Tunnelling for a Better Life

EDITED BY

Jinxiu Yan
Tarcisio Celestino
Markus Thewes
Erik Eberhardt

WTC 2024
ITA-AITES
Shenzhen, China

CRC Press
Taylor & Francis Group

TUNNELLING FOR A BETTER LIFE

Tunnelling for a Better Life contains the contributions presented at the ITA-AITES World Tunnel Congress 2024, which was held from 19-25 April 2024 in Shenzhen, China. As urbanization accelerates, the pivotal role of tunnels and underground spaces in fostering environmental sustainability and improving quality of life becomes ever more pronounced. These underground structures serve as sustainable solutions to the challenges posed by rapid urban growth. By seamlessly integrating into urban landscapes, they alleviate congestion, reduce pollution, and enhance overall mobility, thus contributing to a greener and more sustainable urban environment. Moreover, tunnels and underground works provide vital support for various urban functions, such as accommodating economic activities, providing safe shelters during emergencies or disasters, and facilitating efficient utility management. They address immediate urban needs and lay the foundation for a better and more resilient future.

By focusing on the latest trends in tunnelling and underground engineering, and looking ahead to the era of low-carbon and intelligent technology, the papers in this book illustrate the transformative potential of tunnels and underground works in shaping a better life for present and future generations. The contributions cover a comprehensive range of topics on tunnel engineering, showcasing the latest advancements, insights, and innovations across the following areas:

1. Planning and General Aspects
2. Design and Methodology
3. Geotechnics, Geology and Geophysical Prospecting
4. Ground Stability and Consolidation
5. Support and Lining
6. Conventional Tunnelling
7. Mechanized Tunnelling (TBM, shield)
8. Immersed Tunnels
9. Waterproofing and Drainage
10. Instrumentation and Monitoring/Testing and Inspection
11. Digital and Information Technology
12. Machine Learning
13. Underground Caverns/Underground Space Use
14. Operational Safety, Maintenance and Repair
15. Contractual Practices and Risk Management

Tunnelling for a Better Life is a must-read for professionals, engineers, owners, and other stakeholders worldwide in tunnelling and underground engineering.

Taylor & Francis
Taylor & Francis Group
http://taylorandfrancis.com

PROCEEDINGS OF THE ITA-AITES WORLD TUNNEL CONGRESS 2024 (WTC 2024),
19–25 APRIL 2024, SHENZHEN, CHINA

Tunnelling for a Better Life

Edited by

Jinxiu Yan
China Railway Academy

Tarcisio Celestino
Universidade de São Paulo

Markus Thewes
Ruhr-University Bochum

Erik Eberhardt
University of British Columbia

CRC Press
Taylor & Francis Group
Boca Raton London New York Leiden

CRC Press is an imprint of the
Taylor & Francis Group, an **informa** business
A BALKEMA BOOK

Designed cover image: Gangxia North Station of Shenzhen Metro Line 14. (c) Shenzhen Metro Group Co., Ltd. Used with permission

First published 2024
by CRC Press/Balkema
4 Park Square, Milton Park, Abingdon, Oxon, OX14 4RN

and by CRC Press/Balkema
2385 NW Executive Center Drive, Suite 320, Boca Raton FL 33431

CRC Press/Balkema is an imprint of the Taylor & Francis Group, an informa business

© 2024 selection and editorial matter, Jinxiu Yan, Tarcisio Celestino, Markus Thewes and Erik Eberhardt; individual chapters, the contributors

Typeset by Integra Software Services Pvt. Ltd., Pondicherry, India

The right of Jinxiu Yan, Tarcisio Celestino, Markus Thewes and Erik Eberhardt to be identified as the authors of the editorial material, and of the authors for their individual chapters, has been asserted in accordance with sections 77 and 78 of the Copyright, Designs and Patents Act 1988.

The Open Access version of this book, available at www.taylorfrancis.com, has been made available under a Creative Commons Attribution-Non Commercial-No Derivatives (CC-BY-NC-ND) 4.0 license.

Although all care is taken to ensure integrity and the quality of this publication and the information herein, no responsibility is assumed by the publishers nor the author for any damage to the property or persons as a result of operation or use of this publication and/or the information contained herein.

British Library Cataloguing-in-Publication Data
A catalogue record for this book is available from the British Library

Library of Congress Cataloging-in-Publication Data
A catalog record has been requested for this book

ISBN: 978-1-032-80042-4 (hbk)
ISBN: 978-1-032-80113-1 (pbk)
ISBN: 978-1-003-49550-5 (ebk)
DOI: 10.1201/9781003495505

Tunnelling for a Better Life – Yan, Celestino, Thewes & Eberhardt (Eds)
© 2024 The Editor(s), ISBN 978-1-032-80042-4
Open Access: www.taylorfrancis.com, CC BY-NC-ND 4.0 license

Table of contents

Preface xxxvii

Acknowledgements xxxix

WTC 2024 Organization xli

Planning and general aspects

Multilateral institutions and governance of urban underground space 3
N. Bobylev, Y.-K. Qiao & F.-L. Peng

Forecast and trends related to key personnel for mechanised excavation with TBMs 8
F. Bove

The common duct in New Taipei City 13
H.C. Chao, C. Song, T. Ko, I.K. Chiu & Y.C. Lin

Progress and prospect of urban tunnel engineering in China 20
X. Chen

New chemicals with reduced carbon footprint 28
F. Couturier, D. Matioszek & T. Boursier

City Rail Link – City Rail Link: Managing challenges on the pioneer underground metro project in New Zealand 33
F. Dudouit

Nuclear decommissioning in the UK: Cross-sector collaboration and learning with the tunnelling and underground space sector investigating alternative approaches to reactor dismantling and graphite retrievals 41
D. Garbutt & M. Knights

Planning of alignment & proposed actions for tunnel collapse in diverse ground conditions on the steepest railway curves in the Eastern Ghats, India 47
R. Gupta, L. Kumar & A. Kumar

Comparison of carbon footprint emissions in tunneling projects using innovative methods 57
P. Jarast & V. Nasri

Collaboration in Moscow Metro development: Analysis of joint construction efforts by Russian and Chinese builders 65
V.P. Kivlyuk, A.I. Paschenko, D.S. Konyukhov, L. Xue, J. Zhou, S.N. Vinogradov, K.V. Orlov, Y. Song, J. Huo, Y. Lyu, Z. Gu & T. Wang

The application of technology for resource utilization, reduction, and harmless treatment of subway shield tunneling waste soil 72
J. Lei, H. Long, K. Jia, T. Song & H. Pan

Development and prospects of railway tunnels in China 78
X. Li, S. Tian, W. Wang, J. Gong & H. Wang

Differentiated driving effects of China's green transportation facilities assessment policy 87
Y. Liu & W. Qiu

Planning and execution of horizontal directional coring method for future tunnelling works 96
F. Mahony, K. Goh & C. Veeresh

Theory meets practice: Evaluating discrepancies between theoretical settlement projections and actual measurements in tunnelling projects with tunnel boring machines 101
E. Navarro, E. Salvador & F. Diez

Geotechnical and tunnel engineer's role on the success of major tunnel projects delivery 109
J. Pan, D. Och, A. Kuras & G. Bateman

TBM traffic tunnels for sustainable infrastructure 116
S. Pompeu-Santos

Underground space use layout planning using multi-source spatial data 125
Y.K. Qiao, Z.Y. Li, N. Bobylev & F.L. Peng

Tunnelling in a green country – Brenner Base Tunnel study case: Decision and solutions in construction lot H41 Sill Gorge-Pfons 132
I. Zamberlan & C. Schwarz

Technical challenges and countermeasures of plateau railway tunnels 139
Y. Zhao, T. Zhu & G. Yan

Design and methodology

Observational method and calibration of design safety factors to optimize technical-economical solutions in tunnelling projects 149
A. Antiga, M. Lorenzi & A. Lucia

Design of Ontario Line South Tunnel 158
M. Bakhshi, V. Nasri, T. Maalouf

Design challenges in conventional tunnelling on the Sotra Link Project in Norway 164
G. Barbieri, G. Bella, E. Trivellato, S. Agrillo & M. Giani

(I)-TM: I-System's tunnelling method – four years of application in most challenging ground in India 173
H. Bineshian

Segment design for Australia's largest diameter TBM tunnel 182
S.F. Chau, H. Asche, D. Oliveira, J. Shepherd & C. D'Hondt

Review of key technologies for design of Dalian Bay Undersea Tunnel 193
Z. Chen, H. Chen & M. Lu

Design of tunnel brace and retaining structure on East Artificial Island of Shenzhen-Zhongshan Link 200
H. Chen, C.N. He, X.D. Lai & L. Yu

Sustainability of Shihmen reservoir by desilting tunnel in Taiwan 209
C.E. Chiang, P.S. Kuo, H.T. Chiang & Y.J. Lin

Advanced countermeasure for encountering heavy gas influx in new Wu-shan-ling divert water tunnel 214
K.H. Chou, S.H. Wang, C.H. Chen & T.H. Chen

The "hybrid" tunnel. An innovative solution for urban tunnel in soils. The case of Américo Vespucio Oriente AVO1, in Santiago de Chile 220
J.M. Galera, M. de Cabo & G. Ibarra

The effect of the movement joint on the seismic response of the cross-passage intersection in segmental tunnel lining 228
G. Giordano, D. L'Amante & G. Fantauzzi

Development of sustainable criteria for the Italian railway tunnel design 235
F. Iacobini & A. Pranno

Analysis on applicability of seismic calculation methods for shield tunnel in Shanghai area 240
X.X. Li & H. Chen

Validation of joint non-linear numerical analysis with large-scale physical testing for arched cut and cover tunnels at HS2 project (UK) 247
M. Li, S. Psomas & N. Al Haddid

Innovative application of low-carbon and energy-saving technology in underground space: A case study of erlangshan tunnel on Sichuan-Tibet expressway 256
G. Lin, J. Zheng, J. Wang & F. Yang

Low carbon emission design concept and method for tunnels and underground engineering 261
G. Lu, J. Liu, Y. Zhao, S. Shi & Z. Zhang

Design of the REM Aéroport de Montreal's P5 ventilation shaft 270
M. Mains, J. Lee & V. Nasri

Tunnels and stations design of Montreal Blue Line 277
V. Nasri

Influence of calculation method on the design of the secondary lining 285
J. Ortuta & M. Bakoš

Research on smart design and innovation of Jiaozhou bay second tunnel 292
L. Qu, X. Li, M. Tan, H. Jiang, M. Xiao & W. Sun

Application of a confinement-dependent spalling criterion for tunnels in highly stressed brittle rock 300
M. Rahjoo & E. Eberhardt

Practical considerations of shale swelling impact on underground structures liner design for Ontario Line transit project in Toronto, Canada 308
M. Rahjoo & V. Nasri

How to consider the effects of longitudinal joint imperfections on internal forces in segmental tunnel linings 315
F. Rauch & O. Fischer

Athens metro "Piraeus" station: Numerical analysis versus observational method 323
K. Sampsakis-Bakopoulos & N. Gerolymos

Karanga-a-Hape Station MC21 Junction – Collaborative solutions for complex geology and geometrical constraints - Tackling the challenges at Karanga-a-Hape Station caverns 329
A. Sarathchandran, G. Charlesworth & R. Graafhuis

Design of temporary cofferdam and deep excavation for cofferdam tunnel of Shenzhen-Zhongshan Link 337
Z. Shi, C.N. He, L. Yu & Q.W. Xia

Comparative effects of twin-stacked tunnel excavation on adjacent structure using different simulation models 345
N. Sittiamornporn, P. Jongpradist, C. Phutthananon, A. Chayaroon & P. Malaisree

Key technology of Submarine railway tunnel in complex environment and high-water pressure 352
C. Song, W. He, S. Lv & Y. Yu

Development and innovation of design method for railway tunnel support system in China 360
S. Tian, D. Liu, Y. Zhang & X. Li

Maungawhau mined tunnels - Collaborative design – Management of design amendments for Maungawhau mined tunnels for improved construction schedule outcomes 368
H. Toi, R. Gong, D. Wang & G. Charlesworth

"SINTEF-TriPOD" in underground design – A demonstration for two projects in Norway 377
N. Trinh & E. Grøv

Automatic computation for design of tunnel shafts 385
C.K. Tsang, A. Koay & T. Sia

Case study about adjacent three-arch tunnel 390
H. Tseng, K. Kuo & T. Chu

Optimizing the tunnel ventilation design related to respirable dust in tunnelling by using CFD 396
R. Wei, R. Galler & C. Weiß

Study on the mechanism of tunnel structure damage under the combined effects of fault creep and earthquakes 402
Z. Xia, S. Jia, J. Wang & Q. Wang

Theory and practice of total safety factor method for tunnel support structure design 406
M. Xiao, B. Xie, C. Xu, K. Wang & Z. Deng

Considerations of the coefficient of subgrade reaction forces on seismic response displacement method of a double-circular shield tunnel 416
M. Xu & T. Manabe

Analysis of key technologies in structural design of prefabricated station of Shenzhen Metro 424
Z. Xu, D. Meng, R. Liu & M. Li

Addressing design challenges in large diameter tunnels with big openings in deep soft ground: Innovative solutions and analysis techniques 432
J. Yuan, V.C.S. Goh & C. Maxcia

Aseismic mechanism of laminated shear energy dissipation structure in tunnels during an earthquake 441
X. Zhang, A. Cao, Y. Jiang & X. Wang

Geotechnics, geology and geophysical prospecting

An improved simplified solution for the characteristic line of tunnels in strain-softening rocks 451
M. Anthi, Th. Pferdekämper & G. Anagnostou

Estimation of tunnel support loads due to large deformation in squeezing ground conditions 457
K. Arora & M. Gutierrez

Tunnelling in weak sandstone: A case study of Subansiri Lower Hydroelectric Project (2000 MW) 467
M.S. Chouhan & S. Potnis

Correlation of empirical classification systems in squeezing anisotropic environment and optimisation of underground supports in a headrace tunnel; a case study from Tanahu Hydropower, Nepal 476
E. Christakis, B. Parajuli, P. Yao & R.K. Adhikari

Hydro-geo-mechanical properties for water flow prediction in tunnelling 485
M. Coli & R.E. Rizzo

3D Geological reconstruction and application of tunnel face 493
D. Duan, H. Bai, W. Li & W. Qiu

Study of microgravity survey to predict the Bukit Timah rock head for tunnelling in Singapore 501
T.E.S. Ernest, C. Veeresh, J. Kumarasamy & K.H. Goh

Rock drilling aerosol deslagging technology and CFD-DEM two-way coupling numerical simulation of weak surrounding rock geology 509
S. Guo

Uninterrupted continuous forecasting in mechanized tunnelling in rock 517
J. Hecht-Méndez, T. Dickmann & D. Krueger

Limits on the estimation of the EPB face pressure. A concrete example based on Kalman filter approach 523
C. Iasiello, A. Flor & P. Fantini

Experimental study of rheological characteristics of bentonite-based drilling fluids 529
S. Javarone, M. Palombini, M. Cinelli, I. Bavasso & D. Sebastiani

Optimized electrical exploration for predicting geological transitions ahead of a tunnel based on harmony search algorithm 536
M. Kang, K. Kwon, S. Park, Y. Choe & H. Choi

High resolution resistivity imaging for assessment of geological conditions ahead of tunnel face in a complex geology 542
S.L. Kapil

Tunnel engineering application of assessment technology of karst development degree based on hydrochemical kinetics and fractal theory 548
C. Li, J. Wu, Q. Li, W. Yu & S. Lu

Model test and analysis of failure mechanism of deep high sidewall tunnel from splitting failure to zonal disintegration 556
F. Li, Q. Zhang, G. Xin & G. Long

Development and test of directional coring drilling system for advanced geological exploration 565
J. Liu

Geological risks in TBM tunneling and its prediction by HSP method 572
S. Lu, Y. Xiao & X. Wang

Rock abrasiveness in the studies of são paulo metro: Tests, classification systems, parameters obtained from various lithotypes and their relationship with weathering degree 579
M.D. Monteiro, H C. Rocha, G.B. Robbe & A.M. de Almeida

Phased prediction method for construction period of secondary lining construction time of tunnel in squeezed rocks 584
L. Ning

Ground characterisation of the Sydney Basin for tunnelling works 591
D.J. Och, J. Pan, I.T. Graham, N. Walker, A. Kuras & G. Alvarado

Chengdu-Guiyang High-speed railway—Yujingshan Mountain Tunnel crossing giant karst cave and underground river 598
W. Qing, Y. Yu, J. Zheng, Y. Zhu & Y. Wang

Tunnel behavior in soft soils subjected to pore water pressure drawdown 608
A. Santos, R. Pérez-Léon, J. Rodríguez-Rebolledo & B. Caicedo

The deformation characteristics of soft soil layers with different sand content and the time and space effects of foundation pit excavation on the tunnels below 616
C. Shen, M. Miao, C. Huang, Y. Dong & J. Fan

Non-invasive tunnelling investigations using muon tomography 625
C. Steer & L.F. Thompson

Empirical correlations between ground's mechanical properties and I-system 629
C. Upadhye, S. Potnis & B. Hoss

Research on key technology of design of long tunnel in water-rich karst platform of compound syncline basin 638
H. Wang, M. Wang, H. Fu, P. Li & Z. Li

Numerical simulation of the mechanism of strain rockburst under true triaxial loading and unloading conditions 647
Y. Xue & H. Tian

Sequential 3D geological information system using re-grid of voxel model based on exploration data ahead of the tunnel face 655
S. Yoshikawa, Y. Aono, K. Saito & T. Nishi

HSP Method-based advanced geological prediction and tunneling parameter pre-control technology for super-large diameter pipe-jacking project 660
Z. Zhao, F. Lan, B. Wang, L. Meng, X. Wang & S. Lu

Ground stability and consolidation

Excavation induced settlement in Sydney area 671
G. Alvarado, S. Sadeghian & Y. Dong

A modified approach to assess tunnel excavation stability 678
S. Anwar & G. Charlesworth

Study on crosslink-induced Xanthan Gum biopolymer treated soil as a subsea tunnel backfill grout for saline condition permeability control 685
J. Bang, D.-Y. Park, J. Kim, S. Im & G.-C. Cho

Fixing of unstable water-saturated soils by artificial freezing for construction of inter-tunnel joints during metro construction 689
E.A. Deplagni, V.P. Kivliuk & D.S. Konyukhov

Factors impacting thawing-refreezing around tunnels in permafrost soils 695
S. Gavhane & S. Potnis

Deformation characteristics of long and narrow deep foundation pit with partition walls 705
H. Geng, S. Guan, Z. Chen, G. Dai & Z. Li

Disturbance effect and surrounding rock pressure characteristics of loess shield tunnels 711
X. Han, P. Wang, Z. Chen, H. Feng, H. Cui & F. Ye

Numerical simulation of polymer grouting for rock fracture: Influence of isocyanate index on grout propagation 718
M. Hao, J. Zhang, L. Zou & X. Li

Dynamic soil response around a shallow rectangular tunnel and adjacent building 726
Z. He & S.P. Gopal Madabhushi

Chemical-combined jet grouting for mass treatment of break-in area in Vietnamese urban underground construction 732
H.Q. Le, H. Oyama & P.N. Do

A systematic deformation control methodology for underground space construction in close proximity to an existing metro station 740
J. Li, R. Wen, W.W. Yang & W.F. Mou

Study on diffusion mechanism of backfill grouting in sand and clay stratums 747
S. Li, F. Ye, T. Xia, K. Ying & X. Han

Influences of stress-dilatancy rule on the derivation of ground response curve for deep-buried tunnels 755
J. Liang, J. Chen, J. Ma, H. Yang & L. Huang

The use of jet grouting technology: An overview of the different applications in tunnelling 760
P. Lunardi, G. Lunardi, G. Cassani, M. Gatti, L. Bellardo & C.L. Zenti

Stability analysis of surrounding rock in a highway tunnel crossing a Water-Rich fault fracture zone 769
S. Luo, X. Xie & D. Zhu

Selection of an ontological model for phyllite tunnel based on on-site measured 777
J. Ma & J. Zhang

Analysis of stability of rock column between cut & cover metro station and NATM tunnels 783
S. Maiti, M. Khare & S. Potnis

The freezing technique for the world's longest railway tunnel 789
A. Marottoli, M. Ianeselli, R. Marrazzo, A. Gallotto, G. Vecchione, M. Cavolo & F. Gallo

Stability of portal slopes of a diversion tunnel after the Kahramanmaraş, Turkey (Türkiye) February 6, 2023 Earthquakes 798
A.A. Mert & F. Caliskan

Numerical analysis of the deformation of undersea tunnel crossing fault zone 806
J. Ni, J. Zhang, H. Huang, D. Zhang, & L. Zhang

Research on surrounding rock by shallow tunnelling in Boulder-Cobble Mixed formation: Instability characteristics and control strategies 813
Y. Qin

Practical approach for the control of surface settlements due to TBM tunnelling during excavation by following up of monitoring 822
V. Rattia, H. Rocha, A. Dantas, T. Mendes & A. Assis

Jet grouting soil improvement to excavate a tunnel under passing the A4 Milano-Venezia motorway for the extension of the line 1 of the Milan metro 828
M. Silvestri, D. Chirulli, A. Antiga & P. Coppola

Study on the mechanical behavior of the vertical pre-reinforcement 836
Y. Tatebayashi, N. Tamura, T. Amemiya, K. Kawata & N. Isago

Marble sludge in two-component grout applications 842
C. Todaro, A. Carigi, M. Cardu & D. Peila

Study of support design and construction results of unconsolidated in Aso Caldera 848
T. Tomita, T. Ano, H. Nagamatsu, H. Hirano & H. Tabata

State of the art of soil conditioning technology for earth pressure balance shield tunnelling 857
Z. Wan, S. Li, S. Zhao, K. Qiu & S. Hao

Numerical prediction of tunnelling-induced displacement field in large and very shallow tunnels 865
W. Yang, D. Zhang & D. Boldini

Stability numerical investigation of laminated and randomly discontinuous flat roof 871
P. Yiouta-Mitra & E. Vougioukas

Responses of a shallow tunnel in liquefiable ground subject to multiple shakings 877
J. Zhang, E. Bilotta, Y. Yang & Y. Yuan

Failure mechanism of reinforced faces and design method of advanced supports for tunnels excavated by the full-face mechanized method 882
X. Zhang, M. Wang & L. Yu

Key technologies and safety analysis of deep foundation pit construction in a sea area 890
Z. Zhao & S. Gao

Data-driven stability analysis and uncertainty quantification of surrounding rock mass for tunnel 897
H. Zhao & L. Zhang

Study on settlement deformation of existing structures under ultra-large diameter shield tunnel 906
M. Zou, C.L. Zhen & X. Xie

Support and lining

Rock bolt design, A numerical parametric study 917
S. Anwar, A. Mann & S. Sadeghian

The effect of a frictional interface in a preliminary yielding support for a deep tunnel 926
L. Batocchioni, V. González & S. Miliziano

Numerical calculation approach for the design of segmental tunnel lining equipped with inflatable O-ring sealing 932
M. Bazzani, F.D. Santis, P. Fantini, M. Daniele & S. Pesa

The mechanism, functioning and installation of reinforced ribs of shotcrete in Norwegian Method of Tunnelling (NMT) 941
R. Bhasin & M. Shabanimashcool

Shotcrete structural behaviours as tunnel support in hard jointed rocks – Swedish state of the art 946
Y. Chang & C. Höök

Study on the influence of cracks on mechanical behaviors of tunnel lining of high speed railway with a speed of 400 km/h 953
P. Chen, K. Liu & C. Yan

Design and verification of shear key support system for segmental lining openings at cross passages using non-linear finite element model 962
J.T. Chong

Environmental and economic advantages in using HPFRSCC in tunnelling 969
M. Coli, M. Francini, L. Martelli & M. Tanzini

Structural and sustainability requirement with high performance fibre reinforced precast segment carbon counting example 977
B. de Rivaz

Research on reinforcement measures for soft plastic loess tunnel base 983
Q. Deng

Analytical solution to failure history of segment joint with inclined steel bolt 991
X. Dong, B. Du & X. Chen

Numerical analysis of two deep circular shafts at a former gas works site on the London Power Tunnels Phase 2 scheme 1000
J. Ellis, O. Brown, A. Simic, R. Kundan & J. Coupland

Comparative analysis of simplified solutions for the radial joint behaviour of segmental tunnel linings with finite element numerical modelling 1008
A. Emadi & A.R. Gomes

Steel lining support in headrace tunnel of Uma Oya Project, Sri Lanka 1015
A.R. Farshbar, A. Noorzad, P.V. Yuvaraju & B. Rejith Kumar

Durability of two-component backfill grout: An experimental study 1021
M.D. Felice, A.D. Giulio & N. Valiante

Tangential resistance between primary and secondary lining with PVC waterproofing sheet membrane 1027
L. Forlingieri, C. Hu, M. Morosi & A. Zanichelli

Carbon reduction in conventional tunnelling by advanced design 1036
A. Gakis, P. Salak & F. Wilhelmstoetter

Advanced joint non-linear design analysis and verification of the arched cut and cover tunnels at high speed 2 project (UK) 1044
N.A. Haddid, S. Psomas & M. Li

The stiffness of circular joints and its effect on the deformation of the tunnel segmental lining along the longitudinal direction 1053
X. Han, F. Ye & P. Oreste

Comparison of structural load-bearing performance between precast and cast-in-place permanent linings 1062
K. Kikuchi, A. Kusaka, Y. Koizumi, T. Watanabe & Y. Tatsumi

Development and application of highly adaptable lining equipment for complex tunnels with variable sections 1071
J. Liu

Mechanism of anchor cable in super-span tunnel and its design method 1078
J. Liu, G. Lu, Y. Zhao & S. Shi

Using orthogonal flexible support structure to deal with large deformation of soft surrounding rock tunnel: A case study 1086
Y. Liu & W. Qiu

Study on railway tunnel lining anti-crack surface reinforcement strengthening and design method 1092
Z. Liu, X. Xing & L. Gong

An innovative primary support system of steel shotcrete composite structure in the tunnel 1098
J. Lu & M. Li

Stress analysis of high geothermal tunnel lining structures considering different cooling measures 1105
M. Luo, Z. Yuan, L. Fan, L. Tao & Y. Zeng

Thrust jack loading of large diameter precast segmental tunnel lining 1112
M.A. Mooney, H. Zheng, C. Naito, S. Quiel & Z. Ouyang

Computational approaches towards segmental linings with a reduced environmental impact 1118
G.E. Neu, V. Gudžulić & G. Meschke

Snowy 2.0 - Support design for intersections between access tunnel and caverns 1126
X.-P. Nguyen, P.-L. Tonioni, A.-N. Blaise, R. Taherzadeh, D. Galli & G. Cardone

Research on high-quality and high-durability of tunnel lining by mixing volcanic glass powder 1135
M. Nomura, S. Tomoto, T. Shiina, N. Mitsui, S. Yoshida & D. Hanaoka

Achieving high load-bearing capacity linings in sprayed concrete and segmental linings with high-performance steel fibres 1144
D. Oliveira

EN 14488-3 notched panel versus EN 14651 notched beam testing for pre-construction trial conformance testing of Sprayed Concrete Linings (SCL) 1151
C. Peaston & B.D. Rivaz

Tunnel lining design in hard rock conditions. application of observation method. A case study of a large-scale tunnel cavern for underground train station 1159
M. Petkov, P. Hansson & J. Pilbacka

Risk assessment and large diameter segmental lining design in swelling ground 1167
S. Sánchez, M. Mains, C. Álvarez, E. Barrouillet, C. Garrido & M. Ferreres

The numerical analysis for the segments floating mechanism of the large-diameter shield tunnel in the Rich Water Strata 1174
Z. Shi, J.-F. Xu & X.-Y. Xie

Analysis of composite shell lining based on laminated theory 1183
W. Shuyi

Singapore's land transport authority: 25 years of sprayed concrete lining tunnelling 1189
A. Sim, K.B. Chang, M. Marotta, C.K. Poh & M. Mohiadeen

Design of precast bolted universal segmental tunnel lining for the London Power Tunnels phase 2 scheme 1199
A. Simic, O. Brown & J. Ellis

Value engineering of concrete mix to save 230 tonnes of steel fibre for the west section of the Thames Tideway Tunnel 1207
J. Su, S. Sheth, A. Ellison & C. Barret

Dynamic response characteristics of ultra-shallow buried metro station structures under surface vibration load 1216
L. Tao, L. Deng, Y. Zhang & Z. Jia

Mechanical response and fault-resistant design of urban shallow subway tunnel under normal fault 1224
L. Tao, J. Liu, Z. Wang & M. Shi

Analytical solution for longitudinal response of cross-fault mountain tunnels based on foundation beam model 1231
L. Tao, M. Qiu, H. Zhang, Z. Jia, C. Shi

Experimental study on mechanical properties of grouted π-type SCCS arch 1238
Z. Wang, W. Li & Y. Cai

Study on deformation joint width of mining tunnel under the operation of a normal fault 1244
Q. Wang, D. He, J. Chen, P. Geng & H. Shen

Analysis of issues in the theory and calculation methods of composite lining for hard rock tunnels 1250
N. Wang & X. Yang

Analysis of mechanical behavior and engineering suggestions for double-arch tunnel without middle drift 1258
C. Wang, D. Zhang & Y. Li

A mechanical analysis model for tunnels crossing active fault zones 1267
M. Wang, X. Zhang & L. Yu

Study on mechanical characteristics of a DDCI connection structure for longitudinal joints 1276
M. Xiao, J. Chen, G. Xue, Z. Yan & S. Wang

Research on support parameters of the second Jiaozhou Bay Subsea tunnel based on the total safety factor method 1282
M. Xiao, W. Sun, L. Chen & L. Jin

Research on the airproof performance of shield tunnel segment sealing gasket based on laser surface microstructure 1291
M. Xiao, G. Xue, J. Chen, C. Zhang & S. Wang

Research on the application of marine engineering mass concrete with anti-cracking agent 1297
B. Xie, W. Xu, Y.J. Wang, J. Zhang, W. Jin & J. Liu

Development and application of wall-climbing grinding robot for tunnel lining steel formwork 1303
K. Yan

Retrospective analysis of the design and manufacture of a case of steel fibre reinforced segmental lining in view of the actual behaviour of some rings on site 1312
Z. Yang, Z. Gu & P. García de Haro

Robustness evaluation on non-circular segmental tunnel linings: Case study on quasi-rectangular shield tunnel 1321
Y. Ye, Z. Liu & X. Liu

The effect of polypropylene fiber on the strength and crack propagation of foam concrete 1326
R. Yin, Q. Li, X. Zeng & W. Qiao

Research on construction technology of drilling and blasting tunnel based on load adjustment control technology 1333
G. Ying, R. Zheng, Y. Xing & W. Chen

Construction and applicability of using double supports in a large overburden ground conditions as a countermeasure to suppress displacements 1340
S. Zhai, D. Abeyawardena, H. Aoki, S. Ohmori & N. Isago

Mechanical evolution mechanism of primary support under steel arch frame corrosion in subsea tunnel 1347
Y. Zhang, S. Tian, M. Wang & L. Yu

Effect of excavation on the pipe roof deformation under the action of the pipe roof-beam support system 1356
W. Zhao, Q. Bai & D. Pi

Study on horizontal earth pressure of segment considering the influence of backfill grouting pressure 1365
J.-L. Zhong, X.-C. Zhong, Y.-Z. Jian & F.-D. Li

Impact of base rock deterioration on the mechanical characteristics of loess-expansive mudstone tunnel lining structure 1373
H. Zhu

Conventional tunnelling

Crystalline silica exposure in tunnel construction: Identifying barriers to safe practices 1383
F. Anlimah, V. Gopaldasani, C. MacPhail & B. Davies

Design and construction optimisation of the Karanga-a-Hape Station mined tunnels and bored tunnel cross passages on the City Rail Link project 1390
V. Balakumarasingham, P. Daudibertières, E. Chatoux & W. Okada

Experiences during tunnelling in extreme ground conditions in the Himalayas - Excavation of Rohtang Tunnel, India 1399
R. Bernard

The impact of ramp width on tunnel face stability during ramp excavation 1405
Q. Chen & Y. Cui

Deep underground mined cavern excavations in Auckland city centre, New Zealand 1412
T. Cheung, W. Okada & S.F. Chau

Construction of Girgaon Station of Mumbai metro line – 3, a combination of cut & cover and conventional tunnelling and mix of social and technical challenges in congested urban environment 1418
S.G. Dalvi, R.R. Kumar, S.K. Gupta & A. Rawat

Challenges in the conventional tunnel mixed-face execution 1424
T. de Sá Lima, B. Scodeler & E.P. Filho

Research on key technologies for the construction of extra long tunnels on green roads in karst peak cluster areas 1429
Z. Dong, B. Guo, Y. Zhou, Mengyan & S. Xing

Challenges and lessons learned from 100 km of major hydropower tunnels in Bhutan 1437
T. Dorji, D. Brox & S. Wangdi

Design and construction considerations for cross passages in Bangkok subsoil 1446
O. Duangsano, A. Sramoon, A. Asanprakit, A. Chayaroon & N. Phienwej

Construction of underground rail tunnel above deep tunnel sewerage system 1455
H.M. Fong, Q. Li & C. Veeresh

A study of merits and demerits of steel decking verses concrete decking for traffic management and construction logistics during construction of underground metro stations for Colaba-bandra-seepz (line 3) in Mumbai, India 1461
S.K. Gupta, R.R. Kumar, D. Binnar & S. Vishwakarma

Automatic blasting design and construction system optimized for geological conditions 1469
R. Hemmi, Y. Ide, K. Kakimi, T. Shizawa & F. Ito

Effect of focusing tube geometry and abrasive flow rate on rock drilling width 1475
H.-J. Hwang, Y. Cha, J. Kim, C. Park & G.-C. Cho

Development of advanced tunnel blasting and shotcrete as automated tunnel construction system 1479
K. Iwano, T. Aoyagi, T. Yamagishi, T. Mega & T. Inuzuka

Unforeseen excavation of mixed face soil conditions in a hard rock drill and blast road tunnel 1486
P.D. Jakobsen, H. Nilsen & A.K. Lund

Evaluation of removable time of tunnel lining formworks using surface wave techniques 1492
K. Kato, C. Kuroda, N. Utagawa & K. Ohno

Construction of desilting chambers and connecting tunnels for Vishnugad Pipalkoti He Project (444mw) in adverse geological conditions and very remote location - A case study 1499
R.K. Khali

Construction of tunnel T-49A on Dharam – Qazigund section of Udhampur-Srinagar-Baramulla New BG railway line project in highly adverse geological conditions- A case study 1507
R.K. Khali & S. Yalal

Construction of a new tunnel in proximity to an in-service tunnel by implementing measures to control blasting vibration and ground displacement 1517
Y. Kobayashi, T. Ishii, T. Koma, K. Nakano & Y. Kinomura

Cross passage tunnel excavation by core cutting machine (Stitching) and hydraulic rock splitters in hard rock at Mumbai Metro Station Line-03 (Aqua Line) 1526
A. Kumar Saw, S. Potnis, M.J.C. & M. Roy

Test and research on load spectrum of tunnel drill jumbo 1532
X. Liu

Experimental study of step method construction in soft and broken surrounding rock section of super-long and large section tunnels 1540
Y. Liu, Y. Wang, T. Zhu, M. Tian & Q. Cheng

Innovative practice of mechanized and intelligent construction technology for railway mountain tunnel drilling and blasting method 1549
K. Liu, Y. Yu, Y. Li & X. Liu

The Brenner Base Tunnel: An overview of the excavation types used in the project 1561
D. Marini, G. Venditti, D. Unteregger, R. Insam & R. Marazzo

Key construction technologies for high-speed railway tunnels that with shallow buried depth and gentle slope in loess platform 1569
W. Mi, Y. Wang, H. Zhang, X. Miao, J. Zhang & M. Zhang

Construction procedures of the tunnel for the extension works of Madrid Metro Line 3 from Villaverde Alto to El Casar 1579
M. Núñez & J. Zurdo

Deformation failure characteristics and control measures of shallow loess tunnel of water-rich stratum: A case study 1586
K. Tang & J. Qiu

Impacts of the February 2023 Kahramanmaraş, Turkey earthquakes on outlet works in rock formations 1594
P. Uygur, Ö. Öztürk, E. Dumlu & F. Çalışkan

Research and development support for the construction of the big circle line on the example of the line's intersection with the existing facilities of the Moscow metro 1602
V.V. Viazovoi, R.A. Evtushenko, D.S. Konyukhov & D.S. Petunina

Evaluation of impacts on existing structures induced by deep excavations in Bangkok MWA project 1610
P. Vonghirunyika, W. Kroehong, T. Yonjoho, K. Kandavorawong, A. Chayaroon, O. Duangsano & P. Jongpradist

Mechanized tunnelling (TBM, shield)

Investigation of vibration patterns generated during rock cutting tests 1621
U. Ates, H. Copur & A. Shaterpour-Mamaghani

Bio-polymer sodium alginate application as an eco-friendly additive in slurry TBM excavation 1630
A. Bae, Y.J. Shin, Y. Choe, S. Kim & H. Choi

More efficient, cost-effective and reliable Slurry Treatment Plants (STPs) for mechanized tunnelling operations in the Asia-Pacific region 1634
K. Bai & G. Vogt

An evaluation of using different excavation methods related to specific geologic conditions in the Istanbul area 1641
C. Balci & N. Bilgin

Critical issues in selecting conventional and mechanized tunnelling methods, lessons learned from the past 1648
N. Bilgin & C. Balci

Computational modeling of cutting disc-rock interaction in mixed ground conditions 1654
S.N. Butt, J. Rostami & G. Meschke

Pumice mineral using as a backfill grout injection in TBM excavations 1663
U.C. Çalışkan, S. Beyhan & H. Ergin

Performance analysis of TBM excavation parameters related to small-diameter horizontal and inclined tunnels 1669
M. Cardu, C. Todaro, O. Farzay, A.D. Giovanni & S. Saltarin

Wear prediction of disc cutter tools during shield tunnelling in composite stratum based on improved deep learning method 1675
J. Chang, D. Zhang & H. Huang

A modified foam half-life time test method for EPB shield tunnelling 1682
Z. Chen, A. Bezuijen & Y. Fang

Automatic excavation system for directional control in shield tunneling using machine learning techniques 1687
J. Chen, H. Kamada, N. Takamoto, H. Sugiyama, S. Yamamoto & T. Aoyama

Influence analysis and control measures of super-large diameter shield tunnel undercrossing the existing tunnel in upper-soft and lower-hard composite stratum 1694
J. Chen, Z. Lv & H. Lou

Influence of TBM cutter configurations on gravel excavation characteristics revealed by discrete element method 1698
Y.-F. Chen, T.-T. Wang & F.-S. Jeng

Research on the application of high-strength burn-free building blocks made from shield muck 1705
H. Chen, Y. Xiao, B. chen, A. Lin & X. Liu

The key technology of large section pipe jacking for main structure of station in complex water-rich sand bed 1711
B. Cheng, W. Huang, X. Shuai & Y. Tan

Box jacking construction technology for large cross-section box culverts passing under existing high-speed railways 1719
C. Cheng, J. Wang & Y. Li

City Rail Link – bored tunnel challenges in Auckland city centre, New Zealand 1728
T. Cheung, S.F. Chau, T. Ireland & S. Eratne

Research and application of multi-curve small turn continuous belt conveyor 1737
L. Cui, H. Xu, J. Shen, J. Cheng, P. Song, Q. Qin & W. Yang

Slurry treatment technology based on calcium oxide and seawater of extra-large diameter slurry balance shield machine in Zhuhai area muddy silty clay stratum 1742
R. Dong, Z. Zhou & W. Liao

Field monitoring and numerical modelling of ground heaves due to shield tunnelling in soft ground conditions 1750
O. Duangsano, A. Chayaroon, P. Yensri, A. Asanprakit & N. Phienwej

Research and application of key technologies for the TBM tunnel construction under extremely complex geological conditions 1759
H.H. Feng & K.R. Hong

Evaluations and considerations on the squeezing rock tunnelling in twin TBM tunnel of Rishikesh to Karanprayag railway project in Himalaya 1768
M. Forooghi, V. Bansal, M. Tajik, S. Jain, S. Batuman & P. Aggarwal

Structural behaviour machenism of vertical jacking method on large sections and influencing factors analysis 1777
Y.-M. Gao, X. Liu, Z. Liu, G. Ramos & J. Turmo

Research on the automatic and synchronous construction technology of fully prefabricated internal structures inside large-diameter shield tunnels 1784
Z. Ge, Z. Tang, C. Chen & X. Liu

The Sicilian job, 21 TBMs simultaneously at work to modernize the railway infrastructure of the largest island in the Mediterranean Sea 1792
R. Grandori & R. Bono

Evaluating TBM design and performance, 30 years apart: The Lesotho Highlands Water Tunnel, phase 1 and phase 2 1800
B. Grothen

Load condition effect based on functional model for the ultimate bearing capacity of segmental lining 1806
C. Guo, R. Dong, X. Dong, C. He & Y. Cai

Negligible ground surface movement with EPB TBMs in Singapore marine clay and fluvial sand 1814
G.C. Hangadi, L.J. Pakianathan, C.K. Poh, J. Lim & R. Koh

Development and application of supersized tunnelling technology for China's large-scale construction of underground infrastructure 1820
S. Hu, J. Hoss & W. Sun

Failure analysis and coping suggestions for TBM tools under complicated geological conditions 1828
H. Huan Feng, S. Ying Wang, L. Wei Yang & Y. Dong Yang

Construction method for rapid construction of station by use of large-diameter shield tunneling machines expanding small-diameter shield tunnels and its application 1837
L. Huang, K. Jia, J. Zhang, D. Yu & T. Song

Breaking the tunnel vision: Generalizing TBM performance prediction across projects 1843
S. Huang, R. Sousa & G. Korfiatis

Study on soil discharge efficiency of earth pressure balance shield tunneling in deep buried depth sandy strtum 1850
S. Huang, X. Zhong, Z. Zhou & T. Feng

Muck discharge efficiency depending on soil conditioning by laboratory-scale model test 1860
B. Hwang, A. Bae, D. Lee, K. Lim & H. Choi

Use of biomass as soil conditioner to improve clay rheology in EPB tunneling 1866
M. Ishaq, B. Appleby, J. Rostami, J. Samaniuk

TBM jamming and statistical estimators: Case of a long and deep tunnel 1875
D. Kasal, A. Flor, F. Amadini & A. Oss

Construction of a Horseshoe-shaped trenchless tunnel using the rectangular element propulsion method 1884
D. Koizumi, T. Shimotsu & T. Tanaka

Decision-Making approach for parallel earth pressure balance machine advancements for tunnel construction 1893
N. Kumbhar & S. Tirpude

Short launch of TBM to overcome economic and logistic difficulties in Sri Lanka 1902
D. Lees, J. Sánchez, Y. Chengzhi, S. Banda, D. Denman & P. Muniyandy

Adaptability design and application of TBM cutterhead in Beishan extremely hard rock geological conditions 1909
J.F. Li

Real time estimation and early warning of rock mass strength and integrity in TBM tunneling 1916
Q. Li, L. Du, Y. Yang, X. Zhao, Y. Zhao, Y. Quan & S. Su

Three-dimensional centrifuge modelling of the effects of TBM on adjacent piles 1926
X. Liang & S. Haigh

Geotechnical dimensioning of TBMs and new technological challenges 1935
G. Lunardi, G. Cassani, M.C. Gatti & A. Zimbaldi

Line 2 y Ramal - Red Básica Metro Lima y Callao – Conditioning of different types of soils encountered during the tunnel excavations with 2 TBMs (EPB and Variable Density) 1944
J.L. Magro, M. Calleja, R. Bono & S. Iacullo

Large diameter slurry TBM tunnels with very low cover: A comparison of approaches 1953
M. Mains, S. Sánchez, L. Içik & C. Mora

The mechanised excavation of the exploratory tunnel of the Brenner Base Tunnel: The major challenges 1959
D. Marini, A. Lussu & G. Venditti

Excavation management system for mechanized tunnelling in urban areas 1967
M. Marotta, J. Kumarasamy, A. Sim, C.K. Poh & K.B. Chang

Advancing mechanized tunneling through integrated digital design, simulation, and data-driven techniques 1974
G. Meschke, Y. Zendaki, A. Alsahly & B.T. Cao

TBM design and special features for boring through highly squeezing ground 1981
M. Monina, M. D'Ambrosio & F.D. Rossi

The application of tunnel boring machines in the execution of incline and decline tunnels in mining projects 1987
M. Nasiri, H. Moammeri & G. Stripp

Soil conditioning for TBM performance advancement in mixed geology 1994
E.D. Negro, A. Boscaro, E. Barbero, A. Menghini & C. Butterworth

Tunnel excavation with EPB: Development of new conditioning agents to reduce the amount of water required for soil conditioning 2003
E.D. Negro, A. Boscaro, E. Barbero, C. Todaro & D. Peila

Managing tunnelling risks in urban environment using first earth pressure balance/variable density slurry Tunnel Boring Machine (TBM) in Hong Kong for the MTR East Rail Line Cross Harbour Extension of the Shatin Central Link project 2012
N. Ng, D. Kwork, K. Kwork & D. Jacques

Is a large TBM diameter unfavourable under squeezing conditions? 2020
A.N. Nordas, T. Leone & G. Anagnostou

Developments in large diameter subaqueous tunnels 2028
O. Ozgur, T. Ma & J. Cheung

Design and construction excellence at Tuen Mun-Chek Lap Kok Link tunnels: An engineering marvel beyond boundaries 2035
W.H. Patrick, E. Baranger, K. Choi, P. Thompson & A. Raine

TBM Sub-sea tunnelling in the Arabian Gulf 2043
G. Peach, H. Vigil & K.S. Al-Khayareen

Green TBM: Design targets, features and power efficiency 2049
A. Petriccioli, L. Tafuri & R. Grandori

On the interplay between face extrusion and shield loading in squeezing conditions 2056
Th. Pferdekämper & G. Anagnostou

Research on curved tunneling and bending angle calculation of articulated shield tunneling machine 2062
W. Qiao, X. Zhou & X. Liang

Analysis of motion characteristics of large-sized irregular particles in long pipelines 2070
Z. Ren, S. Wang, Y. Wang & X. Zhou

Experimental study and simulation verification of slurry penetration process 2076
Z. Ren, L. Ye, X. Zhou, Y. Wang & S. Wang

Passage of TBM EPB under buildings with deep foundations, with physical interference 2082
H. Rocha, F. Hirata, G. Robbe, W. Giannotti & T. Pires

TBM performance in rock conditions of water diversion tunnel constructions (Mae Ngad-Mae Kuang tunnel) in Chiang Mai Province, Thailand 2087
K. Sarapagdee, A. Laddakul & T. Saelao

A new AFTES guideline: Suitability and selection process of pressurized TBMs in urban contexts 2099
M. Schivre & F. Renault

JWPCP effluent outfall tunnel in Los Angeles, California – Anticipated challenges and slurry TBM performance in the soft ground section of the alignment 2108
M. Scialpi, M. Piemontese, R. Schürch, M. Kendall & N. Karlin

A review of deterministic approaches in the performance evaluation of Raise Boring Machines (RBMs) 2116
A. Shaterpour-Mamaghani, H. Copur, C. Balci & D. Tumac

Distinctive considerations in the design and construction of large diameter TBM-built tunnels in urban environment – a UK perspective 2122
S. Shen

Smarter, larger, leaner, greener – trends of the tunnelling industry towards a sustainable future in the United Kingdom 2130
S. Shen & A.V. Serin

Tunneling successes in West Los Angeles - Purple Line Project Section 3 2139
E. Sillerico, M. Ellwood, C. Davis, A. del Amo & E. Whitman

Application of EPB-TBM dual-mode shield tunneling technology in Shenzhen Metro 2148
T. Song, J. Yang, L. Huang, J. Lei, K. Jia, J. Huang & J. Lu

A newly developed reduced CO_2 backfill grout system for TBM operations 2157
M.A. Sposetti

Successful tunnelling in the desert, Wakrah and Wukair Drainage Tunnel, Doha, Qatar 2162
J.B. Stypulkowski & K.S.F.S. Al-Khayareen

TBM design for operation in gassy formation 2170
L. Tafuri, O. Bonfanti & A. Lisardi

Successful steering control with partial soil excavation for station crossing of a 13.08 m diameter EPB TBM in Lodz, Poland 2179
M. Tomaszewski, S. Nortoft, F. Bove & M. D'Ambrosio

Planning, design and construction for mechanised cross passage excavation 2185
C.K. Tsang, T.J. Sia, Z.G. Zhang, L. Sun & K. Chen

A study on intelligent assembly technology for Mid-partitions in shield tunnels and application 2193
H. Wang

Creative design for Herrenknecht TBM used in Jiangyin Jingjiang Yangtze River crossing tunnel construction 2202
H. Wang, R. Jin, G. Lin & W. Sun

Research on settlement control of large diameter shallow buried shield tunnel crossing railway and reservoir embankments 2209
J. Wang, S. Yan, C. Wang, Q. Yang, J. Sun & S. Xue

Slaking characteristics of clay blocks and the influence of dispersant 2215
S. Wang, H. Zhu & P. Liu

Revealing inherent mechanism affecting loess-metal interface adhesion properties: Insights from macro- and atomic-scale tests 2222
B. Wu, W.-C. Cheng & X.-D. Bai

Challenges and solution of super large diameter TBM tunnel construction in urban center 2229
X. Xiao, L. Jiao & Y. Li

Research on vertical dry tailings conveying technology and equipment of shaft boring machine 2239
C. Yang

Study on classification prevention and control technology of hard rock rockburst in TBM construction 2244
Y. Yang, L. Du, C. Gong, Y. Song, Q. Li & M. Wang

Prediction model of TBM tunneling speed based on geological parameters 2253
Y. Yang, L. Du, R. Tang, F. Wei & H. Zhang

Research on prefabricated metro station structure and key assembly technologies 2262
X. Yang & F. Lin

Numerical investigation of the excess pore water pressure generated by TBM tunnelling in saturated and unsaturated aquifers: A comparable study 2271
C. Zhang & A. Bezuijen

Launching technology with shallow overburden for super-large diameter slurry shield 2280
B. Zhang, H. Wang, X.B. Xie, Y.Y. Lu & Z. Chen

Experimental research on foam performance and intelligent injection control of foam additive system of tunnel boring machine 2286
C. Zhang & Y. Zhai

Visualization study on stability of shield tunnel face with transparent soil model 2294
H. Zhao, Z. Jia & Y. Liu

Application study of combined machining in the cutterhead design for hard rock tunnel boring machine 2302
M.B. Zhou

Shield self-driving technology and its application 2309
W. Zhou, M. Hu, H. Wu, B. Wu & J. Lu

Research on frontier technology of shield machine/hard rock machine selection and mode innovation 2316
W. Zhu, J. Wang & W. Xie

Development and application of a synchronous shield tunnelling technology combining advancement and segment fabrication 2323
Y. Zhu, Y. Zhu, X. Bi, X. Wang, Z. Zhang, J. Chen, Y. Qin & S. Duan

Immersed tunnels

Achieving sustainable immersed tunnel projects 2333
J. Baber

Research on fire resistance limit standard of steel-encased concrete immersed tunnel structure 2342
P. Cao, S. Song, M. Wu, S. Jiang & E. Liu

Stability and deformation analysis of dry dock slope in Haihe Tunnel, Tianjin, China 2349
C.N. He, Y. Qu, E.C. Qing & J.Q. Shen

Research on online intelligent prediction of service status of immersed tunnel based on artificial intelligence 2358
H. Ding & P. Cao

Key developments of world's immersed tunnel design and construction solutions 2366
A. Doorduyn, Y. Li, H. de Wit, M.T. Hart & W. Chen

Structural optimization design of seamless expansion joint based on finite element analysis 2376
W. Jiang, S. Zhang, Y. Wang, R. Bao & J. Shan

Analysis and research on seismic effects of immersed tunnel joints of Shenzhen-Zhongshan Link 2388
Z. Li, Z.J. Chen & H. Chen

Seismic resilience assessment for longitudinal response of immersed tunnels 2394
X. Li & H. Yu

Void detection method and its application for steel shell-concrete interface of immersed tube tunnel 2400
S. Li, Y. Zhang & S. Feng

Assessment of operational limits for tunnel element transport using a shallow draft semi-submersible barge 2407
M. Lin, Z. Ying, W. Shen & X. Wang

Research and application of steel intelligent manufacturing of Shen-Zhong Link steel sandwich immersed tunnel 2414
H. Long, W. Rui & Y. Xie

Research and application of transportation and landing technology for Shen-Zhong Link super large steel shells of immersed tunnel 2421
H. Long, W. Rui & G. Zhang

Innovative research on key technologies for dredging construction of immersed tunnel 2429
D. Ma, P. Zhang, Z. Li & Y. Yao

Immersed tunnels – knowledge sharing in the past showing the way towards sustainable solutions in the future 2434
T. Olsen

Small-scale model test for the dynamic behavior of submerged floating tunnels considering the coastal connection with subsea bored tunnels 2442
J. Park, S.-J. Kang, J.-B. An, J. Kim & G.-C. Cho

Mechanical behaviors of steel-concrete-steel immersed tunnel composite structures 2450
S. Song, X. Nie, J. Fan, Y. Guo & H. Zhang

Key technologies of concreting construction of super-wide steel-concrete-steel sandwich immersed tunnel element tubes in Shenzhen–Zhongshan Link 2457
Z.-X. Su, X.-D. Wu, C.-L. Zhang & S.-Y. Song

Experimental study on the typhoon resistance by placing Shenzhen-Zhongshan Link immersed tunnel element on the seabed 2466
S.-P. Sun, Q.-A. Ou Yang, W.-H. Li & J.-J. Ma

Assessing the suitability of coarse sand for the sand flow method in immersed tunnel foundations 2475
X. Szadkowski, M. van der Molen, R. Hermsen & R. Montijn

Ventilation and smoke exhaust technical scheme of super wide section immersed tunnel 2483
X. Yang, L. Cheng & M. Zhong

Fire prevention and rescue technologies used in ultra-wide cross-section immersed tunnel 2487
X. Yang, L. Yin, M. Zhong & L. Cheng

Quantitative detection method and practice of voids at the interface of steel-shell concrete with complex structure 2492
H. Zhao, G. Liu, Z. Fan, L. Sun, L. Meng & L. Wang

Research on settlement calculation method for DCM composite foundation of immersed tunnel in Shenzhen-Zhongshan Link 2500
J.-J. Zhou, F.-Y. Xia, Z.-J. Chen, X.-N. Gong, D. Liu & J.-L. Yu

Waterproofing and drainage

Next generation tunnel waterproofing 2509
Y. Boissonnas

Mitigation of the sources of infiltration in the segment sealing gasket 2517
G. Bomben

Analysis of cement grout hydraulic erosion in a homogeneous fracture 2522
H. Duan & L. Zou

Seepage and drainage study of underwater tunnel connecting section with combined method 2529
H. Fu, K. Hu, Y. Wu, Y. Yu & W. Liu

Comparison of double shell and sprayed single shell waterproofing methods in tunneling 2539
I.U. Gök, E. Karahan & B. Ünver

Constitutive model of aged EPDM rubber in subsea shield tunnel 2548
C. Gong, C. Xie, Y. Ge & J. Song

Research and application of joint waterproofing technology for prefabricated metro station structures 2554
M. Huang, Q. Fan, X. Yang & L. Fang

Innovative waterproofing system for shallow underground structures 2561
D.S. Konyukhov, T.E. Kobidze & O.B. Krymov

Tunnel drainage system and the possibility of non-destructive remediation 2567
J. Ortuta & V. Tóth

Step effects of hydraulic pressure of tunnels in loess under high-pressure seepage 2575
J. Qiu, K. Tang, Z. Zhao, Y. Bai, N. Zhang, Y. Chen & S. Ding

ITAtech design guidance chapter for composite Sprayed Concrete Lined (SCL) tunnels waterproofed with sprayed membranes 2584
J. Su

Self healing materials for preventing tunnel crystalline damage: Anti-calcium leaching, mechanical performance, self-healing mechanism 2593
Y. Tong, F. Ye, C. Tian, Y. Jiang, J. Zhang, H. Wang, B. Wu & X. Han

Analysis of viscous fingering between water and cement-based grout in tunnels 2602
S. Zhang, F. Johansson & L. Zou

Analysis of cement grout propagation with varying fracture apertures 2610
L. Zou, G. Zirgulis, A.N. Ghafar, U. Håkansson & V. Cvetkovic

Instrumentation and monitoring/testing and inspection

Design and development of tunnel liner void detection system 2619
A. An, W. Luo, G. Tian, Y. Xu, L. Gao & J. Zheng

Tunnel condition assessment: State-of-the-art 2624
S. Behbahani, J. Steinkuehler, J. Rostami, X. Wang & T. Iseley

Ground movement due to shaft construction and dewatering at Bengeworth road for the London Power Tunnels 2 scheme 2630
O. Brown, A. Simic & J. Ellis

Application of Acoustic signal to quantify the damage of the lesser Himalayan sandstone under unconfined compression loading and its implementation in the micromechanical damage-plasticity model 2639
S. Chajed & A. Singh

Tunnel detection and monitoring technology based on terrestrial laser scanning 2644
Y.-J. Cheng, C. Wang & W.-G. Qiu

Bored tunnels: Automated extraction of segment edge location from scan data 2650
J. Douglas, O. Côté & S. Jain

Cavity detection model from GPR images considering reinforcing bars in tunnel segment lining 2658
C. Hwang, S. Yang, S. park, H. Kim & H. Choi

Combination of modelling and monitoring in assessing stability of a tunnel constructed in highly deformable rock and fragilized by fire 2664
T. Kazerani & E. Garin

Field measurement of pile transient lateral response to advancing tunnel 2672
C.M. Khoo, H. Mohamad, B.P. Tee & M.F. Ghazali

Model experiment on load-bearing performance and failure process of newly proposed invert to reduce volume of excavation 2681
Y. Koizumi, A. Kusaka, N. Isago, K. Kawata, T. Otsu & N. Mikami

A noncontact mobil system using camera module for tunnel inspection 2689
C. Lee, D. Kim & D. Kim

Tunnel indirect monitoring and damage identification method based on SET-Swin transformer 2696
Q. Li, X. Xie & K. Zeng

Effectual approach to characterize rock fracture: Insight from calculating method of fractal dimension 2702
B. Li, W. Zhang, Y. Xue, K. Li, J. Zhao, Y. Chen, R. Kong & G. Wang

Research on integrated monitoring platform of composite steel-concrete immersed tunnel 2717
X. Mao, Z. Zhang & L. Li

Study for health monitoring of mountain tunnels operation using distributed fiber optic sensing technology 2724
H. Nonaka, Y. Miyajima, N. Sakamoto, Y. Taira, T. Yamamoto, M. Imai, K. Koike, K. Kishida, H. Shinbo & J. Kawabata

Development of wear detection device using dye 2731
Y. Omae, Y. Imaoka, H. Ueda, A. Nakamoto & R. Fukui

Structure health sensing network layout and monitoring based on wireless sensor network in undersea tunnel 2737
L. Ouyang, H. Huang, D. Zhang, C. Wang & S. Zhu

Innovative shaft inspection system for the Gotthard Base Tunnel 2745
M. Puglia, P. Spohn, K. Wachter, L. Chelini & S. Xiao

Fault diagnosis system for tunnel boring machines based on electrical energy monitoring 2751
Y. Qin, C. Zhang, S. Huang, Z. Wu, H. Shen & J. Sun

Pivotal role of instrumentation & monitoring in construction of Mumbai Metro Line 3 in an urban setting 2757
A. Rawat, R.R. Kumar & S.K. Gupta

Geotechnical instrumentation for road tunnels: Success cases in Colombia 2763
V. Restrepo, H. Salazar & J. Piedrahita

Analysis of laboratory tests for the determination of the clogging risk in mechanized tunnel excavation in fine-grained soils 2771
D. Sebastiani, S. Mangifesta, A. de Lillis & S. Miliziano

Information entropy based Robust Sensor Placement (RSP) method for wireless sensing of shield tunnel deformation 2778
J. Shi, H. Huang & Z. Guan

Design and key features of shaft and tunnel excavation monitoring system implemented in Singapore's Deep Tunnel Sewerage System Phase 2 Project 2784
A.K.K. Soe, L.L. Woo, K. Khin, P.C. Koh, A. Maxwell & E. Valdez Jr

Research on concrete strength detection method based on digital drilling and machine learning 2792
R. Wu

Development and application of similar materials to cobble stratum for solid-fluid coupling model test 2800
W. Zan, W. Zhang & Q. Yang

Study on the deformation and stress law of single shell lining in subsea rock tunnels 2809
W. Zhang

Using the acoustic emission and infrared thermal imager to identify the precursor of rock violent failure 2817
S. Zhu, D. Zhang, H. Huang, C. Wang & L. Ouyang

Digital and information technology

BIM Modelling & reality capture in underground drill and blast caverns 2825
P.R. Antón, I.J.F. Teixeira, A. Barbetta, B.B. Vieira & F. Abreu

The Sotra Link Project (Norway): An application of the BIM methodology in tunneling design and construction 2834
G. Barbieri, E.D. Panicis, G. Bella, D.D. Femina, A. Biagi & M. Giani

INFRA-BIM interoperability for Tunnel Renewal 2841
M. Catapano, A. Poli, R. Roncoroni & A. Reis

Design and implementation of a mobile welding robot for TBM cutterhead: Enhancing efficiency, precision, and safety 2848
P. Chen, J. Chen, J. Mao, J. Shu, M. Yang & S. Guo

Enhancing management and construction quality for a 5km long sandwich immersed tunnel through digital and intelligent methods 2857
W. Chen & J. Liu

Digital strategies-driven optimization of infrastructure maintenance: The case study of the rehabilitation of a disused tunnel in northern Italy 2863
F. Foria, E. Moschetti, M. Calicchio, V. Grigoras & B. Boyaci

Intelligent technologies and applications on TBM tunnel construction 2868
W. Guo, K. Hong, P. Gao & F. Li

Research and application of the bim-based fine management in shield tunnelling construction of rail transit engineering 2876
Y. Huang, Z. Zhang, K. Jia, H. Lai & Y. Li

Innovative design and practice of full life cycle of complex underground engineering equipment based on digital twin 2885
F. Liu

Research on intelligent construction technology and grading method of railway shield tunnel 2893
G. Lu, T. Wang, J. Liu & W. Wang

The interface between construction site and Tunnel Information Model: The case of the Brenner Base Tunnel 2902
D. Marini & G. Venditti

Integrated design of precast concrete linings for mechanized tunnels 2910
A. Menozzi, B. Tiberi, D. Maturi & R. Comini

Data-driven underground construction management: a case study of the Big Circle Metro Line in Moscow 2917
M.D. Nadot, V.V. Vyazovoy, M.A. Lvovskaya & A.G. Polyankin

Research on construction collaborative control method based on drilling and blasting tunnel equipment 2920
Q. Nianwen, Z. Miaojun, J. Weiliang

Trusted elements in the digital model of the tunnel 2927
G. Paskaleva, P. Beronneau & T. Bednar

Why is it worth using BIM in tunnelling? 2935
F. Robert & N. Dias

Digital automation in the structural modelling process for tunnel linings – A digital tool-based case study 2944
A. Shivasami & G. Heath

Demonstration of parametric analyses in ground models by applying programming logics using a digital tool named ParaRanger 2951
A. Shivasami, R. Nair & L. Dunbar

Streamline field management processes to improve labor productivity and reduce material loss 2959
H. Umeyama, S. Kitagawa, T. Arai, T. Fukuda, S. Taniguchi, F. Ito & H. Nagamatsu

Research on integrated management platform of shield construction based on digital twin and application in subway engineering 2965
X. Wang, J. Wang, Y. Zhang & S. Jiang

A study of digital quantitative evaluation system for the safety risk management in the construction activities of transportation hubs 2972
R. Wen, D. Gao, W. Yang & W. Mou

Research on data management and analysis of BIM technology 2980
Y. Zhaofeng

A study on 3D reconstruction of tunnel based on NeRf: A case study of Shanghai Metro Line 18 Tunnel 2985
Z. Zheng, Y. Xue, Y. Guo, J. Liu & L. Zhao

Machine learning

Development of a hard rock TBM performance prediction model using RMR input parameters 2995
A. Dardashti, J. Rostami, R. Ajalloeian, J. Hassanpour & A. Salimi

Performance analysis of supervised algorithms on encoded data for predicting tunnel strain classes 3005
A. Dewangan, D.R. Sahoo & J. Karlovsek

Automatic classification and segmentation of tunnel cracks based on deep learning and visual explanations 3014
Y. Feng, X. Zhang, S. Feng, Y. Zhao & Y. Chen

TBM machine parameters estimation: From design approach to on-field results. A concrete example based on Kalman Filter approach 3023
C. Iasiello & J. Rodríguez-Sánchez

An intelligent decision support system for tunnel structural defects maintenance with combining knowledge graph and deep learning 3029
F. Jia, Y. Xue, Q. Zhang & L. Qu

Prediction of disc cutter wear considering ground conditions and TBM operating parameters 3037
Y.S. Kang, S.J. Park, J.H. Hwang, J.P. Hong & T.Y. Ko

Leakage prediction and post-grouting assessment in headrace tunnel of a hydropower project 3044
T.B. Katuwal, K.K. Panthi, C.B. Basnet & S. Adhikari

A novel machine-learning model for estimating disc cutter life in TBMs considering individual cutter travel lengths 3053
D. Kim, Y. Shin, D. Kim, C. Lee, K. Kwon & H. Choi

Segment segmentation of tunnel ring point clouds using 3D deep learning 3059
W. Lin, B. Sheil, X. Xie, K. Li & G. Niu

Forecasting the driving speed of the TBM using machine learning algorithms 3067
M. Miller, Y. Fang, H. Luo, Y. Wang, G. Xu, B. Leng, S. Kharitonov, V. Akulich, Y. Ma & F. Zou

Intelligent tunnel asset management of CERN underground facilities 3073
V.D. Murro, A. Ouyang, J.A. Osborne & Z. Li

Research and practice of digital lean construction mode of tunnelling based on shield self-driving technology 3079
L. Pei, H. Wu, M. Hu, J. Lu, B. Wu & G. Li

Study on machine learning method for supporting conventional tunnel engineering judgement 3086
K. Sakai, S. Miyanaga & M. Yamagami

Assessment of TBM performance in different types of rocks using supervised learning techniques 3095
H. Samadi, J. Hassanpour, J. Rostami & A. Moghbeli

Hyperspectral imaging features for concrete compressive strength assessment: Experimental study 3104
C. Wang, H. Huang, M. Zhou & S. Zhu

An energy-efficient tunnel ventilation control algorithm combining dynamic neural network and fuzzy control 3113
H. Wang, Z. Li, Y. Zhang & J. Zhang

Intelligent surrounding rock classification and mechanical parameters analysis method based on drilling parameters of tunnels 3122
M. Wang, S. Zhao, W. Yi & X. Peng

Investigation on surrounding rock quality prediction based on incomplete multi-source dataset and tree-augmented naive Bayesian network 3131
C. Wu, H. Huang, H. Tong, M. Zhou, L. Zhang & Y. Tong

Machine learning-informed soil conditioning for mechanized shield tunneling feature engineering, model selection, and uncertainty quantification 3139
X. Yuan, S. Wang & T. Qu

Underground caverns/underground space use

Planning and support estimation of underground powerhouse in the Himalayas 3149
S. Adhikari, C.B. Basnet, K.K. Panthi & T.B. Katuwal

A conceptual framework for the creation of an integrated planning system for the strategy of implementing technologies for underground urban construction 3157
V. Agafonov, D. Konyukhov & E. Kulikova

Deep powerhouse caverns design development and challenges – Snowy 2.0 experience 3160
I. Ching, M. Diederichs, B. Chapman & G. Cardone

Minimising impacts on the local habitat in relocation and construction of a large cavern for track crossover at Acharya Atre Chowk Metro Station of the Colaba-Bandra-Seepz (Line 3) in Mumbai, India 3169
S.K. Gupta, R. Mittal, M. Dange & R. Tilak

Innovation practice of indoor space of rail transit hub 3174
L. Ji, Y. Li, K. Wei, Y. Deng & Y. Fu

Hexane section and its section combination honeycomb type underground structure system. Design and implementation of the program study 3180
Q. Jiao, L. Guo & W. Chen

Harnessing the potential of underground space for climate-neutral cities: Energy geostructures in metro tunnels 3187
A. Koliji, E. Garin, T. Kazerani, B. Schenk & J. Senn

Research on complete technologies for the construction and utilization of super large caverns in Hong Kong 3194
Y. Li, Z. Hong, W. Li & F. Xu

Challenges in planning, design, and construction of the underground power plant station cavern Kühtai 2 3202
A. Morocutti, P. Wetzlinger & R. Steiger

The use of underground space in greater Kuala Lumpur 3207
T.-A. Ooi & C.-M. Khoo

SMART tunnel revisited – after 15 years in operation 3215
T.-A. Ooi & C.-M. Khoo

Large diameter surge shaft in weak foliated rock mass; excavation and support with real-time investigation and pre-excavation support strategy in the lesser Himalayan Slate 3223
B. Parajuli, E. Christakis, A. Marasini & X.-Y. Yang

Gangxia North Hub innovation highlights 3232
X. Qie & L. Qi

Contract Korsvägen - part of the new Westlänken Commuter Rail Project in Gothenburg, Sweden. Challenges of drill & blast Tunnelling and cut & cover construction in heterogeneous ground conditions 3236
K. Rieker

The cross river rail project as a PPP model in Brisbane, Australia. Experiences in cavern construction for 3 underground stations and tunnelling with double shield machines 3243
K. Rieker

Mechanized shaft sinking with VSM: Developing underground space for U-Park® systems 3249
P. Schmäh, S. Frey & M. Peters

Snowy 2.0 – Implementation of a "twin numerical model" as computational tool of the "observational method" during the excavation of a large cavern under high in situ stress 3255
P.L. Tonioni, A. Toussaint, P. Lignier, K. Thermann, A. Lambrughi & I. Ching

Rock engineering in Sweden - Mining, hydropower and railways 3262
P. Vedin, T. Dalmalm & J. Brantmark

Integration of stations and cities plan and research on technological innovation of Shenzhen Dayun comprehensive transportation Hub 3267
M.-S. Wang, C. Liu, R.-Z. Fei, W.-R. Liu, Y.-Y. Fu & Y.-Z. Deng

Comprehensive development and utilization of underground space of Xiangya Road River-crossing Tunnel project in Changsha City 3276
H. Wang, J. Ma, X. Zhang & M. Zhou

A broad review of cavern engineering approach in meta-sedimentary rock in Northern Hong Kong 3282
J.C.F. Wong, L.W.H. Tsang, H.H.M. Suen, D.C.W. Mak, F.K.L. To & H.H.C. Poon

Key technology for the construction of the Shen-Zhong Link tunnel under the existing operating expressway 3290
X. Zhou, X. Cheng & Q. Xu

Operational safety, maintenance and repair

The 365 km tunnels assessment along ASPI Motorways Network – Key findings addressing risk analysis procedures and structural conditions evaluation and strategy of interventions 3303
C. Alessio, L. Baccolini, D.D. Fiore, M. Conte, M. Mazzola & D. Peila

Conservative rehabilitation interventions of masonry highway tunnels along the historic Genoa-Po valley motorway in Genoa (Italy) 3312
C. Alessio, R. Pittalis, A. Poli, G. Attianese, B. Chiaia, D. Ferretti, E. Zanazzi, L. Ferrari & E. Coisson

Colle Marino left tunnel renewal project: The first case-history of full lining reconstruction - from invert to crown - under difficult geotechnical conditions and future developments for working under traffic 3320
C. Alessio, B. Spigarelli, M. Mazzola, C. Ceccarelli, A. Poli & P. Iuculano

Lessons learned from longitudinal ventilation worldwide and CFD-based solutions 3328
A.B. Amado, Y. Zhao & E.Q. Ruiz

Italian guidelines for the risk classification, safety evaluation and monitoring of existing tunnels: An overview 3333
A. Carigi, C. Todaro & G. Silvestri

A computer-vision-based model updating strategy for shield tunnels with cracks 3342
X. Chang, Y. Zhang & Y. Fu

Evolution of safety situation and repair scheme for punctured shield lining 3350
Z. Dai, R. Hu & Z. Wang

Smart tunnel in industry 5.0: Improving road tunnel resilience by dynamic risk analysis 3359
A. Focaracci, L. Martirano & F. Zacchei

Tunnel asset management: Risk analysis through the MIRET approach 3365
F. Foria, G. Miceli & M. Calicchio

Tunnel renewal strategy – The evaluation of the advantages through LCA 3371
S. Frisiani, M. Pierani, F. Magnelli, L. Baccolini & A. Poli

Development of cementitious repair material for tunnel concrete structures of operating railroad in salt-affected environment 3379
Y. Kose, K. Miyake, A. Hosoda, M. Saito & H. Utsugi

Ventilation for a long underground road tunnel system from a modern perspective 3388
T.K. Lam & E. Hataysal

Study on fire smoke exhaust strategy in daliangshan no.1 super-long expressway tunnel 3394
F. Lan, H. Zou, L. Wu, Y. Wang & Y. Deng

Positioning and autonomous control of intelligent hydrodemolition robot 3401
W. Liang

Research on information perception mechanism and evaluation method of tunnel lighting environment 3409
B. Liang, J. Niu & C. Qin

Research and realization of equivalent lighting environment for tunnels 3418
B. Liang, C. Qin & J. Niu

A numerical investigation on the long-term stability of tunnels excavated in the upper stratum of expansive layer 3428
S. Ma, Y. Cui

Subway ventilation system design and the importance of predicting the long-term wall surface temperature 3437
I.K. Mbaye

Approach in structural fire resistance of the existing North-South Railway Tunnel in Brussels 3444
B.D. Pauw, C. Timperman & S. Devriese

A seismic damage classification for post-damage assessment of rock tunnels 3451
D.A. Reddy & A. Singh

The numerical-physical coupling method in investigation of the response of the tunnel structure under fire scenarios 3456
L. Wang & Z. Yan

Research on fire compartmentation of hyperscale public area in underground rail transit hub 3465
K. Wei, L. Ji, Y. Fu & Y. Deng

Experimental study on the applicability of the combined tunnel ventilation system of complementary ventilation and shaft 3472
Y. Xin & Y. Wang

Study on the influence of longitudinal slope on the temperature field inside railway tunnels in cold regions and engineering counter measures 3480
C. Yang, S. Tian & Z. Ma

The impact of landscape belt design inside extra-long highway tunnel on driving comfort: A driving simulation study 3489
F. Ye, J. Liu, W. Zhu, E. Su, X. Wen, X. Han, Z. Jiao & P. Sun

Full life cycle multi-hazard scenarios and structural response analysis of metro shield tunnels 3497
T. Yu, Z. Yan & H. Zhu

Research on China's extra-long separate construction tunnel emergency evacuation and rescue technology 3504
Y. Yuan & S. Chen

Concept of a thermoelectric power system in high geothermal tunnel: Preliminary design with numerical simulation 3511
Y. Yuan, P. Cui & Q. Wang

Development and application of complete equipment for mechanized construction of defect remediation in existing railway tunnels 3520
W. Yuan, F. Gui, L. Zhang & P. Zhang

Research trend and prospect of reconstruction and expansion technology of existing highway tunnels 3528
Z. Zhang

Reliability study of full jet longitudinal smoke exhaust system for a road tunnel over 5 km long 3538
X. Zhang, L. Tao, M. Luo & Y. Zeng

Resilience assessment of shallow-buried subway stations under earthquake disasters 3545
C. Zhang, D. Zhang & Z. Huang

Contractual practices and risk management

Development of a tunnel asset management tool from a risk-based approach 3557
C. Alessio, D. Di Fiore, L. Baccolini, B. Chiaia & M. Conte

SMART-Systemic approach to risk management of tunnels 3567
E. Andrés Marulanda

Risk management of tunnel projects: From qualitative to quantitative probabilistic risk analysis 3572
A. Antiga, M. Chiorboli & M. Dotti

Strong financial and improved procurement strategies for the success of the Grand Paris Express 3581
A. de Pommerol

A methodology of risk management to urban tunnels and its application to Bogota subway 3585
J. Esteban Alarcón G & A.P. de Assis

The use of a reference cost system for contracting underground public works 3594
E.A.P. Filho, C.K. Miyazato & P.M. Neto

Development of an early contractor involvement selection tool for public owners 3600
C.P. Friedinger & P. Sander

Pawtucket CSO tunnel design build - From managing risk and quality to design and construction innovations 3608
I. Halim, S. Polycarpe & V.E. Gall

Comprehensive risk management for slurry shield TBM tunneling using fuzzy set theory 3617
K. Kwon, M. Kang, H. Park, Y. Ma & H. Choi

Geotechnical risks management associated with a tunnel launch in complex geological conditions 3623
C.L. Ng, C.M. Khoo & N.A. Abdul Rahman

Comparing underground construction risk for urban transportation and hydropower projects – A lender's technical advisor's perspective 3632
A. Noble

Underground risk and ESG aspects in pumped hydro and hydropower projects – what worries the lenders? 3639
A. Noble

Research on risk management and control of undersea tunnel construction based on blockchain technology 3647
L. Qu, S. Liu, M. Tan & H. Huang

Study on the major risk control elements under EPC management mode of rail transit 3652
Z. Shi, J. Huang & L. Ding

Tunnel Euralpin Lyon Turin: The design and contract challenges for a modern Alpine base tunnel 3659
D. Stocker, P. Gilli & M. Falanesca

Risk limiting in urban tunnel contracts 3668
H. Wagner

Author index 3673

Taylor & Francis
Taylor & Francis Group
http://taylorandfrancis.com

Tunnelling for a Better Life – Yan, Celestino, Thewes & Eberhardt (Eds)
© 2024 The Editor(s), ISBN 978-1-032-80042-4
Open Access: www.taylorfrancis.com, CC BY-NC-ND 4.0 license

Preface

The World Tunnel Congress 2024 and the 50th ITA-AITES General Assembly are held in Shenzhen, China, from 19–25 April, 2024. The China Civil Engineering Society (CCES) is honoured to host this prestigious and significant event which is not only a milestone in the history of the ITA, marking its 50th anniversary but also a testament to the enduring commitment and collaboration within the international tunnelling community.

With the visionary theme of "Tunnelling for a Better Life," WTC2024 is set to spotlight the pivotal role of tunnelling and underground works in creating sustainable, efficient, and resilient environments. This theme is a call to the global community to leverage the latest in innovation and technology, addressing the era's most pressing challenges, including climate change, urbanization, and the quest for low-carbon, intelligent infrastructure solutions.

The proceedings encompass a wide array of critical topics in tunnelling and underground space, reflecting the latest trends, insights, and innovations. WTC2024 has received more than 1,000 abstracts and 540 full papers by authors from 46 different countries. After the peer review by the Scientific Committee which was composed of 145 experts from 39 countries, 486 papers from 40 countries were accepted for publication in the WTC2024 Proceedings. From integrating low-carbon technologies to applying intelligent systems in the design, construction, and management of tunnelling and underground works, the contributions within these pages showcase a forward-looking approach to tackling the complexities of modern urban development. The sustainable solutions presented within the proceedings illuminate a path toward resilient, low-carbon, and eco-friendly practices, reflecting our commitment to minimizing environmental impact and underscoring our dedication to efficiency and progress in the intelligent and digital era. The WTC2024 proceedings will inspire and guide our community toward realizing the potential of underground spaces to create a better, more sustainable life for present and future generations.

As we gather in Shenzhen, a city renowned for its dynamic innovation and rapid growth, we are reminded of the power of collaboration and the importance of knowledge exchange in advancing our field. The WTC2024 serves as a platform for experts, practitioners, and stakeholders from across the globe to come together, share insights, and forge partnerships that will drive the future of tunnelling and underground space development.

On behalf of the organizing committee and the CCES, we express our deepest gratitude to all participants, contributors, and sponsors who have made this event possible. As we celebrate the 50th ITA-AITES anniversary, WTC2024 in Shenzhen will provide invaluable opportunities for the international tunnelling community to explore the depths beneath our cities and the heights of our aspirations for a sustainable future and a better life.

Yi Jun
Chair of the WTC2024 Organizing Committee
President of the China Civil Engineering Society (CCES)
Shenzhen, April 2024

Taylor & Francis
Taylor & Francis Group
http://taylorandfrancis.com

Tunnelling for a Better Life – Yan, Celestino, Thewes & Eberhardt (Eds)
© 2024 The Editor(s), ISBN 978-1-032-80042-4
Open Access: www.taylorfrancis.com, CC BY-NC-ND 4.0 license

Acknowledgements

Reviewers
The Editors wish to extend their gratitude to all the members of the Scientific Committee for their unwavering dedication and invaluable contributions.

Sponsors
The Organizing Committee and the Editors wish to extend their gratitude to the congress sponsors for their help and support.

Taylor & Francis
Taylor & Francis Group
http://taylorandfrancis.com

Tunnelling for a Better Life – Yan, Celestino, Thewes & Eberhardt (Eds)
© 2024 The Editor(s), ISBN 978-1-032-80042-4
Open Access: www.taylorfrancis.com, CC BY-NC-ND 4.0 license

WTC 2024 Organization

Organizing Committee

Yi Jun	Chair	China
Shang Chunming	Co-chair	China
Tang Zhong	Co-chair	China
Jinxiu Yan	Co-chair	China
Olivier Vion	Member	France
Li Jiqin	Member	China
Guo Shanyun	Member	China
Zhu Hehua	Member	China
Chen Xiangsheng	Member	China
Gao Wei	Member	China
Peng Limin	Member	China
He Chuan	Member	China
Lei Shengxiang	Member	China
Zhu Weibin	Member	China
Feng Shouzhong	Member	China
Hong Kairong	Member	China
Pei Liefeng	Member	China
Huang Hongwei	Member	China
Tan Zhongsheng	Member	China
Wang Bin	Member	China
Qiu Wenge	Member	China
Fu Helin	Member	China

ITA-AITES Executive Council (2022-2025)

Arnold Dix	President	Australia
Jinxiu Yan	Past President	China
Andres Marulanda	First Vice-President	Colombia
Hangseok Choi	Vice-President	Korea
Jamal Rostami	Vice-President	USA
Ioannis Fikiris	Vice-President (2023-2026)	Greece
Sindre Log	Member	Norway
Damian McGirr	Member	UK
Monika Mitew-Czajewska	Member	Poland
Andrea Pigorini	Member	Italy

Klaus Rieker	Member	Germany
Sanja Zlatanic	Member	USA
Gérard Seingre	Member	Switzerland
Thomas Dalmalm	Member	Sweden
Rick Lovat	Member (2023-2026)	Canada

International Advisory Committee

Jairo Pascoal Júnior	Brazil
Rick Lovat	Canada
Søren Degn Eskesen	Denmark
Michel Deffayet	France
Lars Babendererde	Germany
Ioannis Fikiris	Greece
Rakesh Kumar Khali	India
Giuseppe Lunardi	Italy
Nobuharu Isago	Japan
In-Mo Lee	Korea
Ooi Teik Aun	Malaysia
Zaw Zaw Aye	Myanmar
Abidemi Agwor	Nigeria
Tom Melbye	Norway/ Switzerland
Jeyatharan Kumarasamy	Singapore
Thomas Dalmalm	Sweden
Felix Amberg	Swizerland
Aphichat Sramoon	Thailand
Nick Chittenden	UAE
Ross Dimmock	UK
Martin Knights	UK
John Reilly	USA
Shani Wallis	USA

Scientific Committee

Jinxiu Yan	China	(Chair)
Tarcisio Celestino	Brazil	(Co-Chair)
Markus Thewes	Germany	(Co-Chair)
Erik Eberhardt	Canada	(Co-Chair)
Han Admiraal	The Netherlands	
Jasmin Amberg	Switzerland	
Pengtao An	China	
Lars Babendererde	Germany	
Jonathan Baber	Australia	
Karin Bäppler	Germany	
Mikhail Belenkiy	Russian Federation	
Adam Bezuijen	The Netherlands	
Nuh Bilgin	Turkey	

Nikolai Bobylev	Russia
Nichole Boultbee	Canada
Rune Brandt	Switzerland
Wout Broere	The Netherlands
Andrea Bruschi	Italy
Werner Burger	Germany
Christian Butron	Sweden
Clayton Chan	Hong Kong, China
Shougen Chen	China
Jason Chin	Hong Kong, China
Elena Chiriotti	France
Nick Chittenden	UAE
Jens Classen	Germany
Massimo Coli	Italy
Antonia Cornaro	Austria
Jesper Peter Dahl	Denmark
Thomas Dalmalm	Sweden
Bart De Pauw	Belgium
Michel Deffayet	France
Nicola Della Valle	Italy
Laurence Delplace	Belgium
Jeanne Doreau-Malioche	France
Heinz Ehrbar	Switzerland
Amanda Elioff	USA
Conrad W. Felice	USA
Vojtech Gall	USA
Robert Galler	Austria
Etienne Garin	Switzerland
Giuseppe M. Gaspari	Canada
Anne-Merete Gilje	Norway
Alexandre Gomes	Australia
Piergiorgio Grasso	Italy
Eivind Grøv	Norway
Caixia Guo	China
S.K. Gupta	India
Michael Halwachs	Germany
Choi Hangseok	South Korea
Marcel't Hart	The Netherlands
Siamak Hashemi	Iran
Jafar Hassanpour	Iran
Ole Hededal	Denmark
Karl Gunnar Holter	Norway
Hongwei Huang	China
Roy HUNG Kin-chung	Hong Kong, China
Lars Christian Ingerslev	USA
Nobuharu Isago	Japan
Kumarasamy Jeyatharan	Singapore
Chaojun Jia	China

Su Jiang	UK
Yusheng Jiang	China
Berkan Kayadan	Denmark
Rakesh Khali	India
Chee-Min KHOO	Malaysia
Rakesh Kumar	India
Gyanendra Lal Shrestha	Nepal
Eric Leca	France
Siew Wei Lee	Hong Kong, China
Anna Lewandowska	Poland
Charlie C. Li	Norway
Liping Li	China
Jian Liu	China
Sindre Log	Norway
Rick Lovat	Canada
Zhao Lu	China
Giuseppe Lunardi	Italy
Jason Mann	Canada
Daniele Martinelli	Italy
Camilo Marulanda	Colombia
Andrés Marulanda E.	Colombia
Cátia Matos	Sweden
Alessandro Menozzi	Italy
Mehmed Mesihović	Bosnia and Herzegovina
Monika Mitew-Czajewska	Poland
Michael Mooney	USA
Tone Nakstad	Norway
Verya Nasri	USA
Matthias Neuenschwander	Switzerland
William Newns	New Zealand
Pekka Nieminen	Finland
Bjørn Nilsen	Norway
David J. Och	Australia
Henki Ødegaard	Norway
David Oliveira	Australia
Yoshikazu Ota	Japan
Casper Paludan-Müller	Denmark
Krishna Kanta Panthi	Norway
Jairo Pascoal Júnior	Brazil
Noppodol Phienwej	Thailand
Giorgio Piaggio	Chile
Sandeep Potnis	India
Eric Premat	France
Sanjay Rana	India
Florent Robert	France
Hugo Cássio Rocha	Brazil
Jan K.G. Rohde	Norway
Jamal Rostami	USA

Petr Salak	Czech Republic
Pekka Särkkä	Finland
Magali Schivre	France
Thomas Schoenborn	Norway
Roberto Schuerch	Switzerland
Gérard Seingre	Switzerland
D.K. Sharma	India
Andrew Shaw	UK
Daljit Singh	India
Thor Skjeggedal	Norway
Panos Spyridis	Germany
Raymond Leslie Sterling	USA
Robert Sturk	Sweden
Pavel Szereda	Denmark
Gary Tang	New Zealand
Per Tengborg	Sweden
Alun Thomas	Denmark
Carmine Todaro	Italy
Zvonko Tomanovic	Montenegro
Michael Tonnesen	Denmark
Jorn Treldal	Denmark
Ilkka Vähäaho	Finland
Gonzalo Diniz Vieira	Portugal
Harald Wagner	Thailand/Austria
Shuying Wang	China
Dazhi Wen	Singapore
Sallo Van der Woude	The Netherlands
Xiaochun Xiao	China
Shuan Xiao	Switzerland
Shulin Xu	Italy
Saffet Yagiz	Kazakhstan
Jinjun Yang	China
Shenyan Yao	Australia
Haitao Yu	China
Dongmei Zhang	China
Fengshou Zhang	China

Taylor & Francis
Taylor & Francis Group
http://taylorandfrancis.com

Planning and general aspects

Taylor & Francis
Taylor & Francis Group
http://taylorandfrancis.com

Tunnelling for a Better Life – Yan, Celestino, Thewes & Eberhardt (Eds)
© 2024 The Author(s), ISBN 978-1-032-80042-4
Open Access: www.taylorfrancis.com, CC BY-NC-ND 4.0 license

Multilateral institutions and governance of urban underground space

Nikolai Bobylev*
Saint Petersburg State University, Saint Petersburg, Russia
Herzen State Pedagogical University of Russia, Saint Petersburg, Russia

Yong-Kang Qiao & Fang-Le Peng
Tongji University, Shanghai, China

ABSTRACT: Multilateral institutions are the international organizations that are formed by three or more countries. These institutions usually work on development issues addressing global agenda. Urban underground space, traditionally and predominantly being a responsibility of a city government, is fast becoming an issue of global importance and co-operation. Globalization of urban underground space has been facilitated by technological complexities and innovation. Tunnelling and underground space development has been increasingly executed by global businesses, operating across countries and continents. In response to this "globalisation" trend of urban underground space development, this research is looking into the work that has been already done by variety of multilateral institutions and international organisations, setting out agenda and needs for further discussion on urban underground space at a global level.

Keywords: Globalization, Governance, Institutions, Planning, Urban Underground Space

1 INTRODUCTION

The term *Governance* refers to the set of formal and informal institutions, government, business, civil society that influence a decision-making processes (Rhodes, 1996, 1997, Tretter, 2008, Berggruen & Gardels, 2012). A sustainable governance can be understood as binding political decisions to the benefit of future generations that include state and non-state actors through steering mechanisms, cooperation, and coordination (Driessen et al, 2012, UN Habitat, 2002).

Multilateral institutions are the international organizations that are formed by three or more countries. These institutions usually work on development issues addressing global agenda. The present global agenda is set out by the United Nations via Agenda 2030 and the Sustainable Development Goals (United Nations, 2023). Global development agenda addresses most pressing contemporary problems planet Earth is facing: climate change, biodiversity loss, sustainable and resilient urbanization. This formal and informal agenda reflects international consensus on major challenges, and is supported by the overwhelming majority of national governments, public and private sector, the latter via gaining prominence ESG (Environmental and Social Governance) campaign.

Numerous institutions work on global challenges agenda. Many international institutions set to address a planetary perspective, and aim to align current governance systems with the contemporary global challenges, such as global environmental change and earth-system transformations.

It has been argued that major global challenges can and should be addressed at a global level of governance (e.g. Earth System Governance research alliance, 2023). While it seems obvious, that challenges like climate change and ocean plastic should be addressed at a global level via multilateral agreements, it is less obvious that more localised problems, like urbanisation, should have any global governance framework.

In this paper, we will explore the case of urban underground space as a part of urbanisation process, investigate associated levels of governance, and specific issues that are relevant at the global level.

2 URBAN UNDERGROUND SPACE AS A PART OF GLOBAL AGENDA

Urban areas are at the forefront in driving global environmental change, and these areas are themselves heavily affected by global change, namely

*Corresponding author: n.bobylev@spbu.ru

DOI: 10.1201/9781003495505-1

climate change, land degradation, biodiversity loss. There has been a growing understanding in the recent decades that cities must become greener, smarter, more resilient, energy efficient and compact to address the above challenges. Urban underground space is widely accepted as an important asset for a sustainable urban development, primarily addressing resiliency, energy efficiency, and land use (Peng et al, 2021, Volchko et al, 2020, ITA Working Group 20, 2023, Bobylev et al, 2023).

Construction sector has been accounting for nearly 40% of global CO_2 emissions (for large cities the figure is about 70%) (OECD, 2022), hence, buildings and structures are central to the low-carbon global transition. Climate strategies have been already developed in many cities. Climate change adaptation requires addressing floods and flash floods in urban areas, which tops agenda in many cities. The flood protection infrastructure, including subsurface infrastructure, has been the key element of adaptation plans (Tianming, et al, 2021). Sustainability and resilience has been a part of most cites' development strategies, and urban underground space is an important dimension to these policies (Qiao et al, 2019).

Urban underground space is a part of the global environment and development agenda. Firstly, urban underground space is indispensable for a compact, sustainable urbanisation and a three-dimensional city. Secondly, urban underground space is important in addressing climate change adaptation and mitigation agendas. Thirdly, urban underground space is relevant to a few Sustainable Development Goals, it is interlinked with many issues like energy and environment, that eventually affect global progress on the goals. Fourthly, underground space is a big player in energy sector, which impacts many globally important issues, from climate to economy, equality, poverty, human-wellbeing, ecosystems health. Underground space provides geothermal energy, allows energy storage and transit, is a part of urban energy efficiency agenda via transport infrastructure and buildings thermal performance (Akhmetzyanov et al, 2021, Lin et al, 2022).

3 MULTILATERAL INSTITUTIONS

This section presents state-of-the-art and briefly describes international multilateral institutions that are relevant to urban underground space. We start with global international organisations that are focused on urban underground space.

The International Tunnelling and Underground Space Association is a non-governmental, non-profit organization founded in 1974, comprising currently 78 member nations (International Tunnelling and Underground Space Association, 2023), the Association has a Special Consultative Status with the Economic and Social Council of the United Nations.

The Associated Research Centers for Urban Underground Space is an international, non-governmental organization founded in 1996, the organisation has been holding biannual professional conferences focused on urban underground space planning and development (Associated Research Centers for Urban Underground Space, 2023).

We continue with the major international organisations where countries are members, we pick the most relevant ones to the urban underground space.

The United Nations Human Settlements Programme (UN-Habitat) is the United Nations designated agency that leads and co-ordinates implementation of the sustainable urban development agenda (UN-Habitat, 2023). Urban underground space has been regularly mentioned in its programmatic documents like Habitat III and New Urban Agenda, however there has not yet been any specific action, guide, or policy campaign focused on subsurface use.

The World Bank is an international financial institution with 189 member countries, it leads several affiliated organisations that are working on reducing poverty and building prosperity in developing countries (World Bank, 2023). The World Bank has been financing projects and producing analytical reports that involve discussions on urban underground space.

The Organisation for Economic Co-operation and Development is an intergovernmental organisation with 38 member countries, founded in 1961 to stimulate economic progress and world trade (Organisation for Economic Co-operation and Development, 2023). Urban underground space has been a part of the Organisation urban policy, as well as some regional and country reports.

The United Nations Office for Disaster Risk Reduction was created in 1999, in 2020 it has published Words into Action: Implementation Guide for Land Use and Urban Planning (United Nations Office for Disaster Risk Reduction, 2020) a series of guidelines, based on global expertise, communities of practice, and networks of Disaster Risk Reduction practitioners. The guidelines provide practical, specific advice on implementing the Sendai Framework for Disaster Risk Reduction 2015-2030, it includes a substantial part on urban underground space focusing on combatting floods.

The International Energy Agency is an autonomous intergovernmental organization, established in 1974, that works on policy and data on the global energy sector; it is governed by the 31 member countries and affiliates 13 associated countries (International Energy Agency, 2023). Urban underground space and subsurface features in the reports by this Agency on District energy networks, Geothermal energy, and CO_2 storage.

We move further to a lower, but more focused level of specific multilateral projects and ad-hoc initiatives that significantly contributed to the knowledge on urban underground space.

The European Cooperation in Science and Technology project named "SUB-URBAN – A European network to improve understanding and use of the

ground beneath our cities" has published city surveys of 29 European countries to reflect the state-of-the-art in suburban planning (Campbell et al., 2017).

The NeTTUN project financed by the seventh Framework Programme for the European Commission united 23 industrial, research and development organisations across 9 countries in Europe to investigate the construction, management and maintenance of tunnels (NeTTUN, 2016).

4 CURRENT AGENDA OF THE MULTILATERAL INSTITUTIONS

The current agenda of the above named multilateral institutions related to urban underground space is formed as a response to major global challenges and issues on which those institutions have been working. Thus, urban underground space itself has been yet not on the global institutions agenda, but rather features as one of the issues, tools, options, items of attention, or responses to well-known global challenges like climate, energy, poverty, etc. Professional associations and specific projects dealing directly with subsurface use and tunnelling represent the only international institutions that feature urban underground space as a distinct global agenda item.

Major global interdisciplinary institutions, like World Bank, has been gradually increasing presence of urban underground space in their reports. Now it is very clear that urban underground space not just has been mentioned, but have a detailed description and a clear link to the problem solution or phenomenon which a particular report is discussing. This observation can be interpreted as urban underground space gradually moving towards becoming of one of the distinct issues on global agenda as presented by major international development institutions.

For now, urban underground space has been mentioned as a secondary topical item in the reports, the primarily items of those reports are listed below. The list below was obtained by screening, reading, and interpreting reports of the above named organisations as presented on their websites, the reports issued during and after 2020 were read and analysed (only major development organisations, International Tunnelling and Underground Space Association, Associated Research Centers for Urban Underground Space were excluded). The list below includes themes that urban underground space addresses, and it was sufficiently detailed and explained how in a particular report. The themes are listed alphabetically:

- Advancing Climate Action
- CO_2 storage resources and their development
- District energy networks and engineering infrastructure
- Emergency Response
- Geothermal energy
- Livable city
- Thermal energy storage
- Transformative climate adaptation action
- Transforming cities
- Transforming the urban space
- Transit-oriented development
- Underground hydrogen storage
- Urban development (guides, best practices)
- Urban development overview (regional, national)
- Urban public spaces
- Urban regeneration
- Urban resilience
- Urban transit

It can be observed that this themes indeed include some major global challenges, as well as some specific responses to them, like transit-oriented development. However, some major global agenda issues are missing, like climate change mitigation. The latter example suggests that there is a lot of room and a certain urgency that underground space professional community make aware global policy players of high relevance of urban underground space to (in this example) climate change mitigation by providing renewable energy and energy efficient buildings and structures.

5 GLOBAL AGENDA FOR URBAN UNDERGROUND SPACE

Global agenda for urban underground space has been evolving in the recent decade, based on conceptualising subsurface and urban underground space as asset (Maring & Blauw 2018), partially renewable resource (Parriaux, 2006), and an origin of geosystem services (van Ree, & van Beukering, 2016). This has been quite different from actual absence of any concept of subsurface use in prior decades, and the use of underground space on the first come first served basis (Admiraal & Cornaro, 2016, Grecksch, 2021).

Still evolving concept of geosystem services is focusing on abiotic components and services of the environment (Gray, 2018; Fox et al, 2020). Nature-based solutions are a concept for integrating a range of ecosystem-based approaches in order to address a range of societal challenges (Busha & Doyon, 2019). Both concepts are very relevant to the global agenda for urban underground space, which can be defined as a sustainable, frugal and rational use of urban underground space resources, recognising the limits of their renewability and current and future value to humankind.

Figure 1 Illustrates the value of subsurface defined through geosystem services. The main categories of geosystem services are: 1 – biotic services directly supporting ecosystems; 2 – abiotic services directly supporting ecosystems; 3 – abiotic services supporting man-made infrastructure and indirectly influencing ecosystems; and 4 – abiotic services supporting man-made infrastructure and not related to ecosystems (i.e. to specific types of biomes and distinct living environments (Bobylev, et al, 2022).

Figure 1. Categorization and visualization of geosystem services (from Bobylev, et al, 2022).

6 GOVERNANCE OF URBAN UNDERGROUND SPACE

Governance of urban underground space is relevant primarily at a national and regional (city) levels. National level provides building codes, planning laws, technology norms. Regional and city level regulates spatial plans, environmental permissions, buildings, structure, and infrastructure design approvals, as well as energy and groundwater use permissions and quotes.

Global governance of urban underground space might be required to (1) archive progress on global challenges where urban underground space supports this progress, (2) governance of urban underground space itself, conceptualising it as a global challenge or an important asset. The first avenue was detailed in sub section "4. Current agenda of the multilateral institutions", and it is obvious that this part of the urban underground space governance agenda has already gain some attention and policy documents. The second avenue, global governance of urban underground space has not been yet addressed by international policy community, except of occasional mentioning by underground space professionals.

Global governance of urban underground space should be based on the global agenda for urban underground space (section 4), and address potential conflicts and competing interests by stakeholders. Agenda for these interests and stakeholders themselves could have regional and geographical specifics, this agenda has not been yet conceptualised.

We offer some more insights in competing interests and potential conflicts in urban underground space at a global level. Firstly, urban underground space has some non-renewable resources (section 4), and, therefore, general sustainability approach based on the rights of future generation would apply at a global level. Secondly, urban underground space use impacts a number of the Sustainable Development Goals, and thus affects global progress towards their implementation. Thirdly, urban underground space use (and subsurface use in general) in one particular area might impact its use in another area. Urban underground heat island, groundwater depletion, groundwater barrage effects are good examples. Here we can mention environmental risks, associated with e.g. nuclear waste storage, carbon dioxide deposition, deep geothermal energy use. All these potential conflicts and impacts might have transboundary context in particular locations, and hence quite relevant to global governance. In this regard, Convention on Environmental Impact Assessment in a Transboundary Context (United Nations Economic Commission for Europe, 1991) is quite relevant and to certain extend represent a blueprint to one of the aspects of urban underground space global governance. The Convention was signed in Espoo in 1991 and entered into force in 1997, so far it has been mainly used in the air pollution context.

7 CONCLUSIONS

Urban underground space has been emerging as one of the themes on the global development agenda. Our research has shown that urban underground space has been gaining increasing attention and traction by the global multilateral institutions and international organizations. We have reviewed activities and reports by five major global intragovernmental organizations and have listed prime thematic areas of their work that feature urban underground space. Urban underground space has not been yet a subject of global governance, but rather an important component of many solutions to contemporary global problems, predominantly climate change, sustainable and resilient urbanization, energy.

Governance of urban underground space has been placed on national, regional, and municipal agendas. Global governance agenda for urban underground space has been steadily emerging, mainly based on a need for a rational use of subsurface resources, accompanied by a forming vision for underground space as a global asset for groundwater and carbon dioxide storage.

Urban underground space has been a part of the global environment and development agenda, we expect that in the years to come its presence in a wider dialogue on major global challenges will increase.

ACKNOWLEDGMENTS

Dr. Nikolai Bobylev would like to acknowledge the funding by the Russian Science Foundation No 23-27-00034, https://rscf.ru/en/project/23-27-00034/ on Ecological safety of the underground space of urban areas burdened with accumulated environmental damage.

REFERENCES

Admiraal, H. & Cornaro, A. (2016), 'Why Underground Space Should be Included in Urban Planning Policy—And How This Will Enhance an Urban Underground Future', Tunnelling and Underground Space Technology, 55: 214–20. https://doi.org/10.1016/j.tust.2015.11.013

Akhmetzyanov A, Bobylev N, Wende W (2021) Geothermal energy in urban planning. IOP Conf. Series: Earth and Environmental Science 703 (2021) 012036. 17th World Conference ACUUS 2020 Helsinki. IOP Publishing. doi:10.1088/1755-1315/703/1/012036

Associated Research Centers for Urban Underground Space, 2023, https://www.acuus.org/

Bobylev N, Guo D, Benardos A, (2023) Urban underground space use in a climate neutral city; In: Expanding Underground - Knowledge and Passion to Make a Positive Impact on the World Proceedings of the ITA-AITES World Tunnel Congress 2023 (WTC 2023), 12-18 May 2023, Athens, Greece. Edited By Georgios Anagnostou, Andreas Benardos, Vassilis P. Marinos Copyright 2023; ISBN 9781003348030. Pages 9–13. https://doi.org/10.1201/9781003348030.DOI:10.1201/9781003348030-2.

Bobylev N, Syrbe R, Wende, W (2022) Geosystem services in urban planning. Sustainable Cities and Society (2022), doi:https://doi.org/10.1016/j.scs.2022.104041

Busha O., Doyon A. 2019. Building urban resilience with nature-based solutions: How can urban planning contribute? Cities 95 (2019) 102483.

Campbell, D., de Beer, J., Mielby, S., van Campenhout, I., van der Meulen, M., Erikkson, I., Ganerod, G., Lawrence, D., Bacic,M., Donald, A., Radu Gogui, C., Jelenek, J., 2017. Geoscientists and urban decision-makers: European COST Sub-Urban Action (TU1206). Procedia Engineering 209: 4–11.

Driessen, P.P.J., C. Dieperink, F. van Laerhoven, H.A. C. Runhaar and W.J.V. Vermeulen (2012) 'Towards a Conceptual Framework for The Study of Shifts in Modes of Environmental Governance – Experiences From The Netherlands.' Environmental Policy and Governance 22 (3): 143–60.

Earth System Governance research alliance, 2023, https://www.earthsystemgovernance.org/what-we-do/

Fox, N., Graham, L. J., Eigenbrod, F., Bullock, J. M., & Parks, K. E. (2020). Incorporating geodiversity in ecosystem service decisions. Ecosystems and People, 16(1), 151–159.

Gray, M. 2018. The confused position of the geosciences within the "natural capital" and "ecosystem services" approaches. Ecosystem services, 34, 106–112. https://doi.org/10.1016/j.ecoser.2018.10.010

International Energy Agency, 2023, https://www.iea.org/

International Tunnelling and Underground Space Association, 2023, https://www.ita-aites.org/

ITA Working Group 20: Urban Problems, Underground Solutions, 2023. Urban Underground Space for Resilient Cities. ITA REPORT N32/APRIL 2023 N° ISBN: 978–2–9701670–1–3

Kevin Grecksch (2021), 'Out of sight – out of regulation? Underground space governance in the UK', Journal of the British Academy, 9(s10): 43–68.

Lin D, De Vos J, Maruyama T, Bobylev N, Cui J (2022) Metro-Related Transfers: A Review of Recent Literature. Journal of Urban Planning and Development, American Society of Civil Engineers. ISSN 0733–9488. DOI: 10.1061/(ASCE)UP.1943-5444.0000858.

Maring, Blauw (2018) Asset management to support urban land and subsurface management. Science of the Total Environment 615 (2018) 390–397

NeTTUN, 2016, https://nettun.org/

Nicolas Berggruen, Nathan Gardels. Intelligent Governance for the 21st Century: A Middle Way between West and East. Polity, 2012, 200 p.

OECD, 2022. Decarbonising buildings in cities and regions. OECD Urban Studies, OECD Publishing, Paris.

Organisation for Economic Co-operation and Development, 2023, https://www.oecd.org/

Parriaux, A., Tacher, L., Kaufman, V. and Blunier, P., 2006. Underground resources and sustainable development in urban areas. The Geological Society of London.

Peng, F. L., Qiao, Y. K., Sabri, S., Atazadeh, B., Rajabifard, A., 2021. A collaborative approach for urban underground space development toward sustainable development goals: Critical dimensions and future directions. Frontiers of Structural and Civil Engineering, 15(1), 20–45.

Qiao, Y. K., Peng, F. L., Sabri, S., Rajabifard, A., 2019. Low carbon effects of urban underground space. Sustainable cities and society, 45, 451–459.

Rhodes, R. (1997). Understanding Governance: Policy Networks, Governance, Reflexivity and Accountability. Open University Press

Rhodes, R.A.W. (1996) 'The New Governance: Governing without Government.' Political Studies 44 (4): 652–67.

Tianming, G.; Bobylev, N.; Gadal, S.; Lagutina, M.; Sergunin, A.; Erokhin, V. (2021). Planning for Sustainability: An Emerging Blue Economy in Russia's Coastal Arctic? Sustainability 2021, 13, 4957. https://doi.org/10.3390/su13094957

Tretter E. M. Scales, regimes, and the urban governance of Glasgow //Journal of Urban Affairs. 2008. Vol. 30. №. 1. C. 87–102.

UN-Habitat, 2023, https://unhabitat.org/

UN-HABITAT. The Global Campaign on Urban Governance. Concept Paper. 2nd Edition.

United Nations Economic Commission for Europe, 1991, Convention on Environmental Impact Assessment in a Transboundary Context. https://unece.org/fileadmin/DAM/env/eia/documents/legaltexts/Espoo_Convention_authentic_ENG.pdf

United Nations Office for Disaster Risk Reduction, 2020, https://www.undrr.org/words-into-action/implementation-guide-land-use-and-urban-planning

United Nations, 2023, Sustainable Development Goals https://sdgs.un.org/goals

van Ree, C. C. D. F., van Beukering, P. J. H., 2016. Geosystem services: A concept in support of sustainable development of the subsurface. Ecosystem Services, 20, 30–36.

Volchko, Y., Norrman, J., Ericsson, L.O., Nilsson, K.L., Markstedt, A., Öberg, M., Mossmark, F., Bobylev, N., Tengborg, P., 2020. Subsurface planning: Towards a common understanding of the subsurface as a multifunctional resource. Land Use Policy, 90, 104316.

World Bank, 2023, https://www.worldbank.org/

Tunnelling for a Better Life – Yan, Celestino, Thewes & Eberhardt (Eds)
© 2024 The Author(s), ISBN 978-1-032-80042-4
Open Access: www.taylorfrancis.com, CC BY-NC-ND 4.0 license

Forecast and trends related to key personnel for mechanised excavation with TBMs

Fabrizio Bove*
Seli Overseas, Rome, Italy

ABSTRACT: Some of the crucial questions in order to carry out a proper planning of a new tunnel boring machine (TBM) project, as well as budgeting, are "how many experienced positions do we need to cover a complete TBM bore? Do we need all at once? What could be a rule of thumb's ratio between highly experienced (key personnel) and unexperienced?".

In order to proceed with an adequate management of a TBM project, an analysis of the key positions needed at different stages is proposed, starting from the acceptance of the TBM in factory up to the last phase, i.e. the final disassembly of the machine on site. Additionally, a differentiation of the highly skilled and experienced critical positions needed according to the various types of available TBMs in the market is highlighted.

Eventually, a career path in order to optimise the continuous supervision and goals is suggested, as well as the impact on personnel of the increasing automatizations, data analysis, robotics and remote controlling is also discussed.

Keywords: key personnel, planning, key position, career, management, budget

1 INTRODUCTION

In every organization or company, the importance of personnel is commonly emphasised with the same words, i.e. *human capital* and, more often, *human resources,* which in the last decades has been universally adopted.

Concurrently, the sharp distinction between white and blue collars is going to lose practical meaning within the tunnelling industry. Regardless of what we can nowadays address as an old-fashioned differentiation, a new approach is needed to achieve the expected results within a lean management perspective.

Moreover, considering that physiological oscillations and peaks related to the demand of personnel are cyclical in the market of infrastructures and tunnels, a temporary shortage of it needs to be properly addressed and managed.

It is also worth to point out that, within a TBM project, the overall cost of personnel (labour and staff) can be estimated to be around 40%-50% of the whole construction costs. This value is greater than the same cost of TBM, usually being around 15%-20%.

Eventually, a new perspective focusing on the key personnel, intended as the minimum "core" specialized technicians needed to achieve the goals, can both reduce the costs and allow to better manage the project. Indeed, a proper choice as well as management of the staff that "makes the difference", being able to properly lead the ongoing tasks in every phase, is demanded.

2 KEY POSITIONS RELATED TO TBM

An assessment of the core number of qualified personnel in order to properly execute a TBM drive since the beginning, i.e. starting with the factory acceptance test (FAT) up to the termination of the TBM project, usually being the disassembly of the same machine, is carried out in this paragraph.

It is worth to point out that the current trend leads to present in tender phase also the resumes of some key positions, being a paramount parameter for the project's award: in certain cases it can be a contractual requirement not only for the managers, but also for some critical technicians, like tunnel superintendents, TBM operators etc. and, additionally, a list of minimum requirements should be fulfilled, like years of experience in a certain role as well as specific experience related to the proposed TBM type, that for this purpose can be grouped in earth pressure balance (EPB), slurry, shielded TBMs for hard rock (simple shield and double shield) and open TBMs.

*Corresponding author: f.bove@selitunnelling.com

DOI: 10.1201/9781003495505-2

Hence, what is a key position within a TBM project? First and foremost, it is a role with qualified experience in a specific field of TBM excavation, whose skills are mandatory to properly carry out the project. For the sake of clarity, also a project manager, a safety manager or a senior accountant are key positions; nevertheless, they are not necessarily needed with a dedicated focus and consolidated experience in TBMs, although a previous experience in this field will surely enhance value to the ongoing project.

Eventually, a general summary of these key positions is presented hereby:

- TBM senior engineer: usually he's a civil engineer with overall experience in TBM and general helicopter view of all phases of the project. A dedicated focus is needed for the driving parameters, soil conditioning, grouting and interaction between the TBM, the soil or rock mass as well as the surface and any interface.
- Plant manager: this position is usually covered by a mechanical engineer with overall experience in TBM assembly, disassembly, maintenance, and spare parts management. Moreover, a general overview of conveyors, locomotives or multiservice vehicles (MSVs) and equipment is also needed.
- TBM superintendent: he's the leader of the ongoing process of excavation, with sound knowledge of all internal processes, machineries and TBM operations. An attention to the logistics and general arrangement and organization of the site is also needed.
- Shift supervisor: he's in charge of the shift into the tunnel, with sound knowledge of all internal processes, machineries and TBM operations.
- Chief electrician: he's supervising any electrical equipment in TBM, with sound experience in high and medium voltage cables and junctions.
- Programmable Logic Controller (PLC) electronic: usually he's an electronic engineer able to properly set the parameters into the PLC as well as troubleshooting.
- Chief mechanic: he's supervising any mechanical work in TBM as well as the daily and weekly maintenance, highly experienced in the various components of the machine and, usually, also in hydraulics.
- TBM operator: he's the driver of the machine. Further to have clear the concepts of alignment, pressures, thrust, rotation of the cutterhead, penetration rate, surface settlements, soil conditioning etc., he's able to fine tune the advance according to the geology in situ.
- Erector operator: he's in charge of assembling the ring according to the tolerances (gaps and offsets), giving as result of his task the final and permanent product of the project, i.e. the lining, entirely visible.
- Grouting operator: is the person in charge of the injection of the backfilling, coping with the expected quality of cement as well as entirely filling the volume of the gap between excavation and lining. Although the cement injection is not visible like the lining, this is the other final product of the excavation.
- Mud engineer: this position is requested only for slurry machines. Usually, he's in charge for the adjustment of the slurry fluid as well as for the supervision of the slurry treatment plant (STP).
- Conveyor mechanic: he's a mechanic with specific experience in the alignment, extension, maintenance, vulcanization, junction and repair of continuous conveyors.
- Cutterhead mechanic: he's a mechanic in charge of the cutters or rippers replacements and the check of the buckets, to prevent any possible wear of the surface of the cutterhead and, concurrently, optimizing the dressing of the cutting tools. A long experience with different TBMs as well as with many types of soils and rocks is needed.
- TBM surveyor: an experienced land surveyor able to connect the external benchmarks and open traverse with the guidance systems of the TBM and any possible articulation of the same machine.
- TBM senior electrician: he's an experienced electrician able to deal with the majority of routinary electric tasks into the machine.
- TBM senior mechanic: as for the senior electrician, he's an experienced mechanic able to deal with the majority of mechanical parts into the machine.

3 THE VARIOUS STAGES OF THE PROJECT

If one considers the evolution of a whole project with one TBM, the personnel needed at different phases can vary both in terms of total number as well as related to the key positions (see Figure 1).

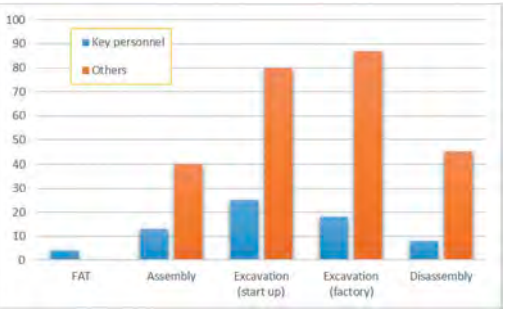

Figure 1. No. of personnel (key and others) at different stages.

For example, during the assembly phase, roughly ten key personnel will be needed to manage the entire process, especially mechanics and electricians. Once the TBM will be ready to bore, the same whole team also guarantees a smooth transition to

the excavation phase, with some "additions" during the learning curve that is usually identified with the first 200 m of excavation.

Once that TBM has started a regular advance, i.e. similar to an underground factory, the number of key personnel can be reduced and, thus, replaced with less experienced and trainee workers. This is possible because, during this factory phase, the attention is more focused towards a proper scheduling and refurbishment instead of troubleshooting, optimization, training etc. thus allowing a slight reduction of personnel.

Moreover, it is worth noting that the number of key personnel in every phase can be adjusted according to the customized TBM itself as well as the whole context of the project (logistic, critical tasks, "reaction" of the machine to the excavation etc.), as shown in Figure 2.

Additionally, some optimizations can be carried out in case of twin TBMs or more than one TBM located in the same area, for example using the same chief mechanic, PLC electronic, chief electrician and plant manager for both machines instead of one per TBM.

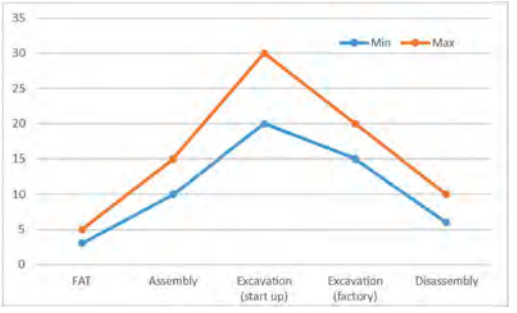

Figure 2. Estimation of possible ranges of key personnel at different stages.

4 DIFFERENT POSITIONS ACCORDING TO TBM TYPES

Looking to the different types of TBM available in the market and, although the TBM customization is still impacting the market, a sort of "common floor" with a forecast for key personnel needed according to the different type of TBM can be listed (see Table 1). Usually, EPBs and Slurry TBMs need a little bit more units of key personnel than hard rock TBMs, shielded or open, especially regarding the lining and grouting operations.

Obviously, regardless the type of TBM, some positions can be "overlapped" by the same person if this same technician has more than one skill and, concurrently, the TBM does not have critical issues to be fixed in that peculiar field. Some examples that are worth to be highlighted in terms of optimization and lean management are shown hereby:

- PLC electronic and chief electrician can be covered by the same technician.
- Experienced mechanics and electricians can be reduced if the TBM has no major and continuous failures. Moreover, it is worth to point out that current industrialization process regarding the TBM production, less customized and more industrial if compared to some decades ago, has the result of less adjustments needed as well as a reduction of breakdown occurred during the excavation, enhancing again the idea that less mechanics and electricians are needed.
- The number of cutterhead mechanics needed depend on the geology: it is heavily related to the hardness of the rock mass as well as the abrasiveness of the soil itself (quartz content) and it can be adjusted according to the different geological formations foreseen (or directly experienced) along the TBM axis.

5 THE CAREER PATH

In this paragraph a possible and "theoretically perfect" evolution for a trainee is proposed since the beginning of his activity in TBM, as shown in Figure 3.

It is quite straightforward that, according to a progressive increasing experience, a general overview of the different tasks allows a better understanding and control of the entire process of excavation day by day. Hence, a deep and direct knowledge of the majority of the most critical TBM tasks, acquired by actual experience in the different roles, plus the needed soft skills for a leading position, can bring a technician to lead the whole excavation process as TBM superintendent.

To better focus on the choice of these roles, it is worth considering that the suggested steps at the beginning, i.e. grouting operator and erector operator, have been included because they generate the output of a TBM ride, i.e. the permanent and visible result of the work of excavation, as already mentioned. Hence, a proper injection of the void between the lining and excavation and, moreover, the installation of the concrete rings without gaps and offsets are essential to achieve the expected results in terms of quality.

After having been trained in these tasks, a long-term experience as TBM operator is suggested, since the position needs a deep knowledge of the majority of TBM technique, in terms of guidance parameters (thrust, torque, rotation etc.), cutterhead dressing, alignment to the theoretical axis, earth pressure, muck removal, over-excavation and so on.

6 MANAGEMENT, REWARDS AND COMMITMENT

A proper management of the personnel should be carried out also using some rewards, that usually can

Table 1. Key positions related to TBM type.

Position	EPB	Slurry	Shielded TBM	Open TBM
TBM Senior Eng.	1	1	1	1
Plant Manager	1	1	1	1
TBM Superintendent	1	1	1	1
Chief electrician	1	1	1	1
PLC electronic	1	1	1	1
TBM senior electrician	2-4	2-4	2-4	2-4
Chief mechanic	1	1	1	1
TBM senior mechanic	2-4	2-4	2-4	2-4
Shift supervisor	1 per shift	1 per shift	1 per shift	1 per shift
TBM operator	1 per shift	1 per shift	1 per shift	1 per shift
Erector operator	1 per shift	1 per shift	1 per shift	
Grouting operator	1 per shift	1 per shift		
Mud engineer		1		
Conveyor mechanic	1	1	1	1
Cutterhead mechanic	1	1	1	1
TBM surveyor	1	1	1	1

have a financial impact roughly estimated being around 10%-20% of the total cost of personnel.

In any case it has to be considered within a bigger context of optimization of the project, i.e. a sound reduction in terms of time for completion. It is straightforward that the anticipation of the termination can positively impact in the rental costs as well as in the reduction of the whole cost of personnel.

Some measures that can be implemented are listed hereby:

- Bonus on milestones (TBM ready to bore, final disassembly, station crossing etc.).
- Bonus related to the meters excavated beyond the contractual minimum requirements.
- Final reward at breakthrough.

To avoid any possible jeopardization of the project, any reward applied should be connected to the fulfilment and accomplishment of any quality, safety and environmental requirement and regulation.

Eventually, a higher level of key personnel management also needs bonds and adjustments ad personam as well as a strong commitment with the company, sharing the passion of carrying out any task to create value for all the stakeholders and the community.

7 THE FUTURE

Looking to the future, it is clear and straightforward that also the TBM market is oriented toward an increasing automatization, thus progressively reducing the manual and physical work: it means that the human action will be switched day-by-day toward a direction of control and supervision. Some of the ongoing and possible evolutions are listed as follow:

– robotic inspection of the cutterhead,
– remote guidance of the multiservice vehicle (MSV),
– automatization of the TBM driving,
– transportation into the back-up automatized and erection of the segments semi-automatic,
– semi-automatic analysis of "big data" regarding excavation, monitoring, environmental and safety parameters with automatic alerts.

Finally, according to these incoming changes, a reduction of the total number of personnel mainly carrying out manual works inside the tunnel can be expected because of automatization. Conversely, further checks in terms of maintenance, control and analysis of data will be needed, thus bringing to a renewal and adjustment of key personnel's skills toward data analysis and control.

8 CONCLUSIONS

After a general overview of different aspects, like type of machines, phases of the project, implementation of an optimized career, current trends and future expectations it is worth to note that a proper forecast and management of the key personnel is one of the core aspects of a successful project.

Moreover, because of this analysis, the number of key personnel can be properly set and adjusted according to two parameters mainly:

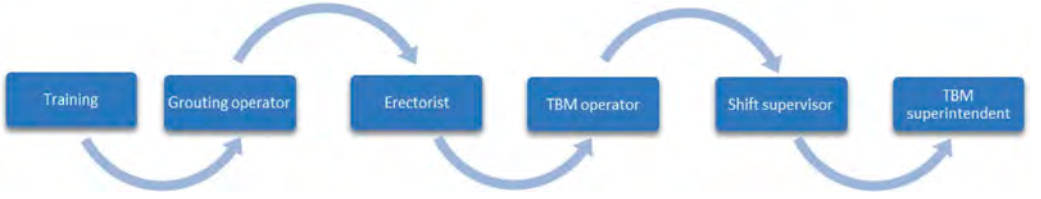

Figure 3. A proposal of career path.

- the different stages of the project,
- the TBM type,

Additionally, some additional adjustments can be also carried out according to the logistics.

Eventually, for a better management of the projects, a career path for key personnel is needed, as well as a strong commitment and shared values between the company and the human capital.

REFERENCES

Crespo, C., Rodríguez, F., 2023. Integration of robotics in underground mining construction works. In: Expanding Underground. Knowledge and Passion to Make a Positive Impact on the World – Anagnostou, Benardos & Marinos (Eds), 1st edition, CRC press, Taylor & Francis, London, U.K., pp. 2414–2421.

Duszynski, D., 2020. Soft Costs Are a Hard Burden on the US Tunnel Industry. Resource Erectors (accessed on Sept. 30, 2023).

Grandori, R., 2022. Intervista. In: Gallerie e Grandi Opere Sotterranee, No. 144, December 2022, Italy, pp. 5–6.

Grandori, R., Castelli, L., Bono, R., 2022. WeView - An Integrated Data & Elaboration System of Global Underground Projects. ITA AITES World Tunnel Congress, WTC2022 and 47th General Assembly Bella Center, Copenhagen, Denmark

Johannessen, S., Askilsrud, O. G., Bruland A., 2020. The Meråker Project - 10 Km of tunnel in 12 months. Publication 11: TBM Tunnelling, Norwegian Tunnelling Society, Norway, pp. 85–89.

Tunnelling for a Better Life – Yan, Celestino, Thewes & Eberhardt (Eds)
© 2024 The Author(s), ISBN 978-1-032-80042-4
Open Access: www.taylorfrancis.com, CC BY-NC-ND 4.0 license

The common duct in New Taipei City

Hsiao-chou Chao*, Chihkuang Song & Tsean Ko
Moh and Associates, Inc., Chinese Taipei

I-Kung Chiu & Yu-Chun Lin
Public Works Department, Chinese Taipei

ABSTRACT: Conventionally, underground utility lines are installed separately and are managed by different authorities. This approach can sometimes lead to challenges in coordination, communication, and efficiency, as different entities or organizations may have their own procedures, standards, and timelines. Renewal, relocation, and maintenance of various pipelines would involve repetitive excavations, frequent traffic interruption, and inevitably shorten the lifetime of the roads. The common duct, as an underground structure that accommodates two or more types of public utilities such as power transmission lines, telecommunication lines, storm sewers, sanitary sewers, tap water pipes, natural gas pipes, and oil pipes, was introduced to Taiwan in the late 1990s. The common duct system offers a solution for constructing a more resilient and sustainable urban environment. With more than twenty years of persistent endeavors, all major cities in Taiwan have successfully developed their common duct network plans and initiated the construction of these systems. As the completion of a common duct system network in a complex urban environment is anticipated to take a substantial amount of time, any change in urban development during the period has the potential to impact the objectives or functions of the planned common duct system network. To adapt to changes, ensure relevance, and maintain the effectiveness of the system network plan over time, it is necessary to conduct a consistent and diligent process of review and revision subsequent to its initial announcement. In New Taipei City, the phase I and phase II initial plans of common duct system network was announced in 2008 and 2012, respectively. The first comprehensive review was carried out and completed in 2016 and the second began in 2021. Methods and results of the comprehensive reviews that meet the public demand, quality of road service, and align with major infrastructural projects are summarized in this article.

Keywords: Resilient City, Common Duct, Main Duct, Supplier Duct, Expert Questionnaire, Analytic Hierarchy Process

1 OVERVIEW

The common duct is an underground structure designed to house and protect multiple types of public utility lines, such as water pipes, power cables, gas main, and telecommunication cables. In general, there are two types of common duct: the main duct and the supplier duct. The main duct serves as a pathway for regional public utility lines. The supplier duct, which can further be divided into branch duct, cable trough, and duct bank, is used to accommodate the public utility lines that deliver the services to the users.

Common duct is an essential part of modern city infrastructure. As maintenance, renewal, and expansion of utility lines can be conducted within the common duct, adverse impacts such as construction noises, traffic interference, and the need for pavement repair resulting from excavation can be significantly reduced or even avoided. Furthermore, the resilience of a city can be enhanced significantly by establishing a common duct network. The experience of the Kobe earthquake in 1995 demonstrates that common ducts can offer effective protection for utility lines, with power supply recovering in 14 days, telecommunication in 7 days, and tap water supply in 42 days in the aftermath.

As shown in Figure 1, located on the northern part of the island, New Taipei City comprises a total area of about 2,053 km^2. As a city that has undergone intensive development, building new common duct network in the congested and limited underground space poses challenges for all parties involved. This paper introduces the background for development of the common duct network in New Taipei City, the current status, the method for reviewing and updating the planned network, and critical design and construction issues.

*Corresponding author: hsch.chao@maaconsultants.com

DOI: 10.1201/9781003495505-3

Figure 1. Twenty nine administrative districts in New Taipei City.

2 DEVELOPMENT OF COMMON DUCT NETWORK

2.1 *Background*

To enhance the quality of life, integrate various public utility lines, improve effectiveness for road management and traffic safety, as well as maintain urban aesthetics, the Common Duct Act of Taiwan was issued in 2000. In New Taipei City, the feasibility study for common duct network commenced in 2004, followed by phase I and Phase II planning. Results of the planning, as the blueprint for follow up development, were announced in 2008 and 2012, respectively.

The time frame for completing the common duct system is anticipated to be lengthy as the system network covers a large area of the city and involves significant amount of construction activities such as excavation, relocation of existing pipelines, and traffic diversion. In alignment with new requirements that might arise from change of urban development or regional plan, or development of new transportation infrastructure, a regular review and update of the common duct system network is required after its announcement. According to the Common Duct Act, a comprehensive review is required every 3 to 5 years. Chronological events related to the development of the common duct system network for New Taipei City are listed in Figure 2. The scope of the work generally required to be implemented for a comprehensive review is provided in Table 1.

Figure 2. Chronological events for the development of common duct system network in New Taipei City.

Table 1. Scope of the comprehensive review.

No	Item
1	Collect, supplement, and analyse fundamental information
2	Evaluate requirements for capacity and life span
3	Update common duct network system
4	Develop alignment plan
5	Configure cross-sections for auxiliary facilities
6	Develop specifications and guidelines for planning and design
7	Study schemes for structural type selection and construction
8	Conduct construction impact evaluation
9	Budget estimate and cost sharing method study
10	Economic benefit analysis
11	Develop construction plan
12	Develop draft of autonomy ordinance for maintenance and management
13	Prepare for incorporating common duct into public utility database
14	Prepare document for obtaining approval and making announcement

2.2 *The first comprehensive review*

The first comprehensive review for the common duct system network was implemented and completed in 2016. Results of the comprehensive review indicated that the total length of completed common duct at the time was approximate 120.5km, comprising main duct 2.64km, branch duct 18.11km, cable trough 3.16km and duct bank 96.6km.

Results of the first comprehensive review also indicated that there are eight sub-networks with the total length of 6.3km, which were not included in the initial system network announced in 2012, were completed with new urban development and road construction projects. Table 2 summaries the status of the common duct network at the completion of the first comprehensive review and the revised common duct network is demonstrated in Figure 3. As shown in Table 2 and Figure 3, among the twenty six sub-networks seventeen have completed, three were under construction, and the rest were pending.

Ownership of the completed common ducts was transferred to the Maintenance Office of New Taipei City Government for follow up management, maintenance, and usage fee collection.

Table 2. Status of common duct system setwork by the 1st comprehensive review.

Sub-network	Total Length (km)				Status
	Main duct	Supplier Duct			
		Branch	Cable Trough	C.C. Box	
1	2.64	9.2	-	-	Completed
2	-	4.2	-	-	Completed
3	-	-	-	3.98	Completed
4	-	1.5	-	-	Completed
5	-	-	-	1.9	Completed
6	-	-	1.1	11.9	Completed
7	-	-	2.1	-	Completed
8	-	1.7	-	1.0	Completed
9	-	-	-	8.2	Completed
10	-	1.5	-	13.9	Completed
11	-	-	-	16.8	Completed
12	-	-	-	1.5	Completed
13	-	-	-	0.9	Completed
14	-	-	-	8.1	Completed
15	-	-	-	12.7	Completed
16	-	-	-	12.1	Completed
17	-	-	-	0.9	Completed
18	-	-	-	125.3	Under construction
19	-	13.2	0	0	
20	-	26.3	-	9.8	
21	-	-	-	17.0	Pending
22	-	-	-	26.4	Pending
23	-	-	-	5.4	Pending
24	-	61.1	-	-	Pending
25	-	-	-	26.6	Pending
26	-	-	-	5.2	Pending

2.3 *The second comprehensive review*

In response to the change of urban development after 2016, the second comprehensive review commenced in 2021. As illustrated in Figure 4, three target schemes and five functional indexes were specified as the baseline criteria for scoring and selection of the routes for updating the common duct network. The five functional indexes are (a) level of road service, (b) level of repetitive excavation occurrence, (c) level of demand for pipelines, (d) number of major infrastructural projects to be implemented along the candidate routes in the future, and (e) level of road width. The three target schemes required to be met include (1) the demand for various types of pipeline, (2) build the common duct in association with the to be implemented infrastructure projects, and (3) promote the quality of road service.

Development of the common duct system network follows the two-stage procedures outlined in Figure 5. In the first stage, the roads with width greater than 20m were identified and selected, followed by generation of a preliminary system network as shown in Figure 6. In the second stage, expert questionnaire and Analytic

Figure 3. Common Duct System Network updated after the first comprehensive review.

Hierarchy Process (AHP) were applied to determine the relative importance in terms of weights among the five functional indexes and three target schemes for each of the road sections in the preliminary system network.

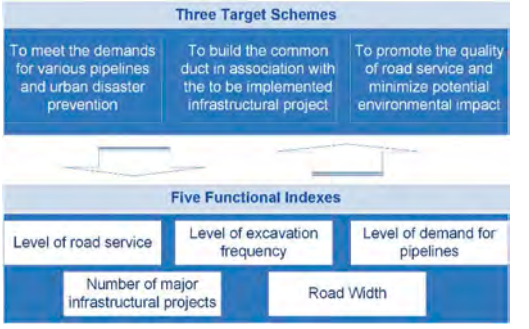

Figure 4. The baseline criteria for selection of the routes for common duct system network.

The weights of the three target schemes and five functional indexes determined by expert questionnaire and AHP method are listed in Tables 3 and 4, respectively. The weighted score for each of the road sections can be calculated by summing the product of the weight and the index value corresponding to each of the five functional indexes. Calculation of the weighted score is demonstrated by examples of three road sections listed in Table 5. It is expected that road section with weighted score greater than zero should be incorporated into the common duct network.

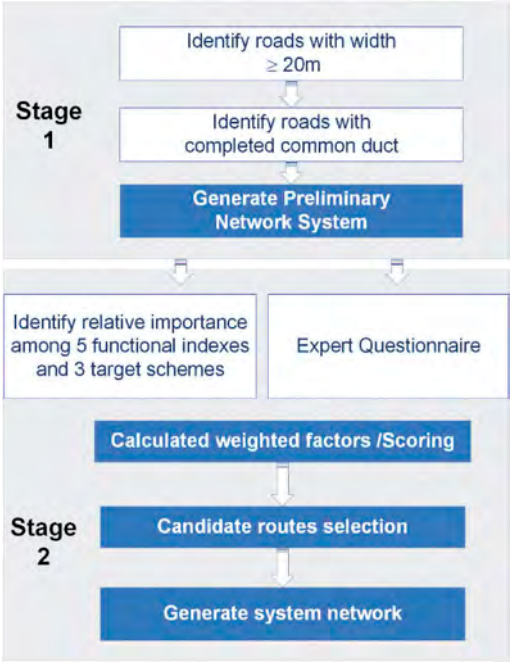

Figure 5. The two-stage procedures for developing the common duct system network.

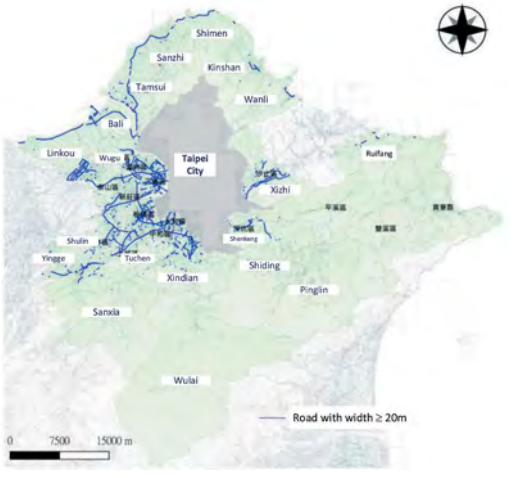

Figure 6. Preliminary common duct system network developed in the second comprehensive review.

Results of the revision for common duct system network in New Taipei City are demonstrated by the tentatively developed sub-network in Xinchung, Luzhou, Wugu, and Taishan districts as shown in Figure 7. The solid black line and red line represent existing and planned routes, respectively, in the common duct network that has been announced at the completion of the first comprehensive review. The solid purple line and blue line represent the routes of common ducts that would be added after the second comprehensive review (mid-term report, 2023).

Table 3. Relative importance among three target schemes.

Target Scheme	Description	Weight
1	To meet the demands for various pipelines and urban disaster prevention	0.415
2	To build the common duct in association with the to-be constructed major infrastructural project	0.244
3	To promote the quality of the road service and minimize potential environmental impact	0.341

Table 4. Relative importance among 5 functional factors.

Functional index	Description	Weight
1	Level of road service	0.191
2	Level of excavation frequency in recent years	0.217
3	Level of demand for various types of pipelines	0.201
4	Number of major infrastructural project to be implemented in the future	0.216
5	Road width	0.175

3 ALIGNMENT OF COMMON DUCT NETWORK

In principle, main common duct shall be placed under median strip with its horizontal alignment consistent with the road. Horizontal alignment is allowed to be adjusted under the circumstance such as crossing over existing underground facilities. In consideration of the space required for installation of retaining structure for excavation work, the clearance between the main duct and adjacent structures shall be no less than 2m.

Branch duct shall be placed under sidewalk or mixed lane. To provide sufficient space for construction of retaining structures and connection of pipelines to the user end, the clearance between the branch duct and the border of private land shall be no less than 1m. The radius of curvature of the branch duct shall not exceed the allowable radius of curvature of the pipelines to be incorporated.

Cable trough also shall be installed under sidewalk or mixed lane. To provide sufficient space for connecting pipelines to the user end, the clearance between the cable trough and the border of private land shall be no less than 30cm.

For main duct constructed by cut and cover method, the overlying depth of soils shall be no less

Table 5. An example of calculation for weighted score.

No. / Road Section		24 Sanchung Sanhe rd. sec. 2	25 Sanchung Sanhe rd. sec. 3	26 Sanchung Sanhe rd. sec. 4
Level of road service	Original value	NA	NA	NA
	Index value	0	0	0
Level of excavation frequency (each/year)	Original value	9	14	25
	Index value	-1	-1	0
Level of demand for pipelines (number of types)	Original value	7	8	10
	Index value	1	1	2
Major infrastructures to be built (number)	Original value	1	1	1
	Index value	1	1	1
Road width	Original value	21	27	25
	Index value	0	1	0
Has the common duct been built already?		No	No	No
Weighted Score		0.20	0.38	0.62

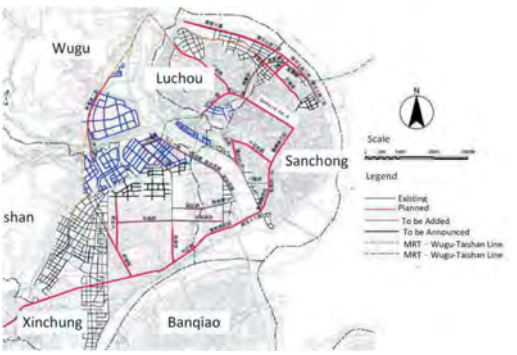

Figure 7. Tentatively developed common duct system network in Xinchung, Luzhou, Wugu, and Taishan districts.

than 2.5m and 1.0m for standard section and special section, respectively. The special section of common duct refers to the entrance, ventilation port, material input port, and diversion section. The clearance height shall be no less than 220cm. For main duct constructed by bored tunnelling method, the overlying depth of soils shall be no less than the diameter of the tunnel. The clearance to the adjacent underground structure shall be no less than 1.0m.

For branch duct, the allowable minimum slope is no less than 0.2% for the purpose of drainage. In consideration of cable installation or maintenance, the slope of a branch duct shall not exceed 1:3 (vertical to horizontal) when the vertical alignment is required to go up or go down to avoid crossing paths with another underground facilities. In general, the height clearance of branch duct shall not exceed 150cm. Nevertheless, this limitation can be eased under circumstances such as change of road alignment, varied width of sidewalk, or extra demand for pipeline capacity.

4 SELECTION OF THE TYPE OF COMMON DUCT

The type of common duct can be selected based on (1) the properties of pipelines to be incorporated, (2) the structural type, and (3) the widths of road and sidewalk.

For main duct, the box shaped structure will be selected when it would be constructed by cut and cover method. The circular shaped structure will be selected if the alignment of main duct crosses features such as underpass, large size box culvert, river, or underground rapid transit and is required to be constructed by bored tunnelling or pipe jacking methods.

The supplier common ducts with the type of branch duct, cable trough, or duct band usually are installed under the sidewalk or mixed lane. The criteria for selection of the type of supplier duct is demonstrated by Figure 8. For road with width less than 15m, a cable bank would be selected and installed on one side. For road with width greater than 15m, the type of supplier duct would be determined based on the width of sidewalk. The common duct can be installed on both sides of the road under the sidewalk or mixed lane.

For roads with existing pipelines, such as water main, telecommunication cable, or storm sewer, it is required to develop a scheme for allocating the common ducts in a congested underground space,

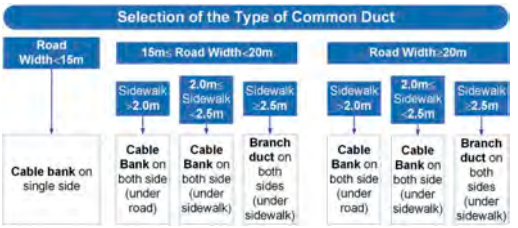

Figure 8. The criteria for selection of the type of supplier duct.

considering the issues involving constructability, future inspection and maintenance. Figure 9 illustrated an example where the layout of common ducts and other types of pipelines are integrated under a 20m-wide road with 1.5m-wide sidewalks. In Taiwan, the BIM and Smart technology are commonly used in the design, construction and maintenance for common duct. Detailed introduction to the application of BIM can be found in the work of Yu et.al. (2021, 2022).

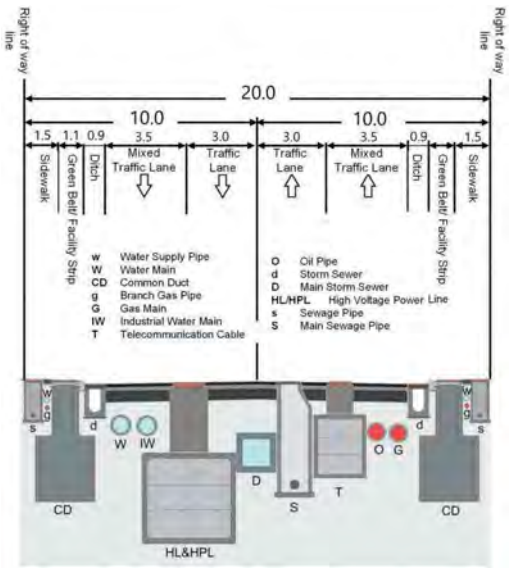

Figure 9. An example demonstrating the integrated layout of common duct and other types of pipelines for road with width 20m.

5 CONSTRUCTION SCHEME

Main common duct is usually constructed by cut and cover method, bored tunnelling method, and pipe jacking method. The box-shaped main ducts with the depth ranges from 5m to 8m as shown in Figure 10-(a), (b), (c) and (d) can be constructed by cut and cover method. The circular-shaped main ducts as shown in Figure 11(a) and (b) can be constructed by bored tunnelling or pipe jacking methods. The supplier ducts such as branch duct or cable trough as shown in Figure 12(a) and (b) are usually installed under sidewalk or mixed lane and constructed by open cut and cast in place method. To ensure construction quality and safety, the underground works need to follow the practice of geotechnical engineering with comprehensive geotechnical investigation, analysis, design, and instrumentation and monitoring. Auxiliary measures such as ground improvement for protection of the buildings in the proximity would be required as per the results of analysis and design.

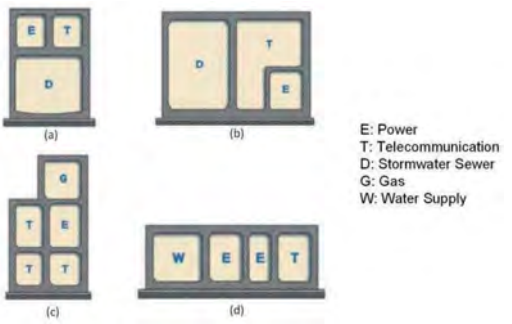

Figure 10. The types of main duct with box shape.

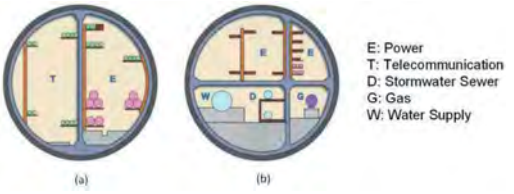

Figure 11. The configuration of main duct with circular shape.

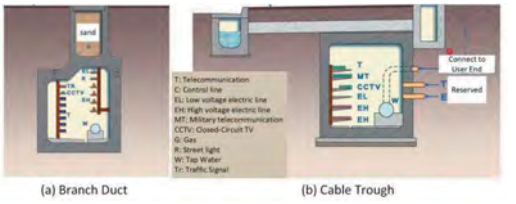

Figure 12. The configuration of branch duct and cable trough.

6 CONCLUSIONS

The initial plans of common duct system network for New Taipei City were announced and released in 2008 and 2012, respectively, as the blueprint for future

development. To adapt to changes of urban development, ensure relevance, and maintain the effectiveness of the system network over time, the announced plan is subject to periodic review and revision. In New Taipei City, the first comprehensive review and revision was completed in 2016, and the second are expected to be completed in early 2024.

The development of an integrated common duct system network in limited underground space and a congested urban environment is a challenging task. The planning and design must be able to address the public demand for pipelines, align with the construction schedule of major infrastructure projects on the routes of network, and meet the requirements for high-quality road services. Five functional indexes, including level of road service, level of repetitive excavation occurrence, level of demand for pipelines, number of major infrastructural projects to be implemented along the candidate routes in the future, and level of road width were selected as the criteria for evaluation. The AHP method was implemented to evaluate the relative importance for each of the indexes and based on which to develop the system network. The persistent effort invested in this endeavor is expected to contribute to the creation of a more resilient and sustainable urban environment, and ultimately leading to an improved quality of life for all.

ACKNOWLEDGMENTS

The authors are grateful to Dr. Za-Chieh Moh for his support in preparation of the manuscript and to all the colleagues who have contributed their efforts to this project.

REFERENCES

The comprehensive review for the common duct system network of New Taipei City – Midterm Report, 2023, Public Works Department, New Taipei City Government.

Instruction for Construction of Underground Power Cable, 2002, Taiwan Power Company.

Yu, C.J., Chin, C.H., Chien, D., Yang, C.C. Yu, C.M., Hsien, H.A., 2021, Smart Road Management: Integrated Intelligent Road Management System, submitted to the 16th REAAA Conference, Manila, Philippines.

Yu, C.J., Cheng, K.Y., Chen, J.T., Lin, C.H., 2022. Case Study of Applied BIM Technology in New Taipei City Sanying Metro Line, Proceedings of the 9th Civil Engineering in the Asia Region (CECAR 9), India.

Tunnelling for a Better Life – Yan, Celestino, Thewes & Eberhardt (Eds)
© 2024 The Author(s), ISBN 978-1-032-80042-4
Open Access: www.taylorfrancis.com, CC BY-NC-ND 4.0 license

Progress and prospect of urban tunnel engineering in China

Xiangsheng Chen*
College of Civil and Transportation Engineering, Shenzhen University, Shenzhen, China
Key Laboratory for Resilient Infrastructures of Coastal Cities (MOE), Shenzhen University, Shenzhen, China
State Key Laboratory of Intelligent Geotechnics and Tunnelling, Shenzhen, Guangdong, China
Underground Polis Academy, Shenzhen University, Shenzhen, China

ABSTRACT: Since the beginning of the new century, with the continuous progress of China's urbanization, China's urban tunnel engineering has achieved rapid development. This paper firstly summarizes the challenges faced by the current urban tunnel engineering in China, and introduces the relevant key technologies of tunnel construction according to the above challenges. For example, mechanized metro's under-excavated station, a prefabricated subway station technology and double carbon resource utilization technology of urban tunnel. The engineering applications of these technologies are introduced in China. Among them, Shasan Station is the first mechanized metro's under-excavated station with double-hole combination pipe jacking at home and abroad. It adopts a construction method of transforming large into small and dividing into parts, ultimately forming an integrated underground space. Then, the key technologies of dual-carbon resource utilization and low-carbon operation and maintenance of urban tunnels are mainly introduced, including waste soil/slurry resource utilization. The intelligent, integrated and modular muck resource equipment technology is developed, and the muck is separated into coarse aggregate, fine sand, mud cake and water for recycling by using the processes of mud and sand separation and solid and liquid separation. The technology has been used on a large scale in Shenzhen subway. Finally, some suggestions are given for the future development direction of urban tunnel engineering in China.

Keywords: Underground Space Development, Intelligent, Review, Technical equipment

1 INTRODUCTION

With the rapid development of the economy, cities are facing "urban diseases" such as traffic congestion and environmental pollution. The development of underground space is an important approach to addressing these issues. Urban tunnel projects are a vital component of underground space development, significantly improving the city's surface traffic conditions, enhancing traffic efficiency, and alleviating road congestion. Therefore, many construction methods and technologies have been developed for the construction of urban tunnel projects.

The pipe jacking method, recognized for its fully mechanized excavation and trenchless construction advantages, has experienced rapid development in recent years (Sterling, 2020). It has found extensive applications in the construction of urban underground infrastructure (Chen et al., 2021; Sun et al., 2019; Zhang et al., 2016). However, the utilization of the pipe-jacking method in subway station construction is infrequent due to the limited size of the pipe-jacking machine, which fails to meet the spatial requirements of the station structure (Yang et al., 2022). The possibility of using a smaller-sized pipe-jacking machine for constructing an integral underground structure has been considered, although the impending construction of tunnels presents considerable challenges (Gao et al., 2019; Wang et al., 2023).

As the core component of the subway system, the prefabricated subway station has many advantages such as rapid construction, flexible layout and sustainable development (Luo et al., 2022; Yang and Lin, 2021). However, with the rapid construction and expansion of prefabricated subway stations, how to ensure their safety, reliability and operation efficiency has become an urgent problem to be solved (Tao et al., 2022). In this context, the prefabricated subway station monitoring has become a key task. Through the comprehensive monitoring of the prefabricated subway station, the status information of the station structure, including the key parameters such as vibration,

*Corresponding author: xschen@szu.edu.cn

DOI: 10.1201/9781003495505-4

deformation and stress, can be obtained in real time (Qiu et al., 2023). This not only helps to ensure the structural safety of prefabricated subway stations, but also provides important data support to help subway operators in operation and maintenance management and decision-making.

The issue of ecological efficiency in construction processes is a major challenge in Urban Tunnel Engineering. Currently, over 5000 km of urban tunnels are under construction in China (Ding et al., 2014; Zhang et al., 2020), leading to a significant increase in the emission of waste spoils from urban underground spaces, tunnels, and building foundations (de et al., 2017). Severe environmental, resource, and safety issues are generated because of the increase (Mao et al., 2021; Xue et al., 2015). Statistics indicate that several billion cubic meters of these waste spoils were emitted annually in China, making them one of the most difficult types of solid waste to dispose of and recycle (Xiao et al., 2021). Taking Shenzhen as an example, the city generates over 100 million cubic meters of construction waste each year, of which waste spoils account for more than 70%. Despite this, the bulk of this waste is predominantly managed through external landfilling, with a low recycling rate (Chen et al., 2022; Qiu et al., 2020).

This paper first summarizes the challenges faced by current urban tunnel engineering in China, and then introduces the relevant key technologies of tunnel construction based on the mentioned challenges. For example, the under-excavated station of mechanized metro, prefabricated subway station technology, and the double carbon resource utilization technology of urban tunnels. The aim is to provide reference for future urban tunnel engineering construction.

2 PRESENT CHALLENGES OF URBAN TUNNEL ENGINEERING

2.1 *Challenge of tunnel construction adjacent to existing structure*

The intensive development of underground spaces has become a crucial strategy for addressing issues like the scarcity of urban land resources and road traffic congestion. However, the construction of urban tunnels faces constraints due to existing structures and underground pipelines, leading to a reduction in safety distances. Additionally, a subway station in Shenzhen (Wang et al., 2023 and 2024) and an underground parking in Zhengzhou (Gao et al., 2019) are being constructed using small-section rectangular pipe-jacking tunnels, requiring the construction of multiple tunnels with zero spacing. The primary challenge in constructing tunnels in close proximity to existing structures lies in the intelligent control of construction machinery. The insufficient intelligence in existing construction machinery hinders the timely acquisition of critical data, such as geological conditions and the responses of existing structures, needed to guide construction. This limitation impedes effective control of construction disturbances, thereby increasing construction risks.

2.2 *Challenge of prefabricated underground structure construction*

Prefabricated underground structures face various challenges owing to the special environmental and functional requirements of underground structures, especially in terms of waterproofing and seismic resistance. There are waterproofing challenges for prefabricated underground structures. Prefabricated underground structures are assembled from precast components, and the joints are prone to be weak links in waterproofing. In addition, compatibility and durability degradation between different materials may lead to leakage. Finally, the complex hydrogeological environment that underground structures have to cope with increases the difficulty of waterproofing. Seismic performance challenges exist for prefabricated underground structures. The joint stiffness between precast components may be lower than that of conventional cast-in-place structures, affecting the overall seismic performance. Due to the special characteristics of prefabricated structures, the uncertainty of their seismic response increases and requires special analysis and design. During earthquakes, the joints between precast components may fail, affecting the overall structural stability. The joint design should be optimized so as to improve the seismic performance. Finally, a long-term monitoring and maintenance mechanism for prefabricated underground structures should be established to ensure their safety and durability.

2.3 *Challenge of the utilization of urban tunnel waste for low-carbon and large-scale resource recovery*

The utilization of urban tunnel waste for low-carbon and large-scale resource recovery presents a host of challenges. First and foremost, there's a need to develop resource recovery methods specifically tailored for urban tunnel waste, facilitating the separation and targeted utilization of multi-phase spoil. Moreover, traditional stabilizing materials like cement have significant drawbacks, including high energy consumption and substantial pollution (Yang et al., 2022). The challenge is exacerbated by the low-value, difficult-to-utilize clay content in the spoil, which makes cement-based stabilization not only energy-intensive but also less effective and costly, thus impeding its widespread adoption. Consequently, this necessitates the innovation of new, low-carbon functional materials for extensive application. Furthermore, the current lack of viable resource recovery methods for waste spoil impedes the large-scale use of processed materials. The

complexity and variability of the spoil also present difficulties in equipment adaptability, particularly with the clay content. This issue is compounded by the limited space at construction sites, where traditional resource recovery equipment, often bulky and inefficient, becomes impractical. Addressing these challenges is crucial for advancing sustainable urban tunnel construction.

3 KEY CONSTRUCTION TECHNOLOGY

3.1 *Construction of a subway station using the pipe-jacking method*

3.1.1 *Construction scheme*

Taking the Shasan Station of Shenzhen Metro Line 12 as a case study, this paper introduces the pipe-jacking construction scheme employed for this subway station. The station has a width of 22.6 meters, a height of 13.53 meters, and a buried depth of 7 meters. Notably, the middle section of the station traverses beneath a large rainwater box culvert, extending 70 meters, which was constructed using the pipe jacking method. However, challenges emerged due to a mismatch in geometrical dimensions between the existing rectangular pipe-jacking machine and the requirements for the station's structural cross-sections. To address this issue, a transformative approach is proposed, involving the division of the cross-section of the subway station into two smaller sections representing the left and right substructures of the station, as illustrated in Figure 1. Subsequently, suitably sized rectangular pipe-jacking machines are employed to sequentially construct the left- and right-line tunnels, maintaining a clearance of about 5 to 10 cm. Finally, a structural transformation is applied to the left- and right-line tunnel, making them to form an integral subway station space.

The pipe-jacking section of the station was constructed using a customized super-large rectangular pipe-jacking machine, which excavated the left- and right-line tunnels sequentially. Following tunnel excavation, temporary sidewalls between the left- and right-line tunnels were removed, and middle pillars, transverse beams, and longitudinal beams were retained to form the integral structure of the subway station, as depicted in Figure 2.

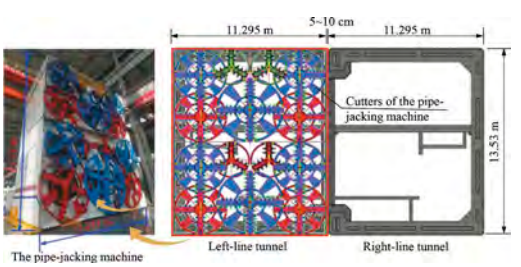

Figure 1. Construction scheme of the Shasan station.

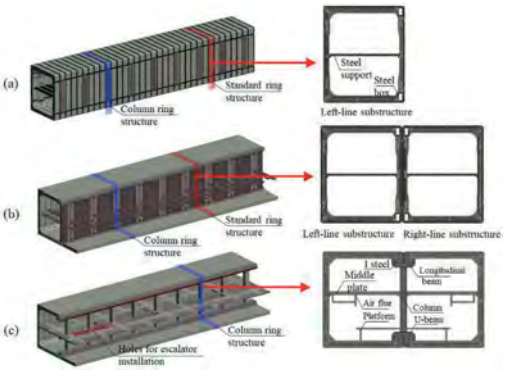

Figure 2. Construction procedure. (a) Left-line substructure, (b) right-line substructure, (c) permanent structure.

The construction sequence using the pipe-jacking method involves the following steps:

(a) Assemble the left-line substructure in the launching shaft, synchronously jack each ring of the substructure using the pipe-jacking machine, and excavate the soil until reaching the receiving shaft.
(b) Lift the machine from the receiving shaft, transport it back to the launching shaft, and repeat the process until the right-line substructure is completed.
(c) Insert four I-steels into the reserved steel box of both the left- and right-line substructures. Pour post-cast concrete into the box to complete the construction of the longitudinal beam. Cut and remove the temporary sidewalls, replacing them with the longitudinal beams and middle plate. Post-cast the upper and lower U-beams after removing the remaining temporary sidewalls and steel supports.

3.1.2 *Key techniques*

1) Jacking super-large rectangular tunnel with shallow buried depth underpass near a box culvert

The Shasan station is situated beneath an urban main road and a large rainwater box culvert. The jacking construction of super-large section rectangular left- and right-line substructures inevitably causes ground surface deformation and differential settlement of the culvert. To mitigate the environmental impact, the following measures can be implemented. Firstly, optimizing the construction sequence by jacking the twin rectangular boxes successively in the same direction proves effective in minimizing ground deformation (Wu et al., 2020). Additionally, employing a horizontal isolation pipe roof and a vertical isolation wall proves to be beneficial in alleviating the environmental impact (Wu et al., 2017; Gao et al., 2022).

2) Jacking the right-line tunnel in close proximity to the left-line tunnel
   Precise control of the pipe-jacking machine's attitude during the jacking process is crucial for the approaching construction, achievable through several measures. Firstly, implementing a longitudinal screw connection between the machine and the three-ring tunnels enhances both longitudinal stiffness and facilitates balance by providing counterweights for the machine. Secondly, the hinge-jointed hydraulic cylinder between the front and rear shields assists in adjusting the attitude during construction. Lastly, grouting holes designed on the machine's side allow the injection of high-pressure bentonite into the soil, enhancing control over the horizontal clearance of the left- and right-line tunnels. Moreover, adjusting the grouting pressure difference in these holes can further contribute to controlling the machine's roll angle.
3) Structural transition
   The left- and right-line tunnels are separated from each other, which are needed to be integrated into a whole station structure through structural transition. The structural transition encompasses both vertical and horizontal mechanical transformations. Critical elements for the vertical mechanical transition include pre-buried steel boxes on the top and bottom plates of the left- and right-line tunnels, columns integrated into temporary side walls, and inserted I-steels within the steel boxes. Following the vertical structural transition, continuous longitudinal beams and supporting columns replace temporary side walls to bear vertical loads. Horizontal mechanical transition involves the removal of temporary steel beams after constructing the middle plate of the station.

3.2 *A multi-scale monitoring and safety assessment of a prefabricated subway station*

Assembling process of large and heavy prefabricated structures may lead to significant strain/stress concentration, and hence may damage these prefabricated components in the form of cracks presented in concrete structures. In this study, we have established a multi-scale monitoring and safety assessment of a prefabricated subway station integrating internal distributed fiber optic sensors and machine vision technologies. A number of prefabricated subway stations including Shapu station, Longxing station, and Pingxi station were monitored using the above-mentioned sensing technologies. Typical distributed fiber optic sensor-based monitoring system is shown in Figure 3(a), where the sensor cables were mounted along steel rebars of prefabricated structures.

Continuous distributed strain field inside prefabricated structures can be directly obtained from fiber optic sensors. Monitored strain distributed in continuous space is shown in Figure 4 and the related spatial resolution of collected strain is 1 mm. Strain change of vault (as shown in Figure 3a) at the different

Figure 3. Application of distributed fiber optic sensors for monitoring large scale prefabricated structures inside subway station (a) position and installation of distributed fiber optic sensors, and (b) transportation and assembling process of vault structures.

assembling steps can be clearly obtained and the potential positions with high stress/strain concentration are also very clear. Therefore, the distributed fiber optic sensors can be used for detecting potential defective positions of prefabricated structures.

The monitoring system also include machine vision equipment and a number of single planar targets as

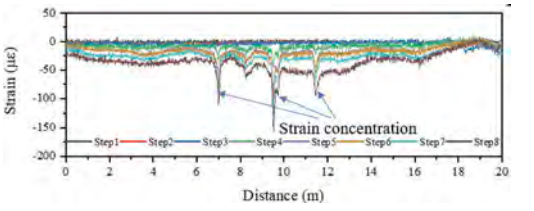

Figure 4. Monitored strain distribution of internal surface inside vault structures.

shown in Figure 5, which were used for tracking the lateral and vertical movement of the whole prefabricated subway stations automatically. The monitoring system is wireless and the monitoring frequency is 50 Hz. The maximum measurement error is less than 0.4 mm within a monitoring distance of 50 m.

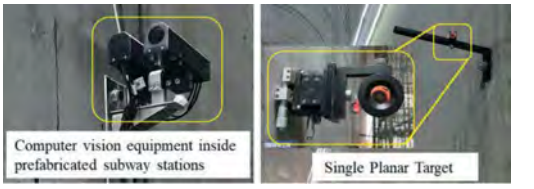

Figure 5. Machine vision-based displacement filed monitoring system in prefabricated subway stations.

Typical monitored settlement of Shapu station during construction process is shown in Figure 6. All obtained settlement data are in continuous, as the machine vision equipment is real-time online automatic monitoring system. It is also seen that the settlement data of different prefabricated structures present slightly difference (less than 5 mm), which is resulted from the difference in overburden pressure of upper soil during backfilling process.

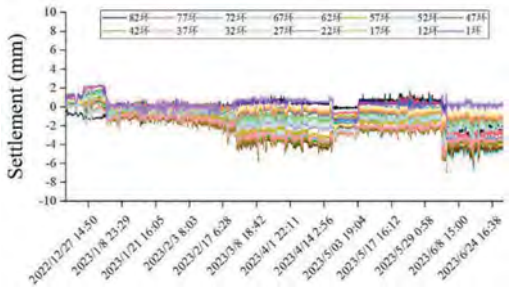

Figure 6. Typical settlement data of prefabricated subway station in construction process.

3.3 *Double carbon resource utilization of urban tunnel*

3.3.1 *Resource utilization methods of solidified tunnel waste*

To facilitate the large-scale application and absorption of tunnel waste, multiple types of solidification and resource utilization methods have been developed.

(1) Utilization of geopolymeric flocculation-solidification soil and flowable fill materials
In the construction of shield tunnels, the direct on-site reduction and solidification of engineering spoil with low sand content and no value for sand-mud separation can significantly reduce the volume of material that needs to be transported off-site. This allows the spoil to be efficiently transformed into fill material in a single step, as shown in Figure 7. Additionally, after flocculating and concentrating the original tunnel waste slurry, further flocculation-solidification processing can be applied to produce flowable fill materials.

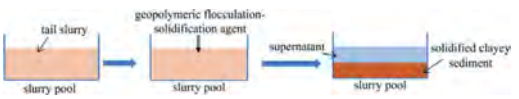

Figure 7. Schematic diagram of the process for producing mud flocculation-solidification soil (Sun et al., 2023).

By adding geopolymeric-based flocculation-solidification agents directly into the waste mud ponds, it is possible to swiftly create flocculated and solidified soil. Throughout this process, the negative charges of slurry particles are neutralized by Al (OH)3 colloid from flocculants, causing the slurry system to become unstable. Simultaneously, CPAM, characterized by its long-chain structure, captures slurry particles and forms flocs in the solution. Flocculation enhances the growth of the strength of solidified sediments by densifying the sediment. Upon hydration of geopolymeric particles, the hydrates fill the gaps within the flocs, leading to decreased fluidity and further strengthening. Figure 8 illustrates the mechanism of the combined effect of geopolymeric flocculation-solidification.

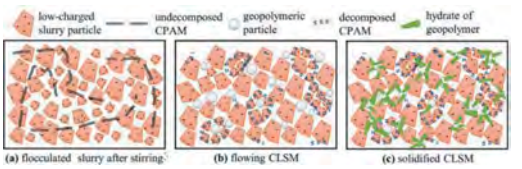

Figure 8. Mechanism of geopolymeric flocculation-solidification (Sun et al., 2023).

(2) Underwater anti-dispersal(lightweight) fill material
To enhance the performance of existing conventional grouting backfill material slurries, the development of underwater anti-dispersion fill materials aims to address issues caused by conventional grout backfill material slurries, such as separation, loss of cementitious materials, insufficient compactness, voids, and inadequate durability, especially in water-rich geological conditions. The process involves using an anti-dispersion agent, which is a high-dose coagulant, to fully encapsulate geomaterials and tunnel waste particles. This ensures that the slurry does not disperse during underwater casting and that the strength of the solidified body is successfully formed. By introducing high polymer bubbles, the weight of the solidified waste can be effectively reduced, while also decreasing the amount of material used. This approach aims to achieve the goal of large-scale, low-carbon utilization.

(3) One-step building material
The current method of mechanically dehydrating slurry and utilizing the resultant filter cake for

Figure 9. Underwater anti-dispersion mud slurry filler for underwater casting.

roller-compacted fillers or as building materials — through processes like further crushing, water addition, solidifying agent incorporation, and stirring — is energy-intensive, costly, and highly inefficient. However, integrating the processes of flocculation, pressure filtration, and solidification can significantly enhance the resource utilization efficiency of the filter cake. The solidified filter cake can then be directly extruded to form building materials or fillers. Research has demonstrated that a geomaterial-based method combining flocculation, pressure filtration, and solidification notably improves the dewatering performance of tunnel waste slurry. Under low-pressure filtration conditions, the volume of dewatered slurry treated with geomaterial flocculation-solidification agents increases by 25%, and the drainage rate by 40%. Additionally, geomaterials display superior solidification efficiency, resulting in stronger solidified soil. Employing high-pressure filtration further aids in expelling water from the solidified soil, thereby densifying its structure. Tests indicate that tunnel waste slurry treated with this geomaterial-based flocculation-pressure filtration-solidification method can achieve a strength of 10 MPa, satisfying the standards required for conventional building material blocks.

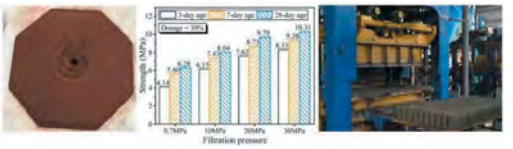

Figure 10. One-step building material (Sun et al., 2023).

(4) Road construction filling disposal
A substantial amount of tunnel waste requires more extensive disposal methods. It is estimated that road construction filling applications can accommodate over 50% of shield tunnelling spoil. Due to the modification and cutting effects on soil bodies during the shield tunnelling process, the properties of the spoil are weakened, making it unsuitable for direct use in road subgrade construction. The use of a flocculation - pressure filtration-solidification method can rapidly improve the quality of tunnel waste spoil, bringing it up to the standards required for subgrade applications. Additionally, by integrating the use of geosynthetic materials, the performance of road subgrades filled with tunnel waste spoil can be further enhanced. Theoretical derivations and calculations required for filling applications are conducted to obtain analytical solutions, thereby guiding practical engineering applications (Sun et al., 2020; Sun et al., 2015).

3.3.2 *Tunnel waste treatment equipment*
Tunnel waste, influenced by construction methods and geological types, displays considerable variability in its slurry and spoil characteristics. For efficient and low-carbon resource utilization of shield waste, it is crucial to identify its unique properties and match them with suitable low-carbon resource utilization technologies. This strategy can significantly enhance the efficiency of tunnel waste resource utilization. The phase separation equipment traditionally used in engineering construction for processing surplus mud and spoil characterized by a large footprint, low reliability, high noise levels, poor adaptability to various spoil types, low automation, complex operation, and substantial labor requirements urgently requires an upgrade to intelligent control systems. The upgrading and retrofitting of this equipment entail the modularization of the resource utilization process for shield construction spoil. This modularization includes developing distinct modules for screening, sand washing, flocculation concentration, and pressure filtration. Through model optimization, pipeline design, and other measures, the processing efficiency of surplus mud and spoil can be greatly improved.

Figure 11. Integrated tunnel waste resource utilization equipment.

4 CONCLUSIONS

In the realms of construction technology of a subway station using the pipe-jacking method, prefabricated station technology, and tunnel muck recycling technology, the prospective developmental pathways in China unfold as follows:

(1) Intelligent Construction. With the relentless progression of technology, the integration of artificial intelligence, big data, and the internet of things in subway construction is poised to gain widespread adoption. The utilization of these technologies holds the promise of boosting construction efficiency, cutting down costs, and ensuring safety—a pivotal trajectory for the forthcoming evolution of subway construction.
(2) Green Construction. As environmental consciousness reaches new heights, the paradigm of green construction emerges as a pivotal trend in the future of subway construction. This

encompasses the adoption of eco-friendly construction materials, the minimization of environmental impacts during construction, and the optimization of construction organization to realize objectives such as energy reduction, pollution mitigation, and environmental protection.

(3) Information Management. Given the diverse specialties and trades involved in subway construction, information management assumes paramount importance in ensuring construction safety and efficiency. Moving forward, information management will be an indispensable tool in subway construction, involving real-time monitoring of construction sites, live collection and analysis of construction data, and remote control and management of the construction process.

In conclusion, the developmental trends in subway station pipe-jacking construction technology, prefabricated station technology, and tunnel muck recycling technology encompass intelligent construction, green construction, and information management. The progression of these technologies holds the promise of enhancing the safety, reliability, and efficiency of subway construction, thereby propelling the rapid development of urban underground space in China.

ACKNOWLEDGMENTS

The research work described herein was funded by the National Natural Science Foundation of China (Grant Nos. 52090084 and 51938008).

REFERENCES

Chen R, Li L, Yang K, et al.Quantitative methods for predicting underground construction waste considering reuse and recycling. Environmental Science and Pollution Research, 2022, 29(3): 3394–3405.

Chen, X., Ma, B., Najafi, M., Zhang, P., 2021. Long rectangular box jacking project: A case study. Undergr. Space. 6, 101–125.

de Magalhães r F, Danilevicz Â m F, Saurin T A. Reducing construction waste: A study of urban infrastructure projects. Waste management, 2017, 67: 265–277.

Ding L, Zhang L, Wu X, et al.Safety management in tunnel construction: Case study of Wuhan metro construction in China. Safety science, 2014, 62: 8–15.

Gao, H., Wu, J., Yang, W.S., Su, D., Wu, Y.Z., Chen, X.S., 2022. Study on restraining effect of seperation wall on carrying-soil effect of pipe jacking. Modern Tunnel Technology. 59(S1): 1120–1126.

Gao, Y., Feng, C., Cheng, P. 2019. Application of structural cut and convert method to underground space development. Tunnel Construction. 39(03): 398–406. (in Chinese)

Luo, Z., Guo, J., Han, J., Wang, Y., 2022. Research on the construction safety risk assessment of prefabricated subway stations in China. Engineering, Construction and Architectural Management.

Mao R, Bao Y, Duan H, et al.Global urban subway development, construction material stocks, and embodied carbon emissions. Humanities and Social Sciences Communications, 2021, 8(1): 1–11.

Qiu, T., Chen, X., Chen, K., Su, D., Shen, J., Wang, L., Zheng, Z., 2023. An adaptation resilience assessment framework for key components of prefabricated underground stations. Tunnelling and Underground Space Technology 136, 105037.

Qiu W, Liu Y, Lu F, et al.Establishing a sustainable evaluation indicator system for railway tunnel in China. Journal of Cleaner Production, 2020, 268: 122150.

Sterling, R. L., 2020. Developments and research directions in pipe jacking and microtunneling. Undergr. Space, 5, 1–19.

Sun X, Han J, Fei J, et al.Geosynthetic-stabilized flexible pavements: Solution derivation and mechanistic-empirical analysis[J]. Geotextiles and Geomembranes, 2020, 48(4): 468–478.

Sun X, Han J, Kwon J, et al.Radial stresses and resilient deformations of geogrid-stabilized unpaved roads under cyclic plate loading tests[J]. Geotextiles and Geomembranes, 2015, 43(5): 440–449.

Sun, Y., Wu, F., Sun, W., Li, H., Shao, G., 2019. Two Underground Pedestrian Passages Using Pipe Jacking: Case Study. J. Geotech. Geoenviron. 145(2), 05018004.

Tao, L., Shi, C., Ding, P., Li, S., Wu, S., Bao, Y., 2022. A study on bearing characteristic and failure mechanism of thin-walled structure of a prefabricated subway station. Frontiers of Structural and Civil Engineering 16, 359–377.

Wang, L., Chen, K., Chen, X., Su, D., Liu, S., Sun, B., Li, W., Yang, W.,Zhou, S., 2024. Low-carbon effects of constructing a prefabricated subway station using a trenchless method: A case study in Shenzhen, China. Tunn. Undergr. Space Technol. 144, 105557.

Wang, L., Chen, X., Su, D., Liu, S., Liu, X., Jiang, S., Gao, H., Yang, W., 2023. Mechanical performance of a prefabricated subway station structure constructed by twin closely-spaced rectangular pipe-jacking boxes. Tunn. Undergr. Space Technol. 135, 105062.

Wu, J., Su, D., Qiu, T., Xiong, H., 2020. Analysis of the settlement superposition effect induced by combined pipes jacking in mined metro station. Modern Tunnel Technology. 57(S1): 485–492. (in Chinese)

Wu, Y., Xu, R.Q., Duan, J.C., Xu, X., Zhu, Y.H., 2017. Environmental effects caused by construction of rectangular jacking pipes with large section, small space and shallow overburden. Modern Tunnel Technology. 54(05): 78–85.

Xiao J, Shen J, Bai M, et al.Reuse of construction spoil in China: Current status and future opportunities. Journal of Cleaner Production, 2021, 290: 125742.

Xue X, Zhang R, Zhang X, et al.Environmental and social challenges for urban subway construction: An empirical study in China. International Journal of Project Management, 2015, 33(3): 576–588.

Yang J, Zeng J, He X, et al.Sustainable clinker-free solid waste binder produced from wet-ground granulated blast-furnace slag, phosphogypsum and carbide slag[J]. Construction and Building Materials, 2022, 330: 127218.

Yang, X., Lin, F., 2021. Prefabrication technology for underground metro station structure. Tunnelling and Underground Space Technology 108, 103717.

Yang, Y.F., Liao, S.M., Liu, M. B., Wu, D.P., Pan, W.Q., Li, H., 2022. A new construction method for metro

stations in dense urban areas in Shanghai soft ground: Open-cut shafts combined with quasi-rectangular jacking boxes. Tunn. Undergr. Space Technol. 125, 104530.

Zhang, D., Liu, B., Qin, Y., 2016. Construction of a large-section long pedestrian underpass using pipe jacking in muddy silty clay: A case study. Tunn. Undergr. Space Technol. 60, 151–164.

Zhang N, Duan H, Sun P, et al.Characterizing the generation and environmental impacts of subway-related excavated soil and rock in China. Journal of Cleaner Production, 2020, 248: 119242.

Tunnelling for a Better Life – Yan, Celestino, Thewes & Eberhardt (Eds)
© 2024 The Author(s), ISBN 978-1-032-80042-4
Open Access: www.taylorfrancis.com, CC BY-NC-ND 4.0 license

New chemicals with reduced carbon footprint

Francois Couturier*, Dimitri Matioszek & Thomas Boursier
SNF, Andrezieux, France

ABSTRACT: Chemicals are widely used in any tunnelling projects for many purposes and benefits. One recent challenge, quite common across many industries, is the reduction of carbon footprint of chemicals. The ISCC+ certification (International Sustainability and Carbon Certification) was set up some years ago and is now well recognized and adopted by chemical manufacturers. ISCC+ is based on traceability of biobased or recycled feedstocks used by chemical manufacturers. As a side benefit of ISCC+ certification, it is possible for chemical manufacturers to provide data about emission factor reduction for each chemical. Suppliers of feedstocks are more and more proposing alternatives to fossil resources, and these alternatives are derived from virgin biomass, circular materials, or renewable ones. Some chemicals for tunnelling having reduced carbon footprint are already commercially available. The reduction can be even more than 100%, depending on feedstocks. The paper also provides detailed explanations on ISCC+ certification.

Keywords: Bio-based chemicals, Tunneling additives, Carbon footprint

1 USE OF CHEMICALS IN TUNNELING PROJECTS

Tunnel Boring Machines (TBM) are high technical equipment that can not work without chemicals, whatever the TBM type. The following cases illustrate the benefit of chemicals in 2 closed shield TBM types, Earth Pressure Balance (EPB) and slurry machines.

1.1 *Chemicals for EPB machines*

Ground treatment in EPB is essential for safety and use of foaming agent to control pressure is necessary. By reducing permeability of excavated material, operational conditions become safe and work goes faster. The foaming agent dosing depends on soil conditions and can be as high as 80%. Foaming agent provides more benefits like reduced abrasion and less clogging. During transport to the surface level, the soil and foam blend has to be conditioned with polymers that bring viscosity control and water absorption to cope with water spills. Efficient lubricants are required since loss of lubricant leads to failure. Technical greases are provided for lubrication and they can withstand wash out, water and dust presence. Sealants are necessary at several TBM locations to make sure that water, soil and backfilling material do not enter in the TBM inner space.

1.2 *Chemicals for slurry machines*

Bentonite mud is permanently injected through nozzles in the excavation chamber, making a slurry once mixed with soil particles. In order to cope with slurry viscosity variation, chemicals are added to the slurry. Presence of groundwater requires viscosification with polymer additives, and presence of swelling clays requires fluidification. Another drawback of clays is that they stick to the tools, and fluidifiers will help detach and suspend them in the circulating slurry.

At the slurry treatment plant, chemicals are used to treat and recycle water. Typically, coagulants and flocculants provide fast settling of soil and bentonite particles, leaving clear water ready for reuse and preparation of fresh bentonite mud.

The list of chemicals above mentioned is not exhaustive and many other chemicals are used at some other locations on the tunnel jobsite.

1.3 *Some other uses of chemicals*

Whether it is during tunnel boring or during repair sessions, waterproofing grouts are necessary to prevent water from flowing to the work zone. During tunnel life, some cracks are appearing, from millimeter to centimeter size, and require various injection material. Chemist have been able to set up specific formulations able to penetrate the crack with

*Corresponding author: fcouturier@snf.com

DOI: 10.1201/9781003495505-5

adjustable parameters like setting times, depth penetration, adherence, mechanical strength and resistance to incoming waterflow.

Concrete for segment is a material made mainly of mineral components, but it contains also chemical additives, such as superplasticizers. These specialty chemicals are specifically designed to decrease water demand, enhance cement hydration during curing, reduce shrinkage, improve workability, and achieve the requested plasticity.

Upstream, the sand that is used in concrete may not be from 100% natural origin. Indeed, sand aggregates in construction formulations are more and more "manufactured sands", due to depletion of natural sand deposits. While the crushing process drives grading and shape, clay mineralogy of source rock dictates fines properties and additives adsorption. Some specific chemicals provide solutions to overcome fines and swelling clays deleterious impacts on concrete and mortar performance.

Backfilling materials are necessary to fill the void between concrete segments and the ground, in order that ground pressure is equally distributed over the external segment surface. Chemicals known as stabilizers and retarders are used to improve the backfilling material properties: the final mix has to get the same strength as the surrounding ground and it shall fill every void before the setting time is reached.

Soil consolidation is sometimes necessary to prevent ground collapse when TBM is entering weak zones, and several options are available, including use of specific chemicals able to bring mechanical properties. These chemicals can also be used when TBM meets fractured areas with many cavities to fill.

Ultimately, tunnel boring is not just a mechanical action, but also a series of chemical reactions.

2 TOWARDS MORE SUSTAINABLE CHEMICALS

The chemical industry is still a recent industry with many new processes to be invented. Over the past 100 years it has supplied chemicals to various downstream industries, and today any manufactured good needs some chemicals in its manufacturing process, as catalyst or upstream component. The role of chemical industry will be even more critical in solving modern challenges, like energy transition, or feeding more people, or coping with growing urbanization. Extracting minerals for batteries, like lithium and nickel, is not possible without mining chemicals, feeding the world population is not possible without fertilizers and pesticides, treating wastewaters or producing potable water is not possible without coagulants, flocculants and disinfection agents.

2.1 *Transition to sustainable chemistry*

A massive move towards sustainable chemicals is on its way. Use of fossil resources for chemical production will significantly decrease in the next decade. Alternatives like use of agriculture or forestry biomass, use of biogenic wastes and residues to make feedstock chemicals are already existing. Many processes have been developed over the past 10 years to move from a linear economy to a circular one, leaving less waste and maximising reuse. Successful processes have led to pilot plant, and now full size plants. This is a large scale approach, and here are some examples taken from various countries and industries.

2.2 *Some recent moves to sustainable chemicals*

2.2.1 *Sustainable Aviation Fuels (SAF)*

The aviation industry has set up goal of carbon footprint reduction, in order to keep growing without increasing its carbon emissions. Options like electric or hybrid vehicles are not yet available like in the car industry or limited to small aircrafts. Biomass-derived jet fuel is one option that comes now into reality. Some routes to sustainable fuels are ethanol to olefins route, and synthetic gas-based kerosene. The 3 key points are as follows: feedstock shall be largely available, given the size of the market; in the same time feedstock supply shall not reduce land surfaces currently in use for food production; and new SAF shall work with the existing petro-based fuel infrastructures. Ethanol route is currently having the lead in the USA, since ethanol can be produced from sugar feedstocks like molasses, but also from cellulosic sources like bagasse (a waste from cane sugar process), or forestry waste, or rice straws. In the UK one project is moving fast using ethanol route, with ethanol made from residual gases coming from surrounding industries, like a nearby steel manufacturing plant. SAF are also a reality in Asia, with Singapore hosting the world's largest manufacturing SAF plant in terms of capacity.

2.2.2 *Bionaphta in Europe*

One of the biggest biorefinery in Europe is located in Rotterdam. It produces sustainable fuel for road transport and aviation, but also bionaphta to reduce the carbon footprint of plastic industry. The Rotterdam plant is processing wasted cooking oils and fats from animal origin, some of these arriving directly by boat. After a pretreatment step, purified oils are sent to a reactor producing biodiesel, biopropane and bionaphta. There is another biorefinery in Finland producing bionaphta from crude tall oil, a waste from paper pulp production.

2.2.3 *Bio-based polypropylene in Japan*

On its path to carbon neutrality, the Japanese chemical industry has to address the issue of the fragmentation of its main petrochemical complex that are operated by several chemical companies which makes decision for change and investments

more complicated. Despite this, decarbonation of the chemical industry has started in Japan, pushed by the Green Growth Strategy initiated at government level. Naphta from fossil origin can be replaced by naphta from biomass, waste plastic and residual gases containing carbon dioxide. There are many forests near Shunan city, where a large petrochemical facility is located. Fast growing trees are planted to provide cost competitive biomass. Biomass naphta is produced and used near Osaka to make polypropylene.

2.2.4 *Bio and recycled plastics in France*
One start-up in France started in 2014 to study casein as a possible source for making plastics. After years of research, a pilot plant has been made to finetune the manufacturing process. An industrial plant has started in 2022, now producing a 100% bio-based and biodegradable plastic, targeting single-use plastics and water-soluble plastics. Another French company has found and patented a technique to turn polyethylene terephthalate (PET) from packagings or textiles to new plastics, using enzymes in specific reactors to degrade PET. The new plastics have the same properties as the ones from fossil origin.

2.2.5 *Practical case at SNF*
SNF is a 40-year-old company headquartered in France and operating 23 plants worldwide. Figure 1 illustrates the very recent changes in its supply chain. With more and more raw materials now available from bio or recycled sources, SNF is now able to manufacture most of its end products, known as water soluble polymers, with reduced carbon footprint.

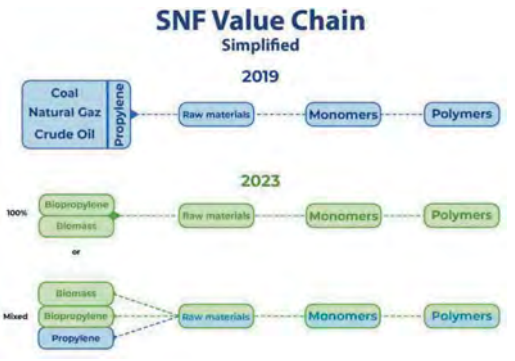

Figure 1. SNF value chain in 2019 and 2023. Most of raw materials and finished goods are now available with some part of biomass or recycled sources.

Whether managed by start-ups or large chemical companies, there are hundreds of new chemicals coming every year in industrial quantities to fuel the sustainable growth of the chemical industry, in its effort to help reduce carbon dioxide emissions.

3 MEASURING SUSTAINABILITY IN CHEMICALS

International Sustainability and Carbon Certification (ISCC+) is a certification for counting carbon emission and it is currently used by many industries across the globe. It covers all sustainable feedstocks, including agricultural and forestry biomass, biogenic waste and residues, circular materials and renewables. With currently over 8000 valid certificates in more than 120 countries, ISCC is among the world's largest certification systems.[1] Industries like food, plastics, packaging, textiles, chemicals are using ISCC certification.

3.1 *ISCC+ in the chemical industry*

ISCC+ certification in the chemical industry does not require a physical separation of flows coming from biomass or recycled sources and flows from fossil origin. It is not necessary to duplicate storage tanks for raw materials and finished goods or having specific reactors and feeding and discharging lines. ISCC+ certification can be implemented with no significant investment. In case the company has already traceability in place, like ISO 9001 is requesting, implementation of ISCC+ certification is light. Most of chemical manufacturers having ISCC+ certification have chosen the mass balance approach: certified and non-certified raw materials, having same chemical and physical properties, can be mixed during the manufacturing process but have to be separated in the bookkeeping. Final products are made from mixed raw materials, and it is possible to allocate some parts of the certified raw materials in the final products. Through the certification, certified raw materials cannot be allocated twice. Final products may have from 0 to 100% certified sustainable share.

3.2 *Emissions from cradle to gate*

Manufacturers of chemicals have first figured out their own emissions, with a split between direct emissions, known as scope 1, encompassing emissions from company activities, and undirect emissions, known as scope 2, related to emissions coming from consumption of electricity, steam and gas. At the company level, scope 1 and 2 emissions can be monitored and reduced. They are already at a low level since they often go along with operating cost reduction.

Scope 1 and 2 count was not satisfactory for end user, because indirect emissions upstream or downstream in the company value chain were not taken into account.

Progressively data on scope 3, dealing with these indirect emissions out of company scope, have been made available.

It is then now common to communicate data from cradle to gate, which counts emission from raw materials extraction to the shipment at the gate of the company. This approach gives a partial life cycle assessment, since upstream transport to user and end of life steps (like waste management) are not counted. But it can be taken as a reliable data by the next user, who can then add its own emission count and pass it downstream to the next customer.

3.3 *Practical cases on 3 tunneling additives*

Some chemicals used in tunnelling are already available with certified raw materials, proving that decarbonation in the chemical industry is not anymore at the stage of white papers and company announcements. Three examples of tunnelling additives having certified raw materials are reported below. All three are manufactured by SNF in Andrezieux, France. For each, Product Carbon Footprint (PCF) is calculated separately with either fossil raw materials (PCF1) or certified raw materials, when available (PCF2). PCF is expressed in kilogram of carbon dioxide equivalent per metric ton of finished product (kg CO_2e/mt), on a cradle to gate basis.

3.3.1 *Soil conditioner*

FLOSET CE 630 N is a soil conditioner used in EPB machine providing stabilization of the mix made of soil particles and foaming agent. It comes as a liquid, known as inverse emulsion since the polymer itself is dispersed in oil. The main raw materials are acrylamide, acrylic acid, caustic soda and oil and all four are now available as ISCC+ certified origin. PCF1 is 946, PCF2 is slightly negative, at -71. The negative value for PCF2 is possible since certified raw materials either contained biogenic carbon dioxide (when from biomass) or prevented carbon dioxide emission (when recycled).

3.3.2 *Mud fluidifier*

FLOSET CT 39 is a fluidifier used in slurry TBM in presence of clays. It has dispersive and deflocculating properties, and can easily be dosed in the bentonite mud. It comes as a liquid, with 44% solid content. The balance is water, since water is used as a solvent in the polymerization step. Its main raw materials, acrylic acid and caustic soda, are both available as ISCC+ certified origin. PCF1 is 512 and PCF2 -456. With such a negative value, the product itself can be considered as a carbon sink.

3.3.3 *Flocculant at the slurry treatment plant*

FLOPAM AN 923 SH is a flocculant that is dosed at the slurry treatment plant to help settle bentonite and ground particles, leaving clear water for recycling. PCF1 is 2000 and PCF2 is 203. As a powder, its manufacturing process requires more energy than for the 2 products above, since it includes drying and grinding steps, using gas and electricity. However, PCF1 is kept at reasonable level because product is made in France, where electricity is mainly from nuclear origin, having a low carbon footprint.

As we can see from Figure 2, results for carbon footprint reduction are not the same between products: in the case of FLOSET CE 630 N and FLOPAM AN 923 SH, it is possible to fully offset the carbon emission when moving from fossil to biomass or recycled sources. For FLOSET CT 39, the use of sustainable resources allows to go well beyond offsetting carbon footprint.

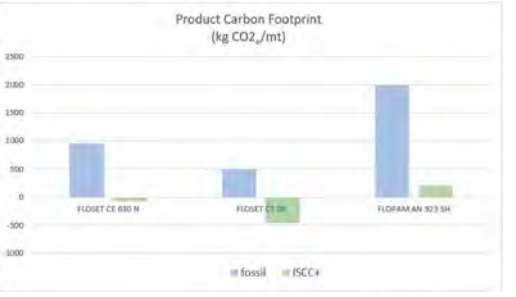

Figure 2. Product carbon footprints with fossil and ISCC+ certified sources, as of July 2023.

In Europe, these 3 chemical products are already available for sale in their reduced carbon footprint version. There is an extra cost for raw materials from biomass or recycled sources, mainly because the availability of biomass or recycled feedstock is low. Arable land is kept first for human and cattle feeding. In a second priority, arable land is used to provide feedstocks to make biofuels, like in countries importing crude oil. Forestry biomass is also competing with other uses, like wood pellets for home heating. As for recycled sources, collection networks are not yet developed enough, and the manufacturing units processing recycled feedstocks are recent (higher depreciation) and designed with a smaller capacity. Some of these units are located next to their source of raw materials (like the bionaphta plant in Finland using tall oil from the local pulp mills) but far from their customers, making overall logistics more expensive, unlike the petrochemical platforms built decades ago and well optimized. Extra costs passed on to the end user for the 3 chemicals listed above are currently in the order of 50% to 100%, and we believe that they will gradually decrease in the short term, at the same time as upstream capacities increase. However, in the medium term, it is likely that some extra costs will persist since fossil resources remain the cheapest ever found so far.

In a broader perspective, it is very likely that by 2030, most of the chemicals used directly at the tunnel construction site will be available from biomass or recycled sources.

4 CONCLUSIONS

The chemical industry has already achieved good results in its way to decarbonation. As early adopter of ISCC+ certification, it is now able to supply chemicals having some parts of raw materials from biomass or from recycled origin. Despite chemicals play an essential role in tunnels construction, their contribution to the total carbon dioxide emission during project's life is probably not the major one. The effective reduction of the global carbon footprint in tunnel construction will first come from the use of low carbon cement, given the vast quantities of concrete used in tunneling and their high contribution to the global carbon dioxide count. Since zero carbon cement will not be largely available soon, use of chemicals having a low or negative carbon footprint is a way to reduce immediately the project carbon footprint.

REFERENCES

1 https://www.iscc-system.org

Tunnelling for a Better Life – Yan, Celestino, Thewes & Eberhardt (Eds)
© 2024 The Author(s), ISBN 978-1-032-80042-4
Open Access: www.taylorfrancis.com, CC BY-NC-ND 4.0 license

City Rail Link – City Rail Link: Managing challenges on the pioneer underground metro project in New Zealand

Francois Dudouit*
Alliance Project Director, Link Alliance, Auckland, New Zealand

ABSTRACT: City Rail Link (CRL) is New Zealand's first underground metro. It is a turnkey project which will be a game-changer for Auckland by doubling the number of people who live within 30-minutes of the city centre. In mid-2019, the Link Alliance, an alliance comprised of the client City Rail Link Ltd and six other New Zealand-based and international constructors and designers, was chosen to deliver the stations, tunnels, and systems. An alliance delivery model with strong integration with the future asset owners, Auckland Transport and KiwiRail, was chosen because of the challenges associated to the size of the project, its complexity, and the risks. The scope of the alliance works includes designing and building two new underground stations and one redeveloped aboveground station, 1.6km twin underground running tunnels, electrical and mechanical equipment and rail systems, as well as testing and commissioning. The technical and engineering feats required so far have been significant, as has the focus on risk management.

Link Alliance is building in the centre of busy Auckland, using a variety of construction methodology including TBM excavation through anchors and large underground excavation in East Coast Formation Bay soil. All of this while in close proximity to live rail infrastructure surrounded by people who live and work in the area. While the alliance has needed to be innovative and adaptable, we have remained clear that people are at the heart of what are doing. We are a culturally diverse team and have developed a unique and inclusive culture which embraces Māori values, looking after our team and stakeholders, and reaching clear sustainability goals.

Decarbonisation in a growing city like Auckland requires continued and focused improvement of urban transport, as well as a commitment to sustainability goals during construction and operational phases of largescale infrastructure projects like the one we're building. From the design stage of the CRL, decarbonisation was prioritised and formally integrated across management systems so that all decisions considered carbon footprint implications.

Keywords: Alliance, Risks, Mining, TBM, Sustainability

1 GENERAL DESCRIPTION OF THE PROJECT

City Rail Link (CRL) is a railway project which will be a game changer for Auckland's transport network when it opens to the public. It is a 3.45km long railway link that will connect the existing Waitematā Station (Britomart) to the North Auckland Line at Maungawhau Station (formerly Mount Eden).

CRL will fundamentally change the dynamics of the existing railway network towards a metro-type operation. Waitematā Station (Britomart) is located close to Auckland's seafront and is presently a terminus, however once the CRL opens, station modifications mean that it will enable traffic through in both directions.

Between Waitematā (Britomart) and Maungawhau stations, two new underground stations are being built – Te Waihorotiu and Karanga-a-Hape – enabling central Auckland, New Zealand's biggest employment hub, to be properly connected by rail.

CRL will double the number of people within 30 minutes of the city centre. When fully operational, 54,000 passengers an hour will use CRL stations at peak times, which is equivalent to 16 lanes of motorway. The project will help reduce vehicular

*Corresponding author: francois.dudouit@linkalliance.co.nz

DOI: 10.1201/9781003495505-6

Figure 1. Overview of the City Rail Link.

congestion, decarbonize Auckland, and deliver significant economic benefits.

Link Alliance is completing all the design and system engineering works, the construction of three stations, the associated running tunnels, the connections to the existing railway lines, all electrical and mechanical equipment and rail systems, and finally the testing and commissioning.

Civil construction is essentially complete. It included Tunnel Boring Machine (TBM) excavation, mining at Maungawhau Station and the 32-metre deep Karanga-a-Hape Station, and top-down and bottom-up cut-and-cover methodology at Te Waihorotiu Station and Karanga-a-Hape Station entrances requiring inter alia significant diaphragm wall and piling works.

Ultimately, because we are a railway project, expertise in systems engineering and in railway development have been fundamental requirements.

Being New Zealand's first metro and building within an already densely populated inner city, CRL has specific challenges which are addressed by innovation and investing in people. Link Alliance has more than 2,000 team members involved in building the CRL. We have brought in experience from round the world as well as building up expertise within the country.

Delivery of the heavy civil works started mid-2019 and progressed well in a covid-19 environment, with the project now delivering architectural, and systems fit-out.

2 ULTIMATELY A RAILWAY PROJECT

Link Alliance is the first construction organisation in New Zealand to gain a Rail Operators and Rail Access provider licence under NZ's Railway Act 2025. Meeting the requirements for this as well as planning, controlling, and coordinating work within the Link Alliance Rail Network has required significant innovation and finding solutions for unique and New Zealand-first challenges.

Railway systems works are being carried out in two distinct environments: the first is defined by the newly built underground structures and the second is adjacent to the existing North Auckland Line (NAL). The phasing of works is dependent on scheduled block of lines (planned periods without commuter rail traffic) and takes place within a very strict regulatory framework.

The transition from heavy civil towards fit-out works is an important phase in the life of the project. It required great attention upstream during design phases of the civil and systems packages, engineering, and in preparation of works, to ensure that integration would be successful and that the project progresses as planned.

Moving towards the testing and commissioning phase of the project – scheduled to start in 2024 – will be another critical transition. The systems teams, which have been integrated into the project from the start, are defining the tests to verify subsystems, systems integration, and validation.

Testing and commissioning plans are being developed in collaboration with the future owners and operators of the CRL: Auckland Transport for the stations and KiwiRail for the rail infrastructure. This integration will help to secure successful testing and commissioning processes and successful handover.

Although CRL links together Auckland's rail network and will fundamentally change the network's dynamics towards a metro-type operation, it is technically a network extension. In particular, the technology of the main systems, such as signalling, remains unchanged. The rolling stock supplied by Auckland Transport is also the same, which will limit risk during the testing and start-up phases.

3 RISKS ASSOCIATED WITH THE PROJECT

There are multiple, interconnected, significant risks that have required careful management including consenting, utilities works, ground conditions, design development, productivity, and interfaces with other infrastructure and construction activity. In addition, being a railway project has meant that we have also had to manage risks associated with systems integration, testing and commissioning. Integration of new infrastructure within Auckland's transport network is another risk which must be managed.

Because this is the first underground metro project in New Zealand, relevant stakeholders have also needed to ensure they have capacity to accept and manage a type of asset that's the first of its kind in the country. Risk associated with this has been mitigated by working closely with stakeholders including the future asset owners, Auckland Transport and KiwiRail.

Two key decisions – made from the outset – have facilitated significant mitigation of project risk: the adoption of an alliance model to deliver most of the works, and making this alliance responsible for civil and system works, including testing and commissioning. Both decisions have enabled the removal of interfaces and helped to optimize the project.

The performance of the alliance is essentially measured collectively, where all risks are shared between partners except for a limited number associated to well defined events. The Variation Benchmarking Register (VBR) defines events giving (or not) the right to adjust the TOC (Target Outturn Cost) and time to completion.

Regarding ground conditions, only a limited number of Extreme Geological Conditions give right to variation. Such conditions must be significant subsurface conditions that are included in the Geotechnical Baseline Report (GBR) and are outside the parameters specified for that subsurface condition.

The relevant subsurface conditions included in the GBR are associated with dangerous gas, excessive groundwater inflows (limited to specific tunnel areas) and only for the TBM tunnel, excessive concretionary interbeds and volcanic rock, ground and groundwater contamination, and unknown manmade obstructions. For example, ground anchors were known to exist under Aotea Centre and the risk of poor TBM progress in that area is named as a shared risk.

The mechanism of risk sharing requires that a comprehensive and efficient risk management process is in place to reduce the alliance partners exposure to additional costs and consequent pain, which in return impacts negatively the margin of the constructors and designers.

4 WHY SELECT AN ALLIANCE MODEL? WHAT ARE THE BENEFITS?

The first call to possible tenderers was made at the beginning of 2017 as part of a 'design & construct' contract for the civil, electrical, and mechanical part of delivering the main stations and tunnels (initial C3 contract scope). During the selection process, various events prompted the client to change its approach: the tender was relaunched in June 2018 in the form of a 'competitive alliance'. Project requirements were also scaled up to provide for a predicted increase in patronage. In particular, allowances were requested for nine-car trains, instead of Auckland's current six-car capacity.

Link Alliance signed the C3 contract in July 2019. While starting C3 works, it continued to develop and cost the rail systems and connection to the existing railway network (initially planned in two additional contracts: C5 and C7). These additional works were integrated into the original contract in September 2020.

It is rare to have a single entity oversee delivering the whole of civil and systems works, including testing and commissioning. However, the decision to have a single entity has definitively permitted removal of interfaces and to optimize design and delivery.

Link Alliance includes seven New Zealand and international companies: City Rail Link Ltd (the client); three construction partners Vinci Construction Grands Projets, Downer NZ and Soletanche Bachy International and three design partners WSP, AECOM and Tonkin + Taylor. Future asset owners - Auckland Transport and KiwiRail - are project partners by way of a stakeholder agreement with City Rail Link Ltd.

Link Alliance is a truly international organisation with our people employed by many different companies from both New Zealand and overseas.

The project's mission is clear. We are working to 'transform Auckland with a rail network people love to use'.

The alliance relies on some key principles: performance requirements are collectively held between client, contractors and designers (one team), the project is governed by a Project Alliance Board (PAB) with representatives from all parties, decisions taken are best for project and at PAB level unanimously, alliance participants share all risks (except for a few identified in the agreement), liability between parties is limited to the fee and there is no possible recourse to arbitration nor litigation. A target cost with a pain and gain sharing mechanism has also been set up to drive financial performance.

Figures 2 & 3. Link Alliance – One Team.

Consequently, the alliance model strongly drives participants to find solutions and mitigate measures together while focusing primarily on performance and delivering the project with the best possible outcomes across a range of objectives. Eight Project Objectives were defined to drive high performance in terms of health, safety and wellbeing, collaborative relationships and stakeholder engagement, programme, performance of the team, best value (cost), sustainability and environment, social outcomes, and legacy. Key Result Areas (KRA) with financial incentives were also developed.

The alliance's induction helps team members to understand the project scope, what the project's core objectives are, how an alliance works and the importance of our objectives and charter – the document which sets out the project's overarching mission, values, and accepted behaviours for working together as one team.

Stakeholders have been involved in the project's planning and design process, fostering a sense of ownership, and ensuring best-practice integration of the rail network and improved accessibility. The intensity of construction within urban residential and business environments has also meant that stakeholders are kept front of mind and environmental impact is mitigated by going above and beyond consent compliance.

During the covid-19 pandemic, New Zealand closed its borders for more than two years and several lockdowns were required in Auckland in adherence with a zero covid policy. Despite this challenging environment, the alliance has maintained progress, including the final TBM breakthrough taking place in line with the original contracted programme date. Strong performance during covid-19 restrictions can largely be attributed to the alliance model and an unwavering commitment to keeping our team safe and well.

Beyond significant technical and engineering challenges and the innovations required to deliver the CRL, the project has developed a unique and inclusive culture which embraces Māori values.

The CRL project has established a partnership with mana whenua through the CRL Mana Whenua Forum, made up of eight Māori iwi (tribes), to ensure that Māori values, culture and vision are respected and deeply integrated into the project. In particular, the architecture and naming of the stations are the result of this strong collaboration.

Key values are set out in the alliance's charter. These include Hui ē tāiki ē (working together as one team where trust, respect, collaboration and inclusion are valued); Pono tauutuutu (holding each other accountable through being reliable, responsible, decisive and committed); Aroha tauutuutu (Caring for each other through wellbeing initiatives, being supportive, making work enjoyable and being mindful of our wider community) and Marohi te tū (being inspired through passion, empowerment, being courageous and proud of the project we're all delivering).

The size and scale of the CRL means that we have been able to significantly contribute to leaving a legacy. Over 9,000 people have been inducted onto Link Alliance works and the alliance focuses on delivering programmes that upskill employees, support qualifications and licence achievement, improve wellbeing and financial literacy, provide opportunities for school and university student engagement and a Māori and Pasifika youth internship programme. As well as this, we have focused on investing in social procurement to enable delivery of values above and beyond commercial value and positively impact on communities for generations to come. To date, over $112 million of our total spend has been with Māori and Pasifika businesses.

5 CHALLENGES ASSOCIATED TO THE UNDERGROUND WORKS

5.1 *Description of the geology*

The CRL's tunnel alignment is underlain by East Coast Bays Formation (ECBF), which is the local representative of the Waitematā Group. Waitematā Group sediments were uplifted at the end of the Miocene and eroded. During the uplift process, some faulting and folding occurred, while the ancestral Waitematā River and associated streams also cut into the sediments, typically following weakened zones that were created during the uplift period.

The Waitematā Group is partially covered by a variety of terrestrial deposits and shallow marine sediments assigned to the relatively thin Pliocene to Holocene age Tauranga Group. At the southern end of the project, located just below the extinct Maungawhau volcano, the cut and cover tunnels pass through fractured to compact layers of basalt, as well as layers of very plastic volcanic ash deposits.

Figure 4. Waitematā group sandstones cliff within Auckland.

The depositional characteristics of the ECBF are consistent over a large area resulting in the typical lithologies being widespread across Auckland, although some exceptions can be noted. The most significant variations are the coarser and typically stronger sandstone layers, the uncemented sand phases and the rarer concretionary nodules. Uniaxial compressive strength of the ECBF is generally between 2 and 5 MPa, but in very cemented areas it can exceed 50 MPa. On the other end of the scale, in uncemented areas the mechanical properties are quite low.

6 TBM TUNNELS

6.1 *Description*

The twin bored tunnels MC30 and MC20 connect all four CRL stations: Maungawhau, Karanga-a-Hape, Te Waihorotiu and Waitematā. Each bored tunnel is about 1.6km long and follows a 3.5% downward slope.

Figure 5. Longitudinal geological section of the bored tunnels.

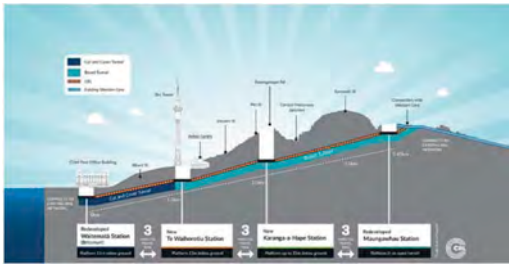

Figure 6. Longitudinal section of the bored tunnels.

In the past, several tunnels had been excavated with a TBM in the ECBF: Ōrākei Main Sewer, Rosedale Outfall and the Waterview Connection.

Based on these experiences, we selected an Earth Pressure Balance (EPB with the following characteristics: drilling diameter of 7.15m; a maximum pressure of 4 bar; a cutting wheel equipped with "rippers" and cutters for hard layers and with an opening percentage of 44% to overcome possible clogging. A single machine was selected to construct both tunnels. The TBM was named in memory of Dame Whina Cooper, a nationally respected leader who fought for many years for the rights of Māori people.

Figure 7 & 8. Dame Whina Cooper TBM (left) & MC30 bored tunnel (right).

Spoil from the TBM was carried out by a conveyor belt with a capacity of 600 tonnes/hour and tunnel transport was mainly achieved by electric vehicles on tyres (contributing to a better tunnel environment and improved sustainability outcomes).

Tunnel lining consists of precast rings, 30cm thick and reinforced with steel fibres, except for special areas where reinforced cages are used.

6.2 *Underground challenges and technical solutions*

6.2.1 *The passage of the Aotea Centre anchors*

Several decades ago, anchors were installed during construction of Aotea Centre (a large performing arts and events centre located in the heart of Auckland) and left in the ground. Investigation work was necessary to ensure the number, position, length, technical characteristics of the anchors, and confirm that they were no longer under tension. In total 26 anchors were identified as clashing with the tunnel. The major impact was on the first tunnel drive for MC30, however some anchors also intersected the second tunnel.

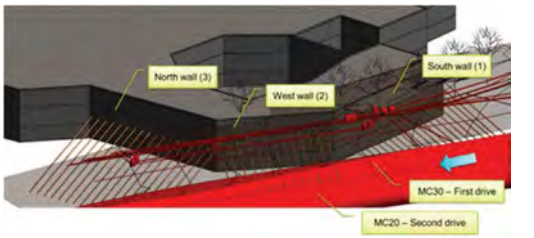

Figure 9. Aotea Centre anchors intersecting the TBM tunnels.

For the first tunnel drive this resulted in 64m of tunnel impacted. Each anchor was made up of seven 15mm diameter strands and had an overall diameter equal to 60mm.

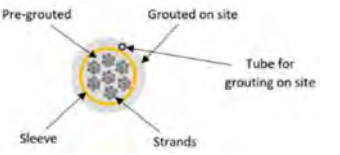

Figure 10. Anchors details.

Due to access and utilities diversion issues, it was hardly feasible to remove these anchors from the surface. The solution was therefore to cut and remove these obstructions from the TBM.

To facilitate this task, the TBM cutterhead was designed with bespoke knives and the screw conveyor with several access hatches. The operating instructions of the TBM have been adapted to this area: three stops were programmed in advance for inspection and possible removal of anchors. These stops were specifically programmed to avoid hyperbaric intervention. Regardless, training and documentation were completed to allow hyperbaric work if deemed necessary and a process was established to decide if additional stops were required.

Figures 11, 12 & 13. Anchors in the cutterhead chamber (left and center) & Tungsten knives on the cutterhead (right).

The TBM parameters were carefully monitored for any sign of cutterhead or screw conveyor torque increase. No such increase was observed. The passage of the anchors on both TBM drives was carried out without long stops and the TBM was able to progress at a very satisfactory average rate of 10m/day, validating the technical choices.

6.2.2 *An alignment with very tight radius (140m)*
The TBM and tunnel equipment were designed for an unusual tight radius, with 110m radius capability for the articulation of the shield. Two lengths of tunnel rings were selected: 1.1m and 1.6m. The first one was used in the tight curves and second one enabled the team to plan for better productivity in the other areas of the alignment. The outcomes in terms of TBM steering in these very tight curves were satisfactory.

On the second drive, the TBM was launched in a 140m radius curve. Knowing the challenges to efficiently steer a TBM in the launching phase, a 24m long launching cavern/stub tunnel was excavated and the shield was held in place in a curved in situ concrete cradle at launch.

Figure 14. The Launching stub tunnel on a 140m curve.

6.2.3 *A complex interface at the TBM launching site*
The TBM was launched at the Maungawhau Station site, a complex site due to other critical works being carried out at the same time: mined tunnels and station civil works. A 40-tonne temporary steel bridge was used to span over the MC50 tunnel entrance and to enable the crossing of the TBM gantries and associated logistics. In addition, the TBM had to be launched along a curved and 3% downhill alignment. For the second TBM drive, the shield was assembled on a 60m^2 tiny platform next to an 8m deep trench. Because no methodological steps could be left to chance, all were performed in four dimensions (with the fourth dimension being time).

Figures 15 & 16. TBM Launching area at Maungawhau, a busy area with several interfaces.

6.2.4 *A challenge to optimize TBM assembly and reassembly*
Significant efforts were required to optimize TBM assembly and reassembly and to save time the shield was delivered to the site in a full section, assembled away from the launching area and then transported (450 tonnes) to a launching cavern, the steel ring was assembled inside the tailskin at the factory, all gantries equipped with boogies and rail wheels to enable a fast transition from the slab surface to the tunnel lining, a caterpillar system embedded in the gantries to enable the 130m long back up to travel back in the tunnel after each break out, no disconnection of the gantries between each drive, embedded jacks in the steel rings to optimize the station crossing.

Figures 17 & 18. Shield transport down to the portal.

7 ACHIEVEMENTS

The first TBM drive (MC30) was completed in December 2021. After the start-up phase, the TBM achieved an average travel rate that was 30% better than the 15m/day initially planned. During the covid-19 restriction period, New Zealand borders were closed. Link Alliance could not rely on experienced tunnellers coming from abroad and consequently focused on investing in training people in New Zealand to build professional and efficient tunnel teams. The progress achieved demonstrates the success of this strategy. Lessons learnt during the first phase realised improved productivity on the second drive (50% better than planned), which was completed in September 2022.

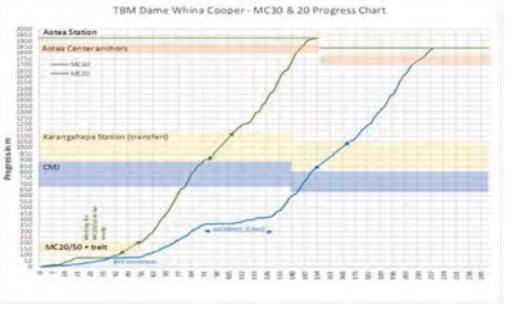

Figure 19. TBM progress curves tunnels MC30 & MC20.

Figures 20 & 21. TBM breakthrough in MC20/MC30 cavern (left) & TBM crossing Karanga-a-Hape (right).

8 MINED TUNNELS

8.1 *Description*

Several critical and significant underground structures had to be mined:

- The two 230m long train platforms at Karanga-a-Hape Station (excavated section 76m^2), the five associated adits and connecting tunnels to the two station entrances: Beresford Square and Mercury Lane.
- At Maungawhau Station, four rail tracks merged underground into two rail tracks to enable trains to run both directions on the North Auckland Line. This requirement necessitated the design and construction of a conical tunnel to connect MC30/MC60 tracks and a conical cavern to connect MC20/MC50 tracks, as well as a tunnel dedicated to the MC50 track.
- Four cross passages between Maungawhau and Te Waihorotiu stations to connect the two bored tunnels MC20 and MC30.

8.2 *Challenges and technical solutions*

8.2.1 *Underground structures at Karanga-a-Hape station*

The reference design for this deep station was based on an access to the middle of the train platforms by inclined adits. The design was simplified by providing access to the farthest points of the platforms using the two entrance shafts. This change resulted in simplified construction methodology, savings and CO^2e reduction.

The tunnels are located in well cemented and strong ECBF layers, which enabled excavation in two phases with a road header, ground support limited to bolts and shotcrete, and efficient tunnelling operations.

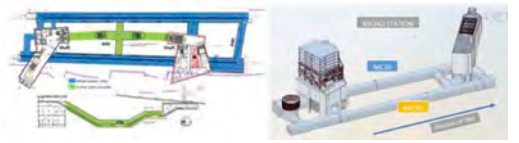

Figure 22. Karanga-a-Hape Station reference design and as-constructed design.

During the design stage, special attention was paid to the intersections between adits and tunnels. They are complex structures, particularly considering that the sections of the adits and the tunnels are quite similar. They required careful modelling to optimize them structurally and enable safe and efficient construction sequencing. Additional ground supports and the use of spilling were required to address two specific challenges: the cover of strong ECBF above the tunnels could be reduced in some areas to about 2 metres, and the presence of a fault with fractured material.

Figure 23. MC20, Adits 4 & 5 connections to Beresford Square shaft.

Figures 24 & 25. Karanga-a-Hape tunnel lining construction (left) & tunnel excavation (right).

8.2.2 *Underground structures at Maungawhau station*

The design for this station was optimized by shifting the location of the tunnel portal and reducing the lengths of the tunnels. These changes resulted in 45% less tunnel works, faster excavation, savings and CO^2e reduction. These design changes also enabled earlier TBM launches.

Figure 26. Maungawhau reference design.

At Maungawhau, the ECBF is weaker and the tunnels intersect lenses of uncemented material. Excavation proceeded in two phases, but with shorter advances and stronger support including the use of lattice girders and canopy tubes. An excavator was sufficient for excavating this material.

Figure 27. Maungawhau as-constructed design.

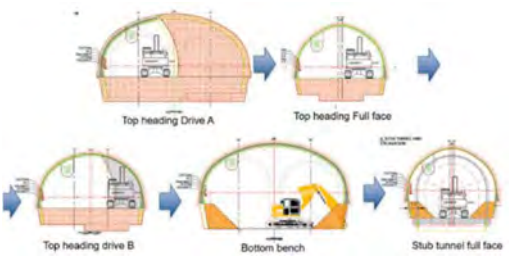

Figure 28. MC20/50 cavern sequence of the excavation works.

The ground support and the sequence of works were carefully designed (the MC20/50 with a 18m span is so far the largest cavern ever built in ECBF in Auckland), and heavy monitoring was in place during construction in order to ensure that construction of the Maungawhau portal and tunnels would not affect a main critical water supply line to Auckland – named Huia 2 – with a 1.4m diameter.

8.2.3 *Achievements*

All mining works were completed safely with minimum movements and settlements, and within programme tolerance. Achieving mining work in time was critical so that the TBM could pass through Karanga-a-Hape Station on its way to Te Waihorotiu Station.

9 THE SUSTAINABILITY CHALLENGE

Early in the CRL project's development, we understood the immense opportunity to benchmark sustainability outcomes to that will leave a lasting legacy for New Zealand for generations to come.

We drew strongly from Te Ao Māori (the Māori worldview) and used Infrastructure Sustainability Council (ISC) certification to externally validate our sustainability practices. In fact, we adjusted our ISC manual so it included mana whenua cultural interests – a world first.

To ensure decarbonisation was prioritised by alliance participants, sustainability was formally integrated across the management system so that all decisions, including design, construction, whole-of-life cost, procurement and change management considered carbon footprint implications.

Industry-leading decarbonisation measures that have contributed to this reduction include reducing the amount of cement in concrete, changing the mined tunnel designs at Maungawhau and at Karanga-a-Hape stations to reduce excavation, material reuse, using self-adjusting 'smart' lighting and ventilation systems to reduce station operational footprints.

The integration of decarbonisation into decision-making has yielded a projected 60,500 tCO2e reduction in total carbon footprint over the CRL's 100-year design lifespan, a 19% reduction which reduces the expected carbon payback time once the CRL is operational to under six years. Once operational, CRL is projected to reduce Auckland's transport emissions by 28,000 tCO2e, every year.

According to ISC criteria the project has reached 'leading' level. This is the highest possible level for the design phase and the project score is the best ever measured in New Zealand.

10 CONCLUSIONS

City Rail Link, New Zealand's first underground metro project, is associated with challenges and has several valuable lessons. Its successful delivery adopting an alliance model thus far has been enabled by well-defined and shared values and objectives, strong organisational set-up, state of the art construction methods, innovations, careful design and works preparation, risks management, sustainability, and a steadfast focus on the ultimate goal: delivery of a safe and reliable rail system.

Tunnelling for a Better Life – Yan, Celestino, Thewes & Eberhardt (Eds)
© 2024 The Author(s), ISBN 978-1-032-80042-4
Open Access: www.taylorfrancis.com, CC BY-NC-ND 4.0 license

Nuclear decommissioning in the UK: Cross-sector collaboration and learning with the tunnelling and underground space sector investigating alternative approaches to reactor dismantling and graphite retrievals

Daniel Garbutt*
Magnox, Nuclear Decommissioning Authority, London, UK

Martin Knights
London Bridge Associates, London, UK

ABSTRACT: Magnox, part of the Nuclear Decommissioning Authority (NDA) overseen by H.M United Kingdom (UK) Government's Department of Energy Security and Net Zero, is tasked with decommissioning the UK's nuclear reactor fleet which includes the 22 first-generation graphite core Magnox reactors. The previous strategy for decommissioning the Magnox reactors, reviewed in the 1990s, was to defer reactor dismantling for approximately 85 years after reactor shutdown. This involved preparing each reactor for many decades of quiescence; the Care and Maintenance (C&M) phase. In 2019 the NDA Board approved a change to the Magnox reactor decommissioning strategy from blanket deferral to Site Specific Strategies. This enables a combination of continuous and deferred decommissioning to be applied on a site-specific basis, avoiding fleet wide quiescence, and instead creates a rolling programme of decommissioning. The revised strategy involves reactor dismantling being brought forward at some sites, which creates opportunities to develop new technologies and innovative approaches such as the retrieval and possible processing of nuclear materials such as contaminated asbestos, irradiated steels, and graphite to allow for potential beneficial re-use. Magnox has identified cross-sector learning and collaboration as one of the ways of being able to meet the aims of its mission effectively and efficiently. Currently Magnox is engaged with the Tunnelling, Mining, and Underground Space sector to establish an understanding of what technology or methodology transfers from these sectors may be feasible to aid in reactor dismantling (which includes graphite core retrieval). Taking learning from industries that have experience of working in hazardous confined spaces and utilising extractive processes.

Keywords: Planning: Nuclear Decommissioning, Sustainability, Technology Transfer, Robotics and Automation, Cross-Sector Collaboration, Innovation

1 INTRODUCTION

Magnox, part of the Nuclear Decommissioning Authority (NDA) overseen by H.M United Kingdom (UK) Government's Department of Energy Security and Net Zero, is tasked with decommissioning the UK's nuclear reactor fleet which includes the 22 first-generation graphite core Magnox reactors, see Figure 1.

In 2019 the NDA board approved a change to the Magnox reactor decommissioning strategy that moved away from the blanket deferral to site specific strategies. The approach now consists of a combination of continuous and deferred decommissioning. This has resulted in reactor dismantling being brought forward at some sites and is creating opportunities to develop innovative approaches and technologies such as the retrieval and possible processing of a variety of nuclear materials which may allow for beneficial re-use.

Figure 1. Magnox sites on great britain in the UK.

*Corresponding author: Dan.Garbutt@magnoxsites.com

DOI: 10.1201/9781003495505-7

In 2021, Magnox initiated the implementation of a programmatic approach to align with its new strategic direction. As a part of this initiative, the organisation established the Strategic Enablers Programme, focused on examining site-specific strategies for continuous reactor dismantling and identifying critical factors essential for driving overall strategic change.

Within the Strategic Enablers Programme, Magnox developed a research and development, innovation, and engagement process (RDIE) to identify opportunities aligned with priority areas, supporting the achievement of new mission objectives, Figure 2, and adhering to the NDA benefits framework. These benefits encompass a safer, greener, faster, cheaper, skills-enhancing, and knowledge-creating approach.

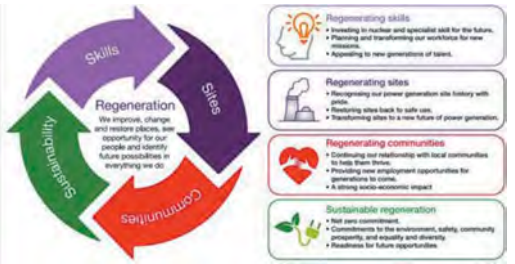

Figure 2. Magnox mission (Magnox 2022).

The programme facilitates pathfinder projects that undergo the RDIE process, showcasing potential benefits. These agile, sprint-type projects aim to deepen understanding within specific opportunity areas, potentially paving the way for larger-scale research, development, technology transfer, or implementation programmes.

In contrast to traditional approaches within the nuclear sector, the NDA and Magnox recognise the significance of cross-sector collaboration in effectively addressing decommissioning challenges through a system-of-systems perspective. This understanding has led Magnox and NDA to engage with diverse industries to enhance their capabilities in addressing the overall decommissioning mission.

Magnox is currently spearheading a "lead and learn" approach to reactor dismantling, with ongoing work at Trawsfynydd in North Wales. The team at Trawsfynydd adopts a pragmatic dismantling approach based on current knowledge and requirements, setting a benchmark for future improvements in dismantling other designated reactors.

To achieve these improvements, Magnox actively collaborates with other sectors to explore relevant approaches, processes, and technologies that may be transferable to the dismantling of designated reactors. Specifically, the organisation has engaged with experts in the tunnelling and underground space sector to investigate potential applicability of techniques used in mining and tunnelling to the Magnox mission. The rationale behind this collaboration lies in the similarities between the challenges posed by confined space hazardous operations and extractive technologies in the underground space sector, and those encountered during reactor dismantling and handling of core materials.

As this project progresses a deeper understanding of the opportunities will emerge, however in this paper the efforts of building understanding between the nuclear decommissioning sector and the underground space sector will be outlined and how this intends to foster improved project scoping and delivery in time. The authors intend an update paper to follow.

2 THE GRAND CHALLENGES

Sitting behind the strategy and the programmes objectives of Magnox and this specific project are the NDA Grand Challenges. These challenges are:

Reducing our waste and reshaping the waste hierarchy

- finding new ways to drive the waste hierarchy, increasing recycling and re-use to reduce volumes sent for disposal.

Intelligent infrastructure

- using autonomous technology to manage assets and buildings proactively and efficiently.

Moving humans away from harm

- reducing the need for people to enter hazardous environments using autonomous systems, robotics, and wearable technology.

Digital delivery

- adopting modern approaches for putting data to work, to improve planning, training, and aid decision-making.

These challenge themes are deliberately broad and they're applicable across the NDA group, across different market sectors and have wider societal benefits. There will be areas where the nuclear sector already excels and so it would naturally take a lead in driving innovation, for example, in radioactive waste and radiation-related safety. However, it is acknowledged that the NDA group actively need to seek opportunities to collaborate and partner more widely and work with other sectors. This project sits as an example where Magnox, part of NDA, has experience and understanding in one key area but requires expertise and experience of another sector to compliment and drive a collaborative project to possible innovation.

3 VALUE FRAMEWORK

When collaborating across different sectors, it's crucial to understand the driving forces behind the approach to programmes. In cases like metro systems, new railways, and utility development, the benefits are clear. Simply put, creating, or upgrading underground assets improves services or utilities, leading to better lives for the local or

national population. Nuclear decommissioning focuses on removing assets that no longer serve the people or the nation. Still, it's essential to ensure benefits for both in carrying out these programmes. The primary task has been based around defining the benefits that guide this programme of work. To do this, the collaborative team including Magnox, London Bridge Associates, OTB, and GCG has outlined and understood the landscape of benefits for a nuclear decommissioning project. This process aligns the underground space sector with Magnox's established principles.

Decisions made by the NDA group must offer value for money. This means using resources in a way that maximizes overall value, not just minimizing costs. The value framework doesn't make decisions, but it helps develop criteria to evaluate options (NDA, 2021) (see Figure 3).

Figure 3. NDA value and benefits framework (NDA 2021a).

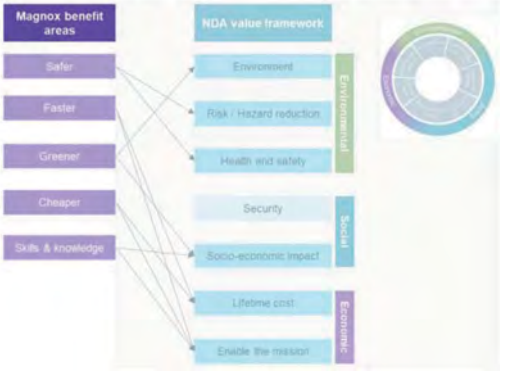

Figure 4. Magnox benefits aligned to nda value framework.

Magnox has aligned a benefits framework with the NDA value framework. This forms the foundation of Magnox's RDIE process, enabling Magnox to assess developmental areas that align with its mission (depicted in Figure 4).

4 SCOPE

Undergoing a strategic shift, Magnox is actively devising an optimal roadmap for dismantling reactors. This strategic transition presents a range of potential options for selecting the subsequent decommissioning site. This approach is deliberately designed for flexibility and a comprehensive grasp of the full spectrum of activities. The scope of this project spans three distinct stations within that strategy, each marked by its own set of characteristics, while maintaining a certain level of consistency across the entire fleet. This standardised approach enables the systematic accumulation of knowledge that can be readily applied to any advantageous scenario that may arise.

4.1 *Reactor sites*

Among the sites under consideration are Dungeness A (DNA), Hunterston A (HNA), and Oldbury (OLD). The rationale behind choosing Oldbury (Figure 5) stems from its structural resemblance to the Advanced Gas Reactors (AGRs), particularly concerning reactor vessel assembly. This alignment positions Oldbury as a potential hub for generating synergies as the purview over AGRs decommissioning transitions to the stewardship of the NDA and Magnox.

Figure 5. Oldbury reactor buildings.

Dungeness A emerges as a prime contender within the ongoing decommissioning trajectory, making it a judicious candidate for in-depth investigation. Adding to its appeal is the presence of geologically intriguing conditions that warrant exploration.

In stark contrast, the Hunterston A reactors deviate from the conventional configuration of the Magnox Fleet. These reactors, positioned sitting above ground, feature a distinctive characteristic: the placement of the

fuel rod assembly at the bottom, bucking the trend. This unique orientation, that can be described as an "upside-down" setup compared to the rest of the fleet, sets Hunterston A apart as a departure from the established norm and a key candidate for investigation.

4.2 *Establishing intelligence*

Magnox's objectives for this project are to explore feasible mining and tunnelling techniques applicable to accessing the reactor, dismantling it, and retrieving the graphite and other materials within the assembly. Central to this endeavour is the development of a pragmatic strategy to address risks and uncertainties inherent in utilising mining or tunnelling methods for reactor dismantling and graphite and other material retrievals.

To achieve these goals, it is necessary to understand the capabilities required in terms of personnel, processes, and technology to effectively execute potential options. Equally crucial is a comprehensive understanding of the planning prerequisites, data requirements, and the progression of concept development, design, and construction needed to actualise these potential options.

While Magnox has a substantial history of decommissioning facilities, the objective of this project is to explore these facets in the context of potential novel solutions, which are previously uncharted by the organisation. This exploration is accompanied by a rigorous assessment of the sustainability implications. Magnox's overarching mission is environmental remediation and sustainability via resource management. Thus, any strides toward circular economy benefits are integral, and this is encompassed as part of the benefits framework.

Additionally, Magnox seeks to gauge the technological readiness of the wider infrastructure sector to meet potential demands associated with executing a programme of this nature. In essence, the collective aim is to cultivate insights and a broad understanding of the risks and opportunities intrinsic to alternative methods for reactor dismantling using mining and tunnelling methods and technologies.

5 OPTIONS DEVELOPMENT

The options development process is currently in hand. The processes began with bringing the integrated team together to understand the Magnox mission along with a site visit to Oldbury to assess the reactor buildings and the site layout, this was followed by a session of key questions and targeted information requests by the London Bridge Associates lead supply chain partner team. This information gathering exercise has enabled the integrated teams to understand the limitations of the scope and grow appreciation of the direction from which Magnox is growing its intelligence.

The LBA team is adopting a "sensing" or intuitive approach to this high-level review of potential options i.e., bringing together a bespoke team of experienced engineers whose expertise includes mining, tunnelling, construction, mechanical & electrical plant equipment, and robotics in a nuclear environment. The teams innate experience enables a collaborative development by blending intuition and technical skills working with subject matter experts within Magnox to jointly review ideas & concepts; deciding on options; subsequently testing their feasibility and outline methodologies. The team is encouraged to step outside their conventional thinking, collaboratively challenge one another and are encouraged to visit the world of the possible rather than the conventional solutions. This high-level approach to developing ideas and options is a basis for progressive workshops to jointly:

a) Agree which ideas to take forward for further review.
b) Establish ideas assess their feasibility and develop. Options.
c) Review current & future technologies.

In addition, an assessment of risks, procurement strategies, programme delivery and costs will be undertaken.

5.1 *Technology development and transfer*

The scale of the nuclear decommissioning mission in the UK is vast and complex, the timescales run in the century scale. This can provide challenges in development of approaches that may become obsolete or embed risk in future activities for decommissioning. This means that the strategic approach that the NDA and Magnox must take is one based on understanding the current technology landscape but with a view to how this can be developed towards addressing some first of a kind complex challenges decades in the future. This means there is a degree of horizon scanning required as well as uptake of the role of influencing the development of the technology and innovation ecosystem to meet the needs of the nuclear decommissioning sector. This culminates in a flexible strategy that requires room to investigate multiple technology and process strands, this crucially makes room for rapid learning and agile change of direction, with banked learning from experience, when areas of investigation reach the limitations of their strategic value and are no longer viable to progress. The aim is to build understanding of where to encourage development and investment across the supply chain and within other government bodies or where to adopt technologies and processes from other sectors.

As outlined by the Grand Challenges, removing humans from harm is a key focus. The NDA invests significantly in various collaborations and technology developments with regards to robotics and automation, including Artificial Intelligence (AI) and Machine Learning (ML) to address this focus, see Figure 5. The Robotics and Artificial Intelligence Collaboration Hub (RAICo1) facility was established by NDA through Sellafield along with the United

Kingdom Atomic Energy Agency (UKAEA), the National Nuclear Laboratory (NNL) and the University of Manchester. This facility and the approach which is supports is focused around bringing where possible end to end process and technology that is supported through robotics and AI and focused on various nuclear applications.

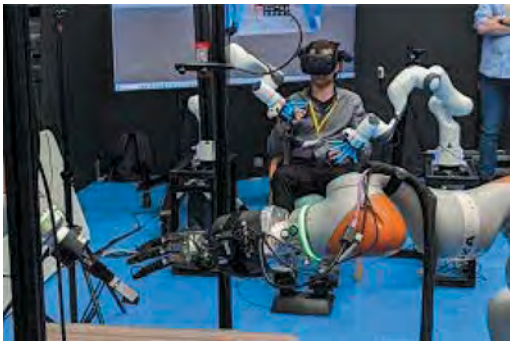

Figure 6. Tele-existence robotics development for nuclear decommissioning (NDA 2022).

As part of this project Magnox is utilising the learning at RAICo1 and the Automated Sort and Segregation (Auto-SAS) collaboration within the NDA estate to understand how this may be part of a broader technology picture that includes processes and technologies from the mining and tunnelling sector. The aim is to build a picture of to what extent there is a plug and play ability, or where further investment within the technology and innovation supply chain is needed to meet feasible options outlined in this project's work. This ultimately will provide Magnox with an intelligence upon which to base any decisions on where to develop its capability in this area.

5.2 *Systems thinking for innovation*

Evolving systems thinking wider than the nuclear silo is acknowledged in the Grand Challenges. Therefore, building an approach that acknowledges the interconnected and interoperable aspects of the sociotechnical landscape within which nuclear interacts is a pragmatic way of progressing the mission.

It's important to underscore that the overarching objective of this project is to overcome constraints in thinking about reactor dismantling and material retrieval. Constraining nuclear-related challenges within existing safety and regulatory confines, whilst intended to enhance safety, can inadvertently hinder innovation.

This becomes evident when building the picture of the decommissioning approach, where certainty, safety and security are perceived as coming from established regulated existing approaches, however there are no established consistent existing approaches to graphite cored commercial reactor dismantling so far. This therefore dictates we must not constrain thinking in developing an approach as security, safety and certainty can come from other sectors and be just as relevant and robust for the nuclear decommissioning mission.

5.3 *Balancing opportunity and risk*

Opportunities and risks evolve as understanding develops, they can grow from singular ideas at the very beginning of a programme to fully detailed, researched, evidenced, and justified statements as time goes on. The pursuit of reducing assumptions through targeted development of opportunities and risks as early on as possible is aimed at providing certainty and clarity for decision making and project execution at later stages.

This project is broadening the opportunity landscape and the perception of risk of those opportunities in relation to using mining and tunnelling methods and technologies for reactor dismantling and material retrievals. Outside the box thinking and feasibility development work are vital stages in planning of major national programmes of work.

The pursuit of value is an important driver; however, it is necessary to build a comprehensive understanding of what value means to the work being carried out and the ecosystem within which it resides. This approach provides the client organisation with the ability to build overall intelligence. They can then cost effectively target deeper dives into areas which provide enough justification to form a possible solution or be considered as part of a wider system of solutions. This approach is an effective tool for transferring understanding and capability form one sector to another; enabling the development of a collaborative understanding of the opportunities and risks as well as reducing assumptions and challenge constraints. The earlier these activities begin the greater the data to inform options and support programme development towards well balanced and understood decisions based on defined benefits with clear value.

6 CONCLUSIONS

The decommissioning of nuclear reactors and the nuclear estate is the most significant infrastructure project in the United Kingdom, lasting centuries. This endeavour's social, economic, and technical impacts have the capacity to mirror the transformative influence of the industry's inception on society, science, and engineering.

This project is an example of the approach to thinking cross-sector in relation to the challenges presented by the nuclear sector. The NDA and therefore Magnox have recognised that this way of working can offer a wide range of benefits to its programmes as well as providing a catalyst for further innovation and sustainable approaches across sectors.

On long term projects such as nuclear decommissioning a flexible but programmable approach is required that balances both risk and opportunity, it is vital to explore ideas and develop learning through an agile strategy. Progression to effective outcomes is rarely linear in nature, however through taking the approach outlined in this paper Magnox recognises that value can be achieved and retained at all points in its strategic journey.

Building relationships across sectors are an essential step in approaching system engineering challenges, these relationships may vary in format, but they are very rarely a waste of resource as they all tend to move the intelligence and understanding of the programme forward and unlock potential and enable ideas.

ACKNOWLEDGMENTS

The authors would like to acknowledge the wider integrated teams that have been crucial in building intelligence and understanding in this new area of technical collaboration between sectors. The support and endorsement from teams across the Magnox sites that fully embrace taking a different look at challenges has facilitated our supply chain partners in open-minded investigation. The professionalism and enthusiasm of our supply chain partners is of great value to the team at Magnox and we would like to thank London Bridge Associates, OTB Engineering and Geotechnical Consulting Group for their insights.

REFERENCES

Magnox 2022, Integrated Decommissioning and Waste Management Strategy 2022, Magnox. https://www.gov.uk/government/publications/magnox-integrated-decommissioning-and-waste-management-strategy

NDA 2021, Nuclear Decommissioning Authority Strategy 2021. ISBN 978-1-5286-2451–0

NDA 2021a, Nuclear Decommissioning Authority Value Framework, August 2021 https://www.gov.uk/government/publications/nda-value-framework-how-we-make-decisions

NDA 2022, Nuclear Decommissioning Authority Innovation Strategy 2022. https://www.gov.uk/government/publications/nda-innovation-strategy

Tunnelling for a Better Life – Yan, Celestino, Thewes & Eberhardt (Eds)
© 2024 The Author(s), ISBN 978-1-032-80042-4
Open Access: www.taylorfrancis.com, CC BY-NC-ND 4.0 license

Planning of alignment & proposed actions for tunnel collapse in diverse ground conditions on the steepest railway curves in the Eastern Ghats, India

Rishabh Gupta*
Assistant Manager, RITES Limited, Gurugram, India

Lalit Kumar
General Manager, RITES Limited, Gurugram, India

Amit Kumar
Joint General Manager, RITES Limited, Gurugram, India

ABSTRACT: In 1960, the Indian Railway successfully completed the Kothavalasa–Kirandaul (KK) BG line, East Coast Railway (ECoR) primarily built to transport iron ore. Currently, ECoR is planning for doubling line (a new railway line parallel to existing one) in Kothavalasa–Kirandul line section. This 445 km long railway line has more than 58 existing tunnels and 45 tunnels are proposed for second line. The existing railway line passes through one of the steepest vertical gradients of 1 in 60 (uncompensated) upto (8 Degree Curve). This region is thinly populated and has dense forests. Proposed line is planned to increase freight capacity of the section. RITES Limited was assigned the task of conducting the feasibility study, preparing Detailed Project Reports (DPR) and further was awarded with Project management consultancy (PMC) for tunnel construction for the Kothavalasa–Kirandul line section. This paper focuses on a specific 51 km segment between Boddavara-Karakavalasa section of KK line (Andhra Pradesh), which includes methodology, challenges, and recommendations for planning project with similar conditions.

Furthermore, a detailed case study of Cavity formation during tunnel construction in adjacent section ie. Jarati-Malliguda of KK Line in which RITES is PMC for Railways is discussed highlighting unexpected geological conditions that were not initially anticipated during the feasibility stage and how they were treated. The study becomes crucial as the region lies in intense rainfall frequency zone ie.175 days a year that could further potentially impact the nearby construction activities being held at site.

Keywords: Doubling Line, Steepest Gradient, Feasibility, Adjacent operational tunnel, Intense rainfall

1 INTRODUCTION

RITES Limited was awarded the work to study the proposed alignment of 51-kilometer stretch within the Boddavara-Karakavalasa section of the KK railway line, fixing location of portals, conducting Geological & Geo-technical investigations and preparation of Detailed Project Report. This focuses on its planning procedures and methodology of a railway doubling project. Further the PMC works for one of the sections in connection with adoption of parallel doubling in Manabar - Jarati - Malligura section of KK line (Odisha) is discussed to shed light on unexpected geological conditions that were not initially foreseen during the project's feasibility stage and its treatment with solutions without hampering project quantities.

2 LOCATION OF PROJECT

KK Line pierces through three states of India i.e.. Odisha, Andhra Pradesh & Chhattisgarh. The line has a length of 445 km, out of which 138 km lies in Andhra Pradesh up to Gorapur which will be joining South Coast Railway, rest of the line will remain in the Rayagada division of East Coast Railway 131 km. lies in Odisha up to Khadapa, 176 km lies in Chhattisgarh up to Kirandul. The KK section is classified. as a Group E-special class line in which speed should be below 100 km/h. The doubling of this line will be for capacity augmentation and contribute to growth in the regions, steel plants and ore mines in states. This line is mainly used for freight purposes which is a huge profit benefiting Waltair Division. Nearly 3,000 crore (US$

*Corresponding author: rishabhgupta141@gmail.com

DOI: 10.1201/9781003495505-8

380 million) of profit comes through this line.The location of the project is shown in Figure 1.

The project discussed in this paper lies in Koraput district of Odisha (Southeastern Region of India) which lies in the eastern ghats of India with hills up to 900-950 m height with Koraput at 870 m elevation above Mean Sea Level (MSL).

Figure 1. Location of the Project.

3 GEOLOGY OF THE PROJECT LOCATION

This region is a part of Eastern Ghats Mobile Belt (EGMB), covering parts of Odisha, Andhra Pradesh, Tamil Nadu, and a small part of Karnataka. It comprises of a typical assemblage of charnockite and khondalite groups, migmatitic gneisses, granitoid, and pegmatite, all metamor-phosed to high-grade granulite facies. The principal rock units of the eastern ghats are the granite gneisses, the charnockite series, the khondalite series, and the Granites. The charnockite series and the khondalite series are more in proportion in the hill ranges, whereas the granite gneisses are more in proportion in the plains between the hill ranges and the east coast. Three main stratigraphic units have been recognized in this area. They are the granite gneisses, the charanockite series and the khondalite series. Detailed mapping and geotechnical investigations further supported the observations. Refer Figure 2 for geological classification of the project location.

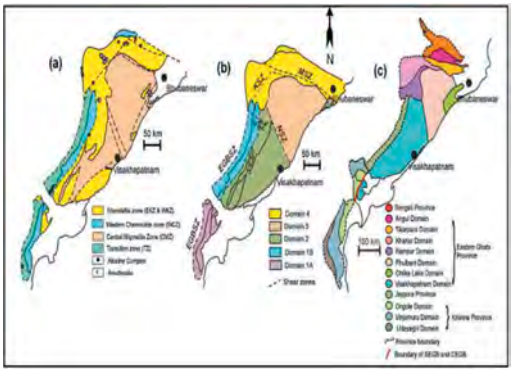

Figure 2. Geology of the project area.

4 METHODOLOGY FOR PLANNING ALIGNMENT

4.1 *General Methodology*

Initially the data and information available from employer and generated from desk study is analysed and a base alignment is plotted on google earth. Based on these studies, the alignment is proposed by establishment of a digital terrain model for the tunnel route of the project on SRTM or ASTER. Further locations are decided for geotechnical investigations, and the data collected form site is analysed and then preliminary designs are prepared. The design of tunnels along with other submission such as, method statement for construction activities, safety tunnel, design of surveillance systems, quality assurance plan, EIA and environmental mitigation plan, maintenance and safety manual is submitted in Pre final design submission stage. Final design submission is made by incorporating the comments from client. Figure 3 depicts the flowchart for steps of alignment study. Further, cost estimate is submitted for construction of tunnel for the project.

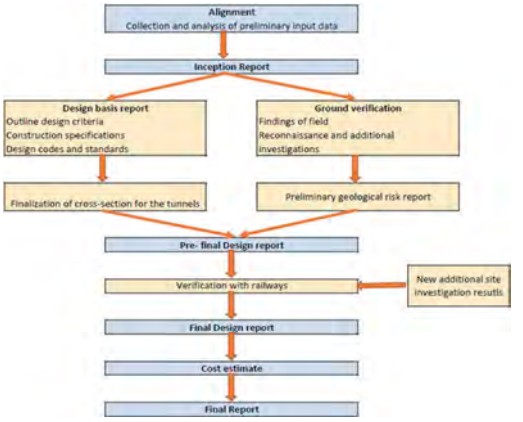

Figure 3. Flow chart summarizing methodology of study.

4.2 *Site Reconnaissance Studies and Observations*

Input Data by Railways: At the outset, the railways handed over an alternative route to RITES Limited for an initial assessment of its viability and to evaluate its techno-economic implications in contrast to following the existing route in parallel. Existing alignment drawings with bridge and tunnel GADs were also provided for review and references.

4.2.1 *Site Studies & Verification for Existing Alignment*

The existing alignment is 51km from Boddavara-Karakavalasa. The section is having five stations i.e. Boddavara(Ch:33), Shivlingapuram (Ch:45), Tyada (Ch:51), Chimdipalli (Ch:63), Borra (Ch:72) and Karakavalasa (Ch:83).Gosthani River, Gurubedda Nadi, Pedda Gedda are the major streams flowing

through the project area (Detour portion). Chinna Gedda Nala, Kodi Gedda Nala, Burudha Gedda Nala, Kakadi Gedda Nala and Anjoda Nala Gosthani River, Gurubedda Nadi, Pedda Gedda are the major rivers crossing the alignment. The topography of the area is varied with waterfalls, meandering rivers, green forests, mountains, hills and undulating plains. The tunnels were unlined in portions from Shivlingapuram to Chimdipalli with deep valleys in right and high cuttings in the left in majority of section. There were some patches of slope stability arrangements at station yards & intermediate locations.

4.2.2 *Site Studies & Verification for Detour Alignment*

- The detour alignment is matching with starting and ending station of the section ie. Boddavara and Karakavalasa whereas intermediate 5 stations are proposed at new locations.
- For all new stations, the yard has been kept at 1 in 1200 grade than existing 1 in 260 and the station Building side 100m and on the other side 50m wide strips of Land has been proposed for acquisition to accommodate necessary Rail Infrastructure. Also, Two new High Level Passenger Platforms of 400m x 7m along with minimum Passenger amenities have been proposed on UP Loop & DN Loop which are connected by FOB.
- After Boddavara Station (Ch:33), the ghat section starts and route stipulating to deep valleys ranging from 30-120 m requirement of huge retaining walls, long viaducts, and huge filling.
- New Shivlingapuram Station (Ch:48) is planned at lower level at north side of existing station, double maintenance of stations at same location.
- After Shivlingapuram Station, ghat section further continues right hand of existing line with deep valleys ranging from 150-220 m requirement of huge retaining walls, long viaducts, and huge filling.
- New Chimdipalli Station (Ch:61) is planned at right side of existing yard, which involved huge filling as existing yard has falling valley at right side making it construction unfeasible and O&M issues during operation.
- The detoured new Gummakota Station (Ch:74) & New Mulapadu Station (Ch:93), building has been planned on right hand side of the Yard. After station boundaries, ghat section continues and alignment negotiates both right- and left-hand curves. The proposed alignment passes through Over Head Power Line of different types at eight locations, Where adequate clearance is not available at the crossing point suitable shifting/diversion has been proposed.
- New Adaru Station (Ch:111), has been planned on right hand side of the Yard and after station boundaries, the ghat section continues with proposal of long viaduct of nearly 100 spans.
- The proposed detour doubling route will meet the existing Main Line of Existing Karakavalasa station. The existing station Yard is at 1 in 400 grade and the same grade has been followed for proposed remodeling.

4.2.2.1 Comments on Detour Alignment

- Majority of portions of detour alignment is through deep valleys with long viaducts, high retaining walls, huge fillings leading to huge width of additional land acquisition as filling slope is (2H:1V) as per railway standards.
- As the location is water charged area, hydrological studies for the new locations of bridge to be studied in detail and new routes to be made for construction leading to further deforestation in green field areas.
- Although the proposed new upline alignment would have higher speed ie. 110kmph as compared to existing alignment ie. 45kmph, but it must be noted that for efficient working of system, the whole system needs to be in sync, if either part is updated the system shall not function with expected outputs.
- As the project is detour alignment, proposal for railway safety in tunnels shall require additional adits, cross passages, and escape tunnels wherever applicable.
- Out of 7 stations in detour alignment there are 5 new stations, leading to double maintenance of stations at nearby locations, also stations are located on majorly fillings whereas current stations are made on verge of cutting, huge fillings must be planned for new locations and land acquisition could be a nuisance during execution.
- Railways had done additional land acquisition in past during execution of existing alignment by acquiring wider width at each structure for future doubling, but as the proposed alignment is detour, the benefit of available land acquisition cannot be redeemed.
- Further issues for land acquisition in forest areas, environmental impact on flaura and fauna and most importantly new access roads in approaches for construction may tend to deteriorate more the sustainability quotient of project in case of a complete detour alignment.

Recommendation for Parallel Alignment Study

Further on discussion with pros and cons of the detour alignment, it was decided to study an alternate parallel alignment from Boddavara-Karakavalasa, and comparative studies shall be conducted for choosing the best alignment for the project location. The proposed alignment shall be designed parallel to the existing line to share the existing infrastructures, electricity, water supply, signalling systems and approach roads which would overall bring a huge impact on project cost when compared to detour alignment.

4.2.3 *Methodology for Parallel Tunnel Alignment Study*

To study the parallel alignment with different types of structures all throughout the alignment. it was not possible to propose a railway line with a fixed distance from existing line. Hence, the criteria to make decisions on proposed alignments was to decide its distance from existing railway line as mentioned in below Table 1.

Table 1 . Centre to Centre Track Distances Structure wise.

S No.	Structure	Distance from Ex. Alignment
1	Tunnels & Its Approaches	25-35 m at Tunnels and 15-25 m at approaches
2	Major Bridge	20 m
3	Station Yard	Min. 5.3 m
4	Open Earthwork Sections	Min 6.5 m

(I) Tunnel & Its Approaches Centre to Centre distance b/w proposed and existing tunnels.

During the excavation of a cavity the ratio between the major and the minor principal stress increases in the adjacent rock. The new state of stress depends on the shape and the dimensions of the cavity, the initial state of stress in the rock, and various other factors. The rock is anticipated to be fairly intact all throughout alignment as majority of sections has unlined tunnels. Therefore, the state of stress in the rock surrounding the tunnel should be approximately the same at different stations, and the normal stress parallel to the centreline of the tunnel should have approximately the same value in every profile.

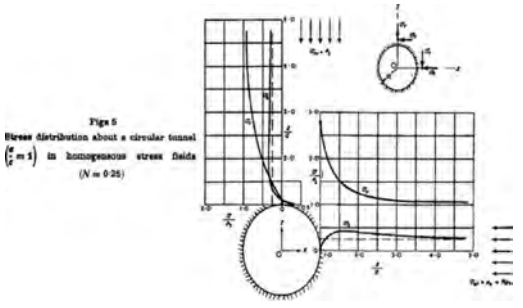

Figure 4. Stress Distribution in Circular (Tunnel) (a/c=1) Reference KARL TERZAGHI and F. E. RICHART, JR.

With below mentioned parameters, the ratio of x/a becomes ineffective for horizontal tangential stress ratio and vertical stress ratio at wall portion of tunnel. Furthermore, the ratio of c/a becomes less ineffective for horizontal tangential stress ratio for said parameters, however it shows positive trend along vertical stress ratio but overall with such given horizontal distance between two tunnels, it is evident that the stress ratio are in permissible ranges as shown in Figure 4.

Let us assume poisons ratio of surrounding rock = 0.2

The overburden at tunnel portal from crown (z) = 10 m

Clear Center to Center Distance b/w tunnels (x) = 25 m

The Width to Height Ratio (a:c) = 9:9 = 1:1

Excavated diameter of the proposed tunnel, D = 9 m

The safe distance b/w proposed, and existing centerlines is calculated as below-

Distance from center of proposed tunnel to minimized stress zone = 2.5 x D = 22.5m

Radius of existing tunnel = 0.5 x D = 4.5m

Length of existing trolley refuge (trolley refuges are also towards proposed tunnel) = 3.5m

Margin for overbreak's due to over excavations = 2m

Safe distance b/w proposed and existing tunnel = 32.5m

Further, there are some aspects which are not quantifiable directly at planning stage to decide the alignment.

The are –

- Progressive loosening of surrounding rock mass around existing tunnel over a period post construction.
- Loosening leads to reduction in C, phi and E values of the geology.
- Impact of vibration on surrounding rockmass due to running of train.
- Hydrogeological wakening of rock mass over period (especially in unlined tunnel portions).
- Quality and health of existing lining in tunnels.

Hence, the adopted safe distance b/w center lines of proposed and existing tunnels are 35m.

Additionally, Tunnel orientation relative to dip and strike is an important consideration in tunnel design and construction. In general, it is recommended to orient the tunnel perpendicular to the strike of the rock layers which would create more stable tunnel. Furthermore, if the tunnel is being constructed through a region with a lot of faults, it may be necessary to orient the tunnel at an angle to the strike of the rock layers to avoid crossing the faults. Tunnels that are oriented parallel to the strike of the rock layers are more likely to be flooded whereas Tunnels that are oriented perpendicular to the strike of the rock layers are more likely to experience rockfalls.

(II) Minor Bridges: The criteria for fixing Standard RDSO spans for minor bridges depends on two criteria:

- If the proposed bridge is upstream of the existing bridge, then in that case the inner

clearance of the box shall be matched with the existing structure (here it is Hume pipes) to avoid any surge on walls of minor bridge.

- If the proposed bridge is downstream of the existing bridge, then in that case the inner clearance of the box can be enlarged or kept same as mentioned above with the existing structure.

(III) Major Bridges: Existing major bridges were constructed with wide open footings and hence safe centre to centre distance of 20m was decided for proposed parallel major bridges. It was proposed to minimize the impact on existing bridges during construction of proposed bridges. Also to avoid the overlapping of foundations as large open foundations are proposed in existing bridges, so adequate distance of 20 m is proposed to have a safe distance during construction and long term loading patterns in foundations of existing and proposed bridges. Also, it was decided to consider the same span configuration of the proposed major bridges to existing bridges to provide same waterway of upstream portions. However, precautions need to be taken when in curve, it must be ensured that the pier doesn't fall in nallah contours which can lead to scouring. Therefore, detailed hydrological studies is required for finalization of proposed bridge piers w.r.t existing bridges.

(IV) Station Yards: The gradients under station limit are proposed to be the same of the existing levels to provide switchovers, points and crossing across the yard limits. Also, the centre to center distance between loop and main lines for new lines have been kept minimum 5.3 m as per latest SOD (BG) of Indian Railways.

(V) Open Earthwork Sections: The track center distance between proposed embankments to existing embankments is kept minimum to 6.5 m for coach clearances in curves, drains and retaining structures wherever required.

4.2.3.1 Remote Sensing Technology for Geological Mapping

The project gets started with the planning phase by sketching the first plan in an Arc GIS software. ArcGIS surface analysis was used to generate contours, slope, aspect, and hill shade from DEM and then photogrammetric maps were prepared to facilitate portal locations and other studies. Two main groups of rock types are recorded along the proposed alignment i.e., Khondalite group and Charnockite group. The geological map of study area had been prepared based on Remote Sensing Technique along with ground truth verification using Geographical Information System software.

A geological map (Figure 5) is showcasing the final output.

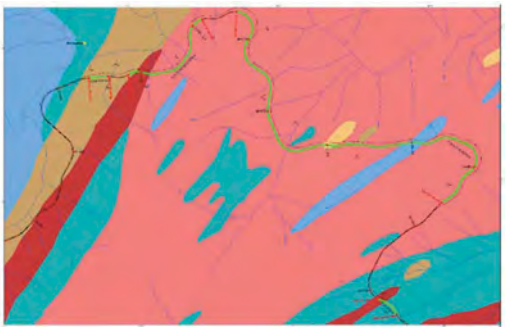

Figure 5. Geological Map of Project Location.

4.2.3.2 Site Studies & Verification for Parallel Alignment

(I) Boddavara (Ch:33), to Shivalingapurm (Ch:45), is lying in flatter terrain to start with for early 3-4 kms and remaining section in ghat section after Tunnel-1. While travelling through alignment along increasing chainage, the general trend is to have deep valley (50-100m) on the right-hand side and uphill slopes on the left. Therefore, the alignment was proposed to the left in this section and no scope of cut & connection was found in this section.

After Tunnel-1A (Ch:36): there is a non-perennial waterfall at the left of existing alignment so to plan a structure and track center at waterfall location the proposed alignment was set to offset 100 m towards the hill side with following points. (Figure 6)

- The alignment towards the right side is not suitable as the valley is about 50m deep and would involve construction of large number of bridges. (Option **Green**)
- Also, the existing radius of curve is 218.8 m (i.e., minimum) with an 8-degree curve so providing an offset track with lesser radius is not practical and feasible.
- The other option is to propose bridge between existing line and Boddavara waterfall. This brings the proposed alignment closer to the rock fall zone of the fall and increases the risk for long term to the train operations. (Option **Blue**)
- Another option was to propose alignment with offset of 100 m from existing line by providing underneath tunnel considering adequate vertical and lateral cover at Boddavara fall, so that rock fall zone and water ingress is avoided. Although the tunnel length would increase but the option was best suited for future durability of structure and cost maintenance at this location. (Option **Red**)

But on subsequent discussions with ECoR, it was finalized for providing offset of 35-40 m from the existing line to the left to avoid land acquisition issues and restrict levels difference between existing and proposed alignments and ways for waterfall diversion were also explored to provide construction feasibility during rainfall season.

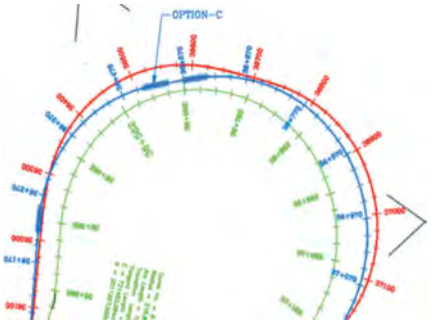

Figure 6. Option comparison at Boddavara Waterfall.

(II) Shivalingapuram to Tyda section is lying comparatively at a higher elevation with no accessibility from nearby roads except for in Tyda station.

(III) Tyda to Chimdipalli station is majorly covered with tunnels adjacent to vertical steep rocks and deep valley. Also, there has been an incident of failure of pier at existing bridge locations (Br. No 249) leading to huge economic loss. The Chidmipalli station lies just adjacent to T-29 and is non- accessible from any nearby road.

(IV) The joint site observations and terrain information available presents the fact to follow left side alignment from Shivlingapuram to Chimdipalli and no cut & connection location was feasible.

(V) The Borra station lies just adjacent to T-38B and is easily accessible from the main road. It is one of the biggest tourist spots in Andhra Pradesh and there are certain reasons for keeping the alignment to the left side.The cover to Borra caves is thin towards the right of the existing alignment. Further, there are karst cavities present to right of the alignment. Also, the alignment from Borra to Karakavalasa region is inhabited by descent amount of population with villages situated to the right of the alignment.

4.2.3.3 Comments over Parallel Alignment

- Major section is in cutting through competent rock mass; therefore, it can be assumed that that 2H:1V or steeper can be provided with minimum support along the alignment in cutting heights more than 6-8 m.
- The area is water charged, hydrological studies for the existing bridges can be referred in detail and this may be useful in estimating proposed bridges configurations.
- The proposed new upline alignment is designed with higher speed i.e., 60kmph as compared to existing line speed i.e., 45kmph.Therefore, upline speed is enhanced by a slight percentage, the overall system is benefitted as currently the upline speed was 40-45 kmph and downline speed was restricted to 30-35 kmph to avoid derailment.
- The most important benefit from this parallel alignment was that the existing tunnels could be useful for escape tunnel and portions where the existing tunnel is opening, there adits are provided for efficient safety rescue exits.
- Out of 5 stations in existing alignment all stations are planned in vicinity of the existing alignment using same station buildings and providing 3-4 lines (main + Loop) as per requirement. No requirement of land acquisition was required within station top point limits. Railways had already done additional land acquisition in past during execution of existing alignment by acquiring wider width at each structure for future doubling, the benefit of available land acquisition can be therefore redeemed.

Figure 7. Existing, Parallel & Detour Alignment on Google Earth.

Figure 7 depicts the alignments of existing (**white**) proposed detour(**magenta**) and proposed parallel(**red**) at a glance. The merits and demerits of detour and parallel alignment are discussed in detail, prima facie through details mentioned in Table 2 and the cost comparison for both the alignments was done on costing based on recent awarded works in East Coast Railway zone and the results stated that the detour alignment was 43 % more costlier than the parallel alignment as per rates worked out in year 2021-22. The information regarding rates and costing is sensitive and cannot be made public. Therefore, Parallel alignment is far more feasible and economic as compared to Detour alignment and it was approved by railways in due discussions and currently construction for doubling is in progress.

Table 2 . Comparison of Existing vs Detour & Parallel Alignment.

S. No	Point of consideration	Existing Alignment at Site	Detour Alignment	Parallel Alignment by RITES
1.	Route Length	51 km with 5 stations	92 km with 7 stations (2 old and 5 new)	51 km with 5 Stations
2.	Gradient	1 in 60 (uncompensated)	1 in 80 (compensated on curves)	1 in 60 (Uncompensated
3.	Max. degree of Curvature	8 degrees	6.48 degrees	8 degrees
4.	Tunnel length	17.5 km	16.15 km	27 km
5.	Minor Bridges	204	34	78
6.	Major Bridges	16 (length -1.05 km)	20 (length -8.174 km)	8 (length -0.6 km)
7.	Road Crossings	One crossing near Borra, No ROB and RUB	Four Crossing, 3 ROB and 7 RUB	One crossing near Borra, No ROB and RUB
8.	Speed	45 km/hr	110 km/hr	55-60 km/hr
9.	Station Gradient	1in 260 in all stations and 1 in 400 at Karakavalasa.	1 in 1200 in all stations and 1 in 400 at Karakavalasa.	1in 260 in all stations and 1 in 400 at Karakavalasa.

5 CASE STUDY OF CAVITY FORMATION ON ACCOUNT OF GEOLOGICAL SURPRISE AND ITS TREATMENT

Efficient planning and geotechnical investigations during the feasibility studies does not rule out guarantee non-occurrence of geological overbreak's in tunnelling. Therefore, a case study in similar project area of a cavity overbreak is discussed in this segment of technical paper and the solutions devised to address these challenges were formulated considering the adjacent operational tunnel, utilizing the allocated quantities specified in the contract to prevent non-scheduled variations, and, most importantly, project schedules.

5.1 *Geological /Geotechnical Studies During Pre-Excavation of Tunnel-1*

Tunnel-1 was planned with 320 m total length with extended. cut & cover boxes both sides with offset distance of 28-30 m c/c with the existing alignment. The tunnel portal was planned at an overburden cover of 8m and maximum cover at mid portion was 53 m. The alignment in this section is running almost perpendicular to the strike direction of the rock with steep dipping, such orientation of the rock mass is generally a fair condition for tunnelling.

Two boreholes were performed at the portals and Geophysical surveys (Seismic Refraction Tomography) were also conducted at the portal location and detailed geological mapping at existing tunnel and proposed portal locations. Water table met in both the boreholes ranging in depth from 10 to 13.5m depth and seepage to minor inflow of water also recorded along the existing cutting & inside tunnel which indicates possible occurrence of water during construction. The Seismic depth probe reveals four-layered model having different seismic velocities

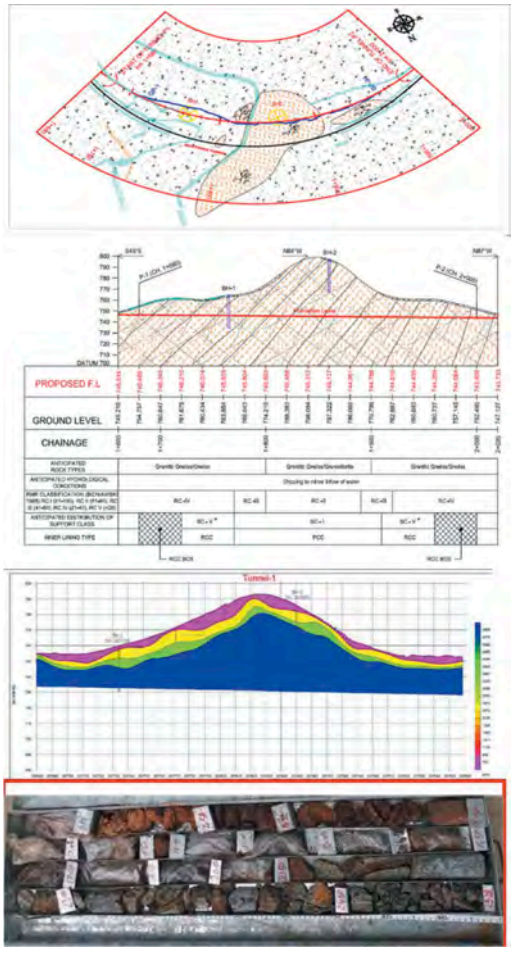

Figure 8. Tunnel 1 (a) Details Geological Plan (b) Geological L-section (c) SRT results (d) core photographs.

with varying thickness. Refraction results indicates that the area is generally covered by 1.0m to 10.0m thick layer of overburden comprises of topsoil (compact nature) with boulders/cobbles/fragment of weathered Granite/Granodiorite in silty/sandy matrix having seismic velocity of the order of 700 to 1178 m/sec.

5.2 *Construction Methodology, Face Mapping and Cavity Formation at Tunnel-1*

Tunnel portal locations both sides showed gentle slope terrain covered with varying thickness of overburden material underlying the basement rocks, therefore SC-V was proposed for initial patch of tunnel portal for a length of 50 m at start of P1 location (Ch:1+680). Refer Figure 9 for detailed support arrangements.

SR. NO	CONSTRUCTION SEQUENCE - HEADING & BENCHING - CLASS 5	REMARKS
1.	Advance of face by top heading for complete length of tunnel or as per the proposed excavation methodology by contractor.	"x" = (1.5 m)
2.	Muck removing from face and dumping it to the designated yard.	
3.	Scale down all loose blocks/fragments using Boomer before spraying shotcrete.	
4.	**1st layer shotcrete** - Spraying of minimum thickness 50mm of Grade M25 on the exposed rock surface.	Sealing shotcrete of 50 mm at rock surface.
5.	Installation of 1st layer Wire mesh (150x150x8mm) on the initial shotcrete layer and fixing it firmly on the undulated surface ensuring there is no gap between rock surface and wire-mesh.	
6.	Install the lattice girder and the wiremesh on the outer surface of lattice girder. At no time shall the face be advanced beyond "x" metres of the last erected lattice girder.	"x" = 1.5 m
7.	Install fore poling through lattice girder at every "x" metre, wherever required.	"x" = 4.0 m. 25Ø, L= 6.0m
8.	**2nd layer shotcrete** - Spraying Final layer shotcrete to cover lattice girder, w/mesh and forepoles ensuring complete lattice girder is embedded in shotcrete.	Application of final 150mm layer shotcrete of Grade M25.
9.	Install rock bolts (SN/SDR) as per the rock support given in respective drawings.	25Ø, L=6 m @1.5 m c/c, Fy=210 KN
10.	Benching excavation to be done as per site specific condition but limited to maximum 50 m beyond top heading.	
11.	After steps 1 to 10, the same cycle shall be repeated.	

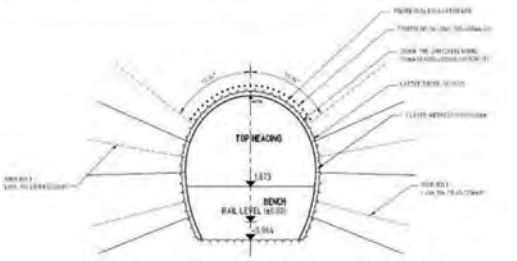

Figure 9. Support Class V construction methodology and Typical Tunnel Cross section with class V support arrangements.

Instrumentation & monitoring during tunnel operation: During the tunnelling operation, below safety instruments were installed for monitoring the behaviour of tunnel and its impact on the surrounding structures. The instrument monitoring systems were following types –Surface monitoring system such as inclinometer to monitor stability of portal slopes. These instruments were installed on the portal ground surface in the array. Bi-reflex target, MPBX, pressure cell, strain gauge, etc. Bi-reflex target (BRT) –Measures deflection, and settlement and was used in traversing. Multipoint borehole extensometer (MPBX) – used for measuring differential settlement. Pressure cells were installed in the tangential direction in the primary lining measures the strain in the rock mass and stress in the shotcrete, Pressure cell installed in the radial direction measures the hoop stress in the primary lining of shotcrete. Strain gauges (SG) – Measures the compression and tension in the primary lining.

Figure 10. Pre-Cavity Photograph of Proposed & Existing Tunnel -1.

Cavity Formation: On 30th May 2022, at (Ch:1700) the vertical cover was 6-8 m and the rockmass of the face was in damp condition with little seepage observed on the face. Seepage in the basic enclaves was favourable for slipping the rock along the joints due to smooth slickenside nature of the joints. Refer Figure 10, the figure was taken before cavity formation.

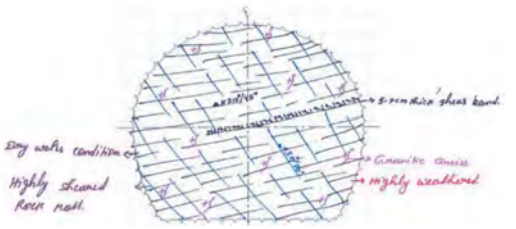

Figure 11. Face Mapping at RD 20 m i.e., Ch:1700.

Excavation for Round length-1m at this chainage completed at morning shift and all the support system installed by evening. Detailed face mapping is attached in Figure 11 which shows intermediate shear band with highly sheared rock mass. Since night it continued heavy rainfall for more than 3 days and the work was suspended. At this stage, the excavated face was pierced 20 m inside from the portal starting point. Suddenly on 4th Day when the rainfall stopped in morning 8 am, a cavity occurred at face and all the support provided at the face were dismantled. Huge quantity of loose rockmass cum debris came down which damaged lastly installed LG, forepoles and other supports as provided. Immediately at 9pm once again loose rockmass came down and damaged another set of LG with forepoles and rockmass covered up till crown portion. No further activities done at that night shift because it was risky to approach the face.

The cavity is visible in the upper part of the top heading. Fortunately, no casualties occurred during face

Figure 12. Damaged LG, Forepoles, Wire Meshes at RD 20m.

instability (Figure 12). The relieving outcome was that the instruments installed in initial 20 m, showed very little deformation results and were in permissible limits. However, the overbreak extended further beyond 22 m (Ch:1722) ie. RD 20m to RD 42m in increasing chainage and complete daylighting of tunnel at the mid-section occurred which can be seen in Figure 13 below.

Figure 13. Complete Daylighting of Tunnel b/w Ch:1700 - Ch:1722.

5.3 *Recommendations for treatment*

- For different reasons no work was carried out to stabilize till it was confirmed no further movement is observed for two days, luckily no further rain occurred at site location. As the track centre between two tunnels was nearly in the range of 25-28 m in this section it was decided to excavate the muck at 60-degrees with temporary slope stability arrangement of 50 mm shotcrete and one layer wire mesh (150x150x6) at required patches so that lateral cover to existing tunnel is not breached. Continuous monitoring of existing tunnel was being done and results were within permissible deformations and showed settling trends. The upper slope and the adjacent slopes were temporary contoured in such a way for efficient discharge of water. Also, relief holes were proposed in slope walls for dissipation of water pressures.
- The portion looked like a discontinuous tunnel section, for which a proposal for Cut & cover box was planned in the mid portion to reinstate the ground and to ensure continuity between initial length of tunnel with the remaining leftover length. The temporary slopes stabilized during muck removal were although provided temporary support arrangements, but due to the region experiencing high intensity rainfalls, the location was vulnerable for future failures, so to provide a box structure and to reinstate the ground conditions above it was the prime goal to cater the situation. However, there were major problem in providing cut & cover box firstly limited site conditions due to muck disposal hill on both sides of existing tunnel. Also, Gantry machine fixing for outer and inner lining for cut & cover box was not possible in the mid tunnel location due to non-availability of horizontal clearance for mobilization of gantry machine. Additionally, the contract under execution is item rate contract, so additional quantities of cut & cover box would have led to deviation in contract, so the proposal need to be made so that the provided quantity for the 20 m section could be utilized for minimum variation and optimization of project quantities.

Figure 14. Synoptic view of NATM, Open Damaged portion of T-1.

Solution Proposed

Therefore, a proposal was made keeping in view the above points by providing a support arrangement of lattice girder at 1m spacing centre to centre with base plates and wire mesh encircling the lattice upper portion tied with tie rods. The wire mesh was fixed to bent down fore poling and existing wire mesh. Galvanized iron sheet was placed as outer shuttering and shotcrete M25 was shot from inside so to provide a tunnel profile up to 150 mm thickness (50mm +100mm) in two layers. This thickness was provided to counter any possibility of shortcomings during operation and to ensure the inner profile of gantry to meet at the time of secondary lining throughout the chainages. Refer Figure 15 at next page.

Furthermore, Support Class V was assumed at this length, however with this scheme saved an additional layer of wire.

mesh, lattice girder nos., shotcrete thickness, rock bolts 6m lengths (1000no.s).

Figure 15. LG, Wire mesh & GI sheets for outer shuttering of Gantry.

- The outer face of the cut & cover was wrapped in water proofing membrane 2mm thick and tunnel excavation material from support class 5 was backfilled on the cut & cover location contoured in such a way that the natural ground conditions, water channel routes are reinstated to original.
- Furthermore, after due removal of muck from the mid portion which took nearly 40 days, false portal was made at Ch:1720 and further working for Tunnel -1 was commenced as competent rock mass was encountered as can be seen in Figure 16 and probe holes confirmed the same. An average round length of 3-4 m was with minimum support requirement as predicted in pre-construction phase.

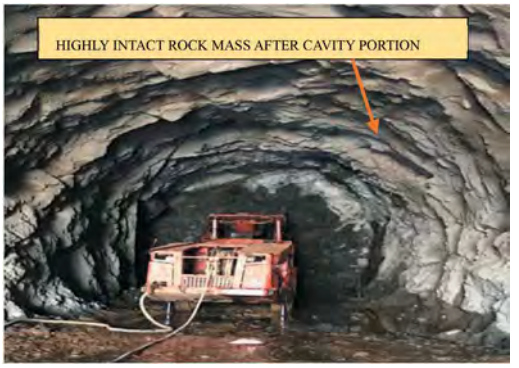

Figure 16. Highly competent rockmass at & beyond Ch:1720 (T-1).

6 CONCLUSION

The parallel doubling project in Indian Railways is a major initiative to increase the capacity and efficiency of the country's rail network.

Here are some of the benefits of the parallel doubling project:

- Increased capacity: The project will double the capacity of the affected rail lines, allowing for more trains to run simultaneously.
- Utilization of available land boundaries in extent of existing railways alignment leading to reduction in menace in comparison to new land proposal plans.
- Reduced congestion: The project will help to reduce congestion on both freight and passenger lines, improving the efficiency of the rail network.
- Improved travel experience: The project will improve the travel experience for passengers by reducing overcrowding and delays.
- Boosted economy: The project will help to boost the Indian economy by making freight transportation more efficient and reducing transit times.

However, the only disadvantage and the most challenging work is that the working operation of existing tunnel gets impacted and existing structures needs to be monitored closely for any deformation due to parallel construction activities. Due planning for alignment is mandatory for any project and criteria mentioned in this paper are recommended to be followed. Furthermore, it must be practiced that a comprehensive detailed study of borehole investigation along with geological mapping and geophysical surveys and results must be correlated as whole which is mandatory. For instance, a patch of T-1 with complete loose rock mass and soon after 15-20 m, excellent quality granitic gneiss occurred for them or extend of remaining tunnel. The challenges encountered during the planning and construction of this project are poor geology, less overburden, rainfalls & water ingress, steepest alignment cavity overbreak, and parallel tunnel Accordingly, the railway team, PMC as well as the construction team, had managed well. The planning, design, and construction process adopted for this section will be helpful for future tunnelling in the parallel tunnelling projects (Doubling) for railways.

REFERENCES

i. Railway board, Ministry of Railways, 2020. Indian railway permanent way manual. Indian Railways Institute of Civil Engineering, Pune.
ii. Rao, A. B., 2002. An engineering feat- construction of Koraput- Rayagada new railway line. Bhubaneshwar: SE Railway.
iii. Stresses In Rock About Cavities by Karl Terzaghi and F.E. Richart, Jr.
iv. Railway Tunnels November 2018: Indian Railways Institute of Civil Engineering, Pune.
v. Detailed Project Report of Boddavara-Karakavalasa section East Coast Railway, RITES Limited
vi. Mindlin, R. D., 1940. Stress distribution around a tunnel. *Trans. Am. Sot. Civ. Engs*. 105: 1117–l 140.

Tunnelling for a Better Life – Yan, Celestino, Thewes & Eberhardt (Eds)
© 2024 The Author(s), ISBN 978-1-032-80042-4
Open Access: www.taylorfrancis.com, CC BY-NC-ND 4.0 license

Comparison of carbon footprint emissions in tunneling projects using innovative methods

Pegah Jarast & Verya Nasri*
AECOM, New York, USA

ABSTRACT: Climate change has long been one of the global issues related to energy consumption, and greenhouse gas emissions caused concern. Construction industry is a big contributor to carbon footprint emissions. In U.S., the construction processes generate the third highest greenhouse gas (GHG) emissions among industrial sectors. Hence, construction organizations need to manage and mitigate their carbon-related risks in the carbon-constrained future. The carbon footprint emissions in the construction stage are mainly from the raw materials supply, transport, and the construction activities. Among various construction processes, tunnel construction results in a significant amount of carbon emissions since almost all tunnels are lined with concrete materials and they utilize various types of high energy-consuming equipment for excavation. In order to identify and mitigate carbon emissions in tunneling projects, it is required to reliably estimate carbon footprints of all materials and construction activities in these projects. Improvements in reducing the carbon emissions in a tunnel project comes in three forms- improvement in equipment, replacement of materials or changes in the design. Improvement in equipment means developing non-fossil fuel powered vehicles for mined tunnels. The substitution of components such as cement replacements, fibers or GFRP rock bolts and new design concepts such as permanent sprayed concrete linings or Composite Shell Linings (CSL). The purpose of this paper is to evaluate carbon footprint emissions of different tunneling construction method and reviewing the state-of-the-art in terms of carbon costing for tunnel projects before going on to illustrate the potential benefits of these innovations as well as highlighting successful projects using them. Total saving in CO2 emission of a tunnel project is calculated in order to have a better comparison of the impact of each of these improvements.

Keywords: Tunnelling, Carbon footprint, GHG, Greenhouse gases, Life cycle assessment, LCA, Lining, concrete mixture, TBM

1 INTRODUCTION

Carbon footprint analysis is becoming more and more popular in every industry due to increasing concerns about global warming and greenhouse gas (GHG) emissions. The construction industry is a major producer of CO2 emission. Huang et al (2018) reported that in 2009, the total CO2 emission of the global construction sector (which includes building and infrastructures) was 5.7 billion tons, contributing 23% of the total CO2 emissions produced by global economic activities. In the U.S., the construction processes generate the third highest greenhouse gas (GHG) emissions among industrial sectors. It is therefore important that this sector significantly reduces its consumption of energy and materials. One of the most relevant activities within this sector is tunneling construction. The significant impact of the construction industry largely arises from the embodied carbon in the primary construction materials – cement and steel and utilizing various types of high energy-consuming equipment. Improvements in reducing the carbon emissions in a tunnel project come in three forms: improvement in equipment, replacement of materials, or changes in the design. Improvement in equipment is materialized by developing non-fossil fuel-powered vehicles for mined tunnels. Replacement of material comprises cement replacements and using supplementary cementitious materials, use of fibers instead of rebar, or GFRP rock bolts instead of steel rock bolts, while new design concepts can include changing the design from cast-in-place lining to permanent shotcrete lining, reducing lining thickness or any design strategy to lower material consumption. In addition, to achieve a comprehensive understanding of whole-life carbon of a tunnel project, the induced carbon during Use & Maintenance stage of the tunnel and improvements in reducing the carbon emissions in this stage should be analysed.

*Corresponding author: Verya.Nasri@aecom.com

DOI: 10.1201/9781003495505-9

This paper starts by reviewing the state-of-the-art methods for estimating carbon emission in tunnel projects before going on to illustrate the potential benefits of these innovations highlighting successful projects. Total savings in CO2 emission of a tunnel project is calculated to compare the impact of different improvement strategies.

2 METHODS OF CARBON EMISSION REDUCTION

2.1 *Design optimization*

Innovative design and techniques can significantly reduce the carbon footprint of tunnels. However, introducing new and not universally accepted concepts always face client resistance due to the absence of established design codes and production standards, and limited data on their performance.

As previously explained the main source of carbon emission is material (cement and steel). Thus, minimizing the use of materials for temporary support (which accounts for 35 % of the total carbon footprint) in favor of using them for permanent support is the key step of a sustainable design.

In traditional design, the tunnel lining consists of a temporary lining and a cast in-place secondary lining installed later as the permanent lining. Steel mesh is used as reinforcement. This is known as the Double Shell Lining approach (DSL) (Thomas 2019b). Figure 1 shows the detail of traditional lining.

Permanent Sprayed Concrete Linings (PSCL) have increasingly been used in recent years in which all the concrete sprayed is considered part of the permanent works. The lining consists of several passes of sprayed fiber-reinforced shotcrete, sometimes with a spray applied waterproofing membrane (SAWM) sandwiched in between. ITAtech has produced a report on Sprayed Applied Waterproofing Membranes, explaining the technology, its merits, and its weaknesses, and presenting case studies (ITAtech 2013). Figure 2 shows the detail of the PSCL lining.

2.2 *Carbon reduction through materials*

Research shows that more than 80 % of the CO2 emissions in the construction phase of a tunnel are attributable to construction materials (cement and steel). Thus, reducing the need for cement and steel can make a significant contribution to reducing CO2 emissions. In some cases, this comes along with a reduction in construction costs.

2.2.1 *Reduction of portland cement using supplementary*

Cementitious Materials

90 % of CO2 emission of conventional concrete mixtures comes from the Ordinary Portland Cement (OPC). Therefore, we can control a very large portion of our CO2 emission issues in concrete by paying attention to the amount of cement, the type of cement, and the amount and the type of Supplementary Cementitious Materials (SCM) which can replace OPC.The CO2 emission of a material can be calculated using the following formula:

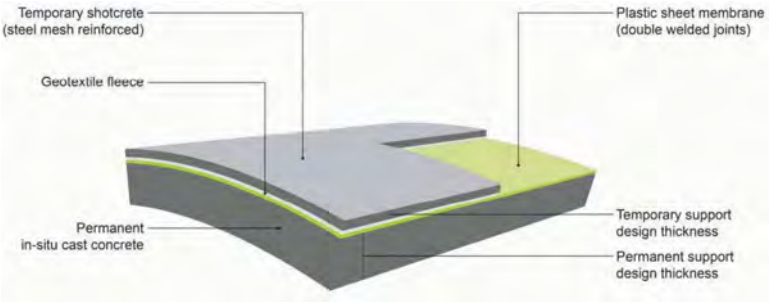

Figure 1. Traditional lining design.

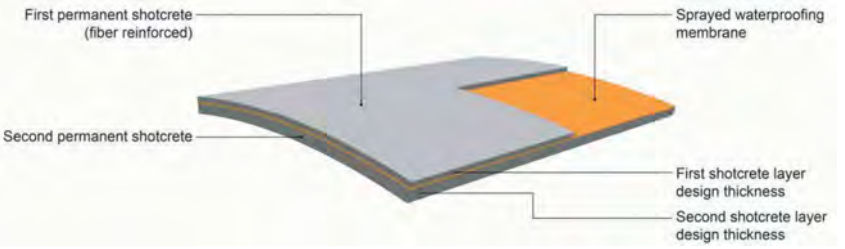

Figure 2. Optimized lining design.

Mass of CO2eq = CO2eq Factor × Material quantities (1)

where CO2eq factor is the amount of equivalent CO2 per pound or kg of material which is obtained from Environmental Product Declarations (EPDs).

Table 1 shows the CO2 eq factor for different types of cement and SCMs. As shown in Table 2 using Portland Lime Cement (PLC) instead of Ordinary Portland Cement reduces the CO2 emission by 7 % while using high SCM mixtures can reduce the CO2 emission by 45 %. A mixture is considered high SCM when: slag is greater than 50 % of total cementitious materials; or when fly ash is greater than 30 % of total cementitious materials; or when slag is greater than 40 % and fly ash is greater than 20 % of total cementitious materials. High levels of cement replacement by SCMs can result in lowering the early strength of concrete. High early-strength concrete is required for stripping segments from the formwork. For example in precast segmental tunnel linings, 13-15 MPa compressive strength is often required within 5-6 hours of casting for a safe stripping procedure. This is the focal point of today's industry research, and so far, the only solution has been using of Alkali-Activated Binders (AABs) produced with sodium carbonate. The concern with the use of AAB is the risk of the alkali-silica reaction (ASR) and long-term durability issues.

Table 1. CO2eq factor for different types of cement and SCMs.

Cementitious Materials	CO_2eq Factor
Ordinary Portland Cement (OPC)	0.92
Portland Limestone Cement	0.85
Ground Granulated Blast-Furnace Slag	0.15
Fly Ash	0.0093
Silica Fume	0.014

2.2.2 *Using steel fiber reinforcement instead of steel rebar*

Steel fiber reinforcement can significantly reduce the embodied carbon in tunnel linings, compared to rebar. Rebar mass in unit concrete volume of tunnel segments, for example, ranges between 90 to 160 kg/m3. Using Equation (1) and considering the CO2eq factor of 1.85 for steel, the carbon emission of rebar is about 166.5 to 296 kg/m3. In comparison, the steel fiber mass in unit concrete volume (fiber content) of tunnel segments is often 40 kg/ m3 or less. Considering the CO2eq factor of steel fiber is 0.88, carbon emission of fiber reinforcement in concrete segments is calculated as 35.2 kg/m3. This results in a 5 to 8 times reduction in CO2 emission when rebar is replaced by steel fiber.

2.2.3 *Optimizing aggregate gradation*

Traditionally, aggregates are designed according to ASTM standards based on coarseness factor charts which can be unreliable at times. Tarantula Curve (Taylor 2015) is a new and effective tool that was developed based on all workability tests including slump, the box test, ICAR Rheometer, visual observation, and float test. This helps optimize the aggregate amount in the concrete mixture and thus reduce the cement paste volume (total cementitious content and water). The carbon emission due to aggregate optimization can be reduced by up to 14 % because of the optimized use of cementitious paste.

2.3 *Improvements in equipment*

The impact of the operation of construction machinery (carbon emission from fuel and electricity) is relatively small compared to the main sources of carbon emissions of tunnels which are construction materials (concrete and steel). However, for highly mechanized tunnel projects the carbon emission of construction equipment is still significant because of the size of tunneling projects.

Construction sites are ideal for alternative fuels since the vehicles do not have to travel far from the refuelling sources. CO2 emission reduction by alternative fuel vehicles also causes a reduction in the demand for ventilation. However, it presents different fire hazards compared to fossil fuel vehicles.

Great improvements have been made in this area by equipment manufacturers. For example, Normet unveiled in 2019 a battery-powered spraying robot as part of its SMARTDRIVE electric vehicle range. Nasta in Norway has teamed up with Hitachi, Siemens, and Sintef to look at hydrogen fuel cell-powered excavators. Epiroc and Volvo have launched ranges of electrically powered drill rigs, loaders, and trucks while mining. In Norway, Stattnett is building the first "fossil (fuel) free" tunnel, a 4 km cable tunnel northeast of Oslo (Thomas, 2019a).

Moreover, the optimization of consumption time, controlling the direction and flow of the energy stream and timely shutting down the extra internal combustion engine drives in the system is also important methods to control CO2 emissions (Song and Xia, 2022).

There are two common sources of emission for equipment; the diesel fuel consumed to move in and out of the tunnel in every cycle and the electricity consumed by the equipment during operation. Explosives which may be used during the drilling and blasting advancing method is another source of CO2 emission.

To have an idea, the accumulated quantity of CO2 emission due to the articulated trucks used to remove the rock from a tunnel is presented in Figure 3 (Rodriguez, R. 2020). The tunnel taken as a reference is a double tube tunnel in Northwest of Spain with a slope of about 1% upwards. The depth was 125 m in average.

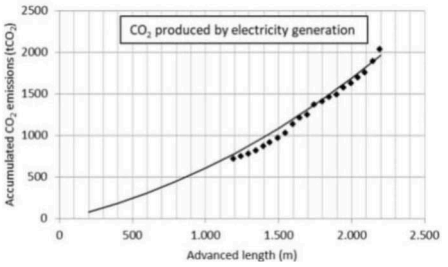

Figure 3. CO2 produced by muck pile transportation [Rodríguez et al., 2020].

To have an idea, the accumulated quantity of CO2 emission by the mobile electric generators used in the reference tunnel is presented in Figure 4 (Rodriguez, R. 2021).

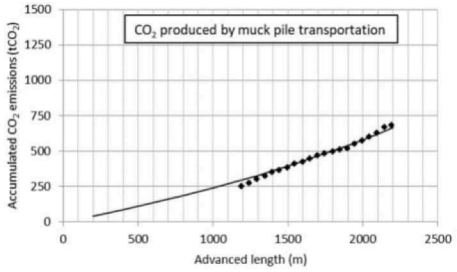

Figure 4. CO2 produced by electric generators [Rodríguez et al., 2020].

Various types of TBMs have specific power requirements. Table 4 shows the total cutter head power for different TBM diameters. The CO2 per kWh for electric power packs using hydraulic motor depends on the area and it changes between 106 and 750 grams of CO2 per kWh (EIA, 2017).

Table 2. Total Power of TBM for Different Tunnel Diameter [Adapted from Robbins, 2017].

No.	Tunnel Diameter	Cutter Head Power	Total Power
1	11.5 ft	1,340 kW (1,836 hp)	2,010 kW
2	13 ft	2,100 kW (2,816 hp)	3,200 kW
3	14.1 ft	2,345 kW (3,143 hp)	3,517 kW
4	14.1 ft	960 kW (214.5 hp)	1,440 kW
5	15.1 ft	1,260 kW (1,690 hp)	1,890 kW
6	15.8 ft	2,275 kW (3,050 hp)	3,413 kW

As an example, assuming TBM has an average production rate of 100 ft per 20-hour shift to allow 4 hours for maintenance and total CO2 emission for 100 ft advancement of a 13 ft tunnel can be calculated as following:

$$3200\ kW \times (106 - 750)\ grCO2/kWh \times 20\ hr/100ft = 6{,}780 - 48{,}000\ kg.CO2/100ft = 222 - 1575\ kg\ CO2/m$$

2.4 *Reduction of operational carbon*

Tunnels are energy intensive pieces of infrastructure once they are in operation. They require continual maintenance, periodic major refurbishments and upgrades, while lighting, ventilation and a multitude of additional systems use energy 24 hours a day. Operational Carbon is simply the carbon that is used during operation of the tunnel (i.e. when it is built).

It is clear that the energy used in the life of a tunnel is dependent of how well it is designed and built and then how well it is operated. But they are not mutually exclusive activities and to a great extent the ability of an operator to manage his assets energy consumption efficiently is governed by the quality of the product with which he is supplied.

Figure 5 shows the GHG emissions of different stages (processes) in 100 years. The 4-km long Chinese double-track four-lane highway tunnel emits around 375.5 thousand tons of CO2 eq. The tunnel ventilation and lighting at operation stage plays a leading role in the life cycle which shares a proportion of 56.12% of the total emissions. The maintenance stage contributes about 12.99% of the emissions while the construction stage is responsible for 30.89% of the GHG emissions. The three processes with the highest GHG emissions at construction stage are casting & lining (27.25%), rock support (25.33%) and road work (22.03%). Moreover, tunneling and waterproof & drainage process are responsible for 8.54% and 8.47% of the GHG emission at construction stage. A similar case of GHG emission ratio over its whole life cycle is the Swedish Norra Lanken Tunnel, whose GHG emission contributions are 36% (construction stage), 56% (operation stage) and 8% (maintenance stage) (Miliutenko et al., 2012).

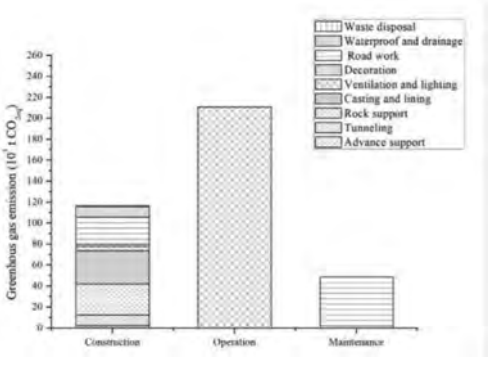

Figure 5. GHG emissions in different stages (processes) of the tunnel [Guo et al. 2019].

3 CASE STUDY

Montreal Blue Line Extension (PLB) project consists of five stations and a 9.3 m diameter TBM tunnel.

The tunnel is approximately 6 km long. The tunnel is 15 m deep on average and will be excavated through the rock. The baseline design included temporary shotcrete as initial support and a section with Cast in Place (CIP) concrete using Ordinary Portland Cement (OPC) concrete mixture as the final lining.

Figure 6 shows the geometry of the final lining of the baseline design. Table 3 presents the mixture design for temporary shotcrete, CIP arc, and CIP invert slab.

To reduce carbon emissions, an alternative case was suggested (Jarast et al, 2023). In this case, while a similar internal geometry was assumed, CIP lining was replaced with a thin low-carbon permanent shotcrete lining which acts as both initial support and final lining.

Figure 7 shows the geometry of the section for this case. In this design, 27 % of the cementitious material was replaced by slag and silica fume (22 % slag and 5 % silica fume which is considered a moderate SCM mix). Table 4 presents this shotcrete mixture design. Using Formula 1 presented in section 2.2.1, the embodied carbon footprint for the unit volume of baseline concrete mixture and low-carbon shotcrete mixture can be calculated. Table 5 and Table 6 summarizes the detail of CO2 emission calculation for the baseline design and low carbon shotcrete design, respectively. The quantities of materials are picked from Table 3 and Table 4.

Based on the geometry of the tunnel presented in Figure 6 and Figure 7, the volume of shotcrete, and the invert slab per 1m of the tunnel can be calculated. Having these quantities together with the information presented in Table 5 and Table 6, the total CO2 emission per 1 m length of the tunnel can be estimated. Table 7 and Table 8 summarizes this calculation.

4 CONCLUSION

This paper presents the state-of-the-art methods in terms of carbon costing for tunnel projects and

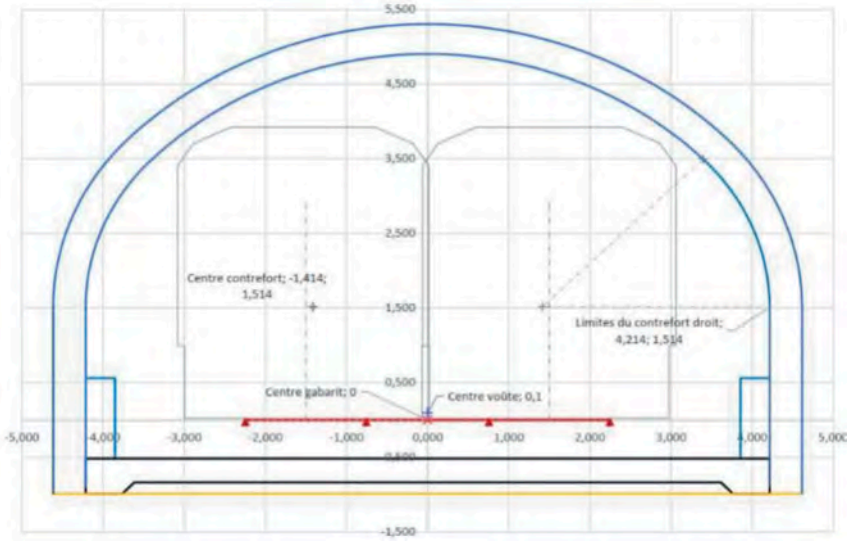

Figure 6. Tunnel geometry-low carbon design.

Table 3. Low carbon shotcrete mixture design.

	Cementitious material (kg/m³)	Portland Cement (kg/m³)	Aggregate (kg/m³)	Water/ Cement	Rebar (kg/m³)	Fiber- (kg/m³)	Admixtures (kg/m³)	Total (kg/m³)
Temporary shotcrete	475	475	1430	0.38	-	20	4.5	2108
CIP arc	415	415	1800	0.41	62	-	3.94	2451
Invert	415	415	1786	0.41	76	-	3.94	2451

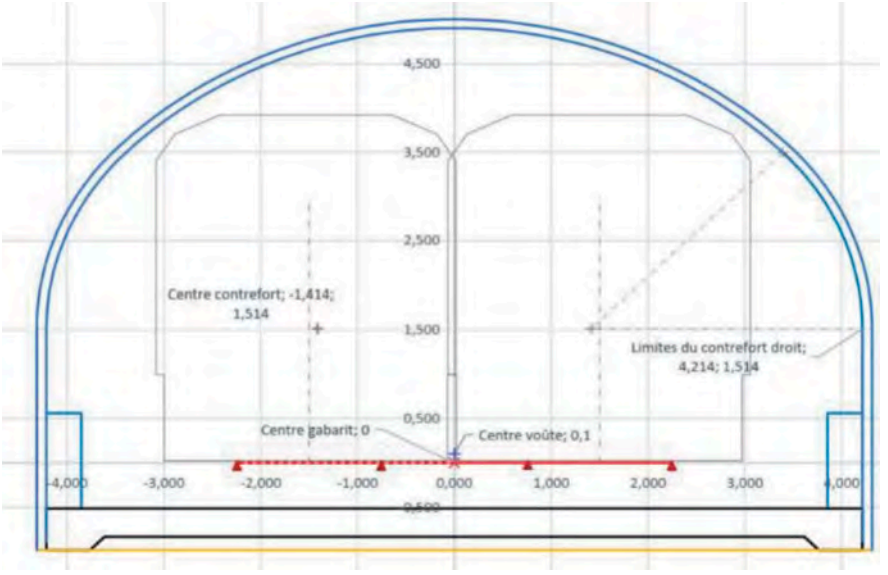

Figure 7. Tunnel geometry-low carbon design.

Table 4. Low carbon shotcrete mixture design.

	Portland Cement (kg/m^3)	Slag (kg/m3)	Silica Fume (kg/m^3)	Aggregate (kg/m^3)	Water/ Binder	Rebar (kg/m^3)	Fiber-Dramix 3D 65/35BG (kg/m^3)	Admixtures (kg/m^3)	Total (kg/m^3)
Shotcrete-SCM	346.75	104.5	23.75	1430	0.38	-	40	4.51	2129

Table 5. CO2 emission of baseline design.

		Temporary shotcrete		Arch concrete		Invert concrete	
Components	CO_2 eq Factor	Mass/m^3 (kg)	CO_2 eq/m^3 (kg)	Mass/m^3 (kg)	CO_2 eq/m^3 (kg)	Mass/m^3 (kg)	CO_2 eq/m^3 (kg)
Ordinary Portland Cement (OPC)	0.92	475	437	415	382	415	368
Admixtures	1.67	4.5	7.5	3.94	6.6	3.94	6.3
Aggregate	0.006	1430	8.6	1800		1786	
Steel bar	1.85	-	-	62	114.7	76	140.6
Fiber	0.86	20	17.2	-	-	-	-
		Total:	470.3		513.9		539.7

illustrates the potential benefits of these innovations as well as highlighting successful projects using them.

Considering the scale of tunnel projects, this reduction in CO2 emission is significant and should not be ignored or underestimated. The steps toward improving sustainability include using electrically powered vehicles in the tunnel, using cement replacements in concrete to the maximum extent possible, using fiber reinforcement instead of steel

Table 6. CO2 emission of low carbon design.

		Arch-Shotcrete- SCM		
Components	CO_2 eq Factor	Mass/m^3 (kg)	CO_2 eq/m^3 (kg)	% Replacement by mass
Ordinary Portland Cement (OPC)	0.85	346.75	295	
Ground Granulated Blast-Furnace Slag	0.1466	104.5	15	22%
Fly Ash	0.093	0.0	-	0%
Silica Fume	0.014	23.75	0.3	5%
Admixtures	1.67	4.51	7.5	1%
Aggregate	0.006	1430	8.6	
Steel bar	1.85	-	-	
Fiber-3D 65/35BG	0.86	40	34.4	
	Total		361	

Table 7. Total embodied carbon footprint per 1 m length of the tunnel- Baseline design.

	Thickness (mm)	Volume (m^3) /1m tunnel	CO_2 eq/m^3 (kg)	CO_2 eq/1 m length (ton)
Temporary shotcrete*	325	5.9	470.3	2.8
CIP arc concrete	400	7.03	513.9	3.61
Invert concrete	320	2.854	539.7	1.54
			Total =	7.9

Table 8. Total embodied carbon footprint per 1 m length of the tunnel- Low carbon design.

	Thickness (mm)	Volume (m^3) /1m tunnel	CO_2 eq/m^3 (kg)	CO_2 eq/1 m length (ton)
Permanent Shotcrete Lining*	160	1.8	361	0.65
Invert Concrete	32	2.854	361	1.03
			Total =	1.68

reinforcement, and implementing new design methods such as replacing the conventional design with temporary shotcrete and CIP final lining with a thin permanent shotcrete lining design.

REFERENCES

Cardu, M., Seccatore, J., 2016. Quantifying the difficulty of tunnelling by drilling and blasting. Tunn. Undergr. Space Technol. 60 (2016), 178–182.

Cho, S.; Chae, C. 2016, A study on life cycle CO2 emissions of low-carbon building in South Korea. Sustainability, 8, 579.

Chun Guo, Jianfeng Xu, Lu Yang, Xiong Guo, Jixuan Liao, Xin Zheng, Zhenhua Zhang, Xiaofeng Chen, Kun Yang, Mingnian Wang, 2019. Life cycle evaluation of greenhouse gas emissions of a highway tunnel: A case study in China, Journal of Cleaner Production, Volume 211, Pages 972–980, ISSN 0959-6526, 10.1016/j.jclepro.2018.11.249.

EIA (2017), U.S. Energy Information Administration, available at:https://www.eia.gov/tools/faqs/faq.cfm?id=74&t=11, (Jan 10, 2017)

Fremo, O., 2015. Life Cycle Assessment of the Byasen tunnel in Trondheim, Norway. Master Thesis. Norwegian University of Science and Technology, Department of civil and transport engineering. Trodheim (Norway), 103pp.

Jarast, P., Bakhshi, M., Nasri V., 2023. Carbon footprint reduction in Montreal Blue Line Extension, Rapid Excavation & Tunneling Conference (RETC) 2023, Boston (USA), 580–588.

Jarast, P., Bakhshi, M., Nasri V., 2023. Carbon footprint emissions of different tunneling construction methods. World Tunnel Congress (WTC) 2023, Athens (Greek), 65–73.

Huang, L., Bohne, R., Bruland, A., Drevland, P., Salomonsen, A., 2013. Life Cycle Assessment of

Norwegian standard road tunnel. In: The 6th International Conference on Life Cycle Management in Gothenburg.

Huang, L., Drevland, P., Bohne, R., Liu, Y., Bruland, A., Manquehual, C.J., 2020. The environmental impact of rock support for road tunnels: The experience of Norway. Sci. Total Environ. 712, 136421.

Huang, L., Krigsvoll, G., Johansen, F., Liu, Y., Zhang, X., 2018. Carbon emission of global construction sector. Renew. Sustain. Energy Rev. 81(Part 2) pp.1906–1916.

ITAtech 2013. Design guideline for spray applied waterproofing membranes, ITAtec

Lee, J., Shim, J.A., Kim, K.J., 2016. Analysis of environmental load by work classification for NATM tunnels. J. Korean Soc. Civ. Eng. 36 (2), 307–315.

Li, X., Liu, J., Xu, H., Zhong, P., 2011. Calculation of endogenous carbon dioxide emission during highway tunnel construction: A case Study. International Symposium on Water Resource and Environmental Protection, May 2011, Xian (China), pp. 2260–2264.

Lovat, R. (2017). "TBM Design Consideration: Selection of Earth Pressure balance or Slurry Pressure balance Tunnel Boring Machines."

Maxam, 2015. "Riodin technical brochure", Maxam Europe S.A., Madrid (www.maxam.net).

Miliutenko, S., Akerman, J., Bjorklund, A., 2012. Energy use and greenhouse gas emissions during the Life Cycle stages of a road tunnel - the Swedish case norra lanken. Eur. J. Trans. Infrastruct. Res. 12 (1), 39–62.

Rodríguez, R., Tosal, A., P´erez, F., Díaz-Aguado, M.B., 2017. Advancing rate and carbon footprint related to different excavation methods in conventional tunnelling (Fabares tunnel, Asturias, Spain). International Conference on NexGen Technoclogies for Mining and Fuel Industries 2017 (NxGnMiFu 2017). February 15-17, 2017, Vigyan Bhawan, New Delhi, India.

Rodríguez, Rafael & Pérez, Fernando. (2020). Carbon foot print evaluation in tunneling construction using conventional methods. Tunnelling and Underground Space Technology. 108. 103704. 10.1016/j.tust.2020.103704.

Shillaber, C., Mitchell, J., Dove, J., 2016b. Energy and Carbon Assessment of Ground Improvement Works. 2016 II: Working model and example. J. Geotech. Geoenviron. Eng. 142 (3) pp. 04015083-1 –04015083-9.

Song, Z., Xia, Z., 2022. Carbon Emission Reduction of Tunnel Construction Machinery System Based on Self-Organizing Map-Global Particle Swarm Optimization With Multiple Weight Varying Models. IEEE Access. 10. 1–1. 10.1109/ACCESS.2022.3173735.

Taylor, P., 2015. Blended aggregates for concrete mixture optimization, The Report of Federal Highway Administration, FHWA, Washington DC, USA, 2015.

Tavakoli, Razieh & Najafi, Mohammad & Tabesh, Amir & Ashoori, Taha. (2017). Comparison of Carbon Footprint of Trenchless and Open-Cut Methods for Underground Freight Transportation. 45–55. 10.1061/9780784480892.005.

Thomas, Alun. 2019a. Achieving sustainability in underground construction through innovation. Proceedings of the Institution of Civil Engineers - Civil Engineering. 173. 1–26. 10.1680/jcien.19.00018.

Thomas, A.H. 2019b. Sprayed concrete lined tunnels. CRC Press, Boca Raton, USA, ISBN: 9780367209759 -www.crcpress.com

Xu, J., Guo, C., Chen, X., Zhang, Z., Yang, L., Wang, M., Yang, K., 2019. Emission transition of greenhouse gases with the surrounding rock weakened – A case study of tunnel construction. J. Cleaner Prod. 209, 169–179.

Xu, J., Guo, C., Chen, X., Zhang, Z., Yang, L., Wang, M., Yang, K., 2019. Emission transition of greenhouse gases with the surrounding rock weakened – A case study of tunnel construction. J. Cleaner Prod. 209, 169–179.

Tunnelling for a Better Life – Yan, Celestino, Thewes & Eberhardt (Eds)
© 2024 The Author(s), ISBN 978-1-032-80042-4
Open Access: www.taylorfrancis.com, CC BY-NC-ND 4.0 license

Collaboration in Moscow Metro development: Analysis of joint construction efforts by Russian and Chinese builders

V.P. Kivlyuk, A.I. Paschenko & D.S. Konyukhov*
JSC «Mosinzhproekt», Moscow, Russia

Liqiang Xue, Jimin Zhou, S.N. Vinogradov, K.V. Orlov, Yangchun Song, Jiuyuan Huo, Yongfang Lyu, Zhiqiang Gu & Ting Wang
CRCC Rus, Moscow, Russia

ABSTRACT: Over the last 12 years the length of the Moscow Metro has grown 1.5 times. More than 200 km of new lines, 109 stations and 11 electric depots have been built. In March 2023, the Big Circle Line – the most ambitious project of the Russian Metro and the largest metro ring line in the world – was put into operation. Mosinzhproekt Joint Stock Company is the general designer and general contractor of the construction. Within the framework of the Agreement between the Government of the Russian Federation and the Government of the People's Republic of China on Encouragement and Mutual Protection of Capital Investments, the limited liability company 'CRCC Rus', a subsidiary of the Chinese railway construction corporation CRCC in the Russian Federation, is taking part in the construction of the Moscow Metro. For the construction of Moscow Metro facilities, the said Chinese company manufactured six tunnel boring mechanised complexes, five of them with a diameter of 6.25 m and one with a diameter of 10.8 m. These shields ensured sediment-free tunnelling in the difficult mining, geological and hydrogeological conditions of Moscow's dense urban development, including the use of unique measures to ensure safe completion of tunnelling operations: 11 tunnels of the South-Western and Eastern sections of the Big Circle Line under the operating stations Michurinsky Prospekt and Prospekt Vernadskogo, under the motorways Michurinsky Prospekt, Leninsky Prospekt, Prospekt Vernadskogo, under the railway tracks of the Kyiv direction, the Nagatinsky flood of the Moscow River, the Museum-Reserve 'Kolomenskoye'; 6 tunnels of the Kommunarskaya line, including one under main underground communications and city motorways - Moscow Ring Road and Kaluga Highway. The Chinese company built 5 metro stations in excavations up to 30 m deep in dense urban development. The report presents in detail the experience of joint work of Mosinzhproekt JSC and 'CRCC Rus' LLC on construction of underground transport infrastructure facilities in the city of Moscow.

Keywords: Tunnelling, TBM, Big Circle Line, Chinese metro builders, Metro construction, Moscow Metro, Russian metro builders

1 INTRODUCTION

The programme for the development of urban transport adopted by the Moscow government envisages intensive expansion of its underground component – the metro, the first line of which was put into operation on 15 May 1935 (Zertsalov, Konyukhov, Merkin, 2015; Neutatz, 2013; Naumov, Kusyy, 2006). Currently, the Moscow Metro consists of 14 lines with a total length of more than 460 km (in double-track) with 263 stations. It is among the world's leading metros in terms of construction rates and a number of operational indicators, for example, in terms of train frequency – during peak hours it is no more than 90 seconds, and on the Big Circle Line (the largest metro ring line in the world), which was commissioned in 2023, it is 80 seconds. Over the last 12 years, the Moscow Metro has been expanding at an unprecedented pace, with maximum involvement of scientific, technical, material and labour resources, with intensive application of the achievements of world metro construction. As a result, the length of the Moscow Metro has grown 1.5 times. More than 200 kilometres of new lines, 109 stations and 11 electric depots were built. The works are carried out in the shortest possible time and with high quality. A large-scale system of research and design, construction and installation and auxiliary organisations is involved. By 2027, according to the Moscow Government's plans

*Corresponding author: konuhovds@mosinzhproekt.ru

DOI: 10.1201/9781003495505-10

(Postanovlenie …, 2012), 25 more stations and 58 km of lines are to be built (Figure 1).

Figure 1. Moscow metro with development perspective up to 2027 (https://2023god.com/karta-metro-moskvy-v-2023-godu-novye-stancii/).

It is planned to extend the Sokolnicheskaya line southwards by 2.4 km and build another station – Potapovo. The extension of the Lublinsko-Dmitrovskaya line to Fiztech station and the Solntsevskaya line westwards to Vnukovo airport, near which the metro station of the same name will be located, has been completed. In 2024 it is expected to open a new line – Troitskaya. After 2023, the Arbatsko-Pokrovskaya line will be extended northwards to Golianovo station, and the Rublyovo-Arkhangelskaya and Biryulevskaya lines will be opened in stages.

2 METRO CONSTRUCTION IN THE PRC AND CRCC COMPANY

For a long time, the cooperation between Moscow metro builders and foreign ones was limited to exchange of experience, scientific and technical achievements, purchase of imported tunnel boring equipment, etc. In recent years, the scale and pace of metro construction in the capital have led to the involvement of foreign contracting organisations directly in construction works. Chinese metro builders were the first in this case, which is quite natural, given the achievements in this field, as well as the long-standing professional ties between Russian and Chinese metro builders, who have been cooperating since the very beginning of metro construction in China.

The pace at which subways are being built in the People's Republic of China shocks the world. The first underground in Beijing began construction three decades later than in Moscow, in 1965. Xue Liqiang, a representative of the CRCC, admits that it was the Moscow Metro that became a benchmark for them, and that their teachers were specialists from Russia. But here is the case when the student surpassed the teacher. If in 2006 the Chinese capital had 114 km of metro, in 2012 it had 442 km, and in 2015 – 708 km. By 2020, the goal was set to bring the length of the underground in Beijing to 1050 km. And this is only in one city! The length of the metro network in China exceeds 8.7 thousand kilometres. The Underground operates in 43 cities. The annual growth is substantial. An important role in its implementation is played by the Chinese railway construction corporation China Railway Construction Corporation Limited – CRCC (https://english.crcc.cn/). This mega-scale construction company, established in November 2007 in Beijing, is one of the most powerful and largest general construction groups in the world, operating not only within the PRC, but also in more than 130 countries and regions around the world, engaging in contracting, planning and design consultancy, etc., as well as in the construction industry. CRCC has a complete production chain including research, planning, survey, investigation, design, construction, supervision, operation, maintenance, investment and financing; playing a leading role in the design and construction of tunnels and urban railway transport in particular. It employs 267,000 professionals, operates four in-house design institutes, and has accumulated vast experience at home and abroad, recognised by many international professional awards and distinctions. CRCC has extensive experience with information modelling technologies. The company has developed high-quality and up-to-date software for these purposes.

3 MOSCOW METRO FACILITIES BUILT BY 'CRCC RUS'

Within the framework of the Agreement between the Government of the Russian Federation and the Government of the People's Republic of China on the Encouragement and Mutual Protection of Capital Investments, CRCC's subsidiary in the Russian Federation, CRCC Rus LLC (https://moscow.cataloxy.ru/firms/www.crcc.cn.htm), participates in the construction of the Moscow Metro. To date, 11 tunnels of the South-Western and Eastern sections of the Great Ring Line have been built in Moscow under the existing stations Michurinsky Prospekt and Prospekt Vernadskogo, under the motorways Michurinsky Prospekt, Leninsky Prospekt, Prospekt Vernadskogo, under the railway tracks of the Kyiv direction, Nagatinsky flood of the Moscow River, the Museum-Reserve 'Kolomenskoye'; 6 tunnels of the Kommunarskaya line, including one under main underground communications and city motorways – Moscow Ring Road and Kaluga Highway. The Chinese company built 5 metro stations in excavations up to 30 m deep in dense urban areas.

The participation of 'RCC Rus' in the construction of the largest project of Moscow metro builders – the Big Circle Line – occupies a special place. The tender was open, everyone could take part in it. The Chinese firm won. In January 2017, a contract was signed between Mosinzhproekt JSC and the Chinese company 'CRCC Rus', under which foreign specialists (mainly employees of the 16th CRCC department) built three stations of the Third Metro Interchange Loop – the Big Circle Line (BCL, 69 km, 31 stations and two electric depots) in Moscow. Chinese specialists were involved in the construction of the stations: Aminievskaya (including the crossing tunnels with tunnelling structures and dead ends behind the station), Michurinsky Prospekt and Prospekt Vernadskogo: a double-track tunnel from Nagatinsky Zaton station to Klenovy Boulevard and further – to the transition chamber, single-track tunnels towards Kashirskaya station. At the same time, 'CRCC Rus' is engaged only for the main construction (tunnelling works), while finishing and installation of equipment, engineering fills (installation and testing of traffic control systems and other precision transport systems) are the responsibility of Russian specialists.

The section from Prospekt Vernadskogo station to Aminievskaya station (including Michurinsky Prospekt station) of the Great Ring Line (Figure 2) is 4.63 km long.

Engineering and geological conditions of the construction site belong to the III (complex) category of complexity – geological processes are widespread and have a decisive impact on the choice of design solutions, construction and operation of facilities.

In geomorphological respect the site belongs mainly to Teplostanskaya upland, dissected by deep erosion valleys, gullies, ravines. The above-mentioned remnant-erosional upland has a pronounced stepped character, the lower stages are covered with fluvioglacial and lake-glacial sediments and, connecting with alluvial terraces, represent a plain, within which the northwestern part of the route section is located; the southeastern part of the route section is located on moraine hills within the middle stage of the upland. The natural gentle undulating accumulative relief of the fluvioglacial plain, in some places moraine, is technogenically modified, relatively planned by the existing development. The technogenic impact on the geological environment is manifested in the corresponding technogenic lithogenesis. As a result of landfilling of the territory, a layer of technogenic bulk soils was formed.

Figure 2. Route of the section between Prospekt Vernadskogo and Aminievskaya stations.

Quaternary soils are underlain by a sandy-clay layer of Mesozoic sediments. These sediments in the lower part of the section are represented by clayey rocks of the Middle and Upper Jurassic overlying Upper Carboniferous carbonate rocks. The upper part of the Jurassic sediments section is composed of clayey sands, in some places changing into strongly sandy clays. The Upper Jurassic sands are overlain everywhere by Cretaceous sediments, represented by sands easily liquefied under very low destructive stresses, often floating. Below are Upper Carboniferous sediments represented by clays and limestones.

Hydrogeological conditions are characterised by the spread of the Meso-Cenozoic sediments water-bearing complex represented by several horizons. Practically everywhere two, and in some areas – three aquifers are traced, confined to relatively well permeable sands in alluvial sediments and sandy interlayers in the Don-Moscow water-glacial sediments, forming a single first above-marine aquifer complex from the surface. Clayey moraine sediments serve as a relative aquifer.

The depth of groundwater occurrence of the first surface water-bearing complex in this area is 5-10 m, increasing up to 15 m in some places on the watershed slopes. At lower watersheds groundwater is revealed at a depth of 3-10 m from the surface, in local areas – even at a depth of up to 3 m. The amplitude of changes in groundwater levels is 2-4 m, and in some areas – more than 5 m, and is clearly manmade. Spreading of weakly permeable moraine and cover tuffs from the surface is very favourable for formation of water table, usually at the depth of 2-3 m.

The second supra-Jurassic aquifer complex is formed by aquifers confined to marine sands of Cretaceous and Jurassic age.

The aquifer complexes are hydraulically connected along the river valleys. Their static levels coincide near the valleys and differ at the watersheds, with the levels of the supra-Jurassic aquifer complex being 3-7 m lower. The depth of the level of the supra-Jurassic aquifer complex varies from 12 to 33.5 m. The sustained regional water table, represented by a thick mass of Jurassic clays, lies at a depth of 100 to 115 m, depending on the relief. Below it lies the Balkovsko-Podolskoye water-bearing complex. The water-bearing rocks are organogenic limestones with subordinate interlayers of clays, marls and dolomites. Absolute elevations of the roof of the Balkovsko-Podolsky aquifer are 90-80 m. The lower water table of the Balkovsko-Podolsky horizon is represented by Rostislavl clays and marls.

Thus, the geotechnical conditions are in general quite complicated, especially in connection with the adopted design and technological solutions.

All three mentioned stations are shallow-buried and were built in the excavation for two-track tunnels.

The Aminievskaya shallow-buried station is located as part of the south-western section of the BCL in the Ochakovo-Matveevskoye district of Moscow, at the intersection with the Kyiv direction of the Moscow railway. Depth of embedment is 15 m. The structural scheme is three-span, with two rows of columns and an island platform 163 m long and 12 m wide. The axis of the station is orientated parallel to the nearby Aminievskoe Highway. The station should provide pedestrian connections with the railway platform and through the underground passage – with the opposite side of Aminievskoe Highway (Figure 3).

Two underground concourses access both sides of Aminyevskoye Shosse to bus stops, residential neighbourhoods and public buildings.

The length of the crossing between Aminyevskaya and Michurinsky Prospekt stations is about 1,473 m. The tunnel route passes under the Kyiv direction of the Moscow railway, the Ochakovka River and Michurinsky Prospekt station of the Kalininsko-Solntsevskaya line of the Moscow Metro. Depth of embedment – 19.5-34.3 m.

The Prospekt Vernadskogo station (Figure 4) has a depth of 17.3 m. Engineering and geological conditions of the projected construction site belong to the III category of complexity. The structural scheme is three-span, with two rows of columns on a 12 m wide island platform. The station has four underground levels. In the central part of the platform there are stairs for transfer.

Michurinsky Prospekt station has a unique layout due to the complex topography of the site and the elevated transfer to the newly built Michurinsky Prospekt station of the Kalininsko-Solntsevskaya line. It is one of the deepest for shallow stations (depth of 19.4 m, 7 underground levels). The structural scheme is three-bay with two rows of columns on a 14 m wide island platform. The architectural solution realised in it is dedicated to the Russian-Chinese friendship.

Lifts were installed at all three stations – without them nowadays station complexes in Moscow are simply not built.

In addition to the described sections of the Moscow Metro, 'CRCC Rus' successfully completed the excavation of 9 tunnels with a diameter of 6.25 m of the South-West section of the Great Ring Line, including the application of unique measures to ensure safe completion of tunnelling works in the area of existing structures.

Work was carried out along the Kaluga Highway in Greater Moscow (Kommunarka district) Ulitsa Novatorov metro station – Stolbovo metro station on the section from Ulitsa Novatorov station to Kommunarka station (Figure 5), including in the area of existing city infrastructure facilities.

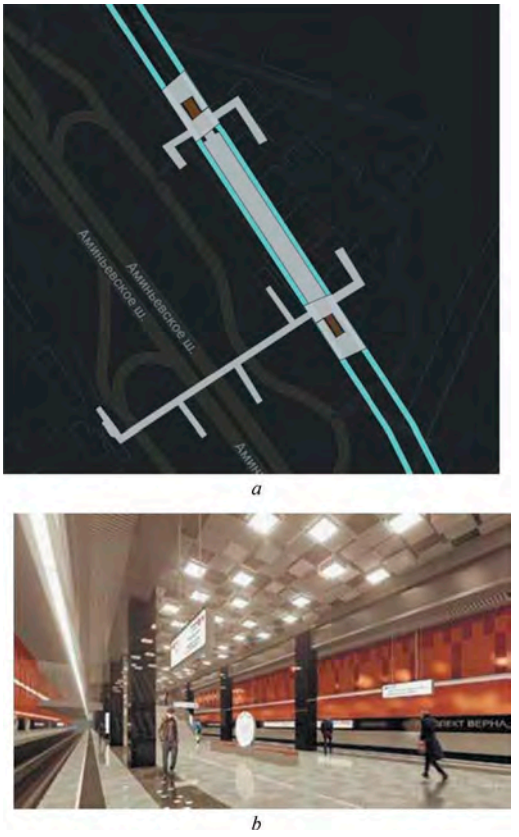

Figure 3. Aminyevskaya station of the BCL: a – location; b – interior of the station platform.

Figure 4. Prospekt Vernadskogo station of the BCL.

Complex works – bottomless tunnelling in difficult hydrogeological conditions under dense urban development (Mazein et al., 2019), under the Nagatinsky Zaton of the Moscow River, under the territory of the Kolomenskoye Reserve Museum – were carried out on the Eastern section of the BCL: metro sections between the stations Kashirskaya and Nizhegorodskaya, on the section from the Nagatinsky Zaton station to the Klenovy Boulevard station and further to site No. 2 (Figure 6). For the period of

tunnelling, geotechnical monitoring (Merkin et al., 2021) and scientific and technical support of construction (Konyukhov, 2022; Kulikova, Potapova, 2022) were organised.

Figure 5. Metro section between Ulitsa Novatorov and Kommunarka stations.

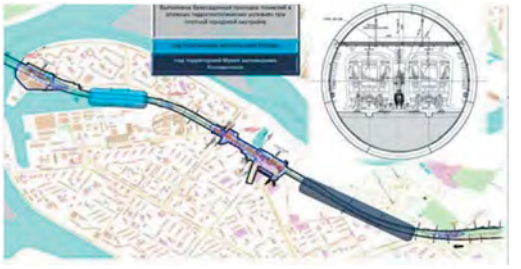

Figure 6. Eastern section of the BCL.

4 CHINESE BUILDING INDUSTRY BASE AND TUNNELLING EQUIPMENT AT MOSCOW METRO FACILITIES

In the Russian Federation, 'CRCC Rus' has set up in-house production of high-precision tunnel lining. For this purpose, 12 sets of tooling moulds for 6.0/5.4 m diameter lining and 4 sets of tooling moulds for 10.5/9.6 m diameter lining are used. More than 14,000 tunnel lining rings with a diameter of 6.0/5.4 m and 1,500 tunnel lining rings with a diameter of 10.5/9.6 m have been manufactured and installed (Figure 7).

For the construction of metro facilities in Moscow, the company 'CRCC Rus' manufactured in the PRC in accordance with the customer's specifications and delivered to Russia six TBMs: 6.25 m diameter – 5 units, 10.8 m diameter – 1 unit (Figure 8). The technical characteristics of the specified TBMs are as follows (data for 10.8 m diameter TBMs given in brackets): rotor diameter, m – 6.28 (10.8); diameter of TBM shell, m – 6.25 (10.84); length of TBM head part, m – 9.5 (11.4); total length of TBM, m – 87 (68); total weight, tonnes – 460 (1700); power, kW – 1750 (6000).

For transportation from China to Russia, the panel complexes were disaggregated into 14 and 40 elements for 6.25 m and 10.8 m diameter and 2 to 130 t and 5 to 180 t respectively.

Figure 7. Chinese-made high-precision tunnel lining blocks.

Figure 8. General view of the head part of the pobeda TBM.

In addition, CRCC delivered five ZOOMLION T8030-25U (https://cranemarket.com/specs/tower-cranes/zoomlion/t8030-25u) full-swing tower cranes with increased lifting capacity: maximum lifting capacity up to 25 t, maximum boom length 50 m, maximum crane height 45 m, as well as two grapple units for the construction of wall-in-ground enclosures.

Two TMPCs (ZTE6250 DZ399, name Eugenia; ZTE6250 DZ401, name Polina) are used for tunnelling the CRCC tunnels. A 10-metre long 10-metre long TBM (the name Pobeda as a symbol of the long-standing friendship between the two countries, based on mutual support and trust, as a reflection of our countries' contribution to the victory in World War II) was used to bore a 3-km tunnel on the BCL section between Nagatinsky Zaton and Klenovy Boulevard stations. Its design was carried out by Chinese colleagues according to the technical specifications developed by Mosinzhproekt specialists in accordance with the hydrogeological conditions at the construction site and taking into account the accumulated experience of

using 10-metre shields in Moscow. This is the third 10-metre TBM used in Moscow for the construction of double-track transport tunnels. This method of tunnelling makes it possible to avoid construction of tunnelling structures and ventilation shafts, respectively, without freeing up additional construction sites, which is very important, given that the line section passes near the Kolomenskoye Museum-Reserve.

The tunnels between Aminievskaya and Michurinsky Prospekt stations were tunnelled with the help of 6-metre TBMs Evgeniya and "Daria", from Aminievskaya station to site No. 6 located in front of Davydkovo station was tunnelled with the similar TBM Maria. The same Galina (ZTE6250DZ400) and Polina (Figure 9) traversed the tunnels between Prospekt Vernadskogo and Ulitsa Novatorov stations.

Figure 9. TBM Polina.

All of the above shields ensured non-sudden tunnelling in difficult mining, geological and hydrogeological conditions of dense urban development of Moscow, including the use of unique measures to ensure safe completion of tunnelling works.

In general, since 2017 'CRCC Rus' has carried out the following scope of works: tunnelling of tunnels with the use of 6.25 m diameter TBMs – 15 tunnels with a total length of 19800 m, the same with 10.8 m diameter – 2 tunnels (200 m), construction of the main structures of station complexes at 5 stations (225000 m3). In addition, 'CRCC Rus' carried out design works for the South-West section of Prospect Vernadskogo station – Kuntsevskaya station of BCL.

5 SCIENTIFIC AND TECHNICAL COOPERATION BETWEEN RUSSIAN AND CHINESE METRO BUILDERS

Interaction between Chinese and Russian metro construction specialists was not limited only to solving production tasks. The exchange of scientific and technical experience is of great value. From 15 to 18 November 2019, the 1st International Conference on Underground Space Research and Utilisation (EUUS2019, https://www.earthsciencematters.com/first-international-conference-on-the-exploitation-and-utilization-of-underground-space-euus2019-in-wuhan-china/) was held in Wuhan (PRC). This conference was organised by the Institute of Rock and Soil Mechanics, Chinese Academy of Sciences (IRSM-CAS) and the State Laboratory of Geomechanics and Geotechnical Engineering (SKLGME), with the participation of 30 research institutes and enterprises. The delegation of Mosinzhproekt JSC took part in the conference (Figure 10) with a report devoted to the analysis of the parameters determining the value of the soil overshoot coefficient during mechanised tunnelling (Konyukhov, Polyankin, 2019). Based on the analysis of engineering-geological and technological factors, the specialists of Mosinzhproekt JSC developed recommendations for determining the over-excavation factor depending on the type of soil and diameter of the TBM (Konyukhov, 2022; Kulikova et al., 2022).

Figure 10. The delegation of Mosinzhproekt JSC.

6 CONCLUSION

The experience of joint Russian and Chinese metro builders in laying new lines and constructing underground metro stations of the Moscow Metro has demonstrated the productivity and efficiency of such cooperation. A rational distribution of design and construction works has been worked out, taking into account the capabilities and experience of the parties. This opens up great prospects for further industrial cooperation. In particular, there are prospects for joint metro construction works in Africa, Asia and the Middle East.

A high social and economic effect has also been achieved directly in Moscow. For example, thanks to the launch of the new BCL Aminievskaya, Michurinskiy Prospekt and Prospekt Vernadskogo stations, local residents will be able to save up to 40 % of their daily travelling time in the city, the existing metro stations will be significantly relieved: Prospekt Vernadskogo station of the Sokolnicheskaya line – by 25 %, and Michurinskiy Prospekt station of the Kalininsko-Solntsevskaya line – by 35%.

The joint labour of Russian and Chinese metro builders has a great future.

REFERENCES

Konyukhov D.S., Polyankin A.G., 2019. Evaluation of parameters that define a quantity of excess excavation ratio in TBM tunnel excavation. 1st International Conference on Exploration and Utilization of Underground Space. 15-18 November 2019. Wuhan, China.

Konyukhov, D.S., 2022. Analysis of mechanized tunnelling parameters to determine the overcutting characteristics. Mining Science and Technology (Russian Federation), 2022, 7(1), pp. 49–56.

Konyukhov, D.S., 2022. Safety of existing buildings during underground mining. Mining Informational and Analytical Bulletin, 2022, (8), pp. 158–167.

Kulikova, E.Yu., Konyukhov, D.S., Potokina, et al., 2022. Analytical method for calculating the coefficient of technological soil sampling in the organization of mining and construction works with the use of mechanized tunneling. Mining Informational and Analytical Bulletin, 2022, (6), pp. 305–315.

Kulikova, E.Yu., Potapova, E.V., 2022. Synthesis of managerial decisions to the effect of underground construction safety. Mining Informational and Analytical Bulletin, 2022, 2022(2), pp. 62–69.

Mazein S.V., Pankratenko A.N., Polyankin A.G., et al., 2019. Soil improvement in tunnel face using foam reagents in EPB TBM. Tunnels and Underground Cities: Engineering and Innovation meet Archaeology, Architecture and Art – Peila, Viggiani & Celestino (Eds). Taylor & Francis Group. London, 2019,pp. 2663–2670.

Merkin, V.E., Pichugin, A.A., Medvedev, G.M., et al., 2021. Comprehensive Automated Geotechnical Monitoring System and Experience in its Application in the Construction of Underground Facilities. Soil Mechanics and Foundation Engineering, 2021, 58(3), pp. 230–236.

Naumov M.S., Kusyj I.A. Moskovskoe metro. Putevoditel'. 2-e izdanie, ispravlennoe i dopolnennoe. M.: Vokrug sveta, 2006. 360 p. (In Rus.).

Nojtatc D. Moskovskoe metro: ot pervykh planov do velikoj strojki stalinizma (1897–1935)/per. s nem. YU.A. Petrova. M.: Rosspehn, 2013. 783 p. (In Rus.).

Postanovlenie Pravitel'stva Moskvy ot 4 maya 2012 goda No 194-PP «Ob utverzhdenii Perechnya ob"ektov perspektivnogo stroitel'stva Moskovskogo metropolitena». (In Rus.).

Zercalov M.G., Konyukho D.S., Merkin V.E., 2015. Ispol'zovanie podzemnogo prostranstva. M.: ASV, 2015. 416 p. (In Rus.).

Zercalov M.G., Konyukhov D.S., Merkin V.E., 2015. Ispol'zovanie podzemnogo prostranstva. M.: ASV, 2015. 416 p. (In Rus.).

Tunnelling for a Better Life – Yan, Celestino, Thewes & Eberhardt (Eds)
© 2024 The Author(s), ISBN 978-1-032-80042-4
Open Access: www.taylorfrancis.com, CC BY-NC-ND 4.0 license

The application of technology for resource utilization, reduction, and harmless treatment of subway shield tunneling waste soil

Jiangsong Lei
Shenzhen Metro Group Co., Ltd, Shenzheny, China

Hongde Long & Ke Jia
Shenzhen Metro Construction Group Co., Ltd., Shenzhen, China

Tiantian Song
Shenzhen Metro Group Co., Ltd, Shenzheny, China

Haijun Pan*
Shenzhen Metro Construction Group Co., Ltd., Shenzhen, China

ABSTRACT: The undisturbed soil of the metro shield tunnel is cut and mixed by the shield machine, and foam agent and water are added to produce a large amount of shield muck with high moisture content and poor properties. The direct transportation and disposal of shield tunneling slag not only occupies land resources, but also has potential environmental pollution and landslide risks. The rock layer where the shield tunneling slag is located itself is a natural resource containing crushed stone, fine sand, and clay, and it is a waste of resources to transport and dispose of. In order to solve this problem, a technology that uses a complete set of processing equipment to screen, precipitate, and filter shield tunneling soil has been proposed. This technology can reduce the amount, resource, and harmless use of shield tunneling soil on site, protect the ecological environment, reduce transportation noise and dust disturbance, and save engineering construction costs. The technology was applied in the fourth phase project of Shenzhen Metro, which reduced the transport volume of shield spoil by 50%, produced 4.6 million cubic meters of aggregate, saved 170 million euros, reduced carbon emissions by 54,520 tons, and reduced land occupation by 1.93 km^2. This technology can provide a reference for the green, low-carbon, and low-cost treatment of various tunnel projects' waste soil.

Keywords: shield tunneling slag, resource reuse, emission reduction

1 INTRODUCTION

Along with the continuous progress of urbanization, it has become a general trend to solve the problem of urban traffic congestion through the development of rail transit. According to the China Urban Rail Transit Association, the mileage of rail transit in operation in China has exceeded 10,000 km, and the kilometers of lines under construction have exceeded 6,000 km, of which the proportion of underground lines is over 70%. While the development of urban rail transit brings great convenience to the public, its construction and excavation process also affects the environment in a non-negligible way. Most of the city subway tunnels are constructed by shield method, and the slag production is also growing with the increasing mileage of subway construction, for example, the Shenzhen Metro produces about 4 million cubic meters of slag on average per year. In the past, the slag disposal method is mainly landfill elimination, taking up a lot of land resources, and transportation costs are high, also brings dust, groundwater pollution and other environmental problems. To carry out the slag resourcefulness, minimization, harmless treatment, take the slag as a kind of "urban mineral resources", can greatly reduce the exploitation of natural resources, protect the urban ecological environment, provide significant social, environmental and economic benefits.

In the aspect of slag resource utilization research, Hangzhou Wall Material Innovation Office used construction slag as raw materials to explore the industrialization of new recycled slag wall materials approach. A feasibility study on the use of slag for the preparation of cement mixes was carried out by Hao et al. at Zhengzhou University, China. At the same time, Zhang et al. investigated the feasibility of low-temperature

*Corresponding author: panhaijun@shenzhenmc.com

DOI: 10.1201/9781003495505-11

burnt clay as a cement mix, and found that the clay used has high activity under the condition of 550-600□ burnt. Clay wrought at this temperature range has higher cementitious strength values when used as a mixing material in cement. Yu and others from Guangxi Brick Industry Co., Ltd. have produced a series of lightweight unburned hollow bricks that satisfy national standards using soil curing technology. Prof. Wu of Wuhan University of Technology studied the preparation and pollutant filtration performance of multi-functional ceramic grains with shield tunneling slag base. The prepared slag ceramic grains were light brown in color, with smooth surface and intact enamel layer, and the interior was loose and porous, honeycomb-like, with a small number of connecting holes. Li et al. used shield tunneling slag as the main raw material, supplemented with magnesium oxide, to produce a moderate strength and excellent performance ceramic granule for phosphorus removal from water at a relatively low temperature. However, little research has been done on large-scale resourcefulness, minimization, and harmless treatment of shield tunneling slag in situ at worksites.

This paper provides a reference for the efficient disposal of slag in other underground tunnel projects by introducing the application of in-situ large-scale resourcefulness, minimization and harmlessness treatment technology of shield tunneling slag in Shenzhen Metro.

2 SHIELD TUNNELING SLAG TREATMENT PROCESS METHOD SELECTION

Shenzhen Metro mainly compares the following shield tunneling slag treatment methods.

2.1 *Plain sedimentation method*

The method is the most primitive one, mainly through tedding, or building slag pool sediment filter, etc., to make the slag water content reduced to meet the requirements before transportation, as shown in Figure 1. The method occupies a large area, is greatly affected by weather and other influences, and all the slag still needs to be transported and then landfilled, so it is inefficient and cannot meet the needs of subway shield construction.

Figure 1. Plain sedimentation method site photos.

2.2 *On-site mechanical and drying*

This method is mainly composed of multi-stage screening (slurry separation), flocculent settling, filter pressing and other processes, the input equipment mainly includes screening machines, belt (plate) filter presses and other equipment, as shown in Figure 2. This method occupies a relatively small site, the water content of the mud cake after filter-pressing is low, clear water discharge can be realized, and materials such as sand and stone screened out can be reused without being affected by the weather, etc., and the actual slag that needs to be transported out is greatly reduced. The dual filter press configuration allows for a throughput of 400-500 cubic meters per day.

Figure 2. Mechanical dewatering and drying equipment constructed on site by shenzhen metro.

2.3 *Consolidation method*

The method is to add environmentally friendly stabilizing curing agent in the slag, through mechanical mixing to make the curing agent and slag fully mixed, so that it is transformed into immobile state, or to form a tight joint. This technology enables the slag to be disposed of in a shorter period of time. This method takes up a small area and has a high treatment efficiency, but causes an increase in the size of the outgoing slag and an additional road occupation due to the landfill. More than 1,000 cubic meters per day of handling capacity can be achieved. Figure 3 shows solidification equipment on site.

3 SHIELD TUNNELING SLAG RESOURCEFULNESS, MINIMIZATION, HARMLESS TREATMENT IN SHENZHEN METRO APPLICATION

The main components of shield tunneling slag are crushed stones, fine sands, clay, etc., which have great potential for resource utilization in engineering

Figure 3. Solidification equipment used on site by shenzhen metro.

construction. Taking Shenzhen Metro Line 14 as an example, there are about 4.95 million cubic meters of shield tunneling slag, and the sandstone content in the garbage reaches more than 40%, indicating huge potential for resource utilization and reduction. In Shenzhen, the main method used for resource utilization, reduction, and harmlessness treatment of shield tunneling slag is on-site mechanical dewatering and drying.

3.1 *The main techniques and processes*

The efficient resource utilization and reduction treatment technology for shield tunneling slag involves equipment consisting of a feeding system, a screening system, a sand washing and whirling system, and a filtering system. The shield tunneling slag undergoes processes such as screening, whirling, flocculation, filtering, and tail water treatment to reduce the moisture content and improve the content of sand and mud cake (as shown in Figure 4). The equipment uses a raw shield tunneling slag as input, which is conveyed by the feeding conveying module to the feeding screening module for the first step of processing. The feeding screening module contains functions such as uniform feeding, vibrating particle size classification, and multi-stage high-pressure spray cleaning, producing clean coarse sand aggregate that can be used for on-site construction or sold; the screened off sand-water mixture is processed by the sand washing and whirling module to produce clean medium and fine sand that can be used for Shielding Grouting or sold for other on-site uses; the muddy water obtained after whirling enters the flocculation module for treatment, and the clarified water is used in the clear water pool; the precipitated muddy water enters the filtering module and is dehydrated to obtain a dry mud with low moisture content (less than 30%) that can be directly transported for use or as a raw material for resource utilization products such as self-burning bricks. The clarified water from the flocculation module and the accelerated flocculation module is recycled within the system. If the shield tunneling slag contains too much moisture, the system needs to discharge water. The advanced catalytic oxidation water treatment module is used to treat the water to achieve discharge after reaching the standard.

Figure 4. Schematic diagram of slag treatment process.

3.2 *Key techniques*

3.2.1 *Efficient dilution defoaming technology*

According to the different fluidity (density) of shield tunneling slag, vertical slag lifting equipment is used to send the shield mud to the mixing and stirring device, and at the same time, defoamer (dosing between 0.05-0.1%) is added and stirred through the defoamer dosing device, so as to defoam and deodorize the residual foaming agent of the shield tunneling slag, and also to effectively promote the separation of mud and sand. Figure 5 and Figure 6 present the slag water before and after treatment, respectively.

Figure 5. The slag water before treatment.

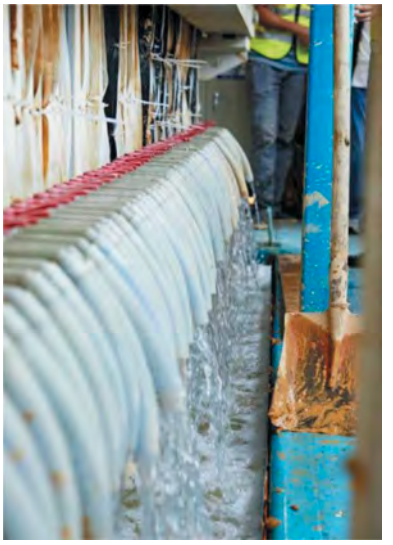

Figure 6. The slag water after treatment.

3.2.2 *High-efficiency sand and mud separation technology*

The screening system receives wet slag from the shield tunneling slag pit, and through gravity separation, screens and recovers medium-fine sand ranging from 0.2 mm to 6mm for reuse. The fine sand and mud smaller than 0.2 mm will enter the mud pit and be pumped by a plunger pump to an automatic high-pressure circular box filter press for dewatering treatment, resulting in mud cakes with a moisture content of 20% to 35% and clear water. The separated clear water will enter the clear water pool and be pumped back to the screening system by a pressure pump for recycling. The sand produced from the separation of mud and sand meets the requirements for resource utilization. Figure 7 illustrates the separation equipment of sand and mud.

Figure 7. The separation equipment of sand and mud.

3.2.3 *High-efficiency mud concentration technology*

The overflowed slag after gravity sorting by cyclone is pumped to the concentration tank, and through the center feed pipe and splitter inside the concentration tank, the slag is concentrated and drained with high efficiency, so that when the slag is concentrated to more than 25% concentration, it is discharged to the transfer pool, and the clean water obtained from concentration is sent to the clean water tank to wait for reuse (as shown in Figure 8).

Figure 8. Concentrated slag.

3.2.4 *High-efficiency filter press dewatering technology*

First, the slag is quickly concentrated by a high-flow slag pump, and then filled into the chamber of the filter press, which can shorten the filtration time. Then, the high-pressure plunger pump is started to mechanically dewater the slag under high pressure, resulting in a moisture content of about 30-35% in the dry mud after filtration. The entire filtration and dewatering process takes about 20-30 minutes. After completion, the system will automatically unload the filter plates, and the dry mud will automatically fall onto the conveyor belt for transportation to other processes. Figure 9 presents the effect of filter press dewatering.

Figure 9. Filter press dewatering.

3.2.5 *The slag water harmless treatment technology*

The clear water obtained through the flocculation module and accelerated flocculation module can be recycled within the system. If there is too much moisture in the shield tunneling slag, the system

needs to discharge water. When the indicators such as surfactants in the shield tunneling slag water exceed the standard, the slag water treatment module needs to be activated to use advanced catalytic oxidation water treatment technology to treat the shield tunneling slag water to meet the standard before clear water discharge.

3.2.6 *Equipment intelligent, integrated, modular design technology*

To solve the problems of equipment ground adaptability and system intelligence, integration, and modularization, and further improve the efficiency and ability of shield tunneling slag processing, firstly, the type and quantity of equipment configuration are determined based on detailed geological investigation of each area and the prediction results of shield tunneling slag properties and proportion of rock and mud. When configuring, equipment with adjustable parameters are selected as much as possible, and parallel settings are used to improve the system's self-adjusting ability. Then, through intelligent equipment development, modular design of subsystems (as shown in Figure 10), and integrated assembly simulation based on BIM (as shown in Figure 11), the configuration and installation plan of the shield tunneling slag processing system are determined in combination with the site and geological conditions. After on-site assembly and commissioning are completed, the intelligent central management platform developed during the equipment operation process can achieve intelligent central control of the system. Not only can it monitor the running status of each module, but it can also issue commands to each module to adapt to different operating conditions in a timely manner. It can achieve one-person operation of all equipment in the control room, and the system can operate automatically with chain start-stop, status monitoring, and automatic alarm functions. Each module and the central control platform can interactively exchange information, adjust operating parameters based on module feedback information, and greatly improve equipment adaptability. The efficient resource utilization technology for shield tunneling slag truly achieves intelligence, integration, and modularization of shield tunneling slag resource utilization.

Figure 10. Main module construction.

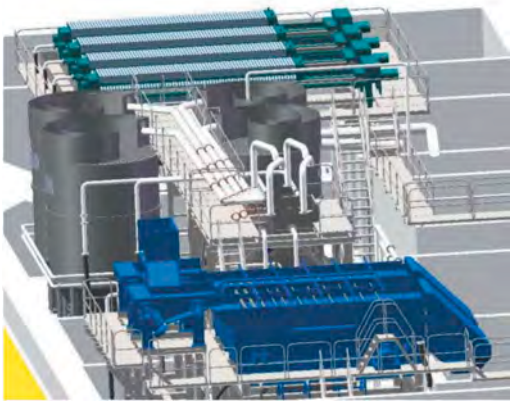

Figure 11. BIM modeling of shield tunneling slag treatment equipment.

3.3 *Main technical parameters*

3.3.1 *System parameters*

(1) System floor area: about 800 m^2 (pure equipment takes up about 470 m^2).
(2) System processing capacity: 1400 m^3/d.
(3) Installed power: about 800 kw.

The system processing capacity can be matched according to the construction capacity of the shield machine.

3.3.2 *Product particle size range*

(1) Coarse sand particle size range: ≥3mm.
(2) Fine sand particle size range: 74um~3mm.
(3) Filter cake particle size range: ≤74um.

The particle size range can be adjusted as needed.

3.3.3 *Product separation effect*

(1) The moisture content of coarse sand and fine sand is less than 30%, and they do not drip during transportation.
(2) The separated filter cake has a moisture content of less than 30%, and it does not drip during transportation.
(3) The coarse sand aggregate and medium-fine sand are clean; the fine sand contains less than 5% clay.

The moisture content and clay content can be adjusted as needed.

3.4 *Application in shenzhen metro*

Based on the resource utilization, reduction, and harmless treatment technology of mechanical dewatering and drying method, Shenzhen Metro has promoted and constructed 84 sets of shield tunneling slag treatment facilities in the Line 12, Line 13, Line 14, and Line 16, as well as the branch line of Line 6,

treating over 10 million cubic meters of shield tunneling slag. It has achieved significant economic, social, and environmental benefits.

(1) In terms of economic benefits, it realizes resource reuse and reduces construction costs. Taking the Phase IV project of Shenzhen Metro as an example, the resource utilization disposal produces approximately 2.3 million cubic meters of resource products, with a potential resource value of about 140 million yuan, and reduces over 3 million cubic meters of slag that needs to be transported and disposed of externally. By reducing the volume of slag transportation through reduction disposal, the cost of external transportation during construction is reduced. Taking Line 14 of Shenzhen Metro as an example, the reduction rate after treatment is approximately 40%. Compared to traditional direct disposal, the use of shield tunnel wet soil along the entire line can reduce transportation costs by 127.68 million yuan.
(2) In terms of social benefits, by recycling and reducing the actual amount of slag transportation through resource utilization and reduction disposal, it reduces the occupation and impact on road resources and land resources during construction, realizes resource recycling, and enhances public happiness.
(3) In terms of environmental benefits, this technology can reduce emissions from slag transportation, landfill occupation, land and water pollution, promote ecological civilization construction, and explore the path to carbon peaking in the industry. Taking the Phase IV project of Shenzhen Metro as an example, the actual reduction in landfill area for slag is approximately 1,150 acres (calculated based on a 3-meter landfill). Calculated based on an average round trip of 25 km and 2 trips per day, it is equivalent to reducing carbon emissions by over 180,000 tons, which is equivalent to the carbon sequestration of 90,000 poplar trees in Xinjiang in one year.
(4) In terms of resource recycling, the obtained crushed stone and fine sand aggregate are directly used in concrete, grouting, and other projects, and the obtained filter cake is used to produce non-burning building materials, such as non-fired bricks, wall panels, and ceramisite. The obtained clean water is recycled in the screening, sand washing, and construction processes.

4 CONCLUSIONS

The technology based on mechanical dewatering and drying method for the resource utilization, reduction, and harmless treatment of shield tunneling slag has changed the traditional method of directly transporting and dumping slag, which that once could only be discarded can now be utilised as a resource. If further research and development is conducted on large-scale resource utilization technologies for the filtered mud cakes, such as manufacturing bricks, ceramic particles, and board materials, zero discharge of shield tunneling slag can be achieved. This technology has strong innovative demonstration effect and reproducibility, and has been widely applied in water tunnel and other shield tunneling projects. It can also be applied in other shield tunneling projects to improve resource utilization, environmental friendliness, and low-carbon levels in related fields.

Tunnelling for a Better Life – Yan, Celestino, Thewes & Eberhardt (Eds)
© 2024 The Author(s), ISBN 978-1-032-80042-4
Open Access: www.taylorfrancis.com, CC BY-NC-ND 4.0 license

Development and prospects of railway tunnels in China

Xu Li*
Southwest Jiaotong University, Chengdu, China
China Railway Economic and Planning and Research Institute Co., Ltd., Beijing, China

Siming Tian, Wei Wang & Jiangfeng Gong
China Railway Economic and Planning and Research Institute Co., Ltd., Beijing China

Huiwu Wang
China Railway Eryuan Engineering Group Co., Ltd., Chengdu, Sichuan, China

ABSTRACT: Briefly introducing the achievements in the development of railway tunnel construction in China. By 2022, the operating mileage of railways in China has reached 155,000km, including 17,873 railway tunnels that have been put into operation, with a total length of 21,978km; There are 3,025 railway tunnels under construction, with a total length of 7,704km. Through large-scale railway tunnel engineering practice, China has achieved a series of achievements in tunnel design theory and methods, tunnel standard system, unfavorable geological tunnel construction technology, risk management system, and disaster prevention and rescue technology. Especially in recent years, China's railway large-section tunnel mechanization construction technology has made great progress. A large number of tunnel projects have been built in complex environment areas such as soft rock deformation with high ground stress, rock explosion with hard rock, high ground temperature, and high-pressure water-rich karst, making outstanding contributions to railway construction and economic and social development in China. Based on the problems faced in the construction of railway tunnels in China, this paper proposes prospects for the support system, design methods, intelligent construction, and other aspects of railway tunnel construction in China.

Keywords: Railway Tunnel, Design Theory, Standard System, Risk Management

1 INTRODUCTION

In recent years, China's railway system has experienced significant advancements in terms of the expansion of its operating road network, the establishment of standardized systems, the improvement of transport services, and the promotion of scientific and technological innovation. These developments have resulted in notable accomplishments. As of the conclusion of 2022, the total operational distance of China's railway system amounted to 155,000 kilometers (Excluding Taiwan Province data, as well as subsequent references). Notably, the high-speed railway network accounted for 42,000 kilometers [1]. This extensive high-speed rail infrastructure stands as the most expansive globally, significantly enhancing the accessibility of travel for a wide range of individuals.

The rapid development of China's railway system has correspondingly led to significant advancements in railway tunnel construction, yielding numerous notable achievements. Initially, it is noteworthy to mention that the magnitude of the tunnels that have been utilized is substantial. As of the conclusion of 2022, China boasted a network of 17,873 operational railway tunnels, spanning a collective distance of 21,978 kilometers. This figure encompasses 4,178 tunnels specifically designed for high-speed railways, which account for a total length of 7,032 kilometers. Furthermore, the theory of tunnel design is undergoing continuous development, with the standard system experiencing ongoing improvement and construction technology advancing rapidly. In recent years, there has been a continuous emergence of tunnel design theories and methods in China that exhibit distinct characteristics. These include the surrounding rock deformation control method, mechanized large-section design method, and total safety factor method. As a result, a complete set of tunnel design standards for each speed target value has been formed, and various tunnel construction technologies, especially

*Corresponding author: lixucq@sina.com

DOI: 10.1201/9781003495505-12

unfavorable geological treatment technologies, have developed rapidly. Furthermore, a considerable quantity of significant tunnel projects have been constructed. China has successfully undertaken various tunnel projects in challenging terrains such as plateaus, cold regions, loess areas, and urban complex environments. These achievements have been recognized through prestigious accolades including the Fidyk Prize and the World Tunnel Association Award, highlighting China's significant global impact in the field of railway tunnel construction.

2 OVERVIEW OF RAILWAY TUNNELS

Based on statistical data, it is observed that as of the conclusion of 2022, China had a substantial network of operational railway tunnels, numbering 17,873 in total. These tunnels collectively spanned a distance of 21,978 kilometers. Notably, among these tunnels, 4,178 were specifically designated for high-speed railways, covering a total length of 7,032 kilometers. The magnitude of this infrastructure undertaking is noteworthy. Simultaneously, there is a considerable proliferation of ongoing and prospective tunnel initiatives. In China, there is currently an ongoing construction of 3,025 railway tunnels, collectively spanning a distance of 7,704 kilometers. Currently, there are 5,376 railway tunnels in the phase of planning and design, encompassing a cumulative length of 13,221 kilometers [2]. In China, a significant railway tunnel project has been undertaken, encompassing the construction of numerous railway tunnels that are currently underway or planned for future development. These railway tunnels exhibit several notable features, including their considerable length, diverse construction techniques, and significant challenges encountered during their construction.

2.1 *Extra-long railway tunnel*

The Dayaoshan Tunnel on the Heng-Guang double track in China commenced operations in 1987. Spanning a length of 14.295km, this tunnel holds the distinction of being the inaugural extra-long railway tunnel constructed in China. Over the subsequent three decades, a significant quantity of exceptionally lengthy railway tunnels have been constructed in China [3]. As of the conclusion of 2022, China has successfully constructed and put into operation a total of 259 railway tunnels of extended length. These tunnels collectively span a distance of 3498 kilometers. Among these tunnels, there are 12 that have a combined length of 283 kilometers. The Guanjiao Tunnel holds the distinction of being the longest among them, measuring 32.690 kilometers in length. Furthermore, it is worth noting that there are currently 26 tunnels being constructed, each spanning a distance of over 20 kilometers. Collectively, these tunnels will amount to a total length of 692 kilometers. The presence of numerous extensive tunnels indicates a substantial enhancement in China's proficiency in tunnel construction and utilization.

2.2 *Diversification in construction methods*

The primary method employed in China's railway tunnel construction predominantly involves the utilization of borehole-blasting techniques, intending to acquire a comprehensive understanding of the New Austrian Tunnelling Method (NATM) concept. In recent years, the construction industry in China has witnessed significant advancements in the field of large-scale construction equipment. As a result, there has been a notable increase in the construction of tunnels using large-diameter Tunnel Boring Machines (TBM) and shield technology. This shift in construction practices signifies a gradual transition from manual labor-intensive methods to mechanized approaches. Regarding the topic of Tunnel Boring Machines (TBM), it is noteworthy that the construction of the Xikang Railway Qinling Tunnel spanned from 1995 to 1999. This tunnel, measuring a length of 18 kilometers, required the utilization of two TBMs for its successful completion. The length of construction for a single Tunnel Boring Machine (TBM) was 5.2 kilometers, achieving a monthly progress peak of 531 meters. Between 2008 and 2015, the West Qinling Tunnel of the Lanzhou-Chongqing railway spanned a total length of 28 kilometers. This tunnel was constructed using two TBMs, each with a construction length of 12.7 kilometers and a highest monthly progress of 833 meters [4]. The Shiziyang Tunnel of the Guangzhou-Shenzhen-Hong Kong high-speed railway, which commenced construction in 2009, holds the distinction of being the inaugural shield tunnel for a high-speed railway project situated underwater. It is noteworthy for its ability to withstand a maximum water pressure of 0.67 megapascals. The construction of the Shiziyang Tunnel, a railway tunnel, commenced in 2016. At that time, it held the distinction of being the largest shield tunnel in China. The tunnel boasted a shield outer diameter measuring 13.1 meters and was designed to withstand maximum water pressure of 0.78 Mpa.

2.3 *Difficulty in tunnel construction*

China's expansive landmass and the intricate geological and environmental circumstances surrounding tunnel construction have necessitated the implementation of numerous tunnel projects in hazardous mountainous regions, karst water-abundant areas, loess regions, cold climates, urban environments with complex surroundings, and sea-crossing zones. During the tunnel construction in the aforementioned areas, numerous challenges are encountered, including but not limited to high stress rockburst, significant deformation, elevated ground temperature, high-pressure water influx, intense seismic activity, frost susceptibility in cold regions, and close proximity to existing structures.

Consequently, the construction process is characterized by considerable difficulty.

3 ACHIEVEMENTS IN THE DEVELOPMENT OF RAILWAY TUNNELS

Through the large-scale construction of railway tunnels in the last 40 years, China's railway tunnel has made a series of achievements in survey means, design theory, standard system, disaster prevention and rescue, mechanization, and complex environment construction technology.

3.1 *Continuous innovation in survey methods*

In order to find out the geological conditions of the tunnel accurately, the railway tunnel survey methods in China have been continuously innovated, and an integrated survey technology of "air-sky-ground" has been formed. The so-called "air-sky-ground" integrated survey technology refers to a comprehensive survey method composed of satellite platforms such as high-resolution images, thermal infrared remote sensing, multi-spectral lithology remote sensing, aviation platforms such as aerial photography, aerial geophysical exploration, unmanned aerial vehicles, three-dimensional tilt photography, and ground platforms such as three-dimensional laser scanning, ultra-deep horizontal drilling, kilometer-level vertical drilling and high-precision ground geophysical exploration. Compared with the traditional survey, the "air-sky-ground" integrated survey technology can greatly reduce the workload of operators in the process of deep-buried long tunnel survey, greatly improve the efficiency of survey work, improve the accuracy of survey work, reduce the exploration cost, and provide a basis for formulating a reasonable tunnel project plan[5].

3.2 *Continuously developing design theory*

The concept of New Austrian Tunnelling Method (NATM) was first introduced in China during the 1970s. Subsequently, NATM gained significant popularity and was extensively employed in the construction of tunnels throughout the country. This adoption of NATM played a pivotal role in facilitating the successful completion of numerous large-scale railway tunnel projects in China, thereby making notable contributions to the field of tunnel construction in the country. In recent years, significant progress has been made in the evaluation and classification of surrounding rock stability and the design of surrounding rock deformation control in China's railway tunnel construction. This progress has been achieved through the assimilation and application of concepts from the "New Austrian Tunnelling Method," "Norwegian Tunnelling Method," and "New Idea Method," as well as through the consideration of China's unique topography, geological conditions, and diverse characteristics of railway tunnels. These efforts have led to the development of tunnel construction methods that are specific to China, thereby advancing the theoretical framework and methodologies for railway tunnel design in the country.

3.2.1 *Standard design method of surrounding rock stability classification*

The primary design methods employed in China's railway tunnel construction include the utilization of standard design and analogy design approaches. Based on extensive engineering experience, it is suggested that the self-stability of the surrounding rock be adopted as a criterion for developing a comprehensive classification system. Furthermore, standard design parameters are proposed based on the classification of the surrounding rock. For a considerable duration, the design and construction of railway tunnels in China have been heavily influenced by the conventional design approach that relies on the classification of surrounding rock stability. This method has played a crucial role in facilitating the extensive development of railway infrastructure in the country. However, during the process of construction, the rock formations exposed during excavation do not necessarily align with the expected characteristics of the surrounding rock. This discrepancy makes it challenging to accurately assess and interpret the conditions on-site. Additionally, the supporting parameters can vary in strength, leading to potential weaknesses or strengths in the overall structure. In recent years, extensive scientific research and testing have been conducted by railway builders in China to enhance and reinforce the quantitative classification of surrounding rock. The refinement of the elastic wave velocity range of surrounding rock with different lithology is achieved through the introduction of the basic quality index (BQ). Additionally, the concept of surrounding rock sub-level is proposed. Based on the findings regarding the self-stability characteristics of the surrounding rocks under various combined conditions, the rocks of Grade III, IV, and V are classified into two sub-grades. The sub-grade division standard is determined based on the index combination corresponding to each sub-grade. Consequently, the BQ value range for each sub-grade of the surrounding rocks is established. The findings have been incorporated into the 2016 edition of the Design Code for railway tunnels, providing valuable guidance for the design and construction processes of railway tunnels.

3.2.2 *Mechanized large section design method*

The tunnel construction team of Zhengzhou-Wangao High-speed Railway Hubei Section, through carrying out scientific research and field practice related to large-scale tunnel mechanized large-section supporting construction, summarized and put forward the

related methods of railway tunnel mechanized large-section design and construction. Using qualitative and quantitative methods, palm surface stability is divided into three types: stable, temporary stable, and unstable, and the advanced support measures (including palm surface shotcrete, advanced small pipe, pipe shed, tunnel face anchor, advanced grouting, etc.) are determined according to the evaluation results of palm surface stability. In the design method of tunnel support, the load-structure model is used to calculate, the surrounding rock pressure of shallow buried and eccentric compression section is adopted according to the formula value of tunnel design code, and the deep buried section is determined according to the measured values of deformation and stress [6].

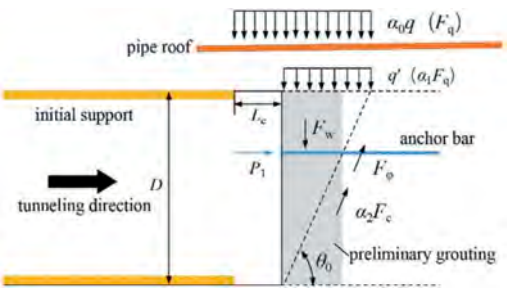

Figure 1. Design model of advance support in palm surface.

3.2.3 *Total safety factor method for tunnel supporting structure design*

Xiao Mingqing and his team have developed the "total safety factor method for tunnel supporting structure design" based on their extensive experience in tunnel engineering design, construction, and research. The conceptual framework of this methodology is as follows: The relationship between the supporting structure and the surrounding rock is commonly understood as the interaction between the acting force and the reaction force. However, the coordination of deformation between these elements is often not taken into strict consideration, resulting in a significant simplification of the problems that need to be addressed. The determination of whether the tunnel requires support and the calculation of the necessary supporting force necessitate the utilization of numerical analysis incorporating various constitutive models that accurately reflect real-world conditions. Simultaneously, the safety and deformation of the supporting structure itself are assessed using the load-structure model. This integration of modern and traditional analysis methods enables the achievement of safety evaluation and quantitative design of supporting parameters. The figure below illustrates the calculation model for determining the total safety factor of a composite lining structure.

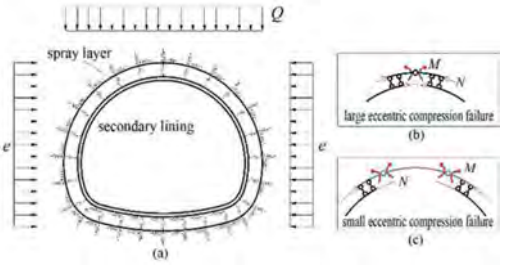

Figure 2. Calculation model of total safety factor method.

3.3 *The standard system is improving day by day*

From the 1980s to the beginning of this century, the construction standard of China's railway tunnel was relatively low, with a common speed of 120km/h for railway tunnels in mountainous areas. The tunnel excavation area is generally 50 ~ 60m^2 for single track and 80 ~ 100m^2 for double track. After entering the 21st century, with the rapid development of high-speed railways and intercity railways, the tunnel section has gradually increased, and the excavation section of the high-speed railway tunnel can reach 160 m^2. The maximum excavation span of Beijing-Zhangjiakou high-speed railway Badaling Great Wall underground station tunnel is 32.7m, and the excavation area is 494.4m^2, It is the largest traffic tunnel in the world at present. Through the engineering practice of various tunnel sections and various geological and environmental conditions, a complete set of technologies for building railway tunnels under different regional environments, different climatic characteristics, and different geological conditions has been formed.

After recent years' development, China's railway tunnel has established the standard system of high-speed railway with the speed of 250km, 300km and 350km/h, and a series of standard systems of railway tunnel with the speed of 120km, 160km and 200km/h, and has successively issued relevant specifications 20 Yu Ben and compiled 46 sets of general standard drawings. China railway tunnel has formed a systematic standard system from survey, design, construction, acceptance to operation and maintenance, which has provided strong technical support for the development of China railway tunnel.

3.4 *The disaster prevention and rescue system has further matured.*

Railway tunnel is a semi-closed structure, which will seriously threaten the safety of passengers in case of fire and other accidents. With the continuous development of railway tunnels, China's railway tunnel implements the development concept of "people-oriented" and attaches great importance to the disaster prevention and rescue of railway tunnels. Based on absorbing and digesting foreign advanced tunnel disaster prevention and rescue concepts and related

technologies, and fully combining China's national conditions and economic and social development level, this paper puts forward the general principle of "people-oriented, safe evacuation, self-help first and convenient rescue", compiles the Code for Design of railway tunnel Disaster Prevention and Evacuation Rescue Project, determines the main standards of China's railway tunnel disaster prevention and rescue project, and fills the gap of China's railway tunnel disaster prevention and rescue. Through the engineering practice of a batch of extra-long tunnels, emergency rescue stations and other facilities inside and outside various types of tunnels have been built, and a disaster prevention and evacuation rescue system covering civil structural facilities, electro-mechanical facilities, monitoring system, management system and evacuation mode has been gradually established.

In recent years, through the practice of tunnel engineering in plateau areas, research on disaster prevention and rescue of tunnels in high-altitude areas has been carried out. Combined with the characteristics of difficult evacuation and rapid spread of smoke in high altitude areas, the disaster prevention and rescue principles and engineering schemes of tunnels in plateau areas have been further put forward.

3.5 *The mechanization of tunnel construction has been continuously improved*

The mechanized construction of railway tunnels in China has experienced significant advancements. Before the 1950s, the construction of railway tunnels in China primarily relied on manual excavation and manual operation. During the latter part of the 1950s, there was a gradual introduction of small-scale rock drilling machines, as well as digging and loading equipment. Consequently, small-scale mechanized construction began to emerge as a prominent practice. During the 1980s, there was a gradual introduction of foreign advanced multi-arm drilling equipment to implement large-scale mechanised supporting practice. Since the year 2000, China has made significant progress in the independent development and production of various equipment, such as multi-arm drilling rigs, wet spraying manipulators, and integrated machines for anchor drilling and injection. These advancements have resulted in a notable reduction in labor intensity during construction, enhanced operational safety, and improved construction efficiency. Consequently, China has established a comprehensive equipment system that encompasses advanced geological prediction, excavation, loading, support, inverted arch construction, waterproofing, secondary lining, and maintenance.

Furthermore, alongside the progressive mechanization of the borehole-blasting technique, there has been notable advancement in China's shield and tunnel boring machine (TBM) tunnels. China has employed tunnel boring machine (TBM) technology for the construction of various railway tunnels, including the Xikang Railway Qinling Tunnel, Southwest Railway Mogouling Tunnel, Lanzhou Railway Zhongtianshan Tunnel, and Lanzhou-Chongqing Railway West Qinling Tunnel. The TBM construction method has emerged as a significant option for the construction of exceptionally long tunnels in mountainous regions. The shield method is extensively employed in tunnel projects that traverse intricate urban environments and underwater regions.

In a broad sense, significant advancements have been made in the mechanization of tunnel construction, leading to a continuous enhancement in the level of construction mechanization. Consequently, this has resulted in a substantial reduction in the physical exertion required by construction workers and a notable improvement in the overall quality of construction.

3.6 *Rapid development of tunnel technology in complex environment*

China has a vast territory, and it is inevitable to build a large number of railway projects in special areas such as dangerous mountainous areas, karst areas, loess areas and severely cold areas. The construction of railway tunnel faces a series of problems such as high-ground stress, high ground temperature, high-intensity earthquake, karst water inrush, collapsible loess, and freezing injury. In recent years, through the technical research of tunnel builders in China, a large number of tunnel projects have been built in the above-mentioned complex environment areas, marking a new step in the construction technology of railway tunnels in China.

—— Through the engineering practices conducted in Chenglan Railway Yue Longmen Tunnel, Lanyu Railway Muzhailing Tunnel, and Cheng Gui Railway Gaopo Tunnel, our country has successfully identified the deformation mechanisms associated with different types of large deformations, including high-stress extrusion, high-stress rock mass expansion bending, and fractured rock mass extrusion. Consequently, a grading evaluation standard and prediction method have been proposed for implementation during the survey and design stage as well as the construction stage. Moreover, the concept of "optimising tunnel shape, active reinforcement, grading control, and strengthening support" has been established as a comprehensive approach to address these deformation challenges.

—— China has developed a rockburst grading identification standard for the initial stage of survey and design and detailed judgment during construction, based on the engineering practice of Bayu Tunnel in Lalin railway. The principle of active disposal, known as "early warning first, active control, more machines and fewer people, ensuring safety," has been proposed. Additionally, the principle of "predicting before construction" has been put forth specifically for rock burst tunnels. The utilization of extensive mechanization in the rock burst tunnel construction is evident, aiming to maximize the

safety of the workers involved. A comprehensive technical system for the treatment of rock burst engineering is established, incorporating an active support system consisting of a prestressed anchor and a high-strength protective net.

—— China has developed a classification system for high ground temperature and standards for assessing thermal damage. This has been achieved through the implementation of railway projects in high-ground temperature environments, including Lari railway, Da Rui railway, and Lalin Railway. Notably, the Sangzhuling Tunnel in the Lalin railway represents the world's highest rock temperature in a traffic tunnel. The proposed principle for waste management involves enhancing geological forecasting, implementing measures to prevent and control thermal damage, providing comprehensive cooling support, appropriately adapting materials, and reinforcing labor safety. This principle aims to establish a comprehensive system for preventing and controlling damp heat in the construction environment of high geothermal tunnels. By employing ventilation cooling, ice cooling, and mechanical refrigeration, the physical and mental well-being of operators is effectively safeguarded. An operational safety guarantee system has been established for high-ground temperature tunnels during their operational period.

—— China has made significant advancements in the construction technology of collapsible loess through the implementation of high-speed railway projects in Zhengxi, Baolan, and Yinxi regions. The presence of water causes a transformation of loess from a solid state to a more fluid state, thereby increasing the construction risk and posing challenges for settlement control. The pressure distribution law and deformation characteristics of the surrounding rock in high-moisture loess cross-section tunnels have been identified through scientific research. Consequently, a large-section construction technology for high-moisture loess tunnels has been proposed, thereby addressing the technical deficiency in the construction of loess tunnels with high moisture content both domestically and internationally. This development has resulted in the establishment of a comprehensive technical system for constructing loess tunnels under varying moisture content conditions.

—— China's railway underwater tunnels have made significant advancements in terms of engineering practices, as exemplified by the Liuyang River Tunnel in the Wuhan-Guangzhou railway, the Shiziyang Tunnel in the Guangzhou-Shenzhen-Hong Kong High-speed railway, and the Shantou Bay Tunnel in the Shantou-Shantou High-speed Railway. These tunnels have evolved from initial breakthroughs to encompass larger diameters, higher water pressures, and more intricate geological conditions. The ongoing construction of the Jintang subsea tunnel within the Yongzhou railway encompasses a comprehensive length of 16.2 kilometers. This tunnel is designed to be buried at a maximum depth of 85 meters, with a diameter measuring 14 meters. Additionally, it is engineered to withstand a maximum water pressure of approximately 0.85 megapascals. This particular subsea high-speed rail tunnel holds the distinction of being the longest in terms of length, while also experiencing the highest water pressure among all such tunnels globally.

4 ICONIC ENGINEERING

Here are some projects that have been completed or are under construction in China.

4.1 *Xinguanjiao tunnel of Xige Second Line*

Xinguanjiao Tunnel is the key project of the second line of Qinghai-Tibet railway from Xining to Golmud, with a total length of 32.69km, a maximum buried depth of 910m, and an average elevation of 3600m. It is designed as two parallel single-line tunnels with a line spacing of 40m and a design speed of 160km/h, and is constructed by the borehole-blasting method, with a total length of 10 inclined shafts of 15350m. It is the first railway tunnel with a length exceeding 30km in China. Construction started in November 2007 and it was put into operation in December 2014. It is the first long tunnel at high altitude in China and the first long tunnel at high altitude in the world. With the completion of Guanjiao Tunnel, the cross-ridge line in this section was shortened by about 37km, and the train running time was shortened from 2 hours to 20 minutes. Figure 3 shows the entrance of the Xinguanjiao Tunnel.

Figure 3. Guanjiao tunnel.

The construction of tunnels has presented numerous technical challenges, including the need for long-distance ventilation in plateau regions, the deformation of wide fault zones within specific areas, the occurrence of high-pressure water gushing from water-rich zones in lengthy sections, as well as the implementation of disaster prevention, evacuation, and rescue measures to ensure safety during the operation of exceptionally long tunnels in plateau environments[7]. Despite these challenges, a comprehensive set of construction techniques specifically designed for high-altitude, extra-long tunnels has been successfully developed and implemented. The project received numerous

accolades both domestically and internationally, including the ITA Major Engineering Award, FIDIC Excellent Engineering Award, Qinghai Science and Technology Progress Award, China Railway Society Science and Technology Award, China Construction Industry Association and Construction Enterprises Association Science and Technology Award, and China Civil Engineering Zhan Tianyou Award. The construction of the Guanjiao Tunnel has significantly advanced tunnel technology in China and has offered valuable technical assistance for the development of extra-long tunnels exceeding 30 kilometers, particularly those situated at high altitudes within the country.

4.2 *Beijing-Zhangjia high-speed railway new badaling underground station tunnel*

The Badaling tunnel, situated within the Beijing-Zhangjiakou high-speed railway, holds the distinction of being the lengthiest tunnel. Spanning a total distance of 12.01 km this tunnel boasts a design speed of 250 km/h. It consists of a single tunnel accommodating two railway lines. The tunnel has a minimum depth of 4m and a maximum depth of 432m. The route consistently traverses significant landmarks such as Juyongguan, Shuiguan, and the Badaling Great Wall. The Badaling Great Wall Station is an underground station that forms part of the Beijing-Zhangjiakou high-speed railway. It is situated within the new Badaling tunnel, approximately 3km from the tunnel exit. The station is located below the Guntiangou parking lot in the Badaling Scenic Area and is close to the Badaling Great Wall. The transportation system consists of two stations that are served by four lines. The side platform has an effective length of 470m, and the overall construction area spans 68,300 m2. The rail surface is buried at a maximum depth of 102m, while the tunnel excavation at both ends has a maximum span of 32.7m and a maximum cross-sectional area of 494.4 m^2. This tunnel currently holds the distinction of being the largest traffic tunnel. The subterranean section of the station comprises a compact subterranean excavation complex, consisting of three tiers arranged in a vertical sequence: the platform tier, the entrance tier, and the exit tier. This complex encompasses a total of 78 cavernous spaces of varying sizes, 88 cross-sectional areas, and 63 intersections. The rock wall thickness between caves is limited to a minimum of 1.2 meters. In 2016, the world witnessed the commencement of a remarkable project - an underground excavation high-speed railway station. This project stands out due to its unprecedented construction scale, buried depth, excavation span, cross-section area, and the intricate cavern structure it entails. Figure 4 presents a cross-sectional perspective view of the Badaling underground station, while Figure 5 illustrates a schematic cross-sectional view of the super-long tunnel associated with the Badaling underground station.

Figure 4. Perspective view of Badaling underground station.

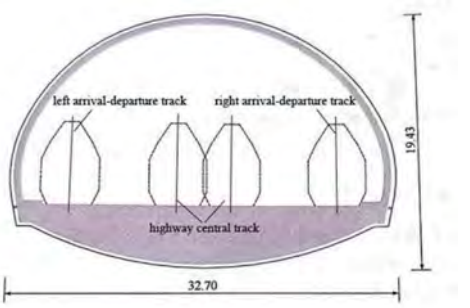

Figure 5. Schematic cross-section of the super-long tunnel in Badaling underground station.

The Badaling Great Wall Station holds the distinction of being the inaugural subterranean high-speed railway station in China. The five characteristics of this phenomenon encompass strict adherence to environmental protection measures, deep burial of waste materials, a lengthy operational lifespan, the presence of densely constructed caverns, and a geological setting that is considered to be of low quality. Throughout the construction process, there are four technical challenges that need to be addressed. These challenges include disaster prevention, rescue and evacuation measures, environmental and cultural relics preservation, as well as the construction of super-large span tunnels and dense cavern groups. The environmental protection technology of constructing tunnels through the Great Wall and scenic spots has been established through scientific research. Additionally, the development of environmental construction for deep underground stations has also been undertaken. This study proposes the component design method for the surrounding rock bearing arch of a super-long-span tunnel, the new construction method of V-shaped excavation for a super-long-span tunnel, the new technology of high-performance fast tensioning prestressed anchor cable, and the theory and control standard for step-by-step deformation control of a super-long-span tunnel. These advancements contribute to the development of a construction

technology for super-long-span tunnels and dense tunnel groups with weak broken surrounding rock. The findings of this study serve as a valuable technical reference for future projects of a similar nature [8].

4.3 *Cheng Gui railway Yujingshan tunnel*

The Yujingshan Tunnel, located on the Cheng Gui Motorway railway, is a dual-track tunnel designed to accommodate speeds of up to 250km/h. It spans a total length of 6,306 meters. The tunnel structure unveils a substantial karst cave and an intricate subterranean network of rivers. The line runs along the top of the karst cave hall, with a length of 95m, a width of 230m perpendicular to the line, and a height of 50 ~ 120 m, showing a "broad bean" shape, a dome-shaped top and a karst cave volume of 1.08 million square meters. The bottom of the cave hall is a slope-filling body of 30m~90m, and a large underground river develops at the bottom of the slope body, with a river surface width of 10 ~ 15m, a flow rate of 70m3/s in rainy season and a height difference of 120m from the surface of the underground river to the rail surface. The underground river is the only water source for downstream hydropower stations, and its ecological environment is sensitive. This giant cave and underground river system are extremely rare in the world of engineering construction, and it is praised as "the first cave of China's high-speed railway" by the industry. Faced with a series of problems such as structure, foundation form, construction organization, operation and maintenance, etc., during the construction process, innovative measures were gradually improved through repeated research and demonstration tests, which solved the above problems, and several disposal technologies filled the gaps at home and abroad.

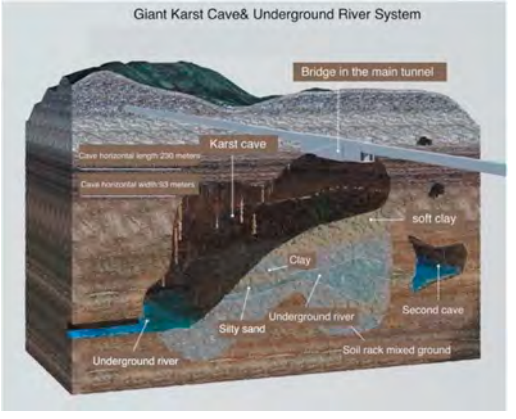

Figure 6. Schematic diagram of karst treatment of Yujingshan tunnel in Cheng Gui railway.

4.4 *Yongzhou railway Jintang cross-harbour tunnel*

The Ningbo railway starts from Ningbo East Station in the west, passes through Beilun District of Ningbo City, Jintang Island, Cizi Island and Fuchi Island of Zhoushan City, and reaches Baiquan Station of Zhoushan Island. The main line is 76.4km long, of which the newly-built line is 70.1km long. Jintang subsea tunnel starts near Taishan West Road, Beilun District, Ningbo City, passes through Sigu Mountain to the north, then enters the sea on the west side of Qingzhi River, passes through Jintang Waterway, lands on Jintang Island in Zhoushan on the north side of Dapukou, and ends near Jin Shun Cement Preproducts Co., Ltd., Jintang Town, Dinghai District, Zhoushan City. The total length of the tunnel is 16.18km, with a single-hole and double-line layout. The shield tunnel passes through Jintang Waterway by shield method, with a length of 11.21km. The land on both sides of the tunnel is constructed by open excavation and mining method, with a length of 3.617km at the Beilun side, 1.313km at the Jintang side, and a total length of 0.04km at both sides of the tunnel. The stratum through which the tunnel passes mainly includes silty soil, silty clay, silty sand, and weakly weathered tuff. The maximum buried depth of the land section is about 250m, and the maximum water pressure of the sea section is about 0.85MPa[9].

5 OUTLOOK

5.1 *Steadily promote intelligence*

In recent years, there has been a gradual decline in the presence of skilled construction technicians at tunnel sites due to the persistent rise in labor costs. Consequently, there has emerged a practical necessity to explore the possibility of substituting human labour with automated machinery in tunnel engineering construction. The reduction or absence of human presence is an inevitable trajectory in the future of tunnel engineering construction and development.

Based on the prevailing construction demand, technical proficiency, and developmental stage of railway tunnel construction in China, significant progress has been made in the accumulation and enhancement of tunnel design and construction methods under diverse geological conditions. This advancement is primarily attributed to the testing and implementation of an intelligent construction system. Notably, the breakthrough in tunnel intelligent construction technology theory, which is based on deep learning, has enabled the realization of a self-learning and self-adaptive intelligent tunnel construction system. Consequently, an intelligent tunnel construction system has been established, incorporating dynamic perception, implementation

analysis, accurate decision-making, and independent execution. This development holds great potential for the comprehensive promotion and achievement of intelligent tunnel construction.

5.2 *Further improve the construction technology of complex tunnels.*

With the in-depth development of China's railway construction, the main battlefield of railway construction in the future will be concentrated in the dangerous mountainous areas in the west, which will face more prominent geological and environmental problems. Although we have made some breakthroughs in high-stress environment, high-intensity earthquake resistance and high ground temperature, the intensity and scale of bad geology will exceed our understanding in future railway tunnel construction. Therefore, we should strengthen the summary of railway construction technology in the complex environment in China and form a complete set of technologies to prepare for railway construction in China.

5.3 *Further improve the level of tunnel operation and maintenance.*

The number of railway tunnel projects in China has been steadily increasing over the years. Consequently, there has been a corresponding rise in lining defects and diseases. This has brought attention to the heightened risk and pressure associated with the safe operation of high-speed railway tunnels. There is a pressing need to develop intelligent monitoring, maintenance, and disease treatment technology for tunnels based on Internet of Things (IoT) technology, as the current maintenance capacity falls significantly short of the demand for tunnel operation and maintenance. This study encompasses the investigation and advancement of a structural health monitoring system specifically designed for tunnel and underground engineering. Additionally, it focuses on the development of an intelligent decision-making system for evaluating tunnel conditions based on big data analysis. Furthermore, it aims to enhance tunnel and underground engineering maintenance practices through the utilization of efficient technology and intelligent equipment.

REFERENCES

1. China railway Group 2022 Railway Bulletin
2. GONG Jiangfeng, WANG Wei, LI Xu, et al. Statistics of railway tunnels in China by the end of 2022 and overview of key tunnels of projects newly put into operation in 2022[J]. Tunnel Construction, 2023, 43(4): 721.
3. TIAN Siming, WANG Wei, YANG Changyu, et al. Development and prospect of railway tunnels in China in recent 40 years[J]. Tunnel Construction, 2021, 41 (11): 1903.
4. QI Mengxue Development, current status, and prospects of TBM tunneling technology in China[J]. Tunnel Construction, 2021, 41(11): 1964.
5. Xu Qiang, Dong Xiujun, Li Weile.Integrated Space-Air-Ground Early Detection,Monitoring and Warningsystem for Potential Castastrophic Geohards[J].Geomatics and Information Science of WuhanUniversity, 2019 (7):957–966.
6. LIU Ke. Key design technology for large cross-section mechanized construction of mountainous tunnels[J]. Tunnel Construction, 2022, 42(4): 703.
7. ZHANG Xuzhen.Large deformation treatment technology of Guanjiao Tunnel[J]. Journal of Shijiazhuang Tiedao University (Natural Science), 2011,24(1):17–20.
8. ZHAO Yong, YU Zufa, CAI Jue, et al. Design Concept and Implementation Path for Badaling Great Wall Station of Beijing-Zhangjiakou High-speed Railway[J]. Tunnel Construction, 2020, 40(7): 929–940.
9. TANG Xiongjun,XIAO Mingqing,JIAO Qizhu, MAO Sheng. Investigation of Overall Design and Key Technology of Jintang Subsea Tunnel of Ningbo Zhoushan Railway[J].Railway standard design, 2021(10)

Tunnelling for a Better Life – Yan, Celestino, Thewes & Eberhardt (Eds)
© 2024 The Author(s), ISBN 978-1-032-80042-4
Open Access: www.taylorfrancis.com, CC BY-NC-ND 4.0 license

Differentiated driving effects of China's green transportation facilities assessment policy

Yang Liu*
Key Laboratory of Transportation Tunnel Engineering, Ministry of Education, School of Civil Engineering, Southwest Jiaotong University, Chengdu, China

Wenge Qiu
Key Laboratory of Transportation Tunnel Engineering, Ministry of Education, School of Civil Engineering, Southwest Jiaotong University, Chengdu, China
Chengdu Tianyou Tunnelkey Co, Ltd, Chengdu, China

ABSTRACT: The Ministry of Transport of China issued the *Green Transportation Facilities Assessment Technical Requirements* in 2017, aiming to promote green transportation facilities in China. This study uses the fuzzy Delphi method to evaluate the differentiated driving effect of this policy on the green initiative of mountain tunnel builders. One hundred thirty first-line builders from twenty-one mountain tunnels in southwest China participated in the survey. The screening thresholds of the first layer indicators are 7.27, 7.01, 6.99, and 7.07, respectively. First-line builders are most motivated to promote green concepts, but their motivation to save resources is insufficient. Among the various ways to promote the green concept, the government's strategic planning and supervision mechanism are more effective than private financing, education, training, and publicity activities. Mountain tunnel builders prefer to protect the eco-environment by safeguarding wildlife habitats, reducing polluting gas emissions, and controlling dust and light pollution. Rational planning of land resources and water resources is the core of saving resources in tunnel construction sites, and the use of recycled materials has also been recognized. Compared with intelligent equipment, energy-saving equipment, and technologies can better stimulate the green initiative of mountain tunnel builders. The widespread application of renewable energy is less motivating. The study results can provide evidence from first-line tunnel builders to adjust and improve *China's Green Transportation Facilities Assessment Policy.*

Keywords: Green assessment policy, Mountain tunnel builders, Green initiative, Fuzzy Delphi method, Differentiated driving effects

1 INTRODUCTION

nChina has achieved the world's fastest growth in transportation facilities over the past few decades. In 2019 alone, China built 330,000 kilometers of roads (new, rebuilt, and expanded), 8,000 kilometers of railways, and 1,710 kilometers of tunnels (Ministry of Transport of China., 2019). Such large-scale construction of transportation facilities has caused severe environmental problems and has attracted the attention of senior government officials.

To guide the construction of green transportation facilities, China promulgated the *Green Transportation Standard System* in 2016, and the *Green Transportation Facilities Assessment Technical Requirements* in 2017 (Ministry of Transport of China., 2016; Ministry of Transport of China., 2017). There are also many well-established green building assessment tools and methods globally. The Leadership in Energy and Environmental Design Building Rating System (LEED), established and implemented by the United States, is the most complete and influential assessment standard in building environmental assessment, green building assessment, and building sustainability assessment around the world (USGBC., 2000). The Building Research Establishment Environmental Assessment Method (BREEAM) issued by the UK is the first and most widely used green building assessment method globally (British Institute of Architecture., 1990). Because of its core concept of "adopting measures to local conditions and balancing benefits", this method has been widely used in more than 76

*Corresponding author: liuyangtunnel@my.swjtu.edu.cn

DOI: 10.1201/9781003495505-13

countries. The German sustainable building evaluation standard overcomes the limitation of the first generation of green building evaluation standards. It comprehensively evaluates the sustainability of buildings from three dimensions ecology, economy, and society (DGNB., 2007).

The effectiveness of the newly promulgated policies in promoting green buildings and green transportation facilities should be tested. There have been many related studies, and the results provide a scientific basis for policy improvement. For example, Gao et al. (2016) evaluated the effect of the *Air Pollution Prevention and Control Action Plan* by cost-benefit analysis. The results proved the policy's cost-effectiveness as its benefit-cost ratio reached 6.32. To understand the impact of the *Emission Control Policy* on public health, soil acidification, and climate, Zhao et al. (2011) quantified the results of policy implementation in two situations. It proposed that the *Emission Control Policy* should include not only common pollutants but also VOCs and CO_2. Xu et al. (2019) used scenario analysis to evaluate urban development to determine whether Chinese urban planning policies meet the goals of sustainable urbanization. Yang et al. (2020) quantified the effect of open biomass burning on surface PM 2.5 during periods of heavy smog monitored by satellite and ground observation data. The results showed that the burning ban policy effectively reduced the occurrence of fires and reduced the PM 2.5 concentration in the whole area by 48.1% during the harvest season. Hu et al. (2020) discussed whether the Chinese ecological red line policy could achieve a balance between urban construction land and green space. After implementing this policy, the amount of urban soil grew, indicating that the policy has achieved a balance between land saving and land sharing.

The above-mentioned analysis methods used the results to infer the policy's impact and effect. It has limitations in evaluating the application effects of policies in different scenarios. Nor can it reflect the green initiative preferences of the direct implementers of the policy. Therefore, this study explores the differentiated driving effects of *China's Green Transportation Facilities Assessment Policy* on mountain tunnel builders. The study results will provide reliable suggestions for policy improvement.

2 GREEN TRANSPORTATION FACILITIES ASSESSMENT POLICY

The Ministry of Transport of China issued the *Green Transportation Facilities Assessment Policy* in 2017. The assessment system given by this policy is a framework structure containing three layers of indicators. The first layer indicators are conceptual, showing the four main directions of green transportation facilities assessment—Green concept, Eco-environment protection, Saving resources, energy-saving, and low-carbon. The second layer indicators are refined based on the first layer and give thirty subdivided green transportation facilities assessment fields. The third layer of indicators gives sixty-one specific requirements of green transportation facilities assessment.

The green concept is further subdivided into four second-layer indicators and eight third-layer indicators (Table 1). Adhering to green and sustainable development is the prerequisite for building green transportation facilities. Firstly, the central and local governments should establish strategic planning to develop green transportation facilities (1.1.1, 1.1.2, and 1.1.3). Secondly, governments should also establish special funds to build green transportation facilities and broaden private financing channels (1.2.1 and 1.2.2). Thirdly, governments at all levels should organize and launch education, training, and publicity activities on green transportation facilities in various forms to expand the influence of the green development concept at the grass-roots level (1.3.1, 1.3.2, and 1.4.1).

Table 1. Green concept.

First layer	Second layer	Third layer
1 Green concept	1.1 Strategic planning	1.1.1 Implement a green transportation facilities development plan and develop the green design, construction, and maintenance plan based on system theory and cycle cost.
		1.1.2 Implement energy conservation assessment and environmental impact assessment.
		1.1.3 Establish an energy conservation and emission reduction management system and assessment mechanism.
	1.2 Special funds	1.2.1 Establish a special fund for green transportation facilities development.
		1.2.2 Implement the PPP development model and expand green transportation facilities financing channels.
	1.3 Education and training	1.3.1 Organize and launch green transportation facilities with special technical consultation.
		1.3.2 Launch education and training activities, such as green design, green construction, green maintenance, etc.
	1.4 Publicity	1.4.1 Launch green transportation facilities publicity activities through the Internet, newspapers, special seminars, etc.

Eco-environment protection includes ten second-layer indicators and twenty-five third-layer indicators (Table 2). The assessment of eco-environment protection first pays attention to the protection of wildlife habitat and the effect of ecological restoration (2.1.1~2.3.2). In addition, soil and water protection, pollution gas emission control, and dust control are also the key points of the eco-environment protection assessment (2.4.1~2.7.2). Finally, the station location should be reasonably arranged to avoid excessive sound and light pollution (2.8.1~2.10.2).

The saving resource is subdivided into eleven second-layer indicators and sixteen third-layer indicators (Table 3). The core of saving resources is to conserve land and water resources (3.1.1~3.6.1). Reduce the amount of earthwork excavation and excessive planning of temporary ground. Build drainage and storage systems following local conditions. Recycle the construction and domestic sewage. In addition, attention should also be paid to the reuse of recycled materials and waste materials (3.7.1~3.8.1). In particular, the recycling rate of tunnel slag is an essential indicator of

Table 2. Eco-environment protection.

First layer	Second layer	Third layer
2. Eco-environment protection	2.1 Habitat protection	2.1.1 Avoid nature reserves, wildlife habitats, wetlands, and other ecologically sensitive areas. If it's impossible to avoid, ecological protection schemes are given.
		2.1.2 Set up signs like no honking in wild animals' living areas. Build passageways suitable for wild animals' life.
	2.2 Ecological restoration	2.2.1 Formulate ecological restoration plans in the affected areas.
		2.2.2 Plant local green plants that are easy to grow and resistant to adversity. Introducing exotic species should be demonstrated.
		2.2.3 Plant vines above the protection work.
		2.2.4 Construction and domestic waste should be strictly harmless treatments.
		2.2.5 Including greening projects and animal passageways in the daily maintenance plan. Formulate a perfect conservation plan.
	2.3 Vegetation restoration	2.3.1 Slopes and tunnel openings are covered with green plants.
		2.3.2 The survival rate of green plants in mountainous areas is more than 90%.
	2.4 Water protection	2.4.1 Select construction and management techniques that are conducive to water protection.
		2.4.2 No asphalt or concrete mixing station is set up in the water source protection area. No materials or wastes containing harmful substances are piled up or dumped.
		2.4.3 Set up sedimentation tanks to treat the wastewater of concrete mixing stations and tunnel construction.
	2.5 Soil protection	2.5.1 Build permanent and temporary protection works to protect the exposed surface.
		2.5.2 Greening tunnel waste dump site. Set up blocking facilities if the waste dump site is near the water area.
		2.5.3 Use an environment-friendly snowmelt agent to remove snow. Use environment-friendly snow removal technology like microwave technology instead of traditional chloride-type snowmelt agents.
	2.6 Pollution gas emission	2.6.1 Use technologies like warm mix asphalt mix to reduce emissions of toxic gases such as asphalt fumes and sulfur oxides.
		2.6.2 The exhaust emission of construction machinery reaches the national standard.
	2.7 Dust control	2.7.1 Use dust removal measures like encapsulation, covering, and water spraying to transport powder materials such as lime and fly ash.
		2.7.2 Use ready-mixed concrete process. Sprinkle water to remove dust on the construction site, material yard, and footpath.
	2.8 Station layout	2.8.1 Mixing stations, power stations, and material yards are located downwind of the prevailing wind in sensitive areas.
		2.8.2 The distance between the concrete mixing stations and residential areas is 300 meters. The distance between the asphalt mixture mixing stations and residential areas is 200 meters.
	2.9 Sound pollution	2.9.1 Reasonable arrangement of construction time and methods of strong noise radiation machinery.
		2.9.2 The noise level of sensitive points such as residential areas, schools, and hospitals near the construction area needs to meet the national standard.
	2.10 Light pollution	2.10.1 Avoid shooting the lighting beam into the sky or outside the construction area at night.
		2.10.2 Control the illumination of lighting facilities; do not disturb the nearby ecological environment and residents' normal life.

Table 3. Saving resources.

First layer	Second layer	Third layer
3 Saving resources	3.1 Land use	3.1.1 Coordinate the use of various channels.
		3.1.2 Make full use of wasteland, abandoned land, and inferior land; try to avoid farmland and residential areas.
		3.1.3 Centralized layout of communication, power supply, and monitoring cables.
	3.2 Earthwork	3.2.1 Select suitable tunnel section style and parameters to reduce the amount of excavation and waste dump.
	3.3 Temporary ground	3.3.1 Use wasteland, abandoned land, and service areas as temporary construction land. Strictly control its boundary.
		3.3.2 Restore the original function of the temporary construction land after use.
	3.4 Drainage and storage	3.4.1 Integrated design of drainage and storage projects.
		3.4.2 The drainage works are in harmony with the natural water system.
	3.5 Sewage treatment	3.5.1 Set up sewage treatment facilities. Recycling construction wastewater and domestic sewage.
		3.5.2 Use reclaimed water for cleaning operations. Water consumption depends on the amount of dust and weather conditions.
	3.6 Saving water	3.6.1 Use equipment or measures containing water-saving technology in construction and daily life.
	3.7 Recyclable material reuse	3.7.1 Use construction waste such as fly ash, coal gangue, and slag to replace part of the pavement materials.
	3.8 Old pavement material reuse	3.8.1 Old pavement materials such as asphalt, and cement reuse.
	3.9 Tunnel slag use	3.9.1 The utilization rate of tunnel slags is over 80%.
	3.10 Material storage	3.10.1 Build a special material shed for storing cement, asphalt, sandstone, and other materials.
	3.11 New materials	3.11.1 Use new materials, such as polymer concrete, high-strength lightweight concrete, natural asphalt, etc.

Table 4. Energy-saving and low-carbon.

First layer	Second layer	Third layer
4 Energy-saving and low-carbon	4.1 Energy-saving technology of mixtures	4.1.1 Warm mix asphalt pavement accounted for more than 10%.
	4.2 Construction energy-saving measures	4.2.1 Use energy-saving construction equipment with frequency conversion function.
		4.2.2 Use centralized power supply in the construction areas. Build substations to replace diesel power generation.
		4.2.3 Improve the utilization rate and load rate of construction machinery, and reduce unit energy consumption.
	4.3 Energy-saving system	4.3.1 Use power supply and distribution system with energy-saving technology.
		4.3.2 Use an intelligent lighting control system.
		4.3.3 Use LED and other new energy-saving lamps.
		4.3.4 Use an energy-saving information board.
		4.3.5 Use an intelligent ventilation control system to monitor the exhaust concentration, wind speed, and traffic flow in the tunnel in real time.
	4.4 Renewable energy	4.4.1 Use renewable and green energy such as solar, wind, geothermal, etc.
		4.4.2 Lighting equipment powered by renewable and green energy accounts for more than 15%.
	4.5 Natural gas mixing station	4.5.1 Use clean energy instead of coal and diesel in mixing stations.

green transportation facilities (3.9.1). Finally, the introduction and use of new materials in the future construction of green transportation facilities cannot be ignored (3.11.1).

The energy-saving and low-carbon indicators include five second-layer indicators and twelve third-layer indicators (Table 4). Applying various energy-saving technologies is critical in assessing green transportation facilities, such as warm-mix asphalt technology, energy-saving frequency conversion equipment, and a centralized power supply system (4.1.1~4.2.3). In addition, the construction of intelligent and energy-

saving power supply systems, lighting systems, information systems, and ventilation systems should be comprehensively promoted (4.3.1~4.3.5). Finally, the assessment of green transportation facilities should also focus on using renewable and clean energy such as solar, wind, and geothermal energy (4.4.1~4.5.1).

3 METHODOLOGY

3.1 *Fuzzy Delphi method*

The fuzzy Delphi method is essentially a feedback-based anonymous consulting method. This method can avoid some of the possible disadvantages of a group decision. With the fuzzy Delphi method, the loudest or most senior person does not have the opportunity to control the group's will because everyone's opinions are collected. The final decision owner can ensure that essential views are not ignored by collecting thoughts from all group members. Therefore, the fuzzy Delphi method has been widely applied to business, NGOs, military, education, health care, and other fields and has achieved good decision-making results (Zangenehmadar et al., 2016; Mclennan et al., 2017; Brunt et al., 2018; Salmon et al., 2018; Fritschy et al., 2019; Mirata et al., 2020; Grace et al., 2021). Figure 1 shows the survey process of the fuzzy Delphi method.

This study established a survey team of the *Green Transportation Facilities Assessment Policy*. This team is responsible for the organization, coordination, collection, summary, feedback, and necessary explanation during the whole survey process. The survey team transformed sixty-one third layer indicators into questionnaire questions. The survey team invited 130 first-line builders with years of experience in mountain tunnel construction in southwest China. The team distributed the prefabricated questionnaire to each respondent and explained the grading rules. The respondents were asked to assess their initiative to implement each policy indicator based on their work experience. The scores ranged from zero to ten. Zero is extremely reluctant, and ten is extremely willing. The questionnaire survey was conducted anonymously, and the respondents were not allowed to discuss with others either.

Through three rounds of Distribution-Collection-Analysis-Feedback, the consensus of all respondents was obtained. The centroid method processed the collected questionnaire results (Figure 2).

The steps are as follows:

1) Calculate the triangle fuzzy numbers (TFNs) of each third layer indicator (Qiu et al., 2020).
   After three rounds of surveys, the green initiative of mountain tunnel builders in implementing the third layer indicators has been collected by questionnaires. Calculate the green initiative assessment results' arithmetic mean for each third layer indicator (Equation (1)).

$$I_{fa} = \frac{I_{f1} + I_{f2} + \cdots + I_{fn}}{n} \tag{1}$$

   Where I_{fa} is the arithmetic mean value, I_{fn} is an independent assessment result, and n is the number of respondents. The minimum value (I_{fmin}), arithmetic mean value (I_{fa}) and maximum value (I_{fmax}) of the green initiative assessment results constitute the TFNs ($T_i = (I_{fmin}, I_{fa}, I_{fmax})$). The TFNs represent the respondents' consensus for the green initiative level of a specific indicator.
2) Convert the TFNs into a single value S_i.Equation (2) is used to convert the TFNs into a single value S_i.

$$S_i = \frac{I_{fmin} + I_{fa} + I_{fmax}}{3} \tag{2}$$

3) Calculate the green initiative threshold of each third layer indicator.The S_i represents the green initiative of each third layer indicator. A threshold (S_t) is needed to determine which indicators are the green initiative preferences of the mountain tunnel builders. The arithmetic

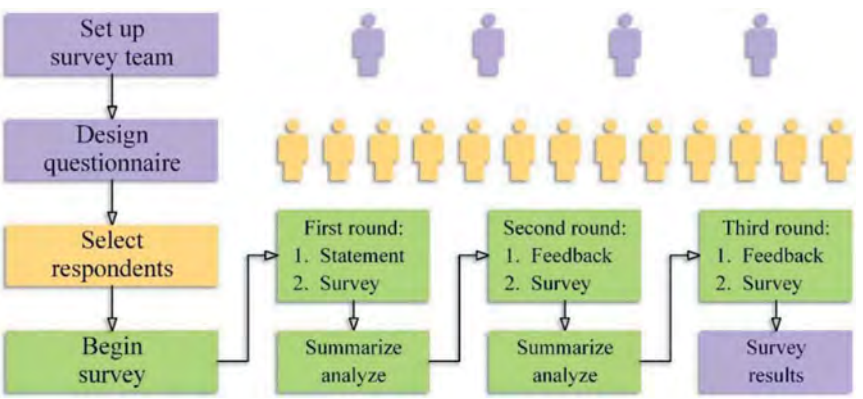

Figure 1. The survey process of the fuzzy Delphi method.

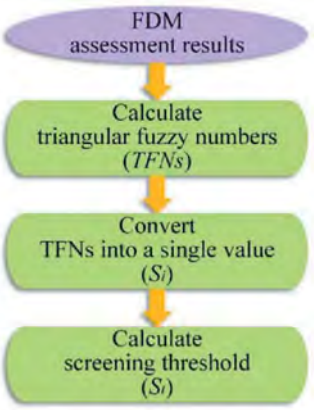

Figure 2. Calculation steps of the centroid method.

mean value was calculated as the green initiative threshold (Equation (3)).

$$S_t = \frac{s_1 + s_2 + \cdots + s_n}{n} \tag{3}$$

3.2 *Data sources*

Inviting enough practitioners from related industries as respondents is the most critical step to ensure the reliability of the fuzzy Delphi method assessment results.

3.2.1 *Study area*

With the continuous progress of China's basic transportation construction, the central tunnel construction has been transferred from the plain eastern sight to the western mountainous area. Soon, many super long and deep mountain tunnels will be built in southwest China. Therefore, it is of great significance to explore whether *China's Green Transportation Facilities Assessment Policy* can motivate the green initiative of mountain tunnel builders. The respondents of this study came from twenty-one mountain tunnels under construction in southwest China. All the respondents invited to join this survey have years of experience in mountain tunnel construction. Therefore, their opinions and consensus are deemed professional and reliable.

3.2.2 *Respondents*

One hundred thirty mountain tunnel builders in southwest China were invited to complete the questionnaire. These respondents mainly come from four positions: project manager, technician, environmental inspector, and constructor (Table 5). The project manager is the core of mountain tunnel construction management, responsible for schedule, quality, safety, and cost. Each tunnel project should be staffed with 2~3 technicians responsible for writing construction plans, monitoring deformation, and supervising the construction process. The environmental inspectors have only been deployed in recent years. They are mainly responsible for reviewing pro-environmental plans, checking their effectiveness, and rectifying requirements. Among all the tunnel builders, the number of constructors is the largest, and they are directly responsible for various construction tasks. The work content of these four positions runs through the whole process of mountain tunnel construction. Therefore, the feedback from respondents in these four positions is honest and meaningful. The survey results can reflect whether *China's Green Transportation Facilities Assessment Policy* can drive the green initiative of mountain tunnel builders.

4 RESULTS AND DISCUSSION

This study transformed China's green transportation facilities assessment indicators into a questionnaire and used the fuzzy Delphi method to conduct the survey. The one hundred and thirty respondents who participated in the survey came from twenty-one mountain tunnel projects in southwest China. The respondent's work location and work content can ensure the professionalism and reliability of the survey results. After three rounds of survey and feedback, seven questionnaires with apparent errors or incompleteness were eliminated, and finally, one hundred and twenty-three valid questionnaires were obtained. The survey results will reflect the different driving effects of China's green transportation facilities assessment indicators on the green initiative of mountain tunnel builders.

Table 5. Position, educational background, and the work content of respondents.

Position	Educational background	Content	Numbers
Project Manager	Bachelor or master in management	Organization, management, schedule, quality, safety, and cost.	40
Technician	Bachelor or master in tunnel engineering	Construction plans writing, deformation monitoring, and process supervision.	30
Environmental Inspector	Bachelor or master in environmental engineering	Review the pro-environmental plans, check the effects, and give rectification requests.	30
Constructor	Bachelor of tunnel engineering	All site construction tasks.	30

4.1 *Green concept*

As shown in Figure 3, the green concept contains eight third-layer indicators, and the green initiative threshold of mountain tunnel builders is 7.27.

Only three third-layer indicators have scores above the threshold (1.1.1, 1.1.2, and 1.1.3). All three indicators are related to strategic planning. It shows that mountain tunnel builders believe that systematic strategic planning and supervision mechanisms from the government are the primary means to drive the construction of green transportation facilities. On the contrary, two indicators related to special funds received the lowest score of 6.72 (1.2.1 and 1.2.2). It is because the mountain tunnel builders doubt whether the government's special funds can be directly used in engineering projects, and it is difficult for the construction of public transportation to attract private investment. Three indicators related to education, training, and publicity scored close to the threshold (1.3.1, 1.3.2, and 1.4.1). It shows that these three indicators can also drive the green initiative of mountain tunnel builders, but the driving effect is limited.

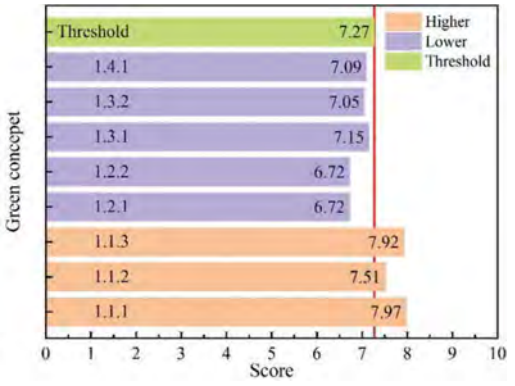

Figure 3. Green concept.

4.2 *Eco-environment protection*

As shown in Figure 4, the eco-environment protection contains twenty-five third layer indicators, and the green initiative threshold of mountain tunnel builders is 7.01.

Seventeen indicators have green initiative scores above the threshold, and the remaining eight are below the threshold. All indicators related to habitat protection have been recognized by mountain tunnel builders (2.1.1 and 2.1.2). Especially indicator 2.1.2 got the highest score of 7.64. It shows that the mountain tunnel builders believe that the first consideration in protecting the eco-environment is to ensure wild animals' normal life and migration. The ecological and vegetation restoration indicators have obtained differentiated assessment results (2.2.1~2.3.2). The mountain tunnel builders are more willing to implement ecological and vegetation restoration by transplanting native species and strengthening daily maintenance (2.2.2 and 2.2.5). Indicator 2.2.4 received the lowest score of 5.24. The construction and domestic waste harmless treatment requires the addition of new equipment, which means an increase in costs. All three indicators related to water protection scored higher than the threshold (2.4.1~2.4.3). On the contrary, only one of the three soil protection-related indicators scored above the threshold (2.5.3). In comparison, mountain tunnel builders have a higher green initiative in water protection. Reducing air pollution is also one of the core concerns of builders when building green transportation facilities. All the indicators related to pollution gas emission control and dust control have gained a high consensus (2.6.1~2.7.2). However, the method of reducing air pollution in sensitive areas by rationally arranging the location of the mixing station has not fully stimulated the green initiative of the builders (2.8.1 and 2.8.2). The land suitable for station layout in mountainous areas is limited, so it isn't easy to balance efficiency and environmental protection. Only one of

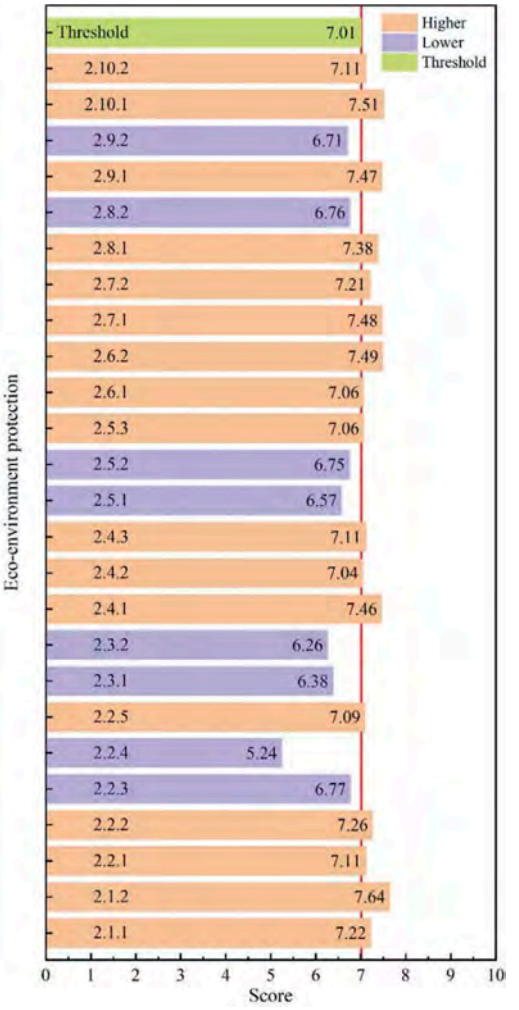

Figure 4. Eco-environment protection.

the four indicators related to sound and light pollution fell below the threshold (2.9.1~2.10.2). Compared with light pollution, noise generated by construction machinery is more difficult to prevent.

4.3 *Saving resources*

As shown in Figure 5, the saving resources contain sixteen third-layer indicators, and the green initiative threshold of mountain tunnel builders is 6.99.

The mountain tunnel builders first paid attention to the economical use of land resources. The land available for arranging stations in mountainous areas is highly scarce. Therefore, indicators such as using wasteland and abandoned land and centrally positioning pipelines have been recognized (3.1.2~3.1.3). The indicator related to earthwork excavation fell below the threshold (3.2.1). This is because the outline size of the tunnel depends on traffic planning and train selection. The mountain tunnel builders believe that the temporary ground should be strictly managed but have little initiative for restoring its original function (3.3.1 and 3.3.2). All the indicators related to the construction of drainage and storage facilities and sewage treatment scored higher than the threshold (3.4.1~3.5.2). On the contrary, mountain tunnel builders have little initiative to use water-saving equipment and methods in construction and daily life (3.6.1). The mountainous area has abundant surface water systems and water resources. The mountain tunnel builders prefer to prevent water pollution rather than save water. The mountain tunnel builders encourage recyclable materials such as fly ash and coal gangue in tunnel construction (3.7.1). However, there is little interest in recycling old pavement materials (3.8.1). Similarly, the mountain tunnel builders also questioned whether the utilization rate of the tunnel slag could meet the required standard (3.9.1). Finally, mountain tunnel builders are eager to use new materials such as polymer concrete, high-strength lightweight concrete, and natural asphalt to construct green tunnels (3.11.1).

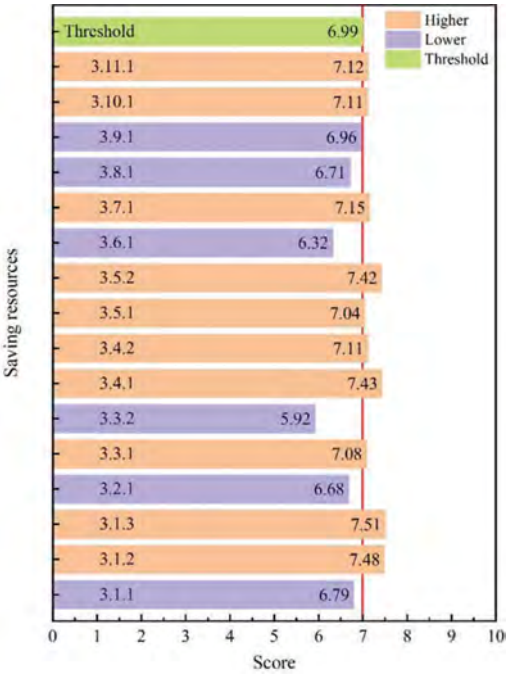

Figure 5. Saving resources.

4.4 *Energy-saving and low-carbon*

As shown in Figure 6, the energy-saving and low-carbon contain twelve third-layer indicators, and the green initiative threshold of mountain tunnel builders is 7.07.

The energy-saving warm mix asphalt technology scored the highest and won the greatest consensus among mountain tunnel builders (4.1.1). There are only one of the three indicators related to energy-saving construction technology scored below the threshold (4.2.1). Purchasing frequency conversion equipment means additional costs and mountain tunnel builders are more willing to save energy by increasing the existing equipment's utilization rate and full load rate (4.2.2 and 4.2.3). The use of energy-saving systems is the key to constructing green transportation facilities. Three indicators related to energy-saving equipment were scored above the threshold (4.3.1, 4.3.3, and 4.3.4). However, mountain tunnel builders have limited green initiatives for using intelligent devices (4.3.2 and 4.3.5). The failure rate of intelligent equipment is high, and it isn't easy to guarantee the stability of tunnel commuting. The use of renewable energy such as solar, wind, and geothermal has also failed to gain consensus among mountain tunnel builders (4.4.1). The lighting equipment is an exception (4.4.2). There is a lack of construction machinery that uses renewable energy as fuel, and if there is, it is expensive. The mountain tunnel builders are also not enthusiastic about using clean energy to replace coal and diesel in the mixing station (4.5.1). The main reason is the lack of a stable, clean energy supply and insufficient power.

5 CONCLUSIONS

This study conducted a questionnaire survey based on the fuzzy Delphi method among one hundred and thirty first-line builders from twenty-one mountain tunnels in southwest China. The purpose is to clarify the differentiated driving effects of *China's Green Transportation Facilities Assessment Policy* on the green initiative of mountain tunnel builders. The results showed:

1) Compared with private financing, education, training, and publicity, the government's strategic planning and supervision mechanism can better drive the green initiative of mountain tunnel builders.

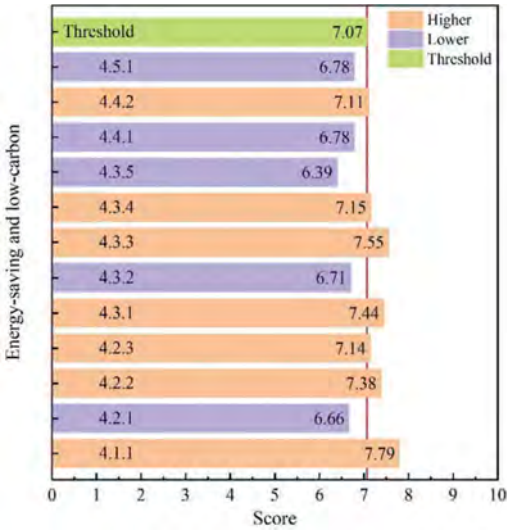

Figure 6. Energy-saving and low-carbon.

2) The mountain tunnel builders believe that the key to eco-environment protection is wild animals' habitat protection, water protection, pollution gas emission control, dust control, and light pollution prevention.
3) The mountain tunnel builders believe that saving resources should focus on land planning, drainage and storage, and recycled and new materials.
4) Compared with intelligent equipment, energy-saving equipment, and technologies can better stimulate the green initiative of mountain tunnel builders. In addition, the widespread use of renewable energy is not recognized.
5) The study results will provide valuable suggestions for adjusting and improving *China's Green Transportation Facilities Assessment Policy.*

ACKNOWLEDGMENTS

The authors gratefully acknowledge the financial support of the Big Data-driven Structural Disasters Prediction and Maintenance in Hazardous Geological Regions of Subsea Tunnels (51991395).

REFERENCES

Ministry of Transport of the People's Republic of China, 2019. Statistics Bulletin 2019. http://www.mot.gov.cn/. (Accessed August 2021).

Ministry of Transport of the People's Republic of China, 2016. Green Transportation Standards System. http://www.mot.gov.cn/. (Accessed August 2021).

Ministry of Transport of the People's Republic of China, 2017. Green transportation facility assessment technical requirements. http://www.mot.gov.cn/. (Accessed August 2021).

United States Green Building Council, 2000. Leadership in Energy and Environmental Design Building Rating System. https://www.usgbc.org/. (Accessed September 2021).

British Institute of Architecture, 1990. Building Research Establishment Environmental Assessment Method. https://www.architecture.com/. (Accessed July 2021).

German Sustainable Building Council, 2007. German sustainable building evaluation standard. https://www.dgnb.de/en/. (Accessed July 2021).

Gao, J., Yuan, Z., Liu, X., Xia, X., Huang, X., Dong, Z. (2016). Improving air pollution control policy in China–A perspective based on cost-benefit analysis. Sci Total Environ, 543(Pt A), 307–314. doi:10.1016/j.scitotenv.2015.11.037

Zhao, Y., McElroy, M. B., Xing, J., Duan, L., Nielsen, C. P., Lei, Y., Hao, J. (2011). Multiple effects and uncertainties of emission control policies in China: Implications for public health, soil acidification, and global temperature. Sci Total Environ, 409(24), 5177–5187. doi:10.1016/j.scitotenv.2011.08.026

Xu, Q., Zheng, X., Zheng, M. (2019). Do urban planning policies meet sustainable urbanization goals? A scenario-based study in Beijing, China. Sci Total Environ, 670, 498–507. doi:10.1016/j.scitotenv.2019.03.128

Yang, G., Zhao, H., Tong, D. Q., Xiu, A., Zhang, X., Gao, C. (2020). Impacts of post-harvest open biomass burning and burning ban policy on severe haze in the Northeastern China. Sci Total Environ, 716, 136517. doi:10.1016/j.scitotenv.2020.136517

Hu, T., Peng, J., Liu, Y., Wu, J., Li, W., Zhou, B. (2020). Evidence of green space sparing to ecosystem service improvement in urban regions: A case study of China's Ecological Red Line policy. Journal of Cleaner Production, 251. doi:10.1016/j.jclepro.2019.119678

Zangenehmadar, Z., Moselhi, O. (2016). Prioritizing deterioration factors of water pipelines using Delphi method. Measurement, 90, 491–499. doi:10.1016/j.measurement.2016.05.001

McLennan, J. V., Mackway-Jones, K. C., Horne, S. T., Body, R. (2017). Predictors of massive blood transfusion: a Delphi Study to examine the views of experts. J R Army Med Corps, 163(4), 259–265. doi:10.1136/jramc-2016-000702

Brunt H, Barnes J, Longhurst J. Enhancing Local Air Quality Management to maximize public health integration, collaboration and impact in Wales, UK: A Delphi study[J]. Environmental Science & Policy, 2018, 80:105–116.

Salmon, G., Tombs, M. (2018). Teaching undergraduate medical students Child and Adolescent Psychiatry (CAP): a Delphi study on curriculum content. BMC Med Educ, 18(1), 315. doi:10.1186/s12909-018-1427-4

Fritschy, C., Spinler, S. (2019). The impact of autonomous trucks on business models in the automotive and logistics industry–a Delphi-based scenario study. Technological Forecasting and Social Change, 148. doi:10.1016/j.techfore.2019.119736

Mirata, V., Hirt, F., Bergamin, P., & van der Westhuizen, C. (2020). Challenges and contexts in establishing adaptive learning in higher education: findings from a Delphi study. International Journal of Educational Technology in Higher Education, 17(1). doi:10.1186/s41239-020-00209-y

Grace M, Balzan M, Collier M. Priority knowledge needs for implementing nature-based solutions in the Mediterranean islands[J]. Environmental Science & Policy, 2021, 116:56–68. doi:10.1016/j.envsci.2020.10.003

Qiu, W., Liu, Y., Lu, F., Huang, G. (2020). Establishing a sustainable evaluation indicator system for railway tunnel in China. Journal of Cleaner Production, 268. doi:10.1016/j.jclepro.2020.122150

Tunnelling for a Better Life – Yan, Celestino, Thewes & Eberhardt (Eds)
© 2024 The Author(s), ISBN 978-1-032-80042-4
Open Access: www.taylorfrancis.com, CC BY-NC-ND 4.0 license

Planning and execution of horizontal directional coring method for future tunnelling works

Fahmi Mahony*, Kh Goh & C. Veeresh
Department of Geotechnical and Tunnels, Land Transport Authority (LTA), Singapore

ABSTRACT: The proposed Cross Island Line (CRL) is a high-capacity underground Mass Rapid Transit (MRT) system with a total route length of 56km. A section of the alignment crosses under one of Asia's busiest runways at Singapore Changi International Airport. Site investigation is an essential component for a better understanding of geotechnical uncertainty which is a key risk for underground tunnelling works. Ground investigations using conventional vertical bore holes along the alignment has limitations along runways and taxiways and closure of runway and taxiways affects the airport operations. To mitigate geotechnical uncertainty during future tunnelling, Horizontal Directional Coring (HDC) technology was adopted. In HDC, continuous cores along the future tunnel route allows comprehensive understanding of ground condition along the alignment. Due to limited amount of subsoil information, it is challenging to plan the HDC trajectory as the technology requires directional steering only in rock stratum. This paper presents various challenges, advantages and disadvantages in executing the HDC under runway 1 of Singapore Changi International Airport.

Keywords: Horizontal Directional Coring, HDC, Tunnel, Gravity Survey

1 INTRODUCTION

The geology along the tunnel alignment plays a dominant role in planning designing and constructing the tunnel, significant risks arise for tunneling construction are associated with uncertainty in the ground. Site investigation is an essential component for a better understanding of geotechnical uncertainty which is a key risk for underground tunnelling works. A section of the cross island (CRL) alignment under crosses the busiest runway at Singapore Changi International Airport.

Based on geological map of Singapore, Changi International Airport Runway 1 resides on Bukit Timah Granite formation. This is intrusive type of igneous rock formed more than 230 million years ago. The upper zone of the Bukit Timah Granite is generally weathered and has been decomposed into residual soils. Bukit Timah Granite has undergone weathering processes over time and the degree of weathering improves with depth. The upper portion of the Bukit Timah Granite Formation is mostly weathered and comprises completely weathered granite to residual soil. The slightly weathered and fresh granites are found at the larger depth of the Formation. The weathering of the Bukit Timah Granite is gradational with depth range and sharp boundary between completely weathered layer (GV) and moderately weathered granite (GIII) is often observed. The rock head level is generally undulating with frequent valleys and commonly follows the topography.

Ground investigations using conventional vertical bore holes along the alignment has limitations along runways and taxiways and closure of runway and taxiways affects the airport operations. Alternative investigation methods using geophysical investigations are explored, microgravity survey has been carried out along the alignment where the access for bore hole drilling is limited. However, due to airport environment there are concerns on reliability of these investigations as the area is consists of numerous services and airport operations. To verify the gravity survey data and enhance the confidence level, Horizontal Directional Coring (HDC) has been considered.

In HDC, conventional boring process is adopted, and the main difference is the steerable core barrel mounted to a drill string attached to drill rig. The steerable core barrel makes it feasible to control the direction of coring in sub-vertical or horizontal direction along the alignment within the rock. In HDC, heat treated drilling rods are used which can withstand bending to between 5ºand 9º for every 30 m (a radius of 200m) along the drilling trajectory. (See Figure 1).

*Corresponding author: muhammad_fahmi_mahony@lta.gov.sg

DOI: 10.1201/9781003495505-14

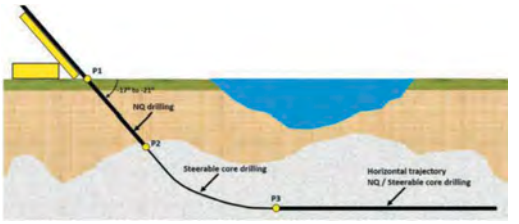

Figure 1. Horizontal direction coring methodology (Veeresh et al 2018).

From the available literature review, it is noted that majority of past projects where HDC was carried out is mostly in hilly terrains focused on determining the rock quality, fracture zones by obtaining the continuous cores along the known tunnel alignment either placing HDC alignment above or on side of the tunnel with known geological information. In current project HDC is carried out in the Airport environment where subsoils information from direct drilling is limited the objective of conducting HDC was to determine the geological condition along the tunnel alignment and validate the geophysical information.

Information from microgravity survey rockhead profile results was used to plan the suitable HDC inclination angle, and curvature portion to determine the appropriate horizontal drilling trajectory. For HDC it is noted that the curvature must be in competent rock (GIII or better). The gravity survey helps to characterise rock profiles around the future alignment. This technique measures minute variations in the gravitational pull of the Earth by using a gravity meter and interprets the presence of massive objects and of voids in the ground. If there exist some material below the ground having density that is lower or higher than surrounding ground (such as a cavity or a subsurface cave), the gravity shows a relatively low anomaly. The denser rock material will have more gravitational attraction. Gravity survey requires at least few boreholes to help with processing and interpretation of the rockhead. See Figure 2 interpreted rockhead profile from gravity survey.

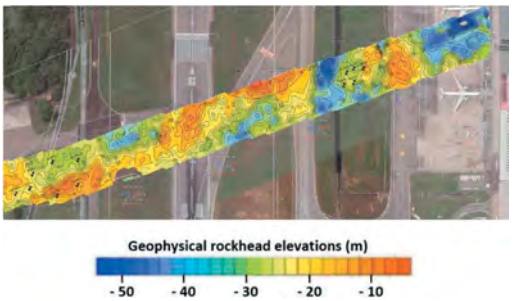

Figure 2. Interpreted rockhead profile.

After the identification of the drilling trajectory, a drilling tolerance envelope must be decided. Typical tolerance envelope for HDC trajectory is within the range of 2m to 7m radius (Veeresh et al 2018). To ensure that drilling is travelling along the planned designed alignment and within the tolerance envelope, a survey equipment, Devitool^{TM} from the HDC specialist was used to record the drilling trajectory in the borehole at regular intervals. The survey equipment uses three high-accuracy magnetometer and accelerometers to acquire three-dimensional borehole position, inclination, azimuth, tool face direction and magnetic dip angle.

2 ADVANTAGES AND CHALLENGES OF HDC

One of the main advantages is the continuous core sample along future alignment which provides valuable information on the geological condition and this reduces tunnelling risk during construction. Other advantages include, High drilling accuracy and able to drill up to 2km, pilot hole which can branch out to 30 multiple branches.

One of the main challenging aspects of HDC is the risk of a broken drill string and getting stuck in the borehole, this may cause the drilling to end prematurely and form a possible obstruction during tunnelling. This risk can be overcome by planning the HDC trajectory outside the tunnel envelope. Another major risk is encountering intermediate layers of soft ground along the alignment, in such situations it is difficult to control the direction of HDC and may have to abandon the drilling works. Localised grouting of soft ground is possible but if the soft stretch is longer it may be difficult to continue the HDC. From the past experience lengths of up to 40m of soft ground are grouted and drilling is able to continue.

Keeping in view the risk associated with HDC, trajectory should be planned with aim to reduces excessive curvatures which can potentially induce drilling stress on the drill rods, and alignment should be within rock strata as much as possible.

Figure 3. Broken drill string.

3 INVESTIGATION RESULTS AND DISCUSSION

From the gravity survey and available borehole data, the aim for HDC was to drill 1m above the north-east of the future tunnel while maintaining drilling within

a 5m envelope to ensure the trajectory does not intrude into the future tunnel alignment. See Figure 4.

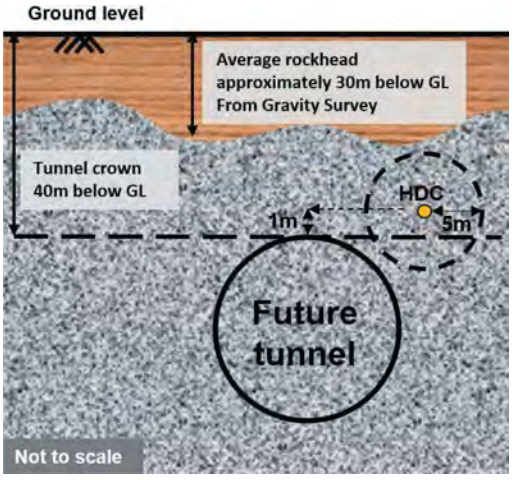

Figure 4. HDC tolerance envelope.

The location plan for the site was strategically placed above the future tunnel alignment for better logistical planning and reduce unnecessary plan for curvature which induces stress on the drill rods. Stress on the drilling rods will impact the machine capability of drilling further. The plan was to terminate at 610m (horizontal distance) from the start location which was 225m away from the runway centreline. The end drilling point targeted before the apron of the cargo complex. The HDC undercrossed live runway, taxiway and drain box culvert. To mitigate the risk of casing stuck in the soft ground, various layers of casing with different sizes was installed, depending on the soil conditions. For examples, large size (140mm in diameter) PW-casing can be installed in loose sand layers, followed by medium-size (115mm in diameter) HW-casing installed in dense sand & residual soil layers, and finally the smallest (76mm in diameter) NW-casing in highly weathered rock layers. The joint screw of casings shall be checked to minimize the failure at the casing joints.

Drilling commenced with an 21° inclination section for approximately 60m before encountering the rock. This translated to approximately 22m below ground level. NW drill casing is then socketed 3m into rock to ensure the inclination degree is maintained before further coring was carried out up to 82m in drilling length before the curvature section using steerable barrel.

Drilling encountered highly fractured rock and multiple core loss between 104.8m – 112.5m. See Figure 5. Flushing and conditioning of borehole prevented the drill string to reach the bottom hole (114.8m). Grouting was proposed to overcome fractured zone. Upon comparing with the longitudinal section from the gravity survey results, drilling may have encountered a weak zone.

Grouting was proposed as mitigation measures between 104m – 114.8m. The single valve (one way) Van Ruth grouting and water control packer was set at 104m where good quality rock was observed. In theory the volume of grouted section was 49L. In actual, over 200L of grout was pumped into the hole and allowed to set for 60 hours. Packer was retrieved successfully when drilling resumed. Between 109m and 114m, fresh rock was sampled implying that the hole may have deviated from the from the original trajectory. Survey was conducted to verify the trajectory and found that hole had deviated slightly but still within the designed alignment.

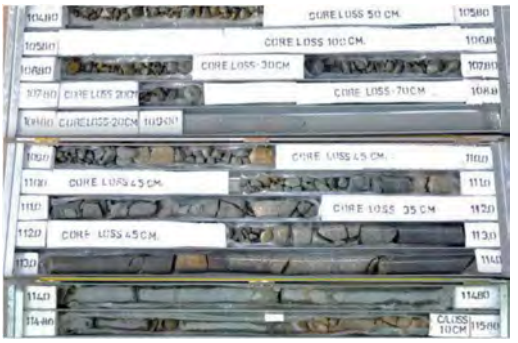

Figure 5. Weak zone core sample.

Drilling continued as planned and successfully cored through underneath Changi Airport Runway 1 which was in operation. Between 321m and 324.6m, brittle rhyolite was encountered and grouting between this section was conducted for 4 times without success. Grout appears to have slipped into the fractured area without any sign of grout sample being retrieved after re-drilling. Drilling parameters were not stable with high torque and high-water pressure being observed. The water pressure for HDC must not exceed 40 bars or risk bursting the sliding packer that is fitted on the HDC barrel. The function of the sliding packer is to hold the core barrel by packing on the borehole wall to control the direction of the drilling.

It was then decided to conduct a side-tracking (branch out) without having to exit the entry point of the HDC. See Figure 6. Branching out or side-tracking can only be conducted at good quality rock section and shall begin with NQ core barrel placed at the apex of curvature along the drilling trajectory. Drilling must be conducted at low in rpm and water pressure for branch out to be successful.

The objective of branching out is to lower the trajectory within the tolerance envelope (See Figure 7) with hope drilling can be overcome previous weak zone and continue with the rest of the drilling as planned.

Branching out was conducted successfully (See Figure 8), however similar weak zone was encountered at 319m before the earlier 321m zone. Drilling experienced high rotation torque which prevented the hole from advancing further. Grouting was

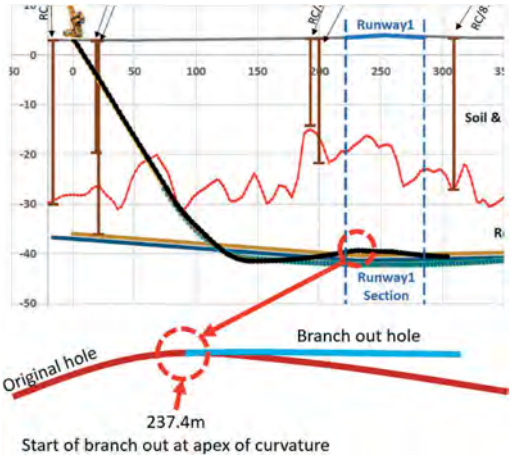

Figure 6. Prominent peak at 237.4m.

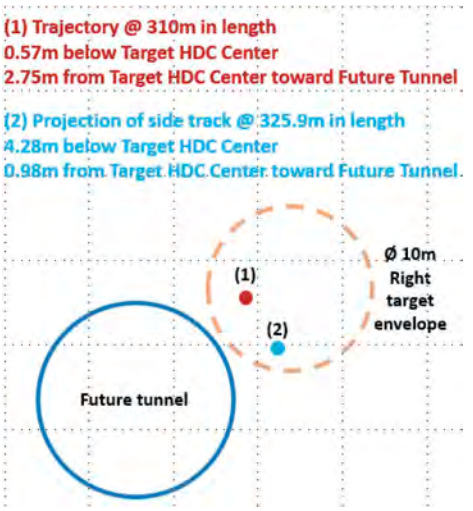

Figure 7. Original hole based on last survey point vs projected trajectory.

carried out between 315m and 322.7m and grout volume pumped was 10 times more than the theoretical volume. When re-drilling was conducted, grout sample was encountered at 290m and towards the end of the hole the no grout sample was retrieved. Drilling again experience high rotation torque prevented the advancement of the drill hole. The hole was terminated prematurely, and the team explored the possibility of second side track and move the drilling trajectory towards the north-west of the future tunnel without the need for intrusion.

Extensive planning and discussion were held to ensure the success of side tracking while maintaining the principle of HDC drilling parameters. Before the side tracking was conducted, the original hole and the first side track hole had to be grouted from 180m onwards to the hole end. See Figure 9.

Figure 8. Side tracking core sample.

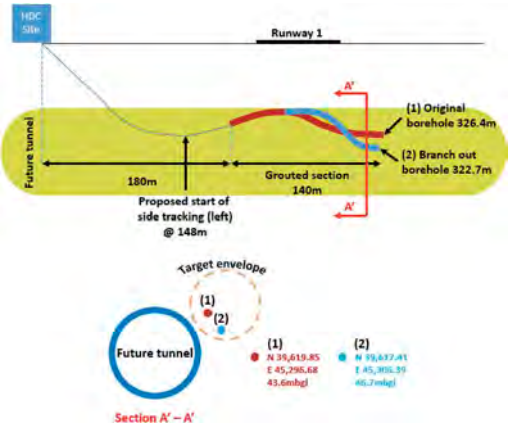

Figure 9. Grouted section (longitudinal section).

The left side tracking was conducted at the lowest apex of the drilling trajectory and the objective is to cross the drilling trajectory to the north-west envelope without having to intrude into drilling path of future tunnel. See Figure 10.

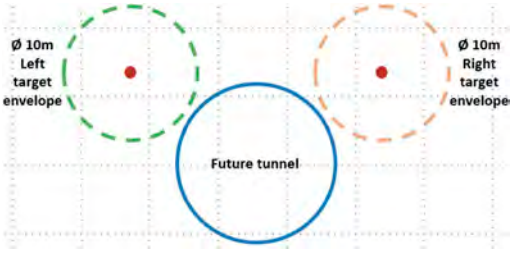

Figure 10. Moving the trajectory from the right to left envelope.

The side tracking when as planned and successfully drilled underneath the runway for 3rd consecutive time before entering to the north-west of the drilling envelope. Upon reaching 587m highly fractured zone were encountered where solid core recovery (SCR) range from 0% to 28%. SCR is referred to as length of core recovered as solid cylinders which is then expressed as percentage of the length of the core run.

Drilling continued with limited core recovery to 607.3m. As a result of the fractured area, the core barrel was jammed on three occasions despite conditioning the drill hole with higher viscosity drilling fluid to stabilise the hole. Higher force was applied on the machine and hydraulic pressure was closed to machine limit at almost 280 bars. The high force forces the machine to stop. The jammed took 5 days before it was finally recovered. This gives indication that further drilling may increase the risk of drilling string getting stuck or potentially break along the hole. Having considered drilling have achieved the intended end point, it was then decided to terminate the HDC. Specialist projected the coordinates based on the drilling trend and the last survey point indicated that drilling is still within the tolerance envelope.

The total drilling length including the two-side tracking was approximately 870m and 93% of the drilling was coring through granite. The final isometric view of all the 3 holes is shown in Figure 11.

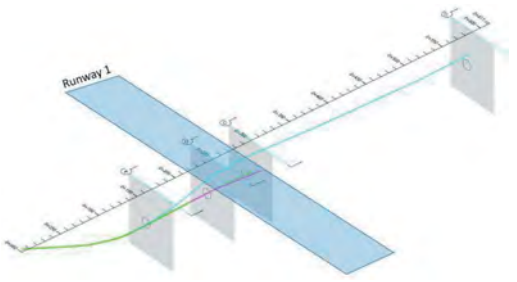

Figure 11. Isometric view of the entire holes.

4 CONCLUSIONS

A section of the cross island (CRL) alignment under crosses the busiest runway at Singapore Changi International Airport. Ground investigations using conventional vertical bore holes along the alignment has limitations along runways and taxiways and closure of runway and taxiways affects the airport operations. The HDC, which avoids any impact to airport operations is used to determine the geological condition along the future tunnel alignment. The HDC method has proved that multiple branching out or side tracking within the main hole can be carried even despite moving the trajectory against the natural deviation. In this study, HDC has branched out twice to explore deeper depth and moving the drill trajectory to the north-west of the future tunnel alignment. The gravity survey data has helped in determining likely depth of rockhead to plan HDC trajectory. HDC is successfully carried out under the runway without any impact to the operations of airport.

ACKNOWLEDGMENTS

The Authors would like to extend their appreciation to Changi Airport Group for facilitating the site work during the COVID-19 pandemic and ensuring that the works are carried out smoothly and safely.

REFERENCES

C.Veeresh, Fahmi Mahony, KH Goh, Cai Jun Gang (2018). "Planning and Execution of Horizontal Directional Coring Method for Future Tunnelling Works". Underground Singapore 2018.

Christopher Brook (2013). "Horizontal Directional Ground Investigation – Reducing Tunnelling Risks by Minimising Geological Uncertainty". Tunnelling and Underground Construction Society (Singapore) 2013.

Chan, M.P (2012). "The use of Horizontal Directional Coring Technique for Ground Investigation of Tunneling Projects in Hong Kong," Masters Dissertation. June 2007.

Association of Geotechnical & Geoenvironmental Specialists (Hong Kong) (2012) Ground Investigation Guidelines - 04.9 – Horizontal Directional Coring.

Tunnelling for a Better Life – Yan, Celestino, Thewes & Eberhardt (Eds)
© 2024 The Author(s), ISBN 978-1-032-80042-4
Open Access: www.taylorfrancis.com, CC BY-NC-ND 4.0 license

Theory meets practice: Evaluating discrepancies between theoretical settlement projections and actual measurements in tunnelling projects with tunnel boring machines

Elena Navarro*
TYPSA/AZTEC, Austin, USA

Eduardo Salvador & Fernando Diez
TYPSA, Madrid, Spain

ABSTRACT: The construction of tunnels using tunnel boring machines (TBMs) is a complex process that requires accurate predictions of ground movement to ensure safety and avoid costly delays. However, discrepancies between theoretical projections and actual measurements are common, leading to significant challenges during construction. This paper presents a comprehensive evaluation of settlement projections in tunnelling projects using the East Crosstown West Extension (ECWE) Project in Toronto as a case study. The study compares predicted settlements during the design phase with actual settlements measured during construction using readings of instruments installed on-site.

The paper reveals important insights into settlement behaviour in different ground conditions, including rock, soil, and mix-face conditions. Maximum settlements at the surface, volume loss, and shape parameter values for each case were analysed. To evaluate ground movement during the design phase, the methodology involved calibration of Volume Loss and Settlement Trough using three-dimensional Finite Element Models (FEM) and calculation of greenfield settlement at 100 m intervals along the tunnel alignment by empirical models including parameters obtained from the FEM. Automated Data Acquisition and Monitoring System (ADAMS) was used during construction to collect and process data from various types of instruments, enabling us to monitor behaviour in real-time, predetermine trends, and trigger alarms. This system proved to be a powerful tool for evaluating ground movement during construction on tunnelling projects.

Overall, our findings highlight the importance of evaluating theoretical settlement projections against actual measurements and the need for accurate predictions of ground movement during tunnelling projects. The methodology and monitoring system presented in this paper contribute to the advancement of theory and practice in the field.

Keywords: Tunnelling, TBM, Settlement Projections, Volume Loss, Simulation, Monitoring

1 INTRODUCTION

Metrolinx (Mx) and Infrastructure Ontario (IO), two provincial government agencies are leading the project to deliver the Toronto subway expansion for the Ontario Ministry of Transportation. The Advance Tunnel for Eglinton Crosstown West Extension (ECWE) Project includes 6.3 km of internal 5.75 m diameter twin bored tunnels that include open cut excavations for the launch and extraction shafts. The tunnel runs from the Renforth Drive to the Extraction Shaft near Scarlett Road, through urban areas and challenging mixed-face (soil and rock) conditions.

Ground induced movements due to tunnelling and potential impacts depend upon the anticipated magnitude of settlements, their spatial distribution, as well as the type and proximity of Existing Adjacent Structures (EAS), Existing Adjacent Utilities (EAU), and other facilities. TYPSA completed the tunnel design to the highest standards to ensure that the excavation of the tunnels does not cause impact on EAS, EAU, and the highway operations.

2 GEOTECHNICAL CONDITIONS

The schematic longitudinal profile of the bored tunnels includes the distribution of the rock/soils/mix-face conditions (soils and rock) along the tunnel excavation.

*Corresponding author: elnavarro@typsa.es /enavarro@aztec.us

DOI: 10.1201/9781003495505-15

2.1 *Rock conditions – sound Georgian Bay Shale*

The bedrock within the confines of the tunnel zone can generally be described as slightly weathered to fresh shale, commonly referred as "Georgian Bay Shale", of Ordovician age. The Total Core Recovery (TCR) in the bedrock typically reaches 100%, while the Rock Quality Designation (RQD) ranges from 48% to 100% with an average value of approximately 82%. Based on the RQD values, the quality of the rock mass can be described as ranging from fair to excellent. Average value of the UCS is over 15 MPa. Schistosity is almost horizontal. No major faults have been detected along the tunnel.

In general, tunnelling works are located within the sound rock except on the transition areas between rock to soils and vice versa (mixed-face conditions). The weathered rock thickness ranges from 0 m to 7.6 m.

Elevated horizontal in-situ stresses are a known characteristic of the Georgian Bay Shale. A design major principal horizontal stress of up to 4.0 MPa was recommended. Based on the available information and the wide range on the major principal stress, a sensitivity analysis of the influence of the horizontal in-situ stress on the induced movements (analysed in terms of the horizontal to vertical in-situ stress ratio, K0) was performed using values from 1.5 MPa to 4.4 MPa.

2.2 *Soils conditions*

Native soil is typically silt and clay tills (cohesive and non-cohesive) with SPT-N values ranging between 7 blows per 300 mm penetration to 50+ blows per 150 mm penetration. The cohesive tills are typically stiff to very stiff and the non-cohesive tills are typically dense to very dense (competent soils).

2.3 *Mixed-face conditions*

Native soil is typically silt and clay tills (cohesive and non-cohesive) with SPT-N values ranging between 7 blows per 300 mm penetration to 50+ blows per 150 mm penetration. The cohesive tills are typically stiff to very stiff and the non-cohesive tills are typically dense to very dense (competent soils).

2.4 *Groundwater conditions*

The soils typically present in the tunnel alignment have been identified as aquitards (tills) and water bearing (granular materials). Based on the rock quality and the hydraulic conductivity of the shale, negligible water ingress was assumed within the rock sections.

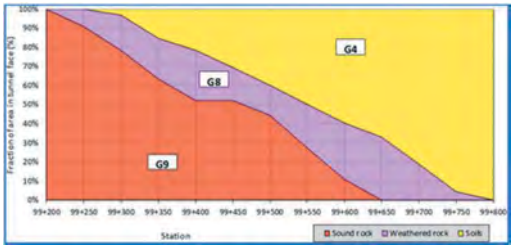

Figure 2. Mixed-face distribution of materials at Martin Grove.

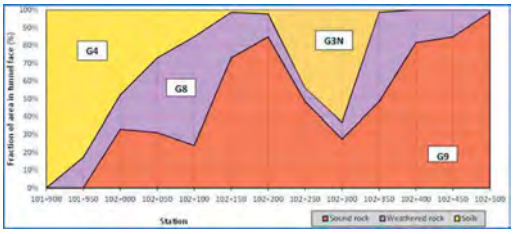

Figure 3. Mixed-face distribution of materials at Royal York.

3 INDUCED SETTLEMENTS – APPLICATION OF THEORY

The methodology of the complete analysis included the following sequence:

- Volume loss (VL) and settlement trough calibration by numerical models (3D FEM) at selected

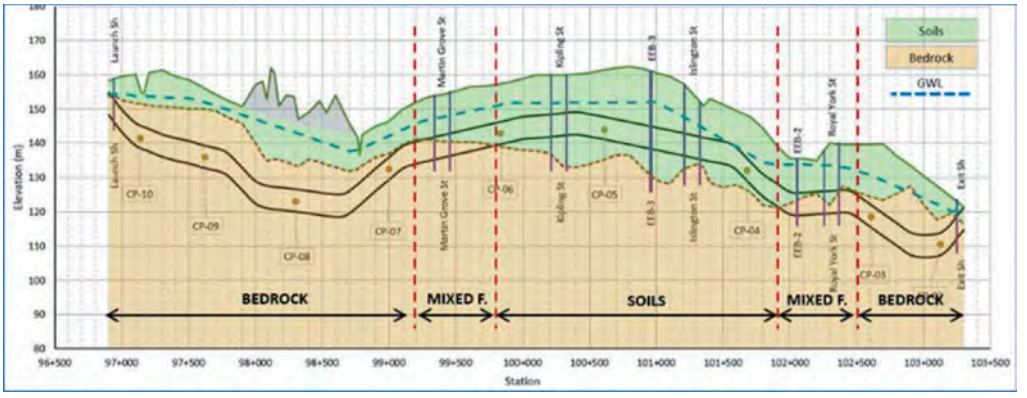

Figure 1. Geological longitudinal profile of the bored tunnels.

sections along the bored tunnel alignment (twelve sections in total).
- Greenfield settlement calculation performed at 100 m intervals along the tunnel alignment by empirical models including VL and the other parameters obtained from the 3D FEM.
- Zone Of Influence (ZOI) definition as per outermost 1mm settlement contour line.
- Estimation of induced movements (settlement, joint rotation, and angular distortion) for each EAS and EAU based on the estimated induced movements.
- Assessment of the magnitude of impact for all Existing Adjacent Utilities (EAU) and Existing Adjacent Structures (EAS) EAS and EAU.

The two main parameters for the ground movement analysis, other than the tunnel dimensions and depth, are the Volume Loss (VL) and the shape parameter (K). VL and K are empirical parameters that are dependent on ground properties, as well as the performance of tunnelling operations.

The settlement analysis was based on an empirical estimation using the usual Gaussian distribution curve (Figure 3), using parameters previously obtained from complex finite elements model (PLAXIS 3D) following good industry practice references such as Boscardin and Cording (1989), New and O'Reilly (1982 and 1991).

The settlement cross-sectional curve and the maximum settlement can be obtained using the following equations:

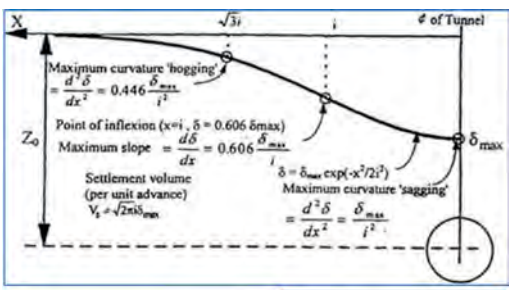

VL = Volume Loss
D = Tunnel Diameter
℈h = horizontal strain
i = Kz; Distance from the centreline of the tunnel to the inflection point, (K: settlement trough shape factor; z: depth of the tunnel centreline).
S = Settlement at distance "y" from the centreline of the tunnel

Figure 4. Representation of settlement through using a Gaussian Curve (New and O'Reilly, 1991).

Different recommendations available in the bibliography, as well as numerous values of VL from previous projects and references in Toronto area have been reviewed. However, 3D Finite Element Models (FEM) were developed at selected sections along the bored tunnel alignment to calibrate the VL and parameter K considering the conditions of ECWE Project. These models included the specific geotechnical conditions at each section, the construction sequence of the tunnel (at every ring excavation cycle), TBM lining and grouting, and the effect of the first tunnel on the settlements induced by the second tunnel.

A total of twelve sections in sound rock, in soils, and in mix-face conditions were analysed by 3D FEM for the Volume Loss (VL) calibration and settlement trough estimation. 3D Finite Element Models' design parameters and geometry:

- Long-term (drained/effective stresses) behaviour of cohesive materials and rock.
- Ground behaviour models:
- Soils: Hardening soil model with small-strain stiffness.
- Rock: Hoek and Brown model.
- Ratios between horizontal and vertical in-situ stresses of rock above 3.5 (up to 4.5).
- The diameter of the tunnel is taken as the external excavation diameter (6.58 m).
- The distance between the two parallel tunnels is 10.90 m (between axes).
- Depth of the tunnels and GWL and strata taken from the Geotechnical profile.
- Assumed horizontal ground surface, strata, and ground water level.
- Model boundaries are stablished to avoid affecting the results.
- 40 rings (68m excavation) and 96 stages in total.
- The settlement trough is obtained after the first and second tunnel excavation.

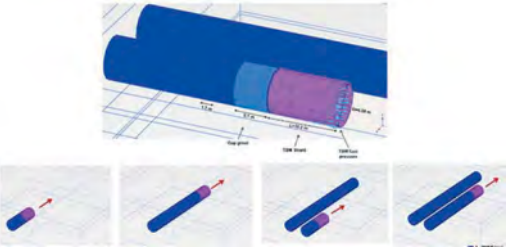

Figure 5. FEM model used to calibrate the settlement parameters VL and K.

The following values are measures and analysed:

- Maximum settlement Smax (mm)
- Volume of the trough A (m^3/m)
- Ratio between the volume of the settlement trough and the total excavated volume (Volume Loss, VL)
- Shape of the curve and inflection point (parameter k)

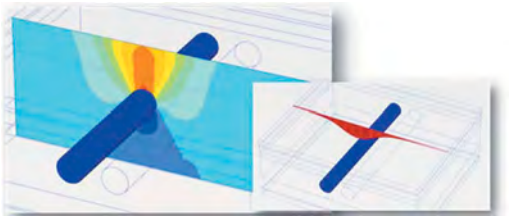

Figure 6. Settlement after one tunnel excavation.

Figure 7. Settlement after two tunnel excavation.

- Influence of first tunnel excavation over the settlements induced by the second tunnel (parameter f_{2T}).

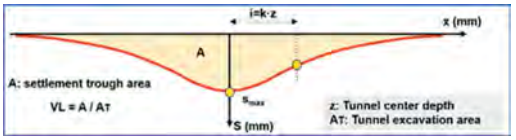

Figure 8. Parameters taken from the Gaussian Curve obtained on the FEM.

4 THEORETICAL SETTLEMENT PROJECTIONS

Three sections in sound rock, four sections in soil, and five sections in mix-face conditions were analysed by 3D FEM for the Volume Loss (VL) calibration and settlement trough estimation.

Tunnelling in rock:

- The high horizontal stress of the rock produces a slight heave (<1 mm) at ground surface.
- Settlements are found to be negligible (<1 mm) in all cases.
- No volume loss VL.

Tunnelling in soils:

- Settlements depend on the ground conditions encountered at the tunnel face (proportion of gravels and fine sands and silts) being higher on gravels formation since these materials are stable with lower TBM face pressure.
- Considering the TBM face pressures from the face stability analysis, all settlements obtained are lower than 10mm (7.5 mm at the most

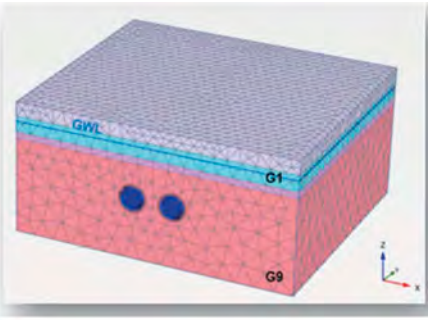

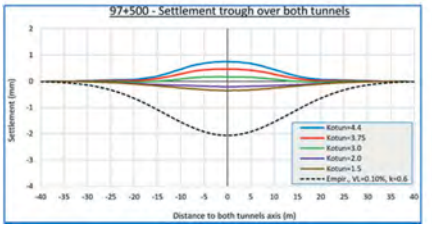

Figure 9. Tunneling in rock – 3D FEM and settlement trough.

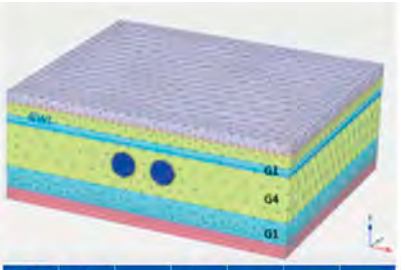

P_f (kPa)	S_1 (mm)	V_{L1}	S_T (mm)	V_{LT}	K	f_{2T}
85	4.9	0.25%	7.3	0.26%	0.49	1.01
100	3.0	0.16%	4.6	0.16%	0.52	1.01
115	2.2	0.12%	3.4	0.12%	0.53	1.01

- P_f: Face pressure (EPB mode)
- S_1: Maximum settlement at surface after construction of the first tunnel
- V_{L1}: Volume Loss induced by the construction of the first tunnel
- S_T: Maximum combined settlement at surface after construction of the second tunnel.
- V_{LT}: Volume Loss induced by the construction of both tunnels
- K: Settlement trough parameter
- $f_{2T} = S_T / (2 \cdot S_{1T})$. Two-tunnels factor

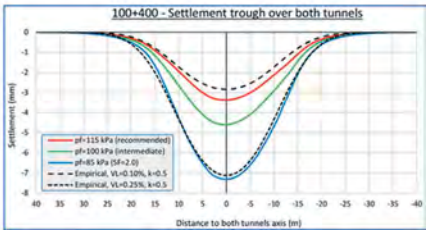

Figure 10. Tunneling in Soils – 3D FEM and settlement trough.

unfavourable hypothesis). The second tunnel induces slightly higher settlements (around 10%) that the first tunnel.

- The volume loss VL when both tunnels are excavated varies within the range 0.15% to 0.30% depending on the adopted face pressure. VL is lower for fine sands and silts and higher for gravels.
- The shape parameter K is between 0.50 and 0.60 depending on the tunnel depth and type of soil.

Tunnelling in mixed-face conditions:

- In general, the calculations show similar results for soils (gravels or fine sands and silts). However, with over consolidated glacial tills the behaviour differs mainly on the ground movements caused by the second tunnel, most likely due to the decompression caused by the first tunnel.
- Considering the TBM face pressures from the face stability analysis, all settlements obtained are lower than 10mm (8.6 mm at the most unfavourable hypothesis). The second tunnel induces slightly larger settlements (around 10%) than the first tunnel.
- The volume loss VL when both tunnels are excavated is found to be around 0.10% - 0.15%.
- The shape parameter K has been found to be between 0.45 and 0.65 depending on the on the cover thickness and on the type of soils.

Where the tunnel is excavated in soils and mix-face conditions (rock and soil), settlement calculations have been performed at 100 m intervals by empirical models including VL and the other parameters obtained from the 3D FEM.

The settlement curves from each tunnel have been added up to obtain the maximum settlement envelope. Figure 12 summarizes greenfield settlement results at 100 m intervals along the tunnel alignment when excavation in soils and mix-face conditions.

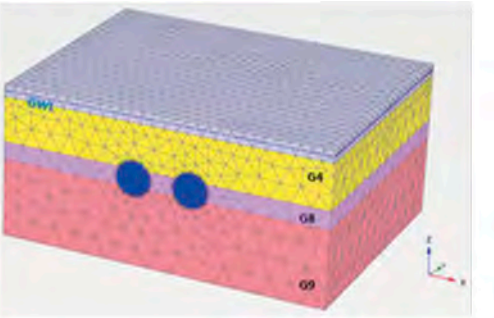

P_f (kPa)	S_1 (mm)	V_{L1}	S_T (mm)	V_{LT}	K	f_{2T}
EPB 140	1.6	0.09%	2.3	0.09%	0.62	0.93
EPB 155	1.1	0.07%	1.7	0.07%	0.66	0.98
EPB 170	0.8	0.05%	1.3	0.05%	0.72	1.00
Air 120	1.7	0.10%	2.4	0.09%	0.63	0.93
Air 130	1.3	0.08%	2.0	0.08%	0.65	0.96

- P_f: Face pressure (EPB mode)
- S_1: Maximum settlement at surface after construction of the first tunne
- V_{L1}: Volume Loss induced by the construction of the first tunnel
- S_T: Maximum combined settlement at surface after construction of the second tunnel.
- V_{LT}: Volume Loss induced by the construction of both tunnels
- K: Settlement trough parameter
- $f_{2T} = S_T / (2 \cdot S_{1T})$. Two-tunnels factor

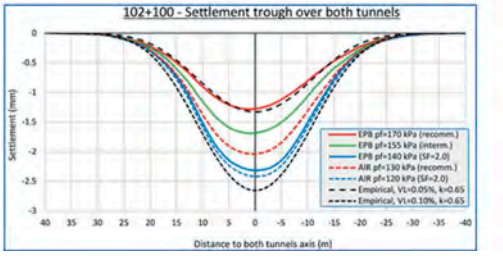

Figure 11. Tunneling in mixed face conditions – 3D FEM and settlement trough.

5 LIMIT OF MOVEMENTS, REVIEW AND ALERT LEVELS

Assessment of the strain, settlement, and angular distortion acting on each EAS and EAU and the magnitude of the impact of the Construction Activities on these Monitored Facilities.

- Existing Adjacent Structures (EAS): All structures which could be impacted by Construction Activities, including but not limited to properties, buildings, railways, roads, and excavations.
- Existing Adjacent Utilities (EAU): All utilities and utility ducts which could be impacted by Construction Activities, including temporary construction activities.
- Monitored Facilities: Temporary structures (including piles, struts, and tie-backs), permanent structures, utilities, THESL, roadways, highways, existing buildings, bridges, HONI towers and any other entity impacted by the Works.
  Data obtained on a continuous basis from all monitoring instruments installed and transmits immediate notifications of exceedances of any Limits of Movement recipients.
- Limit of Movement: The maximum values of displacement, deflection, distortion, settlement, heave, rotation, slip, and strain that shall not be exceeded.
- Alert Level: The instrumentation reading indicating the maximum permissible ground or structural movement due to Construction Activities, the maximum groundwater level permitted during construction, the maximum allowable load or stress imposed on members of a support of excavation system, or the maximum permissible vibration level.

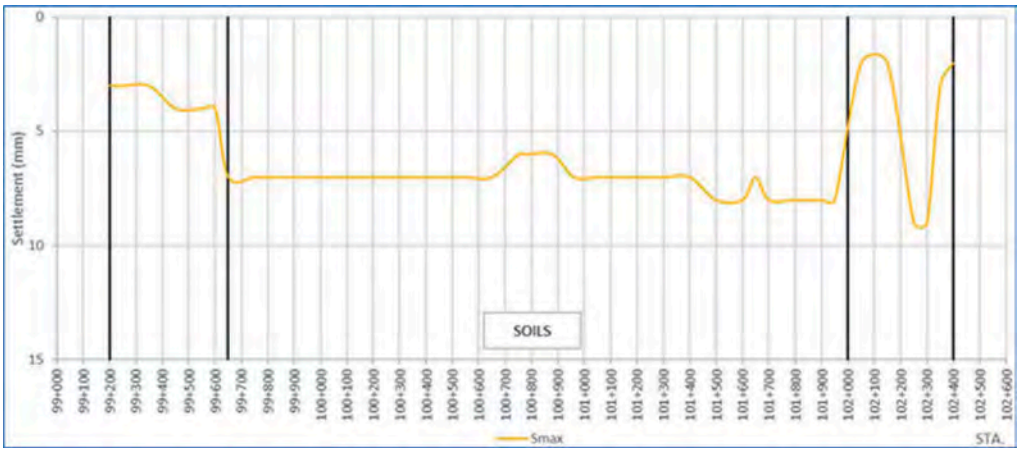

Figure 12. Settlement due to tunnel construction in soils and mix-face conditions.

- Review Level: The instrumentation reading at which requires the assessment of the need to modify construction means and methods to limit further movement.

The response action plan (RAP) provides action guidelines for instrumentation trigger events for all Monitored Facilities, including all infrastructure associated with each facility. The specific contingency plans implemented depends on the specific structure and situation encountered.

If the triggered level is confirmed, an Initial Assessment led by the RAP Implementation Team will make sure that the applicable teams and specialists are informed of the trigger event along with the potentially affected structures, or the potential implications of the event. This team will meet within 24 hours of the confirmed trigger event. The RAP implementation team will assess the mitigation measures to be implemented if deemed necessary as each event is evaluated in a case-by-case scenario.

6 INSTRUMENTATION AND MONITORING DURING CONSTRUCTION (ADAMS)

Ground settlements are a result of a combination of ground movements including in soils, ground movement towards the face and lateral ground movement towards the shield, tail and shield grouting pressure, and in-situ earth and water pressure; in rock, in situ stress relief is due to overcut and shield conicity that causes inwards movement prior to installation of the segmental lining and tail grouting.

The Earth Pressure Balance Tunnelling Boring Machines (EPB-TBMs) guarantee the stability and reduction of risk by creating a balance of pressure with its surroundings and the immediate support generated by the ring's installation and injection behind the completed liner rings.

Construction is supported by an extensive Instrumentation & Monitoring Plan to ensure no impact. Monitored facilities, including structures, buildings, roadways, pavement structures and non-pavement surfaces, along the alignment are monitored by the following instruments:

- BMP (Building Monitoring Points) on buildings and selected utilities.
- SMP (Surface Monitoring Points), MPBX (Multiple Point Borehole Extensometer) and ST (Surface Targets) for pavement surface, non-pavement surface and roadways.
- UMP (Utility Monitoring Point) and VM (Vibration Monitor) for selected utilities.
- RP (Reflector-Less Point).
- WEC has established an Automated Data Acquisition and Management System (ADAMS). ADAM is a GIS web-based system that receives, interprets, organizes, and stores real-time monitoring data obtained on a continuous basis from all calibrated monitoring instruments installed on the Project. ADAMS also transmits automatic notifications of exceedances of any Limits of Movement via phone and email to identified recipients.
- Baseline readings are obtained on a regular basis, at least twice a week, for a minimum of 1 month prior to the TBM being within 100 m of an instrument location.
- Automated instruments (MPBX, RP) collect data every 15 minutes and readings are uploaded to ADAMS in real-time.
- Manual instruments (BMP, SMP, ST, SPZ) are monitored at specified frequencies according to the proximity of the instrument to the TBM face. All manual readings are uploaded to ADAMS within 4 hours of the reading.

  Monitoring reports are prepared highlighting any response level exceedances, plots of active instruments and related construction activities including

the position of the TBM, monitoring results and identification of trends to predict future results.

GIMP instruments are periodically updated in ADAMS, and it is customized to suit the specific Review and Alert levels of each instrument. The system can be accessed online, and Construction personnel, engineers, consultants, and client representatives can access.

Daily Monitoring Reports (DMR) include the plots in seven (7) days of data acquisition prior to issuance. Baseline, Monthly and As-Built Monitoring Reports (BMR, MMR, ABMR) include complementary detailed comprehension of the instrumentation information.

7 PREDICTED SETTLEMENTS VS ACTUAL SETTLEMENTS

Table 1. Instrumentation and monitoring observed per reach.

Material & Stations (1)	Instruments (2)	Dates of Monitoring (3)
ROCK 96+950 to 99+200	ST-14E; MPBX-7E; RP-45 ST-10W; RP-24	From 21-7-2022 to 24-10-2022
MIX-FACE 99+200 to 99+600	MPBX-23E; SMP-63E; SMP-69E; SMP-78E; SMP-83E; ST-41E; ST-45E SMP-68W; SMP-74W; SMP-75W; SMP-83W; SMP-88W; SMP-93W; SMP-97W	From 9-11-2022 to 3-04-2023
MIX-FACE 99+600 to 99+800	ST-50E; ST-59E; ST-68E ST-36W; ST-45W; SMP-A11_7; SMP-A11_8	From 31-1-2023 to 18-04-2023
SOILS 99+800 to 100+400	ST-68E; ST-77E; ST-86E; ST-95E; ST-105E; ST-104E; ST-118E SMP-A11_7; SMP-A11_8; ST-54W; ST-63W; ST-74W; ST-81W; ST-88W	From 7-02-2023 to 9-07-2023

(1) *Stations are chosen for the purpose of comparison behaviour of those ground conditions distinguished in this paper (rock, mix-face, and soils) and are limited to the extent of available monitoring at this stage of the construction (STA 100+400).*
(2) *Instruments shown on the table are those that have been comparable to the theoretical analysis based on their location although there are many other instruments along the shown stations.*
(3) *These dates are considered representative for the purpose of analyzing the influence of the TBM excavation and generally include a range of dates before and after each TBM passes by the reviewed instruments.*

Table 2. Predicted settlements (theory) vs actual settlements (construction).

Material & Stations	TBM (1)	Settlement Prediction (mm)	Measurements (2) (mm)
ROCK 96+950 to 99+200	TBM-E	<1	-1.1 to -0.3
	TBM-E & TBM-W		-0.3 to 1.3
MIX-FACE 99+200 to 99+600	TBM-E	1.5-2.5	0.2 to 3.5
	TBM-E & TBM-W	3.0-4.0	0.2 to 4.0
MIX-FACE 99+600 to 99+800	TBM-E	2.0-3.0	0.4 to 0.8
	TBM-E & TBM-W	3.0-7.0	0.5 to 6.0
SOILS 99+800 to 100+400	TBM-E	2.0-5.0	0.4 to 2.6
	TBM-E & TBM-W	3.5-7.5	0.7 to 10.3

(1) *TBM-E refers to East Westbound TBM and TBM-W refers to West Westbound TBM (first and second TBM respectively).*
(2) *Measurements shown are not intended to be maximum and minimum overall readings but a representative range during the analysed timelines. Measures associated with TBM loss pressure events if any are not considered for comparison purpose. Positive values (+) show settlement, negative values (-) show heave.*

8 CONCLUSIONS

- **While TBMs are excavating in rock materials**: Both heaves and settlements have been observed as predicted during the design due to the high horizontal stress. Readings are negligible, below 1.0-1.5mm, and comparable with the design.
- **While TBMs are excavating in mix-face conditions (sound rock, weathered rock, and soils)**: The lower range of readings shows values below settlement prediction while the upper range of readings shows values very similar (around +/- 1mm difference) to those predicted for both cases, when the first TBM has passed through and when both TBMs have passed through.
- **While TBMs are excavating in soils**: A wider range of readings are available which are in general lower than those obtained with the empirical approach and numerical models when only one of the TBM has passed through. However, once both TBMs have passed through, the upper range of representative measures reach higher values than predicted in average. Those differences do not usually exceed +/- 3mm though which means no concerns in terms of potential design impacts.

In summary, and based on the results, the actual measurements available at this stage indeed show accurate predictions of ground movement during tunnelling. Evaluating ground movement during the design phase using three-dimensional Finite Element Models for volume loss calibration has been key to make possible the settlement estimation to be aligned with the real ground behaviour while tunnelling. This has also allowed for optimization in terms of mitigation measures (no mitigation measures were proposed).

The Automated Data Acquisition and Monitoring System used during construction to collect and process data is also allowing an immediate and continue response to calibrate TBM parameters on real time and adjust tunnelling excavation to control and limit induced movements.

ACKNOWLEDGMENTS

The authors wish to thank the Contracting Authority and their Technical Advisors for their continue collaboration, technical understanding, and agile design submission approvals and follow-up during construction.

Thanks also to WestEnd Connect Construction Joint Venture for their daily support, advise, and constructive supervision during design stages and easy teamwork during construction phase.

Finally, our greatest appreciation to all at TYPSA's team, which provided their expertise and unflagging efforts for the design, unbeatable leadership and guidance as well as providing daily feedback during construction to facilitate an effective engineering of record.

REFERENCES

Boscardin and Cording (1989) "Building Response to Excavation Induced Settlement";

New and O'Reilly (1982) "Settlements Above Tunnels in the United Kingdom – their Magnitude and Prediction";

New and O'Reilly (1991) "Tunnelling Induced Ground Movements; Predicting their Magnitude and Effects";

Tunnelling for a Better Life – Yan, Celestino, Thewes & Eberhardt (Eds)
© 2024 The Author(s), ISBN 978-1-032-80042-4
Open Access: www.taylorfrancis.com, CC BY-NC-ND 4.0 license

Geotechnical and tunnel engineer's role on the success of major tunnel projects delivery

Jiping Pan*, David Och & Antoni Kuras
WSP Australia Pty Ltd, Sydney, Australia

Geoff Bateman
Sydney Metro, Sydney, Australia

ABSTRACT: Successful delivery of major tunnel project with minimum risks to all stakeholders begins at the early stages of the project inception from preliminary study to reference design. This paper presents authors' experience as Technical Advisor (TA) role for Sydney Metro City & Southwest project, Australia with respect to managing Client's expectations and community acceptance through technically feasible solutions with minimum delivery risks. The project faced several challenges related to indigenous, geological, geotechnical, and subsurface boundary constraints. Indigenous heritage sites were assessed with alignment modified prior to Tender; geological and geotechnical issues like rock conditions were addressed during the ongoing design phases; additionally, the presence of specific features like historical brickpits site, Sydney Harbour needed careful consideration in the planning to ensure the safety and stability of the tunnelling process. All these constraints have been carefully managed and mitigated to ensure the successful completion of the project while minimising any adverse impacts on the environment and local communities.

Keywords: Major tunnel project, TBM, Geotechnical and tunnel engineer, Technical Adviser, Tunnel alignment

1 INTRODUCTION

Sydney Metro is Australia's biggest public transport project. By 2030, Sydney will have a network of four metro lines, 46 stations and 113km of new metro rail.

Sydney Metro City & Southwest is Stage 2 of this project extending metro rail from the end of Sydney Metro Northwest at Chatswood. It features a twin 15.5km tunnels along with seven new underground stations between Chatswood and Sydenham. The line is extended beyond Sydenham with an upgrade of the existing Sydney Trains heavy rail line to Bankstown.

Construction began in 2017 with the first tunnel boring machine (TBM) in the ground before the end of 2018. This line is due to open in 2024 with the capacity to run a metro train every two minutes each way through the centre of Sydney.

Transport for NSW engaged the design joint venture (DJV) of WSP and AECOM, with architectural support from Cox and HASSELL together with constructability support from Rail Planning Services as Technical Advisor for the Sydney Metro City & Southwest works.

Figure 1. Sydney Metro – stage 1 & stage 2 alignment.

This paper explores the role of the Technical Advisor (TA) in identifying and mitigating risks during alignment optimisation in the project on behalf of Sydney Metro Authority, in particular for the tunnel and underground stations. It describes the

*Corresponding author: Jiping.Pan@wsp.com

DOI: 10.1201/9781003495505-16

typical challenges and associated solutions to manage the risks with due diligence, environments, heritage, and construction. It draws upon the author's experience of undertaking TA roles regarding geotechnical and tunnelling issues.

2 GEOTECHNICAL CONSIDERATIONS

Understanding the geology along the project alignment is a key to the successful and cost-effective delivery of the project, therefore, geotechnical site investigations are very essential in early stage of tunnelling projects.

Construction of underground stations and tunnels is a complicated process in any situation and involves huge costs which would multiply if proper planning were not exercised before starting the actual excavation. The excavation methods are intimately linked with the type of ground materials to be excavated. Choice of the right method will, therefore, be possible only when the nature of the rocks and the ground all along the alignment is fully known. This is one of the most important objectives of geological investigations.

2.1 *Desktop study*

A geotechnical desktop study has been undertaken to gather and collate relevant geotechnical information available along the proposed rail corridor. This study would provide basic information of the stratigraphy, identified and inferred vertical linear fault zones expected as well as gaps of geological information within the proposed rail corridor.

Findings from this desktop study include:

- Proposed running tunnels will be predominately within Hawkesbury Sandstone, which is typically a highly abrasive medium to coarse-grained sandstone with common clay seams;
- A section of the alignment from Sydenham to Redfern will encounter Ashfield Shale in tunnel;
- The proposed Central Station, Pitt Street Station, Martin Place station, Barangaroo Station and Victoria Cross Station will be constructed within Hawkesbury Sandstone;
- The proposed Waterloo Station and Crows Nest station will be constructed within Ashfield Shale (residual), Mittagong Formation and Hawkesbury Sandstone;
- Several identified and inferred vertical linear fault zones are expected along the project corridor;
- Relatively high horizontal in-situ stress levels within the Sydney Basin strata.

2.2 *Geotechnical site investigation*

Following the gap analysis of all existing available information (including the available borehole information collected in the desktop study) a suite of geotechnical investigations was proposed. These investigations broadly included: geophysical survey under the Sydney Harbour; drilling of drilling of boreholes on land and under the Harbour; and field/laboratory testing. These investigations have focused on the harbour crossing, proposed stations locations, tunnel portal/dive sites and potential fault zones. The site investigations included:

- 36 "on-land" boreholes to depths of between 20 m and 64 m below the ground surface along the proposed tunnel alignment;
- 23 overwater boreholes under Sydney Harbour, in water depths of about 14 m to 23m;
- 30 overwater cone penetrometer tests (CPTs) probed the sediments along the proposed harbour crossing;
- Bathymetry and geophysical investigation under the Harbour
- In-situ stress testing in 4 on-land boreholes and 2 overwater boreholes;
- 14 groundwater monitoring holes.

2.3 *Geological structures along the project corridor*

Understanding the structural condition of the rock is important to tunnelling projects. This includes the extent and attitude of major structural features such as folding, faulting, unconformities, jointing and shearing planes.

It is obvious that with the help of above information, the engineers could propose a number of alternative tunnel routes to connect the two places, and in most cases, even decide about the general run of the tunnel.

The deformation of rock discontinuities is a fundamental component of the performance of a jointed rock mass. The rock structures or discontinuities within the Ashfield Shale, Mittagong Formation and Hawkesbury Sandstone and cross cutting dykes can be generally summarised in Table 1 and the typical geological conditions (Figure 2).

2.4 *Geotechnical interpretive report*

To provide geotechnical advice for the design of the tunnel alignment, locations of station caverns, tunnel portals, groundwater control, and construction associated risk management, a ProjectWise Geotechnical Interpretative Report (GIR) is prepared, which covers the following:

- Project wise topography and geology;
- Geotechnical profiles at the locations of the proposed stations, dive structures, portals and running tunnels;
- Characterisations of soils and rocks along the alignment;
- Characterisation of harbour sediments;
- In-situ stress regime;

- Geotechnical design parameters;
- Groundwater;
- Contamination.

These provided project specific geotechnical and geological information for the team in consideration of tunnel alignment, station locations, and groundwater control measures.

Table 1. Geo-structures identified along the project corridor.

Name	Description	Potential locations
Martin Place Joint Swarm	A concentration of structural features such as faulting, sub-vertical joint swarms. It has been recorded to contain closely spaced jointing, and zones of crushing and shearing.	In vicinity of Pitt Street Station and Martin Place Station
GPO Fault Zone	Multiple crush zones and closely spaced jointing and faulting with normal and reverse fault offsets. The width of the principle shear zones of the fault likely to vary from less than 10 m to over 20 m in width.	Tunnels between Martin Place Station and Barangaroo Station
Luna Park Fault Zone	Up to 3 m wide 'crushed' zones and closely spaced sub-vertical jointing and faulting/shear zones. The faulting shows normal and reverse movement as well as strike-slip movement. Widely spaced joints are encountered either side of the fault zone.	Crossover cavern at north of Barangaroo Station and tunnels under the harbour
Low Angle Thrust Faulting	Low-angle usually parallel to cross bedding will be encountered across the alignment associated with the sub-vertical geological structures.	Various locations
Dykes	Great Sydney Dyke, Ultimo Dyke and other Pittman Dykes, generally up to 6 m in width and comprises various intrusive materials such as basalt, alkali olivine basalt, or dolerite in various sources.	Central Station, tunnel at various locations

3 HARBOUR CROSSING

The Sydney Harbour crossing is a key element of Sydney Metro, City & Southwest. Limited geotechnical information existed, therefore, detailed geophysical/geotechnical investigations to facilitate early planning and design work were undertaken for three potential options to construct the harbour crossing, which would involve either full rock face excavation by Tunnel Boring Machine, mixed face Tunnel Boring Machine or the installation of immersed tubes. Concurrently with the development of the concept design phases, site investigations were carefully staged. This approach allowed for real-time adjustments as both geological interpretation and the concept design evolved. A wealth of geophysical and geotechnical data was meticulously gathered to characterise the terrain beneath the harbour floor. This extensive data acquisition aimed to identify potential geotechnical challenges associated with tunnelling beneath the harbour.

The primary objectives of these site investigations were threefold: to delineate the seabed profile, determine sediment thicknesses, and predict the topography of the underlying rock (Figure 3), as documented by Och et al. (2017). The results of these investigations revealed a significant deviation from the originally anticipated rock profile. This deviation, based on prior technical literature, indicated that the underlying rock profile may, on average, be situated 12 metres deeper than initially presumed.

In response to these significant findings, a collaborative effort ensued between geotechnical engineers and tunnel engineers. They embarked on the task of devising a series of revised metro alignments. These revised alignments aimed to identify the most optimal route for the running tunnel, capitalising on the newly interpreted seabed and bedrock profiles. The overarching goal of this endeavour was to elevate the running tunnel alignment, ensuring the shallowest possible rail level at Victoria Cross Station, while maintaining the necessary ground and rock cover for the metro running tunnels beneath the harbour.

In the development of these alignment options, meticulous attention was given to various design criteria, encompassing track alignment, running tunnel cover requirements, and the placement of cross passages beneath the harbour. The application of these guidelines led to the generation of 12 alignment options, from which nine options were selected for further in-depth assessment.

Key factors considered in the option study for tunnel alignment under the harbour included:

- Depth to the next station;
- Placement of mined cross passages and low point sump;
- Spacing between cross passages;
- Sediment thickness with a minimum 1-meter rock cover;
- Speed restrictions;
- Minimum radius of curvature;
- Length of the tunnel beneath the harbour;
- Assessment of geotechnical risks related to trenching and deep excavation;
- Opportunities for locating a nearby ventilation shaft.

Figure 4 below provides a visual representation of the preferred alignment in conjunction with the geological conditions.

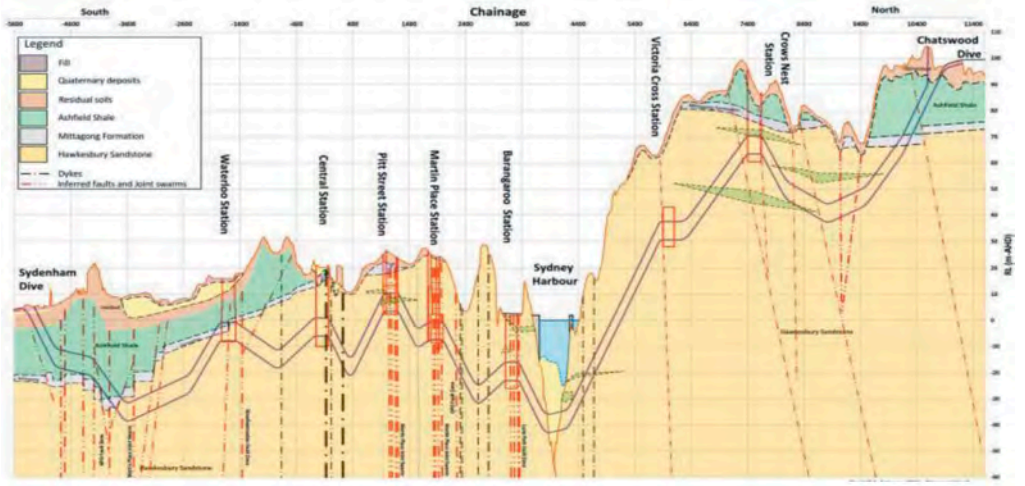

Figure 2. Graphical geological interpretation model, Sydenham (Downline) – Central – Chatswood (Upline).

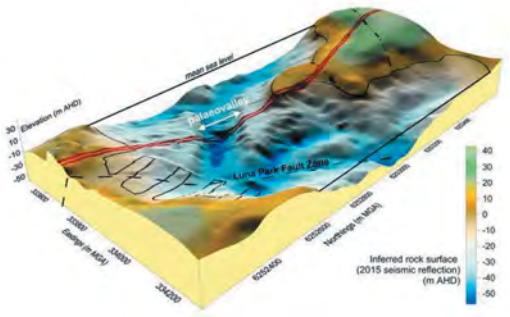

Figure 3. Palaeogeographical rock surface -Seismic Reflection Survey (projected alignment in red) (Och et al 2017).

Figure 4. Interpretative geological long-section of the conditions along the proposed Sydney Harbour crossing (Och et al 2017).

The harbour site investigation including underwater drilling, seismic reflection survey provides sufficient geotechnical information for reference design and selection of construction method of harbour crossing from the three options described above (details were discussed by the authors in a paper presented to WTC 2017 (Och et al 2017)).

4 BUILDINGS, INFRASTRUCTURE AND UTILITIES

Construction of the running tunnels, station caverns and underground structures will cause ground movement with the potential to cause damage to the existing buildings, infrastructure and utilities. Buildings and infrastructure that falls within construction induced settlement troughs (zone of influence) will be affected to varying degrees depending on a number of factors including their relative position, form of construction and current condition. It is the responsibility of geotechnical engineer and tunnel engineer to minimise material adverse impacts on existing ground conditions or the performance of any existing infrastructure and utilities.

All existing buildings, tunnels, roads and utilities within the zone of influence of underground construction need to be evaluated for potential movement and distortion due to induced ground movement. In this context, the zone of influence is defined as the envelope within a 3mm settlement contour (i.e. commensurate with survey accuracy). Assets that fall outside of this zone generally do not need to be assessed.

4.1 *Assets information collection*

To enable the impact assessment, identification of the assets along the project corridor to establish a database is the first task to be carried out. Information in relation to buildings and infrastructure within the zone of influence has been obtained from the following sources:

- Walking through inspection along the project corridor;
- Aerial photography/imagery for the project area;

- As-built drawings obtained from public and private properties;
- Development applications from councils for future developments;
- Targeted building basement surveys;
- Roads and Maritime Services (RMS) including as-built information of existing road tunnels and future proposed road tunnels;
- Sydney Trains (as-built information from plan rooms);
- Utility authorities and companies.

In cases where as-built drawings are not available, preliminary assumptions have been applied in respect of the building foundation type and depth based on past project experience and engineering judgement.

4.2 *Existing buildings*

To be able to assess impacts of ground surface settlement induced by tunnelling works, settlement of contours along the alignment have been generated by green-field approach. This is considered as adequate at reference design stage. The approach taken to assess affected buildings applies analytical methods to filter buildings of concern. The processes have been divided into three phases of assessment:

- Preliminary assessment (level 1);
- Second order assessment (level 2) and
- Detailed evaluation (level 3).

The intent of the first two phases of evaluation is not to precisely quantify the effect of settlement, but to determine which buildings are potentially at risk of damage and thus require further evaluation. For this reason, only the preliminary assessment and second order assessment has been undertaken at the planning stage.

Well established and industry recognised criteria have been used at preliminary assessment - level 1 (CIRIA, 1996). The application of these criteria provides a means of demonstrating that Sydney Metro City & Southwest can be constructed without causing unacceptable effects to impacted buildings.

In total, about 1000 buildings were found to lie within the zone of influence of construction induced settlement (i.e., 3mm settlement contour). Of which, 253 buildings were identified within 10 mm or greater contour and were further taken forward for further review. Further assessments of these 253 buildings, 46 were identified as requiring a more rigorous level 2 assessment. This level 2 assessment also applies greenfield predictions of settlement to assess impacts. However, at this stage calculations are undertaken to estimate the angular distortion and horizontal strain that would occur beneath the foundations of critical buildings were they to follow the estimated settlement trough. The calculated angular distortion and horizontal strain are assessed in combination to determine an appropriate damage category based on the Boscardin and Cording (1989) method. From the subsequent level 2 assessments all of these buildings were predicted to have negligible/ slight risk ratings.

4.3 *Brickpits*

The history of brickpits in St. Peters, as well as across Sydney, is characterised by their pivotal role in the region's early brickmaking industry during the late 19th and early 20th centuries. These clay excavation sites were instrumental in supplying raw materials for the construction of countless buildings that define the city's architectural heritage. However, a significant issue arose when these brickpits were abandoned and repurposed as landfills, a common practice during the mid-20th century. The subsequent filling of these sites with various waste materials, including construction debris and industrial waste, has posed a significant challenge for future infrastructure projects, particularly tunnels due to their hidden locations and without the use of historical airphotos they would remain unidentified (Figure 5).

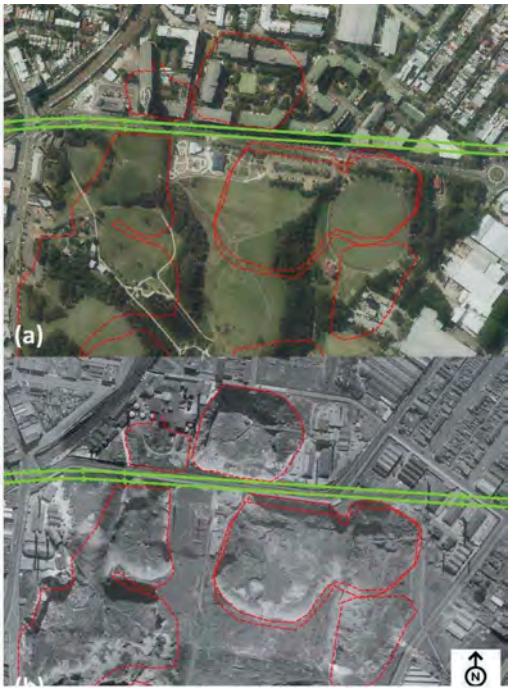

Figure 5. This image highlights the piles used to support the unit development (http://www.waterway.com.au/projects/piling/sydney-park-village-piling).

A noted finding was a property near to Erskineville that had a unit complex constructed above what was identified as a historic brickpit from historic air photography assessments. During early stages of reference design, a graphic was found during searches of piles used to found the complex on (Figure 6) but

further assessment could not confirm the depth these piles were piled to and therefore, was identified as a key risk.

4.4 *Existing tunnels*

Unlike building structures, there are no well-defined methods of risk assessment for existing tunnels. In part, this is because it is difficult to assess the effect of tunnel excavation on existing tunnels using empirical methods. As such detailed numerical modelling and analysis may need to be undertaken at a preliminary stage to judge the degree of damage that could be caused to existing tunnels from construction of adjacent underground metro infrastructure.

To develop the Reference Design critical sections have been identified that have warranted particular attention to prove, with a high level of certainty, the feasibility of their construction and method of support; as well as the acceptability of excavation impacts to existing nearby underground existing tunnels.

Fifteen existing tunnels in proximity to the Sydney Metro City & Southwest alignment have been identified as requiring assessment. Of these, six were analysed using numerical modelling given their close proximity to the Sydney Metro City & Southwest alignment. It has been concluded from the results that the impacts from the metro construction on these existing tunnels in terms of imposed movement will be acceptable.

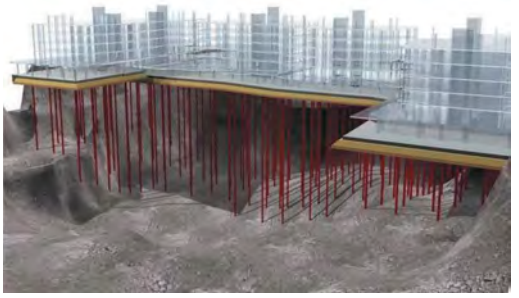

Figure 6. Airphoto comparison (a) 2017 (TfNSW) and (b) 1943 (RTA – TfNSW) of the Erskineville – St Peters area highlighting brick pits and recent developments. (http://www.waterway.com.au/projects/piling/sydney-park-village-piling).

4.5 *Utilities*

A comprehensive staged assessment has been diligently conducted to evaluate the utilities associated with the Reference Design. The primary objective of this assessment has been to discern and highlight utilities of paramount significance. This determination has been influenced by several critical factors, including their functional importance, physical dimensions, spatial proximity to the metro alignment, and their heritage status.

In the context of the Reference Design, a subjective evaluation has been meticulously undertaken to appraise the anticipated repercussions arising from ground movements induced by metro construction activities. This evaluative approach has entailed the judicious application of engineering expertise and fundamental principles, complemented by insights gleaned from prior analogous projects.

Notably, established criteria widely acknowledged within the industry have been thoughtfully considered. These criteria encompass various aspects, such as the material composition of pipes and cables, the length of piles, the nature of joints, and the methodologies employed for backfilling. These parameters serve as essential yardsticks for gauging the relative risks associated with utilities.

A preliminary assessment was systematically carried out, encompassing a total of 95 utilities of substantial significance that lie beyond the purview of future metro stations and tunnel excavations. From this initial pool, a judiciously chosen subset of 15 utilities was identified for further, in-depth examination. The outcomes of this extended evaluation affirm that, while the majority of the scrutinised utilities are unlikely to suffer adverse impacts attributable to the Sydney Metro City & Southwest Project, certain exceptions do exist. Notably, major water tunnels, exemplified by the City Tunnel spanning from Potts Hill to Moore Park, and several other brick-lined stormwater tunnels of heritage significance necessitate meticulous protection measures.

5 INDIGENOUS HERITAGE AND BRICKPIT

The originally proposed metro alignment had running tunnels under the Newtown-St Peters area, which was referred to as the 'Kangaroo Ground'. Local Aboriginal peoples, the Gadigal and Wangal, hunted kangaroo on the grasslands here, and fished and camped at the swamps, creeks and rivers that crisscrossed the area (City of Sydney, 2018).

The north-west part of the park is on the edge of a Wianamatta Shale from which brickmaking clay was extracted in the 19th and 20th centuries and buried below man-made reserves but identified in historic air photography.

To avoid the potential impacts on the indigenous heritage land, the tunnel alignment was revised from the initial location further north relative to the constructed location under Sydney Park Road (Figure 5).

6 DISCUSSIONS

The Sydney Metro City & Southwest project was a significant endeavour that involved the construction of new metro rail lines, underground stations, and tunnels in Sydney, Australia. We focused on the importance of a coordinated, multi-disciplinary approach in managing risks and making critical

decisions during the planning and execution of such a complex infrastructure project.

The success of the Sydney Metro City & Southwest project hinged on the collaboration of various disciplines, including geotechnical engineering, tunnel engineering, architecture, and heritage preservation. This coordinated effort ensured that risks were identified and mitigated effectively, and that the project aligned with the diverse requirements and challenges it faced.

One of the fundamental aspects of this multi-disciplinary approach was geotechnical considerations. Understanding the geological conditions along the project's alignment was crucial for cost-effective and successful tunnel construction. The geotechnical desktop study provided valuable information about the types of rock and soil encountered, potential fault zones, and in-situ stress levels. This knowledge was essential for selecting appropriate excavation methods and optimising tunnel routes.

Geotechnical site investigations followed the desktop study, involving drilling boreholes, conducting field and laboratory tests, and assessing the structural condition of the rock. These investigations provided data that informed the project's design parameters, including tunnel alignment, station locations, and groundwater control measures.

The Sydney Harbour crossing, a key element of the project, exemplified the need for a multi-disciplinary approach. Limited initial geotechnical information prompted detailed geophysical and geotechnical investigations to determine the best approach for tunnel construction under the harbour. The collaboration between geotechnical and tunnel engineers allowed for the adjustment of alignment options, accounting for the reinterpreted seabed and bedrock profiles.

The consideration of existing buildings, infrastructure, and utilities was another critical aspect of the project. A multi-disciplinary team assessed potential ground movements and their impacts on surrounding structures. Buildings, tunnels, and utilities within the project's zone of influence were evaluated for risks and potential damage, with a focus on minimising adverse effects.

Furthermore, the project's engagement with Aboriginal Indigenous heritage and the recognition of these brickpits buried along the alignment underscored the importance of a multi-disciplinary approach. A coordinated effort between heritage experts, geologists, engineers, and environmental specialists ensured that the project respected and preserved cultural heritage and were not impacted by buried historical sites (Figure 7).

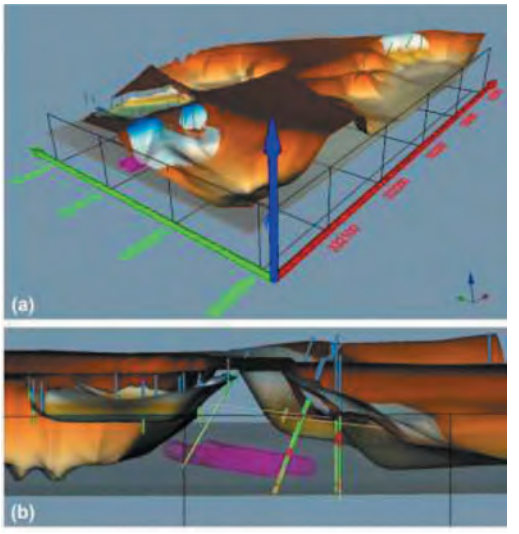

Figure 7. 3D modelling of the Erskineville - St Peters brickpit area that defined passage for the tunnel design to align through. Note the tunnel (white sloped lines picked up in historic mapping by the successful tenderer), following investigation defined the pit transfer tunnel did not impact on the metro running tunnels below.

7 CONCLUSIONS

In conclusion, the Sydney Metro City & Southwest project exemplifies the significance of interdisciplinary collaboration in effectively managing risks and addressing complex challenges in infrastructure development. Geotechnical assessments and site investigations, alongside adaptive planning, played pivotal roles in overcoming major obstacles such as Sydney Harbour crossing, building basements and brickpits. Furthermore, the project's commitment to heritage preservation and cultural sensitivity highlights the value of a holistic approach in achieving its objectives.

ACKNOWLEDGMENTS

The authors extend their gratitude to the Sydney Metro Authority, and the collaborative efforts of the Technical Advisor (WSP AECOM JV) and Transport for New South Wales (TfNSW) team were instrumental in achieving these results.

REFERENCES

Boscardin M. D. and Cording E. J. (1989). "Building Response to Excavation-Induced Settlement," Journal of Geotechnical Engineering, American Society of Civil Engineers, Vol. 115, No. 1.

CIRIA (1996). "Prediction and effects of ground movements caused by tunnelling in soft ground beneath urban areas," Construction Industry Research and Information Association, Project Report 30.

City of Sydney (2018) "History of Sydney Park", https://www.cityofsydney.nsw.gov.au/histories-local-parks-playgrounds, published 16 November 2018.

Och D. J., Pan J., Kuras A. et al (2017) "Sydney Metro - Site Investigation and Ground Characterisation for the Sydney Harbour Crossing", Proceedings of the World Tunnel Congress 2017 – Surface Challenges – Underground Solutions. Bergen, Norway.

Tunnelling for a Better Life – Yan, Celestino, Thewes & Eberhardt (Eds)
© 2024 The Author(s), ISBN 978-1-032-80042-4
Open Access: www.taylorfrancis.com, CC BY-NC-ND 4.0 license

TBM traffic tunnels for sustainable infrastructure

Silvino Pompeu-Santos*
SPS Consulting, Lisbon, Portugal

ABSTRACT: Three innovative and very cost-effective concepts for the construction of tunnels using the TBM technique are presented: the TISB concept for tunnels in soft soil, in seismic areas; and the TMG and TMF concepts for railway and road tunnels, respectively. Some application examples are presented that show the benefits that can be obtained by using these concepts in creating sustainable infrastructure around the world.

Keywords: Traffic Tunnels, TBM, TISB, TMG, TMF, Sustainability

1 INTRODUCTION

Sustainability is a fundamental issue in the construction of infrastructure nowadays, whereby the use of natural resources to satisfy present needs should not compromise the satisfaction of the needs of future generations.

Thus, today, the concerns of decision-makers focus on building of infrastructure with increasingly reduced costs in terms of life cycle, that is, infrastructure that consume ever smaller amounts of materials and are as reliable as possible, to prevent incidents from occurring.

In this context, tunnels play a significant role, as they are increasingly used in the construction of transport infrastructure, for both railway and roadway networks.

The TBM ("Tunnel Boring Machine") technique is currently most used, providing significant savings in terms of cost and construction time, making it common for a TBM to build more than 0.5 km of tunnel per month.

The TBM technique has also other advantages. In urban areas, for example, it allows the reduction of impact on the surface, practically eliminating the need for use surface space. In underwater tunnels, the TBM technique also allows the reduction of the environmental impact, allowing for non-disturbance of the sea bed.

With the technological progress that has taken place, there are now different types of TBMs (Open-Face, EPB, Mixshield, etc.), adapted to specific conditions, of the ground, which make possible to excavate in all types of conditions.

Therefore, the TBM technique is nowadays also the most promising for tunnel construction in the future. However, despite the progress made, the construction of TBM tunnels still faces important challenges.

With regard to rail and road TBM tunnels, major challenges are, among others: i) improving the reliability of structural safety when built on soft ground in seismic areas, ii) improving safety during operation, as well as iii) reducing construction costs.

To face these challenges, three new concepts were recently developed by the author: the TISB concept, that is, "Tunnel of Improved Seismic Behavior"; the TMG concept, that is, "Tunnel Multiple Gallery"; and the concept TMF, that is, "Tunnel Multi-floor".

The TISB concept makes it possible to provide adequate structural safety to TBM tunnels built on soft ground in seismic areas, while the TMG and TMF concepts, for rail and road TBM tunnels respectively, allow, with adequate arrangements of the tunnel's cross section and the adoption of innovative additional measures, a significant improvement in safety during operation and at the same time a significant reduction in construction costs.

This paper presents the most relevant aspects of the author's book dedicated to this theme, entitled "Innovation in TBM Traffic Tunnels" (ISBN 9780367701635) (Pompeu-Santos, 2023), recently published, in March 2023, by Taylor & Francis (UK).

2 CHALLENGES IN TBM TUNNELS

2.1 *TBM tunnels in soft ground in seismic areas*

As in TBM tunnels the connections between precast segments have no tensile strength, ductility is low (they are a kind of "LEGO"), therefore they are suitable for stiff ground (rock, stiff clay, compacted sand, etc.), where stability is essentially ensured by the surrounding ground and the precast segments fundamentally serve as a finishing.

*Corresponding author: pompeusantos@sapo.pt

DOI: 10.1201/9781003495505-17

In the case of TBM tunnels built on soft ground (alluvia, soft clay, loose sand, etc.), in seismic areas, there is the risk of collapse due to horizontal movements of the soil during earthquakes, unless very thick precast segments are used.

Soil treatments, sometimes adopted to improve seismic behavior, are very expensive and sometimes being impractical, do not always guarantee structural reliability.

The adoption of seismic joints in the transitions to the stiff ground, as in the case of the Eurasia Tunnel, in Istanbul, Turkey (Figure 1) (Schmid et al., 2020), solves the problem in those areas, but not the effects of transverse displacements of the tunnel, nor the ovalization of the sections along the tunnel.

In addition, in the case of tunnels formed by two or three tubes connected by transverse tubes that act as cross passages between them, the relative displacements between the main tubes during earthquakes can risk the collapse of the connections to the transverse tubes.

To overcome these limitations, the TISB concept was recently developed by the author.

Figure 1. Eurasia Tunnel. Seismic joints.

2.2 *Conceptual solutions and safety during operation of rail tunnels*

In conventional railway TBM tunnels, after the construction of the outer wall, a filling is placed at the base, creating a platform for the circulation of the trains, with the two directions of traffic placed side by side.

However, to satisfy safety requirements (EU, 2008; UIC, 2003), the installation of two traffic directions side by side is only possible in short tunnels. In tunnels longer than 1 km, due to the chock of the piston effects of trains in opposite directions, their speed will have to be quite limited. Furthermore, it requires the adoption of complex ventilation systems (transverse or semi-transverse) to control the flow of smoke inside the tunnel in fire situations.

It has therefore become common, particularly in tunnels included in High-Speed lines, to adopt the dual-tube tunnel solution, in which two separate tunnels are built, each for one direction of traffic, and a system of cross passages, regularly spaced, interconnecting the two tubes, for access by emergency personnel and the rescue of users in incident situations. In these situations, users will leave the incident train and move to the other railway tube through the cross passages, to later be evacuated via another train.

The safety measures in the dual-tube tunnels are generally quite complex. A remarquable case is the Gotthard-Base Tunnel, in southern Switzerland (Figure 2) (Anagnostou, 2013) opened to traffic in 2016, with tubes of 8.40m in inner diameter and 9.40m in diameter of the excavated section, and 57.1 km extension, the longest traffic tunnel in the world.

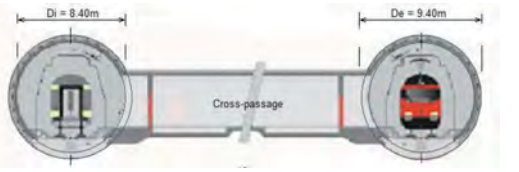

Figure 2. Gotthard-Base Tunnel. Cross-section.

In this tunnel, safety during operation is based on two large MFSs ("Multi-Functional Stations"), located about thirds of the length of the tunnel, which include emergency stops for trains in each tube, track crossings, ventilation shafts with giant fans at the ends and galleries with direct access to the outside. In the event of an incident, the evacuation of users is carried out using emergency trains permanently parked next to the tunnel portals.

Despite all these measures, the recent derailment of a train inside the tunnel meant that it will be out of operation for several months.

In long underwater tunnels, it is usual to use the three-tube tunnel solution, in which, in addition to the two railway tubes, a third tube is adopted, placed between the other two, to serve as a service gallery for the evacuation of users and the access for emergency services in incident situations, all three connected by cross passages.

This is the case of the Channel Tunnel, built in the 90s, with railway tubes with an inner diameter of 7.60m and an excavated section of 8.80m in diameter (Figure 3) (Getlink, 2021), and a length of 50.5 km, still today one of the longest in the world.

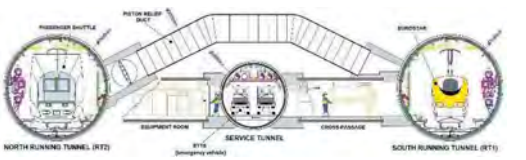

Figure 3. Channel Tunnel. Cross-section.

The tunnel is provided with longitudinal ventilation through ventilation buildings installed in the portals. To alleviate the piston effect of the trains, regularly spaced 2.0m diameter relief ducts were created, connecting the railway tubes, however, the system did not prove to be effective and was neutralized.

For fire-fighting, a classic system through fire trucks was originally adopted, which, after some setbacks, was replaced by a modern WFS ("Water Based Fire Fighting System") based on high pressure water mist nozzles, installed in 4 "safe stations" in each of the railway tubes. In the event of an incident, the evacuation of users is carried out using wheeled vehicles specially designed for this tunnel, which circulate inside the service gallery. At thirds of the tunnel length two large caverns were also created for the installation of train crossings.

This tunnel has already suffered several incidents, some with serious consequences.

However, with the progress made in the technology of TBMs and the possibility of building tunnels with large diameters, the solution of the mono-tube dual-gallery tunnel also emerged, in which a single TBM tube, provided with a separating wall in the middle, houses two independent railway galleries, placed side by side. This is the case of the Groeneheart Tunnel, in the Netherlands, opened to traffic in 2005, with an inner diameter of 13.30m and an excavated section of 14.87m in diameter (Figure 4) (Bouygues, 2001), and a length of 7.2 km.

In the event of an accident or fire inside one of the rail galleries, users leave the incident gallery and enter the adjacent gallery through emergency doors regularly arranged along the separation wall, to later be rescued by another train. However, the escape doors open directly into the adjacent gallery, which can make it difficult to control smoke entry into that gallery.

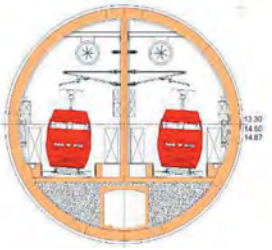

Figure 4. Groeneheart tunnel. Cross-section.

The separation wall has openings at the top to relieve the piston effect of the trains. Ventilation is of longitudinal type, with jet fans. In operation for almost two decades, the tunnel has not yet experienced any significant incidents.

In short, different conceptual solutions (with three, two or one tube) and different safety concepts can be adopted in rail tunnels. In solutions with two or three tubes, safety systems are in general quite complex and expensive. The aforementioned mono-tube solution proved to be very economical, although its safety concept has some weaknesses.

To overcome these limitations, the TMG concept was recently developed by the author.

2.3 *Conceptual solutions and safety during operation of road tunnels*

In conventional road TBM tunnels, after the construction of the outer wall, a filling is placed at the base, creating a platform for the circulation of vehicles (cars, trucks, etc.), with the two directions of traffic placed side by side. However, as in railway TBM tunnels, the installation of two directions of traffic is only possible in short tunnels with a single lane in each direction.

In fact, when there are two or more lanes in each direction, the required diameter would be so large that it would become impractical. Furthermore, in tunnels longer than 0.5 km, to comply with safety requirements: ventilation, firefighting, etc. (EU, 2004), placing bidirectional traffic on the same tube requires very complex and expensive technical systems.

Thus, as in railway tunnels, the double-tube tunnel solution is now commonly used, in which the tunnel is formed by two separate tubes, each for one direction of traffic, the two being interconnected by regularly spaced cross passages. In incident situations, users leave the incident tube and move through the cross passages to the adjacent tube, from where they will later be evacuated by conventional buses.

There are several remarkable cases of this type of solution, for example, the Changjiang Tunnel in Shanghai (China), opened to traffic in 2009, formed by two tubes with excavated diameter of 15.43m and internal diameter of 13.70m (Figure 5) (Huang, 2009), with 3 lanes each and efficiency indexes (ratio between the roadway cross-sectional area and the internal cross-sectional areal) of 0.45. In the middle of the lower part of each tube there are also galleries for the installation of an express train.

In this tunnel ventilation is of the semi-transverse type, with ventilation buildings at the portals and a duct along the upper part of the road galleries, in addition to jet fans, regularly distributed. The firefighting system is relatively complex, using fire trucks that enter through the portals of the non-incident tunnel tube.

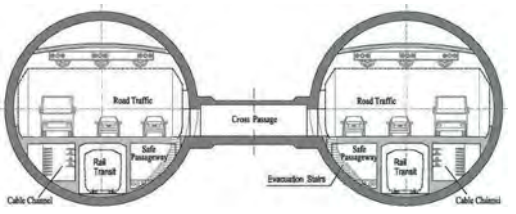

Figura 5. Changjiang tunnel. Cross-section.

The evacuation system is also quite complex, given the need to make the evacuation of users from the road

galleries compatible with that of the railway galleries, being carried out through the non-incident tunnel tube, which is accessed through the cross passages.

With the development of TBMs with increasingly larger diameters, the mono-tube dual-deck tunnel solution also began to be adopted in road tunnels, in which a single large-diameter tunnel with an adequate arrangement of the cross-section houses two overlapping road galleries, each for one direction of traffic, which are connected to each other through vertical galleries, or to the outside through evacuation galleries. Safety systems are diverse and generally quite complex.

An outstanding example is the SR99 Tunnel, in Seattle (USA), opened to traffic in 2019, with two lanes in each direction, 17.50m in diameter of the excavated section (the second largest in the world) and 15.70m in inner diameter (Figure 6) (Jiang et al., 2019), and an efficiency index of 0.47. There are also cases of tunnels of this type with smaller diameters, but with limitations on the height of the vehicles that can use them.

A solution with three lanes in each direction was also developed (and the respective TBM was designed), the Orlovski Tunnel, in Saint Petersburg (Russia) with an excavated section of 19.25m in diameter, but it was not built.

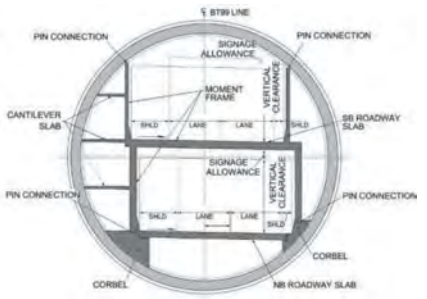

Figure 6. SR99 tunnel. Cross-section.

In the SR99 Tunnel, the ventilation system is of the semi-transverse type, with regularly distributed jet fans and four giant fans in the portals with a ventilation duct placed next to the road galleries. The fire-fighting system is a WFS, based on high pressure water mist nozzles and organized in sections. The evacuation of users in the event of an incident is carried out through escape doors that give access to longitudinal evacuation galleries, which lead to the tunnel portals.

In short, in road tunnels, in addition to the dual-tube solution, the mono-tube solution with superimposed road galleries is also being adopted. In both cases, the safety concepts are quite complex and expensive.

Regarding costs, although the cross-sectional areas of mono-tube and dual-tube tunnels are similar, the unit cost (ratio of the overall construction cost to the excavation volume) of tunnels with smaller diameters is higher, in addition to the need to build a system of cross passages between the two tubes, so their cost will in principle be higher.

To respond to these challenges, the TMF concept was recently developed by the author.

3 THE TISB, TMG AND TMF CONCEPTS

3.1 *The TISB concept*

The TISB ("Tunnel of Improved Seismic Behavior") concept is an innovative solution for TBM tunnels, when the referred tunnels are built in soft ground, in seismic areas, allowing the tunnel be provided with adequate resistance and ductility, without a significant increase in construction costs. It will also allow for the strengthening of existing TBM tunnels, using them as external formwork for the execution of the interior strengthening.

The TISB concept is illustrated in Figure 7 (INPI, 2008).

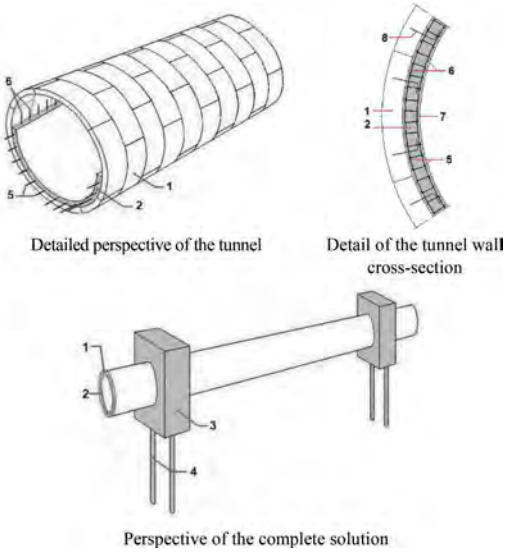

Figure 7. Illustration of the TISB concept.

In the TISB concept, the tunnel is formed by two concentric tubes; an outer tube (1), which is a conventional TBM tunnel, and an inner tube (2), which is subsequently built inside the outer one.

The outer tube (1) is thus formed by precast segments mounted by the TBM, while the inner tube (2) is subsequently cast, using the latter as outer formwork. Within the thickness of the inner tube (2) longitudinal reinforcement bars (5) and transverse reinforcement bars (6) are laid, both in two layers, which are confined by confinement bars (7), so as to provide the tunnel with adequate strength and ductility. Reinforcement bars (8) protruded from the precast segments connect the two tubes.

Where the tunnel can be subjected to significant vertical displacements (for example, due to an increase or decrease in the height of the overburden on weak soil), the tunnel will be provided with supports, regularly spaced along the tunnel axis. Those supports are composed of groups of piles (4) with great horizontal ductility, arranged in the longitudinal and transverse directions, which are anchored at the top in large blocks of jet-grouting (3) surrounding the outer tube (1), and at the base in the stiff ground below, so to resist vertical loads, while allowing horizontal movements of the tunnel during earthquakes, functioning as a kind of "movable bearings".

The TISB concept thus leads to the obtaining of monolithic structures (joints are eliminated) with appropriate resistance in both longitudinal and transverse directions and great ductility under earthquakes. It will also be very effective if liquefaction and cyclic mobility phenomena occur. In addition, the tunnels will be provided great structural redundancy (robustness), which could be useful in the case of scenarios not foreseen in the design phase.

3.2 *The TMG concept*

The TMG ("Tunnel Multi Gallery") concept, for TBM railway tunnels, allows, with a suitable arrangement of the tunnel cross-section, that a mono-tube tunnel provides the capacities there are normally offered by two or three parallel tubes and adopts an innovative safety concept, thus, significantly reducing construction costs and improving safety during operation.

The TMG concept allows in a mono-tube TBM tunnel the creation of two independent and isolated railway galleries and a service gallery at the bottom, inside which appropriate means are installed that create a very reliable system for local access of the emergency personnel and the evacuation of users to out of the tunnel in the event of an accident or fire inside the tunnel. The TMG concept is illustrated in Figure 8 (INPI, 2009a).

In the TMG concept, after executing the circular wall (1) by the TBM, a slab (3), placed slightly above the bottom of the tunnel and the entire width, and a separating wall (2), placed in the middle of the tunnel and its entire height, are built, so as to form two independent rail galleries, placed side by side (4) (5), one for each track, and a service gallery (6) below. In both sides of the tunnel, vertical access galleries (7), regularly spaced and provided with escape doors (8) are created, allowing for the safe passage of people between the railway galleries and the service gallery (6), in the event of an accident or fire inside the tunnel.

Inside the service gallery (6), emergency vehicles (9) of monorail type are installed, which are parked at the tunnel portals, to provide local access for emergency personnel and the evacuation of users out of the tunnel. In long tunnels large openings are also created, at adequate distances, in the separating wall, provided with sliding fire doors (10), to allow trains to pass from one traffic gallery to the other, when it will be necessary to isolate a section of a railway gallery.

A variant B to the basic TMG concept can also be adopted, in which the vertical access galleries (7), instead of being placed on the outer side of the railway galleries, are placed in the middle of the tunnel, at the separating wall.

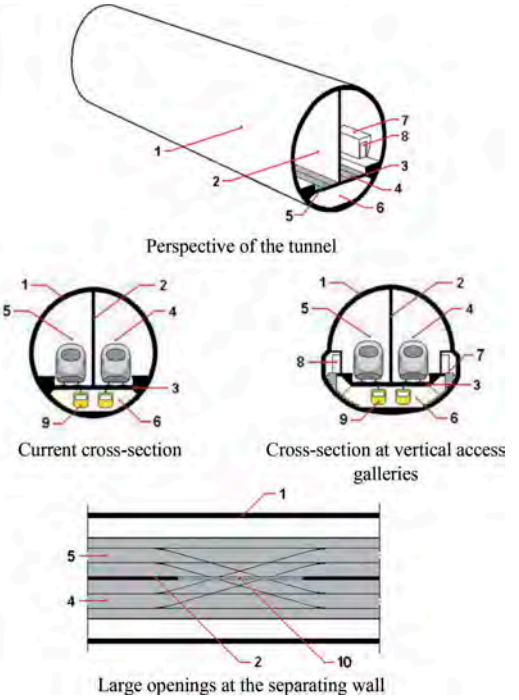

Figure 8. Illustration of the TMG concept.

Although in variant B there is a slight local reduction in the cross-section of the railway galleries, the need to make openings in the outer wall of the tunnel is avoided.

The variant B of the TMG concept is illustrated in Figure 9 (Pompeu-Santos, 2014).

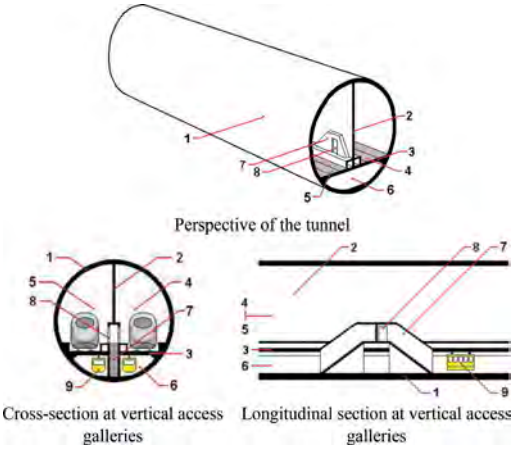

Figure 9. Illustration of variant B of the TMG concept.

3.3 *The TMF concept*

The TMF ("Tunnel Multi Floor") concept, for TBM road tunnels, allows, with a suitable arrangement of the tunnel cross-section, that a mono-tube tunnel provides the capabilities there are normally offered by two parallel tubes and adopts an innovative safety concept, thus, significantly reducing construction costs and improving safety during operation.

The TMF concept allows in a mono-tube TBM tunnel the creation of two independent and isolated road galleries and a service gallery at the bottom, inside which appropriate means are installed to create a very reliable system for local access of the emergency personnel and the evacuation of users to outside, in the event of an accident or fire inside the tunnel.

The TMF concept is illustrated in Figure 10 (INPI, 2009b; EPO, 2011).

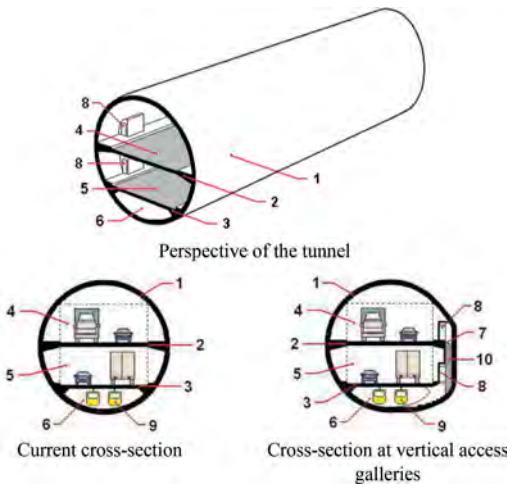

Figure 10. Illustration of the TMF concept.

In the TMF concept, after executing the circular wall (1) by the TBM, two slabs (2) (3) are built at its full width, one placed roughly at half the height of the tunnel and the other placed slightly over the bottom of the tunnel, so as to form two superimposed road galleries (4) (5), one for each direction of traffic, and a service gallery (6) below.

In one of the sides of the tunnel, vertical access galleries (7), regularly spaced and provided with escape doors (8) in both road galleries, are also created, allowing for the safe passage of people to the service gallery (6), in the event of an accident or fire inside the tunnel. Inside the service gallery (6), emergency vehicles (9) of monorail type are installed, which are parked at the tunnel portals, to provide local access for emergency personnel and the evacuation of users to out of the tunnel.

3.4 *Tunnelling based on TISB, TMG and TMF concepts*

When using TISB, TMG and TMF concepts, some essential conceptual aspects are mentioned (Pompeu-Santos, 2023).

As for structural safety, tunnels based on TISB, TMG and TMF concepts will be analyzed as composite structures, considering the precast segments and the cast insitu elements working together to cope with actions, in accordance with the relevant structural codes.

As for the inner diameter of the tunnels, in the case of rail tunnels it will essentially depend on the speed of the trains, which however will only be relevant in tunnels on High- Speed lines (from 250 km/h), being 11.50m, 12.00m and 12.50m, respectively for speeds of 250, 300 and 350 km/h. Rail tunnels will be of two types: Alternative A tunnels, based on the basic TMG concept and Alternative B tunnels, based on variant B of the TMG concept. In the case of road tunnels, inner diameter will essentially depend on the number of lanes in each traffic gallery and their width and height.

Ventilation in both rail and road tunnels is of the longitudinal type, with jet fans regularly distributed along the length of the traffic galleries, which push the air in the traffic direction. They are activated (automatically) when the pollution particles exceed the established limits (in the road tunnels) and in the fire situations. In these situations, only the fans downstream the fire are activated. The service gallery of the tunnels has its own ventilation system, with ventilators operating at both ends, which are permanently active.

For fire-fighting, traffic galleries are equipped with active detection systems and WFSs ("Water Based Fire Fighting Systems"), with high pressure water mist nozzles distributed along the tunnel and grouped in sections of about 30m.

In road tunnels the nozzles are distributed along the entire length of the tunnel, being activated those of the sections adjacent to the fire. In rail tunnels, the nozzles are distributed along "emergency stations" (at least the length of the trains), spaced about 5 km apart, being activated the nozzles of the sections on the vicinity of the fire. The adoption of WFSs will also make it possible to reduce the level fire protection of concrete and technical equipment.

Safety in operation is based on the service gallery, which aims to: i) be a "safe place" for users in the event of an accident or fire, and ii) provide access to emergency services and the evacuation of users out of the tunnel. Therefore, even in very long tunnels, no access to the outside will be necessary along the length of the tunnel. Emergency services and users will never make use of the traffic galleries of the tunnel.

Both rail and road tunnels are provided with escape doors and vertical access galleries spaced about 400m (there is no significant advantage to using smaller

spacing), to provide escape for users, who are evacuated via EMEVs ("Emergency Monorail Electric Vehicles), which circulate inside the service gallery suspended from the roofing slab (Figure 11).

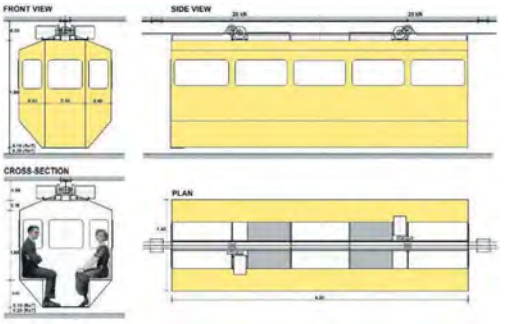

Figure 11. Lay-out of the emergency vehicles (EMEVs).

EMEVs" have (in principle) capacity for 20 people each and are grouped in "trains", in numbers according to the needs. In road tunnels the EMEV "trains" have 2 units each while in rail tunnels its number is 5, in principle. The number of EMEV "trains" will be 2 or 4, in tunnels up to 10 km, or more than 10 km in length, respectively.

Rail tunnels are also equipped with large openings in the separating wall, spaced about 10 km, to allow trains to pass to the other track in case of need.

Costs of the tunnels can be estimated based on the unit construction costs of tunnels already built, taken into account their specific conditions. Given the specificities of the TMG and TMF concepts, compared to conventional rail and road TBM tunnels, cost reductions of around 25-30% can be expected.

4 SOME APPLICATION EXAMPLES

4.1 *Alternative solution for the Gibraltar Strait tunnel*

According to the official lay-out (Pliego, 2005), the Gibraltar Strait Tunnel will link Cape Malabata, near Tanger, north of Marocco, with Punta Paloma, west of Tarifa, south of Spain. It will be 39 km long, of which 28 km under the sea, and goes very deep, until elevation -400 (Figure 12). The maximum slopes will be of 2.5%. The maximum speed of the trains will be of 120 km/h.

The geological conditions along the tunnel consist mainly of formations called flysches, consisting of clayey materials and sandstone, which are overlaid by post-flysches formations, consisting of shallow granular deposits.

The construction of the tunnel faces major challenges. It has go very deep, more than 400 meters

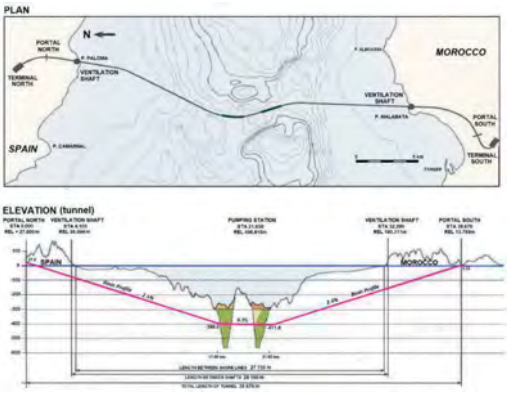

Figure 12. Gibraltar strait tunnel. Plan and longitudinal section.

below sea level, and to cross two paleo-channels in the middle, about 1 km wide each, mostly composed of deposits of clayey brescia and bioclastic sand, which are weak materials. To note also that the area is very seismic-prone, and severe earthquakes have been known to occur.

The basic layout of the tunnel is a three-tube solution, identical to the Channel Tunnel (see, Section 2.2), with railway tubes 7.5m inner diameter and a service tunnel 4.8m inner diameter.

Based on TISB and TMG (variant B) concepts, an alternative solution was developed by the author (Figure 13) (Pompeu-Santos, 2016).

In the alternative, the tunnel is a mono-tube TBM tunnel 11.5m inner diameter, inside which two independent railway galleries, placed side by side, and a service gallery below, are created (Figure 13). The cross-section of each railway gallery is about 36 m^2, identical to that of the railway tubes in the basic layout.

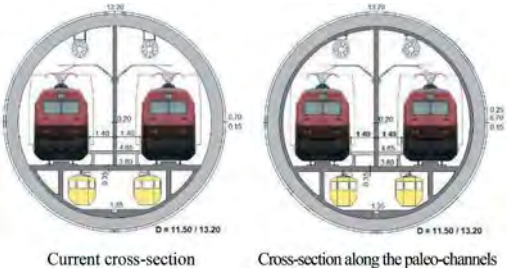

Figure 13. Gibraltar Strait Tunnel. Alternative solution cross-section.

In the section of the tunnel along the paleo-channels, the tunnel cross-section is enhanced with an interior cast insitu concrete vault, creating an inner tube with a wall thickness of 0.25m (Figure 13). The inner tube is reinforced with

longitudinal and transverse reinforcements dully confined, in order to provide the tunnel with adequate ductility under earthquakes.

Vertical access galleries are created in the middle of the tunnel (Alternative B tunnel) (see Section 3.2), with escape doors on the emergency walkways of both railway galleries, spaced about 400m apart. The service gallery is equipped with EMEV type emergency vehicles (see Figure 11), to allow local access for emergency personnel and the evacuation of the users to outside in the event of an accident or fire inside the tunnel.

As mentioned above (Section 3.4) ventilation of traffic galleries is longitudinal, with jet fans distributed along the upper part. For fire safety, the traffic galleries are equipped with WFSs installed along 7 "emergency stations", spaced about 5 km. The separating wall is provided with 3 large openings spaced about 10 km, so that trains can change tracks.

It can be seen that the alternative solution is much more cost-effective; the cost is much lesser and the safety in operation is much higher.

4.2 *Proposal for a road tunnel under the Tagus River in Lisbon*

A new crossing of the Tagus River in Lisbon, Portugal, is being looked for a long time, to allow the closure of the Lisbon's inner ring, being located west of the existing 25 de Abril (suspended) Bridge, on the Algés-Trafaria corridor (Figure 14) (Pompeu Santos, 2020, 2023). Several solutions have already been suggested, namely an immersed tunnel.

Major challenges to be faced are the very-prone seismic conditions of the site (to be remembered the 1755 Lisbon earthquake, one of the most destructive in history) and the bad characteristics of the ground.

The site is characterized by the existence of alluvial deposits of large thickness along the river bed, composed of various complexes of mud and sands, which extends from elevation -20 until elevation -75.

Figure 14. Location of the Algés-Trafaria tunnel.

Underlying the alluvial deposits there are bedrock formations composed of basalts and limestone, which extend through the north bank. On the south bank there are Miocene formations composed mainly of sands and clays (Figure 15).

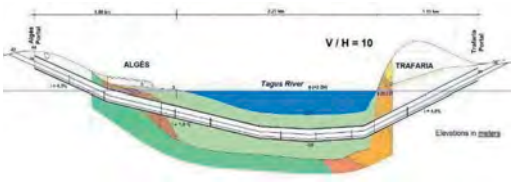

Figure 15. Proposal for the Algés-Trafaria tunnel. Longitudinal section.

Based on the TISB and TMF concepts, a TBM solution was developed by the author (Pompeu-Santos, 2020, 2023).

Given the orographic conditions of the ground, the tunnel will be 5.0 km long, 2.25 km of which under the river, and maximum gradients of 4.8% (Figure 15).

The inner diameter is 14.20m, whereby, using precast segments 0.55m thick (≈ Di/25) and a gap of 0.15m to be filled with jet-grouting, the excavated diameter will be 15.60m (Figure 16), a common size today.

Inside the TBM tunnel, two superimposed road galleries with 4.85m of free height and a service gallery 2.00 m high are created. Each road gallery has two lanes 3.50m wide and 4.35m high (0.50m for signage installation), an emergency lane 2.50m wide and an inner edge 0.70m wide, in addition to emergency walkways in the two sides 1.20 m wide.

These features give the tunnel an efficiency index with an impressive value of 0.56, much higher (25 to 30%) than most TBM road tunnels built.

To improve the seismic behavior of the tunnel, in the section where it crosses the alluvial layers, it will be enhanced with an inner tube of confined concrete cast insitu with 0.25 m wall thickness, which also incorporates the cast insitu concrete elements already foreseen (Figure 16).

Each road gallery has 12 escape doors, placed on one side of the tunnel, approximately 400m apart, which provide access to the service gallery below, through vertical access galleries.

The vertical access galleries will be built through local dismantling of the precast segments of the TBM tube and casting new concrete walls in-situ. In the cases where there is water pressure around, jet-grouting injections will create a kind of "cake" to allow work to be carried out safely.

As mentioned (Section 3.4) ventilation is longitudinal by pairs of jet fans, distributed along the upper part of the road galleries. For fire safety, traffic galleries are equipped with WFSs, with nozzles installed along their entire length, which are grouped in sections. For safety during operation the users

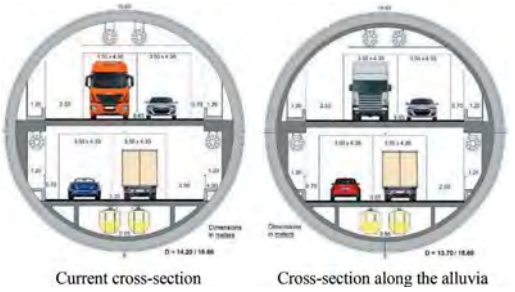

Figure 16. Proposal for the Algés-Trafaria tunnel. Cross-sections.

escape to the service gallery through the vertical access galleries, from where they are moved to outside through emergency vehicles of the EMEV type.

The cost of the tunnel was estimated from the unit construction costs of TBM road tunnels, taking into account the specific conditions of the tunnel, leading to a cost of around 400 million euros, a much lower value (about 1/3) than the estimated cost of an immersed tunnel in that location.

5 CONCLUSIONS

Building sustainable infrastructure, that is, infrastructure with increasingly lower costs and greater reliability in terms of its life cycle, is a major concern for current decision-makers.

As shown, the TISB, TMG and TMF concepts are innovative developments that allow obtaining very reliable and economical solutions in tunnel construction using the TBM technique.

Thus, these concepts can be of great benefit when applied to the construction of tunnels in rail and road networks around the world, significantly improving structural safety and safety during operation, and reducing construction costs and, consequently, materials consumption, contributing to more sustainable infrastructures.

REFERENCES

Anagnostou G., Ehrbar H., 2013. Tunneling Switzerland. Swiss Tunneling Society (STS), Zurich, Switzerland, 2013.

Bouygues, 2001. Avec le Plus Grand Tunnelier, Bouygues Construction, Va Realiser l' Ouvrage de Groenehart, Pays-Bas (With the Largest TBM, Bouygues Construction to Build the Groenehart, Netherlands). Communiqué (in French), Bouyges Construction, January 2001.

EPO, 2011. Tunnel Multi-Floor (TMF). EPO, European Patent EP 2317074 A1, November 2011.

EU, 2004. Safety in Roadway Tunnels. EU Directive 2004/54CE, April 2004.

EU, 2008. Safety in Railway Tunnels. EU Decision 2008/163CE, January 2008.

Getlink, 2021. The Channel Tunnel - A Unique Infrastructure in the World. getlinkgroup.com, 2021.

Huang R., 2009. Overview of Shanghai Yangtze River Tunnel Project. Geotechnical Aspects of Underground Construction in Soft Ground, Taylor and Francis, 2009.

INPI, 2008. Túnel de Comportamento Sísmico Melhorado (Tunnel of Improved Seismic Behaviour). INPI, Portuguese Patent n.103421 (in Portuguese), July 2008.

INPI, 2009a. Túnel de Galeria Múltipla (Tunnel Multi-Gallery). INPI, Portuguese Patent n. 103769 (in Portuguese), January 2009.

INPI, 2009b. Túnel Multi Piso (Tunnel Multi-Floor). INPI, Portuguese Patent n. 103748 (in Portuguese), August 2009.

Jiang Y., Herten A., 2019. SR99 Tunnel in Seattle. Structure Magazine, January 2019.

Pliego J. M., 2005. Opening Session - Briefing Document, Proceedings of the UN-ITA Workshop Systematic Ground Probing and Treatment in Mechanised Tunnelling, Madrid, Spain, January 2005.

Pompeu-Santos S., 2013. The TMG and TMF Concepts: The Right Approach for Large Tunnel Crossings. Proceedings of the WTC2013- Underground, the Way to the Future, Geneva, Switzerland, June 2013.

Pompeu-Santos S., 2014. New Trends in the Tunnels of the Future. IABSE Symposium Engineering for Progress Nature and People, Madrid, Spain, September 2014.

Pompeu-Santos S., 2016. *Sustainable TBM Tunnels for Tomorrow.* Second International Conference on Concrete Sustainability (ICCS2016), Madrid, Spain, June 2016.

Pompeu-Santos S., 2020. Innovative Concepts in TBM Tunnels. Tunnel Engineering – Selected Topics (Chapter 7), IntechOpen, UK, April 2020.

Pompeu-Santos S., 2023. Innovation in TBM Traffic Tunnels. Taylor and Francis, UK, 2023.

Schmid R., Wagner D., 2020. Eurasia Tunnel Istanbul - Sealing Injections against High Water Pressure. Tunnel magazine, June 2020.

UIC, 2003. UIC Code779–9: Safety in Railway Tunnels. UIC, 2003.

Tunnelling for a Better Life – Yan, Celestino, Thewes & Eberhardt (Eds)
© 2024 The Author(s), ISBN 978-1-032-80042-4
Open Access: www.taylorfrancis.com, CC BY-NC-ND 4.0 license

Underground space use layout planning using multi-source spatial data

Yong-Kang Qiao* & Zi-Yu Li
Research Center for Underground Space and Department of Geotechnical Engineering, Tongji University, Shanghai, China

Nikolai Bobylev
Chair of Geoecology, Institute of Earth Sciences, Saint Petersburg State University, Saint Petersburg, Russia

Fang-Le Peng
Research Center for Underground Space and Department of Geotechnical Engineering, Tongji University, Shanghai, China

ABSTRACT: Underground space use is a widely accepted solution to sustainable urban development. The orderly use of urban underground space requires deliberate preliminary layout planning, otherwise ad hoc underground space uses will inevitably confront many challenging issues in planning, design, construction and investment processes. Conventionally, the layout planning of urban underground space relies merely on the subjective judgements of urban planners. Such an approach increases the risks of unreasonable layout planning in the master planning process that involves hundreds of land parcels and heavy workload. To address the deficiency in layout planning, this paper proposes a new approach for the master planning of urban underground space use driven by multi-source spatial data, analytical hierarchy process method and geographic information system. In particular, the data-driven layout planning approach will facilitate laying out the integrated land use purposes, development depth and key areas of underground space use. Taking the city of Zhengzhou, China as a case study, this paper will first interpret the general considerations of underground space use planning focusing on integrated use and development depth, then use multi-source spatial data, including urban planning data, land use data, metro system data, population data, real estate data, etc., to demonstrate the applicability of the proposed approach to achieve deliberate layout planning of urban underground space use.

Keywords: Underground space use, layout planning, spatial data, integrated use, development depth

1 INTRODUCTION

Underground space plays a key role in urban development in particular terms of sustainability and resilience (Bobylev, 2009; Qiao et al., 2022; Sterling and Nelson, 2013). Taking China as an example, the newly built underground space infrastructures nationwide summed up to 1.07 billion square meters during 2016–2020 (CSCCAE et al., 2020), and the amount of urban underground space (UUS) uses in Chinese mega cities such as Beijing and Shanghai have already exceeded 100 million square meters. Such a huge amount of both built capital and future increments beneath a city is likely to cause management chaos with many challenging issues in planning, design, construction and investment processes. Therefore, deliberate preliminary layout planning is required for the orderly use of urban underground space.

The planning of UUS use in China originated from the planning of civil defense facilities dating back to 1990s. since 2000s, the planning of UUS for civil uses began to spread in major Chinese cities. As of 2020, 191 out of 341 prefecture cities in China had completed or were preparing for UUS planning. Nevertheless, the conventional layout planning of urban underground space relies merely on the subjective judgements of urban planners. For instance, common planning criteria include that UUS use should be arranged surrounding metro stations in urban core areas, a higher UUS development density should be introduced to an area with high floor area ratio, etc. However, such subjective approaches could increase the risks of unreasonable layout planning in the master planning process. This is because that the master planning of UUS use generally involves hundreds of land parcels and heavy workload, and that the layout of UUS use are attributed to by multiple factors hence subjective judgements are difficult to perform.

In this context, data-driven and intelligent planning approaches are proposed to address the deficiency in

*Corresponding author: iamqyk@163.com

DOI: 10.1201/9781003495505-18

conventional layout planning of UUS use (Peng et al., 2023). This paper is also intended for this direction. Specifically, it proposes a data-driven approach for the master planning of urban underground space use aided by multi-source spatial data, analytical hierarchy process method and geographic information system. In particular, the data-driven layout planning approach will focus on the key aspects of UUS use layout, including the integrated land use purposes, development depth and key areas of underground space use.

The proposed approach will be illustrated with a case study of the Chinese city of Zhengzhou. The UUS planning of Zhengzhou began in 2017, and completed the first version of review draft in 2018, in which UUS layout planning was mainly performed by the aforementioned subjective judgements. However, there was a planning revolution around 2019 in China with the objective of establishing territorial spatial planning system. For this reason, the first review draft was not put aside and the planning process was suspended. It was not until 2021 that the planning was restarted. In this round, multi-source spatial data, including urban planning data, land use data, metro system data, population data, real estate data, etc., was used to facilitate the deliberate layout planning of urban underground space use under the framework of territorial spatial planning system. Compared with the first draft in 2018, the data-driven approach was deemed as more efficient, convincing and scientific. Against this background, this paper will take the city of Zhengzhou as a case study to demonstrate the applicability of the proposed approach to achieve deliberate layout planning of urban underground space use, which will provide references for the data-driven and intelligent UUS planning.

2 GENERAL CONSIDERATIONS OF UNDERGROUND SPACE USE LAYOUT PLANNING

In practice, there are at least two levels of UUS planning: master planning and regulatory detailed planning. Unlike UUS regulatory detailed planning that is often treated as a statutory and contractual instrument for guiding and regulating developers' behaviors in the use of UUS, UUS master planning puts more emphasis on outlining the development strategies and priorities in terms of integrated use type, scale, location, and depth (Peng et al., 2021). Since this paper focuses on the layout planning of UUS use, this part only introduces the general considerations of UUS planning from the perspectives of integrated use type, location, and depth.

2.1 *Integrated UUS use*

UUS is usually used as civil defense, public service, transportation, parking, municipal and industrial storage facilities. In the level of UUS master planning which is mainly drafted at land parcel scale, it is quite common that the underground space below a land parcel will be planned for multiple uses either integrated horizontally or vertically. This is also a major characteristic of UUS planning distinctive from surface planning. In general, the degree of UUS use integration can be divided into the following three categories based on the conditions of land use properties, locations, development requirements and other relevant factors.

(1) Comprehensive integration, refers to the UUS planned with diverse use types and direct connections with metro stations and surrounding underground buildings. It mainly exists in the key areas and nodes (such as central business districts and commercial centers) of UUS development, and is usually characterized with a UUS use combination form of public service + parking + transportation + utility tunnel + others. Another distinguishing feature is the required high connectivity.
(2) Compound integration, refers to the UUS planned with mixed use types but low connectivity. It is usually characterized with a UUS use combination form of public service + parking + transportation + others. The interconnectivity between planned UUS and surrounding underground buildings is encouraged under this category.
(3) Simple use, refers to UUS with relatively single use type and lack of connectivity. It is the major category of planned UUS use in UUS master planning.
(4) Restricted use, refers to UUS uses are not encouraged for common uses such as commercial and parking. Special uses, such as relic storage and exhibition, transportation tunnels, should be well-reasoned before and during planning process.

2.2 *Development depth*

Different UUS planning levels have different purposes and approaches for development depth control. UUS master planning expects to control and optimize the use of UUS from the surface down to 100 meters or even deeper below a city, while UUS regulatory detailed planning pays more attention to the number of underground floors to be built by private developers or public sectors.

As regards UUS master planning, due to the differences in development stages, demands and geological conditions, cities varied in the vertical stratification standards of UUS development. For example, Beijing, one of the largest Chinese cities, divided its underground space into four layers: shallow layer (0–10 m), sub-shallow layer (10–30 m), sub-deep layer (30–50 m) and deep layer (deeper than 50 m); while Tongren, a less-populated city, was planned with three layers: shallow layer (0–10 m), sub-shallow layer (10–30 m) and deep layer (30–50 m). Evidently, the definition of deep underground layer is different between Beijing and Tongren. Similarly, such a difference also exists between international jurisdictions, such as Tokyo (40 or 10 m below the bearing layer of

foundation piles) and Singapore (30 m). In addition, there are some cities delineated different depth limits for the shallow layer. Prior approximately 2016, the adoption of 10 m was popular among Chinese cities to define the shallow underground layer. But with the demand for UUS grew, particularly the underground parking demand, more residential compound and commercial centers were built with three or more underground floors. This tendency drove more cities to adopt 15 m as the limit of shallow layer of UUS use.

Considering the aforementioned facts and the Standard for Urban Underground Space Planning (GB/T 51358-2019, 2019), this study adopts the following vertical stratification standard: shallow layer (0–15 m), sub-shallow layer (15–30 m), sub-deep layer (30–50 m) and deep layer (deeper than 50 m). Different depths correspond to different major categories of UUS uses. Specifically, shallow layer is more suitable for UUS uses intended for frequent daily activities of inhabitants, sub-shallow layer favors underground transportation facilities due to worse accessibility, sub-deep layer is usually planned as a long-term development reservation, and deep layer is often reserved for special underground facilities.

The development depth of a land parcel is influenced mainly by two factors: the degree of UUS use integration and the amount of UUS development demand. For the first factor, a higher degree of integration implies that more underground floors are required to accommodate various facilities types because the same type of facilities tend to share the same floor. For the second factor, it is apparent a larger development depth can bring more space to accommodate a higher UUS demand. To determine the demand of land parcel, we can refer to the findings of Peng et al. (2019), which used Osaka as a case and revealed that UUS demand or developed UUS area is strongly related with passenger flow rate and land price.

3 METHODOLOGY

The methodology for data-driven UUS layout planning involves the determination of planning decision supporting model, weight calculation method and index system.

3.1 *Planning decision supporting model*

Through the analysis in Section 2, it is clear that the UUS layout planning for integrated UUS use and development depth is a typical problem of multiple criteria decision analysis (MCDA), which is usually solved by Eq. (1).

$$S = \sum_{j=1}^{n} \left(\sum_{i=1}^{n} A_i B_i \right) C_j \qquad (1)$$

Where, S is the calculation value of the planning objective ($0 \le S \le 1$); A_i is the quantitative value of the i-th index; B_i is the weight of the i-th index; C_j is the weight of the j-th theme.

After obtaining the calculation value S, the layout planning can be made by setting reclassification criteria to the calculation value. Specifically, the layout of integrated UUS use and development depth will all be reclassified into four categories as mentioned in Section 2.

3.2 *Weight calculation method*

As a useful decision-making management tool, analytic hierarchy process (AHP) was introduced by Saaty (1980) to deal with multiple criteria problems. AHP follows a procedure of (1) determining the judgment matrix, and (2) calculating the priority vector of the judgement matrix to obtain the weights of multi-criteria.

3.3 *Index system*

As analyzed in Section 2.1, the degree of UUS use integration is influenced by land use properties, locations, development requirements and other relevant factors. Therefore, this study established the index system listed in Table 1 for UUS layout of integrated UUS use. The index system consists of four indicators, namely urban centrality, surface land use, rail transit and area functionality. Following the AHP procedures, the weights of these four indicators were calculated as 0.48, 0.09, 0.16 and 0.27, respectively based on the judgment matrices determined by experts from Tongji University and Zhengzhou Urban Planning Design & Survey Research Institute. Table 1 also lists the sub-indicators used in this study. It can be seen that these sub-indicators are all qualitative expressions. To make it computable in GIS platform, it is necessary to find a suitable scoring approach to translate these qualitative expressions into quantitative values that should reflect the relative importance of sub-indicators. Therefore, AHP is used again to transform them into quantitative scoring values, which are normalized in the field of 'score' of Table 1.

Section 2.2 mentioned that influential factors of the development depth include the degree of UUS use integration and the amount of UUS development demand, and the latter is strongly related with passenger flow rate and land price. The first indicator is derived from Table 1. However, the data of passenger flow rate is usually quite difficult to obtain or to forecast, particularly for cities just about to develop urban rail transit systems. To solve this problem, we need to find other data types to replace this data. According to Peng et al. (2019), the number of transfer lines is highly correlated with passenger flow rate (Pearson Correlation = 0.902). Moreover, the passenger volume is also related with local population. Therefore, we can replace passenger flow rate with the sub-indicators of population and the number of transfer lines. Similarly, we replace land price with the sub-indicator of real estate price. As listed in Table 2, the sub-indicators for development depth planning is weighed as 0.4, 0.2, 0.2 and 0.2, respectively based on AHP method.

Table 1. Index system for integrated UUS use planning.

Indicators	Weights	Sub-indicators	Scores
Urban centrality	0.48	City centers	1
		City sub-centers	0.48
		District centers	0.23
		Others	0.07
Surface land use	0.09	Commercial service	1
		Culture, sports, medical	0.58
		Green, plaza, transportation	0.58
		Residential	0.13
		Others	0.09
Rail transit	0.16	Within 300 m of a station	1
		Within 500 m of a station	0.55
		Within 800 m of a station	0.32
		Others	0.08
Area functionality	0.27	Level I	1
		Level II	0.51
		Level III	0.25
		Level IV	0.13
		Others	0.06

Table 2. Index system for development depth planning.

Indicators	Sub-indicators	Weights
Integration degree of UUS use		0.4
UUS demand	Population	0.2
	Real estate price	0.2
	Number of transfer lines	0.2

4 A CASE STUDY OF ZHENGZHOU

4.1 *Overview of the case study area*

Zhengzhou, the capital city of Henan Province, is located in the central and northern part of Henan Province. It has a history of 3,600 years and is one of the eight ancient capital cities of China. The urbanization of Zhengzhou in the modern sense began after the founding of People's Republic of China. With the construction of Longhai Railway and Beijing-Guangzhou Railway, two of the most important artery railways in China, Zhengzhou has gradually become an important city with the best transportation location, vast hinterland market, abundant human resources and rich historical and cultural heritage in the Central Plains. As of 2020, the city's GDP reached 1.2 trillion yuan ($187 billion) with a population of over 12.6 million. The amount of underground buildings in Zhengzhou's main urban area reached 43.8 million square meters.

With the advent of the new century and the proposal of Belt and Road Initiative, Zhengzhou has risen to become a national central city and the core city of the Central China City Cluster, which puts forward higher requirements for its urban development in particular terms of compact, liveable, green and resilient city. These requirements were also viewed as the objectives of UUS planning in Zhengzhou. The total area of UUS planning set in 2021 was 1,239 square kilometres with a planned population of approximately 8 million.

Table 3. Multi-source spatial data for integrated UUS use planning in Zhengzhou.

Indicators	Illustration
Urban centrality	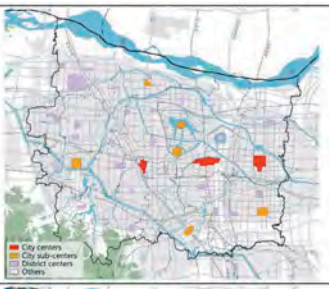
Surface land use	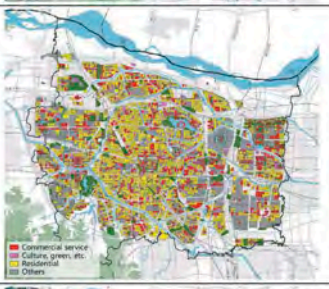
Rail transit	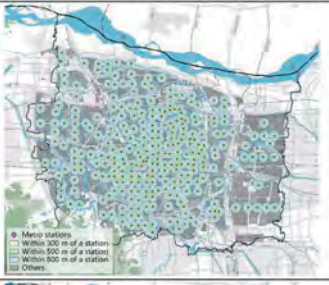
Area functionality	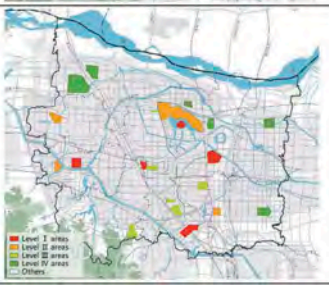

4.2 *Layout planning for integrated UUS use*

Based on the methodology introduced in Section 3, we collected the required multi-source spatial data for integrated UUS use planning. The data is listed in Table 3, which were mainly obtained from planning authorities.

With the aid of GIS platform and AHP, the calculation results of the planning objective of integrated UUS use were derived as shown in Figure 1, based on which the main urban area of Zhengzhou was divided into four categories as shown in Figure 2.

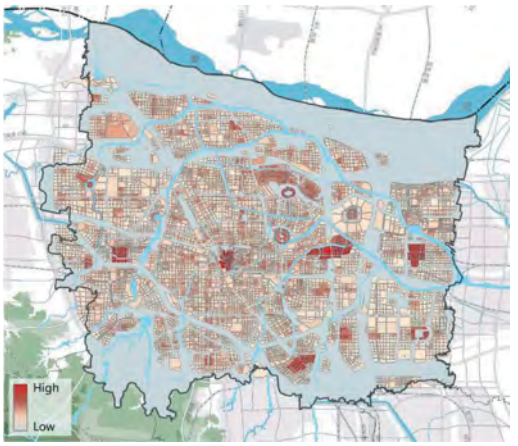

Figure 1. Calculation results of the planning objective of integrated UUS use.

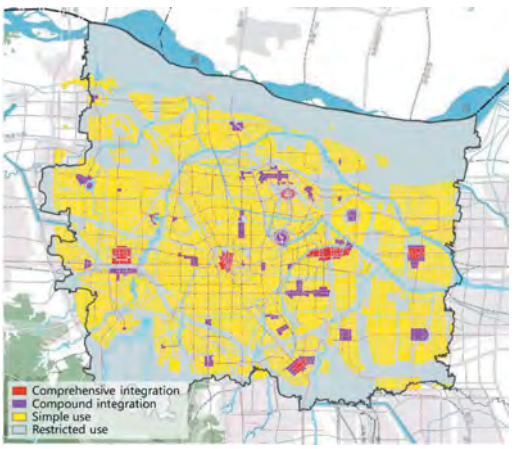

Figure 2. Reclassification results of integrated UUS use in Zhengzhou.

4.3 *Layout planning for development depth*

The required multi-source spatial data for development depth planning was collected and presented in Table 4. The calculation results of the planning objective of development depth were derived as shown in Figure 3, and reclassified into four categories as shown in Figure 4.

Table 4. Multi-source spatial data for development depth planning in Zhengzhou.

Indicators	Illustration
Integration degree of UUS use	
Population	
Real estate price	
Number of transfer lines	

4.4 *Overall layout planning for UUS use in Zhengzhou*

Based on the layout planning of integrated UUS use in Figure 3 and that of development depth in Figure 4, we can delineate the key areas for UUS use and development in Zhengzhou as shown in Figure 5, which includes four city-center-level areas and 17

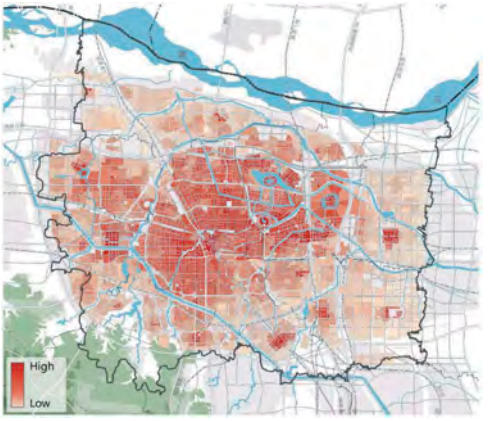

Figure 3. Calculation results of the planning objective of development depth.

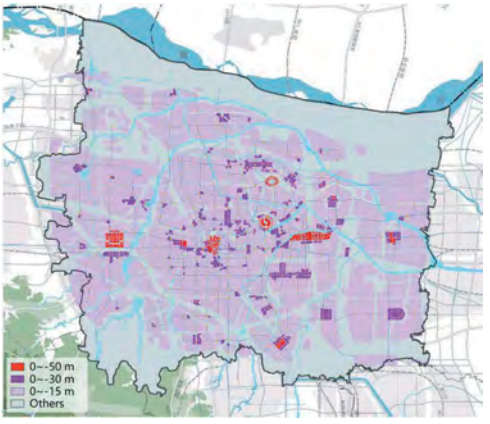

Figure 4. Reclassification results of development depth in Zhengzhou.

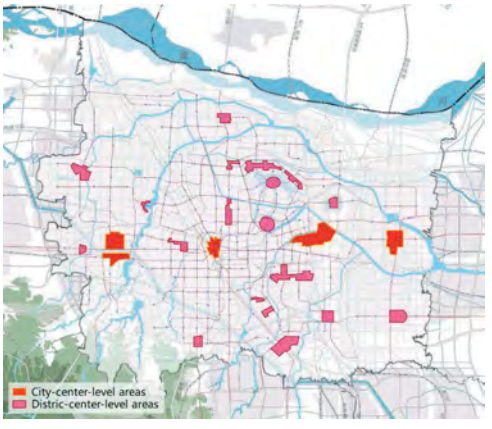

Figure 5. Overall layout planning of key areas of UUS use in Zhengzhou.

district-center-level areas. Furthermore, these results can also provide valuable references for mapping out the planning structure of UUS use in Zhengzhou.

5 CONCLUSION

In the era of smart city development, newly emerged urban planning tendencies are driving urban underground space (UUS) planning to shift from conventional approaches to data-driven technologies.

This paper presents a straightforward approach of data-driven layout planning for UUS use, which is comprised of a planning decision supporting model, i.e. multiple criteria decision analysis, an AHP-based weight calculation method and an index system. The index system for integrated UUS use planning consists of four indicators, namely urban centrality, surface land use, rail transit and area functionality, while that for development depth include integration degree of UUS use, population, real estate price, number of transfer lines. The case study of Zhengzhou, China proved that the proposed data-driven approach for UUS planning is practical.

However, it should be mentioned that this paper just showed a tentative attempt for data-driven UUS master planning. In fact, there are a lot of research work to be done in the future. For instance, UUS use can be influenced by more complicated factors, and these factors should be incorporated into this approach. Moreover, intelligent planning algorithms need to be developed to integrated these factors among which the relations are likely to be nonlinear. Nevertheless, findings of this paper can still provide some insights for UUS planning.

ACKNOWLEDGMENTS

The authors acknowledge gratefully the support provided by the National Natural Science Foundation of China (Grant No. 42201284, 42071251).

REFERENCES

Bobylev, N., 2009. Mainstreaming sustainable development into a city's master plan: A case of urban underground space use. Land Use Policy, 26(4): 1128–1137

CSCCAE (Center for Strategic Consulting of Chinese Academy of Engineering), Sub-society for Underground Space of Chinese Society of Rock Mechanics and Engineering, Chinese Society of Urban Planning, 2020. Blue book of urban underground space development in China 2020: Public edition.

GB/T 51358-2019, 1999. Standard for urban underground space planning. Ministry of Housing and Urban-Rural Development of the People's Republic of China.

Peng, F.L., Dong, Y.H., Wang, W.X., Ma, C.X., 2023. The next frontier: data-driven urban underground space planning orienting multiple development concepts. Smart Construction and Sustainable Cities, 1, 3.

Peng, F.L., Qiao, Y.K., Sabri, S., Atazadeh, B., Rajabifard, A., 2021. A collaborative approach for urban underground space development toward sustainable development goals: critical dimensions and future directions. Frontiers of Structural and Civil Engineering, 15 (1), 20–45.

Peng, J., Peng, F.L., Yabuki, N., Fukuda, T., 2019. Factors in the development of urban underground space surrounding metro stations: A case study of Osaka, Japan. Tunnelling and Underground Space Technology, 91: 103009

Qiao, Y.K., Peng, F.L., Luan, Y.P., Wu, X.L., 2022. Rethinking underground land value and pricing: A sustainability perspective. Tunnelling and Underground Space Technology, 127, 104573.

Saaty, T., 1980. The analytic hierarchy process. McGraw-Hill, New York.

Sterling, R., Nelson, P., 2013. City resiliency and underground space use. In Proceedings of 13th ACUUS International Conference Advances in Underground Space Development, Singapore, November 7-9, 2013, pp. 43–55.

Tunnelling for a Better Life – Yan, Celestino, Thewes & Eberhardt (Eds)
© 2024 The Author(s), ISBN 978-1-032-80042-4
Open Access: www.taylorfrancis.com, CC BY-NC-ND 4.0 license

Tunnelling in a green country – Brenner Base Tunnel study case: Decision and solutions in construction lot H41 Sill Gorge-Pfons

Ivan Zamberlan* & Christian Schwarz*
Brenner Basistunnel BBT SE, Innsbruck, Austria

ABSTRACT: In the construction lot H41 Sill Gorge-Pfons of the Brenner Base Tunnel, decisions have been taken in order to reduce the pressure on the environment and the regional population living in the project area. In cooperation between the contractor and the client, innovative and eco-friendly logistical solutions for the transport of spoil as well as for the manufacture and transport of tubbing were implemented.

The contractor decided to optimize the production of segmental liner by building a factory directly on the construction site, avoiding transportation on the existing highway. They made a reinforced earth to increase the available area built with spoil material. An automatic tubbing production system using local quarry material on the site was established.

Using the exploratory tunnel built in an earlier stage of the project, the client decided to transport the spoil to a deposit site located further from the construction site but with a minor impact on the environment and the resident population. A large-capacity conveyor belt system approximately 30 km long was built, allowing a completely automatic underground material transfer.

The conveyor belt runs through three different construction lots and therefore three different contractors, each of whom must provide management of their own section, are involved. This presents a challenge to all participants for an optimal coordination among the three different contractors to provide smooth service of the conveyor belts and consequently undisturbed TBM advancements.

The reduction in the number of trucks coming to the construction site via the congested highway and the introduction of the conveyor belt system lead to a minor CO_2 emission. These decisions achieved great benefits for the environment and for the regional population.

Keywords: Environment, Conveyor belt, Spoil material, Logistics, TBM, Brenner Base Tunnel

1 INTRODUCTION

The Brenner Base Tunnel is a straight, flat railway tunnel connecting two countries (Italy and Austria) in the heart of Europe. The BBT runs for 55 km between Innsbruck (in Austria) and Fortezza (in Italy). Thanks to the low gradient of 4 ‰ - 7 ‰ and the relatively flat course of the line, the tunnel cuts the route length between Fortezza and Innsbruck by 20 km, from 75 km down to 55 km. Since suitable expansion of the line is not possible, due to the steep ascent to the Brenner pass at 1,370 meters above sea level and the many curves in the current route as it winds through the landscape, a railway tunnel, the Brenner Base Tunnel, is being constructed at the very base of the Brenner massif. The construction of the Brenner Base Tunnel is segmented in several lots to allow a great parallelism of work and optimized tender (Insam et. al, 2022) (Figure 1).

2 THE TUNNEL SYSTEM

Two single-track main tubes run between Innsbruck and Fortezza, set about 40 to 70 metres apart. This distance is necessary to keep the rock mass stable. Smaller tunnels connecting the two main tubes are located every 333 m. They are used for logistics but also for emergency rescue.

A peculiar feature is the exploratory tunnel, which runs from one end to the other. This tunnel lies between the two main tunnels and about twelve metres below them. The exploratory

*Corresponding author: ivan.zamberlan@bbt-se.com; christian.schwarz@bbt-se.com

DOI: 10.1201/9781003495505-19

Figure 1. BBT route, the different lots are marked with different colors, on the left the city of Innsbruck and on the right the city of Fortezza is located.

Source: BBT SE

tunnel is meant for geological prospection, as a service and logistics tunnel during the construction phase and as a maintenance and drainage tunnel during the operational phase (Figure 2). Each 20 km an emergency stop is located, which provides a dense number of cross cuts between the main tunnels and a direct exit to the surface.

In total, the tunnel system for the Brenner Base Tunnel will comprise about 230 km of tunnels.

3 EXCAVATION METHODS

The choice of excavation method depends on the geology of the mountain, on geotechnical findings and forecasts, and on construction logistics and economic considerations.

For the BBT project the drill and blast method and the mechanical excavation are used in a ratio of 50% and 50% circa.

In total 9 TBMs, mainly shielded TBMs, but also open gripper TBM, are used. The far-reaching stretches of the main tunnel are excavated with shielded TBMs and tunnel support using precast concrete tubbing rings are installed.

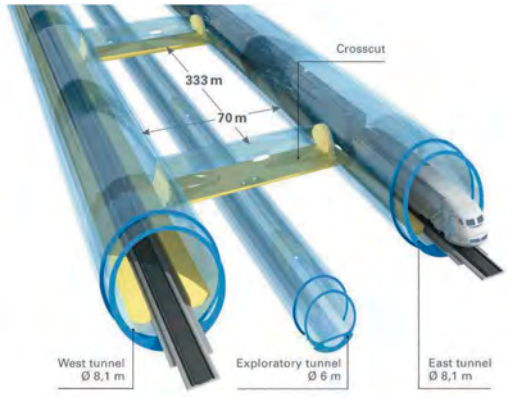

Figure 2. BBT tunnel system.

Source: BBT SE

4 BUILDING IN A PROTECTED ENVIRONMENT

4.1 *General considerations*

The construction of the Brenner Base Tunnel is accompanied by comprehensive environmental measures.

Austria and Italy are implementing numerous environmental measures during the construction of the Brenner Base Tunnel also because there are strict environmental regulations. The high-capacity rail line itself is contributing to the protection of the Alps. Even the construction process is as environmentally friendly as possible.

A series of decision are taken in order to reduce the impact of the construction phase. Dust and noise at the construction sites are kept as low as possible, tackled in terms of minimization and mitigation.

4.2 *Noise reduction*

Firstly, the deployed equipment has a low level of emitted noise, in the tunnel and on the surface. Further, the turbines used to ventilate the tunnel are housed in their own caverns built in the rock. However, noise emission is not entirely avoidable, so noise protection baffles and walls have been erected to protect against noise pollution. Where construction sites are located close to populated areas, construction hours are limited to consider the needs of the local residents. This is the case on the surface as well as underground when excavation underneath a village the excavation has to be stopped during the night hours.

4.3 *Air pollution control*

Air pollution caused by construction site traffic is also minimised. Firstly, all vehicles and construction machinery must comply with the latest technical standards. However, several additional motorway slip roads have been provided in the project area: they allow the construction site to

be supplied exclusively over the primary road network, thus effectively eliminating additional traffic through local residential areas. A dedicated access tunnel, the Saxener tunnel (1km ca.), was built for the construction site in Wolf near Steinach am Brenner. All site traffic exits the A13 Brenner motorway at the Plon road maintenance depot and travels through the Saxener tunnel directly to the construction site in Wolf. The town of Steinach is therefore not burdened with construction site traffic.

Further, a dedicated railway siding was built for the Wolf construction site in 2016. Construction materials and machinery can be directly delivered and discharged by train. In the upcoming construction lot H53 this railway siding will be used intensively, especially for the haulage of tubbings.

On the construction site itself air pollution is mainly caused by dust. All site roads and temporary storage areas on the construction sites are watered down to reduce dust. Vehicles and construction machines are cleaned regularly. Material transport within the construction sites takes place largely via conveyor belts, on which the material is also sprayed with water to avoid dust. Further, a strategic placement of facilities on the construction site avoid dust beforehand. In the Innsbruck area the quite strong *foehn* wind is a common phenomenon. E.g. the placement of the handling area of the dry components for cement and mortar in a wind shielded area is a smart, cheap, and effective measure.

5 SPOIL MATERIAL: COST OR RESOURCE?

5.1 *Conditions at the Brenner Base Tunnel*

The construction of the Brenner Base Tunnel involves the excavation of about 21.5 million cubic meters of spoil. Depending on the quality, this will either be landfilled or recycled. The processing and recycling of the material helps to preserve resources. The processed material can be used for the production of concrete for inner linings and base slabs as well as shotcrete. Since the tunnel spoil is very diverse due to varying geological conditions, the amounts of recyclable tunnel spoil also vary as construction proceeds. When more material is processed than is required for re-use, it is used as aggregate to produce concrete in other sectors.

The processing into concrete aggregates is done *in situ* on the construction sites in dedicated gravel plants and concrete production factories. Doing so, the environmental impact is reduced threefold:

First, the amount of aggregate delivered to the construction site is reduced.

Second, the volume of deposits necessary and the impact on the landscape is reduced.

Third, the amount of spoil transported to the landfills are reduced.

5.2 *Reinforced earth*

At the construction site Ahrental the material properties of the spoil do not allow a use as aggregate neither for segmental liner nor shotcrete, so it has to be deposited. The capacity of the landfill directly at the Ahrental portal is about 2.5 M m³. In the previous construction lot H33 the deposit Ahrental was mostly filled and some room was left for logistical reasons to the current lot. This deposit was built predominantly with the classic 2:3 slopes and mostly considered as a deposit only.

However, in the construction lot H41 the deposit is reshaped in a meaningful manner to optimise the logistics and infrastructure for construction site in an intermediate state of the landfill and emphasize its additional value as a construction site. The current contractor desired a remodelling of the shape of the deposit, i.e. a steepening of the slope in order to create a larger surface on its top. The steeper slope, however, comes with further reinforcement for stability reasons (Figure 3).

Since it was planned to fill the deposit entirely by the end of the construction lot this measure describes an anticipation of works. The larger surface creates the conditions to build directly on the construction site the factory for the segmental liner, that would not have been possible otherwise, due to the confined construction area.

Therefore, this is a win-win-situation, for the BBT SE company on the one side, by reducing the transportation impact on the environment for the segmental liners and avoiding the costs for the reinforced earth. On the other side the contractor, has reduced its cost for the purchase and constant supply of segmental liners and gained the independence of logistic risks on public streets. Overall, this measure is cost-neutral and beneficial for all parties.

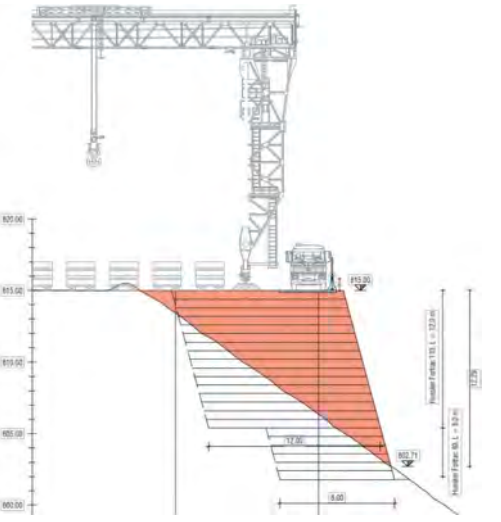

Figure 3. Crosssection of the reinforced earth.
Source: ARGE H41 Sillschlucht – Pfons

The construction of the reinforced earth allowed for the creation of an additional 5,300 square metres (Figure 4; dark brown) of construction site area, which was used to house the segmental liners store.

These, piled in stacks of 12 pieces each, add up to a total weight of around 120 tonnes. The reinforced earth also houses one of the two lanes of the overhead crane dedicated to the handling of segmental liners (red). The maximum height of the reinforced soil is 23 m with a filling volume of approximately 40,000 m³.

Figure 4. Plane view of tubbing factory (yellow) and tubbing storage (red) on the reinforced earth.

Source: ARGE H41 Sillschlucht – Pfons

The two main tube headings towards the south in the construction lot H41 are excavated by two quasi identical single shield tunnel boring machines. In the east tunnel 8398 m and in the east tunnel 8108 m of tunnel has to be drilled and equipped with segmental liners. The tubbing design defines 6 segmental liners and a length of 1,95 m per ring, which results in ca. 50,800 elements in approximately 2.5 years. These figures describe the work load of the factory and the constant logistic effort to stack produced new liners, handle them and load them for transport to the heading, which requires a finely planned logistics just for the tubbing transport.

6 CONVEYOR BELT LOGISTICS

6.1 *Logistics at the Brenner Base Tunnel*

The construction of the Brenner Base Tunnel is segmented in several construction lots awarded to various contractors in individual tenders. However, the BBT SE as the client summarizing all lots and aims at generating value in cooperation between the lots, especially in logistics this is beneficial.

In the proximity of the city of Innsbruck only little percentage of the spoil is deposited, with one bigger landfill of 2.5 M m³ volume and some smaller ones. These landfills were mayorly used during a previous construction lot and only little is left for the current construction lot. The biggest landfill of the Brenner Base Tunnel is located in the Padaster valley near the neighbouring lot in Wolf, which is capable of taking the spoil of its own lot and excess material from another lot.

The two portals of the two construction lots Ahrental H41 and Wolf H52 are only 20 km apart and linked by a highway and a federal street. However, these streets are already prone to congestions and a smooth transport is key to the success of any construction, but to this in particular. In addition, the legal constraints are, that transport by truck is forbidden during the night and on weekend, which conflicts with a 24/7 progress on the construction site. Furthermore, the environmental aspect is considerable.

The two lots are already linked since the breakthrough of the exploratory tunnel happened more than 3 years ago on 06.07.2020 and this was incorporated in the logistic management of the lot.

6.2 *Logistics at construction lot H41 Sill Gorge-Pfons*

Aim of the logistics for the spoil transport was to create safe, redundant, eco-friendly, high capacity system, which is capable of handling four main headings and deliver spoil to two landfills (Ahrental and Wolf/Padaster valley). In the construction lot H41 Sill Gorge-Pfons the two main tunnel headings in the east and west tube to the north are excavated by the drill and blast method and stretched over about two or three kilometres respectively. The two main tunnel headings to the south are excavated by two quasi identical tunnel boring machines (also called "TBMs") and stretch over more than eight kilometres in each tube. Due to the different excavation method the spoil is differently composed in its grain size distribution. A drill and blast heading creates a rather wide graded spoil composition, whereas a TBM heading produces a rather narrow graded spoil. By leading the spoil throw crushers the grain size curve is homogenized and the material is suitable for the transport by conveyor belt.

Another criterion for the conveyor belt logistics at the construction lot H41 was to enable the merge and separation of material flow without interfering in running conveyor belts. This is crucial in order to have really independent headings, whose performance does not depend on the state of the conveyor belt. Finally, the established conveyor belt system comprises 4 sources of material (headings), 2 distribution hubs, and two exits (portal Ahrental and Wolf/Padaster valley).

Under consideration of the above-mentioned boundary conditions the contractor H41 developed the following solution transporting the spoil through the exploratory tunnel (Figure 5).

In the lot H41 alone the length of all conveyor belts sums up to more than 34,7 km distributed over

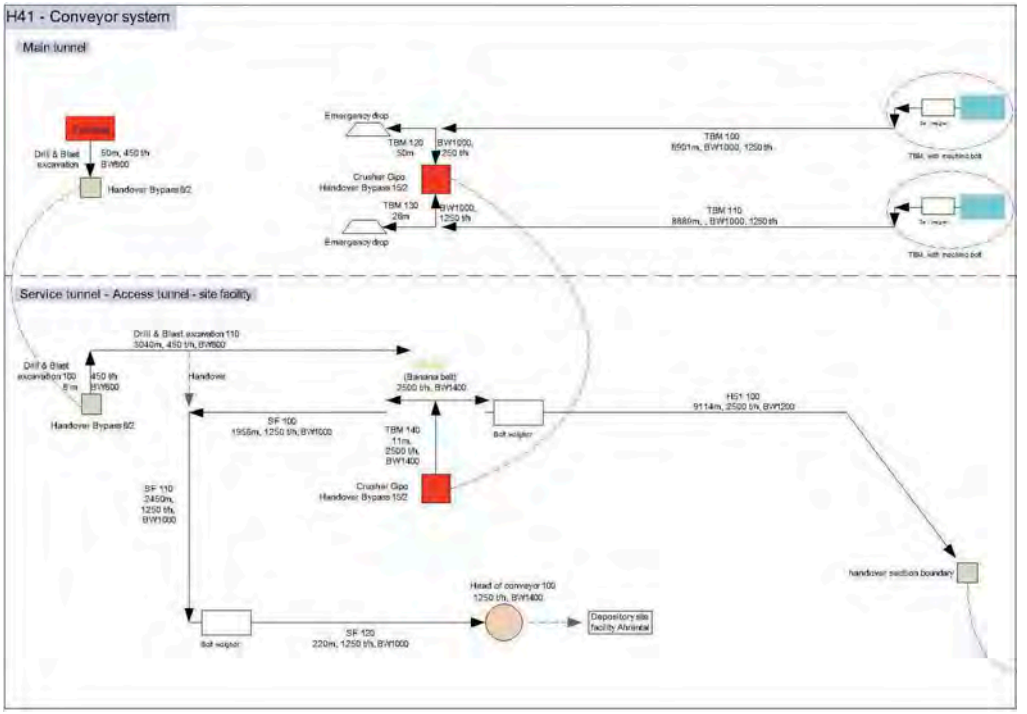

Figure 5. Conveyor belt system of the construction lot H41.
Source: ARGE H41 Sillschlucht – Pfons

20 conveyor belts. The maximal capacity towards the lot H52 in the south is 2,500 to/h and to the construction site Ahrental 1,250 to/h. During the construction phases 4.5 M to will be transported to Padaster valley via the conveyor belt in the exploratory tunnel and about 1.0 M to will be discharged at the construction site Ahrental.

6.3 *Logistics at construction lot H52 Hochstegen*

At the underground border between the lots H41 and H52 the spoil passes to the contractor of H52, who has to transport it to the surface and finally into the Padaster valley deposit without further manipulation. In addition to this, the lot H52 is in operation as well with its own headings. Its spoil has to be transported as well with the same conveyor belt system from the underground to the surface and then to the Padaster valley.

In the construction lot H52 17 belts are operated and sum up to about 26 km. Their design varies from a about 9 km long flat conveyer belt equipped with 3 boosters, to about 4 km long ascending (+300 m) conveyer belts equipped with 3 boosters, and a set of shorter conveyer belts for distribution purposes underground and on the deposit to the different heads (Figure 6).

In the future the upcoming lot will incorporate the conveyer belts for its two TBM drives into this system.

6.4 *Joint logistics*

Each conveyor belt system is a complex arrangement on its own, but all systems have to operate together as a unique system, rather than two systems joint together. However, the construction lots are awarded by independent tenders and therefore the contractors and their conveyor belt manufacturer are not the same. The detailed planning of the logistic concept (e.g. the conveyor belt system) is done by the contractor and the underlaying conception may differ. BBT SE as client of both contractors took care of the tender process and it is still taking care of the execution process, to make sure that the relevant parameters in both lots are identical. These are mainly the capacity of the conveyer belt, the regulation and interdependence of the individual conveyor belts (e.g. emergency stop, regular de- and acceleration). Regular meetings and exchange of experiences between the client and both contractors and their conveyor belt manufacturer are crucial during the total duration of the construction phase (BMA, 2022).

Further challenge will be the transition of contractors from lot H52 to H53 on the same construction site Wolf, right after completion of H52. No service interruption of the conveyor belt system is allowed during this phase, since the lot H41 will continue to excavate and transport material to the lot border to (then) H53.

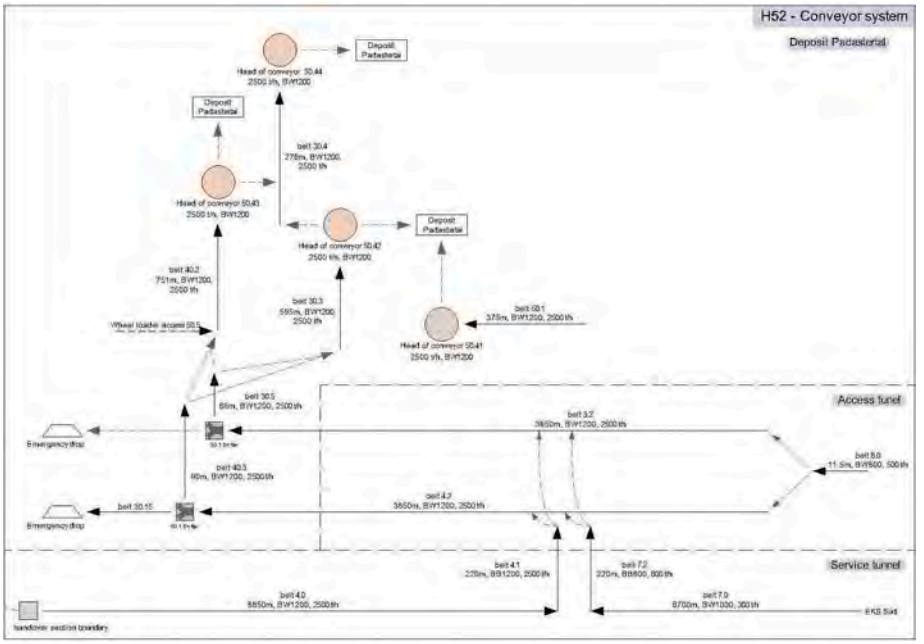

Figure 6. Conveyor belt system of the construction lot H52.
Source: BBT SE based on AN H52 Swietelsky Tunnelbau Gmbh & CoKG

This is a win-win solution for both the client and the contractor. BBT SE reduces its costs, thanks to the optimised material flow. The deposit capacity near portal Ahrental is limited and the transport length and costs would increase if a truck rather than a conveyor belt logistics is implemented. Furthermore, the public acceptance would rise, as this is a more sustainable solution. The contractor will gain a 24/7 available constant flow of spoil out of its headings, due to the redundancy within the systems. In case of unavailability of the conveyor belts from the neighbouring lot, the material flow can be diverted and discharged to the other construction site, and vice versa.

Further, a safer work environment, due to the reduced number of trucks in the tunnels is created. The amount that is expected to be transported in Padaster valley is about 4,5 M tons. To remove this amount of material about 180.000 full loaded trucks would be necessary. Assuming a full load truck emission of 0.9 kg/km and an unloaded truck emission of 0.7 kg/km, this would result in an emission of 7,200 tonnes of CO_2.

A further 1 M tonnes of spoil material is planned to be transported to the Ahrental portal by conveyor belt. This material is used to complete the deposit and shape its final form for its purpose after the construction. The majority of the surface will be given back to the original owners and a small part will serve as an access and emergency area for the emergency stop Innsbruck.

6.5 *Padaster valley*

Another advantage of using the spoil material, that would otherwise not be reusable, is in the form of the final arrangement of said material. The Padaster valley was originally a wild, inhabited V-shaped valley, with no significant economic activities due to its narrow, closed shape (Figure 7).

Figure 7. View of the Padaster valley spoil disposal site at the beginning of construction.
Source: BBT SE

Once the deposit will be completed, the valley will be resettled in a U-shape, which also allows the creation of pastures and the establishment of economic activities within the valley. This results in a significant increase in the economic value of the area affected by the deposit works. The creation of the deposit was also the reason for carrying out work to secure and revitalize the Padaster stream. A holding basin was created in the stream to secure the settlement at the mouth of the valley.

Figure 8. View of the Padaster valley spoil disposal site during the construction.

Source: BBT SE

At the moment the preparatory construction works like the excavation of the spoil removal tunnel and the completion of the holding basins are over. The disposal of the tunnel spoil is currently ongoing (Figure 8). These works are accompanied by the construction of a basal and peripherical drainage lines together with extension and maintenance of an extensive geotechnical and hydrological surveyance system.

After the completion of the disposal of the tunnel spoil, the Padaster valley will be completely restored. Firstly, the entire valley will be replanted, with different site-specific composition of seeds, depending on altitude and water saturation in the soil and a variety of trees and bushes, depending on the specific location. E.g. reforestation or meadow. Finally, the Padaster stream, which runs underground during the construction phase, will be brought back to the surface again and will create a worthy habitat (Figure 9).

7 CONCLUSIONS

In conclusion, with these two examples, an attempt has been made to show that important measures to protect the environment can be taken at large construction sites, without this necessarily entailing higher costs. Through careful management, safeguarding the environment and gaining public support at the same time is possible. In the next few years, more and more attention will be devoted to the protection of the environment in the entire construction industry. Especially in the realisation of large projects, this will be crucial to maintain public support in terms of environment protection.

Figure 9. Model of the Padaster valley spoil disposal site after completion.

Source: BBT SE

ACKNOWLEDGMENTS

The authors would like to thank all their colleagues at the BBT SE for their support and effort. Further acknowledgement to the contractor for providing additional figures and information.

REFERENCES

Insam et. al. 2022, The Brenner Base Tunnel - an overview of the status of the project, ITA-AITES World Tunnel Congress, WTC2022 and 47th General Assembly Bella Center, Copenhagen 22-28 April 2022

Bundesministerium für Arbeit (BMA) Sektion II - Arbeitsrecht und Zentral-Arbeitsinspektorat, Arbeitsinspektion AI, 2022, Gefahrenstellen an verketteten Maschinen und Anlagen

Tunnelling for a Better Life – Yan, Celestino, Thewes & Eberhardt (Eds)
© 2024 The Author(s), ISBN 978-1-032-80042-4
Open Access: www.taylorfrancis.com, CC BY-NC-ND 4.0 license

Technical challenges and countermeasures of plateau railway tunnels

Yong Zhao & Tingyu Zhu
Tibet Railway Construction Corporation, Lhasa City, China

Gaoming Yan
School of Civil Engineering, Beijing Jiaotong University, Beijing, China

ABSTRACT: With the implementation of the Chinese strategy to become a strong transportation nation and the rapid development of our social economy, the national railway network is gradually extending to mountainous areas with relatively weak transportation infrastructure, such as the Qinghai-Tibet Plateau. This has led to the need for the construction of a large number of ultra-long and deeply buried tunnels in the plateau region. The extremely complex and variable environmental characteristics and engineering geological conditions in this area pose significant challenges to the safe construction and long-term operation of these tunnels under construction or planned. In light of this issue, this paper provides a detailed analysis of the major technical challenges faced in the construction of railway tunnels in high-altitude areas. These challenges mainly include disasters caused by crossing active fault zones, high ground stress rock bursts and large deformations in soft rocks, disasters caused by high permeability and sudden water and mud inflows, as well as the high-altitude (water) temperature damage. To address the aforementioned challenges, this paper proposes disaster prevention and control strategies and mechanized intelligent construction technologies from both theoretical and technical perspectives to cope with tunnel construction challenges in the extreme plateau environment. The results can provide a reference for the efficient construction and safe operation of ultra-long and deeply buried tunnels in high-altitude areas.

Keywords: Plateau Railway Tunnels, technical challenges, countermeasures, intelligent construction technologies

1 INTRODUCTION

The Qinghai-Tibet Plateau is an important ecological security barrier in our country. However, the relatively weak transportation infrastructure hampers the development of the Qinghai-Tibet Plateau region. Accelerating the construction of a regional highway network and railway network in the Qinghai-Tibet Plateau is of great significance for the development of Tibet and the long-term stability of the country. With the continuous advancement of major national strategies such as "Building a Strong Transportation Nation" and "Western Development," a large number of significant transportation infrastructure projects are gradually being carried out in the Qinghai-Tibet Plateau and surrounding areas. Tunnel engineering, due to its safety and environmental characteristics, has been widely used in transportation infrastructure construction. There is an urgent need to construct a large number of ultra-long and deep-buried tunnel projects, such as a plateau railway tunnel line where the tunneling rate is as high as 82.6%. The Qinghai-Tibet Plateau region is the most geologically, topographically, and morphologically complex area in the world. Under the strong coupling of internal and external forces, the tectonic plates along the route are the most active, with the most intense fault activities, the strongest earthquake intensities, the most significant topographical changes, and the most developed natural disasters (Figure1). All of these pose extremely severe challenges for tunnel engineering.

The extreme environment of tunnel construction on the Qinghai-Tibet Plateau is mainly reflected in three aspects: environmental characteristics, geological features, and engineering characteristics. In terms of environmental characteristics, most areas are located at altitudes between 3000 and 5000 meters. Influenced by high altitude, significant terrain differences between mountains, and the impact of monsoons and westerly winds[1], these areas exhibit characteristics of high cold and oxygen deficiency, with complex and variable weather conditions.

DOI: 10.1201/9781003495505-20

Figure 1. Plate tectonics and movement in the Qinghai-Tibet Plateau.

From a geological perspective, the Qinghai-Tibet Plateau is located in a zone of compression and collision between the Indian Plate and the Eurasian Plate. The relatively rigid Indian Plate continues to push strongly in northeast direction. On the northern side, oceanic crusts successively diminish and close, continental crusts collide and merge, and the relatively plastic Qinghai-Tibet region is strongly uplifted and compressed, forming complex land crust blocks with converging and nested structures[2-3]. This geological context results in extremely high ground stress, high seismic intensity, frequent earthquakes, the presence of ultra-high-pressure water, and high ground (water) temperatures in tunnel engineering in the Qinghai-Tibet Plateau region. Table 1 lists some representative plateau ultra-long and deeply buried tunnel that have been constructed in the Qinghai-Tibet Plateau region.

Table 1. Ultra-long and deeply buried tunnels that have been constructed in the Qinghai Tibet Plateau.

Tunnel projects	Length/m	Altitude /m	Problem
Galongla Tunnel	3310	3700	Fault, water inrush
Milin tunnel	11560	3076	Water-rich moraine layer, high ground stress, high ground temperature
Gangmulashan tunnel	11660	3128	Rockburst, high ground temperature
Bayu tunnel	13073	3465	Rockburst
Gongduoding tunnel	13590	3116	Water inrush, rockburst, high ground temperature
Sangzhuling tunnel	16449	3581	High ground temperature, rockburst
Muzhailing tunnel	16670	3116	Fault, large deformation, water and mud inrush
Guanjiao tunnel	32690	3500	Karst and fault, water inrush

In terms of engineering characteristics, the depth and length of tunnels in the Qinghai-Tibet Plateau region far exceed the standards specified in current regulations. Taking a certain plateau railway under construction as an example, there are as many as 15 tunnels with lengths exceeding 20 km, the longest of which is 42.4 km. There are 31 tunnels with depths exceeding 1000 meters, and their cumulative length accounts for over 70%. Compared to traditional short and medium tunnels, as tunnel depth and length increase significantly, the deep and complex geological environment differs greatly from the shallow rock conditions. Ground stress, ground temperature, and underground water pressure will significantly increase, resulting in distinctly different engineering characteristics for deep tunnels.

2 DISASTER OF TUNNELS CROSSING ACTIVE FAULT

2.1 *Technical challenges*

Active faults, typically refer to faults that have been active since the Quaternary period (Late Pleistocene) and are likely to remain active in the foreseeable future[4]. Crossing these active faults poses immeasurable hazards to tunnels. During earthquakes, the fault movement results in longitudinal and transverse displacement of tunnels, reducing the arch effect and making the tunnel structure prone to overall collapse. For instance, in the 1906 San Francisco earthquake with a magnitude of 8.3, the tunnels crossing the San Andreas Fault experienced localized displacements of up to 240 cm. The Wenchuan earthquake in 2008 led to severe damage in tunnels near the fault zone, including lateral displacement, secondary lining collapse in upper sidewalls and crowns, as shown in Figure 2. The Longxi tunnel experienced relative vertical displacement of about 100 cm due to the earthquake. In 2022, the Menyuan earthquake caused

(a) Collapse of tunnel vault

(b) Dislocation of lining

Figure 2. Seismic damage in transverse fault tunnels.

overall shifts and twists in the Daliang tunnel and Qilian Mountain Tunnel. Particularly in the Daliang tunnel, the structure was severely damaged, with a relative displacement of 2.8 meters, a vertical deformation difference of 0.6 meters in the track, and approximately 350 meters of the tunnel structure severely damaged, causing track deformation and rendering the tunnel completely unusable.

The Qinghai-Tibet Plateau has a complex stress distribution, widespread active structures, intense seismic activity, and numerous active fault zones. Taking a certain plateau railway as an example, it crosses 11 active fault zones, including the Xianshuihe fault, Jinsha River fault, and Jiali-Polong fault. Therefore, when constructing tunnels in the Qinghai-Tibet Plateau region, it is essential to employ scientific tunnel design, rational construction methods, and stringent safety management measures to minimize the risk of tunnel disasters caused by the sliding and creeping of tunnels crossing active fault zones.

2.2 *Engineering strategies*

2.2.1 *Advanced forecasting techniques*

For complex geological tunnels, a comprehensive advanced geological forecasting approach combining long, medium, and short distances, along with physical drilling, is followed. Various forecasting techniques complement and verify each other. Long and medium-distance advanced geological forecasting involves the use of integrated geophysical methods such as seismic wave method, electromagnetic method, and induced polarization method. Various devices such as TSP, HSP, GRP, TRT, and TST are employed. Advanced drilling methods include advanced geological core drilling and deepening blast hole method, with a minimum drilling length of 50m for complex geological conditions. Especially for the detection of fault and other disaster-causing structures(as shown in Figure3), an expert team led by Shucai Li and others has developed high-energy, wide-frequency controllable excitation methods and seismic source prototypes[5,6]. The detection range has been increased from 100m to 130m. A constrained full waveform inversion method has been proposed, overcoming the theoretical bottleneck of precise wave velocity calculation and achieving accurate fault detection.

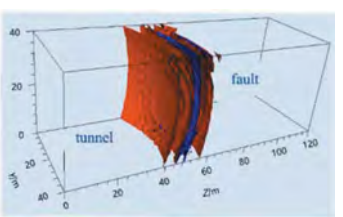

Figure 3. Detection imaging of fault-induced disaster structures.

2.2.2 *Aseismic measures*

Due to the severity of damage caused by faults to tunnels, construction is primarily based on the principle of avoiding active faults, which is also the most effective measure against fault-related tunnel damage. However, due to requirements for track smoothness, it is unavoidable to encounter tunnels crossing active faults. Currently, there are several strategies for seismic reduction in tunnels crossing active faults. One is to improving surrounding rock conditions, which can reduce the relative displacement between surrounding rock and tunnel structure. Methods include grouting reinforcement of surrounding rock. Three commonly used methods for grouting reinforcement are full-ring interval grouting, full-ring grouting, and partial grouting[7]. The second is to alter lining structure properties. Techniques such as enlarging the tunnel across faults, segmenting the lining, and setting joints between sections can be employed. For example, the Wushaoling railway tunnel, constructed in 2004, adopted a construction plan involving an enlarged section size at the fault crossing area[8]. The third is to introduce seismic isolation structures. These structures are placed between the tunnel and surrounding rock to reduce seismic energy transfer between the surrounding rock and lining. In complex geological sections, lightweight and flexible seismic isolation materials can be placed between the surrounding rock and lining structure. These layers can absorb seismic energy, reducing the seismic impact on the tunnel lining[9]. Common materials for these isolation layers include rubber or foam concrete. The isolation layer can be placed between surrounding rock and lining or between initial support and secondary lining.

Considering the current design for seismic resistance in tunnels crossing faults, there are very few examples specifically addressing the design of large cross-section tunnels crossing active faults, and these designs have not been validated in major earthquakes. Reinforcing surrounding rocks and seismic damping layers significantly influence the seismic response, whereas their effect on fault displacement is relatively small[10]. Setting flexible joints reduce uneven tunnel deformations and mitigate damage to tunnel structures caused by fault displacements. However, these designs cannot guarantee the requirements for tunnel alignment, especially for railway lines. They also present challenges for structural waterproofing. Therefore, the principle of "reserving space, optimizing sections, segmental design, and operational monitoring" should be applied in fault zones. In future research on seismic resistance in tunnels crossing active faults, factors such as fault displacement, fault damage zones, surrounding rock pressure, and strong seismic effects should be considered. The main design approach should focus on active prevention and control by enhancing the structural adaptability and deformation capacity. The research should propose a multi-level variable seismic reduction structure system for tunnels crossing active faults to minimize the impact of fault displacements and seismic effects on the tunnel.

For operational tunnels, active fault segments should be closely monitored. This includes routine monitoring requirements along with additional health monitoring during the operational phase, including tunnel settlement and deformation, lining deformation, and structural stress (initial support and secondary lining contact pressure, secondary lining reinforcement stress, concrete stress). Furthermore, research should be conducted on monitoring, early warning technology during fault seismic events, emergency dispatching of train operations, and rapid restoration plans to ensure safe operation.

3 HIGH PERMEABILITY, SUDDEN WATER INRUSH, AND MUD INRUSH

3.1 *Technical challenges*

The climate characteristics of multiple periods of change, high altitudes, sparse rainfall, and heavy snowfall on the Qinghai-Tibet Plateau have created unique surface features such as large ice lakes and plateau-type karst formations. Taking a certain plateau railway as an example, there are as many as 227 major faults along the tunnel alignment, extensive plateau karst sections spanning 58 km, and predicted water pressure reaching 7 MPa. This complex environment makes the tunnels highly susceptible to major geological disasters, such as sudden water inflow and mudslides, as shown in Figure4.

The prevention and control of sudden water inflow and mudslide disasters in the complex and high-energy environment of the plateau railway face the following challenges.

Geological environment is extremely complex. The geological environment within the tunnels is extremely complex, and the mechanisms and evolution patterns of water inflow and mudslide disasters are not clear. There is an urgent need to break through the disaster identification technology to clearly understand the mechanisms causing these disasters from the source.

In high-risk sections, the danger of manual monitoring is high. There is a pressing need to overcome real-time online monitoring technology and intelligent early warning platforms to achieve automatic monitoring and intelligent warnings.

There is a need to develop new materials, technologies, and intelligent equipment suitable for high-pressure environments for large-flow water sealing, rock reinforcement, and active prevention and control of water inflow and mudslide disasters.

There is a lack of scientific management tools for risk assessment. Innovation is needed in dynamic and accurate risk assessment methods, breakthroughs in safety management, and emergency rescue technology systems.

These above challenges have brought a series of technical difficulties to tunnel construction in plateau regions.

Figure 4. Sudden water inrush in the tunnel.

3.2 *Engineering strategies*

The key to actively controlling sudden water inflow disasters in deep and long tunnels on the plateau lies in the correct balance between “draining” and “blocking”. Specific response strategies should be classified based on geological conditions and stratum types.

For karst strata on the plateau, considering various information sources such as different karst forms, water pressure, water volume parameters, and safety distances, a construction control optimization scheme based on a disaster control decision-making model is developed. This scheme integrates key indicators such as pressure relief amount, drainage point layout, and pressure relief timing to propose construction control techniques for sudden water inflow and mudslides. It establishes proactive sealing and drainage standards, accompanying construction processes, and suggests dynamic responses and optimization methods for key parameters at multiple levels and stages.

Regarding fractured zones and faulted zones, a multidimensional evaluation approach, including the stability of fractured zone surrounding rocks and the performance evaluation of anti-inrush structures, is implemented. This approach involves a tailored grouting reinforcement technology system, focusing on the stability of fractured zone surrounding rocks. It incorporates environmental modifications, rock mass improvements, and the enhancement of structural water-resistant properties. Ultimately, a comprehensive and proactive control technology system is established, integrating advanced drainage and pressure reduction with proactive grouting reinforcement for effective control of sudden water inflow and mudslides in tunnels within fractured zones and faulted zones.

4 ROCKBURST AND LARGE DEFORMATION DISASTERS UNDER HIGH STRESS ENVIRONMENT

4.1 *Technical challenges*

The Qinghai-Tibet Plateau is located in the compression-collision zone between the Indian plate and the Eurasian plate. The region experiences intense modern tectonic movements and internal and external dynamic forces, resulting in significant geological features such as strong crustal

deformation and concentrated crustal stress. The high-stress environment in these high-altitude areas is exceptionally prominent. For example, the maximum ground stress in the Bayu tunnel of the Lalin railway is 52.4 MPa. In a certain large railway tunnel construction sites, the estimated maximum ground stress is around 75 MPa, while in planned large hydropower station tunnel sites, it is approximately 100 MPa. The exceptionally high levels of ground stress are evident. In such high-stress environments, tunnel is affected by construction unloading, making it susceptible to disaster risks such as rock bursts and significant deformations [11]. Rock bursts are dynamic instability disasters characterized by the brittle fracture of intact hard rocks. Based on the timing of occurrence, rock bursts can be classified into immediate-type and delayed-type. Immediate-type rock bursts typically occur within 6 to 8 hours after excavation, while delayed-type rock bursts occur over a longer period, often spanning weeks, months, or even longer. For example, in the Gangmula tunnel of the Lalin railway, certain sections of the tunnel bottom experienced sudden rock bursts even two years after operation, causing the floor to uplift by 38.9 cm and interrupting rail traffic for 11 days. Since rock bursts often accompany the ejection of surrounding rock fragments, the crater depth of intense rock bursts can exceed 3 meters. Considering the sudden and random nature of rock burst occurrences, effectively avoiding harm to personnel and equipment during the construction period and ensuring the long-term safety of support structures pose significant technical challenges. Large deformations refer to significant plastic deformations occurring in fractured and soft rock, characterized by high values, rapid rates, long durations, and high support loads [12]. Large deformations can lead to engineering problems such as cracking, spalling, and even intrusion limitations in support structures. For instance, in the Muzailing tunnel, some sections experienced deformations exceeding 2 meters, leading to a high support replacement rate of 30%. Therefore, comprehensive and effective control of surrounding rock deformations becomes a key aspect of deformation disaster control technology.

4.2 *Engineering strategies*

Considering that rock bursts and large deformations disasters are closely related to high-stress environments and the stress state of surrounding rocks, the prevention and control techniques for these two disasters can be implemented based on the principle of "prevention as the main focus, combined prevention and control, actively improving the stress state of surrounding rocks, and strengthening timely and reliable rock support". "Prevention as the main focus" focuses on accurate prediction and warning of high stress environment and disaster characteristic indicators, evaluating the risk of disaster occurrence, and improving the pertinence of disaster prevention and control measures. At present, the prediction and warning technology for rock burst mainly focuses on the precise perception of rock burst surrounding rock fracture information and accurate identification of fracture process[13], and the first high-precision microseismic intelligent monitoring system in the world has been developed. It can accurately concretize the probability of rock burst events, achieve quantitative warning and evaluation of rock bursts, and solve the problem of "undetectable, inaccurate, and incomplete measurement" of rock bursts. Figure 5 is a typical application case of rock burst microseismic prediction and warning technology in tunnels. In terms of in-situ stress environment prediction technology, we actively develop new technologies such as parameter inversion while drilling with rock drilling rigs and borehole acoustic testing to solve the problems of traditional technologies such as long time consumption, large process interference, and delayed feedback. "Combined prevention and control" focuses on comprehensive prevention and control of the entire tunnel area and construction process. It is mainly manifested in the use of "prevention" measures for the surrounding rock in front of the palm. This includes improving the ground stress conditions through advance hole stress release before excavation, using advance hole loosening blasting to reduce the brittleness of hard rock, and using advance grouting and pre-support to improve the quality of soft rock. These measures alleviate the risk and degree of disaster occurrence. The surrounding rock behind the face of the tunnel is mainly treated with "treatment" measures, which include optimizing construction methods and providing timely support to the surrounding rock to ensure effective disaster management. Specific measures include controlling the excavation cycle size, implementing energy dissipation protection nets. Additionally, employing large-section excavation, enhancing the mechanical properties of supporting materials or components, and shortening the closure time for support structures are used to control the early deformation rate of soft rocks. The core of disaster prevention and control technology is to actively improve the stress state of the surrounding rock, which means to enhance the self-stability of surrounding rock and achieve the goal of self-stability of surrounding rock through the active improvement of the stress state of surrounding rock. For example, using electronic digital detonators, directional shaped charge blasting, and precise control blasting of tunnel contour helps alleviate the stress concentration in the excavation contour of surrounding rock. Utilizing high-performance support materials and components and pre-stressed anchor rods (cables) provides effective support force for the surrounding rock [14], timely improving the stress state of the surrounding rock and enhancing its ability to resist deformation (Figure 6). "Strengthening the timely and reliable support of surrounding rocks" emphasizes the timeliness of support time and the reliability of quality, mainly achieved through large-scale mechanized rapid construction technology, such as the mechanized supporting construction technology of the entire tunnel process, which can achieve mechanized and unmanned operations of various types of support such as sprayed

concrete, prestressed anchor rods, and steel supports. The rapid construction technology of the anchor mesh support system based on the drilling injection anchor mesh integrated machine can achieve the full process mechanization of rock burst energy dissipation protection net, pre-stressed anchor rod and other support operations. The technology has been preliminarily applied in the Duoji tunnel (Figure 7), reducing the laying time of the energy dissipation protection net from 5 hours manually to 5 minutes. this significantly improves the rock burst protection capability of the support and the safety of construction personnel.

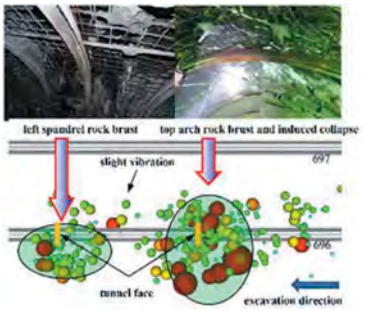

Figure 5. High precision microseismic intelligent monitoring system.

Certainly, deepening the understanding of the disaster mechanisms in the surrounding rocks of tunnels in the high-stress environment of the Qinghai-Tibet Plateau, studying long-term perception, monitoring, and early warning of rockbursts, especially delayed-type rockbursts, optimizing excavation profiles, adapting support designs, and developing fully mechanized and unmanned robotic construction technologies for tunnels, are still pressing technical directions that need to be addressed.

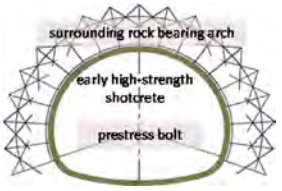

Figure 6. High performance support system.

Figure 7. Mechanized Construction of Anchor Mesh Support.

5 HIGH GEOTHERMAL TEMPERATURE DAMAGE

5.1 *Technical challenges*

The Qinghai Tibet Plateau is rich in geothermal resources. In most areas, the ground temperature ranges from 40 to 60°C, and in certain areas, it can even reach up to 90°C [15]. The construction of deep buried long railway tunnels in the region will inevitably be plagued by high geothermal temperatures. For example, during the construction period of the Sangzhuling tunnel on the Lalin railway, the highest ground temperature recorded was 89.9°C. In the construction of Layue tunnel, high-temperature hot water gushing up to 92.6 ℃ occurred. High geothermal temperature can be divided into two types based on the type of heat source: high rock temperature and high water temperature. The impact of high geothermal temperature on the thermal damage of tunnel engineering is mainly reflected in two aspects [16]. Firstly, it deteriorates the construction environment inside the tunnel. The high temperature and high humidity construction environment can affect the efficiency of construction workers and equipment, leading to efficiency reduction. The high water temperature environment can also induce the risk of burns and other injuries to construction workers. The second is the deterioration of the mechanical performance of the support structure. High temperature environments can deteriorate the mechanical properties of materials such as sprayed concrete and anchor grouting materials, leading to a decrease in the mechanical performance of the support structure and endangering its safety.

5.2 *Engineering strategies*

The prevention and control measures for high-temperature heat damage in tunnels can be implemented in accordance with the principles of “deepening geology, controlling heat sources, combining drainage and water sealing techniques, comprehensive cooling, monitoring and warning, and system guarantee”. “Deepening geology” refers to the use of comprehensive exploration techniques in all aspects to grasp the distribution patterns and characteristics of ground temperature in the tunnel site and excavation area, providing guidance for targeted control in the future. Detection techniques mainly include outside detection and inside detection. Outside detection can use the integrated exploration technology of “space, sky, and earth” to grasp the distribution range and characteristics of high-temperature areas, while inside detection can use three-dimensional geological radar, transient electromagnetic, and deep circulation blast holes The combination of “long distance medium distance short distance” techniques such

as borehole temperature measurement and infrared photography of the surrounding rock of the face can refine the distribution and development degree of heat sources. “Controlling heat sources” refers to the use of targeted heat source control measures based on different types of heat sources to reduce the heat dissipation of the heat source. For high-temperature water, control measures such as drilling and sealing, centralized drainage are mainly used. For hot water drainage pipes, insulation treatment is required (Fig. 8). For high-temperature surrounding rocks, spray insulation concrete is mainly used for heat source control. “Combining drainage and water sealing techniques” refers to the treatment based on the development level of high-temperature hot water. When the hot water is ≤ 50 ° C, the inflow is ≤ 60m^3/h, or the hot water is ≤ 70 ° C, the inflow is ≤ 30m^3/h, a centralized drainage method can be used. In other cases, blockage is the main method, such as curtain grouting, sequential grouting, top water grouting, and so on. It is necessary to develop grouting materials specifically designed for sealing high-temperature hot water tunnels. These materials should enable rapid solidification under high-temperature and high-pressure water environments, effectively sealing water pathways in the surrounding rocks. “Comprehensive cooling” refers to the use of techniques such as enhanced ventilation, localized cooling, and the integration of cold water to achieve targeted cooling control for different geothermal levels and various regions (Table 2). “Monitoring and warning” involve comprehensive, fully automated, and intelligent monitoring and sensing of high-temperature environments inside the tunnel. This system provides feedback and guidance for engineering measures based on the collected data. “System guarantee” ensures construction safety by strengthening occupational health training for workers, enhancing individual protective measures, providing well-equipped rest rooms and medical facilities inside the tunnel, and establishing emergency plans and their simulation mechanisms. Meanwhile, a new high-temperature support structure needs to be adopted, consisting of materials such as heat-resistant sprayed concrete, high-temperature waterproof board, insulation layer, reinforced lining, to ensure the long-term stress safety of the structure in high-temperature environments.

Figure 8. Heat source control.

Table 2. Cooling measures for different sections of high geothermal tunnels.

Surrounding rock and high temperature groundwater temperature	t<40°C	40°C<t<60°C	60°C<t<80°C	t>80°C
tunnel working face section	Use local fans	Use local fans, ice cooling (temperature 60°C, ventilation distance 4000m, ice consumption: 40 tons/day)	Use local fans, use a refrigerator to cool down	Use local fans, use a refrigerator to cool down
Tunnel body section	Drain with cover, thermal insulation air duct	Local grouting, thermal insulation drainage ditch, thermal insulation air duct	Full section grouting, thermal insulation drainage ditch, thermal insulation air duct	Full section grouting, thermal insulation pipe drainage, thermal insulation air duct
The section outside the tunnel	1~2 wind turbines, 1~2 air ducts to enhance ventilation	Use 2~3 turbines and 2~3 air ducts to enhance ventilation	Use 3 turbines and 3 air ducts to enhance ventilation	Use 3 turbines and 3 air ducts to enhance ventilation

Note: When the rock temperature and groundwater temperature exceed 60 °C, a refrigerator is required for mechanical cooling

6 CONCLUSION

The complex climatic conditions and active geological structures in the Qinghai-Tibet Plateau have led to various technical challenges in the construction of these ultra-long deep-buried tunnel projects, including high seismic intensity, high ground stress, high seepage pressure, high geothermal heat, inadequate ventilation, and so on. These challenges seriously threaten the safety of the construction and long-term operation of the projects. This paper summarizes the main difficulties encountered in completed and ongoing tunnel projects in the Qinghai-Tibet Plateau region, as well as the current main prevention and control techniques. It proposes a disaster response concept centered around "active prevention and control", construction techniques led by mechanization and intelligence, and long-term safe operation and emergency support technologies. These provide technical support and theoretical references for the safe construction and long-term operation of ultra-long deep-buried tunnels in the Qinghai-Tibet Plateau.

REFERENCES

[1] Huang L, Chen J, Yang K, et al. The northern boundary of the Asian summer monsoon and division of westerlies and monsoon regimes over the Tibetan Plateau in present-day[J]. Science China Earth Sciences, 53 (4):866–878.

[2] Zhang Peizhen,Wang Weitao,Gan Weijun, et al. Present-day deformation and geodynamic processes of the Tibetan Plateau [J].Acta Geologica Sinica, 2022,96(10):3297–3313.

[3] Zhu Tao. Effects of Eurasian plate motions on mantle convective velocity and horizontal shear stress fields at the base of the lithosphere beneath Mainland China [J]. Earth Science Frontiers,2017,24(05):192–206.

[4] Wu Zhonghai, Zhang Xudong, Han Shua, et al.. Quaternary faulting and deformation mechanism of the western Qiangtang block in northern Ngari,Tibet [J]. Acta Geologica Sinica. 2022, 96(11): 3760–3783.

[5] Li Shucai, Li Xiaozhao, Jing Hongwen, et al. Research Development of Catastrophe Mechanism and Forecast Controlling Theory of Water Inrush and Mud Gushing in Deep Long Tunnel [J]. China Basic Science, 2017;19(3):27–43.

[6] Wang Jianhua, Li Shucai, Li Liping et al. Dynamic evolution characteristics and prediction of water inflow of karst piping-type water inrush of tunnels [J]. Chinese Journal of Geotechnical Engineering, 2018,40(10):1880–1888.

[7] Shen Yusheng Gao Bo, et al. Study on the interval grouting pre-reinforcement scheme of mountain tunnel[J]. China civil engineering journal. 2011, 44 (S1): 186–191.

[8] Dong Qinyin, Song Jianping. Design and construction of F7 moveable faultage on Wuqiaoling tunnel[J]. Tunnel Construction. 2005(03): 58–61.

[9] Yan, Gaoming, Zhao, Boming, Wang, Zijun, Gao, Bo. Simplified analytical solution for responses of fault-crossing tunnels with flexible joints under fault movement[J]. Structures, 2022, 45: 984–998.

[10] Yan, Gaoming, Shen, Yusheng, Gao, Bo, Zheng, Qing, Fan, Kaixiang, Huang, Haifeng. Damage evolution of tunnel lining with steel reinforced rubber joints under normal faulting: An experimental and numerical investigation[J]. Tunnelling and Underground Space Technology, 2020, 97: 103223.

[11] He Manchao, Ren Shulin, Tao Zhigang. 2022. Disaster prevention and control methods for deep buried tunnels[J]. Journal of Engineering Geology, 2022,30 (6): 1777–1797.

[12] Zhao Yong. Tunnel Design Theory and Method-[M]. Beijing: China Communications Press, 2019.

[13] Feng Xiating, Xiao Yaxun, Feng Guangliang, et al. Study on the development process of rockbursts[J]. Chinese Journal of Rock Mechanics and Engineering,2019,38(4): 649–673.

[14] Tian siming,Wu Kefei, Liu Dagang, et al. Study on Design Method for Active Support for Plateau Railway Tunnels in High Energy Geological Environment[J].Journal of The China Railway Society,2022,44(3): 39–63.

[15] Jin Chunshuang, Fu Xiugen, Chen Wenbin, et al. Measurements of borehole heat flow in northern Tibet[J].Chinese Journal of Geophysics,2019,62(8): 3095–3105.

[16] Hu Yunpeng, Wang mingnian, et al. Field test of thermal environment and thermal adaptation of workers in high geothermal tunnel[J]. Building And Environment, 2019,160:106174–106174.

Design and methodology

Taylor & Francis
Taylor & Francis Group
http://taylorandfrancis.com

Tunnelling for a Better Life – Yan, Celestino, Thewes & Eberhardt (Eds)
© 2024 The Author(s), ISBN 978-1-032-80042-4
Open Access: www.taylorfrancis.com, CC BY-NC-ND 4.0 license

Observational method and calibration of design safety factors to optimize technical-economical solutions in tunnelling projects

Andrea Antiga*, Massimo Lorenzi & Antonello Lucia
More Engineering Srl, Milan, Italy

ABSTRACT: Tunnel design is a practice involving countless uncertainties and many failure modes. Often, the knowledge of the geological structure, the hydro-geological conditions, the mechanical properties and the behaviour of the soil/rock is only fulfilled during construction. The reduction of uncertainties progresses during excavation. For these reasons, a solution based only on the knowledge available at the time of the design phase can be unsafe or uneconomic. Conversely, information collected during excavation can be used to adapt the original design to comply with the actual conditions following an "observational approach".

The paper will also provide some reflections on the potentials of the Observational Method in underground works also with reference to its use into projects according to a "lump sum" logic.

Keywords: observational method, risk, lump-sum, claim

1 INTRODUCTION

Doubtless, tunnel design involves much higher uncertainties than any other civil engineering work. A lot of tunnel projects reported significant cost overruns and contractors claims in percentage much greater than other civil construction works.

To be underground means that the context is difficult to know. To realize what "difficult to know" means we have to compare a tunnel with a surface structure.

Even in a comprehensive exploration program we can test only a small fraction of the total ground to be affected by the tunnel construction. We can recover a relatively miniscule drill core volume that is less than 0.0002 % of the volume of rock mass that one has to consider in tunnel design.

It is therefore obvious that ground conditions account for the largest element of technical and financial risk in tunneling projects. Risk minimization implicates decisions about what is required to excavate the ground, to control the ground during the process of excavation and to support that ground as the tunnel advances; each of these decisions are closely related to one's knowledge of ground conditions and one's expectations about how that ground will behave and/or react to the process of tunneling.

From a design viewpoint, uncertainties can be categorized into two macro-categories: parameter uncertainty and model uncertainty. Each source of uncertainty can potentially result in unsatisfactory performance with associated casualty and economic loss, so it is necessary to explicitly evaluate and quantify parameter uncertainty and model uncertainty.

In order to design safe structures, safety factors are used in most design codes in different formats. Ideally, these safety factors are calibrated such that they ensure sufficient reliability for a wide range of cases.

In the recent decades, tunneling design codes have developed considerably. The tunneling engineering practice has developed from experience-based decisions to rational design criteria. In many aspects, geotechnical design Codes have followed developments in structural engineering. Besides design approaches based on reliability theory (i.e., the probabilistic approach) has developed considerably.

Tunnel design rules are usually borrowed from the geotechnical ones.

2 FORESEEABLE AND UNFORESEEABLE UNCERTAINTIES

When we deal with ground conditions the "unknown" usually exist in inverse proportion to the amount and quality of the geotechnical investigations.

In the development of a project of an underground work we can distinguish various levels of knowledge about hazards and uncertainties and consequently about a risk event's occurrence.

We can have:

1. uncertainty associated to the tunnel section in which specific situations, nevertheless certain, will

*Corresponding author: a.antiga@more-engineering.it

DOI: 10.1201/9781003495505-21

occur; for example, it is not known the actual distribution of rock types along tunnel alignment, the extent of fault areas, the exact area of sudden water in flows, etc. but it is certain that them will happen;
2. uncertainty associated to the precise intensity with which certain situations, expected by type (and as maximum value), will occur; for example, having to go through a certain rock mass, there are uncertainties about the maximum magnitude of the acting loads and of the consequent convergences, even though it is possible to assume a priori the extreme situations of reference;
3. uncertainty related to the possible occurrence of completely unforeseen situations. In this category we must include unfortunate geological feature, the presence of which was missed during the design stage and requires partial or total redesign of the project; we have also to include a type of geomechanical behavior that was not predicted in the design.

We can define the first two uncertainties as "expected tunneling hazard". Usually, only foreseeable uncertainties, which can be quantified, are directly considered in design. We can prepare the tools for dealing with them during the design phase and therefore they are manageable during construction and lead to the modification of quantities within a specific standard solution already identified in the project. The third is an uncertainty that we could qualify as "unforeseeable". It can make the typical solutions imagined in the project no longer valid (i.e. it affects the final reliability). It cannot be easily quantified and should be implicitly considered in the design assumptions.

It must be highlighted that it is practically impossible to completely remove uncertainty inherent in tunnel design. It is equally true that increasing awareness of these existing uncertainties and their consequences is a basic input of a reliability view.

Lack of awareness of the uncertainties can result in unsuitable design solution and therefore designers must focus on thinkable consequences of design assumptions.

It is always important to remember that an "expected tunneling hazard" is a controlled hazard and small unforeseen hazards can be worse than big foreseen hazards.

The three first and fundamental steps in the development of a tunnel project are: (1) characterization of the underground layers and geometry, (2) choice material parameters (3) choice of a suitable computational model.

Different designers would make different choices in these three phases leading to conclusions between optimistic or pessimistic and consequently the reliability of the resultant designs can significantly diverge.

2.1 *Geological and geotechnical/geomechanical uncertainties*

The first obvious, but not always respected, rule to mitigate the "geo" uncertainties is to prepare a plan of investigation in an appropriate manner.

The most effective strategy to reduce geotechnical risk is to minimize the unforeseen and site investigations are the basis on which the risks associated with the project are identified; on the other side without enough information from site investigations the inherent risks would be unacceptably high. It would be obvious to conclude that a lot of time and economic effort need to be concentrated in site investigations.

An effective site investigation program is of major significance to obtain the necessary information essential for construction; we should increase our knowledge about possible hazard to be ready to treat them in a right way. Hence, an in-depth site investigation program would ensure that the project sees fewer change; resources dedicated to site investigations should be considered as an investment and when it comes to the geotechnical scope of work established for a tunneling project, one should not be thinking about reducing costs.

Nevertheless, a balance needs to be identified in determining the extent of site investigation. Soil investigations can be carried only to the extent that is judiciously possible, compatibly with time and budget available. It is necessary to establish a balance between the resources spent through site investigations and the losses prevented by them. Anyway, we can surely state that a good investigative program is helpful in reducing costs of works in percentage much higher than the cost of the additional exploration (Figure 1).

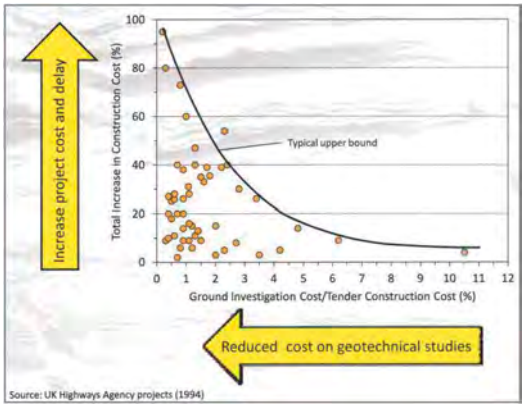

Figure 1. UK Highways Agency – Increase in construction cost vs ground investigation cost.

With an adequate geological and geotechnical knowledge, it is possible to better refine the project in the context of the uncertainties of type 1) and 2) and reduce as much as possible the uncertainties of type 3).

We should remember that residual uncertainties can lead to excessively conservative design approaches, higher provisions for risks and higher exposure to the risk of contractual claims. Any apparent economy in terms of cost could result in bigger residual geotechnical risks.

2.2 *Model uncertainties*

Model uncertainty can be defined as the ratio of the actual quantity to the quantity predicted by a model (Lacasse & Nadim, 1996).

In tunneling practice, site investigation is used as a basis for the definition of a ground model that is an idealized representation of the real geotechnical/geomechanical conditions. Site variability is considered by specifying different soil layers and through the choice of characteristic values of soil parameters. Creating a ground model involves the combination of the data gathered during the ground investigation with previous local experience and subjective judgement.

For design based on calculations, three main types of calculation models can be distinguished: analytical, semi-empirical and numerical.

An additional challenge of modern codes, as EC7, is that it is not prescriptive of the type of analysis to be used in design and encourages the use of numerical analysis. However, it does not specify as to the partial factors should be applied in numerical analysis. For example, the introduction of partial factors on soil strength, or partial material factors, implies that the soil's characteristic strength should be reduced by the relevant partial factor, and this can be achieved in two different ways: at a suitable stage during an analysis, or at the beginning of an analysis. They give different results but there is no guidance on which of these two approaches is more appropriate to apply (Potts & Zdravkovic, 2012).

Another tricky phase in the utilization of numerical models is soil-structure interaction in a semi-probabilistic framework (please refer to §4). When this is carried out with non-linear constitutive models of soils, the stiffness of soil depends on the characteristics of resistance and would be altered in presence of their factorization with partial factors. Furthermore, in these analyses, factoring the resistance soil parameters would modify the soil stiffness-resistance ratio by altering the distribution of stresses. Even the factoring of loads would involve an unnatural alteration of the conditions of plasticization of the soil and, consequently, an unrealistic redistribution of stresses.

For these reasons, the soil-structure interaction analyses must be carried out without any factorization of these parameters, thus using their characteristic values. The safety margin is then introduced by appropriately factorizing the stresses resulting from the interaction analysis.

This aspect is well explained in the recent Italian Codes (NTC 2018). It is not well addressed in most other Codes, first the Eurocode 7, and involves potential critical issues in numerical modeling with soil-structure interaction; this can, for example, occurs when "design approach 3" (for which the entire calculation is performed with the design values of the actions and the design shear strength) is used.

Moreover, the existence of wide variety of calculation methods is one of the main constraining factors of harmonizing design practice and procedures. It is difficult to obtain targeted safety level when a calculation model is used with a set of code-given partial factors, without consideration of the degree of reliability of different models.

The inherent uncertainties resulting from simplifications should lead to redundant conservatism. On the other side, advanced calculation methods require a great number of parameters and factors that can make those methods not appropriate for practical applications.

Lambe (1973) highlighted that using advanced models which parameters are based on unrepresentative number of soil tests may be even less reliable than using simplified models for which the amount of data is enough.

From a practical point of view, the appropriate model can be described as one offering the most favorable balance between the reliability of prediction and the necessary data for its application.

It is important to keep all these in mind when choosing a model to be used in the calculation and also to pay attention to EC7 that states "It should be considered that knowledge of the ground conditions depends on the extent and quality of the geotechnical investigations. Such knowledge and the control of workmanship are usually more significant to fulfilling the fundamental requirements than is precision in the calculation models and partial factors".

The choice of the geotechnical model, the calculation scheme, the constitutive law of the soil, must be commensurate with the quantity and quality of the geotechnical data, since the reliability of the result is conditioned by the weakest link in the chain.

3 DESIGN BY CALCULATION

In the design phase, to deal with the uncertainties, the typical approach, known as 'predefined design', is to attempt to eliminate the uncertainty by assuming a conservative condition, derived from the data available before construction.

Various possible methods, inherited by design of structures, can be used to consider uncertainties and to ensure an adequate margin of safety; the main ones are:

1. the global safety factor method,
2. the semi-probabilistic method (partial safety factors)
3. the probability-based calculation method.

In all three cases, the final design is determined prior to construction, based on ground parameters that take account of uncertainties inherent in natural soil/rock.

The development of the safety philosophy in geotechnical design went through a first phase where "global safety factor method" was adopted (nowadays practically abandoned) to move toward reliability-based methods (i.e. probabilistic-based method).

In the European countries, the main documents providing guidance on the method of reliability assessment and the reference reliability levels in the geotechnical field are EN 1990 and EN 1997.

The main aim of the Eurocodes has been to harmonize the design practice across Europe and provide unified framework for design. Unusual or high-risk structures are beyond their scope.

For tunnel design the codes are very poor and designers refer to geotechnical rules.

Eurocode EN 1997 states that it contains rules for "tunnels in hard non-fractured rock and not subjected to special water tightness or other requirements"; for other tunnels it is necessary to consider alternative provision and rules, but no specific indication is given.

Furthermore, there is no consensus on the choice of a commonly accepted targeted safety level. Reference levels of safety factors provided in Eurocodes may be subjected to a change in the national normative annexes. Moreover, in the respect of a general mandatory framework, Eurocodes allow for the use of different approaches to ensure sufficient reliability level.

The Italian Codes (NTC 2018) are congruent with Eurocodes.

3.1 *Global safety factor design*

Traditionally, geotechnical and tunnel design have been based on "global safety factor" method that has been sustained by a vast amount of experiences. It introduces a safety factor that is defined as a ratio between total resistance and total force and must be kept a value, higher than 1, given by experience. Values for different applications are empirically based and represent commonly accepted representation of the safety level for a given structure.

The use of global safety factor has been associated mostly with Allowable (working) Stress Design framework.

Although this approach can be easily and intuitively understood it doesn't represent an objective measurement of reliability as it does not directly account for various uncertainties. In theory, large uncertainties, arising from data and model, require large safety factors. However, the safety factors established in design Codes are not calibrated to consider different levels of uncertainty.

Since it is not a logical and reliable approach numerous studies have been undertaken in recent years to develop probabilistic approaches that deal with uncertainties in a methodical way. In the last few decades, efforts have been made to substitute "global safety factors", i.e., deterministic design, with reliability-based design.

3.2 *Probabilistic-based design*

The "probabilistic-based design" (i.e. "reliability-based design") is a way of handling foreseeable uncertainties by an explicit introduction of "probability density functions" (PDF) of know variables, i.e. relating to loads, material parameters and resistance.

One of the main characteristics is that parameters are defined over a range of values, not as a specific value, as in a deterministic approach.

In civil engineering the probabilistic method (level 3) is practically impossible to use, both for the number of independent random variables, and for the difficulty of knowing the PDF.

It would be possible to use a simplified probabilistic method (level 2), reducing the number of independent random variables to those that have the greatest effect on the value of the dependent variables, However, in current practice even level 2 methods are difficult to apply, since the designer does not have the data and knowledge of statistics and probabilities to apply it.

In any of the previous cases, the main downside is of course the lack of necessary data, especially, concerning PDF of geotechnical parameters.

Nowadays most design are based, for safety analysis, on the probabilistic method of "level 1" (or "partial safety factor" or "semi-probabilistic") and on the concepts of Limit State, as a demarcation between desired and adverse states of the structure.

This is the method formally used by the Technical Codes for Construction in most of the world countries (i.e. Eurocode 7, NTC, 2018 etc.).

4 OBSERVATIONAL METHOD

Observations have been used by engineers to deal with uncertainties and to observe the performance of structures since the early days of civil engineering.

Terzaghi & Peck (1948) discussed the first thoughts and ideas behind this process in geotechnical engineering. They suggested a new design procedure where information obtained during the construction phase is used to optimize the design.

The interest for the application of the observational method has increased in Europe during the last couple of decades, mainly due to the drive for competitiveness in the construction industry, as well as an increasing demand on reducing time and costs.

According to Nicholson et al (1999) the observational method is: "A continuous, managed, integrated, process of design, construction control, monitoring and review which enables previously defined modifications to be incorporated during or after construction as appropriate. All these aspects have to be demonstrably robust. The objective is to achieve greater overall economy without compromising the safety."

Eurocodes 7 and the Codes of the main European countries state that Limit States could be verified by mean of the "the observational method" when prediction of geotechnical behavior is difficult.

It states that before construction is started "the range of possible behaviour shall be assessed, and it shall be shown that there is an acceptable probability that the actual behaviour will be within the acceptable limits". This asks for a probabilistic approach and makes the rigorous application of the method difficult. In the Italian Code (NTC, 2018) the word "acceptable probability" is not present (!) so the use of this approach is easier.

The approach is based on a design that is improved step by step during excavation by means of observations and data collection on soil-structure interaction that allow to acquire useful elements for a better understanding of the geological and geotechnical reference model.

An Observational Method design assumes that the ground conditions will be near to a "reference value" of the predicted conditions, but alternative designs or contingency measures are prepared in case conditions should turn out to be worse than predicted.

Essentially, it is a method for reducing the risk in the construction phase based on preventive design analysis.

This approach identifies that uncertainty has two components, risk and opportunity: the ground conditions could turn out to be better than expected or worse and therefore brings enormous potential in terms of reducing risks and optimizing the costs of the works. The basic idea behind the OM is to balance reliability with economy by allowing design modifications at the construction phase, where design is done for expected conditions, but steps are taken to safeguard against the occurrence of less favorable ones. The most important aspect distinguishing the OM from just "learn-as-you-go" approach, often confused by engineers, is the preparation of fallback scenarios for every predicted unfavorable situation considered previously.

These scenarios should be realistic and possible to implement without delay and all possible modes of failure should be accounted.

During the design implementation a rigorous monitoring and observation strategy is used to check and confirm the actual conditions found during construction. Performance indicators are selected for monitoring, related to the critical risks. Peck (1969) stressed the importance of making right observations regarding measuring phenomena governing the behavior of the project; measuring the wrong quantities may cause significant problems. The issue noticed by Peck (1969) still rings true now that, not infrequently, less effort goes to the significance of data obtained from monitoring than the preparation of formal reports and documents based on them.

The choice of the calculation parameters for the "reference design" is one of the most debated item and conditions the possibility that the Observational Method is cheaper, with the same safety conditions, compared to a traditional approach. There are, essentially, two approaches (Figure 2):

1. based on 'most probable' conditions. Contingency measures are prepared before construction and are implemented if observed behaviors exceed critical limits;
2. based on a "most unfavorable" set of parameters. Observations during construction are used to actively optimize the design.

There are, obviously, intermediate approaches.

Peck (1969) adopted the "most probable" conditions and then reduced the design to "moderately conservative" parameters, where triggers were exceeded. CIRIA [4] considers a "safer" approach to design by adopting a "progressive modification" of the design starting with the design based on "moderately conservative parameters", and then reverting to "most probable" conditions through field observations. CIRIA uses the terms "most probable" and "most unfavorable" to describe the range of soil conditions as illustrated in Figure 2.

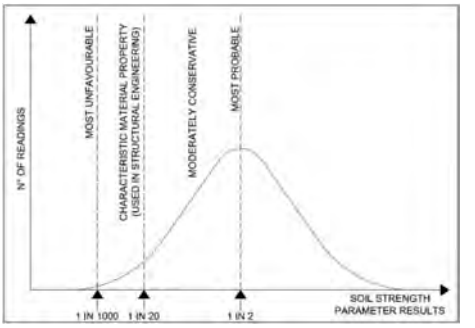

Figure 2. Gaussian distribution.

The "most probable" is a set of parameters that represent the probabilistic mean of all the data.

The "most unfavorable" parameter represents the 0.1% fractile (it represents the worst value that the designer believes might occur in practice).

The "moderately conservative parameter" is not a precisely defined value. It is a cautious estimate of a parameter, worse than the probabilistic mean but not as severe as the most unfavorable. In assessing these parameters, the designer should carefully consider the quality of the site investigation data and assess its suitability. It could be associated to the "characteristic value" of geotechnical parameters that Eurocode 7 defines as a "cautious estimate of the value affecting the occurrence of the limit state". It should ideally result in prediction of the upper 5% fractile.

The establishment of the initial design based on the "most probable" ground conditions drew most concerns. Muir Wood (2000) underlined as sometimes the concept of "most probable" situation is mistakenly associated with the situation that will be overcome with little probability; actually, most probable is equivalent to 50% probability. Almost all subsequent authors, suggest starting with an initial "moderately conservative design", to be relaxed to a "most probable" condition during construction, should the observed behavior warrant it.

In the observational approach, the suitable limits of behavior, is a "serviceability" calculation. These provide the predictions that can be monitored and reviewed.

Since a tunnel is excavated "step by step", we obtain a lot of information on tunnel behavior during the construction and we can improve the original design during excavation: the application of the observational method is a standard method in tunneling design and construction. It is also true that often the application is not formally congruent with all the Code's indications and it would be better to speak of observational approach.

5 THE POTENTIAL OF THE OBSERVATIONAL METHOD

The use of the Observational Method allows, in general terms, a reduction of the risk present in the construction of an underground work.

If we compare an "Observational Method design" with a "predefined design" we must highlight that less conservative ground parameters should be applied.

In a "predefined design" we proceed using the "most unfavorable" (worst scenario) set of parameters; in the case of the Observational Method we should proceed using a less unfavorable set of parameters ("most probable" according to Peck, "moderately conservative" for other authors).

Basically, we can work with safety factors lower than those used in a predefined design without reducing the real safety of the project. This is made possible by the knowledge acquired gradually during the work.

To clarify this concept, let us analyze the Figures 3 and 4 in which Gaussian distribution of load and resistance is represented. If one design based on the "most unfavorable" set of parameters and apply a similar factor of safety that we would for the most probable condition, we will fall in the first category described by Peck (1969), i.e. a wasteful or over-conservative design (Figure 3). On the other hand, designing for the "most probable" decreases the degree of conservatism and would be more economical (Figures 3 and 4). However, as Peck stated, it is, to some extent, a gamble; otherwise, if not there would be no need of using the word "probable".

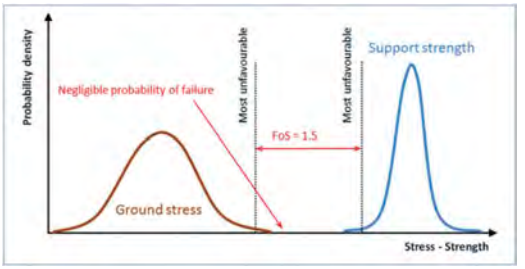

Figure 3. "Most unfavorable" set of parameters.

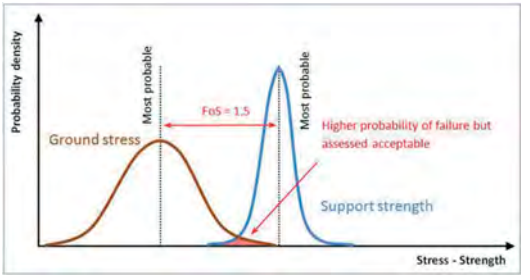

Figure 4. "Most probable" set of parameters.

By adopting an observational approach and a working hypothesis of the most probable conditions, one could say that it is at least a risk-controlled "gamble".

The objective of the observational method is to deal with uncertainties, and not reduce factors of safety, so if we properly monitor the ground behavior during excavation, contingencies may then be put in place if we realize that our "gamble" has failed (Oliveira 2015).

6 RISKS ALLOCATION

Noted that residual "geo" uncertainties and consequently "geo" risks tend to prevail despite robust site investigations and advanced calculation models, a contract should incorporate a mechanism to determine how to deal with residual risks and should give a clear allocation of risks for the case they occur. It is also clear that uncertainties of types 1, 2 and 3 (with reference to chapter 2) must be treated in a different manner and the choice of the contractual form implies a different allocation of risk to the Owner or Contractor. In general, in simplified terms, we can identify two most common forms of contract: 1) unit prices contract and 2) lump sum contract. The use of one or the other contractual form involves a different way of managing uncertainties and any unforeseen events (Klee 2015). In unit prices contract it is easy to deal with large variations of quantities in a reasonable manner, as regulation mechanisms are built into the contract. The experience shows that unit prices contracts are suitable to deal also with 'unexpected geological conditions', as long as the 'unexpected' element results only in variations in the quantities of work activities, that is for uncertainties of type 1) and 2). This means that all necessary work activities must have quantities and preferably also 'standard capacities' for regulation of the construction time. If "truly unforeseen" geological features (that is uncertainties of type 3), for which there are no methods and quantities available in the contract, occur the unit prices contract must be supplemented by special agreement. Unit price contract allocates all or most of the risk for the ground conditions to the Owner. For this reason, for underground construction where the impact of changed ground conditions can be very severe, Owners in many cases are reluctant to shoulder all the geological risk. For purposes of financial planning, many Owners prefer awarding lump sum (i.e fixed price) contracts. Fixed price contracts, with all risk for ground conditions allocated to the Contractor, may have an apparent predictability of cost, which may be attractive to the Owner. However, this type of contract imposes risks on the Contractor that may at best be difficult to quantify, at worst disastrous if the "truly unforeseen" occurs (i.e type 3). Such risks may become an Owner problem, no matter the contract text, if the Contractor is not able to bear the loss and complete the project. Therefore, also lump sum contracts for underground projects may not provide the intended predictable cost. 'Adjustable fixed price' contracts, combining unit rate and fixed price, may prove to be more suitable than fully fixed price

contracts, and easier to handle than unit prices contracts. According to the FIDIC ITA Task Group 10, risk allocation and risk dependent costs can be shown in a simple way as in Figure 5. It suggests that a fair risk allocation is likely to produce the lowest construction cost (FIDIC–ITA 2014). It is evident that, from a contractual point of view, the types of uncertainties described above must be addressed in a different way. In the case of uncertainties of (type 3), one must think a subdivision of the risk that involves in a decisive manner the Owner. History shows that the attempt to transfer the total geotechnical risk to Contractor does not liberate the Owner of his final responsibilities. In the event of a high level of losses, the Contractor will look for all possible ways to terminate the contract in advance; this can impact on the total costs, quality, safety of the entire project. Fair risk sharing between the Owner and the Contractor helps to reduce potential claims and therefore the total project costs. We can say that for the uncertainties of type 1) and 2) we cannot speak of unforeseen or unforeseeable.

In other words, there is the certainty of not knowing exactly anything, but moving in known areas for which the actors (Owner and Contractor) can evaluate and quantify the existing risk.

Figure 5. FIDIC Task Group 10. Lowest construction cost.

In any case, these uncertainties do not allow to precisely define the cost of the work. Therefore, it is necessary to find contractual mechanisms that distribute the risk of this non-definition on Owner and Contractor in a different way, also attributing a "risk premium" to the higher risk that one of the two is willing to charge. The theoretical ideal allocation of risk in a contract is that point where the sum of the risk premiums is minimized, the point where each party takes on the risk for which it is best placed to control and manage those risks. For the uncertainties of type 1) and 2) a lump sum contract could be assumed. It is necessary to define the risk assignment limit to establish what conditions were expressly or impliedly "foreseen" within the contract. This can be done by the Geotechnical Baseline Report (GBR) (ASCE 2007).

The Geotechnical Baseline Report is a document where contractual statements describe the geotechnical conditions predicted (or to be assumed) to be met during construction. It has to be viewed as a tool for defining those conditions that should be considered 'reasonably foreseeable' (i.e. uncertainties of type 1) and 2)).

The contractual statements are referred to as "baselines", and they should be considered as the reference point for risk evaluation and pricing. In fact, the tenderer needs to know 'with a sufficient degree of certainty' the risk that he is going to price, while the employer needs to know what he is going to pay for. Both parties must evaluate the cost of known conditions and to estimate the contingencies that should be included either in the contract price or in the Owners' budget.

The "baselines" serve as contractual references to establish where conditions encountered during construction that are significantly more adverse, onerous and time consuming, may be considered as 'unforeseen' (i.e type 3).

Risks associated with conditions consistent with or less adverse than the "baselines" are allocated to the Contractor, and those more adverse than the baselines are accepted by the Owner (Figure 6).

Figure 6. Baseline.

It is important to describe the possible range of property values or ground behavior. The recommended approach is to indicate the expected range of conditions and uncertainty, but then state a specific baseline (upon which bidders may rely) that has been established for contractual purposes. The baseline may be expressed as a maximum value, a minimum value, an average value, a histogram distribution of values, or a combination of them.

The Owner may decide to allocate certain risks and costs to the Contractor by baselines that are more adverse (higher "risk premium"). This will usually result in an increased bid price. Alternatively, the Owner may choose to share the risks and costs through less adverse baselines and utilization of either alternative payment provisions or a change order process, if the more adverse conditions materialize. To be useful for risk allocation, a geotechnical baseline must clearly establish the boundaries of those conditions that are expected and define how they are measured. The GBR has come into use in some countries, and there are encouraging benefits of its use. The British Tunnelling Society and the Association of British Insurers, which represent insurers and re-insurers on the London-based insurance market, issued their the "Code of Practice for

Risk Management" and the GBR concept is adopted in this code (BTS ABI 2003).

7 FINAL CONSIDERATIONS

In summary, the adoption of Observational Methods helps in mitigating the geotechnical risks.

It is therefore established that by proceeding with an observational approach, two important advantages can be obtained.

1. Verification, during construction, of the solutions defined during the design phase.
2. Calibration of the input parameters and the consequently of the safety factors in consideration of the knowledge acquired during the works.

In general, only the advantage 1 is exploited, i.e. the predefined design solutions are refined. Therefore, its potential, above all in terms of possible reduction of the overall costs of the work, is generally not fully exploited in the planning and construction phase. It is standard practice to limit its use to refine the application of the stabilization interventions and construction methods defined by a "predefined" design.

In other words, a "basic" design is developed based on the available data, and then in the construction phase this design is adapted to the real conditions found on site without modifying the safety factors as it would be possible by the greater information that are gradually acquired.

Depending on the specific problem, the parameter uncertainty, or model uncertainty or both can be updated through back analysis.

Generally, The OM is applied in the context of a unit prices contract with all risks are accepted by the Owner, without fully exploiting the opportunities provided by the method.

Therefore, there is a large "not exploited" reservoir of potential optimization of the total cost of the work. It is often suggested that cost uncertainty should be allocated to the party best able to anticipate and control that uncertainty, usually replacing the term 'uncertainty' by 'risk' although variability, ambiguity and systemic uncertainty may also be involved.

On this basis, a tentative conclusion is that lump sum contracts are appropriate when sources of uncertainty are controllable by the Contractor, i.e. types 1) and 2) that are within baseline. An interesting analysis of Ward and Chapman (2011) concludes that a lump sum contract is usually risk efficient in allocating Contractor controllable uncertainty. An important conclusion is that even where Owner and Contractor share similar perceptions of project cost uncertainty, fixed price contract may be inefficient for the Owner, if the Contractor is more risk averse than the Owner. In this situation, the Contractor will require a higher premium to bear the risk than the Owner would be prepared to pay for avoiding the risk. It is equally true that in the case of lump sum contracts all the uncertainties, even within the baseline, are the responsibility of the Contractor and consequently the Contractor may be driven to maintain a high 'risk premium' and then do not convenient offer for the Owner. For this reason, this type of risk should be mitigated by appropriate contractual architecture. On the other hand, under a fixed price contract, the Contractor is motivated to manage project costs downwards to formulate a competitive offer; it should be able to generate, an 'opportunity discount' for example, by increasing efficiency or using the most cost-effective approaches. With the use of the Observational Method, one could exploit precisely this enhancement linked to the good work of the Contractor.

The definition of aggressive baselines involves high risks for the Contractor and the consequent attribution of a higher "risk premium" (i.e. expensive offer for the Owner).

This premium could be balanced by allowing the Contractor to use an Observational Method with optimization of the interventions. By exploiting the potential of the Observational Method, the Contractor could be able to manage all the risk (within the baseline) and could generate benefits for both Owner and Contractor. For that purpose, it is strategic to build a sufficient flexibility into the contract so that design can be adapted during construction according to "geo" properties encountered within an observational approach. With the use of the Observational Method, the Owner could use a more aggressive baseline because thanks to the possibility of refining the "safety factors" (without reducing the overall safety of the work) there is a possible premium for the Contractor. This could allow for more aggressive lump sum bids and therefore an overall advantage for the Owner. Ultimately, we want to highlight how moving within the limits of the uncertainties of type 1) and 2) then definable by the Geotechnical Baseline Report and controllable, the contract could also be a lump sum thus attributing all the risk to the Contractor. Within the baseline, the Contractor would have the possibilities to evaluate and quantify the risk and considering a possible refining of the "safety factors" (made possible by the greater knowledge acquired during construction and therefore without reducing the overall safety of the work).

It must be emphasized that for a "right" use of the Observational Method, that wants to enhance all the potentials of the same, it is necessary that Owner and Contractor provide a team of expert designers able to support the mutual interests. The processes of design and construction need to be integrated, and close co-operation is required between all those involved in the project. Definitely, increasing investments in engineering design would allow a control of cost and time overrun and a certain reduction of the overall cost of the project.

REFERENCES

ASCE, Essex R., 2007. Geotechnical Baseline Reports for Construction: Suggested Guidelines. ASCE. Avestedt, L.

Bogusz W. and Godlewski T. 2019. Philosophy of geotechnical design in civil engineering – possibilities and risks. Bulletin of the Polish Academy of Technical Sciences, vol. 67, no. 2.

Baecher, G.B. and Christian, J.T, Reliability and Statistics in Geotechnical Engineering. John Wiley & Sons, (2003).

Bolton, M.D. 1981. "Limit state design in geotechnical engineering", Ground Eng., 14(6), 39–46.

ABI, 2003. The Joint Code of Practice for Risk Management of Tunnel Works in the UK. British Tunnelling Society (BTS) and the Association of British Insurers (ABI).

Ciria 1999. Report 185 - Observational Method.

Christian, J.T. 2004. Geotechnical Engineering Reliability: How Well Do We Know What We Are Doing?", J. Geotech. Geoenviron. Eng., Vol. 130, No. 10.

Eurocode 0 (BS EN 1990–1:2006) "Basis of structural design".

Eurocode 7 (BS EN 1997–1:2004) "Geotechnical design - Part 1: General rules".

International Society for Soil Mechanics and Geotechnical Engineering (ISSMGE) 2017 – Joint TC205/TC304 Working Group on "Discussion of statistical/reliability methods for Eurocodes" – Final Report.

Klee, L. 2015. International Construction Contract Law. Wiley & Sons.

Lacasse, S. & Nadim, F., 1996. Uncertainties in characterizing soil properties. Uncertainty in the Geologic Environment: from Theory to Practice, pp.49–75.

Lambe, T.W. 1973. "Predictions in soil engineering". Geotechnique 23, No. 2, 149–202.

Muir Wood, A. 2000. Tunnelling: Management by design. E & FN Spon, London.

Müller, R., 2013. Probabilistic stability analysis of embankments founded on clay. KTH, Royal Institute of Technology.

Nicholson, D., Tse, C.M., Penny, C. 1999. The Observational Method in ground engineering: principles and applications. Report 185. CIRIA.

NTC -Norme tecniche per le costruzioni 2018.

Oliveira, D. 2015. Linkedin Post.(link: www.linkedin.com/pulse/observational-method-geotechnical-engineering-david-oliveira/)

Patel, D. et al. 2007. The Observational Method in Geotechnics. Proceedings of the 14th ECSMGE: Madrid, Spain. Vol. 2, 365–370.

Peck, R. B. 1969. Advantages and limitations of the Observational Method in applied soil mechanics. Geotechnique, 19: 171–187.

Potts, D. M. & Zdravkovic, L. 2012. Accounting for partial material factors in numerical analysis Geotechnique 62, No. 12, 1053–1065.

Prästings, A 2016. Aspects on probabilistic approach to design: from uncertainties in pre-investigation to final design KTH Royal Institute of Technology. Stockholm.

Ward, S. & Chapman C. 2011. How to Manage Project Opportunity and Risk – John Wiley and Son Ltd.

Tunnelling for a Better Life – Yan, Celestino, Thewes & Eberhardt (Eds)
© 2024 The Author(s), ISBN 978-1-032-80042-4
Open Access: www.taylorfrancis.com, CC BY-NC-ND 4.0 license

Design of Ontario Line South Tunnel

Mehdi Bakhshi*, Verya Nasri & Toufic Maalouf
AECOM, New York, USA

ABSTRACT: The Ontario Line is a 15.6-km stand-alone rapid transit line with fifteen stations that will connect the Ontario Science Centre to the Exhibition (Ontario Place) with numerous connections to the broader transit network. The southern stations and tunnel, also known as Ontario Line South (OLS), will be the first portion of the Ontario Line to be designed and constructed. OLS consists of 6.7 km of twin bored tunnels between the Exhibition portal to Don Yard portal (west of the Don River), seven new stations, six underground and one at-grade stations to be integrated with existing underground stations. The tunnel will be excavated by a 6.8-m hybrid shielded rock TBM, capable of operating in open mode when in relatively competent rock and operating in EPB mode when the tunnel is passing through potential buried valleys. TBM excavation will be supported by a precast fiber-reinforced concrete segmental lining system. This paper presents geological conditions in the Georgian Bay formation, alignment, excavation sequence, design of lining, and geotechnical instrumentation and monitoring for the OLS bored tunnels.

Keywords: Concrete, Fiber, Lining, Rock, Segment, TBM

1 INTRODUCTION

Ontario Line is a 15.6-km long rapid transit project. The project will consist of fifteen proposed new stations that will have several connections to the existing stations. Ontario Line South is the south underground portion of the project that runs from Exhibition portal to Don Yard portal, as shown by red line in Figure 1. The tunnel length between the two portals is approximately 5.9 km. This portion will consist of five underground stations (King Bathurst, Queen Spadina, Osgoode, Queen, Moss Park and Corktown). These stations will be connected by two twin TBM tunnels. The TBM tunnel is lined with fiber-reinforced concrete. While the project includes cut-and-cover structures such as portals, headwalls, shafts, station, and underground station structures constructed using the sequential excavation method (SEM) with a roadheader, this paper will exclusively focus on the design and construction of the main tunnels.

Figure 1. Overview of Ontario Line South (OLS) project.

2 GEOLOGICAL CONDITIONS

The site geological conditions consist of the following layers. The shallowest layer is a granular fill layer underlain by modern alluvial deposit and coarse textured lacustrine deposit. These deposits are underlain by glacial till deposits (plastic and non-plastic). These native deposits are underlain by the bedrock. The interpreted stratigraphic profile indicates that the bedrock surface generally slopes down from approximately 80 m at the west to about 65m at the east end except a buried bedrock valley with lowest bedrock surface of about 40 m that was identified in the vicinity of the Don River. The rock belongs to the Georgian Bay formation which consists of shale, limestone, dolostone and siltstone. The fractured rock layer is called Type 16 in this project consists of decomposed or highly weathered shale and Type 17 rock is the competent rock found underneath. The horizontally bedded Georgian Bay Formation regionally contains consistent sets of vertical or sub-vertical discontinuities and horizontal to sub-horizontal bedding discontinuity. Location of tunnel

*Corresponding author: mehdi.bakhshi@aecom.com

DOI: 10.1201/9781003495505-22

with respect to the geological layers are shown in Figure 2. The majority of the tunnel will be excavated in type 17 competent rock.

3 TUNNEL EXCAVATION METHOD

The selection of the Earth Pressure Balance (EPB) TBM excavation method for OLS was based on a comprehensive analysis of geotechnical, settlement, groundwater, wear, and gassy conditions. The project alignment intersects Type 17 and 16 bedrock units, resulting in the majority of the tunnel being excavated in excellent rock face conditions. Nevertheless, pressurized TBMs excel in controlling settlement and face stability when encountering discontinuities like joints and shear faults. Furthermore, they are the optimal choice for addressing geotechnical conditions, such as the potential presence of buried valleys, especially on the eastern side of the project alignment. This selection not only facilitates the implementation of an optimal face stability pattern but also ensures settlement levels below attention thresholds near tall and heritage buildings in Downtown Toronto. Given the groundwater level and low hydraulic conductivity, groundwater pressure does not affect the choice of TBMs. However, addressing groundwater is more effective with pressurized TBMs compared to open-shield TBMs. The selected TBMs are pressurized single shields equipped with cutter discs, as indicated by geotechnical reports that suggest a very low wear potential for the rock mass, reinforcing the suitability of the TBM excavation method. Additionally, geotechnical investigations have confirmed the presence of methane and hydrogen sulfide gas within the shale bedrock, necessitating that the TBM excavation method meet the requirements for a "gassy tunnel". OLS tunnels will be constructed in an easterly direction, starting from the Exhibition Portal, passing through Queen Station, and concluding at Don Yard Headwall. At Don Yard, the shields are abandoned in the ground, and the TBMs are disassembled from within the tunnels.

4 SPACEPROOFING

The selected configuration for the OLS project consists of two twin-tube tunnels with an inner diameter of 6.05 meters (Figure 3). The inner diameter of the tunnel's precast segmental rings is determined by various factors, including the Vehicle Dynamic Envelope (VDE) on curves, track structure, duct banks, electrical conduits, walkway platforms, track center spacing, overhead catenary envelope, and fire life safety cabinets and equipment. Construction tolerance is considered 100 mm.

5 PRECAST SEGMENTAL LINING

The TBM tunnel will be lined with a watertight circular one-pass lining system with precast concrete segmental rings. These rings are available in two types, each designed with a different width to accommodate varying minimum curve radii. Type 1 rings have a width of 1.7 meters suitable for minimum curve radius of 200m, while Type 2 rings are 1.2 meters wide suitable for a minimum curve radius of 141m. Both ring types have a thickness of 270 mm, ensuring structural capacity for all governing load cases. As depicted in Figure 4, each ring is composed of seven ordinary segments, one large key segment, and one reverse-key segment. The key and reverse-key segments have dimensions similar to ordinary segments, leading to a 6+0 ring configuration. Ordinary segments have an arc angle of 60 degrees, while the reverse-key segment features an arc angle of 63 degrees, along with a slightly greater

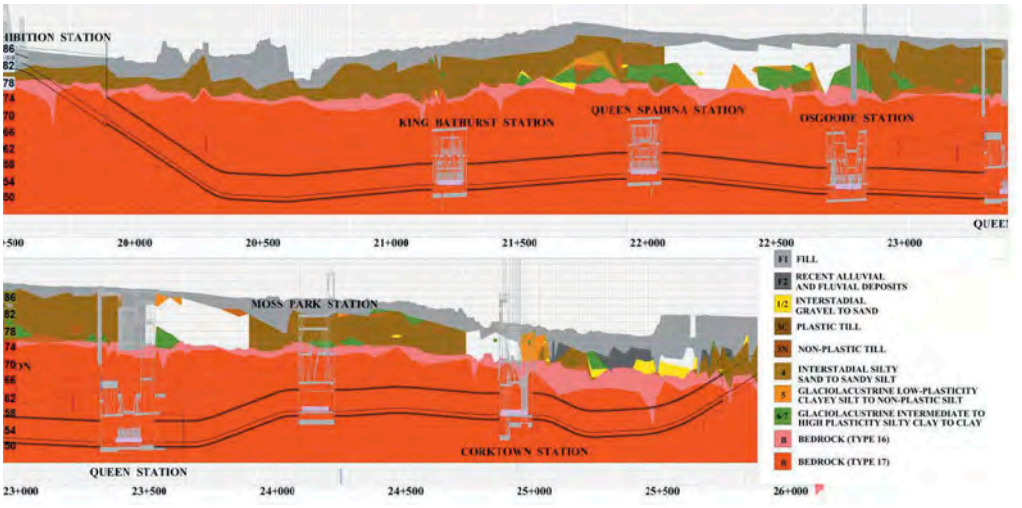

Figure 2. OLS tunnel profile.

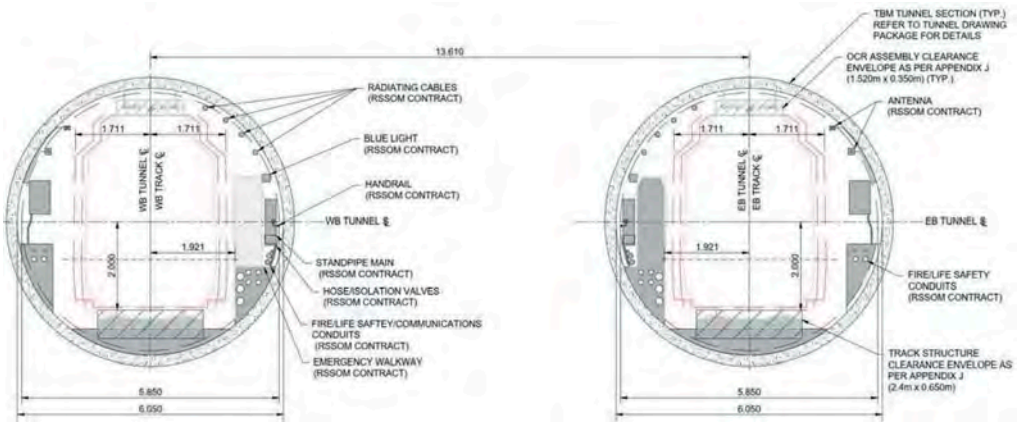

Figure 3. Tunnel spaceproofing.

curved length than other ordinary segments. Consequently, the key segment features an arc angle of 57 degrees and a slightly shorter curved length compared to the ordinary segments. To create staggered longitudinal joints, the angles between the joints of ordinary segments and the tunnel axis are set at 8 degrees. For key segment joints, this angle is slightly adjusted to 10 degrees. Rings are tapered to negotiate alignment curvatures. The calculation of the ring taper takes into account the smallest curve radius along the alignment, the ring's length, and the tunnel's outer diameter. As a result, the total ring taper is 56 mm or ±28 mm at the centerline of both types of rings.

The designed ring geometry is optimized to prevent crucifix joint formation during TBMs' tangent and curved drives, thereby reducing the risk of groundwater infiltration. Using a universal ring system offers several advantages, such as simplifying segment production through a single formwork set for each ring type, resulting in substantial cost savings. In presented configuration, as shown in Figure 5, ordinary segments have a parallelogram shape, while the key and reverse-key segments are trapezoidal. This rhomboidal segment system stands out as the most advanced when compared to other systems like hexagonal, rectangular, and trapezoidal systems. It offers several advantages, including the prevention of crucifix joints, improved sealing performance, continuous ring assembly from bottom to top, and compatibility with a dowel connection system.

Longitudinal and circumferential joints are designed as entirely flat joints. This design promotes efficient load transfer between segments and rings, enhancing joint watertightness. Furthermore, tapered longitudinal joints reduce early gasket friction during segment insertion in the ring assembly phase, making it easier to use fast connecting dowels in circumferential joints. This makes tapered longitudinal joints, hence rhomboidal segments, a preferred choice over rectangular ones.

Designed ring configuration also facilitates the ring assembly phase. As shown in Figure 4, the key segment's longitudinal joints are along the lines originating from a point 1500 mm directly below the tunnel center point.

This eccentricity facilitates the large key segment insertion during ring assembly.

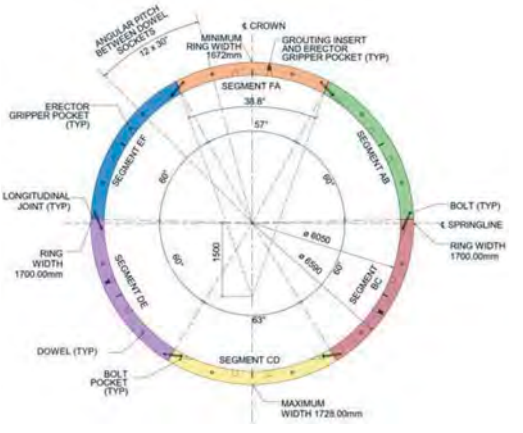

Figure 4. Ring geometry.

The key draw distance is designed so that the minimum gap between the key ring and the reverse key ring is 30mm as shown in Figure 6.

Bolts are used as connection devices between precast segments in longitudinal joints and dowels act as connectors of segments in circumferential joints. The insertion of the dowels is automatically performed by the TBM erector, which saves construction work and manpower during ring installation. Dowel type is modified Optimas SOF-FAST 110 with yield and ultimate pullout capacities of 110 and 160 kN, respectively (Figure 7). This type of dowel reduces the possibility of cracking caused due to joint

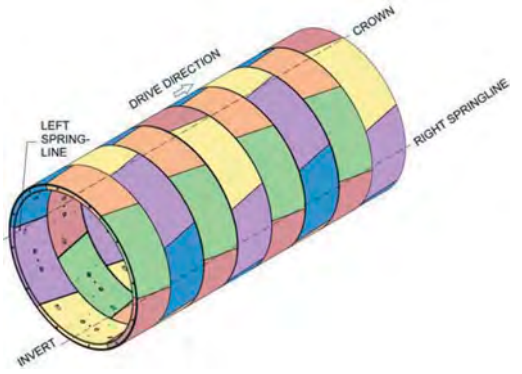

Figure 5. Successive rings on a tangent alignment.

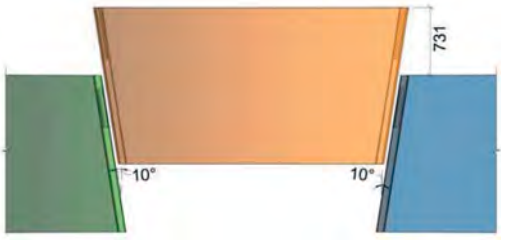

Figure 6. Plan view of key draw.

misalignment by limiting the joint offsets and improves sealing performance of gaskets by limiting joint gaps.

Figure 7. Dowels at circumferential joints.

The segment joints will be sealed using EPDM glued gasket. The gasket profile is Datwyler/Sealable M38596 type "Portland". The sealing performance of the gasket is checked by obtaining the maximum groundwater pressure present along the entire alignment. The capacity of the gasket is checked by accounting for the relaxation factor for 100-year service life of tunnel and maximum potential gaps and offsets between segment gaskets as 5 mm and 10 mm, respectively. At these specified tolerances and considering a design gap of 1mm for the glued gasket groove construction tolerance, the tested water pressure resistance of the designed gasket profile is 15 bar, which provides a safety factor of around 2.1 at the location of maximum groundwater pressure in the alignment.

The guidelines provided in ACI 533.5R-20, ACI 544.7R-16 and the ITA WG2 (2019) were followed for the structural design and analysis of precast concrete segments using the load and resistance factor design (LRFD) design method Temporary and permanent load cases considered during the various stages of construction and at the final service stage are considered for design. For production and transient stages, segments are designed for formwork stripping (demolding), storage (stacking), transportation and handling load cases. Segment stacking is shown in Figure 8. For the construction stage, the considered load cases are TBM thrust forces, tail-skin and secondary grouting. The TBM thrust pad width is 900mm, and the thrust pad contact length with the segment along the thickness is 175 mm. TBM is designed using a 12-pad configuration (two pads per segment, as shown in Figure 9) which increases the gap between the pads and the longitudinal joints (which should be 200mm minimum). The theoretical eccentricity (also called mechanical eccentricity) is 35mm for a 270mm thick segment. We consider that we can correct 20mm thanks to the articulation, so it becomes 15mm. The construction tolerance is considered as +/- 30mm. While both linear elastic and nonlinear FEM simulations can be performed, the amount of stresses developed due to maximum/exceptional combinations of forces and eccentricities often exceeds tensile strength of FRC segments. It can be concluded that only nonlinear analyses can truly capture response of the FRC segments after cracking. Serviceability limit state (SLS) condition is the main concern as crack width opening dimension under jack forces may exceed the limits specified by project's design criteria which is commonly taken between 0.25-0.30mm.

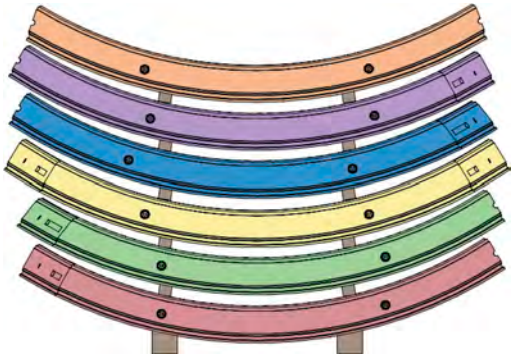

Figure 8. Segment stacking.

The next load cases to be analyzed are tail-skin and secondary grouting load cases. FE Analysis was performed on one segmental ring loaded under the governing grout pressure gradient anticipated in the alignment. This analysis produces axial and shear

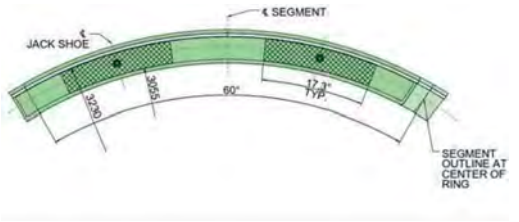

Figure 9. Jack pads on a typical segment.

forces and bending moments which constitutes the structural demand. The governing load cases during the final service stage include earth pressure and groundwater load, and the longitudinal joint bursting. Two-dimensional finite element analyses were conducted for both load cases. The appropriate strength reduction factors and load combinations were applied for each case.

The precast tunnel segments are designed as fiber-reinforced concrete (FRC). Compared to conventionally reinforced concrete segments, FRC segments have superior crack control and offer cost savings hence the preferred solution for this project. The minimum compressive strength of the concrete at 28-day and at the time of stripping (demolding) was designed as 50 MPa and 12 MPa, respectively, to satisfy the demands of all governing load cases and to satisfy the durability requirements of the project. The design of the concrete mixture results in an optimized concrete performance that achieves a high early-age strength for stripping (demolding) and a high-performance concrete for long-term durability.

The type of fiber chosen for this mix design is cold-drawn wire ASTM A820 type I steel fiber. It has a strength of 2200 MPa, which is the highest strength for commercially available fibers in the market. Specified fibers are glued in clips, have double hooked ends, a minimum length of 60 mm, a maximum diameter of 0.75 mm, and an aspect ratio (length/diameter) of 80. The minimum specified content of steel fiber for reinforcing typical segments is 40 kg/m^3. The limit of proportionality (LOP) and minimum specified residual flexural strengths at the stripping (demolding) age are LOP = $f_{R,1k}$ = 1.7 MPa and $f_{R,3k}$ = 2.4 MPa. The LOP and minimum specified residual flexural strengths at 28-day are LOP = $f_{R,1k}$ = 3.8 MPa and $f_{R,3k}$ = 4.6 MPa.

6 CROSS-PASSAGES

To satisfy NFPA 130 fire protection and life safety requirements, this project has three cross-passages between the two tunnels from Corktown Station to the Don Yard Portal as well as openings in the segments into an egress shaft at the Ordnance Street Emergency Egress Building between Exhibition Portal and King-Bathurst Station. Shear bicones are added in the circumferential joints of the rings at and around the opening areas into segments to take additional developed shear forces. Four SOF-SHEAR 375 bicones with shear capacity of 375 kN are placed on circumferential joints of segment, two around each dowel, which makes it 24 bicones per ring. As shown in Figure 10, six to eight bicones from cut rings will be removed in the opening areas, and remaining bicones take the shear force.

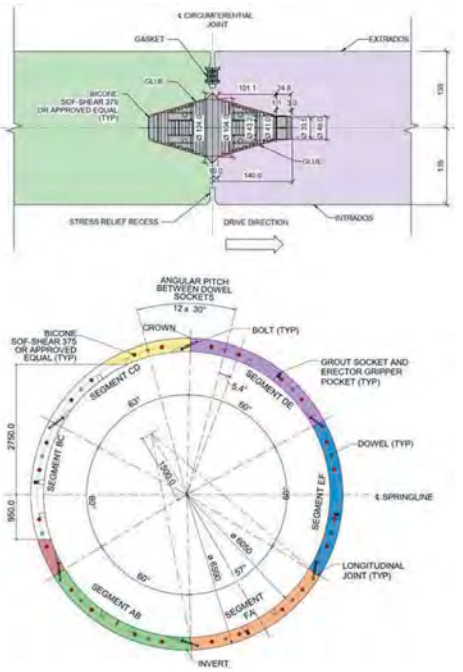

Figure 10. Bicone configuration at cross-passages.

7 GEOTECHNICAL INSTRUMENTATION

Since this project is being built in a densely populated area of Downtown Toronto, it is important to monitor the ground movements caused by underground construction to prevent any impact to the adjacent existing structures and make sure the initial

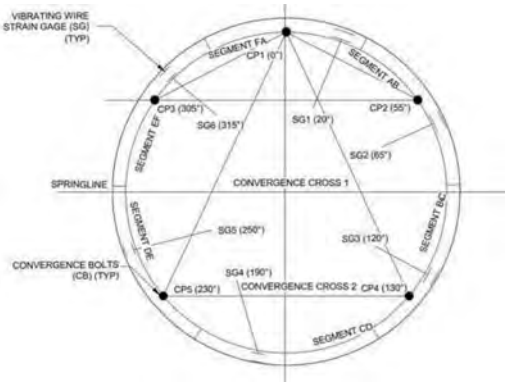

Figure 11. Instrumented Rings.
(SG: Strain Gauge, CP: Convergence Point)

and permanent supports perform as expected. The TBM segmental lining will be equipped with strain gauges (SGs) and convergence bolts as shown in Figure 11. Each instrumented ring will have six strain gages and five convergence bolts. The instruments will be installed all the critical locations.

In addition to these instrumented rings, the project will have surface monitoring program consisting of Multi-Point Borehole Extensometers (MPBXs), Ground Settlement Monitoring Points (GMPs), Manual Inclinometers (INCs), Vibrating Wire Piezometers (VWPs) as well as structure, rail and utility monitoring points.

8 CONCLUSION

The 15.6-km Ontario Line South (OLS) project is a significant enhancement to the public transit system in the Greater Ontario providing faster and more reliable access to rapid transit within Ontario and reduces traffic congestion in the area. The site's geology comprises various layers, including granular fill, alluvial deposits, glacial till, and bedrock. Excavation for the Ontario Line South project will predominantly occur in the competent Type 17 rock of the Georgian Bay formation.

For the underground section, an excavation method using Earth Pressure Balance (EPB) was selected based on optimal face stability, settlement control, and addressing geotechnical challenges, because of efficiency in excavating through rock discontinuities, potential buried valleys, and gas presence in the shale bedrock. The TBM tunnel from the Exhibition portal to Don Yard consists of two twin tunnels that have an inner diameter of 6.05 m and a ring thickness of 270 mm. With two types of rings, 1.2 m and 1.7 m in ring length, the entire alignment can be negotiated using universal segmental rings.

The optimized ring geometry and connection systems as well as gasket, fiber reinforcement and all other major characteristics of segmental rings are presented. It is expected that the segment production to begin in mid-2024 and tunnel construction starts between late 2024 and early 2025.

REFERENCES

ACI 533 5. 2020. Guide for Precast Concrete Tunnel Segments. American Concrete Institute (ACI).

ACI 544 7. 2016. Report on Design and Construction of Fiber-Reinforced Precast Concrete Tunnel Segments. American Concrete Institute (ACI).

ITA WG-2 Report No. 22. 2019. Guidelines for the design of segmental Tunnel Linings. International Tunnelling and Underground Space Association (ITA). Chatelaine, Switzerland. ISBN: 978-2-970-1242-1-4.

Tunnelling for a Better Life – Yan, Celestino, Thewes & Eberhardt (Eds)
© 2024 The Author(s), ISBN 978-1-032-80042-4
Open Access: www.taylorfrancis.com, CC BY-NC-ND 4.0 license

Design challenges in conventional tunnelling on the Sotra Link Project in Norway

Guido Barbieri*, Gianluca Bella, Edoardo Trivellato, Salvatore Agrillo & Matteo Giani
Pini Group SA, Lugano, Switzerland

ABSTRACT: In the perspective of easing the amount of traffic between Øygarden and Bergen along the existing Riksveg 555 (West Norway), the Sotra Link Project (SLP) will consist of 11 km of tunnels between Nye Kolltveit and Drotningsvik, 3 pedestrian/bicycle tunnels, 19 underpasses, 23 tunnel portals, 22 bridges and 24 kilometres of two-lane access roads. Concerning the underground works, the infrastructure will be established as a 4-lanes road and two parallel single-tube one direction tunnels. The present paper aims to introduce the general design approach for the mentioned main tunnels. The permanent rock support, realised with conventional tunnelling based on drill & blast, is evaluated through the NGI Q-system, that provides a useful recommendation to dimension the long-term lining. Afterwards, this paper focuses on representative tunnel sections where specific evaluations are required due to very low overburden conditions, undercrossing of existing infrastructures, extended fault zones and possible squeezing phenomena. These challenges are approached by detailed numerical analyses and overcome by adopting tunnelling solutions such as partial excavation phasing, specific tunnel face support and customized linings.

Keywords: Conventional Tunnelling, TBM, Numerical Modelling, Detailed Design, Rock Support

1 INTRODUCTION

The Sotra Link Project (SLP) is the largest and most complex road infrastructure project developed by the Government of Norway within its National Transport Plan 2018-2029. It represents one of Norway's priority infrastructure projects, including design, financing, realization and maintenance of several surface and underground works between the city of Bergen and the Sotra island in West Norway, along the existing Riksveg 555 (Rv.555). The whole project includes 9 km of highway and a suspension bridge (30 m wide/ 900 m long, including towers 144 m high) between the municipalities of Øygarden and Bergen. The road system includes 12.5 km of tunnels (Kolltveit, Straume, Knarrvika, Drotningsvik and ramp tunnels from/to the main Drotningsvik tunnels), 19 roads and pedestrian underpasses, 23 tunnel portals, 22 bridges and viaducts, and 14 km of pedestrian and bicycle paths. Moreover, BIM approach has been adopted for the Sotra Link Project, involving all phases of the design process that currently entered the Detail Design phase (Barbieri et al., 2024; Barbieri et al., 2023).

The current paper deals with geotechnical challenges and tunnelling experience gained during the design phase of some relevant underground structures. Geotechnical complexities are related to the design of technical solutions for rock support of tunnels characterized by low overburden with loose shallow deposits and interferences with new and existing nearby structures or tunnels in expected fault zone with swelling potential. The detailed design overcomes these challenges by accurate finite element analyses, leading to a suitable dimensioning of customized linings, together with partial excavation phasing and specific tunnel face support. This paper deals with two relevant case studies with reference to Drotningsvik main tunnels.

Chapter 2 concerns the design of the North and South tunnel stretches close to Kiplevatnet Lake, where partial front reinforcement and surface grouting are a foreseen due to very low overburden and presence of existing and future viaducts. Another relevant case is exposed in chapter 3: it deals with a main tubes section located into an expected fault zone where a full front reinforcement and partial excavation phasing are specifically designed. For both cases, numerical analyses are exposed and main results are given.

The status of the works is exposed in chapter 4 and main conclusions are summarized in chapter 5.

*Corresponding author: guido.barbieri@pini.group

DOI: 10.1201/9781003495505-23

Figure 1. General overview of the SLP (Webuild Value Digital Magazine).

2 KIPLEDALEN SECTION

The present chapter shows the challenges associated to the design of the permanent rock support of Drotningsvik Tunnel in correspondence of the existing railway viaduct, part of the Rv.555, and Kiplevatnet lake. The complexities of the project are shown, and the design assumption are exposed together with the main results.

2.1 *General overview*

The Drotningsvik Tunnel reference section (North tube and South tube) is 30 m long and it is located within an area interested by the presence of the Kiplevatnet lake. In the area, a hydraulic pipe collecting the discharge coming from Kiplevatnet lake is also found in correspondence of a section at the kilometric point 8+135 of the project chainage. The reference section

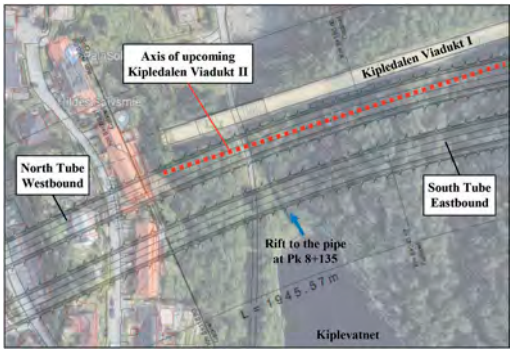

Figure 2. Kipledalen section plan view.

comprehends an existing viaduct (Kipledalen Viadukt I) and a future pedestrian bridge (Kipledalen Viadukt II) to be built after the tunnel excavation.

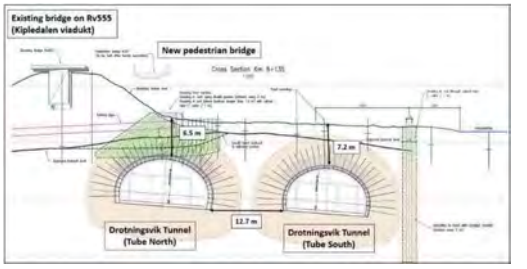

Figure 3. Kipledalen cross section (km 8+135).

2.2 *Main challenges and geotechnical characterization*

The main challenges of the project consist of the low overburden conditions (approx. 6/7 m) together with the undercrossing of existing relevant infrastructure (Kipledalen Viadukt I) and new one (Kipledalen Viadukt II). Relevant core drillings allowed to define three main units: i) *rockfill* consisting of wet sandy soil with some gravel (0÷3.3 m depth), ii) *weathered bedrock* (3.3÷9.2 m depth), iii) *good rock mass* (>9.2 m depth). Starting from laboratory data (σ_{ci}) and a Q-value describing the rock mass quality (Using the Q-system, NGI, 2015), Mohr Coulomb properties are estimated by means of RocData v5.0 (Table 1).

Table 1. Geomechanical properties of the soil/rock units.

	Rockfill	Weathered bedrock	Good rock mass
γ (kN/m^3)	20	29	29
φ (°)	42	30	40
c' (kPa)	10	70	4500
E (MPa)	75	1500	6000
v (-)	0.25	0.20	0.17
Ψ (°)	12	0	10
Q (-)	-	0,14	290

2.3 *Numerical modelling*

Bidimensional finite element (FE) analyses of transversal sections have been performed by means of RS2v.9.0 (RocScience Inc.), under plane strain conditions to estimate stresses and displacements on the concrete support during the excavation phases. Proper sizes were assigned to the model (170 m x 70 m) to avoid boundary effects, and soil/rock was discretized by 26′000 triangular meshes densified in the most relevant clusters. Boundary conditions consists in hinges along horizontal boundary and rollers along vertical boundaries. An elastic-perfectly plastic Mohr-Coulomb criterion was adopted as constitutive law. Acting on the safe side, rock bolts have not

been modelled, and largest excavation tunnel sections are considered. Shotcrete linings have been modelled as composite liner reproducing the excavation sequence. Two FE models have been considered:

– model n.1: 'shallower' interface rock/soil + existing bridge + new pedestrian bridge. This scenario represents a cross section close to km 8+126.
– model n.2: 'deeper' interface rock/soil + existing bridge. This scenario represents a cross section close to km 8+135.

The complexity of in-situ state of stress led to carry out some sensitivity analyses for two different cases (Table 2).

Table 2. Geomechanical scenario assumed for the FE models (i.p.=in plane; o.p.=out of plane).

Case	Rockfill	Weathered bedrock	Good rock mass
1	k_0=0.33 (i.p.)	k_0=1.00 (i.p.)	k_0=1.00 (i.p.)
	k_0=0.33 (o.p)	k_0=1.00 (o.p)	k_0=1.00 (o.p)
2	k_0=0.33 (i.p.)	k_0=0.50 (i.p.)	k_0=0.50 (i.p.)
	k_0=0.33 (o.p)	k_0=0.50 (o.p)	k_0=0.50 (o.p)

In "case 2" the *weathered bedrock* is assumed to be looser than in "case 1" because of the k_0 reduction from 1.0 to 0.5, both in plane and out of plane. For this reason, acting on the safe side, a higher deconfining ratio is assumed in "case 2" for an unsupported span equal to 3.0 m. The model steps and deconfining ratios λ assumed are summarized in Table 3.

Table 3. Finite element model steps.

Step	Description
1	Initialization with the load of the existing bridge
2	North tube: excavation of the tunnel face (case 1, case 2: λ = 30%)
3	North tube: unsupported span = 3 m from the tunnel face (case 1: λ = 60%, case 2: λ = 80%)
4	North tube: excavation far from the tunnel face (λ = 100%) and lining activation
5	South tube: excavation of the tunnel face (case 1, case 2: λ = 30%)
6	South tube: unsupported span = 3 m from the tunnel face (case 1: λ = 60%, case 2: λ = 80%)
7	South tube: excavation far from the tunnel face (λ = 100%) and lining activation
8	Activation of the loading due to the new pedestrian bridge (just for model n.1)
9	Seismic analysis

The FE model of the tunnel cross sections is given in the Figure 4 below for model n.1.

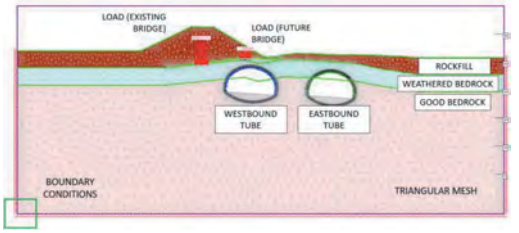

Figure 4. FE model, geometry loads and boundary conditions (km 8+126).

Ground improvements due to grouting are considered in the FE model for the North Tube at km 8 +135 (weathered bedrock overburden 1.0m) for the model n.2, and an increase of the shear strength properties is assessed for both loosen backfill and weathered rock (Table 4).

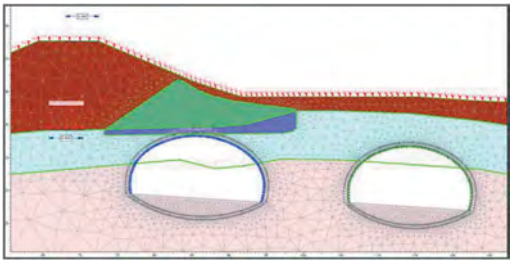

Figure 5. Detail of the FE model with ground improvement above the North Tube, tunnel section km 8+135: treated backfill (green) and treated weathered bedrock (purple).

Concerning the loosen backfill, grouting effect was evaluated by an increment of unconfined compressive strength with an efficiency of 50%, with a consequent rising of effective cohesion.

On the safe side, friction angle value remained constant. Concerning the weathered bedrock, grouting effect was evaluated by an increase of RQD and joints' roughness and alteration - *Jr/Ja* in Barton's definition of Q value (Barton et al., 1974). Improved shear strength parameters assumed, in particular, that failure in the weathered rock could not necessarily occur on joints/or discontinuities, which may result cemented by grouting.

Seismic action and fire occurrence are also taken into account as Accidental Limit State conditions.

Table 4. Re-evaluation of geotechnical properties due to ground improvements.

	untreated		treated	
Soil/rock properties	Rockfill	Weathered bedrock	Rockfill	Weathered bedrock
φ (°)	42	30	42	67
c' (kPa)	10	70	70	100

The pseudo-static analysis is used to consider the seismic input, as last numerical step. According to the Norwegian Public Road Administration Handbook N400 and Eurocode EN 1992-1-2, the effects of fire are considered by properly decreasing the strength concrete properties and a liner section reduction.

2.4 *Numerical results and rock support design*

Numerical analysis showed that the case n.2 is the most critical for the design of the shotcrete linings both for Ultimate Limit State and Accidentally Limit State. Total displacement for the critical cross section at km 8+135, where ground improvement is foreseen above the North Tube, are approx. 1 cm on the lining, and less than 8 mm on the road and slope (Figure 6). These values are not considered critical.

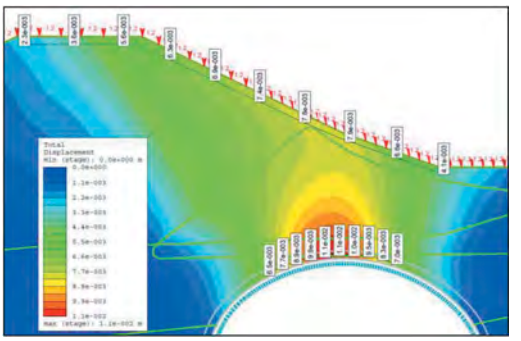

Figure 6. Total displacement above the North Tube, tunnel section km 8+135, case n.2.

Ultimate limit state verifications designed both tunnel sections, while spiles and tunnel front supports are calculated by analytical approaches based on the limit equilibrium methods (Anagnostou and Kovari, 1994). Rock supports for the North and South tubes are summarized in Table 5 and 6, and Tables 7 and 8, respectively.

Table 5. North Tube. Rock support (part I).

North Tube (class V)		
Shotcrete	Steel mesh	Radial bolts
FRC B35 E1000, thickness=250mm (150mm 1st layer; 100mm 2nd layer) + 600mm unreinforced shotcrete for RRS or lattice girders	1 x K335 (8/8; 150/150)	Fully grouted rock bolting φ25, L=4/5m, spacing transversal and longitudinal 1.5m

A longitudinal section of the North tube with the designed support is shown in Figure 7.

Eventually, the grouted schemes adopted for both tubes are represented in the figures below.

Table 6. North Tube. Rock support (part II).

North Tube (class V)		
Spiling	RRS or steel arches	Face support
Self-drilling hollow bolts* Titan 73/56, L=8m, transversal spacing=0.3m, longitudinal spacing=1.5m	RRS dimension D60/(6+4) Φ20, long. Dist.=1.5m or equivalent lattice girders	FRC B35 E1000, thickness=100mm Fiberglass bolts* Φ25, L=12.0m, overlap=6.0m, spacing 1.20x1.20m

**temporary safety measures.*

Table 7. South Tube. Rock support (part I).

South Tube (class IVb)		
Shotcrete	Steel mesh	Radial bolts
FRC B35 E1000, thickness=200mm (150mm 1st layer; 50mm 2nd layer) + 400mm unreinforced shotcrete for RRS or lattice girders	-	Fully grouted rock bolting φ20, L=4/5m, spacing transversal and longitudinal 1.5m

Table 8. South Tube. Rock support (part II).

South Tube (class IVb)		
Spiling	RRS or steel arches	Face support
Self-drilling bolts* φ32, L=6m, transversal spacing=0.3m, longitudinal spacing=1.5m	RRS dimension D40/(6+2) Φ20, long. Dist. =1.5m or equivalent lattice girders	FRC B35 E1000, thickness=100mm Fiberglass bolts* Φ25, L=12.0m, overlap=6.0m, spacing 1.20x1.20m

**temporary safety measures.*

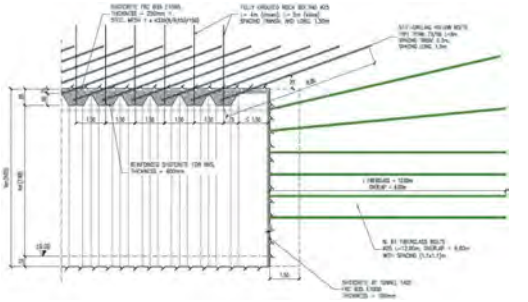

Figure 7. Longitudinal section of the North tube and designed rock supports.

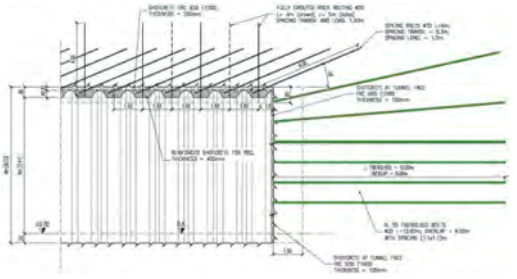

Figure 8. Longitudinal section of the South tube and designed rock supports.

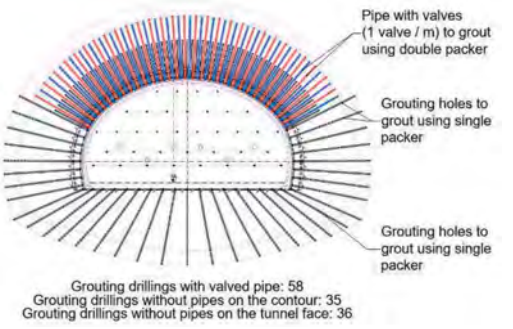

Figure 9. North tube: grouting scheme.

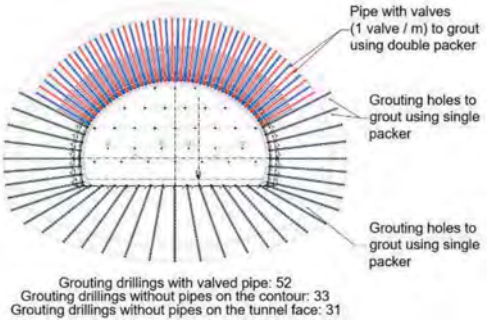

Figure 10. South tube: grouting scheme.

3 FAULT ZONE SECTION

The design of the second relevant section of Drotningsvik Tunnel is described in this chapter: specific solutions issued from numerical modelling were required to overcome the advancement in critical geotechnical conditions. In particular, surveys from in-situ core drillings, together with surficial mapping of local geology, induced to consider a subvertical fault zone, with a longitudinal extent of weathered and highly fractured rock mass estimated at 20-30 m. This portion of the main tubes is located around 550 m western than Kiplevatnet area and it is to be excavated later – being the advancement direction from East to the West. In the following, numerical modelling is described and permanent lining solutions are presented.

3.1 *General overview*

The current designed support is expected for a maximal extension of 30 m. It is located between two junctions, connecting each main tube with the relative exit ramps. These two large sections are, in general, expected in good quality rock mass with reduced fracturing. On the contrary, the small valley/rift in between includes a zone with an extended peatbog – see indications in Figure 11. Core-drillings in this area show evidence of a significant core loss, highly fractured rock with infillings below the foreseen overburden of main tunnels, equal to 35 m. Figure 12 reports the retrieved rock cores from -40 to -50 m below the ground surface, at the kilometric point 7+590 of the project chainage.

Figure 11. Plan view of presumed fault zone section.

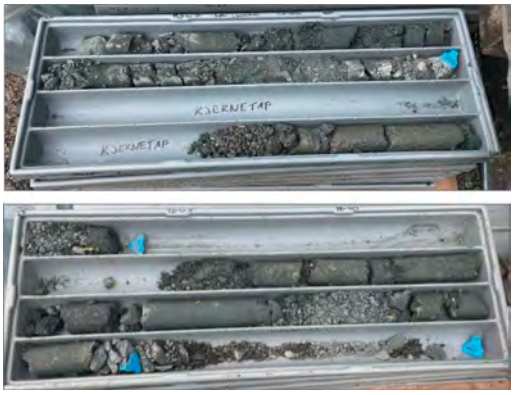

Figure 12. Retrieved core-drillings from Plan view of presumed fault zone section.

3.2 *Main challenges and geotechnical characterization*

The analysed tunnel portions are characterized by the absence of nearby structures and a regular terrain profile in the transversal section. Nonetheless, the extremely poor conditions estimated for the surrounding bedrock constitute the main challenge for tunnels advancement in this area. Q-system

defines a rock mass quality of class G, defined as *exceptionally poor*. Within these conditions, NGI's Handbook for geotechnical modelling based on the Q-system (Using the Q-system, NGI, 2015) attributes a Q value equal to 0.005: this class requires necessarily a special evaluation for excavation and lining design (e.g., by numerical modelling), overcoming the empirical indications of NGI's Rock Support Chart. With the Q-value defined above and laboratory data on undisturbed rock matrix (e.g., σ_{ci}), a Mohr-Coulomb failure criterion is estimated via RocData v5.0, for a tunnel case at 35 m of overburden, assuming the following geotechnical parameters (Table 9).

Table 9. Geomechanical properties of the rock mass.

	Exceptionally poor rock mass – Class G
γ (kN/m^3)	27
φ (°)	30*
c' (kPa)	100
E (MPa)	500
v (-)	0.20
Ψ (°)	0
Q (-)	0.005

**Due to the high presence of joints, friction angle was taken equal to that of clayey infilled material, assuming preferential failure mechanisms along these discontinuities.*

Together with the surrounding weak geotechnical conditions, the risk assessment conducted before the Detailed Design phase reports a high risk of swelling potential for clay minerals, if rock mass conditions show a favourable environment. Considering the actual fracturing, a swelling pressure acting permanently on the outer lining was taken into account and assumed equal to 500 kPa, according to available data of confined swelling tests on local amphibolitic gneiss.

Besides the particularly weak properties of the bedrock at this location, general design is further challenged by the enlargement of the South main tube section and the presence of the Northern ramp. Concerning the first point, the standard section foreseen in main tubes must be widened to an upper class of typological geometry (according to the reference Tunnelling guidance – Håndbok N500 *Vegtunneler*): this aspect requires a front opening which cannot be executed in full section. Numerical modelling had also to include the study of a suitable section division with proper safety measures for the first excavation. Concerning the second topic, the excavation and lining of the Northern ramp must be also included: it stretches from kilometric point 7+668 in the East-West direction and it crosses the potential fault zone northern to the North main tube – see Figure 11 with the identification of each tunnel.

3.3 *Numerical modelling*

A finite element (FE) model of the transversal section has been developed in PLAXIS 2D v.2023.1 (Bentley Systems Inc.), under plane strain conditions. According to the Tender Design phase, three typological tunnel geometries have been considered, respectively, for the South main tube (Eastbound), the North main tube (Westbound) and the Northern ramp, with different values of transversal span at the excavation perimeter, resumed in Table 10.

Table 10. Tunnel sections and front excavation design.

Designed tunnels	Max. longitudinal span [m]	Front opening
South main tube	18.80	Partialized
North main tube	13.50	Full section
Northern ramp	10.05	

A wide extension was attributed to the numerical model (400 m x 150 m) to prevent boundary effects. Boundary conditions were imposed preventing horizontal displacements along the vertical sides and vertical displacements at the lower model limit. Surrounding rock mass was discretized by 9′170 triangular 15-noded mesh elements and 76′100 nodes, properly densified around the excavations. An elastic-perfectly plastic Mohr-Coulomb criterion was assumed as constitutive law, with stiffness and shear strength parameters reported in Table 9. A gravity field stress is considered to define the in-situ stress state, assuming for this rock mass an initial earth pressure coefficient $k_0 = 1.5$ (e.g. Simonsen and Li, 2019). Besides acting on the safe side for the design of structures, this value is also considered more suitable for this higher overburden (35 m), compared to k_0 adopted for Kipledalen Section – see Table 2. As detailed in section 3.4, the initial k_0 value, together with the general poor rock quality and swelling potential in permanent condition led to include, for each section's opening, the excavation and support design of an invert, in order to prevent overloads at the sidewalls.

Table 11 resumes the model general phasing, while Table 12 and Table 13 include, respectively, the detailed excavation and advancement in full section and in partial section mode – with values of applied deconfining ratios.

In general, Table 12 and 13 both indicate that front advancement is foreseen at most 6 m ahead of the invert. Figure 13 shows FE model of the cross section. In the following, Figure 14 provides the details of partial openings for the South main tube.

3.4 *Numerical results and rock support design*

The FE model showed that invert yielded as crucial to verify Ultimate and Serviceability Limit states for each section: a proper design of its distance relatively to the front advancement was essential to

Table 11. Finite element model steps.

Step	Description
1	Initialization with a uniform superimposed dead load = 20 kPa (assuming worksite's engines).
2	North tube excavation and permanent support installation. See Table 12 for detailed design of opening in full section.
3	South tube excavation and permanent support installation. See Table 13 for detailed design of opening in partial section.
4	Norther ramp excavation and permanent support installation. See Table 12 for detailed design of opening in full section.
5	Uniform load activation = 500 kPa around outer lining simulating the swelling pressure in permanent conditions.

Table 12. Phasing in full section excavation.

Phase	Description
1	Front opening (except invert) + 1.5 m of unsupported length: $\lambda = 60\%$
2	Lining installation – see details in section 3.4
3	Repetition of Phase 1 reaching 4.5 m of supported excavation + 1.5 m of unsupported length: $\lambda = 80\%$
4	Invert opening for 4.5 m + 1.5 m: $\lambda = 80\%$
5	Invert lining – see design details in section 3.4: $\lambda = 100\%$

Table 13. Phasing in partial section excavation.

Phase	Description
1	Partial front opening + 1.5 m of unsupported length: $\lambda = 60\%$.
2	Lining installations: permanent on the outer perimeter and temporary on the inner wall to be demolished – see Figure 14a.
3	Repetition of phases 1+2 along the entire fault zone: $\lambda = 100\%$.
4	Full front opening (except invert) with 1.5 m of support + 1.5 m of unsupported length: $\lambda = 65\%$ within the excavated volume – see Figure 14b.
4	Invert opening with 1.5 m of support + 1.5 m of unsupported length: $\lambda = 65\%$ within the excavated volume – see Figure 14c.
5	Invert lining: $\lambda = 100\%$.

assure the short-term front stability – with the initial opening excluding systematically the invert volume. Meanwhile, the invert guarantees the long-term static verification of the entire retaining structure, reducing load concentrations at the sidewalls base.

Table 14 in the following resumes the maximal forces calculated in the lining, both for Ultimate and

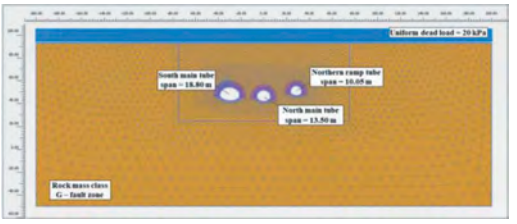

Figure 13. Bidimensional FE model and geometry loads.

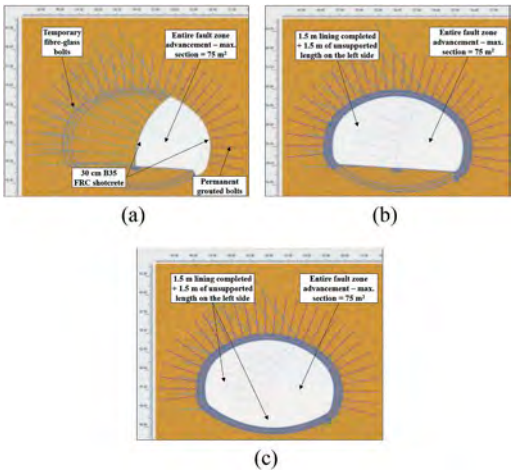

Figure 14. Partial excavation phasing for South main tube.

Serviceability Limit states, together with the efforts in concrete and steel rebars. No cracking was evaluated in any lining part. Numerical analysis confirms that South main tube results the most loaded section.

Table 14. Maximal forces and efforts in permanent lining.

In-lining acting forces	Limit States Ultimate	Serviceability
Axial force, N (kN)	17′800	13′180
Bending moment, M (kN.m)	3′080	2′280
Shear force, V (kN)	950	705
Efforts in concrete and reinforcing bars (Serviceability Limit state)		
Concrete compression (MPa)	20.3	
Steel compression (MPa)	125	
Steel traction (MPa)	106	

Contour plot of total displacements after swelling pressure activation is shown in Figure 15:

Design modelling calculates relatively high displacements around tunnels, in particular occurring before lining installation, while the unsupported advancement of 1.5 m length occurs. Even if maximum displacements are equal to 43 and 78 mm,

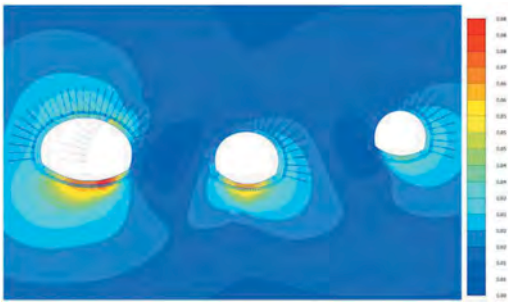

Figure 15. Total displacement around tubes at kilometric point 7+590.

respectively in vault and invert of South main tube, relative lining displacements are estimated equal to 13 and 7 mm, thus respecting imposed limits on vertical deflexions (Tunnelling guidance – Håndbok N500 *Vegtunneler*). Nonetheless, total displacement values overmentioned should be taken into account during drill and blast operations at the advancement. Concerning surface settlements, a displacement of about 1 cm is calculated, which does not constitute any particular vulnerability due to the absence of nearby structures.

Table 15 and Table 16 resume the design for permanent rock support for the fault zone crossing. As done for Kipledalen section, spiles and front supports (i.e., fibre-reinforced shotcrete, fiberglass bolts) are dimensioned by analytical approaches based on the limit equilibrium methods (Anagnostou and Kovari, 1994).

Table 15. Fault zone rock support (part I).

Shotcrete	Steel mesh	Radial bolts
FRC B35 E1000, thickness=300mm (100mm 1st layer; 100mm 2nd layer; 100mm 3rd layer) + 600mm unreinforced shotcrete for RRS or lattice girders	2 x K335 (8/8; 150/150)	Fully grouted rock bolting φ25, L=5m, spacing transversal and longitudinal 1.0m

A longitudinal section of the Fault zone lining solution, applied to the South main tube with divided section, is shown in Figure 16.

4 WORKSITES ADVANCEMENTS

The excavation of the Kolltveit tunnel started in July 2023 from West to East (Figure 17-a-b), and the completion of both North and South tubes is scheduled by April 2024. The Drotningsvik tunnel

Table 16. Fault zone rock support (part II).

Spiling	RRS or steel arches	Face support
Self-drilling bolts* φ32, L=6m, transversal spacing=0.2-0.3m, longitudinal spacing=1-2m	RRS** dimension D60/(7+5) Φ28, Base = 1.5 m laying on shotcrete. Dist.=0	FRC B35 E1000, thickness=100mm Fiberglass bolts* Φ25, L=20.0m, overlap=10.0m, spacing 0.70x0.70m

* *temporary safety measures.*
** *RRS applied to vault, sidewalls and invert – see Figure 16.*

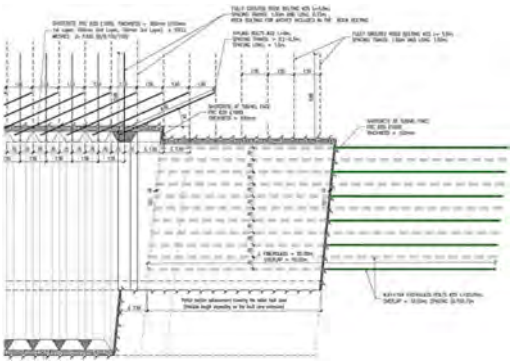

Figure 16. Longitudinal section of the designed solution.

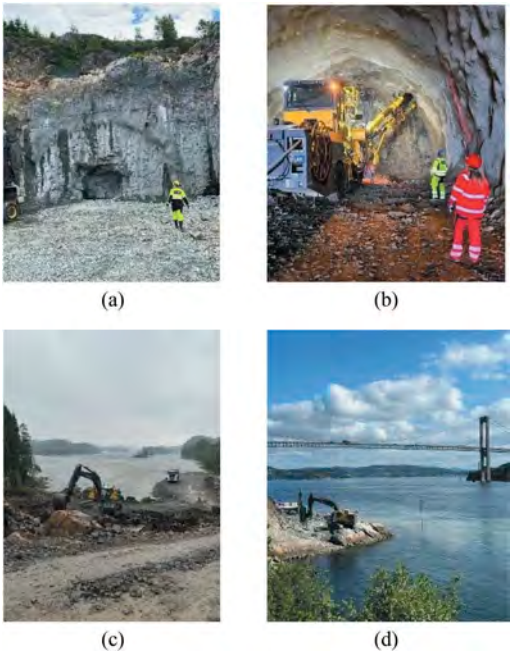

Figure 17. (a) View of Westbound West portal and (b) drill & blast excavation of the Kolltveit tunnel. (c) Filling works of the Storavatnet lake. (d) View from the Knarrvika side of the realization of the foundation of new Sotra bridge.

is currently under excavation, and it will be completed by August 2026, while the realization of the tunnel ramps started in 2024 in order to be completed by June 2026. Rocks excavated from the blasting of the Drotningsvik tunnel portals have been partially used to fill the Storavatnet lake (Figure 17-c). In March 2023 works for the foundation of the new bridge on Knarrvika side started (Figure 17-d), while the completion of the suspended structure is foreseen by September 2026. The excavation of the Straume and Knarrvika tunnels is scheduled to start in 2024 to be completed by March 2026 and July 2025, respectively, including the access portals.

5 CONCLUSIONS

The main geotechnical challenges and the tunnelling experiences gained during the design phase of some relevant underground structures for the Sotra Link Project are presented in this paper. Numerical modelling was a key tool to simulate many excavation phases in heterogeneous rock-masses allowing the evaluation of the potential impact of the excavation works on nearby structures. A comprehensive monitoring system during the construction of all the surface and underground structures will allow to confirm the assumption made during the design phase and eventually permit optimizations, with a reduction in project costs. Currently, the modelling and delivery tasks are in line with the project scheduling. The PPP contract was awarded in September 2021 for a total value of about 2 billion €. The design phase of the whole project is expected to finish in 2024, and the infrastructure will be opened in 2027.

REFERENCES

Anagnostou, G., Kovari, K., 1994. The Face Stability of Slurry-shield driven Tunnels, Tunnelling and Underground Space Technology, vol.9(2), Elsevier (Eds.), pp. 165–174.

Barbieri, G., Giani, M., De Panicis, E., et al, 2023. BIM and tunnelling - a Norwegian application: the Sotra Link Project, ASET & Avestia Publishing (Eds.) – Proceedings of the 8th International Conference on Geotechnical Research and Engineering (ICGRE 2023), Lisbon, Portugal, pp. 1–7.

Barbieri, G., De Panicis, E., Bella, et al, 2024. The Sotra Link Project (Norway): application of the BIM methodology in tunnelling design and construction, (Eds.) Proceedings of the World Tunnel Congress (WTC2024), Shenzhen, China, pp. 1–6.

Barton, N., Lien, R., Lunde, J., 1974. Engineering classification of rock masses for the design of tunnel support. In: Rock Mechanics and Rock Engineering, vol. VI, Springer Verlag, pp. 189–236.

EN 1992-1-2: Eurocode 2: Design of concrete structures.

Håndbok N400 Bruprosjektering (Bridge design). Statens vegvesen Vegdirektoratet (Norwegian Public Road Administration), 2015. ISBN: 978-82-7207-680-0.

Håndbok N500 Vegtunneler (Tunnelling guidance). Statens vegvesen Vegdirektoratet (Norwegian Public Road Administration), 2016. ISBN:978-82-7207-697-8.

ISRM (1978): Suggested methods for the quantitative description of discontinuities in rock masses. International Journal of Rock Mechanics, Mining Sciences & Geomech. Abstr. 16(3), pp. 319–368.

Norwegian Geotechnical Institute (NGI), 2015. Using the Q-system. Rock mass classification and support design.

Opsal, O.L., 2017. Shear strength of dry tills from the southern half of Norway in relation to bedrock geology. Norwegian Journal of Geology, vol.97(2), pp. 145–169.

Simonsen A.L.L., Li C.C., 2019. Updated In Situ Rock Stresses in Norway Based on Recent Estimations and Measurements. Institutt for geovitenskap og petroleum, Norges teknisk-naturvitenskapelige universitet (NTNU). CRC Press.

Webuild Value Digital Magazine, “Norway’s record-setting plan for the roads of tomorrow” (Online). 2022. Available from: Norway highways: a new complex road project - We Build Value.

Tunnelling for a Better Life – Yan, Celestino, Thewes & Eberhardt (Eds)
© 2024 The Author(s), ISBN 978-1-032-80042-4
Open Access: www.taylorfrancis.com, CC BY-NC-ND 4.0 license

(I)-TM: I-System's tunnelling method – four years of application in most challenging ground in India

H. Bineshian*
Principal, Technical Director, Amberg Engineering AG, Australia

ABSTRACT: This paper is a brief technical note on (I)-TM; I-System's tunnelling method, a hybrid method that contains integrated classification and characterisation systems. This feature has made (I)-TM an all-in-one package for underground works from pre-design to post-construction phase. Due to having integrated I-System, it borrows the feature of being applicable for any medium under any condition. Classification and characterisation in pre-design using I-System assists in ground zoning along tunnel alignment, ground behaviour identification for each zone, diagnosis of associated ground hazards, determination of required support systems for each zone, structural dimensioning, and finally structural verification of design. In construction, employment of I-System enables designer to prescribe required measures and to optimise the design while post-excavation damage is assessed and required precautionary action prescribed. (I)-TM proposes suitable excavation technique with safe pull length, active support system configuration for optimised stability, efficient instrumentation technique for monitoring, intelligent prevention technique for avoiding and controlling hazards, and high-performance forecasting technique for prediction of ground ahead of tunnel face for a safe and optimised advance. This paper is a brief outcome of 4 years application of (I)-TM in design and construction of most challenging tunnels in India including T01 of USBRLP.

Keywords: (I)-Class, (I)-GC, (I)-TM, I-System, SRH, ViD

1 INTRODUCTION

A tunnelling method is an approach, which is used in the construction of underground structures. It should be applicable in both rock and soil under any challenging ground condition. A tunnelling method must be backed with a strong concept to assist in design procedure proceeded by construction that makes the tunnelling optimised in terms of cost, time, and safety for the desired life of structure. However, existing tunnelling methods are unclear in their approach and most of them remained as a hypothesis only; they are referred to as an excavation technique (ET) or as a supporting technique; though, they must shoulder a greater responsibility than that of being functioned. It has not been well defined how to employ existing tunnelling methods; besides, they failed to be trusted for application in all media and under all conditions due to their limitations. It is expected, a tunnelling "method" to provide a procedure for accomplishing construction of tunnels systematically but none of the existing tunnelling methods having this feature. Uncertainties in definition of the tunnelling methods forms different understanding for designers, engineers, and geologists that causes misapplication. In some countries, tender documents of tunnelling projects are floated based on the name of some particular methods of tunnelling for execution while the definition of the method is not understood by the clients and it remained unclear for contractors. Some of the existing methods are based on valuable concepts but as they lack in a clear approach for application, they remain as theory. Contrary, some other methods having an approach in execution but their concept is not comprehensive enough to make them suitably applicable for all types of media in which the tunnels are placed; therefore, they make the tunnelling procedure costly and inefficient. (I)-TM (Bineshian, 2022a) is proposed as a practical tunnelling method to overcome the challenges involved with existing tunnelling methods' incomprehensible concept and incomplete approach. (I)-TM includes concept and approach that makes it applicable for tunnelling in any medium under any condition with an accurate evaluation and precise recommendations that can be

*Corresponding author: DrBineshian@outlook.com

DOI: 10.1201/9781003495505-24

applied from pre-design to post-construction phases. In full form, (I)-TM is I-System's (Bineshian, 2019, 2021b) Tunnelling Method that is fully based on I-System's (index of ground-structure) classification and characterisation. This paper aims to provide an outcome of employment of (I)-TM since its first introduction in 2019, including T01 of USBRLP (Mahi et al, 2022).

2 TUNNELLING

2.1 *Tunnel Excavation Techniques*

Excavation Techniques (ETs) in tunnelling are not same as tunnelling methods. ETs are employed in tunnelling methods as an important part and can be categorised into 4 main types; Manual, Mechanised Excavation (ME), Drill and Blast (DnB), and Open Cut (OC). Manual excavation includes partial-sequential digging (PSD) and/or partial-sequential excavation (PSE) using manual tools for small- to medium-scale openings respectively in multiple sequences without the use of explosives maintaining the stand-up time and maximum unsupported span in a safe range; e.g., pilot and enlargement, heading and benching (HnB), etc. ME includes medium- to large-scale excavation using machines (e.g., continuous-miner, excavator, hydraulic-hammer, roadheader, rotary drum cutter, shearer, TBM, etc.) without explosives. It is employed when the ground is poor and blasting is not advisable. It also can be employed when the ground is competent but excavation machineries result in better performance in excavation than blasting. DnB is the most common technique for small- to large-scale excavation of tunnels using parallel-, V-, or angle-cut. Only controlled or engineered blast should be employed in DnB for tunnels; uncontrolled blast in tunnelling is destructive, which deteriorates the rock mass and downgrades the ground class, damages the structure in vicinity, generates hazards, increases the cost, and affects the safety. OC is employed in tunnelling when overburden is shallow. It is used for semi-surface spaces executed from surface of ground. OC is applicable in semi-surface metro stations and shallow tunnels executed from surface. Sequential Excavation Method (SEM) is a "method of excavation" employed in tunnelling rather than a "tunnelling method", which can be used in either Manual, ME, and DnB.

2.2 *Tunnelling methods*

A tunnelling method is an approach having a concept for optimised design and a procedure for safe construction. They are categorised using two bases; the medium in which the tunnels are constructed in (including rock-, soil-, and underwear-tunnelling) and the concept that they are developed based on (including civil- and mining-tunnelling) (Bineshian, 2022a). Rock tunnelling is used for construction of tunnels at any depth in rock mass that includes any concept-based tunnelling method. Employment of ETs depend on concept of method, site condition, and availability of skilled team, materials, equipment, and machinery. Main hazards involved with rock tunnelling generally include gravity-driven, time dependant, block fall, and rock-burst behaviour. Its concept is to utilise rock mass capacity under active load conditions by employment of active measures. Soil tunnelling is used for construction of tunnels in a granular and porous medium. Except DnB, all other ETs can be employed in soil tunnelling. Soil tunnelling like rock tunnelling can include any tunnelling methods. Main hazards in soil tunnelling include gravity-driven failure, slush flow, and settlement in large openings. Soil tunnelling concept is based on stabilisation of ground under passive load and consequently utilisation of passive measures; however, the design is quite inefficient if the arch pressure effect is neglected. Underwater tunnelling including but not limited to IMT (Immersed- tube Tunnel) is referred to as methods for tunnels on/under the bed of sea, river, ocean, lake, etc. that overburden is an individual column of water or water column + ground overburden. ET can be chosen in a similar way for rock and soil tunnelling. Hazards involved with rock and soil tunnelling are applicable for underwater tunnelling. Civil tunnelling is a group of tunnelling methods based on permanent life concept employed in civil works rather than mining. Civil tunnelling generally includes; Conventional, CnC, NATM, NMT, Pipe/box jacking, and SCL. Conventional tunnelling's concept is mainly based on an assumption of a passive stress state. A system of stiff support measures designed for the worst scenario of load is used to absorb the passive load; the same is applied along the entire length of the tunnel. DnB and/or ME is used as ET while in smaller cross sections or in challenging conditions, Manual excavation is applied. Typical sequences employed is; 1- heading excavation in a short pull, 2- placing rigid ribs, 3- lagging, 4- backfilling, 5- applying further measures at heading, 6- execution of drainage system at heading, 7- benching excavation, 8- installation of rib-legs, 9- invert excavation, and 10- ring closure. CnC tunnelling is usually used in soil in the urban areas. Load configuration in design of structure is the combination of live and passive loads from surface. Typical CnC sequences include construction of; 1- concrete diaphragm walls, 2- pin piles, 3- decking, 4- open cut excavation within the span of diaphragm walls, 5- traverse struts, 6- final concrete floor, 7- final concrete walls, 8- final internal structure fitting/s, 9- backfilling, and 10- surface restoration. NATM is used for deep conditions like mountain tunnels. It is based on maintaining the load-bearing capacity of ground and minimising support needs. Due to lack of any clear sequences or stages in NATM it is better to be called a "tunnelling concept" rather than a "tunnelling method". It is

crucial to understand the mechanical behaviour of ground before opening and monitoring after opening. Consequently, support measures are optimised based on mechanics of the ground, geomechanical hazards that may be encountered with, and pre- and post-excavation observation/s. The observation/s is based on sophisticated instrumentation and monitoring of displacement, deformation, strain, and stress. Moreover, regular face mapping, probing, and exploratory holes are conducted to obtain correct input data to classify and evaluate the ground and finally to identify the failure mechanism/s and associated geomechanical hazards. NMT is developed for hard rock while uses Q for classification and employs cross-hole seismic tomography for characterisation. It does not employ a new concept in tunnelling and actually it is similar to NATM for hard rock. The excavation method employed is DnB and ME. Like NATM, it is based on ground-support interaction evaluation. Unlike NATM, the application of monitoring or instrumentation techniques is only required in critical cases as it is developed for hard rock that may not need a monitoring system. Primary and final supports are fibre reinforced shotcrete (FRS) and fully grouted corrosion protected rock bolts; however, in poor to very poor grounds, it may be supplemented by pre-excavation grouting, crown spiling, and encased rib in shotcrete. Primary supports are part of final support system. It is not suitable to be employed for time-dependent behaviour such as squeezing, swelling, and heaving, as a thick layer of load-bearing ring of FRS or encased rib is rigid enough to stop controlled deflection, while load is accumulated behind the measures due to ground response that may cause sudden collapse. Pipe jacking or box jacking is based on installation of steel tubes with diameters usually between 1000 and 7000 mm. It is usually employed in soil or soft rock in the urban areas to prevent disturbing the surface traffic or considering other conditions/limitations. Key elements in pipe jacking include end shafts/pits, thrust walls, and pipe/box segments. In this technique pipes/boxes are pushed through the ground from the end shafts/pits. Thrust wall in the end shafts/pits is used to produce reaction forces during jacking. The main concept in this method is to maintain the virgin stresses untouched; thus, less deterioration is applied after jacking; therefore, induced stresses are not generated or the underground space is less disturbed. The ground material is removed using Manual or ME. SCL is described as NATM in Europe or SEM in North America. Shotcrete is the main support. Plain or reinforced cast-in-situ final lining may be used. Main sequences in SCL comprises; 1- SEM followed by immediate shotcreting, 2- drilling drainage holes, 3- instrumentation/monitoring, 4- invert closure (soft ground), and 5- further support measures (if required). SCL is classified into 3 categories; single shell lining (primary and final in one shell), double shell lining (primary + final), and composite shell lining (primary + waterproofing membrane + final). Depending on thickness and stiffness of the lining, deformation of ground can be allowed to release the load behind the primary lining around the periphery of tunnel; however, by increasing stiffness of final lining, deformation can be controlled to prevent deflection and consequently to prevent failure caused by strain softening. Like NATM, SCL is not recommended in shallow conditions due to passive load and short stand-up time. It is not suitable for tunnelling in plastic medium due to occurrence of excessive deformation and loosening bond strength between particles of ground; the result is gravity-driven failure or slush flow in presence of water. Mining tunnelling is a group of underground methods developed for extraction of ore from ground. Mining tunnels mainly include access tunnels, adits, caverns, drifts/strikes, exploration tunnels, extraction tunnels, galleries, haulage tunnels, shafts, stopes, ventilation/wind tunnels, and winzes. Unlike civil tunnels, their life is considered to be short/temporary depending on volume and value of ore to be extracted and usually it is less than that of considered life for civil tunnels. It is influenced by concept of temporary use and lowering cost of tunnelling to improve margin of benefit out of extraction. Mining tunnelling employs temporary support; however, most of measures used in civil tunnels are invented in mining tunnelling method. ETs in mining are generally DnB, Manual, or ME. DnB in mining is not as costly as it is in civil tunnelling as less control is applied.

3 (I)-TM: I-SYSTEM'S TUNNELLING METHOD

3.1 *Design approach and design procedure*

A design approach in tunnelling contains four phases; empirical, theoretical, seismic, and observational that are dependent on ground classification and characterisation (Figure 1a). Design procedure defines tunnel design in seven stages as shown in Figure 1b. By completion of the design procedure, tunnel's design is complete and it is ready for implementation; however, a tunnelling method is required for construction, but the design outcome would be more accurate and appropriate if the design procedure started based on a tunnelling method. Tunnelling method should have a comprehensive concept and principal components to make the implementation of the design practicable in a safe and efficient manner in the medium in which the tunnel is designed for and under the condition/s that it is predicted to be faced with. In absence of a right tunnelling method, tunnelling procedure may differ from the design's output and perceptions that it was based on. This is happening in tunnelling works due to mismatch between the design and practice because of complex of challenges and varieties of surprises and difficulties involved with underground works. Instead,

a comprehensive tunnelling method can properly address them and tie its concept with the design procedure. It means that only having initial investigations and studies or predictions for mechanical properties of ground as input is not enough for a good for construction design in tunnelling while one of the important inputs prior to design is to have a comprehensive tunnelling method in mind that matches the design with its principal components. Thus, a tunnel design procedure in a healthy design approach is quite dependent on a tunnelling method's concept, which is comprehensive enough to direct the design as well as construction. The proposed design procedure (Bineshian, 2021a) explained here is fully dependent on I-System, which provides a detailed classification and characterisation for underground as well as surface and semi-surface structures. I-System's output for underground structures is a tunnelling method, which is called (I)-TM (Bineshian, 2022a).

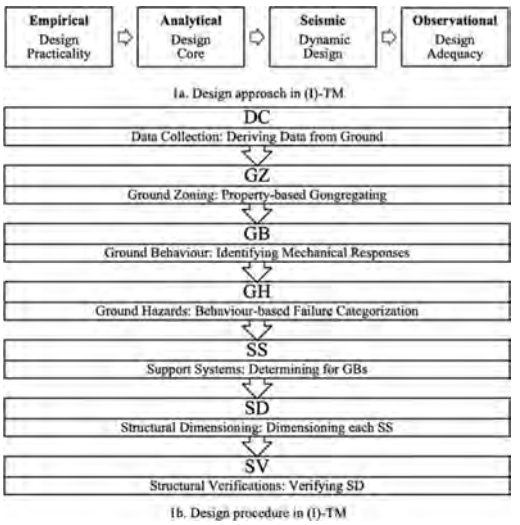

Figure 1. Design approach and design procedure in (I)-TM.

3.2 *Application of (I)-TM*

None of the existing tunnelling methods are comprehensive enough to be employed for all media and under all conditions. (I)-TM has been developed to address these issues and limitations. (I)-TM is applicable for rock and soil tunnelling, civil and mining tunnelling, and practicable under any challenging condition and ground behaviour including but not limited to time-dependent, squeezing, swelling, heaving, plastic, visco-elastoplastic, burst prone, gravity-driven, under water table, etc. from pre-design to post-construction phases (Figure 2). It assists in saving in cost by providing optimised practical design and does not neglect effect of primary measures in final design. It is a hybrid tunnelling method, which combines I-System's classification and characterisation with construction method all together for a comprehensive range of applicability and ease of use in pre-design, design, construction, and post-construction phases.

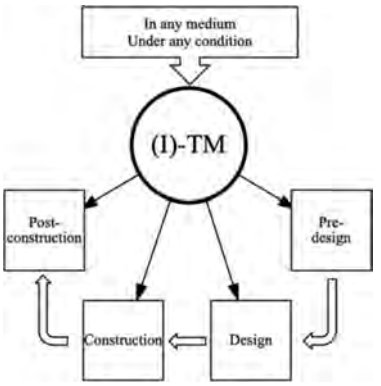

Figure 2. (I)-TM's application.

3.3 *Concept of (I)-TM*

The concept of (I)-TM includes a comprehensive range of components to facilitate with achievement of optimised design and construction of tunnels and underground spaces by means of engaging following ten important aspects (Figure 3 a and b):

1. Comprehensiveness in application
2. Permanent life expectancy for tunnel structure
3. Flexibility of contract to ease construction management and variation of quantities
4. Utilisation of surrounding ground's load-bearing capacity
5. Assumption of arch pressure effect for any depth
6. Controlled release of deformation in plastic ground
7. Primary measures as part of final measures
8. Using I-System in design procedure
9. Employing I-System in construction
10. 10-Post-excavation damage assessment to minimise induced deterioration (e.g., ViD; Bineshian, 2021c)

A brief list of recommendations proposed by I-System in its (I)-Class outputs for underground spaces, which is employed in (I)-TM when ground is indexed (classified and characterised using I-System) is provided here:

I. Active pre-/post-excavation support system (SS):
– Pre-excavation measures including systematic horn-bolting, crown periphery spiling, forepoling, piperoofing, pre-excavation grouting/injection, face bolting, etc. to control the stress state ahead of face, to utilise arching effect, and to

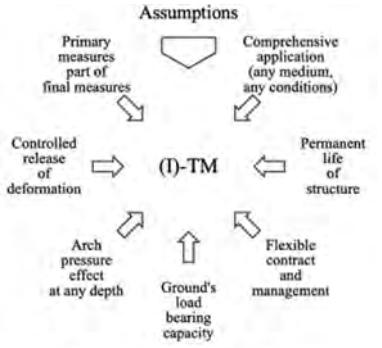

3a. Main assumptions implemented in (I)-TM

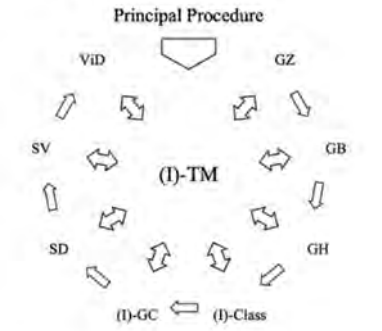

3b. Principles of method in design and construction procedure

Figure 3. Main concept in development of (I)-TM.

increase stand-up time for application of post-excavation measures.
- Post-excavation measures including systematic bolting, rigid-ribs, lattice-girder, FRS, drainage holes, SRH (Bineshian, 2020), etc. - rather than a passive system - to stabilise the opening.
- Ring closure or invert closure to make a full load-bearing ring to improve the load-bearing capacity of surrounding ground when the ground is weak and requires further assistance at right time.
- Mechanism of a thin elastic shell using application of a layer of FRS immediately after opening or as a post-advancement load-bearing shell that reduces the deflection of the underground space under loading when crown deflection should be prevented.

II. Provision of suitable ET and advice on safe pull length by I-System that suits the assessed condition that is compatible with proposed support systems (SS) to obtain a safe and optimised advance at face. PSD and PSE technique/s are proposed to reduce deflection at crown or at walls and to maintain stand-up time when full-face or heading and benching (HnB) does not work efficiently due to scale effect or weak ground properties and existence of passive response of ground-structure.

III. Use of efficient instrumentation technique (IT) for monitoring of ground-structure's mechanical response to excavation-induced stresses and deformations/deflections and to provide required support measures in terms of type and dimensioning to modify requirement/s as per observations before and/or after excavation and application of measures in an optimised manner in a suitable period and right time based on diagnosed hazards (GH) and identified ground behaviour (GB).

IV. Application of intelligent prevention technique (PT) to avoid geomechanical hazards, which is essentially predicted based on the ground behaviour by I-System.

V. Exploitation of high-performance forecasting technique (FT) including geophysical systems (e.g., Electrical Resistivity Tomography, Multi-channel Analysis of Surface Waves, Seismic Refraction Tomography, Tunnel Seismic Prediction) and/or probing (e.g., drilling blind holes and logging) and/or coring systems (e.g., exploratory coring to log the encountered strata ahead of the tunnel face) to predict the geomechanical condition ahead of face to prevent surprise incidents and to get ready for challenges ahead.

Technical proposals and recommendations provided in I to V are included in (I)-Class's outputs when I-System is used for classification and characterisation of ground at face of tunnel or underground space. (I)-Class and (I)-GC are I-System's outputs for classification and characterisations respectively (Bineshian, 2021b). I-System is embedded in (I)-TM, which is employed also in pre-design, design, construction, and post-construction phases that forms the principles of (I)-TM. Observations and re-evaluations to optimise the ongoing work and revising the design is a regular practice in (I)-TM that should be repeatedly conducted till the work is completed (Section 3.4) to improve the efficiency and performance of tunnelling.

3.4 *Utilisation diagram of (I)-TM*

(I)-TM is an intelligent tunnelling method, which is employed from pre-design studies to end of construction and even after construction during the exploitation period for maintenance planning and resolutions for probable incidents. Its examined concept comprises a comprehensive design approach and an extensive range of practical solutions for a safe and optimised execution as an "all-in-one" package for tunnelling in any media and under any challenging condition. It is developed to be employed for tunnelling at any depth (shallow to deep), in any ground type (rock to soil), through any medium with various mechanism (continuum-, discontinuum-, or porous-mechanics), with any physical features (isotropic, anisotropic, homogenous, or heterogeneous), and under any condition and challenges (underwater, plastic, brittle, ductile, burst-prone, time-dependent, etc.). Tunnelling using (I)-TM is proved to be safe and optimised when I-System is applied and design is well-reviewed/revised as per observations, assessments,

and outputs of I-System during the construction phase. Derivation of the input data from ground (face of tunnel or underground space) is important and determinative due to its effect on accuracy of outputs of I-System; however, required data for I-System is confusion-free and easy to derive (Data Collection (DC) in the design procedure. (I)-TM's performance in design and practice is examined in tunnelling works in India. Utilisation flowchart of (I)-TM for design and construction phase is presented in Figure 4.

Utilisation of (I)-TM in construction is as followings:

1. Apply I-System for fresh face at tunnel to evaluate ground-structure condition (this is called indexing the face or classification and characterisation of the ground)
2. Advance at face and implement the recommendation/s of (I)-Class or use (I)-GC estimates for design revision
3. Repeat the steps 1 and 2 and advance at tunnel or underground space's face for one more pull.

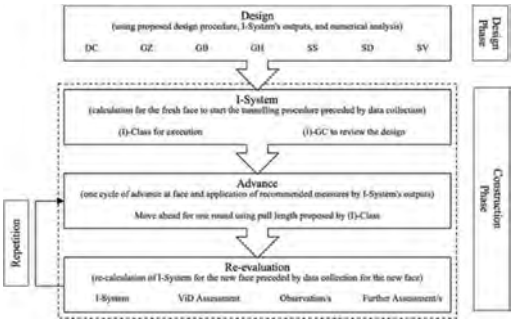

Figure 4. (I)-TM flowchart for design and construction phases.

3.5 *I-System: Index of ground-structure*

I-System as the first-ever classification that is applicable in both rock and soil medium, takes into consideration the most important features of ground-structure (Figure 5a) while it provides an accurate and precise prediction for ground behaviour for varieties of challenging conditions (Figure 5b). It has been verified against varieties of ground conditions to ensure that its outputs are credible (Bineshian, 2021b). It includes five key indices and two impact factors to enable appropriate modelling of ground-structure mechanical response to the full (Figure 6a) that is based on easily derivable main properties (key geomechanical, geostructural, geohydrological, geotechnical, geophysical, and geometrical features) and determinant seismic and excavation factors affecting the ground-structure response (Figure 6a). (I)-Class and (I)-GC are demonstrated in Figures 6b and 6c respectively. I-System Software is developed as an engineering package for calculation of (I), classification of ground with (I)-Class, and characterisation of ground properties with (I)-GC. I-System Software also assists in (I)-TM with further utilities for configuring the systematic bolting, advising for the safe pull length in advancing at a face, measuring the GCD as ground conductivity designation (Bineshian, 2022b), identifying Squeezing, Swelling, and Heaving (SSH) ground from non-SSH ground (Bineshian, 2020), and assessing ViD (Bineshian, 2021c) as vibration-induced damage.

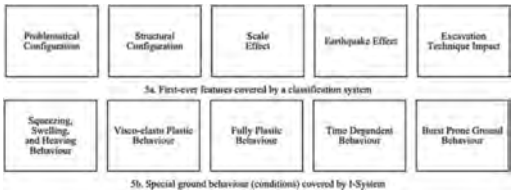

Figure 5. Most important features of I-System (Bineshian, 2021b).

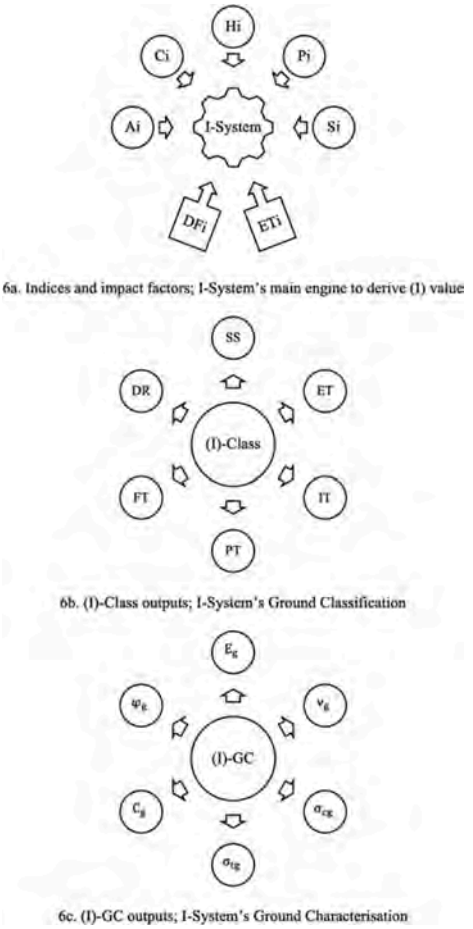

Figure 6. I-System and its main outputs.

3.6 *(I)-TM vs The existing tunnelling methods*

A comparison of (I)-TM and the existing tunnelling methods based on their concept is presented in Table 1 as a quick reference (aspects 1 to 7 in Section 3.3 are considered as comparison criteria). Further comparison of (I)-TM and the existing tunnelling methods based on the principles in design and construction procedure is presented in Table 2 (aspects 8 to 10 in Section 3.3 are considered as comparison criteria). Tables 1 and 2 are shown after Section 6.

4 TUNNEL T01 – USBRLP – INDIA

Tunnel T01 with 3209 m length is a single tube tunnel and the most challenging segment of the USBRL Project of Indian Railways; a project of national importance and the largest project in the construction of a mountain railway since independence of India. Lithology along the alignment contains claystone, dolomite, limestone, mudstone, sandstone, shale, siltstone, scree, alluvium, and colluvium in a clayey and silty matrix and hosting mica family minerals including muscovite. T01 is crossing Reasi Thrust of Main Boundary Thrust of over critical thrust wedge of lower Himalayas; an active fault zone as one of the major Himalayan thrusts that is displaced above the Indian lithosphere (Mahi et al, 2022). From August 2016 till March 2022, T01 faced with 16 major failures with at least 46,000 m^3 discharge of high pressure mix of debris and water (liquified ground) containing fully saturated crushed and sheared dolomite in a matrix of calcite, clay, and silt. This resulted in a huge loss of time (almost 67 months), resources, and machineries without any advance at faces. Due to this, Client decided to switch to (I)-TM from NATM and Conventional and to employ a design based on I-System instead of RMR and Q. Appropriate study in February 2022 revealed that the mechanical response of ground at both faces is visco-elasto plastic (VP) to fully plastic behaviour with almost zero stand-up time that requires pre-excavation measures to increase the stand-up time, a rigid response to absorb the passive load configuration, and a special ET to advance. The new design implemented from 2022/05/01 after 2012 days of unsuccessful tunnelling and accordingly safe and optimised advance at both faces resumed. 512 mm/day advance obtained and breakthrough achieved on 2023/12/20. In design procedure for T01, Ground Zoning (GZ) using I-System determined a single zone. Ground Hazards (GH) for associated GB is derived using I-System; then, by running I-System analysis required Support System (SS) is defined as a proper response to GB and a suitable control of the associated GH. (I)-GC as characterisation output provided the mechanical properties of ground used for Structural Dimensioning (SD) and Structural Verification (SV). Three principles of solution for T01 based on I-System and (I)-TM includes; application of active pre-excavation measures (including perforated piperoofing and glass fibre face bolting injected by PU-2C), employment of passive rigid post-excavation system (including rigid ribs encased in a thick layer of FRS), and controlling the thrust ahead of the face using buttress at face of the tunnel. GCD (Bineshian, 2022b) is conducted before and after pre-excavation injection to measure ground conductivity and to assess solidification quality respectively as a criterion to judge against opening the face and commencing the advance after each round of piperoofing. Drainage holes are applied at back chainages of face whenever required to release hydrostatic pressure built behind the faces. PSD/PSE using ME in a system of HnB with short pull length of maximum 800 mm applied. Safe operation achieved by implementing the right method of prediction and the risk in advancement is minimised. The only way to achieve the acceptability of risk is to control them. To serve this purpose, Tunnel Seismic Prediction (TSP; Choudhary and Bineshian, 2022) is employed to forecast geological condition ahead of the faces at T01 as part of the prescribed solution for T01 as per I-System and (I)-TM. The result's accuracy is scrutinised during excavation and it is found that the matching between anticipated and actual encountered condition is almost 90%. Figure 7 Represents the geological profile of T01 as encountered condition. Figure 7 is placed after Section 6.

5 CONCLUSIONS

This is concluded that misdiagnosis of ground behaviour will lead to great loss in valuable time and resources in tunnelling specially in challenging ground and under hazardous condition. Moreover, it is proven that employment of expensive machineries and complicated set up in design will not help if they are inapplicable for the ground's mechanical configuration. Incidents and frequent failures and loss of time and resources in T01 are examples of incorrect diagnosis of mechanical behaviour, failure of inapplicable classifications, inapt tunnelling method, improper design, inappropriate method statement, and irrelevant machineries and equipment. Implementable design and its elements and applicable associated method statement, which is adopted from 2022/05/01 in T01 and its successful outcome is clear evidence that proves importance of correct understanding of mechanical behaviour using a pertinent classification and characterisation called I-System and appropriateness of (I)-TM as a comprehensive tunnelling method. A design, which is proved that the most challenging tunnel in India can be constructed using easily and locally available machineries, equipment, and materials if the mechanical behaviour of ground is well identified and suitable classification and tunnelling method is adopted.

Table 1. Conceptual comparison of (I)-TM and the existing tunnelling methods (see Figure 3a).

Tunnelling Method	Application						Employing (Conceptual)						
	In Phases				In Medium		Under Special Conditions (Figure 5b)	Permanent Life Expectancy for Tunnel Structure	Flexibility of Contract for Execution	Surrounding Ground's Load Bearing Capacity	Arch Pressure at Any Depth	Controlled Release of Deformation in Plastic Ground	Primary Measures as Part of Final Measures
	Pre-design	Design	Construction	Post-construction	Rock	Soil							
Conventional	N/A	N/A	**A**	N/A	**A**	**A**	N/A	N/A	N/A	N/A	N/A	N/A	N/A
CnC	N/A	N/A	**A**	N/A	**A**	**A**	N/A	N/A	N/A	N/A	N/A	N/A	N/A
NATM	N/A	N/A	**A**	N/A	**A**	N/A	N/A	N/A	N/A	**A**	C/A	C/A	N/A
NMT	N/A	N/A	**A**	N/A	C/A	N/A	N/A	N/A	N/A	**A**	N/A	N/A	**A**
Pipe/box Jacking	N/A	N/A	**A**	N/A	N/A	**A**	N/A	N/A	N/A	N/A	**A**	N/A	N/A
SCL	N/A	N/A	**A**	N/A	C/A	N/A	N/A	N/A	N/A	**A**	C/A	N/A	N/A
(I)-TM	**A**	**A**	**A**	**A**	**A**	**A**	**A**	**A**	**A**	**A**	**A**	**A**	**A**

A Applicable C/A Conditionally Applicable N/A Not Applicable

Table 2. Comparison of (I)-TM and existing tunnelling methods.

Tunnelling Method	Recommendations in Construction Procedure						Embedded Classification	Embedded Characterisation	Post-excavation Damage Assessment
	Support System	Excavation Technique/s	Instrumentation Technique/s	Prevention Technique/s	Forecast Technique/s	Stages in Construction			
Conventional	N/I	N/I	N/I	N/I	N/I	N/I	N/I	N/I	N/I
CnC	N/I	N/I	N/I	N/I	N/I	N/I	N/I	N/I	N/I
NATM	N/I	N/I	N/I	N/I	N/I	N/I	N/I	N/I	N/I
NMT	P/I	N/I	N/I	N/I	**I**	N/I	**I**	N/I	N/I
Pipe/box Jacking	N/I	N/I	N/I	N/I	N/I	N/I	N/I	N/I	N/I
SCL	P/I	N/I	N/I	N/I	N/I	N/I	N/I	N/I	N/I
(I)-TM	**I**	**I**	**I**	**I**	**I**	**I**	**I**	**I**	**I**

N/I Not Included in the method I Included in the method P/I Partially Included in the method

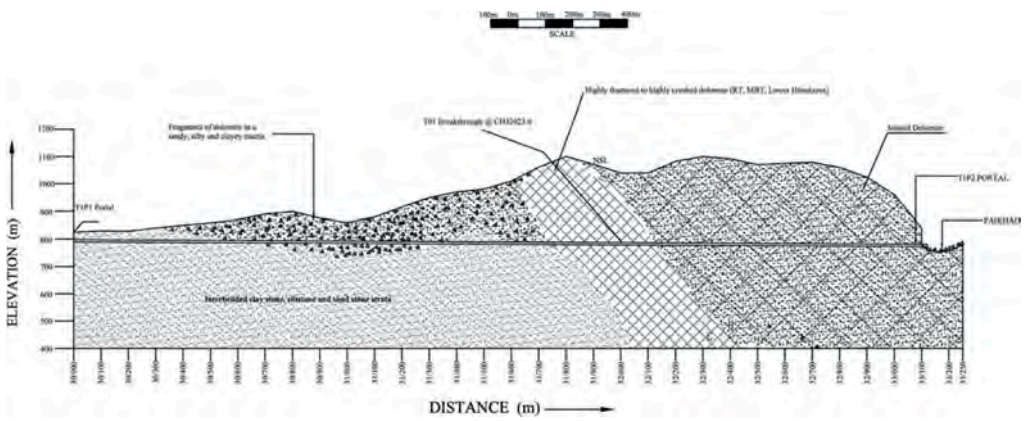

Figure 7. Geological profile of T01 along the alignment – encountered.

6 NOMENCLATURES

(I)-Class	I-System's Ground Classification
(I)-GC	I-System's Ground Characterisation
(I)-TM	I-System's Tunnelling Method
A_i	Armature Index
C_g	Cohesion of ground
C_i	Configuration Index

CnC	Cut and Cover Tunnelling Method
DC	Data Collection
DF_i	Dynamic Forces Impact Drill and Blast
DR	Design Remark/s
E_g	Deformation Modulus of ground mass modulus
ET	Excavation Technique/s
ET_i	Excavation Technique Impact
FT	Forecast Technique/s
GB	Ground Behaviour
GCD	Ground Conductivity Designation
GH	Ground Hazards based on failure categorisation
GZ	Ground Zoning based on ground properties
H_i	Hydro Index
HnB	Heading and Benching - an excavation technique
I-System	Index of Ground-Structure (Bineshian, 2019, 2021b)
IMT	Immersed-tube Tunnel
IT	Instrumentation Technique/s
ME	Mechanised Excavation
NATM	New Austrian Tunnelling Method
NMT	Norwegian Method of Tunnelling
OC	Open Cut excavation
P_i	Properties Index
PSD	Partial-Sequential Digging
PSE	Partial-Sequential Excavation
PT	Prevention Technique/s
SCL	Sprayed Concrete Lining
SD	Structural Dimensioning for each SS
SEM	Sequential Excavation Method
S_i	Strength Index
SRH	Stress Release Holes (Bineshian, 2020b)
SS	Support System
SSH	Squeezing/Swelling/Heaving (Bineshian, 2020b)
SV	Structural Verification
TBM	Tunnel Boring Machine
ViD	Vibration-induced Damage or blast-induced damage
ν_g	Poisson's Ratio of ground
σ_c	Unconfined Compressive Strength of intact ground
σ_{cg}	Unconfined Compressive Strength of ground mass
σ_{tg}	Uniaxial Tensile Strength of ground mass
φ_g	Internal Friction Angle of ground

REFERENCES

Bineshian, H, 2019. I-System; A quick introduction. Proceedings of the 8th IndoRock-2019 Conf, Delhi, India, 254–271.

Bineshian, H, 2020. SRH System – Stress Release Hole/s; A substitution to conventional yield support system. JOEG, XLV (1&2), 1–16.

Bineshian H, 2021a. Design approach for tunnels using engineering classification with reference to I-System. EGCON 2021, Proceedings of Int Conf on Recent Advances in Geotechnics, Keynote Lecture, 56–74.

Bineshian H, 2021b. I-System: Index of Ground-Structure: 2021 Edition. JOEG, XLVI (1), 1–50.

Bineshian H, 2021c. Vibration-induced Damage Assessment; New practical methods applicable for engineered blasting. TAI Journal, 10 (1): 5–14.

Bineshian, H, 2022a. (I)-TM: I-System's Tunnelling Method – An Introduction. TAI Journal, 11 (1): 40–49.

Bineshian H 2022b. GCD – Ground Conductivity Designation – 2022 Edition (A testing method to quantify ground's hydraulic conductivity and solidification quality), TAI Journal, 11 (2): 9–13.

Choudhary, K, Bineshian, H, 2022. High-accuracy long-range seismic prediction during tunnel construction phase using TSP and correlation with geotechnical/ geomechanical calculations using I-System; A recommended prediction technique in (I)-TM. Proc Int Conf on Engineering Geology and Geotechniques for Safe and Sustainable Infrastructures, EGCON 2022, Kolkata, India.

Mahi, S, Bineshian, H, Gupta, S, Hegde, R K, 2022. An Overview of the Success in Resolving the Years-lasting Problem of USBRLP's T01 Tunnelling in Himalayas' MBT within the RT Zone by Employing I-System and (I)-TM. Proc Int Conf on Engineering Geology and Geotechniques for Safe and Sustainable Infrastructures, EGCON 2022, Kolkata, India.

Tunnelling for a Better Life – Yan, Celestino, Thewes & Eberhardt (Eds)
© 2024 The Author(s), ISBN 978-1-032-80042-4
Open Access: www.taylorfrancis.com, CC BY-NC-ND 4.0 license

Segment design for Australia's largest diameter TBM tunnel

Shu Fan Chau*
Aurecon, Auckland, New Zealand

Harry Asche & David Oliveira
Aurecon, Brisbane, Australia

Justin Shepherd & Christian D'Hondt
Acciona, Sydney, Australia

ABSTRACT: The Western Harbour Tunnel is Sydney's newest road tunnel project, and it includes twin three-lane tunnels driven under Sydney Harbour by TBM. The tunnel passes through a jointed and stress-relieved rock before encountering Pleistocene alluvial material under the Harbour. The analysis methods and some of the segment details for this tunnel, which will feature the world's largest diameter steel fibre reinforced concrete (SFRC) segments, are described herein. At each cross-passage opening, the design philosophy is to use a combination of effective shear transfer structural elements to allow the safe tunnel lining opening with minimum construction inconvenience. The segment opening and the cross-passage design considerations are also described.

Keywords: TBM tunnel, cross passage, undersea, steel fibre reinforced concrete, lining segment, precast

1 INTRODUCTION

The Western Harbour Tunnel (WHT) is a new crossing under Sydney Harbour, linking Rozelle Interchange to the Warringah Freeway in Sydney, Australia. The twin 6.5 kilometre motorway tunnel will have three lanes in each direction and will create a western bypass of the Sydney CBD, taking pressure off the Sydney Harbour Bridge, The Sydney Harbour Tunnel, Anzac Bridge and Western Distributor corridors. The WHT is being delivered in two stages (Figure 1). Stage 2 will be delivered in partnership by Transport for NSW and ACCIONA, with the designer AECOM AURECON Joint Venture (JV). Stage 2 will use several roadheaders to excavate the northern section and two Tunnel Boring achines (TBMs) to construct the southern section.

The 1.5 kilometre long twin TBM tunnels are located between Birchgrove and Waverton and pass beneath Sydney Harbour. A short section of the TBM tunnel under the Harbour is within soft/ mixed ground conditions. There are 11 nos. mined cross passages between the two TBM tunnels. The tunnels have an ID of 14.15 metre and will be constructed by two 15.7 metre mixshield (slurry) machines, both advancing from the assembly caverns at the south. Tunnel internal structures include a box culvert for facilitating tunnel construction logistics and subgrade backfill to the road level. Figure 2 shows the TBM tunnel and cross-passage layout plan, and Figure 3 shows the TBM tunnel cross-section.

The segmental lining design consists of precast Steel Fibre Reinforced Concrete (SFRC) segmental rings for most of the tunnel alignment, with short lengths of conventional steel bar reinforced precast

Figure 1. WHT overview (image from https://caportal.com.au/rms/wht/).

*Corresponding author: shufan.chau@aurecongroup.com

DOI: 10.1201/9781003495505-25

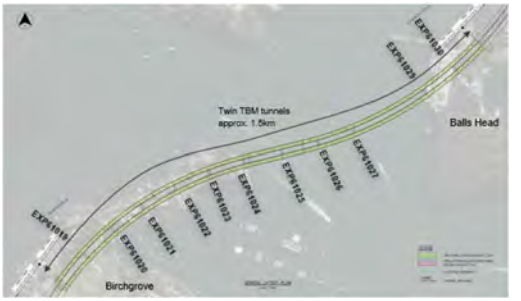

Figure 2. WHT TBM tunnel and cross passage layout plan.

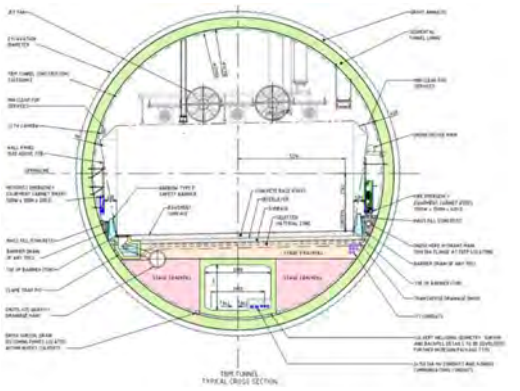

Figure 3. WHT TBM tunnel cross-section.

concrete segmental rings at cross passages only to cater to the lining opening effect. This paper focuses on the design philosophy and challenges in designing the SFRC segmental lining for this mega TBM, Australia's largest diameter TBM tunnel project. Some segment details, including segment shapes and joints, are presented. The under-sea TBM tunnel stability, including flotation, face pressure and blowout, are also discussed. While this paper was being written, the cross-passage design was ongoing. However, the design considerations for the cross passage and segment openings are also described.

2 DEVELOPMENT OF SFRC LINING ON MEGA TBM TUNNELS – A BRIEF LITERATURE REVIEW

In the last 20 years, Steel Fibre Reinforced Concrete (SFRC) lining use has become increasingly popular in TBM tunnel projects, including small-size utility/water tunnels, medium-size metro tunnels, and large-diameter road tunnels. The key factors driving development of SFRC linings include:

- Design aspect: Including fibre reinforcement in the concrete mix results in a noticeable increase in the post-cracking tensile residual properties, allowing the removal of conventional bar reinforcement.
- Construction aspect: Fibre reinforcement facilitates a cost-effective lining segment production process, with reduced potential for damage, and reduces post-drilling clash risks.

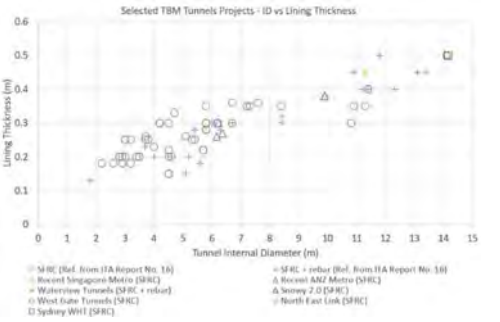

Figure 4. TBM tunnel ID vs lining thickness (SFRC and mega TBM tunnel projects).

ITA (2016) has reported a list of TBM tunnel projects worldwide that adopt SFRC segment lining design in combination (or not) with conventional rebar. The internal tunnel diameter and segmental lining thickness of these projects are graphically presented in Figure 4, together with some of the recent metro TBM projects with SFRC lining in Australia, New Zealand and Singapore. In the ITA data set, SFRC alone and hybrid use peters-out at just over 11m diameter and 13m diameter respectively.

However, the use of mega TBMs with a cut diameter of more than 14 metre rapidly increases. Up to 2023, more than 40 tunnelling projects worldwide have used a mega TBM. The segmental linings for most of these mega TBM tunnels have traditional steel rebar reinforcement (FHWA 2020). The mega TBM tunnels with SFRC lining recently completed or being constructed in Australia and New Zealand are also shown in Figure 4, with details summarised in Table 1.

According to Ireland et al. 2019 and Chau et al. 2020, Melbourne's West Gate Tunnels (WGT) segmental lining is the largest diameter SFRC segmental lining without rebar ever completed (tunnel excavation and lining completed in mid-2023). There are many benefits associated with steel fibre reinforcement for large-diameter tunnels. Besides manufacturing cost benefits, reduced damage during construction has also been observed on the WGT project. Chau et al. 2020 also summarised the critical design philosophy for designing SFRC segments for mega TBM tunnels, including:

- Need for empirical and numerical analyses to PAS8810, a specific concrete segmental lining code. This approach overcame many design challenges and confirmed the SFRC segmental lining, including eliminating radial and circumferential joints steel reinforcement.
- Specification of material and segment testing to verify the design approach and assumptions.

Table 1. Recent ANZ Mega TBM Tunnels with SFRC Segments.

Project	Waterview Tunnels	West Gate Tunnels	North East Link	Western Harbour Tunnels
Location	Auckland, New Zealand	Melbourne, Australia	Melbourne, Australia	Sydney, Australia
TBM Dia. (m)	14.46	15.6	15.6	15.7
Lining ID (m)	13.1	14.1	14.1	14.15
Lining Thk (m)	0.45	0.5	0.5	0.5
Segment width (m)	2.0	2.4	2.4	2.4
Material Types	SFRC + joint rebar	SFRC	SFRC	SFRC
Project Status	Completed 2017	Tunnels completed 2023	Under construction	Under design and construction

3 GEOLOGICAL AND HYDROGEOLOGICAL CONDITIONS

A series of marine-based geotechnical investigations have been provided by Transport for NSW, including seismic survey data, boreholes and cone penetration tests (CPT) within the Harbour Crossing. A construction-phase targeted marine GI has also been undertaken. The geology along the alignment of the WHT TBM tunnels is shown in Figure 5.

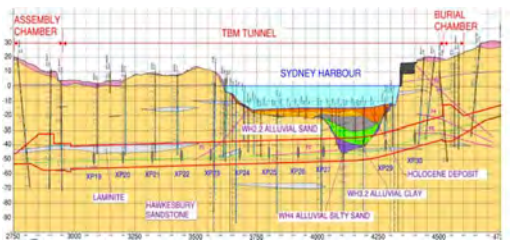

Figure 5. Geological long section along TBM alignment.

TBM tunnels will be excavated mostly in Hawkesbury Sandstone, except for a short 180 metre section of soft ground (alluvial soil of Pleistocene age), where the tunnels cross a paleochannel under the harbour. This paleochannel has been progressively infilled with marine sediments. The boundaries for the harbour sediments show the Pleistocene units WH2.1, WH2.2, WH3.2, and WH4, filling the bulk of the paleochannel eroded into the bedrock. In the Hawkesbury Sandstone, due to stress relief in the eroded palaeovalley, geological features, including laminite beds, dykes, and thrust faults, have been identified from the existing and recently completed marine boreholes.

The face of the TBM is anticipated to encounter the following geology:

- Harbour Sediments, WH3.2: mostly firm to very stiff, clay and silty clay, interbedded with sandy fine soils.
- Harbour Sediments, WH4: Fluvial sandy silts and sands, interbedded with stiff to very stiff silt and clay layers.
- Hawkesbury Sandstone, ranging from massive to jointed and stress relieved,
- Dykes and thrust faults in the Hawkesbury Sandstone.

The groundwater head to tunnel crown ranges from 35m to 45m. Hawkesbury Sandstone is characterised as a dual porosity aquifer where groundwater potential is dominated by secondary alteration, such as joints, fractures, faults and bedding planes, whilst the intact Hawkesbury Sandstone is mainly "impermeable".

Figure 6 illustrates the magnitude and variability of rock mass permeability along the tunnel alignment. Rock mass permeability is higher around the valley that forms the Harbour, where the rock has experienced stress relief and valley bulging. In these areas, existing open discontinuities and developed valley-side joints increase the defect aperture, potentially increasing groundwater flow.

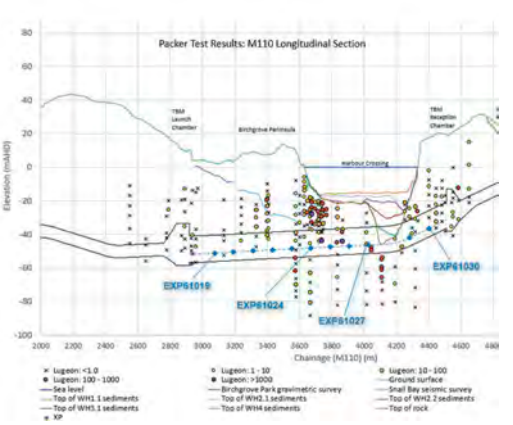

Figure 6. Water packer test results along TBM alignment.

4 WHT SEGMENTAL LINING

The WHT tunnel is currently the largest diameter TBM tunnel project in Australia. The WHT segmental lining design follows a similar design philosophy

to WGT (Ireland et al. 2019, Chau et al. 2020) with project-specified considerations. It adopts SFRC-only segments for the tunnel alignment, except for RC segments at cross-passage opening locations. The WHT tunnel will be the world's largest diameter steel fibre reinforced concrete (SFRC) segment upon completion.

4.1 *SFRC lining properties*

The design compressive strength of the segment concrete is 65 MPa. The design characteristic residual flexural tensile strengths of the SFRC is *fR1* of 4.0 MPa and *fR4* of 4.0 MPa. The characteristic splitting strength is 6.0 MPa. All the design parameters for the SFRC are to be verified by testing. The steel fibre has been specified to be hook-ended with a minimum diameter of 0.75 millimetre, have an aspect ratio (l/d) of 40 to 80, and have a minimum tensile strength of 1800 MPa. However, experience has shown that a fibre tensile strength of 2200 MPa will likely be required and beneficial.

The specified design concrete compressive strength for Waterview Tunnels is 55 MPa (Chau et al. 2017), and for WGT is 50 MPa (Chau et al. 2020), although higher strengths have been achieved in practice for demolding time requirements. The specified design concrete compressive strength in WHT is higher than other recent mega TBM tunnel projects in the Australia – New Zealand region but generally consistent with what is actually used in the precast yard. The SFRC design properties and concrete mix design have been coordinated with the project segment precast team based on the same concrete mix design in another local TBM tunnel project, the Sydney Metro West – Central Tunnelling Package (SMW-CTP). The 28-days mean compressive strength and the splitting strength based on SMW-CTP production testing are 85 MPa (with a standard deviation of 4.29 MPa) and 9.8 MPa (with a standard deviation of 1.35 MPa), respectively. Considering a higher strength concrete mix design will be used for the project, higher design SFRC properties are therefore considered in the WHT tunnel segmental lining design.

4.2 *Segment and ring configuration*

The tunnel's internal diameter is 14.15 metre. The lining thickness is 500 millimetre, and the nominal length of a ring is 2400 millimetre. There are ten segments in a ring at an even 36-degree angle subtended by rhomboidal segments (8 nos.) and two trapezoidal segments, the key and the counter key. The radial joint angle for the rhomboidal segments is 5 degrees, and the radial joint angle for the key and adjacent segments is 10 degrees, with a key segment insert variant angle of 7.5 degrees to achieve a workable key draw distance. The segment ring is a universal taper ring with taper of 60mm (+/-30mm) so that the key can be built in all 20 possible locations. The schematic developed plan view of the ring arrangement is shown in Figure 7.

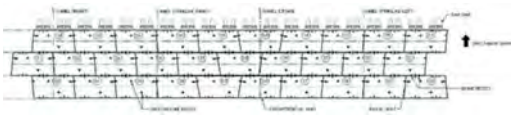

Figure 7. Schematic view of the developed intrados.

4.3 *Rhomboidal segments*

Rhomboidal segment arrangement has been widely used in metro-sized TBM tunnels. However, based on the available information, the segments of mega TBM tunnels are more commonly rectangular, including the WGT and Waterview tunnels. For WHT, the preferred ring configuration was to use rhomboidal segments together with circumferential joint dowels to improve the precision of the ring build and to lessen the potential for leakages through the lining joints under high water pressures. As far as the authors know, WHT is the second largest TBM tunnel with a rhomboidal segment ring arrangement, after the Santa Lucia Tunnel in Italy, despite the BART tunnel in San Jose, US, potentially using a mild joint angle of 2º. A detailed study has been undertaken to compare the rectangular and rhomboidal segment arrangements regarding ring stiffness and bursting stresses at circumferential joints.

4.3.1 *Ring stiffness*

Muir-Wood's equivalent ring stiffness due to the number of joints cannot explicitly account for the inclination of the joint. The approach proposed by Janssen (1983) (Figure 8) considers the joints as an equivalent concrete short column with a width and height equal to the effective width of the joint. Rotational stiffness expressions (M/q) are then developed for varying degrees of contact as the joint rotates. However, the maximum allowable moment across the joint is equivalent to the maximum axial force acting at the extreme fibre of the equivalent short-column concrete section ($N*h_j$ - Nhj/2 in the theoretical model and shown as a plateau in the graph of Figure 8). For a slanted joint, the axial force acting perpendicular to the joint is anticipated to be slightly less than a flat joint, as there will be a component of this load acting parallel to the joint. As a result, the slanted joint will reduce the maximum moment and therefore, the equivalent rotational stiffness will be slightly reduced.

The above conclusion has been confirmed using two simple numerical models developed to compare the rhomboidal segments with the rectangular segments (Figure 9). Only a single ring (i.e. uncoupled) was modelled, as the aim is to compare the impact of the slanted joints without the effects of ring connectors (dowels or bolts). Considering that bending moments are a function (double derivative) of the deflections, the same conclusion applies to the flexural

performance. These results are consistent with the expectation discussed above, which, in turn, indicates a slight reduction in overall stiffness between the rhomboidal and rectangular segments for a single ring, i.e. when the effect of connectors is ignored.

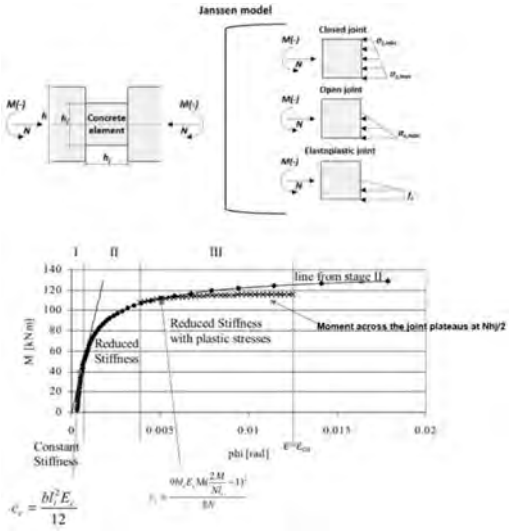

Figure 8. Janssen (1983) joint model.

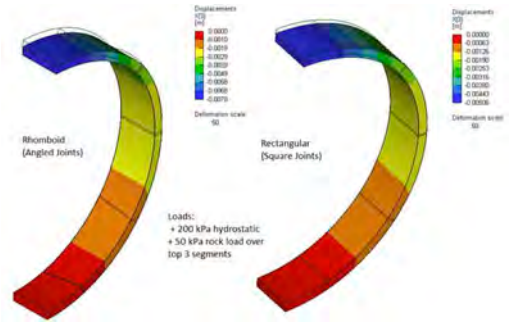

Figure 9. Comparison of single ring (uncoupled) behaviour – rhomboidal vs rectangular.

4.3.2 *Bursting stresses at circumferential joints*

Circumferential joint bursting/splitting stress due to TBM thrust loads is a critical case for joint design, as the edge distance from the ram shoes on one side of the rhomboidal segment is less than that on the rectangular segment.

A non-linear model using the software Midas was adopted to analyse the relevant cases. The model has boundary restrictions at the trailing edge and considers a single segment only. However, its neighbouring segments' confining effects are included by compression-only springs. A non-linear analysis has been undertaken with elasto-plastic models that can represent the concrete material's compressive (crushing) and tensile (cracking and splitting) behaviour. The principal compressive stress, principal tensile stress and cracking from both rectangular and rhomboidal segment models are shown in Figure 10.

Additional models have also been carried out using concrete specialist software called ATENA (Figure 11). Three segments have been included in the ATENA models, with all three loaded. These models allow for the contact of the longitudinal (radial) joints to be included more explicitly, capturing normal compressive and shear stresses (friction) that may develop.

The modelling by both Midas and ATENA indicates that both rhomboidal and rectangular segments are within acceptable limits for estimated cracking but with evidence that the rhomboidal configuration has a potentially greater risk of corner cracking and damage mostly due to the uneven stress distribution on the reacting circumferential joint. However, this risk is only marginally higher than the rectangular segments, and the benefits of the expected better ring-build outcomes of the rhomboidal segments outweigh the slight risk increase. A detailed discussion of ram load and circumferential joint performance is included in Section 4.4.

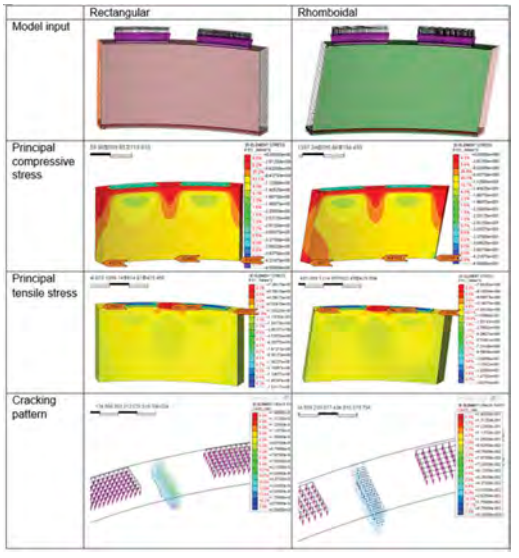

Figure 10. Modelling comparison between rectangular and rhomboidal segments (by Midas).

4.4 *Segment joints*

The WHT tunnel circumferential and radial joint design has eliminated the joint steel ladder/ reinforcement requirement. Figure 12 shows the joint details.

4.4.1 *Temporary ram load and circumferential joints*

There will be 20 pairs of thrust cylinders (2 pairs per segment). The design considered a concrete pad of 1662 x 320 millimetre at the circumferential joint

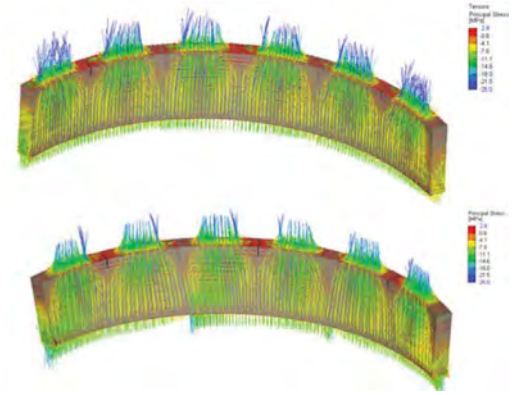

Figure 11. 3D ATENA model results – rectangular (top) vs rhomboidal (bottom).

at the leading edge, and the ram shoe size of 1350 x 545 millimetre is advised by the construction team, giving a maximum working pressure magnitude of over 22 MPa (unfactored for a thrust of 194 MN) and 27 MPa (thrust of 233 MN) for an emergency case, i.e. full thrust. The ram shoe is oversized, so full contact with the bearing area is achieved via the concrete pad, irrespective of ring roll or eccentricity.

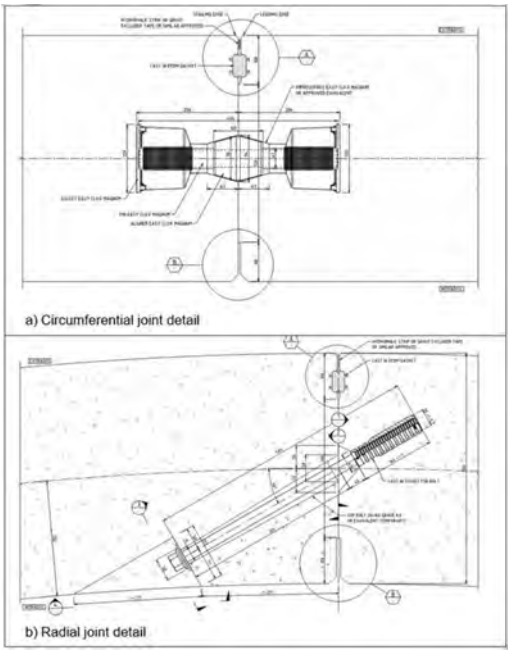

Figure 12. Circumferential joint and radial joint details.

The segment has been checked for bearing, bursting, and compressive loads as an equivalent short column. Adequate resistance to crushing and splitting is demonstrated by the Guyon (1972) method; however, the section is highly utilised, indicating a risk of cracking should poor ring build occur. FEM non-linear analysis of the ram loading on the critical segment (S8, with ram shoe closest to segment edge) has been undertaken in Midas (Figure 13). The model considers the gasket groove, caulking groove details, ram shoe positioning tolerance, and ring roll. These models have been run for both the SLS cases to determine crack widths and the ULS cases to confirm structural capacity.

The FEM model, however, indicates a zone of plasticity that develops between the ram shoes as a result of the elastic deformation of the concrete under maximum design ram loading. The depth of the cracked zone is about 105mm. The maximum crack width is estimated at 0.05mm, with all micro cracks conservatively summed into one single crack. With the removal of the ram load, it is observed that more than 50 percent of the cracked elements observed during the ram loading stage are closed (as shown in green in Figure 13).

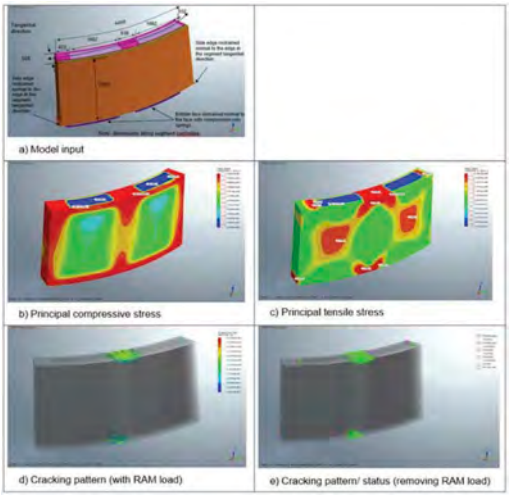

Figure 13. 3D Midas ram load and circumferential joint model.

The FEM analysis confirms that steel ladder reinforcement is not required for the circumferential joints for the 500 millimetre thick SFRC segment.

4.4.2 *Radial joints*

The lining is subject to bursting stresses from hoop loads on the radial joint and TBM ram forces on the circumferential joint. At ULS, numerical modelling was used to determine bursting stresses. Where SFRC is employed, the resistance is initially based on the tensile splitting strength of the concrete applied over the segment depth to resist the bursting force. The effects of joint rotation on the load distribution at the joints is considered for

the worst load-deflection combinations, including the effects of lipping. The analysis has been undertaken using Midas with elasto-plastic constitutive models used to represent the compressive and tensile behaviour of the concrete, similar to the circumferential joint model. The FEM model has also incorporated the guide rods and recesses. The general arrangement of the model and result is in Figure 14. The FEM models confirmed that the maximum tensile stress is lower than the first crack stress in all realistic cases. There are localised stresses near the bottom face where tensile stresses exceed the capacity however, these are not in the bursting zone and are due to the proximity to the boundary supports. This confirms no radial joint bar reinforcement is required.

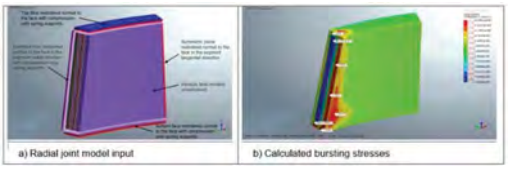

Figure 14. 3D Midas radial joint model.

4.5 *Segment handling and stacking*

The segments are produced in a precast yard and transported to the tunnel construction site to build the tunnel ring. There is a series of handling, stacking and transportation processes, as summarised in Table 2.

The age, segment loading, and supporting conditions are different in each stage. A structural check on the SFRC segments has been undertaken to ensure no adverse effects on the segments occur during all stages. The minimum concrete strength for each handling and stacking case is then specified. The design has been coordinated with the construction team to facilitate segment production logistics and programme planning. This is achieved by determining the required minimum concrete strength to proceed to the next stage of handling/ stacking. The handling and stacking loads are based on the self-weight of the segments and their dynamic impacts - the maximum number of segments to be lifted and placed during the stacking process has been limited. As the handling and stacking are temporary load cases, load factors of 1.2 on segment self-weight and a dynamic factor equal to 2.0 are adopted. A 50 millimetre maximum tolerance for stacking spacer position is also considered. The planning and design of the precast facilities, including the segment production carousel, is currently being developed collaboratively. However, the design cases will be reviewed if the construction eventually requires a segment lifting arrangement different from the current design assumptions.

Table 2. Segment stacking and handling stages.

Step	Stage	Typical Schematic	Plant supporting segments	Min. concrete UCS (MPa)
1	Segment casting and initial curing		Segment mould	12
2	Demoulding		Vacuum pad (2/3 pads)	12
3	Lifting table extrados facing up		Lifting table	12
4	Turning of segment		Turning table	12
5	Lifting table intrados facing up		Lifting table	12
6	Initial stacking in buffer area (max. stack of 3 segments, with max. 1 segment per lift)		Grab	12
7	Transfer in group of 3 to external staging area		Conveyor	25
8	Transfer to storage yard by main portal crane – max. 2 segments per lift		Gantry crane & grab	25
9	Consolidate stacks to 6 segments – max. 2 segments per lift		Gantry crane & grab	25
10	Consolidate to 10 segments max (1 ring) – max. 2 segment per lift		Gantry crane & grab	25 (upper 4 segments) /50 (lower 6 segments)
11	Transport to tunnel site by road vehicle – max. stack of 2 segments		Truck	50
12	Transport from tunnel site storage to TBM – max. stack of 2 segments		MSV	65

5 UNDERSEA TBM TUNNELS STABILITY

Generally, a bored (TBM) tunnel or an immersed tunnel (IMT) can be selected for a subaqueous road tunnel. Compared to the immersed tunnel, using a TBM excavating beneath the seabed does not require dredging and marine access. This difference made the TBM solution more favourable than the IMT option in the WHT Project, considering environmental concerns and constraints in the existing shipping fairways at Sydney Harbour.

A short section of the TBM tunnels is to be bored in soft/ mixed ground under Sydney Harbour. It is essential to understand the soil/ ground cover to achieve subaqueous tunnel stability in terms of structural integrity, tunnel flotation resistance and construction phase blowout prevention.

5.1 *Tunnel flotation*

The TBM tunnels have been checked against flotation. The soil cover shall always provide sufficient stabilising actions against the uplift force acting on the tunnel. This is particularly important for under harbour tunnels as the water level is always above the seabed (soil surface). The model and formulas adopted for the WHT flotation check are described in Lo et al. (2012). The flotation check also meets the following BS EN 1997-1:2004 requirement:

$$V_{dst,d} \leq V_{stb,d} + R_d \quad (1)$$

Where Vdst,d = destabilising permanent and variable vertical actions

Vstb,d = stabilising permanent vertical actions

Rd = any additional resistance to uplift

The partial factors for the flotation check are derived from PAS 8810:2016 Table 11 and 12 (Limit State UPL) and are listed in Table 3.

Due to the short-term effects, soil friction has been considered during the construction stage. In the operational stage, soil friction has been ignored, and a 2 metre seabed scouring/washout has been assumed.

Table 3. Flotation ULS partial factors.

Element		Partial factor
Actions	Self-Weight	0.9
	Water Pressure	1.0
Ground Parameters (taken as the reciprocal of the specified value)	Weight density (soil density)	1.15
	Angle of shearing resistance	1.25
	Effective cohesion	1.25
	Undrained shear strength	1.4
	Unconfined strength	1.0

5.2 *Face pressure and blowout*

The DAUB (2016) guide describes the mechanisms associated with face instability and provides a diagram of the allowable pressures at the tunnel crown to mitigate the risks, as shown in Figure 15. The ability to control pressure in a slurry TBM is known to be good, and the expected deviation of 20 kPa between the pressure set by the operator and the actual pressure ("Deviations" in Figure 15).

5.2.1 *Lower face pressure limit*

The lower face pressure limit is to prevent tunnel face cave-in failure. DAUB (2016) provides a formula (DAUB Equation 4) to estimate a minimal support force:

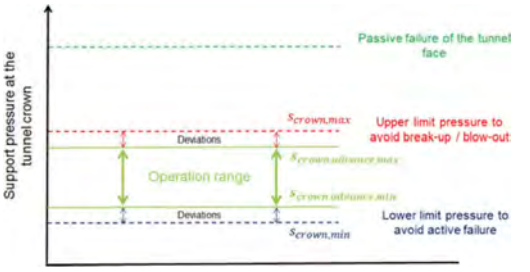

Figure 15. Allowable operational pressures at the crown (DAUB Figure 9).

$$S_{ci} = \eta_E E_{ci} + \eta_w W_{ci} \quad (2)$$

Where,

η_E safety factor for earth pressure force (=1.5) [-]

η_W safety factor for water pressure force (=1.05) [-]

Sci required face pressure (circular tunnel face) [kPa]

Eci face pressure due to earth pressure [kPa]

Wci face pressure due to groundwater pressure [kPa]

For undrained behaviour, the stability number (N) proposed by Broms & Bennemark (1967) is used to estimate the face pressure at the tunnel axis. The critical stability number (Ncr) delivers the support pressure at collapse, and a safety factor of 1.5 shall be included in the calculation. The soil within a vertical opening is stable if the stability number is lower than 6.

$$N = \frac{\sigma_{v,\,axis} - S_{ci,\,axis}}{c_u} \quad (3)$$

Where,

N is stability number [Ncr/1.5];

$\sigma_{v,axis}$ is the vertical stress at tunnel axis [kPa]

$S_{ci,axis}$ is the face pressure at tunnel axis [kPa]

Cu is the undrained shear strength of soil [kPa]

For drained materials, the face pressure due to the earth pressure can be estimated based on the face stability study by Anagnostou & Kovari (1996), which is based on the force equilibrium approach for a sliding wedge at the TBM front face.

$$E_{ci} = F_0 \gamma' D - F_1 c' \quad (4)$$

where E_{ci} face pressure due to earth pressure [kPa]

F_0, F_1 dimensionless coefficient, read from nomograms in Figure 11

D tunnel diameter

c' soil cohesion

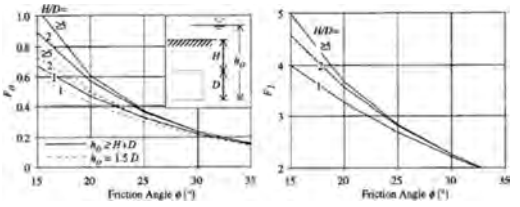

Figure 16. Nomograms for dimensionless coefficient F0 and F1, from Anagnostou & Kovari (1996).

5.2.2 *Upper face pressure limit and blowout*

The upper face pressure limit is defined as a limiting pressure to avoid a break-up of the overburden or blowout of the support medium.

DAUB (2016) gives the upper support pressure limit to less than 90% of the total vertical stress at the tunnel crown (DAUB Equation 5), where this total vertical stress is the minimum, particularly using minimum water levels.

$$1 \leq \frac{0.9\text{x}\sigma_{v,\,crown,\,min}}{S_{crown,\,max}} \qquad (5)$$

where

$\sigma_{v,\,crown,\,min}$ is Total vertical stress in the tunnel crown considering the minimal unit weight of the soil [kPa]

$S_{crown,\,max}$ is Maximal allowable pressure in the tunnel crown due to break-up safety/blow-up safety [kPa]

The above formula only considers the overburden stress and ignores the shear strength, which is conservative. Lo et al. (2012) provide an alternative method to estimate the limit pressure for a blowout using a limit equilibrium model (Figure 17). This limit equilibrium analysis can be carried out either drained or undrained, but the undrained analysis is more conservative. In this case, the loading conditions impose positive excess pore water pressures that reduce the shear strength of the soil. The analysis is performed with minimum water levels.

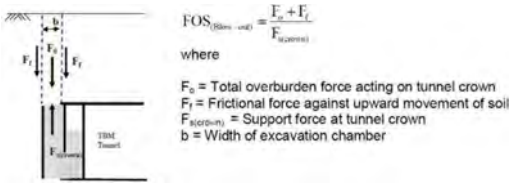

Figure 17. Factor of safety against blowout failure (Figure 7 in Lo et al. 2012).

Figure 18 shows the specific situation for WHT. The slurry pressure is applied to the cuboid of soil at the crown. Resistance to uplift includes the weight of the soil (saturated density) and the water pressure applied at the seabed, as well as frictional and cohesive components applied to the four remaining along the cuboid of soil. An overall factor of safety of 1.2 against blowout failure shall be maintained. In WHT soft ground, the maximum face pressure is equal to:

$$S_{crown,max} \leq \frac{D \cdot b \cdot (\gamma \cdot h_s + \gamma_w \cdot h_w) + 2 \cdot (D + b) \cdot h_{3.2} \cdot c_{3.2}}{1.2 \cdot \mathrm{D} \cdot \mathrm{b}} \qquad (6)$$

where

$S_{crown,max}$ is the maximal allowable pressure in the tunnel crown due to break-up safety/blowout safety [kPa]

D is TBM tunnel [15.7 m]

b is the length of slurry pressure – Adopted 13.5 m

$c_{3.2}$ is undrained shear strength of WH3.2 [80 kPa]

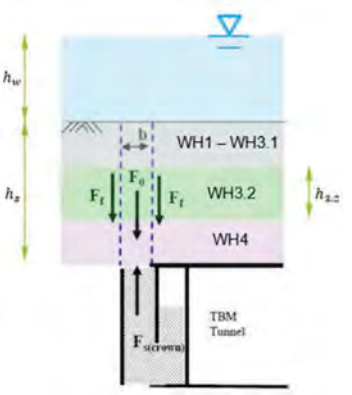

Figure 18. Lo et Al. 2012 model for WHT.

5.2.3 *Numerical analysis of face pressure*

To verify the minimum and maximum face pressure in the mixed/ soft ground under Sydney Harbour, a PLAXIS 3D analysis has been undertaken. The model simulates the excavation of 2.4 m and simultaneously applies face pressure and shield pressure (on the front shield length) and installation of 2.4 m lining at the rear of the TBM shield. The "safety" calculation type (i.e. phi/c' reduction) has been completed in PLAXIS to obtain the factor of safety (FoS) to check the stability of the face pressure model. Under the minimum face pressure of 400 kPa at the crown and maximum face pressure of 530 kPa at the crown, the FoS are 1.25 and 1.21, respectively. Figure 19 shows the analysis results on the ground plastic points and ground movement shading from the maximum face pressure model. A sensitivity model is also run to evaluate the ultimate blowout failure pressure, which is 580 kPa (about 2 bars above hydrostatic pressure) at the crown and with a factor of safety of 1.072.

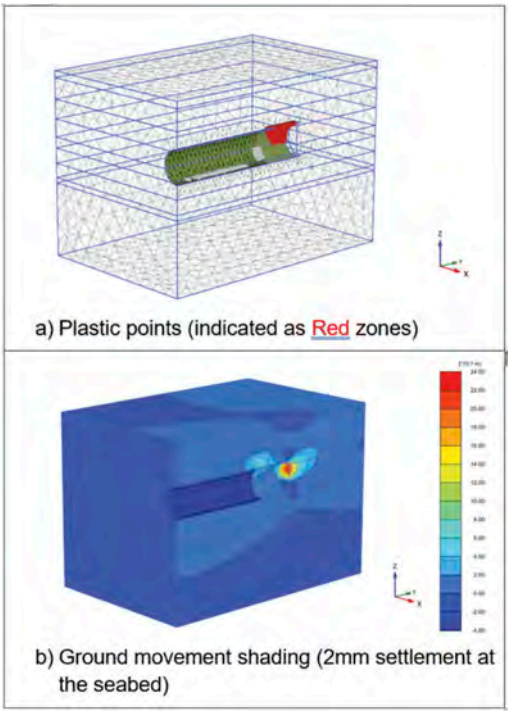

Figure 19. 3D face pressure model results (max. face pressure).

6 CROSS PASSAGES AND SEGMENT OPENING

The TBM section has eleven cross passages with a typical spacing of 120m (Figure 5). However, the separation between cross passages XP27 and XP29 is 260m. No cross passage is in the soft ground location, and all cross passages have been laid out to ensure they will be in competent rock. The soft ground cross passage has been eliminated to reduce the significant construction risks of tunnel opening and cross-passage excavation through the soft ground under the Harbour. Assessment has also demonstrated that the operational, fire, and life safety requirements are still met with the greater separation between XP27 and XP29.

Cross passages in road tunnels are for emergency pedestrian movement from the incident tunnel to the non-incident tunnel. The spaceproofing of the cross passages provides the following elements:

- Civil/ Structural: segment opening and collar, emergency egress, comms pit, wall elements, fire-rated doors, internal structures, and drainage.
- MEP (Mechanical, Electrical and Plumbing): Deluge main, Deluge manifold, electrical equipment room (EER), mechanical ventilation equipment, ITS, and lighting.

Cross passages have two different profiles: those with EER and those without EER. The cross-passage's cross-sectional area is similar to a typical metro-size mainline tunnel. The cross passages between the TBM tunnels are in competent rock. They will be excavated by impact hammers with rock bolts and shotcrete as primary support and cast in-situ fibre-reinforced concrete secondary lining. Probing and grouting processes are required for groundwater inflow control before segment lining opening and cross-passage excavation. The cross-passage excavation support and lining are under design development.

Mega TBM tunnel linings are normally associated with significant axial hoop forces. The high lining hoop forces from the opening segment rings must be transferred through high-capacity shear structural elements to the adjacent non-opening segment rings or external structures during segment opening. This is typically accomplished using heavy and large steel structures (such as steel segments, straight and arched beams, jacked props, etc.). Measures are also required to limit the segmental lining deformation due to the larger collar excavation area at the segment extrados compared to the smaller segment opening size. Harding and Treweek (2016) have summarised and discussed the major solution types of segment opening support and their load path mechanism and key features. Chau et al. (2023) further elaborates upon the segment opening support systems to include the WGT solution, which adopts a combination of shear bi-cones and shear key as the segment opening support system for the high shear force transfer and using non-opening RC segment rings for supporting jambs. Such a support system allows the segment opening with minimum construction inconvenience. Bi-cones are a proprietary product evenly distributed around the circumferential joint. Shear keys used in West Gate Tunnels comprise a seamless steel pipe installed in a post-cored hole from segment intrados through/across the circumferential joint and encapsulated within high-strength grout. The design of the segment opening support for WHT is still under development. However, it may adopt similar principles as WGT from Chau et al. (2023), with additional project specific construtability inputs and coordination to improve construction planning and efficiency and reduce construction safety risk.

7 CONCLUSIONS

Steel fibre-reinforced concrete segments have been widely used in tunnelling projects. Typically, as a minimum, steel ladders or reinforcement are required at radial and circumferential joints to resist the high bursting stresses in segmental lining design.

The Western Harbour Tunnel (WHT) project in Sydney is Australia's largest diameter TBM tunnel project, currently under design and construction. The WHT TBM tunnels pass through jointed and stress-relieved rock and a section of soft ground under

Sydney Harbour, with a 35 metre to 45 metre water head above the tunnel crown. The segment design has used different empirical and numerical analyses to overcome many design challenges and confirmed the SFRC lining design for the tunnel alignment. This makes the WHT the world's largest TBM tunnel (15.15 metre tunnel OD) using SFRC segmental lining without radial and circumferential joints steel ladder/ reinforcement. The WHT project further develops steel fibre segmental tunnel lining design for mega TBM tunnels, which results in a cost-effective, durable and sustainable segmental lining design.

ACKNOWLEDGMENTS

The paper is published with permission from Transport for NSW, which the authors would like to gratefully acknowledge. The design and construction of the project is currently being undertaken by Acciona with the designer joint venture AECOM AURECON JV.

REFERENCES

Anagnostou, G., and Kovari, K., 1996. Face Stability Conditions with Earth-Pressure-Balanced Shields, Tunnels and Underground Space Technology Vol. 11, No. 2, pp. 165–173, 1996.

Asche H and Ireland T., 2013. Segmental Lining Design for Large Diameter Road Tunnels. Rapid Excavation and Tunneling Conference, June 2013. pp 866–877.

Broms B.B. and Bennermark H., 1967. Stability of clay at vertical openings. Journal of Soil Mechanics. And Foundations Division. ASCE, 193(SM1), 71–94.

Chau, S.F., Ireland, T. & Eratne, S., 2017, Waterview Connection Tunnels – Post Construction Review, Proc. of 16th Australasian Tunnelling Conference 2017, 30 October - 1 November, Sydney, Australia.

Chau, S.F., Ireland, T., Lu, L., Gauffre, J., & Cole-Hawthorne, C., 2023, Design and Construction of Segment Opening on Mega TBM Tunnel, Proc. of 18th Australasian Tunnelling Conference 2023, 6-8 October, Auckland, New Zealand.

Chau, S.F., Ireland, T., Asche H, Muir, J., & Clarke, B., 2020, SFRC Linings of Mega TBMs, Proc. of 17th Australasian Tunnelling Conference 2020 1, 10–13 May, Melbourne, Australia. pp 319–331.

DAUB, 2016. Recommendations for Face Support Pressure Calculations for Shield Tunnelling in Soft Ground. 2016, Deutscher Ausschuss für unterirdisches Bauen e. V. (DAUB).

FHWA, 2020, Precast Concrete Segmental Liners for Large Diameter Road Tunnels Literature Survey and Synthesis, U.S. Department of Transportation Federal Highway Administration, FHWA-HIF-20-035, September 2020.

Guyon, Y. 1953. Prestressed concrete, English edn. London: Contractors Record and Municipal Engineering

Harding, A and Treweek, D, 2016. Effective opening support for cross passages. Proceedings of World Tunnel Congress 2016. 22-28 April, San Francisco, US.

Ireland TJ and Asche HR, 2011. Developments in Segmental Lining Design. In proceedings of Rapid Excavation and Tunneling Conference, June 2011. pp 450–462.

Janssen, P. 1983. Tragverhalten von Tunnelausbauten mit Gelenktubbings. Report No. 83-41, University of Braunschweig. Department of Civil Engineering, Institute for Structural Analysis.

T. Ireland, S.F. Chau, H. Asche, J. Muir & B. Clarke (2019), Steel Fiber Segmental Linings for Mega TBMs, Proc. of the Rapid Excavation and Tunneling Conference 2019, 16–19 Jun, Chicago, US.

ITA, 2016, Twenty Years of FRC Tunnel Segments Practice: Lessons Learnt and Proposed Design Principles, ITA Report No 16, April 2016.

Lo, Y. C. Joseph, Chau, S.F., Lau, D.W. David, Li, S.F. Eric (2009) Design and Construction of Shotcrete Lining at Tunnel Intersection of Po Shan Road Drainage Tunnels, Proceedings of Hong Kong Tunnelling Conference 2009, IMMM, Hong Kong.

Lo, J., Frew, R., Tsang, C.K., Wong, J., and Choi, K., 2012. Discussion on Soil Cover for a Subaqueous Bored Tunnel, ITA-AITES World Tunnel Congress 2012, Bangkok, Thailand.

Model Code for Concrete Structures 2010. FIB bulletin No. 65. (Sections 5.6 and 7.7 only).

Morgan HD, 1961. A Contribution to the Analysis of Stress in a Circular. Tunnel. Geotechnique 11(3): 37–46.

PAS 8810: 2016. Tunnel Design – Design of concrete segmental tunnel linings – Code of practice. British Tunnelling Society.

GEO (Golder Associates) 2009. Ground control for slurry TBM tunnelling, Geotechnical Engineering Office (GEO) Report No 249, 2009, Golder Associates HK.

Tunnelling for a Better Life – Yan, Celestino, Thewes & Eberhardt (Eds)
© 2024 The Author(s), ISBN 978-1-032-80042-4
Open Access: www.taylorfrancis.com, CC BY-NC-ND 4.0 license

Review of key technologies for design of Dalian Bay Undersea Tunnel

Zhengjie Chen*, Hong Chen & Ming Lu
Shanghai Tunnel Engineering & Rail Transit Design and Research Institute, Shanghai, China

ABSTRACT: The Dalian Bay Undersea Tunnel is the first immersed tunnel in the cold ocean of northern China. The immersed section is 3035 meters long, divided into 18 elements. This paper provides a detailed exposition of key technologies for design, such as the concrete structure durability technology of the immersed tunnel in the cold marine environment of northern China, the fully flexible segmental element scheme, the closure joint constructed by segment jacking method, and the restoration scheme for immersed elements passing beneath the breakwater, which will offer reference and inspiration for the future design and technological application of immersed tunnels in China.

Keywords: Immersed tunnel, Closure joint, Breakwater, Durability

1 PREFACE

The Dalian Bay Undersea Tunnel is located in Dalian City, Liaoning Province, China (Figure 1). It passes beneath the Dalian Bay, connecting the Zhongshan District on the south bank and the Ganjingzi District on the north bank, and effectively breaks the traffic bottleneck caused by the 'C'-shaped spatial structure of Dalian city. It is part of the urban rapid road that runs through Dalian city from north to south, connecting the eastern core area and the Jinpu New Area, thus holds significant importance in alleviating traffic congestion, promoting the integration of both banks, and establishing the Dalian coastal economic zone. This project is the first large-scale cross-sea tunnel project implemented in the PPP mode in China, and it is also the first immersed tunnel in the cold ocean of northern China.

In view of the characteristics and requirements of this project, a series of key technology research have been completed, such as the concrete structure durability technology for the immersed tunnel in the cold marine environment of northern China, the fully flexible segmental element scheme, the jacking segment method for the construction of closure joint, and the restoration scheme for immersed elements passing beneath the breakwater and so on, laying a solid foundation for the tunnel opening to traffic on May 1, 2023.

Figure 1. Project location.

2 PROJECT SCHEME

As shown in Figure 2, the Dalian Bay Undersea Tunnel project begins at the Planned Road 20 in Suoyuwan on the north bank of Dalian Bay, extends southward beneath the Dalian Bay waters, the Ganjingzi western channel, and the northern breakwater of Dalian Harbor, and ultimately reaches the land at the dock basin between the Berth 3 and Berth 4 of Dalian Harbor on the south bank. From there, it continues eastward along Ganglong West Road to Renmin Road. The total length of the main line of the project is about 5098.227m (K0+208 ~ K5+306.227).

Figure 2. Project layout plan.

*Corresponding author: chen.zhengjie@stedi.com.cn

DOI: 10.1201/9781003495505-26

Figure 3. Visual representation of the tunnel.

Based on the urban rapid road standard, the main line of the tunnel has six lanes in bi-direction with a design speed of 60km/h (Figure 3). The tunnel is constructed by the immersed tube method. Vehicles carrying flammable, explosive, toxic chemicals, and other hazardous materials are prohibited from passing through the tunnel. The design life of the tunnel is 100 years.

The main line of the tunnel has a smooth plane line, with a total of 2 horizontal curves, where a R-1050m horizontal curve is set in the immersed section, and a R-320m reverse horizontal curve is set in the cut and cover section on the south bank.

The longitudinal section of the main line of the tunnel is roughly in the shape of a "W" (Figure 4), with a maximum longitudinal slope of 4%.

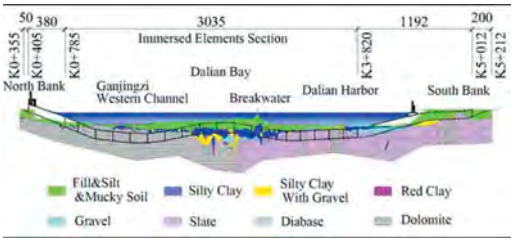

Figure 4. Longitudinal section (unit: m).

The total length of the tunnel section is 4857m, including an immersed section of 3035m (consisting of one 135m long straight element, twelve 180m long straight elements, and five 148m long curved elements), a north-bank cut and cover section of 380m, a south-bank cut and cover section of 1192m, a north-bank open section of 50m, and a south-bank open section of 200m. The immersed section adopts gravel bed foundation with a thickness of 1.3m. The bottom of immersed elements from K0+785 to K2 +100 is directly on the bedrock (highly weathered and moderately weathered dolomite). The bottom of immersed elements from K2+100 to K2+840 is on the cohesive soil (Local treatment is carried out by using block stones for replacement), and the bottom of immersed elements from K2+840 to K3+820 is directly on the bedrock (highly weathered and moderately weathered slate).

According to the process requirements for immersed tunnel construction, two dry docks are set up on the north bank to serve as prefabrication sites for immersed elements during the construction phase.

A total of four equipment areas are built along the entire tunnel line, one on the north bank and three on the south bank.

A total of two ventilation equipment rooms are set up along the entire tunnel line, which are respectively arranged in the north bank equipment area and the south bank equipment area. Two tall exhaust towers and a set of short air shafts are arranged on the ground.

A management center is arranged for the tunnel on the north bank.

3 KEY TECHNOLOGIES FOR DESIGN

3.1 *Concrete structure durability technology for the immersed tunnel in the cold marine environment of northern China*

The environmental category of this tunnel is both marine chloride environment and freeze-thaw environment. Therefore, the impact on concrete brought by the above two environmental categories must be considered for the technical performance requirements of concrete.

1) According to the "Standard for Design of Concrete Structure Durability" (GB/T 50476—2008), the environmental categories and action levels of this project are confirmed as I-B, III-C, III-E, II-E, and V-D. The waterproofing and durability design indexes for concrete structures are shown in Table 1.
2) For this project, the frost resistance index is selected as the concrete frost resistance indicator, and it is proposed that the concrete frost resistance index DF shall reach 80%. Furthermore, considering the project construction schedule and the requirements of winter construction, it is also proposed for this project that the critical strength of concrete frost damage shall not be less than 70% of the design strength.
3) As another important component of the durability of the concrete structure, the specific requirements for the minimum thickness of concrete cover are put forward. Taking the immersed section as an example, for water-facing surfaces of the top slab, bottom slab, and sidewall, the thickness shall be 70mm; for the non-water-facing surfaces, the thickness shall be 50mm; and for either side of the middle wall, the thickness shall be 50mm. For the special range where sidewalls of the north-bank cut and cover section are in the splash area, the minimum thickness of the concrete cover shall be increased to 120mm, and the stainless steel reinforced mesh that does not come into contact with the regular steel reinforced cage is set up in the cover.

Table 1. Waterproofing and Durability Design Indexes for Tunnel Concrete.

Project site		Immersed section, shore section
Site environment		The outer side is in contact with seawater-containing soil, while the inner side is exposed to the marine atmospheric environment.
Concrete strength class		≥C45 (28 days of age) ≥C50 (56 days of age)
Concrete impermeability level		P8~P12
Control of cementitious materials	Type of cementitious materials	PO, PI, or PII cement with low heat of hydration + high-quality fly ash (≥ Grade II fly ash) + superfine slag powder (≥S95) and other ultra-fine mineral admixtures
	Consumption of cementitious materials (kg/m^3)	380~480
	w/b	≤0.34
Concrete chloride diffusion coefficient (m^2/s) (detected by the RCM method)		≤ 6.5 x 10^{-12} (28 days of age) ≤ 4.5 x 10^{-12} (56 days of age)
Depth of rapid carbonization (cm)		≤2
Alkali content (kg/m^3)		≤3
Chloride ion content (%)		≤0.08
Sulfur trioxide content (%)		≤4
Air content inconcrete(%)		≤7

On the other hand, for the concrete structures in the splash area or the water level fluctuation area, its exterior surface is coated with a solvent-free epoxy anticorrosive coating, combined with an aliphatic polyurethane coating, serving together as a special durability measure. The solvent-free epoxy anticorrosive coating has a thickness of 600μm and is characterized by its ability to be applied in dry, humid, and underwater environments at room temperature. In humid and underwater environments, it can cure within 24 hours and provide a good overlapping transition with the polyurea waterproof coating on the top slab of cut and cover tunnel. The applicable aliphatic polyurethane coating has a thickness of 80μm. Its excellent resistance to UV aging and salt mist makes it suitable as a surface protection coating for the marine concrete structure with an outdoor service life of ≥15 years. Additionally, this coating also exhibits outstanding recoatability, facilitating future maintenance, repairs, and recoating of the coating.

3.2 *Fully flexible segmental element scheme*

1) Cross section of the element

As shown in Figure 5, the cross section of the element is designed to have 2 tubes and 1 gallery. The outer dimensions of the element are 33.4m (width) × 9.7m (height), with a clear height of 6.90m for the traffic tubes and a clear width of 12.65m for a single tube. Both the top and bottom slabs of the element have a thickness of 1.4m, the middle wall has a thickness of 0.6m, and the sidewall has a thickness of 1.25m.

Considering factors such as concrete weight, steel content of the structure, water density, construction loads, and element fabrication errors, the freeboard height of the element after outfitting is calculated to be within the range of 100mm to 200mm.

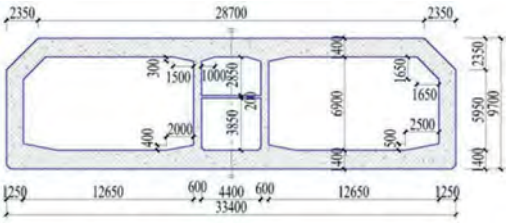

Figure 5. Element cross section (unit: mm).

2) Element selection scheme

This project adopts a fully flexible segmental element scheme, which is the first of its kind in China. The feature of full flexible segmental element is mainly reflected in the structures of an element joint (between two elements) and a segment joint (between two segments of a single element), which enables effective reduction in longitudinal forces on the element structure, and allows for better adaptation to uneven foundation settlement.

Currently, the maximum length for a segmental element can reach 180m. Compared to the shorter monolithic element, it not only reduces the number of elements and the times of immersion, but also correspondingly decreases construction risks. In this project, the 180-meter-long standard straight element is divided into 8 segments; the 135-meter-long straight element is divided into 6 segments; and the 148-meter-long curved element is divided into 7 segments.

In this project, a total of 19 flexible element joints are set. Each element joint mainly consists of the

end steel shell, vertical steel shear keys (VSK1~2 in Figure 6), horizontal reinforced concrete shear keys(HSK1~2 in Figure 6), GINA gasket, OMEGA seal, fireproof structure and so on.

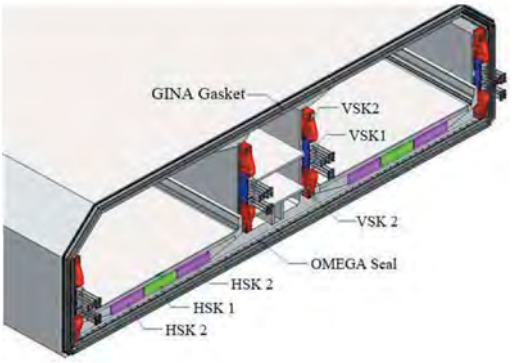

Figure 6. Schematic diagram of a flexible element joint.

In this project, a total of 119 flexible segment joints are set. Each segment joint consists of the OMEGA seal and its embedded part, shear bar, temporary pre-stressed pipe, middle-buried waterstop, sand blocking device, fireproof structure and so on, as shown in Figures 7-8.

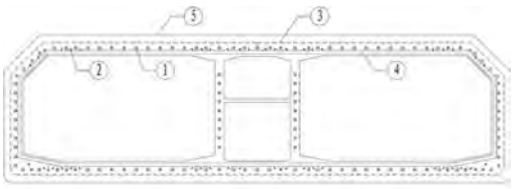

Figure 7. Typical cross-section arrangement of a segment joint.

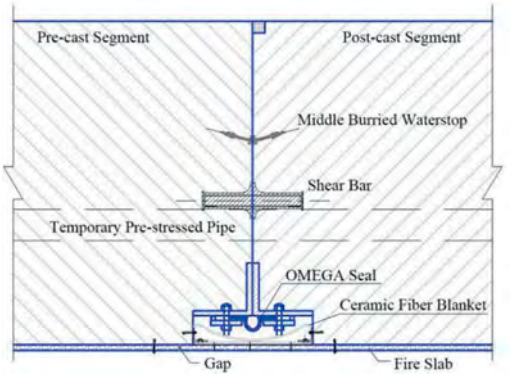

Figure 8. Longitudinal section of top slab at the segment joint.

The segment joint can transmit compression, but not tension. Furthermore, the segment joint can transmit vertical and horizontal shear forces through the special shear bar distributed on the top slab, bottom slab, side wall and middle wall. According to longitudinal force calculation results of the immersed elements structure and bearing capacity test results of the special shear bar, 124 sets of special shear bars are installed at part of the segment joints and 68 sets of special shear bars are installed at the other segment joints.

Before the element is floated, it needs to be tensioned using temporary pre-stressed cables to connect longitudinally segments within the element as a whole. And it shall also be ensured that during construction processes like floating and sinking, the compressive stress at each segment joint is not less than the minimum compressive stress required. The pre-stressed pipes are symmetrically arranged along the element centerline, with 24 pre-stressed pipes arranged on the top slab and 22 pre-stressed pipes arranged on the bottom slab (including 2 reserved pipes respectively).

Vacuum grouting is carried out in the pre-stressed pipe after the temporary pre-stressed cable is tensioned. The pre-stressed anchor heads at both ends of the element are equipped with sealing covers capable of withstanding 0.4MPa water pressure.

After the element is sunk into position for a period of time, the temporary pre-stressed cable at the segment joint is cut to release the pre-stressing force, so that the segment joint becomes a flexible joint that can adapt to certain deformation. The principle of cutting temporary pre-stressed cables is to cut all temporary pre-stressed cables of an element at a batch. Before cutting, it shall be ensured that the backfill coverage, and at least the first layer of ballast concrete, have been completed, and the settlement is also stabilizing (with a change rate not exceeding 0.5mm/day).

Monitoring data indicates that the change in settlement before and after the cutting of temporary pre-stressed cables is not greater than 1mm.

3.3 *Closure joint constructed by segment jacking method*

In this project, diverging and converging ramps are set within the south-bank dock basin, with a gradual change in the cross section. The boundary mileage between the immersed section and the cut and cover section on the south bank is set at K3+820, located at the northern end of the dock basin. The north-south length of the dock basin is about 660m. After the temporary cofferdam is set up at the northern end of the dock basin, the concrete can be cast-in-place at the cut and cover section in it, as shown in Figure 9.

According to the construction schedule, immersed elements are sunk one after another from north to south. So as to meet the requirement of the construction period, the closure joint is arranged accordingly at the south bank side. The bottom elevations of the

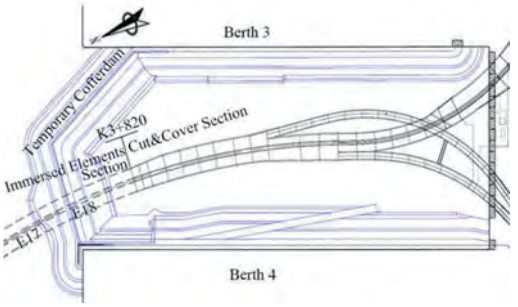

Figure 9. South-bank dock basin tunnel layout plan.

southernmost three elements (E18 to E16) gradually deepen from south to north, with elevations ranging from -25.7 to -27.1m.

The closure joint constructed by segment jacking method is a new type of closure joint. The joint is located at the junction of the immersed section and the cut and cover section. This closure joint structure primarily consists of an external sleeve, jacking segment, waterstop structure, pushing device, locking structure, and post-cast strip structure (Figure 10). During construction, under dry working conditions, the external sleeve structure connected to the cut and cover section is poured first, and then the jacking segment structure is constructed a certain distance away from the external sleeve. Next, push the jacking segment into the external sleeve and install the water stop structure, then fill the site with water. Once the final element is sunk to position, the jacking segment is pushed out using the reserved pushing device for initial compressive connection. Subsequently, the water inside the element joint compartment is discharged, achieving hydraulic compressive connection. After then, install the locking structure. Close the water inlet valve of the jacking segment and discharge water. Pour reinforced concrete at the post-cast strip between the jacking segment and the external sleeve, conduct backfill coverage, and grouting for the foundation of the jacking segment. Finally, remove the bulkhead to complete the closure joint.

By comparison, this project adopts the closure joint constructed by segment jacking method, considering simpler structure fabrication, the main work completed in a dry working environment and minimal underwater works, which assures construction quality, a shorter construction period, limited affection by water depth, and lower construction costs.

In this project, the main components of the closure joint constructed by segment jacking method are as follows:

1) The external sleeve is a cast-in-place reinforced concrete structure. It has a maximum width of 36.23m, a height of 12.70m, and an initial engagement length with the jacking segment of about 2.95m. The lateral internal gap between the external sleeve and the jacking segment is

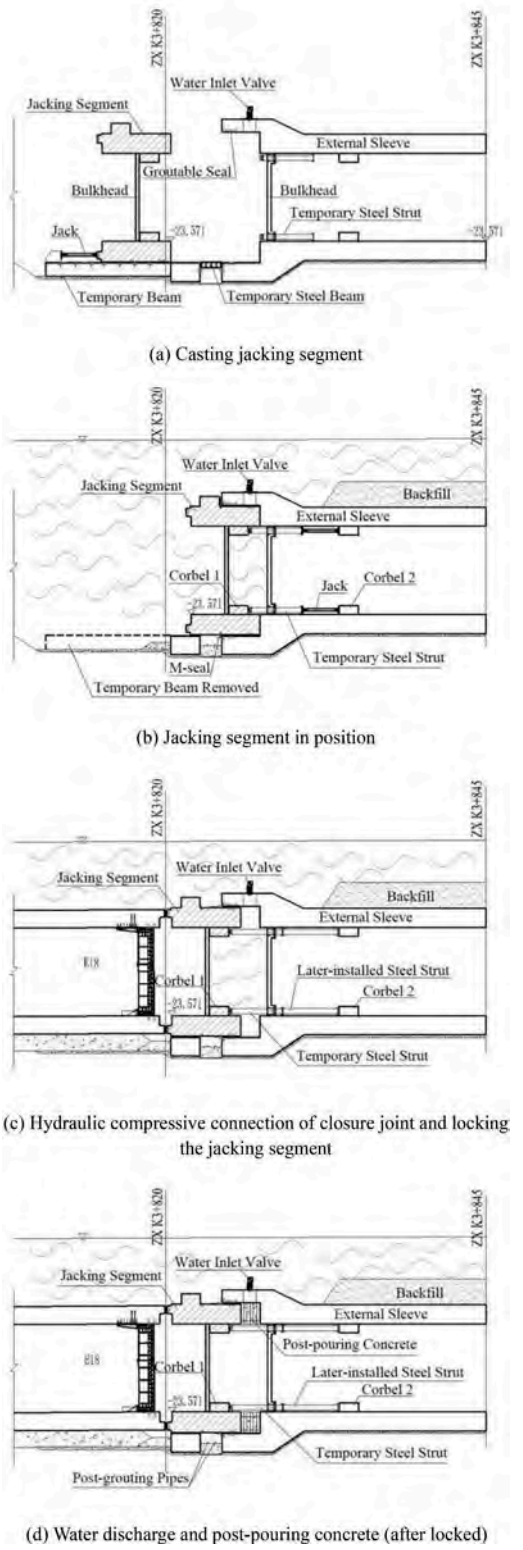

Figure 10. Diagram of construction sequence for segment jacking method (unit: m).

designed with a spacing of 100mm in the engagement range. A reinforced concrete bulkhead is set up in the external sleeve.

2) The jacking segment is a reinforced concrete structure with two tubes and one gallery, having a width of 34.03m, a height of 10.05m, a length of 5.75m, and a bottom elevation of the bottom slab is -25.171m (the top elevation -23.571m). A reinforced concrete bulkhead is set up in the jacking segment. The end face of the jacking segment that connects the immersed element is equipped with the end steel shell, embedded part of vertical steel shear keys, and embedded part of horizontal concrete shear keys etc. A sliding plate structure consisting of mirror-finished stainless steel plate and polytetrafluoroethylene plate is set up at the bottom of the jacking segment, with a sliding friction coefficient of about 0.1. The jacking segment is pushed out in the water for a distance of about 1.5m.
3) The structure adopts two waterstops (Figure 11): M-seal and groutable seal. Waterstops are arranged along the outside of the jacking segment, with one ring each, forming a dual-sealed ring. The circumference of each exceeds 87m. With the design water pressure, the M-seal meets the water-tightness requirement when streching out by 1.5m ± 0.1m; the groutable seal, when grouted (with water), expands to seal the gap between the jacking segment and the external sleeve, thus meeting the water-tightness requirement.

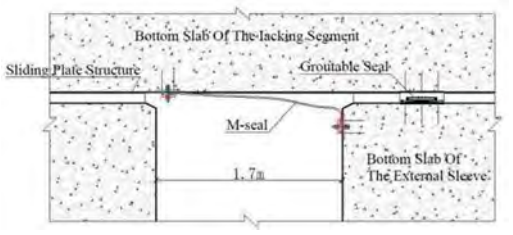

Figure 11. Diagram of the longitudinal section of two waterstops after the jacking segment is pushed out.

4) The pushing device consists of 4 pushing jacks behind the bulkhead of the external sleeve, along with the temporary steel strut and reinforced corbel 1 and corbel 2, as shown in Figure 12.If necessary, the pushing device can also use the steel corbel for pulling back.

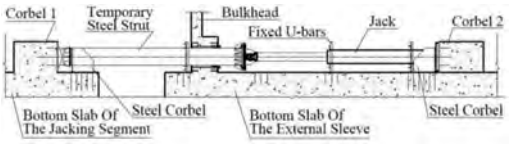

Figure 12. Pushing device structure.

5) The locking structure uses 24 temporary steel struts combined with later-installed steel struts. Each individual steel strut can withstand an axial force of 550t.
6) The post-cast strip uses self-compacting compensating shrinkage concrete with a layered pouring process.

Considering that the jacking segment method is being applied for the first time in China, the pushing process test and the waterstop watertightness test were done on small-sized models before design. This provided reliable calculation parameters and optimization suggestions for the design and construction of the closure joint.

The measurement data after breakthrough survey indicates that the axial horizontal deviation of the jacking segment is no more than 3mm, and the elevation deviation is no more than 2mm; the relative horizontal deviation from the end of element E18 is about 17mm, and the relative elevation deviation is 38mm, both of which meet the requirements.

3.4 *Restoration scheme for immersed elements passing beneath the breakwater*

In this project, the immersed section passes beneath the northern breakwater of Dalian Harbor, with an angle of about 57° between the tunnel axis and the breakwater axis. This breakwater was originally constructed between 1908 and 1918, featuring a gravity-type cubic structure with a top width of 6m and a breakwater top elevation of 3.64m. Before the sinking of immersed elements, it is necessary to dismantle about 420 meters of the northern breakwater of Dalian Harbor to carry out the underwater foundation trench construction for the immersed elements. This breakwater will be restored after the immersed elements are sunk to position.

A special breakwater of about 64.6m in length is restored on the top of the immersed tunnel. It adopts a lightweight caisson structure form. By widening the bottom width of the breakwater and adding side loads to it, this mitigates the partial load under wave action, decreases the stress on the breakwater foundation, and solves issues related to excessive localized stress and uneven settlement of immersed elements. Compared to the high foundation gravity-type cubic structure, this scheme is featured with less cost, faster construction speed, and a smaller offshore footprint. The lightweight caisson structure has been verified through ocean physical model tests, confirming that the stress on it meets the requirement.

Specifically, a bed of 10 to 100kg riprap is first laid on the immersed tunnel, with a top elevation of -12.0m. The lightweight caissons are situated on the riprap bed, with four caissons arranged in total, as shown in Figure 13. The dimensions of a single lightweight caisson are about 16.0m x 25.5m x 14.7m (length x width x height), with internal compartments arranged in a 4x3 layout. Overhanging plates with an

overhanging width of 2.0m are set up for the bottom slabs on the south and north sides. The caisson breast wall is a reinforced concrete structure, with a top elevation of 3.64m.

To ensure uniform force distribution across the cross-section of the immersed element, the outer edge lines of stacked loads on the north and south sides of the lightweight caisson are perpendicular to the tunnel axis. The stacked load is composed of 10-100kg block stones with a minimum width of about 12m, a top elevation of -8.0m and a side slope of 1:2. At the north side (facing the ocean), 400~500kg block stones are used for protection, while at the south side (facing the dock basin), 100~200kg block stones are used for protection.

On the other hand, block stone replacement is applied to the cohesive soil foundation of the immersed elements within the breakwater area, with a replacement thickness ranging from 2.0m to 6.0m based on the longitudinal structural calculations.

Following the implementation of the above plan, the cumulative settlement of the element E12 ranges from -33.9mm to -19.8mm, all of which fall within the allowable range of design.

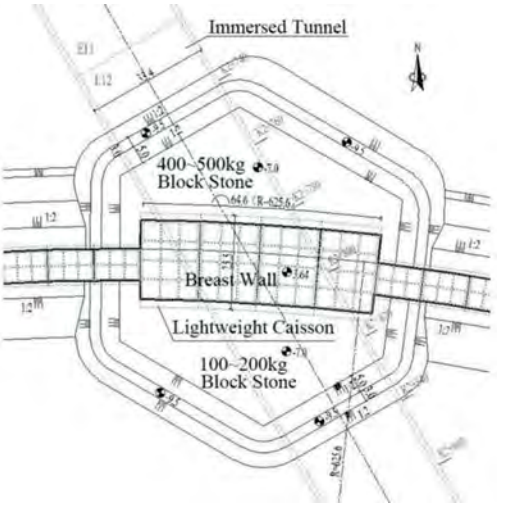

Figure 13. Breakwater restoration plan (unit: m).

4 CONCLUSIONS

The Dalian Bay Undersea Tunnel is another milestone success in the development of immersed tunnels in China. In response to the construction conditions and requirements of the Dalian Bay Undersea Tunnel, this paper elaborates on a series of key technical research achievements completed by the design team. These key technologies have not only laid a solid foundation for its smooth opening to public traffic but also provided more references and insights for the design and technical application of immersed tunnels in China.

Tunnelling for a Better Life – Yan, Celestino, Thewes & Eberhardt (Eds)
© 2024 The Author(s), ISBN 978-1-032-80042-4
Open Access: www.taylorfrancis.com, CC BY-NC-ND 4.0 license

Design of tunnel brace and retaining structure on East Artificial Island of Shenzhen-Zhongshan Link

Hong Chen, Chun Ning He*, Xiao Dong Lai & Long Yu
Shanghai Tunnel Engineering & Rail Transit Design and Research Institute, Shang Hai, China

ABSTRACT: For the Shenzhen-Zhongshan Link, the East Artificial Island is built in the estuary on the Shenzhen side, and the tunnel excavation is carried out in the soil layer that is backfilled and preloaded on the island. Considering that the original marine silt layer in the estuary is widely and unevenly distributed, thick, with low strength and high compressibility, the tunnel brace and retaining structure and respective measures are proposed. The tunnel passes between the pier 53 and pier 54 of the existing Guangzhou-Shenzhen Coastal Expressway, where the tunnel excavation is about 46m wide and 15.5m deep. The outer edge of the retaining structure is only about 1.0m from the nearest point of the pier. Through analysis and comparison, the design schemes and measures are proposed such as interlocked steel pipe piles with bored pile driven inside, rotary jet piles between pipe piles as water stop, bracing servo systems with appropriate ground improvement. These measures were finally successfully implemented to minimize the risk of pier deformation during the tunnel excavation. The monitoring data showed that the deformation of the pier of the Guangzhou-Shenzhen Coastal Expressway caused by the excavation works was below the horizontal displacement limit of 5mm required by the transportation and management authority.

Keywords: Complex ground conditions, marine silt layer, interlocked steel pipe piles, bracing servo system, ground improvement

1 PREFACE

Located in the core of Guangdong-Hong Kong-Macao Greater Bay Area, the Shenzhen-Zhongshan Link directly connects the Shenzhen Special Economic Zone and Zhongshan City. As a sea crossing project integrating "tunnel, artificial island, bridge and underground interchange", the project connects with the Jihe Expressway in the east, passes through the south side of Shenzhen Airport and the Pearl River estuary, and finally reaches the Zhongshan Xinlong Interchange in the west, where it connects with Zhongkai Expressway. The project has total length of 24km with eight lanes in both directions. The project is designed according to expressway standards with a design speed of 100km/h.

According to the function and traffic organization of the project, the east artificial island is constructed in the estuary on the Shenzhen side. The main tunnel on the island connects to the Coastal Expressway Phase II in the east and to the cofferdam tunnel in the west. The design mileage of the main tunnel is between K5+695 and K6+550. The total length of the tunnel is 855m, of which the open section is 395m long and the cut and cover section is 460m long. See Figure 1.

2 DIFFICULTIES IN THE CONSTRUCTION OF THE TUNNEL ON EAST ARTIFICIAL ISLAND

2.1 *Complicated geological conditions*

The engineering site is at Pearl River estuary, where the geological condition is complex and changeable. The soil layer distribution is extremely uneven. The soil layers in the site include silt, clay, mucky clay, residual soil, completely weathered granite, and strongly weathered granite from top to bottom.

The silt is widely distributed, which belongs to marine sedimentary and is characterized by high water content, large pore ratio, low shear strength, high sensitivity, high compressibility, local underconsolidation, and poor permeability. Even after the construction and preloading of the East Artificial Island, the parameters of the silt layer are still relatively poor with internal friction Angle as 9.4° and soil cohesive strength as 6.5kPa, and the layer is distributed in the range of the excavation depth to 12m below the excavation bottom with thickness about 1.8-8m, having a relatively deep depth.

Therefore based on the detailed survey and the supplementary survey data, it is necessary to select the brace and retaining structure reasonably with

*Corresponding author: he.chunning@stedi.com.cn

DOI: 10.1201/9781003495505-27

Figure 1. Tunnel on East artificial Island.

regard to the characteristics of silt layer such as uneven distribution, layer thickness and depth. And according to the results of excavation stability check calculation, the type and length of the retaining structure are determined, and appropriate ground improvement measures are proposed to ensure the excavation safety.

2.2 *Constraints of the existing Guangzhou-Shenzhen coastal expressway*

The Guangzhou Shenzhen Coastal Expressway is a north-south artery in the Pearl River Delta. It is constructed according to highway standards, with eight lanes in both directions with design speed 100km/h. The expressway was completed and opened to traffic in December 2013. See Figure 2.

Figure 2. Existing Guangzhou-Shenzhen coastal expressway.

The main tunnel on the East Artificial Island runs under the Guangzhou-Shenzhen Coastal Expressway, and passes between the pier 53 and pier 54. The structural width of the main tunnel is about 46m, the excavation depth is about 15.5m, and the outer edge of the retaining structure is only about 1.0m from the nearest pier. Considering the complex geological conditions and working conditions of island construction and backfilling on the original marine silt layer at the tunnel site, it is necessary to carefully design the retaining structure and make a reasonable construction organization so as to minimize the potential deformation risks of the bridge piers during the construction. The horizontal displacement limit of the piers during excavation must be less than 5mm required by the transportation and management authority.

See Figures 3 and 4 for photos of the construction phases of the East Artificial Island and the tunnel.

Figure 3. Bird's-eye view of construction of the East Artificial Island and tunnel excavation.

Figure 4. Excavation passing through Guangzhou-Shenzhen Coastal Expressway.

3 DESIGN OF TUNNEL BRACE AND RETAINING STRUCTURE ON EAST ARTIFICIAL ISLAND

3.1 *Overall construction process for tunnel on the island*

The locations of the tunnel on East Artificial Island, the cofferdam tunnel and the Coastal Expressway are shown in Figure 5.

To avoid the mutual interference by the construction of the East Artificial Island and the temporary cofferdam, the eastern end of temporary cofferdam is located approximately 130m from the Coastal Expressway.

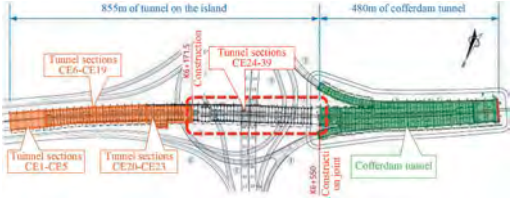

Figure 5. Schematic diagram of overall construction process of the tunnel on the Eastern Artificial Island and cofferdam tunnel.

The overall construction of the East Artificial Island progresses from the east side of the Coastal Expressway to the west side. The tunnel on the island is also constructed in sections with the formation of the island. The backfill thickness for the construction of the island is 8m. To avoid the impact of the backfilling loading on the safety of the operation of the Coastal Expressway, the tunnel on the island is divided into two sections at the mileage of K6 +171.5m, a distance of approximately 161.5m to the east of the Coastal Expressway.

So the tunnel on the island and the cofferdam tunnel are roughly constructed in three phases. The cofferdam is constructed first. The eastern section of the tunnel on the island is commenced when the island is roughly completed. The western section of the tunnel begins to construct after the completion of cofferdam tunnel and the eastern section of the tunnel.

3.2 *Design standard and principles*

(1) The safety level of the excavation shall be determined based on the surrounding environmental conditions, excavation depth, and the function of brace and retaining structure.
The tunnel on East Artificial Island consists of 39 structure sections (CE1-CE39) from east to west. The excavation safety level and deformation control standards for each structural section are detailed in Table 1.
(2) The reasonable brace and retaining system shall be designed according to the excavation safety level, depth and engineering geological conditions.
(3) Calculations shall be conducted on the strength, deformation, stability and impermeability of the brace and retaining structure.
(4) When determining the depth of the retaining structure, calculations shall be carried out on anti-sliding, anti-overturning, overall stability, anti-uplift and anti-piping stability. For the weak soil areas, vertical bearing capacity, deformation, and stability calculations shall also be checked, and reasonable measures shall be taken for the ground improvement.

3.3 *Design of the brace and retaining structure of the tunnel on the island*

For the retaining structure of the tunnel, depending on the depth of excavation, there are six types: slope excavation, single row steel sheet pile, double row steel sheet pile, bored pile + mixing pile water curtain + rotary jet grouting pile between the bored pile, interlocked steel pipe pile with bored pile driven inside + rotary jet pile between pipe piles, and diaphragm wall. Concrete and steel pipe braces are arranged according to different depths. See Figure 6.

Table 1. Control standards for excavation deformation.

Section (safety level)	Maximum horizontal displacement on top of retaining structure	Maximum horizontal displacement of retaining structure	Maximum ground settlement
CE4-CE 11 (L1)	min(1%H, 80mm)	min(1% H,80mm)	0.25%H
CE12-CE23 (L2)	min(0.4%H, 50mm)	0.3%H	0.25%H
CE24-CE29 (L2)	min(0.4%H, 50mm)	0.3%H	0.25%H
CE30 (L1)	min(0.2%H, 30mm)	0.3%H	0.25%H
CE31-CE32 (L1)	min(0.2%H, 30mm)	0.18%H	0.15%H
CE33-CE39	min(0.2%H, 30mm)	0.3%H	0.25%H

Note: H presents the depth of excavation.

Considering the poor quality of bored piles and rotary jet grouting pile construction in the backfilling of sand layer, silt, and sandy soil of island, long casing is adopted to drive through the silt layer to ensure the quality of the pile. A row of mixing pile is set at the outer side of the bored piles to cut off the water, and the rotary jet grouting pile is set between the bored piles to stop the possible seepage between the bored piles and the mixing pile to ensure the water stopping effect. See Figure 7.

To control the deformation of the retaining structure and to minimize uneven settlement during the long-term operation, the weak soil at the bottom of the excavation is reinforced with skirts and strips.

The calculation of the retaining structure simulates the whole construction process according to the principle of load increment method. The finite element method of elastic foundation rod system is adopted to simulate the actual construction process of excavation, bracing, and dismantling, and the structural analysis is carried out according to the principle of "deformation first, brace later". According to the calculations, both the maximum horizontal displacements and all the stability calculations meet the requirements of the code.

4 DESIGN NODE OF TUNNEL PASSING THROUGH GUANGZHOU-SHENZHEN COASTAL EXPRESSWAY

4.1 *Brace and retaining structure design scheme*

In combination with the analysis of the impact of the backfilling of the East Artificial Island and the tunnel excavation on Guangzhou-Shenzhen Coastal

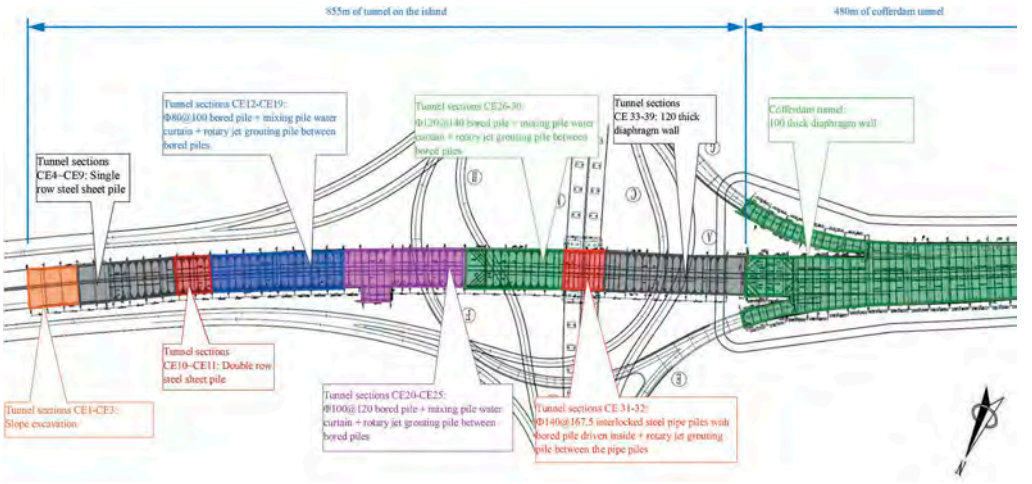

Figure 6. Layout of tunnel retaining structure on the island (dimension unit of retaining structure indicated in the figure: cm).

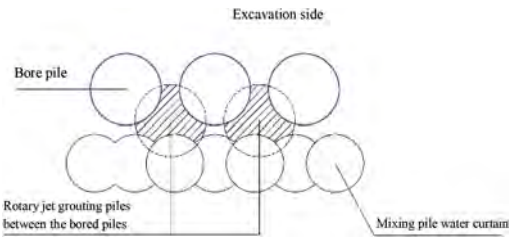

Figure 7. Schematic diagram of bored pile, mixing pile water curtain, and rotary jet grouting pile.

Expressway, the design scheme of the retaining structure and the construction organization design are optimized to minimize the potential deformation risks of the bridge piers. The tunnel retaining structure is designed as combined together with the protection structure of the Coastal Expressway in the construction of the East Artificial Island. The specific design is as the followings:

(1) The Φ140cm interlocked buckle steel pipe piles are set at the pier side every 167.5cm. The pile length is 27.1-30.1m. The bored piles are driven inside the steel pipe piles to increase the stiffness of the retaining structure. The rotary jet grouting piles are set on the outer side for water stop between the pipe piles.

(2) There are four braces, e.g., one concrete brace + three steel pipe braces. All of the steel pipe braces are provided with the servo system. The brace servo system is an intelligent horizontal displacement control system, composed of hardware equipment and software programs. It is suitable for projects with strict control requirements for deformation of retaining structure during excavation. The system can realize 24h real-time monitoring, low voltage automatic servo and high voltage automatic alarm, providing comprehensive and multiple safety guarantees for the excavation. The excavation profile passing through Guangzhou-Shenzhen Coastal Expressway refers to Figure 8.

(3) Considering the complex geological conditions and working conditions of backfilling the island on the original estuary silt layer, in combination with supplementary survey data, skirt + strip rotary jet grouting pile is used to improve the area from the top of the silt layer to the bottom of the excavation about 12m. The skirt width is 5m, the strip width is 5m, and the spacing is 5m. The improvement range extends appropriately along the tunnel to both sides of the bridge. See Figure 9.

(4) As the second steel pipe brace is basically located at the center of the bridge pier abutment, the soil between the interlocked steel pipe pile and abutment is reinforced with rotary jet grouting piles, so as that the second steel pipe brace and the reinforced soil may be formed as a lateral constraint for the abutment.

(5) To ensure effective control of the displacement, settlement, and inclination of the piers of Guangzhou-Shenzhen Coastal Expressway during the artificial island backfilling and excavation, safety evaluation of the operation status of the existing bridge is conducted before construction. And based upon the evaluation, the special construction scheme is formulated to ensure the safety of the bridge. The construction monitoring runs through the whole construction process, which provides timely the monitoring information. And measures shall be taken timely to control the displacement of bridge piles and to ensure the safe operation of the Coastal Expressway.

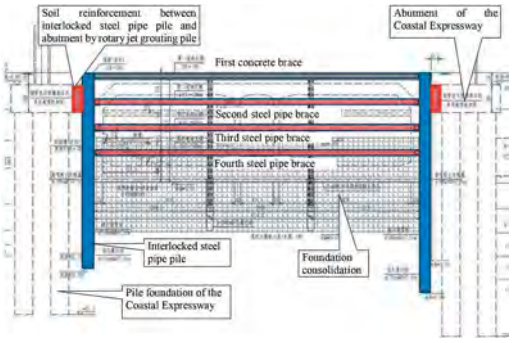

Figure 8. Cross section of brace and retaining structure of the tunnel passing through Coastal Expressway.

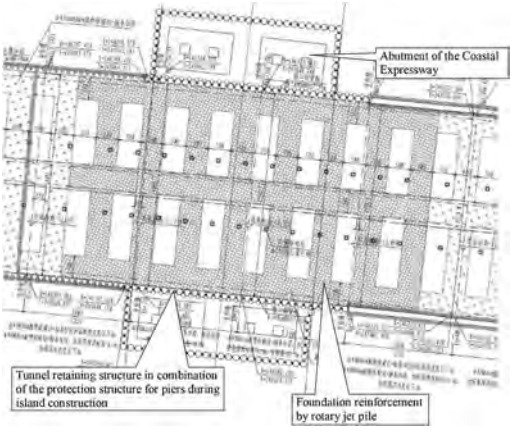

Figure 9. Layout of excavation reinforcement at the location of tunnel passing through Coastal Expressway.

4.2 *Calculation and analysis*

In addition to the calculation and analysis by the finite element method of elastic foundation rod system, 3D finite element model is also used to study the impact of island construction and tunnel excavation on the existing Guangzhou-Shenzhen Coastal Expressway. Considering the linear elasticity of the material, the soil and abutment are simulated with solid units, the retaining structure of excavation is simulated with plate elements, and the pile and brace structure are simulated with beam elements. The calculation model and working conditions refer to Table 2 for in detail, and the calculation results refer to Figures 10-13.

The calculation shows that: Impacts of construction of the East Artificial Island and excavation of tunnel on the pile foundation of Coastal Expressway are as follows: Horizontal additional displacement 4.32mm < 5mm (towards the side of the excavation), and vertical additional displacement -0.685mm < 5mm (settlement), showing a relatively small impact. After applying the additional bending moments, shear forces, and axial forces, the calculation of pile foundation of Coastal Expressway still meets the design requirements both in ultimate limit state and serviceability limit state.

The 2D finite element model is also used for parallel check analysis. In the analysis, the soil is modelled with soil hardening model, the brace structure is simulated with anchor elements, and other structures are simulated with beam elements, considering the linear elasticity of the material. The working conditions calculation is the same as the 3D model. The calculation results refer to Table 3.

According to the calculation results, the impacts from the east artificial island construction and the tunnel excavation on the pile foundation of Coastal Expressway are as follows: Horizontal additional displacement 3.88mm < 5mm (towards the side of the excavation), and vertical additional displacement -0.937mm < 5mm (settlement), showing a little impact.

4.3 *Comparative analysis of monitoring data*

4.3.1 *Brace axis force*

The envelope values of each brace obtained by the finite element method of elastic foundation rod system are as follows: The axis force of the first concrete brace is 2796kN, the axial force of the second steel pipe brace is 2535kN, the axis force of the third steel pipe brace is 2264kN, and the axis force of the fourth steel pipe brace is 944kN.

The measured axis forces of each brace during the excavation measured are shown in Figure 14:

(1) The axis force of the first brace gradually increases with the excavation. After the second steel pipe brace is installed, the axis force decreases, and then gradually increases with the next excavation. After the third steel pipe brace is installed, the axis force of the first brace tends to be stable.
(2) Upon the application of bracing servo system, the steel pipe brace axis force is timely adjusted based on monitoring data, and the axis force of each steel pipe brace becomes relatively stable.
(3) The brace axis forces monitored on site are not beyond the design envelope values, which are approximately 70-85% of the design envelope values.
(4) According to the axis force change curve, it can be seen that the steel pipe brace failed to be installed in time due to the rainstorm weather during the construction, which is particularly obvious in the first brace axis force curve. The on-site excavation and brace installation must follow in queen, and brace shall be done with the excavation progress.
(5) Some steel pipe braces may experience looseness in the pre-applied axis force during the excavation. In this situation, the load must be strictly applied in levels according to the excavation conditions and be adjusted at any time according to the axis force monitoring curve.

Table 2. List of working conditions analysed by 3D finite element models.

	Calculation model	Descriptions of working conditions
Working condition 1	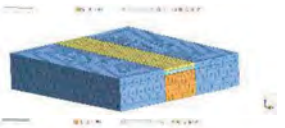	With pile foundation and abutment provided, calculate initial ground stress, and clear the displacement
Working condition 2	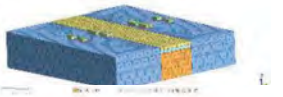	Island backfilling, preloading, and consolidation for 90 days
Working condition 3	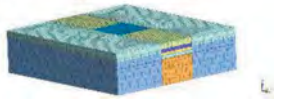	Loading/unloading
Working condition 4	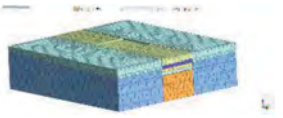	Construction of retaining structure and foundation reinforcement
Working condition 5-1	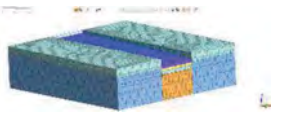	Excavation is carried out step by step from top to bottom with the erection of corresponding brace
Working condition 5-2	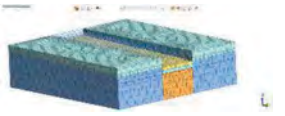	
Working condition 5-3	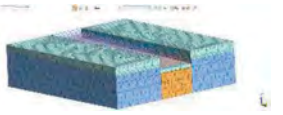	
Working condition 5-4		
Working condition 6	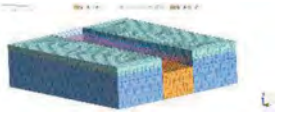	Cast the bottom slab and remove the fourth brace

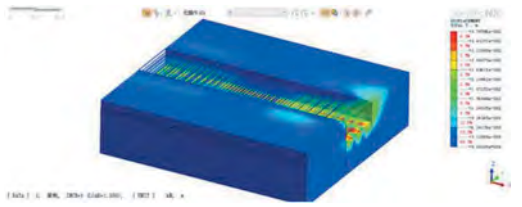

Figure 10. Diagram of overall deformation (mm).

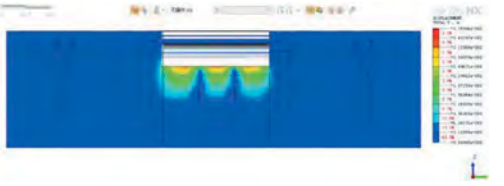

Figure 11. Profile of overall deformation (abutment position) (mm).

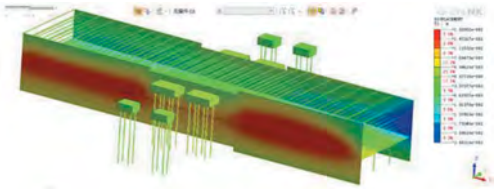

Figure 12. Horizontal displacement of structure (mm).

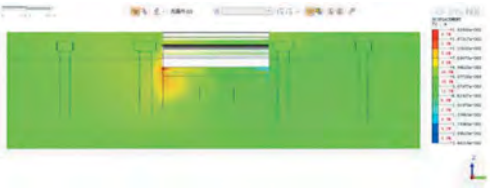

Figure 13. Profile of horizontal displacement of the structure (mm).

Table 3. List of main analysed working conditions of 2D finite element models.

	Calculation model	Descriptions of working conditions
Working condition 2	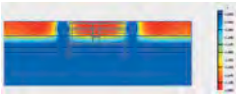	$U_v$max=-1.82mm, $U_h$max=-2.86mm
Working condition 3	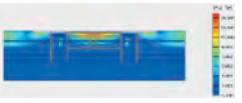	$U_v$max=0.3mm, $U_h$max=0.671mm
Working condition 6	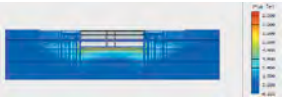	$U_v$max=-0.788mm, $U_h$max=3.78mm

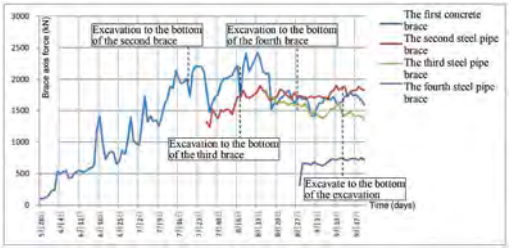

Figure 14. Brace axis force monitoring curve.

4.3.2 *Horizontal displacements of soils*

According to the monitoring data of the horizontal displacement as the monitoring sections of ZQT62, 64, and 65, see Figures 15-18, it can find that:

(1) When excavating to the bottom of the second steel pipe brace, at a depth of about 4.5m, the horizontal displacement of each sections within depth of 15m is basically between the calculated values of the soil structure model and the load structure model; while below 15m the horizontal displacement is close to the calculated curve of the soil structure model.
(2) When excavating to the bottom of the third steel pipe brace, at a depth of about 8.5m, the horizontal displacement of each sections within the depth of 13m is basically between the values calculated by the soil structure model and the load structure method; while below 13m, the displacement is relatively consistent with the calculated curve of the soil structure model.
(3) When excavating to the bottom of the fourth steel pipe brace, at a depth of about 12m, the horizontal displacement of each sections within the depth of 18m is more consistent with the soil structure model; while below 18m, the displacement is between the calculated values of the soil structure model and the load structure model.
(4) When excavating to the bottom of the fourth steel pipe brace, at a depth of about 15.5m, the horizontal displacement of each sections within the depth of 18m is more consistent with the soil structure model; while below 18m, the displacement is between the calculated values of the soil structure model and the load structure model.

The soil layer in the excavation is relatively complex, with a thickness of 3.3~6.3m of silt layer. The spatial differences in soil layer distribution, the different soil layer parameters selected for the two calculation methods, and possible deviations in soil layer parameters result in slight deviation between the calculated values and measured values.

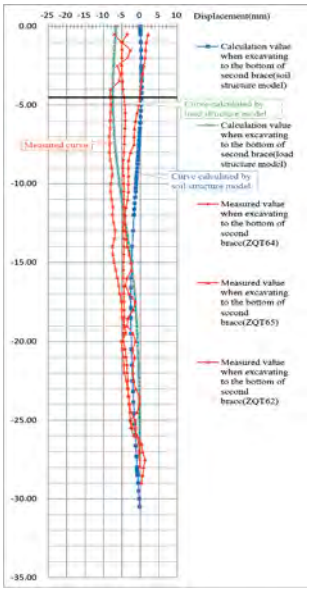

Figure 15. Horizontal displacement when excavating to the bottom of second brace.

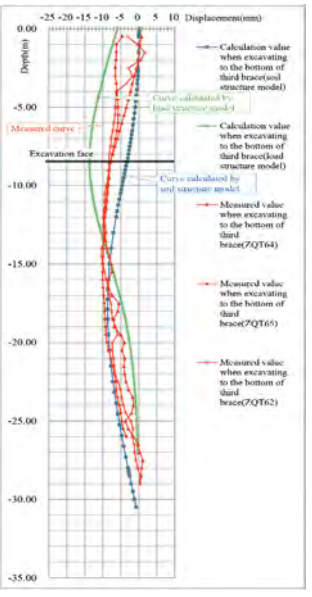

Figure 16. Horizontal displacement when excavating to the bottom of third brace.

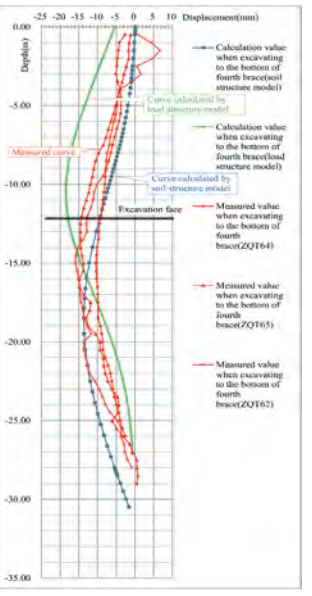

Figure 17. Horizontal displacement when excavating to the bottom of fourth brace.

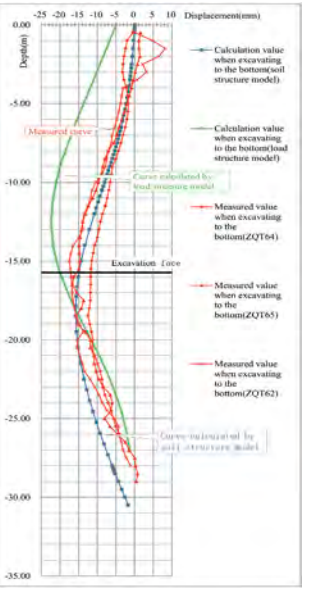

Figure 18. Horizontal displacement when excavating to the bottom of the excavation.

4.3.3 *Horizontal displacement of piers*

The horizontal displacement monitoring curves of pier 53 and pier 54 of Coastal Expressway (see Figure 19)shows that before the tunnel excavation, the horizontal displacement of the piers caused by island backfilling and preloading is about 1.4-2.6mm towards the outside of the excavation, and the horizontal deformation is relatively stable before the excavation. With the tunnel excavation, especially after excavating to the second brace, the horizontal displacement curve of the piers change significantly and begin to gradually deform towards the excavation. When excavating to the bottom, the horizontal displacement of the piers is about 0.4~3.4mmm, which meet the horizontal displacement limit of 5mm required by the transportation management authority.

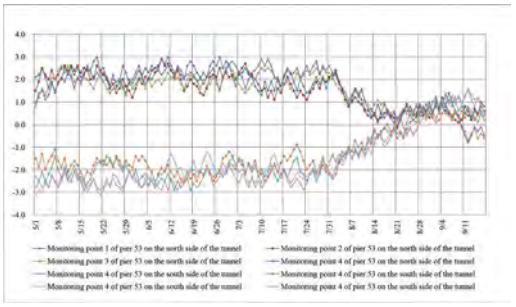

Figure 19. Horizontal displacement time curves of piers 53 and 54.

5 CONCLUSION

This paper presents the design scheme for tunnel excavation after island backfilling and preloading on the existing marine silt layer, focusing on the brace and retaining scheme for the tunnel passing through the Coastal Expressway. Based on the analysis of on-site monitoring data, the stress and deformation characteristics of the excavation are obtained. The successful construction of the tunnel excavation passing through Coastal Expressway, not only ensures normal operation of the Coastal Expressway, but also provides reference for similar projects in the future.

For the tunnel passing through the Coastal Expressway, the following conclusions are obtained:

(1) The retaining structure in combination with the protection structure of the Coastal Expressway during the island construction and the bored piles driven into the interlocked steel pipe pile greatly improve the rigidity of the retaining structure, and the displacement of the retaining structure is controlled effectively.

(2) With the favourable conditions of the second steel brace located at the center of the pier abutment, the soil between the interlocked steel tube pile and the abutment is reinforced with rotary jet grouting piles, which can effectively form lateral constraints on the abutment and minimize the horizontal displacement of the abutment and pile foundation.

(3) The steel bracing servo system automatically compensates for the brace axis force and actively regulates the brace axis force, effectively controlling the displacement of the retaining structure.

(4) According to the calculation results of the load structure model and the soil structure model, as well as the comparative analysis of monitored data, the horizontal deformation of the excavation is basically between the calculated values of two models.

(5) In the design of the brace and retaining structure, the effects of the excavation method and sequence on the displacement and stress conditions of the brace and retaining system shall be considered. During construction, the dynamic engineering monitoring and timely analysis of the monitoring results shall be carried out, and the data shall be collected to provide a basis for scientific research and structural design.

Tunnelling for a Better Life – Yan, Celestino, Thewes & Eberhardt (Eds)
© 2024 The Author(s), ISBN 978-1-032-80042-4
Open Access: www.taylorfrancis.com, CC BY-NC-ND 4.0 license

Sustainability of Shihmen reservoir by desilting tunnel in Taiwan

Chen-En Chiang, Pao-Sheng Kuo, Hsien-Tsung Chiang & Yan-Jhih Lin*
Geotechnical Engineering Department, SINOTECH Engineering Consultants Ltd., Chinese Taipei

ABSTRACT: Earthquake and typhoon are two major natural hazards in Taiwan. Earthquake-triggered landslide in mountainous areas accompany with torrential rainfall supply large amount of sediment to river basin and cause sediment accumulation of reservoir. Considering strategies can be used to reduce sediment delivery or prevent sediment deposition, hydraulic desilting has proven to be the most effective and economical method. Shihmen Reservoir is the main water conservation facility in northern Taiwan and the catchment area is 763.4 km^2. After 60 years of operation, the storage volume reduced from 3.09×10^8 m^3 to 2.09×10^8 m^3 because of sever siltation. To solve the problem, Water Resources Agency (WRA) decided to construct a desilting tunnel which is bypass Shihment dam in 2017. The tunnel is completed in February 2023 and operated while typhoon Haikui attacking Taiwan. About 2×10^5 m^3 silt was discharged by this event and it consider a great success to achieve the objective for the project.

Keywords: Shihmen Reservoir, Sediment, Desilting tunnel

1 INTRODUCTION

1.1 *Project background*

Shihmen Reservoir is the main water conservation facility in northern part of Taiwan with the function of irrigation, electric power generation, water supply, flood prevention and tourism. Shihmen dam impounds the water from Dahan River with the watershed area of 763.4 km^2 (Figure 1). Due to the extreme hydrological events happened frequently, large amount of sediment is flushed into the reservoir. According to the annual sedimentation survey, the average of 3.42×10^6 m^3 silt move into the reservoir every year. The capacity of the water conservation decreases from 3.09×10^8 m^3 to 2.05×10^8 m^3(in 2023),which means only 66% of its original storage volume is remained.

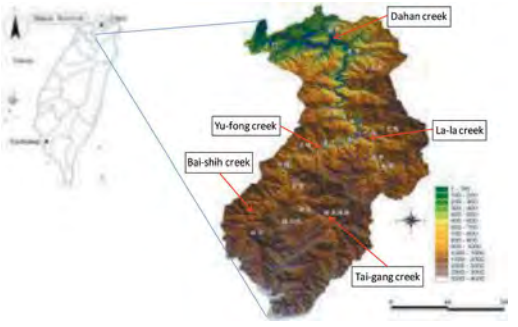

Figure 1. Location and watershed area of Shihmen Reservoir.

Considering the strategies used to reduce sediment delivery or prevent sediment deposition, hydraulic desilting has been proven to be the most effective and economical method. Therefore, Water Resources Agency (WRA) planned to build a desilting tunnel for the Shihmen Reservoir. The basic design has been completed in 2017 and D&B contract is started in November 2017 with USD $120 million of contract price. The construction has completed in February 2023.

1.2 *Objectives*

Two major objectives arise from the desilting tunnel. (1)To enhance the desilting capability and decrease sediment of the reservoir; (2)To enhance the flood-discharging capability to ensure the safety while extreme hydrological events happened.

The desilting tunnel, which is a bypass tunnel of the reservoir, is expected to discharge 6.4×10^5 m^3 silt per year. Furthermore, the desilting tunnel is designed to provide another 600 m^3/s flood-discharging capability for Shihmen reservoir as well. The comparisons of sediment discharge and flood prevention capacity before and after the desilting tunnel is completed shown as Table 1.

*Corresponding author: fcjooyclin@mail.sinotech.com.tw

DOI: 10.1201/9781003495505-28

Table 1. Capacities with/without the desilting tunnel.

Item	Without desilting tunnel	With desilting tunnel
Sediment discharge capacity [10^3 m^3/yr]	2,070	2,710
Flood prevention capacity [m^3/s]	14,100	14,700

2 STRATEGIES AGAINST SEDIMENTATION

In general, three different strategies are considered for reservoir sediment management: (1) Reduce sediment delivery (watershed management); (2) Prevent sediment deposition (route sediments through or around storage); (3) Increase or recover volume (removal of deposited sediments)

Figure 2 shows a variety of sediment management techniques proposed by Kondolf et al. (2014) including the three strategies. A combination of several measures from these categories is necessary to maintain reservoir capacity and achieve reservoir sustainability. In overall, hydraulic desilting is the most effective and economical method to release sediment out of reservoir.

To solve the problem of severe siltation at Shihment Reservoir, WRA proposed an integrated desiltation strategies as shown in Figure 3. By the combination of mechanical removal, dredging, and hydraulic discharge, the sediment discharge amount is up to 2.07×10^6 m^3/yr.

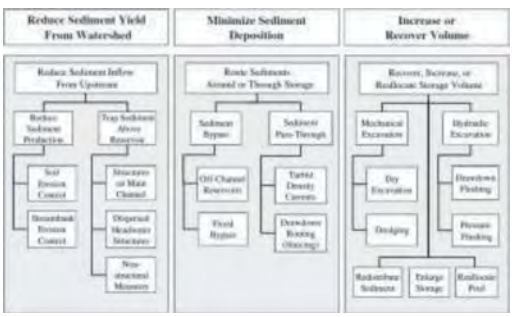

Figure 2. Diagram of sediment management options for reservoir sustainability (Kondolf et al.2014).

It should be especially noted for the hydraulic desilting passway, which is reconstructed from existing penstock in 2012 and works as a bottom outlet for the dam with a discharge capacity of 300 m^3/s, has been desilt 3.1 million m^3 of sediment during the typhoon period in 2013-2016. After the installation of this hydraulic desilting passway, the ratio of desilting during a typhoon event could reaches to about 30% in average in Shihmen Reservoir (Table 2).

After Amuping desilting tunnel and Dawanping sluicing tunnel are completed, the average of total sediment discharge amount will raise to 3.42×10^6 m^3 and equal to the annual income.

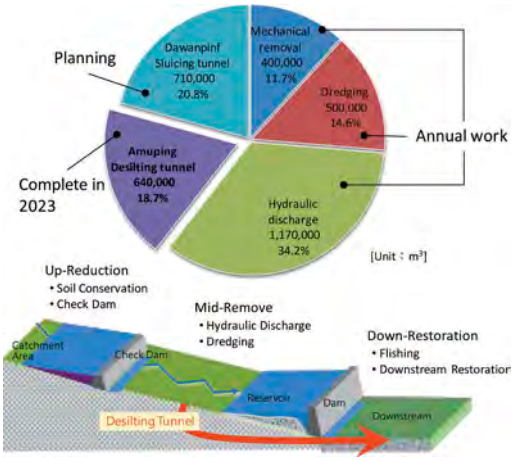

Figure 3. Integrated desiltation strategies for Shihmen Reservoir.

Table 2. Comparison before and after the hydraulic desilting passway completed.

	Year	Typhoon	Ratio of desilting
Without desilting passway	2008	Fung-wong	12.9%
		Sinlaku	26.5%
		Jangmei	17.9%
	2009	Morakot	14.3%
	2010	Fanapi	3.0%
	2011	Saola	15.0%
With desilting passway	2013	Soulik	34.3%
		Trami	37.2%
	2015	Soudelor	36.7%
		Djuan	37.4%
	2016	Megi	21.1%

3 DESIGN CONCEPTS OF DESILTING TUNNEL

3.1 *Layout of desilting tunnel*

According to annual silt survey started from 1963, the shihmen reservoir has been silted by several typhoon events (Figure 4). Therefore, to solve the problem of sedimentation at midstream and upstream as well, the intake of desilting tunnel are arranged at Amuping area where is midstream of the reservoir and 7 km far from the dam.

The desilting tunnel consists of intake structure, adit, desilting tunnel, sifting facilities, outlet structure, and deposition pool. The general layout is shown in Figure 5. The intake structure is 80 m long and situated at Amuping area. The length of the desilting tunnel is about 3,702 m with a varied slope from 10% to 2.863%. The typical cross section of the desilting tunnel is overturn-D type with 8 m in width and 7 m in height as Figure 6. Some information and scales about the tunnel are listed in Table 3. A 306 m long adit is connected to desilting tunnel at

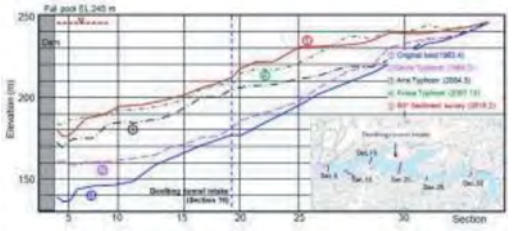

Figure 4. Profile of annual silt survey with tunnel intake location.

millage of 0k+309 serves as the access route during construction period and also works as the maintenance route after completion. The cross section of the adit is as same as main tunnel.

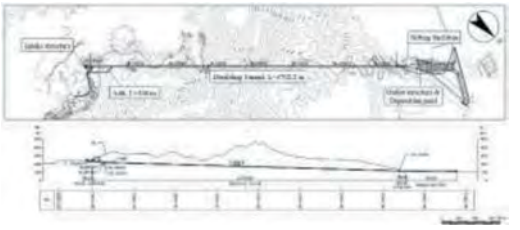

Figure 5. General layout of dedilting tunnel at shihmen reservoir.

In addition, some criteria need to be followed while designing. (1) The design flood-discharging capability for tunnel is 600 m^3/s and the maximum discharge is 700 m^3/s.

(2) Ensure the required freeboard in the tunnel and the safety of operation while desilting operate (The freeboard remains 25% with 600 m^3/s and 15% with 700 m^3/s). (3) To avoid the flow chock happening, the shape of intake is designed as streamline shape. The width at the entrance of tunnel is 14.2 m. The designed plan of intake structure is shown in Figure 7. (4) The design storage of deposition pool is 2×10^5 m^3

For tunneling, the process of excavation is by drill and blasting which is based on NATM(New Austrian Tunneling Method) method. Measuring is the first step and then drill and buried the bomb, blasting and remove the rock, then use the support material such as Lattice Girder, shotcrete and rock bolt to stabilize the cutting face. Repeat the cycle until the tunnel go

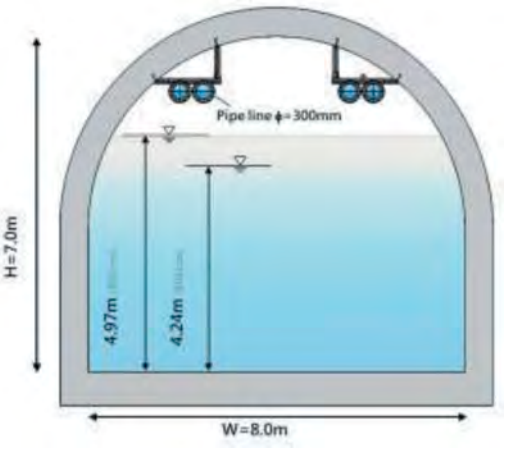

Figure 6. Typical cross section of the desilting tunnel.

through and then construct the concrete lining. The process of excavation shown in Figure 8. Considering the flow velocity is up to 20m/s in tunnel, the invert is design as flat and increase thickness and strength of concrete lining.

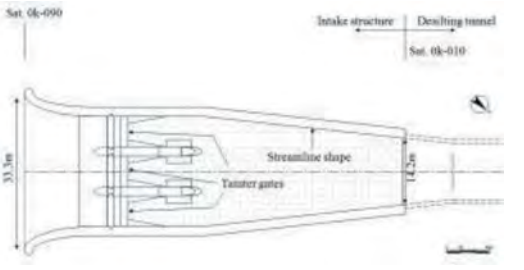

Figure 7. Plan view of intake structure.

For control and operation needed, there are three tainter gates designed in front of intake structure with WxH=6.5m x 5.3m. The gates are closed in normal time to against reservoir water and are opened simultaneously while discharge. Also three tainter gates are arranged in the end of deposition pool with WxH=18.0m x 11.3m and might be the widest tainter gate in Taiwan. The gates are also closed in normal period to contain the silt and opened before desilting process.

Table 3. Information and scales of desilting tunnel.

Sat.	0k-010 ~ 0k+000	0k+000 ~ 0k+070	0k+070 ~ 0k+110	0k+110 ~ 0k+150	0k+150 ~ 0k+200	0k+200 ~ 3k+692
Width [m]	14.2~12	12	12~8	8	8	8
Height [m]	11.1~8	8	8~7.5	7.5	7.5~7	7
Lining thickness [cm]	80	80	60	60	60	60
Slope [%]	10	10	10	8~2.863	2.863	2.863
Flow velocity [m/s]	9.7~11.9	11.9~16.1	16.1~17.0	17.0~17.7	17.7~17.9	17.9~20.2
Section type	Var.			Std.		

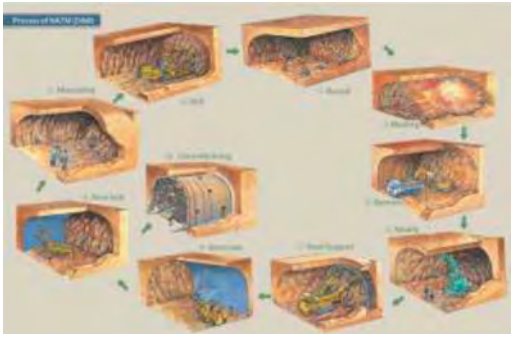

Figure 8. Process of excavation by NATM.

3.2 *Multifunction of desilting tunnel*

The desilting tunnel works as a transportation channel in which four steel pipes are installed and the sediment dredged by the upstream dredging boats is transported via the pipes at usual time. Then the sediment will be screened by sifting facilities at the exit of the tunnel and be separated into coarse sand, fine sand and silt respectively. The percentage of coarse sand and fine sand is expected over 50%.

The coarse sand and fine sand are valuable and can be used as the mixing materials for concrete. On the other hand, the rest of silt will be stored in the deposition pool and be discharged to the downstream during typhoon or heavy rainfall period.

Furthermore, the desilting tunnel can be used as an access road which provides the trucks pass by during drought period. The mechanical machines can dig directly on the river bed at intake area. The multifunction of the desilting tunnel is shown in Figure 9.

3.3 *Reused by sifting facilities*

According to the efficiency concern, three vibrating screen, three sand washers and three sand separators are designed to install, along with the area about 6,000 m^2 including the storage area. The sediment is separated by the facilities and can be divided into 4 parts:

- Gravel or wood, which retained above No.4 (4.76 mm) sieve.
- Coarse sand, which passing the No.4 and retained on the No.18 (1.00mm) sieve.
- Fine sand, which passing the No.18 and retained on the No.200 (0.074mm) sieve.
- Silt, which passing the No.200 sieve and store in the deposition pool.

The process and layout of the sifting facilities are shown as Figure 10. The vibratory screen with No.4 sieve screened out gravel and wood first. The rest is transported to sand washers and sand separators, then be separated into coarse sand and fine sand. The coarse and fine sand can be sold and reused as construction or concrete material. The by the shifting facilities, we can enhance the amount of desilting and solve the problem of silt elimination as well.

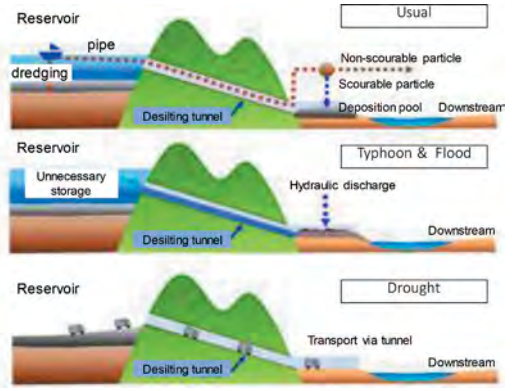

Figure 9. Multifunction of the desilting tunnel.

Figure 10. The arrangement of sifting facilities.

4 PLANNING OF OPERATION

In 2012, WRA reconstructed the penstock of the existing power plant as a hydraulic desilting passway for Shihmen Reservoir and operate during typhoon period. After the desilting tunnel is completed in 2023, this tunnel will be the first priority to drain with 600 m^3/s and flush the siltation in deposition pool during the typhoon period. As the inflow increasing, the spillway and drainage tunnel will be operated to the purpose of flood-discharge. The desilting penstock will be operated then and discharge high density currents with 300 m^3/s at the bottom of the reservoir. The flood-discharge and desilting plan is shown as Figure 11. In addition, to ensure the water-supplying, Zhongzhuang Reservoir, which is located downstream of Shihment dam and was completed in 2017, can provide 6 days of water for New Taipei City while desilting tunnel operationg.

For the operation of intake tainer gates, the opening will be limited and contolled base on the designe flood-discharging capability(600cms).

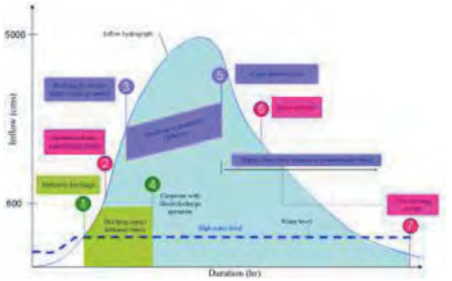

Figure 11. Operation planning of the desilting tunnel.

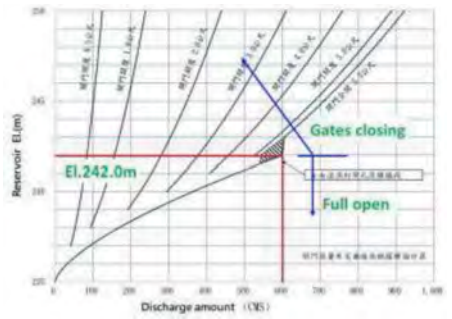

Figure 12. The operation for the intake tainter gate.

(1) Intake structure and cofferdam (2022.6)

(2) Concrete lining for the desilting tunnel (2021.6)

(3) Outlet and deposition pool structure

Figure 13. Photos for the construction period.

According to the analysis, the gates can be full open with discharge amount reaches 600cms while the storage elevation of 242.0m for Shihmen reservoir. Then the gates should be closing down with the storage level is raising up, for this operation is totally contrary to normally concepts. The operation for the intake tainter gates is shown in Figure 12.

5 CONCLUSION

Extreme hydrology events have occurred frequently, large amount of sediment is flushed into the Shihmen Reservoir. The capacity of the water conservation decreases from 3.09×10^8 m^3 to 2.09×10^8 m^3(in 2023) in the past 60 years, which is 66% of its designed storage volume. It is predicted that heavy rainfall and landslide may cause reservoir to lose capacity more severely and may even cut-off water supply.

In order to sustain the life and ensure the safety of Shihmen Reservoir, WRA has completed many measures such as soil erosion control of the upstream areas, digging, dredging, flushing and sluicing. Considering all of the remediation measures, hydraulic desilting proves to be the most economical and rapid method.

Taking effectiveness and economical efficiency into account, a desilting tunnel is planned to construct and is expected to enhance the desilting and flood-discharging capability. The purpose is to deal with 6.4×10^5 m^3 silt per year and provide 600 m^3/s flood-discharging capability. After 5 years of contruction (some photos are took while construction period shown in Figure 13), the tunnel was completed in February 2023 and looking forward to operate in the furture.

REFERENCES

Northern Region Water Resources Office, WRA, MOEA (2016). Desilting Tunnel Project of Shihmen Reservoir (First Stage) The Basic Design Report of Amuping Tunnel.

Taiwan Construction Research Institute (2014). Flexibility Assessment of Sediment Removal at Amuping Tunnel.

Northern Region Water Resources Office, WRA, MOEA (2015). Feasibility Study of Amuping Desilting Tunnel Project for Shihmen Reservoir.

Chien-Hsin Lai (2017). Hydraulic desilting of reservoir in Taiwan. In Proceedings of 2nd IWSBT.

Kondolf, G.M, Gao, Y., Annandale, G.W., Morris, G.L. Jiang, E., Zhang, J. Cao, Y., Carling, P., Fu, K, Guo, Q., Hotchkiss, R., Peteuil, C., Sumi, T., Wang, H.-W., Wang, Z., Wei, Z., Wu, B., Wu, C., Yang C.T. (2014). Sustainable sediment management in reservoirs and regulated rivers: Experiences from five continents. Earth's Future, 2(5), 256–280.

AuthorSurname C. and AuthorSurname D. A conference paper. In Proceedings of the conference, pages 12–34, Sydney, Australia, 2014.

Tunnelling for a Better Life – Yan, Celestino, Thewes & Eberhardt (Eds)
© 2024 The Author(s), ISBN 978-1-032-80042-4
Open Access: www.taylorfrancis.com, CC BY-NC-ND 4.0 license

Advanced countermeasure for encountering heavy gas influx in new Wu-shan-ling divert water tunnel

Kun-Hsien Chou*
CECI Engineering Consultants, Inc., Chinese Taipei

Shih-Hui Wang
Raito Engineering Corp., Chinese Taipei

Cheng-Hsun Chen & Tsung-Hai Chen
CECI Engineering Consultants, Inc., Chinese Taipei

ABSTRACT: Old Wu-shan-ling divert water tunnel is located on the right bank of Zengwen river in Tainan city. The divert water tunnel is an important hydraulic facility connected the Tsengwen river to Guantian river for the water resources of Wushantou reservoir and Chianan irrigation system. It is operated more than 80 years. For the aging lining problem of this old tunnel and long-term consideration for stable water supply, it is necessary to build up a new Wu-shan-ling tunnel. The new Wu-shan-ling tunnel is 3,422m in length. The cross section of the tunnel is 5.4m in width. The geology of the tunnel is the alluvium, Yenshuikeng Shale, Tangenshan Sandstone and several fault zones. It is reported that there were several hazards including gas explosions, leaks, and water inrush disasters during construction period of the old tunnel. Therefore, this project was at the risk of gas burst during the construction. Through the advanced countermeasure for encountering heavy gas influx, the new tunnel was completed and is operated. There was no casualties or incidents due to gas influx during construction time. This paper will take this tunnel as an example to illustrate the advanced countermeasure including risk assessment of encountering gas, gas investigation, gas concentration management threshold value and precautions and strategies against gas hazard.

Keywords: Divert water tunnel, Gas influx, Strategies against gas hazard

1 INTRODUCTION

The new Wu-shan-ling divert water tunnel is approximately 3,422 m long and 5.4 m width with the horseshoe shape profile, which is designed to hold the flow rate of 56 m3/s. As shown in Figure 1, through the new intake and divert water tunnel, the tunnel starts from the east weir construction in the Tsengwen River, where is around 80 m to the downstream side of the existing Wu-shan-ling divert water tunnel east intake weir to the west output located in the upstream side of the Wushantou Reservoir, Jiangziliao nearby, which is about 150 m to the southwest of the existing Wu-shan-ling divert water tunnel exit.

Figure 1. Site location of this project.

2 TOPOGRAPHY AND GEOLOGY

The strike of the mountain range and the drainage pattern in the district is mainly along the southwest direction. Connecting the watershed of the Tsengwen River on the east to the watershed of the Wushantou Reservoir on the west, the planned tunnel was bored through the branch in the south of the Alishan

*Correspoding author: kschou@ceci.com.tw

DOI: 10.1201/9781003495505-29

mountain range. The level of the district is between 400 to 700 m with the Western stratigraphic region on the east and the hill zone on the west.

Strikes of strata in the concerned area are also primarily along the southwest direction. From the east to the west end of the tunnel, strata are recent Alluvium, Yenshuikeng Shale, Tangenshan sandstone, Liuchunghsi Formation and Kanhsialiao Formation (Figure 2). Among these strata, except for the Tangenshan sandstone is composed of thick dense sandstone, others mainly consist of shale or mudstone.

Figure 2. Project geological profile.

3 RISK ASSESSMENT OF ENCOUNTERING TOXIC/ INFLAMMABLE GAS IN THE TUNNEL

The survey record indicated that encountered strata may contain explosive gas and it is very likely to be exposed in the toxic gas while tunnelling. Figure 3 demonstrates the assessment on the risk of encountering the toxic gas along the tunnel, which is approached by considering the explode history record of the excavation in the stratum, the type of the tectonics activity and drilling reports in the design stage. It can be found that there is risk to be endangered by the gas all along the underground alignment, the section 1k+170~1k+260 and 1k +870~2k+350 are even in the high risk region.

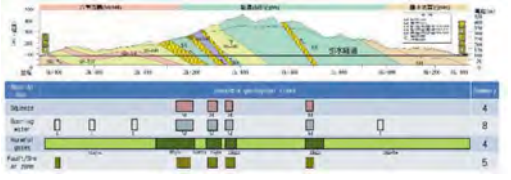

Figure 3. Risk assessment of the special geological condition may encounter.

4 GAS INVESTIGATION

In order to investigate high gas leak potential strata, including Liuchunghsi Formation anticline, Lunhou fault zone and Tangenshan sandstone, sets of the in-situ test in the borehole and lab test were conducted to evaluate the methane concentration and the potential leak gas amount. The test includes resistivity logging measurement, borehole imaging, mud logging and measurement while drilling (MWD) technique. With the result of recording the level of gas brought up in the mud and the composition analysis in the laboratory, the relationship between potential concentration of leak gas, amount, strata attitude and fracture features can be established and the geological model and the feature of potential gas leak strata can be evaluated. The photograph of in-situ tests is shown in Figure 4. Figure 5 is the demonstration of the possible methane concentration evaluation during the excavation of east tunnel section in Tangenshan sandstone.

Figure 4. Photographs of the resistivity logging measurement, borehole imaging.

5 PRECAUTIONS AND STRATEGIES AGAINST TOXIC GAS HAZARD

According to the construction experience of the existing Wu-shan-ling divert water tunnel in 1920s and the investigation outcome in each stages, it can be foreseen that during the excavation of the tunnel, the hazard of inflammable gas might be quite high. Therefore, it is necessary to devise precautions and strategies against toxic gas hazard in the design stage. Based on measures against the inflammable gas in the past, primary principles can be summarized as: (1) Enhance the ventilation, (2) Monitor diligently, (3) Shorten the round length, (4) Decrease the explosion/ vibration, (5) Strengthen the support and (6) Protect immediately. Once the above measures cannot reduce the inflammable gas concentration, auxiliary methods must be applied to prevent from the enlargement of dangers. Besides the aforementioned principles, implementation of the safety regulations and equipment, the control of fire and escape plan while encountering the inflammable gas are even vital to ensure the security of property and life safety. Figure 6 illustrates the primary principles against inflammable gas.

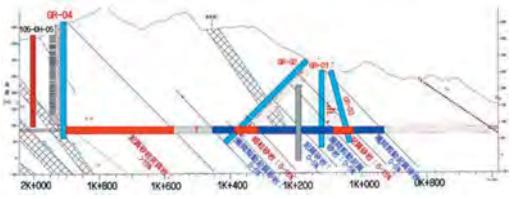

Figure 5. Evaluation of possible methane concentration during the excavation of east section tunnel in Tangenshan sandstone.

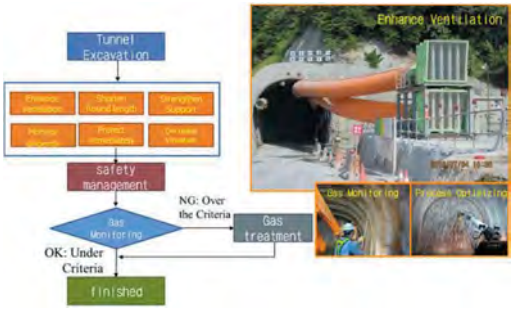

Figure 6. Principle against inflammable gas.

(1) Enhance The Ventilation:Based on the relative experience, enhancing the ventilation is the most effective way to remove the toxic gas. Sufficient air amount and velocity can dilute the inflammable gas into the safe range and remove it, which ensures the workplace safety and property security. The new Wu-shan-ling divert water tunnel is approximately 3,422 m long with the workface in two ends, therefore the maximum construction length of each end has to be less than 2,000 m. The independent ventilation system is installed for each side with the control system and ventilation ducting to send in the fresh air and remove the dust and polluted air.

(2) Monitor diligently: Fixed gas detectors (Figure 7) are installed in every 250 m along the tunnel with all cables connected to the automatic record monitor and warning system outside the tunnel. The automatic warning system sends the alarm and light, once the detected gas concentration reaches the toxic gas concentration warning threshold value (5,000 ppm, 0.5% or LEL=10%). Furthermore, the toxic gas detection should be implemented with the portable gas detector with particular emphasis on workfaces, safety shoulders, U-turn lane and locations where the toxic gas might accumulate when drilling the blasthole and before and after the blast. Figure 7 shows the photograph of fixed, portable gas detector and the measurement. The record of the toxic gas measurement is displayed in Figure 8.

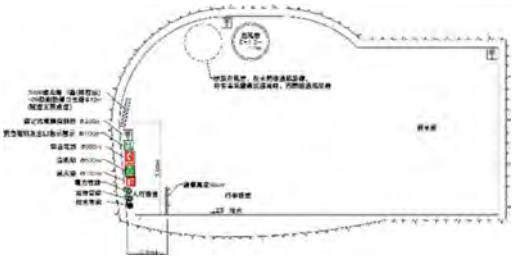

Figure 7. Location of the automatic gas detector.

Figure 8. Site photographs: (a) fixed gas detector, (b) portable gas detector and (c) gas measurement.

(3) Shorten the round length:Based on the estimated amount of the inflammable gas leak, the length of the daily excavation round is found to possess a positive correlation to the leak amount. Therefore, it is suggested to keep the round length less than 1 m whenever the excavation may encounter with the toxic gas in the front (gas concentration less than 2,500 ppm, 0.25% or LEL=5%) and decrease the volume of excavation mass and the gas leak with the immediate installation of the support after the excavation according to the experience and geological condition in the site.

(4) Decrease the explosion/vibration:For the concern of safety, it is necessary to install precisely the required blasthole length, distance and apply the design amount of explosives as the construction plan.

(5) Strengthen the support:The amount of the inflammable gas soars as the result of the increase in the porosity of the surrounding rock plastic zone after the excavation of tunnels. By means of reinforcing the support for suppressing the large tunnel deformation, the surrounding rock plastic zone and the amount of inflammable gas leak can be reduced. Therefore, installing the forepoling or the pipe roof depending on the rock condition to stabilize the excavation face and reduce the excessive tunnel deformation can be feasible in the high inflammable gas hazard section.

(6) Protect immediately:Spraying the shotcrete right after the excavation of each advancement step to seal the surrounding uncover rock not only prevent the rock from falling, weathering and deformation but block the path of gas leak. In addition, reducing the usage of rock bolts in

common sections except for the portal, over-excavated section and the geological fracture zone with ensuring the security and functionality of the tunnel can efficiently block the path for inflammable gas intrusion.

(7) Auxiliary methods:If the toxic gas amount keeps exceeding the safe range, auxiliary methods such as the air-tight shotcrete, auxiliary blowing machine, compensation grouting and spray type air-tight layer can be conducted to restrain the toxic gas leak. To reduce the risk of encountering the inflammable gas leak, the air shaft can be set in the high gas leak potential section.

6 INFLAMMABLE GAS TUNNEL SAFETY MANAGEMENT

The inflammable gas tunnel safety management includes the management of fire, personnel, gas concentration detection and emergency plan, which is designed to secure the operator with periodical monitoring the operation environment and taking counter-measures and procedures according to the measured gas concentration. Table 1 demonstrates the regulation of personnel safety management. The frequency and location of the gas measurement are shown in Figure 9.

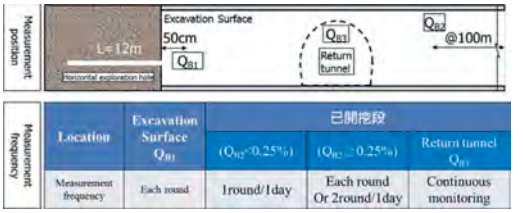

Figure 9. Frequency and location of the gas measurement.

Auxiliary methods that can be applied in the situation, which the indistinct decrease of the inflammable gas concentration after the additional ventilation, are introduced as follow. For the gas constantly leak from the workface, the compensation grouting should be considered if necessary. If the measured gas concentration exceeds the range, the source, path and the reason of the inflammable gas should be found out through additional measurements. For the case of the gas accumulation due to the limitation of the space, the auxiliary blow machine can be installed. Preventive air-tight methods such as the air-tight shotcrete, compensation grouting in excavated sections and spray type air-tight

Table 1. Regulation of personnel safety management.

Gas CH_4					Fire control			Gas treatment (Ventilation. Sucktion)
Volume Ratio	LEL	PPM	State	Gas Monitoring	Worker	Fire	Vehicles	
<0.25%	<5%	<2500	Normal	Portable/Fixed Detection *Geologist *Supervisor *Worker	**Noamal** *Signature *Flop *RFID	*No Smoking *Ban lighter	*Explosion-proof lighting, Phone, Switch	Normal
0.25%~0.50%	5%~10%	2500~5000	Attention (Stop welding)	Portable/Fixed Detection *Geologist *Supervisor *Worker *Testing Commissioner	**Conditional access** *Pure cotton jacket *Antistatic clothing	*No Mobile Phone *No Welding	*No Vehicles *Flame Extinguisher in Mixing Vehicle *Use portable gas detection before engine start-up	Enhance the Ventilation
0.50%~1.00%	10%~20%	5000~10000	Warning (Stop blasting)	Portable/Fixed Detection *Geologist *Supervisor *Worker *Testing Commissioner		*No Blasting		
1.00%~1.50%	20%~30%	10000~15000	Withdraw (stop work)	Fixed Detection *Testing Commissioner (Portable)	withdraw Forbiding	*Cut off the power supply	*Set aside the equipment and walk away *Drive back to the parking lot and pull out the key	Total Enhance the Ventilation1.0M/S (Suction Well)
≧1.50%	≧30%	≧15000	Forbiding (Power-off)	Fixed Detection	Forbiding			

Table 2. Gas concentration management threshold value and according actions.

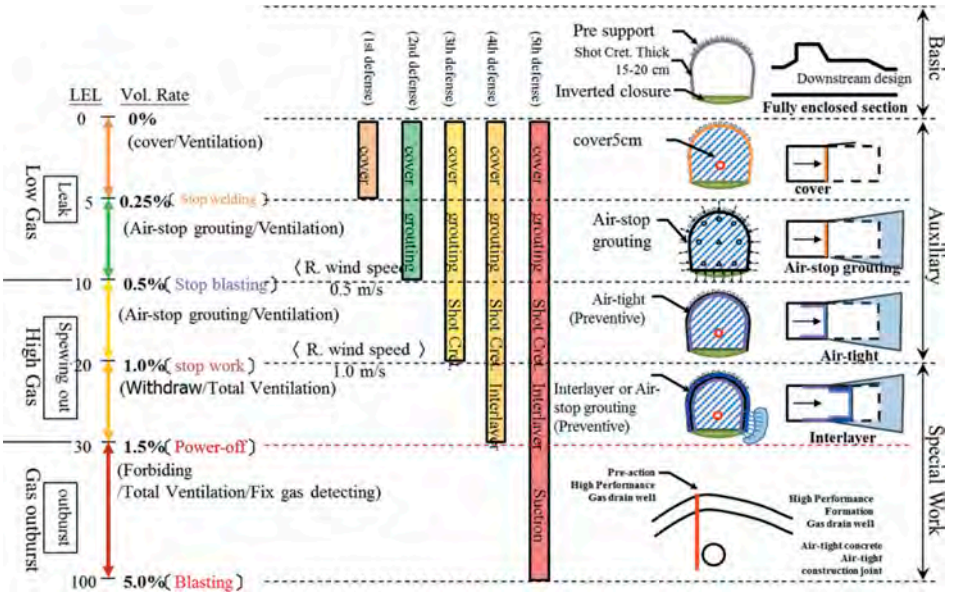

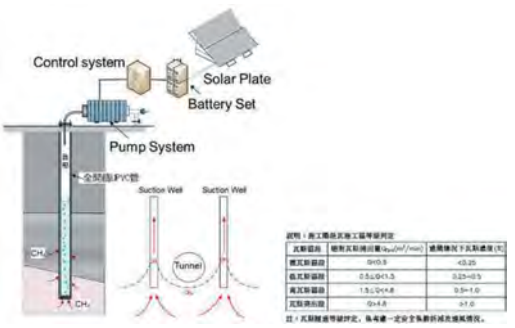

Figure 10. Illustration of the air shaft.

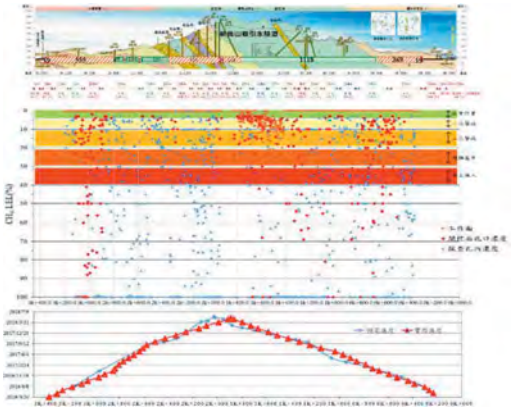

Figure 11. Record of the gas concentration measurement during the construction.

Figure 12. Photograph of the completion ceremony.

Figure 13. Completed photos.

layer can be conducted for the case of inflammable gas leaks from the excavated sections. The contractors should decide the feasible method and apply it after the agreement from the responsible entities in accordance with the site condition. Table 2 lists the gas concentration management threshold value and its actions. The illustration of the air shaft used in this project is shown in Figure 10. Figure 11 is the record of the gas concentration measurement during the each advancement step.

7 CONCLUSIONS

Construction had encountered the gas leak multiple times, some of which even reached the warning and action threshold value. With the prudence and conscientiousness of all crews, the tunnel construction was completed in 23 May 2018. The photograph of the completion ceremony is shown in Figure 12. The completion date is 2020/6/20 and the completed photos are shown in Figure 13. The construction safety can be severely affected if the rock porosity increases due to the tunnel excavation disturbance and the massive toxic gas leaks with high concentration to reach the range of explosion. With the thorough ventilation, fire and personnel management and fixed/portable gas detector, the new Wu-shan-ling divert water tunnel construction effectively reduced the risk of the toxic gas blow up.

REFERENCES

Doyle B R2001 Hazardous gases underground: applications to tunnel engineering. New York.

Taiwan Construction Research Institute2007 Gas Explosion Treatment Technology in Tunnel.

CECI Engineering Consultant Inc. Taiwan 2015 Proposal of New Wu-Shan-Ling Divert Water Tunnel.

Public Construction Commission, Executive Yuan, 2003 Establishment of Tunnel Rock Mass Classification System and Tunnel Engineering Database in Taiwan, Appendix 2 - Reference Manual of Auxiliary Construction Methods for Mountain Tunnel Engineering.

HO,TAI-YUAN, 2004. "Investigation and treatment countermeasures for flammable gases encountered during tunnel construction", CECI ENGINEERING TECHNOLOGY vol. 63.

Taiwan Chia-Nan Irrigation Association2016, Report on countermeasures for encountering flammable gases in New Wu-shan-ling Divert Water Tunnel (first edition).

Taiwan Chia-Nan Irrigation Association, Temporary high-performance relief well construction project results report (first edition), 2017.

Tunnelling for a Better Life – Yan, Celestino, Thewes & Eberhardt (Eds)
© 2024 The Author(s), ISBN 978-1-032-80042-4
Open Access: www.taylorfrancis.com, CC BY-NC-ND 4.0 license

The "hybrid" tunnel. An innovative solution for urban tunnel in soils. The case of Américo Vespucio Oriente AVO1, in Santiago de Chile

Jose Miguel Galera*
Systra Subterra Ingeniería, Madrid, Spain

Manuel de Cabo
Systra Subterra Ingeniería, Madrid, Spain
Subterra Ingeniería, Santiago de Chile, Chile

Guillermo Ibarra
Subterra Ingeniería, Santiago de Chile, Chile

ABSTRACT: The "Américo Vespucio Oriente" Concession (AVO 1) is part of ambitious program, promoted by the Chilean Ministry of Public Works, to close this Ring Road to highway standard in Santiago de Chile. The project integrates this 8,278 m highway with three lanes in each direction, of which 7,678 m are underground, in a dense urban area of the city.

The underground works combines 3 main construction methods:SEM and NATM tunnel: La Pirámide and Mapocho Branch (2,100 + 415 m).Cut & Cover tunnel: 2,891 m in a pile trench with two subway platform levels."Hybrid" tunnel: 2,687 m between Apoquindo and Tobalaba.

The construction works began in November 2017 and its completion was done in July 2022, with a final budget of 900 MUSD.Based on the set of conditioning factors, a highly innovative hybrid tunnel section solution was designed to the fit the tunnel layout under an existing boulevard, as well as each of the seven existing connections with exit/enter branches.

The hybrid tunnel enables two roads overlapped with three lanes each. Level -1 platform is resolved by means of a NATM tunnel, while Level -2 has been constructed as a conventional trench-type structure using 1.00x1.00 m handmade piles with different spacings and a minimum embedment of 3.5 m, which are braced at their head by a post-tensioned slab between both levels. The gap between piles is reinforced by means of a lining wall.The hybrid tunnel has crossed below two existing underground parkings as well as under metro line 1. For that purpose, an improvement using jet-grouting from the deepest parking level was done.The paper describes the main design facts as well as the experiences during its construction.

Keywords: Urban tunnel, Soil tunnel, Innovation, Large tunnel

1 INTRODUCTION

The "Americo Vespucio Oriente Concession, Section Av. El Salto-Príncipe de Gales", known with the acronym AVO 1, is part of the ambitious public-private partnership program promoted by the Chilean Government, through its Ministry of Public Works, to close the Americo Vespucio Ring Road, surrounding the city of Santiago with a highway standard. Figure 1 shows a general plan of the AVO 1 project.

The project addresses the challenge of integrating in an urban dense area a subway highway with three lanes in each direction over a length of 8,278 m, of which 7,678 m run through tunnels. Considering the construction method used the following three sections can be distinguished:

– Conventional NATM & SEM tunnel: 2,100 m under San Cristóbal hill, known as La Pirámide Tunnel, that includes 415 m of Mapocho Branch Tunnel. These are two conventional tunnels of 3 and 2 lanes in the branch, with a bifurcation cavern. The La Pirámide tunnels also crosses under the Mapocho River and it has its exit afterwads, in the area known as "Punto Limpio" in Vitacura. Before, just besides the river's defense walls, there is a ventilation shaft (ϕ15 m and 32.5 m depth).

*Corresponding author: jmgalera@systra.com

DOI: 10.1201/9781003495505-30

Figure 1. Location and general layout of AVO1 concession in Santiago de Chile.

– Cut & Cover tunnel: 2,891 m of cut & cover tunnel in a pile trench with two subway platform levels located along the pre-existing central boulevard park of Americo Vespucio Avenue. In this section there are seven inbound and outbound branches. At the main one, located in the junction with Kennedy Avenue, there are five mined branches that were constructed using NATM method (Branches 1C, 5, 5A, A and A1).
– "Hybrid" tunnel: 2,687 m of the Hybrid Tunnel, configured in an innovative solution also under the central boulevard park of the avenue, in which the level -1 of the tunnel (North traffic direction) has been constructed using NATM & SEM method, while the level -2 below, has been excavated using a pile diaphragm wall. In this section there are two exit branches and five entrance branches, built using NATM method.

Figure 2 shows a detailed scheme of these three construction typologies used for the construction of AVO1.

The construction works began in November 2017 and its completion was done in July 2022, with a final budget of 900 MUSD.

Figure 2. Construction typologies used for the constructions of AVO1.

2 DESCRIPTION OF THE HYBRID TUNNEL

The Cut & Cover section, under the central boulevard park of Americo Vespucio Avenue, should have cross under two underground existing parkings as well as under the Santiago Metro Line 1 located between these two parkings, at Apoquindo Avenue. This stretch approximately 400 m length was initially designed using a mined German construction method, but after having initiated the construction works, it was decided to continue using mined methods till the end of the concession towards the South.

Based on the existing conditioning factors, a highly innovative hybrid tunnel section solution was designed to the fit the tunnel layout under the existing boulevard, including the junctions with seven exit/enter branches.

The hybrid tunnel enables two roads overlapped of three traffic lanes each. The Level -1 platform, that houses northbound traffic, is resolved by means of a NATM/SEM tunnel, while Level -2, that houses southbound traffic, has been constructed as a conventional trench-type structure using 1.00x1.00 m handmade piles with different spacings and a minimum embedment of 3.5 m, which are braced at their head by a post-tensioned slab between both levels. The gap between piles is reinforced by means of a lining wall..As it has been described previously, the hybrid tunnel crosses under two underground parkings as well as under metro line 1. In this area a ground improvement using jet-grouting from the deepest parking level, was done.

Figure 3 shows the hybrid tunnel concept, while Figure 4 shows its dimensions. At it can be appreciated the tunnel is 13.20 m of inner width and 5.0 m clearance, at both traffic level. In the junction sections the inner width, at Level -1, has reached 22.6 m.

3 GEOLOGY, HYDROGEOLOGY AND GEOTECHNICS

Santiago de Chile is located on a plain area known as the "Santiago basin" belonging to the Chilean Intermediate Depression. This depression is limited to the N by the Chacabuco Mountain Range, the Andes to the East, the Paine narrows to the South and the Coastal Mountain Range towards the West. Within the basin there are several pre-Andean reliefs, including the Cerro San Cristóbal Hill, where the La Pirámide Tunnel is located, in which the rock substratum outcrops.

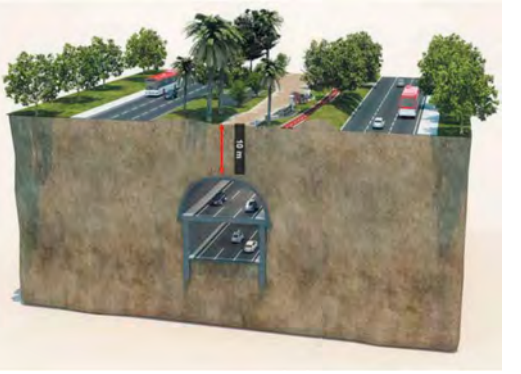

Figure 3. The "hybrid" tunnel concept.

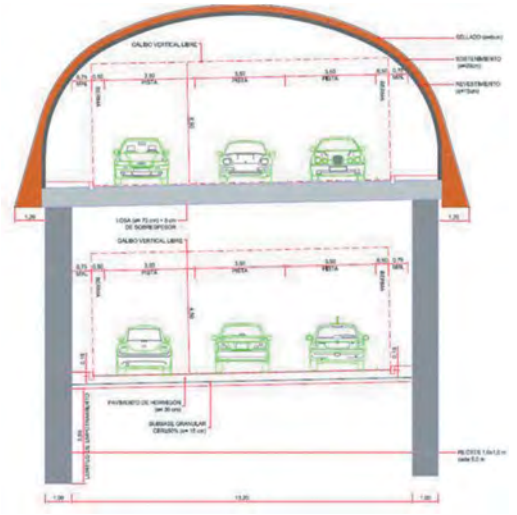

Figure 4. Cross section of the hybrid tunnel.

These reliefs are constituted by stratified volcanic and continental rocks from the Abanico Formation (Upper Cretaceous to Oligocene) as well as intrusive rocks from the Miocene.

The Santiago basin is filled with recent alluvial materials known as the Maipo system, in the South city, and the Mapocho system, towards the North.

Figure 5. Contact between the 2nd deposit and the 1st deposit units of the Mapocho River alluvial gravels.

The Cut & Cover and "Hybrid" Tunnel sections are located in the Mapocho River Gravel Unit. This unit has traditionally been divided into two formations: the "2nd deposit", the most recent one, and the "1st deposit", the oldest and therefore deepest unit. In the Figure 5 the contact between both units is shown at the tunnel excavation face.

While the Level -1 of the tunnel has been entirely excavated in the more recent and shallower "2nd deposit" gravels, the excavation of the Level -2 was done partially also in the lower "1st deposit" gravels. In the exit/entrance branches also some anthropic fills were encountered.

From the hydrogeological point of view the "Hybrid" tunnel is located in the Aquifer Unit UH2 (Mapocho Alto Upper System) that is a free surface aquifer, that includes both stratigraphical units, and that in this area has a thickness ranging 20 and 40 m, with a permeability is on the order of 1E-5 m/s. The water table is located just below the tunnel lower slab.

Figure 6 shows a geological longitudinal cross section of the tunnel, in which the "2nd deposit" has been represented in light green, while the "1st deposit" is shown in dark green.

From the geotechnical point of view, the main difference between both stratigraphical levels is the greater plasticity of the final fraction in the case of the "1st deposit", which is older one.

Table 1 shows the main geotechnical data of all the units involved in the tunnel construction.

Chile is one of the countries with the highest seismicity due to its geotectonic context in a subduction zone. For the quantification of seismic actions, standards NCh 433-Of-96 and NCh 2475 have been considered, as well as the Highway Manual, Volume 3 (Directorate of Roads, Ministry of Public Works).

The Maximum Ground Acceleration obtained is Ao = 0.3 g. and a Seismic Design Deangulation has been considered for the underground works of θs =3.5 x 10-4 for the cut & cover and hybrid section.

4 CONSTRUCTION METHOD

The "hybrid" tunnel combines two different construction methods at each construction section.

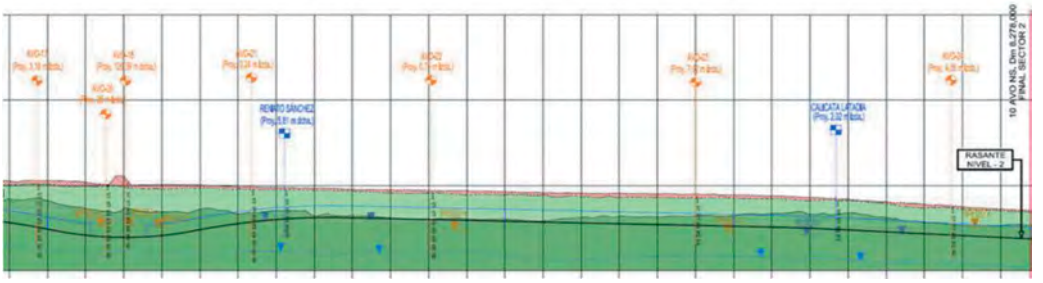

Figure 6. Geological cross section of the hybrid tunnel ("2nd deposit" in light green and "1st deposit" in dark green).

Table 1. Geotechnical parameters of the ground.

Unit	Stress Ratio K_0	Density kN/m3	Def. Modulus MPa	Cohesion kPa	Friction Angle º
Anthropic Fills	0,5	17,0	20	10	33
2ª Deposit	0,65	22,5	100 (Z ≤ 5 m) 42 x Z0.55 (5 < Z < 17 m) 55 x Z0.53 (Z ≥ 17 m)	25	45
1ª Deposit	0,65	22,5		35	48

While the upper level, Level -1 platform, is excavated using NATM/SEM method, the lower level, Level -2, has been constructed as a conventional trench-type structure.

In the case of the Level -1, depending on the tunnel inner width, that has ranged between 13.2 and 22.6 m in one of the existing junctions, full face NATM method or SEM (two and three excavation phases) were used. In all the cases a systematic elephant foot was used.

For the Level -2, the trench-type section consists in the construction of 1.0x1.0 m handmade squared piles, spaced 5.0 m, with a minimum embedment of 3.5 m. These piles are braced at their head by a post-tensioned slab located between both levels. The gap between piles is reinforced by means of a final lining wall and a lower non-strut slab completes the section. Figure 7 illustrates the construction sequence.

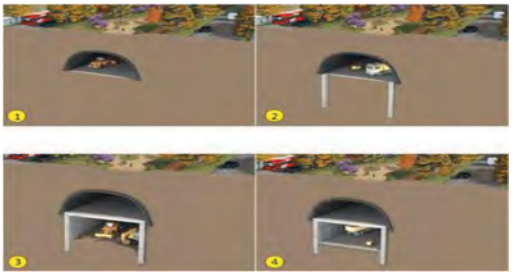

Figure 7. Hybrid tunnel construction sequence.

The support and lining applied at Level -1 the following:

a) Support (Primary lining), composed by:
- 5 cm shotcrete SH-30 seal reinforced with 4-5 kg/m3 of synthetic macrostructural fibres
- HEB-160 steel sets with elephant foot spaced one meter
- 25 cm of 25 cm SH-30 shotcrete with the same number of fibres as before.

If those cases in which due to the width larger than 13.2 m, two or three excavation phases were used, the temporary supports between excavation phases have been
- 20 cm of SH-30 shotcrete with the same amount of fibres
- HEB-160 metal frames each meter

b) H-30 concrete slab 80 cm thick
c) Lining (Final lining), composed by 30 cm of H-30 shotcrete reinforced with 1.5 kg/m3 of fire-resistant polypropylene fibres

The support and lining used for the Level 2, was the following:

- 1x1 m square piles embedded in the ground 3.5 m, spaced 5 m. The amount of steel reinforcement is 145 kg/m3
- The piles are capped at the head by the intermediate concrete slab
- The level -2 platform is configured with a rigid concrete pavement (H-30) with a thickness of 45 cm
- Lining wall between piles composed by wire mesh and 10 cm of H-30 shotcrete reinforced with 1.5 kg/m3 of fire-resistant polypropylene fibres

In the Figure 8 the constructive sequence of the hybrid tunnel is shown. It must be considered that do not correspond to the same given section, but they are really representative of each construction phase.

Figure 8. Typical constructive sequence of the hybrid tunnel section.

In the first image the excavation of the top-heading (Level -1) is shown. As it can be observed in this case three asymmetrical excavation phases can be observed, while the second image, show the demolition of two temporary support diaphragms using three symmetrical excavation phases. The third image shows several hand excavated piles close to the elephant foot at the floor of the Level -1, while in the fourth one, the construction of the intermediate slab is shown.

Finally, images fifth and sixth, show respectively the Level -1 once the final lining is completed and the

aspect of Level – 2, excavated between piles diaphragm walls and with the final lining wall between piles.

Due to the reduced height at both sides of the Level – 1 tunnel, one of the most peculiar aspects of these solution has been the necessity to used hand excavated piles with a squared shape of 1.0 m, as is illustrated in the Figure 9.

Figure 9. Aspect of a final hand excavated squared pile and a moment of its construction.

A real important aspect of the construction method has been the determination and definition of the safety distances between excavation phases, in those cases in which Level-1 has been constructed using more than one excavation phases.

Figure 10, taken for the stress-strain analysis of a given section, show the gap stablished between the three excavation phases, that was defined with a minimum distance of 15 m between them; and the minimum distance in which it was allowed to start the demolition of the temporary support diaphragms, established in 25 m.

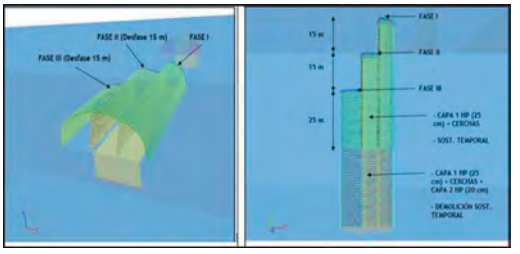

Figure 10. Minimun excavation gaps between excavation phases of Level 1 and the demolition of the temporary support diaphragm.

5 EXAMPLE OF THE DESIGN OF A SUPPORT AND LINING SECTION

The design of the Hybrid Tunnel has been carried out in accordance with Chilean regulations and using AASHTO for structural design.

Tridimensional numerical models have been developed for each section of the tunnel, simulating the different phases of excavation and support of the tunnel, the execution of the lining and the intermediate structural slab, for Level -1. Afterwards, the execution of the piles, and the excavation of the Level -2, allowing the obtention of the following variables to be quantified:

- Induced settlements and deformations on the surface
- Requests induced in support and coating
- Stresses in the piles and dimensioning of the sections

The calculation tool used was FLAC 3D, while for the structural dimension of all the structures, FAGUS7, CEDRUS7 and our own software were used.

Following an example of the design process used for one of the complex sections is shown. In this case the Level -1 has four traffic lanes so the excavation width of the top heading is 20.4 m. Figure 11 shows, at the left image, the aspect of the model developed, while at the right image the stratigraphy in the transversal section is illustrated. As it can be seen at the surface there is a layer in red, 1.45 m thick, that corresponds to the anthropic fills, the 2nd deposit is represented in green, with a total thickness of 14.2 m, and finally, in blue this unit corresponds to the 1st deposit of the Mapocho alluvial gravels.

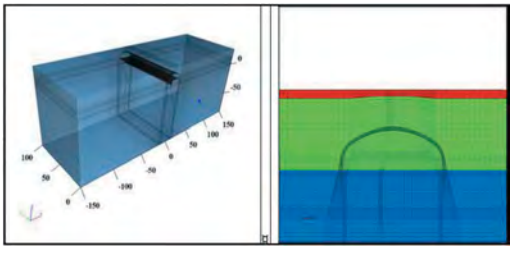

Figure 11. General aspect of the 3D numerical model, and distribution of the stratigraphical units.

Figure 12 shows the detail of the model in a transversal cross section, in which as can be observed, all the elements, except de shotcrete seal, have been considered:

- First shotcrete layer (SH-30) of 25 cm and HEB-160 steel arch spaced 1 m
- Second shotcrete layer (SH-30) of 20 cm
- Final lining of 30 cm of H-30
- Temporary support composed by 20 cm SH-30 and HEB-160 spaced 1 m
- Intermediate structural slab 80 cm thick of H-30

At the same manner, Figure 13 shows all the structural elements that have been included at Level -2. In particular:

- Piles 1x1 m spaced 5 m, with a total length of 8.6 m
- Lower slab composed by 45 cm of concrete H-30

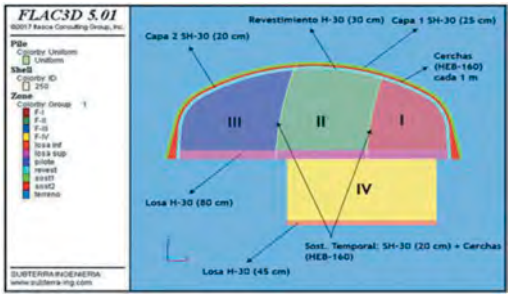

Figure 12. Detail of all structural elements included in the 3D numerical model at Level 1.

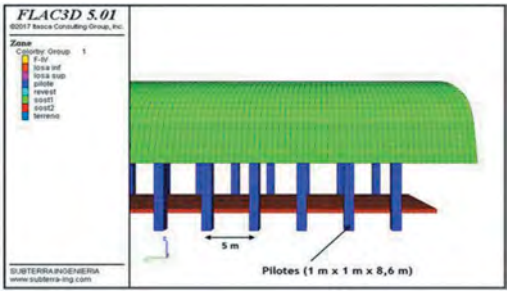

Figure 13. Detail of all the structural elements included in the 3D numerical model at Level 2.

For this analyzed section, the following results for the ground were obtained:

- The maximum deformation at the section with a value of 94 mm in the final excavation phase
- The maximum semi-convergence at the top heading is 6 mm at the right tunnel wall (Level -1), which reaches a maximum of 10 mm between the piles of level -2
- The ground plasification can be considered to be moderate

For this analyzed section, the following results for the ground were obtained:

- The maximum deformation at the section with a value of 94 mm in the final excavation phase
- The maximum semi-convergence at the top heading is 6 mm at the right tunnel wall (Level -1), which reaches a maximum of 10 mm between the piles of level -2
- The ground plasification can be considered to be moderate
- The maximum subsidence at the surface is 80 mm

Figure 14 illustrate these four results.

Concerning the solicitations to the structural elements, the following result were obtained:

- The maximum compressions in the shotcrete are 9.4 MPa (FS>2.7)
- In the steel sets, the maximum axial force obtained is 59.7 t and the maximum bending moment is 0.8 t.m, both in the final phase.
- In temporary support, the maximum axial force is 44.1 t and the maximum bending moment is 1.92 t.m.
- The maximum stresses in the piles are 83.4 t and 81 t of bending moment and shear stress, respectively.

Figures 15, 16 and 17 shows graphically these results at the support elements.

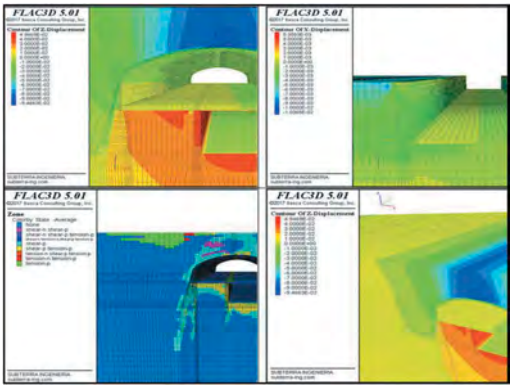

Figure 14. Results of the model including deformations (upper row) yielded elements and subsidence (lower row).

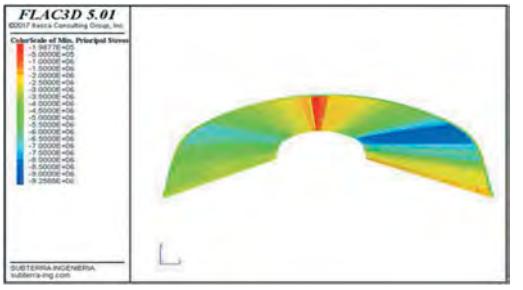

Figure 15. Compression at the shotcrete support.

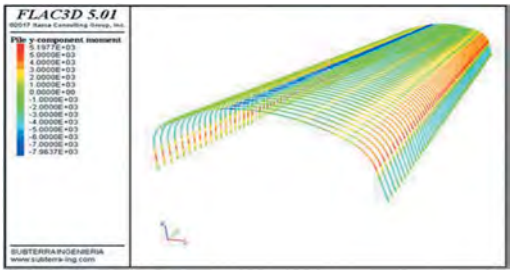

Figure 16. Bending moment at the HEB 160 steel arches.

Figure 17. Shear stresses at the piles.

6 THE UNDERPASS OF THE APOQUINDO NORTH PARKING

Following the underpass below the Nort Apoquindo car-parking is described, as the most challenge part of the project, just at the boundary between the Cut & Cover stretch and the starting of the "Hybrid" tunnel.

As can be seen at Figure 18, after the Cut & Cover, with no colour at the left, it was necessary to make a 22.6 m wide cavern at the level -1 to incorporate on of the entrance branches, coming from Los Militares Street (Los Militares N) at the surface. The normal 3-lane tunnel has been shadowed in a different brown colour.

Figure 18. Layout of the entrance branch Los Militares.

At the end of this 4-lane section, Figure 19 shows the bifurcation with the entrance branch of Los Militares N branch.while Figure 20 shows the bifurcation cavern.

Figure 19. Hybrid tunnel portal at the ending of the cut & cover tunnel.

Figure 20. Bifurcation cavern of Los Militares N entrance branch.

The minimum distance between the foundation of the Level -3 of the existing Nort Parking of Apoquindo and the vault of the tunnel is 3.5 m.

For this reason, a Jet-grouting treatment from level -3 of the parking was designed, while the excavation of the Level -1 of the hybrid tunnel was decided to do it using SEM (Sequential Excavation Method) with two lateral side-drifts and central gallery, with excavation round lengths of 1.0 and keeping a minimum distance between them of 10 m.

Figure 21 shows two sections, the first one right on the abscissa where both tunnels are individualized, while the second corresponds to the final cavern section, just before the mentioned bifurcation.

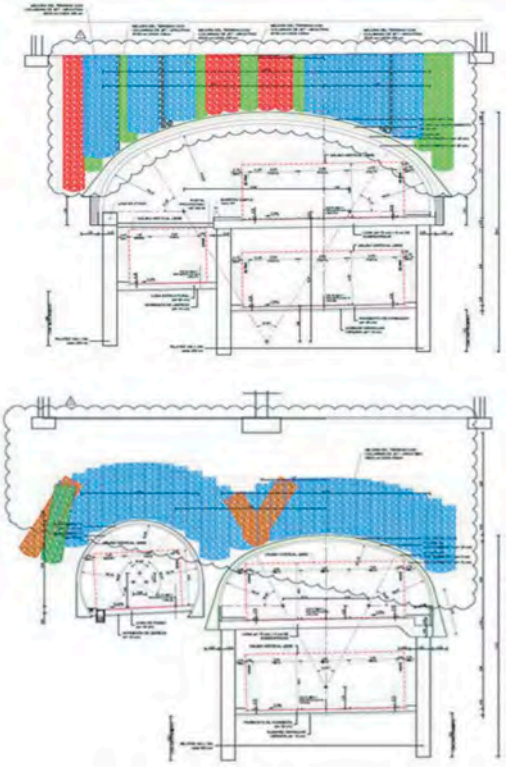

Figure 21. Cross section fo the bifurcation cavern Los Militares N, just under the north apoquindo parking.

This figure also shows the jet grouting carried out prior to the excavation of the tunnel from the deepest level of the existing parking.

During the existence of close structure located just above the tunnel (between 3.5 and 8.0 m) a strict control of deformations was done, including:

– in the tunnel (convergences and vault topographical levelling)
– in the parking, topographical levelling
– on the surface, topographical levelling

The maximum deformation induced in the North parking lot at its -3 level has not exceeded 27 mm.

Figure 22 shows the deformation measured at the abscissa Dm 5+725,4 (control line 16) and the abscissa Dm 5+696,9 (control line 22).

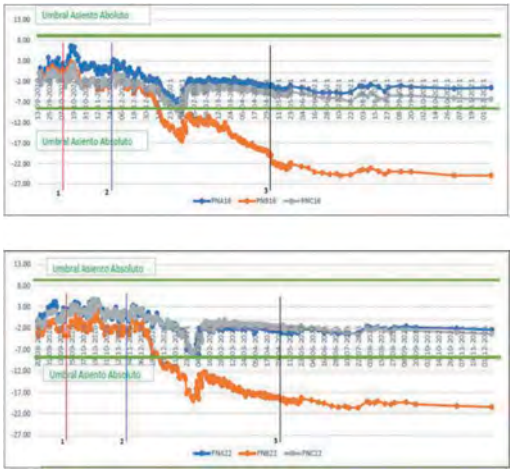

Figure 22. Deformation measure at the Level 3 of the north apoquindo parking.

Figure 22 corresponds to the date of the excavation of the top heading, 2 to the date of the finalization of the excavation, and 3 to the demotion of the temporary support diaphragms.

As it can be observed, the deformation was always moderate and without causing any damage to the existing parking.

7 CONCLUSIONS

The "Américo Vespucio Oriente" Concession (AVO 1) is an ambitious program to improve the mobility conditions in the city of Santiago de Chile, using the underground space and freeing up space on the urban surface for other uses, in a dense urban area of the city. The construction works started in November 2017 and where finished in July 2022.

The project supposes 7,7 km of tunnel, but considering the length of the exit and entrance branches, the total tunnel length is almost 10 km. For its construction three different tunnel construction methods have been used, SEM and NATM, Cut & Cover, and what has been called the "Hybrid" tunnel.

The hybrid tunnel enables two roads overlapped with three lanes each. Level -1 platform is resolved by means of a NATM tunnel, while Level -2 has been constructed as a conventional trench-type structure.

This innovative construction method has made possible to preserve all the existing park located at the central boulevard of the avenue, decreasing the environmental impact of the project.

REFERENCES

Cabo, M., Galera, J.M., Santos D., Richmagui, R., Iñigo, L. E., García L.F., Gómez, P., Fernández, M. et al, 2022. The construction of tunnels for the Americo Vespucio Oriente 1 project in Santiago de Chile, World Tunnel Congress 2022 (WTC 2022), Conpenhague, 2.

Fernández, J.C., 2003. Respuesta sísmica de la cuenca de Santiago. Servicio Nacional de Geología y Minería, Carta geológica de Chile. Serie Geología Ambiental N º 1.

Gomes, A., González, E., R.M., Herrera, J., 2019. Experiences with the use of the conventional mined excavation method in the Santiago metro - Chile 2019. Symp.Tunnelling under Adelaide, South Australia AGS and ATS.

Kuster, J., Nuñez, R., Chavez, E., Galera, J.M., Santos, D., 2017. Santiago Expressway. Tunnel & Tunnelling, Abril 2017.

Kuster, J., Nuñez, R., Chavez, E., Galera, J.M., Santos, D., 2020. The construction of the tunnel Kennedy in Santiago de Chile. A major challenge of an urban tunnel in soils. Tunnels and Underground Cities: Engineering and Innovation Meet Archaeology, Architecture and Art. CRC Press. World Tunnel Congress 2019.

Sellés, D., Gana, P., 2001. Geología del área de Talagante-San Francisco de Mostazal, regiones Metropolitana de Santiago y del Libertador General Bernardo O'Higgins. Servicio Nacional de Geología y Minería. Carta Geológica de Chile. Serie Geológica Básica, N°74.

Vergara, L., Verdugo, R., 2015. Condiciones geológicas-geotécnicas de la cuenca de Santiago y su relación con la distribución de daños del terremoto del 27F. Obras y Proyectos, No.17.

NCH 433-OF-96. Norma Chilena Oficial. Diseño sísmico de edificios. Instituto Nacional de Normalización. Inn.

Manual de Carreteras, 2020. Volumen 3. Instrucciones y criterios de diseño. Junio.

Tunnelling for a Better Life – Yan, Celestino, Thewes & Eberhardt (Eds)
© 2024 The Author(s), ISBN 978-1-032-80042-4
Open Access: www.taylorfrancis.com, CC BY-NC-ND 4.0 license

The effect of the movement joint on the seismic response of the cross-passage intersection in segmental tunnel lining

Gabriele Giordano*, Diego L'Amante & Giorgio Fantauzzi
SYSTRA France, Paris, France

ABSTRACT: Cross-passages intersections in segmental tunnel lining are critical components in underground tunnels that need a specific design, particularly when they are subjected to the earthquake effects. During seismic events, these intersections are subjected to significant dynamic loading, which can potentially lead to structural damage and compromise the overall integrity of the tunnel. This is particularly true for tunnels located in highly seismic zones., such as the Asian section of the Ring of Fire.

This paper presents the case of a specific structural movement joint between the cross-passage and the main tunnel collar designed to mitigate the seismic effects on the tunnel. The seismic joint allows relative displacement between the collar and the secondary lining of the cross passage. This significantly reduces the seismic induced stresses in the segmental lining in the proximity of the opening.

The movement joint is designed as a disconnection between the secondary lining of the cross-passage and the collar. The gap between these two structures is stuffed with rubber sheets, the waterproofing of the joint is assured by means of a steel-edged rubber waterproof strip. This paper presents the simplified 3D FEM analysis carried out, concerning this joint and the consequences in terms of the seismic induced stresses in the segmental lining at the proximity of the opening.

The use of such a movement joint can be seen as a valid mitigation measure, and it can significantly enhance the seismic resilience of the tunnel structure, improving safety and durability.

Keywords: TBM, Tunnel openings, Earthquake, 3DFEM Analysis

1 INTRODUCTION

The intersections of cross-passages and segmental tunnel linings are critical components in underground tunnels that need to be specifically designed to withstand seismic events. During earthquakes, these intersections are subjected to significant dynamic loading, which can cause structural damage and compromise the overall integrity of the tunnel. For such reason, the movement joint can be considered as a valid solution to allow displacements between the main tunnel collar and the cross-passage section by reducing the risk of significant cracking on the main tunnel segmental lining at the proximity of the opening during the seismic event.

The aim of this paper is to study the impact of the use of the movement joint on the internal forces of the segmental lining at the proximity of the cross-passage opening. A simplified FEM analysis is carried out in order to set out in a pragmatic way the use of such kind of joint between the collar and the cross-passage in a seismic analysis. Two different FEM models are built, and the results compared. One with a fixed connection between the collar and the cross-passage section and a second one with the movement joint.

2 STRUCTURAL DETAIL OF THE MOVEMENT JOINT

Unlike the main tunnel, the lining of the cross-passage is continuous, except that the secondary lining is disconnected from the main tunnel collar by a structural joint. Details are shown in the figure below.

In this case, the gap between the secondary lining and the portal is filled with nitrile cork rubber sheets, and it is barred by steel-edged rubber strip and waterproof strip. Moreover, the steel reinforcement of the connection portal is not connected with the secondary lining steel reinforcement of the cross-passage. The steel reinforcement of the connection collar is illustrated in the figure hereafter.

The movement joint represents a real structural disconnection between the connection collar and the cross-passage section. Therefore, in the FEM modelling, the movement joint works only in compression and not in traction. All FEM modelling hypothesis are introduced in the following paragraph.

*Corresponding author: ggiordano@systra.com

DOI: 10.1201/9781003495505-31

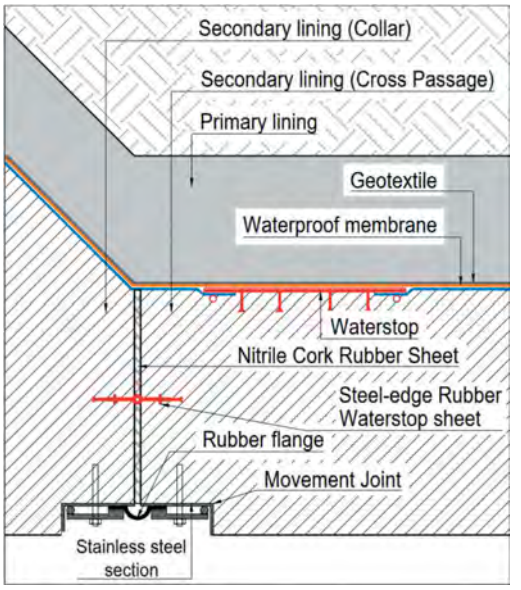

Figure 1. Movement joint details.

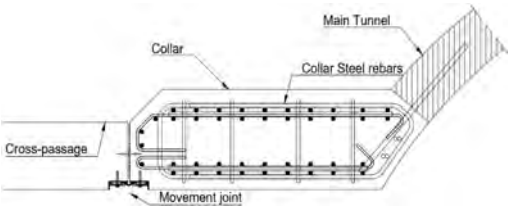

Figure 2. Example of a connection collar steel reinforcement with the movement joint at the intersection between the main tunnel and the cross passage.

3 FEM MODELLING

The structural analyses are calculated using SOFISTIK finite element structural code. The software fits all the engineering application fields, ranging from 2D Slab design to 3D building and bridge design and tunnel design. The software provides the possibility of design according to Eurocodes and many other design codes, plus interactive post-processing and 64-bit solver.

The 3D model used in this analysis is shown in the figure hereafter. Please note that the tunnel rings numbering scheme is depicted in the figure hereafter.

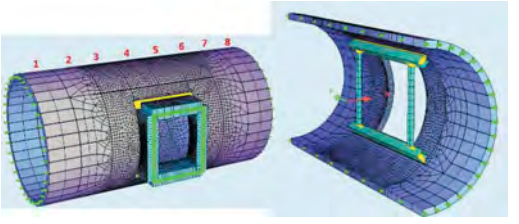

Figure 3. Sofistik model and tunnel rings numbering.

The actual cross-passage (CP) construction staging can be resumed as follow:

- Excavation and segmental lining installation of the two TBM tunnels.
- Ground improvements at the CP location.
- Installation of the steel frame in the TBM tunnel.
- Cutting and opening of the segmental lining.
- CP Excavation and temporary support installation.
- CP Final lining installation.

3.1 *The main tunnel*

The tunnel is modelled by a sequence of C40/50 reinforced concrete plate elements representing continuous rings 1.6m long. The ring thickness is 30cm equivalent to the segmental lining thickness. A total of 8 rings are used in the analysis.

The cutting line of the segmental lining corresponds to extrados of the cross-passage (about 3.4m wide and 4.3m high). In total, 4 rings of the main tunnel are affected by the cut. A focus on the opening is illustrated in the figure hereafter.

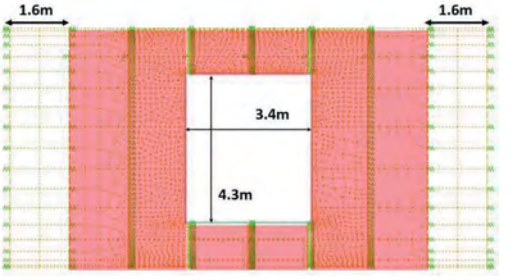

Figure 4. Cross-passage opening in the sofistik model.

3.1.1 *Contact surface between rings and dowels*

The concrete-concrete contact between the rings is modelled in the 3D FE model and will only transfer normal horizontal forces. Joints are modelled so that no tensile normal forces can be transferred (compression only).

The contact surface is considered on the whole contour of the ring with a thickness of 190 mm (the effective width of the joints).

Additionally, 18 dowels (3 per segment) are regularly spaced on the main tunnel contour.

The stiffness of a dowel is calculated from the elastic limit of the element, corresponding to 160 kN of shear force for a limit displacement of 30 mm, i.e.:

$$k = (160\ \text{kN})/(30\ \text{mm}) = 5333\ \text{kN/m} \quad (1)$$

3.1.2 *Main tunnel support stiffness*

The soil-structure interaction is modelled by the use of springs. The used spring stiffness in the hyperstatic reaction method in Sofistik at the Main tunnel segmental is calculated by Galerkin's formula:

$$k_R = E/R(1+\nu) \quad (2)$$

$$k_T = 1/3k_R \quad (3)$$

Where k_R is the radial stiffness (kPa/m), k_T is the tangent stiffness (kPa/m), R is the curvature radius of the tunnel (m), E is the ground Young modulus (kPa) and ν is the Ground Poisson ratio (-).

3.2 *The main tunnel collar*

The cast in place connection beam is modelled by beam elements. Moreover, in a simplifying and conservative way from the structural point of view the upper beam is modelled as a straight plate with a width of 1.2m instead of a U-shape geometry. The collar is fixed to the main tunnel segmental lining. Please refer to the Figure 2 and the figure hereafter.

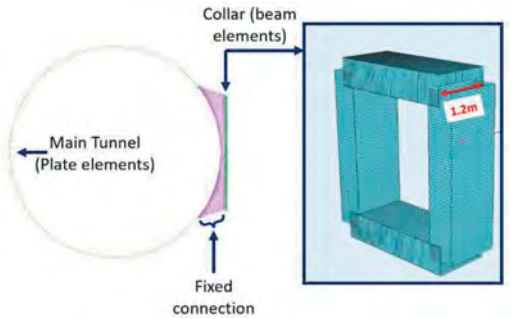

Figure 5. The collar in the sofistik model.

The collar support stiffness representing the contact with the surrounding ground is modelled as for the main tunnel by the use of springs. In this case the stiffness of the springs is calculated according to Vesic 1961.

3.2.1 *Movement joint*

As introduced in paragraph §2, the movement joint is modelled by the use of springs at the surface contact of the collar with the cross-passage. These springs can only work under compression loads and don't react to traction forces. The spring working law aim is to represents the effect of the structural disconnection between the main tunnel collar and the cross-passage. This aspect is clearly illustrated in Figure 2 in which a steel reinforcement of the collar is totally disconnected from the cross-passage one.

3.2.2 *Fixed joint*

The fixed joint is also modelled by the use of springs at the surface contact of the collar with the cross-passage. In this case springs can work both in compression and traction. This working law represents a "classic" junction solution between the collar and the cross-passage section in which the steel reinforcement can be considered as continuous between these two elements. A typical case of fixed joint is illustrated in the figure hereafter.

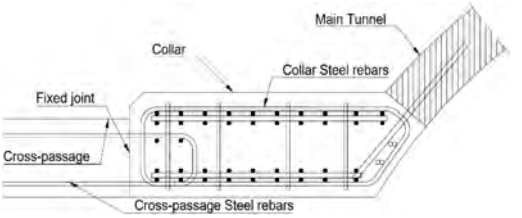

Figure 6. Example of fixed joint between the collar and the Cross Passage Section.

3.3 *The metallic temporary structure*

The metallic temporary structure used in the model is shown in Figure 3. This structure is composed by two horizontal beams with a square hollow section 400x400mm and two vertical columns which have the same shape but a reduced section i.e. 200x200mm. This structure plays a key role during the phase of the main tunnel opening. Its main role is to support the stresses of the main tunnel segments interested by the opening during the temporary phase of the opening, before the concrete collar is constructed and acquire il full strength. The Sofistik modelling allows to design this structure and to optimize its position.

3.4 *The model loads*

The tunnel loading is modelled in Sofistik by a combination of static loads described hereafter.

3.4.1 *The geostatic loads*

The earth and water pressure applied on the Sofistik model are calibrated with the results issued from a geotechnical FEM analysis calculated in the same section using the software Plaxis 2D. This calibration allows to obtain similar axial force and bending moment in the segmental lining studied with the two different softwares.

3.4.2 *The seismic load*

The seismic calculation approach presented hereafter is based on an internationally recognized method which performs the seismic analyses according to ITA/AITES guidelines for the design of Segmental tunnel linings 2019 and to ITA/AITES Seismic design and analysis of underground structures, 2001. According to this method, the seismic response of a tunnel is dominated by the surrounding ground response and not by the inertial properties of the tunnel structure itself, as "for most underground structures, the inertia of the surrounding soil is large relative to the inertia of the structure".

Therefore, the underground seismic design is based on the free-field deformation of the ground and its interaction with the structure, in contrast to the design of the surface structures. Further studies (for example using 3D full dynamic modelling) should be carried out to better investigate the negligibility (or not) of inertial effects in function of the dimensions and thickness of the structure.

The applied methodology foresees the application of a distortion to the ground to deform the underground structures and obtain the stresses acting in the lining in case of a seismic event.

The starting point of the study is the site-specific design acceleration at surface, $a_{max,S}$. For the specific case, a value of 0.9 g has been considered.

In order to consider the depth of the tunnels, the ITA/AITES Seismic design and analysis of underground structures, 2001 defines the peak acceleration at the tunnel depth ($a_{z,max}$): the procedure consists in the determination of a reduction coefficient C for the peak acceleration on the surface depending on the tunnel depth as shown in the equation here below:

$$a_{z,max} = C\, a_{max,s} \quad (4)$$

Where, $a_{z,max}$ is the peak acceleration at the tunnel depth (m/s^2), C is a reduction coefficient (-) and $a_{max,S}$ is the site-specific design acceleration at surface.

The value of $a_{z,max}$ is used to determine the γ_{max} (maximum shear deformation in free-field condition) from the peak ground velocity V_s which is a function of the earthquake magnitude and distance from the seismic source, as shown in following equations:

$$\gamma_{max} = V_S / C_S \quad (5)$$

$$V_S = k\, a_{z,max} \quad (6)$$

Where, γ_{max} is the maximum shear deformation in free-field condition (-), V_s is the peak ground velocity (m/s), C_s is the apparent propagation velocity (km/s) and k is the ratio of peak ground velocity to peak ground acceleration.

The main input parameters used in the calculation illustrated in this paper are resumed in the following table.

Table 1. Input for the seismic analysis.

Tunnel overburden (m)	15
Type of surrounding ground	Soft Rock
Moment magnitude (M_w)	8.5
Source to site distance (km)	< 20
Gravity acceleration (m/s^2)	9.81
$a_{max,S}$ (g)	0.9
C	0.9
$a_{z,max}$ (g)	0.796
k (cm/s/g)	127
Vs (m/s)	1.01
Cs (km/s)	0.775
γ_{max} (-)	0.0013

A FEM modelling is carried out with the aforementioned parameters and the seismic induced stresses in the segmental lining are analysed.

Subsequently, the simulation of the earthquake effects in Sofistik are simulated by the application of lateral forces to the model to reproduce the same seismic distortional effects on the main tunnel issued by the previous analysis.

The two following load-cases are considered in the Sofistik analysis.

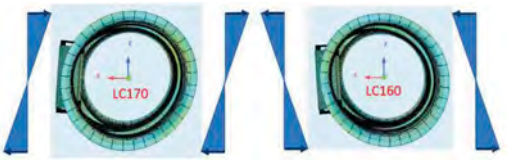

Figure 7. Sofistik loadcases for the seismic analysis.

3.5 *The model phasing*

The tunnel is modelled by a sequence of seven consecutive stages. The calculation steps consider the history of loads and deformations from previous phases.

For the calculation of the crack width at the serviceability limit states (SLS), the quasi-permanent combination is used. In the ultimate limit state (ULS) calculation all the loads are factored by a coefficient of 1.35. In the accidental limit state (ALS) calculation al the loads are factored by a coefficient of 1.00.

The Sofistik phases are:

- Phase 110 – Initial state: Initialization of the stresses on the Main tunnel segmental lining.
- Phase 120 – The temporary metallic structure is installed.
- Phase 130 – The cross-passage opening is excavated.
- Phase 140 – The collar is constructed (activated) and the metallic structure deactivated.
- Phase 150 – The collar is loaded with the geostatic loads described in paragraph §3.4.1.
- Phase 160 – A distortion in X direction is applied to the main tunnel in order to simulate the earthquake effects.
- Phase 170 – A distortion in -X direction is applied to the main tunnel in order to simulate the earthquake effects.

The paper focuses on the results of phases 160 and 170 in order to study the effects of the two different types of joints on the segmental lining stresses results at the proximity of the opening.

This phasing is used for both the models, one with the fixed joint and the other one with the movement joint.

3.6 *The model results*

The results in terms of internal stresses of the segmental lining at the proximity of the cross-passage opening are described in this paragraph

for both the model with the fixed joint and the one with the movement joint at ring number 5 and 6. In the following images the point A represents the intersection between the segmental lining and the collar.

The results shown for the seismic analysis represent the worst-case scenario in terms of internal stresses in the main tunnel segmental lining, i.e. the load-case LC 160.

N.B. The tunnel rings numbering is illustrated in Figure 3. The results in terms of stresses illustrated in this paragraph refer to the centrelines of ring number 5 and 6. Point A represents the stress distribution in ring 5 at the collar's upper beam.

3.6.1 *Fixed joint*

The main results in terms of axial forces and bending moment in the segmental lining are shown in the figures hereafter.

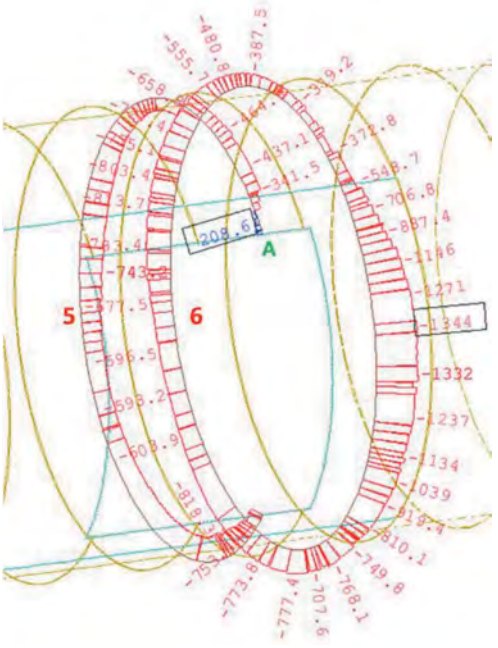

Figure 8. Sofistik results – Axial force for the seismic analysis – Fixed joint.

3.6.2 *Movement joint*

The main results in terms of axial forces and bending moment in the segmental lining are shown in the figures hereafter.

3.6.3 *Results comparison*

The maximum internal stresses comparison between the two models are resumed in the tables below for both the main tunnel lining segments analysed (n.5 & n.6) and for point A.

NOTA: Compression values are shown as negative.

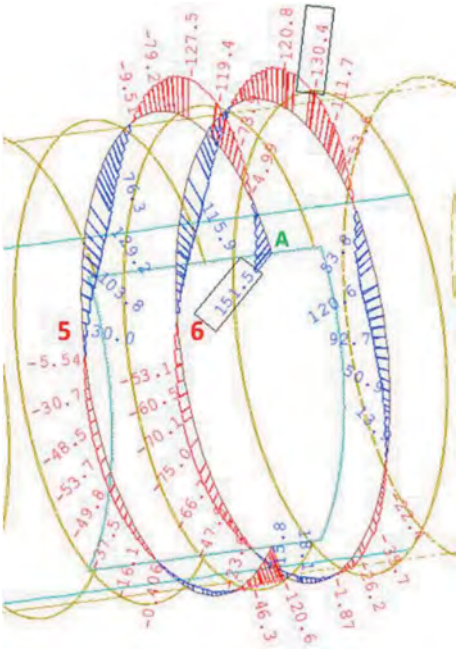

Figure 9. Sofistik results – Bending moment for the seismic analysis – Fixed joint.

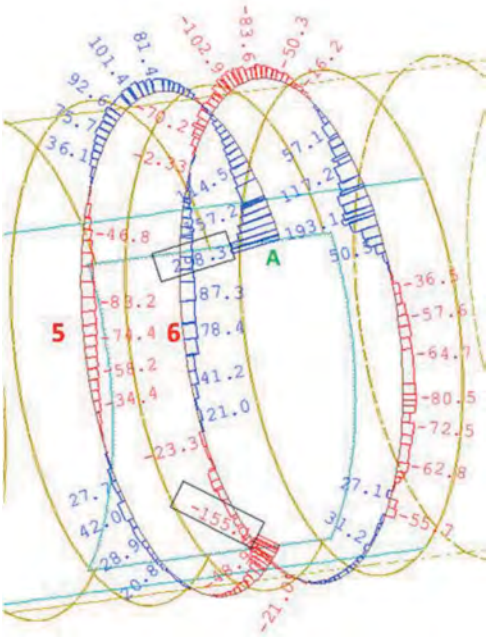

Figure 10. Sofistik results – Shear force for the seismic analysis – Fixed joint.

4. CONCLUSION

Table 2 summarizes the results of the seismic analysis carried out and shows the variation in terms of

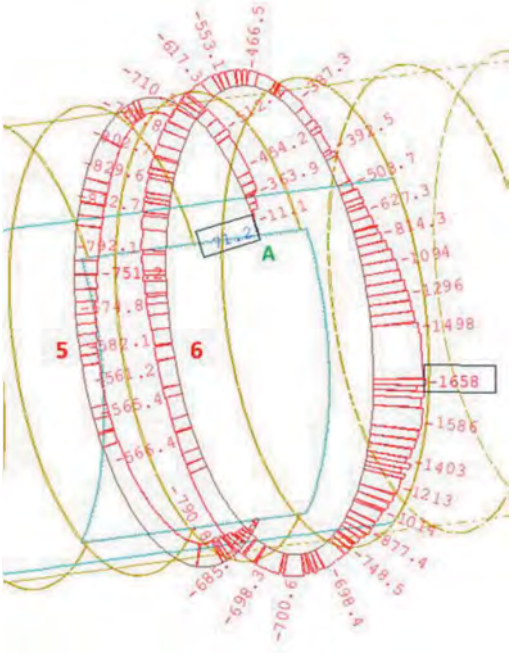

Figure 11. Sofistik results – Axial force for the seismic analysis – Movement joint.

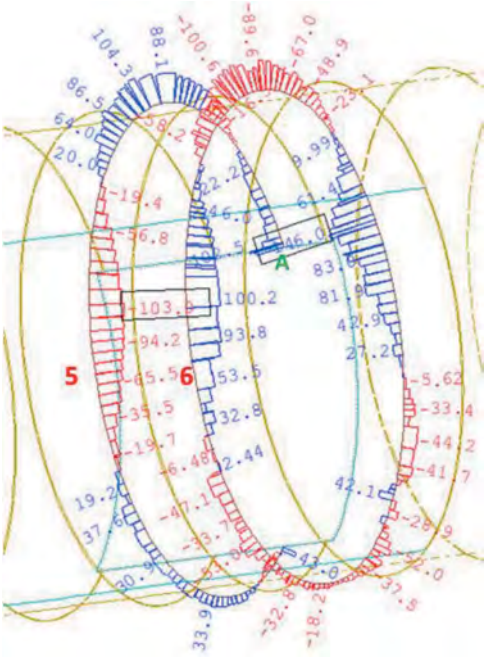

Figure 13. Sofistik results – Shear force for the seismic analysis – Movement joint.

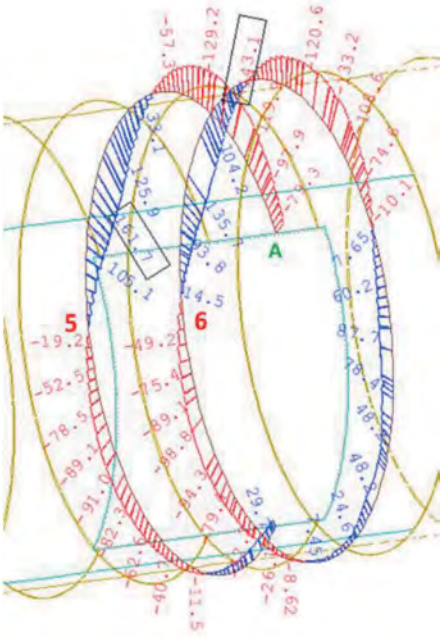

Figure 12. Sofistik results – Bending moment for the seismic analysis – Movement joint.

internal stresses in the segmental lining for both solutions (fixed joint and movement joint).

Table 2. Internal stresses comparison between the F.J. and M.J. models.

	Fixed Joint	Movement Joint	Variation (%) F.J. &&& M. J.
N min (kN/m) ring n.6	-1344	-1658	+ 23.3 %
N max (kN/m) Ring 5 & at point A	+208.6	+71.2	- 65.9 %
M max (kNm/m) ring n.5	151.5	161.7	+ 6.73%
M max (kNm/m) ring n.6	-130.4	135.7	+4.06%
M max (kNm/m) at point A	151.5	-79.3	- 47.6 %
V max (kN/m) ring n.5	298.3	104.3	- 65.0 %
V max (kN/m) ring n.6	193.1	146.0	- 24.4 %
V max (kN/m) at point A	298.3	102.5	- 65. 6 %
Maximum Collar seismic displacement (mm)	0	5	-

The movement joint solution leads to a general reduction of the internal stresses at the opening. For instance, at the point A, the maximum values of both the axial traction and shear force drop by more

than 60% and the maximum bending moment by about 50%.

However, we can observe a small increase of the bending moment in the remaining part of the segmental lining ring n.5 (+ 7%) and in the adjacent ring n.6 (+4%). At the same time, we can observe a slight increase of the compression level in the ring n.6 and no changes of the compression level in the ring n.5 between the two solutions. In terms of bending moment, these increases remain small and easily manageable with the steel cage foreseen for the main segmental lining, especially for the ring n.6 in which the increment of axial force leads to a global safety factor increase for the whole ring. The relative displacements between the structures remain small and don't affect the stability of the cross passage.

The findings of this study suggest that the use of the movement joint, designed as a disconnection between the secondary lining of the cross-passage and the collar is a valid mitigation measure for cross-passage intersections in segmental tunnel lining. The simplified 3D FEM analysis carried out shows that the use of such a movement joint can significantly reduce the seismic induced stresses in the segmental lining, which can help to prevent structural damage and improve the overall integrity of the tunnel. Further studies are still required for the full understanding of the problem, future lines of research could be focused on more complex 3D FEM seismic analysis such as a full dynamic modelling and collecting real cases results or carrying out physical experiments to validate the model.

REFERENCES

Zhang, Yuan, Bao, Yu, Bilotta, 2019. Shaking table tests on the intersection of cross passage and twin tunnels. Soil Dynamics and Earthquake Engineering 124 (2019) 136–150. Amsterdam, Netherlands.

Zhang, Yuan, Bilotta, 2019. Analytical solutions for seismic responses of the tunnel in a shaft-tunnel junction under transverse excitations. Soil Dynamics and Earthquake Engineering 127 (2019) 105826. Amsterdam, Netherlands.

Liao, Xu. 2013. The Reasonable Layout of Cross Passages for Qianjiang River Tunnel based on seismic analysis. Tongji University, Shanghai, China.

ITA/AITES, 2019. Guidelines for the Design of Segmental Tunnel Linings.

Y.M.A. Hashash, J.J. Hook, B. Schmidt, J.I-C. Yao. Seismic design and analysis of underground structures. ITA/AITES, 2001.

Tunnelling for a Better Life – Yan, Celestino, Thewes & Eberhardt (Eds)
© 2024 The Author(s), ISBN 978-1-032-80042-4
Open Access: www.taylorfrancis.com, CC BY-NC-ND 4.0 license

Development of sustainable criteria for the Italian railway tunnel design

Franco Iacobini & Annalisa Pranno*
Rete Ferroviaria Italiana – Infrastructure Department, Rome, Italy

ABSTRACT: In recent years, RFI has been developing the challenging topic of sustainable for railway infrastructures drowning up the change management program "Sustainability on-the-go". The program consists of ten guidelines and the first of them concerns the railway infrastructure design through the revision and the definition of standards in terms of sustainability and Life Cycle Assessment. To achieve these goals, RFI improved its Manual Standard (Civil Work Design Manual and Civil Work Technical specification for construction) in an integrated approach to implement a systemic vision of sustainability. Starting from the planning phase and then moving on to the design phase and finally to construction, RFI provides in its manuals the indications for sustainable structures.

This paper will focus on sustainability topics provided in the tunnel section of RFI Civil Works Design Manual. Overall, in the new changeling approach the design and the construction of a railway tunnels have to enhance the integration in the territory and to promote the development of the socio-territorial context. In particular, the manual has been updated providing solutions to reduce soil and resources consumption and allowing the reuse of materials and equipment. For example, the reuse of the TBMs and their component has been included. Further studies are in progress even for the definition of a LCA analysis for a tunnel, allowing a quantitative assessment of the potential environmental impacts in addition to the current required.

Keywords: Sustainability, Design, Standard, Tunnelling, RFI

1 INTRODUCTION

In October 2015, 193 United Nations countries, including Italy, signed the 2030 Agenda to define commitments to achieve the 17 global Sustainable Development Goals (SDGs) by 2030. The SDGs are intend to lead a change in the development of economic, social and environmental model and, in particular, to arrive at a way of construction that is more resilient, inclusive and economically sustainable.

Further to that, at the European level, the Green Deal defines a new growth strategy with the aim to transform the European Union into an efficient economy without net greenhouse gas emission by 2050 and a reduction of around (50-55)% by 2030 too. In this new vision of infrastructural development, Ferrovie dello Stato Italiane Group, that is one of the largest industrial companies in Italy for the mobility system, contributes in a relevant way to the SDGs. The objectives of the 2030 Agenda in which the railway infrastructures have a significant impact are a lot, such as "Good jobs and economic growth", "Industry, Innovation and Infrastructure", "Reduce inequalities", "Sustainable cities and communities", "Responsible consumption" and "Climate Change" (Figure 1).

Figure 1. The SDGs relevant to the railway infrastructures.

Moreover, Ferrovie dello Stato Italiane Group counts more than 15 subsidiaries and one of the main ones is Rete Ferroviaria Italiana (RFI), as the manager

*Corresponding author: a.pranno@rfi.it

DOI: 10.1201/9781003495505-32

of the national railway infrastructure. The network managed by RFI has an extension of approximately 16800 km. The tunnels over 100 meters are 1630 and about 1536 km long, which over 50% double track (Figure 2). The particular orographic conformation has made Italy the European country with the largest number of railway tunnels and also in the next future a great number of tunnels will be put in service.

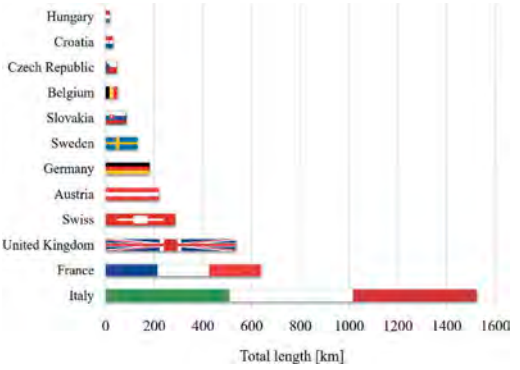

Figure 2. European railway tunnel asset.

The transportation systems are a fundamental part of our society and key sectors for the environment, due to the greenhouse gas emissions, the impact on the soil and resources and, in general, for the resilience of the country. The infrastructure's role is an essential component for the environment in particular for their long service lives.

In fact, RFI, according to the SDGs, plays a fundamental role to act the national recovery and resilience plan and up to 2026 more than three hundred kilometres of new tunnels will be put in service. The underground construction industry is the future for the development of sustainability approaches, as part of the solution to the increasing demand for space and natural resources. The main aim of RFI is to review and define its standards in terms of sustainability and Life Cycle Assessment (LCA).

2 CIVIL WORKS DESIGN MANUAL

RFI has been improving its Civil Works Design Manual and Civil Works Technical Specifications to achieve the objectives of the first guideline of its sustainability program.

In particular, the Civil Works Design Manual and the Civil Works Technical Specification are divided into different sections. The manual contains the technical requirements for the civil works design, in order to unify and to standardize the design. The objective is to provide a significant advantage in terms of costs and a improvement in the maintenance in order to gain in efficiency and timing for the entire lifetime. As a single reference document, it gathers all the project requirements of the sector issued in recent years. The fourth section of the RFI Civil Works Design Manual concerns the design of new tunnels. In this paper the sustainability topics of the RFI Civil Works Design Manual for tunnels are illustrated.

2.1 *Sustainable management of excavated soil and rock*

Railway infrastructure design and construction have been widely promoted also through the national recovery and resilience plan. Accordingly, a large amount of infrastructure-related excavated soil and rock (ESR) is generated, particularly from the construction of underground works. In order to comprehend the importance of the topic, it is essential to provide an estimate of the quantities of ESR that will be produced by the tunnel sections of the RFI Civil Works Design Manual. For example, for mechanized excavation sections (Figure 3), the quantitative of ESR volumes correspond to approximately 74000 cubic meters per km for the single-track and about 127000 cubic meters per km of tunnel for the double-track (speed 200÷250 km/h).

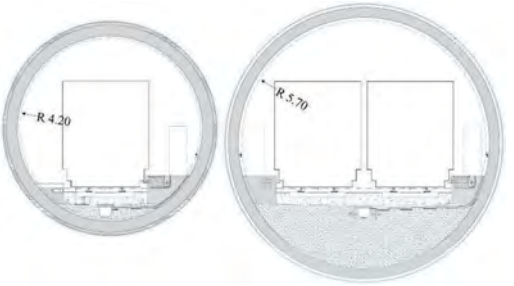

Figure 3. Standard section for mechanized excavation (speed 200÷250 km/h).

Due to the large quantities of ESR that are excavated and removed from the tunnelling, the manual establishes that, starting from the first design phase, the management of the ESR have to be analysed to protect the environment and pursue the principles of circular economy, preserving their value as resources over time. Besides, the manual was updated to examine and support innovative technological solutions that maximize the reuse of excavated material. Reuse can occur within the same projects and/or at external sites, but anyway the waste management has to be limited to a residual condition. The management of ESR requires consideration of both environmental and social sustainability, as well as technical and economic factors. According to the physical and geotechnical properties of the material produced after the excavation process (muck), it can be used for:

- production of concrete (aggregates), for good quality muck;
- new embankments or road works, for fair quality muck;

– for filling, backfilling or environmental/land reclamation, for low quality muck. Instead, ESR that cannot be reused is usually stored in a temporary storage sites, if necessary, and then delivered to final storage sites. To sum it up, reusing excavated materials has two primary environmental advantages: a decrease in waste disposal and a decrease in the amount of raw materials extracted.

2.1.1 *Authorization process*

The reuse of ESR or the identification of the final storage has to be defined in the phase of the design. Furthermore, the plan of the use of ESR have to be assessed according to the specific legislation. For example, according to legislation, to identify the most suitable alternative for reuse, it's necessary to develop experimental site-specific studies for the mechanized excavation with additives. During the design phase, the samples were taken from the geognostic surveys and experimental site-specific studies were conducted with the additives that were expected to be used in the construction phase. Both environmental compatibility and eco-toxicological and conditioning studies were conducted as part of the studies.

2.1.2 *RFI's best practices for the new railway lines*

A sustainable and efficient management of ESR has been planned for the design of several new high-speed and high-capacity railway lines, of which some projects are already in the construction phase. Considering one of these, for example, a new high-capacity line of more than twenty kilometres long, consisting mainly of underground works, it can be estimated that there is approximately five and half million cubic meters of ESR in bench from mainly granitic and phyllite rock formation and, in the final design, it is provided to fully reuse them. The excavated materials were divided into classes of use (Figure 4). The class A is identified for the good quality of muck that can be used for the production of concrete (aggregates) for structures and precast tunnel segments, but also for new embankments. After that, the class B is for fair quality muck that can be used for new embankments. Last, the class C is used for filling, backfilling or final storage.

ESR were produced from both: conventional excavation, with or without consolidation at the excavation face; mechanized excavation, bored by an earth pressure balance shield with or without using additives for soil conditioning.

For the conventional excavation sections with consolidation at the excavation face, the average percentage of fiberglass, polyvinyl chloride and cement is estimated and the average percentage of anthropic inclusions respect the limitations of legislation. The vegetal soil, on the other hand, has been preserved since the opening of the construction site. At the end of the works, it will be utilized for naturalization, which will restore the territory to its original state.

Figure 4. Reuse of excavated soil and rock.

For the mechanized excavation, for the nature of the additives used (foams) and through the treatments of crushed and screened, the ESR will be delivered to the final storage sites without any additives thanks to the drying and natural biodegradation process. Moreover, various logistical solutions have been implemented to reduce the number of trucks on the roads during the transport of excavated materials.

2.2 *Sustainable management of water resources*

The management of water resources is also relevant to pursue the objectives of sustainability. First of all, to preserve the purity of waters, in the railway infrastructure projects the tunnel drainage system provides a separation between the waters from rock/soil and the waters from the railway platform. The management of the water resource plays a fundamental role especially for the tunnel built by conventional excavation. To take a specific example, in conventional excavation, there is a polyvinyl chloride waterproofing membrane between primary and secondary linings. The waterproofing and drainage system intercepts water by the waterproofing of the tunnel crown, and it is collected from the longitudinal drainage pipes. The water is conveyed through transversal connecting pipes to a dedicated collection pipe. The inspection wells are also provided for maintenance. This system is separated from the drainage of the railway platform water (Figure 5).

It is important to analyze the opportunity to reuse and enhance water resources in different phases of the project and it is related to the possible interference with the aquifers present. In addition, it is relevant to enhance potentially drained water whenever possible and always in compliance with the technical, economic, and functional requirements of the project.

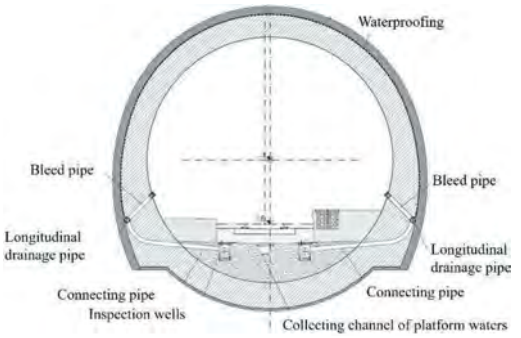

Figure 5. Drainage systems for conventional excavation sections.

In fact, any possible solutions should be studied to evaluate their recovery, valuation, and reuse.

To maximize the sustainable management of drained water resources, the following should be carefully assessed:

- the quantities of inflows;
- the chemical-physical quality;
- any contamination with which water may come in contact.

The aim is to identify the possible reuse of waters that can be used for agricultural, potable, industrial, fire, and other types. The full round waterproofing is an excellent solution to avoid an environmental impact on water resources. For the waterproofing in the tunnel crown, the water is conveyed through lateral collectors or a single collector under the invert and, in this case, it is configured as a drainage system with filtration motion towards the tunnel. In RFI Civil Works Technical Specification, the waterproofing have to be guaranteed by the installation of a polyvinyl chloride waterproofing membrane between the primary and secondary linings with a thickness of minimum two millimeters, accompanied by a layer of geotextile outside in order to regularize the laying surface. For a sustainable railway investment from a technical, economic and environmental perspective, it is relevant the problem of the groundwater lowering due to the possible drainage during excavation. In order to excavate safely, it is necessary to find a technical compromise. For this purpose, it is fundamental to control instability resulting from the entrance of water into the tunnel, which may necessarily lead to a lowering of the groundwater during construction, and to minimize the impact on the hydraulic conditions at the boundary. After an appropriate evaluation, if it is not possible to adopt a full round waterproofing, the first mitigation intervention consists of reducing the volumes of water drained by the tunnels.

2.2.1 *RFI's best practices for the new railway lines*

Considering a new high-capacity line of about ten kilometers long, consisting mainly of underground works, the estimated number of water sources in the area of study is approximately two hundred. For the tunnels, it is provided a full round waterproofing system. Mitigation measures are implemented in the project, including replacing preventive measures and waterproofing the rock mass formation during the phase of construction. Moreover, the environmental monitoring system of the project is combined with a specific monitoring of water resources. The water resources were analyzed for the period before the construction (two years before), are analyzing during the construction phase, and will be monitored also after the realization of the works (for at least two years). The plan of water sources monitoring is relevant for the hydrogeological, geological and geotechnical information. These information are useful for the identification of measures and interventions to be acted, such as waterproofing of rock mass formation, preventive replacement interventions and, if necessary, emergency interventions. The plan (Figure 6) includes for example:

- measurements of chemical-physical parameters, such as temperature, specific electrical conductivity, fixed residue, red-ox potential, pH, turbidity, amount of oxygen;
- measurements from piezometers and wells;
- flows measures;
- hydro-chemical and isotopic analysis.

Figure 6. Water sources monitoring system.

For the specific chemical-physical water treatment for waters that come from tunnels, the waters need to be treated before being re-entered in the receivers, as provided in the RFI Civil Works Technical Specification. In conclusion, the sustainability elements of the project's construction site have been identified. Water collection and regimentation systems are used to reuse water as a resource. Treatment plants, for the waters from precipitation for instance, to reuse them as water for example for construction site toilets. Further treatment and accumulation plants for waters from the tunnelling, for the industrial reuse. Energy-efficient systems are utilized to decrease the energy consumption.

2.3 *Use of "remanufacturing" for the TBM*

The construction of a tunnel is interested by a series of actions: excavation, support of the cavity and removal of muck. Performing all of these activities

can be done through various methods, which are often combined together. The construction of a tunnel can be achieved through several conventional and mechanized methods. Considering the technological advancement of the industry, the TBM is definitively more used than in the past for the construction of new tunnels. The cost of a TBM, if newly built, is however averagely high, also related to the forecast of the high demands for the TBMs in the next years. For the protection of environmental and to pursue the principle of circular economy, the RFI Civil Works Design Manual provides that solutions that allow the reuse of the TBMs or their components through a process of "remanufacturing" which can be adopted since the design phase. This process is capable of establishing a complete new life cycle for the product, guaranteeing a quality level that is equivalent to the original one. The process of "remanufacturing" is defined by the "ITAtech Guidelines on rebuilds of machinery for mechanized tunnel excavation" and it is mentioned in the RFI Civil Works Design Manual. The process consists of five main phases, which are:

- complete disassembly of TBMs to their single part level;
- cleaning of all parts;
- cataloguing of all parts and visual and/or instrumental inspection;
- reconditioning parts that are worn or obsolete;
- reassembling and final testing for product certification and quality. Due to the complexity of the TBMs context, different methods of "remanufacturing" can be adopted for each component of the TBM, always preserving the environment. For example, laser cladding, welding or other methods can be adopted to repair the screw conveyor when the wear amount exceeds the fixed threshold (Figure 7).

Figure 7. Screw conveyor before and after the remanufacturing process.

The reuse of a TBM is at the moment provided in one construction procurement.

3 CONCLUSIONS

In this paper the sustainability topics for tunnels are illustrated. It is provided an overview about the reuse of excavated soil and rock, the management of the water resources and regarding to the remanufactured TBMs. Moreover, analysis are in progress to achieve the aim of the realization of sustainable tunnels through a systemic vision.

Further studies are in progress even for the definition of a LCA analysis for a tunnel, allowing a quantitative assessment of the potential environmental impacts. These results can be useful in addition to the current required regulations and standards and to completely update the manual standards.

REFERENCES

ITAtech REPORT n.5-V2, March 2019. ITAtech Guidelines on Rebuilds of Machinery For Mechanized Tunnel Excavation, ITAtech Activity Group Excavation, pp. 7–12 (section 2, 3, 4 and 5)

RFI, 2023. Civil Works Design Manual, Section IV – Tunnels, for the sustainable management of excavated soil and rock and for the sustainable management of water resources, p. 185 (subsection 4.8.5 and 4.8.6).

RFI, 2023. Civil Works Design Manual, Section IV – Tunnels, for the use of "remanufacturing" for the TBM, p. 134 (subsection 4.8.2.3.1.3).

RFI, 2023. Civil Works Technical Specification, Section V - Concrete and Steel Works, pp. 10–12 (subsection 5.5.3 and 5.5.4)

RFI, 2023. Civil Works Technical Specification, Section VI - Earthworks and Excavations, p. 17 (subsection 6.5.3.3).

RFI, 2023. Civil Works Technical Specification, Section XVIII - Use of Recycled Aggregates and Lime Treatments for Earthworks, p. 44 (subsection 18.6.7).

Tunnelling for a Better Life – Yan, Celestino, Thewes & Eberhardt (Eds)
© 2024 The Author(s), ISBN 978-1-032-80042-4
Open Access: www.taylorfrancis.com, CC BY-NC-ND 4.0 license

Analysis on applicability of seismic calculation methods for shield tunnel in Shanghai area

Xin xing Li* & Hong Chen
Shanghai Tunnel Engineering and Rail Transit Design & Research Institute, Shanghai, China

ABSTRACT: At present, national and local standard have presented definitely some pseudo-static methods for lateral seismic design methods for shield tunnel in Shanghai area. These methods include response displacement method, response acceleration method, equivalent earthquake acceleration method and equivalent inertia force method. In the seismic design of field tunnel projects, there are some problems in using these methods. It includes how to select a suitable method and the results of different calculation methods are different. Based on a project case of shield tunnel, lateral seismic design using five different calculation methods is given separately in the paper. According to the results of dynamic time-history analysis, the causes of error on the calculation results of displacement and internal force are analysed. The Applicability of methods is studied in detail in terms of calculation model, determination of equivalent load, results error, and project application. The result shows that the response acceleration method has the minimum result error by compared with the dynamic time-history method. The response acceleration method is recommended as the recommended method for seismic design of underground tunnel in Shanghai area.

Keywords: Shield tunnel, Seismic design, Calculation method, Response displacement method, Response acceleration method

1 INTRODUCTION

The seismic design of underground structures is not taken care seriously until the underground station has been damaged by the Kobe earthquake in Japan. Subsequently, it sparked a widespread research trend. With the vigorous development of subway construction in major cities nationwide, China has also put forward clear requirements for the seismic design of underground structures, including subways. In 2011, the Ministry of Housing and Urban-Rural Development issued the "Notice on the Issuance of Technical Points for Seismic Design Special Demonstration of Municipal Public Facilities (Underground Engineering)", which stated that in areas with a seismic intensity of six degrees or higher seismic defence zones, urban rail transit projects with a total construction area exceeding 10,000 square meters, such as underground stations, must undergo a special seismic design demonstration. Therefore, the research on seismic design methods for underground engineering structures has become an important concern for engineering designers (Liu et al., 2007; Tao et al., 2012; Li et al., 2014).

In recent years, Shanghai has been gradually developing and improving seismic design standard for underground structures, including the subway interval shield tunnel. In 2009, Shanghai issued the "Seismic Design Standard for Underground Railway Structures" (Shanghai, 2009), which provides two equivalent seismic load methods for circular tunnels and other underground structures. These two methods are the equivalent horizontal seismic acceleration method and the equivalent inertial force method. The national standard issued in 2014 explicitly states the seismic design requirements for subway interval shield tunnel structures (China, 2014). It recommends two quasi-static calculation methods as seismic design methods, namely the response displacement method and the response acceleration method. The response displacement method is further divided into two cases based on the determination of seismic loads (Li et al., 2016). In the soft soil of Shanghai area, due to the specific geological conditions, it is very important to research on how to select the appropriate method among these available seismic calculation methods for specific underground tunnel projects, as well as to understand the differences and patterns in results obtained from different calculation methods.

Taking the case of circular shield tunnel projects in Shanghai subway, this paper conducts the lateral seismic calculations through the use of the response displacement method, the response acceleration method, the equivalent horizontal seismic acceleration

*Corresponding author: lxxxinyue@163.com

DOI: 10.1201/9781003495505-33

method, and the equivalent inertial force method. With the dynamic time-history analysis method as the standard, the results are compared and analysed in multiple aspects to identify the errors and its underlying causes. The analysis aims to further explore the rationality and applicability of seismic calculation methods and provide guidance in selecting suitable seismic calculation methods for shield tunnel structures in Shanghai.

2 SEISMIC DESIGN METHODS IN THE STANDARD

2.1 *Response displacement method I*

The response displacement method considers several loads, including the shear forces from the surrounding soil layers, the seismic earth pressure generated by the relative displacement of the soil layers, and the inertial forces on the structure under seismic action. To account for the constraint of the surrounding soil layers on the structure, a ground spring is introduced in the calculation model of the response displacement method (Liu et al., 2007), as shown in Figure 1.

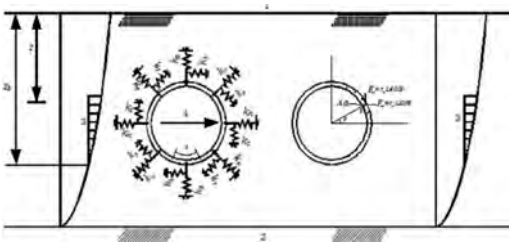

Figure 1. Schematic of response displacement method.

According to section 6.6.4 of the national standard (China, 2014), when evaluating the relative displacement of soil layers without conducting seismic safety assessment for the engineering site, the simplified calculation formula provided in Appendix E can be used to determine the variation curve of displacement with depth and calculate the relative displacement of the soil layers.

This method is called the response displacement method I. In this method, the variation curve of displacement with depth is simplified as a cosine function curve, and the corresponding shear stress variation curve is a sine function curve. If no other information is available, the peak ground acceleration provided in the code can be selected and multiplied by the corresponding adjustment coefficient to determine the peak acceleration of the structural element.

2.2 *Response displacement method II*

The calculation models and principles of the response displacement method I and the response displacement method II are consistent, with the main difference being the different methods for determining equivalent seismic loads.

According to the national standard (China, 2014), for the response displacement method, if seismic safety assessment has been conducted for the engineering site, the relationship between displacement and depth obtained from the assessment can be used to calculate the relative displacement of soil layers. This method is called the response displacement method II. In this method, the free-field displacement, shear stress, and acceleration at a certain depth, as well as the dynamic shear modulus of the corresponding soil layer at that depth, are all obtained through one-dimensional soil layer seismic response analysis.

2.3 *Response acceleration method*

The response acceleration method uses a soil-structure model to apply the horizontal effective inertial acceleration obtained from one-dimensional soil layer seismic response analysis at the time of maximum relative displacement of the top and bottom plates of the structure. The acceleration is applied at the corresponding depth positions in the soil and structure, simulating the seismic action through the generated horizontal inertia force (Liu et al., 2007). This method can reflect the interaction between the soil and structure, and consider the influence of complex cross-sectional structural forms and geological conditions, as shown in Figure 2.

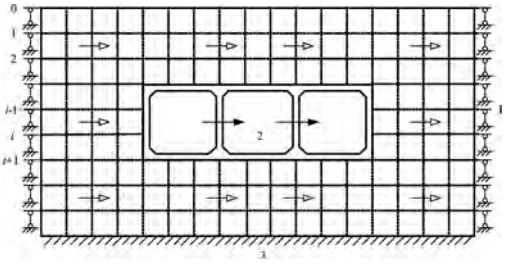

Figure 2. Schematic of response acceleration method.

In the calculation model, the soil is represented by plane strain elements, and the structure is generally represented by beam elements, although other element types can be used as needed. When calculating the structural response under seismic action only, the bottom boundary of the model is fixed, and the vertical displacement at the two side boundaries of the model is constrained while the horizontal displacement is free.

2.4 *Equivalent horizontal seismic acceleration method*

The equivalent horizontal seismic acceleration method is an equivalent seismic load method proposed for analysing the seismic response of

underground structures based on the plane strain problem. It belongs to the soil-structure method, and the load is determined according to the principle of equal ultimate action effect (Shanghai, 2009). The equivalent seismic load is determined based on the principle of equal the maximum bending moment of the main components. At the same time, the maximum bending moment of the remaining components, as well as the maximum axial force and maximum shear force of each component, are calculated by multiplying a correction factors.

For circular structures of subway interval tunnel in Shanghai, by using the equivalent horizontal seismic acceleration method, the seismic acceleration is uniformly distributed in the horizontal direction. This horizontal seismic acceleration is then taken as the equivalent seismic load. The load distribution and calculation diagram can be seen in Figure 3.

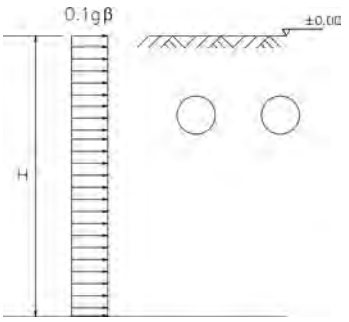

Figure 3. Calculating model of equivalent acceleration method.

In the diagram, H represents the total thickness of the soil layers surrounding the subway tunnel. It has a significant impact on the seismic response of the structure. Typically, H is taken as 70m. β is the coefficient for the equivalent horizontal seismic acceleration load.

The equivalent horizontal seismic acceleration method is a simplified calculation method for seismic loads based on the response acceleration method. It can also directly reflect the interaction between the soil and structure.

2.5 *Equivalent inertial force method*

The equivalent inertial force method belongs to the load-structure method, and the load is determined according to the principle of equal ultimate action effect (Shanghai, 2009). The equivalent seismic load is determined based on the principle of equal the maximum bending moment of the main components. At the same time, the maximum bending moment of the remaining components, as well as the maximum axial force and maximum shear force of each component, are calculated by multiplying a correction factors.

For circular structures of subway interval tunnel in Shanghai, by using the equivalent inertial force method, the seismic inertia force is applied at the node of the structure in the horizontal direction. The horizontal seismic inertia force and the corresponding triangular distributed horizontal soil resistance are then taken as the equivalent seismic load. The interaction between the structure and the soil is simulated by springs in the load-structure model.

The load distribution and calculation diagram can be seen in Figure 4. In the diagram, K represents the foundation coefficient of soil, P_f represents the maximum value of the horizontal soil resistance distributed in a triangular shape, which can be determined by the equilibrium condition with the equivalent seismic load in the horizontal direction, and F_1 represents the equivalent horizontal seismic inertial force acting on the lining segments.

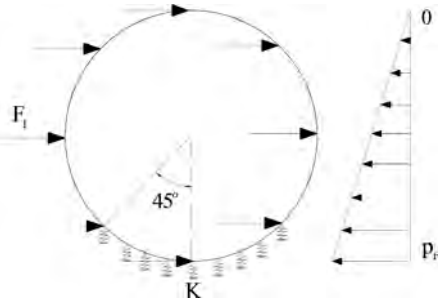

Figure 4. Calculating model of equivalent inertia force method.

3 CASE ANALYSIS AND COMPARISON

3.1 *Engineering examples and conditions*

The circular structure of a certain subway interval tunnel in Shanghai is constructed using the shield method. The outer diameter of the structure is 6.6 meters. The inner diameter of the structure is 5.9 meters. The width of the structure ring is 1.2 meters. The thickness of the segments is 0.35 meters. The thickness of covering soil is 20.0 meters, as shown in Figure 5. The segment material is high-strength concrete C55, and it is assembled with straight joints. The lining consists of six segments, including one

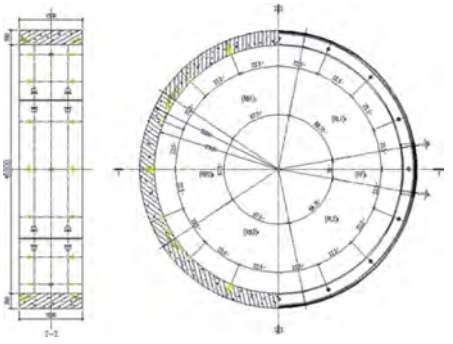

Figure 5. Cross section of subway station.

small top segment, two adjacent segments and three standard segments. The seismic analysis considers the coefficient of the joint effect and the dynamic modulus correction factor for the structural material.

The dynamic calculation parameters for the selected typical soil layers in the Shanghai area are shown in Table 1. The site category is classified as Category IV, and the nonlinear dynamic properties of each soil layer are represented by the Davidenkov fit curves (ZHANG et al., 2010).

The seismic design intensity is 7 degrees. The acceleration time history curve for the earthquake motion is taken at a 70m depth of underground with a 50-year exceeding probability of 10%, as shown in Figure 6.

Table 1. Parameters of different soil layers in Shanghai area.

NO.	Soil	Thickness /m	Depth /m	Gravity density / (kN/m^3)	Velocity of shear-wave /(m/s)
1	Artificial fill	1.88	1.88	17.3	127
2	Silty clay	0.8	2.68	18.5	126
3	Mucky silty clay	1.8	4.48	17.1	125
4	Clayey silts	1.7	6.18	18.4	125
5	Mucky silty clay	3.8	9.98	17.1	124
6	Mucky clay	7	16.98	16.6	147
7	Clay	7.2	24.18	17.4	192
8	Silty clay	2.6	26.78	19.4	235
9	Sandy silt	8.2	34.98	18.9	255
10	Silty clay mixed with silt	7.8	42.78	18.3	373
11	Silt sand	11.9	54.68	19.6	410
12	Silt sand mixed with coarse sand	19.02	73.7	19.8	433

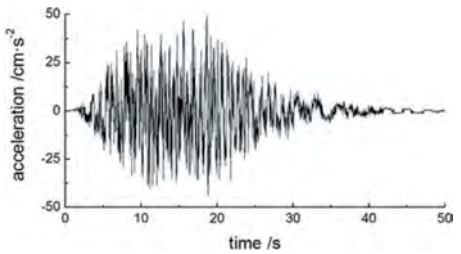

Figure 6. Time history of earthquake motion.

3.2 *Equivalent load parameters of different methods*

According to the design peak ground acceleration standard (Li et al., 2014) to the response displacement method I, the peak ground acceleration a_{max} is taken as 0.1g for a site of Category IV with a seismic design intensity of 7 degrees. The peak displacement u_{max} of the seismic motion is calculated as 0.105m. These values are considered as the basic parameters to determine the seismic load in the response displacement simplified method.

The basic parameters of seismic motion load to the typical soil conditions in the Shanghai is the same for both the response displacement method II and the response acceleration method. It is obtained from one-dimensional seismic response analysis. The distribution curve of the maximum relative displacement at the top and bottom of the structure, occurring at the time T=5.56s, is shown in Figure 7. The two red lines represent the depth of the top and bottom of the circular tunnel structure.

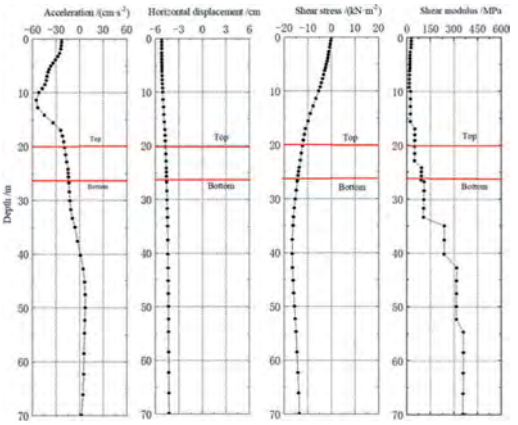

Figure 7. Load parameter distribution curve.

The relevant load parameters for the equivalent horizontal seismic acceleration method and the equivalent inertial force method of subway interval tunnel are obtained through table lookup and calculation. The acceleration coefficients and inertial force coefficients for different soil layer are shown in Table 2.

For the equivalent horizontal seismic acceleration method, the seismic acceleration load coefficient β is 0.2421. It is an important parameter to determine the applied acceleration load.

For the equivalent inertial force method, the seismic inertial force coefficient k_c is 0.68278. The maximum horizontal resistance of the triangular distribution strata P_f is 37.54kN. These two parameters are key parameters that contribute to the calculation of the equivalent seismic load in the equivalent inertial force method.

3.3 *Calculation results of different methods*

Seismic analysis of interval shield tunnels in typical soil conditions of the Shanghai was performed using six different seismic design methods: the response displacement method I, the response displacement method II, response acceleration method, the equivalent horizontal seismic acceleration method, the

Table 2. Load Parameters of two different methods.

NO.	β_{0i}	acceleration coefficients β_i	k_{0cli}	inertial force coefficientsk_{cli}
1	0.2	0.162475	0.7	0.56866
2	0.23	0.186846	1.1	0.89361
3	0.255	0.207155	1.115	0.90580
4	0.195	0.158413	0.8	0.64990
5	0.255	0.207155	1.115	0.90580
6	0.28	0.227464	1.2	0.97485
7	0.21	0.170600	0.9	0.73114
8	0.23	0.186846	1.1	0.89361
9	0.18	0.146227	0.7	0.56866
10	0.205	0.166536	0.9	0.73114
11	0.18	0.146227	0.7	0.56866
12	0.18	0.146227	0.7	0.56866

equivalent inertial force method, and dynamic time history method. The maximum values of horizontal relative displacement of the top and bottom of the structure Dx_{max}, axial force N_{max}, shear force Q_{max}, and bending moment M_{max} were obtained. The summary of these results is presented in Table 3. The results obtained from the dynamic time history analysis method were taken as the standard, and the calculation errors of the five different pseudo-static methods were compared. The summary of these comparison results is presented in Table 4.

Table 3. Calculation results of six different methods.

NO.	seismic design methods	Dx_{max} /mm	N_{max} /kN	Q_{max} /kN	M_{max} /(kN·m)
1	response displacement method I	3.69	99.3	35.1	52.3
2	response displacement method II	1.45	28.7	12.9	18.8
3	response acceleration method	1.42	56.3	18.4	20.8
4	equivalent horizontal seismic acceleration method	0.56	26.6	14.1	8.0
5	equivalent inertial force method	5.8	39.2	23.6	40.0
6	dynamic time history method	2.14	82.3	29.3	31.5

From the two tables mentioned above, for the error of maximum horizontal relative displacement at the top and bottom of the structure, the maximum error observed in the equivalent inertial force method is 171.0%, while the minimum error observed in the response displacement method II is -32.2%. For the error of maximum axial force of the structure, the maximum error observed in the equivalent horizontal seismic acceleration method is -67.7%, while the minimum error observed in the response displacement method I is 20.7%. For the

Table 4. Results error of different methods.

No.	seismic design methods	Results error /%			
		Dx_{max}	N_{max}	Q_{max}	M_{max}
1	response displacement method I	72.4	20.7	19.8	66.1
2	response displacement method II	-32.2	-65.1	-56.0	-40.3
3	response acceleration method	-33.6	-31.6	-37.2	-34.0
4	equivalent horizontal seismic acceleration method	-73.8	-67.7	-51.9	-74.6
5	equivalent inertial force method	171.0	-52.4	-19.4	27.0
6	dynamic time history method	——	——	——	——

error of maximum shear force of the structure, the maximum error observed in the response displacement method II is -56.0%, while the minimum error observed in the equivalent inertial force method is -19.4%. For the error of maximum bending moment of the structure, the maximum error observed in the equivalent horizontal seismic acceleration method is -74.6%, while the minimum error observed in the equivalent inertial force method is 27%. The overall comparison of relative errors calculated by different methods is shown in Figure 8.

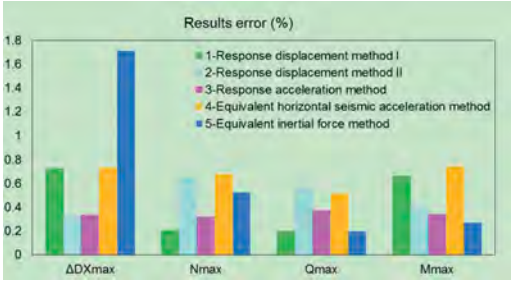

Figure 8. Comparison of relative error of calculation results.

From the overall results, in terms of the relative errors of displacement, axial force, shear force, and bending moment, the response displacement method II and the response acceleration method show relatively smaller errors compared to the dynamic time history method. The error range of the response displacement method II is from -30% to -65%. The error range of the response acceleration method is from -30% to -40%. Additionally, the overall error of the response acceleration method is slightly smaller than that of the response displacement method II. On the other hand, the equivalent horizontal seismic acceleration method and the equivalent inertial force method show larger relative errors, with the response displacement method I being slightly better than them.

Among the five pseudo-static seismic calculation methods, the response displacement method II and

the response acceleration method are relatively better calculation methods. They show smaller relative errors compared to the dynamic time history analysis method. The response acceleration method is slightly better than the response displacement method II.

4 ANALYSIS ON APPLICABILITY OF SEISMIC CALCULATION METHODS IN SHANGHAI AREA

To the calculation methods and models, the response displacement method I, the response displacement method II, and the equivalent inertial force method belong to the load-structure models. They do not consider the interaction between the structure and the soil, and only achieve the constraint effect of the soil on the structure by setting up connecting springs. At the same time, the value of the spring stiffness has a significant impact on the calculation results. The response acceleration method and the equivalent horizontal seismic acceleration method belong to the soil-structure models. Both methods can consider the combined action of the structure and the soil, only apply an acceleration load, and are not affected by the spring stiffness parameters.

To the equivalent seismic loads, the response displacement method I, the equivalent horizontal seismic acceleration method, and the equivalent inertia force method do not require inputting seismic motion loads for seismic response analysis of soil layers. The peak acceleration of the ground design seismic motion in Shanghai site is set to 0.1g when using the equivalent horizontal seismic acceleration method and the equivalent inertia force method. The response displacement method I can achieve the actual set peak value through modification based on the peak ground acceleration. On the other hand, both the response displacement method II and the response acceleration method require seismic response analysis of the site soil by inputting seismic motion loads. At the same time, both methods can also ensure that the peak ground design seismic motion matches the actual peak value.

To the calculation results, the calculation results of the response displacement method I, the response displacement method II, and the response acceleration method do not require modification, while the results of the equivalent horizontal seismic acceleration method and the equivalent inertia force method need to be appropriately adjusted to achieve relative stability.

Compared with the results of dynamic time history analysis method, the error of the results for the response displacement method II and the response acceleration method are generally comparable, usually around 30%, which is acceptable in engineering applications. The error of the results for the response displacement method I is generally around 40%. However, the error of the results for the equivalent inertia force method and the equivalent horizontal seismic acceleration method can be as high as 70% or even larger, which generally exceeds the acceptable range in engineering applications.

To the engineering design and practical application, the cross-section of an interval tunnel is generally not a circular structure. Sometimes the cross-section corresponding to different construction methods is often irregular, such as a horseshoe shape, a four center circle, a five center circle, etc. Compared with other methods, the response acceleration method can be applied to irregular cross-sections and has a wide range of engineering applications.

Based on the above analysis, among the five pseudo-static seismic design methods commonly used for circular shield tunnel structures in Shanghai area, the response acceleration method is recommended to use as the first choice, followed by the response displacement method II. In cases where the corresponding seismic motions cannot be obtained, the response displacement method I can be considered.

5 CONCLUSIONS

In response to circular shield tunnel structures in Shanghai's soft soil areas, a comparative analysis was conducted on five recommended pseudo-static lateral seismic design methods in current standard. Using the results from dynamic time-history analysis as the reference, the following conclusions were drawn:

(1) Among the five pseudo-static methods, the method with the smallest error in the results is the response acceleration method, followed by the response displacement method II. The methods with the largest errors are the equivalent horizontal acceleration method and the equivalent inertia force method. The error in the first two methods is generally around 30%, which is acceptable in engineering applications.

(2) For the equivalent horizontal acceleration method and the equivalent inertia force method, their equivalent seismic loads are not based on soil seismic response analysis, and the internal force results are determined based on the principle of equal maximum bending moments. In addition, a correction factor needs to be introduced for adjustment, resulting in significant calculation errors in both methods.

(3) The response acceleration method can directly reflect the soil-structure interaction, avoiding the influence of factors such as springs. Its equivalent load is based on the results of soil seismic response, and the working model is simple. It is suitable for irregular sections and has a wide range of engineering applications.

(4) For the seismic design of circular shield tunnel structures, it is recommended to prioritize the use of the response acceleration method, followed by the response displacement method II. In situations where it is not possible to obtain

corresponding seismic motion data, the response displacement method I can be considered.

REFERENCES

Jun Koizumi, Wenjun Zhang & Dajun Yuan, 2009. Seismic Research and Calculation Examples of Shield Tunnels, China Architecture and Building Press, Beijing, China.

Lianjin Tao, Wen pei Wang, Bo Zhang, et al, 2012. Difference law study of seismic design methods for subway structures. China Civil Engineering Journal, 45 (12):170–176.

MOHURD GB 50909-2014, 2014. Code for seismic design of urban rail transit structures - Part 6: Seismic response calculation, Ministry of Housing and Urban-Rural Development of the People's Republic of China, Beijing, China.

MOHURD GB/T 51336-2018, 2018. Standard for seismic design of underground structures - Part 6: Seismic calculation and checking, Ministry of Housing and Urban-Rural Development of the People's Republic of China, Beijing, China.

Rushan Liu, Shaoqing Hu, Hongbin Shi, 2007. Study on seismic loading of pseudo-static approach used in the seismic design of underground structure. Chinese Journal of Geotechnical Engineering, 29(2): 237–242.

SHURCMC DG/TJ 08-2064-2022, 2022. Standard for seismic design of subway structures - Part 5: Earthquake action and structures seismic checking, Shanghai Housing and Urban-Rural Construction Management Committee, Shanghai, China.

Xinxing Li, Hong Chen, Zhengjie Chen, 2014. Study on Applicability of Design Method for Seismic Analysis of Subway Station. China civil engineering journal, 47 (S2):322–327.

Xinxing Li, Hong Chen, 2016. Comparison and analysis of three lateral seismic design pseudo-static methods for subway station. New Technology, Development & Application in Engineering for Seismic prevention and Disaster Mitigation – Proceedings of the 9th National Symposium on Earthquake Prevention and Disaster Reduction Engineering, Hefei, China, pp. 258–265.

Yajun Zhang, Hongliang Lan, Yonggao Cui, 2010. Statistical studies on shear modulus ratios and damping ratios of soil in Shanghai area. World Earthquake Engineering, 26(2): 171–175.

Tunnelling for a Better Life – Yan, Celestino, Thewes & Eberhardt (Eds)
© 2024 The Author(s), ISBN 978-1-032-80042-4
Open Access: www.taylorfrancis.com, CC BY-NC-ND 4.0 license

Validation of joint non-linear numerical analysis with large-scale physical testing for arched cut and cover tunnels at HS2 project (UK)

Mengxiao Li*, Sotiris Psomas & Nayef Al Haddid
COWI UK LTD

ABSTRACT: High speed 2 (HS2) Project C3 includes 2 twin arched Cut and Cover precast concrete tunnels ('Green Tunnels'), totalling 5.3km in length. In these structures the precast concrete arched roofs and the precast walls (piers) are connected via concrete-to-concrete knuckle (pin) joints, the verification of which required advanced numerical analysis and physical testing. To demonstrate the significance of the knuckle joint performance, the main findings of the joint non-linear response were initially summarised, then the study focused on the experimental large-scale (full element thickness) testing carried out in CERIB (France) aiming to validate the behaviour under the installation tolerances of combined twist and lip. The test results have been analysed by adopting a non-linear Finite Element model representing the actual scale of the test specimens. The numerical model also considers the non-linear material properties and the reinforcing steel bars. By comparing the results between the physical tests, numerical test simulation and the back-analysis of FE model of the structure, some very useful conclusions can be drawn related to the reliability of the design.

Keywords: Non-linear numerical analysis, physical testing, knuckle (pin) joints, precast concrete arched roof, cut and cover tunnel, HS2 project

1 INTRODUCTION

The HS2 Green Tunnels are constructed using the cut-and-cover approach and comprise precast reinforced units, including arched roofs and side walls, along with cast-in-situ base slabs. The design represents an innovative and sustainable precast arch solution, and the benefits it offers in terms of cost saving, safety risk reduction and sustainability improvement are discussed in Smith et al. (2023) [1]. The design methodology for fire resistance and the analysis of physical fire tests are detailed in Psomas et al. (2023) [2]. The connection between the roof unit and the wall is made through a concrete-to-concrete knuckle/pin joint. To analyse the structural behaviour of the joint under loading, a full-scale 2D finite element (FE) numerical model was created in the FE structural analysis software LUSAS. Figure 1 shows half of a full-scale tunnel model. To accommodate installation deviations, the design allows for joint movement, such as a lip and twist, up to 10mm, which is also considered in the numerical model analysis [3]. Detailed analysis and findings about the full-scale tunnel model are presented by Al Haddid et al. (2024) [4].

The joint behaviour was initially investigated based on the numerical results from the full-scale tunnel model and further validated through a series of physical tests. This paper focuses on the analysis of the physical tests and the calibration of the numerical modelling approach. Section 2 describes the physical test setup. The test simulation numerical model, which adopts the same modelling approach as the full-scale tunnel model, is presented in Section 3. A comparative study between the tests and numerical simulation results is conducted to assess the effectiveness and reliability of the modelling approach and is presented in Section 4.

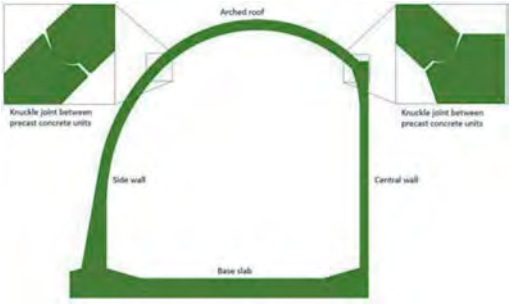

Figure 1. Half of a full-scale tunnel FE numerical model in 2D.

*Corresponding author: mxli@cowi.com

DOI: 10.1201/9781003495505-34

2 PHYSICAL TESTING

Physical tests were carried out at CERIB in France, involving two types of test specimens representing the two types of tunnels. The key distinction between the two lies in the joint thickness: for type 1, the thickness is 350mm, and for type 2, it is 400mm. This design difference is attributed to the varying depth of the backfilling along the tunnel alignment. For each type, multiple tests were performed, considering various configurations within the allowable design tolerances [5]. This paper specifically concentrates on the tests carried out for type 1.

2.1 *The test sample*

The test sample consists of two straight reinforced concrete panels, with one representing the roof and the other representing the wall. These panels are vertically positioned with a pin joint in the middle. The geometry of the pin joint aligns with the actual joint geometry between the roof and the wall of the tunnel. Each panel is 2.49m long and 1m high, as shown in Figure 2.

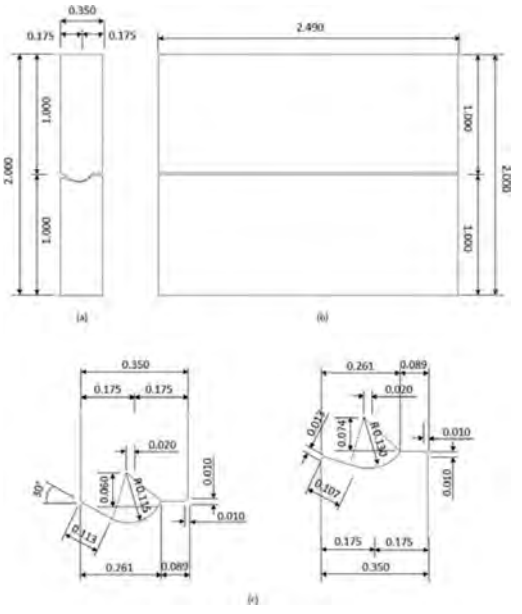

Figure 2. Geometry and dimensions of the test sample for type 1 (a) transversal section (b) Longitudinal elevation (c) detail of pin-joint for top panel (left) and bottom panel (right); unit in m.

To investigate the performance of the pin joint under various configurations, capturing the allowable design lip and twist at the joint, the following scenarios were established and tested:

Regarding the material properties, the concrete is specified to achieve a C50/60 strength at 28 days. Cylinders were cast simultaneously with the test samples and were tested on the day of testing. Table 2 displays the averaged concrete strength obtained from the cast test samples. The reinforcement cages within the test samples were designed to adhere to the specifications of the units.

Table 1. The pin joint configurations.

Case no.	Lip & twist	Description	Diagram
1	0 mm	Perfect alignment where the axes of both panels are precisely aligned.	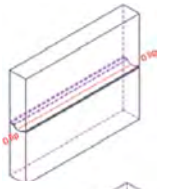
2	+10 mm	At one end, the top panel's pin joint aligns with the bottom panel's pin joint, but at the opposite end, the top panel's pin joint axis is shifted inward by 10mm compared to the bottom panel's pin joint axis.	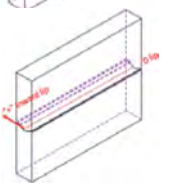
3	-10 mm	At one end, the top panel's pin joint aligns with the bottom panel's pin joint, but at the opposite end, the top panel's pin joint axis is shifted outward by 10mm compared to the bottom panel's pin joint axis.	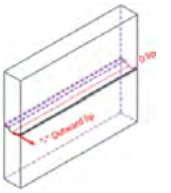

Table 2. Averaged concrete properties of the test samples for type 1.

Compressive strength (Mpa)	47.8
Splitting tensile strength (Mpa)	3.1
Elastic Young's modulus (Gpa)	28.3

2.2 *The test set-up supporting frame*

Figure 3 illustrates the test set-up supporting frame installed to maintain the vertical alignment of the sample, in front view (Figure 3a) and in side view (Figure 3b). In cases of misalignment, it ensures the initial eccentricity is achieved. The frame includes a metal plate supporting the bottom panel and four metal columns welded to the plate along the longitudinal sides of the sample. In all configurations, the bottom panel consistently aligns with the frame, while the position of the top panel varies depending on the specific configuration being tested.

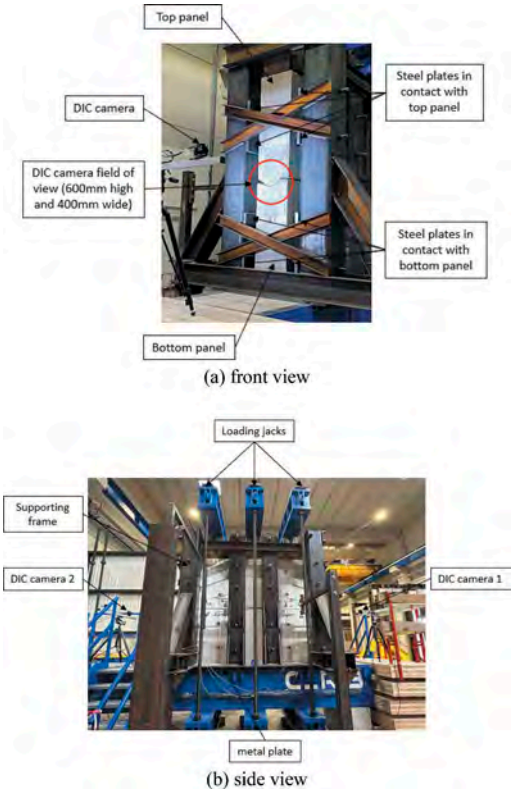

Figure 3. The test set-up.

Additionally, four steel plates are affixed to each column to provide lateral support to the top and bottom panels. It is important to ensure that the behaviour of the pin joint between the top and bottom panels of the test accurately represents the actual joint behaviour in a real-world scenario. The presence of a gap between the steel plate and the concrete surface, allowing for a certain degree of movement, can significantly impact the theoretical joint rotation. Therefore, a comparative analysis between the test simulation numerical model and the full-scale tunnel numerical model was undertaken to investigate the appropriate gap, and the results are presented and discussed in Section 3.2. To explore the pin joint behaviour more precisely during the test, two stereo digital image correlation (DIC) cameras are positioned on the front and back sides of the sample. They can capture a field of view that is 600mm in height and up to 400mm in width in the pin joint area. The surface is covered with thirteen dark speckles stamped within the field of view on a 150mm×150mm grid. The detailed location of the targets is shown in Section 4 Figure 11.

2.3 *Loading*

The load is applied to the test sample using three jacks, each with a capacity of 3000kN, distributed across a steel slab with dimensions of 200mm×300mm ×2490mm placed on top of the top panel. The load is applied in multiple steps, as shown in Figure 4.

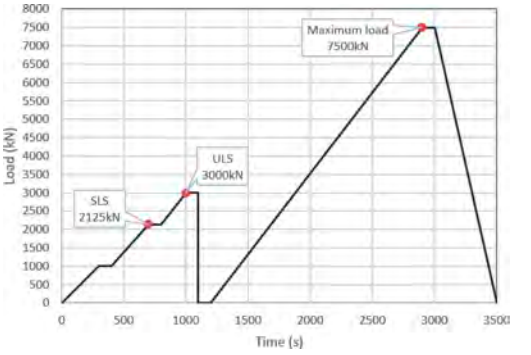

Figure 4. Graph of load vs time and major loading stages.

3 NUMERICAL TEST SIMULATION

The physical tests are numerically simulated using LUSAS to validate the reliability of the modelling approach.

3.1 *Modelling approach*

The test simulation model includes two materials: concrete, modelled using shell elements, and steel reinforcement, modelled using bar elements. To facilitate a better comparison with the actual design of the full-scale tunnel model, the numerical model is developed in 2D. In cases with lip and twist, where perfect alignment exists on one side and lip on the other side, only the side with the lip is modelled. This side is considered critical based on the pre-numerical analysis of the full-scale tunnel model and physical test observations. The geometry of the numerical simulation model is shown in Figure 5.

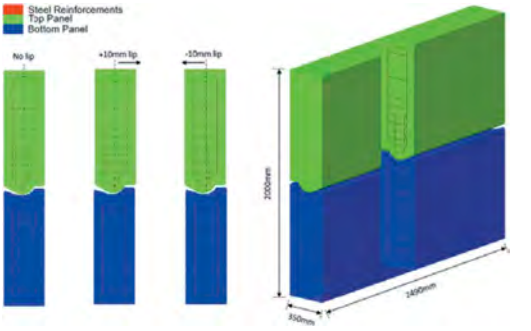

Figure 5. Geometry of the numerical simulation models.

To simulate the concrete performance more accurately, the smoothed multi-crack concrete model in LUSAS is adopted (Figure 6). This model is a plastic-damage-contact model in which damage

planes form according to a principal stress criterion. The softening curve for tensile failure is determined by the specification of a fracture energy per unit area.

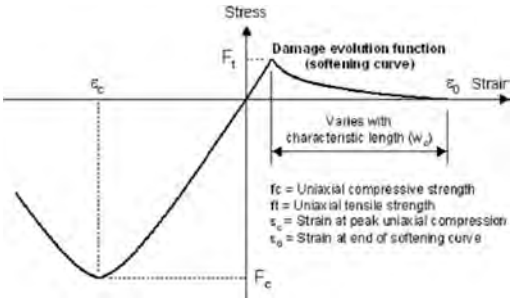

Figure 6. Stress/strain curve for concrete model in LUSAS.

The fracture energy required to propagate a tensile crack of unit area G_F is calculated based on FIB Model Code [6] for Concrete Structures 2010 cl. 5.1.5.2:

$$G_F = 73 \times f_{cm}^{0.18} \quad (1)$$

Where, f_{cm} is the mean compressive strength (Mpa). According to BS EN 1992-1-1 [7] Table 3.1:

$$f_{cm} = f_{ck} + 8 \quad (2)$$

The strain at peak uniaxial compression ε_{c1} is estimated according to BS EN 1992-1-1:

$$\varepsilon_{c1} = 0.7 \times f_{cm}^{0.31} \leq 2.8 \quad (3)$$

The mass density for reinforced concrete is assumed to be 2500kg/m³, and Poisson's ratio is assumed to be 0.2. The Young's modulus, the uniaxial compressive strength and the uniaxial tensile strength are obtained from cylinder tests on the testing day, as provided in Table 2. The reinforcement is modelled using a linear steel material model. The pin joint contact is modelled using the slideline feature in LUSAS, offering the advantage of not requiring prior knowledge of the contact point between two elements. Penetration, a term in contact analysis defining the relative overlap of meshes on separate contact surfaces, is influenced by the properties of the slideline. The design permits concrete surface crushing at the joint and assumes the maximum penetration to be between 1.0mm and 1.50mm at the SLS stage. The uniformly distributed line load applied to the top of the panel is calculated based on the capacity of the three jacks, totalling 9,000kN, and the loaded area of 300m×2490mm. The analysis begins with self-weight loading only and then proceeds with an increment of 1% of the total external applied load. Table 3 demonstrates the key loading stages with the corresponding load factors calculated as a percentage of the design forces divided by the total applied force.

The base of the bottom panel is fixed in the vertical direction. The side supports are modelled using

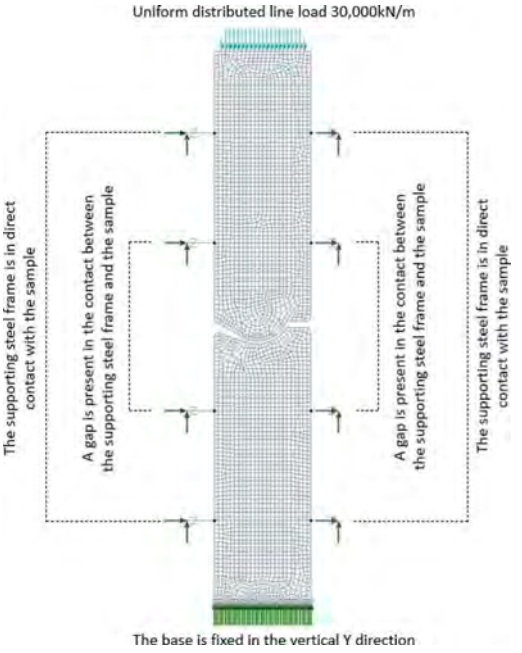

Figure 7. Numerical test simulation model.

Table 3. Key loading stages.

Loading stage	Design force/(kN)	Load factor
SLS	2125	0.24
ULS	3000	0.33
Max	7500	0.83

joint contact with compression only stiffness, which is estimated based on the property of the steel supporting frame. As mentioned in Section 2.2, allowing some movement of the panels near the joint is necessary to capture the actual joint behaviour in a real-world scenario. Therefore, a gap is left at the lateral supports for the four middle rows, while the four top and bottom rows maintain direct contact with the sample, as shown in Figure 7.

3.2 *Assessment of the gap for lateral support*

This section investigates the appropriate gap left between the steel plate and the concrete surface near the joint and assesses the impact of the gap on joint performance. Results from the analysis of case 3 (i.e., with a -10mm lip and twist) are presented here, as the influence of the gap is more significant compared to other cases. Four distinct scenarios were examined, considering gap sizes of 0mm (no gap), 1mm, 3mm and 5mm. To mitigate any potential impact of mesh density on the results, a consistent mesh density was applied to the pin joint area across all cases. Figure 8 presents stress contour plots (i.e., vertical compression and horizontal tension) and the joint contact length at

the ULS stage. These results are then compared to those obtained from the full-scale tunnel numerical model, as shown in Figure 9.

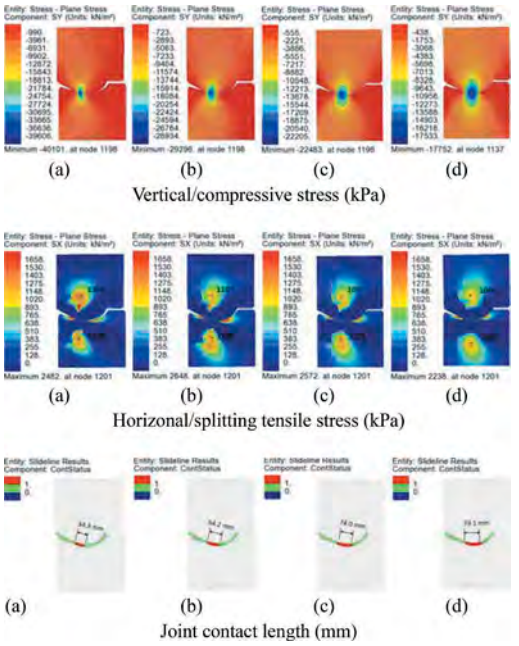

Figure 8. Results from test simulation model (a) no gap; (b) 1mm gap; (c) 3mm gap; (d) 5mm gap.

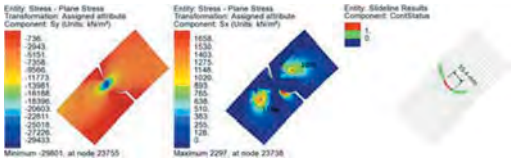

Figure 9. Results from full-scale tunnel model.

It can be observed that the compressive stress concentration occurs at the joint contact area. The maximum compressive stress SY significantly decreases with an increase in gap size, from 40.1Mpa in the case with no gap to 17.8Mpa in the case with a 5mm gap. Additionally, the contact length increases from 34.3mm in the no-lip case to 79.1mm in the 5mm gap case. This implies that a larger gap allows more joint movement towards the centre of the panel, increasing the contact area and alleviating stress concentration, resulting in more even stress distribution within the structure. The splitting tensile stress is another critical factor that impacts the design. It is noticed that localised high tensile stress appears next to the joint contact zone, but this is not the focus of this study. The area of interest lies in the splitting tensile stress zone, a distance away from the compression zone, which impacts the reinforcement design for enhancing the tensile capacity of the concrete structure. The maximum tensile stress SX is highlighted in the top and bottom panels. Although it decreases as the gap increases, the reduction is not as significant as observed in the compressive stress. Comparing the stress distribution between the test simulation and the full-scale tunnel model, it can be seen that the scenario assuming a 1mm gap for lateral support exhibits a similar joint contact length, distribution of compressive stress and tensile stress. Therefore, a 1mm gap was determined and adopted for both the physical test and numerical model.

4 PHYSICAL TEST VS NUMERICAL SIMULATION

This Section presents the physical test and numerical simulation results for two cases: case 1, with no lip and twist, and case 2, with a +10mm lip and twist (Figure 10).

The DIC camera recorded displacement data for the thirteen targets within the pin joint area is used to analyse the joint behaviour for each case. Figure 11 shows the locations of the target points. In the numerical model, nodal displacements in similar locations are selected for comparison with the physical test results.

Figure 10. Test sample of case 1: no lip and twist (left) and case 2: +10mm lip and twist (right).

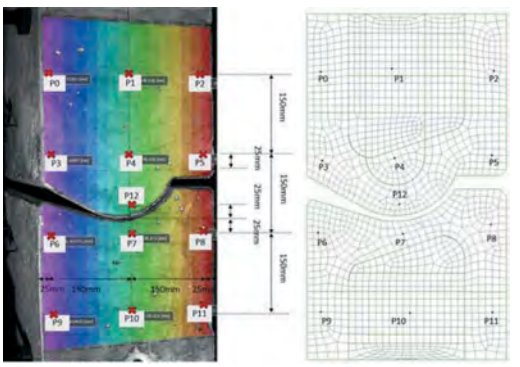

Figure 11. Targets within the pin joint area of the test sample (left) and the numerical model (right).

4.1 *Case 1: No lip and twist*

As shown in Figure 11, targets P12 and P7 are located 25mm above and below the centre of the joint in the top and bottom panels, respectively. The vertical differential displacement between these two targets can be used to estimate whether concrete crushing appears at the joint contact and to what extent during the test. The numerical model allows for concrete surface overlapping/penetration at the joint, assuming the maximum penetration is between 1.0mm (Figure 12a) and 1.50mm (Figure 12b) at the SLS design stage. Compressive strain developed in the 25mm depth of the concrete section in the top and bottom panels under loading is also considered. The concrete displacement is calculated based on the displacement between P12/P7 and the point at the edge of joint centre of each panel, P12′/P7′.

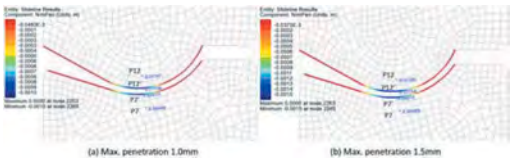

Figure 12. Penetration at the joint and vertical displacements of the selected nodes at the SLS stage in the numerical model.

Figure 13 illustrates the differential displacement between P12 and P7 obtained from the physical test, as well as the joint penetration and concrete displacements from the numerical model. It can be observed that the compressive strain within the concrete is minimal and can be neglected. The physical test results reveal a disparity between the displacements recorded by DIC 1 and DIC 2. This discrepancy arises because achieving perfect alignment between the two panels during the test is challenging, given factors such as the precise placement of elements and vertical alignment of the jack on top of the panel. Additionally, the two systems measure the displacement of opposite faces at a distance of 2.5m, introducing a certain level of expected variation in measurements. Overall, the differential displacement at the SLS stage ranges between 1.0mm and 1.5mm, showing good agreement with the design assumption made in the numerical model regarding concrete surface penetration.

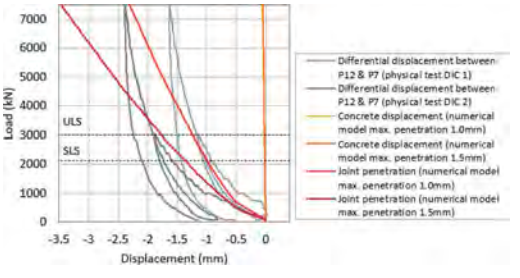

Figure 13. Comparison of penetration at the joint between physical test and numerical model.

The vertical and horizontal displacements of each target within the top and bottom panels from the physical test are compared to that of the corresponding nodes in the numerical model and are presented in Figure 14. Numerical contour plots of von Mises stresses with the deformed shape at key loading stages are also provided (Figure 15) to further illustrate the joint performance under loading.

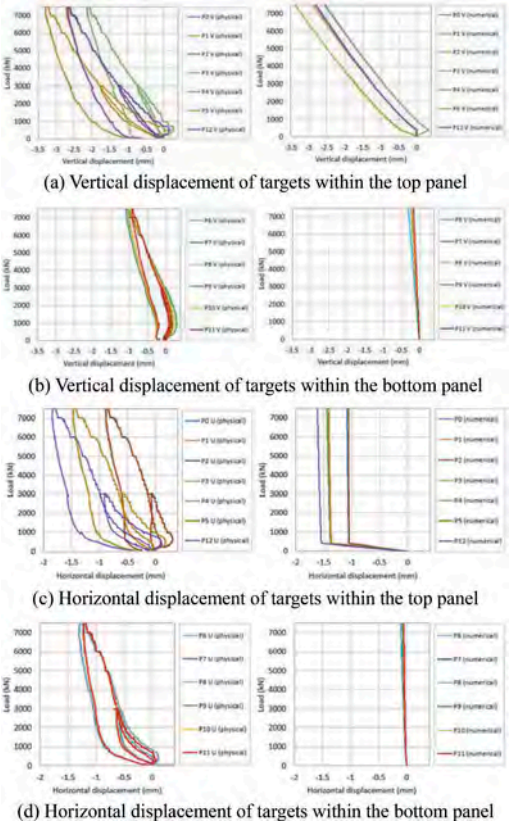

Figure 14. Comparison of displacement of targets between the physical test and numerical model.

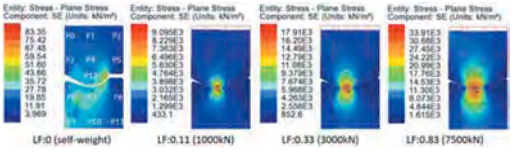

Figure 15. Numerical contour plots of von Mises stresses.

It can be observed that there is a significant downward movement of the top panel in the initial loading stages in the numerical model. This is due to the initial gap between the two panels. Once the joint contact is established, the displacement is reset to 0, making it comparable with the physical test displacement, as contact is present in the initial stage in reality. For the top panel, P2 and P5 exhibit the largest

vertical movement, reaching up to 3.25mm under the max loading of 7500kN, while P0 and P3 show the least vertical movement. P12, positioned closest to the joint centre, experiences the largest horizontal movement, decreasing as it approaches the lateral supports that restrict the panel's lateral movement. A similar trend is observed in the numerical model. For the bottom panel, there is little difference in displacements between targets observed in both physical and numerical results. Additionally, relatively smaller displacements are observed in the numerical model compared to the physical test. As mentioned above, imperfections in the test setup impact the results, whereas the numerical model presents an idealised scenario. However, overall, the joint behaviours match between the physical and numerical results. The major movement appears in the top panel, a clockwise rotation, reducing the opening on the right-hand side of the joint.

4.2 *Case 2: +10mm lip and twist*

This section focuses on case 2 (i.e., with a 10mm lip and twist) and discusses the differences in joint performance between case 1 and case 2. Similar to the observations in the numerical model of case 1, concrete displacements within the 25mm section in the top and bottom panels are small (Figure 17). Due to the initial 10mm lip, the joint contact is not established at the centre of the panel; hence, there is zero penetration through the centre of the panel at the SLS stage in the numerical model, as shown in Figure 16a and 16b. Although the physical test displays a differential displacement between the two targets (P12 and P7), it is considerably smaller compared to those observed in case 1 (e.g., 0.2mm vs 1.0mm at SLS), aligning with the findings in the numerical model.

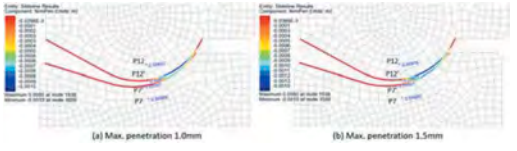

Figure 16. Penetration at the joint and vertical displacements of the selected nodes at the SLS stage in the numerical model.

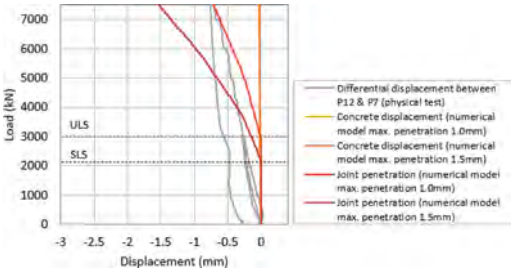

Figure 17. Comparison of penetration at the joint between physical test and numerical model.

Comparing Figures 15 and 18, the contour plots of von Mises stresses for case 1 and case 2 also reveal the distinct location where initial joint contact is established and its impact on the stress distribution.

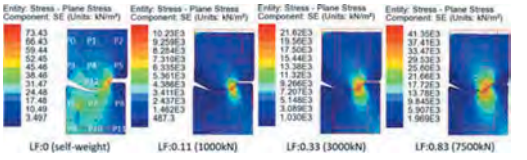

Figure 18. Numerical contour plots of von Mises stresses.

Figure 19 presents a comparison of vertical and horizontal displacements of targets in the top and bottom panels between the physical test and numerical model for case 2.

As can be observed in Figure 19(a) and 19(c), all the targets within the top panel exhibit similar vertical and horizontal displacements. This suggests that joint rotation is not significantly induced by the movement of the top panel, which is different from what has been observed in case

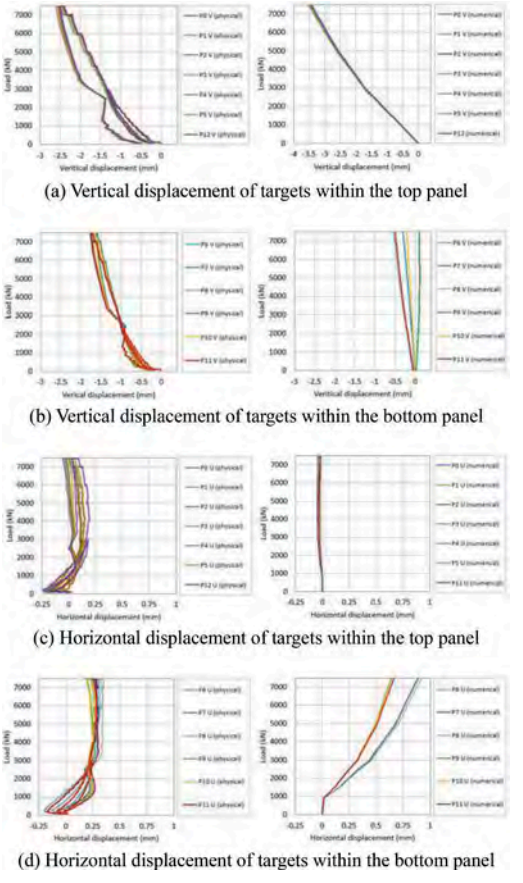

Figure 19. Comparison of displacement of targets between the physical test and numerical model.

1. For the bottom panel, case 1 exhibits a slight anti-clockwise movement, whereas case 2 shows movement in the opposite direction (clockwise) which is caused by the initial off-centre joint contact that results in imbalanced loading from the top panel onto the bottom panel. Figure 20 presents numerical contour plots of displacements of the bottom panel with deformed shapes for both case 1 and case 2, offering further insight into the differences in movement of the bottom panel.

It is important to note that there is slight difference in the displacement of the bottom panel between the physical test and the numerical model. Specifically, positive horizontal movements are observed in both cases, but the magnitude in the numerical model is higher. Regarding vertical displacement, targets on the left-hand side of the panel (i.e., P6 and P9) exhibit positive displacement in the numerical model but negative displacement in the physical test. This indicates that the rotation of the bottom panel in the physical test is not as pronounced as in the numerical model. However, since the top panel in the physical test experiences some anticlockwise rotation (i.e., positive displacements shown in Figure 19(c)), resulting in a joint contact/rotation similar to that obtained in the numerical model. Once again, there are other potential factors contributing to the differences between the test and numerical results, stemming from deviations during test setup or measurements.

In Figure 21, the vertical and horizontal strain distribution plots at the ULS design stage from the physical test and numerical model are presented. The location of the contact zone confirms the findings on joint rotation derived from the analysis of the displacement data of targets within the pin joint area. There is also alignment in the magnitude and distribution of the vertical compressive strain. For the horizontal strain, it is observed that in the physical test, positive/tensile strain also appears at the contact (i.e., edge of the concrete surface), while only negative/compressive strain is shown in the numerical model. This discrepancy maybe attributed to the concrete surface condition of the test sample, where minimal cracks appear and develop, resulting in tensile strain at the contact concrete edge.

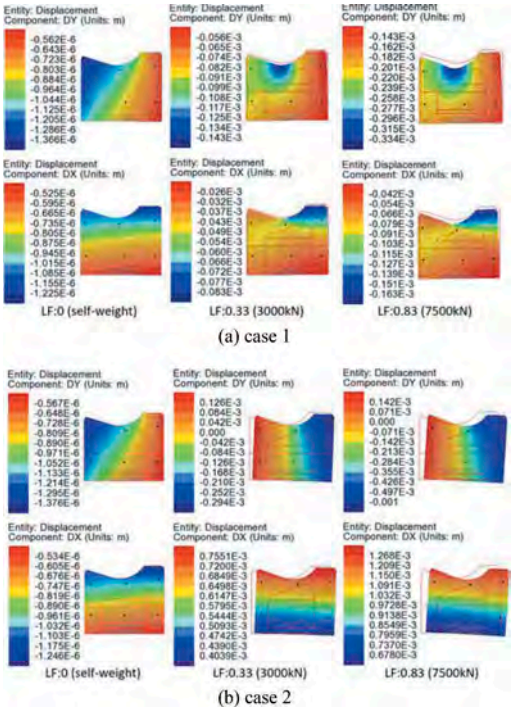

Figure 20. Comparison of displacements of the bottom panel between case 1 (a) and case 2 (b).

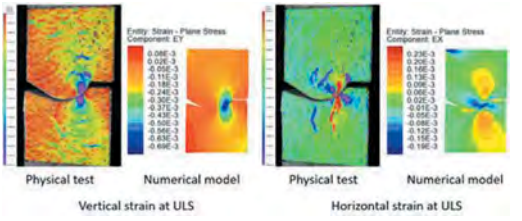

Figure 21. Comparison of strain distribution between physical test and numerical model.

5 CONCLUSIONS

In conclusion, this paper presents a comprehensive validation of joint non-linear numerical analysis through large-scale physical testing for arched Cut and Cover Tunnels in the HS2 project in the UK. The study focused on the investigation of knuckle/pin joints connecting precast concrete arched roofs and walls. The physical tests were carried out on specimens representing configurations within allowable design tolerances. The numerical simulation model incorporated non-linear material properties of concrete, capturing the complexities of the pin joint. The investigation also delved into the assessment of the lateral support gap, determining the appropriate gap size to approximate the real-world joint behaviour. Comparative analyses between the results of physical test results and numerical simulations demonstrated a high level of agreement, validating the reliability and effectiveness of the design modelling approach. Although imperfections in the test set-up and variations in measurements between different monitoring systems could contribute to some disparities in the results obtained from physical tests and the numerical model. The joint behaviours, including vertical and horizontal displacements, as well as stress distributions, showed an overall alignment between the physical and numerical outcomes. This research contributes significantly to the understanding pin joint performance. The integrated approach of numerical analysis and physical testing presented in this paper serves as a valuable reference for engineers and researchers involved in the design and construction of similar structures.

ACKNOWLEDGEMENTS

The Authors would like to thank HS2 and EKFB Green Tunnels Team for granting permission to publish and for their support, respectively. Special thanks go to CERIB for the fruitful discussions regarding the physical test setup and the interpretation of the test results.

REFERENCES

[1] Smith, E. and Psomas, S., 2023. Innovative and sustainable twin arch solution for High Speed Two Green Tunnels. In High Speed Two (HS2): Infrastructure Design and Construction (Volume 3) (pp. 187–202). ICE Publishing.

[2] Psomas, S., Al-Haddid, N. and Monckton, H., 2023. Fire design analysis for the Green Tunnels at High Speed 2 project (UK). In Expanding Underground-Knowledge and Passion to Make a Positive Impact on the World (pp. 861–869). CRC Press.

[3] Green Tunnels – SNC-673 – Design Report on Lip and Twist tolerances to support SCEW 4040 departure, document no: 1MC07-CEK-TN-SPE-CS07_CL13-600001.

[4] Al-Haddid, N., Psomas, S. and Li, M., 2024. Advanced Joint Non-linear Design Analysis and Verification of the Arched Cut and Cover Tunnels at High Speed 2 project (UK). In Tunnelling for a Better Life. CRC Press.

[5] CERIB Test Protocol.

[6] fib Model Code 2010 for Concrete Structures 2010.

[7] BS EN 1992-1-1, BSI.

Tunnelling for a Better Life – Yan, Celestino, Thewes & Eberhardt (Eds)
© 2024 The Author(s), ISBN 978-1-032-80042-4
Open Access: www.taylorfrancis.com, CC BY-NC-ND 4.0 license

Innovative application of low-carbon and energy-saving technology in underground space: A case study of Erlangshan tunnel on Sichuan-Tibet expressway

Guojin Lin*, Jianguo Zheng, Jun Wang & Feng Yang
Sichuan Highway Planning, Survey, Design, and Research Institute Ltd

ABSTRACT: China has the largest amount of road tunnels around the world. While road tunnels greatly improve the traffic conditions in the mountainous areas, they demand enormous energy for lighting, ventilation and fire rescue. Erlangshan tunnel with the length of over 13km is the first super-long tunnel on the Sichuan-Tibet highway. Erlangshan tunnel has 4 inclined shafts with a total length of 8001m. Several innovative applications of low-carbon and energy-saving technologies are used to reduce the demand for energy in tunnel operation. i) The elevation difference between the top and bottom of the inclined shaft is utilized for water diversion and power generation, and the annual power generation of 4 million kWh is realized to meet all demands for lighting. ii) The natural wind formed by the pressure difference between two slopes of Erlangshan Mount and between the portal of inclined shaft and the tunnel is utilized. The inclined shafts are used as natural ventilation passages for auxiliary ventilation, thus, the tunnel ventilation can save 15% of energy and about 2.1 million kWh of electricity annually. iii) A rescue access between the inclined shafts is used as the high-level fire-water pond, so that the fire-water pond outside the tunnel in winter is not frozen and the pumping equipment is saved.

Keywords: Low-carbon and energy-saving technology, Erlangshan tunnel, power generation, natural wind

1 INTRODUCTION

With the rapid economic development in China, the transportation in eastern China has matured, and massive highway construction is carried out in the western China (Chen et al. 2019a; Xu et al. 2020). As the China's terrain is three-ladder shaped (high in the west and low in the east), more than two thirds of the country is occupied by mountains. Thus, a large amount of road tunnels must be constructed from the second ladder (average altitude 1000-2000m) to the first ladder (average altitude 4500m) (Chen et al. 2019b).

For the purpose of improving the transportation conditions of Ganzi, a Tibetan autonomous prefecture, and the Tibet Autonomous Region, the transportation construction of China has been gradually extended from the Sichuan Basin to the Qinghai-Tibet Plateau, with the altitude sharply rising from approximately 600m to 4,000m. There are extremely complicated conditions of geology and topography, and the tunnel accounts for 70% of the section (Wang et al. 2023a). The larger the tunnel scale is, the higher the energy consumption of the tunnel, and the higher the safety risk of the tunnel during its operation arising out of harsh climate conditions is. Meanwhile, green energy, such as hydropower, wind energy, and solar energy, is abundant in western Sichuan province, so it is critical to how to use the green energy to solve huge energy consumption of the tunnel (Wang et al. 2023b; Zhao et al. 2023).

This paper presents a case study of Erlangshan tunnel, which employs the low-carbon and energy-saving technology to fully utilize the underground space, and the energy consumption during operation is greatly reduced. Erlangshan tunnel is the longest tunnel on the Ya'an-Kangding Express, which is part of the famous Sichuan-Tibet highway. The existing inclined shaft space of Erlangshan tunnel is fully developed for the application of green energy, so 6.1 million kWh of electricity for tunnel operation can be saved per year. 122 million kWh of electricity for 20 years of operation can be saved, equivalent to 15,000 TCE, and the CO_2 emission is reduced by 1,216,300t. The investment in the Project is only increased by RMB5.5 million, but RMB78.5 million is saved. A perfect combination of

*Corresponding author: 316605958r@qq.com

DOI: 10.1201/9781003495505-35

tunnel construction and clean energy utilization is realized, with an ideal quality rate of 100% and zero casualties in construction. In the context of "Carbon peak and Carbon neutralization" strategy, the effect of energy saving and emission reduction is significant, and both economic and social values are highly and widely praised by the public, which are very helpful for similar projects in the world.

2 ENGINEERING BACKGROUND

With an average elevation exceeding 4,000 meters, the Qinghai-Tibet Plateau is known as "the Third Pole of the Earth". Sichuan-Tibet Expressway is the most convenient route to Tibet, which has the most complex geological conditions. The Ya'an-Kangding Express is 134.46km long, and it is an important part of the Sichuan-Tibet Expressway. The Ya'an-Kangding expression lies in the west of Sichuan basin, and it is located at the intersection of the Logmenshan Mountain and Qinghai-Tibet Plateau. Due to the large elevation difference, a lot of mountain tunnels have to be constructed to pass through the eastern border of the Qinghai-Tibet Plateau and the Henduanshan Mountain. There are 30 tunnels with the total length of 69533m in the express, and the ratio of the tunnel length to the length of the total express is as high as 52%. Erlangshan tunnel with the length exceeding 13km is the keystone project, the construction of the tunnel commenced in September, 2012 and ended in December, 2017, i.e. it takes 63 months to finish the tunnel construction.

The left line of Erlangshan tunnel is 13549 in length, and the right line is 13406m in length. The tunnel with four inclined ventilation shafts is the second longest tunnel in southwest China, and the fourth-longest tunnel in China. The total construction volume of Erlangshan tunnel is shown in Table 1.

The total length of four inclined shafts reaches 8001m and it ranks the first in China, as shown in Figure 2.

The huge tunnel greatly improves the transportation of Tibet by offering safe and fast traveling, but it inevitably produces massive energy consumption, and the annual power consumption by tunnel ventilation and lighting is 10.37 million kWh and 3.63 million kWh, respectively. Besides, the fire-water pond outside the tunnel is easily frozen in winter and has poor reliability, posing serious safety hazards to the tunnel's fire protection.

The traditional inclined shafts and underground fan rooms of an extra-long tunnel are only used for mechanical ventilation during operation.

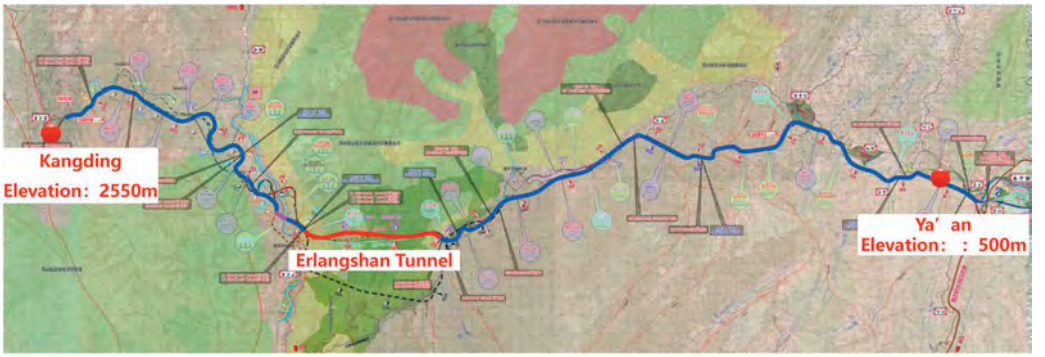

Figure 1. Geological location of Erlangshan tunnel.

Table 1. Construction volume of Erlangshan tunnel.

Entities		Length (m)	Slope (gradient %/length m)	Elevation of the shaft entrance	Elevation of the shaft exit
Tunnel	Left line	13459	2/7005. -0.50/6477	1464.30	1572.21
	Right line	13406	2/6995. -0.50/6444	1464.50	1572.35
Shaft at Ya'an	Air supply	2305	12.58/2305	1850	1550
	Air exhaust	2246	12.96/890	1665	1560
Shaft at Kangding	Air supply	1716	13.57/1716	1890	1600
	Air exhaust	1734	13.41/1734	1890	1610

Figure 2. Layout of the shaft of Erlangshan tunnel.

To solve the problems of high energy consumption and low reliability of fire protection during operation, creative thinking is used and a series of innovative low-carbon and energy-saving technologies for inclined shafts are developed to utilize the topography, meteorology, hydrology at the tunnel site and the elevation difference between two ends of shafts.

3 INNOVATIVE APPLICATIONS

3.1 *Inclined shafts for power generation*

Fossil fuels (e.g. coal and petroleum) have been extensively used by humans for almost a century, releasing a lot of greenhouse gases (GHGs), e.g. CO_2. These GHGs are responsible for global warming. In the 20th century, the global average temperature was increased by 0.6℃. In the 21st century, the global warming trend has been further aggravated. To counteract global warming, the United Nations established the *United Nations Framework Convention on Climate Change* in 1992, and on April 22, 2016, the Paris Agreement was formally signed by 175 parties. Reducing carbon emissions, protecting the Earth, and protecting our homeland have become an international consensus.

Erlangshan tunnel exploits the shaft at Kangding to generate power, which has never been done in similar projects. The inclined shaft is located at the upstream of the Wuligou River as shown in Figure 3. The elevation difference between the two ends of the inclined shaft is as high as 192m. The abundant water of Wuligou River was controlled by a dam, a water diversion pipeline is set in the inclined shaft to divert water from the river at the portal of inclined shaft to the underground fan room at the bottom of inclined shaft, as shown in Figure 4. A generator set is installed in the fan room to generate power as shown in Figure 5, and the tailwater from power generation

Figure 3. Relation between the shaft and Wuligou River.

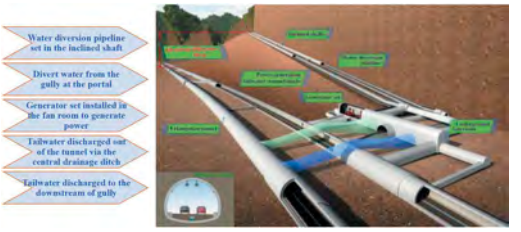

Figure 4. Procedures to generate hydraulic power.

Figure 5. Power generator in the underground fan room.

is discharged out of the tunnel via the central drainage ditch. The abundant rainfall and a large catchment area (19km^2) in the region ensure stable power generation, the installed capacity is 730 kW and the annual power generation of 4 million kWh is realized, meeting all requirements for lighting.

3.2 *Inclined shafts for auxiliary ventilation*

The Erlangshan Mountain is the first natural barrier on the Ya'an-Kangding Express and it is the watershed of the Qingyi River and the Dadu River. The eastern slope of the Erlangshan Mountain has a humid subtropical climate with an annual rainfall of over 2,000mm, while the western slope is located in a famous dry-hot valley and has subtropical monsoon climate, with an annual rainfall of only 660mm. Thus, Mount Erlang is called "rainscreen of western Sichuan" with a distinct difference in the climate between two ends.

Figure 6. Climate difference between two ends of the Erlangshan tunnel.

Before the tunnel construction, two years of meteorologic observation was carried out, and the direction and magnitude of nature wind was closely recorded. As shown in Figure 7, the data analysis

indicates that the wind blows from the entrance of the tunnel to the exit with the probability of 63%, and it blows in the reverse direction with the probability of 37%. The direction of the nature wind also varies with seasons, and it blows from the portal of shaft to the bottom in summer, while a chimney effect dominates in the winter, and the wind blows from the bottom to the portal of the winter.

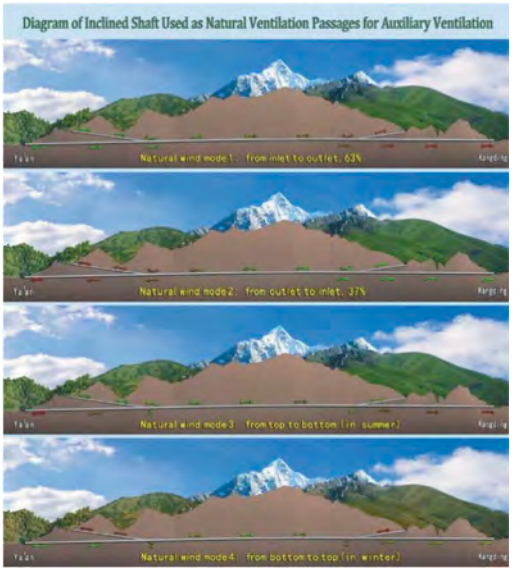

Figure 7. Mode of nature wind.

The inclined shafts bring about the motion of natural wind, and inclined shafts are used as the natural ventilation passages for auxiliary ventilation of the tunnel during operation, so that the ventilation requirements can be met during the period of low traffic volume. The annual energy consumption of ventilation is reduced by 15% and 2.1 million kWh of electricity is saved per year.

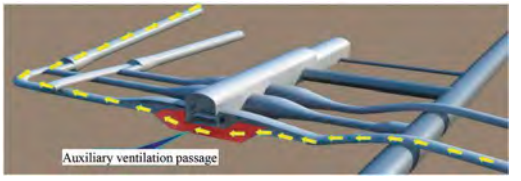

Figure 8. Auxiliary ventilation passage.

3.3 *Water pond for fire protection in the inclined shaft*

The water pond provides the water for the fire rescue of the highway tunnel. As shown in Figure 9, the conventional tunnel fire water supply usually adopts a constant high pressure water supply system with a high-level water pool. The water supply is designed to accumulate water in the reservoir, and then use a water pump to pump the water to the low-level pool to form a backup water source. Then, use a water pump to lift the backup water source to the high-level pool to form a constant high pressure water supply.

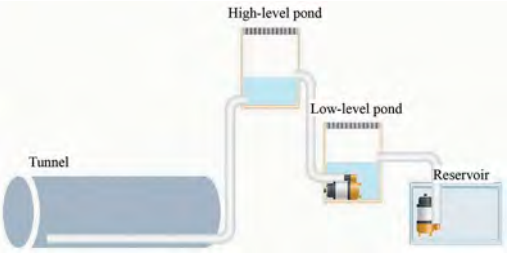

Figure 9. Conventional fire water supply system.

The high-level pond is usually placed in a high slope and buried in the soil to keep the elevation difference and avoid being frozen. The work is difficult and expensive to finish and it also destroys the surroundings.

To solve the problem that the fire-water pond outside the tunnel is frozen in winter, a high-level fire-water pond is set in the inclined shaft. The passage between inclined shafts, which served as the rescue access during construction, is used as the high-level fire-water pond of the tunnel, and a branch pipe is set for the pipeline of water diversion and power generation to supply water for the fire-water pond, and the pond is always filled with water to realize fire protection with artesian water, without requiring a lot of pumping equipment; the year-round positive

(a) Location of the high-level pond

(b) Diagram of the fire water supply system

Figure 10. Fire water supply of Erlangshan tunnel.

temperature and head water differential in inclined shafts ensure safety and reliability of the system.

In the Erlangshan tunnel, the existing inclined shaft space is fully utilized for the application of green energy, so 6.1 million kWh of electricity for tunnel operation can be saved per year. 122 million kWh of electricity for 20 years of operation can be reduced, equivalent to 15,000 TCE, and the CO_2 emission is reduced by 1,216,300 tons. The investment in the project is only increased by RMB5.5 million, but RMB78.5 million is saved; both economic and social benefits are remarkable.

4 CONCLUSION

In the Project, the existing space of inclined shafts and underground fan room of the Erlangshan tunnel is fully used, and the inclined shafts for tunnel ventilation are first utilized for water diversion and power generation to supply power for tunnel lighting; inclined shafts are first used as natural ventilation passages for auxiliary ventilation; a high-level artesian water pond for fire protection of the tunnel is first set in the inclined shaft. And 6.1 million kWh of electricity for tunnel operation can be saved per year. 122 million kWh of electricity for 20 years of operation can be reduced, equivalent to 15,000 TCE, and the CO_2 emission is reduced by 1,216,300 tons; in the context of "Double Carbon" strategy, the effect of carbon reduction is significant.

The low-carbon and energy-saving innovative application of inclined shafts realizes the low-carbon operation of the Extra-long Highway Tunnel. No safety accidents occurred during the construction. The ideal quality rate is up to 100%.

The Project won the following awards: grand prize of CHTS Science & Technology Award 2021, 2021 China National Quality Engineering Award, 2021 Civil Engineering Li Bing Award of Sichuan Province, first prize of 2020 CHSDA Excellent Design Award of Highway Traffic, second-class achievement prize of 2020 Green Construction Design Level Evaluation of China, and "Safety Engineering" of 2018 Highway and Waterway Construction Project of China, and applied for 7 patents.

REFERENCES

Chen, Z.Q., He, C., Xu, G.W., Ma, G.Y., Wu, D. 2019a. A case study on the asymmetric deformation characteristics and mechanical behavior of deep-buried tunnel in phyllite. Rock Mech Rock Eng 52:4527–4545

Chen, Z.Q., He, C., Xu, G.W., Ma, G.Y., Yang, W.B. 2019b. Supporting mechanism and mechanical behavior of a double primary support method for tunnels in broken phyllite under high geo-stress: a case study. Bull Eng Geol Environ 78:5253–5267

Wang, X., Wang, M.N., Jiang, R.L., Xu, J.N., and et al. 2023a. Impact of battery electric vehicles on ventilation design for road tunnels: A review. Tunnelling and Underground Space Technology, 134: 105013

Wang, Y. D., Du, P.X., Chen, Y.Y., Hua, S.H. and et al. 2023b. Mixed ventilation approach combined with single-shaft complementary system for highway tunnels, Tunnelling and Underground Space Technology, 132: 104927

Xu GW, He C, Wang J, Chen ZQ (2020) Study on the mechanical behavior of a secondary tunnel lining with a yielding layer in transversely isotropic rock stratum. Rock Mech Rock Eng 53:2957–2979

Zhao, S.Z., Yang, H.R., Li, Y.Z., Ingason, H., and et al. 2023. Theoretical and numerical study on smoke descent during tunnel fires under natural ventilation condition. Tunnelling and Underground Space Technology, 142: 105414

Tunnelling for a Better Life – Yan, Celestino, Thewes & Eberhardt (Eds)
© 2024 The Author(s), ISBN 978-1-032-80042-4
Open Access: www.taylorfrancis.com, CC BY-NC-ND 4.0 license

Low carbon emission design concept and method for tunnels and underground engineering

Gang Lu & Jianyou Liu
China Railway Engineering Design Consulting Group Co., Ltd., Beijing, China

Yong Zhao
Sichuan Tibet Railway Co., Ltd., Tibet, China

Shaoshuai Shi
China Railway Economic and Planning Research Institute Co., Ltd., Beijing, China

Zhenbo Zhang
Shijiazhuang Tiedao University, Shijiazhuang, China

ABSTRACT: At present, the design concept of tunnel and underground engineering is to reduce the construction cost under the condition of ensuring engineering safety, and economy is the main assessment index of engineering construction scheme comparison. With the implementation of China's carbon emission and carbon neutrality strategy, reducing carbon emission has gradually become the goal pursued by the project construction. Therefore, in the process of comparing engineering design scheme and construction scheme, carbon emission will gradually become an important indicator of engineering construction scheme comparison. Based on the carbon emission coefficient method, gives the tunnel and underground engineering survey and design, build and the operation of carbon emission calculation method, with the shield tunnel, tunnel and underground engineering and low carbon design concept and method, combined with the engineering case, from the application of low carbon effect, from earthwork excavation and supporting structure materials of the hole layout of low carbon effect. Relying on the practice of Beijing-Zhangjiakou high-speed railway project, the implementation effect of low-carbon design concept is analysed. The main conclusions are as follows: (1) the carbon emission of materials is relatively large in the construction process of shield tunnel; (2) Proposed low-carbon design concepts for tunnels and underground engineering, including the application of prefabricated structures, the use of group cave layout design scheme, gabion ecological retaining walls, ventilation and lighting of underground stations, and green operation of large-scale facilities; (3) The prefabricated structure replaces cast-in-place structure and the group hole arrangement replaces single-hole large-section scheme with significant low-carbon effect. The research shows that the proposed low-carbon design concept and method of tunnel and underground engineering has a good application prospect, and is of great significance to promote the low-carbon design of tunnel and urban underground engineering.

Keywords: Tunnel engineering, Carbon emission patterns, Low carbon design, Carbon emission coefficient method

1 INTRODUCTION

By the end of 2021, there will be 17,532 railway tunnels in operation, with a total length of about 21,055 km, and 8,644 railway tunnels under construction and planning, totalling 21,680 km, the construction of which will generate a large amount of carbon emissions. (Gong et al., 2022) With the implementation of the strategies of carbon peaking and carbon neutrality, the transport sector is a key focus area of the above strategies. Tunnels are the most energy-intensive part of the transport infrastructure and it is particularly important to analyse their carbon emissions from a life cycle perspective.(Miliutenko et al., 2012). The carbon

*Corresponding author: tzydglg@126.com

DOI: 10.1201/9781003495505-36

reduction, carbon saving and carbon sink role of tunnels and underground engineering has a broad prospect, and it is of great significance to analyze the carbon emission law of tunnels and underground engineering as well as the design concepts and methods to reduce carbon emission to achieve the target of "Carbon Peak and Carbon Neutral" in China.

There is no unified standard for tunnel carbon emissions, and the problem of calculating tunnel carbon emissions is more prominent, mainly reflected in the lack of a unified boundary, and the range of carbon emissions calculation varies greatly among different studies. Huang et al. (2015) analysed the impact of tunnel excavation using drilling and blasting methods on the environment.

Xu et al. (2016) studied the emission of tunnels during the physicochemical stage. Guo et al. (2016) studied the carbon emissions of ventilation equipment and materials during tunnel construction. Xiao et al. (2018) analysed the electricity consumption of shield tunnels using the emission coefficient method. Wang et al. (2019) investigated the carbon emissions from the physical and chemical phases of shield tunnelling in metro projects. Dong (2016) calculated the carbon emissions of a shield tunnel in Hengqin New Area by preparing a quota. Fei et al. (2017) studied the carbon emissions during the production, construction and operation phases of a road tunnel material. Chen (2017) considered carbon emissions from vehicle operation in the calculation of carbon emissions during the operation period of road tunnels. He (2015) established a carbon emission quota list for civil engineering of cut-and-cover metro stations based on the life cycle assessment theory, and analysed the impact of burial depth and station width on the carbon emissions of the construction process. Li et al. (2016) established a metro life cycle carbon emissions measurement model, which divided the life cycle into five phases: production of building materials, transport of building materials, on-site construction, operation and maintenance, and carried out a case study. Huang (2019) analysed the carbon emissions from the production-transportation-construction of prefabricated components for shield tunnels with other materials.

Based on the carbon emission coefficient method, this paper gives the calculation method of carbon emission of tunnels and underground projects, analyses the main factors of carbon emission in the process of engineering construction, puts forward the concepts and methods of low-carbon design of tunnels and underground projects, and analyses the low-carbon effect of assembled structure and group hole arrangement in conjunction with case studies. It also relies on the engineering practice of Beijing-Zhangzhou high-speed railway to analyse the implementation effect of low-carbon design concept. Through the above research, it can provide a basis for the low-carbon design of tunnels and urban underground engineering and promote the application of low-carbon design.

2 CALCULATION METHOD FOR CARBON EMISSIONS FROM TUNNELS AND UNDERGROUND ENGINEERING

In tunnel and underground engineering, the entire life cycle mainly includes the survey and design stage, construction stage, and operation stage. This article provides carbon emission calculation methods for different stages based on the carbon emission coefficient method.

2.1 *Carbon emissions during tunnel survey and design phase*

The survey phase mainly involves carbon emissions generated by on-site drilling, survey, and other work. The design phase mainly involves the energy consumption of designers and equipment such as computers during the design process. The carbon emissions of personnel and labor force are the product of the total number of working days of labor force and the carbon emission factor of working days. By calculating the number of working days required for each job, the total number of working days of the labor force can be calculated. Some scholars have also conducted research on the carbon emissions generated by the labor force. (Wang et al., 2012)

2.2 *Carbon emissions during tunnel construction phase*

The calculation range of carbon emissions during the tunnel construction phase includes the carbon emissions generated by completing various sub projects and the carbon emissions generated during the implementation of various measures and projects; The calculation time boundary should be from the start of the project to the completion and acceptance of the project. According to the GB/T 51366 Calculation Standard for Building Carbon Emissions, the formula for calculating carbon emissions during the construction phase is as follows:

$$C_{JZ} = \frac{\sum_{i=1}^{n} E_{jz,i} EF_i}{A} \quad (1)$$

Where, C_{JZ} is the carbon emissions per unit area of the construction phase ($kgCO_2/m^2$); $E_{jz,i}$ is the total energy use of type i in the construction phase (kWh or kg); EF_i is the carbon emission factors for energy type i ($kgCO_2$/kWh or $kgCO_2$/kg);A is the building area (m^2).

The energy consumption during the construction phase includes four stages: production materials, material transportation, construction machinery, and labor consumption.

Taking a certain subway shield tunnel as an example, the outer diameter of the segment is 6m, the thickness is 0.3m, and the ring width is 1.5m. It is prefabricated with C50 concrete, and the total length of the section is 3500m. The proportion of carbon

emissions from materials used during construction and the carbon emissions from machinery used are shown in Figure 1-2.

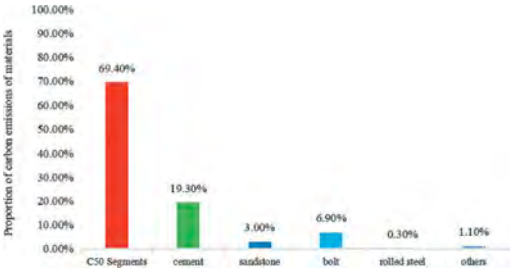

Figure 1. Carbon emission of shield construction.

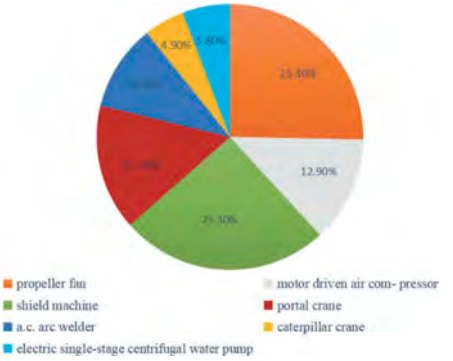

Figure 2. Proportion of energy consumption and carbon emission of construction equipment.

2.3 *Carbon emissions during tunnel operation phase*

The calculation range of carbon emissions during the operation phase should include the carbon emissions of HVAC, lighting and elevators, renewable energy, railway tunnels, and underground engineering carbon sink systems during operation. The carbon emissions during the operation phase are determined based on the different types of energy consumption and carbon emission factors of each system. The total carbon emissions per unit building area (C_M) are calculated using the following formula:

$$C_M = \frac{[\sum_{i=1}^{n}(E_i EF_i) - C_p]y}{A} \quad (2)$$

$$E_i = \sum_{j=1}^{n}(E_{i,i} - ER_{i,i}) \quad (3)$$

Where, C_M is the carbon emissions per unit of engineering area during the operation phase ($kgCO_2/m^2$); E_i is the annual energy consumption of the i-th type of building (unit/year); EFi is the carbon emission factor for Class i energy; $E_{i,j}$ is the i-th energy consumption of the j-type system (unit/year); $ER_{i,j}$ is the i-th type of energy consumed by the j type system provided by the renewable energy system (unit/year); I is the type of terminal energy consumed, including electricity, gas, oil, et; J is the energy consumption system, including heating, air conditioning, lighting systems, etc; C_p is the annual carbon reduction of the green space carbon sink system ($kgCO_2$/year); Y is the engineering design life (years); A is the building area (m^2).

The energy consumption of the HVAC system during the operation phase includes cold source energy consumption, heat source energy consumption, transmission and distribution system energy consumption, and end air treatment equipment energy consumption. The greenhouse gas emissions generated by the use of refrigerants in HVAC systems should be calculated using the following equation:

$$C_r = \frac{m_t GWP_r}{1000 y_e} \quad (4)$$

Where, C_r is the carbon emissions generated by the use of refrigerants (tCO_2/year); R is the type of refrigerant; m_t is the refrigerant charging capacity of the equipment (kg/unit); y_e is the service life of the equipment (years); GWP_r is the global warming potential of refrigerant r.

3 LOW CARBON DESIGN CONCEPTS FOR TUNNELS AND UNDERGROUND ENGINEERING

The construction process of tunnels and underground projects is a carbon emission process. In order to achieve the goal of "carbon peak and carbon neutrality", the principle of reducing carbon emissions should be implemented in the feasibility study, preliminary design, construction drawing design, and construction process of the project, and design schemes, construction methods, and building materials with lower carbon emissions should be selected. From the perspective of low-carbon design, the following three principles should be followed: firstly, reduce emissions, that is, reduce pollutant emissions and energy consumption during the construction process, and achieve the goal of reducing emissions by saving raw materials and improving prefabrication rates; The second is multi convergence, which refers to the integration of comprehensive management methods from multiple aspects, reducing the building area and increasing vegetation coverage; The third is durability, which refers to the development of corrosion-resistant and carbonization resistant building materials with high reliability and toughness. The principle of green design guides the construction direction of tunnels and underground engineering, and the low-carbon design concept requires the use of various low-carbon technologies to achieve it. The implementation path of the low-carbon design concept includes low-carbon line selection and station setting technology, low-carbon building design technology, low-carbon structural

design technology, low-carbon ventilation and air conditioning technology, and low-carbon waterproof and drainage technology. The principles of low-carbon design and the implementation path of low-carbon design concepts for tunnels and underground engineering are shown in Figure 3-4.The engineering design concept with the goal of reducing carbon emissions is to reduce carbon emissions as one of the main goals pursued by the project. While ensuring safety, in the process of comparing and selecting engineering design solutions, the principle of minimizing carbon emissions is replaced by the previous principle of minimizing economic costs. The focus is on considering the carbon emissions throughout the entire life cycle of the project, analyzing the total energy consumption and proportion of carbon emissions in each stage, and optimizing the design comparison, The ultimate design concept is to achieve energy-saving and carbon reduction in tunnels and underground engineering. The design concepts for energy conservation and carbon reduction in tunnel and underground engineering are presented from four aspects: the application of prefabricated structures, optimization of excavation methods for large underground spaces, design of green retaining walls such as edges and slopes, and green operation.

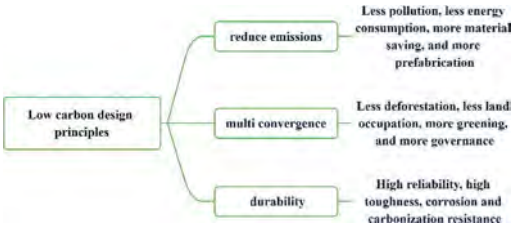

Figure 3. Low carbon design principles.

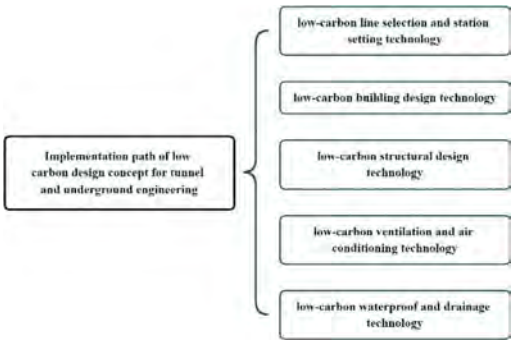

Figure 4. Implementation path of low carbon design concept for tunnel and underground engineering.

3.1 *Application of prefabricated structures*

During the tunnel excavation process, including advanced support, earthwork excavation, construction and demolition of temporary structures, construction of initial support, secondary lining and other structures, and grouting reinforcement, each process generates energy consumption. Especially in the process of shotcrete, there is a high loss of materials and a large amount of dust, which requires measures such as dispersing water to reduce dust. Adopting prefabricated structure, compared with cast-in-place, it has better maintenance conditions, fewer materials, lower material loss, and saves template energy consumption. Therefore, prefabricated structure has good carbon reduction ability. Taking the single hole and single track tunnel in the subway section as an example, the carbon emissions of prefabricated structures and cast-in-place structures will be analyzed.

The design of a shield section of Beijing Subway is as follows: the excavation radius of the shield cutter head is 3.2m, the outer diameter of the C50 shield segment is 6.2m, the inner diameter is 5.5m, the thickness is 350mm, the ring width is 1.2m, and the grouting thickness is 1.0m. There are 24 bolts between the segments.

A single track and single hole section of Beijing Subway. The design situation is as follows: a horseshoe shaped cross-section with a soil cover thickness of 6.51-10.33m, and the cross-section is shown in Figure 3. The grouting thickness is 1.5m; The initial support is made of C25 concrete with a thickness of 300mm; The secondary lining concrete adopts C40 concrete with a thickness of 300mm.

The carbon emissions during the construction phase of single hole and single line tunnels in the subway section of the above two types of construction are closely related to material consumption, transportation, installation, etc. This section only considers carbon emissions from material usage.

Based on the design of two tunnel sections, the consumption of various materials can be calculated separately, and combined with existing research (Li et al., 2022), the carbon emission factors for the same material can be given, as shown in Table 1 below.

Table 1. Materials carbon emission factor.

Material type	carbon emission factor (kg/m^3)	Material usage (m^3)	
		shield tunnel	mined tunnel
C25 concrete	289.44	/	8.37
C40 concrete	432.29	/	6.00
C50 concrete	563.89	6.43	0
cement mortar	400.94	12.82	48.55

For prefabricated segments of shield tunnels, excess losses are not considered for shield segments and bolts, and 10% losses are considered for grouting; For underground tunnels, 20% loss is considered for the initial support of spraying, 5% loss is considered for the secondary lining, and 10% loss is considered for grouting. Based on Table 1 and Equation (1) above, the carbon emissions of the shield tunnel segment are calculated to be 9337.31kg, and the emissions of the underground tunnel are 27,389.59kg.

The carbon emissions of prefabricated pipe segment structures are 34.09% of the carbon emissions of concealed excavation support structures. It can be seen that prefabricated structures have certain advantages and application prospects in carbon reduction.

3.2 *Design scheme for group caves*

With the intersection of multiple lines and multi-functional transportation types, stations are currently in a large-scale state. The design of a large space can create a good underground environment, but it will inevitably be accompanied by large-scale earthwork excavation. According to the station function, a dispersed layout scheme of group tunnels is adopted, which is to set up tunnel groups composed of independent tunnels. The support effect of rock walls and slabs between the group tunnels is fully utilized to improve the overall stability of the group tunnels, reduce tunnel excavation volume, and reduce tunnel support costs. Compared with direct excavation of large sections, it has better energy-saving and carbon reduction functions.

Next, relying on the Badaling Great Wall railway station Project of Beijing Zhangjiakou High speed Railway (see Figure 4), and considering different earthwork excavation quantities and tunnel support structures, the carbon emissions of two schemes of single tunnel and group tunnel layout are analyzed. The single hole layout is to design the four tracks, platform, and station hall of the station in a super large span tunnel, with a tunnel excavation span of 44m and a height of 27m. A concrete medium slab is set up in the single tunnel, with the upper layer being the station hall layer and the lower layer being the platform layer. The layout scheme of group tunnels is to set independent tunnels to form a group of tunnels according to the Functional requirement of the station. Nine single tunnels are arranged within the range of 90m in length and 44m in width to give full play to their respective functions and make full use of the supporting role of rock walls and slabs between the group tunnels to improve the overall stability of the group tunnels.

The construction process of the above two types of tunnel construction is closely related to carbon emissions and material usage, transportation, and installation. This section considers material usage and carbon emissions from soil and rock excavation.

Based on the design of two types of tunnel sections, the consumption of various materials and the amount of earthwork excavation can be calculated separately. Combined with existing research (Li, 2022), the carbon emission factors for the same material and earthwork excavation can be given, as shown in Table 2 below.

Table 2. Materials and earthwork carbon emission factor.

Material type	carbon emission factor (kg/m^3)	Material usage (m^3) Large-span single-hole tunnel	Group tunnel
earth-rock excavation	17.95	972.58	831.85
C40 concrete	432.29	348.61	116.21

Based on Table 1 and Equation (1) above, the emission of a single large-span tunnel is calculated to be 168182.92kg, and the emission of a group tunnel is 65,167.33kg.

The carbon emissions of group tunnel are 38.75% of the carbon emissions of single tunnel. It can be seen that group tunnel has certain advantages and application prospects in carbon reduction.

3.3 *Green retaining wall design of side slope*

Gebin ecological retaining walls are used as retaining structures for tunnel slopes, waste disposal areas, and other structures. On the one hand, they can maintain the stability of the stacked waste soil, and on the other hand, they can penetrate water and provide necessary growth beds for vegetation growth, laying a solid foundation for surface environmental greening. Choosing the waste soil from tunnel excavation as the filling material in the gabion not only achieves the reuse of waste soil, but also saves the production of traditional concrete retaining walls, which has important prospects for carbon reduction applications. Below is an example to show the carbon reduction situation of Gebin Ecological Barrier.

Design Overview: The retaining wall is 10m long and 8m high, with a base width of 4.5m and a cross-sectional area of 22.5m^2. The total filling volume of gabion is 225m^3. The size of the Gebin unit is 2m × 1m × 1m, mesh size 8cm × 10cm, steel wire diameter 2.7/3.7mm, coated with Galfan and plastic. The density of gabion is 9.5kg/m^3, and the equivalent density of filled stone is 1750kg/m^3. The traditional plan considers concrete retaining walls with a R_{ck} rating of 45, an equivalent cross-sectional area of 18.9m^2, and a total filling volume of 189m^3.

The transportation of materials for two types of retaining walls also has carbon emissions. Generally,

when using tunnel waste, the transportation distance of waste slag for Gebin ecological retaining walls is smaller than that of traditional concrete retaining wall materials. Therefore, the carbon generated by material transportation for Gebin ecological retaining walls is smaller than that of traditional concrete methods. Due to significant differences in transportation distances between different projects, the carbon emissions during the material transportation process of the two options will be ignored in the following text.

According to research results (Wang, 2012; Zhang, 2018), the carbon emission factors per unit of building materials ($1m^3$ concrete, 1t steel, 1t PVC) required for the two types of retaining walls are 363.7kg, 2062.4kg, and 9019.1kg, respectively.

The source of stone used to fill the mesh box in the retaining wall in the case is the waste slag from the tunnel. The total amount of stone to be filled (considering a 5% loss) is $225m^3 \times 1750kg/m^3 \times 1.05=413.44t$, the total amount of gabion (considering 5% loss) is $225m^3 \times 9.5kg/m^3 \times 1.05=2.24t$, the total amount of concrete required for traditional concrete retaining walls (considering 5% loss) is $189m^3 \times 2300kg/m^3 \times 1.05=456.44t$.

According to equation (1), the carbon emissions of Gebin ecological retaining wall and traditional concrete retaining wall are calculated to be 617.8kg/m and 7217.7kg/m, respectively. The carbon emissions of Gebin ecological barrier walls are only 8.6% of the carbon emissions of traditional concrete barriers, reducing carbon emissions by over 90%. It can be seen that the Gebin ecological barrier has good carbon reduction and environmental protection effects.

3.4 *Design of green operation mode for stations*

During the operation of the station, energy will be consumed. Taking Beijing as an example, the total annual power consumption of the operating network in early 2020 was 2.19 billion kilowatt hours, including train traction, power lighting, and station energy consumption. Scholars have conducted explorations on low-carbon and green operation models from the perspectives of train operation management mode (Yu, 2022), introduction of green and clean energy such as photovoltaic power generation or ground source heat pumps (Zhu, 2021), and low-carbon design of equipment such as vehicles, ventilation, and air conditioning (Li, 2022).

From this, it can be seen that there is still great room for improvement in green operation of stations, especially underground stations. Research on station energy consumption shows that the energy consumption of ventilation and air conditioning systems, lighting equipment, and escalators accounts for over 80% of the station's energy consumption (Shi, 2022). For underground stations, combining the characteristics of warm winter and cool summer in the ground, utilizing the train piston wind effect to transfer the heat from the ground into the station space can effectively reduce energy consumption and carbon emissions in terms of temperature control; Stations can also reduce energy consumption and carbon emissions in terms of station lighting by adopting photovoltaic power generation, introducing intelligent lighting systems, and cleverly utilizing ground light; The introduction of intelligent control systems for large-scale equipment can intelligently control the operation of equipment based on passenger flow characteristics, achieving manned operation and unmanned suspension, effectively reducing energy consumption and carbon emissions.

4 LOW CARBON DESIGN PRACTICE - TAKING THE BEIJING ZHANGJIAKOU HIGH SPEED RAILWAY AS AN EXAMPLE

Relying on Beijing Zhangjiakou High speed Railway, the application effect of typical carbon reduction design concept is introduced from four aspects: Tsinghua Garden Tunnel, New Badaling Tunnel and Badaling Great Wall railway station, slope green protection, and energy saving operation mode of Badaling Great Wall railway station.

4.1 *Tsinghua garden tunnel*

The Tsinghua Garden Tunnel of Beijing Zhangjiakou High speed Railway is located in Haidian District, Beijing. It enters the ground from the south of Xueyuan South Road to the south of Fifth Ring Road, north of Qinghua East Road, and exits the ground from the south. The total length of the tunnel is 6020 m, with an inner diameter of 11.1 m and an outer diameter of 12.2 m. It successively passes through 7 main municipal roads and 106 important municipal pipelines in total, including Xueyuan South Road, North Third Ring Road, Zhichun Road, North Fourth Ring Road, Chengfu Road, Qinghua East Road, Shuangqing Road, and also passes through 3 subway lines, namely Line 10, Line 12, and Line 15, The entire line runs in close parallel with Metro Line 13, which is currently one of the high-risk large diameter shield tunnels with the highest number of important buildings and structures traversed by China Railway.

During the practice of Tsinghua Garden Tunnel Project, many technologies were adopted based on the low-carbon design concept to reduce carbon emissions. These technologies include low-carbon route selection technology for tunnels, carbon reduction construction technology for shield tunnels based on fully prefabricated assembly, carbon reduction construction technology for deep and large shield wells based on permanent utilization of underground walls, green environmental protection treatment technology for large-diameter slurry shield tunneling mud, zero water reduction construction technology for tunnels based on grouting sealing. In addition, carbon sinks are further offset by setting up the Jingzhang Site Park on the ground of the tunnel. The application of these low-carbon design technologies helps to reduce the

impact on the environment and promote the development of underground engineering towards a more sustainable and environmentally friendly direction.

4.1.1 *Fully prefabricated structural design*

Tsinghua Garden Tunnel shield segments, structures under the track and auxiliary grooves are all prefabricated and assembled structures. It is the first tunnel in China that has been fully prefabricated and assembled, and an assembly robot has been developed, which has realized the industrialized, mechanized, professional and intelligent construction of shield segments, structures under the track and auxiliary grooves.

Compared with cast-in-place structures, prefabricated structures are produced in a factory with better curing conditions, higher concrete strength, and better quality, resulting in less material usage; Secondly, centralized manufacturing and maintenance of prefabricated structures result in low material loss and low energy consumption for measures; Thirdly, the prefabricated structure saves a lot of template consumption and energy consumption during template installation and dismantling. In addition, the prefabricated structure also avoids dust and wastewater pollution generated by cast-in-place construction. The calculation and analysis show that the carbon emission of prefabricated structure is 246.4kg/m less than that of cast-in-place structure, the shield section of Tsinghua Garden Tunnel is 4.45km long, and the carbon emission of prefabricated structure under track is 1096.5t less. After the promotion of this technology, based on the planned length of 387km of railway shield tunneling, it will reduce carbon emissions by 95,300 tons.

4.1.2 *Increase in surface greening area*

The Tsinghua Garden Tunnel eliminates the division of the old Beijing-Zhangjiakou Railway from the city, and cancels the level crossings such as Sidaokou and Wudaokou, which significantly reduces the traffic congestion in the area and reduces the automobile exhaust emissions. In the fifth ring road of Beijing Zhangjiakou High speed Railway, large diameter shield tunnels are used to penetrate the urban core area. At the same time, the old Beijing–Zhangjiakou Railway ground line is demolished and transformed into Beijing Zhangjiakou Heritage Park and urban green belt, integrating tunnel construction into urban development, significantly reducing noise and vibration pollution, and releasing urban space. The planned Jingzhang Ruins Park is 9km long and about 20m wide, adding 180000 square meters of green belt area to Beijing, with an annual carbon sequestration of over 2000 tons.

4.2 *New badaling tunnel and badaling great wall railway station*

The new Badaling Tunnel is a control project of the whole line of Beijing-Zhangjiakou Railway, with a total length of 12.01km. It continuously passes through Juyong Pass, Shuiguan, Badaling Great Wall and other important scenic spots, passes through the Great Wall three times, and passes through the century old Beijing Zhangjiakou Railway and Shifosi Village with ultra shallow burial. It is the longest tunnel along the line, the most stringent environmental protection requirements, and the most tense construction period.

Badaling Great Wall railway station is an underground station in the Badaling Tunnel, located below the Guntiangou Parking Lot in Badaling, Yanqing, Beijing, and adjacent to Badaling Great Wall. The station has a total length of 470m, a total width of 80m, an underground construction area of 398,500 square meters, a buried depth of 102m on the track surface, and a passenger lifting height of 62m. It is currently the largest high-speed railway underground station in China in terms of burial depth and lifting height; The most complex underground excavation tunnel group station in China currently has multiple levels of stations, a large number of tunnels, complex tunnel types, and dense intersection nodes; The single tunnel excavation span of the crossover section at both ends of the station reaches 32.7m, making it the largest single arch excavated railway tunnel in China.

In the design process of Badaling Great Wall railway station, a number of low-carbon design technologies were applied to reduce carbon emissions and improve environmental protection. These technologies include: green line selection technology of underground station line, green design technology of underground station building selection, low-carbon construction technology of tunnel based on self-bearing of surrounding rock, groundwater cleaning and sewage separation drainage and sewage treatment technology of water source protection area, air dust removal and purification technology of tunnel in scenic spot, reduction and recycling technology of tunnel spoil, energy saving and emission reduction technology of underground station making full use of ground temperature, train piston wind and solar energy, and green design technology of underground engineering blanking. Through the application of these low-carbon design technologies, the construction of Badaling Great Wall railway station has greatly reduced the impact on the environment and reduced a lot of carbon emissions.

4.2.1 *Optimization of station location selection*

Based on the green route selection technology of underground station line, Badaling railway station has studied three station schemes, namely Guntiangou, Chadaocheng underground station and Chengjiayao ground station. The distance from the entrance of the Great Wall Trail is approximately 6km from the ground station and 2km from the underground station of Chadaocheng; Guntiangou Underground Station is only 250m away from the Great Wall Cableway Dengcheng Pass and 800m

away from the Great Wall Walkway Dengcheng Pass, which is 6km shorter than the ground station. This plan is to set up a station underground at the entrance of Badaling. It takes only 30 minutes for tourists to travel from the urban area to the scenic spot by car. Therefore, a large number of tourists give up taking buses and minibuses and choose to take high-speed rail to visit the scenic spot. According to the annual transport of 2.6 million tourists and the average travel distance of 70 kilometers, the carbon emissions of Badaling tourists alone will be reduced by 1820 tons each year.

4.2.2 *Station architectural design plan*

During the design period, the advantages and disadvantages of 9 layout schemes, including single tunnel, triple arch, three tunnels, dome, and group tunnels, were compared and analyzed. The carbon emission analysis of each scheme was also supplemented. Now, an example is given to compare the carbon emissions of single tunnel centralized layout and group tunnel dispersed layout.

The single-hole centralized arrangement (referred to as the large-span scheme) is to design the four-lane, platform and station hall of the station in a super-large-span tunnel. The tunnel excavation span reaches 44 m and the height reaches 27 m. A concrete medium plate is set up in the large-span tunnel, the upper layer is the station hall layer, and the lower layer is the platform layer. The scattered layout scheme of group holes is to set up independent tunnels to form a tunnel group according to the functional requirements of the station, and make full use of the supporting role of rock walls and rock plates between the group holes to improve the overall stability of the group holes.

Comparing the two schemes, the emission of a single tunnel with a large span is 182.8 t/m; The emission of group tunnel is 77.8 t/m; The carbon emissions of group tunnel are 42.57% of the carbon emissions of single tunnel. The large span scheme has an excavation area of 1023.7m^2/m per linear meter, while the group tunnel scheme has an excavation area of 844.8m^2/m per linear meter. The station platform is 450m long, and the dispersed arrangement scheme of group tunnels reduces rock excavation by 80000 m^3 compared to the centralized arrangement scheme of single tunnels, saving energy consumption for slag transportation and land for slag stacking, and reducing carbon emissions during the construction period by about 17000 tons.

4.2.3 *Optimization of structural design methods*

Due to the need of setting the crossover line, the excavation span of the tunnel at both ends of the Badaling Great Wall Station is 32.7 m, and the excavation area is 418.9 m^2. According to the collapse arch theory, the thickness of the secondary lining of the tunnel reaches 2m, the excavation span of the tunnel will increase to 36.3m, and the excavation area of the tunnel will reach 622.9m^2. Low-carbon construction technology of tunnel based on self-bearing of surrounding rock. The self-bearing theory of surrounding rock of super-long-span tunnel, the component design method of bearing arch of surrounding rock, the self-bearing support measures of pre-stressed anchor net supporting rock shell and the excavation method of super-long-span tunnel are put forward. The self-bearing of surrounding rock is realized. The new method has reduced the tunnel span by 8%, the excavation area by 20%, and the lining thickness by 70%.The thickness of secondary lining is successfully reduced to 0.6m, and the excavation per meter of the maximum span is reduced by 125.77m^2. In total, the excavation amount is reduced by 20,500 m^3, and the carbon emission is reduced by 4400 tons.

4.2.4 *Station stealth design scheme*

The Badaling Great Wall Station is located in the world cultural heritage protection area. How to realize the station function, facilitate the convenient travel of tourists, and avoid the impact on the scenic environment, and integrate with the natural and cultural landscape is the focus of design thinking. In order to shorten the travel distance of tourists as much as possible and reduce the damage to the surface vegetation of the scenic spot, the tunnel method is adopted to cross the scenic spot. The Badaling Great Wall Station adopts the underground station scheme, and the only surface entrance and exit top is also covered with green vegetation. Reduce the area of 40,500 m^2, the annual increase in carbon sinks of about 1500 tons.

5 CONCLUSIONS

With the implementation of China ‘s carbon emission and carbon neutralization strategy, reducing carbon emission has gradually become the goal of engineering construction. The calculation method of engineering carbon emission is given, and the low-carbon design concept and method of tunnel and underground engineering are put forward. Based on the case of Beijing-Zhangjiakou high-speed railway, the effect of the above low-carbon design scheme is analyzed. Through the above research, the main conclusions are as follows:

(1) The calculation method of carbon emission coefficient in three different stages of survey and design, construction and operation in tunnel and underground engineering is established.
(2) The carbon emission law in the construction process of tunnel and underground engineering is analyzed. The material carbon emission of supporting structure accounts for a large proportion in the construction process.
(3) The low-carbon design concept of tunnel and underground engineering is put forward, including the application of prefabricated structure, the design scheme of group hole layout, gabion ecological retaining wall such as side slope,

ventilation, lighting and green operation of large facilities in underground stations.

(4) Combined with engineering cases, the rationality of low-carbon design of prefabricated structure replacing cast-in-place structure and group hole arrangement replacing single hole large section scheme is compared and analyzed.

(5) The implementation of the Beijing-Zhangjiakou high-speed railway case shows that the proposed low-carbon design concept of tunnel and underground engineering has a good application prospect.

REFERENCES

Chen L. J., 2017. Research on carbon emission characteristics and impact mechanisms of highway tunnel traffic. Master Thesis. Chongqing Jiaotong University, Chongqing, China. (Chinese)

Dong H. M., 2016. Research on the preparation method of carbon emission quota for shield tunnel construction - Taking the Maluzhou traffic tunnel project in Hengqin new area as an example. Master Thesis. Guangdong University of Technology, Guangzhou, Guangdong, China. (Chinese)

Fei, L., Zhang, Q., Xie, Y., 2017. Study on energy consumption evaluation of mountainous highway based on LCA. IOP Conference Series: Earth and Environmental Science. 69: 012036.

Gong J. F., Tang G. R., Wang, W., et al,2022. Statistics of China's railway tunnels by the end of 2021 and design & construction overview of Gaoligongshan tunnel. Tunnel construction (in both Chinese and English). 42 (3):508–517(Chinese)

Guo, C., Guo, X., Xu J. F., et al,2016. Research on carbon emission boundary of tunnel construction ventilation system. Proceedings of the 2016 China Tunnel and Underground Engineering Conference (CTUC) and the 19th Annual Conference of the Tunnel and Underground Engineering Branch of the Chinese Civil Engineering Society. (Chinese)

He X. T., 2015. Research on the calculation methods and major parameters on CO_2 mission during the construction of urban mass transit open-cut station. Master Thesis. Beijing Jiaotong University, Beijing, China. (Chinese)

Huang, L, Bohne RA, Bruland A, et al,2015. Life cycle assessment of Norwegian road tunnel. Int. J. Life Cycle Ass. 20, 174–184.

Huang X. H., 2019. Carbon emission measurement and reduction analysis in the embodied stage of metro civil engineering. Master Thesis. South China University of Technology. Guangzhou, Guangdong, China. (Chinese)

Li, M., Zhang, J., Cui T. R., et al,2022. Research and application of green and low-carbon innovation in Beijing subway. Locomotive electric drive. (03): 29–36. (Chinese)

Li, Y., He, Q., Luo, X., et al,2016. Calculation of lifecycle greenhouse gas emissions of urban rail transit systems: A case study of Shanghai Metro. Resources, Conservation and Recycling. S0921344916300416.

Li Y. H., Zhang, Y., Duan H. B., et al,2022. Research on environmental impact assessment and emission reduction potential of metro construction: A case study in Shenzhen. Environmental Engineering. 40(05): 184–192 +236. (Chinese)

Miliutenko, S., Åkerman, J., Björklund, A., 2012. Energy use and greenhouse gas emissions during the life cycle stages of a road tunnel-the swedish case Norra Länke. European Journal of Transport and Infrastructure Research. 12(1): 36–92.

Shi Z. H., Ding S. K., 2022. Green and low-carbon development strategies for urban rail transit. Urban rail transit. (09):14–17. (Chinese)

Wang, X., 2012. Life cycle assessment for carbon emission of residential building. Master Thesis. Tianjin University, Tianjin, China. (Chinese)

Wang Y. S., Huang X. H., 2019. Quantitative analysis of embodied carbon mission in metro shield tunnel. Journal of Civil Engineering and Management. (3): 12–18. (Chinese)

Wang, Z., 2012. Study on calculation and impact factors of carbon emissions from residents' consumption. PhD Thesis. University Of Science and Technology of China, Hefei, Anhui, China. (Chinese)

Xiao S. H., Ma Z. D., 2018. Application of carbon emission calculation method for construction projects in shield tunnel construction. Construction Economics. (1), 36–42. (Chinese)

Xu J. F., Guo, C., Guo, X., et al2016. Research on the calculation model of Carbon Emissions during the Physicochemical Stage of Tunnels. Proceedings of the 2016 China Tunnel and Underground Engineering Conference (CTUC) and the 19th Annual Conference of the Tunnel and Underground Engineering Branch of the Chinese Civil Engineering Society. Chengdu, Sichuan, China, pp. 64–72.

Yu, X., 2022. Research and prospect of green and low-carbon technology for urban rail transit. Modern Urban Rail Transit. (08): 1–6.

Zhang, X. C., 2018. Research on the quantitative analysis of building carbon emissions and assessment and assessment methods for low-carbon buildings and structures. PhD Thesis. Harbin Institute of Technology, Harbin, Heilongjiang, China. (Chinese)

Zhu, M., Sun X. H., Chen X. S., et, al, 2021. Green, efficient, and intelligent construction of underground metro station. Tunnel Construction (in both Chinese and English). 41(12): 2037–2047.

Tunnelling for a Better Life – Yan, Celestino, Thewes & Eberhardt (Eds)
© 2024 The Author(s), ISBN 978-1-032-80042-4
Open Access: www.taylorfrancis.com, CC BY-NC-ND 4.0 license

Design of the REM Aéroport de Montreal's P5 Ventilation shaft

Michael Mains*
AECOM, Burnaby, Canada

Jaeseoung Lee & Verya Nasri
AECOM, New York, USA

ABSTRACT: The Réseau Express Métropolitain (REM) is a new 67km automated light rail project with 26 new stations. It is the largest project undertaken by the City of Montreal in over 50 years and once completed will be 4th largest automated network in the world. The ADM P5 shaft is located at the western terminus of the project's underground airport branch, which consists of two underground stations, and roughly 250m of cut and cover, 3 km of TBM, and 300m of drill and blast tunnels. The shaft is approximately 42m deep with a challenging 24m in soft saturated soils overlying limestone and shale bedrocks. The shaft was designed using deep internally braced and permanent secant pile walls over bolt supported rocks. The innovative approach of integrating the ground support into the permanent structure with a novel semi-drained design allowed for an accelerated construction schedule, reduced carbon footprint, and significant savings in material quantities and costs. This paper presents the state-of-the-art design approach of the P5 shaft, and the innovative solutions employed to overcome complex site and geo-structural conditions.

Keywords: Deep Excavation Design, Permanent Secant Piles, Rock Support, Airport Tunnel

1 INTRODUCTION

The Réseau Express Métropolitain (REM) is a new regional light rail project located in the City of Montreal, Canada. The project adds 67km of new double track and 26 new stations and will connect Montreal's South Shore, North Shore, West Island, and the Pierre-Elliot Trudeau International Airport with the city's downtown core. The project, illustrated in Figure 1) effectively doubles Montreal's existing metro network which, for context, consists of roughly 70km of double track across four lines. The project has been widely recognized for its numerous innovations not only from a project delivery and finance perspective, but also from an engineering and technical perspective. Among these innovations is the design and construction of the project's P5 Ventilation shaft located at the Pierre-Elliot Trudeau Airport (denoted herein as the ADM P5 Shaft). This paper provides an overview of the shaft's design and the innovations implemented to overcome significant site and geologic constraints.

Figure 1. REM key plan with P5 Shaft location identified.

2 CONTEXT

2.1 *Project location*

The ADM P5 shaft is located at the end of the approximately 3km long EPB TBM tunnel which makes up the project's underground airport branch. The shaft is one of three underground structures on this branch (the other two being stations) and serves as one of two ventilation points for the entire tunnel branch of the project. A more detailed plan of the airport branch alignment is shown in Figure 2 below.

2.2 *Geological and hydrogeological setting*

The subsurface conditions at the P5 shaft location consists of approximately 20m of soft saturated soils overlying bedrock with a groundwater table located approximately 7m below grade. The upper soft ground stratigraphy consists of approximately 3m of fill over

*Corresponding author: Mike.Mains@AECOM.com

DOI: 10.1201/9781003495505-37

Figure 2. REM airport branch alignment.

5m of soft clayey silt with SPT N values in the range of 0 to 2. The soft clay overlays a more competent 10 to 12m thick layer of dense gravel/sand and/or glacial till with SPT N values in the order of 28 to 64.

The rock horizon is located at a depth of approximately 20m. The top 4 to 5m of rock is highly weathered and consists of very poor quality calcareous shale with limestone bands and an RQD in the range of 0 to 48%. For the purposes of design, this upper 5m of rick is treated as soil. The rock underlying the weathered zone is competent and consists of approximately 50% limestone and 50% bedded shale with RQD in the range of 88% to 100%.

3 DESCRIPTION OF THE ADM P5 STRUCTURE

The ADM P5 shaft consists of one level of above grade superstructure and nine underground levels which contain six floors of mechanical and electrical equipment, most notably two jet fan and damping systems for tunnel ventilation each weighing over 34 tonnes. The bottom of the shaft connects to the turnback tunnel of the REM airport station located roughly 300m away. The shaft had to be designed to accommodate a strict over height restriction of 18m during construction and an encroachment limit of only 5m beyond the structure's perimeter due to its location at the airport. The structure is rectangular in plan with a rough footprint of 21m long by 18m wide.

3.1 *Support of Excavation (SOE)*

The shaft required an approximate 42m deep excavation, 24m of which was in soft soils and very poor-quality rock. Due to the higher permeability and relatively shallow groundwater, the support of excavation in this softer ground had to consist of a watertight shoring system. Further, strict encroachment limitations prevented the use of tie-backs and forced an internal bracing to support ground loads.

Ultimately 22m long secant piles with concrete walers, braced internally with temporary pipe struts was selected as the most appropriate SOE solution. The secant piles would be installed from a 3m deep pre-excavated platform to reach a total depth of 25m from surface. The reinforcement in each secondary pile would then be extended 3m upward and encased in a cast-in-place concrete wall so that grade could be reinstated to its original level. The secant piles were embedded 1.0m into the underlying competent rock and a 1.0m rock bench was left in place to aid toe anchors in ensuring stability of the pile toe.

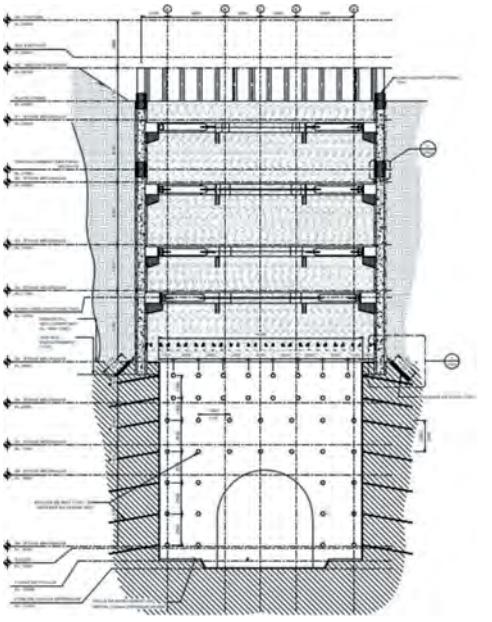

Figure 3. SOE system for the ADM P5 shaft.

The bottom 17m of excavation was in competent bedrock and could be supported by much lighter support consisting of 4m long CT rock bolts spaced at 1.8m to 2.5m center with 100mm of steel fiber reinforced shotcrete.

3.2 *Permanent structure*

The internal structure consists of a multi-level steel structure, with all the levels being underground except the first floor which is above grade to provide the access to the shaft. The main lateral force resisting systems are moment frames in both directions for the above grade structure and direct load transfer to the ground for the below grade structure. An isometric view of the permanent structure is shown in Figure 4.

One of the major innovations of the P5 shaft design was to incorporate the secant piles, walers, and rock support into the permanent structure and to provide a "semi-drained" structure. The design team recognized early on that providing a fully tanked

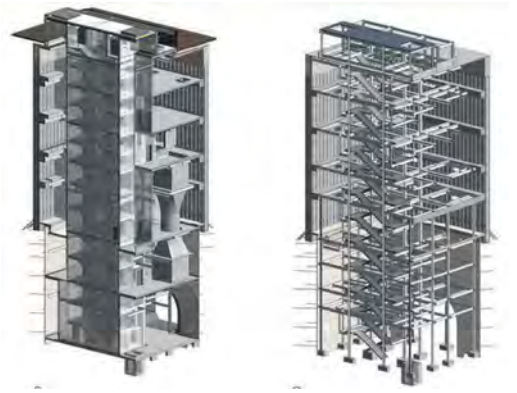

Figure 4. Isometric view of the P5 permanent structure.

below grade structure designed to support 35m of hydrostatic pressure would lead to prohibitively large structural elements. On the other hand, a fully drained structure would require constant and permanent dewatering and would lead to prohibitively large operating costs over the life of the structure.

The solution ultimately adopted was to fully waterproof the upper 25m of the shaft while leaving the underlying rock portion drained. A steel girder system would provide both the lateral capacity for ground, seismic and hydrostatic loads as well a carry all gravity loads for the upper five floors. The underlying rock's hydraulic conductivity was low enough that relieving hydrostatic pressures would require a very low flow rate that could be easily managed throughout the life of the structure. Thus, no ground or hydrostatic loads needed to be carried by the lowest four levels of structural framing if this portion of the shaft was drained. The only lateral loads experienced by the steel frame in rock are those resulting from restraining seismic drift of the structure thereby allowing a considerable reduction in all structural elements in this lower half of the shaft.

This allowed for the SOE system to be incorporated into the final structure which led to significant material cost savings, allowed for an accelerated construction schedule, and lowered the carbon footprint of the structure.

4 DESIGN

The ADM P5 Shaft has been designed according to Load and Resistance Factor Design (LRFD) for a design life of 125 years. The design process was a collaborative effort between the architectural, MEP, structural, and geotechnical disciplines. All coordination was done through a regularly updated and clash detection BIM model covering all disciplines. Since the majority of the structural elements serve both as temporary SOE as well as permanent structure, the final structural design had to be fast-tracked. Normally in a design-build context, it is beneficial to begin construction of the temporary SOE while design of the final structure proceeds concurrently. For the ADM P5 shaft, all later stage analyses like seismic, special case loads, and detailing had to be fully flushed out prior to construction of any element of the shaft. Collaboration in the BIM environment and weekly coordination meeting allowed the design team to arrive at the final design configuration in the least possible number of iterations.

4.1 *3D Soil-Structure Interaction (SSI)*

Upon completion of the architectural design along with some preliminary sizing of structural members, it was possible to determine the minimum space proofing required for the shaft excavation. This allowed the SSI to proceed in parallel to the permanent structure design thereby fast tracking the design of the overall structure.

The SSI modelling, using PLAXIS 3D as shown in Figure 5, confirmed the stability of the excavation, predicted excavation induced deformations, and allowed for the determination of structural demands throughout the entire excavation sequence.

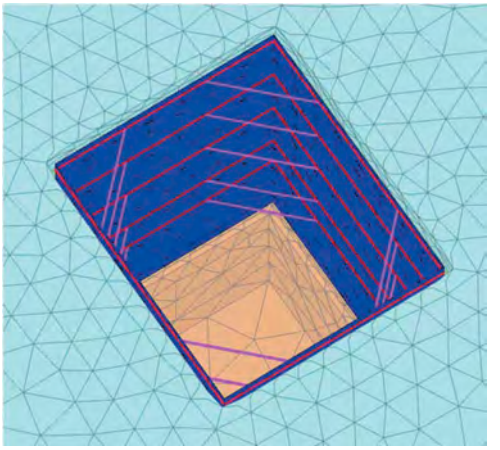

Figure 5. 3D plaxis model.

Two SSI models were developed. The first model was carried out with the secant piles modelled as linear elastic plates with isotropic stiffnesses. This model approximated more or less the real "global" behaviour of the shaft and was thus considered suitable for the deformation analyses. However, a limitation of the linear-elastic constitutive model is that secant pile plate will continue to pick up load regardless of whether the structural capacity of that element is exceeded. Secant piles have very high bending resistance about the horizontal axis but have very little bending capacity about the vertical axis. It is, therefore, necessary to prevent the secant pile plates in the model from spanning between the shaft

corners and artificially lowering the structural demands in the walers. Thus, a second model where the k22 stiffness was set to a negligible value to ensure that all bending about the vertical axis is concentrated on the walers and that the correct forces would be considered in design. The moment and shear envelopes in the scant pile wall as well as the strut loads of this second model were then extracted and used in the structural calculations. The directionality of bending stiffness is illustrated in Figure 6.

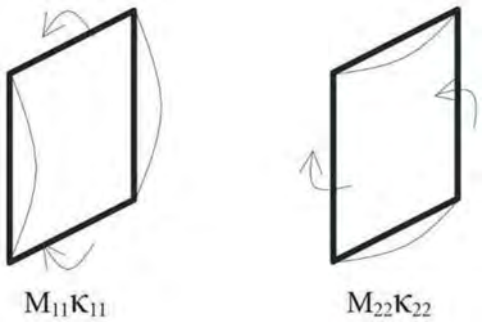

Figure 6. Schematic of bending stiffness in the wall plate.

4.2 *Secant pile wall design*

The secant pile wall consists of alternating unreinforced primary piles and W610 reinforced secondary piles with an average center to center pile spacing of 700 mm.

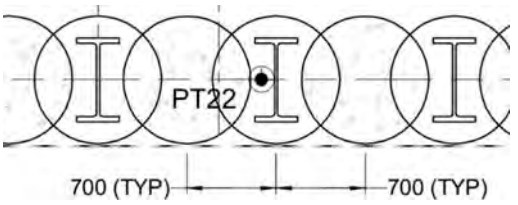

Figure 7. Typical secant pile layout.

The structural capacity of the secant piles was verified against the forces extracted from the SSI model as well as those extracted from a secondary limit equilibrium model which accounted for a seismic load case. Two approaches were used. The first was to treat the secant pile like a composite concrete and steel column subject to both bending and compression. The second approach was to verify the concrete and wide flanges independently using a strain compatibility approach.

Similar to a traditionally reinforced concrete beam or column, the compressive forces tended to have a beneficial impact on the capacity of the member when using the composite member approach.

Compression in the secant pile originated from two sources. First were the gravity loads generated by the structure itself. In the ADM P5 shaft, the gravity loads from the top five levels were transferred directly into the secant pile walls, causing compression. Although these gravity loads were easily calculated, there will always be uncertainty with respect to how fast the gravity loads are shed into the surrounding soils by friction.

The second source of compression was the down-drag originating from negative skin friction. As excavation of the shaft proceeds, the surrounding ground settles and tries to pull the secant pile wall down with it. In the case of the ADM P5 shaft, the toes of the secant piles were socketed into stiff bedrock preventing this downward movement from occurring. This created a compression in the wall.

In the finite element calculation, the assumptions required to be conservative when estimating down-drag were not the same as those required to be conservative when calculating bending moments. For example, higher interface friction between the wall and ground produced higher compression but lower bending forces. Thus, it is often better to ignore compression when using the composite member capacity calculation.

However, with secant pile lengths exceeding 23m, the down-drag compression can be significant and potentially govern when using the strain compatibility method.

Therefore, as a due diligence measure both scenarios (compression and no compression) were verified using both the composite member and strain compatibility approaches.

4.3 *Rock support design*

Competent rock is located for roughly the bottom 17m of excavation which is supported by 4m long CT rock bolts spaced at 1.8m to 2.5m centres with 100mm of steel fiber reinforced shotcrete.

The rock support was designed both empirically and with the use of the finite element method. The overall stability of the excavation was demonstrated in the 3D SSI model using conservative rock mass properties without modelling the rock reinforcing elements.

Subsequently, the rock reinforcing was design using the empirical method based on the Q system support chart and Barton's (2013) recommendations for shaft support design as shown in Figure 8.

The permeability of the rock was very low, except for at localized joints which may produce higher levels of seepage. The rock support is treated as a drained system and to prevent hydrostatic build-up, infiltration at these locations is directed down behind the shotcrete to a sump located below the invert slab by way of strip drains. Additionally, a provision for additional injection grouting was included in the design to mitigate the risk of encountering zones with higher-than-expected fracturing and seepage. A spray-on waterproofing membrane (Masterseal 345) was also incorporated into the design to prevent

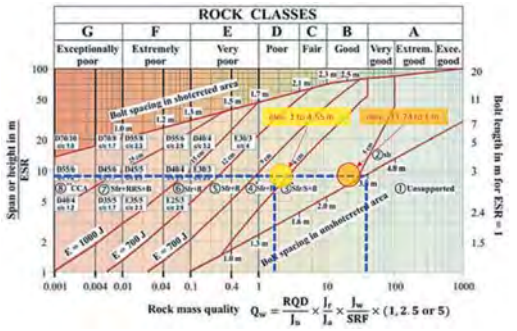

Figure 8. Rock support selection based on barton (2013).

any dampness from infiltrating into the shaft interior space in the permanent condition.

Similar to the secant pile wall, this reinforced rock perimeter wall is incorporated into the final structure, which meant that all elements needed to withstand a 125-year design life. The primary degradation mechanism for rock bolts is corrosion, which was mitigated by using CombiCoat® protected CT-bolts which provide at least a 125-year design life. See Figure 9 for rock support details.

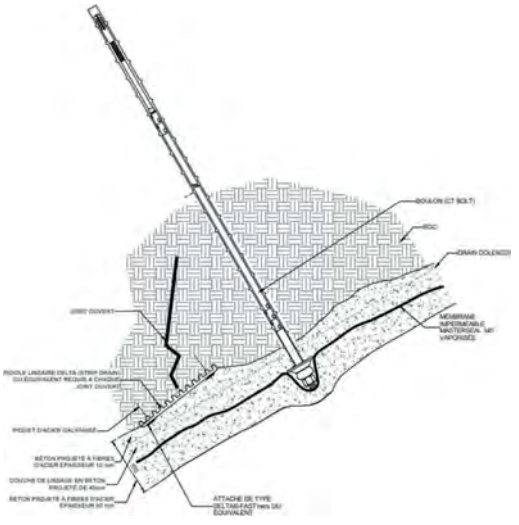

Figure 9. Rock support schematic.

4.4 *Permanent structure design*

In order to capture the various load states associated with a complex build-out sequence, the permanent steel frame was designed using a combination of 3D structural analysis using the RAM Structural system V17 software with additional 2D frame analyses to model the walers and excavation support frame.

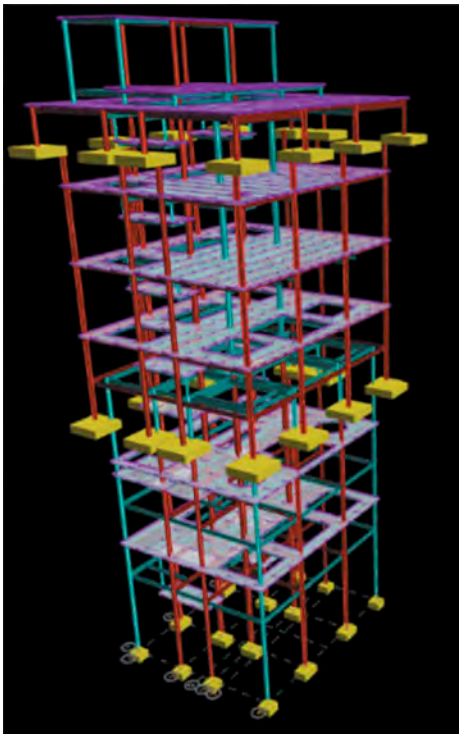

Figure 10. 3D structural model.

The structural frame at each floor in the soft ground portion supports all lateral earth pressure, hydrostatic, and seismic loads. Since the walers are used for both the temporary and permanent conditions, the temporary corner struts at each level had to be installed at the same elevation as the floor frame which would eventually support all lateral loads in the system. Consequently, the walers had to be designed to support these loads with multiple cases of differing support locations in different load and construction scenarios.

To optimize member sizes, compression girders were separated into two categories. First, static members were defined which would carry all lateral loads transferred after removing the temporary corner struts. Second, additional seismic members were added to carry eventual extreme loads cases like seismic, which could be installed after temporary strut removal. Both member types would also act as the principle girders in the gravity load framing. These additional seismic struts were required on two levels since the loads on these two levels generated under the seismic condition were too large to be carried by reasonably sized members as shown in Figure11.

To design these main strut girder elements, the 3D structural analysis was used to determine the gravity loads and lateral loads required to restrain the seismic drift of the full 45m “tall” structure. Multiple 2D frame analyses of all load scenarios we then

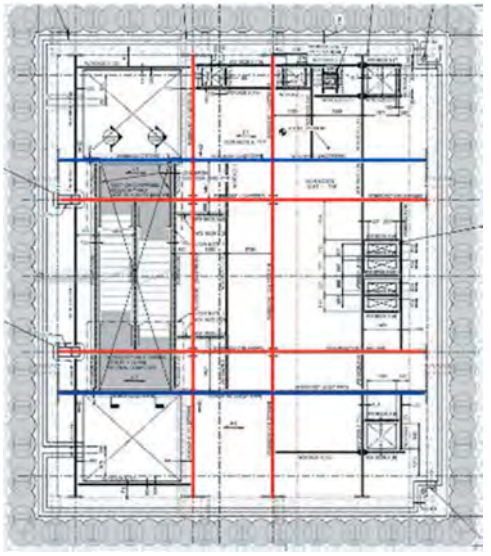

Figure 11. Example lateral support system with static struts shown in red and seismic struts shown in blue.

carried out to determine the axial loads in the struts, including from seismic earth pressures. The results of the 3D and 2D modelling were then used in a combined stress analysis to properly size the lateral support elements.

4.5 *Waler design*

Concrete walers were designed to support all four levels of internal bracing. Although the supply chains for large steel members were already established for the REM project due to several other steel framed stations on the project nearing completion, large cross-section steel walers would still have been associated with long lead times. Since waler construction was on the critical path, long lead times would cause unacceptable delays to the schedule. Consequently, concrete walers were selected to provide an overall faster construction schedule. Additionally, cast-in-place concrete can more easily accomodate eventual deviations of the secant piles from their theoretical position, thus were more adaptable to the Field condition.

To save space, connections of all temporary and permanent steel elements were embedded into the concrete, as illustrated in Figure 12.

Figure 12. Strut knife plate connection embedded in waler.

4.6 *Waterproofing design*

The waterproofing system at the ADM shaft was designed using two philosophies. The upper secant pile portion of the shaft is, in theory, already watertight. However, eventual defects can potentially be found at the joints between primary and secondary piles which can cause minor leakage. Thus, the secant piles are first covered with an initial layer of shotcrete to preserve the pile's concrete. Strips of Delta Drain MS-20 are then placed at all joints to direct any eventual leakage down to an internal drainage system inside the shaft. Since the shaft's primary use is for MEP support equipment, two additional protections in the form of a Dolenco Drain mat and an impermeable layer of Masterseal 345 is layered on top of the drain to protect the shaft from dampness. The waterproofing is then capped with an additional layer of shotcrete for durability. Figure 13 provides a cross section of this configuration.

A similar system was implemented in the lower rock portions of the shaft. Since this part of the project was drained, all seepage captured by the drain mat could be carried down below the invert slab, which is underlain by 600mm of free draining gravel fill. This under-slab drainage directs water to a 2.5m deep sump from which it can be pumped-out of the shaft to the storm water discharge system.

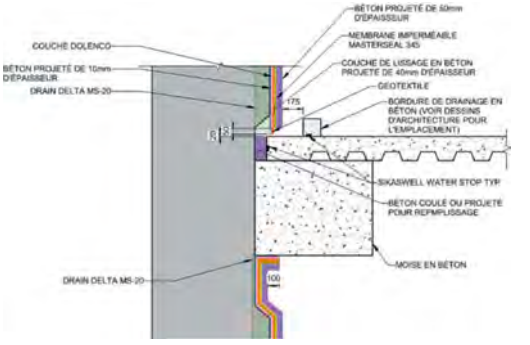

Figure 13. Waterproofing system in secant pile shaft.

5 CONCLUSIONS

The design of the REM ADM P5 Ventilation Shaft was a particularly interesting endeavor due to its significant depth and limited working area. Its location at the Pierre-Elliot Trudeau International Airport imposed strict height and encroachment restrictions which in large part drove some of the fundamental principles of the design. The design of the SOE and permanent structure also had to incorporate potential construction issues such as supply chain influences and secant pile installation tolerances.

The design team was not only able to accommodate these challenges, but also implemented considerable innovations such as a novel "semi-drained" shaft condition and the incorporation of SOE elements into the permanent structure design.

The project demonstrated how strong collaboration between engineering disciplines and innovation in design can lead to significant benefits in cost and schedule for a project even when the design schedule is fast-tracked.

REFERENCES

Barton, N, 2013. Integrated empirical methods for the design of tunnels, shafts and caverns in rock, based on the Q-system. 3rd Int. Symp. on Tunnels and Shafts in Soil and Rock, SMIG/ Amitos,17p. Nov. 2013, Mexico City.

Nasri, V., Rey, A., (2023), Tunnels and Underground Stations of Montreal Réseau Express Métropolitain (REM). Tunneling Association of Canada Conference, Toronto, Canada, September 24–26, 2023.

Lee, J., Gupta, S., Bhargava, A., and Nasri, V. (2022), Design and Construction of Technoparc Station in Montreal. International Tunneling Association World Tunnel Congress 2022, Copenhagen, Denmark, September 2- 8, 2022.

Motallebi, M., Bhargava, A., and Nasri, V. (2023), Permanent Secant Pile Wall for Underground Transit Station. International Tunneling Association World Tunnel Congress 2023, Athens, Greece, May 12-18, 2023, PP 752–760.

Nasri, V., Rey, A., Fortin, T. (2020), Design and Construction of the Deepest North American Underground Station - Station Édouard-Monpetit, Montreal, Canada. International Tunneling Association World Tunnel Congress 2020, Kuala Lumpur, Malaysia, September 11- 17, 2020.

Tunnelling for a Better Life – Yan, Celestino, Thewes & Eberhardt (Eds)
© 2024 The Author(s), ISBN 978-1-032-80042-4
Open Access: www.taylorfrancis.com, CC BY-NC-ND 4.0 license

Tunnels and stations design of Montreal Blue Line

Verya Nasri*
AECOM, New York, USA

ABSTRACT: The development of the Montreal metro Line 5 also known as Blue Line Extension toward the northeast are located between the existing Saint-Michel station and Anjou. It consists of 6-km long single double track tunnel, five new stations and six auxiliary structures. Most of tunnel length (5.5 km) will be excavated by a 9.6 m diameter shielded rock TBM and supported by a precast segmental tunnel lining system. Based on the project master schedule, the five stations will be built first and then the TBM will skid through the already built stations. For the inter-station tunnels, the shielded rock TBM excavation method with segmental liner installation was selected based on the existing geotechnical challenges, evaluation of the project construction cost, schedule and risk, noise, and vibration. TBM will be fitted for probing and pre-excavation grouting to control water inflow into the tunnel during the excavation in fractured limestone and shale formation under the downtown of Montreal where lower rock quality and high water infiltration rates are anticipated. The latest development in segmental liner technology and the latest segmental liner design code ACI PRC-533.5-20 were used for the design of the tunnel segmental liner of this project. The stations and auxiliary structures will be built using the controlled drill and blast method or roadheader. Two thin layers of shotcrete separated by a layer of spray on membrane will be used as the initial and final liner of the stations and auxiliary structures resulting in significant construction cost and time savings. This paper presents major design aspects of the TBM tunnel and mined station caverns of this major project in Montreal, Canada.

Keywords: TBM Tunnel, NATM Tunnel, Rock Cavern, Shaft, Transit Tunnel, Sustainability

1 INTRODUCTION

The extension of the Blue Line metro is an integral part of the Montreal strategic plan for the development of public transit (Nasri, et al., 2023). The Société de Transport de Montréal (STM) plays the role of public body initiating and managing the project. This major infrastructure project provides for the addition of five underground stations and seven auxiliary structures connected by nearly 6.0 kilometers of a double track tunnel (Bakhshi and Nasri, 2022). It also includes an underground storage track and maintenance facility. The project cost is estimated at about $6.4 billion CAD and its expected service date is in 2029. For the first time in North America, Blue Line extension metro system is designed with a single side-by-side track tunnel without a separating center wall. This will be the first use of a TBM in the history of the STM which will speed up the excavation process, reduce noise and vibration impacts and contribute to the infrastructure quality of extended section of Blue Line.

The extension of the Blue Line of the Montreal metro will allow approximately 25,600 users during the morning peak period to benefit from a reliable and fast service, and above all from improved access to the infrastructure network of public transport. This will be equivalent to removing 5,300 cars from the city streets and reducing the travel time between the two ends from currently 40 minutes by bus to only 15 minutes. Each station will have a main entrance and a secondary entrance located diagonally at each of the intersections and connected by underground pedestrian walkways. To ensure that they are universally accessible, the stations will all be equipped with escalators and elevators in main entrances. The final design of the project is completed, and the underground work package is now out for bid.

Construction will begin with underground stations and auxiliary structures, followed by the excavation of tunnels to connect them. Most of the tunnel (5.5 km) will be excavated by a - 9.6 m diameter shielded rock TBM and supported by precast segmental lining system and a segment of the tunnel (about 0.5 km) will be excavated by roadheader and supported by shotcrete initial and final liners. The underground stations and

*Corresponding author: verya.nasri@aecom.com

DOI: 10.1201/9781003495505-38

auxiliary structures shafts will be excavated by drill and blast method and their tunnels will be mined using roadheader and supported by shotcrete initial and final liners following the New Montreal Tunneling Method used in the construction of REM project (Nasri et al., 2021). Figure 1 shows the layout of the tunnel, underground stations, and auxiliary structures.

2 GEOLOGICAL SETTINGS

Based on the geological map of the island of Montreal and as shown in Figure 2, the project route would be in the following geological formations

- Deschambault formation only for the small portion of the tunnel in the south.
- Montreal (Saint Michel and Rosemont members) formation.
- Tetreauville formation in the north.
- Intrusive in the form of dykes and/or sills which can be present in the rock mass randomly.

The Deschambault formation consists typically of a bioclastic crystalline limestone, thick-bedded, cross-bedded, containing several coquina and fragmented shell beds. Limestone is light grey to dark, slightly brown, and varies from very fine to very coarse grained. Bedding is irregular and the numerous basins and tabular cross bedding are accentuated by the presence of argillaceous laminae. Otherwise, shale beds are sparse or non-existent, although more present at the top of the formation.

The Montreal Formation is predominantly limestone with thin shale interbeds. It is made up of a wide variety of lithologies (semi-crystalline, micritic or crystalline limestones), but clayey limestone in thin and irregular beds and very bioturbated predominates. The formation is subdivided into two wildlife areas corresponding to two members: the member of Saint-Michel at the base, and the member of Rosemont at the top. The Rosemont member is defined as the upper member of the Montreal Formation. The Rosemont member is mainly composed of limestone with thin interbedded shale. It consists of a wide variety of lithologies (semi-crystalline, micritic or crystalline limestones), but typically includes argillaceous limestone with wavy bedding. Its chemical composition indicates that it is slightly dolomitic.

The Tétreauville formation consists of a dense, dark bluish gray limestone, occurring in beds of 2 to 15 cm, alternating with beds of shales of 2 to 6 cm. The limestone is clayey, micritic, clean and in places contains crystalline lenses a few centimetres thick. Generally, the shale and limestone beds are very clearly separated from each other, which distinguishes this formation from other units of the Trenton group. When exposed to air, limestone takes on a characteristic light yellowish colour. In several places, a strong smell of petroleum emanates from the rock.

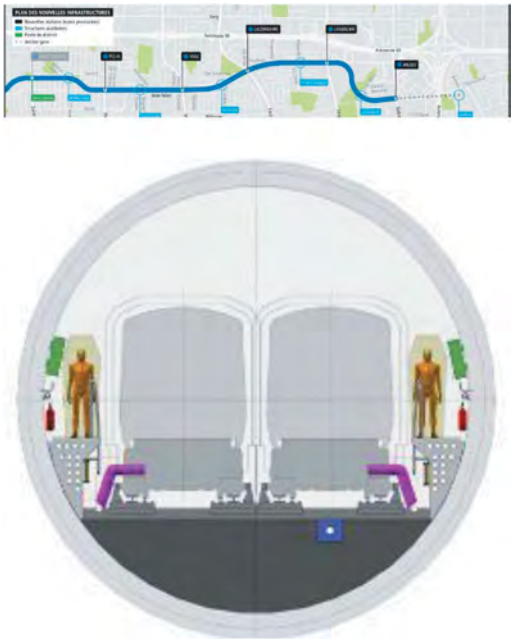

Figure 1. Layout of the tunnel, underground stations, auxiliary structures, and the tunnel section.

The intrusive rocks mainly include gabbro, syenites and carbonatites. They occur in the form of sills and dykes that are distributed randomly in the surrounding sedimentary rocks. When intact, these rocks are generally more resistant and more abrasive than their sedimentary host to which they have sometimes induced a slight contact metamorphism.

The sedimentary formations in Montreal area form a series of open northeast/southwest trending synclinal and anticlinal folds characterized by shallow dips. The project is located along the southeast flank of the Villeray anticline, parallel to its axis that is plunging towards northeast. Given the structural complexity of the Island of Montreal and the probable extension of the pre-identified faults (named Saint-Vincent-de-Paul I and II), these faults could potentially be encountered along the northern part of the tunnel route. There are signs of a glaciotectonic phenomenon in the area of one of the auxiliary structures which causes tilting of large rock fragments from 1 to more than 3 m thick.

Except a few meters of fractured/weathered zone observed on the top of the bedrock and at the locations of localized fractured zones, the rockmass is competent in general with RQD>75. The quality of bedrock usually gets better with increase in depth due to increase in fracture spacing. In the competent rock mass, the discontinuities have fair to good surface quality. Based on the Rock Mass Rating (RMR) Classification system, the rockmass is mostly classified as Classes II and III, with occasional Class IV. Using the Geological Strength Index (GSI) rockmass

Figure 2. Geological Map of the project route.

characterization method, the GSI of the rockmass varies in the range of 47-77, corresponding to the RMR Classes of III to II.

The results of laboratory tests on intact rock samples give the average range of values of 25-27 KN/m^3, 90-120 MPa, 40-50 GPa, and 0.8-1 for Unit Weight, Uniaxial Compressive Strength, Young Modulus, and Cerchar Abrasivity Index, respectively. The groundwater table is approximately at the interface of soil and rock. The hydraulic conductivity varies between 4 x 10^{-4} cm/sec to 1 x 10^{-6} cm/sec. Typically, the hydraulic conductivity of rock mass reduces with increasing depth. Majority (about 85%) of Lugeon readings are small (Lugeon values less than 5). High horizontal stress condition is present in Montreal Formation with K_0 in the range of 1.5-2.5.

3 PRECAST SEGMENTAL LINING

The rolling stock used for this project are running on pneumatic wheels and are energized by third rail. The internal diameter of the tunnel is determined as 8,600 mm considering construction tolerance of 100 mm on the radius. This tolerance which is required by ACI 533.5R-20 includes production tolerances of segments, tolerances of placement of ring centrelines and ring ovalization following the ring erection. For TBM tunnel, a watertight circular one-pass lining system with precast concrete segmental rings is adopted. The size of the segmental ring is defined by the internal diameter, thickness, and length of the ring. The internal diameter of the tunnel is determined as 8,600 mm after the space-proofing exercise. The thickness of segments is initially considered as 350 mm, which was validated for structural capacity against all governing load cases. Length of the segmental rings is 1.80 m, which was optimized considering the alignment curvature (curve radius of 250 m) and the efficiency of tunnel works. As shown in Figure 3, the ring geometry consists of seven (7) ordinary segments and one small key segment, almost 1/3rd of the size of the ordinary segments. This configuration is referred to as a 7+1 ring. The arc angle and curved length of the reverse key segment are designed slightly smaller than other ordinary segments. Consequently, the arc angle and curved length of the key segment is slightly larger than one-third (1/3rd) of the ordinary segments. Together with tapered longitudinal joints of segments, this optimized design inherently prevents creation of crucifix joints in the tunnel, despite all relative rotations of the ring during TBM navigation of curve and tangent drives (Figure 4). To create staggered longitudinal joints, the angles between ordinary segment joints and tunnel axis is considered as 80. The ring taper is designed based on the radius of the tightest curve in the alignment, the length of the ring, and the outer diameter of the tunnel. Total ring taper is 100 mm or ±50 mm at the centreline of the key and reverse-key segments.

The proposed segmental ring geometry and configuration have an important advantage over any other segmental ring configurations. The proposed ring configuration inherently prevents the creation of crucifix joints, which are more susceptible to groundwater leakage. In comparison to ring designs in which some of relative rotations of the ring are prevented to negate crucifix joints, this optimized ring design allows for all possible relative ring rotations. This leads to less deviation from theoretical tunnel alignment, a more accurate lining installation, and less construction tolerances required for the segmental rings, which directly impacts the gasket watertightness resistance and sealing performance of tunnel.

A universal ring system is proposed for the TBM tunnel, and the key segment can be located anywhere in the tunnel for turning the ring into any desired direction: up, down, left, right, and their combinations (Figure 5). The main advantage of this system is the simplification of segment production and ring installation because of the requirement of only one type of formwork set, which yields significant cost savings. The segmental ring geometry is designed as rhomboidal or parallelogrammical-trapezoidal segments, consisting of ordinary segments in the shape of parallelogram, a normal key, and a reverse key segment in the shape of trapezoid (Figure 4). In comparison with other (i.e. hexagonal, rectangular and trapezoidal systems) systems, the rhomboidal segment system is the most advanced system because it prevents crucifix joints, has a higher sealing performance, features a continuous ring build from bottom to top, and is compatible with a dowel connection system.

The tapered longitudinal joints provide a major advantage over rectangular systems by preventing early gasket friction during segment insertion in the ring assembly phase, which facilitates the use of fast connecting dowels in circumferential joints. Longitudinal and circumferential joints are designed as completely flat joints, which are advantageous for load transfer between the segments and the rings,

compared to other types of joints. In addition, flat joints are proven to have superior sealing performance. Bolt connection was designed for the longitudinal joints and dowels were chosen for connecting rings in the circumferential joints, as these require less construction work for the segment formwork and less manpower in the tunnel during the installation, when the insertion is automatically performed by the TBM erector. The SOF-FAST dowel system was designed and chosen as the dowel connection device system for circumferential joints. This type of dowel reduces construction tolerances and offsets between segments of adjacent rings and limits ring roll and segment stepping, all of which improve gasket performance and reduce the possibility of cracking due to joint misalignment. The gasket for sealing joints between segments is designed as an anchored gasket, which offers a much higher pull-out resistance, compared to a conventional glued gasket system. The designed gasket provides a water pressure resistance exceeding the maximum groundwater pressure in the entire alignment, by accounting for the relaxation factor for tunnel service life (125 years) and any potential gaps and offsets between segment gaskets due to construction tolerances. At the specified gap and offset of 5 mm and 10 mm respectively, the water resistance of the designed gasket profile is 10 bar, which provides a safety factor of more than 3 at the location of maximum groundwater pressure in the alignment.

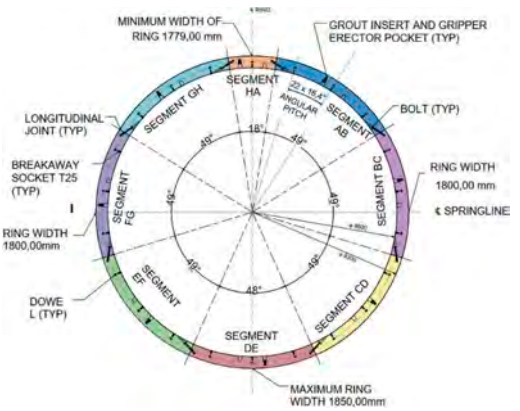

Figure 3. Geometry and configuration of the segmental ring.

Figure 4. Developed plan on intrados of the ring in tangent alignment.

From the structural design point of view, performed analysis and design procedures follow the latest ACI codes (ACI 533.5R-20 and ACI 544.7R-16) and the ITA guideline (ITA Report no. 22, 2019), and satisfies the intended objectives of the project during construction and service life of the tunnel. The structural design was carried out using the load and resistance factor design (LRFD) design method recommended by the aforementioned codes. Precast tunnel segments are designed to be made of very high-strength, double hooked-end fibre-reinforced concrete (FRC). FRC segments are superior for crack control and more cost effective overall and are therefore the preferred solution for this project. Minimum compressive strength of the concrete at 28-day and at the time of stripping (demoulding) was designed as 60 MPa and 15 MPa, respectively, to satisfy the structural demand for governing load cases and the durability of the tunnel for its intended service life. An optimized concrete mixture was designed for production of segments to achieve a high early-age strength for stripping (demoulding) and a high-performance concrete for long-term durability. Designed steel fibre satisfies the serviceability requirements by limiting time-dependent effects of creep on crack opening. Ductility requirements are guaranteed in conventional fibre dosages of less than 40 kg/m^3, by providing an ultimate bending moment higher than the cracking bending moment. Minimum required fibre content for segment reinforcement of 40 kg/m^3 and residual flexural strengths of 4.8 MPa at 28 days and 2.4 MPa at the time of formwork stripping were designed based on the required structural demand, obtained from analysis discussed above.

4 UNDERGROUND STATIONS AND AUXILIARY STRUCTURES

The new line has five underground stations and seven auxiliary structures. The stations have typically a cut and cover main entrance box and a mined tunnel which contains the station side platforms. This tunnel in excavated by roadheader and supported by permanent bolt and shotcrete liner. The auxiliary structures are located between the stations to provide emergency exit according to the NFPA 130 requirements. They are also used to house a tunnel ventilation plant and a tunnel drainage facility. Figure 6 shows a typical underground station and auxiliary structure.

For the support of excavation system, the design included shotcrete with rock bolts. Prior to bolting, a first layer of 5cm of steel fibre reinforced shotcrete, designed specifically for the cold Montreal temperature, is sprayed onto the rock. The rock bolts are installed on top of this first layer. The shotcrete and the bolts represent the initial support of the excavation. Once the rock bolts are installed, a spray-on waterproofing membrane is applied on top of this first shotcrete layer and the rock bolts' end hardware. This is later covered by an additional 5cm of steel

fibre reinforced shotcrete. Figure 7 shows the details of the initial liner with bolt and shotcrete, spray-on waterproofing membrane and the shotcrete final liner. With the spray-on waterproofing membrane, the designed support system represents both the initial and the final liner.

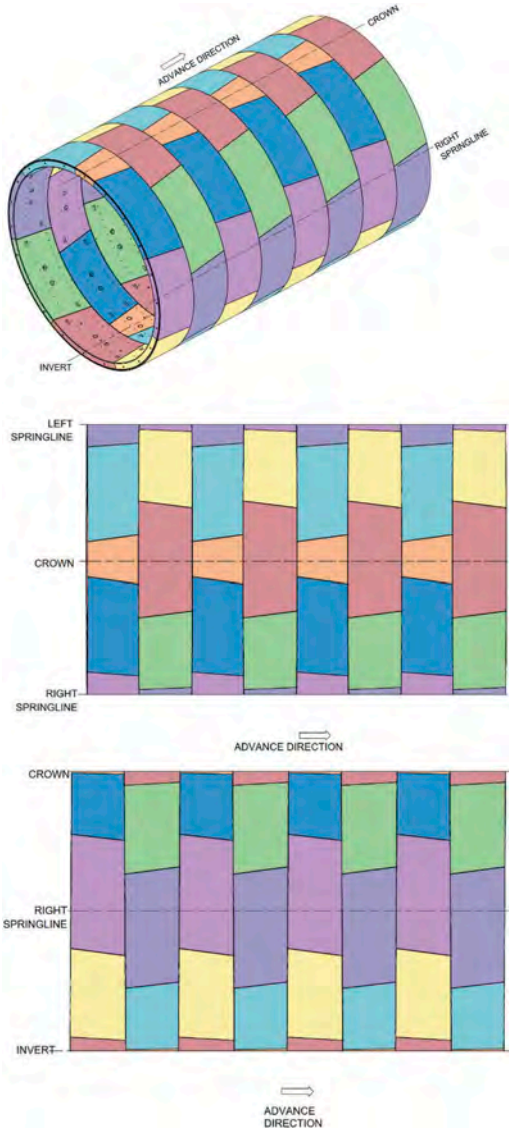

Figure 5. Negotiation of tunnel alignment by rotation of key segment in a tangent drive (from top to bottom, isometric view, plan view, elevation view).

The first use of this configuration in North America was for a pump station cavern in Indianapolis, but the first use of this approach for a major transit station in North America was in the Edouard Montpetit Station, Montreal (Nasri et al., 2020). Advantages of this configuration are numerous, both in terms of design and constructability, compared to the typical approach consisting of an initial temporary support, a sheet membrane, and a permanent cast in place concrete final liner. Effectively, the initial liner, which would typically be considered only as temporary support, now serves as both temporary and permanent, as this configuration allows load transfer from the initial lining to the final lining. As a result, the overall lining thickness is reduced compared to a typical design. In terms of constructability, the use of a spray-on waterproofing membrane instead of typical sheet membrane represents labour saving, less logistics with no formwork, and is much easier to work with, particularly where excavation configuration varies. Note that the selected spray-on membrane is not well-suited for cases with high water inflow and large water head.

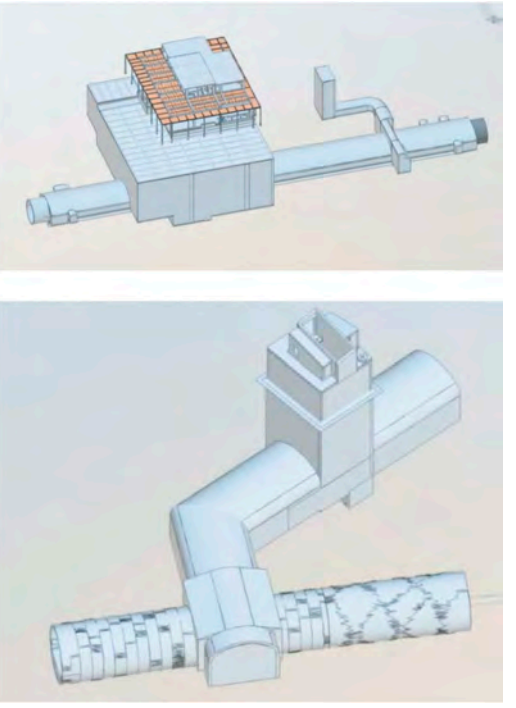

Figure 6. Typical underground station (top) and auxiliary structure (bottom).

Durability has always been a critical factor in the permanent structure design for transit systems. The durability requirements for this project include a lifespan of 125 years. Hence, all materials used as part of the permanent structure and lining had to be selected or designed accordingly.

Durability of the rock bolt is ensured using CombiCoat® protected CT-bolts, as manufactured by Vik Ørsta. The main degradation mechanism for rock bolts is corrosion, against which the protective properties of the CombiCoat® coating system include

hot dip galvanizing, phosphating, and epoxy powder coating. In addition to these protective layers, the rock bolts will be fully grouted, which means that they are not expected to be exposed to oxygen. In terms of durability, these fully grouted CombiCoat® CT-bolts are designed to last at least 150 years as estimated by the research group SINTEF in 2016.

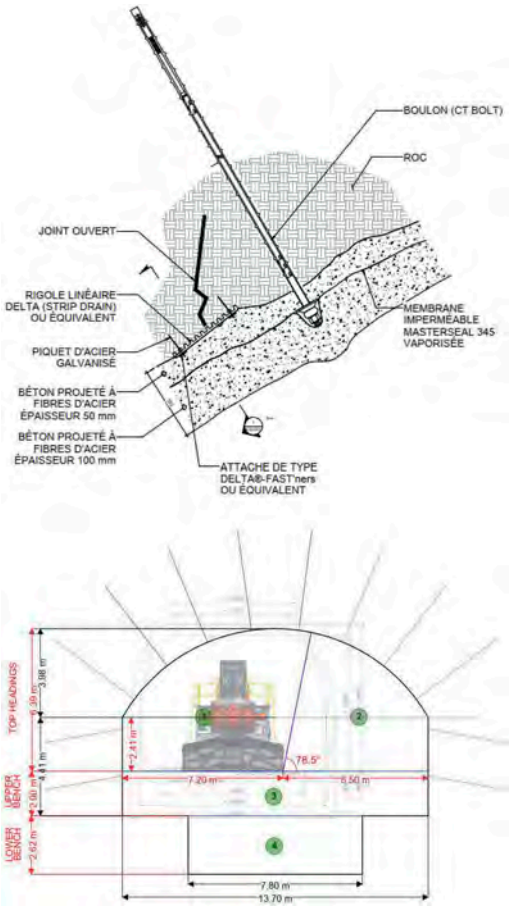

Figure 7. Initial and final liner system (top) and excavation sequence (bottom).

The steel fibre reinforced shotcrete main degradation mechanisms include corrosion of the steel fiber, mainly by the effect of carbonation and the ingress of chlorides, sulfide/acid attack, granular alkali reaction, and freeze and thaw cycles. The durability requirement for this project is higher than the normative ACI or Eurocode standards. As such, the design was developed based on an exposure class type of approach. The mix designs were developed using laboratory-based formulations designed to resist the different degradation mechanisms identified above. The formulations were based on various tests as specified by Fib 34, including ASTM C1202, NT Build 492-99, ASTM C457 and AASHTO TP-95-14.

For waterproofing, MASTERSEAL® 345 spray-on membrane manufactured by BASF was selected for this project since it has been used on numerous tunneling projects with design service life more than 100 years. This membrane is based on a copolymer of ethylene and vinyl acetate mixed with fast setting cement which forms a layer of polymer (plastic) and acts as a barrier against water penetration. Water can diffuse through the membrane in the form of steam, but if water pressure is applied, the long chain polymers are brought together, and the water movement is prevented. This membrane was designed specifically for use in underground structures. In addition to its inherent durable chemical composition, the key component of this membrane in terms of durability resides in the fact that it is sandwiched between two layers of steel fiber reinforced shotcrete, limiting its exposure to temperature changes and UV rays, which would be the two main degrading mechanisms.

5 CARBON FOOTPRINT REDUCTION

The construction industry is a major producer of CO2 emissions. Huang et al. (2018) reported that in 2009, the total CO2 emission of the global construction industry including building and infrastructures was 5.7 billion tons, accounting for 23% of the total CO2 emissions produced by global economic activities. The significant impact of the construction industry largely arises from the embodied carbon in the primary construction materials, cement and steel. IEA (2020) reported that in 2019, the cement industry emitted 2.4 billion tons of CO2 corresponding to around 7% of world energy sector emissions which is approximately 1/3rd of total CO2 emission of the construction industry. In addition, approximately half of the global steel production is directed towards the construction industry, and 44% of construction industry's steel consumption is used for reinforcement. This represents a contribution of 1.5% to the world's CO2 emissions, solely originating from steel rebar. Among various construction processes, tunnel construction results in a significant amount of CO2 emissions because almost all tunnels are lined with reinforced concrete and utilize various high energy consuming equipment for excavation. Embodied carbon and high energy consumption can be minimized through three distinctive ways. The first method includes decreasing the overall quantity of reinforced concrete utilized through design optimization. The second approach is lowering the embodied carbon within each unit volume of the reinforced concrete by reducing the usage of portland cement and steel rebar. This can be established by substituting portland cement in the concrete mix by supplementary cementitious materials (SCM), opting for fibre reinforcement in lieu of rebar, and aggregate grading optimization using Tarantula Curve (Taylor, 2015) which reduces the cement paste in the unit

volume of concrete. The third approach involves enhancing equipment efficiency through the development of excavation and construction machines powered by non-fossil fuels. This last approach already applies to TBM tunnels; hence, the first two methods should be employed in bored tunnels to minimize the carbon emissions.

The focus of this section is on the calculation and reduction of embodied carbon of precast concrete segmental lining system. The evaluation of CO2 emission reduction is carried out by comparing the carbon emissions of a baseline design, featuring conventional reinforcement and concrete mix designs, to an optimized design with a low-carbon concrete mixture.

A typical bored tunnel with the size and geological conditions of the Blue Line tunnel often has a concrete lining thickness of 400 mm when reinforced with rebar. A typical mix design to achieve 50 MPa concrete includes 475 kg/m^3 of ordinary portland cement and a water-to-cement (w/c) ratio of 0.38. Also, a typical reinforced concrete segment in this size, have at least 80 kg/m^3 of steel rebar. In comparison, the structural design was optimized with reducing the segment thickness to 350 mm and using ground granulated blast furnace slag and silica fume SCMs as partial cement replacement by 22% and 5%, respectively. In addition, steel fibre with a dosage of 40 kg/m^3 is designed as standalone reinforcement. The reduction in segment thickness achieved with fibres can be primarily attributed to the concrete cover requirements of 60-75 mm on both intrados and extrados rebar to ensure the durability against corrosion when designing according to Canadian code CSA A23.1:19 (2019). In contrast, when subjected to chloride exposure, corrosion in steel fibre reinforced concrete is limited to just a few millimetres from the surface, and nonetheless, does not lead to spalling cracks and is not regarded as a durability issue. The CO2 emission of the baseline and the optimized final mix designs for unit volume of concrete can be calculated using the following Equation.

$$\text{Mass of CO2eq} = \text{CO2eq Factor} \times \text{Material Quantities} \quad (1)$$

where CO2eq Factor is the amount of equivalent CO2 per unit mass (1 kg) of material from Environmental Product Declarations (EPDs). In this design, EPA 530-R-08-007 (2008), Life 365 (2010), and Hammond and Jones (2008) were used as references for CO2eq factors of cementitious materials while CO2eq factor of steel fibre was taken from the supplier's EPD. Table 1 summarizes the detail of CO2 emission calculation for the unit volume of baseline concrete mixture designs. As shown in this table, embodied carbon of the baseline and the optimized final mix designs are 601 and 387 kg CO2eq/m^3, respectively. Now considering the design optimization using a 350 mm thick segment in comparison with the baseline lining thickness of 400 mm, embodied carbon of these two options for a unit length of tunnel, and total embodied carbon are calculated and summarized in Table 2. Results of calculations indicate that in Blue Line tunnel segments, using structural design optimization, adopting a moderate SCM concrete mixture and opting for fibre reinforcement in lieu of rebar, the embodied carbon is reduced by 44%. The total carbon saving through design optimization is 13,177 tons of CO2eq.

Although Designer has successfully adopted a 70% cement replacement by ground granulated blast furnace slag in the concrete mix design in cast-in-place tunnel lining applications, such high slag content has proven to be challenging for precast segments. This is because precast applications, and especially precast tunnel segment production, require very high early-strength requirements of 13-15 MPa within 6-24 hours of casting for safe stripping from formwork. Achieving such high early-strength using high dosages of slag has posed difficulties. Nonetheless, for the upcoming projects, increasing the slag content to 40-45% are being considered for precast concrete segments. Together with use of 5% silica fume, it is expected that around 50% of cement can be replaced by SCM for future projects. This level of cement substitution holds a significant potential for carbon footprint reduction in the future.

Table 1. Embodied carbon in unit volume for the baseline and the optimized final mix designs.

		Baseline Reinforced Concrete Mixture (OPC)			Moderate SCM Concrete Mixture with Fiber		
Mix Design Components	CO_{2eq} Factor	Mass (kg/m^3)	CO_{2eq} (kg/m^3)	% Replacement by Mass	Mass (kg/m^3)	CO_{2eq} (kg/m^3)	% Replacement by Mass
Portland Cement	0.92	475.0	437		346.8	319.1	
Slag	0.1466	0.0	-	0%	104.5	15.3	22%
Fly Ash	0.093	0.0	-	0%	0	0	0%
Silica Fume	0.014	0.0	-	0%	23.8	0.3	5%
Admixtures	1.67	4.5	7.5	1%	4.5	7.5	1%
Aggregate	0.06	1430	85.6		1430	85.6	
Steel bar	1.85	80.0	148.00		-	-	
Steel Fiber	0.88	-	-		40	36.4	
		Total	601		Total	387	

Table 2. Calculation of total embodied carbon footprint of the Blue Line tunnel segmental lining for the baseline and optimized designs.

	Ring width (m)	Tunnel Length (m)	D_{out} (m)	D_{in} (m)	Ring Volume (m^3)	Total Concrete Volume (m^3)	CO_{2eq} (kg/m^3)	CO_{2eq} Per 1m of Tunnel (ton)	Total CO_{2eq} (ton)
40 cm thick Segment-OPC	1.8	4086	9.4	8.6	20.4	46212	601	6.8	27,773
35 cm thick Segment-SCM	1.8	4086	9.3	8.6	17.7	40210	387	3.8	15,568

6 CONCLUSION

The extension of the Montreal Blue Line metro toward the northeast consists of a 6-km long two-track tunnel, five new stations and seven auxiliary structures. These underground stations and auxiliary structures will be built first using mainly roadheader when practical, and drill and blast excavation method. Then, TBM will be used to excavate tunnels connecting these structures. This is the first time in North America that a Metro system is designed with a single side-by-side track tunnel without a separating centre wall. For supporting the excavation of stations and auxiliary structures two thin layers of shotcrete combined with permanent rock bolts and a sandwiched layer of spray-on waterproofing membrane are used for both initial and final liners of these underground structures resulting in a more sustainable solution and an optimized design and construction process. The final design of the project is recently completed, and the construction is planned to start at the beginning of 2024.

REFERENCES

AASHTO TP 95-14. 2014. Standard Method of Test for Surface Resistivity Indication of Concrete's Ability to Resist Chloride Ion Penetration. American Association of State Highway and Transportation Officials, Washington, DC, USA.

ACI 533.5R. 2020. Guide for Precast Concrete Tunnel Segments. American Concrete Institute (ACI). Farmington Hills, MI, USA.

ACI 544.7R. 2016. Report on Design and Construction of Fiber-Reinforced Precast Concrete Tunnel Segments. American Concrete Institute (ACI). Farmington Hills, MI, USA.

ASTM C457. 2016. Standard Test Method for Microscopical Determination of Parameters of the Air-Void System in Hardened Concrete. Annual book of ASTM standards, 4(2). Washington, DC, USA.

ASTM C1202. 2018. Standard Test Method for Electrical Indication of Concrete's Ability to Resist Chloride Ion Penetration. Annual book of ASTM standards, 4(2). Washington, DC, USA.

Bakhshi, M., and Nasri, V. 2022. Design of Montreal Metro Blue Line Extension Tunnel. North American Tunneling 2022 (NAT 2022). Philadelphia, PA, June 19-22, 2022.

CSA A23.1:19 (2019). Concrete Materials and Methods of Concrete Construction. CSA Standard. Toronto, ON, Canada.

EPA 530-R-08-007 (2008). Study on Increasing the Usage of Recovered Mineral Components in Federally Funded Projects Involving Procurement of Cement or Concrete. EPA Report to Congress, p. 225.

Hammond, G.; Jones, C. (2008), Inventory of Carbon & Energy (ICE), University of Bath version 1.6a.

Huang, L., Krigsvoll, G., Johansen, F., Liu, Y., Zhang, X. (2018). Carbon emission of global construction sector. Renewable and Sustainable Energy Reviews, Rev. 81 (Part 2), pp. 1906–1916.

IEA (2020). Energy Technology Perspectives 2020. The International Energy Agency. https://www.iea.org/reports/energy-technology-perspectives-2020.

ITA WG-2 Report No. 22. 2019. Guidelines for the design of segmental Tunnel Linings. International Tunnelling and Underground Space Association (ITA). Chatelaine, Switzerland. ISBN: 978-2-970-1242-1-4.

Life 365 (2010). Service Life Prediction Model for Reinforced Concrete Structures Exposed to Chlorides, version 2.0.

Nasri, V., Rey, A., Fortin, T. 2020. Design and Construction of the Deepest North American Underground Station - Station Édouard-Montpetit, Montreal, Canada. ITA-AITES World Tunnel Congress 2020 (WTC 2020). Kuala Lumpur, Malaysia, Septembre 11-17, 2020.

Nasri, V., De Nettancourt, X., Patret, P., Mitsch, T. 2021. Design and Construction of Réseau Express Métropolitain in Montreal. AFTES International Congress 2021, Paris, 6-8 September 2021.

Nasri, V., Bakhshi, M., Maurel, G., and Saghaee, R. (2023), Montreal Metro Blue Line Extension Tunnels and Caverns. International Tunneling Association World Tunnel Congress 2023, Athens, Greece, May 12-18, 2023, PP 1640–1647.

NFPA 130. 2017. Standard for Fixed Guideway Transit and Passenger Rail Systems. National Fire Protection Association. Quincy, MA.

NT Build 492. 1999. Chloride Migration Coefficient from Non-Steady-State Migration Experiments. Finland: NORDTEST.

Taylor, P. (2015). Blended aggregates for concrete mixture optimization, The Report of Federal Highway Administration, FHWA, Washington DC, USA, 2015.

Tunnelling for a Better Life – Yan, Celestino, Thewes & Eberhardt (Eds)
© 2024 The Author(s), ISBN 978-1-032-80042-4
Open Access: www.taylorfrancis.com, CC BY-NC-ND 4.0 license

Influence of calculation method on the design of the secondary lining

Juraj Ortuta* & Martin Bakoš
Amberg Engineering Slovakia, s.r.o., Bratislava, Slovakia

ABSTRACT: Tunnels have become among the most complex structures in the mountainous terrain of the country. Here, it is not only the complexity of the actual implementation that is at issue, but also the complexity of the actual design preparation of such a structure. The first design problems occur right at the beginning, which relates to the engineering-geological survey and the description of the environment in which the tunnel will be implemented. Another problem is the static calculation itself, which involves the values determined by the geologist, which must be unified in a certain way for the sake of idealization. The static calculation is currently carried out using the finite element method, in which it is possible to simulate the stamping process as well as the actual construction of the tunnel.

This paper will deal specifically with the effects of different calculation procedures on the sizing of the secondary lining and the influence of these procedures on the result, which mainly affects the economic aspects related to the optimization of the design.

Keywords: Calculation method, Secondary lining, Numerical modelling, Geotechnical aspect

1 INTRODUCTION

One of the signs of a modern state is also advanced infrastructure and developed transport system. The priority of every government is to connect large agglomerations using a road network, especially a motorway network. This effort has been transferred to the development of motorways across territories which are not always associated with an ideal topography. Financial problems and price increases are associated with this, mainly due to poor geological conditions and several other resulting problems, such as the delay in construction, or completing of already started construction sections.

Tunnels are among the most complex structures in the mountainous relief of the countryside. This is not only about the complexity of the implementation itself, but also about the complexity of the design preparation of such an object. The first design problems appear at the very beginning. They relate to the engineering-geological survey and the description of the environment in which the tunnel will be built. Another problem is the static calculation itself, which includes the values determined based on survey results, which must be unified in a certain way due to idealisation. Currently, the static calculation is mainly done using the Finite Element Method, where it is possible to simulate the tunnel excavation process, as well as the construction of the tunnel itself.

The paper will dedicate itself to the influence of different calculation procedures on the dimensioning of secondary lining and the influence of these procedures on the results, which affects the economic aspects associated with the optimisation of the design.

2 SEARCHING FOR CORRECT VIEWING OF ROCK MECHANICS

The development of underground construction engineering at the beginning of the 20th century, but especially after the Second World War, brought with it increased requirements for soil and rock mechanics from the point of view of finding and processing such methods of designing reinforcement for the lining of underground workings, which would be technically and economically subordinate to the practice. A significant shortcoming was the fact that rock mechanics only dealt with one side of the problem, namely the issue of rock pressure acting of the lining, while the other side, the design of reinforcement, was pushed aside. The theories of structural mechanics were developed without respect to the specifics that will appear in the case of excavation

*Corresponding author: jortuta@amberg.sk

DOI: 10.1201/9781003495505-39

support as a building structure in the underground. Therefore, the old calculation procedures, not respecting the significant differences in the behaviour of reinforcement in comparison with other building structures, persisted.

In underground construction, this problem is manifested in the still used method of analogy based on empirical experience and not exact knowledge of natural processes. This leads to the overdimensioning of structures to secure the static calculation in case of unexpected or unknown influences. Exact mathematically refi ned theories of building structures collide with shortcomings in the knowledge of the processes existing in the rock mass. This raises several ambiguities in the function of reinforcement as such, mutual influence of rock environment and reinforcement and the like.

Rock mechanics has passed through several stages of its development. In the first stage, it was the recognition of explanatory functions. That is, the effort to find theories clarifying the processes that a geotechnical engineer encounters underground. The second stage is associated with the effort to find out the causes of rock pressures and other phenomena underground. The development of the cognitive function was the cause of the development of in situ observations, the development of laboratory methods, mathematical and physical modelling. Of course, this stage is still alive and still requires a lot of work. But it also forms a transition to the third stage, the prognostic stage. This highest stage of the development of science strongly demands that science flexibly responds to changes in natural and technical conditions during the implementation of underground constructions.

3 THEORETICAL BASES

Determining the load acting on the lining of underground structures has always been one of the basic and most difficult tasks of a geotechnical engineer. In contrast to the tasks faced by a static engineer in the framework of building and building structures with relatively precisely given external loads, the role of the geotechnical engineer in underground construction is incomparably more difficult. It is not only due to the indeterminacy of the load acting on the structure, but mainly to a different concept of the function of the lining.

The current understanding of the lining as an interacting and stabilising element in the rock-lining system assumes that our knowledge of the strength and deformation properties of rocks forming the rock mass and the material of the lining meets the requirements for solving the task. But here we encounter a whole range of difficulties, even though research (mainly in situ) of rock properties from the point of view of the stability of underground workings is still developing. All of this is mainly related to the fact that the rock as a representative of the mass fulfils the role only partially, because its strength and deformation properties in most cases do not correspond to the behaviour of rock blocks. This difference between the behaviour of the element and the whole system is primarily the result of the complex genesis and the process of development of the rock mass that it passed through during its existence. These are internal as well as external influences. One of the most important is the influence of tectonic processes, which caused several discontinuities, and thus a change in its mechanical properties. These circumstances, together with other anomalous changes in stress in space and time, created a very complex system of variables which must be considered in a certain way in the static calculation. In this phase, it is usually necessary to use the experience of e geotechnical engineer and correct the numerical result with the empirical factor.

Currently, there are several theoretical solutions which are usually offered without a critical approach and without further defi ned conditions of validity, and thus the applicability of the solution. However, the experience of the person solving the problem plays a very important role here.

4 MATHEMATICAL MODELLING IN GEOTECHNICS

The rock mass through which the underground working is driven, must be examined as a system with its structure given by the number of elements and mutual relations, i.e. focus on structure and behaviour. If the examination of these regularities of the real systems is difficult or even impossible, the original system is replaced with another, simplified, a so-called model. This model can be real (modelling with equivalent materials) or abstract (mathematical). An analogy must exist between the original and the model so that the model can forecast the development of the original. The basis is to decide which model is most appropriate for the given task. Even though one of the basic characteristics of a person is the ability to create abstract models corresponding to objective reality, the mathematical formulation of the models is very complex and sometimes even impossible. It follows from this fact that no model system can contain all the properties of objective reality. Therefore, deviations between the behaviour of the original and the results obtained from the model must always be considered. To maintain the acceptable degree of adequacy between the original and the model, the model is constructed to produce approximately the same behaviour as the original. Therefore, the model must be constantly verified and supplemented, especially when new information is obtained (for example, during design or during the actual excavation).

Geotechnical problems and the necessity for mathematical modelling can be divided into four areas according to the amount and quality of information (Figure 1). For creating models, area 4, within which the maximum amount of knowledge and a lot of data

is available, is ideal. In area 3, it is customary to relay on statistical processing of data and the search for empirical correlations. Unfortunately, most geotechnical tasks are from areas 1 and 2. Models created within these areas should not become routine, as they cannot be fully verified and require a pragmatic approach. It is often better to create several simple models than one complex model. Simple models can subsequently be improved and modified.

However, it is necessary to understand that the mathematical model is only a tool for understanding and solving the model. It is necessary to perceive not only its strengths, but also its weaknesses. It is important to realise that the mathematical model is not a solution, because it only imitates reality, and even not completely exactly.

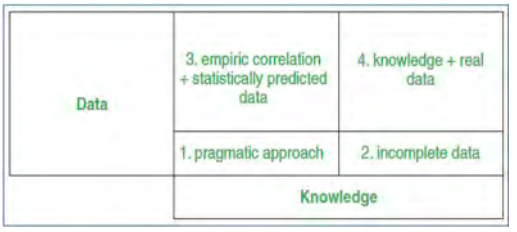

Figure 1. Representation of problem classification.

5 DEVELOPMENT OF MATHEMATICAL MODEL AND CALCULATION METHOD USED

Choice of material constitutional relationship and subsequent input of rock or soil parameters into the calculation is one of the most important and at the same time most problematic tasks in the modelling of the structure using the Finite Element Method. The main task of the material model is to describe the behaviour of the rock or soil as reliably as possible. Therefore, the correct choice of the material model is directly connected with the correct modelling (Figure 2).

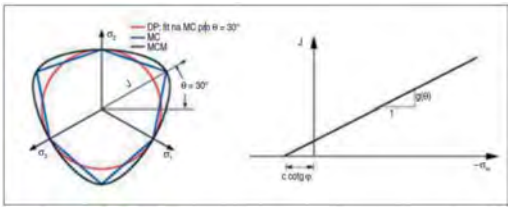

Figure 2. Projection of plasticity surfaces onto the deviator and meridian planes.

Material models can be divided into two groups, namely linear and non-linear. For the calculations of larger structures, non-linear models are the only option to minimise the uncertainty of the result, because linear soil models, for example, in the calculations of underground structures such as tunnels (Figure 3), provide completely unrealistic results.

Modelling using the Finite Element Method is a rather complex process. Most geotechnical engineers try to solve a complicated task on the first attempt. Subsequently, if the task does not converge, it is difficult to find the cause and a new model must be developed.

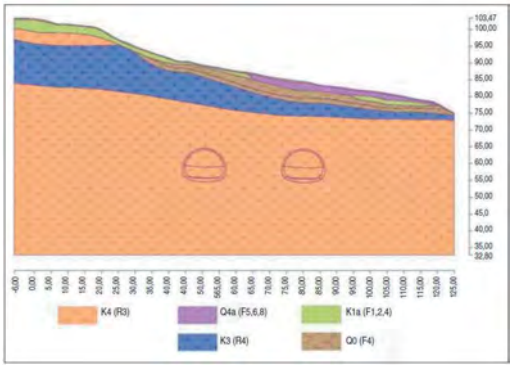

Figure 3. Double-tube tunnel model, overburden thickness in the model ranging from 20–25m, excavation width 12.6m and height 10m, axial distance between tunnel tubes 30 metres.

The modelling procedure could be summarised in several points:

1. Complete modelling of the structure.
2. Soils/rocks and contact elements are entered as elastic ones (linear models).
3. Generation of a coarse network.
4. Modelling of all calculation phases.
5. Calculation of all phases.
6. First assessments:
   - If the calculation ended with an error, the structure is probably entered incorrectly (the beam has many internal joints, the rockbolts are not fixed in the structure, etc.).
   - If the calculation ended in the last phase, it is necessary to check the deformations, and thus also the reality of the specified parameters. In the case of a plastic model of the soil, deformations are always greater than in the case of elastic one. If they are already large at this stage, adjustment is needed, and it is not necessary to approach the calculation with a non-linear model.
   - If the calculation ended without errors and the deformations correspond to reality, it is possible to proceed further.
7. Changing the linear material model to a non-linear one (Mohr-Coulomb, Drucker-Prager, Hardening Soil Model, etc.).
8. Calculation of all phases and repeated assessment according to point 6.
9. Refinement of the finite element mesh and final calculation.

When choosing the right non-linear rock model, it is necessary to have as much engineering-geological information as possible about the place where the structure will be located. It assumes that every constitutive relationship describing the material has certain limitations. Mohr-Coulomb, Drucker-Prager, as well as the modified Mohr-Coulomb model can be included in the group of models based on the classical Mohr-Coulomb fracture conditions. A common feature of these models is unlimited elastic deformation under the assumption of geostatic state of stress (Figure 2).

The second group of models consists of the Hardening Soil Model, the modified Cam Clay, the generalised Clam Clay and a hypoplastic model. These models already have a consolidation mechanism built in them, and their use is unsuitable for calculation in a location that is disturbed by cracks or fractures.

6 MODELLING OF THE CONSTRUCTION PROCEDURE AND ASSESSMENT OF THE SECONDARY LINING

As part of the study, a static calculation of a double-tube tunnel (Figure 3) was carried out using a geotechnical approach. The GEO5 2023 program, the Tunnel module was used as the software.

The tunnel overburden is 24 metres high, and the geology covers the entire rock environment. There are genetically diverse Quaternary soils there, passing into the bedrock. These are representatives of the Cretaceous rock, from marlstone to limestone.

In general, a variably thick eluvial layer characterised by gravelly to stony clay is developed on the surface of the bedrock. The thickness is affected by erosive processes in the past. The geotechnical parameters used in the calculation correspond to these assumptions.

The primary lining was modelled and, in the next stages, also the secondary lining. This was statically assessed based on internal forces determined by calculation.

The first variant represented a geotechnical approach, where the overall composition of the double-shell lined tunnel is already considered within the framework of the creation of the model.

The second variant was an assessment commonly used in practice, namely the modelling of the excavation procedure with the involvement of contact stresses, while the calculation of the primary lining was the last step of the construction phase and the calculated contact stresses were transferred to the classic static assessment of the secondary lining.

A (geotechnical approach):
(Model creation phases, the part of which is also secondary lining)

1. Determination of primary geostatic state of stress.
2. Modelling of the excavation of the top heading of the lefthand tunnel tube (LTT), installation of anchors, the activation of the excavation.
3. Installation of the top heading vault primary lining made from fresh concrete.
4. Increasing the material characteristics of hard concrete for the top heading.
5. Modelling of the excavation of the side walls, installation of anchors, the activation of excavation.
6. Installation of fresh concrete primary lining of walls.
7. Increasing the material characteristics of hard concrete for top heading.
8. Modelling of the excavation of the top heading of the righthand tunnel tube (RTT), installation of anchors, the activation of the excavation.
9. Installation of the top heading vault primary lining made from fresh concrete.
10. Increasing the material characteristics of hard concrete for top heading.
11. Modelling of the excavation of the side walls, installation of anchors, the activation of excavation.
12. Installation of fresh concrete primary lining of walls.
13. Increasing the material characteristics of hard concrete for top heading.
14. Modelling of the LTT secondary lining.
15. Modelling of the RTT secondary lining.
16. Removing anchors from the model.
17. Removing primary lining from the model, simulating its degradation.
18. Loading of the lining with temperature: summer.
19. Loading of the lining with temperature: winter.

B (static approach):
(Creation phases for the determination of contact stresses)

1. Determination of primary geostatic state of stress.
2. Modelling of the excavation of the top heading of the LTT, installation of anchors, activation of the excavation.
3. Installation of the top heading vault primary lining made from fresh concrete.
4. Increasing the material characteristics of hard concrete for the top heading.
5. Modelling of the excavation of the side walls, installation of anchors, the activation of excavation.
6. Installation of fresh concrete primary lining of walls.
7. Increasing the material characteristics of hard concrete for top heading.
8. Modelling of the excavation of the top heading of the RTT, installation of anchors, the activation of the excavation.
9. Installation of the top heading vault primary lining made from fresh concrete.
10. Increasing the material characteristics of hard concrete for top heading.

11. Modelling of the excavation of the side walls, installation of anchors, the activation of excavation
12. Installation of fresh concrete primary lining of walls.
13. Increasing the material characteristics of hard concrete for top heading

The main difference from an optimisation point of view is that in the static approach to the overall assessment, the contact stresses are fully transferred to the secondary lining. It is caused by the fact that within the model, a theoretical layer (representing the waterproofing which prevents seepage) is introduced between the primary and secondary linings, eliminating shear forces. In this way, the interaction of the primary lining is eliminated, and the secondary lining is dimensioned for the total, often even unrealistic, load.

In the geotechnical approach, this usual view was not applied to the optimisation and the waterproofing layer was omitted. It is the fact that shear forces are also transferred to the secondary lining, but by retaining the primary lining, the overall load on the secondary lining was reduced to such an extent that the overall dimensioning assessment was much more favourable.

The output of the geotechnical approach to the calculation of the secondary lining according to approach **"A"** provides the internal forces, based on which the reinforcement will be designed (Figure 4).

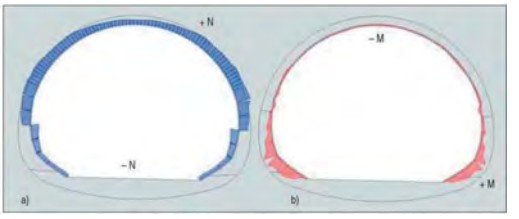

Figure 4. The resulting distribution of internal forces in the secondary lining without the influence of temperature on approach A (maximum values: a) normal force (N) 259.9kN; b) bending moment (M) 22.7kNm).

The result which is required for the design of the reinforcement in the case of a combination of geotechnical calculation and classical static calculation according to approach **"B"**, is, as mentioned above, the pattern of distribution of contact stresses (Figure 5), which will be transferred to the model of the secondary lining. Subsequently, a calculation is carried out to determine the internal forces and the reinforcement is designed (Figure 6).

In the statics practice, the method of designing and assessing structures according to limit states has been used in recent decades. Reaching one of the limit states (bearing capacity, deformation, formation of cracks) depends on many factors.

Calculations according the first group of limit states are made regarding the breaking of the critical cross-section of the lining. The critical cross-section is understood as that part of the lining in which the bearing capacity will be exhausted under a certain way of stressing. When it is assumed that the lining will be used in elasticity (the formation of plastic joints is not allowed here), the critical cross-section is determined by the overall loadbearing capacity. The calculation will therefore prove that the loadbearing capacity of the lining is sufficient when interacting with the rock mass and ensures permanent stability.

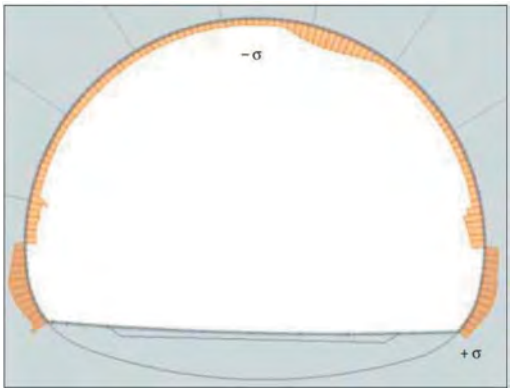

Figure 5. Distribution of calculated contact stresses for approach B (maximum value: σ = 352.8kPa).

Calculations according to the second group of limit states are made with a focus on the strain in the lining, the formation and behaviour of cracks. This is used for checking whether the deformation of the lining does not exceed the limit values which would cause problems during normal tunnel operation. By calculating the occurrence and behaviour of cracks. It is demonstrated that the utility of the tunnel will not be impaired by the permeability of the lining or the corrosion of the reinforcement.

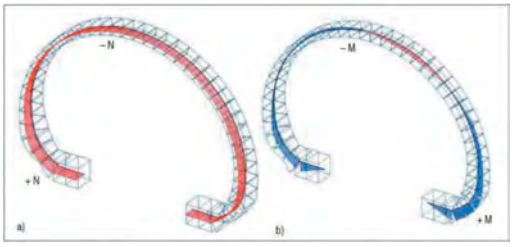

Figure 6. The resulting distribution of internal forces in the secondary lining without the influence of temperature for approach B (maximum values: a) normal force (N) 1592.48kN, b) bending moment (M) 869.24kNm).

While the assessment of the lining according to the first limit state is strictly required, the assessment of the occurrence and behaviour of cracks is usually only part of the static calculation of the lining

regarding the requirement for resistance against inflows of groundwater.

7 TWO APPROACHES

After determining/calculating the internal forces in the secondary lining, it was possible to proceed with the reinforcement design and the overall static assessment of the reinforced concrete structure.

The first differences already appeared in the magnitude of the calculated values. However, the checking on the distribution of forces and states of stress showed the correctness of the calculation and thus confirmed the theory, how important it is to take into consideration the behaviour of the rock mass from the point of view of rock mechanics and interaction with the structure being designed.

An important difference is that in the geological calculation of cross-sectional forces, the gradual degradation of the primary lining was considered already during the calculation. This degradation was introduced directly as a calculation step with gradual loss of strength characteristics. This degradation is represented in the model by the omission of the primary lining as an element and replacing it with a surface to which the material parameters are introduced. This means that when the primary lining was carried out using C20/25 concrete grade, its degradation represents a reduction of the parameters to the values of C12/16 concrete. For concrete as such, the uniaxial pressure is clearly given, and with the help of the Hoek-Brown criterion it was possible to calculate the parameters needed as an input to the calculation.

Since a double- shell tunnel is in question, it is appropriate to retain the interaction of the primary lining, which loses its function over time, but never loses it completely. In this way, it is possible to reduce the mechanical properties over time, but at the same time does not lose them completely.

The Table 1 summarises the overall assessment (due to space, it is only a part of the table).

The results show that during the further strengthening and stabilisation of the rock vault, such values of the strength characteristics were achieved where it was possible to completely omit the reinforcement and it was sufficient to use unreinforced concrete. In the most stressed places, where reinforcement was necessary, it

Table 1. Comparison of loads for both calculations.

Calculation with maintaining degraded primary lining								
Point	Quantity	Caracteristic load per m'	Maximum load per m'	Addition to char. load by prem. load	Partial coefficient	Coefficient for variable part of load	Design load per m'	
1	N (kN)	-924	-2108.4	-1184.4	1	0.9	-1989.96	assessment
	V (kN)	20.6	3.7	-16.9	1.35	1.5	2.46	without reinforcement
	M (kNm)	10.3	-58.7	-69	1.35	1.5	-89.595	
2	N (kN)	-947.9	-1899.9	-952	1	0.9	-1804.7	assessment
	V (kN)	90.2	197.9	107.7	1.35	1.5	283.32	without reinforcement
	M (kNm)	-13	-71.1	-58.1	1.35	1.5	-104.7	
3	N (kN)	-983.6	-1890.9	-927.3	1	0.9	-1798.17	assessment
	V (kN)	-100.7	-166.7	-66	1.35	1.5	-234.945	without reinforcement
	M (kNm)	-13	-71.1	-58.1	1.35	1.5	-104.7	
4	N (kN)	-939.3	-2180.4	-1241.1	1	0.9	-2056.29	assessment
	V (kN)						9.66	without reinforcement
	M (kNm)	5.8	-58.7	-64.5	1.35	1.5	-88.92	
5	N (kN)	-963	-1841	-878	1	0.9	-1753.2	assessment
	V (kN)	-82.6	-138.2	-55.6	1.35	1.5	-194.91	without reinforcement
	M (kNm)	32.1	-40.4	-72.5	1.35	1.5	-65.415	
6	N (kN)	-898.7	-1905.7	-1007	1	0.9	-1805	assessment
	V (kN)	-87.9	-189.3	-101.4	1.35	1.5	-270.765	without reinforcement
	M (kNm)	8.8	-85.2	-94	1.35	1.5	-129.12	
7	N (kN)	-951.9	-1958.9	-1007	1	0.9	-1858.2	assessment
	V (kN)	107.5	190.4	82.9	1.35	1.5	269.475	without reinforcement
	M (kNm)	-10.9	-69.3	-58.4	1.35	1.5	-102.315	
8	N (kN)	-949.5	-1974.8	-1025.3	1	0.9	-1872.27	assessment
	V (kN)	-64	-146.9	-82.9	1.35	1.5	-210.75	without reinforcement
	M (kNm)	-10.9	-69.3	-58.4	1.35	1.5	-102.315	

Calculation with applying full size contact stresses to the secondary lining								
Point	Quantity	Caracteristic load per m'	Maximum load per m'	Addition to char. load by prem. load	Partial coefficient	Coefficient for variable part of load	Design load per m'	
1	N (kN)	-926.32	-1251.17	-324.85	1	0.9	-1218.685	assessment
	V (kN)	74.86	101.07	26.21	1.35	1.5	140.376	without reinforcement
	M (kNm)	29.47	39.89	10.42	1.35	1.5	55.415	
2	N (kN)	-930.66	-1257.08	-326.42	1	0.9	-1224.438	assessment
	V (kN)	73.86	99.64	25.78	1.35	1.5	138.381	without reinforcement
	M (kNm)	17.32	38.23	20.91	1.35	1.5	54.747	
3	N (kN)	-936.27	-1264.72	-328.45	1	0.9	-1231.875	assessment
	V (kN)	72.43	97.71	25.28	1.35	1.5	135.701	without reinforcement
	M (kNm)	-8.71	36.57	45.28	1.35	1.5	56.162	
4	N (kN)	-910.42	-1229.48	-319.06	1	0.9	-1197.574	assessment
	V (kN)	158.5	214.72	56.22	1.35	1.5	298.305	without reinforcement
	M (kNm)	68.7	92.83	24.13	1.35	1.5	128.94	
5	N (kN)	-943.56	-1274.59	-331.03	1	0.9	-1241.487	assessment
	V (kN)	70.6	95.33	24.73	1.35	1.5	132.405	12/150
	M (kNm)	-17.43	37.35	54.78	1.35	1.5	58.640	
6	N (kN)	-975.07	-1316.77	-341.7	1	0.9	-1282.6	assessment
	V (kN)	-82.42	-111.8	-29.38	1.35	1.5	-155.397	12/150
	M (kNm)	147.94	200.07	52.13	1.35	1.5	277.914	
7	N (kN)	-969.23	-1308.93	-339.7	1	0.9	-1274.96	assessment
	V (kN)	-91.89	-124.34	-32.45	1.35	1.5	-172.727	12/150
	M (kNm)	168.97	228.59	59.62	1.35	1.5	317.540	
8	N (kN)	-965.49	-1303.95	-338.46	1	0.9	-1270.104	assessment
	V (kN)	-78.24	-105.94	-27.7	1.35	1.5	-147.174	16/150
	M (kNm)	187.81	254.21	66.4	1.35	1.5	353.144	

Table 2. Amount of reinforcement determined for both calculation procedures.

Geotechnical calculation of internal forces secondary lining section length 12,5 m							
pol.	ds	ks	L	length total [m] B 500B			
	mm		m	ds = 12	ds = 16	ds = 18	ds = 20
1	12	166	10.900	1809.40			
2	20	83	9.500				788.50
3	12	166	5.900	979.40			
4	18	166	3.500			581.00	
5	18	166	3.300			547.80	
6	18	166	5.600			929.60	
7	18	166	3.500			581.00	
8	10	4814	–	2108.20			
9	12	148	11.400	1687.20			
10	16	112	11.400		1276.80		
11	12	48	3.350	160.80			
12	12	48	1.000	48.00			
13	16	26	3.850		100.10		
14	16	26	1.500		39.00		
15	16	20	3.500		70.00		
16	16	20	1.500		30.00		
17	12	483	1.500	724.50			
length total			[m]	7517.50	1515.90	2639.40	788.50
unit weight			[kg/m]	0.888	1.579	1.998	2.466
weight			[kg]	6675.54	2393.61	5273.52	1944.44
total weight [kg]				16287.1			

Calculation of internal forces based on contact stresses secondary lining section length 12,5 m									
pol.	ds	ks	L	length total [m] B 500B					
	mm		m	ds = 12	ds = 16	ds = 20	ds = 25	ds = 28	beam
1	16	166	10.900		1809.40				
2	25	166	10.900				1809.40		
3									
4	20	166	3.500			581.00			
5	28	166	3.300					547.80	
6	20	166	5.600			929.60			
7	20	166	3.000			498.00			
8	12	4814	–	1660.00					
9	12	148	11.400	1687.20					
10	16	100	11.400		1140.00				
11	12	48	3.350	160.80					
12	12	48	1.000	48.00					
13	16	26	3.850		100.10				
14	16	26	1.500		39.00				
15	16	15	3.500		52.50				
16	16	15	1.500		22.50				
17	12	23	1.500	34.50					
beam	-	6	–						3300.00
length total			[m]	3590.50	3163.50	2008.60	1809.40	547.80	3300.00
unit weight			[kg/m]	0.888	1.579	2.466	3.853	4.834	1.000
weight			[kg]	3188.36	4995.17	4953.21	6971.62	2648.07	3300.00
total weight [kg]				26056.4					

was possible to proceed at least to its profile reduction (Table 2).

After drawing the reinforcement of one block in detail, it was demonstrated how important it is to know how to correctly connect geotechnics with classical statics and to find the right moment when the calculated values are transferred from the mathematical model to the final assessment of the critical cross-section.

A correctly chosen method of modelling and its subsequent interpretation usually leads to optimisation, which is associated with savings. In this case, almost 37% of the reinforcement within the block is saved and that is only because the mathematical model contained the entire construction process and considered all aspects of the rock environment together with elements that are part of the excavation and lose their function only gradually.

8 CONCLUSION

At the beginning of any static geotechnical calculation, it is necessary to ask the basic questions which modelling is associated with and on which the next procedure depends what will be modelled and what results provided by the static calculation are expected. Each such analysis has its own specifics that must be respected. It is important to be aware of this principle during the individual phases of static calculation and construction of underground workings.

As it was shown in the paper, the correct interpretation of the behaviour of rock mass leads to optimisation of the design and economic savings in the implementation of the working.

It should also be pointed out here that the usual structural element used in double skin lining is intermediate foil insulation. This, in addition to its primary function of waterproofing, prevents the transfer of shear loads from the primary to the secondary lining. In the classical calculation procedure, the contact stress is given to the model, which is calculated to form a "minimum" layer where shear is allowed to occur. In the optimization construction of the computational model, this layer is neglected, and the secondary lining was also loaded with shear forces. Thus, the secondary lining was loaded to the maximum (although in a real situation this will not be the case). However, a comparative calculation showed that the stress reduction while keeping at least a minimum function of the primary lining was such that it was worth proceeding with retaining the shear stresses, without undersizing the cross section and retaining all the necessary properties to ensure stability.

It is important to emphasise that the correct description of the mechanical properties of rock is mainly based on experience, but not least also on theoretical training, already at university. Without these fundamentals, it is impossible for a geotechnical engineer to fully understand what the nature is trying to tell him, but it is for a completely other discussion.

REFERENCES

Aldorf, J., 1999. Mechanics of underground structures. Ostrava, .

Chabroňová, J., 2012. Rock mechanics. Bratislava, ISBN 978-80-227-3685-5.

Herle, I., 2003. Fundamentals of mathematical modelling in geomechanics, Praha, .

Tunnelling for a Better Life – Yan, Celestino, Thewes & Eberhardt (Eds)
© 2024 The Author(s), ISBN 978-1-032-80042-4
Open Access: www.taylorfrancis.com, CC BY-NC-ND 4.0 license

Research on smart design and innovation of Jiaozhou bay second tunnel

Liqing Qu, Xiang Li, Minglun Tan & Hua Jiang*
Qingdao Guoxin Jiaozhou Bay Second Submarine Tunnel Co., Ltd, Qingdao, China

Mingqing Xiao & Wenhao Sun
China Railway Siyuan Survey and Design Group Co.,Ltd, Wuhan, Hubei, China

ABSTRACT: The Second Jiaozhou Bay subsea tunnel has many characteristics, such as such as super long, super large, super deep, complicated geology, difficult ventilation and smoke extraction, difficult evacuation and rescue, complicated cross-straits connection, and many restrictions on construction conditions. In order to build the second Jiaozhou Bay subsea tunnel scientifically, safely and economically, combining with the characteristics of the project, this paper studies the key issues of the ultra-long undersea tunnel such as the site-selection, the construction-method, the burial-depth, the section-arrangement, the ventilation and smoke extraction, the evacuation and rescue, and draws the following main conclusions. 1) The concept of geological route selection should be emphasized in the overall design of ultra-long undersea tunnel, which is the key to reduce construction and operation risks, control investment and guarantee the construction period. 2) It is an important content of the overall design of ultra-long undersea tunnel to compare and select the appropriate construction method and determine the reasonable burial depth according to the specific geological and construction environment conditions. 3) The second Jiaozhou Bay subsea tunnel is arranged by two main tunnels and an intermediate service tunnel. The air duct is set on the top of the main tunnel in the sea section, and the innovative ventilation scheme of section 2.5 is put forward. The service tunnel is also used as the fresh air channel, which solves the ventilation problem of the ultra-long undersea tunnel. 4) A management center is set up at the entrance of both ends of the tunnel, and an emergency management station is set up at the entrance of the service tunnel. Moreover, a complete evacuation and rescue system composed of the service tunnel, the transverse passage of people and vehicle, the evacuation stairs and longitudinal escape channel on the lower part in shield section, which can ensure the operation safety of the ultra-long undersea tunnel.

Keywords: Subsea road tunnel, The overall design scheme, Select routes according to geology, The service tunnel, Selection of construction method, Ventilation and disaster prevention

1 INTRODUCTION

As an effective way to solve the problem of traffic blocking on both sides of the sea, subsea tunnel has gradually become the main way to cross the strait (bay) with its remarkable advantages such as small impact on the marine environment, all-weather traffic, and no impact on the sea channel [1-5]. At present, the longest subsea tunnel in the world is the Seikan Tonneru subsea (railway) tunnel in Japan, which was built from 1971 to 1988, with the total length of the main tunnel of 53.9 km. After 2000, China's underwater tunnels entered a stage of rapid development. By the end of 2021, there were about 260 underwater tunnels under construction in China, covering railway, highway, subway, municipal and other fields, involving shield method, drilling and blasting method, immersed tube method and other construction methods. Qingdao Jiaozhou Bay Tunnel is the longest subsea road tunnel in operation at present in China, with a total length of 7,797 m, which was constructed by drilling and blasting method [6-8].

Second Jiaozhou Bay Subsea Tunnel is located between the existing Jiaozhou Bay Tunnel and the Jiaozhou Bay Cross-sea Bridge (Figure 1). It is an all-weather cross-sea channel connecting the main urban area of Qingdao and the New Area on the west shore. It adopts the 3-tunnel layout with "two-way six-lane main tunnels + intermediate service tunnel". The main line (the southern route) tunnel is 14,373 m long, with a design speed of 80 km/h, and its function is positioned as an urban expressway, with a lane width of 3.5 m+2×3.75 m, and net lane-height of 4.5 m. Second Jiaozhou Bay Subsea

*Corresponding author: jianghua142857@126.com

DOI: 10.1201/9781003495505-40

Tunnel is the largest subsea road tunnel in Asia at present, and it is also the longest subsea road tunnel in Asia. Its section undersea is about 10.5 km long. The condition in the sea area don't allow to set a vertical shaft there. It has many characteristics, such as super length, super size, super depth, complex geology, difficult ventilation and smoke exhaust, difficult evacuation and rescue, complex connection on both the banks, and many restrictions on construction conditions. See Table 1 for its project construction scale.

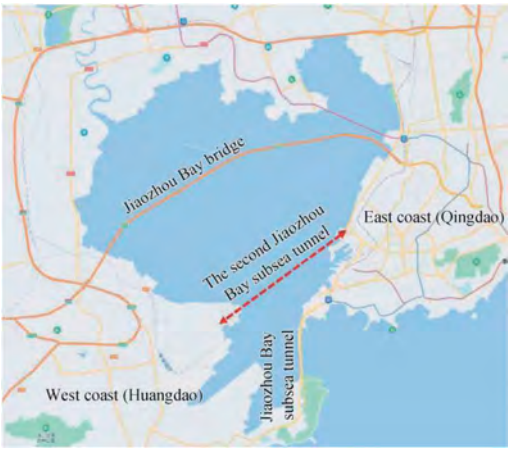

Figure 1. Location map of the second Jiaozhou Bay subsea tunnel.

Table 1. Scale of project construction.

Item	Length (m)
Southern route of main line tunnel	14,373
Northern route of main line tunnel	14,323
Service tunnel (including inclined shaft)	10,874
Ramp S1	509
Ramp S3	293
Ramp N3	557
Ramp C	452
Ramp D	468

In combination with the second submarine tunnel in Jiaozhou Bay, this paper studies the overall design scheme of the tunnel from the aspects of tunnel site selection, buried depth selection, construction method selection, service tunnel setting, tunnel cross-section layout, ventilation and smoke exhaust and evacuation rescue of super long submarine tunnel, so as to provide reference for similar engineering design.

2 PROJECT CONSTRUCTION CONDITIONS

2.1 *Marine environment*

Jiaozhou Bay is located in Qingdao City on Shandong Peninsula, which is a harbor shore with typical mountainous bedrock, and whose geomorphic pattern is obviously controlled by structure and lithology. The water depth of the bay is shallow in the northwest and deep in the southeast. The submarine terrain inclines from north to south, with a large belly and a small mouth. A deep-water trough with a depth of 30~40 m at the mouth of the bay extends into the bay in a north north-west direction. There are five waterways (east-west) in the bay from east to west that converge at the mouth of the bay and then lead to the open sea. The raised positive landforms are between the waterways, which are the main channel for the ebb and flow of the tide in Jiaozhou Bay.

2.2 *Engineering geology*

2.2.1 *Geological structure near the site*

The bedrock in Jiaozhou Bay can be generally divided into sedimentary rock distribution area and igneous rock area. The surface layer is mostly covered by Quaternary strata, and the bedrock in some low-lying areas of the seabed is exposed. There are many fault zones distributed in the areas near the site, such as Cangkou Fault, Xindao Fault, Pishikou Fault, Wanggezhuang Fault, etc. Affected by the faults, the rocks in the fault zones are mostly broken. And there are fault gouge and mylonite formed in most of the zones, and mainly broken zones and cataclastic rocks on both sides of the fault zones, forming permeable channels, which have a great impact on the tunnel construction.

2.2.2 *Characteristics of rock and soil mass in the site area*

As shown in Figure 2, on the north side of the lithologic boundary is mainly breccia sedimentary rock, with bedrock surface elevation of -50 ~ -70 m, and on the south side is mainly granite and tuff igneous rock formation, with bedrock surface elevation of -10 ~ -30 m. The Quaternary overburden above the bedrock surface mainly includes silt, silty clay, medium coarse sand, coarse sand and gravelly sand.

2.3 *Hydrogeology*

In the sea area, the permeability coefficient of rock stratum is 0.003~0.282 m/d, which is slightly ~ weakly permeable; the permeability coefficient of sand layer and breccia layer is 5~40 m/d, which is medium~strong permeability; the permeability coefficient of silt and clay layer is 0.05 ~ 1 m/d, which is weak permeability. The slightly weathered zone of the local bedrock has developed with tensile fractures. The hydrological test results show that its comprehensive permeability coefficient is up to 20 m/d, and there is a possibility of water gushing. According to the analysis results of groundwater sampling, the environmental action level of marine chloride is III-E, and the chemical corrosion level is V-E.

3 RESEARCH ON TUNNEL SITE AND ROUTE LOCATION SCHEME

3.1 *Tunnel site scheme*

According to the plan of Qingdao high-speed highway network, the Second Jiaozhou Bay Subsea Tunnel starts from Huaihe East Road on the side of Huangdao in the west and is laid toward the east under Liugongdao Road. After crossing Jiaozhou Bay, it is connected to the existing Hang'an Viaduct. The geological conditions in Jiaozhou Bay are complex. The bedrock in the sea area north of the lithological boundary shown in Figure 2 is sedimentary rock, and the igneous rock in the south. Meanwhile, the boundary divides Cangkou fault into the middle section and the south section, and according to the seismic safety evaluation, it is predicted that the fault quantity in the middle section is large. According to the geological structure and geological conditions of the site, and the connection requirements for the road network on the both banks, two tunnel site schemes of the southern route and the northern route are proposed, and the landing points of the two schemes on Huangdao bank are basically the same.

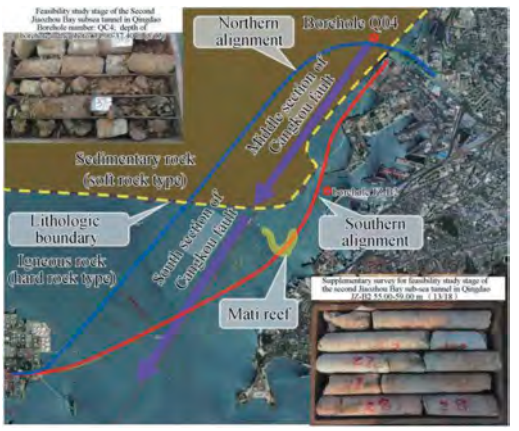

Figure 2. Tunnel address scheme in Jiaozhou Bay.

According to the southern route scheme, after entering the sea from the Huangdao shore, the tunnel obliquely crosses the southern section of the Cangkou fault, underpasses the Mati Reef, bypasses the sedimentary rock area, and lands at the freight yard on the west side of Qingdao Port. The tunnel is mostly located in the igneous rock stratum, and the minimum clear distance between the route location and the lithologic boundary is about 200 m. The northern route plan is set on the west side of Cangkou Fracture. After crossing the middle section of Cangkou Fracture at a large angle, it lands at both banks of Haibo River. The tunnel is partially located in igneous rock and partially located in sedimentary rock. It crosses the lithologic boundary twice.

3.2 *Construction scheme of tunnel in sea area section*

The longitudinal section of this scheme is shown in Figure 4. The drilling and blasting method is used for the tunnel to cross the Huangdao land area and the sea area on the Huangdao side with good integrity of surrounding rock. The shield method is used to cross the muddy soil and broken rock strata on the Qingdao side (geological survey shows that the rock mass near the Cangkou fracture is broken). At the granite section with good surrounding rock near the boundary between granite and tuff, the shield receiving chamber is built by expanding excavation to realize shield receiving.

4 STUDY ON THE OVERALL SCHEME OF TUNNEL ENGINEERING

4.1 *Deeply buried tunnel and longitudinal section scheme*

4.1.1 *Study on burial depth of the drilling and blabsting section of the tunnel in the sea area*

If the burial depth of subsea tunnel is too shallow and the bedrock cover at the top is too thin, the stability of surrounding rock is poor, the risk of collapse and water gushing during construction is high. Therefore, the cost of supporting measures is high, the construction progress is slow, and the water leakage during operation is large, but the energy consumption of vehicles during operation is reduced. When the tunnel is deeply buried, the surrounding rock is stable, but the slope increases, the fuel consumption

Figure 3. Schematic diagram of the northern and southern route scheme.

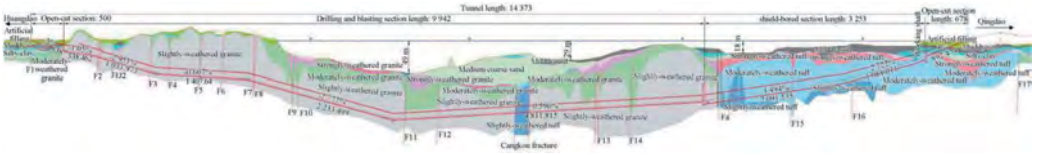

Figure 4. Longitudinal section.

of vehicles increases during the operation period, and the function of connecting lines on the two banks may not be realized. Therefore, the burial depth of the tunnel should be reasonably determined. At present, the methods for determining the burial depth of subsea tunnels at home and abroad mainly include Norwegian subsea tunnel construction experience method, Japanese minimum water inflow method and numerical calculation analysis method[9-14].

According to the Norwegian experience method, the surrounding rock quality of the granite section of the Huangdao side of this tunnel is good. The minimum thickness of the overburden rock of the tunnel in the section with shallow water depth (average 13 m) is 25 m, and that in the secction with deep water depth (maximum 49 m) is 30 m. The quality of surrounding rock in the sea area at the Qingdao end is poor, and the minimum thickness of the overburden rock of the tunnel is 40 m.

According to Japan's calculation formula of the minimum water inflow, and taking three working conditions, namely, the deepest point 49 m of the sea area, the average depth of the Huangdao sea area 20 m + the strong permeable overburden 8 m, and the water depth of the west side of the Cangkou fault 30 m + the strong permeable overburden 45 m, to calculate, the results show that the overburden thicknesses with the minimum water inflow is 25 m, 20 m, and 40 m respectively.

The FLAC 3D software is used to calculate the displacement and bending moment of the supported vault in the initial stage under different overburden rock thicknesses of the tunnel roof, and analyze the displacement of the vault and relationship between bending moment of lining and the overburden thickness, to determine the minimum overburden thickness of the tunnel. According to the calculation results, the minimum overburden thickness of the tunnel in the section with the thick Quaternary overburden or strongly weathered layer should be 30 m.

According to the above analysis results and combined with the construction experience of Jiaozhou Bay subsea tunnel in Qingdao, the design principle of overburden rock thickness of this project is comprehensively determined as follows:

① When the total thickness of water depth + weak overburden is greater than 30 m, the minimum overburden rock thickness of the tunnel is 30 m;

② When the total thickness of water depth + weak overburden is less than 30 m, the minimum overburden thickness of the tunnel is 25 m;

③ Reliable technical measures shall be taken to ensure construction safety in the section with insufficient overburden rock thickness.

4.1.2 *Longitudinal section scheme for the sea area section*

According to Code for Design of Urban Underground Road Engineering [15], the maximum allowable longitudinal slope of the main line tunnel of this project is 5%, and the general value is 3%. Due to the limitation of the minimum overburden soil thickness for shield at the sea entering point at the Qingdao end, the longitudinal slope of 4% is adopted locally, and the maximum longitudinal slope of other sections is less than 3%. According to the above-mentioned design principle of overburden rock thickness, combined with the burial depth of bedrock surface in the sea area section, two longitutinal section schemes are studied. According to Scheme 1, the lowest point is located in the middle of the drilling and blasting section in the sea area (shown by the purple dotted line in Figure 5), and the lowest point elevation of the route is -112 m. According to Scheme 2, the lowest point of the longitutinal section of the route moves about 1.0 km to the west based on Scheme 1, and the lowest point elevation is about -115 m.

The elevation of the lowest points of the two schemes and the minimum overburden rock thickness of the tunnel are basically the same. Considering that the tunnel is excavated from west to east in the drilling and blasting section during the construction period, the section about 5 km from the lowest point to the east in Scheme 2 is constructed down the slope, and the drainage pipeline leaking during the operation period is short (about 1.0 km shorter than that in Scheme 1), so Scheme 2 for the longitudinal section is recommended after comparison for selection.

Considering that reducing the burial depth of the lowest point can improve the operating conditions and reduce the fuel consumption of vehicles, on the basis of Scheme 2, the schemes of reducing the minimum overburden rock thickness by 10 m and by 20 m respectively compared with the recommended scheme are studied. According to the research results [16] of the influence of automobile road slope on the fuel consumption of 100 kilometers, the oil consumption after the tunnel burial depth is reduced is estimated. Assuming that the traffic volume is 80,000 vehicles/day, when the tunnel burial depth is reduced by 10 meters, the annual fuel consumption can be reduced by about RMB 14 million yuan. According

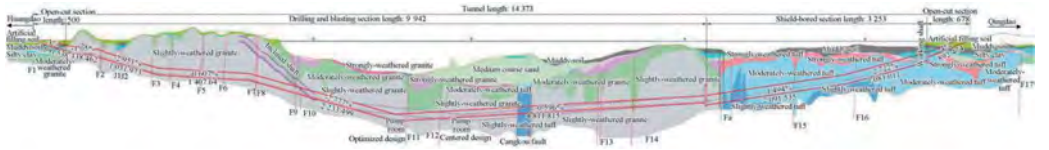

Figure 5. Longitudinal section of the tunnel.

to the 100-year cycle calculation, assuming that the yield is 5%, the corresponding present value is RMB 278 million yuan. When the burial depth of the tunnel is reduced by 20 m, the present value corresponding to the reduced fuel consumption cost is RMB 556 million yuan. However, when the overburden rock thickness decreases by 10 m and by 20 m, due to the relative deterioration of surrounding rock, the cost of strengthening the supporting structure and grouting for water blocking will increase, and the construction period will be extended. According to calculation, the project cost will increase by about RMB 400 million yuan and RMB 600 million yuan respectively (the impacted range is about 800 m), and the construction period will be extended by 6 months and 12 months respectively. It can be seen that it is unreasonable to further reduce the overburden rock thickness in terms of life-cycle cost, construction safety and duration.

5 VENTILATION AND SMOKE EXHAUST SCHEME

5.1 *Operation ventilation standard*

Considering the long distance, large construction scale and long construction period of this tunnel, values for the ventilation is taken according to PIARC2019 standard, and the ventilation standard of 2 times /h is added, as shown in Table 2.

Table 2. Ventilation and health standards.

Traffic Conditions	Vehicle Speed (km/h)	CO Concentration (cm^3/m^3)	Dust Concentration (m-1)	NO_2 Concentration (cm^3/m^3)
Normal	80~50	70	0.005	1
Normal	40~30	70	0.007	1
Whole course block	20	70	0.007	1
Local block (2 km)	10	70	0.007	1
Closing the tunnel		200	0.012	——

Usually, the tunnel is dominated by buses and small- and medium-sized trucks. Under special conditions, large trucks can pass. Because the tunnel building length exceeds 14km, in order to improve the fire safety of tunnel, it is designed according to 50MW for the fire scale of large trucks, and the critical wind speed is 2.4 ~ 3.1 m/s.

5.2 *Operation ventilation scheme*

Due to the requirements of environmental assessment and navigation in Jiaozhou Bay, no ventilation shaft is set in the sea. After a ventilation shaft is set in the offshore position in the Huangdao land section, the length of the ventilation section of the sea area section tunnel is about 10.5 km, which is the road tunnel with the longest ventilation section in China. Combined with the actual situation and cross-section layout of this tunnel, three ventilation schemes are put forward:

Scheme 1: A vertical shaft is set up on the Huangdao shore for ventilation in two sections.

Scheme 2: 2.5-section ventilation mode of setting a vertical shaft on Huangdao bank: the vertical shaft on the Huangdao shore is used for air supply and exhaust, and the top air duct of the service tunnel and the main line tunnel in the sea area section is used to supplement air supply and exhaust.

Scheme 3: 2.5-section ventilation mode of setting a vertical shaft on the Huangdao shore for the northern route: A centralized purification machine room is set in the sea for the southern route, while the air supply and exhaust are supplemented by the air ducts at the top of the service tunnel and the main line tunnel in the sea area.

The ventilation mode of Scheme 2 is shown in Figure 7. In this scheme, a air supply and exhaust shaft is only set up on the Huangdao shore. The whole length of the tunnel is divided into two large ventilation sections. The sea area section is divided into two small ventilation sections by using the service tunnel (fresh air duct) and the top air duct (exhaust duct) of the main line tunnel, the ventilation mode is between 2 sections and 3 sections, so it is called 2.5-section ventilation.

The comparison results of various ventilation schemes are shown in Table 3.

All three schemes can achieve the ventilation effect of the design standard, in which the installed power and operating energy consumption are considered. 2.5-section ventilation is recommended.

5.3 *Fire smoke exhaust scheme*

According to the current "Code for Fire Protection Design of Buildings" [17], the tunnel with a length greater than 3,000 m shall adopt sectional longitudinal or key smoke exhaust methods. The tunnel

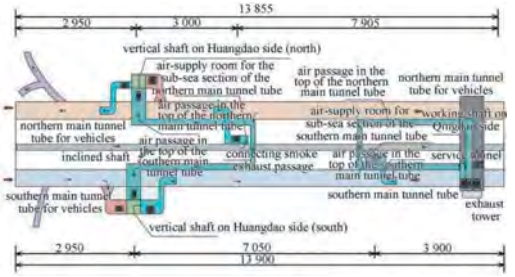

Figure 6. Ventilation mode of section 2.5 with a shaft on the shore of Huangdao.

Table 3. Comprehensive comparison table of operation ventilation scheme.

Comparison Item	Scheme 1:	Scheme 2:	Scheme 3:
Ventilation section length	2-section ventilation	2.5-section ventilation	2.5-section ventilation for northern route + purification for southern route
Maximum wind speed of 20 km/h	2,950 m, 10,950 m	2,950 m, 7,950 m, 3,000 m	2,950 m, 7,950 m, 3,000 m
Total installed power	4.6 m/s	3.6 m/s	4.6 m/s
100-year operating expenses	11,400 kW	8,314 kW	9,644 kW
100-years equipment cost	RMB0.96bn	RMB0.85bn	RMB0.89bn
Others	simple	an air supply room set in the sea, and complicated control	an air-supply machinroom and a purification machine room set in the sea, and complicated control

lengths of land sections for the northern and southern are 2,973,m and 3,146,m respectively. After comprehensive comparison for selection of the longitudinal smoke exhaust and key smoke exhaust in the land area from the aspects of smoke exhaust effect, people evacuation and equipment configuration, it is recommended to adopt the longitudinal smoke exhaust scheme, and while two smoke exhaust ports for the northern route is added so that the length of the longitudinal smoke exhaust section does not exceed 3,000 m.

The tunnel in the sea area section between the ventilation shafts on both shores of the river is about 10.5 km long. In order to solve the problem of smoke exhaust in the super-long ventilation section, three schemes, namely, the sectional longitudinal smoke exhaust scheme (Scheme 1) with the top smoke exhaust duct + the connecting flue (that is, the flue connecting the north and south tunnels with a distance of about 3,500 m); the sectional longitudinal smoke exhaust scheme (Scheme 2) of setting the smoke exhaust duct combined with the service tunnel; and the key smoke exhaust scheme (Scheme 3), are studied. The advantages and disadvantages of the three schemes are shown in Table 4.

All three schemes can meet the requirements of Code for Fire Protection Design of Buildings. Considering that this tunnel is a super-long subsea tunnel in a city, there are as many as 350 smoke outlets in the

Table 4. Selection table of comprehensive comparison of smoke extraction schemes in sea section.

Comparison Item	Scheme 1	Scheme 2	Scheme 3
Smoke exhaust effect	The longest spread range of smoke reaches 3 km, and the smoke exhaust effect is poor when a fire occurs in the blocking condition.	The longest spread range of smoke reaches 3 km, and the smoke exhaust effect is poor when a fire occurs in the blocking condition.	Theoretically, the upstream and downstream smoke shall be controlled above the clear height, but the requirement for the air tightness of the smoke exhaust system is high.
Smoke-influenced range	large	large	small
People evacuation	One-way evacuation from upstream of fire source	One-way evacuation from upstream of fire source	Evacuation from both upstream and downstream of fire source.
Exhausted smoke volume	Greater than 300 m^3/s	Greater than 300 m^3/s	Theoretically, greater than 240 m^3/s
Civil work investment	A smoke exhaust duct is added at the top of the sea area section, which will increase the civil work cost by RMB 130 million yuan.	The service tunnel section is increased by 25 m2, which will increase the civil work cost by RMB 350 million yuan.	Same as Scheme 1
Number of smoke outlets	Totally there are 6 groups of smoke outlets	Totally there are 6 groups of smoke outlets	Totally there are 370 groups of smoke outlets.
Control model	In case of fire, a group of smoke outlets downstream of the fire source shall be opened, and the control mode is simple.	In case of fire, a group of smoke outlets downstream of the fire source shall be opened, and the control mode is simple.	In case of fire, six groups of smoke outlets downstream of the fire source shall be opened, with many mode combinations and complicated control.
Reliability	high	high	low

conventional key smoke exhaust mode (the spacing between smoke outlets is 60 m), which requires extremely high air-outlet sealing and installation, and the control in case of fire is complicated and the reliability is low. The longitudinal smoke exhaust control is simple, which is applicable for tunnels with infrequent traffic congestion. The line connection condition at both ends of this project is good, and a perfect traffic monitoring system is set there. A toll station is set at Huangdao entrance and a inspection booth is set at Qingdao entrance, which can avoid frequent traffic jams. Moreover, the sectional longitudinal smoke exhaust scheme of the top smoke exhaust duct + connecting flue does not need to increase the section of the service tunnel, which can reduce the civil work cost by RMB 220 million yuan compared with Scheme 2. After comprehensive comparison, it is recommended to adopt sectional longitudinal smoke exhaust scheme of the top smoke exhaust duct + connecting flue (Scheme 1), as shown in Figure 7.

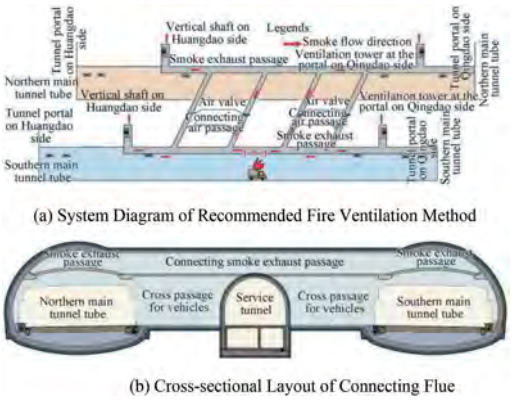

Figure 7. Schematic diagram of fire smoke extraction scheme.

6 CONCLUSIONS AND SUGGESTIONS

By studying the key problems in the overall design of Second Jiaozhou Bay Subsea Tunnel Project, the following conclusions are obtained:

(1) For subsea tunnels under complex geological conditions, a reasonable tunnel site is very important for the project construction. Through detailed comparison for selection of schemes of southern and northern routes, Second Jiaozhou Bay Subsea Tunnel Project highlighted the geological concept of route selection, based on which the southern route scheme with relatively good engineering geology was selected, which is of great significance for controlling project investment, reducing project risk and ensuring construction period.

(2) Super-long tunnels may cross various geological units or strata with very different properties. It is one of the important contents of the overall design to compare and choose the construction methods, select the appropriate construction methods by section and determine the reasonable burrial depth in combination with the specific geological and construction environment conditions. According to the specific construction conditions, the Second Jiaozhou Bay Subsea Tunnel adopted the construction methods of drilling and blasting, shield and cut-and-cover excavation. Through the research of reasonable buried depth, taking into account the tunnel construction and operation conditions, the tunnel longitutinal section layout was reasonably determined.

(3) In extra-long subsea tunnel, a service tunnel generally has the functions of advanced leading pilot tunnels, auxiliary tunnels for construction, operation maintenance, and emergency rescue. The layout of two main tunnels plus one intermediate service tunnel is adopted in the sea area section in Second Jiaozhou Bay Subsea Tunnel, and an air duct is set at the top of the main line tunnel. According to the requirements of this project, the 2.5-section ventilation technology is innovatively put forward, and the service tunnel is used as the fresh air passage, which solves the ventilation problem of the 10.5km-long ventilation section of the tunnel without increasing the investment in civil work, and can provide reference for similar tunnel projects in the future.

(4) A perfect evacuation and rescue system is formed through making full use of the management centers set at the openings at both ends of the tunnel, the emergency management station at the Huangdao end, the service tunnel, the pedestrian and vehicle cross-passages, the evacuation stairs in the shield section and the longitutinal evacuation passages at the lower floor, so as to ensure the operation safety of the super-long subsea tunnel in case of traffic accidents and fire conditions.

REFERENCES

[1] Editorial Department of China Journal of Highway and Transport. Review on China's Traffic Tunnel Engineering Research: 2022[J]. China J. Highw. Transp., 2022, 35(4): 1–40.

[2] XIAO Mingqing. Representative Projects and Development Trend of Underwater Shield Tunnels in China[J]. Tunnel Construction, 2018, 38(03): 360–367.

[3] QIAN Qihu, CHEN Jian. Analysis of Tunneling Risks of Large-Diameter Shield and Thoughts on Its Challenges[J]. Tunnel Construction, 2021,41 (02):157–164.

[4] DAI Hongbo, JI Yuguo. Statistical Analysis of Chinese Large-Diameter Shield Tunnel and State-of-Art and Prospective of Comprehensive Technologies[J]. Tunnel Construction, 2022, 42(05): 757–783.

[5] CHEN Jianqin, FENG Xiaoyan, WEI Huai, et al. Statistics on Underwater Tunnels in China[J]. Tunnel Construction, 2021, 41(03): 483–516.
[6] ZHOU Shuming. Design and Construction of Jiaozhou Bay Subsea Tunnel in Qingdao[J]. Tunnel Construction, 2013, 33(01): 38–44.
[7] TANG Xiongjun, XIAO Mingqing, JIAO Qizhu, MAO Sheng, et al. Investigation of Overall Design and Key Technology of Jintang Subsea Tunnel of Ningbo-Zhoushan Railway[J]. Railway Standard Design, 2021, 65(10): 20–25.
[8] LI Zhe, JIANG Yuan, JIANG Lijie, et al. Research on Development Strategy of Tunnel and Underground Construction Technology and Equipment in China[J]. Tunnel Construction, 2021, 41(10): 1717–1732.
[9] T S Dahl, Nilsen B. Stability and rock cover of hard rack subsea tunnels[J]. Tunneling and Underground Technology, 1994(2): 151–158.
[10] Arid Palmstrom. The challenge of subsea tunneling[J]. Tunneling and Underground Technology, 1994(2): 145–150.
[11] WEI Liyuan. Study on Stability of Surrounding Rocks and Selection of Overburden Thickness for Underwater Tunnels[D]. Shandong University, 2010.
[12] QIAN Qihu. Challenges in Construction of Underwater Tunnels and Countermeasures[J]. Tunnel Construction, 2014, 34(06): 503–507.
[13] LV Ming, Grφv E, Nilsen B, et al. Experience of Norwegian Subsea Tunneling[J]. Chinese Journal of Rock Mechanics and Engineering, 2005(23): 4219–4225.
[14] Ministry of Housing and Urban-Rural Development of the People's Republic of China, General Administration of Quality Supervision, Inspection and Quarantine of the People's Republic of China. Code for Fire Protection Design of Buildings: GB 50016-2014[S]. Beijing: China Planning Press, 2018.

Tunnelling for a Better Life – Yan, Celestino, Thewes & Eberhardt (Eds)
© 2024 The Author(s), ISBN 978-1-032-80042-4
Open Access: www.taylorfrancis.com, CC BY-NC-ND 4.0 license

Application of a confinement-dependent spalling criterion for tunnels in highly stressed brittle rock

Masoud Rahjoo
The University of British Columbia, Vancouver, Canada
AECOM, Burnaby, Canada

Erik Eberhardt*
The University of British Columbia, Vancouver, Canada

ABSTRACT: Tunnelling experiences in highly stressed brittle rock suggest that commonly used numerical tools, and more specifically the rock strength criteria available, need to be revised for robust prediction and design where stress fracturing is encountered (e.g., spalling, strainbursting). Missing is the recognition that brittle failure is sensitive to confinement, exhibiting extensional fracturing under low confinement and shear fracturing under high confinement. Conventional rock strength criteria such as Mohr-Coulomb and Hoek-Brown were developed based on experiences and observations dominated by shear failure of weak or heavily fractured rock masses. This paper reviews the influence of confinement on spalling and the application of a confinement-dependent extensional fracturing criterion with a shear transition derived for brittle rock failure. The criterion is developed for use with 3-D numerical stress analyses and is validated against results assessing the location and depth of failure for spalling observed during the advance of a deep tunnel in massive rock. Comparisons using conventional rock strength criteria and their adaptation for brittle rock failure show that these can either significantly under- or over-estimate the depth and extent of failure if they do not adequately capture the susceptibility to spalling initiation under low confinement at the tunnel boundary or the limiting influence of confinement on suppressing stress fracturing as failure extends into the rock mass away from the tunnel boundary.

Keywords: Tunnelling, High stresses, Spalling, Depth of brittle failure, Confinement dependency

1 INTRODUCTION

Tunnels in highly-stressed massive rock are susceptible to brittle fracturing, resulting in behaviours ranging from progressive non-violent spalling and dilative bulking to sudden and violent strainbursting. These conditions have pushed engineers and designers to the limits of conventional empirical and numerical design capabilities. Of issue is that the rock strength criteria most commonly used, Mohr-Coulomb and Hoek-Brown, were developed based on experiences and observations in lower-stress environments where instability was dominated by shear failure of weak and heavily jointed or faulted rock masses (Kaiser & Kim, 2008). A common misconception in the use of these criteria is that brittle fracturing is associated with tensile stresses and shear fracturing is associated with compressive stresses. This gave rise to the use of shear-based criterion with tension cut-offs (e.g., Mohr-Coulomb, see Labuz & Zang, 2012; Hoek-Brown, see Hoek & Martin, 2014).

However, evidence from laboratory and field observations shows that brittle failure occurs through extensional fracturing under low confinement where the rock is tangentially compressed (Eberhardt et al., 2016). Also missing in existing strength criteria is the recognition that brittle failure is sensitive to confinement, exhibiting extensional fracturing under low confinement and shear fracturing under high confinement (Figure 1a). The challenge for robust design where brittle failure conditions are expected reduces to the development of a strength criterion that is capable of assessing both extensional and shear failure.

Efforts to account for extensional fracturing include Martin et al.'s (1999) use of the Hoek-Brown criterion with brittle parameters (m = 0, s = 0.11) and Diederichs' (2002) multi-linear envelope separating spalling from shear failure as a function of confinement. The latter is commonly referred to as the "s-shaped"

*Corresponding author: erik@eoas.ubc.ca

DOI: 10.1201/9781003495505-41

criterion, and its application makes use of the Hoek-Brown yield criterion to simulate crack initiation and a subsequent "residual strength" threshold to reflect the transition to shear (Diederichs et al., 2010).

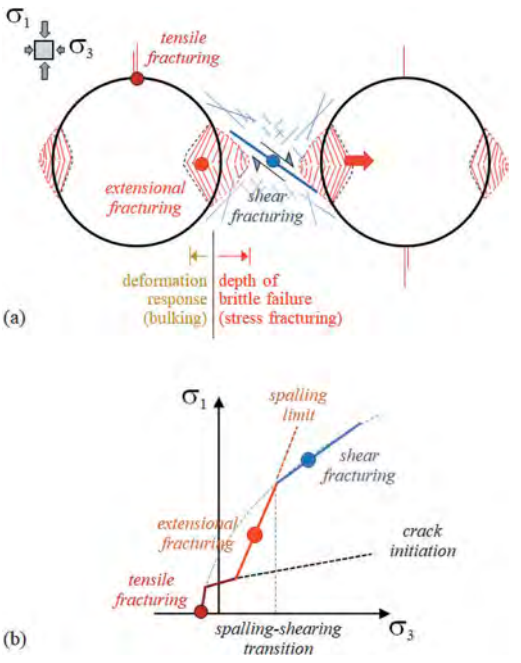

Figure 1. (a) Illustration of low-confinement dominated by extensile brittle fracturing (spalling) and high-confinement dominated by shearing. (b) Conceptualization of spalling criteria (after Diederichs, 2002).

This paper applies these principles, for which we present the application of a confinement-dependent extensional and shear fracturing criterion derived for brittle rock failure. First, we provide a short review of the influence of confinement on brittle fracturing and efforts to develop a corresponding criterion. We next present the criterion together with its parameterization and then results assessing the location and depth of failure for spalling observed during the advance of the Mine-By Experiment (MBE) tunnel at the Atomic Energy of Canada Ltd.'s Underground Research Laboratory (AECL-URL). Results are compared against the use of the conventional Hoek-Brown criterion and its use with brittle failure parameters. The findings demonstrate that the consideration of confinement on stress fracturing is critical for evaluating the location and depth of spalling around a tunnel in highly stressed brittle rock.

2 CONFINEMENT-DEPENDENT SPALLING CRITERIA

2.1 *Extensional fracturing and spalling initiation*

In a review of existing strength criteria and their use for brittle rock, Rahjoo (2019) noted that the use of Mohr-Coulomb and Hoek-Brown limits the consideration of extensional fracturing to tensile loading conditions that transit to shear fracturing right at $\sigma_3 = 0$. In reality, however, extensional fracturing also occurs in compression under low confinement. At the laboratory scale, this has been characterized in terms of the crack initiation and crack damage stress thresholds (Bieniawski, 1967; Martin, 1997; Eberhardt et al., 1998). At the tunnel scale, Read & Martin (1996) thoroughly investigated the damage zone and spalling that developed in the massive granitic rock around the AECL-URL's MBE tunnel. They characterized the spalling mechanism as initial cohesion loss followed by the mobilization of friction. Martin (1997) suggested that the crack initiation threshold would be an appropriate criterion for determining the extent of a damage zone. He proposed the following criterion for crack initiation, σ_{ci}:

$$\sigma_1 - \sigma_3 \geq \sigma_{ci} \tag{1}$$

Comparing this with the Hoek-Brown criterion (Eqn. 2), where σ_c is the uniaxial compressive strength, Martin et al. (1999) suggested that it can represent crack initiation if using the brittle parameters, m = 0 and s = 0.11 (Eqn. 3):

$$\sigma_1 = \sigma_3 + \sqrt{m\sigma_c + s\sigma_c^2} \tag{2}$$

$$\sigma_1 = \sigma_3 + \sqrt{0.11\sigma_c^2} \tag{3}$$

As a design parameter, σ_{ci} marks the stress at which new cracks initiate and begin to propagate (Diederichs et al., 2010), and near the excavation boundary where confining stresses are low and crack propagation can easily transition to unstable crack propagation and spalling, it represents the lower bound long-term in-situ rock strength under which spalling initiates (Martin, 1997; Diederichs et al., 2004).

2.2 *Confinement and spalling limit*

Wawersik & Fairhurst (1970) noted that adding moderate confining pressures could eliminate the development of spalling in laboratory compression testing. The importance of confinement in limiting crack propagation and spalling has been demonstrated experimentally and numerically by various authors, as summarized by Eberhardt et al. (2016). Read et al. (1998) considered an upper limit for the effect of low confinement on unstable cracking potential based on the ratio of minimum to maximum principal stresses:

$$\frac{\sigma_3}{\sigma_1} \leq R_{spalling}, \; R_{spalling} = 0.05 - 0.1 \tag{4}$$

This ratio defines a limit for stress states under which microcracks can easily grow, coalescing to form macro-scale fractures. It also defines a transition from extensional fracturing to shearing. The combination of the crack initiation criterion and spalling limit (Eqns. 1 and 4) defines a dual criterion that characterises the favourable stress state for spalling. This is reflected in Diederichs (2002, 2007), who proposed a composite in-situ strength envelope for brittle rock, with segments corresponding to a lower bound strength of crack/damage initiation under low confinement, an upper bound strength involving shear under high confinement, and a transition zone between these related to the spalling limit (Figure 1b).

2.3 *Formulation and implementation*

Rahjoo (2019) extended the work of Read et al. (1998) and Diederichs (2002, 2007) to develop and formulate an integrated 3-D confinement-dependent strength criterion that captures both extensional and shear fracturing, and their sensitivity to σ_3 as well as σ_2, both of which act as confinement in 3-D. However, as a first step towards validation, as well as the equally important step of parameterization, a simplified version is presented here aligned with Read et al. (1998) utilizing Eqns. (1) and (4).

These are implemented using the 3-D boundary element program EX3 by Rocscience. Although the use of the boundary element method restricts the analysis to elastic stresses and, therefore, does not account for the effect of stress redistribution as failure progresses, this is generally acceptable for brittle failure in massive rock (Martin et al., 1999). Of specific interest to the analysis of spalling failure, the computational efficiency of the boundary element method allows for a more straightforward implementation of a user-defined spalling criterion and visualization of the 3-D spalling that develops, which requires a very fine mesh discretization and stress grid.

To implement, we need to define a mathematical formulation that uniquely gives each of the zones defined by extensional stress fracturing (i.e., spalling) and shearing under compression. These are as follows:

$$crack\ initiation:\ \sigma_1 \geq N_{ci}\sigma_3 + \sigma_{ci} \tag{5}$$

$$spalling\ limit: \sigma_1 \geq N_{sp}\sigma_3 \tag{6}$$

$$spalling/shearing\ transition:\ \sigma_3 \leq \sigma_{ss} \tag{7}$$

$$compressive\ stress:\ \sigma_3 \geq 0 \tag{8}$$

In the above, N_{ci} is the crack initiation gradient, N_{sp} is the spalling limit gradient, and σ_{ss} is the spalling to shear transition stress. These are discussed in more detail later in the paper when describing the parameterization of the model.

Next, we need a summation method. It is noted that different numerical analysis software have different functionality with respect to allowing user-defined criteria. In EX3, filtering of the different zones can be achieved by applying a log10 function. This is implemented as:

$$log10(\sigma_1 - N_{ci}\sigma_3 - \sigma_{ci} + 1) \times log10\big(\sigma_1 - N_{sp}\sigma_3 + 1\big) \times log10(\sigma_3 + 1) \tag{9}$$

$$log10(\sigma_1 - N_{ci}\sigma_3 - \sigma_{ci} + 1) \times log10(-\sigma_3 + \sigma_{ss} + 1) \times log10(\sigma_3 + 1) \tag{10}$$

Eqn. (9) makes use of the spalling limit and Eqn. (10) uses the spalling/shearing transition limit. In the 3-D stress analysis program Map3D, implementation is similar except a sign function can be used instead of log10.

3 VALIDATION CASE

3.1 *AECL-URL Mine-By Experiment*

The Mine-by Experiment (MBE) tunnel at the AECL Underground Research Laboratory in Pinawa, Manitoba, Canada, provides a pioneering case study on the progressive failure and spalling of brittle rock. The MBE was carried out at a depth of 420 m in massive, sparsely fractured granite (Martin, 1997). The 3.5 m-diameter circular tunnel was excavated in 50 increments over its 46 m length using perimeter drilling and hydraulic rock splitters to break out the rock. Sixteen triaxial accelerometers were installed around the MBE tunnel to record crack initiation via microseismic events (Read & Martin, 1996). Figure 2a shows the V-shaped notch that formed by stress-induced extensional fracturing at the tangentially compressed but laterally low-confined zones in the roof and floor of the tunnel.

Figure 2b shows the progressive development of the notch as the tunnel face was advanced. The data showed that the microseismicity belonging to each advance of the face did not extend further than 2 times the tunnel diameter behind the tunnel face (Read & Martin, 1996). Thus, any spalling that occurred farther than several meters behind the face (e.g., the difference between profiles 3 and 5 in Figure 2b) might be related to either time-dependent fracturing or stress change caused by time-dependent formation of the V-shaped notch. As such, profile 3 was used for the validation exercise.

Figure 2c and d show the calculated stress paths by Read & Martin (1996) for a point in the tunnel

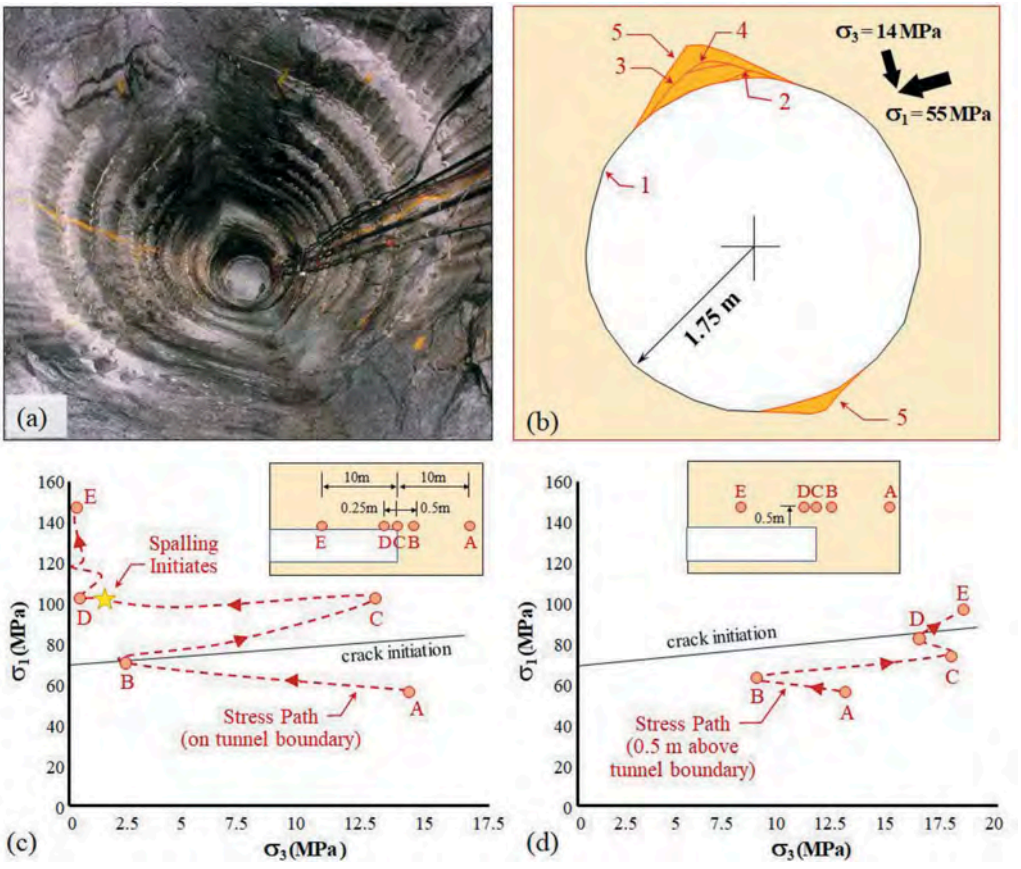

Figure 2. (a) MBE tunnel showing the final shape of the spalling breakout in the crown and invert of the tunnel. (b) Sequence of the progressive development of the spalling geometry. Profiles 1 to 4 were the surveyed boundaries when the face was 0.24 m, 0.5 m, 3.5 m and 10 m ahead of the section, respectively. Profile 5 represents the long-term depth of spalling after several months when the tunnel excavation was completed and the section was 24 m behind the tunnel face. (c) Stress path for a point located just above the tunnel boundary at the maximum compressive stress concentration in the roof. The first visual signs of spalling failure are observed just past point D, 0.5 m behind the tunnel face. (d) Stress path for a point located 0.5 m above the tunnel roof, showing the influence of increased confinement on suppressing the development of crack initiation and spalling. After Read & Martin, 1996).

roof at 0 and 0.5 m above the tunnel boundary, respectively. These show that the stress path exceeds the crack initiation stress just ahead of the tunnel face, with visible spalling initiating and developing 0.5 m behind the face (Figure 2c). Deeper within the rock mass above the tunnel boundary (Figure 2d), the crack-initiation stress is exceeded after the tunnel face is well beyond the surveyed section, but confinement acts to suppress and stop the depth of spalling.

Thus, the validation exercise for the confinement-dependent spalling criterion developed incorporates three targets: (i) the distance from the face where spalling initiates (0.5 m); (ii) the depth of spalling (0.25 m for profile 3; see Figure 2b); and (iii) the lateral extent of spalling around the perimeter (as shown in Figure 2b).

3.2 *Model parameterization*

The 3-D in-situ stress input was assigned as reported by Read & Martin (1996): σ_1 = 55 MPa, σ_2 = 48 MPa and σ_3 = 14 MPa, with σ_1 rotated 19 degrees from horizontal (see Figure 2b). The properties of the LdB pink granite were reported as having a σ_c of 213 MPa and Hoek-Brown properties of m = 30.8 and s =1. Figure 3a shows the predicted distance from the face, depth and extent of spalling if using the assessed Hoek-Brown properties for the MBE. These show that spalling would not be expected if peak strength values are used. It has been well established that peak strength values are not appropriate for brittle failure and spalling analyses as the failure process initiates well below this at the crack initiation stress (Martin, 1997). Figure 3b shows the results of using only the crack initiation criterion in

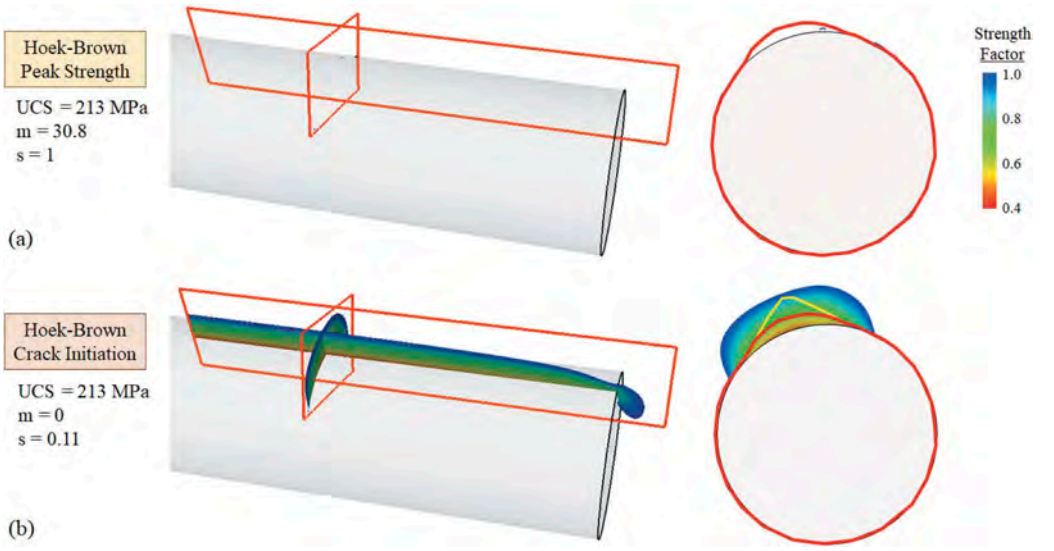

Figure 3. 3-D stress and spalling analysis results assuming: (a) Hoek-Brown peak strength values for LdB pink granite, and (b) Hoek-Brown crack initiation values (m=0, s 0.11). Shown are the predicted extent and depth of spalling (strength factor < 1) in the tunnel roof along a longitudinal plane and those in a cross-sectional plane 6 m from the tunnel face. The cross-sectional plane corresponds with the advance from profile 3 to 4 (see Figure 2b), and shows the measured extent and depth of spalling outlined in red.

Eqn. (1). Without a spalling limit (or a spalling/shearing transition limit) to account for the suppressing influence of confinement, the results overpredict the distance from the face where spalling begins, indicating spalling at the face, as well as the extent and depth of spalling.

Proceeding with the parameterization of the confinement-dependent spalling criterion implemented using Eqns. (9) and (10), four input parameters are required: σ_{ci}, N_{ci}, N_{sp} and σ_{ss}. Eberhardt et al. (1998) determined a σ_{ci} of 0.4 to 0.5 σ_c from acoustic emission and strain measurements performed on LdB pink granite. Hoek & Martin (2014) more generally report a range of 0.4 to 0.6 σ_c, for a range of brittle rock types. A value of 0.5 σ_c was used for σ_{ci} in this study. The crack initiation gradient, N_{ci}, generally ranges from 1 to 1.5 where lower values are associated with more brittle rock dominated by crack opening (i.e., low friction) and higher values correspond to conditions with more bulking where friction develops between the spalled pieces. It can be calculated based on the Mohr-Coulomb relationship:

$$N_{ci} = (1 + \sin\phi)/(1 - \sin\phi) \qquad (11)$$

where ϕ is the internal friction angle. The value of N_{ci} = 1 is used here for the case of the MBE as the spalling observed did not result in significant dilation and bulking. The spalling gradient, N_{sp}, ranges from 10 to 15 as per Diederichs (2002) and Diederichs et al. (2004). A value of 13 was used in this study, but it was found to be non-sensitive relative to the spalling to shear transition stress, σ_{ss}. The value for σ_{ss} was determined from triaxial test data for LdB pink granite by analysing the peak strength, volumetric dilation (i.e., crack damage threshold), and plastic volumetric dilation, also referred to as the crack volumetric strain by Martin (1997). Figure 4a shows that the values derived have increasing trends with increasing confinement but reach a plateau beyond a σ_3 of 15 MPa (Figure 4b). As such, σ_{ss} was set at 15 MPa (see Rahjoo, 2019 for the full procedure).

4 SPALLING ANALYSIS RESULTS

Figures 5-7 present the results of the 3-D stress and spalling analysis using the confinement-dependent spalling criterion, implemented using Eqn. (10). Figure 5 shows the results in perspective view, highlighting the depth of spalling along a longitudinal profile. This shows the notch starting to develop 0.5 m behind the tunnel face, matching the visual observations by Read & Martin (1996). Figure 6 shows why the notch does not form right at the tunnel face, as the σ_3 confinement is higher at the face where the stresses rotate around the edges of the tunnel boundary. The importance of 3-D stress rotation with respect to spalling as a tunnel face advances is discussed in Eberhardt (2001). Thus, the results in Figures 5 and 6 confirm that the confinement-dependent spalling criteria correctly predicts the first validation check involving the distance from the face where spalling initiates (i.e., 0.5 m).

Figure 7 confirms that the confinement-dependent spalling criteria predict the other two validation

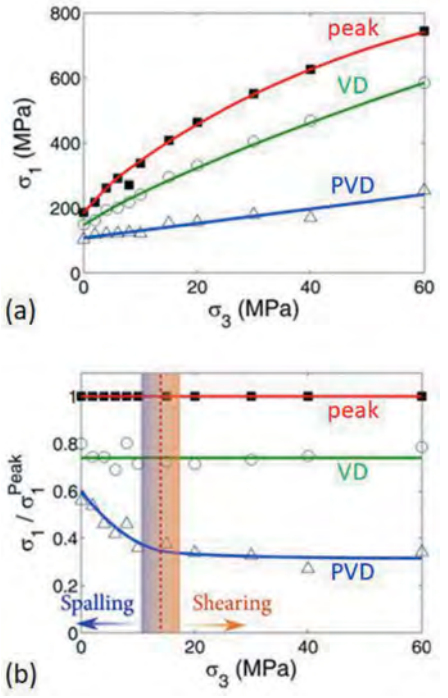

Figure 4. (a) Strength of LdB Pink Granite at peak strength (peak - red), volumetric dilation (VD - green) and plastic volumetric dilation (PVD - blue) under confining stresses ranging from 0 to 60 MPa. The data is derived from Lau & Gorski (1991). (b) Determination of the spalling to shearing transition using the ratio of σ_1/σ_1^{peak}, calculated here as σ_3 = 15 MPa for LdB pink granite. See Rahjoo (2019) for the full procedure.

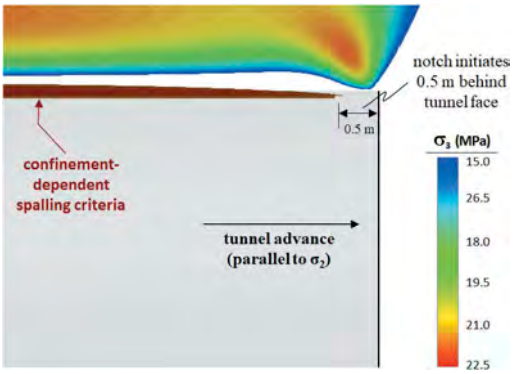

Figure 6. 3-D stress and spalling analysis results plotted on a longitudinal profile showing the distance from the tunnel face where spalling initiates (at 0.5 m). The model-predicted spalling is shown in dark red and is plotted together with the σ_3 confinement contours.

checks: that the depth of spalling several meters behind the tunnel face, beyond its influence on the redistributed stresses, is 0.25 m (agreeing with profile 3 in Figure 2b as reported by Read & Martin, 1996); and the lateral extent of spalling around the perimeter at the same location matches the measured tunnel profile (again, agreeing with that shown in Figure 2b). As shown by the σ_3 contours in Figure 7, the depth of spalling is limited by the confinement levels when they reach the spalling to shearing transition stress of 15 MPa. It is worth noting that using Eqn. (9), a similar result is obtained but with a slightly shallower depth for the notch.

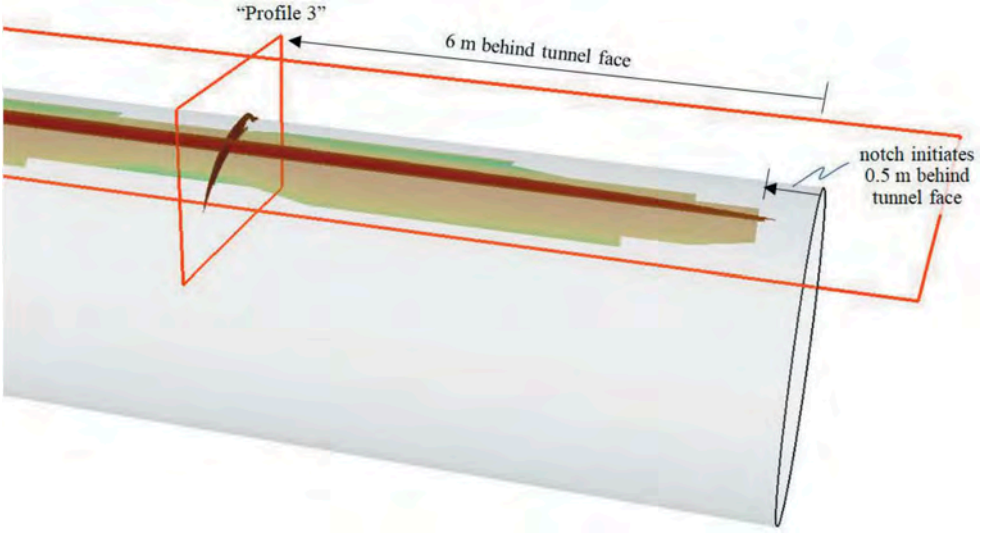

Figure 5. 3-D stress and spalling analysis results applying the confinement-dependent spalling criterion, implemented via Eqn. (10) with inputs: σ_{ci} = 106.5 MPa, N_{ci} = 1, N_{sp} = 13 and σ_{ss} = 15 MPa. The locations where spalling is modelled as developing are indicated by the coloured areas. The extent of spalling on the tunnel boundary is in light brown to green. In dark red is the depth of spalling as projected on a longitudinal plane along the tunnel roof, as well as a cross-sectional plane 6 m from the tunnel face, corresponding with the advance from profile 3 to 4 (see Figure 2b). The results for these two projection planes, outlined in bright red, are provided in Figures 6 and 7, respectively.

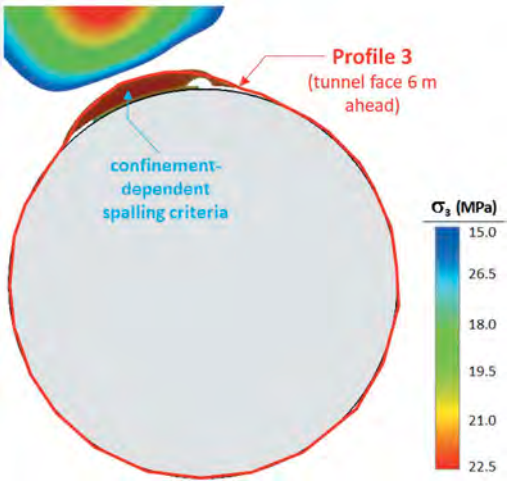

Figure 7. 3-D stress and spalling analysis results plotted on a cross-sectional plane coinciding with "Profile 3" from Read & Martin (1996), including the measured tunnel profile outlined in bright red (see also Figure 2b). Plotted is the model-predicted extent and depth of spalling in dark red together with the σ_3 confinement contours.

5 CONCLUSIONS

Determining the depth of stress fracturing and spalling is essential for designing a deep tunnel in massive brittle rock. However, doing so requires numerical tools and rock strength criteria developed for brittle failure. Commonly used rock strength criteria, such as Mohr-Coulomb and Hoek-Brown, were developed based on experiences and observations dominated by shear failure and need to be revised for robust prediction and design where spalling is encountered. Missing is the recognition that brittle failure develops under high compressive stresses, for example, those tangential to the tunnel boundary, and is sensitive to confinement, exhibiting extensional fracturing under low confinement (near the tunnel boundary) and being limited by higher confinements (deeper into the rock mass) that suppress the spalling process.

A formulation was presented applying crack initiation and spalling limit principles in the form of a confinement-dependent spalling criterion developed for brittle rock failure. The criterion can easily be implemented into any numerical modelling software that allows user-defined criteria. When properly parameterized, it can provide the potential location, depth and lateral extent of spalling as required for excavation and ground support design, and pillar dimensioning. This was demonstrated using a 3-D boundary-element stress analysis against the measured location and depth of spalling failure observed during the advance of the MBE tunnel at the AECL-URL.

The validation exercise demonstrated that the criterion could correctly predict the distance from the face where spalling was initiated, the depth of spalling, and the lateral extent of spalling around the tunnel perimeter. Results were compared against the use of the Hoek-Brown criterion using peak strength values and brittle fracture strength parameters. These were found to significantly under- and over-predict the observed spalling, respectively. Our findings thus demonstrate that the consideration of the role of confinement on extensional fracturing is critical for evaluating the location and depth of spalling around a tunnel in highly stressed brittle rock.

ACKNOWLEDGMENTS

This work was made possible through funding provided by the International Caving Research Network (ICaRN), Rio Tinto Centre for Underground Mine Construction (RTC-UMC), Natural Sciences and Engineering Research Council of Canada (NSERC) and Mitacs. The authors would also like to thank Rocscience for providing access to EX3 through their educational and research support program.

REFERENCES

Bieniawski, Z.T., 1967. Mechanism of brittle rock fracture: Part II - Experimental studies. Int. J. Rock Mech. Min. Sci. 4(4), 407–423.

Diederichs, M.S., 2002 Stress induced damage accumulation and implications for hard rock engineering. In: Hammah, R. et al. (Eds.), NARMS-TAC 2002: Mining and Tunnelling Innovation and Opportunity, Toronto. University of Toronto Press, pp. 3–12.

Diederichs, M.S., 2007. Mechanistic interpretation and practical application of damage and spalling prediction criteria for deep tunnelling. Can. Geotech. J. 44(9), 1082–1116.

Diederichs, M.S., Carter, T., Martin, D., 2010. Practical rock spall predictions in tunnels. In: Eberhardt, E. (Ed.): Tunnel Vision Towards 2020: Proceedings, World Tunnel Congress 2010. Tunnelling Association of Canada, Vancouver.

Diederichs, M.S., Kaiser, P.K., Eberhardt, E., 2004. Damage initiation and propagation in hard rock tunnelling and the influence of near-face stress rotation. Int. J. Rock Mech. Min. Sci. 41(5), 785–812.

Eberhardt, E., 2001. Numerical modeling of three-dimensional stress rotation ahead of an advancing tunnel face. Int. J. Rock Mech. Min. Sci. 38(4), 499–518.

Eberhardt, E., Diederichs, M.S., Rahjoo, M., 2016. Pre-peak brittle fracture damage. In: Feng, X-T. (Ed.), Rock Mechanics and Engineering, Volume 1: Principles. CRC Press/Balkema, Leiden, pp. 623–657.

Eberhardt, E., Stead, D., Stimpson, B., Read, R.S., 1998. Identifying crack initiation and propagation thresholds in brittle rock. Can. Geotech. J. 35(2), 222–233.

Hoek, E., Martin, C.D., 2014. Fracture initiation and propagation in intact rock – A review. J. Rock Mech. Geotech. Eng. 6(4), 287–300.

Kaiser, P.K., Kim, B-H., 2008. Rock mechanics challenges in underground construction and mining. In: Potvin, Y.

et al. (Eds.), Proceedings of the First Southern Hemisphere International Rock Mechanics Symposium. Australian Centre for Geomechanics, Perth, pp. 23–38.

Labuz, J.F., Zang, A., 2012. ISRM suggested method for rock failure criteria: Mohr–Coulomb failure criterion. Rock Mech. Rock Eng. 45(6), 975–979.

Lau, J.S.O., Gorski, B., 1991. The Post-Failure Behaviour of the Lac Du Bonnet Pink Granite. Mining Research Laboratories, Ottawa, ON, Canada.

Martin, C.D., 1997. The effect of cohesion loss and stress path on brittle rock strength. Can. Geotech. J. 34(5), 698–725.

Martin, C.D., Kaiser, P.K., McCreath, D.R., 1999. Hoek-Brown parameters for predicting the depth of brittle failure around tunnels. Can. Geotech. J. 36(1), 136–151.

Rahjoo, M., 2019. Directional and 3-D confinement-dependent fracturing, strength and dilation mobilization in brittle rocks. PhD Thesis, Geological Engineering, The University of British Columbia, Vancouver, BC, Canada.

Read, R.S., Chandler, N.A., Dzik, E.J., 1998. In situ strength criteria for tunnel design in highly-stressed rocks masses. Int. J. Rock Mech. Min. Sci. & Geomech. Abstr. 35(3), 261–278.

Read, R.S., Martin, C.D., 1996. Technical summary of AECL's Mine-by Experiment, Phase 1: excavation response. Atomic Energy of Canada Limited Report, Pinawa, MB, Canada, AECL–11311.

Wawersik, W.R., Fairhurst, C., 1970. A study of brittle rock fracture in laboratory compression experiments. Int. J. Rock Mech. Min. Sci. 7(5), 561–575.

Tunnelling for a Better Life – Yan, Celestino, Thewes & Eberhardt (Eds)
© 2024 The Author(s), ISBN 978-1-032-80042-4
Open Access: www.taylorfrancis.com, CC BY-NC-ND 4.0 license

Practical considerations of shale swelling impact on underground structures liner design for Ontario Line transit project in Toronto, Canada

Masoud Rahjoo*
AECOM, Burnaby, British Columbia, Canada

Verya Nasri
AECOM, New York, New York, USA

ABSTRACT: The swelling-prone Georgian Bay Shale in the Greater Toronto Area, Canada, will host several underground transit projects. Swelling may apply excessive pressure on the support system of the underground structures. Investigating the short-term and long-term swelling impacts on the initial and final liners, respectively, is critical for a successful design. Driven by osmosis and diffusion processes, swelling in shale initiates only when all the prerequisites are available; namely, the outward salinity difference exists, the water is accessible, and the 3D confining stresses applied to a volume of shale are below the suppression stress threshold. This paper reviews the fundamental swelling behaviour characteristics, explains the numerical modelling approach, and discusses the practical considerations of swelling impacts on liner design.

Keywords: Swelling, Time-dependent Behaviour, Suppression Stress, 3D confinement, PLAXIS, RS2

1 INTRODUCTION

Several underground transit projects are being designed and constructed in the Greater Toronto Area, Canada. The host rock is the Georgian Bay Shale, which has swelling characteristics. Swelling, also known as Time-Dependent Deformation (TDD), may apply excessive pressure on the support system of the underground structures. Therefore, it is critical to investigate swelling impacts on the initial and final liners. This paper reviews the fundamental swelling behaviour characteristics, explains the numerical modelling approach selected for the Ontario Line South (OLS) project, and discusses the practical considerations of swelling impacts on liner design.

2 SWELLING CHARACTERISTICS OF GEORGIAN BAY SHALE

The swelling phenomenon in the Georgian Bay Shale is driven by osmosis and diffusion processes (Lee and Lo, 1993). Swelling initiates if all three prerequisites are available, including the existence of outward salinity difference, accessibility of water, and lack of 3D confinement. Rahjoo et al. (2023) provided a comprehensive summary of these prerequisites and the scenarios for swelling initiation and suppression, as shown in Figure 1.

Figure 1. Prerequisites for swelling initiation in shaly rocks in southern Ontario, Canada (Rahjoo et al., 2023).

In Figure 1, the Swelling condition is noted by S, and the three No-Swelling (NS) Conditions are

*Corresponding author: masoud.rahjoo@aecom.com

DOI: 10.1201/9781003495505-42

noted by NS Salinity (NS S), NS Water (NS W), and NS Confinement (NS C). No-Swelling Type Salinity (NS S) is when there is no or negligible outward salinity difference between the pore and ambient fluids. So, even with a reduction of 3D confinement and extra access to water, the swelling would not initiate. As soon as an outward salinity difference is introduced, swelling will occur. No-Swelling Type Water (NS W) is when there is limited access to water. So, even with the reduction of 3D confinement and the potential existence of an outward salinity gradient, swelling would not initiate. As soon as water is accessible, swelling may occur. No-Swelling Type Confinement (NS C) is when the 3D stress state confines the shale. So, even with extra access to fresh water, the swelling would not initiate. As soon as stress is relieved, swelling will occur. The stress relief should happen in a 3D sense, and swelling would not arise unless the 3D confining stresses applied to a volume of shale drop below a suppression stress threshold.

Swelling behaviour, upon its initiation, has two aspects of time-dependency and confinement-dependency, as will be discussed next. Before getting to them, we should remember that shales are bedded and exhibit anisotropy (commonly transverse isotropy). The anisotropy is an inherent characteristic of the time-dependency and confinement-dependency of shales.

2.1 *Time-dependency*

As shown in Figure 2, swelling strain increases linearly over the logarithm of time. The swelling strain and its rate are higher perpendicular to the bedding (black curve) compared to tangential (parallel) to the bedding (red curve). This effect is the direct consequence of the inherent transverse isotropy of shales. The swelling rate decreases over time, and the maximum is expected to occur in the early days and months after swelling initiation rather than in years. Still, swelling strain can increase to several times the 1-year swelling strain over the lifetime of the tunnelling projects.

There are some constraints on swelling from chemical and mechanical perspectives. From a chemical perspective, the driving force behind swelling is the salinity gradient. So, the process naturally stops when there is no salinity difference between the water in the pores and the ambient water. The salinity difference is mainly affected by the shale composite and accessibility to fresh water over time. From a mechanical perspective, swelling results in the elongation of the sample. So, the shale sample eventually cracks (most probably tangential to the beddings) after reaching a specific extensional strain. The chemical and mechanical constraints point to an upper-bound swelling strain over time despite the high swelling rates at the early stages of swelling initiation.

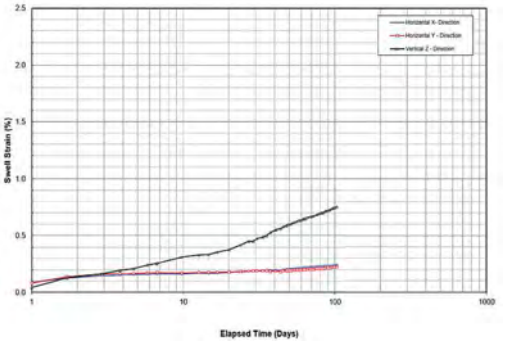

Figure 2. A linear increase of swelling strain over logarithm of time. the example belongs to a free swell test. (Rahjoo et al., 2023). note the higher swelling strain and swelling rate perpendicular to the bedding (black curve) compared to tangential to the bedding (red curve).

2.2 *3D confinement-dependency*

Swelling strain decreases linearly over the logarithm of confinement. Confinement, whether the stress is applied perpendicular or tangential to the bedding, suppresses swelling, i.e., suppression is a multi-directional phenomenon. Again, this is the direct consequence of the inherent transverse isotropy of shales and the fact that swelling is a volumetric increase of pores size.

The multi-directional suppression effect of confinement is critical from a practical perspective: the rock around the underground excavation experiences radial unconfinement but tangential compression/tension. The radial stress reaches the original in-situ stress within a specific distance from the excavation perimeter. The potential swelling is limited to the rock surrounding the excavation. The induced tangential compression, however, acts to suppress swelling. Therefore, the swelling would only initiate in the laterally deconfined rock surrounding the excavation if the rock is sufficiently confined tangentially. The swelling is more expressed in the rock that is unconfined both radially and tangentially, especially considering the ease of access to fresh water via the opened fractures. Please recall that swelling would not occur even in the tension zones if water accessibility and salinity gradient prerequisites are not met.

2.3 *Design considerations*

The possibility of the scenarios that could initiate swelling should be carefully assessed in the early stages of the design of new excavations. The success of the swelling mitigation strategy is directly associated with suppressing the prerequisites, i.e., eliminating or diminishing any of the outward salinity gradient, 3D unconfinement, or water accessibility. The interaction between the in-situ conditions and construction sequences should be assessed to determine how the three swelling mitigation means can be used effectively and successfully. The cost-benefit evaluation of swelling suppression methods may lead to the allowance of a controlled swelling stage during construction as

a mitigation strategy, which is very cost-effective in many projects. It is only after the exhaustion of all possible means of mitigation strategies that the designer moves to control swelling by enhancing the support system's structural performance.

3 NUMERICAL MODELLING OF SWELLING BEHAVIOUR

3.1 *Swelling model selection*

For the OLS project, we decided to use PLAXIS2D to investigate swelling and its impacts on lining design. Among the swelling models available in PLAXIS2D, we selected the Anagnostou model (1993), as it considers the 3D confinement-dependency of swelling behaviour. A similar model exists in RS2. The time-dependency and confinement-dependency of this model are as follows:

$$(\in)_p = \left(\in_\sigma^\infty\right)_p \left(1 - e^{-A_0 t}\right) \tag{1}$$

$$(\in)_t = \left(\in_\sigma^\infty\right)_t \left(1 - e^{-A_0 t}\right) \tag{2}$$

$$\left(\in_\sigma^\infty\right)_p = -k_{qp} \log\left(f(\sigma)/f\left(\sigma_{\boldsymbol{sup}}\right)\right) \tag{3}$$

$$\left(\in_\sigma^\infty\right)_t = -k_{qt} \log\left(f(\sigma)/f\left(\sigma_{\boldsymbol{sup}}\right)\right) \tag{4}$$

$$f(\sigma) = \sigma_p k_{pt} + (\sigma_{t1} + \sigma_{t2}) \tag{5}$$

$$f\left(\sigma_{\boldsymbol{sup}}\right) = \sigma_{q0p} k_{pt} + 2\sigma_{q0t} \tag{6}$$

$$k_{pt} = k_{qp}/k_{qt} \tag{7}$$

In which, $\left(\in_\sigma^\infty\right)_p, A_0, k_{qp}, k_{qt}, \sigma_{q0p}$ and σ_{q0t} are the input parameters. σ_p, σ_{t1}, and σ_{t2} are the magnitudes of stress perpendicular and tangential to the bedding. Equation (6) enforces an implication to the Anagnostou model that a relation exists between $\sigma_p^{u-\sup}$ and $\sigma_t^{u-\sup}$ (the values of the uniaxial stress that suppresses swelling perpendicular and tangential to bedding, respectively) as:

$$\sigma_p^{u-\sup} k_{pt} = \sigma_t^{u-\sup} = \sigma_{q0p} k_{pt} + 2\sigma_{q0t} \tag{8}$$

In Anagnostou model, the ratio k_{pt} defines the ratio of $(\in)_p/(\in)_t$, $\left(\in_\sigma^\infty\right)_p/\left(\in_\sigma^\infty\right)_t$, and $\sigma_t^{u-\sup}/\sigma_p^{u-\sup}$.

3.2 *Swelling model restrictions*

The Anagnostou model comes with a few restrictions. The first restriction is that σ_{q0p} and σ_{q0t} can take any value if they satisfy Equation (8). For the sake of simplicity, we select $\sigma_{q0t} = 0$, so that Equation (8) reduces to:

$$\sigma_p^{u-\sup} k_{pt} = \sigma_t^{u-\sup} = \sigma_{q0p} k_{pt} \tag{9}$$

Therefore:

$$\sigma_{q0p} = \sigma_p^{u-\sup} = \sigma_t^{u-\sup}/k_{pt} \tag{10}$$

The second restriction is that the model uses an exponential function for time-dependency per Equations (1) and (2). The exponential functions come with upper bound values of $\left(\in_\sigma^\infty\right)_p$ and $\left(\in_\sigma^\infty\right)_t$. More importantly, the strain rate of the exponential function is quite different from the observed logarithmic trend of swelling (see Figure 2).

The abovementioned three restrictions are carefully considered during model calibration. The first restriction concerning an upper bound value for swelling strain $\left(\in_\sigma^\infty\right)_p$ is addressed by using a new logarithmic function to find the upper bound value for the project's lifetime. The new logarithmic function is defined as (Rahjoo et al. 2023):

$$\in = m_1 \log(m_2 t + 1) \tag{11}$$

$$m_1 = SP_\sigma / \log(100 - \bar{t}) - 1 \tag{12}$$

$$m_2 = (90 - \bar{t})/10\bar{t} \tag{13}$$

SP_σ is the Swelling Potential defined as the difference between strains measured 100 and 10 days after initiation:

$$SP_\sigma = \in_{100} - \in_0 \tag{14}$$

$\bar{t} > 0$ is the time at which we have $\in = SP_\sigma$, and has an upper bound of $\bar{t} < 90$.

100-120 years is a typical lifetime for ordinary tunnelling projects in North America. This lifetime gives an upper bound for swelling strain $\left(\in_\sigma^\infty\right)_p$ that should be considered in numerical modelling.

The second restriction concerning the strain rate of the exponential function is addressed by dividing the modelling timeframe to two periods, one for short-term swelling and one for long-term swelling, each section having its own A_0 and $\left(\in_\sigma^\infty\right)_p$. For a given $\in_\sigma^\infty, A_0$ controls the slope of the swelling curve (i.e., swelling strain versus time) as we have $\partial \in / \partial t = \in_\sigma^\infty A_0$. Also, A_0 controls the time at which 0.95% of $\in_\sigma^\infty$ is reached, i.e., time at $0.95 \in_\sigma^\infty \approx 3/A_0$. The swelling rate is essential for the first period as it has its highest rate right after initiation. Construction sequencing and the lag between excavation and support installation are critical factors for the selection of an appropriate end date for the first modelling period. Therefore, the input parameters for this two-period model should be selected according to the construction specifications of each project. In other words, for a similar host rock, the input parameters used for an SEM cavern could differ from those used for a TBM tunnel due to the difference in their construction specifications. As a result, knowledge of construction specifications is a prerequisite for model calibration.

4 NUMERICAL INVESTIGATION FOR OLS PROJECT

The Ontario Line Southern Civil, Stations and Tunnel project is a design-build-finance contract for the southern portion of the Ontario Line, from Exhibition/Ontario Place to the Don Yard portal. The OLS project includes seven stations (one above-ground and six underground) and a six-kilometre tunnel from Exhibition to Don Yard portal. The project layout is shown in Figure 3.

Figure 3. Ontario Line Southern Civil, Stations & Tunnel Project.

4.1 *Model geometry and excavation sequencing*

The geometry and stratigraphy of an SEM cavern model for the OLS Project is shown in Figure 4. The phases defined in the model are listed in Table 1. The model is symmetric, and the snapshot is cropped in Figure 4. Note that the geometry and design presented here belong to the tender design and will be updated for construction design stage.

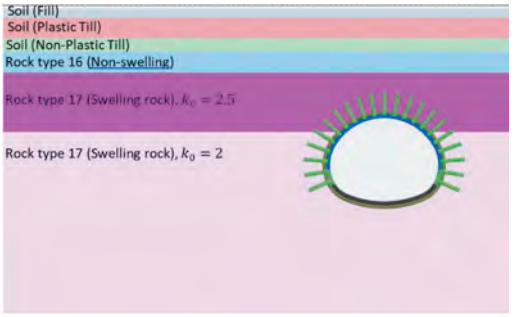

Figure 4. Geometry and stratigraphy of the SEM cavern model.

4.2 *Swelling model calibration*

The calibrated input parameters are listed in Table 2. Remember that $\sigma_{q0t} = 0$, and $k_{pt} = k_{qp}/k_{qt} = 3$. The calibrated time-dependent behaviour is shown in Figure 5.

4.3 *Swelling initiation in numerical model*

Above a certain depth, the in-situ stress level sits below the suppression stress criterion given as (Equations (5) and (6)):

$$f(\sigma) = f(\sigma_{sup}) \tag{15}$$

To differentiate and eliminate the swelling that had already happened in geological time in the naturally low-confined over-burden, a historic swelling phase is considered in the numerical model (see Table 1), after which displacements are set to zero before the excavation phases. As a result, the naturally low-confined zone consumes a portion of its swelling potential in this historic swelling phase.

Table 1. Modelling Phases in PLAXIS2D.

Phase	Relaxation/ TTD
In-situ Stress State Initialization	-
Historic Swelling Initialization	TDD for 100 Days
Excavation of the Top Heading,	Top Heading: 60%
Shotcrete and bolts	Top Heading: 100%
Short-term TDD	TDD for 30 Days
Excavation of the Top Bench	Top Bench: 70%
Shotcrete and bolts	Top Bench: 100%
Short-term TDD	TDD for 30 Days
Excavation of the Bottom Bench	Bottom Bench: 80%
Shotcrete and bolts	Bottom Bench: 100%
Short-term TDD	TDD for 30 Days
Excavation of the Invert	Invert: 100%
Shotcrete	-
Short-term TDD	TDD for 10 Days
Long-term TDD	TDD for 80 Days
Installation of Final Lining	
Long-term TDD	TDD for 120 Days
Long-term TDD Until 120 Years	TDD for 43700 Days

Table 2. Calibrated input parameters for PLAXIS2D model.

TDD Period	k_{qp}	k_{qt}	σ_{q0p}	A_0	$\left(\in_{\sigma}^{\infty}\right)_p$
1st Period (Day 0 to 100)	0.01071	0.00357	800	0.06	0.018
2nd Period (Day 100 to 44000)	0.02142	0.00714	800	0.001	0.036

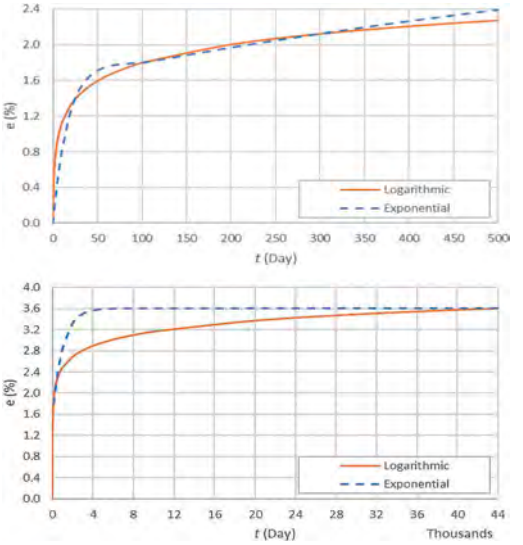

Figure 5. The modelled exponential vs lab-based logarithmic time-dependency of swelling strain perpendicular to bedding.

4.4 *Lining specifications*

Based on the load requirements of the permanent lining, the lining thickness increases from 40 cm at the crown to 80 cm at the invert. In the model, three lining sections are considered with 40cm, 60cm, and 80 cm thicknesses. The permanent lining properties are listed in Table 3.

Table 3. Properties of the permanent lining.

Support Element	Properties	
Lining (Cast-in-place)	PLAXIS Element	Plate, elastic
	Drainage type	Non-porous
	Young's modulus E	33 E+06 kN/m^2
	Poisson's ratio v	0.2
	density	25 kN/m^3
Top Section	thickness	0.4 m
Middle Section	thickness	0.6 m
Bottom Section	thickness	0.8 m

4.5 *Results and discussion*

The numerical analysis shows that the magnitudes of total displacements at the springlines and invert are more significant than at the crown. Every excavation sequence is followed by a short-term TDD, which quickly vanishes. Liner responses to long-term TDD show increases in the maximum value of axial and shear forces, as well as bending moment, as seen in Figures 6 to 8.

Ground response to long-term TDD shows increase in the magnitude of total displacement, as shown in Figure 9. An increase in the magnitude of displacement in the invert over time (TDD-induced) is noticeable, although it is very small. The long-term TDD is only observed in the invert with a magnitude of 2.5mm over the course of 4000 days (approximately from day 300 to day 4300), which vanishes afterwards. Similar observations are made investigating the displacement of the liner.

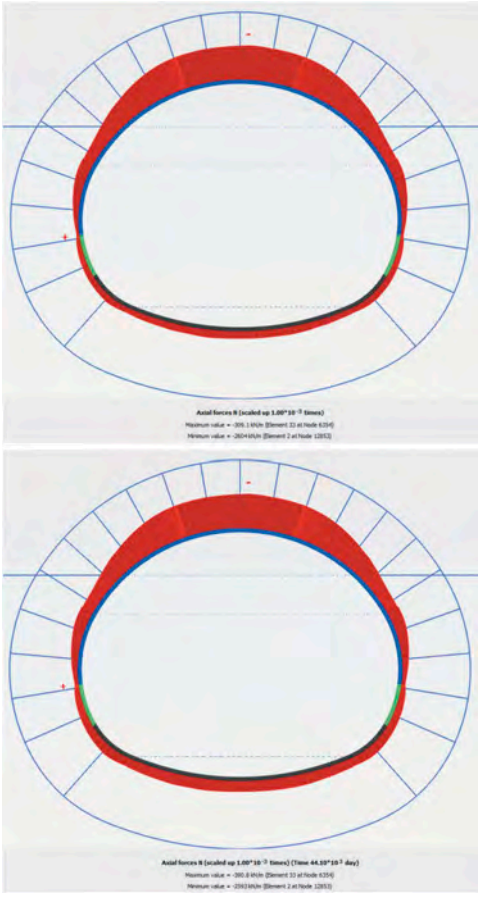

Figure 6. Axial force in the sem cavern model liner over time. top) after installation of permanent liner, after TDD for 180 days, Bottom) after TDD for 44000 days.

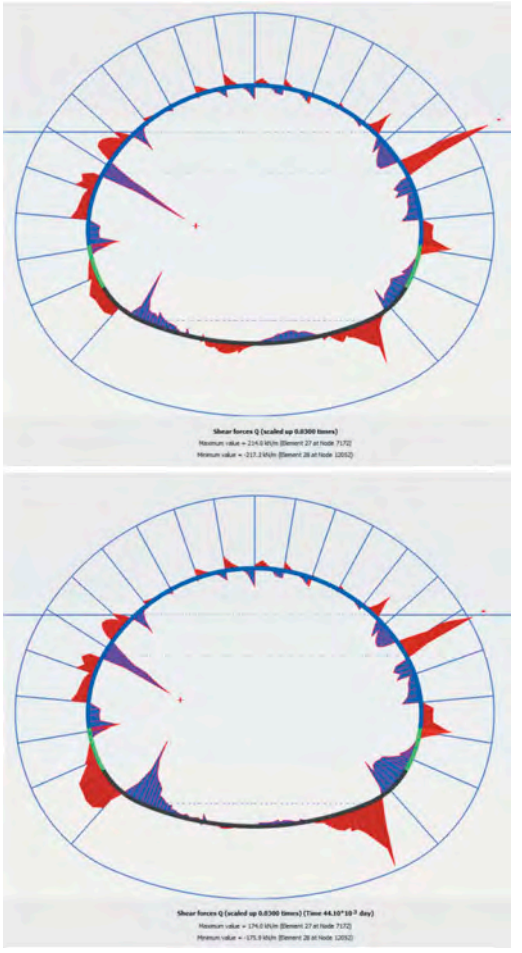

Figure 7. Shear force in the sem cavern model liner over time. top) after installation of permanent liner, after TDD for 180 days, Bottom) after TDD for 44000 days.

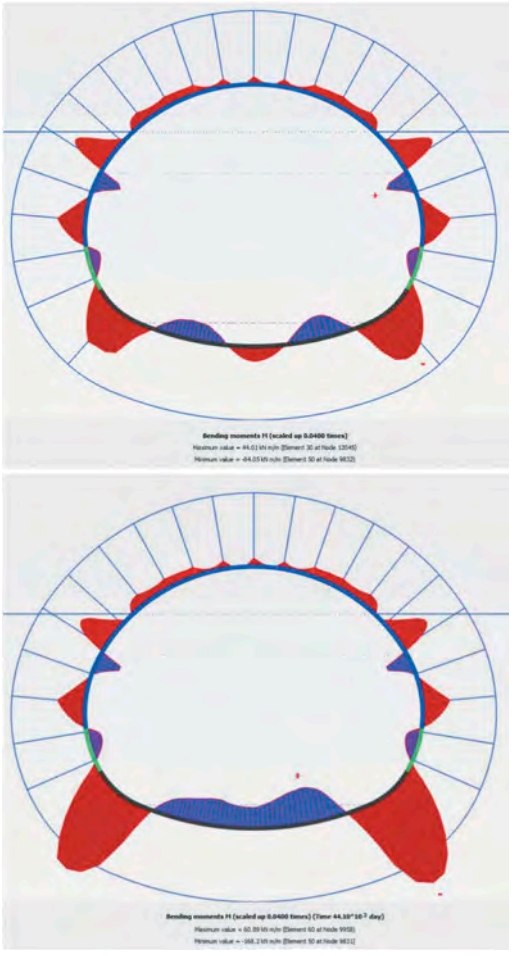

Figure 8. Bending moment in the sem cavern model liner over time. top) after installation of permanent liner, after TDD for 180 days, bottom) after TDD for 44000 days.

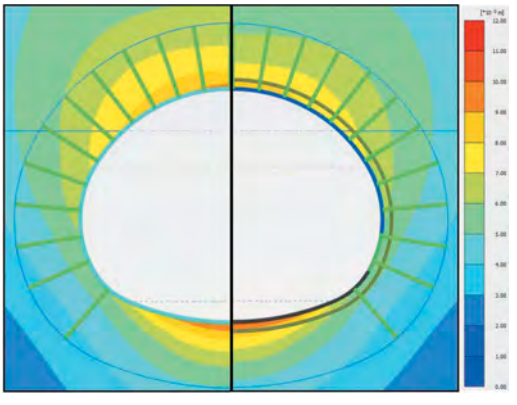

Figure 9. Total displacement contour in the sem cavern model over time. left) after installation of permanent liner, after TDD for 180 days, right) after TDD for 44000 days.

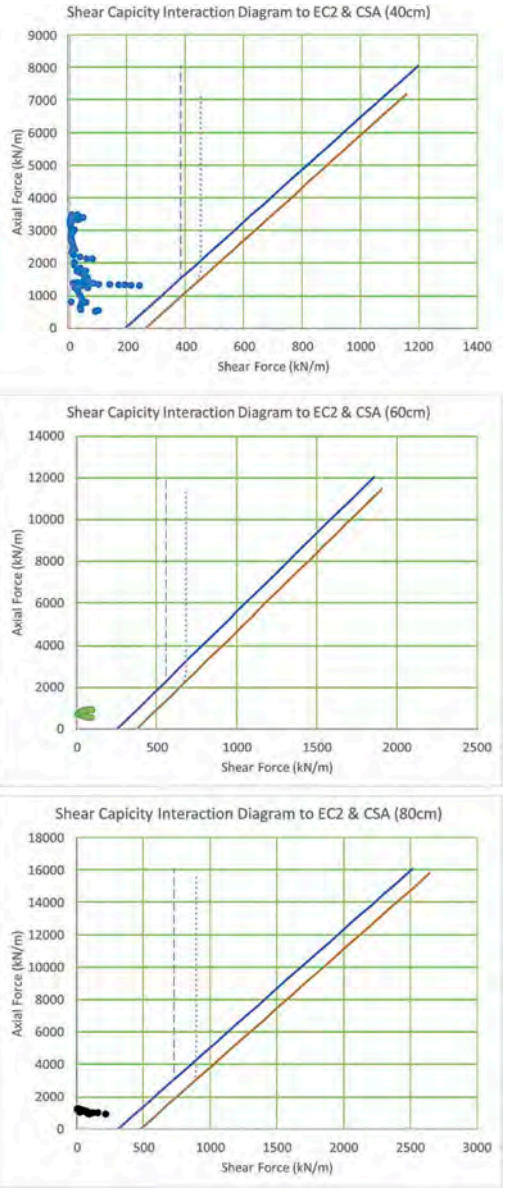

Figure 10. Axial force-shear force diagrams for the sem cavern lining. data is plotted for the 40cm, 60cm, and 80cm lining sections. data after 44000 days is used.

The demand vs capacity of the lining is investigated using the interaction diagrams for each lining section (40cm, 60cm, and 80 cm sections, as shown in Figures 10 and 11. Demand data falls below the acceptable limits of the capacity of the designed lining. Overall, the time-dependent displacements are found to be suppressed by the 3D confinement around the excavations, and in cases where a small amount of swelling mobilizes, it vanishes over the course of 2000 days.

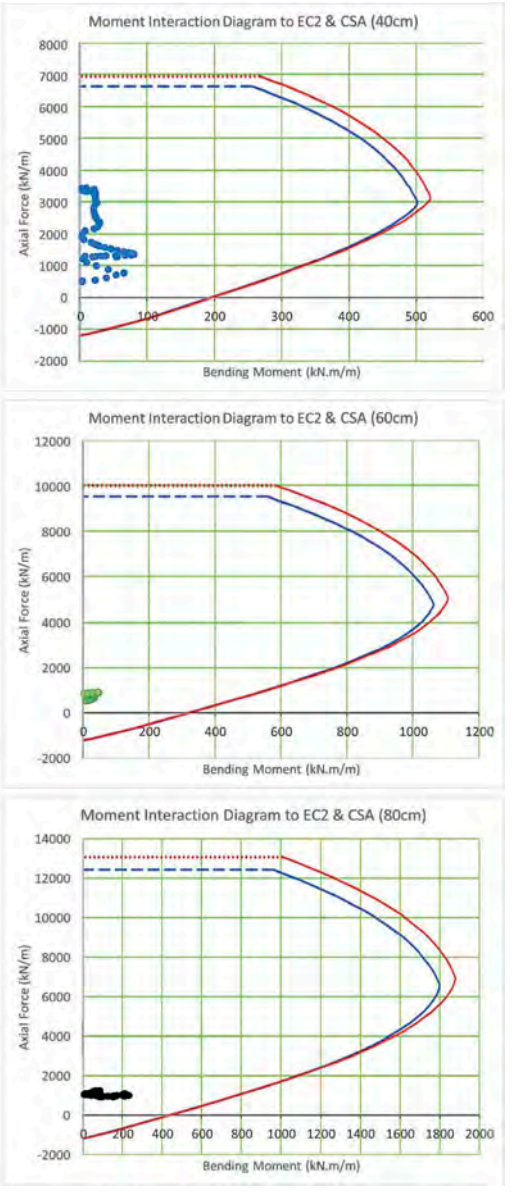

Figure 11. Axial force- moment diagrams for the sem cavern lining. data is plotted for the 40cm, 60cm, and 80cm lining sections. data after 44000 days is used.

5 CONCLUSION

Swelling in shale initiates only when all the pre-requisites are available and may apply excessive pressure on the support system of the underground structures. Upon initiation, the swelling has the highest strain rate right at the beginning. Hence, the primary mitigation strategy against the potential swelling impacts is giving the ground enough relaxation time after excavation and before installation of the permanent lining.

In this paper, we present the results of our investigation of swelling for an SEM cavern of the OLS Project that will be developed in the swelling-prone Georgian Bay Shale in the Greater Toronto Area, Canada. The numerical modelling results show that the alterations in the swelling-induced deformation and load/ bending moment of the lining over the project's lifetime are negligible. Our interpretation of the results is that the induced tangential compressive stresses around the excavation and the increase of radial compressive stresses in the rock due to lining-rock interaction over time contribute to the suppression of swelling.

ACKNOWLEDGMENTS

The authors would like to acknowledge the contributions of the Tunnelling Team at AECOM and their constructive discussions; especially Dr Mahdi Soudkhah and Mr Mahmoud Sepehrmanesh. Special thanks to the PLAXIS scientific support team Dr Richard Witasse, Dr Tuan-Anh Bui, and Mr Micha van der Sloot.

REFERENCES

Lee, Y. N., Lo, K. Y., 1993. The Swelling Mechanism of Queenston Shale. Canadian Tunnelling 1993, The Tunnelling Association of Canada, 75–97.

Rahjoo, M., Nasri, V., Sepehrmanesh, M., and Soudkhah, M., 2023. Design aspects of swelling of shales for tunnelling projects in Southern Ontario, Canada. Expanding Underground Knowledge and Passion to Make a Positive Impact on the World, WTC 2023. CRC Press, 2023. 2177–2185.

Anagnostou, G. 1993. A model for swelling rock in tunnelling. Rock Mechanics Rock Engineering 26, 307–331.

Tunnelling for a Better Life – Yan, Celestino, Thewes & Eberhardt (Eds)
© 2024 The Author(s), ISBN 978-1-032-80042-4
Open Access: www.taylorfrancis.com, CC BY-NC-ND 4.0 license

How to consider the effects of longitudinal joint imperfections on internal forces in segmental tunnel linings

Fabian Rauch* & Oliver Fischer
Chair of Concrete Structures, Technical University of Munich, Munich, Germany

ABSTRACT: Small geometrical imperfections are inevitable when assembling concrete segments to a circular segmental tunnel lining. As a result, small translational and rotational contact imperfections occur in the longitudinal joints between the segments. As these imperfections sum up, they can significantly influence the internal forces in the lining. While the normal forces are not very sensitive to imperfections, the bending moments and, consequently, the stresses in the lining can be significantly increased. In structural design, imperfections are typically taken into account in local analyses (e.g. stress distribution at joints). In the overall calculation of internal reactions, however, imperfections are mostly neglected or considered with approaches that strongly simplify the structural behavior. A more accurate and realistic investigation of this influence is achievable with numerical models that explicitly include the longitudinal joints and potential imperfections with contact formulations. Therefore, first, a suitable modeling strategy was developed. However, these calculations are time-consuming if many combinations have to be considered and only supported by limited available calculation programs. Therefore, it is shown and verified how imperfections can be considered in a simplified way with one-dimensional bedded beam models and rotational springs. The simplified approach's results approximate well the numerical model's results with discrete joints and contact formulations.

Keywords: FEM, structural design, imperfections, assembly, tolerances, TBM

1 INTRODUCTION

Mechanized tunneling by placing curved reinforced or steel fiber concrete segments to form a circular segmented lining is nowadays a state-of-the-art tunnel construction technique that is widely used (Fischer et al., 2014).

One essential construction step of this method is the assembly of about five to 13 (Grübl, 2012) segments into a ring within the cover of the TBM shield, after which the segments are connected through several joints (Figure 1).

The number of joints with one surface axis in the longitudinal direction ("longitudinal joints") equals the number of segments. Two further joints connect the neighboring rings ("circumferential joints"). The joint surfaces can be of different shapes. Flat shapes are nowadays state-of-the-art for longitudinal joints, while several options exist for circumferential joints (DAUB, 2013) (DAUB, 2023).

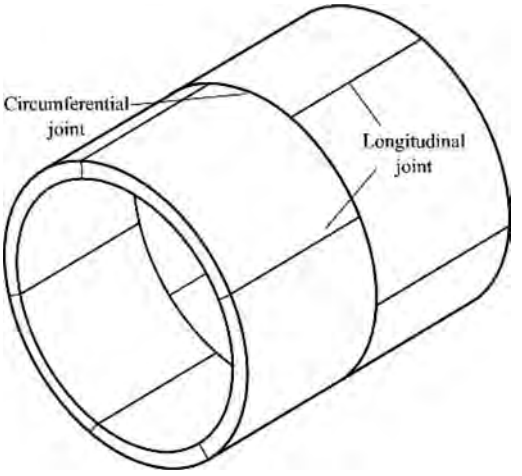

Figure 1. Segmental structure and nomenclature.

*Corresponding author: fabian.rauch@tum.de

DOI: 10.1201/9781003495505-43

For ring assembly, experienced TBM operators usually bring the segments into their foreseen position with the help of visual control and simple auxiliary means. Sometimes built-in components that assist the operators during assembly (e.g. guiding rods, tongue/groove) are used. These methods ensure satisfactory assembly quality, and watertightness is commonly achieved.

However, a completely accurate assembly of these large segments is not possible. Small irregularities and geometrical imperfections in the longitudinal and circumferential joints are inevitable (OEVBB, 2009). Although they do usually not adversely affect functions like watertightness, they can cause incomplete contact between two joint surfaces. Both translational and rotational imperfections are possible (Figure 2).

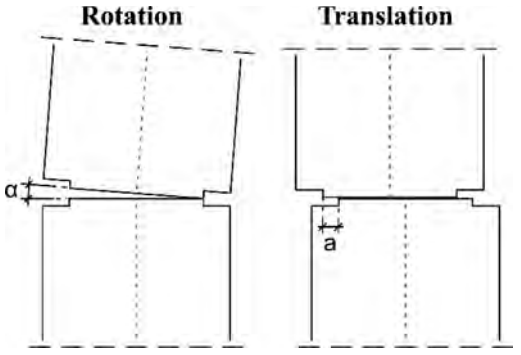

Figure 2. Rotational and translational imperfections.

Such imperfections, which were all within the permissible tolerances, were measured in a recent structural monitoring project of the authors (Rauch and Fischer, 2022), which was the starting point for investigations on the influence of geometrical joint imperfections on the internal forces in a segmental tunnel lining. The imperfections in this study are those caused by assembly inaccuracies. Although some mechanisms overlap, imperfections due to production tolerances are not considered here, as they are generally kept as low as possible.

Imperfections in circumferential joints can lead to local stress peaks due to inaccurate longitudinal supports. They can cause damage to the concrete segments during TBM advance when the longitudinal jacking forces act on the lining. This was already discussed e.g. in (Behnen et al., 2016), and is therefore not further studied.

The general, qualitative mechanisms regarding the influence of longitudinal joint imperfections on the internal forces become visible by analyzing the situation in Figure 2. Both rotational and translational imperfections cause an incomplete contact of the two joint surfaces. Their center lines do not match, and an initial eccentricity is already included in the structure before loading. When normal forces develop in the lining, these initial eccentricities cause additional bending moments.

Former investigations regarded the local resistance of longitudinal joints with geometric imperfections (Cavalaro et al., 2011) and the general influence of joint imperfections on the linings' structural behavior (Schotte, 2016). To the authors' best knowledge, a systematic analysis of the effects of longitudinal joint imperfections on the stresses and internal forces along the linings' circumference compared to a perfectly assembled ring has yet to be carried out. This is necessary to assess their significance for structural design.

Due to the large number of possible combinations and the resulting great effort, experimental studies are not feasible for this analysis. Numerical investigations are the better-suited approach.

Therefore, a modeling strategy had to be developed as a first step to reproduce the influence of longitudinal joint imperfections on segmented linings realistically and accurately in a numerical model. Further requirements of the modeling strategy were a short calculation time and eligibility for parametric studies. An advanced and a simplified modeling strategy were established and can be used depending on software availability and available calculation time.

The model development, the established strategies, and the (validating) results of the first calculations are presented in this paper.

2 LONGITUDINAL JOINT IMPERFECTIONS

Longitudinal joint imperfections can appear in the forms shown in Figure 2. Theoretically, as a third form, it is also possible that the two surfaces of a joint have no contact. This is possible if the segments of neighboring rings interact and stabilize each other via friction. However, the corresponding mechanisms differ from those in Figure 2; therefore, this third case is not considered in this study. Except for some special cases, it is almost always necessary to combine rotational and translational imperfections in an imperfect ring assembly (Figure 3) for geometrical compatibility.

To cause longitudinal joint imperfections, the segments have to be rotated and translated. These movements also cause "global" deformations; consequently, the form of the segmented lining differs from a perfect circle. This is called "initial ovalization" and was e.g. described in (Baumann, 1992) (Figure 3).

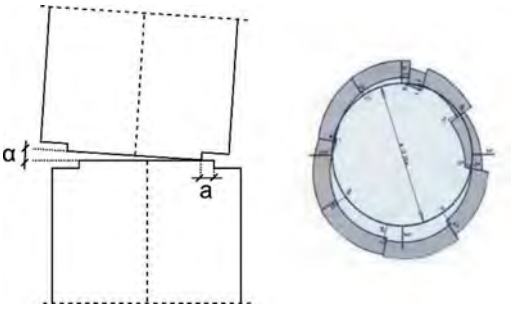

Figure 3. Left: combined rotation and translation, right: initial ovalization (OEVBB, 2009).

2.1 *Imperfections in structural design*

In structural design, when dimensioning the longitudinal joints for partial (concentrated) compression stresses and tensile splitting forces (Schmidt-Thrö et al. 2019), the negative influence of imperfections on stresses and internal forces can be considered by an extra eccentricity due to assembly inaccuracies (ITA, 2019). This value has to be set project-specific, but it should generally be around ± 10 mm (e.g. (DB Netz AG, 2002)).

Regarding the effects of longitudinal joint imperfections on internal force development, to the best knowledge of the authors, no explicit recommendations are available. Performing calculations on an elliptical-shaped ring is a thinkable way to consider initial ovalizations, but this does not reproduce well the real situation. Generally, it is indirectly tried to keep the influence of longitudinal joint imperfections low through other recommendations (e.g. small tolerances).

2.2 *Limit values*

To consider a realistic parameter range for translational and rotational imperfections as well as for initial ovalizations in the study, limit values are set according to guidelines and literature. There is no direct, generally valid relation between the three values. Therefore, one limit for each must be set and checked separately for any model input parameter combination. The modeling strategy presented in this paper was developed and tested for and within these limit values.

Relevant guidelines on segmental tunnel linings (e.g. (ITA, 2019), (DAUB, 2013), (DAUB, 2023), (OEVBB, 2009), (DB Netz AG, 2002), (BMDV, 2022)) do provide limit values for assembly misalignments (translational imperfections). A realistic range should be of ± 10 mm. Due to geometrical compatibility, this value indirectly also narrows down rotational imperfections and ovalizations. However, separate limit values are set.

(Cavalaro et al., 2011) assumed possible segment rotations of up to 0.4°. (Schotte, 2016) reported measured values of up to about 0.1°. (OEVBB, 2009) considers values below 0.225° as feasible. The limit is set to ± 0.3° to consider the possible range.

The third limit value regarding the initial ovalization is set to 0.5% of the inner diameter, according to (DAUB, 2013) (DAUB, 2023).

3 ADVANCED MODELING STRATEGY

The FEM software ABAQUS/CAE 2017 (Dassault Systemes, 2016) is used for the "advanced" model. In this advanced model, the different mechanisms relevant to this study are included in a more realistic and detailed way. Some of the corresponding modeling strategies were developed during investigations for a Master's Thesis (Dreier, 2023) that the authors of this paper supervised.

3.1 *General model configuration*

The focus of the study is on the influence of joint imperfections. Therefore, the model detailing is increased around this aspect. Other model components that are usually important for tunnel structures are not relevant to this study, e.g. soil parameters or groundwater. Therefore, the model basis is a bedded beam model ((Behnen et al. 2012), (Behnen et al., 2015)) (Figure 4). In this model, the soil-(tunnel)structure-interaction (SSI) is considered in a simplified way by springs. The radial spring stiffness is determined according to (Duddeck, 1980). The tangential spring stiffness, simulating the tangential SSI, is set to 2.5 % of the radial spring stiffness to increase numerical stability but is not expected to occur in reality (DAUB, 2013) (DAUB, 2023). Because a shallow tunnel is modeled in this case, a 90-degree area around the tunnel crown remains unbedded.

In bedded beam models, the concrete segments are typically modeled as one-dimensional straight beam chains to approximate the circular form. In the studied case of this paper, 96 beams formed the ring. The longitudinal joints are modeled in a simplified way with hinges that connect these beams. Rotational springs are applied to these hinges to account for the rotational stiffness of the longitudinal joints. The corresponding moment-rotation-relation was established by (Janßen, 1983), adapting the findings of (Leonhardt and Reimann, 1965) for tunnel linings. The earth and water pressure are applied to the tunnel explicitly through active loads.

However, because of the simplified approach with hinges and rotational springs, one-dimensional models do not include the actual longitudinal joint geometry. Therefore, explicit modeling of longitudinal joint imperfections is not possible. At least a two-dimensional model is required. That is why, in this study, two- and three-dimensional beam models are used to model longitudinal joints and their imperfections realistically, as presented in the next section.

The concrete segments are modeled with an elastic material model. A more accurate elastic-plastic

concrete material model (Sargin, 1971) leads to no significant changes in the results. Reinforcement bars were not considered in this model.

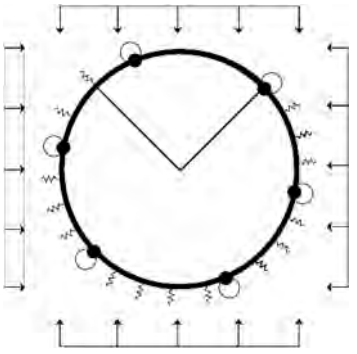

Figure 4. Bedded beam model.

3.2 *Longitudinal joint modeling*

The joint area is modeled with its actual geometry. The only geometrical simplification regards the transition area from joint surfaces to segment body. These are considered rectangular, although, in reality, they are sometimes inclined. This had no significant effect on the results. Bolts and gaskets were not included as they were not expected to significantly influence the studied mechanisms.

The interaction of two joint surfaces is modeled with surface-based contact in ABAQUS/Standard. The normal and the tangential behavior of two interacting surfaces in contact must be defined. The various options and settings for contact simulation can significantly impact the results and must be selected carefully.

The parameters and settings for numerical longitudinal joint simulations of (Schmidt-Thrö, 2019) are used to ensure a realistic behavior perpendicular to the joint surface. These values were calibrated on an extensive experimental study. The normal contact behavior is defined by the pressure-overclosure relationship of "hard contact." This minimizes penetration of two surfaces and does not allow for tensile stress transmission across them (ABAQUS Documentation, 2006, 30.1.2). The penalty constraint enforcement method was used with a stiffness scale factor of 300 (Schmidt-Thrö 2019).

The tangential behavior is simulated by a penalty friction formulation (ABAQUS Documentation, 2006, 30.1.5). The friction coefficient for the Coulomb friction model is set to 0.4. This is slightly below the range of 0.5-0.7 proposed for concrete-concrete friction in (fib, 2013) because the concrete surface of lining segments is expected to be exceptionally smooth and regular due to the high production tolerances and the normally used steel formworks.

To model longitudinal joint imperfections, the segments are rotated and arranged with an offset (translated) according to predefined values. These values are within the limit values of section 2.2 and ensure that overlapping of the joint surfaces is avoided (geometrical compatibility).

3.3 *Test results and model selection*

The presented modeling strategy is applied to an example case of a recently built shallow segmented tunnel (Rauch and Fischer, 2022) to test the strategy and investigate the influence of longitudinal joint imperfections on the internal forces of the lining. The modeling parameters of the example case are listed in Table 1. The models' geometry and the loading situation are presented in Figure 5, as well as the geometric details of the longitudinal joints.

A two-dimensional and a three-dimensional model are created. The mesh size is set following a sensitivity analysis, and the model is meshed regularly and evenly distributed. The CPE4R element type is used for 2D calculations, and the C3D8R element type is used for 3D calculations.

Table 1. Model parameters and values.

Parameter	Value
Oedometric modulus (soil)	45 MPa
Concrete elastic modulus	36,000 MPa
Concrete strength	C 45/55
Concrete density	2,500 kg/m³
Segment length	1.2 m
Segment thickness	45 cm

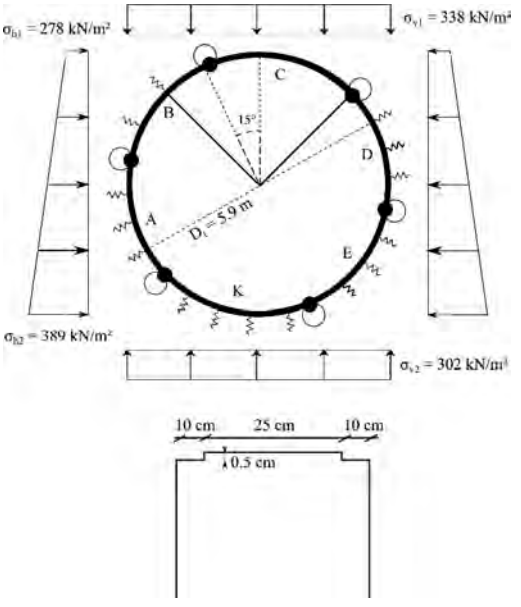

Figure 5. Example case, upper: model geometry and loads., lower: longitudinal joint detail.

3.3.1 *2D vs. 3D model*

The results of the two-dimensional (2D) and the three-dimensional (3D) model are compared in Figure 6.

The model dimensionality has no significant influence on the linings' normal forces. However, they do have a small effect on the bending moments. While the qualitative trends are similar, there are some differences regarding the quantitative values. The maximum bending moment magnitude is 14 % higher in 3D than in 2D. Except for a slight influence of the general differences between 2D and 3D models, this is ascribed to the fact that the longitudinal joints show a slightly stiffer behavior in 3D than in 2D (Schmidt-Thrö, 2019).

However, both models deliver adequate results to reproduce the structural behavior and can be used to study the influence of longitudinal joint imperfections. The 2D approach is used for further calculations and analyses to reduce modeling and computation time.

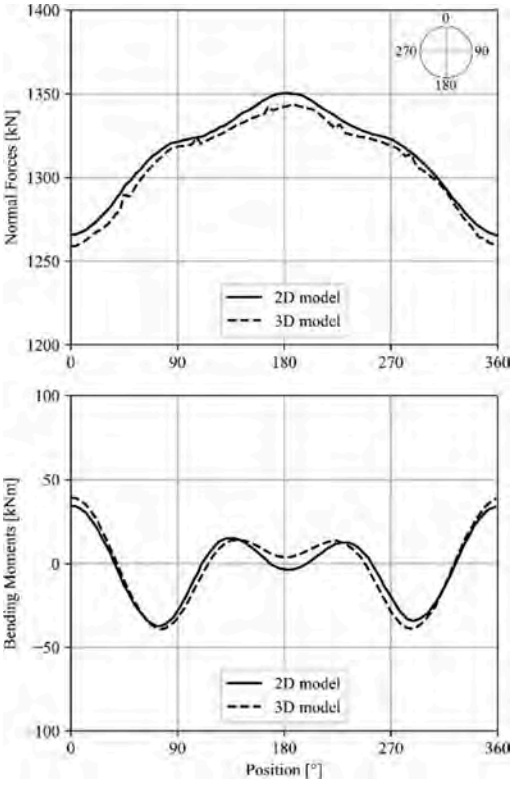

Figure 6. Effect of model dimensionality on internal forces with explicit longitudinal joint modeling.

3.3.2 *Perfect vs. imperfect assembly*

To illustrate the mechanisms, the results of the example case with one full-ring configuration of imperfections are presented. The applied imperfections are shown in Table 2. A positive value corresponds to a clockwise rotation. Translational imperfections were added within the limit values to ensure the required geometric compatibility.

The internal forces get disturbed when applying this configuration to the example case (Figure 7). The effect of imperfections is much smaller on normal forces than on bending moments. The difference in normal force magnitude is about 4.5 %. Although some minor qualitative changes occur, the overall trend and the magnitude remain similar to the normal forces in perfectly assembled segments.

Table 2. Rotational imperfections.

Segment	Rotation in [°]
A	-0.04
B	-0.06
C	0.09
D	-0.11
E	0.11
K	0.01

This is not the case for bending moments. The bending moments change strongly both qualitatively and quantitatively. E.g., although almost no bending moments resulted in the tunnel invert of a perfectly assembled model, significant bending moments have now developed. The bending moments differ almost everywhere along the circumference, also in their sign.

Generally, in this and other analyzed examples, the bending moments are increased due to the longitudinal joint imperfections. The peak bending moments almost triple. Since the normal forces remain pretty similar, this results in significantly higher stresses in the segmented lining, which is not desirable.

Of course, it is also possible that different configurations of imperfections have no influence or even reduce stresses in segments. However, since the actual assembly imperfections can neither be predicted in advance nor steered accurately, it should generally be tried to avoid them by ensuring an accurate segment assembly and considering auxiliary means to keep (additional) lining stresses low.

4 SIMPLIFIED APPROACH

With the strategy presented in section 3, it is possible to simulate the influence of longitudinal joint imperfections on the linings' internal forces. However, this strategy is costly and requires advanced numerical modeling software. A simplified approach would be beneficial to perform more calculations in a shorter time and consequentially enable more extensive systematic parametric studies – and to allow for potential applications in engineering practice. As an essential requirement, a simplified approach must

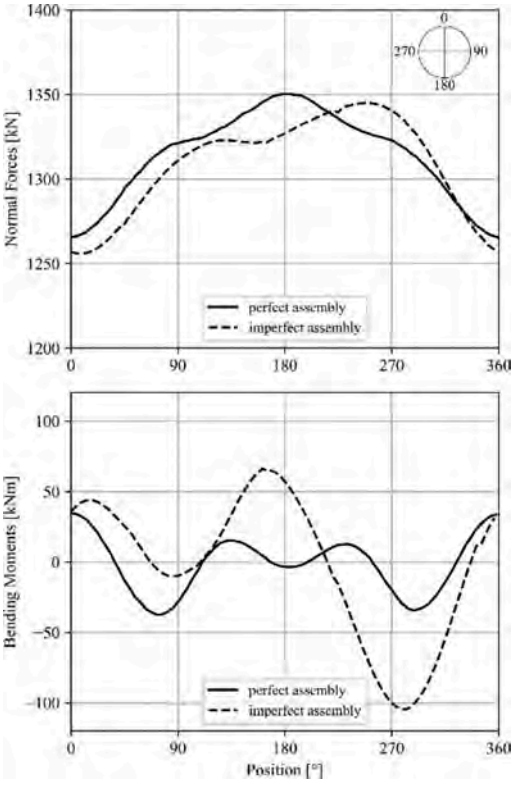

Figure 7. Influence of longitudinal joint imperfections on internal forces.

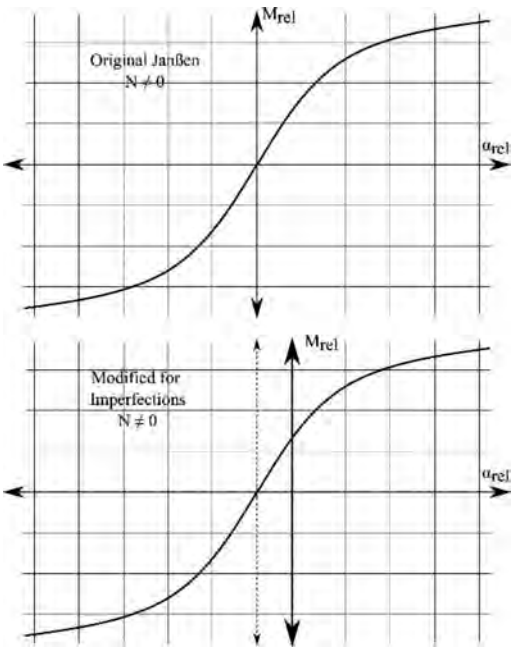

Figure 8. Original and modified moment-rotation-relation.

also reproduce the influence of longitudinal joint imperfections similar to the advanced strategy with satisfying accuracy.

Such a simplified approach is presented and compared to the results of section 3.

4.1 *Simplified modeling and simulation strategy*

In the simplified approach, the dimensionality of the model is again reduced to one (1D). Because of the one-dimensionality, the longitudinal joints cannot be modeled explicitly anymore. Still, as mentioned, their stiffness can be considered with rotational springs and the moment-rotation-relation proposed by (Janßen, 1983) (Figure 8). The rest, e.g. loads, radial springs, etc., is modeled similarly to section 3. Since no surface contact is required anymore, this approach is feasible with almost any software. Here, the software SOFiSTiK (Sofistik, 2018) is used for the calculations with the simplified approach.

The original formulation of (Janßen, 1983) applies to perfectly assembled rings and complete contact between two flat joint surfaces before loading. When loading starts, the angle α between two neighboring joint surfaces is $\alpha_0 = 0$. Then, the formulation induces the formation of bending moments that develop due to the rotational stiffness of the joints when opening and closing (which means α gets smaller or greater than one ($\alpha \lessgtr 0$)). It defines a relation between moments and rotations and is reversible in both directions.

Now, to account for longitudinal joint imperfections, the moment-rotation-relation is modified. When loading starts, the joints are not closed but opened by an angle $\alpha_0 \neq 0$ (Figure 3). This angle is the difference between the rotational imperfections of two adjoining segments. Because the original formulation by (Janßen, 1983) is reversible, $\alpha_0 \neq 0$ equals $\alpha \lessgtr 0$. Graphically, this means the vertical axis in Figure 8 is moved horizontally. Consequently, additional bending moments develop in the lining due to the initial eccentricities caused by the imperfections when a normal force is applied to the longitudinal joint.

4.2 *Comparison and validation*

To validate the simplified approach, it is applied to the same example case of section 3, and the results are compared to the results of the advanced two-dimensional model with explicit joints. The model configuration can again be found in Table 1, Table 2, and Figure 5.

The results are shown in Figure 9. When considering imperfections, the normal forces resulting from the simplified approach correspond well to the normal forces of the two-dimensional contact model both qualitatively and quantitatively. Once again, it can be seen that the quantitative effect of

longitudinal joint imperfections on normal forces is also small when using the simplified approach.

The bending moments for imperfect assemblies calculated by the two approaches do not agree to the same extent, but similarities can be observed in the two lines. First, with both models, the bending moments are increased significantly compared to the assembly without imperfections. Also, the general qualitative trends are the same in both models. Second, the agreement of the four peak values – important for further studies – is quite satisfactory, especially if put in relation to the peak values of the perfectly assembled model. The observations in different examples were similar.

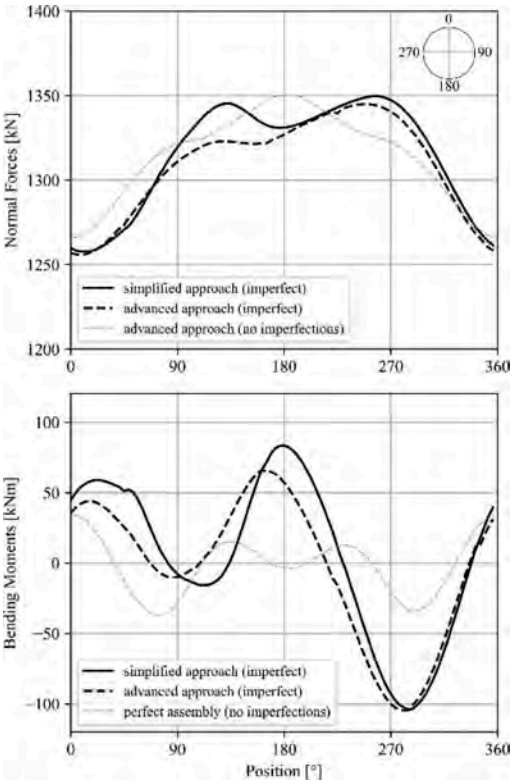

Figure 9. Comparison of simplified (1D) and advanced (2D) approach.

However, the comparison also shows some disagreements. Although the four peak values have similar magnitudes, they still do not equal each other. Also, the bending moment distribution is slightly shifted to the right in Figure 9, which means it is rotated clockwise on the lining circumference.

Two reasons are found that contribute to these deviations. First, the general model configuration of the two approaches is not exactly the same, even if no imperfections are modeled. Also, although the basic idea is the same, the interaction of two joint surfaces through contact and the simplified consideration with a rotational spring are not equal. Second, as shown e.g. in Figure 3, modeling the imperfect linings with real geometries requires to include some translations into the model due to geometrical compatibility. This is not possible with one-dimensional beams and rotational springs. This reason should influence the results and could be the leading cause for the observed differences.

Altogether, the simplified approach yields results that reproduce the structural behavior of a segmented lining under the influence of longitudinal joint imperfections in a realistic way. Although there are some disagreements with the results of the two-dimensional model with explicitly modeled longitudinal joints, the results of the simplified approach are satisfying, especially if put in relation to magnitudes of internal forces in perfectly assembled linings. Especially qualitative trends are reproduced accurately. The simplified approach's advantages, which are mainly quicker and easier-to-get results, have to be considered for model selection. By applying either the simplified approach or the two-dimensional model, one gets a good impression of the influence of longitudinal joint imperfections and the resulting trends. Both models can be used for further studies e.g. for systematic investigations on how sensitive the internal forces of models with different parameters react to longitudinal joint imperfections.

5 CONCLUSIONS AND OUTLOOK

A modeling strategy was established to consider the effects of longitudinal joint imperfections on the internal forces in segmental tunnel linings. First, an advanced model was presented. It consists of a two- and a three-dimensional bedded beam configuration that includes longitudinal joints explicitly with their actual geometry. The interaction of two adjoining joint surfaces is considered with a calibrated contact formulation. It was found that the dimensionality has no significant influence on the results.

Then, a simplified approach was presented. The corresponding model consists of a one-dimensional bedded beam. The longitudinal joints are modeled with hinges and rotational springs whose behavior has been described by means of a widely used moment-rotation-relation. To consider longitudinal joint imperfections, this relation was modified.

Both approaches were applied to an example case. Although there were some differences in the results of the two models, they both reproduced the basic mechanisms accurately. They gave the same general trends: while longitudinal joint imperfections have a low influence on the linings' normal forces, they strongly disturb the bending moments, which can increase significantly. As a consequence, the stresses increase, which is not desirable. Because of that, longitudinal joint imperfections should generally be minimized.

The approaches were tested on several example configurations, and the results of one of them were

presented. As a next step, a more systematic study is carried out to analyze the influence of longitudinal joint imperfections on the internal forces under different boundary conditions.

ACKNOWLEDGMENTS

The authors thank Stephan Dreier for his contributions to this paper during the work on his Master's Thesis.

REFERENCES

ABAQUS Documentation Online. 2006. Version 6.6-1. https://classes.engineering.wustl.edu/2009/spring/mase5513/abaqus/docs/

Baumann, T., 1992. Tunnelauskleidungen mit Stahlbetontübbings (Tunnel linings with reinforced concrete segments, in German). Die Bautechnik, 69(1),11–20.

Behnen, G., Nevrly, T., Fischer, O., 2012. Bettung von Tunnelschalen (Bedding of tunnel linings, in German). In: Laackmann, K. et al. (eds): Taschenbuch für den Tunnelbau 2013, VGE Verlag, Essen, Germany, pp. 235–282.

Behnen, G., Nevrly, T., Fischer, O., 2015. Soil-structure interaction in tunnel lining analyses. Geotechnik, 38 (2),96–106. http://dx.doi.org/10.1002/gete.201400010

Behnen, G., Fischer, O., Schmidt-Thrö, G., 2016. Scheibenbemessung der Pressenkraftdurchleitung bei TVM-Vortrieben. (Design of segmental linings for longitudinal force application, in German). Beton- und Stahlbetonbau, 111(11),694–705. http://dx.doi.org/10.1002/best.201600045

BMDV Bundesministerium für Digitales und Verkehr, 2022. ZTV-ING 2022: Zusätzliche Technische Vertragsbedingungen und Richtlinien für Ingenieurbauten - Teil 7 Tunnelbau - Abschnitt 1 Geschlossene Bauweise.

Cavalaro, S., Blom, C., Walraven, J., Aguado, A., 2011. Structural analysis of contact deficiencies in segmented lining. Tunn. Undergr. Sp. Tech. 26(6),734–749. http://dx.doi.org/10.1016/j.tust.2011.05.004

Dassault Systemes. 2016. Simulia, Dassault Systèmes, ABAQUS/CAE 2017, San Diego: Dassault Systèmes.

Dreier, S. 2023. Numerical analysis of the structural behaviour of segmental tunnel linings under explicit consideration of longitudinal joint imperfections, (In German). Master's Thesis. Technical University of Munich, Munich, Germany. (unpublished)

DAUB Deutscher Ausschuss für Unterirdisches Bauen, 2013. Recommendations for the design, production and installation of segmental rings.

DAUB Deutscher Ausschuss für Unterirdisches Bauen, 2023. Recommendations for the design, production and installation of segmental rings. (in preparation)

DB Netz AG, 2002. Eisenbahntunnel planen, bauen und instand halten. (Design, construction and maintenance of railway tunnels, in German). Updated 2014.

Duddeck, H. (ed), 1980. Empfehlungen zur Berechnung von Tunneln im Lockergestein (1980). (Recommendations on the calculation of tunnel linings in soft soil, in German). Die Bautechnik, 57 (10),349–356.

fib fédération internationale du béton. 2013. fib model code for concrete structures 2010.

Fischer, O., Nevrly, T., Behnen, G., 2014. Fertigteile im Tunnelbau. (Segments for tunnel linings, in German). In: Bergmeister, K. et al.: Betonkalender 2014, Ernst & Sohn, Berlin, Germany, pp. 233–302. http://dx.doi.org/10.1002/9783433603352.ch

Grübl, F., 2012. Segmental Ring Design: New Challenges with High Tunnel Diameters. Muir Wood Lecture. Proceedings of the World Tunnel Congress 2012, Bangkok, Thailand.

ITA International Tunnelling and Underground Space Association, 2019. Guidelines for the design of segmental Tunnel Linings. ITA Report No. 22.

Janßen, P., 1983. Tragverhalten von Tunnelausbauten mit Gelenktübbings. (Structural behavior of segmental linings with longitudinal joints, in German). PhD Thesis, TU Braunschweig, Braunschweig.

Leonhardt, F., Reimann, H., 1965. DafStb Heft 175: Betongelenke – Versuchsbericht, Vorschläge zur Bemessung und konstruktive Ausbildung. (Concrete joints: experimental study, design recommendations, construction, in German). Ernst & Sohn, Berlin.

OEVBB Österreichische Vereinigung für Beton- und Bautechnik, 2009. Richtlinie Tübbingsysteme aus Beton. (Guidelines on concrete segments for segmented linings, in German).

Rauch, F., Fischer, O., 2022. Structural monitoring of Segmental Tunnel Linings: towards safer and more resource-efficient tunnels. Civil engineering design, 4 (1-3), 62–71. http://dx.doi.org/10.1002/cend.202100053

Sargin, M., 1971. Stress-strain Relationship for Concrete and the Analysis of Structural Concrete Sections. Solid Mechanics Division University of Waterloo, Waterloo, United Kingdom.

Schmidt-Thrö, G., 2019. The bearing behaviour of the longitudinal joint of reinforced segmental linings, in German. PhD Thesis, Technical University of Munich, Munich, Germany.

Schmidt-Thrö, G., Tabka, B., Smarslik, M., Scheufler, W., Fischer, O., Mark, P., 2019. Experimental analysis of concrete elements under partial area strip loading. Civil engineering design, 1 (1). 23–38. http://dx.doi.org/10.1002/cend.201900001

Schotte, K., 2016. Verification of the Performance of Segmental Tunnel Linings Using Strain and Ovalisation Monitoring. PhD Thesis. University of Ghent, Ghent, Belgium.

Sofistik, 2018. Sofistik AG, Sofistik: Service Pack 2018-10 Build 22. Nürnberg, Germany.

Tunnelling for a Better Life – Yan, Celestino, Thewes & Eberhardt (Eds)
© 2024 The Author(s), ISBN 978-1-032-80042-4
Open Access: www.taylorfrancis.com, CC BY-NC-ND 4.0 license

Athens metro "Piraeus" station: Numerical analysis versus observational method

Konstantinos Sampsakis-Bakopoulos* & Nikos Gerolymos
IPP Design & Construction of Underground Works, National Technical University of Athens, Athens, Greece

ABSTRACT: Piraeus, Europe's busiest passenger port and primary gateway to the Greek islands, required a vital metro connection to address the significant tourist influx and resulting traffic congestion during the summer. The inclusion of Piraeus in the Line 3 extension project not only met this demand but also served as a compelling case study for exemplary infrastructure development. The station's underground location, just 40 meters from the sea and 2 meters from the historic ISAP terminal, presented intricate challenges. These challenges involved managing surface traffic diversion and adhering to regulatory guidelines for settlements due to the station's proximity to the ISAP terminal. To overcome the complex hydrogeological conditions and limited surface area, the construction employed the cut-and-cover method with diaphragm walls and prestressed steel struts as temporary support. This approach ensured stability and structural integrity while providing an opportunity for an in-depth case study on implementing the cut-and-cover method in challenging hydrogeological conditions. An array of geotechnical monitoring instruments was meticulously installed, which played a pivotal role in measuring the displacements of the diaphragm walls and nearby structures, variations in groundwater levels due to dewatering processes and settlements arising from the construction activities. By exploiting geological and geotechnical data, finite element analyses were performed to compute the displacements of all monitored points. The focus was on comparing the measured with the computed response in terms of the wall's displacements. The results derived from the aforementioned analysis were in satisfactory agreement with the measured values, affirming the reliability and accuracy of the applied methodologies.

Keywords: Metro Station, Monitoring System, Diaphragm Wall, Settlements, Finite Element Analysis, Piraeus

1 INTRODUCTION

The growing tourist influx and the traffic congestion in the area, especially during the summer months made it indispensable for Piraeus to be connected via metro to the centre of Athens and the airport. Thus, Piraeus became one of the 6 stations of the Line 3 extension and was inaugurated in October of 2022 after numerous delays and challenges that arose during the construction of the station.

2 RETAINING STRUCTURE

The Piraeus station is situated adjacent to the terminal of line 1 within the Piraeus port area and is part of the most recent extension of the Athens Metro Line 3. The station is positioned in close proximity, approximately 2 meters, to the ISAP station on its eastern side, while on its western side lies the sea at a distance of 40 meters.

Figure 1. Top view of the Piraeus station outline.

Numerous challenges arose during the construction of the Piraeus station, encompassing various aspects. Firstly, the proximity of the station to the aged and historically significant ISAP terminal building posed a distinct challenge. Additionally, the station's proximity to the Piraeus port led to prevailing hydrogeological conditions, resulting in a water table that reached surface level.

*Corresponding author: sampsakiskostas@gmail.com

DOI: 10.1201/9781003495505-44

This circumstance gave rise to several complications due to the additional pressure exerted by water on the station's diaphragm walls, necessitating careful consideration of the additional load. Moreover, the excavation process induced water due to the head difference. This water flow led to increased pore water pressures beneath the excavation level and subsequent reduction of effective stresses, thereby creating potential risks of uplift. To address these challenges, the construction implemented 80cm thick diaphragm walls, that were constructed in 240cm panels, reaching a depth of 38m, with the reinforced concrete portion spanning up to 29.5m depth.

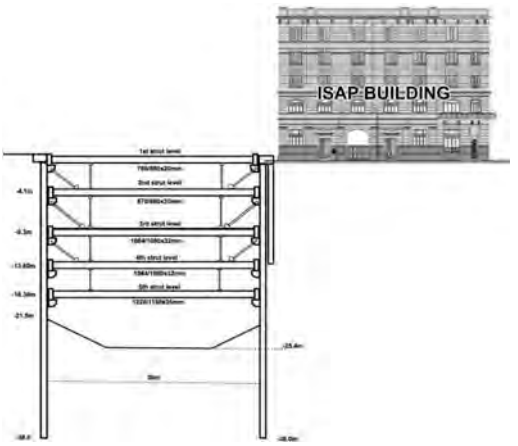

Figure 2. Side view of the retaining structure.

Figure 3. Retaining structure with emphasis in the struts during the construction phase.

To reinforce the diaphragm walls, a system of five rows of prestressed struts was installed. These struts were progressively added as the excavation deepened, allowing for minimal movements and deformations to prevent an active state. Specifically, the Piraeus station incorporated a total of five rows of prestressed metal supports within its primary trench. The horizontal spacing between the struts was equal to 5.4m, although slight variations in distance occurred in certain areas, especially the corner sections of the station. A visual representation depicting the arrangement of the struts relative to the station trench, both vertically and horizontally, can be observed in Figure 2 and Figure 3.

3 GEOLOGICAL CONDITIONS AND DESIGN PARAMETERS

3.1 *Geological conditions*

Based on the findings of the geotechnical investigations, which involved sampling and pressure borings, the geological formations encountered within the construction vicinity of the Piraeus station primarily consist of recent Quaternary sediments. Furthermore, in certain deep positions, the presence of the *Marl of Piraeus* formations has been identified. The stratigraphic succession of these units (also seen in Table 1), arranged according to their depth, is as follows:

- [AL] Artificial/Alluvial Deposits
- [SW] "Alipedon" Marsh Deposits
- [PT] Coastal Deposits
  - [PT-CN] Conglomerate-breccia-microconglomerate, exhibiting varying degrees of cementation from light to strong
  - [PT-SD] Sands, silty Sands, silty Sandstones
  - [PT-SM] Silts, sandy Silts, sandy Siltstones
- [NM] Marl of Piraeus
  - [NM-CN] Conglomerate-breccia- microconglomerate, occasionally featuring sandstone horizons or layers of calcite silt in specific locations.

3.2 *Idealized geotechnical profile*

The design of the GDP-2 section (Table 1), developed utilizing stratigraphy within the study area and encompasses a wide spectrum of anticipated geotechnical conditions. Upon this section, geotechnical calculations were conducted to facilitate the design process for the excavation, temporary support systems, and permanent construction of the Piraeus Station. Specifically, in the construction of the GDP-2 section a unification of the fractional relatives approach was employed between the geotechnical formations sands-sandstones and silts-siltstones. This procedure was also used for the slightly and strongly bound cobblestones of the coastal deposits but also of the cobblestones of the *Marl of Piraeus.*

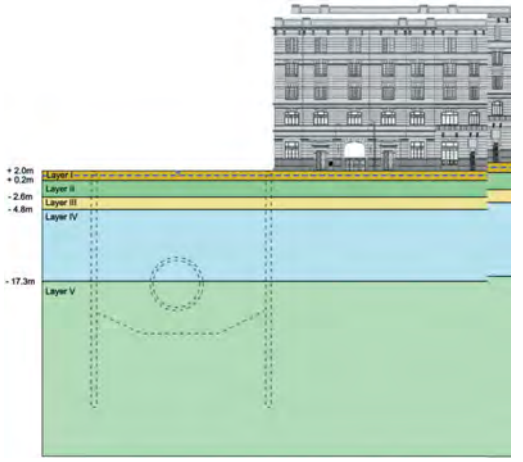

Figure 4. Stratigraphic representation of the idealized geotechnical profile GDP-2.

The area that was simulated in Plaxis was the section A-A' (as shown in Figure 1) of the deep excavation, while the subsequent calculations and simulations that took place were based on the stratigraphy of the ideal design section GDP-2, the elements of which are presented in the following table:

Table 1. Stratigraphic Succession in GDP-2.

Idealized Geotechnical Profile GDP-2	
Layer I	Level from +2 to +0.20m (Artificial/Alluvial Deposits)
Layer II	Level from +0.20 to -2.60m ("Alipedon" Marsh Deposits)
Layer III	Level from -2.60 to -4.80 m (Conglomerate-breccia)
Layer IV	Level from -4.80 to -17.30 m (Silty Sands, Sandstones)
Layer V	Level > -17,30 m (Sandy Silts, Siltstones)

3.3 *Geotechnical design parameters*

The geotechnical design parameters utilized in this study were established in accordance with the guidelines outlined in paragraph 2.4.5.2 of Eurocode 7, specifically the Geotechnical Design Part 1: General Rules. These parameters were estimated by considering the outcomes and derived values from laboratory tests, as well as the findings from field tests. This comprehensive approach ensured the incorporation of reliable and relevant data to accurately determine the geotechnical design parameters for the project.

All the values of the geotechnical design parameters that will be implemented in this thesis are summarized in Table 2.

4 MONITORING SYSTEM

Given the extensive nature of projects of such magnitude, continuous monitoring is imperative throughout both the construction phase and after its completion. In line with this requirement, the Piraeus Station implemented a comprehensive array of monitoring instruments to track movements, settlements, and potential deformations that may arise.

Consequently, the Automated Monitoring System (AMS) program was implemented, encompassing the measurement and recording of various data points, including:

- Vertical and horizontal movements of buildings and structures, facilitated by a volumetric measurement system and a 3D movement measurement system (BNOS0282 & BNOS0285).
- Monitoring the level and water pore pressures of groundwater through the utilization of piezometers (BNHC07 & BNHC08, BNBP0050 &BP244).
- Tracking horizontal movements of the diaphragm walls of the trench via the installation of inclinometers (BNDF06).

This study incorporated data obtained from the previously mentioned piezometers, inclinometers, and the 3D movement measurement system to enhance the accuracy of simulating the authentic conditions that prevailed during the construction of the project. By leveraging the measurements

Table 2. Geotechnical design parameters.

Layer Parameters	Layer I	Layer II	Layer III	Layer IV	Layer V	Units
Unit Weight, γ	19	20	23	21.5	20.5	kN/m^3
Friction Angle, φ	28	26	40	36	34	°
Cohesion, c	10	0 (5)	5	10	45	kPa
Dilatancy Angle, ψ	9	0	12	12	10	°
E_{50}^{ref}	40	10 (80)	190	190	110	MPa
E_{oed}^{ref}	30	8 (64)	165	165	110	MPa
E_{ur}^{ref}	120	30 (240)	570	570	330	MPa
Permeability, k	10^{-5}	$3{\cdot}10^{-6}$	$8{\cdot}10^{-6}$	$5{\cdot}10^{-6}$	$4{\cdot}10^{-8}$	m/s

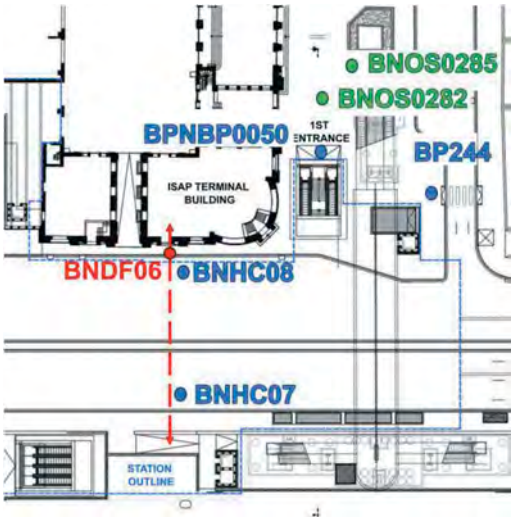

Figure 5. Monitoring instruments and their position in the studied analysis.

obtained from these monitoring instruments, a more robust and realistic representation of the project's construction environment is expected to be achieved.

5 NUMERICAL ANALYSIS AND COMPARISON BETWEEN FINITE ELEMENT CALCULATIONS AND MONITORED DATA

5.1 *Parametric investigation*

Analyses were performed with the finite element code PLAXIS for plane strain conditions, in terms of effective stresses, and for fully coupled flow deformation properties of the soil.

A parametric investigation was carried out with the aim of matching the calculated movements with those measured by the inclinometers and the geodetic targets. A total of 6 scenarios were considered regarding the estimated geotechnical and hydraulic conditions (strength and deformability parameters of the soil, excavation levels, groundwater level, water pumping inside the trench etc). By pursuing this approach, the study aimed to ascertain the closest possible approximation of shared conditions, thereby facilitating the final comparison of data from the instruments employed by the GDP organs. The main features of the scenarios that were examined are summarized in Table 3.

In Figure 6 the deformed meshes of the finite elements at the final stage of the construction stage is presented as calculated by Plaxis for the 1st,2nd,4th and 6th scenario.

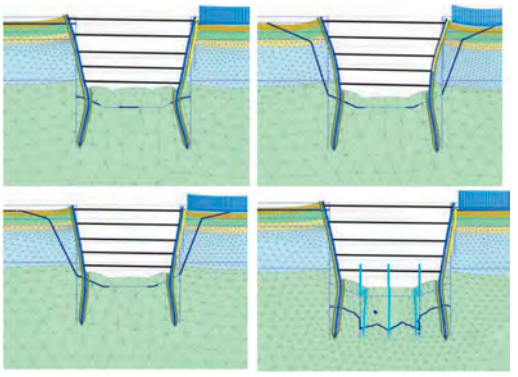

Figure 6. Deformed meshes of the different scenarios (Upper Left:1st scenario, Upper Right: 2nd scenario, Lower Left: 4th scenario, Lower Right: 6th scenario).

5.2 *Results from finite element caclulations*

The maximum values of the calculated displacements in the retaining wall and on the ground surface near the station are presented in Table 4.

5.2.1 *Horizontal displacements of diaphragm wall and inclinometer*

The best comparison between calculated and measured displacements from the monitoring data in the retaining wall is achieved with scenarios 3, 4 and 6. The distributions of said movements are shown graphically in Figure 7.

The smallest deviation for the maximum horizontal movement of the wall results for the 6th scenario and is approximately 20%. On the contrary, the horizontal movements which have resulted from the analyses

Table 3. Parametric Investigation with the altered parameters.

	Scenarios					
Changes	1st	2nd	3rd	4th	5th	6th
Excavation depth level	D.S	M.D	D.S	D.S	M.D	D.S
Grownwater level	Init.+0m	C.o.D	C.o.D	C.o.D	Init.+0m	Init.+0m
Water Pumping	No	No	No	No	Yes	Yes
Calculation Type	P-FCFD	P-C	P-C	P-C	P-FCFD	P-FCFD
Properties of Layer II	Initial	Initial	Initial	Incr.	Init.	Init.

*D.S (Design Study), M.D (Monitoring Data), C.o.D (Cone of Depression), P-FCFD (Plastic-Fully Coupled Flow Deformation), P-C (Plastic-Consolidation), Init. (Initial). Incr. (Increased)

Table 4. Maximum values of the calculated displacements.

Results of Parametric Investigation		Scenarios 1st	2nd	3rd	4th	5th	6th
Maximum Horizontal Displacement of Diaphragm Wall (mm)	East	24.7	21.9	18.9	18.7	27.2	18.8
	West	21.8	21.4	17.6	17.4	25.1	18.4
Maximum Surface Settlements (mm)	East	17.7	23.1	25.4	18	29.5	16.3
	West	9.3	16	21.2	12	14.3	9.8

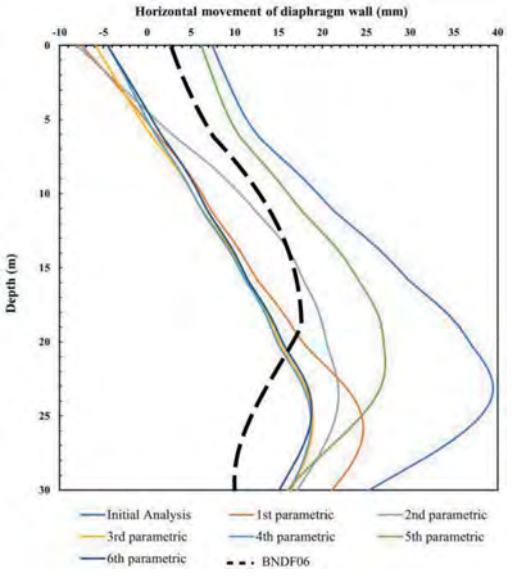

Figure 7. Horizontal displacement of the diaphragm wall compared with readings from inclinometer BNDF06.

that used the excavation levels obtained by the monitoring data are slightly increased, but without exceeding the action limit or alarm limit. Therefore, both scenarios of the parametric investigation regarding the regulations set by Attiko Metro are considered safe.

5.2.2 *Vertical displacements and geodetic targets*

During the construction of the station, the settlements were the most important monitoring size, due to the proximity of the ISAP building to the eastern side of the station trench. The strict limits for the settlements that had to be taken under consideration posed formidable challenges to the project's execution. Specifically, the settlement action limit was 22mm, while the alarm limit was 33mm.

The calculated maximum ground surface settlement based on the initial analysis model exceeded not only the caution limit, but also the alarm limit. As a result, the set of assumptions/considerations regarding the geotechnical and hydraulic conditions is judged as

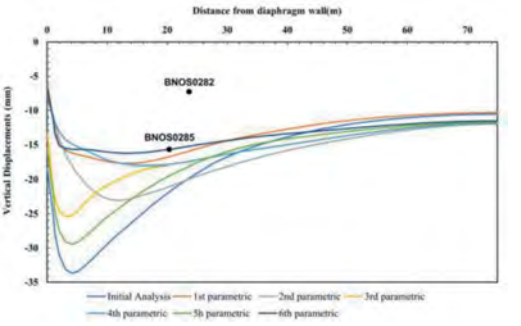

Figure 8. Settlement curves in the east bank of the excavation in comparison with readings from the 3D movement measurement system.

unrealistic. In Figure 8 the calculated distributions of surface settlements from the 6 scenarios are shown and compared to those measured by the prismatic targets BNOS0282 and BNOS0285. It is observed that the measured behaviour is more favourable even than the forecasts of the most optimistic scenario.

5.2.3 *Water pressure, groundwater level and piezometers*

Without a doubt, the measurements provided by the vibrating wire piezometers and the standpipe piezometers were of paramount importance in terms of comparison, aiming to achieve a more precise simulation through the analyses.

Figure 9 shows the estimated water table level (scenarios 2, 3and 4) in comparison with the readings from the piezometers BP244 and BNBP0049. It is observed that the measured groundwater level is identical to the initial one (before start of construction activities) at distances from the wall longer than 15 m.

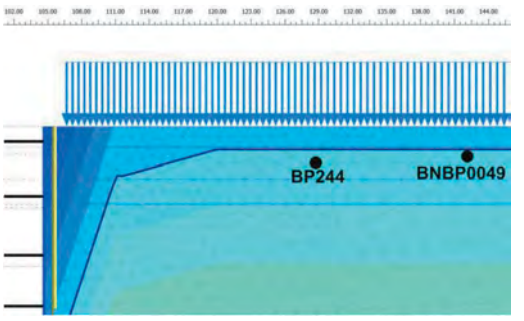

Figure 9. Groundwater level during its depression.

Figure 10 shows the calculated time series of the pore pressure at the upper (-37.6 m) and lower (-39.6 m) positions of the BHNC08 piezometer and are compared with the corresponding measured ones. The comparison or scenarios 2, 4 and 6 is very satisfactory, in contrast to the predictions based on the original analysis model, which show a huge

deviation from the measured behaviour. This justifies to a significant extent the errors as well the large movements based on the original analysis model.

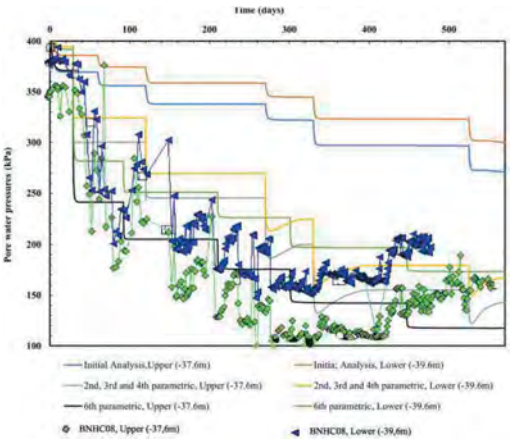

Figure 10. Pore water pressure at the Upper and Lower positions within the vibrating wire piezometers.

6 CONCLUSIONS

Two-dimensional numerical analyses of the excavation and temporary retaining structure were examined, the aim which was the matching of the calculated with the measured displacements in the retaining wall and on the ground surface. The effect of crucial factors in the behaviour of the temporary support system of the station was investigated parametrically, such as: the stiffness of characteristic soil layers, the pumping conditions and groundwater level, the numerical method used (coupled mechanics - hydraulic analysis or undrained behaviour - consolidation). From the results of the analyses, it was found that the factors with the dominant role are the pumping conditions and groundwater level as well as the excavation step in combination with the depth of the struts placement.

ACKNOWLEDGEMENTS

The authors thank Attiko Metro S.A. for its valuable assistance during the preparation of the present paper.

REFERENCES

[1] Attiko Metro SA, Extension of Line 3: Haidari – Piraeus - Geotechnical Investigation Results Evaluation Report (Section from K.P 1+418 to K.P 8+969) Technical Report, 2013.
[2] Attiko Metro SA, Extension of Line 3: Piraeus Station (Geotechnical Evaluation of Design Parameters Report), 2015.

Tunnelling for a Better Life – Yan, Celestino, Thewes & Eberhardt (Eds)
© 2024 The Author(s), ISBN 978-1-032-80042-4
Open Access: www.taylorfrancis.com, CC BY-NC-ND 4.0 license

Karanga-a-Hape Station MC21 junction – Collaborative solutions for complex geology and geometrical constraints - Tackling the challenges at Karanga-a-Hape Station caverns

Arun Sarathchandran*
AECOM Australia, Sydney, Australia

Geoffrey Charlesworth
AECOM Australia, Brisbane, Australia

Rhys Graafhuis
Tonkin and Taylor, Auckland, New Zealand

ABSTRACT: The geometry and geology at the southern end of Karanga-a-Hape Station combine to create a challenging set of constraints for design and construction. These were effectively negotiated through the design phase via a collaborative approach between the construction and design teams. Challenges included: development of the overall sequence in order to develop an efficient geometry for the installation of pre-support over the junction in the area; managing the design in response to discovery of a large, fractured fold hinge traversing the junction; refinement of the design through collaboration with the construction-team to manage the risks associated with the junction breakthroughs.

Keywords: Fold, canopy tube

1 INTRODUCTION

The City Rail Link (CRL) Project includes the design and construction of two underground rail stations; a redevelopment of an existing surface rail station; two new rail tunnels; and connections to the existing North Auckland Line (NAL). The twin tunnels connecting the stations extend from Albert Street to Newton where they bifurcate through a grade separated interchange with terminations at Mt Eden Station and between Mt Eden Road and Normanby Road bridges. Connections to the NAL are via east and west grade separated connections.

The twin tunnels were driven northwards from Mt Eden towards the CBD via TBM drives (using a single TBM, first along MC30, then MC20). Karang-a-Hape Station is aligned roughly north-south along Pitt Street, with the intersection with Karang-a-Hape Road over the approximate mid-point of the station. The station layout comprises two station shafts, one at Mercury Lane in the south, and one at Beresford Square in the north, two platform caverns and five connection adits. The two platform tunnels (MC20 and MC30) and adits have been mined using roadheaders. Sub-zone MC21 encompasses the junction between a ventilation adit at the southern end of the station, and the MC20 platform tunnel (Figure 2).

Figure 1. Overall scheme layout.

The MC21 Junction geometry is influenced by the need to connect ventilation rooms in the Mercury Lane shaft with the southern end of both platform tunnels via MC20 and the adit linking the end of each platform cavern. Four ducts are routed through MC21 totalling 16 sqm. providing tunnel ventilation supply and over track exhaust connections for both platform caverns link the over-track exhausts. The

*Corresponding author: Arun.Sarathchandran@aecom.com

DOI: 10.1201/9781003495505-45

solution results in an oversized platform cavern through the MC21 junction, and a local trench into the adjoining ventilation adit (see Figure 3).

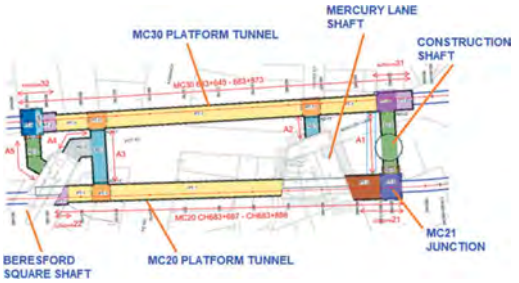

Figure 2. Karang-a-Hape Station layout.

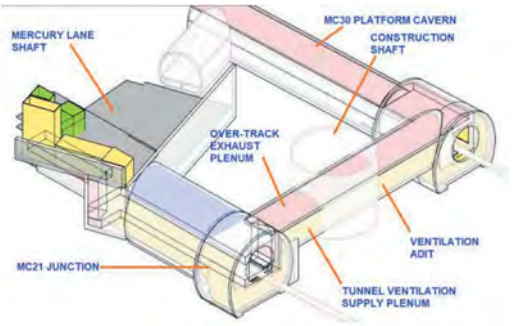

Figure 3. Karang-a-Hape Station – Geometry at south end.

The mined tunnels are designed with a two-pass lining system, an initial, temporary primary support shell, within which cast insitu concrete linings are installed. The platform caverns are approximately 15m span, and 11-14 m high. The ventilation adit is approximately 9m span, and 7-9m high. The mined station caverns and adits are designed as drained structures, with a groundwater pressure relief system.

2 GROUND CONDITIONS

2.1 *Geological profile*

The geological profile in the vicinity of MC21 consists of fill and alluvium over the sedimentary rocks of the East Coast Bays Formation (ECBF). The ECBF was formed during the Early Miocene, and consists of the following major units in the vicinity of MC21:

- Predominantly interbedded very weak, sandstone and siltstone (EU2). Typical unconfined compressive strength (UCS) values for un-weathered EU2 is 1-5MPa.
- Well cemented volcaniclastic, polymitic sandstones and conglomerates (EU3), typically weak to moderately strong and more massive than EU2.
- Channelised Sandstone (EU3cs) - around Karang-a-Hape Road there is a very specific sequence of conglomeratic sandstone (2-3m thick) grading up into fine sandstone (c.8m thick).

The topography, and rockhead levels, drop away rapidly to the south, such that cover over the crown on MC21 narrows to less than 1m. An inferred geological section along the southern end of the MC20 platform cavern is shown in Figure 4.

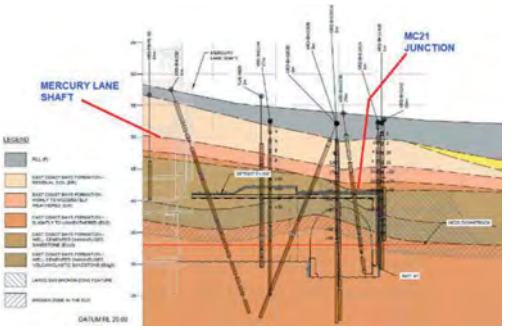

Figure 4. MC21 geological long section.

2.2 *Geological structure*

A normal fault zone was identified during the site investigations, and subsequently mapped during excavation of the tunnels running through the MC21 junction and the Mercury Lane Shaft, Adit 1 and MC30 tunnel (Figure 5). Zones of brecciated rock were encountered within the fault zone, particularly in areas where shear zones intersected. Either side of the fault, zones of blocky rock mass were observed, this graded laterally into massive sandstone (Figure 6). The fault zone varied between 6 to 12m in width and displayed up to 5m vertical offset of the EU2 unit below the Channelised Sandstone. A number of discrete shear zones where observed within the fault zone, these where infilled with 30 to 50mm of highly plastic clay gouge. Defects within the massive rock massive comprised very widely spaced (5 to 10m) orthogonal joint sets.

2.3 *Groundwater*

The Karanga-ā-Hape Station area is located in the upper reaches of the ridge line that runs northwards, towards the Waitemata Harbour area. Within this zone the groundwater regime is relatively complex, with four to five levels of perched groundwater systems identified, and a suspected fault-bounded groundwater network, where perched tables are gradually under-drained in cells towards the underlying regional groundwater level. The mined station caverns and adits are designed as drained structures, with a groundwater pressure relief system.

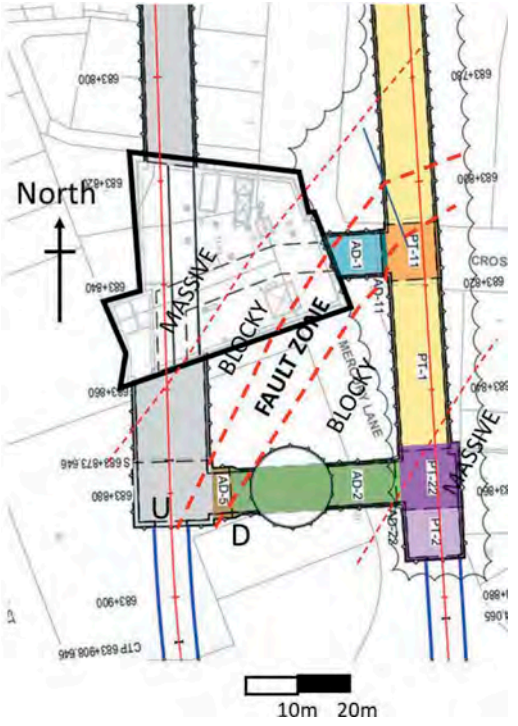

Figure 5. Mapped shear zone associated with normal faulting.

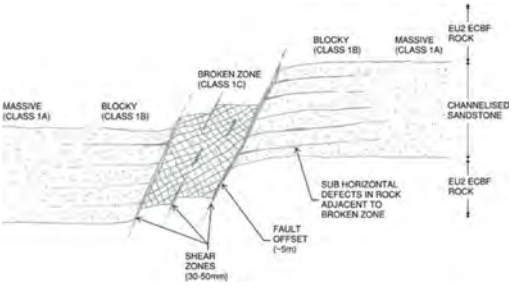

Figure 6. Typical rock classes in the Channelised Sandstone. Zones of broken brecciated rock occurs where shear zones intersect. A zone of blocky rock occurs sub-horizontal defects adjacent to the fault intersect the sub-vertical orthogonal joint sets. Sketch courtesy of A Thorpe.

3 DEVELOPMENT OF MC21 SEQUENCE AND GEOMETRY

3.1 *Geometry*

The geometry and sequence for the MC21 junction was developed as a close cooperation between the design and construction teams, acknowledging the proposed general arrangement, the expected ground conditions, interfaces with adjacent structures, and construction programme. The platform caverns at the southern end of the station were accessed via a temporary construction shaft from surface (Figure 2), with the caverns to be constructed prior to TBM transit. The southern station entrance and plant building, the Mercury Lane Shaft, was constructed top-down, lagging behind tunnel construction.

Options for advancing MC21 access from the direction of the ventilation adit were considered, with a phased construction of the arch profile over the top of the junction under spiles rejected in favour of an approach from the north from the direction of the Mercury Lane Shaft. This offered the following advantages:

- Enabled the use of canopy tubes in the area of non-existent to limited rock cover over the junction of the adit.
- Allowed for break-in from the direction of the adit under mature sprayed concrete (f'c > 20MPa) installed in MC21.

Approach from the north was achieved via a construction adit driven through the base of the partially excavated Mercury Lane Shaft (see Figure 7).

Figure 7. Construction access for MC21.

The geometry local to the junction was developed in response to inferred rockhead levels extending south from the Mercury Lane Shaft consisted of (from south to north, see Figure 9):

- Skewed headwall and entry to MC21 under 4m long rock-bolts and shotcrete. The profile here widened as it exited the Mercury Lane Shaft footprint, and transitioned from the narrow construction adit span to a split top-heading for the platform cavern (Figure 10).
- Expansion of the profile (maintaining the split top-heading) under spiles, shotcrete and lattice girders in an area of reducing rock head cover, in order to create sufficient space for the installation of canopy tubes southwards.
- Continuation of the split top-heading southwards under the canopy tubes through the area of the junction with the adit, with the primary support consisting of lattice girders and shotcrete.

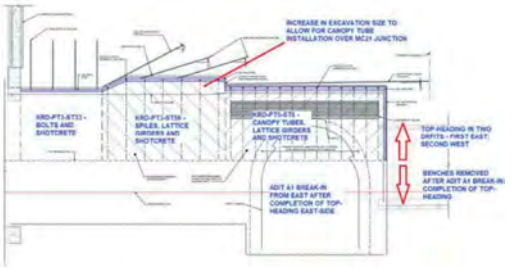

Figure 8. MC21 Arrangement of primary support types.

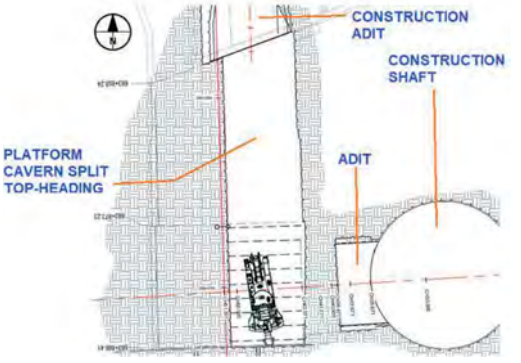

Figure 9. Platform cavern split top-heading layout.

The adit enters MC21 from the east, with the crown level of the adit approximately 2m below that of the platform cavern. This allows break-in of the adit below the level of the canopy tubes over MC21, inside collar reinforcement installed in MC21 prior to the break-through.

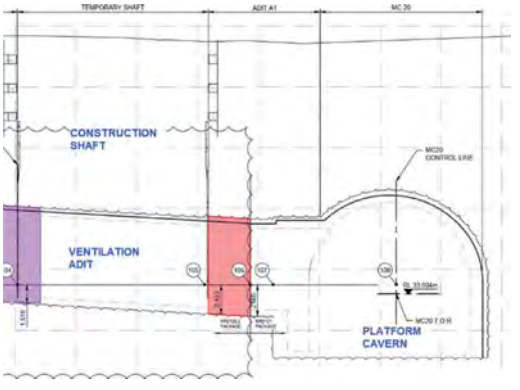

Figure 10. Section along the ventilation adit.

3.2 *Construction sequence*

The base-line construction sequence for excavation and primary support was developed in response to the geometry and ground conditions described above, and involves the following steps:

A. Break-out from the construction shaft to east and west. The drive to the west terminates short of MC21 (Figure 9).
B. Access into the northern section of MC21 via a construction adit driven through the unexcavated base of the Mercury Lane Shaft. This enables excavation of MC21 whilst top-down construction of the shaft proceeds (Figure 8).
C. Split top heading down the eastern side of MC21.
D. Break-in of the adit top-heading into the completed eastern side drift in MC21 (Figure 11).
E. Top-heading completed by drift down the western side of MC21. The walls of the Mercury Lane Shaft in the southwest corner require a pillar of rock to be maintained for support. The pillar to be safely removed after the structure at the B2 Level constructed (Figure 12).
F. Removal of the rock pillar adjacent to Mercury Lane Shaft, and completion of the top-heading, after construction of the shaft B2 level structure.
G. Closure of access through the construction access through the Mercury Lane Shaft, and backfill of the adit, allowing shaft construction to continue.
H. Excavation of benches from the direction of the construction shaft and ventilation adit.

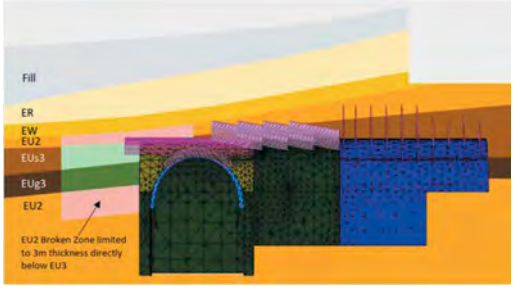

Figure 11. MC21 adit break-through.

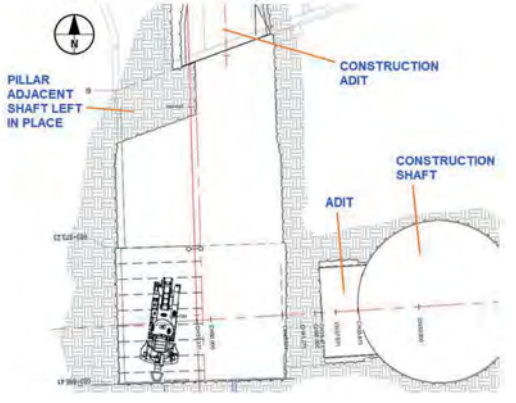

Figure 12. MC21 western side drift.

4 PRIMARY SUPPORT DESIGNS

4.1 *Ground model for MC21*

The design of the MC21 Zone, which encompasses the junction with Adit A1 and interfaces with the Mercury Lane shaft to the north, relies predominantly on numerical analyses conducted using the 3D Plaxis software. Figure 13 presents an illustration of the 3D Plaxis model. To assess the reliability of the design, the following two distinct ground models were developed.

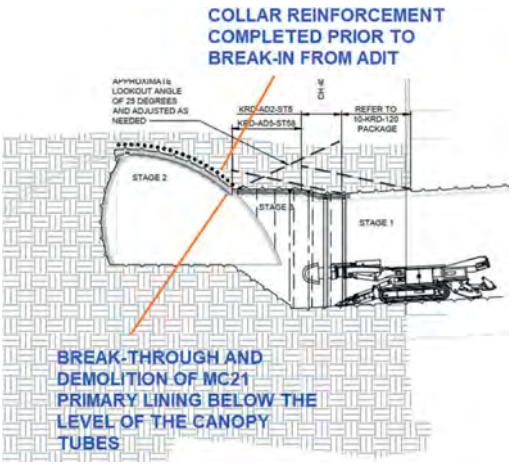

Figure 13. Long section of the modelled geometry with broken zone intersection the tunnel at ventilation adit MC20 cavern junction.

4.1.1 *Characteristic-Case (Model #1)*

This model is constructed based on inferred geological data from boreholes and face mapping. It comprises a fractured and folded zone, roughly 10 meters wide, with a prevailing orientation of approximately NE-SW and a dip to the SE. The geological strata affected by this zone include the beds of EU3 and the overlaying and underlying layer of EU2, which extends up to 3 meters below the base of the EU3. The rock-mass strength parameters for this zone are derived from a Geological Strength Index (GSI) of 40, in accordance with a characteristic, observation-based condition.

4.1.2 *Lower-bound ground model (Model #2)*

This model maintains the same geometric characteristics as the characteristic-case model but incorporates rock-mass strength parameters corresponding to a lower-bound condition. The rock-mass strength parameters for this zone are based on a GSI of 25. Additionally, the fractured zone in this model extends to a greater depth compared to the characteristic-case.

4.2 *Geotechnical parameters*

To model the stiffer unload/reload behaviour compared to the initial loading modulus, hardening soil constitutive model was adopted for the design. However for EU3 rock unit, geotechnical data suggests no substantial difference between loading and unloading modulus hence loading/unloading modulus was kept the same for EU3 rock. Parameters adopted for numerical modelling are shown in Table 1 below.

Table 1. Parameters adopted for numerical modelling.

Unit	*γ (kN/m³)*	*ϕ' (°)*	*c' (kPa)*	*E_{50} (MPa)*	*E_{ur} (MPa)*
Fc2	*19*	*28*	*8*	*20*	*60*
ER	*18*	*30*	*7*	*20*	*60*
EW	*19*	*35*	*25*	*100*	*300*
EU2	*20*	*40*	*100*	*400*	*1000*
EU_u3	*21*	*45*	*400*	*2500*	*6500*
EU_g3	*21*	*45*	*400*	*3500*	
Fault Zone (FZ)					
EU2 (FZ) GSI 55	*20*	*40*	*25*	*200*	*500*
EUs3 (FZ) GSI 40	*21*	*40*	*60*	*400*	*1000*
EUg3 (FZ) GSI 40	*21*	*40*	*60*	*600*	

4.3 *Numerical modelling*

The presence of a broken rock zone as shown in Figure 5, coupled with reducing rock cover towards the southern end, combined with the complex geometry of the tunnel makes the analysis a three-dimensional problem. Consequently, a detailed three-dimensional numerical modelling of the cavern intersection was undertaken using Plaxis 3D software with geological surfaces imported from a Leapfrog model to generate a more accurate representation of the geological conditions of the area. Moreover, the 3D model also facilitated an evaluation of how the broken zone influenced the surrounding rock mass. Figure 13 shows a long section of the modelled geometry in Plaxis 3D.

Outline details of the support types developed for application in the MC21 Zone are listed in Table 2. To mitigate tunnel face stability concerns, a split heading approach was adopted through the area of the junction. Canopy tubes were positioned in a nearly horizontal orientation in order to maximise cover.

Figure 14 shows the excavation sequence adopted in Plaxis 3D with partial drifts with top-heading tunnel advances varying from 1.8m for rock bolted support to 1m for tunnel advance under canopy tubes.

Table 2. Summary of primary support types.

Cavern – Zone	Primary support	Sequence
MC21 – North of the junction with Adit A1	150-200 thk. fibre-reinforced shotcrete. 4m long rock-bolts.	Top-heading and bench
MC21 – North of the junction with Adit A1 – Area of reducing cover	Profile expands to facilitate installation of canopy tubes to the south. 150-300 thk. fibre-reinforced shotcrete. Spiles in the crown, 4m long rock-bolts on sidewalls and bench.	Top-heading and bench
MC21 – Junction with Adit A1	Single round of canopy tubes across the intersection and over the southern headwall of the platform cavern. 150-350 thk. fibre-reinforced shotcrete. Lattice girders at 1m centres. 4m long rock-bolts on sidewalls and bench.	Split top-heading and bench
Adit A1	Spiles from east and west over break-through. 300 thk. fibre-reinforced shotcrete. Lattice girders at 1m centres. 4m long rock-bolts on sidewalls and bench.	Top-heading and bench

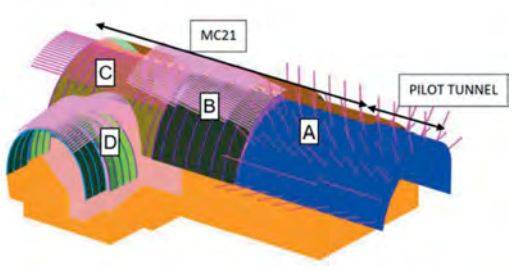

Figure 14. Mining sequence adopted A). East Side drift under rock bolts B). Spile support with elevated crown to enable canopy tube installation at intersection zone C). Complete side drift under canopy tube D). Adit excavation and break-in.

4.4 *Analysis results*

4.4.1 *Tunnel deformations*

Figure 15 shows a contour plot of ground convergence deformations on the primary tunnel liner. Maximum deformation occurs above the intersection zone and coincides with the location of the fractured zone. The total displacement at the tunnel crown was estimated to be in the order of 20 to 30mm.

4.4.2 *Surface settlement*

The surface settlement was estimated to be approximately 20mm. Maximum settlement is expected directly above the MC20-Adit junction, coinciding with the location of the fault or broken zone modelled. Figure 16 illustrates the projected contours of ground settlement upon completion of tunnel mining operations.

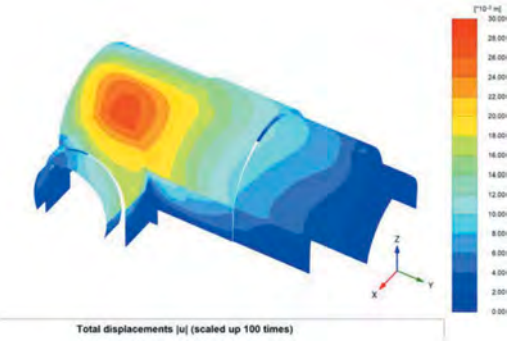

Figure 15. Predicted ground convergence at tunnel crown.

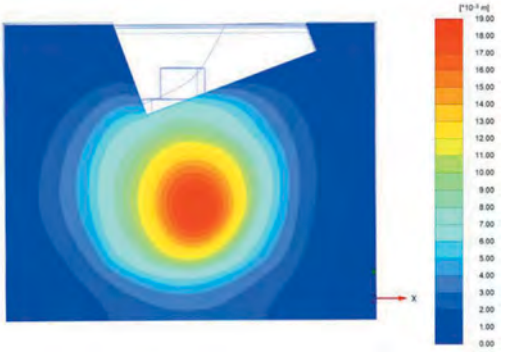

Figure 16. Maximum predicted surface settlement at MC21 junction.

5 DESIGN REFINEMENTS

5.1 *Refinements in response to observed conditions*

Following the commencement of construction, and subsequent to additional ground investigations, the design was further refined. The significant observations and ground investigation data were assessed, and the following conclusions drawn:

- Higher rockhead extending further south, enabling an active support design to be extended southwards (Figure 17).
- Better than previously adopted characteristic strength parameters for the broken-EU3 zone inferred to affect the eastern side of the MC21 junction.

- Observations from the MC30 excavations suggesting that at least locally, that the broken-EU3 was unstable/meta-stable when exposed in the face, with sliding of blocks on sub-vertical joints noted during excavation.
- Observations of persistent inflows from probeholes drilled into the MC21 junction zone from the direction of Adit A1.

The subsequent design refinements allowed for the following changes:

- Extension of the section under bolts and shotcrete southwards (Figure 17).
- Adoption of full width top headings south from the shaft to the end of MC21, and increase in height of the top heading. These refinements supported by a requirement for mandated ring cut and buttress and face dowels in the area under the canopy tubes; rock bolts in the areas below the canopy tubes.
- Elimination of lattice girders in the primary support linings north of the area of the adit junction.
- Elimination of the need to retain the rock pillar adjacent to the Mercury Lane Shaft, allowing for opening up of the full top-heading face to the south of the shaft. This required the opening up of a panel of the top-heading in stages adjacent to the shaft wall (Figure 18).
- Development of additional mitigations to deal with the potential for poor ground at the face, or at the locations of the primary support elephants feet.

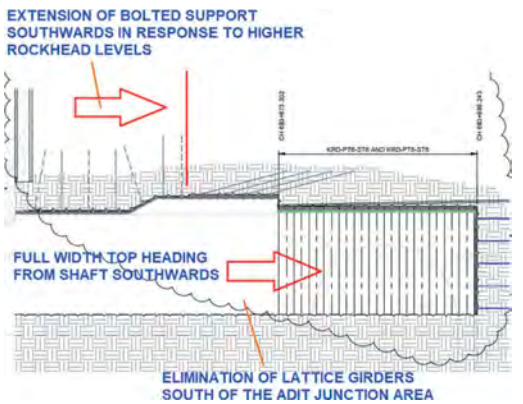

Figure 17. MC21 refinements.

5.2 *Numerical model refinements*

5.2.1 *Full face top heading*

Following the commencement of tunnelling, improved geological parameters and an updated geological model with higher rock-cover extending further south were developed. This enabled extension of the bolted solutions further south, and exploration of the potential to move to a full width top-heading advance. The 3D numerical model was updated to a full-face model to

Figure 18. Initial widening of MC21 profile south of the Mercury Lane Shaft.

test whether a full-face advance through the area of the junction could be supported. Modelling results showed with improved geological parameters that a full-face advance was feasible with ground movements and shotcrete lining loads within acceptable limits. Bending moments within the canopy tubes were also within acceptable limits for the full face heading as shown in Figure 19. A further sensitivity check conducted with more unfavourable ground conditions showed the requirement of a widened elephant footing at the top heading invert level, a detail subsequently added to the design as a mitigation measure.

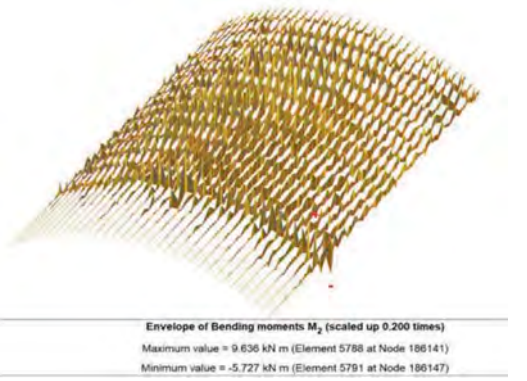

Figure 19. Canopy tube bending moment envelop after the end of tunnelling.

A series of 2D models were also modelled for different sections and lining capacities were compared with the 3D modelling results, both were comparable and within capacity limits except at the intersection zone where the 3D model captured the force redistribution of the intersection area more realistically. Subsequently a reinforced section around the breakin area was designed to account for tensile stresses at the breakout zone (see Figure 20).

5.2.2 *Elimination of lattice girder for spile support*

In the original design, lattice girders were assumed to act as reinforcing elements especially for early

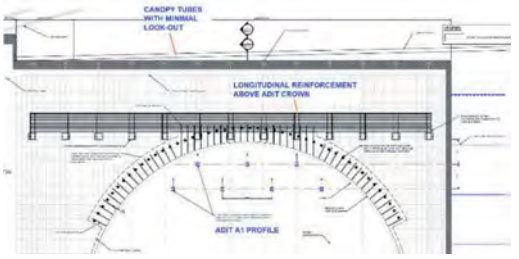

Figure 20. Junction reinforcement detail.

age shotcrete to provide sufficient flexural capacity to accommodate additional loading transferred from spiles. A series of numerical modelling checks were conducted by assuming spile loads acting on the shotcrete shell as eccentric loads as well as a uniformly distributed load acting on the entire spiled cross section. The loading on the shotcrete lining was conservatively assumed as a wedge load acting on the lining in addition to ground load. Early age shotcrete strength was defined as 8MPa and the results showed that combined ground loads acting on shotcrete are within the capacity limits, hence allowing for the elimination of lattice girders from the sections under spiles immediately north of the junction with Adit A1.

6 CONCLUSIONS

The primary support designs for the Karanga-a-Hape Station MC21 Junction excavation were developed and refined through close collaboration between the construction, geotechnical and tunnel design teams, with feedback leading to improved designs leading to enhanced cost and schedule outcomes. Ground conditions were challenging, as the junction location corresponds to an area of low cover, and a normal fault zone. The initial designs and sequences were developed to enable opening up of the junction from the north, allowing for the installation of canopy tubes tight to the cavern profile through the area of low cover. This in turn allows the break-in from the east of the ventilation adit beneath a mature cavern arch with a reinforced collar zone. The designs were further refined as construction proceeded to respond to local higher than expected rock cover, and better than originally predicted fault zone parameters. This paper has outlined the core principles behind the primary support design, the design challenges for the cavern excavation as well as the strategies employed to enhance the design and construction schedule. The successful completion of this project highlights the collaborative efforts between the design and construction teams, ultimately resulting in a highly favourable outcome.

REFERENCES

Chang, Y., Stille, H., 1992. Influence of early-age properties of shotcrete on tunnel construction sequences. Shotcrete for Underground Support VI, American Society of Civil Engineers, pp. 110–117.

John, M., Mattle, H., 2002. Design of Tube Umbrella. Tunel - ROCNIK, Czech Tunneling Committee and Slovak Tunnelling, Vol. 3, no. 11, pp. 1–11,.

John, M., Mattle, H., 2003. Factors of shotcrete lining design. Tunnels & Tunnelling International, Vol. 35, no. 10, pp. 42–44.

NZS 3101, 2006. Concrete structures standard. Standards New Zealand, Wellington, New Zealand.

Tunnelling for a Better Life – Yan, Celestino, Thewes & Eberhardt (Eds)
© 2024 The Author(s), ISBN 978-1-032-80042-4
Open Access: www.taylorfrancis.com, CC BY-NC-ND 4.0 license

Design of temporary cofferdam and deep excavation for cofferdam tunnel of Shenzhen-Zhongshan Link

Zheng Shi, Chun Ning He*, Long Yu & Qiao Wang Xia
Shanghai Tunnel Engineering & Rail Transit Design and Research Institute, Shang Hai, China

ABSTRACT: Considering the layout of the interchange ramp on the East Artificial Island of Shenzhen-Zhongshan Link, the width and construction difficulty of the immersed tube tunnel, as well as the influence of Fuyong Wharf and other factors, a temporary cofferdam is built in the sea on Shenzhen side as the water retaining structure, then the open excavation and the structure of the cut and cover tunnel with widened and diverging section is implemented within the cofferdam, to ensure the construction feasibility of the tunnel with variable cross-section and large-span and the adaptability of the curved and widened tunnel elements. The engineering geology of the Pearl River estuary is complicated, and the soil layers are variable and unevenly distributed. The cofferdam and island are built on soft silt layer with the maximum thickness of 15m in the sea. The elevation of the formed land area is 5-7.5m lower than the sea level. The maximum depth of excavation is up to 23m below the sea level, and the excavation width is up to 70.7m at the widest. The construction safety of the cofferdam and excavation must be ensured, which poses great challenges to the engineering construction. This paper provides a detailed introduction to the engineering scope and structural form of the cofferdam, design scheme and calculation method of the cofferdam and retaining structure, serving as references for similar projects in the future.

Keywords: cofferdam tunnel, double-row steel sheet pile cofferdam, marine environment, complicated geological conditions, extra-wide excavation

1 PREFACE

Shenzhen-zhongshan Link is located in the core of Guangdong-Hong Kong-Macao Greater Bay Area, which directly connects Shenzhen Special Economic Zone and Zhongshan City. As a sea-crossing link integrating "tunnel, artificial island, bridge and underground interchange", the project connects with the Jihe Expressway in the east, passing through the south side of Shenzhen Airport and the Pearl River estuary, and finally reaches the Zhongshan Xinlong Interchange in the west, where it connects with Zhongkai Expressway. The project is 24km long in total with eight lanes in both directions. The project is designed in highway standards with a design speed of 100km/h. The sea section is an immersed tube tunnel, the standard element of which is 46m wide.

According to the function and traffic organization of the project, the East Artificial Island is built on the side of Shenzhen, which connects with the existing Guangzhou-Shenzhen Coastal Expressway through an underwater interchange. According to the overall arrangement, the Ramp F and G respectively merge into the immersed tube tunnel. The element width in the merging area gradually increases from a standard width of 46m to 70.7m; and then the Ramp F and G are separated from the immersed tube tunnel and connect to the island interchange. See Figure 1.

Figure 1. Location relationship between cofferdam tunnel and tunnel under east artificial island.

*Corresponding author: he.chunning@stedi.com.cn

DOI: 10.1201/9781003495505-46

In order to reduce the total length and the width of the widened immersed tube section, to minimize the risk of the tunnel element construction, and to ensure the construction feasibility of tunnel structure with variable cross-section and large-span, it is considered to build a cofferdam tunnel on the west side of the East Artificial Island, without affecting the interconnection arrangement. This means to construct a temporary cofferdam in the estuary, and to implement the excavation and structure of the cut and cover tunnel with widened and diverging sections within the cofferdam. Upon completion of the main structure. the temporary cofferdam will be removed after the backfill and coverage, and restored to the original seabed surface.

2 DIFFICULTIES IN CONSTRUCTION OF COFFERDAM TUNNEL

2.1 *Complicated environmental conditions*

The tidal current in the estuary is of irregular semi diurnal type, in reciprocating motion. The average tidal range is 0.85-1.70m and 2.30-3.20m at the maximum.

The region is in the subtropical marine monsoon climate zone. Affected by the alternating influence of Eurasia and tropical oceans, the weather and climate are complex and changeable, and it is vulnerable to the gale and rainstorm brought by tropical cyclones from June to October every year.

The engineering geological conditions in the Pearl River estuary are complicated and changeable. The soil layers include silt, clay, mucky clay, residual soil, completely weathered granite, and strongly weathered granite from top to bottom, and are in extremely uneven distribution. The maximum thickness of the surface silt in the area where the cofferdam constructed is up to 15m.

2.2 *Constraints from existing wharf*

The north side of the cofferdam tunnel is adjacent to the Fuyong Airport Wharf. The minimum clear plane distance from the temporary cofferdam to the wharf is only approximately 49m. During cofferdam tunnel construction, the normal operation and safety of the wharf shall be guaranteed.

2.3 *Challenges in construction of cofferdam and extra-wide excavation*

During island backfilling and land-forming construction in the silt layer, the following requirements shall be fully considered including the ground bearing capacity, flexural and shear bearing capacity, anti-erosion and anti-seepage, and stability requirements of cofferdam structure. As a temporary work, the cofferdam's economy and ease of demolition shall also be considered.

Different from the traditional excavation, after forming the land, the land elevation is 5~7.5m lower than the sea level, the deepest excavation of the tunnel is 23m below the sea level, the widest is 70.7m, and the excavation is close to the temporary cofferdam. The excavation design shall consider the influences of backfill load of cofferdam, and the water level fluctuation as well.

Considering the site conditions and according to the construction organization plan, it is required to build a trestle in the middle of the excavation. The trestle is 14m wide, running longitudinally and serving as a heavy load passage during the construction.

In view of the above complex construction environment and load conditions, the safety of cofferdam and excavation must be ensured in the such an extra-wide excavation for the cofferdam tunnel, which brings strict requirements for design and construction.

See Figure 2~4 for site photos of the temporary cofferdam and tunnel excavation.

(a)Cofferdam closing (b)Land formation

Figure 2. Bird's-eye view of cofferdam.

Figure 3. Bird's-eye view of excavation in cofferdam.

Figure 4. Excavation and support arrangement in cofferdam.

3 DESIGN OF TEMPORARY COFFERDAM

3.1 *Determination of temporary cofferdam scope*

The scope of cofferdam shall be determined by comprehensively considering the layout of interchange ramps, width and construction difficulty of tunnel elements, impacts on adjacent Fuyong Wharf, feasibility of constructing tunnel structure with variable sections and large-span and other factors.

Considering that the tunnel axis on Shenzhen side is located on a horizontal curve, and some of the tunnel elements are curved, two schemes as long cofferdam and short cofferdam are proposed to minimize the total length and the width of the widened immersed section as possible or to make all the tunnel elements straight.

3.1.1 *Long cofferdam scheme*

As the straight element will be more convenient for prefabricating, towing, sinking, and installation, the western end of the cofferdam in the long cofferdam scheme follows the principle as all the tunnel elements are straight. That is, all the widened and curved tunnel section need to be cast-in-situ in the cofferdam. According to the layout of the route, the tunnel section starts at mileage K7+672.6 as the straight section with standard width; the end mileage of the cofferdam is at K7+730. The starting mileage of the cofferdam at K6+513 is determined based on the mileage of Eastern Artificial Island wall at K6+560.So the long cofferdam scheme is approximately 1217m long along the tunnel axis, and the formed land area is approximately 249,000m^2. As the cofferdam encroaches into the Dachan Waterway and Airport Branch Waterway, the construction of the long cofferdam scheme is planned in two phases and three sectionsto minimize the impact on the waterways, as shown in Figures 5 and 6. However, in the construction of Phase I, temporary diversion measures are still required for the Dachan Waterway and Airport Branch Waterway. The length of the route need to be diverted and dredged will be 6.1km, and the dredging volume will be 1,776,600 m^2.

The Section I on the west side (K7+270~K7+730) and Section II on the east side (K6+513~K6+958) of Phase I will be constructed firstly; after the cofferdam is completed, the cut and cover tunnel sections between K7+330~K7+665 and K6+550~K6+885 respectively in the cofferdam will be constructed simultaneously.

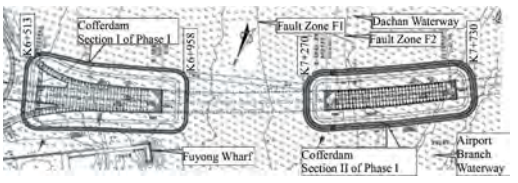

Figure 5. Layout of long cofferdam scheme (phase I).

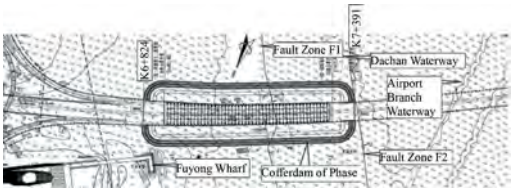

Figure 6. Layout of long cofferdam scheme (phase II).

The cofferdam Phase II is between the mileages of K6+824 and K7+391. Upon completion, the cut and cover tunnel sections will be constructed between the mileages of K6+885 and K7+330 in the cofferdam. The two phases construction of cofferdam and the corresponding tunnel structure will take about 63 months.

3.1.2 *Short cofferdam scheme*

As the long cofferdam scheme has a longer distance into the sea area and encroaches both of the Dachan Waterway and Airport Branch Waterway, a short cofferdam scheme is proposed to ensure the smooth operation of elements towing and sinking. This scheme may also minimize the impact on the wharf during the construction, minimize the impact on the Pearl River flood control and avoid construction risks. The western end mileage of the cofferdam changes to be at K7+072, and the starting mileage of the cofferdam to be as same as the long cofferdam scheme at K6+513. So the cofferdam is approximately 559m long along the tunnel axis and the formed land area is approximately 80,000m^2. See Figure 7.

The short cofferdam will be completed in one stroke. Upon completion, the construction of cut and cover tunnel sections between K6+550~K7+030 in the cofferdam will begin. The total construction period will be approximate 25 months.

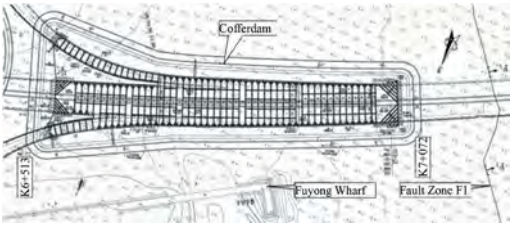

Figure 7. Layout of short cofferdam scheme.

3.1.3 *Comprehensive comparison of temporary cofferdam scope*

For the short cofferdam scheme, six tunnel elements still remain in the curved section. The width of these elements varies in the range of 46~55.46m. To facilitate the selection of construction equipment, cost control and reduce construction difficulty, the length of curved and widened elements shall be considered based on the principle of equivalent drainage volume to standard elements during floating transportation.

Considering the safe operation of underwater interchange, difficulty in construction of tunnel element, construction period and cost, impact on water conservancy, flood control, navigation channels and other factors, the short cofferdam scheme is recommended.

3.2 *Selection of cofferdam structure*

According to the practical cases of cofferdam tunnel construction, the main types of cofferdam include: steel pipe pile cofferdam, steel sheet pile cofferdam, wood pile cofferdam, membrane bag sand cofferdam and the others.

Table 1. Comparison of temporary cofferdam structure types.

Cofferdam type	Applicable conditions	Features
Double-row steel sheet pile cofferdam	Suitable for soft ground areas with strong adaptability to ground	(1)Low soil usage, strong erosion resistance. (2)Small settlement. (3)The overall stiffness is relatively high, bringing good safety and stability of the cofferdam. (4)The steel sheet piles can be leased and recycled after completion. (5)The construction process is relatively complex.
Double-row wooden pile cofferdam	Suitable for soft ground areas with strong adaptability to ground	(1)Low soil usage, strong erosion resistance. (2)Small settlement. (3)Good safety and stability of the cofferdam. (4)The wooden piles may be more economical. (5)The construction process is relatively complex.
Membrane bag sand cofferdam	Suitable for areas with high soil and rock content, with moderate adaptability to ground	(1)Large amount of sand and soil. (2)The settlement may be relatively high. (3)Higher requirement for the bearing capacity of the ground. (4)The cross-section is large and has a significant impact on the marine environment. (5)The construction process is relatively simple.

The selection of cofferdam structure type and materials shall be based on the requirements of water depth, flow velocity, geological conditions, tunnel structure type and other considerations. The selection shall not only consider the applicable conditions, advantages and disadvantages of different types of cofferdams, but also consider the characteristics of the project. Due to high cost, the steel pipe pile cofferdam is not considered. Table 1 shows the comparison of different types of cofferdams. From the comparison table and the characteristics of the project, the double-row steel sheet pile cofferdam is adopted thanks to its features of fast construction speed, convenient demolition, and high cost-effectiveness.

3.3 *Cofferdam structure design*

3.3.1 *Standard and principle of design*

(1) The lifetime of the cofferdam shall be 2-3 years, and according to *Design Specifications for Cofferdam in Water Resources and Hydropower Engineering* (SL 645) and *Classification and Flood Standards for Water Resources and Hydropower Engineering* (SL 252), the cofferdam level shall be Level 4.

(2) The designed flood recurrence period shall be 5-10 years, with a 10-year high water level of 2.85m and a 10-year low water level of -1.28m taken as the design standard. Wave forces shall be considered based on a 10-year recurrence period. The designed normal water level shall be +0.52m, and the maximum designed water retaining height shall be 8m.

(3) The cofferdam must undergo verification calculations such as anti-sliding, anti-overturning, depth of penetration, anti-seepage, and overall stability of the cofferdam; the bearing capacity of the structural components of the cofferdam must be verified according to the most unfavourable load combination during in use.

3.3.2 *Cofferdam structure design*

The scope of the cofferdam is determined between the mileageK6+511.5 andmileage K7+072. The length of the cofferdam along the tunnel axis is 560.5m, and the perimeter of cofferdam is about 1393.4m. The cofferdam is designed to be constructed in one stroke. The width of the cofferdam is about 206m on the east side and 116m on the west side. See Figure 8.

The width of double-row steel sheet pile cofferdam is 10m, and the top elevation of the cofferdam is+3.00m. The top elevation of the outer row steel sheet pile is+6.00m. The pile length is 30-33m.The top elevation of the inner row steel sheet piles is +3.00m, and the pile length is 27-30m, driven into the fully weathered layers. The cross-section of the steel sheet pile is 750 × 225 × 14.5mm, and the

material is Q390BZ. Steel tie rods with a diameter of 60mm are used to connect the inner and outer rows of steel sheet piles at a spacing of 1.5m. The elevation of the steel tie rods is +1.5m.

To effectively resist the power of wave currents and typhoons, a L-shaped buttress retaining wall is installed along the cofferdam. The thickness of the retaining wall is 200mm, and the height is 2m. The buttresses are set every 1.5m, with a thickness of 150mm and a height of 1.5m.

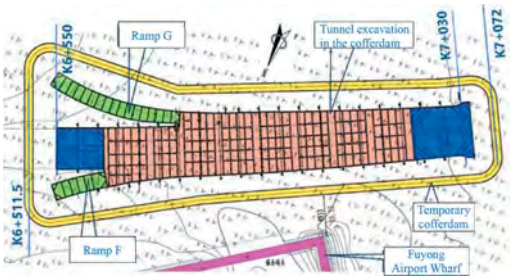

Figure 8. Schematic diagram of cofferdam tunnel.

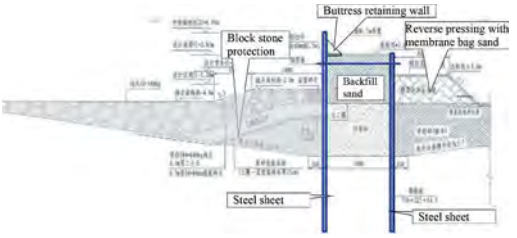

Figure 9. Typical cross-section of cofferdam.

To avoid erosion of the outer slope bottom of the cofferdam, multiple layers of different specifications of block stones are set on the slope surface for dumping and filling. Reverse pressing with membrane bag sand is set on the inner side of the cofferdam, and the slope surface is protected by membrane bag concrete. See Figure 9.

The engineering geological condition is complex and soil layers are unevenly distributed. The surface layer is composed of Holocene marine sediment, with a thickness of 5.2-15.0m, presenting poor engineering properties, high water content, high compressibility, rheological properties, and thixotropy. The differential weathering of the bedrock is significant, and the rock layers are with large fluctuations and uneven thickness of the weathered layer. To ensure the stability of the cofferdam, the surface silt is removed in layers within a range of 8m below the seabed surface and replaced with medium to coarse sand before the construction of the cofferdam. After the cofferdam is constructed, the remaining silt between the double row steel sheet piles is reinforced with rotary jet grouting piles.

3.3.3 *Cofferdam structure calculation*

A 2D load structure model is established for calculation. The stratum is simulated by loads and springs, the beam elements are used for the steel sheet pile and cable elements for steel tie rods. Only vertical restraint is applied to the bottom of the steel sheet piles, and all horizontal springs simulating lateral constrains as compress-only springs only (without tension). The spring ultimate bearing capacity considered the relationship with passive soil pressure. Different values of spring stiffness are specified based on specific positions and action forms. See Figure 10.

In the design, typical sections are taken and calculated based on different construction conditions and assumptions of high and low water levels. All of the normal stress and shearing stress of steel sheet piles and steel walings, and normal stress of steel tie rods meet the design requirements. In the calculation, a soil model is also used to conduct numerical simulation analysis and parallel verification of the double-row steel sheet pile cofferdam according to the construction processes (see 4.2 Support and retaining structure design for details).

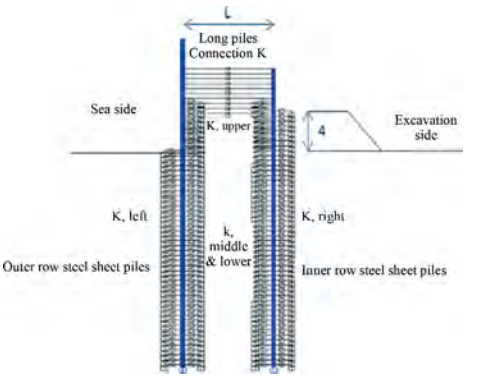

Figure 10. Assumptions of calculation constraint conditions.

Table 2. List of stability calculations and safety factors of cofferdam.

Serial number	Stability calculation	Safety factor
1	Anti-sliding stability	1.1
2	Anti-overturning stability	1.35
3	Overall stability	1.35
4	Depth in soil	1.25
5	Anti-seepage stability of steel sheet piles	1.5
6	Anti-piping stability of cofferdam body	2.0

Note: The stability calculations are based on the combination of high and low water levels + 10-year recurrence period and wave forces of 10-year recurrence period.

Various stability calculations are conducted on the steel sheet pile cofferdam according to relevant specifications. All of the calculation results meet the design requirements.

3.3.4 *Sub-cofferdam design*

During construction, in order to provide the conditions for the connection of tunnel element as early as possible, a sub-cofferdam is added on the west side of the cofferdam.

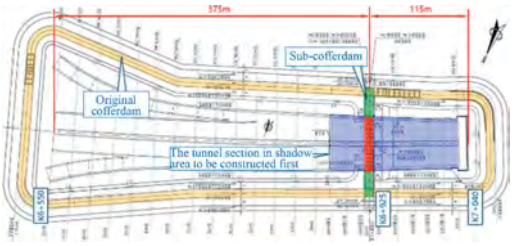

Figure 11. Layout plan of sub-cofferdam.

The sub-cofferdam is at mileage K6+925, where the double row steel pipe pile cofferdam is used between the tunnel structure and the original cofferdam, and the buttress retaining wall is used on the top of the tunnel structure.

The width of the double row steel pipe pile cofferdam is 10.5m; the top elevation of the cofferdam is +3.00m; the top elevation of the outer row of steel pipe pile is +6.00m; the top elevation of the inner row of steel pipe pile is +3.0m; and the bottom elevation of the steel pipe piles is -24m. The outer diameter of the steel pipe pile is Φ820, and the thickness is 16mm, and its material is Q355B. The steel pipe piles are connected by locking buckles. The full length of the gap inside the locking buckles is sealed by grouting. The inner and outer steel pipe piles are supported by the HW200×200×8×12 steel support at a spacing of 2.0m, and the center elevation is +2.5m. See Figure 11.

The top elevation of the buttress retaining wall is +6.0m, and the thickness of the wall is 600mm. The 400mm thick buttresses are set at a horizontal spacing of 4.7~5.6m cross the tunnel. The inner and outer sides of the retaining wall are respectively protected by bag sand and membrane bag sand backfilling.

The overall construction process of the cofferdam tunnel with additional sub-cofferdam is adjusted as shown in Figure 12:

Process 1: After dewatering within the cofferdam, level the site and carry out the retaining structure construction. First implement the main tunnel excavation ① on the west side and then carry out the excavation of Ramp F and Ramp G on the east side. In the construction process, it shall ensure that the tunnel excavation ① as soon as possible to form the conditions for tunnel element connection.

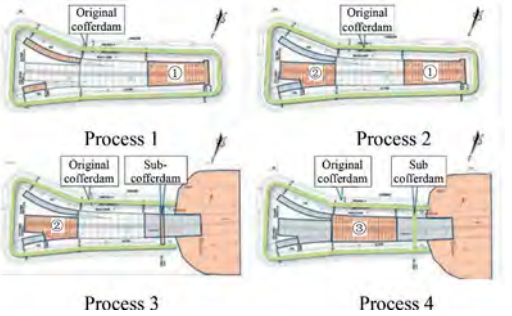

Figure 12. Overall construction process of cofferdam with additional sub-cofferdam.

Process 2: After the completion of the excavation of Ramp F and G on the east side, implement the main tunnel excavation ② in sequence.

Process 3: After the completion the main tunnel excavation ①, construct the sub-cofferdam at mileage K6+925. Upon the connection of the sub-cofferdam with the original cofferdam, ingress water into the west side of the sub-cofferdam and dismantle the original cofferdam on the west side. The corresponding work will be prepared for tunnel element immersing and installation.

Process 4: Construction the main tunnel excavation ③.

4 SUPPORT AND RETAINING STRUCTURE DESIGN

4.1 *Standard and principle of design*

(1) Determine the safety level of the excavation works based on the surrounding environmental conditions, excavation depth, support and retaining structure and other considerations.
(2) Select a reasonable support and retaining structure based on the safety level, excavation depth, and engineering geological conditions.
(3) The support and retaining structure must be verified by strength, deformation and stability check.
(4) When determining the depth of the retaining structure, it must be verified by anti-sliding, anti-overturning, overall stability, anti-uplift and anti-

Table 3. Control standard for excavation deformation.

Safety level of excavation	Maximum horizontal displacement on top of the retaining structure	Maximum horizontal displacement of the retaining structure	Maximum settlement of the earth surface
First level	min(0.2% H,30mm)	0.3%H	0.25%H

Note: H presents the excavation depth.

piping stability. For these weak soil areas, vertical bearing capacity, deformation, and stability calculation must also be carried out, and reasonable measures such as ground improvement should be taken into account.

4.2 *Support and retaining structure design*

The design mileage of the tunnel in the cofferdam is K6+550~K7+030. The tunnel is 480m long with 26 structural segments. The support and retaining structure is made of a 1m thick diaphragm wall + concrete support + steel support. See Figure 13.

Table 4. List of tunnel support and retaining structures.

Scope	Depth of excavation	Form of support and retaining structure
K6+550~K6+918 Main tunnel	13.21~16.60m	Two concrete supports and one Φ80cm steel support
K6+91~K7+030 Main tunnel	16.60~17.96m	Two concrete supports and two Φ80cm steel supports
FK1+268~FK1+329.198 RampF	12.38~13.84m	One concrete support and two Φ80cm steel supports
GK0+485~K0+330.355 RampG	9.79~14.04m	One concrete support and two Φ80cm steel supports

Different from these traditional land excavations, the tunnel excavation is close to the cofferdam, which is only about 8m between the excavation and the membrane bag sand of the cofferdam, and the water level fluctuates greatly outside the cofferdam. So the design of the excavation shall consider both the impact of the stacking load of the cofferdam, and the impact of water level fluctuations.

In addition to using the conventional elastic foundation rod system finite element method for calculation and analysis, a 2D soil structure interaction model is established for typical cross-section to carry out re-checks according to the overall construction process of

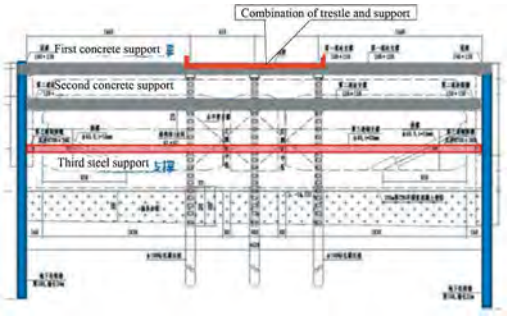

Figure 13. Typical cross-section of support and retaining structure for the cofferdam tunnel.

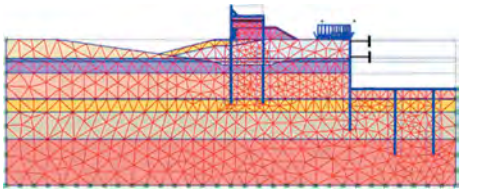

Figure 14. Computational model and grids.

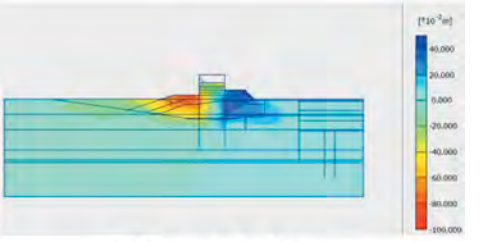

(a)Horizontal displacement

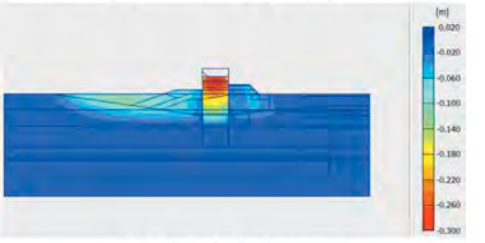

(b)Vertical displacement

Figure 15. Cloud diagram of deformation of double-row steel sheet pile cofferdam after backfilling to elevation +3.0m.

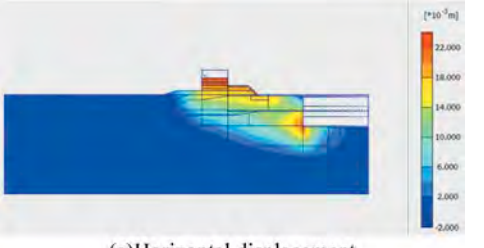

(a)Horizontal displacement

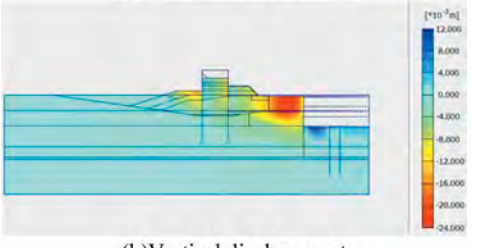

(b)Vertical displacement

Figure 16. Cloud diagram of deformation of double-row steel sheet pile cofferdam during excavation.

the cofferdam and excavation. The 2D physical element is used for the soil, and the HS model is used for the constitutive models of soft soil and sand; steel sheet piles are simulated using plate elements, and steel tie rods are simulated using point-to-point anchor elements, both of which are calculated using linear elastic models.

The interaction between steel sheet piles and the surrounding soil is simulated by the software's built-in interface element. The support and retaining structure is designed based on the calculation results of the elastic foundation rod system finite element method in combination with verification results of the soil model, so as to ensure the engineering safety. See Figure 14~16.

4.3 *Trestle design*

Considering the constraints of site conditions as well as the construction organization plan, a trestle is required in the middle of the tunnel excavation. The trestle goes longitudinally and has a width of 14m, it is impossible to avoid the support system in both plane and vertical profiles. Therefore, the trestle is designed with the first concrete support system to ensure the safety of the excavation and trestle while saving engineering investment.

As the trestle serves as a heavy load traffic passage for the excavation in construction, to ensure the safety, an overall calculation of the excavation support and trestle is carried out based on a 3D finite element model. The first support, together its tie rods, and lattice columns are strengthened in the design according to the calculation results. See Figures 17, 18.

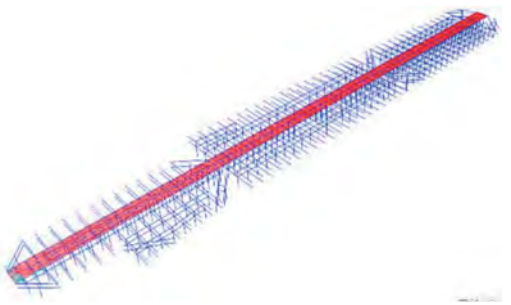

Figure 17. Schematic diagram of 3D model of trestle and support structure.

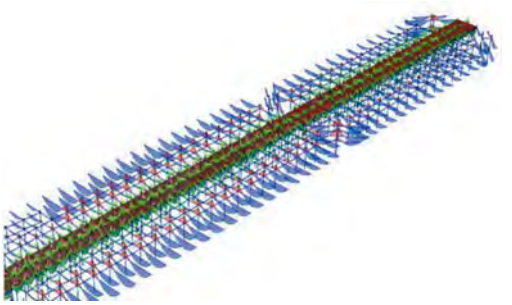

Figure 18. Schematic diagram of bending moment of the first support and longitudinal beam of trestle.

5 ANALYSIS OF THE IMPACT OF COFFERDAM TUNNEL CONSTRUCTION ON FUYONG WHARF

The Fuyong Wharf of Shenzhen Airport is close to the cofferdam. The filling material for the wharf is basically block stone. The minimum clear distance between the wharf and the temporary cofferdam is about 49m, where the tunnel is at the mileage of K6 +857. The tunnel excavation depth is 16.4m, and the excavation width is 65.50m.

To accurately reflect the additional deformation impact on wharf caused by the construction of temporary cofferdam, tunnel excavation, the plane elastic-plastic finite element analysis is adopted to simulate the construction process.

The calculation results show that: during the whole construction, the maximum additional vertical displacement of the wharf is about 28mm (settlement), and the maximum additional horizontal displacement is about 27.6mm, less than the control requirement of 30mm. See Figure 19. The actual displacement measured during construction is within 10mm.

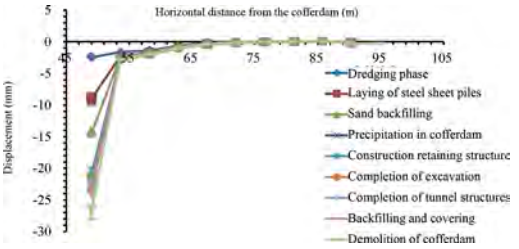

Figure 19. Settlement curve of wharf.

6 CONCLUSION

The construction of double row steel sheet piles for the temporary cofferdam started in May 2018, and the tunnel structure was completed in January 2022. During the construction, it has experienced severe weather impacts such as typhoons and rainstorm many times.

Following the principles of economic rationality, safety and reliability, and relying on practical engineering experiences, targeted design schemes and treatment measures have been adopted for the temporary cofferdam and excavation support and retaining structures according to the characteristics of the project to ensure the smooth construction of the tunnel in the cofferdam, and good economic, social, and technical benefits have been achieved. It also provides a reference and an experience for the future construction of tunnels in the cofferdams in complex marine environmental conditions.

Tunnelling for a Better Life – Yan, Celestino, Thewes & Eberhardt (Eds)
© 2024 The Author(s), ISBN 978-1-032-80042-4
Open Access: www.taylorfrancis.com, CC BY-NC-ND 4.0 license

Comparative effects of twin-stacked tunnel excavation on adjacent structure using different simulation models

Nattavich Sittiamornporn, Pornkasem Jongpradist* & Chana Phutthananon
Department of Civil Engineering, Faculty of Engineering, King Mongkut's University of Technology Thonburi, Bangkok, Thailand

Arthit Chayaroon
Geotechnical and Foundation Engineering Co., Ltd, Bangkok, Thailand

Phattarawan Malaisree
MAA Consultants Co., Ltd, Bangkok, Thailand

ABSTRACT: The increase in transportation in urban areas has made it inevitable to excavate the twin-stacked tunnels and consequently affect adjacent structures. Therefore, an appropriate evaluation of the impact of tunnel excavation on the nearby building has been necessary to prevent the damage that may occur to the structure. In current engineering practice, there are various methods with different degrees of complexity to assess the impact on the building. This study presents a comparison of the effect caused by twin-stacked tunnel excavation on adjacent pile-supported structures by using three different simplified analysis methods. The results reveal that each method gives different results and the distance between the tunnels and the nearest pile affects the computed results. This study indicated that the tunneling analysis with the loaded pile method (FEM-LP) is more appropriate and conservative for the building impact assessment of the piled supported structures. The tunneling in green field (FEM-GF) conditions is proven to not be the conservative method.

Keywords: Tunneling, Interaction, Finite element, Pile supported structure

1 INTRODUCTION

The execution of tunnel construction projects within densely populated urban zones induces soil displacement, unavoidably posing a potential hazard to nearby building structures (Sirivachiraporn and Phienwej, 2012; Duangsano et al., 2023). A comprehensive impact assessment becomes imperative for mitigating risks and preventing resulting damages. Past research (Boscardin and Cording, 1989) has commonly utilized building movements, such as settlement, horizontal displacement of the building at diverse column positions, and distortional angularity, as practical measures to evaluate and classify potential risks of structural damage. A predominant assumption in practical applications is that column settlement equates to soil surface settlement at the same position due to tunneling in the absence of buildings, resulting in a conservative evaluation. Empirical solutions, such as Gaussian equations or normal probability curves (Loganathan and Poulos, 1998), are often employed for preliminary assessments to estimate soil settlement.

The Finite Element (FE) method stands out as another widely adopted technique for appraising soil movement resulting from tunnel construction, enabling the simulation of more realistic tunnel-soil-structural interactions, particularly in twin tunneling scenarios. However, achieving highly accurate results demands a complete FE modeling, involving a detailed analysis of the entire structure. To streamline this complexity, a simpler simulation method entails selecting representative portions of the structure for settlement analysis. Two prevailing approaches for impact assessment

*Corresponding author: pornkasem.jon@kmutt.ac.th

DOI: 10.1201/9781003495505-47

thus involve: 1) estimating soil movement values through the analysis of tunnel construction simulations only (Greenfield condition: without the presence of buildings), as exemplified by Bilotta et al.'s research (Bilotta et al., 2017), and 2) simplifying the model of nearby structures by analyzing only specific representative parts, such as applying force to thin plate elements to estimate the impact of the structure's weight on evaluation (Mirhabibi and Soroush, 2012).

In regions with soft soil where structures rely on pile foundations, similar concepts have been applied for impact assessment. Considering the connection between columns and piles, the representative components in this context are the piles. However, the interaction among tunneling, soil, and piles becomes intricate depending on the relative position of the pile tip and the tunnel (Jongpradist et al., 2013; Heama et al., 2021). The assumption conventionally employed in impact assessments may no longer be valid. This study aims to assess soil and pile settlements derived from FE simulations of twin-stacked tunnel excavation using models with varying complexities. The calculated settlements and the corresponding buildings impact assessment (BIA) on piled-supported are compared and discussed.

2 ANALYSIS CONCEPTS FOR BIA

2.1 *Simulation models*

In this study, to indicate the different effects of different types of modeling assumptions on nearby existing piles due to twin-stacked tunneling, a total of three types with different degrees of complexity in FE modeling was considered. The complexity involves the existence of the structural parts (i.e., different types of modeling of the existing pile structure) in each modeling assumption which provides a significant dissimilarity of impact on the obtained FE results. Referring to the study of Mirhabibi and Soroush (2013), it is revealed that the type of structure has an important effect on the structural behavior. However, the above-mentioned study considered solely the structures beyond the soil surface without considering the piling support. Therefore, the pile-supported structure is the main focus of this study. The FE analyses with differences in pile-supported structure assumptions including (1) FE modeling of tunneling under the greenfield condition (FEM-GF), (2) FE modeling of tunneling incorporated with pile existence (FEM-P), and (3) FE modeling of tunneling incorporated with loaded pile existence (FEM-LP) are considered. Detailed components involved in FE modeling of each considered case can be illustrated in Figure 1.

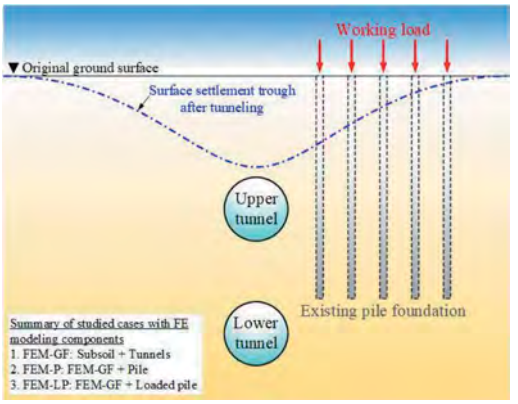

Figure 1. Schematic diagram of considered twin-stacked tunneling adjacent pile structures.

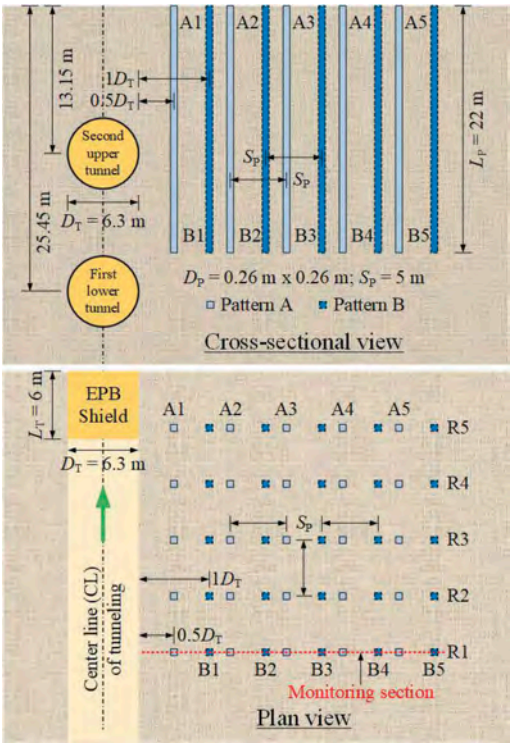

Figure 2. Cross-sectional and plan views of considered problems.

In addition, to take into account the effect of the relative position of the pile tip to the tunnel on the behavior of the existing pile in the evaluation, two patterns of pile arrangement (i.e., Pattern A and Pattern B) as presented in Figure 2 were adopted. Pattern A represents the pile position in which the tips of the nearest pile row are located in the influencing zone of tunneling as proposed by Jongpradist et al.

(2013). In contrast, the pile arrangement used for Pattern B is designed for the case in which the tips of the closet pile row are located out of the influencing zone.

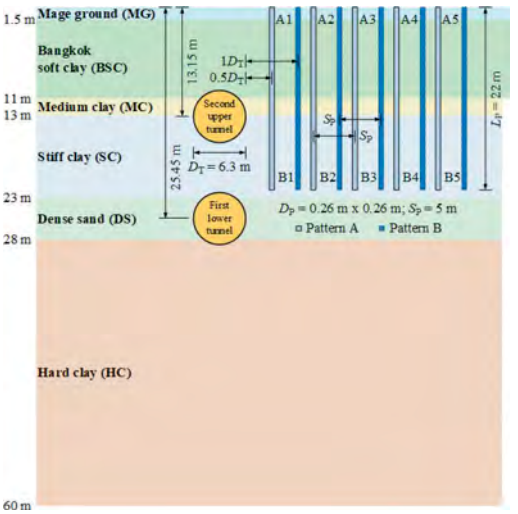

Figure 3. FE mesh for 3D numerical modeling of considered problems.

2.2 *Considered problem in the study*

For the current study, a history case of twin-stacked tunnel excavation was chosen from section CS-4C of the Chaloem Ratchamongkhon Line, Bangkok MRTA project in Thailand. The subsoil profile of the selected twin-stacked tunnel analyzed in this study is shown in Figure 3 which consisted of a 1.5-m-thick made ground (MG) layer followed by a 9.5-m thick Bangkok soft clay (BSC) layer and a 2-m-thick medium clay (MC) layer. These above-stated layers were placed on a 10-m-thick stiff clay (SC) and 5-m-thick dense sand (DS) layer which was situated on the hard clay (HC) layer with a thickness of 32 m. This selected section composed an excavation of the twin-stacked tunnel (i.e., lower southbound and upper northbound tunnels) with a vertical clearance of 6 m as also depicted in Figure 3. The outer diameter (D_T) of both tunnels was 6.3 m and the concrete lining was 0.3 m thick and 1.2 m wide. The lower and upper tunnels were respectively excavated at the depth of –25.45 m and –13.15 m below the ground surface by a mechanized method using the earth pressure balance (EPB) shield with a shield length (L_T) of 6 m. For the existing pile structures, a 5 × 5 pile group of a single pile with a spacing of 5 m located aside from the twin-stacked tunnel was considered. The pile with a square cross-sectional area of 0.26 × 0.26 m^2 and a length of 22 m was considered for both pile arrangement patterns. For Pattern A, a clearance between the nearest pile row and tunnel equals to 3.15 m (0.5D_T) while for Pattern B, the distance of 6.3 m (1D_T) was considered.

3 FINITE ELEMENT ANALYSIS

The FE software PLAXIS 3D was adopted in this study to investigate the tunnel-pile-soil interaction for assessing the impact of twin-stacked tunneling on the response of an adjacent existing piled structure. The obtained responses of the adjacent existing structure owning to the tunnel construction computed by several modeling assumptions were discussed and compared to highlight the influence of using different conditions in the analysis.

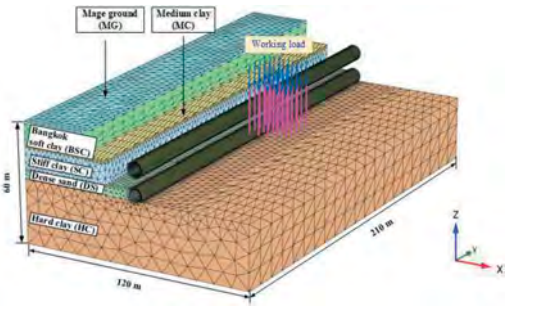

Figure 4. 3D FE mesh.

3.1 *FE modeling details and material properties*

Figure 4 presents an example of FE mesh in the case of a twin-stacked tunnel adjacent to an existing loaded pile (considered as FEM-LP for this study). The bottom boundary of the FE mesh was assigned at a depth of 60 m below the ground surface. The other FE mesh dimensions were 120 m in the transverse direction and 210 m in the longitudinal direction. The above-stated FE modeling dimensions were considered for all cases of this study and can provide satisfactory FE results without any boundary effects (Phutthananon et al., 2023). For the displacement boundary, a fixed constraint was applied only for the FE modeling bottom while for the four side boundaries, the movement was restrained only in the horizontal direction. In terms of drainage boundary conditions, all boundaries are set to be impermeable surfaces, except for the top surface of FE modeling (freely drained boundary). The soil was modeled with the 10-noded tetrahedral elements while the modeling of tunnel lining was simulated by the 6-noded triangular plate elements. For simulating the soil characteristics, the Hardening Soil (HS) constitutive model was used for all layers. The required input soil parameters for HS model used in this study (see Table 1 and 2) are adopted from the study of Likitlersuang et al. (2014) which were completely calibrated through drain triaxial and oedometer testing results of collected soil samples at the project site. The information related to the calibration results can be found in the previous study (Surarak et al., 2012). The tunnel lining was modeled as a linear elastic behavior using plate elements. The required properties of tunnel

lining and pile utilized in this study were followed from the past study (Lueprasert et al., 2017a; 2017b; Phutthananon et al., 2023): Young's modulus of 31 GPa, Poisson's ratio of 0.2, and unit weight of 24 kN/m^3. The pile was modeled using embedded beam elements with 3-noded line elements. The concrete pile material with a unit weight of 24 kN/m^3 is assumed to be a linear elastic behavior with Young's modulus of 31 GPa and Poisson's ratio of 0.2.

Table 2. The input HS model parameters for the last three soil layers (Likitlersuang et al., 2014).

Parameter	Unit	SC	DS	HC
Depth	m	13-23	23-28	28-60
γ	kN/m^3	19.5	19	20
E_{50}^{ref}	kPa	8500	38000	30000
E_{oed}^{ref}	kPa	9000	38000	30000
E_{ur}^{ref}	kPa	30000	115000	120000
m	(-)	1	0.5	1
c'	kPa	25	1	40
ϕ'	degree	26	27	24
ψ	degree	0	0	0
ν_{ur}	(-)	0.2	0.2	0.2
R_f	(-)	0.9	0.9	0.9

Table 1. The input HS model parameters for the first three soil layers (Likitlersuang et al., 2014).

Parameter	Unit	MG	BSC	MC
Depth	m	0-1.5	1.5-11	11-13
γ	kN/m^3	18	16.5	17.5
E_{50}^{ref}	kPa	45600	800	1650
E_{oed}^{ref}	kPa	45600	850	1650
E_{ur}^{ref}	kPa	136800	8000	5400
m	(-)	1	1	1
c'	kPa	1	1	10
ϕ'	degree	25	23	25
ψ	degree	0	0	0
ν_{ur}	(-)	0.2	0.2	0.2
R_f	(-)	0.9	0.9	0.9

3.2 *FE analysis procedures*

The FE modeling procedure of the considered problem can be divided into two main phases. As for the first phase, the initial stress state of the subsoil was simulated using the combination of the coefficient of earth pressure at rest and soil unit weight. Then, a set of single concrete-driven piles was simulated based on the wished-in-place method prior to the tunnel excavation. After finishing the pile installation, only for the FEM-LP case, the application of axial loading was then applied. The allowable load of the single pile was set to be equal to the ratio of the ultimate capacity of the single pile over the safety factor of 2.5 (Phutthananon et al., 2023). In the second phase, tunnel excavation was simulated following the "step-by-step" approach (Do and Dias, 2022) together with the "AG-shell" method (Lueprasert et al., 2017b) in which the tunneling advancement rate of 1.2 m in each step (equivalent to tunnel lining width) was considered. The simulation of tunnel excavation as mentioned earlier can be partitioned into three minor steps. In the first minor step, the soil elements within the desired excavation area were deactivated simultaneously with the modeling of the application of face pressure. Then, the shell elements with the calibrated contraction ratio were activated to stand for the mechanized tunneling procedure. These aforementioned processes were iterated until the EPB shield advancement was achieved corresponding to the shield length of 6 m (equal to 5 rings). As for the second minor step, modeling of tail void grouting considering the liquid state of grouting was considered by simulating using the radial pressure. Finally, the hardening stage of tail void grouting was modeled by utilizing the solid elements, and the shell elements to represent the tunnel lining were activated. Note that the required properties of EPB shield and grouting material are adopted from the past work of Phutthananon et al. (2023). For more detailed information about EPB advancement modeling, it can be found in the previous studies (Lueprasert et al., 2017b, 2023; Phutthananon et al., 2023).

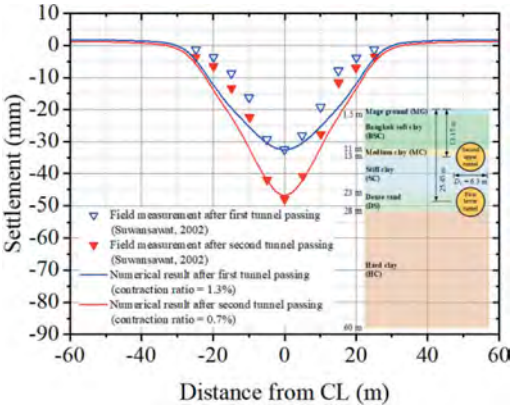

Figure 5. Calibration of tunneling simulation.

4 FE ANALYSIS RESULTS

4.1 *Calibration of tunneling simulation*

Figure 5 shows the suitable contraction ratios for tunneling simulation of the lower southbound and upper northbound tunnels were first determined by adjusting the contraction ratios to match with the field measurement. From the analyses, the contraction ratios of 0.6% and 1.3% were found suitable for the simulation to replicate the settlement patterns observed in the actual twin-stacked tunneling in this

study. These two values were used throughout all subsequent analyses.

4.2 *Pile/soil settlements*

The computed transverse settlement distribution along the transverse section R1 from different analysis modeling are compared in Figure 6 for Patterns A and B, respectively. The magnified figure of the results near the centerline of the tunnel is also included in the figure. Note that section R1 cuts through the piles. For the positions at which the piles are located, the pile settlements are presented.

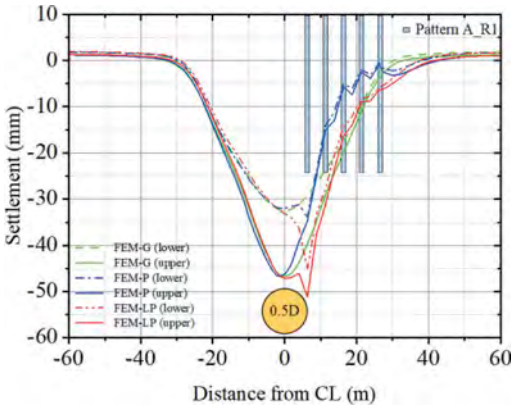

Figure 6. Transverse settlement profile at section R1 of Pattern A.

For the FEM-GF case, the symmetry normal-distribution shape settlement profile is seen. The settlement trough from the excavation of the lower tunnel expands to the distance from the tunnel center (from center to point of inflection) of approximately 30 m ($\approx 5D_T$) while that from excavation from the upper tunnel induces the settlement increase to the distance of 20 m from tunnel centerline.

It is clearly seen that, compared to the greenfield (FEM-GF), the settlement distribution of the side with the piles (right side in the figure) differs significantly. The settlements from the FEM-P case are generally smaller than those of the FEM-GF case, except at pile A1 for lower tunnel excavation. This implies that the ground was reinforced by the embedded piles. The larger settlement at pile A1 from the excavation of the lower tunnel is due to the stability loss of the pile tip since pile A1 is considered to be in the influencing zone or the lower tunnel excavation as suggested by Jongpradist et al. (2013). The pile must settle to mobilize the shaft resistance along the pile and compensate for the end-bearing resistance. However, after the excavation of the upper tunnel, no significant settlement increase is seen from the position of pile A1.

Larger settlements are seen for the case of FEM-LP, compared to the FEM-P case. This indicates that the application of the loads on the pile head significantly affects the computed results. Moreover, the larger settlement at pile A1 is more noticeable. The settlement increase due to the excavation of the upper tunnel is seen even for greater distance from the center line. Considering the BIA, the pile/soil settlements at the pile positions in section R1 from different analysis methods are plotted in Figure 7. It is clear that the used analysis assumption has a great impact on the computed settlements and their profile.

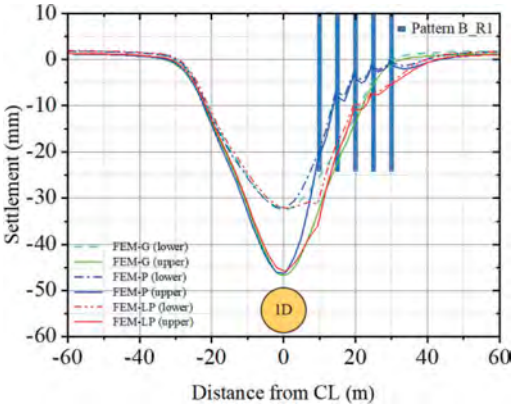

Figure 7. Pile settlement of Pattern A.

Figure 8 Shows the results of cases for pile settlement of Pattern B. Similar tendencies to those of Pattern A are seen. However, the settlement of the nearest pile (B1) is not much greater than the soil settlement at the same position of the FEM-GF case, particularly from the FEM-P case. This emphasizes the significance of the relative position between the pile and the tunnel.

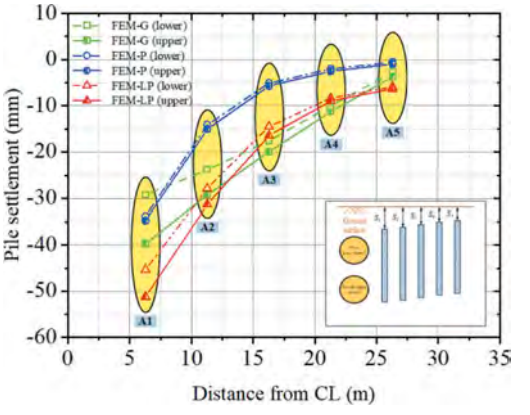

Figure 8. Transverse settlement profile at section R1 of Pattern B.

The pile/soil settlements at the pile positions in section R1 of Pattern B from different analysis methods are plotted in Figure 9. Compared to those

of Pattern B in Figure 7, the pile settlements computed from the FEM-P are the smallest. However, the results of the FEM-LP and FEM-GF become close. In terms of pile settlement prediction, the FEM-GF can be considered to be the conservative and yet simplest.

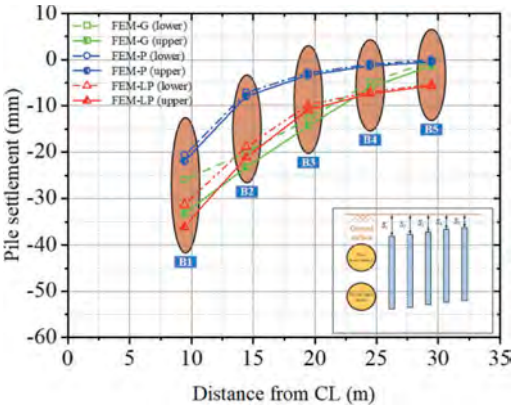

Figure 9. Pile settlement of Pattern B.

4.3 *Differential settlement*

The differential settlements (S_d) between two piles along section R1 are illustrated in Figures 10 and 11 for Patterns A and B, respectively.

For Pattern A, the computed S_d from FEM-GF becomes the smallest. As expected, the maximum S_d occurs at bay 1 which is closest to the tunnel. For the FEM-P case, since the settlements from Pile A1 to the farther side do not much change during the excavation of the upper tunnel, almost the same S_d for excavation of the lower and upper tunnels are thus seen. An increase in S_d from the excavation of the lower tunnel to that of the upper tunnel is noticed for the FEM-LP case. Among the three models, the FEM-LP case offers the largest computed S_d.

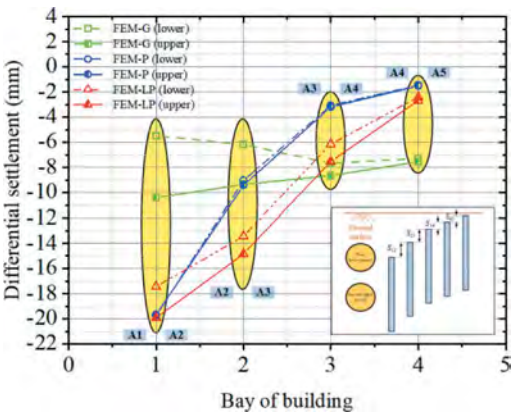

Figure 10. Differential settlement of Pattern A.

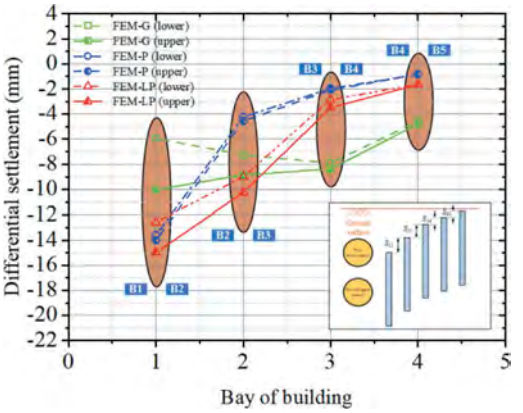

Figure 11. Differential settlement of Pattern B.

For Pattern B, a similar tendency to that of Pattern A is noticed. It seems that, in terms of differential settlement, the FEM-GF is not conservative and the FEM-LP gives the largest computed S_d.

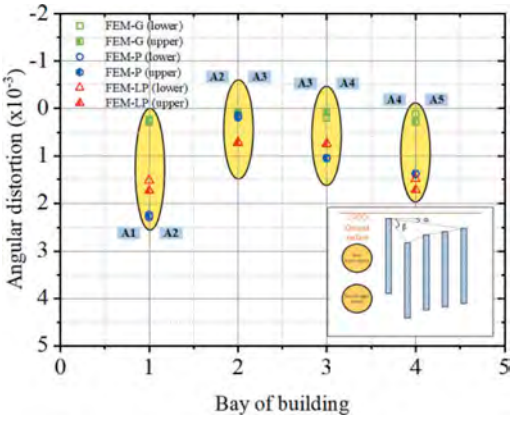

Figure 12. Angular distortion of Pattern A.

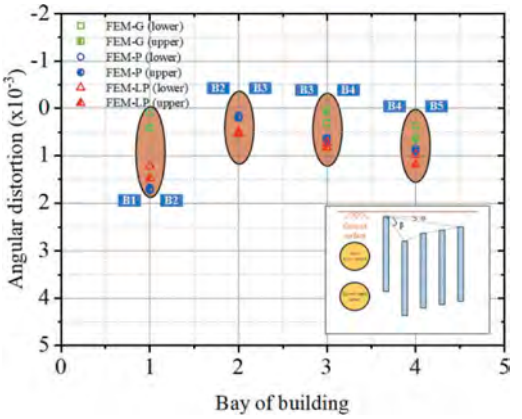

Figure 13. Angular distortion of Pattern B.

4.4 *Angular distortion*

Angular distortion (β) is defined as the ratio of the differential settlement between two piles to the tilting of the pile structure. Figures 12 and 13 depict the β of all bays of the building at section R1 for piles of both Patterns A and B, respectively. The magnitudes β of from Pattern A are larger due to a closer spacing to the tunnel. For both patterns, the largest β are from the FEM-P method. However, the results from the FEM-LP are not much different from those of the FEM-P.

5 CONCLUSIONS

The study compared the BIA of twin-stacked tunneling adjacent to nearby piled structures by employing simplified methods with different levels of complexity in the analysis. The conclusions drawn from the study are;

1. Different analysis methods provide different evaluations, yet, the relative position of the piles and the tunnel has a great impact on the evaluation.
2. It is evident that the green filed consderation which is believed to provide the conservative evaluation and commonly used in the practice, becomes unsuitable for the piled structures, particularly when the piles are situated in the influencing zone.
3. From the results presented in this study, it is postulated that the FEM-LP can be considered the simplified method providing the conservative evaluation of all considered items.

ACKNOWLEDGMENTS

This research was supported by the King Mongkut's University of Technology Thonburi (KMUTT) and the Thailand Science Research and Innovation (TSRI) under Basic Fundamental Fund: Fiscal year 2024 (Project: Advanced Construction Towards Thailand 4.0).

REFERENCES

Bilotta, E., Paolillo, A., Russo, G., Aversa, S., 2017. Displacements induced by tunnelling under a historical building. Tunnelling and Underground Space Technology. 61, 221–232.

Boscardin, M.D., Cording, E.J., 1989. Building response to excavation-induced settlement. Geotechnical Engineering. 115, 1–21.

Do, N.A., Dias, D., Golpasand, M.R.B., Dang, V.K., Nait-Rabah, O., Pham, V.V., Dang, T.T., 2022. Numerical analyses of twin stacked mechanized tunnels in soft grounds – Influence of their position and construction procedure. Tunnelling and Underground Space Technology. 130, 104734.

Duangsano, O., Yensri, P., Chayaroon, A., Timpong, S., Jongpradist, P., 2023. Tunnelling impacts and mitigation on existing structures for Bangkok MRT Orange Line. Geomechanics and Tunnelling. 16(3), 272–280.

Heama, N., Jongpradist, P., Lueprasert, P., Suwansawat, S., Jamsawang, P., 2021. Comparative effects of adjacent loaded pile row on existing tunnel by 2D and 3D simulation models. Geomechanics and Engineering. 27(2), 151–165.

Jongpradist, P., Kaewsri, T., Sawatparnich, A., Suwansawat, S., Youwai, S., Kongkitkul, W., Sunitsakul, J., 2013. Development of tunneling influence zones for adjacent pile foundations by numerical analyses. Tunnelling and Underground Space Technology. 34, 96–109.

Likitlersuang, S., Surarak, C., Suwansawat, S., Wanatowski, D., Oh, E., Balasubramaniam, A., 2014. Simplified finite-element modelling for tunnelling-induced settlements. Geotechnical Research. 1(4), 133–152.

Loganathan, N., Poulos, H.G., 1998. Analytical prediction for tunneling-induced ground movements in clays. Geotechnical and Geoenvironmental Engineering. 124, 846–856.

Lueprasert, P., Jongpradist, P., Jongpradist, P., Schweiger, H.F., 2023. Structural responses of a tunnel lining due to an adjacent loaded pile. International Journal of Civil Engineering. 21, 1027–1043.

Lueprasert, P., Jongpradist, P., Jongpradist, P., Suwansawat, S., 2017a. Numerical investigation of tunnel deformation due to adjacent loaded pile and pile-soil-tunnel interaction. Tunnelling and Underground Space Technology. 70, 166–181.

Lueprasert, P., Jonpradist, P., Suwansawat, S., 2017b. Tunneling simulation in soft ground using shell elements and grouting layer. International Journal of GEOMATE. 12 (31), 51–57.

Mirhabibi, A., Soroush, A., 2012. Effects of surface buildings on twin tunnelling-induced ground settlements. Tunnelling and Underground Space Technology. 29, 40–51.

Mirhabibi, A., Soroush, A., 2013. Effects of building three-dimensional modeling type on twin tunneling-induced ground settlement. Tunnelling and Underground Space Technology. 38, 224–234.

Phutthananon, C., Lertkultanon, S., Jongpradist, P., Duangsano, O., Likitlersuang, S., Jamsawang, P., 2023. Numerical investigation on the responses of existing single piles due to adjacent twin tunneling considering the lagging distance. Underground Space. 11, 171–188.

Sirivachiraporn, A., Phienwej, N., 2012. Ground movements in EPB shield tunneling of Bangkok subway project and impacts on adjacent buildings. Tunnelling and Underground Space Technology. 30, 10–24.

Soomro, M. A., Ng, C.W.W., Liu, K., Memon, N.A., 2017. Pile responses to side-by-side twin tunnelling in stiff clay: Effects of different tunnel depths relative to pile. Computers and Geotechnics. 84, 101–116.

Surarak, C., Likitlersuang, S., Wanatowski, D., Balasubramaniam, A., Oh, E., Guan, H., 2012. Stiffness and strength parameters for hardening soil model of soft and stiff Bangkok clays. Soils and Foundations. 52(4), 682–697.

Suwansawat, S., 2002. Earth pressure balance (EPB) shield tunneling in bangkok: ground response and prediction of surface settlements using artificial neural networks. Doctoral Dissertation. Massachusetts Institute of Technology, Massachusetts, USA.

Tunnelling for a Better Life – Yan, Celestino, Thewes & Eberhardt (Eds)
© 2024 The Author(s), ISBN 978-1-032-80042-4
Open Access: www.taylorfrancis.com, CC BY-NC-ND 4.0 license

Key technology of submarine railway tunnel in complex environment and high-water pressure

Chaoye Song*, Weiguo He, Shuqing Lv & Yong Yu
China Railway Liuyuan Group Co. Ltd, Tianjin, China

ABSTRACT: A submarine tunnel is generally characterized by its large scale, a complex site environment with high water pressure, and a lack engineering experience. The success or failure of the project is directly tied to the design scheme. In current research and practice, the water pressure of shield tunnelling is approximately 0.8MPa. However, the Zhujiangkou Tunnel of the Shenzhen-Jiangmen Railway faces an extreme geological environment, with a water-rich sand layer and hard granite, and water pressure exceeding 1.0MPa. In this study, we analyzed the key technologies in the design of a long and large submarine railway tunnel design. This includes construction method selection, section design, waterproofing and drainage system design, complex geological response in the sea area, durability design, and evacuation. We employ methods such as geological analysis, engineering analogy, and comprehensive comparison based on the engineering background of the Zhujiangkou tunnel. A combination of the shield and mining methods is proposed to account for the diverse geological conditions in different sections. The drainage system in the mining section can be maintained by implementing advanced grouting to control displacement and ensure its effectiveness. Both the durability design of the tunnel structure and the limit of the bearing capacity are treated with equal emphasis. The conclusions drawn from this study provide technical support for decision-making on interval schemes and serve as a reference for similar projects.

Keywords: Railway tunnel, Submarine tunnel, Shield and mining combination method, Waterproofing and drainage, Durability

1 INTRODUCTION

With the rapid development of China's economic construction, railroad construction has entered a new period of high-speed development. At present, China's "four vertical and four horizontal" high-speed railway network has been completed ahead of schedule. Tunnels, as essential crossings over rivers and seas, offer inherent advantages over other engineering types like bridges. They prove superior in bad weather prevention, operation cost reduction, maintenance, and national defence strategy considerations in Zhang, 2021 and Zhou et al., 2019.

Railroad submarine tunnels are generally large, with a complex site environment and a lack of engineering experience. The success or failure of a project is directly related to the design program. At present, there is no completed undersea railroad tunnel in China, and there are limited design standards and technical studies on cross-harbour tunnels. Foreign developed countries initiated submarine tunnel constructions as early as the 1930s. Examples includes Japan's closed submarine railroad shield tunnel and the Netherlands' Rotterdam immersed tube tunnel. In 1988, Japan completed the world's longest strait railroad tunnel, the Aokikan Tunnel, using the drilling and blasting method, with a total length of 54 km in Zhang et al., 2017. Representative projects of submarine tunnels constructed by the shield tunnel method include the Anglo-French Channel Tunnel (49.2 km) and the Danish Grand Channel Project (7.9 km), both are railroad tunnels with double-tube diameter of 8.5 m in circular section in Li & Mu, 2009 and Wang, 2014.

In China, the Liuyang River tunnel of the Wuhan-Guangzhou high-speed railway is the first underwater high-speed railway tunnel with a large span (14.8 m) and excavation section (170 m^2), constructed using the mining method in Huang et al., 2011. The Lion's Bay Tunnel of the Guangzhou-Shenzhen-Hong Kong high-speed railway, at a length of 10.8 km, is the longest underwater high-speed railway tunnel in China, employing the shield tunnel technology of "tunneling toward each other, docking in the middle of the ground, and disintegration in the hole" in Li, 2010. Although research on submarine tunnel projects mainly focuses on feasibility analysis(Guo, 2022;Huang & Liu, 2006;Wang, 2008;Qu, 2009), program selection (Song, 2020;Tian et al., 2008;Zhang, 2013), and overall design(Tang et al., 2021;Wu, 2021;Han et al., 2021), there is limited systematic introduction to the key

*Corresponding author: scyesky@126.com

DOI: 10.1201/9781003495505-48

technology of designing submarine tunnels across the sea. This paper combines the specific project of the submarine tunnel in the Pearl River Estuary of the Shenzhen River Railway and introduces in detail the design key technology of the extra-long railroad submarine tunnel in the complex site environment. Figure 1 illustrates the alignment plan of the Pearl River Estuary tunnel. The aim is to provide important guidance for the safe and smooth construction of the project and offer reference material for similar projects.

Figure 1. Alignment plan of the Pearl River Estuary tunnel.

2 PROJECT OVERVIEW

2.1 *Tunnel design overview*

The Zhujiangkou Tunnel serves as the pivotal component of the new Shenjiang Railway, crossing the sea area of Zhujiangkou and linking Humen in Dongguan with Nansha in Guangzhou. Covering a total length of the tunnel is 13.69 km, with approximately 11 km crossing the sea, the tunnel adheres to the standard of a two-lane high-speed railroad. The line spacing is set at 4.6 m, and the design speed is targeted at 200 km/h. The tunnel is comprised of distinct sections, including a 5520 m mine tunnel, a 6520 m shield tunnel (3590 m on the Humen side and 2930 m on the Wanhaisha side), and a -1650 m cut-and-cover tunnel (including two working shafts), along with one inclined shaft.

2.2 *Geological conditions and environment*

2.2.1 *Geological structure*

The tunnel site is situated along the northwest-oriented Lion's Ocean Fracture Bundle and Baini-Shawan Fracture, and the survey revealed three sets of fracture zones, F1, F2, F3-1, F3-2, and seven secondary fracture zones, as shown in Figure 2.

Figure 2. Location map of the Pearl River Mouth tunnel fault zones.

2.2.2 *Geological conditions*

The site is in the downstream of the Pearl River waterway, characterized by a predominantly deltaic plain geomorphology. The maximum water depth of the sea section is approximately 18 meters. The geological conditions for tunneling through the stratigraphy are complex and variable. On both sides of the land section, the bedrock surface is low. The Cretaceous Baihetong terrestrial clastic rocks to gravelly sandstone dominate the Humen site, while the Nansha side features metamorphic rocks transitioning from Aurignacian metamorphic rocks to schist. The sea area in the middle exhibits a slightly weathered bedrock rock surface undulation, primarily based on Yanshan late intrusive rocks granite. The saturated compressive strength averages about 70 MPa for slightly weathered granite and schist, with potential maximum values exceeding 200 MPa, indicating significant strength variations.

Groundwater at the site encompasses are four main types: upper stagnant water, loose rock-like pore water, weathered bedrock pore fissure water, and bedrock fissure water, These are predominantly weakly water-rich, with locally moderate water richness. Projections estimate the maximum water influx in the main hole of the mine section to be 150,000 cubic meters per day, and that the maximum influx in the sloping shaft to be 10,000 cubic meters per day. The sea area is characterized as a marine chloride corrosion environment, with an environmental action level of L3 and a salt crystallization action level of Y2.

2.2.3 *Environmental conditions*

Environmental conditions along the planned fairways in the Pearl River Estuary Tunnel are detailed in Table 1 and Figure 3. The tunnel site traverses the sea area encompassing the Dongguan Yellow Lip Fish Nature Reserve. The land areas on both sides are densely populated and complex, featuring pipelines and notable sensitive sites such as the Weiyuan Island Battery, Museum of Naval Battles historical relics and monuments, Nansha Tin Hau Temple, as well as wetland parks. The areas carry high environmental protection requirements.

2.3 *Design features and criteria*

(a) The construction of a long cross-harbour railroad tunnel spanning 11 km across the sea poses significant construction risks and demands rigorous operational measures for disaster prevention and evacuation;
(b) The tunnel operates at considerate depth, exposed to substantial water pressure. The maximum water depth across the sea is 18 m, and the deepest point of the tunnel reaches 115 m;
(c) The main structure is designed with a service life of 100 years;
(d) The structural waterproof grade is designated as Grade II; and

Table 1. Planning channel grade table.

Channel Name	Planned channel class	Representative Ship Type	channel bottom elevation/m	Distance from the top of the tunnel/m
Taiping River Channel	River I	3000t class general cargo ship	-8.52	23.64
Humen River Channel	coastal waterway	100,000t class general cargo ship 225,000t cruise ship	-16.26	63.1
Nanbeitai River Channel	coastal waterway	10,000t class bulk carriers	-11.45	85.57
Zhenxiang River Channel	River I	3000t class general cargo ship	-5.03	66.11
Zhenxiang North branching stream	—	100t class cargo ships	-2.03	86.71
Longxuenan River Channel	River I	5000t class general cargo ship	-9.52	20.48

Table 2. The permeability coefficient of stratum.

Geotechnical number	Geotechnical name	Natural density (g/cm^3)	Cohesion (kPa)	internal friction angle(°)	permeability coefficient, K(m/d)	Poisson's ratio	Lateral pressure coefficient	compressive strength(MPa)
1-5	filler sand;	1.97	0	26	10	0.30	0.43	/
8-4	Medium, coarse, gravel sand	2.00	1	34	15	0.30	0.40	/
8-5	Round gravel	2.05	0	35	30	0.25	0.33	/
17-1	Fully weathered granodiorite	1.92	22	21	0.1	0.28	0.40	/
17-2	Strong weathered granodiorite	2.03	30	26	0.15	0.25	0.33	/
17-3	Cracked and strongly weathered granodiorite	2.21	50	28	1.0	0.2	/	/
17-4	Medium-weathered granodiorite	2.58	70	30	0.1	/	/	50
17-5	Microweathered granodiorite	2.68	120	35	0.08	/	/	110

Figure 3. Location map of the Pearl River Mouth tunnel fault zone.

(e) The seismic intensity of the structure is assessed 7 degrees, and seismic structural measures are implemented in accordance with an 8-degree standard.

3 INTERVAL TUNNEL METHOD SELECTION AND DESIGN

The selection of a construction method for submarine tunnels is a critical determinant of project success. Commonly used methods include the mine method, shield tunnel method, and immersed tube method. The choice among these methods hinges on factors such as site geological conditions, adjacent structures, tunnel function, as well as project cost, duration, and risk. Given the specific conditions of the tunnel in question, the primary consideration is between the mine method and the shield tunnel method.

3.1 *Full shield tunneling method scheme*

The tunnel adopts a single-hole, two-lane design with a shield outer diameter of 12.8 m. The water shield section spans a total length of 11,940 m, divided into east and west sections of 6,950 m and 4,990 m, respectively. The east section uses two shields, initiating construction from both ends and meeting in the middle, Conversely, the west section employs a single shield, with the two ends of the banked section constructed using the open excavation method, totaling 1,650 m. The total construction period is about 52.5 months, with a project cost of 3.887 billion RMB shown in Figure 4.

3.2 *Combination scheme of shield tunneling method and mine method*

The scheme involves a single-hole, two-lane design, utilizing shield tunnel construction at both ends of the water section and the mine method in the hard rock section in the middle. The mine method section spans a total length of 5,520 m, with construction through the Nansha Island shore sloping shaft. The sloping shaft has a length of 1,160 m. The shield method section spans a total length of 6,520 m, divided into east and west sections of 3,590 m and 2,930 m, respectively. Two composite mud-water balanced shields are used, initiated from the two ends of the shield shafts towards the sea, with the shield method concluding in mines. The demarcation of disintegration is performed using the shield method. Cut-and-cover construction is applied at both ends of the shore section, totaling 1,650 m. The total construction period is approximately 56 months, with a project cost of 3.086 billion RMB shown in Figure 5.

For comparison between the two schemes,

Shield tunnel section at both ends: The full shield tunneling scheme has a relatively short upper soft and lower hard formation with low water pressure. In contrast, the combined scheme has a slightly higher water pressure, requiring high waterproofing standards.

Intermediate tunnel section: The combined scheme's mine tunnel passes through various faults, i.e. F2 fault and f1-f6 secondary faults, posing risks of sudden mud and water influx, with grouting challenges and high costs. The shield tunnel in the full shield scheme traverses a long upper, soft and lower hard formation, incurring tool wear and frequent knife changes. Attention is need for the unknown risk of locally unproven hard rock intrusion which may affect the attitude and operating parameters of shield tunneling. The combined scheme anticipates a leakage of approximately 2600 m³ per day in the mine method section, resulting in higher operating costs. The construction cost of the full shield scheme is 805 million yuan higher than that of the combined scheme.

After comprehensive comparison, both the full shield method and the combination of the shield method and the mine method are technically feasible, with comparable construction periods. The combination scheme entails slightly higher construction risk at the shield tunnel ends. However, considering the synergies between the shield and mine methods and an overall cost reduction of 800 million yuan, the recommended implementation plan is to adopt the shield method and mine method.

4 TUNNEL CROSS-SECTION DESIGN

4.1 *Shield method section*

In adherence to the requirement for a minimum effective area of tunnel clearance (not less than 90 m^2), the proposed inner diameter of the shield tunnel is 11.7 m. The effective clearance area above the tunnel rail surface is 74.05 m^2. The profile section layout is shown in Figure 6.

Considering factors such as tunnel depth, economy efficiency and shield segment joint forms, the concrete segment is designed with varying thickness of 600 mm and 550 mm, resulting in a ring width of 2.0 m. The lining comprises 9 rings with a universal wedge ring and a 40 mm double-sided wedge.

4.2 *Mining method*

The selection of mining method section is primarily based on the intended function and construction risk. To address the substantial groundwater pressure in the sea section, a composite lining structure is adopted.

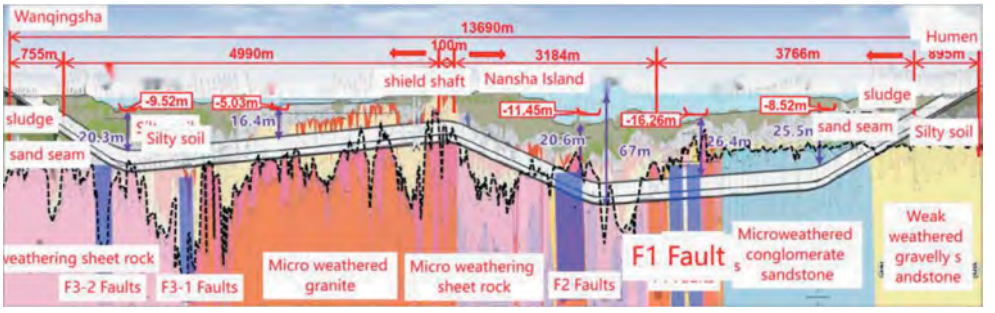

Figure 4. Vertical sectional drawing of shield mines combination tunnel.

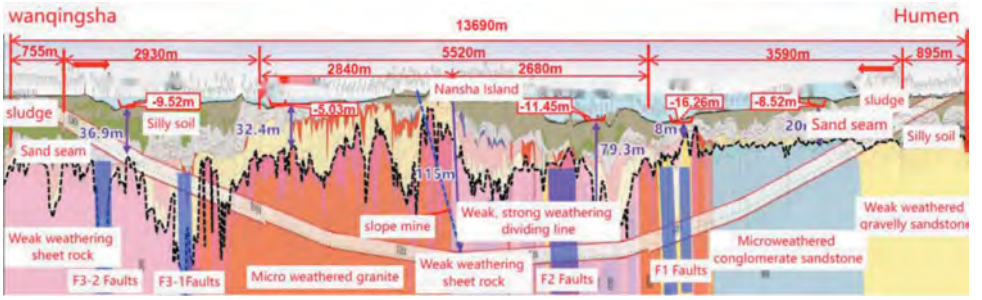

Figure 5. Construction organization plan of shield mines combination tunnel.

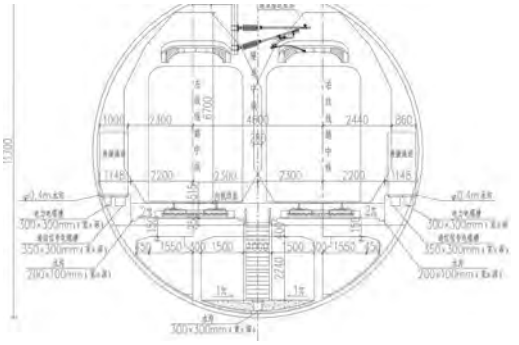

Figure 6. Single hole double line shield section view.

The tunnel section takes on a horseshoe shape, featuring an inverted arch for added support. Either spray anchor or grid steel frame support is implemented, with the second lining constructed as a reinforced concrete structure. The effective internal clearance area above the double line section of the mine method is 81.37 m^2. The profile of the single-hole and double-line mine is shown in Figure 7.

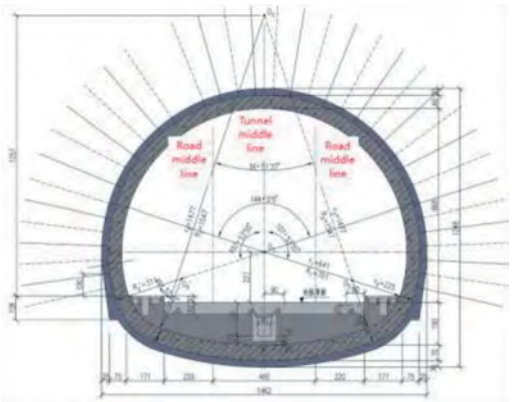

Figure 7. Single hole double line mine profile.

5 WATERPROOF AND DRAINAGE DESIGN

The tunnel, characterized by a vast sea span and significant water seepage, presents a substantial challenge to drainage capacity during both construction and operation. The tunnel's waterproof grade is designated as secondary, with a maximum hydrostatic pressure of approximately 1.15 MPa in the mine section and around 1.06 MPa in the shield section.

5.1 *Mine method tunnel waterproof and drainage*

To ensure the effective management of water ingress and drainage in the mine method tunnel, a comprehensive set of measures is implemented:

- Utilization of advanced geological forecasting system analysis to analyze and anticipate potential challenges related to water ingress and drainage;
- Improvement of the permeability coefficient of surrounding rock to control and manage permeability effectively;
- Implementation of drainage measure post-tunnel grouting to maintain controlled drainage rates: not exceeding 0.4 m^3/dm in the mine section; not exceeding 0.2m^3/dm in other sections;
- Integration of a maintainable drainage system into the tunnel, directing water towards a bottom drainage ditch;
- Establishment of longitudinal shafts at intervals of 100 m to facilitate later dredging and maintenance operations;
- Utilization of C50 and P12 waterproof concrete for the secondary lining, enhancing the tunnel's waterproofing properties.

During the construction process, the water inflow and pressure test are conducted to assess and monitor conditions. Selection of different grouting schemes is based on advanced geological forecast results. For local fissure development, the scheme involving local section advanced pre-grouting + radial supplementary grouting in the sections with low water pressure. Implementation of surrounding curtain grouting + radial supplementary grouting where water pressure and water output are controlled. Adoption of the scheme involving full section grouting + radial supplementary grouting in

sections where surrounding rock is extensively broken, fault rock is seriously weathered, or fault mud is present.

5.2 *Shield method tunnel waterproof design*

The Zhujiankou shield tunnel is bifurcated into east and west sections, experiencing varying maximum water pressure. In the western section, the maximum water pressure is 0.88 MPa, and in the eastern section, it reaches 1.06 MPa, making it the highest in the world presently. The waterproof design of segment joints is very important for the later-stage operation safety of the tunnel.

For segment joint waterproofing design, a typical approach in domestic underwater shield tunnel involves using an elastic gasket on the outside with a water pressure of 0.8 MPa, along with a water expansion stop on the inside. Due to the limited durability of 0.8 MPa, the tunnel opts for two EPDM elastic gaskets on the outside to ensure tightness in the shield tunnel joints.

Adopting a segmented fine design concept, the joint of the shield segment in the shield tunnel poses a challenge in assembling segments under ultra-high water pressure. The accuracy of segment assembly becomes a crucial factor limiting the waterproof performance of the joints, as shown in Figure 8.

Figure 8. Double channel EPDM elastic gasket joint waterproof design.

6 DOCKING DESIGN FOR SEA AREA

In the sea area, two common methods for shield machines to dock on the seabed are civil docking and mechanical docking. To ensure smooth construction, the docking position of the shield and the mining method is selected in the microweathered granite layer with good rock integrity. The microweathered rock layer's coverage thickness in this section is greater than two times the hole diameter, with a longitudinal length of about 30 m. The receiving scheme is shown in Figure 9.

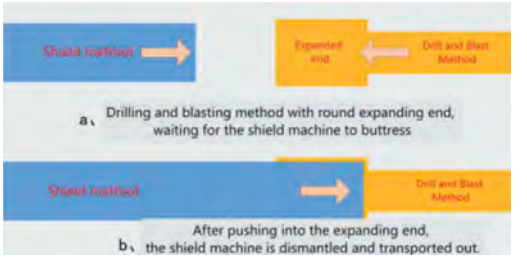

Figure 9. Design of Submarine Docking Enlargement Chambers.

Considering the potential adjustments to the theoretical docking mileage of the shield and the mine may during actual construction, the shield machine adopts the "double-shell" mode. This approach allows the shield machine to receive and synchronize in situ disassembly independently of the mine section's progress, facilitating a retreat from the whole body akin to a 'golden shell".

7 DURABILITY DESIGN

7.1 *Design principles*

Durability is a critical consideration in the design of the tunnel structure, with equal emphasis on both the durability and the limit design of bearing capacity. The design should meet the requirements of repairability and considered reserved reinforcement space to enhance the undersea tunnel's service life. Key components such as the reinforced concrete structure and drainage system, segment connecting components, and segment sealing material, collectively form a durability system. The failure of any of these components not only directly affects the normal use of the engineering but may also accelerate the deterioration of other parts, making the service life of the tunnel dependent on the weakest link of the durability system.

7.2 *Durability design of mine method tunnel support structure*

The mine method tunnel adopts a composite lining structure, where the secondary lining is designed for both bearing capacity and durability under the entire load. While the durability of the initial support lacks a quantitative implementation standard, it serves as an auxiliary measure to further improve the overall durability and structural safety of the project.

(a) Durability design measures for the initial support

In the mining tunnel, advanced curtain grouting is used to block the groundwater, thereby reducing soil permeability and the water pressure behind the lining. Grouting recommendations include the use of ordinary cement slurry, sulphaluminate slurate, and other grout materials with proven durability, controlling the amount of cement-water glass double slurry. For

sections with weak surrounding rock, the initial support incorporates an "8" bar grid steel frame, ensuring shotcrete impermeability not less than P6 through the application of the wet spray process. The net protective layer, both inside and outside the steel frame, is designed to be not less than 40 mm.

(b) Durability design for the secondary lining

Concrete strength and structural measures are reasonably selected based on environmental action grade considerations. The second lining adopts C50 and P12 reinforced concrete, with a specified crack width limit of 0.15 mm and a net protective layer thickness of 60 mm.

To control the hydration heat of molded concrete, the design opts for ordinary Portland cement with low hydration heat, maintaining a water-cement ratio within 0.36 and controlling the amount of cementing material within the range of 360 ~ 480 kg/m. A significant proportion of high quality fly ash (20 ~ 30 % of the cementing material) is incorporated to enhance concrete properties. The curing time for concrete is not less than 14 days, followed by humidification curing until reaching 50 % of the standard strength at 28 days and lasting not less than 7 days. Additionally, polypropylene fiber is introduced with a dosage of 0.9 kg/m³to further enhance the crack and seepage resistance of concrete.

(c) Durability design of the waterproof and drainage control system

Evaluation of the seawater resistance of the 2 mm thick ECB waterproof coil and water stop involves soaking in a 10 % NaCl solution and 23°C for 168 hours. The tensile strength retention rate should not be less than 80 %, and the pull elongation rate should not be less than 90 %.

7.3 *Durability design for shield tunnel structure*

The durability design of the shield tunnel focuses primarily on the segment structure, joint sealing material, and connecting bolts. Past projects have shown that corrosion resistance protection was not adequately emphasized. Taking Shenzhen Qianwan cable tunnel, completed in 2005, concrete test results in February 2014 were satisfactory without the need for repair. However, corrosion rates averaged 80 %, with bolts experiencing an average corrosion rate of 92.3 %, and bolt gaskets facing an average corrosion rate of 99.5 %, leading to loosening and water leakage in some severely corroded bolts.

1) Shield segment durability design measures

The Zhujiangkou Tunnel, enduring a marine corrosive environment for extended period, requires additional anti-corrosion measures to meet its 100-year design life. Traditional methods involve applying epoxy resin waterproof material to the outer structure surface. However, in shield tunneling, this material is susceptible to damage from the shield tail brush, affecting anticorrosion performance. To address this, the project adopts silane impregnated anticorrosion design, allowing hydrophobic material to attach to the concrete structure's air holes without blocking pores. The epoxy resin coating, with a thickness of up to 3.5 mm, poses challenges in meeting the assembly accuracy requirements for the pipe piece, particularly concerning the ring and longitudinal seam gap deviation (≤ 2 mm). To address this issue, the shield segment of the project adopts a silane impregnated anticorrosion design, as shown in Figure 10.

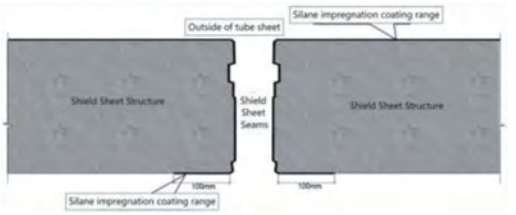

Figure 10. Silane impregnation anticorrosion design of segment.

Silane impregnation leverages its permeability to penetrate the concrete structure to a certain depth, allowing hydrophobic material to attach to the air holes without blocking the pores. Through this treatment, it prevents the entry of corrosive mediums while enabling water vapor to permeate freely. This ensures the permeability of the segment structure, ultimately achieving an effective anti-corrosion effect. This technology resolves interference concerns caused by epoxy resin and other processes on segment assembly accuracy. Additionally, it proves effective in avoiding the impact of shield tail brush scraping, meeting the stringent anticorrosion requirements of shield tunnels.

The segments adopt C55 and P12 reinforced concrete, with a crack width limit of 0.15 mm and a net protective layer thickness of 50 mm. Durability indexes, including concrete cement ratio, dosage of cement material, and chloride ion diffusion coefficient, are strictly controlled. Admixtures such as polycarboxylic acid high-performance water reducer, steel rust inhibitor, fly ash, and polypropylene fiber are utilized. Proper temperature and time during steam curing and pool maintenance are ensured.

2) Durability design measures of bolt and joint sealing material

(a) At present, shield bolts usually use coating for anticorrosion, constrained by coating thickness limitations and insufficient protection life. The project adopts for 316L stainless steel bolts with chlorine salt corrosion resistance and passivated surfaces.

(b) Micro-expansion cement mortar is used to seal the bolt hand hole.

(c) Materials such as sealing ket, water stop, and others at the joint are selected for seawater resistance, with consideration for embedding inside the segment.

8 CONCLUSIONS AND SUGGESTIONS

The Zhujiangkou Tunnel, a pivotal project for the Shenzhen-Jiangmen Railway, stands as China's deepest and most water pressure-intensive mine and shield tunnel combination submarine tunnel. With increasing depth and pressure, new technical challenges emerge. This paper employs geological analysis, engineering analogy, and comprehensive comparison to scrutinize key technical aspects in the intersection design across the sea:

(1) It is proposed that a combination of shield and mine methods tailored to the geological conditions of different sections is adopted. The layout design employs a single hole and double-line configuration.
(2) The drainage control should be emphasized, ensuring the maintenance of the drainage system. Use of a double ternary ethylene propylene elastic gasket layout for large-diameter, ultra-high water pressure shield tunnels is recommended to enhance assembly accuracy and achieve effective sealing and waterproofing.
(3) The durability design of the tunnel structure and the limit design of bearing capacity should be treated equally. Silane impregnation anticorrosion technology is introduced to safeguard against external damage, such as shield tail brush scraping, meeting the anti-corrosion requirements for shield tunnel.
(4) A combined submarine docking technology that is independent of project progress is introduced. Through the "double shell" mode, the shield machine can autonomously receive and synchronize in-situ disassembly.

The enormity of undersea tunnel construction necessitates high standards, promoting the advancement and innovation of tunnel construction technology in China. Although construction has commenced, challenges persist, including limited experience and elevated safety risks. The design technology issues discussed in this paper will require further exploration, accumulation, and summarization in the future practice endeavors.

REFERENCES

Zhang Chaoyong, 2021. Research on the Construction Scheme of Ningbo-Zhoushan Railway. Mode. Railway Standard Design. 65 (7):1–6(inChinese).

Zhou Yuzheng, LIN Haibo, 2019. Study on the Scheme of Hangzhou bay-crossing Bridge and Tunnel between Jiaxing and Ningbo Section of the Tong-Su-Jia-Yong Railway. Mode. Railway Investigation and Surveying. (3): 89–94 (in Chinese).

Zhang Jiuchang, SHI Junling, QU Yunteng, 2017. Technical specifications and operation of Seikan submarine tunnel. Mode. Chinese Railways. (5):91–96. (in Chinese)

Li Yan, MU Huansen, 2009. The channel tunnel: construction process and innovation experiences. Mode. Journal of Engineering Studies. 1(1):90–96. (in Chinese)

Wang Mengshu, 2014. Tunneling by TBM/shield in China: state-of-art, problems and proposals. Mode. Tunnel Construction. 34(3):179–188. (in Chinese).

Huang Kan, DING Guohua, PENG Limin, et al, 2011. Safety accessment of Liuyanghe tunnel construction through weathered slot. Mode. Journal of Central South University. 42(3):803–809. (in Chinese)

Li Guangyao, 2010. Technology for slurry shield to passing through up-soft-down-hard stratum in construction of Shiziyang tunnel. Mode. Railway Standard Design. (11):89–94. (in Chinese)

Guo Qiang, 2022. Study on the Route Scheme of Xifeng to Xiuwen Section of Chongqin-Guiyang Rialway. Mode. Railway Investigation and Surveying. (4):105–108 (in Chinese).

HUANG Jun, LIU Hongzhou, 2006. Feasibility research on shield scheme of sumerged tunnel. Mode. Highway. 6 (6):190–194. (in Chinese).

Wang Mengshu, 2008. Current developments and technical issues of underwater traffic tunnel-discussion on construction scheme of Taiwan strait undersea railway tunnel. Mode. Chinese Journal of Rock Mechanics and Engineering. 27(11):2161–2172. (in Chinese).

Qu Shouxin, 2009. Preliminary conclusions of construction technology in Xiamen Xiangan subsea tunnel. Mode. Engineering Science. 11(7):24–30. (in Chinese).

Song Yi, 2020. Selection of design of Su'ai Subsea Shield Tunnel in Shantou. Mode. Tunnel Construction. 40 (10):1391–1398(inChinese).

Tian Yuanjin, GUO Xiaohong, LIAO Chaohua, et al, 2008. Proposal selection of Dalian bay subsea tunnel. Mode. Journal of China and Foreign Highway. 28(3):124–128. (in Chinese).

Zhang Yueling, 2013. Proposal selection of planning programs for Bohai strait tunnel. Mode. Railway Economics Research. (1):12–16. (in Chinese).

Tang Xiongjun, XIAO Mingqing, JIAO Qizhu, MAO Sheng, 2021. Investigation of Overall Design and Key Technology of Jintang Subsea tunnel of Ningbo-Zhoushan Railway. Mode. Railway Standard Design. 65 (11):20–25(in Chinese).

Wu Qiang, 2021. Summary of Shantou Bay Cross-Harbour Tunnel Design for Shantou-Shanwei Railway. Mode. Railway Standard Design. 65 (10):38–43(in Chinese).

Han Huxuan, MENG Qingyu, ZHU Zhankui, ZHAO Fuquan, 2021. Study on Overall Scheme and Node Control Technology Scheme of NO.1 Tunnel for Jakarta-Bandung High Speed Railway in Indonesia. Mode. Railway Standard Design. 65(10):6–13(in Chinese).

Tunnelling for a Better Life – Yan, Celestino, Thewes & Eberhardt (Eds)
© 2024 The Author(s), ISBN 978-1-032-80042-4
Open Access: www.taylorfrancis.com, CC BY-NC-ND 4.0 license

Development and innovation of design method for railway tunnel support system in China

Siming Tian*
China Railway Economic and Planning Research Institute, Beijing, China
School of Qilu Transportation, Shandong University, Jinan, China

Dagang Liu
School of Civil Engineering, Southwest Jiaotong University, Chengdu, China

Yiteng Zhang & Xu Li
China Railway Economic and Planning Research Institute, Beijing, China
School of Civil Engineering, Southwest Jiaotong University, Chengdu, China

ABSTRACT: The design method of tunnel support system is an important way to ensure the safety of tunnel support structure construction, help tunnel construction efficiently and achieve the goal of green and low-carbon construction. This paper systematically reviews the development history of railway tunnel support system design in China from three dimensions of tunnel support system design concept, support type and design method, and points out the characteristics of the development of design concept from emphasizing the support to emphasizing the surrounding rock, support type from passive support to active support, and design method from empirical method to quantitative analysis method. This paper also expounds the innovative achievements in the design of advanced support of the face and anchorage support of the tunnel body in the analytical method, summarizes the problems still faced in the design of tunnel support system at the present stage, and puts forward that the whole-process intelligent dynamic design method based on the multi-information data of the construction period and the intelligent algorithm as the core is an important direction for the future development. The key technologies involved in intelligent dynamic design, such as sample database construction, intelligent algorithm model and safety evaluation method of supporting structure, are introduced.

Keywords: Railway tunnel, Supporting system, Design method, Empirical design method, Quantitative analysis method, Intelligent dynamic design method

1 INTRODUCTION

The tunnel support system is an important measure to maintain the clearance of the tunnel cross-section, prevent the deterioration of tunnel surrounding rock quality, withstand various external loads of the tunnel, and ensure the safety of tunnel construction. Therefore, scientifically designing the tunnel support system, selecting reasonable support types and parameters, is of great significance for the safe, economic, and efficient construction of the tunnel, and achieving the goal of green and low-carbon construction of the tunnel.

Since the establishment of the People's Republic of China, Chinese railway tunnels have been developing for more than 70 years, especially in the past 40 years. During this period, China's railway tunnel support system design has been based on the continuous reference, digestion and absorption of foreign advanced concepts and experiences, fully combined with the actual conditions and characteristics of railway tunnel construction in China, and through a large number of engineering practices and summaries. Continuous innovation and breakthroughs have been made in the support design theory and method, and the level and quality of China's railway tunnel support design have been continuously improved, demonstrating the international influence of China's railway tunnel construction (Tian et al., 2021).

This article reviews the development process of China's railway tunnel support system design, summarizes the main innovative achievements of China's railway tunnel support system design, and proposes development directions and prospects based on the current technical difficulties and challenges faced by

*Corresponding author: tsmd@163.com

DOI: 10.1201/9781003495505-49

railway tunnel engineering. This has positive significance for further improving the design level of China's railway tunnel support system.

2 DEVELOPMENT OF DESIGN METHODS FOR RAILWAY TUNNEL SUPPORT SYSTEMS IN CHINA

For tunnel engineering, a complete support system consists of two parts: surrounding rock and support structure (Guan, 2011). Therefore, how to understand the position and role of surrounding rock and support structure in the design of tunnel support system is the core and key of tunnel support system design.

It should be pointed out that the understanding of surrounding rock and support structure in tunnel support design is not achieved overnight, but gradually deepens with the continuous development of tunnel support technology and construction technology. The design concept of support system varies depending on the understanding during different periods. Throughout the development process and characteristics of China's railway tunnel support system design, it can be roughly divided into three stages.

2.1 *Stage 1: Before the 1980s*

At this stage, China's railway tunnels continue to use the traditional mining method construction concept, and the support technology mainly adopts simple wooden support + integral lining. The support construction is mainly manual. Due to the low efficiency and poor timeliness of support, it is often difficult to ensure the stability control of the surrounding rock. To ensure the reliability of the support design, the surrounding rock load is considered as a relaxation (collapse) load, and the lining structure is considered as the main bearing unit, assuming that the lining structure bears all the load. The design method is generally based on empirical methods, and a formula for calculating the relaxation load of surrounding rock has also been studied and proposed, starting to apply the load structure method to support design. The surrounding rock load considered in this stage of support design is the most unfavourable working condition, and the bearing unit is single, so the safety redundancy of support parameters is often too high.

2.2 *Stage 2: From the 1980s to the end of the 20th century*

At this stage, the construction concept of the New Austrian Tunnelling Method (NATM) was gradually applied and promoted in Chinese railway tunnels, and the support technology was transformed into a composite lining structure system of "primary support + secondary lining". The primary support components were mainly sprayed concrete and mortar anchor rods, and special sections were supplemented with steel support. The support construction method gradually developed into small-scale mechanized or single-process large-scale mechanized construction. Due to the fact that anchor-spray support can effectively control the deformation and stability of the surrounding rock, the design of support during this period gradually emphasizes the study of deformation loads on the surrounding rock, and both the primary support and secondary lining are considered as load-bearing units. It is believed that the two work together to bear all the loads. The design method is mainly based on empirical methods for primary support, while the load structure method is mainly used for secondary lining. At the same time, the surrounding rock structure method, which can consider the synergistic effect of the two, has also begun to be applied in design. Although the quality of support design in this stage has been significantly improved compared to the first stage, there are still some deficiencies in the self-bearing effect of the surrounding rock in the design.

2.3 *Stage 3: Since the beginning of the 21st century*

At this stage, China's railway tunnels have been continuously developed and influenced by new materials, construction equipment, artificial intelligence and other technological fields. Support technology has gradually introduced new support components such as early high-strength sprayed concrete and prestressed anchor rods (cables). Support construction has gradually evolved into a large-scale mechanized or even intelligent construction mode throughout the entire process, further improving the timeliness and quality of support construction, The active control effect of support on the stability of surrounding rock is becoming more prominent, and the design concept of active support is becoming increasingly mature, emphasizing the main role of rock anchor support system in bearing, and using secondary lining as a safety reserve. The design method focuses more on the synergistic bearing capacity of surrounding rock and support structure and the spatiotemporal effects of their support effects, and the level of support design has also been continuously improved.

3 MAIN ACHIEVEMENTS OF DESIGN METHODS FOR RAILWAY TUNNEL SUPPORT SYSTEMS IN CHINA

In recent years, Chinese scholars have gradually formed a new method for designing tunnel support systems with active support control of surrounding rock deformation as the core, based on the characteristics of railway tunnel construction in China and through continuous exploration, practice, and summary.

3.1 *Design method for deformation control of tunnel surrounding rock*

In response to the problem of controlling the deformation of surrounding rock in tunnels, a design method for controlling the deformation of surrounding rock in

railway tunnels is proposed (Zhao, 2019). The core idea of this method is to take the stability of the surrounding rock as the premise, control the deformation of the entire process of the surrounding rock as the goal, and use scientific support measures as the means to achieve the synergistic effect between the support structure and the tunnel surrounding rock, in order to fully utilize the self-bearing capacity of the surrounding rock and achieve a safe, economic, fast, and durable tunnel stability structural system.

This method assumes that the surrounding rock is composed of a combination of shallow and deep layers. Shallow surrounding rock refers to the loose zone surrounding rock that is disturbed and unstable around the tunnel, and the load generated by this part of the surrounding rock needs to be fully borne by the support structure; Deep surrounding rock refers to the surrounding rock outside the loose zone that is in a stable or temporarily stable state. This part of the surrounding rock is composed of a structural layer and a load layer, and the load generated is mainly deformation load. The magnitude of the load mainly depends on the control level and force transmission effect of the structural layer. Based on the load transfer effect of the composite surrounding rock, the final force of the support structure can be analysed, and then the design of the support structure can be carried out.

Based on the composite surrounding rock load effect, the calculation model shown in Figure 1 can be used to analyse the support reaction force. r_c is the thickness of the deep surrounding rock structure layer; r_b is the thickness of the shallow surrounding rock; r_a is the excavation size of the tunnel.

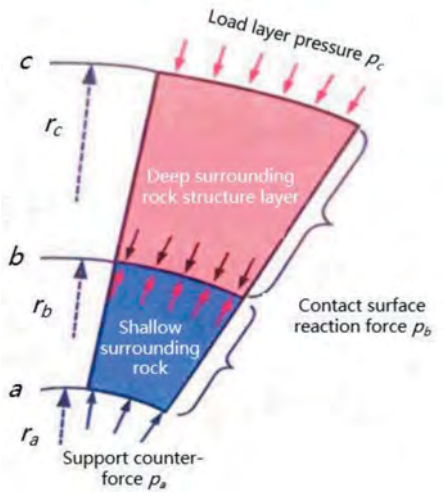

Figure 1. Calculation model of composite surrounding rock load.

Take a group of structural layers for analysis, with a focus on supporting radial loads. Assuming the support reaction force is p_a, the contact reaction force between the structural layer and the shallow surrounding rock interface is p_b, and the load applied to the structural layer by the load layer is p_c.

The support load p_a comes from the self-weight load p_1 of the shallow surrounding rock and the deformation load p_2 of the structural layer, respectively.

$$p_a = p_1 + p_2 \tag{1}$$

The self-weight load p_1 directly acts on the support, and the structural layer deformation load p_2 is transferred to the support structure through the shallow surrounding rock. The self-weight load of shallow surrounding rock is:

$$p_1 = \gamma_1 h_1 \tag{2}$$

Where, γ_1 is the weight of shallow surrounding rock; h_1 is the thickness of the shallow surrounding rock.

If the deformation load of the structural layer is related to the pressure of the load layer and its own parameters, it can be expressed as:

$$p_2 = \alpha p_c + \beta \mu_i \tag{3}$$

Where, α is the pressure transfer coefficient of the load layer; β is the deformation load transfer coefficient of the structural layer, both of which are related to the geometric and material parameters of the analysis problem; μ_i is the deformation amount of the structural layer.

Therefore, the focus of support load calculation is shifted to the determination of deformation load transfer parameters α and β for the structural layer and shallow surrounding rock. Reference (Zhao, 2019) specifies the parameter determination of α and β.

3.2 *Tunnel mechanized large section design method*

Based on the characteristics of mechanized large-section construction in tunnels, a design method for mechanized large-section support in railway tunnels has been proposed, which mainly includes two aspects: advance support design and tunnel body system support design (Wang, 2018).

In terms of advanced support design, the mechanical mechanism of various advanced support measures such as advanced pipe roof, tunnel face bolt, and advanced pre-grouting were systematically analysed. Based on the analysis of the ultimate mechanical balance of the tunnel face surrounding rock, a calculation and analysis model for advanced support was constructed, which can achieve the quantitative design of various advanced support parameters.

As shown in Figure 2, the height and width of the tunnel face is D and B, respectively; the length of the unsupported span is L_e. According to the force analysis of the tunnel face, the equations for the stability coefficient of the tunnel face is derived based on the limit equilibrium method as follows:

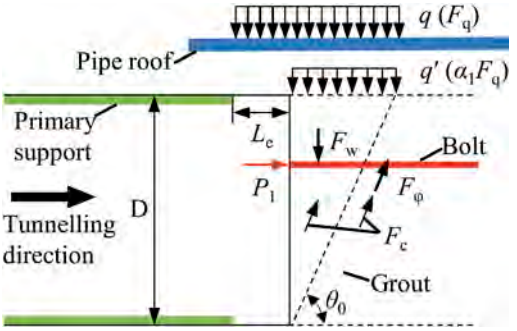

Figure 2. Calculation Model for Advance Support of Tunnel Face.

$$K = \frac{P_1 + \beta_1 F_c}{\beta_2 (F_w + \alpha_1 F_q)} + \beta_3 \geq [K] \tag{4}$$

$$F_c = \frac{cBD}{\sin\theta_0} + 2D^2 \cot\theta_0 \left[c + \lambda \left(\frac{2}{3} q + \frac{D\gamma}{3} \right) \tan\varphi \right] \tag{5}$$

$$F_w = \frac{D^2 B \gamma \cot\theta_0}{2} \tag{6}$$

$$F_q = qB(D\cot\theta_0 + L_e) \tag{7}$$

$$\beta_1 = \frac{1}{\sin\theta_0 \tan\varphi + \cos\theta_0} \tag{8}$$

$$\beta_2 = \frac{\sin\theta_0}{\sin\theta_0 \tan\varphi + \cos\theta_0} \tag{9}$$

$$\beta_3 = \frac{\cos\theta_0 \tan\varphi}{\sin\theta_0} \tag{10}$$

$$\theta_0 = \frac{\pi}{4} + \frac{\varphi}{2} \tag{11}$$

Where, K is the face stability coefficient; $[K]$ is the design stability coefficient of tunnel face, with the value of 1.15; F_c is the shear force on the failure surface; F_w is the weight of tunnel face; F_q is the vertical force exerted by the underlying ground; c is the cohesion of the ground; q is the earth pressure; γ is the bulk density of the ground; θ_0 is the failure angle of tunnel face; λ is the lateral pressure coefficient; β_1, β_2 and β_3 are the coefficients related to φ; P_1 is the support force of face bolt; α_1 is the load transfer coefficient of pipe roof.

In terms of support design for the tunnel system, a calculation formula for the deformation load of surrounding rock under deep burial conditions was proposed through statistical analysis of the contact pressure samples of the surrounding rock on the on-site support structure. Based on this, a load structure model was used to design the support structure.

The deformation load of the surrounding rock is as follows:

$$q = \alpha \cdot B \cdot e^{0.5s - \frac{15}{H}} \tag{12}$$

$$e = \lambda q \tag{13}$$

Where, q is vertical deformation pressure; e is the horizontal deformation pressure; α is the correction factor (α =1.2); B is the tunnel span; s is the level of surrounding rock; H is buried depth of tunnel; λ is lateral pressure coefficient.

3.3 *Total safety factor method for tunnel support structure design*

In response to the overall safety evaluation of composite lining structures, the total safety factor method for tunnel support structure design has been proposed for railway tunnels (Xiao, 2020). This method suggests that when the composite lining structure is designed using the safety factor method, the total safety factor should include the respective contributions of the initial support and secondary lining. In the design, the relationship between the surrounding rock and support structure is regarded as the relationship between force and reaction force. The characteristic value of surrounding rock pressure is used as the load value for support design, and the support structure is divided into four calculation models: spray layer, anchor bolts - surrounding rock bearing arch, anchor bolt, and secondary lining. The safety factors of spray layer, anchor bolt-surrounding rock bearing arch, and secondary lining are calculated using the load structure method, as shown in Figure 3. Finally, based on the actual engineering situation, the total safety factor of the support structure is given.

After calculating the safety factors of anchor bolt-surrounding rock bearing arch, spray layer and secondary lining respectively according to the above model, the lower limit value of the total safety factor of the structure can be approximately calculated as follows under the condition that no tensile failure occurs:

Construction phase (without secondary lining):

$$K_c = \eta K_1 + K_2 \tag{14}$$

Where, K_1 and K_2 are the safety coefficients of anchor bolt-surrounding rock bearing arch and the spray layer when they bear the design value of all surrounding rock pressure; η is the correction factor for the safety factor of the anchor bolt-surrounding rock bearing arch.

During the operation phase, when using durable or non-durable anchor bolts, calculated according to Eq. (15) and Eq. (16) respectively:

$$K_{op} = \eta K_1 + \xi K_2 + K_3 \tag{15}$$

$$K_{op} = \xi K_2 + K_3 \tag{16}$$

Where, K_3 is the safety factor of secondary lining under the design value of all surrounding rock pressure; ξ is the adjustment coefficient of spray layer bearing capacity.

The total safety factor during the construction period is recommended to be not less than 1.8 when the spray layer is steel fiber concrete or steel frame,

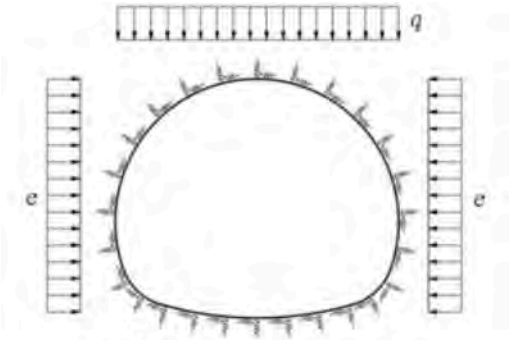

(a) Spray layer calculation model

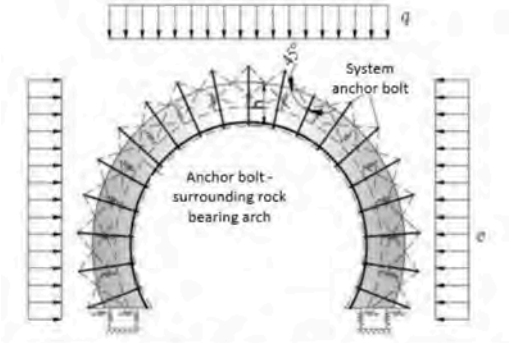

(b) Calculation model of anchor bolt - rock bearing arch

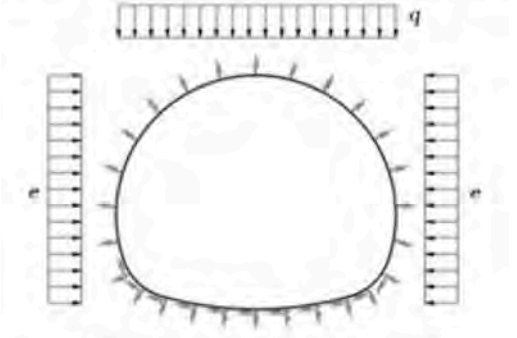

(c) Calculation model for secondary lining

Figure 3. Calculation model of total safety coefficient method for composite lining.

and not less than 2.1 when the spray layer is plain concrete.

The overall safety factor during the operating period is recommended to be not less than 3.0 when the secondary lining is reinforced concrete and not less than 3.6 when the secondary lining is plain concrete.

3.4 *High performance active support design method for tunnels*

Combining the support characteristics of new support components such as early high-strength shotcrete and prestressed anchor bolts (cables), a high-performance active support design method has been developed for railway tunnels(Tian et al., 2022), as shown in Figure 4. This method categorizes the instability of surrounding rock into two categories: the overall deformation instability of soft rock and the sliding instability of key blocks in hard rock. In terms of deformation instability control, the goal is to control the overall deformation of surrounding rock in three-dimensional space, with the improvement of surrounding rock stress and mechanical parameters by support as the core, and the comprehensive effect of spatiotemporal factors on the deformation of surrounding rock and support forces (such as the age strength of sprayed concrete) is considered, the mechanical analysis model and design method of the supporting system is established; In terms of controlling the instability of block sliding, with the goal of controlling the stability of key blocks, a local load mechanics analysis model was established through mechanical balance analysis of block self-gravity, shear resistance of sliding surface, radial and tangential forces of support, etc., to guide the design of anchor- spray support structure.

A quantitative design method for prestressed anchor bolts based on active control of surrounding rock deformation is mentioned in the high-performance active support design method. The specific process is as follows:

(1) Calculation model of surrounding rock layers

Based on the ideal elastic-plastic solution of the surrounding rock, a calculation model for the surrounding rock layer considering the reinforcement area of prestressed anchor bolts was established, as shown in Figure 5. And the final deformation value of the surrounding rock is obtained through the circle layer calculation model, as shown in Eqs. (17) ~ (20).

$$\mu_0 = R_0 \sin\varphi \left(\frac{1+\upsilon}{E'} + \frac{1+\upsilon}{E}\frac{R_p^2}{R_L^2} - \frac{1+\upsilon}{E'}\frac{R_p^2}{R_L^2} \right) \times \left[\frac{(P_0 + c\cot\varphi)(1-\sin\varphi)}{c'\cot\varphi'} \right]^{\frac{2}{M_{\varphi'}}} \tag{17}$$

$$R_p = R_0 \left[\frac{(P_0 + c\cot\varphi)(1-\sin\varphi)}{c\cot\varphi} \right]^{\frac{1}{M_\varphi}} \tag{18}$$

$$M_\varphi = 2\sin\varphi/(1-\sin\varphi) \tag{19}$$

$$M_{\varphi'} = 2\sin\varphi'/(1-\sin\varphi') \tag{20}$$

Where, c, φ, E, υ represents the original surrounding rock cohesion, internal friction angle, elastic modulus, and Poisson's ratio; c', φ', E' represents the cohesive force, internal friction angle, and elastic modulus of the surrounding rock in the reinforcement area; P_0 is the initial geostress; R_L refers to the reinforcement range of prestressed anchor bolts; R_0 is the radius of the tunnel.

For non-circular cross-section tunnels, the equivalent circle calculation method can be used to convert them into circular tunnels for analysis, and the value of R_0 is as follows:

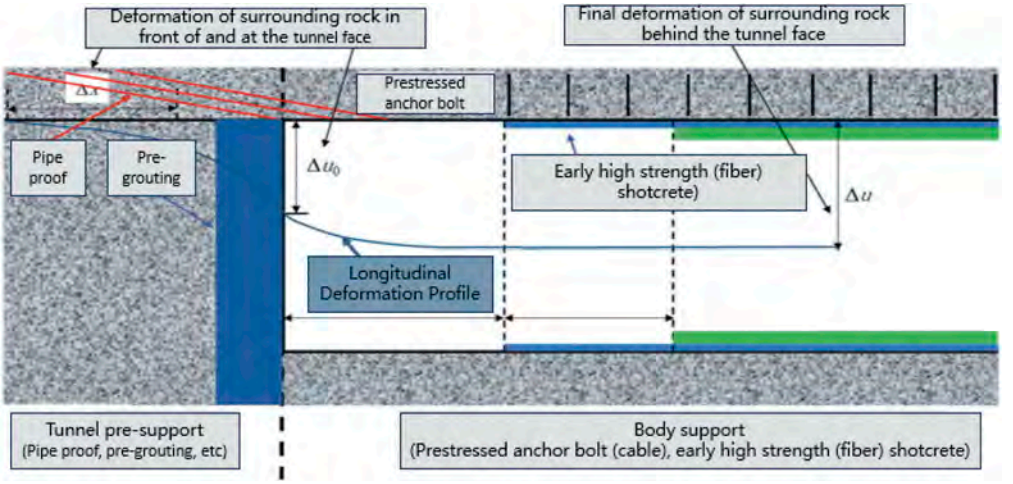

Figure 4. Schematic diagram of high-performance active support design principle.

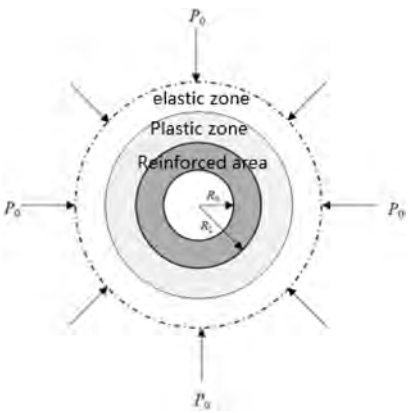

Figure 5. Calculation model for the surrounding rock layer.

$$R_0 = \frac{h+b}{4} \tag{21}$$

Where, h and b are the height and span of the horseshoe shaped tunnel section.

(2) Determination of the reinforcement range of prestressed anchor bolts

Considering the length, spacing and prestress value of prestressed bolts, the calculated thickness of the continuous pressure zone under the supporting action of multiple prestressed bolts is established, as shown in Eq. (22).

$$R_L = L - \frac{S_r - B}{2\tan\varphi_p} \tag{22}$$

Where, B is the width of the base plate; S is the circumferential spacing of the anchor bolts; L is the length of the free section of the anchor bolts; φ_P is the diffusion angle; R_L is the thickness of the compression zone.

The calculation method of additional stress in the reinforced area is shown in Eq. (23).

$$\Delta\sigma_3 = \frac{F}{S_l S_r} \tag{23}$$

Where, F is the pre tightening force of the anchor bolts; S_l and S_r are the longitudinal and circumferential spacing of the anchor bolts.

The calculation method for the mechanical parameters of the surrounding rock in the reinforcement area is shown in Eqs. (24) ~ (29).

$$E' = E + \Delta E \tag{24}$$

$$\Delta E = A_E(\Delta\sigma_3 + 1)^{B_E} \tag{25}$$

$$\varphi' = \varphi + \Delta\varphi \tag{26}$$

$$\Delta\varphi = A_\varphi \ln(\Delta\sigma_3 + 1) + B_\varphi \tag{27}$$

$$c' = c + \Delta c \tag{28}$$

$$\Delta c = A_c(\Delta\sigma_3 + 1)^{B_c} \tag{29}$$

Where, A and B represent the undetermined fitting coefficients of the calculation model of the mechanical parameters of each surrounding rock respectively, which can be obtained according to the indoor triaxial test.

(3) Control criteria for surrounding rock deformation

According to Technical code for monitoring measurement

of railway tunnel (China Railway Eryuan Engineering Group Co., 2007), the required control criteria for surrounding rock deformation control are selected, as shown in Table 1 and Table 2.

(4) Design process of pre-stressed anchor bolts

Determine the grade of surrounding rock in the design area based on the geological conditions and rock grade parameters in actual engineering, and

Table 1. Ultimate relative displacement of primary support for tunnels with a span of 7m<B≤12m.

Surrounding rock grade	Buried depth of tunnel *h* (m)		
	h≤50	50<h≤300	300<h≤500
Horizontal relative clearance change of arch foot (%)			
II	——	0.01~0.03	0.01~0.08
III	0.03~0.10	0.08~0.40	0.30~0.60
IV	0.10~0.30	0.20~0.80	0.70~1.20
V	0.20~0.50	0.40~2.00	1.80~3.00
Relative settlement of the arch (%)			
II	——	0.03~0.06	0.05~0.12
III	0.03~0.06	0.04~0.15	0.12~0.30
IV	0.06~0.10	0.08~0.40	0.30~0.80
V	0.80~0.16	0.14~1.10	0.80~1.40

Table 2. Ultimate relative displacement of primary support for tunnels with a span of B<7m.

Surrounding rock grade	Buried depth of tunnel *h* (m)		
	h≤50	50<*h*≤300	300<*h*≤500
Horizontal relative clearance change of arch foot (%)			
II	——	——	0.20~0.60
III	0.10~0.50	0.40~0.70	0.60~1.50
IV	0.20~0.70	0.50~2.60	2.40~3.50
V	0.30~1.00	0.80~3.50	3.00~5.00
Relative settlement of the arch (%)			
II	——	0.01~0.05	0.04~0.08
III	0.01~0.04	0.03~0.11	0.10~0.25
IV	0.03~0.07	0.06~0.15	0.10~0.60
V	0.06~0.12	0.10~0.60	0.50~1.20

select the deformation control values of the surrounding rock according to the engineering needs.

According to the deformation control criteria of surrounding rock, the required reinforcement parameters are solved, and the scope of reinforcement and the lifting ratio of mechanical parameters are determined.

According to the calculation model of the reinforcement range of the prestressed bolts, the length and spacing of prestressed bolts are determined.

The prestress value of the prestressed bolt is determined according to the calculation model of the lifting rate of the mechanical parameters in the reinforcement range of the prestressed bolt.

4 DEVELOPMENT DIRECTION OF SUPPORT SYSTEM DESIGN FOR RAILWAY TUNNELS IN CHINA

The essence of tunnel support system design is to control the change process of tunnel construction mechanic's state. In fact, there are many factors affecting the change of tunnel construction mechanic's state. In addition to geological objective factors, it is also closely related to construction method, support timing, support closing distance and other construction human factors. How to comprehensively consider the comprehensive influence of various factors in the design of support systems, in order to achieve dynamic and precise design of support, has become an important direction for design development.

With the continuous improvement of digitalization, informatization, and intelligence in tunnel construction, it is possible to use multi-source information data obtained during the construction period to carry out precise and dynamic design of tunnel support systems. Based on this, some experts and scholars have conducted active research and exploration on the dynamic design and intelligent decision-making methods of informationization throughout the entire process of tunnel support construction (Tian et al., 2023). The core idea is to use the information of all elements in the entire construction process to construct an information sample database, and use artificial intelligence algorithms to find the nonlinear mapping relationship between various elements in the entire construction process and the safety of the support structure. By quantitatively evaluating and analysing the safety of the support structure, and based on the set optimization feedback rules, reasonable optimization decisions are provided for the design and construction control of the support system. The key technical steps of this method mainly include the following four aspects:

(1) The Expression of All Element Information in the Whole Construction Process and the Construction of a Sample Database

The expression of all element information in the entire construction process refers to the qualitative or quantitative expression of indicator information for various element indicators that affect the safety of support structures during the construction process. By collecting the above indicator information, an information sample database can be constructed, providing a foundation for the learning and training of intelligent algorithm models.

(2) Training and Selection of Intelligent Algorithm Models

The purpose of using an intelligent algorithm model is to provide a nonlinear mapping relationship between various elements in the entire construction process and the safety degree of the support structure. Essentially, it is to predict the safety index information of the support structure based on the indicator information of each element. Therefore, it is advisable to use supervised learning regression machine learning algorithms for implementation.

(3) Quantitative Evaluation and Analysis of the Safety Degree of Support Structures

For the surrounding rock mainly characterized by deformation and instability, the deformation of the support structure is the most intuitive indicator reflecting the safety of the support structure. The deformation value of the support structure can be directly obtained through monitoring and

measurement methods, and the stress of the support structure can be obtained through the stiffness matrix displacement method from the deformation of the support structure. Based on this, the safety of the support structure can be uniformly measured and evaluated. For the surrounding rock mainly characterized by sliding and instability, the safety of the support structure should be quantitatively evaluated based on mechanical analysis such as the weight of the sliding block, the radial and tangential forces provided by the support, and the three dimensional indicators of anchor bolts axial force, sprayed concrete stress, and shear force at the contact surface between sprayed concrete and surrounding rock.

(4) Intelligent Decision Feedback Mechanism for Support Optimization

When the safety evaluation redundancy of the support structure is high, it is necessary to develop corresponding intelligent decision feedback rules for support optimization, guiding the machine to carry out automatic iterative optimization and feedback work on the support, in order to find the optimal support parameters and construction control plan for designers to make decisions. Support optimization mainly takes safety, efficiency, green and low-carbon as feedback goals, prioritizing the optimization of support components and parameters with low efficiency and long-time consumption until the safety redundancy of the support structure meets expectations.

5 CONCLUSIONS

Overall, the design of China's railway tunnel support system has undergone more than 40 years of development, with constantly improving design theories and methods. It has gradually evolved from traditional emphasizing support concepts and experiential design methods to highlight surrounding rock concepts and quantitative analysis design methods, and has formed many original technical achievements, greatly improving the design level and quality of China's railway tunnel support system. However, there are still a lot of technical challenges to be overcome in further improving the accuracy of tunnel support system design and meeting the dynamic requirements of support design during construction, which is also an important direction for the future development of tunnel support system design.

REFERENCES

China Railway Eryuan Engineering Group Co., L., 2007. Technical code for monitoring measurement of railway tunnel. China Railway Publishing House Co. Ltd., Beijing.

Guan, B., 2011. Key Points for Tunnel Engineering Design. China Communications Press Co., Ltd., Beijing.

Tian, S., Li, S., Liu, D., Wang, M., 2023. Research on Dynamic Design and Intelligent Decision-making Method for Whole Process Informatization of Tunnel Active Support System. Journal of the China Railway Society.

Tian, S., Wang, W., Yang, C., Liu, C., Wang, M., Wang, K., Ma, Z., Lyu, G., 2021. Development and Prospect of Railway Tunnels in China in Recent 40 Years. Tunnel Construction 41, 1903–1930.

Tian, S., Wu, K., Liu, D., Wang, M., Wang, Z., Dong, Y., 2022. Study on Design Method for Active Support for Plateau Railway Tunnels in High Energy Geological Environment. Journal of the China Railway Society 44, 39–63.

Wang, Z., 2018. Innovation and Future Apllication of Mechanized and Intelligentized Construction Technology for High-speed Railway Tunnels: ACase Study of Hubei Section on Zhengzhou-Wanzhou High-speed Railway. Tunnel Construction 38, 13.

Xiao, M., 2020. Total Safety Factor Method of Tunnel Support Structure Design. China Communications Press Co., Ltd., Beijing.

Zhao, Y., 2019. Tunnel Design Theory and Method. China Communications Press Co., Ltd., Beijing.

Tunnelling for a Better Life – Yan, Celestino, Thewes & Eberhardt (Eds)
© 2024 The Author(s), ISBN 978-1-032-80042-4
Open Access: www.taylorfrancis.com, CC BY-NC-ND 4.0 license

Maungawhau Mined Tunnels - Collaborative design – Management of design amendments for Maungawhau Mined Tunnels for improved construction schedule outcomes

Howard Toi*
SMEC Australia, Brisbane, Australia

Richard Gong
Geoinventions, Brisbane, Australia

Dian Wang
AECOM Australia, Perth, Australia

Geoffrey Charlesworth
AECOM Australia, Brisbane, Australia

ABSTRACT: This paper describes the challenges faced in the design of primary supports for the City Rail Link Maungawhau Mined Tunnels through extremely to very weak sedimentary rocks of the East Coast Bay Formation. The tunnels, designed to accommodate the rail alignments, including turn-outs, TBM transits and launches, were excavated by road headers in an area of low cover. The primary support designs were a mixture of passive lattice girders and sprayed concrete and active designs utilizing rock-bolts, executed in an intricate sequence to accommodate the complex geology, geometry and schedule constraints. One of the particular challenges involved the excavation and support of large tapered caverns to accommodate the track turnouts. These are efficient in terms of excavation volumes but require attention to design and construction detailing to successfully complete. The design was amended in the lead-up to construction, and through the early stages of construction, in order to optimise the schedule outcomes, which had been affected by supply-chain issues stemming from the Covid-19 pandemic.

Keywords: Sprayed concrete lining, tapered cavern

1 INTRODUCTION

The City Rail Link (CRL) Project includes the design and construction of two underground rail stations; a redevelopment of an existing surface rail station; two new rail tunnels; and connections to the existing North Auckland Line (NAL). The twin tunnels connecting the stations extend from Albert Street to Newton where they bifurcate through a grade separated interchange with terminations at Mt Eden Station and between Mt Eden Road and Normanby Road bridges. Connections to the NAL are via east and west grade separated connections.

The twin tunnels were driven northwards from Mt Eden towards the CBD via TBM drives. The initial, complex geometry at Mt Eden was negotiated in cut and cover and mined tunnels. The mined tunnels (Maungawhau Mined Tunnels, previously known as the Mt Eden Mined Tunnels) were excavated by mechanical excavators and roadheaders. The Maungawhau Mined Tunnels consist of:

Figure 1. Overall scheme layout.

*Corresponding author: Howard.Toi@smec.com

DOI: 10.1201/9781003495505-50

- MC30/MC60 Cavern: Accommodating the convergence of two tracks (MC30 and MC60) into turnouts to a single track (MC30). The northern end of the cavern was arranged to allow for the launch of the TBM along the MC30 alignment.
- MC20 Stub Tunnel: Excavated through a highly skewed headwall and arranged to allow for the launch of the TBM along the MC200 alignment southwards.
- MC50 Mined Tunnel: Excavated through a highly skewed headwall mined northwards towards the MC20/MC50 Cavern,
- MC20/MC50 Cavern: Accommodating the convergence of two tracks (MC20 and MC50) into turnouts to a single track (MC20). The northern end of the cavern was arranged to allow for the launch of the TBM along the MC20 alignment.

Figure 2. Maungawhau Mined Tunnel layout.

The mined tunnels are designed with a temporary primary lining, within which cast concrete, drained, secondary linings are constructed. This paper focuses on the challenges associated with the design, and design refinements for, the primary support two turn-out caverns.

2 TAPERED CAVERN GEOMETRY

One of the particular challenges involved the excavation and support of large tapered caverns to accommodate the track turnouts. The tapered caverns are efficient in terms of excavation volumes but require attention to design and construction detailing to successfully complete.

The MC30/MC60 Cavern profile gradually tapers over a length of 12m from the portal wall with a maximum cavern span of approximately 13m. The cavern profile maintains a constant profile for about 35m towards the northern end. A stub tunnel at the end of the MC30/MC60 cavern facilitates launch of the MC30 TBM (Figure 3).

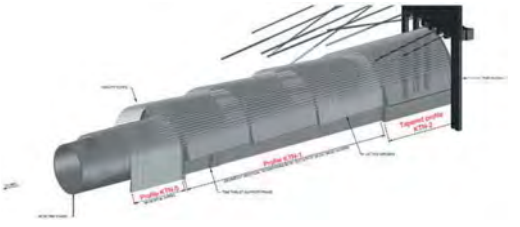

Figure 3. MC30/MC60 cavern arrangement.

The MC20/MC50 tapered cavern profile extends approximately 54 m north from the southern headwall. The maximum cavern span is approximately 17 m and is located at the southern headwall. The cavern profile then reduces to the north terminating in a short stub similar to that for MC30/60 (Figure 4).

Figure 4. MC20/MC50 cavern arrangement.

3 PRIMARY SUPPORT DESIGNS

3.1 *Ground conditions*

Ground conditions at the two caverns generally comprises East Coast Bays Formation (ECBF), including the following units:

- Highly to moderately weathered EBCF rock (EW).
- Slightly to unweathered extremely weak, poorly cemented sandstone (EUs1).
- Predominantly interbedded very weak, sandstone and siltstone (EU2). Typical unconfined compressive strength (UCS) values for un-weathered EU2 is 1-5 MPa.

EUs1 was often washed away during borehole drilling resulting in zones of core loss. When recovered, it appeared in boreholes as sand, or where recovered as a full core stick can be easily peeled by a knife and broken by hand. Typical geological sections at the two caverns are shown in Figures 5 and 6.

At MC30/MC60 cavern, a significant amount of EUs1 was encountered in the face and above crown. For MC20/MC50 cavern, the dominant rock type is EU2 within the cavern face, with significant EW and EUs1 above the crown at the cavern's widest span near the southern headwall.

3.2 *Turn-out caverns - Proposed support types*

The extremely weak uncemented sandstone EUs1 was recognized as being potentially unstable, posing a significant risk of instability. Low rock cover was also expected above both caverns. A passive support system was proposed for areas affected by significant lenses of EUs1 and in areas of low rock cover. Details for the proposed primary support types for each of the caverns are listed in Table 1.

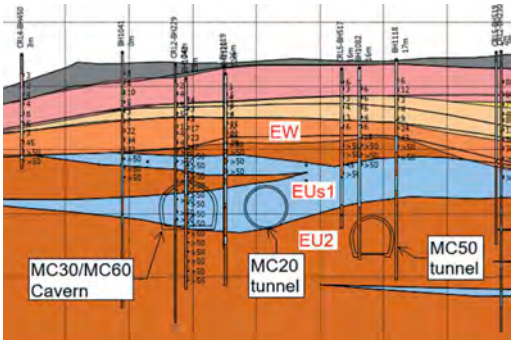

Figure 5. Typical geological section for MC30/MC60 cavern.

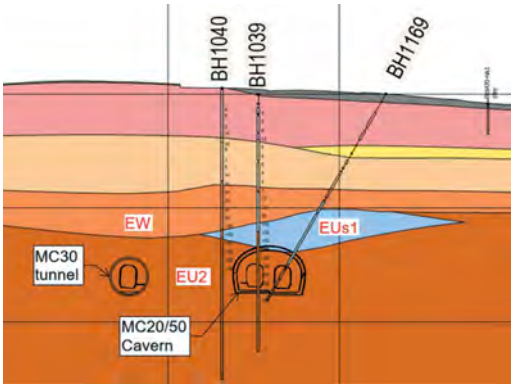

Figure 6. Typical geological section for MC20/MC50 cavern.

Table 1. Proposed primary support types.

Cavern – Zone	Primary support	Sequence
MC30/60 (see Figure 7)	200mm thk. fibre reinforced shotcrete with lattice girders. Pre-support consisting of canopy tubes. Glass reinforced plastic (GRP) face dowels. Allowable advance in top-heading 1.1m	Top-heading and bench
MC20/50 – Low cover area at south (see Figure 8)	200-350mm thk. fibre reinforced shotcrete with lattice girders. Pre-support consisting of spiles. Glass reinforced plastic (GRP) face dowels. Allowable advance in top-heading 1.1m	Split top-heading and bench; becoming full width top-heading as span reduces
MC20/50 – EU2 crown pillar > 3m thk.	4m long rock-bolts with 100-150mm thick fibre reinforced shotcrete	Top-heading and bench

Each tapered cavern narrows northwards in the direction of the TBM drives. Key dimensions are listed in Table 2.

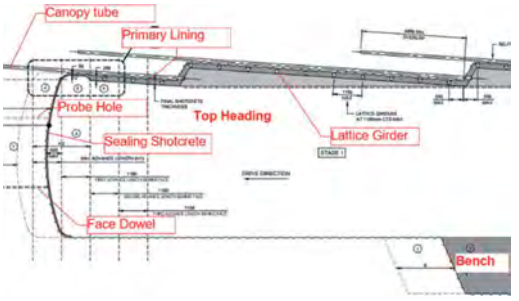

Figure 7. Primary supports for MC30/MC60 cavern.

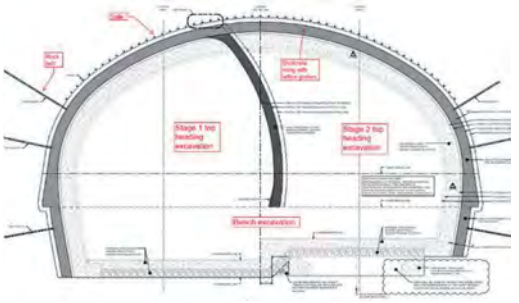

Figure 8. Primary supports for MC20/MC50 cavern tapered profile KTN-3.

Table 2. Approximate cavern dimensions.

Cavern – Zone	Span (m)	Height (m)	Comment
MC30/60	13	8	Excavation profile varies to follow canopy tube look-out
MC20/50	17	10	Southern most section, narrows northwards; Profile KTN3
MC20/50	13	8	Central section, identical geometry to MC30/60 Cavern
MC20/50	10	8	Northernmost section

3.3 *Ground relaxation*

To address the three-dimensional arching effect near the advancing tunnels, the Convergence Confinement Method (CCM) was employed. Ground relaxation in CCM is evaluated by numerical analysis using Plaxis 2D and 3D Finite Element (FE) modelling. A Plaxis 3D model was developed to simulate the process of tunnel excavation and lining installation with time dependent stiffness, as indicated in Figure 9. For the Plaxis 2D analysis, ground

relaxation associated with tunnel excavation is modelled by the multiplier Mstage which controls stepwise ground stress and associated ground deformation of the excavation. Mstage value corresponding to the excavation stage and subsequent ground support are assessed based on the comparison of the 2D and 3D analysis results. The ground relaxation study for the MC30/MC60 cavern was used a basis for subsequent mined tunnel designs. The MC30/60 simplified ground model assumed for the 3D analyses is illustrated in Figure 10.

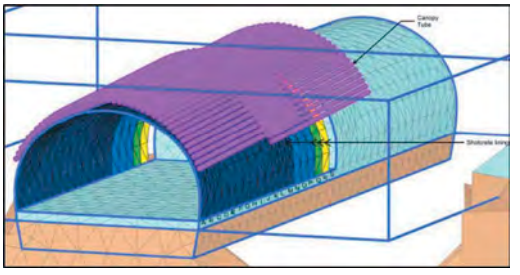

Figure 9. Plaxis 3D model for ground relaxation assessment.

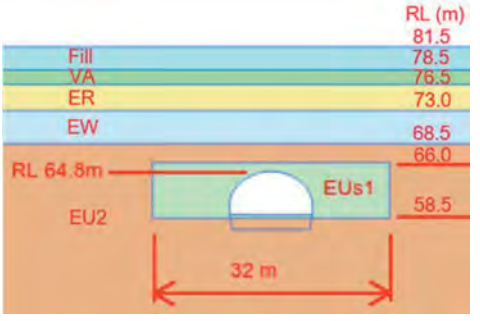

Figure 10. Analysis model for MC30/MC60 cavern.

Canopy tubes are required for the MC30/MC60 Cavern, and were included in the 3D model as embedded beams above the tunnel crown. They are spaced at 350mm intervals, have a length of 15m, and feature a 4m overlap. In the analysis, the primary lining thickness is set at 200mm. This assumes that the full lining thickness will be attained through the application of two sprays, the initial spray measuring 50mm, followed by a second spray of 150mm.

The 3D modelling considers both lining thickness and stiffness build-up with time, and age of sprayed concrete. Advance rate is assumed to be 2 rounds per day, while advance length is 1.1m per round. Thicknesses and ages of the respective lining segments (1.1m per segment) behind Advance N are indicated in Figure 11.

Advance ID	N	N-1	N-2	N-3	N-4
Lining Thickness (mm)	0	50	200 (50/150)	200 (50/150)	200 (50/150)
Age (days)	NA	0.5	1.0/0.5	1.5/1.0	2.0/1.5

Figure 11. Assumed shotcrete build-up.

Shotcrete stiffness build-up with time is assessed based on the research by Chang and Stille (1993), as shown in the equation below:

$E = aE_{28}e^{c/t^{0.7}}$, where

E_{28} = 27.4 GPa (shotcrete modulus at 28 days)

a = 1.062

c = -0.446

In the analysis, the overall stiffness of a full-thickness lining segment is evaluated to be a weighted average of the first and second layers.

John and Mattle (2003) investigated the effects of shotcrete creep and rock mass behaviour and stress re-distribution on tunnel deformation and derived the computational or hypothetical modulus of shotcrete from ground deformation.

Two scenarios to investigate the effect of modulus on deformation were used (see Figure 12):

- Option 1: Modulus determined based on Chang and Stille.
- Option 2: Similar to Option 1 but lower modulus values used for shotcrete with ages ≤ 2 days (John and Mattle; 2003).

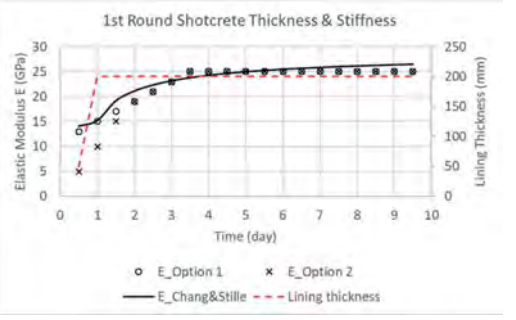

Figure 12. Shotcrete lining thicknesses and stiffness.

The Plaxis 3D analysis simulates tunnel excavation/lining installation time intervals of half day steps until 9.5 days (19 time steps) until the total excavation length reaches 20.9m (19x1.1m). Theoretically the simulation requires 19 lining stiffness values corresponding to the 19 time steps. The increase of lining stiffness after 3 days becomes less significant and hence seven property cases are adopted in the simulation to characterise build-up of lining thickness and stiffness. The modulus values evaluated in accordance with Chang & Stille and

those adopted in the analysis are indicated in Figure 11 for the 1st round (Round 1) shotcrete lining from Day 0.5 to Day 9.5. The other rounds (Rounds 2, 3, …, 18) follow the same pattern for both lining thickness and stiffness build-up, having their respective starting time (Day 0.5, 1, 1.5, …, 9) to Day 9.5.

3.3.1 *Plaxis 2D analysis*

Plaxis 2D models were developed using the same cavern profile and ground profile as that of Plaxis 3D. The ground relaxation considering 3D effect near tunnel face is represented by the parameter Mstage in Plaxis 2D analysis. Ground relaxations (Mstage) for the excavation and 50mm shotcrete stages are assessed by comparing deformations at tunnel crown from the 2D and 3D analyses. Ground relaxation for the full thickness young shotcrete is assumed to be 100%.

- Excavation stage: Excavation prior to applying shotcrete lining is modelled in Plaxis 2D. Mstage assumed in the analysis increased from 0 at intervals of 0.1, i.e. Mstage = 0, 0.1, 0.2, 0.3, … until the 2D analysis reaches similar deformation to 3D. The corresponding Mstage is then assigned as the Mstage for the excavation.
- 50mm shotcrete stage: Following the analysis of the excavation using the Mstage determined above, a 50mm shotcrete lining is applied and analysed. Under the same approach, Mstage is progressively increased (0.1, 0.2, 0.3, …) until the 2D analysis has similar deformations to the 3D model, and the corresponding Mstage is then assigned for the initial shotcrete stage. Modulus of the 50mm shotcrete is assumed to be 15GPa for Option 1 and 5GPa for Option 2.

3.3.2 *Analysis results*

Plaxis 3D deformation profile: The estimated deformation profiles at tunnel crown from 3D analyses are plotted in Figure 13 for Option 1 and Figure 14 for Option 2. Deformations at the mid-point of the nearest round to the face (0.55m to tunnel face) and 2nd nearest round (50mm shotcrete round, 1.65m to tunnel face) are also shown.

Figure 13. Deformation profile from 3D analysis - Option 1.

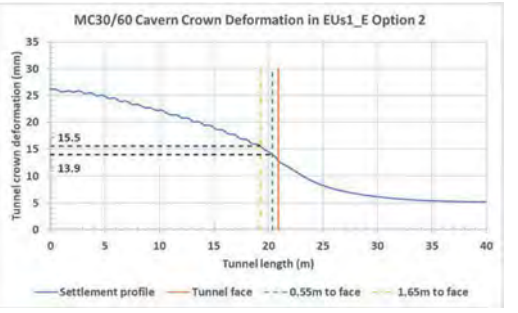

Figure 14. Deformation profile from 3D analysis - Option 2.

The results indicate that deformations are not very sensitive to the shotcrete modulus adopted.

Plaxis 2D Mstage for the excavation round (0.55m to tunnel face): For the initial excavation, tunnel crown deformations associated with ground relaxation (Mstage) from Plaxis 2D analysis are plotted in Figure 15. Plaxis 3D result for the excavation round is 13.9mm as presented above. An Mstage-value of 0.57 (rounded to 0.55 for the purpose of further analysis) closely matches the 3D analyses.

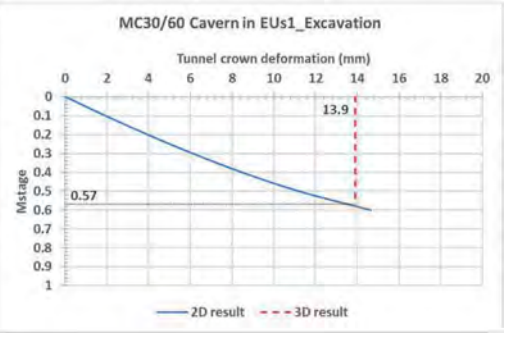

Figure 15. Ground reaction for excavation stage.

Plaxis 2D Mstage for 50mm shotcrete (1.65m to tunnel face): Following analysis of the tunnel excavation using Mstage = 0.55 as determined above, a 50mm shotcrete lining is applied and the analysis continues with varying Mstage of 0.1, 0.2, 0.3, …, etc. Modulus of shotcrete is assumed to be 15GPa (Option 1) and 5GPa (Option 2) respectively to assess the impact on analysis results. The difference of deformations from the two cases is small. Hence, the deformation at the initial shotcrete stage are not considered sensitive to the shotcrete modulus. Plaxis 3D result for the 50mm shotcrete round is 15.5mm as presented above. Mstage-values of 0.22 for Case 1 and 0.25 for Case 2 closely match the 3D analyses. An Mstage-value for the 50mm shotcrete stage of 0.25 was adopted for design.

3.4 *Mined tunnel construction sequence*

Defining the overall construction sequence was critical given that the proposed tunnels are in close proximity

The following sequence was assumed for design: a) first the MC30/MC60 Cavern (assumed that TBM launch from the northern end of the cavern could then proceed at any time, independent of the mined tunnel works); b) followed by the MC50 Mined Tunnel; c) the MC20 Stub Tunnel; and finally d) the MC/20 Cavern.

3.5 *Primary lining design*

Polypropylene fibre reinforced shotcrete (PFRC) was used as the principal element for the primary lining for the mined caverns and tunnels. The PFRC was designed in accordance with the methodology in NZS 3101 for steel fibre reinforced concrete (SFRC).

The characteristic stress-strain relation for PFRC is shown in Figure 16 as extracted from NZS 3101 for SFRC. Design strength parameters are as follows:

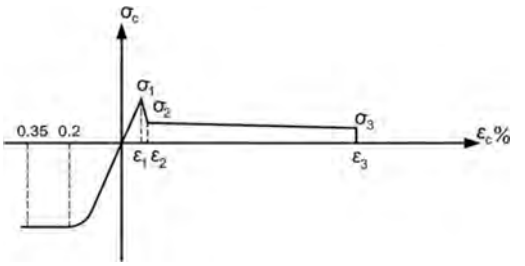

Figure 16. Characteristic stress-strain relation for PFRC.

- Characteristic compressive strength, fc' = 30MPa
- Peak flexural tensile strength, σ_1 = 4.8MPa
- Residual flexural tensile strength σ_2 = 2.0MPa
- Residual flexural tensile strength σ_3 = 1.5MPa

Bending moment (M) and axial force (N) interaction diagrams were developed based on the stress-strain relationship shown above. It is assumed that plane section of a structural member remains plane after straining. Rectangular parabolic stress distribution is assumed in the compression zone, with a bi-linear stress distribution in the tension zone. Strength reduction factors of 0.85 for flexure and 0.75 for compression were applied. The M-N interaction diagram for a typical 200mm thick PFRC lining is shown in Figure 17 together with design moments and axial forces from Plaxis with an overall load factor of 1.35.

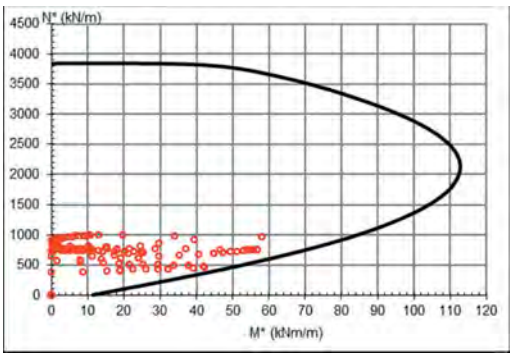

Figure 17. Structural capacity of 200mm PFRC lining.

3.6 *Canopy tube & spile design*

Fore-poling pre-support was employed for tunnelling in EUs1 dominant rock, or in areas where rock cover < 3m was anticipated. For the MC30/MC60 Cavern, fore-poling typically comprising canopy tubes as described in Section 3.3 were installed. The canopy tube design was based on the beam model suggested by John and Mattle (2002). Ground load is assessed using Terzaghi silo method. Unsupported length for beam span calculation is taken as 2 times advance length L. Comparison with the Plaxis 3D analysis indicates that calculation based on the beam model is conservative. Similarly, the same method is applied to the canopy tubes employed elsewhere (MC20 Stub Tunnel, MC50 Mined Tunnel) and spile design for tunnels and caverns.

3.7 *Face stability analysis*

Tunnel face stability was analysed in accordance with the method suggested by Anagnostou and Kovari (1997). The method assumes a three-dimensional wedge slides from the face of the excavation into the tunnel opening. The following assumptions are used to determine face stability.

- Driving forces result from the self-weight of the sliding wedge and any additional acting on the wedge. The additional load is derived from maximum block sizes according to wedge analysis or from the silo theory if the excavation is in weak ground.
- Resisting forces are provided by friction and cohesion on both the sliding and the side planes.

Factor of safety (FoS) for face stability, i.e. the ratio of resisting force to driving force was required to be at least 1.5. The analyses indicated that for the MC30/60 Cavern located in EUs1 dominant ground, the required FoS for the top heading cannot be achieved without reinforcement of the face. As a result GRP dowels 9m long with 4m minimum overlap at 1.5m spacing were specified. Figure 18 shows indicative arrangement of face dowels for MC30/MC60 Cavern.

For the MC20/MC50 Cavern, the face ground conditions were anticipated to be EU2 material. Face stability assessments show that the factor of safety is likely to be adequate for the top heading excavation in EU2 ground conditions or partial top heading excavation in EUs1/EW ground conditions.

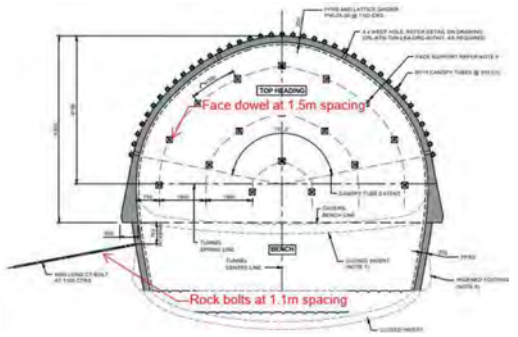

Figure 18. Tunnel face dowel arrangement for MC30/ MC60 cavern.

4 OPTIMISATION OF SUPPORT DESIGNS AND SEQUENCE

4.1 *MC30/MC60 Cavern*

4.1.1 *Optimisation of primary support designs*

The excavation of MC30/MC60 Cavern was on the critical path in the construction program. In order to optimise the schedule outcomes, the design was amended in the lead-up to construction, and through the early stages of construction.

The MC30/MC60 Cavern profile was carefully selected for allowing the re-use of secondary lining formwork in the MC20/MC50 Cavern. The tapered section was constructed by travelling shutters with inserts in the crown to achieve the required profiles. Additional formwork segments could be included at the footings to increase the cavern height as required.

The primary support geometries naturally respond to the proposed secondary lining geometries, and hence determination of lattice girder geometries became critical. The lead times for the lattice girder significantly increased due to the supply-chain issues stemming from the Covid-19 pandemic. In order to meet the construction program, the lattice girders were ordered based on the setout in the early stage of the primary support design. Each lattice girder round features unique geometry and was divided into several standardised segments of varying lengths to ensure constructability. Due to its complexity, the setout of the lattice girder was executed using the Navisworks BIM model.

4.1.2 *MC30/MC60 Cavern excavation sequence*

The MC30/MC60 Cavern tapered section has the largest span of approximately 13 m. The presence of extensive EUs1 at the tapered section in an area of low cover added further complexity to the excavation. Therefore, the excavation for the tapered section was undertaken in two stages: top heading and bench, as indicated in Figure 18. Bench excavation only commenced after the completion of the top heading excavation. Following the preferred construction sequence, bench excavation only commenced after the completion of the top heading excavation. The bench excavation design sequence was modified in the early construction stages to incorporate berm excavation adjacent to the top heading shotcrete lining footings. This design amendment allowed for a minimum width of 2.2 m at the centre of the cavern to accommodate construction traffic and facilitate efficient spoil management during excavation. Subsequently, the removal of berms and construction of the bench shotcrete lining were carried out simultaneously at two locations, optimising the overall schedule outcomes. Figure 19 shows the typical section of modified bench excavation with berms supporting the top heading lining.

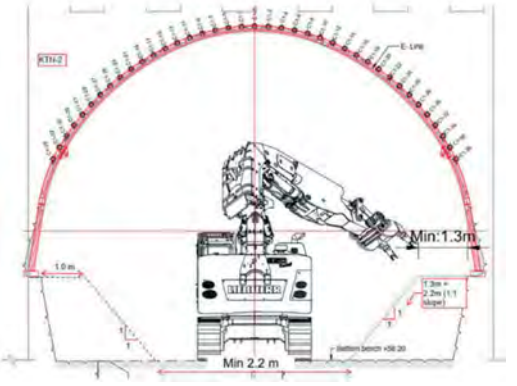

Figure 19. Typical section of modified bench excavation.

4.2 *MC20/MC50 cavern*

4.2.1 *Optimisation of primary support designs*

Similar to the tapered cavern for MC30/60, the design development of the MC20/MC50 primary support accommodates varying geometry, with the cavern narrowing northwards as the MC30 and MC50 tracks converge. In order to further reduce the excavation volumes, the tapered cavern profile was designed to have the eastern invert level about 1m higher than the western invert level. The difference in invert levels gradually reduces along the cavern.

Weaker ground conditions, extensive EW/EUs1 zones and reduced rock cover above the cavern crown at the tapered section was also a challenge to be managed. Figure 20 shows the anticipated ground conditions at the MC20/MC50 Cavern tapered section. Monitoring data from the MC30/MC60 Cavern excavation was used to assess EUs1 properties, and the performance of the installed support. Measured deformation in the inclinometers installed within the canopy tubes was in the order of 2 mm to 9 mm, and typically less than 5 mm as compared to the predicted deformation of 18 mm. The ground movement data was used to refine the EUs1 geotechnical parameters and justify the use of a larger tunnel advance for

MC20/MC50 Cavern excavation. The initial tunnel advance increased from 1.10 m to 1.35 m during design development and was revised to 1.80 m during construction based on the ground monitoring data.

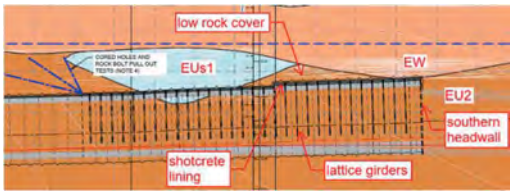

Figure 20. Anticipated ground conditions – MC20/MC50 cavern tapered section.

Similar to the MC30/MC60 cavern primary support, the setout and geometries of the lattice girder in the tapered section are complex. Each lattice girder round features unique geometry and was divided into six standardized segments of varying lengths at the tapered section, where partial top headings were required, to ensure constructability. Given its intricate nature, the setout of the lattice girder was executed using the Navisworks BIM model. Figure 21 presents a typical section of the lattice girder setout for MC20/MC50 Cavern.

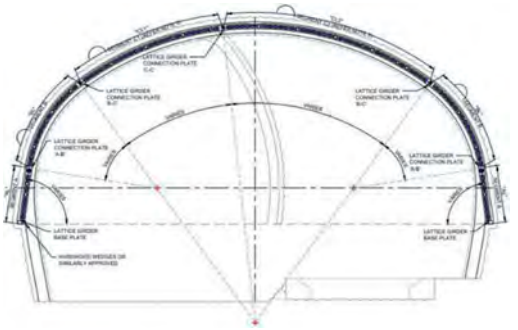

Figure 21. A typical section of the lattice girder setout for MC20/MC50 cavern.

The transition from the MC50 Tunnel to the MC20/MC50 Cavern involves a rapid increase in profile from the single track MC50 into the largest span within the cavern. A GRP spile system was adopted to provide pre-support and reinforcement in the area of the transition, which corresponds to an area of very limited rock cover (see Figure 20). The use of GRP spiles facilitated smoother excavation at the transition zone. Figure 22 presents the primary supports at transition from the MC50 Tunnel to the MC20/MC50 Cavern.

Stability of the rock pillar between the MC30 TBM tunnel and MC50 Mined Tunnel where these tunnels intersect the southern headwall of the MC20/MC50 Cavern, as illustrated in Figure 23, was addressed

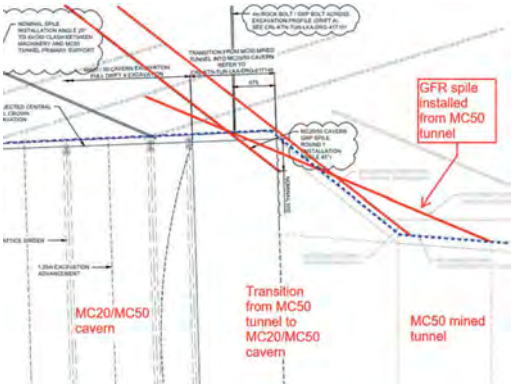

Figure 22. Primary supports at transition between MC50 mined tunnel and MC20/MC50 cavern.

through reinforcement of the pillar. The pillar width gradually reduces to approximately 0.5 m at the headwall. GRP dowels were installed as part of the temporary headwall and MC50 primary support system, effectively "stitching" the pillar prior to the MC20 TBM breakout.

A segment of the MC50 secondary lining, approximately 8 meters long, along with the permanent headwall of the MC20/MC50 Cavern, were constructed in advance of the MC20 TBM breakout. This preventative measure was taken to withstand the thrust exerted by the TBM and the pressure from the surrounding ground at the junction. The MC50 KTN-8 secondary lining consists of a 700mm thick reinforced concrete side wall engineered to withstand the force of the TBM drive and to provide additional support to the rock pillar. The permanent headwall of the MC20/50 Cavern features a 600mm thick reinforced concrete wall, complete with openings to accommodate the MC50 Mined Tunnel and MC20 TBM Tunnel.

4.2.2 *MC30/MC60 Cavern excavation sequence*

The excavation for the tapered section of the cavern was executed in multiple stages to optimise the construction schedule as follows:

1) Stage 1 top heading from MC50 was mined until the cavern section where the primary supports change from passive support to active support.
2) Northbound top heading with active support was mined for the rest of the cavern. Concurrently, an escape structure was constructed within the Stage 1 top heading area to facilitate the safe evacuation of workers in the event of an emergency.
3) Stage 2 top heading (Southbound) was mined while Northbound top heading excavation was carried out simultaneously to improve the excavation program.
4) Bench (only commenced after the completion of the top heading was mined) completed utilizing a similar approach to that adopted for MC30/60, allowing for advances on multiple fronts.

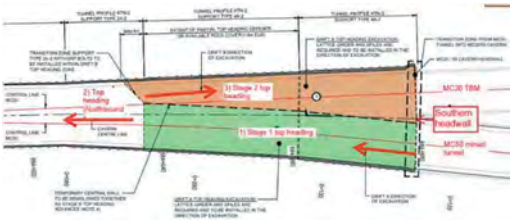

Figure 23. MC20/MC50 cavern excavation sequence.

5 CONCLUSIONS

The Maungawhau Mined Tunnels excavation faced a series of design and construction challenges, including intricate geometry, challenging ground conditions and unforeseen disruptions in the supply-chain due to the Covid-19 pandemic. This paper has outlined the core principles behind the primary support design, the design challenges for the cavern excavation as well as the strategies employed to enhance the design and construction schedule. The successful completion of this project highlights the collaborative efforts between the design and construction teams, ultimately resulting in a highly favourable outcome.

REFERENCES

Anagnostou, G., Kovari, K., 1997. Face stabilization in closed shield tunnelling. Rapid Excavation and Tunneling Conference, Las Vegas, NV, USA.

Chang, Y., Stille, H., 1992. Influence of early-age properties of shotcrete on tunnel construction sequences. Shotcrete for Underground Support VI, American Society of Civil Engineers, pp. 110–117.

John, M., Mattle, H., 2002. Design of Tube Umbrella. Tunel - ROCNIK, Czech Tunneling Committee and Slovak Tunnelling, Vol. 3, no. 11, pp. 1–11,.

John, M., Mattle, H., 2003. Factors of shotcrete lining design. Tunnels & Tunnelling International, Vol. 35, no. 10, pp. 42–44.

NZS 3101, 2006. Concrete structures standard. Standards New Zealand, Wellington, New Zealand.

Tunnelling for a Better Life – Yan, Celestino, Thewes & Eberhardt (Eds)
© 2024 The Author(s), ISBN 978-1-032-80042-4
Open Access: www.taylorfrancis.com, CC BY-NC-ND 4.0 license

"SINTEF-TriPOD" in underground design – A demonstration for two projects in Norway

Nghia Trinh* & Eivind Grøv
SINTEF AS, Trondheim, Norway

ABSTRACT: Many rock engineering projects today may face rock mechanics challenges such as particularly complicated profile or excavation plan, located near to existing infrastructure and thus pose a high risk to such structures, and complicated geological conditions. In such situation, there may be no similar existing experience to lean on. Thus, empirical methods have limitations and uncertainties in such cases. Therefore, SINTEF has developed a rock engineering tool to deal with the challenges. The tool is a combination of Investigation, Numerical modelling, and Monitoring. We use the term "SINTEF-TriPOD" for the methodology, and through projects it has proved to be a reliable tool.

This paper presents the application of the SINTEF-TriPOD for two important infrastructure projects in Oslo, Norway, which are Follo Line metro project (4 billion USD) and a fresh water supply project (approximately 1.2 billion USD).

Keywords: Stress measurement, Numerical modelling, Monitoring, Metro railway, Water supply, Underground complex

1 INTRODUCTION

Many rock engineering projects today may face rock mechanics challenges such as particularly complicated profile or excavation plan, located near to and thus cause a high risk to existing structures, and complicated geological conditions. In such situation, there may be no similar existing experience to lean on. Thus, empirical methods have limitations and uncertainties in such cases. Therefore, SINTEF has developed a reliable rock engineering tool to deal with the challenges. The tool is a combination of Investigation, Numerical modelling, and Monitoring:

- Investigation: The investigation can be rock stress measurements before and during construction (hydraulic fracturing from rock surface, 2D and 3D over-coring), different geological surveys, drill holes, and geological engineering mappings to evaluate the rock mass quality. Obtained information is used for the second component of the "SINTEF-TriPOD" – a numerical model.
- Numerical model: Establish a comprehensive numerical model, normally 3D numerical model is preferred as the model can handle complicated geometry and construction plans and methods. Simulations are to be carried out in certain order with clear objectives for each simulation steps. This is done to follow the planning and construction closely, helping the project team in making correct decision.
- Monitoring: To improve the numerical model even further, stress and displacement are monitored continuously, and comparing them to the modelled values. The model is calibrated, verified, and improved with the observations made in the surveillance program. This gives us a reliable tool to help for decision making during implementation of the project.

We use the term "SINTEF-TriPOD" for the methodology, as shown in Figure 1.

This paper presents the application of the "SINTEF-TriPOD" for two important infrastructure projects in Oslo, Norway, which are Follo Line metro project (4 billion USD) and a fresh water supply project (approximately 1.2 billion USD).

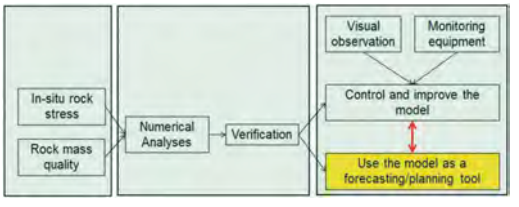

Figure 1. Three components of the "SINTEF-TriPOD" methodology.

*Corresponding author: nghia.trinh@sintef.no

DOI: 10.1201/9781003495505-51

2 FOLLO LINE PROJECT

2.1 *Project information*

BaneNOR (Norwegian National Rail Administration) has decided to construct the Follo Line Project with new railway tunnels connecting Oslo and Ski. The excavation period commenced in 2015, and it was opened for operation in early 2023. In 2015, the estimated cost of the project was 25 billion Norwegian kroner (NOK) (Kruse, 2017). The location and layout of the Follo Line project and the junction is shown in Figure 2.

The project comprises a 22 km long twin-tube-tunnel to be excavated mainly with tunnel boring machines (TBM, D = 9.96 m), but also by drill & blast and drill & split (D = 9.5 m). The drill & blast and drill & split tunnel section was in the first part of the Follo Line tunnels, near Oslo Central Station, and where the Follo Line tunnels go below the Ekeberg tunnels. Vertical distance between Follo Line tunnels and Ekeberg tunnels in this junction was just less than 4 m, as shown in Figure 2. This made the construction of the intersection to be very challenging. In addition, the Ekeberg tunnels have high traffic as part of European highway No.18 and No.6. Thus, the construction of the Follo Line tunnels in this intersection is performed with the following requirements from The Norwegian Public Roads Administration (SVV):

- No negative effect on the stability of the Ekeberg tunnels.
- No stopping of traffic in the Ekeberg tunnels during the construction of the Follo Line tunnels. Thus, the stability of the existing tunnels must be ensured at all time.
- Any risk of instability in the existing tunnels must be detected beforehand to make necessary precaution actions.

Since 2014, SINTEF assisted Bane NOR in dealing with the rock mechanics challenges and safety requirements for the construction of the mentioned intersection in this project. To meet the requirements from SVV and to study the stability of the existing Ekeberg road tunnels and the Alna river tunnel in connection with the construction of the Follo Line tunnels, SINTEF used a comprehensive approach, which is a combination of three components: Investigation – Numerical modelling – Monitoring, forming a rock mechanic tool for the project.

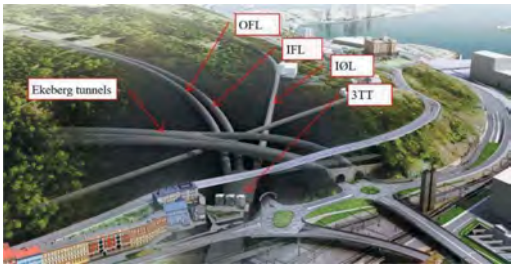

Figure 2. Junction between Ekeberg tunnels (existing) and the Follo Line tunnels with the following names: Inbound Østfold Line (IØL), Inbound Follo Line (IFL), Outbound Follo Line (OFL), 3-Tracks Tunnels (3TT) (BaneNOR, 2021).

2.2 *Investigations*

Detailed description of the geological conditions and different surface and sub-surface investigations have been presented in Holmøy et al. (2015). This paper briefly presents the in-situ rock stresses measurements and rock mass properties.

In pre-excavation stage, SINTEF carried out stress measurements in 2011 and 2012. During excavation of the Inbound Østfold Line (IØL), in 2016 when the tunnelling face was at chainage 1890, an additional 3D stress measurement was carried out to obtain the in-situ stress condition at the site. The measuring method was over-coring method, as described in Trinh et al. 2016. The measurements in 2011, 2012, and 2016 were 3D- and 2D-stress measurements. Results from the 3D-stress measurements are given in Table 1.

Table 1. Results from 3D-stress measurements carried out by SINTEF.

Year	Measure stress 3D overcoring	Value (MPa)	Trend (Degrees)	Plunge (Degrees)
2011	Sigma 1	9.9±1.9	N248.4	24
	Sigma 2	7.5±1.9	N145	27
	Sigma 3	1.9±2.8	N14	61
2016	Sigma 1	21.6±2.1	N338	35
	Sigma 2	17.3±3	N224	27
	Sigma 3	10.9±0.9	N104	61

The in-situ stress level measured in 2016 was much higher than the measurements in 2011, sigma 1 was twice and sigma 3 was 5 times higher than the measurements in 2011. This may be explained by a local weakness zone or maybe existing caverns/ tunnels or the existing Alna river tunnel not too far away from the location of 2016 measurements. Comprehensive calibrations of the numerical model with result of stress measurements in 2011 and 2016 were done during planning and early construction stages of the Follo Line project. It was found that all the numerical model results with input from 2016 measurement gave far higher values than the results obtained from 2D stress measurements measured in the existing infrastructure, whilst with input from the 2011 measurement, the numerical model results fitted quite well. Thus, it was decided that the results from the stress measurement in 2011 can be used as a representative in-situ stress for input in the numerical model for this project. In-situ stress for the model was estimated based on the measurement in 2011. At elevation zero, the sigma in east-west direction was 10 MPa, north-south 6 MPa, vertical 4.5 MPa, and the stress had gravitational gradient.

During early establishment of the model and simulation, the input for rock mass properties have been estimated based on mapping and laboratory tests. Results of this model were verified with the registered data obtained from monitoring equipment (stress change and displacement in connection with the tunnelling progress). Through certain construction progress, a very comprehensive calibration and testing of the model with collected data from monitoring equipment were carried out. This work was done with weekly excavation reports and monitoring data. Result of this calibration was that the rock mass properties used in the initial analyses were updated. The updated inputs of the rock mass properties for the 3D numerical model are rock mass Young's modulus (Em) = 10 GPa, Poisson's ratio = 0.15, internal friction angle = 55 degrees, and cohesion = 2 MPa.

2.3 *Numerical model*

Based on the scanning of the existing tunnels and the drawings of the planned Follo Line tunnels, a 3D numerical model was established, as shown in Figure 3. FLAC3D (Itasca, 2021) code was used to model a 3D picture of the crossing of these tunnels. Geometry of the Ekeberg and Follo Line tunnel system is presented in Figure 3. When constructing the geometry for the simulations, the excavation method and sequence were modelled as per a specific process according to the contractor's plan.

The excavation method was conventional "drill and blast" in the area outside the crossing. Whilst near or under the existing tunnels, the excavation method "drill and split" was applied to minimise damage to the rock mass around the tunnel. In the "drill and blast" sections, a normal pull length of 5 m for each blasting round was used. In the "drill and split" section, a pull length of 2.5 m for each splitting round was used. Thus, in the model geometry, the Follo Line tunnels were divided into every 5 m and 2.5 m in the "drill and blast" and "drill and split" area, respectively. By doing this, every excavation step was simulated to obtain the whole development of stress distribution and displacement from the starting of the construction process.

Simulation process in this project is as follow:

- Simulation 1: No excavation in the model. This simulation was dedicated to obtain the original in-situ stress condition within the site boundary.
- Simulation 2: All existing tunnels were excavated to model the existing condition, before the construction of the Follo Line tunnels. This simulation was done to obtain the existing stress situation and deformation and verify with the observation and 2D measurements in the existing tunnels. This step was considered as an early verification of the model.
- Simulation 3: This was the most complicated simulation for the project, where all the planned excavation steps and sequences were strictly followed: 63 simulation steps for the excavation of the Inbound Østfold Line, 58 simulation steps for the Inbound Follo Line (IFL) and Outbound Follo Line (OFL), 65 simulations steps for the "Three tracks" tunnel.

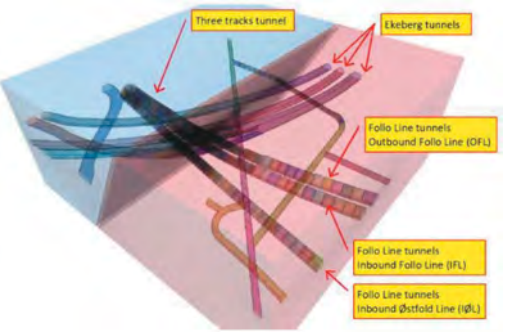

Figure 3. Geometry of the 3D numerical model for the intersection between Follo Line tunnels and Ekeberg tunnels.

Some results of the 3D-model are shown in Figures 4 to 6. According to the figures, the following comments were made:

- The maximum stress component (sigma 1, as shown in Figure 4) around the tunnel was estimated to increase slightly from about 12 MPa (in-situ original condition) to about 17.5 MPa. In the critical area (the horizontal rock pillar between Follo Line tunnels and Ekeberg tunnels), the model estimated the same amount of stress increase.
- The minimum stress component (sigma 3, as shown in Figure 5) around the tunnel decreases from about 5 MPa (in-situ original condition) to about 2.5 MPa. The reduction is approximately 2.5 MPa.
- The tunnel excavation results in a displacement of about 2 to 3 mm around the tunnel, as shown in Figure 6. Below the existing Alna river tunnel, the model showed that displacement in the new tunnel is from 4 mm to 6 mm. It is thus expected that the maximum displacement in the junction will be 4 to 6 mm after completion of the construction of Follo Line tunnels.
- Before excavation of the Follo Line tunnels, the model result showed yield elements in the floor of the Ekeberg tunnels; whilst after excavation of the Follo Line tunnels, the model results showed slightly more yield elements in the horizontal pillar.
- In general, the model results showed that there is a certain impact from the excavation of the Follo Line tunnels on the Ekeberg tunnels. However, the amount of change was estimated to be modest (stress change of about 5 MPa, and the displacement change of 2 to 6 mm depending on excavation stage). Model results gave an impression of overall stable condition for both tunnel systems.
- A monitoring system consisting of extensometers and long-term-door-stopper monitoring (LTDM)

were installed at key locations for better control of the stability situation. The monitoring system will be presented in the next chapters.

Figure 4. Distribution of sigma 1 at final excavation stage – Vertical section along IFL (negative value means compression).

Figure 5. Distribution of sigma 3 at final excavation stage – Vertical section along IFL (negative value means compression).

Figure 6. Distribution of displacement at final excavation stage – Vertical section along IFL.

2.4 *Monitoring of stress and displacement*

In this project, it was very important to capture the stress and displacement development in a very early stage, well before any instability problem may appear. The purposes to get early information were:

- Early information can be used to calibrate the numerical model, improving the model during the early construction so that the model becomes a reliable tool for testing the critical excavation stages – excavation close to or directly below the Ekeberg tunnels.
- The stress redistribution and displacement development in the rock mass can be followed from the beginning, so that any "unexpected development" can be detected in a good time for further study and actions.
- Early registered data from monitoring equipment can be used with the corresponding rock mass behaviour observed during the construction to design and test the warning system well before the construction progress to the critical area – under the Ekeberg tunnels.

Description of the monitoring program and warning system can be found in Trinh et al. (2016 and 2021). The locations of the monitoring system are presented in Figure 7.

Data from monitoring equipment was used to control the quality of the numerical model, to make the model becoming a reliable forecasting tool. Results from the numerical model were compared with the stress data from the monitoring devices, the data from two critical LTDMs ("LTDM-Pillar" and "LTDM-Floor") are presented in Figures 8 and 9. These two LTDMs were installed to monitor the stress evolution in the existing Ekeberg tunnels as a result of the excavation of the Follo Line tunnels. The LTDMs were installed at the most critical locations, where the Follo Line tunnels were at their closest to the Ekeberg tunnels – less than 4 m vertical distance. Both LTDMs were installed in May 2015, when the excavation of the Follo Line tunnels was still a very long distance away (more than 150 m) and, therefore, having practically no influence on the Ekeberg tunnels. Early installation of the LTDMs provided a good possibility of obtaining, from the start, the evolution of induced stress in the Ekeberg tunnels as the excavation of the Follo Line tunnels approached. Any abnormal change or evolution of stresses during the excavation progression could be detected early enough to implement appropriate precautionary measures, if necessary. The early monitoring data were also used for model verification.

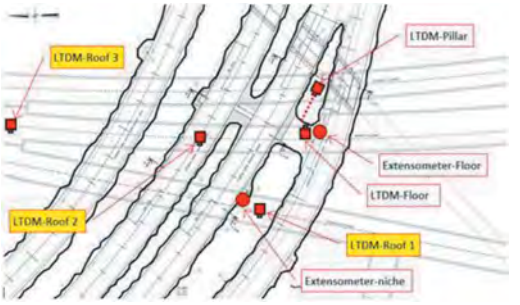

Figure 7. Locations of monitoring equipment for monitor the stress and displacement (Trinh et al. 2021).

The results from the numerical model and the recorded data at the "LTDM-Pillar" show that they fit relatively well as shown in Figure 9. The model results versus the monitoring data for the "LTDM-

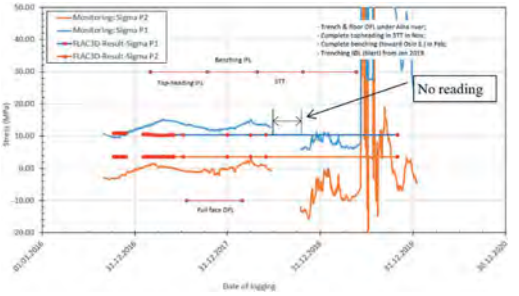

Figure 8. Comparison of stress from monitoring (LTDM-Pillar) versus numerical model.

Floor" are presented in Figure 10. As can be seen from the figure, the model results did not fit well before September 2017. After September 2017, the stress in this location quickly increased, and the model results fitted better with the monitoring data. A possible explanation for this could be joint movement and better rock contact to increase the stress evolution. After the "no reading" period, data from the LTDMs became unreliable as pointed out in Trinh et al. (2021).

Displacement result from the numerical model was compared with the data from "Extensometer-Floor", as shown in Figure 10. The verification of the numerical model with the displacement monitoring data can be divided into three periods:

- Before September 2017: Displacement monitoring in this period is presented in Figure 9. This period includes both the non-critical excavation stages and part of the critical excavation stage which started in February 2017 with the top heading. During the non-critical excavation stages when excavation was relatively far from the junction, the displacement results from the numerical model fit well with the monitoring data. During the critical excavation stage, the numerical model displacement prediction was approximately 0.5mm greater than that from the monitoring data. This numerical model result was acceptable due to: (a) The difference being only 0.5mm, (b) The model result and monitoring data show the same evolution pattern, and (c) Full face excavation was implemented in the model whilst in reality only top heading excavation was carried out. Thus, it is reasonable that displacement in the numerical model is higher than the registered data from the "Extensometer-Floor". This concludes that for this period, the numerical model appears to be a reliable tool for planning, construction, and decision-making. The model can be used for predicting displacement and stability evaluation of the upcoming critical excavation steps.
- Between September 2017 and March 2018: Displacement monitoring in this period is as shown in Figure 10. During this period, the benching in the IFL tunnel was excavated producing full face conditions as simulated in the numerical model. The results from the numerical model and the recorded data were almost identical during this period, which demonstrates a very good match between the numerical model and the actual recorded data. With this level of accuracy, the numerical model proved to be a reliable and an important tool for evaluating the stability condition at the junction during the critical excavation stage. The monitoring data indicates that the excavation of tunnel bench can cause 0.5 mm of displacement above the tunnel.
- After March 2018: Critical excavation had already been completed in February 2018. After March 2018, the excavation activities were (a) at Three-Tracks Tunnel (3TT) with approximately 30m span, and (b) excavation of a small trench in the floor of the OFL and IFL tunnels by drill and blast. During this period, the numerical prediction gave 1.0 to 1.5mm displacement less than that from the monitoring data. It seems that the numerical model was unable to fully calculate the displacement caused by drill and blast in the Three-Tracks Tunnel (3TT), which was approximately 100m away from the extensometer. Studying the excavation progress in the 3TT and the monitoring readings during the same period, the displacement caused by the 3TT excavation was estimated to be approximately 0.5mm at the "Extensometer-Floor" location. The additional 1mm displacement recorded at "Extensometer-Floor" occurred during the excavation of the trench in the floor of the OFL and IFL tunnels. This excavation was by drill and blast, directly below the extensometer. Even though the size of the trench was only 1m x 1m, it had a greater influence on the displacement than the excavation of the 3TT with a 30m span. This is most likely due to the much shorter distance to the excavated trench compared to that from the 3TT which was 100m away. Displacement for the whole period from 2016 to 2019 is as shown in Figure 11.

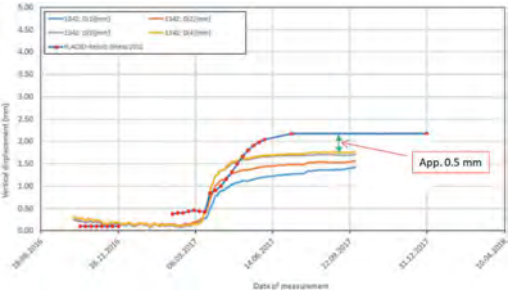

Figure 9. Displacement registered by the "Extensometer-Floor" versus predicted value from numerical model – Just before critical excavation steps.

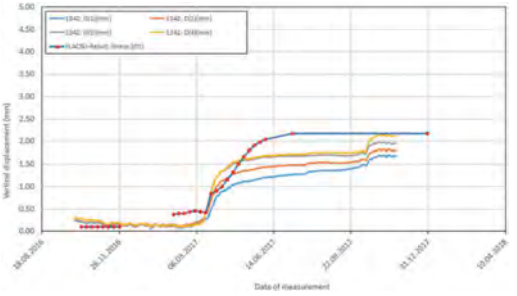

Figure 10. Displacement registered by the "Extensometer-Floor" versus predicted value from numerical model – During critical excavation steps.

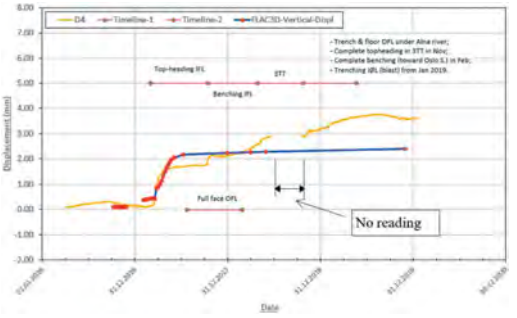

Figure 11. Comparison of displacement from monitoring versus numerical model for 4 years.

3 NEW WATER SUPPLY PROJECT

Oslo is the fastest growing city in Europe. The prognosis indicate that the population growth will continue. Today 90% of the water supply to Oslo is from a limited source named Maridalsvannet and its water treatment plant is at Oset. This makes the city very vulnerable to incidents that strike either the source or the treatment plant. The Oslo Municipality Water and Sewage Administration (VAV) is therefore in the process of building a secondary water supply. According to the plan, by 1st January 2028 the new water supply to Oslo will be ready. The new water treatment plant is located at Huseby. The treatment plant consists of six large caverns with cross sections BxH varying between 20m x 24m to 26m x 43 m. In addition, an assembly chamber for a TBM is being excavated within this underground complex. The treatment plant consists of three different levels and is a complicated system of caverns and connecting tunnels. The volume is approximately 1 million m3 which is all excavated in a relatively small area (Mørck et al., 2022).

Based on initial geological investigation and design, it was expected that the geological conditions were not very favourable in this underground treatment plant. The plan was to use heavy rock support with arches of lattice girders in combination with rock bolts and sprayed concrete. As a reference, similar but smaller and less complicated caverns nearby were built using the same rock support concept. There were also identified several weakness zones, adding the reason for the need of the designed lattice arches.

VAV found it necessary to follow-up the effect the excavation of such a large volume on such a small area could have on the stress conditions in the rock mass and the potential deformations in the caverns. In collaboration with the contractor Skanska, SINTEF was engaged to model the development of the stress redistribution and displacement before starting the actual excavation. The same "SINTEF-TriPOD" procedure was applied in this project as in the Follo Line project. The whole campaign is as follows:

- Investigation: Rock stress measurements were carried out before construction (hydraulic fracturing from rock surface and 3D over-coring in an existing cavern nearby) and during early stage of construction (2D and 3D over-coring). Different geological investigations were made, including drill holes and geological engineering mappings were made before and during early stage of construction to evaluate the rock mass quality.
- Numerical model: Comprehensive 3D numerical model was established. In this project, FLAC3D program was used. Several simulations were carried out including simulation of original condition, simulation of up-to-date excavation progress, simulation with and without rock support. This was to follow the planning and construction closely, helping the project team in making correct decision.
- Monitoring: Stress-meters, extensometers, and instrumented bolts were installed in this project. Stress and displacement were monitored continuously and comparing them to the modelled values. The model has been calibrated, verified, and improved during construction of the project.

Examples of simulation result are presented in Figures 12 and 13.

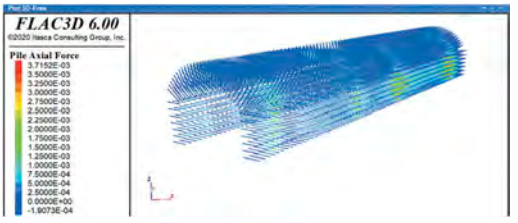

Figure 12. Axial force in the systematic bolts. The result indicated that maximum axial load in bolts is 0.37 ton, whilst the capacity of the bolts is design to be more than 30 tons.

During early stages, displacement result from the numerical model was almost identical to the monitoring data at MPBX1, as shown in Figure 14. At MPBX2, the displacement result in the numerical model (3 mm) was higher than the monitoring data (less than 1 mm), as shown in Figure 15. This is an expected result due to a conservative assumption used in the numerical model. The model results versus the monitoring data for the stress were not as good as those for the displacement, as can be seen in Figures 16 and 17. Stress results in the model were only comparable to the monitoring data in term of the order of magnitude. Due to the differences only about 5 to less than 10 MPa, stress results from the numerical model were acceptable from the practical point of view. Despite of the stress result, general impression of the model results, displacement monitoring, in-situ observations, it is concluded from the early stage that the numerical model can be used as a reliable tool for the planning and construction.

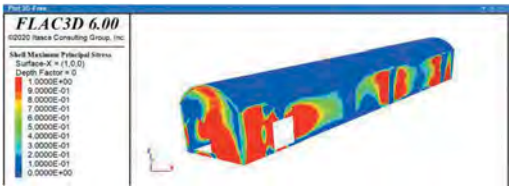

Figure 13. Minor principal stress (due to mathematical convention in FLAC3D this is named as "maximum principal stress") in sprayed concrete. Red areas indicate tensile stress is larger than tensile strength of the sprayed concrete.

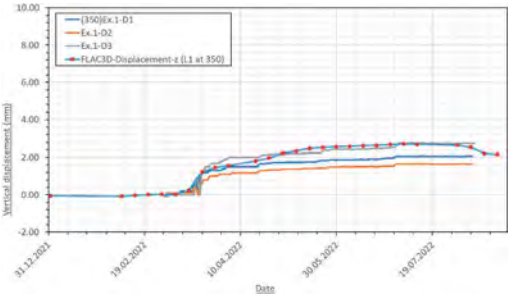

Figure 14. Deformations modelled versus recorded deformations in extensometer MPBX1.

The comprehensive simulations and the monitoring gave the project owner's site team the confidence to reduce the amount of rock support in the caverns. The caverns are now supported by 20 cm thick sprayed concrete applied in two layers and rock bolts with length between 5 m and 6 m applied between the two rounds of sprayed concrete (lattice girders were planned originally). Based on the results from the numerical model, a list of areas has been identified for frequent visual inspection throughout the excavating process. So far, fracturing of sprayed concrete has been found, which could be due to overloading, but may also be shrinkage. No or very little spalling of sprayed concrete have been found. Actual construction is as shown in Figure 18.

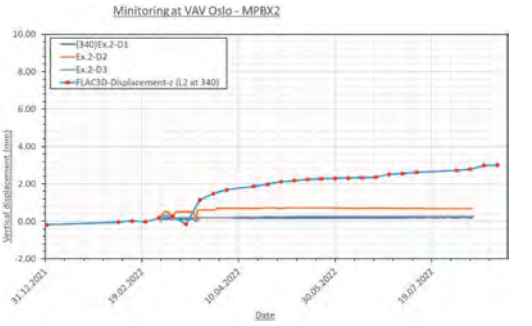

Figure 15. Deformations modelled versus recorded deformations in extensometer MPBX2.

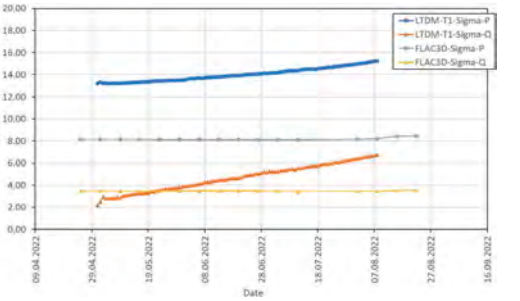

Figure 16. Stress modelled versus stress obtained in LTDM-T1.

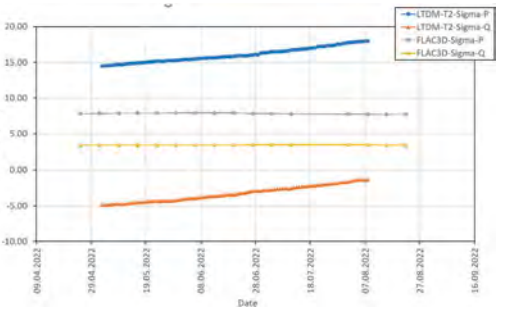

Figure 17. Stress modelled versus stress obtained in LTDM-T2.

4 CONCLUDING REMARKS

The Follo Line project was successfully excavated in 2019. Experience from the construction was that the entire rock mechanics procedure (the "SINTEF-TriPOD") was working smoothly providing reliable information for evaluation of the safety situation for both the new and existing tunnels. With help from

Figure 18. Photo from the end wall in one of the halls. The picture shows the rock support of the end wall in the roof and the upper part of the wall (Mørck et al., 2022).

other components, the 3D numerical model established for the Ekeberg and Follo Line junction demonstrated that it is a reliable tool for planning and construction of such complicated crossings.

The application of the "SINTEF-TriPOD" to the New Water Supply project provided vital inputs to optimise the rock support for the underground complex. Project cost saving from the optimisation process was estimated to be more than 100 million Norwegian krone. It is also expected a lot of time saving from construction work with the reduction of the rock support.

The described rock mechanic toolbox (the "SINTEF-TriPOD") in this paper can be divided into three components, which are:

- Investigations: Stress measurements 2-D and 3-D, laboratory tests, and geological mapping. The investigations provide input parameters for the numerical model.
- Numerical model: Comprehensive numerical model (two- and/or three-dimension) was established for stability analyses of the project. The numerical model should be able to include as much as possible the geometrical details such as existing and future tunnels, and the construction sequence was simulated carefully. The obtained results were used for model calibration in the existing tunnels and evaluation of the overall stability related to the construction of the new tunnels.
- Monitoring: A monitoring program was established to monitor the displacement and stress change at the junction during the construction of the Follo Line tunnels. The monitoring program was established for stability monitoring and the data was also used for model calibration.

With successfully application in these projects, it is believed that the "SINTEF-TriPOD" toolbox, which is a combination of three components (Investigation, Numerical model, and Monitoring), is an important tool for dealing with challenged rock engineering projects.

ACKNOWLEDGMENTS

The authors would like to express sincerely thanks to Bane NOR and VAV Oslo for permission to prepare and publish this paper.

REFERENCES

Kruse HC 2017 Bane NOR presentation in "Supplier Meeting 2 February 2017". (https://www.banenor.no/contentassets/c0667e70caf7487f999232196f66cd2d/4.-follo-line-project—hans-christian-kruse_en.pdf). Access on 06 August 2020.

BaneNOR Homepage 2021 (https://www.banenor.no/Prosjekter/prosjekter/follobanen/om-follobaneprosjektet/innhold/2018/bane-nor-lyser-ut-fire-nye-kontrakter-i-follobanen/). Last accessed 2021/03/10.

Holmøy K.H., Trinh Q.N., Backer L., 2015 3D-numerisk analyse, Follobanen/Ekebergtunnelene FJELLSPRENGNINGSTEKNIKK, BERGMEKANIKK CONFERENCE 2015, S Engen ed pp 26.1–12 (Tekna, Oslo, Norway).

Trinh Q. N., Holmøy H. K., Larsen T., and Myrvang A. 2016 Continued rock stress and displacement measurements 6combined with numerical modeling as an active, realistic rock engineering tool. RS2016 Symposium, 7th International Symposium on In-Situ Rock Stress, Johansson, E., Raasakka, V. ed (RIL, Tampere, Finland) pp. 181–93.

Itasca Homepage 2021 (https://www.itascacg.com/software/downloads/flac3d-5-01-update. Last accessed 2021/05/25).

Trinh Q. N., Holmøy, K. H. and Sagen H. W. (2021) Challenging Infrastructure Project Assisted by Monitoring and Numerical Modelling as the Follo Line Tunnels were Excavated Below Existing Tunnels. Journal of Rock Mech Rock Eng 54, pp 1671–85.

Mørck I., Thorsen S., Grøv E., Trinh Q.N. 2022 New water supply oslo – caverns for the new water supply: rock support, stress and strain development. FJELLSPRENGNINGSTEKNIKK, BERGMEKANIKK CONFERENCE 2022, S Engen ed pp 39.1–21 (Tekna, Oslo, Norway).

Tunnelling for a Better Life – Yan, Celestino, Thewes & Eberhardt (Eds)
© 2024 The Author(s), ISBN 978-1-032-80042-4
Open Access: www.taylorfrancis.com, CC BY-NC-ND 4.0 license

Automatic computation for design of tunnel shafts

C.K. Tsang*, Andrew Koay & Tong Sia
SMEC Australia Pty Ltd, Melbourne, Australia

ABSTRACT: Tunnel shafts are often used for launching the tunnel excavation and the selection on types of retaining structure based on the function of the shafts and excavation depth are critical for the project schedule as it usually falls on the critical path of construction program. The design of excavation and lateral support system for tunnel shafts using 2D finite element software typically involves the development of cross sections with all geometric parameters of ground and groundwater profiles, retaining structures and temporary supports. These together with the engineering properties of soil and rock, loadings are input to the 2D finite element software for modelling the construction stages to calculate the forces and bending moment for structural design. Normally several rounds of iterations are run to develop the most economical engineering solution. The human operation of the process is time consuming and always create a lot of errors. An innovative solution by automatic computation using Python script and smart input data file is developed to automate the manual processes. This paper describes the method by automatic creation of Plaxis 2D finite element models for shaft retaining structure design using Plaxis' remote scripting Python wrapper, Python script and smart input data file. Through this automated process, designers were able to reduce the time used to set up a model significantly, while also eliminating other human errors from tedious work particularly when several schemes need to be performed before an economical solution is developed.

Keywords: Tunnel, Shaft, Automatic Computation, Python

1 INTRODUCTION

Tunnel shafts are often used for launching the tunnel excavation and the selection on types of retaining structure based on the function of the shafts and excavation depth are critical for the project schedule as it usually falls on the critical path of construction program. The design of excavation and lateral support system for tunnel shafts using 2D finite element software typically involves the development of cross sections with all geometric parameters of ground and groundwater profiles, retaining structures and temporary supports. These together with the engineering properties of soil and rock, loadings are input to the 2D finite element software for modelling the construction stages to calculate the forces and bending moment for structural design. Normally several rounds of iterations are run to develop the most economical engineering solution. The human operation of the process is time consuming and always create a lot of errors. Instead of spending most of the engineer's time in doing the computer operation for the numerical analyses, this is more important for engineers to use the time to review the design assumptions, input parameters and interpretation of the analysis results.

Considering the application programming interface (API) is available in Plaxis 2D and Plaxis 3D, this enables remote scripting using Python. Therefore, an innovative solution by automatic computation using Python script for Plaxis input and output is developed.

This paper describes the method by automatic creation of Plaxis 2D finite element models for shaft retaining structure design using Plaxis' remote scripting Python wrapper, Python script and smart input data file. Through this automated process, designers were able to reduce the time used to set up a model significantly, while also eliminating other human errors from tedious work particularly when several schemes need to be performed before an economical solution is developed.

2 DESIGN WORKFLOW

The design of deep excavation and lateral support system using Plaxis 2D modelling typically involves the selection of several cross sections for analysis. Engineering judgement needs to be applied when choosing the locations of these cross sections to ensure that the critical combinations of topography, ground

*Corresponding author: ck.tsang@smec.com

DOI: 10.1201/9781003495505-52

and groundwater conditions, structural geometry, excavation depth and loading conditions are selected.

Currently, the design of tunnel shaft involves deep excavations typically follow design workflow as shown in Figure 1. The steps for Plaxis analysis are summarised below:

a) Pick a representative geological cross-section and import the geometry into the model, then input all the soil/rock properties.
b) Draw all the structural elements (such as retaining walls, struts/anchors/slabs, plunge columns, tension piles, internal primary structure), loads, water levels, excavation levels. Then, calculate all the structural properties for the various elements and input it into the model.
c) Mesh the model
d) Set up all the construction stages from the beginning to the end of construction. This includes activation/deactivation of various structural and soil elements, load conditions, setting water conditions (includes water levels and boundary conditions)
e) Run the model
f) Review the outputs after the model has finished running
g) Export the outputs for reporting as well as use by structural engineers for the design of elements.

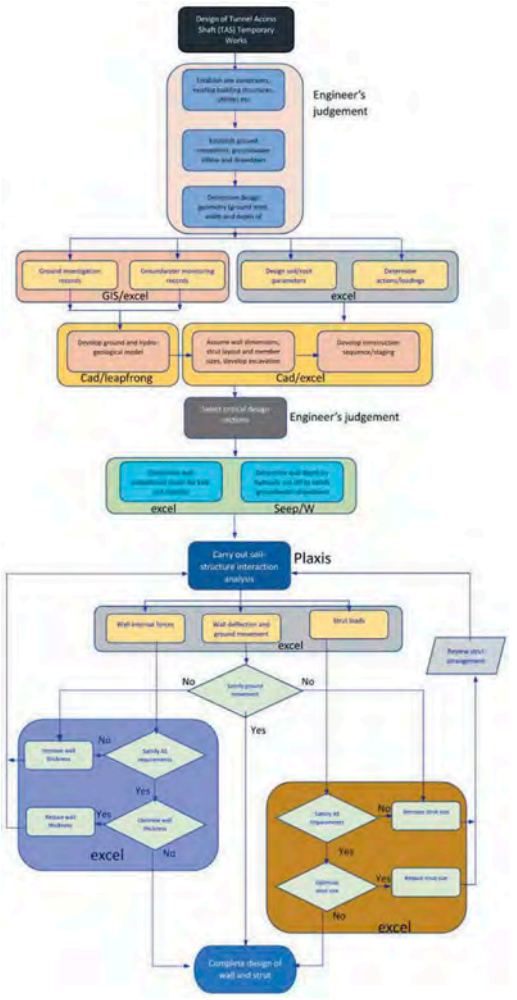

Figure 1. Design workflow for deep excavation and lateral support system.

For a typical tunnel shaft design, a geotechnical engineer is required to build and setup dozens of typical plaxis models for a detailed calculation with different input datasets, it will be very time-consuming to do it manually.

Python can be utilized to help the process, starting from reading and sorting the input data, building and running the model, up to plotting the analysis output.

3 PYTHON APPLICATION

Python is an interpreted, object-oriented, high-level programming language with dynamic semantics. This can be used in a vast domain of applications. It was designed to be easy to understand and easy to use. As a dynamically typed language, Python is very flexible to engineering software. The Plaxis 2D has already a Python API built-in within their program, thus enables remote scripting using Python for automatic computation. To activate the Plaxis Python environment, it needs to select Plaxis built-in python interpreter which contains all the functionalities required to operate Plaxis.

3.1 *Automatic computation developments*

The automation development in this paper mainly covers from steps b) to d) as described in Section 2. The aim of the automation procedure is to create a user-friendly general-purpose procedure which can be used for the majority of deep excavation problems. This has the benefit of not having to redevelop scripts for each new problem, and the end-user only needs to learn how to use the script once.

Due to the prevalence of Excel use in the engineering profession, the numerous calculation facilities it possesses as well as the ease of using data from other worksheets, it was decided early on during the development phase that the user input/GUI interface should be in Excel as much as possible, with the Python script simply reading the inputs from the Excel input sheet.

The followings are developed to facilitate the automatic computation using Plaxis model for tunnel shafts design on excavation support and lateral system:

- D1 - Plaxis input data file in excel format
- D2 - Python script_1 to read input from the excel input date file to set up the model programmatically in Plaxis
- D3 – Python script_2 to carry out batch run of models

- D4 – Plaxisimport excel add-in to export Plaxis results to excel file to plot envelops of bending moment/shear force/deflection and strut loads

The script that is developed is highly capable and supports the definition of many different structural elements involved with deep excavations including retaining walls, struts, anchors, slabs, 2 pass systems (including internal walls and setting up the interface between internal walls and external retaining walls), plunge columns (for top-down excavation problems) and tension piles. It also supports the definition of both phreatic water levels (with varying dewatering angles) as well as setting up steady-state seepage. It is designed to be flexible enough to allow for various construction sequencing which can cater for most deep excavation problems.

With the above developments, the workflow for automatic computation using Plaxis programme is streamline into 4 stages as shown in Figure 2.

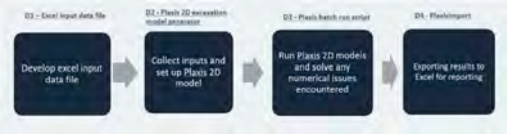

Figure 2. Simplify workflow for Plaxis analysis.

3.2 *Excel input sheet*

The Excel input sheet (see Figure 3 below) which allows users to set up all the construction staging, excavation geometry, structural properties. These are arranged in different sheets for convenience. The first tab contains instructions for the end users on how to install and use the automation procedure. The second tab contains global properties such as excavation geometry (width), options to define two pass walls (including defining interface properties between the internal wall and retaining walls) and options to define a jet grout block.

The third tab allows the user to input the excavation sequence which involves defining the excavation level supports that will be installed/removed and water conditions.

The fourth to ninth tab allows the user to define the geometry and properties of various structural elements (retaining wall, struts/anchors/slabs, internal wall, plunge columns, tension piles) and loads.

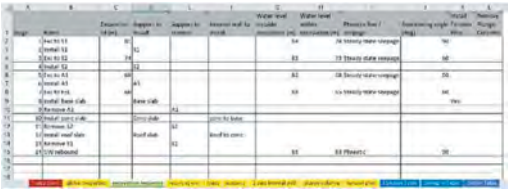

Figure 3. Excel input sheet.

3.3 *Plaxis Python scripts*

In order to read Excel files, the openpyxl (https://pypi.org/project/openpyxl/) library has to be imported. This is used to read the Excel input sheet, with the data then stored in Python lists and variables. An excerpt is shown below in Figure 4.

Figure 4. Excerpt of Plaxis Python script.

The script first imports the selected Excel file and a base Plaxis file (which contains the geological layering as well as the soil/rock properties already input)

Plaxis includes a remote scripting API functionality which allows the user to control all Plaxis functions using Python rather than using the Plaxis GUI.

Using the Plaxis documentation, the script was set up in a way to do the following in Plaxis the following order:

a) Draw all the structural elements in the model and define their properties
b) Mesh the model
c) Define all the construction staging in the model – including excavation, activating/deactivating structural elements and changing water conditions.
d) Save the ready-to-run model

The end user can conveniently run the script directly from Plaxis as shown in Figure 5.

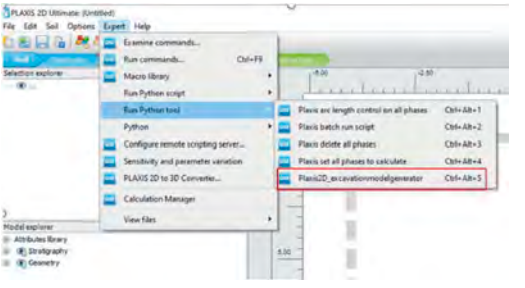

Figure 5. Running the Plaxis Python script.

A sample of a ready-to-run model generated by the script is shown in Figure 6.

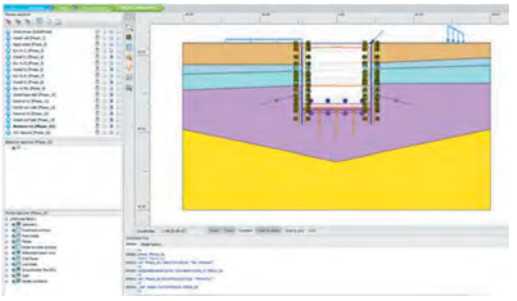

Figure 6. Finished ready-to-run model generated by the Plaxis Python script.

Another Python script is developed for Plaxis batch run that enable the programme to run multiple Plaxis files overnight without supervision. It is designed to automatically increases basic iteration parameters if stages fail (due to numerical issues) to avoid failed runs. If there are real failures happening in the model those will fail to run and the script will skip those stages. Engineers can inspect the finished models the next day rather than having to manually monitor the models running.

The Plaxis batch run script can be called from Python tool in Plaxis as shown in Figure 7.

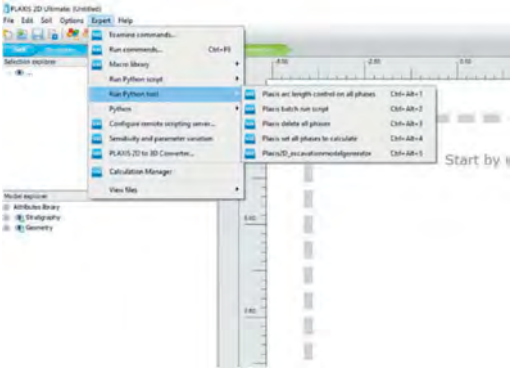

Figure 7. Plaxis Python tool for Plaxis batch run script.

4 PLAXISIMPORT

The excel add-in Plaxisimport is developed to generate stage by stage charts and summary tables for all structural elements. The output strut loads and internal forces of the retaining walls can be used for structural capacity check. The excel add-in function is shown in Figure 8. Some examples of automatic out from Plaxis to excel are shown in Figures 9-11.

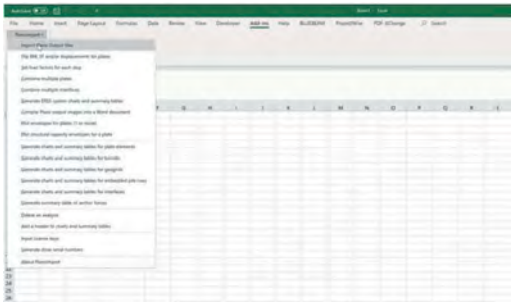

Figure 8. Excel add-in Plaxisimport.

Figure 9. Output of struct loads in excel.

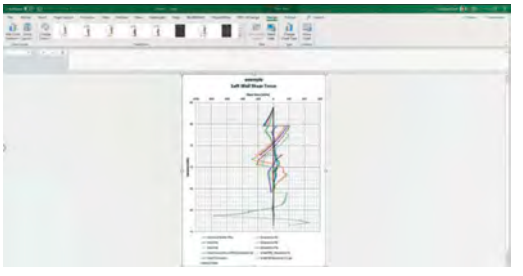

Figure 10. Output of shear force envelope.

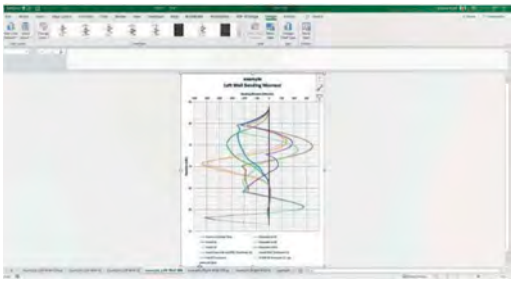

Figure 11. Output of bending moment envelope.

5 CONCLUSION

An automated procedure to generate ready-to-run Plaxis 2D finite element models for tunnel shaft design on excavation and lateral support design has been achieved using a combination of Plaxis' remote

scripting Python wrapper, Python script and a smart Excel input data file. This allows for a complex manual procedure which takes up to a few days to be simplified to a process taking less than an hour (filling up an Excel input sheet and then running the script in Plaxis), which saves a lot of precious engineer time as well as reducing the amount of user errors that can happen when setting up the models.

The key objective of the automatic computation for Plasix analysis is to reduce the engineer's input in carry out time consuming numerical model input and output for structural design excavation and lateral support system.

- Improve efficiency in design delivery
- Reduce human error during the setting up of plaxis model
- Optimise the design by carryout out more analyses covering full range of design input variables

REFERENCES

Andrew Koay, CK Tsang and Joo Sia Tong., 2023. Automatic Computation for Design of Excavation and Lateral Support System. Proceedings of the 14th Australia and New Zealand Conference on Geomechanics, Cairns 2023 (ANZ2023).

Z. Farook, C. Matthews, M. Skinner, M. Brown., 2019. Automation in geotechnical design – applications and case studies. Proceedings of the XVII ECSMGE-2019, Reykjavik, Iceland.

Brinkgreve, R.B.J., Brasile, Sandro., 2022. Automatic Finite Element Modelling and Parameter Determination for Geotechnical Design. Workshop Numerische Methoden in der Geotechnik

B.A. Yogatama, B.A. Tirta, 2021. Python Application in Geotechnical Engineering Practice. Simposium Nasional Teknologi Infrastruktur Abad ke-21 Using Plaxis Remote scripting with Python wrapper, Bentley Communications.

Tunnelling for a Better Life – Yan, Celestino, Thewes & Eberhardt (Eds)
© 2024 The Author(s), ISBN 978-1-032-80042-4
Open Access: www.taylorfrancis.com, CC BY-NC-ND 4.0 license

Case study about adjacent three-arch tunnel

Hoteng Tseng* & Kwojane Kuo
T.Y.Lin Taiwan Consulting Engineers, Inc., Chinese Taipei

Tihju Chu
New Taipei City Government, Chinese Taipei

ABSTRACT: 3D LiDAR scanning monitoring technology can quickly scan the object. It has high-density and high-precision scanning object's three-dimensional spatial data characteristics without reflection prism. At present, Ground-based laser scanner has been widely used in the sliding collapse of hillside slopes, highway bridges, and tunnel for deformation monitoring purpose, i.e., Mass Rapid Transit (MRT) tunnels and hydraulic engineering tunnels. If a new tunnel project is built in a relatively young geological age or in a deformation-oriented stratum, surrounding rock disturbance caused by tunnel excavation may affect the safety of neighboring areas and construction workers. Traditional tunnel convergence deformation measurement cannot fully reflect the full impact of tunnel excavation disturbance. It is also impossible to fully control the deformation behavior mode of rock mass after excavation. This paper presents a comprehensive monitoring study of an adjacent excavation and shallow-covered tunnel consisting of a three-arch tunnel in the Xindian area of northern Taiwan. The displacement of the surrounding rock of the tunnel is reduced due to the effective application of the central RC wall. The paper aims to explain the application of the optical scanning monitoring results, to provide the overall circular displacement trend of the tunnel and the equivalent displacement contour map along the tunnel, which can provide accurate tunnel safety monitoring, and establish a new thinking on tunnel safety monitoring for adjacent construction of tunnel. The 3D LiDAR scanning monitoring results can be effectively applied in subsequent similar cases.

Keywords: Ground-based LiDAR, Adjacent excavation, Shallow-covered tunnel, Three-arch tunnel

1 PREFACE

As road tunnels in the metropolitan area usually pass through densely residential and densely populated areas, land acquirement tends to be limited. The case of this article is about a two-arch, one-way and two-tube road tunnel (with an excavation diameter of about 13 m) in the Xindian area of northern Taiwan. Due to traffic network planning, a light rail Mass Rapid Transit (MRT) tunnel (with an excavation diameter of about 12 m) must be set up between these two road tunnels. Because the land use is limited, the spacing between each two arches of this three-arch tunnel is only about 1.5 m. The three-arch tunnel of this project is adjacent to each other but the geological material is very weak in strength. After the tunnel is excavated, the central rock pillar may not be able to support the load of rock cover above. Therefore, the small-section central pilot method (height × width = 6 m × 6.5 m) for excavation is applied and a five-arch tunnel is thus formed, which is the first of its kind in Taiwan. A central reinforced concrete (RC) wall (width 1.5 m) is constructed between the eastern and western pilots to provide sufficient compressive and shear strength to reduce tunnel excavation deformation. The multi-arch tunnel has the characteristics of shallow coverage, weak rock mass strength and multi-arch adjacent construction. The rock mass disturbance caused by each round of tunnel excavation may impact the surrounding completed tunnels, which makes the deformation behavior of tunnel surrounding rock more complex.

2 INTRODUCTION TO PROJECT CASE

Due to traffic network planning requirements, the tunnel of this case is designed to consist of two one-way and two-tube road tunnels and one light rail MRT tunnel:

2.1 *Tunnel section configuration*

Figure 1 is the tunnel configuration layout. The shape and dimension of the tunnel section are mainly subject to two factors: spatial configuration and tunnel excavation stability, as well as economic

*Corresponding author: httseng@tylin.com.tw

DOI: 10.1201/9781003495505-53

considerations. As this tunnel is a shallow-covered one and the rock load comes from the weight of the covering soil, a close-to-circular cross-section is adopted for the tunnel cross-section shape rather than a flat cross-section. The arrangement of clearance and the configuration of relevant facilities within the section are mainly based on the design criteria and required to meet the spatial requirements for driving, maintenance, facilities, etc. Therefore, the tunnel section is designed to be the minimum section which meets the above-mentioned considerations.

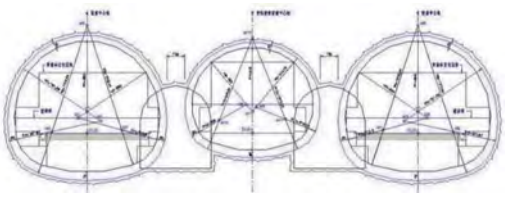

Figure 1. Tunnel configuration layout.

2.2 *Regional geology and terrains*

Figure 2 shows the location and geological map of the studied area. This Xindian area has a mountainous topography. The rock mass is weak in cementation and highly deformable due to weathered rock-soil. Therefore, the main discontinuous surface is the interface among stratification, earth covering and bedrock. The exposed strata in this area are mainly the Miocene coastal facies or Nanchung formation of continental facies. The coastal facies are composed of white or gray-white sandstone and thin layers of sandstone, siltstone and shale, and carbonaceous shale. The rock mass is weakly cemented. The main discontinuous surfaces are thus stratification while the jointing is not well-developed. As the structural weak surfaces are not well-developed, the rock mass is regarded as a homogeneous isotropic material.

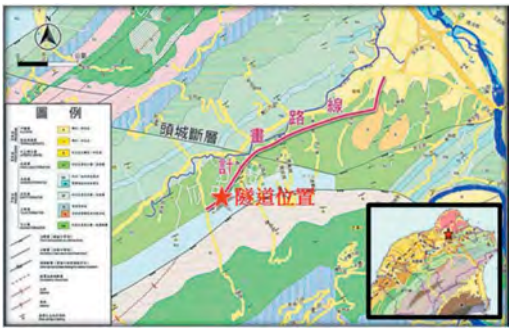

Figure 2. Case location and geological map.

2.3 *Strength parameters of rock mass material*

Table 1 shows the design parameters of various rock mass supports. The factors affecting the strength and deformability of rock mass include the following: stratum, lithology, single pressure strength, geological strength index (GSI) and coverage depth, etc. Therefore, there will be quite a lot of permutations and combinations of rock mass parameters. According to the geological survey results, the input parameters required by the numerical calculation software are the basis for tunnel support stress analysis and verification. During the analysis, the 2D plane strain element is used to simulate soil, the beam element is used to simulate shotcrete and trussed steel supports, and the cable element is used to simulate rock bolts. Meanwhile, it is assumed that the soil is a homogeneous and isotropic material, the elasto-perfectly plastic model is adopted as the constitutive model, and the Mohr-Coulomb criterion is adopted as the material failure criterion.

Table 1. Parameter table for numerical analysis of various rock masses.

Mileage	South side of main line 0k+125~0k+220			North side of main line 0k+200~0k+300	
Rock class	BIV	BV	BVI	Ci(s)	Cii(s)
Unit weight (kN/m^3)	22	22	22	22	22
Core single pressure (MPa)	5	4	3	0.25	0.15
GSI	45	35	25	-	-
mi	13	13	13	-	-
D	0	0	0	-	-
Cohesion (kPa)	105	80	58	73	44
Internal friction angle (°)	42.2	37.4	31.8	29.4	29.4
Elastic modulus (E) (MPa)	300	200	150	50	50
Poisson's ratio (v)	0.3	0.3	0.3	0.3	0.3
Volume modulus (K) (MPa)	250	167	125	83	83
Shear modulus (G) (MPa)	115.4	76.9	57.7	38.5	38.5

The volume modulus is $K = \frac{E}{3(1-2\nu)}$, and the shear modulus $G = \frac{E}{2(1+\nu)}$.

2.4 *Stress behavior of central pillar*

Based on the analysis grid in the analysis with finite difference program *Flac*, different sections, i.e. upper, middle and lower ones, are selected, and the axial force (P) and bending moment (M) of different sections are simplified to be analyzed with vertical stress σy. The material stress formula is shown as Equations (1) and (2), and the symbols are explained as shown in Figure 3. In the formula, A is the unit area of the central wall (1.5 m×1.0 m), and y is the distance from $\sigma y1$ and $\sigma y2$ to the center of the central wall. From Equations (1) and (2), the axial force and bending moment values of the central wall in

different sections and different construction steps are obtained, which can be used for the reinforcement design of the central wall.

It can be learned from Figure 4 as well that the stress of the central wall is concentrated and symmetrical, and the displacement change tends to move toward the slope due to the impact of west slope. Therefore, the displacement on west side is larger than on the east side, and the displacement of the central wall itself is that the upper part is larger than the lower part, and the west side is larger than the east side.

$$\sigma_{y_1} = \frac{P}{A} - \frac{My}{I} \tag{1}$$

$$\sigma_{y_2} = \frac{P}{A} + \frac{My}{I} \tag{2}$$

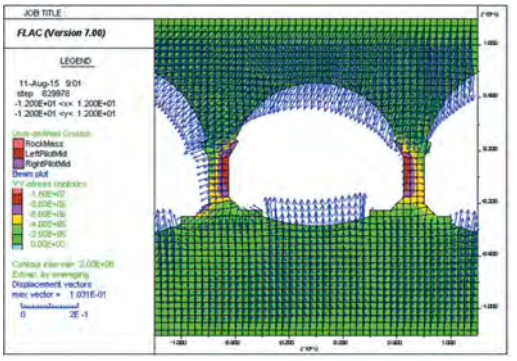

Figure 3. Vertical stress and displacement distribution of central wall.

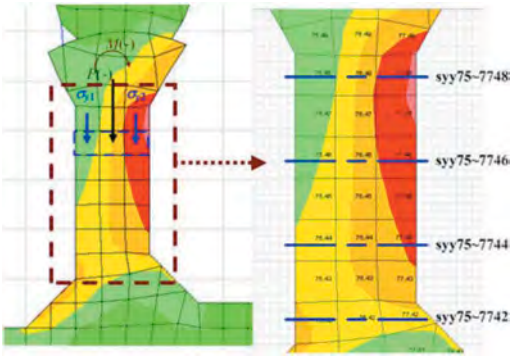

Figure 4. Axial force bending moment symbol of central wall.

3 RESULTS FROM SCANNING AND MONITORING TECHNOLOGY

The 3D LiDAR scanning technology has been sprouting since 1970s. It was first developed by National Aeronautics and Space Administration (NASA). The 3D LiDAR Scanner can quickly scan the object to be measured to obtain high-density, high-precision 3D spatial data with a relative coordinate system without reflection prism. Such an instrument which quickly obtains comprehensive spatial 3D information is a brand-new surveying tool.

3.1 *3D LiDAR scanning and monitoring*

The point cloud data obtained by 3D LiDAR scanning is stacked over multiple periods to obtain coordinate changes of the same position. In other words, the displacement of the said position can be obtained. Regarding the equivalent displacement contour of the eastbound tube of the central pilot as shown in Figure 5, the X-axis on the contour represents the tunnel mileage distance, and the Y-axis is the left and right side walls and roof arch of the tunnel section expanded to the plane. Different colors on the contour represent the displacement changes after tunnel excavation. It can be supplemented by scanning result images to initially evaluate changes in anomalies.

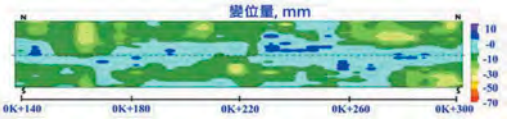

Figure 5. Equivalent displacement contour of surrounding rock on the eastbound tube of the central pilot.

The larger displacements are located at both the upper and lower parts of the equivalent displacement contour (i.e. the left and right side walls of the tunnel). The tunnel roof has no obvious change as the pipe umbrella roofing method has a relatively good supporting effect. The displacement in some mileage areas of the tunnel roof appears to expand outward (blue-purple in the equivalent displacement contour) due to extrusion of the left and right side walls of the tunnel. In addition, it is obvious that the eastern entrance (0K+260~300) and the western entrance (0K +140~160) have large displacements after tunnel excavation due to shallow coverage on the terrain and the position of the unsymmetrical load area.

3.2 *Tunnel duration curve*

To organize the deformation data of tunnel excavation, Figure 6 shows the duration curve of both eastbound and westbound tubes of the central pilot. Overall, the maximum displacement δ_{max} are 29 mm, 38 mm, and 16 mm for eastern entrance, western entrance, and intermediate section, respectively. The displacement at the eastbound tube is slightly larger than the westbound tube by about 1.9~3.3 mm.

Figure 7 Shows the MRT tunnel duration curve. Since the MRT tunnel was excavated after the construction of the central RC wall between the east and west sides was completed, the maximum displacement δ_{max} is only 6 mm in two months after this tunnel was bored through (on March 18th, 2018). It is obvious that the central wall plays an effective role in mitigating the displacement of the rock mass. Afterwards,

there is continual displacement due to the construction of adjacent tunnels. At the initial stage, the maximum displacement δ_{max} caused by the eastbound-tube tunnel construction is up to 10~15 mm; then the maximum displacement δ_{max} caused by the westbound-tube tunnel construction is up to 20~25 mm. The weakened rock mass, caused by rainfall event (July through September, 2018), results in the increment displacement $\Delta\delta_{max}$ of the tunnel rock mass by about 15~20 mm during the rainfall event period. The final displacement δ_{max} of the rock mass is about 35~45 mm.

Figure 8 shows the duration curve of the eastbound-tube tunnel. The MRT tunnel has been bored through at the time of the construction of the eastbound tube, which was thus negligibly affected by the MRT tunnel. The maximum displacement δ_{max} is about only 9.5 mm in 1.5 months after this tunnel was bored through (on June 15th, 2018), and the maximum displacement δ_{max} gradually increases from 13 mm to 40 mm because of the subsequent rainfall events and the westbound-tube tunnel construction. It is assessed that the terrain ridgeline also affects bedrock that is weakened by rainfall. The road portions affected are mainly between 0K+168 to 264. Figure 9 shows the duration curve of the westbound-tube tunnel. Both the MRT and eastbound-tube tunnels have been bored through at the time of the construction of the westbound tube. However, the construction period was in the rainy season. Overall, the maximum displacement

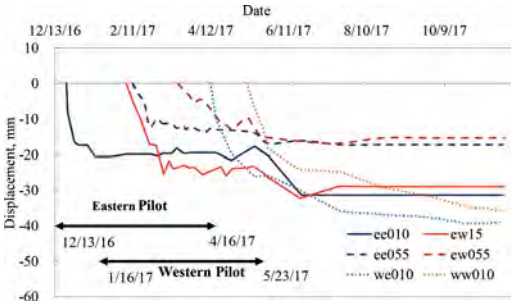

Figure 6. The duration curve of both eastbound and westbound tubes of the central pilot (eastern entrance, intermediate section and western entrance).

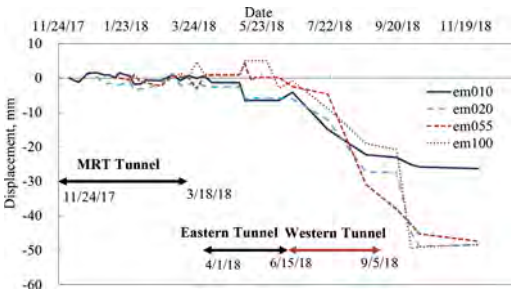

Figure 7. The duration curve of the MRT tunnel (eastern entrance, intermediate section and western entrance).

δ_{max} are 19.5 mm, 29.6 mm, and 16 mm for eastern entrance, western entrance, and intermediate section, respectively. It is assessed that the weakened bedrock, caused by rainfall, results in the increment displacement $\Delta\delta_{max}$ by about 10~15 mm.

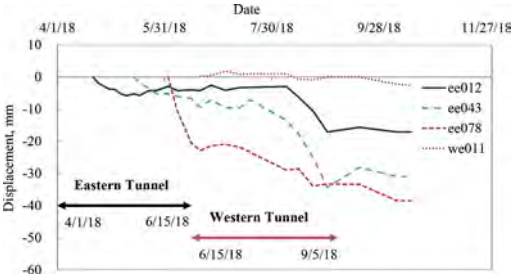

Figure 8. The duration curve of eastern-tube tunnel (eastern entrance, intermediate section and western entrance).

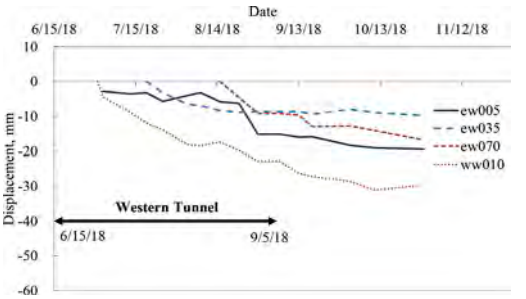

Figure 9. The duration curve of westbound-tube tunnel (eastern entrance, intermediate section and western entrance).

3.3 *Tunnel surrounding rock radial displacement*

To organize the deformation data of tunnel excavation, Figure 10 shows the radial displacements of the surrounding rock at the eastern entrance, intermediate section, and western entrance of both eastbound and westbound tubes of the central pilot (facing to eastern entrance). On the whole, the terrain at the eastern entrance is a valley with two high sides; thus the displacement is affected by the unsymmetrical load. The southern side wall of the eastbound tube has larger deformation, while the northern side wall of the westbound tube has larger deformation. The intermediate section is less affected by the terrain behavior due to the unsymmetrical load. Because the terrain at the western entrance is higher in the south, and lower in the west, the displacement is thus also affected by the unsymmetrical load.

The full-section displacement monitoring results of the tunnel provided by the 3D LiDAR scanning technology can obtain the displacement of the tunnel in all directions. It contributes to reasonable assessment for the deformation behavior. The overall terrain is characterized by higher rock cover on the southern side and lower rock cover on the northern side. Therefore, most of the radial displacements are

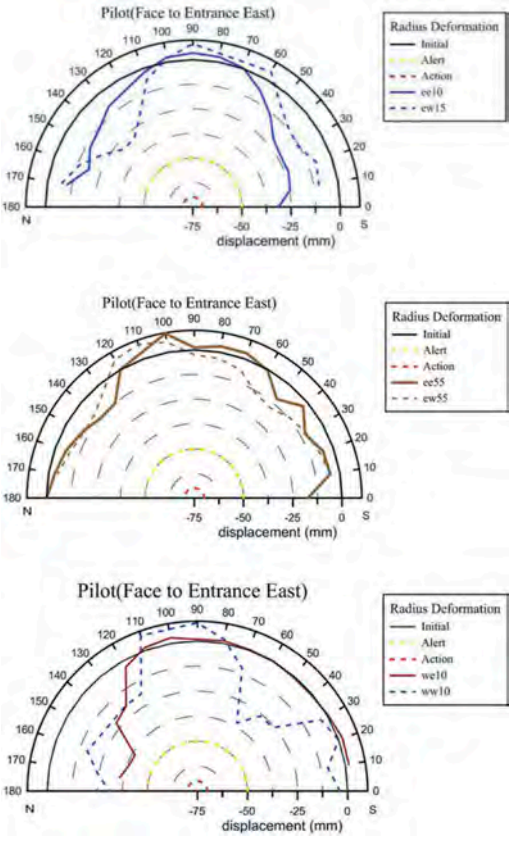

Figure 10. The radial displacements of the surrounding rock at both eastbound- and westbound-tube tunnels of the central pilot (eastern entrance, intermediate section and western entrance).

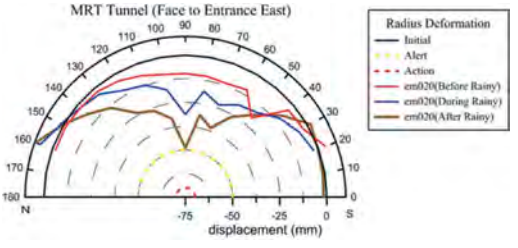

Figure 11. The radial displacement of the surrounding rock at the eastern entrance of the MRT tunnel (before and after the rainy season).

inwardly squeezed in the southern side, and has an external expansion phenomenon in the northern side (Figures 12 and 13 are relevant to eastbound- and westbound-tube tunnels). The displacement of the weakened bedrock, caused by rainfall, mainly occurred above the junction (about 3 m above the springing line of the side walls) between the central wall and the outer support of the tunnel. The weakest support stiffness is at this junction. From the

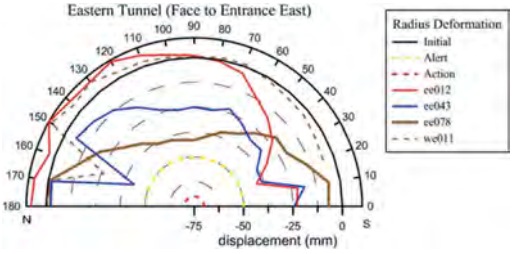

Figure 12. The radial displacement of the surrounding rock at the eastbound-tube tunnel (eastern entrance, intermediate section and western entrance).

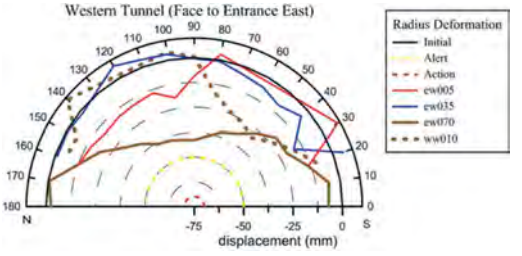

Figure 13. The radial displacement of the surrounding rock at the westbound-tube tunnel (eastern entrance, intermediate section and western entrance).

monitoring results of the radial displacement contour of the MRT tunnel in Figure 11, it can be seen that the displacement range is consistent. Using 3D LiDAR scanning technology can provide a safety monitoring for adjacent tunnel excavation construction and can have better control in the deformation behavior of rock mass after tunnel excavation. It can maintain tunnel construction safety, and provide reference basis for on-site construction adjustment and design correction.

4 CONCLUSION

This paper highly recommends the use of 3D LiDAR scanning technology for tunnel construction monitoring and tunnel surrounding rock displacement monitoring. It is also applied to multi-arch tunnel, adjacent construction, and cases of shallow-covered tunnels of which the geological rock strength are weak. Through 3D LiDAR scanning technology, it can quickly obtain high-precision, high-density, and comprehensive 3D spatial coordinate information of tunnels after tunnel excavation.

After the scanning and monitoring data are processed and analyzed, more rock mass displacement around the tunnel can be controlled. For the entire tunnel construction safety monitoring, a complete excavation disturbance behavior mode for surrounding rock can be provided. It can also be applied to more complex excavation disturbances such as special geological structures. The blind spots in

traditional monitoring systems for tunnel excavation can be greatly improved, thus providing more comprehensive monitoring results.

As the effective monitoring and central walls are appropriately leveraged in tunnel surrounding rock displacement, the average displacement is within a range of 25~30 mm for the central pilot with an average excavation diameter of 6.5 m. After the completion of the double central wall, it can effectively inhibit the average displacement of the rock mass to be less than 6 mm for the MRT tunnel with an average excavation diameter of 12 m. The weakened rock mass, caused by rainfall event, resulted in the increment displacement Δ_{max} of the tunnel rock mass increases by about 10~20 mm during the rainfall event period. Due to the adjacent construction and shallow coverage factors, the increment displacement Δ_{max} of the tunnel rock mass also increases by about 10~20 mm. Due to the results of the full-section scanning data of the 3D LiDAR, the overall radial displacement trend is obtained and the equivalent displacement contour is provided along the alignment of tunnel. These monitoring results help taking effective and comprehensive control over the deformation behavior of the surrounding rock of the tunnel. These results can provide a reference for on-site construction adjustment and design correction. If these data combined with more rigorous numerical simulation and feedback design, it is a great help to modern tunnel construction technology.

REFERENCES

Hsiao, K. H., Yu, M. F., Liu, J. K., Tseng, Y. H., 2003. Preliminary study of ground based LiDAR application to terrain changes after collapsing. In: Proceedings of the Taiwan Geographic Information Society Annual Meeting & Academic Conference, Taipei City, Chinese Taipei. (In Chinese)

Kuo, K. J., Tseng, H. T., Jhan, R. H., Huang, C. H., 2015. The case study for center pillar of three-arch tunnel. In: The 14th Cross-Strait Tunnel and Underground Engineering Academic and Technical Seminar, Yilan County, Chinese Taipei. (In Chinese)

Kuo, L. C., Shih, T. Y., 2004. Study of ground based LiDAR data overlay-a case study of the collapsed ground in Chutung. In: The 23rd Conference on Surveying Theories and Application. National Chung Hsing University, Taichung City, Chinese Taipei, pp. 323–332. (In Chinese)

Lemy, F., Yong, S., and Schulz, T., (2006). A case study of monitoring tunnel wall displacement using laser scanning technology. The 10th IAEG International Congress.

Stephanie F., Mark D., and Matthew L., (2010). Geotechnical and operational applications for 3-dimensionallaser scanning in drill and blast tunnels, Tunnelling and Underground Space Technology, 25 (5),614–628.

Tseng, H. T., Kuo, K. J., Gao, Z. H., Jhan, R. H., 2014. Discussion on the design case of three-arch small clearance tunnel. In: The 13th Cross-Strait Tunnel and Underground Engineering Academic and Technical Seminar, Guangxi Province, China. (In Chinese)

Tseng, H. T., Lee, L. Y., Gao, Z. H., Jhan, R. H., Huang, C. H., 2016. New thinking for construction safety monitoring during adjacent excavation. In: The 15th Cross-Strait Tunnel and Underground Engineering Academic and Technical Seminar, Hunan Province, China. (In Chinese)

T.Y.Lin Taiwan Consulting Engineers, Inc., 2012. Geological drilling and testing service outcome report for design technical services for the second phase of Ankeng Road No. 1 in Xindian District, New Taipei City (Rose Road to Antai Road, and Anho Branch). (In Chinese)

United Geotechnical Engineering Consulting Co., Ltd, 2018. Safety assessment report for the second phase of Ankeng Road No. 1 in Xindian District, New Taipei City (Rose Road to Antai Road) (In Chinese)

Tunnelling for a Better Life – Yan, Celestino, Thewes & Eberhardt (Eds)
© 2024 The Author(s), ISBN 978-1-032-80042-4
Open Access: www.taylorfrancis.com, CC BY-NC-ND 4.0 license

Optimizing the tunnel ventilation design related to respirable dust in tunnelling by using CFD

Ranzhu Wei*, Robert Galler & Christian Weiß
Montanuniversität Leoben, Leoben, Austria

ABSTRACT: Fine dust and toxic gases produced by blasting underground are mainly removed by mechanical ventilation. Among them, the removal of respirable dust with diameters of less than 5 μm is important for the occupational safety of the miners. Respirable dust is difficult to settle on the ground resulting in an unacceptably long lasting dust removing process. Therefore, to effectively remove the respirable dust, understanding the movement pattern of dust particles under mechanical ventilation is important. In this paper, computational fluid dynamics software Ansys Fluent is used to simulate the dust particle generation and mechanical ventilation inside the tunnel. The movement characteristics of diffusion, sedimentation and accumulation of dust particles are monitored by particle location and concentration at different time periods after the blasting takes place. These simulations provide more understanding of respirable dust particle movement under mechanical ventilation and offers further guidance on optimization of tunnel ventilation design.

Keywords: Optimization tunnel ventilation, Dust movement, Tunnel construction, Mechanical ventilation, Numerical simulation

1 INTRODUCTION

Tunnel blasting is a common and cost-effective method of excavation in tunnel construction. However, during this process a large amount of dust is produced reducing visibility and adversely affecting the working environment inside the tunnel. Potential irreversible health hazards can be caused by inhalation of quartz dust for tunnel construction workers. There is a high chance of getting Pneumoconiosis or respiratory malignancy if working in a high quartz dust concentration place for a long time (Erol et al., 2013). There has been considerable literature linking quartz dust exposure to lung cancer and the data shows that silica dust greatly increases the risk of death from respiratory and cardiovascular disease (Chen et al., 2012; Chen et al., 2019; Ulvestad et al., 2001; Keramydas et al., 2020). Quartz is a kind of ultra-fine particle. It is light in texture and easy to suspend in the air. Because of the small diameter, respirable dust particles are difficult to settle on the ground, so it often takes a long time to remove the dust resulting in a significant impact on the duration of a tunnel construction and the cost of the construction project. It is impossible to visually observe respirable dust, so the concentration is mainly obtained by on-site measurements. Due to the limited number of on-site sampling equipment and complex actual building conditions, computer fluid dynamics simulation is widely used to investigate the air flow and the dispersion pattern of respirable dust inside the tunnel. The two-phase gas-solid flow model is most widely used to investigate the movement of particles with air (Yin et al., 2020; Hua et al., 2020; Zhang et al., 2021).

Researchers have used numerical modelling methods to simulate the effect of the location of and air flow rate of ventilation ducts on respirable dust removal effect. Guo et al put the ventilation duct at the bottom, vault and haunch of the arch and compared the dust concentrations of personnel respiratory regions (Guo et al., 2023). Xie investigated the effect of the angles of the force ventilation duct on dust removal performance (Xie et al., 2022). Liu adjusted the air flow rate of the force ventilation duct and compared the dust concentration in the working area and effective dust control distance to predict the optimal range of air flow rate (Liu et al., 2021). Hu investigated the maximum air flow rate for dust removal and found the increasing dust concentrations with excessive air flow rate due to the entrainment effect (Hu et al., 2020). Nie and Liu studied the change of diffusion distance of dust over time under mechanical ventilation conditions after tunnel blasting and proposed optimal suggestions on air flow rate to shorten the dust diffusion distance (Nie et al., 2022; Liu et al., 2019).

Therefore, in this paper, movement patterns of respirable dust particles under mechanical ventilation after tunnel blasting will be studied based on discrete

*Corresponding author: ranzhu.wei@unileoben.ac.at

DOI: 10.1201/9781003495505-54

phase particle tracking technology in CFD software Ansys Fluent. In addition, the air velocity and dust distribution characteristics at different distances from the working face along the tunnel will be analysed and compared with the actual measurements in the tunnel. The air velocity and dust distribution characteristics were correlated, and dust transport patterns are explained at a microscopic level. Analysing respirable dust movement characteristics can provide guidance on optimization of respirable dust removal and tunnel ventilation design.

2 GEOMETRIC MODEL ESTABLISHMENT AND SOLUTION

Kaprun tunnel is a road tunnel under construction in the altitude of 786m and the tunnel part chosen for air flow and dust movement analysis is 113.35 meters long and the duct is at the left side of the construction direction as shown in Figure 1.

Figure 1. Kaprun tunnel cross section.

2.1 *Geometric model and meshing*

The physical model of the tunnel is established in SpaceClaim by considering a 1:1 equal scale of tunnel under construction in Kaprun Austria with the length of 113.35 m and the duct is 61 m from the working face, as shown in Figure 2 (a). The cross section of the tunnel is shown in Figure 2 (b), with the following dimensions: 4.2 m in width and 6.54 m in height. The pressed-in ventilation duct with a radius of 1.6 m is located on the left side of the tunnel 0.25 m from the side wall and 4.5 m from the ground. The air velocity of the duct outlet is 9 m/s.

In numerical modelling, the quality of mesh is crucial to the accuracy of the simulation results. Cell size used in current model is 0.2 m with the element

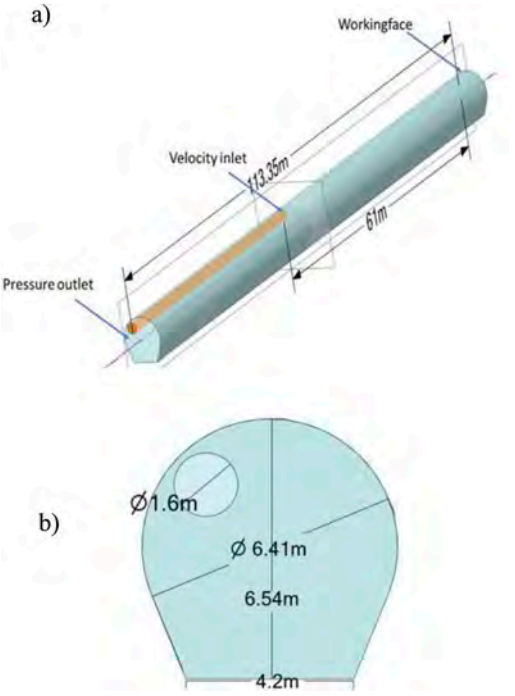

Figure 2. Physical model a); Cross section details b).

number of 4078296 and the "Orthogonal Quality" value for the adopted mesh is 0.213, which corresponds to "Good" quality in the mesh metrics spectrum.

2.2 *Boundary conditions*

Based on air flow rate measurement of the duct outlet in Kaprun tunnel and literatures reviewing about dust transport after tunnel blasting, the air flow parameters and discrete phase model settings are listed in Table 1 (Shi et al., 2022; Xie et al., 2023; Yang et al., 2022).

Table 1. Boundary conditions.

Parameter name	Parameter setting
Solver	Pressure-based solver
Viscous model	k-epsilon model
Inlet boundary type	Velocity inlet
Inlet velocity	9 m/s
Outlet boundary type	Pressure outlet
Near-wall treatment	Standard wall function
Particle size distribution type	R-R distribution
Min. particle diameter	1 um
Max. particle diameter	5um
Mass flow rate	0.03 kg/s
Injection type	Surface

The mathematical models used for this paper for simulating gas–solid two-phase flow in the FLUENT is discrete phase model (DPM). Large number of

particles are injected from the working face. Dust particles from blasting are considered as a discrete phase, the air flow field in the tunnel space is considered as a continuous phase. The air flow is analysed in simulation by vectors and air flow velocity along the tunnel. The dust particles are analysed by dust particle concentration and dust location monitor.

3 ANALYSIS OF THE AIRFLOW AND DUST SIMULATION RESULTS

3.1 *Analysis of the distribution of the air flow field in the tunnel*

The air velocity of 30 measurements points in 5 cross sections at different distances from the working face are measured in Kaprun tunnel. As shown in Figure 3 (a), the measurement cross sections are 46 m, 61 m, 76 m, 91m and 113m from the working. Each cross section has 6 measurement points in the height of 1.25 m and 2.5 m, 1.5 m left and right from the central of the tunnel shown in Figure 3 (b).

The development of the air flow for the central of the duct is shown in Figure 4 (a). Air velocity of 9 m/s is generated from the outlet of the duct. Since in the Kaprun tunnel the duct outlet is 61m far away from the working face, eventually a backflow occurs even before reaching the working face. To bbetter understand the change of air flow direction occurring next to the duct outlet, contours of the axial air flow component are shown in cross sections 40, 50,60 m from the working face in Figure 4 (b). Figure 5 present the air velocity development for the 6 measurement points in each cross section along the tunnel. The orange points in Figure 5 are the data from the onsite measurement and the curve is air velocity along the tunnel from simulation. The calculated results indicate good congruence with the field measurements for most of the measurement points. The velocity is generally decreasing along the tunnel and there is a sharp decrease of air velocity before and behind the ventilation duct. The air velocity

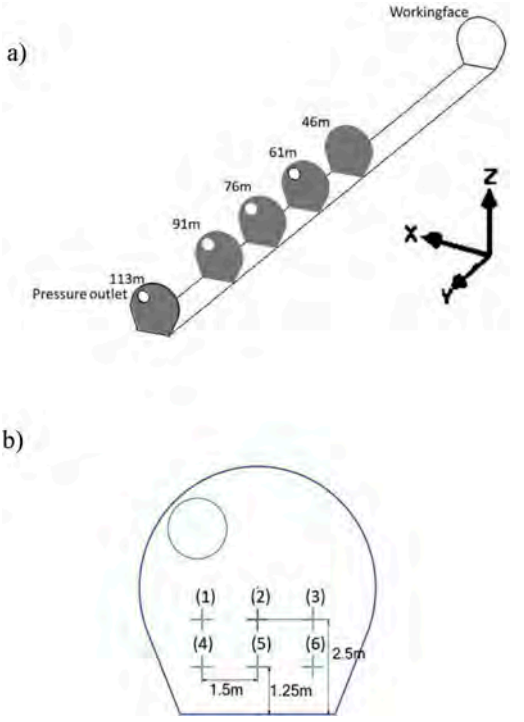

Figure 3. Location of measurement planes (a); measurement positions (b).

before the ventilation duct mostly ranges from 3-5 m/s while the velocity after the ventilation duct is stable at about 0.5-0.6 m/s.

In Figure 4 (a) and (b), at approximately 55 meters from the working face, the air flow exhibits a downward trajectory, eventually collides with the ground at about 49 m from the working face and backflow phenomenon occurring within a zone spanning 50-60 meters from the working face. Within the zone of 40-50 meters from the working face, here is a pronounced reduction in the air velocity along the

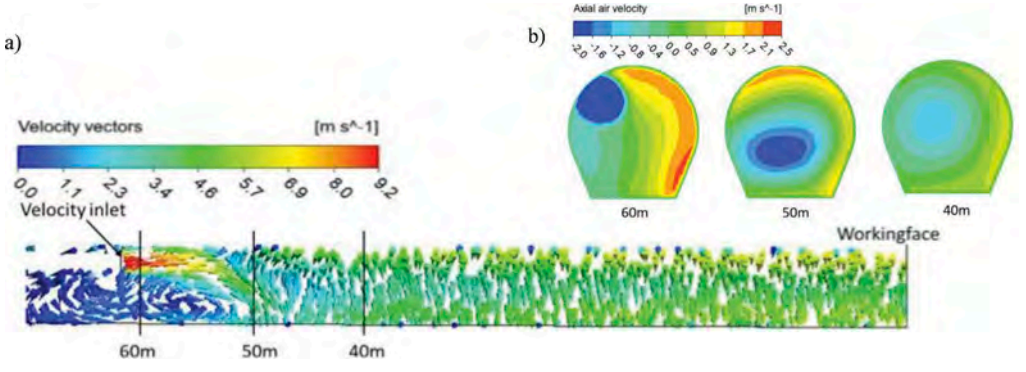

Figure 4. Air velocity vectors in length cut (a); contours of axial velocity for three cross sections (b).

y-axis and the airflow primarily exhibits a rotational motion predominantly confined within the tunnel. Since the measurement points are generally distributed in the middle of lower half of the cross section, this leads to a local peak at 50 meters at points 1 and 2 shown in Figure 5 compared to points 4, 5, 6. This peak is attributed to the collision and subsequent backflow phenomena of the ventilation duct. For the zone of 0-40 meters from the working face, the back flow disappears, and the air velocity tends to be stable at 3-5 m/s. However, due to the high turbulence and the rotation of the airflow, the air velocity of 0-40 meters away from the working face at point 2 which is in the central of the cross section is lower than other measurement points.

With 61 m the ventilation duct is relatively far from the working face, compared to the usual construction site where the distance is often shorter (20 - 40 m). Backflow appears along the duct wall and insufficient amount of air flow reaches the working face.

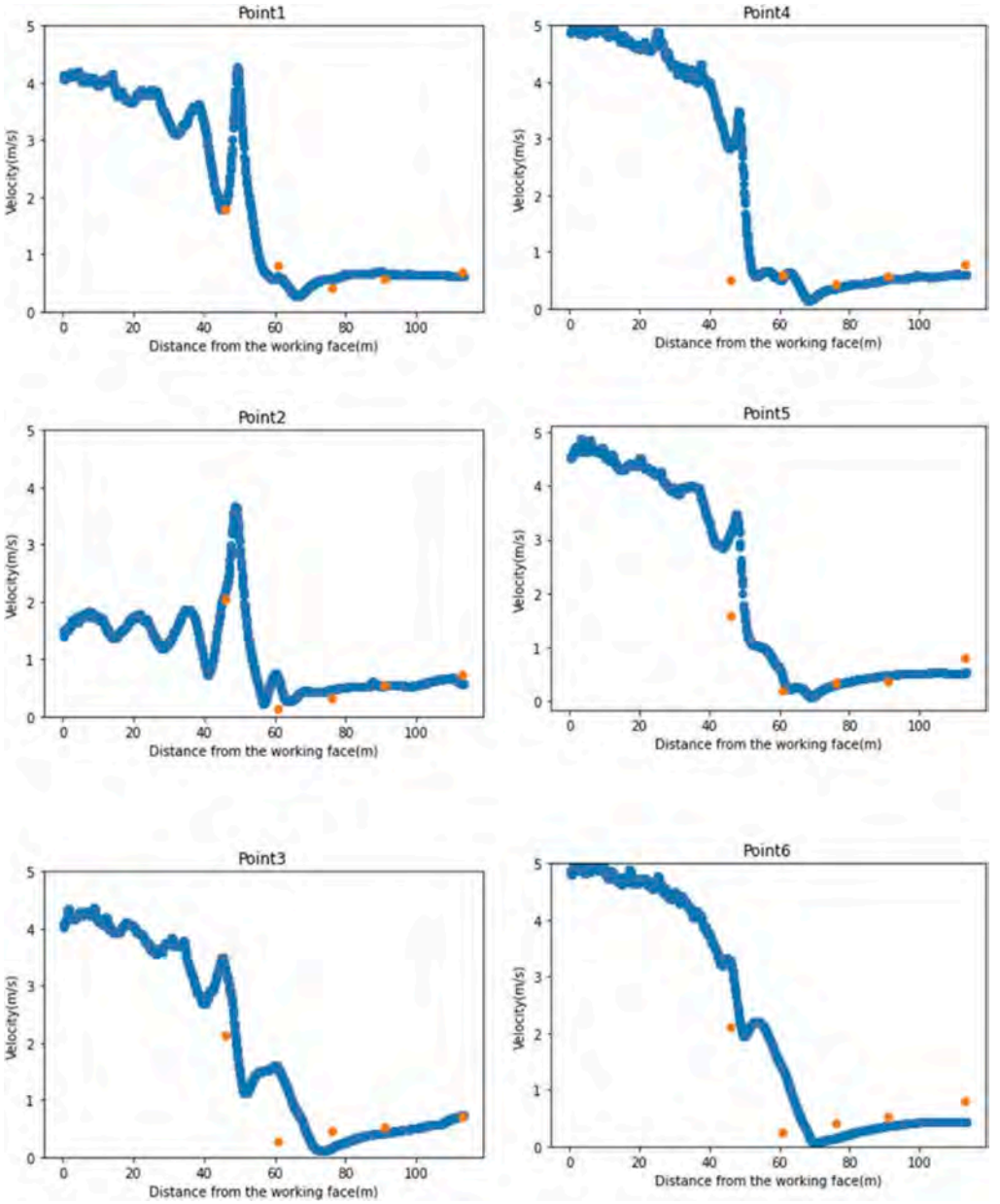

Figure 5. Comparison of simulated air velocity magnitude with measured air velocity at the six measurement points.

3.2 *Analysis of respirable dust movement in the tunnel*

To better analyse the dust particle movement, particle concentration in different cross section along the tunnel is compared in a 5 min simulation as shown in Figure 6 and dust particle location is recorded at 1,3,5 minutes in CFD-post for better visualization of particle location in Figure 7.

As shown in Figure 6 and Figure 7, at 1 minute the dust particle moving distance is 10m with highest dust concentration of 150mg/m^3. At 3 minutes, high dust concentration zone near the working face is decreasing and dust moving distance is about 100 m. The dust has not reached the tunnel outlet so the concentration near the outlet is still low, about 5 mg/m^3. At the moving front of the dust cloud (80-100m from the working face) dust concentration can reach up to 60 mg/m^3. At 5 minutes after the ventilation, high dust concentration zone next to the working face has disappeared. Dust particle is fully distributed inside the tunnel. And because of the insufficient air flow in axial direction, high concentration dust zone occurs after 80 m from the working face with the maximum dust concentration of 60-80 mg/m^3.

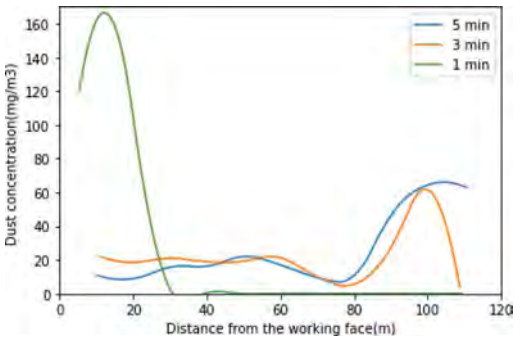

Figure 6. Length profile of cross-sectional averaged dust.

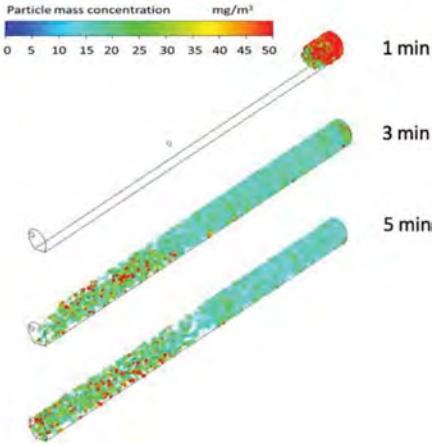

Figure 7. Spatial distribution of model dust particles.

4 CONCLUSIONS

In this paper, the CFD simulation method is used to simulate air flow and respirable dust particle movement is modelled using surface particle injection with the diameter of less than 5 micrometres. The following conclusions are reported from the air flow and dust particle movement simulation results:

1. The air flow velocity along the ventilation duct with the air velocity of 9 m/s, Air velocity after 70 m from the working face stable at 0.5-0.7 m/s and the maximum air velocity downstream of the ventilation duct can reach 4-5 m/s. The simulated air velocities of the measurement points are in good agreement with the actual measurement data inside the tunnel.
2. One minute of the blast the dust is still accumulated within 10m near the working face with the highest dust concentration of 150 mg/m^3. After 3 minutes of ventilation, the dust particles have been observed to disperse over approximately 100 meters. High dust concentration zone occurs at 80-100 meters from the working face, with the maximum dust concentration of 60 mg/m^3. At 5 minutes after the ventilation, dust particles are fully distributed inside the tunnel. High dust concentration zone occurs between 80 m and 110 m with the maximum concentration of 72 mg/m^3 because of insufficient air flow in the y direction reaching the working face.
3. The simulation and measurement results of air flow and respirable dust particle movement with the long distance of 61 m between ventilation ducts and the working face with air velocity 9 m/s provide reference on air movement for large scale tunnel construction project with a relatively long distance between the ventilation duct outlet and the working face. According to the air velocity and dust concentration results, it is evident that a ventilation duct with an air velocity of 9 m/s is insufficient for a complete dust transport. Backflow occurs next to the ventilation duct outlet preventing a strong air flow from reaching the working face. However, the efficiency of dust removal can be enhanced through better positioning of the duct and an increased air flow rate for this situation.

REFERENCES

Chen, W., Liu, Y., Wang, H., Hnizdo, E., Sun, Y., Su, L., Zhang, X., Weng, S., Bochmann, F., Hearl, F.J. and Chen, J., 2012. Long-term exposure to silica dust and risk of total and cause-specific mortality in Chinese workers: a cohort study. PLoS medicine, 9(4), p.e1001206.

Chen, X., Guo, C., Song, J., Wang, X. and Cheng, J., 2019. Occupational health risk assessment based on actual dust exposure in a tunnel construction adopting

roadheader in Chongqing, China. Building and Environment, 165, p.106415.

Erol, I., Aydin, H., Didari, V. and Ural, S., 2013. Pneumoconiosis and quartz content of respirable dusts in the coal mines in Zonguldak, Turkey. International Journal of Coal Geology, 116, pp.26–35.

Guo, J., Li, A., Gao, R., Hou, Y., Wang, T., Li, J., Yin, Y. and Che, L., 2023. Analysis and comparison of airflow-respirable dust control and innovative ventilation environment in drilling construction tunnels. Atmospheric Pollution Research, p.101908

Hua, Y., Nie, W., Liu, Q., Yin, S. and Peng, H., 2020. Effect of wind curtain on dust extraction in rock tunnel working face: CFD and field measurement analysis. Energy, 197, p.117214.

Hu, S., Liao, Q., Feng, G., Huang, Y., Shao, H., Gao, Y. and Hu, F., 2020. Influences of ventilation velocity on dust dispersion in coal roadways. Powder Technology, 360, pp.683–694.

Keramydas, D., Bakakos, P., Alchanatis, M., Papalexis, P., Konstantakopoulos, I., Tavernaraki, K., Dracopoulos, V., Papadakis, A., Pantazi, E., Chelidonis, G. and Chaidoutis, E., 2020. Investigation of the health effects on workers exposed to respirable crystalline silica during outdoor and underground construction projects. Experimental and Therapeutic Medicine, 20(2), pp.882–889.

Liu, Q., Cheng, W., Liu, L., Hua, Y., Guo, L. and Nie, W., 2021. Research on the control law of dust in the main ventilation system in excavated tunnels for cleaner production. Building and Environment, 205, p.108282.

Liu, Q., Nie, W., Hua, Y., Jia, L., Li, C., Ma, H., Wei, C., Liu, C., Zhou, W. and Peng, H., 2019. A study on the dust control effect of the dust extraction system in TBM construction tunnels based on CFD computer simulation technology. Advanced Powder Technology, 30(10), pp.2059–2075.

Nie, W., Sun, N., Liu, Q., Guo, L., Xue, Q., Liu, C. and Niu, W., 2022. Comparative study of dust pollution and air quality of tunnelling anchor integrated machine working face with different ventilation. Tunnelling and Underground Space Technology, 122, p.104377.

Shi, J., Zhang, W., Guo, S. and An, H., 2022. Numerical modelling of blasting dust concentration and particle size distribution during tunnel construction by drilling and blasting. Metals, 12(4), p.547.

Ulvestad, B., Bakke, B., Eduard, W., Kongerud, J. and Lund, M.B., 2001. Cumulative exposure to dust causes accelerated decline in lung function in tunnel workers. Occupational and Environmental Medicine, 58(10), pp.663–669.

Xie, Z., Xiao, Y., Zhao, Q. and Lin, J., 2022. Transient analysis of dust exposure under different supply airflow angle in a blasting tunnel based on CFD. Energy Reports, 8, pp.45–52.

Xie, Z., Ruan, C., Zhao, Z., Huang, C., Xiao, Y., Zhao, Q. and Lin, J., 2023. Effect of ventilation parameters on dust pollution characteristic of drilling operation in a metro tunnel. Tunnelling and Underground Space Technology, 132, p.104867.

Yin, S., Nie, W., Guo, L., Liu, Q., Hua, Y., Cai, X., Cheng, L., Yang, B. and Zhou, W., 2020. CFD simulations of air curtain dust removal effect by ventilation parameters during tunneling. Advanced Powder Technology, 31(6), pp.2456–2468.

Yang, X., Yu, H., Wang, Y. and Cheng, W., 2022. Investigation of dust pollution control rules in tunnel excavation based on modularized airflow diverging system. Building and Environment, 221, p.109356.

Zhang, S., Nie, W., Guo, C., Peng, H., Ma, Q., Xu, C., Zhang, H. and Liu, Q., 2021. Optimization of spray dust suppression device in return air tunnel of a coal mine based on CFD technology. Building and Environment, 203, p.108059.

Tunnelling for a Better Life – Yan, Celestino, Thewes & Eberhardt (Eds)
© 2024 The Author(s), ISBN 978-1-032-80042-4
Open Access: www.taylorfrancis.com, CC BY-NC-ND 4.0 license

Study on the mechanism of tunnel structure damage under the combined effects of fault creep and earthquakes

Zhipeng Xia, Sijia Jia, Jianhong Wang & Qi Wang
School of Qilu Transportation, Shandong University, Jinan, Shandong, China

ABSTRACT: Fault creep in active fault zones poses a serious threat to tunnel structure safety, and when coupled with seismic effects, it can easily lead to tunnel disasters. Therefore, it is urgent to study and understand the tunnel structure damage mechanism under the combined effects of fault creep and earthquakes. Taking a railway tunnel crossing a specific fault zone as the engineering background, this study explores the tunnel structure damage mechanism under fault creep and seismic effects through indoor model tests and numerical simulations. The research findings indicate: (1) Under fault creep, the deformation of tunnel structures generally follows an "S" shaped distribution pattern along the longitudinal direction; (2) Under the combined effects of fault creep and earthquakes, stress concentration occurs in the tunnel lining structure at the fractured zone of the fault, necessitating special consideration for seismic design within the range of the left and right arches of the lining structure at the boundary of the fractured zone; (3) A comparison of seismic effects in different directions shows that under the coupling of longitudinal and transverse seismic and fault creep, the stress variation trends are basically consistent. Compared to seismic effects, fault creep has a greater impact on the safety of tunnel lining structures. The study is expected to provide fundamental support for the safe design of tunnels crossing active.

Keywords: active fault tunnel, fault creep, model experiment, seismic analysis, seismic direction

1 INTRODUCTION

In recent years, China has accelerated the pace of its transportation infrastructure construction, inevitably requiring tunnel construction to traverse geological structures such as faults and fractured zones. Active faults can experience fault creep and strong seismic activity, leading to serious tunnel structural damage. Therefore, studying the influence of fault creep and intense seismic activity on tunnel structures, and understanding the mechanism of tunnel structure damage, is of great significance for improving the safety and stability of tunnel structures crossing faults.

In high-intensity earthquake areas, tunnels crossing faults may experience not only the detrimental effects of fault creep but also severe seismic activity, exacerbating tunnel damage. Existing studies largely focus on either strong seismic activity or fault creep, with limited research on the structural damage mechanism under the coupled effects of fault creep and earthquakes. Therefore, it is necessary to conduct research on the dynamic response of tunnel structures under fault creep and seismic activity.

Based on the engineering background of a tunnel crossing an active fault, this paper adopts the method of model test and finite element numerical simulation. Firstly, the deformation and stress of tunnel structure under fault creep are studied based on experiments. Secondly, the structural response of tunnels under the coupling action of earthquake and fault creep in different directions is studied, which provides the research basis for exploring the deformation mechanism and failure mechanism of tunnels crossing active faults.

2 ENGINEERING BACKGROUND

The tunnel is located in a typical plateau landform area, and the tunnel site area has a high level of strong earthquake activity, and passes through a number of deep and large active fault zones, among which the surrounding rock of F9-1 fault zone is IV level, and the broken zone is V level. The dip Angle of the fault zone is 75° and the width of the fault zone is 12m. The maximum buried depth of the tunnel is about 1215m, the longest diameter is 12m, and the lining is made of C40 concrete with a thickness of 80cm. The tunnel crossing F9-1 fault zone will be directly affected by strong earthquake and fault dislocation, resulting in the cumulative deformation and serious damage of the tunnel.

DOI: 10.1201/9781003495505-55

Figure 1. Geological profile of the fault zone.

3 EXPERIMENTAL STUDY OF CREEP EFFECT

In order to find out the structural response and failure mechanism of the tunnel crossing the fault zone under creep, this experiment takes the tunnel project crossing the F9-1 fault zone as the prototype to build a surround-rock tunnel model, and uses an independently developed fault dislocation testing machine to conduct model tests.

3.1 *Test model*

The surrounding rock tunnel model mainly includes four parts: fault upper wall rock, fault fracture zone, fault footwall wall rock and tunnel structure. The overall length of the model is 1200mm, the section diameter of the tunnel model is 200mm, the width of the fault fracture zone model is 200mm, and the inclination Angle is 75°. The strength of the surrounding rock is 0.917MPa, and the strength of the fracture zone is 0.056MPa. The surrounding rock tunnel model is shown in Figure 2.

Figure 2. Test model.

3.2 *Test loading*

In order to simulate the creep slip of the upper wall fault under deep buried conditions, the fault dislocation test device developed in this study was used (Figure 3). In the test, the vertical cylinder of the fault dislocation test device was used for constant velocity displacement loading control, and the surrounding rock of the hanging wall was driven to make upward displacement dislocation at a control rate of 2mm/min, and the load was carried out step by step by 2mm. When the displacement dislocation reached 10mm, the test was stopped, and the structural damage patterns of the tunnel and surrounding rock were observed. The model loading status was shown in Figure 4.

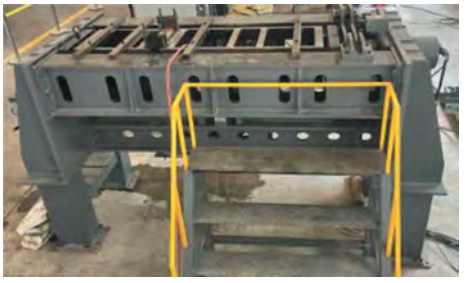

Figure 3. Test device.

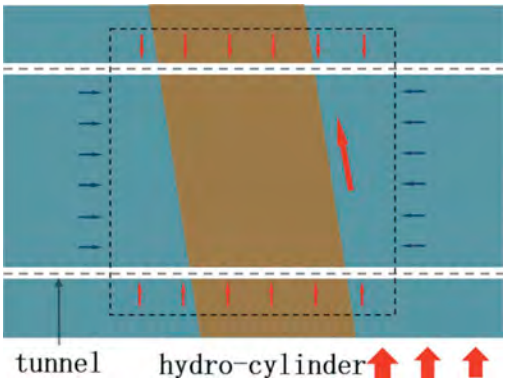

Figure 4. Test loading.

3.3 *Result analysis*

3.3.1 *Failure phenomenon analysis*

Figure 5 shows the failure of tunnel structure under the action of fault dislocation in model test and numerical analysis. As can be seen from Figure 5, the tunnel failure range caused by fault dislocation is concentrated near the slip plane, the tunnel arch bottom first occurs tensile failure, and the fracture instability occurs along the fault dip direction. The failure trend of the tunnel structure is basically consistent between the model test and the numerical simulation.

Figure 5. Damage of tunnel structure.

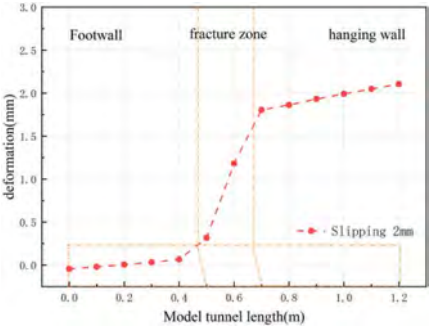

Figure 6. Comparison of vertical deformation results.

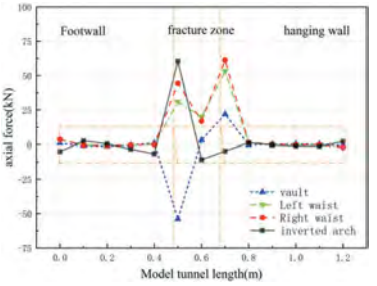

Figure 7. Axial force change.

3.3.2 *Tunnel deformation*

As can be seen from Figure 6, when the upper disk is displaced upward by 2mm, the vertical deformation of the tunnel gradually increases along the lower disk, crushing zone and upper disk. Figure 7 shows that the maximum axial force in the model test occurs at the junction of the fracture zone and the surrounding rock of the footwall, and it is necessary to pay attention to the seismic fortification of the lining structure within the junction of the fracture zone.

4 TUNNEL STRUCTURE RESPONSE UNDER EARTHQUAKE AND CREEP COUPLING

The tunnel and surrounding rock numerical model is established based on the test model. The forced displacement method is used to simulate the creep slip of fault, and the displacement is applied to the surrounding rock of the upper wall. The seismic action is simulated by applying the seismic load along the axial and transverse direction to carry out the seismic time history analysis.

4.1 *Tunnel vertical deformation*

Figure 9 shows the vertical distribution curve of the vertical deformation of the tunnel through the fault zone under the coupling of earthquake and fault creep in different directions. Obviously, the curves can be divided into three parts: basic stability, non-

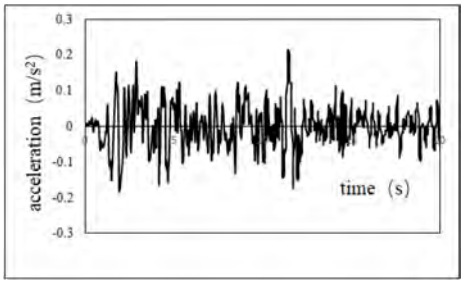

Figure 8. Time-acceleration curve.

uniform deformation and overall creep, and the overall distribution is "S", which is basically consistent with the vertical distribution of tunnel structure deformation under creep. In addition, the results of tunnel deformation under the coupling effects of longitudinal and lateral earthquakes and fault creep are close to those under creep, indicating that creep is a control effect affecting structural safety.

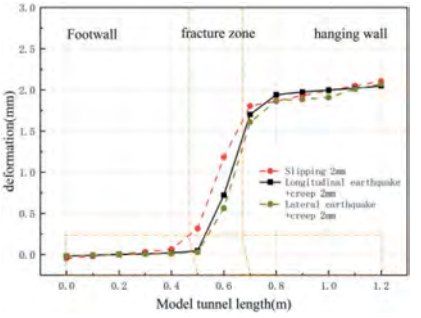

Figure 9. Strain comparison.

4.2 *Principal stress*

Figure 10 shows the tunnel stress cloud map under the coupling effect of longitudinal and transverse earthquake and fault creep slip. It can be seen from Figure 10 that under the coupling effect of earthquake and creep slip, the tunnel will produce stress concentration at the left and right arches under the coupling effect of earthquake and creep slip, and significant tensile stress appears in the tunnel. The tensile stress of the left and right arches and the stress at the junction between the fault and the surrounding rock are larger, so the seismic fortification of the left and right arches of the lining structure should be emphasized when considering the junction of the lining structure and the fracture zone.

Figure 11 shows the longitudinal variation curves of the axial stress and lateral stress of the tunnel arch under the coupling effects of longitudinal and transverse earthquake and fault creep. As can be seen from the figure, the axial stress is larger and the lateral stress is smaller under the coupling effect of lateral earthquake and fault creep, while the lateral stress is larger

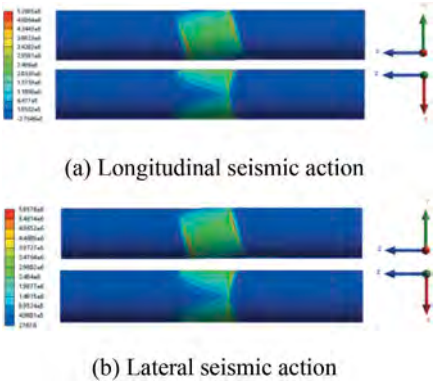

Figure 10. Main stress nephogram of tunnel.

and the axial stress is smaller under the coupling effect of lateral earthquake and fault creep. However, the variation trend of tunnel structural stress under the two conditions is basically the same, indicating that creep is a control effect affecting structural safety, and the impact of earthquake on tunnel structure is relatively small.

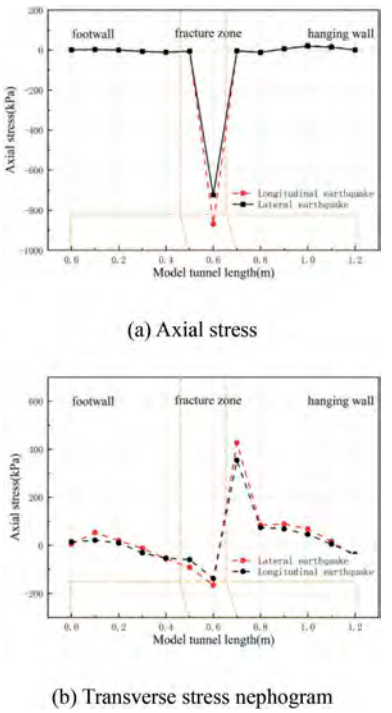

Figure 11. Change curve of tunnel principal stress.

5 CONCLUSIONS

(1) Under the action of creep, the deformation of tunnel structure is generally "S" type distribution along the longitudinal distribution, and the stress concentration occurs at the interface between the fracture zone and the surrounding rock of the footwall; With the increase of the amount of dislocation, the tunnel invert will crack first, resulting in the overall instability of the tunnel.

(2) Under the coupling action of earthquake and dislocation, stress concentration occurs at the junction of the fracture zone of the tunnel structure, and the first principal stress at the waist of the left and right arch is much greater than that at the arch and invert, so it is necessary to pay attention to the seismic fortification of the left and right arch of the lining structure at the junction of the fracture zone.

(3) Compared with the seismic action in different directions, the stress variation trend under the coupling action of longitudinal and transverse earthquakes and fault creep is basically the same, indicating that creep is a control effect affecting structural safety, and seismic action has relatively little influence on tunnel structure.

ACKNOWLEDGMENTS

This research was partially funded by the National Natural Science Foundation of China (approval number: 52130808,52178390) and the National Key Research and Development Plan project (Grant number:2021YFB2600800).

REFERENCES

Chen J, Shi X, Li J. Shaking table test of utility tunnel under non-uniform earthquake wave excitation[J]. Soil Dynamics and Earthquake Engineering, 2010, 30 (11):1400–1416.

He Chuan, Geng Ping. Challenges and countermeasures of railway tunnel construction in strong earthquake active fault zone [J]. China Railway, 2020, No.702(12): 61–68.

He Chuan, Li Lin, Zhang Jing, et al. Study on earthquake damage mechanism of tunnel crossing fault fracture zone [J]. Chinese Journal of Geotechnical Engineering, 2014, 36(03):427–434.

Wang WL, Wang TT, Su JJ, et al. Assessment of damage in mountain tunnels due to the Taiwan Chi-Chi Earthquake[J]. Tunnelling and Underground Space Technology, 2001, 16(3):133–150.

Chen Junbo, Wang Tianqiang, Geng Ping et al. Dynamic response analysis of cross-fault tunnel under creep slide-strong earthquake superposition [J/OL]. Railway standard design: 1–12[2023-10-26].

Cui Zhen, Sheng Qian, LI Jianhe et al. A preliminary study on deformation and failure mechanism of cross-active fault tunnel under the action of creep slip fault-strong earthquake sequence [J]. Rock and soil mechanics, 2022, 43 (05): 1364–1373.

Tunnelling for a Better Life – Yan, Celestino, Thewes & Eberhardt (Eds)
© 2024 The Author(s), ISBN 978-1-032-80042-4
Open Access: www.taylorfrancis.com, CC BY-NC-ND 4.0 license

Theory and practice of total safety factor method for tunnel support structure design

Mingqing Xiao, Biting Xie*, Chen Xu, Kejin Wang & Zhaohui Deng
China Railway Siyuan Survey And Design Group Co, LTD
National & Local Joint Engineering Research Center of Underwater Tunneling Technology

ABSTRACT: The tunnel support systems worldwide primarily rely on an "experiential design" approach, where modifications and validations are based on measurement information during implementation. However, this "empirical design" lacks quantitative analysis of the safety of supporting structures, leading to conservative approaches that can have adverse effects on engineering economics. To address these limitations, a research method called "Total Safety Factor Method" has been developed. This method focuses on tunnels approaching or reaching the failure stage and combines modern numerical analysis techniques with traditional load structure methods. It aims to integrate the surrounding rock load, support structure, and various parameters related to support design. These parameters include the necessity of support, the type of support (systematic or local), the magnitude of support force, structural calculation models, calculation methods, values of the safety factor, deformation analysis of support structures, and dynamic adjustment methods of support parameters. This comprehensive approach has been successfully applied to numerous tunnel projects in China, such as the Yichang to Xingshan High-Speed Railway, Ningbo to Zhoushan Railway, and Jiaozhou Bay Second Submarine Tunnel. The rationality of Total Safety Factor Method has been verified through field tests, model tests, numerical calculations, and other rigorous means. By employing this design method, engineers can quantitatively calculate the parameters of tunnel support structures, thereby ensuring a more precise and efficient approach to tunnel construction and improving the full life cycle safety and cost-effectiveness of tunnel projects.

Keywords: Total Safety Factor Method, Stability of surrounding rock, Design value of surrounding rock pressure, Anchor bolt-surrounding rock bearing arch

1 INTRODUCTION

The existing design theories abroad, represented by the New Austrian Tunnelling Method, New Italian Tunnelling Method, and Norwegian Tunnelling Method, have played a crucial role in promoting the development of tunnel engineering technology. The concept of the New Austrian Tunnelling Method (L V et al., 1989) proposed by Austrian scholars in the 1950s was based on tunnel engineering experience and the theory of rock mechanics and has become one of the new technological symbols of modern tunnel engineering. New Italian Tunnelling Method, also known as the Rock and Soil Control Deformation Analysis Method (LUNARDI, 2008), is an extension of the concept of the New Austrian Tunneling Method. It is mainly used in tunnel excavation in weak strata to pre reinforce and control the deformation of surrounding rocks in weak strata. The New Austrian Tunneling Method and the New Italian Tunneling Method are mainly based on design concepts and do not propose clear support parameter design methods. The Norwegian tunnel construction method, abbreviated as NMT, is a refinement, supplement, and development of the New Austrian Tunneling Method. It refers to the classification of surrounding rock and the selection of support based on the Q-value of the surrounding rock quality index, and the summary of charts that can quantitatively select support parameters based on multiple tunnel cases. Its essence is still the engineering analogy method, and Norwegian tunnel engineering mainly focuses on rock strata, with relatively single engineering conditions.

With the rapid development of China's transportation infrastructure construction, China has built the world's largest number, largest construction scale, and most complex technical conditions of tunnel engineering. However, there is still no internationally recognized tunnel design method with Chinese characteristics. The tunnel design specifications in China are no longer suitable for the current development requirements of tunnel construction technology in terms of load values for deep buried tunnels. Moreover, the design of tunnel support structures is still in the stage of "engineering analogy as the main method and

*Corresponding author: 983126144@qq.com

DOI: 10.1201/9781003495505-56

theoretical calculation as the auxiliary". It cannot achieve quantitative design of support parameters so that it is impossible to analyse and evaluate the safety and economy of tunnel support structures, which greatly restricts the development of tunnel construction technology. Meanwhile, with the rapid development of intelligent tunnel construction technology, existing design methods can no longer match it, it is becoming the weakest link in intelligent tunnel construction. Therefore, it is urgent to make an improvement in the design method of tunnel support structure.

Currently, a multitude of scientific research endeavours have been undertaken by domestic experts and scholars to investigate the stress characteristics and bearing capacity of tunnel support structures. Notable contributions include studies such as "Deformation and stability control technology throughout tunnel construction" and "Design method for high-speed railway mechanized large cross-section tunnels" (WANG, 2018). These efforts primarily focus on intelligent classification of surrounding rock and the coordination mechanism of supporting deformation in the context of tunnel construction. However, there is a lack of specific and well-defined design methods for the quantitative design of tunnel support structures. This absence hinders the direct guidance of engineering design processes. In this regard, Total Safety Factor Method for tunnel support structure design has made significant progress in establishing a quantitative design system for tunnel support structures. This approach enables the transition from "analogue design" to "quantitative design" of tunnel support structures. Its implementation has played a constructive role in advancing the development of tunnel engineering design technology. By incorporating Total Safety Factor Method into the design process, engineers can now rely on a systematic and quantifiable approach for designing tunnel support structures. This advancement not only enhances the accuracy and efficiency of tunnel construction but also contributes to improving the overall safety and cost-effectiveness of tunnel.

2 THEORY OF TOTAL SAFETY FACTOR METHOD

Total Safety Factor Method (XIAO,2020a), proposed in 2017, takes the tunnel approaching or reaching the failure stage as the research object, and organically integrates the surrounding rock, load, and support structure with a combination of numerical analysis method and load structure method. A set of quantifiable design methods for calculating support structure parameters has been developed based on the main theme of "whether the tunnel needs support, system support or local support, support force values, structural calculation models, safety factor calculation methods and values, analysis of support structure deformation and dynamic adjustment of support parameters" (Figure 1).

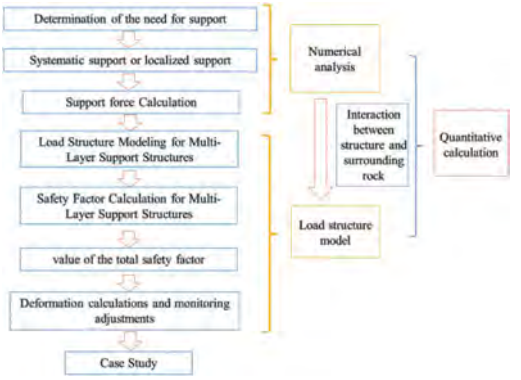

Figure 1. Technical route of total safety factor method.

In addition, systematic research has been conducted based on Total Safety Factor Method including support structure types and optimization of support parameters for high-speed railway double track tunnels (XIAO,et al.,2018), safety analysis of existing tunnel support structures(XIAO,et al.,2019), comparison of tunnel section forms, design of support parameters for high ground stress soft rock large deformation tunnels and ultra large span tunnels. Total Safety Factor Method was used to explore several current hot and controversial issues (XIAO,2019), including the design concept of tunnels(XIAO,2020b), the role of anchor rods, the distinction between the bearing bodies of multi-layer supporting initial support and secondary lining, the optimization method of support parameters, the setting and protection layer of steel frames, the early strength of sprayed concrete, and the selection of support types.

2.1 *Determination of the need for support*

There is a wide range of caves without any support but can be basically self-stabilizing, such as caves, loess kiln caves, etc., which leads to the theoretical study of the stability of tunnel surrounding rock and the need for support. Based on this, the concept of critical stable section of tunnel and the method of analysing the stability of tunnel surrounding rock based on critical stable section are proposed, which can quantitatively analyse the self-bearing capacity of surrounding rock (XIAO and XU,2020).

As shown in Figure 2(a), the critical stable section of a tunnel is the largest section that has the same depth of burial and similar geometry as the centre of the designed excavation section, and the surrounding rock can achieve self-stability with the designed safety factor under the unsupported condition and basically can maintain its original shape. The critical stability section can be used to determine the stability of the surrounding rock in the unsupported condition of the designed tunnel. The study determines that the damaged area with depth greater than 1m in the side wall area and 0.5m in the arch area after

tunnel excavation is the potential collapse area of the tunnel and takes this as the criterion for critical stability section.

When the excavation section is smaller than the critical stabilizing section, as in Figure 2(b), it is considered that the surrounding rock in the section plays a supporting role for the critical stabilizing section, which can be regarded as a part of the supporting structure. When the excavation section is larger than the critical section, such as Figure 2(c) and (d), the surrounding rock cannot be self-stabilized, and it is necessary to meet the design requirements for the safety factor through engineering support measures.

2.2 *Systematic support or localized support*

Based on the distribution characteristics of the surrounding rock damage zone after unsupported tunnel excavation, the criteria and methods for the division of local support and system support (XIAO and XU,2021)are as follows:

① When there is no potential collapse area in the tunnel, it is judged that the tunnel is self-stabilized. When the designed section is smaller than the critical stabilizing section, and the strength safety factor of the surrounding rock in the section when it is used as a supporting structure is greater than or equal to the design value, the tunnel does not need support.

② When the designed section is smaller than the critical stabilizing section, but the strength safety factor of the surrounding rock in the section when it is used as a supporting structure is less than the design value, or the designed section is larger than the critical stabilizing section, and the potential collapse range of the arch wall accounts for less than 30%, the tunnel can adopt the local support scheme.

③ When the proportion of potential collapse range of the arch wall is between 30% and 60%, zoned unequal strength support can be adopted.

④ When the proportion of potential collapse range of arch wall is more than 60%, equal strength system support can be adopted.

2.3 *Support force calculation*

Without considering the role of chance factors, the tunnel surrounding rock pressure from construction to destruction of the whole life cycle will generally go through four stage: the construction stage, the working stage, the failure stage, and the post-failure stage (XIAO and XU,2019a; XIAO,et al.,2023; XU, et al.,2019) (as shown in Figure 3). When using the total factor of safety method for design, only the most unfavorable case of the surrounding rock pressure needs to be found. Therefore, it is proposed to adopt the design value of the surrounding rock pressure as the design support force and thus solve the difficult problem that the actual surrounding rock pressure is difficult to determine.

In the tunnel surrounding rock pressure full life stage three (destruction stage), due to the support measures on the surrounding rock support role, only when the destruction of the area of the surrounding rock formed by the loose load is greater than the support can provide the ultimate bearing capacity in order to determine the failure of the support structure, to maintain the limit of the surrounding rock equilibrium state of the support force can be referred to as the minimum support. surrounding rock pressure design value in the minimum support based on the design value should have a certain safety reserve and should not be less than 1.4, so that as far as possible to envelope the service period surrounding rock pressure but not too conservative to affect the economy. Based on the minimum support force $P_{i\min}$ should have a certain safety

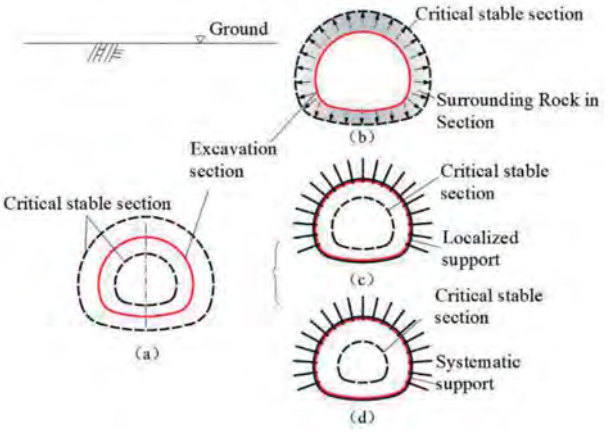

Figure 2. Schematic diagram of critical stabilized section of the tunnel and division of support scheme.

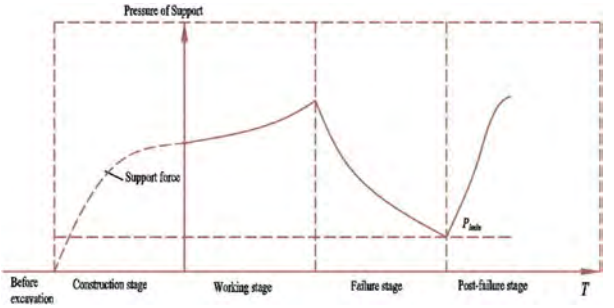

Figure 3. Schematic diagram of the change process of tunnel surrounding rock pressure over the whole life cycle.

reserve, and should not be less than 1.4, so that as far as possible to envelope the service period of the pressure of the surrounding rock, but not overly conservative impact on the economy. The safety reserve coefficient can be adjusted according to the importance of the project, the strictness of deformation control and the accuracy of geotechnical parameters and constitutive modeling and other factors.

2.4 *Load structure modelling and safety factor calculation for multi-layer support structures*

After obtaining the design value of surrounding rock pressure, the tunnel support structure can be used to calculate the internal force using the load structure method. Since the tunnel support structure is generally a multi-layer structure composed of bolt-rock bearing arch, shotcrete layer, and secondary lining layer, it is necessary to establish the calculation models of single-layer structure and multi-layer structure respectively. In each load structure model, the surrounding rock pressure is taken as the design value of all the surrounding pressure, and the safety factor K_1 of the bolt-rock bearing arch, the safety factor K_2 of the sprayed concrete layer, and the safety factor K_3 of the secondary lining are all calculated according to the breakage stage method of the current tunnel design specification (XIAO and XU,2019b; XIAO,2018).

2.5 *Methodology for calculating total safety factor*

The coefficient of safety of each layer of the structure itself is calculated using the breaking stage method, and the total coefficient of safety of the multi-layer structure includes the contribution of each layer of the structure, which needs to be considered after considering the coordination of deformation and the sequence of damage between each layer of the structure.

(1) Assumptions for calculation of total safety factor

The bearing structure of multi-layer supporting consists of two or three layers. Assuming that the structure of each layer is an ideal elastic-plastic material and linear-elastic structure, when a cross-section of one of the structural layers reaches the breakage stage first, it can continue to maintain the strength, until a cross-section of both the shotcrete layer and the second lining reaches the breakage stage, or the second lining has two or three (three when the load and structure are symmetrical, otherwise two) breakage cross sections, before reaching the overall structural design strength.

(2) Calculation formula of total safety factor

After calculating the safety factors of bolt-rock bearing arch, shotcrete layer and second lining respectively according to the above method, the lower limit value of the total safety factor of the supporting structure can be approximated as follows:

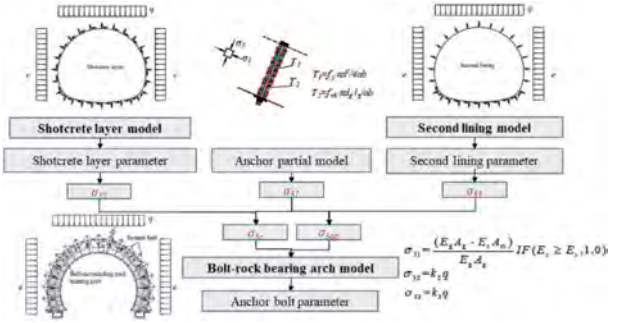

Figure 4. Calculation model and calculation idea of total safety factor method for tunnel support structure design.

Construction stage (no second lining):

$$K_c = \eta K_1 + K_2 \tag{1}$$

Operation stage:

When using durable anchors,

$$K_{op} = \eta K_1 + \xi K_2 + K_3 \tag{2}$$

When using non-durable anchors,

$$K_{op} = \xi K_2 + K_3 \tag{3}$$

In the formula, K_1, K_2, K_3 are the safety factor of the bolt-rock bearing arch, shotcrete layer and second lining when they bear all the design values of the surrounding rock pressure, η is the correction coefficient of the safety factor of the bolt-rock bearing arch, ξ is the adjustment coefficient of the bearing capacity of the shotcrete layer.

According to the assumption of "ideal elastic-plastic material and linear-elastic structure" mentioned above, η can be calculated according to Eq. (4) by considering only the difference in ultimate strains between the surrounding rock and concrete materials.

$$\eta = \frac{\varepsilon_u + E_0}{\sigma_1} \tag{4}$$

Where ε_u is the ultimate strain of concrete, E_0 is the modulus of elasticity of the anchor rock bearing arch, σ_1 is the compressive strength of the anchor rock bearing arch under the action of supporting force.

Although the shotcrete layer and second lining have similar structural materials, their section shapes (e.g., the second liner has a superelevation arch and the shotcrete layer does not have a superelevation arch) and damage patterns may be different, and it is possible that the first broken cross-section of each layer of the structure does not appear one after another, or the damage patterns of the shotcrete layer structure are different in the construction period and the operation period (from the tensile damage to the compressive damage). According to many calculations, when the shotcrete layer and second lining are both under pressure, can generally be taken as 1.0. When the shotcrete layer and the second liner have different damage patterns, needs to be calculated according to the specific situation, and the design should try to avoid the vegetative concrete structure for tensile damage.

Theoretically, under the premise of the same total safety factor, there can be a variety of support parameter programs. Due to the differences in the strength and stiffness of each layer of structure in different support schemes, the structure of each layer does not always reach the most unfavorable cross-section strength at the same time, so the total safety factor obtained by the above formula is the minimum safety factor of the overall structure, and the actual load carrying capacity is generally higher than the above calculation results.

2.6 *Value of total safety factor*

(1) Suggested values for the construction stage

Different from the ground structure, the initial tunnel support (or anchor bolt-spray support) is subjected to the pressure of surrounding rock, blasting vibration and other loads from the time of the applying. With the hardening strength of shotcrete (or anchor mortar) gradually increased, the pressure of surrounding rock is also gradually increased. It must be ensured that the support structure during the construction period has a suitable safety, so that it is recommended that total safety factor during the construction stage should not be less than 1.5 ~ 1.8.

(2) Suggested values for the operation stage

Considering the structural characteristics of the tunnel project, the characteristics of the loading and calculation model, the construction quality and other major factors, the total safety factor during the operation period is recommended as follows:

①When only the primary load is considered, the total safety factor is 50% higher than that of a single structural component.

For multi-layer supporting, when the secondary lining adopts reinforced concrete, the total safety factor is recommended to be not less than 3.0; when the secondary lining adopts plain concrete, the total safety factor is recommended to be not less than 3.6.

For shotcrete-anchor permanent support, when the shotcrete layer is made of steel fiber concrete or steel frame with relatively good ductility, and it is recommended that the total safety factor is not less than 3.0. When the shotcrete layer is made of plain concrete, it is recommended that the total safety factor is not less than 3.6.

②When adopting the combination of "main load + additional load", total safety factor can be reduced by 15% to 20% compared with the value of "only considering the main load".

2.7 *Deformation calculations and monitoring adjustments*

To ensure that the safety of the supporting structure meets the predetermined objectives of the design, dynamic optimization and adjustment of the design support parameters must be carried out according to the results of on-site monitoring and measurement.

The deformation value monitored during construction is essentially the deformation value of the supporting structure, and the control value of on-site monitoring can be derived by calculating the allowable deformation value of the supporting structure. The allowable deformation value of the supporting structure refers to the structural deformation value of the supporting structure under the premise of having a safety factor corresponding to the design of structural strength. The ultimate deformation value of the supporting structure refers to the structural deformation value when the shotcrete layer of the supporting structure has the first broken cross-section (plastic

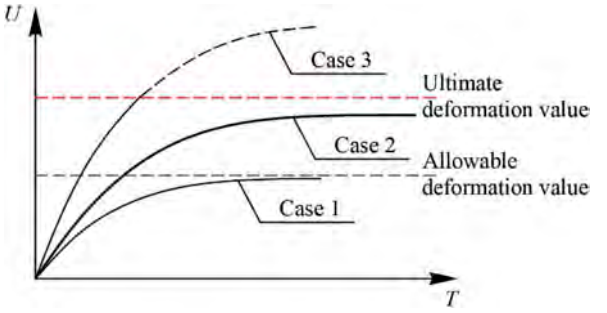

Figure 5. Comparison of measured and calculated displacement-time curves.

hinge), i.e., the structural deformation value when the structural safety factor of the shotcrete layer is 1.0.

During the construction process, the measured displacement-time curve (u-t curve) should be compared with the calculated u-t curve (Figure 5) as the basis for judging the reasonableness of the design parameters. According to the relationship between the measured value and the calculated allowable deformation value, it is divided into three cases, and corresponding adjustment measures can be taken to dynamically adjust the support stiffness and support timing (XIAO and XU, 2019c).

3 CASE STUDY

Taking the two-lane tunnel of China's 350km/h high-speed railroad as an example, which is excavated by the full-section method without considering the influence of tectonic geostress, and the support parameters of Class Ⅳ surrounding rock under the working condition of 400m burial depth are designed according to the principle of Total Safety Factor Method. The physical mechanics index of surrounding rock is according to the lower 1/3 quartile of the range value of physical mechanics index in the "Railway Tunnel Design Code (TB 10003-2016)", which is shown in Table 1.

Step 1: Judgment of whether the tunnel needs to be supported or not.

The finite element model is established, and the critical stabilized section of the tunnel is only 2.9m under the condition of 400m depth of Class Ⅳ surrounding rock, while the excavation span of the tunnel of the high-speed railway is 14.7m, support is needed.

Step 2: Discriminate between systematic support and local support.

The convergence of finite element model is poor under the condition of 400m burial depth of Ⅳ class surrounding rock, and there is a large range of tensile damage zone around the hole, so it is judged that system support is needed after tunnel excavation.

Step 3: Design value of surrounding rock pressure.

Calculate the minimum support force $P_{i\min}$is 115.5kPa, due to the high structural importance of high-speed railroad tunnels, deformation control is more stringent, so the load safety factor takes 2.0, the design value of surrounding rock pressure q=231kPa, e=155.5kPa.

Step 4: Formulate the parameters of the support structure and account for the calculation results of the safety factor.

According to the experience, the support parameters shown in Table 2 are initially formulated and

Table 1. Table of physical and mechanical index of surrounding rock.

Surrounding rock level	Bulk weight (kN/m^3)	Elastic resistance coefficient (MPa/m)	Elasticity modulus (MPa)	Poisson's ratio	Internal friction angle (degree)	Cohesion (MPa)
Ⅳ	21.0	300	2.87	0.33	31.0	0.367

Table 2. Table of Parameters of tunnel support for two-lane tunnel of 350km/h high-speed railroad.

	Initial support								
	Shotcrete		Archor bolt			Steel frame	Second lining		
Project	Strength grade	Thickness (cm)	Length (m)	Diameter (mm)	Spacing (m×m)	Specification	Spacing (m)	Strength class	Thickness (cm)
Parameters	C30	20	3	25	1.5×1.2	Φ22@150	1.2	C30	40

Table 3. Table of calculation results of safety factor.

Project	Shotcrete layer		Bolt-rock bearing arch in construction stage		Bolt-rock bearing arch in operation stage				
	Discount factor	Safety factor	Discount factor	Safety factor	Discount factor	Safety factor	Second lining	Initial support	Total
Safety factor	1.0	2.72	1.0	2.02	1.0	3.27	3.38	4.74	9.37

the safety factor is calculated, and the results are shown in Table 2.

Total Safety Factor Method was used to calculate the safety factors of the anchor rock bearing arch, the shotcrete layer and the second liner respectively, the calculation results are shown in Table 3.

Step 5: Deformation monitoring allowable deformation value and limit deformation allowable value.

Through previous measurement experience, the surrounding rock pressure-time relationship curve after support is simplified as an exponential function (Eq. 5).

$$P_i = P_0 \cdot e^{-0.385/t} \tag{5}$$

Where: P_i is the surrounding rock pressure at any moment; P_0 is the surrounding rock pressure when the support is stabilized; t is time.

The variation curve of elastic modulus of shotcrete in relation to age is obtained in the laboratory as in Eq. 6.

$$E(t) = 24.7(1 - 0.37e^{-0.008t} - 0.63e^{-0.095t}) \tag{6}$$

The allowable deformation value of the structure under the design value of the surrounding rock pressure is calculated by the variable stiffness incremental method, and then the surrounding rock pressure is increased until the first plastic hinge appears in the shotcrete layer, so that the allowable value of the ultimate deformation of the structure can be obtained, and the results of the calculation are shown in Table 4.

Table 4. Table of deformation value calculation results.

Project	Allowable deformation value (mm)		Limit deformation allowable value (mm)	
	ΔUy	ΔUx	ΔUy	ΔUx
IV	21.0	300	2.87	0.33

The above obtained tunnel excavation allowable deformation value and limit deformation allowable value, construction can be monitored through the site, evaluation of the safety of the support structure, and dynamic adjustment.

4 ENGINEERING APPLICATIONS AND PRACTICES

To validate the rationality of Total Safety Factor Method, a comprehensive large-scale tunnel structure model test system was developed, focusing on structural testing. Various working conditions, including unsupported cavern, shotcrete layer, bolt-rock bearing arch structure, spraying and anchoring combination structure, and second lining, were simulated. Single-layer and multi-layer supporting structure bearing tests were conducted under these conditions. The model tests involved monitoring the internal stress and strain of the surrounding rock, tunnel displacement, and anchor strain. The damage state and load-bearing capacity of both the surrounding rock and supporting structure were analysed, and their deformation and force characteristics were studied. To facilitate the tests, a model testing device and monitoring schematic diagram were employed (refer to Figure 6).

Table 5 presents a comparison between the theoretical and experimental results of the load carrying capacity for each working condition in the model tests. The test results show a disparity ratio between the theoretical and experimental load carrying capacities ranging from 13% to 27%, and a disparity ratio of ultimate load carrying capacity ranging from 19% to 44%. Notably, the test results exhibit higher values than the theoretical results, indicating that the theoretical design adopts a conservative approach. Total Safety Factor Method demonstrates enhanced accuracy in predicting structural breakage locations and the overall structural state. The theoretical results of the calculations, although conservative, are not excessively so. As a result, this method is deemed suitable for application in the design of actual engineering structures. Overall, the model tests provide empirical evidence supporting the practicality and effectiveness of Total Safety Factor Method, further affirming its merit as a reliable tool for designing tunnel support structures.

Meanwhile, Numerous field tests have been conducted in the Laolingang, Wanjiashan Tunnel, and Xingshan East Tunnel of the Yichang to Xingshan High-Speed Railway project. These tests specifically focused on analysing the surrounding rock contact pressure and the performance of the initial support

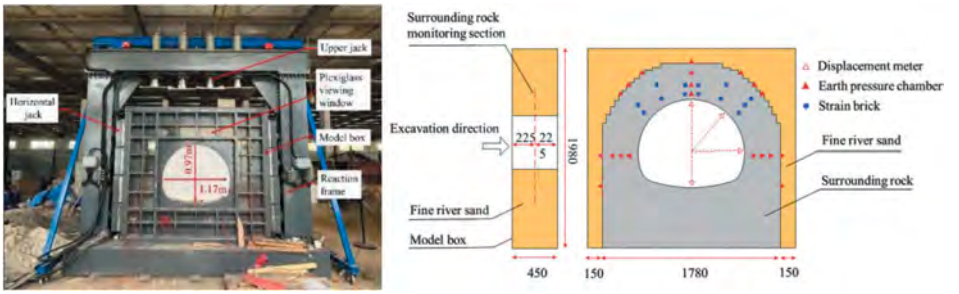

Figure 6. Model testing device and monitoring schematic diagram.

Table 5. Comparison table of theoretical and experimental results of load carrying capacity for each working condition.

Project	Design load capacity			Limit load capacity		
	Test value/ kPa	Theoretical value /kPa	Disparity ratio /%	Test value/ kPa	Theoretical value /kPa	Disparity ratio /%
Unsupported	/	/	/	/	/	/
Shotcrete layer 2cm	100	73	-27.00%	180	126	-30.00%
Shotcrete layer 4cm	140	108	-22.86%	360	232	-35.56%
Second lining	120	90	-25.00%	260	144	-44.62%
Bolt-rock bearing arch	90	65	-27.78%	100	77	-23.00%
Encrypted bolt-rock bearing arch	140	100	-28.57%	220	141	-35.91%
Shotcrete layer 2cm &Bolt-rock bearing arch	160	144	-10.00%	270	199	-26.30%
Shotcrete layer 2cm &Encrypted bolt-rock bearing arch	200	155	-22.50%	450	334	-25.78%
Multi-layer supporting	220	191	-13.18%	400	326	-18.50%

system. The results of the field tests indicate that the designed value of the surrounding rock pressure exceeds the measured pressure. This observation highlights that the designed value adequately accounts for the most unfavourable loading conditions. It demonstrates the capability of the design to encompass extreme scenarios. Moreover, the design safety factor aligns well with the actual working conditions. This finding confirms that the optimized support parameters derived from Total Safety Factor Method meet the requirements of safety factor.

The extensive field tests provide substantial evidence supporting the robustness and reliability of Total Safety Factor Method in designing tunnel support structures. It installs confidence in the practical application of this method in engineering projects. Overall, the field tests conducted in the Laolingang, Wanjiashan Tunnel, and Xingshan East Tunnel underscore the effectiveness of Total Safety Factor Method, ensuring the satisfaction of safety factor requirements and enhancing the stability and security of tunnel construction projects.

Theoretical results based on Total Safety Factor Method were applied to the engineering design of Yichang to Xingshan High-speed Railway, Ningbo to Zhoushan High-speed Railway (TANG, et al.,2019), Shenzhen Airport (Hezhou) to He'ao Expressway (XIAO,et al.,2022), and Qingdao Jiaozhou Bay Second Submarine Tunnel(XIAO, et al.,2023), as shown in Figure 7,which realized the design of the support structure of high-speed railway tunnels and multi-cavity tunnels with small clearances in space based on the premise of the safety factor analysis. In addition, the results are also applied to the safety assessment of the Sichuan-Tibet Railway tunnel, the general map of tunnels in the railroad industry, and the concealed subway station.

5 CONCLUSIONS

The Total Safety Factor Method has been verified through various means, such as on-site testing, modelling tests, and numerical calculations. These practical applications have demonstrated the effectiveness and

Table 6. Comparison table of theoretical and measured results.

Number	Type	Lithology	Construction zone	Section	Depth	Measured rock pressure	Theoretical rock pressure	Measured shotcrete safety factor	Designed shotcrete safety factor
1	IIa	Mafic granodiorite	Wanjiashan Tunnel inclined shaft	DK39 +620	244	8.32	8.42	16.04	14.26
2	IIIa	Dolomitic limestone	Laolingang Tunnel inlet	DK17 +200	115	33.01	10	6.64	22.16
3	IIIa	Mafic granodiorite	Wanjiashan Tunnel inclined shaft	DK39 +500	210	10.01	39.5	2.47	2.35
4	IVb	Dolomitic limestone	Laolingang Tunnel inlet	DK17 +280	143	70.42	117	13.83	4.91
5	IVk1	Mudstone	XingShan east Tunnel inclined shaft	DK90 +750	779	317.66	800	0.95	0.93
6	IVk1	Carbonaceous shale	Xingshan east Tunnel flat guide exit	DK94 +450	570	457.61	634	2.63	1.15
7	IVk1	Carbonaceous shale		DK94 +400	528	/	597.3	2.5	1.22

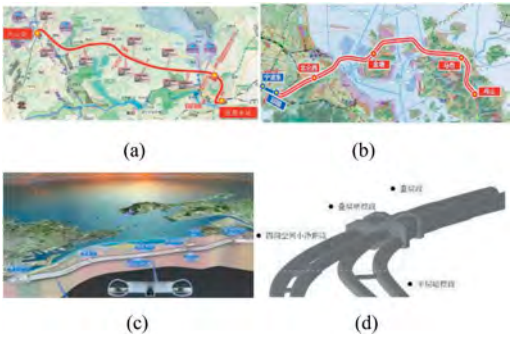

Figure 7. (a) Yichang to Xingshan High-speed Railway (350km/h) (b) Ningbo to Zhoushan High-speed Railway (250km/h) (c) Qingdao Jiaozhou Bay Second Submarine Tunnel (d) Shenzhen Airport (Hezhou) to He'ao Expressway.

reliability of Total Safety Factor Method in designing tunnel support structures. The method has proven its ability to ensure the safety and stability of tunnels while considering both technical and economic aspects. Building on these successful implementations, there are plans to further expand the application of Total Safety Factor Method in the railway system. Efforts will be made to establish industry standards and specifications, aiming to promote widespread adoption of this tunnel design method. This initiative reflects China's commitment to independent innovation and showcases the country's advanced levels of engineering expertise.

In conclusion, Total Safety Factor Method has gained recognition and validation through its application in various tunnel projects in China. With continued development and standardization, it is expected to become a widely adopted design method for tunnels, characterized by its remarkable technical and economic advantages.

REFERENCES

Rabcewicz LV, 1956. Effect of modern constructional methods on tunnel design. Water Power Dec. Vienna, Austria.

PIETRO Lunardi, 2008. Design and Construction of Tunnels: Analysis of Controlled Deformation in Rock and Soils. Berlin Heidelberg, Germany.

WANG Zhijian, 2018. Research on Key Technology of Large Cross-sectional Mechanized Construction of Zhengzhou-Wanzhou High-speed Railway Tunnel. Tunnel Construction, 38(08):1257–1270.

XIAO Mingqing, 2020. Total Safety Factor Method of Tunnel Support Structure Design. China Communications Press Co.Ltd. Beijing, China.

XIAO Mingqing, CHEN Libao, XU Chen, et al, 2018. Calculation Study of Support Parameters of High-speed Railway Tunnel. Tunnel Construction, 38(03): 406–413.

XIAO Ming-qing, XU Chen, WANG Shao-feng, 2019. Calculation and Study on the Structure Safety of Railway Tunnel Standard Drawings of China. Railway Standard Design, 63(01):92–98.

XIAO Mingqing, 2019. Exploration on the Several Problems of Tunnel Design with the Total Safety Factor Method. Journal of Railway Engineering Society, 36 (01): 65–69.

XIAO Mingqing, 2020. Design of Railway Tunnel Support Structure Based on Overall Safety Factor Method. China Railway, (12): 82–88.

XIAO Mingqing, XU Chen, 2020. Discussion on stability analysis method of tunnel surrounding rock based on critical stable section. Rock and Soil Mechanics, 41(05): 1690–1698.

XIAO Mingqing, XU Chen, 2021. Study on the Criterion and Method for Distinguishing Local Support and Systematic Support of Tunnel. Railway Standard Design, 65(10):44–49.

XIAO Mingqing, XU Chen, 2019. Research on the Representative Value of Deep Buried Tunnel Surrounding Rock Pressure Based on Total Safety Factor Method. Journal of Railway Engineering Society, 36(02):64–69.

XIAO Ming-qing, XU Chen, YANG Jian, et al, 2023. Study on identification technology of tunnel surrounding rock failure zone based on continuous discontinuous analysis theory. Rock and Soil Mechanics. 1–10 [2023-10-16].

XU Chen, XIAO Mingging, XIE Biting, et al, 2023. Universal Calculation Method for Design Values of Tunnel Surrounding Rock Pressure under Different Burial Depth Conditions. Journal of Railway Engineering Society, 40(06): 62–68.

XIAO Mingqing, XU Chen, 2019. Modification and Application of Design Method for Total Safety Factor of Multi-layer supporting Tunnel. Tunnel Construction, 39 (03): 421–429.

XIAO Ming-qing, 2018. Discussion on Design Method of General Safety Factor of Multi-layer supporting Tunnel. Journal of Railway Engineering Society, 35(01): 84–88.

XIAO Mingqing, XU Chen, 2019. Study on Allowable Deformation Value of Tunnel Based on Total Safety Factor Design Method[J]. Journal of Railway Engineering Society, 36(12): 48-52+70.

TANG Xiongjun, XIAO Mingqing, JIAO Qizhu, et al, 2021. Investigation of Overall Design and Key Technology of Jintang Subsea Tunnel of Ningbo-Zhoushan Railway. Railway Standard Design, 65(10): 20–25.

XIAO Mingqing, XU Chen, ZHENG Qiang, et al, 2022. Study on the Support Structure Design of Spatially Small-spaced Four-tube Section of He'ao Tunnel. Modern Tunnelling Technology. 59(02): 1–10.

XIAO Mingqing, SUN Wenhao, QU Liging, et al, 2023. Study on General Design of Second Jiaozhou Bay Subsea Tunnel. Tunnel Construction, 43(02): 199–216.

Tunnelling for a Better Life – Yan, Celestino, Thewes & Eberhardt (Eds)
© 2024 The Author(s), ISBN 978-1-032-80042-4
Open Access: www.taylorfrancis.com, CC BY-NC-ND 4.0 license

Considerations of the coefficient of subgrade reaction forces on seismic response displacement method of a double-circular shield tunnel

Min Xu* & Takashi Manabe
Science Solutions Division, Mizuho Research & Technologies, Ltd, Chiyoda-ku,Tokyo, Japan

ABSTRACT: In this paper, we investigate the seismic analysis of the cross-section of a double-circular shield tunnel using the seismic esponse displacement method. In the seismic response displacement method, we consider the ground displacement during an earthquake as the displacement of the ground spring. We discuss the calculation method of the coefficient of subgrade reaction used in the seismic response displacement method by comparing it with the results obtained from 3D dynamic FEM analysis. Specifically, we effectively estimate the coefficient of subgrade reaction by thoroughly examining the ground deformation obtained from the 3D dynamic FEM analysis.

Keywords: Seismic response displacement method, Coefficient of subgrade reaction, Double-circular shield tunnel, 3D dynamic analysis, M-K method

1 INTRODUCTION

In the seismic response displacement method, the interaction between the shield tunnel segments and the ground during an earthquake is simulated by utilizing ground springs. However, there has been no established method for determining the ground spring constants, making it one of the significant areas of investigation until now.

The authors conducted an analysis using the 3D dynamic finite element method (FEM) and the 2D beam-spring model based on M-K method in the response displacement method for the cross-sections of a double-circular shield tunnel. In the case of the 2D beam-spring model based on M-K method[1),2)], they compared the results obtained using ground spring constants for cases where tangential shear stresses are not fully transmitted of the traditional shear Stress in the tangential direction and where they are fully transmitted. These ground spring constants were calculated from FEM analysis[1)]. The results indicated that careful attention is required in determining ground spring constants for the double-circular shield tunnel.

This study focuses on the determination of ground spring constants using the FEM analysis model. It estimates ground spring constants for the general-section segment and the gull-section segment of the double-circular shield tunnel using respective methods. It then conducts analyses using the response displacement method and compares the results with those obtained through the 3D dynamic FEM analysis method. Regarding subgrade reaction forces, the study considers four calculation methods, 1) The unit forced displacement method using the FEM analysis model (referred to as the δ=1m method); 2) The unit load method using the FEM analysis model (referred to as the F=1kN method); 3) The theoretical solutions for cases where tangential shear stresses in the ground are not fully transmitted to the lining (referred to as the Full-slip method) based on 2D elastic theory[1)]; and 4) Theoretical solutions for cases where tangential shear stresses in the ground are fully transmitted to the lining (referred to as the No-slip method) based on 2D elastic theory[1)]. Furthermore, the shield tunnel model is implemented using the beam-spring model based on M-K method. The beam-spring model is a structural model that represents the segment body as a beam element, the segment joint as a spring with rotational components, and the ring joint as a shear spring. The rotational spring constant of the segment joint is calculated using the Murakami-Koizumi method (M-K method)[2)]. The interaction between the tunnel and the ground is expressed using ground springs. The schematic diagram is shown in Figure 1.

2 THE RESPONSE DISPLACEMENT METHOD FOR A DOUBLE-CIRCULAR SHIELD TUNNEL[1)]

The seismic analysis of shield tunnels in semi-infinite horizontal layered ground often employs the response displacement method using the beam-spring model based on M-K method[2)], which is

*Corresponding author: min.xu@mizuho-rt.co.jp

DOI: 10.1201/9781003495505-57

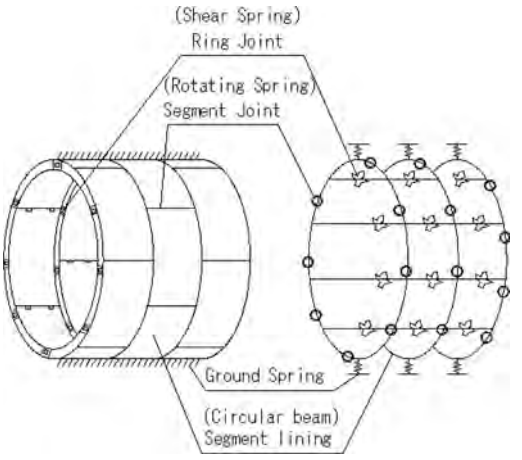

Figure 1. Schematic diagrams of the beam-spring model based on M-K method.

a relatively straightforward computational approach and widely used in the seismic design of underground structures. In this method, seismic ground displacements obtained from one-dimensional overlapping reflection theory, as shown in Figure 2, are input as ground spring displacements, the method directly applies circumferential shear forces and conducts the analysis. For a double-circular shield tunnel with an external diameter of 3.15m at a depth of 14.0m in semi-infinite horizontal layered ground, as illustrated in Figures 3 and 4, the authors have previously compared the results of the 3D dynamic FEM analysis and the 2D M-K method of beam-spring model's response displacement method. When comparing the results of both methods to those obtained from the 3D dynamic FEM analysis, it was found that the results of both methods are nearly identical for the general-section segment of the tunnel, excluding the gull-section segment. However, differences in sectional forces appeared in the gull-section segment.

Regarding the 2D M-K method of beam-spring model, the authors calculated subgrade reaction coefficients for the No-slip method, including previously established subgrade reaction coefficients for the Full-slip method, as shown in Figure 2. They conducted analyses using both sets of coefficients. When comparing the results of these analyses with the 3D dynamic FEM analysis results, it was observed that the differences in the gull-section segment were small, but the differences in the general-section segment were significant[1]. Based on the above findings, it is evident that in the analysis of the response displacement method for double-circular shield tunnels, different estimation methods are required for calculating the subgrade reaction coefficients for the general –section segment and the gull-section segment.

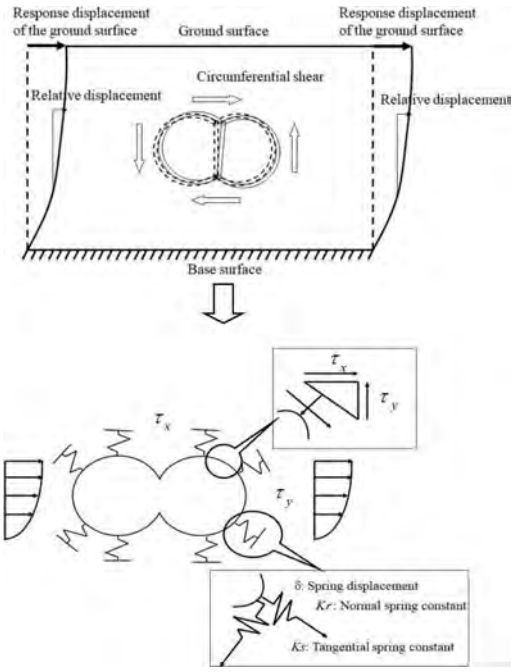

Figure 2. Schematic diagrams of the response displacement method using the 2D beam spring model based on M-K method.

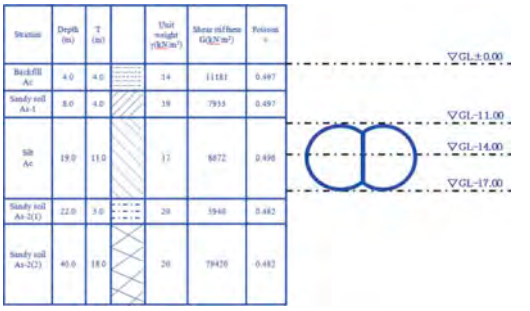

Figure 3. Ground distribution map.

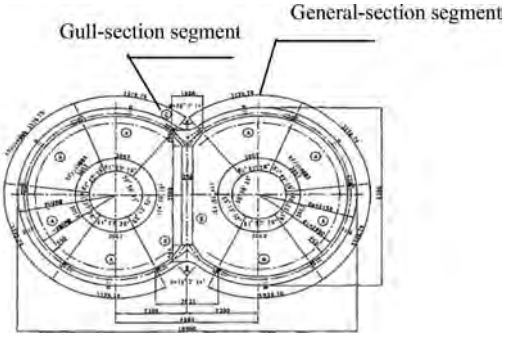

Figure 4. Shield tunnel structural diagrams.

3 CALCULATION METHOD FOR SUBGRADE REACTION COEFFICIENTS

There are several methods to determine subgrade reaction coefficients. In this context, the four calculation methods were used, which are δ=1m method, F=1kN method, Full-slip method and No-slip method. They are used to calculate subgrade reaction coefficients. These coefficients are then utilized in response displacement based analyses (Case 1 to Case 4). The results from these analyses are compared with the results from the 3D dynamic FEM analysis (Case 5) to assess the methods for calculating subgrade reaction coefficients.

3.1 *δ=1m method (Case1)*

Here, a finite element analysis (FEM) model of the cavity ground was created as shown in Figure 5[3]. Unitary forced displacements were applied at various points within the cavity. Subsequently, ground spring constants around the segments in contact with the ground were determined from the resulting forces. In the previous analysis (Case 1), only horizontal forces (in the X-direction of the global coordinate system as depicted in Figure 5) were considered for subgrade reaction calculations. However, in this analysis, unitary forced displacements were applied in both horizontal and vertical directions (in the Y-direction of the global coordinate system shown in Figure 5), and subgrade reaction forces were calculated. The calculated subgrade reaction forces in the global coordinate system were transformed into the element coordinate system (tangential-normal direction) as shown in Figure 6.

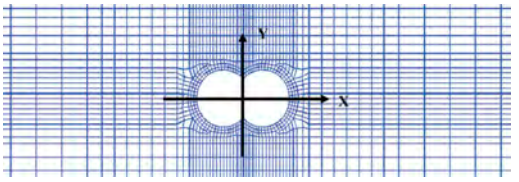

Figure 5. Illustration of the FEM calculation model.

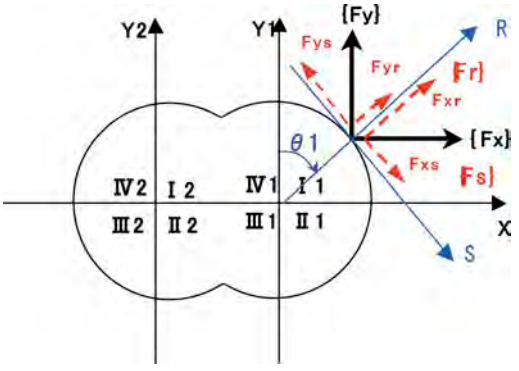

Figure 6. Illustrations depicting the global coordinate system and element coordinate system.

These subgrade reaction forces were used as the ground spring constants for Case 1, and analysis was conducted using the response displacement method.

The subgrade reaction forces, estimated using the δ=1m method for various points within the cavity, as presented in Figure 7, are depicted in Figures 8 and 9. Specifically for δ=1m, the subgrade reaction forces for general-section segments of the double-circular shield tunnel increase with depth. In other words, the left and right subgrade reaction forces for general -section segments are symmetrical with respect to depth.

It may be assumed that the same ground spring constants can be set for segments at the same depth. However, the subgrade reaction forces for gull-section segments at the same depth differ from those of general-section segments, suggesting that different ground spring constants must be assigned.

Here, as for the ground spring constants in the response displacement method, the subgrade reaction forces in the X and Y directions were converted into segment element coordinate systems, and their absolute values were calculated. The distribution of the estimated ground spring constants is shown in Figures 10 and 11. As depicted in Figure 10, the shield tunnel is divided into five segments. The average values of subgrade reaction forces at various points within each segment were calculated. The ground spring constants were then determined based on these average values, and the response displacement method analysis was conducted. The calculated ground spring constants are presented in Table 1.

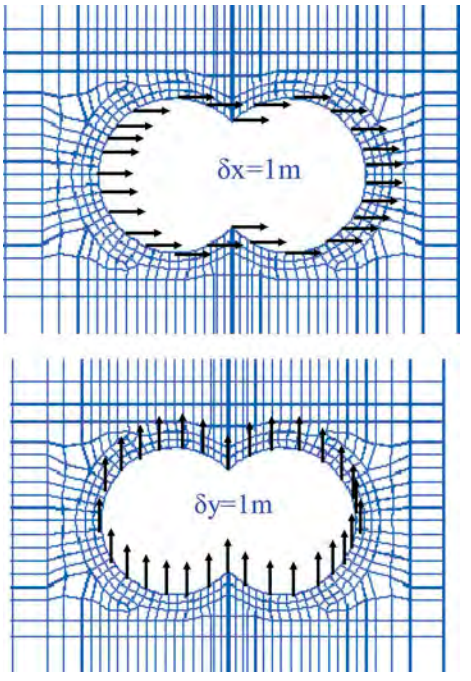

Figure 7. Illustrations of the δ=1m method calculation model.

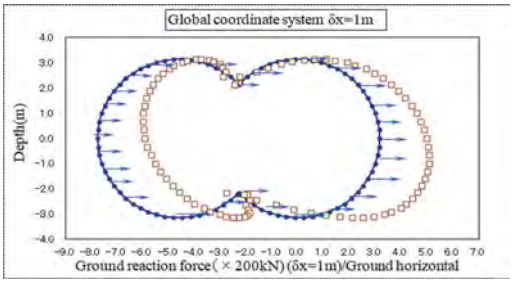

Figure 8. Distribution of subgrade reaction forces in the global coordinate system for δx=1m.

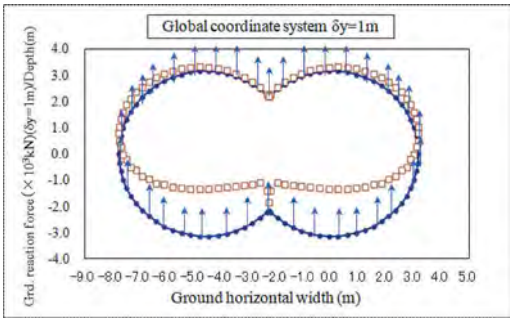

Figure 9. Distribution of subgrade reaction forces in the global coordinate system for δy=1m.

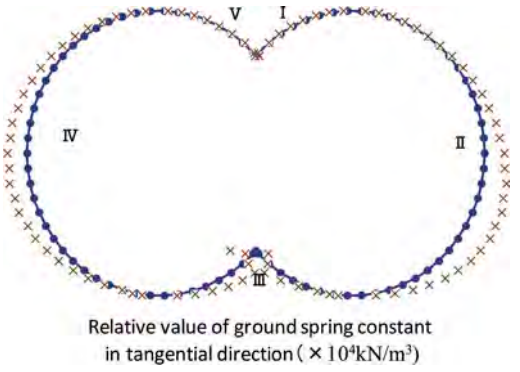

Figure 10. Distribution of tangential ground spring constants calculated by the δ=1m Method.

3.2 *F=1kN Method (Case2)*

Next, as shown in Figure 12, a unit load was applied to each point within the cavity[4], and the values of ground displacement were calculated. The estimated ground displacements at various points within the cavity are illustrated in Figures 13 and 14.

Here, as for the ground spring constants in the response displacement method, the subgrade reaction forces in the X and Y directions were converted into segment element coordinate systems, and their absolute values were calculated. The distribution of the

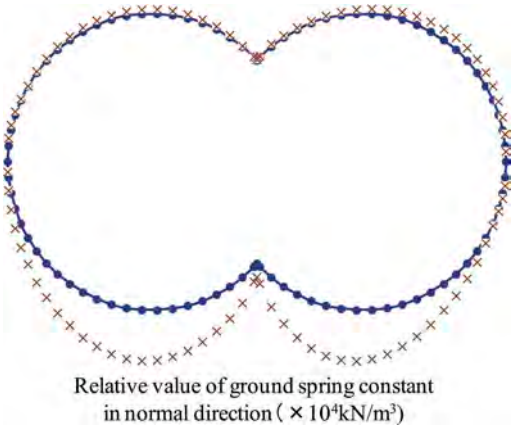

Figure 11. Distribution of normal direction ground spring constants calculated by the δ=1m method.

Table 1. Results of ground spring constants calculated by the δ=1m method (kN/m³).

δ=1m	I	II	III	IV	V
Tangential Direction	5.200 ×10²	3.550 ×10³	1.420 ×10⁴	3.098 ×10³	4.471 ×10²
Normal Direction	5.342 ×10²	4.290 ×10³	2.240 ×10⁴	4.708 ×10³	5.758 ×10²

estimated ground spring constants is shown in Figures 15 and 16. As in the case of Case 1, values from each point were used to divide the shield tunnel into five segments, and the average ground spring constants for each segment were calculated. The response displacement method analysis was then conducted using these calculated ground spring constants. The results are presented in Table 2.

3.3 *Full-slip Method (Case-3) and No-slip Method (Case-4)*

In 2D elastic theory, the relationship between the lining and the surrounding ground is depicted in the Figure 17. [5]

Here, the variables and parameters mentioned are,

P: Load(kN);

λ: Side pressure coefficient;

σ_R: Radial stress acting on the lining (N/mm^2);

$\tau_{R\theta}$: Tangential stress acting on the lining (N/mm^2);

u_s: Radial displacement of the lining (m);

v_s: Tangential displacement of the lining.(m);

E: Deformation modulus of the ground (kN/m^2);

E_s: Elastic modulus of the tunnel lining (kN/m^2);

ν: Soil's Poisson's ratio;

ν_s: Tunnel lining's Poisson's ratio;

I_s: Sectional second moment of area per unit width of the lining (m^4);

A_s: Cross-sectional area per unit width of the lining (m^2);

R : Outer radius of the lining (m)

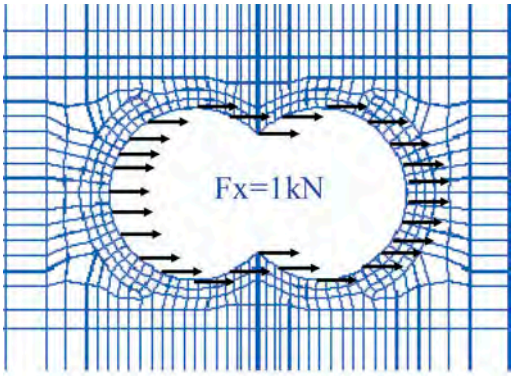

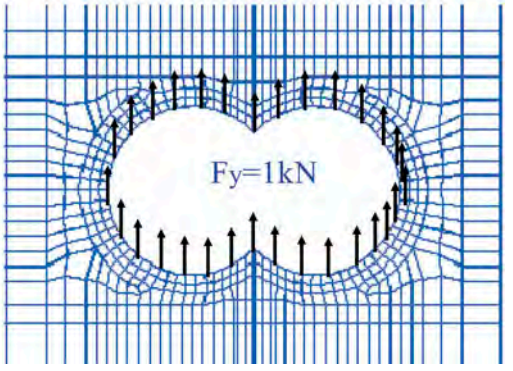

Figure 12. Illustrations of the F=1kN method model.

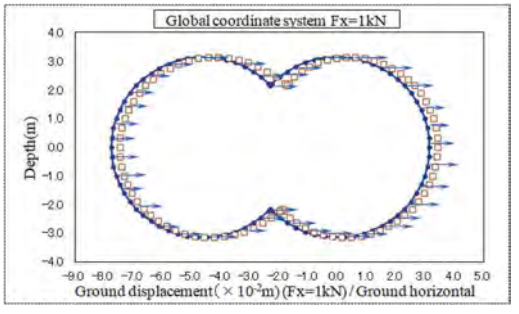

Figure 13. Distribution of ground displacement in the global coordinate system for Fx=1kN.

The theoretical solutions for cases where tangential shear stresses in the ground are not fully transmitted to the lining (referred to as the full-slip method) based on 2D elastic theory. The calculation formula for the full-slip method is relatively commonly used in various design guidelines[6]. The model is shown in Figure 17. The calculation formula is shown in Equation (1).

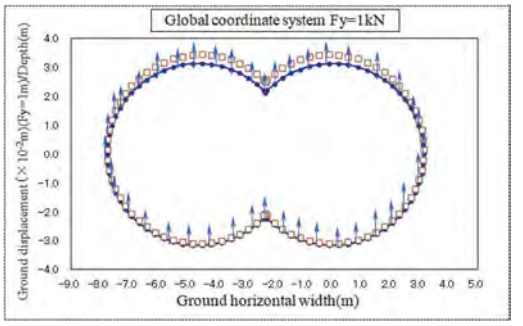

Figure 14. Distribution of ground displacement in the global coordinate system for Fy=1kN.

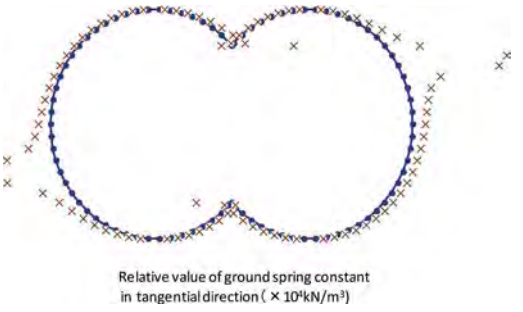

Figure 15. Distribution of tangential ground spring constants calculated by the F=1kN method.

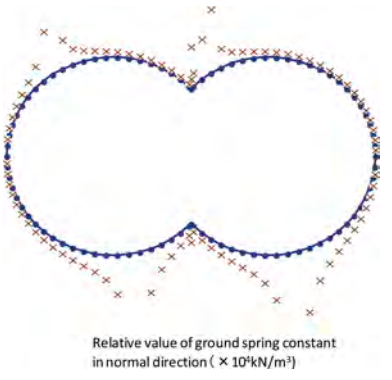

Figure 16. Distribution of normal direction ground spring constants calculated by the F=1kN method.

$$K_r = \frac{3E}{(1+\nu)(5-6\nu)R},\ K_s = \frac{1}{3}K_r \qquad (1)$$

Here, the variables and parameters mentioned are

K_r: Normal direction subgrade reaction coefficient (kN/m³);

Table 2. Results of ground spring constants calculated by the δ=1m method (kN/m³).

δ=1m	I	II	III	IV	V
Tangential Direction	1.360 ×10³	5.282 ×10³	4.384 ×10⁴	1.147 ×10⁴	4.305 ×10³
Normal Direction	7.580 ×10³	7.918 ×10³	2.286 ×10⁴	8.243 ×10³	1.492 ×10³

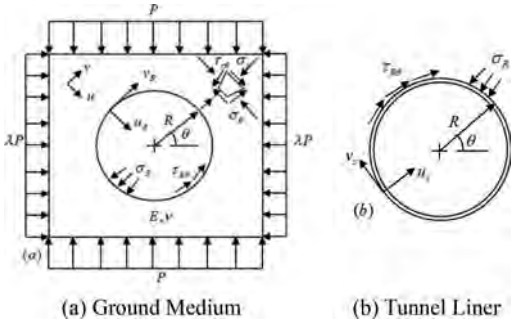

Figure 17. Image representation of 2D elasticity theory.

K_s: Tangential direction subgrade reaction coefficient (kN/m³);
E: Ground deformation modulus ($E=2(1+\nu)G$) (kN/m²);
R: Radius to the center of the segment (m);
ν: Poisson's ratio

$$\text{Normal direction}: K_r = \frac{(13-12\nu)E}{R(1+\nu)(3-4\nu)} \quad (2)$$

$$\text{Tangential direction}: K_s = \frac{(11-12\nu)E}{R(1+\nu)} \quad (3)$$

In the model of the 2D elastic theory method, these parameters are used in the equations and calculations for the Full-slip method and related analyses. Additionally, the calculation formula for the No-slip method is shown in Equation (2) and (3).

By using the methods mentioned above, the ground spring constants obtained using the Full-slip method and No-slip method for the ground conditions as shown in Table 3 are presented in Table 4.

Table 3. Ground property values.

Stratum		Thickness (m)	Unit weight γ (kN/m³)	Shear sti. G (kN/m²)	Poisson
B.fill	AC	4	14	11181	0.497
S. soil	AS-1	4	19	7933	0.497
Silt	AC	11	17	8672	0.496
S.soil	AS-2 (1)	3	20	5940	0.482
S.soil	AS-2 (2)	18	20	79420	0.482

Table 4. Ground spring constants calculated by the Full-slip method and No-slip method (kN/m³).

	Full-slip	No-slip
Tangential direction	2.856E+03	2.918E+04
Normal direction	8.569E+03	4.011E+04

4 CALCULATION RESULTS AND DISCUSSION

We conducted an analysis using the response displacement method with the subgrade reaction coefficients determined for each case (Case1 to Case4). The resulting section forces at the positions shown in Figure 18 and the section forces from the 3D dynamic FEM analysis (Case5) are presented in Table 5 to Table 10. The section force distribution for Case1 is shown in Figure 19. The section force distribution trends for each case are nearly the same. From the analysis results presented in Table 5 to Table 10, it can be observed that the bending moments of the upper gull-section segment at position (1) are nearly the same as those from the 3D dynamic FEM, but differences appear in axial and shear forces. At position (2), where the upper gull-section segment connects to the general-section segment, differences in section forces are apparent. At positions (3), (4), and (5), the bending moments for the general-section segment are almost the same, but differences appear in axial and shear forces. At position (6), where the lower gull-section segment connects to the general segment, the section forces are almost the same.

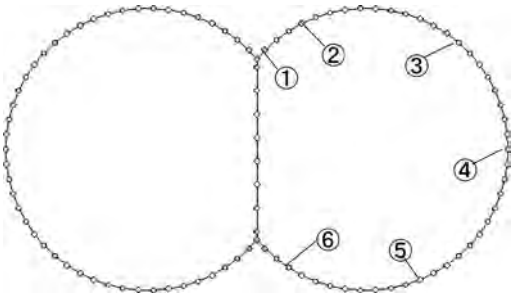

Figure 18. Cross-sectional force display positions.

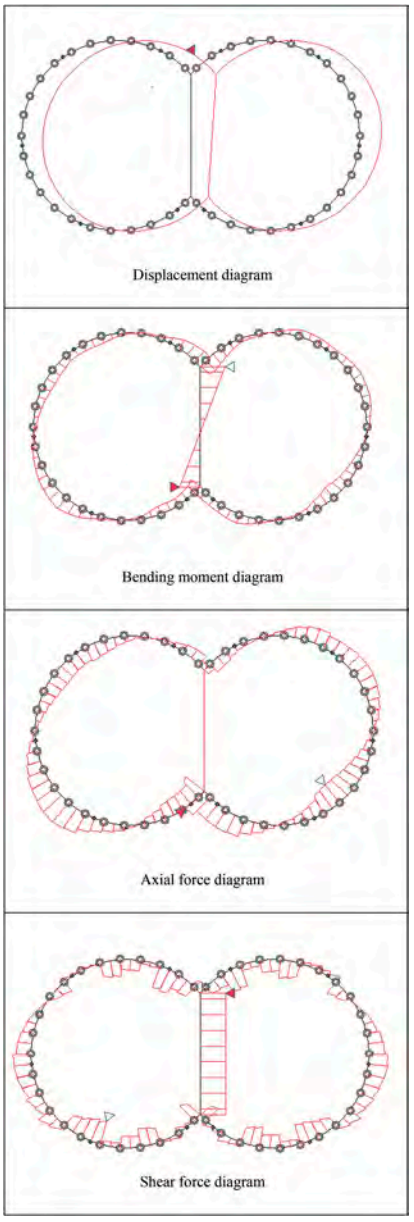

Figure 19. Cross-Sectional Force Distribution Diagrams in Case1.

Table 5. Comparison of Sectional forces at position-(1).

Position	Case	Bending.M (kNm)	Axial F. (kN)	Shear F. (kN)	Method
(1)	1	173.850	-60.824	-28.414	δ=1m
	2	175.890	-64.951	-34.957	F=1kN
	3	167.770	-67.083	31.636	Full-slip
	4	176.800	-111.870	50.926	No-slip
	5	171.720	-138.630	19.676	3D FEM

Table 6. Comparison of sectional forces at position-(2).

Position	Case	Bending.M (kNm)	Axial F. (kN)	Shear F. (kN)	Method
(2)	1	105.45	-18.781	128.93	δ=1m
	2	102.67	-21.343	132.72	F=1kN
	3	98.516	-25.535	126.990	Full-slip
	4	91.305	-59.722	141.070	No-slip
	5	138.470	-130.730	50.651	3D FEM

Table 7. Comparison of sectional forces at position-(3).

Position	Case	Bending.M (kNm)	Axial F. (kN)	Shear F. (kN)	Method
(3)	1	-71.94	69.744	52.302	δ=1m
	2	-70.378	72.986	49.215	F=1kN
	3	-68.418	66.615	48.012	Full-slip
	4	-67.077	138.170	37.464	No-slip
	5	-141.700	125.620	6.3407	3D FEM

Table 8. Comparison of sectional forces at position-(4).

Position	Case	Bending.M (kNm)	Axial F. (kN)	Shear F. (kN)	Method
(4)	1	-18.146	17.198	86.342	δ=1m
	2	-20.143	15.377	86.335	F=1kN
	3	-19.005	14.347	83.802	Full-slip
	4	-24.847	10.065	90.942	No-slip
	5	-32.455	40.799	103.600	3D FEM

Table 9. Comparison of sectional forces at position-(5).

Position	Case	Bending.M (kNm)	Axial F. (kN)	Shear F. (kN)	Method
(5)	1	85.673	-46.454	-131.96	δ=1m
	2	85.708	-58.568	-129.87	F=1kN
	3	83.348	-51.284	127.100	Full-slip
	4	81.310	-143.600	133.620	No-slip
	5	107.92	-102.31	99.174	3D FEM

5 CONCLUSIONS

In this study, we conducted an investigation into the proper configuration of ground spring constants in

Table 10. Comparison of sectional forces at position-(6).

Position	Case	Bending.M (kNm)	Axial F. (kN)	Shear F. (kN)	Method
(6)	1	-103.310	166.350	61.371	δ=1m
	2	-101.46	164.400	56.928	F=1kN
	3	-103.010	151.330	58.658	Full-slip
	4	-96.818	189.080	53.602	No-slip
	5	-119.450	117.240	82.134	3D FEM

the response displacement method for a shield tunnel with double-circular cross-sections. Analyses using the response displacement method with 3D dynamic FEM and a 2D beam-spring model based on M-K for the double-circular shield tunnel. For the 2D beam-spring model based on M-K method, we considered various cases, including applying unit displacements or unit loads in horizontal or vertical directions. We determined the ground spring constants for each case and compared the results obtained using the response displacement method with those from the 3D dynamic FEM analysis. As a result, it was found that the subgrade reaction forces for the general-section segments of the double-circular shield tunnel increase with depth. In other words, as the depth of the ground increases, the relative displacement responses become smaller, but the subgrade reaction coefficients become larger. Additionally, for general-section segments, the left and right subgrade reaction forces of the overlapping circular shape are symmetric. Therefore, it is sufficient to set the same ground spring constants for segments at the same depth.

However, for segments at the same depth, the subgrade reaction forces for the gull-section segments and the general-section segments are different, requiring the use of different ground spring constants. This study verifies the possibility of calculating ground spring constants from the response displacement method for the overlapping circular shield tunnel, but it is important to analyze and understand the characteristics of these springs with precision.

REFERENCES

1) Min Xu and Takashi Manabe, 2007, Considerations of the Coefficient of Subgrade Reaction on Seismic Deformation Method of Double-o-tube Shield Tunnel, Collection of papers from the 4th Japan-China Shield Technology Exchange Conference, pp.46–52 (in Japanese).
2) Hirotoino Murakami and Atushi Koizumi, 1978, Study On Load Bearing Capacity And Mechanics Of Shield Segment Ring, Japanese Journal of JSCE, No.727 (in Japanese).
3) Jsce,2006, A seismic Design of Cut and Cover Tunnel, Tunnel library 9 of JSCE, Maruzen Co., Ltd. (in Japanese).
4) =Kazuhiko Kawashima, 1995, A seismic Design of underground structures, Kashima Publishing, (in Japanese).
5) Einstein, H.H. and Schwartz, W., Simplified Analysis for Tunnel Support, Proc. ASCE, GT4, (1979), 499–518.
6) For example, 1997, Railway Structure Design Standard/ Explanation Shield Tunnel, Railway Technical Research Institute (in Japanese).

Tunnelling for a Better Life – Yan, Celestino, Thewes & Eberhardt (Eds)
© 2024 The Author(s), ISBN 978-1-032-80042-4
Open Access: www.taylorfrancis.com, CC BY-NC-ND 4.0 license

Analysis of key technologies in structural design of prefabricated station of Shenzhen Metro

Zhuang Xu, Dong Meng & Renpu Liu
Shenzhen Metro Group Co., Ltd., Shenzhen, China

Mengting Li
Beijing Urban Construction Design and Development Group Co., Ltd., Beijing, China

ABSTRACT: This paper takes the prefabricated station under the inner support system of Shenzhen Metro as the engineering background. The key design techniques for prefabricated middle plate, beams and columns in station were proposed. And the influence of geological conditions on the deformation, stress, and joints internal forces of the station structures was analyzed. Research shows that the design of prefabricated middle plates, beams and columns in station includes three key techniques: overall flow assembly process, stress analysis of prefabricated middle plate, and design of large open pore in the precast middle plates, beams and columns system. Among them, the overall flow assembly process of prefabricated station needs to solve the problem of continuous flow assembly in the vertical direction of the foundation pit and the longitudinal direction of the station. The stress of prefabricated middle plates mainly includes three stages: factory prefabrication, lifting and transportation, on-site assembly, and normal use. The design of large pore in prefabricated middle plates needs to consider the shear effect between the prefabricated plates, so that the prefabricated plate, the laminated layer, and the longitudinal beam form an overall bearing horizontal force in the plane of the middle plate. For the overall structure of prefabricated subway station, the geological conditions have a significant impact on the internal forces of the roof span, arch foot support, and top corner joints, while the impact on the internal forces of the side walls is relatively small. The top corner joints of a prefabricated subway station are the weak part. When the station is located in a fill layer, the top corner joints need to be strengthened in design, and when the station is located in a hard plastic layer, the safety reserve of the top corner joints is sufficient.

Keywords: Shenzhen Metro, prefabricated station, key design techniques, geological conditions, internal forces and deformation analysis

1 INTRODUCTION

In recent years, prefabricated subway station technology has been promoted nationwide. Since the first prefabricated station in China was applied at Yuanjiadian Station on Changchun Metro Line 2 in 2012, prefabricated station technology has been applied in cities such as Jinan, Shanghai, Guangzhou, Harbin, Qingdao, Shenzhen, and Wuxi in China. The construction process of prefabricated stations involves prefabricating components in the factory and using "building blocks" on site to assemble each component into a whole using connecting joints. Compared with cast-in-place stations, this construction method has advantages such as high production efficiency, good construction quality, less labor, and minimal environmental impact. The research work related to prefabricated subway stations is the theoretical and technical support for its promotion and application.

Yang[1-7] conducted a systematic study on the design, calculation methods, component partitioning, joint types, joint mechanical properties, stiffness characteristics, structural static and dynamic characteristics, and station waterproofing of prefabricated stations. Ding[8-9] analyzed the stress and deformation mechanism of a single ring structure of a prefabricated station after being assembled into a ring, and studied the horizontal and vertical seismic responses of the prefabricated station, which showed that the prefabricated station structure has excellent seismic performance under earthquake and meets seismic requirements. Peng et al. [10] analyzed the entire construction process of prefabricated station structures through a combination of numerical simulation and on-site measurement. Tao et al. [11] established a three-dimensional solid model to study the effects of different support methods on structural internal forces, stresses, and deformations.

DOI: 10.1201/9781003495505-58

The prefabricated station in Changchun is based on an anchor cable support foundation pit system, where the floor slab and beam columns adopt a cast-in-place plan. The existing literature on prefabricated stations mainly focuses on the stress characteristics of joints and prefabricated peripheral lining structures, while there is less research and application on the mid floor structure system under the internal support foundation pit support system. This article takes prefabricated stations in Shenzhen as the research object, and conducts research on the key structural design of prefabricated middle plate beams and columns. Subsequently, the influence of geological conditions on the force deformation of prefabricated stations was analyzed. Through the study of prefabricated middle plates in prefabricated stations, the full section assembly of subway stations has been achieved, which improve the assembly rate of subway stations and the efficiency of on-site flow assembly. This provides valuable experience and methods for the subsequent design of prefabricated station structures.

2 PROJECT OVERVIEW

The prefabricated station section of Shenzhen Metro adopts a column arched structure section without column platform in the station hall. The total length of the station is 260 m. The two ends of the station are reinforced concrete cast-in-place structures, and the middle section of the station is 194 m long and adopts a prefabricated structure. The prefabricated station is an underground two-story structure with a single arch and large span structure, as shown in Figure 1. The structural dimensions of the station include a total width of 22.3 m, a height of 17.35 m, a top plate thickness of 1.2 m, a side wall thickness of 0.8 m, a bottom plate thickness of 1 m, a middle plate thickness of 0.45 m, and a station ring width of 2 m.

The first ring structure, using prefabricated components, consists of bottom plate A, side wall block B, top plate C, middle plate, and middle column. The joint between the bottom plate and the side wall is called the AB joint, and the joint between the side wall and the top plate is called the BC joint. The fertilizer trough between the main structure and the enclosure is transmitted through screws and concrete.

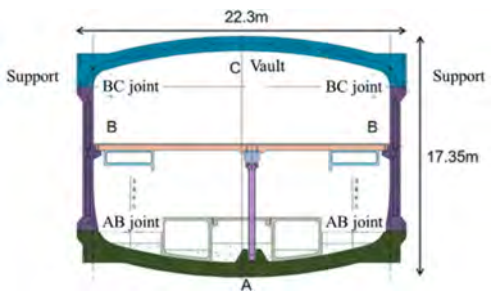

Figure 1. Cross-section of prefabricated station.

According to the structural characteristics of prefabricated stations, the design of prefabricated middle plate beam column structures has the following key and difficult points:

1) Adopting a prefabricated middle plate beam column system. The research on the assembly process of the entire prefabricated station is a key focus.
2) The design of the middle plate needs to meet the stress requirements of lifting construction, assembly construction, foundation pit stress conversion, normal use, and other working conditions, which are significantly different from cast-in-place structures. The stress analysis of the middle plate is the focus of the middle plate design.
3) There are large holes in the middle board. The design and stress analysis of large openings using a prefabricated middle plate beam column system is a difficulty in middle plate design.

3 RESEARCH ON KEY TECHNOLOGIES FOR DESIGN OF PREFABRICATED MIDDLE PLATE BEAMS AND COLUMNS

3.1 *Research on assembly steps*

The difficulties in the assembly process of assembled stations under the prefabricated middle plate beam column system need to solve the vertical and vertical continuous flow assembly problems of the foundation pit and the station. The key to vertical flow assembly of foundation pits is to combine the dismantling and replacement of the support system within the foundation pit. The prefabricated structural plates assembled first are used to form the replacement support of the foundation pit, and then the support of adjacent foundation pits is removed, providing installation conditions for the subsequent assembly of prefabricated plates; The key to the vertical continuous flow assembly of the station is to use the support spacing to advance the assembly of the bottom plate, center column, and center beam in the station, providing conditions for the vertical ring assembly of prefabricated components in the foundation pit. By connecting the vertical components of the foundation pit with the vertical assembly of the station, a flow assembly process for the full section prefabricated station under the open excavation and internal support foundation pit support system is formed. The vertical flow construction sequence of prefabricated stations is shown in Table 1.

Compared with the cast-in-place subway station foundation pit, the horizontal spacing of the support and the width of the diaphragm wall of the prefabricated station have been increased (the steel support spacing of the cast-in-place station foundation pit is generally 3 m, and the width of the diaphragm wall is generally 6 m). To ensure the stress feasibility of foundation pit support, finite element modeling

Table 1. The longitudinal construction steps.

Construction steps	Step 1	Step 2	Step 3
Content	Foundation pit excavation and support	Advance assembly of base plate A1-A10 blocks	Assembly of central column, central beam, and first ring
Illustration		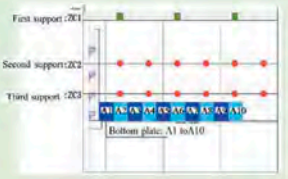	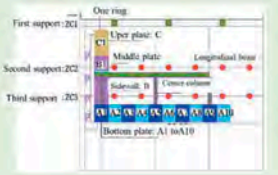
Construction steps	Step 4	Step 5	Step 6
Content	Dismantle the second and third supports, assemble side wall blocks and middle plates	Assembly of remaining side walls and middle plates	Enter the next cycle of assembly

analysis was conducted on the stress of the support before and after the assembly of the middle plate, as well as the deformation of the retaining structure, as shown in Figure 2. The concrete grade of the enclosure structure is C35, the wall thickness is 0.8 m, the maximum size of the plate shell unit used is 0.8 m, the soil volume weight is 19.5 kN/m^3, and the lateral pressure coefficient is 0.55. The calculation results are shown in Table 2. The calculation analysis shows that the horizontal displacement of the retaining structure in the above working conditions is less than the control value (30mm), meeting the requirements for deformation control of the foundation pit. The Q345 steel support for foundation pit support has an outer diameter of 800 mm and a wall thickness of 16 mm. The calculated stable stress ratio is 0.68 (less than 1), and the bearing capacity meets the requirements. Therefore, increasing the horizontal spacing of the prefabricated station foundation pit support and the width of the ground connecting wall, as well as meeting the stress requirements of the flow assembly process for the enclosure and middle plate.

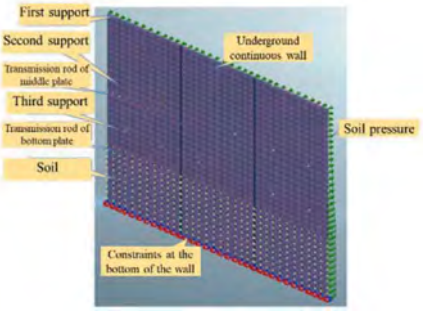

Figure 2. Load- structure finite element calculation model.

3.2 *Stress analysis of prefabricated middle plate under different working conditions*

There are differences in the design of prefabricated mid slabs between subway stations and cast-in-place stations, and prefabricated middle slabs need to cover various stress conditions during the design stage. The prefabricated middle

Table 2. Axial force of support at middle plate and deformation of retaining structure.

Construction conditions	Condition 1	Condition 2	Condition 3	Condition 4
Description	Excavation of foundation pit	Replace the bottom plate and remove the third support	Assemble the first middle plate and remove the second steel support	Subsequent middle plate assembly
Deformation of enclosure (mm)	3.41	7.22	7.94	7.72
Support/Replacement axial force (kN)	2267 (Second support)	2450 (Second support)	3342 (Middle plate support)	3455 (Middle plate support)

plate undergoes three stages: factory prefabrication, lifting and transportation, on-site assembly, and normal use. For the above stress stages, the calculation conditions are as follows: lifting construction, assembly, foundation pit stress conversion, pouring of composite layer construction, decoration, equipment installation construction, short-term low water level during normal use, and long-term high water level during normal use. Considering that the equipment load borne by the middle plate in the equipment room area is greater than the crowd load borne by the public area, the middle plate in the equipment area is selected for calculation, as shown in Figure 3. The calculation results for each working condition are shown in Table 3. From Table 2, it can be seen that the axial force of the middle plate support replacement is 1671 kN-1727.5 kN per linear meter. In addition, in the first stage (condition 1 to condition 3), the internal force control condition of the prefabricated middle plate is the pouring middle plate composite layer, and its reinforcement ratio meets the requirements of bearing capacity and crack control. In the second stage (condition 4 to condition 6), the control condition is the high water level during the use stage, and the reinforcement ratio also meets the requirements for bearing capacity and crack control. The deformation calculation shows that the deformation of each working condition meets the stiffness requirements, and the maximum deflection of the prefabricated middle plate during the construction stage is the pouring composite layer working condition.

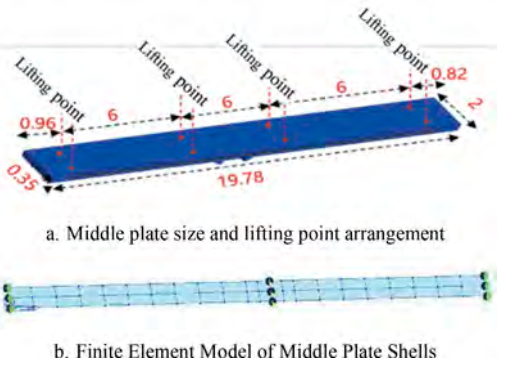

a. Middle plate size and lifting point arrangement

b. Finite Element Model of Middle Plate Shells

Figure 3. Middle plate size and graphic calculation model.

3.3 *Design and stress analysis of large holes in middle plate*

The stairs, escalators, and equipment in the station need to have large holes in the middle plate, such as the size of the hole in the escalator is 12m × 6m. In prefabricated stations, the opening design of the middle plate not only needs to meet the stress requirements during the use stage, but also needs to meet the stress requirements during construction stages such as transportation, lifting, and assembly. The design plan diagram of the large hole position in the middle plate during the construction and application phase is shown in Figure 4.

According to the force analysis results of the standard middle plate, the most unfavorable

Table 3. Results of middle plate's internal force under various working conditions.

Construction conditions	Condition 1	Condition 2	Condition 3
Description	Hoisting construction	Assembly and force conversion of foundation pit	Pouring laminated layer
Bending moment of support (kN·m)	45	202	243
Bending moment in the span (kN·m)	32	195	235
Shear force (kN)	39.5	130	166
Deformation in the span (mm)	0.56	11	13
Construction conditions	Condition 4	Condition 5	Condition 6
Description	Decoration and equipment installation	Normal use under low water levels	Normal use under high water levels
Bending moment of support (kN·m)	284	315	392
Bending moment in the span (kN·m)	277	307	243
Shear force (kN)	202	208	198
Deformation in the span (mm)	7	8.5	10

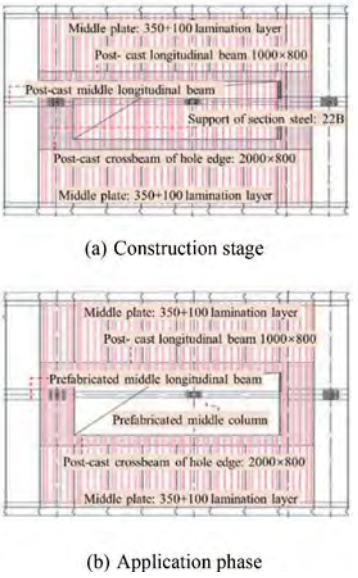

Figure 4. Plane graphic of middle plate opening large hole.

working condition (pouring composite layer working condition) is selected for the construction stage analysis of the middle plate opening large hole. The finite element models were established to analyze the stress of single mid plate and steel support. Figure 5 shows the finite element model of prefabricated mid plate and section steel support at each stage, and the calculation results are shown in Table 4. The results indicate that the composite component composed of prefabricated middle plate and section steel support during the construction stage can meet the requirements of bearing capacity and crack control by reinforcing according to the standard plate. During normal application stage, the reinforcement of the longitudinal beam and crossbeam at the hole edge meets the requirements for bearing capacity and cracks.

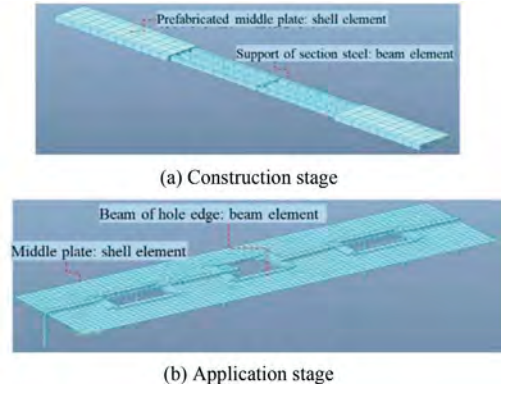

Figure 5. Calculation model of middle plate opening large hole.

Table 4. Bending moment and shear force of middle plate under vertical load.

Conditions	Construction stage		Application stage	
Location	Prefabricated plate	Section steel	Longitudinal beam	Transverse beam
Bending moment of support (kN·m)	--	39	614	3062
Bending moment in the span (kN·m)	171	--	308	--
Shear force (kN)	87	17	339	1036

4 ANALYSIS OF THE INFLUENCE OF GEOLOGICAL CONDITIONS ON THE INTERNAL FORCES OF PREFABRICATED STATION STRUCTURE

4.1 *Station structural model*

The assembled station strata model is shown in Figure 6. Considering the influence of boundary effects on the structural model, the depth of the soil in the model needs to be selected at least 3 times the height of the station, and the horizontal boundary needs to be selected at least 5 times the width of the station. The horizontal and vertical sizes of the model are 162 m and 54 m, respectively, with a longitudinal length of 2 m. Fixed constraints are set at the bottom and surrounding boundaries of the soil, while the upper boundary is free. The elastic constitutive model is used for concrete materials, and the Mohr Coulomb constitutive model is used for soil materials. The main structure adopts C50 concrete material, and the ground connecting wall adopts C35 concrete material. The model joint adopts the joint mode proposed by Lin [12], which uses beam spring element simulation and multiple joint stiffness iterations to obtain accurate joint stiffness.

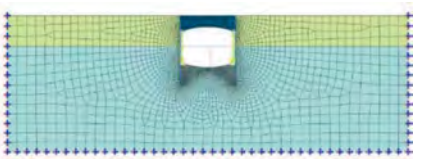

Figure 6. Stratum-structure calculation model.

In order to better analyze the impact of different geological conditions on the station structure, representative soft and hard soil layers are selected for analysis. Four types of strata, namely fill soil, soft plastic silty clay, hard plastic silty clay, and completely weathered sandstone, were studied. The selection of elastic modulus and Poisson's ratio for different soil properties is shown in Table 5.

Table 5. Strata parameters.

Strata	Elastic modulus E/ (MPa)	Poisson's ratio υ
Fill soil	15	0.4
Soft plastic silty clay	30	0.35
Hard plastic silty clay	45	0.3
Completely weathered sandstone	60	0.25

4.2 *Analysis of internal force and deformation of prefabricated station structure*

Figure 7 shows the horizontal displacement deformation of the station in a completely weathered sandstone formation. For the prefabricated station structure studied in this paper, the BC joint is relatively close to the arch foot, which is the weak point of structural deformation. Therefore, the horizontal displacement of the arch foot needs to be focused on.

Figure 8 shows the vertical displacement deformation of the station in a completely weathered sandstone formation. The vertical settlement of the top plate is greater than that of the bottom plate. Excessive deformation of the structure can affect the stability of the station and result in displacement exceeding the limit. Therefore, this paper selects the horizontal displacement and mid span settlement of the top plate at the arch foot support as the analysis objects for structural deformation.

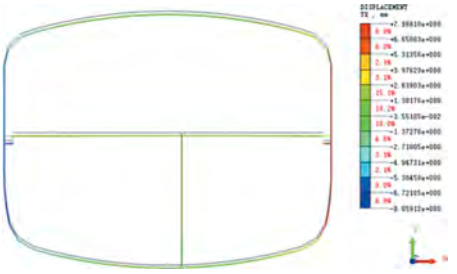

Figure 7. Horizontal displacement of station.

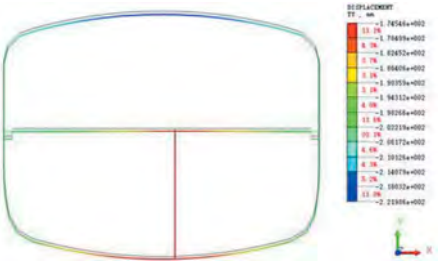

Figure 8. Vertical displacement of station.

Figures 9 and 10 show the distribution of bending moment and axial force at stations in completely weathered sandstone formations. It can be seen that the position where the larger bending moment is located is the mid span of the top plate, the arch foot support and bottom plate support, and the mid span of the bottom plate. The extreme bending moment occurs in the span of the top plate. The larger values of axial force are concentrated at the supports of the top and bottom plates. The extreme value of axial force occurs at the position of the arch foot support of the top plate. Therefore, this paper selects the arch span and arch foot support for analysis.

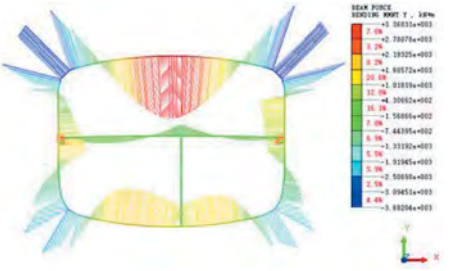

Figure 9. Bending moment of station.

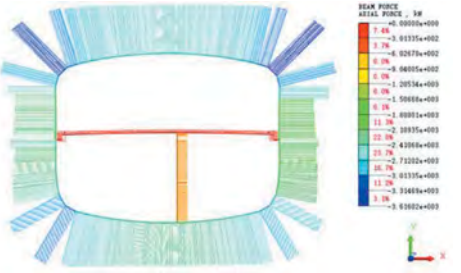

Figure 10. Axial force distribution of station.

4.3 *The influence of geological conditions on the stress of station structure*

Figure 11 shows the curves of the settlement of the arch crown and the horizontal displacement of the arch foot support in different strata. It can be seen that as the stratum hardens, the horizontal displacement of the arch foot support and the settlement of the arch crown decrease. For the mid span of the top plate, the settlement of the arch crown in fully weathered sandstone is 10.42 mm smaller than that of the fill, and the horizontal displacement of the arch foot support is reduced by 2.56 mm.

Figure 12 shows the bending moment values at the arch and support under different geological conditions. The axial force values at the arch and support under different geological conditions are shown in Figure 13. For the mid span of the top slab, the bending moment of completely weathered sandstone has decreased by 1640 kN·m compared to that of the filled soil, and the axial force has increased by 428 kN. For

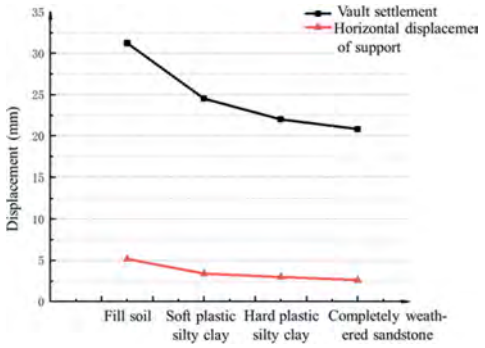

Figure 11. Horizontal displacement of bearing and settlement curve of vault for different soil.

the arch foot support, the bending moment of completely weathered sandstone has decreased by 337 kN·m compared to that of the filled soil, and the axial force has increased by 853 kN.

It can be concluded that the geological conditions have a significant impact on the structural stress. The harder the formation, the more favorable the structural stress. When the elastic modulus E of the soil layer is 15 MPa, the mid span bending moment of the top plate reaches 5536 kN·m. It is recommended to strengthen the structural design in this formation. In relatively hard soil layers (E>60 MPa), the bending moment value is small, the axial force value is large. The slightly hard strata are favorable for structural stress, and are suitable for the structural cross-section form presented in this article.

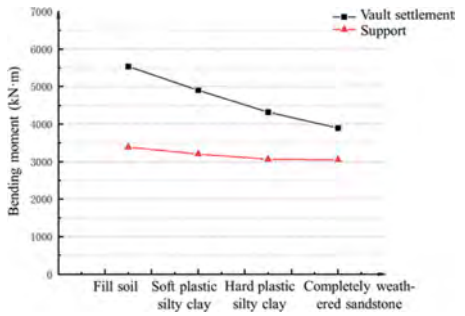

Figure 12. Bending moment of bearing and arch crown of different soil.

By comparing the redundancy of bending moment and shear force values, it is possible to compare the redundancy of joint stiffness under different geological conditions. The joint redundancy of structures under different geological conditions is shown in Table 6. The following conclusions can be drawn: 1) As the soil layer hardens, the redundancy of bending moment and shear force of the BC joint and the AB joint increases, indicating that the hardening of the soil layer has a positive impact on the structural stress. 2) The change of soil layer has a significant impact on the redundancy of the BC joint, while it

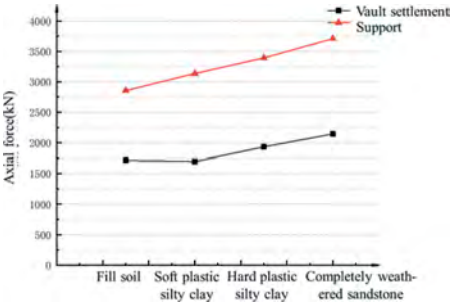

Figure 13. Axial force of different soil.

has a smaller impact on the redundancy of the AB joint. When the formation changed from fill soil to completely weathered sandstone, the bending moment redundancy of the BC joint increased from 5.7% to 40.74%, which increase 35.04%. While the AB joint increased from 48.04% to 49.78% as the formation becomes hard, only an increase of 1.74%. 3) The redundancy of the BC joint in the fill layer is very small, only 5.7%. In this soil layer, measures such as increasing the size of the tenon can be taken to enhance the joint stiffness, such as joint reinforcement design or soil improvement.

Table 6. Connector redundancy of bearing of different soil.

Formation condition	BC joint Bending moment	BC joint Shear force	AB joint Bending moment	AB joint Shear force
Fill soil	5.70%	57.59%	48.04%	38.18%
Soft plastic silty clay	25.29%	60.35%	48.34%	41.49%
Hard plastic silty clay	34.04%	67.61%	48.38%	51.93%
Completely weathered sandstone	40.74%	75.30%	49.78%	54.37%

5 CONCLUSION AND SUGGESTIONS

Taking the prefabricated subway station project in Shenzhen as the engineering background, the key and difficult problems in the prefabricated middle plate, beam, and column scheme of the prefabricated subway station were studied. The mechanical properties of station structures under different geological conditions were analyzed, and the main conclusions are as follows:

1) A flow assembly sequence under the open excavation of the internal support system is proposed for the prefabricated middle plate of prefabricated stations, which improves the section assembly rate and assembly efficiency. At present, the assembly

efficiency of this process in Shenzhen is 2 days to complete 3 complete rings.

2) The prefabricated middle plate is used in the prefabricated station. The design of prefabricated middle plate needs to be combined with factors such as the force conversion requirements of open excavation of foundation pits, the lifting of prefabricated components, and the assembly process of stations.
3) The deformation of the single arch large span non-column arch roof station structure is mainly reflected in the top plate support and bottom plate support. Both undergo outward horizontal displacement, but the horizontal displacement is relatively small. The top and bottom plates mainly experience downward settlement, and the vertical settlement of the top plate is greater than that of the bottom plate.
4) As the stratum hardens, the redundancy of bending moment and shear force of the BC joint and the AB joint increases, but the influence of stratum change on the BC joint is greater than that of AB joint. When designing prefabricated station joints, the BC joint between the roof and side wall should be given special attention.

REFERENCES

[1] Yang Xiuren, Huang Meiqun. Research strategies on new prefabricated technology of underground subway station[J]. Urban rapid rail transit, 2018, 31(01): 78–85.

[2] Yang Xiuren, Huang Meiqun, LIN Fang. Research on bending resistance characteristics of grouted mortise-tenon joint for prefabricated metro station structure[J]. China Civil Engineering Journal, 2020, 53(02): 33–40.

[3] Yang Xiuren, Huang Meiqun, LIN Fang, et al. Experimental method of grouted mortise-tenon joint for prefabricated metro station structure[J]. Urban Rapid Rail Transit, 2019, 32(05): 83–90.

[4] Yang Xiuren, LIN Fang, Huang Meiqun. Experimental research on flexural rigidity of grouted single mortise-tenon joints for prefabricated metro station structures[J]. China Civil Engineering Journal, 2020, 53(03):38–43.

[5] Yang Xiuren. Research and application of prefabricated structure construction technology for metro station[J]. Tunnel Construction, 2022, 42(03): 345–354.

[6] Yang Xiuren. Design technology and method of open-cut prefabricated underground structures of urban rail transit[J]. Tunnel Construction, 2022, 42 (03): 355–362.

[7] Yang Xiuren, HUANG Meiqun. Calculation and analysis method of overall action effect of open-cut prefabricated tunnel structures[J]. Tunnel Construction, 2022, 42(03): 372–377.

[8] Ding Peng, Yang Xiuren, GAO Xiangyu, ZHAO ji, SHI cheng, WU Shang. Horizontal and vertical seismic response of single-arch and large-span prefabricated subway stations [J]. Journal of Heilongjiang University of Science & Technology, 2018, 28(06): 630–637.

[9] Ding Peng, Tao Lianjin, Yang Xiuren, et al. Force transfer and deformation mechanism of single ring structure of prefabricated subway station[J]. Journal of Southwest Jiaotong University, 2020, 55(5): 1076–1084, 1110.

[10] Peng Zhiyong, Yang Xiuren, Huang Meiqun, et al. Mechanical behavior of prefabricated underground station structure in construction stage[J]. Tunnel construction, 2022, 42(3): 398

[11] Tao Lianjin, LI Zhuoyao, Yang Xiuren, et al.Research of the mechanical behaviors of subway station structure assembled with prefabricated elements based on ABAQUS[J]. Modern tunnelling technology,2018, 55 (5): 115–123.

[12] Lin Fang, Mechanical property analysis of top arch joint for prefabricated underground metro station structure based on in-suit monitoring[J].Tunnel construction,2022,42 (3):430:430–436.

Tunnelling for a Better Life – Yan, Celestino, Thewes & Eberhardt (Eds)
© 2024 The Author(s), ISBN 978-1-032-80042-4
Open Access: www.taylorfrancis.com, CC BY-NC-ND 4.0 license

Addressing design challenges in large diameter tunnels with big openings in deep soft ground: Innovative solutions and analysis techniques

Jinrong Yuan*, Vince Chee Siong Goh & Claudia Maxcia
COWI Singapore Pte Ltd. Singapore, Singapore

ABSTRACT: This paper discusses the design challenges and innovative solutions of segmental lining for a large diameter bored tunnel with big opening in soft ground at a depth of 50m. One of the main challenges in the design is to design a temporary support system for the opening that would not disrupt concurrent tunnelling works. To achieve this, it was necessary to transfer the maximum ground load applied on the cutting rings to the adjacent rings and minimize the temporary support. Therefore, 3D structural FEM analysis was carried out to simulate the load transfer and tunnel lining behaviour as well as the stress states of all radial and circumferential joints. In addition, investigation on the ground loading applied on tunnel lining with different tunnel depth was carried out using 2D/3D Plaxis. The analyses results show that the circumferential dowels and bicone significantly contributed to load transfer between the cutting and adjacent rings, the soil arching effect may reduce the ground loading applied on the tunnel lining by 20~30%, which allow for a reduction in the required reinforcement and a smaller temporary support system. The study provides valuable insights into the design and analysis of a segmental lining for a large diameter bored tunnel in soft ground with openings. The findings can be applied to similar tunnel projects in soft ground conditions.

Keywords: Large diameter tunnel, Segmental lining, TBM tunnelling, Opening, Soil arching effect, Deep tunnel

1 INTRODUCTION

Global cities are experiencing rapid urbanization as rural populations migrate to urban areas. According to the United Nations 2022 World Cities Report (UN-Habitat, 2022), the world's cities are projected to add 2.2 billion people by 2050, with nearly 90% of this growth occurring in Asia and Africa (S. Vardakos, S. Zlatanic, S. M. Wongkaew & A. Bauer, 2023).

Large diameter tunnels, particularly single bores for transit, rail, and roadway applications, are well-suited to meet the demands of high-capacity transportation projects, especially in densely populated urban areas where surface and right-of-way space is at a premium. It is capable of accommodating multi-lane roadway traffic or multi-modal services, thereby eliminating the need for multiple tunnels with cross connections. In comparison to dual bored tunnel, which typically necessitate the construction of cross-passages at specific intervals, a single bored tunnel offers the flexibility to incorporate cross passages, thereby reducing evacuation times in the event of an incident within the tunnel.

Current practice in tunnel design tends to very a great deal, depending on national or owner-imposed design requirements, local tradition and practice and the experience of the tunnel designer. There are no universally accepted guidelines on how to assess the safety of a tunnel or the acceptability of a design and this means that engineering judgement and experience play a very large role in the design of tunnel.

2 CHALLENGES OF LARGE DIAMETER BORED TUNNEL

The benefits of large diameter tunnels are counterbalanced by challenges in their design and construction, necessitating careful planning, alternative analyses, and innovative, performance-based engineering solutions.

2.1 *Non-uniform ground conditions within the advancing face*

Large diameter tunnels frequently encounter intricate and demanding ground conditions. The expanded

*Corresponding author: jiyu@cowi.com

DOI: 10.1201/9781003495505-59

excavation size increases the likelihood of encountering various geological formations, thereby presenting a substantial challenge. These ground conditions may encompass soft soils, rock formations, mixed face conditions, weak rock masses, fault zones, and more. Understanding the geotechnical properties of the ground and devising suitable support systems to maintain stability becomes imperative.

2.2 *Ground control and settlement risks*

Impacts to adjacent buildings/utilities due to settlement are key risks associated with large diameter tunnel. It is very important to recognize that the volume loss will be smaller and does not scale with the square of the tunnel diameter, as is often the case with smaller diameter tunnels. Volume losses in such cases are often found to correlate better with the diameter of a large tunnel (S.Vardakos, S.Zlatanic, S. M. Wongkaew & A. Bauer., 2023)

2.3 *Higher hood force and thrust force in the segmental lining*

The increased size of these tunnels presents new technical challenges to both designers and contractors, such as increased pressure due to soft ground or weak rock, will significantly increase hoop force and TBM thrust force in the tunnel segmental lining, which pose challenges in the design of segmental ling, especially for radial joints and circumferential joints.

2.4 *Provision of internal structures*

Large tunnels often necessitate the inclusion of internal structures for functional purposes, which can adversely affect the structural integrity of the lining. For instance, consider a TBM road tunnel requiring a ventilation slab with supports at shoulder level, potentially leading to unacceptable localized loading of the lining. The design of the segments must carefully address such concerns. In the case of larger TBM tunnels, solutions may need to account for significant internally induced forces.

2.5 *Opening in the segmental lining*

Another challenge for designers to consider is the provision of structural openings to accommodate future underground infrastructure or other purpose. The presence of these openings can have a substantial impact on stress distribution within the segmental lining of large diameter tunnels. Consequently, strengthening work is typically required around the openings for both temporary and permanent cases in order to maintain the overall integrity of the tunnel structure. Advanced analysis techniques can be used to optimise the structural designs in these areas to ensure cost effective solutions.

2.6 *Greater risks of lining uplifting, stepping and ovalisation*

Large tunnels passing through poor ground with rich underground water content entail greater risks of lining uplifting, stepping, and ovalisation due to buoyancy during segment erection. In the case of larger diameter tunnels, increasing the number of segments per ring is a common practice to reduce their size and weight for ease of delivery and handling within the TBM during erection. While having more segments per ring allows for greater flexibility and lining deformation, it also increase the risks affecting the lining's integrity.

3 GROUND LOADING CONSIDERATION FOR LARGE DIAMETER BORED TUNNEL

A tunnel can be expected to experience permanent loads (i.e. dead loads, earth pressure, surcharge loads, etc.), live loads (i.e. vehicular loads, live load surcharges, etc.), or transient loads (i.e. earthquake, superimposed deformations, blast, fire, construction loads, etc.).

Ground movements due to tunnelling, either TBM or sequential excavation are inevitable and can be attributed to: (1) Ground movement towards the face; (2) Radial movement towards the shield; (3) Ground movement towards the tail void; and (4) Deformation of the lining.

Deformation of the tunnel lining results in a reduction in ground stress acting on the tunnel linings. After excavation, the ground requires time to redistribute, and even longer for consolidation to reach the final stress state.

The ground loadings imposed on the tunnel lining are a function of the stress variation with tunnel depth, ground-lining relative stiffness, tunnel geometry, and construction sequence. As Per AASHTO-LRFDTUN-1 (2017), the vertical earth pressure for tunnels in soft ground may be taken as the pressure resulting from the total height of ground directly over the tunnel crown, if the height of ground over the tunnel crown is two times or less the excavated width of the tunnel. If the height of ground directly over the tunnel crown is greater than two times the excavated width of the tunnel, the arching action of the soil should be evaluated to determine if an increase in pressure is necessary. Similar, ITA working group 2 recommends that reduced earth pressure for bored tunnel can be adopted in accordance with Terzaghi's formula (WG2 ITA (2000)).

Peck (1969) defined the two principal requirements of a tunnel lining and illustrated the factors influencing the development of ground loading on the lining. The key points are summarized as follows (R. J. Mair & R. N.Taylor (1997)):

- By the time the lining is installed, soil displacements have inevitably occurred (the ground

having moved radially towards the tunnel and axially towards the face).

- The short-term ground loading experienced by the tunnel lining is inversely proportional to the magnitude of soil displacements that have occurred prior to its installation.
- The circumferential flexibility of the lining may allow a further reduction in the loading, although this is generally small since most completed rings are generally relatively stiff circumferentially.
- The short-term ground loading acting on the tunnel lining can be taken to correspond to when the tunnel face has moved away from the lining by approximately 2 tunnel diameters, i.e. when the three-dimensional effects of the tunnel heading are no longer evident.
- Any further increase in ground loading on the lining depends on the soil type. In the case of sandy soils, tunnel excavation and lining erection take place under drained conditions, and hence little or no increase in ground loading would be likely (unless caused by additional grouting). In clays, however, the ground loading will increase as excess pore pressures dissipate.

Arching effect is one of the most universal phenomena encountered in soils both in the field and in the laboratory (Terzaghi, 1943). This effect is most recognized in underground structures, for example, underground conduits. Underground openings can be built utilizing the arching action to account for the reduction in the overburden pressure.

Hsien-Jen Tien (1996) carried out a literature study on the arching effect and summarized the arching effect as follows:

(1) Arching is a phenomenon existing widely in nature and man-made construction. It is an important issue for geotechnical engineers and researchers to comprehend and recognize in their studies and design.
(2) The arching effect can be defined as follows: "If a portion of an otherwise rigid support of a geomaterial mass yields, the adjoining soil moves with respect to the remainder of the soil mass. This movement is resisted by shearing stresses which reduce the pressure on the yielding portion of the support while increasing the pressure on the adjacent rigid portions." Arching can also occur when one portion of a yielding support moves more than adjoining parts. Generally speaking, arching is stress redistribution occurring in a geomaterial mass.

Practice and literature show that moderate changes in earth loads may be responsible for large changes in predicted lining loads. This becomes especially critical for large diameter tunnels. Grübl (2012) highlights that for large diameter tunnels with segmental lining, a marginal change of lateral pressure leads to notable changes of ring bending moments. As soil-structure interaction models can capture soil arching and redistribution of ground stresses, they can be a practical method in estimating ground loads acting on lining. The Orlovsky-Tunnel study showed through FE calculations that a 25% reduction of earth loads should be possible versus conventional methods (Grübl, 2012).

When numerical analyses are performed for the design of a tunnel lining the designer should consider the different stress states that the tunnel lining needs to accommodate starting from the initial ground stress regime, the change in stress during excavation, and the change in groundwater pressure. The estimation of ground loads becomes more complicated as the tunnel diameter increases and the probability of encountering ground of mixed stiffness becomes higher compared to smaller diameter tunnels. In that context, the use of geotechnical numerical models versus the conventional practice of empirically derived stress reduction due to arching, becomes more relevant than before. Further research should be performed to identify the instances when the use of numerical modelling for calculation of earth loads is necessary and provide the designers practical information for the application of this methodology.

The Convergence Confinement Method (CCM) (Marc Panet, Jean Sulem, 2022) is a design principle used for tunneling in soft ground conditions. The method aims to control and manage ground movements and deformations by achieving a balance between convergence (deformation) and confinement (support).

Convergence refers to the inward movement or deformation of the ground around the tunnel. The CCM recognizes that some level of convergence is inevitable in soft ground tunneling. However, excessive convergence can lead to instability and potential failure. The goal is to control and manage the convergence to ensure it remains within acceptable limits.

Confinement refers to the support provided to the tunnel lining to resist the pressure exerted by the surrounding ground. The CCM emphasizes the need for a robust and effective support system, typically achieved through the use of segmental lining, shotcrete, or other forms of structural support. The support system should be designed to provide sufficient stiffness and strength to prevent excessive deformations and maintain stability.

The key principle of the CCM is to achieve a balance between convergence and confinement. By carefully designing the support system and controlling ground movements, a state of equilibrium can be achieved where the deformations are controlled within acceptable limits, and the stability and integrity of the tunnel are maintained.

The CCM emphasizes the importance of continuous monitoring of ground and tunnel behavior during and after construction. Monitoring techniques such as instrumentation, geodetic measurements, and ground surface surveys are used to assess

convergence, ground settlements, and other relevant parameters. This information allows for real-time adjustments to the support system, if necessary, to ensure the desired balance between convergence and confinement is maintained.

Overall, the Convergence Confinement Method provides a systematic approach to tunnel design in soft ground conditions. It focuses on achieving a controlled and balanced interaction between the tunnel lining and the surrounding ground to maintain stability, control deformations, and ensure the safety and functionality of the tunnel structure.

4 SEGMENTAL LINING DESIGN AT OPENING LOCATION

Design of railway or road bored tunnels always calls the need for opening in the segmental lining, for instance, for cross passage or future underground infrastructure, design of opening in the bored tunnel segmental ling especially in large diameter bored tunnel in soft ground with deep overburden under high groundwater table proves to be a challenging task.

In order to construct opening, the tunnel segmental lining at opening location is required to be removed and temporarily supported during construction stage and connected to the cross passage in permanent stage.

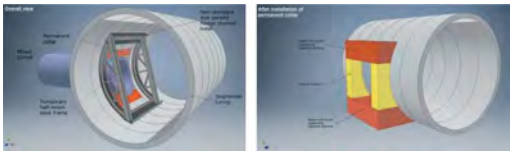

Figure 1. Support for tunnel opening. left: temporary right: permanent.

The relevant tunnel rings are opened by removing the filling segments so that they no longer act as a closed structural system. The hoop forces must be supported temporarily during construction and permanently after completion by other structural elements. This can be accomplished either by using steel segments, which remain in the structure permanently and form part of the tunnel lining, or with special concrete segments. In case of special concrete segments these either must be temporarily supported with a suitable structure during construction, or permanently coupled during and after construction. Temporary support can be provided by, for example, an appropriate steel structure or by using dowels to couple the segments. In the final stage, a concrete frame which forms part of the permanent cast-in-place lining will carry the forces around the opening (See Figure 1).

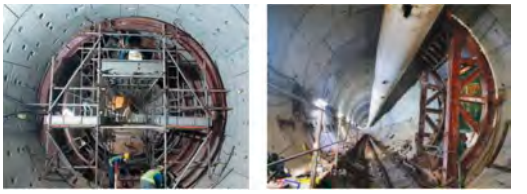

Figure 2. Temporary steel support for tunnel opening (left: Hamster cage Right: Half-moon).

Various methods, such as steel support frames of hamster cage, half-moon (See Figure 2), or steel segments, can be used to provide the rigidity to bear the loads which need to be conducted around an opening in a segment-lined tunnel. Each solution has advantages and dis-advantages, and some methods have limits with regard to their applicability.

In Singapore MRT tunnel, the hamster cage temporary support was commonly adopted as temporary support for opening in the past. One of the disadvantages of this solution is that these steel structures extent into the tunnel space and, thus, could disrupt construction work in the main tunnel. The time required to install and remove, the construction and the cost of the steel components are also disadvantageous. In order to overcome the disadvantage, some of the projects proposed different steel frame of half-moon or/curved steel frame for the opening with innovative design approach considering the load transfer to adjacent ring through the circumferential joints of dowel or/and bicone.

This half-moon/curved steel frame eliminate risks associated with the traditional “Hamster cage” internal bracing, difficult and potentially dangerous to build due to having to lift heavy steel structure and provide sufficient working platform for concurrent activities in the bored tunnel and therefore significantly improved the construction progress.

For permanent stage, the permanent collar will be designed to carry the loads from the cut segment lining from the time when the temporary steel frame is removed until permanent stage. These loads will be carried by bending and torsion in the beam and column members of the rectangular frame and the design actions will be locked into the structural members for the entire design life.

5 CASE STUDY

A case study was carried out to study on the design and analysis of the large diameter bored tunnel with large opening in the segmental lining to be built in soil conditions of old alluvium (OA) at depth of 50 m from ground level in Singapore. This study involves discussion of the magnitude of ground loads on the tunnel lining and its influence on the opening set design of the segmental lining with 3D geotechnical and structural analysis.

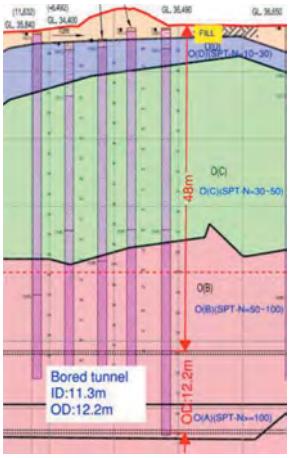

Figure 3. Soil profile for large diameter tunnel analysis.

The proposed segmental lining with 11.3 m internal diameter comprises 9 standard segments and 1 key segments (9+1). The segment thickness is 450 mm thick and steel fibre reinforced (sfrc).

Th ground conditions of the studied section is illustrated in Figure3, based on the geological information, the large diameter tunnel at this section is envisaged to be driven through Old Alluvium overlain by Fill materials. Old Alluvium consists of ill-assorted masses of semi-consolidated sand, gravels, pebble beds and silty clay beds. Old Alluvium was categorized and divided into 5 sub-layers (OA(A) to OA(E)), according to its weathering grade and strength based on SPT N-Values with OA(A) being unweathered and OA(E) as residual soil.

A series of openings of 4.0m wide x 5.6 m height will be created on the segmental lining to facilitate the future connection with the future underground infrastructure (see Figure 4), the tunnel horizon at openings will be in OA(B) or better with about 4 times tunnel diameter ground cover to the tunnel crown.

According to the project requirement, the proposed design of load transfer elements and associated temporary support systems at the opening locations shall allow concurrent TBM tunnelling work. Hence, the stability of the cut ring will be maintained by transfer of axial load to adjacent segments through special segments(steel-concrete grout composite segments and SFRC-rebar reinforcement hybrid precast segments) as well as high shear capacity dowels and bicones for the circumferential joints during construction period between the breaking of the segment to form an opening, and the installation of the permanent reinforced concrete collar.

Both short-term construction and long-term permanent stages considered in the analysis.

During construction stage, the special segments in conjunction with bolts, shear bicones and high strength dowels along the circumferential joints to ensure the axial load transfer mechanism to be achieved.

To further enhance the stability of the system, additional steel temporary props will be installed in conjunction with all the aforementioned measures.

During the long-term permanent stage permanent RC collar will be carrying the permanent loads induced onto the segmental lining over time.

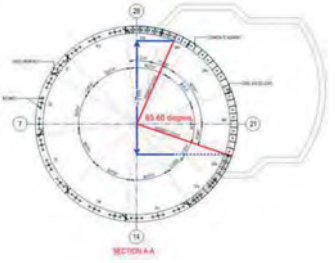

Figure 4. Large diameter tunnel section with opening.

5.1 *Ground relaxation in the segmental lining design*

As discussed in section 3 above, tunnel excavation necessarily results in direct stress release towards the excavation accompanied by arching of the ground around it before ground supports are installed. For deep tunnel excavation the eventual load for which supports need be designed can be far less than the load corresponding to original ground stresses before excavation. Theories for assessment of arched loading may be used to establish appropriate loading for design of supports in granular materials. For excavations in clay soils with lower permeability, pore water pressures changing towards equilibrium values with time bring about gradually increasing load on excavation supports.

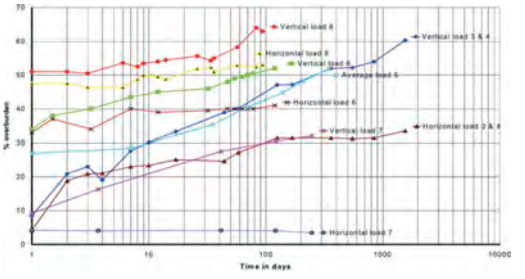

Figure 5. Recorded time related loading on tunnel in London clay (London Underground, 2007).

Figure 5 shows the measurement of ground load on London Underground tunnel linings in London Clay (London Underground, 2007), which shows that the actual load on the tunnel at 1000 days is less than 65% overburden. These measurements confirm the important point highlighted by Peck (1969) that in reality the tunnel lining is not subjected to the original in-situ ground stresses as if it had been "wished into

Table 1. Comparison of soil parameters for OA(B) and London Clay.

Soil Type	Unit weight [kN/m^3]	Drained modulus [MPa]	Undrained modulus [MPa]	Undrained shear strength [kPa]	Friction angle [°]	Cohesion [kPa]
London Clay	20	Min. 36.4	Min. 45	Min. 65	23	0
OA(B)/OA(A)	20.5	200	230	250	34	20

place". The soil displacements that occur prior to installation of the lining clearly have a major influence in reducing both the short-term and long-term ground loading to much lower values than the original in-situ stresses. Particularly in the case of highly over-consolidated clays.

Comparing with London clay, OA(B)/OA(A) is cemented stiff material similar to London Clay (see Table 1), the ground load on the tunnel for the case study is expected not more than that in London clay (65%).

Plaxis 2D and 3D analysis were carried out to study on the ground-structure interaction and ground relaxation. In Plaxis 2D model, different overburden of bored tunnel were assumed to study the effective stress influence height above the tunnel versus overburden, the bored tunnel lining was only considered as "Wished-in-place" without construction sequence considered, the soil relaxation is only result from the soil-structure interaction due to the differential stiffness. Refer to Figure6 for the total displacement around the tunnel.

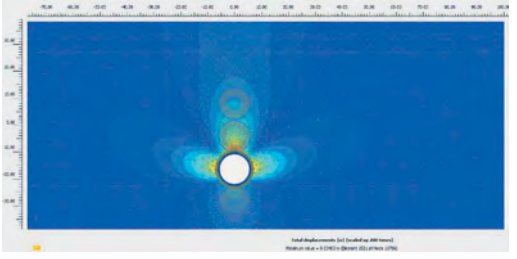

Figure 6. Plaxis 2D model for tunnel overburden at 4D.

From the Plaxis 2D analysis, following findings are observed:

- Ground cover lesser than 2D (D is the tunnel external diameter), the soil arching effect is insignificant. The soil pressure acts on the tunnel is close to in-situ stress.
- Ground cover greater than 2D, the soil arching effect tends to more notable. In this study of 4D ground cover, approximately 20% of soil relaxation is expected (See. Figure 7).
- Influence height of effective stress increase with tunnel overburden, but not more than 2D (See Figure 8), which indicates the extent of soil relaxation and disturbance of soil is about 2D, the stress beyond 2D will not be affected.

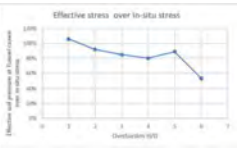

Figure 7. Soil pressure over in-situ stress for different tunnel overburden.

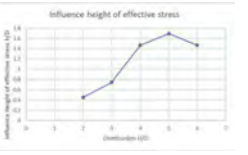

Figure 8. Influence height of effective soil pressure for different tunnel overburden.

Plaxis 3D analysis was adopted to simulate the future underground infrastructure excavation and tunnel boring works to obtain the relevant ground stresses that serves to be the input in the tunnel structural model.

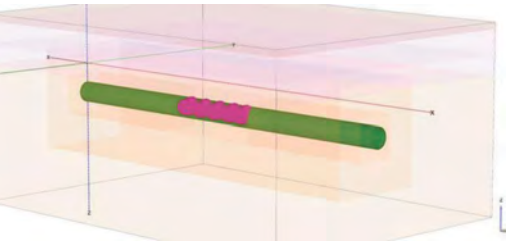

Figure 9. Plaxis 3D model for bored tunnel with openings.

The Mohr-Coulomb constitutive model is used for various soil strata. Only undrained analysis is conducted due to the short completion time of the openings. Undrained (B) is adopted for analysis which does not have a cap and yield surface. Linear-elastic and perfectly plastic conditions are used in the analysis; hence deformations and effective stresses were used to ensure that the overall results make sense and do not stray far from initial conditions.

Figure 9 shows the idealised finite element model. The future underground infrastructure have been split into 2 phases (1 & 2) to show the relative sequence of excavations. This is in correspondence to carrying out excavation only in alternative opening to mitigate the risk of concurrent excavation within close proximity. The opening excavation is simulated with wished-in-place techniques to conservatively estimate the ground stresses for bored

tunnel lining design. The envisaged construction sequence as follows:

- Apply surcharge
- Apply ground volume Loss
- Install bored tunnel lining & deactivate soil clusters
- Phase 1 Excavate & install primary lining
- Phase 1 Install permanent lining
- Phase 2 Excavate and install primary lining
- Phase 2 Install permanent lining

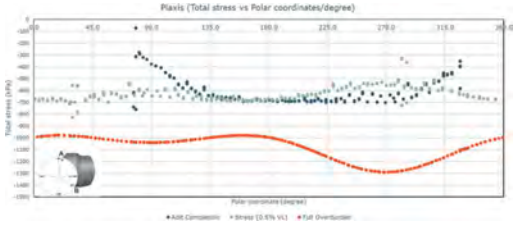

Figure 10. Ground load generated from Plaxis 3D.

Equivalent moment of inertia of segmental lining has considered Muir Wood Tunnel lining reduction to account for the segmental radial joints (Refer to Equation (1).

$$I_{eq} = I_{joint} + I_{full}\left(\frac{4}{n}\right)^2 \leq I_{full}. \qquad (1)$$

Where I_{eq} is the equivalent moment of segment

I_{joint} is the moment of inertia of segment radial joint

I_{full} is the moment of inertia of full segment thickness

n is the number of main segments (excluding key segment)

Plaxis 3D analysis shows that the ground load on the bored tunnel is only 65%~70% of the in-situ stress in the temporary stage (see Figure 10).

Based on Plaxis 2D and 3D analysis, arching ground load of 80% of full overburden (i.e 20% ground relaxation) was considered for short-term temporary construction stage is deemed to be appropriate.

For permanent stage, full overburden ground load will be considered in segmental lining design.

5.2 *3D structural analysis with opening for temporary stage*

Bedded-shell spring models have been set up in LUSAS (version 19.1) to derive the structural forces, i.e. the bending moments, hoop forces and shear forces in the segmental tunnel lining as well as the shear force and tension force in the joints.

The soil load derived from Plaxis analysis together with all temporary and permanent loadings

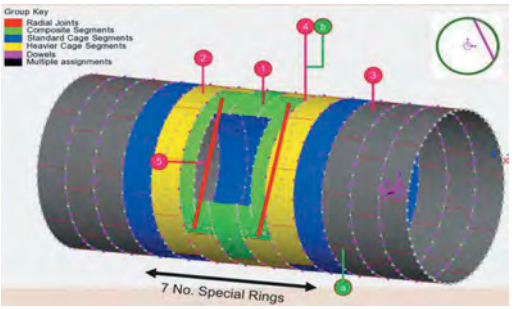

Figure 11. 3D bedded-shell spring model setup.

are applied to the structural model (see Figure11) with different load combinations, at temporary stage, no soil and water pressure loads have been applied at all the excavated regions to simulate the loss of confinement.

The soil-structural interaction is modelled with a set of ground radial and tangential springs. The radial ground reaction spring value Kr is derived with Duddeck and Erdmann's empirical formulas:

$$K_r = \frac{E_c(1-v)}{(1+v)(1-2v)R}$$

Where E_c is the drained Young's modulus of the surround ground;

v is the Poisson ratio of the surround ground;

R is the extrados radius of the tunnel.

The tangential stiffness has considered as one third of radial springs stiffness as per Dixon (1971) for soft ground.

The rotational springs with spring stiffness magnitude derived according to Leonhardt (1966) have been adopted to model the radial joints between the segments.

At the circumferential joints, connection has been modelled via coupled-shear springs without rotational stiffness (thus no moment transfer). The shear force-displacement curves of the connectors have been input based on the direct shear test carried out in the laboratory by the suppliers.

Additional internal temporary propping system consist of two vertical steel props connected to the non-standard segments have been modelled as beam elements connected to the shell elements of the ring (See Figure12).

5.3 *3D structural analysis with opening for Permanent stage*

In the permanent stage, the hoop load from the cut segments will be transferred to the permanent RC collar upon the removal of the temporary prop. The stability of the tunnel will be improved at this stage as the permanent

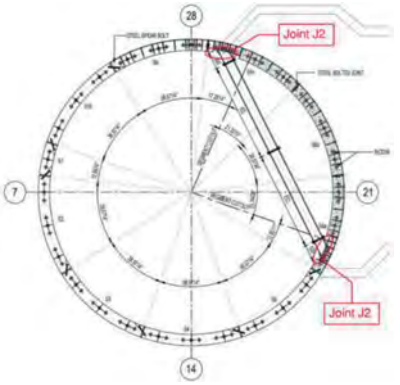

Figure 12. Temporary support for opening.

concrete collar and adit structures provide additional lateral restraint to the tunnel. The regions where the ground support was lost during the temporary stage has been casted with concrete at this stage (See Figure13).

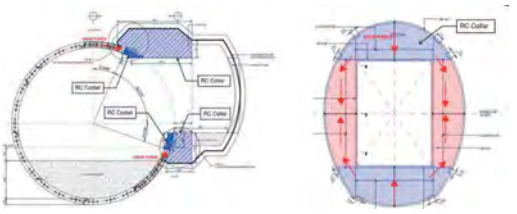

Figure 13. Load path of opening (elevation and section view.

The RC collar is modelled with as a volume element using LUSAS v19.1. Due to the line of symmetry, only half the collar is modelled and it is fixed along the Global Y axis at the axis of symmetry. Only the permanent lining is modelled for this permanent case model and it is assumed that the full ground load will be transferred to this permanent lining in the long-term

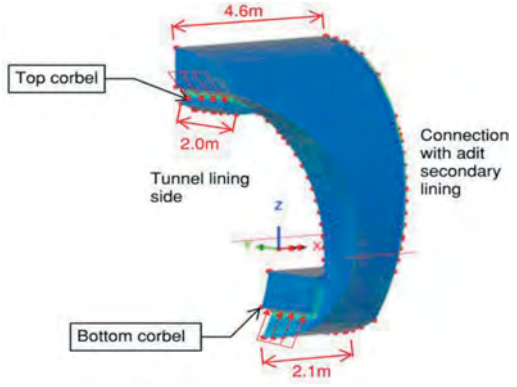

Figure 14. Permanent RC collar model geometry.

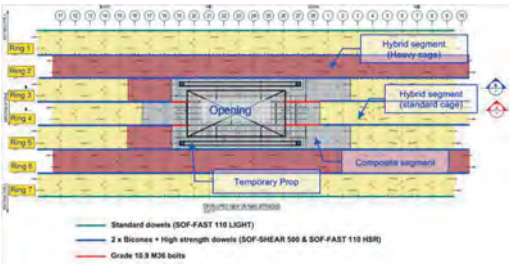

Figure 15. General ring arrangement for opening.

case. A tetrahedral mesh with quadratic interpolation is used. The model geometry is shown in the Figure 14.

5.4 *Analysis results and segmental lining design*

The results of 3D structural analysis of the tunnel opening segmental lining (temporary stage and permanent stage) have been evaluated and studied carefully due to the presence of singularities in finite element analysis (FEA) especially at sharp corners or sudden change in boundary conditions that does not represent the reality.

The structural design of segmental lining and check for the joints were carried out based on Eurocodes and Singapore codes and specifications.

The segment types and joints connection details are shown in Figure15.

6 CONCLUSIONS AND RECOMMENDATIONS

Design of openings in segmental linings for large diameter tunnels, particularly in soft ground with substantial overburden and high groundwater tables, presents intricate challenges, the need for concurrent tunnelling works during opening construction further complicates the design process.

There are no generally accepted standards or guidelines for the detail design of precast segmental lining, especially for ground loading consideration in deep tunnel, which depends on geological conditions, tunnel stiffness, tunnel depth, excavation method etc., hence, experience of the tunnel designer with engineering judgement is important.

Arching is an important issue for geotechnical engineers and researchers to comprehend and recognize in their studies and design.

The case study shows that the ground relaxation increase with overburden, for 4 times tunnel diameter overburden, 20% soil relaxation is expected, while soil arching effect is not significant when overburden is less than 2 times tunnel diameters, the influence height of effective stress increase with tunnel depth, but not more than 2 times tunnel diameter, which means soil arching can be considered if tunnel overburden is deeper than 2 times tunnel diameters, this is in line with studies of previous researchers (e.g. Terzaghi, 1943).

Effective load transfer mechanisms are critical to maintaining structural stability. Various methods, such as steel support frames, bicones, shear dowels, and bolts, play vital roles in transferring hoop forces around openings. Careful selection and design of these elements are essential for safe and robust construction. Hybrid and composite segments, incorporating steel reinforcement and specialized connections, prove effective for opening creation. These segments enhance load transfer capabilities and overall structural integrity.

Tunnel hoop force around the opening may be transferred to adjacent rings though circumferential joints and significantly simplify the temporary support for the opening during construction stage and therefore eliminate the obstruction of concurrent tunnelling works. Sophisticated 3D structural analysis modelling with appropriate software, realistic boundary condition assumptions, and correct inputs, and interpretation, post-processing of the outputs by experienced engineer are critical to successful design of the segmental lining and joints connections.

The design of permanent collar requires to consider the hoop force transferring during the design life, the permanent collar significantly contributes to long-term stability of the tunnel at opening location.

REFERENCES

S. Vardakos, S. Zlatanic, S.M. Wongkaew & A. Bauer. Large diameter TBM tunnels – Trends in planning and design. Proceedings of the ITA-AITES World Tunnel Congress 2023(WTC2023), pp.2030~2038, Athens, Greece

FHWA-HIF-20–035,U.S Department of Transportation Federal Highway Administration, Precast Concrete segmental liners for large diameter road tunnels, literature Survey and Synthesis, 2020

American Association of State Highway and Transportation Officials (AASHTO) (2017). "LRFD Road Tunnel Design and Construction Guide Specifications First Edition", AASHTO-LRFDTUN-1, Washington, DC.

Working Group No.2 International Tunnelling Association-(ITA)-Guidelines for the Design of Shield Tunnel Lining

Grübl, F. (2012). "Segmental Ring Design: New Challenges with High Tunnel Diameters", AITES/ITA.

Terzaghi, K. (1943) Theoretical Soil Mechanics, John Wiley and Sons, New York, pp. 66–76.

R. J. Mair, R. N.Taylor(1997), Theme lecture: Bored tunnelling in the urban environment, 14th International Conference on Soil Mechanics and Foundation Engineering (Hamburg),pp.2353–2385

Peck, R. B. (1969). Deep excavations and tunnelling in soft ground. Proc. 7th International Conference Soil Mechanics and Foundation Engineering, Mexico City, State of the Art Volume, pp. 225–290.

Hsien-Jen Tien(1996), A Literature Study of the Arching Effect, Submitted to the Department of Civil and Environmental Engineering in Partial Fulfillment of the Requirements for the Degree of Master of Science at the MASSACHUSETTS INSTITUTE OF TECHNOLOGY

Marc Panet, Jean Sulem, 2022, Convergence-Confinement Method for Tunnel Design, Springer Tracts in Civil Engineering, Switzerland

London Underground, 2007, Manual of Good Practice-Civil Engineering-Deep Tube Tunnels and Shafts, 2007

Tunnelling for a Better Life – Yan, Celestino, Thewes & Eberhardt (Eds)
© 2024 The Author(s), ISBN 978-1-032-80042-4
Open Access: www.taylorfrancis.com, CC BY-NC-ND 4.0 license

Aseismic mechanism of laminated shear energy dissipation structure in tunnels during an earthquake

Xuepeng Zhang* & Anting Cao
State Key Laboratory of Strata Intelligent Control and Green Mining Co-founded by Shandong Province and the Ministry of Science and Technology, Shandong University of Science and Technology, Qingdao, China
College of Energy and Mining Engineering, Shandong University of Science and Technology, Qingdao, China

Yujing Jiang
State Key Laboratory of Strata Intelligent Control and Green Mining Co-founded by Shandong Province and the Ministry of Science and Technology, Shandong University of Science and Technology, Qingdao, China
School of Engineering, Nagasaki University, Nagasaki, Japan

Xingda Wang
State Key Laboratory of Strata Intelligent Control and Green Mining Co-founded by Shandong Province and the Ministry of Science and Technology, Shandong University of Science and Technology, Qingdao, China
College of Energy and Mining Engineering, Shandong University of Science and Technology, Qingdao, China

ABSTRACT: The longitudinal seismic response of a tunnel during an earthquake cannot be ignored aspect same as the transversal seismic response. A novel laminated shear energy dissipation (LSED) structure is proposed for the longitudinal aseismic design in this paper. The LSED structure is composed of thin steel plate and rubber layer bonded alternately aiming at improving the longitudinal seismic performance of the tunnel by changing the connection mode between the linings. The laboratory compression-shear test on the LSED structure is carried out. Results show that a better deformation capacity in the horizontal direction because of the small horizontal stiffness of the rubber layer in the structure, and a larger vertical bearing capacity in the vertical direction because of the rigidity of the thin steel plate. A three-dimensional refined numerical model of LSED structure-tunnel lining-surrounding ground is established using the finite element software ABAQUS. The seismic response analysis is carried out by using the dynamic time history method. The research results showed that the installation of LSED structure could effectively reduce the seismic response of the lining with the seismic mitigation rate of more than 45%.

Keywords: Tunnel, Seismic performance, Laminated shear energy dissipation control, Earthquake

1 INTRODUCTION

Statistics on earthquake damage to underground structures indicate that tunnels and other underground engineering are not entirely resistant to seismic forces. Numerous historical earthquakes, such as the 1923 Kanto earthquake, the 1996 Kobe earthquake, the 1999 Chi-Chi earthquake, the 2008 Wenchuan earthquake, the 2016 Kumamoto earthquake, and the 2022 Menyuan earthquake, have caused varying degrees of damage to tunnel structures (Asakura et al., 1996; Sayed et al., 2019; Shen et al., 2014; Yu et al., 2016; Zhang et al., 2018; Wang et al., 2021; Chen et al., 2023). These global instances of tunnel seismic performance emphasize the importance of focusing on the seismic safety and aseismic design of underground structures, particularly in seismically active areas.

The primary objective of aseismic design, as pursued in various studies, is to reduce the stress induced by earthquakes on tunnel linings or release seismic energy by implementing mitigation measures at the connections between the lining and ground or between lining spans. Presently, two main approaches-seismic isolation technology and seismic reduction technology-are used to protect underground structures from earthquake damage. Seismic isolation technology involves incorporating an isolation system between the tunnel lining and the ground to reduce the transfer of seismic energy from the

*Corresponding author: zhangxuepeng0722@126.com

DOI: 10.1201/9781003495505-60

ground to the tunnel structure (Li, 2012; Providakis, 2009; Xin et al., 2019). The use of an isolation layer, frequently employing foam, concrete, rubber, and similar materials, has proven effective in reducing seismic damage to underground structures through theoretical and experimental studies (Konagai et al., 2001; Xu et al., 2016; Hasheminejad et al., 2008; Li et al., 2019). Seismic reduction technology involves incorporating structures such as flexible joints between tunnel segments or at lining connections (Ding et al., 2006; Yu et al., 2013; Kawamata et al., 2016; Yu et al., 2017). While seismic reduction technology is primarily used in subway tunnels, it is seldom applied in mountain tunnels. However, recent seismic investigations of ring crack damage in tunnels resulting from the 2016 Kumamoto earthquake and the 2008 Wenchuan earthquake have highlighted the significance of considering longitudinal performance in mountain tunnels, which mainly experience axial compression and tension during earthquakes. As a result, longitudinal seismic mitigation technologies are crucial for improving the seismic performance of mountain tunnels, particularly for long tunnels constructed in recent years, to protect the lining from severe damage (Atsushi et al., 2009; Cui et al., 2015; Yu et al., 2016; Zhang et al., 2018; Savigamin and Bobet, 2021).

Flexible joints for mountain tunnels can be installed at the primary or secondary lining connections. However, research on longitudinal flexible joints is still in its initial stages, with current studies primarily focused on the tunnel portal section (Cui et al., 2013, 2020; Ma, 2018). Ding et al. (2019) have also noted that there are few countermeasures for tunnel longitudinal deformation, with existing tunnel engineering only considering individual cases. It should be mentioned that the stiffness of flexible joints made with isotropic materials like rubber or foam concrete may be weakened, leading to larger local deformations and potential leakage due to differential surrounding pressure (Yu et al., 2013; Zhang et al., 2022). Therefore, seismic design of tunnels with flexible joints needs careful consideration, allowing for differential movements, resisting static and dynamic loads, and ensuring the integrity of the entire lining structure in the axial direction. To enhance the overall seismic performance of tunnel structures, it is necessary to conduct aseismic optimization designs of existing tunnel lining connections. In light of these challenges, a new type of laminated shear energy dissipation (LSED) structure is proposed to modify the connection mode of the lining and improve the aseismic performance of tunnel structures. The LSED structure's energy absorption body consists of both an elastic layer and alternating steel plates. In the radial direction of the tunnel cross-section, the LSED structure remains nearly rigid to avoid compromising the radial stress-bearing capacity provided by the surrounding rock. With the implementation of the LSED structure, the tunnel lining gains flexibility in the longitudinal direction. The aseismic efficacy of this proposed structure requires further investigation before its application in underground structures.

Hence, a fine three-dimensional (3D) finite element model is developed using numerical methods to investigate the aseismic longitudinal performance of the LSED structure in conjunction with the tunnel lining and surrounding rock. In this study, 18 cases are considered to analyze the structure's aseismic mechanism, considering both internal influencing factors such as the rubber shear modulus, steel plate dimensions, structure number, and structure installation location, as well as external influencing factors including seismic wave parameters and surrounding rock grade. These cases provide a comprehensive evaluation of the LSED structure and its effectiveness in mitigating seismic effects on the tunnel system.

2 MECHANICAL PRINCIPLE OF LSED STRUCTURE

2.1 *Design of LSED structure*

Figure 1 illustrates the schematic design diagram of the LSED structure, which comprises two main components: the energy absorption body (A in Figure 1) and the connecting parts (B in Figure 1). The energy absorption body is composed of an elastic rubber layer (A1 in Figure 1) that provides deformation capability and a steel plate (A2 in Figure 1) that offers high rigidity. These layers are stacked alternately to form the energy absorption body. The connecting parts are constructed using L-type steel-reinforced concrete slabs. The energy absorption body is connected to the L-type connecting parts through flange plates (C in Figure 1).

The horizontal equivalent stiffness, denoted as K_h is a crucial parameter for evaluating the anti-shear characteristic of the LSED structure. The stiffness is influenced by various factors, including the rubber shear modulus, rubber layer thickness, rubber layer number, and steel plate dimensions. To calculate this stiffness, a method similar to the approach used for natural laminated rubber bearings in building structures can be employed (Liu et al., 2022), as illustrated in Equation (1).

$$k_h = \frac{GA}{T_r} \tag{1}$$

where G is the shear modulus of rubber, A is the effective area of rubber inside, and T_r is the total thickness of rubber inside.

2.2 *Aseismic principle of LSED structure in tunnel*

Figure 2 depicts three models of tunnel lining connections, illustrating the presence or absence of longitudinal aseismic measures. In these models, the lining is simplified as a spring-mass system with circumferential stiffness (k_s) and

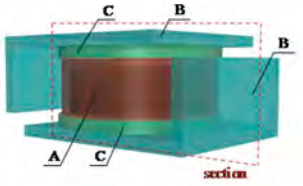

(a) panorama of the LSED structure

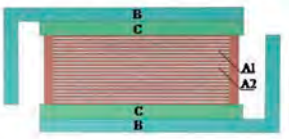

(b) sectional view of the LSED structure

Figure 1. Schematic design diagram of the laminated shear energy dissipation structure (Symbol A denotes energy absorption body; symbol A1 denotes elastic rubber layer; symbol A2 denotes steel plate; symbol B denotes L-type steel-reinforced concrete slab; and symbol C denotes flange plate).

axial stiffness (k_t). The static and dynamic forces acting on the lining can be decomposed into axial force $H(t)$ and vertical force $V(t)$.

(a) Lining without aseismic measures

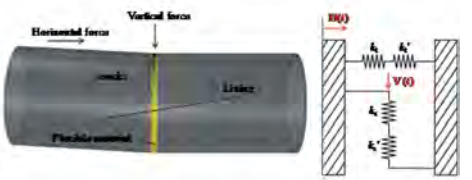

(b) Lining with isotropic flexible joints

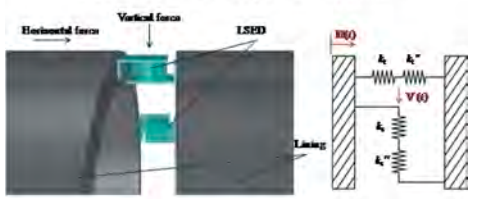

(c) Lining with LSED structure

Figure 2. Lining connection models with/without longitudinal aseismic measures.

In Figure 2a, the connection between the tunnel linings is rigid, without any aseismic measures. In this case, the lining's axial and circumferential stiffness values are solely determined by the lining k_t and the lining circumferential stiffness k_s.

To mitigate the negative effects of rigid connections, flexible joints with isotropic characteristics, such as rubber or foam concrete, are commonly used in current longitudinal seismic design between tunnel linings (Hasheminejad et al., 2018; Xu et al., 2011; Li et al., 2019), as shown in Figure 2b. In this case, the mechanical model can be simplified as two springs connected in series, considering both the horizontal and circumferential directions. Due to the flexible characteristics of the joint, a significant amount of energy can be absorbed by the flexible joint along the axial direction of the tunnel, effectively mitigating seismic damage. However, it should be noted that the elastic deformability of the flexible joint is much greater than the rigidity of the lining. This increased deformation has the potential to compromise the integrity of the entire tunnel structure, including the functionality of the waterproof layer.

To mitigate the isotropic effect of the flexible joint, a transversely isotropic model is proposed, as depicted in Figure 1. This structure exhibits different stiffness properties in the horizontal and vertical directions. The thin steel plate provides significant vertical bearing capacity, while the rubber component maintains good deformation allowance in the horizontal direction. The aim is to ensure that the structure can withstand large vertical loads while allowing for deformations in the horizontal direction. Figure 2c illustrates the lining connection model incorporating the LSED structure. The orientation of the laminated layers aligns with the circumferential direction of the tunnel, while the horizontal direction runs parallel to the axial direction of the tunnel. By implementing the LSED structure, the aim is to achieve improved seismic performance by effectively managing both vertical load-bearing capacity and horizontal deformation allowances. The mechanical model with the LSED structure can be expressed as

$$\begin{cases} H(t) = k_t{}''u_t{}'' = k_t u_t = k_{lt} u_{lt} \\ k_t{}'' = \frac{k_t}{k_t + k_{lt}} \\ V(t) = k_s{}''u_s{}'' = k_s u_s = k_{ls} u_{ls} \\ k_s{}'' = \frac{k_s}{k_s + k_{ls}} \end{cases} \tag{2}$$

where $k_t{}''$ and $k_s{}''$ are the equivalent horizontal and circumferential stiffness of lining and the LSED structure in series; $u_t{}''$ and $u_s{}''$ are the overall horizontal and circumferential displacement of lining and the structure in series; k_{lt} and k_{ls} are the horizontal and circumferential stiffness of the LSED structure; u_{lt} and u_{ls} are the horizontal and circumferential displacement of the LSED structure. The LSED structure, with its flexible rubber component in the horizontal direction, exhibits similar energy absorption capabilities as a flexible joint. However, what sets it apart from a flexible joint is its ability to maintain circumferential rigidity due to the increased stiffness of the steel plate. This circumferential rigidity ensures the integrity of the entire tunnel structure and protects the waterproof layer.

By combining the energy absorption performance of the rubber component and the circumferential rigidity provided by the steel plate, the LSED structure offers a balanced solution that effectively mitigates seismic damage while preserving the overall structural integrity of the tunnel system.

3 NUMERICAL SIMULATION ON ASEISMIC PERFORMANCE OF THE LSED STRUCTURE IN TUNNELS

3.1 *Numerical model establishment of the lining – ground - LSED structure system*

The seismic response of the LSED structure-tunnel-ground system is analyzed using the full dynamic time history analysis method with the finite element analysis software ABAQUS. The numerical model of the system is illustrated in Figure 3. In the model, the upper and lower L-type slabs of the LSED structure (highlighted in red in Figure 3) are connected to the left and right sides of the lining cross-section, respectively. The LSED structure is distributed along the circumference of the lining, and the remaining joint area is filled with elastic material. The numerical model has dimensions of 80 m in width (cross-sectional direction), 60.996 m in length (axial direction), and 80 m in depth (vertical direction), with a buried depth of 36.4 m. To eliminate boundary effects on the tunnel response, the distance between the ground boundary and the lining is more than five times the tunnel diameter. The tunnel cross-section is circular, with inner diameters of 3 m and a thickness of 0.6 m. Construction joints occur at regular intervals of 10 m along the axial direction of the tunnel. In the numerical model, the LSED structure is only installed at the middle construction joint to highlight its seismic performance.

The proposed structure has dimensions of 0.996 m in length, 0.6 m in width, and 0.421 m in thickness to meet the requirements for tunnel lining thickness. The energy absorption body consists of 19 steel plates and 20 rubber layers, each with dimensions of 0.6 m in length, 0.6 m in width, and 0.2355 m in thickness. The steel plates and rubber layers are generated by establishing the overall model before assigning parameters in different regions. This approach reduces the number of node elements in the model, improving convergence and

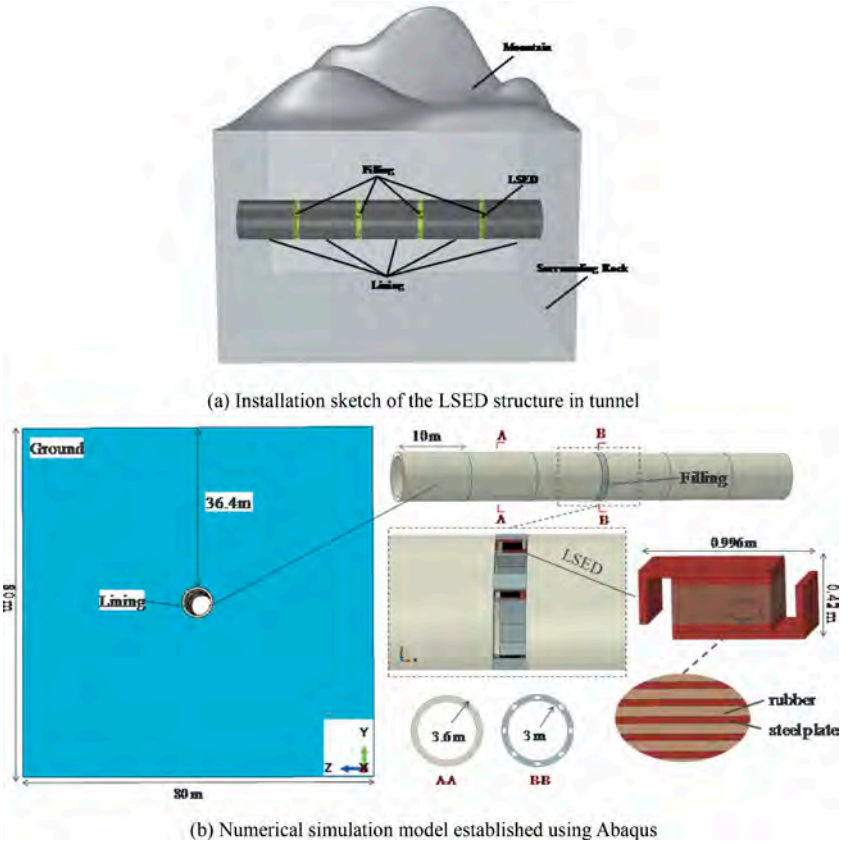

(a) Installation sketch of the LSED structure in tunnel

(b) Numerical simulation model established using Abaqus

Figure 3. Model sketch for the LSED structure - lining - ground system.

minimizing errors compared to establishing separate steel plates and rubber layers and setting binding contacts between them. To simplify the contact between the LSED structure and the filling material, the cross-section shape of the energy absorption body is designed as a square, and the rubber protective layer is not included in the numerical model as it has a negligible influence on the tunnel response.

The meshing of the model is shown in Figure 4. The size of soil elements is chosen to be less than 1/6 to 1/8 of the minimum wavelength to ensure proper wave propagation through the elements (Kuchlemeyer et al., 1973). Mesh refinement is performed near the contact areas between the surrounding rock and the lining, as well as between the LSED structure and the lining.

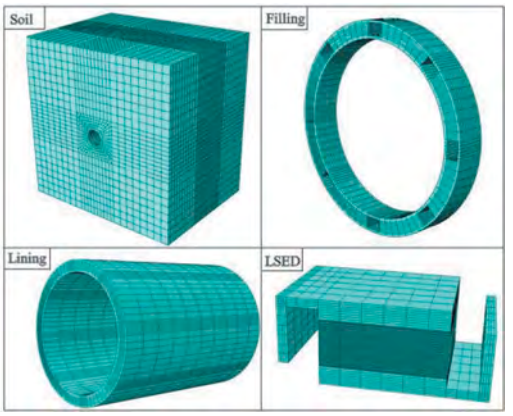

Figure 4. Meshing of model.

3.2 *Material model*

The surrounding rock is discretized using a 3D 8-node reduced integration element (C3D8R) with the Mohr-Coulomb model, where the damping ratio of the rock is set as 0.05. The tunnel lining and filling at the joint are also discretized using a 3D 8-node reduced integration element (C3D8R) and assumed to have an elastic behavior. Detailed properties of the ground-lining system are provided in Table 1. For the LSED structure, the rubber material is considered almost incompressible and characterized using the 3D 8-node hybrid element (C3D8H) with the first-order strain energy function constitutive model (Mooney-Rivlin). This model accurately describes the mechanical properties of rubber materials with deformations below 150%. The constants C1 and C2 in the Mooney-Rivlin model can be calculated based on the rubber shear modulus, while the coefficient D1, which affects the compressibility of the rubber, is set to zero (Du et al., 2006). The steel plate material is discretized using the 3D 8-node element (C3D8) and assumed to follow an elastic behavior with a density of 7850 kg/m³, an elastic modulus of 206 GPa, and a Poisson's ratio of 0.3. To simulate the bolt connection, the L-type steel-reinforced concrete slab is set to have a binding contact with the lining end face. Surface-to-surface contact with finite sliding is established at the connections between linings at the construction joint, between the ground and the lining, and between the ground and the filling. The contact is modeled using tangential penalty friction and normal 'Hard' contact conditions (Wang et al., 2022). Please refer to Table 1 for more detailed properties of the ground-lining system and the LSED structure.

3.3 *Boundary condition*

To simulate free field motion and account for the elastic recovery performance of the semi-infinite media outside the artificial boundary, a viscous-spring artificial boundary is applied to all boundaries except the upper boundary of the model. This boundary condition involves the application of a viscous damper and a spring to the boundary node of the finite element model. The viscous-spring artificial boundary is designed to maintain good stability at both high and low frequencies (Du, 2006). It effectively mimics the behavior of the surrounding media beyond the artificial boundary and allows for

Table 1. Properties of the LSED-tunnel-ground system for numerical simulation.

					LSED structure			
		Ground	Lining	Filling	steel plate	rubber 1	rubber 2	rubber 3
Density (kg/m^3)		2100	2400	100	7850	930	930	930
Elastic modulus (GPa)		2.4	30	0.0001	206	-		
Shear modulus (MPa)		-	-	-	-	0.286	0.486	1.086
Poisson's ratio		0.31	0.2	0.1	0.3	-	-	
Friction angle(°)		30	-	-	-	-	-	
Cohesion yield stress (MPa)		0.3	-	-	-	-	-	
Shear wave velocity (km/s)		2.924	-	-	-	-	-	
Mooney-Riviling	C_1 (MPa)	-	-	-	-	0.130	0.221	0.494
	C_2 (MPa)	-	-	-	-	0.0130	0.0221	0.0494
	D_1 (MPa)	-	-	-	-	0	0	0

accurate simulation of the elastic recovery response. By implementing this boundary condition, the model can effectively reproduce the dynamic characteristics of the free field and ensure that the seismic response analysis captures the realistic behavior of the system.

The input motion of the shear wave is vertically applied at the bottom boundary of the model. Figure 5 displays the seismic wave from the Trinidad earthquake. To simplify the calculations, the acceleration concentration portion between the 7th and 10th seconds is selected as the input wave. In ABAQUS, instead of directly applying the seismic wave, an equivalent node force is applied at the bottom node of the artificial boundary surface. This equivalent node force is determined based on the velocity and displacement time history of the seismic waves (Huang, 2015), allowing for a realistic representation of the input motion. By using this approach, the seismic response can be accurately captured while reducing computational complexity and simplifying analysis process.

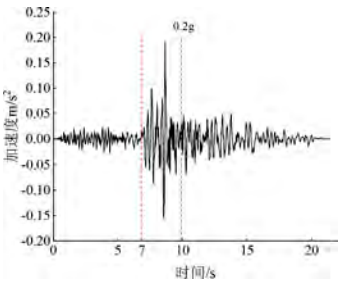

Figure 5. Trinidad seismic wave.

3.4 *Seismic response result*

In this study, the monitoring surface is chosen as the right end face of the third lining section. Considering the model's geometry and boundary conditions, the seismic response of the cross-section exhibits axisymmetric behavior. To analyze the seismic response, five monitoring points are strategically placed, namely the crown, spandrel, haunch, springing line, and invert, as depicted in Figure 6. Using a finite element model, we obtained the seismic responses of the tunnel-ground system with and without the LSED structure. We evaluated the differences between these responses by examining the maximum principal stress and strain energy within the tunnel lining structure.

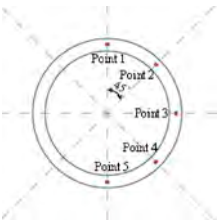

Figure 6. Monitoring points arrangement of the lining.

Figure 7 illustrates the time histories of the maximum principal stress and strain energy at the five monitoring points. A comparison between the model with and without the LSED structure is shown, represented by the dotted line and solid line, respectively. The results indicate a significant reduction in both the maximum principal stress and strain energy for the model with the LSED structure, accompanied by a smaller variation in amplitude. This highlights the effectiveness of the LSED structure in reducing the seismic response of the tunnel lining under earthquake forces. Further evidence supporting the good seismic performance of the structure can be observed from Figure 8, which displays the maximum principal stress contour of the third and fourth lining sections. To quantify the seismic mitigation achieved by the LSED structure, we define the seismic mitigation rate as the percentage change between the seismic response of the tunnel lining with the LSED structure and that without it. Figure 9 presents the seismic mitigation rates at the various monitoring points: 46.09% at the crown (Point 1 in Figure 7), 46.94% at the spandrel (Point 2), 45.07 % at the haunch (Point 3), 46.75% at the springing line (Point 4), and 46.72% at the invert (Point 5). These findings highlight the excellent aseismic performance of the LSED structure in tunnel seismic design.

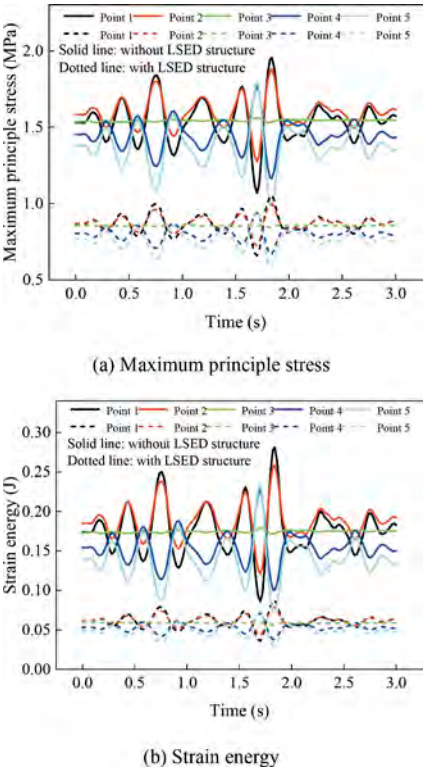

Figure 7. Time history curve of maximum principle stress and strain energy at each monitoring point.

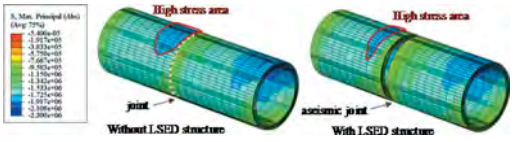

Figure 8. Contour of the maximum principal stress at the third and fourth lining section.

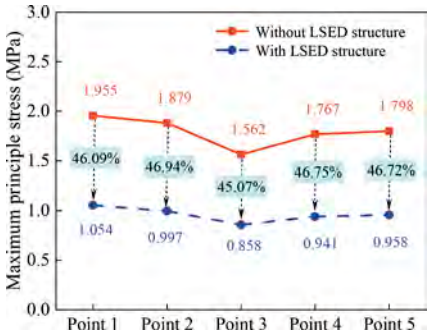

Figure 9. Seismic mitigation rate at each monitoring point.

4 CONCLUSIONS

This paper proposes a laminated shear energy dissipation (LSED) structure to enhance the axial aseismic performance of tunnel structures. As tunnels are susceptible to longitudinal seismic response, the LSED structure, composed of alternating thin steel plates and rubber layers, is installed at the cross-section boundary of the secondary lining to improve deformation ability and rigidity resistance. The mechanical properties of the LSED structure are verified using a spring-mass model, and a three-dimensional numerical model of the LSED structure-tunnel lining-surrounding rock system is developed for seismic response analysis. The research results show thatthe LSED structure exhibits high vertical bearing capacity due to the rigidity of the thin steel plate, while maintaining good deformation allowance in the horizontal direction through the elastic characteristics of the rubber component. Seismic response analysis shows that the LSED structure significantly reduces the maximum principal stress and strain energy of the tunnel compared to the case without the structure. Subjected to Trinidad seismic waves, the seismic mitigation rate exceeds 45%.

ACKNOWLEDGMENTS

This work was supported by the National Natural Science Foundation of China (grant number 52109132); and the Shandong Provincial Natural Science Foundation (grant number ZR2020QE270).

REFERENCES

Asakura, T., Sato, Y., 1996. Damage to mountain tunnels in the hazard area. Soils and Foundations, Japanese Geotechnical Society, Special Issue, 301–310.

Atsushi, K., 2009. Seismic research and example of shield tunnel. Translated by Zhang Wenjun, Yuan Dajun. Beijing: China Architecture and Building Indusitry Press.

Cui, G.Y., Wang, M.N., Yu, L., Lin, G.J., 2013. Model test study of shock absorption joint damping technology of crossing stick-slip fracturl tunnel. Chinese Journal of Rock Mechanics and Engineering. 32(8), 1603–1609. (in Chinese)

Cui, G.Y., Liu, W.D., Ni, S.Z., Wang, M.N., Lin, G.J., 2015. Analysis of seismic damage and mechanism of general section of highway tunnel in Wenchuan earthquake. Rock and Soil Mechanics. 36(S2), 439–446. (in Chinese)

Cui, G.Y., Li, P.Y., Wang, M.N, Zhu, C.A., 2020. Model tests for safety of stick-slip fault tunnel in strong earthquake area using rigid-flexible com. Journal of Vibration and Shock. 39(5), 194–207. (in Chinese)

Chen, P.L., Geng, P., Chen, J.B., Gu, W., 2023. The seismic damage mechanism of the Daliang tunnel by fault dislocation during the 2022 Menyuan Ms6.9 earthquake based on unidirectional velocity pulse input. Engineering Failure Analysis. 145, 107047.

Du, X.L, Zhao, M., Wang, J.T., 2006. A stress artificial boundary in fea for near-field wave problem. Chinese Journal of Theoretical and Applied Mechanics. 38(1), 49–56. (in Chinese)

Du, X.L., Huang, J.Q., Zhao, M., Jin, L., 2014. Effect of oblique incidence of SV waves on seismic response of portal sections of rock tunnels. Chinese Journal of Geotechnical Engineering. 36(8), 1400–1406.

Ding, J.H., Jin X.L., Guo, Y.Z., Li, G.G., 2006. Numerical simulation for large-scale seismic response analysis of immersed tunnel. Engineering Structures. 28, 1367–1377.

Ding, X.L., Zhang, Y.T., Zhang, C.J., Yan, T.Y., Huang, S. L., 2019. Review on countermeasures and their adaptability evaluation to tunnels crossing active faults. Hazard Control in Tunnelling and Underground Engineering. 1(1), 25–40. (in Chinese)

Hasheminejad S.M., Miri A.K., 2008. Seismic isolation effect of lined circular tunnels with damping treatments. Earthquake Engineering and Engineering Vibration. 7 (3), 305–319.

Hao, X., Zhang, Q., Sun, Z., Wang, S., Yang, K., Ren, B., Zhang, X., 2021. Effects of the major principal stress direction respect to the long axis of a tunnel on the tunnel stability: physical model tests and numerical simulation. Tunnelling and Underground Space Technology. 114, 103993.

Kuchlemeyer, R.L., Lysmer, J., 1973. Finite element method accuracy for wave propagation problems. Journal of the Soil Mechanics and Foundations Division. 99 (5), 421–427.

Konagai, K., Kim, D.S., 2001. Simple evaluation of the effect of seismic isolation by covering a tunnel with a thin flexible material. Soil Dynamics and Earthquake Engineering. 21(4), 287–295.

Kawamata, Y., Nakayama, M., Towhata, I., Yasuda, S., 2016. Dynamic behaviors of underground structures in E-Defense shaking experiments. Soil Dynamics and Earthquake Engineering. 82, 24–39.

Li, T.B., 2012. Damage to mountain tunnels related to the Wenchuan earthquake and some suggestions for aseismic tunnel construction. Bulletin of Engineering Geology and the Environment. 71, 297–308.

Li, C., Chen, W., 2019. Seismic isolation effect of foamed concrete layer along the longitudinal direction of a mountainous tunnel. Vibroengineering Procedia. 23, 76–80.

Wang, J.N., Zhang, J.Y., Zhuang, H.Y., Yang, J., Li, C., 2022. Numerical investigation on seismic performance of a shallow buried underground structure with isolation devices. Earthquake Research Advances. 2, 100171.

Providakis, C.P., 2009. Effect of supplemental damping on LRB and FPS seismic isolators under near-fault ground motions. Soil Dynamics and Earthquake Engineering. 29, 80–90.

Shen, Y.S., Gao, B., Yang, X.M., 2014. Seismic damage mechanism and dynamic deformation characteristic analysis of mountain tunnel after Wenchuan earthquake. Engineering Geology. 180, 85–98.

Sayed, M.A., Kwon, O.S., Park, D., Nguyen, Q.V., 2019. Multi-platform soil-structure interaction simulation of Daikai subway tunnel during the 1995 Kobe earthquake. Soil Dynamics and Earthquake Engineering. 125, 105643.

Savigamin, C., Bobet, A., 2021. Seismic response of a deep circular tunnel subjected to axial shear and axial bending. Tunnelling and Underground Space Technology. 112, 103863.

Wang, T.T., Kwork, O.A., Jeng F.S., 2021. Seismic response of tunnels revealed in two decades following the 1999 Chi-Chi earthquake (Mw 7.6) in Taiwan: A review. Engineering Geology. 287, 106090.

Xin, C.L., Wang, Z.Z., Zhou, J.M., Gao, B., 2019. Shaking table tests on seismic behavior of polypropylene fiber reinforced concrete tunnel lining. Tunnelling and Underground Space Technology. 88, 1–15.

Yu, H.T., Yuan, Y., Qiao, Z.Z., Gu, Y., Yang, Z.H., Li, X. D., 2013. Seismic analysis of a long tunnel based on multi-scale method. Engineering Structures. 49, 572–587.

Yu, H.T., Chen, J.T., Bobet, A., Yuan, Y., 2016. Damage observation and assessment of the Longxi tunnel during the Wenchuan earthquake. Tunnelling and Underground Space Technology. 54, 102–116.

Yu, H.T., Yuan, Y., Bobet, A., 2017. Seismic analysis of long tunnels: A review of simplified and unified methods. Underground Space. 2, 73–87.

Zhang, X.P., Jiang, Y.J., Sugimoto, S., 2018. Seismic damage assessment of mountain tunnel: A case study on the Tawarayama tunnel due to the 2016 Kumamoto Earthquake. Tunnelling and Underground Space Technology. 71, 138–148.

Zhang, Y.J., Huang, H.W., Zhang, D.M., Ayyub, B.M., 2022. Deformation recoverability of longitudinal joints in segmental tunnel linings: An experimental study. Tunnelling and Underground Space Technology. 124, 104475.

Geotechnics, geology and geophysical prospecting

Taylor & Francis
Taylor & Francis Group
http://taylorandfrancis.com

Tunnelling for a Better Life – Yan, Celestino, Thewes & Eberhardt (Eds)
© 2024 The Author(s), ISBN 978-1-032-80042-4
Open Access: www.taylorfrancis.com, CC BY-NC-ND 4.0 license

An improved simplified solution for the characteristic line of tunnels in strain-softening rocks

M. Anthi*, Th. Pferdekämper & G. Anagnostou
ETH, Zürich, Switzerland

ABSTRACT: We present an analytical solution for calculation of the characteristic line for tunnels excavated in strain-softening rock masses obeying the Mohr-Coulomb criterion, with linear uniaxial compressive strength decay. The derivation is based on the simplifying assumption that the strains inside the plastic zone are completely plastic. This significantly simplifies the mathematical formulation, enabling the derivation of closed-form solutions. The accuracy of the simplified solutions is evaluated by comparing their predictions with rigorous solutions obtained by numerical finite-difference analyses.

Keywords: ground response curve, tunnelling, strain-softening, Mohr-Coulomb

1 INTRODUCTION

The characteristic line in strain-softening rock masses can be determined by numerical methods with rigorous treatment of the deformations in the plastic zone, or by analytical or semi-analytical methods involving certain simplifications (for comprehensive reviews see, *e.g*., Guan *et al*. 2020, Ghorbani and Hasanzadehshooiili 2019). From a theoretical perspective, the rigorous methods are robust. However, in general, these are too complex for practical use, due to the need to solve differential equations. The mathematical treatment can be significantly simplified by neglecting the elastic strains that develop during yielding (Egger 1974, Panet 1976), but Guan *et al*. (2007) showed that this simplification underestimates the tunnel wall displacement by 20-40% compared to rigorous methods (Alonso *et al*., 2003).

In this paper, we propose an improved simplifying solution for the characteristic line, adopting Kovári's (1985) approach, which derived characteristic lines for perfectly plastic rocks (no softening) completely neglecting the elastic strains within the plastic zone. The improvement achieved by the new solution is illustrated by means of comparative analyses considering older approximate solutions as well as numerical results obtained for the rigorous formulation by the finite differences method presented by Lee and Pietruszczak (2008). Furthermore, the paper discusses some interesting features of the characteristic line in addition to aspects of the stability in the case of strain softening.

2 PROBLEM STATEMENT

We consider a deep cylindrical tunnel with radius a, crossing homogeneous and isotropic rock under a hydrostatic *in-situ* stress field (Figure 1). The tunnel is supported by a uniform pressure σ_a, while the far field stresses are equal to the *in-situ* stress σ_0. Under these assumptions the system fulfils rotational symmetry. We are looking for the relationship between the support pressure σ_a and the radial displacement u_a of the tunnel wall.

The rock mass is taken as a linearly elastic, softening plastic material obeying the Mohr-Coulomb yield criterion. A linear decrease in the uniaxial compressive strength f_c with the deviatoric plastic strain γ^{pl} will be assumed (Figure 2):

$$f_c(\gamma^{pl}) = \begin{cases} f_c^p - \left(f_c^p - f_c^r\right)\frac{\gamma^{pl}}{\gamma^r}, & if\ \gamma^{pl} \le \gamma^r \\ f_c^r, & if\ \gamma^{pl} \ge \gamma^r \end{cases}, \quad (1)$$

where f_c^p and f_c^r denote the peak and residual strength values, respectively; γ^r is a material constant representing the deviatoric plastic strain at which the residual strength is attained; and γ^{pl} is the deviatoric plastic strain.

Following Alonso *et al*. (2003), the latter is defined as follows:

$$\gamma^{pl} = \varepsilon_t^{pl} - \varepsilon_r^{pl}, \quad (2)$$

where $\varepsilon_t{}^{pl}$ and $\varepsilon_r{}^{pl}$ represent the tangential and radial plastic strains, respectively. For the sake of simplicity, we assume that the friction angle is constant.

*Corresponding author: maria.anthi@igt.baug.ethz.ch

DOI: 10.1201/9781003495505-61

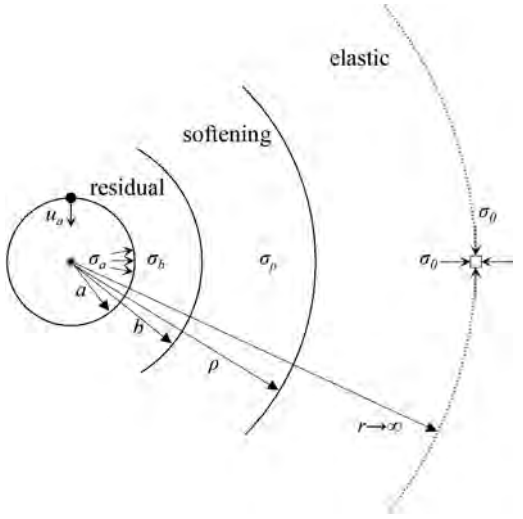

Figure 1. Problem setup and zones of the stress field in a strain softening rock mass.

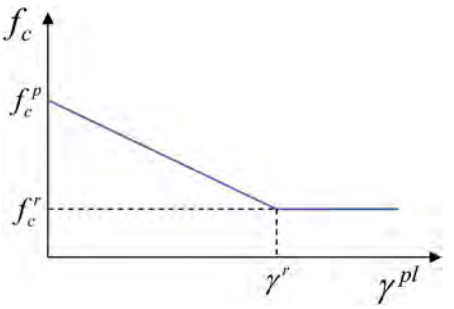

Figure 2. Strength over deviatoric plastic strain.

Furthermore, considering that in most cases the dilatancy angle is small, a non-associated flow rule with zero plastic volumetric strains will be considered.

3 DERIVATION

We will determine the radial displacement of the tunnel wall that occurs when the radial stress at the tunnel wall decreases from its *in-situ* value σ_0 to the support pressure σ_a. With decreasing radial stress, the rock mass initially remains elastic and, at a certain support pressure σ_ρ, starts experiencing plastic deformations. Further radial stress reduction results in the formation of a zone of radius ρ where the rock mass experiences plastic shearing, and its strength decreases according to the softening law of Figure 2. The deviatoric plastic strain at the excavation boundary may reach γ^r at a certain support pressure σ_b; in this case, a further decrease in the support pressure ($\sigma_a < \sigma_b$) will result in the formation of an inner plastic zone up to a radius b, where rock strength equals residual strength. So, the system consists in general of three zones, hereafter referred to as the elastic zone (an infinite body with a cylindrical hole), the softening zone and the residual zone (thick-walled cylinders) (Figure 1). The characteristic line can be determined by considering these three system components separately, taking account of the radial stress and radial displacement continuity conditions at their interfaces.

For simplicity, the abbreviation

$$\bar{\sigma}\ldots = \sigma\ldots + f_c^p/(m-1), \tag{3}$$

where m is a function of the friction angle (m = (1 +sinφ)/(1-sinφ)), will be used below for all stresses. The elasticity solutions for a cylindrical tunnel in combination with the condition that the stress state at the boundary ρ of the plastic zone fulfils the yield condition with the peak strength parameters leads to the following expressions for the radial stress σ_ρ and for the radial displacement u_ρ (*cf., e.g.*, Vrakas and Anagnostou, 2014):

$$\bar{\sigma}_\rho = \frac{2\bar{\sigma}_0}{m+1}, \tag{4}$$

$$u_\rho = \rho\frac{\bar{\sigma}_0}{E}\frac{(1+\nu)(m-1)}{m+1}, \tag{5}$$

where E and ν denote the Young's modulus and the Poisson's ratio, respectively.

Under the assumptions made (negligible elastic strains in the plastic zone and negligible plastic volumetric strains), the volume of the plastic zone is constant and consequently the radial displacements fulfil the following condition (Kovári 1985):

$$u_a a = u_\rho \rho = u(r)r = \text{ constant}. \tag{6}$$

Introducing u_ρ from Eq. (5) into Eq. (6) leads to the following expression for the radius ρ of the plastic zone as a function of the displacement u_a of the tunnel boundary:

$$\frac{\rho}{a} = \left(\frac{m+1}{(1+\nu)(m-1)}\frac{u_a E}{a\bar{\sigma}_0}\right)^{1/2}. \tag{7}$$

The tangential stress σ_t fulfils the yield condition $\sigma_t = m\sigma_r + f_c(\gamma^{pl})$, where σ_r is the radial stress and $f_c(\gamma^{pl})$ and γ^{pl} are given by Eqs. (1) and (2), respectively, whereby the strains on the r.h.s. of Eq. (2) are obtained from the kinematic relationships with u after Eq. (6). This leads to $\gamma^{pl}(r) = 2\rho u_\rho/r^2$; at the tunnel wall, $\gamma^{pl} = 2\rho u_\rho/a^2$.

Introducing σ_t from the yield condition into the equilibrium condition $d\sigma_r/dr = (\sigma_t - \sigma_r)/r$ results in a differential equation for the radial stress, the solution of which for the boundary condition $\sigma_r(a) = \sigma_a$ provides the stress field in the form $\sigma_r = f(r/\rho, \sigma_a)$. This equation in combination with the condition $\sigma_r(\rho) = \sigma_\rho$ results in a relationship between support pressure σ_a and radius ρ of the plastic zone. More specifically, considering the linear decay part of the softening relation (Figure 2), we obtain:

$$\frac{\bar{\sigma}_a}{\bar{\sigma}_0} = \frac{2}{m+1}\left(\left(\frac{\rho}{a}\right)^{1-m} + \frac{f_c^p - f_c^r}{\gamma^r E}\frac{(1+\nu)(m-1)}{m+1}\left(\left(\frac{\rho}{a}\right)^2 - \left(\frac{\rho}{a}\right)^{1-m}\right)\right) \quad (8)$$

Eq. (8) holds provided that there is not yet a residual zone, which means that the plastic shear strain at the tunnel wall (which equals $2\rho u_\rho/a^2$ as mentioned above) is less than γ^r. This is the case as long as the radius of the plastic zone is less than a critical value ω:

$$\frac{\rho}{a} \le \omega = \max\left\{1, \sqrt{\frac{\gamma^r E}{\bar{\sigma}_0}\frac{m+1}{2(1+\nu)(m-1)}}\right\}. \quad (9)$$

If the last r.h.s. term of this equation is less than 1, then $\omega = 1$ and a residual zone develops from the start of plastification (see Anthi *et al.*, 2024, for details). The support pressure at the onset of the formation of the residual zone (that is σ_b) can be obtained from Eq. (8) with $\rho/a = \omega$.

If $\sigma_b > 0$, then for $\sigma_a < \sigma_b$ (or, equivalently, for $\rho/a > \omega$) a residual zone develops. The outer radius of the residual zone (b) is such that the support pressure exerted by the residual zone upon the softening zone equals to σ_b and, consequently, $\rho/b = \omega$ or $b = \rho/\omega$. It can be obtained from the bearing capacity equation of a fully plastified thick-walled cylinder that exhibits a uniform strength (the residual strength f_c^r), is loaded at its outer boundary by σ_b and is supported at its inner boundary by σ_a (see, *e.g.*, Kovári 1985):

$$\frac{b}{a} = \frac{\rho/\omega}{a} = \left(\frac{\sigma_b + \frac{f_c^r}{m-1}}{\sigma_a + \frac{f_c^r}{m-1}}\right)^{\frac{1}{m-1}}. \quad (10)$$

Solving this equation with respect to σ_a provides the following expression for the support pressure in the presence of a residual zone, that is for $\rho/a > \omega$:

$$\frac{\bar{\sigma}_a}{\bar{\sigma}_0} = \left(\frac{\bar{\sigma}_b}{\bar{\sigma}_0} - \frac{f_c^p - f_c^r}{\bar{\sigma}_0}\frac{1}{m-1}\right)\left(\frac{\rho/a}{\omega}\right)^{1-m} + \frac{f_c^p - f_c^r}{\bar{\sigma}_0}\frac{1}{m-1}. \quad (11)$$

The non-trivial (plastic) part of the characteristic line can be computed analytically by considering the displacement as an independent parameter (observing the condition $u_a E/a/\bar{\sigma}_0 \ge (1+\nu)(m-1)(m+1)$ in order that $\rho \ge a$) and first computing ρ from Eq. (7). Subsequently, if ρ fulfils the inequality (9), then σ_a is determined from Eq. (8); else σ_b is computed first (from Eq. 8 with $\rho/a = \omega$) and introduced afterwards into Eq. (11), which finally provides σ_a. An inspection of the equations above readily reveals that the characteristic line can be expressed as follows:

$$\frac{\bar{\sigma}_a}{\bar{\sigma}_0} = f\left(\frac{u_a E}{a\bar{\sigma}_0}, \frac{f_c^p - f_c^r}{\bar{\sigma}_0}, \frac{\gamma^r E}{\bar{\sigma}_0}, \varphi, \nu\right). \quad (12)$$

The derivation outlined above can be applied for arbitrary softening laws as well as for Egger's (1974) and Panet's (1976) simplifying assumption regarding the elastic strains in the plastic zone (Anthi *et al.*, 2024).

4 ERROR

To assess the error of the proposed solution, we use Lee and Pietruszczak's (2008) numerical predictions as benchmarks. Figure 3 shows the error in the convergence of an unsupported cavity, calculated as follows:

$$error = \frac{u_{a,simplified} - u_{a,exact}}{u_{a,exact}} \cdot 100\% \quad (13)$$

The error is given as a function of the dimensionless parameter $\gamma^r E/\sigma_0$, which governs how rapidly the strength drops to its residual value, for two values of the normalised peak strength f_c^p/σ_0, characterising

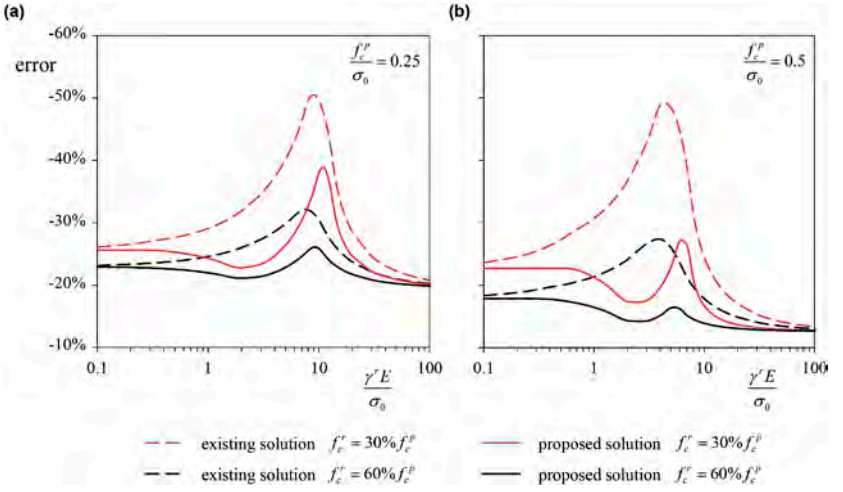

Figure 3. Error of the proposed and of the older analytical solution over the dimensionless factor $\gamma^r E/\sigma_0$ (unsupported tunnel, $\varphi = 30°$, $\nu = 0.3$).

heavy and moderate squeezing conditions (Figures 3a and 3b, respectively), while comparing two values of the residual strength f_c^r as a percentage of the peak strength f_c^p, with red and black curves, respectively.

Each diagram presents two sets of curves. The continuous curves show the error of the simplified solution proposed in this paper, while the dashed curves hold for the former simplified solution. Both solutions underestimate the convergence of the unsupported tunnel, however, the proposed solution exhibits a smaller error. In general, the error increases with decreasing f_c^r and $f_c^{\ p}/\sigma_0$. For materials with either low or high values of $\gamma^r E/\sigma_0$ (indicating rather brittle or rather perfectly plastic behaviour, respectively), the simplified solutions converge. For intermediate values of $\gamma^r E/\sigma_0$ (softening behaviour) the proposed solution outperforms the existing one significantly. While the existing simplified solution reaches an error of 50%, the solution introduced in this paper maintains an error of less than 30% approximately.

5 CHARACTERISTIC LINES

Figure 4 illustrates the effect of the two softening parameters $(f_c^p - f_c^r)/\bar{\sigma}_0$ and $\gamma^r E/\bar{\sigma}_0$. It presents normalised characteristic lines for three values of the strength decay $(f_c^p - f_c^r)/\bar{\sigma}_0 = 0.75,\ 0.5,\ 0.25$(black, blue and orange curves, respectively) and $\gamma^r E/\bar{\sigma}_0 = \infty, 12,\ 6,\ 3$and 0. The latter expresses how rapidly strength decreases with plastic deformations. The uppermost curve in each set of same colour ($\gamma^r E/\bar{\sigma}_0 \to 0$) holds for a brittle plastic material characterised by a sudden decrease in strength at the onset of yielding. The lowermost line ($\gamma^r E/\bar{\sigma}_0 \to \infty$) is common to all sets and holds for a perfectly plastic

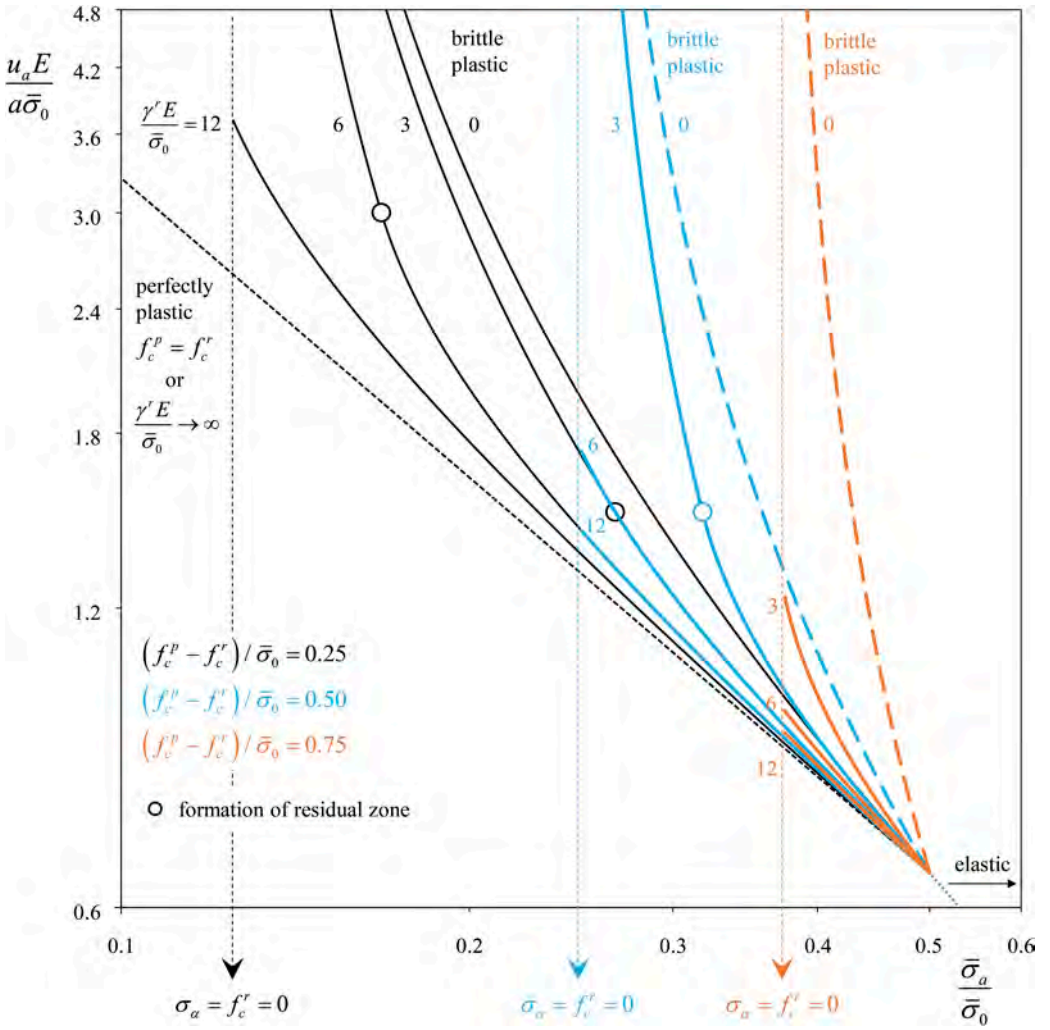

Figure 4. Normalized characteristic lines ($\varphi = 30°$, $\nu = 0.3$).

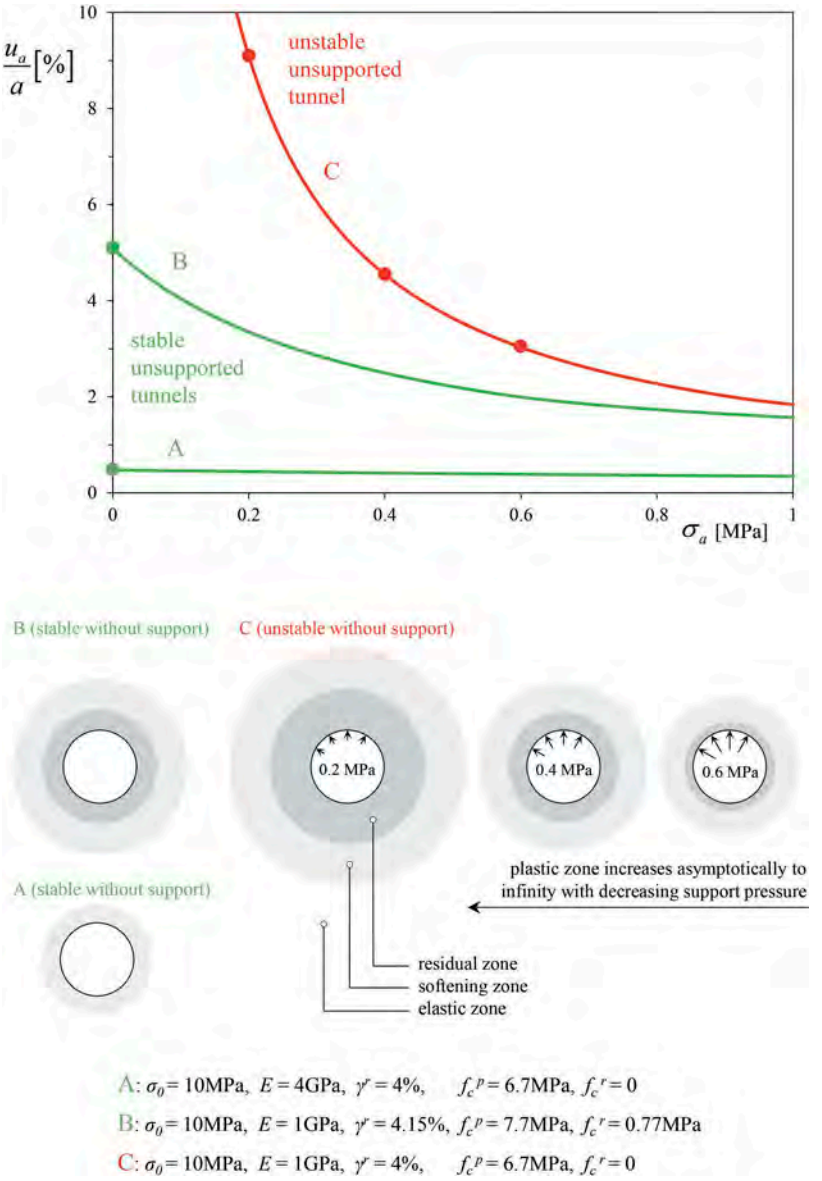

Figure 5. Characteristic lines illustrating stable and unstable conditions (φ = 30°, ν = 0.3). The presented plastic zones correspond to the marked points of the characteristic lines.

material; it is identical with Kovári's (1985) characteristic line, a straight line in the double-logarithmic diagram. Each characteristic line starts at $\bar{\sigma}_a/\bar{\sigma}_0 = (f_c^p - f_c^r)/\bar{\sigma}_0/(m-1)$, which is the value of $\bar{\sigma}_a/\bar{\sigma}_0$ when $\sigma_a = 0$ and $f_c{}^r = 0$. Lower values are not considered because they correspond to negative support pressures and therefore lack physical meaning.

As expected, with decreasing $(f_c^p - f_c^r)/\bar{\sigma}_0$-value, the effect of $\gamma^r E/\bar{\sigma}_0$ becomes smaller as all lines move towards that of the perfectly plastic material (lowest straight dashed line).

The convergence of an unsupported opening in a rock with zero residual strength stabilises to a finite value, despite the zero residual strength, if $\gamma^r E/\bar{\sigma}_0$ is so large that a residual zone does not form. In the cases of Figure 4, this is true for: $\gamma^r E/\bar{\sigma}_0 = 12$ and $f_c^p/\bar{\sigma}_0 = 0.25$; $\gamma^r E/\bar{\sigma}_0 = 12$ or 6 and $f_c^p/\bar{\sigma}_0 = 0.5$; $\gamma^r E/\bar{\sigma}_0 = 12, 6$ or 3 and $f_c^p/\bar{\sigma}_0 = 0.75$. Otherwise, *i.e.* if $\gamma^r E/\bar{\sigma}_0$ is small enough that a residual zone with zero uniaxial compressive strength develops, equilibrium is not possible and, therefore, the displacements increase asymptotically to infinity as the support pressure tends to zero (Panet, 1976).

To gain a better understanding of the dimensionless representation of the characteristic lines of Figure 4, we focus on the set of blue curves ($i.e.(f_c^p - f_c^r)/\bar{\sigma}_0 = 0.5$), examining three cases:

- complete strength loss ($f_c{}^r = 0$) and $\gamma^r E/\bar{\sigma}_0 = 12$, which is high enough that a residual zone is not formed around the unsupported opening (see characteristic line A and corresponding plastic zone in Figure 5);
- partial strength loss ($f_c{}^r = 0.10\ f_c{}^p$) and a$\gamma^r E/\bar{\sigma}_0 = 3$, which is low and allows residual zone formation around the unsupported opening (curve and plastic zones B in Figure 5); and
- complete strength loss ($f_c{}^r = 0$) with the same low $\gamma^r E/\bar{\sigma}_0$ of 3, leading to the formation of a zone with zero strength around the unsupported opening (curve and plastic zones C in Figure 5).

In cases A and B, the unsupported opening is stable, whereas in case C, equilibrium is impossible without support (displacements tend towards infinity).

Since curves B and C of Figure 5 correspond to the same normalised curve of Figure 4, one may say that the normalised diagram of Figure 4 presents characteristic lines for cases that are qualitatively different from the constructional viewpoint (stable vs. unstable unsupported openings).

The comparison of the case A (stable without support) with case C (stable without support), which are different only with respect to E (4 and 1 GPa, respectively) shows again that the stability of an unsupported opening also depends on Young's modulus.

6 CONCLUSIONS

An improved analytical solution was derived for assessing tunnel convergences in strain-softening rock masses obeying Mohr-Coulomb yield criterion with linear strength decay during softening.

The characteristic lines are expressed in a dimensionless form, which enables the analysis of qualitatively different cases, *i.e.* stable and unstable unsupported openings, by one and the same characteristic line. Specifically, for a given cavity support pressure and strength drop f_c^r/f_c^p, stable conditions are characterised by a finite dimensionless convergence of the cavity. Otherwise, the convergence tends towards infinity. If the strength at the tunnel wall becomes equal to zero, the tunnel cannot be stable without support.

The derivation of closed-form characteristic lines was made possible by adopting the simplifying assumption of disregarding the elastic strains within the plastic zone. It was shown that the proposed solution consistently outperforms the simplified solution found in the existing literature. However, both analytical solutions underestimate the tunnel convergence compared to rigorous results obtained from the FD model suggested by Lee and Pietruszczak (2008).

REFERENCES

Anthi, M., Pferdekämper, T., Anagnostou, G. (2024). Analytical solutions for cavity contraction in strain-softening materials with linear or exponential strength decay. *Engineering Reports* (under review).

Alonso, E., Alejano, L. R., Varas, F., Fdez-Manín, G., Carranza-Torres, C. (2003). Ground response curves for rock masses exhibiting strain-softening behaviour. *Int. J. Num. Anal. Meth. in Geomech*., 27, 1153–1185.

Egger, P., "Gebirgsdruck im Tunnelbau und Stiitzwirkung der Ortsburst bei Uberschreiten der Gebirgsfestigkeit," Advances in Rock Mechanics, Proceedings of the Third Congress of the International Society for Rock Mechanics, Vol. 2, Part B, National Academy of Sciences, Washington, D.C., 1974, pp. 1007–1011.

Ghorbani, A., & Hasanzadehshooiili, H. (2019). A comprehensive solution for the calculation of ground reaction curve in the crown and sidewalls of circular tunnels in the elastic-plastic-EDZ rock mass considering strain softening. *Tunnelling and Underground Space Technology*, 84, 413–431.

Guan, Z., Jiang, Y., & Tanabasi, Y. (2007). Ground reaction analyses in conventional tunnelling excavation. Tunnelling and Underground Space Technology, 22(2),230–237.

Guan, K., Zhu, W., Liu, X., and Wei, J. (2020). Finite Strain Analysis of Squeezing Response in an Elastic-Brittle-Plastic Weak Rocks Considering the Influence of Axial Stress. *Tunnelling Underground Space Tech*. 97, 103254. https://doi.org/10.1016/j.tust.2019.103254

Kovári, K. (1985). The determination of the characteristic line from straight line nomograms. *Fifth Int. Conf. on Num. Meth. in Geomech*., Nagoya, 1741–1746.

Lee, Y., Pietruszczak, S. (2008). A new numerical procedure for elasto-plastic analysis of a circular opening excavated in a strain-softening rock mass. *Tunnelling and Underground Space Technology*, vol. 23, 588–599.

Panet M. (1976). Analyse de la stabilité d'un tunnel creusé dans un massif rocheux en tenant compte du comportement après la rupture. Rock Mechanics, 8, 209–223

Vrakas, A., Anagnostou, G. (2014). A finite strain closed-form solution for the elastoplastic ground response curve in tunnelling. *Int. J. Numer. Anal. Meth. Geomech*., vol. 38, 1131–1148.

Tunnelling for a Better Life – Yan, Celestino, Thewes & Eberhardt (Eds)
© 2024 The Author(s), ISBN 978-1-032-80042-4
Open Access: www.taylorfrancis.com, CC BY-NC-ND 4.0 license

Estimation of tunnel support loads due to large deformation in squeezing ground conditions

Ketan Arora*
Department of Mining Engineering, Indian Institute of Technology (IIT) Kharagpur, India

Marte Gutierrez
Civil and Environmental Engineering, Colorado School of Mines, Golden, CO, USA

ABSTRACT: During tunnel excavation, the accumulated wall displacement and the tunnel support load result from both the tunnel advance and the time-dependent behavior of the surrounding rock mass. One approach to analyze the interactions between tunnel wall displacement and support load is the Convergence-Confinement Method (CCM) using analytical closed-form solutions or empirical Longitudinal Displacement Profiles (LDP). This approach neglects the influence of time dependency on ground response, resulting in delayed deformation increasing significantly within time after the excavation stage. Failure to consider the added delayed displacements in the preliminary design can result in a false selection of the installation time and the support system type, causing safety issues, cost overruns, and project delays. Considering the time-dependent ground response, this paper discusses a revised CCM to estimate the tunnel's support system loads in squeezing ground conditions. The proposed approach combines laboratory-scale physical model test results and observations from the squeezing tunnels worldwide. The first part of this paper explains the CCM and the improvement offered to extend the methodology for squeezing tunnels. The second paper presents the validation of the proposed method.

Keywords: Convergence Confinement Method, Tunnel Support System, Squeezing ground

1 INTRODUCTION

Squeezing ground conditions during tunnel excavation leads to large ground deformations that may continue even after excavation (Barla 1995). In such situations, the load imposed by the ground on the tunnel support system also increases gradually. The ultimate support requirements can be two to three times more in squeezing ground than the same tunnel cross-section in non-squeezing conditions (Jethwa, J. L., Singh, B., & Singh 1984). Hence, estimating the deformations due to squeezing beforehand is vital to ensure safe, efficient, and economical tunnel construction (Barla 2000).

Squeezing ground conditions are associated with clay-rich minerals at a low ratio of rock-mass strength to the in-situ stress at the tunnel location (Terzaghi 1946; Wood 1972). Reported examples of such tunnels include but are not limited to, the John Street Pumping Station Tunnel in Canada (Lo et al. 1987), the Still Water Tunnel in the United States (Phien-wej and Cording 1991), the Uluabat Project Tunnel in Turkey (Bilgin and Algan 2012), and the Laodongshan Tunnel in China (Cao et al. 2018).

Numerous approaches have been proposed in the literature over the years to study tunnel squeezing, which included experimental techniques (Semple 1973; Mesri et al. 2015; Arora et al. 2019, 2021b, a; Arora 2020), numerical analyses (Dusseault and Fordham 1993a; Bonini et al. 2009; Barla et al. 2012; Kabwe et al. 2020), analytical methods (Kallhawy 1974; Ghaboussi and Gioda 1977; Gioda 1981, 1982; Sulem et al. 1987; Pan and Dong 1991; Gioda and Cividini 1996; Singh et al. 2018), and empirical equations (Terzaghi 1946; Deere et al. 1970; Barton et al. 1974; Singh et al. 1992; Goel et al. 1995; Aydan et al. 1996; Schubert 1996; Hoek and Marinos 2000; Manh et al. 2015; Vrakas et al. 2018; Arora et al. 2021c). According to the International Society of Rock Mechanics (ISRM), the most appropriate method for designing tunnels in squeezing ground conditions should incorporate field observations, numerical techniques, and conventional closed-form solutions (ISRM 1994). The methodology must consider ground deformation due to elastoplastic behavior, creep, consolidation, progressive damage and other physical phenomena.

Despite the commendable efforts of researchers over the years to study tunnels in squeezing ground

*Corresponding author: ketanarora@mining.iitkgp.ac.in

DOI: 10.1201/9781003495505-62

conditions, tunnels continue to encounter many engineering surprises (Wang et al. 2019). This lack of definite progress is primarily due to the existing approaches' critical assumptions and limited applicability. For example, the analytical methods proposed in the literature attribute squeezing with the creep and assume no volumetric deformations (Pan and Dong 1991; Gioda and Cividini 1996). However, several past researchers have observed that rocks experience significant volumetric changes during creep (Dusseault and Fordham 1993b; Fabre and Pellet 2006; Arora 2020). Similarly, numerical methods also require a reliable constitutive model for the time-dependent behavior of the rock derived with minimum assumptions (Bonini et al. 2009). On the other hand, the empirical methods are case-specific, hold discrepancies, and are derived from limited field and laboratory experimental observations (Arora et al. 2021c).

From the limitations of the different approaches, it is evident that squeezing phenomena have yet to be extensively studied. An applicable, reliable criterion for squeezing would improve the understanding and, more importantly, could guide the tunnel engineers in designing squeezing-resilient support systems. This paper discusses a convergence-confinement method (CCM) to estimate the loads on the tunnel's support system in squeezing ground conditions. CCM is prevalent in tunnel design, but its application remains limited in squeezing ground conditions. The first part of this paper explains CCM and the proposed extension of the methodology for squeezing tunnels. The second part presents the validation of the proposed method.

2 CONVERGENCE-CONFINEMENT METHODS (CCM)

Tunnel excavation is a three-dimensional (3-D) process involving geomaterial excavation at in situ stress and geostatic conditions. Tunneling mechanically leads to stress redistribution around the excavation boundary and further leads to ground deformation. It is well-studied that the closer the tunnel cross-section is to the tunnel face, the lesser the stress redistribution (Su et al. 2011; Zheng et al. 2016). The tunnel support system design must anticipate the ground deformations and keep the tunnel convergence within the safe limit. Researchers have proposed various analytical and numerical solutions for tunnel design considering the 3-D effects of the excavation (Zhang et al. 2008; Vlachopoulos and Diederichs 2009; Su et al. 2011; Lü and Low 2011; Vrakas and Anagnostou 2016; Hedayat and Weems 2019). Such analysis methods are a primary tool for quickly assessing the system's behavior. Most of the methods are based on the popular and widely used convergence-confinement method (CCM) (Paraskevopoulou and Diederichs 2018).

CCM is a way to incorporate 3-D rock-support interaction response in tunnels into a two-dimensional (2-D) plane model (AFTES 1983). The method requires the study of the following three components:

a) *Ground reaction curve* (GRC) relating radial internal support pressure p_i and tunnel wall displacement (convergence) u.
b) *Support Characteristic Curve* (SCC) relating convergence provided by the support p_i to the support convergence.
c) *Longitudinal displacement profile* (LDP) relating convergence of the tunnel boundary u to the distance from the tunnel face x_f. The LDP approximates the 3-D deformation of the tunnel in a 2-D model.

GRC and SCC are derived analytically in a typical CCM, while the LDP is considered for the unsupported tunnel. Figure 1 illustrates the calculation of the stresses on the liner using CCM. Figure 1a shows an advancing tunnel in an isotropic stress-state p_o. For a given position of tunnel face, the liner is installed at some distance behind the tunnel face, creating a 'lag' in Figure 1a. The tunnel cross-section 1-1′ at the lag distance from the face is shown in Figure 1b. Figure 1c shows GRC, LDP and SCC for the tunnel excavated in an anisotropic stress state. In the plot, internal pressure on the tunnel boundary p_i is normalized with p_o, and tunnel convergence u and distance from the face x_f are normalized with respect to the tunnel radius R. Support stress calculation using CCM by converting the 3-D tunnel problem into a simplified 2-D problem is elaborated in the following steps:

At the time of support installation

a) Point 1 in Figure 1c represents the lag distance, i.e., the longitudinal distance between the tunnel face and the cross-section (AA' in Figure 1a) at which the tunnel support is installed.
b) In Figure 1c, point 1 is projected on the LDP through a horizontal line to reach point 2. Point 2 represents section 1-1′ on LDP.
c) Point 2 is projected on the convergence axis to obtain point 3, representing the tunnel's convergence before support installation. If the tunnel does not advance further, this will be the ultimate convergence of the tunnel cross-section 1-1′. The SCC will govern any increment in tunnel convergence beyond this point.
d) The convergence point of the previous step is marked on the GRC as point 4, and its projection of the internal pressure axis will provide support pressure p_f supplied by the tunnel face to section 1-1′ (point 5).
e) As the tunnel advances further, the longitudinal distance of section 1-1′ from the tunnel face will increase. Once the tunnel excavation is complete, the position of this section is defined by point 6 in Figure 1c and represented by point 7 on the LDP. The critical point to be considered in the further analysis is that the LDPs are defined for unsupported

tunnels, and in this case, section A-A' was supported as the tunnel advanced by distance x_f.

f) Project point 7 on the LDP vertically to the SCC in Figure 1c to get point 8. This point represents the load carried by the support system and the total convergence of the tunnel. The support pressure is represented by the 9 in Figure 1c.

Using the steps mentioned above, tunnel designers have determined the support system's design load for a given allowable convergence. However, in squeezing ground conditions, the surrounding ground continues to converge even after the excavation.

The LDP of the tunnel also changes due to the time-dependent behavior of the material. This paper presents a new approach for estimating the loads on the tunnel support system in squeezing ground conditions. A time-dependent LDP is incorporated in the CCM, which accounts for the increase in support load with time. The new methodology and the changes included in the existing CCM (defined above) are discussed in the following section.

3 METHODOLOGY

3.1 *A time-dependent LDP*

One major shortcoming of the CCM technique described above is that the time-dependent behavior of the ground material around the tunnel boundary is not explicitly considered. Time-dependent closure in squeezing ground can have a considerable impact on support loading. Failure to account for these additional loads can result in unforeseen failures, causing safety concerns, ultimately leading to tunnel collapse

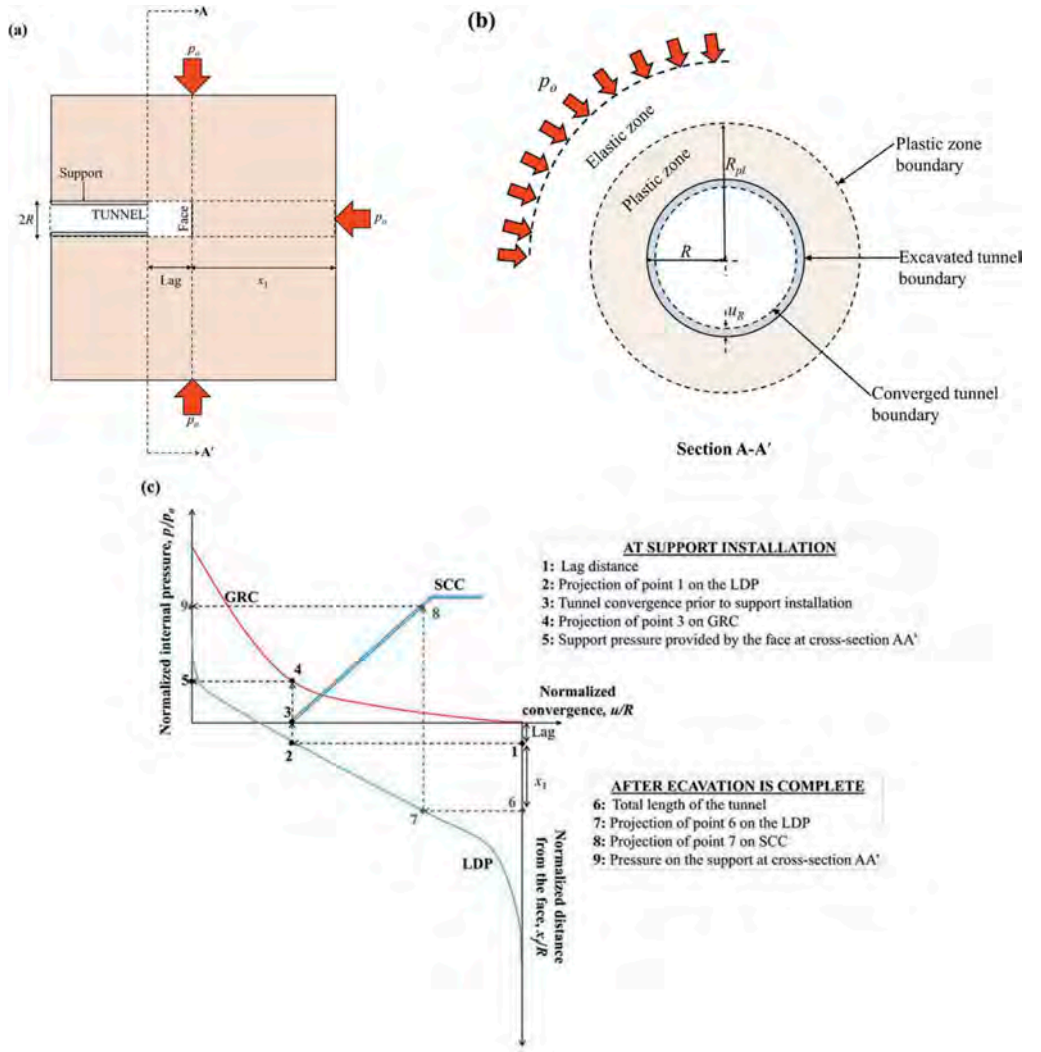

Figure 1. Schematic diagram of (a) an advancing tunnel of radius R in isotropic stress p_0, (b) tunnel cross-section A-A' and (c) plot showing GRC, SCC and LDP for section A-A'.

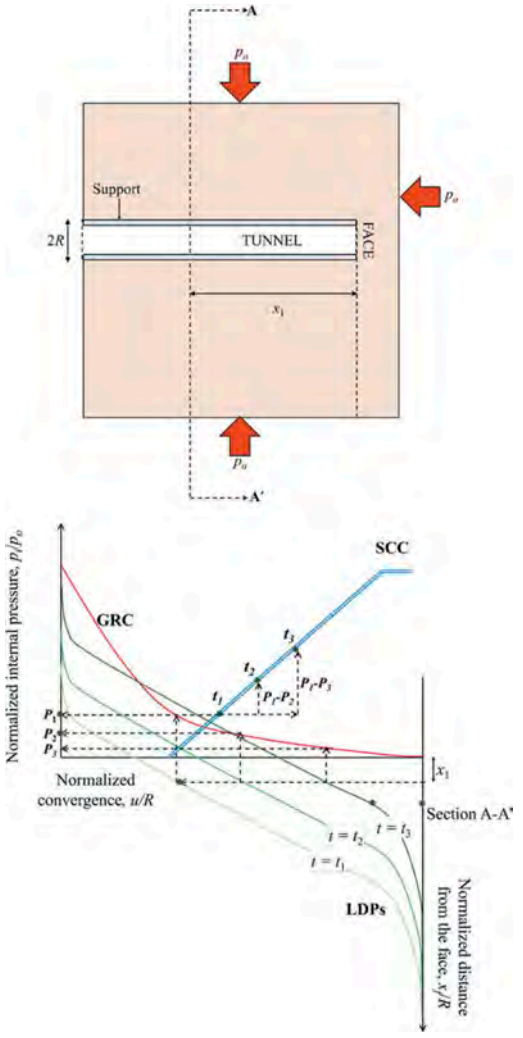

Figure 2. Application of the time-dependent LDP in CCM to estimate the post-excavation squeezing loading on the tunnel support system.

(Arora 2020). Gschwandtner & Galler (2012) suggested applying CCM in squeezing ground to investigate the behavior of different support systems (e.g., combinations of shotcrete and rock-bolts) with time.

One possible way of introducing the time-dependent behavior in the CCM is by introducing time-dependent LDP. Based on their experimental observations, Arora et al. (2021b) proposed the following time-dependent LDP for the tunnels in squeezing clay-rich rocks:

$$\frac{u}{R}(t) = a - b(d)^t \qquad (1)$$

where, for any tunnel cross-section, u/R is the normalized tunnel convergence (in percentage) for a tunnel with a radius R; a and b are the model parameter; d is the time-factor for squeezing ground conditions equal to 0.98; and t is the time (in hours) after excavation is complete. The model parameter a is a function of in-situ stress at tunnel level p_o and distance of the tunnel cross-section from the face x_f. Parameter b was observed to be a function p_o and independent of x_f. Hence, a and b can be expressed as:

$$a = f\left(X, \frac{p_o}{\sigma_c}\right) \qquad (2)$$

$$b = h\left(\frac{p_o}{\sigma_c}\right) = 1.22\left(\frac{p_o}{\sigma_c}\right)^{1.913} \qquad (3)$$

where $X = x_f/R$ is the normalized distance of the tunnel cross-section from the face; p_o is the isotropic stress at the tunnel location before excavation and σ_c is the unconfined compressive strength of the geomaterial at the tunnel location. For a given ratio of p_o/σ_c, parameter a was observed to increase linearly with an increase in X. Also, for a given tunnel cross-section (constant X), parameter a increases with an increase in ratio p_o/σ_c. The correlations presented in Equation (2) and (3) are based on the experimental observations from physical model tests on cubical synthetic mudstone specimens by Arora et al. (2021b).

3.1 *Revised CCM*

The inclusion of the time-dependent LDP in the CCM to determine post-excavation increment in design support pressure due to squeezing ground is presented in Figure 2. Consider a tunnel cross-section 1-1′ at a distance x_1 from the tunnel face. The LDPs for the tunnel at three different times t_1, t_2 and t_3 in hours ($t_3 > t_2 > t_1$) are shown in the plot in Figure 2. The points on the three LDPs representing tunnel cross-section A-A' are projected on the GRC as shown in Figure 2.

For the tunnel cross-section A-A', the normalized reduction in ground pressures due to squeezing are marked as P_1, P_2 and P_3 at time t_1, t_2 and t_3, respectively, in Figure 2. In Figure 2, it can observed in Figure 2 that that from time t_1 to t_2, the decrease in ground pressure is P_1-P_2. This research considers that this difference in ground pressure is directly transferred to the support, as shown in Figure 2.

The stability of the tunnel support system in the squeezing can be checked using the proposed CCM. The first step is to determine the tunnel's LDP infinite time and mark the convergence for this unsupported tunnel cross-section on the LDP. Then this LDP is projected vertically on the GRC to find the reduction in ground pressure. This pressure reduction is projected on the SCC as an increment. If the new point crosses the yield after increment, the support has failed.

4 EXTENSION OF THE TIME-DEPENDENT LDP

The approach proposed in this paper to estimate the squeezing loads on the tunnel support system utilizes a time-dependent LDP. The parameters a and b for this LDP are well defined by Arora et al. (2021b) for synthetic mudstone at different stress to strength ratio p_o/σ_c and normalized distance from the tunnel face X. The dependency of the parameter a and b on material properties should be calibrated for broader applicability.

The parameters a and b can be defined as follows: At time $t = 0$ and for $d = 0.98$ hours in Equation (1), the convergence can be determined by the following equation,

$$\left(\frac{u}{R}\right)_i = a - b \tag{4}$$

where $(u/R)_i$ is the convergence of the tunnel at time $t = 0$ hours, i.e., the ground has not squeezed yet. Similarly, as the time approaches infinity in Equation (1), the convergence reduces as,

$$\left(\frac{u}{R}\right)_u = a \tag{5}$$

where $(u/R)_u$ is the ultimate convergence of the tunnel due to squeezing and non-squeezing factors. The ultimate convergence as defined by Hoek & Marinos (2000) for the tunnels excavated in squeezing ground conditions can be defined by the following equation:

$$\left(\frac{u}{R}\right)_u = 0.2\left(\frac{p_o}{\sigma_{cl}}\right)^2 \tag{6}$$

Equation (6) is defined for the tunnel cross-section at a considerable distance from the tunnel face. However, for tunnel cross-sections closer to the face, Equation (6) changes to,

$$\left(\frac{u}{R}\right)_u = 0.2\left(\frac{p_o}{\sigma_{cl}}\right)^2 F_L \tag{7}$$

where σ_{cl} is the long-term compressive strength of the geomaterial at the tunnel location; F_L is the long-term tunnel face factor introduced to convert the 3-D problem into 2-D defined by Vlachopoulos & Diedrichs (Vlachopoulos and Diederichs 2009) as,

$$F_L = 1 - \left[1 - \frac{1}{3}\exp(-0.15R^*)\right]\exp\left(-\frac{3X}{2R^*}\right) \tag{8}$$

In the above equation, R^* is the ratio of the extent of the long-term plastic zone radius R_{pl} to the excavated tunnel radius R. The plastic zone radius R_{pl} can be defined as (Hoek and Marinos 2000),

$$R_{pl} = 1.25R\left(\frac{p_o}{\sigma_{cl}}\right)^{0.57} \tag{9}$$

Combining Equation (5) and (7) yields,

$$a = 0.2\left(\frac{p_o}{\sigma_{cl}}\right)^2 F_L \tag{10}$$

Similarly, the convergence of the tunnel immediately after the excavation can be defined by the following equation:

$$\left(\frac{u}{R}\right)_i = 0.2\left(\frac{p_o}{\sigma_{cs}}\right)^2 F_S \tag{11}$$

where σ_{cs} is the short-term compressive strength of the geomaterial at the tunnel location. The major difference between short-term and long-term compressive strength is that the latter considers the effect of creep, progressive breakdown of individual rock pieces under high stress and groundwater percolation. The parameter F_s is defined as,

$$F_S = 1 - \left[1 - \frac{1}{3}\exp(-0.15R^*)\right]\exp\left(-\frac{3X}{2R^*}\right) \tag{12}$$

where R^* is the ratio of the extent of the plastic zone R_{pl} in the short-term to the radius of the excavated tunnel R. To determine short-term R_{pl}, σ_{cl} is replaced by σ_{cs} in Equation (9).

Using Equation (4), (10) and (11) results in,

$$b = 0.2\left[\left(\frac{p_o}{\sigma_{cl}}\right)^2 F_L - \left(\frac{p_o}{\sigma_{cs}}\right)^2 F_S\right] \tag{13}$$

Substituting a and b in Equation (10) and (13), respectively into Equation (1), a generalized time-dependent LDP for the tunnel is obtained as follows

$$\frac{u}{R}(t) = 0.2\left\{\left(\frac{p_o}{\sigma_{cl}}\right)^2 F_L - \left[\left(\frac{p_o}{\sigma_{cl}}\right)^2 F_L - \left(\frac{p_o}{\sigma_{cs}}\right)^2 F_S\right]0.98^t\right\} \tag{14}$$

The above LDP can be incorporated in CCM as described above to estimate the time-dependent squeezing load on the tunnel support system.

Considering the effect of time in the interactions of support load and tunnel pressure is essential to have a safe and economic support system. Using long-term response alone will be unsafe if shear strength increases with time because actual failure can occur at a lower strength and at an earlier time (i.e., using long-term shear strength is unconservative). For ground where shear strength decreases with time, long-term shear strength will be uneconomical because the actual shear strength at failure will be larger than the long-term shear strength.

5 APPLICATIONS OF THE PROPOSED CCM

The model presented in this paper is applied to the Yacambu´-Quibor tunnel in the State of Lara in Venezuela. This tunnel is recognized as one of the most challenging tunnels ever excavated. The primary reason for the difficulty was the squeezing. The project, geology and the significant issues are briefly discussed in the following section.

5.1 *Yacambu´-Ouibor tunnel*

The 5-m diameter and 24.3-km long tunnel was designed to carry water through the Andes from the Yacambu dam in the wet tropical Orinoco basin to the semi-arid yet fertile Quibor basin in western Venezuela. The tunnel was located in silicified and graphitic phyllites at depths of up to 1270 m below the surface. As per the descriptive method of classifying rock, Yacambu´-Quibor tunnel location had five classes of rock identified as A, B C, D1 and D2. The class A rock predominantly was silicified phyllite with small amounts of calcareous and/or graphitic phyllite. Class B rock had calcareous silicified phyllite with intervals of graphitic phyllite. In the class C rock, Graphitic phyllite with some intervals of silicified phyllite was found. The class D1 rock was tectonically deformed, folded and sheared form of classes A, B and C. The highly squeezing class D2 had class D1 rock with clay gouge in contact. Several tunnel sections along class D2 rock experienced severe squeezing problems, creating technical, financial and political conflicts between the client and contractors (Hoek and Guevara 2009).

In 1976, ineffective attempts were made to counter the squeezing by using an open-face TBM and a heavy support system. For the next 28 years, several shapes of tunnels cross-section and support type were analyzed to overcome the difficulties encountered during construction. In 2004, the agreement on the use of yielding support with circular cross-section was cleared by the owner's and the contractor's conflicts. The emphasis was placed on developing a routine construction procedure, irrespective of the rock conditions encountered at the face. Figure 3 shows the longitudinal cross-section along the alignment of the Yacambu´-Quibor tunnel. Eight contractors constructed the tunnel in more than 32 years, and the breakthrough was finally achieved in July 2008.

5.2 *Study of the most challenging tunnel cross-section*

Hoek & Guevera (Hoek and Guevara 2009) identified the most challenging tunnel segments of the tunnel alignment based on the combination of overburden and rock mass properties. The analysis was carried out for a 5.2-m diameter section of the Yacambu´-Quibor tunnel mined at a depth of 1000 m below surface in class D2 rock. The short-term and long-term properties of the class D2 rock as considered in their analysis are summarized in Table 1.

Figure 4 Shows the short-term and long-term ground reaction curves (GRCs) for the Yacambu´-Quibor tunnel in D2 rock as monitored in the field (Hoek and Guevara 2009). Calculating the GRC for short-term and long-term rock mass properties has only been applied to the plastic zone. It is assumed that long-term changes due to displacement-induced damage, air and water circulation, and the like will be restricted to this zone. Upon comparing the

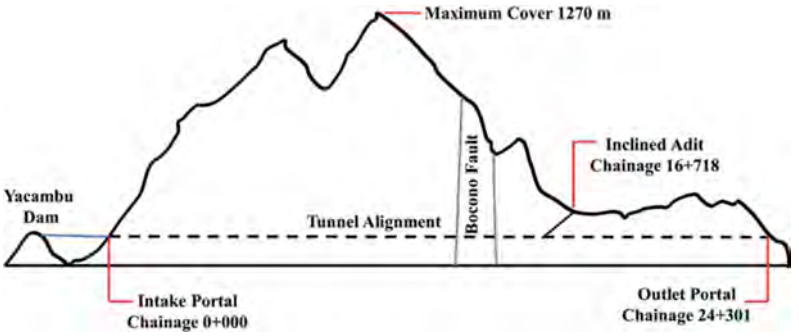

Figure 3. Cross-section along the alignment of the Yacambu´-Quibor water conveyance tunnel in Venezuela.

plotted GRCs, there is a significant amount of squeezing that the rock experiences with time, and designing the tunnel considering short-term properties as design parameters will be disastrous.

The model-generated short-term (at t = 0 hours) and long-term LDPs are plotted in Figure 5 for the studied tunnel alignment using the properties in Table 1 and Equation (1) through (14). It can be seen in Figure 5 that the difference between short-term and long-term convergence is between 2.5% to 15% for X, varying between 0 to 20. This longitudinal displacement profile is based on the combination of experimental study by Arora et al. (2021b) and field observations of Hoek & Marinos (2000). The extent of the plastic zone R_{pl} was 9.90 m and 12.98 m, respectively, considering the short-term and long-term properties listed in Table 1.

Table 1. Short-term and long-term properties of D2 rock along Yacambu´-Quibor tunnel's alignment.

Property for tunnel section in D2 rock	Short-term value	Long-term value
Depth below surface H	1000 m	
Unit weight of rock mass Υ	0.026 MN/m^3	
In situ stress p_o	26 MPa	
Cohesive strength c	1.26 MPa	0.84 MPa
Friction angle ϕ	21.2°	17.4°
Rock mass compressive strength σ_c	3.68 MPa	2.29 MPa
Elastic modulus E	1.65 GPa	0.93 GPa

From several years of experience and field observations, tunnel designers determined that, for the deepest sections of the tunnel in the poor-quality rock, the tunnel would be circular and that it would be lined with a high-quality shotcrete lining (Hoek and Guevara 2009). The shotcrete was mixed at surface batching plants adjacent to the portals and transported by rail to the faces, where it was applied as a wet mix. The tests on in-situ drilled shotcrete cores provided a uniaxial compressive strength of 30 MPa with a minimal standard deviation. The shotcrete had no fiber added as a reinforcing material, as the lining was under compressive loading only. The only parameters to be decided were the thickness of the lining and the timing.

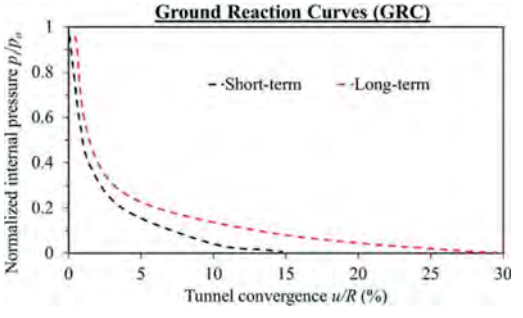

Figure 4. Ground reaction curves (GRCs) for the critical section of the Yacambu´-Quibor tunnel for the short-term and long-term properties, as Hoek & Guevera (2009) reported.

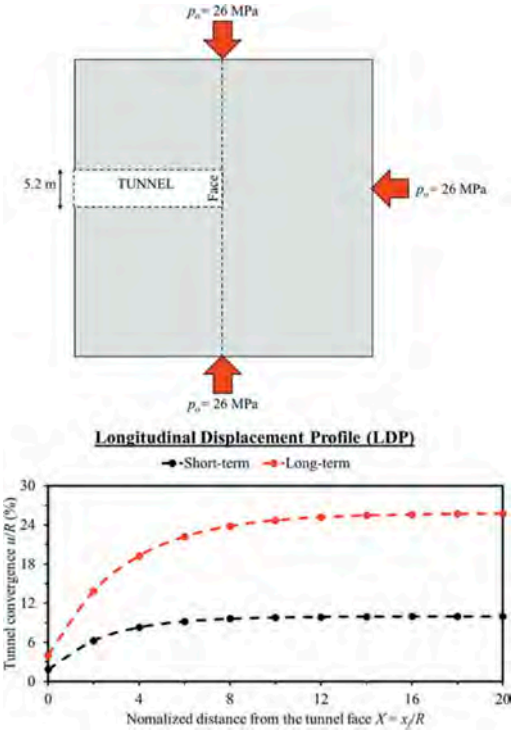

Figure 5. Short-term (t = 0 hours) and long-term (t = ∞ hours) Longitudinal Displacement profiles (LDPs) for the critical zone of Yacambu´-Quibor tunnel.

In this study, the stability analysis of the tunnel liner thickness between 0.2 m to 1.0 m has been studied. The unconfined compressive strength of the shotcrete is taken as 30 MPa, and the shotcrete is installed 2 m behind the face. The shotcrete's Support Characteristic Curves (SCC) were determined by the methodology defined by Hoek & Brown (1980). The increment in load due to squeezing ground conditions was determined as per the procedure discussed in section 3.2. Figure 6 shows the CCM for the critical cross-section of the Yacambu´-Quibor tunnel. It can be observed from the CCM analysis that, due to squeezing, the change in p_i/p_o is 0.13. This change will be added to the tunnel support system per the proposed method. If the support does not yield due to this stress increment, it is stable against the squeezing.

Figure 6 Also shows the SCC for shotcrete liner thickness 0.2 m to 1 m. Considering that the tunnel did not advance after installing the shotcrete liner, it will be reasonable to assume that all stresses on the

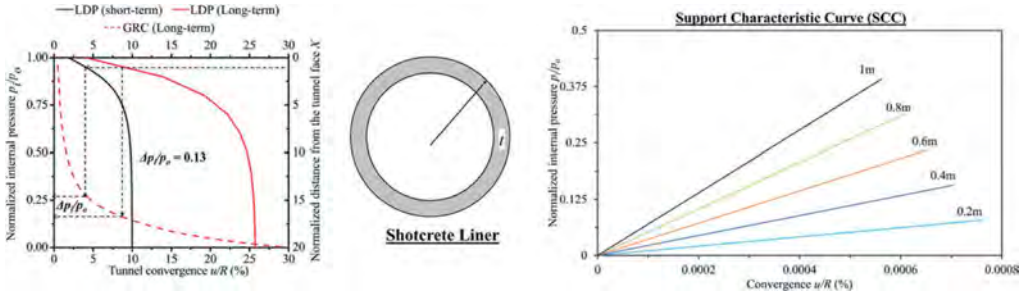

Figure 6. CCM for the Yacambu´-Quibor tunnel along with SCC for the tested shotcrete liners for different shotcrete thickness.

liner will be due to squeezing. It can be seen from the SCC of shotcrete in Figure 6 that the 0.2 m shotcrete will yield when subjected to p_i/p_o increment of 0.13. The 0.4 m thick shotcrete liner will be on the verge of yielding and should be considered a primary tunnel support system. The shotcrete liner having a thickness of 0.6 m and more will take the additional squeezing load without yielding. This 0.6 m liner thickness is the same as the actual thickness of shotcrete used in constructing the Yacambu´-Quibor tunnel (Hoek and Guevara 2009). Based on these results, the application and validity of the proposed method for estimating the squeezing load on the tunnel support system are demonstrated for the Yacambu´-Quibor tunnel.

6 CONCLUSIONS

Convergence Confinement Method (CCM) is one of the popular techniques for the three-dimensional study of tunnel construction. However, most CCM studies do not consider the ground time-dependent behavior around the tunnel boundary. The revised CCM proposed in this paper can be used to estimate tunnel support loads in squeezing ground conditions. The methodology considers time-dependent behavior due to creep and progressive breakdown of individual rock pieces under high stress.

The method is relatively simple and requires only the ground's short-term and long-term strength parameters, which can be easily determined through laboratory tests.

The methodology has been derived from laboratory-scale physical model tests and observations from the hundreds of tunnels excavated in a highly overstressed squeezing zone. Hence, the method is reliable and will have broader applicability. The applicability and validity of the proposed procedure were verified using the Yacambu´-Quibor tunnel.

It is envisioned that the proposed time-dependent CCM will contribute to tunnel design and construction theory and practice in squeezing ground, mainly if used in conjunction with tunnel monitoring and laboratory data.

ACKNOWLEDGMENTS

The authors wish to gratefully acknowledge the support from the University Transportation Center for Underground Transportation Infrastructure (UTC-UTI) at the Colorado School of Mines for funding this research under Grant No. 69A3551747118 from the US Department of Transportation (DOT). The opinions expressed in this paper are those of the Authors and not of the DOT.

REFERENCES

AFTES groupe de travail numerio 7 (1983) Recommendation sur l'emploi de la methode convergence-confinement. Dans Tunnels et ouvrages souterrains 59:218–238

Arora K (2020) Experimental study of tunnels in squeezing ground conditions

Arora K, Chakraborty T, Rao · K Seshagiri (2019) Experimental Study on Stiffness Degradation of Rock Under Uniaxial Cyclic Sinusoidal Compression Loading. Rock Mech Rock Eng 52:4785–4797. https://doi.org/10.1007/s00603-019-01835-3

Arora K, Gutierrez M, Hedayat A (2021a) New physical model to study tunnels in squeezing clay-rich rocks. Geotechnical Testing Journal 44:1–25. https://doi.org/10.1520/GTJ20200081

Arora K, Gutierrez M, Hedayat A, Cruz EC (2021b) Time-Dependent Behavior of the Tunnels in Squeezing Ground: An Experimental Study. Rock Mechanics and Rock Engineering 2021 54:4 54:1755–1777. https://doi.org/10.1007/S00603-021-02370-W

Arora K, Gutierrez M, Hedayat A, Xia C (2021c) Tunnels in squeezing clay-rich rocks. Underground Space 6:432–445. https://doi.org/10.1016/J.UNDSP.2020.07.001

Aydan Ö, Akagi T, Kawamoto T (1996) The squeezing potential of rock around tunnels: Theory and prediction with examples taken from Japan. Rock Mech Rock Eng 29:125–143. https://doi.org/10.1007/BF01032650

Barla G (1995) Squeezing rocks in tunnels. ISRM News Journal 2:44–49

Barla G (2000) Tunnelling under squeezing rock conditions. Tunnelling Mechanics - Advances in Geotechnical Engineering and Tunnelling, Eurosummer-School in Tunnel Mechanics 169–268

Barla G, Debernardi D, Sterpi D (2012) Time-Dependent Modeling of Tunnels in Squeezing Conditions.

International Journal of Geomechanics 12:697–710. https://doi.org/10.1061/(ASCE)GM.1943-5622.0000163
Barton N, Lien R, Lunde J (1974) Engineering classification of rock masses for the design of tunnel support. Rock mechanics 1974 6:4 6:189–236. https://doi.org/10.1007/BF01239496
Bilgin N, Algan M (2012) The performance of a TBM in a squeezing ground at Uluabat, Turkey. Tunnelling and Underground Space Technology. https://doi.org/10.1016/j.tust.2012.05.004
Bonini M, Debernardi D, Barla M, Barla G (2009) The mechanical behaviour of clay shales and implications on the design of tunnels. Rock Mech Rock Eng 42:361–388. https://doi.org/10.1007/s00603-007-0147-6
Cao C, Shi C, Lei M, et al (2018) Squeezing failure of tunnels: A case study. Tunnelling and Underground Space Technology. https://doi.org/10.1016/j.tust.2018.04.007
Deere DU, Peck RB, Parker HW, et al (1970) design of tunnel support systems
Dusseault MB, Fordham CJ (1993a) Time-dependent Behavior of Rocks. Comprehensive rock engineering Vol 3 119–149. https://doi.org/10.1016/B978-0-08-042066-0.50013-6
Dusseault MB, Fordham CJ (1993b) Time-dependent behavior of rocks. Comprehensive rock engineering Vol 3. https://doi.org/10.1016/b978-0-08-042066-0.50013-6
Fabre G, Pellet F (2006) Creep and time-dependent damage in argillaceous rocks. International Journal of Rock Mechanics and Mining Sciences 43:950–960. https://doi.org/10.1016/J.IJRMMS.2006.02.004
Ghaboussi J, Gioda G (1977) On the time-dependent effects in advancing tunnels. Int J Numer Anal Methods Geomech 1:249–269. https://doi.org/10.1002/NAG.1610010303
Gioda G (1981) A finite element solution of non-linear creep problems in rocks. International Journal of Rock Mechanics and Mining Sciences & Geomechanics Abstracts 18:35–46. https://doi.org/10.1016/0148-9062(81)90264-3
Gioda G (1982) On the non-linear 'squeezing' effects around circular tunnels. Int J Numer Anal Methods Geomech 6:21–46. https://doi.org/10.1002/NAG.1610060104
Gioda G, Cividini A (1996) Numerical methods for the analysis of tunnel performance in squeezing rocks. Rock Mech Rock Eng 29:171–193. https://doi.org/10.1007/BF01042531
Goel RK, Jethwa JL, Paithankar AG (1995) Tunnelling through the young Himalayas — A case history of the Maneri-Uttarkashi power tunnel. Eng Geol 39:31–44. https://doi.org/10.1016/0013-7952(94)00002-J
Gschwandtner GG, Galler R (2012) Input to the application of the convergence confinement method with time-dependent material behaviour of the support. Tunnelling and Underground Space Technology 27:13–22. https://doi.org/10.1016/J.TUST.2011.06.003
Hedayat A, Weems J (2019) The Elasto-Plastic Response of Deep Tunnels with Damaged Zone and Gravity Effects. Rock Mechanics and Rock Engineering 2019 52:12 52:5123–5135. https://doi.org/10.1007/S00603-019-01834-4
Hoek E, Brown ET (1980) Underground Excavations in Rock. CRC Press
Hoek E, Guevara R (2009) Overcoming squeezing in the yacambú-quibor tunnel, venezuela. Rock Mech Rock Eng 42:389–418. https://doi.org/10.1007/s00603-009-0175-5
Hoek E, Marinos P (2000) Predicting tunnel squeezing problems in weak heterogeneous rock masses. Tunnels and Tunnelling International Part 1-2:1–20
ISRM (1994) Comments and recommendations on design and analysis procedures for structures in argillaceous swelling rock. International Journal of Rock Mechanics and Mining Sciences 31:535–546
Jethwa, J. L., Singh, B., & Singh B (1984) 28 Estimation of ultimate rock pressure for tunnel linings under squeezing rock conditions—a new approach. In: In Design and Performance of Underground Excavations: ISRM Symposium—Cambridge, UK,. pp 231–238
Kabwe E, Karakus M, Chanda EK (2020) Isotropic damage constitutive model for time-dependent behaviour of tunnels in squeezing ground. Comput Geotech 127:103738. https://doi.org/10.1016/J.COMPGEO.2020.103738
Kallhawy F (1974) Finite element modeling criteria for underground opening in rock. International Journal of Rock Mechanics and Mining Sciences: Geomechanics Abstracts 11:465–472
Lo KY, Cooke BH, Dunbar DD (1987) Design of buried structures in squeezing rock in Toronto, Canada. Canadian Geotechnical Journal 24:232–241. https://doi.org/10.1139/t87-028
Lü Q, Low BK (2011) Probabilistic analysis of underground rock excavations using response surface method and SORM. Comput Geotech 38:1008–1021. https://doi.org/10.1016/J.COMPGEO.2011.07.003
Manh HT, Sulem J, Subrin D, Billaux D (2015) Anisotropic Time-Dependent Modeling of Tunnel Excavation in Squeezing Ground. Rock Mechanics and Rock Engineering 2015 48:6 48:2301–2317. https://doi.org/10.1007/S00603-015-0717-Y
Mesri G, Febres-Cordero E, Shields DR, Castro A (2015) Shear stress-strain-time behaviour of clays. http://dx.doi.org/101680/geot1981314537 31:537–552. https://doi.org/10.1680/GEOT.1981.31.4.537
Pan YW, Dong JJ (1991) Time-dependent tunnel convergence—II. Advance rate and tunnel-support interaction. International Journal of Rock Mechanics and Mining Sciences & Geomechanics Abstracts 28:477–488. https://doi.org/10.1016/0148-9062(91)91123-9
Paraskevopoulou C, Diederichs M (2018) Analysis of time-dependent deformation in tunnels using the Convergence-Confinement Method. Tunnelling and Underground Space Technology 71:62–80. https://doi.org/10.1016/J.TUST.2017.07.001
Phien-wej N, Cording EJ (1991) Sheared shale response to deep TBM excavation. Eng Geol 30:371–391. https://doi.org/10.1016/0013-7952(91)90069-W
Schubert W (1996) Dealing with Squeezing Conditions in Alpine Tunnels. Rock Mech Rock Engng 29:145–153
Semple RM (1973) THE EFFECT OF TIME-DEPENDENT PROPERTIES OF ALTERED ROCK ON TUNNEL SUPPORTREQUIREMENTS. - ProQuest. University of Illinois at Urbana-Champaign
Singh A, Kumar C, Kannan LG, et al (2018) Estimation of creep parameters of rock salt from uniaxial compression tests. International Journal of Rock Mechanics and Mining Sciences 107:243–248. https://doi.org/10.1016/J.IJRMMS.2018.04.037
Singh B, Jethwa JL, Dube AK, Singh B (1992) Correlation between observed support pressure and rock mass quality. Tunnelling and Underground Space Technology 7:59–74. https://doi.org/10.1016/0886-7798(92)90114-W
Sulem J, Panet M, Guenot A (1987) An analytical solution for time-dependent displacements in a circular tunnel.

International Journal of Rock Mechanics and Mining Sciences and 24:155–164. https://doi.org/10.1016/0148-9062(87)90523-7

Su Y-H, Li X, Xie Z-Y (2011) Probabilistic evaluation for the implicit limit-state function of stability of a highway tunnel in China | Elsevier Enhanced Reader. Tunnelling and Underground Space Technology 26:422–434. https://doi.org/https://doi:10.1016/j.tust.2010.11.009

Terzaghi K (1946) Rock defects and loads on tunnel supports. In: Rock tunneling with steel supports. Proctor, R. V., White, T.L. (Eds.), Commercial Shearing and Stamping Company, Youngstown, OH, pp 45–92

Vlachopoulos N, Diederichs MS (2009) Improved Longitudinal Displacement Profiles for Convergence Confinement Analysis of Deep Tunnels. Rock Mech Rock Engng 42:131–146. https://doi.org/10.1007/s00603-009-0176-4

Vrakas A, Anagnostou G (2016) Ground Response to Tunnel Re-profiling Under Heavily Squeezing Conditions. Rock Mechanics and Rock Engineering 2016 49:7 49:2753–2762. https://doi.org/10.1007/S00603-016-0931-2

Vrakas A, Dong W, Anagnostou G (2018) Elastic deformation modulus for estimating convergence when tunnelling through squeezing ground. https://doi.org/101680/jgeot17P008 68:713–728. https://doi.org/10.1680/JGEOT.17.P.008

Wang X, Lai J, Garnes RS, Luo Y (2019) Support System for Tunnelling in Squeezing Ground of Qingling-Daba Mountainous Area: A Case Study from Soft Rock Tunnels. Advances in Civil Engineering 1–18. https://doi.org/10.1155/2019/8682535

Wood AMM (1972) Tunnels for roads and motorways. Quarterly Journal of Engineering Geology 5:111–126. https://doi.org/10.1144/GSL.QJEG.1972.005.01.12

Zhang P, Yin JJ, Nordlund E, Li N (2008) Determination and verification of the longitudinal deformation profile in a horse-shoe shaped tunnel using two-stage excavation. In: 5th International Conference and Exhibition on Mass Mining, Luleå Sweden 9-11 June 2008. Luleå, Sweden, pp 845–854

Zheng YL, Zhang QB, Zhao J (2016) Challenges and opportunities of using tunnel boring machines in mining. Tunnelling and Underground Space Technology 57:287–299. https://doi.org/10.1016/J.TUST.2016.01.023

Tunnelling for a Better Life – Yan, Celestino, Thewes & Eberhardt (Eds)
© 2024 The Author(s), ISBN 978-1-032-80042-4
Open Access: www.taylorfrancis.com, CC BY-NC-ND 4.0 license

Tunnelling in weak sandstone: A case study of Subansiri Lower Hydroelectric Project (2000 MW)

Mohammed Shakeel Chouhan
Vice President – Projects, Patel Engineering Limited, Patel Estate, Jogeshwari (W), Mumbai, Maharashtra, India

Sandeep Potnis
Professor & Head, Tunnel Engineering Program, MIT World Peace University, Pune, Maharashtra, India

ABSTRACT: The Subansiri Lower, *the largest under construction Hydro Electric Project in India having installed capacity of 2000MW,* stands as a prominent run-of-river scheme strategically situated near the gorge mouth of the Subansiri River, which forms a natural boundary between the states of Arunachal Pradesh and Assam. Being a significant right bank tributary, the Subansiri River contributes around 11% of the total discharge of the mighty Brahmaputra River. At present, the project is in its final stage of construction, gearing up to harness its full potential. This ambitious venture encompasses a complex network of tunnels. The Hydraulic Headrace Tunnel (HRT) complex boasts an impressive arrangement of 08 parallel tunnels, while the Surge Tunnel comprises an additional 08 tunnels, each boasting a finished diameter of 9.5 m. The geological composition of the project region primarily comprises fragile sandstone from the Middle Siwalik group of rocks. Nestled within the delicate Outer Himalayas, the project site is demarcated by the imposing Main Boundary Fault to the north, and the formidable Main Frontal Fault to the south. The rocks in this area exhibit an Unconfined Compressive Strength (UCS) ranging from 10 to 25 Mpa under dry conditions and 2 - 7 Mpa under saturated conditions. Tunnelling operations in this geological setting have faced significant challenges due to the soft nature of the rock mass, lack of fissility, and the presence of a higher percentage of fine grain matrix, resulting in low cutting rates and substantial dust generation. Innovative engineering solutions, including the use of road headers and twin cutters, were adopted for excavation, and dust suppression techniques were implemented. However, the formation of slush due to water usage for dust suppression posed difficulties in muck handling. Rock mass classification using the Rock Mass Rating (RMR) system was limited in addressing the rock's massive and weak nature. Hence, a hindrance-based classification approach was introduced, considering factors like rock support and excavation difficulty. This approach offered a more comprehensive understanding of the challenges encountered during tunnelling. This paper presents a detailed case study of the tunnelling operations undertaken in the Subansiri Lower HEP, focusing on the unique geological complexities of weak sandstone and the innovative engineering solutions applied to ensure successful tunnel construction. The study sheds light on the specific challenges faced during tunnelling in weak sandstone and provides valuable insights for similar projects in comparable geological conditions.

1 INTRODUCTION

The Subansiri Lower HE Project (2000MW) is a run-of-river scheme and is located near the gorge mouth of the river Subansiri bordering both the states of Arunachal Pradesh and Assam. Subansiri River, contributing about 11% of total discharge, is a major right bank tributary of great Brahmaputra River. It originates in the high Himalayan ranges in southern Tibet. As per the study on "Reassessment of Hydroelectric Potential "carried out by CEA during 1978-87, a total of 25 hydroelectric schemes with a potential of 6892MW, have been identified in the Subansiri Basin. Subansiri Lower H.E project is around 471 kilometers from Guwahati and 16 kilometers from Gogamukh, a small town on NH-52. The dam is located on the river Subansiri, 2.3 kilometers upstream of Gerukamukh Village on the Assam-Arunachal Pradesh border. The dam's left abutment is in Assam, and its right abutment is in Arunachal Pradesh. The proposal proposes to use 91m of gross head by building a 166m high concrete gravity dam with a surface powerhouse with a capacity of 2000MW. The stored water is routed to the powerhouse via eight 9.5 Dia horse shoe shaped head race tunnels and an 8m diameter steel walled pressure shaft. After flowing through the turbine in the powerhouse, the water will be dumped back into the river via tail race channel (Figure 1 &2). Because this is a run-of-the-river scheme, there will be a constant flow of water even during the lean season in the river system.

DOI: 10.1201/9781003495505-63

Figure 1. Project layout.

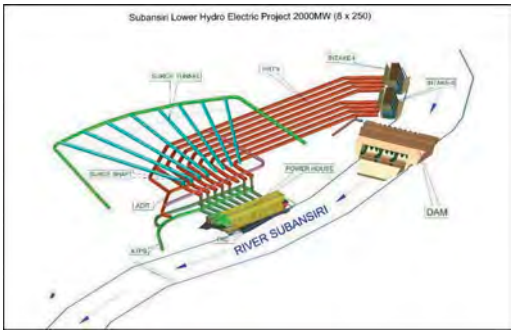

Figure 2. 3-D View of Subansiri Lower Hydroelectric Project.

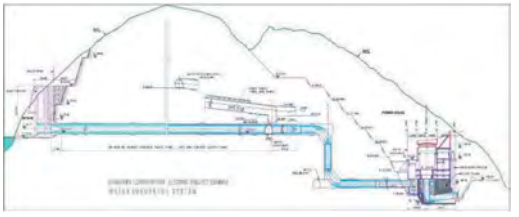

Figure 3. Water conduction system (L-Section) for Subansiri Lower Hydroelectric Project.

2 LITERATURE REVIEW

1. Geotechnical Challenges of Tunneling in Weak Sandstone: A Case Study by A. Smith and B. Johnson: The geotechnical difficulties encountered during a tunneling project in brittle sandstone are covered in this case study. It emphasizes the value of ground improvement methods, site-specific description, and support systems.
2. Strength and Deformation Characteristics of Weak Sandstone for Tunneling by M. Patel and S. Gupta: This study paper provides a thorough examination of weak sandstone's strength and deformation characteristics. It investigates laboratory testing techniques and how they apply to tunneling operations.
3. Numerical Modeling of Tunneling in Weak Sandstone by J. Wang and X. Li: In this paper, the main topic is the simulation of weak sandstone tunneling using numerical modeling. It talks about modeling techniques like the finite element method for predicting ground behavior and evaluating tunnel stability.
4. Numerical Modeling of Weak Rock Tunneling by H. Kang and H. Konietzky: The behavior of tunnels in weak rock is examined and predicted using numerical modeling in this research. It investigates several modeling strategies and their uses.
5. Tunnel Support Systems for Weak Sandstone: A Review by R. Sharma and N. Verma: In this review paper, numerous tunnel support systems are analyzed along with how well they work with weak sandstone conditions. It talks about the efficiency and effectiveness of ground reinforcement procedures.
6. Tunnel Support Design in Weak Rocks: A Case Study by M. Ghosh and S. Das: This case study investigates the difficulties encountered with constructing a tunnel through brittle rock and the engineering of tunnel support systems. The significance of site-specific assessments and monitoring is emphasized.
7. Influence of Geological Features on Tunnel Stability in Weak Rock" by L. Li and C. Tang: This study investigates the effects of fault zones and joint systems on the stability of tunnels in weak rock. It talks about the necessity of thorough geological studies and suitable countermeasures.
8. Ground Improvement Techniques for Weak Sandstone Tunnels by K. Tan and G. Lim: This study investigates soil reinforcement and grouting as ground enhancement techniques to increase tunnel stability in sandstone that is brittle. It explores real-world applications while presenting case studies.
9. Grouting Techniques for Weak Rock Tunneling by P. C. Chiu and K. Soga: This study discusses grouting methods for strengthening the stability of tunnels in brittle rock. It talks about the uses of different grouting techniques and how effective they are.
10. Tunneling in Sandstone with Varying Strength: Lessons from Field Projects by E. Chen and H. Liu: The tunneling efforts in sandstone rocks with varying strengths are discussed in this publication's insights learned section. It highlights the importance of flexibility and ongoing observation.
11. Instrumentation and Monitoring of Weak Sandstone Tunnels by S. Das and P. Kumar: In order to determine the behavior of weak sandstone during tunnel construction, this paper highlights the significance of equipment and monitoring. It

addresses methods for gathering data, analyzing it, and reducing risks.

12. Instrumentation and Monitoring in Weak Rock Tunnels by M. Karakus and H. K. Kim: This study focuses on the significance of monitoring and instrumentation systems in identifying and controlling the hazards related to tunneling in weak rock. It offers perceptions into the gathering and interpreting of real-time data.
13. Case Studies of Tunnels in Weak Sandstone by D. Zhao and L. Wu: These case studies highlight tunneling initiatives carried out in brittle sandstone deposits across the world. It offers understanding into the problems encountered and the solutions put into practice in varied circumstances.
14. Case Studies of Weak Rock Tunneling Projects by D. Hoek and E. Marinos: A collection of case studies from weak rock tunneling projects from all around the world are presented in this paper. It highlights the difficulties encountered and the lessons discovered via these undertakings.
15. Tunneling in Soft Rock – Subansiri Hydroelectric Project, Arunachal Pradesh, India. - by Arvind Garg, Alok Kumar Rahul, and Dr. Devojit Bezbaruah: The study highlights the importance of comprehensive geological and geotechnical investigations for tunneling projects. Mechanical excavation methods should be carefully chosen and accompanied by proper ventilation plans. the project faces significant challenges due to the weak sandstone rock type found in the region. The rock exhibits unique characteristics such as low uniaxial compressive strength (UCS) and the presence of fine-grained matrix and carbonaceous material, resulting in reduced tunneling efficiency. Furthermore, the limitations of existing rock mass classification systems must be acknowledged in challenging geological conditions. This literature review explores the geological setup of the area, construction methods, and the challenges encountered during tunnel excavation, including dust generation and water use. Additionally, it discusses the limitations of conventional rock mass classification systems like RMR and Q-system and presents an alternative classification approach based on hindrances during tunneling.
16. Challenges in Weak Rock Tunneling and Their Mitigation Measures: A Review by V. R. Sastry and G. R. Reddy: This review study explores the numerous difficulties that can arise while tunneling through brittle rock formations. It talks about ground improvement techniques, grouting procedures, and support systems as examples of mitigating strategies.
17. Tunneling in Weak Rock - A Review by R. Gertsch and F. F. B. Zettler: In-depth analysis of tunneling in weak rock is provided in this work, with a focus on geotechnical considerations, rock mechanics, and case studies. It goes through how weak rocks are categorized, what makes them weak, and how geological circumstances affect tunnel stability.
18. Rock Mass Classification for Weak Sandstone Tunneling by A. Gupta and S. Rajan: The classification of rock masses for weak sandstone is covered in this article. It talks about the difficulties in describing diverse formations and how they affect tunnel design.
19. Rock Mass Classification Systems for Weak Rock Tunnels by E. Hoek: This study covers strategies for classifying rock masses that are particularly pertinent for tunneling through weak rock. It examines the Hoek-Brown failure criterion and how to use it to evaluate tunnel stability in weak rock.
20. Issues and Challenges in Construction of Hydro Tunnel in Extreme Geological conditions in India – An Empirical Study by Rakesh Kumar Khali and Dr. Sandeep Potnis: This review explores the numerous difficulties geological challenges encountered during the construction of the Vishnugad Pipalkoti Head Race Tunnel project, which navigates through a geologically intricate landscape characterized by dolomitic limestone and slate formations, thrust zones, shear zones, and fault zones. These geological challenges profoundly influence excavation procedures, safety measures, and project timelines. The HRT, located in an area dominated by dolomitic limestone and slate, requires a nuanced understanding of these geological units and their implications for tunnel construction. The adoption of Tunnel-Boring Machines (TBMs) stands as a vital solution to mitigate risks and ensure project success in the face of extreme geological conditions.

3 REGIONAL GEOLOGY OF THE PROJECT AREA

The entire project is made of sandstone from the middle Siwalik Formation. The sandstone is medium to fine grained, soft having typical salt and paper texture. It is massive to moderate joint and current bedded at places. Stringers and lenses of carbonaceous materials as well as concretionary nodules (of much harder sandstone) are also present occasionally. Due to the soft nature of the rock valley slopes are deeply dissected by streams (nallahs) controlled by the master joints.

The rock units are aligned in NE-SW trend with folded and local window structures. The project area is separated by two major tectonic plates namely main boundary fault (MBT) at about 9 km U/s of the dam site at north and Himalayan frontal thrust (HFT) at about 5 km D/s of the project layout. MBT, the northerly dipping fault demarcates the tectonic boundary between the Lesser Himalayas and Sub Himalayas while HFT, the north dipping low angle thrust has brought the Siwalik group of rocks in juxtaposition with recent alluvium of Brahmaputra plains.

4 OVERALL STRATIGRAPHIC SUCCESSION OF THE AREA ARE AS FOLLOWS:

Table 1. Stratigraphy of project area.

Age	Formation	Rock Type
Recent to Sub Recent (0.01 million Year till date)	Alluvial & Terrace Deposit	Boulders, Pebbles, Silt & Sands (Unconsolidated)
Pleistocene (0.01 - 1.80 million Year)	Younger Parts of Dihing beds & Upper most Siwalik	Weakly consolidated beds of Sandstone, Mudstone & Pebbles showing slight dips
Pliocene (1.8 - 5.3 million Year)	Siwalik (Upper) Dihing Namsangs	Sandstone, Conglomerate, Pebbles beds
**********Unconformity**********		
Miocene (5.3 - 23.8 million Year)	Middle Siwalik Lower Siwalik (Equivalent to Tipams, Surmas)	Sandstone, Siltstone, Claystone
Project Location		
**********Unconformity**********		

5 LITHOSTRATIGRAPHIC SUCCESSION OF THE PROJECT AREA

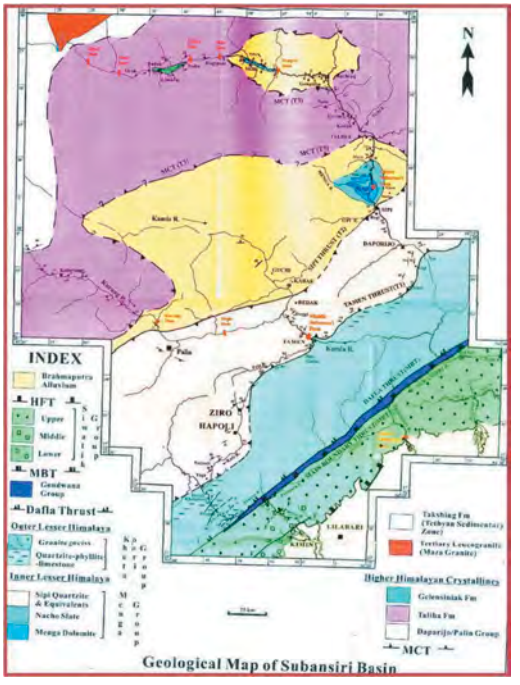

Figure 4. Geological map of subansiri basin.

6 SITE GEOLOGY

The Subansiri Lower HEP site is predominantly composed of sandstone from the middle Siwalik formation, also known as the Subansiri formation. These sandstones exhibit a medium to fine grain texture, characterized by a typical "salt and pepper" appearance, and possess a soft and friable nature. At various locations, the sandstone forms massive beds, while occasional occurrences of stringers and carbonaceous materials are also observed. Notably, the sandstone exhibits embedded rounded pebbles of quartzite and lenses of pebbles originating from concretionary nodules with diagenetic origins. Upon conducting a petrological analysis of the rock, it is revealed that the sandstone primarily consists of quartz (3-5%) and feldspar (5-8%), along with trace amounts of chlorite, biotite, and muscovite (approximately 3-5%). The fine-grained matrix is composed of quartz, calcareous, and carbonaceous material, constituting approximately 15-20% of the rock's composition. Comparison of UCS values during investigation and construction stages is illustrated in Figure 5. Geotechnical characteristics of discontinues observed in during underground excavation are given in Table 2.

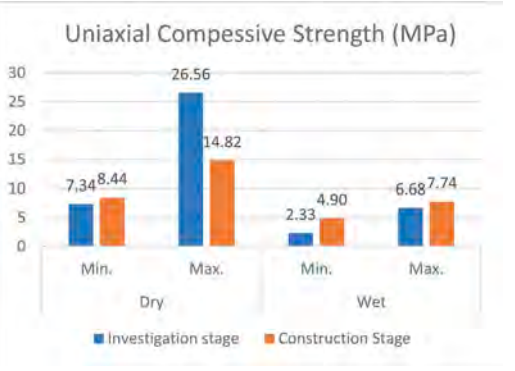

Figure 5. Comparison of uniaxial compressive strength determined during investigation & construction stage.

7 HEAD RACE TUNNEL (HRT)

Two sets of tunnels, each comprising 4 no's horse shoe shaped HRT of 9.5M dia. each are constructed on right bank of Subansiri River with their intakes located between 180m and 445m upstream of dam axis keeping invert at EL. 160M. The total length of HRT designed for excavation is 7124m. The longest tunnel, HRT-1 having 1164m length and HRT-8 having shortest length of 608m have been completed. HRT is aligned almost NNE - SSW cutting subparallel to obliquely to the bedding planes. The lateral cover between consecutive two tunnels is 21M, and rock cover over tunnels varies from 40m to 150m. Head race Tunnel are envisaged to convey water from Intake to pressure shaft then to power House

Table 2. Discontinuities characteristics of HRT.

Discontinuous	Orientation	Persistence (m)
S1	100°-150°/55°-75°	5-15
S2	200°-260°/35°-60°	4-6
S3	300°-350°/35°-70°	2-10
S4	010°-040°/45°-75°	3-8

Discontinuous	Spacing	Aperture	Condition
S1	Widely to very widely	Tight to partly open	Rough Planar
S2	20 cm to very widely	Tight to partly open	Rough to Slightly rough
S3	very Widely	Tight to partly open	Rough planar to slicken sided
S4	20 cm to very widely	Tight to partly open	Rough planar to Smooth

8 SURGE TUNNELS (ST)

Eight nos. of horse shoe shape inclined surge tunnels of finished 9.5 m Dia of length varying from 400m to 485m have been located above HRTs. The surge tunnels are on the slope of 1:10 thus the elevation varies from EL 212 to EL 171.5. Each Surge Tunnel relates to HRT by a 9.50m Dia circular Surge Shaft. The rock cover between crown of HRTS and invert of surge tunnels varies from 9 m to 44 m. Wherever the rock cover is minimal, steel ribs are provided in HRTS as adequate support measures as per design drawings. Surge tunnels have also been negotiated all through similar geological conditions as observed in HRTS. During the progressive excavation of surge tunnels (01 to 08), shear seam/zone having thickness from 10cm to 50cm associated with fractured/shattered rock mass were observed.

9 METHOD OF EXCAVATION, ROCK MASS CONDITION AND TUNNELABILITY

Due to the weak nature of Siwalik sandstone's low UCS value (25.85 MPa in dry condition & 7.11 MPa in wet condition), poor tensile strength (1.12 MPa in dry condition & 0.30 MPa in wet condition), low modulus of elasticity (3.29 MPa in dry condition & 1.15 MPa in wet condition), and proximity of tunnels, mechanical method was used instead of drilling and blasting. Road header and Drum cutters are the two prominent machines being used for the excavation of HRT and Surge Tunnel by adopting heading and benching method. Road header T3.20 of Wirth from Germany is being used for the excavation of the tunnels. The average cutting rate of Road Header observed at site is 6.69 cum/hr. and pick consumption is 0.15 pick/cum. Road Header takes approximately 8-10 hrs. in cutting 1m stretch of heading area of 60 sqm. The monthly average progress of Road Header is 20m to 25m.

The most common underground partial face excavation machine for soft to medium strength rock is the road header. In addition to their higher and more versatile adaptability, road heeders are often lower capital cost systems than most other mechanical excavators. Because of their increased cutting power density and smaller cutting drum, they can extract rock that is harder and more abrasive than continuous miners and borers.

Figure 6. Road header's performance parameters by manufacturer.

Road Header: WIRTH Road Header T3.20

- Total Weight: 131 Ton.
- Length: 16.59 M; Height: 3.94 M
- Maximum Cutting Height: 0.92 M to 7.60 M
- Maximum Cutting Width: 9.6 M
- Total Install Power: 1000 V (485 Kw)
- Number of Picks: 144 No's.

Figure 7. Road header's performance parameters by manufacturer.

Figure 8. Road header.

Drum Cutter ERC 1500xl (Attached to Kobelco 380XDLC):

- Gross Weight: 40 Ton.
- Drum Cutter Weight: 2.5 Ton.
- Rotation Speed: 75 rpm.
- Max. Operating Pressure: 350 bar.
- Number of Picks: 48

Figure 9. Drum cutter.

The observed cutting rates of the twin cutter machines and road headers were notably lower than the rates predicted by manufacturers. Table 3 provides a summary of the cutting rates of various rock cutting machines used in Siwalik sandstone, the primary tunnelling medium for both the HRT and Surge Tunnels.

Table 3. Cutting rate of equipment.

	Cutting rate m^3/hr.		
Machine Type	Max	Min	Average Cutting rate m^3/hr
WIRTH Road Header T3.20	9.96	4.04	6.69
Drum Cutter ERC 1500xl (attached to Kobelco SK380XDLC):	3.62	0.39	2.01

10 THE LOW CUTTING RATE ARE MAINLY ATTRIBUTED TO FOLLOWING REASONS

a) The rock's characteristics, which range from marginally jointed to huge and lack fissility, constitute a problem. The rock cutting process has distinct obstacles. Because the rock cutting machine grinds the rock rather than chipping it, more energy is required. Cut more efficiently. This increased energy requirement affects the overall cost and time required for tunnel excavation. In addition to the energy considerations, the rate of cutting is significantly influenced by the presence of various geological features, including discontinuities such as joints, faults, and bedding planes. Their spacing and orientation concerning the direction of tunnelling, play a crucial role in determining the machine's performance. Proper analysis and understanding of these geological characteristics are vital for optimizing the cutting process and ensuring smooth progress during tunnel excavation. Gehring (1997), Thuro and Spaun (1996a & 1996b), and Verhoef (1997) have extensively studied the impact of geological factors on the efficiency of rock cutting machines. Their research provides valuable insights into designing effective cutting strategies and improving tunneling operations in similar rock formations.

b) A large amount of energy is lost due to the cushioning effect of the matrix due to the presence of 15-20% fine-grained matrix and carbonaceous materials. As a result, cracking the rock necessitates a tremendous amount of energy. Furthermore, this position impedes fracture propagation throughout the cutting process, resulting in unsatisfactory results.

c) The cutting process generates large quantities of dust, causing a significant challenge in tunnel excavation. Measurements of fine dust near the tunnel face have shown levels as high as 85-90 mg/m². The excessive dust generation results in poor visibility at the face, leading to intermittent excavation halts to remove the dust through the ventilation system installed in the tunnel. The need for frequent interruptions to clear the dust has a detrimental impact on the productivity of the rock cutting machine. The constant start-and-stop nature of the excavation process not only consumes valuable time but also increases wear and tear on the cutting equipment, further affecting overall efficiency. Efficient dust control measures, such as improved ventilation systems and dust suppression techniques, are essential to mitigate these issues and enhance the productivity of the rock cutting process. Proper dust management not only ensures a safer working environment for the crew but also contributes to maintaining a smooth and uninterrupted tunnel excavation process.

d) The use of water for dust suppression had a detrimental effect, as it led to the formation of slush, making it challenging to handle the generated muck. The combination of water with the dust created a muddy and sticky mixture, significantly impacting the flow of excavated material and

causing handling difficulties. The presence of slush and muck not only slows down the excavation process but also poses a risk of clogging machinery and equipment. Furthermore, the handling issues increase the time and effort required for waste removal, further contributing to reduced productivity.

11 GEO-MECHANICAL CLASSIFICATION OF ROCK MASS

The geo-mechanical classification of the rock mass, known as Rock Mass Rating (Bieniawski, 1976), has been adopted for the Head Race Tunnels and Surge Tunnels. The distribution of rock classes at the negotiated tunnel grade is provided in the Figure no. 9. Notably, much of the tunnel rock falls under class-III. It is essential to apply the RMR system to assess the geomechanics characteristics of the rock mass and plan the tunnelling process accordingly. Classifying the rock mass into different categories helps in understanding its behavior, stability, and the potential challenges that may arise during excavation.

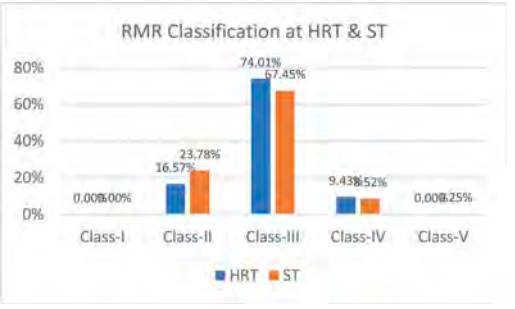

Figure 10. Comparison of rock class based on RMR classification at HRT & ST.

12 ROCK CLASSIFICATION BASED ON THE HINDRANCE

Given the limitations and challenges associated with traditional classification systems, an alternative approach to categorizing underground excavations is adopted based on the concept of hindrance. This method divides underground excavations into different classes to differentiate the difficulties and hindrances encountered during excavation work, which are often influenced by the properties of the materials encountered. The classification of excavation is established in relation to the hindrance it poses to the progress of excavation works, primarily caused by the type and amount of rock support installed within the tunnel heading zone. As the excavation progresses, the characteristics of the rock mass and the need for rock support can vary significantly, affecting the overall difficulty and complexity of the tunnelling process. By categorizing underground excavations based on the hindrance factor, engineers and tunnelling teams can gain a better understanding of the challenges they are likely to face at different stages of the project. This approach allows for more targeted planning and selection of appropriate excavation methods, support systems, and safety measures.

Factors such as the rock mass quality, jointing patterns, presence of groundwater, and expected ground convergence play a vital role in determining the class of excavation. As the excavation class changes, adjustments to the support systems and excavation techniques may be necessary to ensure safe and efficient progress throughout the tunnelling process.

Overall, this hindrance-based classification system provides a practical and adaptable framework for evaluating and managing the complexities of underground excavations, promoting successful project execution while mitigating potential risks and challenges encountered in varying geological conditions.

13 THE UNDERGROUND EXCAVATION CLASSES, DESIGNED TO CATEGORIZE THE LEVEL OF HINDRANCE ENCOUNTERED DURING EXCAVATION WORK, ARE AS FOLLOWS:

Class IIIA: The implementation of support measures significantly impedes the advancement of heading excavation to the extent that support installation becomes an integral component of the work cycle. The support system entails the utilization of steel fiber-reinforced shotcrete (SFRS) applied in one or multiple layers, combined with a configuration of patterned rock anchoring or rock bolting in both heading and benching zones. This configuration may encompass the option of incorporating wire mesh as reinforcement for the shotcrete.

Class IIIB: The implementation of support measures introduces a certain level of interference and deceleration to the progress of excavation activities. The support system entails the utilization of steel fiber-reinforced shotcrete (SFRS) applied in one or multiple layers, combined with a configuration of rock anchoring or rock bolting in both heading and benching areas. This configuration may include the option of incorporating wire mesh as reinforcement for the shotcrete.

Class IV: When implementing support in this category, the excavation process encounters considerable delays in both heading and benching activities. The support strategy involves incorporating sturdy steel ribs within both these sections. Alongside these ribs, wall plates and a continuous lagging system are promptly positioned at the forefront of the excavation site. To reinforce stability, a meticulous rock anchoring approach is applied to the entire cross-sectional area. In certain scenarios, complete encasement of the steel ribs in shotcrete might be necessary, supplemented by the inclusion of wire mesh reinforcement if the lagging component is omitted. This comprehensive support method ensures the

structural integrity of the excavation despite the notable hindrance it introduces to the work process.

Class V: Excavation in this category necessitates a simultaneous installation of support for both heading and benching, ensuring the protection of the ongoing work. The support system is characterized by the incorporation of steel ribs within both these sections, accompanied by the utilization of invert bracing or struts. Additionally, wall plates and continuous lagging are promptly placed at the freshly exposed surface after any segment of the cross section is excavated. For enhanced stability, a systematic rock anchoring technique is implemented, providing reinforcement to the steel ribs and lagging. In specific circumstances, the steel ribs might require complete envelopment in shotcrete, with the potential inclusion of wire mesh reinforcement, particularly when lagging is not utilized. This comprehensive support approach guarantees the structural integrity of the excavation process, allowing it to proceed despite the need for simultaneous support installation. The allocation of different underground excavation classes based on hindrance to the head race tunnel (HRT) and surge tunnel (ST) is illustrated in the figure below.

Despite the various engineering classifications of the rock mass, there is no strong correlation observed between the percentage of the engineering classification and the percentage of hindrance class. The hindrance class is influenced by a combination of factors beyond the engineering classification, such as the specific tunnelling method used, geological variations within the tunnel alignment, and the effectiveness of support systems implemented. As a result, the hindrance class provides a more comprehensive understanding of the challenges encountered during excavation, considering a broader range of factors than the engineering classification alone. This reinforces the significance of adopting the hindrance-based classification approach to better address the complexities of underground excavation and ensure successful project execution.

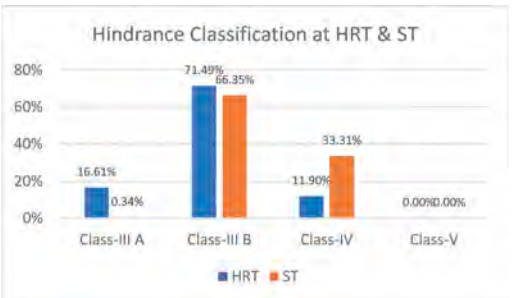

Figure 11. Comparison of rock class based on hindrance classification at HRT & ST.

14 CONCLUSIONS

The Subansiri Lower Hydro Electric Project (HEP) presents a unique case study of tunnelling in weak sandstone, which has posed several geological and engineering challenges during its construction. The soft and friable nature of the sandstone, coupled with the lack of fissility and the presence of fine-grained matrix and carbonaceous matter, has significantly impacted the tunnelling operations. To tackle these challenges, innovative engineering solutions and support systems were employed to ensure the successful construction of the project.

The use of mechanical excavation methods, such as road headers and twin cutters, proved effective in handling the weak sandstone. However, the low cutting rates observed were primarily attributed to the massive nature of the rock mass and the grinding effect during excavation. The substantial generation of dust during the cutting process led to poor visibility at the tunnel face, resulting in intermittent excavation halts for dust removal. This hindered the productivity of the rock cutting machines and required additional time and effort for waste removal.

The engineering classification of the rock mass using the Rock Mass Rating (RMR) system provided valuable insights into the geomechanics characteristics of the rock, but it was limited in addressing the specific challenges posed by the weak sandstone. As a result, an alternative hindrance-based classification approach was adopted, considering various factors, including the type and amount of rock support installed within the tunnel heading zone. This classification proved to be more relevant in assessing the difficulty and complexity of the excavation process.

Excavation classes were established based on the hindrance approach, providing a practical framework for evaluating and managing the challenges encountered during tunnelling. The support systems used in these classes, including steel fiber-reinforced shotcrete and rock anchoring or rock bolting, played a crucial role in ensuring the stability and safety of the tunnel structures.

Despite efforts to correlate the engineering classification of the rock mass with the hindrance classes, no strong correlation was observed. This highlights the significance of considering a broader range of factors beyond the engineering classification to better understand the challenges of underground excavation.

Overall, the case study of tunnelling in weak sandstone at the Subansiri Lower Hydro Electric Project has provided valuable insights and lessons for similar projects in comparable geological conditions. The successful application of innovative engineering solutions and hindrance-based classification approaches has contributed to the safe and efficient construction of the tunnels. By addressing the specific challenges posed by weak sandstone, the project has made significant progress towards its completion and has added to the knowledge base for future tunnelling endeavors in similar geologies.

REFERENCES

1 Bieniawski, Z. T. (1976) Rock mass classifications in rock engineering. proc. of the Sym. on Exploration for Rock Engineering, Johannesburg, 97-106.

2 Tunnelling Association of India, India Infrastructure," TAI, India Infrastructure records.

3 CEA Report on Subansiri Lower Hydro Electric Project (October-2021).

5 Barton, N., lien, R. and Lunde, J. (1974).

6 Engineering Classification of Rock Masses for the Design of Tunnel Support. NGI Publication No. 106, Os lo, 48.

7 Gehring, K. 1997 Classification of drillability, cuttability, borability and abrasivity in tunnelling. Felsbau 15: 183–191.

8 Krishnan M.S. (1956). Geology of India and Burma. Higginbotham's Ltd. Madras 604pp.

9 Le Fort P. (1975). Himalayas: The collided range. Present knowledge of the continental arc. Am. J. Sci. 2751–44

10 Sinha Roy, S. (1976). Tectonic elements in the eastern Himalaya and geodynamic model of evolution of the Himalaya. Geological Survey of India, Misc. Publ., 34, 57–74.

11 Thuro, L. and Spaun, G. (1996a). Drillability in Hardrock drill and blast tunneling. Felsbau 14: 103–109.

12 Thuro, L. and Spaun, G. (1996b). Introducing destruction work' as a new rock property of toughness referring to drillability in conventional drill and blast tunneling. In G. Barla (ed.) Eurock'96.

13 Verhoef, P, n.W. (1997). Wear of Rock Cutting Tools. Implication for the site investigation of rock dredging projects. Rotterdam, Brookfield: Balkema, 340pp.

14 Wadia D.N. (1957). Geology of India. Mc Millan and Co. Ltd. London 536 pp.

15 Geotechnical Challenges of Tunneling in Weak Sandstone: A Case Study by A. Smith and B. Johnson.

16 Strength and Deformation Characteristics of Weak Sandstone for Tunneling by M. Patel and S. Gupta.

17 Numerical Modeling of Tunneling in Weak Sandstone by J. Wang and X. Li.

18 Numerical Modeling of Weak Rock Tunneling by H. Kang and H. Konietzky.

19 Tunnel Support Systems for Weak Sandstone: A Review by R. Sharma and N. Verma.

20 Tunnel Support Design in Weak Rocks: A Case Study by M. Ghosh and S. Das.

21 Influence of Geological Features on Tunnel Stability in Weak Rock by L. Li and C. Tang.

22 Ground Improvement Techniques for Weak Sandstone Tunnels by K. Tan and G. Lim.

23 Grouting Techniques for Weak Rock Tunneling by P. C. Chiu and K. Soga.

24 Tunneling in Sandstone with Varying Strength: Lessons from Field Projects by E. Chen and H. Liu.

25 Instrumentation and Monitoring of Weak Sandstone Tunnels by S. Das and P. Kumar.

26 Instrumentation and Monitoring in Weak Rock Tunnels by M. Karakus and H. K. Kim.

27 Case Studies of Tunnels in Weak Sandstone by D. Zhao and L. Wu.

28 Case Studies of Weak Rock Tunneling Projects by D. Hoek and E. Marinos.

29 Tunneling in Soft Rock – Subansiri Hydroelectric Project, Arunachal Pradesh, India. - by Arvind Garg, Alok Kumar Rahul, and Dr. Devojit Bezbaruah

30 Challenges in Weak Rock Tunneling and Their Mitigation Measures: A Review by V. R. Sastry and G. R. Reddy.

31 Tunneling in Weak Rock - A Review by R. Gertsch and F. F. B. Zettler.

32 Rock Mass Classification for Weak Sandstone Tunneling by A. Gupta and S. Rajan.

33 Rock Mass Classification Systems for Weak Rock Tunnels by E. Hoek.

34 Issues and Challenges in Construction of Hydro Tunnel in Extreme Geological conditions in India – An Empirical Study by Rakesh Kumar Khali and Dr. Sandeep Potnis.

Tunnelling for a Better Life – Yan, Celestino, Thewes & Eberhardt (Eds)
© 2024 The Author(s), ISBN 978-1-032-80042-4
Open Access: www.taylorfrancis.com, CC BY-NC-ND 4.0 license

Correlation of empirical classification systems in squeezing anisotropic environment and optimisation of underground supports in a headrace tunnel; a case study from Tanahu Hydropower, Nepal

Eirinaios Christakis*
Tractebel Engin. GmbH, Bad Vilbel, Germany

Bibash Parajuli, Pengcheng Yao & Radha Krishna Adhikari
PowerChina Chengdu Engin. Corp. Ltd, Chengdu, China

ABSTRACT: The headrace tunnel of Tanahu Hydropower Project was excavated in the Benighat Slates of the Lesser Himalayan zone, located at West-Central Nepal. The tunnel runs underneath a high overburden massif that comprises thinly foliated Slates with distinct presence of multiple sheared zones, characterised by anisotropy. Geotechnical information retrieved for the construction of the adjacent underground powerhouse was utilised for the numerical analysis, whereas the design for the temporary support was initially based on Bieniawski's RMR system. For the design and the in-situ assignment of reliable support measures to ensure underground stability, a realistic evaluation that resembles the actual geological regime is significant. Should difficult ground conditions hinder excavation and geological uncertainty contributes to the unforeseeable, the necessity for the most adaptive classification system becomes apparent. Rock-mass classification systems are the basis for the real-time evaluation of underground stability, and a supplementary tool, wherever design parametrization is based on limited pre-excavation information or lacks of realistic numerical analysis. Moreover, the risk for overestimation or underestimation in case of erroneous rock-mass assessment might lead to over-supporting (uneconomical and time consuming) or under-supporting (entails instability risk). For the particular tunnel, the distribution of support classes based on RMR was found unsuitable to address anisotropy and squeezing phenomena. In order to deal with similar classification shortfalls, temporary supports were re-designed based on Q-system. Researchers have developed empirical correlations between classification systems, which cannot always reflect specific geological conditions. Hence, the authors attempt to develop relevant correlations between Q, GSI and RMR which derive from statistical analysis; and recommend the most optimal equations compared to equations from other researchers. The parallel use of two or more classification systems for the particular underground environment provides a more reliable assessment tool, and subsequently assures the assignment of optimal rock support measures.

Keywords: Squeezing ground, Rock mass classification, Correlation, Tunnel support, Slate, Anisotropy

1 INTRODUCTION

A fundamental tunnelling aspect that assures underground stability, is that the extent of applied rock support should reflect the behaviour of the excavated rock mass, whilst rock mass behaviour is reflected by the used classification approach. The comprehension of the actual physical and mechanical rock mass characteristics plays an important role in determining the actual rock support requirements and their limitations. However, considering the self-supporting capacity of rock mass, its geomechanical behaviour and the principal economic factors of tunnelling, i.e., time and cost; there is always space for the optimisation of support measures. The selection of tunnel rock support should be based on the sound understanding of rock mass characteristics, the stress regime, and stability issues (i.e. the geotechnical risk) that may arise (Nilsen & Thidemann, 1993).

Several classification systems have been developed throughout the years focusing to the inclusion and the quantification of the most important factors/parameters which influence stability, aiming to provide a realistic evaluation of rock mass quality. Apart from selecting the optimal support, classification systems in tunnelling intend to assess rock mass behaviour under particular in situ stress conditions in order to adopt a safe excavation strategy. In other words, an attempt to quantify rock mass quality. From the beginning of 20th century, empirical

*Corresponding author: renos.christakis@tractebel.engie.com

DOI: 10.1201/9781003495505-64

approaches for rock mass classifications have set the basis for support design, for underground structures and open excavations. The most prevalent classification systems such as RMR, Q, and GSI are employed in the engineering practice since long time now. These classification systems constitute the quantitative estimation of rock mass quality, linked with empirical design rules in order to assess adequate rock support measures (Palmstrøm, A., 2009).

2 EMPIRICAL CLASSIFICATION SYSTEMS

Bieniawski developed Rock Mass Rating (RMR) in 1973. RMR classification system is based on the algebraic summation of six geomechanical parameters, emphasising on the intact strength, the blockiness, the characteristics of discontinuity surfaces, the groundwater conditions, and the orientations of the structural planes with respect to the underground structure. Thus, RMR derives from the following equation.

$$RMR = A1 + A2 + A3 + A4 + A5 + B \qquad (1)$$

A1 corresponds to rates related to the intact rock strength, A2 relates to RQD, A3 refers to the spacing of discontinuities, A4 comprises a series of joint surface condition parameters (i.e. persistence, aperture, roughness, infill material and weathering), A5 represents groundwater conditions, and B is the rating adjustment for joint orientations. The derivative value ranges from 0 to 100, and with reference to the excavation span, they define specific stand-up times, the optimal excavation guideline, and recommend estimated rock support measures.

In 1994, Hoek introduced the Geological Strength Index (GSI). GSI evaluation is based on the observation of the rock structure system -and in particular, to its interlocking degree, in conjunction with the quality of joint surface conditions. Since then, a number of system updates included the consideration of weak or jointed rock masses (1998 and 2000), and also special classifications for heterogeneous masses (e.g. flysch). For an ample variety of geological conditions, GSI system facilitates the determination of rock mass properties, aiming to provide estimates for the rock mass strength and its deformation modulus, whilst the system can be used as part of the empirical Hoek-Brown failure criterion. The validity of the index depends on a precondition; rock mass exhibits isotropic behaviour, without considering structural failures. The values derive from matrix charts by combining the primary factors of the index (i.e. the visual estimate of structure and surface conditions), represented in the form of diagonal contours (ranging between 0-100).

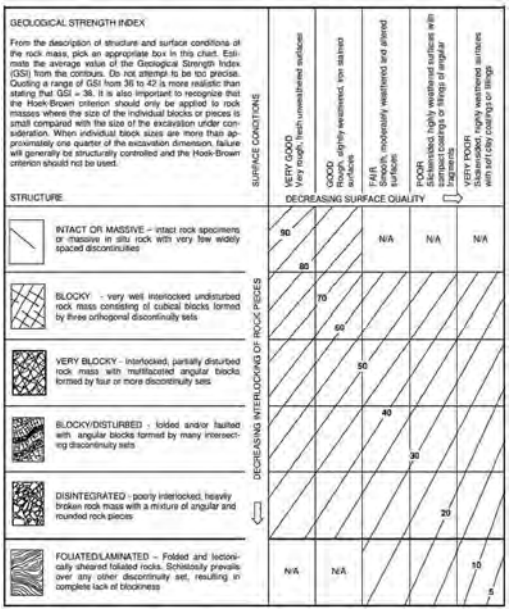

Figure 1. General GSI matrix chart (Marinos et al., 2005).

In 1974, Barton et al. developed the first version of Q-system at the Norwegian Geotechnical Institute, based on a large number of tunnelling reference data, taking into consideration the stability of the underground openings. The system has been updated several times by integrating more reference cases until lately (latest update 2022); aiming to provide a realistic description of rock mass quality, and at the same time, recommend design guidelines, and the estimation of rock support (with respect to the size of the opening, and the purpose of the structure). Q-value comprises the product of three fundamental geomechanical characteristics: i) the degree of jointing, i.e. the quotient of RQD and the number of joint sets (J_n); ii) joint friction, i.e. the quotient of joint roughness (J_r) and the joint alteration (J_a); and iii) the stress regime, i.e. the quotient of groundwater regime (J_w) and the effect of stress (SRF or stress reduction factor).

$$Q = RQD/Jn \times Jr/Ja \times JW/SRF \qquad (2)$$

The derivative ranges on the logarithmic scale, and support measures are assigned considering the excavation's span and purpose, based on a schematic chart.

2.1 *Correlation between classification systems*

Considering the variable degree of geological uncertainty and the complexity of an underground excavation, neither a particular system, nor can any index explicitly "*describe*" rock mass or simulate the behaviour of rock mass under particular circumstances. None of them can be viewed as panacea on its own. In several cases, rock mass, the stress

regime and the salient features of an excavation would set the path and point out the factors to be considered, in order to address geotechnical risk and assure stability. The use of a single system entails the risk of disregarding or undervaluing an important stability factor that might lead to an imprecise assessment of the geomechanical conditions.

Provided that classification parameters from each system overlap to some extent, numerous researchers attempt to correlate different systems by developing corresponding equations, opting to better understanding the ground reaction on applied supports for specific rock classes. The majority of the equations are resultants of statistical analysis based on data collected from case studies of various projects, various lithologies and geomechanical regimes. The following tables summarise the most common correlation equations between the three main empirical classification systems, i.e. Q, RMR and GSI. It shall be noted that every equation relates to particular geographical, geological and stress conditions.

Table 1. Correlation equations between Q, GSI and RMR.

Equation		Researcher
$RMR = 9\ln Q + 44$	(3)	Bieniawski (1976)
$RMR = 5.9\ln Q + 43$	(4)	Rutledge et al. (1978)
$RMR = 5.49\ln Q + 55.2$	(5)	Moreno (1980)
$RMR = 5\ln Q + 60.8$	(6)	Cameron & Budavari (1981)
$RMR = 10.5\ln Q + 41.8$	(7)	Abad et al. (1984)
$RMR = 3.7\ln Q + 53.1$	(8)	Sari & Pasamehmetoglu (2004)
$RMR = 8.15\ln Q + 44.88$	(9)	Laderian & Abaspoor (2012)
$RMR = 8.09\ln Q + 43.08$	(10)	Rafiee (2013)
$RMR = 4.52\ln Q + 43.6$	(11)	Khana & Sayeed (2015)
$RMR = 6.63\ln Q + 35.53$	(12)	Castro et al. (2010)
$RMR = 6.4\ln Q + 49.6$	(13)	Kumar et al. (2004)
$RMR = 2.8\ln Q + 45.19$	(14)	Cosar (2004)
$RMR = 5.37\ln Q + 40.48$	(15)	Hashemi et al. (2010)
$RMR = 4.52\ln Q + 43.63$	(16)	Ali et al. (2014)
$GSI = RMR - 5$	(17)	Bieniawski (1989)
$GSI = 0.5RQD + 1.5Jc$	(18)	Hoek et al. (2013)
$GSI = 0.42RMR + 23.07$	(19)	Cosar (2004)
$GSI = 1.35RMR - 16.4$	(20)	Irvani et al. (2013)
$GSI = 0.73RMR - 4.38$	(21)	Singh & Tamrakar (2013)
$GSI = 1.21RMR - 18.61$	(22)	Zhang et al. (2019)
$GSI = 6e^{0.05RMR}$	(23)	Osgoui & Unal (2005)
$GSI = 1.61\ln Q + 42.99$	(24)	Cosar (2004)
$GSI = 5.96\ln Q + 47.85$	(25)	Deak et al. (2014)
$GSI = 12.64\ln Q + 28.54$	(26)	Sadeghi et al. (2020)
$GSI = 0.5RQD + 52Jr/(Jr + Ja)$	(27)	Hoek et al. (2013)
$GSI = 9\ \log \mathrm{Q} + 44$	(28)	Hoek et al. (1995)

(*Continued*)

Table 1. (*Continued*)

2.2 *Methodology and metrics*

Three classification systems -as described in the preceding chapter have been utilised for the evaluation of rock mass quality, and for correlation purposes. For each advanced face, during the geological mapping task, geologists calculated three separate values with reference to the respective classification systems (i.e. RMR, Q and GSI). Recorded values were tabulated for statistical processing in line with the linear regression approach; aiming to produce optimal correlation equations between two systems (should this be feasible), and evaluate the degree of accuracy for those equations. In addition, to select the most suitable and realistic mathematical expression (i.e. equations from Table-1 with the highest correlation and the lowest error coefficients, including the produced optimal correlation from project data), regression analyses were also performed between the theoretical rock mass quality derivatives and the actual values which were assigned during the tunnel mapping process. The following metrics were utilised for data analyses.

The Mean Absolute Percentage Error (MAPE) is calculated in order to define the degree of accuracy of the produced equations; hence, it provides a comparison index between the forecasted value (*calc*.) and the actual values as those measured in the tunnel (*act*.). The MAPE value for a particular data population (n), expresses the average of the absolute percentage errors based on the following equation.

$$MAPE = \frac{1}{n} \times \sum_{1}^{n} \left| \frac{act. - calc.}{act.} \right| \qquad (29)$$

The Mean Absolute Error (MAE) corresponds to the absolute difference's average between the in-situ recorded (*act.*) and calculated values (*calc.*). Therefore, MAE measures the average of the residuals in a dataset population (n) of rock quality predictions, where all individual differences have equal weight. MAE value is given by the following equation.

$$MAPE = \frac{1}{n} \times \sum_1^n |act. - calc.| \qquad (30)$$

The Root Mean Squared Error (RMSE) is a quadratic index which measures the average magnitude of the error for a data set (n), and defines data concentration (their proximity) around the optimal regression line, based on the equation.

$$RMSE = \sqrt{\frac{\sum_1^n (act. - calc.)^2}{n}} \qquad (31)$$

The coefficient of determination (R^2) or R-squared in linear regression analysis, indicates the level of variation by measuring the square of the correlation between the actual site values (x) and the values produced by the theoretical equation (y). The validity and trend of a linear relationship of the analysed data sets is quantified with values ranging between 0 and 1.0. The closest to 1.0 the R^2 is measured, the more reliable the theoretical correlation is. R^2 derives from the correlation coefficient formula (Pearson's R index).

$$r = \frac{n(\sum^x y) - (\sum^x)(\sum^y)}{\sqrt{[n\sum^{x^2} - (\sum^x)^2][n\sum^{y^2} - (\sum^y)^2]}} \qquad (32)$$

3 GEOLOGICAL BACKGROUND OF TANAHUN PROJECT

Tanahun Hydropower Project is a storage type project located at Tanahun District of Gandaki Province in the West-central Nepal. The main salient features of this project comprise a 140-metres high RCC gravity dam, the underground powerhouse (89x22x51m), a 25.5m wide underground surge system, and its 1418m long headrace tunnel (HRT). The excavation shape of headrace tunnel is horse-shoe, excavated in two phases (i.e. top heading and benching) along a 2% gradient, with an average span of 10.2m.

The tunnel runs along medium to high overburden (minimum 70m and maximum 695m). Almost 60 to 70% of the headrace tunnel passes through rock cover of greater than 300m, which means high vertical stresses and a risk of high deformation magnitudes. The excavation was carried out with conventional drill and blast method (D&B), and in exceptional cases of weak rock mass, with mechanical means (i.e. use of hydraulic breaker and excavator). The average advance length per drill & blast round is less than 1.8m, and the excavation commenced from the powerhouse towards the power intake (Dam area).

Based on the preliminary investigation conducted during the design stage of the project, the anticipated lithology of the HRT consists of Benighat Slate series of the Upper Nawakot group (Lesser Himalayan sequence). Benighat Slates overlay a series of very thick bedded, massive, blue-grey Dolomite (Dhading formation). The encountered lithology during the excavation phase substantiated the literature references as well as the results of the design stage. Dhital (2015) describes Benighat Slate as light grey to black and green-grey formation, containing very thinly (<1mm) cleaved varieties. Carbonaceous Slate is regarded as special continuous formation, where weak zones parallel to foliation are playing an important role to its anisotropic behaviour. Moreover, its deformability and strength directly depends on the cleavage plane orientation with respect to the principal stresses. It is important for numerical modelling, to conceive rock mass characteristics and its anticipated behaviour, in order to facilitate the adoption of realistic design parameters. Such parameters would allow the precise analysis of probable failure mechanisms and deformation thresholds. Thus, the lack of proper understanding of those characteristics and the inaccurate determination of failure mechanisms entails the risk of an uncertain numerical model (Marinos, 2014).

Considering the purpose of the underground structure in conjunction with the anticipated geomechanical conditions, the tunnel will be permanently supported with concrete lining segments (lining thickness 0.50-0.90m, depending on the encountered rock mass conditions). The temporary supports include the application of reinforced shotcrete (with steel fibres or embedded wire mesh), ranging from 50 to 200mm depending upon the support classes; 4 to 6m long fully grouted passive rock bolts; and steel supports in stretches of very poor or extremely poor rock mass (lattice girders or H-beams). A typical tunnel profile and its characteristic lithology are shown in Figure 2.

Figure 2. Typical carbonate Slate; overburden 380m (approx.).

It is notable that in almost 55% of the tunnel stretches, the encountered rock mass quality necessitated the installation of steel ribs or lattice girders.

Numerous shear zones of ranging thickness (from few centimetres up to 300cm) were encountered during the top-heading stage, influencing the tunnel's stability. A number of prevailing geomechanical parameters such as the distinct anisotropy, the localised low intact strength, the joint spacing (very thin to laminated), the

intense shearing and folding in conjunction with the high overburden; resulted in the increment of anisotropic strain and consequently to several low-squeezing incidents that led to localised defects of the temporary support shell. Defects had localised characteristics and consisted of swayed lattice girders, shattering or bulging of bearing plates, and shotcrete cracks or detachments. It is worth to note, there was no significant groundwater activity apart of scattered damp/wet areas of dripping (i.e. flow<1.0 lit/min.).

Considering the encountered deformations, in order to optimise the temporary support strategy (prevent support inadequacies or even avoid oversupport), the numerical model was re-assessed based on the real-time excavation data, the design of the temporary support was reviewed, and the NGI's Q classification system replaced RMR for the remainder of the excavation. Few examples of defects are illustrated in the Figure 3, below.

Figure 3. Rock support defects due to low squeezing.

Panthi (2006) states that the strength of intact rock for Slates reaches the lowest possible margin when schistosity dips with 45° degrees. In particular, for the entire HRT, Slate's schistosity strikes parallel to tunnel drive, dipping with 40° to 50° to the SW wall, an additional critical squeezing factor. When the underground opening exhibits anisotropy as governing stress mode, it can lead to a situation where the applied supports may experience variable magnitudes of support pressures around their periphery. (Shrestha & Panthi, 2014). Very poor rock masses with distinct persistent schistosity, tend to react in an elastic - perfectly plastic mode. However, under high overburden conditions, a poor quality anisotropic formation might behave in a quasi-isotropic mode whilst the anisotropic factor is gradually outweighed, resulting in squeezing failure. In that case, the Slate's low strength plays a major role for the occurring deformation. In stretches of medium strength, minor chimney and shear failures occurred close to the advancing face. The magnitude and attitude of profile deformation was closely monitored with a dense network of convergence stations alongside with daily routine observations. The maximum deformation in some sections reached nearly 200mm having a maximum strain of 2.5% which indicates minor squeezing, whereas the average strain values range between 0.5 and 0.7%, a figure which reflects to the defects of the temporary support elements.

4 CORRELATION OF FACTUAL CLASSIFICATION DATA

The classification data relate to specific geological-geomechanical conditions. In brief, data were collected from a 1070 m tunnel stretch that comprises medium strong, light grey to black micro-folded Slate. Table 2 presents the summary of the geomechanical properties of the excavated rock mass. A typical cleaved, micro-folded Slate encountered in many excavated faces is shown in Figure 4.

Table 2. Particular geomechanical properties of research.

Overburden	120-695m
Groundwater	Dry to damp, with localised scattered drippings (<1.0 lit/min)
Structure	Intense foliation (crenulation cleavage); spacing <60mm (average 10-40mm); foliation dips 45°, striking parallel to tunnel alignment
Discontinuities	Persistence: 1-3m Separation: tight to 2mm (localised 3-6mm) Roughness: smooth, planar to undulating Infilling: graphite, patches of clay, quartzite Weathering: slightly weathered to unweathered
Tectonic features	Shear bands parallel to foliation (10-200cm)

For reference, the data range of rock mass quality based on the geological mapping records are summarized below.

For the statistical analysis of the factual values and for the three classification systems, geologists mapped 548 tunnel faces and assigned values for each system separately. Regression analysis was conducted for the data couples resulted from classification systems, for all three combinations (Q-RMR, RMR-GSI, and Q-GSI). These data were interpolated in order to generate the best fit curve. Each combination was evaluated based on five regression modes: i) exponential, ii) linear, iii) logarithmic, iv) power, and v) 2nd order polynomial.

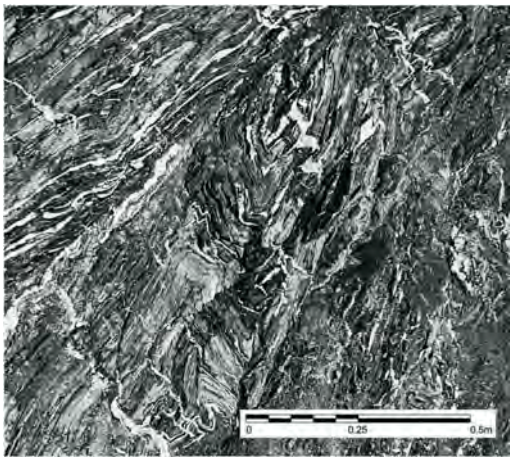

Figure 4. Typical cleaved Slate; close up photograph.

Table 3. Actual rock mass quality values (548 data).

	Highest value	Lowest value	Mean value	Most frequent value
Q-value	1.44	0.016	0.184	0.07
RMR	53	31	40	39
GSI	49	20	34	31

Such curve may provide a reliable correlation between two classification systems.

4.1 *Factual Q-RMR evaluation*

Five different possible regression curves were evaluated, in order to conclude to the most reliable (the highest possible R^2 derivative). With reference to the mapped Q and RMR factual values, the highest coefficient of determination results from the power equation, and equals to R^2=0.5965, therefore R=0.772, a relatively acceptable value.

$$RMR = 49.411 \times Q^{0.1084} \tag{33}$$

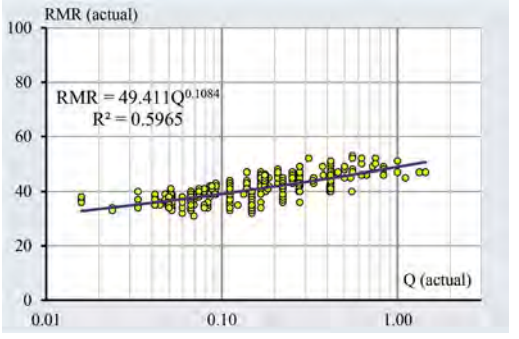

Figure 5. Correlation between Q and RMR actual values.

4.2 *Factual RMR-GSI evaluation*

The same evaluation approach was adopted to define the relationship between the RMR and GSI mapped values (factual data). Similar to the preceding correlation analysis, the highest coefficient of determination results from the logarithmic equation, and equals to R^2=0.4047, therefore R=0.636, a relatively low value, not highly recommended for a reliable correlation between RMR and GSI.

$$GSI = 38.466 \ln RMR - 108.96 \tag{34}$$

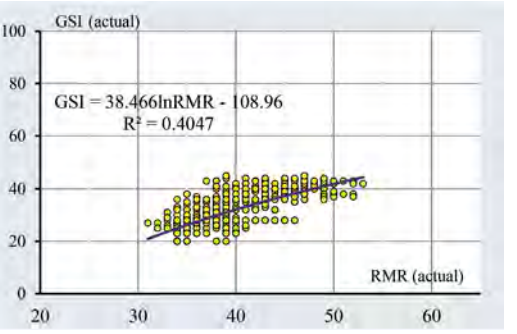

Figure 6. Correlation between RMR and GSI actual values.

4.3 *Factual Q-GSI evaluation*

With respect to the relationship between Q and GSI (minimum index) mapped factual data, there is no coefficient of determination that exceeds 0.30 (R<0.5477), an indication of very low reliability between these classification systems. The coefficient of the power equation equals to R^2=0.30, therefore R=0.5477.

$$GSI = 42.902Q^{0.147} \tag{35}$$

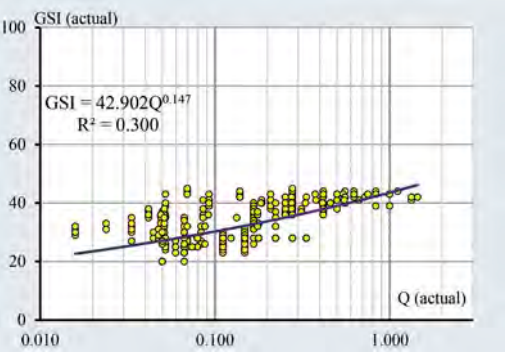

Figure 7. Correlation between Q and GSI actual values.

5 EVALUATION OF LITERATURE CORRELATIONS

Aiming to evaluate the accuracy of the literature equations included in Chapter 2.1 (Table 1) with

respect to the real rock mass data, and compare with the most reliable equations which derived from the factual evaluation process (Chapter 4), analyses were conducted, and the metrics of the most reliable equations are summarised below.

Table 4. Evaluation of accuracy.

Equation		MAPE (%)	MAE	RMSE
Q to RMR				
$RMR = 49.411 \times Q^{0.1084}$	(33)	6.31%	6.51	7.78
$RMR = 2.8 \ln Q + 45.19$	(14)	6.86%	2.72	3.19
$RMR = 6.4 \ln Q + 49.6$	(13)	10.5%	4.17	4.84
	(5)	11.6%	4.38	5.28
RMR to GSI				
$GSI = RMR - 5$	(17)	14.1%	4.53	5.18
No reliable equation from actual data correlation				
Q to GSI				
$GSI = 5.96 \ln Q + 47.85$	(25)	16.6%	5.26	6.21
No reliable equation from actual data correlation				

With respect to the correlation equations between RMR and GSI, and between Q and GSI, the metrics derivatives produced relatively high mean absolute percentage errors (MAPE>14.1%). In addition, the most optimal correlation equations for these combinations, which resulted from the actual recorded values (equations 34 and 35) show relatively low coefficients of correlation (Pearson's index). Thus, they are both considered unreliable.

With respect to the Q-RMR correlation, the comparison of the three most-reliable literature equations (i.e. Cosar, 2004; Moreno, 1980; and Kumar et al., 2004) and the power regression model of the actual values (eq. 33) are illustrated in Figure 8, below.

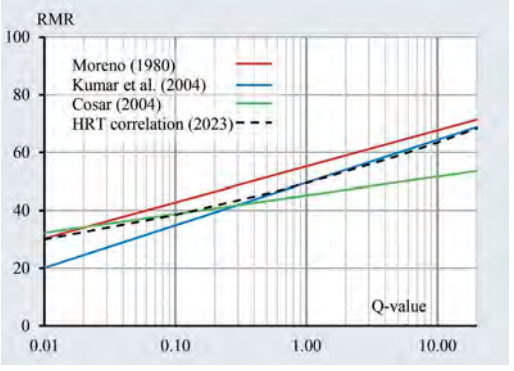

Figure 8. Best optimum Q-RMR correlation equations.

For very poor to extremely poor rock masses (Q<0.4), Cosar's equation (14) is marginally matching to the logarithmic regression line equation (33). Both equations have similar MAPE, whereas Cosar's equation shows lower absolute error values. Equation (14) utilised reference data from a Schist formation under medium stress regime, and its correlation coefficient is 0.818. On the other hand, for better rock mass qualities (Q>0.2), Kumar et al. equation (13) is converging to the linear regression line of equation (33). Equation (13) has utilised reference data mainly from Schists and Gneiss formations under squeezing conditions, and its correlation coefficient is 0.55.

6 CONCLUSIONS AND RECOMMENDATIONS

The scope of rock mass classification systems constitute an attempt to quantify rock mass quality, to shed light in the anticipated ground behaviour, and to provide support quantitative estimates for the design of an underground structure. Given the fact that the rationale and foundation of each system differs; it is essential for the end user to be well-aware of those, and in addition to consider their limitations (Palmstrøm & Broch, 2006). Another critical factor that is directly influencing the classification derivatives and subsequently may result in inaccurate or unrealistic design, relates to the degree of subjectiveness (i.e. how biased estimates can lead to misinterpretation), and how conservative or not a field practitioner could be. Therefore, the question: "*which is the best or reliable classification system?*" is invalid, and the authors suggest an alternative: "*which is the most suitable system for site specific use?*". As Young et al. (2021) recently underline, the characterisation and classification of rock mass should incorporate geology, and at the same time, should be tailored to specific rock mass types. Hence, no system can equally and accurately reflect each site's particular geological conditions.

6.1 *Shortfalls and limitations*

The reference data from which Q-system was established were obtained from metamorphic and igneous hard, jointed rocks, including weakness zones, aiming to provide an average estimate for the necessary rock support. The system considers the stress regime and in particular accounts for squeezing ground, and the dimensions of the underground opening. However, considering the scarcity of data from weaker formations and the small number of references under squeezing ground conditions; for the design and the evaluation of support measures Barton (2022) himself recommends the contribution of numerical methods, supplemented with monitoring. A basic shortfall of the system lies in the RQD dependency, where in weak rock masses the parameter turns practically meaningless.

The majority of reference cases which RMR derives from, relate to sedimentary formations. The system also aims to provide a crude estimate for the necessary rock support. In the RMR the stresses and

tectonic regime are not considered, whereas the influence of fault zones/weak zones is ambiguous. However, some parameters included in the system may represent fault conditions, although the complicated structure and composition of these features are generally difficult to characterize and classify (Palmstrøm, 2009). In addition, similar to Q-system, RMR is also dependent upon RQD, and subsequently tends to fail when addressing poor quality rock mass (and heterogeneity, as well).

GSI system excludes RQD in terms of a quantitative metric, whilst the system focuses on the structural composition and surface discontinuity conditions. It should be highlighted that its main objective is the estimate of rock mass properties, and specifically its strength; and not the direct recommendation of support measures. Provided that GSI does not rely on quantified parameters, its derivative results through a visual examination process. However, the system is not applicable to anisotropic rock masses or massive rock masses with few very wide spaced discontinuities with respect to the dimension of the opening (Marinos, 2005), but works quite well with poor quality rock masses. Moreover, GSI does not consider the stress and groundwater regime.

6.2 *Applicability of classification systems to the HRT*

With reference to the site specific conditions (i.e. Tanahu HPP Headrace Tunnel), the field geologist was expected to map excavated workfronts and assign classification indices in a low to moderately strong Slate (i.e. a metamorphic rock), characterised with foliation and cleavage, intersected by numerous shear or weakness zones, under a high stress environment with prominent long-term and slow response deformation due to mild-squeezing. In general, a very poor to extremely poor rock mass. Moreover, the margins that stresses exceed rock mass strength were considered inexplicit, rendering the threshold between anisotropy and pseudo-isotropy also fluid.

In order to produce a realistic quantifiable index, that adapts to the encountered geology and also assure safe and economical excavation, many key-authors of rock engineering (Bieniawski, 1989, and Palmstrøm, 2009) recommend the simultaneous use of two systems. Considering the particular geological conditions and the aforementioned shortfalls and limitations of each classification system, the authors recommend the "collaboration" of Q-system with the parallel application of GSI as the most suitable systems that could result in realistic rock mass evaluation. The selection of a suitable system is the key-tool for the conceptual geological model, the foundation for precise parametrization, and an important factor for the uncertainty risk mitigation when conducting analytical numerical methods. Instead of relying on a crude figure (i.e. an index value), a more analytical description of each system's input parameters provide additional clarity to the actual or anticipated rock mass behaviour.

Further to this, with respect to the excavation of the 2nd phase (bench), the authors highly recommend a diligent and coherent monitoring strategy. Such strategy should include:

i. the geodetic survey of optical target stations (convergence stations as those installed during the excavation of the top-heading phase and new stations where necessary), and
ii. the installation of multi-point borehole extensometers (MPBX) in stretches under the highest overburden, and stretches of considerable deformation.

Geodetic survey of the convergence targets will provide information about supplementary deformation that may occur during benching phase. MPBX instruments will also monitor profile displacements, as well as they will determine deformation behaviour within the rock mass and provide an estimate of the extent of plasticity zone. Consistent monitoring plays and important role for the early detection of displacements beyond the assigned stability thresholds, and predispose the modification of supports or the installation of supplementary measures.

6.3 *Optimal correlation equations*

It is evident from the regression analyses, as well as from the comparison with the available literature correlations, that the applicability of an existing equation relates to the range of the encountered rock mass type and quality, and the stress regime. Therefore, for very poor to extremely poor Slate in a squeezing environment, Cosar's (2004) equation (14) provides a satisfactory correlation output. However, for better quality Slates (poor or fair), Kumar's (2004) equation (13) is mostly recommended. The most optimal Q-RMR correlation equation recommended for generic purpose in poor or worse quality Slates is equation (33).

Table 5. Recommended Q-RMR correlation equations.

Equation		Application
$RMR = 49.411 \times Q^{0.1084}$	(33)	Generic quality Slate; squeezing
$RMR = 2.8 \ln Q + 45.19$	(14)	Slates Q<0.4
$RMR = 6.4 \ln Q + 49.6$	(13)	Slates, schists; squeezing

However, no matter how perfect the regression metrics will be, no mathematical expression can simply "*translate*" and quantify geology from one system to another. In addition, the applicability of any correlation is linked to site-specific and geological conditions, and is subject to the discretion of the field practitioner. Hence, correlations should be used with caution, always with reference to their

database source, and only for validation purposes. As such, they cannot replace the direct use of any classification system.

REFERENCES

Abad, J., Calera, B., Chacon, E., Gutierrez, V., Hidlgo, E., 1984. Application of geomechanical classification to predict the convergence of coal mine galleries and to design their supports. 5th Int. Congress on Rock Mechanics, Melbourne, 15–19.

Ali W., Mohammad N., Tahir M. 2014. Rock mass characterization for diversion tunnels at Diamer Basha Dam, Pakistan – a design perspective. Int J Sci Eng Technol. 3: pp. 1292–1296.

Barton, N., 1995. The influence of joint properties in modelling jointed rock masses. Keynote lecture, 8 ISRM Congress, 3: 1023–1032.

Bieniawski, Z.T., 1984. Rock Mechanics Design in Mining and Tunnelling, 272.

Bieniawski, Z.T., 1989. Engineering Rock Mass Classifications. John Wiley and Sons, PA.

Cameron-Clarke, I.S., Budavari, S., 1981. Engineering Geology, Correlation of rock mass classification parameters obtained from bore core and in situ observations, 19–53.

Castro-Fresno, D., Diego-Carrera, R., Ballester-Muñoz, F., Álvarez-García, J., 2010. Correlation between Bieniawski's RMR and Barton's Q Index in Low-Quality Soils. Revista de la Construccion. 9. 107–119. 10.4067/S0718-915X2010000100012.

Cosar, S., 2004. Application of rock mass classification systems for future support design of the Dim tunnel near Alanya. MSc Thesis, Middle East Technical University, Ankara, Turkey.

Deak, F., Kovacs, L., Vasarhelyi, B., 2014. Geotechnical rock mass documentation in the Bataapati radioactive waste repository. Central European Geology, Vol. 57, Issue 2, pp:197–211.

Dhital, M.R., 2015. Lesser Himalaya of Gandaki Region. Geology of the Nepal Himalaya. Regional Geology Reviews. Springer, Cham.

Hashemi, M., Moghaddas, S., Ajalloeian, R. 2010. Application of Rock Mass Characterization for Determining the Mechanical Properties of Rock Mass: a Comparative Study. Rock Mech Rock Eng 43, pp 305–320, https://doi.org/10.1007/s00603-009-0048-y

Hoek, E., Kaiser, P.K., Bawden, W.F., 1995. Support Underground Excavations in Hard Rock (Balkema).

Hoek, E., Carter, T.G., Diederichs, M.S., 2013. Quantification of the Geological Strength Index Chart. 47th US Rock Mechanics & Geomechanics Symposium ARMA, 13–672.

Irvani, I., Wilopo, W., Karnawati, D. 2013. Determination of Nuclear Power Plant Site in West Bangka Based on Rock Mass Rating and Geological Strength Index. Journal of SE Asian Appl. Geol 5(2): pp. 78–86.

Khanna, R., Sayeed, I., 2015. Empirical correlation between RMR and Q systems of rock mass classification derived from Lesser Himalayan and Central crystalline rocks. Int. Conference on Engineering Geology in New Millennium 2015, New Delhi, India.

Kumar, N., Samadhiya N. K., Anbalagan R., 2004. Application of rock mass classification systems for tunnelling in Himalaya, India. International Journal of Rock Mechanics and Mining Sciences, Vol. 41, Sup.1, pp. 852–857, ISSN 1365-1609.

Laderian, A., Abaspoor, M.A., 2011. The correlation between RMR and Q systems in parts of Iran. Tunnelling and Underground Space Technology, S0886779811000770.

Marinos, V., Marinos, P., Hoek, E., 2005. The geological strength index: applications and limitations Bulletin of Engineering Geology and the Environment, vol. 64, no. 1, pp. 55–65.

Marinos, V., 2014. Tunnel behaviour and support associated with the weak rock masses of flysch. Journal of Rock Mechanics and Geotechnical Engineering, Vol:6, Issue:3, pp 227–239.

Moreno Tallon E., 1980. Aplicación de las Clasificaciones Geomecánicas a los Túneles de Pajares. II Curso de Sostenimientos Activos en Galerías y Túneles. Fundación Gomez-Parto, Madrid.

Nielsen, B., Thidemann, A., 1993. Rock Engineering. Hydropower Development vol. 9, Norwegian Institute of Technology.

Osgoui, R., Unal, E. 2005. Rock reinforcement design for unstable tunnels originally excavated in very poor rock mass. 31st ITA-AITES World Tunnel Congress, Istanbul, Turkey, pp. 291–296.

Palmstrøm, A., Broch, E., 2006. Use and misuse of rock mass classification systems with particular reference to the Q-system. Tunnels and Underground Space Technology, 21, pp. 575–593.

Palmstrøm, A., 2009. Combining the RMR, Q, and RMi classification systems. www.rockmass.net, 25p.

Panthi, K.K., 2006. Analysis of geological uncertainties analysis related to tunnelling in Himalayan rock mass conditions. Doctoral Thesis, Department of Geology and Mineral Resources Engineering, Norwegian University of Science and Technology.

Rafiee, R., 2013. Tunnels stability analysis using binary and multinomial logistic regression (LR). J. Geol. Min. Res. 5, 97–107.

Rutledge, J.C., Perston, R.L., 1978. Experience with engineering classifications of rock, Proceedings of Int. Tun. Symp., Tokyo, Japan.

Sadeghi, S., Sharifi Teshnizi, E., Ghoreishi, B., 2020. Correlations between various rock mass classification/characterization systems for the Zagros tunnel-West Iran. Journal of Mountain Science 17

Sari, D., Pasamehmetoglu, A.G., 2004. Proposed support design, Kaletepe tunnel, Turkey. Engineering Geology 72, 201–216.

Singh, J. L., Tamrakar, N. K., 2013. Rock mass rating and geological strength index of rock masses of Thopal - Malekhu River areas, Central Nepal Lesser Himalaya. Bull. Dep. Geol. 16, pp: 29–42.

Yang, B., Mitelman, A., Elmo, D., Stead, D., 2021. Why the future of rock mass classification systems requires revisiting their empirical past. Quarterly Journal of Engineering Geology and Hydrogeology, 55 (1), qjegh2021–039.

Zhang, Q., Huang, X., Zhu, H., Li, J., 2019. Quantitative assessments of the correlations between rock mass rating (RMR) and Geological Strength Index (GSI). Tunnel Underground Space Technology 83, pp:73–81.

Tunnelling for a Better Life – Yan, Celestino, Thewes & Eberhardt (Eds)
© 2024 The Author(s), ISBN 978-1-032-80042-4
Open Access: www.taylorfrancis.com, CC BY-NC-ND 4.0 license

Hydro-geo-mechanical properties for water flow prediction in tunnelling

Massimo Coli* & Roberto Emanuele Rizzo
Department of Earth Sciences, University of Florence, Firenze, Italy

ABSTRACT: Tunnelling projects often face challenges related to water inflow leading to operational safety issues, destabilisation, and increased costs. Accurate prediction of water flow is therefore critical. This study aims to provide guidance on how to achieve this goal by examining hydro-geo-mechanics principles for predicting water flow in tunnelling and highlighting the role of geology in rock mass discontinuities data collection. This study discusses the role of geology in rock mass discontinuities data collection. Understanding the geological setting is crucial for collecting appropriate discontinuities data. We present an overview of different data collection techniques, including information gathered from discrete and confined outcrops, and those collected from more continuous outcrops. It discusses data collection from borehole, hydraulic tests (e.g., Drill Stem Tests), and tracer tests, for 1D and 2D data to derive the rock mass zone. Furthermore, discontinuities statistical distributions for different rock types, such as stratified and non-stratified rocks, are discussed. The next aspect discussed in this study is fracture network attributes such as connectivity, transmissivity, and permeability. Connectivity and transmissivity of discontinuities can be used to derive the permeability tensor from discontinuities data in rock masses. The study provides details on how to use the fracture network data to derive estimation of the permeability tensor from, including a comparison of different methods, In conclusion, this study provides insights into hydro-geo-mechanics principles for predicting water flow in tunnelling. The discussion on discontinuities data collection, statistical distribution, and permeability tensor derivation provides valuable information for tunnel engineers to accurately predict and control water flow during tunnel excavation. The study emphasises the importance of considering the hydro-geo-mechanical behaviour of the rock mass in predicting water flow and provides a comprehensive understanding of the various techniques used in the process.

Keywords: Tunnelling, water, faults and fractures, permeability, inflow prediction

1 INTRODUCTION

Recent advances in tunnel engineering have facilitated the construction of long base-tunnels that face high water heads, presenting unique safety and environmental concerns. Water inflows, and more critically, inrush during tunnel construction, not only pose significant risks to both human life and machinery but also lead to project delays and increased costs. This is particularly true for tunnels executed with tunnel-boring machines (TBMs), which require comprehensive pre-construction knowledge of rock mass properties to optimise performance.

From an environmental standpoint, safeguarding natural water bodies has gained prominence, guided by regulatory frameworks such as the European Union's Water Framework Directive and more recently the principle of 'Do No Significant Harm' (DNSH). These frameworks mandate stringent environmental considerations for infrastructural projects. In Europe, the Hydrogeological Excavation Code (HEC) is increasingly recognized as the authoritative technical guide for balancing water body protection with the technical and economic sustainability of tunnel projects (Coli & Tanzini, 2016; Coli et al., 2019a; Coli & Martelli, 2021).

Given these complexities, preliminary investigations must rigorously define the characteristics of natural water bodies and rock mass permeability (Figure 1). Such data enables the prediction of potential water linkages, inflows, or inrushes, thereby informing the design of effective countermeasures to ensure both construction safety and environmental protection (Coli & Martelli, 2021). Additionally, accurate predictions can facilitate the recovery of fresh water from the rock mass for beneficial uses, such as potable water supply or agricultural irrigation.

Many geological formations contain extensive networks of discontinuities (bedding, joints and fractures) that developed in lithification or in response to tectonic stress. Tectonic strain can be generated by various mechanisms: regional tectonic deformation,

*Corresponding author: coli@unifi.it

DOI: 10.1201/9781003495505-65

flexure over large folds or diapirs, local deformation around larger faults, or high-pressure fluids injected into the formation. Fractures and joints develop in response to the strain may be vertical Mode 1 dilatant, or inclined Mode 2 and Mode 3 shear, depending on the in situ stress state and fluid pressure at the time of deformation (Anderson, 1951). Such features can also interact with pre-existing lithological boundaries, thus forming a dense network of discontinuities.

Within the scope of preliminary investigations, the characterisation of such discontinuities in rock masses takes on paramount importance for multiple reasons (Figure 1). Firstly, the orientation, length, and aperture of these discontinuities must be accurately mapped. Traditional methods such as field surveys and mapping of exposed outcrops, together with advanced techniques like remote sensing, laser scanning and seismic imaging, can be utilised for this purpose (Welch, 2023). Secondly, detailed characterisation of the discontinuity network such as density and connectivity can also shed light on the hydraulic properties of the discontinuities, such as their transmissivity and permeability (Rizzo et al., 2017).

Networks of discontinuities have a major impact on fluid flow, especially when the host rock has low primary permeability (Figure 1). They will provide important long-distance conduits for water flow, influencing both the volume and velocity of inflows and potentially leading to water inrush — a critical safety hazard during tunnelling. They will also have a significant impact on the strength and elastic properties of the fractured rock mass as a whole (the "bulk rock" properties), potentially introducing planes of weakness in the rock mass. It is, therefore, important to incorporate the discontinuity networks into any 3D models of the geology that may be used for hydromechanical models, essential for predicting the directional flow of water through the rock mass.

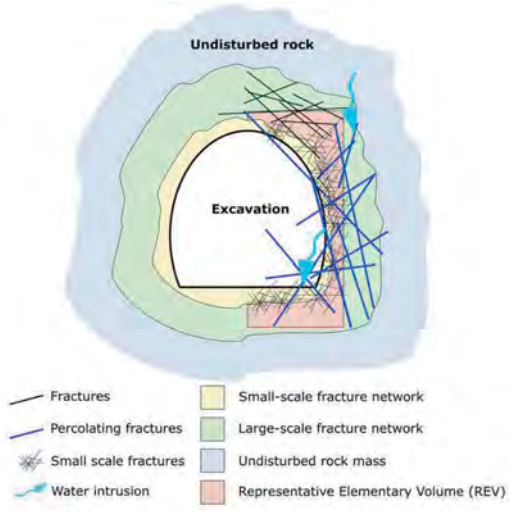

Figure 1. Schematic of an underground excavation. The coloured areas contour the scales of interest for the discontinuity intersect the excavation. The REV incorporates the representative property for the rock-mass. Black lines indicate fractures at the large- (continuous) and small-scale (dashed), while blue lines show connected and percolating fractures. Light-blue arrows indicate the water flow (elaboration by the Authors).

2 GEOLOGICAL FEATURES

2.1 *Overview*

Fluid flow through rocks with low matrix permeability (0.1–several mD's) rely for a large part on networks of connected discontinuities such as fractures formed around structurally deformed zones (Bons et al., 2012; Smit et al., 2023; Gomez-Rivas et al., 2014; Sachau et al., 2015). Therefore, the importance of accurate characterisation of the discontinuities has been consistently emphasised both in the literature (e.g., Hoek & Brown, 1980; Bieniawski, 1989; Hoek, 1994; Pelizza & Soldo, 1995; Hoek, 2018) and at international meetings (most recently at the ISRM Conference in Iguazu, Brazil, in 2019).

Discontinuities in hard rock masses vary in nature depending on the rock type. These can be categorised as follows:

- *Massive*: Includes metamorphic, plutonic, and carbonate platform rocks, as well as sedimentary formations.
- *Regularly Bedded*: Features sedimentary and volcaniclastic rocks.
- *Regularly Alternating*: Characteristic of flysch and turbidites, but also of volcanic lava flows.
- *Irregularly Alternating*: Also typical of flysch and turbidites but with less predictable patterning.
- *Complex*: Includes debris, tectonically disrupted formations, scaly-fabric, schistosity planes, and fault-rocks.

2.2 *Discontinuity systems*

Discontinuities are not randomly distributed in rock masses; rather, they tend to occur in organised systems, sets, and families depending on the type of rock mass (Figure 2). It is also important to recognise that these networks evolve through geological time, and an observed network represents a snapshot in that evolution. Typically, the smaller features (joints and fractures) develop earliest, and then grow to form faults, so the ratio of larger to smaller fractures will generally increase through time. It is therefore necessary to consider the physical processes by which fracture networks develop, and the effect that this will have on their relationship on different scales, when characterising discontinuities size distributions. Therefore, outcrop characterisation of the discontinuity assemblage is essential to recognise and categorise these features.

- *Sedimentary Rocks*. In sedimentary formations, bedding planes act as primary discontinuity, often supplemented by joint systems and additional fracture. These features play a significant role in connected porosity, permeability, and fluid flow in the rock mass (Berre et al., 2019; Garland et al., 2012; Narr et al., 2006). Mechanical stratigraphy and lithology are particularly critical in carbonate sequences, affecting fracture systems and patterns (see Figure 2 as example) (Faÿ-Gomord et al., 2018; Laubach et al., 2009; Nelson, 2001; Sun & Pollitt, 2021; Suo et al., 2012).
- *Granitic Rocks*. Granitic rock masses typically exhibit a homogeneous distribution of fractures due to their intrinsic physical and chemical properties (Velde et al., 1991). Primary discontinuities, mainly fractures, are attributed to cooling and solidification processes (Cloos, 1922). These features often necessitate meticulous mapping and multidisciplinary risk assessment, particularly in tunnelling projects, with a specific attention to weathered bands (Thuro & Scholz, 2003).
- *Metamorphic Rocks*. Metamorphic rocks manifest discontinuities in various forms, including anisotropic foliation planes, unloading structures, and tectonic fractures (Özbek et al., 2018; Ramsey & Huber, 1983; Liu et al., 2020). These features can be complex, particularly in basement reservoirs that have undergone multiple episodes of tectonism and diagenesis (Liu et al., 2020).
- *Volcanic Rocks*. Volcanic rocks display a complex range of discontinuities, influenced by deformation around the volcanic edifice and cooling processes (Vitale & Isaia, 2014; Fuller & Sharp, 1992; Lodge & Lescinsky, 2009). In massive lava flows, fractures often appear as sub-vertical, columnar structures and are guided by thermal contraction and isotropic stresses (Lodge & Lescinsky, 2009).

Understanding the intricacies of discontinuity systems across various rock types is paramount for geological exploration, accurate modelling of fluid flow, and risk assessment in tunnelling and reservoir characterization. The distinctiveness of each rock type necessitates a multidisciplinary approach, integrating geological, hydrogeological, and geomechanical investigations.

2.3 *Statistical analysis of discontinuities*

When characterising the network of discontinuities in rock masses, most data collection techniques are limited to collecting data over a narrowly defined range of scales. Data smaller than this scale range are often unobservable due to resolution limitations (known as censoring), while discontinuities exceeding the scale range are omitted due to truncation — essentially, they are too large/long and thus are only partially included into a dataset.

The selection of an appropriate statistical distribution to model the dataset is crucial for making reliable predictions about the attributes at both small and large scales (Figure 2). The prevalent method for inferring statistical attributes of discontinuities involves calculating the slope of a regression line, often using data plotted on a bi-logarithmic scale (Rizzo et al., 2017). This method assumes that, for a given value of x (e.g., the length or aperture of a discontinuity), the corresponding y-values (the dependent variable) are normally distributed with a constant variance σ^2 (Kreyszig 1970). Various statistical distributions can model discontinuity attributes, including Log-normal, Exponential, Gamma, or inverse Power Law distributions (Hoek et al., 1995; Barton & Zoback, 1992). To find the correct statistics underlying our data, it is also fundamental to adjust the observed distribution of discontinuity attributes (e.g., length, aperture, and orientation) for sampling biases. The first type of bias arises from the probability of intersecting a fracture within the sampling area, which could be a tunnel or an outcrop. This bias is influenced by the fracture dip. The second type of bias is associated with the limitations of observational resolution, encompassing truncation — omitting small attributes — and censoring — failing to capture large attributes due to sampling area limitations. The ultimate aim of statistical analysis is to determine which statistical distribution — be it Log-normal, Exponential, Gamma, or Power Law — most accurately represents the macro- and meso-scale discontinuity attributes; this, in turn, allow us to build accurate upscale models of the discontinuity's networks (Rizzo et al., 2017).

Many authors (see Barton & Zoback, 1992 and references therein) have proposed that discontinuities at all scales in the Earth's crust exhibit self-similar behaviours. The self-similarity of a random variable conforms to an inverse Power Law distribution (Mandelbrot, 1977). Fractal geometry offers a framework for describing these features, which are irregular across all scales. The transformation from one scale to another depends on a specific parameter known as the fractal dimension (often denoted a D). This non-integer slope of the Power Law curve serves as a measure of the distribution's irregularity. Notably, self-similar distributions are scale-invariant, meaning that their features maintain a consistent appearance across different scales. If discontinuities like faults and fractures conform to Power Law distributions, this has significant implications for understanding the network structure of these discontinuities and their impact on the hydro-mechanical properties of the rock mass. More notably, if a Power Law distribution is confirmed that implies a scale-invariance of observed attributes, thus allowing us to directly upscale the observed network of discontinuities.

If a distribution does not follow a Power Law or Exponential distribution, key statistical parameters like the mode, median, mean, and variance can represent the discontinuities, specific to different

systems or sets of discontinuities. The choice of statistical distribution may also be influenced by the type of rock mass in question (Coli et al., 2007). The mode is usually the preferred statistical parameter for characterising rock masses (Bieniawski 1989). The variance also serves as a useful parameter for sensitivity analyses, especially when incorporating the Excavation Support Ratio (ERS) concept, as proposed by Grimstad & Barton in 1993. These parameters can help in selecting the appropriate statistical percentile values, in relation to the target of the project, thus enhancing the reliability of rock mass characterization.

Data should be systematically collected, focusing on systems, sets, and families of discontinuities. Depending on the scale of work, one may observe 1 to 3 discontinuity systems; within each system, 1 to 5 sets; and within each set, 1 or 2 families. The orientation or 'attitude' within these categories often exhibits a spectral distribution around a modal or median value.

Persistence varies widely based on the rock formation. For example, in bedding planes, persistence is practically infinite. In ubiquitous joints, persistence is constrained in one direction by bed thickness but can extend up to a few tens of metres in the opposite direction. In massive rocks, first-generation discontinuities are generally straighter, wider, and more persistent than subsequent generations, with scales ranging from tens to hundreds of metres. Notably, in neotectonics fracture bands, persistence can extend to hundreds or even thousands of metres. Such variations in persistence are crucial for an accurate *water flow* assessment and should be meticulously documented.

3 MODELLING THE ROCK-MASS PERMEABILITY

The nature of a hard rock-mass is inherently heterogeneous and discontinuous, which has important implications for what is known as the 'scale effect.' Specifically, as the size of the excavation expands, the area factor increases according to the square of the size, while the volume factor increases cubically. This non-linear scaling can lead to complex behaviours that must be accounted for in both study approaches and engineering solutions. Often, the size of the excavation exceeds that of individual rock blocks defined by their natural discontinuity patterns. These variations in size relationships can lead to diverse responses from the rock-mass, prompting the need for specialised study methods to address the unique challenges they present (Hoek & Brown, 1980).

The hydro-mechanical behaviour we observe in the rock mass varies based on the spacing of these discontinuities and the relative size of the excavation: it may focus on the properties of intact rock, extend to the broader rock mass, or even centre on a specific discontinuity.

To carry out a precise investigation — whether focused on hydro-mechanical behaviour or geomechanical stability — it is crucial to understand the 3D geo-structural configuration of the rock mass. This understanding is especially important in relation to the scale at which engineering projects and geological structures are observed. Such comprehension allows us to categorise the rock mass into four primary zones of interest, as reported in Coli & Pinzani (2014). These zones influence the methods we choose for modelling rock behaviour:

– *Very Near Field*: Defined by a single, well-understood discontinuity.
– *Near Field*: Defined by several known discontinuities.
– *Far Field*: Defined by a pervasive network of discontinuities, resembling a continuum.
– *Very Far Field*: Defined by omnipresent discontinuities coupled with distinctive regional tectonic structures, such as faults, thrusts, and fracture corridors.

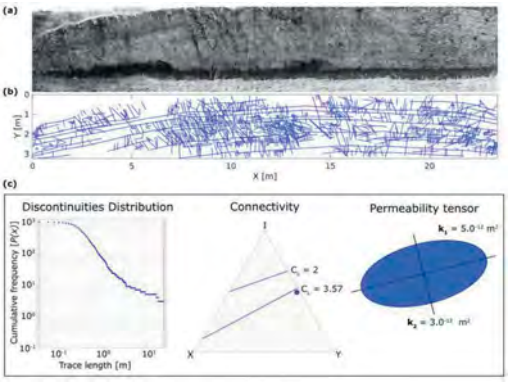

Figure 2. Example of discontinuity analysis performed on an outcrop analogue. (a) A vertical section of the Meso-Cenozoic carbonate unites of the Apulian foreland (Canale di Pirro, Apulia, Italy). (b) Trace of the discontinuities – fractures and bedding plane. (c) Example of data derived from outcrop analysis using the software FracPaQ (Healy et al., 2017): from left to right, statistical distribution of discontinuities; connectivity (blue dot) of the discontinuity network; and permeability tensor estimated using Oda (1986) (elaboration by the Authors).

A conventional approach to modelling these complex, spatially variable discontinuity networks involves statistical description. Statistical models allow us to account for key properties like density, orientation, and connectivity. Specifically, the intensity and density distribution can be characterised using cumulative density distribution functions P21 or P20 (Dershowitz & Herda, 1992). These functions describe the areal or mean linear intensity and density of discontinuities of a given size or larger. We then use these statistical properties to inform key

attributes of the bulk rock mass, such as its porosity and permeability (important for flow modelling), or its failure strength and elastic moduli (relevant for geomechanical modelling).

In particular, determining the permeability in hard rock masses requires a comprehensive analysis of discontinuity data, emphasising connectivity and transmissivity. Crucial discontinuity attributes, such as spacing/frequency, roughness, and notably, aperture (critical due to its cubic impact as per Lomize, 1951), need to be statistically assessed (Coli & Modugno, 1996). Based on this data, a tensor representing the bulk permeability of the rock mass can be derived using methodologies like those of Snow (1969), Oda (1986), and Kiraly (1969; 1978; 2002). These tensors then aid in estimating the potential impact and anticipated water influx for tunnel sections (Figure 2). For instance, when modelling the rock-mass permeability using these bulk methods, the following assumptions are generally made:

- The analysed rock mass is considered to have low primary (matrix) porosity; thus, the fluid flow occurs entirely within the discontinuities.
- Despite natural discontinuities having complex surfaces and irregular apertures, they are modelled by a parallel plate model—i.e., individual fractures lie in a single plane and have a constant hydraulic aperture (Rizzo et al., 2017).

One of the most common methods to estimate bulk permeability of rock masses is based on the combination of the cubic law and the crack-tensor formulation as expressed in Figure 2c according to Oda (1986) and Brown & Bruhn (1998). The permeability tensor incorporates information about discontinuity size (length and aperture), orientation and spatial densities. In recent developments, a novel analytical method for estimating the bulk permeability of rock masses has emerged, based on the work of Saevik & Nixon (2017). This innovative approach employs a straightforward formulation centred on the connectivity within the discontinuity network (Figure 2b). Factors like density and size distribution of observed features do influence connectivity, but it also encapsulates other geometric attributes such as spacing distribution and anisotropy of the discontinuity network. Importantly, connectivity exerts a significant, nonlinear impact on overall rock permeability; fluid flows far more easily through a network of interconnected discontinuities than through isolated fractures (Balberg et al. 1991; Berkowitz 1995; Odling et al. 1999).

While the two aforementioned analytical methods offer quick estimations of bulk permeability, they have the limitation of not explicitly accounting for stress conditions. However, their speed makes them widely preferred over more time-consuming numerical simulations. In addition to these methods, equations from Barton et al. (1985) and Wei et al. (1992) highlight the role of surface roughness in constraining water flow within a discontinuity, leading to a laminar flow pattern. These laminar flow patterns are best described by Darcy's Law (Coli et al., 2019b). Moreover, Barton et al. (1985) included the impact of in-situ stresses, and Wei & Hudson (1988) integrated the influence of depth-induced stress into their permeability equations. Building on these foundational methods and equations, the permeability values obtained can then serve multiple practical purposes. They can be incorporated into empirical charts for quick reference (Heuer, 1995; Marinos, 2001), used in analytical studies to fine-tune models (Goodman et al., 1965; Perrochet, 2005), or applied in numerical simulations like Finite Element Method (FEM) and Distinct Element Method (DEM) for detailed analyses of water flow in tunnel sections (as compared in Rutqvist et al., 2009a; 2009b; Coli et al., 2018).

Instead of using the bulk properties of the rock mass, a more sophisticated approach is to build an "explicit" stochastic model, comprising a series of geometric objects representing individual discontinuities, also known as a Discrete Fracture Network model or DFN (Dershowitz et al. 2000). The discontinuities in the DFN do not correspond directly with those actually observed on outcrop; instead, a DFN model has the same overall statistical and geometrical properties as the real discontinuity network. Key properties that a DFN encloses are the density and the size distribution, as well as the connectivity of the different elements — fractures, faults, and bedding planes — composing the network of discontinuities.

DFN models are invaluable tools for simulating flow and exploring both hydraulic behaviour and interactions between hydraulic and mechanical elements (Thomas et al., 2020). A range of methods exists for calculating mechanical and hydraulic properties in these models, including approaches like boundary element methods (Tuckwell et al., 2003), discrete element methods (Lisjak & Grasselli, 2014), finite difference methods (Karimi-Fard et al., 2004; Erhel et al., 2009a), and others such as finite elements (Vohraliket al., 2007), finite volume (Koudina et al., 1998), and virtual element methods (Benedetto et al., 2017). Some approaches combine both *continuum* and *discontinuum* theories to tackle various challenges, such as arrest, force, and displacement solutions, as well as the dynamics and contact between elements (e.g., Berrone et al., 2015; Maillot et al., 2016). DFN studies are crucial for determining permeability tensors in fractured rock masses. These tensors, which represent the rate at which fluid can move through a material, are calculated based on the geometry of the network and interconnectivity of discontinuities. For large-scale models where representing each discontinuity is impractical, effective, or 'equivalent' permeability tensors are employed. The process of upscaling

these properties to a larger model necessitates the use of a Representative Elementary Volume (REV) — a sufficiently large and intricately fractured and faulted volume that can encapsulate the rock mass essential characteristics. In rocks with sparse discontinuities, finding an appropriate REV is challenging because properties become highly dependent on scale. The size of an REV varies with the geological context and the scale of the engineering project (Franciss, 2010; Gustafson, 2012). Conceptually, an REV can be thought of as a cube, where each side is ten times longer than the modal block (*Bv*) as defined by the discontinuity network (Coli & Pinzani, 2014).

4 DISCUSSION

4.1 *Significance of the observations*

The advancements in rock-mass hydro-mechanical modelling, as discussed in this paper, have significant implications for real-world scenarios and elucidate several critical facets of hard rock excavations and their inherent heterogeneity. Firstly, the unveiled complexities surrounding the scale effect accentuate the necessity of adaptive approaches in geological and engineering analyses. Scale effects, characterised by the intricate relationship between excavation sizes and the behaviour of rock masses, serve as a fundamental parameter influencing engineering decisions, especially in tunnelling projects.

4.2 *Future work*

The journey to understand and model rock-mass behaviour, though extensive in our current research, opens avenues for future innovative explorations. A promising direction lies in the realm of technological advancements, specifically, the development of automated or semi-automated tools. By leveraging the prowess of deep learning segmentation techniques, it is conceivable to rapidly extrapolate a discontinuity network from images of outcropping rocks. This automated extraction could, in turn, facilitate more accurate and efficient calculations of an appropriate REV, grounded in geo-structural data, streamlining processes that currently demand significant manual intervention.

5 CONCLUSIONS

The presented work has examined the intricacies of rock-mass behaviour, focusing specifically on scale effects and the permeability of discontinuities in hard rock masses. By discussing the use of both analytical and numerical methods, we have highlighted the complexities involved in understanding and modelling the hydro-mechanical behaviour of rock formations for tunnelling projects.

While analytical methods offer quick insights into the hydro-mechanical properties of discontinuity networks, more sophisticated tools like numerical Discrete Fracture Networks (DFNs) provide practical advantages. These are particularly beneficial for large-scale projects and in areas with variable properties. Here, DFNs can more effectively incorporate the hydraulic behaviour and mechanical interactions within rock masses. The importance of correctly acquiring and statistically treating data from available outcrops cannot be overstated, as this information directly feeds into both analytical and numerical models.

The potential applications of the observations presented in this work are noteworthy. For engineers, these insights could serve as valuable reference points in tunnelling projects, emphasising considerations of both safety and cost. Looking ahead, numerous avenues for further research exist, from the development of automated analysis tools to the exploration of these methods in various geo-engineering and geo-energy contexts.

REFERENCES

Anderson, E. M. (1951). The dynamics of faulting. Transactions of the Edinburgh Geological Society, 8(3), 387–402.

Balberg, I., Berkowitz, B., & Drachsler, G. E. (1991). Application of a percolation model to flow in fractured hard rocks. Journal of Geophysical Research: Solid Earth, 96(B6), 10015–10021.

Barton, N.R., Bandis, S., Bakhtar, K., 1985. Strength, deformation and conductivity coupling of rock joints. Int. J. Rock Mech., 22: 121–140.

Barton, C. A., and Zoback, M. D. (1992), Self-similar distribution and properties of macroscopic fractures at depth in crystalline rock in the Cajon Pass Scientific Drill Hole, J. Geophys. Res., 97(B4), 5181–5200

Benedetto, M., Borio, A., & Scialó, S. (2017). Mixed virtual elements for discrete fracture network simulations. Finite Elements in Analysis and Design, 134, 55–67.

Berkowitz, B. (1995). Analysis of fracture network connectivity using percolation theory. Mathematical geology, 27, 467–483.

Berre, I., Doster, F., & Keilegavlen, E. (2019). Flow in fractured porous media: A review of conceptual models and discretization approaches. Transport in Porous Media, 130, 215–236

Berrone, S., Pieraccini, S., Scialo, S., & Vicini, F. (2015). A parallel solver for large scale DFN flow simulations. SIAM Journal on Scientific Computing, 37(3), C285–C306.

Bieniawski, Z.T. 1989, Engineering Rock Mass Classification. John Wiley & Sons Inc., 251 pp, ISBN 0-471-60172–1.

Bons, P. D., Elburg, M. A., & Gomez-Rivas, E. (2012). A review of the formation of tectonic veins and their microstructures. Journal of Structural Geology, 43, 33–62.

Brown, S. R., & Bruhn, R. L. (1998). Fluid permeability of deformable fracture networks. Journal of Geophysical Research: Solid Earth, 103(B2), 2489–2500.

Cloos E. (1922). Tektonik des Granits von Gorkau (Kr. Nimptsch) im Schlesien. Abh. Preuss. Geol. Land., 89:93–102.

Coli M. & Martelli L. (2021) Preliminary Investigations and the Financial Sustainability of Underground Project. Mechanics and Rock Engineering, from Theory to Practice, IOP Conf. Series: Earth and Environmental Sciences, 833 012170, 8 pp. http://doi:10.1088/1755-1315/833/1/012170

Coli M., Martelli L. & Staffini P. (2019a) Hydrogeological Excavation Code, a value-added methodology for water safeguarding. In Tunnel and Underground Cities: Engineering and Innovation meet Archaeology, Architecture and Art, Peila D., Viggiano G. & Celestino T. eds. Taylor & Francis Group, London, 4417-4424. ISBN 978-1-138-38865-9

Coli M., Piccini L. & Muscedra M.M. (2019b) Tunnelling and karst systems: a review. Rock Mechanics for Natural Resources and Infrastructure Development, Fontoura, Rocca & Pavòn-Mendoza (Eds), CRC Press-Balkema, Proceeding in Earth and Geoscience, 6, 504–511. ISBN 978-0-367-42284–4.

Coli, M. & Modugno, C. 1996, Classificazione geomeccanica preliminare di un sito: approccio deterministico o possibilistico? GEAM, 89, 111–119.

Coli, M. & Pinzani, A. 2014, Tunnelling and hydrogeological issues: a short review of the current state of the art. Rock Mech Rock Eng 47/3, 839–851. https://doi.org/10.1007/s00603-012-0319-x

Coli, M., Tanzini, M. 2016. Water safeguarding in tunnelling: for execution and environment. Proc. GEOSAFE2016, 1st International Symposium on Reducing Risks in Site Investigation, Modelling and Construction for Rock Engineering, Xi'an, China 25–27, May 2016: 274–287.

Coli M., Furesi D. & Cantini C. (2007) Stima della venute d'acqua durante l'esecuzione di una galleria sulla base di studi geostrutturali. GIGS, Riunione annuale, Urbino 2007, Atti, Rend. Soc. Geol. It. 4,204-206. ISSN 2038–1689.

Coli M., Coli N., Pinzani A., Pranzini G. & Tanzini M. (2018) Water inflow prediction in tunnelling on the base of Geostructural Survey. Geomechanics and Geodynamics of rock-mass, EUROCK-2018, San Pietroburgo (Russia), V. Litvinenco ed., CRC Press, Taylor & Francis Group, London, Balkema, 1129–1135. ISBN: 978-0-429-46176-7 (eBook).

Dershowitz, W. S., & Herda, H. H. (1992, June). Interpretation of fracture spacing and intensity. In ARMA US Rock Mechanics/Geomechanics Symposium (pp. ARMA-92). ARMA.

Dershowitz, B., LaPointe, P., Eiben, T., & Wei, L. (2000). Integration of discrete feature network methods with conventional simulator approaches. SPE Reservoir Evaluation & Engineering, 3(02), 165–170.

Erhel, J., J. de Dreuzy, and B. Poirriez (2009a), Flow simulation in three-dimensional discrete fracture networks, SIAM J. Sci. Comput.,31(4),2688–2705, doi:10.1137/080729244.

Faÿ-Gomord, O., Verbiest, M., Lasseur, E., Caline, B., Allanic, C., Descamps, F., Vandycke, S., & Swennen, R. (2018). Geological and mechanical study of argillaceous North Sea chalk: Implications for the characterisation of fractured reservoirs. Marine and Petroleum Geology, 92, 962–978.

Franciss, F.O. 2010 Fractured Rock Hydraulics. CRC Press, Taylor & Francis Group, A. Balkema Book, 179 pp.

Fuller, C. M., & Sharp Jr, J. M. (1992). Permeability and fracture patterns in extrusive volcanic rocks: Implications from the welded Santana Tuff, Trans-Pecos Texas. Geological Society of America Bulletin, 104(11), 1485–1496.

Garland, J., Neilson, J. E., Laubach, S. E., & Whidden, K. J. (Eds.). (2012). Advances in carbonate exploration and reservoir analysis. Geological Society, London, Special Publications, 370, 1–15.

Goodman, R.E., Moye, D.G., Van Schalkwyk, A., Javandel, I. 1965. Groundwater inflow during tunnel driving. Eng. Geol., 2: 39–56.

Gomez-Rivas, E., Corbella, M., Martín-Martín, J. D., Stafford, S. L., Teixell, A., Bons, P. D., Griera, A., & Cardellach, E. (2014). Reactivity of dolomitizing fluids and Mg source evaluation of fault-controlled dolomitization at the Benicàssim outcrop analogue (Maestrat basin, E Spain). Marine and Petroleum Geology, 55, 26–42.

Grimstad, E. & Barton, N. 1993, Updating the Q-System for NMT. Proc. Int. Symp. On sprayed Concrete – Modern use of the Wet Mix Sprayed Concrete for Undergrond Support, Fagerns, Kompen, Opsahi and Berg eds, Norwegian Concrete Ass., Oslo.

Gustafson, G. 2012, Hydrogeology for rock engineers. Published by BeFo with ISRM sponsorship, Sweden, p 171.

Healy, D., Rizzo, R.E., Cornwell, D.G., Farrell, N.J., Watkins, H., Timms, N.E., Gomez-Rivas, E. and Smith, M., 2017. FracPaQ: A MATLAB™ toolbox for the quantification of fracture patterns. *Journal of Structural Geology*, *95*, pp.1–16.

Heuer, R. 1995. Approche quantitative, théorique et empirique, del Ronald E. Heuer, sur le venues d'eau en tunnel. Rapid Exc. and Tunn. Conf., San Francisco, Cal., June - 18–21.

Hoek, E. 1994. The Challenge of Input data for Rock Engineering. Letter to the Editor, ISRM Journal, 2/2

Hoek, E., 2018, Practical Rock Engineering, Rocscience, Hoek's Corner, 2018 edition https://static.rocscience.cloud/assets/resources/learning/hoek/1966-Rock-Mechanics-Introduction.pdf

Hoek, E. & Brown, T. 1980, Underground Excavations in Rock. Inst. Min. Metall., London, 527 pp.

Hoek E., Kaiser P.K., Bawden W.F. 1995 Support of underground excavation in hard rock. A.A. Balkema, Rotterdam, 215 pp.

Karimi-Fard, M., Durlofsky, L., & Aziz, K. (2004). An efficient discrete fracture model applicable for general purpose reservoir simulators. SPE Journal SPE-88812-PA, 9(2), 227–236.

Kiraly L (1978) La notion d'unité hydrogéologique. Bulletin du Centre d'Hydrogéologie, 2, 83–216.

Kiraly, L. 1969. Anisotropie et hétérogénéité de la perméabilité dans les calcaires fissurés. Eclogae Geol. Helv., 62/2: 613–619.

Király, L., (2002). Karstification and Groundwater Flow. In: Proceedings of the Conference on Evolution of Karst: From Prekarst to Cessation. Postojna-Ljubljana. 155–190.

Koudina, N., Gonzalez Garcia, R., Thovert, J.-F., & Adler, P. (1998). Permeability of three-dimensional fracture networks. Physical Review E, 57(4), 4466–4479.

Kreyszig, E., 1970. No. 519.5. In: Wiley New York (Ed.), Introductory Mathematical Statistics: Principles and Methods.

Laubach, S. E., Olson, J. E., & Gross, M. R. (2009). Mechanical and fracture stratigraphy. AAPG Bulletin, 93, 1413–1426.

Lisjak, A., & Grasselli, G. (2014). A review of discrete modeling techniques for fracturing processes in discontinuous rock masses. Journal of Rock Mechanics and Geotechnical Engineering, 6(4), 301–314

Lodge, R. W., & Lescinsky, D. T. (2009). Anisotropic stress accumulation in cooling lava flows and resulting fracture patterns: Insights from starch-water desiccation experiments. Journal of Volcanology and Geothermal Research, 185(4), 323–336.

Lomize, G.M. (1951). Water flow through jointed rock. Gosenergoizdat, Moscow.

Maillot, J., P. Davy, R. Le Goc, C. Darcel,and J.R. de Dreuzy (2016),Connectivity, permeability, and channeling in randomly distributed and kinematically defined discrete fracture network models, Water Resour.Res.,52, 8526–8545

Mandelbrot, B. B., (1977) Fractals, Form, Chance and Dimension, W. H. Freeman, New York.

Marinos, P., (2001) Tunnelling and mining in karstic terrain; an engineering challenge. Geotechnical and Environmental Application of Karst Geology &Hydrology. Beck & Herring (eds), Balkema publ., 3-16.

Narr, W., Schechter, D. W., & Thompson, L. B. (2006). Naturally fractured reservoir characterization. Society of Petroleum Engineers.

Nelson, R. A. (2001). Geological analysis of naturally fractured reservoirs. Gulf Professional Publishing.

Pelizza, S. & Soldo, L. 1995, Nel mondo del tunnelling la catena progettuale è indebolita dalle scarse indagini preliminari. Cocis, luglio-ottobre, 24–26.

Perrochet, P. 2005. Confined flow into a tunnel during progressive drilling: An analytical solution. Ground Water, 43(6): 943–946.

Rizzo, R. E., Healy, D., & De Siena, L. (2017). Benefits of maximum likelihood estimators for fracture attribute analysis: Implications for permeability and up-scaling. Journal of Structural Geology, 95, 17–31.

Oda, M. (1985) Permeability tensor for discontinuous rock masses. Geotechnique, 35, 483–495.

Odling, N.E., Gillespie, P., Bourgine, B., Castaing, C., Chiles, J.P., Christensen, N.P., Fillion, E., Genter, A., Olsen, C., Thrane, L. and Trice, R., (1999). Variations in fracture system geometry and their implications for fluid flow in fractures hydrocarbon reservoirs. Petroleum Geoscience, 5(4), pp.373–384.

Özbek, A., Gül, M., Karacan, E., & Alca, Ö. (2018). Anisotropy effect on strengths of metamorphic rocks. Journal of Rock Mechanics and Geotechnical Engineering, 10(1), 164–175.

Rutqvist, J., Bäckström, A., Chijimatsu, M., Feng, X.T., Pan, P.Z., Hudson, J., Jing, L., Kobayashi, A., Koyama. T., Lee, H.S., Huang, X.H., Rinne, M., Shen, B. (2009a). A multiple-code simulation study of the long-term EDZ evolution of geological nuclear waste repositories. Special Issue: THE DECOVALEX-THMC PROJECT (Safety assessment of nuclear waste repositories). Environ Geol., 57: 1313–1324.

Rutqvist, J., Barr, D., Birkholzer, J.T., Fujisaki, K., Kolditz, O., Liu, Q.S., Fujita, T., Wang, W., Zhang, C.Y. (2009b). A comparative simulation study of coupled THM processes and their effect on fractured rock permeability around nuclear waste repositories. A multiple-code simulation study of the long-term EDZ evolution of geological nuclear waste repositories. Special Issue: THE DECOVALEX-THMC PROJECT (Safety assessment of nuclear waste repositories). Environ Geol., 57: 1347–1360.

Sachau, T., Bons, P. D., & Gomez-Rivas, E. (2015). Transport efficiency and dynamics of hydraulic fracture networks. Frontiers of Physics, 3, 63.

Sævik, P. N., & Nixon, C. W. (2017). Inclusion of topological measurements into analytic estimates of effective permeability in fractured media. *Water Resources Research*, *53*(11), 9424–9443.

Smit, F. W. H., Stemmerik, L., Smith, M. E., Staudigel, P. T., Lüthje, M., Welch, M., van Buchem, F. S. P., & Swart, P. K. (2023). The importance of fault damage zones for fluid flow in low-permeable carbonate rocks–Fault-related compaction fronts in the Danish North Sea. Marine and Petroleum Geology, 148, 105993.

Snow, D.T. 1969. Anisotropic permeability of fractured media. Water Resources Res., 5.

Sun, S., & Pollitt, D. A. (2021). Optimising development and production of naturally fractured reservoirs using a large empirical dataset. Petroleum Geoscience 27(2), petgeo2020–079.

Suo, C., Peng, S., Chang, S., Duan, R., & Wang, G. (2012). A new calculating method of the curvature to predict the reservoir fractures. Procedia Environmental Sciences, 12, 576–582.

Thomas, R. N., Paluszny, A., & Zimmerman, R. W. (2020). Permeability of three-dimensional numerically grown geomechanical discrete fracture networks with evolving geometry and mechanical apertures. Journal of Geophysical Research: Solid Earth, 125, e2019JB018899. https://doi.org/10.1029/2019JB018899

Thuro, K. & Scholz, M. 2003. Deep weathering and alteration in granites – a product of coupled processes. GeoProc 2003 International Conference on Coupled T-H-M-C Processes in Geosystems: Fundamentals, Modelling, Experiments and Applications. Royal Institute of Technology (KTH), Stockolm, Sweden.

Tuckwell, G. W., Lonergan, L., & Jolly, R. J. H. (2003). The control of stress history and flaw distribution on the evolution of polygonal fracture networks. Journal of Structural Geology, 25(8), 1241–1250.

Velde, B., Dubois, J., Moore, D., & Touchard, G. (1991). Fractal patterns of fractures in granites. Earth and Planetary Science Letters, 104(1), 25–35.

Vitale, S., & Isaia, R. (2014). Fractures and faults in volcanic rocks (Campi Flegrei, southern Italy): insight into volcano-tectonic processes. International Journal of Earth Sciences, 103, 801–819.

Vohralik, M., Maryška, J., & Severýn, O. (2007). Mixed and nonconforming finite element methods on a system of polygons. Applied numerical mathematics, 57(2), 176–193.

Wei Z.Q., Hudson JA (1988) Permeability of jointed rock masses. Rock Mechanics and Power Plants, 613–626, Romana (ed.), Balkema, Rotterdam. ISBN 9061918278.

Wei, Z.Q., Egger, P., Descoeudres, F. 1992. Cyclic hydromechanical normal behaviour of rock joints. Proc. ISRM Fractured and Jointed Rock Masses, 2, Lake Tahoe: 389–398.ASTM D2938-95, 1995. Standard test method of unconfined compressive strength of intact rock core specimens.

Welch, M.J. (2023). Using Geomechanical Models to Simulate the Growth of the Fracture Network in the Ekofisk Formation of the Kraka Structure, Danish Central Graben. In: Welch, M.J., Lüthje, M. (eds) Geomechanical Controls on Fracture Development in Chalk and Marl in the Danish North Sea. Petroleum Engineering. Springer, Cham.https://doi.org/10.1007/978-3-031-35327-7_7

Tunnelling for a Better Life – Yan, Celestino, Thewes & Eberhardt (Eds)
© 2024 The Author(s), ISBN 978-1-032-80042-4
Open Access: www.taylorfrancis.com, CC BY-NC-ND 4.0 license

3D Geological reconstruction and application of tunnel face

Dongya Duan*, Hengbin Bai & Wei Li
Chengdu Tianyou TunnelKey Co, Ltd., Chengdu, China

Wenge Qiu
Chengdu Tianyou TunnelKey Co, Ltd., Chengdu, China
MOE Key Laboratory of Transportation Tunnel Engineering, Southwest Jiaotong University, Chengdu, China

ABSTRACT: The most authentic geological information is exposed on the tunnel face, and the identification of rock integrity is an important basis for classifying the surrounding rock of the tunnel face. To solve the many shortcomings of traditional manual sketching, it is proposed to use image processing technology and point cloud processing technology to extract the structural characteristics of the surrounding rocks on the tunnel face. A 3D data acquisition instrument combining a camera and a laser radar has been developed for collecting tunnel face data. To adapt the collected data from the instrument, an algorithm was developed to establish a 3D model of the tunnel's invert and identify the structural planes of the surrounding rocks based on differences in their normal vectors. Simultaneously, a convolutional neural network was trained to automatically extract structural plane features from the 2D tunnel face images. Finally, the results of the 3D model identification and image feature extraction were synthetically evaluated to achieve automatic recognition of the joint structures of the tunnel face's surrounding rocks.

Keywords: Tunnel face, 3D reconstruction, Convolution, Convolutional Neural Network Tunnelling

1 INTRODUCTION

The geological information of the tunnel affects the safety and efficiency of the project. There is a significant discrepancy between the surrounding rock exposed during tunnel excavation and the geological survey results. When the surrounding rock exposed during excavation is found to be worse than the results of geological investigation, it may lead to unreasonable support parameters, resulting in increased project cost and prolongation of construction time. The geological structure of the surrounding rock during the excavation stage of the tunnel is closely related to the safety of the tunnel excavation. The traditional method of obtaining the surrounding rock structural information by manual sketching is incomplete and unable to form a 3D model. This kind of product has great limitations in evaluating the safety of the tunnel. At the same time, measurement results are affected by personnel experience and subjective judgment, and different personnel may obtain different results, making it difficult to evaluate the grade evaluation of the surrounding rock of the working face (Yang et al., 2009).

With the development of photography and laser scanning technology, non-contact measurement methods have gradually been applied in the field of tunnel engineering. Digital photography technology has received widespread attention due to its convenience, speed, and easy data storage. Leng (2009) used monocular vision method to study the extraction of geological information from tunnel face images and visualized the geological structure of the excavated part of the tunnel. Chen et al. (2017) established a high-precision 3D model of the tunnel face by single-camera binocular technology, which realized the automated extraction of rock mass spacing and roughness. Li et al. (2022) used Unet neural network algorithm for automatic identification of traces in tunnel face image. Combined with the strength information to realized the classification of surrounding rock in palm face. However, digital camera image acquisition is greatly affected by the environment, and in the complex and harsh working environment of the tunnel. There are problems such as image quality is difficult to guarantee and it is difficult to match the same name points on the image (Li et al., 2018).

*Corresponding author: 1196761682@qq.com

DOI: 10.1201/9781003495505-66

Laser scanning can directly obtain the 3D coordinate information of the object surface to be measured. According to the three-dimensional coordinates, a high-precision 3D model can be directly established. Therefore, it is widely used in the acquisition of surrounding rock structural plane. Song et al. (2013) investigated the advantages and disadvantages of 3D laser scanning technology and digital photography technology in geological cataloging work. Although it lacks in real images compared with digital camera technology, 3D laser scanning technology can better obtain holographic data of geological structural surfaces. Fekete et al. (2010, 2013) detailed a method to establish a tunnel perimeter rock based on the 3D point cloud data of the tunnel face and surrounding wall. And use the model to evaluate the stability of the surrounding rock. However, laser scanning has the defect of not being able to obtain the surface texture information of the rock mass due to its own characteristics.

In this paper, a portable tunenl face rock information acquisition device that combines a small laser scanning device with a camera is used. Laser scanning has strong anti-interference ability and can obtain 3D coordinate information of the detected object surface. The camera can obtain the shape and color information of the detected object surface. This equipment can be used to realize the fast and high-quality acquisition of the surrounding rock information and the establishment of high-precision 3D model of the tunnel face. This article proposes an automated identification method for the joint information of the surrounding rock of the tunnel face, which provides support for the compilation of tunnel geological information.

2 METHOD OF CONSTRUCTING 3D MODEL OF TUNNEL FACE

2.1 *Collecting tunnel face data*

Before establishing a high-precision 3D model of the tunnel face, it is necessary to collect the geological information data of the surrounding rocks of the tunnel face. TK-SEG(smart eye geology) and external lighting are used to collect raw data. TK-SEG is a self-developed equipment that combines laser lidar and camera, as shown in Figure 1. The data collection process is carried out after the completion of excavation muck transport. Adopting image processing technology based on multi-view geometric projection, the overlap rate of neighboring images needs to be more than 30%. In order to avoid the effect of insufficient image overlapping area caused by manually rotating the camera, the equipment is combined with the gimbal to realize automatic data acquisition. To obtain the best data, the equipment needs to be leveled before acquisition, and the surface of the object should be as vertical as possible when collecting data. The equipment is placed near the center axis of the tunnel, and the whole tunnel surface image is automatically captured through the rotation of the gimbal at the erection position. The placement position when collecting data is shown in Figure 2.

Figure 1. Equiment for collecting data.

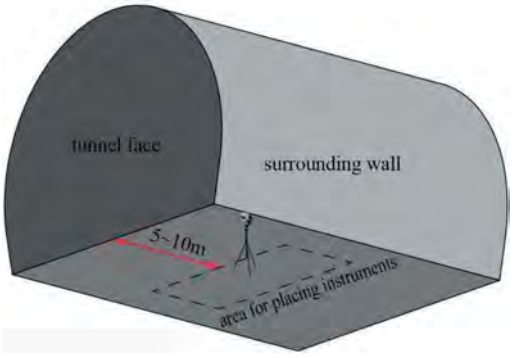

Figure 2. Area for placing instruments.

2.2 *Create 3D model of the tunnel face*

SFM (Structure from Motion) technology is used to realize 3D reconstruction of tunnel surrounding rock based on tunnel face image data. A camera is used to take a sequence of highly overlapping photos of the same object from multiple angles to obtain the feature points of the neighboring photos. The spatial structure equation of the feature points of the photographed object is constructed by using the geometric projection relationship, and the spatial position relationship between the feature points of the photographed object and the camera is obtained by solving the equation. In this paper, SMART EYE software is applied to reconstruct the 3D model of the tunnel face. The scene information such as the camera position is obtained by matching the feature points in the neighboring pictures of the tunnel surface and calculating with the projective theorem. Then the scene information is combined with the original pictures to get the 3D

point cloud of the object. Finally, the Poisson Surface Reconstruction algorithm is used to connect the point cloud to form a triangular mesh to construct a 3D surface to complete the reconstruction of the image.

To determine the scale of the reconstructed tunnel face model, it is necessary to combine the separate 3D models of the tunnel face created by the camera and laser lidar. The distance and angle relationship between the instrument and the surrounding rock acquired by laser lidar is utilized to determine the scale of the image 3D model. Matching the excavation mileage with the model enables the model to be positioned in the design line. The image and laser 3D model are shown in Figure 3.

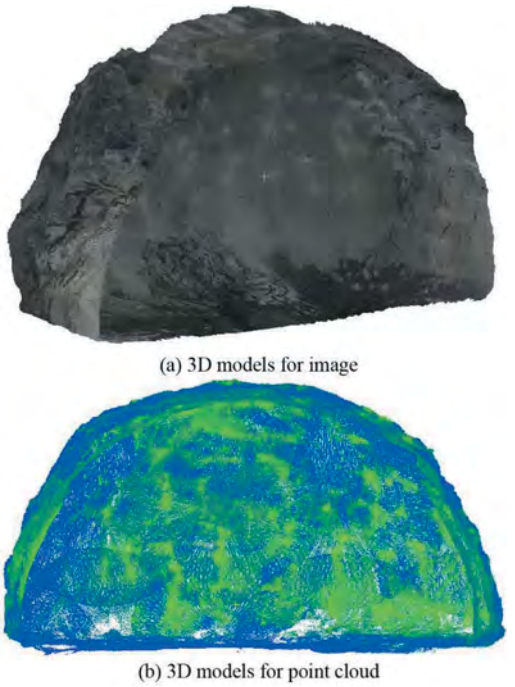

(a) 3D models for image

(b) 3D models for point cloud

Figure 3. Reconstruction model of tunnel face.

2.3 *Classification of reconstructed models*

The reconstructed 3D model includes tunnel face and surrounding wall. Both of these are valuable for identifying joints on the tunnel face. However, it is necessary to classify both in the model for accurate analysis. After determining the dimensional relationship between the model and the design contour, the reconstruction model is positioned with the mileage information to determine the correspondence between the model and the mileage of the designed line. The normal vectors of the triangular mesh of the tunnel face have obvious parallel relationship with the design line, and the normal vectors of the triangular mesh of the surrounding wall have obvious perpendicular relationship with the design line. The tunnel face and surrounding wall in the model are segmented by utilizing the corresponding relationship. The result of tunnel face and surrounding wall segmentation is shown in Figure 4.

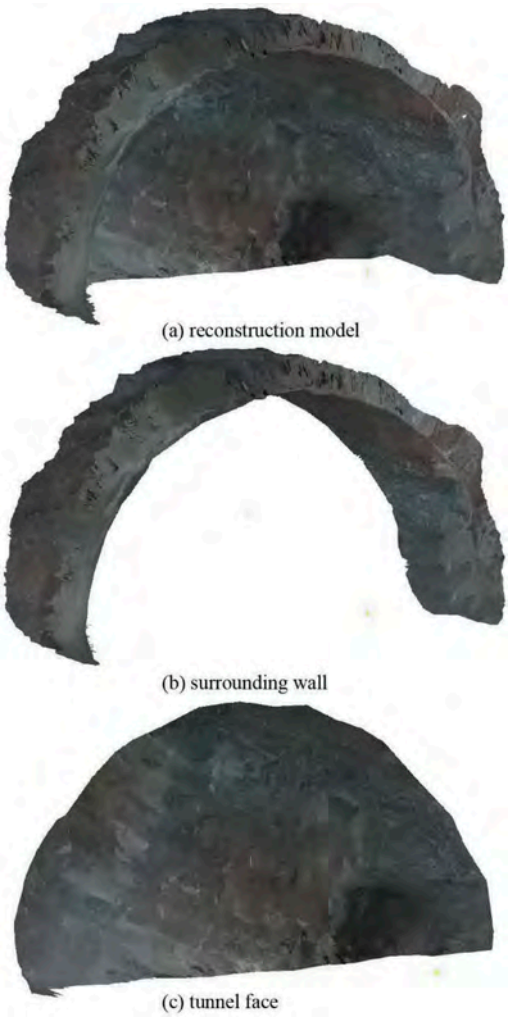

(a) reconstruction model

(b) surrounding wall

(c) tunnel face

Figure 4. Result of reconstruction model classification.

3 METHOD OF CONSTRUCTING 3D MODEL

3.1 *Structural surface recognition based on 3D model*

In the reconstructed model of the tunnel face that has been localized, the occurrence of the structural surfaces in the tunnel face can be obtained directly. Based on the feature that the normal vector orientations of different structural surfaces have large differences, the structural surfaces are recognized from the point cloud of tunnle face. It is realized as follows: (1) The structural surface of the tunnel face model is divided into small closed regions. (2) The closed regions with the same normal vectors are aggregated using a clustering algorithm. (3) The

boundaries between the different aggregated regions are the 3D traces of the structural surface. After the structural surface 3D traces are aggregated and eliminated, the projection algorithm is used to project the 3D traces onto the 2D image of the tunnel face. The two-dimensional structural surface traces of the tunnel face can be obtained. The structural surface identification and projection are shown in Figure 5.

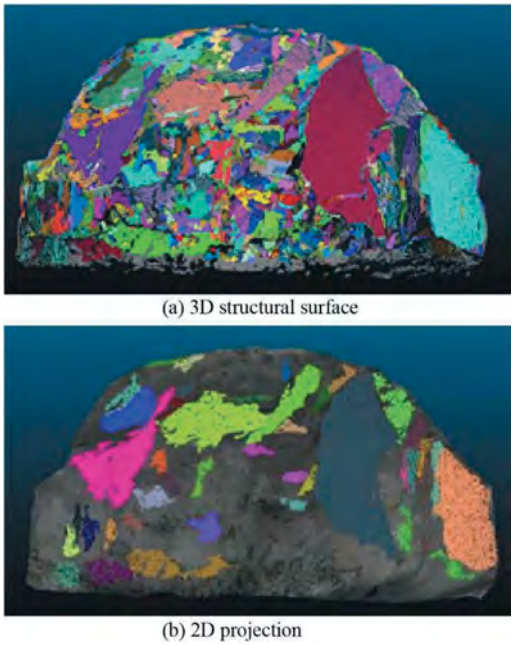

(a) 3D structural surface

(b) 2D projection

Figure 5. Structural surface recognition and projection.

3.2 *Extraction of palisade nodules based on CNN*

Traditional image processing techniques and machine learning algorithms utilize contour extraction and feature point matching to identify the structural surface of the tunnel face. However, the scenes targeted are single, the scope of application is narrow, and the correct rate is low. The different lighting and different acquisition angles will have a great impact on the results of image processing, and the extracted contour contains a lot of noise. Convolutional Neural Networks (CNN) is one of the most effective means to carry out image recognition research, which can accomplish the extraction of complex image features. Therefore, this paper chooses the CNN training software to recognize and extract the perimeter rock joint traces in the tunnel face image. The training process is as follows:

(1) Training dataset: Geological engineers annotate the generated tunnel face images with structural surface traces, and the annotated structural surface trace image data are recorded in the form of text. The annotated text and images are summarized to form a dataset together with the original images, as shown in Figure 6.

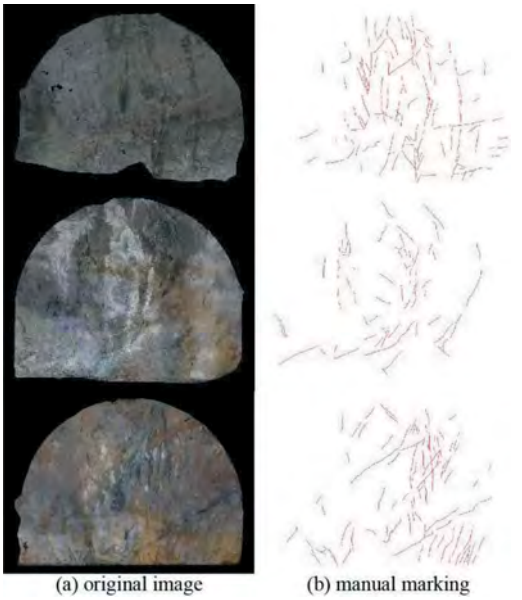

(a) original image (b) manual marking

Figure 6. Structural surface recognition training.

(2) Expansion of the dataset: The tunnel face images are large in size, which are directly used for training and have higher requirements for hardware equipment. It is necessary to crop the images into small-sized images and exclude the tunnel face images that do not contain structural surface trace annotations. To increase the diversity of the dataset, the training image will be randomly rotated, flipped, mirrored, and adjusted for brightness and saturation. Annotated image data needs to be processed simultaneously to maintain consistency.

(3) CNN training: CNN is used to obtain the output by forward computing the inner product of the inputs and the weights. The weights are updated iteratively by back propagation algorithm. Finally combined with gradient descent method to get the weights that make the whole network optimal. Therefore, the dataset image is cropped to 800×800 pixel size. Supervised learning using CNN. The training is stopped after the software recognition effect reaches the design accuracy requirement or the design number of times. The training results are shown in Figure 7.

(4) joint feature extraction: the feature image obtained through the CNN is a probability distribution map, which needs to be processed in order to obtain the pending structural surface area. This paper adopts the Conditional Random Field algorithm (CRF) to mark the structural surface image. The steps of the algorithm are as follows:
Set the random variable $X_i \in L = \{l_1, l_2, \cdots, l_L\}$ to denote the label of pixel i and form a random vector X according to $X_1, X_2, \cdots, X_N, N$ denotes the number of pixels in the image.

Assuming the image $G = (V, E)$, where $V = \{X_1, X_2, \cdots, X_N\}$, the global observation is I. The Gibbs is used to transform $G = (V, E)$ to $P(X = x|I) = \frac{1}{z(I)}\exp(-E(x|I))$. In the fully-connected CRF model, the labeling x_i energy is denoted as $E(x) = \sum_i \varphi_u(x_i) + \sum_{i<j} \varphi_p(x_i, x_i)$. $\varphi_u(x_i)$ is a unitary energy term representing the partirioning of pixel i into labels x_i energy. $\varphi_p(x_i, x_i)$ is the energy of simultaneous segmentation of pixel points i, j into x_i, x_j .Thresholding judgment is performed for the obtained $E(x)$. The pixel points with probability greater than 0.5 are retained. The final imageis obtained as shown in Figure 8.

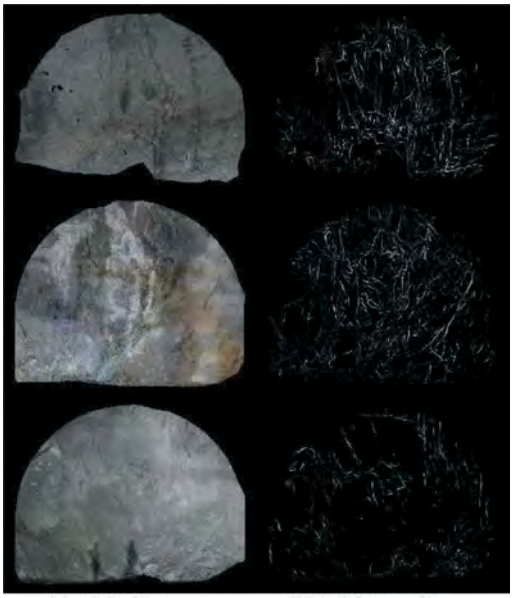

(a) original image (b) training results

Figure 7. CNN training result.

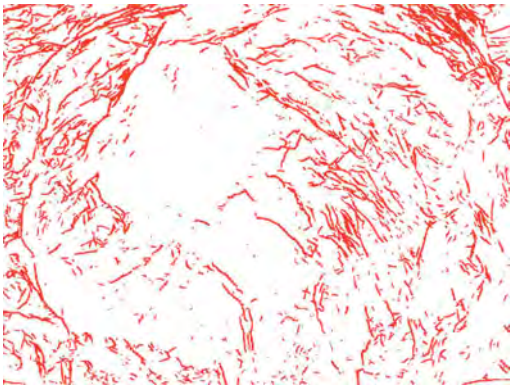

Figure 8. Probabilistic threshold maps for structural surface.

(5) Burr rejection and joint grouping: The connected regions are extracted in the thresholded labeled image and line refinement is applied to the extracted connected regions to obtain irregular lines with single pixel widths. The training-acquired joint traces are used to determine the degree of overlap with the traces of structural surfaces projected onto a 2D plane by 3D model identification. Calculate the minimum closure rectangle overlap rate of the both using the absolute difference of their angles, and eliminate areas with closure areas less than the preset threshold.

When grouping joint traces, the overlap of 0° and 360° results in the inability to cluster using Euclidean distance. Equation (1) is used to compute the angle based on the uniform reference axis. And Equation (2) is used to map the angle to the circumference to obtain the coordinate points of the position.

$$\theta = \arctan\frac{y_2 - y_0}{x_2 - x_0} - \arctan\frac{y_1 - y_0}{x_1 - x_0} \tag{1}$$

Where: x_0, y_0 are the coordinates of the origin.

$$P(x, y) = (\sin\theta, \cos\theta) \tag{2}$$

Coordinate points are used as data input for clustering using Meanshift algorithm. The first three groups with the highest number are taken as retained nodes. The remaining groups are taken as cluttered structural surfaces. The recognition effect obtained after clustering is shown in Figure 9.

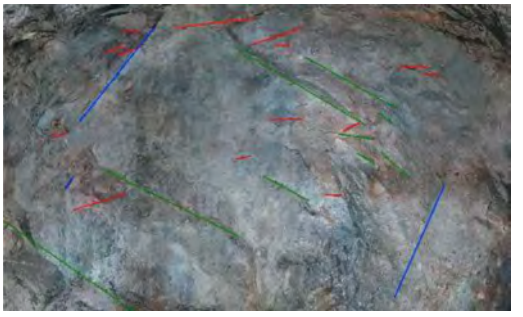

Figure 9. Result of geological sketching on tunnel face.

4 APPLICATION OF GEOLOGICAL RECONSTRUCTION

4.1 *Calculate the rock integrity*

The BQ method is used to evaluate the surrounding rock, which is based on two indicators: rock mass hardness and integrity. The hardness of the rock mass is determined by the uniaxial saturated compressive strength R_c of the surrounding rock. The integrity of

the rock mass is determined by the rock integrity index K_v. Calculate BQ through Equation (3). The R_c can be obtained directly through the strength test of surrounding rock. The K_v is the research objective of this paper. There is a corresponding relationship between K_v and J_v. The J_v is the number of structural surfaces per cubic meter of rock volume. The formula for calculating K_v from J_v is shown in Equation (4) (Hu et al., 2010).

The spacing method is a commonly used method to measure the J_v. After the convolutional neural network algorithm extracts and groups the joint traces of the tunnel face, the distance between each group of joint traces can be obtained and the average value can be obtained by making virtual measuring lines. Then the J_v is calculated by Equation (5). As can be seen from Equation (5), the default assumption is that the length of the normal calculation line of each group of joints is 1m. But the distribution of joints in the actual rock mass is uneven. There is obvious dispersion between the spacing of the joints. When the group of joints is diagonally intersected with the surface of the unit body, the length of its calculation line is greater than 1m. So the actual calculation of the value of J_v is multiplied by the correction coefficient of 1.05~1.1.

$$\mathrm{BQ} = 90 + 3R_c + 250K_v \tag{3}$$

$$\begin{cases} K_v \approx 0.75 (J_v < 3) \\ K_v = 0.75 - \frac{J_v - 3}{35} (3 < J_v < 10) \\ K_v = 0.55 - \frac{J_v - 10}{50} (10 < J_v < 20) \\ K_v = 0.35 - \frac{J_v - 20}{75} (20 < J_v < 35) \\ K_v = e^{-0.054 J_v} (35 < J_v) \end{cases} \tag{4}$$

$$J_v = S_1 + S_1 + \cdots + S_n + S_k \tag{5}$$

Where: S_n is the number of joints per meter of measuring line in the nth group of joints, S_k is the number of joints per meter of measuring line in the non-grouped joints.

4.2 *Joints analysis of tunnel face*

Eighteen sets of tunnel face data were collected in the test tunnel to analyze the integrity of the surrounding rock. The information of the surrounding rock at the tunnel face was collected by using the TK-SEG equipment. The 23 images were automatically collected at one tunnel face. Some of the tunnel face images are shown in Figure 10. After importing the raw data into TK-SEG software, the 3D model of the tunnel face was obtained as shown in Figure 11.

Based on the aforementioned method, the joints of the tunnel face are obtained as shown in Figure 12(a). The tunnel face contains two groups of joints. The main direction of Group 1 joint inclination is 49°, the joint spacing is 0.51 m, the average length is 2.85 m. The main direction of Group 2 joint inclination is -8°, the joint spacing is 0.79 m, the average length is 3.26 m. The J_v of surrounding rock mass is 3.55, and the K_v is 0.73. Compared with the sketch results of geological engineers (Figure 12 (b)), the software recognition results can identify the corresponding joint traces. It has been proven that this method is feasible and accurate for use in tunnels.

Figure 10. Original image of tunnel face.

Figure 11. 3D reconstruction result of tunnel face.

4.3 *Analysis of rock intergrity of tunnel face*

In the test tunnel of 18 groups of tunnel face surrounding rock joint information as shown in Table 1. The data results show that the excavation exposed tunnel face surrounding rock K_v is in the range of 0.66~0.75. The integrity of the rock mass is complete and more complete. Overall, the integrity of surrounding rock mass in the test section is relatively

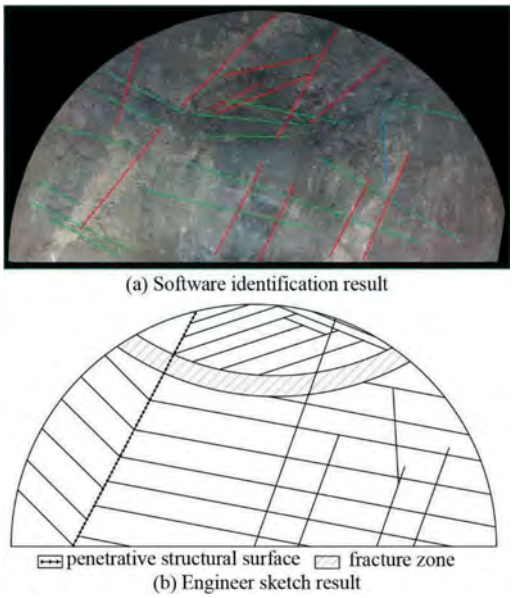

Figure 12. Result of identifying joints.

good. This situation is conducive to tunnel excavation. The 150m test section was constructed for a total of 46 days. The construction progress proves the accuracy of the method used in this article in identifying the integrity of surrounding rock.

Compared with the manual measurement method, the method of this paper can flexibly and quickly obtain the information of surrounding rock joints. Combined with the information of surrounding rock strength, it can carry out the work of enclosing rock classification.

Table 1. Integrity of 18 tunnel faces.

tunnel faces	joint inclination/°			joint spacing/m			J_v	K_v
	1	2	3	1	2	3		
01	4	-76		1.34	1.61		1.50	0.75
02	18	72		0.75	2.02		2.01	0.75
03	-3	38		0.55	3.53		2.31	0.75
04	2	-86		0.84	8.73		1.44	0.75
05	2	-71		0.62	2.86		2.16	0.75
06	22	89		0.41	1.21		3.59	0.73
07	58	3		1.14	0.56		2.93	0.75
08	-1	-59		0.65	2.05		2.23	0.75
09	9			1.03			1.07	0.75
10	1	-75		1.11	0.69		2.59	0.75
11	-1	-67		0.5	1.05		3.25	0.74
12	-3	34	-71	0.77	0.55	4.25	3.69	0.73
13	6	-85	-32	0.66	1.42	1.56	3.15	0.74
14	7			0.49			2.24	0.75
15	7			0.25			4.40	0.71
16	4	-57	83	0.39	1.8	2.06	3.97	0.72
17	8	-30	66	0.59	0.35	1.01	6.10	0.66
18	4	-68	55	0.6	0.74	0	3.32	0.74

5 CONCLUSIONS

On the basis of image recognition technology, this article proposes to use convolutional neural network algorithm to automatically extract the structural features of surrounding rock in the surrounding rock image of the tunnel face. A method for identifying the integrity of surrounding rock is established. And this method is applied to the integrity analysis of surrounding rock in test tunnel. The conclusion is as follows:

(1) Using a combination of photography and laser to obtain images of the tunnel face and 3D coordinates of the surrounding rock surface. 3D reconstruction of tunnel face images using SFM technology. The combination of images and spatial information obtained by laser enables the determination of model scale. Simultaneously achieve positioning on the design line. This method solves the shortcomings of two technical methods in data collection and model building, and has good application value.

(2) The method based on convolutional neural network training can quickly and automatically extract the features of surrounding rock structural surface under the condition of guaranteeing the recognition accuracy. Combined with the J_v, the method of recognizing the integrity of surrounding rock at the tunnel face is established. The accuracy and feasibility of the method are verified in the field application of test tunnel.

(3) The surrounding rock classification in the tunnel face is a research hotspot, which is an important parameter for determining the rationality of tunnel design. The research content of this paper is mainly the recognition of perimeter rock integrity, which is only a part of the parameters of surrounding rock classification. The following work will study methods for automatically obtaining other parameters required for automatic analysis of surrounding rocks.

REFERENCES

Chen, J.Q., Li, X.J., Zhu, H.H., 2017. Automatic extract of rock mass spacing and roughness based on point clouds. Chinese Journal of Underground Space and Engineering. 13(1), 133–140.

Fekete, S., Diederichs, M., 2013. Integration of three-dimensional laser scanning with discontinuum modelling for stability analysis of tunnels in blocky rockmasses. International Journal of Rock Mechanics and Mining Sciences. 57, 11–23.

Fekete, S., Diederichs, M., Lato, M., 2010. Geotechnical and operational applications for 3-dimensional laser scanning in drill and blast tunnels. Tunnelling and Underground Space Technology. 25, 614–628.

Hu, X.W., Hu, S.M., Lu, Y., et al,2010. Measurement of volumetric joint count and its application in surrounding rock classification. Journal of Yangtze River Scientific Research Institute. 27(6), 30–34.

Leng, B., 2009. Research of tunnel face geology information system based on digital image. PhD Thesis. Southwest Jiaotong University, Chengdu, Sichuan, China.

Li, C.M., Lv, M., Yuan, Q., et al, 2022. Repid classification technology of surrounding rock of tunnel face based on three-dimensional reconstruction and unet neural networks. Tunnel Construction. 42(1), 33–40.

Li, S.C., Liu, H.L., Li, L.P., et al, 2018. State and trends of dangerous rock prevention and control during tunnel construction. China Journal of Highway and Transport. 31(10), 1–18.

Song, Y., Wang, X.L., Li, Y., et al, 2013. Contrast research on application of 3-dimensional laser scanning technology and digital imaging geology catalog system in acquisition of rock mass information of tunnels. Tunnel Construction. 33(3), 197–202.

Yang, T.H., Yu, Q.L., Chen, S.K., et al, 2009. Rock mass structure digital recognition and hydro-mechanical parameters characterization of sandstone in fangezhuang coal mine. Chinese Journal of Rock Mechanics and Engineering. 28(12), 2482–2489.

Tunnelling for a Better Life – Yan, Celestino, Thewes & Eberhardt (Eds)
© 2024 The Author(s), ISBN 978-1-032-80042-4
Open Access: www.taylorfrancis.com, CC BY-NC-ND 4.0 license

Study of microgravity survey to predict the Bukit Timah rock head for tunnelling in Singapore

Tan Egk Sze Ernest*, C. Veeresh, J. Kumarasamy & K.H. Goh
Land Transport Authority, Singapore

ABSTRACT: Singapore is a land scarce country with complex infrastructure and a sophisticated underground transportation network which is generally to construct using bored tunnels in difficult geological conditions. Many areas of the island's subsurface consist of Bukit Timah Granite (BTG) Formation, ranging from intact rock to completely weathered residual soils. The Bukit Timah Granite Formation is one of the oldest geological formations which is an intrusive type of igneous rock formed more than 230 million years ago. Top portions of Bukit Timah Granite are generally weathered and decomposed into residual soils. As the water seeps through fractures of granite mass below the weathered soil, chemical process takes places and as a result, the subsurface of the rock is eroded leaving numerous boulders in place. Deep tropical weathering and variability in bedrock level of the Bukit Timah Granite Formation is well established and the inherent complexities pose challenges to the tunnelling works. Tunnelling through rock induces rapid cutterhead wear and incurs high costs. Thus, mapping of the subsurface stratigraphy along the tunnel alignment is an important aspect for safe and economical tunnelling. In recent years, gravity surveys have been successfully employed as a non-intrusive means to predict the underground stratigraphy. Several gravity surveys have been conducted in Singapore to determine the rockhead elevation for tunnelling projects and have achieved varying degrees of success. This paper presents a study on the methodologies adopted in the implementation and interpretation of these surveys and identifies factors that may have contributed to the accuracy of predicted results. Findings from this study are useful for future projects to identify the suitability of gravity surveys for tunnelling projects in Bukit Timah formation.

Keywords: Geophysical, Rockhead, Microgravity Survey, Tunnelling, Bukit Timah Granite

1 INTRODUCTION

In a land scarce country like Singapore, efficient utilisation of space above and underground is critical. Singapore boasts a sophisticated underground transportation network that is constantly being expanded to service ever-growing needs. Many areas of the island's subsurface consist of Bukit Timah Granite (BTG) Formation, ranging from intact rock to completely weathered residual soils. The Bukit Timah Granite Formation is one of the oldest geological formations which is an intrusive type of igneous rock formed more than 230 million years ago. Top portions of Bukit Timah Granite are generally weathered and decomposed into residual soils. As the water seeps through fractures of granite mass below the weathered soil, chemical process takes places and as a result, the subsurface of the rock is eroded leaving numerous boulders in place. Deep tropical weathering and variability in bedrock level of the Bukit Timah Granite Formation is well established (Shirlaw et al., 2000) and the inherent complexities pose challenges to the tunnelling works. Tunnelling through rock induces rapid cutterhead wear and incurs high costs. Thus, mapping of the subsurface stratigraphy along the tunnel alignment is an important aspect for safe and economical tunnelling. Site investigation to determine the underground geology using bore hole drilling is challenging and inaccessible in several areas due to site constraints and use of reliable non-intrusive methods is an attractive alternative in such conditions. In recent years, microgravity surveys have been successfully employed as a non-intrusive means to predict the underground stratigraphy.

The microgravity survey is a geophysical technique that detects minute fluctuations in the Earth's gravitational field due to variations in the density of subsurface material. Utilisation of the gravity technique for subsurface exploration began in the early twentieth century (Nabighian et al., 2005). Improvements in the precision of gravity data acquisition over the past few decades have increased the popularity of gravity

*Corresponding author: ernest_tan@lta.gov.sg

DOI: 10.1201/9781003495505-67

surveys. Through the reduction and interpretation of gravity data, it is possible to predict the presence of subsurface geological structures such as faults, rock intrusions, dykes, and sills (Saibi, 2017).

Several projects have used gravity surveys in Singapore to determine the soil and rock interface. However, the results of these surveys achieved varying degrees of success in terms of accurately predicting the rock level when comparing with reference boreholes. This study is aimed to achieve a better understanding of the factors which influence the test results and interpretations from various microgravity surveys carried out. The methodology of data collection, processing and interpretation is presented, followed by the project-specific details of each gravity survey in the following sections. Various aspects that affect the microgravity survey results are discussed and findings from this study are useful for future tunnelling projects to accurately determine the rock profile for safe and economical tunnelling.

2 MICROGRAVITY SURVEY

Fundamentally, the underlying concept behind gravity surveys is to measure the deviation of locally observed gravitational acceleration from its theoretically computed value. In gravity surveys, the common unit of measurement is the 'gal', which is equivalent to gravitational acceleration of 0.01 m/s2. In gravity survey measurements, fluctuations in gravitational acceleration can range from several hundred milligals (mgal) to several microgals (µgal). The term 'microgravity' may be used when the accuracy of measurements is better than 0.05mgal, and if the spacing between survey stations is less than 100m (Omnes, 1976). Gravity measurements are performed using a gravimeter, which consists of a mass suspended from a highly sensitive spring. Fluctuations in gravity alter the position of this mass because of the extension or contraction of the spring, and a restoring force is then automatically applied to the mass to bring it back to its original position. The magnitude of this restoring force is proportional to the gravitational force exerted on the mass, and the observed gravity at that location can be obtained after correction for natural instrument drift and removing the effects of the earth's tides.

The field procedure for data acquisition generally requires establishing a base station. The base station should preferably be at an open location with level ground and with no obstructions and easily accessible. The gravity readings from this base station are then recorded and compared with an absolute gravity station linked to the International Gravity Standardisation Network 1971 (IGSN71). Thereafter, gravity readings are taken in a loop, starting from the base station, and successively moving to the next survey station. The loop ends at the original base station where a second reading is taken; this allows for correction of the gravimeter's instrumental drift.

The collected gravity data will be subjected to additional corrections (i) Free air correction: to account for the gravity difference due to elevation at which the reading was taken (ii) Bouguer correction: the gravity due to the subsurface material between sea level and the measurement point and (iii) Terrain correction: the effects of localized changes in topography. The final gravity anomaly value after accounting for the above effects was termed as 'Terrain Corrected Bouguer Anomaly (TCBA)'.

In gravity data interpretation, the TCBA is split into two components: regional and residual components of the gravity anomaly. The regional component is attributed to widespread and deep-seated mass distributions (Mickus et al., 1991), while shallower subsurface mass distributions constitute the residual component. Typically, the regional anomaly is not expected to vary significantly across a small survey site. The residual anomaly data is then subjected to inverse modelling which predicts the subsurface geological structure as a function of sedimentary thickness variation (Wahyudi and Kadir, 2018), based on an assumed density contrast.

3 MICROGRAVITY SURVEY TEST RESULTS

In this section, the microgravity surveys from four different sites are presented: (1) Bishan Park, (2) Central Catchment Nature Reserve, (3) Blackmore Drive and (4) Changi Airport. These surveys were performed by the same geophysical specialist company between 2015 and 2022, using the Scintrex CG5 or CG6 Autograv Gravity Meter.

3.1 *Gravity survey at Bishan Park*

The site location is shown in Figure 1 and is situated at a public park. A total of 225 survey points were demarcated for this site, with an average square

Figure 1. Survey boundaries and borehole layout at Bishan Park.

spacing of 10 m. The topography was slightly undulating, with ground levels varying between 3.1 to 9.9 meters above the Singapore Height Datum (SHD). Terrain correction was applied during the gravity data reduction process.

Four boreholes were used for control to calibrate the regional component of the gravity anomaly by assuming that the variation follows a smooth first order polynomial as a function of the site coordinates. A final mean density contrast of -650kg/m^3 was adopted in the 3D depth model, based on the estimated difference between the mean density of rock and the less dense overlying weathered soils. The final depth model was then verified against the reference boreholes, shown in Table 1.

3.2 *Gravity survey at Central Catchment Nature Reserve (CCNR)*

Table 1. Gravity predicted versus actual rockhead at bishan.

Borehole	Ground Level Elevation/ mSHD	Actual Rockhead Elevation/ mSHD	Predicted Rockhead Elevation from Gravity Data/ mSHD	Difference between Predicted and Actual Rock Level/ m
BH-1a	7.9	-17.1	-17.8	0.7
BH-2a	7.4	-8.6	-7.4	1.2
BH-3a	5.7	-14.8	-13.8	1.0
BH-4a	8.2	-12.3	-11.8	0.5

The location of the gravity survey is shown in Figure 2. The survey site was located at a nature preservation site and mostly consists of moderately dense foliage. A total of 254 survey stations were set out, with an average square spacing of 15 meters. The terrain was moderately hilly, with ground elevations varying from 14.4 m to 39.3 m above the SHD.

A total of 20 reference boreholes along the proposed tunnel alignment were adopted for calibration and control of the regional anomaly distribution across the site. To derive the mean density contrast of the residual component, soil densities obtained from lab testing of 12 boreholes located at the southern half of the survey location were initially utilized to determine the average difference in bulk densities between Timah Granite rock and overlying soil layers. This resulted in a sample density contrast of -747kg/m3. However, in the 3D depth model, a final adopted mean density contrast of -950kg/m3 was adopted in order to optimize the correlation with the actual borehole rockhead elevations, which is presented in Table 2.

Horizontal Directional Coring (HDC) was also carried out at CCNR to verify the subsurface stratigraphy along the tunnel alignment. Since the HDC was performed within the survey area, results could be used to compare against the gravity rockhead predictions.

Figure 2. Survey boundaries and borehole layout at CCNR.

Table 2. Gravity predicted versus actual rockhead at CCNR.

Borehole	Ground Level Elevation/ mSHD	Actual Rockhead Elevation/ mSHD	Predicted Rockhead Elevation/ mSHD	Difference between Predicted and Actual Rock Level/ m
BH-1b	25.0	-6.5	-23.0	16.6
BH-2b	29.9	-24.4	-35.0	10.6
BH-3b	30.3	-13.2	-17.5	4.3
BH-4b	30.8	-7.7	10.0	17.7
BH-5b	31.1	-9.9	-16.0	6.1
BH-6b	32.3	5.3	-3.0	8.3
BH-7b	33.4	4.4	3.0	1.4
BH-8b	35.3	7.8	3.0	4.8
BH-9b	36.3	6.3	5.0	1.3
BH-10b	21.7	-21.8	-19.0	2.8
BH-11b	32.3	-4.9	6.0	10.9
BH-12b	31.4	-2.3	3.0	5.3
BH-13b	31.0	-2.5	2.0	4.5
BH-14b	29.6	-0.3	-5.0	4.7
BH-15b	25.0	-13.3	-35.0	21.7
BH-16b	23.6	-15.3	-14.0	1.3
BH-17b	20.0	-9.8	-12.0	2.2
BH-18b	15.7	-1.4	-7.0	5.6
BH-19b	15.3	-5.9	2.0	7.9
BH-20b	31.4	-15.8	-7.5	8.3

3.3 *Gravity survey at Blackmore Drive*

The surveyed location can be seen in Figure 3 and is located within a moderately built-up residential district. A total of 565 survey stations were demarcated

for the gravity survey at an average spacing of 8 m. The elevation of the site varies from 11.7 m to 28.5 m above the topographic datum. Terrain corrections were applied to correct for the undulations in terrain. Situated close to the survey areas are the following structures: (1) An underground rapid transit station at the north boundary of the survey area, and (2) A ten-storey condominium complex located along the north-eastern boundary of the site.

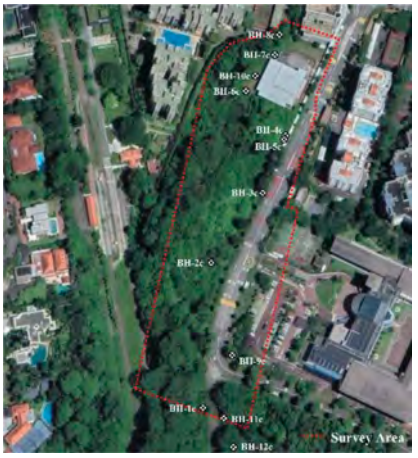

Figure 3. Survey boundaries and borehole layout at Blackmore.

There were 27 boreholes located within proximity of the survey area, 12 of which were terminated in rock, while the remaining 15 either terminated at a shallow depth or did not encounter rock. All available borehole laboratory data from these boreholes were used to determine the average densities of the following soil layers:

(a) Rock strata,
(b) soil between Rock and the topographic datum,
(c) soil between the existing ground level and the topographic datum.

Bouguer corrections were performed based on the density data above the topographic datum to allow for a more accurate correction. Additional corrections for the surrounding structures were also performed to refine the gravity data. For the rapid transit station, the negative gravity contribution due to underground voids was defined based on an as-built 3D model, while the condominium complex was simulated by considering the full three-dimensional outline of the structure, with an assumed bulk density of 300kg/m^3. This value was adopted based on the specialist's previous project experience and was deemed to be representative of concrete shell structures.

The final density contrast adopted for the 3D depth model was -608kg/m^3, which was based on the difference between the rock density and residual soils below the topographic datum. Comparison between predicted and actual rock rockhead elevations are presented in Table 3.

Table 3. Gravity predicted versus actual rockhead at Blackmore Drive.

Borehole	Ground Level Elevation/ mSHD	Actual Rockhead Elevation/ mSHD	Predicted Rockhead Elevation from Gravity Data/ mSHD	Difference between Predicted and Actual Rock Level/m
BH-1c	24.2	-25.3	-44.2	18.9
BH-2c	24.0	-30.8	-48.1	17.4
BH-3c	18.7	-42.5	-36.1	6.4
BH-4c	16.2	-65.3	-53.9	11.4
BH-5c	16.3	-62.2	-52.9	9.4
BH-6c	15.0	-42.2	-31.6	10.6
BH-7c	14.8	-42.1	-52.8	10.7
BH-8c	12.4	-58.7	-47.0	11.7
BH-9c	23.9	-52.6	-48.5	4.1
BH-10c	15.0	-37.0	-35.3	1.7
BH-11c	24.6	-48.6	-42.1	6.5
BH-12c	24.7	-46.9	-45.0	1.9

3.4 *Gravity survey at Changi Airport*

The gravity survey boundaries are shown in Figure 4. A combined total of 1038 stations were marked out at an average station spacing of 10m. The terrain was relatively flat, with ground levels only varying between 2.5 m to 4.9 m above the topographic datum.

A total of 15 boreholes were located within the survey area. An additional five boreholes outside of the data coverage was also used to calibrate the mean density contrast between residual soils and rock. A mean density contrast of -730kg/m3 was derived from the sample test results, and this value was adopted as the final mean density contrast input into the depth model as it proved to have a good correlation with the actual borehole rock levels, shown in Table 4.

Horizontal Directional Coring performed at the site was within the bounds of the gravity survey and the HDC results were compared against the gravity predicted rockhead depth.

4 DISCUSSION

The interpreted rockhead profiles for Bishan and Changi achieved close matches to the reference boreholes. Furthermore, horizontal directional coring performed at Changi Airport first encountered the rock at approximately -19.3mSHD, which was comparable to the rock level predicted from the gravity survey results (-18.0mSHD). Figure 5(a) shows the location of the HDC trajectory and location of the first encounter with rock, while Figure 5(b) overlays the location with the rockhead model interpreted from gravity results.

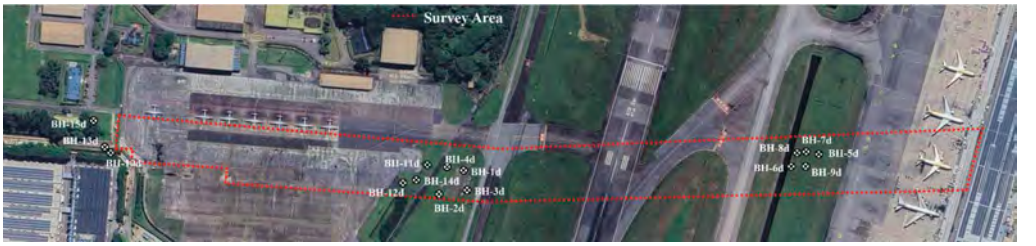

Figure 4. Survey boundaries and borehole layout at Changi Airport.

Table 4. Comparison between gravity predicted and actual rockhead elevation at Changi Airport.

Borehole	Ground Level Elevation/ mSHD	Actual Rockhead Elevation/ mSHD	Predicted Rockhead Elevation from Gravity Data/ mSHD	Difference between Predicted and Actual Rock Level/m
BH-1d	2.9	-27.6	-27.4	0.2
BH-2d	3.1	-16.9	-19.4	2.5
BH-3d	2.8	-19.3	-19.9	0.6
BH-4d	3.0	-29.8	-27.2	2.6
BH-5d	3.1	-21.6	-21.0	0.6
BH-6d	3.0	-28.0	-30.0	2.0
BH-7d	3.1	-27.5	-31.8	4.3
BH-8d	2.9	-29.0	-32.2	3.2
BH-9d	3.1	-29.5	-28.0	1.5
BH-10d	2.6	-21.9	-26.0	4.1
BH-11d	3.1	-26.2	-25.5	0.7
BH-12d	2.9	-23.1	-21.5	1.6
BH-13d	2.7	-25.9	-26.0	0.1
BH-14d	3.0	-21.8	-26.0	4.2
BH-15d	4.7	-30.1	-30.0	0.1

On the other hand, surveys at CCNR and Blackmore encountered situations where the predicted gravity rock profile deviated significantly from the actual borehole rock level. A summary of the predictive errors across the four survey sites are presented in Table 5.

HDC runs were also carried out in CCNR along the trajectories shown on Figure 6(a). The horizontal drilling encountered rock at -5.5mSHD, while the gravity model predicted the actual rock elevation to be at 0mSHD at the same location, incurring an absolute error of 5.5m and a percentage error of 18% (Figure 6(b)).

4.1 *Factors affecting gravity predictions of rockhead*

4.1.1 *Depth to rockhead*

The comparison between actual and predicted rockhead level across the four gravity surveys is shown in Figure 7(a). A line of unity was also plotted for reference to indicate a case where the interpreted gravity data matches the actual rock level. The same data above was expressed in terms of the absolute difference between the actual and predicted rockhead elevations in Figure 7(b) to illustrate the relationship more clearly between rockhead depth and prediction error. This reduction in absolute accuracy with depth is expected due to an increased possibility of encountering both lateral and longitudinal density variations that deviate from the input mean density contrast.

The difference between predicted and actual rockhead elevations were also plotted as a percentage of the total depth to the rock. For easy reference, the

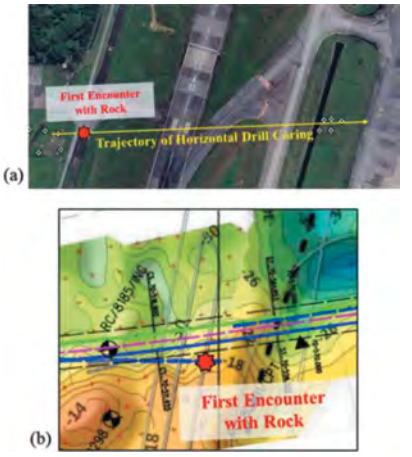

Figure 5(a). HDC Alignment within Changi, Figure 5(b): HDC first encounter with rock superimposed on gravity model.

Table 5. Summary of gravity prediction errors compared to actual rockhead level across survey sites.

Survey Area	No. of BH	Difference between gravity prediction and actual rockhead depth (% of verification BH)			
		<3m	3m to 5m	5m to 10m	>10m
Bishan	4	100	0	0	0
CCNR	20	25	20	30	25
Blackmore	12	16.7	8.3	25	50
Changi	15	73.3	26.7	0	0

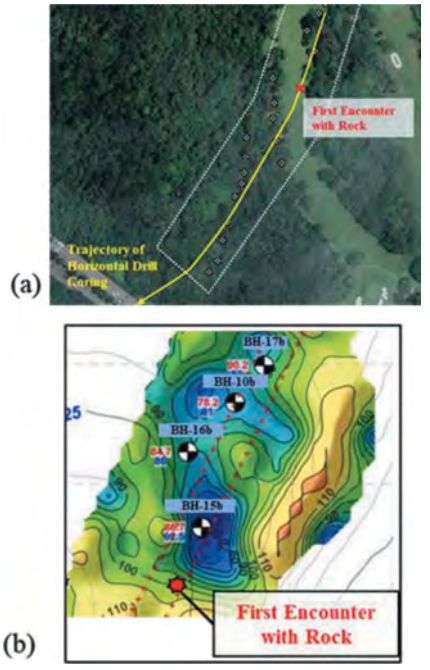

Figure 6(a). HDC Alignment within CCNR, Figure 6(b): HDC first encounter with rock superimposed on gravity model.

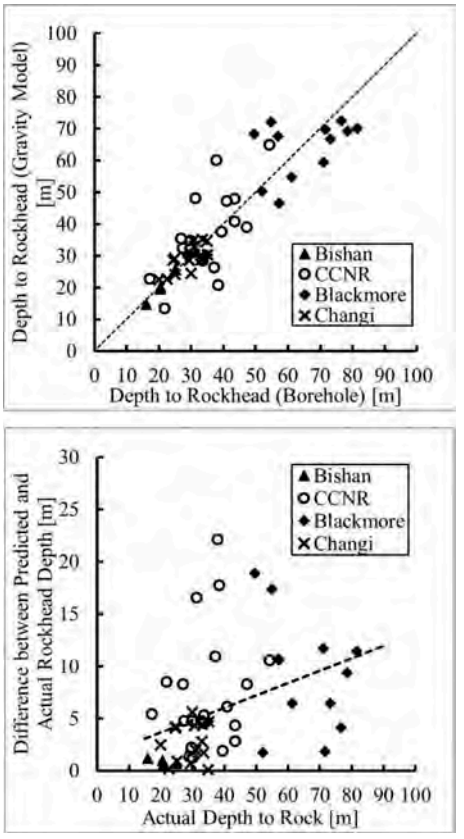

Figure 7(a). Borehole rockhead with model rockhead elevations, Figure 7(b) Correlation between absolute error from gravity model and actual depth to rock.

results for each individual site were plotted separately in Figures 8(a) to 8(d). Across each of the four sites, most prediction errors were clustered between 0 to 20%. However, there were outlier predictions from the surveys at Blackmore and CCNR which deviated between 30% to 60% from the actual rockhead depth. These outliers could be largely attributed to the steep and undulating rock at several locations which had significant influence on the gravity predictions; this will be discussed in Section 4.1.2. Figure 9 shows the combined results from all sites. A consistent trend line of approximately 15% error across all four sites is observed, and a majority of the data had predictive uncertainties of below 20%. This is to be expected, as the rockhead model is developed based on the residual gravity anomaly distribution which is an expression of the thickness of soil layers above the rock. A greater thickness of overlying soils would logically result in a proportionately increased absolute uncertainty in the depth to rockhead. The average prediction error is generally in agreement with a study performed by Nyquest (2001) to determine the depth to Precambrian bedrock in Montana, USA, where an average prediction error of 3% to 17% was observed for bedrock depths between 20 to 70 meters below ground level.

On the other hand, Abbott and Louie (2000) also reported a potential 50% depth estimation error in their gravimetric study on the depth to bedrock in Nevada, USA, due to a lack of rock and soil density contrast data, thus highlighting the importance of gravity data correction and reduction with sufficient background understanding of actual density contrasts between rock and soil.

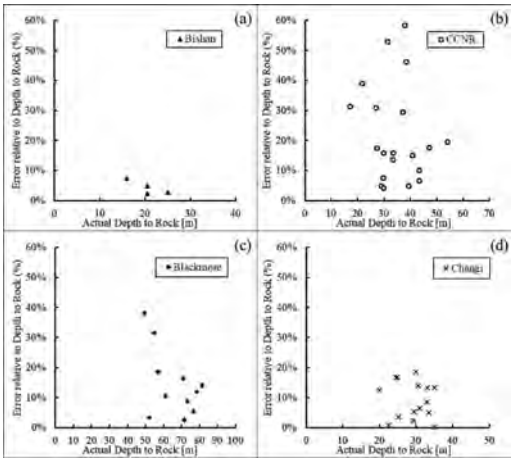

Figure 8. Correlation between percentage error from gravity model and actual depth to rock for individual sites: (a) Bishan, (b) CCNR, (c) Blackmore and (d) Changi.

4.1.2 *Undulations in rockhead*

For each of these microgravity surveys, the survey points were spaced between 8 to 15 meters in both directions. The observed gravity data was based on discrete points and relies on interpolation methods to derive the continuous gravity anomaly distribution across the survey area. As such, the gravity fluctuations caused by steep and sudden changes in the rock level in between gravity stations may not be precisely reflected in the survey data.

For example, the gravity rockhead predictions for CCNR indicated that the rockhead varied up to 55 meters across the survey area. Results from the 3D depth model (Figure 10) demonstrated that there could be steep undulations in the rock exceeding 20 meters in elevation within a lateral span of 10 meters at the location of BH-15b. The survey stations which were spaced 15 meters apart would not be able to precisely capture the effects of the gravity anomaly due to the lateral and longitudinal influence of the steeply sloping rockhead compared to a borehole, which is effectively a point prediction. Consequently, a significant difference of 21.7m was observed between the actual and predicted rock depth.

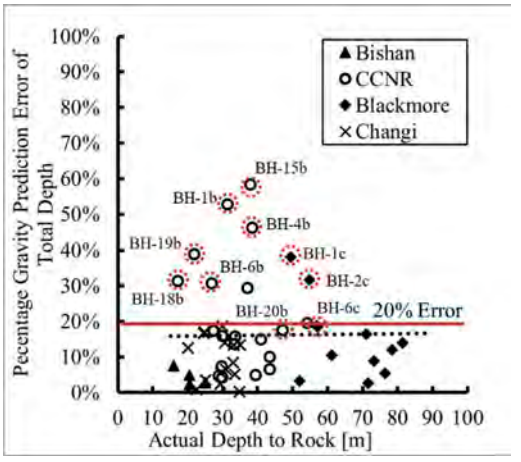

Figure 9. Correlation between percentage error from gravity prediction and actual depth to rock.

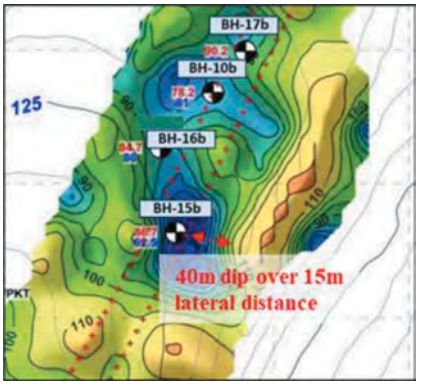

Figure 10. Depth inversion gravity model of CCNR.

It was also noted that in cases where the difference between predicted and actual rockhead varied significantly, these data points often manifested as outliers from the 20% error margin discussed in the previous section. These data points are identified in Figure 9 (circled in red).

Noting that steep inclinations in rockhead could result in incorrect gravity predictions, a two-stage approach could potentially be adopted when planning gravity surveys:

i) An initial gravity survey can be conducted based on a larger station spacing between (e.g., 15 meters). Gravity data correction and reduction is to be carried out to establish the residual anomaly distribution across the site. Ideally, several reference boreholes should be drilled within the site to allow for site-specific calibration of the regional anomaly.

ii) Identify areas within the site encountering significant fluctuations in the residual anomaly over a short distance, as this indicates potential locations with steep rockhead inclinations that may not result in accurate predictions.

iii) Perform a second gravity survey at these locations with a reduced spacing between stations. The residual anomaly distribution may then be refined based on a higher number of data points within the identified zone, allowing for greater resolution of the rockhead 3D depth model.

4.1.3 *Underground structures*

Density contrast between rock and soil is a key parameter affecting the data interpretation. The presence of subsurface voids (e.g., underground basements) should be carefully accounted as the contribution to the gravity anomaly could be significant. For the case of Blackmore Drive, the void from the underground rapid transit station void was reported to have an influence of up to 0.328mGal. For reference, the Bouguer Anomaly was observed to have a maximum variation of 0.8mGal across the site, between 33.11 to 33.91mGal. A 0.328mGal contribution from an underground void could result in fluctuations of up to 40% of the range of rockhead elevations. It was also noted that the predicted rock elevation at the location of the closest reference borehole to the station structure, BH-8c, experienced a significant difference of 11.69m between predicted and actual depth to rock. Figure 11 indicates the location of the underground station with respect to BH-8c.

4.1.4 *Density variations in soil and rock*

In the depth inversion model, a single value of density contrast is input to correlate the rockhead model with the residual anomaly map. To provide a reasonable estimate across the survey area, average density values were computed from lab results from soil sampling of boreholes throughout each site.

Figure 11. Proximity of MRT station to BH-8c.

However, this merely provides a best estimate average density contrast between rock and the overlying soils. Natural variations in soil and rock densities across the site would thus have an impact on the final predicted rockhead level. This could be another underlying reason for locations where the bedrock was predicted to be relatively uniform, but still resulted in significant percentage deviation from the true rockhead level.

5 CONCLUSIONS

Microgravity surveys were carried out at four different sites in Singapore with the objective of profiling the depth to rock, achieving varying degrees of success. The following inferences and conclusions can be made from the case studies of these surveys:

- When considering the prediction error as a percentage of the actual depth to rockhead, it was noted that the average error was relatively consistent at approximately 15% and was not significantly impacted by the rockhead depth. Additionally, majority of gravity predictions were observed to produce prediction errors of less than 20% of the total depth to rock.
- Steep undulations in the rockhead level will influence the accuracy of gravity predictions. This was observed at multiple borehole locations in CCNR and Blackmore Drive. Due to the spacing of the survey points which varied between 8 meters to 15 meters, the resolution of gravity data may be affected, especially if a steep change in rockhead elevation occurs over a relatively short distance between survey points. Gravity fluctuations due to these geological structures may not be effectively captured as the assumed gravity anomaly distribution between points is generated using interpolation techniques.
- Underground voids (e.g., Basements, storage tanks) have a significant impact on the observed gravity anomaly located nearby to the void, and proper corrections should be applied based on an accurate three-dimensional representation of the void geometry.
- As there will be natural variations in the soil and rock densities across the site, this could give rise to uncertainties in the gravity prediction as a single best estimate value of the density contrast between rock and soil is assumed in the inverse modelling process.

REFERENCES

Abbott, E.A., Louie, J. N., 2000. Depth to bedrock using gravimetry in the Reno and Carson City, Nevada, area basins. Geophysics. 65(2), 340–350.

Mickus, K.L., James, W.C., 1991. Regional gravity studies in southeastern California, western Arizona, and southern Nevada. Journal of Geophysical Research Atmospheres. 96(B7), 12333–12350.

Nabighian, M.N., Ander, M.E., Grauch, V.J., Hansen, R.O., Lafehr, T.R., Li, Y., Pearson, W.C., Peirce, J.W., Phillips, J.D., & Ruder, M.E., 2005. Historical development of the gravity method in exploration. Geophysics. 70(6), 63–89.

Nyquest, D.L., 2001. A depth to bedrock model of the Hellgate Canyon and Bandmann Flats area East Missoula Montana using constrained inversion of gravity data. Graduate Student Theses. University of Montana, MT, USA.

Omnes, G., 1976. Microgravity and its applications to civil engineering. Innovations in subsurface exploration of soils. 581, 42–51.

Saibi, H., (2018). Microgravity and its applications in geosciences. In: Gravity book, Intech Edition. Chapter 3, 41–72.

Shirlaw, J.N., Hencher, S.R and Zhao, J. (2000) Design and construction issues for excavation and tunnelling in some tropically weathered rocks and soils. Invited lecture Proceedings GeoEng2000, Melbourne, Australia. 19-24 November 2000. Technomic Publishing, PA, USA. Volume 1: 1286–1329.

Wahyudi, E., Kadir, W., 2018. Inverse Modeling of Gravity Data with Two Layers Density in Sedimentary Basin Structure. Journal of Physics: Conference Series, Bandung, Indonesia. Volume 1090. 012048.

Tunnelling for a Better Life – Yan, Celestino, Thewes & Eberhardt (Eds)
© 2024 The Author(s), ISBN 978-1-032-80042-4
Open Access: www.taylorfrancis.com, CC BY-NC-ND 4.0 license

Rock drilling aerosol deslagging technology and CFD-DEM two-way coupling numerical simulation of weak surrounding rock geology

Shuaitao Guo*
China Railway Construction Heavy Industry Corporation Limited, Changsha Hunan, China,

ABSTRACT: To solve the problem caused by weak surrounding rock that is easy to soften or argillize when exposed to water, the technology of drilling aerosol and slag discharge is put forward here, i.e. discharging cuttings formed during the process of drilling through high-speed aerosol forming in the combination of HP air and LP water, so as to realize heat dissipation and dust reduction. To improve the efficiency of aerosol deslagging and avoid blockage and jamming, CFD-DEM two-way coupling simulation method is adopted here to analyze the interaction between the flow field inside the drill bit and cuttings during the process of aerosol deslagging for rock drilling bit, and the contribution of different parts to pressure loss. The distribution and movement trajectory of cuttings under different air flows and pressures are studied to determine the critical pressure required for deslagging, which is then compared with experimental test results. As shown by the result, the critical pressure required for deslagging is 7.5 bar, which basically matches the experimental results, providing a research method and theoretical basis for the design of rock drilling aerosol deslagging bit.

Keywords: Weak Surrounding Rock, Drill Bit, Deslagging and Two-way Coupling

1 INTRODUCTION

Depending on the prosperity of China's transportation industry, railway tunnel construction is becoming increasingly widespread. In the process of tunnel drilling construction, unreasonable construction technology may affect the stability and safety of the tunnel structure provided that weak surrounding rock is encountered in such a low-strength geological environment [1]. Hence, studying the drilling and deslagging technology in weak surrounding rock geological environment has great significance for tunnel construction. The weak surrounding rock is characterized by broken and loose state, prone to poor stability and easy softening or argillization when exposed to water, bringing great challenges to tunnel drilling construction [2]. In the geological environment of complexity such as the weak surrounding rock, conventional mechanical spiral deslagging and hydraulic deslagging may easily trigger outburst and pipe jamming [3]. Therefore, wind deslagging is generally adopted for drilling and deslagging of the weak surrounding rock.

Multiple studies have been carried out on wind deslagging from boreholes at home and abroad. Huber N [4] et al. simulated the particle transport process in a horizontal pipe by means of simulation and then obtained the movement trajectory of particles in the horizontal pipe. Muschelknantz [5] and Matsumoto [6] respectively put forward empirical and semi-empirical formulae for the prediction of critical wind velocity of pneumatic transport through simulation of such pneumatic transport. Wang Yilong analyzed the influencing factors of gas lift deslagging from gas drainage boreholes by combining simulation and test, and concluded the influence law of coal dust particle size, air volume and quantities of cuttings on deslagging [7]. Zhang Yu designed a drill pipe structure to prevent jamming for drilling in soft coal seams, by adopting a special spiral blade structure to obtain a better deslagging capacity and jamming prevention performance [8]. For challenges encountered in mining of soft outburst coal seams, Li Jia optimized the parameters of rib drill pipe through gas-solid two-phase coupling method to obtain the optimal combination of parameters by using range analysis method. The deslagging efficiency of the optimized rib drill pipe structure can reach 15.77%[9]. Zhang Wei simulated the borehole deslagging process by means of numerical simulation. The critical wind velocity increases logarithmically and the pressure loss also increases with the increase of solid-gas ratio. [10] Wang Yonglong analyzed the critical conveying wind velocity of coal debris particles group and the solution to pressure loss of drilling system through the theoretical research on the borehole deslagging mechanism

*Corresponding author: 893318677@qq.com

DOI: 10.1201/9781003495505-68

and the time effect of blockage. As shown by the results, the soft outburst coal seam is challenged with large fracture zone area distribution and large expansion deformation of hole wall during drilling, resulting in increased friction coefficient of hole wall, decreased deslagging space, higher transportation resistance of coal debris and increased pressure loss [11].

Most of the researches about borehole deslagging for weak surrounding rock adopt wind deslagging home and abroad. Excessive dusts however will be generated during the drilling process, which contaminates the construction environment and affects the health and safety of workers. To come up with a resolution, an appropriate amount of water is added into the HP air to form a high-speed aerosol. The deslagging using aerosol can not only avoid softening of weak surrounding rock exposed to water, but also effectively reduce dust spread. However, due to the limited research on aerosol deslagging at home and abroad, there is no simulation and experimental analysis methods for actual working conditions. Hence, this paper mainly analyzes the theory and simulation of aerosol deslagging technology in rock drilling holes, and compares the result with test data, aiming to provide an effective method for the study of aerosol deslagging technology in rock drilling holes in weak surrounding rock geology.

2 BASIC THEORIES

2.1 *Pneumatic transport process*

Aerosol deslagging is essentially a pneumatic transport process. Pneumatic transport uses the energy of airflow to transport granular materials along the direction of airflow. Pneumatic conveying can be divided into suction type and pressure-feeding type according to the working principle. Suction type refers to conveying by negative pressure below atmospheric pressure, while pressure-feeding type refers to conveying materials through the HP air that is above atmospheric pressure. The pressure-feeding type is usually preferred to in the borehole wind deslagging. In pneumatic transport analysis, for spherical solid particles with a diameter d, the expression of particle suspension velocity can be derived according to the mechanical relationship between gravity and buoyancy balance in the suspended state [12]:

$$v_n = \sqrt{\frac{4gd(\rho_s - \rho_a)}{3C\rho_a}}$$

Where, vn represents the suspension velocity of spherical particles, m/s; g represents the acceleration of gravity, m/s^2; d represents the diameter of particles, m; ρs represents the density of particles, kg/m^3; ρa represents the density of air, kg/m^3; C represents the resistance coefficient of particles, generally taken as 0.44. In fact, the motion of drilling cuttings in the process of discharging with airflow is extremely complicated. In the vertical direction, there are not only gravity and buoyancy, but also components of mutual collision force between particles in the vertical direction, upward component of turbulence acting on particles, acting force generated by velocity difference between upper and lower surfaces of particles, and components of thrust generated by irregular shape of particles in the vertical direction.

2.2 *Basic assumptions*

In the process of borehole deslagging, air is taken as gas phase and drilling cuttings particles are taken as solid phase. Generally, the volume fraction of drilling cuttings particles is relatively large, so the interaction between particles cannot be neglected. To accurately simulate the deslagging process, it is necessary to simulate through fluid-discrete element coupling. The discrete element method is an engineering numerical method that can be used to simulate the motion of dense particle flow. Using the discrete element method necessitates the following assumptions:

(1) Solid particles are spherical, without considering the irregular shape of the particles;
(2) The solid particles are rigid in properties, without considering the deformation of particles;
(3) The contact between particles is point contact;
(4) Crushing and bonding of particles are not considered.

2.3 *Aerosol deslagging process*

Borehole aerosol deslagging is a complex physical process. As shown in Figure 1, air and water are atomized in the aerosol mixing block, and then enter the drill pipe and inner hole of the bit for deslagging after passing through the pipeline system. Atomization is a physical process in which liquid droplets turn into water mist under the action of gas impact, providing aerosol preparation for deslagging process. High-speed aerosol serves to discharge rock debris formed during drilling in the deslagging process. This paper mainly studies these two processes. The whole physical process from atomization to deslagging is of complexity since the slenderness ratio of the system is too large, and the direct simulation calculation is costly. To improve the simulation efficiency and catch up with the project schedule, the two processes are independently studied, and the aerosol distribution obtained through atomization simulation functions as the input for the deslagging process.

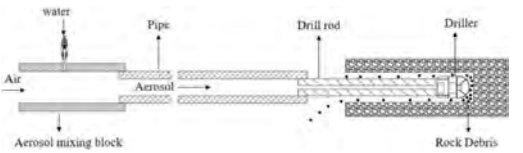

Figure 1. Schematic diagram of aerosol deslagging device.

3 ATOMIZATION SIMULATION

To simulate the atomization process of liquid droplets, a VOF multiphase flow model describes the mixing of air and water, and a VOF-Lagrange transformation model captures the breakage of liquid film and peels off small droplet particles from the free surface to obtain the size distribution of water mist.

3.1 *Calculation model and boundary conditions*

The 3D model of the water-gas mixing device comprises of a gas mist mixing block and a built-in nozzle as shown in Figure 2, which are geometrically cleaned and simplified. The fluid area inside the water-gas device and the inner wall surface of the pipeline contacting the fluid are reserved. Other non-contact surfaces are deleted, and the CFD geometrical model of the water-gas mixing device is obtained by pumping out the cavity, as shown in Figure 3.

The geometric model is meshed, with a total of 885,422 elements, as shown in Figure 4.

The air inlet boundary is the flow inlet, which is set according to the volume flow of 3,000L/min under standard atmospheric conditions. The liquid water inlet boundary is also the flow inlet, which is set corresponding to a volumetric flow of 1 L/min and an outlet pressure of 12.5 bar. To precisely capture the droplet fragmentation, adaptive grids and adaptive time steps are used for the purpose of simulation.

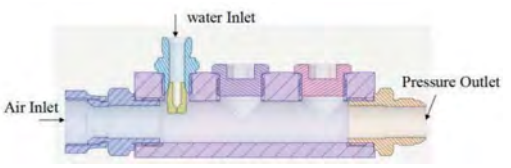

Figure 2. Solid model of water-gas mixing device.

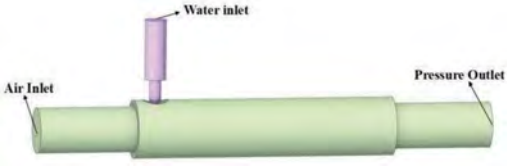

Figure 3. CFD Geometric model of water-gas mixing device.

Figure 4. CFD grid model of water-gas mixing device.

3.2 *Numerical simulation results and analysis*

The liquid enters the aerosol mixing block from the built-in nozzle to form a liquid column, which is mixed with high-speed air. The internal velocity nephogram of the aerosol mixing block is shown in Figure 5. The air flow rate near the liquid column is about 20m/s. The pressure nephogram is shown in Figure 6. The pressure distribution in the whole aerosol mixing block is relatively uniform, around 12.5bar, indicating that the liquid column has little influence on the surrounding pressure field. Under the action of airflow impact, the liquid column changes from jet shape to liquid film and large-diameter liquid droplets. It is a primary atomization process, as shown by the frame line in Figure 7a. The diameter distribution range of droplet particles is 0.042mm-0.109mm. Due to the large velocity difference between liquid droplets and surrounding air, the air force acting on the liquid film and large-diameter liquid droplets in the spray exceed their own surface tension in the airflow. The liquid droplets are quickly broken again to generate smaller diameter liquid droplets. The size of the atomized particles after droplet fragmentation is shown by the outline in Figure 7b, with a droplet particle diameter ranging from 0.004 mm to 0.109 mm and an average particle diameter of 0.06 mm.

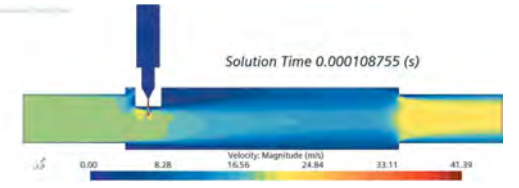

Figure 5. Velocity nephogram in aerosol mixing block.

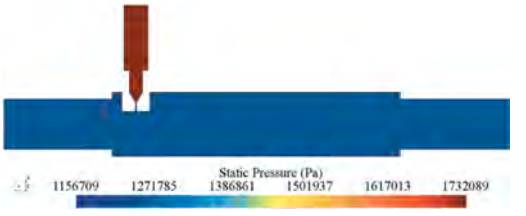

Figure 6. Pressure nephogram in aerosol mixing block.

4 SIMULATION OF AEROSOL DESLAGGING

The schematic diagram of the deslagging process of the drill pipe in working state is shown in Figure 8, in which, high-speed aerosol enters the borehole bottom 6 through the inner cavity 1 of the drill pipe and the inner cavity 5 of the bit, driving rock debris to be discharged out of the borehole through the annular channel 4 formed

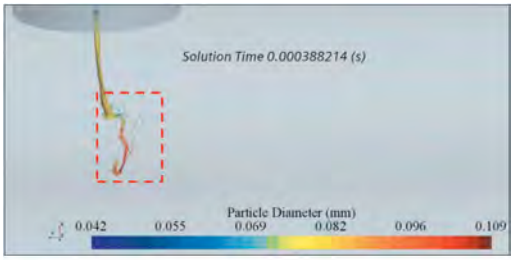

a Nephogram of atomized particle size-primary atomization

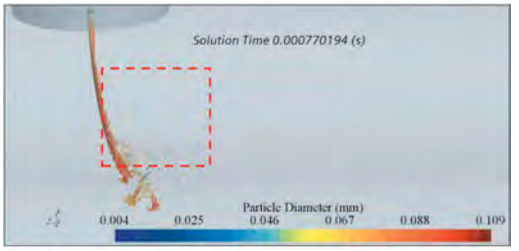

b Nephogram of atomized particle size-secondary atomization

Figure 7. Size nephogram of water vapor atomization particle.

by the outer wall 3 of the drill pipe and the inner wall 2 of the borehole. The gas-liquid-solid three-phase coupling is involved in aerosol deslagging, indicating that the ideal gas model can serve to deal with the flow of gas phase, the discrete multiphase model can deal with the mixing of water and mist and the discrete element model can deal with the motion of drilling cuttings particles. The gas and liquid phases are described by Eulerian method, and the granular phase is described by Lagrangian method.

1-inner cavity of drill pipe; 2-borehole wall; 3-outer wall of drill pipe; 4-annular channel; 5-drill bit; 6-borehole bottom

Figure 8. Schematic diagram of deslagging process of drill pipe.

4.1 *Geometric model and grid division*

The calculation model of drill pipe and the local scale-up grid model are shown in Figure 9. The length L1 of drill pipe is 4.5m, the diameter d1 of inner hole of drill pipe is 8mm, the outer diameter d2 of drill bit is 45mm, the inner diameter d3 of borehole is 49mm, and the drilling depth L2 is taken as 0.2m.

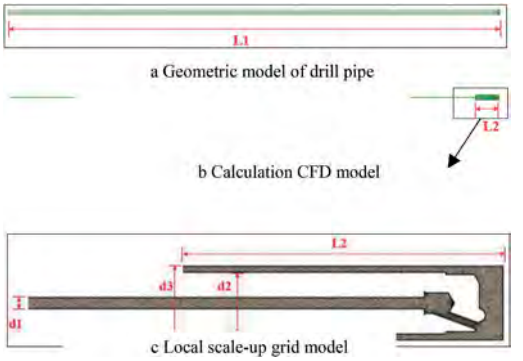

a Geometric model of drill pipe

b Calculation CFD model

c Local scale-up grid model

Figure 9. Calculation model of drill pipe.

4.2 *Boundary conditions*

The inlet boundary serves as the drill pipe inlet, which is a aerosol two-phase flow. With reference to the atomization simulation results, the average diameter of water mist particles is taken as 0.06 mm, with an deviation of ±0.05 mm, indicating that the diameter ranges from 0.01 mm to 0.1 mm, the volume fraction of water mist is 0.4%, and the corresponding volume flow rate is 1 L/min. The annular channel outlet adopts the pressure outlet boundary condition so that its pressure is atmospheric pressure. A particle injector is provided on the wall surface at the bottom of the borehole. Since the drilling speed is 3m/min, the rock debris generation rate is calculated as 0.2357kg/s, and the particle diameter is taken as 1mm. The material parameter settings are listed in Table 1.

4.3 *Analysis of coupling numerical simulation results*

4.3.1 *Analysis on sectional pressure loss of deslagging system*

The pressure loss of deslagging system can be divided into the pressure losses of drill pipe inner hole, drill bit inner hole, borehole bottom area and borehole annular channel by components, as shown in Figure 10, corresponding to the pressure losses of section AC, section CD, section DE and section EB respectively. The pressure loss in the bottom area of the borehole includes the pressure loss caused by the diffusion of airflow from the outlet of the drill bit hole at the bottom of the borehole, the pressure loss caused by the reverse direction of airflow when encountering the bottom of the borehole and the pressure loss resulting in the drilling cuttings acceleration.

Table 2 shows the pressure loss and proportion of each component of deslagging system under different drill pipe inlet pressures. It can be seen that in the aerosol deslagging system, the pressure loss of the inner hole of drill pipe accounts for the largest proportion, accounting for about 47%, due to the long length of drill pipe and the small diameter of inner hole. The proportion of pressure loss in the bit borehole and the

Table 1. Parameters of rock debris granular materials.

Object	Poisson's ratio	(kg/m^3) Density (kg/m^3)	Shear modulus (pa)	Collision recovery coefficient	Static friction coefficient	Rolling friction coefficient	Particle diameter (mm)
Debris particle model	0.29	2.5×10^3	1.48×10^{1}°	0.5	0.25	0.17	1mm

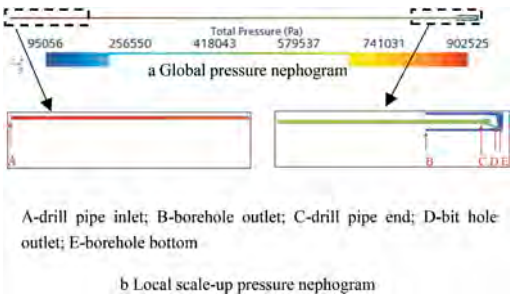

Figure 10. Pressure nephogram of deslagging system.

bottom area of the drill hole is equivalent, approx. 25%. The borehole annular channel has the smallest proportion of pressure loss, which is less than 3%.

Besides, as the inlet pressure of drill pipe decreases, the proportion of pressure loss in the inner hole of drill pipe and bit increases, while that in the bottom area of borehole and annular channel of borehole decreases.

4.3.2 *Analysis of critical deslagging pressure*

The velocity nephogram of debris particles under different deslagging pressures is shown in Figure 11. It can be seen that the velocity of debris particles in the annular channel decreases with the decrease of deslagging pressure. When the deslagging pressure is 10bar, 9bar and 7.5bar respectively, the debris particles are evenly distributed in the annular channel without occurrence of any particle deposition. Provided that the deslagging pressure drops to 5bar, all debris particles cannot be suspended in the airflow, but caused to deposit in the gravity direction, resulting in blockage of the annular channel, as shown by the box line in the figure. The average velocity curve of debris particles is shown in Figure 12. Provided that the deslagging pressure is 5bar, the average velocity of debris particles is only 0.2m/s, approaching stagnation, which will lead to particles accumulation in the annular channel. Where the deslagging pressure increases to 7.5bar or above, the average velocity of debris particles reaches more than 5m/s, ensuring that the particles can be discharged smoothly. Therefore, the critical pressure of aerosol deslagging is 7.5bar, and the corresponding volume flow rate in standard atmospheric state is 1,884L/min under the working condition of drilling speed at 3m/min.

The flow field velocity nephogram of the annular channel in the deslagging system is shown in Figure 13. It indicates that the maximum hole velocity in the drill bit is caused by the sudden change of hole area in the drill bit. By comparing the velocity nephograms under different deslagging pressures, it can be seen that with the decrease of deslagging pressure, the internal velocity and gas flow rate of the deslagging system also decrease accordingly. Since the drilling speed remains constant, the deslagging flow rate remains unchanged. According to the empirical formula $m=0.2396e^{\circ\cdot 235Va}$ for solid-gas ratio m and critical deslagging wind velocity Va, where solid-gas ratio m represents the ratio of mass flow rate of cuttings against air mass flow rate, and Va represents the critical deslagging wind velocity, so that the critical deslagging wind velocity under different deslagging pressures can be obtained[13]. The wind velocity V of the annular channel calculated by simulation is extracted for comparison, as shown in Table 3, indicating that when the deslagging pressure is 5bar, the critical deslagging wind velocity calculated by the formula is 18.9m/s and the wind velocity in the annular channel is 15.3m/s, which are less than the critical deslagging wind velocity, resulting in

Table 2. Pressure loss and proportion of components of deslagging system under different working conditions.

		Inner hole of drill pipe		Inner hole of drill bit		Bottom area of borehole		Annular channel of borehole	
P_A (bar)	Q (L/min)	Pressure loss (bar)	Proportion (%)	Pressure loss (bar)	Proportion (%)	Pressure loss (bar)	Proportion (%)	Pressure loss (bar)	Proportion (%)
10	2667	4.1	46	2.1	23	2.6	29	0.14	1.57
9	2228	3.7	47	1.9	23	2.2	28	0.17	2.14
7.5	1884	3.1	48	1.7	26	1.5	23	0.17	2.62
5	1286	2.1	54	1.2	30	0.6	15	0.07	1.76

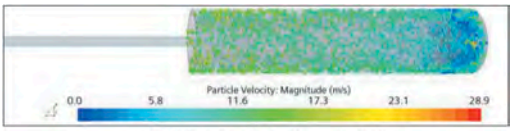

a Particle velocity nephogram -10 bar

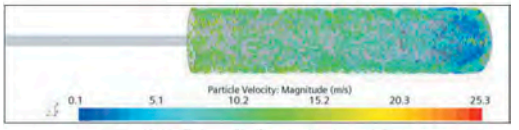

b Particle velocity nephogram -9 bar

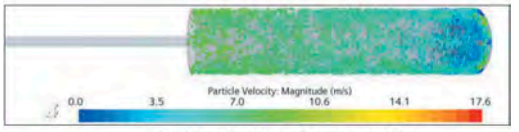

c Particle velocity nephogram -7.5 bar

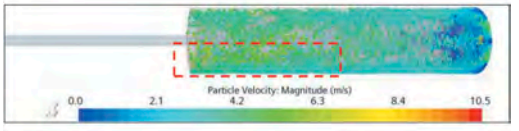

d Particle velocity nephogram-5 bar

Figure 11. Debris particle velocity nephogram under different deslagging pressures.

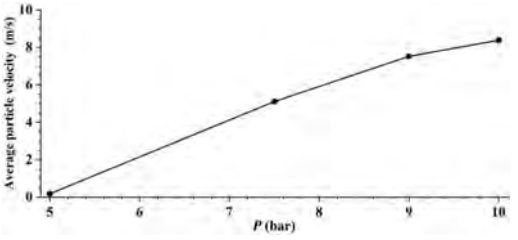

Figure 12. Average velocity curve of rock debris particles.

blockage in the annular channel. When the deslagging pressure is 7.5bar, 9bar and 10bar respectively, the wind velocity in the annular channel is greater than the critical deslagging velocity, indicating that the smooth discharge is expected, and the result obtained is consistent with the above results analyzed based on the debris particle velocity nephogram.

4.3.3 *Influence of water mist flow on deslagging performance*

The content of water mist in aerosol deslagging will produce certain influence on the deslagging performance. The gas velocity in the annular channel is obtained by simulation calculation under different

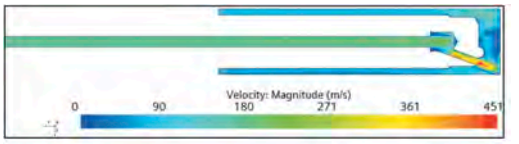

a Flow field velocity nephogram -10bar

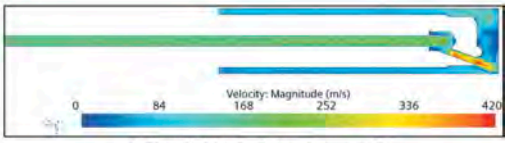

b Flow field velocity nephogram -9bar

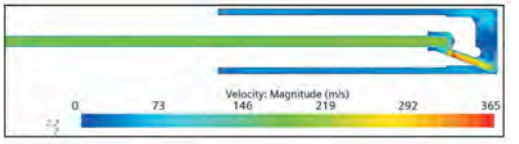

c Flow field velocity nephogram -7.5 bar

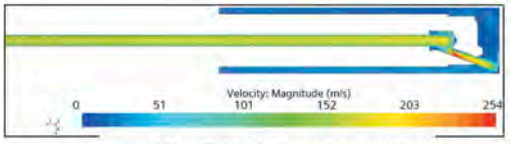

d Flow field velocity nephogram -5bar

Figure 13. Flow field velocity nephogram under different deslagging pressures.

Table 3. Critical deslagging velocity at different solid-gas ratio.

P/bar	Mass-solid(kg/s)	Mass-air(kg/s)	m	*Va*	*V*
5	0.2357	0.01253	18.9	18.9	15.3
7.5		0.02217	10.6	16.1	33.0
9		0.03633	6.5	14.0	54.1
10		0.04141	5.7	13.5	61.4

water mist flow rates at deslagging pressures of 10 bar and 7.5 bar, respectively, as shown in Figure 14. As shown by the figure, under the condition of constant deslagging pressure, the deslagging gas velocity in the annular channel decreases with the increase of water content. According to the above analysis that deslagging wind velocity is critical to the deslagging performance, the smaller the deslagging wind velocity, the more difficult it is to discharge slag, indicating that the increase of water mist flow is adverse to the deslagging effect.

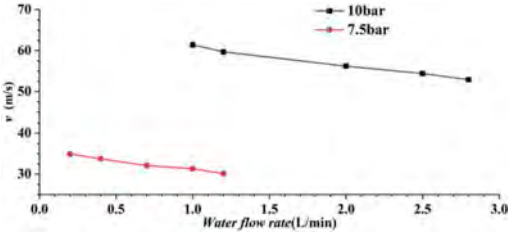

Figure 14. Velocity curve of deslagging gas under different water mist flow rates.

4.4 *Test validation*

The aerosol deslagging device is carried out on ZYS1133 wall drill jumbo for testing. The drilling object is precast cement pier, and the drilling distance of a single drill pipe is 4 m, which takes 3 min for drilling. The borehole deslagging test process is shown in Figure 15, and the drilling distances are 0.1m, 1m, 2m and 3m respectively. During the drilling process, the aerosol carrying the drilling cuttings is exhausted, so that the dust is kept under well control.

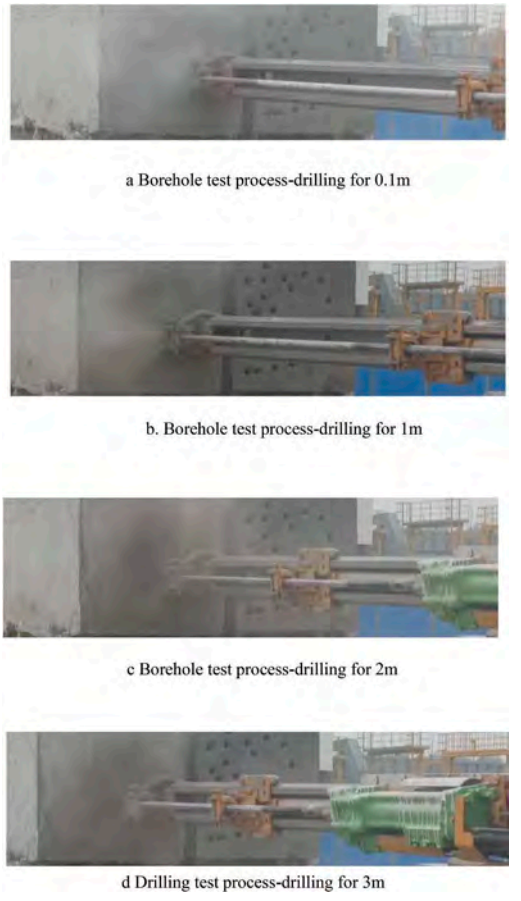

Figure 15. Field borehole deslagging test.

The test principle of aerosol deslagging is shown in Figure 16. First, the external atmosphere and external water enter the aerosol mixing block through the flowmeter and flow regulating valve respectively to crush and atomize the liquid droplets, thus generating HP airflow containing water mist that enters the bottom of the borehole through the inner hole of the drill pipe for deslagging. The test system has tested three effective parameters, including the flow rate of external water Q_{water}, the flow rate of external air before compression Q_{air} and the pressure P at the inlet of drill pipe.

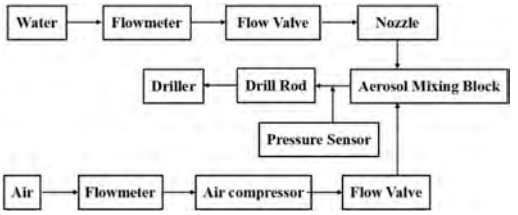

Figure 16. Test principle.

4.4.1 *Test for critical deslagging pressure*

The test data under different deslagging pressures are shown in Table 4. It can be seen that when the external water flow is 1L/min, the flow rate of external air is 2,570L/min and 1,810L/min respectively, without borehole blockage provided that the deslagging pressure is respectively 10bar and 7.5bar. The blockage in the borehole under the condition that the deslagging pressure is 5bar and the flow rate of external air is 1,350L/min indicates that the critical deslagging pressure is 7.5bar under such working condition, agreeing with the simulation results.

Table 4. Test data of critical deslagging pressure test.

P(bar)	Q_{water} (L/min)	Q_{air} (L/min)	Drilling jamming
10	1	2570	No
7.5	1	1810	No
5	1	1350	Yes

4.4.2 *Comparative analysis of test results and simulation under different water mist flow rates*

The influence of water mist flow rate on air flow rate under deslagging pressures of 10bar and 7.5bar is tested respectively for comparing with the simulation results. The deslagging gas flow rate decreases with the increase of moisture content in aerosol, and the simulated air flow rate is slightly greater than the measured value, as shown in Figure 17. The comparison of test and simulation values is shown in Table 5. Compared

with the measured data, the simulated value is greater, with an error within 5%, falling in the allowable engineering error range.

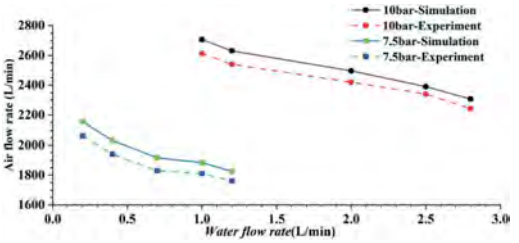

Figure 17. Comparison curve of deslagging gas flow between test and simulation.

Table 5. Comparison of deslagging gas volume under different water mist contents.

P(bar)	Q_{water} (L/min)	Q_{air} (L/min) Measured Value	Simulation Value	Errors
7.5	0.2	2063	2157	4.56%
	0.4	1940	2033	4.64%
	0.7	1830	1926	4.70%
	1	1810	1884	4.09%
	1.2	1761	1825	3.63%
10	1	2613	2706	3.56%
	1.2	2540	2631	3.58%
	2	2420	2496	3.14%
	2.5	2340	2390	2.14%
	2.8	2242	2307	2.90%

5 CONCLUSION

This paper has studied the aerosol deslagging process by combining numerical simulation and experiment:

1) In the aerosol deslagging system, the pressure loss in the inner hole of drill pipe accounts for the largest proportion (approx. 47%), the pressure loss in the inner hole of drill bit and the bottom area of borehole is equivalent, accounting for about 25%, and the pressure loss in the annular channel of borehole accounts for the smallest proportion (less than 3%).
2) When the moisture content of aerosol is 1L/min and the drilling speed is 3m/min, the critical drill pipe inlet pressure required for deslagging is 7.5bar, and the corresponding air flow rate for deslagging is 1,810L/min.
3) The air velocity for deslagging will decrease with the increase of water mist content. The increased content of water mist is adverse to the deslagging effect.
4) Through simulation of the working conditions under diverse water mist flows, the air flow at the inlet is extracted for comparison with the test results, with the obtained simulation error falling within 5%, which in turn validates the accuracy of the simulation.

REFERENCES

[1] Zhang Yuekun, Zhang Jianchao and Guo Wenwu. Large-scale Mechanical Equipment for Tunnel Drilling and Blasting Construction [J]. Engineering Machinery, 2018, 49(8):4–10,87.
[2] Hao Jinxin. Tunneling Construction Technology for Weak Surrounding Rock Tunnel Project [J]. Sichuan Building Materials, 2023, 49(5):138–140.
[3] Qiao Anzhen. Research on Drilling and Deslagging of Small Aperture Anchor Holes in the Floor of Deep Mine Roadways [D]. Jiaozuo: Henan Polytechnic University, 2017.
[4] Wang Yilong, Cai Feng, Zhao Qingquan and Wang Zongchao. Study on Simulation Test for Gas Lift Deslagging from Long Boreholes for Bedding Gas Extraction [J]. Coal Mine Safety, 2022.53 (10):184–190.
[5] Huber, Sommerfeld M. Modeling and numerical calculation of dilute-phase pneumatic conveying in pipe system [J]. Powder Technology, 1998, 99(1):90–101.
[6] Muscheknautz E, Wojahn H. Auslegung pneumatischer Förderanlagen[J]. Chemie Ingenieur Technik, 1974, 46(6):223–225.
[7] Matsumoto S, Kikuta M, Maeda S. Effect of particle size on the minimum transport velocity for horizontal pneumatic conveying of solids[J]. Journal of Chemical Engineering of Japan, 1977, 10 (4):273–279.
[8] Zhang Yu. Design of Anti-jamming Drill Pipe for Drilling in Soft Coal Seams [J]. Coal Safety, 2023, 42 (04):226–231.
[9] Li Jia. Research on Deslagging Mechanism and Drill Pipe Optimization of Mining Ribbed Drill Pipe [D]. Qingdao: Shandong University of Science and Technology, 2016.
[10] Niu Guoqing and Zhang Wei. Study on Critical Wind Velocity and Pressure Loss of Pneumatic Deslagging in Boreholes along Coal Seam [J]. China Safety Science Journal (CSSJ), 2013, 23(11):60–65.
[11] Wang Yonglong, Liu Chun, Sun Yuning, Song Weibin and Wang Zhenfeng. Study on Drilling Cuttings Migration Mechanism and Pore-forming Technology in Gas Extraction Borehole [J]. Journal of Safety and Environment, 2015, 15(04):89–93.
[12] Zhang Peng. Simulation Study on Hydrodynamic Characteristics and Control of Pneumatic Conveying of Granular Materials [D]. Hefei: Hefei University of Technology, 2003.
[13] Yang Yongliang, Li Zenghua, Gao Wenju and Pan Shangkun. Study on Simulation Experimental for Pneumatic Deslagging from Coal Seam Boreholes [J]. Journal of Mining and Safety Engineering, 2006, 23 (04):415–418.

Tunnelling for a Better Life – Yan, Celestino, Thewes & Eberhardt (Eds)
© 2024 The Author(s), ISBN 978-1-032-80042-4
Open Access: www.taylorfrancis.com, CC BY-NC-ND 4.0 license

Uninterrupted continuous forecasting in mechanized tunnelling in rock

Jozsef Hecht-Méndez*, Thomas Dickmann & Dirk Krueger
Amberg Technologies AG, Regensdorf, Switzerland

ABSTRACT: The history of seismic exploration in tunnelling began in the early 1990s and continues until today. Especially in mechanised tunnelling, technologies are advancing. Digital construction requires a digital ground model that must be adapted during the construction to reassess newly gained knowledge about the ground risk. In fast tunnelling with average daily rates of 20-30 metres, geological surprises must no longer play a significant role. The innovative TSP 603-Impact system ensures seismic exploration wirelessly in the TBM area. With TSP-Impact, a mechanical source rapidly transmits high-energy seismic waves from the TBM's shield into the rock mass, enabling a prediction range of 100 metres or more. Wireless transceivers convert the signals into digital data and send them to a tablet. This procedure is carried out at the end of each stroke of the TBM. Thus, reflection-seismic data from different spatial positions on a possible fault can be collected and analysed. Flexible and subsequent installation of the system in the TBM makes it independent and yet easy to operate. Once the data from 20 strokes has been collected, it can be uploaded to the cloud with a unique encrypted identifier for data protection. If no trained site personnel are available to process the data, the data can very quickly reach an authorised expert who will process it and return with a geological forecast after 2 to 3 hours. The 3-D velocity distributions of P- and S-waves can be surface rendered to focus particularly on anomalies characterised by low-velocity zones. A geological model of the predicted area completes the picture. This allows the size and extent of the anomaly to be determined, preventing the risk of failure and collapse in the tunnel with an accuracy of 85-90%. With such a TSP operation once a week, continuous geological prediction can ensure smooth tunnelling.

Keywords: TSP, In-tunnel seismics, geological characterization, risk mitigation

1 INTRODUCTION

During the last three decades, the use of seismic techniques for geological characterization in tunnelling has established as a suitable and reliable methodology. By integrating data obtained from in-tunnel seismic surveys with targeted probe drillings, the existing digital geological model can be improved by reassessing information about the rock mass condition as the excavation moves forward (Dickman et al., 2018). In-tunnel seismics can be applied in all types of tunnelling methods. However, in case of mechanized tunnelling in rock, some special requirements should be fulfilled to apply these techniques with minimum to no impact in the production cycle.

Modern mechanized tunnelling using Tunnel Boring Machines (TBMs) may achieve advance rates of up to 20-30 meters per day, or even more. These high advance rates pose challenges for geological investigations. Firstly, the excavation may reach hazardous zones without sufficient early warning. Secondly, the limited available time for geological investigations adds to the complexity.

Current TBMs are equipped with rigs for probe drilling the rock mass ahead while the TBM is in standstill. This process is commonly integrated in the project execution. In many cases, probe drilling is carried out on a regular basis, even if the geological baseline report does not indicate a hazard zone nor the rock composition does change. These boreholes are time-consuming and give a rather limited view of the dimension of the geological conditions ahead of the cutter wheel. In order to profit from in-tunnel seismics in the TBM environment, an execution with an uninterrupted production cycle becomes necessary. Moreover, due to the high advance rates, the prediction of the rock condition should cope with the speed of excavation. This challenge can only be met, and the process can only be appropriate to the TBM environment if rapid seismic data acquisition procedures and continuous interpretation and prediction for the job site are put in place.

2 TUNNEL SEISMIC PREDICTION (TSP)

The TSP method is based on the principle of reflection seismics. It is used to image the structural features of the surrounding rock from inside the tunnel by excitation, reception and evaluation of elastic

*Corresponding author: jhecht@amberg.ch

DOI: 10.1201/9781003495505-69

body waves. The method requires a controlled seismic source, which usually consists of small explosive charges in conventional tunnelling. They are blasted in 1.5 m deep boreholes drilled into a tunnel wall. As a rule, 24 boreholes are used (Figure 1).

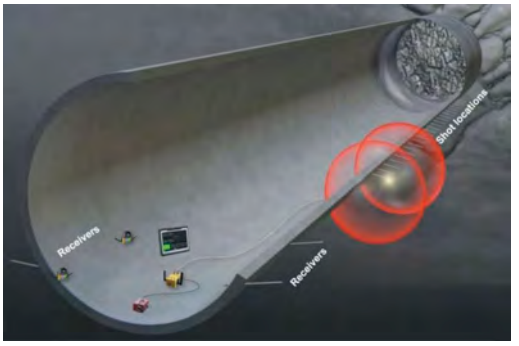

Figure 1. Schematic visualisation of a standard TSP layout in conventional tunnelling.

The wavefronts initiated by the blasts are travelling through the ground as compressional or P-waves and as shear or S-waves. They are partially reflected at and partially transmitted through interfaces of different physical properties. The wave and its type are measured with 3-component sensors (accelerometers) installed on both tunnel walls, commonly 4 receivers. By capturing the reflected elastic waves and their corresponding travel time, information about the rock mechanical parameters of the ground can be derived and important technical parameters such as the dynamic Young's modulus (Edyn), Poisson's ratio, shear modulus and bulk modulus can be determined.

2.1 *TSP 603-Impact system*

The TSP 603-Impact system comprises two main elements. One is the TSP 603 wireless system that acquires and processes seismic data in the tunnel. The other is the TSP-Impact as a seismic wave source. The TSP 603 wireless system includes special transceivers which convert the analogue signal picked up by the sensors installed in the rock mass into digital data achieving microsecond accuracy of sync among the transceivers. The data is then transferred to a field tablet where it can be immediately visualised for quality control. The use of wireless transceivers enables easier and safer operation of the TSP system in the TBM environment. At the same time, the use of more receivers/transceivers ensures higher data density. The receivers are additionally equipped with an electronic compass sensor (MEMS) to detect and measure the precise spatial position of the 3-component accelerometers once installed (Figure 2).

The TSP-Impact is a pneumatically driven impact hammer, which has been specially designed for the high-energy excitation of seismic waves in the underground. It replaces the use of explosives as a seismic wave generator and saves the drill holes where the small explosive charges were otherwise detonated. This means an enormous advantage for TBM tunnelling. For its operation, the controlled impact hammer source simply needs a mains power supply of 230V and compressed air supply of 7 bar. The impact hammer can be easily installed into a TBM's framework.

Figure 2. Two TSP 603 wireless transceivers attached to TSP receivers deployed 1.5 m deep in boreholes through the grout hole of precast segments.

Figure 3. Controlled impact hammer of TSP-Impact. The impact cylinder, in which the impact mass is accelerated, is coupled to the lateral rock wall through an opening in the TBM's shield shell by the feed cylinder below.

The hammer can be mounted directly on the framework of the TBM or on a bracket. In any case, a minimum clearance for proper operation of the hammer is necessary. It must be ensured that the hammer's impact cylinder can couple to the bare rock wall through an opening in the TBM's shield

(Figure 3). Once the hammer is mounted, it remains there for the duration of the complete excavation or exploration section.

The hammer works according to the Stretch-Shot-Relax pattern once the TBM has completed its stroke and come to a stop. From its rest position it stretches into the striking position up to the lateral rock wall, where its impact head is prestressed to the rock mass (Stretch). In the striking position, the impact mass is accelerated inside the cylinder and hammers against the prestressed impact head (Shot). 3 to 8 shots are taken in the same place, each recorded individually. The digital data traces of the repetitions at the same point are later vertically stacked to improve the signal-to-noise ratio. The nominal energy of each shot is about 130 Joule. With help of an intelligent routine, the user can evaluate the data quality after each shot and finish the data acquisition at this position. Next, the hammer is decoupled from the tunnel wall (Relax). The entire Stretch-Shot-Relax procedure takes maximum five minutes, while it is completely operated and controlled remotely from a field tablet using a dedicated data acquisition and control software.

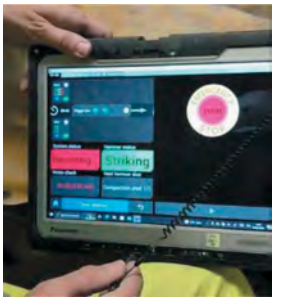

Figure 4. Easy to use data acquisition and control software on a field tablet.

2.2 *The seismic source – Explosives vs TSP-Impact*

With TSP, the seismic waves must be generated by a point source. Both, explosives, and TSP-Impact satisfy this requirement. However, the energy transferred by the explosives to the media is larger. Repeated hammer blows on the same spot help indirectly increase the energy transferred to the ground. The difference in energy leads to a more rapid attenuation of the waves as they pass through the medium, so that the penetration depth is lower when using TSP-Impact. When using TSP-Impact, prediction ranges of up to 100 m ahead of the face can be achieved, while up to 250 m are possible when using explosives.

Another difference is the signal bandwidth. Normally, explosives have a wider bandwidth from 100 Hz to 3,000 Hz, whereas with TSP-Impact the bandwidth can be between 100 Hz and 1,750 Hz. The frequency range of the useful signal has a major influence on the spatial resolution. The higher the prevailing frequency, the higher the resolution, i.e., the ability to identify successive reflectors depending on the wavelength.

Figure 5 shows the amplitude spectrum of data recorded with explosives and TSP-Impact (left and right, respectively) with the same receiver at the same location in Switzerland's Hagerbach Test Gallery. Here, the lithology consists of competent schist. The bandwidths of the significant signals are 100 - 1,150 Hz and 100 - 850 Hz, respectively, with most of the energy around 500 Hz for both source types. Given the anelastic attenuation or absorption of seismic waves, the high frequency component of the signal generated by explosives may be rapidly attenuated by the medium, so the signal frequency of reflections from distant areas (e.g. > 20 - 50 m from the face) is likely to be in a similar range, i.e. 100 - 250 Hz. Therefore, a similar spatial resolution can be expected for both data sets, resulting in very similar results.

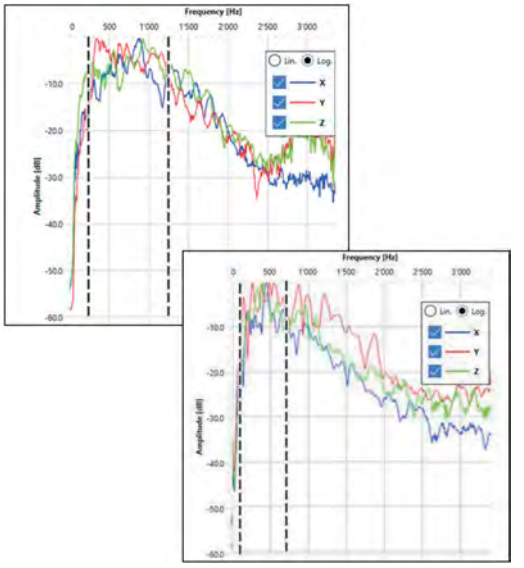

Figure 5. Amplitude spectrum, left: explosive; right: TSP-Impact.

2.3 *Uninterrupted data acquisition and processing*

To fully integrate geological prediction into mechanised tunnelling, the deployment of the measurement system and data acquisition must be carried out quickly so that the tunnelling cycle is not delayed. The use of a pneumatic impact hammer not only fulfils time and safety requirements, but also the demands for efficiency and prediction quality. Full integration of the system into the production cycle is achieved by installing the receivers at a specific location and using the TSP impact hammer during short breaks between each stroke (Figure 6). After a number of shot points have been recorded, the back receivers can be moved

forward in a roll-along fashion. This continuous use of the hammer in short breaks after each stroke always ensures a consistent geological prediction. Any downtime is reduced to a minimum.

As soon as twenty shot points have been recorded, the data can be sent to the processing centre via the cloud. Processing takes place immediately so that initial results are quickly available. If further data is collected at more shot points, it can be sent for processing and merged with previous data. In this way, the results are constantly regenerated, and the accuracy of the results is continuously improved.

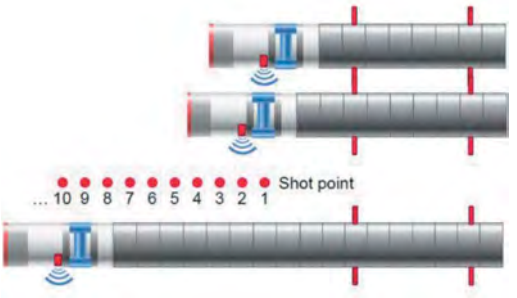

Figure 6. Continuous data recording using TSP-Impact.

3 THE USE OF TSP 603-IMPACT IN THE RISHIKESH – KARNAPRAYAG RAILWAY LINE PROJECT

3.1 *Project description*

The Rishikesh - Karnaprayag Railway Line Project is a 125 km single-track railway line under construction in the Uttarakhand state of India (Figure 7). The project was commissioned by the national enterprise Rail Vikas Nigam Limited (RVNL) and it comprises the construction of 17 tunnels, 35 bridges and 12 stations. Tunnel Package 4 includes the excavation of two main tunnels of about 15 km and an escape tunnel of 0.7 km. 10.5 km of tunnels are currently under construction by two single shield TBMs for hard rock with a 9.1 m diameter each. The construction work is done by the Indian contractor Larsen and Toubro.

Figure 7. Project location overview.

3.2 *Campaign selection and local geology*

To date, more than 25 TSP campaigns have been carried out with the impact hammer source. The TSP hammer was installed in a special niche behind the TBM shield (see Figure 3). In this article, campaigns no. 7 and no. 8 are selected for further discussion. The face positions of those campaigns are at chainage 49,376 m and 49,445, respectively.

According to the Geotechnical Baseline Report and previous field work, a sheared/fault zone was expected along these chainages. The rock mass rating was estimated at RMR< 20 resulting in rock mass class V.

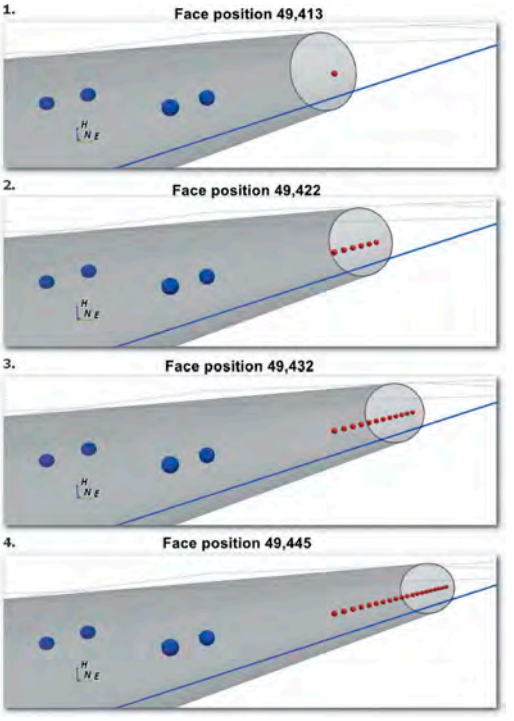

Figure 8. Tunnel model at 4 different face positions. Blue and red dots are receivers and shot points, respectively.

The inspection of the tunnel face during the excavation, which was carried out at two different stations before the problematic zones were encountered, revealed that it was a highly jointed and slightly weathered quartzite phyllite with strong to medium strength.

3.3 *Tunnel definition in Amberg TSP Ease software*

The TSP software makes it possible to take into account both planning information and the current tunnelling status. As soon as the tunnel axis has been entered in project coordinates, the tunnel model can be defined. Data acquisition begins at a specific position with the first blow of the hammer. The impact position refers to the current position of the tunnel face. Figure 8 shows the tunnel model in various positions of the tunnel face as the TBM moves forward.

After each TBM stroke of 1.7 metres, the next shot position is reached and the impact source can be coupled and seismic data recording proceeds. As segments are installed by the TBM or other tasks are carried out between each lift, seismic data acquisition does not cause any additional downtime, which means that the geological investigations are fully integrated into the production cycle.

3.4 *Results*

Seismic results can be obtained as tables, charts, and 2D/3D figures. Figure 9 shows the property charts of the seismic P- and S-wave velocities, Vp and Vs, respectively, and dynamic Young's Modulus (Edyn) of campaign #7. The position and the extent of the changes in the individual parameters are determined by the spatial position of the reflectors extracted by the software. The seismic reflectors correspond to boundaries at which a high acoustic impedance contrast exists. Hence, a large part of the wave energy was reflected to the receivers. The plane representing the boundary intersects with the tunnel axis. This correspond to the position where the change is expected along the prediction range. Decreasing values in seismic velocities or in the elastic parameters are commonly associated to weakness zones were for instance increasing fracturing, fault zones, cavities or any unfavourable ground condition might be expected.

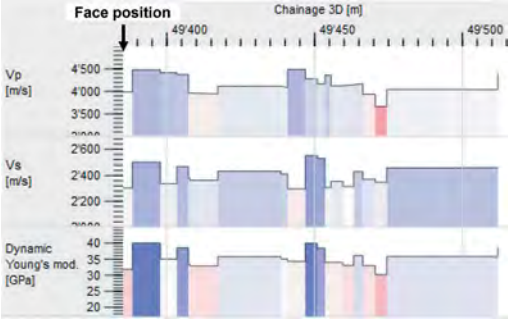

Figure 9. P and S-wave velocities and dynamic Young's modulus of campaign #7.

Figure 10 depicts longitudinal and horizontal planes from the 3D models of the Vp distribution for campaigns #7 and #8, top and bottom, respectively. On the upper part of each figure, Edyn charts are shown indicating the changes in GPa of the modulus. In campaign #7, Edyn values between 35 and 40 GPa dominate throughout most of the model. These values are related to the medium strong rock mass. Two anomalies in the velocity field are observed at the left-hand side of the tunnel axis, starting around 19 m from the axis, and extending for about 20 m, laterally. The reflectors defining the start of these two zones intercept the axis at chainage CH 49,407 and 49,466. The second anomaly has the lowest Vp and Edyn values: 3,630 m/s and 30 GPa, respectively. Lower Edyn values are associated with decrease in rock mass stiffness due to increasing fracturing, fault zones, etc.

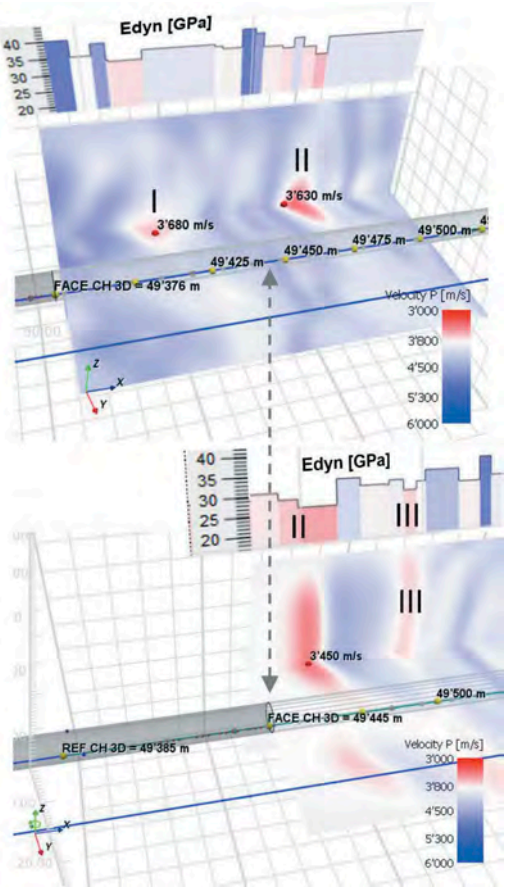

Figure 10. Longitudinal and horizontal 2D sections extracted from the 3D model of the Vp distribution. Top: campaign #7, bottom: campaign #8. On top of each figure, charts of Edyn variation in GPa are superimposed along the prediction range.

Campaign #8 was performed after 69 m excavation ahead of campaign #7, partially overlapping the prediction range of that campaign and shortly before the probable occurrence of the second anomaly. The result of campaign #8 not only confirmed the existence of a weak zone at the same location, but also enabled a more precise visualisation of the spatial distribution of the anomaly. According to the new result, the weakness zone reaches the tunnel section, and its influence area is two times larger at the tunnel level, 16 m instead of 8 m. The latter is based on the interception of the reflectors with the tunnel axis. Velocity and elastic values are slightly lower, Vp= 3,450 m/s and Edyn= 27 GPa.

Figure 11 shows the correlation between the TBM Contact Force (CF) and Edyn values obtained from Campaign #7 and #8 between chainages CH 49,440 and CH 49,500, approximately. According to the construction site personnel, CF has become an important parameter that allows conclusions to be drawn about the quality of the rock mass. Dropping

CF is an indicator of decreasing rock mass quality. For instance, CF < 4,000 KN is well correlated with poor rock mass. The lower the CF, the poorer the rock mass. In turn, increasing CF values are then associated with a rock mass of higher quality.

Along the selected chainages, the most significant CF drop is observed between CH 49,468 and CH 49,480, with CF values < 3,000 KN. This zone is in good agreement with the velocity anomaly (II) observed in the results of both TSP campaigns covering these chainages. Outside from this section, CF values > 4,000 KN dominate. Edyn values are in good agreement along most of the depicted section. However, in campaign #7 some opposite trend is observed between CH 49,452 and CH 49,464. Since this section lies in the far-field forecast of campaign #7 and is obviously embedded between two strong reflectors, one of which has a significant Edyn rise at around CH 49,446 and the largest drop from CH 49,466, sufficient resolution was not achieved to obtain reflectors that would better match this section. In fact, the influence of anomaly II can already distort the result for earlier chainages.

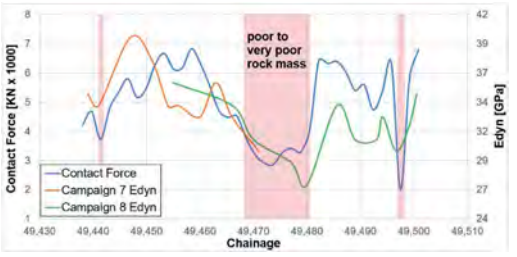

Figure 11. Diagram of TBM Contact Force versus Edyn as per Campaign #7 and #8 along selected chainages.

4 CONCLUSIONS

The new mechanised seismic source overcomes the current challenges posed by TBM tunnelling, namely the immediate identification of hazard zones and data acquisition without disrupting the production cycle and without downtime.

The percussion hammer is suitable for tunnelling with TBMs. It enables fast data acquisition during TBM stops for other activities.

In the present case study, critical areas such as shear/fault zones according to the GBR have not yet been encountered. However, areas with low to very low rock strength were encountered in these sections. These zones were correctly identified in various seismic campaigns and in some cases in exploratory boreholes and confirmed by the parameters logged by the TBM.

The information obtained from probe drills did not always match the TBM parameters, as was the case in some seismic campaigns, mainly due to the low to very low data quality.

Although much less energy is released into the ground with the impact hammer compared to explosives, sufficient spatial resolution is still achieved to identify geological structures that could be unfavourable for excavation. The penetration depth is naturally affected by this. However, this disadvantage is compensated for by uninterrupted data acquisition. This was demonstrated by the results of the two seismic measurements presented in this article. The first campaign made it possible to identify a possible weak zone in the far field about 90 metres before hitting it. In the subsequent campaign, which was carried out after about 70 metres of excavation, the weak zones were confirmed. The results of the second seismic campaign clarify the spatial extent and arrangement of this zone much better.

The TBM parameters, especially the contact force, corresponded well with the predicted zone of weakness.

ACKNOWLEDGMENTS

The authors would like to thank the site team of the contractor Larsen and Toubro, who actively supported the use of the TSP 603-Impact System in the Package 4 lot. The readiness for continuous operational use is in place and is also supported by the client RVNL.

REFERENCES

Dickmann, T., Krueger, D., Hecht-Méndez, J., 2018. Optimization of Tunnel Seismic operations for fast and continuous investigations ahead of the face. Proceedings of the ITA-AITES World Tunnel Congress (WTC) 2018 and 44th General Assembly Dubai, UAE 21-26 April 2018.

Tunnelling for a Better Life – Yan, Celestino, Thewes & Eberhardt (Eds)
© 2024 The Author(s), ISBN 978-1-032-80042-4
Open Access: www.taylorfrancis.com, CC BY-NC-ND 4.0 license

Limits on the estimation of the EPB face pressure. A concrete example based on Kalman filter approach

Cosimo Iasiello & Alberto Flor*
Systra-SWS, Trento, Italy

Paolo Fantini
Systra-SWS, Turin, Italy

ABSTRACT: The estimation of face pressure in urban tunnelling is a challenging task due to the complex geotechnical conditions and the need to protect existing infrastructures. This paper proposes a methodology to correct the geotechnical parameters (soil cohesion and friction angle) based on the measured pressure applied by the tunnel boring machine (TBM). The methodology is applied to a real case study of a 4 km tunnel excavated in soft soils in Paris. The results show that the proposed methodology can be used to calibrate the ranges of values for TBM face pressure and to provide possible design countermeasures despite the obvious discrepancies between the estimated and measured face pressures. These discrepancies can be attributed to the inherent complexity of TBM follow-up engineering in urban settings, where engineering decisions, predictions from analytical models, and contingent requirements may be incomparable.

Keywords: Tunnelling, TBM, Performance prediction, Face pressure, Kalman Filter

1 INTRODUCTION

In many cases, the excavation of urban tunnels has to deal with low overburden, soft soils, productive groundwater tables, and pre-existing or future constructions inside its geotechnical zone of influence. The envelope of these constraints results in the current adoption of closed mode tunnel boring machines (TBM) capable of managing the external geotechnical condition by the application of a confinement pressure at the face, as shown in Leca et al (2007), Zizka et al. (2016), and AFTES (2018). Moreover, in urban areas, where EPB are employed, the face pressure plays a fundamental role to control the surface settlements and possible problems on the existing infrastructures, in particular buildings.

The estimation of the face pressure, during the design stage is based on the geotechnical parameters, employing analytical or numerical models. In most cases the estimation of the geotechnical parameters is quite difficult and a small change in loads could lead to have different settlement estimations. During the construction, the face pressure is continuously monitored, normally referring the value to the tunnel crown, and compared with the designed value.

The aim of this paper is to:

- discuss a methodology to estimate the possible variation of the geotechnical parameters that play a fundamental role in the face pressure estimation based on the analytical formulation proposed.
- Apply the methodology to a real case, in order to assess the buoyancy and the limits of the findings and to establish also the possible variation of the parameters compared with the observed ones.
- Employ the so-called Unscented Kalman Filter (UKF) approach taking as reference the Face Pressure measured during the TBM tunnel execution.

The limits of this statistical method are then analysed.

2 DATASET AND METHODOLOGY

The real data used for comparison with the statistical models belong to an urban excavation for the city of Paris.

The utilized dataset comprises of all the TBM execution parameters, aggregated per lining ring, together with geomechanical information of the ground.

*Corresponding author: aflor@systra.com

DOI: 10.1201/9781003495505-70

The total number of rings is 2223 and the total length of the tunnel is approximately 4 km, with a cover of 15 meters on average, with minimum cover of 7 m and maximum cover of 21 meters.

The design confinement face pressure was evaluated along the alignment in an iterative way, as the minimum allowed pressure that guarantees tunnel face stability, contrast to waterhead in the chamber, and limitation of induced effects on pre-existing structures. Moreover, given the undrained behavior of the excavated soils, the confinement pressure also limits the insurgence of excess pore pressures and long-term subsidence induced by their consolidation.

The design process started with the assessment of the admissible volume loss every 20 m.

The confinement pressure was estimated according to this volume loss. The design pressure profile was then smoothened to obtain a constant value stretching on less than 75 m and a gradual pressure transition.

3 METHODOLOGY

In this work we propose a methodology that aims to correct the geotechnical parameters (soil cohesion and friction angle) based on the measured pressure applied by the TBM.

In the following paragraphs, the data of the already completed excavation are used to investigate the limits of validity of the proposed methodology. The discussion is a critical review of the effective application in an under-construction project.

The methodology process starts with the assessment of the admissible face pressure in undrained conditions. For this reason, the formula collected in Broms (1967) was used to establish the face design:

$$N = \frac{\sigma_s + \gamma h - \sigma_T}{c_u} \qquad (1)$$

where:

N= stability number (minor than 2 to keep the deformations in the elastic field)

γ= Soil unit weight

h= tunnel cover

σ_s= is the surcharge on the top of the ground

σ_t= is the face EPB face pressure

c_u= undrained cohesion

Figure *1* shows the distribution of the face pressure according to Equation (1). It is possible to see the formula seems to have a quite good fit with the measured values for the first 1000 rings but does not show a good trend for the last 1000 rings aproximately. For this reason, the application of the approach based on drained parameters was considered as well, employing the analytical formula collected in Kolymbas (1998) with approach shown in Amemiya et al. (2014).

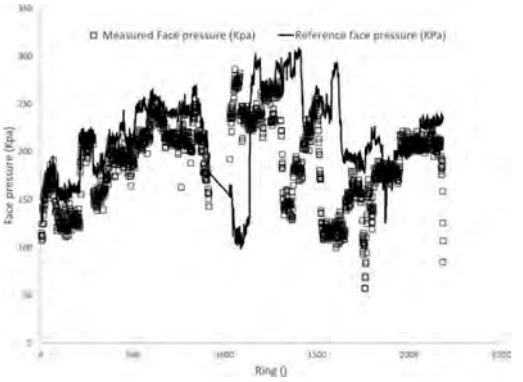

Figure 1. Distribution of the face pressure vs measured along the alignment for undrained parameters.

The approach employed in this paper for the estimation of the face pressure is shown in equation (2).

$$pf = \alpha \left(\frac{\gamma h}{tg\ (45 + \frac{\varphi}{2})} + \ c\ k_p \right) \qquad (2)$$

where:

- pf is the applied face pressure,
- γ is the soil unit weight,
- h is the cover from the tunnel crown,
- c is the cohesion,
- φ is the friction angle.
- Kp is the passive earth coefficient
- α is a coefficient between 0.5 and 1.0.

By employing Equation (2), one can model in a very simple but effective manner both the soil properties (with c and φ) and the human factor (coefficient α). The proposed formula for the estimation of the front pressure could be further expanded to better reflect the different agents. In this simplest form it allows nonetheless to take into account choices that may not be dictated by calculations (for instance Client demands related to other factors).

The proposed procedure consists of three iterative steps:

1. Estimation of reference face pressure based on the Equation (2).
2. Variation of the values for the alfa factor, cohesion and friction angle and comparison with measured value.
3. Prediction of the new value of face pressure.

This methodology allows to calibrate the ranges of values for TBM face pressure and, so provide the possible designed countermeasures. For example, depending on the geological conditions, it is possible to vary the face pressure between lower and upper values.

4 KALMAN FILTER METHODOLOGY

The Kalman Filter is a mathematical tool for finding the best estimate for the state of a system in a discrete time process that is assumed as a linear stochastic differential equation (Salimi et al. (2016)). Following the approach of Innaurato (2001) we could consider the following discrete nonlinear time system:

$$x_{k+1} = f(x_k) + w_k \tag{3}$$

$$y_k = h(x_k) + v_k \tag{4}$$

Where $k \in \mathbb{R}$ labels the discrete timesteps, $x_k \in \mathbb{R}^{n_x}$ is the unknown state of the system and $y_k \in \mathbb{R}^{n_y}$ corresponds to the output data. In this paper $x_k$are:

- c_k: estimated cohesion;
- φ_k : estimated friction angle;
- α_k: estimated value of alfa.

Whereas y_k are the observed EPB face pressure values.

In order to provide an adequate initial model, all previous information on the input parameters x_k must be assessed. This previous information will come with an associated error of modelling w_k that can be represented probabilistically by means of a multivariable Gaussian probability density function with zero mean and covariance matrix Q_k.

On the other hand, the error related to face pressure values (v_k) is usually given by the manufacturer of the TBM, so it also turns out to be an independent and Gaussian random variable, with zero mean and covariance matrix R_k. The nonlinear functions f and h represent the dynamic process and the measurement model, respectively. The estimation of the state consists in elaborating an outlook of x_k employing y_k for each time k. For this reason, the interest of the user should be focused on obtaining the probability distribution function (PDF) of x_k conditioned to y_k or, in other words, the probability of reproducing the observed measurements (TBM face pressure) with a particular set of input parameters. The probability of a parameter set given the observations is:

$$p(x_k|\mathbb{Y}_{k-1}) = \int p(x_k|x_{k-1})p(x_{k-1}|\mathbb{Y}_{k-1})dx_{k-1} \tag{5}$$

The application of the Bayes Theorem to the observations leads to the updated equation of the parameters set, which is:

$$\mathrm{p}(x_k|\mathbb{Y}_k) = \frac{p(y_k|x_k)p(x_k|\mathbb{Y}_{k-1})}{p(y_k|\mathbb{Y}_{k-1})} \tag{6}$$

Where:

$p(x_k|Y_k)$ is the probability of a certain estimation for the set of geotechnical parameters given the observed measures. This term is also known as the a-posteriori PDF.

$p(y_k|x_k)$ is the probability of computing the observed measures through the application Equation (2) given a certain set of geotechnical parameters.

$p(x_k|Y_{k-1})$ is the probability of a certain estimation for the set of geotechnical parameters given the previous observed measures. This term is also known as a-priori probability.

$p(y_k|Y_{k-1})$ in Equation (6) is the normalised probability or so-called scale factor so the $p(x_k|Y_k)$ could be between 0 and 1.

In this way expressions (5) and (6) represent the fundamental estimation of the Bayesian system of the Equations (3) and (4) depending on time k. The approach is depicted schematically below:

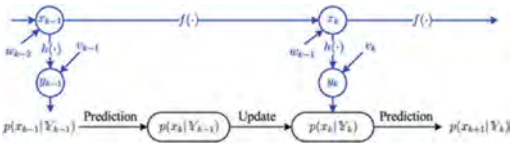

Figure 2. Principles of Bayesian Filter.

However, Equations (5) and (6) cannot be used in a simple way to find the PDF of a random vector belonging to a very nonlinear system, since a computationally demanding random sample simulation procedure must be adopted. This issue can be addressed by using the first two statistical moments (mean and covariance) of a Gaussian probability density function assumed for the parameter vector x_k. This procedure then aims for finding the PDF of the parameter's estimation. In this case the search problem is easier to solve by implementing the approach previously mentioned, with the unknown parameter standing for x_k at time k. The new equations (5) and (6) can be expressed in terms of the Kalman filter as the predictions:

$$\hat{x}(k|k-1) = E[(f(x_{k-1}|\mathbb{Y}_{k-1})] \tag{7}$$

$$P^x_{(k|k-1)} = Cov[(f(x_{k-1}|\mathbb{Y}_{k-1})] + Q \tag{8}$$

and the updated formulation can be expressed as:

$$\hat{y}(k|k-1) = E[(h(x_k)|\mathbb{Y}_{k-1})] \tag{9}$$

$$P^y_{(k|k-1)} = Cov[(x_k|\mathbb{Y}_{k-1})] + R \tag{10}$$

$$P^{xy}_{(k|k-1)} = Cov[x_k, (h(x_k)|(\mathbb{Y}_{k-1})] \tag{11}$$

$$\hat{x}(k|k) = \hat{x}(k|k-1) + P^{xy}_{(k|k-1)}(P^{y}_{(k|k-1)})^{-1}(y_k - \hat{y}(k|k-1)) \tag{12}$$

$$\hat{x}(k|k) = \hat{x}(k|k-1) + P^{xy}_{(k|k-1)}(P^{y}_{(k|k-1)})^{-1}(y_k - \hat{y}(k|k-1)) \tag{13}$$

As shown in Figure 3, the Kalman filter employs a recursive prediction-update procedure to obtain the mean and covariance of x_k from measurements. Equations (9)-(13) show how this implementation depends on the determination of the mean and covariance of the random state vector through the nonlinear functions f (·) and h (·).

Figure 3. Principle of Kalman Filter technique.

Nonlinear systems, such as those commonly encountered in geotechnical engineering, present a challenge for state estimation. However, significant research has been conducted in recent years, leading to the development of various Kalman Filter algorithms for nonlinear systems. Three of the most prominent algorithms are the Extended Kalman Filter (EKF), the Unscented Kalman Filter (UKF), and the Ensemble Kalman Filter (EnKF).

In this work, we use the UKF, which is a variant of the Kalman Filter that employs the Unscented Transform (UT) to propagate the state distribution through the nonlinear system (see for instance Julier (2004)).

The UT uses a set of deterministically chosen sigma points to represent the mean and covariance of the state distribution. These sigma points are propagated through the nonlinear system, and the resulting mean and covariance are calculated using a weighted average. To generate the sigma points, we consider the initial mean and covariance of the state distribution (red ellipse in Figure 4). The sigma points are then propagated through the nonlinear system to obtain a new set of points, which are used to calculate the mean (the "star" point at the right of Figure 4) and covariance (ellipse in Figure 4) of the transformed state distribution.The UKF is applied to both the prediction and update steps of the Kalman Filter algorithm. In the prediction step, the UKF is used to propagate the state distribution through the nonlinear process function f. In the update step, the UKF is used to update the state distribution based on the nonlinear measurement function h.

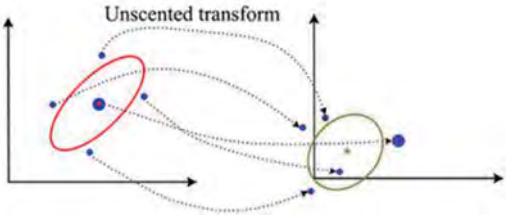

Figure 4. Uhlmann unscented transformation based on reference Julier (2004).

5 LIMITATIONS

The main drawback of the method is the assumption of normal distribution for the coefficients and the noise on the measured quantity (pressure) being white noise.

In practice both these assumptions are wrong since:

- Human intervention dictates the effective choice of TBM face pressure, be it because of buildings on the surface or other criteria.
- The encountered soil properties do not follow a normal distribution, as shown in Figure 5.

As an example, by looking at the design phase information of the soil cohesion, Figure 5, it is obvious that that the Normal distribution built on the parameters calculated on the samplings (mean and standard deviation, with amplitude proportional to the histogram area) and the normal distribution fitted on the data (amplitude, mean and standard as free parameters) are very different .

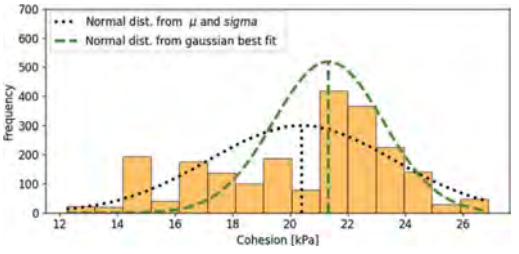

Figure 5. Distribution of designed values of cohesion.

On the other hand, the distribution of friction angle values shows that both the normal distributions (the optimized one and the one constructed with the original distribution parameters) (Figure 6). This means that the gaussian approximation is still valid for the friction angle.

6 RESULTS

Despite the limitation described in the previous paragraph, reference (the value applied during excavation) and estimated values for pressure are in good accord, see Figure 7.

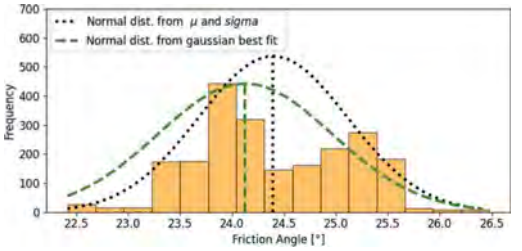

Figure 6. Distribution of designed values of friction angle.

The main difference between the two sets of data is in the extreme values (both low and high). These differences are not of significant interest, as they are not due to limitations of the methodology, but to specific field conditions.

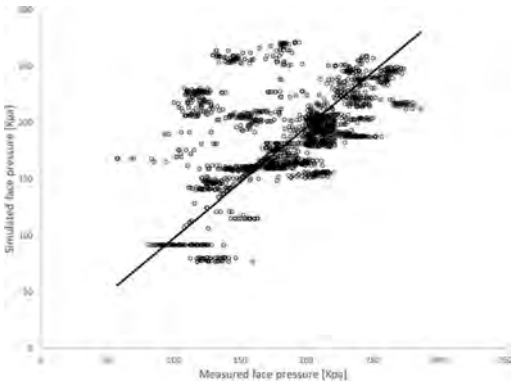

Figure 7. Correlation between measured and simulated face pressure.

Figure 8 shows the comparison between the reference face pressure and the estimated one where the small differences are always within the prescription established by the designer in terms of lower and upper threshold which normally are within a tolerance of +/- 0.2-0.3 bar i.e. the natural pressure oscillation in the chamber of an EPB type TBM.

Figure 9 shows the absolute error expressed in % between the simulated and the measured face pressure values; it is possible to see how the majority of the values are within the 50 KPa which is the value normally recommended in the engineering practice. The absolute error is about zero for the first 200 rings approximately with some peaks between rings 1000 and 1800. These differences are due to particular conditions of EPB advancing with lower pressure in order not to damage the existing structures as it was a Client's requirement, and they could not be efficiently considered in a mathematical forecasting model.

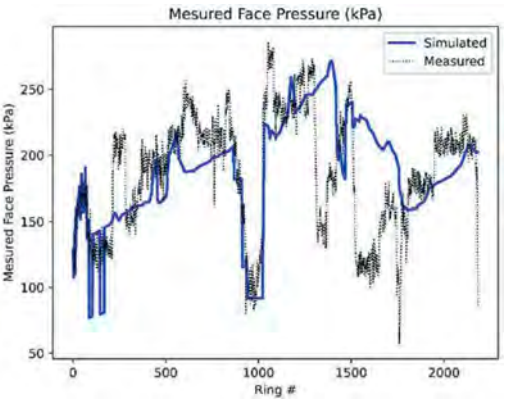

Figure 8. Correlation between measured and simulated for all rings.

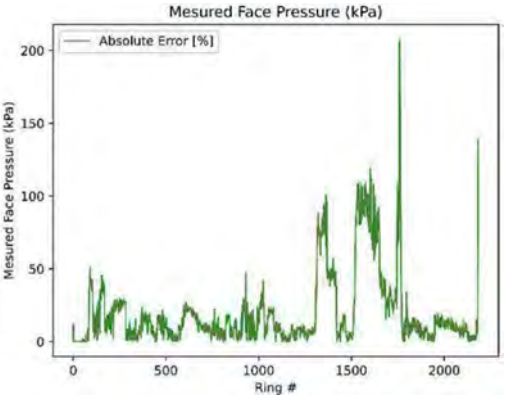

Figure 9. Measured face pressure absolute error (%) depending on the studied ring.

7 CONCLUSIONS

From the above considerations, the following conclusions can be drawn:

- The estimation of the TBM face pressure during the design stage is very important to efficiently forecast volume loss and hence the settlements onto the existing structures. The most employed methods are the analytical formulations which give a good estimation in almost ideal conditions.
- the estimation carried out in this paper, through the application of probabilistic estimators (Unscented Kalman Filter, UKF) showed that this technique constitutes a powerful and versatile calculation tool that allows to obtain very satisfactory adjustments. During the iteration process of the UKF, it has been possible to observe the special relevance of the maximum and minimum limits of each parameter to be estimated and entered in the filter.

The proposed Kalman filter methodology for estimating face pressure in urban tunnelling settings showed promising results in this case study based on a very simple analytical formulation. However, some limitations were apparent, with notable discrepancies between the estimated and measured face pressures. These discrepancies can be attributed to the inherent complexity of TBM follow-up engineering in urban settings, where engineering decisions, predictions from analytical models, and contingent requirements may be incomparable.

Despite these limitations, the proposed methodology has the potential to provide a more robust and reliable approach to face pressure estimation in urban tunnelling. Further testing on other datasets is warranted to validate its effectiveness in a wider range of conditions.

REFERENCES

Leca, Eric, New, B. 2007. Settlements induced by tunnelling in Soft Ground. Tunnelling and Underground Space Technology. 22. 119–149.

Zizka, Z., Thewes, M., 2016. Recommendations for face support pressure calculations for shield tunnelling in soft ground. German Tunnelling Committee (ITA-AITES), Cologne, Germany.

AFTES, 2018. Prise en compte des effets induits par le creusement sur les constructions avoisinantes dans la conception et la réalisation des ouvrages souterrains— GT16R2F1.

Broms, B. B., and Bennermark, H. (1967). Stability of clay at vertical opening. *J. Soil Mech. Found. Div. ASCE* 96 (1), 71–94. doi:10.1061/jsfeaq.0000946

Kolymbas, D. 1998. Geotechnik – Tunnelbau und Tunnelmechanik. Eine systematische Einführung mit besonderer Berücksichtigung mechanischer Probleme. Springer-Verlag: Berlin, Heidelberg.

Amemiya, K., Kakimi, K., Kusumoto, K. & Sasaki, T. 2014. Application of a spherical tunnel face to full-face tunnel excavation by drill and blast. In: Proceedings of the 8th Asian Rock Mechanics Symposium. Rock Mechanics for Global Issues – Natural Disasters, Environment and Energy, Sapporo, Japan, 14.-16. October 2014.

Salimi, A.; Rostami, J.; Moormann, C.; Delisio, A. Application of non-linear regression analysis and artificial intelligence algorithms for performance prediction of hard rock TBMs. Tunn. Undergr. Space Technol. 2016, 58, 236–246.

Innaurato N, Oggeri C, Oreste P. "Validation techniques in tunnelling: the complementary approach of modelling, monitoring and excavation performance evaluation". Proceeding of the AITES-ITA 2001 World Tunnel Congress, 2001, p 217–26.

Julier S.J. and J. K. Uhlmann, "Unscented filtering and non-linear estimation," in Proceedings of the Ieee, vol. 92, no. 3, march 2004 isbn 0018-9219/04.

Tunnelling for a Better Life – Yan, Celestino, Thewes & Eberhardt (Eds)
© 2024 The Author(s), ISBN 978-1-032-80042-4
Open Access: www.taylorfrancis.com, CC BY-NC-ND 4.0 license

Experimental study of rheological characteristics of bentonite-based drilling fluids

Stefano Javarone, Marta Palombini & Matilde Cinelli
GEEG, Geotechnical and Environmental Engineering Group, Rome, Italy

Irene Bavasso
GEEG, Geotechnical and Environmental Engineering Group, Rome, Italy
Department of Chemical Engineering Material Environment, Sapienza University of Rome, Italy

Diego Sebastiani*
GEEG, Geotechnical and Environmental Engineering Group, Rome, Italy
Department of Structural and Geotechnical Engineer, Sapienza University of Rome, Italy

ABSTRACT: Bentonite and polymer-based drilling slurries are widely used in numerous geotechnical applications such as Slurry Shield TBM tunnelling, MicroTunnelling, Horizontal Directional Drilling and other trenchless technologies, piles and diaphragms constructions. In all cases, the rheological characteristics of the fluids must be correctly adjusted to ensure the stability of the excavation, proper lubrication and transportability of the excavated material. To date, there are several international standards and many best practices, empirical abacuses and indications for the definition of rheological properties of drilling fluids. However, there is often a lack of correlation between the results of different tests or measurements that can be carried out in laboratories using rheometers, viscometers and other sensitive and accurate equipment, and the rapid measurements that are widely used on site. The study presented in this paper involves the systematic performance of laboratory tests and rapid measurements on a natural bentonite used in the construction of tunnels and other underground works. The aim is to provide a broad overview of the rheological characteristics of drilling fluids prepared at different bentonite dosages, a series of correlations between the results of laboratory tests carried out using different mixing speed and mixing time. The results of the study support a better selection of the correct properties during drilling, an informed choice of the most appropriate measuring instruments and a more accurate measurement and control of the rheological properties of drilling fluids.

Keywords: Excavation, Viscosity, Marsh, Mixing, Rheology, Slurry

1 INTRODUCTION

Bentonite and polymer-based drilling slurries are used extensively in various geotechnical applications such as Slurry Shield TBM tunnelling, Microtunnelling, Horizontal Directional Drilling and other trenchless technologies, piles and diaphragms constructions. The crucial aspect in all these applications is to appropriately adjust the rheological properties of the fluids. This adjustment is necessary to guarantee excavation stability, adequate lubrication and the efficient transportation of the excavated materials.

Drilling fluids can be oil-based, synthetic-based and water-based: such fluids have different characteristics but, among them, water-based drilling fluids are environmentally friendlier and cheaper than oil-based and synthetic ones (Liu et al., 2022).

Bentonite fluids are a particular type of water-based drilling fluids obtained by mixing water and bentonite, a natural volcanic clay. These fluids are commonly employed in tasks involving soil excavation as they are able to stabilize the hole walls by creating a protective barrier and ensuring the transportability of the excavated material (Chiarelli, 2014).

The essential element in the preparation of these fluids lies in the interactions between clay and water. When dry clay, which is composed of stacked plate-like structures, comes into contact with water, it undergoes a series of transformations. These transformations involve various stages, including hydration, dispersion, gelation,

*Corresponding author: diego.sebastiani@geeg.it

DOI: 10.1201/9781003495505-71

aggregation, and flocculation, as explained by Muller-Vonmoos et al. (1989).

Furthermore, these fluids typically exhibit pseudoplastic behaviour, although there are exceptions. Pseudoplasticity means that they require the application of a certain level of stress, known as the yield point or yield stress (represented as τ_0), to initiate flow. Below the yield stress the sample does not flow but behaves elastically (Steffe, 1996). When forces exceed the shear stress, the behaviour of the material can exhibit either pseudoplastic or Newtonian characteristics, as illustrated in Figure 1. Pseudoplasticity can be better understood by considering that the system is composed of molecules that can arrange themselves into lattice structures. To disrupt or "break" these structures, stress levels equal to or exceeding the yield point are required. This means that the material can transition between a solid-like and a liquid-like state depending on the applied stress. Whether this plasticity is reversible or not depends on the material capacity to re-establish the lattice structure after deformation (Luckham and Rossi, 1999).

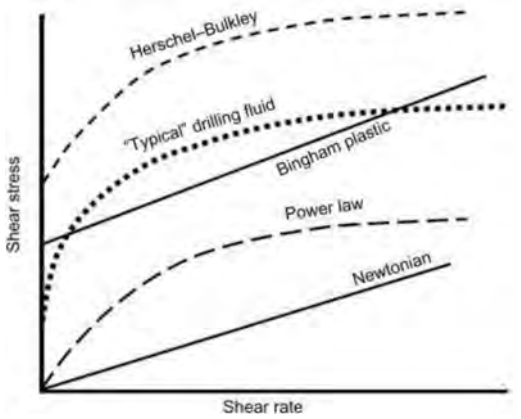

Figure 1. Shear stress vs shear rate and main rheological behaviour of fluids (modified after Braun and Rosen, 1999).

The concentration of bentonite in fluid formulations is restricted because excessive amounts of powder can lead to issues such as the creation of a thick filter cake and formation damage. To address these challenges, the inclusion of polymers and other additives can be beneficial (Saboori et al., 2019). These additives serve multiple purposes, including the achievement of a thinner filter cake on the wellbore wall, reducing the potential for damage and fluid loss, and improving the rheological properties of the fluid (Song et al., 2016).

The intricate interaction between clay and water is of the utmost importance in the formulation of bentonite fluids. Its understanding plays a crucial role in tailoring these fluids for diverse applications, ranging from their use as drilling fluids in the oil industry to soil stabilization in civil engineering projects. The literature contains some information, including results from experimental tests and theoretical explanations, that shed light on the rheological properties of bentonite drilling fluids (Ettehadi et al., 2022).

This study aims to offer supplementary insights into the rheological properties of bentonite drilling fluids. In particular the main objectives are: i) the investigation of the influence that mixing parameters adopted on site, such as time and rpm (round per minute), have on the properties of bentonite drilling fluids and ii) the definition of a correlation between the apparent viscosity and the results of easily accessible tests such as the Marsh cone, offering a valuable way to swiftly assess the parameter without resorting to more advanced instruments like rotational rheometers.

2 MATERIALS AND METHODS

To investigate the rheological properties, a natural bentonite was selected and different fluid samples were prepared by mixing it in varying concentrations with water.

The first step was the bentonite characterization in terms of Atterberg limits, water content, dry residue over 75 μm and swelling index; then different fluids were prepared adopting different mixing conditions, varying mixing speed and mixing time, and tested in terms of rheological parameters such as Marsh viscosity, API filtrate and filtercake. Also, a rheological analysis with a rotational rheometer was performed.

In the following paragraphs the testing methods and the models used are described.

2.1 *Mixing and concentration*

2.1.1 *Bentonite sample characterization*

Liquid limit values were determined with the Casagrande apparatus, following the ASTM D4318 (ASTM-D4318-17, 2017), in duplicate. The water content of the powder was measured using a thermobalance Gibertini mod. crystaltherm, at 105°C until constant weight of the dry sample. The dry residue over 75 μm was determined on the dry powder weighting the residue retained over a standard sieve of 200 Mesh, and calculated as (1):

$$dry\ residue\ \% = \frac{W_{residue}}{W_0} \cdot 100 \qquad (1)$$

where W_0 is the initial weight of the powder, and $W_{residue}$ is the residue retained after the sieving.

The wet residue was determined on a 5% solution of bentonite, passed through a standard sieve of 200 Mesh. The wet residue (2) was dried overnight at 105°C and weighted to obtain an indication on the insoluble minerals fraction, using the following formula:

$$wet\ residue\ \% = \frac{W_{driedresidue}}{W_0} \cdot 100 \qquad (2)$$

where W_0 is the initial weight of the powder, and $W_{dried\ residue}$ is the residue retained after the sieving of the slurry and dried overnight.

The swelling index was determined following the standard ASTM D5890 (ASTM-D5890, 2019).

The pH of the bentonite slurry was determined using a pH test strip.

2.1.2 *Bentonite slurries preparation*

Different bentonite fluids were prepared at different rpm and mixing times using an orbital mixer Giorgio Bormac AM 20-D ARGOlab with a three-blade rotating stirrer positioned about 2 cm from the bottom of a 5 L plastic can with a 17 cm diameter. Every sample was prepared filling the can with tap water weighing 2500 g. The study can be divided into two main phases. The two different phases involved different concentration of bentonite as well as mixing parameters. In the first phase it was investigated the effect of different mixing parameter (Table 1) on the bentonite slurries properties described from the American Petroleum Institute (API-13B-RP1, 2015).

Table 1. Mixing parameters.

Bentonite weight %			5% wt	6% wt	7% wt
Fixed time: 15 min	Mixing speed (rpm)	750	✓	✓	✓
		1000	✓	✓	✓
		2000	✓	✓	✓
Fixed rpm: 1500	Mixing time (min)	5	✓	✓	✓
		10	✓	✓	✓
		15	✓	✓	✓

For the second phase the mixing parameters were fixed, (Table 2) varying only the bentonite concentration.

Table 2. Second phase mixing parameters.

Bentonite weight %		6.0% wt	6.5% wt	7.0% wt	7.5% wt
Fixed time: 20 min	Fixed rpm: 1500	✓	✓	✓	✓

2.2 *Rheological tests*

The bentonite slurries obtained at different dosages were subjected to the Marsh cone test at t = 0 h (immediately after the active mixing phase, T_0) after 1 hour, 3 hour and 24 hours of steady state. This assessment aimed to observe any distinct effects on the hydration phase of the bentonite slurry due to the different mixing parameters specified. The Marsh cone test was conducted following the guidelines outlined in API 13B-RP1 specifications. The retention capacity of the bentonite slurries was determined by assessing the fluid loss both immediately after T_0 and after a 24-hour period, following the guidelines outlined in API 13B-RP1 specifications.

The rheological characteristics of bentonite fluids have been analysed using a rotational rheometer. A rotational rheometer is an instrument used to study the rheological properties of various types of fluids. These fluids are placed between a rotor and a stator, which can have different geometries. The fluid placed between the rotor and stator is set in motion by the rotation of the rotor. A second device measures the torque required to keep the plate in motion, and from this measurement, the applied stress on the fluid (shear stress, τ) can be determined. Meanwhile, the rotational speed provides information about the shear rate, $\dot{\gamma}$ (Sartori, 2013).

2.3 *Common yield stress models for drilling fluids*

Aqueous suspensions of clay that possess a relatively high particle concentration have traditionally been described according to Bingham's theory. The Bingham model is the simplest constitutive equation for viscoplastic fluids. Another model extensively adopted to describe the behavior of bentonite fluid viscosity is the the Herschel-Bulkley (H-B) model. This model was used in this study to describe the rheological behaviour of the bentonite slurry.

Typically, the H-B model, described by eq. (3) and (4), is used for many suspensions since Newtonian plastic, shear thinning, shear-thickening and Bingham can be considered as a special case of the model.

$$\tau = \tau_0 + K \cdot \dot{\gamma}^n \tag{3}$$

$$\eta = \frac{K \cdot (\dot{\gamma})^n + \tau_0}{\dot{\gamma}} \tag{4}$$

Where τ is the shear stress; τ_0 is the yield stress or yield point; η is the viscosity; $\dot{\gamma}$ is the shear rate; n is the flow behaviour index and n is the consistency coefficient.

3 RESULTS AND DISCUSSION

3.1 *Bentonite characterization*

In the first part of the study, we characterized bentonite powder (Table 3), identifying its water content, residue at 75 microns both dry and wet. Regarding the water absorption properties of this bentonite, the liquidity limit and swelling index were analysed. The liquid limit is quite high, standing at around 430%.

The bentonite selected in this study can be categorized as a natural sodium bentonite. Generally, the higher the content of montmorillonite in the natural bentonite, the more the card-like structure can expand, resulting in a higher liquid limit (while the plastic limit remains relatively unchanged), thereby increasing the plasticity index (the range between the liquid limit and

Table 3. Bentonite characterization.

Type		Natural Sodium Bentonite
Physical state		Powder
Colour		Yellow
Water Content	%	13.0
Dry residue over 75 microns	%	16.8
Wet residue over 75 microns	%	3.3
Swelling index	mL	25
Liquid limit	%	430
pH sol. 5% @25°C		9

the plastic limit). Consequently, bentonite with a higher capacity for water absorption requires less bentonite powder in the water mixture to achieve a specific viscosity. However, pure bentonites (with an exceptionally high montmorillonite content) are rare and expensive. It is well known (Madsen and Muller-Vonmoos,1989) that due to their card-like structure, bentonites sol takes time to expand, and the particles require more time to disperse and swell. As a result, the viscosity increase over time is slow.

3.2 *Mixing optimization*

The preparation of a bentonite-based fluid initially involved the adoption of three different dosages of bentonite powder. In Figure 2 the results of Marsh viscosity are reported and the same behaviour on the API filtrate analysis can be observed.

Furthermore, it's important to note that extending the mixing time did not impact either the fluid loss or the thickness of the cake (Figure 3).

On the other hand, as rpm changes (mixing energy), there is a slight decrease in viscosity. The decreasing trend of viscosity with the increase of rpm adopted is in opposition to what expected (Figure 4) probably because the natural bentonite could be characterized by a low Na/Ca ratio as pointed out by the swelling analysis (25 mL). By enhancing the mixing efficiency there is a greater availability of Ca ions into solution. Such ions are recognized to have an adverse effect on the swelling and rheological properties of the bentonite fluid.

Using a typical electric motor curve as an example for a generic mixer, we generated a curve for the laboratory agitator based on the available data. To assess the laboratory findings, we compared them to the standard mixing speed and duration used in the field, taking into account the associated energy consumption taking as reference the previous part. Three scenarios were considered. The first scenario, representing the typical values used for on-site preparation, involved mixing at 1200 rpm for 20 minutes and re-mixing for 5 minutes. In the second scenario, mixing occurred at 1400 rpm for 10 minutes, followed by re-mixing for 2 minutes and 30 seconds.

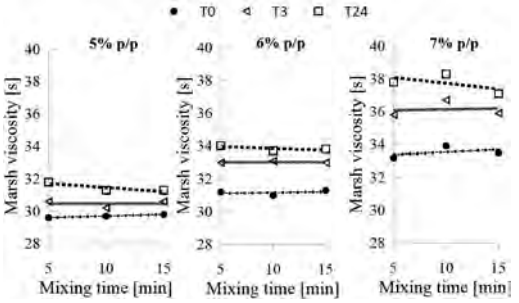

Figure 2. Marsh viscosity comparison immediately after mixing, hydrated 3 hours and 24 hours.

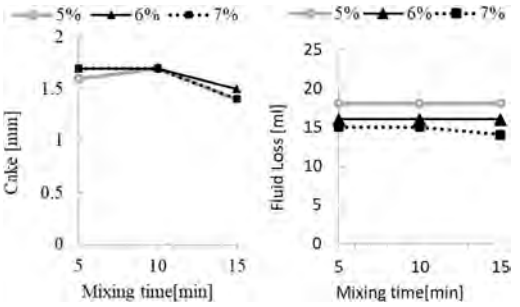

Figure 3. Fluid loss and cake thickness comparison for different %wt, immediately after mixing.

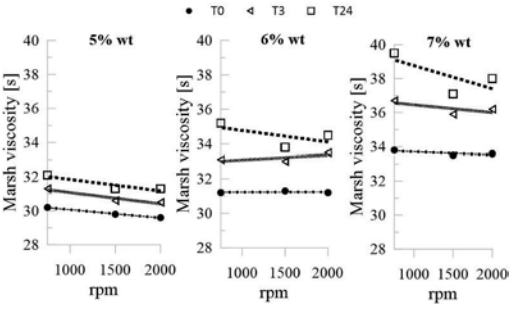

Figure 4. Marsh viscosity comparison immediately after mixing, hydrated 3 hours and 24 hours.

The third scenario involved mixing at 1600 rpm for 7 minutes and 30 seconds, with a subsequent re-mixing time of 2 minutes. It's worth noting that in Italy, the electricity cost for businesses typically falls within the range of 8 to 9 cents per kWh. The resulting percentage savings compared to the on-site preparation procedure are presented in Table 4.

The results show that it is possible to reduce the energy consumption optimising mixing time and mixing speed. It's important to notice that these results are obtained from laboratory apparatuses and they need to be adjusted if compared to field ones, taking into account specific field conditions.

Table 4. Cost options and savings.

	rpm	Time mix [min]	Remix time [min]	Cost [€]	Save [%]
1st possibility	1200	20	5	0.15-0.17	0
2nd possibility	1400	10	2.5	0.08-0.09	45%
3rd possibility	1600	7.5	2	0.06-0.07	58%

3.3 *Rheological measurement*

To investigate the rheological characteristics of bentonite fluids they were subjected to progressively escalating shear rates, spanning from 250 s^{-1} to 2000 s^{-1}. The primary objective was to analyse the transformation of these fluids, transitioning from a gel-like state to a more liquid state, which occurs when the stress level exceeds the threshold causing the breakdown of the fluid's network structure, ultimately resulting in a more gel-like consistency. In this instance, the aim was to attain a Marsh viscosity goal of 40 seconds Figure 5.

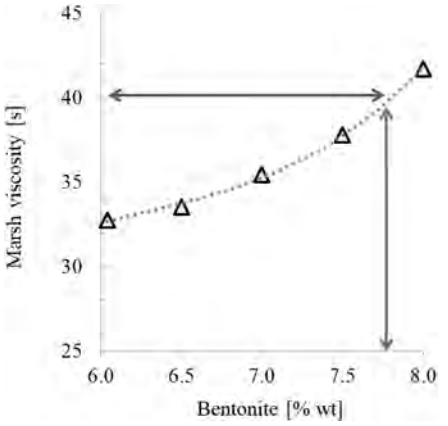

Figure 5. Individuation of the concentration to a marsh viscosity target of 40s.

The Herschel-Bulkley model was chosen as the best fit for characterizing the rheological properties of the studied bentonite fluids. This decision was based on minimizing errors between model-calculated and observed viscosities in experimental data. The suitability of this model is evident when analysing graphs of shear rate changes from 0 to 100 s^{-1} and back to 0 for various bentonite concentrations. The study examined different concentrations to understand how the thixotropic loop varies with increased bentonite powder content. During the decreasing shear rate phase, the Herschel-Bulkley model, supported by several studies (Yang, et al.) (Ren, et al., 2021) (Mellak, et al., 2014), effectively describes the fluids behaviour.

The fitting results, displayed in the Figure 6, demonstrate a strong alignment between the Herschel-Bulkley model and the experimental rheometer data. An n value of less than 1 reveals the existence of pseudoplastic behaviour, signifying that viscosity rises as the shear rate diminishes.

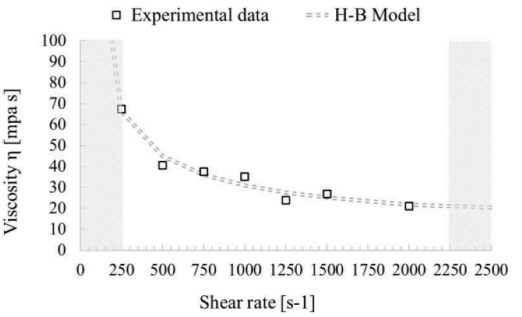

Figure 6. H-B model applied to the experimental data.

Studying bentonite fluid behaviour beyond the initial gel structure breakdown is essential for understanding its thixotropic rheological properties. Traditional models like the Herschel-Bulkley model are insufficient to capture the complex behaviour observed when shear rates are gradually increased and then decreased in thixotropic fluids, leading to the creation of a "thixotropic loop" in shear stress-shear rate graphs (Franceschini, et al., 2022).

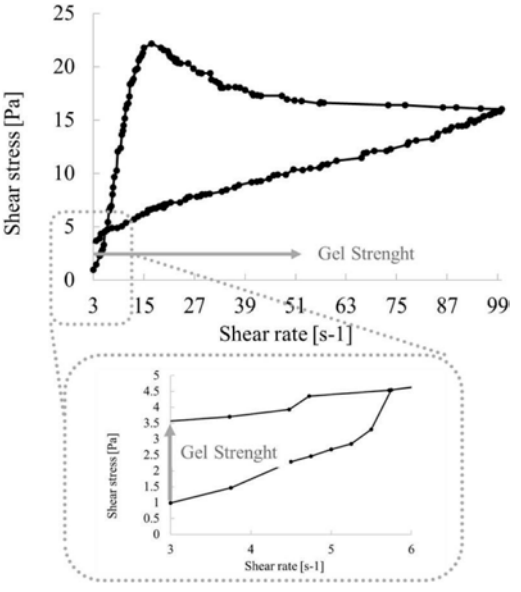

Figure 7. Hysteresis shear rate/shear stress cycle.

In the region of decreasing shear rates, the Herschel-Bulkley model is commonly used and referred to as the "steady state flow" zone. However, when examining the area of increasing shear rates, known as the "transient flow" zone, a different trend emerges (Franceschini, et al., 2022). Here, shear stress initially

rises linearly with shear rate, but as the shear rate continues to increase, shear stress decreases before returning to the steady state flow zone. This phenomenon is more pronounced with higher bentonite concentrations. The combination of transient flow and steady state flow forms the thixotropic loop, and its size grows with increasing bentonite content, indicating the materials degree of thixotropy (Yang, et al.) (Ren, et al., 2021). This degree of thixotropy is a measure of the energy required for bond dissociation per unit time and volume. The magnitude of the hysteresis area in the loop indicates whether the material has a gel-like structure under static conditions, resulting in increased rheological parameters and resistance to creep. In the case of bentonite fluids, the gel structure is related to swelling due to the insertion of water molecules between montmorillonite trilayer elements and particle interactions based on the electrical double layer theory (İşçia, et al.). At higher concentrations, particle aggregation into clusters occurs, forming a more complex network called a flocculate. The arrangements of particles contributing to the gel structure include edge-to-face and edge-edge arrangements, driven by electrostatic attractions or repulsions within the double layer. The transient flow zone is characterized by a "stress overshoot" peak, representing the elongation and resistance of the microstructure before its rupture due to increased shear rates (İşçia, et al.). Unlike the steady state flow zone, the transient flow zone is complex and challenging to describe with models like the Herschel-Bulkley model. It's worth noting that the fluid cannot fully recover its original characteristics after being subjected to increased and then decreased shear rates, leading to changes in the shear force required for new flow. The hysteresis area increases as the bentonite content in the fluid rises, indicating higher thixotropy (Yang, et al.). Regarding the hysteresis areas (Table 5), as anticipated, their value increases as the bentonite content in the fluid increases because the material is more thixotropic.

Table 5. Values of hysteresis (thixotropy) areas for different concentrations of the Bentonite N.

Concentration	%	6.5	7.0	7.5
Area	J/m3 s	551	644	651

After conducting a study on the rheological behaviour of bentonite fluids at different concentrations, an attempt was made to establish a correlation between the viscosity values measured with the Marsh cone (expressed in seconds) and the apparent viscosity values obtained with a rheometer. Based on literature studies (Pitt, 2000), it was established that the viscosity measured with the Marsh cone can be considered as the effective viscosity of a fluid subjected to a shear rate on the order of 2000 s^{-1} (ranging from 1500 to 2500 s^{-1}). Therefore, all four types of bentonite fluids at varying concentrations were subjected to a rotational rheometer at shear rates of 1000, 1500, and 2000 s^{-1} to obtain measurements of apparent viscosity (Figure 8).

Subsequently, the obtained data points were analysed to establish a correlation with the Marsh cone times obtained in the previous phase of the study The theoretical background for seeking a linear correlation is based on existing literature, which suggests that Marsh cone viscosity values expressed in seconds can be transformed into viscosity values (referred to as "effective viscosity") expressed in cP using the following empirical expression:

$$\mu = \rho\ (t - 25) \tag{5}$$

Where μ effective viscosity in Centipoise [cP = mPa·s], ρ bentonite fluid density [g/cm^3], t time to Marsh cone [s], 25 is a value that refers to the seconds it takes for a fluid with negligible viscosity at any density.

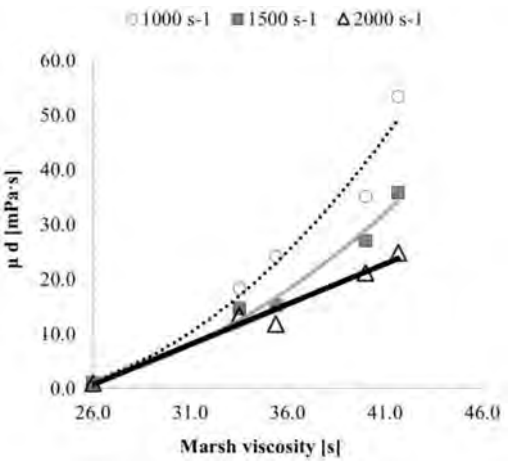

Figure 8. Correlation between Marsh viscosity and effective viscosity (μ) at different shear rate.

The expression suggests a linear relationship between viscosity and Marsh cone time. Table 6 presents the values obtained through rotational rheometer analysis of the optimally concentrated bentonite fluid, subjected to shear rates of 1000 s^{-1}, 1500 s^{-1}, and 2000 s^{-1}, resulting in apparent viscosity measurements.

Table 6. Apparent viscosity and Marsh time results for natural bentonite.

Shear rate [s^{-1}]	Apparent viscosity [mPa s]	Marsh viscosity [s]
1000	35	40.0
1500	27	40.0
2000	21	40.0

4 CONCLUSIONS

The primary aim of this study was to further the body of knowledge related to the rheological properties of bentonite-based drilling fluids.

First, it was evaluated how operative conditions adopted during the mixing step as time and rpm influence the properties of bentonite drilling fluids. The main outcomes were that Marsh viscosity was almost constant at the increase of mixing time, similarly to the results of the fluid loss and the cake thickness. This allows to reduce the energy consumption associated with prolonged mixing operations.

Secondly, a good fit between the Herschel-Bulkley model and the experimental rheometer data was obtained. The n value lower than 1 revealed the occurrence of pseudoplastic behaviour as signifying that viscosity rises as the shear rate diminishes. The hysteresis area increased as the bentonite content in the fluid raised, indicating higher thixotropy of the materials.

Finally, a correlation between the apparent viscosity and the results of Marsh cone tests was investigated, offering a valuable way to swiftly assess the parameter with easily accessible tools.

REFERENCES

API Abu-Jdayil, B. and Ghannam, M., 2014. The Modification of Rheological Properties of Sodium Bentonite-water Dispersions with Low Viscosity CMC Polymer Effect. U.A.E: U.A.E. University, Al-Ain. Vol. Department of Chemical & Petroleum Engineering.

API-13B-RP1, 2015. API 13B-RP1. s.l.: American Petroleum Institute.

ASTM-D4318-17, 2017. Standard Test Methods for Liquid Limit, Plastic Limit and Plasticity Index of Soils. s.l.: Annual Book of ASTM Standards, 2017.

ASTM-D5890-19, 2019. Standard Test Method for Swell Index of Clay Mineral Component of Geosynthetic Clay Liners.

Braun D. B., Rosen M. R., 1999. Rheology Modifiers Handbook.

Chiarelli M., 2014. Horizontal Directional Drilling: ingegneria dei fluidi di perforazione. Strade & Autostrade 2.

Ettehadi A., Ülker C., Altun G., 2022. Nonlinear viscoelastic rheological behavior of bentonite and sepiolite drilling fluids under large amplitude oscillatory shear. Journal of Petroleum Science and Engineering, 208, art. no. 109210, DOI: 10.1016/j.petrol.2021.109210

Franceschini, Claudia, et al., 2022. Produzione di fanghi bentonitici: sperimentazione e modellazione del mixing. s.l.: Facoltà di ingegneria Civile e Industriale.

Galazzo, D., 2007-2008. Caratterizzazione dei fluidi di perforazione per l'impiego nella horizontal directional drilling (H.D.D.). s.l.: Alma Mater Studiorum, Università di Bologna. Vol. Tesi di laurea in moto dei fluidi e prospezioni nel sottosuolo LS.

Guidotti, M., 2012. Fluidi Tempo-Dipendenti. s.l.: Facoltà di Farmacia e Medicina. Vol. http://www.galenotech.org/reologia3.htm.

Hogg, R., 2013. Bridging Flocculation by Polymers. Department of Energy and Mineral Engineering, The Pennsylvania State University, Hosokawa Power Technology Foundation KONA: Powder and Particle Journal. Vol. No.30.

İşçia, S., Uslua, Y.O. and Ece, Ö.I., 2006. The characterizations of rheological, electrokinetical and structural properties of ODTABr/MMT and HDTABr/MMT organoclays. Istanbul, Turkey,: Elsevier.

Jun Li, Wen Zhou, Zhilin Qi, Taotao Luo, Wende Yan, et al., 2019. Morphology and Rheological Properties of Polyacrylamide/Bentonite Organic Crosslinking Composite Gel. s.l.: State Key Laboratory of Oil and Gas Reservoir Geology.

Liu J., Zhang T., Sun Y., Lin D., Feng X., Wang F., 2022. Insights into the high temperature-induced failure mechanism of bentonite in drilling fluid. Chemical Engineering Journal, 445, art. no. 136680. DOI: 10.1016/j.cej.2022.136680

Luckham, Paul F. and Rossi, Sylvia., 1999. The Colloidal and Rheological Properties of Bentonite Suspensions, Advances in Colloid and Interface Science, 82, pp. 43–92. DOI:10.1016/S0001-8686(99)00005-6.

Maxey, Jason., 2007. Thixotropy and Yield Stress Behavior in Drilling Fluids. Houston, Texas: American Association of Drilling Engineers. Vol. National Technical Conference and Exhibition.

Mellak, A. and Benyounes, K., 2014. Modeling and rheological characterization of sludge based drilling oil. s.l.: Faculty of Hydrocarbons and Chemistry, University of Boumerdes, 2014. Vol. 350.

Muller-Vonmoos, M. and Loken, T. The shearing behaviour of clays, 1989. Applied Clay Science, 4, pp. 125–141. DOI:10.1016/0169-1317(89)90004-5.

Papanastasiou, Tasos C., 1987. Flows of Materials with Yield. s.l.: J. Rheol., 1987. Vol. 31 (5), 385–404.

Pitt, M.J., 2000. The Marsh Funnel and Drilling Fluid. Viscosity: A New Equation for Field Use. U. of Leeds,: SPE Drill. & Completion. Vols. Vol. 15, No. 1.

Ren, Jiangtao, Deshun, Yin and Zhai, Ruizhi., 2021. Rheological behavior of bentonite-water suspension at various temperatures: Effect of solution salinity. s.l.: Engineering Geology. Vol. Volume 295.

Saboori R., Sabbaghi S., Kalantariasl A. Improvement of rheological, filtration and thermal conductivity of bentonite drilling fluid using copper oxide/polyacrylamide nanocomposite, 2019. Powder Technology, 353, pp. 257–266. DOI: 10.1016/j.powtec.2019.05.038

Sartori, A. 2013. Metodi di caratterizzazione di nanoparticelle magnetiche per applicazioni di Magneto Fluido Ipertermia", Tesi di Laurea magistrale in bioingegneria. 2013.

Song K., Wu Q., Li M., Ren S., Dong L., Zhang X., Lei T., Kojima Y. Water-based bentonite drilling fluids modified by novel biopolymer for minimizing fluid loss and formation damage, 2016. Colloids and Surfaces A: Physicochemical and Engineering Aspects, 507, pp. 58–66. DOI: 10.1016/j.colsurfa.2016.07.092

Steffe J. F. Rheological Methods in Food Process Engineering, 1996. Second Edition, Freeman Press, 2807 Sill Valley Dr. East Lansing, USA.

Yang, Yi, Li, Xing-Gao and Su, Wei-Lin. Experimental Investigation on Rheological Behaviors of Bentonite-and CMC-Conditioned Sands. Beijing Jiaotong University, Beijing 100044, China: Key Laboratory of Urban Underground Engineering of Ministry of Education.

Tunnelling for a Better Life – Yan, Celestino, Thewes & Eberhardt (Eds)
© 2024 The Author(s), ISBN 978-1-032-80042-4
Open Access: www.taylorfrancis.com, CC BY-NC-ND 4.0 license

Optimized electrical exploration for predicting geological transitions ahead of a tunnel based on harmony search algorithm

Minkyu Kang, Kibeom Kwon & Sangyeong Park
Korea University, Seoul, Republic of Korea

Yongjoon Choe
Georgia Institute of Technology, Georgia, USA

Hangseok Choi
Korea University, Seoul, Republic of Korea

ABSTRACT: Accurate identification of geological transitions during tunnel excavation is vital for ensuring safety and operational efficiency. Recognizing the significance of this critical issue, the present study developed an optimization system based on electrical exploration to analyze the characteristics of geological transitions in front of tunnel faces. The system employed an inverse analysis utilizing the harmony search algorithm to calculate essential attributes, including the distance between the tunnel face and geological transitions, as well as the electrical resistivity of the changing ground. To assess the applicability of the developed system, laboratory experiments were conducted using a soil chamber that simulated ground formations with geological transitions. The experimental findings confirm the system's effectiveness, demonstrating exceptional predictive capabilities within a relatively short data analysis timeframe. Notably, the system's ability to accurately predict the distance between the tunnel face and geological transitions highlights its efficacy in mitigating potential hazards arising from unforeseen geological transitions. As a result, the precise prediction of geological transitions achieved through the proposed method enables proactive implementation of risk management measures.

Keywords: Electrical exploration, Geological transition, Harmony search algorithm, Optimization

1 INTRODUCTION

Over the past few decades, there has been a significant increase in underground infrastructure construction driven by the growing demands for transportation, electricity, water supply, and sewage treatment. However, geological hazards during tunnel excavation can pose risks such as water inflow and collapse, which can severely impact both efficiency and safety (Zhao et al., 2007; Farrokh & Rostami, 2009; Zhao et al., 2014; Rafie et al., 2015; Bai et al., 2021; Xu et al., 2022). Particularly, geological transitions during tunnelling have the potential to induce ground settlement, face collapse, and sinkholes (Toth et al., 2013). Therefore, accurate predictions of these transitions are essential for effective risk management during tunnel construction (Yazdani-Chamzini, 2014).

At the tunnel design stage, geotechnical surveys often fall short in accurately identifying geological hazards along the tunnel route. Consequently, various non-destructive techniques have been developed, including seismology, electromagnetic exploration, and ground-penetrating radar, to detect geological hazards ahead of tunnel construction (Dickmann & Sander, 1996; Grodner, 2001; McDowell et al., 2002; Gong et al., 2019; Caselle et al., 2020). Among these techniques, electrical methods, such as electrical resistivity tomography (ERT), stand out for their cost-effectiveness and efficiency in data analysis at tunnel sites (Kaus & Boening, 2008; Schaeffer & Mooney, 2016; Park et al., 2018; Kang et al., 2022; 2023; Mifkovic et al., 2021; Nie et al., 2023). Specifically, Park et al. (2016) developed a system that utilizes the harmony search (HS) optimization algorithm and electrical resistance measurements to predict anomalies ahead of a tunnel.

Building on prior research, this study aims to develop an optimization system to estimate geological transition attributes. These attributes include the distance from the transition point to the tunnel face and the electrical resistivity of the changing ground. In contrast to the approach taken by Park

*Corresponding author: dldnjfwp@korea.ac.kr

DOI: 10.1201/9781003495505-72

et al. (2016), this study employed the Wenner electrode array, renowned for its low earth resistance, to enhance measurement accuracy.

To validate the effectiveness of the developed system, laboratory-scale experiments were conducted, replicating the transition from rock to soil within a soil chamber. In addition, parametric studies were performed to investigate how prediction accuracy was affected by the characteristics of the geological transition. These characteristics encompassed variables such as the distance between the transition and the tunnel face and the electrical resistivity of the changing ground.

2 BACKGROUND

2.1 *Electrical resistivity*

An optimization system was developed to estimate the characteristics of geological transitions ahead of a tunnel face using electrical resistivity measurements. Electrical resistivity is a property that signifies a material's resistance to electrical current flow. In the context of soil and rock formations, various factors can lead to significant variations in electrical resistivity. These factors encompass porosity, clay content, weathering degree, saturation, as shown in Table 1 (Atkins and Smith, 1961; Brace and Orange, 1968; Timur et al., 1972; Rhoades et al., 1976; Parkhomenko, 2012). For instance, a decrease in porosity reduces electrical resistivity. Consequently, electrical resistivity has been widely employed to determine vital properties of rock and soil formations, as well as to infer the geological structures of ground formations.

Table 1. Correlation between soil conditions and resistivity.

Electrical resistivity of ground	Porosity	Clay content	Degree of weathering	Degree of saturation
High → Low	High → Low	Low → High	Low →High	Low → High

2.2 *Analytical solution for geological transition*

To accurately assess the attributes of a geological transition ahead of a tunnel face using inverse analysis, this study incorporated an analytical solution of electrical resistivity into an optimization algorithm. The well-known analytical solution for ground formations with a geological transition was employed, as represented by Equation 1 (refer to Figure 1) (Takahashi and Kawase, 1990).

$$\rho=\rho_g\left[1+4a\int_0^\infty \frac{\frac{\rho_{trans}-\rho_g}{\rho_{trans}+\rho_g}e^{-2\lambda d_{trans}}}{1-\frac{\rho_{trans}-\rho_g}{\rho_{trans}+\rho_g}e^{-2\lambda d_{trans}}}(J_0(\lambda a)-J_0(2\lambda a))d\lambda\right] \quad (1)$$

The analytical solution involves five variables, including both known and unknown variables. The known variables consist of the measured apparent electrical resistivity (ρ), the electrical resistivity of the surrounding ground (ρ_g), and the electrode spacing (a). On the other hand, the unknown variables comprise the electrical resistivity of the changing ground (ρ_{trans}), the distance between the geological transition and tunnel face (d_{trans}).

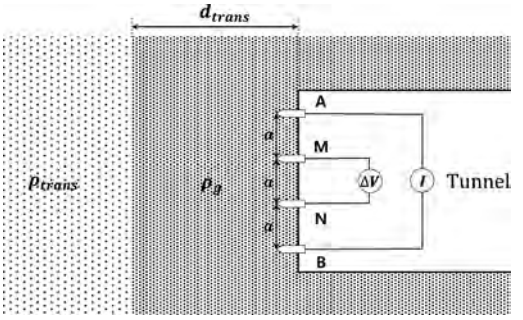

Figure 1. Schematic for the analytical solution of a geological transition.

3 OPTIMIZATION SYSTEM

3.1 *System overview*

This study developed an optimization system to determine geological transition characteristics, such as the electrical resistivity of the changing ground (ρ_{trans}), and the distance from the geological transition to the tunnel face (d_{trans}). The system incorporates an inverse analysis program based on the HS algorithm, which utilizes the analytical solution derived from Equation 1 to estimate these characteristic values of the geological transition. A detailed explanation of the inverse analysis process using the HS algorithm within the proposed system is provided in the subsequent section 3.2.

To enhance the prediction performance of the system, electrical resistivity was measured five times by changing the electrode spacings (a), and these measurements were integrated into the inverse analysis process. Consequently, the measurement equipment must be capable of measuring five electrical resistivity values corresponding to each electrode spacing.

In summary, the developed optimization system is composed of electrodes, a circuit board, a power supply, a measurement apparatus, and a control PC with the inverse analysis capability, as depicted in Figure 2.

3.2 *Inverse analysis procedure*

The developed optimization system utilizes the inverse analysis approach to estimate the unknown variables associated with the characteristics of the geological

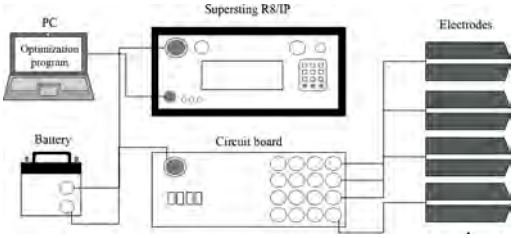

Figure 2. Schematic of the proposed optimization system.

transition. This is achieved by inversely implementing the analytical solution in conjunction with the known variables (refer to Figure 3). To conduct the inverse analysis, the system employs the HS algorithm, which aims to find the optimal condition through a process resembling musical harmony improvisation (Geem et al., 2001).

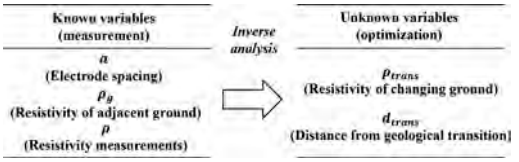

Figure 3. Objectives of the inverse analysis.

The objective function ($f(x)$) of the HS algorithm was defined as the root mean square error (RMSE) between the analytical solution ($\rho_{analytical}$) and the measured electrical resistivity (ρ_a), as shown in Eq. 2. The HS algorithm aims to minimize the objective function values of the harmony memory, which includes the unknown variables. Finally, the characteristics of the geological transition can be obtained using the harmony memory with the minimum objective function. A detailed description of the HS algorithm procedure can be found in Geem et al. (2001).

$$f(x) = \sqrt{\sum \frac{1}{M}\left(\rho - \rho_{analytical}\right)^2} \qquad (2)$$

where M is the number of measurements with different electrode spacings.

4 LABORATORY EXPERIMENTS

4.1 *Experimental setup*

The developed system was validated through a lab-scale soil chamber test designed to simulate a geological transition in front of a tunnel face. A schematic of the experimental setup is shown in Figure 4. The experimental equipment comprised a soil chamber, electrodes, measuring apparatus, and a PC with the inverse analysis program. To enhance prediction performance, five apparent electrical resistivities were measured with electrode spacings of 10, 15, 20, 25, and 30 mm. The experiment employed rock and soil formations such as granite, gravel, silica sand, and weathered granite soil to simulate ground conditions while considering geological transitions. The properties of theses specimens are summarized in Table 2.s

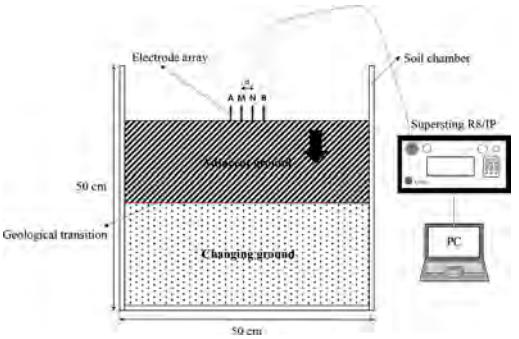

Figure 4. Schematic diagram of the experimental setup.

Table 2. Properties of the rock and soil specimens.

Type	Property	Values
Gravel	Water content [%]	3.03
	Coefficient of uniformity (C_u)	0.6696
	Coefficient of curvature (C_c)	0.8673
	Dry unit weight (r_d) [kN/m^3]	14.396
	Soil type (USCS)	GP
	Electrical resistivity (ρ) [Ωm]	119.665
Silica sand	Water content [%]	31.26
	Coefficient of uniformity (C_u)	0.6384
	Coefficient of curvature (C_c)	1.1697
	Dry unit weight (r_d) [kN/m^3]	14.578
	Soil type (USCS)	SP
	Electrical resistivity (ρ) [Ωm]	76.29
Weathered granite soil	Water content [%]	22.42
	Coefficient of uniformity (C_u)	0.7382
	Coefficient of curvature (C_c)	1.0897
	Dry unit weight (r_d) [kN/m^3]	13.812
	Soil type (USCS)	SP
	Electrical resistivity (ρ) [Ωm]	133.34
Granite	Dry unit weight (r_d) [kN/m^3]	25.064
	Electrical resistivity (ρ) [Ωm]	303.89

Geological transitions were simulated in the soil chamber by filling it with silica sand, gravel, or weathered granite soil and stacking granite blocks. In this setup, the rock and soil formations were arranged in the upper and lower layers, respectively, as shown in Figure 5. Six experimental cases were performed, involving variations in the characteristics of the geological transition, such as the distance between the geological transition and the tunnel face (d_{trans}) and

the electrical resistivity of the changing ground (i.e., soil formations) (ρ_{trans}). Table 3 summarizes the characteristics of the geological transitions in each experimental case.

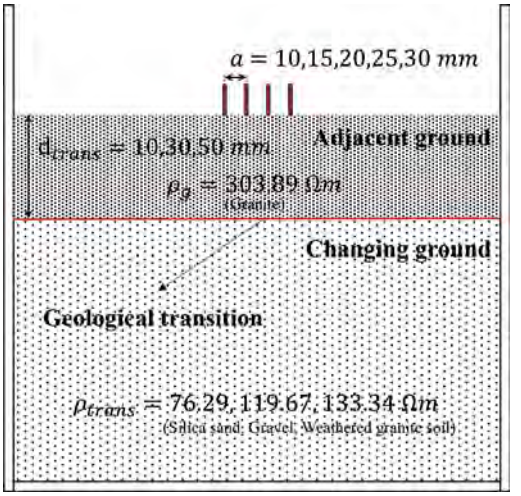

Figure 5. Illustration of the laboratory test cases for predicting geological transitions.

Table 3. Laboratory experimental cases for predicting geological transitions.

Considering the distance (d_{trans})	Values		
Distance [d_{trans}] (mm)	10	30	50
Electrical resistivity [ρ_{trans}] (Ωm)	119.67 (Gravel)		
Considering the changing ground (ρ_{trans})	Values		
Electrical resistivity [ρ_{trans}] (Ωm)	76.29 (Silica sand)	119.67 (Gravel)	133.34 (Weathered granite soil)
Distance [d_{trans}] (mm)	30		

4.2 *Experimental results and discussion*

The optimization results were analysed using two types of graphs: the prediction error graph and the convergence curves, as illustrated in Figures 6 and 7. Prediction errors were calculated by comparing the predicted results with the characteristic values of the simulated geological transition in the soil chamber. In addition, the convergence curves represented the objective function (i.e., Eq. 2) corresponding to each iteration, demonstrating the optimization performance of the developed system. A significant decrease in the convergence curves indicates the high optimization capacity of the system.

To assess the effect of the distance between the geological transition and the tunnel face, the electrical resistivity was measured while varying the distance from the geological transition to the tunnel face during the optimization process. The optimization results are compared in Figure 6. The experimental results show that the prediction error decreased as the tunnel face approached the geological transition, as shown in Figure 6(a). Furthermore, the convergence rate increased along with the shorter distance between the geological transition and the tunnel face (refer to Figure 6(b)). Thus, the geological transition ahead of a tunnel face can be detected more clearly when it is adjacent to the tunnel.

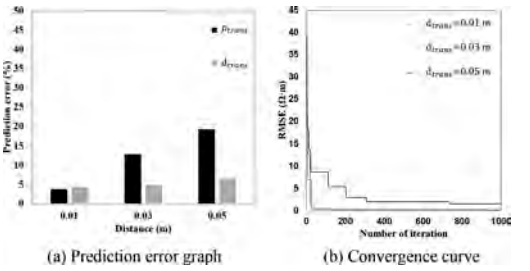

Figure 6. Effect of the distance between the geological transition and tunnel face on the optimization result.

To estimate the effect of the electrical resistivity of the changing ground on the optimization, inverse analysis was conducted using the electrical resistivity measurements corresponding to different materials of changing ground. The optimization results are compared in Figure 7, considering three substances of changing ground. The results showed that the effect of the changing ground on the optimization was negligible, as shown in Figure 7. Nevertheless, the prediction and convergence performance were sufficiently superior to predict the geological transition in front of a tunnel face, regardless of the changing ground.

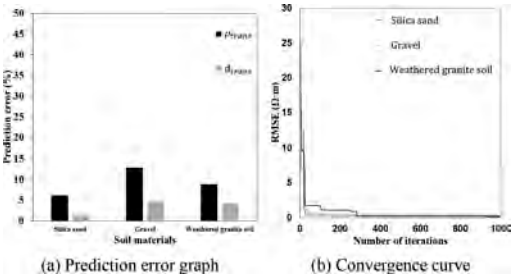

Figure 7. Effect of the changing ground on the optimization result.

5 CONCLUSIONS

In this study, an optimization system was developed for predicting geological transitions ahead of

a tunnel face using inverse analysis combined with the HS algorithm. The developed system is capable of estimating important features, including the electrical resistivity of changing ground, and the distance between the geological transition and the tunnel face, which are crucial for implementing effective risk management strategies. To validate the system, a series of laboratory experiments were conducted, and the findings can be summarized as follows:

1) The developed system was successfully verified through laboratory-scale chamber experiments that simulated geological transitions ahead of a tunnel face. These experiments demonstrated the system's ability to accurately predict the two characteristics of the geological transition.
2) The prediction error of the system decreased when the tunnel face approached the geological transition in the experiments. Thus, tunnel operators can detect geological transitions more accurately when they are in close proximity to the tunnel face.
3) The prediction performance of the system was consistently significant, regardless of the changing ground. This capability enables the effective management of construction risks associated with unforeseen geological transitions by accurately predicting their characteristics.

ACKNOWLEDGMENTS

This research was conducted with the support of the "National R&D Project for Smart Construction Technology (No. RS-2020-KA157074)" funded by the Korea Agency for Infrastructure Technology Advancement under the Ministry of Land, Infrastructure and Transport, and managed by the Korea Expressway Corporation.

REFERENCES

Atkins, E. R., Smith, G. H., 1961. The significance of particle shape in formation resistivity factor-porosity relationships. Journal of Petroleum Technology. 13(03), 285–291. https://doi.org/10.2118/1560-G-PA.

Ayvaz, M. T., 2009. Application of harmony search algorithm to the solution of groundwater management models. Advances in Water resources. 32(6), 916–924. https://doi.org/10.1016/j.advwatres.2009.03.003.

Bai, X. D., Cheng, W. C., Ong, D. E., Li, G., 2021. Evaluation of geological conditions and clogging of tunneling using machine learning. Geomechanics and Engineering. 25(1), 59–73. https://doi.org/10.12989/gae.2021.25.1.059.

Brace, W. F., Orange, A. S., 1968. Electrical resistivity changes in saturated rocks during fracture and frictional sliding. Journal of Geophysical Research. 73(4), 1433–1445. https://doi.org/10.1029/JB073i004p01433.

Caselle, C., Bonetto, S., Comina, C., Stocco, S. 2020. GPR surveys for the prevention of karst risk in underground gypsum quarries. Tunnelling and Underground Space Technology, 95, 103137. https://doi.org/10.1016/j.tust.2019.103137.

Dickmann, T., Sander, B. K., 1996. Drivage concurrent tunnel seismic prediction (TSP). Felsbau. 14(6), 406–411.

Farrokh, E., Rostami, J., 2009. Effect of adverse geological condition on TBM operation in Ghomroud tunnel conveyance project. Tunnelling and Underground Space Technology 24(4), 436–446. https://doi.org/10.1016/j.tust.2008.12.006.

Geem, Z. W., Kim, J. H., Loganathan, G. V., 2001. A new heuristic optimization algorithm harmony search. Simulation. 76(2), 60–68. https://doi.org/10.1177/003754970107600201.

Gong, S. Y., Li, J., Ju, F., Dou, L. M., He, J., Tian, X. Y., 2019. Passive seismic tomography for rockburst risk identification based on adaptive-grid method. Tunnelling and Underground Space Technology, 86, 198–208. https://doi.org/10.1016/j.tust.2019.01.001.

Grodner, M., 2001. Delineation of rockburst fractures with ground penetrating radar in the Witwatersrand Basin, South Africa. International Journal of Rock Mechanics and Mining Sciences. 38(6), 885–891. https://doi.org/10.1016/S1365-1609(01)00054-5.

Kang, M., Kim, S., Lee, J., Choi, H., 2022. FE model of electrical resistivity survey for mixed ground prediction ahead of a TBM tunnel face. Geomechanics and Engineering. 29(3), 301–310. https://doi.org/10.12989/gae.2022.29.3.301.

Kang, M., Lee, J., Kwon, K., Park, S., Choi, H., 2023. Laboratory simulations on hybrid non-destructive survey of electrical resistivity and induced polarization to predict geological risks ahead of a TBM tunnel. Tunnelling and Underground Space Technology 135, 105066. https://doi.org/10.1016/j.tust.2023.105066.

Kaus, A., Boening, W., 2008. BEAM–Geoelectrical Ahead Monitoring for TBM-Drives. Geomechanik und Tunnelbau: Geomechanik und Tunnelbau. 1(5), 442–449. https://doi.org/10.1002/geot.200800048.

McDowell, P. W., Barker, R. D., Butcher, A. P., Culshaw, M. G., Jackson, P. D., McCann, D. M., Arthur, J. C. R., 2002. Geophysics in Engineering Investigations. (Vol. 19). London: Ciria.

Mifkovic, M., Swidinsky, A., Mooney, M., 2021. Imaging ahead of a tunnel boring machine with DC resistivity: A laboratory and numerical study. Tunnelling and Underground Space Technology. 108, 103703. https://doi.org/10.1016/j.tust.2020.103703.

Nie, L., Wang, C., Liu, Z., Xu, Z., Sun, X., Du, Y., Wei, W., 2023. An integrated geological and geophysical approach to identify water-rich weathered granite areas during twin tunnels construction: A case study. Tunnelling and Underground Space Technology, 135, 105025. https://doi.org/10.1016/j.tust.2023.105025.

Park, J., Lee, K. H., Park, J., Choi, H., Lee, I. M., 2016. Predicting anomalous zone ahead of tunnel face utilizing electrical resistivity: I. Algorithm and measuring system development. Tunnelling and Underground Space Technology. 60, 141–150. https://doi.org/10.1016/j.tust.2016.08.007.

Park, J., Ryu, J., Choi, H., Lee, I. M., 2018. Risky ground prediction ahead of mechanized tunnel face using electrical methods: laboratory tests. KSCE Journal of Civil Engineering. 22(9), 3663–3675. https://doi.org/10.1007/s12205-018-1357-z.

Parkhomenko, E. I., 2012. Electrical properties of rocks. Springer Science & Business Media.

Rafie, M., Namin, F. S., 2015. Prediction of subsidence risk by FMEA using artificial neural network and fuzzy

inference system. International Journal of Mining Science and Technology. 25(4), 655–663. https://doi.org/10.1016/j.ijmst.2015.05.021.

Rhoades, J. D., Raats, P. A. C., Prather, R. J., 1976. Effects of liquid-phase electrical conductivity, water content, and surface conductivity on bulk soil electrical conductivity. Soil Science Society of America Journal. 40(5), 651–655. https://doi.org/10.2136/sssaj1976.03615995004000050017x.

Schaeffer, K., Mooney, M. A., 2016. Examining the influence of TBM-ground interaction on electrical resistivity imaging ahead of the TBM. Tunnelling and Underground Space Technology. 58, 82–98. https://doi.org/10.1016/j.tust.2016.04.003.

Takahashi, T., Kawase, T., 1990. Analysis of apparent resistivity in a multi-layer earth structure. IEEE Transactions on Power Delivery. 5(2), 604–612. https://doi.org/10.1109/61.53062.

Timur, A., Hempkins, W. B., Worthington, A. E., 1972. Porosity and pressure dependence of formation resistivity factor for sandstones. In Trans CWLS 4th Formation Evaluation Symposium 30.

Xu, Z. H., Yu, T. F., Lin, P., Wang, W. Y., Shao, R. Q., 2022. Integrated geochemical, mineralogical, and microstructural identification of faults in tunnels and its application to TBM jamming analysis. Tunnelling and Underground Space Technology. 128, 104650. https://doi.org/10.1016/j.tust.2022.104650.

Yazdani-Chamzini, A., 2014. Proposing a new methodology based on fuzzy logic for tunnelling risk assessment. Journal of Civil Engineering and Management. 20(1), 82–94. https://doi.org/10.3846/13923730.2013.843583.

Zhao, J., Gong, Q. M., Eisensten, Z., 2007. Tunnelling through a frequently changing and mixed ground: a case history in Singapore. Tunnelling and Underground Space Technology. 22(4), 388–400. https://doi.org/10.1016/j.tust.2006.10.002.

Zhao, K., Janutolo, M., Barla, G., Chen, G., 2014. 3D simulation of TBM excavation in brittle rock associated with fault zones: The Brenner Exploratory Tunnel case. Engineering Geology. 181, 93–111. https://doi.org/10.1016/j.enggeo.2014.07.002.

Tunnelling for a Better Life – Yan, Celestino, Thewes & Eberhardt (Eds)
© 2024 The Author(s), ISBN 978-1-032-80042-4
Open Access: www.taylorfrancis.com, CC BY-NC-ND 4.0 license

High resolution resistivity imaging for assessment of geological conditions ahead of tunnel face in a complex geology

S.L. Kapil*
President, ISEG & Director DMR Hydro Engineering & Infrastructures Ltd., India

ABSTRACT: Assessment of subsurface geological conditions along tunnel alignment is the most challenging task for tunnelling projects. Extremely rugged, densely forested, and inaccessible topography provides limited scope for investigations, which becomes a cause of concern during execution of these projects. Therefore, a realistic geological prognosis based on a comprehensive survey and investigation is the backbone of any successful project.

Conventional geological mapping and exploration techniques like drilling-drifting are expensive, time-consuming, and provide very limited information. On the other hand, geophysical investigations are fast, economical, and capable of continuous area coverage. In the last two decades, developments in software and hardware have considerably improved the reliability and applicability of geophysical techniques, and now 2D/3D subsurface details can be generated in a fast and economical way. Now it is possible to apply advanced geophysical investigation tools in rugged topography as well as under high slope conditions (> 45°).

Resistivity imaging is a newly developed advanced technique for generating 2D/3D resistivity images of subsurface geology and is capable of identifying the location and geometry of weak/fracture zones in a precise way. In this case study, resistivity imaging was utilized at one of the tunnelling projects in southern India. The investigation of the 6.71 km long tunnel was done utilizing more than 40 drill holes. In general, good quality rock mass consisting of granitic gneiss, biotite gneiss and migmatite with occasional pegmatite veins present in the area. After excavation of about 4 Km length, the tunnel face completely collapsed due to adverse geological conditions and construction was held up for more than two years. Resistivity imaging identified a highly poor rock mass of about 200 m length ahead of the tunnel face. These findings were used for planning the treatment and design of excavation methodology for the inferred zone and the same was crossed successfully.

Keywords: Investigation, Geophysical, Resistivity, Imaging

1 INTRODUCTION

Assessment of subsurface geological conditions along tunnel alignment is the most challenging owing to inaccessibility, thick vegetation cover, high super incumbent cover and geological complexity of the terrain. This results into time and cost overrun due to unforeseen geological conditions during execution. Therefore, realistic geological prognosis based on comprehensive survey and investigation is the backbone of any successful infrastructure project. Acquiring precise details of geotechnical parameters in the investigation stage of project development have great implication in selection of optimum alignment, preparation of cost estimate and design.

The conventional exploration techniques like drilling, drifting, pitting and trenching are expensive, time consuming and provide very limited information. On the other hand, geophysical investigations are fast, economic and capable of continuous coverage of the project area. To minimize the uncertainties in investigation, emerging geophysical techniques are of immense help. These techniques provide precise details of subsurface rockmass conditions and can minimize uncertainties met during construction. Geophysical studies with appropriate technology covering all project components needs to be taken up for minimizing the adverse geological conditions often met during construction.

Two decades back, due to lack of advancements in hardware and software, the geophysical instruments especially for engineering applications were in development stage and relied on basic theories of homogeneous isotropic and sub-horizontal layered

*Corresponding author: shyamkapil@gmail.com

DOI: 10.1201/9781003495505-73

earth. Due to these unrealistic assumptions it was difficult to undertake geophysical surveys under undulated terrain and high slope areas. In the last two decades, development in software and hardware have considerably improved the reliability and applicability of geophysical techniques and now 2D/3D subsurface details can be generated in a fast, economic and precise way. Now it is possible to apply new age geophysical tools in rugged topography as well as on high slope area (>45°). These non-invasive advanced geophysical investigation techniques like resistivity imaging, crosshole seismic tomography and seismic refraction tomography are extremely useful in optimizing and minimizing quantity and locations of direct investigations like drilling and are capable in developing more accurate sub surface geological model of the project components.

2 PROJECT LOCATION

The project is located near Munnar in Idduki district of Kerala and envisages transfer of water from Western Kallar River to the existing Sengulam Reservoir by constructing a 12m high and 80m long concrete gravity weir and a diversion tunnel of 3.5m diameter and 6.8 km length.

Project layout and location is shown in the Figure 1 and Figure 2 respectively. Geological investigations for this scheme were carried out doing extensive drilling along the diversion tunnel and along adits. During construction of tunnel highly poor rock mass was encountered from RD 4095.25m onwards and finally due to loose fall, over break and caving, tunnel face was completely collapsed at RD 4005.0m.

Efforts were made to negotiate the poor rock mass. However because of highly poor nature of rock mass work could not proceed for almost two years. Drilling from surface ahead of tunnel face was also planned. However due to difficult field conditions this could not be taken up. Tunnel face was at a depth of about 200m from surface. As such, in order to assess geological conditions ahead of tunnel face resistivity imaging along the tunnel alignment from surface was taken up.

Figure 1. Project layout.

Figure 2. Project location.

3 GEOLOGY OF PROJECT AREA

The project is located at Anachal near Munnar in Idduki district of Kerala along the western slope of the Western Ghats amidst ridges rising to a moderate level of EL 850M to EL 1100M. The hills are occupied by migmatite group of rocks essentially made up of granitic gneiss, biotite gneiss, migmatite with occasional pegmatite veins which are highly weathered at places. The tunnel is driven through hornblende biotite gneiss and granitic gneiss and intrusive pegmatite. The trend of foliation varies from N 30° to 60° W- S30° to 60° E and dip 60° to 70° towards NE.

4 RESISTIVITY IMAGING

Resistivity surveys have been used for many decades in hydrogeological, mining and geotechnical investigations with some limitations. The resistivity sounding method used since 1920's provides a one dimensional model of the subsurface. The greatest limitation of the resistivity sounding (1D) is that it does not take into account horizontal changes in the subsurface resistivity. A more accurate model of the subsurface is a 2D model where the resistivity changes in the vertical direction, as well as in the horizontal direction along the survey line can be determined. Accordingly, resistivity surveying method has undergone dramatic changes over the last two decades on account of rapid developments in hardware technology and interpretation software.

A major improvement in the early 1990's was the development of two- dimensional (2D) resistivity imaging method that provide a more realistic model of the subsurface in geologically complex areas. In 2D imaging large numbers of electrodes

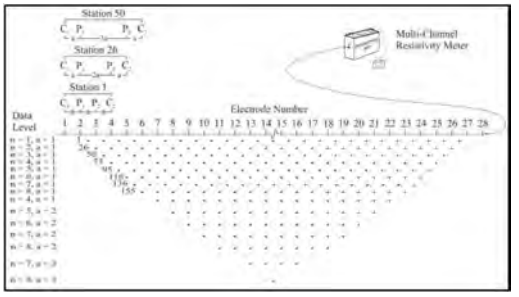

Figure 3. Arrangement of electrodes for a 2D imaging survey for apparent resistivity pseudo section (Loke 2000).

placed over the surface are connected to the instrument through an electronic switching mechanism. Arrangement of electrodes for 2-D Resistivity imaging survey is detailed in the Figure 3.

Data is collected by the instrument automatically for several datum points as per the selected electrode configuration protocols viz. Wenner, Dipole-Dipole, Schlumberger etc. As large data is collected for several datum points, this can be inverted for generation of subsurface image in terms of resistivity. This 2D/3D resistivity image can be interpreted further for assessment of subsurface lithology and can provide fine details about the subsurface. The inversion software can handle resistivity variations in both horizontal as well as in vertical directions. With these developments resistivity imaging has become a powerful tool for geological exploration with more reliability.

Figure 4. Imaging cable crossing the highway.

5 DATA COLLECTION

The tunnel alignment on the surface was crossing the National Highway, NH-49 at number of places. This posed serious problem for laying the imaging cables and was negotiated by making the local arrangement at site by placing cable in between thick rubber sheet and angle iron tied with wire (Figure 4). This was further covered by placing soil sacks and soil. This arrangement helped in smooth data collection without any restriction to traffic movement.

Moreover, tunnel is passing through big boulders and dense plantations and it was very difficult to inject the current with the electrodes available with the imaging system. In order to make good contact with the ground special mild steel electrodes of 1.5m length were fabricated and these were used for data collection. Further, to increase the contact surface area of electrodes, these were driven with hammer in a small pit filled with bentonite, salt water mixture. This mixture was kept ready and poured in between measurements to keep the contact wet.

Figure 5. Installation of longer electrodes in dense forest area.

Resistivity Imaging data was collected in roll-along (Dahlin 1996) manner with four cables each of 200m length with a cumulative length of 800m using eighty-one electrodes with 10m interval. Initially it was planned to cover the entire tunnel length of 2900m in a single layout. However due site difficulties and restriction first imaging line (R1) was terminated after covering a length of 2200m from RD 4309m to RD 2109m. Another imaging line (R2) of 800m was taken up from RD2309m to RD1509m with a overlap of 200m. A total length of 2800m was covered.

ABEM Lund Imaging System was used for field data collection. Instrument was kept in the mid of layout for taking one set of data recording. After completion of one set of data recording first cable & 20 electrodes were shifted after the last cable and the position of instrument kept in the middle of layout and again data set was recorded and this procedure was continued till the requisite length was covered. Data collection in this manner helped in data overlap after every 200m for better depth and lateral resolution. Installation of electrodes in forest area and schematic diagram showing data collection in roll-along manner is shown Figure 5, Figure 6 respectively. Data collection was done utilizing Schlumberger and Dipole- Dipole. The work presented in this paper is from the investigation report (Kapil et al. 2017).

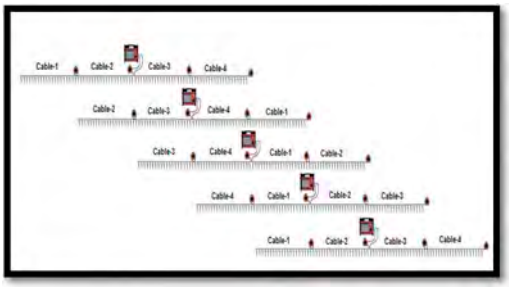

Figure 6. Data collection as per roll along method. protocols.

6 DATA PROCESSING

Data was processed using RES2DINV software in which a finite difference or finite element model of subsurface resistivity distribution is automatically adjusted to minimise the residuals between the model response and measured data (Loke and Dahlin 2002). Two different optimisation methods were tried for data inversion, L2 norm and L1 norm. In L2 norm or least square inversion, square of differences between model response and measured data is minimised. This method gives smooth transitions in resistivity between zones of different resistivity. In L1 norm or robust inversion the absolute differences are minimised. This method is more robust against noise in the data, and gives sharper boundaries between zones of different resistivities (Loke et al. 2003). Data for both Schlumberger and Dipole-Dipole protocols was processed using least square and robust inversion. Schlumberger data did not provide the vertical resolution with clarity. However dipole-dipole data provided the boundaries of poor rockmass with clarity and therefore the same was used for final assessment of geological conditions ahead of tunnel face.

7 RESULTS

7.1 *Imaging line (R1)*

This 2200m long profile was conducted utilizing Dipole-Dipole, Schlumberger and Gradient protocols with 10m electrode spacing in roll-along manner covering the diversion tunnel length from tunnel RD 4309m to 2109m. However out of these protocols the expected poor rockmass boundaries were obtained in dipole-dipole electrode configuration with clarity and the same was used for geological assessment. Maximum penetration depth of about 250m has been achieved in this profile. The resistivity imaging section corresponding to Dipole-Dipole electrode protocol is shown in Figure 7.

Low/high resistivity values on the top are indicating the overburden, boulders and rockmass. Some higher resistivity values are also observed on ground surface in overburden area representing dry soil and boulders. A low resistivity zone having values of 80 to 200 ohm. m from RD 4069m to RD 3795m is clearly visible within the rockmass. This zone corresponds to completely weathered water saturated rockmass representing the location where tunnel face was collapsed. From tunnel face (RD 4005m) length of this zone is about 210m (RD 3795 m). In the balance length of tunnel, resistivity values varying from 600 ohm.m to 4500 ohm.m represents fair to good quality rockmass. Some zones are having resistivity values above 4500 ohm,m and this represents highly competent rockmass.

7.2 *Imaging line (R2)*

This 800m long profile was conducted utilizing Dipole-Dipole and Schlumberger protocols with 10m electrode spacing in roll-along manner covering the tunnel length from RD 2309m to RD 1509m with 200m overlapping with R1 profile. In this profile also poor rockmass boundaries were obtained in dipole-dipole protocol data with clarity and the same was

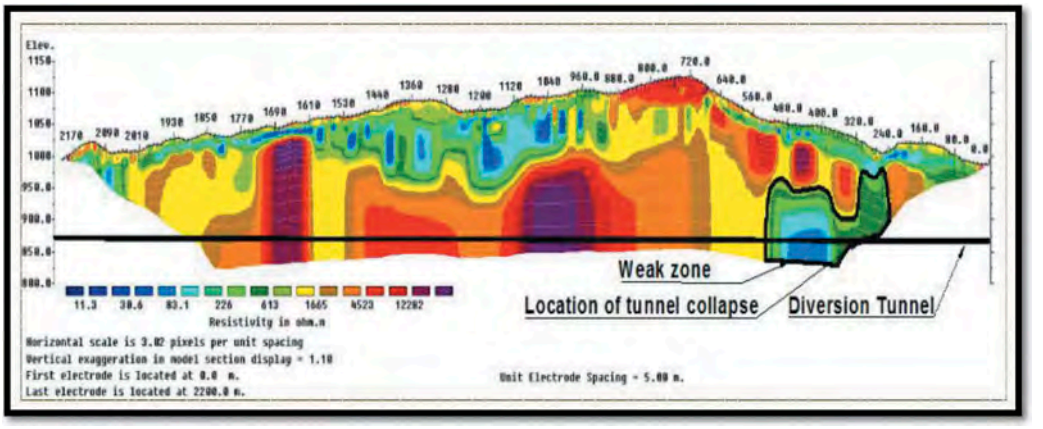

Figure 7. 2D resistivity imaging section along profile R1.

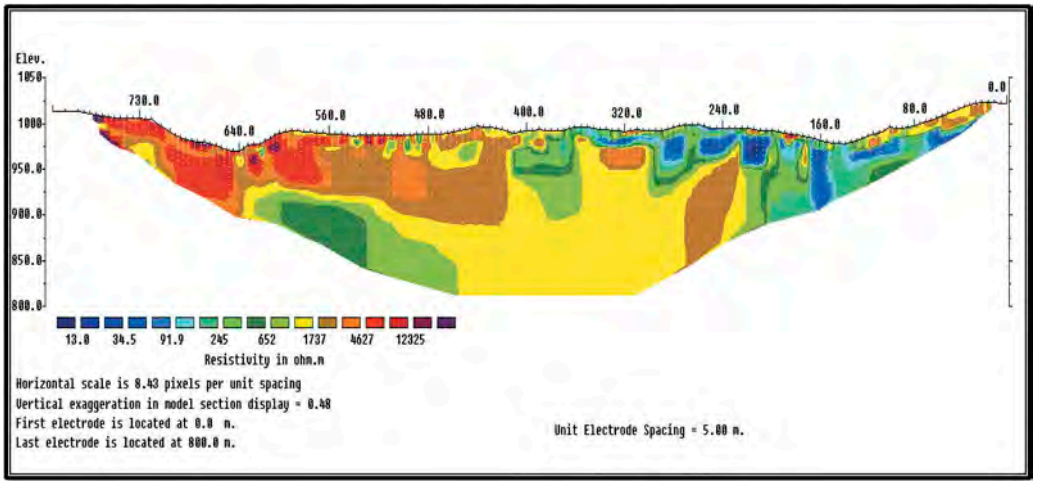

Figure 8. 2D resistivity imaging section along profile R2.

used for geological assessment. Maximum penetration depth of about 180m has been achieved in this profile.

The resistivity imaging section corresponding to this profile is shown in Figure 8.

Low/high resistivity values on the top in general corresponds to overburden representing dry soil, boulders and rockmass. A low resistivity zone of 97m length from RD 2149m to RD 2052m having values of 80 to 200 ohm.m is clearly visible within the rockmass. This zone corresponds to completely weathered, water saturated rockmass. In the balace length of tunnel, resistivity values are varying from 600 ohm.m to 4500 ohm.m representing fair to good quality rockmass. Some zones are having resistivity values above 4500 ohm,m representing highly competent rockmass.

7.3 *Geological section*

On the basis of results of the resistivity imaging profile R1 and R2 a Geological section was developed along tunnel alignment from RD 4039M to RD

Table 1. Anticipated geology in different zones.

Zone	Anticipated Lithology
Zone A	Top soil consisting slope wash material, boulders, weathered rockmass
Zone B	Completely weathered water saturated rockmass . This zone is expected to behave like soil with very loose Migmatite group of surrounding rock.
Zone C	Migmatite group of rock consisting of hornblende, biotite gneiss and granite gneiss with intrusive pegmatites. Moderately jointed fair quality rockmass.
Zone D	Migmatite group of rock consisting of hornblende, biotite gneiss and granite gneiss with intrusive pegmatites. Slightly jointed good quality rockmass.
Zone E	Migmatite group of rock consisting of hornblende, biotite gneiss and granite gneiss with intrusive pegmatites. Strong, massive very good Quality rockmass.

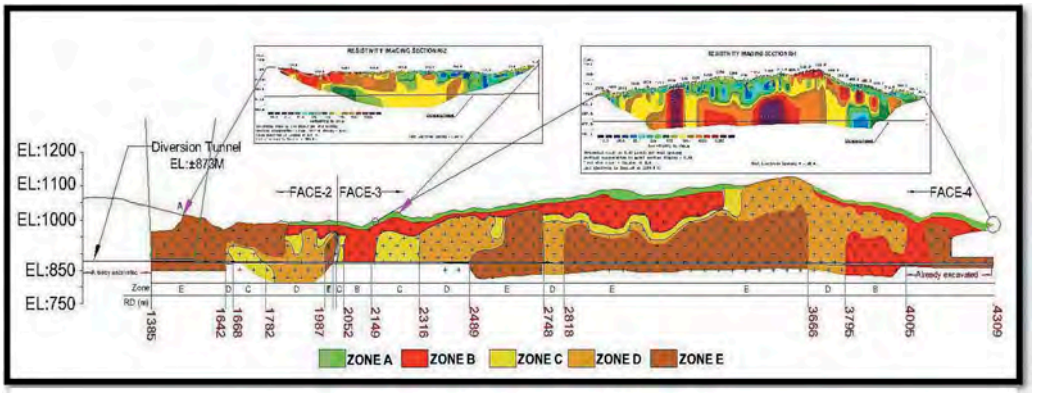

Figure 9. Geological section showing inferred zones.

1385M. Along the tunnel alignment anticipated lithology based on resistivity values has been divided into five zones Zone A, Zone B, Zone C, Zone D and Zone E. The detailed geological description of different zones is given in Table 1. The Geological section showing different zones is shown in Figure 9. Pie chart showing the percentage of different zones is shown in Figure 10.

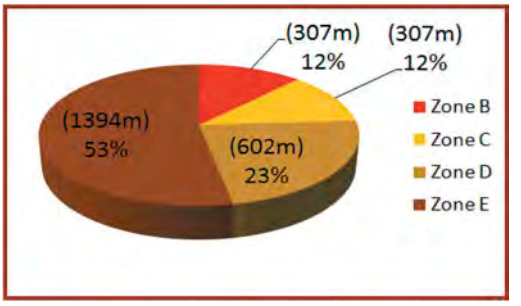

Figure 10. Pie chart showing the % in different zones.

8 CONCLUSIONS

Investigation of the diversion tunnel was done with extensive drilling utilizing more than 40 drillholes. Good quality rockmass was expected as per the drilling data along most of the tunnel alignment at tunnel grade. However adverse geological conditions were met after excavation of about 4 Km tunnel length where good rock mass was predicted based on geological mapping and drilling data. Resistivity imaging from the surface was taken up for assessment of geological conditions ahead of collapsed tunnel face and along the balance tunnel alignment. Keeping in view the rugged topography and presence of large boulders along the tunnel route, longer electrodes of 1.5m length were fabricated and used for current injection. In addition to this for increasing the surface area, these electrodes were installed in a small diameter hole filled with a mixture of bentonite and salt. This arrangement provided a high quality data. Dipole- Dipole protocol data was processed with RES2DINV software using robust inversion. Penetration depth of more than 200m beyond tunnel grade was achieved along most the covered length from RD 4005m to 1385m. Two zones consisting highly weathered rockmass were inferred along the tunnel alignment. Zone 1 is inferred from RD 4005m to RD 3795m and Zone 2 is inferred from RD 2149m to RD 2052m (Figure 9). Zone 1 corresponds to the location where the tunnel face was collapsed completely. Based on results of imaging survey data, planning & excavation methodology was finalized and tunnel excavation was restarted. The zone 1 was crossed successfully after taking adequate measures. Out of the predicted length of 210m of Zone 1, 185m length encountered highly weathered rock mass. This confirmed the reliability of imaging results. Resistivity imaging mapped the poor rock mass with proper location and geometry and this helped in starting the excavation which was pending for more than two years.

These results clearly indicate that resistivity imaging is a powerful tool and capable to provide the subsurface geological conditions in a fast and economic way with reliability. Moreover this also provide the complete details of the subsurface geology which is generally not possible by other methods nor even by drilling.

REFERENCES

Arjwech R and Everett, M. E. (2015). Application of 2D electrical resistivity tomography to engineering projects: Three case studies. *Songklanakarin Journal of Science and Technology*, 37(6), 675–681.

Dahlin, T. (1996). 2D resistivity surveying for environmental and engineering applications. *First Break*, 14(7), 275–284.

Dahlin, T. (2001). The development of DC resistivity imaging techniques. *Computers and Geosciences*, 27, 1019–1029.

Dahlin T., Garian H., & Palm H. (2004). Combined resistivity imaging and RCPT for geotechnical pre-investigation. In *Proceedings NGM 2004*, Ystad, Sweden.

Dahlin T. and Bernstone, C. (1997). A roll-along technique for 3D resistivity data acquisition with multi-electrode arrays. In *Proceedings of SAGEEP'97 (Symposium on the Application of Geophysics to Engineering and Environmental Problems)*, Reno, Nevada, March 23-26, 1997. 2, 927–935.

Griffiths, D. H., & Barker, R. D. (1993). Two-dimensional resistivity imaging and modeling in areas of complex geology. *Journal of Applied Geophysics*, 29, 211–226.

Kapil, S. L., Jyotirmoy, Singh, M. P., & Pandey, N. K. (2017). Report on geophysical investigations involving resistivity imaging and seismic tomography conducted at Sengulam Augmentation Scheme, Kerala. Geophysical Report No:- NH/EG/Geophy/174 (Unpublished).

Loke, M. H., & Barker, R. D. (1996). Practical techniques for 3D resistivity surveys and data inversion techniques. *Geophysical Prospecting*, 44(3), 499–523.

Loke, M. H. (2000). *Electrical Imaging Surveys for Environmental and Engineering Studies: A Practical Guide to 2-D and 3-D Surveys*. Penang, Malaysia.

Loke, M. H., & Lane, J. W. (2004). Inversion of data from electrical resistivity imaging surveys in water-covered areas. *Exploration Geophysics*, 35, 266–271.

Tong, L., & Yang, C. (1990). Incorporation of topography into 2D resistivity inversion. *Geophysics*, 55, 354–361.

Tunnelling for a Better Life – Yan, Celestino, Thewes & Eberhardt (Eds)
© 2024 The Author(s), ISBN 978-1-032-80042-4
Open Access: www.taylorfrancis.com, CC BY-NC-ND 4.0 license

Tunnel engineering application of assessment technology of karst development degree based on hydrochemical kinetics and fractal theory

Cangsong Li & Jian Wu
China Railway Southwest Research Institute Co., LTD. Chengdu, China
China Academy of Railway Sciences, Beijing, China

Qiang Li*, Weigang Yu & Song Lu
China Railway Southwest Research Institute Co., LTD. Chengdu, China

ABSTRACT: During tunnel construction in karst areas of China, geological hazards such as water or mud gushing pose substantial geological risks to tunnel construction. Improper handling of these hazards results in significant safety hazards during the operation stage. Therefore, it is of great significance to enable more accurate prediction and assessment of karst development degree in karst tunnels and thus minimize or prevent hazards in tunnel construction. In the above research, through the study of characteristics of karst forms and karst groundwater revealed in tunnel excavation, the characteristics and action mechanism of karst water-bearing media were unveiled, an assessment model of karst development degree based on hydrochemical kinetic parameters and fractal indexes of karst forms was established, and a hydrochemical kinetics-fractal index assessment technology of karst development degree was proposed. In engineering application in typical karst tunnels including Yaowanggu Tunnel on Jiuzhaigou-Mianyang Expressway, Xingaopo Tunnel on Xuyong-Bijie Railway and Shuangfengya Tunnel on Micang Avenue, the assessment technology of karst development degree based on hydrochemical kinetics and fractal theory was used according to different regional geological, hydrogeological and environmental conditions, and the corresponding hydrodynamic parameters and fractal assessment indexes were obtained for targeted prediction and assessment of karst development degree in tunnels. It played a positive guiding role in the project construction. The application of this technology in tunnel projects above has proved its potential for wider adoption and promotion in similar tunnel projects.

Keywords: Tunnel, Karst development degree, Groundwater chemical dynamics, Fractal theory, Evaluation technology

1 INTRODUCTION

China has the largest number of tunnels which more than 40,000 (Tian Siming et al., 2021), there are some instances of long and deep tunnels located in highly complex geological environments in mountainous regions. Especially, the construction of karst tunnels that traverse karst development areas often confronts geological hazards, including water or mud gushing of varying magnitudes, posing substantial risks to tunnel construction. Improper handling of these hazards will result in significant safety risks during the operation stage.

It is widely acknowledged that karst development necessitates specific conditions, namely the solubility and permeability of the rock, as well as the mobility and erosive properties of water (Zhang Renquan et al., 2018). Hydrogeological conditions such as structure, lithology and karst development horizon are key factors controlling the development of karst water systems (Qin Xiaoqun et al., 2017). Karst water system is affected by tunnel construction, which results in different characteristics of groundwater recharge, runoff and discharge (Li Xiao et al., 2020). To date, how to accurately assess the development of karst and karst groundwater in karst tunnels remains a prevalent and challenging issue in tunnel construction. In the study of the hazard-inducing theory of karst tunnels, unfavorable geological bodies that adversely affect tunnel construction safety when disturbed by construction are defined as hazard-inducing karst structures (He Faliang, 2019). These structures can be categorized into different types, namely dissolution fissures,

*Corresponding author: liq019@qq.com

DOI: 10.1201/9781003495505-74

karst cave cavities, channels and underground rivers (Li Shucai et al., 2018). Many scholars have extensively investigated the hazard-inducing mechanisms of certain typical karst structures through case analyses (Liu Y et al., 2019), theories encompassing geochemistry and fracture mechanics (Wang Ying et al., 2004), as well as model experiments (Li Shucai et al., 2018), and unveiled the hazard-inducing mechanisms of water and mud gushing in karst tunnels. Through the analysis of hazard-inducing mechanisms, typical factors were selected as assessment indexes to establish different water gushing risk assessment models (Yingchao Wang et al., 2017). For assessment of the criticality level of water and mud gushing in tunnels (Mao Bangyan et al., 2010), various methods such as the hierarchical analysis method (Han Xingrui et al., 2018), the expert scoring method (Liu Jian et al., 2004), and the machine learning-based method (Bai Chenghao, 2021) were used and thus a range of risk assessment methods have been developed for evaluating the risk of water and mud gushing hazards in karst tunnels. The assessment technology of karst development degree based on hydrochemical kinetics and fractal theory was developed through the study of fractal characteristics of karst forms and hydrochemical kinetics (Li Cangsong et al., 2017a). The feasibility of this method was further verified based on the engineering applications carried out in recent years.

2 CHARACTERISTICS OF KARST KARST AQUIFER

2.1 *Hydrogeological characteristics of karst water storage structures*

Karst terrain in China has a vast distribution, encompassing a total area of approximately 3.44 million km^2 (Li Datong, 1985). Karst terrain exhibits a more pronounced presence in regions such as Guangxi, Guizhou, eastern Yunnan, and northern Guangdong. However, the extent of karst development and the characteristics of karst functional assemblage can widely differ from one location to another. Based on the analysis, these variations can primarily be attributed to different geological and climatic conditions including different karst geochemical background conditions such as topography, hydrology, vegetation coverage, as well as the intensity of karst dissolution or sedimentation. Generally, karst aquifers are divided into different karst water systems according to the spatial association relationship between aquifer and aquiclude formations, different combinations of surface hydrological network and deeply incised valleys, and the existence of surface and underground watersheds. Different karst water systems not only have different hydrogeological characteristics, but also have different karst water circulation and hydrochemical characteristics due to the different morphology of water storage structures. Generally, the hydraulic connection between different karst water systems is weak or completely absent. From the perspective of water-bearing structure, tunnels traverse geological bodies of monoclinal strata, folds, fracture zones and composite strata. Tunnels that pass through syncline water-bearing structures or fracture structures are particularly susceptible to significant hazards like karst water or mud gushing. This vulnerability arises from the development of fissures within these structures where the existence of highly water-rich media, such as karst channels, is more prevalent. Additionally, based on engineering cases, long and deep tunnels, in particular, frequently encounter a wide range of karst water storage structures.

2.2 *Chemical action mechanism of karst water*

In terms of macroscopic karst landforms, the development and distribution patterns of karst exhibit variations that encompass peak clusters, peak forests, depressions, and dissolution valleys. Based on observations from various karst tunnels, several karst forms are commonly present including dissolution pores, dissolution fractures, dissolution grooves, dissolution channels, karst caves and karst underground rivers. The diverse range of karst forms fully shows the irregularity of karst forms. The karst forms revealed in tunnel excavation exhibit the characteristics of uncertainty and irregularity. When changing the observation scale and magnifying or reducing a karst form of a certain scale by multiplying it exponentially by a factor of 2, a remarkable similarity can be observed between images of large-scale dissolution fractures, pores, and underground river channels, and those of smaller-scale joints and fissures. This similarity indicates that the development of karst forms exhibits a significant characteristic of fractal imagery known as self-similarity. Upon confirming the self-similarity of karst forms, the observation scale and magnification factor were changed through image processing. It was found that the characteristics of each karst form remained unchanged. Consequently, the fractal dimensions of various karst forms can be determined. This finding suggests that karst development forms also exhibit the scale invariance characteristic of fractal images. Due to the properties of self-similarity and scale invariance exhibited by karst forms, the fractal theory can be applied to conduct an in-depth study on their characteristics, so as to explore the underlying laws governing karst development and distribution and integrate macroscopic and microscopic laws.

Based on the chemical kinetics theory of karst groundwater (Cao Yuqing et al., 2017), soluble rock and karst groundwater not only facilitate the dissolution of rock but also induce changes in the hydrochemical composition of karst groundwater through hydrodynamic and hydrochemical processes. The chemical composition of groundwater reflects the hydrogeochemical environment and various physical and chemical reactions or action mechanisms that groundwater undergoes as it migrates through karst

water-bearing media. It becomes a hydrogeological parameter capable of characterizing the process of water-rock interaction and the extent of such reactions.

According to the fractal theory, the hydrogeological characteristics of karst revealed in tunnels are affected by their hydrogeological environment, and there are differences in hydrochemical components, so the composition of hydrochemical ions is random. According to the complexation reaction theory in analytical chemistry, the formation of highly stable new ions through the combination of molecules or ions with metal ions is known as a complexation reaction. By integrating the principles of hydrochemical kinetics, ion pairs are defined through the combination and pairing of common ions in hydrochemical analysis. Subsequently, the cumulative percentage of ion pairs is statistically analyzed. According to paper (Li Cangsong et al., 2018), they also have two significant attributes, i.e. self-similarity and scale invariance of fractal images. This proves the applicability of fractal theory in the chemical composition analysis of karst groundwater.

3 ASSESSMENT TECHNOLOGY OF KARST DEVELOPMENT DEGREE

3.1 *Assessment method based on hydrochemical kinetics-fractal indexes*

The karst development degree can be viewed as varying stages and conditions of karst geological phenomena formed by the dissolution of soluble rocks under the influence of specific internal driving forces and external agents. It represents the ultimate outcome of karstification, yet remains a relative concept. Therefore, both qualitative and quantitative methods should be used for assessment of karst development extent. Finally, a comprehensive assessment index is utilized to describe the extent of karst development. The qualitative assessment coefficient C_{kDq} of karst development degree is determined according to the monograph Groundwater Chemical Kinetics and Fractal Characteristics of Karst Tunnel (Li Cangsong et al., 2017b). The present study primarily focuses on the fractal assessment index C_{kDF} for determining the extent of karst development using Formula (1). This mainly involves calculating hydrochemical fractal assessment index Q_w and microscopic karst form fractal assessment index Q_v.

$$C_{kDF} = \sqrt{Q_w \bullet Q_p} \tag{1}$$

The calculation steps for hydrochemical fractal assessment index Q_w are as follows:

1. collect water samples and analyze the conventional hydrochemical composition of the samples;
2. create the cumulative ion pair percentage - observation scale scatter diagram and the fractal dimension calculation curves;
3. perform regression analysis on the fractal dimension calculation curves; and
4. compute the hydrochemical fractal assessment index using the slope and correlation coefficient indicated in Q_w regression curves.

The calculation steps for microscopic karst form fractal assessment index Q_p are as follows:

1. obtain microscopic karst form photos by taking field photos or scanning rock samples under a microscope;
2. conduct "gray scale processing" of the images;
3. call in fractal images and compute the fractal dimensions using the prediction and assessment system of tunnel karst development degree V1.0 (software copyright No. 2019SR0236368);
4. plot the karst unit area percentage - observation scale scatter diagram curves, and perform regression analysis, and compute the fractal assessment index Q_p of karst development degree according to the fractal dimension and correlation coefficient of fractal curve.

3.2 *Index system*

As described above, karst development is special and complex, and karst forms encountered in tunnel excavation are random. Therefore, it is not easy to accurately define or assess the extent of karst development. So, the assessment index system of karst development degree consists of two parts: qualitative index and quantitative index. The qualitative assessment index (C_{kDq}) of karst development degree is based on the necessary conditions for karst development, and it is obtained by itemized scoring and summing as per assessment indexes by field technicians. The fractal assessment index (C_{kDF}) of karst development degree is computed by using the aforementioned method to analyze the fractal characteristics of both karst form and karst groundwater. For details, please refer to paper (Li Cangsong et al., 2018) and literature (Li Cangsong et al., 2017b).

The assessment model of karst development extent based on hydrochemical kinetics-fractal indexes is established as Formula (2):

$$C_{kD} = 0.3 \times C_{kDq} + 0.7 \times C_{kDF} \tag{2}$$

3.3 *Assessment criteria*

By fully considering the understanding or judgment experience of karst experts on the possibility of karst development, and based on the calculation results of the comprehensive assessment index C_{kD} of karst development degree, recommended assessment criteria for karst development degree are given in Table 1.

Table 1. Recommended assessment criteria for karst development extent.

Extent of karst development	Characteristics of surrounding rock and possibility of karst occurrence	C_{kD}
Not developed	The rock is hard, the rock mass is complete, the structure is not developed, and generally there is no occurrence of karst.	0.0~0.10
Slightly developed	A small number of small dissolution fractures, cracks or pores may be developed in places with good groundwater runoff conditions.	0.10~0.20
Relatively developed	Dissolution grooves and channels may be developed	0.20~0.40
Developed	Karst caves or underground rivers are very likely to develop is the lithology is soluble rock.	0.40~0.80
Very developed	Extra-large filled karst caves or extra-large underground rivers that may have a catastrophic safety impact on tunnels	0.80~1.00

4 ENGINEERING APPLICATION CASES

4.1 *Yaowanggu tunnel*

4.1.1 *Project overview*

Yaowanggu Tunnel is located in Beichuan County, Sichuan Province, China. The left tunnel is 2,030 m long and the right track is 1,994.5 m long. The tunnel site area is in the northwest of Sichuan Basin. Under the control of strata lithology and tectonic process, the topography and landforms in the tunnel site area exhibit distinct characteristics of medium-low mountains, characterized by prominent dissolution and denudation. The tunnel is situated at the southwest end of the water storage structure of Tangwangzhai flat-topped trap syncline. The tunnel body passes through the strata of the Middle Devonian Guanwushan Formation (D_2gn) limestone, the Middle Devonian Yangmaba Formation (D_2y) limestone, the Middle Devonian Ganxi Formation (D_2g) argillaceous sandstone, mudstone and shale in sequence.

4.1.2 *Karst development degree*

1. The karst form of soluble rock exposed in Yangmaba Formation in the tunnel site area, and Figure 1 shows the karst after numerical processing. The fractal dimension of karst in Figure 2 is calculated by the compiled fractal image calculation software. Scatter Diagram of Karst Unit Area Percentage-Observation Scale and Calculation Curve of Fractal Dimension after calculation. After regression analysis of the fractal dimension curve, the linear equation is y = 0.471x+3.016, and the fractal assessment index (Q_p) of karst form is 0.68.

2. Chemical fractal dimension calculation of karst groundwater

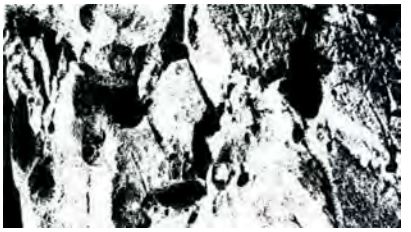

Figure 1. Numerical processing of karst landform.

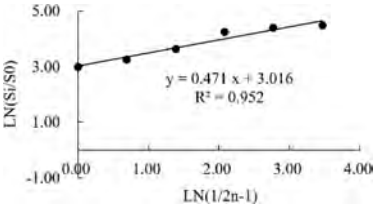

Figure 2. Calculation curve of fractal dimension.

According to the investigation of water samples, which hydrochemical compositions of groundwater points are similar, indicating that the hydrochemical process is mainly dominated by water-rock interaction and rainfall, and mainly controlled by carbonatite dissolution.

In this study, two groundwater sample points are taken as the chemical fractal samples of karst groundwater. The hydrochemical fractal assessment index Q_w of sample points is calculated respectively, and averaged to obtain the karst development assessment index value of karst strata exposed by the tunnel. After calculation, through linear regression

Table 2. Hydrochemical composition analysis of karst groundwater in tunnel.

		K^++Na^+	Ca^{2+}	Mg^{2+}	NH^{4+}	Cl^-	SO_4^{2-}	HCO_3^-	CO_3^{2-}	NO^{3-}	TDS
No.	ph	Unit: mg/L									
S01	7.72	8.46	39.14	5.56	0.28	9.21	9.73	139.36	0.00	2.95	145.02
S02	7.93	8.40	41.23	4.80	0.22	6.91	9.85	145.42	0.00	2.89	147.01

of the fractal dimension curve, the linear equation of two water sample is y=0.966x-1.574 (Figure 3), which indirectly proves that the karst water samples taken in this study have high homology. The fractal assessment index (Q_w) of karst form is 0.87. Therefore, the fractal assessment quantitative index C_{kDF} of karst development degree is obtained according to the formula:

$$C_{kDF} = \sqrt{Q_w \cdot Q_p} = \sqrt{0.87 \times 0.68} = 0.77$$

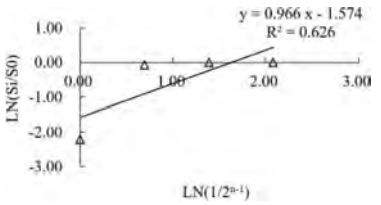

Figure 3. Calculation curve of S01 and S02.

According to the on-site geological survey and regional karst hydrogeological conditions, the tunnel body passing through limestone is the key mileage section for karst and karst groundwater development. According to the previous table, the qualitative assessment index (C_{kDq}) of karst development degree is calculated as 0.76. According to the classification standards for karst development degree of the constructed assessment model, the fractal assessment index C_{kD} of karst development degree is 0.77. Therefore, when the tunnel passes through this stratum section, the karst development degree is "developed", and it is highly likely to develop karst caves or underground rivers.

$$C_{kD} = 0.3C_{kDq} + 0.7C_{kDF} = 0.77$$

4.1.3 *Verification of construction reveal*

In April 2022, the tunnel was excavated to the stratum of Yangmaba Formation at ZK199+306, revealing a karst cave. Then the tunnel was excavated to ZK199+312, revealing a large karst cave again. According to the advanced geological forecast of the tunnel, the karst is developed at ZK199+301~+355 section of the tunnel. In combination with the tunnel excavation exposure, the karst cave extends towards the right line of the tunnel and passes through the vault of the right tunnel. The karst caves at ZK199+296~+306 section belong to the same system as those exposed in this study. In June 2022, the right line of the tunnel was excavated to the tunnel working face at K199+324, revealing a relatively soft rock stratum with extremely developed joints and fissures. The rock stratum is broken as a whole, with yellow mud in the vault and falling blocks. Geophysical prospecting shows that this section is a low-resistance section, and it is inferred that there is a karst or dissolution development zone. The above reveal fully verifies the accuracy of the prediction and assessment conclusions.

4.2 *Shuangfengya Tunnel*

4.2.1 *Project overview*

Shuangfengya Tunnel is located in Tiechang Township and Huitan Township, Nanjiang County, Bazhong City, with a total length of more than 8.5km. The tunnel site area is located in the northeast of Sichuan Basin and at the southern foot of the Micang Mountain in Daba Mountains. The landform is obviously controlled by geological structure and lithology, and is distributed in east-west direction. It belongs to the landform of tectonic denudation-dissolution high and medium mountains. The topographic slope changes greatly, generally ranging from 10° to 35°, and is nearly vertical locally in the form of scarps and cliffs. The exposed section is at one end of Guangwu Mountain, which is on one flank of the syncline and can be regarded as monoclinal karst water-bearing structure.

See Table 3 for the simple analysis data of investigated water samples, and the water sample points are moderately~weakly alkaline. The cations in the water samples are mainly Ca^{2+}, followed by Na^{+}+K^{+}, and Mg^{2+} is less. The anions are mainly HCO_3^{-}, followed by SO_4^{2-}, and Cl^{-} is less. The hydrochemical characteristics of the water sample points belong to bicarbonate and sulfate water with low TDS, short runoff path and good circulation conditions, maintaining a good state of natural freshwater resources.

Table 3. Hydrochemical composition analysis water points in tunnel site area.

No.	Sampling location	K^{+}+Na^{+}	Ca^{2+}	Mg^{2+}	Cl^{-}	SO_4^{2-}	HCO_3^{-}	CO_3^{2-}	TDS
		mg/L							
A01	Underground river at ditch bottom	36.00	80.16	19.46	8.51	115.27	268.49	0.00	393.64
S01	Tunnel working face	78.00	117.84	6.32	14.18	169.07	341.71	0.00	556.26
S02	Tunnel working face	51.00	124.25	7.30	12.76	134.48	346.59	0.00	503.09

4.2.2 *Karst development degree*

According to the above method, and the calculation process will not be described in detail. The fractal dimension of karst calculated results are shown in Figure 4. After regression analysis of the fractal dimension curve, the linear equation is y=0.663x +2.477, and the fractal assessment index (Q_p) of karst form is 0.80.

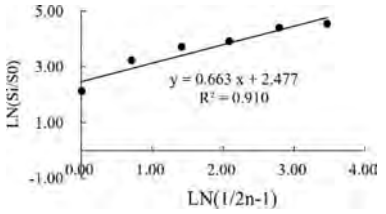

Figure 4. Fractal dimension curve of karst form.

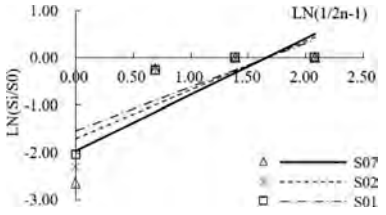

Figure 5. Hydrochemical fractal dimension curve.

According to the hydrochemical analysis data of groundwater samples taken, the calculation curves of fractal dimensions are shown in Figure 5, and their linear equations are y=0.921x-1.533, y=1.029x-1.701 and y=1.187x-1.961 respectively. The average value of fractal assessment index (Q_w) of karst form is 0.93. Therefore, according to the formula, the assessment quantitative index C_{kDF} of karst development degree is 0.86. According to the classification standards for the constructed karst development degree assessment model, the C_{kD} value is 0.83. When the tunnel passes through this stratum section, the karst development degree is "very developed". If the passing lithology is soluble rock, it may cause catastrophic safety impact on the tunnel, such as extra-large filled karst caves or extra-large underground rivers.

4.2.3 *Verification of construction reveal*

(1) Geophysical prospecting forecast results

See Figure 6 for the slice map of HSP test results in ZK51+259~ZK51+159 section within the detection range. There is obvious wave impedance interface and wave velocity reduction in ZK51+259~ZK51+210 section. According to the analysis, within this section, the rock mass is broken, joints and fissures are developed, weak interlayers, fracture zones and karst (solution cracks, etc.) are relatively developed, groundwater is developed, mostly occurring in a linear manner, and the stability of surrounding rock is poor. There is obvious wave impedance interface and wave velocity reduction in some sections of ZK51+305~ZK51+249 section. According to the analysis, within this section, the rock mass is broken, joints and fissures are developed, there are weak interlayers, fracture zones and karst (solution cracks, etc.) in ZK51 +305~ZK51+285 and ZK51+260~ZK51+249, groundwater is developed, mostly occurring in a linear manner and increasing in rainy season, and the stability of surrounding rock is poor.

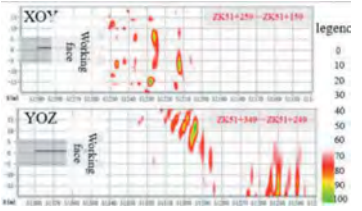

Figure 6. HSP analysis results.

(2) Site exposure

Since the exposure of karst caves at ZK51+258 at the exit of Shuangfengya Tunnel, three large-scale karst caves have been continuously exposed within a range of less than 50m of the tunnel alignment. The surrounding rocks in this section are light yellow and grayish black limestone and shale, which are relatively hard and broken in stratified structure, with developed karst, fracture zones and weak interlayers. There are indeed sinkholes on the surface, which are consistent with the design data. Three large-scale karst caves originate from the same water system, with chainages of ZK51+258, ZK51 +240 and ZK51+220 respectively. The three exposed karst caves all run through the tunnel in a transverse manner and develop along both sides of the side wall and top of the tunnel. The occurrence of karst caves is basically consistent with that of rock strata, i.e. 3°∠85°. The width of the karst cave revealed at ZK51+258 is about 4m, that at ZK51+240 is about 7m, and that at ZK51+220 is about 15m.

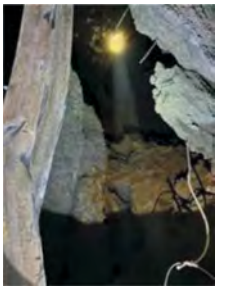

Figure 7. Karst cave revealed in tunnel.

4.3 *Xingaopo Tunnel*

4.3.1 *Project overview*

The Xingaopo Tunnel on Xuyong-Bijie Railway has a total length of 8,100m and a maximum burial depth of about 445m. Soluble rocks are mainly distributed in D3K300+106~D3K301+400 section, with a length of about 1,294m, including limestone interlayers of Maocaopu Formation (T_1m), Feixianguan Formation (T_1f) and Changxing Formation (P_2c). The geological structure of the tunnel site area is complex, and the structural features such as faults and folds are mainly in east-west direction, intersecting with the tunnel alignment at a large angle. Due to strong tectonic action, the stratum rock mass is very broken. Affected by stratum uplift and river erosion, the water system in the tunnel site area is distributed in a dendritic shape, and most of the streams belong to seasonal running water. Lanjia River Gully at the entrance section, Shangyangtang River Gully at DK304+780 and Chashu River Gully at DK306 +300 are the main surface water bodies in the tunnel site area, with relatively abundant water volume.

4.3.2 *Karst development degree*

The fractal dimension of karst is calculated by the compiled fractal image calculation software. After regression analysis of the fractal dimension curve, the linear equation is y=0.579x+2.689, and the fractal assessment index (Q_v) of karst form is 0.75.

According to the hydrochemical analysis data of groundwater samples taken, their linear equations of fractal dimensions curves are y=0.897x-1.496, y=1.055x-1.779 and y=1.103x-1.806 respectively. The average value of fractal assessment index (Q_w) of karst form is 0.92 .The assessment quantitative index C_{kDF} of karst development degree is 0.83. Therefore, according to C_{kD} of 0.79, when the tunnel passes through this stratum section, the karst development degree is "developed", and it is highly likely to develop karst caves or underground rivers.

4.3.3 *Verification of construction reveal*

Based on the prediction and assessment of karst development and forecast analysis, it is confirmed that joints and fissures are developed in rock mass at D3K300+354~D3K300+375 section of Xingaopo Tunnel, with "developed" karst. The tunnel encounters karst caves and cavities, so there is a great possibility of water and mud inrush in the tunnel. According to the comprehensive forecast conclusion, corresponding preventive measures have been taken during construction. When the tunnel working face was exposed to D3K300+364, a large unfilled karst cave with a major axis diameter of about 20m was observed. The karst cave is divided into upper and lower layers. The wall of the upper karst cave is dry and water-free, and its alignment is perpendicular to that of the tunnel. The wall of the lower karst cave is relatively wet and attached with a large number of white carbonate crystals, and its alignment is oblique to that of the tunnel. The revealed karst cave is shown in Figure 8.

Figure 8. Revealed karst cave.

5 CONCLUSIONS

In this study, the hydrochemical kinetics-fractal index assessment technical method of karst development degree and its application in tunnel engineering are analyzed. The research results are as follows:

(1) The water and mud inrush hazards in karst tunnels are the results of comprehensive action of stratum lithology, geological structure and karst groundwater. Its macroscopic karst form, microscopic dissolution traces and karst hydrochemical dynamic characteristics reflect the karst development degree. Therefore, it is feasible to use macroscopic surface karst forms and hydrochemical fractal characteristics of karst groundwater as quantitative assessment indexes of karst development degree.

(2) The application practice of karst tunnels such as Yaowanggu Tunnel, Shuangfengya Tunnel and Xingaopo Tunnel shows that the assessment technology of karst development degree based on hydrochemical kinetics-fractal indexes can be combined with advanced geological forecast means on the basis of accurate identification of hazard-inducing structures in high-risk karst tunnels, and multiple methods are used for comprehensive assessment. In addition, based on the special geological investigation of karst risks, it is conducive to avoiding tunnel karst geological hazards during construction by evaluating potential risks and reasonably supplementing measures such as geological drilling and advanced drilling in the tunnel.

REFERENCES

Bai Chenghao. Research on Intelligent Risk Prediction Method for Water and Mud Inrush Hazards in Karst Tunnels Based on Machine Learning [D]. Shandong University, 2021.

Han Xingrui. Karst Water Bursting in Tunnel and Expert Judging System [J]. Carsologica Sinica, 2004(03): 47–52.

He Faliang. Geological Hazards and Disaster-Causing Structures in Tunnel Construction and Disaster-Causing Modes of Disaster-Causing Structures [J]. Modern Tunnelling Technology, 2019, 56(z1):138–143.

Li Cangsong, Ding Jianfang, Liao Yankai. 2017. Groundwater Chemical Kinetics and Fractal Characteristics of Karst Tunnel [M]. Beijing: Science Press, 1–38.

Li Cangsong, Liao Yankai, Ding Jianfang. Study on Karst Development in Tunnels by Hydrochemical Kinetics--Fractal Index Evaluation Technology [J]. Modern Tunnelling Technology, 2017, 54(06):24–31+44.

Li Cangsong, Wu Fengshou, Zhao Yanjie, et al.Fractal and Hydro-Chemical Characteristics of Microscopic Karst Morphology Based on Dissolution Experiments [J]. Modern Tunnelling Technology, 2018, 55(02):110–120.

Li Datong. 1985. Specification for Map of Soluble Rock Types in China [M]. Beijing: SinoMaps Press, 1–38.

Li Shucai, Pan Dongdong, Xu Zhenhao, et al.A Model Test on Catastrophic Evolution Process of Water Inrush of a Concealed Karst Cave Filled with Confined Water [J]. Rock and Soil Mechanics, 2018, 39(09):3164–3173.

Li Shucai, Xu Zhenhao, et al.Classification, Geological Identification, Hazard Mode and Typical Case Studies of Hazard-causing Structures for Water and Mud Inrush in Tunnels [J]. Chinese Journal of Rock Mechanics and Engineering, 2018, 37(05):1041–1069.

Li Xiao, Qi Jihong, Xu Mo. Analysis on the Characteristics of Small-scale Shallow Karst Water Systems in Typical Tight-narrow Folds and Tunnel Water Inrush in Southwestern China [J]. Carsologica Sinica, 2020, 39(3):9.

Liu Jian, Liu Dan. Groundwater Negative Effects Evaluation for Tunnel Engineering Based on Fuzzy Analytic Hierarchy Process [J]. Environment and Ecology in the Three Gorges, 2009, 2(01):53–56.

Liu Y, Feng Y, Xu M, et al.Effect of an incremental change in external water pressure on tunnel lining: a case study from the Tongxi karst tunnel[J]. Natural Hazards, 2019, 98: 343–377.

Mao Bangyan, Xu Mo, Jiang Liangwen. Preliminary Study on Risk Assessment of Water and Mud Inrush in Karst Tunnel [J]. Carsologica Sinica, 2010, 29(02):183–189.

Qin Xiaoqun, Song Kaiben, Huang Qibo, et al.Groundwater Occurrence Characteristics and Drilling Well Models in Karst Peak Forest Areas, Guangxi, China [J]. Carsologica Sinica, 2017, 36(5):8.

Tian Siming, Wang Wei, Yang Changyu, et al.Development and Prospect of Railway Tunnels in China in Recent 40 Years [J]. Tunnel Construction (in Chinese and English), 2021, 41(11):56.

Wang Ying, Chen Qiang, et al.Water/Rock Interaction Mechanism in Deep-buried Tunnels in Karst Area [J]. China Railway Science, 2004, 25(4):55–58.

Yingchao Wang, et al. Risk Assessment of Water Inrush in Karst Tunnels Based on the Effcacy Coeffcient Method[J].Pol. J. Environ. Stud. Vol.26, No. 4 (2017), 1765–1775.

Zhang Renquan, Liang Xing, Jin Menggui, et al. Fundamentals of Hydrogeology [M]. Beijing: Geological Publishing House, 2018.

Tunnelling for a Better Life – Yan, Celestino, Thewes & Eberhardt (Eds)
© 2024 The Author(s), ISBN 978-1-032-80042-4
Open Access: www.taylorfrancis.com, CC BY-NC-ND 4.0 license

Model test and analysis of failure mechanism of deep high sidewall tunnel from splitting failure to zonal disintegration

Fan Li*
Shandong Hi-speed Group CO.,LTD. Innovation Research Institute
Shandong Key Laboratory of Highway Technology and Safety Assessment

Qiangyong Zhang
Research Center of Geotechnical and Structural Engineering, Shandong University

Gongfeng Xin & Guanxu Long
Shandong Hi-speed Group CO.,LTD. Innovation Research Institute
Shandong Key Laboratory of Highway Technology and Safety Assessment

ABSTRACT: Splitting failure and zonal disintegration often occur in the high sidewall of the underground powerhouse due to excavation-induced unloading, which brings many adverse effects to the construction and support work of the tunnel. We carried out two true three-dimensional geomechanical model tests to investigate the splitting failure and zonal disintegration of rock tunnel with high sidewall under high in-situ stress. The tests result show that with the increase of in-situ stress, the failure mode of the surrounding rock has a tendency to change from splitting to zonal disintegration. The model tests result reveals the formation conditions and failure characteristics of splitting failure and zonal disintegration of high sidewall tunnel, which provides a solid test foundation for further study of the nonlinear deformation and failure mechanism of rock tunnel with high sidewall under high in-situ stress. Then, we proposed a numerical analysis method based on ABAQUS platform. The numerical simulation results effectively reveal the formation condition and failure mechanism of the high sidewall tunnel.

Keywords: High sidewall tunnel, Geomechanical model test, Splitting failure, Zonal disintegration, Finite element method

1 INTRODUCTION

With the growth of underground engineering projects, the depth of excavation has increased, resulting in more and more rock engineering constructions. High sidewall tunnels in brittle rock experience complex and discontinuous deformations during excavation and pose a threat to stability and the construction process. The two most common failure modes are splitting failure and zone disintegration. These specialized failures must be taken into consideration given the risks they pose on long-term stability.

In-situ observations have revealed noticeable differences between splitting failure and zonal disintegration in rock tunnels. Splitting failure refers to a vertical or subvertical fracture at the high sidewall, which manifests as parallel or nearly parallel split cracks. In contrast, zonal disintegration is characterized by an annular layered fault, involving alternating zones of rupture and non-rupture in the surrounding rock of the deep tunnel. These findings highlight the importance of accurately distinguishing between these two phenomena, which could significantly impact the safety and stability of rock tunnels.

Previous studies (Reva, 2002; Li et al., 2008; Tan et al., 2012; Gao et al., 2019; Chanyshev and Belousova, 2018) have only focused on the zonal disintegration phenomenon in rock tunnels, ignoring any possible relationship between this phenomenon and splitting failure.

The geomechanical model test is a crucial tool in investigating the zonal disintegration of subterranean chambers, thanks to its capacity for visualization, intuition, and realism (Chen et al. 2013a, 2013b and

*Corresponding author: lifanll@foxmail.com

DOI: 10.1201/9781003495505-75

2013c; Gao et al., 2018b; Zhu et al. 2019). Additionally, numerical simulation is a computational analysis method that has gained extensive use through the application of computer technology (Zhou and Shou. 2013; Vtorushin, 2016; Gao et al., 2018a; Wu et al., 2019; Li et al., 2023). In our research, we have found that zonal disintegration typically occurs in deep tunnels with depths of over 1,000 meters, while splitting failure occurs in rock tunnels with high sidewalls and depths of several hundred meters. With increasing in-situ stress, does the failure mode of high sidewall rock tunnels shift from splitting failure to zonal disintegration? To test this hypothesis, we conducted two model tests on the failure mechanisms of high sidewall tunnels under high in-situ stress, using the main powerhouse of the Pubugou Hydropower Station as an example. In Model I, we replicated the splitting failure of high sidewall tunnels under high ground stress. Upon increasing the ground stress, we found that zonal disintegration occurred in Model II, confirming the previous hypothesis.

To further investigate this relationship, we propose a numerical analysis method based on ABAQUS platform, utilizing strain gradient theory and continuous damage mechanics to establish an elastic damage softening model and energy damage failure criterion. This method can effectively predict the failure modes of rock tunnels under different in-situ stress and temperature scenarios. These findings contribute to a better understanding of the failure mechanisms of rock tunnels and can serve as a useful reference for future engineering design and construction of such structures.

2 IMPLEMENTATION OF GEO-MECHANICAL MODEL TEST

2.1 *The scheme of the geo-mechanical model*

The Pubugou Hydropower Station's main powerhouse project serves as our engineering background. The underground powerhouse cavern is situated within the granite rock mass on the left bank downstream of the dam axis. The overlying rock mass measures 360m thick, and the main powerhouse's cross-section size is 26.8m x 70.1m. According to the similarity principle (Zhang et al. 2019a) and considering the scale of the main powerhouse and the size of the test system (0.7 m × 0.7 m × 0.7 m), the geometrical similarity of the model test is selected as C_L=C_P/C_M=300. Figure 1 displays the extent and in-situ stress as simulated by the model test. To investigate the correlation between high sidewall tunnels' splitting failure and zonal disintegration, we conducted two model tests. Model I involved normal excavation while Model II involved overloading post-excavation.

An iron-barites-silica cementation material (Zhang et al. 2019b), referred to as IBSCM, has been chosen as an analogous material for the purpose of this study. The mixture proportion of IBSCM, as well as the physical and mechanical parameters of both the granite and the analogous material, are presented in Tables 1. To accurately measure the deformation and stress changes of the surrounding rock during the testing process, three typical monitoring sections, namely stress monitoring sections I and III (to monitor radial and tangential stress respectively), and deformation monitoring section II have been established. In Figure 2, five measurement lines have been arranged for each monitoring section, each of which comprises six measuring points. It is important to note that due to the size of the model, vertical measurement Line C only includes five measuring points. These monitoring sections and measuring lines have been established to ensure precise data collection and accurate analysis of the deformation and stress changes in the surrounding rock during testing.

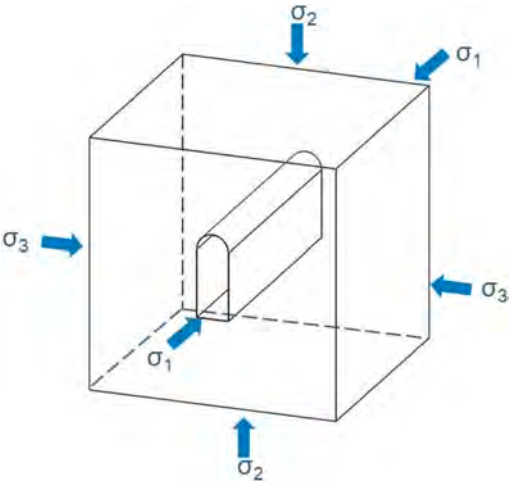

Figure 1. Geo-mechanical model test loading scheme (σ_1=27.30 MPa, σ_2=16.16 MPa and σ_3=15.25 MPa).

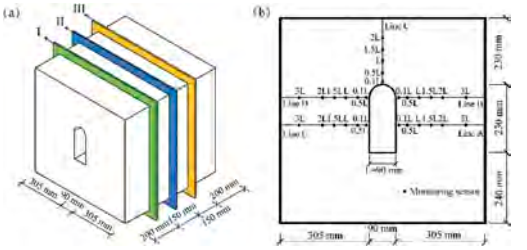

Figure 2. Layout of monitoring sections (a) and monitoring sensors (b) (Unit: mm). Section I: the radial stress monitoring section; Section II: the radial deformation monitoring section; Section III: the tangential stress monitoring section.

Table 1. Components ratio of IBSCM.

Iron powder: Barite powder: Silica sand	Cementing agent concentration (%)	Cementing agent as a percentage of aggregate weight (%)
1:1:0.5	6	5.5

2.2 *Conduct geomechanical model tests*

To ensure the consistency and stability of rock formations, a geomechanical model is created through layering, compacting and air-drying the material (Zhang et al. 2012, 2017, 2020; Wang et al. 2017). This methodology involves dividing the model into ten layers, each 70mm in span, and carving grooves in the model to implant sensors at designated elevations. To maintain cohesion and prevent detachment, each previous layer's surface is chiseled and moistened with alcohol before adding the subsequent layer. This ensures that the layers' interface remains rough and firm, thereby increasing the reliability and accuracy of the geomechanical model's performance.

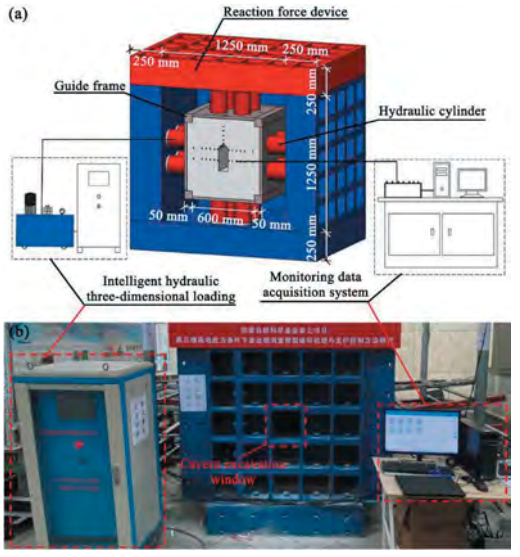

Figure 3. Three-dimensional loading system. (a) Internal schematic diagram; (b) Frontal photo of the system.

Model I is an experiment involving the excavation of a tunnel. To simulate the stress field in an actual engineering site, a self-developed true three-dimensional model test system is used to impose boundary loads on the model (Figure 3). The model is loaded step-by-step until it reaches the design value, after which the load is kept constant and stabilized for 24 hours using a servo-control mode. This process allows for the formation of an initial stress field that conforms to the in-situ field within the model. The subsequent step involves the excavation of the model tunnel. This experiment aims to provide valuable insights into the behavior and performance of tunnels under varying stress conditions, contributing to the development of effective and safe engineering practices.

Model II excavation stage is similar to Model I, but with an additional overloading test conducted after completion. During this geomechanical test, incremental loads are applied to the model until its structural failure, simulating a progressive increase in buried depth. The gravity and tectonic stresses are increased stepwise, each at 0.1 times the initial in-situ stress. Following each loading stage, the model's boundary pressure is maintained for at least 15 minutes until data stabilization. Displacement and pressure of the surrounding rock are recorded at each stage. The overloading test continues until the loading reaches 2.2 times the in-situ stress, when significant tunnel collapse occurs and the test ceases. This experiment advances our understanding of underground conditions and offers insights into avoiding potential collapses in mining operations. It is intended to serve as a valuable reference for geotechnical engineers tasked with subterranean construction planning.

3 GEO-MECHANICAL MODEL TEST RESULTS

3.1 *Model failure phenomenon*

After completion of excavation, boundary loading is maintained for a period of time. The model frame is then disassembled and the model is cut perpendicular to the axis of the tunnel to compare the failure patterns of Model I (after excavation) and Model II (after unloading test), as demonstrated in Figure 4. Observations reveal that splitting failure occurs in the high sidewall tunnel after excavation (burial depth of 360m). However, when in-situ stress is increased to 2.2 times the initial in-situ stress (equivalent to a burial depth of 792m), zonal disintegration arises in the high sidewall tunnel. These findings illustrate the complex behavior of geological materials and the importance of considering various factors during excavation and post-excavation phases to avoid undesirable consequences. Such knowledge can contribute to the development of more efficient and safer underground constructions in the future.

The high sidewall tunnel depicted in Figure 4a shows severe damage due to splitting failure. The model tunnel's both sides display evident longitudinal cracks, whereas the vault exhibits no significant damage. Figure 4b depicts the typical zonal disintegration where the rupture zone and non-rupture zone appear sequentially like onion-skin. The sidewall region shows a twofold increase in the cracks, almost double the size of the excavation phase. Overloading intensifies the tunnel's damage, causing the sidewall area to experience serious collapse. The cracks parallel to the tunnel wall still exist, indicating a hypothesis that with the increase in in-situ stress, the high sidewall tunnel undergoes a failure mode shift from splitting failure to zonal disintegration.

Based on the observation that the high sidewall tunnel's zonal disintegration failure mode is caused

by high in-situ stress. When under extreme stress, the surrounding rock fails abruptly and can cause catastrophic damage. The splitting failure displayed in Figure 4a is characteristic of moderately fractured rock masses with a lower in-situ stress concentration. At this stage, the vault remained intact, and only the sidewall suffered damage. Given that the tunnel remained unaffected by the stress earlier, overloading significantly amplified the sidewall's damage.

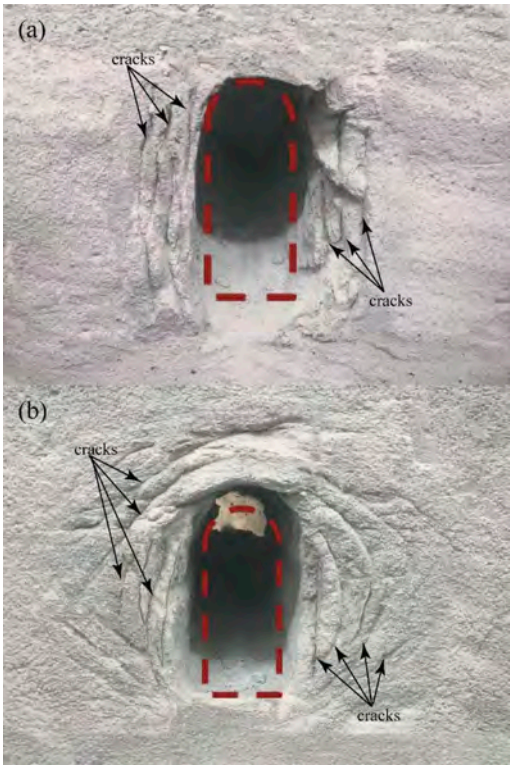

Figure 4. Fracture patterns around the tunnel with high sidewall. (a) Model I; (b) Model II.

In summary, the high sidewall tunnel subjected to a gradual increase in in-situ stress appeared to undergo a failure mode shift from splitting failure to zonal disintegration. In the case of higher stress levels, the material experienced a catastrophic failure leading to severe damage to the tunnel. The findings of this study can be crucial for understanding the mechanics of rock mass failures and preventing catastrophic tunnel damage.

3.2 *Displacement monitoring results*

In this section, the model test results have been transformed into the prototype based on the principles of similitude. The positive value of the convergence displacement towards the tunnel is defined. The radial displacement variation around the tunnel can be derived by joining the data of each measurement point with a smooth curve (Figure 5).

Figure 5 illustrates that:

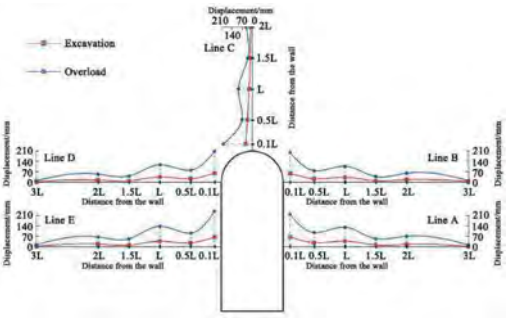

Figure 5. Radial displacement around the tunnel after the excavation and overloading test.

After excavation (as depicted by the red squares in Figure 5), there was noticeable deformation in the circumference of the tunnel, which was directed towards its interior. The nearest measuring point displayed relatively significant displacement, suggesting that the surrounding rock's broken area was consistent with the damage observed during the test. Conversely, the measuring point farthest away from the tunnel sidewall exhibited significantly less displacement compared to other measuring points on the same line, indicating minimal excavation disturbance on the high sidewall tunnel situated 3L away from the tunnel. The measured displacement on lines A, B, D, and E showed a generally oscillating attenuation pattern, which differed greatly from the displacement variations around the shallow tunnel. In contrast, each measuring point's displacement on vertical Line C displayed a monotonic attenuation trend, distinctly contrasting the pattern observed on the horizontal lines. At this stage, the test data did not significantly differ from Model I, demonstrating the occurrence of splitting failure.

The results of our overloading test (indicated by blue circles in Figure 4b) showed that the maximum displacement around the tunnel was 3.7 times larger than in the excavation stage. This suggests that the deformation rate of the surrounding rock is greater than the rate of load increase and that rupture of the surrounding rock is more likely to occur. We observed that the displacement variation of the measuring points on the horizontal lines was consistent with that observed during the excavation stage, undergoing oscillation attenuation, but with a larger vibration amplitude, about three times that of the excavation stage. However, we observed different variation in the vertical displacement of the tunnel vault, which changed into oscillation attenuation. We discovered that zonal disintegration, in which annular layered fractures alternated between the rupture zone and the non-rupture zone, occurred in the high sidewall tunnel. These findings are important for understanding the behavior of surrounding rocks in tunnels under

overloading conditions and can inform the design of future underground structures.

3.3 *Stress monitoring results*

Connecting data from measurement points during excavation and overload stages with smooth curves allows for obtaining changes in radial and tangential stresses around the tunnel, as shown in Figure 6. We can find that:

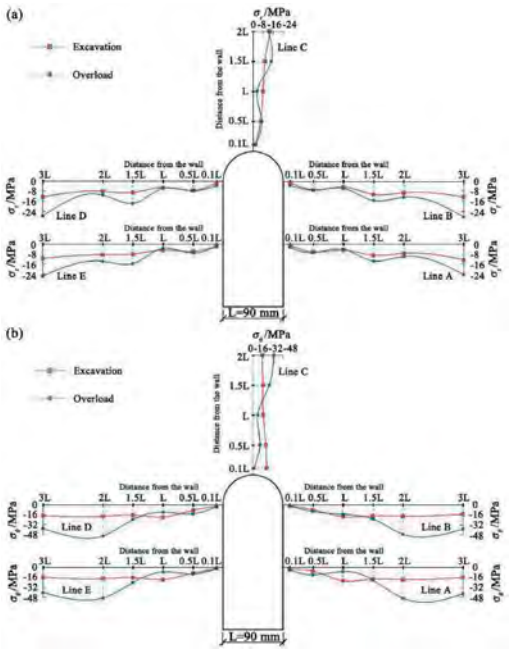

Figure 6. (a) Radial stress around the tunnel after the excavation and overloading test; (b) Tangential stress around the tunnel after the excavation and overloading test.

Following the excavation, the stress release around the tunnel leads to deformation that is focused towards the tunnel. As a result, radial stress around the tunnel decreases, as can be observed from the red squares in Figure 6a. During this phase, the changes in the radial stress data are consistent with Model I, indicating the occurrence of a splitting failure. As in-situ stress increases, damage to the surrounding rock increases, resulting in an increase in the release of radial stress. The farther away from the tunnel sidewall, the less damage occurs to the surrounding rock, resulting in an increased difference between the monitoring data after excavation and overload. During the overload stage, changes in the radial stress of the vault are more prominent. The stress values at 0.1L, 0.5L, and 2L away from the wall remain largely unchanged, while the radial stress decreases as the distance increases from the wall and increases at 1.5L. This change in radial stress from a monotonous increase during excavation (red squares in Figure 6a) to vibration during overload (blue circles in Figure 6a) coincides with zonal disintegration. Overall, these findings suggest that the damage around the tunnel increases with the increase of in-situ stress, and the release of radial stress is concentrated towards the tunnel.

Regarding displacement and radial stress, the change of tangential stress after excavation is similar to that of Model I. During the overload phase, the plastic area around the tunnel expands, causing points L and 1.5L away from the sidewall to enter the plastic phase and decrease their tangential stress. The rock 2L away from the wall remains in the elastic stage, where the tangential stress is still concentrated. In addition, the surrounding rock of the vault also enters the plastic stage from the elastic stage, leading to a release of the tangential stress. The plastic zone extends from the tunnel sidewall to the vault and takes on an approximately circular shape, which aligns with the variation in zonal disintegration. Overall, these findings have important implications for understanding the response of rock masses around tunnels to excavation-induced stress changes, underscored by the stress-induced rock failure patterns, which can help inform the design and safety of underground engineering structures.

4 NUMERICAL SIMULATION OF FAILURE MODE

We have developed a simulation program that utilizes the finite element method to replicate splitting failure and zonal disintegration in the rock surroundings of a tunnel with high sidewalls under high stress conditions. The program incorporates an elastic damage softening model and an energy damage failure criterion, both of which are based on the strain gradient theory and continuous damage mechanics. This section provides an introduction to the simulation program and compares the simulation results with those from the geo-mechanical model test. The aim of this program is to improve our understanding of rock mechanics and to enhance our ability to predict and prevent catastrophic rock failures.

4.1 *Development of the simulation program*

In this section, the model test results have been transformed into the prototype based on the principles of similitude. The positive value of the convergence displacement towards the tunnel is defined. The radial displacement variation around the tunnel can be derived by joining the data of each measurement point with a smooth curve (Figure 5).

When dealing with the elastic damage softening model and simulating splitting failure and zonal disintegration numerically, the influence of strain gradient must be taken into account. However, in general finite element analysis, the element shape function only

achieves first-order continuity, and the second-order derivative value of the displacement within the element after interpolation becomes zero. As a result, applying such a unit analysis does not reflect the impact of strain gradient. Therefore, it is crucial to build the element with higher order continuity, which is required to maintain C^1 order continuity of the displacement of the node and its first derivative. Hermite interpolation function has been used to construct high-order hexahedral elements, from which both the shape function and stiffness matrix of the element have been derived (Zhang, 2015; Li et al. 2021, 2022). This technical advancement forms the basis for considering strain gradient effects in numerical simulation. Our simulation program is developed on the platform of ABAQUS finite element software.

To determine the distribution of the failure zone in the surrounding rock, a criterion must be established to identify element failure. In numerical simulations, two criteria are commonly utilized: the maximum tensile strain criterion and the energy damage failure criterion. The maximum tensile strain of the unit is calculated using equation (1). If the maximum tensile strain ε_{max} is greater than or equal to the ultimate tensile strain ε_{tu}, the element is deemed to have undergone tensile failure. To ensure that the entire calculation remains coherent and continuous throughout the simulation, a residual elastic modulus E_C is applied to the rock mass element where tensile failure has occurred. It is crucial to establish the criterion for determining element failure to accurately obtain the distribution of the failure zone in surrounding rock.

$$\varepsilon_{max} = \frac{2}{\sqrt{3}}\sqrt{|J_2'|}\cos\left(\omega - \frac{\pi}{3}\right) + \frac{I_1'}{3} \tag{1}$$

where

$$\omega = \frac{1}{3}arccos\left(-\frac{3\sqrt{3}}{2}\frac{J_3'}{|J_2'|\sqrt{|J_2'|}}\right) \tag{2}$$

$$\begin{cases} I_1^{'} = \varepsilon_x + \varepsilon_y + \varepsilon_z \\ J_2^{'} = -(e_1e_2 + e_2e_3 + e_1e_3) \\ J_3^{'} = e_1e_2e_3 \end{cases} \tag{3}$$

$$\begin{cases} e_1 = \dfrac{2}{3}\varepsilon_x - \dfrac{1}{3}\left(\varepsilon_y + \varepsilon_z\right) \\ e_2 = \dfrac{2}{3}\varepsilon_y - \dfrac{1}{3}\left(\varepsilon_x + \varepsilon_z\right) \\ e_3 = \dfrac{2}{3}\varepsilon_z - \dfrac{1}{3}\left(\varepsilon_x + \varepsilon_y\right) \end{cases} \tag{4}$$

Where ε_x, ε_y and ε_z are strains in X, Y and Z directions respectively.

If the maximum level of tensile strain experienced by a particular element falls below the ultimate tensile strain, then that unit will not undergo tensile failure. In such cases, the failure criterion of the element is based on the energy damage caused by strain gradient. To account for the influence of the strain gradient term, a formula for calculating the strain energy density of the element has been proposed. This formula is believed to effectively measure the strain energy density of the element, helping experts accurately predict whether or not that element will fail under tensile conditions.

$$\frac{dW}{dV} = \int_0^{\varepsilon_{ij}} \sigma_{ij} d\varepsilon_{ij} + \frac{1}{8}Gl^2 \left(4\eta_{ijj}\eta_{ikk} + 4\eta_{iik}\eta_{kjj} + 4\eta_{iik}\eta_{jjk} + 7\eta_{ijk}\eta_{ijk} + 2\eta_{ijk}\eta_{kji}\right) \tag{5}$$

where σ_{ij} is two order Cauchy stress tensor, ε_{ij} is Eulerian strain tensor, G is the lame constant, l is the internal length parameter, η_{ijk} is strain gradient tensor.

The calculation formulas of elastic strain energy density $(\mathrm{d}W/\mathrm{d}V)_\mathrm{s}$, critical strain energy density $(\mathrm{d}W/\mathrm{d}V)_\mathrm{c}$ and ultimate strain energy density $(\mathrm{d}W/\mathrm{d}V)_\mathrm{u}$ are as follows:

$$\begin{cases} \left(\frac{dW}{dV}\right)_s = \int_0^{\varepsilon_s} \sigma_{ij} d\varepsilon_{ij} \\ \left(\frac{dW}{dV}\right)_c = \int_0^{\varepsilon_o} \sigma_{ij} d\varepsilon_{ij} \\ \left(\frac{dW}{dV}\right)_u = \int_0^{\varepsilon_u} \sigma_{ij} d\varepsilon_{ij} \end{cases} \tag{6}$$

Where ε_s is the yield strain in the process of loading, ε_o is the residual strain in the process of loading, ε_u is the ultimate strain in the process of loading.

The energy damage failure criterion is defined by the variation in strain energy density ($\mathrm{d}W/\mathrm{d}V$). When $(\mathrm{d}W/\mathrm{d}V) < (\mathrm{d}W/\mathrm{d}V)_s$ (ε_s is the yield strain in the process of loading), it remains in the linear elastic phase with no internal damage. Upon exceeding $(\mathrm{d}W/\mathrm{d}V)_\mathrm{s}$ and entering the plastic damage regime, the damage variable d is triggered, leading to the formation of micro-cracks within the material which then begin to propagate as the loading increases. When $(\mathrm{d}W/\mathrm{d}V) \geq (\mathrm{d}W/\mathrm{d}V)_c$, the micro-cracks transition into macroscopic cracks, with the rock mass entering its residual stage while still retaining some of its bearing capacity. Once the ultimate strain threshold $(\mathrm{d}W/\mathrm{d}V)_u$ is reached, the rock mass is no longer able to bear the load, resulting in its failure. As with tensile failure, the failure element is assigned a residual elastic modulus E_s to maintain the overall integrity and continuity of the calculation. It is worth noting that this approach can predict the strength and deformation behavior of materials under complex loading conditions, which is particularly relevant when evaluating the stability of underground structures or geotechnical engineering projects.

4.2 *Establishment of numerical models*

The numerical model's range aligns with that of the physical model delineated in Section 2.1. Figure 7

portrays the numerical model's scales along the X, Y, and Z axes, all of which are 210 m. The three-dimensional computational grid comprises 60000 elements and 67769 nodes. The external loads applied to the numerical model, which appear in Figure 7, reflect consistency with the physical model's boundary conditions and tunnel construction process.

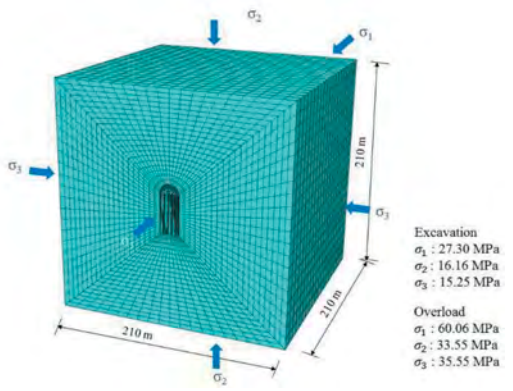

Figure 7. Numerical model generated for the simulation of high sidewall tunnel the excavation and overload.

4.3 *Numerical models' results*

The external loads depicted in Figure 7 are applied to the numerical model. After equilibrating, the nodes' displacement and strain parameters are established at zero to initiate the in-situ stress field. The tunnel is then excavated, and the stress, strain, and displacement fields of the rock surrounding it are calculated. These results are then transformed to the cylindrical coordinate system to visually communicate the distribution of radial stress, strain, and displacement of the rock around the tunnel, as shown in Figures 8 and 9.

The Figures 8 and 9 demonstrate the emergence of spaced apart rupture zones in the surrounding rock. In Figure 8, the rupture zone is distributed on either side of the tunnel, running parallel to the tunnel sidewall. In Figure 9, the rupture zone is shaped like a ring around the tunnel. The numerical simulations of the damage zone range, average radius, and average width were found to closely correspond with the results of the model tests.

The displacement, strain, and stress around the tunnel also reveal the appearance of three layers of rupture zones. Deformation is concentrated in the middle of the sidewall near the tunnel rupture zone, and stress is aligned parallel to the height of the tunnel sidewall. This finding is consistent with Figure 4b, where a vertical crack appears parallel to the wall near the tunnel. Although the two rupture zones forming a ring shape outside the tunnel were similar to the test results shown in Figure 4b, there were two cracks on the vault and four cracks on the sidewall in the model test, indicating greater damage to the surrounding rock

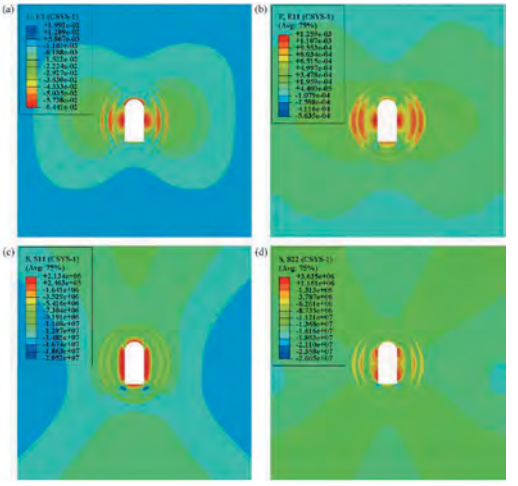

Figure 8. Simulation splitting failure results in terms of the contour of: (a) Radial displacement; (b) Radial strain; (c) Radial stress; and (d) Tangential stress in the surrounding rock of the tunnel.

than in the numerical simulation. This may be due to the constitutive model used in the numerical calculation, which does not account for the damage effect of excavation on the surrounding rock.

The numerical model reveals that the surrounding rock's radial displacement exhibits an oscillating pattern, characterized by the alternating wave crest and trough. These observations correspond with the radial displacement variation measured by the model test. This validation attests to the robustness of the elastic damage softening model and the ABAQUS-based numerical analysis methodology utilized in this study.

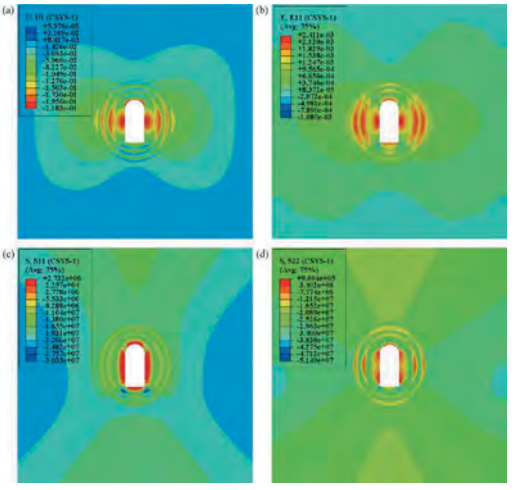

Figure 9. Simulation zonal disintegration results in terms of the contour of: (a) Radial displacement; (b) Radial strain; (c) Radial stress; and (d) Tangential stress in the surrounding rock of the tunnel.

Through numerical simulation, it has been observed that the unloading of an excavation can cause the surrounding rock to rupture. The resulting stress wave from the rock fracture moves away from the tunnel wall, thus creating a new stress field in the adjacent rock. Upon overlaying the original rock mass' stress field, further fracturing may occur, leading to the formation of ruptured and non-ruptured zones. Crack propagation is likely to extend along the direction of maximum principal stress, or the direction of tangential stress. Ultimately, a ring-shaped fracture will form at the elasto-plastic boundary. These observations have significant implications for understanding the behavior of rock masses when subjected to excavation activities.

5 CONCLUSIONS

Using the Pubugou Hydropower Station's main powerhouse as our engineering background, we conducted 3D geo-mechanical model tests on the failure of rock tunnels with high sidewalls due to excavation and overloading. Our research revealed that the failure of high sidewall tunnels would transform from splitting failure to zonal disintegration as in-situ stress increased. During the excavation stage, the displacement and stress of the surrounding rock at the side wall of the tunnel would exhibit oscillation attenuation, while the vault showed a trend of monotonic attenuation. However, in the overload stage, the displacement and stress of the surrounding rock of the high sidewall tunnel underwent wave-like changes in the distribution of peaks and troughs. Finally, we confirmed the zonal disintegration of the high sidewall tunnel by cutting the model body after the overloading test.

Using the elastic damage softening model and energy damage failure criterion, established through strain gradient theory and continuous damage mechanics, we developed a numerical simulation program to analyze the splitting failure and zonal disintegration of high-stress surrounding rock in sidewall tunnels. Our simulation results are in agreement with model test results. The study shows that excavation unloading causes stress redistribution in the surrounding rock, leading to renewed rock mass breakage and newly defined ruptured and non-ruptured zones. Crack propagation occurs along the maximum principal stress direction, forming annular cracks at the elastic-plastic boundary.

ACKNOWLEDGMENTS

Supported by the Natural Science Foundation of China (Grant Nos. 42172292 and 41772282) and Shandong Provincial Natural Science Foundation (No. ZR2023QE312).

REFERENCES

Chanyshev, A. I., & Belousova, O. E., 2018. Inclusion of inhomogeneous deformation and strength characteristics in the problem on zonal disintegration of rocks. In IOP Conference Series: Earth and Environmental Science, Bristol, 1341(1), 012011.

Chen, X. G., Wang, Y., Zhang, Q. Y., Li, S. C., & Nordlund, E., 2013a. Analogical model test and theoretical analysis on zonal disintegration based on filed monitoring in deep tunnel. European Journal of Environmental and Civil Engineering, 17(sup1), s33–s52.

Chen, X. G., Zhang, Q. Y., Wang, Y., Li, S. C., & Wang, H. P., 2013b. In situ observation and model test on zonal disintegration in deep tunnels. Journal of Testing and Evaluation, 41(6), 990–1000.

Chen, X. G., Zhang, Q. Y., Wang, Y., Liu, D. J., & Zhang, N., 2013c. Model test of anchoring effect on zonal disintegration in deep surrounding rock masses. The Scientific World Journal, 2013, 935148.

Gao, Q., Zhang, Q., & Xiang, W., 2019. Mechanism of Zonal Disintegration Phenomenon (ZDP) Around Deep Roadway Under Dynamic Excavation. Geotechnical and Geological Engineering, 37(1), 25–41.

Gao, Q., Zhang, Q., Xiang, W., & Zhang, X., 2018a. Numerical simulation of zonal disintegration for deep rock mass under high geostress. IOP Conference Series Earth and Environmental Science, 170(2), 022154.

Gao, Q., Zhang, Q., Zhang, X., & Zhang, L., 2018b. Geomechanical Model Test and Energy Mechanism Analysis of Zonal Disintegration in Deep Surrounding Rock. Geosciences, 8(7), 237.

Li, F., Zhang, Q., Duan, K., Xiang, W., & Yu, G., 2023. Investigating the mechanism of splitting failure in deep high sidewall cavern based on complex function and strain gradient. Tunnelling and Underground Space Technology, 132, 104910.

Li, F., Zhang, Q., & Xiang, W.. 2021. Mechanism of splitting failure for high sidewall cavern of hydropower station based on complex function and strain gradient. Energies, (14), 5870.

Li, F., Zhang, Q., Xiang, W., & Yu, G., 2022. Failure mechanism and numerical simulation of splitting failure for deep high sidewall cavern under high stress. Geotechnical and Geological Engineering, (40), 175–193.

Li, S. C., Wang, H. P., Qian, Q. H., Li, S., Fan, Q., Yuan, L., … & Zhang, Q., 2008. In-situ monitoring research on zonal disintegration of surrounding rock mass in deep mine roadways. Chinese Journal of Rock Mechanics and Engineering, 27(8), 1545–1553.

Reva, V. N., 2002. Stability criteria of underground workings under zonal disintegration of rocks. Journal of Mining Science, 38(1), 31–34.

Szwedzicki, T., 2003. Rock mass behaviour prior to failure. International journal of rock mechanics and mining sciences, 40(4), 573–584.

Tan, Y. L., Ning, J. G., & Li, H. T., 2012. In situ explorations on zonal disintegration of roof strata in deep coalmines. International Journal of Rock Mechanics and Mining Sciences, (49), 113–124.

Vtorushin, E. V., 2016. Application of mixed finite elements to spatially non-local model of inelastic deformations. GEM-International Journal on Geomathematics, 7(2), 183–201.

Wang, C., Zhang, Q., & Xiang, W., 2017. Physical and numerical modeling of the stability of deep caverns in Tahe oil field in China. Energies, 10(6), 769.

Wu, S., Chen, L., & Cheng, Z., 2019. Macro and meso research on the zonal disintegration phenomenon and the mechanism of deep brittle rock mass. Engineering Fracture Mechanics, 211, 254–268.

Zhang, Q. Y., Duan, K., Jiao, Y. Y., & Xiang, W., 2017. Physical model test and numerical simulation for the stability analysis of deep gas storage cavern group located in bedded rock salt formation. International Journal of Rock Mechanics and Mining Sciences, 94, 43–54.

Zhang, Q. Y., Liu, C., Duan, K., Zhang, Z., & Xiang, W., 2019a. True Three-Dimensional Geomechanical Model Tests for Stability Analysis of Surrounding Rock During the Excavation of a Deep Underground Laboratory. Rock Mechanics and Rock Engineering, 53(2), 1–21.

Zhang, Q., Li, F., Duan, K., Yu, G., & Guo, X., 2020. Experimental investigation on splitting failure of high sidewall cavern under three-dimensional high in-situ stress. Tunnelling and Underground Space Technology, 108(sup1), 103725.

Zhang Q.Y., Li S.C., Li Y. et al, 2012. New method and new technology of model test for underground engineering and its application. Science Press, Beijing, pp 64–79.

Zhang, Q. Y., Zhang, Y., Duan, K., Liu, C. C., Miao, Y. S., & Wu, D., 2019b. Large-scale geo-mechanical model tests for the stability assessment of deep underground complex under true-triaxial stress. Tunnelling and Underground Space Technology, 83, 577–591.

Zhang X T., 2015. The research on failure mechanism and numerical simulate on analysis of zonal disintegration in deep tunnel. PhD Thesis. Shandong University. Jinan, Shandong, China.

Zhou, X. P., & Shou, Y. D., 2013. Excavation-induced zonal disintegration of the surrounding rock around a deep circular tunnel considering unloading effect. International Journal of Rock Mechanics and Mining Sciences, 64, 246–257.

Zhu, G. Q., Feng, X. T., Zhou, Y. Y., Li, Z. W., Fu, L. J., & Xiong, Y. R., 2019. Physical Model Experimental Study on Spalling Failure Around a Tunnel in Synthetic Marble. Rock Mechanics and Rock Engineering, 53(2), 1–18.

Tunnelling for a Better Life – Yan, Celestino, Thewes & Eberhardt (Eds)
© 2024 The Author(s), ISBN 978-1-032-80042-4
Open Access: www.taylorfrancis.com, CC BY-NC-ND 4.0 license

Development and test of directional coring drilling system for advanced geological exploration

Jun Liu*
China Railway Construction Heavy Industry Corporation Limited, Changsha, China

ABSTRACT: Directional coring drilling system is an effective tool for advanced geological exploration in tunnel construction, which can realized the directional drilling and continuous coring, so as to obtain effective geological information. Its key technologies include the design of directional drilling trajectory, and the design of deflection tool which can realize the coring function. A directional drilling trajectory design software is developed. According to the deviation between actual drilling trajectory and design trajectory, the trajectory to be drilled is designed in the form of "arc segment + straight segment", and the appropriate tool face angle and build-up distance of the deflection tool are calculated. Based on the working principle of static Point-the-Bit Rotary Steering System, an deflection tool integrating the functions of guiding, steering, and coring — directional coring tool is developed. Finally, the feasibility of this directional coring drilling system is verified by test. The test results show that this system can realize the effective control of drilling trajectory, achieve the continuous coring in the whole hole section of directional drilling, with low water consumption and high coring rate, and thus it has certain promotion and application value.

Keywords: directional drilling, coring, geological exploration, drilling trajectory design, deflection tool

1 INTRODUCTION

Directional coring drilling system is a high-tech precision drilling system for underground spaces integrating the functions of guiding, steering, and coring. It can realize directional drilling according to the predetermined trajectory and obtain rock core samples continuously. As an indispensable advanced geological exploration tool in major national infrastructure projects such as long mountain tunnels and subsea tunnels, it can accurately obtain the location information of surrounding rock and water area of the rock strata in a tunnel trajectory area, effectively reduce the tunnel construction risks, and provide effective data support for the design and construction decisions of super-long major engineering tunnels.

At present, the directional drilling technology is relatively mature in petroleum industry. Some companies such as Baker Hughes, Schlumberger and Halliburton have their rotary steering drilling tools, the working mechanism of which is to realize the steerable drilling by offsetting the drill bit or main shaft with an offset mechanism [1]. According to different steering modes, rotary steering drilling tools can be divided into two types: Push-the-Bit and Point-the-Bit. Push-the-Bit type means that the offset mechanism offsets the drill bit near the bit to directly provide lateral force to the drill bit. Point-the-bit type means that the offset mechanism directly or indirectly offsets the main shaft connecting with the drill bit to bend it so that the drill bit points the direction of well trajectory control. According to different offset modes, rotary steering drilling tools can be divided into static offset type and dynamic offset type: the static offset means that the offset mechanism does not rotate with the drill string in the process of drilling, and can provide a fixed lateral force in one direction. Dynamic offset type means that the offset mechanism rotates with the drill string in the process of drilling, extends directionally and periodically at a certain position by the control system, and provides steering force by virtue of the supporting reaction. However,, their diameters are large, and these rotary steering drilling tools can only realize the function of directional drilling but not coring.

In the field of geological exploration, drilling and coring in front of the tunnel face with drilling equipment can directly reveal the formation lithology, structure, groundwater, karst, weak interlayer and

*Corresponding author: liujun1@crchi.com

DOI: 10.1201/9781003495505-76

other geological bodies in front of the tunnel face and their properties, being one of the most direct and effective methods of advanced geological prediction [2-3]. However, if the traditional linear coring tool is used, due to the influence of gravity and surrounding rock anisotropy, the drilling trajectory longer than 300 m will be significantly bent, which is difficult to truly reflect the geological characteristics of the tunnel crossing area [4]. Therefore, a directional coring drilling system is required. At present, the directional coring drilling system mainly uses screw drilling tool to realize directional drilling, and then uses traditional linear coring tool to realize coring, that is, discontinuous coring cannot obtain the core of the whole hole section. The working principle of a screw motor is to carry out the directional drilling in cooperation with bend joint and bottom-hole survey tool by using a bottom-hole motor with high-pressure flushing fluid as the power source [5]. Limited by the working principle, the motor is installed at the near bit end, and thus cannot realize the coring function. DEVICO in Norway has mastered the directional coring drilling technology, which can realize continuous coring [6]. However, the company strictly keeps relevant technologies confidential, and only provides technical services without selling products. Its product DeviDrill has realized long-distance directional drilling and continuous coring in Hong Kong [7-9]. But the measurement of actual drilling trajectory cannot be directly obtained by the MWD (measurement-while-drilling) system in the directional coring tool, requiring the combination with other measuring tools.

The composition of directional coring drilling system for advanced geological exploration is introduced, including the directional drilling trajectory design software and directional coring drilling equipment. The software can, according to the deviation between actual drilling trajectory and design trajectory, design the trajectory to be drilled in the form of "arc segment + straight segment", and calculate the appropriate tool face angle and build-up distance of the deflection tool. Based on the working principle of static Point-the-Bit Rotary Steering System, an deflection tool integrating the functions of guiding, steering, and coring — directional coring drilling device is developed. The device can obtain information such as azimuth angle and inclination angle required for the calculation of actual drilling trajectory through its own MWD tool. Finally, the feasibility of the directional coring drilling system for advanced geological exploration is verified by test.

2 DIRECTIONAL DRILLING TRAJECTORY DESIGN SOFTWARE

The calculation of actual drilling trajectory and the design of track to be drilled are characterized by heavy calculation workload, many complicated formulas, and error-prone calculation process, bringing great difficulties to the on-site drilling guidance. In order to keep the deviation between the drilling trajectory and the design trajectory in a small value, it is necessary to calculate the actual trajectory of a borehole according to the data measured by MWD tool, design the trajectory to be drilled according to the deviation between the actual trajectory and the design trajectory, and provide reference values for the proper tool face angle and deflection distance of deflection tool in directional drilling, so as to guide the directional drilling process. Based on MATLAB App Designer, the trajectory design and calculation analysis system of directional coring tool is developed, realizing the functions including the calculation of actual drilling trajectory, the design of trajectory to be drilled, and the visualization of borehole trajectory, etc. The application of the system in directional drilling practice can effectively improve the drilling efficiency and reach the target point faster.

2.1 *Calculation of actual drilling trajectory*

The actual drilling trajectory is a curved form of the borehole axis, presenting a spatial curve. The parameters required for the calculation of actual drilling trajectory include borehole depth, borehole inclination angle and azimuth angle [10], and the calculation methods include tangential method, mean-angle full range method, balanced tangential method, radius of curvature method and minimum curvature method [11]. With mean-angle full range method as the example for introduction, as shown in Figure 1, in the geodetic coordinate system NEG, N is the magnetic north direction, E is the magnetic east direction and G is the gravity direction. O and A are two measuring points. Given the distance L_A from O to A, local geomagnetic declination λ, and coordinates (X_O, Y_O, Z_O) of point O, the azimuth angles of point O and point A α_O and α_A, and the inclination angles θ_O and θ_A, the calculation of the three-dimensional coordinates of point A is shown in Formula 1. Generally, the orifice coordinates are set to (0, 0, 0), and by analogy and iteration according to Formula 1, the three-dimensional coordinates of all measuring points can be obtained, thus the actual drilling trajectory is obtained.

$$XA = LA \sin\frac{\theta_o + \theta_A}{2}\cos\left(\frac{\alpha_o + \alpha_A}{2} - \lambda\right) + X_O \quad (1)$$

$$YA = LA \sin\frac{\theta_o + \theta_A}{2}\sin\left(\frac{\alpha_o + \alpha_A}{2} - \lambda\right) + Y_O \quad (2)$$

$$ZA = LA \cos\frac{\theta_o + \theta_A}{2} + Z_O \quad (3)$$

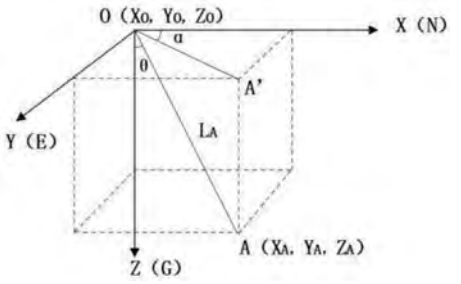

Figure 1. Schematic diagram of actual drilling trajectory calculation.

2.2 *Design of trajectory to be drilled*

In order to reduce the deviation between the actual drilling trajectory and the design trajectory, the trajectory to be drilled is designed in the form of "arc section + straight section", of which the arc section is drilled by directional coring tool, while the straight section is drilled by conventional coring tool. Based on the principle of arc section + straight section as the shortest distance, the optimal trajectory to be drilled is selected, and the tool face angle and deflection distance required for deflection tool are calculated for the guidance of directional drilling.

In the paper, the inclined plane method is used to design the trajectory to be drilled in three-dimensional space, i.e. the design of drilling trajectory on a inclined plane in the space, where the inclined plane is determined by the tangent line of the starting point of deviation correction and the ending point of deviation correction, the radius of curvature R of the curved section is constant and is determined by the build-up rate of deflection tool [11]. As shown in Figure 2, given the coordinates of point a (the end of actual drilling trajectory), inclination angle θ_a and azimuth angle α_a, radius of curvature R of the deflection tool, and the coordinates of target point c, then the angle γ, the distance L_{bc} between point b and c, the coordinates of point m and b, the inclination angle θ_b and azimuth angle α_b at point b can be solved, with the formulas as below. It should be noted that the coordinates of point c are on the design trajectory, and based on the principle of arc section + straight section as the shortest distance, the final coordinates are determined by optimization algorithm.

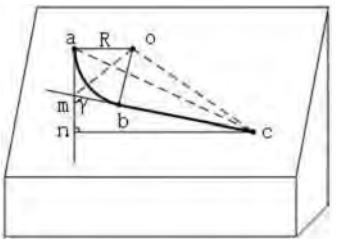

Figure 2. Schematic diagram for calculation of trajectory to be drilled by inclined plane method.

$$\gamma = 2\tan^{-1}\frac{D-\sqrt{D^2+S^2-2RS}}{2R-S} \tag{4}$$

$$L_{bc} = \sqrt{D^2+S^2-2RS} \tag{5}$$

Where

$$\mathrm{D} = \mathrm{L_{ac}}\cos\angle mac \tag{6}$$

$$S = \mathrm{L_{ac}}\sin\angle mac \tag{7}$$

$$L_{ac} = \sqrt{(X_c-X_a)^2+(Y_c-Y_a)^2+(Z_c-Z_a)^2} \tag{8}$$

$$\angle mac = \cos^{-1}\frac{(Z_c-Z_a)\cos\theta_a+(X_c-X_a)\sin\theta_a\cos\alpha_a+(Y_c-Y_a)\sin\theta_a\sin\alpha_a}{L_{ac}} \tag{9}$$

The coordinates of point m are calculated as below:

$$\mathrm{Z_m} = Z_a + R\tan\frac{\gamma}{2}\cos\theta_a \tag{10}$$

$$X_m = X_a + R\tan\frac{\gamma}{2}\sin\theta_a\cos\alpha_a \tag{11}$$

$$Y_m = X_a + R\tan\frac{\gamma}{2}\sin\theta_a\sin\alpha_a \tag{12}$$

The inclination angle, azimuth angle and three-dimensional coordinates of point b are calculated as below:

$$\theta b = \cos^{-1}\left(\frac{Z_c-Z_m}{\sqrt{(Z_c-Z_m)^2+(Y_c-Y_m)^2+(X_c-X_m)^2}}\right) \tag{13}$$

$$\alpha_b = \begin{cases} \tan^{-1}\left(\frac{Y_c-Y_m}{X_c-X_m}\right), \text{if} & X_c > X_m \\ \tan^{-1}\left(\frac{Y_c-Y_m}{X_c-X_m}\right)+\pi, \text{if} & X_c < X_m \end{cases} \tag{14}$$

$$\mathrm{Z_b} = Z_a + R\tan\frac{\gamma}{2}(\cos\theta_a+\cos\theta_b) \tag{15}$$

$$Y_b = Y_a + R\tan\frac{\gamma}{2}(\sin\theta_a\cos\alpha_a+\sin\theta_b\cos\alpha_b) \tag{16}$$

$$X_b = X_a + R\tan\frac{\gamma}{2}(\sin\theta_a\sin\alpha_a+\sin\theta_b\sin\alpha_b) \tag{17}$$

According to the above conditions, the formulas for the calculation of tool face angle ω and deflection

distance L of the deflection tool can be obtained as follows [12].

$$\tan\frac{\omega}{2} = \frac{\sin\gamma\cos(\alpha_b-\alpha_a) - SGN(\theta_b-\theta_a)\sqrt{\sin^2\gamma - \sin^2\theta_a\sin^2(\alpha_b-\alpha_a)}}{\sin(\alpha_b-\alpha_a)\sin(\theta_b-\gamma)} \tag{18}$$

$$L = \gamma R \tag{19}$$

Where

If $x>0$, SGN $x = 1$;
If $x = 0$, SGN $x = 0$;
If $x<0$, SGN $x = -1$;

2.3 *Software interface and application cases*

Based on the above theoretical calculations, a directional coring tool trajectory design and analysis system is developed by using MATLAB App Designer, realizing the functions of parameter input, automatic selection of effective data of the MWD tool, calculation of actual build-up rate and display of calculation results, calculation of actual drilling trajectory and visualization of calculation results, design and calculation of trajectory to be drilled and the visualization of results, calculation and display of actual drilling trajectory end point deviation, calculation and display of recommended deflection tool face angle and deflection distance, etc. The software interface is shown in Figure 3.

With the actual drilling trajectory as the example, the software is tested to verify the feasibility of the software. The design trajectory is a straight line, and it is expected that the initial azimuth angle of 330° and inclination angle of 90° will be maintained in the whole process of drilling, with a final hole in 800 m deep. As shown in Figure 3, the red line is the theoretical design track, and the area surrounded by the blue line is a cylindrical target area with a radius of 5 m. An actual drilling trajectory not exceeding this target area is expected. Input the local magnetic declination, build-up rate of the deflection tool and the measured data of actual drilling trajectory, and click START CALCULATION to obtain deviation between the end point of actual drilling trajectory and the design trajectory of 4.576 m. If the deviation correction is started at this time, the recommended tool face angle of the deflection tool is 341.7°, the deflection distance is 46.94 m, and the distance between the target point and orifice on design trajectory is 283 m. In addition, the software can visually show the actual drilling trajectory and the trajectory to be drilled in three-dimensional space (NEG coordinate system), where the black one is the actual drilling trajectory and the blue one is the design trajectory of "arc section + straight section". The output results of the software can effectively guide directional drilling process.

Figure 3. Software interface.

3 INTRODUCTION AND TEST OF DIRECTIONAL CORING DRILLING SYSTEM

3.1 *System introduction*

The directional coring drilling system includes software and hardware. The software has been introduced above. The hardware mainly includes drilling rig, linear coring tool, directional coring tool, mud pump, hydraulic pump station, source of water, and source of electricity, as shown in Figure 4. The drilling rig is mainly driven by the hydraulic pump station to provide rotary power and propulsion power for the drilling tools. The mud pump is used to provide flushing water for drilling tools for slag removal and cooling in the process of drilling. The drilling tools are the core equipment of the whole system, used for coring. It should be noted that the linear coring tool is only functioned by coring, with relatively mature technology at present. Directional coring drilling tools have the functions of both coring, guiding and correcting deviation, which is an important and difficult point in directional core drilling system.

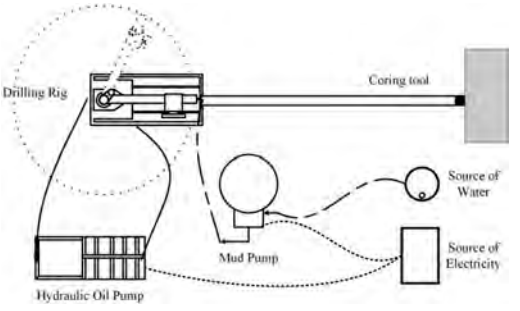

Figure 4. Schematic diagram of directional coring drilling system.

Based on the working principle of static Point-the-Bit Rotary Steering System in the field of petroleum, an deflection tool integrating the functions of guiding, steering, and coring — directional coring tool is developed, with the working principle as below.

The acceleration value is measured by accelerometer. The magnetic force value is measured by magnetometer. The MWD tool integrating accelerometer and magnetometer is connected to the rear end of the inner pipe assembly. The measured data are stored in the MWD inclinometer. The MWD tool can be lowered and refloated along with the inner pipe assembly. After refloating, the measured data is read: azimuth angle α, inclination angle θ and tool face angle γ. In combination with the drilling depth of each measuring point, the actual drilling trajectory can be solved by the directional drilling trajectory design software. Of them, the tool face angle γ represents the degree of rotation of the deflection tool around its own axis, and is an important reference for directional drilling.

(2) Steering principle

The steering principle of directional coring tool refers to the static Point-the-Bit Rotary Steering System, and the schematic diagram is shown in Figure 5. Of them, the eccentric mechanism, thrust bearing and joint bearing determine the deflection deformation of the center shaft, tilting the drill bit connected with the center shaft. Lower it to the bottom of the hole and rotate the whole directional coring tool to change the inclination direction of the drill bit, and ensure the correct inclination direction of the drill bit in combination with the tool face angle measured by the MWD tool. During the formal drilling, the hydraulic anti-rotating mechanism is used to prevent rotation. Finally, the casing will not rotate, but only the drill pipe, center shaft and bit rotate to ensure an unchanged drilling direction.

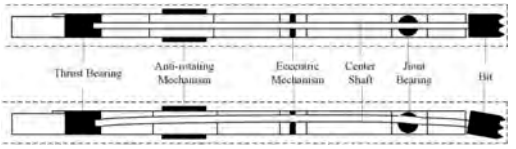

Figure 5. Steering principle of the directional coring tool.

(3) Coring principle

Wireline coring is adopted for the directional coring tool to reduce the time of bit lifting and tripping, and improve the drilling efficiency [13]. The coring principle is the same as that of conventional linear coring tool: the inner pipe assembly is lowered by water pressure in place, then the elastic part enters the locking coupling, and the water pressure rises; during normal drilling, the core enters the inner pipe through the core lifter; when coring is required, the overshot is lowered with water pressure and connected to the inner pipe assembly, then the overshot is lifted upward, forcing the elastic part to contract, disengaging the inner pipe from the outer pipe, and lifting the inner pipe assembly [14].

Based on the above principle, the technical parameters of directional coring tool developed in this paper are shown in Table 1. In the whole drilling process of directional coring drilling, linear coring tool and directional coring tool are used alternately. When it is found that the actual drilling trajectory exceeds the allowable error, the directional coring tool is used for deviation correction. After the completion of deviation correction, linear coring tool is used to continue to drill, so as to ensure that the actual drilling trajectory does not exceed the target area.

Table 1. Technical parameters of directional coring tool.

Parameter Description	Parameter Value	Parameter Description	Parameter Value
Borehole diameter (mm)	76	Maximum build-up rate (°/30m)	>3
Core diameter (mm)	31.5	Measurement parameters and errors	Azimuth angle < ±1° Inclination angle<±0.2° Tool face angle < ±0.2°
Single coring length (m)	3	Maximum drilling speed (m/h)	>1

3.2 *Engineering test*

Testing verification is carried out to verify whether the directional coring drilling system can realize the functions of guiding, steering, and coring in actual working conditions. Aiming at the actual drilling trajectory formed by the directional coring drilling system, MWD tool is used for measurement. The actual drilling trajectory is calculated in combination with the directional drilling trajectory design software. The calculation results are compared with the measurement results of laser tracker (accuracy: 0.01 mm). The accuracy of the measurement results is verified, that is, the guiding function is verified. The actual drilling trajectory is measured by laser tracker, and the direction of deviation correction and the radius of curvature are fitted with Matlab to verify the steering function of directional coring device. In addition, in the test, the drilling rate and core sampling rate of directional coring tool are tested to verify its coring function.

3.2.1 *Test methods*

The directional coring drilling test is carried out with two 4.2m concrete blocks in the plant. The test methods are as follows:

(1) The conventional NQ linear coring tool was used to drill for not less than 2m first, so as to ensure that the anti-rotating mechanism of directional coring tool was already in the borehole and could play an anti-rotating function. In the process of linear coring drilling, the set bit pressure was about 10 kN, the rotating speed was about 304 rpm, and the flow rate was about 55 l/min.
(2) Then the drilling function of directional coring tool was tested. The directional coring tool was carried on a qualified drilling rig after commissioning, and the eccentricity of the eccentric mechanism was adjusted to tilt the drill bit. In order to eliminate the influence of gravity, the directional coring tool was lowered to the hole bottom in a way that the drill bit deflected to the right. Flushing water was supplied, and the anti-rotating mechanism prevented the casing from rotating. In the process of directional coring drilling, the bit pressure was 16-20 KN, the rotating speed was 210-305 rpm, and the flow rate was about 28-35 l/min.
(3) After the completion of drilling, the actual drilling trajectory was obtained by using MWD tool and laser tracker in combination with directional drilling trajectory design software. A comparison for consistency between the direction of actual drilling trajectory and the expectation was carried out. The actual build-up rate was calculated and concluded.

Figure 6. Directional coring drilling engineering test.

3.2.2 *Test results*

Verification of guiding function: The data of MWD tool was input as the directional drilling trajectory design software. The calculated actual drilling trajectory results are shown in Figure 7(a), and the measurement results of laser tracker are shown in Figure 7(b). It can be seen that the data of MWD tool fluctuates more than laser tracker data in xy plane, which may be caused by large measurement error of azimuth angle of MWD tool. In yz plane, the distance between the starting point and the ending point of the borehole as measured by the MWD tool on the vertical plane is about 20.5mm, which is only 2.5% of difference in comparison with the distance of 20mm between the starting point and the ending point as measured by the laser tracker on the vertical plane, indicating a small measurement error of MWD tool in inclination angle.

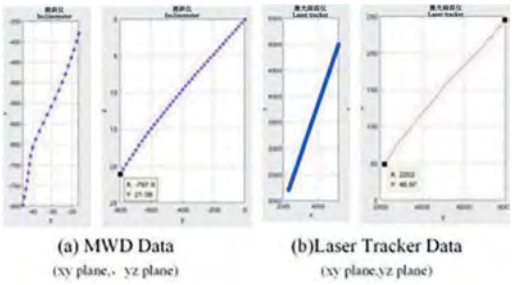

Figure 7. Measurement results of borehole trajectory.

Verification of steering function: The measurement results of laser tracker in horizontal plane are shown in Figure 8(a), with totally 602 measuring points. The last 100 measuring points of the laser tracker were extracted, i.e. about 1.3 m of directional drilling trajectory. The local enlarged view is shown in Figure 8(b). It can be seen that the drilling trajectory tends to deviate to the right from the starting point to the ending point of the borehole, which is consistent with the set direction. Fitting the circle with matlab, as shown in Figure 8(c), the radius of curvature is about 114m, and the corresponding build-up rate reaches 15°/30m. Moreover, it can be seen from Figure 8(c) that the direction of circle center is on the right side of the trajectory, which is consistent with the expected drilling direction.

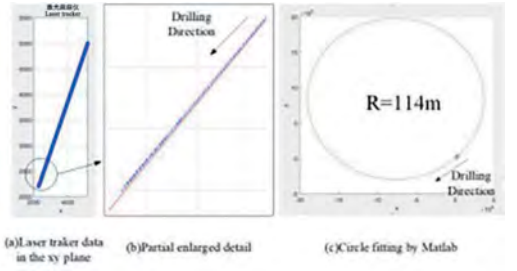

Figure 8. Deviation correction results.

Verification of coring function: The actual boreholes and the cores obtained are shown in Figure 9. As can be seen from the figure,

(1) In the process of drilling, the water returned from the flushing fluid to the outside of the hole is turbid, indicating a high drilling speed.
(2) The geology in the concrete is very uneven, while the hole wall formed by coring drilling is

smooth, requiring high anti-rotating ability of directional coring tool.

(3) Directional coring tool can be directly put into the borehole formed by linear coring tool, without reaming process or replacing mud pumps and other equipment, thus greatly improving the drilling efficiency.

(4) The diameter of the core from linear drilling is 47.3 mm, and that from directional drilling is 31.45 mm. In comparison with the core from linear drilling, the core from directional drilling is more broken. It may be because the core from directional drilling is smaller in diameter and easy to fracture.

(5) In the process of linear coring drilling, the drilling rate was about 2 m/h. In the process of directional coring drilling, the drilling rate was about 1.06-1.18m/h and the coring rate was higher than 90%, realizing continuous coring in the whole hole section.

Figure 9. Coring results.

4 CONCLUSION

Aiming at the drilling needs of directional continuous coring in advanced geological exploration, a directional drilling trajectory design software is developed, which can implement the calculation and visualization of actual drilling trajectory and trajectory to be drilled, the calculation of appropriate tool face angle and deflection distance of deflection tools, effectively guiding the directional drilling process.

In addition, the hardware of directional coring drilling system is introduced, and a deflection tool integrating the functions of guiding, steering, and coring — directional coring tool is developed. Finally, the feasibility of directional coring drilling system is verified by test. As shown by the test results, the directional coring drilling system can effectively control the borehole trajectory and implement continuous coring in the whole hole section of directional drilling. In comparison with screw drilling tool, it consumes less water, requires no special mud pump, saving the equipment replacement time and improving the drilling efficiency. Therefore, it has certain promotion and application value.

REFERENCES

[1] Du Jiansheng. 2009. Study on Mechanical Internal Offset Pointing Rotary Steering Tool and Its Control Method [Doctoral Dissertation] [D]. Beijing: China University of Geosciences.

[2] Li Shucai, Liu Bin, Sun Huaifeng, Nie Lichao, Zhong Shihang, Su Maoxin, Li Wei, Xu Zhenhao. 2014. Research Status and Development Trend of Advanced Geological Prediction for Tunnel Construction [J]. Chinese Journal of Rock Mechanics and Engineering, 33(006):1090–1113.

[3] Lu Chunhua, Yan Taining, H.Г. Yegorov. 2009. New Drilling Tool to Improve Coring Quality in Complex Formations [J]. Geology and Exploration, 45 (02):112–114.

[4] Liu Kun, Deng Jingen, Shen Xuefeng. 2000. Simulation Experiment and Theoretical Research on Borehole Stability of Directional Wells and Horizontal Wells [J]. Journal of Rock Mechanics and Engineering, S1:913–916.

[5] Lu Jiaxing, Wang Yu, Li Xuefei, Liu Bin, Wang Zhiqiao, Zhang Kai. 2019. Design and Research of Microdrilling Test Devices for Downhole Power Drilling Tools [J]. Geology and Exploration, 55 (03):833–839.

[6] Xiang Junwen, Chen Xiaolin, Hu Hanyue. 2007. Continuous Coring Technology for Directional Deflection and Horizontal Drilling [J]. Exploration Engineering (Rock & Soil Drilling and Tunneling), 09:33–36.

[7] Cunningham B, Tam J K W, Tattersall J W, Nip GCY, Seit RKF. Planning of horizontal direction coring for Deep Subsea tunnel[J].

[8] Cunningham B, Tam J K W, Tattersall J W. Horizontal Directional Coring (HDC) and Groundwater Inflow Testing for Deep Subsea Tunnels[J].

[9] Boden A, Bridges G, Tsang CK and Xu J (2018). Experience of horizontal directional coring in Hong Kong. Proceedings of the Institution of Civil Engineers. Civil Engineering 171(4): 179–185.

[10] Li Jing, Zhang Jinchang, Chen Xiaolin. New Model for Calculation of Borehole Trajectory in Geological Exploration [J]. Exploration Engineering (Rock & Soil Drilling and Tunneling), 2011, 38(01):22–24.

[11] Han Zhiyong. Design and Calculation of Directional Wells [M]. Petroleum Industry Press, 1989.

[12] He Yong, Zhang Lin, Yu Wencheng. Calculation and Application of Directional Well Tool Face Angle [C]. China Petroleum Society 2005 Eastern Oilfield Drilling New Technology Seminar. China Petroleum Society, 2005.

[13] Peng Fenfei, Wang Jialiang, Wan Buyan. 2020. Optimization of Key Mechanisms of Wireline Coring Tools for Hard Rock Drilling with Subsea Rig [J]. Geology and Exploration, 56(01):154–162.

[14] Wang Qiang, Zhu Hengyin, Bu Changgen. 2017. Study on a New Electric Directional Coring Tool and Directional Coring Technology [J]. Anhui Geology, 27(002):127–131.

Tunnelling for a Better Life – Yan, Celestino, Thewes & Eberhardt (Eds)
© 2024 The Author(s), ISBN 978-1-032-80042-4
Open Access: www.taylorfrancis.com, CC BY-NC-ND 4.0 license

Geological risks in TBM tunneling and its prediction by HSP method

Song Lu*, Yang Xiao & Xu Wang
China Railway Southwest Research Institute Co., Ltd. , Chengdu

ABSTRACT: In order to realize the real-time prevention and control of geological risks in TBM tunneling, and taking into consideration the construction technology of TBM tunnels and structural characteristics of the TBM machine, the unfavorable geological bodies affecting the construction of TBM tunnels, such as karst, boulder, bedrock relief and structural fracture zone were analyzed so as to develop an advanced geological prediction technology based on HSP method, which uses the rock-breaking vibration of the TBM machine as the seismic source. By developing the software system with the functions of one-click design of parameters, automatic acquisition of wave field information, real-time data processing, detection of geophysical anomalies, and intelligent interpretation of prediction results, we put forward the optimization design scheme for the hardware and software of HSP system, so that the HSP system can be mounted on the TBM machine, and the goal of "real-time geological exploration and reporting while TBM tunneling" can be achieved. This technology has been applied in Guiyang Metro Line 3, Guangzhou Metro Line 18, Fuzhou Metro Line 4, Qingdao Metro Line 8 and other projects, and the karst, boulder, bedrock relief and other unfavorable geological bodies with elastic wave impedance difference have been well predicted. The HSP method-based geological prediction technology, which is based on the "passive source" of TBM construction environment, provides a solution for the real-time perception of geological state in the process of TBM tunneling, making the real-time fusion analysis of geological and construction information possible, and promoting the development of intelligent TBM construction.

Keywords: TBM Construction, HSP method, Rock-breaking Seismic Source, Intelligent identification

1 INTRODUCTION

Urban rail transit, which operates through subterranean tunnels, has gained popularity due to its fast speed, high transportation capacity and low environmental impact. It has become an essential mode of transportation for people to travel. Tunnel Boring Machine (TBM) construction is a prevalent technique in urban rail transit construction and has also been applied to underground infrastructure projects, including underground pipe galleries and pipelines. As urban transportation and underground space construction continue to develop, the need for effective management of geological risks and optimization of engineering design has increased. Consequently, the standards for density and accuracy of geological exploration have become more stringent. Exploration methods primarily based on drilling and in-situ testing are limited in terms of location and number of holes due to site structures, transportation and other constraints. Moreover, the accuracy of surface investigation may not meet the requirements for high-precision investigation due to factors such as time period and funding. Additionally, frequent geological disasters occur due to uncertain geological conditions [1, 2]. While existing geophysical exploration technologies have resolved many engineering problems within their respective detection capabilities, traditional geophysical exploration methods still could not identify the distribution of unfavorable geological conditions (bodies) in TBM construction or adapt to TBM construction scenarios. Furthermore, the unique structure and construction characteristics of TBM will also impact the safety and progress of TBM construction, particularly in complex geological conditions and environments. Hence, ensuring effective management of geological risks during TBM construction is essential for the efficient implementation of the metro construction project using the TBM method.

Based on the technological characteristics of TBM construction, this paper examines significant geological hazards that impact TBM construction, such as karst, boulder and bedrock relief. It discusses geological prediction technology that employs the HSP method which utilizes the rock-breaking vibration of the TBM as the seismic source. Additionally, the paper presents several prediction cases to provide guidance for future TBM construction projects with similar geological conditions.

Fund project: China Railway Major Special Project (cz02-ZX-03, 2020-ZDZX-04-01); Guangxi Science and Technology Development Project (2021AB40119)

*Corresponding author: 178404719@qq.com

DOI: 10.1201/9781003495505-77

2 TECHNOLOGICAL CHARACTERISTICS OF TBM CONSTRUCTION

The TBM method is a highly mechanized tunnel construction technique that employs a TBM to excavate underground. The TBM performs tunneling and mucking while simultaneously controlling the excavation face and surrounding rock to prevent collapse and destabilization. Additionally, the TBM assembles pipe segments to form the lining and carries out grouting behind the wall to construct the tunnel without disturbing the surrounding rocks, as illustrated in Figure 1. The primary principle is to minimize the impact on surface buildings, transportation facilities, and underground pipelines by completing tunneling and lining works to the greatest extent possible without disturbing the surrounding rocks. To attain this objective, the earth or slurry pressure within the pressure chamber is frequently utilized to balance the earth pressure and water pressure exerted on the excavation surface, thereby actively regulating the release of stress and deformation of the surrounding rocks. This aspect constitutes a crucial element of TBM technology.

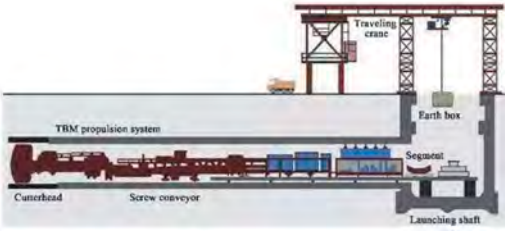

Figure 1. Schematic diagram of TBM construction.

3 ANALYSIS ON GEOLOGICAL RISKS OF TBM CONSTRUCTION

3.1 *Cases of disasters faced by TBM construction*

In TBM construction, safety incidents frequently arise as a result of unfavorable geological conditions. For instance, in one engineering project, a water-earth consolidated block obstructed the screw conveyor, rendering the TBM inoperable. Upon opening the observation hole to address the issue, sand and water surged through the opening of the screw conveyor. In another project, the sudden release of gas in the local formation gap created a groundwater channel, causing the confined water behind the TBM to surge along the channel and into the hole, resulting in a significant collapse of the ground and the TBM being buried. It is evident that determining geological conditions is a crucial aspect of TBM construction for metro lines. Therefore, significant emphasis shall be placed on geological conditions, and geological exploration work shall be carried out beforehand for TBM construction sections. Typical geological hazards that may arise during TBM construction include karst, boulder, bedrock relief, and water-rich structural zone.

3.2 *Risk of karst or dissolution zone*

Based on varying geological conditions and levels of karst development or hazards, karst zones can be categorized into high- and low-risk zones. A geological area that features a rock-soil interface (primarily defined by a heavily weathered rock stratum beneath a soil layer) located within 10 m below the structural floor is classified as a high-risk karst zone. The high-risk karst zone is typically considered to be bounded by a plane range of 3 m away from the main structure boundary, while all other zones are considered low-risk karst zones.

In areas where karst develops, large-scale karst/soil cave groups are typically formed, and the distribution pattern of karst is often irregular. The individual shapes of the karst caves vary. The fillings of the karst/soil caves are mostly rheoplastic or soft plastic, which exhibit low stability. If the groundwater is abundant or flows actively, ground collapse may occur easily [3]. Under such circumstances, TBM construction may result in structural damage, leading to issues such as sinking, "kowtow" and deflection of the TBM, or sudden mud burst or water gushing in the tunnel.

3.3 *Risk of boulders*

The spheroidal weathering of rock mass commonly creates boulders and poses a significant challenge to TBM construction. If an unknown boulder is encountered during TBM excavation, it may act as a major obstacle, akin to a "tiger blocking the road," as illustrated in Figure 3. This will make excavation exceedingly difficult, with the cutterhead frequently getting stuck. The TBM's posture will become challenging to control, and the cutter holder and cutterhead will be deformed easily, significantly impeding the efficiency of TBM construction.

Figure 2. Boulder.

Figure 3. Geological risk of boulder.

3.4 *Risk of bedrock relief*

The bedrock surface is characterized by undulations, often forming distinct strata with a soft top and hard bottom, as illustrated in Figure 4. When the TBM advances to cut the rock stratum at the bottom, severe wear will be caused around the cutterhead, and the TBM posture control will also become difficult. There have been instances where the shield was worn out by the cutterhead.

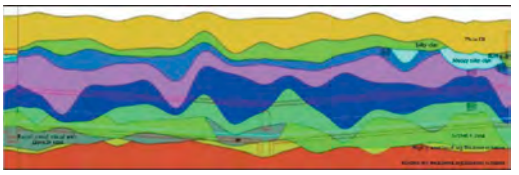

Figure 4. Geological section of an engineering project.

3.5 *Risk of geological structural zones*

The lithology on either side of the fracture zone exhibits significant differences. The fracture zone itself is characterized by a substantial amount of breccia. Shallow fracture zones are typically filled with clay, which has a relatively high stickiness, leading to the formation of mud cakes. If groundwater is abundant, gushing may occur easily during TBM excavation. Furthermore, due to the uneven bedrock surface and the impact of hydrothermal process, the rock strata on either side of the fracture zone may become silicified. Silicified rock is known for its high strength, but it can also cause excessive wear on the cutterhead, as well as cracking of the cutter ring and bolt fracture. For instance, in a previous project, TBM excavation encountered a fracture zone, resulting in slow progress and a 39-day suspension due to a fractured scraper bolt.

3.6 *Other risks*

During urban metro construction, TBM construction often encounters existing structures such as foundation piles and anchor cables that intrude into the construction area. These structures will act as roadblocks, impeding TBM progress and leading to significant wear and tear around the cutterhead. In some cases, they can even make the TBM get stuck or affect the structural safety of nearby buildings.

4 ANALYSIS ON GEOLOGICAL PREDICTION FOR TBM CONSTRUCTION

4.1 *Environmental characteristics of TBM construction*

(1) Space characteristics of TBM construction
The TBM construction environment is highly intricate. Since the TBM occupies a significant portion of the tunnel space behind the working face, the observation space for advance geological prediction is extremely narrow, and the room for laying out geological prediction equipment is insufficient, as illustrated in Figure 5. Consequently, the application of advance prediction methods used in traditional drilling and blasting (D&B) tunnel construction in the TBM construction environment is challenging.

Figure 5. Environment of TBM construction.

(2) Impact of shield segments
Shield segments are the primary assembly components used in TBM construction. Typically, they are constructed from high-strength, impermeable reinforced concrete, with a high reinforcement ratio, high strength and thickness ranging from 30 cm to 50 cm, to ensure reliable load-bearingcapacity and waterproof performance. Once the TBM has excavated a distance of one ring, the erector operator assembles single-layer lining segments using the erector, enabling the tunnel to be formed in one go, as illustrated in Figure 6. However, the complete coverage of the tunnel wall by segments limits the arrangement of geophysical exploration receiving devices, such as geophones and electrodes.

Figure 6. Tunnel segment support.

(3) Environmental noise interference
Vibration interference: Compared with the D&B method, the vibration, noise and other environmental hazards generated by TBM construction are less harmful, but its vibration and noise will still have a certain impact on advance geological prediction. The main sources of vibration and noise include: 1) Large vibration caused by large collision when the cutterhead cuts soil during

TBM tunneling; 2) the mucking mechanism of TBM, including mainly screw conveyor and belt conveyor; 3) several links of the TBM construction involving auxiliary equipment and the treatment and transportation of raw materials and muck. Transportation work involving segment transport trolleys, slurry carts, muck carts and bentonite carts can generate varying degrees of vibration and noise.

Electromagnetic field interference: As described by Maxwell's Electromagnetic Theory, changing magnetic fields can excite vortex electric fields, and changing electric fields can excite vortex magnetic fields. Electronic devices inherently generate electromagnetic fields in their surrounding space. The TBM construction site is equipped with intensive electric equipment, complex electrical circuits and numerous metal components. Its power distribution systems range from high voltage to low voltage and from strong current to weak current, featuring extremely intricate structures and functions. All of these factors contribute to the production of significant electromagnetic interference, which can significantly affect the accuracy of advance geological prediction through electromagnetic methods.

4.2 *Technical requirements for the geological prediction for TBM construction*

Scenario adaptability of prediction methodsThe TBM construction environment poses limitations or challenges to the implementation of commonly used prediction methods for mine tunneling, such as TSP, geological radar method and transient electromagnetic method [4]. The implementation of the geological radar method and the transient electromagnetic method, which involve laying survey lines on the tunnel face, is not feasible. Similarly, the TSP method, which requires blasting source holes and receiving holes in the side walls, is affected by the segments, and the use of explosive sources poses safety risks for the TBM. Therefore, a suitable prediction method for TBM construction scenarios shall consider factors such as field source excitation, measuring point arrangement and noise disturbance capability.

Figure 7. Influence of TBM construction environment on geophysical prediction.

(3) Detection range

The TBM method offers significant advantages over traditional underground excavation methods in terms of engineering progress. Through analysis of statistical data from TBM construction sections of Beijing Metro Lines 5, 4, and 10, as well as Beijing Airport Express, and by disregarding non-advancing operations and solely comparing normal tunneling conditions in TBM construction sections, it is evident that the maximum and average tunneling speeds in TBM construction sections are significantly higher. In fact, they are approximately 5 to 10 times faster than those of the mine tunneling method, as illustrated in Figure 6. In this case, the detection range of the prediction method must meet the requirements of the tunneling speed.

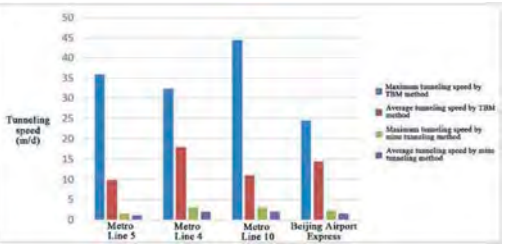

Figure 8. Comparison of tunneling speed between TBM construction and mine tunneling method.

5 GEOLOGICAL PREDICTION METHODS SUITABLE FOR TBM CONSTRUCTION

In TBM construction, conventional advance geological prediction methods primarily include the surface drilling method, geophysical exploration method, and analysis of rock-machine sensing parameters and muck behavior in the tunnel. Each method has its unique characteristics and limitations. For instance, the drilling method's hole layout is restricted by surface buildings and structures. Similarly, the surface geophysical exploration method is susceptible to interference from underground pipelines and urban geophysical exploration sources, which will affect the quality of field source signal reception. Additionally, the rock-machine sensing parameter analysis is typically more accurate when an anomaly is imminent, making it challenging to predict unfavorable geological conditions in advance and gain valuable time for treatment. This paper introduces a real-time advance geological prediction method (HSP method) which uses the rock-breaking vibration of the TBM as the seismic source.

5.1 *Technical principles of HSP method*

This method is based on the elastic wave theory, which utilizes the vibration signals generated by the disc cutter during TBM tunneling as seismic sources [5, 6]. By creating virtual seismic sources [7, 8] through interference phenomena, reflection imaging is performed for geological bodies with differences in elastic wave

impedance (i.e., the product of density and velocity) in front. Unfavorable geological bodies, such as faults, weathered fracture zones, karst and groundwater enrichment zones, exhibit distinct characteristics from surrounding rocks. The reflection characteristics of the wave field propagation are as follows:

$$R_{12} = \frac{\rho_2 v_2 - \rho_1 v_1}{\rho_2 v_2 + \rho_1 v_1}$$

Where, R_{12} is the reflection coefficient, ρ is the medium density, and v is the longitudinal wave velocity of medium.

Figure 9. Geological Prediction with rock-breaking vibration as the seismic source.

5.2 *On-site implementation process of HSP method*

In the implementation process, geophone points are arranged along the tunnel contour. While fixed positions are not necessary, it is important to meet minimum offset requirements to ensure accurate geophone point position data entry into the software system. Rock-breaking vibration signals are continuously collected during TBM excavation to ensure sufficient data volume, typically not less than 8 minutes. The collected data undergoes time-frequency analysis [9], interference analysis, reflection imaging [10, 11], time-depth conversion, anomaly extraction, and geological interpretation to determine the spatial location and range of unfavorable geological conditions (bodies) ahead. This process enables accurate geological prediction.

5.3 *Onboard HSP217T real-time geological prediction system*

Incorporating onboard geological prediction equipment that is suitable for TBM construction environments is an effective approach to enhance the intelligent sensing capabilities for TBM construction. The acquisition control is performed using the industrial control computer located in the TBM control room. The acquisition host is modularized and integrated into the TBM host room, while the large receiving cable is integrated with the TBM structure to form a complete set of onboard prediction equipment. See Figure 10 for further details.

Figure 10. Onboard prediction system.

With a modular design, the software component of the system comprises three distinct modules: (i) the host control and parameter design module, which includes host acquisition control, position parameters of receiving and sending points, data processing parameters, and other relevant parameters that can be set rapidly and efficiently; (ii) the information acquisition, storage and imaging module, which performs data acquisition, processing, and inversion imaging based on the design parameter information, as illustrated in Figure 11, and completes the mapping of geophysical exploration images, abnormal areas and presumed geological risks; and (iii) the anomaly identification and geological interpretation module, which identifies and interprets anomalies in the result images and performs iterative approximation analysis of multiple detections. See Figure 12 for further details on the iterative approximation analysis.

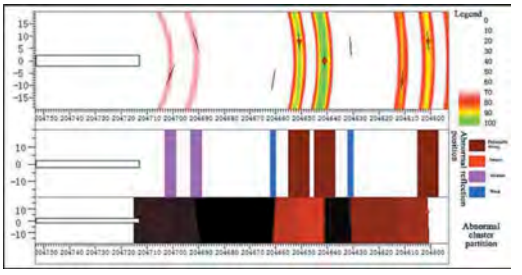

Figure 11. Inversion imaging display interface.

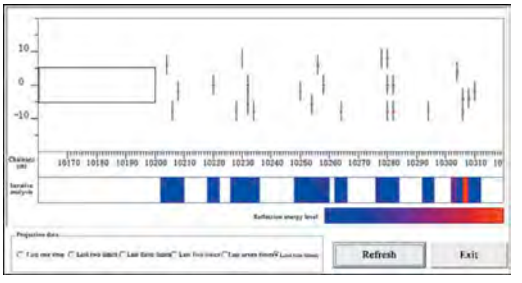

Figure 12. Iterative approximation analysis of multiple detections.

6 CASE ANALYSIS OF PREDICTION BY HSP METHOD

6.1 *Karst prediction*

TBM cluster construction is adopted for Guiyang Metro Line 3. However, due to the presence of a karst zone, risks such as deviation, water burst and mud gushing may be encountered during TBM construction. To mitigate these risks, the HSP method was employed for geological prediction along the entire line. The prediction analysis focused on ZDK24+687 in the Sifanghe Road Station–Zaojiaojing Station Section. In this project, 200 data were collected, with a total of 1,600 channels. Each channel lasted for 0.256 s and the whole process took 15 minutes. The data were processed by interference imaging, as illustrated in Figure 14. The analysis predicted five areas of abnormal reflection. When the TBM entered these areas, excavation parameters and mucking amount became abnormal.

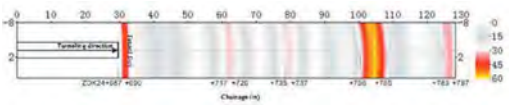

Figure 13. Results of Detection at ZDK24+687 (top view).

6.2 *Boulder prediction*

In Section K6+939~K6+869 of Guangzhou Metro Line 18, the TBM needed to pass through an intensely weathered zone of granite. Preliminary survey data showed that there were boulders in the area. In this case, HSP method was used to perform test at K6+939 of the tunnel face. A total of 300 data were collected, totaling 2,400 channels. Each channel lasted for 0.256 s, and the whole process took 18 minutes. The data were processed by interference imaging, as illustrated in Figure 15. Based on the prediction results, numerous abnormal reflection areas were identified. When the TBM entered these areas, a loud abnormal sound was detected in front of the tunnel face, which was confirmed to be the sound of boulder breakage caused by the cutterhead. The screw conveyor brought out small pieces of boulders, leading to damage of the cutting tools and belts, and necessitating the shutdown of the TBM for maintenance. Multiple spheroidal weathered blocks of granite appeared in the muck. See Figure 14 for detection results.

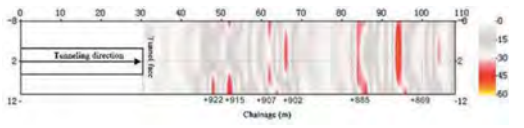

Figure 14. Results of detection at K6+939 (top view).

6.3 *Prediction of bedrock relief*

The Linpu Station-Chengmen Station Section of Fuzhou Metro Line 4 comprises primarily of torso mountains, hilly landform units, and Quaternary deposits as its geomorphic units. The terrain of the torso mountains and hilly landform units exhibits significant fluctuations, and the TBM crossing area is characterized by numerous bedrock intrusions into the tunnel design space. In this test, 300 data were collected at K42+700 of the tunnel face, with a total of 2,400 channels. Each channel lasted for 0.256 s, and the whole process took 18 minutes. The data were processed by interference imaging, as illustrated in Figure 16. Based on the prediction results, one abnormal reflection area was identified. When the TBM entered the area, tunneling was carried out under challenging conditions, including broken stones and bedrock relief, which led to the TBM's shutdown for handling. The specific situation of surrounding rock excavation and exposure is shown in Figure 15.

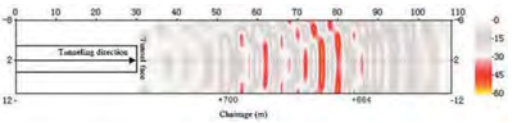

Figure 15. Results of Detection at K42+700 (top view).

6.4 *Prediction of structural fracture zones*

The pilot tunnel in the Dayang Station–Qingdaobei Station Section of Qingdao Metro Line 8 was constructed using dual-mode TBM. The tunnel's top has a minimum cover depth of 29.49 m, and the maximum burial depth of the overburden is 52.49 m (57.94 m below sea level). The overburden primarily comprises of weakly weathered tuff and weakly weathered andesite. To mitigate the construction risks associated with the cross-sea tunnel, the project team defined the chainage for optimal mode conversion and conducted advance geological prediction using the HSP method. Specifically, two anomalies were identified through the prediction process at K1+473, including a minor reflection anomaly and a major anomaly area, as illustrated in Figure 16. During the tunneling process towards the minor anomaly in the hard rock mode, joint fissures emerged within a 2-meter tunnel length range in the direction of 12 o'clock to 1 o'clock, accompanied by localized water seepage. As the tunneling progressed towards the major anomaly, an advance horizontal drilling operation was conducted by the TBM at a distance of 7 meters, revealing a broken stratum ahead. Based on the drilling and prediction outcomes, the TBM mode was appropriately adjusted, enabling it to pass smoothly through the structural fracture zone.

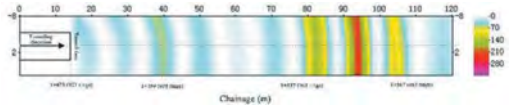

Figure 16. Results of detection at K1+473 (top view).

Figure 17. Photos of exposure by excavation.

Figure 18. Photos of exposure by excavation.

7 CONCLUSIONS

TBM construction is frequently impeded by unfavorable geological conditions, such as karst, boulders, bedrock relief and fault fracture zones, which may result in TBM entrapment, adversely affecting construction efficiency and safety. However, the implementation of conventional advance geological prediction methods in tunnels is hindered by the space environment, geophysical exploration source interference, and segment support mode.

By analyzing the common geological risks and characteristics of TBM construction, this paper discusses an advanced geological prediction technology based on HSP method which uses the rock-breaking vibration of the TBM as the seismic source. Additionally, various cases of unfavorable geological condition prediction are introduced and analyzed. The application results demonstrate that the HSP method can effectively predict common unfavorable geological conditions in the TBM construction environment. Furthermore, since shutdown is not required, this method provides a solution for the real-time perception of geological state in the process of TBM tunneling, making the real-time fusion analysis of geological and construction information possible, and promoting the development of intelligent TBM construction.

Fund project: China Railway Major Special Project (cz02-ZX-03, 2020-ZDZX-04-01); Guangxi Science and Technology Development Project (2021AB40119)

REFERENCES

[1] He Faliang, Lu Song, et al. Construction Prediction Research and engineering Practice of geologically complex Tunnel[M]. Southwest Jiaotong University Press, 2019.

[2] He Faliang, Lu Song, et al. Tunnel construction geological uncertainty[M]. Southwest Jiaotong University Press, 2019.

[3] Li Shucai, Li Shuchen, Zhang Qingsong. Forecast of karst-fractured groundwater and defective geological conditions, Chinese Journal of Rock Mechanics and Engineering, 2007,26(02):217–225.

[4] Li Shucai, Liu Bin, et al. State of art and trends of advanced geological prediction in tunnel construction[J]. Chinese Journal of Rock Mechanics and Engineering, 2014, 33(6):1090–1113.

[5] Lu Song, Wang Xu, et al. Design and Implementation of HSP Realtime Prediction Technology Suitable for TBM Construction[J]. Tunnel Construction, 2019, 39(8): 1255–1261.

[6] Lu Song, Wang Xu, Li Cangsong, et al. Study on Geological Prediction Technology of HSP Method for TBM Tunnel, Modern Tunneling Technology, 2020,56(3):30–35.

[7] Yang Wenjun, Sun Fuli, et al. Application of seismic interferometric migration in Seismic While Drilling-(SWD)data processing[J]. Progress in Geophysics, 2011, 26(2): 602–605.

[8] Zhu Heng, Wang Deli et al. Passive seismic imaging of seismic interferometry[J]. Progress in Geophysics, 2012, 27(2):496–502.

[9] Zhao Jian, Li Yong. Digital Signal Processing[M]. tsinghua university press, 2006.

[10] Wang Jiaying. Geophysical inverse theory[M]. China University of Geosciences Press, 1998.

[11] Wang Huazhong, Feng Bo, et al. Analysis of seismic inversion imaging and its technical core issues[J]. Geophysical Prospecting for Petroleum, 2015, 54(2):115–125.

Tunnelling for a Better Life – Yan, Celestino, Thewes & Eberhardt (Eds)
© 2024 The Author(s), ISBN 978-1-032-80042-4
Open Access: www.taylorfrancis.com, CC BY-NC-ND 4.0 license

Rock abrasiveness in the studies of São Paulo Metro: Tests, classification systems, parameters obtained from various lithotypes and their relationship with weathering degree

Marcelo D. Monteiro*, Hugo C. Rocha, Guilherme B. Robbe & Audrey Melchert de Almeida
Companhia do Metropolitano de São Paulo - Metrô, Brazil

ABSTRACT: The assessment of the abrasivity effects exerted by rocks on cutting tools is of great importance. The consumption of these tools needs to be carefully analyzed, as it can result in increased costs and delays in schedules. In this regard, the Sao Paulo Metro conducts detailed studies to better understand the factors that condition abrasive properties in rocks found in the São Paulo Metropolitan Region.

These studies are carried out through petrographic analysis of rocks, uniaxial compressive strength tests, CERCHAR abrasivity tests and drillability tests. The results are reported using internationally recognized classification systems, such as the equivalent quartz content (eQc), the CERCHAR abrasivity index (CAI), and the rock abrasivity index (RAI).

An aspect of major relevance in the studies was the evaluation of the weathering degree of the rocks and its influence on the results of the abrasivity tests. It was observed that as the weathering degree increases, the abrasivity parameters show lower values. This information is crucial for a proper evaluation of abrasivity. Solely considering mineralogical aspects is not sufficient. It is necessary totake into account the specific geomechanical conditions of the rocks.

Finally, based on the CERCHAR and RAI indexes, estimates of the consumption of cutting tools were made for the studied rocks. The Cantareira Granite proved to be more abrasive, resulting in higher tool consumption compared to the granitic and gneissic rocks of the Embu Complex.

Keywords: abrasivity, cerchar, weathering, cutting tools

1 INTRODUCTION

The study of parameters related to the abrasiveness of rocks and soils is of great importance in the execution of works in rock masses, both for drilling & fire blasting excavations, as well as those mechanized with tunnel boring machines (TBM) or road header machine mainly for assessment of wear on cutting tools and their associated costs. Since the expansion projects for the metro lines in São Paulo (Brazil) started to intercept the rock masses that constitute the basement of the Metropolitan Region of São Paulo, the São Paulo Metro started to develop a line of studies related to abrasivity of rocks and their effects on the consumption of cutting tools, trying to fill the existing gap in knowledge on the subject, both in São Paulo and in Brazil. The studies carried out showed behavior of the local lithotypes that were quite different from those observed in classical studies carried out on the European continent, in particular due to the different physical and chemical conditions of the tropical climate with a temperate climate and a different degree of action of external dynamics.

2 GEOLOGICAL CONTEXT AND SAMPLE SELECTION

The samples for the study were collected throughout the geological-geotechnical investigation campaigns of the Basic and Executive Project phases of the São Paulo Metro, Lines 2, 4, 5 and 6. In the evaluations, we sought to identify the representative lithotypes at depths of interaction with underground excavations.

The geology of the São Paulo Metropolitan Region (RMSP) is represented by three compartments: in stratigraphic order, the Precambrian basement, the Paleogene to Neogene sediments of the São Paulo Basin and the Quaternary covers. As for lithotypes, the geological framework of the RMSP is

*Corresponding author: mdmonteiro@metrosp.com.br

DOI: 10.1201/9781003495505-78

basically made up of metamorphic and igneous rocks, associated with the Embu Complex and the São Roque and Serra do Itaberaba Groups, in addition to bodies of intrusive granitoid rocks.

The Embu Complex is the unit with the highest occurrence in the basement of the RMSP, occurring in its central-southern portion and occupying a range of outcrops with a NE-SW direction, represented by gneisses, amphibolites, migmatites and granite-gneisses (Monteiro et al., 2012).

The intrusive granitoids, in this study represented by the Cantareira Granite, occur as rocks of granodioritic to granitic composition and appear as a large number of batholiths that outcrop in the region, some partially covered by the sediments of the São Paulo Basin. The greater resistance to weathering has caused these rocks to sustain morphological highs (Coutinho 1980, apud Juliani 1992). These rocks are marked by high values of uniaxial compressive strength. Samples of hydrothermalized archosean sandstone from the Resende Formation were selected from the sedimentary soil packages. These were included in this study due to their frequent occurrence in studies. They are sandstones with strong cementation, which makes excavation difficult in relation to the rest of the sedimentary package. These rocks are located next to fault zones, from where they receive input from hydrothermal fluids, especially in the east zone of São Paulo.

3 ABRASIVENESS ASSESSMENT

Historically, abrasiveness studies were restricted to mineralogy and were based only on the amount of quartz mineral present in the samples, based on the Mohs hardness scale (relative) and the Rosiwal hardness scale (absolute), the latter of which supported the development of quartz-equivalent content. Plinninger (2010) mentions that exclusive approaches to these indices based only on the mineralogy of the rock proved to be limited as they did not consider other important characteristics (such as grain size and mechanical resistance); This scenario provided the development and application of other tests and indices to better evaluate the abrasive properties of rocks and soils.

In the international literature, in addition to mineralogical approaches, there are a large number of parameters and tests to evaluate the abrasive properties of soils and rocks (all tests and indices developed have applications depending on specific approaches). In studies carried out in Brazil, the equivalent quartz content (eQc) and the CERCHAR abrasiveness index (CAI) have been used more frequently. In recent years, the application of the drilling rate index (DRI) has been increasing.

3.1 *Equivalent Quartz Content (EQC)*

It is an index developed to indicate the abrasive potential of rocks based on the presence of abrasive minerals. Quartz equivalent is a parameter obtained from petrographic analysis carried out on slides from rock samples in which the percentage of minerals is determined; the value obtained is multiplied by the Rosiwal abrasivity of each mineral.

Equivalent quartz is used by excavation equipment manufacturers and research professionals to identify tool consumption problems.

3.2 *Cerchar Abrasiveness Index (CAI)*

The CERCHAR abrasiveness index is obtained from the homonymous test, developed in the 1970s. The test consists of fixing a rock sample over which a tip made of material with known hardness is slid. The tip is subjected to a weight of 7 kg, which provides a load of 70 N. The surface of the sample where the tip friction is applied is obtained naturally through fresh flat fractures or artificially, in this case, using diamond saw. The friction of the tip with the test surface creates a groove in the sample, leading to wear of the tip, which represents the CERCHAR Abrasive Index (CAI). Values below 1.0 are considered slightly abrasive, values between 1.0 and 2.0 are considered medium abrasive, values between 2.0 and 4.0 are considered very abrasive and values between 4.0 and 6.0 are considered considered extremely abrasive. In practice, we can assume that CERCHAR evaluates primary wear. This is the wear that cutting tools suffer in direct contact with the rock mass and is the most discussed in studies focused on the consumption of these tools.

3.3 *Rock Abrasiveness Index (RAI)*

The rock abrasiveness index (RAI) represents a modification of the quartz-equivalent content (eQc) and is applicable not only to sound rocks, but also to weathered rocks. The RAI is calculated by multiplying the simple compressive strength (RCU) by the equivalent quartz content (eQc), being defined as an index that combines the presence of abrasive minerals with the mechanical properties of the rock (Plinninger, 2010). The RAI stands out for its practicality in obtaining it, since petrography data and RCU tests are usually available in good geological-geotechnical investigation campaigns. Even so, Plinninger (2010) mentions that in the absence of these parameters, eQc can be replaced by X-ray diffractometry and RCU by the point load test. In the rating scale for RAI there are no upper and lower limits. Values below 10.0 are considered as non-abrasive, values between 10.0 and 30.0 are considered as little abrasive, values between 30.0 and 60.0 are considered abrasive, values between 60.0 and 120.0 are considered considered as very abrasive and values above 120.0 are considered as extremely abrasive.

The highest RAI values recorded were in quartzites in South Africa (RAI of 360) and Germany (RAI around 200), but experience indicates that values of up to 400 are admitted as plausible for this parameter. The lowest values are attributed to highly weathered rocks, with low mechanical resistance (Plinninger, 2010).

RAI has been used successfully in Europe, contributing significantly to the assessment of the

abrasive properties of rocks and the prediction of cutting tool consumption.

4 RESULTS AND IMPLICATIONS FOR EXCAVATIONS

Below are presented the results obtained for the evaluated parameters (equivalent quartz - eQc, the CERCHAR abrasivity index - CAI and the rock abrasivity index - RAI), the correlations between these parameters, the influence of the degree of alteration and the application of these in predicting the consumption of cutting tools in underground excavation works in rock masses.

4.1 *Equivalent quartz content results*

The granite units are predominantly within the same occurrence range, between 40% and 50%. These units have a main mineralogical profile represented by quartz (20 – 25%), feldspars (30 – 40% for Cantareira and 40 – 50% for the Embu Complex) and biotite (10 – 20%). Secondary and accessory mineralogy includes zircon, titanite, apatite, epidote, tourmaline, chlorite, sericite, muscovite and opaque minerals. Some samples of these granites presented quartz-equivalent values that differ from the average profile, these are credited to specific variations, such as sample 6175B with 8% tourmaline, contributing to an eQc of 59.30% (Cantareira Granite) and sample 5719 with 6% hornblende and about 35% quartz, resulting in an eQc of 53.33%. At the other extreme, counts of 20% biotite (sample 6115) and the combination of 20% quartz with high amounts of biotite, muscovite and chlorite (sample 5653A) provided eQc values of 43.80% and 40.90%.

The gneisses of the Embu Complex are in a similar range to the granites, however, with a predominant occurrence range of up to 60%. The mineralogical profile of these rocks is more diverse, presenting a wide variety in the quantities of the main mineralogy (quartz, feldspars, amphiboles and biotite). Despite this great variability, the lithotype reaches higher average values than the granitic units. Discrepant occurrences are also observed in this unit; sample 5595B has 15% garnet, a mineral with a high weight for abrasiveness, contributing to an eQc of 58.69%. For sample 5207A, the low amount of quartz (20%) and 28% biotite contributed to the eQc value of 40.07%. Even so, looking at the average values of the three units, it is clear that they are very close. The Cantareira Granite has an average value of 47.96%, the granites of the Embu Complex have 46.94% and the gneisses of the Embu Complex have 52.90%.

For the other lithotypes with more restricted occurrence, an eQc of 99.57% was recorded in the quartz vein sample (5595). This is the highest value among all the samples analyzed in this study and is consistent with what is expected for a sample with 99.5% quartz and 0.5% opaque minerals. High values of eQc are also recorded (and were expected) in the hydrothermalized arkose sandstones of the Resende Formation, with values from 63.18% to 77.00%. These high values occur due to quantities of quartz + feldspars exceeding 80%. Amphibolite samples from the Embu Complex have low eQc values due to the reduced amount of quartz (below 6%), combined with a greater amount of amphibole (between 50 and 60%). For this unit, the average eQc value is 27.70%, the lowest of all units analyzed.

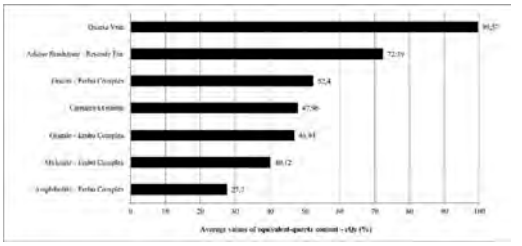

Figure 1. Values of equivalent-quartz content.

4.2 *Cerchar abrasiveness index results*

The unit with the highest CERCHAR values is that of the Embu Complex granites, which have a higher frequency of results between 4 and 6 (extremely abrasive). The Cantareira Granite, with a smaller number of samples, presents results concentrated in relatively close ranges (ranges 4 to 5), indicating compatibility between the granite samples. Despite widespread occurrence among almost all ranges of results, the gneisses from the Embu Complex present a higher frequency of results between ranges 2 and 4 (very abrasive). In relation to the other lithotypes studied, it is possible to observe that the hydrothermalized archosean sandstones present lower values (ranges 0 to 1), being predominantly considered as little abrasive. The amphibolite samples from the Embu Complex had results in ranges 2 and 3 (medium to very abrasive abrasiveness) and the mylonite sample showed high abrasivity, with a value of 4.9. For granite units, in Cantareira the largest number of results above their average is evident. Within this unit, the low value of 3.3 obtained for sample 6116 represents an exception to its standard behavior. The Embu Complex has samples with higher CERCHAR values. Sample 5622, located in the region of the Ponte Grande neighborhood - municipality of Guarulhos, presented a value of 5.7. This is the sample with the highest CERCHAR value recorded in the studies. In general, the two granitic units have CERCHAR abrasiveness results profiles within similar results ranges, with the Embu Complex having higher values between the two units. The hydrothermalized sandstones of the Resende Formation, despite the small number of samples tested, at the 3 different sampling points the results varied from 0.5 to 1.1. It should be noted that these are samples with high quartz-equivalent content (eQc) values. The values for the granitic units are in accordance with the typical CAI values indicated for these rocks in the study by Plinninger et al. (2003).

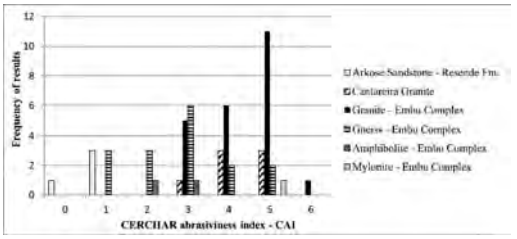

Figure 2. Values of CAI.

4.3 *Comparison between EQC and Cerchar*

Among all the samples used in this study, 44 have quartz-equivalent and CERCHAR results, 24 of which are from igneous rocks, 17 from metamorphic rocks and 3 from sedimentary rocks; This made it possible to compare these parameters. The comparison between the eQc and CERCHAR results obtained on the same samples allowed us to identify the lack of correlation between these parameters, which indicates that abrasive mineralogy is not the only factor that influences the CERCHAR test. Arcosean sandstone samples have high quartz-equivalent values, however, low CERCHAR values. Similar cases also occur in other lithotypes. These results are in agreement with the evolution of this study. Previous initial work with samples from the Metropolitan Region of São Paulo (Monteiro et al., 2011 and Monteiro et al., 2012) already indicated the lack of correlation between these two parameters and this is completely in agreement with the observations of reference works in the European continent, such as Kasling (2000) and Plinninger et al. (2004). In this way, the premise is assumed that just the presence of large quantities of quartz and other abrasive minerals does not necessarily imply the ability to significantly consume cutting tools. The observations of West (1989) and Bieniawiski et al. were not confirmed.

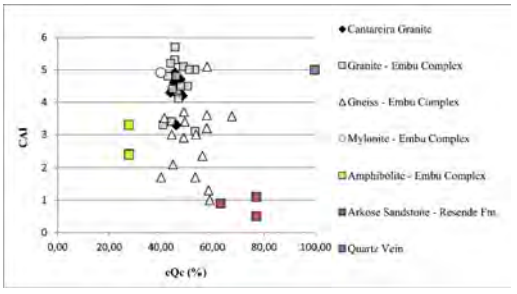

Figure 3. Comparisson between eQc and CAI.

4.4 *Influence of weathering alteration degree*

The studies by Monteiro et al. (2011, 2012) suggest that one of the reasons for the lack of compatibility for the eQc and CERCHAR parameters would be the action of weathering, an agent of external dynamics, which causes changes in rocks, reducing their mechanical resistance, but having little influence on the quartz content-equivalent. This low influence on quartz-equivalent is due to the fact that quartz, the most abundant high-hardness mineral in rocks in this geological context, is significantly resistant to weathering. For the CERCHAR abrasiveness index, rocks with a degree of alteration A1 (sound lithotype geomechanical conditions) presented 80% of results considered as extremely abrasive (ranges 4 to 6) and 20% as very abrasive (ranges 2 to 4). At this degree of change, low abrasive results (ranges 0 to 1) or medium abrasiveness (ranges 1 to 2) are not observed.

When evaluating the results of rocks with alteration degree A2 (little altered rock), it is observed that the percentage of extremely abrasive rocks drops to 67%, while very abrasive rocks increase to 33%. In rocks with degree of alteration A3 (moderately altered rock), the change is even more significant, extremely abrasive rocks drop to 27%, very abrasive rocks remain at 33% and low abrasive and medium abrasive results appear which together total 40% of the results. For the rock abrasiveness index (RAI), a very similar behavior occurs. With rocks in degree of alteration A1, 36% of very abrasive results were recorded (RAI between 60 and 120), 57% of abrasive rocks (RAI between 30 and 60) and 7% of slightly abrasive rocks (RAI between 10 and 30). Moving to the degree of alteration A2, the percentage of very abrasive rocks fell to 8%, abrasive rocks fell to 54% and the percentage of low-abrasive rocks rose to 38%. With the degree of alteration A3, results from very abrasive rocks are no longer recorded, abrasive rocks drop to 20% and the percentage of low-abrasive rocks rises sharply to 80% of the results. By evaluating the average CERCHAR and RAI results for the different degrees of change, the data presented above is consolidated. For CERCHAR there is a small reduction in the average between grades A1 and A2, with a significant drop for grade A3. In the RAI results there is a significant drop across the three degrees of change. These results are compelling and confirm the hypothesis that the action of weathering, through the alteration of rocks, is an incisive and preponderant factor in the loss of abrasive conditions. The degree of change also explains the reason for the lack of similarity in the behavior of eQc versus CERCHAR in studies carried out in São Paulo, compared to studies carried out with rocks from the European continent.

5 CONCLUSIONS

This study applied some of the abrasiveness assessment indices most used by tunnel engineering to rock samples from the São Paulo Metropolitan Region. The quartz-equivalent content (eQc) and the CERCHAR abrasiveness index (CAI) were evaluated. Regarding the evaluated indices, the quartz-equivalent showed that the three main lithotypes are found in approximately the same result range, which is in line with what was expected for all the lithotypes evaluated. For CERCHAR, compatibility was observed between the

granite samples and a large dispersion of values for the gneisses. • No correlation was found between quartz-equivalent and CERCHAR, which indicates that just the presence of abrasive minerals does not necessarily imply an abrasive behavior of the rock (taking into account primary wear). • The mechanical resistance of the rock plays a fundamental role; In this context, the action of alteration on the rocks becomes important, which reduces their geomechanical conditions, but does little to alter the quartz-equivalent content. • CERCHAR values decrease as the degree of rock alteration increases, showing that the evaluation of alteration is fundamental for the study of abrasivity. Rock dismantling in an excavation process begins with the friction of the cutting tool against the rock mass in order to detach a rock fragment (chip). For tools, this is the primary wear and CERCHAR adequately evaluates the action of abrasiveness in this process. After the fragment is released from the mass, it remains under conditions of free friction with the cutting tool and, subsequently, with the internal part of the excavation chamber and with the excavated material transport system. This is secondary wear and the quartz equivalent becomes its best indicator at this stage of the process.

ACKNOWLEDGMENTS

The authors would like to thank Companhia do Metropolitano de São Paulo- Metrô-SP for releasing the data for publication and supporting the studies developed.

REFERENCES

ABGE, 2013. Diretrizes para classificação de sondagens, São Paulo, Brazil.

aSTM D7625–10, 2010. Standard test method for laboratory determination of abrasiveness of rock using the CERCHAR method;

CMSP, 2013. Especificação Técnica de Sondagens, São Paulo, Brazil, 6p.

Coutinho, J.M.V., 1980. "Relações litológicas e estruturais da Bacia de São Paulo com o Pré-Cambriano circunvizinho; In: Aspectos geológicos e geotécnicos da Bacia Sedimentar de São Paulo", ABGE/SBG-SP, São Paulo, Brazil, pp. 15–23.

Juliani, C., 1992. "O embasamento pré-cambriano da Bacia de São Paulo; In: Problemas geológicos e geotécnicos na Região Metropolitana de São Paulo", ABAS/ABGE/SBG-SP, São Paulo, Brazil, pp. 3–20.

Monteiro, M.D.; Rocha, H.C., 2014. "A abrasividade de rochas nos estudos do Metrô de São Paulo: ensaios, classificações, a influência do grau de alteração e considerações sobre o consumo de ferramentas de corte em escavações subterrâneas"; Brazilian Journal of Engineering and Environmental Geology, São Paulo, Brazil, pp. 71–86.

Monteiro, M.D.; Gurgueira, M.D.; Rocha, H.C., 2012. "Geologia da Região Metropolitana de São Paulo"; In: Solos das Regiões Metropolitanas de São Paulo e Curitiba, ABMS, Brazil, pp. 15–44.

Plinninger, R.J., 2010. "Hardrock abrasivity investigation using the Rock Abrasivity Index (RAI)"; Geologically Alive, London, pp. 3445–3452.

Thuro, K, 1997. Prediction of drillability in hard rock tunneling by drilling and blasting; Tunnels for People, Rotterdam, 1997, pp. 103–108.

Tunnelling for a Better Life – Yan, Celestino, Thewes & Eberhardt (Eds)
© 2024 The Author(s), ISBN 978-1-032-80042-4
Open Access: www.taylorfrancis.com, CC BY-NC-ND 4.0 license

Phased prediction method for construction period of secondary lining construction time of tunnel in squeezed rocks

Li Ning*
China Railway First Survey and Design Institute Group Co. Ltd, Xi'an, Shanxi, China

ABSTRACT: The construction time of the secondary lining of the tunnel is often judged by the deformation rate, but in practical engineering, it is often difficult to obtain the later deformation rate after the waterproof board is laid, so it is impossible to accurately judge. In order to obtain the construction time of secondary lining of squeezing surrounding rock tunnel and make the construction of secondary lining more operable, based on the limit value of deformation rate, this paper fits and statistically analyzes the deformation measurement data of 412 squeezing surrounding rock tunnel sections, and obtains the deformation stability time range value of different deformation grades and the prediction method of construction time of secondary lining in stages during construction period. The specific conclusions are as follows: (1) A deformation data processing method is proposed, which can predict the stability of the deformation(u) and the final stability time (t') in the stability stage. (2) Through statistical analysis, the stable range of deformation stability time (t') under different deformation levels and different span conditions is determined, which is used to preliminarily determine the timing of secondary lining construction in the design stage. (3) The stable range value of deformation stabilization time (t') from excavation under different deformation levels and different span conditions is proposed, which can be used to preliminarily determine the construction time of secondary lining in the design stage. (4) Through the test of measured deformation data, the prediction results can be accepted by the project by using the staged prediction method of secondary lining construction time. (5) The construction time prediction method of secondary lining of squeezing surrounding rock tunnel with the stability time (t') of staged deformation as the discriminant index has strong operability, which avoids the operation trouble when the deformation rate is used as the discriminant index and can directly serve the engineering practice.

Keywords: Squeezing rock, Railway tunnel, Construction timing of secondary lining, Deformation classification, Deformation stabilization time, Statistical analysis

1 INTRODUCTION

With the advancement of infrastructure construction in western China, the problem of large deformation of squeezing surrounding rock has become a prominent problem for tunnel builders. Squeezing rocks is a rock mass with significant plastic deformation or rheology in a certain range around the tunnel under high ground stress environment, which has the remarkable characteristics of high ground stress, low strength and strong rheology. Under the action of high ground stress, the squeezing surrounding rock tunnel is prone to large deformation, resulting in support cracking, steel frame distortion, deformation intrusion and even lining cracking and falling block.

Under the condition of large deformation, the construction of secondary lining too early or too late will affect the safety of tunnel construction and structural stability. Therefore, the timing of secondary lining construction is always a hot issue in the study of squeezing surrounding rock tunnel. Taking Wushaoling tunnel as an example, Liu et al. (2008) proposed two discriminant indexes for the timing of secondary lining construction with different deformation levels, that is, the daily deformation and total deformation measured on site based on the ultimate displacement of the tunnel. The slight large, medium and severe large deformation sections reached the secondary lining construction standard after 45-55d, 55-60d and 80-90d of tunnel excavation respectively, which was proposed by Guo et al. (2020). Taking Zhegushan Tunnel as an example, Meng et al. (2017) proposed that it is more appropriate to apply secondary lining after the initial support deformation is 65%-70% of the final convergence value.

Many scholars have also carried out a lot of research work on the time characteristics of tunnel deformation. Zhang et al. (2001) analyzed the displacement-time relationship curve of the whole process of surrounding rock deformation according to the field monitoring data. Yang et al. (2006) carried out curve analysis on the convergence measurement

*Corresponding author: 406639508@qq.com

DOI: 10.1201/9781003495505-79

data of tunnel surrounding rock and summarized the characteristics of deformation aging. Zuo et al. (2018) combined with field monitoring data, according to the classification of surrounding rock, the deformation-time characteristic curve of surrounding rock is divided into three stages of 'bow' type and four stages of 'step' type. Sun et al. (2008) divided the deformation curve of surrounding rock according to the deformation rate of surrounding rock. Based on the field measured data, Liu et al. (2009) analyzed the relationship between the deformation stability time and the surrounding rock grade.

In summary, there are few studies on the timeliness and deformation prediction of surrounding rock applied to the construction timing of tunnel secondary lining. In this paper, through the statistical analysis of the deformation m0o0nitoring data of 412 squeezing surrounding rock tunnel sections, the deformation stability time range values of squeezing surrounding rock tunnels with different deformation grades are obtained. Based on the final deformation stability time statistics, a phased secondary lining construction timing prediction method is proposed. The phased deformation stability time is used as the discriminant index of the construction timing of the secondary lining, which provides a reference for the construction timing of the secondary lining of the squeezing surrounding rock tunnel.

2 DEFORMATION CLASSIFICATION STANDARD AND STATISTICAL SAMPLES

2.1 *Deformation classification standard of squeezing surrounding rock tunnel*

Based on the geological conditions and in-situ stress of squeezing surrounding rock tunnel, the classification standard of deformation potential of squeezing surrounding rock in China is shown in Table 1 (Liu et al., 2020), and the deformation potential is divided into four grades: slight, medium, serious and extremely serious.

Table 1. Classification standard of deformation potential of tunnel in squeezing rock.

Deformation grade (S)	Deformation potential	$G_n=R_{cm}/\sigma_{max}$	Relative deformation (ε/%)
I	Slight	0.3~0.2	2~4
II	Medium	0.2~0.15	4~6
III	Serious	0.15~0.1	6~8
IV	Extremely serious	<0.1	>8

2.2 *Statistical sample*

The measured data of convergence deformation of 412 squeezing surrounding rock tunnels at home and abroad were investigated and counted, including 55 foreign samples (Kimura et al., 1987; Panet et al., 1996; Brox et al., 1999; Phienwej et al., 2007; Barla et al., 2009, 2010,2001; Atgar et al., 2020), accounting for 13 %. There are 357 domestic samples, accounting for 87%, including Liangshui tunnel, (2013a), (2013b), (2018); Muzhailing tunnel, (2017); Wushaoling tunnel (2005); Xinchengzi tunnel, (2016); Lanzhou-Chongqing tunnel, (2018) The excavation span of the tunnel is divided according to the Industry standard of The People's Republic of China (2002): the small and medium span is 5-12 m, and the large span and above is greater than 12 m. The specific sample statistics are shown in Table 2.

Table 2. Summary of statistical samples of measured deformation curve of tunnel in squeezing rock.

Order number	Excavation span	Tunnel name	Nationality	Grade				Total
				I	II	III	IV	
1	medium and small span (5-12m)	Wushaoling tunnel	China	20	17	13	38	88
2		Muzhailing tunnel	China	5	4	2	5	16
3		Maoxian Tunnel	China	8	8	7	15	38
4		Changping Tunnel	China	3	4	4	3	14
5		Jiazhuqing tunnel	China	2	5	3	4	14
6		Saint Martin Tunnel	Italy	3	2	4	8	17
7	Large span and more	Liangshui tunnel	China	2	14	28	4	48
8	(>12m)	Maoyushan tunnel	China	2	6	8	2	18
9		Yangjiaping tunnel	China	2	30	46	10	88
10		Xinchengzi tunnel	China	3	5	8	5	21
11		Tongzhai tunnel	China	-	3	5	4	12
12		Bolu Mountain Tunnel	Turkey	3	4	5	6	18
13		Frejus Tunnel	France	2	3	2	1	8
14		Enasan Tunnel II	Japan	1	1	6	4	12
		Aggregate		56	106	141	109	412

Note: The deformation samples are all sidewall convergence data.

3 DEFORMATION DATA PROCESSING METHOD

3.1 *Deformation time history curve fitting and stable time value method*

From Figure 1, it can be seen that the measured data of surrounding rock is the deformation from the element buried to the laying of waterproof board. The fitting curve of surrounding rock deformation is $u=f(t)$, and the fitting curve of deformation rate is $v=f'(t)$. Observing the deformation rate $v=f'(t)$ curve, t takes day as the unit. When the deformation rate decreases obviously and tends to be relaxed, the t corresponding to the first point A' of the relaxation section along the time coordinate $v<v_l$ is the stable time t_s. At this time, the point corresponding to the deformation fitting curve $u = f(t)$ is point A, and the corresponding u of point A is the stable deformation u_s.

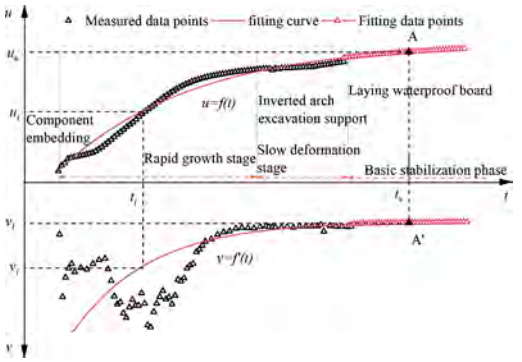

Figure 1. Deformation-time curve of rock.

3.2 *Deformation stability time criterion*

In the squeezing surrounding rock tunnel, the following regulations are formed in the Technical Specification for Railway Squeezing Surrounding Rock Tunnel: the construction of secondary lining should be carried out after the deformation of surrounding rock and initial support is basically stable, and the deformation rate decreases obviously and tends to be moderate. When there is no experience, it can be carried out according to the deformation rate (7d average value). The small span is less than 1 mm/d, and the large span and above are less than 2mm/d, and the secondary lining is strengthened. That is, for small and medium span, v_l=1mm/d; for large span and above, v_l=2mm/d. The engineering practice shows that the tunnel constructed according to this criterion has no lining cracking problem due to extrusion deformation.

3.3 *Deformation prediction in stable stage*

The optimal curve fitting method is used to predict the deformation of surrounding rock in the stable stage, and three typical fault planes are selected to explain the deformation prediction method. Taking the most unstable section 1 of deformation development as an example, based on the analysis of curve characteristics, five function forms are selected for fitting, as shown in Table 3.

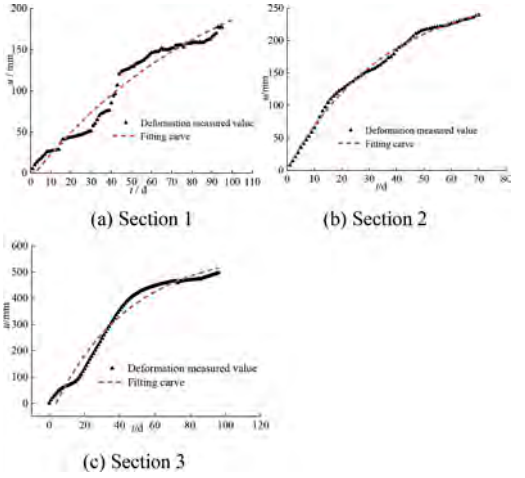

Figure 2. Deformation-time curve of typical section.

Table 3. Deformation-time curve function of section 1.

Function forms	Fitting expression	Correlation coefficient
Power	$u = 4.303 \cdot t^{0.830}$	0.949
Polynomial	$u = -7.57 + 3.07t - 0.01t^2$	0.964
Logarithm	$u = -941.08 + 220.23\ln(t+70)$	0.958
Exponential 1	$u = 332.32e^{-66.72/(t+13.33)}$	0.961
Exponential 2	$u = 290.30 - 296.87e^{-t/95.36}$	0.968

It can be seen from Table 3 that the exponential 2 function form with the largest correlation coefficient can obtain the same results as the other two sections. Therefore, the fitting function form is

$$u = f(x) = A_1 + A_2 \cdot \mathrm{e}^{-t/A_3} \tag{1}$$

In the formula, u is the deformation of surrounding rock (mm); $f(x)$ is in the form of function; t is the measurement time (d); e is a natural constant; A_1, A_2 and A_3 are fitting constants.

In order to predict the deformation u_s and the stability time t_s of the surrounding rock in the stable stage, the function form of the deformation rate curve is obtained according to Formula (1), that is,

$$v = f'(x) = (-A_2/A_3) \cdot \mathrm{e}^{-t/A_3} \tag{2}$$

In the formula, v is the deformation rate of surrounding rock (mm/d); $f'(x)$ is the derivative of $f(x)$.

For $v=v_l$ in Equation (2), the value of t can be obtained.

$$t = -A_3 \cdot \ln(-v_1 \cdot A_3 / A_2) \quad (3)$$

The t obtained by the formula (3) is rounded, and the stability time t_s is obtained.

Substituting t=t_s into formula (2), the stable deformation rate of surrounding rock can be obtained.

$$v_s = (-A_2/A_3) \cdot \mathrm{e}^{-t_s/A_3} \quad (4)$$

Substituting t=t_s into formula (1), the deformation of surrounding rock in stable stage can be obtained.

$$u_s = A_1 + A_2 e^{-t_s/A_3} \quad (5)$$

Sections 1-3 are medium and small span tunnels, and the v_f=1mm. According to the formula (3)-(5), the deformation prediction results of section 1-3 can be calculated and shown in Table 4.

Table 4. Deformation prediction results of typical sections.

Section	Fitting expression	t_s/d	u_s/mm	v_s/ (mm·d^{-1})
1	$u = 290.30 - 296.87e^{-t/95.36}$	109	195.64	0.993
2	$u = 278.548 - 278.058e^{-t/35.664}$	74	243.63	0.979
3	$u = 584.61 - 639.77e^{-t/43.25}$	117	541.84	0.989

4 DEFORMATION STABILITY TIME STATISTICS BASED ON DEFORMATION CLASSIFICATION

In the above deformation prediction method, A_1, A_2 and A_3 have different values in the fitting curves of different sections. In order to establish the relationship between the deformation stability time t_s and the relative deformation of surrounding rock ε_s (ε_s =u_s/a) in the statistical sense, 412 sets of t_s and ε_s data were statistically analyzed. The t_s obtained by the above prediction is calculated from the component embedding. According to the statistical results of Liu et al. (2008), the time from tunnel excavation to component embedding is 1-3 days. In order to obtain the time from excavation to deformation stability and ensure the safety of secondary lining construction, the time of early loss of displacement is increased by 3 days on the basis of the above predicted t_s, that is,

$$t_s' = t_s + 3 \quad (6)$$

In the formula, t'$_s$ is the deformation stability time (d) from excavation; t_s is the deformation stabilization time (d) from the time of the embedded element.

4.1 *Abnormal data elimination method*

The following is a statistical score of the data in the two cases of small and medium span and large span.

In the statistical samples, due to the limitations of on-site construction environment, measurement methods, downtime and other conditions, the statistical data are very discrete. For example, Figure 3 is a scatter plot of the relationship between the deformation stability time and the corresponding relative deformation of 187 small and medium span sections.

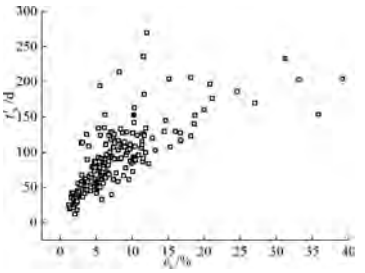

Figure 3. t'_s-ε_s relationship scatter chart of medium and small span tunnel (data before elimination).

In order to ensure the credibility of statistical data, it is necessary to eliminate abnormal data. Based on the deformation classification standard in Table 1, the relative deformation distribution of small and medium-sized tunnel sections is divided into four sections. The coverage rates of 90% and 10% are used as the upper and lower limits of the stability time of the surrounding rock in each section, and the data outside the boundary are eliminated as abnormal data. The upper and lower limits of the four sections are shown in Figure 4.

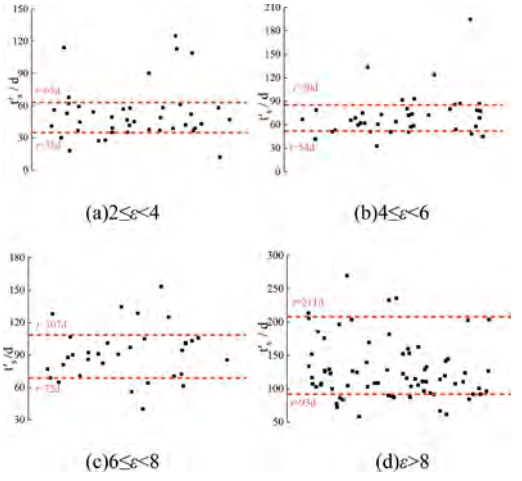

Figure 4. Data processing of deformation stability time of each section of medium and small span tunnel.

The relationship between the deformation stability time and the relative deformation of the small and medium span tunnel after eliminating the abnormal data is shown in Figure 5.

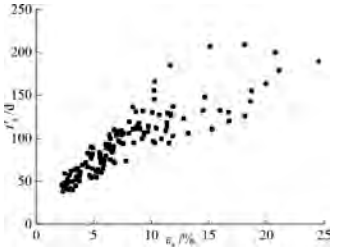

Figure 5. t'_s-ε_s relationship scatter chart of medium and small span tunnel (data after elimination).

After the same method is used to eliminate the abnormal data for 225 large-span and above tunnel sections, the scatter diagram of the relationship between the deformation stability time and the relative deformation of large-span and above tunnels is shown in Figure 6.

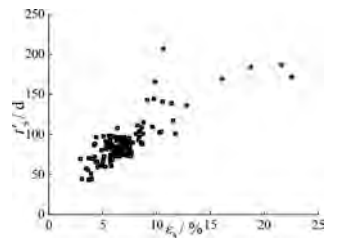

Figure 6. t'_s-ε_s relationship scatter chart of large-span and above tunnel (data after elimination).

4.2 *Statistical analysis of deformation stability time*

The scatter results of the relationship between the deformation stability time and the relative deformation of small and medium-sized and large-span and above tunnels are summarized as shown in Figure 7.

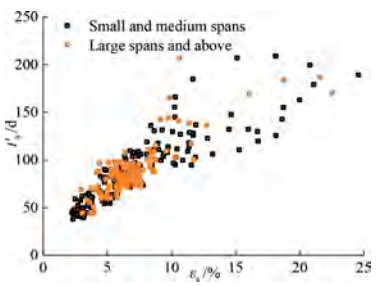

Figure 7. t'_s-ε_s relationship scatter chart of all sections.

It can be seen from Figure 7 that although the relationship between t_s and ε_s is relatively discrete, in general, the deformation stability time of small and medium span and large span and above tunnels increases with the increase of relative deformation. For large-span and above tunnels, the deformation stability time range of each grade is obtained according to the same treatment method, and the deformation stability time of each grade of small and medium-span and large-span and above tunnels is summarized. The results are shown in Table 5.

Table 5. Statistical results of deformation stability time t's (construction time of secondary lining) of different deformation grades (unit:d).

		Span	
Deformation grade	Relative deformation	Medium and small span	Large spans and above
I	$2\leq\varepsilon<4$	$38\leq t<65$	$43\leq t<70$
II	$4\leq\varepsilon<6$	$54\leq t<90$	$59\leq t<98$
III	$6\leq\varepsilon<8$	$72\leq t<107$	$72\leq t<112$
IV	$8\leq\varepsilon$	$t\geq93$	$t\geq93$

Note: When the surrounding rock conditions are good, the relative deformation value is small, and the support stiffness and control measures are relatively strong, the smaller value of the numerical range in the table is taken, otherwise the larger value is taken.

It can be seen from Table 5 that the deformation stability time range of each grade of squeezing surrounding rock tunnel with small and medium span and large span and above is not much different, and the deformation stability time is positively correlated with the relative deformation.

5 PREDICTION OF CONSTRUCTION TIMING OF STAGED SECONDARY LINING DURING CONSTRUCTION PERIOD

5.1 *Prediction method for construction timing of staged secondary lining during construction period*

In the above analysis, ε at different stages of each section corresponds to a t'_s. For this reason, the ε of 20d, 30d, 40d and final stable stage were extracted in stages, and the relationship between ε and t'_s is sought, as shown in Figure 8.

The obtained scatter relationship is fitted by curve fitting, and the exponential 2 function form in Table 3 is also selected. Due to the limitation of various construction conditions on site, the distribution of each scatter point in Figure 8 is observed. It is found that the t'_s corresponding to the same ε is still a range value of a certain interval. The median value of the scatter point is taken to fit the curve, extending to the upper and lower sides and ensuring that the 85% coverage rate takes the range value, as shown in Table 6.

Table 6 can be used to realize the prediction and discrimination of the construction time of the secondary lining in stages. The discrimination method does not consider the deformation grade. The

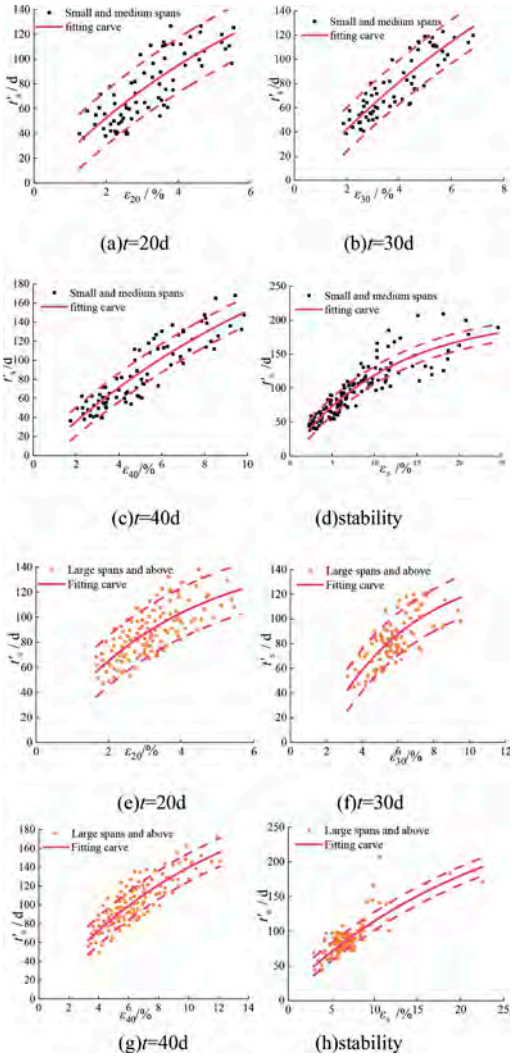

Figure 8. t'_s-ε_s relationship scatter chart of different stages of construction period.

Table 6. Prediction method of construction timing of secondary lining by stages in construction period based on stability time statistics.

Span	Measurement time /d	Fitting expression
Medium and small span	20	$t'_s = 228.58 - 232.07e^{-\varepsilon_{20}/7.231} \pm 22$
	30	$t'_s = 304.62 - 308.92e^{-\varepsilon_{30}/13.37} \pm 18$
	40	$t'_s = 295.53 - 301.33e^{-\varepsilon_{40}/14.81} \pm 15$
	Stability	$t'_s = 207.01 - 203.15e^{-\varepsilon_s/12.99} \pm 13$
Large spans and above	20	$t'_s = 155.17 - 156.19e^{-\varepsilon_{20}/3.62} \pm 20$
	30	$t'_s = 146.05 - 197.51e^{-\varepsilon_{30}/4.92} \pm 17$
	40	$t'_s = 235.84 - 232.32e^{-\varepsilon_{40}/11.33} \pm 15$
	Stability	$t'_s = 307.99 - 292.51e^{-\varepsilon_s/24.18} \pm 12$

difference of different deformation grades is reflected in the actual value of ε in each stage. The deformation grade is high, the value of ε is large, and the predicted t'_s is large.

5.2 *Application test*

The section YDK176+641 of a medium and small span tunnel is selected for inspection. The final stable deformation time of the section is 62d, the final stable deformation is 311.55 mm, and the hole diameter is 6.4 m. According to the measured deformation data of the section, the final stability time is predicted in stages. The measured deformation data of the four stages are converted into relative deformation, and then substituted into the fitting expression of Table 6 respectively, so as to obtain the predicted deformation stability time t'_s of each stage. The test results are shown in Table 7.

Table 7. Test results of prediction method for construction timing of secondary lining by stages during construction period.

Measurement time /d	Measured deformation / mm	Relative deformation / %	Predicted value /d
20	196.41	3.07	76.8±22
30	245.41	3.83	72.6±18
40	276.75	4.32	70.4±15
Stability	311.55	4.87	67.3±13

It can be seen from Table 7 that the predicted deformation stabilization time of the four stages of YDK176+641 section is within the range of the above four intervals, among which the predicted deformation time at stabilization is the closest to the actual deformation stabilization time, and the predicted error values of the four stages can be accepted by the project.

6 CONCLUSION

(1) A deformation data processing method is proposed, which can predict the deformation u_s and the final stability time t'_s in the stable stage.
(2) The exponential function $u = f(x) = A_1 + A_2 \cdot e^{-t/A_3}$ can fully reflect the characteristics of the deformation time history curve of the squeezing surrounding rock tunnel and obtain the maximum fitting correlation coefficient.
(3) The stable range value of deformation stability time t'_s from excavation under different deformation grades and different span conditions is proposed, which can be used to preliminarily determine the construction time of secondary lining in the design stage.

(4) A method for predicting the construction time of secondary lining in stages during construction period based on deformation stability time statistics is proposed. According to the measured relative deformation, the construction time of secondary lining can be predicted in stages and finally determined.
(5) Through the test of measured deformation data, the prediction method of staged secondary lining construction is adopted, and the prediction results can be accepted by the project.

Because there are some differences in the geological conditions, support stiffness, control measures and construction methods of each tunnel in the statistical samples of this paper, the statistical results have a large range of values, and the specific implementation should be reasonably valued according to the engineering conditions.

REFERENCES

Aygar, E.B., 2020. Evaluation of new Austrian tunnelling method applied to Bolu tunnel's weak rocks. Journal of Rock Mechanics and Geotechnical Engineering, 12(3), 541.

Barla G., 2001. Tunnelling under squeezing rock conditions. Eurosummer-school in tunnel mechanics, Innsbruck, 169.

Barla G., 2009. Innovative tunneling construction method to cope with squeezing at the Saint Martin La Porte access adit (Lyon-Turin Base Tunnel), ISRM Regional Symposium-EUROCK. OnePetro.

Barla G., Bonini M., Debernarai D., 2010. Time dependent deformations in squeezing tunnels. ISSMGE International Journal of Geoengineering Case Histories, 2(1) 40.

Brox D. Hagedorn H., 1999. Extreme deformation and damage during the construction of large tunnels. Tunnelling and Underground Space Technology, 14(1): 23.

China Railway First Survey and Design Institute Group Co. Ltd., 2013. Research Report on carbonaceous phyllite support structure and construction technology of Liangshui tunnel. Xi'an, China Railway First Survey and Design Institute Group Co. Ltd., (In Chinese).

China Railway Tunnel Bureau Group Co. Ltd., 2017. Monitoring and safety assessment report of support structure in high stress area of Muzhailing. Guangzhou, China Railway Tunnel Bureau Group Co., Ltd. (In Chinese).

China Railway First Survey and Design Institute Group Co. Ltd., 2005. Research Report on deformation control technology under complex stress conditions in ridge section of Wushaoling Tunnel. Xi'an, China Railway First Survey and Design Institute Group Co. Ltd., (In Chinese).

China Railway First Survey and Design Institute Group Co. Ltd., 2016. Research Report on stress test and analysis of high ground stress complex structure of Xinchengzi tunnel. Xi'an, China Railway First Survey and Design Institute Group Co. Ltd. (In Chinese).

China Railway First Survey and Design Institute Group Co. Ltd., 2018. Research Report on construction technology and application of squeezed surrounding rock tunnel in Lanzhou Chongqing Railway. Xi'an, China Railway First Survey and Design Institute Group Co. Ltd., (In Chinese).

Guo X.L., Tan Z.S., Li L., et al., 2020. Study on the Construction Time of Secondary Lining in Phyllite Tunnel Under High Geo-stress. China J.Highw.Transp.,33(12), 249. (In Chinese).

Industry standard of The People's Republic of China, 2002. Code for construction on tunnel of railway, TB 10204-2002. Beijing, China Railway Publishing House. (In Chinese).

Kimura F., Okabayashi N., Kawamoto T., 1987. Tunnelling through squeezing rock in two large fault zones of the Enasan Tunnel II. Rock Mechanics and Rock Engineering, 20(3), 151.

Liu X.Z., Su J.W., Wang X.X., 2009. Statistical analysis of time effect of surrounding rock of NATM highway tunnel. Chinese Journal of Rock Mechanics and Engineering, 28(S1), 2662. (In Chinese).

Liu Z.C., Li G.L., 2020. The Calculation Method of Surrounding Rock Pressure in Squeezing Rock Tunnel. Journal of Railway Engineering Society, 37(11), 69. (In Chinese).

Liu Z.C., Li W.J., Zhu Y.Q., et al. 2008. Discussion on the timing of secondary lining of soft rock tunnel with large deformation. Chinese Journal of Rock Mechanics and Engineering, (03), 580.(In Chinese).

Liu Z.C., Li G.L., 2020. The Calculation Method of Surrounding Rock Pressure in Squeezing Rock Tunnel. Journal of Railway Engineering Society, 37(11), 69. (In Chinese).

Panet M., 1996. Two case histories of tunnels through squeezing rocks. Rock mechanics and rock engineering, 29(3), 155.

Phienwej, Thakur, Cording E.J., 2007. Time-dependent response of tunnels considering creep effect. International Journal of Geomechanics, 7(4), 296.

Shijiazhuang Tiedao University. 2013. Test report on double layer support and double layer lining of Liangshui tunnel. Shijiazhuang, Shijiazhuang Tiedao University. (In Chinese).

Shijiazhuang Tiedao University. 2018. Research Report on key technology of single track railway tunnel construction in high intensity area. Shijiazhuang, Shijiazhuang Tiedao University, (In Chinese).

Sun Y.C., Shang Y.J., 2008(02). Analysis on spatial- temporal effect of deformation of rock tunnel surrounding rock. Journal of Engineering Geology, 211. (In Chinese).

Yang H.J., 2006(01). Deformation characteristics of tunnel surrounding rock under complex conditions. Journal of Railway Engineering, 57. (In Chinese).

Zhang Y, Zhang Z.X., Hua A.Z., 2001(03). Deformation characteristics of surrounding rock of Expressway Tunnel. South Central Highway Engineering, 12. (In Chinese).

Zuo Q.J., Wu Y.Y., Yan T.X., 2018. Spatial-temporal effect analysis of surrounding rock deformation during construction of extra-large fault face rock tunnel. Journal of Disaster Prevention and Mitigation Engineering, 38(02), 233. (In Chinese).

Tunnelling for a Better Life – Yan, Celestino, Thewes & Eberhardt (Eds)
© 2024 The Author(s), ISBN 978-1-032-80042-4
Open Access: www.taylorfrancis.com, CC BY-NC-ND 4.0 license

Ground characterisation of the Sydney Basin for tunnelling works

David J. Och*
WSP Australia Pty Ltd, Sydney, Australia
School of BEES, UNSW, Kensington, Australia

Jiping Pan
WSP Australia Pty Ltd, Sydney, Australia

Ian T. Graham
School of BEES, UNSW, Kensington, Australia

Nicholas Walker
AECOM, Sydney, Australia

Antoni Kuras
WSP Australia Pty Ltd, Sydney, Australia

Giovanny Alvarado
AECOM, Sydney, Australia

ABSTRACT: Sydney Metro West will double rail capacity between Greater Parramatta and the Sydney CBD, transforming Sydney for generations to come. This once-in-a-century infrastructure investment will have a target travel time of about 20 minutes between Parramatta and the Sydney CBD, link new communities to rail services and support employment growth and housing supply. The Sydney Metro West corridor, encompassing nine stations at Westmead, Parramatta, Sydney Olympic Park, North Strathfield, Burwood North, Five Dock, The Bays, Pyrmont, and Hunter Street in the Sydney CBD, four cross-over caverns, two turnback junction cavern and associated stub tunnels, two service facilities, one dive, and a stabling and maintenance facility at Clyde, is strategically located near other major infrastructure within the geological region known as the Sydney Basin. This basin is characterised by extensive structural and topographic features, including a thick sequence of sediments deposited under both fluvial and marine conditions. The bedrock geology along the Sydney Metro West rail corridor predominantly comprises various soils overlaying the Wianamatta Group shale, predominantly the Ashfield Shale. This formation, in turn, rests atop the Mittagong Formation, which overlays the Hawkesbury Sandstone. However, the corridor is also known to harbour several vertical linear fault zones that cut across both the Ashfield Shale and the Hawkesbury Sandstone. Additionally, dykes ranging from clay to high-strength basalt or dolerite have been identified in the vicinity of the proposed rail corridor, with several likely to intersect with the alignment. Employing rigorous best practices, our team has gathered a wealth of geophysical and geotechnical data to characterise the subsurface geotechnical units beneath various harbour and bay crossings, as well as the stratigraphy aligning with the westward-heading tunnels. This comprehensive analysis has helped identify key geotechnical risks that could arise during the construction of the tunnels and other related underground infrastructure along this corridor.

Keywords: Sydney, Geology, Tunnelling, Geological Structure, Metro, Characterisation

1 INTRODUCTION

Sydney Metro West will provide a direct connection between the CBDs of Parramatta and Sydney, linking new communities to rail services as well as supporting employment growth and housing supply (Figure 1). This state-of-the-art railway helps address Sydney's rapid growth, with the city's population to increase

*Corresponding author: David.Och@wsp.com

DOI: 10.1201/9781003495505-80

above 6 million in the next 20 years. The Sydney Metro West corridor, encompassing nine stations at Westmead, Parramatta, Sydney Olympic Park, North Strathfield, Burwood North, Five Dock, The Bays, Pyrmont, and Hunter Street in the Sydney CBD, four cross-over caverns, two turnback junction cavern and associated stub tunnels, two service facilities, one dive, and a stabling and maintenance facility at Clyde, is strategically located near other major infrastructure within the geological region known as the Sydney Basin. As such, detailed geophysical and geotechnical investigations to facilitate early planning and design work were undertaken on behalf of the Sydney Metro.

The scoping, delivery management and interpretation of the ground investigation and the development of the tunnel alignment design was undertaken by the Technical Advisor (WSP AECOM design joint venture) in collaboration with TfNSW over several stages, namely the Scoping Design, Definition Design, and finally the Early Contractor Involvement (ECI), which the WSP AECOM JV only focused on the ECI delivery of the Central Tunnelling Package (CTP) tender defining the completion of their Technical Advisor appointment.

Tunnelling design and delivery for the project has been separated into three separate packages -; Westmead Station to Sydney Olympic Park Station – Western Tunnel Package (WTP); Sydney Olympic Park Station to The Bays Station – Central Tunnel Package (CTP), and The Bays Station to the Sydney CBD defines the Eastern Tunnel Package (ETP). Several alignment and design options were considered along the length of the corridor that were mainly defined horizontally and vertically by existing infrastructure assets and geological constraints, respectively. The design was predicated on full rock face excavation on the main tunnels heading west by Tunnel Boring Machine (TBM), with the possible use of mixed face TBM excavation heading east.

Following an assessment of the reliance of the historical geotechnical data sourced from earlier iterations of this project, local councils, and other government agencies a staged targeted site investigations based on gaps in geological knowledge was conducted concurrently with the concept design options. This allowed for these boreholes to be adjusted as the geological interpretation and the design developed. The land investigations included cored boreholes and cone penetration testing (CPT) in alluvial lowland areas, along with seismic refraction surveys in areas inaccessible by drilling equipment.

All major boreholes had specific lab testing carried out, along with water pressure and permeability testing (packer and slug testing), down-hole optical and acoustic televiewer of the cored rock to measure defects and in specific key boreholes in-situ stress testing (HSM and over-coring) were undertaken.

The marine intrusive investigations were carried out on Darling Harbour, Johnstone Bay and Iron Cove Bay and included cored boreholes completed

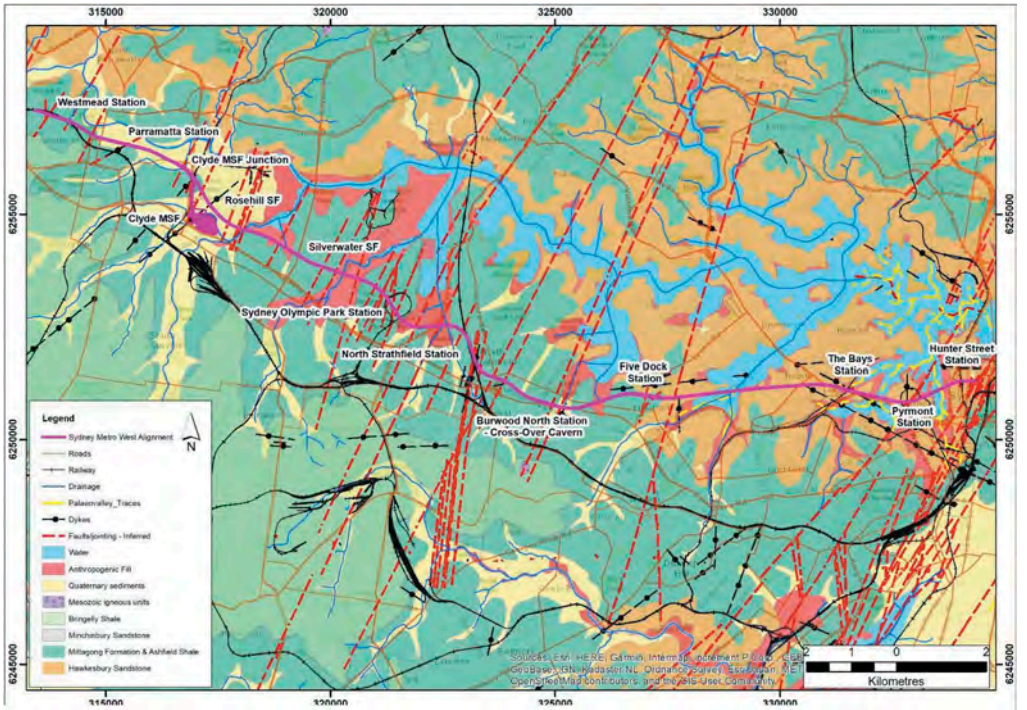

Figure 1. Geological map defining the Sydney Metro West corridor (Colquhoun et al., 2018; Herbert, 1983a; Och et al., 2009).

from jack-up barges. This also included continuous sediment sampling and in-situ tests noted above.

Marine geophysical investigation included seismic refraction and reflection surveys, magnetometer, and side-scan sonar surveys.

These data collected during the investigations allowed both the rock and soil formations along the corridor to be characterised and defined into geotechnical units.

The interpretation of these units and rock head was critical to design development and the identification of the geotechnical risks that could be realised whilst tunnelling below these environments.

This paper describes the site investigation and then focuses on an unknown geological interpretation of ground conditions near to Sydney Olympic Park to inform and influence the design development.

2 REGIONAL GEOLOGY

The project area is situated within the geological region known as the Sydney Basin. During the Permian and Triassic Periods, which occurred approximately 298 to 200 million years ago, the Sydney Basin experienced the deposition of a thick sequence of sediments in both fluvial and marine environments.

At the end of the Late Triassic, there was minor deformation and warping of the basin, followed by a period of tectonic activity from the Jurassic to the Palaeogene. These geological processes contributed to the formation of joints, faults, and the intrusion of igneous dykes (Och et al., 2009).

As a result of these structural weaknesses, major river systems eroded the uplifted eastern margin of the basin, forming deeply incised valleys. During the Pleistocene, there was a rise in sea levels, leading to the infilling of these valleys with sediment.

Subsequently, there was a period of lower sea levels, which resulted in the erosion of most of the Pleistocene valley infill, except for the upper portions of the valleys. In the more recent Holocene era, another sea-level rise occurred, leading to the infilling of the valleys with Holocene sediments. These sediments rest upon the underlying Pleistocene sediments.

Along the proposed Sydney Metro West alignment, the dominant geological units are depicted in Figure 1 and consist of the following formations (Colquhoun et al., 2018; Herbert, 1983a): anthropogenic fill (reclaimed areas), Holocene sediments, Pleistocene sediments, Triassic-age sedimentary rocks of the Ashfield Shale, Mittagong Formation, Hawkesbury Sandstone, and localised igneous dykes.

2.1 *Local geological conditions*

The regional geological units in the project area are shown in Figure 1 and include the following:

- Fill: Reclaimed areas near the harbour and some parklands.
- Holocene sediments: Under-consolidated sediments.
- Pleistocene sediments: Over-consolidated sediments, often sandy clays.
- Residual soils: Weathered siltstone and sandstone rock.
- Wianamatta Group: Ashfield Shale - Claystone, mudstone, siltstone, laminites, and fine-grained lithic sandstone.
- Mittagong Formation: Interbedded shale and fine-grained sandstone.
- Hawkesbury Sandstone: Medium to coarse-grained quartz sandstone.

2.1.1 *Anthropogenic*

Major areas of fill are associated with reclamation works near the harbor foreshores, pond sites, and brick pits. Unnatural topography, such as the Pyramid in Sydney Olympic Park, indicates substantial infilled areas at White Bay, Sydney Olympic Park, Silverwater, and Rosehill (Figure 1). The Johnstons Bay area has a deeper section of fill due to land reclamation, approximately 30m above the alignment. Station boxes, portals, dives, shafts, and Clyde MSF will likely be impacted by fill. Fill material varies from good quality ripped sandstone to poor-quality refuse, such as boiler ash or chemical to putrescible waste material. It can consist of gravels, sands, clays, and may range in consistency from loose to very stiff cohesive material. Asphalt and concrete are also classified as fill.

2.1.2 *Quaternary deposits*

Quaternary deposits are commonly found along the alignment and comprise sands, silts, and clays with varying amounts of organic matter. Some station boxes, dives, and shafts will be impacted by alluvium. Major alluvial areas include The Bays, Powell Creek, Haslams Creek in Sydney Olympic Park, Clyde, Rosehill, and Parramatta. Parramatta has alluvial clays and sands extending from the river into the township with varying layers of fill. Parramatta Park has a small shallow alluvial channel defined by a northerly running creek.

2.1.3 *Bays and Harbour*

Sediments within Darling Harbour, Johnstons Bay, Iron Cove Bay, and the adjoining Parramatta River areas are expected to consist of sands, silts, and clays with shell fragments, organic matter, and anthropogenic content. These sediments result from marine and fluvial processes during the Pleistocene, Holocene, and present age. The sedimentary sequence within the Port Jackson part of Sydney Harbour has been described by (Roy, 1980), (Pells and Wong, 1990) and (Och et al., 2017):

"Pleistocene sediments dominate boreholes in the harbour palaeovalleys and comprise over-consolidated marine sediments. These upper sediments consist of well-sorted medium dense to dense medium-grained sand overlying a thick layer of stiff

silty clay to clay, including shell hash zones. Fluvially derived sediments, including sandy clays, minor sand, and gravel with charcoal layers, are found below and appear to be associated with locally derived slope colluvial deposits.

Holocene sediments consist of loose/soft clayey silt interbedded with fine to medium-grained silty sand and shells. They overlay the relatively flat Pleistocene deposits and fill incised channels formed during the last glacial maximum".

2.1.4 *Residual*

Residual soils develop from in-situ weathering of the parent bedrock and are typically found as a mantle over the weathered bedrock profile on low-relief, gently inclined natural surfaces. Residual soil derived from weathering of shale material consists of medium to high plasticity silty clay, gravelly clay, sandy clay, and silt, with variable consistencies ranging from firm to hard.

The residual Hawkesbury Sandstone soils are thin, typically less than 2m thick, and comprise medium plasticity silty clay to sandy clay. The residual Ashfield Shale soils are around 1.0 to 3.0m thick on ridge tops and thicker below valley floors and river channels. Unlike Extremely Weathered (EW) rock, the Ashfield Shale lacks relict structure and exhibits soil-like properties when remoulded by hand.

2.1.5 *Wianamatta Group*

The Wianamatta Group comprises the Bringelly Shale, Minchinbury Sandstone, and Ashfield Shale. The Sydney Metro West corridor is located within the Ashfield Shale and lower formations.

2.1.5.1 Ashfield Shale

This formation is up to 50 m in thickness at Sydney Olympic Park comprising the four members defined by Herbert and Helby (1980) and Herbert (1983b). The tunnels only align in this formation on approach to stations and service shafts or in areas of major faulting (Homebush Bay Fault Zone – Figure 1) then transition into the lower geological formations between North Strathfield and Westmead. The full profile of the Ashfield Shale members is only encountered at Westmead (partial) and Sydney Olympic Park, but other locations where Ashfield Shale is encountered the profile is defined by the topography and pervading geological structure. The Ashfield Shale encountered along the Sydney Metro West Corridor are characterised below:

- Mulgoa Laminite Member: Up to 11.0 m thick, dark grey siltstone and fine light grey sandstone laminations. Upper levels show micro cross beds and small burrows. Boundary with Minchinbury Sandstone is sharp but not found in this area.
- Regentville Siltstone Member: Up to 15.0 m thick, dark grey sideritic-banded siltstone beneath Mulgoa Laminite. Base is sharp.
- Kellyville Laminite Member: 6.5 m to 9.0 m thick, light-grey siltstone and fine to medium-grained sandstone laminations. Features include micro-crossbeds, coarsening of grain size, and inclined beds. Base is gradational in some boreholes.
- Rouse Hill Siltstone Member: Average thickness of 6m, dark grey to black sideritic claystone-siltstone. Faint pale laminations increase towards the top. Lower 3 m has a ubiquitous light grey-white marker lamination (Och et al., 2020). Basal contact generally grades into Mittagong Formation, but some boreholes show discrete unconformities into the Hawkesbury Sandstone.

The Ashfield Shale generally has a UCS (unconfined compressive strength) ranging from 5 to 40MPa, with a mean value of approximately 25MPa when fresh and normal to bedding. These laminated rocks exhibit high anisotropy, with lower strength parallel to bedding.

2.1.6 *Mittagong Formation*

The Mittagong Formation consists of alternating dark shale and sandstone beds and laminae of varying thickness. It is challenging to map this formation due to its variable thickness and weathered surface occurrence, making it difficult to distinguish from other formations at the published scale.

2.1.7 *Hawkesbury Sandstone*

The Hawkesbury Sandstone is a medium to coarse-grained sandstone. Petrographic analysis shows that it is composed of quartz grains (50% to 80%), clay matrix (5% to 40%), quartz cement (up to 20%), and carbonate cement (0% to 15%, up to 35%) (Cole et al., 2020; Franklin, 2000). The sandstone exhibits three facies' types: massive sandstone, cross bedded or sheet facies, and shale/siltstone interbed "mudstone" facies (Herbert and Helby, 1980).

The cross-bedded facies consists of sets of cross-bedded strata with variable dip angles, typically dipping towards the northeast. Massive sandstone facies lacks crossbedding and may contain channelized erosional features and concentrated shale clasts. The Mudstone Facies includes lenses and continuous beds of shale, siltstone, and laminites within the sandstone, with variable thickness.

2.1.8 *Geological structure*

Deeper weathering and palaeovalleys in the in the upper Triassic formations described above reflects faulting/shear zones, stress relief areas, and valley bulging (Gray, 1982; McNally, 1981). Many variably thick dykes have been encountered cross cutting the alignment (Figure 1) and vary from high strengths through to clays. The contact zones can also result in slight rock strength variabilities at the contact boundaries (contact metamorphism), ranging from highly altered and strong to highly weathered and weak due to preferential weathering across the host rock along with chilling associated cooling during dyke emplacement (Dale, 1989; Dale et al., 1997).

3 GROUND INVESTIGATIONS

During the initial Scoping Design phase through to the Tender stage of the Sydney Metro West project, several tranches of land and bay/harbour geotechnical and geophysical investigations (Table 1) were carried out for the proposed running tunnel alignment options. The vertical alignment of the tunnels was critical as the geology along this corridor were in locations that had very limited sub surface knowledge as it would potentially govern station depths and tunnelling methodology. The ground investigations were based on assessments of historical borehole information and data and the investigations were targeted in areas that were deemed important to the alignment. In areas where no access (swamp lowlands or residential constraints) was avaiable some land-based refraction surveys were undertaken to supplement the knowledge gained from nearby boreholes. Across water crossings geophysical surveys (reflection and refraction) were carried out prior to intrusive investigations being undertaken to assess for any anomalies to allow for better targeting.

Table 1. Sydney Metro West - Ground Investigations (2017 - 2021).

Marine	Land
• 16 – HQ+SPT *(avg. depth 43.0 m)*	• 165-HQ+SPT *(136 deep)* (avg. depth 32.3 m)
• In-situ stress testing	• In-situ stress testing
• Packer/Slug testing	• Packer/Slug testing
• Downhole imaging	• Downhole imaging
• Sediment sampling	• Cone Penetration Testing (CPT 40)
• Geomechanical testing.	• 17 – Test pits
• Sedimentological analysis	• 105 – Environmental BHs
• Geophysics (Reflection/ Refraction)	• Geophysics (refraction)
	• Geological mapping

4 RESULTS

The tunnel alignment spanning from North Strathfield Station to Sydney Olympic Park Station and Parramatta Station traverses diverse geological formations. The elevation profile fluctuates along this path, with Sydney Olympic Park Station being the highest point at 21 m AHD and Newington at 14 m AHD. The tunnel reaches its deepest point beneath Silverwater. The region is characterized by Homebush Bay catchment, where the topography follows undulating patterns with lower areas around Rosehill and Duck Creek (Figure 1).

Geologically, the upper layers consist of reclaimed alluvial plains with varying fill depths overlying interbedded clay, sandy clay, and sand formations. These transitions are especially pronounced around the Ashfield Shale layer, with fill depths ranging up to 6m. The Mittagong Formation, encountered at depth, has alternating siltstones and fine to medium-grained sandstones with layers of shale or sandstone, eventually overlaying the Hawkesbury Sandstone.

The tunnel corridor's geological nature is anticipated to vertically align through Ashfield Shale, progressing to Mittagong Formation, and finally Hawkesbury Sandstone. Throughout, the presence of geological structures like joints, faults, and buried palaeovalleys is evident, possibly influencing the excavation of cross passages. The Homebush Bay Fault Zone (Och et al., 2009) and secondary faults contribute to vertical variations in rock formations, indicating fault displacement and the development of a negative flower fault structure and that splays into a discrete strike-slip fault system to the NNE and SSW shaping the region's lowlands (Figure 2). Similar structures have been identified in projects such as the M4-M5 (Lyons and Grasso, 2022) and M8 (Baxter-Crawford and Lippet, 2023) but are more related to flower-type structures associated with a strike-slip fault system (Woodcock and Rickards, 2003).

5 TBM AND TUNNEL CONSIDERATIONS

The geological characteristics of harbours and lowland swamps along the Sydney Metro West alignment exerted a significant influence on both the horizontal and vertical alignment of the designed tunnel and associated cross passages, as well as the selection of Tunnel Boring Machines (TBMs). The in-house design team worked closely with geological experts to navigate these challenges and optimise the tunnel's alignment and construction methodologies.

Selection of TBMs considers the machine could handle different ground conditions during tunnel driving, including soft sediments, clay, and rock formations. Slurry TBMs was assessed to be the appropriate TBM for the Eastern Tunnel Package (ETP) due to the depth and uncertainties in geological conditions below the Johnstons Bay and Darling Harbour. Double shield TBM technology for both the Central and Western Tunnel Packages (CTP and WTP) was adopted as the design team considered the depth of the TBMs vertically below the lowland areas, namely Iron Cove Bay, Powell Creek, Haslams Creek in Sydney Olympic Park, Clyde, Rosehill, and Parramatta (Figure 1). The full length of tunnelling would be through the described varying rock formations (Figure 2), and therefore, these hard rock TBMs were chosen to ensure safe and efficient excavation and reduced wear on the cutting tools.

6 DISCUSSION

Geological findings significantly influenced tunnel design considerations. The varying geological

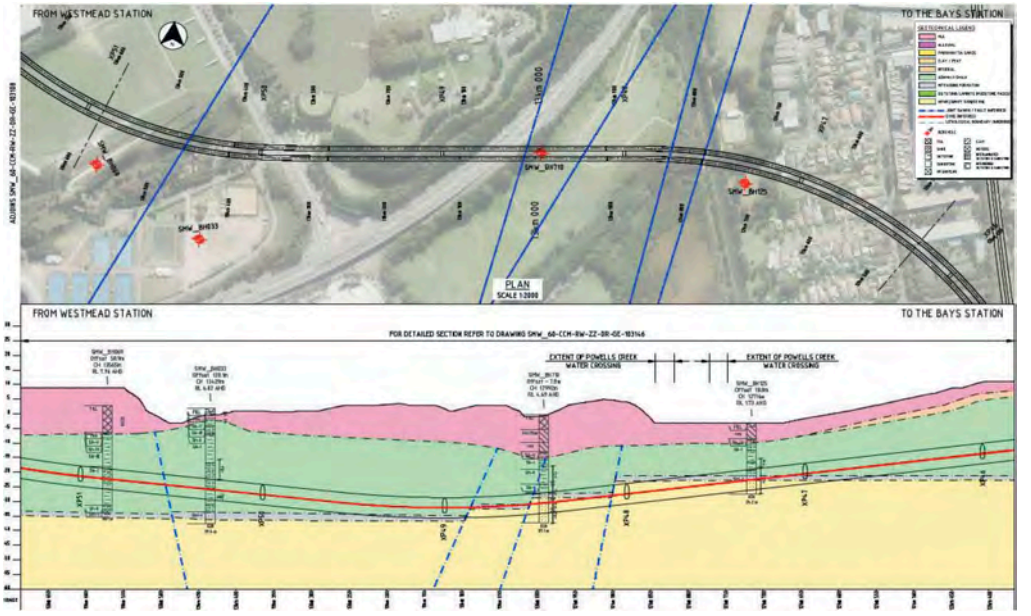

Figure 2. Geological long section highlighting the displacement of the upper Triassic sedimentary rocks of the Sydney basin across the Homebush Fault Zone (Och et al., 2009) across the Powells Creek lowlands between Sydney Olympic Park and North Strathfield.

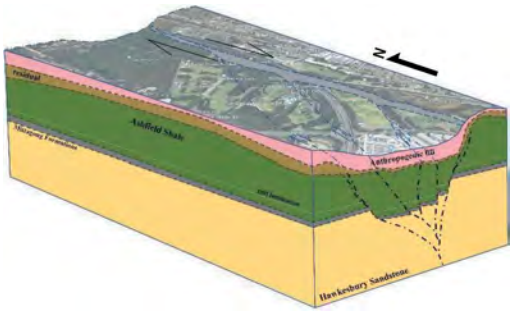

Figure 3. A cross-sectional 3D relief (long axis - north) pictorial depicting associated topography across the Sydney Olympic Park – North Strathfield area with an underlying interpretation of a negative flower structure and geological displacement of the Triassic stratigraphy across the Homebush Bay Fault Zone.

formations necessitated adaptation of tunnelling methodologies and support systems. The presence of major fault systems and other geological structures and hydrogeology introduced complexities for the in-house design team in aligning the tunnels along this corridor. The study of analogous projects informed the understanding of fault systems and their impact on future tunnel construction. Ongoing scientific studies aim to enhance our understanding of subsurface relationships in the Sydney Basin due to the geological and engineering significance of these fault systems (McMillan et al., 2021; McMillan, 2021; Och et al., 2009).

7 CONCLUSION

The success of the Sydney Metro West project hinged on the pivotal roles played by thorough ground investigations across very sensitive areas and the expertise of the in-house design team. Geological complexities, especially in harbours and lowland swamps, underscored the necessity for precise tunnel alignment and TBM selection. The collaborative efforts between geological experts and the design team ensured optimised designs that navigated diverse ground conditions, ensuring both structural integrity and environmental stewardship. The synergy between comprehensive ground investigations and in-house design expertise was instrumental in achieving the project's goals.

ACKNOWLEDGMENTS

The authors extend their gratitude to the Sydney Metro for approving this article, and all the contributors Jonathon Chan, Julian Singh, David McIntyre, Matthias Rheinlander, Peter Dowbiggin, Geoff Bateman, Ben Seaford, Brendan O'Kane, Stuart Allabush, Stephen Roberts, and others who all worked well as a team to facilitate the integration of the

earlier ground investigations into the tunnel design process. The collaborative efforts of the Technical Advisor (WSP AECOM JV) Ground Investigations team (Golder Associates (WSP) - Douglas Partners) and TfNSW team were instrumental in achieving these results.

REFERENCES

Baxter-Crawford, H. and Lippet, A., 2023. Televiewer defect aperture logging for detailed model development – A case study from the M8, Sydney, Australia. In: G. Anagnostou, A. Benardos and V.P. Marinos (Editors), Expanding Underground - Knowledge and Passion to Make a Positive Impact on the World. ITA-AITES World Tunnel Congress 2023 London, pp. 227–234.

Cole, K., Och, D. and Howard, L., 2020. Best practice in controlling respirable crystalline silica in infrastructure, ATS2022, Melbourne.

Colquhoun, G.P., Hughes, K.S., Deyssing, L., Phillips, G., Troedson, A.L., Folkes, C.B. and Fitzherbert, J.A., 2018. New South Wales Seamless Geology geodatabase, version 1 [Digital Dataset]. Geological Survey of New South Wales, NSW Department of Planning and Environment, Maitland.

Dale, M., 1989. The geology and engineering geology of the Great Sydney Dyke, Sydney, NSW. 9130_130 Thesis, University of New South Wales, Sydney.

Dale, M.J., Rickwood, P.C. and Won, G.W., 1997. The geology and engineering geology of the 'Great Sydney Dyke', Sydney, NSW. In: G.H. McNally (Editor), Collected Case Studies in Engineering Geology, Hydrogeology and Environmental Geology. Geological Society of Australia, Sydney, pp. 1–37.

Franklin, B., 2000. Stone: The role of petrography in the selection of sandstone for repair, Material Evidence - Conserving historic building fabric. NSW Heritage Office, Sydney, pp. 1–16.

Gray, N.M., 1982. Direction of stress, southern Sydney Basin. Journal of the Geological Society of Australia, 29: 277–284.

Herbert, C., 1983a. Geology of the Sydney 1:100,000 Sheet 9130. Explanatory Notes. Geological survey of new south wales department of mineral resources, Sydney.

Herbert, C., 1983b. Introduction, Geological Survey of New South Wales, Department of Mineral Resources, Sydney.

Herbert, C. and Helby, R., 1980. A guide to the Sydney Basin, Bulletin 26. Geological Survey of New South Wales, Department of Mineral Resources, Sydney, 603 pp.

Lyons, N. and Grasso, E., 2022. WestConnex M4-M5 Link – Construction of the St Peters Interchange Ramps and Ventilation tunnels through the Woolloomooloo Fault Zone – Case Study, ITA-AITES World Tunnel Congress, WTC2022 and 48th General Assembly Bella Center. ITA-AITES World Tunnel Congress, Copenhagen, pp. 15.

McMillan, T., David, K., Murray, T., Timms, W., Rau, G. and Andersen, M., 2021. Geological Mapping and Geophysical Surveys of the Thirlmere Lakes Area Thirlmere Lakes Research Program 4 (TLRP4).

McMillan, T.C., 2021. Idenifification and hydro-geomechanical characterisation of non-conventional fault zones, University of New South Wales, Kensington.

McNally, G.H., 1981. Valley bulging, Mangrove Creek Dam near Gosford, New South Wales. Quarterly Notes - Geological Survey of New South Wales, 42: 4–11.

Och, D.J., Offler, R., Zwingmann, H., Braybrooke, J. and Graham, I.T., 2009. Timing of brittle faulting and thermal events, Sydney region: association with the early stages of extension of East Gondwana. Australian Journal of Earth Sciences, 56(7): 873–887.

Och, D.J., Pan, J.P., Kuras, A., Thorin, S., Cox, P., Bateman, G. and Skilbeck, C.G., 2017. Sydney Metro - Site Investigation and Ground Characterisation for the Sydney Harbour Crossing, Proceedings of the World Tunnel Congress 2017 – Surface challenges – Underground solutions, Bergen, Norway, pp. 10.

Och, D.J., Thorin, S., Bateman, G., Nicoll, B. and Graham, I.T., 2020. Identification of a fine 'tuff' layer in the Rouse Hill Siltstone Member of the Ashfield Shale: Implications, WTC2020. IAT-AITES, Kuala Lumpur, Malaysia.

Pells, P.J.N. and Wong, P.K., 1990. Site Investigation for the Sydney Harbour Tunnel, 7th Australian Tunnelling Conference: "The underground domain". Institution of Engineers, Australia, Barton, A.C.T, Sydney, pp. 121–131.

Roy, P.S., 1980. Quaternary Geology. In: C. Herbert (Editor), Sydney 100K Geological sheet - Explanatory Notes. Geological Survey of NSW, Sydney, pp. 41–91.

Woodcock, N.H. and Rickards, B., 2003. Transpressive duplex and flower structure: Dent Fault System, NW England. Journal of Structural Geology, 25(12): 1981–1992.

Tunnelling for a Better Life – Yan, Celestino, Thewes & Eberhardt (Eds)
© 2024 The Author(s), ISBN 978-1-032-80042-4
Open Access: www.taylorfrancis.com, CC BY-NC-ND 4.0 license

Chengdu-Guiyang High-speed railway—Yujingshan Mountain Tunnel crossing Giant Karst cave and underground river

Weichen Qing*, Yu Yu, Jieyuan Zheng, Yong Zhu & Yong Wang
China Railway Eryuan Engineering Group Co. Ltd, Chengdu, Sichuan, China

ABSTRACT: Yujingshan Mountain Tunnel, with a total length of 6,306m, is a key part of the Chengdu-Guiyang High-speed Railway Project with a design speed of 250km/h. A giant karst cave was discovered when the tunnel was excavated to about 2km from the entrance. The karst cave is 95m long, 230m wide, and 50m-120m high. Its volume is about 1 million cubic meters. A large underground river develops at the bottom of the cave, with a width of 5-15m, and a flow of 70m^3/s in the rainy season. As Yujingshan Mountain Tunnel is 110m perpendicular to the water surface of the underground river, the project faces four major challenges: construction safety, operation safety, construction period, and environment protection. In order to overcome the challenges, firstly, the underground river was relocated to the outside to maintain the original water channel; secondly, the method of layer-by-layer and zone-by-zone backfilling is adopted to realize quick backfilling; thirdly, a 430 m^2 tunnel with super-large cross section was built in the spoil body; fourthly, a 184m double-track high-speed railway bridge was built in the tunnel. By adopting the above measures, about 1 million cubic meters of spoil was used to backfill the cave, which saves a lot of land; the underground river was relocated to the outside, which maintains the original water channel and protects the original ecosystem; a new structure of integrated tunnel and bridge was created, which ensures the operational safety. The successful construction of this project has shortened the travel time between Chengdu and Guiyang, the two major provincial capitals in southwest China, from 14h to 3h. Meanwhile, it has also accumulated valuable experience of tunnels passing through large karst caves, which is a model of coordinated development of environmental protection and economic construction. The project received the Overcoming the Challenge of ITA Awards 2020.

Keywords: Giant karst cave, Underground river, Tunnel with super-large cross section, Bridge crossing, Environment protection

1 INTRODUCTION

The karsts are widely distributed in China, and the area with karst accounts for about one-third of the country's land area. Karst geology is quite common, and only in Yunnan, Guizhou, and Guangxi provinces, the exposed area of carbonate rocks accounts for about half of the total area of the three provinces. Therefore, karst-fissure-cavities, karst valleys, karst caves, karst channels, underground rivers, etc. might be encountered when tunnels are constructed in karst areas, which pose serious safety hazards to tunnel construction and operation, and may cause structural deformation, water and mud inrush, collapse, and top chip off-falling [1-3].

When tunnels are constructed in karst areas, in order to ensure the safety of the railway, geological exploration measures should be taken first to explore the karst area [4-7], and try to avoid possible karst caves ahead [8]. If it is impossible to avoid them, reasonable treatment measures will be taken. Common treatment methods include bridge or piled raft crossing, shotcrete-bolt support, backfilling/ replacement, grouting reinforcement, etc. Two technical schemes, namely curtain grouting, pipe shed and pipe-jacking culvert, were proposed for the karst cave section filled with soft plastic gray brown silty clay under the new Wulong drainage tunnel of Chongqing-Huaihua Railway[9]. During the construction process of a mountain tunnel of Qianjiang-Changde Railway, a giant karst cave was discovered. The internal situation of the cave was complex, and its overall stability was poor. After comparing multiple schemes, the treatment plan of backfilling the cave with spoils and upper grouting reinforcement was finally selected [10]. A super large karst caves developed at ZK250+135~ +166 section of Yanwan Tunnel, which were treated with measures including backfilling with spoils, bridge crossing, and arch protection [11]. A beam span structure was proposed to cross karst fissures and sections

*Corresponding author: 33635115@qq.com

DOI: 10.1201/9781003495505-81

damaged by karst caves of Xiaosanxia Tunnel on Zhengzhou - Chongqing HSR [12].

The paper takes the construction process of the Yujingshan Tunnel as the research object, which encountered a giant karst cave and an underground river. The karst cave had giant internal space and complex accumulations at the bottom. The railway was located high near the roof of the cave and had a long distance to cross the cave. There is still limited research on crossing this type of karst cave. This paper extensively compares and demonstrates the treatment plans for crossing karst caves, in order to determine the optimal technical solution.

2 PROJECT PROFILE

The Yujingshan Tunnel is located in the Xingwen - Weixin section of Chengdu-Guizhou Railway, within the territory of Weixin County, Yunnan Province. The tunnel has an entrance mileage of D3K277+860 and an exit mileage of D3K284+164, with a total length of approximately 6,306m and a maximum burial depth of 350m. When it was excavated towards the small mileage end of the transverse gallery work area to the D3K279+948 mileage, the upper bench excavation revealed the development of a giant karst cave in front of the lower part of the tunnel face. The karst cave was shaped like a dome and was located about 60m below the ground level. With a plan shape of a broad bean shape, the karst cave is 95m along the route, 230m wide laterally, and 50m-120m high. The sediment at the bottom of the karst cave is 30-90m thick, with a cross slope of 30-40°. It is high on the right side of the route and low on the left side, and a large underground river develops on the low side of the cross slope. The river is 5-15m wide, with a total length of 18km and a flow rate of 70m^3/s in the rainy season. The D3K279+855~+960 section of the railway is suspended near the roof of the karst cave, 40m away from its bottom, and 110m perpendicular to the surface of the underground river. The plane position relationship between the railway and the cave is shown in Figure 1.

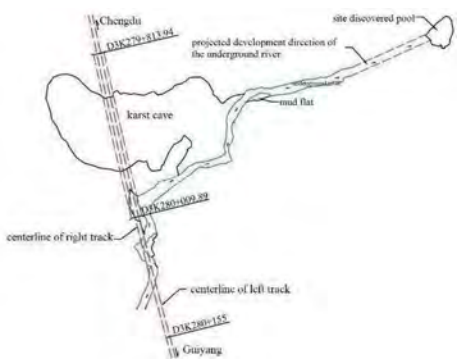

Figure 1. Plane position of relationship between tunnel and cave.

It is rarely seen in the world for a tunnel to pass through such a large and complex karst cave. There are many difficulties in engineering construction, mainly including four major challenges:

(1) It is found by site investigation that the walls of the karst cave are medium to thick layered limestone. Generally the integrity of rock mass is good, but the rock mass is fragmented in some areas, which is extremely unfavorable for the stability of the cave wall, leading to the risk of falling and collapsing on the roof and walls of the cave. As shown in Figure 2, multiple collapsed accumulations are found at the bottom of the cave, with residual sliding marks of collapsed rocks sliding on the surface. The scars in some sections of the cave roof are fresh, which indicates that recent collapses have occurred in the cave. According to the actual measurement of a single boulder at the bottom of the cave, the maximum size of the stone block reaches 8×4×15m, which directly threatens the safety of workers and mechanical equipment inside the tunnel. Therefore, how to ensure the construction safety of the structure crossing giant karst cave is the first challenge.

Figure 2. Cave roof wedge.

(2) The tunnel is 40m above the bottom of the karst cave, with a suspended length of 90m. There is a thick accumulation body at the bottom of the cave, mainly composed of fragmented stones. According to exploration, there are weak interlayers such as soft clay and silt with a thickness of 0-15m distributed among them, with poor regularity. Which reliable structural form should be adopted to meet the strict requirements of the high-speed railway for track settlement control is the second challenge.

(3) Faced with such a rare giant karst cave, no matter what treatment plan is adopted, the difficulty of engineering treatment is extraordinary. In addition, there are only 3 years to the planned opening of Chengdu-Guizhou High-speed Railway. How to

quickly determine the treatment plan and efficiently organize construction to ensure the scheduled opening of Chengdu-Guizhou High-speed Railway is the third challenge.

(4) The water resources in the project location are poor, and the underground river in the karst cave is the main source of production and domestic water for downstream villages, as well as the only water source for downstream hydroelectric power stations. How to maintain the water flow of the underground river, sustain the balance of the existing groundwater network, and protect the original ecosystem is the fourth challenge.

3 RESEARCH ON THE TREATMENT PLANS FOR THE GIANT KARST CAVE

In order to overcome the four major challenges mentioned above, ensure the smooth crossing of the tunnel through the karst cave and guarantee the safety of high-speed rail operation in the later stage, various schemes have been studied and compared, including preliminary comparison of route relocation and in-situ crossing, detailed design of subgrade backfilling, arch bridge crossing, bridge crossing and light protection, bridge crossing and tunnel protection, etc., and eventually the final plan is formed, which consists of diversion of the underground river, backfilling of the giant karst cave, excavation of the backfill body for tunnel construction, and construction of a bridge in the tunnel.

3.1 *Preliminary plans*

Based on previous research and experience, two preliminary plans have been proposed: route relocation and in-situ crossing. In the route relocation plan, in order to avoid the karst cave, the route will be shifted to the right with a length of 5.5km, whose construction period is no less than 3.5 years. Works worth of CNY 431 million will be abandoned and the investment will be increased by CNY 445 million. In addition, geological surveys will be conducted again, which does not rule out the possibility of encountering large-scale karst again. Taken into account the project schedule, investment, and engineering risks, the route relocation plan is not recommended. Therefore, it is suggested to focus on studying the in-situ crossing plan.

3.2 *Detailed design*

After the in-situ crossing plan is determined, in-depth research is conducted on schemes such as subgrade backfilling, arch bridge crossing, bridge crossing and light protection, bridge crossing and tunnel protection treatment, etc., whose specific measures are:

(1) Subgrade backfilling

Firstly, the soft soil on the surface of the accumulated material at the bottom of the karst cave is removed, and the lower side is backfilled. A work platform is provided to reinforce the lower accumulation layer with bored piles. Then the karst cave is backfilled in layers, with a 1:1 slope on both sides of the subgrade. Within the 1:1 slope range of the filling body, grouting pipes are horizontally embedded to solidify the filling material. After the grouting is completed, the outer filling continues, as shown in Figure 3(a).

(2) Arch bridge crossing

Firstly, the cave is backfilled in layers. After it is backfilled to a certain height at the bottom of the beam, to ensure the safety of bridge construction, the upper roof in the bridge construction range above the karst cave is protected before the bridge construction proceeds. Finally, an open-cut tunnel is constructed on the upper part of the bridge to ensure the safety of train operation, as shown in Figure 3(b).

(3) Bridge crossing and light protection

Firstly, the cave is backfilled in layers. After the backfilling is completed, the backfilling body is excavated by sloping and a U-shaped retaining wall is provided at the bottom. To ensure the safety of bridge construction and operation, anchor mesh shotcrete combined with anchor cables is used to strengthen protection on the top wall of the karst cave and improve the self-supporting capacity of the surrounding rock at the cave top. To prevent the peeling of the surface layer of sprayed concrete from affecting operational safety, a lightweight steel structure is installed on the bridge, as shown in Figure 3(c).

(4) Bridge crossing and tunnel protection

The plan of bridge crossing and light protection is relatively mature and feasible. However, to ensure the safe operation of high-speed railway, reduce the rockfall threat of karst cave roof to the track and bridge structure, and minimize safety risks, a treatment plan of bridge crossing and tunnel protection which separates bridge and tunnel has been proposed combined with construction practice. Namely, the karst karst cave is first backfilled in layers. After the backfilling is completed, the upper benches are excavated, which are used as the construction platform for anchor mesh shotcrete on the upper roof and anchor cable protection, and both sides of the backfill body are grouted and reinforced. Then, the lower benches of the tunnel are excavated. After the completion of tunnel construction, under the protection of the tunnel structure, the bridge is constructed as the bearing structure of train and track during operation, as shown in Figure 3(d).

As shown in Table 1, the main advantages and disadvantages of the four schemes mentioned above were compared. The bridge crossing and tunnel protection scheme has the advantages of bridge and tunnel combination, dynamic and static separation, relatively low construction risk, controllable construction cost, and short construction period. It avoids the disadvantages of difficult control of settlement and

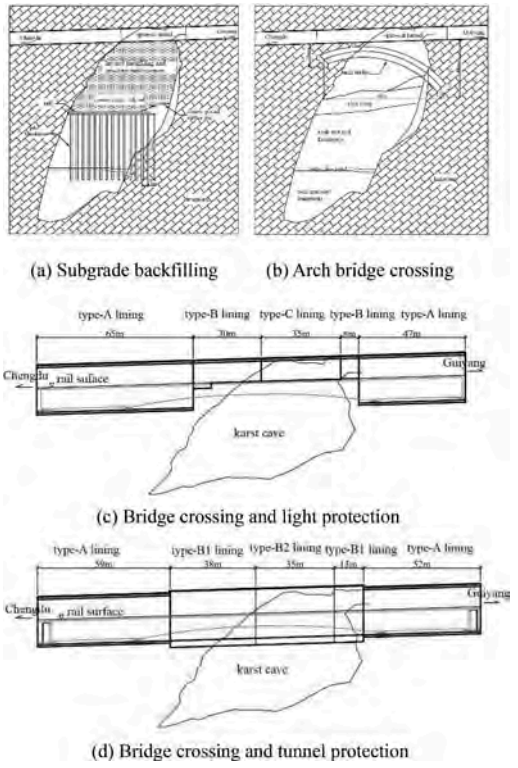

Figure 3. Schematic design.

differential settlement in the subgrade backfilling scheme, difficulty and large amount of foundation excavation of the arch bridge crossing scheme, and low stability of the upper roof of the bridge crossing and light protection scheme. Although this plan also faces the challenges of large tunnel sections and complex construction, the construction technology for tunnels with super-large section is relatively mature and the risks are controllable. Therefore, the bridge crossing and tunnel protection scheme is determined as the implementation plan.

4 TECHNICAL SOLUTION FOR TREATMENT OF GIANT KARST CAVE

4.1 *General technical road map*

Based on the above scheme study, the final solution which includes underground river diversion, backfilling of giant karst cave, excavation of tunnel in the backfill body and construction of bridge in tunnels has been formed. The overall principle is to prioritize the diversion of underground rivers, build a work platform for backfilling the karst cave, then excavate a tunnel with super large cross section, and finally construct a bridge under the protection of the tunnel. The overall technical road map is shown in Figure 4.

4.2 *Underground river diversion*

In order to maintain the original underground water system, the underground river inside the cave is relocated to the outside of the cave before the backfilling of the giant karst cave. A detour drain cavern is set up along the direction of the underground river water flow and 30-50 m away from the right side of the cave wall at the foot of the cave slope, to divert the upstream water of the underground river to the downstream. The drain cavern is about 450m long, as shown in Figure 5. In addition, large block stones are backfilled as a three-dimensional seepage layer for backfilling construction within the range of 3m around the karst cave and 20m at the bottom of the original underground river, to introduce the bedrock fissure water around the cave into the underground river system.

Table 1. Comparison of in-situ crossing schemes.

S.N.	Main Engineering Measures	Advantages	Disadvantages	Additional Investment (CNY 100 million)	Construction Period (years)
1	Subgrade backfilling	the economic cost is relatively low, and the construction period is relatively short	Settlement is difficult to control and it can cause differential settlement, which affects operational safety	3	3
2	Arch bridge crossing	It has good feasibility; Estimated construction period of 42 months	Large amount of tunnel expansion and under cut engineering, long affected section length, causing certain difficulties in construction; The excavation of bridge foundations is difficult and carries high risks	4	3.5
3	Bridge crossing and light protection	It has High feasibility; Estimated construction period of 43 months	Unable to completely solve the stability problem of the upper roof, and there is a potential risk of arch block falling	3.6	3.5
4	Bridge crossing and tunnel protection	relatively low construction risks; Estimated construction period of 41 months	The tunnel excavation has a large cross section and the construction is complex	3.4	3

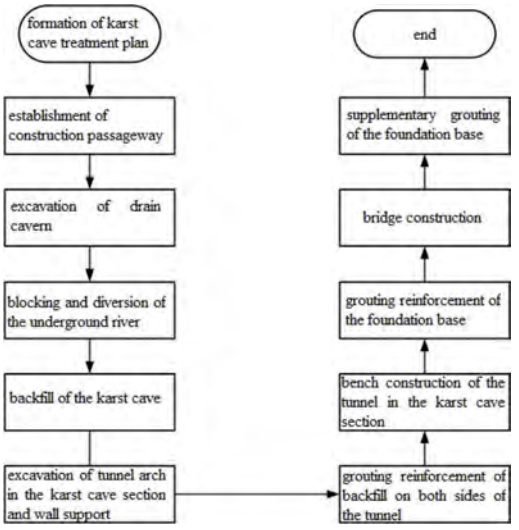

Figure 4. Diagram of underground river diversion.

4.3 *Backfilling of giant karst cave*

Figure 5. Diagram of backfill section of karst cave.

Based on the geological and hydrological conditions of the giant karst cave in the Yujingshan Tunnel and the characteristics of the cavity structure, a multi-channel layered backfilling scheme is proposed to safely and efficiently complete the backfilling with a height of 120m and a total volume of 1.08 million cubic meters, as shown in Figure 6.

(1) The vertical spatial height of the giant karst cave varies from 50m to 120m. Five backfill channels are built vertically inside the cave, with a height difference of 20m between adjacent channels, namely: Channel 4 at 988m elevation, Channel 6 at 1008m elevation, Channel 7 at 1028m elevation, Channel 1 at 1048m elevation, and the upper bench channel at the large mileage end of the tunnel at 1082m elevation.

(2) The hierarchic backfilling scheme is adopted, which means that the giant karst cave is backfilled layer by layer in 5 levels from bottom according to the height difference of every 20m by the 5 backfilling channels.

(3) The backfilling surface is compacted and leveled with construction machinery after every 3m of backfilling to ensure that the backfill material has a certain degree of compaction.

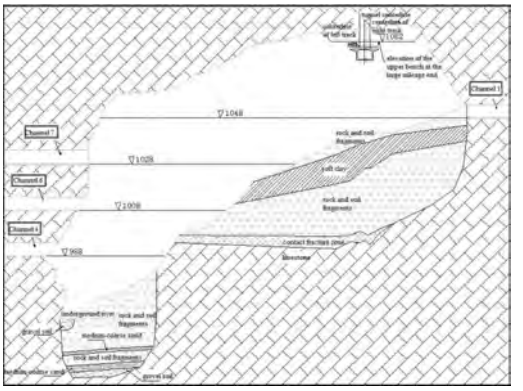

Figure 6. Diagram of backfill section of karst cave.

4.4 *Excavation of the backfill body for tunnel construction*

Bridge crossing is adopted for the D3K279 +813~D3K280+010 section of Yujingshan Tunnel. Type A lining structure is used for D3K279+813~ +872 and D3K279+958~D3K280+010 sections to meet the requirement of bridge structure, construction and maintenance, and in accordance with the relative position relationship between the tunnel and the cave, as shown in Figure 7(a). D3K279+872~ +958 section is located in the backfill body, and adopts the Type B protective structure, as shown in Figure 7(b). The minimum distance between the tunnel floor and the bridge floor is 1.5m, leaving a maintenance space of 1.5m below the bridge floor.

Type A lining section is mainly located at the front and rear positions outside the karst cave along the mileage direction (as shown in Figure 3), and it is constructed by four-bench method, in which controlled blasting is adopted for the first and second benches, and mechanical excavation is used for the third and fourth benches. The supporting measures are as follows: spray C25 concrete with a thickness of 4cm, lay steel mesh and anchor rod, erect I20b steel frame, and sett anchor pipes with lock feet, re-spray concrete to 28cm, and us C35 reinforced concrete for the secondary lining with a thickness of 1 m.

Type B protective structure is located in the backfill body, with an excavation area of 430m2. The support of the excavated stratum has large deformation and high risk of instability, so it is necessary to solve the instability problem in the excavation

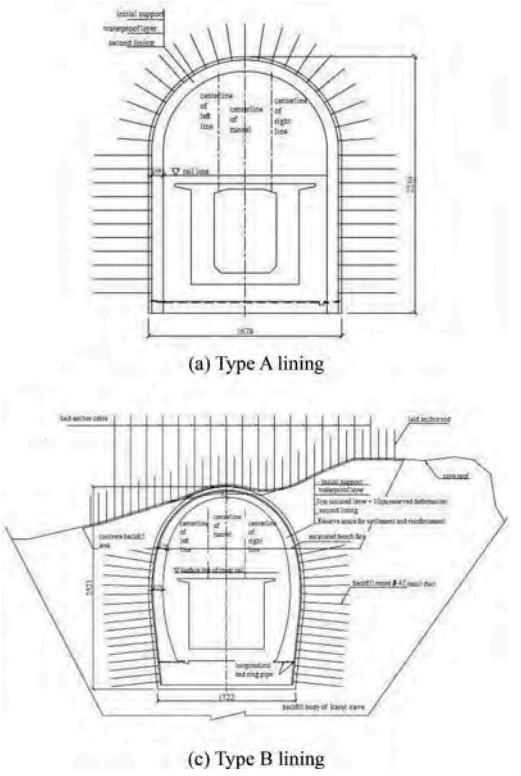

Figure 7. Diagram of different types of lining section (Unit: cm).

process and restrain the deformation of the initial support.

(1) First, the first bench is excavated in the karst cave range, with anchor net spraying and anchor cable protection. In order to ensure the safety of subsequent construction, both sides of backfill body should be reinforced by grouting, as shown in Figure 8.
(2) After the grouting of the backfill body achieves the effect, the lower backfill body is excavated by the bench method, as shown in Figure 9.
(3) Considering the uneven composition of backfill body and the uneven settlement of tunnel foundation, steel pipe grouting is adopted at the tunnel bottom to improve the integrity of backfill body, as shown in Figure 10.
(4) A reinforced concrete tunnel protection bridge is set in the karst cave section, and its initial support is C30 sprayed concrete with a thickness of 40cm, the secondary lining is C35 reinforced concrete, the arch wall of the secondary lining is a variable cross-section with a thickness of 75cm and the bottom plate is 3m thick, as shown in Figure 11.
(5) In order to adapt to the uneven settlement and deformation of the foundation that may occur in the later period and ensure the safety of operation, the tunnel structure is divided into sections every 5m, and wide deformation joints with a width of 2cm are set between adjacent sections.

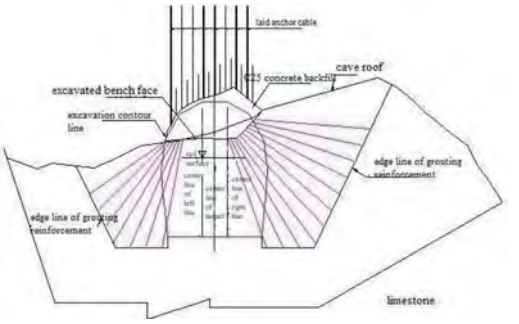

Figure 8. Diagram of the pre-grouting and reinforcement of the backfill body.

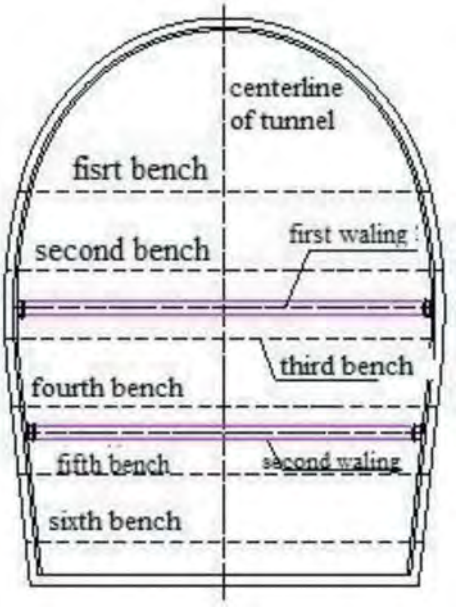

Figure 9. Diagram of bench method construction.

4.5 *Bridge crossing in the tunnel*

The bridge structure adopts (38.85m+108m +38.85m) short-side span prestressed concrete continuous beam, and the concrete strength grade of the beam body is C55. The line on the bridge is a double-track line, with a line spacing of 4.6m, a gradient of +30.00‰ and a design running speed of 250km/h. The ratio of side to mid span of continuous beam is 0.352. The continuous beam is a box girder with a single box, single cell, variable height and variable cross section, and a total length of 185.7m. The 4m long beam section at the mid span near the fulcrum and the full beam section at the side span are of the same beam height, which is 8.8m.

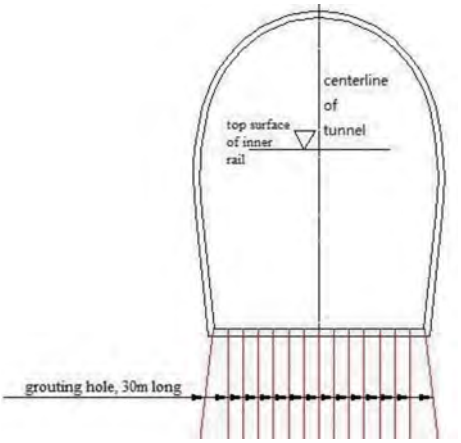

Figure 10. Diagram of tunnel bottom grouting reinforcement.

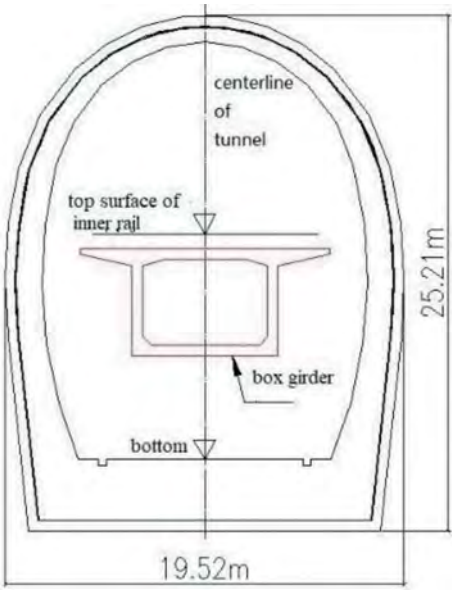

Figure 11. Reinforced concrete protective structure (tunnel).

The beam section with a span of 10m is of equal height, with a beam height of 5m. The schematic diagram of the mid-span section of the bridge is shown in Figure 12, and the bottom edge of the rest of the beams is changed according to Formula (1).

$$y = 5 + \frac{3.8x^2}{2025} \quad (1)$$

The side span, abutment and pier of the bridge are located in the type A cross-section (non-cave backfill

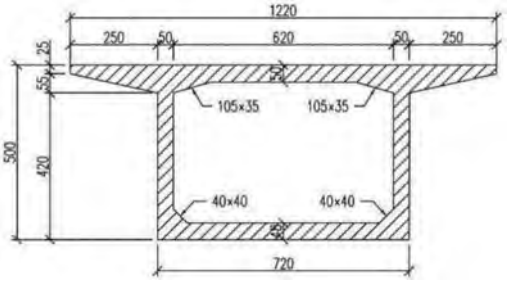

Figure 12. Diagram of midspan section (Unit: cm).

section), and the 108m long mid span crosses the backfill area in the cave. After the tunnel lining in the backfill area, a continuous beam is constructed. The beam body is divided into 0# block, 1# segment, 2# segment and mid-span closure segment (see Figure 13 for details). Continuous beam is constructed by cast-in-place support. First, the cast-in-place bracket is erected below the position of 0# block, after full preloading, the concrete of beam section 0# is poured, then the beam sections 1# and 2# are symmetrically constructed on both sides, and finally the bracket for the mid-span closure section is installed to pour the mid-span closure section, and the corresponding steel beams are tensioned. After the cast-in-place brackets are dismantled, the whole continuous beam system is formed.

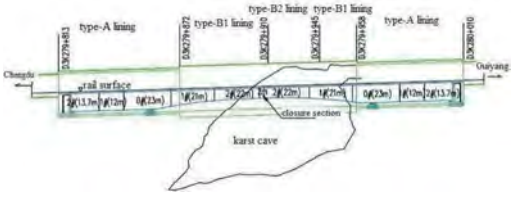

Figure 13. Sectional Layout Profile of Beam.

5 STRUCTURAL SAFETY ANALYSIS AND MONITORING OF SUPER-LARGE SECTION TUNNEL

5.1 *Computational model*

Because it is necessary to excavate a super-large section tunnel (25.21m high and 17.22m wide) in the backfill body, the construction risk is high. The construction process of tunnel mileage D3K279+820~+980 is numerically calculated using finite difference numerical software FLAC3D, and the calculation model is shown in Figure 14.

5.2 *Calculation parameter*

According to the field survey data, the physical mechanics parameters of the stratum and backfill materials are shown in Table 2. C30 high strength shotcrete is used for the initial shotcrete, and C35 reinforced concrete is used for the second lining. See Table 3 for the parameters.

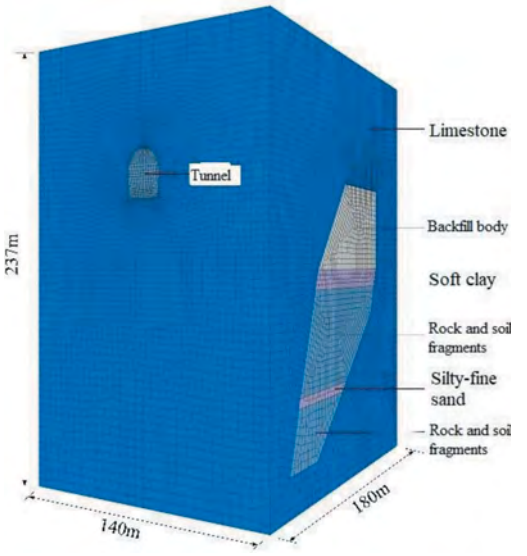

Figure 14. Numerical calculation model.

Table 2. Physical mechanics parameters of rock and soil.

Type	Unit weight γ (kN/m3)	Elastic modulus E(MPa)	Poisson's ratio ν	Internal friction angle φ(°)	Cohesion c(kPa)
Limestone	23.5	6000	0.25	35	3000
Backfill body	23.0	65	0.25	30	200
Soft clay	20.5	15	0.30	7	24
Rock and soil fragments	22.5	60	0.28	36	15
Silty-fine sand	18.0	30	0.35	32	18

Table 3. Material parameters for primary support and secondary lining.

Support type	Unit weight γ (kN/m³)	Elastic modulus E(GPa)	Poisson's ratio ν
Initial support	25.0	28	0.2
Secondary lining	25.5	31.5	0.2

5.3 *Calculation result*

The internal force values of the initial support of the D3K279+915 section are listed in Table 4, and the safety factor of the initial support structure of the tunnel is checked based on the Code for Design of Railway Tunnel [13],. As shown in the table, because the cave itself is relatively stable, the initial supporting structure is less stressed and the safety factor is larger at the vault. The maximum internal force of the initial supporting structure appears at the foot of left wall the tunnel. The maximum bending moment and axial force are -48.5 kN m and -967.3kN respectively, and the safety factor is 11.14.

Table 4. Maximum vault settlement at different sections.

Measure point	Bending moment value/ kN·m	Axial force value /kN	Safety factor	Whether it meets the requirements
Vault	2.9	103.4	117.82	yes
Left arch foot	-30.2	-272.6	29.96	yes
Right arch foot	-27.3	-186.6	38.33	yes
Left wall	46.6	-808.2	12.82	yes
Right wall	38.0	-756.1	14.24	yes
Foot of left wall	-48.5	-967.3	11.14	yes
Foot of right wall	-35.8	-825.3	13.53	yes
Baseplate midpoint	12.2	-627.6	20.46	yes

The internal force values and safety factor of the secondary lining of D3K279+915 section are listed in Table 5. The maximum internal force of the secondary lining structure also appears at the foot of the left wall. The maximum bending moment and axial force are-22.5 kN m and -440.1kN respectively, and the safety factor is 18.65, which meets the specification requirements. Combined with the calculation of internal force and safety factor of the primary support and secondary lining structure, it can be seen that the tunnel structure is reliable and can fully ensure the structural safety during operation.

Table 5. Maximum horizontal convergence at different sections.

Measure point	Bending moment value/ kN·m	Axial force value /kN	Safety factor	Whether it meets the requirements
Vault	1.6	32.5	135.29	yes
Left arch foot	-13.4	-162.3	44.68	yes
Right arch foot	-11.5	-186.6	42.03	yes
Left wall	22.1	-286.4	25.69	yes
Right wall	20.7	-265.3	27.79	yes
Foot of left wall	-22.5	-440.1	18.65	yes
Foot of right wall	-18.1	-429.5	19.76	yes
Baseplate midpoint	-7.8	-527.6	18.18	yes

5.4 *Situation of field monitoring*

(1) At present, the maximum settlement of tunnel bottom is 9.11mm, locating at the large mileage end of the right side of D3K279+885 section, which appears almost 40m away from the profile where the tunnel crosses the cave, mainly because the tunnels on the left and right sides have not entered the karst cave along the profile direction of the tunnel, and the surrounding rock at the bottom of some sections is bedrock, the basement settlement value is small. From the distance of 40m from the profile the bottom of the tunnel is backfill body, which means that the tunnel starts to completely cross the backfill body near this section, so the settlement of the basement is much larger than that of the tunnel bottom located on bedrock.

(2) Due to the uneven soil mass at the lower part of the high fill backfill body, uneven settlement occurs when the tunnel passes through the karst cave. The maximum longitudinal differential settlement at the tunnel bottom appears on the right side of K279+885 section, which is 2.95mm. The settlement on the right side of the tunnel bottom is slightly larger than that on the left side. At present, the maximum left-right differential settlement is 6.94mm at the large mileage end of D3K279+885 section, which meets the design requirements.

6 CONCLUSION AND DISCUSSION

In this paper, the treatment scheme of high-speed railway tunnel crossing giant karst caves is throughly studied. By comparing and selecting four in-situ crossing schemes: subgrade backfilling, arch bridge crossing, bridge crossing and light protection, bridge crossing and tunnel protection, the comprehensive plan is proposed, which consists of diversion of the underground river, backfilling of the giant karst cave, excavation of the backfill body for tunnel construction, and construction of a bridge in the tunnel. Combined with field construction, monitoring and operation verification, the plan has achieved good treatment effect, with various indicators meeting the requirements. Since the operation of the railway at the end of 2019, the tunnel settlement is controllable and the structure is stable, which fully guarantees the safety of high-speed rail operation and fully proves the practicability and reliability of this innovative scheme.

(1) Because the net height of the karst cave is 120m, and the accumulations at the bottom are unstable, it is not only difficult to construct the railway structure after the traditional scaffold platform is used to protect the karst cave, but also the construction period is long, and the safety is not guaranteed as it requires a large number of operating personnel. In this project, a multi-channel layered backfill scheme is proposed, and the spoil of this tunnel is skillfully used to backfill the karst cave completely, which adapts to local conditions and turns waste into treasure. Moreover, the construction is simple and cost-effective as fewer operating personnel is needed. In addition, no casualties and mechanical equipment damage accidents occurred during the construction period.

(2) In order to solve the structural problem of the high-speed railway crossing the giant karst cave, firstly, a 432m2 super-large section tunnel was built in the backfill body, and then a 38m+108m+38m three-span continuous beam was erected in the tunnel as the track bearing structure, which perfectly combined the advantages of the bridge and tunnel structure and embodied the combined design idea of complementary functions.

(3) In order to build a 432m2 super-large section tunnel in soft backfill, high-pressure grouting is firstly used to reinforce the backfill around the tunnel, and then bench method is adopted with five benches from top to bottom. To adapt to the uneven settlement and deformation of the foundation that may occur in the later period, the tunnel structure is divided into sections every 5m, and wide deformation joints are set between adjacent sections, imitating the animal spine structure. Numerical simulated calculation is carried out for the construction and structure of super-large section tunnel, and the deformation and stress of tunnel in karst cave section are within the allowable range of specification and design. At the same time, since the operation, the measured maximum settlement at the tunnel bottom is 9mm, which meets the structural safety requirements.

(4) In order to maintain the original underground water system, a three-dimensional drainage system for underground water is constructed. Before backfilling construction, the underground river in the cave will be diverted to the outside of the cave; In the backfill construction, large stones are used to backfill around the cave and the bottom of the original underground river to form a three-dimensional seepage layer, and the bedrock fissure water around the cave is introduced into the underground river system. Since the operation, the quantity of underground river in the lower reaches is stable, which meets the demand of local villages for production and domestic water and hydropower generation.

(5) The successful construction of this project has broken through the technical bottleneck of tunnel construction in karst areas, developed the construction technology of tunnel passing through giant karst caves, and improved the freedom of high-speed railway line selection in karst areas, which has important guiding significance for railway construction in karst areas.

REFERENCES

[1] Yang Changyu. Analysis on Treatment Measures for Highway Tunnel Passing Through Karst Caves[J]. Modern Tunnelling Technology, 2011, 48(1): 90.

[2] Yang Haokun, Zheng Zhangqing, Zheng Jun. A Study of the Karst-Related Geological Problems of a Metro Tunnel in the Nanjing Eastern Suburb Area[J]. Modern Tunnelling Technology, 2013, 50(5): 12.

[3] Li Shucai, SHI Shaoshuai, LI Liping, et al. Control of Water Inrush In Typical Karst Tunnels In Three Gorges Reservoir Area And Its Application[J]. Chinese Journal of Rock Mechanics and Engineering, 2014, 33(9): 1887.
[4] Zhang Chongmin, Zhang Fengkai, LI Yao. Study of Full Waveform Inversion of Advance Tunnel Geological Prediction by Ground Penetrating Radar[J]. Tunnel Construction, 2019, 39(1): 102.
[5] Hao Shihua, LOU Guochong. The Research of Ground Penetrating Radar Advanced Detection Technologyin Highway Tunnel Karst Area[J]. Highway Engineering, 2017, 42(4): 285.
[6] Han Kan, WANG Bingyong. Research on the Data Analysis and Detection Technology of TSP Advance Forecast[J]. Journal of Railway Engineering Society, 2020, 37(3): 72.
[7] Cheng Qiaojian. Research on tunnel karst over-detection and cavity treatment technology[J]. Highway, 2020, 65(5): 357.
[8] Cao Xiaoyong, Zhang Long, Lin Yongfeng. Study of the Treatment Scheme for a Large, Dry Karst Cave in the Yangqiaoba Tunnel[J]. Modern Tunnelling Technology, 2014, 51(4): 185.
[9] Xiong Jun. Technical Measures for Tunnel Drainage Hole Undercrossing Filling Karst Cave in Karst Area[J]. Railway Engineering, 2021, 61(4): 62.
[10] Liu Tongjiang, Tang Gang, Wang Jun, et al. Treatment Technology of Giant Karst Cave of Gaoshan Tunnel on Qianjiang-Zhangjiajie-Changde Railway[J]. Tunnel Construction, 2019, 39(6): 972.
[11] LI Kun. Case Study on Coping with Super-large Karst Cave in Construction of Yanwan Tunnel[J]. Tunnel Construction, 2015, 35(1): 79.
[12] Zhu Jianwei, Zhu Jianguo. Comprehensive Treatment Techniques for Karst Caves in Xiaosanxia Tunnel of Zhengzhou-Wanzhou High-Speed Railway[J]. Tunnel Construction, 2021, 41(S1): 401.
[13] Code for design of railway tunnel [S]. Beijing: China Railway Publishing House, 2017.

Tunnelling for a Better Life – Yan, Celestino, Thewes & Eberhardt (Eds)
© 2024 The Author(s), ISBN 978-1-032-80042-4
Open Access: www.taylorfrancis.com, CC BY-NC-ND 4.0 license

Tunnel behavior in soft soils subjected to pore water pressure drawdown

Alan Santos*, Raimundo Pérez-Léon & Juan Rodríguez-Rebolledo
Universidade de Brasília, Brasília, Brazil

Bernardo Caicedo
Universidad de Los Andes, Bogotá, Colombia

ABSTRACT: Constructing tunnels in soft soils presents significant challenges due to their unfavorable mechanical properties, which can result in excessive strains and potential damage to the tunnel and surrounding structures. In cities such as Bogotá, Mexico City, Shanghai, Singapore, and Tokyo, an additional phenomenon arises from the consolidation process of the soft soil caused by the reduction in pore water pressure resulting from deep water pumping. This phenomenon alters the total stresses acting on the tunnel lining during operation, leading to increased bending moments, compression, and shear forces. To investigate the behavior of tunnels under these challenging conditions, a numerical simulation using the Finite Element Method (FEM) was conducted and compared with a physical model tested in a geotechnical centrifuge. Two scenarios were simulated: one with the tunnel at the bottom of a compressible layer, resting on the hard layer (Model 1), and another in the middle (Model 2). The Hardening Soil (HS) model was utilized to simulate the behavior of the compressible soil. The results demonstrate agreement between the numerical and physical models. All models indicate an increase in vertical total stress at the top and bottom of the tunnel. Conversely, different patterns of earth pressure at the side walls were observed in each simulation. Furthermore, FEM simulations aided in assessing the influence of the initial stress state on the behavior of the tunnel lining during pore water pressure drawdown.

Keywords: Lowering, Regional subsidence, Geotechnical centrifuge, Hardening soil

1 INTRODUCTION

The consolidation process occurring in clayey soil due to piezometric drawdown from water pumping in underlying aquifers can lead to regional subsidence. According to Kusakabe & Ariizumi (2005) and Rodríguez-Rebolledo et al. (2013), this phenomenon causes an increase in vertical total stress at the top (crown) of a tunnel liner and a decrease in horizontal total stress at its sides. This redistribution of stress results in a significant increase in bending moments and compression forces within the tunnel lining structure.

To investigate the behavior of tunnels under these challenging conditions, a numerical simulation using the Finite Element Method (FEM, Plaxis 2D) was conducted. The findings from this analysis were compared with the results of a physical simulation performed in a geotechnical centrifuge by Pérez-León (2023). Additionally, the influence of the initial stress state on the behavior of the tunnel lining during pore water pressure drawdown was evaluated.

Two scenarios were examined: one with the tunnel located at the bottom of a compressible layer, resting on the hard layer (Model 1), and another positioned in the middle (Model 2).

2 PROTOTYPE DEFINITION

The prototype for this study was defined as a refence case, based on the subsoil conditions in the cities of Bogota and Mexico. Typically, tunnels in these conditions consist of two linings: a primary lining composed of precast segments and a secondary lining made of cast-in-place reinforced concrete.

For the tunnel prototype, an external diameter of 6.0 m, a total thickness of 50 cm (including both linings), and a concrete compression strength of 35 MPa were considered. Figure 1 illustrates the overall characteristics of the prototype used for both the physical and numerical modeling analyses.

3 PHYSICAL MODELLING

3.1 *Centrifuge model*

The physical models were developed and conducted by Pérez-Léon (2023) at the geotechnical centrifuge of *Universidad de Los Ándes*, Colombia.

A beam-type geotechnical centrifuge with the following specifications was utilized: a rotation radius

*Corresponding author: alanrsmbs@gmail.com

DOI: 10.1201/9781003495505-82

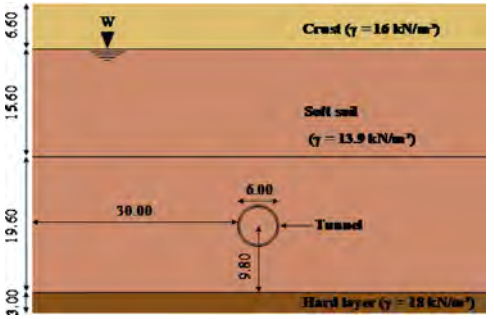

Figure 1. General characteristics of the prototype (dimensions in m).

of 1.90 m (1.70 m effective radius), maximum acceleration of 200 g, maximum model weight of 400 kg, nominal power of 298.3 kW, and data acquisition with 50 channels.

Centrifuge modeling aims to replicate the stress state of the prototype by increasing acceleration N times, resulting in a scaled model 1/N times in the centrifuge (NG, 2014). In addition to replicating in-situ stresses in a reduced model, the geotechnical centrifuge offers the advantage of reducing consolidation time up to $1/N^2$ times.

Considering the dimensions of the prototype (Figure 1) and a flight acceleration of 80 g (N = 80 g), two models were constructed for the geotechnical centrifuge: one with the tunnel at the bottom of the soft soil supported by the hard layer (Model 1, Figure 2.a), and another with the tunnel in the middle of the soft soil (Model 2, Figure 2.b). The model box for the geotechnical centrifuge had dimensions of 0.15 m wide, 0.55 m long, and 0.58 m high, with a front wall made of acrylic measuring 0.064 m thick. Ten holes were drilled on the right side of the box to install pore water pressure transducers at different depths. Another hole was added at the bottom to connect a horizontal water reservoir for water drainage during testing (pore water pressure drawdown). To maintain the water level in the model, a hole was added on the lower left side of the box connected to a vertical water reservoir.

To facilitate water drainage and reduce consolidation time, the superficial part of the soft soil was replaced with a sand layer. Two flexible hoses were added to drain the sand layer through the bottom sand drain (Figure 2). These modifications allowed for maintaining pore water pressure drawdown conditions and reducing the consolidation time from 49 to 16 hours in the model (equivalent to 36 to 12 years in the prototype).

Also, to represent the behavior of lacustrine soft soils more realistically and comply with the maximum permitted daily continuous operating time of 9 hours for the equipment, laboratory reconstituted clay was used. The clay consisted of a mixture of 50% kaolin clay (Caomin P055, a commercial

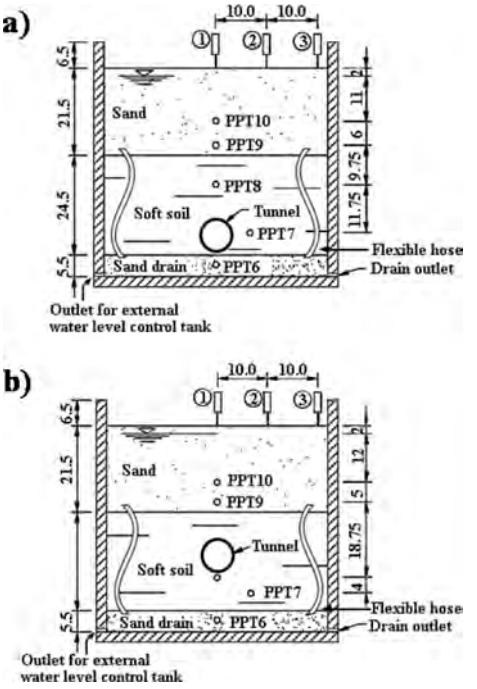

Figure 2. Dimensions and instrumentation for the centrifuge models: a) model 1, tunnel supported by the hard layer; and model 2, tunnel in the middle of the soft soil (dimensions in cm, from rodríguez-rebolledo et al., 2022).

product available in Bogota, Colombia) and 50% diatomaceous soil (50K-50DS) from Bogota (G_S = 2.49, γ = 13.9 kN/m³, e_0 = 2.70, C_c = 0.707, C_u = 0.110, c_v = 28.16 m²/year and k = 7.74×10^{-7} cm/s) (Rodríguez-Rebolledo et al., 2022; Pérez-Léon et al., 2022b).

In summary, the following materials were used in the physical models:

a) Bottom sand drain: composed of coarse sand (D_{50} = 3.0 mm, C_u = 1.89, C_c = 1.02 and k = 8.2×10^{-2} cm/s).
b) Upper sand layer: composed of medium sand (D_{50} = 0.70 mm, C_u = 2.35, C_c = 0.92, γ_{max} = 15.3 kN/m³, γ_{min} = 14.8 kN/m³, γ_{sat} = 19.1 kN/m³, e_{max} = 0.94, e_{min} = 0.56 and k = 2.9×10^{-3} cm/s).
c) Soft soil: laboratory reconstituted clay composed by 50% kaolin clay and 50% diatomaceous soil.
d) Tunnel: aluminum tube with an external diameter of 7.5 cm, 4.85 mm thick and a length of 12 cm (density of 27 kN/m³, Young's modulus of 70 GPa and Poisson's ratio of 0.33).

3.2 *Diatomaceous soil*

According to Ovalle and Arenaldi-Perisic (2020) and Zulaga-Astudillo et al. (2022), diatoms are unicellular algae with a hard and porous cell wall called frustule, composed mainly of silica. When diatoms die, their frustules settle and form diatomaceous soil

(DS), which is present in various aquatic environments worldwide.

Several authors (Zuluaga-Astudillo et al., 2022; Arenaldi-Perisic et al., 2019; Caicedo et al., 2019; Slebi-Acevedo et al., 2021) state that DS has low density, high surface area, elevated porosity, and a high initial void ratio. These characteristics, along with its double porosity (voids between and inside frustules), make DS highly capable of storing water (Palomino et al., 2011; Ovalle and Arenaldi-Perisic, 2020).

Despite the high-water storage capacity of DS, which results in high liquid and plastic limits, it exhibits relatively high values of effective shear strength compared to other fine soils, as reported by Caicedo et al. (2018). Ovalle and Arenaldi-Perisic (2020) explain that this is due to the interlocking of frustules and the highly frictional nature of the contact between them, characterized by their rough and hard surfaces.

3.3 *Model instrumentation*

According to Figure 2, the soil was instrumented with five pore pressure transducers (PPT6 to PPT10) to measure pore water pressure variations along the soil profile, and three Linear Variable Differential Transformers (LVDT's) on the model surface to measure settlements.

For the tunnel lining, as shown in Figure 3, eight earth pressure cells (C) were installed to measure total stresses, one LVDT for vertical convergence, sixteen strain gauges (SG) to quantify strains, moments and axial forces, and five piezometers (PPT) to compute the pore pressure variations around the tunnel.

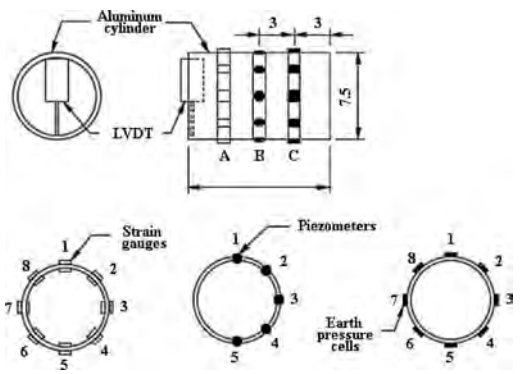

Figure 3. Tunnel lining instrumentation (dimensions in cm, from pérez-léon, 2023).

4 NUMERICAL MODELLING

4.1 *General characteristics*

The numerical models were developed using the Finite Element Method (FEM) with Plaxis 2D software, considering plane strain analysis and utilizing 15-node triangular elements. Due to the problem's symmetry, only half of the model was simulated.

For simulating the soft soil (50K-50DS), the Hardening Soil (HS) constitutive model was employed. The HS model, introduced in the Plaxis software, is based on the theory of plasticity (Schanz et al., 1999; Brinkgreve et al., 2014, 2015). In this model, total strains are calculated using stress-dependent stiffness, which differs for loading and unloading/reloading conditions. Failure is defined by the Mohr-Coulomb failure criterion and incorporates shear hardening and compression hardening. Shear hardening follows a non-associated flow rule, while compression hardening has its own associated flow rule.

4.2 *Material properties*

The mechanical parameters for the 50K-50DS reconstituted soil were obtained, calibrated, and validated for the HS model based on laboratory test results by Pérez-Léon et al. (2022a), as presented in Table 1. To simulate the consolidation process, the drainage condition "Undrained A" was selected, representing undrained material behavior with effective values defining stiffness and strength. The soil was considered incompressible by applying a large bulk stiffness for water, and pore pressures were calculated (Plaxis, 2022).

Table 1. Material properties for 50K-50DS (from pérez-léon et al., 2022a).

Parameter Drainage type	Name Type	Value Undrained A	Unit
Unit weight	γ	13.9	kN/m^3
Secant stiffness in standard drained triaxial test	E_{50}^{ref}	4.2	MPa
Tangent stiffness for primary oedometer loading	E_{oed}^{ref}	2.4	MPa
Unloading/reloading stiffness	E_{ur}^{ref}	18	MPa
Poisson's ratio	ν_{ur}	0.2	-
Power for stress-level dependency of stiffness	m	0.5	-
Cohesion	c'_{ref}	20	kPa
Friction angle	ϕ'	28°	°
Dilatancy angle	ψ	0	°
K_0-value for normal consolidation	K_0^{nc}	0.53	-
Failure ratio	R_f	0.9	-
Reference stress for stiffnesses	p_{ref}	100	kPa
K_0-value	K_0	0.53	-
Over-consolidation ratio	OCR	1	-

As shown in Table 2, the hard layer (HL) and crust were simulated by the Mohr-Coulomb model. The properties of the aluminum tube used in the centrifuge model were considered for the tunnel lining (Table 3), employing a liner-elastic model. Additionally, a strength reduction factor of 1 was assumed for

the lining-soil interface, considering the properties of the surrounding soil.

Table 2. Material properties for hard layer (HL) and crust.

Parameter Drainage type	Name Type	Value HL Drained	 Crust	Unit
Unit weight	γ	18	16	kN/m^3
Young's modulus	E'_{ref}	50	12	MPa
Poisson's ratio	ν	0.33	0.3	-
Cohesion	c'_{ref}	10	24	kPa
Friction angle	ϕ'	45	28°	°
Dilatancy angle	ψ	0	0	°
K_0-value	K_0	0.29	0.53	-

Table 3. Material properties for the tunnel lining and interface.

Parameter Drainage type	Name Type	Value Non-porous	Unit
Unit weight	γ	27	kN/m^3
Young's modulus	E'_{ref}	70	GPa
Poisson's ratio	ν	0.33	-
Strength reduction factor	R_{inter}	1.0	-

4.3 *FEM mesh*

The FEM mesh was generated automatically by the software (Figure 4), with the general element distribution set to fine and a refined region around the tunnel (coarseness factor = 0.3). This resulted in a total of 2,866 elements and 23,638 nodes (Model 1).

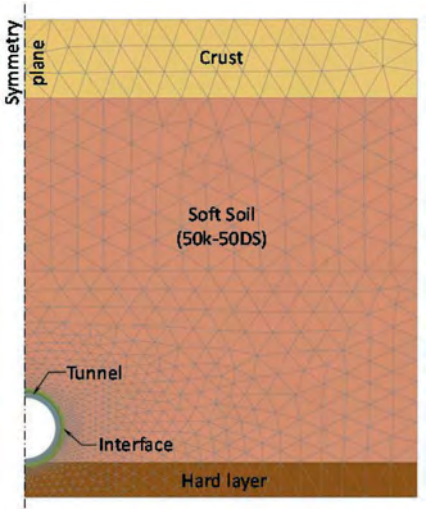

Figure 4. FEM mesh for model 1.

4.4 *Simulation stages*

Three stages were considered for the numerical simulation:

I. Initial phase: During this stage, the initial stress state was determined using the K_0 procedure, and the initial pore water pressure was calculated assuming hydrostatic conditions (phreatic level at a depth of 6.6 m).
II. Tunnel construction: in this stage the tunnel was excavated, and the lining and the interface were activated. The plastic calculation type was applied, neglecting the undrained behavior of soft soil.
III. Pore water pressure drawdown: This stage involved simulating the drawdown of hydrostatic initial conditions to induce regional subsidence. A fully coupled flow-deformation analysis was performed, allowing for a time-dependent analysis of deformations and pore pressure (Plaxis, 2022).

For Stage III, the flow boundary conditions were defined based on hydraulic head, using data obtained from instrumentation of the physical model. Pérez-Léon (2023) noted that complete dissipation of initial hydrostatic conditions was not achieved during physical modeling, as the water level in the horizontal outlet tank resulted in a remaining hydraulic head at the bottom of the model. Consequently, in the numerical modeling, hydraulic heads were adjusted to match the subsidence values obtained in the physical model through superficial LVDT's. The subsidence value obtained for both centrifuge models was approximately 0.75 m. As depicted in Figure 5, for maximum drawdown condition, hydraulic heads of -26.0 m and -6.6 m were defined at the bottom and

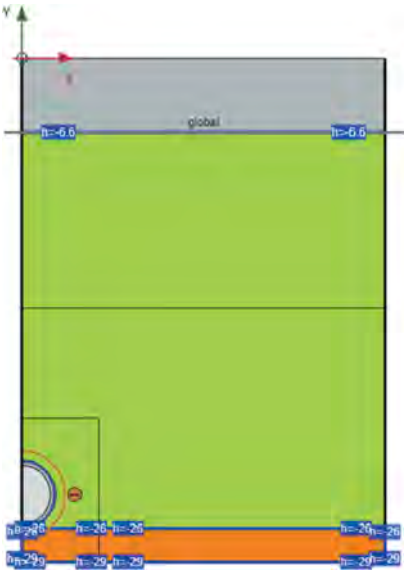

Figure 5. Flow boundary conditions (model 1).

top of the soft soil layer, respectively. Figure 6 illustrates the subsidence versus time curves obtained for both physical and numerical models.

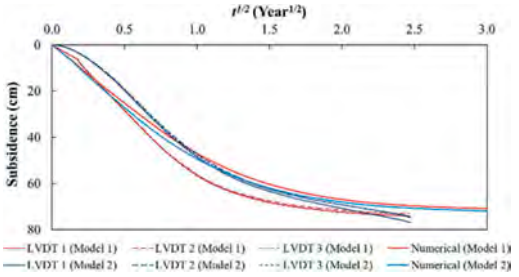

Figure 6. Subsidence along the simulation time (red curves: model 1; blue curves: model 2).

To evaluate the influence of the initial stress state on the tunnel behavior, an additional simulation was held considering for the initial phase the stress calculation by the gravity loading procedure. The results were compared with those obtained by K_0 procedure.

5 RESULTS

5.1 *Piezometric conditions*

Figure 7 Illustrates the piezometric profiles obtained for both Model 1 and Model 2, as well as for the physical and numerical simulations. In general, there is a similar behavior observed between the physical and numerical models. However, a notable difference is observed in the final drawdown condition (U = 100%), where the numerical model shows higher pore pressure values (u) near the sand layer. This discrepancy is also evident in the U *versus* u graphs (Figure 8) for PPT7 and PPT8 (refer to Figure 2). Initially, the u values (for U = 0%) are reasonably similar between models, but a significant difference develops during the consolidation process's final stage (U = 100%) for the deeper piezometers. Nonetheless, these differences do not appear to impact the final magnitude of subsidence, as demonstrated earlier (Figure 6), where similar values were obtained between models.

5.2 *Earth pressure*

Figures 9 and 10 present the earth pressure (P_0) developed around the tunnel lining during the pore water pressure drawdown (U), for the physical and numerical Models 1 and 2, respectively.

For the physical models, not all earth pressure transducers worked properly or gave consistent results, so, considering the symmetry of the problem, only the results from half of the tunnel lining were included. For the numerical model, P_0 values were obtained at the stress points located in the same positions of the transducers.

As depicted in Figures 9 and 10, there is a notable disparity between the measurements obtained from numerical and physical models during the initial phase of consolidation (U = 0%), likely attributed to the diverse methodologies employed in representing tunnel installation. However, as the pore pressure dissipates entirely and the total and effective stresses

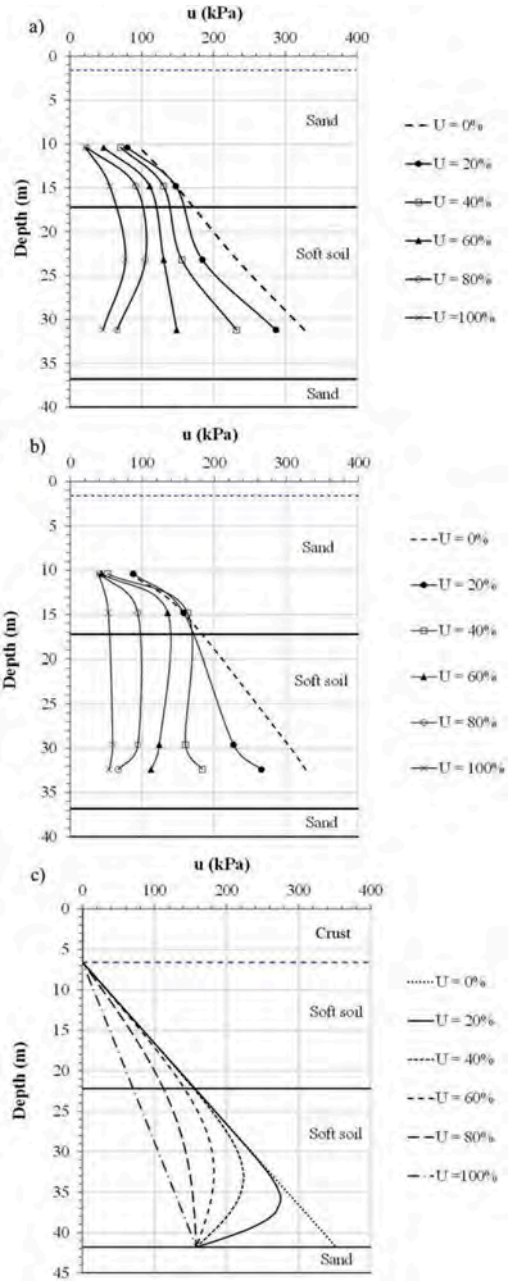

Figure 7. Piezometric profiles for: a) physical model 1, b) physical model 2, and c) numerical modeling.

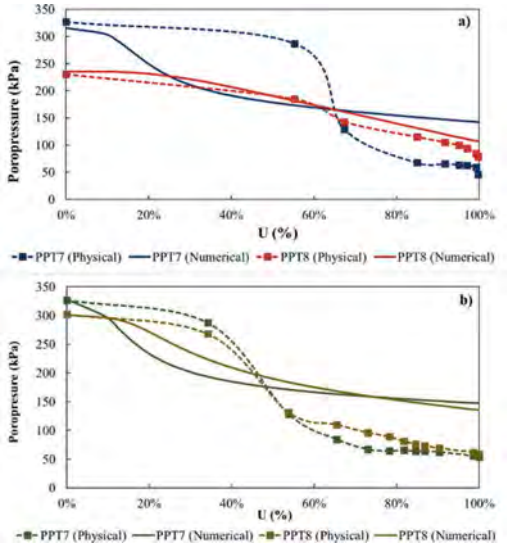

Figure 8. Pore water pressure (u) versus degree of consolidation (U) for PPT7 and PPT8, and for: a) model 1 and b) model 2.

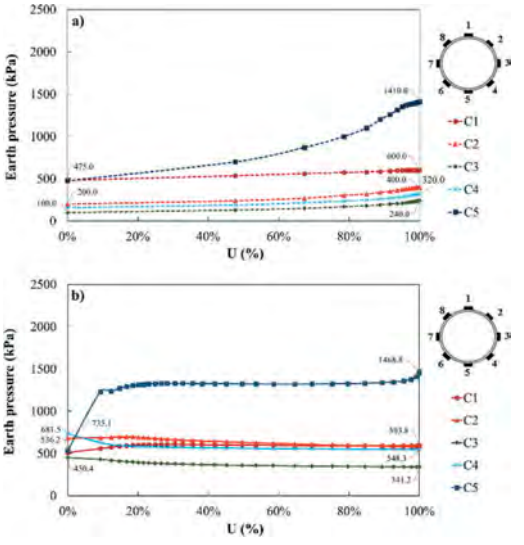

Figure 9. Earth pressures (P_0) versus U, for: a) physical model 1 and b) numerical model 1.

become equivalent (U = 100%), a higher degree of concurrence is observed in the outcomes.

For U = 100 %, the results indicate a significant increase in pressure at cell C5 when the tunnel is supported by the hard layer (Model 1, Figure 9) compared to when it is located within the compressible layer (Model 2, Figure 10). The pressure rises from 285 to 1410 kPa in the physical model (Figures 10a and 9a), and from 574.8 to 1468.8 kPa in the numerical model (Figures 10b and 9b). This can be attributed to the restriction of vertical tunnel movement caused by the hard layer, which also leads to higher pressures at the top of the lining (cell C1): an increase from 500 to 600 kPa in the physical model, and from 487.2 to 593.8 kPa in the numerical model. Moreover, there is congruence between the behavior and magnitude of results obtained from both numerical and physical tools at these two points. Just cell C5 of the physical model (Figure 10a) presents a significant difference with the numerical one, which will be explained later.

On the other hand, cell C3 records the lowest magnitude of earth pressure among all models, as the pressures at this location are primarily influenced by total horizontal stresses. It is noteworthy that physical models demonstrate an increase in lateral pressure during piezometric drawdown, whereas numerical models indicate a decrease. Kusakabe and Ariizumi (2005) published results from a centrifuge model with similar conditions, showing that lateral pressure also decreases during drawdown. However, in that model, the tunnel was fixed to the walls, restricting its vertical displacement. In another experiment conducted by Ma et al. (2010), where half of the tunnel was longitudinally supported by soft clay and the other half by rigid clay, lateral pressures decreased in the case of soft soil but increased for rigid soil.

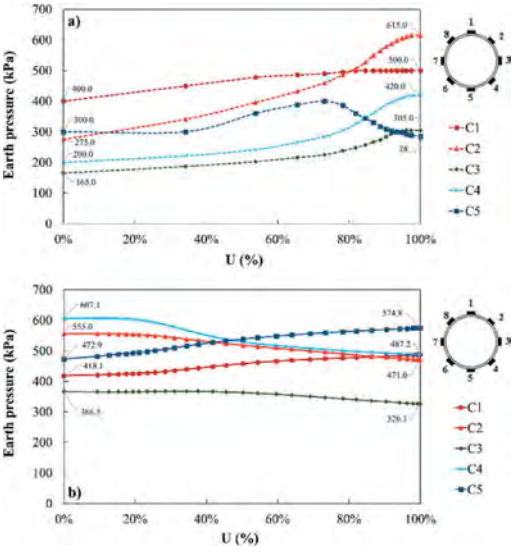

Figure 10. Earth pressures (P_0) versus U, for: a) physical model 2 and b) numerical model 2.

In addition to total horizontal stress, horizontal earth pressure acting in the laterals of the tunnel lining is influenced by the lateral pressure generated by lining deformation. Several factors contribute to the development of this lateral pressure, including: the compression and bending stiffness of the lining, the value of the lateral earth pressure coefficient, and the soil's Poisson's ratio and stiffness. Due to its complexity and to the lack of congruence among the results obtained from various studies, this topic is under investigation.

In physical Model 2, there is a significant increase in pressure in cell C2 during the piezometric drawdown

(Figure 10a). This can be attributed to the tunnel being influenced by the boundary conditions of the model, as it did not descend freely. The decrease in pressure observed in cell C5 during drawdown confirms this, indicating that the soil is unloaded beneath the tunnel. In the study by Kusakabe and Ariizumi (2005), where the tunnel was fixed to the model walls, this trend is consistent for both C2 (increases) and C5 (decreases). The stiffness of the tunnel, being higher than that of the surrounding soil, prevents it from moving vertically in sync with the soil during piezometric drawdown. As a result, negative skin friction develops at the top of the lining where cell C2 is located, as the soil tends to drag down the tunnel. The greater the limitation of the tunnel to move vertically, the greater the magnitude of this negative friction.

5.3 *Initial conditions analysis*

Figure 11 Presents the results obtained for numerical models 1 and 2, where the initial stress state was generated using the gravity loading method. By comparing the results of Model 1 under two different initial stress conditions (Figures 9b and 11a), it is evident that cell C5 exhibit the highest variation. At U = 0%, C5 shows an increase of up to 207%. The other cells display smaller variations ranging from 0.5% to 21% (C2 and C4, respectively). At U = 100%, the variation in C5 decreases significantly to 54%, while the other cells depict smaller alterations. These findings indicate that the support point of the tunnel in the hard layer is highly sensitive to the initial stress conditions. When employing the gravity loading method, the tunnel is installed since the beginning of the analysis, so the tunnel lining's weight and the forces generated by soil self-weight consolidation un top of the lining (negative friction) exert additional pressure on cell C5.

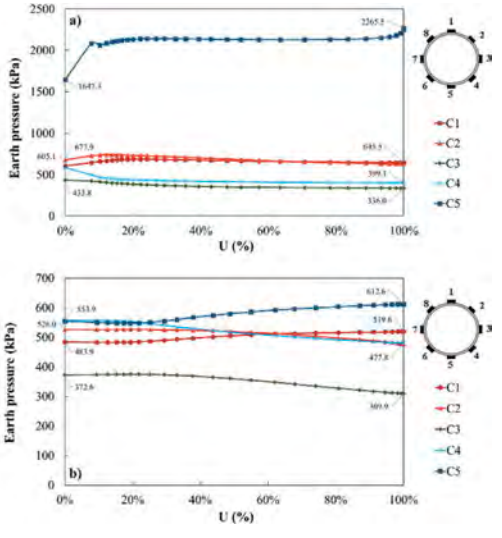

Figure 11. Earth pressures (P_0) versus U, using initial gravity loading procedure for: a) model 1 and b) model 2.

For Model 2 (Figures 10b and 11b), the variations decrease considerably. At U = 0%, C5 exhibits a variation of only 17%, while the other cells range from 1.7% to 16% (C3 and C1, respectively). Under full settlement conditions (U = 100%), instruments experience maximum variations of only 6.7% (C1). These results confirm that for Model 2, the methodology used to calculate initial stresses does not significantly affect the magnitudes of pressures acting on the lining. Furthermore, the obtained variations for U = 0% tend to decrease during pore water pressure dissipation.

In conclusion, despite significant differences in initial pressures between physical and numerical models (considering K_0 procedure), there is a notable similarity at the end of the consolidation process. This similarity can be attributed to the dissipation of excess pore pressure generated during tunnel installation over time. Consequently, all models reach a similar state when total stresses are equivalent to effective stresses.

6 CONCLUSIONS

This paper presents an investigation into the behavior of tunnels in soft soil subjected to regional subsidence. A numerical simulation using the Finite Element Method (FEM) with Plaxis 2D software is performed. The results of this analysis are compared to a physical simulation conducted by Pérez-León (2023) in a geotechnical centrifuge. Moreover, the influence of the initial stress state on the behavior of the tunnel lining during pore water pressure drawdown is assessed. Two scenarios are considered: one with the tunnel located at the bottom of a compressible layer, resting on a hard layer (Model 1), and another positioned in the middle (Model 2).

Flow boundary conditions were established by utilizing hydraulic head data gathered from instrumentation of the physical model. In the numerical modelling phase, hydraulic heads were modified to align with the subsidence values obtained from the physical model. A significant disparity was observed in the ultimate drawdown condition (U = 100%), where the numerical model exhibited elevated pore pressure values near the sand layer. However, these discrepancies do not seem to have an impact on the overall subsidence magnitude, which remained consistent at approximately 0.75 m for all models.

It seems that there was initially a difference between the measurements obtained from the physical and numerical models in terms of earth pressure around the tunnel lining during pore water pressure drawdown. However, as the pore pressure dissipated and the stresses transitioned, there was a higher degree of agreement in the outcomes. Similar conclusions were reached in the numerical simulation when evaluating the

influence of the initial stress state on tunnel behavior, considering gravity loading and the K_0 procedures.

ACKNOWLEDGMENTS

This study was financially supported by the *Coordenação de Aperfeiçoamento de Pessoal de Nível Superior*, Brazil (CAPES) and *Conselho Nacional de Desenvolvimento Científico e Tecnológico*, Brazil (CNPq). Special thanks to Los Andes University (Bogotá, Colombia) for their support and partnership.

REFERENCES

Arenaldi-Perisic, G., Ovalle, C. & Barrios, A., 2019. Compressibility and creep of a diatomaceous soil. Engineering Geology 258 (2019) 105145. https://doi.org/10.1016/j.enggeo.2019.105145.

Brinkgreve, R.B.J., Engin, E. & Swolfs, W.M., 2014. Plaxis 2D Anniversary Edition, Plaxis bv.

Brinkgreve, R.B.J., Kamarswamy, S. & Swolfs, W.M., 2015. Plaxis 3D Anniversary Edition, Plaxis bv.

Caicedo, B., Mendoza, C., López, F. & Lizcano, A., 2018. Behavior of diatomaceous soil in lacustrine deposits of Bogotá, Colombia. J. Rock Mech. Geotech. Eng., 10, 367–379.

Caicedo, B., Zuluaga, D. & Slebi, C., 2019. Effects of micro-features of fossil diatom on the macroscopic behaviour of soils. Géotechnique Lett., 9, 322–327.

Kusakabe, O. & Ariizumi, T., 2005. Physical and numerical modeling of long-term load on a tunnel in soft clay. Geomechanics II: Testing, modeling, and simulation, pp 390–406.

Ma, X.F., Yu, L., Soga, K. & Laver, R., 2010. Centrifugue modelling on long-term behaviour of tunnels in transitional ground. Proceedings of the 7th International Conference on Physical Modelling in Geotechnics, pp 569–574.

Ng, C.W.W., 2014. The state-of-the-art centrifuge modelling of geotechnical problems at HKUST. J. Zheijang Univ.-Sci. 15, 1–21. https://doi.org/10.1631/jzus.A1300217.

Ovalle, C. & Arenaldi-Perisic, G., 2020. Mechanical behaviour of undisturbed diatomaceous soil, Marine Georesources & Geotechnology, DOI: 10.1080/1064119X.2020.1720049.

Palomino, A.M., Kim, S., Summitt, A. & Fratta, D., 2011. Impact of diatoms on fabric and chemical stability of diatom–kaolin mixtures. Appl. Clay Sci. 2011, 51, 287–294.

Pérez-León, R.F., 2023. Interação solo-suporte de túneis construídos em solo mole em processo de adensamento. Doctoral thesis in Geotechnics (in portuguese), Universidade de Brasília, Brasília, Brazil, 117 p.

Pérez-Léon, R.F., Rodríguez-Rebolledo, J.F. & Hormaza, B.C., 2022a. Stiffness and strength parameters for the hardening soil model of a reconstituted diatomaceous soil. European Journal of Environmental and Civil Engineering. https://doi.org/10.1080/19648189.2022.2051077.

Pérez-Léon, R.F., Rodríguez-Rebolledo, J.F., Hormaza, B. C & Silva, A.R.C., 2022b. Modelagem em Centrífuga Geotécnica de um Túnel em Solo Mole em Processo de Adensamento. XX Congresso Brasileiro de Mecânica dos Solos e Engenharia Geotécnica. Campinas, Brazil.

Plaxis., 2022. Plaxis 2D – Reference Manual. Plaxis, Connect Edition V22.02. Bentley Advancing Infrastructure.

Rodríguez-Rebolledo, J.F., Auvinet, G. & Vázquez, F., 2013. Design of tunnel lining in consolidating soft soils. Proceedings of the 18th International Conference of Soil Mechanics and Geotechnical Engineering, Paris, 1765–1768.

Rodríguez-Rebolledo, J.F., Pérez-Léon, R.F. & Homaza, B. C., 2022. Centrifuge modelling of the behavior of a tunnel in soft soil subjected to pore water pressure drawdown. 20th International Conference on Soil Mechanics and Geotechnical Engineering. Sydney, Australia.

Schanz, T., Vermeer, A. & Bonnier, P., 1999. The hardening soil model: Formulation and verification. In Beyond. 2000 in Computational Geotechnics -10 Years of Plaxis. Balkema, pp. 281–296.

Slebi-Acevedo, C., Zuluaga-Astudillo, D., Ruge, J. & Castro-Fresno, D., 2021. Influence of the Diatomite Specie on the Peak and Residual Shear Strength of the Fine-Grained Soil. Appl. Sci., 11, 1352.

Zuluaga-Astudillo, D., Ruge, J.C., Camacho-Tauta, J., Reyes-Ortiz, O. & Caicedo-Hormaza, B., 2022. Diatomaceous Soils and Advances in Geotechnical Engineering —Part I. Appl. Sci. 2023, 13, 549. https://doi.org/10.3390/app13010549.

Tunnelling for a Better Life – Yan, Celestino, Thewes & Eberhardt (Eds)
© 2024 The Author(s), ISBN 978-1-032-80042-4
Open Access: www.taylorfrancis.com, CC BY-NC-ND 4.0 license

The deformation characteristics of soft soil layers with different sand content and the time and space effects of foundation pit excavation on the tunnels below

Caihua Shen, & Miao Miao
College of Civil and Transportation Engineering, Hohai University, Nanjing, PR China

Chaotian Huang
Hangzhou Communications Investment Construction Management Group Co., Ltd, Zhejiang, PR China

Yuxiang Dong
Changzhou Planning and Design Institute, Changzhou, PR China

Jinjia Fan
Hangzhou Communications Investment Construction Management Group Co., Ltd, Zhejiang, PR China

ABSTRACT: According to the characteristics of sandy soft soil layer in Hangzhou, soft soil with different sand content is prepared artificially, triaxial shear experiments are carried out to establish the constitutive equations of different sand content, and the safety characteristics of disturbed deformation of foundation pit excavation in different sandy soil layers are revealed. Combined with the actual project of excavation pit above the existing subway, the three-dimensional numerical simulation technology is used to analyze the influence process of pit excavation on the subway below, and the reasonableness of the simulation method is verified by comparing with the measured values. The influence of excavation depth, excavation width and excavation process on existing underground tunnels in different sand-bearing layers is further analyzed, which can optimize the excavation scheme and provide reference for similar projects in the future.

Keywords: soft soil with different sand content, triaxial shear experiment, foundation pit, tunnel deformation

1 INTRODUCTION

The rheology of soft soil refers to the phenomenon in which the deformation of soft soil changes over time under the influence of external forces. The rheology of soft soil is the primary cause of disturbance and progressive failure during foundation pit excavation, and it also significantly influences the time and spatial deformation effects. The rheological mechanism is very complex, involving creep, relaxation, elastic aftereffect and more. The creep test is relatively easy to implement. Therefore, the creep constitutive equation, which can reflect the stress state, is often constructed to simulate the rheological effect. The rheological deformation in consolidation during construction can be regarded as the combination of instantaneous elastoplastic deformation and creep deformation (creep deformation caused by time effect of soft soil under different stress states), so the full creep constitutive equation that can reflect different stress states can be used to simulate the rheological deformation during construction. During the construction period, the load changes greatly, and the total rheological deformation (because the creep constitutive model is used to simulate the rheological deformation in this paper, the total rheological deformation is collectively referred to as creep deformation) is also obvious. During the operation period, the load is basically unchanged. At this time, the total rheological deformation is mainly the traditional creep deformation, and the overall deformation is relatively slow.

The newly excavated waterway in Hangzhou passes over the Hangzhou Metro Line 1 that has been put into operation. The waterway is located above the existing metro tunnel. The elevation of the crown of the prefabricated segment of the metro

*Corresponding author: 530356828@qq.com

DOI: 10.1201/9781003495505-83

tunnel structure is -9.30m (The ground elevation of the area where the excavation channel is located is 5m), and the minimum distance between the bottom of the foundation pit and the top surface of the tunnel structure is only 4.9m.

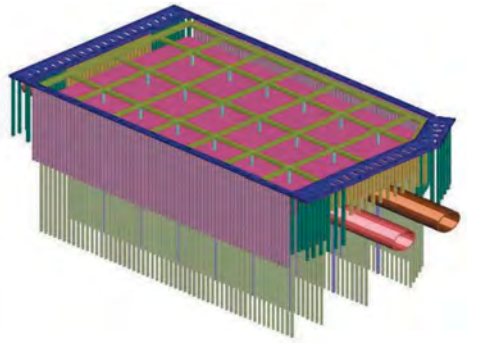

Figure 1. The relationship between the new waterway and existing metro tunnels.

According to the technical code for the safety protection of urban rail transit structures (CJJ/T202-2013), the relative relationship between the newly excavated channel and the subway tunnel is very close:<1.0D (D=6.2m), and the channel excavation is located directly above the subway, which belongs to the strongly affected area: within $0.7h_1$ (h_1=9.4m) directly above and outside the structure, and the impact of channel construction on the subway is special. Excavation disturbance control has become the primary technical problem of construction safety control [1-3].

According to the as-built information, the subway tunnel passes through multiple layers of soft soil with varying sand contents, and the excavation disturbance above the subway tunnel in soft soil has obvious time effect on the surrounding ground and tunnel. Currently, numerous researches being conducted on soft soil, focusing on the deformation and failure caused by creep.

Xu F R[4] et al. (2012) proposed a mechanical model for the creep instability of honeycomb soft clay microstructure to predict the creep deformation characteristics of the soft clay, and found that the deformation instability of soft clay microstructure is related to its stress state, geometry, size and other factors.

Wang Y H[5] et al. (2014) simulated the triaxial creep test of dense sand and loose sand through DEM, and studied the micromechanics involved in the creep process.

Xu R Q[6] et al. (2015) obtained the microstructure data of Zijingang soft soil in the Hangzhou area through SEM (Scanning Electron Microscope) image scanning, studied the pore characteristics of the soft soil, developed a three-dimensional pore calculation model using Image Pro Plus analysis software, and examined the impact of various factors on the calculation of three-dimensional porosity.

Sun M Q[7] (2016) determined the microstructure factor that can indicate the change of soft soil microstructure through the analysis of orientation degree and orientation fractal dimension in soft soil microstructure. By combining the microstructure factor with the one-dimensional creep consolidation differential equation, the one-dimensional creep consolidation differential equation was established.

Ming X[8] et al. (2018) utilized the discrete element method to investigate the creep and stress relaxation process of rockfill. The parameters and appropriate macro responses are derived from the experimental results. The relationship between macro and micro responses is discussed. The micro mechanism of the observed non isochronous phenomenon is also studied.

It can be seen that the creep characteristics of soft soil have a great relationship with the structure of soft soil, and different sand content has great impact on the structure of soft soil [9-11]. Therefore, according to the characteristics of different sand content in the stratum, a creep constitutive model is developed to depict the time effect of excavation construction and The time effect of the operation period; the disturbance influence law of different excavation length, different excavation depth, different excavation sequence and different creep characteristics on the existing subway is simulated and analyzed; the influencing factors and laws of excavation disturbance in the strong influence area above the existing subway are revealed, which provides a reference for the optimization of construction scheme.

2 CONSTRUCTION OF 3D NUMERICAL MODEL BASED ON PROGRESSIVE FAILURE THEORY

2.1 *Establishment of geometric model and working condition determination*

The core area utilizes the sloping+portal reinforcement scheme, and the specific construction sequence is as follows:

(1) Cement mixing piles are used for foundation stabilization in different areas. After the initial setting of cement mixing piles is completed, all bored piles (including uplift piles, retaining piles and column piles+lattice columns) are driven. The cement mixing pile is reinforced in six areas. The unconfined compressive strength in the weak reinforcement area is greater than 0.6MPa, and the unconfined compressive strength in the strong reinforcement area is greater than 1.5MPa. The zoning reinforcement diagram of the core area is depicted in Figure 2. The uplift pile is φ 600@1250 Bored piles, l=40m, 256 in total; The single row of retaining piles parallel to the subway are φ 800@1000 133 bored piles, l=23.5m; The outer side of the double row retaining piles directly above the subway is φ

800@2000 Bored pile with inner side φ 800@1000 67 bored piles, l=9.8m; The outer side of the double row retaining piles above the subway side is φ 800@2000 Bored pile with inner side φ 800@1000 Bored piles, l=18.5M, 64 in total; Column pile is φ 800@10000 18 bored piles, l=40m; Lattice column size is 450 × 450 × 8400 (mm), embedded in the lower column pile. The schematic diagram of bored Piles in the core area is shown in Figure 2.

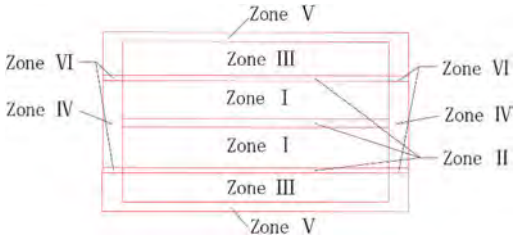

Figure 2. Schematic diagram of reinforcement area of core area.

(2) The core area is divided into seven blocks symmetrically along the direction of the subway tunnel, each with a width of 10m. For each sub pit, first excavate the slope from 3.0m to 1.0m, then excavate pit A to -4.4m elevation, and section steel reinforced concrete (1 m) is poured. The excavation and pouring of pit B have been completed. Excavating the D1 pit to -4.4m elevation, pour plain concrete bedding, and lay section steel reinforcing cages on the base slab. During this period, C1 is excavated synchronously and the above operations are repeated. The 1m section of steel reinforced concrete base layer for pits C1 and D1 was poured as a whole. The later sub pit construction is the same as described above, and the construction sequence is illustrated in Figure 3.

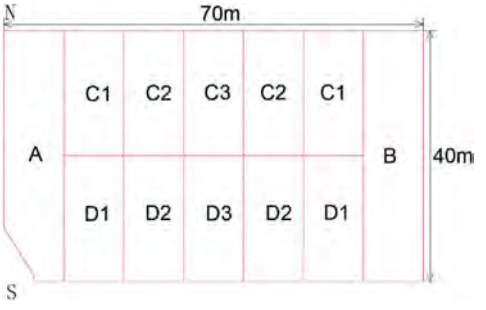

Figure 3. Construction sequence diagram of core area.

The simplified numerical simulation model of foundation pit excavation in the channel core area is shown in the following Figure.

Figure 4. Numerical simulation model diagram of channel excavation above tunnel.

2.2 *Progressive failure simulation method based on creep model and determination of constitutive model parameters*

The progressive failure of soil is the process of soil deformation over time, including short-term sudden failure and long-term slow deformation failure. In order to simulate the entire process of deformation of the channel above the existing subway tunnel during excavation, the generalized exponential creep model is used to replicate the long-term progressive failure deformation of the strata with varying sand content. After determining the equivalent stress of the strata with varying sand content, the creep constitutive equation is adjusted by using the instantaneous equivalent strain corresponding to the equivalent stress as the initial instantaneous strain of the creep constitutive model.

The soft soil parameters in the core area are presented in Table 1 below.

Table 1. Soft soil parameters in core area.

Formation	Es / MPa	Poisson's ratio	Density / kg·m^{-3}	Cohesion / kPa	φ /°
①Silty soil	10.21	0.4	1891	11	29.2
②Silty sand	10.61	0.35	1902	6.6	31.3
③Silty clay	10.65	0.29	1831	1.9	16.2
④Clay	10	0.26	1802	28.1	17.9
⑤Silty clay	10.06	0.23	1871	27.8	17.2
⑥Silty sand	10.69	0.25	1862	6	33.1

The parameters of the retaining structure of the foundation pit in the core area are presented in Table 2 below.

The improved equivalent creep model is utilized to simulate the time effect of the excavation process and operation period. The implicit equation 3 in ANSYS is a commonly used generalized exponential

Table 2. Parameters of foundation pit retaining structure.

Structure	E / MPa	Poisson's ratio	Density / kg·m^{-3}	Cohesion / kPa	φ /°
Semi reinforced soil	90	0.24	2100	3150	45
Reinforced soil	120	0.24	2200	5500	55
Diaphragm wall	17700	0.24	2500	8010	94
Top beam	45000	0.26	2500	8010	94
Coupling beam	30000	0.26	2500	8010	94
Column pile	17700	0.24	2500	8010	94
Lattice column	2780	0.30	2500	8010	94
Uplift pile	5590	0.24	2500	8010	94
Brace	33800	0.26	2500	8010	94
Pier	30000	0.26	2500	8010	94
Cushion	30000	0.24	2500	5020	50

strain rate creep model. The constitutive equation is as follows:

$$\dot{\varepsilon}e = C_1 C_5 e^{(-C_4/T)} \sigma e^{C_2 + C_3} e^{\left[-C_5 \sigma e^{C_3} e^{(-C_4/T)} t\right]} \quad (1)$$

Where: C_1-C_5 represent unknown parameters obtained through fitting. σe is the von Mises equivalent stress and εe is the equivalent strain, and the calculation formula is as follows:

$$\sigma e = \left[\frac{(\sigma 1 - \sigma 2)^2 + (\sigma 2 - \sigma 3)^2 + (\sigma 3 - \sigma 1)^2}{2}\right]^{\frac{1}{2}} \quad (2)$$

$$\varepsilon e = \frac{1}{1+\nu'}\left(\frac{1}{2}\left[(\varepsilon 1 - \varepsilon 2)^2 + (\varepsilon 2 - \varepsilon 3)^2 + (\varepsilon 3 - \varepsilon 1)^2\right]\right)^{\frac{1}{2}} \quad (3)$$

When the creep constitutive parameters are obtained by fitting the creep strain rate duration curve equation, temperature and other effects are not considered. In Formula (2.2-1) $C_2 = 1$, $C_3 = C_4 = 0$, the implicit creep equation is rewritten as:

$$\dot{\varepsilon}e = C_1 C_5 \sigma e \cdot e^{(-C_5 t)} \quad (4)$$

The strain corresponding to the equivalent stress of the formation with varying sand content, as obtained by Formula ($\sigma_e = (1 - K_0)\sigma_1$) is utilized as the initial strain for the creep equation of the formation with different sand content. The creep test curve has been modified, and the creep fitting results of the formation with different sand content are shown in Figure 5.

The specific construction steps and numerical simulation construction sequence of the foundation pit in the core area are presented in Table 3 below.

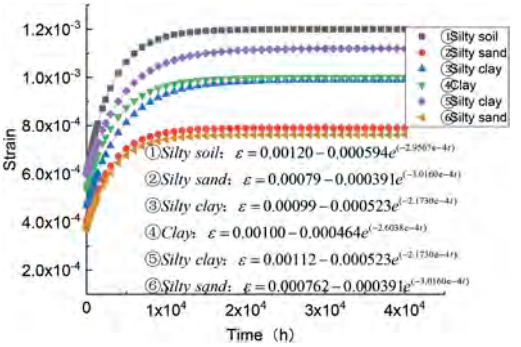

Figure 5. Creep fitting results of each formation.

Table 3. Construction sequence of foundation pit.

Time	Construction content	Last/ day	Remarks Content
2019.12.7~2020.5.8	Pile testing	179	620 days of mixing pile +bored pile construction
2020.5.9~2020.8.7	Shut down	116	
2020.8.8~2021.4.15	MJS construction method pile construction	279	
2120.3.17~2021.7.3	Triaxial mixing pile in zone III, zone IV and zone V	178	
2021.7.28~2021.9.15	Zone I biaxial mixing pile, Zone V high-pressure jet grouting pile	47	
2021.1.9~2021.8.17	Enclosure pile +bored pile	141	
2021.8.18~2021.10.23	Construction of unloading topsoil and retaining structure	67	
2021.10.24~2021.11.3	Pit excavation at East and west sides	10	5 days for each pit
2021.11.4~2021.12.30	Excavate by pit and block and construct the base plate	56	11 days for each pit

3 ANALYSIS ON INFLUENCE LAW OF EXCAVATION LENGTH IN CORE AREA OF CREEP UNIFORM FORMATION ON TUNNEL SAFETY

Assuming that the excavation length of the foundation pit in the core area (other parameters are the same) is 36m (condition 2-1), 40m (condition 2-2) and 44m (condition 2-3), the displacement variation law of the key points of the subway tunnel structure under different excavation lengths of the foundation pit is analyzed. The schedule for excavation construction is shown in Table 4.

Table 4. The schedule of excavation construction.

Construction sequence	Time
Tunnel operation for 7 years and shutdown stage	2800 days
Construction of Zone II and Zone VI	2953 days
Construction of Zone I, Zone III, Zone IV, Zone V and bored piles	3175 days
Excavation of the first layer of soil and construction of retaining structure	3242 days
Pit and block excavation of foundation pit in core area	3308 days

The upward line of the tunnel is located under the center of the foundation pit in the core area. The Y-direction displacement curve of the crown and invert of the tunnel with time during the construction period is depicted in Figure 6.

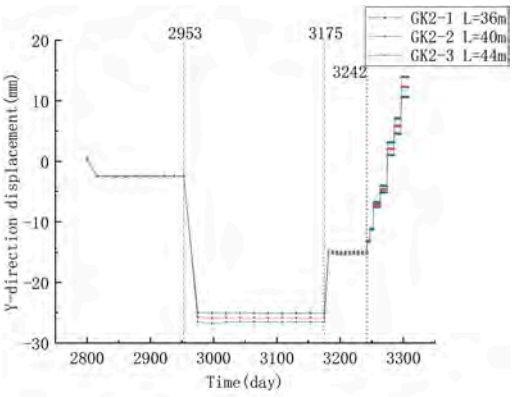

(a) Crown during construction

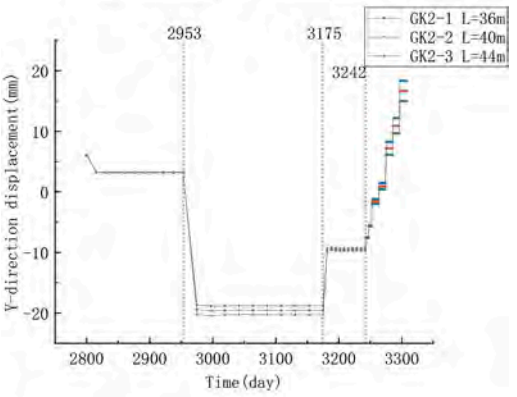

(b) Invert during construction

Figure 6. Curve of Y-direction displacement versus time of tunnel crown and invert during construction period.

As can be seen from Figure 6:

In the core area I, III, IV and V and the bored pile construction stage (3175 days), after the reinforcement of the area where the foundation pit in the core area was not reinforced in the previous stage, the Y-direction displacement of the tunnel crown and invert decreased significantly, and the settlement increased significantly compared with the previous stage. Compared to the previous stage (2953 days), the settlement of the tunnel crown with excavation lengths of l=36, 40 and 44m (GK2-1, 2-2 and 2-3) in the core area was 22.587mm, 23.387mm and 24.141mm respectively, and that of the invert was 21.984mm, 22.789mm and 23.551mm respectively. As the core excavation length L and the area of the reinforced area increase, the settlement of the tunnel crown and invert caused by the reinforcement increases with the increase of the core excavation length L.

Combined with the above figure, it is found that during the second step of excavation, the change in uplift value has exceeded the change of settlement value caused by the reinforcement of the core area. After that, the y-direction displacement of the tunnel with the excavation length of l=44m (GK2-3) in the core area is the largest, followed by l=40m (GK2-2), and l=36m (GK2-1) is the smallest. Although the entire core area has been reinforced, with the increase of the excavation length of the core area, the size of the core area, and the scope of the reinforcement area also increases, but the increase of the excavation scope of the core area leads to the increase of soil rebound deformation caused by excavation, and the reinforcement of the core area is not enough to inhibit the increase in rebound deformation.

The maximum Y-direction displacement of zone 2 and zone 6 after construction was 5.683, 5.730 and 5.776mm (2953 days), which was reduced by 0.404, 0.410 and 0.416mm respectively compared with the previous stage (2800 days). At this time, the variation in the maximum Y-direction displacements increased as the increase of excavation length L. After excavating the first layer of soil and constructing the retaining structure, the maximum Y-direction displacement of 2.681, 2.558 and 2.460mm increased by 2.328, 2.486 and 2.647mm respectively compared with the previous stage (3175 days). At this time, the variation in the maximum Y-direction displacement increased with the increase of the excavation length L; Compared with the previous stage (3242 days), the maximum Y-direction displacement after pit and block excavation in the core area was 15.262, 16.892 and 18.512mm, which increased by 12.581, 14.334 and 16.052mm respectively. At this time, the variation of the maximum Y-direction displacement increased with the increase of excavation length L.

4 ANALYSIS OF INFLUENCE OF EXCAVATION DISTURBANCE ABOVE TUNNEL UNDER DIFFERENT EXCAVATION DEPTHS

Assuming that the excavation depth of the foundation pit is 8.4m (working condition 4-1), 9.4m

(working condition 4-2) and 10.4m (working condition 4-3) respectively, the impact of the excavation depth of the foundation pit on the deformation of the tunnel below is analyzed.

The displacement duration curve of the key points on the lining structure of the subway tunnel is mainly analyzed (the key points include the arch crown, invert (arch bottom) and left and right arch waist of the tunnel below the center of the foundation pit in the core area). The construction time for numerical simulation is shown in Table 4.

(1) During the excavation of the first layer of soil and the construction of the retaining structure (3242 days), the tunnel crown and invert have rebound deformation due to the influence of excavation. Compared with the previous stage (3175 days), the tunnel crown with excavation depths of 8.4, 9.4, and 10.4m (GK4-1, 4-2, and 4-3) in the core area were 10.712mm, 10.705mm, and 10.706mm, respectively; Compared with the previous stage (3175 days), the uplift values of invert are 10.076mm, 10.068mm and 10.070mm respectively. At this time, although the excavation was carried out, only the soil layer within 2m below the ground surface was excavated under the three working conditions, so the uplift values of the tunnel crown and invert under the three working conditions were almost the same.

(2) After 3308 days of pit and block excavation in the core area, the tunnel arch crown and invert experienced rebound deformation, with Y-direction displacement continuing to increase throughout the excavation process. The uplift value also increased significantly. Compared to the previous stage (3242 days), the uplift values of the tunnel arch crown with the excavation depths of 8.4, 9.4, 10.4m (GK4-1, 4-2, 4-3) in the core area are 22.980mm, 27.519mm, 33.349mm respectively; Compared with the previous stage (3242 days), the uplift values of the invert are 21.776mm, 26.267mm and 31.810mm respectively. The uplift value of the tunnel crown and invert caused by excavation increases with the increase of excavation depth in the core area.

Combining with Figure 7, it can be observed that during the process of step-by-step excavation, the uplift value of the tunnel crown and invert caused by excavation increases with the increase of excavation depth in the core area, and the variation of uplift value with the excavation depth in the core area is not linear, and the variation of uplift value increases with the increase of excavation depth.

Under the influence of creep, the minimum Y-direction displacement of the subway during the 7-year operation and shutdown period is 0.333, 0.334, 0.333mm (2800 days), the maximum Y-direction displacement is 6.135, 6.135, 6.135mm (2800 days), and the maximum differential settlement is about 5.8mm.

After completing the pit and block excavation of the foundation pit in the core area, the maximum Y-direction displacement of the three working conditions are 12.478, 17.013 and 22.701mm respectively, which are increased by 10.005, 14.539 and 20.227mm respectively compared with the previous stage (3242 days). At this time, the variation in the maximum Y-direction displacement increases with the increase of the excavation depth.

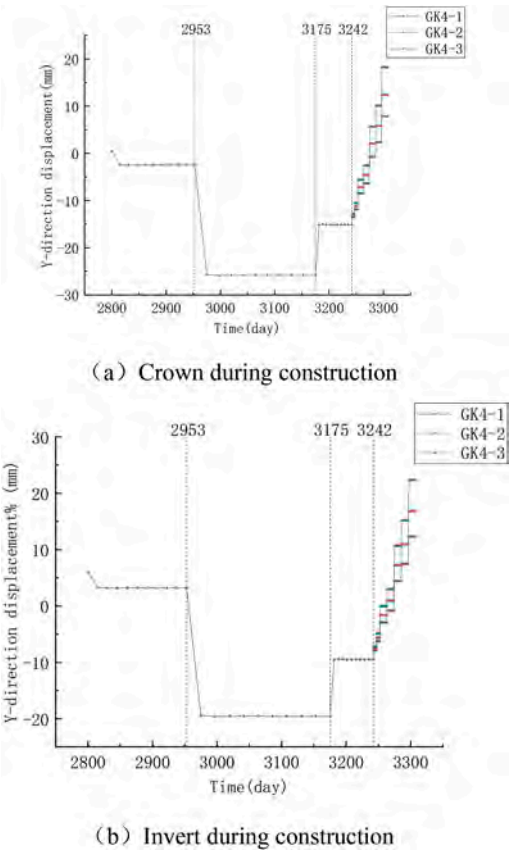

Figure 7. Curve of Y-direction displacement versus time of tunnel crown and invert during construction period.

5 ANALYSIS OF DISTURBANCE EFFECT OF DIFFERENT EXCAVATION SEQUENCE ON EXISTING TUNNEL UNDER FOUNDATION PIT

Assuming that the excavation sequence of the foundation pit in the core area of the channel is different (other parameters remain the same), the impact of the construction scheme on the subway tunnel below is predicted. This paper primarily analyzes the displacement duration curve of the key points on the subway tunnel, which include the arch crown, invert (arch bottom) and the left and right arch waist of the tunnel under the center of the foundation pit in the core area). It also analyzes the changing trends of the x-direction and Y-direction displacement at the

selected positions. The schematic diagram of the block excavation area is depicted in Figure 8, and the excavation sequence parameters for the core area are presented in Table 5.

The three excavation sequences have obvious effects on the displacement curves of the tunnel arch crown and invert over time during the construction period. However, due to the viscoelastic model used in this paper, it can not accurately reflect the cumulative effect of plastic deformation. The excavation sequence is the same for the total deformation of the tunnel crown and invert after excavation, but the real situation is that the plastic deformation of the surrounding rock in the subway tunnel is large due to the excavation disturbance of the soft soil layer. Therefore, in terms of controlling the deformation of the subway tunnel below, different excavation sequences should be optimized and analyzed.

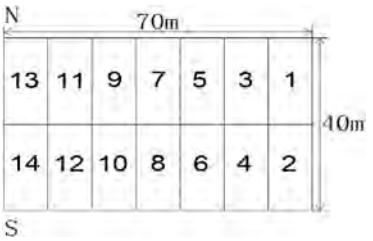

Figure 8. Schematic diagram of block excavation area.

Table 5. Excavation sequence parameters of core area.

Working condition	Excavation sequence
5-1	1、2→3、4→5、6→7、8→9、10→11、12→13、14
5-2	1、2→13、14→4、12→3、11→6、10→5、9→7、8
5-3	1、2、13、14→3、4、11、12→5、6、9、10→7、8

The upward line of the tunnel is located below the center of the foundation pit in the core area. The curve of Y-direction displacement versus time of the arch crown and invert (arch bottom) of the tunnel (s1062 section) during the construction period is shown in Figure 9.

(1) GK5-1 is excavated in a unilateral way, from pit 1 and 2 to pit 13 and 14, and is divided into 7 strips for step-by-step excavation. From the above figure, it can be found that during the excavation of GK5-1 in the core area pit sub-pit and block excavation, the tunnel arch has been bulged by 1.939, 3.324, 5.201, 6.276, 5.447, 3.396, 1.930mm compared to the previous step of excavation, and the tunnel superelevation arch has been bulged by 1.925, 3.290, 4.975, 5.587, 5.130, 5.587, 4.975, 5.587, 5.130, 5.587, 4.975, 4.975, 5.975, 4.975 and 5.975mm respectively, 5.587, 5.130, 3.409, and 1.945 mm, respectively. The uplift values of the tunnel arch and the superelevation arch increased from the edge of the pit in the core area towards the center of the pit and then decreased away from the pit.

(2) During the pit and block excavation of the foundation pit in the core area of GK5-2, the crown of the tunnel was 1.939, 1.936, 4.090, 2.552, 6.699, 3.758 and 6.545mm higher than in the previous excavation. Additionally, the invert of the tunnel was 1.925, 1.922, 4.033, 2.542, 6.281, 3.730 and 5.833mm higher than in the previous excavation. The uplift value of the tunnel crown and invert was the smallest at the edge of the foundation pit in the core area. In the subsequent process of dividing a sub pit into two sides and excavating towards the center of the foundation pit at the same time, the tunnel heave caused by the excavation of the entire sub pit is effectively reduced.

(3) During the pit and block excavation of the foundation pit in the core area of GK5-3, the crown of the tunnel was raised by 3.875, 6.642, 10.457 and 6.545mm respectively, compared with the previous excavation. Additionally, the invert of the tunnel was raised by 3.848, 6.575, 10.012 and 5.833mm respectively, compared with the previous excavation. When a pit is excavated to the center of the foundation pit at the same time without dividing it into two sides, the tunnel uplift value caused by excavation increases significantly, which adversely impacts tunnel deformation control.

The horizontal displacement curve of the arch crown and invert (arch bottom) of the tunnel located below the foundation pit center in the core area during the construction period is shown in Figure 10.

(1) During the pit and block excavation of the foundation pit in the core area of GK5-1, the crown of the tunnel was displaced by -0.019, -0.091, -0.210, -0.292, -0.237, -0.099, -0.007mm respectively compared with the previous excavation, and the invert of the tunnel was raised by -0.068, -0.192, -0.323, -0.361, -0.334, -0.205, -0.070mm respectively compared with the previous excavation. When excavating unilaterally, the horizontal displacement direction of the subway tunnel on the upward line is in the downward line direction.

(2) During the pit and block excavation of the foundation pit in the core area of GK5-2, the displacement of the tunnel crown was -0.019, -0.019, 0.096, -0.274, 0.267, -0.684, -0.321mm respectively compared with the previous excavation, and the displacement of the tunnel invert was -0.068, -0.068, 0.257, -0.637, 0.272, -0.914, -0.395mm respectively compared with the previous excavation. The horizontal displacement of

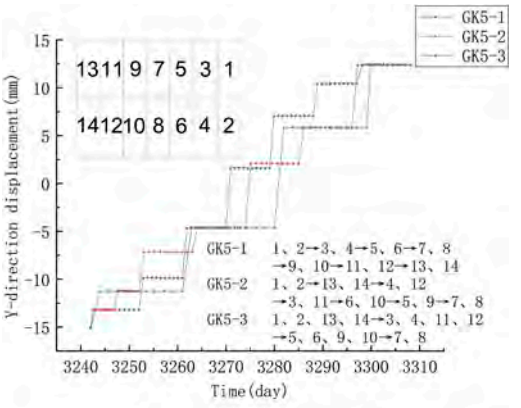

（a）Crown during construction

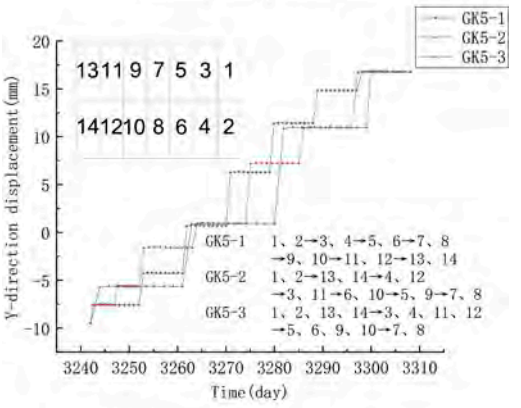

（b）Invert during construction

Figure 9. Curve of Y-direction displacement versus time of tunnel crown and invert during construction period.

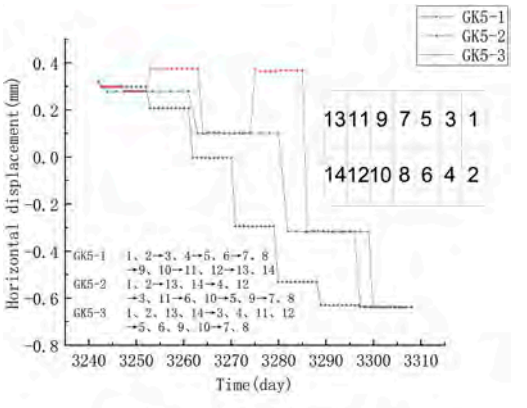

（a）Crown during construction

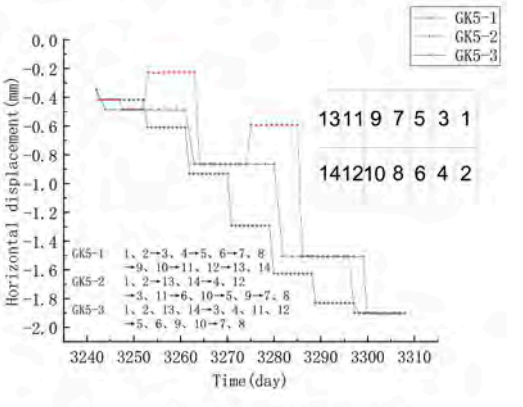

（b）Invert during construction

Figure 10. Curve of horizontal displacement versus time of tunnel arch crown and invert during construction period.

the tunnel crown and invert was the smallest at the edge of the foundation pit in the core area.

(3) During the pit and block excavation of the foundation pit in the core area of GK5-3, the displacement of the tunnel crown was -0.039, -0.178, -0.418, -0.321mm respectively compared with the previous excavation, and the displacement of the tunnel invert was -0.137, -0.380, -0.642, -0.395mm respectively compared with the previous excavation. When excavating both sides simultaneously, the horizontal displacement direction of the uplink metro tunnel is in the downward travel direction. The horizontal displacement variation of the crown and invert of the subway tunnel increases from the edge of the foundation pit in the core area to the center of the foundation pit.

By analyzing the Y-direction displacement versus time curve of the tunnel crown and invert during the construction period, it is evident that the maximum variation in vertical and horizontal displacement occurs when excavating the sub pits (7 and 8 sub pits) in the center of the foundation pit in the core area during the unilateral excavation (GK5-1), and when excavating the sub pits (5, 6, 9 and 10 sub pits) on both sides at the same time (GK5-3), The variation of vertical displacement and horizontal displacement reaches the maximum. When a sub pit is divided into two sides and excavated at the same time (GK5-2), the variation of vertical displacement reaches its maximum when excavating the sub pits on both sides of the foundation pit center in the core area on one side of the subway tunnel on the uplink (6 and 10 sub pits). The variation of horizontal displacement reaches its maximum when excavating the sub pits on both sides of the foundation pit center in the core area on one side of the subway tunnel on the downlink (5 and 9 sub pits), The excavation method of GK5-2 effectively avoids the simultaneous maximum variation of vertical and horizontal displacement, greatly improving tunnel deformation.

In summary, the analysis demonstrates that the excavation depth of the channel core area has a greater impact on tunnel deformation compared to the excavation length of the channel core area.

Therefore, the priority should be given the influence of the excavation depth of the core area on tunnel deformation. Given that the bottom of the channel core area features a steel reinforced concrete composite bottom plate, which belongs to the navigation section that is not easy to be rebuilt, in order to facilitate the navigation of large tonnage ships in the future, the elevation of the foundation pit bottom in the channel core area is finally taken as -4.4m, and the excavation depth is taken as 9.4m.

6 CONCLUSION

In this paper, according to the characteristics of different sand content in the stratum, the generalized exponential creep constitutive model and parameter determination method of soft soil with different sand content are proposed, and the three-dimensional numerical simulation model of rheological deformation of the whole process of excavation of the foundation pit above the subway tunnel in different sand content strata is established, which reveals the influence of different excavation depth, excavation length and excavation sequence of the foundation pit above the subway tunnel on the deformation of the subway tunnel below in the creep soft soil layer. The main conclusions are as follows:

The sequence of excavating the foundation pit above the existing subway tunnel affects the deformation of the existing subway tunnel below. The sequence of excavation for the foundation pit affects the deformation process of the tunnel when the pit is excavated by pit and block. When a pit is divided into two sides and excavated toward the center of the foundation pit simultaneously, it effectively avoids the simultaneous maximum variation of vertical and horizontal displacement, leading to significant improvement in tunnel deformation.

ACKNOWLEDGMENTS

This research has been funded by National Natural Science Foundation of China (Grant No.52278400); the Science and Technology Project of Zhejiang Provincial Department of Transportation (Grant No. 2022-GCKY-12); the Science and Technology Project of Jiangsu Provincial Department of Transportation (Grant No. 2022Y04); The authors gratefully acknowledge these supports.

REFERENCES

[1] Huang H W, Huang X, Schweiger F Helmut. Numerical simulation study on the influence of foundation pit excavation on the underlying operating shield tunnel [J]. China Civil Engineering Journal, 2012, 03: 182–189.

[2] Hu H Y, Zhang Y C, Yang G H, etc. Field measurement and numerical analysis of the impact of foundation pit excavation on existing metro tunnels [J]. Journal of geotechnical engineering, 2014, 36 (supp.2): 431–439.

[3] Guo P F, Yang L C, Zhou S H, etc. Analysis on measured data of uplift deformation of underlying tunnel caused by foundation pit excavation [J]. Geomechanics, 2016, 37 (S2): 613–621.

[4] Xu F R, Liang X Y, Wang F. Micro analysis of creep of honeycomb soft clay [J]. Journal of Lanzhou University of technology, 2012, 38 (03): 119–123.

[5] Wang Y H, Lau Y M, Gao Y. Examining the mechanisms of sand creep using DEM simulations[J]. Granular matter, 2014, 16(5): 733–750.

[6] Xu R Q, Deng Y W, Xu B, etc. Quantitative analysis of 3D porosity of soft soil based on SEM image information [J]. Journal of Geosciences and environment, 2015, 37 (03): 104–110.

[7] Sun M Q. Study on rheological consolidation characteristics of soft soil in Tianjin Binhai New Area [D]. Jilin University, 2016.

[8] Ming X, Juntian H, Erxiang S. DEM study on the macro- and micro-responses of granular materials subjected to creep and stress relaxation[J]. Computers and Geotechnics, 2018, 102: 111–124.

[9] Osipov V I, Sokolov V N . A study of the nature of the strength and deformation properties of clay soils with the help of the scanning electron microscope[J]. Bulletin of Engineering Geology and the Environment,1978,17(1):91–94.

[10] Chen X P, Zhu H H. Experimental study on time effect characteristics of soft soil deformation [D]. Journal of rock mechanics and engineering, 2005,24 (12): 2142–2148.

[11] Yang C, Wang K, Shu W F. One dimensional consolidation rheological properties and model of marine soft soil [J]. Journal of Hunan University of science and Technology (NATURAL SCIENCE EDITION), 2018.33 (1): 28–34.

Tunnelling for a Better Life – Yan, Celestino, Thewes & Eberhardt (Eds)
© 2024 The Author(s), ISBN 978-1-032-80042-4
Open Access: www.taylorfrancis.com, CC BY-NC-ND 4.0 license

Non-invasive tunnelling investigations using Muon tomography

Chris Steer & Lee F. Thompson*
Geoptic Infrastructure Investigations Ltd, Beechcroft Barn , South Warnborough, Hants, UK

ABSTRACT: Muon tomography is a technique that harnesses natural radiation to image large-scale objects in a non-invasive and non-destructive way. This paper reports on the successful application of muon tomography to the imaging of railway tunnels on the UK rail network. The muon tomography is described and a brief resume of the recent and past history of applications of muon tomography is presented. This is followed by a detailed description of the technique to the imaging of railway tunnels. The methods involved in extracting visualisations of the tunnel overburden are outlined and examples of results from recent tunnel surveys are presented. The paper concludes with an outlook of possible future applications of muon tomography to the tunnelling sector.

Keywords: Imaging, Surveying, Mapping

1 INTRODUCTION TO MUON TOMOGRAPHY

Muon tomography is a technique which exploits naturally-occurring radiation in the form of muons. Muons are fundamental particles that are created in the upper atmosphere, they have properties similar to that of a heavy electron (they have approximately 200 times the mass of the electron) which makes them highly penetrating particles capable of passing through tens to hundreds of metres of rock with ease. This, coupled with their relative abundance (at sea level there is 10,000 per m^2 per minute), leads to their suitability for tomographic imaging.

The muon tomography method is analogous to a medical X-ray. With an X-ray, the density information in an object of interest (e.g. a bone in a patient's arm or the root canal system in a patient's tooth) is images by passing a beam of X-rays through the object which are observed by a "detector" (X-ray film) on the other side of the object.

Muon tomography works in the same way except that a muon-sensitive detection system is needed to detect the muons. The key points here however are that muon tomography is a non-invasive and non-destructive method - capable of returning vital information on the structural integrity of objects at a distance and without the need to interact with the object. Furthermore, in the same way as an X-ray can diagnose issues that are otherwise hidden, muon tomography can identify features in, e.g. a tunnel overburden that would otherwise be invisible.

2 MUON TOMOGRAPHY, HISTORY AND APPLICATIONS

Muon tomography isn't a new method, its first documented application was in 1955 when it was used to measure the overburden in a tunnel system around a hydro-electric power station in New South Wales (George, 1955). The technique has most famously been used to identify hidden chambers in pyramids - as depicted in Figure 1 (Morishima et al., 2017).

Muon tomography has also been used in other applications such as imaging volcanos (Tanaka et al., 2014) and imaging sections of the Xi'an's ancient city walls (Liu et al., 2023). A summary of the broad

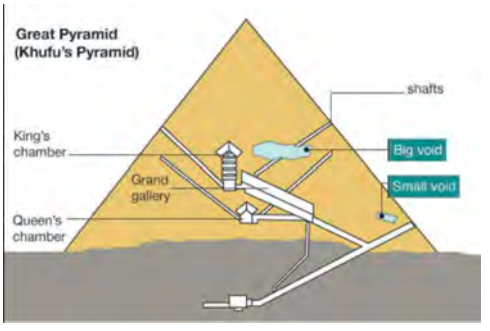

Figure 1. Depiction of voids found in Egyptian pyramid using the muon tomography method.

*Corresponding author: lee.thompson@geoptic.co.uk

DOI: 10.1201/9781003495505-84

range of muon tomography applications has recently been published by the International Atomic Energy Authority (IAEA, 2022).

3 HIDDEN SHAFT LOCATION USING MUON TOMOGRAPHY

The background to this problem lies in the fact that much of the railway infrastructure in the United Kingdom dates back to the Victorian era. The period between the 1850s and early 1900s saw an enormous increase in the UK rail network with a proliferation of track, bridges, tunnels and viaducts being built during this period. Tunnel building methods at that time often involved several additional shafts being created along the length of the tunnel, these were constructed to speed up the construction of the tunnel and were used either to deploy personnel and/or to remove spoil. Importantly, what happened to these shafts when the tunnel was complete is somewhat arbitrary. In some cases the shafts were left open, in others they were bricked over in both the tunnel and on the surface, other shafts have a combination of these approaches.

Due to the age of these tunnels vital documentation on the location of hidden shafts is often incomplete or lost. It is a priority for the UK rail network operator, Network Rail, to have as full an understanding as possible of these hidden shafts since they have potential for dramatic consequences, as evidenced in an event which took place near Manchester in the early 1950s resulting in a loss of life.

Muon tomography is well-suited to the identification, characterisation and, if required, the long-term monitoring of railway tunnel infrastructure since it is capable not only of locating areas of under-density in an overburden but can pinpoint that density deficit and return valuable information on the opacity (effectively the integrated density along the column height above the tunnel) - information which can educate tunnel asset managers and help them to prioritise remedial works.

The potential of muon tomography to return valuable tunnel asset information is highlighted in the following two cases studies.

3.1 *Case study: Alfreton Old Tunnel*

The muon tomography technique was first demonstrated to Network Rail (UK) at the so-called Alfreton Old Tunnel - a disused railway tunnel located in Nottinghamshire, UK. Alfreton Old Tunnel has 3 open shafts to the surface and so is an ideal tunnel for a "proof of principle" application of muon tomography.

Muon sensors, consisting of plastic scintillator, coupled to photomultiplier tubes (light detection devices) were constructed. When a muon passes through the scintillator material a light pulse ("signal") is created that is detected by the photomultiplier. The size and exact time (to a few tens of billionths of a second) are recorded, enabling so-called "co-incidences", i.e. instances of signals seen in two or more sensors separately but at the same time are identified as a muon passing through the system. The exact combination of which sensors see signals give additional information on the trajectory of the detected muon.

This muon detection system was deployed in the Alfreton Old Tunnel and a series of readings taken at regular 5 metre intervals along the tunnel. A full report of the tunnel survey is published in Thompson et al. 2020.

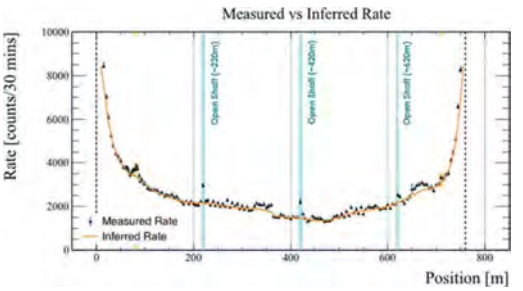

Figure 2. Results of muon tomography scan of Alfreton tunnel.

Figure 2 shows the results of scanning the entire length of the tunnel at 5 metre intervals and with just 30 minutes of data at each point. The "inferred rate" is that predicted to be seen in the muon sensor system (via computer simulations) assuming a certain geology for the tunnel. The 3 open shafts (indicated by blue vertical lines) are clearly visible in the data, a highly significant excess of muons compared to that which would be expected with a full overburden is observed in each case.

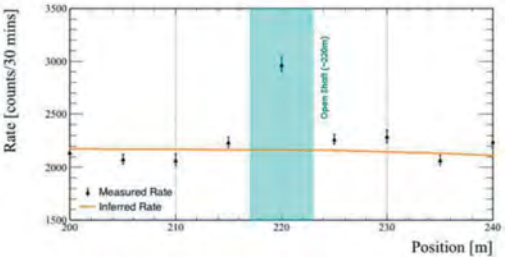

Figure 3. Muon sensor system data around open shaft.

Figure 3 shows a zoom in of the data around 220 metres, here the statistical significance of the open shaft observation is very high - 11 standard deviations, with just 30 minutes of data. Figure 2 shows other features visible in the data: the discontinuity at approx. 350 metres was due to a system replacement

and is understood, there is also some indication of an elevated muon rate around 650-700 metres which may reflect incorrect modelling of the overburden close to the tunnel portal. However, of particular interest is the deviation in the data around 80 metres, which is illustrated in greater detail in Figure 4.

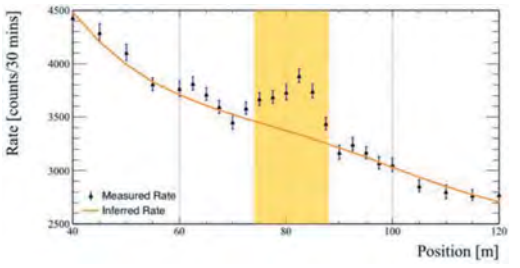

Figure 4. Data from the suspected hidden shaft region.

The elevated muon rate in this region is indicative of a hidden shaft. When reported back to Network Rail it was confirmed that there is a suspected hidden shaft in the area - information that wasn't provided to the Geoptic team prior to reporting the results of the field trial. Having identified a hidden shaft Geoptic were subsequently contracted to take further measurements around this point. The results from this second study are depicted in Figure 5 which indicates that the hidden shaft is centred at the tunnel crown with a diameter of approximately 3.5 metres, the data also indicates that the overburden of the shaft is equivalent to 1 metre of standard density rock (5 metres of rock at 1 standard deviation), which suggests that the feature is highly likely to be a hidden shaft with minimal backfill material.

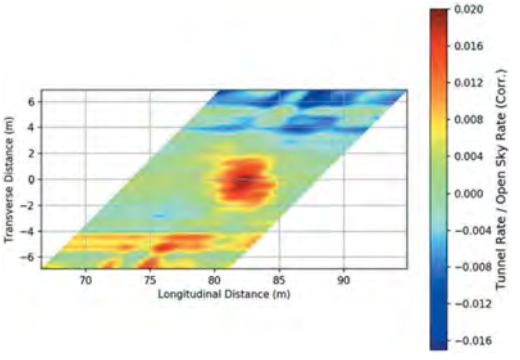

Figure 5. Visualisation of the hidden void in the Alfreton tunnel.

This case study ably demonstrates the potential for muon tomography not only to identify objects of interest but to characterise them also. Muon tomography is also capable of monger-term monitoring of a region of interest to determine, for example, if water ingress is taking place since this would result in density changes that the muon sensors would detect.

4 INSTRUMENTATION AND DATA VISUALISATION

Since this initial project with Network Rail, Geoptic has been contracted to perform studies of many other tunnels across the UK. In total over the past year, we have spent more than 120 days or nights in tunnels performing imaging surveys using muon tomography. These programmes of work have resulted in improvements to instrumentation and also a more refined data analysis and reporting system.

Figure 6. Image of two muon systems on railway tracks.

In terms of instrumentation, as depicted in Figure 6 above, Geoptic has developed a ruggedised IP68 TRL9 system that can be deployed directly onto a Permaquip trolley and rolled into a rail tunnel. In addition to the above, borehole instrumentation is also available.

Since the initial body of work at Alfreton, Geoptic's software techniques - used both in the initial stages of any tunnel visualisation project to educate measurement times, and in the data-processing phase of any project - have undergone considerable refinements and improvements. This is exemplified in Figure 7 which illustrates results from a recent tunnel campaign where a number of features were identified and visualised. Figure 7 is a 2D slide through a 3D image of the area of interest.

5 OTHER TUNNELLING APPLICATIONS

To date, from a civil engineering perspective, Geoptic has applied the muon tomography

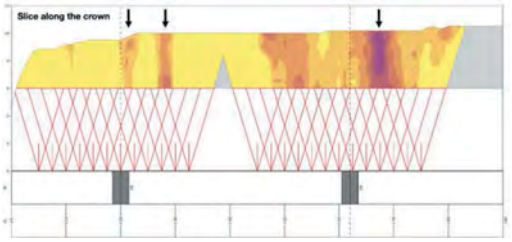

Figure 7. 2D slice through a 3D tunnel overburden density reconstruction.

technique to the location and characterisation of hidden shafts in the UK's railway infrastructure. However, it is clear that a non-invasive imaging tool such as this has many applications in the broader engineering sector and, indeed, studies into applications such as the use of muon tomography for safety and safeguarding in the nuclear waste sector are underway. In the context of the World Tunnel Congress we see applications in areas such as: TBM look ahead, long-term monitoring of voids post detection, structural evaluation of viaducts and bridges, detection and delineation of underground mine workings adjacent to rail lines (using the borehole sensors mentioned in Section 4), identification of geological voids, sinkhole detection and monitoring, determination and evaluation of hydrological conditions.

6 SUMMARY

Muon tomography is a powerful non-invasive imaging technique capable of returning detail on density changes in an overburden without the need to make contact with the object of interest. Geoptic has successfully pioneered the application of muon tomography to the identification and characterisation of hidden shafts and voids in railway tunnels on the UK's rail network. A number of other potential applications are outlined.

REFERENCES

E.P. George, 1955. "Cosmic rays measure overburden of tunnel", Commonwealth Engineer 455.

G. Liu et al. (2023). High-precision muography in archaeogeophysics: A case study on Xi'an defensive walls. Journal of Applied Physics. Vol. 133, January 7, 2023. doi: 10.1063/5.0123337.

International Atomic Energy Agency, 2022. Muon Imaging Present Status and Emerging Applications, IAEA-Tecdoc-2012.

Morishima, K., Kuno, M., Nishio, A. et al., 2017. "Discovery of a big void in Khufu's Pyramid by observation of cosmic-ray muons. Nature 552, 386–390. http://dx.doi.org/10.1038/nature24647

Tanaka, H., Kusagaya, T. & Shinohara, H., 2014. Radiographic visualization of magma dynamics in an erupting volcano. Nat. Commun 5, 3381. http://dx.doi.org/10.1038/ncomms4381.

L. F. Thompson, et al., 2020. "Muon tomography for railway tunnel imaging", Phys. Rev. Research 2, 023017

Tunnelling for a Better Life – Yan, Celestino, Thewes & Eberhardt (Eds)
© 2024 The Author(s), ISBN 978-1-032-80042-4
Open Access: www.taylorfrancis.com, CC BY-NC-ND 4.0 license

Empirical correlations between ground's mechanical properties and I-system

Chiraag Upadhye* & Sandeep Potnis
MIT World Peace University, India

Bineshian Hoss
Amberg Engineering AG, Australia

ABSTRACT: Design procedure for underground structures, particularly tunnels, relies on engineering classifications as a significant part of empirical and observational approach. Every system, technique, or method has specific scope and limitations due to the vast complexity of natural and physical characteristics of ground i.e., soil mass, rock mass or mixed ground. The Index of Ground-Structure abbreviated as I-System is a comprehensive approach for the classification and characterization of ground. It provides recommendations for support systems, excavation techniques, instrumentation techniques, prevention techniques, forecasting techniques, and design considerations. Using I-system, hundred number of cases are computed. It involves data collection for project located in Indian subcontinent in the Himalayas to evaluate parameters such as the Armature Index, Configuration Index, Hydro Index, Properties Index, Strength Index, Dynamic Forces Impact, and Excavation Technique Impact. This data is computed using I-System Software to obtain ground characterization parameters. Parametric study of the equations of the (I)-GC parameters is interpreted by regression analysis. The results obtained from I-system are compared with Geo-mechanical properties derived from the lab test results on samples. This analysis leads to improve the accuracy of the existing correlations.

Keywords: I-System, (I)-GC, Geomechanical Properties, Regression Analysis

1 INTRODUCTION

Mega projects such as tunnel construction involves number of activities, which are to be carried out at various stages of project. While infrastructure projects like tunnels are proposed, a Detailed Project Report is prepared to check its feasibility. Numerous investigations are conducted to analyse the ground i.e., the medium through which tunnels are constructed. Also, additional geological as well as geotechnical investigations are carried out in the further stages of the project. All this process is performed with the sole purpose of defining the ground in terms of its properties, strength, and character.

For the same reason there has been a development of rock mass classification such as RQD, RMR, Q, and most recently I-System (Bineshian, 2019, 2021). These systems particularly RMR, Q, and I-System include information on strength of the intact rock material, the condition of discontinuities, the orientation and frequency of discontinuities, the influence of subsurface groundwater. All these systems are based on the empirical approach and were primarily developed for classification of ground and estimation of supports for the underground structures; however, I-System unlike other systems is applicable for underground, semi-surface, and surface structures in rock and soil providing classification as well as characterisation of ground.

2 I-SYSTEM – A BRIEF OVERVIEW

The "Index of Ground-Structure" or I-System (Bineshian, 2019, 2021) is a comprehensive classification and characterization system for ground (rock and soil). It differs conceptually from other classifications due to its applicability to a wide range of ground conditions and structures, as well as its comprehensiveness in providing accurate and precise prediction of ground behaviour based on several geomechanical hazards (failure mechanisms) studied during development.

Its design and practice range includes underground structures (caverns, deep or underground metro

*Corresponding author: sharmachiraag98@gmail.com

DOI: 10.1201/9781003495505-85

stations, exploration and grouting galleries, mine stopes, shafts, tunnels of any type or method, underground spaces, underground storages, wells, and so on), semi-surface structures, and surface structures. It is the first classification that takes into account the problematical and structural configurations of the ground, the scale effect of openings, the negative effect of earthquakes, and the influence of excavation techniques (Bineshian, 2021). Furthermore, it is the first classification that carefully predicts special ground behaviour such as Squeezing, Swelling, and Heaving (SSH), Time Dependent (TD), Viscoelastic Plastic (VP), fully plastic, gravity driven (GD), and Burst Prone (BP) condition.

2.1 *I -System input data*

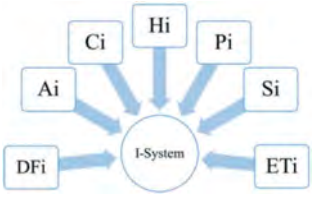

Figure 1. I-System's indices and impact factors.

I-System contain important indices that will allow for comprehensive modelling of ground-structure behaviour. It has five indices that define the mechanical response of ground to the structure. It also contains two impact variables that characterise the influence of Dynamic Forces (DF_i) and Excavation Technique (ET_i) on structure. In I-System Figure 1 indices and impact factors are based on easily derivable main properties (i.e., key geomechanical, geostructural, geohydrological, geotechnical, geophysical, and geometrical features) and determinant seismic and excavation factors affecting ground-structure response. Eq 1 depicts I-System mathematically as "(I)". The indices and impact factors for (I) are defined in Eq 2 to 8 as follows:

$$(I) = (A_i + C_i + H_i + P_i + S_i) \times DF_i \times ET_i \quad (1)$$

$$A_i = (a_{dn} + a_{ds} + a_{di}) \times a_{da} \times a_{dd} \times a_{df} \times a_{dp} \quad (2)$$

$$C_i = C_{pc} \times C_{sc} \quad (3)$$

$$H_i = h_{gc} \times h_{gs} \quad (4)$$

$$P_i = \left[p_{cc} + p_{dc} + \left(p_{ps} \times p_{pm}\right)\right] \times p_{bw} \,\&\, p_{bw} = f(V_p, V_s) \quad (5)$$

$$S_i = S_{cs} \times S_{se} \quad (6)$$

$$DF_i = f(PGA_{SD}, ERZ, MSK) \,\&\, PGA_{SD} = f(PGA, SF, MSF) \quad (7)$$

$$ET_i = f(ET, PPV) \quad (8)$$

2.2 *I-System's value*

I-System value ranges from 0 to 100 and categorizes the ground-structure interaction into ten classes as (I)-01 to (I)-10, from worst to Best. The indices A_i, C_i, H_i, P_i, and S_i account for 20% of the overall score of 100. (DF_i) and (ET_i) are variables with values ranging from 1 to 0.75 and 1 to 0.50, respectively, that influence the sum of indices Figure 2.

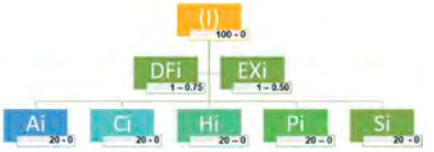

Figure 2. I-System's indices and impact factors.

I-System is distinctive due to its outputs that is (I)-Class and (I)-GC Figure 3

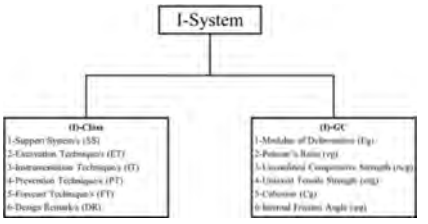

Figure 3. I-System's classification output.

2.3 *(I)-GC; I-System's ground characterization*

I-System's Ground Characterisation abbreviated as "(I)-GC" characterises the mechanical properties of ground (rock or soil mass) by evaluating most important ground properties including Modulus of Deformation (E_g), Poisson's Ratio (ν_g), Unconfined Compressive Strength (σ_{cg}), Uniaxial Tensile Strength (σ_{tg}), Cohesion (C_g), and Internal Friction Angle (ϕ_g). Quantified values provided as output of (I)-GC are estimations based on empirical correlations. (I)-GC's output provides most important input values required in design approach and procedure for underground structures. These empirical equations are developed and examined by author for several cases.

$$Eg = e^{0.05\times(I)} - 1 \quad (9)$$

$$\nu g = 0.5 - 0.004 \times (I) \quad (10)$$

$$\sigma cg = 0.007 \times \sigma c \times e^{0.05\times(I)} \quad (11)$$

$$\sigma tg = -\sigma cg \times e^{(0.04\times(I)-4)} \quad (12)$$

$$Cg = 0.002 \times \sigma cg \times e^{0.05\times(I)} \quad (13)$$

$$\Phi g = 15 + 0.55 \times (I) \quad (14)$$

This study improvises the accuracy of the (I)-GC's parameters and adopts specific methodology. The Parameters include three Geo-mechanical properties of the ground as follows:

i. Modulus of Deformation of the ground (E_g),
ii. Cohesion of the ground (C_g), and
iii. Internal Friction Angle of the ground (φ_g).

The author of I-System mentioned in his study that the empirical equations which are developed are examined by author for several cases. However, the author stated that the accuracy of these empirical equations may be improvised for better results. As any empirical study depends on the frequency and variety of the cases, the more they are the better results shall be obtained. Assessing the point, the paper focuses to improve the accuracy of the results of the following ground properties.

3 DATA COLLECTION

The USBRL-T01 (Udhampur Srinagar Baramulla Rail Line Tunnel-01) Project is one of the most critical tunnel projects in India where currently I-System is being implemented and hence was selected for the data collection. The T01 Tunnel has two portals viz. P1 and P2. Portal P1 is located at the start of the project i.e., towards Udhampur side and portal P2 on the other side. The overview of the project is described in Section 2.1.

A unique set of procedure is developed to execute the research in this research. Initially, a thorough study to understand I-System's definition, structure, chronology and procedure is accomplished. A framework of process shown in Figure 4 is planned in order to compare the results of I-System and the actual results of the on-site data of the ground properties collected from the reference documents of the project.

For the derivation of the I-Value, the inputs parameters in terms of five indices and two impacting factors are decided based on the actual ground condition. The Table 1 below shows different documents referred for deriving inputs of indices.

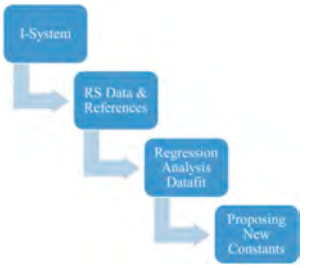

Figure 4. Framework.

Table 1. References for input parameters.

Indices	**References**
Armature Index (A_i)	Geo-logical Face Maps
Configuration Index (C_i)	Geo-logical Face Maps/Consultancy Report
Hydro Index (H_i)	Geo-logical Face Maps
Properties Index (P_i)	Physical Ground Inspection/Geophysical Investigation Report/ Standard References
Strength Index (S_i)	Geo-logical Face Maps and Tunnel Cross Section Drawings
Impacting Factors	**References**
Excavation Technique Impact (ET_i)	Geo-logical Face Maps/Refer Table
Dynamic Forces Impact (DF_i)	IS 1893-1 (2002)/Refer Table

3.1 *USBRL – T01*

Tunnel T01 is an important segment of the Udhampur - Srinagar - Baramulla Railway Project (USBRLP) as Indian Railways 'most challenging project. USBRLP with 326 km railway line will provide an alternative and a reliable transportation system to union territory of Jammu and Kashmir (J & K) with the Indian Railway network from Jammu to Baramulla. It has been declared as a project of national importance and the largest project in the construction of a mountain railway since independence of India. It passes through the young Himalayas with tectonized zones including major thrust faults. The client for USBRLP project is Northern Railway (NR) and the project is in the last stage of progress in the balance length from Katra to Banihal.

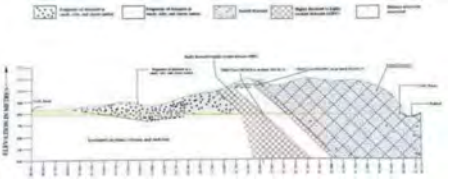

Figure 5. Longitudinal tunnel profile T01.

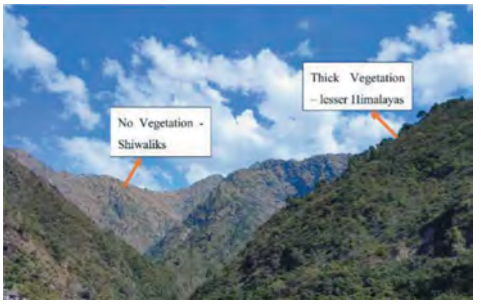

Figure 6. USBRL T01 regional topography.

Tunnel T01 includes a single tube tunnel as critical part of the project that has been assigned to Konkan Railway Corporation Limited (KRCL). T01 is crossing the Reasi Thrust (RT) at its 336 m length between CH31804 to CH32140. RT is part of Main Boundary Thrust (MBT) of lower Himalayas. MBT is an active fault zone as one of the major Himalayan thrusts, which is incorporated within the Himalayan over - critical thrust wedge. It is displaced above the Indian lithosphere. The displacement is along the most of MBT's length. T01 with 3209 m length is the most challenging and hazardous tunnel in USBRLP with portal one (P1) chainage at CH29950 and portal two (P2) chainage at CH33159. T01 along its length, crosses through claystone, dolomite, limestone, mudstone, sandstone, shale, siltstone, and scree, alluvium, and colluvium materials in a clayey and silty matrix. Claystone, mudstone, sandstone, shale, and siltstone in T01 contains mica family minerals including muscovite.

Figure 7. T01 P2 tunnel face.

They mechanically deform non - uniformly, which resulting in convergence as a proof of squeezing behaviour.

Figure 8. Crushed dolomite mixed with PU-2C grout.

The construction work of the tunnel T01 is in progress from both the ends. From Km 30/000 to 31/822 rock mass strata is interbedded Sandstone and clay stone after that 31/768 to up-to face is highly fractured and crushed dolomite. From km 33/159 (T1P2) in the initial stretch, the rock mass strata are represented by highly jointed and fractured greyish/whitish cherty dolomite up to km 32/159. After these strata got deteoraited represented by highly sheared greyish/whitish cherty dolomite When the excavation reached at Chainage 32/140 on 28 August 2016 first collapse occurred with huge flow of water along with material of sheared rock mass. Part of face at this Chainage towards left side had intact rock mass and highly sheared and fractured rock mass in the centre and towards the right side of the face. Probably this was the beginning of the shear zone. Approximately 5000 cum material along with water moved towards portal from the face.

Figure 9. Face butt at T01 P1 tunnel face.

During the excavation from both P1 and P2 end some minor over-break/small cavity have been

recorded in face logs after each round length at various locations and some major failure/large cavity/ collapses have also been recorded at both the ends.

3.2 *Creation of data pair*

The Data pairs created for the USBRL T01 project are abbreviated as **TDP** (T01 Data Pairs). A total of 100 number of cases are selected for computation and analysed after purification of the data pairs. The next procedure is to obtain the values of the geomechanical properties of the corresponding chainages of 100 cases from the Geotechnical Investigation Report (GIR) and Geological Face Maps of the project which are Uniaxial compressive strength of Intact rock (UCS), Rock Quality Designation (RQD), Geological Strength Index (GSI), Hoek and Brown Constant (m_i), Disturbance Factor (D), Intact Modulus (E_i), Unit Weight (Υ_{rm}).

3.3 *Purification of data pair*

A total of 100 cases of TDP data pairs were plotted in a scatter plot between (I)-Value vs geomechanical property. The plot highlighted the data pairs not following the trend. As per the principles of rock mechanics the value of geomechanical property included in this study that are (Eg, Cg, ϕg) shall always increase with increase in strength of the ground. This means that the values of these geomechanical properties should increase/decrease with increase/ decrease in (I)-Value.

Based on such conditions a purification technique was applied to eliminate the data pairs.

i. The data pairs representing lower value than the previous data pair were eliminated in an increasing trend and vice versa if necessary.
ii. The data pairs far away from the trend were eliminated.
iii. For the data pairs showing different Y values for same X values, the Data pairs obtaining better Coefficient of Multiple Determination (R^2) value were selected.

4 COMPUTATION OF DATA PAIRS

4.1 *Evaluation of data pairs for modulus of deformation of the ground (Eg)*

The Data pairs created for the USBRL T01 project are abbreviated as TDP (T01 Data Pairs). A total of 100 number of cases are selected for computation and are analysed after purification of the data pairs.

The Figure 10 is the window of I-System's Software in which the input parameters are seen for the underground structure. The window also has options to refer to the nomenclature for better understanding and be confusion free while selecting the input

Figure 10. I-system's software input window for representation.

parameters. Once all the inputs are checked as accepted by the user the compute button will become active. By clicking on the compute button, the window of computation will be generated by the software as shown in Figure 11

Figure 11. I-system's software output window for representation.

I-System's software calculates the values of six geomechanical properties as shown in the Table 2 which is the report generated by the software. It also plots the graphs for whole range of I-Value i.e., from (0-100) as described in Figure 12 defined by the original Eq. 9 - 14

To derive the actual rockmass parameters of the site, RSData Software by Rocscience which is based on Generalized Hoek and Brown Failure Criterion is used.

Table 2. Input and output parameters for RS Data.

Input Parameters	Output Parameters
Material type	Tensile strength (MPa)
Intact Modulus (MPa)	Uniaxial Compressive strength (MPa)
UCS of Intact rock (MPa)	Modulus of Deformation (GPa)
GSI	Cohesion (MPa)
(Hoek and Brown constant) mi	
Disturbance Factor (D)	

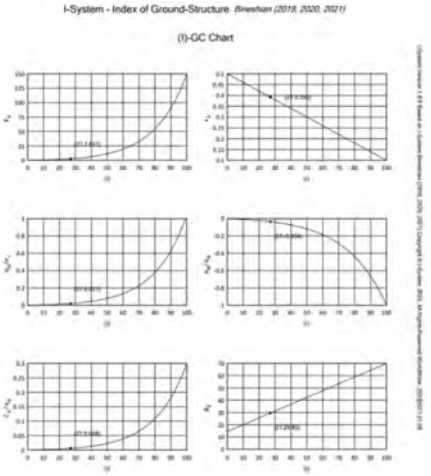

Figure 12. I-system's software I-(GC) graphs for representation.

The data pairs are in the form of (X, Y) where X represents the (I)-Value and Y represents Modulus of Deformation of the ground (Eg).

The range of X i.e. (I)-Value varies from (20-40).

The range of Y i.e. Modulus of Deformation of the ground (Eg) varies from (1.0 - 5.0 GPa). The TDP data pairs are sorted as per the ascending (I)-Value.

Table 3. TDP Data Pair Summary.

Modulus of Deformation of the ground Eg TDP Summary			
(I)-Value	Eg (GPa) I-System	Eg (GPa) RS Data	Total Data Pairs
24	2.320	1.204	1
26	2.669	2.409	13
27	2.857	1.204	19
27	2.857	3.392	6
27	2.857	4.752	2
30	3.482	3.392	5
30	3.482	4.752	47
Total Data Pairs			100

The Table 3 summarizes total case count of 100 cases for the Modulus of Deformation of the ground (E_g) based on the (I)-Value and sorted as purified and un-purified in black and red colour respectively. Out of 100 cases 39 cases were eliminated and 61 cases were selected for regression analysis with maximum coefficient of multiple determination value (R^2) as 0.999

4.2 *Evaluation of data pairs for cohesion of the ground (C_g)*

The initial chainages of the USBRL project were constructed with conventional as well as NATM methods. Both the methods produced numerous failures and collapsed for several times. Due to termination of various agencies, the project has insufficient data for evaluation of Cohesion of the ground from the site and hence a modification or correlation cannot be established using the TDP data pairs. Though the need to modify the original equation due to ultra conservative output by the (I)-GC for the Cohesion of the ground (C_g) expressed by Eq. 15 is assessed.

To propose the modification to improve the accuracy of the original equation of Cohesion of the ground (C_g), the source data presented in Table 4 has been obtained from the standard reference notes and geotechnical references.

Table 4. Reference data for cohesion of the ground.

(I)-Value	(I)-Class	Cohesion C_g (KPa)
100 – 91	(I) - 01	1101 – 1350 or greater
90 – 81	(I) - 02	876 – 1100
80 – 71	(I) - 03	676 – 875
70 – 61	(I) - 04	501 – 675
60 – 51	(I) - 05	351 – 500
50 – 41	(I) - 06	226 – 350
40 – 31	(I) - 07	126 – 225
30 – 21	(I) - 08	76 – 125
20 – 11	(I) - 09	51 – 75
10 – 0	(I) - 10	25 – 50 or lesser

The data pairs for performing regression analysis are formed using the data presented in the Table 4. The data pairs are in the form of (X, Y) where X represents the mean (I)-Value of the range presented in the Table 5 and Y represents the mean value of the Cohesion of the ground (Cg) in KPa. The range of X i.e. (I)-Value varies from (0-100). The range of Y i.e., Cohesion of the ground (Cg) varies from (25.0 - 1350.0) KPa.

Table 5. Data pairs for cohesion of the ground.

(I)-Value X	Cohesion of the ground C_g (KPa) Y
95.50	1225.50
85.50	988.00
75.50	775.50
65.50	588.00
55.50	425.50
45.50	225.50
35.50	175.50
25.50	100.50
15.50	63.00
5.00	37.50

4.3 *Evaluation of data pairs for friction angle of the ground (°)*

The original Equation of the (I)-GC for the Friction angle of the ground has produced very accurate and precise results when compared with the actual value of the geotechnical references. Hence, after the thorough assessment and the analysis of the results the original equation and the constants are kept same represented in the Eq. 17

$$\Phi g = 15 + 0.55 \times (I) \quad (17)$$

The data pairs for performing regression analysis are formed using the data presented in the Table 4. The data pairs are in the form of (X, Y) where X represents the mean (I)-Value and Y represents Friction angle of the ground (ϕ_g) in degrees. The range of X i.e. (I)-Value varies from (0-100). The range of Y i.e., Cohesion of the ground (C_g) varies from (15°-70°).

Table 6. Data Pairs for Friction angle of the ground.

(I)-Value X	Friction angle of the ground ϕ_g (°) Y
100	70.00
90	64.50
380	59.00
70	53.50
60	48.00
50	42.50
40	37.00
30	31.50
20	26.00
10	20.50
0	15.00

5 ANALYSIS AND RESULTS

In this study, DataFit 9.1 software is used to perform data plotting, regression analysis and statistical analysis. It is a science and engineering tool that simplifies the tasks of data plotting, regression analysis (curve fitting) and statistical analysis. It reports the general as well as statistical information about each solved regression model automatically.

Plotting of Scatter Data using DataFit 9.1software

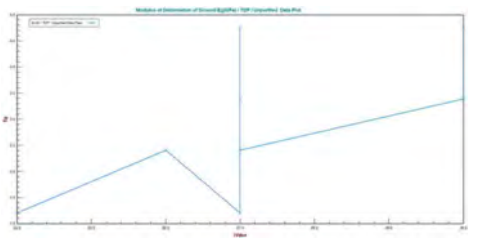

Figure 13. Scatter data plot for Eg Unpurified data pairs.

The next process after formation of the Data Pairs viz. TDP was the sorting and plotting of the of the Scatter Data as shown in the Figure 4 for the Modulus of Deformation (Eg). The Scatter Data plot highlights the need to for the purification of the data pairs. As some TDP data pairs do not follow the trend are tending to create diversion of the relation. The purification of TDP data pairs is executed as per the conditions mention in section. 2.3.

5.1 *Regression analysis of TDP data pairs for modulus of deformation of the ground (E_g)*

The regression analysis performed using DataFit 9.1 software has yielded that in the range of (I)-Value (24 - 27) corresponding to (I)-Class - 03 which represents poor ground conditions, the value derived from the RS Data software represented by red colour plot in Figure 14 for the Modulus of Deformation of the ground is representing conservative value than the result derive from the original (I)-GC's Equation of (Eg), represented by black colour plot in Figure 14. The original and new constants are described in the Table 7 derived as the result of the regression analysis performed using Non-linear Model in the form of exponential curve.

Table 7. Equation details for Eg.

Eg-Modulus of the Deformation of the ground (GPa)							Y=Exp (a*x)-b
			Original Constant		Proposed New Constant		
Sr. No.	Data Pair	Case Count	a	b	a	b	R^2 Value
1	TDP	61	0.05	1.00	0.07	4.50	0.999

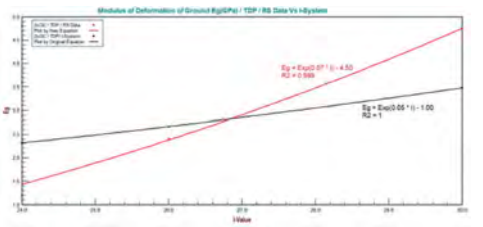

Figure 14. New equation Vs original equation plot for Eg.

5.2 *Regression analysis of data pairs for cohesion of the ground (Cg)*

The regression analysis performed on the data pairs described in Table 8 using Non-linear Model in the

form of exponential curve plotted in red colour shown in Figure 15.

Table 8. Equation details for Cg.

Cg-Cohesion of the ground (KPa)							Y=Exp (a*x)*b
			Original Constant		Proposed New Constant		
Sr. No.	Data Pair	Case Count	a	b	a	b	R^2 Value
1	Ref	10	0.05	0.002	0.03	73.0	0.981

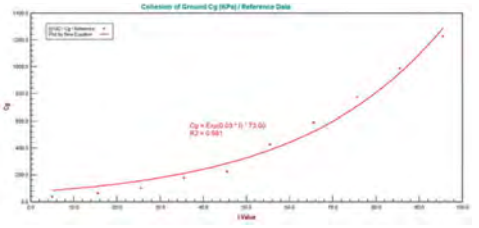

Figure 15. New equation Plot for Cg.

5.3 *Regression analysis of data pairs for friction angle of the ground (ϕg)*

The regression analysis performed on the data pairs described in Table 9 using linear Model and plotted in black colour shown in Figure 16.

Table 9. Equation details for ϕg.

Cg-Cohesion of the ground (KPa)					Y=Exp (a*x)*b
			Original Constant		
Sr. No.	Data Pair	Case Count	a	b	R^2 Value
1	TDP	11	0.55	15.00	1.00

6 CONCLUSION OF THE STUDY

6.1 *Deriving new constant*

The original equations of the (I)-GC's properties in I-System are in exponential as well as linear form mentioned in the **Eq. (18-20).**

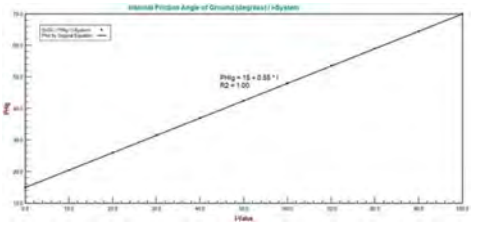

Figure 16. Original equation plot for ϕg.

Table 10. Statistical summary of the analysis.

Sr. No.	Properties	Constants a	b	Coefficient of Multiple Determination (R^2)
1.	Modulus of Deformation of the ground (E_g)	0.07	4.50	0.999
2.	Cohesion of the ground (C_g)	0.03	73.00	0.981
3.	Friction angle of the ground (ϕ_g)	0.55	15.00	1.00

$$Eg = e^{0.05\times(I)} - 1 \quad (18)$$

$$Cg = 0.002 \times \sigma cg \times e^{0.05\times(I)} \quad (19)$$

$$\Phi g = 15 + 0.55 \times (I) \quad (20)$$

After the thorough analysis and its interpretation, the New Equation for the (I)-GC's Modulus of Deformation of the ground (E_g) proposed for the (I)-Value ranging between 20-40 is

$$Eg = e^{0.07\times(I)} - 4.50 \quad (21)$$

After the thorough analysis and its interpretation, the New Equation for the (I)-GC's Cohesion of the ground (C_g) proposed for the (I)-Value ranging between 0-100 is

$$Cg = e^{0.03\times(I)} \times 73.00 \quad (22)$$

After the thorough analysis and its interpretation, the Original Equation for the (I)-GC's Internal Friction Angle of the ground (ϕ_g) proposed to keep same for the (I)-Value ranging between 0-100 is

$$\Phi g = 15 + 0.55 \times (I) \quad (23)$$

ACKNOWLEDGMENTS

Expressing my sincere gratitude to inventor of I-System, Dr Bineshian Hoss and all his team of USBRL T01 for their immense support and guidance. Also thanking Dr Sandeep Potnis for his continuous guidance and strong support. Lastly to my colleague Mr Karan Lakhlani for being together in this journey.

REFERENCES

AFTES, Recommendations on the Convergence-Confinement Method. Versión 1. AFTES, Paris. 1984. Austrian Society for Geomechanics, Guideline for the Geotechnical Design of Underground Structures

Bineshian, H. SRH System-Stress Release Hole/s A substitution to conventional yield support system.

Bineshian, H. (2022). (I)-TM: I-System's Tunnelling Method-An Introduction (Vol. 11, Issue 1).

Bineshian, H. (2021a). Chronology of Development of I-System A Brief History. In Journal of Engineering Geo-logy: Vol. XLVI (Issue A).

Bineshian, H. (2021b). Ground Characterisation for Design using I-System Software Case Studies. In Journal of Engineering Geo-logy: Vol. XLVI (Issue A).

Bineshian, H. (2021c). I-System: Index of Ground-Structure. In Journal of Engineering Geo-logy: Vol. XLVI (Issue A).

Bineshian, H. (2021d). Vibration-induced Damage Assessment New Practical Methods Applicable for Engineered Blasting InfraBlast CommBlast Commercial Blasting near commercial area ManDigg Manual Digging (small scale excavation without use of explosives or NonEx-Break) (Vol. 10, Issue 1).

Bineshian, H, Rasouli, V, Ghazvinian, A (2013). 'Proposed constants for Bieniawski's strength criterion for rocks and coal', IJRSG, 2 (3): 12–21.

Bineshian, H., Ghazvinian, A., Bineshian, Z. (2012). Comprehensive compressive-tensile strength criterion for intact rock. Journal of Rock Mechanics and Geo-Technical Engineering, 4(2), 140–148.

Carranza-Torres, C (2004). 'Elasto-plastic solution of tunnel problems using the generalized form of the Hoek-Brown failure criterion', Int J Rock Mech Min Sci 41 (Suppl 1): 629–639.

Choudhary, K., Bineshian, H., Dickmann, T., Gupta, S., Hegde, R. K. (2021) Long Range Underground Prediction of Ground Behaviour/Hazards at Tunnel T13 in USBRL Project using TSP. Journal of Engineering Geology, 46(1).

CRC Press 13: 978-0-8153-8662-9, 2020. Ground Characterization and Structural Analyses for Tunnel Design. CRC Press Taylor and Francis Group, Boca Raton, FL.

Duddeck, H. (1988), "Guidelines for the Design of Tunnels", ITA Working Group on General Approaches to the Design of Tunnels, Tunnelling and Underground Space Technology. Vol. 3. No. 3.

Hoek, E., Diederichs, M. S. (2006). Empirical estimation of rock mass modulus. International Journal of Rock Mechanics and Mining Sciences, 43(2), 203–215. ijrmms. 2005.06.005

Hoek, E., Carranza-Torres, C., Corkum, B. (2002), "Hoek-Brown failure criterion, 2002 edition", Proceedings of the 5th North American Rock Mechanics Symposium. Toronto, Canada.

Hoek, E., Brown, E.T. (1997), "Practical estimates of rock mass strength", International Journal of Rock Mechanics and Mining Sciences. Vol. 34. No. 8., pp. 1165–1186.

Palmström, A., Singh, R. (2001). "The Deformation Modulus of Rock Masses" comparisons between in situ tests and indirect estimates (Vol. 16, Issue 3).

Tunnelling for a Better Life – Yan, Celestino, Thewes & Eberhardt (Eds)
© 2024 The Author(s), ISBN 978-1-032-80042-4
Open Access: www.taylorfrancis.com, CC BY-NC-ND 4.0 license

Research on key technology of design of long tunnel in water-rich karst platform of compound syncline basin*

Hailin Wang & Muqun Wang
Hunan Provincial Communications Planning, Survey & Design Institute Co., Ltd, Changsha, China

Helin Fu
School of Civil Engineering, Central South University, Changsha, China

Pin Li & Ziyu Li
Hunan Provincial Communications Planning, Survey & Design Institute Co., Ltd, Changsha, China

ABSTRACT: In order to solve the design problem of the long tunnel of the water-rich karst platform in the compound syncline basin, the long tunnel with strong karst development – Yuanguping Tunnel is taken as an engineering example, the karst hydrogeology and surrounding environment topography and geomorphology are fully verified, and the comprehensive treatment of the karst in Yuanguping Tunnel is carried out for a long time by the method of engineering analogy, so as to ensure the safety of the tunnel construction and operation. The key design technologies are as follows: (1) The key design technologies such as drainage tunnel, drainage branch tunnel and grouting water plugging are adopted to solve the water gushing problem of the karst tunnel; (2) Drainage tunnels are set on both sides of the tunnels to solve the problem of groundwater backfilling tunnels in Huangyuxi Reservoir and Baiyangping Depression; (3) Combined construction of flue and drainage tunnel is adopted, with the upper layer as the smoke drainage area and the lower layer as the water drainage area to solve the problem of disaster prevention and smoke drainage in the long tunnel. The design case of this paper can be used as a reference for similar tunnels.

Keywords: Syncline, Karst, Rich water, Drainage tunnel, Back irrigation

1 INTRODUCTION

Karst is one of the common diseases when building highway tunnels in limestone areas. Its surface morphology is mainly characterized by solution cracks, solution grooves, sinkholes, and corroded depressions, and locally, there are karst funnels, skylights, shafts, karst trough valleys, and compound development of different karst forms. The development forms of underground karst are mainly joint fissures, dissolution, karst fissures, karst caves and karst water passages. The degree of karst development is controlled by lithology, folds, faults, groundwater and topography. It can be divided into three grades: strong, medium and weak. At present, the karst development grade of highway karst tunnels built in China is mostly weak or medium, the design treatment cost is not high, and the treatment measures are relatively mature (Zhao et al., 2022, Li et al., 2020, Wu et al., 2021). For tunnels with large karst bodies and strong karst development in general, there is still a lack of experience in engineering treatment. At present, a lot of research has been carried out on the problem of karst in the industry, mainly focusing on the advanced prediction of single karst (Zhang et al., 2020, Cheng, 2020, Yan, 2021, Zhou et al., 2017) and the treatment measures of karst (Zhu and Zhu, 2021, Guan and Yang, 2018, Wang et al., 2020, Jiang and Zhang, 2022). However, there are few research reports on the comprehensive treatment measures that are mainly karst and accompanied by other problems such as high pressure and rich water.

Yuanguping Tunnel of Zhangguan Expressway passes through Wuling Mountain area. The surrounding rock of the whole tunnel is mainly argillaceous limestone, and the overall karst development is very strong. In addition, the groundwater in the tunnel area is very rich, which is a high-pressure water-rich zone. The tunnel passes through 8 folds and 7 fault zones, and the geological conditions are very complicated. In summary, the Yuanguping Tunnel of Zhangguan Expressway faces many problems such as strong karst, high pressure and rich water, and complex geological

*Corresponding author: 253484901@qq.com

DOI: 10.1201/9781003495505-86

conditions. Its key design and treatment technology are worthy of reference for similar projects in the future.

2 ENGINEERING OVERVIEW AND RISK ANALYSIS

Yuanguping Tunnel is one of the control projects of Zhangjiajie-Guanzhuang Expressway. The highway belongs to the section of the national highway G59 Hohhot-Beihai Expressway. It is located in the northwest of Hunan Province and spans the Wuling Mountain area. The terrain is undulating and the geological conditions are complex. The tunnel is located at the junction of Yuanguping Town and Jinyan Tujia Township in Yongding District, Zhangjiajie City, Hunan Province. The entrance of the tunnel is located at 600 meters to the south of Quanjiayu in Jinyan Township, and the exit of the tunnel is located at about 150 meters to the northwest of Ganxiwan in Yuanguping Town. The Yuanguping Tunnel is arranged in a double-hole separated layout. The pile number of the left line is ZK14 + 178 ~ ZK19 + 329, with a length of 5151 m, and the pile number of the right line is K14 + 185 ~ K19 + 312, with a length of 5127 m. It is an extra-long tunnel with a longitudinal slope of 8 ‰ and a maximum burial depth of 423 m. The surrounding rock of the tunnel area is mainly argillaceous limestone. At present, the plane line of the tunnel is basically set along the groundwater watershed, and the amount of water is relatively small. And the tunnel line position is basically perpendicular to the direction of the maximum horizontal ground stress, which is conducive to tunnel support and surrounding rock stability, as shown in Figure 1. Although the route selection has been fully considered, the design and construction risk of Yuanguping Tunnel is still huge.

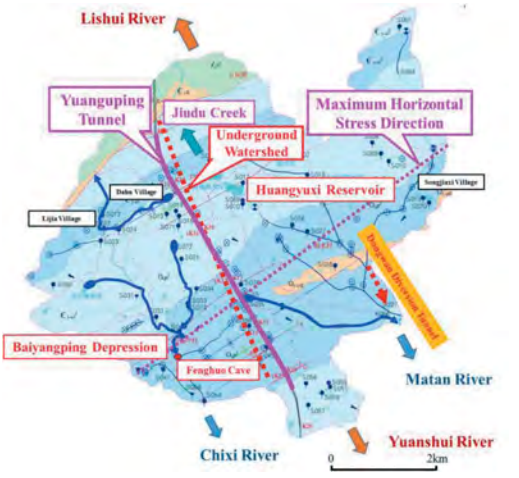

Figure 1. The plane of the tunnel.

2.1 *Topography*

The site of the tunnel is a medium-low mountain tectonic dissolution karst platform landform. The mountain is ridge-shaped, with some peak-shaped and hilly mountains, including micro-topography such as upland, karst, hills and flats. The mountain area accounts for more than 80 % of the total area. Various external dynamic geological processes denuded and accumulated the ground in the tunnel site area, forming an approximately flat uniform surface, which formed a relatively flat karst platform landform with steep cliffs around the top of the mountain, as shown in Figure 2. The surrounding rock of the whole tunnel is mainly argillaceous limestone, and the overall karst development is strong. The average line karst rate is 21.3 %, as shown in Figure 3.

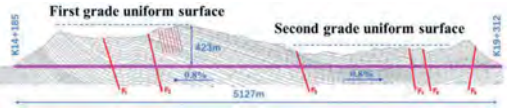

Figure 2. Karst terrace.

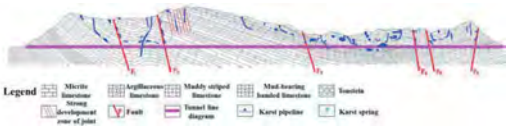

Figure 3. Strong karst.

2.2 *Compound syncline and large water inflow*

A total of 8 folds are developed in the Yuanguping Tunnel. Among them, the Guojiajie syncline (f23) is the largest, which is a regional controlled fold, and the rest are secondary folds, which are caused by the influence of locally developed fault structures, and the development scale is slightly smaller. Most of the area of the tunnel is located in a large composite syncline tectonic belt composed of several sub-level anticlines and synclines, as shown in Figure 4.

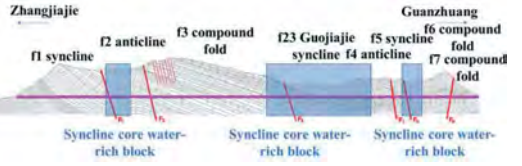

Figure 4. Compound syncline.

The water system of the working area belongs to the Yuanshui River system, a tributary of the Yangtze River. The main rivers are Quankou Creek (Gaojia Creek), Chixi River and Leigong Creek. Most of the rivers flow from northwest to southeast. Due to the wide distribution of carbonate rocks, the surface streams are mostly recharged by springs and underground river outlets, showing the characteristics of alternating distribution of open and ambush streams. Most of the tunnel site is in a water-rich area, and the surrounding surface has long-term running water. The slope catchment area is large, and the surface runoff dissipates quickly during rainfall. Most of the surface runoff flows into vertical karst pipelines such as karst funnels and sinkholes, and then discharges through horizontal karst pipelines. There is surface water in the depression ponds and gullies along the Dahu Village in the northwest of the working area. A small part of surface runoff, such as Mula River and Hanshui River, flows into Lishui River from southeast to northwest. Seasonal water flow exists on both sides of the tunnel and in the gullies at the foot of the slope at the inlet and outlet ends.

2.3 *Surface reservoirs and karst depressions*

In addition to the surface streams, the upper Huangyuxi Reservoir and the lower Huangyuxi Reservoir are located on the left side of the ZK15 + 150-890 section of the Yuanguping Tunnel, which is 0.6 km away from the left line of the tunnel entrance section. The reservoir capacity of the upper Huangyuxi Reservoir is 138,000 m^3, which is discharged through the lower Huangyuxi Reservoir. The reservoir capacity of the lower Huangyuxi Reservoir is 547,000 m^3. The two reservoirs are mainly irrigated and have benefits such as flood control and fish farming. The total irrigated area is 650 mu and approximately 450 people are protected. The F2 fault developed at ZK15 + 660 of tunnel strikes northeast and crosses Huangyuxi Reservoir and Yuanguping Tunnel. Geological survey shows that the fault bandwidth is 2-5 m. The influence bandwidth of the fault is tens of meters, and the rock mass on both sides is nearly vertical, and the rock mass in the zone is broken, and the joint fissures are developed. This zone is easy to become a water gushing channel for tunnels and reservoirs. The flood level of the upper Huangyuxi Reservoir is 804.74 m, which is discharged through the lower Huangyuxi Reservoir. The dam crest elevation of the lower Huangyuxi Reservoir is 788.65 m, and the flood level is 788.32 m. The design elevation of the tunnel is about 510 m, and the head difference is about 279 m, as shown in Figure 5 and Figure 6. The reservoir will pose a potential threat to the construction and later operation of the tunnel. Under the action of fault F2, the cracks generated by it will establish a hydraulic connection between the lower Huangyuxi Reservoir and the lower aquifer, which will increase the risk of water gushing in the tunnel.

Figure 5. Head height difference.

Figure 6. Huangyuxi Reservoir.

Figure 7. Baiyangping Depression.

Baiyangping Village on the southwest side of the K17 + 000-K18 + 00 section of the right line of the tunnel is the main catchment area of groundwater in the right area of the tunnel, as shown in Figure 7. The river is about 3km long, and there are many sinkholes, F3, F4 fault zones and joint cracks. Water flows into the river all the year round. The catchment depression area in Baiyangping Village is large. The lowest groundwater level elevation is 575m, about 1.5km from the right line of the tunnel. The design elevation of the tunnel is about 508m, and the water level difference is 67m.

2.4 *Risk analysis of Yuanguping Tunnel*

The tunnel stratum is dominated by carbonate rocks. The tunnel site area is a typical karst platform landform. The karst development is strong, and the possibility of hall-type karst caves is very large. It crosses the Guojiajie compound syncline water storage structure, and the groundwater in the core section of the syncline is rich and the pressure is large. The Yuanguping Tunnel is a water-rich karst platform tunnel with a compound syncline basin structure. The water-rich volume is huge, which is easy to cause mud and water inrush. The design and construction

risk is large, and the tunnel construction is extremely likely to expose karst pipeline water or underground river. The horizontal distance between the left line of the tunnel entrance and Huangyuxi Creek is about 780 m, and the head difference is 278 m, with high head pressure. The F2 fault developed at K15 + 660 on the left side of the tunnel entrance passes through the Huangyuxi Reservoir and Yuanguping Tunnel. The geological survey shows that the fault bandwidth is 2-5 m, and the influence bandwidth of the fault is tens of meters. The rock mass on both sides is nearly vertical, and the rock mass in the zone is broken, and the joints and fissures are developed. This zone is easy to become a water gushing channel between the tunnel and the reservoir. The reservoir water of Huangyuxi Reservoir is easy to flow backward along the fault zone, forming a major water gushing accident. The catchment depression area in Baiyangping Village on the right side of K17 + 000-K18 + 00 section of the tunnel exit is large, and the water volume increases sharply and the discharge is not smooth in the rainy season. Under natural conditions, because the tunnel is located in the underground watershed, the groundwater flows from the tunnel to both sides. However, after the tunnel excavation, the groundwater on both sides of the tunnel can pour into the tunnel along the groundwater pipeline, F3 and F4 fault zones and joint fissures, forming a huge water gushing in the tunnel. Yuanguping Tunnel should focus on solving the problem of high pressure and rich water; in addition, the length of Yuanguping Tunnel is more than 5000 m, so it is necessary to solve the problem of disaster prevention and smoke exhaust. In general, the main problems solved by Yuanguping extra-long tunnel are karst, high pressure and rich water, disaster prevention and smoke exhaust.

3 KEY DESIGN TECHNOLOGIES OF YUANGUPING EXTRA-LONG TUNNEL

3.1 *Treatment of karst water*

3.1.1 *Drainage tunnel*

The high-pressure water-rich tunnel structure can be directly subjected to high water pressure by anti-water pressure lining, or the high water head can be avoided by reducing the water head. The strong karst development section of Yuanguping Tunnel accounts for a high proportion of the total length of the tunnel, and through the syncline core, and the tunnel water inflow is 270,000 m^3/d. If the anti-water pressure lining structure is adopted, the tunnel structure will bear a high water head of 50-250 m. The cost of the anti-water pressure lining is shown in Table 1.

According to the head pressure of each section of Yuanguping Tunnel, if the anti-water pressure lining of 'mainly blocking' is adopted, the tunnel needs to be equipped with 800m long KSY-2.5 lining, 400m long KSY-2.0 lining, 1100m long KSY-1.5 lining and 1000m long KSY-0.7 lining. It is expected that the whole tunnel will increase the investment of 574 million yuan, and the economic and energy-saving benefits will be reduced. Moreover, there are many engineering cases of serious diseases or even structural damage after the completion of high-head tunnels at home and abroad. For example, the Yuanliangshan Tunnel of the Chongqing-Huaihua Railway adopts a lining structure with thickness of 1.2 m, and a double-layer rail is set inside to strengthen the

Table 1. Investment risk table of anti-water pressure lining.

Serial number	Lining name	Design head height	Secondary lining thickness	Single hole linear meter cost of the main structure (considering full head anti-water pressure lining during operation)	Estimate of single tunnel linear meter for surrounding rock reinforcement measures (encountered in the construction of high water pressure)	Single hole estimation extension index (lining + grouting)
1	KSY-0.7	70m	65/70cm	118000	——	118000
2	KSY-1.0	100m	75cm	153000	——	153000
3	KSY-1.5	150m	100cm	154000	3.5 m reinforcement ring 0.15 filling rate 34000 (radial grouting)	208000
4	KSY-2.0	200m	115cm	193000	4 m reinforcement ring 0.15 filling rate 40000 (radial grouting)	233000
5	KSY-2.5	250m	145cm	208000	4.5 m reinforcement ring 0.15 filling rate 48000 (radial grouting)	256000

stiffness of the tunnel structure, but the lining cracks and leaks seriously after completion. After the completion of Huayingshan Tunnel of Guanglin Expressway, a sudden mud gushing and water inrush accident occurred, resulting in the interruption of traffic in this direction of the tunnel. The Smart Tunnel in Malaysia passes through the karst area, and is closed after two years of operation due to structural damage. Hundreds of large-scale water and mud gushing occurred in the construction of the new Dabashan Tunnel on the second line of Xiangyu, which caused many shutdowns on site. Finally, a drainage tunnel was added to reduce the potential energy pressure and reduce the influence of high water head on the lining structure.

It can be seen that the risk of failure of the anti-water pressure lining structure is large, and the cost of anti-water pressure lining is high, so the economy of large-scale use in this project is unreasonable. It is proposed to adopt the scheme of "discharge-based and limited discharge." On the premise of not changing the regional hydrology, the hydrodynamic pressure of groundwater around the tunnel is reduced by parallel discharge tunnels, as shown in Figure 8. So as to solve the problem of water gushing (mud inrush) caused by uncovering karst pipelines or karst development sections in tunnel construction or insufficient drainage capacity of tunnel central ditch in the operation stage, so as to solve the problem of high pressure and rich water in Yuanguping Tunnel. Horizontal branch holes are set up in the strongly developed karst section to assist drainage, as shown in Figure 9.

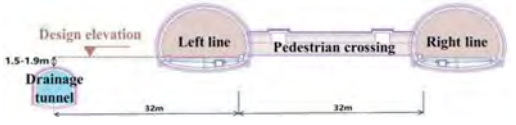

Figure 8. Drainage holes.

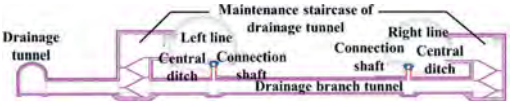

Figure 9. Drainage branch holes.

The transverse branch tunnel is set at the connection part between the discharge tunnel and the main tunnel. The discharge tunnel is connected to the main tunnel by the lower connection mode, which is perpendicular to the main tunnel and the discharge tunnel. The transverse branch tunnel is located below the inverted arch of the main tunnel, forming a separated interchange structure with the main tunnel. The central ditch of the main tunnel can be discharged into the transverse branch tunnel through the shaft, and the maintenance and repair of the discharge tunnel can enter the discharge tunnel from the ladder that perpendicularly intersects the main tunnel.

3.1.2 *Drainage tunnel size*

The control factors of the discharge tunnel section are as follows: ① The maximum drainage volume is determined according to the rainstorm condition of 270,000 square/d; ② The construction requirements of the discharge tunnel are determined according to the operation size of the medium-sized slag skimmer. In addition to considering the drainage capacity, the convenience and mechanization level of construction should also be considered. Considering the current mechanical application of mine engineering, it is proposed to use the slag skimmer with the dump truck to carry out the slag discharge construction. At present, the construction space generally required by the medium-sized crawler slag skimmer is about 4×4m. Combined with the requirements of dump truck transportation, the section to be adopted in this project is an arched section of 4.8m×5m (width × height). The standard discharge tunnel adopts a straight wall circular arch section with a cross-sectional area of 22 square meters. The longitudinal slope of the discharge tunnel is 0.4 %. The discharge capacity is greater than the maximum water inflow of the Yuanguping Tunnel, which is 270,000 m^3/d, and has a certain surplus to meet the drainage requirements. The size of the drainage branch tunnel is set at 2.4m×2.9m. Since the transverse tunnel is short, it can be constructed by small machinery.

3.1.3 *Pre-design of grouting scheme*

After advanced geological prediction, in view of the water-rich areas such as filling large karst caves and water-rich joint fissure dense zones where water inrush (mud) may occur, measures such as full-section deep hole pre-grouting and surrounding grouting after excavation can be taken in combination with the actual situation to carry out grouting and water plugging reinforcement treatment. The tunnel passes through a large filled karst cave or cave with poor self-stability, a contact zone between soluble rock and non-soluble rock, a dense zone of water-rich joint fissures, and a bedrock section with extremely developed groundwater. There are 2/3 full holes in the advanced exploration hole or the total water output is greater than 15m^3/h. Combined with the core and water pressure analysis, it is determined that when there is a possibility of mud and water inrush, the grouting reinforcement measures of the full section surrounding rock 6m ahead of the excavation line are adopted, as shown in Figure 12. The tunnel passes through the dense zone of water-rich joint fissures and the bedrock area where groundwater is extremely developed. Through the advanced geological prediction results, it is judged that there is no possibility of water inrush in the tunnel, but the surrounding rock is weak and the self-stabilizing ability is poor, which is prone to collapse accidents. After excavation, the full-ring radial grouting reinforcement of 3m outside the excavation line is adopted, as shown in Figure 13.

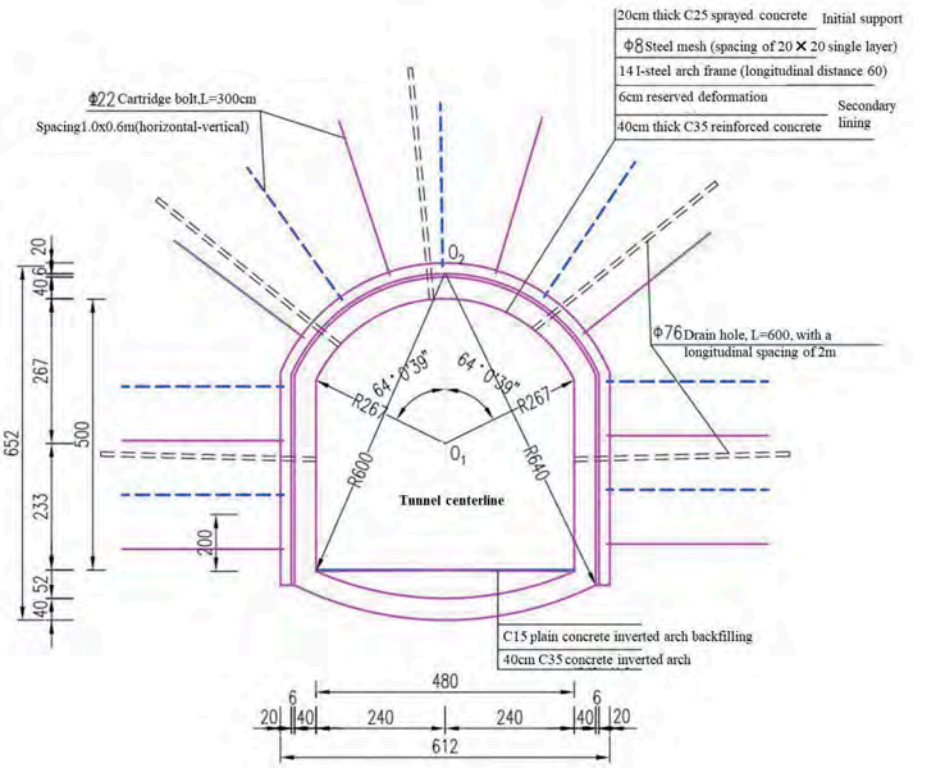

Figure 10. Cross-section of the drainage hole.

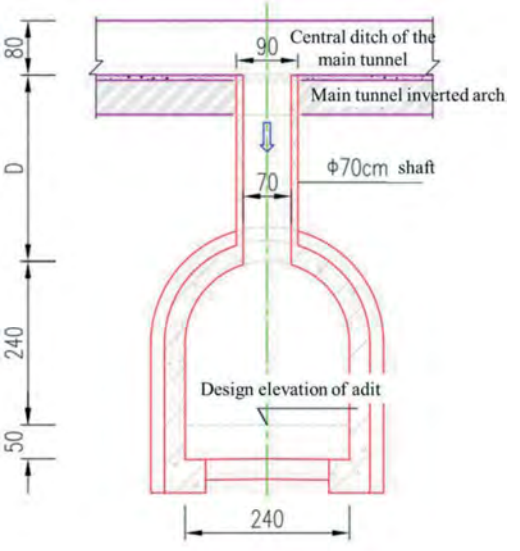

Figure 11. Cross-section of drainage branch hole (unit: cm).

According to the geological survey data, the pre-grouting, post-excavation grouting and supplementary grouting measures are designed for the grouting reinforcement of surrounding rock in the tunnel. In the actual construction, the grouting scheme and paragraph should be adjusted in time according to the proved water volume, water pressure and dynamic changes.

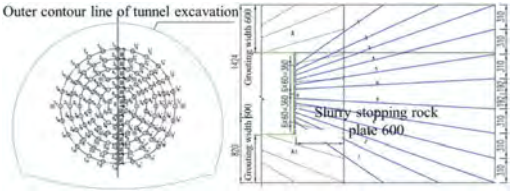

Figure 12. Advanced curtain grouting (unit: cm).

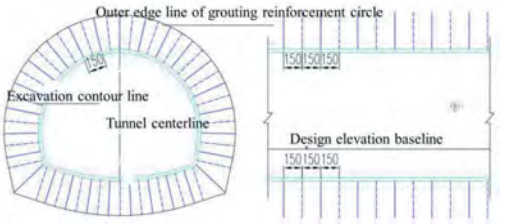

Figure 13. Radial grouting reinforcement (unit: cm).

3.2 *Groundwater backflow treatment in Huangyuxi Reservoir and Baiyangping Village*

Huangyuxi Reservoir with local land for irrigation and aquaculture is located 600m to the left of tunnel K15+150-890 section. The reservoir capacity is 547,000 m^3, and the height difference between the bottom of the reservoir and the tunnel pavement is 278 m. The reservoir water of Huangyuxi Reservoir is easy to flow backward along the fault zone, forming a major water inrush accident. Because the main groundwater flow direction of this section is located on the left side of the tunnel, the drainage system layout on the left side of the tunnel should be strengthened. The P1 drainage tunnel is set up on the 33 m left side of the Zhangjiajie end of the tunnel, P1K14 + 192 ~ P1K16 + 610, 2418 m long; The karst depression of Baiyangping Village on the right side of the exit section of the tunnel is the main water accumulation area of groundwater. Its ground elevation is above 600 m, and the terrain is relatively gentle. There is a risk that groundwater in the Baiyangping Depression pours into the tunnel along the karst channel and joint fissures, forming a huge water gushing in the tunnel. The drainage setting on the right side of the tunnel should be strengthened. A P2 drainage tunnel is set up at 33 m on the right side of the Guanzhuang end, P2K16 + 500 ~ P2K19 + 325, 2825 m long, as shown in Figure 14. The key measures of transverse branch tunnel, anti-water pressure lining and grouting water plugging are adopted at the core of the syncline and fault fracture zone. The transverse branch tunnel of water discharge is set at a spacing of 500m.

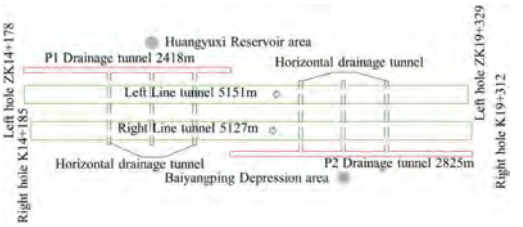

Figure 14. Floor plan of the drainage hole.

3.3 *Disaster prevention and smoke exhaust*

The length of the Yuanguping Tunnel is 5151 m. According to the provisions of Article 10.2.7 of the "Guidelines for Design of Ventilation of Highway Tunnels," the maximum travel length of fire smoke in the tunnel should not be greater than 5000 m. Therefore, a smoke exhaust duct was set up at the Zhangjiajie end of the tunnel.

The left hole of the tunnel is set at ZK14 + 680, and the right hole is set at K14 + 700. The connecting air duct is perpendicular to the main hole, as shown in Figures 15 and 16. According to the calculation, the air volume required for tunnel exhaust is 244m^3/s, and the wind speed in the exhaust duct should not be greater than 13 ~ 20m/s, so the clearance area of the exhaust duct should not be less than 18m^2. From the perspective of construction space and structural safety, the proposed section of the exhaust flue is a 4.8m×4.6m (width × height) straight wall arch section, with a section area of 22.1m^2. In order to reduce the scale of the project, the combined construction of the smoke exhaust duct and the water discharge tunnel is adopted. In the P1K14 + 192 ~ P1K14 + 715 section of the water discharge tunnel, the water discharge tunnel structure and the smoke exhaust duct structure are combined and set as the smoke discharge tunnel. The upper layer is the smoke discharge area, and the lower layer is the

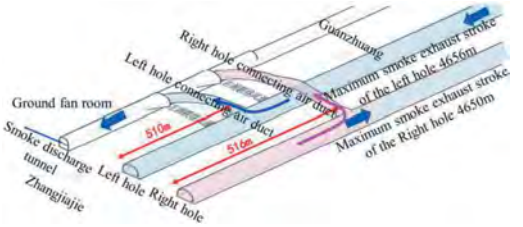

Figure 15. Smoke exhaust channel.

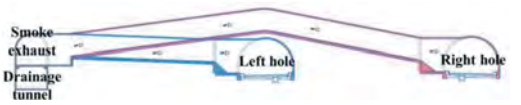

Figure 16. The relationship between the smoke drainage hole and the main cave.

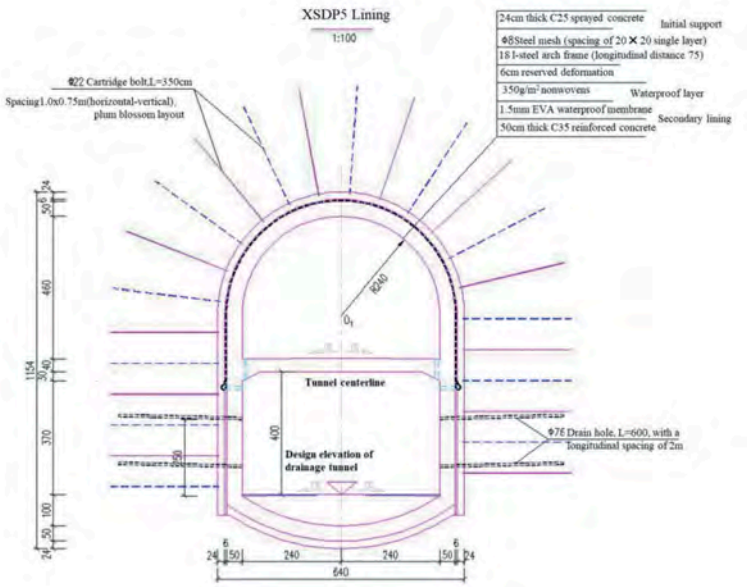

Figure 17. Section of smoke and drainage hole (unit: cm).

water discharge area, so as to realize the independent function partition, as shown in Figure 17. An axial flow fan is installed at the opening of the smoke exhaust channel to fully exhaust smoke.

4 CONCLUSIONS AND SUGGESTIONS

In order to solve the design problem of the extra-long tunnel in the water-rich karst platform of the compound syncline basin, this paper takes Yuanguping extra-long tunnel with strong karst development as an engineering example. The conclusions are as follows:

(1) The 'discharge-based, limited discharge' scheme is adopted. The problem of high pressure and rich water in Yuanguping Tunnel is solved by setting parallel discharge tunnel and discharge branch tunnel to reduce the hydrodynamic pressure of groundwater around the tunnel, and grouting and water plugging measures are adopted in the high risk section of water and mud inrush.

(2) The P1 discharge tunnel (P1K14 + 192 ~ P1K16 + 610) is set up on the left side of the Zhangjiajie end of the tunnel, which is 2418 m long. It solves the problem that the groundwater of the Huangyuxi Reservoir on the left side of the Zhangjiajie section is poured backward along the fault zone to form a major water inrush accident. The P2 drainage tunnel (P2K16 + 500 ~ P2K19 + 325) is set up at 33 m on the right side of the Guanzhuang end, which is 2825 m long. It solves the problem that the groundwater in the Baiyangping Depression on the right side of the Guanzhuang section pours into the tunnel along the karst channel and joint fissures to form a huge water gushing in the tunnel.

(3) The P1K14 + 192 ~ P1K14 + 715 section of the discharge tunnel combines the structure of the discharge tunnel with the structure of the smoke exhaust duct. The length of the joint construction section is 523 m. The Zhangjiajie end of the discharge tunnel is set to be double-layer. The upper layer is the smoke exhaust area, and the lower layer is the discharge area, which realizes independent functional zoning. On the basis of reducing the scale of the project, the problem of disaster prevention and smoke exhaust in extra-long tunnels of more than 5 kilometers is fully solved.

REFERENCES

Cheng, Q. J., 2020. Research on advance detection of tunnel karst and karst cave treatment technology. Highway. 65(05), 357–362.

Guan, Z. Y., Yang, C. S., 2018. Optimal application of advanced pre-grouting technology in high-pressure water-rich karst tunnels. Tunnel Construction (Chinese and English). 38 (S1), 136–141.

Jiang, Y., Zhang, Q. Q., 2022. Research on Karst Treatment Technology of Guinan High-speed Railway Tunnel.

Western Communications Technology. (07), 177-178 +185.

Li, F. T., Li, H. M., Hu, Z. P., et al, 2020. Karst Development Law and Engineering Effect Analysis of Liaoshan Tunnel of Ehan Expressway. China Karst. 39(04), 592–603.

Wang, J., Wang, L. J., Ma, J. X., et al, 2020. Analysis of treatment measures for highway tunnels crossing large karst caves in karst areas. Journal of Underground Space and Engineering. 16(S2), 964-970+998.

Wu, Y. B., Yin, R. C., Lei, M. T., et al, 2021. Karst collapse formation evolution model and prevention countermeasures under the influence of tunnel engineering in Zhongliangshan area of Chongqing. China Karst. 40 (02), 246–252.

Yan, J., 2020. Selection and practice of several main geophysical prospecting methods for advanced geological prediction of karst tunnels. Tunnel Construction (Chinese and English) 40(S1), 327–336.

Zhao, S. Z., Huang, X., Xu, Z. H., et al, 2022. Research on Karst Development Characteristics and Karst Cave Treatment Technology of Qiyueshan Tunnel. Tunnel Construction (Chinese and English). 42(07), 1289–1299.

Zhang, S. X., Sun, L., Wang, L., 2020. Advanced geological forecast and treatment technology for water-rich section of karst tunnel. Highway. 65(12), 163–165.

Zhou, L., Li, S. C., Xu, Z. H., et al, 2017. Tunnel comprehensive advanced geological prediction technology and its engineering application. Journal of Shandong University (Engineering Science Edition). 47(02), 55–62.

Zhu, J. W., Zhu, J. G., 2021. Comprehensive Treatment Technology of Karst Cave in Small Three Gorges Tunnel of Zhengwan High-speed Railway. Tunnel Construction (Chinese and English). 41(S1), 401–406.

Tunnelling for a Better Life – Yan, Celestino, Thewes & Eberhardt (Eds)
© 2024 The Author(s), ISBN 978-1-032-80042-4
Open Access: www.taylorfrancis.com, CC BY-NC-ND 4.0 license

Numerical simulation of the mechanism of strain rockburst under true triaxial loading and unloading conditions

Yadong Xue & Hengjiao Tian*
Tongji University, Shanghai, China
Key Laboratory of Geotechnical and Underground Engineering, Ministry of Education, Shanghai, China

ABSTRACT: Rockburst represents a prevalent hazard in the excavation of deep tunnels, posing substantial risks such as severe economic losses, casualties, equipment damage, and schedule delays. Among the various forms of rockburst, strain rockburst is notably common, underscoring the critical importance of investigating the impact of three-direction pressure value variations on its intensity. To delve into this phenomenon, numerical simulations were conducted utilizing 3DEC software to monitor and analyze kinetic energy, joint friction work, total strain energy, and overall energy release across 10 distinct working conditions. Concurrently, a network of 10 monitoring points was established, with a specific focus on scrutinizing velocities and displacements at points 4 and 10. The findings reveal a consistent pattern in the influence of both the maximum compressive stress (σ_{max}) and the minimum compressive stress (σ_{min}) on the occurrence of rockburst intensity. As these stresses increase, so does the intensity of rockburst. Conversely, the intermediate compressive stress (σ_{int}) exhibits minimal impact on rockburst intensity. In practical terms, managing and controlling the maximum compressive stress (σ_{max}) and minimum compressive stress (σ_{min}) emerges as a pivotal strategy to mitigate rockburst intensity. This research not only sheds light on the governing principles behind rockburst occurrence but also provides valuable guidance for engineering applications in the realm of rockburst control.

Keywords: Rockburst, Deep tunnels, 3DEC software, Numerical simulation, Rockburst control

1 INTRODUCTION

With the swift advancement of infrastructure development in western China, the prevalence of deep-buried tunnels is on the rise. Among the formidable challenges faced during the construction of these tunnels, rock burst stands out as a particularly severe disaster (Lijie et al., 2021, Dong et al., 2017).

The incidence of rock bursts is typically characterized by its randomness, suddenness, and destructive nature. Rockbursts can result in significant economic losses, casualties, equipment damage, and schedule delays, among other consequences. Categorized by their breeding mechanisms, rockbursts are broadly classified into three types: strain rockbursts, strain structure surface slip rockbursts, and fracture slip rockbursts. Among these, strain rockbursts are most commonly observed in underground engineering, particularly in hard rock tunnels or deep mining operations (Li et al., 2019, Yang et al., 2020, Yinghua and Fei, 2020). The formation process of rockbursts is intricate, lacking a comprehensive theory to fully explain it. Consequently, rockbursts have garnered considerable attention from scholars due to their complex and unpredictable nature.

In the past three decades, the research on the mechanism of rock explosion has been carried out from various angles, mainly including engineering phenomena (TAN, 1989), indoor tests (He et al., 2019, He et al., 2015, Su et al., 2018), theoretical analyses (LI, 1997, Li, 2019, ChunlinLi, 2021), numerical simulations (Yu et al., 2022, Yi et al., 2021, Zhang et al., 2020) and so on. Early research on rock bursts mainly from the engineering phenomenon. Bingrui et al. (2011) through the microseismic monitoring signal characteristics of the research on rock bursts. Chongyan et al. (2020) through the granite specimens containing round holes under different lateral load rock burst simulation tests, the use of micro-cameras, acoustic emission (AE) system and infrared thermography and other monitoring systems, analyse the rock burst process of acoustic emission timing, frequency, spatial and temporal characteristics and thermal imaging of the temperature transport law. He et al. (2019) studied the effect of stiffness on

*Corresponding author: 2010hjtian@tongji.edu.cn

DOI: 10.1201/9781003495505-87

the strain rupture of laminated sandstone with different inclination angles through indoor tests. ChunlinLi (2021) considered the development process of rockbursts from the energy point of view, and accordingly gave the supporting structure to prevent rockbursts should be designed with high load and displacement bearing capacity at the same time. Engineering phenomena have been of great help in the study of early rockbursts, but it is difficult to explain the intrinsic reasons for the occurrence of rockbursts. Indoor tests have a complex test programme development, test operation is difficult, and can not provide timely guidance to the field. Theoretical analysis to consider the problem can not be too complex, using many approximations and assumptions. In contrast, numerical simulation to consider the problem can be more complex and comprehensive, to obtain more information, with theoretical research and experimental research part of the advantages.

According to the research conducted by scholars in the field, numerical simulation methods primarily include the finite element method and the discrete element method. Given that rock burst involves significant deformation within a short time frame, the discrete element method proves more advantageous compared to the finite element method. PFC stands out as a representative discrete element software; however, the calibration process can be quite intricate to achieve a particle aggregate resembling the macroscopic properties of the rock body in the field. Both 3DEC and PFC are products of Itasca, yet 3DEC software distinguishes itself by not requiring complex calibration. It has the capability to directly utilize the macro-parameters of the rock, streamlining the simulation process. Additionally, the built-in functions of 3DEC software facilitate the easy retrieval of energy data for each component. Given the strong correlation between rock bursts and energy, employing 3DEC software for numerical simulation presents a significant advantage.

In this study, the 3DEC software was employed to explore the impact of variations in the three principal stresses on the severity of rockbursts, considering actual ground stress conditions. This was achieved by simulating the behavior of the rock mass under loading and unloading conditions. Ten distinct working conditions were simulated in the numerical tests, and the observed patterns from these tests contribute valuable insights for a more comprehensive understanding of the mechanisms governing strain rockbursts.

2 3DEC NUMERICAL SIMULATION

3DEC is primarily intended for analysis in rock engineering projects, ranging from studies of the progressive failure of rock slopes to evaluations of the influence of rock joints, faults, bedding planes, etc. on underground excavations and rock foundations. 3DEC is ideally suited to study potential modes of failure directly related to the presence of discontinuous features. Both manual and automatic joint generators are built into 3DEC to create individual (and sets of) discontinuities that represent jointed structure in a rock mass. A wide variety of joint patterns can be generated in the model. In addition, a discrete fracture network (DFN) generator is included in 3DEC. Rockburst processes are intricately linked to energy dynamics, and the 3DEC software's built-in functions facilitate the straightforward acquisition of energy values. Additionally, the 3DEC software allows for the direct input of macro-mechanical parameters. Consequently, utilizing 3DEC software for rockburst analysis offers distinct advantages.

2.1 *Energy relations in 3DEC*

The total energy balance can be expressed in terms of the released energy (W_r), which is the difference between the work done at the boundary of the model and the total stored and dissipated strain energies (Salamon, 1984):

$$W_r = W - (U_c + U_b + W_j + W_p) \tag{1}$$

where, W_r denotes released energy, W denotes total boundary loading work supplied to the system, U_c denotes total stored strain energy in material, U_b denotes total change in potential energy of the system, W_j denotes total dissipated energy in joint shear, and W_p denotes total dissipated work in plastic deformation of intact rock.

A second calculation of released energy can be made based on the kinetic energy, mass damping work, the work performed at viscous boundaries, and the strain energy in excavated material:

$$W_r = U_k + W_k + W_v + U_m \tag{2}$$

where, U_k denotes current value of kinetic energy in the system, W_k denotes total work dissipated by mass damping, W_v denotes work done by viscous (non-reflecting) boundaries, and U_m denotes total strain energy in excavated material.

Usually, the second form of the released energy is particularly useful for dynamic problems because the released kinetic energy is easily calculated.

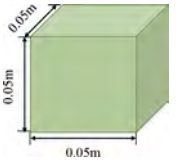

Figure 1. Rock specimen size.

Table 1. Mechanical parameters related to blocks in rock samples.

Density (d) /(kg/m^3)	Bulk modulus (K) /(Pa)	Shear modulus (G) /(Pa)	Cohesion (c) /(Pa)	Internal friction angle (φ)/ (°)	Tensile strength (σ_t)/ (Pa)
2700	2.44×10^{10}	2.18×10^{10}	3.73×10^{7}	33.69	5×10^{6}

Table 2. Mechanical parameters related to joints in rock samples.

Joint type	Normal stiffness (k_n)/(Pa/m)	Tangential stiffness (k_s)/ (Pa/m)	Cohesion (c) /(Pa)	Internal friction angle (φ)/ (°)	Tensile strength (σ_t)/ (Pa)
virtual joints	3×10^{12}	1.5×10^{12}	4×10^{7}	33.69	5×10^{6}
the newborn joints	3×10^{12}	1.5×10^{12}	8.37×10^{6}	5	0

2.2 *Numerical test programme*

2.2.1 *Numerical modelling*

Numerical simulations were carried out using 3DEC software, the software version used was 3DEC 7.0, and the dimensions of the simulated rock samples in terms of length, width and height were 0.05m×0.05m×0.05m as shown in Figure 1.

For numerical simulations, the relevant mechanical parameters of the rock mass (block) in the 3DEC model are shown in Table 1, and the relevant mechanical parameters of the joints in the 3DEC model are shown in Table 2.

In the above simulations, the blocks are modelled using the Mohr-Coulomb constitutive model, and all blocks are assigned the corresponding mechanical parameters. joints are modelled using the default Mohr-Coulomb constitutive model, and all joints are assigned the corresponding mechanical parameters.

2.2.2 *Loading and unloading programmes*

In the simulation of rockbursts, the cubic rock specimen is initially subjected to loading on all six faces using 3DEC software, and the process extends over 2000 steps. Subsequently, it undergoes unloading from one of the lowest compressive stress values (simulating real-life tunnel excavation conditions), and this phase continues for 4000 steps. The loading and unloading processes are illustrated in Figure 2.

In Figure 2, σ_{max} represents the maximum compressive stress, σ_{int} represents the intermediate compressive stress, and σ_{min} represents the minimum compressive stress. It is worth noting that here there is a difference between σ_1, σ_2, and σ_3 and the maximum principal stress, intermediate principal stress, and minimum principal stress in the stress state of a point in space. The maximum principal stress, intermediate principal stress and minimum principal stress reflect the stress state of a very small point, while the rock specimen has a certain spatial scale, when this scale is relatively small, σ_1, σ_2, σ_3 can be approximated as the maximum principal stress, intermediate principal stress and minimum principal stress.

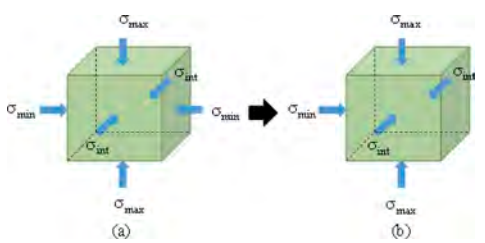

Figure 2. (a) Rock sample loading process (b) Rock sample unloading process.

A total of 10 working conditions were simulated for 3DEC numerical simulation. Among them, σ_{max} =60MPa, σ_{int}=40MPa, σ_{min}=30MPa are used as the most basic working conditions to study the effect on the intensity of rockburst when σ_{max}, σ_{int}, σ_{min} are changed. In the process of unloading, it is assumed that the compressive stress at each face after unloading is $\sigma_{max\text{-}u}$, $\sigma_{int\text{-}u}$, $\sigma_{min\text{-}u}$ and in order to simulate the real excavation better, the maximal compressive stress will be increased (assumed to be increased by 15MPa), the intermediate compressive stress will remain basically unchanged, and the minima will be reduced to zero. The 10 working conditions are shown in Table 3.

2.2.3 *Layout of monitoring points*

For the 3DEC simulation, a total of 10 points were selected as monitoring points on the unloading surface, and the locations of the 10 monitoring points are shown in Figure 3. The detailed coordinates of each point are P1(0.025, 0, 0),P2(0.025,0,0.0125),P3(0.025,0,0.025),P4(0.025,0,-0.0125),P5(0.025,0,-0.025),P6(0.025,0.025,0),P7(0.025,0.025,0.0125),P8(0.025,0.025,0.025),P9(0.025,0.025,-0.0125),P10(0.025,0.025,-0.025).

2.2.4 *Monitoring variables*

During the numerical simulation, the changes in the values of the following variables after unloading were monitored mainly at 10 monitoring points. It mainly contains kinetic energy, block strain energy, boundary loading work, joint friction work, joint strain energy, shear strain energy on joints, tensile strain energy on joints, total strain energy, total energy released, X displacement and X velocity.

Table 3. Numerically simulated information on 10 working conditions.

Working Condition No.	σ_{max} (MPa)	σ_{int} (MPa)	σ_{min} (MPa)	σ_{max-u} (MPa)	σ_{int-u} (MPa)	σ_{min-u} (MPa)
1	60	40	30	75	40	0
2	70	40	30	85	40	0
3	80	40	30	95	40	0
4	90	40	30	105	40	0
5	60	45	30	75	45	0
6	60	50	30	75	50	0
7	60	55	30	75	55	0
8	60	40	25	75	40	0
9	60	40	20	75	40	0
10	60	40	15	75	40	0

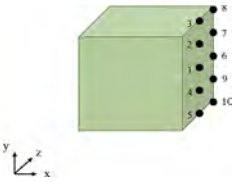

Figure 3. Schematic of the location of the 10 monitoring points.

3 NUMERICAL SIMULATION TEST RESULTS AND ANALYSIS

3.1 *Numerical simulation results*

After 2000 steps of loading and 4000 steps of unloading considering the most basic condition (σ_{max}=60MPa, σ_{int}=40MPa, σ_{min}=30MPa), the velocity vector of the rock specimen is shown in Figure 4, and the displacement cloud of the rock specimen in the X-direction is shown in Figure 5.

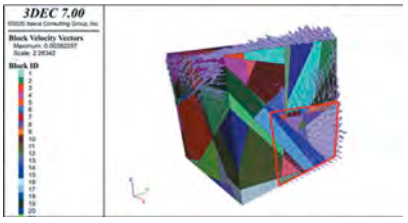

Figure 4. The velocity vector of the rock specimen (σ_{max} =60MPa, σ_{int}=40MPa, σ_{min}=30MPa).

In Figure 4, due to the existence of joints, the whole model is not symmetric when generating blocks, so the velocity vector diagram is not symmetric either. In the model, the velocity vector inside the red frame line points to the direction of the outer normal of the unloading surface, indicating that the block has a tendency to move outward, i.e., the rock burst phenomenon. In Figure 5, the displacement of each block on the unloading surface after the end of unloading is also visualised.

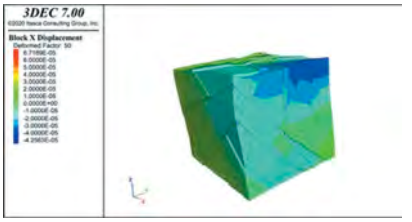

Figure 5. The displacement cloud of the rock specimen in the X-direction (σ_{max}=60MPa, σ_{int}=40MPa, σ_{min}=30MPa).

3.2 *σ_{max} Laws of influence on rockburst*

The initial combination of compressive stresses when considering the law of maximum compressive stress σ_{max} on rockburst is (σ_{max}=60MPa,σ_{int}=40MPa, σ_{min}= 30MPa),(σ_{max}=70MPa,σ_{int}=40MPa,σ_{min}=30MPa), (σ_{max}=80MPa,σ_{int}=40MPa,σ_{min}=30MPa), and (σ_{max}=90MPa,σ_{int}=40MPa,σ_{min}=30MPa).

3.2.1 *The effect of σ_{max} on energy*

The effect of maximum compressive stress σ_{max} on kinetic energy, joint friction work, total strain energy, and total energy released is shown in Figure 6.

As can be seen from Figure 6, with the increase of σ_{max}, all kinds of energy overall show a more obvious trend of increase. The increase in energy to a certain extent can increase the intensity of rock bursts, so from the energy point of view shows that the increase in σ_{max} will increase the intensity of rock bursts.

3.2.2 *The effect of σ_{max} on velocity*

When researching the X-velocity, point 4 and point 10 in the red box line of Figure 4 are mainly selected as the focus of attention. The effect of the maximum compressive stress σ_{max} on the X-velocity of point 4 and point 10 is shown in Figure 7.

As can be seen from Figure 7, with the increase of σ_{max}, the velocity of point 4 and point 10 shows a more obvious trend of increase. The magnitude of the velocity can also reflect the intensity of the rock burst to a certain extent, so from the point of view of the velocity indicates that the increase of σ_{max} will increase the intensity of the rock burst.

3.2.3 *The effect of σ_{max} on displacement*

The effect of the maximum compressive stress σ_{max} on the X-displacement at point 4 and point 10 is shown in Figure 8.

As can be seen in Figure 8, the displacement of point 4 and point 10 shows an increasing trend with the increase of σ_{max}. The magnitude of the displacement can also reflect the intensity of the rock burst to a certain extent, so from the point of view of the displacement indicates that the increase of σ_{max} will increase the intensity of the rock burst.

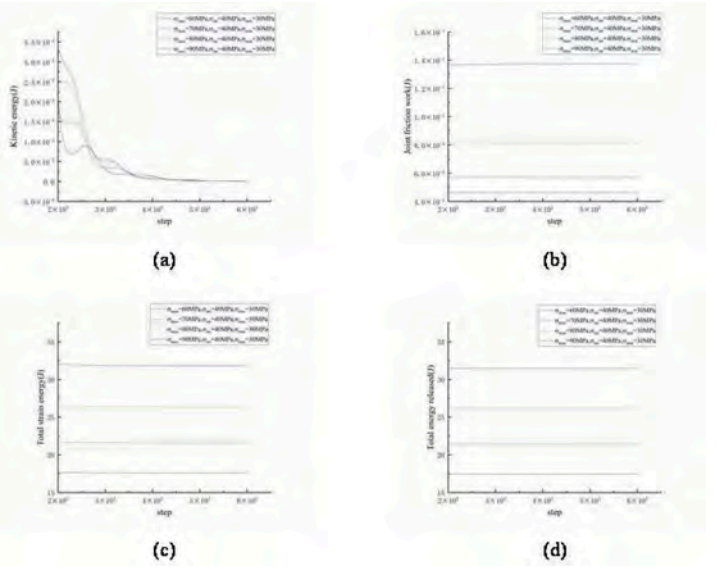

Figure 6. The influence by σ_{max} on energy (a) kinetic energy, (b) joint friction work, (c) total strain energy, and (d) total energy released.

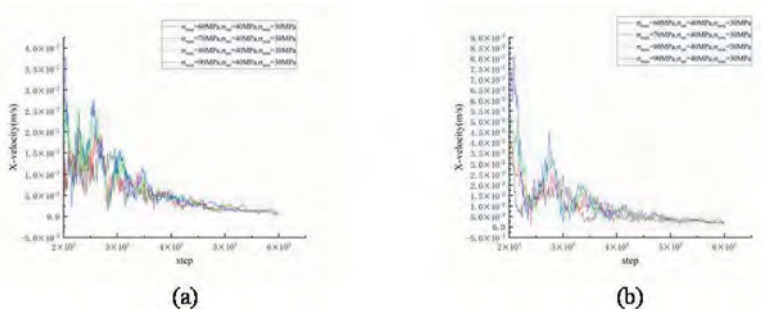

Figure 7. The influence by σ_{max} on X-velocity (a) at point 4, (b) at point 10.

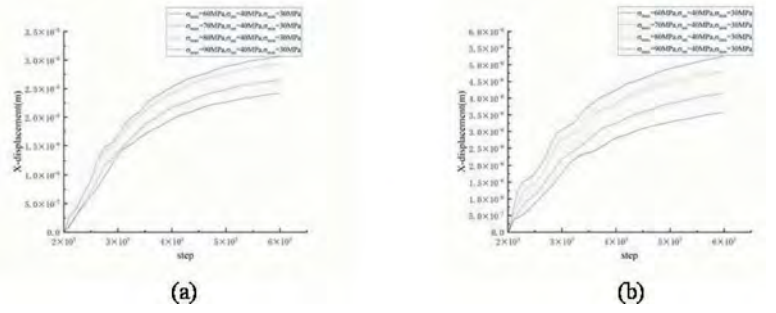

Figure 8. The influence by σ_{max} on X- displacement (a) at point 4, (b) at point 10.

3.3 *σ_{int} Laws of influence on rockburst*

Considering the law of intermediate compressive stress σ_{int} on rockburst, its initial compressive stress combination is (σ_{max}=60MPa, σ_{int}=40MPa, σ_{min} =30MPa),(σ_{max}=60MPa,σ_{int}=45MPa,σ_{min}=30MPa), (σ_{max}=60MPa,σ_{int}=50MPa,σ_{min}=30MPa), (σ_{max} =60MPa, σ_{int}=55MPa, σ_{min}=30MPa).

3.3.1 *The effect of σ_{int} on energy*

The effect of intermediate compressive stress σ_{int} on kinetic energy, joint friction work, total strain

energy, and total energy released is shown in Figure 9.

As can be seen from Figure 9, with the increase of σ_{int}, all kinds of energy overall show a more obvious trend of increase except kinetic energy. There is very little change in kinetic energy in the Figure. Compared with other types of energy, kinetic energy is more directly reflect the intensity of rock bursts. Therefore, from the energy point of view shows that the increase of σ_{int} has little effect on the intensity of rock bursts.

3.3.2 *The effect of σ_{int} on velocity*

The effect of the intermediate compressive stress σ_{int} on the X-velocity of point 4 and point 10 is shown in Figure 10.

As can be seen from Figure 10, with the increase of σ_{int}, the velocity of point 4 and point 10 does not change significantly. The magnitude of the velocity can also reflect the intensity of the rock burst to a certain extent, so from the point of view of the velocity shows that the increase of σ_{int} has little effect on the intensity of the rock burst.

3.3.3 *The effect of σ_{int} on displacement*

The effect of the intermediate compressive stress σ_{int} on the X-displacement at point 4 and point 10 is shown in Figure 11.

As can be seen from Figure 11, with the increase of σ_{int}, the displacement of point 4 and point 10 increases insignificantly. The magnitude of the displacement can also reflect the intensity of the rock burst to a certain extent, so from the point of view of the displacement shows that the increase of σ_{int} has little effect on the intensity of the rock burst.

3.4 *σ_{min} Laws of influence on rockburst*

When considering the minimum compressive stress σ_{min} on rock bursting law, its initial compressive stress combination is (σ_{max}=60MPa, σ_{int}=40MPa,σ_{min}=30MPa),(σ_{max}=60MPa,σ_{int}=40MPa,σ_{min}=25MPa),(σ_{max}=60MPa,σ_{int}=40MPa,σ_{min}=20MPa),and(σ_{max}=60MPa,σ_{int}=40MPa, σ_{int}=15MPa).

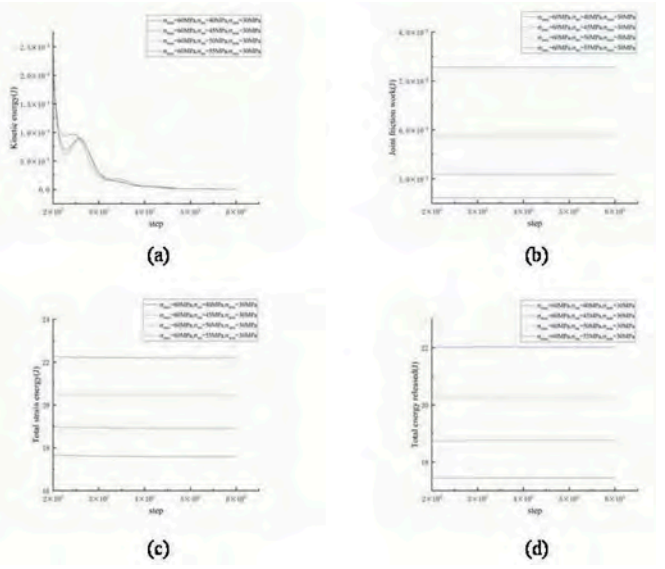

Figure 9. The influence by σ_{int} on energy (a) kinetic energy, (b) joint friction work, (c) total strain energy, and (d) total energy released.

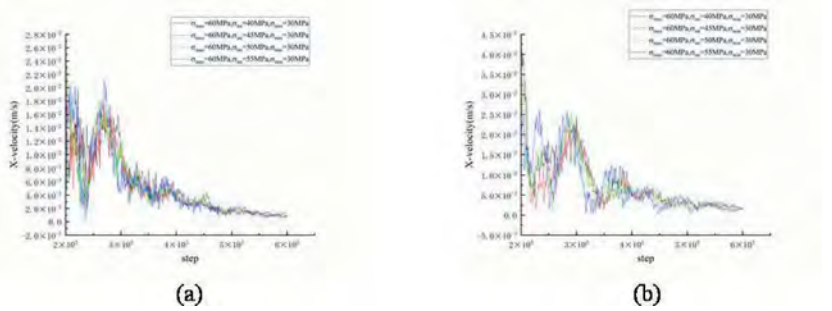

Figure 10. The influence by σ_{int} on X-velocity (a) at point 4, (b) at point 10.

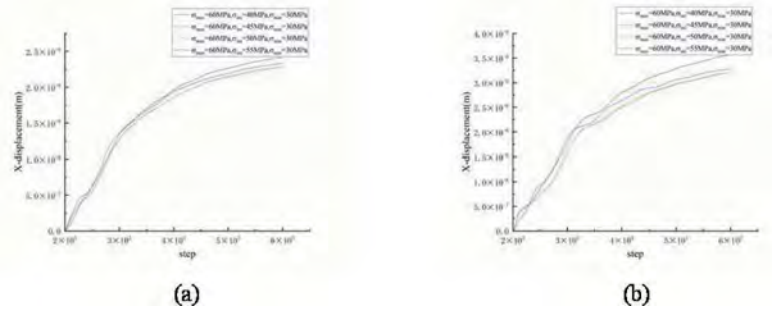

Figure 11. The influence by σ_{int} on X- displacement (a) at point 4, (b) at point 10.

According to the processing and analysis of the relevant data, it is found that the influence of σ_{min} on the intensity of rock bursts is similar to the rule of σ_{max}, i.e., with the increase of σ_{min}, the intensity of rock bursts will also increase accordingly.

4 CONCLUSIONS

Rockburst is one of the common disasters encountered during deep tunnel excavation, and the main conclusions obtained from numerical modelling of the rockburst process using 3DEC discrete element software are as follows:

(1) Considering 10 different compressive stress combinations under the conditions of 3DEC numerical modelling. The kinetic energy, joint friction work, total strain energy, and total energy released were monitored and analysed. A total of 10 monitoring points were set up and the analyses were focused on the relevant velocities and displacements of point 4 and point 10 among them.
(2) The effects of the maximum compressive stress σ_{max} and the minimum compressive stress σ_{min} on the intensity of the rockburst show the same pattern. As the value increases, the intensity of the rockburst increases accordingly.
(3) The intensity of rockbursts is not sensitive to changes in the intermediate compressive stress σ_{int}. That is, with the increase in the value of the intermediate principal stress σ_{int}, the intensity of rock bursts does not change significantly.
(4) The practical engineering can be achieved through certain means mainly to reduce the maximum compressive stress σ_{max} and minimum compressive stress σ_{min} method to control the intensity of rock explosion.

ACKNOWLEDGMENTS

This research was funded by the National Natural Science Foundation of China (Grant No. 52078377). We are grateful to anonymous reviewers for their constructive reviews on the manuscript, and the editors for carefully revising the manuscript.

REFERENCES

Bingrui C, Xiating F, Xionghui Z, et al. 2011. Real-Time Microseismic Monitoring and Its Characteristic Analysis During TBM Tunneling in Deep-Buried Tunnel. Chinese Journal of Rock Mechanics and Engineering [J], 30: 275–283.

Chongyan L, Guangming Z, Wensong X, Xiangrui M 2020. Experimental study on rockburst and its spatio-temporal evolution criterion in high stress roadway. Journal of China Coal Society [J], 45: 998–1008.

Chunlinli C 2021. Principles and methods of rock support for rockburst control. Journal of Rock Mechanics and Geotechnical Engineering [J], 13: 46–59.

Dong W, Tian-Bin L, LIANG-WEN J, et al. 2017. Analysis of the Stress Characteristics and Rock Burst of Ultra Deep Buried Tunnel in Sichuan-Tibet Railway. Journal of Railway Engineering Society [J], 34: 46–50.

He M, Ren F, Cheng C 2019. Experimental and numerical analyses on the effect of stiffness on bedded sandstone strain burst with varying dip angle. Bulletin of Engineering Geology and the Environment [J], 78: 3593–3610.

He M, Ribeiro E Sousa L, Miranda T, Zhu G 2015. Rockburst laboratory tests database - Application of data mining techniques. Engineering Geology [J], 185: 116–130.

Li C 2019. Rockburst conditions and rockburst support Charlie. Chinese Journal of Rock Mechanics and Engineering [J], 38: 674–682.

Li D, Zhang J, Wang C, et al. 2019. Assessing Rockburst Hazards Using a Self-Developed Real-Time Microseismic Monitoring System in a Deep-Sea Goldmine. Ieee Access [J], 7: 134360–134371.

Li G 1997. The Mechanism of Compression-Shear Damage for Rock Mass with Its Application to Rockburst. Chinese Journal of Geotechnical Engineering [J]: 49–55.

Lijie D, Kairong H, Jiaxing W, et al. 2021. Rockburst Characteristics and Prevention and Control Technologies for Tunnel Boring Machine Construction of Deep-buried Tunnels. Tunnel Construction [J], 41: 1–15.

Salamon M DG 1984. Energy Considerations in Rock Mechanics: Fundamental Results. Journal of the Southern African Institute of Mining and Metallurgy [J], 84: 233–246.

Su G, Hu L, Feng X, et al. 2018. True Triaxial Experimental Study of Rockbursts Induced By Ramp and Cyclic Dynamic Disturbances. Rock Mechanics and Rock Engineering [J], 51: 1027–1045.

Tan Y 1989. Study on the formation mechanism of rockburst. Hydrogeology and Engineering Geology [J]: 34–38, 54.

Yang J, Yang X, Zhou J, et al. 2020. Comparative Study of the Excavation Damage and Rockburst of the Deeply Buried Jinping II Diversion Tunnels Using a TBM and the Drilling-Blasting Method. Advances in Civil Engineering [J], 2020.

Yi C P, Nordlund E, Zhang P, et al. 2021. Numerical modeling for a simulated rockburst experiment using LS-DYNA. Underground Space [J], 6: 153–162.

Yinghua W, Fei L 2020. Numerical Simulation Analysis of the Rockburst Mechanism in the Tunnel with High Geostress. Modern Tunnelling Technology [J], 57: 46–54.

Yu Z, Shi X Z, Zhang ZX, et al. 2022. Numerical Investigation of Blast-Induced Rock Movement Characteristics in Open-Pit Bench Blasting Using Bonded-Particle Method. Rock Mechanics and Rock Engineering [J].

Zhang Z H, Gao W L, Li K P, Li B J 2020. Numerical simulation of rock mass blasting using particle flow code and particle expansion loading algorithm. Simulation Modelling Practice and Theory [J], 104.

Tunnelling for a Better Life – Yan, Celestino, Thewes & Eberhardt (Eds)
© 2024 The Author(s), ISBN 978-1-032-80042-4
Open Access: www.taylorfrancis.com, CC BY-NC-ND 4.0 license

Sequential 3D geological information system using re-grid of voxel model based on exploration data ahead of the tunnel face

Shuro Yoshikawa* & Yasuhisa Aono
Institute of Technology, Shimizu Corporation, Tokyo, Japan

Kanji Saito
Nagoya Branch, Shimizu Corporation, Nagoya, Japan

Takuro Nishi
Institute of Technology, Shimizu Corporation, Tokyo, Japan

ABSTRACT: Social demands, such as improving productivity, reforming work styles, and ensuring workplace safety, are prevalent during mountain tunnel construction projects. Therefore, it is necessary to undertake an advanced information-based approach to mountain tunnel construction to address these social demands. Here we address an aspect of this advanced information-based approach by developing a new three-dimensional (3D) modeling system, SG-ReGrid®, which updates 3D geological models using exploration data, such as advanced boring and seismic surveys that are conducted during construction, and requires minimal time and effort compared with conventional software. The 3D modeling system has the ability to identify potential geological risks that may be present ahead of the tunnel face, thereby making it possible to propose design changes in a timely manner and contribute to worksite safety. Furthermore, we are also considering improving the efficiency and generalization of the system to better address the above-mentioned social demands. We demonstrate the effectiveness of the modeling system by first presenting the system configuration and then providing an example application at the Shitara Dam Seto Shitara Line tunnel construction site in Japan.

Keywords: 3D geological model, Sequential update, Visualization, Exploration data, Mountain tunnel

1 INTRODUCTION

The early prediction of geological hazard risks, such as fault zones, significant rock cracks, and groundwater inrush, is required to ensure workplace safety and effective construction schedule management during the construction of mountain tunnels. Therefore, a number of efficient technologies have been developed to explore the state of the rock mass ahead of the tunnel face. For example, the S-BEAT® seismic exploration system is a fast, low-cost surveying method that is undertaken during construction, whereby the sound source is generated by a hydraulic rock-breaker at the tunnel face (Nishi and Wakabayashi, 2016; Yoshikawa et al., 2021). The seismic system has a negligible impact on construction cycle times because it uses existing rock bolts and common rock-breakers during survey.

There are various types of forward exploration ahead of the tunnel face, such as seismic reflection survey and advanced boring. Geological expertise is often required to spatially visualize and interpret the geological conditions ahead of the tunnel face using these various datasets. However, if rapid integration and three-dimensional (3D) modeling of these seismic, boring, logging, and other datasets can be undertaken, then the geological conditions ahead of the tunnel face will be easier to understand and assess. Furthermore, from a social perspective in Japan, it is necessary to deal with labor-saving costs that are related to construction work, shortage of engineers, and productivity improvements, including BIM/CIM (building/construction information modeling), which are mainly promoted by the Ministry of Land, Infrastructure, Transport and Tourism.

We address the above-mentioned issue by developing a new 3D modeling system, SG-ReGrid®, whereby the initial voxel model is re-gridded using exploration data acquired during tunnel construction. We also present an example application of the system at a tunnel

*Corresponding author: s-yoshikawa@shimz.co.jp

DOI: 10.1201/9781003495505-88

construction site to demonstrate its effectiveness in identifying geological hazards ahead of the tunnel face.

2 NEW 3D MODELING SYSTEM

An overview of the proposed 3D modeling system is shown in Figure 1. The initial model is first created using pre-construction geological surveys that are incorporated into commercially available software packages and mainly interpreted by geological specialists. The target volume where the updates to the geological model are sequentially performed then has to be determined. This initial model (solid model) of the target volume is converted into a voxel model and then input to the model update section (the 3D modeling system). The mode of the voxel model, such as the geological classification of the rock, can be changed according to the purpose of the exploration surveys in this section. Therefore, the elastic-wave (P-wave) velocity structure that is obtained from the pre-construction survey, the rock classification corresponding to the initially designed support pattern, and the lithological classification are used as attribute values for each voxel in the initial voxel model. Sequential updates to the voxel attribute values may include the P-wave velocity structure obtained by advanced boring (hereinafter Br) and active-source P-wave exploration, lithology classification by Br, and strength tests using Br specimens. The physical properties derived from these results and the S-BEAT®-derived reflection surfaces are also classified and included in the updates.

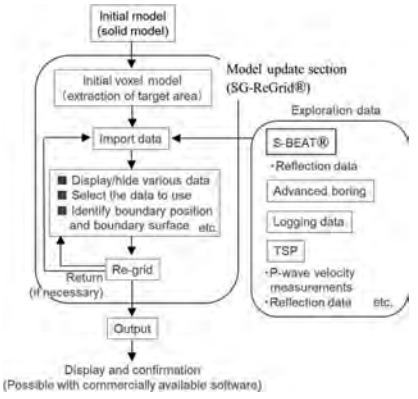

Figure 1. Overview of the 3D modeling system.

The updated geological model can then be output, together with the coordinate and attribute information from the voxel model, and reflected in an analytical model using commercially available software. Furthermore, we can set guidelines on how to input, select, and use various exploration results, with the ultimate goal of enabling non-geological engineers to quickly and easily update the geological models during tunnel construction.

3 SEISMIC EXPLORATION SYSTEM

An example diagram of the unique seismic survey design and exploration process is shown in Figure 2. The system consists of two single-component acceleration sensors (X: longitudinal direction of the tunnel axis), two three-component acceleration sensors (longitudinal (X), transverse (Y), vertical (Z) directions of the tunnel axis), a trigger switch to synchronize the four sensors, and a tablet PC to view and record the sensor data (Figure 3). Each sensor is attached via a jig to the nut of a rock bolt located 10–20 m from the tunnel face.

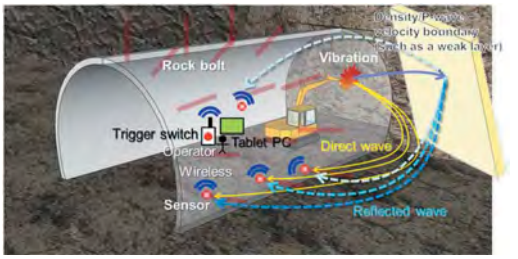

Figure 2. Cartoon of the S-BEAT® seismic survey design for exploring ahead of the tunnel face.

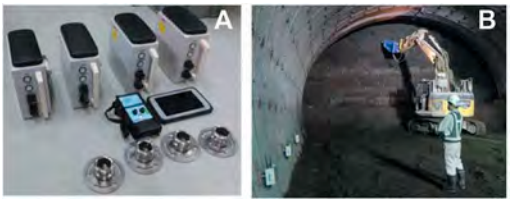

Figure 3. Photographs of the (A) seismic system and (B) on-site surveying.

If the vibration (oscillation) and sensor (receiver) locations in the system, ground P-wave velocity, and reflected-wave arrival times are all known, then the reflected wave is assumed to have originated from a certain point on the isotravel ellipsoid (Ashida et al., 2001). The ellipsoid is created using the vibration and receiving points, which serve as focal points (Figure 4). The installation of multiple sensors means that a point will be formed where the travel-time ellipses overlap if the observed waves reflect from the same point. This overlapping point is a common reflection point and indicates a rock density and/or P-wave velocity boundary. The position and slope of the reflecting surface can be estimated from this overlapping point and the tangent to the point with high reflection intensity, respectively (Figure 4).

The data analysis consists of setting the geometry, performing bandpass filtering, identifying the initial motion of the direct waves (P waves), calculating the rock P-wave velocity, and deconvolution. A single-component sensor is used to calculate the P-wave

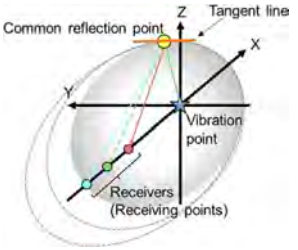

Figure 4. Concept of estimating the reflection point.

velocity. If there is no reference P-wave velocity, then it is assumed to be the P-wave velocity in front of the tunnel face; this value is used in the subsequent reflective surface distribution analysis. A 3D analysis is then performed using the data from the two three-component sensors, whereby the amplitude values (reflection intensity) are weighted according to the directions of reflected wave arrivals in the X, Y, and Z directions. Finally, a 3D map of the imaged reflective surfaces is created. The analysis volume extends 100 m ahead of the tunnel face and ±50 m in both the vertical and transverse directions of the tunnel, with the origin located at the intersection of SL (spring line) and CL (center line) of the tunnel face. Although the penetration depth of the seismic waves depends on the hardness/softness of the rock at the tunnel face, breaker striking produces a weaker vibration than blasting, such that the exploration range is generally up to ~70 m ahead of the tunnel face.

4 AN EXAMPLE ON-SITE APPLICATION

4.1 *Site geology*

An on-site application of the 3D modeling system has been conducted at the Shitara Dam Seto Shitara Line mountain tunnel construction site in Japan. The mountain consists mainly of sandy and siliceous gneiss (and metachert) of the Ryoke metamorphic rock group and diorite intrusions. The key geological concerns before construction included the local distribution of diorite intrusions (due to the difference in strength from the country rocks), weathering of gneiss layers, and the presence of weak layers such as faults. Tunnel construction was initiated with a primary focus on the effects of weathered tunnel faces and partial clay formation; corresponding measures to prevent/mitigate any associated tunnel face collapse were also undertaken. It was therefore necessary to conduct a re-modeling process from the initial model using the exploration results during construction in a timely and accurate manner.

4.2 *Visualization of the exploration data and update of the geological model*

First, we had to determine the update range in the model from the solid model, which was created using general-purpose software (Figure 5A). It is best to limit the update range to the minimum necessary size to shorten the processing time of the model update; the range covered the main and diagonal tunnels at the construction site in the present study (Figure 5B). The initial solid model that was within this range was then converted to a voxel model, which served as the input model for the 3D modeling system.

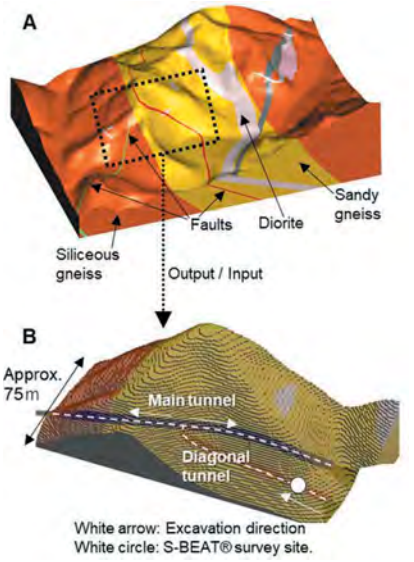

Figure 5. (A) Initial model (solid model) and (B) initial voxel model for SG-ReGrid®.

An example of the modeling system operation is as follows. Br data were obtained along the diagonal tunnel (Figure 6). Fractured strata were recognized 60–65 m from the tunnel entrance in the Br data, thereby prompting the seismic survey to be conducted ~25 m before this weak layer was excavated (Figure 6). The survey results identified five surfaces that were drawn in descending order of reflection intensity (Figure 7). These surfaces are constructed as follows. First, a normal line is drawn from the point at which the reflection intensity is strongest on the radial front of the reflected waves. A surface with an angle that is perpendicular to the normal line is then drawn. This surface is interpreted to represent a rock density and/or P-wave velocity boundary. Incorporating the seismic survey and Br results into the 3D modeling system indicated that the reflection surfaces intersected the weak (fractured) layer (Figure 7). Furthermore, the slope of this reflection surface, which is inclined in the opposite direction of tunnel excavation (i.e., dip slope), highlighted the need to be aware of potential tunnel-face collapse caused by destabilization of this weak layer during excavation.

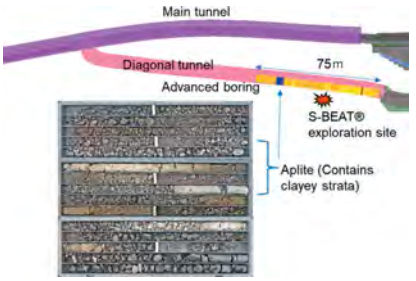

Figure 6. Advanced boring data, and locations of the weak layer (blue) and the seismic survey (star).

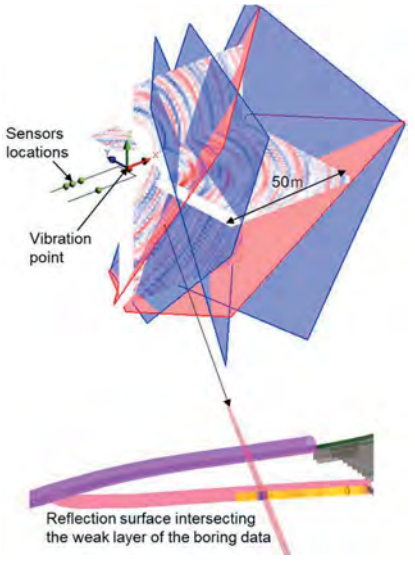

Figure 7. Seismic reflection survey results, which are based on the positions of the boring data and reflective surface.

We then updated the geological model based on these exploration results. We determined that the reflection surface was oriented in the predominant direction of the density and/or P-wave velocity boundary in this area based on past exploration results at multiple sites and added a surface with the same strike and dip (Figure 8A). After moving the boundary surfaces that were parallel to the start and end positions of the weak layer section in the Br data, we defined a newly modeled weak layer in this section (Figure 8B, blue layer). The tunnel face did collapse in this section during excavation (Figure 9). However, construction was safely completed because informed warnings were given well before this weak layer was excavated. The width of the blue layer (weak layer) was increased by ~7 m in the direction of travel based on tunnel-face observations and length of area where tunnel subsidence occurred. We effectively made the necessary design changes because we were able to consider auxiliary construction methods in advance.

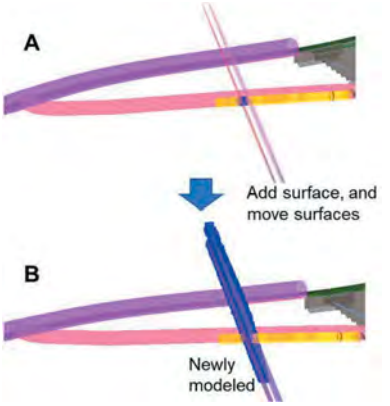

Figure 8. (A) Creating and moving the boundary surfaces (B) subsequent modeling of the weak layer.

Figure 9. Collapse occurred to ~2.0 m depth within the weak layer in the diagonal tunnel.

A similar effect was expected on the tunnel face of the main tunnel owing to the weak layer and its proximity to the diagonal tunnel (20–25 m). The range of this weak layer was initially identified in the main tunnel by creating a plan view and longitudinal section (Figure 10). We then conducted the seismic survey to examine the locations of the weak layers in detail and determine the dominant direction of the boundaries and cracks during the excavation of the main tunnel. The reflected surfaces possessed dip and reverse dip slopes (Figure 10). A V-shaped collapse occurred at the actual tunnel face, as predicted from the reflective surfaces (Figure 11). However, the excavation was completed without any delays owing to the preliminary consideration of face bolting and the long-fore-piling method based on the re-modeling results.

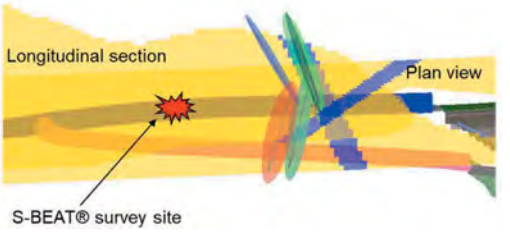

Figure 10. Examining the location of the weak layer in the main tunnel using information in the diagonal tunnel and additional seismic data.

Figure 11. An example of the weak layer in the main tunnel. White lines denote the geological interpretation, indicating fault, Aplite dyke, and major cracks.

5 CONCLUSIONS

We developed a 3D geological model sequential update system, SG-ReGrid®, to predict the geological conditions ahead of the tunnel face and take the necessary precautions during construction. We presented an example application of this update system the Shitara Dam Seto Shitara Line tunnel construction site in Japan, whereby we acquired exploration data along both the diagonal and main tunnels to quickly visualize and re-model the geological conditions during construction. This rapid re-modeling approach allowed us to assess and highlight potential geological hazards lying ahead of the tunnel faces. Furthermore, the 3D imaging of these weak layers provided the ability to smoothly propose design changes to the client, such as the addition of auxiliary construction methods.

We will continue to improve the 3D modeling system through future field applications, whereby we will add additional functions as needed to address the requirements at other tunnel construction environments. We are also working on developing guidelines that will allow non-geologists to update the model information. Furthermore, we are considering improving the software to automate the process based on user-defined thresholds of the input data.

The 3D modeling system is a fundamental technology that improves the accuracy of predictive analysis during tunnel construction. We plan to use this model update technology to predict groundwater flow and associated rock displacement during excavation (e.g., Fukuda et al., 2023).

REFERENCES

Ashida, Y., Matsuoka, T., Kusumi, H., 2001. Seismic imaging technique of looking ahead of tunnel face by use of three components receivers. Japanese Jour. JSCE 680(III-55), 123–129.

Fukuda, T., Yoshikawa, S., Hosono, K., Iwanaga, S., 2023. Development of a ground forecasting system based on the geologic and groundwater conditions in mountain tunneling. Proceedings of World Tunnel Congress, 6pages (Poster presentation: PP_Theme08_09).

Nishi, T., Wakabayashi, N., 2016. Research and development of an exploration method using the vibration during the excavation work. Jour. Japan Soc. Eng. Geol. 56(6), 343–349.

Yoshikawa, S., Aono, Y., Awaji, D., Henmi, R., Adzam, A., Hirano, H., 2021. Improvement of efficiency and generalization of tunnel exploration method. Proceedings of the 15th Japan Symposium on Rock Mechanics, 115–120.

Tunnelling for a Better Life – Yan, Celestino, Thewes & Eberhardt (Eds)
© 2024 The Author(s), ISBN 978-1-032-80042-4
Open Access: www.taylorfrancis.com, CC BY-NC-ND 4.0 license

HSP method-based advanced geological prediction and tunneling parameter pre-control technology for super-large diameter pipe-jacking project

Ziyue Zhao
China Railway Southwest Research Institute Co., Ltd., Chengdu, China

Fu'an Lan
Sichuan Lexi Expressway Co., Ltd., Liangshan Yi Autonomous Prefecture, China

Bin Wang, Lu Meng, Xu Wang & Song Lu
China Railway Southwest Research Institute Co., Ltd., Chengdu, China

ABSTRACT: The super-large diameter pipe-jacking is widely used in the municipal and rail transit works, which has strict technical requirements for real-time and accurate detection or prediction of geological conditions in front of the working face. In view of this, an advanced geological prediction technology based on the HSP method is proposed for the super-large diameter pipe-jacking project for the first time. In this method, the acoustic wave generated in rock breaking by pip-jacking machine is taken as the main transmission signal, and the signal acquisition is completed at the same time of rock-breaking, so as to reduce the influence of geological prediction work on the pipe-jacking construction. In order to verify the geological prediction accuracy of the proposed method, the prediction results are compared with the geological survey data, tunneling parameters and actual excavation conditions, and the results show that the method can effectively distinguish the lithological change area and effectively guide the construction. Based on the prediction results of the HSP method, the fuzzy mathematical theory is used to pre-control the tunneling parameters, and the statistical analysis of the parameters in the abnormal area is carried out to obtain the empirical function, so that it can divide the huge amount of excavation parameters generated in the overall construction process into the characteristic spaces of excavation parameters. And the most realistic results are selected from the ten characteristic spaces of tunneling parameters, so as to analyze the tunneling parameters in different characteristic spaces. Finally, it can provide a reasonable reference range for the actual tunneling parameters and effectively avoid construction risks.

Keywords: Advanced geological prediction, HSP method, Pipe-jacking, Fuzzy mathematical theory

1 INTRODUCTION

With the continuous development of the national economy, the tunnel works in China have a scale ranking first in the world, and municipal pipeline works and underground passage works also keep increasing. The pipe-jacking method can significantly reduce the construction's impact on the surrounding environment and road traffic and has wide application prospects. The super-large diameter pipe-jacking construction involves risks affected by complex geological conditions, and tunnel safety accidents in such construction cause immeasurable losses every year. Therefore, advanced geological prediction for tunnels plays a vital role in judging the geological conditions ahead of the tunnel face. In the rapid emergence of mechanized construction, traditional geological prediction technologies are also being upgraded and improved to adapt to mechanized construction scenarios. For example, onboard HSPs, induced polarization device, and other advanced geological prediction equipment mounted on TBMs have been widely used in various regions of China[1-3].

To avoid tunnel safety risks in pipe-jacking, TBM, and other mechanized construction, this paper will adopt the HSP method-based advanced geological prediction system for guidance of construction. In 2008, Li Cangsong et al.[4] first proposed the passive source HSP (horizontal sonic/seismic profiling) detection technology that uses the vibration signal generated in TBM cutterhead's rock-shearing as the excited seismic source. In 2019, Lu Song, Wang Xu, et al.[5-8] further improved the HSP method to make it more suitable for TBM construction and summarized

DOI: 10.1201/9781003495505-89

detailed treatment process flow and design concepts. For the technology, the elastic waves generated in the TBM cutterhead's strata-shearing are taken as an excitation signal to realize the quick and efficient acquisition of data. However, the modules for site environmental noise processing have still not been studied systematically. In 2021, Zhao Ziyue, et al.[9] started with the study of site environmental noise and improved the detection process flow of the existing HSP method based on the characteristics of TBM construction on the site.

In this paper, Yanziji New Town Comprehensive Pipe Gallery Project in Qixia District, Nanjing City is taken as a case, and the HSP method is adopted for advanced geological prediction detection. The inversion results obtained are compared with the actual geological survey data, and massive tunneling parameters are simultaneously collected for analysis and processing. Finally, the accuracy of the HSP method is verified based on the actual tunneling conditions. In 2009, Song Kezhi, et al.[10] used fuzzy mathematical theory to identify the conditions of tunnel surrounding rock during TBM tunneling, and discussed and revealed the relation between the specific thrust and specific torque of the cutterhead, the correlation of the cutterhead thrust, torque, and cutting depth with geological conditions, as well as the corresponding relation between different surrounding rock conditions and TBM tunneling states. In this paper, based on the test results of the HSP method, the fuzzy mathematical theory is used for tunneling parameter pre-control, and statistical analysis is performed on the abnormal area parameters to obtain an empirical function. The tunneling parameter characteristic spaces generated by massive tunneling parameters throughout the construction process are divided into multiple zones, and the most realistic results are selected from ten tunneling parameter characteristic spaces for the analysis and description of tunneling parameter points in different characteristic spaces. Finally, this paper provides a reasonable reference range for actual construction to avoid construction risks.

2 HSP METHOD-BASED ADVANCED GEOLOGICAL PREDICTION TECHNOLOGY FOR DRILL JUMBO ROCK-BREAKING SEISMIC SOURCE

The HSP method is based on the Huygens–Fresnel principle and Fermat's principle and requires the difference in wave impedance of stratum media as a premise. The strata ahead of the tunnel face are identified according to the propagation characteristics of the elastic wave field, including velocity, amplitude, etc. According to the characterization attributes of different components, densities, and elastic moduli in the underground media, a detailed analysis is conducted based on the characteristics of the underground structure. Based on the observation of the actual tunnel face, the conditions of exposed surrounding rocks are compared. The difference in results is finally summarized for a reasonable adjustment of the inversion parameters, and a result profile reflecting the adverse geological conditions is obtained. Common adverse geological conditions include faults, weathered fracture zones, karst caves, groundwater-enriched zones, etc. The core formula of reflection and transmission characteristics of wave field propagation is as follows:

$$R_{12} = \frac{\rho_2 v_2 - \rho_1 v_1}{\rho_2 v_2 + \rho_1 v_1} \tag{1}$$

Where, R_{12} is the reflection coefficient, $\rho 1$ is the density of the surrounding rock ahead of the tunnel face; ρ_2 is the density of adverse geological (body); v_1 is the longitudinal wave velocity of the surrounding rock ahead of the tunnel face; v_2 is the longitudinal wave velocity of the adverse geological (body).

2.1 *Advanced geological prediction scheme design for super-large diameter pipe-jacking*

Currently, the passive source HSP method-based prediction technologies for TBM construction have been applied in many projects, realizing a breakthrough in prediction method without shutting down a TBM or affecting construction. Among them, the mounted and portable HSP method-based prediction technologies have been widely used in many projects at home and abroad. They support continuous data collection and can form a TBM data database. The rich case experience has allowed the HSP technology to be improved.

Based on the existing HSP technology for TBM construction, the overall scheme design for advanced geological prediction for super-large diameter pipe-jacking is realized, the collection and processing of rock-breaking signals of pipe jacking equipment is improved, the technical process is optimized, and a complete prediction flow chart is developed, as shown in Figure 1.

According to the actual construction environment on the site and the tunneling situation of the pipe jacking machine, the installation position of the HSP

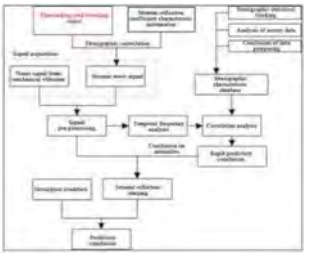

Figure 1. Flow chart of prediction for mechanized construction with drill jumbo.

equipment is reasonably allocated. The onboard equipment is installed on a stable platform to avoid equipment failure due to mud gushing, as shown in Figure 2.

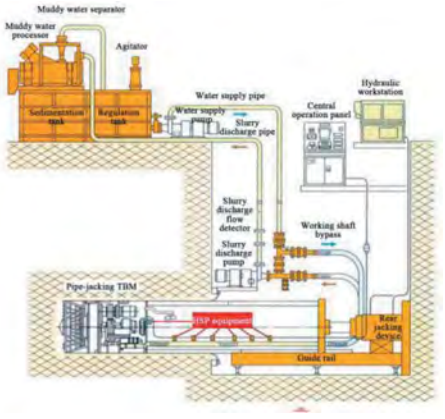

Figure 2. Schematic diagram of onboard HSP equipment.

2.2 *Field testing*

Yanziji New Town Comprehensive Pipe Gallery is located in Qixia District, Nanjing City. It is an important part of Jiangnan Ring Trunk Pipe Gallery of Najing. In the Project, the pipe diameter is 5.4 m (OD). With respect to the geological conditions of the pipe-jacking section, the upper part is clay soil, and the middle and lower parts are harder rock, i.e., the strata are soft at the upper part and hard at the lower part. The strengths of the upper and lower strata are quite different. This is very likely to cause the deflection of the pipe jacking machine's head toward the weaker strata and the continuous ascending of the pipe jacking machine's head. Under severe conditions, this may even cause land upheaval, sharp increase of jacking force, and jacking failure.

The chainage of the tunnel face under test is K0 +658. The original waveform curves collected on the site are subject to data processing and analysis. The inversion analysis results are shown in Figure 3 and Figure 4, the analysis results are shown in Table 1, and the three-dimensional results of the inversion analysis are shown in Figure 5.

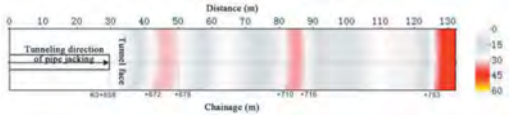

Figure 3. Results of inversion analysis on detection at Chainage K0+658 (0 m position of XOY slice – horizontal tunnel axis slice).

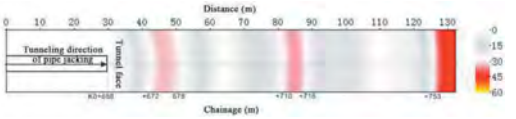

Figure 4. Results of inversion analysis on detection at Chainage K0+658 (0 m position of ZOY slice – vertical tunnel axis slice).

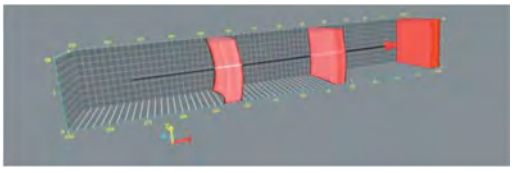

Figure 5. Three-dimensional results of inverse analysis on detection at Chainage K0+658.

Table 1. Test and analysis results.

Detection range	Length (m)	Test result
K0+658~K0+716	58	The detection results show that the local parts in this section have weak reflection anomalies. Analysis suggests that the rock mass in this section is relatively fragmented as a whole, and lithological changes may exist in local areas. In the detection range, chainage sections K0+672~K0+678 and K0+710~K0+716 have weak reflection anomalies, indicating that differences in wave impedance exist in these chainage sections. Comprehensive analysis shows that the detection range is an area of lithological changes and the surrounding rock is of poor stability.
K0+716~K0+758	42	The detection results show that strong reflection anomalies exist in the local parts of the detection range. Analysis suggests that strong reflection anomalies in the section (K0+753~K0+758) may be caused by the difference in wave impedance between the lithological change area and the break-out free face. The rock mass in the detection range is still relatively broken.

Figure 6. Field testing.

According to the comparison of the geological survey data in Figure 7, the HSP detection results of the lithological change area show the existence of anomalies, which is basically consistent with the geological survey results. Strong reflection anomalies exist at the break-out free face, which is consistent with the actual situation. This proves that the HSP method is feasible and effective for pipe-jacking projects.

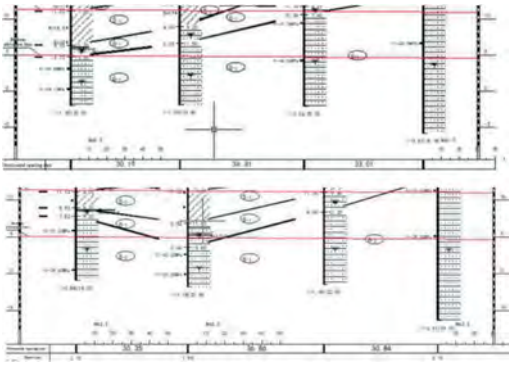

Figure 7. Geological survey data.

3 RESEARCH ON JACKING PARAMETER PRE-CONTROL BASED ON FUZZY MATHEMATICAL THEORY

3.1 *Fuzzy mathematical theory analysis*

During pipe jacking, the observation of the geological characteristics of the surrounding rock is greatly restricted by the construction conditions. The surrounding rock condition can only be judged based on the observation through the geological observation window and the slag discharge situation. The judgment often involves a certain degree of subjectivity and error. Therefore, the data obtained by various means must be fully utilized for the timely judgment of the surrounding rock conditions. Research shows that the analysis of tunneling parameters is conducive to the effective judgment of the geological conditions of the surrounding rock and the objective reflection of changes in the surrounding rock encountered. Therefore, the cutterhead speed, cutterhead torque, total thrust, flow rate in the slurry inlet pipeline, and flow rate in the slurry discharge pipeline are selected as parameters for judging surrounding rock conditions during pipe jacking. These five parameters are grouped in pairs and subject to analysis based on the fuzzy mathematical method, and the most representative parameter models are summarized.

To ensure the accuracy and universality of statistical data, the existing data of each link are expanded in detail to increase the overall data volume. Tunneling time is introduced into the new data, and data is collected at a rate of one data point every 1-3 minutes to ensure data authenticity and effectiveness and reduce the impact of errors caused by the artificial selection of data. Finally, 9968 data sampling points are obtained. Based on this, correlation analysis of various parameters is carried out and the comparison is shown in Figure 8.

It can be clearly seen from the figure that throughout the entire construction stage, strong correlations exist between four pairs of data: the cutterhead torque and the total thrust, the total thrust and the

	1	2	3	4	5
1	1	-0.1109	0.0466	-0.0356	0.0150
2	-0.1109	1	0.3348	-0.0703	-0.0602
3	0.0466	0.3348	1	0.3562	0.3273
4	-0.0356	-0.0703	0.3562	1	0.5146
5	0.0150	-0.0602	0.3273	0.5146	1

Figure 8. Comparison of correlation between parameters.

flow rate in the slurry inlet pipeline, the total thrust and the flow rate in the slurry discharge pipeline, as well as the flow rate in the slurry inlet pipeline and the flow rate in the slurry discharge pipeline. The cutterhead torque and total thrust are commonly used in tunneling parameter research and are very representative parameters. This can reflect the problem of low correlation between the cutterhead torque and total thrust due to human statistical influence in the previous section. With the support of massive data, the interference of human factors is eliminated, and the result generally conforms to the research law of tunneling parameters.

3.2 *Analysis of actual jacking parameters*

During the pipe-jacking process under certain output thrust and torque conditions, the thrust and torque parameters are obtained through the data acquisition system. They collectively constitute a tunneling characteristic space Ω, and the tunneling parameters of each tunneling test constitute a subspace Ωi of space Ω. By plotting the tunneling parameter point (xi, yi) obtained in a test on the plane Ω, the subspace Ωi can be obtained, as shown in Figure 9. In the subspace Ωi, regression analysis on the tunneling parameter point (xi, yi) is carried out to obtain the regression curve y=kx. By controlling the accuracy of the regression analysis, the boundary curves y_1 =kx-b and y_2=kx+b of the prediction interval are obtained. Then, a curve $y_3=k_3x+c$ is made to intersect the curve y=kx at the boundary between the typical mudstone parameters and the typical sandstone

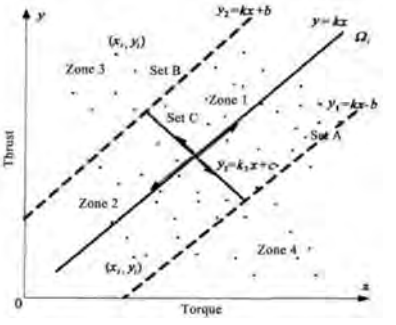

Figure 9. Corresponding relation between tunneling parameters and surrounding rock conditions and their positions in subspace.

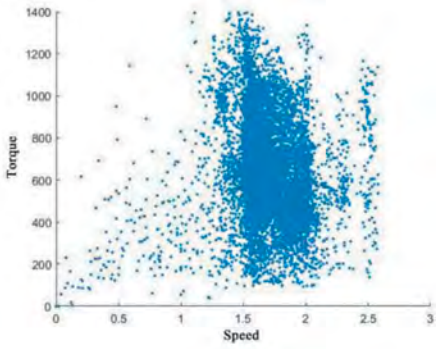

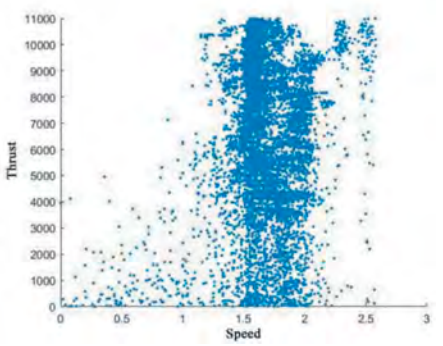

(1) Corresponding relation between speed and torque (2) Corresponding relation between speed and thrust

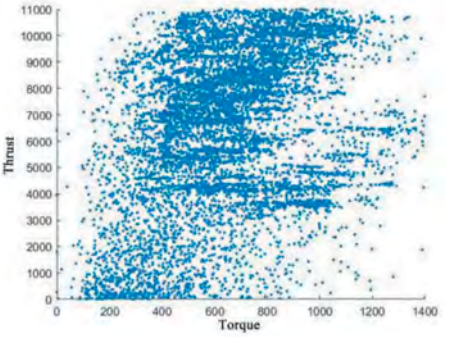

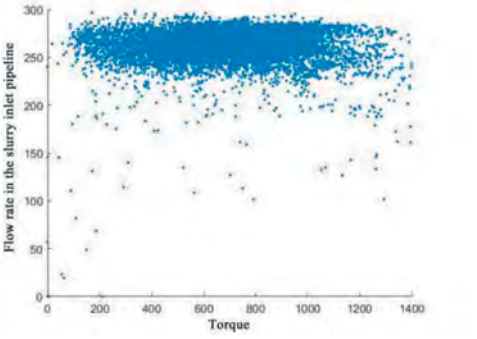

(5) Corresponding relation between torque and thrust (6) Corresponding relation between torque and flow rate in the slurry inlet pipeline

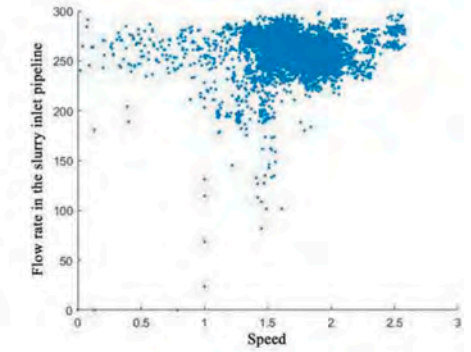

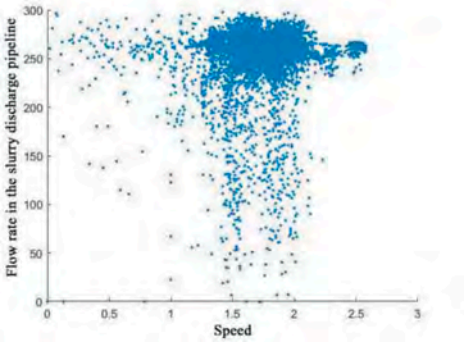

(3) Corresponding relation between speed and flow rate in the slurry inlet pipeline (4) Corresponding relation between speed and flow rate in the slurry discharge pipeline

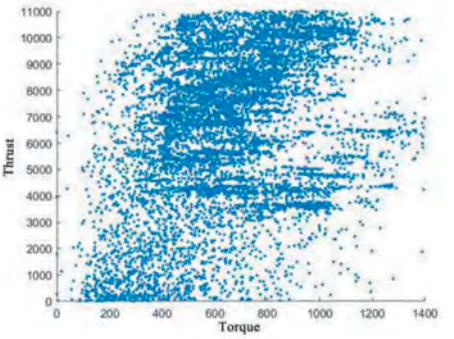

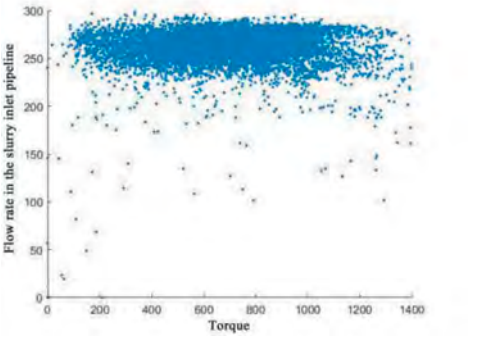

(7) Corresponding relation between torque and flow rate in the slurry discharge pipeline (8) Corresponding relation between thrust and flow rate in the slurry inlet pipeline

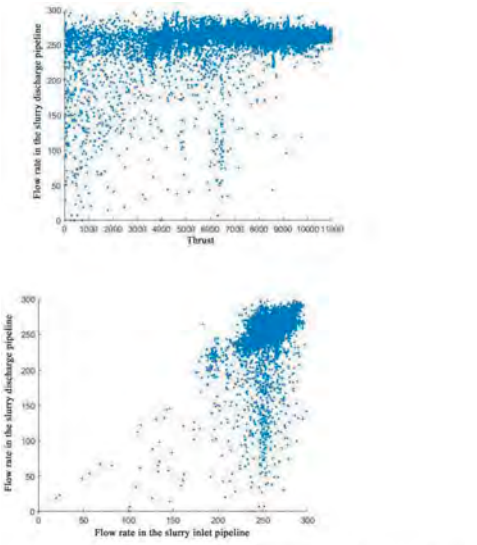

(9) Corresponding relation between speed and flow rate in the slurry discharge pipeline (10) Corresponding relation between flow rate in the slurry inlet pipeline and flow rate in the slurry discharge pipeline

Figure 10. Corresponding relation between tunneling parameters and Their positions in Subspace.

parameters and divide the curve y=kx into two parts. So far, three sets have been established in Space Ω_i, namely A: y_1=kx-b, B: y_2=kx+b, and C: y_3=k_3x+c. They divide Space Ω into four zones, as shown in Figure 9.

Based on the establishment of this relation model and 9968 data, 5 parameters are grouped in pairs and the position of the corresponding relation of each pair is plotted in the subspace. The results are shown in Figure 10 below.

It can be seen from the figure that only Figure 10-(5) and (10) fit the regression model. Since the flow rate in the slurry inlet pipeline and the flow rate in the slurry discharge pipeline are not the parameters of the pipe jacking machine itself, the torque and the thrust are more representative, and the selection of these two parameters is more convincing and consistent with the parameter selection results analyzed by scholars in the industry.

3.3 *Torque-thrust research model*

Taking the torque and thrust corresponding relation as the main research model, the tunneling status of pipe-jacking under different surrounding rock conditions has a certain corresponding relation with the zones in Figure 9. When pipe jacking is carried out in a relatively complete and homogeneous stratum, the cutterhead torque and cutterhead thrust change basically in proportion. Therefore, when the tunneling parameter point (x_i, y_i) falls in Zone 1, the torque and thrust are both relatively high, indicating that the pipe jacking is carried out normally in a hard stratum. When the tunneling parameter point (xi, y_i) falls in Zone 2, the torque and thrust are both low, indicating that the pipe jacking is carried out normally in a soft stratum. When the tunneling parameter point (x_i, y_i) falls in Zone 3, the cutterhead thrust increases abnormally, but the cutterhead torque is very low, indicating that the pipe-jacking cutterhead is held by compressive rocks or is stuck and unable to adjust its displacement normally, or it encounters strong obstacles. When the tunneling parameter point (x_i, y_i) falls in Zone 4, the cutterhead torque increases abnormally, but the thrust is not large, indicating that the surrounding rock is abnormally broken, the tunneling face collapses seriously, and the cutterhead slag outlet is stuck and unable to discharge slag normally, causing the torque to increase abnormally.

Euclidean distance is used for fuzzy discriminant calculation, and the distances (as per the distance from a point to a straight line) between the tunneling parameter point (x_i, y_i) and the points in fuzzy sets (A, B, C) are respectively

$$d_{1i} = \frac{\left|kx_i - y_i - \hat{\sigma}_e u_{1-\frac{\alpha}{2}}\right|}{\sqrt{k^2+1}}, y_i < y_1(x_i) \tag{2}$$

$$d_{2i} = \frac{\left|kx_i - y_i - \hat{\sigma}_e u_{1-\frac{\alpha}{2}}\right|}{\sqrt{k^2+1}}, y_i \geq y_2(x_i) \tag{3}$$

$$d_{3i} = \frac{|k_3 x_i - y_i + c|}{\sqrt{k_3^2+1}}, y_1(x_i) \leq y_i \leq y_2(x_i) \tag{4}$$

Then, each distance is normalized to obtain d_{01i}, d_{02i}, d_{03i}. According to the relation between the normalized distance and the membership degree, the membership degree of the parameter point (x_i, y_i) to fuzzy sets (A, B, C) can be obtained, as shown below

$$\mu_A = \exp\left(\frac{-d_{01i}}{(1-d_{01i})}\right) \tag{5}$$

$$\mu_B = \exp\left(\frac{-d_{02i}}{(1-d_{02i})}\right) \tag{6}$$

$$\mu_C = \exp\left(\frac{-d_{03i}}{(1-d_{03i})}\right) \tag{7}$$

The greater the distance between the parameter point (x_i, y_i) and a fuzzy set, the smaller the membership degree.

(1) When y_1 (x_i) $\leq y_i < y_2$ (x_i), the shield tunneling is considered to be in a normal state. At this time, if $y_i \geq y_3$ (x_i), the smaller the membership degree μ_C, the harder the rock; if $y_i < y_3$ (x_i), the smaller the membership degree μ_C, the softer the rock.
(2) When $y_i \geq y_2$ (x_i), if the membership degree μ_B is close to 1.0, it means that the shield tunneling is basically normal, and the smaller the μ_B is, the greater the possibility that the thrust is higher than that in the normal state.
(3) When $y_i < y_1$ (x_i), if the membership degree μ_A is close to 1.0, it means that the shield tunneling is basically normal, and the smaller the μ_A is, the greater the possibility that the torque is higher than that in the normal state.

The actual parameter data are substituted into the above equations, and sets A and B are obtained as follows:

$$y = 20.28x + 1325.4 \tag{8}$$

$$y = 20.28x - 9807.28 \tag{9}$$

According to the actual parameters on the site, strata 5-3 dense medium sand and 6-2 moderately dense coarse sand of different lithological properties in the geological survey data are distinguished. Combining the field data and empirical parameters, the following equation is obtained:

$$y = -0.04931x + 5885.597 \tag{10}$$

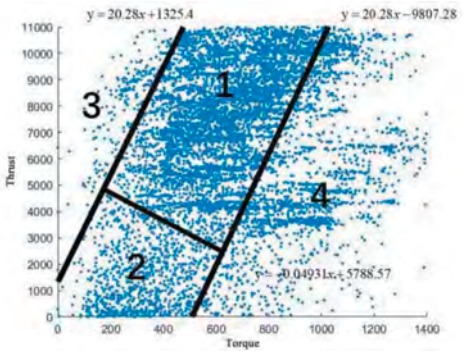

Figure 11. Corresponding relation between actual tunneling parameters and surrounding rock conditions and their positions in subspace.

Based on the corresponding relation in the above figure, when any data falls in Zone 4, it can be identified there is a large abnormal area such as a free face. Such data in subsequent construction requires more attention. When such data continuously falls in Zone 4, the TBM needs to be shut down for processing and analysis of causes.

3.4 *Pre-control analysis*

Based on the above content and overall analysis, the existing parameter patterns are summarized, and the main parameter ranges are divided, as shown in Table 2 below. The mathematical fuzzy method and the clustering analysis method are adopted to establish a torque-thrust model. When the parameter point falls into Zone 1, it is considered that the surrounding rock is hard or the pipe jacking is in the launching stage. When the parameter point falls into Zone 2, the pipe jacking machine is considered to be in a section with the surrounding rock being relatively broken and of poor stability. When the parameter point falls into Zone 3, the pipe jacking machine is considered to be in a normal tunneling stratum. When the parameter point falls into Zone 4, it is considered that the surrounding rock is overall of poor stability and there may exist underground anomalies such as hazardous areas and solution cavities, or free face before break-out. The conditions need to be comprehensively judged based on the geological survey data and other information. The construction contractor needs to pay more attention, strictly monitor the tunneling parameters and slag discharge situation, and be prepared for emergencies.

Table 2. Parameter pre-control analysis.

Parameter range	Cutterhead speed	Cutterhead torque	Total thrust	Flow rate in the slurry inlet pipeline	Flow rate in the slurry discharge pipeline
Normal range	1.6-2.2	6000-10000	400-1000	280-250	260-240
Abnormal areas such as solution cavities	Below 1.4	Below 5000	Above 1200	Below 220	Below 220

4 CONCLUSIONS AND SUGGESTIONS

(1) For the advanced geological prediction scheme design for super-large diameter pipe-jacking, the HSP method-based advanced geological prediction technology is applied for the first time in super-large diameter pipe-jacking. The accuracy of the prediction technology is verified based on the geological survey data, tunneling parameters, and actual tunneling conditions, and it is proved that this technology can be used to identify lithological change areas and guide construction.
(2) Based on the identification results of the HSP method, the fuzzy mathematical theory is used for tunneling parameter pre-control, and statistical analysis is performed on the abnormal area parameters to obtain an empirical function. The

tunneling parameter characteristic spaces generated by tens of thousands of tunneling parameters are divided into multiple zones. Finally, it is determined that the parameter characteristic space established with torque and thrust is the most realistic result.

(3) Based on the parameter analysis results, a parameter characteristic space is established with torque and thrust, providing a reasonable reference range for actual construction to avoid construction risks.

REFERENCES

[1] Rector III, J.W. and Marion B.p. 1991, The use of drill-bit energy as a downhole seismic source: Geophysics 56, 628–634.

[2] James W. Rector III and Bob A. Hardage, 1992, Radiation pattern and seismic waves generated by a working roller-cone drill bit: Geophysics 57, 1319–1333.

[3] Jacon B. U. Haldorsen, Dougkas E. Miller, and John J. Walsh, 1995, walk-away VSP using drill noise as a source. Geophysics: vol. 60, p.978–997

[4] Li Cangsong, Gu Ting, Ding Jianfang, et al. Horizontal sound probing(HSP) geology prediction method appropriated to TBM construction [J]. Journal of Engineering Geology, 2008(S1): 111–115.

[5] Lu Song, Li Cangsong, Wu Fengshou, et al. Application of HSP (horizontal sonic profiling) sound wave reflection method to geological prediction of TBM tunnel of Hanjiang River-Weihe River Water Diversion Project [J]. Tunnel Construction, 2017, 37(2): 236.

[6] Lu Song, Meng Lu, Wang Xu, et al. HSP advance geological forecast method of tunnel technique and image analysis [J]. Modern tunnel technology, 2019 (S01): 6. DOI: CNKI: SUN: XDSD. 0.2019 - S1-021.

[7] Wang Xu, Meng Lu, Yang Gang, et al. Study on influencing factors of multi-source seismic interferometry imaging results for tunnel advance geological prediction [J]. Modern Tunnel Technology, 2019, 56(5):9.

[8] Lu Song, Wang Xu, Li Cangsong, et al. Design and implementation of real-time prediction technology of HSP method for TBM construction [J]. Tunnel Construction (Chinese & English), 2019, 39(8):7.

[9] Zhao Ziyue, You Yuanming, Meng Lu, et al. Improvement and application of horizontal sonic/ seismic profiling method in advance geological prediction of shield tunneling[J]. Tunnel Construction, 2021, 41(8): 1344.

[10] Song Kezhi, Yuan Dajun, Wang Mengshu. Based on the shield tunneling parameters fuzzy discriminant analysis of tunnel surrounding rock [J]. Journal of civil engineering, 2009 (1): 7. DOI: CNKI: SUN: TMGC. 0.2009-01-024.

Taylor & Francis
Taylor & Francis Group
http://taylorandfrancis.com

Ground stability and consolidation

Taylor & Francis
Taylor & Francis Group
http://taylorandfrancis.com

Tunnelling for a Better Life – Yan, Celestino, Thewes & Eberhardt (Eds)
© 2024 The Author(s), ISBN 978-1-032-80042-4
Open Access: www.taylorfrancis.com, CC BY-NC-ND 4.0 license

Excavation induced settlement in Sydney area

Giovanny Alvarado, Somaye Sadeghian & Yang Dong
AECOM Australia, Sydney, Australia

ABSTRACT: Excavations affect the state of in-situ stress in the ground, leading to displacements in adjacent buildings and structures. In Hawksbury Sandstone in Sydney, horizontal stresses are higher than vertical stresses, posing a risk of excavation-induced displacement even in good quality rock. This paper continues the research of other authors and aims to introduce a simplified approach to estimating excavation-induced stress in Hawksbury Sandstone without numerical modeling. In the authors' previous study (to be published in the Australian Geomechanics Journal in 2024), a comprehensive investigation using three-dimensional finite element analysis was conducted to determine the displacement trough at the excavation edge. Ground type, excavation depth, and width were considered as variables in these analyses. In this paper, orientations of the principal in-situ stress and length/width ratio are adopted as variables, and correlations are provided to relate the maximum lateral displacement to the orientation of the locked-in stress as well as the length/width ratio of the excavation. The outcomes of this study offer valuable insights for assessing potential damage to buildings during excavations in Sydney and can be used in preliminary design stages before detailed planning.

Keywords: 3D modelling – FLAC3D – PLAXIS3D

1 INTRODUCTION

Excavations lead to changes in the stress distribution within the surrounding ground, resulting in excavation-induced lateral displacement. Such changes in stress are particularly evident in open excavations in the Sydney region, where the horizontal stress resulting from tectonic activities at shallow depths exceeds the vertical stress. As a result, the existing stress conditions are commonly characterized using established relationships that outline in-situ stress as a function of depth (Pells (2004), Bertuzzi (2014), Oliveira and Parker (2014), Hewitt and Kitson (2022), and Lochaden et al. (2019)). In the previous study by the authors, a simplified process for estimating lateral excavation-induced displacement was proposed. The simple correlations provided to estimate (1) the maximum lateral displacement at the edge of the excavation and (2) the displacement trough along the excavation. Initially, a dataset (as shown in Figure 1) was generated by analyzing 60 finite element models of open excavations conducted in Plaxis3D (V22). Various classifications of Sandstone, depths of excavation, and widths were incorporated into the Plaxis3D models, enabling the computation of displacements at the excavation boundary. The independent variables considered were depth, width, and the class of Hawkesbury Sandstone, and the approach of Least Squares Linear Regression was employed to establish the relationship between excavation-induced lateral displacement and the independent variables. For the sake of simplification, the following assumptions were made: 1) the major and minor locked-in stresses were assumed to be perpendicular to the excavation; and 2) the excavation has a box shape. Figure 2 illustrates these assumptions. Herein, the effect of major and minor locked-in horizontal stress orientation on the lateral excavation-induced displacement is studied. Next, the effect of Length over Width ratio on the estimated lateral displacement is assessed. The paper focused on Hawkesbury Sandstone Class II, III, and IV, with excavation depths

Figure 1. Dataset was created from 60 open-excavation models.

DOI: 10.1201/9781003495505-90

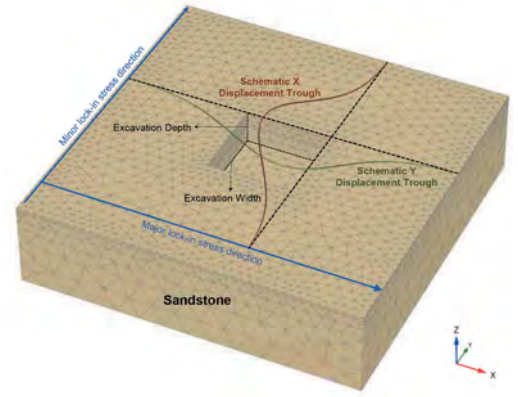

Figure 2. Plaxis3D model.

ranging from 5m to 20m and widths from 10m to 50m. The paper acknowledges certain limitations. It specifies the applicability of the proposed equations to specific conditions, such as the range of sandstone classes, excavation depths, and widths considered in the study. It also emphasizes that the findings pertain to lateral displacement at ground level and do not account for the influence of adjacent excavations on in-situ stress. Despite these limitations, the paper provides a comprehensive and practical approach for assessing excavation-induced lateral displacement in the Sydney region.

1.1 *Maximum displacements*

The paper defined the maximum excavation-induced lateral displacement (δ_{Max}) at the direction of major principal stress as a function of excavation width (W), and excavation depth (D) for different rock class. Equation 1 and 2 were proposed for Sandstone Class III, and II, respectively.

$$\delta_{Max-III}(mm) - 5.94 - 1.16D(m) \\ -0.51W(m) + 3.01\sqrt{D(m) * W(m)} \quad (1)$$

$$\delta_{Max-II}(mm) = -4.63 - 1.13D(m) \\ -0.43W(m) + 2.75\sqrt{D(m) * W(m)} \quad (2)$$

Maximum lateral displacement at the direction of minor principal stress can be estimated from Equation 3.

$$\frac{\delta_{Max(Y-min)}(mm)}{W(m)} = 0.64 * \left(\frac{\delta_{Max(X-max)}(mm)}{W(m)}\right)^2 \quad (3)$$

Where:$\delta_{Max(Y-min)}$: maximum excavation-induced lateral displacement in the direction of the minimum horizontal locked-in stress (mm), see Figure 2

$\delta_{Max(X-max)}$: maximum excavation-induced lateral displacement in the direction of the maximum horizontal locked-in stress (mm)

W: Width of the excavation (m), see Figure 2

1.2 *Displacement trough*

The paper also suggests Equation 4 for X and Y displacement trough (refer to Figure 2). Equation 4 is defined based on δ_{Max} values in section 2.1.

$$\frac{\delta}{\delta_{Max}} = \exp\left(\frac{-4.685\ X^2}{W^2}\right) \quad (4)$$

Where, δ : excavation-induced lateral displacement along the edge of the excavation. δ_{Max}: maximum excavation-induced lateral displacement along the edge of the excavation. W: excavation width in meter. X: distance from the centre of the excavation in meter.

2 FLAC3D MODELS –TO GENERATE DATABASE

In this study and as a continuation of the previous paper, a dataset was generated by analyzing 220 finite difference models of open excavations in FLAC3D 9.00 (Itasca, 2023).

The cases analyzed are depicted in Figure 3. The excavation width was maintained at a constant value of 20 meters, while the excavation length varied within the range of 20 meters to 60 meters in increments of 4 meters (20m, 24m, 28m, 32m, 36m, 40m, 44m, 48m, 52m, 56m, 60m). The analyses were conducted in both Sandstone Class II and III, incorporating different orientations of the major principal stress as an additional variable. The orientations

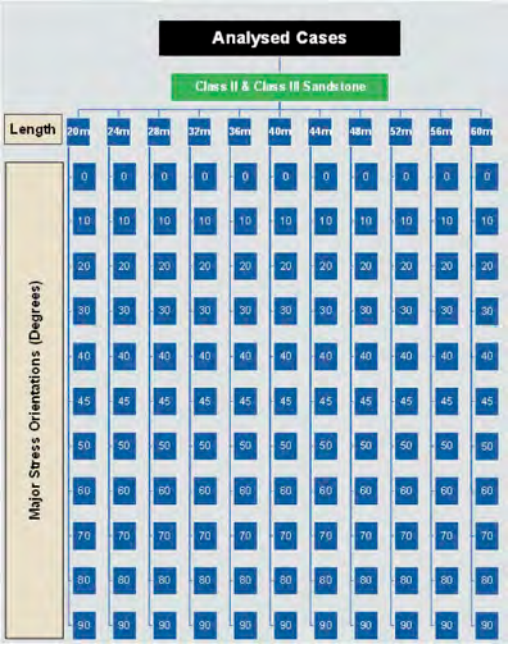

Figure 3. Analysed cases; excavation width and depth are assumed to be constant and equal to 20m.

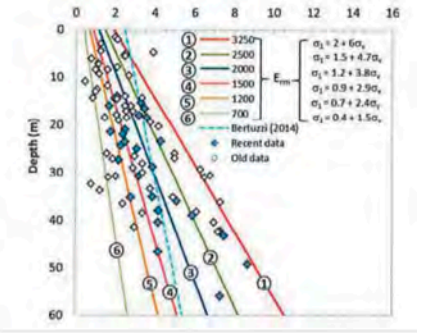

(a) Major principal stress

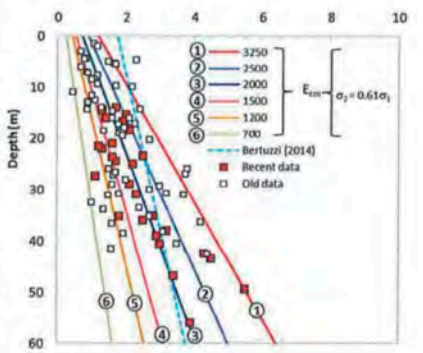

(b) minor principal stress

Figure 4. Major and minor horizonal stress (Oliveira and Parker, 2014).

Table 1. Parameters adopted in the numerical models.

Hawkesbury Sandstone - Class	Unit weight (kN/m3)	Vertical Young's modulus (GPa)	Horizontal Young's modulus- (GPa)	Poisson's ratio
II	24	2.55	3.4	0.2
III	24	3.0	4.0	0.2

Table 2. In situ stress for rock excavation design in Hawksbury Sandstone in Sydney.

	Horizontal In Situ Stress		Vertical Stress (MPa)
Hawkesbury Sandstone - Class	$\sigma_{H-Major}$ (MPa)	$\sigma_{H-Minor}$ (MPa)	σ_V (MPa)
II	$1+3\sigma_V$	$0.6\sigma_{H-Major}$	0.024 x depth (m)
III	$0.7+2.2\sigma_V$	$0.6\sigma_{H-Major}$	0.024 x depth (m)

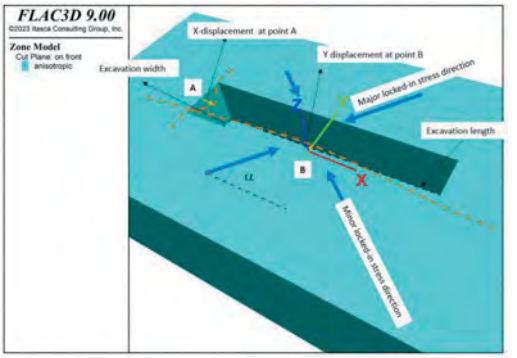

Figure 5. Model geometry.

were varied at angles of α=0, 10, 20, 30, 40, 45, 50, 60, 70, 80, and 90 degrees.

An equivalent continuum approach was adopted for the geomechanical behavior of Hawkesbury Sandstone II and III. The horizontally bedded Hawkesbury Sandstone was modeled with a transversely isotropic elastic model. Table 1 provides the equivalent continuum design parameters adopted in the study. The values in Table 1 were selected based on previous experience in this area.

Regarding Figure 4a and 4b (Oliveira and Parker, 2014), the locked-in stress reported in Table 2 was adopted

The orientation of Major locked-in horizontal stress has defined as a variable with respect to the excavation as shown in Figure 5.

3 LATERAL DISPLACEMENT VERSUS MAJOR PRINCIPAL STRESS ORIENTATION

This section examines the effect of the orientation of the major lock-in stresses (α). Figure 5 illustrates the geometry of the models. Points A and B are designated at the edge of the excavation, positioned at Y=0 and X=0, respectively. α is defined as the angle formed between the major horizontal locked-in stress vector and the X-direction (as depicted in Figure 5).

The orientation of the major locked-in stress varied at angles of α=0, 10, 20, 30, 40, 45, 50, 60, 70, 80, and 90 degrees, and the displacements at points A and B (as indicated in Figure 5) were calculated using FLAC3D.

The excavation width remains constant at 20m in all analyzed cases, while the excavation length varies from 20m to 60m. Figures 6 and 7 present the results from the analyzed cases. Figure 6 showcases the impact of the major locked-in stress orientation on excavation-induced lateral displacements.

Graphs in Figures 6a and 6b display the maximum lateral displacement along the width of the excavation (lateral displacement in the X-direction at point A in Figure 5) for Sandstone Class II and III.

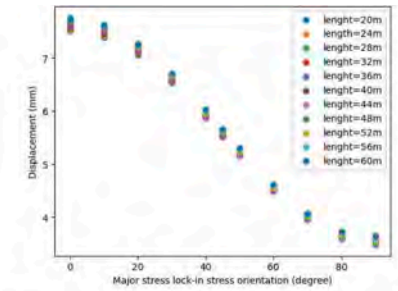

(a) Sandstone Class II – maximum lateral displacement at point A versus α value

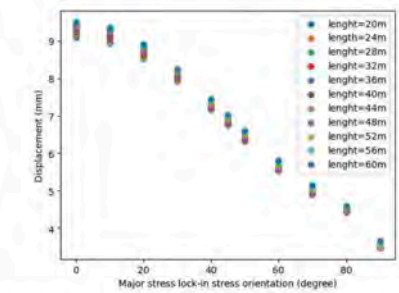

(b) Sandstone Class III – maximum lateral displacement at point A versus α value

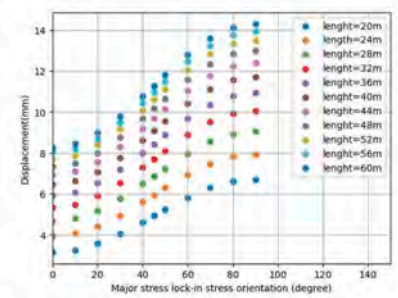

(c) Sandstone Class II – maximum lateral displacement at point B versus α value

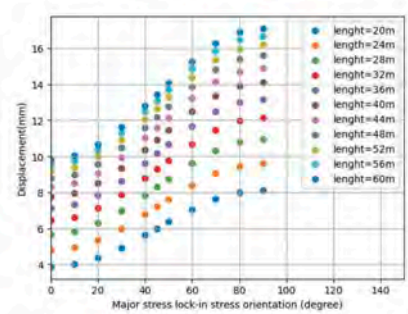

(d) Sandstone Class III – maximum lateral displacement at point B versus α value

Figure 6. Maximum lateral displacement along the excavation length and width versus α value.

Figure 6a demonstrates that the maximum X-displacement at point A occurs when the major locked-in stress aligns with the X-direction, decreasing as α increases from 0 to 90. A similar trend is observed in both Sandstone Class II and III, although lateral displacements are higher in Class III (Figure 6b) compared to Class II.

Figures 6c and 6d depict the maximum lateral displacement along the length of the excavation in the Y-direction (Y-displacement at point B, as seen in Figure 5). Figure 6c indicates that the maximum Y-displacement at point B occurs when the major locked-in stress aligns with the Y-direction, decreasing as α decreases from 90 to 0. Similar trends are observed in both Sandstone Class II and III, with higher lateral displacements in Class III (Figure 6d) compared to Class II.

3.1 *Normalised lateral displacements*

Figure 6 shows that the occurrence of maximum lateral displacements at points A and B is observed at orientations α=0 degrees and α=90 degrees, respectively.

Figure 7 illustrates normalized lateral displacements versus α values. In Figures 7a and 7b, the lateral displacement at point A has been normalized with respect to its maximum value (which occurs at α=0, i.e., when the major horizontal locked-in stress is perpendicular to the excavation width). Figures 7a and 7b show the normalized displacement for excavations in Sandstone Class II and III, respectively.

In Figures 7c and 7d, the lateral displacement at point B has been normalized relative to its maximum value, occurring at α=90 degrees, where the major horizontal locked-in stress is perpendicular to the excavation length (see Figure 5). Figure 7c illustrates the normalized displacement for excavations in Sandstone Class II, while Figure 7d depicts the corresponding values for Sandstone Class III. The normalized graphs have then been used for curve fitting.

3.2 *Curve fitting*

The curve fitting function in Python, utilizing the NumPy library, has been employed to derive the following equations (Equations 5) describing the relationship between the major locked-in stress and the X and Y displacements at points A and B, respectively. Figure 8a illustrates the correlation that can be employed to estimate lateral excavation-induced displacement at point A.

$$x_{disp}(\alpha) = (0.45Sin(\alpha)^2 + \cos^2(\alpha)).\, x_{disp}(\alpha = 0) \quad (5)$$

Where, α is the angle between major locked-in stress and X-direction; x-disp is the lateral displacement at point A (see Figure 5); $x_{disp}(\alpha = 0)$ is the displacement at point A when the major locked-in stress is in X-direction. $x_{disp}(\alpha = 0)$ can be computed using equation 1 and 2 for Sandstone Class II and III, respectively.

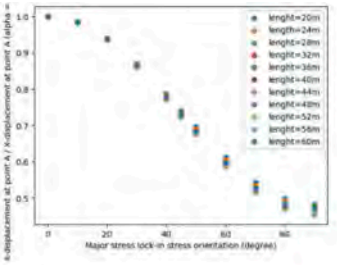

(a) Sandstone Class II – normalised lateral X-displacement at point A versus α

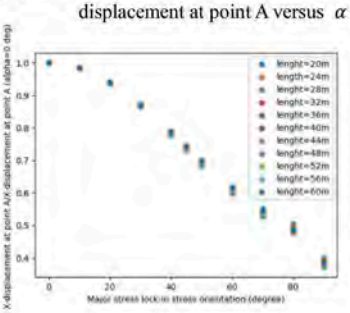

(b) Sandstone Class III – normalised lateral X- displacement at point A versus α

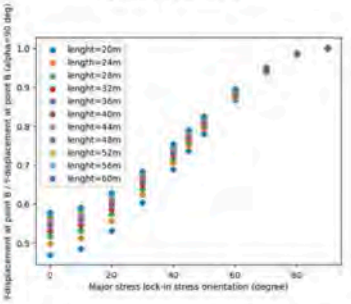

(c) Sandstone Class II – normalised lateral Y- displacement at point B versus α

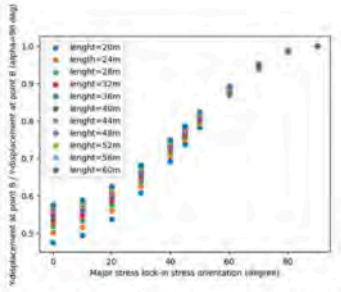

(d) Sandstone Class III – normalised lateral Y-displacement at point B versus α

Figure 7. Normalised maximum lateral displacement along the excavation length and width versus α.

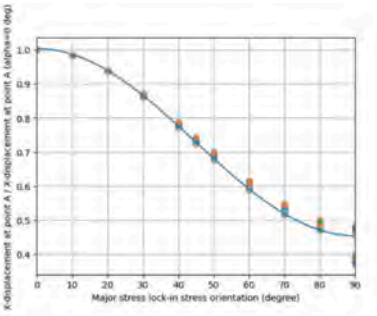

(a) Curve Fitting: Sandstone Class II and III – normalised X-displacement at point A versus α

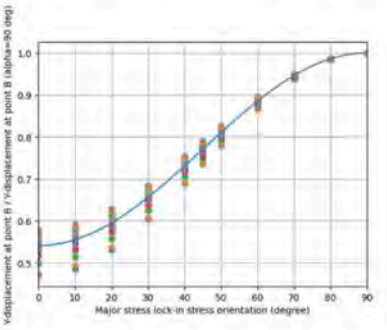

(b) Curve Fitting: Sandstone Class II and III – normalised Y-displacement at point B versus α

Figure 8. Curve fitting.

Equation 6 estimates the lateral excavation-induced displacement at point B as a function of α. In which, α is the angle between major locked-in stress and X-direction; y-disp is the lateral displacement at point B (refer to Figure 5); $y_{disp}(\alpha = 90)$ is the lateral displacement at point B if the major locked-in stress is in Y-direction. $y_{disp}(\alpha = 90)$ can also be calculated using equation 1 and 2 for Sandstone Class II and III, respectively. Figure 8b shows the curve versus the database used to drive this curve.

$$y_{disp}(\alpha) = (0.45Sin(\alpha)^2 + \cos^2(\alpha)).y_{disp}(\alpha = 90) \quad (6)$$

4 LATERAL DISPLACEMENT IN NON-SQUARED SHAPE BOX VERSUS SQUARED SHAPE EXCAVATIONS

In this section, the influence of the Length-to-Width ratio is evaluated in a non-square-shaped excavation. As described in Section 2, the database was created by maintaining excavation width and depth as constant values, both equal to 20 meters. The length of the excavation was initially set at 20 meters (forming a square shape) and progressively increased in

4-meter intervals to reach lengths of 24 meters, 28 meters, and so forth, up to 60 meters. The excavation with dimensions 20 meters by 20 meters is considered the reference case, and the analysis focuses on examining the rise in lateral displacement as the excavation length increases.

The orientation of the major horizontal locked-in stress is assumed to remain constant and perpendicular to the length of the excavation (α=90).

Figure 9 presents the outcomes for Sandstone Class II and Class III. The horizontal axis in Figure 10 represents the excavation length divided by 20 meters, which is equivalent to the excavation length in the square-shaped reference excavation. The vertical axis then depicts the maximum lateral displacement along the length of the excavation (Point B in Figure 5), normalized by the lateral displacement in the square-shaped excavation (2 meters wide by 2 meters long, which serves as the reference excavation).

The blue line in Figure 9 was generated using a curve fitting method in Python and the NumPy library. The derived correlation is expressed by the equation:

$$y_{disp} = y_{disp,ref}.0.91exp(3.2L/20m) \qquad (7)$$

In which B represents the length and width of the reference square-shaped excavation. L is the length of the B(m) x L(m) dimension excavation. This correlation has been established and is suggested for examination in future studies, particularly for other values of B.

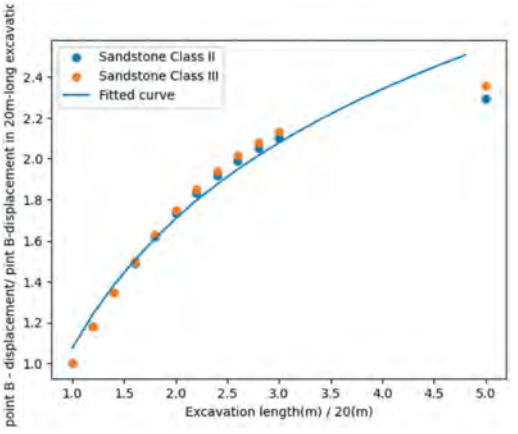

Figure 9. Lateral displacement in a rectangle shape excavation (B(m)-wide x L(m)-long with reference to the square shape excavation of B(m) x B(m).

5 CONCLUSION AND RECOMMENDATION

The suggested approach is summarised as below:

For square shape excavation:

– Calculate the maximum excavation-induced lateral displacement in the direction of the maximum horizontal locked-in stress based on width, depth, and Hawkesbury Sandstone class using Equations 1 to 2
– Calculate the maximum excavation-induced lateral displacement in the direction of the minimum horizontal lock-in stress using Equation 3.
– Modify the calculated value based on theα value using Equation 5 and 6;

For rectangle shape excavation B(m)-wide x L(m)-long:

– Calculate the maximum lateral displacement for B(m) x B(m) square shape excavation using Equation 1 and 2,
– Modify the calculated values for L(m) long excavation, using Equation (7)

The reader should be mindful of the limitations associated with the proposed equations, outlined below:

– Applicability to Specific Rock Classes:
This approach has been formulated for Hawkesbury Sandstone Class II and III. Its generalization to other rock classes may require further investigation.
– Depth and Width Range:
Equations (1), (2), and (3) are valid for excavation depths ranging from 5m to 20m.
Equations (1), (2), and (3) are applicable to excavation widths within the range of 10m to 50m.
– Depth Limitation for Equations (5) and (6):
Equations (5) and (6) were derived based on 20m-wide x 20m-long excavation. Additional studies are needed to assess their suitability for deeper and wider excavations.
– Limited Applicability of Equation 7:
Equation 7 has been developed based on a 20m-wide and 20m-deep excavation. Further evaluation is necessary to determine its applicability to excavations with different dimensions.
– Bedding Plane and Discontinuity Effects:
The proposed equations do not account for the impact of bedding planes and discontinuities. The models in Plaxis3D and Flac3D assume a continuum media.

The equations presented in this paper estimate lateral displacement at the ground level. Consideration of other factors or locations may necessitate additional analysis.

These limitations highlight the need for careful consideration and validation in applying the proposed equations in various geological and geometric contexts.

REFERENCES

Bertuzzi, R. (2014). Sydney Sandstone and Shale Parameters for Tunnel Design. Australian Geomechanics, 49(2).
Hewitt, P., & Kitson, M. (2022). Finite element analysis of a deep excavation: A case study ground response due to deep excavations in Sydney sandstone, 27–38.

Gutierrez, G. A., Sadeghian, S., & Dong, Y. (forthcoming). Simplified excavation-induced lateral displacement assessment in sydney area.

Lochaden, A.LE. & Haberfield C.M. (2019). The effect of the in situ stress field on basement performance – a case study from Sydney, Australia. 13th Australia New Zealand Conference on Geomechanics, 435–440.

Oliveira, D.A.F., & Parker, C.J. (2014). An alternative approach for assessing in situ stresses in Sydney. In Proceedings of the 15th Australian Tunnelling Conference, Sydney, NSW, 17-19 September, 189–194.

Oliveira, D.A.F., & Wong, P.K. (2012). Selection of rock mass design parameters for assessing excavation-induced movements in the Sydney CBD. In Proceedings of the Australia New Zealand Conference – Ground Engineering in a Changing World, 789–795.

Pells P.J.N, et al. (2019). Classification of sandstones and shales in the Sydney region; A forty-year review. Australian Geomechanics, 54(2)

Pells, P.J.N. (1990). Stresses and displacements around deep basements in the Sydney area. Stresses and displacements around deep basements in the Sydney Sandstone. 7th Australian Tunnelling Conference, Sydney, 11-13 September, 241–249.

Pells, P. J. N. (1998). Foundations on Sandstone and Shale in the Sydney Region. Australian Geomechanics, Dec 1998.

Pells, P. J. N. (2004). Substance and Mass Properties for the Design of Engineering Structures in the Hawkesbury Sandstone. Australian Geomechanics, 39(3).

Tunnelling for a Better Life – Yan, Celestino, Thewes & Eberhardt (Eds)
© 2024 The Author(s), ISBN 978-1-032-80042-4
Open Access: www.taylorfrancis.com, CC BY-NC-ND 4.0 license

A modified approach to assess tunnel excavation stability

Sajjad Anwar*
AECOM New Zealand, Auckland, New Zealand

Geoff Charlesworth
AECOM Australia, Brisbane, Australia

ABSTRACT: This paper discusses and proposes modifications to an earlier simplified approach for the preliminary assessment of excavation behaviour in rock tunnelling by Russe (2008). Modifications are proposed so that new graphs can be used for different rock types considering any tunnel shape and in situ stress state. These graphs can be constructed in computer software MS Excel adopting different rock mass conditions, tunnel shapes and in situ stresses. A discussion is presented with example illustration. The new graphs are arranged in the same logical sequence, of rock mass quality based on Hoek et al (2013) method (1); rock mass strength considering material constant, mi and blast disturbance factor, D (2); Stability Factor considers the non-circular tunnel profile and anisotropic stress state (3); and Tunnel Excavation Stability (4) of a rock mass using NGI Q system. Based on these new graphs, the excavation behaviour and effective performance of the tunnel support system can be assessed in relation to spalling, rock bursting and squeezing occurrences.

Keywords: Spalling, squeezing

1 INTRODUCTION

The Russo (2008) simplified approach for the preliminary assessment of the excavation behaviour in rock tunnelling and selection of the support system at the tunnel face based on pre-defined design criteria is a useful tool. However, due to its simplifications, it confined its applications to circular cross section and isotropic stress field (k = 1.0). The assessment of the rock mass strength does not consider the overall behaviour of a rock mass but rather uniaxial compressive strength of the rock mass at the boundary of an excavation. The squeezing and spalling excavation behaviour in rock tunnelling can be attributed to overall behaviour of a rock mass rather than failure propagation at the excavation surface.

To overcome these limitations, modifications are suggested to the Russo (2008) "multiple graph" approach. These modifications create a new "multiple graph" approach to be used for different rock types considering noncircular cross sections and anisotropic stress state. The new graphs are arranged in the same logical sequence as Russo (2008). The sequence and comparison are provided below in Table 1.

Like Russo (2008) the new "multiple graph" approach can be used to assess excavation behaviour and effective performance of the tunnel support system in relation to spalling, rock bursting and squeezing occurrences. These graphs can be constructed in computer software MS Excel adopting different rock mass conditions, tunnel shapes and in situ stress conditions. A discussion is presented with examples illustrated below.

2 NEW MULTIPLE GRAPH APPROACH

The new "multiple graph" approach proposes the use of 4 sub-graphs as shown in Figure 1, each graph is arranged to quantify the corresponding properties presented in Table 1. The first graph is in the lower right quadrant and progress is clockwise through system.

2.1 *Graph 1: Estimation of geological strength index*

Graph I is located at the lower right quadrant in Figure 1. It is used to estimate Rock Mass Fabric (GSI) based on Rock Quality Designation (RQD) and Joint Conditions using NGI (2022) Q system joint surface roughness (Jr) and alteration (Ja) number.

The GSI chart published by Hoek and Marinos (2000) was developed on the assumption that GSI would be estimated based on visual exposure

*Corresponding author: Sajjad.Anwar@aecom.com

DOI: 10.1201/9781003495505-91

Table 1. Comparison of logical sequence in development of multiple graph approach.

Graph	Russo (2008)	Modification
1	Rock block volume + Joint Conditions = Rock mass fabric (GSI)	RQD + Joint Conditions Rock mass fabric (GSI)
2	Rock mass fabric (GSI) + Strength of intact rock = Rock mass strength	Rock mass fabric (GSI) + Strength of intact rock + material constant (mi) + Blast Disturbance factor (D) = Rock mass global strength
3	Rock mass strength + Isotropic circular profile in situ stress = Competency	Rock mass global strength + Anisotropic noncircular profile in situ stress = Stability Factor
4	Competency + Self-supporting capacity (RMR) = Excavation behaviour	Stability Factor + Rock Quality (Q) = Excavation behaviour and Tunnel Stability

observations of the rock mass in the field. It was envisaged that the estimation of the GSI using GSI (2000) chart would be made by qualified and experienced geologists or engineering geologists. When such individuals are available, the use of the GSI charts based on the descriptive categories of rock mass structure and discontinuity surface conditions have been found to work well. However, there are many situations where engineering staff rather than geological staff are assigned to collect data, which means that the mapping of rock masses or core is carried out by persons who are perhaps less comfortable with these qualitative descriptions. Therefore, attempts were made by many researchers to quantify the estimation of the GSI. Hoek et al (2013), Cai et al (2004) Somnez and Ulusay (1999) and Russo (2008) have published quantified GSI charts which incorporate joint surface and rock structure scales.

The authors of this paper have adopted the quantification of GSI method by Hoek et al (2013) due to it user friendly quantification of the GSI based on readily available RQD data from boreholes and observed joint surface condition parameters Jr and Ja from commonly used Q rock mass classification system for tunnelling applications. The correlation relationship is shown below and is graphically represented in Graph I (located at the lower right quadrant in Figure 1):

$$GSI = \frac{52Jr/Ja}{(1 + Jr/Ja)} + RQD/2$$

It should be noted here that the approach to estimate GSI is not recommended in complex and heterogeneous rock masses, such as a flysch, where the specific charts proposed by Marinos and Hoek (2001) should be used for estimating the GSI.

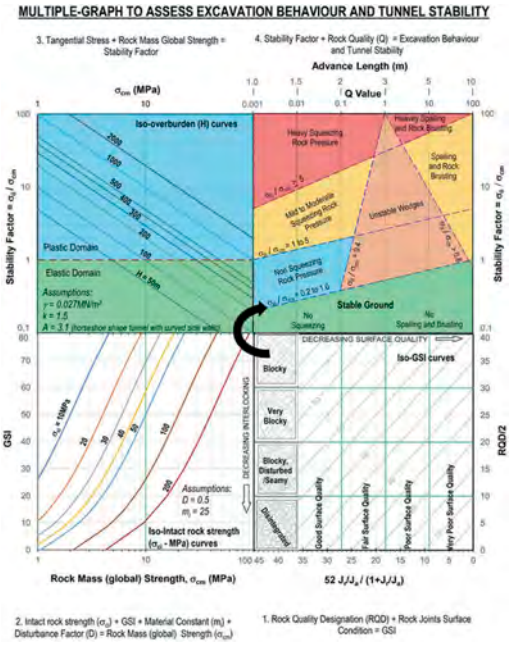

Figure 1. New multiple-graph approach for the preliminary assessment of the excavation behaviour and tunnel support system performance in relation to spalling, rock bursting and squeezing.

2.2 *Graph 2: Estimation of rock mass global strength*

Graph 2 is located in the lower left quadrant in Figure 1. It is used to estimate the rock mass global strength (σcm) based on GSI, rock intact strength (σci), material constant (mi) and blast disturbance factor (D). The estimation of the rock mass global strength is based on the equation of Hoek et al (2002).

Most numerical models can follow the process of fracture propagation and this level of detailed analysis is very important when considering the stability of excavations in rock and when designing support systems. However, to assess the performance of the excavation and tunnel stability it is useful to consider the overall behaviour of a rock mass rather than the detailed failure propagation process. For example, when considering squeezing potential of a tunnel excavation, it is useful to have an estimate of the overall strength of the rock mass rather than a detailed knowledge of the extent of fracture propagation at the excavation surface. The estimation of rock mass global strength using Hoek et al (2002) is provided in Figure 2.

A graphic representation of the rock mass global strength using the above equation is presented in Graph 2, which is located at the lower left quadrant in Figure 1. A value of rock mass global strength is graphically obtained by the intersection of the estimated GSI and intact rock strength curves. An average value of mi of 25 with D = 0.5 is used to

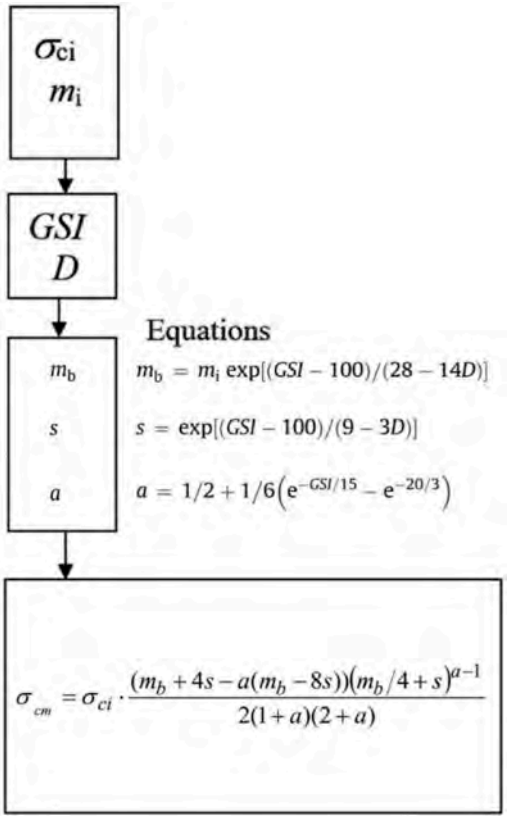

Figure 2. Flow chart for the estimation of rock mass global strength using Hoek et al (2002).

construct the rock strength curves in Figure 1. The curves for a value of mi other than 25 and D other than 0 can be constructed easily using MS Excel worksheets. The reliability of the rock mass global strength estimation is primarily related to both the effective applicability of the Hoek-Brown failure criterion and the occurrence of shear type failure. The guidance for estimating material constant, mi value for rock types and blast distance factor, D, is provided in Figures 3 and 4.

2.3 *Graph 3: Estimation of rock mass stability factor*

Graph 3 is located in the upper left quadrant in Figure 1. It estimates the rock mass Stability Factor based on rock mass global strength (σcm) and maximum excavation induced tangential stress (σΘ). The Stability Factor is simply defined as the ratio between the maximum excavation induced tangential stress (σθ) and rock mass global strength (σcm).

$$\text{Stability Factor} = \sigma\theta/\sigma\text{cm}$$

It is important to note here that the simplified assumption made by Russo (2008) about the circular

Rock Type	Class	Group	Texture: Coarse	Medium	Fine	Very fine
SEDIMENTARY	Clastic		Conglomerates* (21 ± 3) Breccias (19 ± 5)	Sandstones (17 ± 4)	Siltstones (7 ± 2) Greywackes (18 ± 3)	Claystones (4 ± 2) Shales (6 ± 2) Marls (7 ± 2)
	Non-Clastic	Carbonates	Crystalline Limestone (12 ± 3)	Sparitic Limestones (10 ± 2)	Micritic Limestones (9 ± 2)	Dolomites (9 ± 3)
		Evaporites		Gypsum 8 ± 2	Anhydrite 12 ± 2	
		Organic				Chalk 7 ± 2
METAMORPHIC	Non-Foliated		Marble 9 ± 3	Hornfels (19 ± 4) Metasandstones (19 ± 3)	Quartzites (20 ± 3)	
	Slightly Foliated		Migmatite (29 ± 3)	Amphibolites 26 ± 6		
	Foliated**		Gneiss 28 ± 5	Schists 12 ± 3	Phyllites (7 ± 3)	Slates 7 ± 4
IGNEOUS	Plutonic	Light	Granite 32 ± 3	Diorite 25 ± 5		
			Granodiorite (29 ± 3)			
		Dark	Gabbro 27 ± 3	Dolerite (16 ± 5)		
			Norite 20 ± 5			
	Hypabyssal		Porphyries (20 ± 5)		Diabase (15 ± 5)	Peridotite (25 ± 5)
	Volcanic	Lava		Rhyolite (25 ± 5) Andesite 25 ± 5	Dacite (25 ± 3) Basalt (25 ± 5)	Obsidian (19 ± 3)
		Pyroclastic	Agglomerate (19 ± 3)	Breccia (19 ± 5)	Tuff (13 ± 5)	

Values in parenthesis are estimates.
*Conglomerates and breccias may present a wide range of mi values depending on the nature of the cementing material and the degree of cementation, so they may range from values similar to sandstone to values used for fine grained sediments.
**These values are for intact rock specimens tested normal to bedding or foliation. The value of mi will be significantly different if failure occurs along a weakness plane.

Figure 3. Guidelines for estimating material constant, mi for various rock types when laboratory tests are not possible (From Hoek, 2018).

tunnel in isotropic stress field using in-situ stress ratio k = 1 is not adopted to estimate σθ. Instead, an assumed value of k = 1.5 is considered along with horse-shoe shaped tunnel profiles with curved side walls, to estimate tangential stress (σθ) in Figure 1. The tangential stresses, around the horse-shoe shaped tunnel with curved side walls, are estimated using the following relationship developed by Hoek and Brown (1980).

$$\text{Thetangentialstress}(\sigma\theta) = (\text{A} \times \text{k} - \text{–1})\text{Pv}$$

Where A is tunnel shape constant as provided in Figure 5, k is the ratio horizontal/vertical stresses and Pv is overburden stress = γ H, with γ= rock mass density (assumed value = 0.027MN/m^3) and H = overburden.

The value of Stability Factor = 1 in the graph separates the deformation response of the excavation into the elastic (below) and plastic (above) domains. The iso-overburden curves for any in situ stress ratio (k), rock mass density (γ) and tunnel shape using shape constant (A), can be constructed easily using MS Excel worksheets.

2.4 *Graph 4: Estimation of excavation behaviour and tunnel stability*

Graph 4 is located upper right quadrant in Figure 1. This shows the relationship between rock mass strength, in situ stress and rock behaviours in tunnels with rock mass quality (Q).

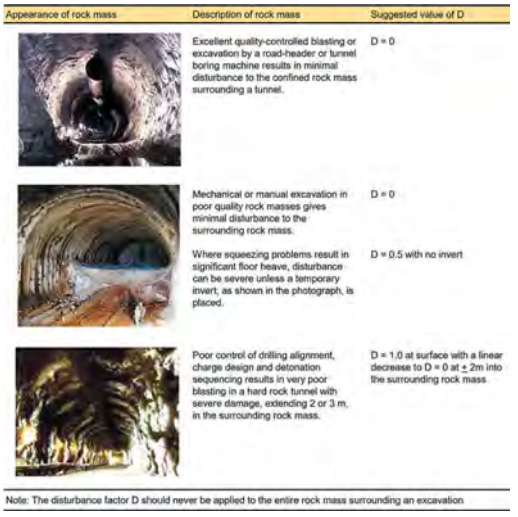

Figure 4. Guidelines for estimating disturbance factor D due to blasting damage (From Hoek et al, 2018).

Figure 5. Shape Factors for Various Tunnel Shapes (From Hoek and Brown, 1980).

The rock behaviour during tunnelling is controlled by rock bursting, wedge failure and squeezing ground pressures. Rock bursting is a sudden fracturing of rock in conjunction with an audible sound. Rock burst can occur as a violent detachment of rock slabs from the face, sidewalls and crown of a tunnel or it may occur as gradual spalling where the rock slabs progressively. In all cases, the failure phenomenon occurs due to overstressing where the rock surrounding the excavation is brittle and massive. For a preliminary estimation of the possibility of stress-driven instabilities of brittle rocks, the region susceptible to spalling/rockburst is marked with $Q > 1$. With respect to the classification proposed by Diederichs et al. (2010) and Cai and Kaiser (2014) the onset for the spalling and rock bursting failure is taken at Stability Factor $(\sigma\theta/\sigma cm) > 0.8$.

The mobilisation of pressure due to failure of the rock mass around a tunnel opening under the influence of in situ stresses can be expressed as squeezing. Squeezing involves pronounced time-dependent deformations and is generally associated with rocks of low strength and high deformability such as, for example, phylltes, schists, serpentines, mudstones, tuffs, certain kinds of flysch, and chemically weathered igneous rocks. For a preliminary estimation of the possibility of squeezing ground, the method proposed by Singh et al., (1992) and Bhasin and Grimstad (1996) is considered. A similar approach is recommended by NGI (2022). In this respect the region on the plot with $Q < 1$ is marked, where squeezing ground pressures may be generated. The stable ground onset is taken at Stability Factor of 0.2 to 1 indicating rock mass strength is 5 to 1 times of the tangential stresses around the opening with increasing Q values.

As the overburden depth increases, the tangential stresses around the opening are also increase, resulting in aggravated squeezing problems. E.g., Singh et al. (1992) have developed an empirical criterion based upon the rock mass quality Q and the height of overburden H for predicting squeezing conditions, i.e., when squeezing occurs:

$$H > 350Q^{1/3}(\mathrm{m})$$

Using this method, at $Q = 1$, the onset overburden depth to cause squeezing ground pressures is 350m compared to $Q = 0.01$, where the onset overburden depth to cause squeezing ground pressures is 75m. With this consideration the stable ground line is drawn starting at $Q = 0.001$ at Stability Factor of 0.2 and terminating at $Q = 100$ at Stability Factor of 1.0. Using the same analogy, the lines for mild to moderate and heavy squeezing ground pressures lines are drawn. The onset for mild to moderate squeezing ground pressures is taken at Stability Factor of 1 to 5 indicating tangential stresses around the opening are 1 to 5 of the rockmass strength with increasing Q values. Heavy squeezing ground pressures onset is taken at Stability Factor of more than 5. The unstable wedges or potential of rock wedge failure zone on the plot is mainly associated with poor to good rock mass quality class with Q value in the range of 1 to 100. The potential of rock wedge failure is subject to relatively low stress condition, i.e., when the failure mechanism at the excavation boundary is dominated by the shear strength of discontinuities rather than material shear strength itself. The region between squeezing ground pressures and spalling and rock bursting is marked as the "Unstable wedges" zone.

3 Q VALUE ASSESSMENT

In the case that the Q values are not available for the application of the multiple graphs, it may be useful to consider the procedure described in the following. The Q-value gives a description of the rock mass stability of an underground opening in jointed rock masses. High Q-values indicates good stability and low values means poor stability. Based on 6 parameters the Q-value is calculated using the following equation:

$$Q = \frac{RQD}{J_n} \times \frac{J_r}{J_a} \times \frac{J_w}{SRF}$$

The six parameters are:

RQD = Degree of jointing (Rock Quality Designation)

J_n = Joint set number
J_r = Joint roughness number.
J_a = Joint alteraytion number
J_a = Joint water reduction factor
SRF = Stress Reduction Factor

In accordance with Hoek et al (1993), the parameters RQD, Jn, Jr and Ja represent the rock mass blockiness and joint surface condition (Q'), conceptually equivalent to the GSI. Consequently, given that the possible ranges of variability the following mean value equation can be used to assess Q' value from GSI.

$$Q' = EXP(GSI - 44)/9$$

Where in Q system$Q' = RQD/JnxJr/Ja$

Finally, to get Q value the active stress (Jw/SRF) value shall be added. In case of dry rock mass condition or drained tunnelling conditions the Jw = 1 is considered. Other values of Jw such as 0.66 for medium inflow to 0.1 for exceptionally high inflow can be used. The SRF values can be approximated from the Stability Factor (σθ/σcm) value as provided in Table 2.

Table 2. SRF estimation.

Stability Factor σθ/σcm	SRF
< 1.0	1
1.0 to 2.0	2.5
2.0 to 3.0	5
3.0 to 5	10
> 5	20

Once the Q' is determined from the GSI, the Q values can reasonably be estimated by combining remaining active stress parameters i.e., Jw and SRF.

3.1 *Practical application of the NEW multiple graph*

The new 'multiple graph' has two main applications:

1) During the preliminary design stages to assess the expected excavation behaviour and tunnel stability issues, in order to devise a plan for detailed analysis.
2) During construction stage, select advance length and support type from Q chart of the NGI (2022) in response to the encountered ground conditions and tunnel face mapped Q values.

Examples 1 and 2 (below in this section) illustrate the application of the new 'multiple graph' approach with reference to the above two main applications.

Example 1: A 10m span horseshoe shaped tunnel (assumed Effective Span Ratio = 1 for the purposes of this example, and the following example) with curved side-wall is located at 160m depth, where in situ stress ratio is determined as 1.5. The site investigation data has shown the ground conditions at tunnel depth and zone within 2 to 3 times of the tunnel span is moderately strong igneous rock with an average intact strength of 40MPa. The rock unit weight, $\gamma = 0.027MN/m^3$. The RQD within the tunnel zone is averaged at 65% with joint surface conditions characterised as smooth, undulating with sandy particles, clay-free thin infillings. Tunnel excavation will be undertaken using drill and blast method.

Solution 1 using Graph 1 lower right quadrant in Figure 1:

- Using NGI (2022) the joint roughness number (Jr) for smooth, undulating surface = 2
- Using NGI (2022) the joint alternation number (Ja) for sandy particles, clay-free thin infillings = 4
- The RQD = 65%

Using Graph 1 which is located lower right quadrant in Figure 1, the GSI is assessed as 50. This indicates rock mass is blocky with poor joint surface quality. The solution 1 illustration is marked in Figure 6.

Solution 2 using Graph 2 lower left quadrant in Figure 1:

- Moderately strong igneous rock with an average intact strength, σci = 40MPa
- Using Figure 3, the material constant (mi) for volcanic rocks = 25
- A blast disturbance factor, D is considered as = 0.5

The intercept of GSI = 50 with σci = 40MPa, read along x-axis given the rock mass (global) strength, σcm = 8MPa. The solution 2 illustration is marked in Figure 6.

Solution 3 using Graph 3 upper left quadrant in Figure 1:

- Tunnel depth, H = 160m
- In situ Stress Ratio, k = 1.5
- Shape factor for a horseshoe shaped tunnel with circular wall using Figure 5 = 3.1
- The rock unit weight, $\gamma = 0.027MN/m^3$

The intercept of σcm = 8MPa with tunnel depth, H = 160m, read along y-axis given the Stability Factor, SF (σΘ/scm) = 2.0. The solution 3 illustration is marked in Figure 6.

Solution 4 using Graph 4 upper right quadrant in Figure 1:

- Using GSI = 50, Q' is estimated in accordance with Hoek et al (1993) = 1.9
- The Stability Factor is 2.0, therefore using Table 2, SRF = 2.5.
- Considering drained conditions, with Jw = 1.0, the Q value is assessed as 1.9 x 1/2.5 = 0.76

The intercept of Stability Factor = 2.0 and Q = 0.76, landed in non-squeezing rock pressure zone, potential for unstable wedge failure. The solution 4 illustration is marked in Figure 6.

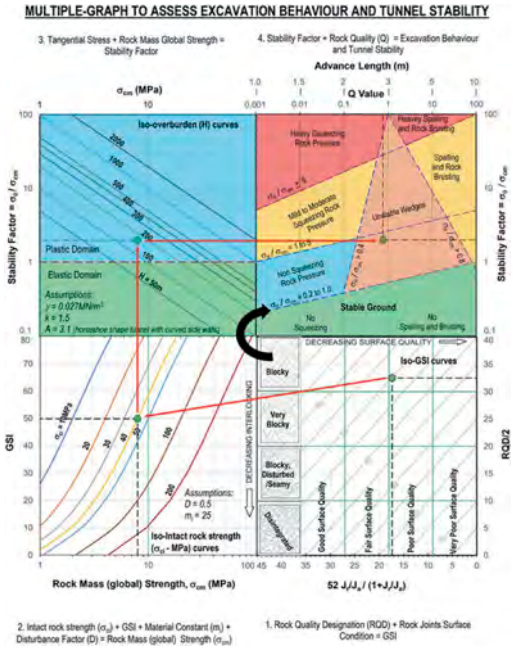

Figure 6. Example 1 – Graphical solution.

In summary, Graph I [Jr = 2, Ja = 4 and RQD = 65% → GSI≈50 (blocky rock mass with poor joint surface condition)]; Graph 2 [GSI≈50 & σci =40MPa → σcm≈8MPa]; Graph III [σcm≈8MPa & H =160m → SF ≈2.0]; Graph IV [SF ≈ 2.0 & Q ≈ 0.8 → (prevalent hazard: wedge instability) → Application of Support Type 5 (i.e., 3.0m long rock bolts with 90mm Fibre reinforced shotcrete) in accordance with Q support chart as shown in Figure 7.

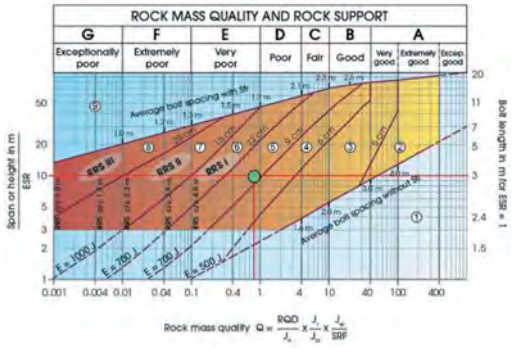

Figure 7. Estimation of support type for example 1.

Example 2: Similar shape of tunnel of Example 1, but located at 500m depth, where in situ stress ratio is assumed 1.5. The site investigation data has shown the ground conditions at tunnel depth and zone within 2 to 3 times of the tunnel span is weak volcanic rock with an average intact strength of 20MPa. The assumed rock unit weight, g = 0.027MN/m^3 and RQD within the tunnel zone is assumed averaged at 10% with joint surface conditions characterised as rough or irregular, undulating with unaltered joint walls, surface staining only. Tunnel excavation will be undertaken using drill and blast method.

Solution 1 using Graph 1 lower right quadrant in Figure 1:

- Using NGI (2022) the joint roughness number (Jr) for rough or irregular, undulating = 3
- Using NGI (2022) the joint alternation number (Ja) for unaltered joint walls, surface staining only = 1
- The RQD = 10%

Using Graph 1, which is located lower right quadrant in Figure 1, the GSI is assessed as 44. This indicates rock mass is disintegrated with very good joint surface quality. The solution 1 illustration is marked in Figure 8.

Solution 2 using Graph 2 lower left quadrant in Figure 1:

- Weak volcanic rock with an average intact strength, sci = 20MPa
- Using Figure 3, the material constant (mi) for volcanic rocks = 25
- A blast disturbance factor, D is considered as = 0.5

The intercept of GSI = 44 with sci = 20MPa, read along x-axis given the rock mass (global) strength, scm = 3MPa. The solution 2 illustration is marked in Figure 8.

Solution 3 using Graph 3 upper left quadrant in Figure 1:

- Tunnel depth, H = 500m
- In situ Stress Ratio, k = 1.5
- Shape factor for a horseshoe shaped tunnel with circular wall using Figure 5 = 3.1
- The rock unit weight, g = 0.027MN/m^3

The intercept of scm = 3MPa with tunnel depth, H = 500m, read along y-axis given the Stability Factor, SF (sq/scm) = 14.4. The solution 3 illustration is marked in Figure 8.

Solution 4 using Graph 4 upper right quadrant in Figure 1:

- Using GSI = 44, Q' is estimated in accordance with Hoek et al (1993) = 1.0
- The Stability Factor is 14.4, i.e.., > 5, therefore using Table 2, SRF = 20.
- Considering drained conditions, with Jw = 1.0, the Q value is assessed as 1.0 x 1/20 = 0.05

The intercept of Stability Factor = 14.4 and Q = 0.05, indicated heavy squeezing rock pressure zone conditions. The solution 4 illustration is marked in Figure 8.

In summary, Graph I [Jr = 3, Ja = 1 and RQD = 10% → GSI≈44 (disintegrated rock mass with very good joint surface condition)]; Graph 2 [GSI≈44 & σci =20MPa → σcm≈3MPa]; Graph III [σcm≈3MPa & H =500m → SF ≈14.4]; Graph IV [SF ≈ 14.4 & Q ≈ 0.05 → (prevalent hazard: heavy squeezing rock

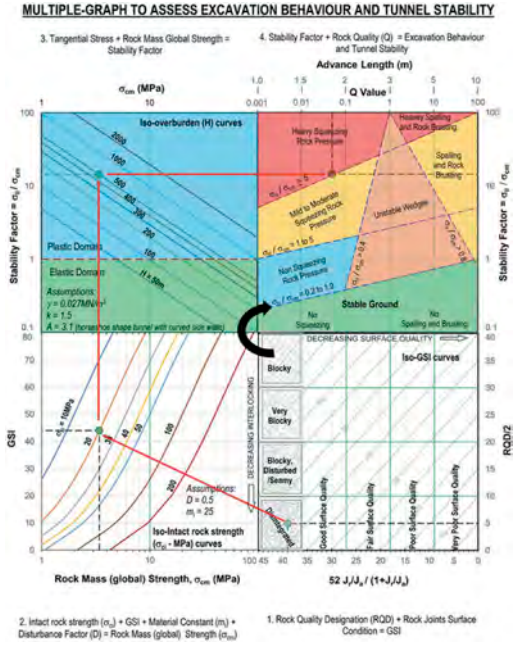

Figure 8. Example 2 – Graphical solution.

pressure) → Application of the Support Type 7 (i.e., 3.0m long rock bolts with 200mm fibre reinforced shotcrete + reinforced ribs of sprayed concrete at 2.9m centres) in accordance with Q support chart as shown in Figure 9.

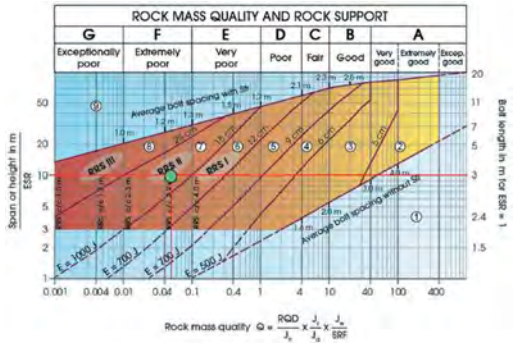

Figure 9. Estimation of support type for example 2.

4 CONCLUSIONS

A modified "multiple graph" approach for the preliminary estimate of the rock mass excavation behaviour and tunnel stability, and consequently, assessment of support type for the probable hazards for tunnelling has been illustrated.

The new modified "multiple graph" approach utilizes simplified assumptions similar to those made under Russo (2008) "multiple graph" approach, i.e., circular tunnel in homogeneous/isotropic rock mass, equivalent continuum modelling, k=1.

Examples are presented to show the application of the new 'multigraph' to predict the stability problems in tunnels in both competent and less competent rocks. The new multigraph approach involves the estimation of stress-strength parameters through simple empirical criteria. The method is based on previous case studies involving rock stress problems and squeezing rock. For the assessed probable hazards, the support system is estimated from the NGI (2022) Q-Chart, which can then be further analysed.

REFERENCES

Bhasin, R. and Grimstad, E. (1996): The use of stress – strength relationships in the assessment of tunnel stability. Tunnelling and Underground Space Technology, 11(1): 93–98.

Cai and Kaiser (2014) In-situ Rock Spalling Strength near Excavation Boundaries. Rock Mech Rock Eng (2014) 47:659–675.

Cai, M., Kaiser, P.K., Uno, H., Tasaka, Y., Minami, M. (2004). Estimation of rock mass strength and deformation modulus of jointed hard rock masses using the GSI system. Rock Mech Min Sci 41(1):3–19.

Diederichs, M.S., Carter, T., Martin, D., (2010). Practical Rock Spall Prediction in Tunnels. ITA World Tunnel Congress Vancouver

Hoek, E. and Marinos, P. (2000). Predicting Tunnel Squeezing. Tunnels and Tunnelling International. Part 1 – November 2000, Part 2 – December 2000.

Hoek, E., Carranza-Torres C.,, Corkum, B., (2002). Hoek-Brown failure criterion, 2002 Edition. Proc. North American Rock Mechanics Society. Toronto, July 2002.

Hoek, E., Carter, T.G., Diederichs, M.S (2013),Quantification of the Geological Strength Index chart, 47th US Rock Mechanics/Geomechanics Symposium held in San Francisco, CA, USA, June 23-26, 2013.

Hoek-Brown (1980) Underground Excavation in Rock

Hoek, E. (2018). Practical Rock Engineering Book

Hoek. E., Brown, E.T. (2018) The Hoek-Brown failure criterion and GSI -2018 edition. Journal of Rock Mechanics and Geotechnical Engineering.

Marinos. P, and Hoek, E. (2002). Estimating the geotechnical properties of heterogeneous rock masses such as flysch. Bulletin of the Engineering Geology & the Environment (IAEG). 60: 85–92.

NGI (2022) Using the Q-system, Rock Mass Classification and Support Design

Russo, G. (2007). Improving the reliability of GSI estimation: the integrated GSI-RMi system. ISRM Proc. SAIMM 108 6 325–338.

Russo (2008) A simplified ration approach for the assessment of the excavation behaviour. TUNNELS ET OUVRAGES SOUTERRAINS - N° 207 - MAI/JUIN

Russo, G. (2009). A new rational method for calculating the GSI. Tunnelling and Underground Space Technology. 24, 103–111.

Russo, G. (2014). An update of the "multiple graph" approach for the preliminary assessment of the excavation behaviour in rock tunnelling. Tunnelling and Underground Space Technology. 41 (2014) 74–81.

Singh, B., Jethwa, J.L., Dube, A.K. and Singh, B. (1992): Correlation between observed support pressure and rock mass quality. Tunnelling and Underground Space Technology 7(1): 59–74

Sonmez, H. and Ulusay, R. (1999). Modifications to the geological strength index (GSI) and their applicability to the stability of slopes. Int J Rock Mech Min Sci. 36, 743–760.

Tunnelling for a Better Life – Yan, Celestino, Thewes & Eberhardt (Eds)
© 2024 The Author(s), ISBN 978-1-032-80042-4
Open Access: www.taylorfrancis.com, CC BY-NC-ND 4.0 license

Study on crosslink-induced Xanthan Gum biopolymer treated soil as a subsea tunnel backfill grout for saline condition permeability control

Jeonguk Bang*, Dong-Yeup Park, Jin Kim, Sanghon Im & Gye-Chun Cho
Department of Civil and Environmental Engineering, Korea Advanced Institute of Science and Technology (KAIST), Daejeon, Korea

ABSTRACT: Subsea tunnels have become indispensable for navigating challenging terrains, but geological and hydro-mechanical challenges mar their construction. Inadequate subsurface exploration can result in accidents like cave-ins, face collapses, and water intrusions. Water intrusions can be particularly devastating due to their high sea levels. While traditional lime-based or cement-based grout materials have been used to tackle the water inflow, environmental drawbacks were inevitable. Biopolymer-based grouts, specifically xanthan gum, have gained attention for their eco-friendliness and durability. This study focuses on the application of cross-linked XG in reducing hydraulic conductivity in marine clay in seawater conditions. Through the consolidation test, the cation cross-linkage induced xanthan gum-treated marine clay showed a significant drop in permeability compared to the untreated sample. The results suggest the possible application of cross-linked xanthan gum as an eco-friendly subsea tunnel grouting for permeability control in saline environments.

Keywords: Water inflow, Hydraulic conductivity, Consolidation test, Permeability

1 INTRODUCTION

Ever since the construction of the Thames Tunnel in London in 1825 to 1843, extensive numbers of subsea tunnels have been constructed and operated to pass through challenging areas. Despite its advantages of not being affected by severe weather above the surface, subsea tunnels encountered drawbacks due to their geological and hydro-mechanical conditions. Insufficient and inaccurate subsurface exploration caused severe accidents such as cave-ins, face collapses, and water intrusions (Guo et al., 2021). In the case of water inrush subsea tunnel, it can lead to significant and catastrophic effects owing to the high water levels of the sea (Xue et al., 2019). For example, the Seikan Tunnel in Japan experienced four disastrous water inflows during its construction, causing casualties, financial losses, and construction delays (Anderson et al., 1994). Therefore, proper exploration before construction and sufficient grouting during construction are needed to prevent water inflow of subsea tunnels.

Grouting is applied to stabilize and reinforce the strata to mitigate unfavourable conditions in subsea tunnelling. A conceptual model of subsea tunnel grouting consists of five stages: backfill grouting and permeation grouting, compaction grouting, primary fracture grouting, secondary compaction grouting, and secondary fracture grouting (Zhang et al., 2014). While conventional grout materials are categorized as lime-based or cement-based grout materials, they can cause pollution due to their high pH characteristics. Other low-pollution grout materials or recycled material-based grouts, such as bulk solid waste (Wu et al., 2022), epoxy resin-modified grout (Wang et al., 2021), or slag-based grout (Perez-Garcia et al., 2019), have been introduced as an alternative.

Recently, biopolymer-based grout materials have been proposed as a pollution-free, environmentally friendly, and durable solution. Biopolymers are biological organism-derived polymers that are eco-friendly and carbon-neutral. Extensive research has suggested biopolymer applications for grout materials, considering its practical effect on hydraulic

* Corresponding authour: jeonguk.bang@kaist.ac.kr

DOI: 10.1201/9781003495505-92

conductivity reduction for infiltration prevention (Momeni et al., 1999; Khatami et al., 2018; Lee et al., 2021; Ryou et al., 2023). Xanthan gum (XG) biopolymer, a bacteria-originated ionic polysaccharide, interacts by attributing the formation of an interconnecting network between clay particles (Kwon et al., 2023). Moreover, XG biopolymers undergo a hardening process in the presence of cations to induce cross-linkage between xanthan gum polymers. This cross-linkage promotes the gelation of XG to form a rigid and bulk-size system (Lee et al., 2023). However, most biopolymer applications are limited to fabricated soil samples in the laboratory and distilled water conditions. This study examined the permeability drop of cation cross-linkage induced XG-treated marine clay's permeability reduction in seawater conditions.

2 MATERIALS AND METHODS

2.1 *Materials*

2.1.1 *Soil: Marine clay*

This study utilized marine clay samples that were bored and sampled near the Ulsan seabed (35° 33′N, 129° 32′E). The sampling depth of 23.0 ~ 23.8 m was used, and its mean grain size (D_{50}) is 19.22 mm. In-situ water contents (w) is 58.55 % with a liquid limit (LL) and plastic limit (PL) of 65.4 % and 23.3 %, respectively, with a specific gravity of 2.71. Figure 1 shows the particle size distribution, and this marine clay can be classified as fat clay with sand (CH) according to the unified soil classification system (USCS). The X-ray diffraction analysis (XRD) quantified the compositing minerals of the marine clay, as shown in Table 1. The soil samples were oven-dried at 130 ± 1 °C for at least 24 h to evaporate the pore water and sieved using no. 40 sieve before use.

2.1.2 *Biopolymer: Cross-linkage induced xanthan gum*

The negatively charged carboxyl group of XG hydrogel forms a bind when it encounters an aqueous solution containing cation. This process is the cross-linkage-induced gelation of xanthan gum with cations such as Na^{+}, Ca^{2+}, and Cr^{3+}. This study utilized trivalent chromium (Cr^{3+}) as a cross-linkage agent since Cr^{3+} is an essential mineral for humans and less toxic than the heavy metal ion hexavalent chromium (Cr^{6+}) (Baruthio et al., 1992). Moreover, a trace amount of sodium chloride (NaCl) was used as a surface-active agent to minimize individual repulsive force and to promote binding between XG and Cr^{3+} (Nolte et al., 1992). A rigid system due to the gelation of Cr^{3+} cross-linked XG (CrXG) is shown in Figure 2.

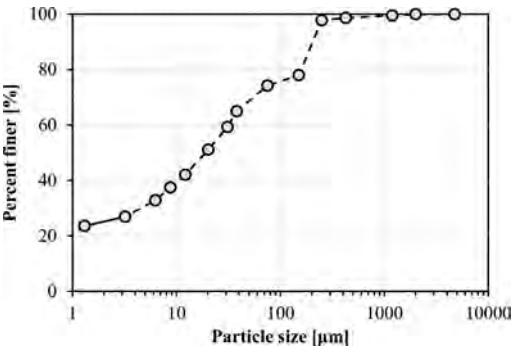

Figure 1. Particle size distribution of marine clay.

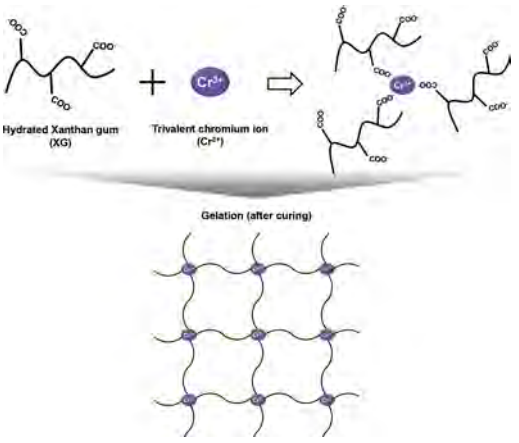

Figure 2. Gelation process of XG and Cr^{3+}.

2.2 *Methods*

2.2.1 *Specimen preparation*

The experimental specimens were prepared using CrXG treated the dried marine clay sample. Dry XG powder (CAS: 11138-66-2; Sigma-Aldrich) with a mass ratio of 1% to the dried marine clay and chromium nitrate nonahydrate (Daejung Chemical Co.) with a mass ratio of 30% to the XG powder was prepared. Research-graded NaCl

Table 1. Composition of minerals in marine clay.

Quartz	Muscovite/Illite	Calcite	Albite	Orthoclase	Kaolin	Chlorite	Pyrite	Halite	Hornblende	Montmorillonite
28.9	24.2	18.7	11.9	7.5	3.4	2.2	1.9	1.3	-	-

with a mass ratio of 10 % to the XG powder was mixed with XG, Cr^{3+} with an initial water content of 58.55 %, corresponding to the in-situ water content. The CrXG hydrogel was thoroughly mixed using a laboratory hand-blender for 1 min before use. Finally, dried marine clay was hand-mixed with the CrXG to reach the desired water content and XG ratio.

2.2.2 *Consolidation test*

The permeability of the CrXG-treated marine clay was measured through a 1D consolidation test according to ASTM D2435-11 (ASTM, 2020). An automatic computerized consolidation test apparatus (Wykeham Farrance; 26-WF3120) with an oedometric cell of diameter and height of 63.5 mm and 20 mm, respectively. A saturated porous plate and wet filter paper (Whatman; Grade 42 filter paper) were placed on the specimen's top and bottom for drainage and equilibrium between seawater. Before testing, the prepared CrXG-treated marine clay specimen was placed and compacted by tamping in 3 layers inside the oedometric cell. The oedometric cell was placed in the consolidation apparatus, and laboratory substitute seawater was poured according to ASTM D1141-98 (ASTM, 2021). Before the test, the initial void ratio was calculated using the specific gravity, initial height, and cell area.

The consolidation was performed with six incremental steps of 12 kPa, 25 kPa, 50 kPa, 100 kPa, 200 kPa, and 400 kPa and three unloading steps of 200 kPa, 100 kPa, 25 kPa. The loading duration was 24 hours for each loading and unloading, and the displacement was measured using a top-mounted linear variable displacement transducer (LVDT). The coefficient of consolidation (c_v) at each loading was analyzed by the log time method (Casagrande et al., 1940). The hydraulic conductivity (k) was computed at each loading step, and the final compressibility index (Cc) and swelling index (Cs) were derived using the void ratio-pressure relation (Terzaghi et al., 1996).

3 RESULTS AND DISCUSSIONS

3.1 *Consolidation behavior of CrXG treatment*

Figure 3 shows the time-displacement curve at 200 kPa loading step for untreated and CrXG-treated marine clay. The final compression of the two cases is almost identical with or without the CrXG treatment. However, the time-displacement curve shape of the CrXG-treated sample depicts a delayed shift. When compared, each case's 50 % compression point at 200 kPa is 123 sec of the untreated sample and 1608 sec of the CrXG-treated sample.

Figure 4 depicts the void ratio-pressure curve for untreated and CrXG-treated marine clay. The compressibility index (C_c) is 0.313 and 0.329 for untreated and CrXG-treated samples. It can be assumed that the compressibility is smaller due to CrXG treatment but almost identical, as it was seen for each loading step. However, the swelling index (C_s) is 0.071 and 0.046 for untreated and CrXG-treated samples, respectively. The difference in the swelling index is due to the hydrophilic XG biopolymer absorbing the seawater in the unloading process. This behavior can be desirable as the XG-treated soil swells to fill the fractures when pressure dissipates.

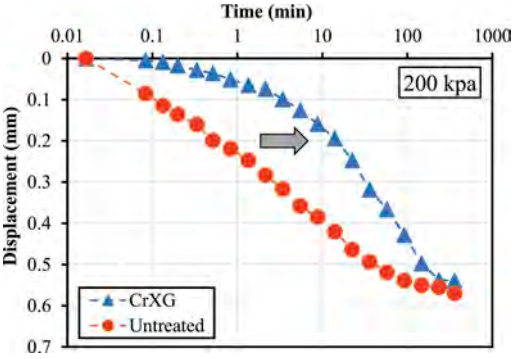

Figure 3. Time-displacement curve at 200 kPa loading.

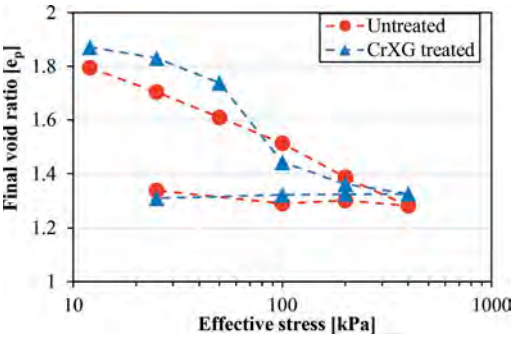

Figure 4. Compression curve.

3.2 *Permeability behavior of CrXG treatment*

As the coefficient of consolidation (c_v) is in inverse proportion to the 50 % compression point at the log-time method (i.e., $c_v=T_vH^2/t_{50}$), the coefficient of consolidation (c_v) is smaller for the CrXG-treated marine clay. Permeability k at each void ratio was computed using the coefficient of volume change (m_v) and coefficient of consolidation (c_v) relationship (i.e., $k=c_v m_v/\gamma_w$). Figure 5. illustrates the computed permeability at each void ratio (e_p). CrXG-treated marine clay depicts a significant permeability drop from the initial treatment, lower than 10^{-7} cm/s. The requirement for a hydraulic barrier is 10^{-7} cm/s (US EPA, 1998; Benson et al., 1999). The treated sample meets the criteria, while the untreated sample was above the limit. The

decrease in the permeability k was caused by the gelation of CrXG hydrogel in the pore space in the marine clay.

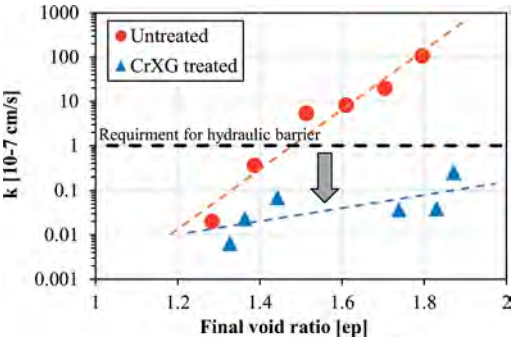

Figure 5. Permeability with a variation in the void ratio.

4 CONCLUSIONS

This study examined the utilization of cation cross-linkage induced xanthan gum biopolymer on the hydraulic conductivity of the marine clay. CrXG demonstrated its potential use as a grout material for subsea tunnels owing to its permeability reduction when the marine clay was treated. The gelation of CrXG hydrogel and its binding characteristic with the clay particles by the attraction of electric forces contributed to the drop in permeability. However, the undrained shear strength and microscopic analysis of CrXG treatment needs to be considered to fully comprehend the CrXG and clay particle interactions.

ACKNOWLEDGMENTS

This work was supported by the National Research Foundation of Korea (NRF) grant funded by the Korea government (MSIT) (2023R1A2C300559611) and Ministry of Oceans and Fisheries (MOF) of the Korean Government (No. 20220364).

REFERENCES

Anderson, G., & Roskrow, B. (Eds.), 1994. The channel tunnel story. CRC Press.

ASTM D1141-98, 2021. Standard practice for the preparation of substitute ocean water. ASTM International, USA.

ASTM D2435-11, 2020. Standard test methods for one-dimensional consolidation properties of soils using incremental loading. ASTM International, USA.

Baruthio, F., 1992. Toxic effects of chromium and its compounds. Biological trace element research, 32, 145–153.

Benson, C. H., Daniel, D. E., & Boutwell, G. P., 1999. Field performance of compacted clay liners. Journal of Geotechnical and Geoenvironmental Engineering, 125 (5),390–403.

Casagrande, A., & Fadum, R. E., 1940. Notes on soil testing for engineering purposes. Harvard University, Cambridge.

Guo, P., Gong, X., Wang, Y., Lin, H., & Zhao, Y., 2021. Minimum cover depth estimation for underwater shield tunnels. Tunnelling and Underground Space Technology, 115, 104027.

He, S., Lai, J., Wang, L., & Wang, K., 2020. A literature review on properties and applications of grouts for shield tunnel. Construction and Building Materials, 239, 117782.

Khatami, H., & O'Kelly, B. C., 2018. Prevention of bleeding of particulate grouts using biopolymers. Construction and Building Materials, 192, 202–209.

Kwon, Y. M., Chang, I., & Cho, G. C., 2023. Xanthan biopolymer-based soil treatment effect on kaolinite clay fabric and structure using XRD analysis. Scientific Reports, 13(1), 11666.

Lee, M., Chang, I., & Cho, G. C., 2023. Advanced Biopolymer–Based Soil Strengthening Binder with Trivalent Chromium–Xanthan Gum Crosslinking for Wet Strength and Durability Enhancement. Journal of Materials in Civil Engineering, 35(10), 04023360.

Lee, M., Im, J., Chang, I., & Cho, G. C., 2021. Evaluation of injection capabilities of a biopolymer-based grout material. Geomechanics and Engineering, 25(1),31–40.

Momeni, D., Kamel, R., Martin, G. R., & Yen, T. F., 1999. Potential use of biopolymer grouts for liquefaction mitigation. Phytoremediation and Innovative Strategies for Specialized Remedial Applications, 5(6),175–180.

Nilsen, B., & Palmstrøm, A., 2001. Stability and water leakage of hard rock subsea tunnels. Modern tunneling science and technology, 497–502.

Nolte, H., John, S., Smidsrød, O., & Stokke, B. T., 1992. Gelation of xanthan with trivalent metal ions. Carbohydrate polymers, 18(4),243–251.

Perez-Garcia, F., Parron-Rubio, M. E., Garcia-Manrique, J. M., & Rubio-Cintas, M. D., 2019. Study of the suitability of different types of slag and its influence on the quality of green grouts obtained by partial replacement of cement. Materials, 12(7), 1166.

Ryou, J. E., & Jung, J., 2023. Characteristics of thermo-gelation biopolymer solution injection into porous media. Construction and Building Materials, 384, 131451.

Terzaghi, K., Peck, R. B., & Mesri, G., 1996. Soil mechanics in engineering practice. John Wiley & Sons.

US Environmental Protection Agency, 1998. Evaluation of subsurface engineered barriers at waste sites. United States Environmental Protection Agency, Washington.

Wang, Y., & Liu, Q., 2021. Investigation on fundamental properties and chemical characterization of water-soluble epoxy resin modified cement grout. Construction and Building Materials, 299, 123877.

Wu, T., Gao, Y., & Zhou, Y., 2022. Application of a novel grouting material for prereinforcement of shield tunnelling adjacent to existing piles in a soft soil area. Tunnelling and Underground Space Technology, 128, 104646.

Xue, Y., Li, Z., Li, S., Qiu, D., Su, M., Xu, Z., … & Tao, Y., 2019. Water inrush risk assessment for an undersea tunnel crossing a fault: An analytical model. Marine Georesources & Geotechnology, 37(7),816–827.

Zhang, D., Fang, Q., & Lou, H., 2014. Grouting techniques for the unfavorable geological conditions of Xiang'an subsea tunnel in China. Journal of Rock Mechanics and Geotechnical Engineering, 6(5),438–446.

Tunnelling for a Better Life – Yan, Celestino, Thewes & Eberhardt (Eds)
© 2024 The Author(s), ISBN 978-1-032-80042-4
Open Access: www.taylorfrancis.com, CC BY-NC-ND 4.0 license

Fixing of unstable water-saturated soils by artificial freezing for construction of inter-tunnel joints during metro construction

E.A. Deplagni*, V.P. Kivliuk & D.S. Konyukhov*
Mosinzhproekt JSC, Moscow, Russia

ABSTRACT: Different variants of freezing of soils around the inter-tunnel assemblies under construction in unstable water-saturated soils are shown and analysed on the basis of the experience gained at various underground construction sites in Moscow. The peculiarities and disadvantages of each variation of freezing methods are considered. In order to minimise the risks of emergencies during mining operations and complications during the creation of ice-loading fence, recommendations have been developed. When freezing soils, granulated solid carbon dioxide ('dry ice') was used as a cold carrier along with aqueous calcium chloride solution. Freezing of soils by 'dry ice' is based on heat extraction from the surrounding ground body by means of solid cryo-agent (carbon dioxide), which is periodically loaded into the freezing column until an ice-loaded enclosure of the required dimensions is created. This method of ground freezing due to low sublimation temperature (-78 °C) allows reducing considerably the duration of the active freezing period and was successfully applied both independently and in addition to the traditional brine method. Examples of practical implementation of the described method are given.

Keywords: ground freezing, underground space development, tunnelling, metro construction, 'dry ice', water-saturated ground

1 INTRODUCTION

Soil stabilization for the construction of inter-tunnel joints in complex engineering and geological conditions is becoming more and more important, as tunnels are driven by TBMs, and the depth of tunnels under construction in Moscow tends to decrease. The geological structure of the city is such that during the construction of deep subways, interconnections were located, as a rule, in clay or limestone, i.e. in soils that did not require special methods of preliminary stabilization. Now, more and more often, the joints are located at a depth of 20 to 35 m, and these depths are mainly water-saturated sands and sandy loam, i.e. running sands (Konyukhov, 2022).

It should be recalled that in the event of a blowout into a mine, the mine must be flooded immediately to avoid subsidence and the associated catastrophic consequences (Kulikova, Balovtsev, Skopintseva, 2023; Kulikova, Konyukhov, 2022). Interconnections are located, as a rule, between tunnels that have been tunnelled, as well as between a tunnel and a tunnelling structure, such as a dewatering plant under construction or a tunnel ventilation plant, which are full enclosing structures of a shaft or an excavation. Flooding of such excavations is problematic and sometimes even impossible due to the huge size of the excavations or the presence of an existing shaft or interconnections nearby.

That is why the construction of interconnections in drift sand under the rock pressure of 0.2-0.35 MPa is a dangerous type of tunnelling work.

For safe mining operations it is necessary to create a closed strong fence around the dikes to prevent the breakthrough of running sands into the excavation.

Artificial freezing of soils is used as a method of temporary stabilization of unstable water saturated soils during construction of underground structures in complex engineering and geological conditions.

Compared to chemical stabilization, cementation, etc., artificial ground freezing is the only controllable method of ground stabilization: the continuity and thickness of the created ice-soil barrier is controlled by hydrogeological and thermometric measurements in specially drilled boreholes.

*Corresponding author: deplani.ea@mosinzhproekt.ru; konuhovds@mosinzhproekt.ru

DOI: 10.1201/9781003495505-93

Nowadays, both the traditional brine freezing method (concentrated aqueous solution of calcium chloride cooled to -20 °C … -25 °C is used as a cold carrier) and zonal freezing with granulated 'dry ice' (granulated solid carbon dioxide) are widely used.

The purpose of this paper is to consider examples of selection of the most reliable and optimal method of freezing of soils around the piles on the basis of analysis of the existing experience at various underground construction objects.

2 OBJECTS INVESTIGATED

2.1 *Object No. 1. Serebryanoborsky tunnels junction*

Tunnel construction at the crossing of the Serebryanoborsky forestry zone and the specially protected recreation area was carried out by a trenchless method – by the Herrenknecht pressurized face EPB TBM.

The left and right transport tunnels with an outer diameter of 13.75 m are double-decked. The upper tier of each of the tunnels is designed for motor transport in one direction and has three traffic lanes, while the lower tier is designed for one metro track. Between the transport tunnels there is a service tunnel with an outer diameter of 6 m for maintenance and processing purposes, also constructed in a trenchless way.

It was also necessary to pretreat/stabilize the soils in a trenchless method at great depth without causing any damage to the environment and landscape.

The interconnection between transport tunnels has a cross-section of 5.5(b) × 6.9(h) metres (Figure 1).

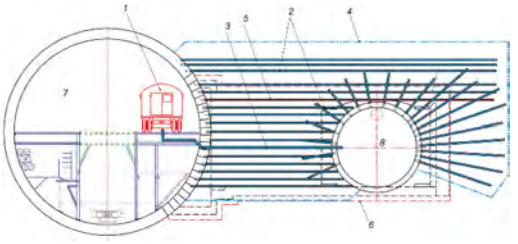

Figure 1. Soil freezing elements on the stage 1: 1 – freezing station (two refrigeration units); 2 – freezing columns; 3 – brine pipeline with a diameter of 140 mm; 4 – conditional boundary of the ice-soil fence; 5 – thermometric well T2; 6 – contour of the tunnelling interconnection; 7 – left transport tunnel; 8 – service tunnel.

The construction plan was to build the interconnection in two phases:

1) from the left transport tunnel to the service tunnel;
2) from the service tunnel to the right transport tunnel.

In the first phase, the interconnection was constructed between the 13.75 m diameter left transport tunnel and the 6 m diameter service tunnel. To freeze the soils around the interconnection, boreholes from the transport tunnel and short counter boreholes from the service tunnel were drilled horizontally using pre-venters (Figure 2), with the freezing station located in the left transport tunnel directly at the interconnection location.

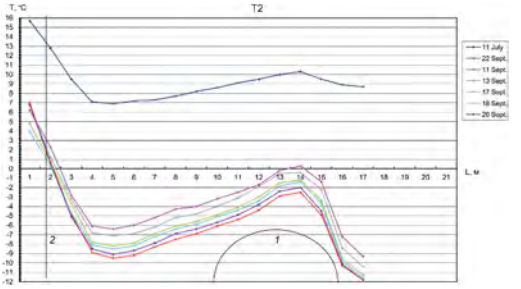

Figure 2. Graph of ground temperature change during freezing of the interconnection between the left transport and service Serebryanoborsky tunnels.

The issue of cold carrier circulation in the columns drilled in the two tunnels was solved in the following way: two horizontal boreholes of 140 mm diameter were drilled from the left tunnel at the level of the interconnection axis for brine pipes, with their entrance into the service tunnel lining. Since the soil at this level is hard loam, the drilling was carried out without any additional reinforcement measures. In this way, a unified spreading network was created for freezing the soils from the two tunnels simultaneously.

Earlier this problem was considered (Taranenko, et al., 2008), but we were forced to return to the Serebryanoborsky tunnels interconnection by a condition that always occurs when soils are frozen between excavations. The issue is, that in the constructed tunnels and excavations, when ventilation is operating, a constant heat influx is created, which complicates the freezing process.(Figure 3).

The thermometric borehole was drilled horizontally from the left transport tunnel and passed in close proximity above the service tunnel. The diagram in Figure 3 shows that at the distance of the borehole above the service tunnel, despite the presence of counter freezing boreholes drilled from the tunnel, as well as near the lining of the transport tunnel, temperature anomalies caused by ventilation were observed. At the same time, the rings of both the service and transport tunnels in the area of works were lined with heat insulation made of 100 mm thick URSA mineral wool mats with a layer of polyethylene film.

An important conclusion follows from this: the contour of the closed ice-ground enclosure around the interconnections under conditions of heat inflow

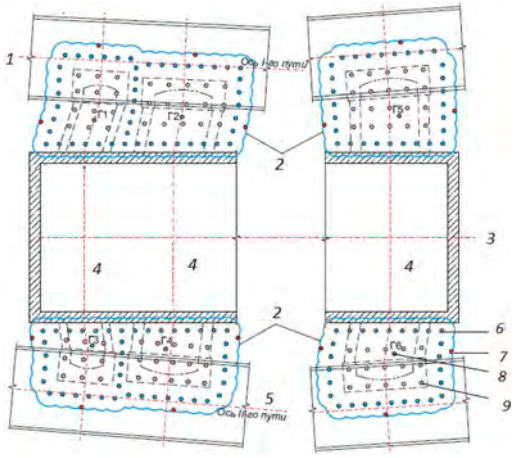

Figure 3. Scheme of ground freezing around the interconnection by the combined method: 1 – axis of the track I; 2 – ice and soil barriers; 3 – installation of tunnel ventilation; 4 – axis of the passage; 5 – axis of the track II; 6 – columns for brine freezing; 7 – thermometric columns; 8 – hydraulic observation wells; 9 – columns for freezing with 'dry ice'.

coming from the ventilation of the constructed tunnels cannot be formed only by vertical, inclined or horizontal freezing boreholes drilled before the lining or tangentially to the tunnel. To create such a contour it is necessary to drill counter boreholes from the constructed tunnels, overlapping the heat flow zone.

2.2 *Object No. 2. Freezing of sidings on the adjacent to the tunnel ventilation installation on the crossing from Karacharovo station to Tekstilshchiki station of the Big Circle Line of the Moscow Metro*

The tunnel ventilation installation consisted of a - 73.25 m long excavation between the constructed tunnels. Four tie-backs had to be constructed from the excavation to the tunnels in frozen ground (Figure 4).

To solve the problem, a two-stage combined method of soil freezing was used, i.e. artificial freezing of soils was carried out both by the traditional brine method and by using granulated 'dry ice'. Drilling of brine freezing wells was carried out both from the surface and with the help of freeze pipes (preventers) drilled from the constructed tunnels (Figure 5).

To optimise the freezing and sinking processes, the work area was divided into compartments corresponding to each interconnection. Soil freezing could be carried out either sequentially in each bay or in parallel, depending on the sequence of mining operations.

The purpose of brine freezing was to create continuous ice-soil contours of the compartments, excluding communication with external water-

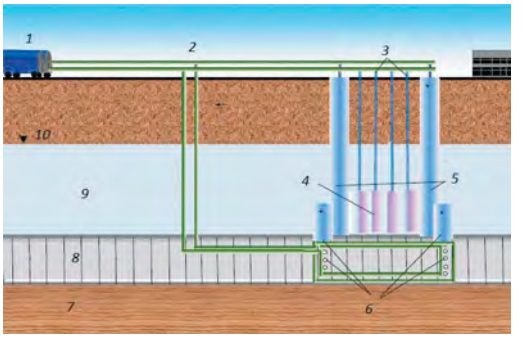

Figure 4. Freezing of soils around the junction by combined method (sections): 1 – ice-soil fence from brine columns; 2 – ice-soil massif frozen with 'dry ice'; 3 – bracing wooden beams; 4 – excavation fence; 5 – columns for brine freezing; 6 – columns for 'dry ice' freezing; 7 – hydro-observation well.

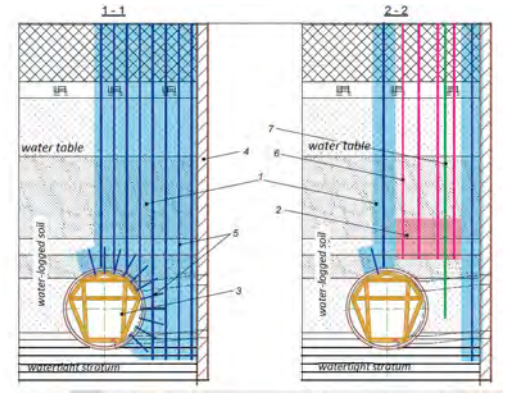

Figure 5. Brine network for simultaneous maintenance of freezing columns drilled both from the surface and from the con-structed tunnel: 1 – freezing station; 2 – brine network; 3 – 'dry ice' filling columns; 4 – ground massif frozen with 'dry ice'; 5 – traditional contour freezing with brine; 6 - columns drilled from the tunnel; 7 – water table; 8 – constructed tunnel; 9 – waterlogged ground; 10 – groundwater level.

saturated soils. The contours of the compartments were frozen to the full depth, up to 2 m into the water-retaining clays.

The purpose of freezing the soils with 'dry ice' was to create a sealed 'slab' above the vault part of each compartment inside the brine contour of the fixed soils 3 m thick in unstable water-saturated soils.

'Dry ice' freezing on each bay was carried out in parallel with the brine method so that the active periods of freezing by both methods ended simultaneously.

Construction of horizontal interconnection at the described object was carried out by trenchless method at a depth of 20-25 m in unstable water-saturated

sands. To exclude the possibility of floatation under pressure of 0.2 MPa into the excavation, it was necessary to create a hermetically sealed ice-load fence around it.

The method of artificial freezing of soils provides the only method of controlling the ice-loading enclosure continuity – water lifting in the intra-circuit hydraulic monitoring well. Therefore, the second stage of freezing, i.e. creation of the ice-loaded slab above the junction, could be started only after the water rise in the in-circuit monitoring well had been recorded. Otherwise, at the second stage, the water in the observation well would have frozen and the control of ice-loading contour continuity would have been lost.

If to exclude freezing of the array by 'dry ice' and to freeze the second stage by brine, then, firstly, it would increase the total freezing period in 1.5-2 times; secondly, as a result of increase of the ground volume due to frozen water, the pressure on the walls of the pit and tunnel lining would increase, as it is practically impossible to perform zone-by-zone freezing by brine; thirdly, it would lead to increase of the number of working refrigeration units.

The use of 'dry ice' as a colder carrier allows reducing considerably the terms of active freezing (4-5 times) in comparison with the traditional brine method, which allows avoiding the general increase of freezing terms. Soil freezing is carried out zonally, which eliminates soil swelling and reduces pressure on the constructed structures.

Besides, in case of accidental damage to the freezing column, which got into the sinking zone, the column is cut off, the bottom of the column is welded to it and freezing continues, while in the case of brine method there is a threat of release of brine circulating in the system into the ground (up to 20 m³), which is fraught with defrosting of the latter. Further use of the damaged column is excluded. In connection with the above, the necessity of two-stage freezing is justified: first, contour freezing (until water rise is detected in the observation well due to the increase in its volume during crystallisation during freezing and, consequently, pressure increase inside the interconnection), and then the creation of a fixed array above the excavation by 'dry ice'.

For the purpose of simultaneous brine freezing both from the surface and from the tunnel, two brine net-works were installed to serve the upper and lower columns for each tunnel, with freezing stations located on the surface (Figure 6).

Two main boreholes were drilled through each tunnel to run the forward and return brine lines underground. Drilling through the tunnels is fraught with the risk of releasing flow earth into the tunnel, so the work was carried out in the following order:

– the interval from the surface to the contact with the tunnel lining was drilled with a D395 bit with the subsequent insertion of a 325 mm diameter pipe; subbasic cementation was performed in the pipe;
– diamond drilling with a diameter of 250 mm was performed with drilling of cement stone in the 325 mm diameter pipe and reinforced concrete tunnel lining;
– 219 mm diameter pipe from the tunnel was lowered into the borehole, it was fixed with a clamping plate; then grouting was performed between the 325 mm and 219 mm diameter pipes;
– a 120 mm diameter hole was cut in the pressure plate; then a 114 mm diameter pipe was lowered into the borehole, welded to the pressure plate and grouted between the 219 mm and 114 mm diameter pipes.

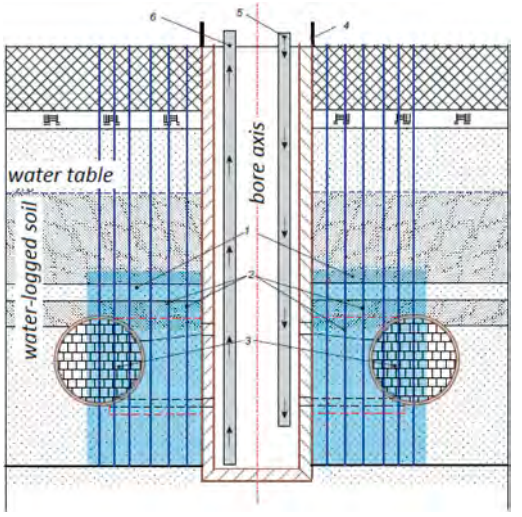

Figure 6. Freezing of soils around the junction by an array in the absence of a water table: 1 – ice-soil array frozen by 'dry ice'; 2 – columns for 'dry ice' backfilling; 3 – battered tunnel sections; 4 – shoring of excavation; 5 – inlet ventilation; 6 – exhaust ventilation.

For the convenience of construction of walkways in the tunnel sections, cast iron rings were laid in the interconnection. In order to exclude the possibility of deformation of the lining, all reinforced concrete and cast-iron tunnel rings located near the excavation were braced with temporary wooden beams.

Despite the favourable performance of the freezing works at the site, the described system has a number of disadvantages:

– the difficulty and danger of main boreholes drilling through the tunnel lining;
– complexity of installation of the brine network in the tunnel due to the presence of numerous wooden beams;
– complexity of maintenance of freezing boreholes in the tunnels, as the descent into the tunnels was located at a distance of about 500 m from the freezing area.

Finally, the main disadvantage of the considered freezing system is the fact that often the enclosing structures of excavations are not airtight, as it was the case at the considered object. In order to stop water entering the excavation, vertical drainage pipes were installed in the flume of the excavation at a height up to the ground surface so that the water would be set at the water table. In addition, it was necessary to caulk the joints between the cast iron tubes in the tunnels to eliminate water dripping. Without these measures, an artificial movement of water in the ground would have been created, preventing the freezing process.

There is one more interesting peculiarity: as it is known, water rise in the intra-circuit monitoring well occurs because water pressure in the contour increases when the ice-ground enclosure is closed. However, if the inter-tubing joints in the tunnel rings located under the freezing contour are not well sealed, the water may completely or partially unload into the tunnel when the pressure increases. And then, instead of the water level rising in the hydro-monitoring well, it is possible to fix a drop in the level, or, even worse, the level will not change.

So, we draw conclusions from the experience gained at the two sites considered:

1. To cover the tunnel zone of heat and heat inflow, it is necessary to drill freezing boreholes, inevitably breaking the tunnel lining.
2. It is necessary to exclude the danger of soil flow into the tunnel when drilling through its lining, and in this case do without a 'telescope' of pipes.
3. It is necessary to exclude artificially created groundwater movement in the freezing zone.
4. It is undesirable to have a brine network in the tunnel because of the difficulty of its maintenance.
5. Finally, it is necessary to minimise the pressure of the frozen massif on the tunnel rings.

It was possible to find an optimal variant of soil freezing for the construction of interconnections, satisfying all the above requirements, at the following object.

2.3 *Freezing of interconnections on the abutment to the drainage unit on the section from Kakhovskaya station to Prospekt Vernadskogo station of the Big Circle Line of the Moscow Metro*

The dewatering installation at this site was a shaft driven using a specialised Herrenknecht VSM 7800/5600 shaft boring system. From the shaft to the tunnels penetrated, it was necessary to construct two tie-backs in water-saturated sands. The task was complicated by the absence of water-retaining clays beneath the tunnels. In such cases it is impossible to create an ice-loaded contour by vertical freezing boreholes. To ensure safe mining operations, an array of frozen ground is usually created.

It was decided to perform zonal freezing of the soil mass by vertical boreholes using granulated 'dry ice' (Figure 7) with drilling through the tunnelled sections that fall within the zone of sidewall construction.

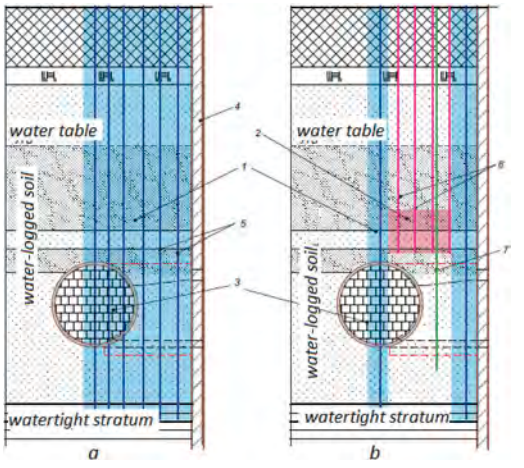

Figure 7. Recommended variant of freezing: *a* – cut along the brine contour; *b* – cut along the junction axis; *1* – ice-load fence from brine columns; *2* – ice-load mass frozen with 'dry ice'; *3* – rubbled tunnel section; *4* – excavation fencing structure; *5* – columns for brine freezing; *6* – columns for freezing with 'dry ice'; *7* – hydro-observation well.

The key idea was to pre-bottom the tunnel sections located in the zone of ice-loaded mass? prior to drilling operations.

First, it allows drilling freezing boreholes from the ground surface through the tunnel with a single bit diameter and not to be afraid of floatation into the tunnel. Second, it reduced the influence of intra-tunnel ventilation on the process of soil freezing, as well as eliminated the 'dripping' of water in the tunnel in the freezing zone. Third, the shoring played the role of a temporary support for the freezing period.

It should be emphasised that 'plugging' does not mean filling the tunnel sections with sandbags. Before drilling, the tunnel sections were densely filled with foam blocks fixed with cement mortar. It was important that no air cavities were left for the possibility of drifting out of the tunnel. Iron-concrete partitions 1 m thick were built at the ends. The sections of the backfill had to be 2 m wider on each side of the bore-hole drilling zone so that the latter would not go be-yond the limits of the backfill as a result of possible deviations during drilling.

The choice of the 'dry ice' freezing method is conditioned by the fact that during soil development in a solid ice-loaded massif, the columns falling into the mining zone are inevitably cut off. Maintaining the array in the frozen state is not difficult for this method of freezing. The fragment of the column, interfering with the junction construction, is cut out,

at the same time, a bottom is welded to the upper part of the column and the ice filling into the above vaulting zone of the interconnection continues, while the ice is poured into the lower part of the column directly from the excavation. In the case of brine freezing, an additional brine network would have to be installed to maintain the ice mass in the under drain zone of the store.

In all freezing columns, 'dry ice' was poured from the bottom of the borehole 3 m deeper than the trough in the development to a depth of 5 m above the vault, with 2 m considered the 'evaporation zone'. Every hour, as evaporation progressed, the 'dry ice' was backfilled to the specified level.

Attention should be paid to the safety of works during freezing with 'dry ice'. During this work, it is strictly forbidden to let people down into unventilated excavations located below the ground surface and within 50 m from the freezing site.

Descent of people is possible provided that there is supply and exhaust ventilation in the excavation with air velocity of at least 0.5 m/s, taking into account that carbon dioxide, formed in the process of sublimation of solid carbon dioxide, is heavier than air and accumulates in low points of the excavation. The ventilation should be continuous, with a backup fan in case of an emergency shutdown.

As the shaft was driven by a mechanised system and represented an additional source of heat flow, freezing boreholes were drilled around the perimeter of the shaft to prevent groundwater movement along the shaft lining. In the future, excavations that involve the construction of tie-ins should also be pre-frozen where possible.

With this type of work technology, there is no need to install cast iron rings in the tunnels in the areas where the interconnections are to be constructed. It is advisable to leave the reinforced concrete tubes with pre-assembled metal insulation.

3 CONCLUSIONS

On the basis of the acquired experience in freezing of soils around inter-tunnelling in unstable water-saturated soils, the following algorithm of these works is recommended:

1. Shore up the tunnel sections falling into the zone of ice-loaded contour or massif above the interconnections with densely laid foam blocks.
2. A combined method of freezing is optimal: first, an ice-load fence should be created around the development contour, controlled by an intra-contour hydraulic observation well, and then a 3-4 m thick array (slab) should be frozen above the junction vault. It is recommended to use the method of creating ice-loaded massif only in conditions when there is no water table under the tunnels for more than 10 m, because when freezing the ground massif the control of its continuity is lost, as there is no possibility to fix the water rise in the hydraulic observation well.
3. The brine contour should be located around the development contour of the disruption at a distance of at least 1 m. In this case, in each ring of the tunnel to avoid the loss of its bearing capacity should be located no more than 1 row of wells with a spacing of at least 1 m.
4. All boreholes should be drilled from the ground surface through the tunnels.
5. In case of ground freezing with dry ice, install ventilation in the excavation. During the works on the joint construction, the tunnel lining should be gradually dismantled.
6. Upon completion of the work, cut off the columns forming the brine contour; weld the bottoms to the upper ones, fill all the columns with cement mortar; the gaps between the columns and the tunnel lining should be injected with cement mortar through the plates welded to the tunnel lining.

REFERENCES

Konyukhov, D.S., 2022. Safety of existing buildings during underground mining. Mining Informational and Analytical Bulletin. 8, 158–167.

Kulikova, E.Yu., Balovtsev, S.V., Skopintseva, O.V., 2023. Complex estimation of geotechnical risks in mine and underground construction. Sustainable Development of Mountain Territories, 2023, 15(1), p. 7–16.

Kulikova, E.Yu., Konyukhov, D.S., 2022. Accident risk monitoring in underground space development. Mining Informational and Analytical Bulletin, 2022, (1), p. 97–103.

Taranenko, I.N., Nikiforov, K.P., Kiselev, V.N., et al., 2008. Iskusstvennoe zamorazhivanie gruntov pri sooruzhenii mezhton-nel'noj sbojki. Metro i tonneli, No 2, 20–23. (In Rus.).

Tunnelling for a Better Life – Yan, Celestino, Thewes & Eberhardt (Eds)
© 2024 The Author(s), ISBN 978-1-032-80042-4
Open Access: www.taylorfrancis.com, CC BY-NC-ND 4.0 license

Factors impacting thawing-refreezing around tunnels in permafrost soils

Sachin Gavhane*
Research Scholar, MIT World Peace University, Pune, India

Sandeep Potnis*
Professor, MIT World Peace University, Pune, India

ABSTRACT: Permafrost system is a fragile state of equilibrium, conditioned by the heat transfer between the ground and atmosphere. Construction and operation of Tunnels in such environment poses unique sustainability challenges and inevitably relies on the comprehensive sensitivity analysis involving thermal, hydraulic and mechanical (THM) behaviours. Freeze-thaw (FT) cycles in permafrost, are characterised by the dynamic thermal loads and stress reversals. This study examines the refreezing of thawed zone around a tunnel in permafrost, using Thermal Module of Rocscience software RS2. The key results indicate that while tunnel causes thawing of permafrost radially around it, conversely, in winters, the tunnel acts as a heat sink, absorbing heat from the surrounding, trying to refreeze the thawed zone. The maximum zone of thawing is reached in July of first year and generally refreezes in 8 FT cycles. However, some cases also prohibit the refreezing. Areas with higher Nthaw (1.29) values or higher FT cycles(60/year), or higher amplitudes (19.5) exhibit slower refreezing rates and more extensive thawed zone that do not refreeze by 8th FT cycle. The study discusses that the effects of the soil thermal properties can be balanced by modulating those of tunnel liner. The study also brings out reduced thawed zone from 4.4m (at 35m) to just 2.1m in crown (at 65m), concluding that confining pressures affect the thermal regime, melting point and soil thermal conductivity. The results indicate that presence of water table actually assists refreezing and reduces the thawing zone (3.3m at crown) compared to the one without (4.4m at crown). The findings on the extent and behaviour of thawing zone could have significant implications on the planning for permafrost tunnels, particularly in India, where recently the Bilaspur-Leh railway line is announced. Given the unique geo-cryology of the region, substantial alignment of the project is likely to face the permafrost conditions.

Keywords: Permafrost, Freeze-Thaw, Finite Element Analysis, Rocscience, N-Factor, Thermal Conductivity, Specific Heat Capacity, Unfrozen Water Content

1 INTRODUCTION

The Indian government recently announced the construction of the Bhanupali- Bilaspur -Leh railway line. Given the unique environment and geo-cryology of the region, a substantial portion of the alignment is likely to face the permafrost conditions. Though Permafrost is no new to the international fraternity, this term is relatively less frequent in Indian context.

S. Nawaz Ali et al (2017) quoted that though Permafrost is an integral component of the Indian Himalayas, but has hardly been ever studied and thus lacks scientific data on its degradation. Gruber, (2012); Gruber et al., (2017) reiterated that the Hindu Kush Himalaya has a wide belt of permafrost visualized by a global model. These authors along with Gautam et al., (2016) and Wu et al., 2017 have further gone on record stating that the permafrost in the Indian Himalayas remains largely unaddressed.

As per Muller (1940), Permafrost is a 'ground' beneath where temperature below freezing has existed continuously for at least two consecutive years". 'Temperature' and 'Time', and not the material characterises the permafrost and hence soil mechanics in these cases is a function of Thermal state. A change in thermal regime causes a phase change in pore fluid state thereby triggering a 'hydraulic' regime in the ground which in turn manifests into 'Mechanical' outcome.

Underground infrastructure development in such regions presents significant yet unique challenges as is seen from the recent spate of floods and landslides in the Manali region. Tunnels, in particular, are affected by the freeze-thaw (FT) cycles that occur in permafrost regions. Taking cue from the studies carried out in China during the construction of the Qinghai-Tibet Railway (that connects Tibet with the rest of China), where more than 550 kilometers of the railway was built on permafrost, it is

*Corresponding author: sandeep.potnis@mitwpu.edu.in; 1032210004@mitwpu.edu.in

DOI: 10.1201/9781003495505-94

high time the scientific and academic community in India take cognisance of this very aspect of the geocryology. While thawing causes the tunnel to settle, refreezing may also cause frost heaving pressure on the tunnel liner which if not factored may cause serious damages to the Tunnel. In this context, the report on Qinghai Highway Line 227 in 2007 by Liu et al., (2011) stated that, the lining structure of the Daban Mountain tunnel is seriously damaged by intrusions; serious transverse/ longitudinal lining cracks, and serious large-scale dislocations at the crown springing levels. Despite these challenges, the construction of tunnels, remains crucial for connecting communities in permafrost regions to the mainland.

2 THE STUDY

Thus, a parametric study was undertaken in 2D plane strain, THM (thermal, hydraulic, and mechanical) coupled analysis, of tunnel constructed in permafrost, using the versatile RS2 Rocscience software. **This paper addresses** the important but hardly studied aspect of influence of varied factors on the refreezing process and the **extent** of thawing zone around the tunnels in Permafrost. In absence of any known Permafrost tunnel in India, this Prelim Research was completed on the what-if location in Ladakh, India. A study site with known soil parameters was chosen at an altitude of 4500 m, Ladakh, India.

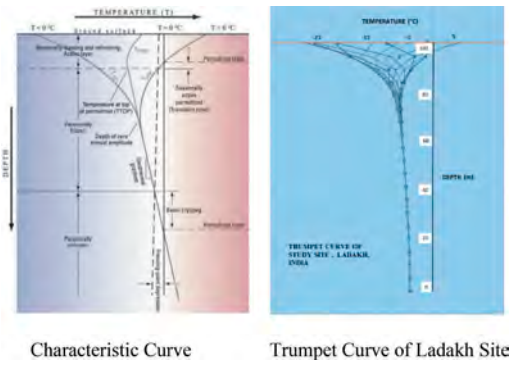

Figure 1. Trumpet curve.

3 STUDY SECTOR AND ENVIRONMENTAL DATA

3.1 *Meteorological data*

The parameters driving the simulations were obtained from the meteorological stations, experimental research station and the literatures published to date and comprised of data from Jan 2008 to Jan 2021. The input data as found at the site represented graphically in Figure 2.

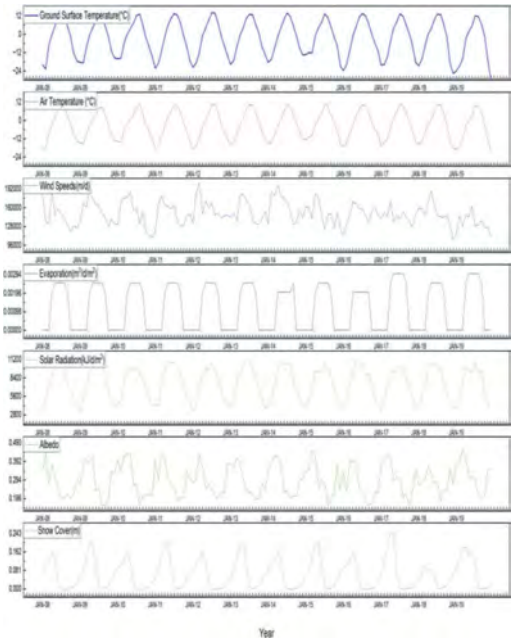

Figure 2. Meteorological input data.

3.2 *Ground surface data*

The ground temperatures in Ladakh are colder than the air temperatures due to the ground albedo as studied by John Wani et al., (2019) published in The Cryosphere. The MAGT at site area varied from -18 to + 12 ° C. Rocscience software provides to obtain realistic conditions of the permafrost, in form of the Initial Temperature grid. Given the geothermal gradient; a bottom flux of 2.44 kJ/day/m^2 was applied. The surface skin temperature obtained at site was then compared to the Initial grid so obtained and the results are close to those of site. *Refer Figure 1(b).*

3.3 *Freezing and thawing indices of surface and air*

The Freezing and Thawing Indices of Surface and Air were calculated and the presence of permafrost was reconfirmed by the Carlson's Approximation Criteria (1952) for existence of permafrost in the area by using, $\frac{I_{st}}{I_{sf}} < \frac{\lambda_f}{\lambda_{th}}; 0.48 < 1.25$

4 METHOD

4.1 *Description of model*

Refer Figure 3. The models are 100x 100 m with four soil layers (BHUKOSH site and well logs). Side boundaries are modelled as adiabatic ones. Top boundary is Free with climatic flux. A Km long, curved horseshoe shape tunnel, with invert to crown 9.21m; composite liner with shotcrete 300 mm thick and Secondary lining of 550mm with 50 cm geotextile and

water proofing membrane was used in numerical model. Piezo line is as per the water table in the area. The 2D section analysed is at 100m chainage from the portal. Mesh of fine graded six noded triangular mesh with gradation factor of 0.1 refined around the tunnel perimeter and in regions of high thermal gradients, is used.

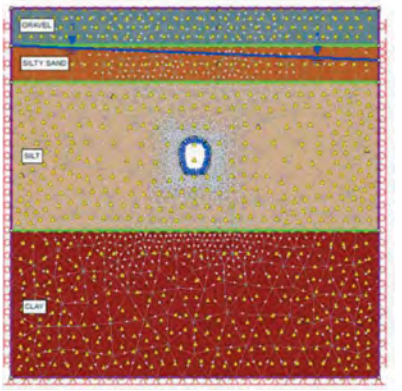

Figure 3. Soil stratigraphy and boundary conditions.

4.2 *Assumptions incorporated in the study*

The permafrost soil is assumed to be Homogenous, isotropic and non-saline. Thermal diffusivity assumed as unity. The climatic conditions/trend generally stays same in a period of 30 years. The tunnel is commissioned in the 2nd year and FT cycles are counted from the month of this particular year.

Table 1. The thermal and hydraulic properties of soil.

PARAMETER	GRAVEL	SILTY SAND	SILT	CLAY
Hydraulic Properties				
Material Behaviour	Drained			
K2/K1	1	1	1	1
Thermal Properties				
Water Content	0.15	0.2	0.3	0.4
Thermal Conductivity Method	Johansen	Johansen	Johansen-Lu	Johansen-Lu
Soil Type	Coarse	Coarse	Coarse	Coarse
Quartz Content	0.67	0.47	0.47	0.47
Heat Capacity Method	Jame Newman			
Include Latent Heat	Yes			
Soil Specific Heat capacity	758	738	886	880
Unfrozen Water Content Function	Simple			

Table 3. Model boundary conditions.

TOP BOUNDARY	TUNNEL BOUNDARY		BOTTOM BOUNDARY
(kJ/ d/m^2)	Initial (°C)	Operation (°C)	kJ/d/m^2
Climate/ Correction	-1.45	12	Geothermal Flux

4.3 *The material and liner properties*

These are as enumerated in Tables 1 to 3. Based on the Parameter to be studied and the objective of the modelling suitable boundary conditions close to actual site conditions were applied.

5 RESULTS AND DISCUSSION

Overall, the maximum extent of the thawing zone was generally reached in the Jul/ Aug month in first year from the tunnel commissioning year. The refreezing commenced from the tunnel perimeter extending radially outwards before the outer fringe started to refreeze and converge. The refreezing fringe is normally non-uniform as the formation of ice crystals during phase change is influenced by the permeability of the soil and its underlying layers. The radial ground around the perimeter up to a distance of 3-4m generally freezes and re-establishes quasi equilibrium state in the 8th F-T cycle under the given conditions in the study area.

Related results are graphically depicted as below and presented/ discussed in succeeding paragraphs. The Graphs are segregated into Uncontrollable (*Refer Figure 4*) and Controllable Parameters (*Refer Figure 5*) and indicate the measurements at crown and invert.

5.1 *Effect of N Factor indices on thawing-refreezing of permafrost.*

A Base model (N*thaw* =1.29; N*freeze*=1.09) was used along with Model-A2 having (N*thaw* 1.29;

Table 2. Tunnel lining properties.

PARAMETER	PRIMARY LINING	SECONDARY LINING
Liner Type	Reinforced Concrete	Reinforced Concrete
Equivalent Young's Modulus(MPa)	28158	30997.2
Equivalent thickness (m)	0.292713	0.549169
Reinforcement Properties		
Type	Lattice girder(3-Bar)ø70,Bar Size 20,30mm Rebar(Europe)ø16	
Section Depth(m)	0.12	0.254
Moment of Inertia (m4)	3.06E+06	6.49E+06
Tensile Strength (MPa)	400	400
Unit Weight (kg/m)	12.5	3.16
Concrete Properties		
Thickness(m)	0.3	0.55
Youngs Modulus (MPa)	25000	30000
Poisson ratio	0.15	0.15
Compressive strength (MPa)	40	40

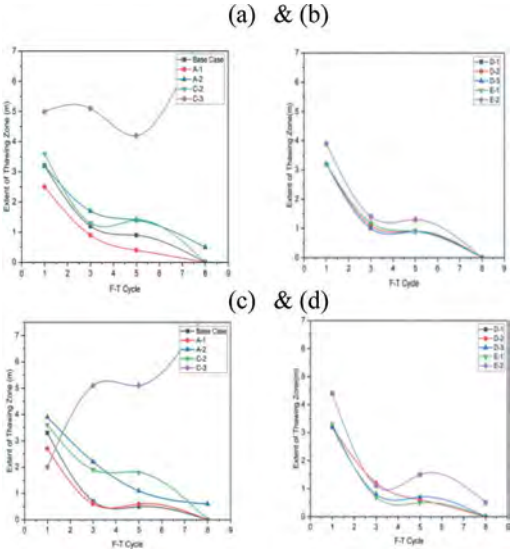

Figure 4. Extent and behaviour of maximum thawing zone due to the effect of uncontrollable parameters.

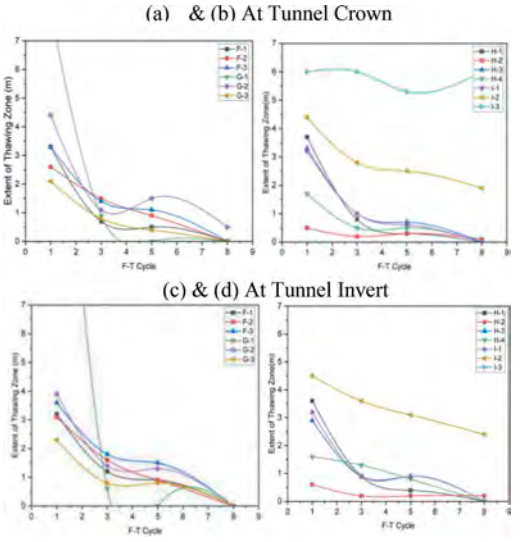

Figure 5. Extent and behaviour of maximum thawing zone due to the effect of controllable parameters.

N*freeze*=0.8) and a Model-A3 having (N*thaw* =0.8; N*freeze*=1.29) to analyse the ibid parameter.

The Results & Discussion are summarised below.

5.2 *Effect of frequency of freeze thaw cycle*

Two models with 60 F-T cycles and 15 F-T cycles each were examined to analyse the extent and the time taken to attain maximum thaw and entire re-freezing respectively.

Table 4. Effect of N factor indices.

Results	Discussion
The thawing zone extent observed was, (i) 3.3m (crown) for N*thaw*=1.09; (ii) 2.7m (crown) for N*thaw*=0.8; (iii) 3.9m (crown) for N*thaw* =1.29. Rate of Refreezing. The radial width of thawed zone from 1st to 3rd FT cycle respectively reduces from: -(i) 2.3 m at crown in 1st FT cycle to 0.7m in 3rd FT cycle for N*freeze* =1.09 compared to; (ii) 0.9m to 0.6m for Nfreeze=1.29 and (iii) 3.3m to 2.2m for N*freeze* =0.8; In Base Case and Case, A-2; *the entire thawed zone refreezes in 8th FT cycle.* With highest N*thaw* and lowest N*freeze* i.e., Case A3; *the thawed zone formed around the tunnel persists.*	A higher N-thaw value indicates a greater thawing, resulting in a more extensive thawed zone. A lower N-freeze value indicates a slower rate of refreezing of the thawed zone and longer duration of thawed conditions and thus more prominent impact on the stability of the ground. On the other hand, a lower N-thaw value and a higher N-freeze value indicate a lesser degree of thawing and a faster refreezing rate, which can result in a shallower and less extensive thawed zone and a lower impact on ground stability.

The results are discussed in Table 5 as following:

5.3 *Effect of amplitude and ambient air temperatures*

This parameter depicts the effect of global warming in permafrost soils. Three cases with increasing amplitude and corresponding increase of T max from the initial 12° C to 14° C and 22° C.

Results & Discussion are summarily enumerated as below in Table 6 along with results of numerical modelling in Figure 6.

5.4 *Effect of soil thermal properties*

Thermal Conductivity (varied through Quartz content(Q); prominent in soils of Ladakh) and Thermal Heat Capacity are studied through three variations.

Results and Discussion**.** The thawing and refreezing rate in the model D-1 is been compared with the other cases. The important results and related discussion points are as below in Table 7.

5.5 *Effect of presence of Water Table (WT) on thawing- refreezing of permafrost*

Two models– base model with water table and base model without water table were examined.

Table 5. Effect of frequency of freeze thaw cycle.

Results	Discussion
Model with 60 F-T cycles/year experiences an unusually larger thawed zone in the first year (6.1m at Invert). The extent of thawing zone increases with every passing F-T cycles. Refreezing time increases as the number of FT cycles increase.	With a high number of FT cycles, the thawed zone around the tunnel shall be deeper and larger, which takes longer to refreeze. In general, each FT cycle causes additional thawing and refreezing. However, as the number of cycles increases, the thermal regime around the tunnel reaches a quasi-equilibrium state, where the rate of thawing balances the refreezing and thawed zone stabilizes. The specific number of cycles required to reach this state will depend on the properties of the soil and the tunnel, as well as the duration and frequency of the freeze-thaw cycles.
Model with 15 F-T cycles/year exhibits consistent and smaller thawed zone. (4.4m at Invert).	From the results of the N factor and the FT cycles the following thumb rule for predicting the freezing/thawing time for the Nth cycle can be derived. *Predicted freezing/thawing time for Nth cycle = Freeze/thaw time taken in the first cycle * N factor (N-1)*

Table 6. Effect of amplitude and ambient air temperatures.

Results	Discussion
The maximum thawing zone occurs in July of first year, with maximum extent around the crown and invert of the tunnel. All other conditions remaining same, the extent of the thawing zone was expected to increase with the increasing amplitude and T*max* and the **results are in conformity**. When amplitude magnitude is 15.5 and T*max* = 12° C, the entire ground refreezes and re-establishes quasi-equilibrium state in the 8th F-T cycle. In Case-C2, only the crown and invert are refrozen in 8th FT cycle, while pockets of unfrozen water 0.6 to 1m wide persists around the sidewall.	A larger amplitude and greater T*max* indicate more extensive thawed zone and vice versa. However, a lower T*min* also means shorter duration of thawed conditions, which means less impact on the ground stability and is thus favourable for tunnels in permafrost. With subsidiary iterations (excluded from the results) this study also found that refreezing occurs faster at locations with amplitude of up to magnitude 8 and Tmax upto10°

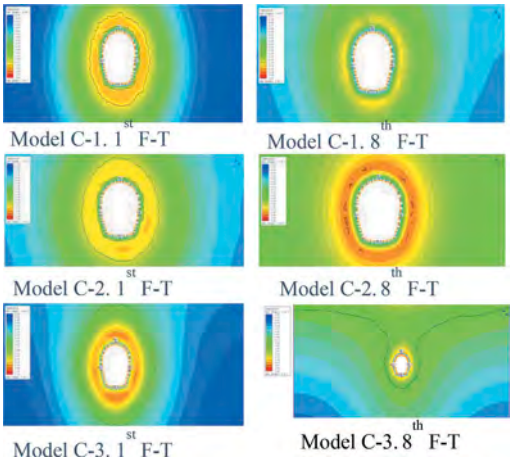

Figure 6. Numerical modelling results of effect of amplitude & ambient temperature.

The important results and related discussion points are as below in Table 8.

5.6 *Effect of shape of tunnel in permafrost*

Three models were considered; one each of horseshoe (base model), circular and rectangular tunnels with WT.

5.6.1 *Results & discussion*

The important results and related discussion points are as below in Table 9 and Figure 7.

5.7 *Effect of depth of tunnel in permafrost*

Three cases of tunnels with horseshoe shape at the depth of 20m, 35m and 65m respectively were considered and numerically modelled. The findings of this study shows that shallow tunnels in permafrost soil may not be feasible unless preconstruction measures such as thermosyphons and ground freezing methods

Table 7. Effect of soil thermal properties.

Results	Discussion
The maximum thawed zone (July of first year) has extent up to - 4.4m at crown, 3.9m each at sidewalls and invert in MODEL D-1(Q:0.47 & C:886 kJ/kt/C); - 3.2m at crown/ invert and 2.9m at sidewalls in MODEL D-2 (Q:0.1 & C:886 kJ/kt/C). Refreezing is achieved - only at the **invert** by 8th FT cycle in MODEL D-1, whereas - in **MODEL D-2-** the thawed fringe around the entire tunnel perimeter refreezes by 8th FT cycles. In **MODEL D-3**(Q:0.47 & C:1772 kJ/kt/C): wherein, the specific heat capacities of soil layers are doubled, **NO MAJOR CHANGE IS OBSERVED.**	Thermal conductivity, reflects the ease with which thermal energy is transferred from one point to another. Specific heat capacity, on the other hand, reflects the capability to store thermal energy. Quartz has a relatively high thermal conductivity hence soils with a higher quartz content conduct heat more easily than soils with lower quartz content. Also, due to lower coefficient of thermal expansion compared to ice, it can lead to differential stresses and cracking with temperature fluctuations. This can cause further destabilization of the soil around the tunnel and increase the potential for thawing and degradation. Results indicate that the soils with higher specific heat capacities have similar effects to those with lower thermal conductivity/quartz content. Thus, in permafrost regions, the Soil thermal properties effects need to be balanced by optimum choice of other parameters such as liner properties/depth and shape of tunnels.

Table 8. Effect of presence of water table (WT).

Results	Discussion
The thawed zone -around crown is 4.4m without WT v/s 3.3m with WT; -around the sidewalls it is 3.9m v/s 3m and for inverts it is 3.9m v/s 3.2m respectively In Model w/o WT the ice layer growth is limited and even in 8th FT cycle the thawed zone around crown and side walls persists with only the Invert refreezing	The Thawing zone is prominently larger for the model without water table. In absence of water table or when the tunnel is above the water table, the thawed zone can persist for longer periods as it leads to a closed system, which allows water to move freely through the soil, promoting further thawing. The lack of ice lenses means that the soil remains unfrozen, leading to extended period of thawing. Only the Invert refreezing is probably due to the capillary rise of water to the freezing front from the Clay in the lower layer.
For the model with water table the frozen fringe grows continuously and the entire thawed zone is refrozen in 8 FT cycles.	A water table above the permafrost tunnel leads to an open system, which promotes the formation of ice crystals, trapping the water and further preventing its free flow through the soil (decreased permeability). Since the water that migrates is replenished continuously by the water table, ice crystals multiply during the freezing period and helps refreezing of the entire thawed zone by eight FT cycles.

are rigorously applied prior to construction and that the excavation is restricted to freezing winter days.

Results. The important results and related discussion points are as below in Table 10.

5.8 *Effect of thermal properties of tunnel liner on thawing- refreezing of permafrost*

The model with average thermal conductivity (λ)and Specific heat capacity(C) was compared with two different models one where conductivity was modulated using insulation and another without insulation but increased Specific heat capacity.

A special case was also considered with a Gravel lining of granitic aggregates of well graded composition 12mm and 20mm densely packed in Gabion baskets of 0.3m width placed around the tunnel lining perimeter prior to secondary lining. *The Thermal properties of the liner can be carefully modulated to control the extent of thawing and rate of refreezing as per this study.*

Results are briefly touched upon and discussed in the succeeding Table 11 and depicted in Figure 8.

5.9 *Effect of inside tunnel temperatures on the extent of thawing*

To study this effect three models with internal tunnel temperatures of 12 °C, 16 °C and 22 °C were modelled to depict the temperatures due to the traffic conditions inside.

Table 9. Effect of shape of tunnel in permafrost.

Results	Discussion
The **circular** tunnel in Model **F-2 has the least maximum thawing zone** in crown and invert **amongst the three**. With just 2.6m in crown and invert the thawing zone is smaller as compared to the rectangular tunnel with 3.6m in crown/invert and 3.5m in sidewalls. While the Model F-1(**Horseshoe**) and Model F-2(**Circular** tunnel) **is refrozen in the 8th FT cycle**, the **rectangular** tunnel **persists with thawing zones** (very few unfrozen pockets) along the perimeter. The refreezing around circular tunnel is more uniform as compared to other cases.	**Circular shapes are more suited in permafrost** environment. One of the likely reasons for this is that circular shape has **least surface area** and **hydraulic perimeter** resulting into **minimum heat exchange coefficient** and least exchange of heat with the surroundings. The **non-circular shapes** can **create stress concentrations at corners or edges**, potentially increasing the risk of damage or failure. A tunnel with a **larger diameter or a flatter profile** result in a **larger thawed zone** and **slower refreezing** and vice versa **The anomaly in a horseshoe-shaped tunnel** of larger thawed zone at inverts compared to the crown, is due to the difference in the curvature of radius of invert vis a vis the crown. **Smaller and steeper radius of curvature leads to larger thawing zones.**

Table 10. Effect of depth of tunnel in permafrost.

Results	Discussion
Though the tunnel at the **depth of 20m** indicates refreezing of the thawing zone in **4th FT cycle**. However, the **thawing zone as a result of construction** shall **merge with the active layer during maximum temperature months** of July/August.	At shallow depth i.e., 20m overburden, **the confining pressure is very low,** which causes the surrounding soils to thaw more easily due to the heat generated by the tunnel. The thawing also results in increased Pore water Pressure thereby reducing the effective stresses to minimum.
The model at **depth 35m**, records the extent of thawing zone as 4.4m at crown and 3.9m at sidewalls and invert respectively. The **refreezing** of the thawing zone occurs ***only at invert*** **after 8 FT cycles.**	In general, an **increase in confining pressure** causes the **melting point of ice** to **decrease**, meaning that ice can melt at a lower temperature than it would at standard atmospheric pressure and well explains the thawed zone. The high confining pressures **also increases the thermal conductivity** of permafrost soils by causing the ice particles in the **soil** to come into **closer contact**.
The model at **depth of 65m** has the **least extent of maximum thawing zone** with just 2.1m at crown, 2.6m at sidewalls and 2.3m at invert.	However, the confining pressure **also have a shielding effect** by **maintaining the structural integrity of the soil**, which prevents further melting **making them more thaw resistant**. This in turn restricts the pore water pressure increasing the overall effective stresses. The test **results for deep tunnels**, are **in good agreement with the findings of Liang Tang et al., (2018)** who observed a strain hardening behaviour in expansive soils(clay) with the increase in the confining pressure.

5.9.1 *Results & discussions*

The discussions on the results are as tabulated below in Table 12.

6 CONCLUSION

The conclusions drawn can be summarised as below**: -**

Permafrost is a four-phase particulate system in a fragile state of equilibrium conditioned by the 'Heat Exchange'. Any change above or disturbance underneath is going to affect its Thermal equilibrium.

The re-establishment of quasi equilibrium by refreezing process around a tunnel in permafrost can be affected by several factors many beyond our control while others could be controlled by an informed choice.

Certain factors beyond control viz the 'Soil Thermal properties' and 'Presence of water table' largely influence not only the extent and behaviour of thawing, but the rate of refreezing and the quantum of differential stresses/ cracking too.

The study on controllable parameter brings out deeper, smaller diameter circular tunnels with modulated thermal conductivity of liner material alongside

Table 11. Effect of thermal properties of tunnel liner.

Results	Discussion
Base Case H1 λ*concrete*=1.95 W/m^2°C; C=1000 kJ/kT/C: This case exhibits a larger extent of thawing reaching up to 3.7m at the crown, 3.8m at sidewalls and 3.6m at invert.. *A higher rate of refreezing was observed and the thawed zone entirely refreezes in the 8th FT cycle.*	The Model H-1 results stated indicate- that with higher thermal conductivity the tunnel shall act as a heat sink in winters promoting heat loss from the surrounding soil and refreezing of thawed zone.
H2 λ*combined*=0.2636 W/m^2°C; C=1000 kJ/kT/C: The maximum extent of thawing zone is drastically reduced to 0.5m-0.8m only. However, a low rate of refreezing was observed and thin *unfrozen fringe continues to remain around the perimeter* even after the 8th FT cycle.	Model H-2 indicate that putting an insulation liner along with the concrete tunnel liner restricts the extent of thawing zone, albeit also slows down the refreezing rate.
H3 λ=1.95 W/m^2°C; C=1916 kJ/kT/C Compared to base case *the maximum extent of thawing zone reduced from 3.7m to an average 3.1m.* The entire thawed zone was refrozen by 8th FT cycle.	The thermal conductivity, specific heat capacity and the coefficient of heat exchange of the tunnel lining significantly controls the heat exchange between the tunnel and the surrounding soil, which affects the size and depth of the thawed zone around the tunnel.
H 4 λ=1.95 W/m^2 C; C=1000 kJ/kT/C plus Gravel Separator: *A substantial reduction in the extent of maximum thawing zone was observed.* The maximum extent of thawing zone was restricted to 1.7m from the earlier 3.7 at the crown; 2.1 m from the earlier 3.8m at sidewalls and only 1.6m from the earlier 3.6m at invert,respectively .Gravel Separator also resulted in a *stable rate of refreezing with uniform frozen fringe and refreezing the entire thawed zone by the 8th FT cycle*.	*Model H-4 indicate that the use of Gravel separator lining with the concrete liner can be an effective method in controlling the thawed zone.* The gravel layer due to high porosity yet strong intra granular arrangement not only reduces the thermal conductivity but also helps segregate the water and ice crystals thereby reducing the thawing around the tunnel. *Gravel use also prevents heaving force from directly acting on the composite liner.*

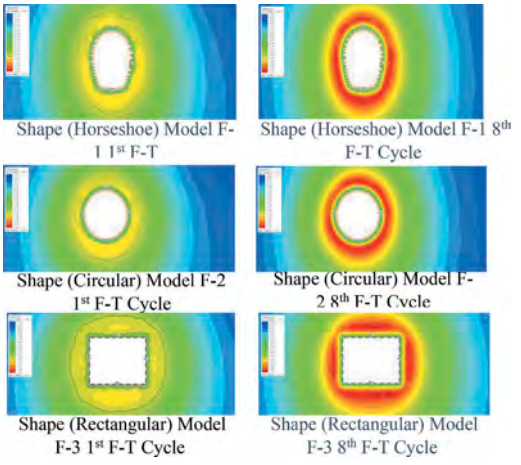

Figure 7. Numerical modelling results of effect of shape of tunnel.

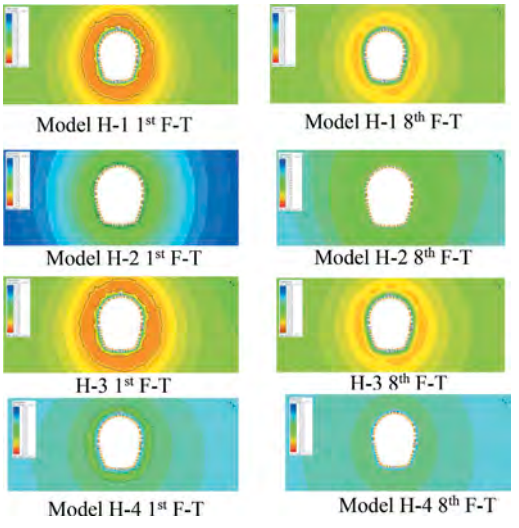

Figure 8. Numerical modelling results of effect of thermal properties of liner.

closely monitored and controlled internal Tunnel temperatures are more apt for such environment.

The findings of the study will help the Permafrost Tunnel engineers in planning tunnels at right depth, to design incorporating correct geometry and shape, in selecting appropriate materials/insulation and implementation of right thermal management & instrumentation scheme. Sometimes simple solutions like a 'Gravel Separator Layer prior to the secondary lining and help separate the particulate phases and prove effective as discussed in the study.

Generalisations on the refreezing of the thawed zone in any particular FT cycles would be ambitious and would differ from case to case depending on the site conditions and above-mentioned causative factors.

Table 12. Effect of inside tunnel temperatures.

Results	Discussion
The extent of the thawing zone was expected to increase with the increasing tunnel temperatures and the results are in conformity.	During operation of the tunnel, the heat generated by the equipment and ventilation systems inside the tunnel lead to a higher heat exchange coefficient between the tunnel and the surrounding environment, resulting in thawing of the permafrost around the tunnel.
The thawing zone ceases to refreeze when the internal tunnel temperature of the tunnel exceeds 12° C.	During the cold winters, the tunnel is supposed to act as a heat sink and absorb heat stored in the surrounding permafrost, leading to refreezing of the permafrost around the tunnel. But this can only happen when Tmax of the ground surrounding the tunnel absorbed during the summers is more than the Tunnel inside temperatures which are generally colder due to the outside cold air suctioned through portals. Hence as seen from the second case the Tunnel can only act as a sink till the inside tunnel temperatures are maintained below the maximum annual average temperature of the ground through artificial cooling. As the inside tunnel temperature increases beyond the annual average, the heat exchange is only one way- from tunnel to the surrounding throughout the year. As a result, the thawing zone only keeps increasing with every passing year as is seen in cases T2(Tunnel temperature 16° C) and T3(Tunnel temperature 22°C) findings.

Finally, while the construction of tunnels remains crucial for connecting communities in permafrost regions to the main land, the results of disturbing the permafrost equilibrium without the ability to anticipate and ensue correctly the changes and their impacts can be catastrophic.

7 LIMITATIONS AND SCOPE FOR FURTHER STUDIES

This study was attempted on the what-if location in Ladakh, India and assumes permafrost soil as isotropic and homogenous. Thermal diffusivity and Salinity in soils excluded can form part of the future studies.

CREDIT AUTHORSHIP CONTRIBUTION STATEMENT

Mr. Sachin Gavhane: Conceptualization, Investigation, Data collection Methodology, Original Draft and Review Prof. Dr. Sandeep Potnis: Guidance, Curation, Supervision and Editing. sandeep.potnis@mitwpu.edu.in, 1032210004@mitwpu.edu.in +91-9890436536

DECLARATION OF COMPETING INTERESTS

It is hereby declared that the authors have no known competing financial interests or personal relationships that could have appeared to influence the work reported in this paper.

ACKNOWLEDGEMENTS

The authors gratefully acknowledge the online help and guidance extended by Dr. Kien Dang, FEM Group Manager, Rocscience, Canada, Permafrost Engineer Mr Konstatin O, University of Calgary, Canada and Mr Sharique Khan, Senior Geotechnical Engineer, Atkins, India as well as the assistance rendered by Miss. Vaishnavi, MIT, WPU, Pune for the Graphics, Tabulation and Presentation of the paper.

REFERENCES

Ayman A. Abed, Solowski W.T.. 2017. A study on how to couple THM behaviour of Unsaturated Soils. Computers and Geotechniques. 92 (2017) 132–155. https://doi.org/10.1016/j.compgeo.2017.07.021.

Potts David M., Wenjie Cui, Zdravkovic L.. 2021. A coupled THM Finite Element Formulation for Unsaturated Soils and a strategy for its non-linear solution. Computers and Geotechnics. 136, August 2021,104221 https://doi.org/10.1016/j.compgeo.2021.104221.

Fredlund D. G., Rahardjo H., Fredlund M.D... 2012. Heat Flow Analysis for Unsaturated Soils. Unsaturated Soil Mechanics in Engineering Practice. Chapter-10. http://dx.doi.org/10.1061/(ASCE)1090-0241(2006)132:3(286)

Vo D., Chung L., Cho J.S., Salem Y.. 2019. A Finite Element Analysis of Tunnel Response to Permafrost Thaw. Tunnels and Underground Cities: Engineering and Innovation. Taylor and Francis Group 2019.

Ling F.. Zhang T. .2004. A numerical model for SEB and Thermal Regime of Active Layer and Permafrost containing Unfrozen Water. Cold Regions Science and Technology. 38 1, January 2004, 1–15 . http://dx.doi.org/10.1016/S0165-232X(03)00057-0

Jin H., Wei Z., Wang S.. Yu Q.. et. Al. 2008.Assessment of Frozen Ground Conditions for Engineering Geology along Qinghai-Tibet highway and railway, China. Engineering Geology. 101(2008)96–109. https://doi.org/10.1016/j.enggeo.2008.04.001.

GuoJie HU., Lin Zhao., et al. 2015. Modelling Permafrost Properties in Quinghai-Xizang (Tibet) Plateau. Earth Sciences China Issue-September 2015. http://dx.doi.org/10.1007/s11430-015-5197-0

Jean Cote,Jean Marie-Konrad. 2005. A generalized thermal conductivity model for soils and construction materials. Canadian Geotechnical Journal, 42, 2, April-2005. https://doi.org/10.1139/t04-106

John Wani1, Renoj J. Thayyen, *2 Chandra Shekhar Prasad Ojha1, and Stephan Gruber. 2021. The surface energy balance in a cold-arid permafrost environment, Ladakh Himalaya, India. The Cryosphere. https://doi.org/10.5194/tc-15-2273-2021.

Tang L., Cong S., Geng L., Ling X.. et.al. 2018. The effect of freeze-thaw cycling on mechanical properties of expansive soils. Cold Regions Science and Technology. 145, January 2018, 197–207 https://doi.org/10.1016/j.coldregions.2017.10.004..

Leger P., Cote M.. and Tinawi R. 1995. Thermal Protection of Concrete Dams subjected to Freeze-Thaw cycles. Canadian Journal of Civil Engineering. 22. https://doi.org/10.1139/l95-067.

Nishimura S. et al., 2009.THM coupled finite element analysis of Frozen soil: formulation and application. Article in Geotechnique http://dx.doi.org/10.1680/geot.2009.59.3.159.

Yu W., Zhang T., Lu Y., et.al. 2020. Engineering Risk Analysis in cold regions: State of the Art and Perspectives. Cold Regions Science and Technology, 171, March 2020. https://doi.org/10.1016/j.coldregions.2019.102963.

.Zhang X, Lai Y., Yu W., Wu Y.. 2003. Forecast Analysis for the Refrozen of Feng Huoshan Permafrost Tunnel on Qing-Zang Railway. Tunnelling and Underground Space Technology. 19 2004 45–56. http://dx.doi.org/10.1016/S0886-7798(03)00085-3.

Lin Z., Xia C., et.al. 2023. Numerical Investigation of the temperature field and frost damages of a frost penetration tunnel considering turbulent convection heat exchange. Tunnelling and Underground Space Technology, 131, January 2023, 104777. https://doi.org/10.1016/j.applthermaleng.2021.116923.

Liu Z., Ye Sun, Yu X.. 2012. Theoretical Basis for Modelling Porous Geomaterials under frost Actions: A Review. Soil Science Society of America Journal, 76, 2, March-12. https://doi.org/10.2136/sssaj2010.0370

Tunnelling for a Better Life – Yan, Celestino, Thewes & Eberhardt (Eds)
© 2024 The Author(s), ISBN 978-1-032-80042-4
Open Access: www.taylorfrancis.com, CC BY-NC-ND 4.0 license

Deformation characteristics of long and narrow deep foundation pit with partition walls

Huiyong Geng & Shouye Guan
China Railway Construction Investment Group Corporation Limited

Zhiwei Chen, Guoliang Dai* & Zhongwei Li
School of Civil Engineering, Southeast University

ABSTRACT: Based on a long and narrow deep foundation pit in Nanjing Jiangbei New Area, a three-dimensional finite element model was established to analyze the effect of setting partition walls on the deformation of a long and narrow foundation pit. The results show that the length of the foundation pit is reduced by setting the partition wall to carry out the partition excavation, which has a good control effect on the overall deformation of the long and narrow foundation pit and can also significantly reduce the horizontal displacement and surface settlement in the long side direction of the foundation pit, especially in the middle area of the long side.

Keywords: Long and narrow deep foundation, Partition wall, Deformation characteristic, Horizontal displacement, Surface settlement

1 INTRODUCTION

The rapid pace of urbanization has led to extensive development of urban underground spaces. There is an increasing construction of complex underground projects, including underground shopping malls, parking lots, and basements of high-rise buildings. As a result, the number of deep foundation pits, particularly long and narrow ones, is increasing due to spatial constraints in urban areas. These long and narrow deep foundation pits are characterized by a large length-to-width ratio and considerable depth, presenting new challenges.

Elongated deep excavations can lead to excessive horizontal displacement and ground settlement, potentially causing damage to nearby structures. Remedial measures must be taken to mitigate these risks. Strengthening the ground and reinforcing support structures are common measures to reduce displacement and surface settlement (Gaba, 1990; Parashar et al., 2007). Additionally, some scholars (Ou et al., 2011) have investigated the effectiveness of installing partition walls connected to diaphragm walls. Research results indicate that partition walls can effectively reduce wall deflection and surface settlement. In a study on deep foundation excavation by Lin et al. (2012), it was found that the horizontal deflection of diaphragm walls is influenced by factors such as construction sequence, spacing of partition walls, and the height of partition walls below the excavation surface.

Hsieh et al. (2012) employed a two-dimensional plane strain analysis method to analyze the deformation characteristics of excavations with partition walls. They derived an equivalent beam model based on the deflection behavior of continuous beams and the principle of superposition. However, excavation is a three-dimensional (3D) spatial problem. Therefore, to gain a better understanding of the deformation characteristics of elongated deep excavations with partition walls, it is necessary to conduct 3D numerical analysis (Wu et al., 2019).

This study utilized numerical simulations conducted with Plaxis 3D software to analyze the impact of partition walls on the horizontal displacement of diaphragm walls and the surface settlement surrounding a long and narrow deep foundation pit in the second phase of the Jiangbei Underground Space Project in Nanjing. The findings of this study can offer valuable insights for the design of future elongated deep excavations.

2 ENGINEERING SITUATIONS AND NUMERICAL MODEL

2.1 *Engineering situations*

The long and narrow deep foundation pit studied in this paper is the H1 ramp foundation pit of the second phase project of Jiangbei Underground Space in

*Corresponding author: daigl@seu.edu.cn

DOI: 10.1201/9781003495505-95

Nanjing, Jiangsu Province, China. The width of this foundation pit is about 31.5 m, the length is 180.3 m, and the excavation depth is about 16 m. The layout of the foundation pit is shown in Figure 1. The shorter side of this foundation pit is reinforced with a diaphragm wall measuring 0.8 m in thickness, featuring a concrete grade of C30. On the other hand, the longer side is fortified with a diaphragm wall that has a thickness of 1.0 m, matching the concrete grade of C30. The diaphragm wall extends to a depth of 37.5 meters. The foundation pit is vertically equipped with three concrete internal supports. The cross-sectional dimensions are 0.8 m × 0.8 mm, and the support depths are 1.4 m, 7.46 m, and 12.46 m, respectively. The horizontal spacing between them is 6 m. The primary form of support is a combination of struts and diagonal braces.

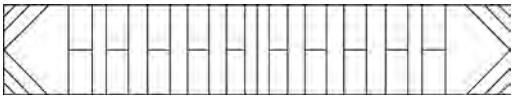

Figure 1. H1 foundation pit plane diagram.

Within the excavation range of this foundation pit, there are a total of 7 soil layers. The basic physical and mechanical parameters of these soil layers are listed in Table 1.

2.2 *Numerical model*

Plaxis 3D software is used for numerical simulation. To mitigate the impact of boundary conditions on the simulation results, the horizontal boundary is set to 5 times the excavation depth, resulting in a model size of 192 m × 241 m. The vertical boundary extends 3 times the excavation depth, equating to 80 m. The surface is unconstrained, serving as a free boundary, while the bottom of the model is entirely fixed. The side boundary of the soil is fixed in the normal direction.

The constitutive model of the soil adopts the HSS model, with specific parameter values listed in Table 1. The basic parameters for the diaphragm wall and concrete support can be found in Table 2.

Table 2. Basic parameters of the diaphragm wall and concrete support.

Type	Size (mm)	γ (kN/m^3)	E (Gpa)
Diaphragm wall	800	25	30
Angle brace	1000×1000	25	32.5
Internal supports	800×800	25	32.5
Tie beam	600×600	25	32.5

The excavation of the foundation pit is divided into three stages. In stage 1, the excavation reaches a depth of -1.7 m, and the first support is constructed. Stage 2 involves excavating to a depth of -7.76 m and installing the second support. Finally, in stage 3, the excavation reaches a depth of -12.76 m, and the third support is constructed.

3 RESULT ANALYSIS (WITHOUT PARTITION WALLS)

3.1 *Horizontal displacement (without partition walls)*

The horizontal displacement contour maps of the diaphragm walls after each excavation stage are shown in Figure 2. From these contour maps, it can be observed that the excavation-induced unloading results in horizontal displacement of the diaphragm wall towards the pit direction. Furthermore, the horizontal displacement increases with the increasing depth of excavation.

Figure 3 presents the horizontal displacement of the ground diaphragm wall at the midpoints of the long side, short side, and corner of the H1 foundation pit as a function of excavation depth. These figures demonstrate that the horizontal deformation patterns of the ground diaphragm wall at these three positions consistently follow similar trends throughout different stages. In the first and second stages, the maximum horizontal displacements are both below 5 mm, with the peak displacement located at the top of the diaphragm wall. During the third stage, a substantial increase in horizontal displacement is observed

Table 1. Basic physical and mechanical parameters of the soil layer.

No.	Soil layer	Thickness (m)	γ(kN/m^3)	c'^{ref} (kPa)	φ'(°)	ψ	E_{oed}^{ref} (MPa)	E_{50}^{ref} (MPa)	E_{ur}^{ref} (MPa)	G_0^{ref} (MPa)	$\gamma_{0.7}$
1	Miscellaneous fill	0.33	18	8	12	0	4.131	5.202	28.66	149.09	3.20E-04
2	Plain fill	3.5	17.85	12	10	0	4.131	5.202	28.66	149.09	3.20E-04
2	Muddy silty clay	8.3	17.56	11.4	12.7	0	2.7864	3.5088	21.68	76.10	3.20E-04
4	Silty clay containing silt	10.7	17.62	11.6	13	0	3.3453	4.2126	24.58	103.57	3.20E-04
5	Clayey silt	6.6	17.99	13.2	15	0	3.7908	4.7736	26.89	128.39	3.20E-04
6	Mealy sand	5	18.76	2	31.7	1.7	7.9623	10.0266	48.52	486.55	3.90E-04
7	Silty fine sand	13.5	18.84	1.8	32.1	2.1	9.3717	11.8014	55.83	658.92	3.90E-04

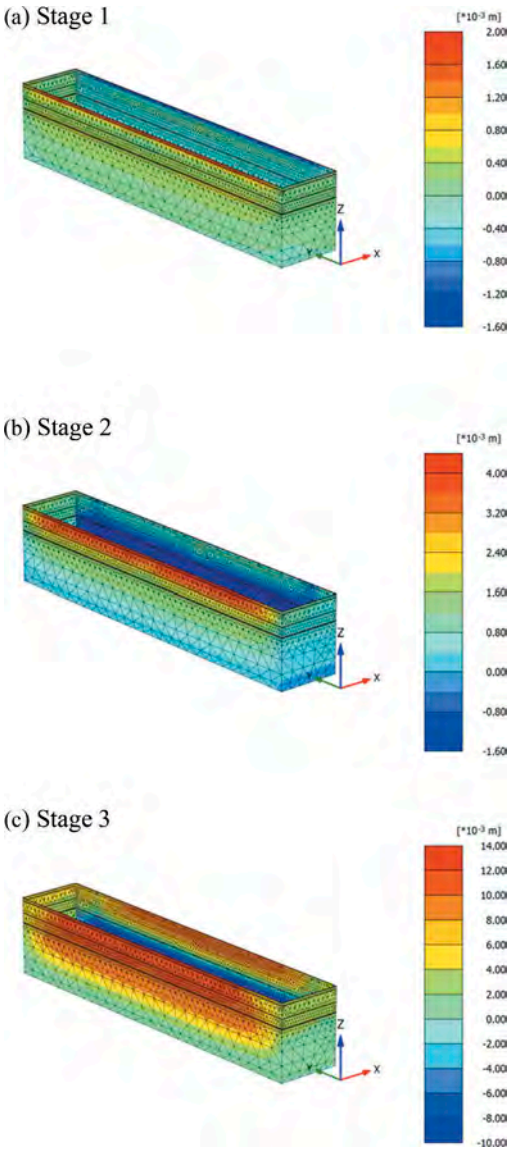

Figure 2. Horizontal displacement contour maps of diaphragm walls at different stages.

compared to the preceding two stages, with the maximum displacement occurring in the middle of the diaphragm wall at a depth of approximately 19 m.

Several studies have investigated the relationship between horizontal displacement (ε) and excavation depth (H) in deep foundation pits. Peck (1969) proposed a control line of ε = 1% H, and Clough (1990) proposed a control line ranging from 0.22% H to 0.5% H. Figure 4 illustrates the relationship between the maximum horizontal displacement (ε) and excavation depth (H) for the H1 ramp foundation pit studied herein. The figure reveals that the maximum horizontal displacement is generally constrained below 0.22% of the excavation depth in each stage.

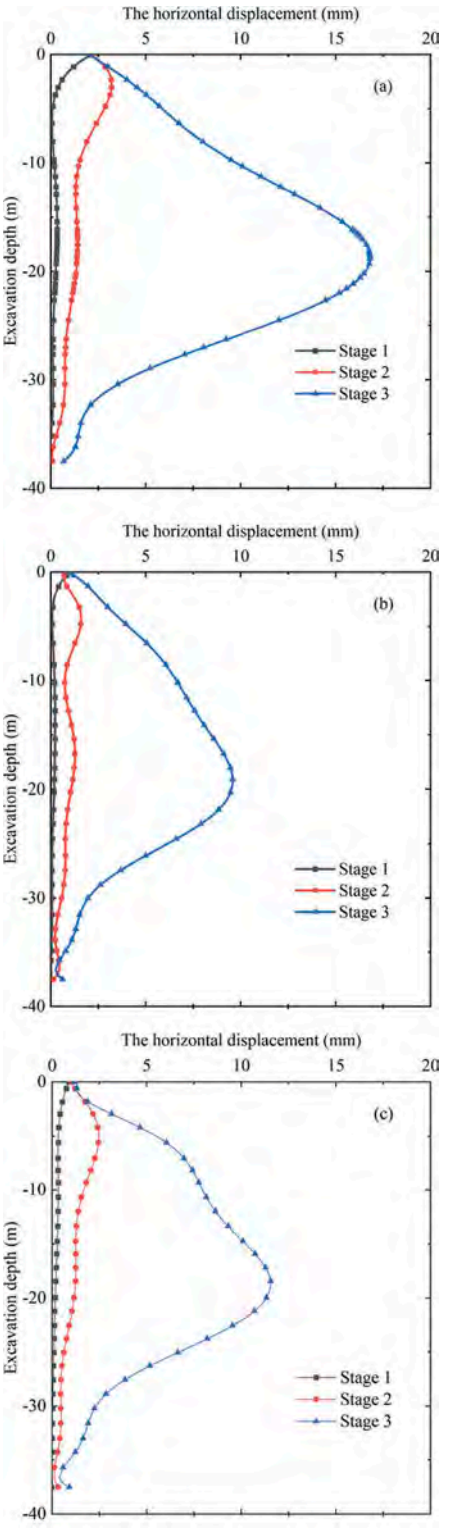

Figure 3. Horizontal displacement with depth at different positions of h1 foundation pit: (a) the long side, (b) the short side, (c) the corner.

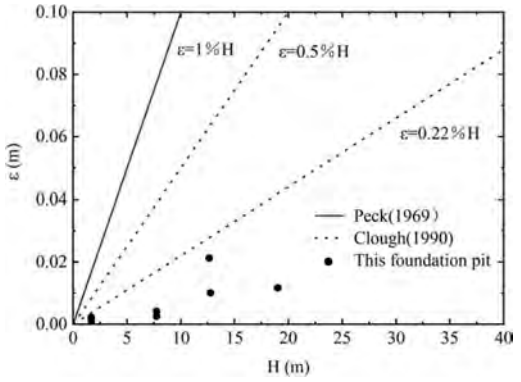

Figure 4. Relationship between maximum horizontal displacement and excavation depth.

3.2 *Surface settlement analysis (without partition walls)*

Figure 5 shows the surface settlement at the midpoint of the long side (a), the midpoint of the short side (b), and the corner (c) of the foundation pit. From these figures, it can be observed that the surface settlement deformation outside the foundation pit mainly concentrates within a range of twice the excavation depth, with the maximum settlement occurring within a range of one excavation depth. The trend of surface settlement exhibits a pattern of initially increasing and then decreasing.

Figure 6 illustrates the correlation between the maximum surface settlement around the foundation pit and the excavation depth across various excavation stages. Clough (1990) and O'Rourke (1993) proposed settlement control lines ranging from ε = 0.15% H to ε = 0.5% H. The figure shows that the settlement points at the corners are distributed below ε = 0.15% H, whereas those in the central area are distributed below ε = 0.24% H.

4 RESEARCH ON EXCAVATION OF PARTITION WALLS

Based on the aforementioned analysis, it can be concluded that the deformation of elongated deep excavations is closely related to the aspect ratio of the excavation, particularly the dimensions of the long side. Therefore, effectively utilizing the spatial effect can achieve efficient control over the deformation of elongated deep excavations and the surrounding environment. One of the most direct measures is to reduce the length of the excavation. Implementing partition walls to reduce the actual length of the excavation can bring about structural changes to the excavation. This point has also been confirmed by Ou et al. (2006).

In order to analyze the influence of partition walls on the deformation characteristics of elongated deep excavations, three additional partition walls were introduced based on the finite element model described in the previous section. The partition walls

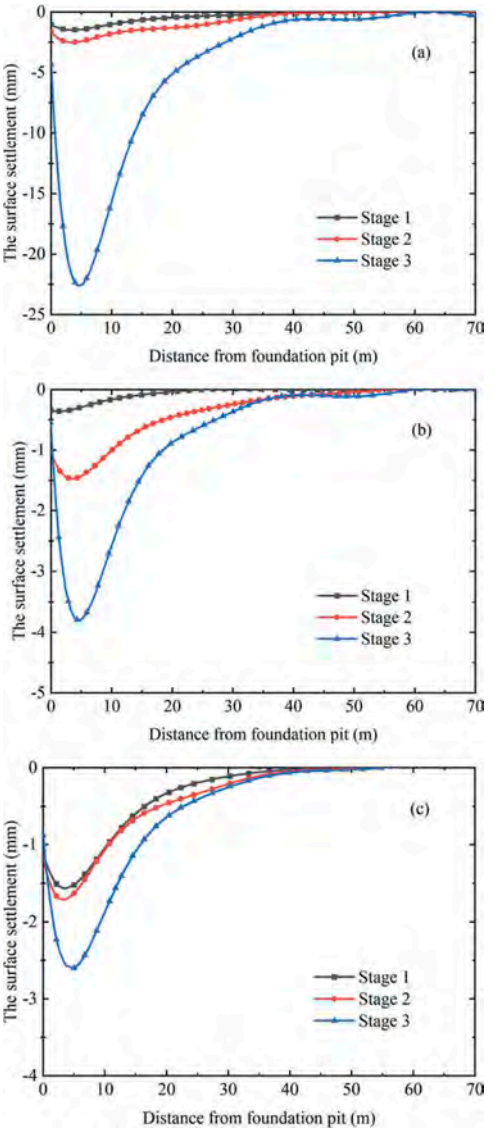

Figure 5. Surface settlement at different positions outside the foundation pit: (a) the midpoint of the long side, (b) the midpoint of the short side, (c) and corner.

consist of diaphragm walls with a thickness of 0.8 m, and their depths at the bottom are consistent with the existing diaphragm wall. Thus, the H1 foundation pit is divided into three regions, namely, A, B, and C, as illustrated in Figure 7. The synchronous excavation method is employed for all the three regions.

4.1 *Comparative analysis of horizontal displacement*

Figure 8 illustrates the horizontal displacement of the diaphragm wall at three excavation stages, comparing the scenarios with and without partition walls. The figure demonstrates that despite the presence of partition walls, the horizontal deformation of

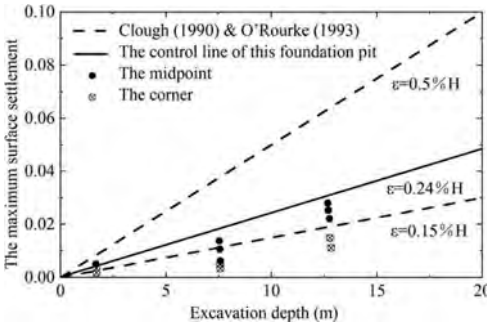

Figure 6. Relationship between the maximum surface settlement and excavation depth.

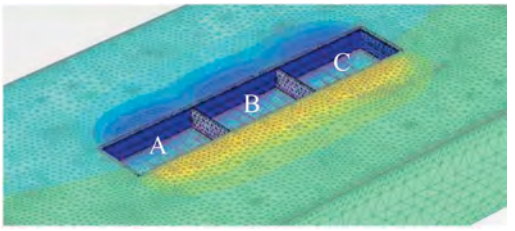

Figure 7. Numerical model with partition walls.

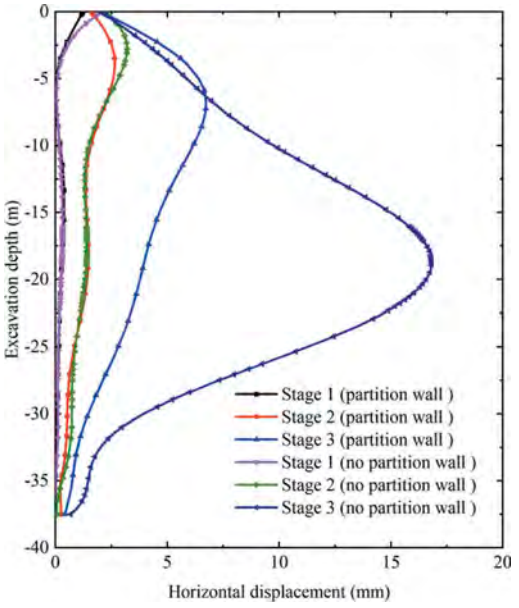

Figure 8. Comparison of horizontal displacement between partition wall and no partition wall.

the diaphragm wall maintains a concave shape, which aligns with the deformation trend proposed by Hsieh et al (2012). The horizontal displacements in regions A, B, and C increase gradually with the depth of excavation, with the maximum deformations occurring near the excavation face. During stage 3, the diaphragm wall exhibits a maximum horizontal displacement of approximately 8 mm with the partition wall.

Figure 9 illustrates a comparative diagram of the maximum horizontal displacements in regions A, B, and C. The figure shows that region B exhibits the largest horizontal displacement regardless of the presence of partition walls. The partition walls result in a maximum horizontal displacement of 9.47 mm for the connected wall in region B, compared to 16.81 mm without partition walls. The partition wall also leads to a significant decrease in the maximum horizontal displacements for regions A and C at each excavation stage, effectively controlling the deformation of the excavation. This suggests that the partition walls, which reduce the length of the excavation, are highly effective in controlling deformation during excavation. Partition walls offer support in the longitudinal direction of the connected wall, effectively restricting horizontal displacement.

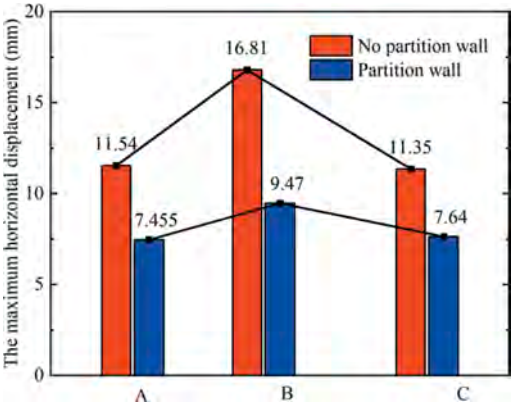

Figure 9. The maximum horizontal displacement of each area.

4.2 *Comparative analysis of surface settlement*

Figure 10 reveals that the ground surface settlement pattern outside the excavation, after the installation of partition walls, resembles that observed when partition walls were present. In both instances, the maximum settlement occurs 5-10 m away from the pit's edge. During Stage 3, the maximum settlement value reaches 22.59 mm without partition walls, whereas with partition walls, the ground surface settlement outside the excavation is only 2.53 mm (11.2% of the former). In the remaining two stages, the ground surface settlement outside the excavation experiences a certain degree of reduction following the installation of partition walls. This suggests that the installation of partition walls effectively controls the ground surface settlement outside the excavation and mitigates its impact on the surrounding environment.

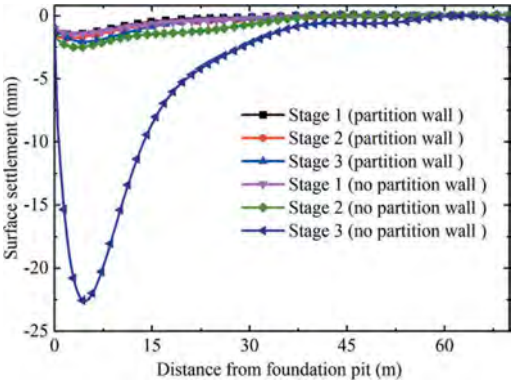

Figure 10. Comparison of surface settlement between the partition wall and no partition wall.

In order to further analyze the influence of partition walls on the surface settlement of the surrounding area in the excavation, the maximum surface settlement values in regions A, B, and C were compared. From Figure 11, it can be observed that after the installation of partition walls, the maximum surface settlement values in regions A, B, and C are all around 2.5 mm. Compared to the case without partition walls, they have reduced by 2.16 mm, 20.17 mm, and 2.14 mm, with reduction rates of 45.45%, 88.85%, and 46.72% respectively. In region B (the central area along the long side of the excavation), there is a significant reduction in the maximum surface settlement, indicating that the partition walls has a noticeable inhibitory effect on the surface settlement in the central area along the long side of the foundation pit.

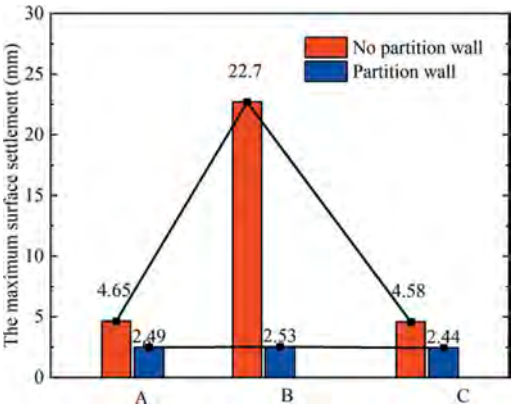

Figure 11. The maximum surface settlement of each area.

5 CONCLUSIONS

(1) The maximum horizontal displacement of the diaphragm wall in each excavation stage of the long and narrow deep foundation pit is generally controlled below 0.22% H, and the maximum surface settlement outside the foundation pit is controlled below 0.24% H. Both the maximum horizontal displacement and the maximum surface settlement occur in the central area along the long side of the diaphragm wall.

(2) The utilization of partition walls to shorten the length of the long and narrow deep foundation pit enables an effective reduction in the horizontal displacement of the diaphragm wall and the surface settlement outside the foundation pit. The central area along the long side exhibits the most substantial decrease, with a 43.66% reduction in the maximum horizontal displacement of the diaphragm wall.

(3) This study focuses solely on examining the impact of installing two partition walls on the deformation characteristics of the long and narrow deep foundation pit. Future research should aim to explore the optimal configuration of partition walls to achieve the most effective deformation control.

REFERENCES

Clough, G. W., 1990. Construction Induced Movements of Insitu Wall, Design and Performance of Earth Retaining Structure. In ASCE, pp. 439–479.

Gaba, A.R. 1990. Jet grouting at Newton station. In Proceedings of the 10th Southeast Asia Geotechnical Conference, Taipei, Taiwan. pp. 77–79.

Hsieh, P. G., Ou, C. Y., & Shih, C., 2012. A simplified plane strain analysis of lateral wall deflection for excavations with cross walls. Canadian Geotechnical Journal, 49(10),1134–1146.

Lin, Y.L., Ou, C.Y., and Hsieh, P.G. 2012. Three dimensional numerical analysis of deep excavations with cross walls. Department of Construction Engineering, National Taiwan University of Science and Technology, Taipei, Taiwan. Research Report GT2012001.

Ou, C. Y., Lin, Y. L., & Hsieh, P. G., 2006. Case record of an excavation with cross walls and buttress walls. Journal of GeoEngineering, 1(2),79–87.

Ou C.Y., Hsieh P.G., and Lin Y.L. 2011. Performance of excavations with cross walls. Journal of Geotechnical and Geoenvironmental Engineering, 137(1): 94–104.

O'rourke, T. D., 1993. Base stability and ground movement prediction for excavations in soft clay. In Retaining structures, pp. 657–686.

Parashar, S., Mitchell, R., Hee, M.W., Sanmugnathan, D., Sloan, E., and Nicholson, G. 2007. Performance monitoring of deep excavation at Changi WRP project, Singapore. In Proceedings of the 7th International Symposium on Field Measurements in Geomechanics. Edited by J. DiMaggio and P. Osborn. ASCE, Reston, Va. pp. 1–12.

Peck, R. B., 1969. Deep excavations andtunnelingin soft ground. In Proceeding of, pp. 215–285.

Wu, B., Peng, Y., Lan, Y., & Meng, G., 2019. Response analysis of excavation of deep foundation pit in metro station of soft soil. In IOP Conference Series: Earth and Environmental Science (Vol. 330, No. 2, p. 022102). IOP Publishing.

Tunnelling for a Better Life – Yan, Celestino, Thewes & Eberhardt (Eds)
© 2024 The Author(s), ISBN 978-1-032-80042-4
Open Access: www.taylorfrancis.com, CC BY-NC-ND 4.0 license

Disturbance effect and surrounding rock pressure characteristics of loess shield tunnels

Xingbo Han, Peiyuan Wang, Ziming Chen, Haolan Feng, Hao Cui & Fei Ye*
Chang'an University, Xi'an, China

ABSTRACT: Subjected to the unique mechanical properties of loess strata, the disturbance from shield tunneling and subsequent stress relocation within this stratum show their own features. In this study, by developing a UMAT subroutine that can characterize the constitutive properties of the loess strata, a FEM method is proposed to simulate the loess behavior during the shield tunneling and validated by experiments, using the user programming of ABAQUS. With this method, the soil behavior and redistribution of stress fields are investigated with varying water contents. Results show that the increase in water content of loess results in the displacement development of the loess stratum being gradual at the beginning, and the displacement increases rapidly after reaching 15% water content. In terms of soil pressure, the built-up pressure at the tunnel shoulder shows a unimodal distribution with the increase in water content. In addition, the pressure differential between the two tunnel shoulders becomes apparent at 20.2% water content. At 25.5% water content of loess, the soil pressure at the tunnel invert reaches its maximum. The pressure built-up at the crown drops with the increase in water content.

Keywords: shield tunnel, loess stratum, secondary development, water content, surrounding rock pressure

1 INTRODUCTION

The safety of tunnel structures is directly influenced by the load or pressure from the disturbed surrounding soil. Therefore, understanding the influence mechanism of construction disturbance on stratum stability, as well as the disturbance caused by soil load, is crucial for guiding safe construction and optimal design of tunnels. A large number of scholars have conducted extensive research through numerical simulations such as the finite element method.

Atkinson and Cairncross (1973) used the finite element method to calculate the ground stability of shallow tunnels. In 1983, Clough et al (1983), who proposed the Finite Element Method, analyzed the soil response of EPB shield tunnel. These early studies mostly adopted linear elastic constitutive, which is still widely used in a large number of recent research. Subsequently, Yang et al (1985) gave a nonlinear finite element calculation process for the plane strain problem of cavern excavation. Lyamin and Sloan (2000), as well as Yamamoto et al (2011), used the M-C nonlinear constitutive model to obtain a more accurate stress solution of surrounding rock in tunnel excavation. The ideal elastic-plastic constitutive was applied by Zheng et al (2008) in the Strength reduction method to calculate the slope safety factor. Then, the three-dimensional models with complex Geometry (Zhang et al., 2022), modified elastic-plastic and viscoelastic-plastic constitutive (Pan et al., 2019; Luo et al., 2018) were applied in the recent research. At the same time, new methods such as node-based finite element method (NS-FEM) (Vo-Minh et al., 2018; Vo-Minh and Nguyen-Son., 2021a; Nguyen and Vo-Minh., 2022) and smooth finite element method based on stable nodes (SNS-FEM) (Vo-Minh and Nguyen-Son., 2021b) have been applied. These methods further consolidate the important position of finite element numerical simulation in tunnel engineering mechanics analysis.

Several studies have been conducted to simulate the stress and deformation characteristics of loess surrounding soil for tunnels. For instance, Hu et al, (2011) used ABAQUS to simulate the stress and deformation characteristics of loess surrounding soil for tunnel Humaling. Song et al. (2018) used the Drucker-Prager model through ANSYS to simulate the mechanical behavior of surrounding soil under immersion by changing material parameters. Lai

*Corresponding author: xianyefei@126.com

DOI: 10.1201/9781003495505-96

et al (2018) used the Duncan-Chang model to study the effect from loess surrounding soil to the structure underwater immersion through secondary development. Pan et al (2019) used FLAC3D to simulate the pressure arch of an unsupported loess tunnel based on the Mohr-Coulomb constitutive model. In these studies, the elastic constitutive model was mostly applied in simulating the tunnel surrounding soil, and only limited conclusions of regularity can be conducted from these simulation works. To address this issue, it is necessary to realize the simulation of reasonable mechanical behavior of loess through secondary development. Therefore, this study intends to use the elastic nonlinear constitutive model which can reflect the characteristics of loess to describe the stress-strain relationship of loess stratum. Then, it is proposed to realize the reasonable simulation of the construction behavior of the loess shield tunnel through the secondary development of ABAQUS. Finally, based on the proposed reasonable numerical simulation method, this study investigates the influence of excavation and water content on the mechanical behavior of tunnel and stratum. The research conclusions are expected to provide support for designing loess shield tunnels.

2 ELASTIC NONLINEAR CONSTITUTIVE OF LOESS AND ITS SECONDARY DEVELOPMENT

The reasonable stress-strain relationship of soil is the key to accurately analyzing geotechnical tunnel engineering problems. The stress-strain relationship of general rock or soil can be expressed as:

$$\{\sigma\} = [D]\{\varepsilon\} \tag{1}$$

Where $[D]$ is the stiffness matrix, which can be expressed as a function of modulus and Poisson's ratio:

$$[D] = f(E, \nu) \tag{2}$$

Where E is the modulus, v is the Poisson's ratio.

As early as 1963, Kondner obtained the stress-strain relationship of soil by using a hyperbolic curve through a large number of triaxial tests:

$$\sigma_1 - \sigma_3 = \frac{\varepsilon_a}{a + b\varepsilon_a} \tag{3}$$

Where the elastic modulus $E=a+b\varepsilon_a$, a, b are constants. This formula can directly reflect the stress-strain relationship of soil by linear elastic relationship.

Subsequently, Duncan and Chang proposed the incremental elasticity model- Duncan—Chang Model. The elastic coefficient in the elastic matrix can change with the change of stress state, which can more reasonably reflect the nonlinear relationship of soil stress and strain:

$$[D] = \frac{E_t}{(1+\nu_t)(1-2\nu_t)} \begin{bmatrix} (1-\nu_t) & \nu_t & \nu_t & 0 & 0 & 0 \\ \nu_t & (1-\nu_t) & \nu_t & 0 & 0 & 0 \\ \nu_t & \nu_t & (1-\nu_t) & 0 & 0 & 0 \\ 0 & 0 & 0 & (1-2\nu_t)/2 & 0 & 0 \\ 0 & 0 & 0 & 0 & (1-2\nu_t)/2 & 0 \\ 0 & 0 & 0 & 0 & 0 & (1-2\nu_t)/2 \end{bmatrix} \tag{2}$$

Where E_t is the tangent modulus of the soil, v_t is the tangent Poisson's ratio.

However, for loess strata, Xie and Xing (2014) pointed out that the stiffness matrix is different from that of general soil, which can be expressed as:

$$[D] = \frac{E}{(1+\nu)(1-2\nu)} \begin{bmatrix} 1-\nu & \nu & \nu & 0 & 0 & 0 \\ \nu & 1-\nu & 0 & 0 & 0 & 0 \\ \nu & 0 & 1-\nu & 0 & 0 & 0 \\ 0 & 0 & 0 & 1-2\nu & 0 & 0 \\ 0 & 0 & 0 & 0 & 1-2\nu & 0 \\ 0 & 0 & 0 & 0 & 0 & 1-2\nu \end{bmatrix} \tag{5}$$

Where the elastic modulus E can be expressed as:

$$\begin{aligned} E = E_t &= (1 - R_f s)^2 E_i \\ &= \left[1 - R_f \frac{(1-\sin\varphi)(\sigma_1 - \sigma_3)}{2c\cos\varphi + 2\sigma_3 \sin\varphi}\right]^2 K p_a \left(\frac{\sigma_3}{p_a}\right)^n \end{aligned} \tag{6}$$

Poisson ratio V_t can be expressed as:

$$\nu_t = \frac{G - F\lg(\sigma_3/p_a)}{\left\{1 - \frac{D(\sigma_1-\sigma_3)}{Kp_a\left(\frac{\sigma_3}{p_a}\right)^n \left\{1 - \frac{R_f(\sigma_1-\sigma_3)(1-\sin\varphi)}{2c\cos\varphi + 2\sigma_3\sin\varphi}\right\}}\right\}^2} \tag{7}$$

In Eq.(6) and (7), E_i is the initial modulus, R_f is the failure ratio, c is the cohesion, φ *is the* angle of internal friction, p_a is the atmospheric pressure, K is intercept of straight lines, n is the slope of straight lines, D, G and F are experimental constant.

Therefore, to describe the mechanical behavior of loess strata under the influence of shield construction more reasonably, the stiffness matrix is constructed in ABAQUS through secondary development.

3 RATIONALITY VERIFICATION OF THE SELF-DEVELOPED CONSTITUTIVE

In this section, the simulated triaxial test results are compared with the indoor triaxial test experiment results to verify the rationality of the self-developed elastic nonlinear constitutive model.

A three-dimensional standard soil sample finite element model with the same size as the indoor sample is established to simulate the conventional

indoor triaxial compression test. Calculations are performed here for two soil samples. One is from reference Gao and Li (2006) (No.1 in Table 1), and the other is from the project site of Xi'an Metro Line 8 with the moisture content of 15.1% (No.2 in Table 1). The height of the specimen is 80mm and the diameter is 39.1mm showing in Figure 1. The numerical model is divided into 25341 elements, and the soil is simulated by C3D8 elements. The relevant parameters of the model are listed as Table 1.

Table 1. Elastic nonlinear constitutive relation of loess stratum.

No.	K	n	R_f	c/kPa	φ/°	G	D	F
1	376	0.35	0.84	38	30	0.466	1.18	0.184
2	216	0.41	0.86	35.95	24.39	0.192	3.41	0.073

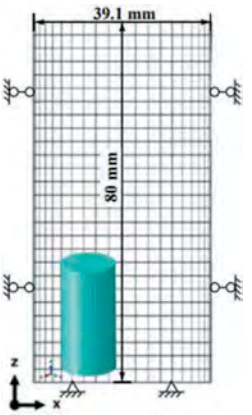

Figure 1. Three-dimensional standard soil sample finite element model.

In the numerical simulation, the displacement of the side (U2 = 0) and the bottom (U3 = 0) of the model is 0, and the top is the free surface. The confining pressures with 100 kPa, 200 kPa, 300 kPa, σ and 400 kPa were applied during the test. After the stress was balanced, a 12 mm displacement load was applied along the Z-axis direction at the top free surface. The comparison between numerical simulation and indoor triaxial test results are shown in Figure 2. It can be seen from both Figure 2 (a) and (b) that the results of the numerical simulation of the loess triaxial test based on the elastic nonlinear constitutive model obtained by secondary development are consistent with the results of the laboratory test. The constitutive bilinear characteristics of loess can be well reflected in numerical simulations. The UMAT subroutine in this study is feasible in simulating loess mechanical problems.

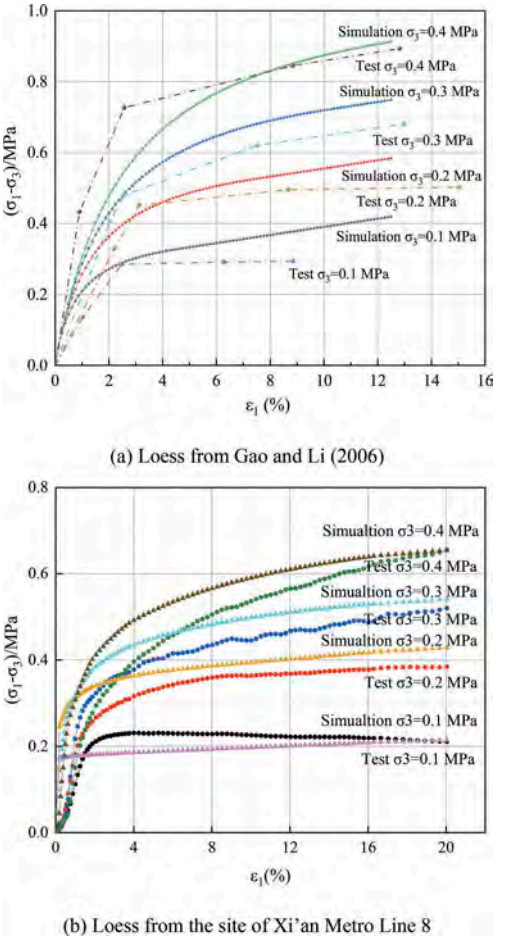

Figure 2. Comparison of numerical simulation and indoor triaxial test results.

4 SOIL DISTURBANCE CHARACTERISTICS OF LOESS SHIELD TUNNEL CONSTRUCTION

4.1 *Modelling*

Based on the elastic nonlinear constitutive model UMAT subroutine, this section studies the soil deformation and surrounding rock pressure of loess strata under shield construction. One section of Xi'an Metro Line 8 was taken as an engineering case. The outer diameter of the segment is 6.2 m with the thickness of 0.35 m. This section of the tunnel is buried in the loess stratum. The buried depth is 15 m. The numerical model adopts the C3D8 element, and the mesh division is shown in Figure 3. The parameters of the loess stratum are listed in Table 1. The parameters of the segment shield shell are listed in Table 2.

The elastic nonlinear constitutive model UMAT subroutine established in Section 2 is used to describe the constitutive relationships of loess. The

Table 2. Model material parameter table.

Materials	Density/(t/m^3)	Young's modulus/Pa	Poisson ratio
Segments	2.6	24 500 000	0.2
Shield shell	7.85	245 000 000	0.2

construction process containing excavation, shield shell supporting and segment assembly are simulated by using life-and-death element method. The soil and the segment are set with binding constraints, and the segment is in contact with the soil. In the model, a fixed constraint is set at the bottom of the soil, and the displacement perpendicular to the plane is 0. A support pressure with the amount of 200kPa was applied on the tunnel front face during the drilling.

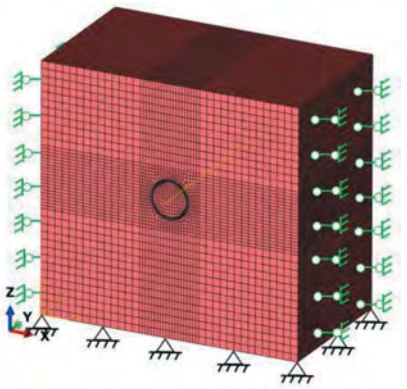

Figure 3. Model grid diagram.

4.2 *Disturbance characteristics of soil and comparison with model test results*

The vertical displacement of soil caused by tunnel excavation is the most significant. According to the calculation of this model, the three-dimensional equivalent surface of vertical displacement of soil after excavation is shown in Figure 4. It is found from Figure 4 that there is a certain range of collapse area above the tunnel face. The soil is displaced towards the direction of the tunnel face. And the closer to the tunnel face, the greater the soil displacement. The boundary of the collapse area is platform-shaped. Then a 1:50 scale indoor experiment was carried out to verify the numerical result The experiment equipment is shown in Figure 5. The detailed parameters of the experiment have been reported by Han et al. (2023). The macroscopic morphology and digital image analysis results of the collapse surface obtained by the test are shown in Figure 6. The collapse area is also obviously characterized by a platform distribution. This also shows that the proposed self-developed constitutive model has applicability.

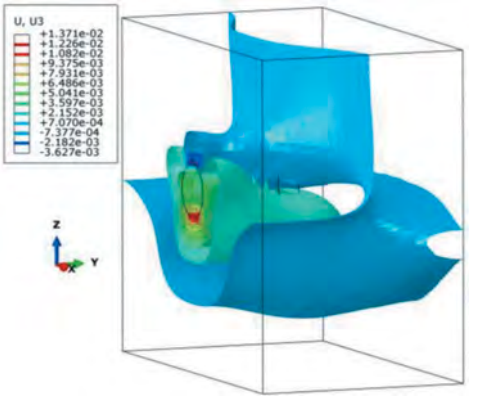

Figure 4. Numerical simulation results of vertical displacement of soil.

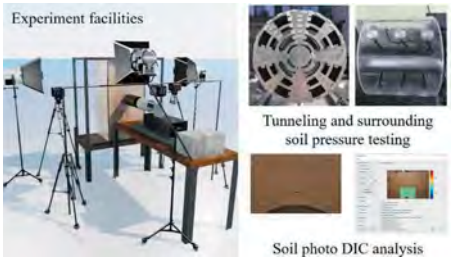

Figure 5. Model test settings.

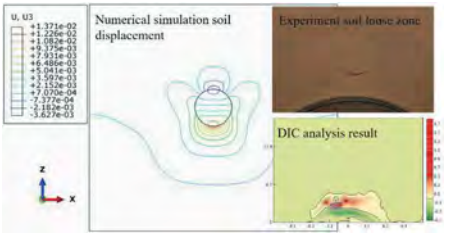

Figure 6. Numerical simulation and model test soil loose area comparison.

4.3 *Surrounding rock pressure characteristics*

In this section, the shield excavation process in the loess stratum is simulated based on the elastic nonlinear constitutive model UMAT subroutine. The surrounding rock pressure corresponding to different excavation steps under the action of self-weight stress is extracted showing in Figure 7. It is found that the surrounding rock pressure under the action of self-weight stress in the vault is the largest, followed by the arch bottom. And the surrounding rock pressure both side wall is the smallest. With the excavation of the tunnel, the distribution law of surrounding rock pressure has changed, and the surrounding rock pressure of the arch shoulder exceeds the vault. In addition, the surrounding rock pressure

of the arch waist also gradually increases. The surrounding rock pressure of the vault measured by the experiment (black stars in Figure 7) is close to the numerical simulation results.

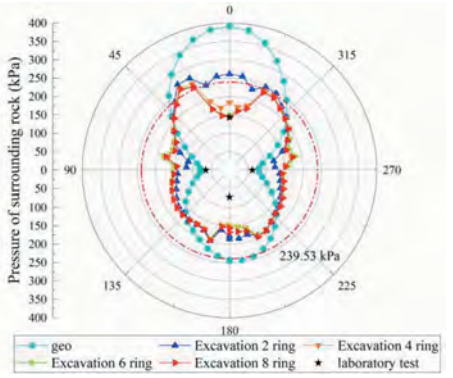

Figure 7. Surrounding rock pressure corresponding to different excavation steps.

5 CHARACTERISTICS OF SURROUNDING ROCK PRESSURE OF LOESS SHIELD TUNNEL WITH DIFFERENT WATER CONTENT

Based on the triaxial test for the loess from the shield tunnel site of Xi'an Metro Line 8, the Duncan-Chang parameters under different moisture contents of the engineering loess strata are measured as shown in Table 3. Subsequently, the above parameters are input into the numerical calculation model. The surrounding rock disturbance and surrounding rock load of loess shield tunnel construction under different water content are analyzed.

Table 3. Parameters of the elastic nonlinear constitutive model of loess with different water content.

Moisture content (%)	*K*	*n*	R_f	*c/ kPa*	*φ/°*	*G*	*D*	*F*
11.8	318	0.5	0.94	45.00	27.91	0.223	3.73	0.087
15.1	216	0.41	0.86	35.95	24.39	0.192	3.41	0.073
16.8	153	0.32	0.81	36.55	23.91	0.169	3.02	0.065
20.2	127	0.26	0.75	30.32	22.45	0.133	2.77	0.046
25.4	92	0.16	0.71	33.96	15.93	0.123	2.65	0.033

5.1 *The overall displacement of soil*

The overall deformations of the soil after tunnel excavation and support under different water contents are shown in Figure 8. It can be seen from Figure 8 that the maximum value of the overall displacement of the soil gradually increases with the increase of the stratum water content. During the shield excavation process, the soil displacement at the tunnel face is the largest. In addition, when the water content increases to 25.4 %, the area with large disturbance has developed to the surface. When the water content exceeds 15 %, the soil displacement develops rapidly. The maximum displacement of the 25.4 % water content formation is about 10 times that of the 11.8 % water content formation (Figure 9).

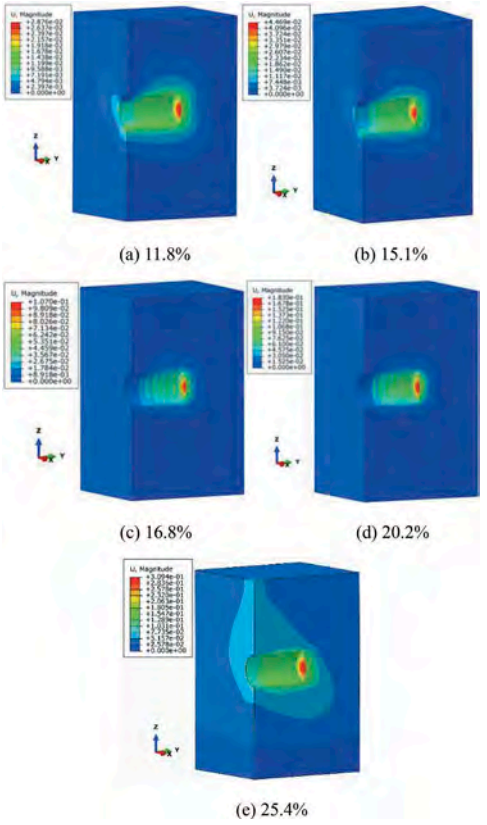

Figure 8. The overall deformation diagram of soil during shield tunneling under different water content loess strata (unit:m).

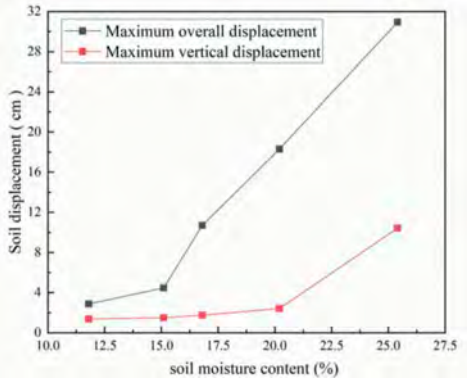

Figure 9. The maximum value of the overall and vertical displacement of the soil during shield tunneling in loess strata with different water contents.

5.2 *Pressure of surrounding rock*

The surrounding rock pressure during shield tunneling in loess stratum with different water contents is extracted and compared, as shown in Figure 10. The formation water contents are 11.8 %, 15.1 %, 16.8 %, 20.2 %, and 25.4 %, respectively.

It can be seen from Figure 10 that the law of surrounding rock pressure distribution during shield tunneling at different water contents situations is similar. With the increase in water content, the surrounding rock pressure gradually increases (the closer the whole is to 239.53 kPa).

The changes of surrounding rock pressure in different directions after the completion of shield tunneling under different water content are compared in Figure 10 (f). It can be seen that, with the increase of water content, the surrounding soil pressure at the arch waist increases first and then decreases. When the water content is 20.2 %, the surrounding rock pressure on both sides of the arch waist increases most significantly. The surrounding rock pressure at the arch bottom increases gradually, and the surrounding rock pressure at the arch bottom is the largest when the water content is 25.4 %. The surrounding

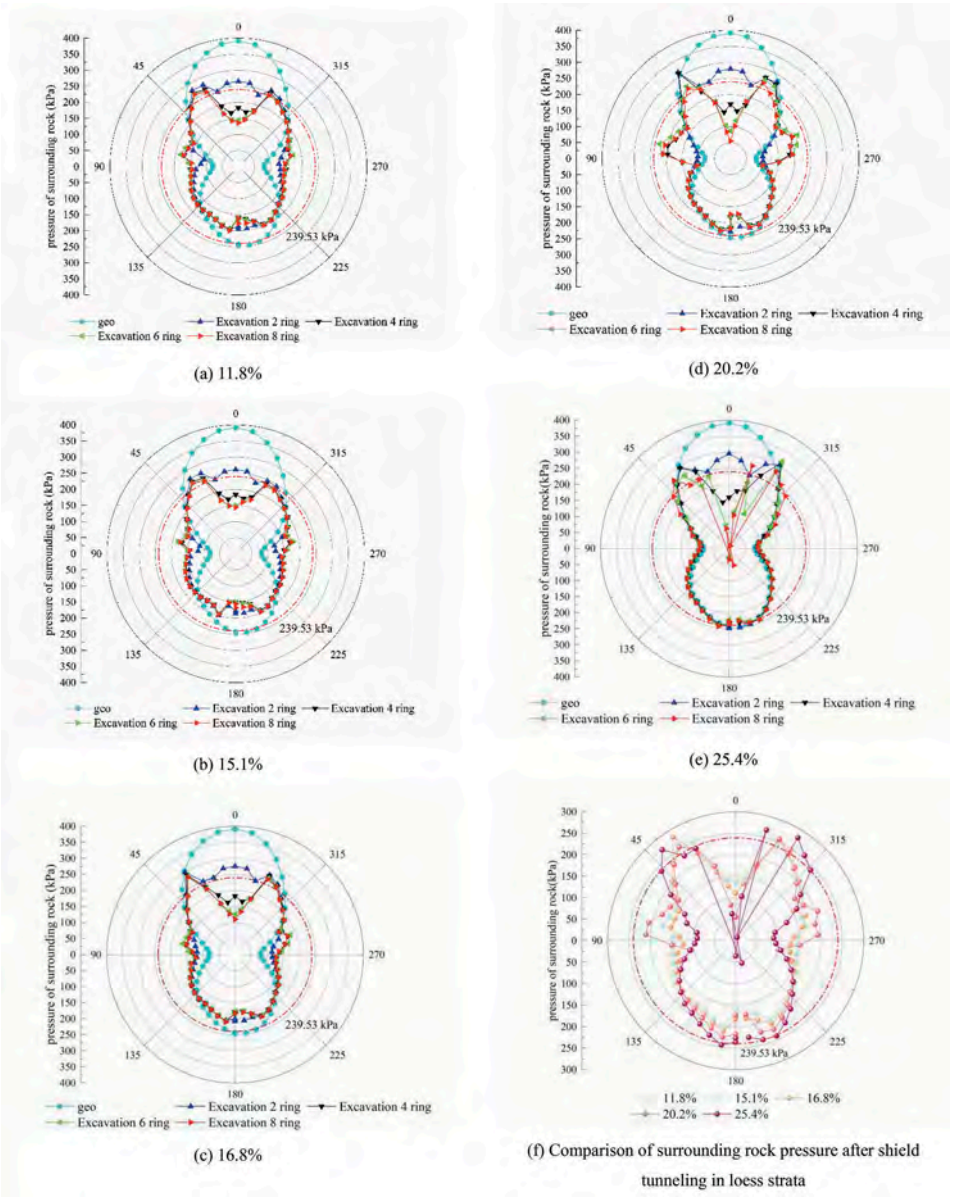

Figure 10. Surrounding rock pressure during shield tunneling in loess strata with different water contents.

rock pressure of the vault decreases from large to small, and from positive to negative. This shows that, with the increase in water content, compressive stress gradually appears in the vault. When the water content is 25.4%, the variation range of surrounding rock pressure of the vault is the largest.

6 CONCLUSION

In this research, we first established an elastic nonlinear constitutive model to reflect the characteristics of loess stratum. Then, we proposed a numerical simulation method for loess tunnel engineering by applying the elastic nonlinear constitutive into the software ABAQUS. The accuracy of the numerical method was verified by comparing it with the triaxial test and the indoor scale experiment. Finally, we studied the influence of excavation and water content on the mechanical behavior of tunnel and stratum in loess area. Detailed conclusions are follows:

(1) The elastic nonlinear constitutive model proposed in this work can reasonably simulate the disturbance law of loess shield tunnel construction to the stratum.With an increase in water content, the maximum value of overall displacement of the loess stratum gradually increases. When water content exceeds 15%, soil displacement develops rapidly.
(2) With an increase in water content, surrounding rock pressure at arch waist increases first and then decreases.
(3) When water content is 20.2%, surrounding rock pressure on both sides of arch waist increases most significantly. When water content is 25.4%, surrounding rock pressure of arch bottom is largest. Surrounding rock pressure of vault decreases from large to small, and vault gradually appears under compressive stress. When water content is 25.4%, surrounding rock pressure of vault changes most.

ACKNOWLEDGMENTS

The research was conducted with funding provided by the National Natural Science Foundation of China (Grant No. 52108360, 52378389, 52378390) and the Fundamental Research Funds for the Central Universities, CHD (Grant No. 300102213206).

REFERENCES

Atkinson, JH., AM Cairncross., 1973. "Collapse of a shallow tunnel in a Mohr-Coulomb material." In *Proceedings of the Symposium on the Role of Plasticity in Soil Mechanics*, *Cambridge*, *UK*, 13–15.

Clough, G. W., B. P. Sweeney., and R. J. Finno., 1983. 'Measured Soil Response to EPB Shield Tunneling', *Journal of Geotechnical Engineering-Asce*, 109: 131–49.

Han, X. B., Feng, H. L., He, Q., et al, 2023. 'Digital lmage Measurement Technology and lts Application in Tunnel lndoor Model Test', Journal of Tongji University(Natural Science), 51: 1344–51.

Hu, S. M., Zhang, D. L., Wang, M. S., 2011. 'The Mechanical Response of the Surrounding Rock Caused by the Excavation of Loess Tunnel with Large Cross Section', China Railway Science, 32: 50–55.

Gao, J.P., Li, F., 2006. Experiments on parameters of duncan-chang model for loess. Journal of Chang'an University (Natural Science Edition) 26: 10–13.

Lai, H. P., Xie, Y. L., Liu, Y. Y., 2018. 'Deterioration mechanism and evaluation technology of structural performance of loess highway tunnel' (Science Press: Beijing).

Luo, Z., B. Hu., Y. W. Wang.,et al, 2018. 'Effect of spatial variability of soft clays on geotechnical design of braced excavations: A case study of Formosa excavation', *Computers and Geotechnics*, 103: 242–53.

Lyamin, AV., and SW Sloan., 2000. "Stability of a plane strain circular tunnel in a cohesive-frictional soil." In *Proceedings of the JR Booker memorial symposium*, *Sydney*, *Australia*, 16–17.

Nguyen, H. C., and T. Vo-Minh. 2022. 'The use of the node-based smoothed finite element method to estimate static and seismic bearing capacities of shallow strip footings', *Journal of Rock Mechanics and Geotechnical Engineering*, 14: 180–96.

Pan, Y., K. Yao., K. K. Phoon., et al, 2019. 'Analysis of tunneling through spatially-variable improved surrounding - A simplified approach', *Tunnelling and Underground Space Technology*, 93: 12.

Pan, H. S., Du, G. Y., Wang, K., 2019. 'Model test and numerical simulation on pressure arch of unlined loess tunnel', Journal of Southeast University (Natural Science Edition), 49: 949–55.

Song, W. L., Lai, H. P., Liu, Y. Y., 2018. 'Analysis of lining cracking of loess highway tunnel based on surrounding rock immersion', China Journal of Highway and Transport, 31: 117-26+50.

T Vo-Minh., L Nguyen-Son - Computers., and Geotechnics., 2021b. 'A stable node-based smoothed finite element method for stability analysis of two circular tunnels at different depths in cohesive-frictional soils', *Computers and Geotechnics*, 129: 17.

Vo-Minh, T., A. Chau-Ngoc., T. Nguyen-Minh., et al. 2018. 'A node-based smoothed finite-element method for stability analysis of dual square tunnels in cohesive-frictional soils', *Scientia Iranica*, 25: 1105–21.

Vo-Minh, T., and L. Nguyen-Son., 2021a. 'A stable node-based smoothed finite element method for stability analysis of two circular tunnels at different depths in cohesive-frictional soils', *Computers and Geotechnics*, 129.

Xie, D. Y., and Xing, Y. C., 2014. Soil Mechanics for Loes Soils (Higher Education Press: Beijing).

Yang, D. L., Huang, W., Wang, Y., 1985. 'The Finite Element Method for Determining the Initial Earth Stress', Journal of Tongji University: 69–77.

Yamamoto, K., A. V. Lyamin., D. W. Wilson., et al, 2011. 'Stability of a circular tunnel in cohesive-frictional soil subjected to surcharge loading', *Computers and Geotechnics*, 38: 504–14.

Zhang, W. G., L. Han., X. Gu., et al, 2022. 'Tunneling and deep excavations in spatially variable soil and rock masses: A short review', *Underground Space*, 7: 380–407.

Zheng, Y. R., Qiu, C. Y., Zang, H., 2008. 'Exploration of stability analysis methods for surrounding rocks of soil tunnel.', Chinese Journal of Rock Mechanics and Engineering: 1968–80.

Tunnelling for a Better Life – Yan, Celestino, Thewes & Eberhardt (Eds)
© 2024 The Author(s), ISBN 978-1-032-80042-4
Open Access: www.taylorfrancis.com, CC BY-NC-ND 4.0 license

Numerical simulation of polymer grouting for rock fracture: Influence of isocyanate index on grout propagation

Meimei Hao*
School of Water Conservancy and Transportation, Zhengzhou University, Zhengzhou, China
Division of Resources, Energy and Infrastructure, Department of Sustainable development, Environmental science and Engineering, Royal Institute of Technology, Stockholm, Sweden

Jia Zhang
School of Water Conservancy and Transportation, Zhengzhou University, Zhengzhou, China

Liangchao Zou
Division of Resources, Energy and Infrastructure, Department of Sustainable development, Environmental science and Engineering, Royal Institute of Technology, Stockholm, Sweden

Xiaolong Li
School of Water Conservancy and Transportation, Zhengzhou University, Zhengzhou, China

ABSTRACT: The grout propagation plays a crucial role in the design of polyurethane grouting for reinforcing and sealing fractured rock. Understanding the influence of isocyanate index on the diffusion process is essential for selection and material modification to improve the grouting effectiveness. In this study, a numerical method was developed to simulate the grout propagation of polyurethane, considering the coupled of reaction kinetics and fluid flow. Furthermore, the influence of the isocyanate index on pressure, diffusion distance, component conversion and density were analyzed. These findings contribute to the preparation and selection of polyurethane grout for practical engineering applications.

Keywords: Polyurethane, Fracture grouting, Isocyanate index, Grout propagation, Numerical simulation

1 INTRODUCTION

In recent years, the increasing use of two-component polyurethane grouting material with self-expanding characteristics has gained great attention, driven by advancements in the modern polymer industry. Unlike traditional grouting materials such as cement and sodium silicate entirely rely on static pressure, the two components of polymer grout, black material (isocyanate) and white material (polyol, blowing agent, catalyst, foam stabilizer, and other additives) chemically react rapidly after mixing, leading to the volume expansion as the primary driving force of polymer grout. With the advantages of rapid reaction, high expansion rate, excellent impermeability, safety and environmental protection over traditional alternatives, the polymer material has been widely used in the repairing of uneven settlement of high-speed railway subgrade, treatment of voids under airport pavements, non-excavation maintenance of highways, quick tunnel repairment, and dam anti-seepage reinforcement (Fang et al., 2019; Guo et al., 2020; Guo and Wang, 2009; Wang et al., 2022; Zhang et al., 2021). Understanding and regulating the diffusion and evolution of polymer grout in rock fractures are of great importance in grouting design.

As a chemical grouting material, the isocyanate index of polyurethane grout significantly impacts on the process of chemical reactions, manifested as an increase in volume and temperature macroscopically. For the grout propagation of polymer material, the molar ratio of NCO to OH, known as the isocyanate index greatly influences the increase in cross-link of

*Corresponding author: haomm1213@outlook.com

DOI: 10.1201/9781003495505-97

polyurethane, hard segment content and unreacted NCO functional groups (Eun and Lee, 2020). Tu et al. (2007) examined the influence of isocyanate index on the density, compressive strength, and thermal conductivity of polyurethane foam, but the presence of physical blowing agent was not considered in their works. Kim et al. (2008) synthesized various types of rigid polyurethane foams with HFC-365mfc as the physical blowing agent, and the effect of isocyanate index on the foam properties such as reactivity, cell morphology, mechanical and dynamic mechanical properties, and thermal properties had been analyzed. For the diffusion patterns of polymer grout in rock fractures, Hao et al. (2018) simulated the diffusion process of polymer grout in rock fractures, and obtained the time-varying characteristics of pressure field and diffusion distance. Li et al. (2019) presented an analytical solution to model the radial transient flow of polymer grout with variable density in a planar fracture and the analytical expressions of the diffusion radius, radial velocity and pressure distribution over time between the fracture walls in self-expanding phase were derived. Liang et al. (2021) established a single radial diffusion model of fracture grouting and analyzed the influence of grouting amount, expansion ratio and aperture on the diffusion patterns of polymer grout in rock fractures. These studies treated the polymer grout as a homogeneous fluid with known density and viscosity variations over time, without considering the intrinsic driving mechanism of chemical reactions. Jia et al. (2022) incorporated chemical reaction kinetic equations into the numerical simulation of the diffusion process of polymer grout in a planar fracture under adiabatic conditions, analyzing the time-varying laws of grout component conversions, temperature, diffusion range, density, pressure and other variables, but did not investigate the influence of isocyanate index of polymer grout material on the grout propagation.

In summary, existing studies mainly focus on the mold filling or free rising process of polyurethane, with simplistic consideration of the external environment and surrounding media conditions compared to the expansion process in the fractures; these studies primarily investigate the influence of operating parameters and external environment on the expansion and diffusion of polymer grout, while paying less attention to the influence of isocyanate index. In our study, coupling the chemical kinetics and grout flow, a numerical model for the spread and expansion of polymer grout in a rock fracture was established. Based on the lubrication theory, the governing equation combining chemical kinetic equation were solved to investigate the propagation of polymer grout in a fracture. Furthermore, the influence of isocyanate indexes on the spread, pressure, conversion and density were analyzed. The results are able to improve the comprehensive understanding of the diffusion process of polymer grout in rock fractures and provides valuable references for choosing material proportions as needed in practical engineering applications.

2 CHEMICAL KINETICS

2.1 *Gelling reaction*

Gelling reaction is the process of isocyanate react with polyol to form polyurethane, as can be seen in formula (1).

$$\underset{\text{Isocyanate}}{n\text{NCO}-\text{R}-\text{NCO}}+\underset{\text{Polyol}}{n\text{HO}-\text{R}'-\text{OH}}\rightarrow -\underset{\text{Polyurethane}}{[\text{O}-\text{R}'-\text{O}-\text{CONH}-\text{R}-\text{NHCO}]_n} \tag{1}$$

The chemical reaction kinetic equation for this reaction, i.e., the rate equation, is:

$$\frac{\mathrm{d}X_{\text{OH}}}{\mathrm{d}t}=A_{\text{OH}}\cdot\exp\left(-\frac{E_{\text{OH}}}{RT}\right)\cdot c_{\text{OH}}^{0}\cdot(1-X_{\text{OH}})\cdot\left(\frac{c_{\text{NCO}}^{0}}{c_{\text{OH}}^{0}}-2\frac{c_{\text{W}}^{0}}{c_{\text{OH}}^{0}}X_{\text{W}}-X_{\text{OH}}\right) \tag{2}$$

2.2 *Blowing reaction*

The blowing reaction refers to the process of reaction between isocyanate and water to produce carbon dioxide, which is a process of rapid expansion of the volume of polymer grout. The chemical reaction equation is as follows:

$$\underset{\text{Isocyanate}}{2\text{R}-\text{NCO}}+\underset{\text{Water}}{\text{H}_2\text{O}}\rightarrow \underset{\text{Urea}}{\text{R}-\text{NH}-\text{CO}-\text{NH}-\text{R}}+\text{CO}_2\uparrow \tag{3}$$

The chemical reaction kinetic equation is:

$$\frac{\mathrm{d}X_{\text{W}}}{\mathrm{d}t}=A_{\text{W}}\cdot\exp\left(-\frac{E_{\text{W}}}{RT}\right)\cdot c_{\text{OH}}^{0}\cdot(1-X_{\text{W}})\cdot\left(\frac{c_{\text{NCO}}^{0}}{c_{\text{OH}}^{0}}-2\frac{c_{\text{W}}^{0}}{c_{\text{OH}}^{0}}X_{\text{W}}-X_{\text{OH}}\right) \tag{4}$$

Where, c_i^0 and X_i denote the initial concentration and conversion of component i respectively, and i takes W, OH and NCO when denoting water, polyol and isocyanate, respectively. A_{OH} and A_{W} are the pre-exponential factors for the gelling and blowing reactions, respectively. E_{OH} and E_{W} are the activation energies for the two reactions, respectively. R is the ideal gas constant, and T is the grout temperature.

3 MATERIAL MODELS

3.1 *Density model*

During the reaction process, the polymer grout is considered as a homogeneous mixture of two gases and three liquids. In this case, the gas part consists of the gaseous physical blowing agent produced by vaporization of the liquid physical blowing agent and the carbon dioxide generated by the blowing reaction. The liquid part is formed by water, the polyurethane mixture and the liquid physical blowing agent dissolved in the grout. Thus, the calculated expression for the density of the polymer grout at any moment is:

$$\rho = \frac{1 + r_{\mathrm{W}}^0 + r_{\mathrm{BL}}^0}{\frac{r_{\mathrm{CO_2}} RT}{PM_{\mathrm{CO_2}}} + \frac{r_{\mathrm{BG}} RT}{PM_{\mathrm{B}}} + \frac{(1-X_{\mathrm{W}})r_{\mathrm{W}}^0}{\rho_{\mathrm{W}}} + \frac{r_{\mathrm{BL}}^0 - r_{\mathrm{BG}}}{\rho_{\mathrm{BL}}} + \frac{1}{\rho_{\mathrm{p}}}} \tag{5}$$

Where, r_{W}^0 and r_{BL}^0 are the initial mass fraction of water component and liquid physical blowing agent, respectively. r_{BG} and $r_{\mathrm{CO_2}}$ are the mass fraction of gaseous physical blowing agent and carbon dioxide, respectively. $M_{\mathrm{CO_2}}$ and M_{B} are the molar mass of carbon dioxide and physical blowing agent, respectively. ρ_{BL} and ρ_{p} are the density of liquid physical blowing agent and polyurethane, respectively. P is the pressure of the grout.

3.2 *Solubility of physical blowing agent*

The solubility of the physical blowing agent in the polymer grout varying with the grout temperature obtained from experiments is as follows:

$$r_{\mathrm{BL}} = 0.03518 + \frac{0.04341}{1 + \exp\left(\frac{T-430.8294}{19.2898}\right)} \tag{6}$$

$$r_{\mathrm{BG}} = r_{\mathrm{BL}}^0 - r_{\mathrm{BL}} \tag{7}$$

4 FLOW CONTROL EQUATIONS

Considering the characteristics of polyurethane material, the following assumptions and simplifications are made: a) The polymer grout is regarded as a viscous fluid. b) The expansion process takes place is in an adiabatic environment, where there is no heat exchange with the external surroundings. c) The polymer grout is fully reacted, and all the gases generated during the reaction are incorporated into the mixture. d) The polymer grout is an isotropic homogeneous continuous fluid, and the flow process is considered as laminar flow. e) The reaction process in the fracture is a two-phase flow with grout and air.

4.1 *Governing equations*

A quasi-3D model developed by Li et al. (2019) was used in this paper, and set the scales of z direction much smaller than those of x and y directions (with order of magnitude differences). The model takes the geometric characteristic of the fracture into account and introduces the assumptions of the Hele-Shaw model to deduce the partial derivatives of the velocity with respect to z at fracture walls and the derived equation is a function of the aperture and the average velocity. The conventional difference scheme for the diffusive term is partly replaced by the derived analytical expression, thus the three-dimensional problem of grout flow in parallel fracture can be transformed into a two-dimensional problem.

The flow of the polymer grout satisfies the following equations:

(1) Mass conservation equation
The flow of the polymer grout satisfies the mass conservation equations:

$$\frac{\partial \rho}{\partial t} + \mathrm{div}(\rho \boldsymbol{u}) = 0 \tag{8}$$

Where, ρ is the density, t is the time, $\boldsymbol{u}$ is the velocity vector, and div is the scatter.
(2) Momentum conservation equationsThe flow of the polymer grout satisfies the momentum conservation equations:

$$\begin{aligned} \frac{\partial(\rho u)}{\partial t} + \mathrm{div}(\rho u \boldsymbol{u}) &= \mathrm{div}(\mu \mathrm{grad} u) - \frac{\partial}{\partial z}\left(\mu \frac{\partial u}{\partial z}\right) + S_u \\ \frac{\partial(\rho v)}{\partial t} + \mathrm{div}(\rho v \boldsymbol{u}) &= \mathrm{div}(\mu \mathrm{grad} v) - \frac{\partial}{\partial z}\left(\mu \frac{\partial v}{\partial z}\right) + S_v \end{aligned} \tag{9}$$

Where, u and $v$are the flow velocities in the x and y directions, respectively; S_u and S_v are the source terms in the x and y directions, respectively; μ is the velocity.
(3) Energy conservation equation
Under adiabatic conditions, the energy conservation equation of the polymer grout is:

$$\begin{aligned} &\left(C_{\mathrm{p}} + r_{\mathrm{CO_2}} C_{\mathrm{CO_2}} + r_{\mathrm{W}} C_{\mathrm{W}} + r_{\mathrm{BG}} C_{\mathrm{BG}} + r_{\mathrm{BL}} C_{\mathrm{BL}}\right)\frac{\mathrm{d}T}{\mathrm{d}t} \\ &= \left(\frac{-\Delta H_{\mathrm{OH}} c_{\mathrm{OH}}^0}{\rho_{\mathrm{p}}}\right)\frac{\mathrm{d}X_{\mathrm{OH}}}{\mathrm{d}t} \\ &+ \left(\frac{-\Delta H_{\mathrm{W}} c_{\mathrm{W}}^0}{\rho_{\mathrm{p}}}\right)\frac{\mathrm{d}X_{\mathrm{W}}}{\mathrm{d}t} - \lambda\left(-\frac{\mathrm{d}r_{\mathrm{BL}}}{\mathrm{d}t}\right) \end{aligned} \tag{10}$$

Where, C_i and r_i is the specific heat capacity and mass fraction of component i, and i takes p, CO_2, W,

BG and BL when denoting polyurethane, carbon dioxide, water, gaseous physical blowing agent and liquid physical blowing agent, respectively. ΔH_{OH} and ΔH_W are the heats of gelling reaction and blowing reaction, respectively. λ is the heat of evaporation of physical blowing agent.

(4) Scalar-transport equations

The component mass conservation equations for the hydroxyl and water components (ignoring the diffusion terms) are as follows:

$$\frac{\partial}{\partial t}(\rho\alpha_F X_{OH}) + \mathrm{div}(\rho\alpha_F X_{OH}\boldsymbol{u}) = \rho\alpha_F Q_{Kin,OH} \quad (11)$$

$$\frac{\partial}{\partial t}(\rho\alpha_F X_W) + \mathrm{div}(\rho\alpha_F X_W\boldsymbol{u}) = \rho\alpha_F Q_{Kin,W} \quad (12)$$

Where α_F represents the volume fraction of grout in a cell, $Q_{Kin,OH}$ and $Q_{Kin,W}$ represent the rate of change of hydroxyl fraction conversion and water fraction conversion, respectively:

$$Q_{Kin,W} = A_{OH}\cdot\exp\left(\frac{-E_{OH}}{RT}\right)\cdot c_{OH}^0\cdot(1-X_{OH})\cdot \left(\frac{c_{NCO}^0}{c_{OH}^0} - 2\frac{c_W^0}{c_{OH}^0}X_W - X_{OH}\right) \quad (13)$$

$$Q_{Kin,W} = A_W\cdot\exp\left(\frac{-E_W}{RT}\right)\cdot c_{OH}^0\cdot(1-X_W)\cdot \left(\frac{c_{NCO}^0}{c_{OH}^0} - 2\frac{c_W^0}{c_{OH}^0}X_W - X_{OH}\right) \quad (14)$$

(5) VOF model

The volume of fluid (VOF) method is employed to accurately track the interface between the grout and air phases. The sum of the volume fractions of the grout phase and air phase of each cell is 1 in the computational domain. Therefore, there are three values representing the volume fraction of the grout phase: $\alpha_F = 1$ means that the cell exclusively contains polymer grout, $0 < \alpha_F < 1$ means that the cell contains both polymer grout and air, and $\alpha_F = 0$ means that the cell only contains air without grout present.The volume fraction of the polymer grout satisfies:

$$\frac{\partial\alpha_F}{\partial t} + \boldsymbol{u}\mathrm{div}\alpha_F = 0 \quad (15)$$

4.2 *Solving process*

- Dissect the solution area, divide the grid cells, and generate information of the number, center and interface coordinates of each cell;
- Set the boundary types and location information of the solution area;
- Initialize the VOF functions, initial pressure, velocity vectors, initial temperature, initial reactant concentrations and initial conversions of each cell;
- Assign material properties such as density and viscosity based on current volume fraction, temperature, pressure and reactant conversions of each cell;
- Calculate and discrete scalar-transport equations based on current temperature, conversions, density, and velocity vectors to obtain current reactant conversions;
- Calculate the energy equation and obtain the temperature field distributions;
- Solve the continuous and momentum discrete equations according to the PISO algorithm to obtain the converged velocity vectors;
- Solve the volume functions of the fluid cells based on the current flow velocity values in each direction;
- Update and output the current fluid volume function values and the values of parameters such as pressure, velocity, density, temperature, and conversion;
- Update the time, and start a new round of solving.

5 NUMERICAL CALCULATION

5.1 *Settings of operating conditions*

The foaming polyurethane grouting material mainly relies on the self-expanding characteristics to achieve the purpose of filling voids, compacting rock, and controlling seepage. During the grouting process, isocyanate reacts with polyol to generate a large amount of polyurethane. Additionally, the reaction between isocyanate and water produces urea and carbon dioxide, which serves as a source of bubbles for foam expansion. Therefore, this paper mainly investigates the influence of isocyanate index on the grout propagation.

The numerical simulation program was developed in Fortran language to accurately solve the expansion process of polymer grout in the fracture. The model size is set as 0.8 m × 0.8 m (the dimension in the z direction has a large order of magnitude difference from those in the x and y directions), with the cell size of 0.01 m × 0.01 m. The bottom, left and right sides of the model are wall boundaries, while the upper side is free surface boundary as shown in Figure 1. Water is chosen as the chemical blowing agent while HCFC-141b serves as the physical blowing agent. The initial pressure is set as 0.75 MPa and initial temperature is 313.15 K. Since the viscosity of the grout does not change much before curing, the constant value of 1 Pa·s is taken here. Furthermore, the initial radius of the grout is set as 0.19 m. Then a series of simulation calculations are carried out.

According to the composition ratio range of polymer grouting material (Li et al., 2021), the isocyanate index varies from 1.12 to 3.62 and the detailed settings are shown in Table 1. The parameters of chemical reaction kinetic models and material properties related are listed in Table 2 and Table 3, respectively (Jia et al., 2021).

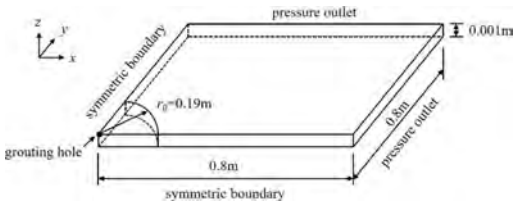

Figure 1. Schematic diagram of the fracture grouting model.

Table 1. Settings of cases.

Numbers	c^0_{NCO}/c^0_{OH}
1	4557.7/4079.6
2	4557.7/2818.3
3	4557.7/2152.7
4	4557.7/1741.4
5	4557.7/1462.1
6	4557.7/1260.0

Table 2. Parameters of chemical reaction kinetic models.

Characteristics	Values
A_{OH}(m^3/mol/s)	2.7
E_{OH}(J/mol)	35000
A_W(m^3/mol/s)	26.0
E_W(J/mol)	42000
$-\Delta H_{OH}$(J/mol/K)	70750
$-\Delta H_W$(J/mol/K)	86000
λ(J/kg)	206800
c^0_W(mol/m^3)	1194.7
r^0_{BL}	0.0359

Table 3. Parameters of material properties.

Characteristics	Values
C_p(J/kg/K)	1800
C_{BG}(J/kg/K)	1000
C_{BL}(J/kg/K)	1159
C_W(J/kg/K)	4200
C_{CO_2}(J/kg/K)	836.6
ρ_p(kg/m^3)	1100
ρ_{BL}(kg/m^3)	1228
ρ_W(kg/m^3)	1000

5.2 *Results and discussion*

The pressure of polymer grout contributes to filling cracks and pores, enhancing the bond with surrounding soil or rock, and providing lateral support and restraint. Studies have shown that it exhibits a three-stage variation of slow increase, sharp increase and gradual decrease in the plane fracture grouting under adiabatic conditions (Jia et al., 2022), indicating the existence of a peak value. Hence, the maximum pressure of the polymer grout deserves further attention. At the same time, component conversion is an important parameter to indicate the degree of reaction. Besides, the density of self-expanding grouting material plays a significant role in its mechanical properties (Li et al., 2022), and the mechanical properties of self-expanding grouting material with different densities are essential in evaluating the repairing effect on underground structures. The decrease in density corresponds to the expansion of the volume, which is crucial for achieving proper filling range and fracture integrity. For the reasons above, to achieve the comprehensive evaluation and optimization of self-expanding grouting materials, it is necessary to take the pressure, diffusion distance, component conversion and density into consideration.

1) Pressure

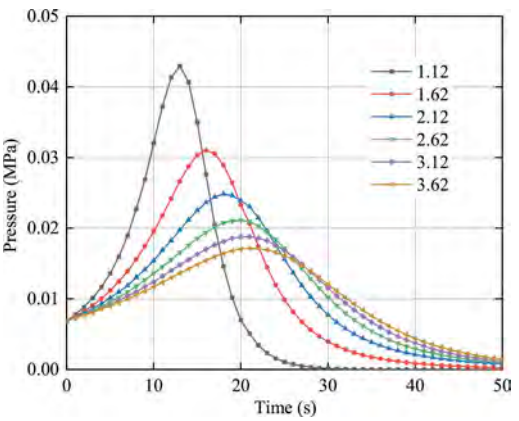

Figure 2. The influence of isocyanate index on pressure at grouting hole.

Figure 2 shows the time-variation curves of pressure at grouting hole for different isocyanate indexes. The pressure of grout increases rapidly and then decreases. And the larger the isocyanate index, the slower the rate of pressure increases and decreases. Besides, it can be seen obviously that the maximum pressure of the polymer grout diminishes as the isocyanate index increases. It may be attributed to the excess isocyanate groups react with polyurethane generated by the gelling

reaction, and at the same time, self-polymerization reaction occurs (Xu et al., 2017), to a certain extent, inhibit the occurrence of the gelling reaction and blowing reaction, which reduce the contribution of carbon dioxide gas generation, i.e., bubble growth to pressure. Therefore, the maximum pressure decrease.

2) Diffusion distance

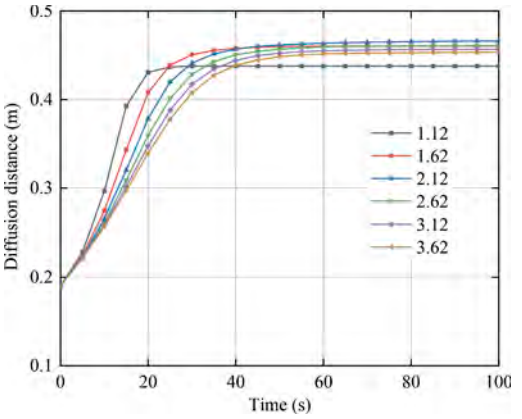

Figure 3. The influence of isocyanate index on diffusion distance from the grouting hole.

Figure 3 illustrates the time-variation curves of diffusion distance from the grouting hole under different isocyanate indexes. The diffusion rate decreases with the increasing isocyanate index due to the inhibitory effect mentioned in (1). However, the final diffusion distance exhibits a pattern of initially increasing and then decreasing as the isocyanate index increases. When it is less than 2.12, as the isocyanate index increases, the increased formation of carbon dioxide gas from the isocyanate-water reaction results in the increase in the final diffusion distance of the grout. For larger values, complete reaction of isocyanate with hydroxyl group and water occurs, and the isocyanate further reacts with polyurethane generated through the gelling reaction, forming allophanate containing urea groups which are much more polar compared to urethano in polyurethane (Sami et al., 2014). Thus, the isocyanate-polyurethane reaction greatly promoted the formation of hydrogen bonds between molecular chains, and then increased the physical cross-linking degree and interaction forces among molecular chains, leading to the molecular chain more difficult to slip. As a result, the final diffusion distance decrease.

3) Component conversion

Figure 4 shows the time-variation curves of component conversion of water and hydroxyl group

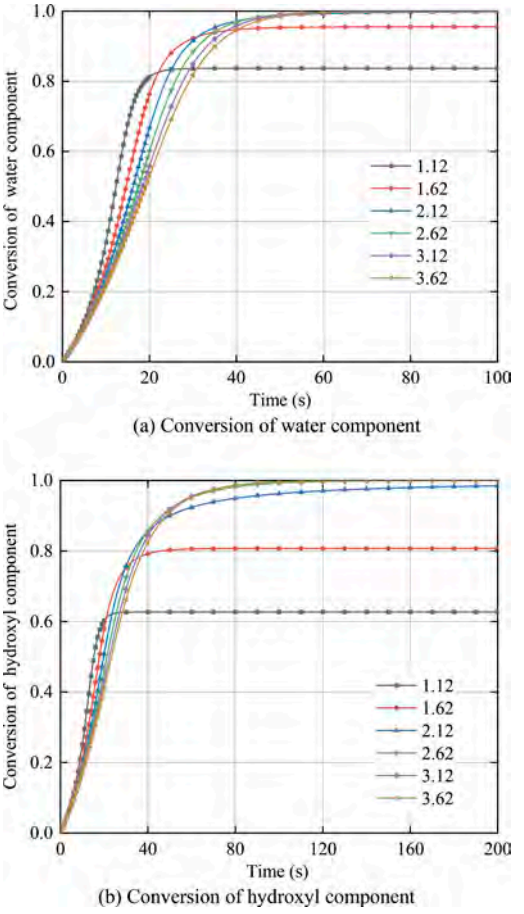

Figure 4. The influence of isocyanate index on component conversion of water and hydroxyl group.

for different isocyanate indexes. It can be seen from the figure that the component conversion gradually increases over time, and finally tends to be stable. The final component conversion of water and hydroxyl group increases with isocyanate index increasing. When the isocyanate index reaches 2.12, the final conversion of the water and hydroxyl components can be almost up to 100%, at this point continue to increase the isocyanate index, the final component conversion is not changing much.

Under the same isocyanate index, the increase rate of component conversion of water is greater than that of component conversion of hydroxyl group, which is mainly because one isocyanate molecule can react with two water molecules, but can only react with one hydroxyl molecule.

4) Density

Figure 5 shows the time-variation curves of density for different isocyanate indexes. The density of grout gradually decreases with the

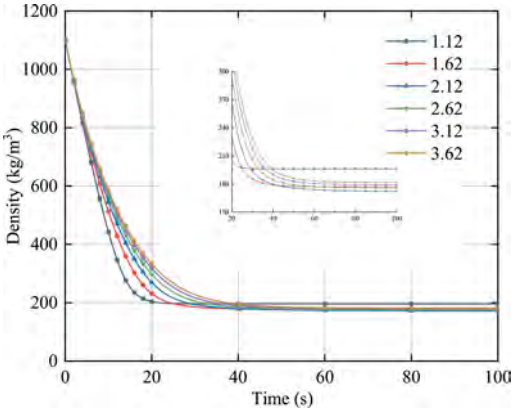

Figure 5. The influence of isocyanate index on the density of polymer grout.

reaction time and the decreasing rate decreases with the increase of the isocyanate index. For the final density, when the isocyanate index is less than 2.12, the increasing of isocyanate index, i.e., the higher proportion of isocyanate, means the more generation of carbon dioxide. The significant volume of gases causes more expansion of the polymer grout, resulting in an increase in volume and then a decrease in final density. However, when the isocyanate index is larger, the hydroxyl group and water molecule are reacted completely by the isocyanate as shown in Figure 4. Excessive isocyanate further reacts with polyurethane to produce allophanate, while self-polymerization occurs to form dimer, trimer and other compounds. Additionally, a large amount of free isocyanate groups with higher density remains uninvolved in the chemical reactions, increasing the final density of the polymer grout.

6 CONCLUSION

In this paper, based on the coupled of reaction kinetics and fluid flow, a simulation model of the flow diffusion of polymer grout in rock fractures was established. The grout propagation of polymer grout under different isocyanate indexes of polymer grout were numerically calculated. The results show that:

As the isocyanate index increases, the maximum pressure of the grout gradually decreases with the increase of isocyanate index. Besides, there is an inflection point in the effect of isocyanate index on spread and curing density. Thus, to obtain a higher expansion performance of polyurethane grout, while considering the reaction rate, it is recommended that the isocyanate index is between 1-2.

Notations

A_{OH}	Preexponential factor for gelling reaction ($m^3/mol/s$)
A_W	Preexponential factor for blowing reaction ($m^3/mol/s$)
E_{OH}	Activation energy for gelling reaction(J/mol/K)
E_W	Activation energy for blowing reaction(J/mol/K)
ΔH	Heat of reaction (J/mol)
λ	Heat of evaporation (J/kg)
C	Heat capacity (J/kg/K)
c	Concentration (mol/m^3)
r	Mass fraction
X	Conversion
M	Molecular weight (kg/mol)
P	Pressure (Pa)
R	Universal gas constant
t	Time (s)
T	Grout temperature (K)
u	Velocity vector (m/s)
S	General source term for conversion equation
μ	Viscosity (Pa · s)
ρ	Density(kg/m^3)

Indices

0	Initial
BL	Liquid phase of physical blowing agent
BG	Gas phase of physical blowing agent
NCO	Cyanate group
OH	Hydroxyl group
W	Water
P	Polyurethane
F	Polymer grout foam

REFERENCES

Eun, J. H., Lee, J. S., 2020. Study on the NCO index and base knitted fabric substrates on the thermal, chemical, and mechanical properties of solvent-less formulations polyurethane artificial leather. Journal of Engineered Fibers and Fabrics, 15.

Fang, H., Su, Y., Du, X., et al., 2019. Experimental and Numerical Investigation on Repairing Effect of Polymer Grouting for Settlement of High-Speed Railway Unballasted Track. Applied Sciences, 9(21).

Guo, C., Cui, C., Wang, F., 2020. Case Study on Quick Treatment of Voids under Airport Pavement by Polymer Grouting. Journal of Materials in Civil Engineering, 32(7).

Guo, C., Wang, F., 2009. Research on polymer injection technology for quick tunnel repairment. Geotechnical Special Publication, pp. 110–117.

Hao, M., Wang, F., Li, X., et al., 2018. Numerical and Experimental Studies of Diffusion Law of Grouting with Expansible Polymer. Journal of Materials in Civil Engineering, 30(2).

Jia, H., Li, X., Hao, M., et al., 2021. Test Method for the Solubility Model of Physical Blowing Agent of Self-Expanding Polymer. Mathematical Problems in Engineering, 1–10.

Jia, H., Li, X., Lu, L., et al., 2022. Study on simulation method for planar fracture grouting of expansive polymer grout based on polymerization reaction mechanism. China Civil Engineering Journal, 55(11), 50–61.

Kim, S. H., Kim, B. K., Lim, H., 2008. Effect of isocyanate index on the properties of rigid polyurethane foams blown by HFC 365mfc. Macromolecular Research, 16(5), 467–472.

Li, X., Hao, M., Zhong, Y., et al., 2019. A Quasi-3D Numerical Model for Grout Injection in a Parallel Fracture Based on Finite Volume Method. Complexity, 4139616:1-4139616: 18.

Li, X., Hao, M., Zhong, Y., et al., 2021. Experimental study on the diffusion characteristics of polyurethane grout in a fracture. Construction and Building Materials, 273.

Li, X., Wan, J., Zheng, D., et al., 2022. Compressive mechanical properties of self-expanding grouting materials with different densities. Construction and Building Materials, 332.

Li, X., Wang, L., Hao, M., et al., 2019. An analytical solution for the radial flow of variable density grout in rock fractures. Construction and Building Materials, 206, 630–640.

Liang, J., Ma, S., Du, X., 2021. Diffusion Model of Parallel Plate Crack Grouting Based on Foaming Expansion Characteristics of Polymer Slurry. Mathematics, 9(22).

Sami, S., Yildirim, E., Yurtsever, M., et al., 2014. Understanding the influence of hydrogen bonding and diisocyanate symmetry on the morphology and properties of segmented polyurethanes and polyureas: Computational and experimental study. Polymer, 55(18), 4563–4576.

Tu, Y.-C., Kiatsimkul, P., Suppes, G., et al., 2007. Physical properties of water-blown rigid polyurethane foams from vegetable oil-based polyols. Journal of Applied Polymer Science, 105(2), 453–459.

Wang, Y., Han, M., Li, B., et al., 2022. Stability evaluation of earth-rock dam reinforcement with new permeable polymer based on reliability method. Construction and Building Materials, 320.

Xu, J., Wu, T., Sun, W., et al., 2017. Generalization and Modelling of Rigid Polyisocyanurate Foam Reaction Kinetics, Structural Units Effect, and Cell Configuration Mechanism. Cellular Polymers, 36(6), 285–312.

Zhang, B., Zhang, X., Zhong, Y., et al., 2021. Research on Fatigue Model of Semi-Rigid Base Asphalt Pavement before and after Polymer Grouting. Advances in Civil Engineering, 1–16.

Tunnelling for a Better Life – Yan, Celestino, Thewes & Eberhardt (Eds)
© 2024 The Author(s), ISBN 978-1-032-80042-4
Open Access: www.taylorfrancis.com, CC BY-NC-ND 4.0 license

Dynamic soil response around a shallow rectangular tunnel and adjacent building

Zhengyao He* & S.P. Gopal Madabhushi
Department of Engineering, University of Cambridge, Cambridge, UK

ABSTRACT: Recent earthquake events indicated that shallow buried structures are susceptible to be damaged during a strong cyclic loading. This is even further critical when considering the adjacent surface building in a congested urban area. With the requirement to minimize the tunnel uplift and building rotation, it is firstly important to understand the dynamic soil behaviour around these structures during the earthquake. In this paper, the main research aim is to investigate the seismic soil response around a shallow, rectangular tunnel that is adjacent to a nearby building founded on loose, saturated sand. The results from two separate dynamic centrifuge tests will be presented. The soil deformations around the tunnel-building system will be obtained by adopting GeoPIV_RG software based on the Particle Image Velocimetry (PIV) technique. Dynamic effects on the soil stiffness due to the earthquake loading will be studied by using the cone penetrometer test (CPT). Finally, the conclusions will be drawn on the effect of the relative building-tunnel lateral distance with the same tunnel buried depth.

Keywords: Cut & cover tunnel, Soil-structure interaction (SSI), Centrifuge modelling, Earthquake engineering

1 INTRODUCTION

Shallow cut-and-cover tunnel has been widely used in congested urban areas. Designing these underground structures is critical and the interaction of the surface building should be accounted for. Recently earthquakes have caused substantially irreparable property and personal losses in the urban city such as 2023 Turkey–Syria earthquake, 2023 Morrocco earthquake and 2008 China Wenchuan earthquake.

Most recently, there are many researchers focus on the dynamic underground structure behaviour subject to seismic loading. Hashash et al. (2001) conducted a state-of-the-art review of the currently understanding of the seismic underground design, and the demand for additional work. This work has been extended by Tsinidis et al. (2020), and Chen et al. (2023) particular for the shield tunnelling. It was observed that the tunnel uplift due to the earthquake-induced soil liquefaction is one of the major concerns for the shallow cut-and-cover tunnel. Early study of the tunnel floatation due to excess pore pressure started by Chou et al. (2008a, 2008b, 2011) as part of the BART project in California. Dynamic centrifuge testing is adopted to study the dynamic soil and tunnel responses. Chian and Madabhushi (2012) studied the effects of the tunnel buried depth on the floatation resistance.

Considering the increasing complexity of the surface structures in the urban area as shown in Figure 1. It is important to consider the dynamic building interaction when analysing the seismic behaviour of the adjacent tunnels. Dashti et al. (2016) and Hashash et al. (2018) adopted centrifuge testing and 3D numerical modelling to study the dynamic interaction between the multi-story structures and the adjacent underground braced excavations subjected to cyclic loading through a series of centrifuge tests and 3D numerical modelling. Miranda et al. (2023) conducted similar work but adopting PIV technique to capture the soil deformation during the cyclic loading.

This research aims to investigate the influence of the lateral building-tunnel distance with fixed tunnel buried depth the dynamic tunnel and soil behaviour subjected to earthquake loading through two dynamic centrifuge tests. Soil shear resistance and surface soil deformations are studied by adopting a high-speed imaging based PIV technique and cone penetrometer test (CPT). The observations from experiments form the basis of understanding the tunnel-building dynamic interaction under liquefied soil.

*Corresponding author: za301@cam.ac.uk

DOI: 10.1201/9781003495505-98

Figure 1. A rectangular motorway tunnel under a wide residential building at Belgrade, Serbia.

2 CENTRIFUGE MODELLING

Centrifuge modelling has been widely adopted to study the seismic structural behaviour under liquefied soil strata. It simulate the prototype non-linear soil stress and strain with a scaled down model by centrifugal accelerating the model in N g-level. Scaling laws for centrifuge testing following Madabhushi (2014) are selected in this study as given in Table 1. Two dynamic centrifuge models were conducted by using the Turner beam centrifuge with a rotational radius of 4.125 m at the Schofield Centre, Cambridge University. Testing g-level is 60 g for both tests. Most recent generalized scaling laws derived by Iai et al. (2005) stated that the soil behaviour is highly depended on the confining pressure after reaching the peak deviatoric stress based on 1 g testing. However, this modified scaling law is not suitable to be applied in the dynamic centrifuge tests as the stress and strain are scaled differently.

Table 1. Scaling laws for centrifuge tests.

Parameters	Model/prototype	Dimensions
Length	N^{-1}	L
Mass	N^{-3}	M
Stress	1	$ML^{-1}T^{-2}$
Strain	1	1
Force	N^{-2}	MLT^{-2}
Seepage velocity	N	LT^{-1}
Time (seepage)	N^{-2}	T
Frequency	N	LT^{-1}
Acceleration	N	LT^{-2}
Velocity	1	LT^{-1}

Note: N, scaling factor

2.1 *Structural design*

The scaled down aluminium tunnel model is designed to represent a two-lane 12 m × 6 m rectangular cut-and-cover motorway tunnel at the prototype scale. The axial stiffness and flexural stiffness of the aluminium tunnel is equivalent to the concrete tunnel with 300 mm wall thickness at the prototype scale. The surface building is simulated as a rigid aluminium black with 6 m span at the prototype scale. This block simulates the dead load of a two-storey residential building and gives approximately 50 kPa contact pressure on the soil strata beneath at the testing g-level. Both transverse edge of the tunnel and building model are attached with polytetrafluoroethylene (PTFE) plates to minimize the in-plane direction friction between the model and the container as this is a 2D cross-section model. Figure 2 shows the installation of the tunnel and building model in test ZA03

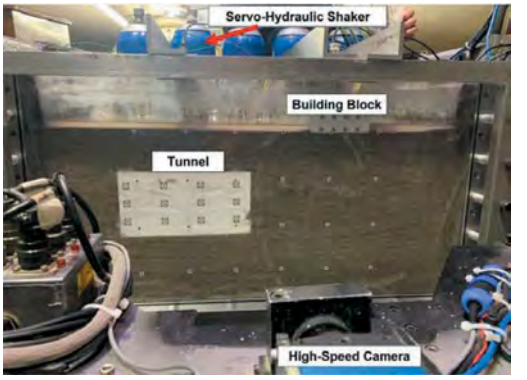

Figure 2. Completed model of test ZA03 before spinning.

2.2 *Test preparation*

Both two tests are prepared in a rigid aluminium container with a Perspex observing window panel. This type of container has been commonly adopted by the previous researchers to study the dynamic buried structural behaviour (Chian and Madabhushi. 2012; Chian et al., 2014; Cilingir and Madabhushi (2011a, 2011b, 2011c)). Hostun HN31 sand (Mitrani, 2006; Haigh et al., 2012) is selected and poured by an automatic sand pouring machine following by Madabhushi et al. (2006). Details of the sand property are given in Table 2. A servo-hydraulic centrifuge shaker designed by Madabhushi et al. (2012) is implemented to apply the scheduled input motion to the centrifuge model.

Table 2. Houstun sand material properties.

Parameters	Value
f (degrees)	33[a]
D_{10} (mm)	0.209
D_{50} (mm)	0.335
e_{min}	0.555[a]
e_{max}	1.01[a]
G_s	2.65[a]
K (m/s)	1×10^{-3}[b]

a Data from Mitrani (2006).
b Data from Haigh et al. (2012)

Both centrifuge model ZA03 and ZA04 are saturated with premixed high viscous methyl cellulose fluid at the designed viscosity. Prior to seismic analysis, it is important to conduct a preliminary static factor of safety (FoS) analysis to ensure the reasonable tunnel buried depth and the tunnel stationary before applying any cyclic loading. This simplified FoS calculation against the vertical floatation shown in Equation (1) does not consider the complex contribution from the adjacent building contact pressure and friction along the soil slip surface, where is the tunnel buoyancy, F_T is the tunnel structural self-weight, F_{Soil} is the effective soil overburden pressure. As the result the tunnel FoS against floatation is calculated as 1.17 for ZA03 and 1.12 for ZA04.

$$FoS = \frac{F_{Soil} + F_T}{F_B} > 1 \quad (1)$$

Table 3. Centrifuge tests configurations.

	Earthquake			
Test ID	Type	Frequency (Hz)	PGA (g)	Lateral distance (m)
ZA03_RD=43%	Sinsweep	100 - 1	0.04	6
	Sinusoidal	1	0.23	
	Sinusoidal	1	0.35	
	Sinusoidal	1	0.06	
ZA04_RD=42%	Sinsweep	100 - 1	0.08	3
	Sinusoidal	1	0.21	
	Sinusoidal	1	0.33	
	Sinusoidal	1	0.05	

Note: Lateral distance, tunnel edge to building edge

The test configurations for both centrifuge tests are summarized in Table 3. The loose Houstun sand are prepared with similar relative density and been fully saturated. Same earthquake sequence is applied to both tests to investigate the effect of the lateral tunnel-building distance on the dynamic soil and structural behaviour.

3 DYNAMIC SOIL RESPONSE

3.1 *Cone penetration test*

Saturated soil shear resistance is particularly critical subjected to cyclic loading. During a rapid cyclic loading such as a strong earthquake, the hypothesis of soil liquefaction being considered as partially drained event that the drainage condition is highly depended on the confining pressure. Earthquake-induced excess pore pressure can significantly damage the interparticle friction and caused substantial loss of soil shear strength. Soil shear resistance will then be recovered with time due to the drain of excess pore pressure.

Figure 3. CPT system adopted in test ZA04.

Two cone penetration test (CPT) is performed at the free-field in test ZA04 to measure the soil shear resistance before and after the earthquakes. This model scale CPT system contains a load cell with capacity of 500 N and maximum testing depth of 200 mm as shown in Figure 3. The measured penetration resistance qc is determined as the measured tip load over the CPT cross-section area. As the results, the CPT measured penetration resistance adjacent to tunnel is shown in Figure 4 at the prototype scale. The load cell output has been processed with an 8th order Butterworth filter under the low pass frequency of 80 Hz to minimize the centrifuge power noise. The measured depth covers the range from the surface to the base of the tunnel.

Soil at the sub-surface has low penetration resistance due to the low confining pressure before the earthquake. This has increased proportionally with the increasing of depth, confirming the uniformity of the soil layer. This CPT penetration resistance profile can be further investigated to determine the soil slip surface frictional resistance against tunnel floatation. Most recently, there are many researchers investigate the orientation of the soil slip surface adjacent to the tunnel (Chian and Madabhushi, 2012). It should be noted that the existence of the building can significantly affect the orientation of the soil slip surface, as well as the soil shear strength due to building's contact pressure.

During the earthquake, saturated soil lost most of the shear capacity due to the excess pore pressure generation, and the frictional resistance along the slip surface significantly reduced. Tunnel is observed to float upward due to the soil shear strength reduction and the excess pore pressure generated along the tunnel lining. It will be interesting to analyse the soil slip surface shear resistance on the building side, as the building contact pressure can minimize the liquefaction ratio beneath the building.

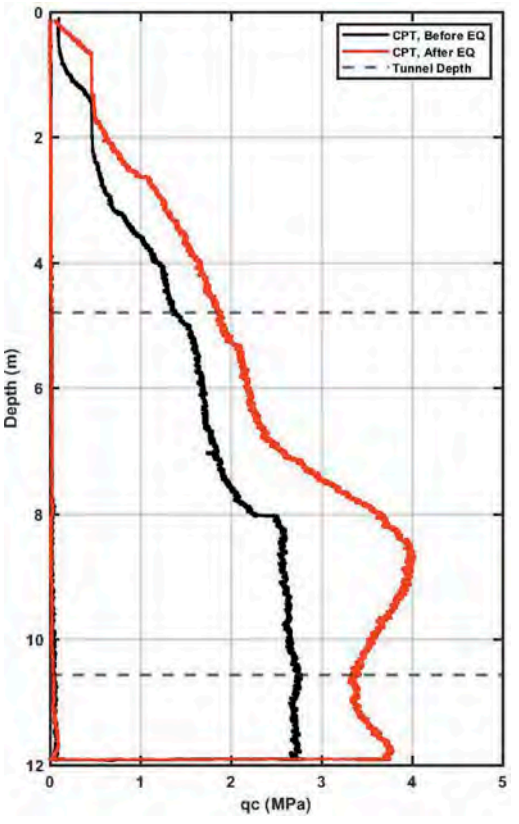

Figure 4. CPT penetration resistance profile for test ZA04.

After the earthquake, excess pore pressure existed in the soil porous media drain by the time and the soil shear strength recovered. The horizontal cyclic loading caused densification to the soil layer, this is supported by the additional CPT penetration resistance profile shown in Figure 4. Tunnel uplift caused circular loop shaped soil movement adjacent to the tunnel side wall. This leads to a reduction of the soil unfactored penetration resistance around tunnel's base depth due to the suction beneath the tunnel during the tunnel uplift. Soil densification also leads to the increasing of the shear strength at the sub-surface. It should be noted that the tunnel has been pushed away from the building during the earthquake. This can cause additional lateral pressure to the soil layer and thereby, increase the CPT measured shear resistance.

3.2 *Soil surface deformation*

Earthquake-induced soil deformation is a primary concern in the congested urban area. Most recent research on the dynamic building behaviour with the shallow foundation in liquefied soil has conducted by Dashti et al. (2010a, 2010b), Dasthi and Bray (2013) and Adamidis and Madabhushi (2018) through a series of dynamic centrifuge tests. Significant building settlements have been widely observed due to the shear strength reduction beneath the foundation. Buried structure floatation during the earthquake has been investigated by Chian and Madabhushi (2012) and Chian et al. (2014) for the circular tunnel, Watanabe et al. (2016) and Miranda et al. (2023) for the rectangular tunnel. It is critical to analyse the soil surface deformation within a buried structure and an adjacent building.

The soil surface deformation within the tunnel-building system is obtained by adopting the Particle Image Velocimetry (PIV) technique. A high-speed imaging-based code GeoPIV_RG designed by Stainer et al. (2016) is implemented to analyse the soil movements during the cyclic loading.

The soil surface profile before the earthquake, after 2 and 4 cycles of shaking as well as the post-earthquake profile for both tests are shown in Figure 5a and 5b at the prototype scale. Soil heave within the tunnel range and the soil settlement within the building range are observed in both tests. It can been seen that the soil deformations are cumulatively built up as more cyclic loading applied to the soil profile. The maximum soil deformations are determined as the difference of the soil final vertical position and the initial position before the earthquake. Maximum soil heave within the tunnel axis is captured as 0.21 m for the test ZA03 and 0.17 m for the test ZA04. Maximum soil settlement within the building axis is captured as 0.6 m for the test ZA03 and 0.54 m for the test ZA04. This present the surface soil profile within the tunnel-building system is more stable when then tunnel-building distance is decreased.

In addition, More uniform soil settlement distribution is observed beneath the building range for the test ZA04 than ZA03. This indicates the building perform less rotation when the tunnel-building distance is reduced. A possible hypothesis is that as the tunnel-building distance is increased, there are less interaction effect to the building from the adjacent tunnel. As the tunnel-building distance is reduced, there are more contribution of the tunnel interaction to the building behaviour during the earthquake as the tunnel lining stiffness is significantly higher than the liquefied soil stiffness. This is a particularly critical phenomenon for the SSI problem, because more interaction between the structures generally caused more susceptible damage during the cyclic loading.

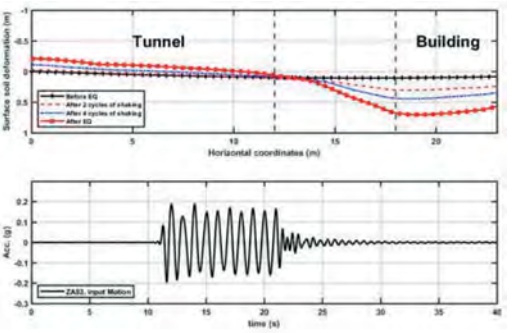

Figure 5a. Surface deformation during the earthquake for test ZA03_EQ2 (Prototype scale)

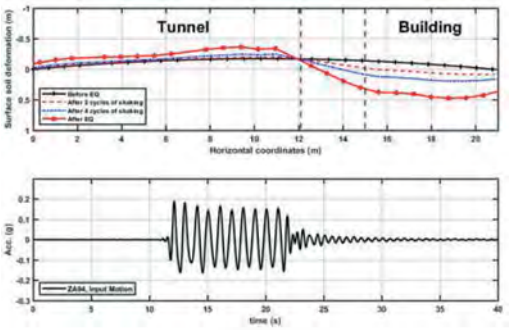

Figure 5b. Surface deformation during the earthquake for test ZA04_EQ2 (Prototype scale)

4 CONCLUSIONS

This paper presents the current research to investigate the effect of the tunnel-building distance under the liquefied soil subjected to earthquake loading. Two dynamic centrifuge tests are conducted to analyse the dynamic soil response within a tunnel-building system by reducing half of the tunnel-building distance. A exemplified 1 Hz 10 cycles sinusoidal input motion with similar PGA is selected from the earthquake sequence for both tests. Soil stiffness and the soil surface deformations during the earthquake are observed in the centrifuge test using a miniature CPT test and a fast imaging based PIV technique respectively.

It can be seen that the frictional resistance along the surface slip surface contribute significantly to the tunnel FoS against floatation at the rest. During the earthquake, this frictional resistance is reduced due to the soil liquefication and recovered after the earthquake with the drainage of the excess pore pressure. Soil profile is more stable when less tunnel-building distance during and after the earthquake. This is proved by the less soil heave along the tunnel axis and less soil settlement below the building and with less building rotation.

This research gives a further understanding of the dynamic tunnel and building behaviour under the liquefied soil. Additional centrifuge outputs such as the excess pore pressure generation along the tunnel lining, the comprehensive soil deformation profile within the tunnel-building system, and the tunnel movements are currently under process and will be presented in the future publications.

ACKNOWLEDGMENTS

The authors would like to appreciate to the technicians at the Schofield Centre for their contribution during the preparation and operation of the centrifuge tests.

REFERENCES

Adamidis, O., & Madabhushi, S. P. (2018). Deformation mechanisms under shallow foundations on liquefiable layers of varying thickness. Géotechnique, 68(7), 602–613.

Chen, X., Shen, J., Bao, X., Wu, X., Tang, W., & Cui, H. (2023). A review of seismic resilience of shield tunnels. *Tunnelling and Underground Space Technology*, 136, 105075.

Chou, J. C., Kutter, B. L., Travasarou, T., & Chacko, J. M. (2011). Centrifuge modeling of seismically induced uplift for the BART transbay tube. *Journal of Geotechnical and Geoenvironmental Engineering*, 137(8), 754–765. 19 434

Chou, J. C., Kutter, B., and Travasarou, T. (2008a). *Centrifuge testing of the seismic performance of a submerged cut-and-cover tunnel in liquefiable soil centrifuge data report for test series JCC01*. Network for Earthquake Engineering Simulation (NEES) Program, Center of Geotechnical Modeling, Univ. of California, Davis, CA.

Chou, J. C., Kutter, B., and Travasarou, T. (2008b). *Centrifuge testing of the seismic performance of a submerged cut-and-cover tunnel in liquefiable soil centrifuge data report for test series JCC02*. Network for Earthquake Engineering Simulation (NEES) Program, Center of Geotechnical 441 Modeling, Univ. of California, Davis, CA.

Chian, S. C., & Madabhushi, S. P. G. (2012). Effect of buried depth and diameter on uplift of underground structures in liquefied soils. *Soil Dynamics and Earthquake Engineering*, 41, 181–190.

Chian, S. C., Tokimatsu, K., & Madabhushi, S. P. G. (2014). Soil liquefaction–induced uplift of underground structures: physical and numerical modeling. *Journal of Geotechnical and Geoenvironmental Engineering*, 140 (10), 04014057.

Cilingir, U., & Madabhushi, S. G. (2011a). Effect of depth on the seismic response of square tunnels. *Soils and Foundations*, 51(3), 449–457.

Cilingir, U., & Madabhushi, S. G. (2011b). A model study on the effects of input motion on the seismic behaviour of tunnels. *Soil Dynamics and Earthquake Engineering*, 31(3), 452–462.

Cilingir, U., & Madabhushi, S. G. (2011c). Effect of depth on seismic response of circular tunnels. *Canadian Geotechnical Journal*, 48(1), 117–127.

Dashti, S., Hashash, Y. M. A., Gillis, K., Musgrove, M., & Walker, M. (2016). Development of dynamic centrifuge models of underground structures near tall buildings. *Soil Dynamics and Earthquake Engineering*, 86, 89–105.

Dashti, S., Bray, J. D., Pestana, J. M., Riemer, M., & Wilson, D. (2010a). Centrifuge testing to evaluate and mitigate liquefaction-induced building settlement mechanisms. *Journal of geotechnical and geoenvironmental engineering*, 136(7), 918–929.

Dashti, S., Bray, J. D., Pestana, J. M., Riemer, M., & Wilson, D. (2010b). Mechanisms of seismically induced settlement of buildings with shallow foundations on liquefiable soil. *Journal of geotechnical and geoenvironmental engineering*, 136(1), 151–164.

Dashti, S., & Bray, J. D. (2013). Numerical simulation of building response on liquefiable sand. *Journal of Geotechnical and Geoenvironmental Engineering*, 139(8), 1235–1249.

Hashash, Y. M., Dashti, S., Musgrove, M., Gillis, K., Walker, M., Ellison, K., & Basarah, Y. I. (2018).

Influence of tall buildings on seismic response of shallow underground structures. *Journal of Geotechnical and Geoenvironmental Engineering*, 144(12), 04018097.

Hashash, Y. M., Hook, J. J., Schmidt, B., John, I., & Yao, C. (2001). Seismic design and analysis of underground structures. *Tunnelling and underground space technology*, 16(4), 247–293.

Haigh, S. K., Eadington, J., and Madabhushi, S. P. G. (2012). Permeability and stiffness of sands at very low effective stresses. *Géotechnique*, 62(1), 69–75.

Iai, S., Tobita, T., & Nakahara, T. (2005). Generalised scaling relations for dynamic centrifuge tests. *Geotechnique*, 55(5), 355–362.

Miranda, G., Nappa, V., Bilotta, E., Haigh, S. K., & Madabhushi, G. S. (2023). Physical modelling of the interaction between a tunnel and a building in a liquefying ground and its mitigation. *Tunnelling and Underground Space Technology*, 137, 105108.

Mitrani, H. (2006). *Liquefaction remediation techniques for existing buildings*. PhD thesis, University of Cambridge, Cambridge, UK.

Madabhushi, G. (2014). *Centrifuge modelling for civil engineers*. CRC press

Madabhushi, S. P. G., Houghton, N. E., & Haigh, S. K. (2006). A new automatic sand pourer for model preparation at University of Cambridge. In *Proceedings of the 6th International Conference on Physical Modelling in Geotechnics* (pp. 217–222). Taylor & Francis Group, London, UK.

Madabhushi, G. S., Haigh, S. K., Houghton, N. E., & Gould, E. (2012). Development of a servo-hydraulic earthquake actuator for the Cambridge Turner beam centrifuge. *International Journal of Physical Modelling in Geotechnics*, 12(2), 77–88.

Stanier, S. A., Blaber, J., Take, W. A., & White, D. J. (2016). Improved image-based deformation measurement for geotechnical applications. *Canadian Geotechnical Journal*, 53(5), 727–739.

Tsinidis, G., de Silva, F., Anastasopoulos, I., Bilotta, E., Bobet, A., Hashash, Y. M., … & Fuentes, R. (2020). Seismic behaviour of tunnels: From experiments to analysis. *Tunnelling and underground space technology*, 99, 103334.

Watanabe, K., Sawada, R., & Koseki, J. (2016). Uplift mechanism of open-cut tunnel in liquefied ground and simplified method to evaluate the stability against uplifting. *Soils and Foundations*, 56(3), 412–426.

Tunnelling for a Better Life – Yan, Celestino, Thewes & Eberhardt (Eds)
© 2024 The Author(s), ISBN 978-1-032-80042-4
Open Access: www.taylorfrancis.com, CC BY-NC-ND 4.0 license

Chemical-combined jet grouting for mass treatment of break-in area in Vietnamese urban underground construction

Hanh Quang Le*
FECON RAITO Underground construction JSC, Vietnam
University of Transport and Communication, Vietnam

Hitoshi Oyama* & Phong Ngoc Do*
FECON RAITO Underground construction JSC, Vietnam

ABSTRACT: Pipe Jacking method has been applying in Vietnam for urban drainage system since the 2000s, typically the wastewater sewer project along Nhieu Loc - Thi Nghe canal started in 2005; wastewater sewer project along Tau Hu - Ben Nghe canal in Ho Chi Minh City. Construction of the wastewater sewer in Ho Chi Minh City started in 2016 and the Yen Xa sewage system project in Hanoi started in 2020.

In the world, the traditional method of soil reinforcement for Pipe jacking is grouting with chemicals to reinforce the break-in and break-out areas. The main material composition is sodium silicate. This method is very effective in sandy soils but shows weakness when it is not effective enough in improving clayey soils and organic soils at locations with pipe jacking diameters larger than 1m (one meter). The geological characteristics of Hanoi and Ho Chi Minh City are sedimentary geology with many layers of soft clay soil. Therefore, after reinforcing with chemical grouting practically, this could not reach the necessary required strength for waterproof objective. Consequently, during the opening of the tunnel eyes, it caused many problems such as: The collapse of the tunnel eye causes the roadbed, the embankment to collapse at the shaft sides, or the sinking of the drilling robot head, contractor must construct a new shaft to rescue. All incidents have a direct impact on urban traffic flow, delaying progress and increasing construction costs.

This paper proposes the solution of combining Chemical grouting and Jet grouting JSG for mass treatment of break-in area. This method was successfully applied in Hanoi and Ho Chi Minh underground drainage system projects, and it has brought remarkable results when it is almost completely overcome the entire collapse incident when cutting the tunnel eye for the pipe jacking construction.

Keywords: Tunnelling, Pipe jacking, Chemical grouting, Jet Grouting, Ground Improvement, Break-in, Urban Underground

1 INTRODUCTION

The tunnel eye is considered to apply Chemical grouting method to stabilize and waterproof technical shaft when cutting tunnel eye. In fact, Chemical grouting method is very useful in sandy soil, but it shows the weakness in clayey soil, especially in soft clay with organic. During the application and construction process, water leakage and landslides at the tunnel eye occur more frequently at the location of the tunnel located in the soft clayey soil layer. In statistic, these incidents are often occurred on the tunnel eye diameter is > 1.0m. Some main causes can be listed as follows:

- Chemical materials do not penetrate evenly in soft clay and difficulty forming gel in soils containing organic material, so the effect of stabilizing the soil mass does not increase significantly, sometimes even causing the soil mass to lose its original state and become weaker.
- The jacking machine causes a front force to cause cracking on improved block, water seeps into the shaft through tunnel eye, causing erosion and instability of soil mass.
- The process of excavation inside the shaft causes displacement, causing cracks in the improved soil block, reducing stability, and creating water seepage paths.

To overcome the main causes of the above problems, the soil mass at tunnel eye must be reinforced with enough strength to avoid overburden pressure and machine pressure when it drives to enter the

*Corresponding author: hanhquangle@googlemail.com; ooyama0203@raito.co.jp; phongdn@fecon.com.vn

DOI: 10.1201/9781003495505-99

shaft. The combination of Jet grouting and Chemical grouting was chosen to research. Jet grouting is added 01 row at least beside shaft wall then chemical grouting. Column diameter Jet grouting is small enough to create a soil-cement wall that is stable enough for the jack drill head to be safely installed and ready to drill. Therefore, the 2-phase jet grouting method jumbo jet special grout (JSG) was chosen with a column diameter ranging from 1.0m (one meter) to 1.2m (one point two meter). The rest of the soil block in front of the tunnel entrance is grouted and improved with chemical grouting.

2 INTRODUCING THE APPLICATION METHOD

2.1 *Chemical grouting method (CG)*

Chemical grouting method uses the main material which is sodium silicate combined with gel-forming additives pumped at low pressure, pumping flow is about 8-16 litters/minute, the material is pumped into the soil. through the drilling rod to the designed location and penetrates the cracks and pores of the soil and then solidifies to create a more stable soil mass and prevent water from seeping through. Figure 1 describe chemical grouting sequency and Figure 2 explains how grout material penetrate into soil.

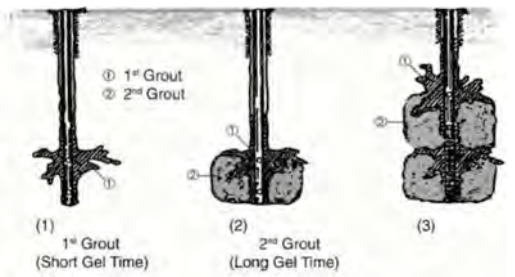

Figure 1. Sequence of chemical grouting.

At the initial stage of injection, outside surface of the rod is shielded and initial penetration area ① is formed. Then within ①, solution flow paths are created radially. (Flow paths create vertical plane).

Along the flow paths plane ① other paths are created in the area ②. Solution further penetrates around these flow paths and solidified will be formed and grow in area ②.

Further injection shall grow the flow paths plane to the area ③ and penetration area will expand outward.

With the method of using Sodium silicate material, the volume of grout pumped can usually be applied according to the void coefficient of sandy soils of 35% or more, clayey soils of 24% or more. Designing the amount of grout to be pumped according to geology according to Japan Grouting association (reference [1]) in Table 1. Details need to carefully consider the characteristics of the soil layers within the treatment area to adjust.

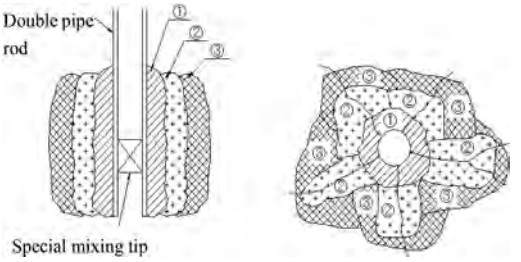

Figure 2. Describes the principle of penetration of chemical liquid into the soil.

Table 1. Standard table for chemical grouting design.

Soil condition	N value	Void ratio %	Filling rate %	Injection ratio %
Sand & gravel	0 ~ 50	40	90	36.0
	50 <	35	90	31.5
Sand	0 ~ 30	45	90	40.5
	30 <	35	90	31.5
Cohesive soil	0 ~ 4	70	40	28.0
	4 ~ 8	60	40	24.0

2.2 *Jet grouting method (JSG)*

The 2-phase jet grouting method JSG uses cement slurry pumped at a high pressure of about 20 Mpa, with a pump flow of about 60 litters/minute. The air phase provides additional support to the slurry fluid to cut the soil to the desired diameter and mix the soil more evenly. Principle of the JSG method is described in Figure 3 (reference [2]).

The application method is most effective in sandy soils and can also be applied to cohesive soils. However, the characteristics of cohesive soils need to be carefully considered, especially soils containing organic humus. Although the method also has limitations when applied to organic clays, in general, with using cement slurry mixing, it can still create a treated soil mass with much better properties than the Chemical grout method.

According to JJGA (reference [2]), selecting design parameters for Jet grouting construction in cohesive soil is refer to Table 2. Standard design strength for improvement structure can be selected from Table 3.

The values in this table were set in accordance with experimental results of the sampled core. (4-week strength). In general, strength suppressing hardening agent is applied to the sandy soil. Standard design strength of an improvement structure in the case such hardening agent is applied to a five layered cohesive soil, or the like is considered to decreases as follows:

JG-2 = JG-1 x 70%;

JG-3 = JG-1 x 50%.

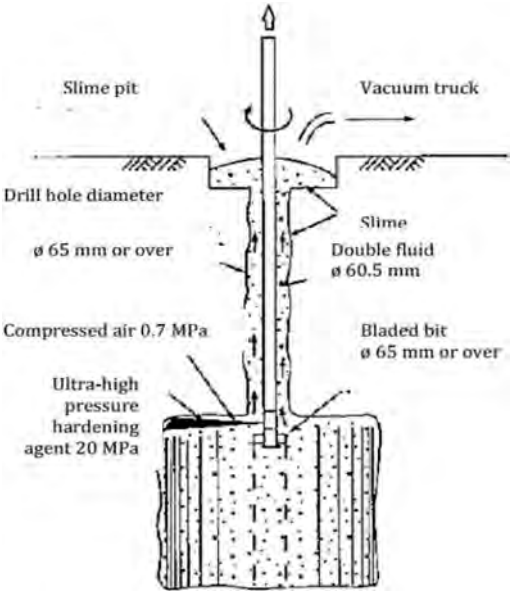

Figure 3. Principle of JSG 2-phase Jet grouting method (JJGA).

Unit weight for an improvement structure is equal to that of original ground. Sand and pebbles are equivalent to the sandy soil. 1-week strength is equal to 30 ~ 40% of 4-week strength.

Coefficient of permeability is approximately the following value, in accordance with lab tests results for sampled core. k = 1 x10^{-6} m/s to 1 x 10^{-7} m/s.

Properties of hardening agent are as follows:

JG-1: strength development type (standard type)
JG-2: strength suppressing type (moderate strength type)
JG-3: strength suppressing type (low strength type)
JG-4: for humic soil
JG-5: for cohesive soil

3 APPLICATION OF CHEMICAL-COMBINED JET GROUTING

Based on geological conditions and underground sewer system design, the sewer system stretches over

Figure 4. Map of Shaft 13.0.

Table 2. Standard table for Jet grouting design.

	Cohesive soil					
Criteria	N < 1	N = 1	N = 2	N = 3	N = 4	Humic soil *
Effective diameter (m) with depth (0m< Z ≤ 25m)	2.0	1.8	1.6	1.4	1.2	-
Withdraw time (min/m)	30.0	2.0	23.0	20.0	16.0	-
Discharge rate (m^3/min)	0.06					

* Need to be studied in case

Table 3. Selecting design strength parameters.

Hardening agent	Soil	Uniaxial compressive strength (MN/m2)	Adhesive strength c (MN/m2)	Adhesion f (MN/m2)	Bending tension force (MN/m2)	Deformation coeffi-cient E50 (MN/m2)
JG-1	Sandy soil	3	0.5			300
	Cohesive soil	1	0.3			100
JG-2	Sandy soil	2	0.4			200
JG-3	Sandy soil	1	0.2	c x 1/3	c x 2/3	100
JG-4	Humic soil	0.3	0.1			30
JG-5	Cohesive soil	1	0.3			100

Table 4. Geological parameters table.

Soil layer	Layer thicknesst (m)	Unit volume weightγt (kN/m^3)	Void ratio e	Internal friction angleφ (°)	Adhesive strengthC (kN/m^2)
1- Road bed	1.40	18.0	-	30.0	0
2- Stiff clay	0.60	18.5	0.841	12.5	28.635
7- Soft clay	4.80	19.8	0.673	17.5	19.417
8- Soft clay, organic	10.20	17.8	1.153	7.5	11.571

a large area, some sewer pipe locations are not located in the geological layer most suitable for the Chemical grouting method. Most of instability problems occur with the location of the tunnel in a layer of loose, flexible clay mud, sometimes mixed with organic matter.

The chemical-combined Jet grouting method was applied in Yen Xa 2 project. This paper analyses requirement of reinforcement on a typical case of Shaft 13.0 (Figure 4) before and after the soil is grouted by chemical to verify the necessary of Chemical-combined Jet grouting method.

3.1 *Typical geological condition at the project*

Result of the study and assessment of geological conditions of the area survey showed the ground structure to a depth of 30m is divided into 21 soil layers. According to geological data, borehole AD-6. Shaft 13.0 is located in stratigraphy including 4 layers, soil characters are shown in the Table 4.

Layer 1: Made ground: beton, brick, sand, sandy clay, roots, organic matter, ect.

Layer 2: . Clay, darkish brown, yellowish brown. Soft to firm.

Layer 7: . Clayey Sand, brown, brownish grey, blackish grey. Soft.

Layer 8: Sandy Clay, brownish grey, blackish grey, greyish; mixed with organic matter. Very soft.

3.2 *Check the thickness of the soil improvement at the tunnel eye reinforced only with chemicals*

3.2.1 *Calculation condition*

Calculation parameter table of the tunnel eye:

Ground elevation:	GL = 0.00 m
Tunnel eye centre depth	H = 11.78 m
Groundwater level	h' = 2.50 m
Water unit volume weight	γ_w = 10.00 kN/m^3
Heavy load on top	q = 10.00 kN/m^2
Tunnel eye diameter	D = 1.30 m
Safety ratio	Fs = 1.20
Improved adhesive strength	c' = 0.012 MN/m^2

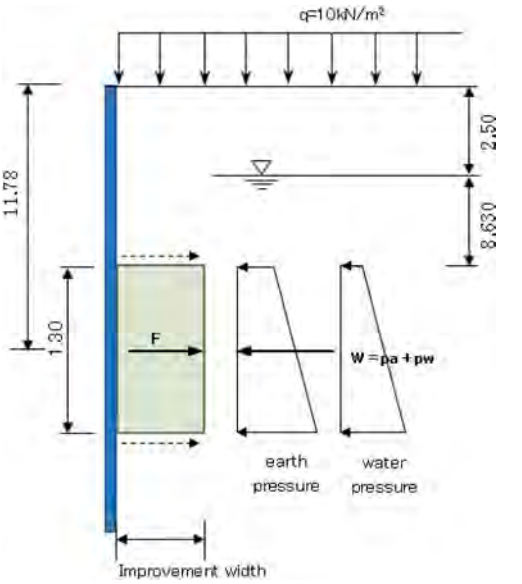

Figure 5. Calculation diagram.

Table 5. Geological parameters table.

Soil layer	Layer thickness t (m)	Unit volume weight γt (kN/m^3)	Underwater weight γt'(kNm^3)	Internal friction angleφ(°)	Adhesive strength C (kN/m^2)	Adhesive after improvement C' (kN/m^2)
1- Road layer	1.40	18.0	8.0	30.0	0.00	0.00
2- Stiff clay	0.60	18.5	8.5	12.5	28.64	28.64
7- Soft clay	4.80	19.8	9.8	17.5	19.42	19.42
8- Soft clay, organic	10.20	17.8	7.8	7.5	11.57	11.57

3.2.2 *Calculation formula for earth pressure and water pressure*

$$K_A = tan^2\left(45^\circ - \frac{\varphi}{2}\right) \quad (pa > 0)$$
$$p_A = K_A \cdot \{(\sum \gamma_t \cdot H) + q\} - 2 \cdot C \cdot \sqrt{Ka}$$
$$w = p_A + p_w$$

Fs = F/W
F = l × C′ x L
W = S x w
L = (Fs x S x w)/(l x c′) = 6.02 m

Where, P_A is earth pressure (kN); P_1 is above the release part (kN); P_2 below the release part (kN); P_w is water pressure (kN).

Using the formula above, earth pressure P_A is calculated as P_1 above the release part and P_2 below the release part, and water pressure P_w is added to calculate the resultant force P

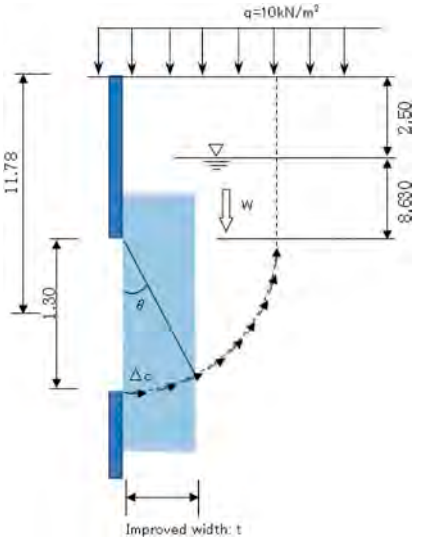

Figure 6. Calculation diagram.

Upper side	P_1 = 167.73 kN
Lower side	P_2 = 188.54 kN
Outside force:	$w = P_A + P_w$ = 178.13 kN/m^2
Open radius:	r = 0.65 m
Adhesive strength after improvement	c'= 11.57 kN/m^2
Perimeter:	l = 4.08 m
Open area:	S = 1.33 m
Required improved thickness	t = 6.10 m

The thickness required to process is quite large, the hole to open the tunnel eye is within the weak organic clay layer, it is not possible to ensure stability when cutting to open the tunnel eye when the jack drill enters the shaft. Therefore, it is necessary to add a layer of jet grouting close to the tunnel eye to ensure stability. Additional Jet grouting to combine with Chemical grouting is considered at shaft location 13.0.

Calculation parameter table of the tunnel:

Ground elevation	GL = 0.00 m
Centre depth of tunnel eye	H = 11.78 m
Groundwater level	h' = 2.50 m
Unit volume weight of water	γ_w = 10.00 kN/m^3
Top load	q = 10.00 kN/m^2
Tunnel eye diameter:	D = OD + (0.15m x 2) = 1.30 m
Safety factor	Fs = 1.70
Design strength	q_u = 1.00 MN/m^2
Adhesive strength after improvement	c' = 0.30 MN/m^2

Calculation formula for moment

$$M_{D1} = \left(\sum_{i=1}^{i}(\gamma_{ti} \cdot H_i) + q\right) \cdot D \cdot \frac{D}{2}$$
$$M_{D2} = \gamma_t \cdot \frac{\pi}{4} D^2 \cdot \frac{4}{3\pi} \cdot D = \frac{\gamma_t \cdot D^3}{3}$$
$$M_R = \frac{c_0 \cdot \pi \cdot D^2}{2}$$
$$F_s \cdot M_D - M_R = \Delta M_R$$
$$\Delta M_R = \Delta c \cdot \theta \cdot D^2 \; => \theta = \frac{F_s \cdot M_D - M_R}{\Delta c \cdot D^2} \; => \theta$$
$$= \sin^{-1}\left(\frac{t}{D}\right) \; => t = D \sin\theta$$

Table 6. Geological parameters table.

Soil layer	Layer thickness t (m)	Unit volume weight γt (kN/m^3)	Weight in water γt' (kNm^3)	Internal friction angle φ(°)	Adhesive strength C (kN/m^2)	Adhesive after improvement C' (kN/m^2)
1-Road bed	1.40	18.0	8.0	30.0	0.00	0.00
2-Stiff clay	0.60	18.5	8.5	12.5	28.64	28.64
7-Soft clay	4.80	19.8	9.8	17.5	19.42	19.42
8-Soft clay, organic	10.20	17.8	7.8	7.5	11.57	300.0

Starting moment	MD1 = 185 kNm
	MD2 = 13 kNm
Resistance moment	MR = 31 kNm
Increasing moment	ΔMR = 305 kN/m^2
From the above	θ = = 0.602 rad

Required improved thickness by Jet grouting t = 0.80 m

When the jacking machine reaches the tunnel eye, the gap between the machine body and the borehole is created as a path for water from the outside to enter the tunnel eye. In addition, the machine pressure may cause damage to soil improvement soil block. Therefore, it is necessary to add a Jet grouting block to ensure the safety of machine arriving.

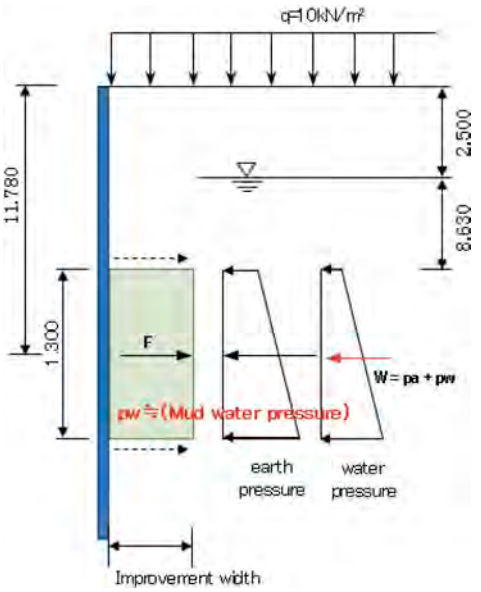

Figure 7. Calculation diagram.

Calculation parameter table of the tunnel:

Ground elevation	GL = 0.000 m
Centre depth of tunnel eye	H = 11.780 m
Groundwater level	h' = 2.500 m
Unit volume weight of water	γ_w = 10.0 kN/m^3
Top load	q = 10 kN/m^2
tunnel eye diameter	D = 1.300 m
Safety factor	Fs = 1.70
Design strength	q_u = 0.16 MN/m^2
Adhesive strength after improvement	c' = 0.08 MN/m^2
Required thickness of excavator length	l + α, l = 1.5 m

Calculation formula for earth pressure and water pressure

$$K_A = \tan^2\left(45^\circ - \frac{\varphi}{2}\right) \quad (pa > 0)$$
$$p_A = K_A \cdot \{(\sum^{\gamma_i} \cdot H) + q\} - 2 \cdot C \cdot \sqrt{Ka}$$
$$w = p_A + p_w$$

Required thickness: α is

$$t = F_s \sqrt{\frac{1.2 \cdot w \cdot r^2}{\sigma_t}}$$
$$t = 1.7. \sqrt{\frac{1.2 \cdot 178.13 \cdot 0.65^2}{53}} = 2.3m$$
$$w = w - pw = p_A + pw - pw = p_A$$
$$\alpha = 1.7. \sqrt{\frac{1.2 \cdot 85.33 \cdot 065^2}{53}} = 1.6m$$

Lateral pressure acting on the shield centre.

Earth pressure P_A; above the release part P_1 and below the release part P_2.

Upper side	P_1 = 167.73 kN
Lower side	P_2 = 188.54 kN
Outside force	w = P_A+P_W = 178.13 kN/m^2
Open radius	r = 0.65 m
Shear strength	σt = 53.00 kN/m^2
Outside force	P_A = 85.33 kN/m^2
Required section length:	t = 2.30 m
Length of machine	+α:= 1.5 +1.6 = 3.10 m
So, necessary improvement section	=3.10 m

The larger of the required section and excavator length + α

On arriving side, the design pipe diameter is 1.0m, the tunnel eye is larger with diameter of 1.3m for pipe jacking machine passing. With a larger pipe diameter, 02 rows of jet grouting could be applied according to stability. Layout Chemical grouting combined Jet grouting on arriving side with designed pipe diameter of 1.0m as Figure 8 and Figure 9 follow.

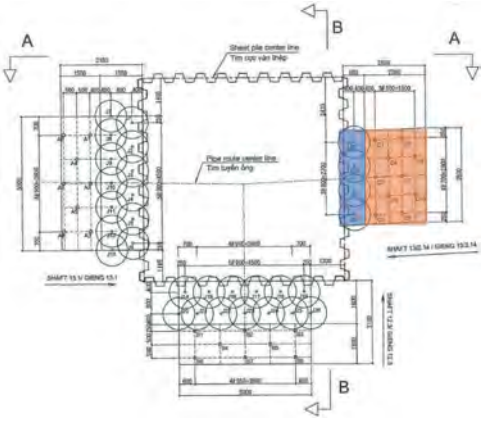

Figure 8. Layout of Chemical grouting and Jet grouting.

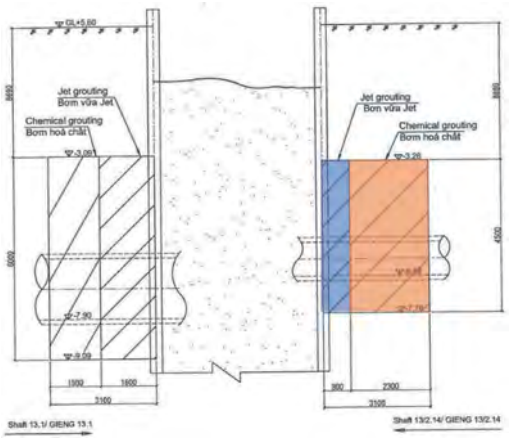

Figure 9. Section of Chemical grouting and Jet grouting (A-A).

According to the layout, quantity of Chemical grout combined jet grout is summarised in table 7.

3.2.3 *Result of construction*

Before applying Chemical grouting and Jet grouting method, field permeability test was conducted to verify coefficient of permeability of chemical grouting (Figure 10). Trial jet grouting was also conducted at project to ensure quality of Jet grouting column, target values were archived, $q_u \geq 1.0$ Mpa, $k \leq 1.10^{-7}$ m/s (Figure 11 and Figure 12).

The results of test are shown in Figure 11 and Figure 12.

According to project quality control policy. After soil improvement by Chemical grouting combined Jet grouting 14 days, small holes were cut on soft eye to check water leakage condition and improved soil

Figure 10. Field permeability test on Chemical grouting and Core sampling on Jet grouting.

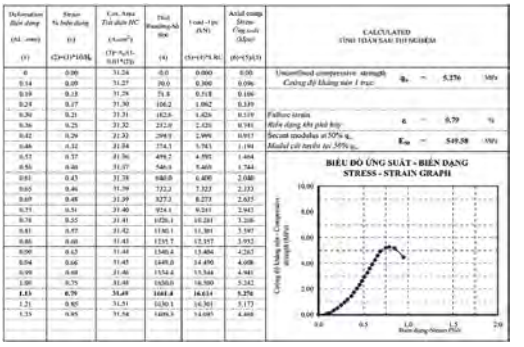

Figure 11. Result of UCS test on Jet grouting sample.

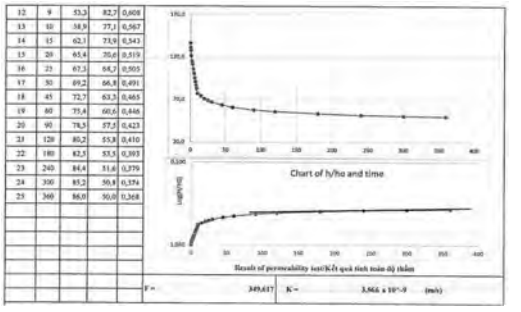

Figure 12. Result of field permeability test.

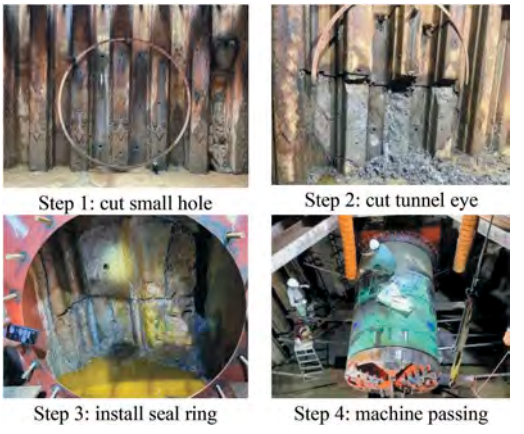

Figure 13. Check water leakage and cut tunnel eye.

Table 7. Quantity of Chemical combined Jet grouting.

Method	Number of holes	Drilling length (m/hole)	Grouting length (m/hole)	Total grouting length (m)	Grouting ratio (%)	Total grout (m3)
Chemical grouting	10	13.38	4.5	45	37	13.4
Jet grouting	4	13.38	4.5	45	100	21.6

condition (Figure 13). If there were no water leakage, tunnel eye will be cut partly. After tunnel eye was cut fully, seal ring will be installed to prevent mud and water increase during machine passing. When machine passed the tunnel eye safely, it will be move to the next jacking span.

4 CONCLUSION AND RECOMMENDATION

Lessons learned from jacking shaft locations where water leakage and subsidence occurred when cutting tunnels eye in Ho Chi Minh City. The technical solution combining Chemical grouting and Jet grouting at the tunnel location was researched and applied from the beginning for the project in Hanoi City, and the quality test results met the requirements. During the process of cutting and opening the tunnel eye for the pipe jacking machine to operate, there was no problem of water leakage causing subsidence from then on. Construction work in deep shaft is guaranteed to be safe.

With a long sewer system over a large area must ensure the slope and design flow, so it is inevitable that the sewer elevation will be within the weak soil layer such as organic clays. Jet grouting method solves the strength of tunnel eye blocks, Chemical grouting method solves the problem of seepage, this combination is completely suitable and can be applied to projects with similar properties.

ACKNOWLEDGMENTS

We would like to sincerely thank the contribution and support of FECON-RAITO underground construction JSC Company during the survey, visit construction, data collection and results analysis process.

REFERENCES

[1] Japan Grouting Association. Grouting Method - Technical Manual 2016.
[2] JJGA Japan Jet Grouting Association. Jet Grout - Jet Grouting Method - JSG/Column Jet Grouting - Technical Manual (20th Edition) Sept 2011.
[3] US Army Corps of Engineers. Chemical grouting Engineering and Design January 1995.

Tunnelling for a Better Life – Yan, Celestino, Thewes & Eberhardt (Eds)
© 2024 The Author(s), ISBN 978-1-032-80042-4
Open Access: www.taylorfrancis.com, CC BY-NC-ND 4.0 license

A systematic deformation control methodology for underground space construction in close proximity to an existing metro station

Jinhua Li*
AECOM Asia Co Ltd, Hong Kong, China

Renxue Wen
Sino-Railway South Constructing Group Co Ltd, Shenzhen, China

Wen Wu Yang & Wing Fei Mou
AECOM Asia Co Ltd, Hong Kong, China

ABSTRACT: The deep excavation or tunnel construction adjacent to an existing metro station will cause additional stress and displacement in the as-built structures, which might affect its functionality and/or even threaten the structural integrity. A systematic deformation control methodology for underground space construction is discussed in this paper, taking the Huangmugang Transportation Hub Project in Shenzhen as an engineering case study. This project is in close proximity to the existing metro line 7 station, which continues under normal operations during the entire course of extensive underground construction activities. For maintaining construction safety at different construction stages, systematic and stringent control of ground and structural deformations become critical, in view of the engineering risk challenges in complex ground and built environments. Staging construction approaches by zones with protective measures and monitoring are discussed. The rationality and effectiveness of the deformation control by ground reinforcement, construction disturbance control and monitoring among other engineering measures are verified. The principle, methodology and relevant experience are of relevance for similar projects.

Keywords: Existing station, Mined tunnel, Deep excavation, Metro protection, Risk assessment

1 INTRODUCTION

With the rapid development of urban construction, the demand for utilization efficiency of traffic resources in urban areas has been increasing. For urban rail transit projects, the expansion and extension of existing metro lines is the main content of development. In this process, new rail transit projects often need to be constructed near various existing structures (such as tunnels and metro stations), resulting in a large number of complicated conditions involving adjacent structures (Zhang et al., 2011). Due to the existence of as-built underground structures, the soil stress of adjacent strata was redistributed during construction activities, which inevitably affected the displacement and stress response of the as-built underground structure (Li, 2009). Therefore, the approach to optimize design and construction sequences of a newly-built underground structure to effectively control the deformation of existing structures have become a key issue.

In recent years, a series of calculation and analysis methods had been applied to deformation control and safety risk assessment of adjacent structures caused by underground space construction (Guo et al., 2015). Theoretical calculation, FEM simulation and monitoring data analysis were adopted to quantify the stress and deformation caused by underground construction, then design optimization and corresponding protective measures have been taken according to the analysis results (Guo, 2015 and Wang et al., 2018). Zhao (2019), Sun (2013) and Feng (2018) analysed the spatial relationship and characteristics between new projects and existing structures, and specified construction methods to be applied to mitigate the risks of close proximity construction on existing structures. Tao et al. (2010) and Liu et al. (2010) studied the pre-construction stage risk assessment, and mitigation of the construction risk in advance through safety rating and systematic risk management.

The previous research mainly studied the deformation mechanism and key construction

*Corresponding author: Maxim.Li@aecom.com

DOI: 10.1201/9781003495505-100

technology of the adjacent existing rail transit structure under common construction conditions (the newly-built underground structure crossing sideways or downwards). However, research on the structural design and in-situ monitoring of new projects under complex construction conditions (the newly-built underground structure crossing both sideways and downwards) is still insufficient. Based on the Huangmugang (HMG) transportation hub project, this paper studies the comprehensive safety impact of a mined tunnel under short distance and deep excavation in close proximity to the existing Shenzhen Metro Line 7 station, and systematic deformation control measures that were applied during construction. According to the in-situ monitoring results, the deformation experienced by the existing station is small and well controlled within a safe range.

2 PROJECT OVERVIEW

2.1 *Project background*

The HMG Transportation Hub Project is located in the northeast of Futian District, Shenzhen, at the intersection of Sungang West Road, Nigang West Road, Huafu Road and Huaqiang North Road. It is a three-line subway interchange hub for the existing Line 7, planned Line 14 and planned Line 24. The existing Line 7 station is laid underground along Huaqiang North Road and Nigang West Road, which is a three-storey underground structure with side stacked platforms. The Line 14 station is laid underground along Huafu Road and Nigang West Road, which was planned to be a three-storey underground one-platform interchange station (with existing Line 7 station). The Line 24 station is laid underground along Sungang West Road and was planned to be a four-storey underground station. The site location of the HMG transportation hub is shown in Figure 1.

Figure 1. Site location of HMG transportation hub.

The existing Line 7 station has a length of 232m, and a width of 21.85m at both ends and 11.7m in the middle. The structure base slab depth of Line 7 station is around 27.6m~28.35m. The Line 14 station is a newly-built station, close to the west side of the existing Line 7 station, with a length of 262m, a width of about 44.6m~81.3m and a base slab depth of about 28.35m~29.1m. This was connected with the Line 7 station after completion. Another newly-built station, for Line 24, has a 70-degree cross relationship with the existing Line 7 station, with a length of 235.2m, a width of 28.2m and a maximum buried depth of 40m. In addition, two metro tunnels for Line 24 passed through the bottom of the Line 7 station. See Figure 2 for the plan-view relationship of the three metro stations at the HMG hub.

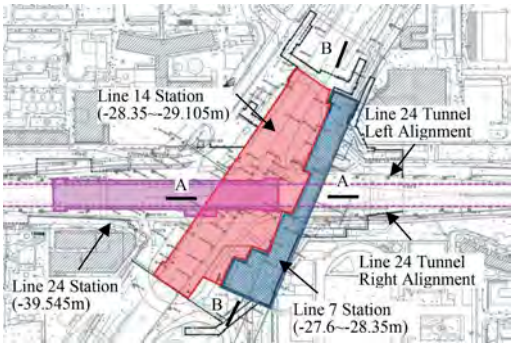

Figure 2. Layout plan of HMG transport hub.

2.2 *Geological conditions*

The project site is located in the Pearl River Delta, with a relatively flat terrain and a ground surface elevation of about 18.5m~25.50m. The geological profile of the station area was identified as: (1) Fill (partially rubble); (2) Soft Clay (SC); (3) Clayey Soil (CS); (4) medium to coarse Sand; (5) Eluvial Soil (ES) on Granite; and (6) Granite with different weathering degrees. The base slab of the newly-built station is mainly located on strongly weathered Granite (SWG) and moderately weathered Granite (MWG), and show characteristics of differential

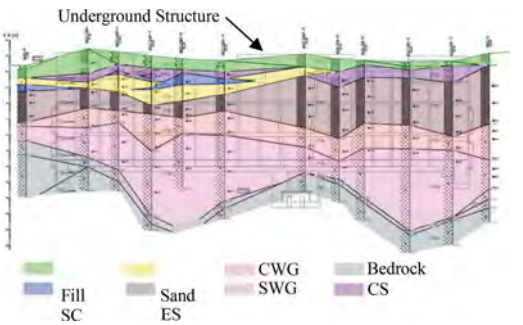

Figure 3. Typical geological profile (B-B).

weathering along the station profile. There are two main sources of groundwater in the stratum: in the Quaternary loose strata and in bedrock fissures, which occur in the Quaternary Sand layer and Granite bedrock, respectively. The relationship between the typical geological profile and the newly-built station structure is shown in Figure 3.

2.3 *Spatial relationship of station structures*

There are two key construction works in the project that obviously affected the existing Line 7 station. One is the construction of the new Line 14 station, which is in close proximity to the existing Line 7 station. The other is the new metro tunnels of Line 24, where both tracks passed through the foundation of the Line 7 station, and the shortest distance between the top of the tunnel and the base slab of the existing station is only 1.9m (Figure 4).

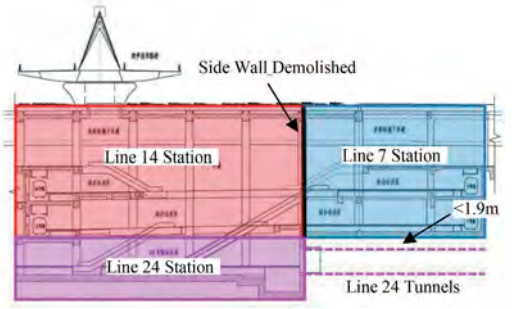

Figure 4. Elevation relationship among 3 stations (A-A).

3 ENGINEERING RISK ASSESSMENT

3.1 *Quantitative risk assessment system*

Since multiple engineering works of the project need to be commenced in complex and challenging conditions, a quantitative risk assessment system was proposed at pre- construction to synthetically identify risks at a high level and to investigate the corresponding risk factors.

The system used is the Analytical Hierarchical Process (AHP) technique, which was developed by Saaty (1977, 1980), and contains a multitude of uncertain variables and multi-level decision making and management mechanisms. The Alternatives and Criteria are chosen according to a Work Breakdown Structures (WBS) and Risk Breakdown Structures (RBS), respectively. Once the calculation is finished, Fuzzy Comprehensive Evaluation (FCE) is used to revise the AHP so that the assessment results could be represented mathematically.

Based on the assessment result, 3 major high level risks are identified:

(1) Deep excavation of new stations
(2) Demolition of Line 7 station side walls
(3) Tunnelling under-crossing Line 7 station

3.2 *Deep excavation of new stations*

In the process of deep excavation, the stress state of the stratum within a certain range is redistributed due to unloading effect, and deformation or ground movement occurs. The change of stress state in the stratum indirectly affected the stress balance system of the existing underground structure itself, which is reflected in the increase of additional internal stress and additional deformation of permanent structures. When deformation or internal force exceeds a certain limit, it may lead to structural damage of the station structure, thus affecting structural safety and serviceability of the rail transit system.

3.3 *Demolition of Line 7 station side walls*

During construction of the Line 14 station, the structural side walls of the existing Line 7 station needed to be demolished to form an open passage between the old and new stations. See Figure 5 for the demolition scope of the side walls, ranging from the first to third floors of the existing Line 7 station.

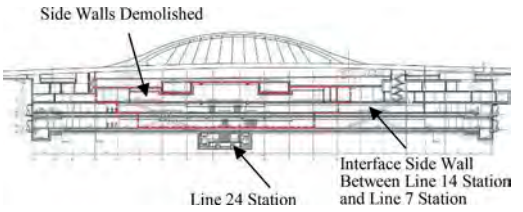

Figure 5. Demolition of side walls of Line 7 station (B-B).

According to previous research on the construction technology and structural behaviour of slab walls opening into an underground metro station, the wide opening of reinforced concrete side walls not only changes the original structural boundary conditions, but also changes its stress distribution (An et al., 2020). The key structural portion of the existing station, as the main loading-bearing component, is working together with the new station structure component to accommodate loading and internal stress transmitted through the structural system. The internal stress transformation of the spatial structure at the station opening interface is quite complicated. Commonly, internal stress around the structural opening is concentrated, which is the weakest portion of the entire structure system. The newly-built structure combined with the opening portion have a significant impact on the spatial stress redistribution (Xie et al., 2012).

3.4 *Tunnelling under-crossing Line 7 station*

After the fourth storey underground excavation work of Line 24 station was completed, two tunnels with diameter of 7.5m passed through and under the base slab of the existing Line 7 station. The purpose of

under-crossing the 7.5m tunnel is to provide launching space for further TBM boring of the Line 24 metro tunnels. Both tunnels were planned to be constructed by conventional mining, with excavation lengths of 48.8m and 39m respectively, as shown in Figure 6.

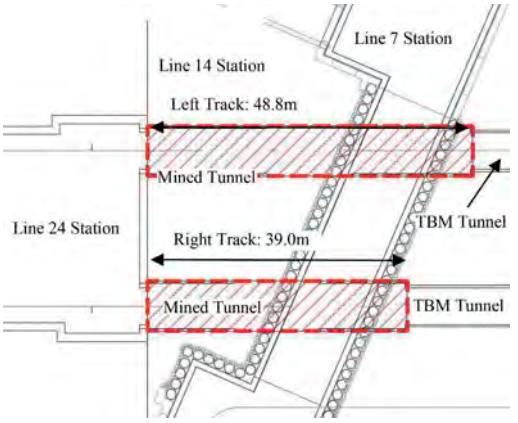

Figure 6. Layout of mined tunnels.

The lower portion of the two mined tunnels will encounter moderately to slightly weathered Granite, while the upper portion of tunnel and Line 7 station foundation are located in strongly weathered Granite. The space between the tunnel and Line 7 station is quite narrow, less than 2m thin. If drilling and blasting is adopted, the vibration generated by blasting will greatly disturb the existing station and strongly weathered Granite stratum. After being disturbed by construction vibration, the strongly weathered Granite stratum will become extremely unstable, gradually softening and disintegrating under the added effect of groundwater. Finally, the strength of the stratum might decline greatly, inducing collapse or excessive deformation in a short time (Zhu, 2013). The collapse of a softened stratum will have a significant influence on the stability of the existing Line 7 station, seriously affecting safety and further operations.

4 SYSTEMATIC DEFORMATION CONTROLS

According to the results of the pre-construction quantitative risk assessment, several key risk factors emerge. As the daily operation of the existing Line 7 station cannot be interrupted during construction, to minimize the impact of construction on the existing stations, based on ALARP principles (Yang et al., 2015), a whole-process risk management system was applied to the project. Scientific and systematic risk management processes and technologies were organized for the engineering design stage, construction stage and in-situ monitoring, so as to control and lower engineering risks into an allowable range.

4.1 *Deep excavation work*

Before the permanent structures of the Line 14 and Line 24 stations are constructed, an ELS system needs to be set up first for deep excavation.

In this project, the deformation of the existing Line 7 station is one of the key controlling factors. Based on engineering practices and related research, the top-down construction method has obvious advantages in controlling ground deformations during excavation (Xie et al., 2014). Compared with other construction methods, the top-down method uses the structural slab as a supporting component, which has high stiffness and relatively small deformation. For this reason, the top-down method was finally adopted and commenced as shown in Figure 7.

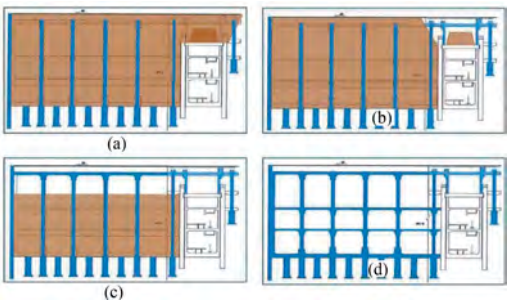

Figure 7. Construction sequences of top-down excavation: (a) Construction of diaphragm wall and structural columns; (b) Excavation of soil overlaying Line 7 station; (c) Excavation of new station area in layers and construction of structural slab; (d) Top-down excavation to base level.

Due to huge volume of excavation work and differential excavation levels, in order to further control the deformation induced by excavation, on the basis of the top-down method, the whole area was excavated by stages and zones, as shown in Figure 8. According to the different depth and risk level, the construction sequence is listed as follows:

(1) Excavation of A portion (excavation depth between 20m~30m);
(2) After completion of A portion, B portion was excavated (excavation depth between 30m~40m);
(3) Finally, two affiliated areas were excavated (excavation depth did not exceed 20m).

4.2 *Side walls demolition*

The demolition of the side walls was commenced after completion of the deep excavation work, to ensure operational and structural safety of the existing Line 7 station. Under the principle of "reinforcing before demolishing, transforming structural system by stages and zones", the demolition and reconstruction of the side walls were divided into stages. Detailed construction procedures are shown in Figure 9.

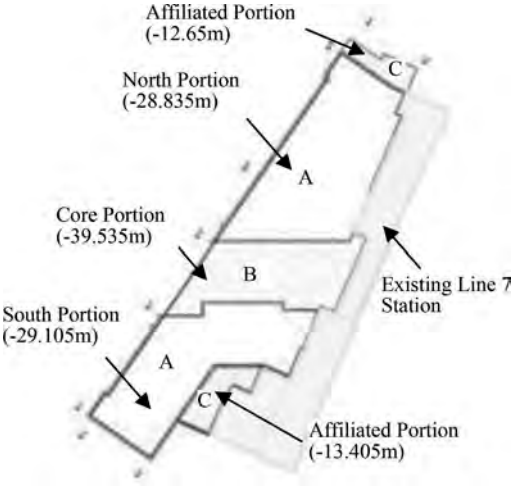

Figure 8. Deep excavation by stages and zones.

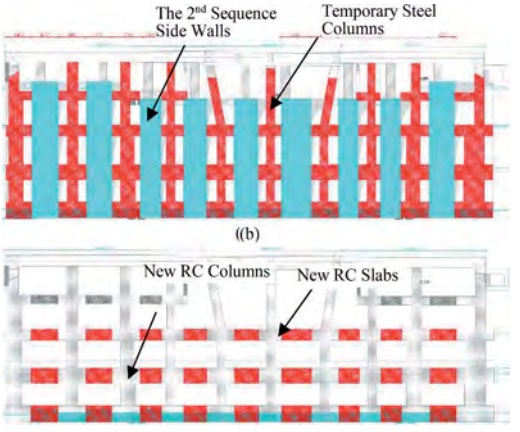

Figure 9. Side wall demolition by stages and zones: (a) Demolition of the first sequence side walls and construction of new RC beams and columns; (b) Demolition of the second sequence side walls and construction of remaining RC beams.

The first stage was mainly commenced inside the existing Line 7 station. After the construction area was completely enclosed, temporary steel columns were erected near the side walls to be demolished in the station. In the second stage, side walls in the first sequence were demolished from top to bottom by the layered and sequential method, and new RC beams and columns were constructed from bottom to top afterwards. In the third stage, the side walls from the second sequence were demolished by the same method, and then the remaining new RC beams were constructed.

4.3 *Tunnelling work*

After demolition and reconstruction of the side walls were completed, the mined tunnels under-crossing the Line 7 station were commenced. As previously noted, the distance between the top of the tunnel and Line 7 station base slab is quite small, and the strongly weathered Granite stratum is easy to soften and collapse during tunnelling. It is crucial to ensure the stratum stability at the top of the tunnel for deformation control of the existing Line 7 station.

Based on a comprehensive comparison of the risk levels of various tunnel supporting methods, use of a large-diameter pipe umbrella combined with small-diameter duct grouting was adopted. The support was arranged across a 120° interval above the tunnel vault. The pipe umbrella is comprised of steel pipes of 108×5mm, with circumferential spacing between pipes of 30cm. Each 6m long steel pipe was pushed into the front of the cave roof at an elevation angle of 1°~2°. The small duct for grouting has a diameter of 42mm and a wall thickness of 3.5mm. Each 3m long duct was arranged at a circumferential spacing of 30cm. The typical section of forepoling support is shown in Figure 10.

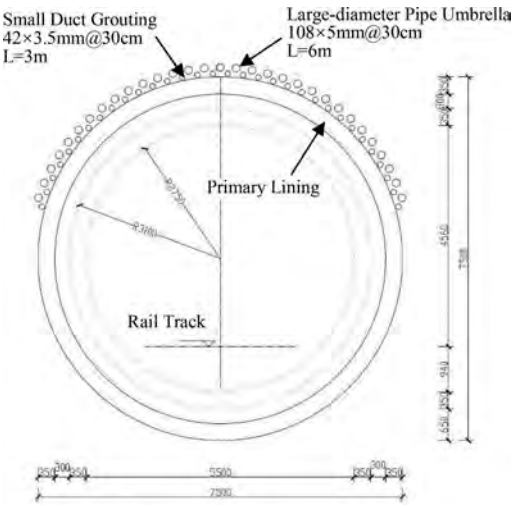

Figure 10. Typical section of forepoling support.

The primary lining of the tunnels also requires strengthening according to the stratum lithology and risk characteristics. Twenty-two grid steel frames with a spacing of 0.5m was fully arranged, and double-layer steel mesh was arranged inside and outside the steel frame, as well as C25P6 shotcrete with a thickness of 350mm.

In addition, the tunnelling parameters have also been strictly controlled and mainly listed as follows:

(1) Before tunnelling, unfavourable geological bodies were detected and forecasted by

comprehensive means of advanced geological drilling and geological radar.
(2) During tunnelling, a benching method was adopted, and the length of the upper and lower benches was strictly controlled.
(3) Tunnel blasting was controlled precisely, with blasting vibration velocities not exceeding 2.5cm/s.

5 DEFORMATION MONITORING RESULTS

The deformation monitoring of the existing Line 7 station was carried out by combining automated and manual monitoring. According to the risk level of construction engineering and surrounding environment, the monitoring level was classified as Grade I. The main monitoring items include vertical and horizontal deformation of the station structure, differential settlement of deformation joints and axial force of temporary steel columns. Within the influence range of transportation hub construction, the monitoring points were set to 5m~10m spacing within one monitoring section.

Monitoring ran through the whole construction process, including the top-down deep excavation, demolition of the Line 7 station side walls and the Line 24 tunnelling by conventional mining. Some monitoring results of each stage are shown in Table 1.

Table 1. Deformation results of Line 7 station (in mm).

	Measured Value/mm			
Monitoring Portion	Excavation Work Completion	Side Wall Demolition Completion	Tunnelling Work Completion	Allowable Value/mm
Side wall (horizontal)	-5.30	-5.45	-7.13	±10.0
Top slab (vertical)	-2.71	-3.22	-6.07	±10.0
Base slab (vertical)	-2.11	-6.32	-7.71	±10.0
Differential settlement	1.52	2.31	3.06	±4.0

As can be seen from the table, although the monitoring data of Line 7 station show an increasing trend with the development of different construction stages, the deformation values of structure portions are still within the allowable safety range.

6 CONCLUDING REMARKS

The construction conditions of the HMG transportation hub project is complicated and encounters engineering challenges with safety concerns of the existing Line 7 station. With application of quantitative risk assessment process, a systematic deformation control method aimed at deep excavation, structure demolition and tunnelling was proposed, and the deformation of the existing stations has been effectively controlled during construction. Thereby, several remarks are derived as follows:

(1) For a complex underground space development project in close proximity to an existing station structure, a top -down excavation method can effectively control the deformation of the nearby stratum and structures. For development projects with complex processes, an appropriate construction method is a crucial factor to mitigate engineering risks.
(2) In similar projects, it is necessary to adhere to the principles of constructing in stages and with benches, and supporting ahead of the face to minimize disturbance induced by construction activities to the pre-existing structures.
(3) For complex underground engineering, it is necessary to comprehensively consider all key risk factors, and consider the relationship between each factor and the construction sequences. This allows for an effective systematic deformation control method to be proposed to reduce engineering risks to a reasonable level.
(4) Dynamic monitoring plays an important role in underground construction engineering, including advanced geological prediction and automatic monitoring, which can timely reflect unexpected geological conditions and risks.

REFERENCES

An, D. H., Shao, W., 2020. Analysis on the effect of the expansion and reconstruction of the metro station on the stress of original structures. Railway Standard Design. 64(11), 129–135.

Feng, G. J., 2018. Protection Countermeasures for metro structure adjacent to deep. Journal of Railway Science and Engineering. 12(2), 393–401.

Guo, D. T., Zhou, C. Y., Xie, L., 2015. Research on static and dynamic performance of the foundation pit excavation adjacent to subway tunnels. Journal of Railway Science and Engineering. 12(2), 393–401.

Guo, L., 2015. The Influence of New Foundation Excavation on the Existing Subway Stations and Its Countermeasures. Journal of Railway Engineering Society. 32(2), 109–112.

Li, X. X., 2009. Security analysis of running metro station structure adjacent to foundation excavation. Rock and Soil Mechanics. 30(S2), 382–386.

Liu, Z. G., Lu, Y. Z., Yang, W. W., 2010. Practical examples of risk management in large tunnel projects: from Hong Kong to Mainland China. Tunnel Construction. 30(S1), 8–14.

Saaty, T. L. 1977. A scaling method for priorities in a hierarchichal structure. J. Math. Psych. 15(3), 234–281.

Saaty, T. L., 1980. The Analytical Hierarchical Process. McGraw-Hill, New York.

Sun, X. D., 2013. Case study on key construction technologies for mined tunnels crossing closely underneath existing metro station. Tunnel Construction. 33(5), 412–418.

Tao, L. J., Xu, Y. J., Wang, W. P., 2010. The safety evaluation of the structure of existing subway station above shielding tunnel traversing. Chinese Journal of Underground Space and Engineering. 6(A01), 1513–1516.

Wang, H. D., Liu, F. M., Peng, H. X., 2018. Safe construction technologies for newly-built metro station foundation pit closely crossing underneath adjacent operation metro station. Tunnel Construction. 38(11), 1836–1845.

Xie, S. Y., Shi, C. H., Peng, L. M., et al, 2012. Numerical simulation analysis on mechanical behaviour during construction at the intersection of metro station and ventilation gallery. Railway Standard Design. 2012(6), 93–97.

Xie, Y. J., Qian, D. L., Wei, X. Y, 2014. Research on deformation law of over-sized deep foundation pit which is adjacent to metro station and constructed by top-down method. Journal of Hefei University of Technology (Natural Science). 37(10):1231–1238.

Yang W. W., Hu Y. M., Tsang C. K., 2015. On risk management of tunnel engineering in whole process, Tunnel Construction. 35(8), 753–758.

Zhao, T. D., 2019. Structural design and monitoring analysis of new-built mined tunnel crossing underneath existing metro station. Tunnel Construction. 39(S02), 253–260.

Zhang, G. L., Han, X. F., Li, Y. H., et al, 2011. Numerical simulation on interaction between new foundation pit and existing metro Station. Tunnel Construction. 31 (003), 284–288.

Zhu, H. H., 2013. Physical and mechanical characteristics of mixed rock eluvium and its effects on metro works and treatment measures. Modern Tunnelling Technology. 50(1):29–33.

Tunnelling for a Better Life – Yan, Celestino, Thewes & Eberhardt (Eds)
© 2024 The Author(s), ISBN 978-1-032-80042-4
Open Access: www.taylorfrancis.com, CC BY-NC-ND 4.0 license

Study on diffusion mechanism of backfill grouting in sand and clay stratums

Sihan Li* & Fei Ye
Chang'an University, Xi'an, China

Tianhan Xia
Zhongshan transportation Breau, Zhongshan, China

Kaichen Ying
Southwest Jiaotong University, Chengdu, China

Xingbo Han
Chang'an University, Xi'an, China

ABSTRACT: Backfill grouting is one of the important components of the shield construction method. The grout diffusion is very complicated under the influence of the physical and mechanical properties of the soil and the properties of the grout itself. In order to understand the diffusion mechanism of grout behind the tunnel segments, a visual grout diffusion model test device is used for indoor test. Two typical soils, sand and clay, are selected and a pure cement grout with a water - cement ratio of 1:1 is prepared. During the grouting process, the grout diffusion distance, seepage pressure and soil pressure are monitored in real time. After 24 hours of grout solidification, the soil in the model cylinder is excavated in layers. Combined with the theory of grout injectability, the injectability of grout in sand and clay is determined. The main conclusions are as follows: the grout mainly undergoes penetration and infiltration diffusion in sand. Due to the adsorption and deposition of cement particles, different extents of filter mud and filter cake appear in each layered sand. The grout mainly undergoes screening and splitting diffusion in clay, and different extents of splitting grout veins appear in each layered clay. Due to the large permeability coefficient of sand, cement grout or fine particle cement grout can be used in practical engineering grouting. The permeability coefficient of clay is small, and chemical grout or grout with good filling property can be used.

Keywords: Backfill grouting, Sand, Clay, Diffusion mode, Indoor test

1 INTRODUCTION

In the 21st century, all countries in the world are promoting and developing shield construction methods and gradually moving toward a new era of longer, larger, deeper, wider and more intelligent shield tunnels of a higher level. As an important component of the shield construction method, the backfill grouting, the adaptability of the grout to the formation(Shirlaw et al 2004; Oreste et al 2021), the reinforcement effect of the grout, and the interplay of the formation-grout layer-segment have also become the focus of research(Katebi et al 2015; Liang et al 2020).

The formation is identified as a porous medium due to its internal pore structure, and the grout is composed of solid particles and water. Due to the different physical and mechanical properties of different strata, the grout diffusion mechanism in the strata is different. Existing related studies have mainly focused on sand and clay formations. Sandy soil (particle size 1-0.05 mm) content greater than 50 % is sand(Li et al 2016; He et al 2016). Sand has good ventilation and water permeability, strong capillary action and fast water operation(Cai et al 2018; Chen et al 2019). China's sand strata are mainly concentrated in the northwestern regions, such as Gansu, Ningxia, Inner Mongolia and Xinjiang(Sun et al 2020). Unlike sand, clay contains very few sand particles, and the main constituents are silica and alumina(Lamber 1958a; Lamber 1958b). The permeability of clay is low, and

*Corresponding author: sihan.Li@chd.edu.cn

DOI: 10.1201/9781003495505-101

water does not pass easily through it. The pores of clay with too small pores are mostly occupied by bound water, and the capillary action is weak(Seed et al 1959; Levoueil et al 1990). China's clay strata are mainly concentrated in the southeastern regions, such as Jiangsu, Zhejiang, Hubei and Guangdong(Weng et al 2011). The diffusion modes of backfill grouting of shield tunnels are divided into four types, namely, filling diffusion, penetration diffusion, compaction diffusion and splitting diffusion(Akbulut et al 2002; Ye et al 2013; Ye et al 2016; Ye et al 2020). However, due to the influence of surrounding strata, grout characteristics, grouting parameters and other factors, the diffusion modes are transformed and doped with each other and there is no obvious boundary(Ye et al 2022). In order to study the grout diffusion characteristics of backfill grouting, it is necessary to observe the diffusion process and the grouting effect(Ying et al 2022). However, because the grouting behind the shield tunnel segment is a concealed project, this process is performed behind the ring segment. Only the in-situ test at the negative ring segment of the shield tunnel shows the diffusion process better, but the in-situ test at the negative ring segment does not simulate the true formation. Therefore, the indoor model tests with strong pertinence and high flexibility have been used by many researchers to study the construction process of backfill grouting. The overall model test can better show the stress situation, and strain, grout diffusion properties and grout effects of the segment by simulating the whole section of the whole grout section. The local model test studies the grout diffusion in some dimensions and then selects the characteristic points to be injected using some segments, soil and grout.

In this paper, we focus on the grout diffusion mechanism in different formations. In the case of sand and clay, a visual grout diffusion model test device was used to perform backfill grouting in sand stratum and clay strata, respectively, and to monitored the change in grout diffusion distance, seepage pressure and soil pressure during the grouting process. The permeability coefficient was measured and analyzed for each layer of soil in the model tube. It is concluded that the penetration and infiltration diffusion modes mainly occur in sand strata, while the screening and splitting diffusion modes mainly occur in clay strata. Combined with the permeability coefficients of sand and clay, the groutability criteria for backfill grouting were determined.

2 MODEL TEST

2.1 *Test device and materials*

2.1.1 *Test device*

The visual grout diffusion model test device consists of an injection device, a model device, a pressure regulator device and a data acquisition device. Due to the high permeability coefficient of sand, the diameter of the model tube is set to 100 mm and the height to 2000 mm. The diameter of the model cylinder used for clay grouting is set to 300 mm and the height to 700 mm to reduce the effect of boundary conditions. The specific test device is shown in Figure 1. The injection device consists of a grout storage bucket, a grout pump and a buffer. The pressure regulator device consists mainly of a three - way interface, a pipeline pressure gauge and a pipeline flow meter. The model device consists mainly of a plexiglass cylinder, frame structure, a shield - tail voiding device and sealing device. The data acquisition device consists mainly of soil pressure gauge and seepage pressure gauge.

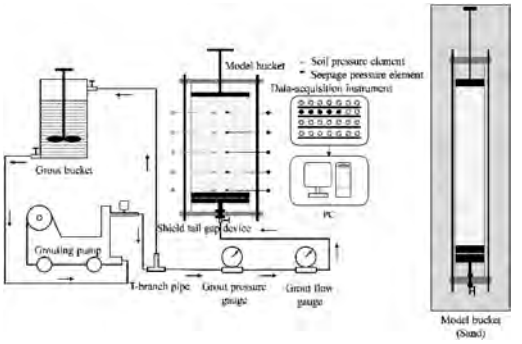

Figure 1. The visual grout diffusion model test device.

2.1.2 *Test material*

The sand is mixed coarse sand with particle size of 0.5 - 1 mm. The clay is made from the soil of the shield foundation pit of the D8KC - 1 section of Xi'an Metro Line 8, and the undisturbed soil is dried and the water content is adjusted by the method of remolding the soil. The relevant parameters of the test soil are shown in Table 1. The grout is pure cement grout with a 1:1 water-cement ratio. The grouting pressure is controlled at 0.2 MPa - 0.4 MPa.

Table 1. Test soil related parameters.

	Moisture content/ %	Specific gravity	Gravity/ $kN \cdot m^{-3}$	Dry unit weight/ $kN \cdot m^{-3}$	Void ratio	Saturation/ %
Sand	20	3.47	19.5	14.4	0.984	62
Clay	20	2.70	15.8	13.1	1.037	55

The cement is selected from a cement plant in Xianyang City, Shaanxi Province, of Hailuo ordinary Portland cement P.O 42.5 grade. The technical indicators are listed in Table 2.

2.2 *Test procedures*

(1) The expansion rubber band is pasted on the lower splint groove of the frame kit and on the

Table 2. P.O 42.5 grade cement technical indicators.

Stability	Setting time/min		Flexural strength/ MPa		Compressive strength/MPa	
Qualification	pre-hardening	final gel	3d	28d	3d	28d
	198	240	5.6	7.5	26.4	45.2

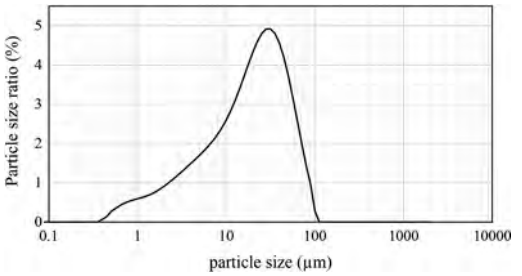

Figure 2. Particle size distribution of cement.

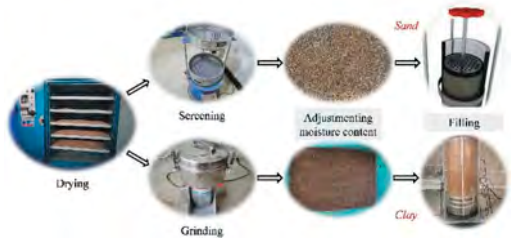

Figure 3. Test soil preparation process.

outer surface of the shield-tail voiding device. Install the waterproof connector and water stop rubber plug for the plexiglass tube, and affix the scale. After the preparation work is completed, the frame structure and the plexiglass tube are assembled sequentially.

(2) The shield tail gap simulation is set to 10 cm. After the shield tail disengagement device is supported by the lower screw, the test soil is filled in every 10 cm layer. Keep the same amount of soil filled each time, and use the same impact strength and compaction times to consolidate the soil.

(3) When the soil is filled to the place where the monitoring element is buried, the soil pressure gauge and the seepage pressure gauge are connected and the waterproof joint is tightened. After the filling is completed, the upper pressure plate is tightened, and the upper and lower nuts of the fastening screw are tightened, and the moisture content monitoring element is inserted from the water stop rubber plug.

(4) The inert iron oxide is chosen as the grout indicator, with a dosage of 5 % of the cement dose. The mixed grout is poured into the grout storage cylinder.

(5) To ensure the initial grout pressure and grout flow rate, the grout pump should be turned on first and the valve at the grout port should be closed. The pressure of the storage grout is not less than 0.2 MPa and then the grout pump is turned off.

(6) Pull down the shield tail disengagement device and turn on all monitoring elements. The grout pump is turned on and the grout pressure is controlled to 0.2 - 0.4 MPa.

(7) After the grouting is completed, the valve at the bottom of the model cylinder is closed to avoid backflow from the grout. After the grout solidifies, the test device is removed and the soil is excavated to find out the diffusion of the grout inside the soil.

The grouting stopping time is controlled. When the pipeline flow meter value does not increase and remains unchanged for 2 min, it indicates that the grout cannot be injected and the grouting is stopped at this time.

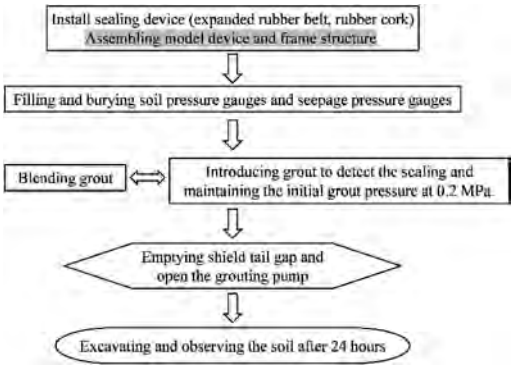

Figure 4. Test procedures.

2.3 *Result analysis*

2.3.1 *Grout diffusion distance*

The diffusion process of the grout was observed and recorded by a high-definition camera, as shown in Figure 5. When grouting in sand, the curve of the grout diffusion distance as a function of time is roughly linear, with an inflection point at 10 s. Within 0 - 10 s, the grout diffusion distance increases sharply, and after 10 s, the grout diffusion rate decreases significantly. This is due to the large aperture size of sand. In the initial grouting stage, the grout is easily permeable and diffuses over long distances. During the subsequent grouting process, the cement particles gradually penetrate and blocked the pores of sand, which reduces the permeability of the sand and makes it difficult for grout to continue to diffuse. Subsequently, only a small amount of very fine cement particles and water infiltrated into the sand under grout pressure. The maximum diffusion distance of the

grout is eventually maintained at 68 cm. When grouting in clay, the time - dependent curve of the grout diffusion distance shows irregular fluctuations. In 0 - 150 s, the grout diffusion rate fluctuates, and after 150 s, the grout diffusion rate is almost 0 and the diffusion distance remains constant. This is due to the small pore size of the clay, which makes it difficult for the grout to penetrate into the clay during the initial grouting stage. Under continuous grout pressure, the grout may be compacted and diffused, which causes the grout diffusion distance increase slowly. It is worth noting that for some time periods, the grout diffusion distance is almost constant. The maximum diffusion distance of the grout is eventually maintained at 55 cm. After waiting for the grout to solidify for 24 hours, the soil in the model tube is excavated in layers to further observe the specific grout diffusion.

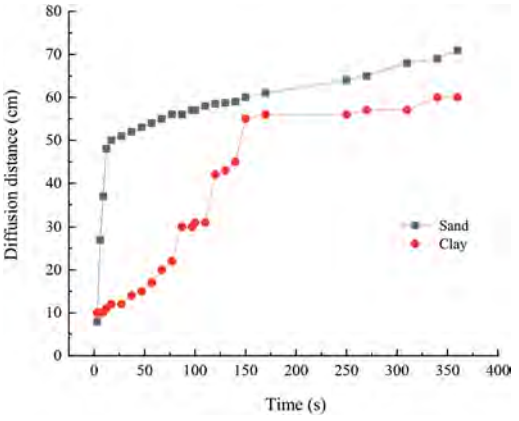

Figure 5. The grout diffusion distance.

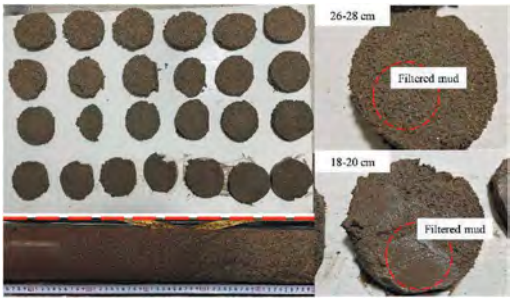

Figure 6. Grout diffusion in sand.

Figure 6 and 7 show the grout diffusion in sand and clay, respectively. The sand in the model cylinder was cut in layers, and it was found that the color of the sand gradually faded away from the grouting hole. 6 - 8 cm is pure cement block and 8 - 10 cm is a mixture of grout and sand. A thick dense filter mud appears at 18 - 20 cm, indicating that the pores of the soil at this location are completely blocked by cement particles, and that the grout has been unable to penetrate into the soil. Filter mud also appears at 26 - 28 cm, but is thin in thickness, indicating that the grout has spread to the site, but at a small value. 54 - 100 cm sand is lighter in color and the position of the grout diffusion cannot be directly observed with the naked eye. Combined with the curves of the grout diffusion distance in sand, it shows that the grout has a seepage and penetration diffusion mode in sand. Observing the grout diffusion in clay, it can be found that at the bottom of the model cylinder, the grout is almost non-diffusive, and the grout only generates water migration at the interface with the soil. In stratigraphic excavations, however, it was found that there were grout veins of different sizes in the clay. At 40 - 50 cm, the thickness and width of the veins are smaller. At 20 - 30 cm, a large thickness of grout veins is found. Combining the grout diffusion situation with the time - dependent curve of the grout diffusion distance, it shows that the grout has undergone screening and splitting diffusion mode in clay.

Figure 7. Grout diffusion in clay.

2.3.2 *Seepage pressure*

The seepage pressure in each layer of sand and clay is extracted as shown in Figure 8 and 9. As the grout diffuses in the sand, the seepage pressure is larger at

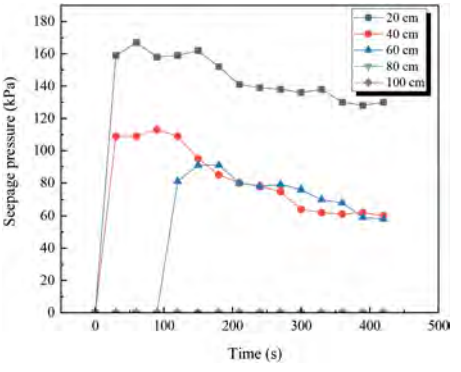

Figure 8. Seepage pressure in sand.

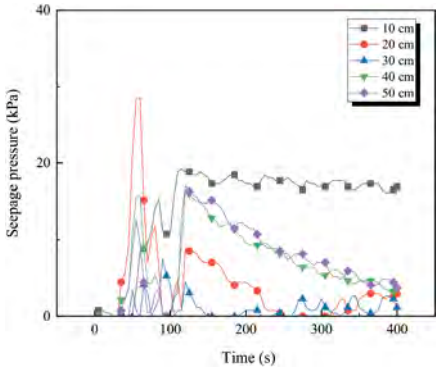

Figure 9. Seepage pressure in clay.

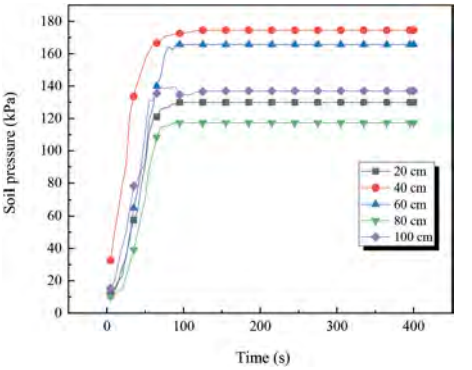

Figure 10. Soil pressure in sand.

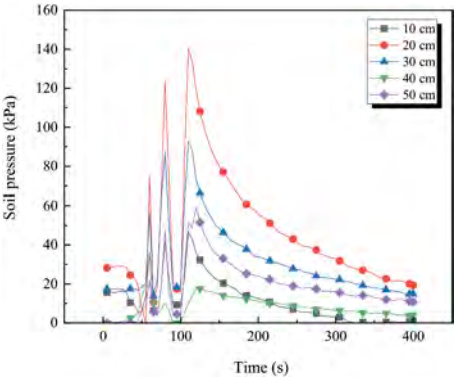

Figure 11. Soil pressure in clay.

20 cm, 40 cm and 60 cm. The increase in the seepage pressure in each layer occurs mainly in the first 30 s, and the seepage pressure shows a slow downward trend after 30 s. This is due to the large pore size of the sand, and during the initial grouting stage, the grout penetrates the sand at a large rate. As the cement particles adsorb and clog, the diffusion rate of the grout decreases and the seepage pressure of each layer decreases. Since the grout does not diffuse to 80 cm and 100 cm, the seepage pressure at these two points is always 0. The increase of seepage pressure in sand shows a linear trend, with a maximum seepage pressure of 163 kPa appearing at 20 cm. As the grout diffuses in the clay, the seepage pressure in each layer shows a stepwise fluctuation trend for the first 150 s. After 150 s, the seepage pressure in each layer gradually remains stable. This is due to the small pore size of clay. Under the grouting pressure, the grout first undergoes pressure screening diffusion. When the clay has a certain extent of compaction, the grout splits and diffuses, resulting in fluctuations in the seepage pressure curve. As grout veins are generated, the clay reduces the grout pressure, resulting in a gradual stabilization of the seepage pressure. It is found that when the grout diffuses in clay, the seepage pressure of each layer is significantly lower than that in sand, with a maximum seepage pressure of 29 kPa appearing at 20 cm.

2.3.3 *Soil pressure*

The soil pressure of each layer in sand and clay is extracted as shown in Figure 10 and 11. As the grout diffuses in the sand, the increase in soil pressure is mainly concentrated in the first 100 s, showing a linear increase trend. After 100 s, the soil pressure in each layer gradually remains stable. The maximum soil pressure in sand is 170 kPa, which occurs at 40 cm. As the grout diffuses in the clay, the soil pressure fluctuates continuously for the first 150 s and decreases after 150 s. This is consistent with the change of seepage pressure in each layer of clay. As the result of the splitting and diffusion of grout, the soil pressure will show a step-like fluctuation as the grout splits the clay and produces grout veins. By comparison, it is found that the soil pressure increases linearly due to the penetration and infiltration diffusion of the grout in the sand. Combined with the grout diffusion in sand and clay, the seepage pressure and soil pressure changes of each layered soil, it can be concluded that the penetration and infiltration occur mainly in the sand. The screening and splitting diffusion mode occur mainly in the clay.

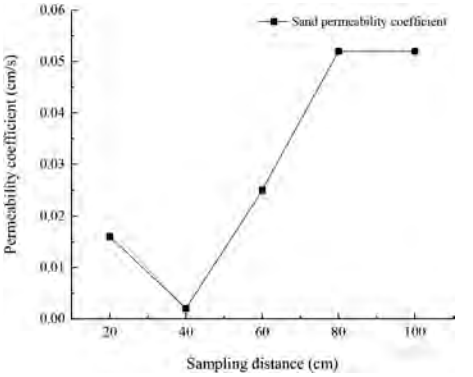

Figure 12. Permeability coefficient of sand.

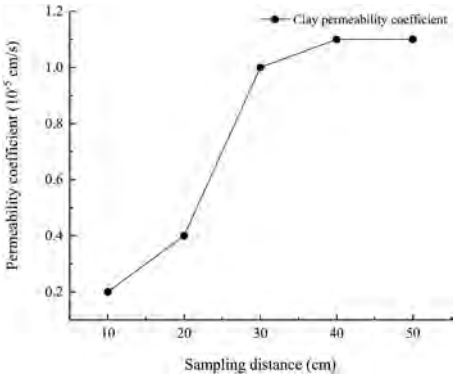

Figure 13. Permeability coefficient of clay.

2.3.4 *Permeability coefficient*

After waiting for the grout to solidify for 24 hours, the soil in the model cylinder was sampled in layers to determine the permeability coefficient of each layer. Figure 12 shows the permeability coefficient for each layer of sand. It can be found that the permeability coefficient of sand is large, at the level of 10^{-2} cm/s. Sand at 40 cm has the smallest permeability coefficient, 0.001 cm/s. The permeability coefficient of sand at 60 cm increases, which that at 80 cm and 100 cm remains constant. This is because the grout diffusion distance in sand is limited, and the generation of the filter mud leads to a decrease in permeability of the sand. Figure 13 shows the permeability coefficient in each layer clay. It can be found that the permeability coefficient of clay is small, at the level of 10^{-5} cm/s. The permeability coefficient of clay at 10 cm is the smallest, which is 0.2×10^{-5} cm/s. The permeability coefficient of clay began to increase after 10 cm and remained stable at 30 cm, with a stable value of 1.1×10^{-5} cm/s. It can also be inferred that the penetration diffusion, infiltration diffusion and screening diffusion of the grout will affect the permeability of the soil and reflect the diffusion mechanism of the grout in terms of the permeability coefficient.

3 PERMEATION DIFFUSION BASIC TYPES AND GROUTABILITY JUDGEMENT

3.1 *The basic types of penetration diffusion*

It is considered that the formation structure is a porous medium with internal pores, and the grout is a mixture of viscous solid particles and water. When penetration diffusion occurs, the solid particles in the grout fill the pores of the soil, but when the pore diameter of the soil is smaller than the solid particle size of the grout, the grout particles cannot enter the stratum, and only the free water and the very small particles in the grout can continue to enter. Therefore, the penetration diffusion is classified into screening (pressure filtration) diffusion, infiltration diffusion and penetration diffusion. The main classification is shown in Figure 14.

Figure 14. Main types of penetration diffusion.

The main controlling factor determining the type of permeation and diffusion is whether the grout particles enter the formation, which depends on the particle size of the grout particles and the pore diameter of the formation.

The specific explanation is as follows:

Grout particles do not diffuse: When the grout particle size exceeds 1/3 of the pore diameter of the formation, the grout particles cannot enter the formation, and only the free water in the grout can penetrate into the formation.

Grout particles diffuse: Based on whether the deposition of grout particles in the process of entering the soil affects the diffusion, it is divided into infiltration diffusion and penetration diffusion. When the grout particles can penetrate into the soil, the pore channels of the soil are gradually filled due to the adsorption and deposition of the grout particles, which hinders the further diffusion of the grout. An obvious filter cake or filter mud is formed at the interface between the grout and the soil. In the penetration diffusion, the pore diameter of the soil is much larger than the diameter of the grout particles. The grout particles can diffuse freely in the soil, and the adsorption and deposition of the grout particles have little effect on the diffusion distance.

3.2 *Groutability judgement*

In the process of grout penetration diffusion, groutability reflects the difficulty of grout particles to enter soil pores, and also determines the basic types of screening diffusion, infiltration diffusion and penetration diffusion. On the one hand, the injection depends on the characteristics of the porous media, and on the other hand, it depends on the properties of grout. The properties of porous media are dominated by its permeability and seepage structure, and the properties of grout are dominated by the gradation distribution and rheological properties of the grout particles. The determination of injectability in the domestic and foreign proposals is not uniform, according to literature investigation. The gradients of the strata and the pore conditions are mostly used to determine whether the grout particles can enter. Landry's theory is used as follows(Landry et al 2000):

$$k = 116(0.7 + 0.034t)(D_{10})^2 \quad (1)$$

$k > 1 \times 10^{-1}$ cm/s, cement grout can be injected into the formation; 1×10^{-1} cm/s $> k > 5 \times 10^{-3}$ cm/s, fine

cement particles can be injected into the formation; 5×10^{-3} cm/s > k > 1×10^{-4} cm/s, chemical grout can be used for grouting.

Combined with the determination of the permeability coefficient for sand and clay in Section 2.3.4, this is determined by Landry's theory of groutability. Since the permeability coefficient of sand is mostly 10^{-1} cm/s, cement grout and fine-grained cement grout can be used. The permeability coefficient of clay is about 10^{-5} cm/s, so cement grout and fine-grained cement grout cannot be injected into the soil. For the backfill grouting of clay shield tunnels, one of the main functions of backfill grouting is to fill the shield tail gap and stabilize the stratum and segment. The groutability of the grout cannot be used as a basis for judging the grouting effect. Therefore, it can be considered to inject chemical grout or find other grout with good filling properties to perform the backfill grouting of the shield tunnel.

4 CONCLUSIONS

In this paper, two typical soils, sand and clay, are chosen to study the diffusion mechanism of grouting grout behind shield tunnel segments. A visual grout diffusion model test device was used to monitor the grout diffusion distance, seepage pressure and soil pressure in real time. After 24 hours of grout solidification, samples were taken to determine the permeability coefficient of each layer of soil, and the groutability of grout in sand and clay was determined by combining the groutability theory. The main conclusions are as follows:

(1) The grout mainly undergoes penetration and infiltration diffusion modes in sand. In the initial grouting stage, the grout diffusion distance in the sand increases linearly. When the cement particles adsorb and plug the pores of the sand, the curve of the diffusion distance with time shows an inflection point, and the increase rate of the diffusion distance decreases. During the grouting process, the seepage pressure in the sand is larger, and the seepage pressure increases faster.

(2) The screening and splitting diffusion modes mainly occur in the clay. In the initial grouting stage, the seepage pressure and soil pressure in the clay fluctuate step by step. After excavating the layered soil, it is found that there are different extents of grout veins in the clay. With the increase of the height of the model tube, the thickness and width of the grout veins decrease.

(3) The permeability coefficient of sand and clay in the model tube was measured by stratified sampling. Combined with the theory of grout injectability, it is found that cement grout or fine-grained cement grout is suitable for backfill grouting in sand. The backfill grouting in clay stratum is suitable for chemical grout or grout with good filling property.

ACKNOWLEDGMENTS

This research work was supported by National Natural Science Foundation of China (NO. 51878060, 448 NO. 52108360), the Fundamental Research Funds for the Central Universities, CHD (NO. 449 300102213206). The financial support is highly appreciated.

REFERENCES

Shirlaw, J.N., Richards, D.P., Ramond, P., et al, 2004. Recent experience in automatic tail void grouting with soft ground tunnel boring machines. Proceedings of the ITA - AITES World Tunnel Congress. Singapore, pp. 22–27.

Oreste, P., Sebatiani, I.D., Spagnoli, G., et al, 2021. Analysis of the Behavior of the Two-Component Grout around a Tunnel Segmental Lining on the Basis of Experimental Results and Analytical Approaches. Transportation Geotechnics. 29, 100570.

Katebi, H., Rezaei, A., Hajialilue, B.M., et al, 2015. Assessment the influence of ground stratification, tunnel and surface buildings specifications on shield tunnel lining loads (by FEM). Tunnelling and Underground Space Technology. 49, 67–78.

Liang, Y., Zhang, J., Lai, Z., et al, 2020. Temporal and spatial distribution of the grout pressure and its effects on lining segments during synchronous grouting in shield tunnelling. European Journal of Environmental and Civil Engineering. 24(1), 79–96.

Li, M.D., Lin, L., Zhang, Z.D., et al, 2016. Review, outlook and application technology design on soil improvement by microbial induced calcium carbonate precipitation. China Civil Engineering Journal. 49, 80–87.

He, J., Chu, J., Liu, H.L., et al, 2016. Research advances in biogeotechnologies. Chinese Journal of Geotechnical Engineering. 38(4), 643–653.

Cai, D.G., Ye, F., Cao., K., et al, 2018. Test of Grout Diffusion of Shield Tunnel Backfill Grouting in Sandy Strata. China Journal of Highway and Transport. 31 (10), 274.

Chen, Z.H., Guo, N., 2019. New developments of mechanics and application for unsaturated soils and special soils. Rock and Soil Mechanics. 40(1), 23–32.

Sun, Y.L., Tang, L.S., Liu, J., 2020. Advances in research on microstructure and intergranular suction of unsaturated soils. Rock Soil Mechanics. 41, 1095–1122.

Lambe, T.W., 1958. The engineering behavior of compacted clay. Journal of Soil Mechanics and Foundations Division. 84(2), 1–35.

Lambe, T.W., 1958. The structure of compacted clays. Journal of Soil Mechanics and Foundations Division. 84(2), 1–34.

Seed, H.B., Chan, C.K., 1959. Structure and strength characteristics of compacted clays. Journal of Soil Mechanics and Foundations Division. 85(5), 87–128.

Levoueil, S., Vaughan, P.R., 1990. The general and congruent effects of structure in natural soil and weak rock. Geotechnique. 40(3), 467–488.

Weng, X., Kresse, O., Cohen, C.E., et al, 2011. Modeling of Hydraulic Fracture Network Propagation in a Naturally Fractured Formation. Spe Production & Operations. 26(4), 368–380.

Kim, J.S., Lee, I.M., Jang, J.H., et al, 2009. Groutability of cement-based grout with consideration of viscosity and filtration phenomenon. International Journal for Numerical and Analytical Methods in Geomechanics. 33(16), 1771–1797.

Akbulut, S., Saglamer, A., 2002. Estimating the groutability of granular soils: a new approach. Tunnelling and Underground Space Technology. 17(4), 371–380.

Ye, F., Liu, Y.P., Gou, C.F., et al, 2013. Capillary penetration diffusion model for backfill grouting of shield tunnel. Journal of Southwest Jiaotong University. 48(3), 428–434.

Ye, F., Chen, Z., Sun, C.H., et al, 2016. Penetration diffusion model for backfill grouting through segments of shield tunnel considering weight of grout. Chinese Journal of Geotechnical Engineering. 38(12), 2175–2183.

Ye, F., Wang, B., Han, X., et al, 2020. Review of shield tunnel backfill grouting tests and its diffusion mechanism. China Journal of Highway and Transport. 33(12), 92.

Ye, F., Xia T.H., Ying K.C., et al, 2022. Optimization method for backfill grouting of shield tunnel based on stratum suitability characteristics. Chinese Journal of Geotechnical Engineering. 44(12), 2225–2233.

Ying, K., Ye, F., Li, Y., et al, 2022. Backfill grouting diffusion law of shield tunnel considering porous media with nonuniform porosity. Tunnelling and Underground Space Technology. 127, 104607.

Landry, E., Lees, D., Naudts, A., 2000. New developments in rock and soil grouting: design and evaluation. Geotechnical News Magazine. 18(3), 38–48.

Tunnelling for a Better Life – Yan, Celestino, Thewes & Eberhardt (Eds)
© 2024 The Author(s), ISBN 978-1-032-80042-4
Open Access: www.taylorfrancis.com, CC BY-NC-ND 4.0 license

Influences of stress-dilatancy rule on the derivation of ground response curve for deep-buried tunnels

Jiguan Liang*
School of Aeronautics and Astronautics, Sun Yat-sen University, Shenzhen, China

Jianying Chen, Jianjun Ma & Hongwei Yang
School of Civil Engineering, Sun Yat-Sen University, (Southern Marine Science and Engineering Guangdong Laboratory (Zhuhai), Guangdong Key Laboratory of Oceanic Civil Engineering, Guangdong; Research Center for Underground Space Exploitation Technology, Zhuhai, China

Linchong Huang
School of Aeronautics and Astronautics, Sun Yat-sen University, Shenzhen, China
School of Civil Engineering, Sun Yat-Sen University, (Southern Marine Science and Engineering Guangdong Laboratory (Zhuhai), Guangdong Key Laboratory of Oceanic Civil Engineering, Guangdong; Research Center for Underground Space Exploitation Technology, Zhuhai, China

ABSTRACT: Ground response curves (GRCs) serve as an important intermediary during tunnelling, as it provides an effective way to evaluate the response of surrounding rock and installation of support structure. The choice of stress-dilatancy rule might cause different description on the behavior of surrounding rock and thus, have strong influence on the resulting GRCs. In order to find out such influences, GRCs based on different stress-dilatancies are calculated under the framework of cavity contraction solution, where the finite strain (Hencky strain) is also assumed. In this study, a bounding surface plasticity model is used as the elasto-plastic driver with a cohesion weakening Mohr-Coulomb bounding surface being introduced. In terms of the stress-dilatancy rule, the stress-dilatancy rule used in the Cam-clay model, Rowe's stress-dilatancy rule and a modified Rowe stress-dilatancy rule are introduced in this paper. Stress distributions and GRCs under different in-suit stresses are calculated by deriving semi-analytical solutions. The resulting stress distributions and GRC are validated by comparison with previous works in the literature. Moreover, GRCs under different in-suit pressures are also derived and investigated to fully evaluate influences of stress-dilatancy selection on GRCs. Results show that: The proposed solution in this paper captures the response of the surrounding rock of deep-buried tunnel reasonably. The GRC calculated in this paper is in good agreement with classical results in the literature and can be used in tunnelling. An inappropriate stress-dilatancy rule may provide inappropriate suggestions for support installation of deep-buried tunnels.

Keywords: Ground response curve, Stress-dilatancy, Bounding surface, Deep-buried tunnel

1 INTRODUCTION

Nowadays, with the rapid development of underground facility constructions and deep mining engineering, more and more deep-buried tunnels (Ou et al., 2021; Yang et al., 2023) are being constructed. The excavation, support and maintenance of deep-buried tunnels rely on the accurate investigation and evaluation on the response of surrounding the rock in depth. And the control of negative effects during tunnelling requires a reasonable description of the behavior of deep-buried rocks.

Cavity contraction solutions are widely used to investigate the repose of surrounding rock after excavation. In particular, solutions based on elasto-plastic models are used very frequently, such as solutions based on the GZZ model (Su et al., 2022), Mohr-Coulomb model (Mo et al., 2020; Pan & Brown, 1996; Vrakas & Anagnostou, 2014), CASM (Yu et al., 2019), Hoek-Brown model (Lee & Pietruszczak, 2008; Pan & Brown, 1996), etc. However, the results of these solutions are highly dependent on the definition of the elastic limit or yield surface (Dafalias, 1986). The bounding surface theory

*Corresponding author: liangjg5@mail2.sysu.edu.cn

DOI: 10.1201/9781003495505-102

calculates the plastic strain increment by exploiting the distance between the current bounding and loading surface (Huang et al., 2022; Kang et al., 2020; Masoumi et al., 2016), and there is no need to define the value of elastic limit. The application of bounding surface theory to the response analysis of deep-buried tunnel could avoid the negative effects of uncertainties of the value of elastic limit. However, the stress-dilatancy rule used in a bounding surface constitutive model has a strong influence on the deformation prediction of rocks under high stress ratios when stress level is low. It has been pointed out that the dilatant response of the surrounding rock affects the stress distribution and displacement of a tunnel (Pan & Brown, 1996). Thus, the choice of stress-dilatancy can affect the effectiveness of the resulting ground response curve (GRC), which is used to design the support structure (Yu et al., 2019). It is necessary to evaluate the influence of stress-dilatancy on the GRCs of deep-buried tunnels.

To this end, cavity contraction solution and GRCs are investigated in this paper. In section 2, a cohesion weakening bounding surface model is introduced to model the surrounding rock of deep-buried tunnels, and the resulting cavity contraction solution is derived to obtain the GRC. The proposed solution and resulting GRC are then validated in section 3. Finally, comparisons are conducted on GRCs obtained from different stress-dilatancy rules, and discussions focus on the influences of stress-dilatancy on GRCs for deep-buried tunnel.

2 METHODOLOGY

This section presents the cohesion weakening bounding surface model, stress-dilatancy rules being used, the derivation of controlling equations, and the boundary conditions.

2.1 *Bounding surface model and stress-dilatancy rules*

The bounding surface model and stress paths during cavity expansion and contraction are presented in Figure 1. The Mohr-Coulomb type bounding surface (Wood, 2003) is written as Equation (1). The movement of the bounding surface is attributed to the cohesion weakening mechanism, as written in Equation (2).

$$\bar{F} = \bar{q} - M(\theta)\bar{p} - M(\theta)\cdot\cot\phi\cdot c(\gamma^p) = 0 \qquad (1)$$

$$c(\gamma^p) = c_r + (c_i - c_r)\exp[-k(\gamma^p/\Upsilon)] \qquad (2)$$

Where, $\bar{p}$ and $\bar{q}$ are image stress on current bounding surface, $M(\theta)$ is the slope of the bounding surface considering the Lode angel, θ. ϕ is the frictional angle and γ^p is the accumulative plastic shear strain. c_i and c_r are the initial and final cohesion. k and Υ are model parameters that controlling the cohesion weakening.

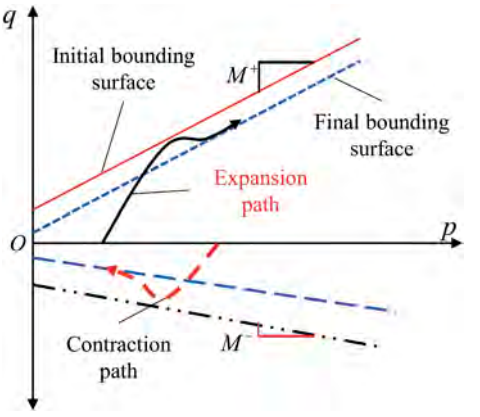

Figure 1. Cohesion weakening bounding surface and stress paths.

In this bounding surface model, a simple but effective mapping rule is introduced to link the image stress and current stress on loading surface (Huang et al., 2022; Kang et al., 2020; Masoumi et al., 2016). Besides, the total plastic modulus, h could be calculated by summarizing two components (Huang et al., 2022; Kang et al., 2020; Masoumi et al., 2016). One component h_b is derived by using consistency on Equation (1), while the other one h_f describes the distance between the current bounding and loading surface. By combining Hoek's law, the incremental elasto-plastic stress-strain matrix around a circular opening could be written as Equation (3),

$$\begin{Bmatrix} \delta\varepsilon_v \\ \delta\gamma \end{Bmatrix} = \begin{bmatrix} a_{11} & a_{12} \\ a_{21} & a_{22} \end{bmatrix} \begin{Bmatrix} \delta p \\ \delta q \end{Bmatrix} \qquad (3)$$

Where, $a_{11} = n_p m_p/h + 1/K$, $a_{12} = n_q m_p$, $a_{21} = n_p m_p$ and $a_{22} = n_q m_q/h + 1/2G$. $\delta\varepsilon_v$, $\delta\gamma$, δp and δq are total volumetric, deviatoric strain increment and increments of both mean and deviatoric stress. n_p and n_q are components of the unit normal vector of the bounding surface. $m_p = d/\sqrt{1+d^2}$ and $m_p = d/\sqrt{1+d^2}$ are components of the unit plastic flow vector, while is the stress-dilatancy $d = \delta\varepsilon_v^p/\delta\gamma^p$. K and G are both elastic bulk and shear modulus and could be calculated by using the Young's modulus and Poisson's ratio. Stress-dilatancy rules considered in this paper are listed in Table 1.

Table 1. Stress-dilatancy rules being considered.

Rowe	$d = \frac{9(M-\eta)}{9+3M-2M\eta}$
Cam-clay	$d = M - \eta$
Modified Rowe (MR)	$d = \frac{9(M(\gamma^p,\theta)-\eta)-B}{9+3M(\gamma^p,\theta)-2M(\gamma^p,\theta)\eta-B}$

Notes: $M(\gamma^p,\theta) = [1 + A\exp(-m\gamma^p)]M(\theta)$ and $B = \alpha\sigma_0/(\alpha+\beta\sigma_0)$ in Table 1. A, m, α and β are model parameters for the modified Rowe stress-dilatancy. σ_0 is the in-suit stress around the circular opening.

When considering the simplified cavity contraction problem (Yu et al., 2019; Mo et al., 2020) as in this paper, the definition of mean, deviatoric stress and the volumetric, deviatoric strain are listed in Equations (4)-(7),

$$p = (\sigma_r + \sigma_\theta)/2 \tag{4}$$

$$q = \sigma_\theta - \sigma_r \tag{5}$$

$$d\varepsilon_v = d\varepsilon_r + d\varepsilon_\theta \tag{6}$$

$$d\gamma = d\varepsilon_\theta - d\varepsilon_r \tag{7}$$

Where, σ_r, σ_θ, ε_r and ε_θ are radial hoop stress and strain components.

2.2 *Controlling equations*

As shown in Figure 2, distributions of both radial and hoop stress varying with the distance r around the circular opening could be written as follows (Yu et al., 2019; Mo et al., 2020),

$$\frac{rd\sigma_r}{dr} + \sigma_r - \sigma_\theta = 0 \tag{8}$$

By combing Equation (3) and Equations (4)-(8), the controlling equations of the mean, deviatoric stress and the volumetric strain around the circular tunnel could be derived as Equations (9)-(1), while an auxiliary variable $\xi = (r - r_0)/r$ being introduced along with Hencky strain ($\varepsilon_r = -\ln(dr/dr_0)$, $\varepsilon_\theta = -\ln(r/r_0)$, $\varepsilon_v = \ln(v/v_0)$) (Chen & Abousleiman, 2013; Yu et al., 2019; Mo et al., 2020).

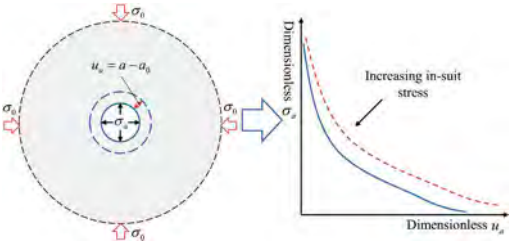

Figure 2. A contracting cavity and its GRCs.

$$\frac{Dq}{D\xi} = \frac{-1}{\left[\frac{(a_{22}+a_{12})}{(a_{21}+a_{11})} + 0.5\right]} \left[\frac{q}{1-\xi-\frac{e^{\varepsilon_v}}{1-\xi}} + \frac{2}{(1-\xi)(a_{21}+a_{11})}\right] \tag{9}$$

$$\frac{Dp}{D\xi} = -\frac{(a_{22}+a_{12})}{(a_{21}+a_{11})}\frac{Dq}{D\xi} - \frac{2}{(1-\xi)(a_{21}+a_{11})} \tag{10}$$

$$\frac{D\varepsilon_v}{D\xi} = -\left[a_{21}\frac{Dp}{D\xi} + a_{22}\frac{Dq}{D\xi} + \frac{2}{1-\xi}\right] \tag{11}$$

By solving Equations (9)–(11) using the Runge-Kutta method, we could also calculate the current position of any rock medium around the tunnel by introducing Equation (11) and integrating as follow,

$$\frac{r}{a} = \int_{\xi(a)}^{\xi} \frac{d\xi}{1-\xi-\frac{e^{\varepsilon_v}}{1-\xi}} \tag{12}$$

2.3 *Boundary conditions and the derivation of GRCs*

The boundary conditions being introduced in this paper are listed in Table 2. To solve Equations (9)–(11), integration is conducted from the far filed to the cavity wall. When support pressure under various combinations of in-suit stress and cavity wall deformation is derived by solving Equations (9)–(11), we could obtain a ground response curve under certain in-suit stress by plotting the radial stress on the cavity wall against the cavity wall deformation, as shown in Figure 2. When all in-suit stresses of our interest are considered, GRCs under various in-suit stresses could be derived and used to design supporting structure of a deep-buried tunnel.

Table 2. Boundary conditions.

Far field	$p_0 = \sigma_0$ $q_0 = 0$ $\varepsilon_{v0} = 0$ $\xi_0 = 1 - r_{\infty 0}/r_\infty$
Cavity wall	$\xi(a) = 1 - a_0/a$

3 VALIDATIONS

In this section, the stress distributions calculated by using the proposed solution in section 2 are validated by comparing with other solutions in the literature. In addition, the ground response curve derived by using the proposed solution is also validated in this section.

3.1 *Validation on stress distributions*

Stress distributions around a circular opening is calculated by using the solution being proposed in section 2, with the modified Rowe stress-dilatancy rule being

used. The resulting distributions of both radial and hoop stress component are presented in Figure 3, which are compared with analytical results provided by Park & Kim (2006) and Lee & Pietruszczak (2008).

Model parameters are the same as in Lee & Pietruszczak (2008) with σ_0=3.0MPa, E=10.0GPa, μ=0.20, ϕ=30°, c_i=0.5MPa and c_r=0.3MPa. As shown in Figure 3, stress components derived in this paper near the tunnel wall ($r/a \leq 2.4$) is the same as those provided by both Park & Kim (2006) and Lee & Pietruszczak (2008). Moreover, the trend of the distribution of both radial and hoop stress are the same for result in this study and provided by Lee & Pietruszczak (2008), while the slight difference on values of stress components and the position of maximum hoop stress might be due to the definition of elastic limit in Lee & Pietruszczak (2008). Moreover, the resulting cavity wall deformation of the proposed solution is a/a_0=0.995, which is very similar to results of a/a_0 =0.998~0.992 in Park & Kim (2006) and Lee & Pietruszczak (2008). In this word, the solution proposed in this paper have the capability to capture the response of rocks around the tunnel reasonably.

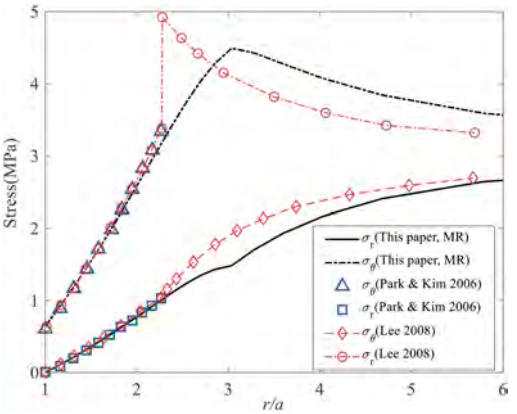

Figure 3. Stress distribution under 3.0MPa in-suit stress.

3.2 *Validation on GRC*

In this section, a GRC obtained by using the proposed solution in this paper under the modified Rowe stress-dilatancy rule is validated through comparing with results provided by Alonso et al. (2003) and Lee & Pietruszczak (2008), as shown in Figure 4. Model parameters are σ_0=20.0MPa, E=10.0GPa, μ=0.25, ϕ=30°, c_i=1.0MPa and c_r =0.8MPa. It is clear in Figure 4 that the GRC derived by this paper shows reasonable agreement with other results. Differences between the proposed solution and other results on medium range support pressures might be attributed to the used of the modified Rowe stress-dilatancy rule (i.e. MR in Figure 4), which could predict higher volumetric deformation under high mean stress level comparing with other stress-dilatancy rules.

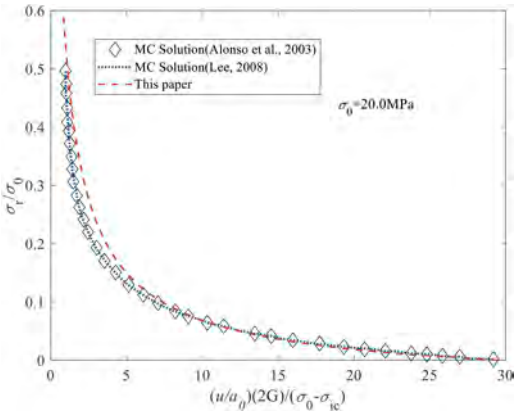

Figure 4. Comparisons between GRCs derived by different solutions.

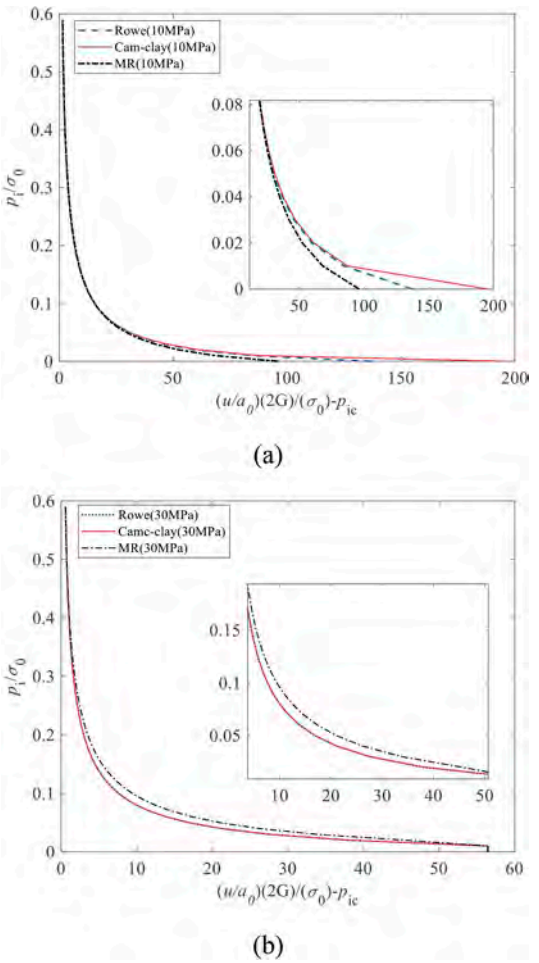

Figure 5. Resulting GRCs under the in-suit stress of (a) 10MPa and (b) 30MPa.

4 COMPARISONS ON GRCS

In this section, GRCs under the in-suit stress of both 10MPa and 30MPa are derived by using same parameters in section 3.1, with all stress-dilatancy rules in Table 1 used. These 2 selective in-suit stresses model the buried depths of approximately 400m and 1200m (Vrakas & Anagnostou, 2014), respectively. The resulting GRCs are shown in Figure 5.

As shown in Figure 5, when the buried depth is shallow with lower in-suit stress, ground response curves calculated by those stress-dilatancy rules are divergent on lower support stresses and convergent on medium to high stresses. MR provide the smallest deformation prediction under low support pressure. This might be caused by the swift convergence of the MR as the plastic strain is large under 10MPa in-suit stress and small support stresses. When the in-suit stress is higher, MR will predict larger deformation under the middle range of support stress, while the deformation predicted by Rowe and Cam-clay stress-dilatancy rule are smaller, since the d value of those 2 rules are only constrained by stress ratio and becomes smaller under large mean stress level. In addition, the deformation of the tunnel wall becomes convergent as support stress increasing. Since the deformation of the tunnel being restricted under high support stresses. As the choice of stress-dilatancy rule determines the deformation of rocks under certain mean stress level, an inappropriate stress-dilatancy rule might result in an inappropriate choice of support structure installation.

5 CONCLUSIONS

In this paper, a cohesion weakening bounding surface model coupled with 3 stress-dilatancy rules is used in the cavity contraction solution, to investigate influence of choices of stress-dilatancy rule on GRCs for deep-buried tunnels. The solution derived in this paper is validated thorough comparing with existing classical solutions on stress distribution around tunnel and GRC of a tunnel. Then GRCs obtained by three stress-dilatancy rules under 10MPa and 30MPa in-suit stress are compared. The proposed solution in this paper shows good agreement with results in the literature, no matter for the stress-strain distributions or the resulting GRC. Since the deformation of rocks under medium and high mean stress level is sensitive to the choice of stress-dilatancy, using an inappropriate stress-dilatancy rule may provide inappropriate suggestions on support installation of deep-buried tunnels.

ACKNOWLEDGMENTS

Financial support from Foundation Research Project of China (Grant: JCKY2020110C096), National Natural Science Foundation of China (No. 51978677, 52278422), and the Shenzhen Science and Technology Project for Sustainable Development (Grant: KCXFZ202002011008532, KCXFZ20201221173207020) are gratefully acknowledged.

REFERENCES

Alonso, E., Alejano, L. R., Varas, F., et al, 2003. Ground response curves for rock masses exhibiting strain-softening behaviour. International Journal for Numerical and Analytical Methods in Geomechanics. 27(13), 1153–1185.

Chen, S. L., Abousleiman, Y. N., 2017. Wellbore stability analysis using strain hardening and/or softening plasticity models [J]. International Journal of Rock Mechanics and Mining Sciences. 93, 260–268.

Dafalias, Y. F., 1986. Bounding surface plasticity. I: Mathematical foundation and hypoplasticity. Journal of engineering mechanics. 112(9), 966–987.

Huang, L., Liang, J., Ma, J., et al, 2022. A dynamic bounding surface plasticity damage model for rocks subjected to high strain rates and confinements. International Journal of Impact Engineering. 168, 104306.

Kang, X., Liao, H., Leng, X., 2020. An enhanced bounding surface plasticity model for soft rock subjected to drained and undrained condition. Computers and Geotechnics. 127, 103742.

Park, K. H., Kim, Y. J., 2006. Analytical solution for a circular opening in an elastic–brittle–plastic rock. International Journal of Rock Mechanics and Mining Sciences. 43(4), 616–622.

Lee, Y. K., Pietruszczak S., 2008. A new numerical procedure for elasto-plastic analysis of a circular opening excavated in a strain-softening rock mass. Tunnelling and Underground Space Technology. 2008, 23(5), 588–599.

Masoumi, H., Douglas, K. J., Russell, A. R., 2016. A bounding surface plasticity model for intact rock exhibiting size-dependent behaviour. Rock Mechanics and Rock Engineering. 49, 47–62.

Mo, P. Q., Fang, Y., Yu, H. S., 2020. Benchmark solutions of large-strain cavity contraction for deep tunnel convergence in geomaterials. Journal of Rock Mechanics and Geotechnical Engineering. 12(3), 596–607.

Ou, G. Z., Jiao, Y. Y., Zhang, G. H., et al, 2021. Collapse risk assessment of deep-buried tunnel during construction and its application. Tunnelling and Underground Space Technology. 115, 104019.

Pan, X. D., Brown, E. T., 1996. Influence of axial stress and dilatancy on rock tunnel stability. Journal of Geotechnical Engineering. 122(2), 139–146.

Su, C., Cai, W., Zhu, H., 2022. Elastoplastic semi-analytical investigation on a deep circular tunnel incorporating generalized Zhang–Zhu rock mass strength. Computers and Geotechnics. 150, 104926.

Vrakas, A., Anagnostou, G., 2014. A finite strain closed-form solution for the elastoplastic ground response curve in tunnelling. International Journal for Numerical and Analytical Methods in Geomechanics. 38, 1131–1148.

Wood, D. M., 1990. Soil behaviour and critical state soil mechanics. Cambridge university press.

Yang, J., Fan, P., Wang, M., et al, 2023. Experimental study on the irreversible displacement evolution and energy dissipation characteristics of disturbance instability of regular joints. Deep Underground Science and Engineering. 2(1), 20–36.

Yu, H. S., Zhuang, P. Z., Mo, P. Q., 2019. A unified critical state model for geomaterials with an application to tunnelling. Journal of Rock Mechanics and Geotechnical Engineering. 11(3), 464–480.

Tunnelling for a Better Life – Yan, Celestino, Thewes & Eberhardt (Eds)
© 2024 The Author(s), ISBN 978-1-032-80042-4
Open Access: www.taylorfrancis.com, CC BY-NC-ND 4.0 license

The use of jet grouting technology: An overview of the different applications in tunnelling

Pietro Lunardi
Lunardi Geoengineering, Milan, Italy

Giuseppe Lunardi, Giovanna Cassani*, Martino Gatti, Luca Bellardo & Carla L. Zenti
Rocksoil S.p.A., Milan, Italy

ABSTRACT: "Jet-grouting" is a jet injection technology that has widely been used in geotechnical works since the 1970s. Nowadays, it is one of the most popular ground improvement techniques due to its applicability in almost all soil types. Its peculiarity is to change drastically ground characteristics, thanks to the effect of very high-speed jets, able to break up the soil and to mix it with cementitious slurry, improving soil's mechanical parameters and reducing its permeability. In the paper, a general overview of the technology will be given, together with the design criteria for the particular tunnelling applications.

Keywords: jet grouting, vertical, sub-horizontal, portal, excavation face

1 INTRODUCTION

Nowadays, jet-grouting technology is one of the most popular ground improvement techniques due to its applicability in almost all soil types. Its peculiarity is to change drastically ground characteristics, thanks to the effect of very high-speed jets, able to break up the soil and to mix it with cementitious slurry, improving soil's mechanical parameters and reducing its permeability. Several techniques and construction processes can be used for jet-grouting execution, depending on the types of fluid injections and on working parameters.

Jet-grouting has a fundamental role in the progress that has been achieved over the last thirty years in tunnel construction (Lunardi, 1986). Jet-grouting treatments can be executed by surface, where space is available and overburden is limited, or directly at the tunnel face. Horizontal jet-grouting made possible to overcome all the difficulties connected with excavation in cohesionless soils. Sub horizontal jet-grouting is used to create a series of columns of improved ground, side by side ahead of the face around the profile of the extrados of the tunnel to be excavated. Jet-grouting technology is also applied for the construction of tunnel portals in cohesionless or slightly cohesive soils too. Tunnelling can be performed with a very low overburden, by jet-grouting shell, arch shaped, thus minimizing the risk of slope instability and providing outstanding results from an environmental and landscape point of view.

*Corresponding author: giovanna.cassani@rocksoil.com

DOI: 10.1201/9781003495505-103

2 JET-GROUTING

The technology involves the injection of a high-speed fluid (water jet or grout jet) through small-diameter nozzles into the subsoil to erode the surrounding soil, while the nozzles are rotated and lifted towards the ground surface at a constant speed. The eroded soil is simultaneously mixed with the injected grout to form the admixture, and a soil-cement column with a quasi-cylindrical shape would be formed after some days of solidification. It is possible to reach columns with diameters ranging between 500 mm and up to 2,500–3,000 mm, owing to the adopted systems, the working parameters and the soil types. Grout pressure, rate of ascent, angular speed, and number and diameters of nozzles are the main parameters to be controlled to obtain the improved soil of the desired shape and size. Soil investigation and field tests must be carefully planned for each application.

2.1 *Classification*

Based on the different methods of fluid injection, jet-grouting technology can be conventionally classified into three basic types of systems (Figure 1):

a) single-fluid system (only grout);
b) double-fluid system (grout and air);
c) triple-fluid system (water, grout and air).

The "single-fluid" system utilizes grout as the cutting jet to achieve cementation of the eroded soil. In the most common case of drilling without casing, a self-drilling monitor will be used, by rotation or roto-percussion system, with the drilling rod equipped both with injection nozzle and with cutting tool. In the "double-fluid" system, a compressed air shroud is introduced around the grout jet to enhance the cutting distance of the grout jet; the construction process is the same of the single-fluid system, adding an additional nozzle for the air. In the "triple-fluid" system, water is used for the cutting jet together with a compressed air shroud, and grout is injected separately through a lower nozzle at a much smaller pressure to mix with the eroded soil. The adoption of a lower viscosity fluid such as water (in comparison with that of grout) allows the cutting distance to be further enhanced, especially in cohesive soils. The three methods are represented in Figure 1 (Cassani et al., 2022).

2.2 *Parameters*

The key jet-grouting operational parameters governing the jetting performance are as follows:

- Characteristics of jetting fluid, i.e. water-cement ratio of grout (W/C).
- Pressure (MPa) and flow rate of jetting fluid (Q = m^3/h).
- Jetting time, which is a function of the traverse velocity of nozzle, and hence the withdrawal rate (m/min) and rotation speed (rpm).
- Characteristics of nozzle: nozzle diameter (mm), number of nozzles (N) and nozzle shape.

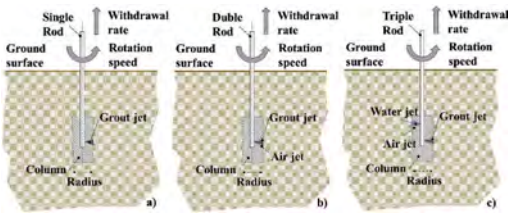

Figure 1. Jet-grouting systems: (a) single fluid; (b) double fluid; (c) triple fluid.

The injection pressure is controlled by pressure gauges; the jet energy and consequently the radius of action mainly depend on pressure. The upper pressure limit is essentially determined by the capacity of the pump used. The number and diameters of nozzles determine the injection capacity: the volume of grout injected into the ground per unit of time and, consequently, the rate of treatment. High flow rates require high power pumps to maintain high pressure. Larger nozzle diameters make more efficient use of the power employed, while large number of nozzles, with the same rates, decreases performance, due to a greater loss of head, so it is preferable to limit the number of nozzles. The water-cement ratio of the grout is the most important parameter regarding the mechanical properties of the treated soil and the initial behaviour of the soil-grout mixture; a low water-cement ratio is extremely important where there is groundwater flow, as this could wash away the cement shortly after injection. The injection time depends on the withdrawal rate and the angular velocity of the drill rod; it is controlled by a timer placed on the drill rig (normally, 1 m every 2–6 minutes and 10–20 rpm). Raising is usually performed in 4–5 cm steps, thus allowing the jet to act on the surrounding ground, for set time intervals. The diameter and the mechanical properties of the ground treated, as well as the time required for treatment, are strongly affected by the withdrawal rate. Table 1 shows the range of jet-grouting parameters commonly adopted for the three conventional jet-grouting systems (Lunardi, 1997a). Typical withdrawal rates, expressed in cm/min, and rotation speed, in rpm, are reported in the table. It is possible to link the flow rate of jetting fluid (Q), the volume (V) and the speed of treatment (v), with the formula V = Q/v; the flow rate Q depends on jetting area, i.e. the number and diameters of nozzles, and on the jet speed, in turn related to the injection pressure (P). Thus, the knowledge of these working parameters allows to evaluate a global design parameter: the "linear specific energy", by the

Table 1. Ranges of jet grouting parameters for conventional jet grouting systems.

Parameters	Single fluid system	Double fluid system	Triple fluid system
Water pressure (MPa)	-	-	30~40
Flow rate of water (L/min)	-	-	80~200
Number of nozzle (n°)	-	-	1.5~3.0
Nozzle diameter (mm)	-	-	1~2
Air pressure (MPa)	-	0.7~1.5	0.7~1.5
Flow rate of air (m^3/min)	-	8~30	4~15
Grout pressure, (MPa)	40~70	30~70	7~10
Flow rate of grout (L/min)	100~300	100~600	120~200
Grout density [g/cm^3]	1.25~1.6	1.25~1.8	1.5~2.0
Number of nozzle (n°)	1~6	1~2	1~3
Nozzle diameter (mm)	1.0~4	2~7	5~10
Withdrawal rate (cm/min)	15~100	10~30	6~15
Rotation speed (rpm)	7~20	2~20	7~15
Specific Energy (MJ/m)	10-20	40-80	120-200

formula E = P Q/v, expressed in MJ/m of linear jet-grouting, or the "volume specific energy", by the formula E = P·Q/(v·V), expressed in MJ/m^3 (according to Tornaghi, 1993). Using these correlations, it is possible to dispose of a rational approach to compare several combinations of working parameters and find the best technical and economical solutions for each application.

2.3 *Context*

From the experiences acquired in several geotechnical works, we can state shot jet-grouting can be successfully performed in any type of soil (Figure 2.a), independently of grain size and permeability, with the exception of very hard cohesive soils whose strength cannot be overcome by the jet (such as stiff silts and clays, with undrained cohesion greater than 0.2–0.5 MPa). This technology has the advantage of being able to treat "stratified soils" too (alternating sands, silts, clays, etc.), providing almost uniform levels of cementation and waterproofing. In fine-grained soils, the outer surface of the columns obtained is normally well defined and fairly regular; in coarse-grained and heterogeneous grounds, this surface is irregular and there is the systematic appearance of "root effect", i.e. grouting through "claquage" outside the radius of action of the jet. The occurrence of still groundwater does not in any way compromise the results of the treatment. When seepage occurs, special precautions, such as the addition of accelerators to the grout, give good results even at the groundwater speed of the order of 0.1 cm/s. The compressive shear strength of jet-grouted soil generally increases from clays to gravels (see Figure 3). Maximum strengths of about 20–30 MPa could be reached in sands and gravels, while in fine-grained peaty soils, it is hard to attain values ten times lower.

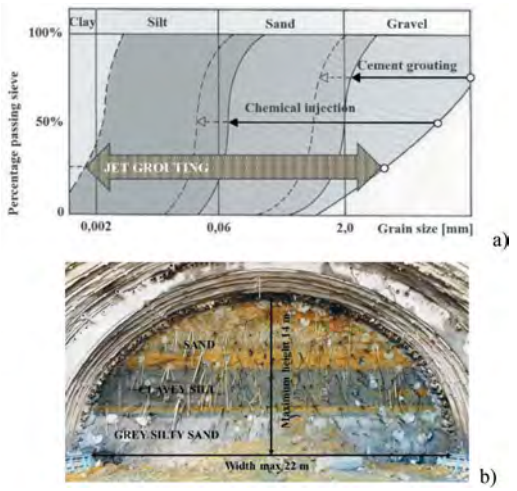

Figure 2. a) Jet-grouting applicability; b) Cassia Tunnel - External track: total length 232 m.

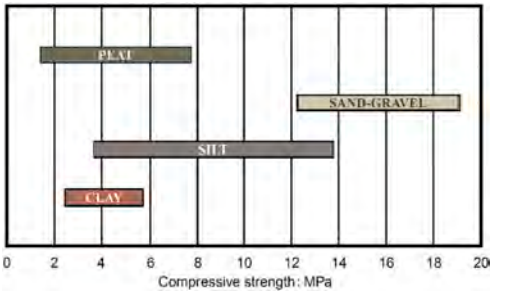

Figure 3. Compressive strength of jet-grouted soils.

2.4 *Design approach and technical specifications*

The design of ground improvement using jet-grouting must involve these main following stages:

a) defining soil investigations and preliminary field tests;
b) choice of grout type and operating parameters,
c) deciding the pattern, shape and size of the grouted volumes,
d) identification of the most appropriate numerical model to study the stress-strain distribution in the soil treated
e) choice of the monitoring and controlling systems.

The most critical aspect is the ones related to the pattern and dimensions of jet-grouting treatments. It is essential to understand that ground volumes treated by jet-grouting are cemented ground and not real structures; there phase to define thickness and required strength, it is necessary to predict the stresses acting on treatments. The treated ground can take compression and shear, and consequently, the application of other types of stresses, i.e. tension, should be avoided. In this case, the insertion of bars and steel sections into improved ground can be achieved, especially for retaining structures, usually before setting takes place, by gravity or using high-frequency vibrators or re-drilling. It must be remembered that the existence of more rigid volumes in the ground may possibly be used to produce a system channelling stresses along a desired direction and these stresses should be carefully considered in dimensioning. The analysis of such problems implies generally the use of the finite element method, since the types of problems connected with jet-grouted ground are clearly non-linear. In addition to this, it is often necessary to analyse structures whose shape changes over time due to excavation or construction operations. This requires starting with the analysis of the natural untreated conditions and passing through an appropriate sequence of stages realistically approximating the actual development of the work. Once the geometry of the treatment is defined and the required strength is fixed, it is necessary to study

the correct pattern, considering the column diameters easily achieved in the geotechnical context of intervention and an appropriate overlapping to ensure the continuity of treatment. The working parameters will be set, based on database experiences in similar contexts or according to the specific energy approach discussed in Section 2.2, and they will be confirmed or fine-tuned by a field test. Designer must define in detail, in addition to the executive technical specifications, the prescribed requirements in terms of diameter, strength and permeability of the soil treated, to be checked by tests.

3 TUNNELLING APPLICATION

The authors when designing a tunnel always apply ADECO-RS approach (Analysis of the controlled deformations in rocks and soils) which is related to one only parameter common to all the excavations, that is the tenso-deformative

behaviour of the system "front of the excavation advancement core" and to the introduction of the concept of preconfinament of the cave and of the "conservative systems" (Figure 4).

Particularly, design has been articulated in:

- An investigation phase, during which the designer, has carried out the categorization of the soil crossed by the tunnel in terms of geotechnical parameters. This step is essential to complete the analysis of the existing natural balance, and to correctly work in the following design phase;
- A diagnosis phase, during which have been prepared theoretical forecasts regarding the deformative answers of the soil to the excavation action. The soil behaviour can be intended in terms of genesis, localization, evolution and entity of the probable reaction which, without intervention of soil improvement, would commence at the excavation face and, as a consequence, in the soil ring at the cavity. From the combined analysis of the deformation behaviour of the system excavation front advancement core and of the cavity, one can infer which will be he homogeneous deformative behaviour in the domain of the three fundamental categories of behaviour (category A: stable front, category B: front stable in short terms, category C: unstable front);
- A phase of therapy, during which, following the predictions made in phase of diagnosis, the designer selects the type of action to be exerted (pre-containment or simple containment) and the necessary interventions, among the three behaviour categories (A, B and C) in order to obtain the complete stabilization of the tunnel, and he perfections the choice in terms of systems, cadence and phases of excavation. Then, he defines the composition of the longitudinal standard sections and the cross sections dimensions, assessing their efficacy by using computation tools.

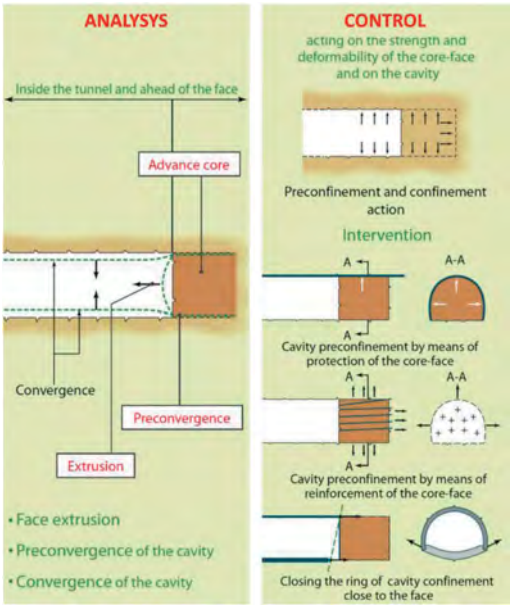

Figure 4. ADECO-RS approach.

3.1 *Portals*

The construction of tunnel portals often involves solving problems that are closely connected with the morphology of the slope to be entered, with the existence of nearby constructions, with the geometry of the structures to be constructed and the type of material involved.

The preparation of a portal site and of the wall to be excavated, very frequently requires substantial cuttings which are of no particular concern when working in rock, but are very problematic when working in soft soils, especially if they are loose. If the decompression caused by excavation in ground with little cohesion is not adequately confined, there is a risk that it will easily and rapidly propagate into the medium with serious effects for the whole

slope. The only way the entrance to the portal of a tunnel can be excavated without decompressing the ground is clearly by creating a structure to confine (or better preconfine) the ground in advance ahead of the future excavation which is capable of conserving the existing natural equilibrium.

The systems available for achieving this goal were to place the following structures at the entrance of the bored tunnel:

- large diameter pile walls, anchored if necessary;
- "Berlin" or soldier pile walls;
- Reinforced Concrete diaphragm walls.

The construction of large diameter piles on slopes tending towards instability is, however, often difficult, if not impossible, because, it is often the case that the morphology of the slopes does not allow the use of the heavy operating machinery required. On the other hand

the lability of Berlin type structures themselves, which rely to a large extent on anchors which reach into stable zones of the ground for their effectiveness, mean that these systems are not always sufficiently reliable. Not even r.c. diaphragm walls are sufficient for the most delicate situations: earth removal and the introduction of water have the effect of reducing the shear strength of the ground with consequences for which there is no remedy in some situations.

These problems were then made worse because the lack of adequate techniques to improve the ground in advance and of suitable operating systems, required bored tunnels to be driven with overburdens measurable in terms of tunnel radii. This required huge portions of the ground to be removed with the risk of triggering ground decompression that is very difficult to confine (Figure 5).

Figure 5. a) very deep cut is made into the slope for a tunnel portal in semi-cohesive soils using conventional systems (anchored Berlin wall; overburden: twice the diameter of the tunnel); b) The same portal as the one above, after it had collapsed because of the decompression induced in the slope.

The availability of a jet-grouting systems for improving ground, introduced in Italy around thirty years ago, allowed to invent and experiment an innovative solution to create preconfinement structures in loose or poorly cohesive soils with properties that would overcome the problems that have been described. The idea consists of creating a confinement shell, before excavation for the portal commences, consisting of rows of columns of ground improved by means of jet-grouting, which geometrically enfold the section of artificial tunnel (see Figure 6). The magnitude and distribution of the treatment are decided on the basis of each specific operating and geotechnical context. A top beam in r.c. joins the tops of the columns to help make it a single rigid structure. Once the earth has been removed for the entrance to the portal, the work is completed with:

- a layer of shotcrete sprayed on the whole surface of the exposed wall;
- drainage pipes placed sub-horizontally through the improved ground to prevent the formation of heads of water behind it.

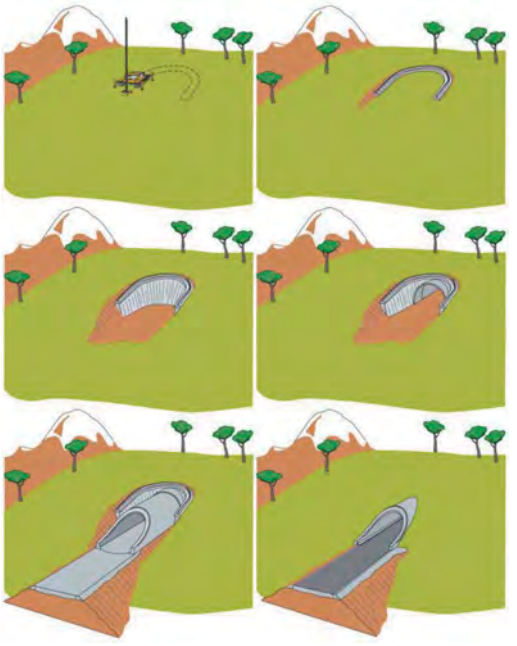

Figure 6. Tunnel portals with shell of improved ground by means of vertical jet-grouting (Lunardi, 2008).

The structure thus built functions by means of the sub-horizontal arches and is subject mainly to compressive and shear stress. The creation of shells of this type is strictly dependent on the subsequent tunnel being driven using horizontal jet-grouting methods. Thanks to the characteristics of this ground preconfinement technology, which requires only minimum overburdens, bored tunnels can be driven with extremely low cover, with many important advantages, including the way it fits unobtrusively into the environment.

3.2 *Sub horizontal jet-grouting columns*

The use of sub-horizontal jet-grouting column inside a tunnel could be performed mainly by two way: around the cavity or at the face and together also (see Figure 7).

Truncated cone 'umbrellas' realized by sub-horizontal columns of jet-grouting as a conservative protective intervention. It creates ahead of the face around the cavity a protective shell. It channels stresses around the outside of the face performing, as the term says, a protective action which conserves the natural strength and deformation characteristics of the ground.

Sub-horizontal jet-grouting is used to create a series of columns of improved ground, side by side ahead of the face around the profile of the extrados of the tunnel to be excavated. An arch of improved ground with considerable strength is created to provide protection to the ground inside the advance core along the longitudinal direction, lightening the load on it and giving it stability; this arch produces cavity confinemnt action occurring along the transverse direction, sufficient to prevent the ground around it from decompressing and consequent deformation from occurring. It therefore allows subsequent tunnelling operations to proceed under the protection of an arch effect already operational and therefore in complete safety.

Reinforcement of the core-face by means of sub-horizontal jet grouting column is a conservative reinforcement intervention. It acts directly on the consistency of the advance core, improving its natural strength and deformation characteristics by means of the reinforcement techniques.

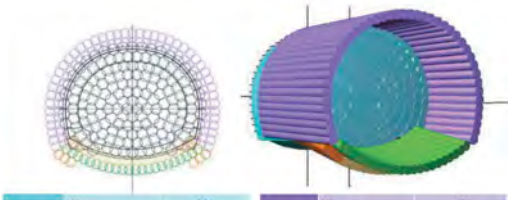

FACE			
	N°	161	
	Diameter [mm]	1350	1400
	$L_{PER.}$ [m]	11,33	
	L_{GROUT} [m]	2,5	0,5
	$V_{THEORETICAL}$ [m]	575,84	123,86
	V_{TOTAL} [m]	699,70	
	$L_{PER.\ TOTAL}$ [m]	1824,13	

CROWN		
	N°	43
	Diameter [mm]	1100
	$L_{PER.}$ [m]	19,33
	L_{GROUT} [m]	16,33
	$V_{THEORETICAL}$ [m]	535,36
	V_{TOTAL} [m]	666,98
	$L_{PER.\ TOTAL}$ [m]	831,19

INVERT 1		
	N°	22
	Diameter [mm]	1100
	$L_{PER.}$ [m]	20,00
	L_{GROUT} [m]	10,50
	$V_{THEORETICAL}$ [m]	219,42
	V_{TOTAL} [m]	219,42
	$L_{PER.\ TOTAL}$ [m]	440

INVERT 2			
	N°	17	6
	Diameter [mm]	1100	1100
	$L_{PER.}$ [m]	15,83	17,83
	L_{GROUT} [m]	8,50	10,50
	$V_{THEORETICAL}$ [m]	137,25	59,84
	V_{TOTAL} [m]	197,09	
	$L_{PER.\ TOTAL}$ [m]	269,11	106,98

Figure 7. Sub-Horizontal jet grouting: intervention map, assessment though 3D analysis and parameters.

4 CASE HISTORY

The solutions described in section 3 have been developed by Prof. Lunardi and his teams more than 30 years ago and from that time applied in a lot of cases. In this section the authors just mention the tunnelling applications of sub-vertical and sub-horizontal jet-grouting columns and they will give more details about one face reinforcement application more recently designed.

The first time that sub-vertical jet-grouting to pre-confine excavation was experimented in 1980 at Sesto San Giovanni (Milan), in an area destined to contain a ventilation chamber 9.80 m deep on a section of the Milan metro line 1 under construction. The first application for the construction of tunnel portals occurred five years later for the T1 portal on the Pontebba side of the S. Leopoldo tunnel on the Pontebba-Tarvisio. railway line. This application was suddenly followed by several application (Lunardi, 2008):

- S. Elia Tunnel (Messina-Palermo motorway): portal on the Messina side under construction, 1986 (Figure 8a).
- Pianoro Tunnel (new high speed/capacity railway line between Bologna and Florence), 1996.
- Gran Sasso Tunnel, Assergi side Portal, xxxx.
- Tunnel No. 2 (Sibari-Cosenza railway line): the use of jet-grouting technology enables tunnel portals to be built in difficult grounds with full respect for natural equilibriums and for the landscape, 1992 (Figure 8b).

Figure 8. Examples of portal of tunnels by jet-grouting shells. (a) S.Elia Tunnel, Messina-Palermo Motorway and (b) Tunnel N2, Sibari-Cosenza Railway Line (Lunardi, 2008).

Horizontal jet-grouting made possible to overcome all the difficulties connected with excavation in cohesionless soils. In this case also a statics design that is congruent with the features of the treated ground was fundamental, namely, a design in which the material is mainly subjected to compressive and shear stresses.

This is the famous 'umbrella' treatment which, by penetrating beyond the face of a tunnel, develops arching in the ground ahead of the excavation. The first application of this technique, which was developed in 1983, was during the construction of the 'Campiolo' tunnel, along the Udine Tarvisio railway line (Figure 9).

The first case was followed by several application:

- Underpass of the Campinas railway yard in Brazil (1987)
- Milan-Chiasso railway line, Monte Olimpino 2 tunnel, (1984)
- The Rome Greater Ring Road: Appia Antica Underpass (Lunardi 2000a), Cassia and Trionfale Tunnels
- Firenzuola tunnel, high speed/high capacity railway line Bologna-Florence (Lunardi, 2000b)
- Road underpass of the Ravone Railway Yard (Bologna, Lunardi & Cassani, 2001)

Figure 9. Campiolo Tunnel, Udine-Tarvisio railway line (Lunardi, 2008).

The most recent and challenging application is the one of the Isarco River Underpass. The southernmost construction lot of the Brenner Base Tunnel is the construction lot know as Isarco River Underpass. This lot links the Brenner Base Tunnel with the existing Brenner line and the railway station in Fortezza. The work has been completed in 2023.Since in this section the tunnel tubes are just a few meters below the surface, a portion of the activities pertaining to this construction lot has been carried out building artificial tunnels. Furthermore, as loose fluvioglacial materials and the groundwater layer crossed, it has been necessary to adopt specific ground consolidation procedures including ground freezing and the so-called jet grouting.

The Isarco River Underpass passes through the alluvial deposit of the valley bottom and through the dejection conoids of the tributary rivers. These loose deposits, heterogeneous both in composition and in granulometry, consist of gravels and rounded sand, with frequent boulders and thick layers of sandy silt. The flanks of the valley are covered by coarse particle size material, composed by slope debris, alluvial sediments and weather material. Figure 10. Shows the geological profile and Table 2 summarizes the geotechnical parameters.

Excavation section C1 (Figure 11 reported a general scheme) has been applied in case of loose soils of quaternary origin. Particularly in the Northern sector, in correspondence of the Debris Flow with unstable behaviour, to underpass the motorway A22 and the SS12; the overburden is ranging between 25 to 30 m. It is applied in the Southern sector too, in correspondence of the detritus conoids where unstable core-face behaviour is expected. This section type considers pre-consolidation intervention around the cavity (blue mark in Figure 11 and at the core-face (red marks in Figure 11), aimed creating the conditions of stability and waterproofing of the natural soil.

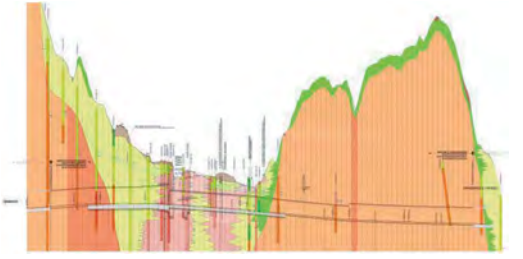

Figure 10. Isarco River Underpass Geological Profile (Lunardi et al. 2018, Lunardi et al. 2019).

Table 2. Soil mass geotechnical parameters.

SOIL TYPE	γ (kN/m^3)	φ (°)	c' (kN/m^2)	E_s (MN/m)
Debris Flow	21,0	30	10	60
Slope Debris	21,0	35	0	60
Alluvional sediments	20,5	36	2	60
Weathered material	21	30	0	30

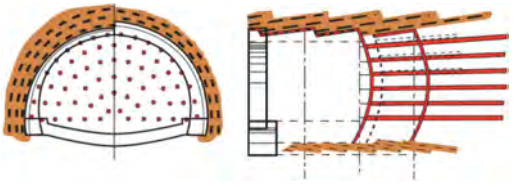

Figure 11. Reinforcements sketch made by jet grouting sub-horizontal columns.

Figure 12. Section C1: Blue marks truncated cone 'umbrellas', red marks core face reinforcements.

The design requires that excavation is performed without reducing the groundwater level, in hydrostatic conditions. For this reason it is necessary to create a grouted arch around the cavity and a plug at the face, so that the advance core is waterproofed. The last requirement has been satisfied tanks to the application of a special jet-grouting technology: Quick set jet grouting - QSJG - based on a "triple-fluid" system. The fluid added to the most common "double-fluid" system is a silicate and its accelerating characteristic was fundamental for "the quick" development of the ground column resistance and waterproofing. Despite to the not ideal conditions for jet grouting application, the adoption of QSJG solve the most critical issues related to this technology (Figure 13). The truncated cone 'umbrellas' realized by sub-horizontal columns create a pre-containment structure in the ground before its excavation, with the creation of "arch effect" which minimizes the deformations. The reinforcement of the core-face by means of sub-horizontal jet grouting column acts directly on the consistency of the advance core, improving its natural strength and deformation characteristics.

Figure 13. Section C1: detail of sub-horizontal jet-grouting column and detail of the excavated ground.

The performed interventions made the cavity and the advance core waterproofed allowing to perform the excavation in hydrostatic condition with a hydraulic head of 25m on the crown key.

The work phases related to this kind of intervention can be summarize as follow:

1) reinforcement of the core-face with sub horizontal columns of ground improved by means of jet-grouting (Figure 14);
2) creation of columns of sub-horizontal jet-grouting in advance in the crown;
3) creation of sub horizontal columns of improved ground under the tunnel floor (Figure 15);
4) full face excavation with steel ribs and shotcrete placed (Figure 16);
5) the face is given a concave shape and is sprayed with shotcrete;
6) the kickers and the tunnel invert are excavated and cast at a distance from the face of ≤ 1 diameter;
7) water-proofing is placed and the final lining is cast at a distance from the face of $\leq 2 \div 3$ diameters.

5 CONCLUSIONS

Jet-grouting has a fundamental role in the progress that has been achieved over the last thirty years in tunnel construction. Jet-grouting treatments can be executed by surface, where space is available and overburden is limited, or directly at the tunnel face. In the paper, the authors rendered a general overview of the technology, together with the design criteria for tunnelling applications such as portals, cavity and excavation face reinforcements.

Figure 14. Reinforcement of the core-face with sub horizontal columns of ground improved by means of jet-grouting.

Tunnelling can be performed with a very low overburden, by jet-grouting shell, arch shaped, thus minimizing the risk of slope instability and providing outstanding results from an environmental and landscape point of view.

Horizontal jet-grouting made possible to overcome all the difficulties connected with excavation in

cohesionless soils. Sub horizontal jet-grouting is used to create a series of columns of improved ground, side by side ahead of the face around the profile of the extrados of the tunnel to be excavated. The authors listed a series of application performed during the latest 30 years and described the most recent and challenging application related to one section of the Isarco River Underpass.

Figure 15. Creation of sub horizontal columns of improved ground under the tunnel floor.

Figure 16. Full face excavation with steel ribs and shotcrete placed.

ACKNOWLEDGMENTS

A short acknowledgement section can be written between the conclusion and the references

REFERENCES

Cassani, G., Gatti, M., Zenti, C.L., Manassero, V., Pelizza, S., Pigorini, A, 2022. Auxiliary methods technology. Ground reinforcing, ground improving and presupport technology. In: Handbook on Tunnels and Underground Works: Volume 2: Construction – Methods, Equipment, Tools and Materials [Chapter 4,]. In Bilotta, E., Casale, R., di Prisco, C.G., Miliziano, S., Peila, D., Pigorini, A., & Pizzarotti, E.M. Eds., 2022. (1st ed.). CRC Press, pp.295–376.

Lunardi, G., Cassani, G., Gatti, M., Bellardo, L., Palomba, A., 2018. Brenner Base Tunnel & Isarco River Underpass Section: several technical and operational solutions. Gallerie e Grandi Opere Sotterranee n° 125, Marzo 2018 pp.33–44. ISSN-0393-1641.

Lunardi, P., 1997. Ground improvement by means of jet grouting. Proceedings of the Institution of Civil Engineers - Ground Improvement, 1, Issue 2, pp65–85.

Lunardi, P., 2000a. Tunnelling under the Via Appia Antica in Rome.Tunnels & Tunnelling International, April 2000

Lunardi, P. 2000b. Tunnelling under the Mugello Racing Circuit incorporating the ADECO-RS approach Tunnel, n. 8 (Dicember).

Lunardi, P., Cassani, G., 2001. Construction of an underpass at the Ravone railway yard in the city of Bologna: aspects of the design and construction. Proceedings of the International Congress "Progress in Tunnelling after 2000", Milan, 10 ÷ 13 June 2001

Lunardi, P., 2008. Design and Costruction of Tunnels – Analysis of Controlled Deformation in Rock and Soils (ADECO-RS). Berlin: Springer.

Lunardi, P., Cassani, G., Gatti, M. (2014). Industrialisation of the construction process for the Solbiate Olona tunnel by using "jet-grouting" technology. Proceedings of the World Tunnel Congress 2014 – Tunnels for a better Life. Foz do Iguaçu, Brazil.

Lunardi, P., Cassani, G., Gatti, M., Bellardo, L., 2019. Brenner Base Tunnel & Isarco River Underpass Section: several technical and operational solutions. Proceedings of the World Tunnel Congress 2019 – Naples, Italy.

Tornaghi, R., 1993. Controlli e bilanci analitici dei trattamenti colonnari mediante jet-grouting, Rivista Italiana di Geotecnica n. 93 (3), pages 217–234.

Tunnelling for a Better Life – Yan, Celestino, Thewes & Eberhardt (Eds)
© 2024 The Author(s), ISBN 978-1-032-80042-4
Open Access: www.taylorfrancis.com, CC BY-NC-ND 4.0 license

Stability analysis of surrounding rock in a highway tunnel crossing a water-rich fault fracture zone

Shiwei Luo & Xiongyao Xie
Key Laboratory of Geotechnical and Underground of Ministry of Education, Tongji University, Shanghai, Chinay
College of Civil Engineering, Tongji University, Shanghai, China

Dexiang Zhu
Yunnan Yunlu Engineering Testing Co. Ltd., Yunnan, China

ABSTRACT: One of the most challenging aspects of tunnel construction is the encounter with unfavourable geological conditions such as fault zones with fractured rock. When crossing fault zones, it is generally necessary to implement advance support to reinforce the fractured rock and block the seepage path, and then use the CD method or CRD method to excavate the tunnel to ensure the stability of the surrounding rock. However, if the CD method is employed for excavation, it would require changing the excavation method and implementing and removing temporary supports during the construction process, which does not align with the requirements of safe and environmentally friendly tunnel construction. The three-bench seven-step excavation method (TSEM) has been widely used in fractured rock excavation as a method that can stabilize the surrounding rock with simple procedures and low cost. Therefore, a comparative study can be conducted on the excavation methods of fault fracture zone surrounding rock. Based on the A Tunnel project in Beibei District, Chongqing, finite element numerical simulation methods were employed to compare the effects of the CD method and the TSEM on the stability of the surrounding rock. The research indicates that the CD method has limited advantages in terms of displacement control, rock stress, and expansion area of the plastic zone. Therefore, it is feasible to replace the CD method with the three-step seven-step excavation method, which has practical implications for similar projects.

Keywords: Fault zones, CD method, Three-bench seven-step excavation method, Numerical simulation

1 INTRODUCTION

In the process of tunnel construction, special geological conditions will be encountered from time to time, and crossing the water-rich fault zone is one of the common ones. Due to the complexity of the mechanical problems involved in tunnelling through a fractured fault zone, traditional mechanical analysis methods are difficult to apply. Therefore, scholars often analyse the stability of highway tunnels crossing fractured fault zones based on numerical computational methods: Wang et al.(2016) utilized numerical simulation methods to investigate the deformation and stress distribution characteristics of surrounding rock in fractured zones with different dip angles and widths of the fault. They combined model experiments to study the tunnel collapse process during construction and found a good agreement between the results of the two approaches. The study by Zuo et al.(2015) indicated that the time-dependent settlement and deformation of the surrounding rock arch can be effectively transformed into a model of sudden instability. According to the criteria for determining sudden instability of the surrounding rock, the obtained state of surrounding rock instability corresponds well to the actual rock failure conditions. This approach has achieved favourable results in analysing the stability of surrounding rock in fractured fault zones. Peng et al.(2022) simultaneously considered the influences of groundwater and blasting on the stability of the surrounding rock. They established a sharp-point sudden instability model for tunnelling through fault zones with abundant water, which was used for analysing the stability of the surrounding rock in fractured fault zones.

Significant research achievements have been made regarding the influence of tunnel excavation methods

*Corresponding author: 2232527@tongji.edu.cn

DOI: 10.1201/9781003495505-104

on the stability of weak surrounding rock: Li et al. (2020) systematically compared the distribution of deformation and plastic zone of surrounding rocks obtained by two excavation methods, cd method and step method; Li et al.(2015) studied the influence of TSEM on the stability of the surrounding rocks of loess tunnels by taking the displacement characteristics as the main entry point and found that significant subsidence occurred on the arches and surface of loess tunnels. Zhou et al.(2021) compared the influences of the Benching method and the CD method on the stability of surrounding rock when crossing coal seams. They concluded that, under conditions allowing for greater subsidence, using the Benching method for tunnel construction is technically feasible and can achieve favourable technical and economic benefits.

In the face of complex geological conditions, it is often necessary to design a variety of excavation methods to cooperate with each other to complete the tunnel excavation, but the excavation methods should not be changed frequently during the tunnel construction process, and the excavation methods of the same tunnel should be simplified as much as possible. Otherwise, it will induce numerous unsafe factors and increase the construction cost. Based on this, the purpose of this paper is to analyse the feasibility of using the three-bench seven-step excavation method (TSEM) to replace the center diagram method (CD method) to excavate the fault zone by using finite element analysis. In order to simplify the tunnel excavation method and improve the technical and economic benefits of tunnel construction.

2 PROJECT OVERVIEW

2.1 *Geological condition*

The tunnel crosses the backslope mountain formed by the Wintang Gorge backslope, and only the Jialingjiang. The tunnel crosses the F1 fault, the fault strikes north-east, tends to the north-west, dipping angle of 60 ~ 85 °, the left side of the lower plate strata for the T_1j^4 (mainly composed of limestone) and a small part of the T_1j^3 (mainly composed of limestone), the right side of the upper plate strata for the T_1j^3. According to a thorough borehole survey, the rock formation in the 0-150m interval exhibits a fractured structure, with the rock core being moderately fragmented.

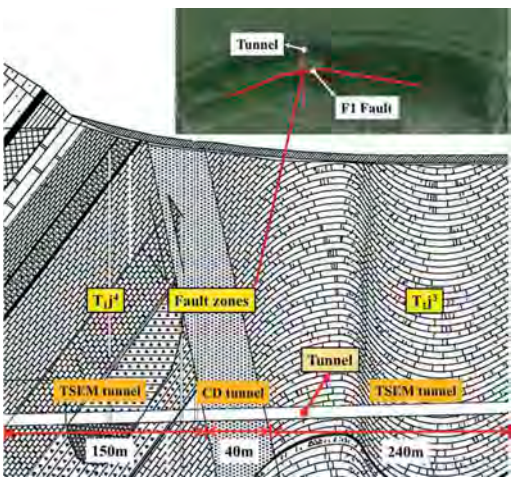

Figure 1. Geological condition.

2.2 *Fault fracture zone xonstruction scheme*

According to Specifications for Design of Highway Tunnels, surrounding rock classification is determined according to rock hardness rock integrity and BQ value comprehensively(Table 1). A total of seven lining schemes and four excavation schemes were designed according to the surrounding rock classification to meet the support and excavation requirements of the emergency stopping zone section from Class III to Class V perimeter rock.

According to Table 2, fault fracture zone corresponds to V surrounding rock (Geologically poor sections), should choose the lining program for the S5a, and its adaptive advanced support programs in the pipe shed or two-layered conduit, excavation methods selected in the CD method. Therefore, it can be determined that the construction program of the fault fracture zone is as follows: firstly, apply pipe shed or two-layered grouting conduit for tunnel arch advanced support, and then use CD method for excavation, lining program selection S5a, of which: two-layered conduit are made of hot-rolled seamless steel pipe, with a single length of 4.5m, a diameter of 42mm, a wall thickness of 4mm, and are arranged within the range of 120 ° on the top of the arch, with an annular spacing of 40cm, of which the outer insertion angle of 10 ° is 10 °. Among them, the outer insertion of slow inclination angle of 10 ° to 15 °, steep inclination

Table 1. Highway tunnel surrounding rock classification.

Surrounding rock classification	Main qualitative characteristics of surrounding rock
III	hard rock,the rock is relatively broken
	the rock is relatively hard, the rock is relatively intact
	the rock is relatively soft, the rock is intact
IV	hard rock,the rock is broken
	the rock is relatively hard, the rock is broken
	the rock is relatively soft, the rock is relatively broken
	the rock is soft, the rock is intact
V	the rock is relatively soft, the rock is broken
	the rock is soft, the rock is relatively broken
	ultrasoft rock

angle of 30 ° to 40 ° up and down the two layers of staggered arrangement (Figure 2);

Table 2. List of tunnel construction scheme.

Excavation Methods	Advanced Support Methods	Surrounding Rock Classification	
		Three-lane Section	Emergency Stop
Three Benching Tunnelling Method	\	III	III
TSEM	Forepoling Bolts	IV, V (Deeply buried and geologically normal sections)	IV
CD Method	One-layered Conduit	V (Geologically poor sections)	\
CD Method/ Double Side Drift Method	Pipe shed, Two-layered Conduit	V (Shallow buried sections)	V

3 THE NEED TO CONDUCT EXCAVATION PROGRAM SELECTION

In the original design, three benching tunnelling method, CD method and double side drift method are adopted for a few III surrounding rocks, fault fracture zones and emergency stopping zones respectively, but the three benching tunnelling method is adopted for most of the IV surrounding rocks and V (Deeply buried and geologically normal sections) excavation. Tunnel left line design statistics are as follows, from the table it can be seen that the use of three TSEM accounted for 73.74% far more than the other two excavation methods(Table 3). Due to the poor physical and mechanical properties of surrounding rocks in V (Shallow buried sections). The resulting surrounding rock pressure is also larger, it is difficult to ensure that after changing the excavation method to guarantee the safety of construction, but for the CD method designed to excavate the V (Deeply buried and geologically normal sections)surrounding rock geological poor section still exists optimization possibilities, consider using three benching tunnelling method to replace the TSEM in the next door method, specifically for the following reasons:

The three benching tunnelling method is simple, fast and more economical. Compared with the CD method, if the step method is used, the amount of temporary support used per meter of tunnel support structure is reduced, the loss of materials is reduced, resulting in the application of temporary support when the cost of manpower, material resources, time are reduced, so in the surrounding rock conditions allow, it is advisable to try to use the step method of construction, in order to shorten the construction period, reduce the cost of the purpose.

Frequent changes in excavation methods for the same tunnel are not economical and may even cause safety problems. If the CD method is replaced by the TSEM, it will reduce the abandoned temporary work on one hand, and simplify the excavation method on the other hand, which is beneficial to the management and economy of the tunnel construction.

The CD method causes secondary disturbance to the surrounding rock when removing the CD method after excavation, while the step method avoids secondary disturbance to the surrounding rock when removing the temporary support, and the number of stress redistribution is reduced.

4 COMPARISON OF EXCAVATION METHODS FOR FAULT FRACTURE ZONES

4.1 *Assumptions and descriptions of the numerical model*

As shown in the Figure 2, the three-dimensional numerical simulation was carried out using Midas GTS NX finite element software. Considering the scope of the rock mass affected by the tunnel excavation, the height of the tunnel section span and the length of the F1 fault, the length of the model was determined to be 60 m, width 100 m and height 100 m. The length of the fault zone was taken to be 40 m according to the geotechnical report, and the stratigraphic model was T_1j^4, fault zone and T_1j^3 from left to right as shown in the figure. It is

Table 3. List of tunnel construction scheme.

Surrounding Rock Classification	III	IV			V		
Length	355	1040			1433		
Excavation Methods	Three Benching Tunnelling Method	TSEM	TSEM	TSEM	CD Method	TSEM	Double Side Drift Method
Excavation Length	355	230.13	650	50	371.75	1251.12	50
Percentage	12.00%	73.74%	\	\	12.57%	\	1.69%

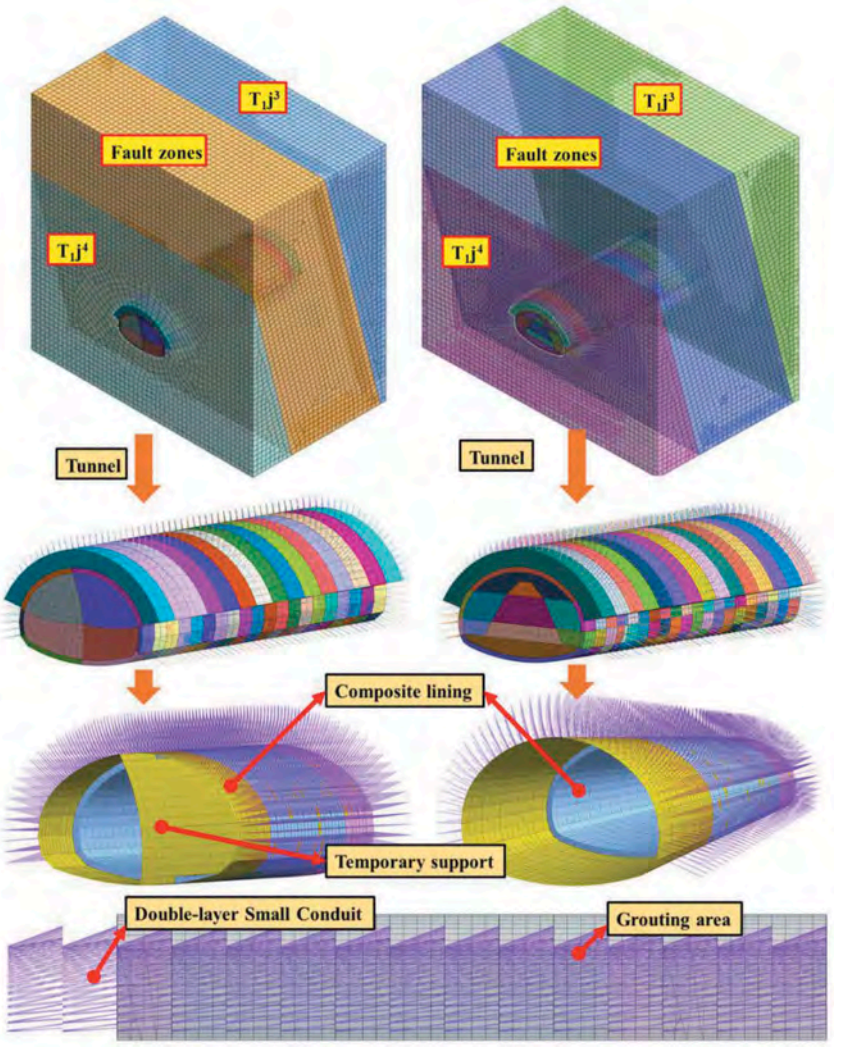

Figure 2. Numerical model.

necessary to select different simulation units and corresponding constitutive models for different simulation objects, the stratum and grouting reinforcement area are simulated by solid units, the constitutive model adopts the Mohr-Coulomb model, the support is simulated by plate units and considered as elastic, and the two-layered conduit are simulated by implanted trusses and considered as elastic. The normal displacements of the left, right, front, back and lower part of the constrained model are used as the displacement boundary conditions.

To simulate the CD method excavation, the arch advanced support (support distance 4m) is constructed first. The excavation was then carried out in the order of drift ① ~④(excavation length 3m). Primary support and temporary support will be applied after each step of excavation is completed. After the primary support was closed, the removal of the temporary support began (removal length 12m). Pouring of the invert after removal of the first temporary support (pouring distance 12m). To simulate the TSEM excavation, the arch advanced support (support distance 4m) is constructed first. The excavation was then carried out in the order of drift ① ~ ⑦(excavation length 3m). Primary support and temporary support will be applied after each step of excavation is completed. Pouring of the invert after the primary support was closed (pouring distance 12m). (Figure 3)

4.2 *Simulation results*

4.2.1 *Displacement*

For both vertical and horizontal displacement values, both excavation method displacements are larger

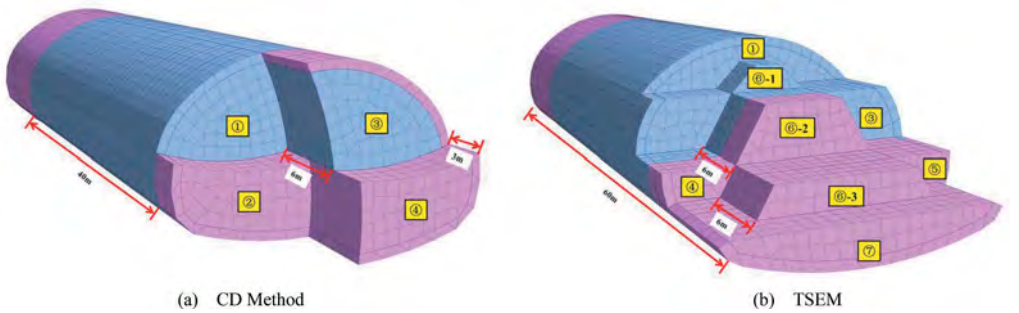

(a) CD Method (b) TSEM

Figure 3. Construction process simulation.

Table 4. Physical and mechanical properties.

	E/MPa	N	γ/ (kN/m^3)	*c* /MPa	φ/°
T_1j^3,T_1j^4	6000	0.35	26.3	0.7	39
Fault Zones	1200	0.35	22.5	0.05	27
Grouting Area	4000	0.35	25	0.2	45
Primary Support	26000	0.2	22	\	\
Lining	30000	0.2	25	\	\
Bolt	200000	0.3	78.5	\	\

within the fault zones and the displacement control of TSEM is weaker than CD method(Figure 4-7). It is noteworthy that sudden changes in displacement were observed for both excavation methods near the stratigraphic junction locations (construction locations 10 and 50) and large displacement differences were observed at both the top and waist of the tunnel. Therefore, when the tunnel crosses the fault zones, the difference in surrounding rock stiffness before and after the fault zones will lead to uneven deformation along the longitudinal direction of the tunnel. Such uneven deformation acting on the lining structure may cause shear damage. The horizontal displacement difference is larger under both excavation methods, and the settlement is larger in the TSEM but it is uniform and the settlement difference is small, which shows some advantages compared with the CD method.

4.2.2 *Stresses*

The principal stress nephogram of the two excavation methods are similar and maximum principal stresses are manifested as compressive stresses. The maximum principal stresses in the side wall at the same monitoring location are larger than those at the top and bottom of the tunnel, and the maximum principal stresses in the fault zones of the side wall at different monitoring locations are smaller than those in the strata on both sides. In summary, the maximum principal stress maxima are located at the side wall of the strata on both sides. The minimum principal stress at the same monitoring position is tensile stress at the top and bottom of the tunnel and compressive stress at the side wall the tunnel; the minimum principal stress at the top and bottom of the tunnel at different monitoring positions is tensile stress, and the range of tensile stress has been

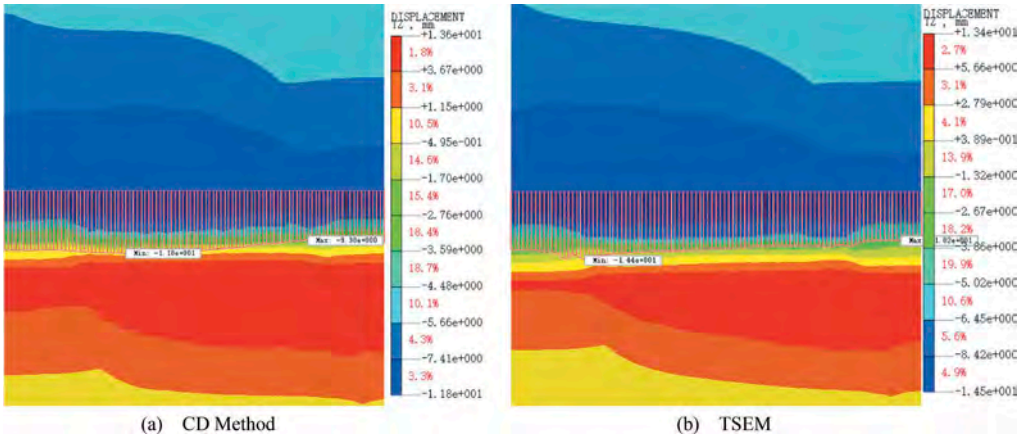

(a) CD Method (b) TSEM

Figure 4. Vertical displacement nephogram.

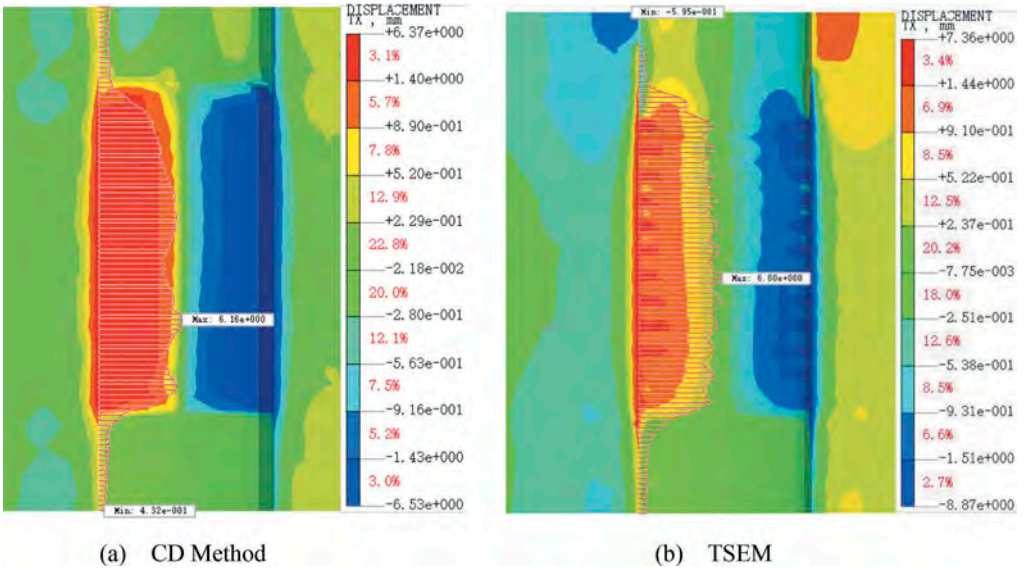

Figure 5. Horizontal displacement nephogram.

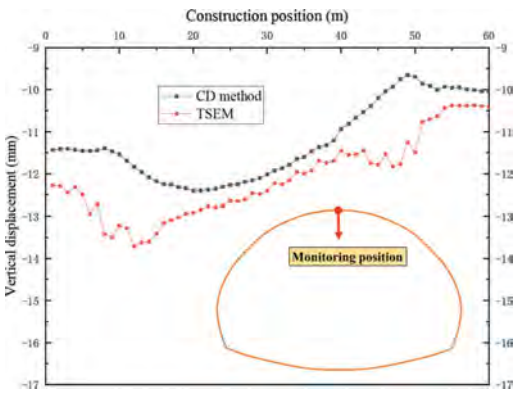

Figure 6. Vertical displacement.

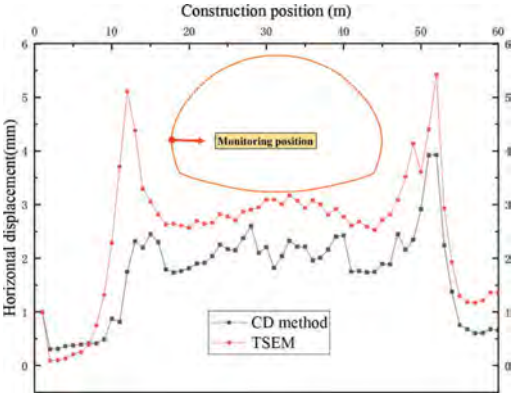

Figure 7. Horizontal displacement.

expanding with the monitoring position from the left to the right; the minimum principal stress at the side wall of the tunnel at the same monitoring position has been compressive stress, but it has been larger in the two sides of the ground layers and smaller in the fault zones.

The plastic zones are observed in the sidewall of the tunnel within the fault zones and its adjacent region. But it is primarily concentrated within the fault zones. Hence, in the comparison of the two excavation schemes, five sets of data of the sidewall within the range of construction steps from primary support closure to tunnel completion in the fault zones were selected for comparison, and Table 5, 6 was obtained based on Equation (1) Moore-Cullen damage criterio.

$$\varphi_p = \sin^{-1}\frac{\sigma_1 - \sigma_3}{\sigma_1 + \sigma_3 + 2c\cot\varphi} \quad (1)$$

Where, σ_1 is maximum principal stress(pa);σ_3 is minimum principal stress (pa); c is cohesion (pa); φ is friction angle (°).

As illustrated in Figure 10, two positions adjacent to the waist and shoulders of the tunnel were chosen as points of comparison. For the comparison position 1, φ_P varies within 3° for both methods after primary support closure, and the surrounding rock at the position 1 is not grouted and reinforced, so φ=27°for the position 1 surrounding rock. Comparing the two excavation methods, both $\varphi_P > \varphi$ after primary support closure, indicating that the rock body has been sheared at this time, but the value of φ_P under the

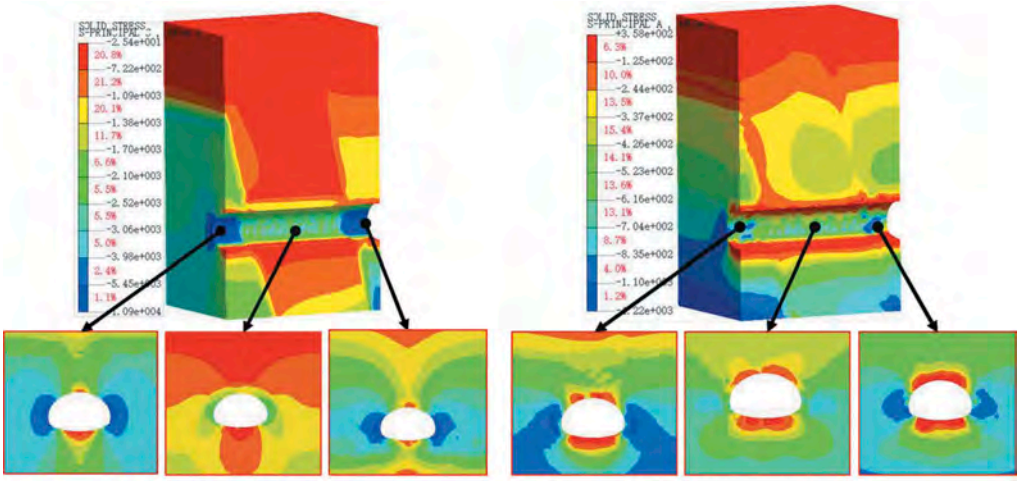

(a) Maximum Principal Stress (b) Minimum Principal Stress

Figure 8. CD method principal stress nephogram.

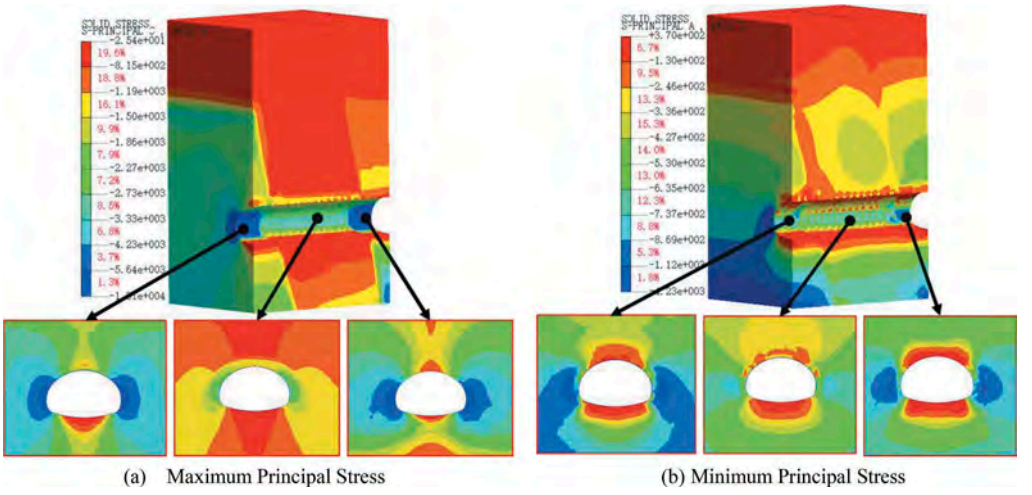

(a) Maximum Principal Stress (b) Minimum Principal Stress

Figure 9. TSEM principal stress nephogram.

three benching tunneling method is greater than that under the CD method, and the surrounding rock is in a more unfavorable state. Therefore, for the excavation of surrounding rock at the position 1, the primary support should be applied earlier for timely control. The rupture angle of the two methods varies within 2° after the primary support is closed, and the surrounding rock at the position 2 is reinforced by grouting, so the surrounding rock φ=27°. Comparing the two excavation methods, there are results $\varphi_P>\varphi$ at different stages, when the CD method is used for excavation to get φ_P are greater than the same stage of the three benching tunneling method with seven steps, which is in a more unfavorable state. In addition, even though there is advanced support for the

Table 5. Comparison position 1 stress state.

	CD Method			TSEM		
Construction Stage	σ_1/ MPa	σ_3/ MPa	φ_P/°	σ_1/ MPa	σ_3/ MPa	φ_P/°
Primary Support Closure	2.078	0.504	35.66	2.067	0.403	40.00
Intermediate Process1	2.131	0.547	34.51	2.110	0.423	39.51
Intermediate Process 2	2.174	0.575	33.89	2.149	0.441	39.08
Lining Closure	2.199	0.594	33.46	2.148	0.440	39.14
Tunnel Completion	2.207	0.604	33.18	2.155	0.449	38.81

Table 6. Comparison Position 2 Stress State.

Construction Stage	CD Method σ_1/ MPa	CD Method σ_3/ MPa	CD Method φ_P /°	TSEM σ_1/ MPa	TSEM σ_3/ MPa	TSEM φ_P /°
Primary Support Closure	1.70	0.15	51.85	2.12	0.26	48.39
Intermediate Process 1	1.80	0.18	51.21	2.18	0.28	48.05
Intermediate Process 2	1.86	0.19	50.87	2.24	0.29	47.82
Lining Closure	1.91	0.20	50.59	2.24	0.29	47.81
Tunnel Completion	1.91	0.20	50.63	2.24	0.27	48.86

surrounding rock of the position 2, shear damage still occurs, and more reasonable advanced support measures with higher strength should be proposed.

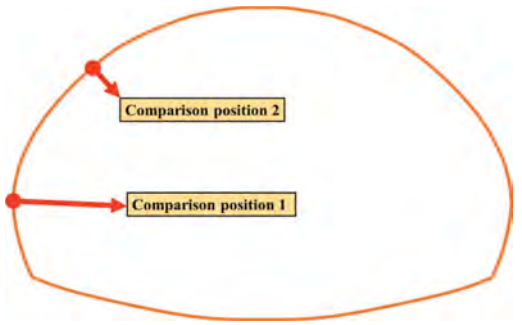

Figure 10. Comparison position.

5 CONCLUSIONS

Summarizing the displacement and stress comparisons, it is considered that TSEM can be used instead of the CD method of excavation. The reasons are as follows:

Displacement convergence value. The CD method has better deformation control ability than TSEM, but for the arch settlement and tunnel peripheral displacement generated under both excavation methods are within the range of the code-recommended recommendations, the TSEM is applicable to the excavation of fault zones under the same conditions.

Displacement difference. Horizontal displacement difference generated under both excavation methods at the stratum junction is larger, but the tunnel top settlement convergence value is larger using the TSEM but the settlement is uniform and the settlement difference is small, which shows some advantages.

Surrounding rock stress. The surrounding rock at the shoulder and waist of the tunnel within the fault zones of are damaged under both types of excavation, but each has its own advantages and disadvantages, and a comparison of the value of φ_P shows that the stress on the surrounding rock at the waist of the tunnel is worse using the TSEM of CD method, and that the stress on the surrounding rock at the shoulder of the tunnel is worse using the CD method of the middle-septal door excavation. The advantages embodied in the CD method are limited. In summary, replacing the CD excavation method with TSEM can greatly reduce the construction process, shorten the construction period, and save the construction cost while being environmentally friendly.

REFERENCES

Wang, Y., Jing, H., Su, H., Xie, J., 2016. Effect of a Fault Fracture Zone on the Stability of Tunnel-Surrounding Rock. International Journal of Geomechanics, 04016135.

Zuo, Q.J., Wu, L., Lu, Z.L., Tan, Y.Z., Yuan, Q., 2015. Instability analysis of soft surrounding rock in shallow tunnel portal under unsymmetrical pressure by catastrophe theory. Rock and Soil Mechanics,36 pp.424–430.

Peng, Y., Liu, G., Huang, Z., Lyu, H., Wu, L., 2022. Study on catastrophe instability criterion of surrounding rock in tunnels blasting crossing water-rich fault zones. China Safety Science Journal(CSSJ)32, pp.104–111.

Li, N., Zhou, Y., Zhao, Y., Li, G., 2020. Analysis of mechanical behavior of double arch tunnel by CD method and benching method. IOP Conference Series: Earth and Environmental Science 580, 012074 (012076pp).

Li, P., 2015. Displacement characteristics of high-speed railway tunnel construction in loess ground by using multi-step excavation method. Tunnelling and Underground Space Technology 51, pp.41–55.

Zhou, G., Zhao, Z., Song, Z., Wang, H., 2021. Stability Analysis and Protection Measures of Large Section Tunnel in Coal Rich Weak Rock Stratum. Geofluids 2021, pp. 1–15.

Tunnelling for a Better Life – Yan, Celestino, Thewes & Eberhardt (Eds)
© 2024 The Author(s), ISBN 978-1-032-80042-4
Open Access: www.taylorfrancis.com, CC BY-NC-ND 4.0 license

Selection of an ontological model for phyllite tunnel based on on-site measured

Jianchi Ma*
Key Laboratory of Transportation Tunnel Engineering, Ministry of Education, Southwest Jiaotong University, Chengdu, China
School of Civil Engineering, Southwest Jiaotong University, Chengdu, China

Junru Zhang
Key Laboratory of Transportation Tunnel Engineering, Ministry of Education, Southwest Jiaotong University, Chengdu, China

ABSTRACT: As a typical layered rock mass, Phyllite has significantly anisotropic physical and mechanical properties compared with homogeneous rock mass. In order to further explore the influence of strength anisotropy of Phyllite on the displacement field of surrounding rock, based on the Dashazui Tunnel of Jinning Expressway, the Finite difference method (FDM) is used to study the difference of displacement field of surrounding rock of Phyllite tunnel under the two constitutive models of Mohr Coulomb and Ubiquitous-joint, and it is verified by the field measured displacement. According to the simulation results of different working conditions, compared with the Mohr Coulomb constitutive model, the Ubiquitous-joint model is more suitable for the actual data of the displacement field of the surrounding rock. The selection of the Ubiquitous-joint model better reflects the phenomenon of concentrated failure in Phyllite tunnels during excavation.

Keywords: Tunnel, Phyllite, Ubiquitous-joint model

1 INTRODUCTION

Phyllite, which is widely distributed in southwest China, is one of the low-grade metamorphic rocks, and is formed by metamorphism of claystone or volcanic tuff. Due to the different proportions of its main components, although the structure is similar, there are still great differences in specific physical and mechanical parameters (Li et al., 2014). As a typical stratified rock mass, its anisotropic mechanical properties are often different from the failure forms of conventional tunnels when tunnel diseases occur (Si et al., 2021; Zan et al., 2023; Wu et al., 2022). In view of its anisotropic mechanical properties, scholars around the world used uniaxial/triaxial compression test, uniaxial creep test, X-ray powder diffraction, electron microscope scanning and Brazil disc splitting test to study, and achieved fruitful results (Xu et al., 2018; Ramamurthy et al., 1993; Ozbek et al., 2018; Hu et al., 2017).

Numerical simulation is widely used in the study of the mechanical behavior of layered rock tunnels, and the treatment of joints is usually divided into explicit and implicit methods. The Ubiquitous-joint model treats the rock as a composite consisting of "matrix" and "joints", and directly considers the strength criterion and flow law of the matrix and joints separately in the constitutive equations, i.e., the treatment of joints is "implicit" (Deangeli & Omwanghe, 2018). Simulation of nodules by modeling them individually, e.g., by 3DEC software is referred to as the display approach. Tien & Kuo (2001) proposed an ontological model for analyzing laminated rock bodies using two independent sets of criteria namely sliding damage controlled by discontinuous surfaces and non-sliding damage controlled by the rock matrix. Saeidi et al., (2014) A new anisotropic strength criterion was proposed for analyzing the strength of transversely isotropic rock bodies by integrating several metamorphic and sedimentary rock mechanical parameters. Shi et al., (2016) introduced two parameters to represent the direction of minimum strength and the anisotropic effect in a laminated rock mass, and accordingly established a strength criterion for laminated rock masses. Fortsakis et al., (2012) investigated the anisotropic

*Corresponding author: 408996541my.swjtu.edu.cn

DOI: 10.1201/9781003495505-105

mechanical behavior of tunnelling in a laminated rock mass by qualitatively dividing the laminated rock mass into rocks and joints. And the destruction of joints often leads to the further development of the surrounding rock fissures, resulting in the deterioration of the surrounding rock, and then the occurrence of surrounding rock instability triggering a series of tunnel diseases (Meng et al., 2013; Wang et al., 2014). In order to further investigate the influence of the phyllite joints on the deformation of the surrounding rock after tunnel excavation, this paper investigates the mechanical behavior of the phyllite tunnels after excavation by means of SEM electron microscopy, triaxial experiments, numerical simulation combined with on-site measurements. And through the study, we find out an intrinsic model that can be used to simulate the centralized damage in the excavation process of phyllite tunnel, which can provide certain reference for future projects.

2 PROJECT OVERVIEW

The Dashazui Tunnel project of Jinyang to Southern Ningnan section of G4216 expressway is the support project of this paper. The tunnel is located in the northeast margin of Hengduan Mountain system in southwest, between Sichuan Basin and Yunnan-Guizhou Plateau, with high terrain in northwest and low in southeast. The Dashazui Tunnel is a two-way four-lane road tunnel with a design speed of 80km/h. The length of the left line tunnel is 3940m, and the mileage of the tunnel is Z3K189+946 and Z3K193 +886 respectively. The length of the right line tunnel is 3974m, and the starting and ending mileage of the tunnel are K189+900 and K193+874 respectively. In this paper, the K1190+463 section of Dashazui Tunnel is taken as the research object, and its surrounding rock is quartz phyllite. According to the field geological survey report, the Angle between K190+463 section and the tunnel axis is 317°, and the dip Angle is 51°.

Figure 1. Section diagram of K1190+463.

3 MECHANICAL PROPERTIES OF PHYLLITE

3.1 *Microstructure analysis*

The macroscopic failure of rock (tensile, shear) has different manifestations at the microscopic level, on the other hand, the microscopic fracture mode also determines the macroscopic failure behavior of rock. The block of rock sample is taken from the engineering site, processed, and then glued to the sample table with conductive adhesive for SEM scanning. The scanning effect of quartz phyllite under electron microscope when magnified to 20000 times is shown in Figure 3. The surface of the sample debris is smooth, and the details are composed of thin layered structures with uniform thickness. The proportion of the sample bedrock is much larger than that of mineral particles, and no scale blastoblastic structure is found. Quartz phyllite based on this project is a macroscopic anisotropic material composed of transverse isotropic planes superimposed.

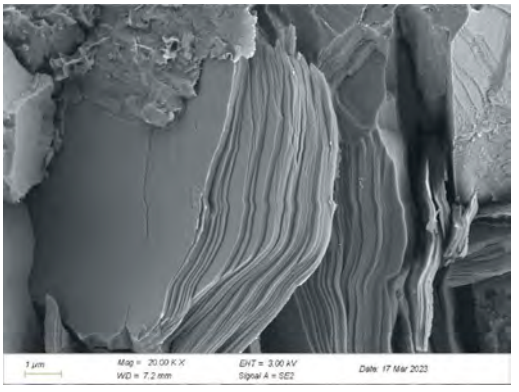

Figure 2. 20,000x electron microscope scan.

3.2 *Uniaxial triaxial compression experiment*

3.2.1 *Sample preparation*

The rock samples used in this study were all taken from the K193+760 mile palm face of Dashazui Tunnel, and the core drilling machine was fixed with bolts on the palm face for sampling. After the sampling was completed, the samples were taken to the laboratory for cutting and processing, and the samples were prepared according to the engineering rock mass test method standard. Finally, 5 rock samples were formed, as shown in Figure 3.

The density of phyllite samples after water absorption was measured by free water absorption method, and the density parameters obtained were as follows:

3.2.2 *Compression experiment*

Two groups of samples were selected for uniaxial compression experiment, and the remaining three

Figure 3. Phyllite sample.

Table 1. Phyllite density parameter.

Sample number	1	2	3	4	5
Saturation density (kg/m3)	2738.34	2712.89	2749.08	2731.68	2737.97
Mean density (kg/m3)	2733.99				

groups were subjected to conventional triaxial compression experiment. The loading rate was controlled by axial displacement and set at 0.1mm/min until the specimens were completely destroyed. According to the sampling depth and subsequent numerical simulation requirements, the confining pressure conditions of the five samples are set as shown in Table 2. According to the experimental results, quartz phyllite is not an ideal elastic-plastic body, and its stress-strain curve can be divided into a compaction stage, an elastic stage and a strength cliff decline stage when the peak strength is reached.

Table 2. Normal triaxial compression test condition table.

Sample number	1	2	3	4	5
Confining pressure (MPa)	0	0	1	3	5

Poisson's ratio and elastic model quantity of phyllite samples can be obtained by calculating the elastic stage of stress-strain curve. Combining the three groups of triaxial test data, the average Poisson's ratio and elastic modulus of phyllite samples are 0.33 and 5.85GPa.By drawing the molar envelope of phyllite samples under different confining pressures, the internal friction Angle of quartz phyllite is 45° and the cohesion is 2.31MPa.

4 NUMERICAL CALCULATION

4.1 *Model building*

The length of K190+463 section of the right line of Dashazui Tunnel was selected as the calculation section, and the tunnel buried depth was 100m. In order to avoid the influence of boundary effect, the distance between the tunnel contour and the left and right borders as well as the bottom boundary was selected to be 4 times the hole diameter according to the Saint-Venant theorem, and the model size was 140m×60m×180m (as shown in Figure 4). The excavation method is three-step method, the circulation footage is 1.5m, and the step length is 6m.

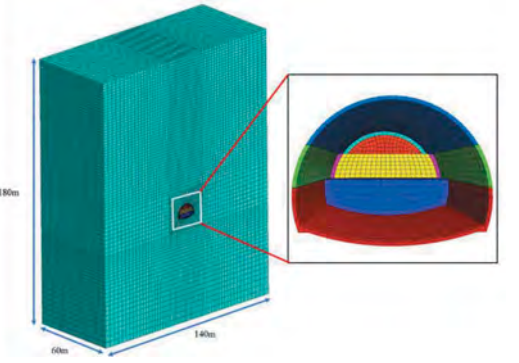

Figure 4. Schematic diagram of numerical calculation model.

Considering the coordinated deformation of shotcrete and I-steel frame, and the primary support is mainly shear failure, the elastic modulus of the grille steel frame is converted to C25 shotcrete by using equivalent stiffness as the initial support parameter. In addition, considering that the secondary lining in actual construction is far away from the face of the palm, the force is mainly borne by the initial support of the tunnel, so only the initial support is activated in the calculation process. Cable unit is used to simulate the bolt. The section of Z5b lining adopts 3m long bolt with 1.2m spacing and plum blossom layout. The initial support parameters are shown in Table 3.

Table 3. Initial support parameter table.

Structure	Elasticity (GPa)	Poisson's ratio	Density (kg/m^3)	Thickness
Initial support	3.19	0.2	2614.06	0.24
Cable	210	0.2	7850	-

4.2 *Mohr Coulomb model parameters*

Considering that the whole surrounding rock is not homogeneous and dense in actual engineering, the surrounding rock parameters obtained by mechanical experiments directly used in numerical simulation will cause large errors. Considering lithology, rock formation occurrence, construction disturbance and other influencing factors, the rock mass strength parameters suitable for numerical calculation should also be reduced by Hoek-Brown strength criterion (E. Hoek et al., 2002). The Hoek-Brown strength criterion is calculated as follows:

$$\sigma_1 = \sigma_3 + \sigma_c \left(\frac{\sigma_3}{\sigma_c} m_b + s \right)^{\alpha} \quad (1)$$

$$m_b = m_i \exp\left(\frac{GSI - 100}{28 - D} \right) \quad (2)$$

$$s = \exp\left(\frac{GSI - 100}{9 - 3D} \right) \quad (3)$$

$$a = \frac{1}{2} + \frac{1}{6}(e^{-GSI/15} - e^{-20/3}) \quad (4)$$

Where: σ1 is maximum principal stress of rock mass failure; σ3 is minimum principal stress of rock mass failure; σ_c is uniaxial compressive strength of rock; mb and s is H-B criterion empirical parameters; a is Coefficient of determining rock mass characteristics. mi is Lithology index; D is disturbance factor; GSI is geological strength index of rock mass.

Among them, since the parameters are selected from the laboratory test, the GSI value is 100, a=0.5, mi=mb. The least square method was used to fit the previous uniaxial compression test and triaxial compression test data mi. The result is that mi=23.31.

Combined with the rock mass structure, weathering degree and structural plane state of the surrounding rock mass on the face of the tunnel construction site, and referring to the quantitative table of GSI index based on the macro-characteristics of rock mass given by Hoek-Brown, the geological strength index of rock mass GSI is determined to be 20. The value of the disturbance factor D is 0.7. Uniaxial compressive strength of rock (σ_c) is 11.04MPa. In addition, a is 0.52 and s is 3.93×10^{-5}. Equation (5) can be used to calculate the deformation modulus of surrounding rock.

$$E_m = \begin{cases} (1 - \frac{D}{2}) \sqrt{\frac{\sigma_c}{100}} 10^{(\frac{GSI-10}{40})}, (\sigma_c \le 100MPa) \\ (1 - \frac{D}{2}) 10^{(\frac{GSI-10}{40})}, (\sigma_c > 100MPa) \end{cases} \quad (5)$$

Taking the H-B strength envelope as the object, the equivalent description of M-C criterion for rock mass strength is expressed by tangential or secant lines of σ1-σ3 curves. The final solution is: E_m =0.39GPa, σ_{cm}=0.92MPa, c=0.12MPa, φ=22.11°.

4.3 *Ubiquitous-joint model parameter*

Ubiquitous-joint model is based on the Mohr Coulomb model, and the joint surface is also subject to the Mohr Coulomb yield criterion. The failure of rock mass may occur in rock matrix and joint plane, or both. (Sainsbury et al., 2008) studied the modification of rock mass parameters of four types of rock mass: carbonate rock, phosphate rock, mica pyroxene and dolomite. The elastic modulus of rock mass is 30%~50% of the intact rock measured by triaxial test, the tensile strength is 36%~56% of the cohesive force, and the cohesive force of joint surface is 1% ~0.1% of the rock mass. The friction Angle of joint surface is 10°~21° smaller than that of rock. The parameters obtained from phyllite triaxial test of Dashazui Tunnel were selected for rock matrix reduction and joint plane parameters, as shown in Table 4.

4.4 *Ubiquitous-joint model parameter*

Under the Mohr Coulomb model, the tunnel arch settlement reaches 21.42mm, invert heave reaches 23.83mm, and the longitudinal displacement is large. The position of the side wall of the tunnel arch foot converges horizontally, and the maximum value reaches 15.15mm. Under the Ubiquitous-joint model, the deformation after tunnel excavation shows asymmetry, the maximum vertical settlement occurs at the left arch waist, and the horizontal displacement of the left arch waist is larger than that of the right arch waist. From the perspective of the plastic zone after excavation, under the Mohr Coulomb model, the failure of surrounding rock is mainly shear, and the development of plastic zone is relatively symmetrical (as shown in Figure 5). Under the Ubiquitous-joint model, the failure form of surrounding rock of the tunnel is mainly shear failure of the joint plane, and the most serious direction of failure is basically perpendicular to the dip Angle of the joint plane, that is, the vertical Angle of the dip Angle of the joint plane has serious damage and large deformation influence range, while the parallel joint plane inclination direction has light deformation and small damage range (as shown in

Table 4. Matrix and joint plane parameters of phyllite rock mass.

	Elasticity(GPa)	Angle of internal friction(°)	Cohesion(MPa)	Poisson's ratio	Tensile strength(MPa)
Rock mass matrix	1.5	45	2.31	0.33	0.92
Joint plane	-	15	0.00154	0.33	0.92

Figure 6). It can be seen that the deformation of phyllite tunnel shows obvious asymmetry under the influence of joint inclination.

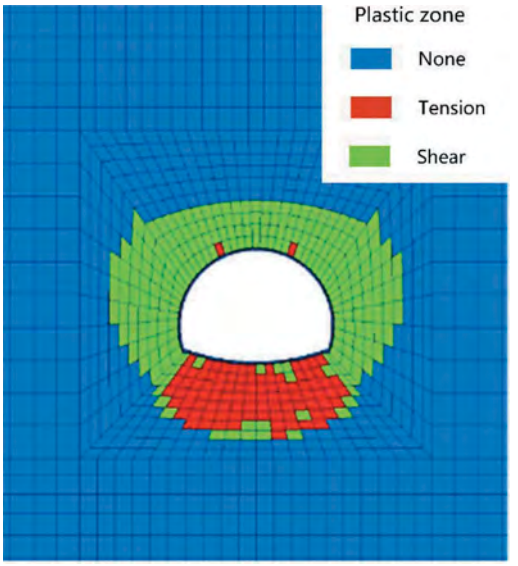

Figure 5. Mohr Coulomb model plastic region cloud image.

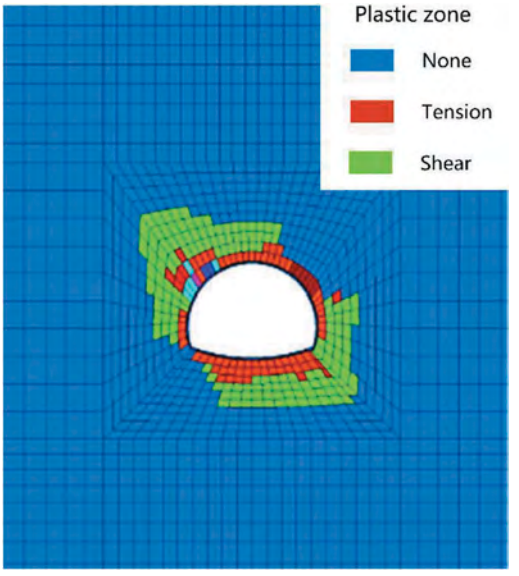

Figure 6. Ubiquitous-joint model plastic region cloud image.

4.5 *On-site measurements*

Comparing the on-site monitoring data of Dashazui Tunnel K193+760 with the numerical simulation results of the above two types of models(as shown in Figure 7), it is obvious that the use of Ubiquitous-joint model is the most suitable for the on-site displacement and deformation characteristics. From the on-site measurement results, the settlement of the left arch waist is larger than that of the right arch waist, the final settlement value of the left arch waist is 22.42mm, and the final settlement value of the right arch waist is 15.18mm. The use of the Ubiquitous-joint model matches the asymmetric deformation of the arch waist of the tunnel on-site. Using the Mohr Coulomb principle model with Hoek-Brown discount parameter, the settlement of the arch top is 21.42mm, which is in good agreement with the on-site monitoring data, but the left and right arch girdle settlements are equal to 19.81mm, and the error of the left arch girdle settlement is more than 40%. In addition, the horizontal convergence of the side wall measured in the field is about 6.81mm, which is relatively close to that calculated by the Ubiquitous-joint model. The horizontal convergence of the side wall calculated by Mohr Coulomb based on the Hoek-Brown reduced parameter is 13.97mm, which is significantly different from the on-site monitoring data. Comprehensive field test data, Ubiquitous-joint model is more suitable for the calculation of phyllite tunnels, and the calculated displacement maps and plastic zones are also in line with the general deformation characteristics of the laminated surrounding rock, the azimuthal displacement in the radial pressure perpendicular to the nodal surface is larger, and the shear damage impact zone is also larger.

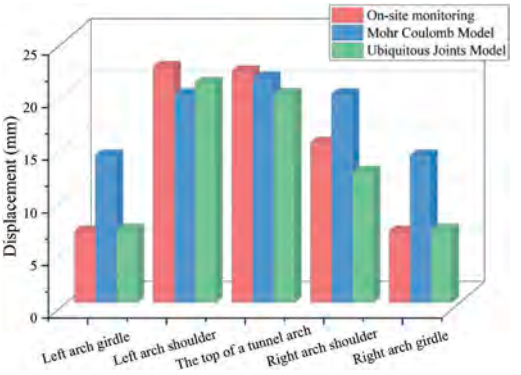

Figure 7. Comparison of on-site measurement and numerical simulation.

5 CONCLUSIONS

This chapter relies on the K190+463 section mileage of the right line of the Dashazui Tunnel Project as the calculation section for numerical simulation, and uses the Mohr Coulomb constitutive model and Ubiquitous-joint model to carry out numerical simulation. The numerical simulation results are verified by field measurement data, and the following conclusions are drawn:

(1) Based on the results of the triaxial compression test, the Hoek-Brown criterion was used to reduce the strength parameters of the rock mass suitable for numerical calculation. The numerical simulation results show that the vertical displacement, horizontal convergence, and the range of plastic zone of the tunnel have certain symmetry.
(2) The joint plane parameters and rock mass matrix parameters are obtained by reducing the rock mechanics parameters using the Ubiquitous-joint model. The numerical simulation results show that the maximum vertical displacement and horizontal displacement of the tunnel do not appear in the vault and side wall because of the joint dip Angle. The range of plastic zone also shows asymmetry.
(3) On-site monitoring data show that the settlement of the left arch girdle in K190+463 section is larger than that of the right arch girdle, and the overall deformation shows asymmetry. The asymmetric deformation indicates that the tunnel excavation section shows some concentrated damage due to the anisotropy of the phyllite rock mass. The results of the numerical simulation using the Ubiquitous-joint model are more consistent with the deformation and damage form of the surrounding rock in the field.

ACKNOWLEDGMENTS

The authors are very grateful for the High-Speed Railway and Natural Science United Foundation of China (U2034205)

REFERENCES

Deangeli, C., & Omwanghe, O. O. (2018). Prediction of Mud Pressures for the Stability of Wellbores Drilled in Transversely Isotropic Rocks. Energies, 11(8), Article 8. https://doi.org/10.3390/en11081944

Fortsakis, P., Nikas, K., Marinos, V., & Marinos, P. (2012). Anisotropic behaviour of stratified rock masses in tunnelling. Engineering Geology, 141–142, 74–83. https://doi.org/10.1016/j.enggeo.2012.05.001

Hu, K., Feng, Q., & Wang, X. (2017). Experimental Research on Mechanical Property of Phyllite Tunnel Surrounding Rock Under Different Moisture State. Geotechnical and Geological Engineering, 35(1), 303–311. https://doi.org/10.1007/s10706-016-0107-6

Li, X. Z., Wang, G. F., & Cao, L. (2014). Test Research on Influence of Water and Mineral Composition on Physical and Mechanical Properties of Phyllite. Applied Mechanics and Materials, 496–500, 2398–2401. https://doi.org/10.4028/www.scientific.net/AMM.496-500.2398

Meng, L., Li, T., Jiang, Y., Wang, R., & Li, Y. (2013). Characteristics and mechanisms of large deformation in the Zhegu mountain tunnel on the Sichuan–Tibet highway. Tunnelling and Underground Space Technology, 37, 157–164. https://doi.org/10.1016/j.tust.2013.03.009

Özbek, A., Gül, M., Karacan, E., & Alca, Ö. (2018). Anisotropy effect on strengths of metamorphic rocks. Journal of Rock Mechanics and Geotechnical Engineering, 10(1), 164–175. https://doi.org/10.1016/j.jrmge.2017.09.006

Ramamurthy, T., Rao, G. V., & Singh, J. (1993). Engineering behaviour of phyllites. Engineering Geology, 33(3), 209–225. https://doi.org/10.1016/0013-7952(93)90059-L

Saeidi, O., Rasouli, V., Vaneghi, R. G., Gholami, R., & Torabi, S. R. (2014). A modified failure criterion for transversely isotropic rocks. Geoscience Frontiers, 5(2), 215–225. https://doi.org/10.1016/j.gsf.2013.05.005

Sainsbury, B.-A., Pierce, M., & Mas Ivars, D. (2008, August 1). Simulation of Rock Mass Strength Anisotropy and Scale Effects Using A Ubiquitous Joint Rock Mass (UJRM) Model.

Shi, X., Yang, X., Meng, Y., & Li, G. (2016). An Anisotropic Strength Model for Layered Rocks Considering Planes of Weakness. Rock Mechanics and Rock Engineering, 49(9), 3783–3792. https://doi.org/10.1007/s00603-016-0985-1

Si, X., Huang, L., Li, X., Gong, F., & Liu, X. (2021). Mechanical properties and rockburst proneness of phyllite under uniaxial compression. Transactions of Nonferrous Metals Society of China, 31(12), 3862–3878. https://doi.org/10.1016/S1003-6326(21)65770-9

Tien, Y. M., & Kuo, M. C. (2001). A failure criterion for transversely isotropic rocks. International Journal of Rock Mechanics and Mining Sciences, 38(3), 399–412. https://doi.org/10.1016/S1365-1609(01)00007-7

Wang, Z., Qiao, C., Song, C., & Xu, J. (2014). Upper bound limit analysis of support pressures of shallow tunnels in layered jointed rock strata. Tunnelling and Underground Space Technology, 43, 171–183. https://doi.org/10.1016/j.tust.2014.05.010

Wu, H., Fan, F., Yang, X., Wang, Z., Lai, J., & Xie, Y. (2022). Large deformation characteristics and treatment effect for deep bias tunnel in broken phyllite: A case study. Engineering Failure Analysis, 135, 106045. https://doi.org/10.1016/j.engfailanal.2022.106045

Xu, G., He, C., Su, A., & Chen, Z. (2018). Experimental investigation of the anisotropic mechanical behavior of phyllite under triaxial compression. International Journal of Rock Mechanics and Mining Sciences, 104, 100–112. https://doi.org/10.1016/j.ijrmms.2018.02.017

Zan, W., Liu, L., Lai, J., Wang, E., Zhou, Y., & Yang, Q. (2023). Deformation failure characteristics of weathered phyllite tunnel and variable-stiffness support countermeasures: A case study. Engineering Failure Analysis, 153, 107553. https://doi.org/10.1016/j.engfailanal.2023.107553

Hoek, E., Carranza-Torres, C., & Corkum, B. (2002). Hoek-Brown failure criterion-2002 edition. Proceedings of NARMS-Tac, 1(1), 267–273.

Tunnelling for a Better Life – Yan, Celestino, Thewes & Eberhardt (Eds)
© 2024 The Author(s), ISBN 978-1-032-80042-4
Open Access: www.taylorfrancis.com, CC BY-NC-ND 4.0 license

Analysis of stability of rock column between cut & cover metro station and NATM tunnels

Swarup Maiti*
PG student, MIT World Peace University, Kharghar, Navi Mumbai, India

Makarand Khare
PG student, MIT World Peace University, Kharghar, Navi Mumbai, India
Director of Terranova Consultants, Mumbai, India

Sandeep Potnis
PG student, MIT World Peace University, Kharghar, Navi Mumbai, India
Head, School of Tunnel Engineering, MIT world Peace University, Pune, India

ABSTRACT: Planning and accommodation of underground metro stations in available land areas is an important aspect of any metro project. Designer has to adopt the innovative solution for station design due to limited space. To accommodate the station box within the available area, station may have to be constructed with the combined construction approach of NATM and cut and cover. In this approach main station box is constructed with a cut and cover method and platform tunnel is constructed with a NATM method. The sequence of construction can be simultaneous or opening of tunnel is carried out from the cut & cover shaft or TBM tunnel excavation is done before station excavation. Any underground excavation has a major influence on the nearby existing structures. This paper covers the various aspects of ground response to the interaction between strutted excavation and NATM tunnel excavation. Study of integrated excavation is carried out with varying the width of rock column between station excavation and NATM platform tunnel. The variations in the geological stratification and impact of different construction sequences are investigated.

Keywords: Earth Retaining System (ERS), secant pile, Platform NATM tunnel, Surface settlement, Underground metro, Rock column, cut and cover structures, deep excavations

1 INTRODUCTION

India has seen a huge development in the metro rail projects in the last 3 decades. Several Underground Metro projects have been constructed and many are in the under-construction and planning phase. Planning and design of the underground metro station is a challenging job. As most of the underground stations are planned in a densely populated area to gain more public ridership. Underground metro stations are usually planned under roads, empty ground. Planning of underground station under existing road has major issue i.e., protection of buildings adjacent to the metro station. One of the underground metro stations were planned in a densely populated area in Mumbai, on narrow roads, and in the station vicinity, several dilapidated buildings were present. Hence few stations were planned to construct with a mixed method of cut and cover for station box and NATM method for Platform tunnel. Owing to the presence of buildings in the vicinity of the station footprint the possibility of a complete cut and cover station was not feasible. Hence the innovative idea of integrated NATM platform tunnel and cut & cover station excavation is adopted in many stations. This study inspires by the same case where the station box is being executed by adopting the methodology of cut and cover method and the platform is being constructed by the NATM tunnelling method [1]. Connection with station box and NATM platform is made with the intermediate cross passages at regular intervals. Research study emphasis on the behaviour of integrated cut and cover excavation and excavation of NATM tunnel using predictable element of soil-structure interaction analysis. The results response of ground under different parameters are presented in this paper.

Alignment of the underground metro is generally planned through a heavily built-up urban area. Many times, important Landmarks and Heritage structures are located nearby or directly above the tunnel

*Corresponding author: swarup.bec.civ@gmail.com

DOI: 10.1201/9781003495505-106

alignment. Owing to land availability constraints, cost of private properties, inadequate available road width, and the very important presence of Heritage buildings planning, and design of metro alignment is important part of any underground metro project.

The alignment of an underground metro project is constructed with twin tunnels by Tunnel Boring Machine (TBM) connecting two stations. The underground stations or shaft are generally proposed to be constructed by adopting the cut & cover construction methodology, and NATM method of construction and ground settlements are to be limited to protect existing buildings.

Due presence of a high-water table, high rise building imposes a higher surcharge load which leads to higher settlements; however, the designer has to control it well within the acceptable limit. In high water table areas generally, excavation is done with a water-tight retaining system to prevent ground settlements due to seepage during excavations. To maintain the water table in the non-excavated area proposal of the recharge well may be required.

The purpose of this study is to carry out the assessment of rock column between cut & cover station and NATM tunnels of one Underground Metro project in Mumbai. This paper provides an analysis for safety of rock column.

- In Preliminary stage, the rock column width was 2.6m based on tender stage GIR.
- During construction stage, after preparing actual GIR, Geotechnical parameters were revised, and rock quality is considered to be poor w.r.t Tender GIR. Rock column width needed to increase for stability of supporting system during excavation.

Following analyses are performed –

a) Rock Column width 4m between cut & cover Station and NATM Tunnel
b) Rock Column width 5m between cut & cover Station and NATM Tunnel

2 LITERATURE REVIEW

The settlement data from TBM tunnelling in varying ground condition which are representative of the Mumbai geology are analysed and presented in this section.

In the year 1958, Martos has examined the settlement trough shape on mining excavations, which was represented by a Gaussian or Normal distribution curve.

On the later stage, Schimdt, and Peck in the year 1969 has shown that surface settlement in the above tunnels were experienced in a similar form. O'Reilly and New has developed the Gaussian mode in the year 1982, by assuming that the ground loss could be represented by a radial flow of material towards the tunnel and that the trough could be related to the ground conditions through an empirical "trough width parameter" (K). The model was guided by an analysis of case history data.

Due to the above assumptions, it was possible to develop equations for vertical and horizontal ground movements that were also presented in terms of ground strain, slope, and curvature (both at, and below, the ground surface). From there on, the equations are being widely used to access the potential impact of tunnelling works during the design stage. The base equation is as mentioned below.

$$S = S_{max} \exp\left(\frac{-x^2}{2(kz)^2}\right) = \frac{AV}{(kz)\sqrt{2\Pi}} \exp\left(\frac{-x^2}{2(kz)^2}\right)$$

Where S = ground settlement at a point; Smax = maximum ground settlement; A = cross-sectional area of tunnel; V = % of ground loss assuming the ground is incompressible i.e., V = Vs/A, where Vs is the volume loss; k = empirical constant also called as trough width parameter; and Z = depth of tunnel axis.

For an example, to determine /predict the ground movement only the following parameters were adopted /considered.

- Clough, O'Rourke and Peck adopted the excavation depth to determine ground movement as it is the only parameter.
- To predict the ground movement wherein the excavation depth is the main parameter in the formula, Bowles considered the area covered by lateral wall movement as a parameter.
- To predict the concave type and spandrel type of settlement profiles, Hsies and Ou used the excavation depth as the only parameter.
- Osman and Bolton adopted the plastic zone, which is completely related to the excavation depth and was the only parameter used in the prediction.

3 DESIGN OF TEMPORARY SUPPORT SYSTEM AND GEOLOGY

In combination of cut & cover and NATM underground metro station construction, there is access Tunnel at regular interval for connection between them. During excavation for access tunnel and Platform tunnel high stresses around the opening are to be checked and controlled. Therefore, rock column stability check is very important. This study has been performed using PLAXIS 2-D finite element analysis program.

As per requirement of Employer, all the tunnel sections shall be complied with Schedule of Dimension (SOD). The profile of Tunnel may be circular, D-Shape or horseshoe and it depends on the ground conditions. Here horse-shoe shape tunnel is considered. Cross sectional area of Tunnel is around 90.4 sqm., width is 11.2m and height is 10m. Overburden (soil mixed with rock) of 18m is considered above tunnel crown in this analysis. Actual geotechnical

profile and information is collected from GIR of project. Class IV and V rock are identified at final excavation level which is 28m below ground. For parallel construction and stability of the system, all the secant pile are terminated 4m below the final excavation level.

For stability analysis, following parameters have been considered in the model –

- Co-efficient of lateral earth pressure=0.5
- The soil is modelled by using Mohr-Coulomb material model
- Using Mohr-Coulomb material model, Rock mass is modelled where the strength and deformation properties are derived using Hoek and Brown criterion based on Hoek and Torres (2002).
- Water table at ground level
- Secant pile (combination of M40 - RCC and M10 - PCC) of 1m dia, 32m depth and 170mm overlap.
- All piles are 32m depth i.e., 4m below from final excavation level.
- 5 level struts are used for supporting of secant pile, horizontal spacing 10m c/c and vertical spacing 4.5m c/c.

Table 1. Properties of structural element.

Structural elements	Grade of Concrete	EA (kN/m)	EI (kN-m^2/m)
RCC Secant Pile (1m diameter)	M40	22.14E +06	645780
Sprayed concrete for primary Tunnel lining 200mm thick	M35	5.19E +06	19720

Table 2. Geotechnical parameters.

Material Type	Unit wt (kN/m3)	Cohesion c (kPa)	Friction angle	Young's modulus E (MPa)	Poisson's Ratio
Soil	18	1	30	12	0.3
Completely weathered rock	20	27	29	423	0.3
Moderately weathered rock	25	148	55	685	0.3

Following construction stages are considered in the model:

1. In-situ stage
2. Installation of Secant Piles
3. Lowering of water table inside the cut & cover box 1m below – 1st level of strut
4. Excavation of soil up to 1m below 1st level strut
5. Installation of 1st level strut
6. Repeat the stage 3, 4, 5 till the last design strut is installed
7. Excavation of NATM tunnel profile
8. Installation of Primary support
9. Installation of full-strength primary tunnel lining along with wire mesh.

Figure 1. Road level plan of station box.

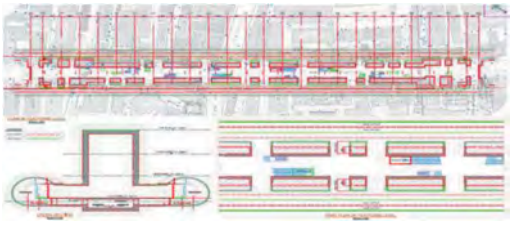

Figure 2. Undercroft level of station box.

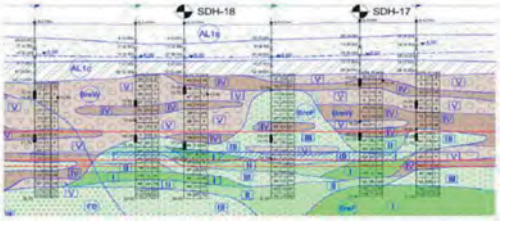

Figure 3. L- Section of geotechnical profile of station box.

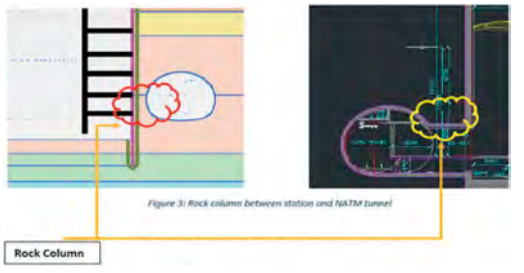

Figure 4. Rock column width.

4 METHODOLOGY

Analysis of the stability of rock column, properties of temporary support system and construction sequence are discussed here.

The geotechnical software PLAXIS 2D was used to study the soil-structure interaction between the cut & cover structure and NATM tunnel and its impact

on rock column stability. The software was used to provide the factor of safety of rock and soil for the proposed construction sequence.

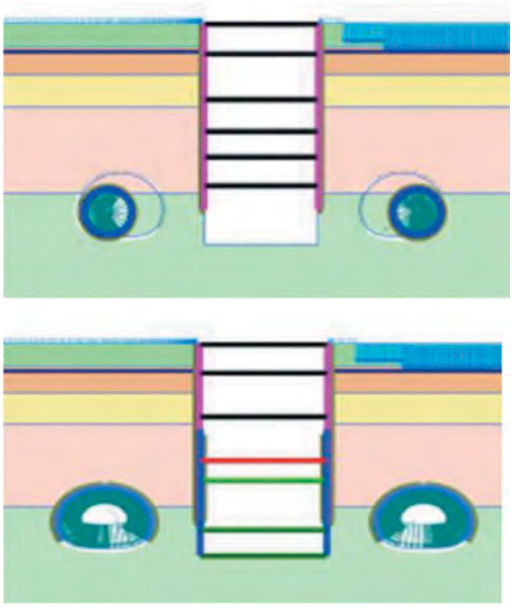

Figure 5. Construction stage PLAXIS 2-D model.

5 ANALYSIS AND RESULTS

Initially rock column of 2.66m width is analysed. The analysis was carried out for this column width, and it was observed that the rock collapses in this scenario. Hence, the width between the cut & cover station box and NATM tunnel was increased to have lower concentration of stresses in the rock column.

Following analysis were performed –

a) Rock column width of 4m between station and NATM Tunnel Plaxis output for Rock column stability (4m wide) considering 30% Relaxation –

Figure 6. Total displacement after final excavation of cut & cover Box: 43mm.

Figure 7. Maximum Total displacement near ground surface after NATM Construction: 50mm.

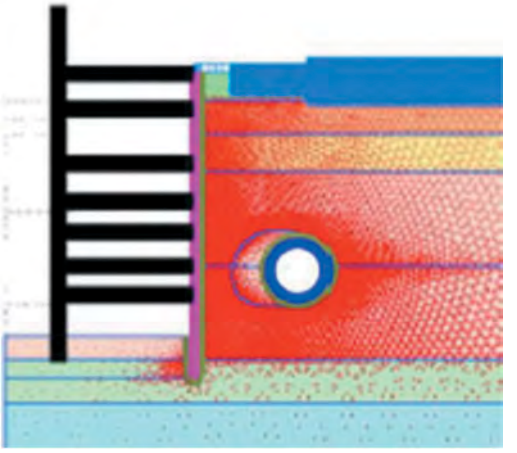

Figure 8. Total stress after final excavation of cut & cover Box.

Maximum value = 1822 kPa
Minimum value = -9982 kPa

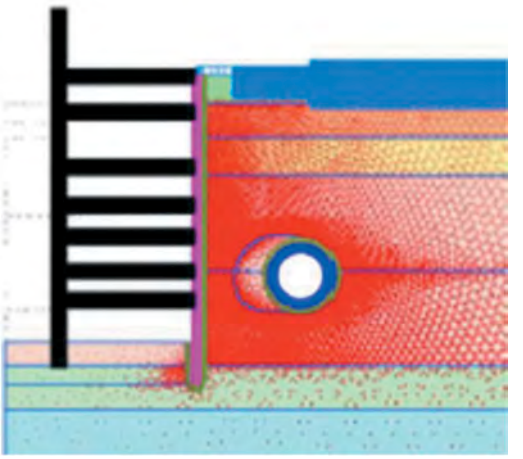

Figure 9. Total stress after construction of NATM lining.

Maximum value = 1895 kPa
Minimum value = -10.10*10^3 kPa

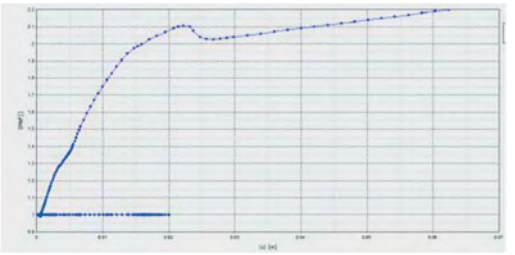

Figure 10. The factor of safety with column width 4m between station and NATM Tunnel.

b) Rock column width of 5m between station and NATM Tunnel Plaxis output for Rock column stability (5m wide) considering 30% Relaxation –

Figure 11. Maximum Total displacement near ground surface after final level excavation of cut & cover Box: 32mm.

Figure 12. Maximum Total displacement near ground surface after NATM construction: 39mm.

Maximum value = 1673 kPa
Minimum value = -8157 kPa
Maximum value = 1787 kPa
Minimum value = -9067 kPa

6 DISCUSSION AND CONCLUSION

To understand the complex soil-structure interaction Two-dimensional FEM modelling is used, involving cut & cover excavation with an adjacent NATM

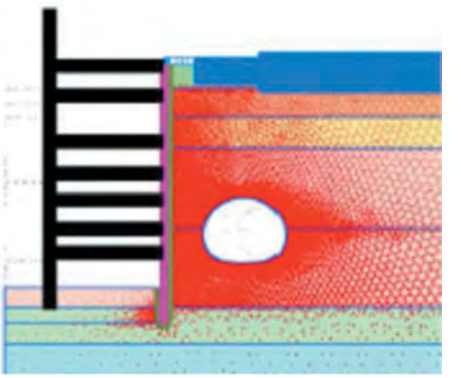

Figure 13. Total stress after final excavation of cut & Cover Box.

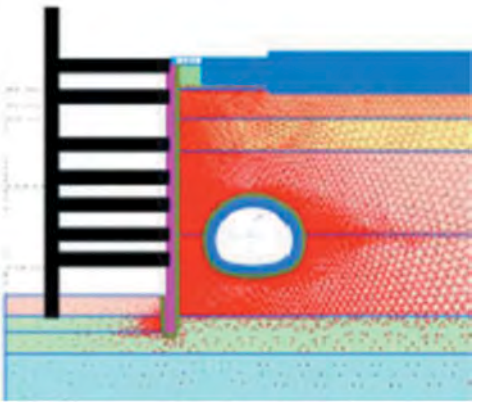

Figure 14. Total stress after construction of NATM lining.

Tunnel. It is observed that the excavation of Tunnel adjacent to the cut & cover box excavation influences the ground behavior along with the behavior of earth retaining system.

Geological stratification has major impact on tunnel design. Increase in rock column width, there is reduce of ground settlement and reduce of total stress.

Excavation of tunnel will cause a short-term loss of ground water due to which the unbalanced load path is imposed on earth retaining system of supporting cut & cover excavation. The unbalanced loading conditions increases the displacement of secant pile on the fair side of tunnel excavation. The loss of ground water can be controlled by installing a grout curtain around the tunnel profile before the start of excavation along with recharge wells.

It is observed that the tunnel excavation induces additional stress on the rock column and causes the rock column deformation. After excavation of tunnel, surface settlements increase immediately. The maximum surface settlements are observed immediately behind the secant pile. The width of rock column appears to have no major effect on the magnitude of maximum surface settlements. The slope of settlement trough is influence by the rock column width.

Table 3. Comparison of result of different rock column.

Rock Column width	Total displacement after final excavation of cut & cover Box	Maximum Total displacement near ground surface after NATM Construction	Total stress after final excavation of cut & cover Box	Total stress after construction of NATM lining	FOS
4m Rock Column width	43mm	50mm	Maximum value = 1822 kPa Minimum value = -9982 kPa [2]	Maximum value = 1895 kPa Minimum value = -10100 kPa	2.2
5m Rock Column width	32mm	39mm	Maximum value = 1673 kPa Minimum value = -8157 kPa	Maximum value = 1787 kPa Minimum value = -9067 kPa	2.8

Table 4. Actual displacement and stress for 5m rock column.

Rock Column width	Total displacement after near ground surface final excavation of cut & cover Box	Total displacement near ground surface after NATM Construction	Total stress after final excavation of cut & cover Box	Total stress after construction of NATM lining
5m Rock Column width	18 mm	21 mm	Maximum value = 903 kPa Minimum value = -5272 kPa	Maximum value = 988 kPa Minimum value = -5887 kPa

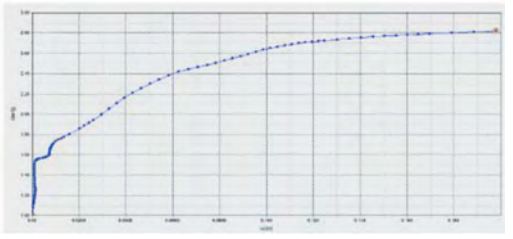

Figure 15. The factor of safety with column width 5m between station and NATM Tunnel.

Adjacent cut & cover excavation has an influence on the behavior of tunnel excavation. Tunnel lining was subjected to higher deformation at the face wall adjacent to the open excavation and deformation increased with reduction in width of the rock column.

From the analysis, it is concluded that the minimum width of rock column between station and NATM tunnel shall be 5m to achieve FOS of 2.8. A sensitivity analysis was carried out for 4m wide rock column, and the analysis was not successful (i.e., FOS<2.5), confirming that the minimum width of rock column shall be 5m for these geological conditions.

REFERENCES

[1] Mechanized Tunnelling in Urban Areas – Design methodology and construction control by Vittorio Gulielmetti, Piergiorgio Grasso, Ashraf Mahtab & Shulin Xu

[2] Martos, F. 1958. Concerning an approximate equation of the subsidence trough and its time factors. International Strata Control Congress, Leipzig, (Berlin: Deutsche Akademie der Wissenschaften zu Berlin, Section fur Bergbau), 191–205

[3] Peck, R. B. 1969. Deep excavation and tunneling in soft ground. 7th International Conference on Soil Mechanics and Foundation Engineering, Mexico City State-of-the-Art volume, 225–290

[4] O'Reilly, M. P. and New, B. M., 1982. Settlements above tunnels in the United Kingdom – their magnitude and prediction. Tunneling'82, London, 173–181.

[5] Clough GW, O'Rourke TD. Construction-induced movements of in situ walls. Proceeding of the design and performance of earth retaining structures, ASCE special conference, Ithaca, New York: 1990, 439–70.

[6] Bowles JE. Foundation analysis and design. 4th ed. New York: McGraw-Hill: 1986

[7] Hsieh PG, Ou CY. Analysis of nonlinear stress and strain in clay under the undrained condition. J Mech 2011; 27(2): 201–13

[8] Osman AS, Bolton MD. Ground movement predictions for braced excavations in undrained clay. J Geotech Geoenviron Engg 2006; 132(4):465–77.

[9] Chakeri H, Hasanpour R., Hindistan M., Unver B. (2010). Analysis of interaction between tunnels in the soft ground by 3D numerical modeling. Bulletin of Engineering Geology and the Environment, 70: 439–448.

[10] Hoek E., Carranza – Torres C. (2002). Hoek – Brown failure criterion, Edition 1, In: Proc. NARMS-TAC Conference, Toronto, 1, 267–273.

[11] Kim S. H., Burd H. J., Milligan G.W.E. (1998). Model testing of closely spaced tunnels in clay. Geotechnique. 48(3), 375–388.

[12] Liu H. Y., Small J. C., Carter J. P., Williams D. J. (2009). Effects of tunneling on existing support system of perpendicularly crossing tunnels, Comput Geotech. 36(5), 880–894.

[13] Perri G. (1994), Analysis of the effects of the new twin-tunnels excavation very close to a big diameter tunnel of Caracas Subway. In: Salam A (ed) Tunneling and ground conditions, Balkema, Rotterdam, 83–90.

[14] Shahrour I., Mroueh H. (1997). Three-dimensional nonlinear analysis of a closely twin tunnels. In: Sixth international symposium on numerical models in geomechanics (NUMOG VI), Montreal, QC, Canada, 2, 481–487.

Tunnelling for a Better Life – Yan, Celestino, Thewes & Eberhardt (Eds)
© 2024 The Author(s), ISBN 978-1-032-80042-4
Open Access: www.taylorfrancis.com, CC BY-NC-ND 4.0 license

The freezing technique for the world's longest railway tunnel

A. Marottoli, M. Ianeselli, R. Marrazzo*, A. Gallotto, G. Vecchione, M. Cavolo & F. Gallo
Brenner BasisTunnel BBT-SE, Bolzano-Fortezza, Italy

ABSTRACT: The Brenner Base Tunnel is a railway tunnel infrastructure under construction as part of an Italian-Austrian civil engineering project. It will connect Fortezza to Innsbruck, running under the Brenner Pass. The 'Isarco River Underpass' construction lot, the southernmost part of the entire infrastructure, overcame the major geotechnical difficulties encountered with the use of innovative technologies. These included artificial ground freezing and pre-consolidation of the excavation faces by means of Quick Set Jet Grouting (QSJG) and Roto Injection Controlled Parameters (RICP).

This article focuses on the adoption of artificial ground freezing technology as a consolidation technique for the construction of the four tunnel stretches connecting four shafts under the Isarco river, where the ground is characterised by the presence of loose debris material.

Artificial ground freezing is a 100% eco-friendly technology that, through the use of special cooling fluids circulating in suitable pipes, directly freezes the water in the ground without any product being injected and dispersed into the soil and/or groundwater.

For the Isarco River Underpass, the 'mixed method' was used, i.e. a rapid-freezing phase using liquid nitrogen followed by a longer temperature maintenance phase using brine, switching between the two phases only once the target temperatures defined by the planner had been reached. Before proceeding with the excavation, the drains inside the excavation core were opened in order to empty it and to verify the effectiveness of the freezing process by noting that water inflow had stopped.

Thanks to this solution, the excavation of the four tunnels under the Isarco River was completed without any particular problem, avoiding more invasive interventions such as the temporary displacement of the river and its subsequent repositioning in its natural location.

Keywords: ground improvement, artificial ground freezing, conventional tunnelling, temperature field, heat transfer

1 INTRODUCTION

The Brenner Base Tunnel is a railway tunnel currently under construction within an Italian-Austrian civil engineering project. It will connect Fortezza to Innsbruck, running under the Brenner Pass.

The Brenner Pass is one of the most important links between northern and southern Europe. At 1,371 metres above sea level, it is the lowest pass in the entire Alpine range and for this reason has always been considered strategic from an economic and commercial point of view. In order to cope with the continuous increase in the amount of goods transported, two major transport infrastructures were built: the historic Brenner railway in the second half of the 19th century and, about 100 years later, the A22 Brenner motorway.

150 years after its inauguration, the existing Brenner railway line continues to play a major role as a connecting axis between Italy and Austria, but its route is very winding and steep, with tight curves and sections with a gradient of 26 ‰. These two factors severely limit train speeds and load ceilings and, considering the cost of the vehicles needed to move the trains, the high consumption of electricity and the long journey times, road transport has been preferred to railway infrastructure for freight haulage, with a consequent increase in environmental impact.

In 1994, the European Union promoted and developed the TEN-T (Trans European Network-Transport) rail transport network, with the aim of shifting the increasingly heavy flow of road traffic onto rail and in order to support the single market, guarantee the free movement of goods and persons and strengthen the growth and competitiveness of the Union. Nine TEN-T corridors have been defined, touching all EU member states and linking the most important seaports

*Corresponding author: Roberta.Marrazzo@bbt-se.com

DOI: 10.1201/9781003495505-107

with railway infrastructure and access to main road arteries.

The Brenner Base Tunnel will be the central element of the Scandinavian-Mediterranean Corridor, running from Helsinki in Finland to Valletta on the island of Malta for a total length of approximately 7,500 km (Figure 1).

Figure 1. European union TEN-T corridors.

The new Brenner Base Tunnel will connect the village of Fortezza, about 50 km north of Bolzano, with the town of Innsbruck in Austria. It is defined as a "Base" tunnel precisely because it will be built at the base of the Brenner Pass at an altitude of 794 m above sea level, with an almost flat and straight route. When completed, it will be 55 km long compared to the 75 km of the existing line, with a maximum slope of approximately 7 ‰ (Figure 2).

Figure 2. Comparison of the existing railway line and the future brenner base tunnel.

On the new track, trains will thus be able to travel at a maximum speed of 250 km/h, cutting journey times from the current 80 minutes to just 25 minutes. Near Innsbruck the new tunnel will connect to the existing bypass around this Austrian city and thus reach a total length of 64 km, holding the record for the longest underground railway link in the world (Marottoli et al., 2022).

2 THE ISARCO RIVER UNDERPASS LOT

The construction of the Brenner Base Tunnel is an important engineering challenge, due to the size and the complexity of the works.

The Isarco underpass construction lot is the southernmost part of the Brenner Base Tunnel before entering the railway station in Fortezza and it is located approximately 1 km north of the town of Fortezza, in the Prà di Sopra neighbourhood (BZ).

The works were awarded in October 2014 to the bidding consortium that included Webuild Italia S.p.a, Strabag S.p.A./AG, Collini Lavori S.p.A. and Consorzio Integra.

The project area lies in the narrow valley floor, which is only a few hundred metres wide and enclosed by steep rock walls. In the middle of this area (Figure 3) we can see the Isarco river, highlighted in light blue, the transport infrastructures of the A22 motorway in green, the State Road 12 in red and the historical Brenner railway line in yellow, all of which therefore represent major interferences with the route of the tunnels, highlighted in blue.

Figure 3. Valley floor and route of the Isarco River Underpass lot.

The works in this lot, which is interdependent with the other lots in the project, include the construction of approximately 4.5 km of two main tubes and two interconnecting tunnels that link to the existing railway line, for a total of approximately 1.7 km. The lot also includes preparatory external works such as rerouting the SS12 state road, the construction of a bridge over the Isarco river, a bridge over the Rio Bianco brook, an underpass below the Brenner railway line, and the construction of the loading/unloading area on the A22, which makes it possible to handle incoming and outgoing transports without interfering with the local road system.

The tunnels are excavated entirely using conventional drilling and blasting techniques and divided into the following main parts (Figures 4):

- line tunnels, even and odd tracks north of the Isarco (in red);
- line tunnels, even and odd tracks south of the Isarco (in green);

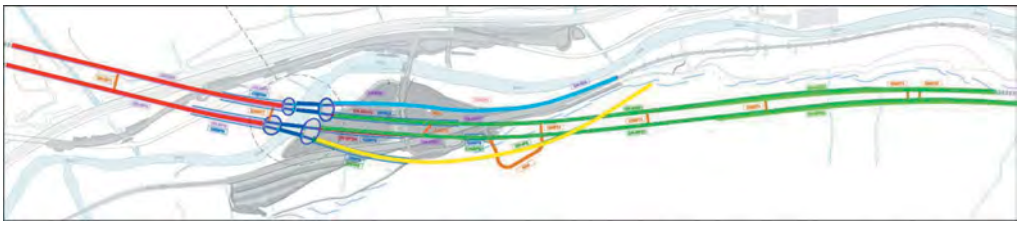

Figure 4. Map of the isarco river underpass lot.

- interconnection tunnel with the existing line, even track south of the Isarco (in yellow);
- interconnection tunnel with the existing line, odd-numbered track south of the Isarco (in light blue);
- line and interconnection tunnels, even and odd tracks, below the Isarco river (4 tunnels, in blue);
- southern entrance portals of the Brenner Base Tunnel, located in the area of Fortezza station;
- emergency exit.

In the Isarco Underpass lot, the tunnels are characterised by generally limited overburdens, single- and double-track excavation sections, and extremely variable geological conditions, ranging from excavations through Brixner granite at the beginning and end of the lot to excavations through scree below the water table to the Isarco Underpass, which is driven through alluvial material also below the water table.

In order to cope with these very different geological conditions, different excavation techniques were used:

- "drill and blast', excavation with explosives: used in the initial and final sections of the lot where the usually compact Brixner granite is present;
- excavation in granular material with advance consolidation: used in sections preceding rock mass characterised by coarse granular material in a sandy matrix with boulders several metres in size, with single-fluid jet-grouting columns and cement injections;
- excavation in granular material with consolidation from ground level: used in the sections near the Isarco River characterised by overburdens of less than 10-12 m in coarse alluvial soils in a sandy matrix with boulders several metres in size, with vertical bifluid jet-grouting columns;
- cut-and-cover tunnels and large shafts (surface area from approx. 800m^2 to approx. 1600m^2) constructed with consolidation from ground level. The shafts were necessary both to execute the freezing work for the river underpass and as starting points for the excavation of the tunnels north of the Isarco. These works were realised with vertical bi-fluid jet-grouting columns for both the walls and the bottom cap, excavated and encased in reinforced concrete with subsequent wall consolidation;
- excavation in granular material with consolidation using artificial ground freezing. This technique will be explored in more detail in the following paragraphs.

3 ARTIFICIAL GROUND FREEZING TECHNIQUE IN THE ISARCO RIVER UNDERPASS

The crucial point of the entire project is the excavation under the Isarco River of four full-bore tunnels, starting from four shafts approximately 30 metres deep and 60-80 metres in diameter (Figure 5).

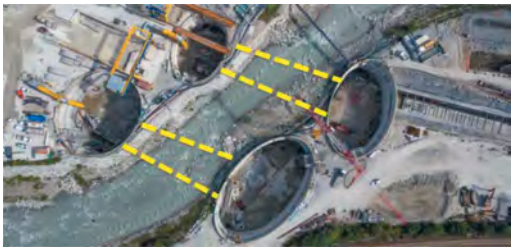

Figure 5. View from above of the 4 large shafts on the banks of the Isarco River.

The final approved project for the Brenner Base Tunnel envisaged the construction of an underpass beneath the Isarco river with cut-and-cover tunnels and the temporary diversion of the river into a specially constructed concrete basin, the bottom of which was lined with river stones embedded in concrete.

According to the executive design, on the other hand, the underpass was to have 4 tunnels driven from underground, hereinafter referred to as GNIDI, GNBDI, GNBPI and GNIPI (Figure 6), driven with full-section excavation from shafts placed laterally to the riverbed, after consolidation works were carried out using soil freezing technology. Pre-consolidation work was necessary in order to reduce underground water flow velocity and facilitate the freezing phase by acting on the permeability of the soil.

Choosing this method avoided the displacement of the Isarco river and protected the local environment, as only minimal in-bed displacement was required during the dry season to allow for the construction of the works to protect the river itself.

In order to use the freezing technique to consolidate the ground around the 4 tunnels connecting the south shafts to the north shafts, a so-called 'mixed method' was adopted, flushing a cooling liquid inside special heat exchangers, hereafter referred to as freezing probes.

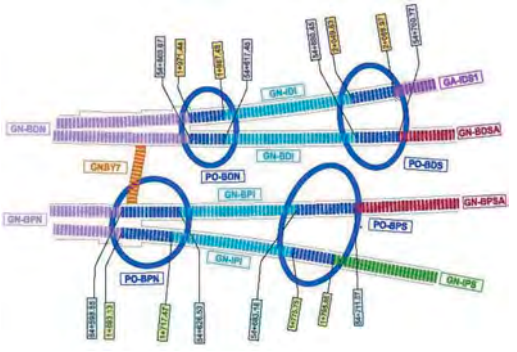

Figure 6. Detail of the map of the isarco river underpass lot.

The starting point for the flushing of the coolant was the walls of the north and south shafts (Figure 7), at the specific section of the tunnel to be driven, in two distinct phases:

- Phase one - liquid nitrogen freezing (open or direct circuit): compressed liquid nitrogen is circulated at a temperature of -196°C inside the freezing probes and dispersed into the environment as a gas at a temperature between -100 and -60°C (Figure 8). In this phase there is an accretion of an ice wall around the area to be excavated, with subsequent closure and achievement of the design thickness and temperature;
- Phase two - brine maintenance (closed or indirect circuit): the brine is an aqueous solution of calcium chloride with a freezing point between -40°C and -50°C, which is circulated at an approximate temperature of -35°C. On leaving the freezer probes, after subtracting heat from the ground and warming up by about 2/3°C, this liquid returns to the refrigeration system to be cooled and sent back to the freezer probes. In this phase, enough calories are extracted from the soil to maintain the geometric dimensions and characteristics of the soil frozen in the previous phase, without increasing its size.

Figure 7. View of the GNBDI south portal and detail of the freezing probes.

Figure 8. View of nitrogen vents.

This 'mixed method' was necessary to optimise execution times, minimise freezing times by using the direct nitrogen cycle, and for subsequent temperature maintenance throughout the excavation, waterproofing and final lining of the tunnels. This choice therefore required two separate and adjacent, but obviously complementary, site facilities to manage these two distinct soil freezing phases (Marottoli et al., 2020).

The liquid nitrogen ($_{N2}$) storage refrigeration plant included four double-walled tanks, with a storage capacity of 50,000 litres/each, connected in series, therefore with a total storage capacity of 200,000 litres. These tanks were equipped with a liquid nitrogen vaporisation and pressure system that allows the liquid nitrogen to be fed to the freezer probes without the use of a pumping system. The 4 tanks were installed not far from the shafts from which the freezing operations preparatory to the excavation of the 4 tunnels were launched. (Figure 9).

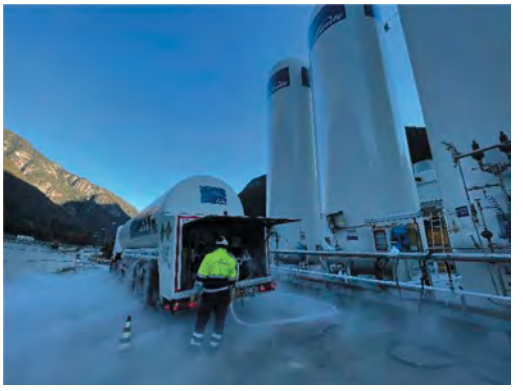

Figure 9. Liquid nitrogen supply to the storage facility.

Compressed liquid nitrogen at -196°C was conveyed from the silos to the two north and south portals at the entrance to the tunnels inside special sealed stainless-steel header pipes that maintained

the nitrogen's physical characteristics until it flowed into the freezer probe.

The brine plant (Figure 10) included three refrigeration units with an installed capacity of 240 kW each, for a total available capacity of 720 kW. Only two of the three installed refrigeration units were used during the freezing maintenance phase, to allow for rotating maintenance of these three pieces of equipment.

Figure 10. Brine storage plant.

The freezing probes consist of two coaxial pipes: the inner pipe, in stainless steel with a diameter of 42 mm and a thickness of 1.5 mm, from which the refrigerant fluid was delivered to the system, and the outer pipe, made of AISI stainless steel with a diameter of 76.10 mm and a thickness of 3.00 mm, through which the refrigerant fluid flowed back to the outside. The two tubes were connected at the head by a special distribution or 'freezing head'.

Prior to the installation of the stainless-steel pipes, sub-horizontal boreholes were drilled from inside the shafts around the perimeter of the future tunnel using drilling equipment specifically designed and engineered for the Isarco River Underpass works; within these boreholes and at the same time as the drilling phase, steel pipes with a diameter of 114 mm were laid, equipped with a disposable drill bit engineered to prevent groundwater from penetrating the pipe itself. These tubes also protected the freezing probes during the subsequent excavation phases.

In order to maintain the interaxis distances according to the design and allow the ice wall to be distributed as evenly as possible, the position of the freezer probes and thus of the corresponding probe holder tubes (114 mm) was constantly measured with a special inclinometer (Gyro by Reflex Instruments) which, by means of gyroscopes and accelerometers, made it possible to detect and three-dimensionally reconstruct the geometry of each individual probe with an azimuth tolerance of 1%.

To verify the effectiveness of the freezing and maintenance phases, temperatures were monitored by thermometric chains inserted inside the tubes used for the consolidation injections, except for several outermost ones.

The thermometer chains were constructed using fibre-optic technology, which allows a high number of measurement points, with continuous measurements every 25 cm along the length of the probe itself, in order to simplify data management.

3.1 *Three-dimensional modelling*

For ground freezing to be successful, the need for additional drilling should be assessed on a case-by-case basis, depending on the actual spacing of the probes. To this end, the deflections of all the boreholes intended to house the freezer probes were measured in order to reconstruct a three-dimensional model (Figures 11).

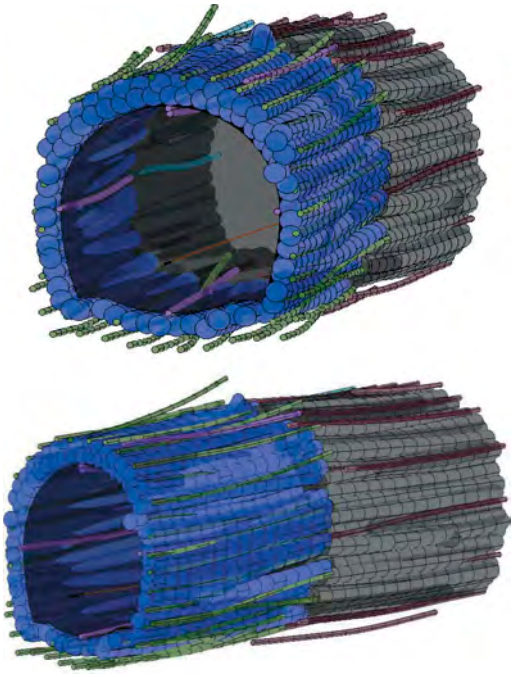

Figure 11. Construction of the 3D model for controlling deviations.

This model also made it possible to assess cases in which the probes came too close to the theoretical excavation profile by taking a minimum distance of 10 cm as a safety reference, below which it was decided not to equip the borehole with the freezer probe, or to equip it with a shorter probe in order to avoid the risk of damaging the probe during excavation operations.

3.2 *Design requirement*

The design requirements for the excavation of the tunnels were defined as follows: a maintained continuous ice wall with a thickness of at least 1.00 m, considering the temperature limit as -10°C with the non-permeability of the ice wall.

For the first requirement, target temperatures for each thermometer probe were defined by the designer as a function of the actual distance from the freezing probes, using a numerical finite element calculation model (TEMP-W from Geoslope).

The calculations to define the target temperatures were carried out considering the actual ground temperatures measured a few days before the start of the freezing treatment by means of the thermometric chains in place, taking into consideration the location of the probes and their position in relation to the excavation profile and verifying, for each of the measuring points, that the thickness of the frozen ground wall had been reached at temperatures not exceeding -10°C.

For each section analysed (every 3 metres), the crown of freezer probes was divided into sectors, each of which monitored by a particular thermometer probe. Each target, therefore, corresponds to the maximum temperature that can be reached in the sensor in order for the planned thickness of frozen ground to be reached at -10°C at the most critical point in the sector. Such critical points can be caused either by excessive spacing between probes, by abnormal deviations, or by failure to achieve continuity between the probes of opposite fronts.

The use of a numerical finite element calculation model is certainly beneficial, as it is more accurate than purely theoretical models, such as that of Sanger & Sayles (1979), as it takes into account all the boundary conditions and various factors that would otherwise not be considered (such as, for example, the overlapping effects of two or more freezing probes on the same sensor). However, it should be noted that there are still uncontrollable variables, such as the reliability of deviation measurements, which risk partially negating the effort required to implement such a sophisticated method.

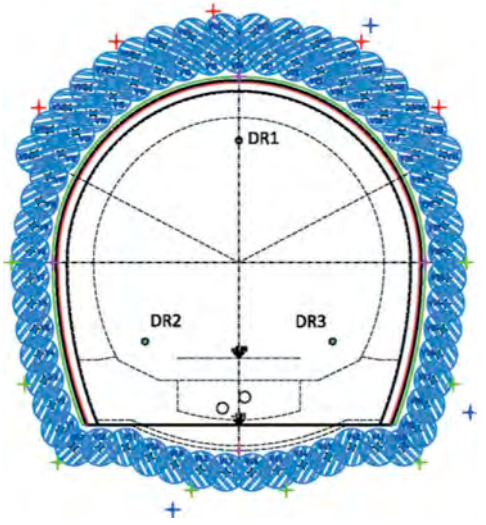

Figure 12. Typical section per executive design showing the location of DR1, DR2 and DR3 drains.

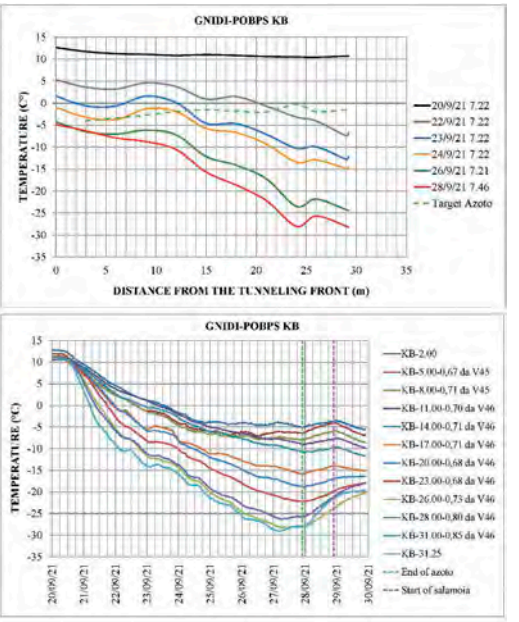

Figure 13 Graphs of the GNIDI KB thermometer probe from the south portal

Figure 13. Graphs of the GNIDI KB thermometer probe from the south portal.

In addition, the thickness of the ice wall is constrained not only by the spacing of the freezing probes but also, and above all, by time and by the quantity of the cooling fluid, and is guaranteed by the analysis of the three-dimensional model and any corrective actions at critical points.

In order to reach the required non-permeability, the drains located within the excavation core, which can be seen in Figure 12, were opened and therefore emptied prior to excavation.

In order to verify the presence of a continuous and therefore impermeable ice wall and, therefore, the effectiveness of the freezing phase, it is crucial that residual flow rates in the soil inside the ice wall be around 0 l/min.

3.3 *Temperature analysis*

Monitoring of the freezing technique implemented for the 4 tunnels was carried out with the following diagrams, evaluating the temperatures recorded by

the sensors of the thermometric probes every 3.00 m and carefully comparing the measured values with the target values foreseen by the designer.

- *Temperature-Distance from the excavation front*, which shows the trend of the temperatures measured along the thermometric probe as a function of the distance from the section at 0 m. This graphic representation makes it possible to visualise any increases or decreases in temperature and to study temperature evolution as the days go by. This diagram also shows the designer-defined target temperatures for each section;
- *Temperature-Time*, which makes it possible to evaluate for each sensor the temperature trend during the entire freezing process.

By way of example, the graphs referring to the freezing and maintenance phases of the GNIDI tunnel, the eastern interconnection tunnel excavated under the Isarco river, for which the first phase of nitrogen freezing began on 20/09/2021 and was interrupted on 28/09/2021 by the southern portal and on 29/09/2021 by the northern portal, thus totalling 9 days. The interruption of the nitrogen flow is followed by a waiting period that allows the freezing probes to reach, along their entire length, a temperature of around -45°C, i.e. a few degrees higher than phase transition (solidification) temperature of the brine. Brine flow therefore started about 24 hours later for both portals.

The following figure shows the graphs referring to the GNIDI KB thermometer probe from the South portal (Figure 13).

The *Temperature-Distance-to-Front-of-Attachment* graph clearly shows that, for this thermometer probe, even before the nitrogen flow was interrupted, temperatures below the target values visible from the green dashed curve were reached along all points of the probe under investigation.

It is important to note that, as the days pass, the temperature along the entire thermometer probe decreases almost constantly, with lower temperatures, even around -20°C, in the sections furthest away from 0 m. This happens because the furthest sections correspond to the overlap zone of the freezing probes, which is about 2 m, where we also have the effect of the probes from the other shaft.

In this area, the freezing probes are actually staggered so as to create an overlap zone necessary to minimise the risk of intersection.

Furthermore, it is useful to point out that the thermometer sensors, evaluated every 3 m, are different from probe to probe due to the inclination of the shaft front and therefore depend on the actual position with respect to it and to the section considered. For example, at the section at 0 m, the KB probe is 2.02 m from the front and the sensor to be considered, therefore, is the sensor at 2.00 m

The *Temperature-Time* graph shows how, when the nitrogen flow is suspended (dashed green line), there is a rise in temperatures within the frozen soil shell, with a subsequent drop again following the start of the holding phase with the brine flushing (dashed pink line).

As the days pass, however, one observes a stabilisation at temperature levels compatible with brine circulation (Figures 14).

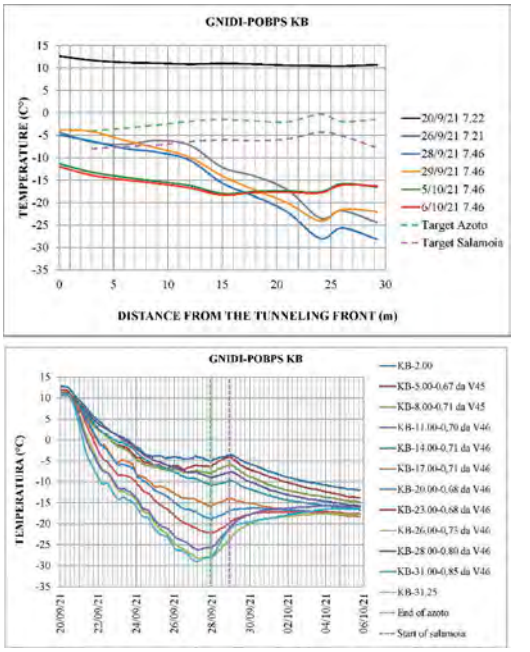

Figure 14. Graphs of the GNIDI KB thermometer probe from the south portal in the immediate brine phase.

Keeping the brine maintenance phase active, after verifying that the design requirements had been met, the excavation phases began with the demolition of the wall and the shaft structure until reaching the area of ground under the Isarco River, which at that point was well consolidated and dry with a visible band of frozen ground within the excavation profile (Figure 15).

The excavation was carried out with conventional methods, using hydraulic hammers on crawler excavators with an average advancement speed of 2.7 m/day, for excavation depths of approximately 1.00 m and a first stage lining with protective ribs and shotcrete at the contour and face, up to completion of the section.

Tunnel excavation operations lead to a rise in temperature, detected by thermometric probes at the excavation progress. As an example, the following figure (Figure 16) shows the progress of the excavation for the KG probe from the north of the GNIDI during different 24-hour windows, with temperatures rising in the sensors as the chainages progress.

Once the actual excavation phase was completed, during which the temperature trends were constantly monitored, the subsequent construction phases of the tunnels were carried out, including the excavation of

the inverted arch in segments of approximately 12.50 m, the laying of waterproofing sheets and the laying of the reinforcement with the subsequent casting of the final lining, up to the completion of the tunnel (Figure 17).

Figure 15. Band of frozen soil within the excavation profile.

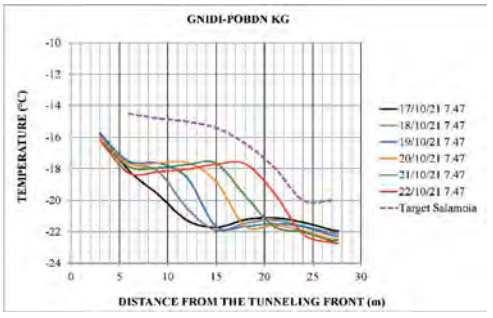

Figure 16. Graph of the GNIDI KG thermometer probe from the north portal during the excavation phases.

Figure 17. Tunnel completion.

It was only after the final lining of the tunnel was completed that brine flushing was stopped, on 08/12/2021, for a total of approximately 70 days.

The timing of the individual work phases for each tunnel section under the Isarco River, which were carried out in partial overlap with each other, was as follows. The preliminary phase, with the pre-consolidation work, permeability tests, measurement of deviations, installation of the freezing probes and equipping of the portals lasted approx. 5 months; the freezing and maintenance phase, with temperature monitoring and drainage tests, lasted approximately 3.5 months and the excavation and lining phase lasted approximately 3 months.

In total, the construction of each individual tunnel took about nine months.

The excavation of the four tunnels under the Isarco River was completed on 07.04.2022 (Figure 18).

Figure 18. Final breakthrough under the Isarco river: GNBDI tunnel on 07/04/2022.

4 CONCLUSIONS

It can therefore be confirmed that the technique of artificially freezing the ground is certainly the best alternative to other consolidation techniques normally used to protect excavations in the presence of water, which would also have involved more invasive and environmentally high-impact interventions, such as temporarily re-routing the river and subsequently returning it to its natural bed. In fact, this technique, where economically feasible, makes it possible to temporarily modify the characteristics of

the soil in terms of both non-permeability and the actual mechanical properties of the soil, both of which are significantly improved, thus enabling the safe excavation and construction of tunnels below the water table and beneath the river bed.

It is important to emphasise that successful freezing takes place in several stages, with the flow of refrigerants being only the final step.

Particular importance must be given to the drilling phase prior to the installation of the pipes and their deflection measurement. In fact, the evaluation of temperature trends can only properly monitor the formation and development of the ice shell, and analyse any anomalies that may occur, if the drilling deflections are measured correctly and as precisely as possible.

REFERENCES

Marottoli, A., Fossati, A. The Southernmost Lot of the Brenner Base Tunnel, the 'Eisack River Crossing'. Swiss Tunnel Congress 2022, 79–94.

Marottoli, A., Manassero, V., Marrazzo, R., Celot, A., Centis, S., Fossati, A., Vanin, A., Pettinaroli, A. Tutti i particolari del congelamento. Le Strade N. 1562/ 11 November 2020, 58–64.

Tunnelling for a Better Life – Yan, Celestino, Thewes & Eberhardt (Eds)
© 2024 The Author(s), ISBN 978-1-032-80042-4
Open Access: www.taylorfrancis.com, CC BY-NC-ND 4.0 license

Stability of portal slopes of a diversion tunnel after the Kahramanmaraş, Turkey (Türkiye) February 6, 2023 Earthquakes

Ahmet Ali Mert* & Fatih Caliskan
General Directorate of State Hydraulic Works, Dams and HEPP Department, Ankara, Turkey

ABSTRACT: This study delves into the stability challenges faced by portal slopes in a diversion tunnel, particularly post-Kahramanmaraş earthquakes in Turkey (February 6, 2023). Geotechnical issues, notably slope failures in portal areas, pose significant threats to tunnel safety and operability. The research analyzes both pre- and post-earthquake scenarios, employing methods like limit equilibrium and pseudo-static analyses. The investigation identifies parameters influencing portal slopes and assesses their behavior under static and dynamic loads. Solutions, including the use of fill and slope flattening (terracing) as a rehabilitation method, are proposed based on comprehensive analyses, field studies, laboratory experiments, and topographic data. The findings contribute valuable insights to combat stability problems in tunnel portal slopes, emphasizing their importance for tunnel safety and longevity. The study aims to guide engineers in developing safer and sustainable solutions for diversion tunnel projects, ultimately enhancing the overall stability and performance of portal slopes.

Keywords: Slope stability, Dams, Diversion tunnels, Earthquakes, Limit equilibrium, Pseudo-static analysis

1 INTRODUCTION

In order Slope stability is an important topic in geotechnical engineering that deals with the assessment of the potential failure or deformation of natural or artificial slopes due to various factors, such as gravity, seepage, external loads, seismicity, and weathering (Day, 2006). Slope stability analysis is necessary for the design and construction of various civil engineering structures, such as dams, embankments, roads, tunnels, excavations, and mines. Slope failure can cause significant economic losses, environmental damages, and human casualties. Therefore, it is essential to evaluate the stability of slopes under different conditions and scenarios using suitable methods and tools.

One of the difficult problems in slope stability analysis is the stability of tunnel portal slopes. Tunnel portals are the openings or entrances of tunnels that connect the underground space with the surface. Tunnel portals are often located on steep slopes that are susceptible to instability due to the excavation process and the presence of weak or fractured rock masses. Moreover, tunnel portals may be exposed to dynamic loads from earthquakes, blasting, or traffic that can generate additional stresses and deformations on the slope. Therefore, tunnel portal slopes need careful design and reinforcement to ensure their safety and functionality (Wang, 2019).

Popescu (2001) conducted a study in which he proposed a concise set of measures to mitigate landslides and recommended a specific format for documenting these landslide remediation efforts (Table 1).

Fatkhiandari et al. (2020) evaluated stability at the Bagong Dam tunnel portals under static and seismic loads using the finite element method. Despite earthquake-induced reductions in the Strength Reduction Factor (SRF), both natural and excavated slopes maintained relative stability.

Oktarina et al. (2023) assessed the stability of Tunnel No. 8 outlet portal under traffic loads, recommending shotcrete reinforcement to prevent instability and landslides in weak rock masses.

Sengkey et al. (2023) analyzed the diversion tunnel portal slopes at Manikin Dam, finding stability issues in the inlet portal slope due to poor mechanical properties of Bobonaro clay.

Huda et al. (2022) studied Lau Simeme Dam's diversion tunnel portals, emphasizing stability under static and earthquake loads. Shotcrete reinforcement was suggested for enhanced stability in poor rock mass conditions.

*Corresponding author: ahmetalimert@utexas.edu

DOI: 10.1201/9781003495505-108

Table 1. Overview of landslide remedial measures (Popescu, 2001).

No.	Category	Remedial Measure
1	Slope Geometry Modification	1.1 Removal of material from the landslide area with potential substitution by lightweight fill
		1.2 Addition of material to maintain stability, using counterweight berms or fill
		1.3 Reduction of the overall slope angle
2	Drainage	2.1 Installation of surface drains to divert water away from the slide area, including collecting ditches and pipes
		2.2 Implementation of shallow or deep trench drains filled with free-draining geomaterials, such as coarse granular fills and geosynthetics
		2.3 Creation of buttress counterforts using coarse-grained materials to achieve a hydrological effect
		2.4 Installation of vertical (small-diameter) boreholes, either pumped or self-draining
		2.5 Establishment of vertical (large-diameter) wells with gravity draining
		2.6 Implementation of sub-horizontal or sub-vertical boreholes
		2.7 Construction of drainage tunnels, galleries, or adits
		2.8 Employment of vacuum dewatering techniques
		2.9 Drainage achieved through siphoning
		2.10 Application of electro-osmotic dewatering techniques
		2.11 Introduction of vegetation planting with a hydrological effect
3	Retaining Structures	3.1 Implementation of gravity-retaining walls
		3.2 Construction of crib-block walls
		3.3 Development of gabion walls
		3.4 Creation of passive piles, piers, and caissons
		3.5 Building cast-in-situ reinforced concrete walls
		3.6 Establishment of reinforced earth-retaining structures with strip/sheet-polymer/metallic-reinforcement elements
		3.7 Installation of buttress counterforts using coarse-grained material to achieve a mechanical effect
		3.8 Deployment of retention nets for rock slope faces
		3.9 Implementation of rock fall attenuation or stopping systems, including rock trap ditches, benches, fences, and walls
		3.10 Use of protective rock/concrete blocks against erosion
4	Internal Slope Reinforcement	4.1 Application of rock bolts
		4.2 Installation of micropiles
		4.3 Implementation of soil nailing techniques
		4.4 Use of anchors, whether pre-stressed or not
		4.5 Application of grouting
		4.6 Creation of stone or lime/cement columns

This study examines stability challenges in diversion tunnel portal slopes, focusing on post-Kahramanmaraş earthquakes in Turkey (February 6, 2023). The earthquakes, magnitudes 7.8 and 7.5, caused widespread damage and numerous fatalities. Portal slope failures pose significant threats to tunnel safety. The research utilizes limit equilibrium and pseudo-static analyses for both pre- and post-earthquake scenarios. Limit equilibrium assesses slope stability by calculating the factor of safety, while pseudo-static analysis simplifies seismic slope stability with constant seismic coefficients (Naseer & Evans, 2020; Hammouri et al., 2008). The investigation identifies parameters influencing portal slopes under static and dynamic loads, proposing solutions such as fill application and slope flattening. Fill material enhances stability by increasing normal stress, reducing pore water pressure, and adding resistance along the potential slip surface (Wang, 2019). The study provides crucial insights for addressing stability issues in tunnel portal slopes, emphasizing thfeir significance for tunnel safety and durability. Intended to guide engineers in developing safer, sustainable solutions for diversion tunnel projects, the research aims to enhance overall stability and efficiency of portal slopes.

2 METHODOLOGY

The dam project involved initial investigations, including 24 foundation borings with a total depth of 1108 m, conducted during the planning stage. These borings were distributed among the dam location (17), two axis locations (17), diversion location (2), spillway route (2), and transmission tunnel (3). In the final project phase, 13 boreholes with a total depth of 400 m were drilled at the dam and construction sites, and 6 boreholes with a total depth of 95 m were drilled at the siphon site on the transmission line. Additionally, 63 pressuremeter tests were performed in 4 boreholes at the dam site.

Parameters for the Rock Mass Rating (RMR) classification method were determined by evaluating field observations, drilling and field studies, literature data, and factors such as weathering, discontinuity conditions, unit boundaries, distribution, and measurements. The RMR method considers parameters related to Rock Quality Designation (RQD), uniaxial compressive strength, joint frequency, joint location, groundwater conditions, and the relationship of the dominant joint system with the slope.

Slope stability analyses were conducted for both inlet and outlet portals, employing the limit equilibrium method for static and seismic conditions (Simplified Bishop, GLE/Morgenstern-Price, Spencer). Pseudo-static slope stability analysis, a simplified approach considering seismic forces as an equivalent static force, was used for seismic conditions. This method assumes instantaneous seismic forces and slope failure under pseudo-static conditions (Duncan and Wright, 2005).

The limit equilibrium analysis involved calculating resisting forces (e.g., frictional forces) and driving forces (e.g., seismic forces, loads) to determine the factor of safety. Analyses considered landslide conditions, landslide prevention support cases, and the aftermath of the February 6, 2023 Kahramanmaraş earthquakes, with corresponding results and recommendations presented.

3 SITE DESCRIPTION

The Ophiolitic complex sediments (Ofk-s) in the project area consist of clay-altered, dispersed, loose, unstable, silicified-radiolarite conglomeratic limestone, and serpentinite blocks. This formation is prevalent at the dam axis, diversion, spillway,

relocation roads, post-siphon end sections of the transmission line, and tunnel portal area. Drillings in this formation (Ofk-s) consistently reveal core percentages between 42% and 71%, with an RQD of 0%, indicating a weak and very weak rock mass.

Numerous landslides, both old and active, along with runoff occurrences are observed at the dam axis, mainly within the sedimentary levels of the Ophiolite Complex (Ofk-s). The high alteration of the unit, coupled with weakly cemented clay, sand, gravel, and block-sized material, leads to water absorption during rainy seasons. This absorption causes clay layers to swell, increasing the mass's weight and resulting in mud flow along the slopes.

Vertical faults have developed in the project area within the Ophiolite Complex and at the junction of this unit and the Midyat Formation. Another important fault is the reverse fault at the junction of the Ultrabasics (Ofk-u) and Volcanites (Ofk -v) within the Ophiolite Complex. The ophiolite unit was observed in the field as weakly to very weakly fractured, fragmented and weathered with the influence of these faults and the Eastern Anatolian fault line.

At the inlet and outlet portals and side slope excavations of the diversion tunnel, it was observed that the unit consists of silicified radiolarite units of the ophiolite complex which is clayified, dispersed, weak-very weak rock in places. The portal location is on the dry stream route and water discharge during rainfall comes to the portal excavation slopes through this stream. This unit is clayified in contact with water such as rain and snow, causing surface flows and landslides.

Below are the obtained geotechnical parameters to be used in analyses.

Table 2. General geotechnical parameters.

Parameters	Cohesion (kPa)	Internal Friction Angle (º)
Very weak altered rock near the surface	25	3
Compacted unsorted material to be used in the embankment	5	25
Rock fill	0	40

It is recommended to place 1.00 m of rockfill on slopes to prevent yielding and ensure stability. Seismic hazard analysis indicates peak ground accelerations: MDE (Maximum Design Earthquake) = 0.28g, OBE (Operation Based Earthquake) = 0.14g. Borehole results on the tunnel route show weathered ophiolite (0.00-11.00 m) and ophiolite complex (11.00-50.00 m). Groundwater level is 1.10 m. Borehole tests include permeability, pressurized water, and standard penetration tests at various levels. Rock core samples underwent uniaxial compressive strength and point loading tests (Table 3).

Geotechnical parameters for the weak rock of the ophiolitic unit in the diversion section are cohesion in the range of 100-200 kPa and internal friction angle in the range of 15°-25°.

For the ophiolite complex (siliceous shale), 75 kPa cohesion, 20° angle of internal friction, 25 kN/m^3 unit volume weight were selected as the strength parameters to be used in the calculations considering the calculations and evaluations made for the values of mi = 7 and GSI = 32, uniaxial compression test result 23 kg/cm^2 from laboratory results, as well as laboratory data and field observations.

3.1 *Tunnel inlet*

Diversion Tunnel entrance and water intake structure excavations had been completed. Although there was a requirement for typical slope reinforcement if necessary for excavations to be carried out in the open, only the first benches of the tunnel entrance portal were supported with mesh steel and shotcrete in the diversion tunnel entrance excavations. Diversion tunnel entrance portal, water intake structure and route excavation slopes were opened in ophiolitic unit which is weak to very weak rock. The excavations were exposed without support for a long time, and landslides and flows occurred on the slopes due to the effect of water and rainwater in the unit. It was observed that the additional benches opened in the diversion tunnel route excavations were very close to the dam plinth route.

3.2 *Tunnel inlet*

The exit excavations of the diversion tunnel had been completed, while conduit excavation had not yet commenced. Despite the necessity for standard

Table 3. Ophiolite complex laboratory test results.

					Point Load Test	
Depth (m)	Unit Weight (g/cm^3)	Uniaxial Compression Strength (kg/cm^3)	Modulus of Elast icity (kg/cm^3)	Poisson's Ratio	Is_{50} (MPa)	q_u (kg/cm^2)
36.20-36.40	2.57	162.9	41681	0.26	-	-
45.40-45.60	2.55	-	-	-	2.13	521.27
47.00-47.80	2.49	23.00	25641	0.25	-	-

Figure 1. View of flows on the right and left slope slopes at the diversion tunnel entrance portal.

slope reinforcement in open excavations, there was an absence of support in the diversion tunnel exit excavations. These excavations, situated in an ophiolitic unit with weak to very weak rock slopes, remained exposed for an extended period without support, resulting in landslides and erosion triggered by water and rainwater. The diversion tunnel exit portal excavation, conducted in proximity to the body skirt, was observed to be opened without diverting the tunnel itself. This proximity to the body, and potentially within it, suggests a deviation from standard excavation practices. Furthermore, water inflows perpendicular to the diversion tunnel route were identified.

Figure 2. View of the diversion tunnel exit portal and slope failure.

The excavations left exposed formed an altered zone in contact with air and water, lead a sliding, and the diversion tunnel exit was closed (Figure 3).

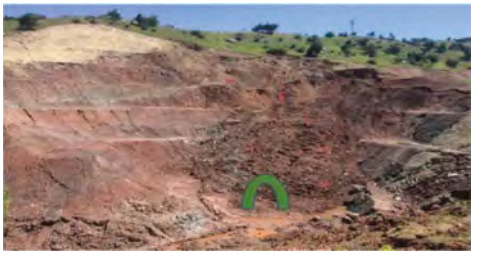

Figure 3. Diversion outlet, in-situ situation on 01.05.2020.

Figure 4. View from the slides on the hillside at diversion tunnel outlet conduit route.

As can be seen in the following figure, during the February 6, 2023 Kahramanmaraş sequential earthquakes, the first M7.5 magnitude earthquake struck the dam area in 0.1g-0.2g ground acceleration range, while it went up to 0.48g during the second M7.8 magnitude shock. This data was observed at the nearest instrumentation station to the dam site (USGS, 2023).

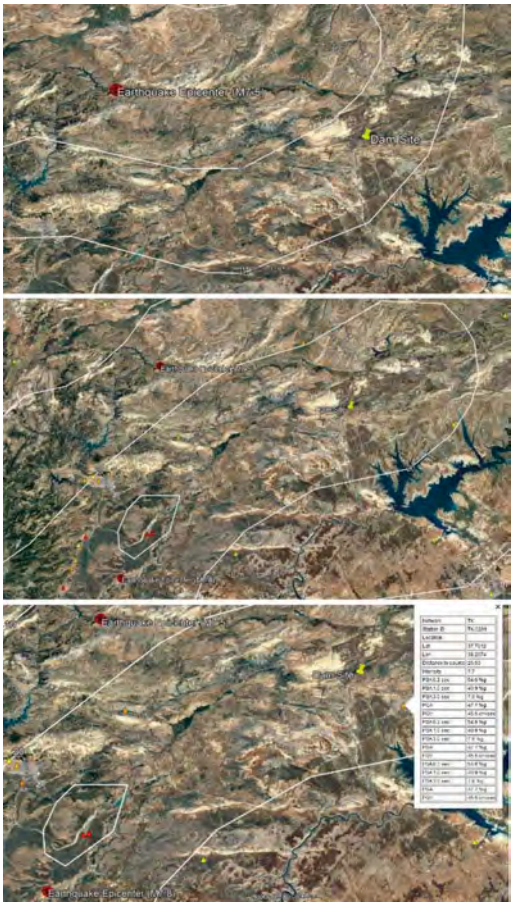

Figure 5. Observed PGA values after M7.5 and M7.8 magnitude earthquakes.

4 SOLUTIONS AND RECOMMENDATIONS

To stabilize the slopes at the diversion tunnel entrance portal, two alternatives were considered. The first involves terracing the slopes at 3H:2V, implementing typical slope support, and incorporating a concrete trapezoidal channel at the base for scour prevention. The existing temporary 1H:1V slopes were part of this alternative. The second alternative proposes a retreat of these slopes, creating a 6.00m base width, constructing a conduit instead of a trapezoidal channel, and covering it with fill before the tunnel entrance. The water intake tower is recommended to be positioned openly on the conduit, away from the portal slope, mitigating potential slope slippage damage.

For the portal excavation, an additional option considers addressing flows at the existing portal location by lowering the excavation slopes and supporting them with a typical support system. In its current state, the portal excavations are at a 1H:1V slope, and flows have occurred. To address this, a design shift to a 3H:2V slope with a 6m high bench and typical support is proposed. The excavation slopes will reach the dam axis and the access road, avoiding the challenges posed by the existing 1H:1V slopes, which are close to the dam plinth line.

The second alternative recommends setting back the temporary 1H:1V slopes on the sides, creating a 6.00m base width, and covering the portal excavation area with fill until the tunnel entrance. The water intake tower is set back 10.00m from the portal to mitigate potential slope slippage risks. The top of the conduit will be backfilled with compacted mineral fill up to the first pallet elevation to form a heel, and the portal slope will be tilted 2H:1V to prevent sliding under the plinth. The excavation slopes are suggested to be arranged with embankment at a 2H:1V slope. Additionally, 1.00m rock filling is recommended to prevent flow and slipping on the embankment, designed in different sections based on the fill load on the conduit.

5 RESULTS AND DISCUSSION

5.1 *Stability analysis*

0.14g ground acceleration (OBE) was used in the seismic (pseudo-static) analyses of slope rehabilitation. For the actual earthquake comparison, the observed PGA of 0.48g was used.

5.1.1 *Inlet*

Geotechnical parameters were determined for the unit in the diversion inlet excavations and slope stability analyses were performed. Necessary alternative studies were carried out to ensure the safety of the slopes and it was aimed to make the slopes safe. Regarding the excavated part of the diversion entrance route, the current situation was mapped and the existing excavation and the structures in the project were processed, and the interaction of the excavations already opened in the field and the body plinth route was evaluated. The following slope stability analyses were performed for the excavations to be carried out at 1H:1V slope gradient. On the ophiolitic complex, which is a weak to very weak rock, a section close to the surface decomposes due to contact with air and water and forms an altered zone. In the analyses, the altered zone formed when the slope surface is left exposed and the situation where the contact of the unit with air and water is cut off with support were also analyzed.

Static and pseudo-static stability analyses are given below for 1H:1V excavation with steel mesh and shotcrete support, where air-water contact on the slope surface is interrupted by weep holes and slope drainage.

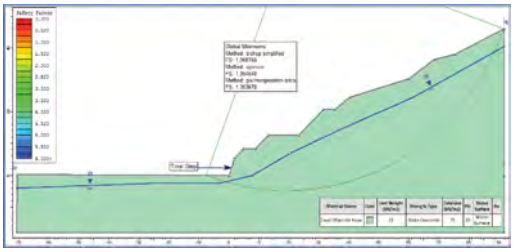

Figure 6. Diversion tunnel inlet 1H:1V supported static stability analysis (FS= 1.35 < 1.5).

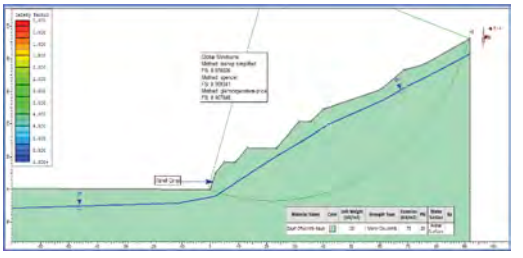

Figure 7. Diversion tunnel entrance 1H:1V supported seismic stability analysis (FS = 0.96 < 1.1).

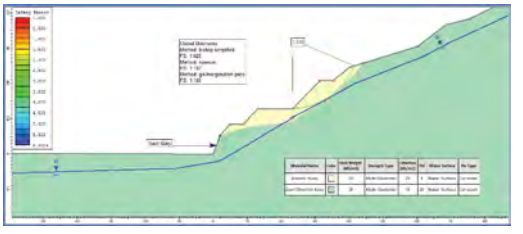

Figure 8. Diversion tunnel entrance 1H:1V unsupported static stability analysis (FS= 1.18 < 1.5).

If the slope is 3H:2V for permanent excavations, the slopes cannot be opened as they reach under the plinth and under the dam body. For this reason, since the portal excavations opened with temporary slope slopes of 1H:1V that do not provide stability, the slope stability will be ensured by constructing a conduit instead of a trapezoidal channel until the tunnel entrance and filling the slopes and conduit with fill and the topography reaching its own slope. Backfill slopes will not be steeper than 2H:1V. It is recommended that 1.00 m of rock fill should be placed on the backfill applied on the slope surface in order to prevent it from collapsing with the current.

Static and pseudo-static stability analyses are given below in case of 2H:1V filling after 1H:1V excavation.

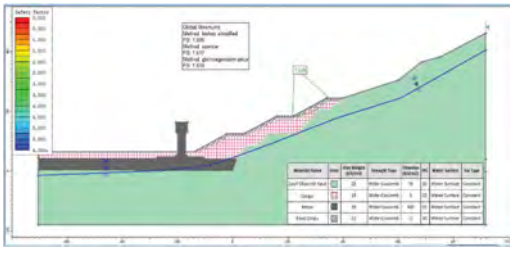

Figure 9. Diversion tunnel inlet conduit section static stability analysis (FS= 1.506 > 1.5).

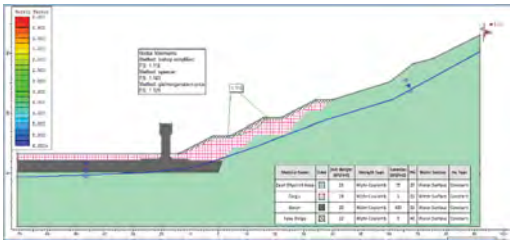

Figure 10. Seismic stability analysis of the diversion tunnel entrance conduit section (FS= 1.118 > 1.1).

It is recommended to apply steel mesh and at least 5cm+5cm shotcrete according to the support type in the project. In the final project, the bolt length is given as 4m, which is not long enough. In this type of soils, the bolts do not work because there is no block, solid rock where the rock bolt will be anchored and the slip surfaces are formed in a wide circle. Due to this reason, it is recommended to lower the slope gradients and reduce the bench heights in terms of stability. In cases where it is not possible to lower the slopes at the entrance section of the diversion (excavations enter into the body), the topography should be brought to its natural slope by passing through a conduit (such as a cut-and-cover tunnel) and backfilling.

The following analysis is not a dam body stability analysis, but an analysis of the interaction between the body and the conduit entrance completed during the construction of the body. According to the height of the body, approximately 4kg/cm^2 load is applied.

Figure 11. Interaction with the body after conduit backfill in static condition (FS=1.54>1.5).

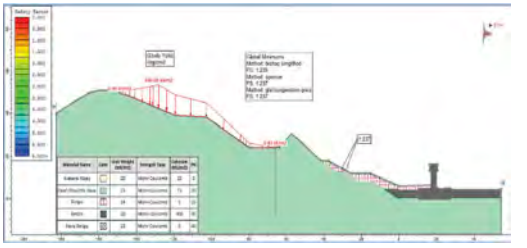

Figure 12. Interaction with the body after conduit backfill for seismic case (FS=1.23>1.1).

Cleaning excavation will be made in the sliding area and it will be covered again with backfill after the conduit. It is recommended that the new slope excavations to be opened by the conduit should be opened with supports and drainage.

The analysis below corresponds to the model in Figure 12, utilizing an actual PGA of 0.48g from the M7.8 magnitude earthquake as the horizontal ground acceleration. Factors of safety below 0.759 are associated with shallow slope failures, and only critical and deep slope surfaces were evaluated, ensuring a minimum factor of safety of 0.759.

Figure 13. Interaction with the body after conduit backfill for seismic case for 0.48g (FS=0.759<1.0).

5.1.2 *Outlet*

Geotechnical parameters were determined for the diversion outlet excavations, and slope stability

analyses were conducted to ensure safety. Mapping the current conditions and evaluating the interaction of the body with existing excavations, particularly those in the field, were part of the assessment. Water flowing perpendicular to the conduit's route will be diverted from upper elevations parallel to the valve chamber access road and released into the stream bed.

Cracks and splits were observed in shaft sections leading to the valve chamber. To preserve the valve room road, the first two slopes from the base were analyzed at a 1H:1V slope, while slopes between the third slope pallet elevation and the valve room access road were analyzed at a 3H:2V slope. Slope stability analyses were conducted for excavations at 1H:1V and 3H:2V slope gradients, considering the altered zone and interruption of the unit's contact with air and water when the slope surface is exposed.

Face portal slope stability analyses were undertaken in two sections—the body and diversion sections—ensuring stability. However, in the interest of brevity, face portal analyses are not included in this paper.

In the analysis performed without support in temporary excavation at the critical section of the diversion outlet, the safety factor was 1.18 due to the effect of the altered zone. As also seen in the field, failures occur from the slope surface (Figure 14).

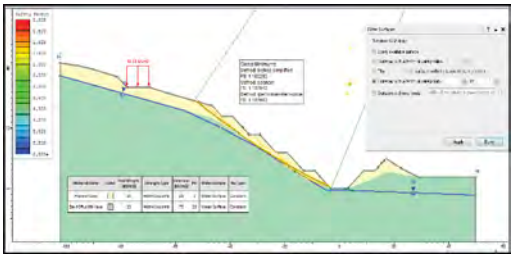

Figure 14. Diversion outlet 1H:1V unsupported static stability analysis (FS=1.18<1.50).

The diversion outlet's critical section underwent analysis with slope reinforcement, utilizing steel mesh and shotcrete during excavations on a 1H:1V slope to obstruct the unit's contact with air and water. It is anticipated that cutting this contact, along with water removal through a drainage system, including head ditches and weep holes in the benches, will prevent the formation of an altered zone. Application of steel mesh, 5cm+5cm shotcrete, and weep holes in the supports was considered. Analysis revealed that the use of short rock bolts did not significantly impact stability, given the wide sliding arc.

Since the safety factor is 1.33 for the first two slope surfaces 1H:1V from the base and 3H:2V for the upper slopes, there will be a stability problem in case of permanent excavation (Figure 15).

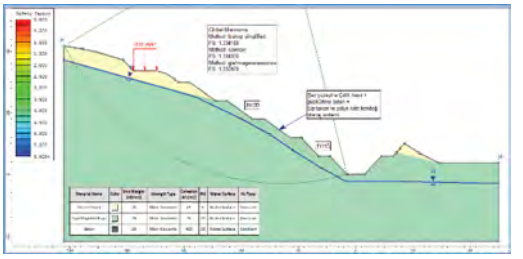

Figure 15. Static stability analysis with diversion outlet 1H:1V support (FS = 1.33 < 1.50).

If filling is done only up to the first bench, stability problems will still persist (Figure 16).

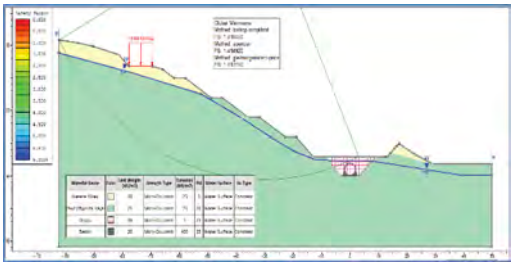

Figure 16. Static stability analysis of backfill up to the first bench at the diversion outlet (FS = 1.41 < 1.50).

The slope heel filling on the slope close to the natural slope of the topography was analyzed below. The case of filling with backfill up to the first two bench elevations and supporting the slope surfaces with 2H:1V slope protection embankment is analyzed. In the slope protection embankment, it is recommended to construct a slope protection cover with 1.00m rock fill against surface runoff.

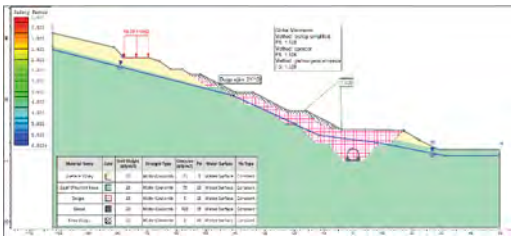

Figure 17. Static stability analysis of embankment up to the first two benches of the diversion outlet (FS = 1.508 > 1.50).

Stability problems will be eliminated if the first two benches are backfilled. The topography approximately reaches its natural slope. Embankments are analyzed as 2H:1V. Embankments should not be constructed at steeper slopes.

Seismic analysis of the slope surfaces in case of 2H:1V embankment and backfilling up to the first two benches is given below.

Figure 18. Seismic condition stability analysis of the embankment up to the first two benches of the diversion outlet (FS = 1.14>1.1).

In accordance with the observed PGA of 0.48g, comparable outcomes to those at the inlet portal were noted, with all factors of safety registering below 1, some marginally so. However, these results are not presented here for the sake of conciseness.

6 CONCLUSIONS

Proposed support by terracing and granular fill is working as seen during site visits, even after the major earthquake sequence in the vicinity of the dam site. This method can be used as a cost-effective method in tunnel projects with similar landslide problems.

On the other hand, the fact that the slopes are failing in the analysis but not in reality might be explained by the following reasons:

- The peak ground acceleration value obtained from the earthquake records is very instantaneous and may not be fully representative of the earthquake on the given site conditions,
- Being conservative when selecting parameters,
- The extent to which the topographic model reflects reality,
- Selection of analysis type and earthquake acceleration,
- Material model and stress-strain behavior.

In addition, the possibility of landslides of invisible size and velocity during site visits should not be ignored.

REFERENCES

Bieniawski, Z. T. (1989). Engineering Rock Mass Classification Mining and Mineral Resources Research Institute. New York, A Willey-Interscience Publication.

Day R.W. (2006). Foundation engineering handbook. McGraw-Hill Companies.

Duncan, J. M., & Wright, S. G. (2005). Soil strength and slope stability. John Wiley & Sons.

Fatkhiandari, I. A., Indrawan, I. G. B., & Karnawati, D. (2020b). NUMERICAL EVALUATION OF TUNNEL PORTAL SLOPE STABILITY AT BAGONG DAM SITE, EAST JAVA, INDONESIA. Journal of Applied Geology. https://doi.org/10.22146/jag.57044

Hammouri N.A., Malkawi A.I.H., & Yamin M.M.A. (2008). Pseudo-static slope stability analysis using a modified dynamic coefficient. Bulletin of Engineering Geology and Environment 67:471–478.

Huda, N., Indrawan, I. G. B., & Wilopo, W. (2022). Stability Evaluation of Diversion Tunnel Portal Slopes at Lau Simeme Dam Site, Indonesia, using Limit Equilibrium Method. Journal of Applied Geology, 7(1), 41. https://doi.org/10.22146/jag.58069

Naseer S., & Evans R. (2020). Stability analysis of slopes using limit equilibrium and finite element methods. In 2nd Conference on Sustainability in Civil Engineering 2020 (pp. 1–8). Department of Civil Engineering Capital University of Science and Technology.

Oktarina, I. M. A., Pramumijoyo, S., & Indrawan, I. G. B. (2023). Slope stability analysis at outlet portal of tunnel No. 8 Jakarta-Bandung high-speed railway, Indonesia. Nucleation and Atmospheric Aerosols. https://doi.org/10.1063/5.0130144

Popescu, M. (2001). A suggested method for reporting landslide remedial measures. Bulletin of Engineering Geology and the Environment, 60(1), 69–74. https://doi.org/10.1007/s100640000084

Sengkey, C. I., Amijaya, D. H., & Indrawan, I. G. B. (2023). Slope stability analyses of the diversion tunnel portals at Manikin Dam, Indonesia, using limit equilibrium and finite element methods. Nucleation and Atmospheric Aerosols. https://doi.org/10.1063/5.0132911

U.S. Geological Survey, 2023, Mw 7.5 - Elbistan earthquake, Kahramanmaras earthquake sequence at https://earthquake.usgs.gov/earthquakes/eventpage/us6000jlqa/executive (Accessed September 18, 2023).

U.S. Geological Survey, 2023, Mw 7.8 - Pazarcik earthquake, Kahramanmaras earthquake sequence at https://earthquake.usgs.gov/earthquakes/eventpage/us6000jllz/executive (Accessed September 18, 2023).

United States Geological Survey (2023). The 2023 Kahramanmaraş, Turkey Earthquake Sequence. Retrieved from https://earthquake.usgs.gov/storymap/index-turkey2023.html (Accessed September 20, 2023).

Wang I.-T. (2019). Stability analysis for tunnel portal slope with weak rock mass by numerical simulation method: A case study in Taiwan. Infrastructures 4(4):70.

Tunnelling for a Better Life – Yan, Celestino, Thewes & Eberhardt (Eds)
© 2024 The Author(s), ISBN 978-1-032-80042-4
Open Access: www.taylorfrancis.com, CC BY-NC-ND 4.0 license

Numerical analysis of the deformation of undersea tunnel crossing fault zone

Jiaze Ni*, Jinzhang Zhang, Hongwei Huang & Dongming Zhang
Department of Geotechnical Engineering, Tongji University, Shanghai, China
Key Laboratory of Geotechnical and Underground Engineering of Ministry of Education, Tongji University, Shanghai, China

Le Zhang
Qingdao Guoxin Second Jiaozhou Bay Subsea Tunnel Co., Ltd., Qingdao, China

ABSTRACT: In recent years, the construction of undersea tunnels has been booming in China, but it is faced with severe challenges, especially when crossing fault zones. Water gushing, rock instability and other accidents often occur during tunnel excavation due to the fracture of fault zones. Relying on the second undersea highway tunnel in Qingdao Jiaozhou Bay, this paper adopts theoretical derivation, statistical analysis and numerical simulation to study the deformation of the undersea tunnel crossing a fault zone. The main work and results of this research are as follows: (1) The distribution laws of influential parameters of Qingdao Second Tunnel crossing the fault zones were counted up. The depth of seawater, grade of surrounding rock, lining type and excavation method of Qingdao Second Tunnel crossing the fault zones were statistically analysed and the distribution range of these parameters was obtained. A characterization method for the angle and width of tunnel crossing a fault zone was proposed, and the angles and widths of Qingdao Second Tunnel crossing fault zones were calculated and counted. (2) Based on a 2D numerical model and the distribution range of the above parameters, a parameter analysis of the deformation of undersea tunnel crossing fault zones was carried out. The influences of the above parameters on the deformation of the tunnel when undersea tunnel crosses a fault zone was revealed.

Keywords: Undersea tunnel, Fault zone, Numerical simulation

1 INTRODUCTION

In recent years, China has planned and constructed several undersea tunnels, including the Xiamen-Xiang'an Tunnel and the Qingdao Jiaozhou Bay Tunnel, etc. China is gradually gaining the capability to construct undersea tunnels with larger cross-sections, longer lengths, and more complex geological conditions. However, Undersea areas often contain unfavourable geological features like fault zones, where rock formations have low strength, poor stability, and high permeability. The fault zones have reduced load-bearing capacity and also serve as pathways for hydraulic replenishment between the tunnel and the seawater above. Therefore, most accidents in undersea tunnels worldwide, such as collapses and water ingress, are fundamentally caused by the presence of fault zones (Wang et al., 2007).

The Finite Difference Method (FDM) is a numerical technique used to approximate solutions to differential equations. FLAC 3D (Three-Dimensional Fast Lagrangian Analysis of Continua), developed by the American company Itasca, is a three-dimensional explicit finite difference program known for its effective simulation capabilities. Many scholars have proposed mature theories and procedures for numerical simulations of crossing through fault zones in undersea tunnels, including model dimensions (Li et al., 2002), displacement constraints (Wang et al., 2011), element types, constitutive models, model parameters, the generation of initial stress field, and excavation simulations (Zarei et al., 2011). However, there are questions about the reliability of the selection of rock mass elements, fault zone parameters and support structure constitutive models.

*Corresponding author: nijz@tongji.edu.cn

DOI: 10.1201/9781003495505-109

Researchers like Kiani et al. (2016) and Sabagh and Ghalandarzadeh (2020) investigated the impact of tunnel cover thickness, fault angle, tunnel diameter, and lining thickness on the stability of surrounding rocks when crossing through fault zones. Xu et al. (2016) revealed the progressive failure process of rock masses in various parts when crossing through fault zones and analyzed the redistribution of stress caused by tunnel excavation. Yang et al. (2015) established finite element models for undersea tunnel seepage with different cover layer thicknesses, conducting research on water inflow, seepage velocity, pore water pressure, and grouting ring parameter selection during crossing through fault zones. Long (2020), compared and analyzed the effects of permeable and impermeable changes when crossing unfavourable geological formations in undersea tunnels using FLAC 3D software. She summarized the development of the plastic zone, pore water pressure field, displacement field, and water inflow.

For the study of structural forces and deformations when crossing fault zones in undersea tunnels, Han et al. (2021) proposed a limit equilibrium model considering the influence of seepage forces and geological interfaces. They compared this model with numerical simulation results and existing failure mechanisms to determine the ultimate pressure on support structures when crossing through fault zones. Zaheri et al. (2020) conducted a three-dimensional numerical simulation study on the interaction between tunnel linings and strike-slip faults, exploring the influence of soil mechanics properties, tunnel layer thickness, tunnel depth, fault dip angle, and their impact on tunnel mechanical performance. Li et al. (2023) identified three typical failure modes when crossing fault zones in tunnel face excavation: face uplift, local failure and sliding collapse based on Material Point Method (MPM) numerical verification experiments. For construction in fault zones, safer construction methods are often adopted, including strengthening the strength and stiffness of initial support and secondary lining (Li et al., 2007), grouting reinforcement (Zhang, 2007), and timely support.

To prevent accidents like collapse and water ingress and ensure the safety of undersea tunnel construction, especially when crossing fault zones, this study conducted the following research based on the Qingdao Jiaozhou Bay Second Undersea Highway Tunnel project,:

(1) Statistically analyzed data from the Qingdao Jiaozhou Bay Second Undersea Highway Tunnel project.
(2) Revealed the structural stress and deformation evolution patterns of undersea tunnels when crossing fault zones based on 2D numerical simulations.

This study employed a systematic approach to scientific research, incorporating methods such as mathematical statistics, theoretical analysis, and numerical simulations. The specific technical approach is shown in Figure 1.

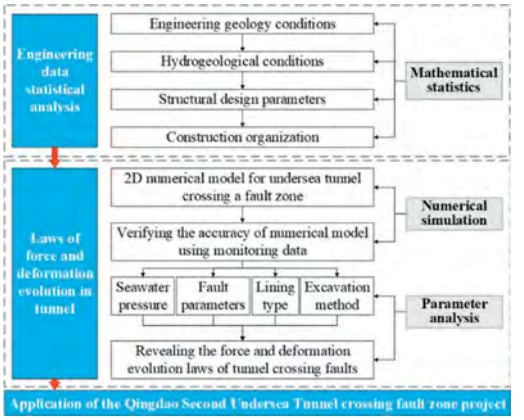

Figure 1. The technical approach of this research.

2 INFORMATION STATISTICAL ANALYSIS OF QINGDAO SECOND UNDERSEA TUNNEL CROSSING FAULT ZONES

2.1 *Project overview*

The Jiaozhou Bay Second Undersea Tunnel Project connects the main urban area of Qingdao with the West Coast New Area. The tunnel is 14,376 meters long and is constructed using a combination of cut-and-cover, drill-and-blast (west) and shield (east) methods. The standard cross-section of the drill-and-blast section in the mainline sea area has a width of about 15 meters and a height of about 10.6 meters. The designed elevation of the bottom plate ranges from -67.3 to -118.8 meters and the thickness of overburden ranges from 50 to 80 meters. Composite lining structure is mainly employed in the drill-and-blast section of the tunnel.

2.2 *The information of fault zones crossed by tunnel*

To study the distribution of the angle and width at which fault zones intersect with tunnels, this research has established formulas (1) and (2) for calculating the angle and width of fault zones on tunnel cross-sections precisely intersecting the centre of a fault zone.

$$\varphi = \arcsin \frac{\cot \alpha}{\sqrt{(\cot \alpha)^2 + (\cot \beta)^2}} \tag{1}$$

$$w = \left| \frac{d_0 \sin \alpha}{\cot \beta} \sqrt{1 + (\cot \alpha)^2 + (\cot \beta)^2} \right| \tag{2}$$

Where φ is the fault angle on the cross-section; w (m) is the fault width on the cross-section; α is the fault angle on the side view; β

is the fault angle on the top view; d_0 (m) is the fault width on the top view and side view.

Table 1. The information of fault zones crossed by tunnel.

Fault	d_0/m	w/m	φ/°	Rock grade	Sea depth/m
f9	64	127	116	V	17.45 ~ 19.78
f10	78	142	114	V	20.06 ~ 21.72
f11	25	32	81	V	45.97 ~ 47.08
f12	40	51	81	IV	40.88 ~ 42.95
fc	226	289	83	III ~ V	17.97 ~ 21.32
f13	20	25	82	V	25.35 ~ 26.20
f14	53	60	84	V	13.76 ~ 14.30
Fa	187	386	86	V	12.42 ~ 17.32
f15	186	768	50	V	8.78 ~ 10.00
f16	56	59	84	V	9.00 ~ 9.12

As shown in Table 1, the Qingdao Second Undersea Highway Tunnel crosses 10 fault zones in the sea area, with an impact distance exceeding 935 meters. Each fault zone has various characteristics in the sea depth above, rock mass grade, angle and width of intersection with the tunnel. This research has compiled data on the sea depth and rock mass grade according to the mileage as well as angle and width on the cross-sections according to the number of fault zones crossed by the Qingdao Second Undersea Tunnel, as shown in Figure 2.

It can be found from the figure that 91% of the mileage of the tunnel crossing the fault zones has a seawater depth of less than 25m, while there are also cases where the seawater depth in the upper part of the fault zones is as high as 45~50m(a). 80% of the surrounding rock grade in the part of the tunnel crossing fault zones is Ⅳ and Ⅴ(b), so the self-stability is poor. Most of the fault zones traversed by Qingdao Tunnel intersect with the tunnel at a high Angle(c), resulting in a shortened hydraulic connection path and weak surrounding rock of the crown. All fault zones traversed by the tunnel cover the entire excavation range in the studied section(d).

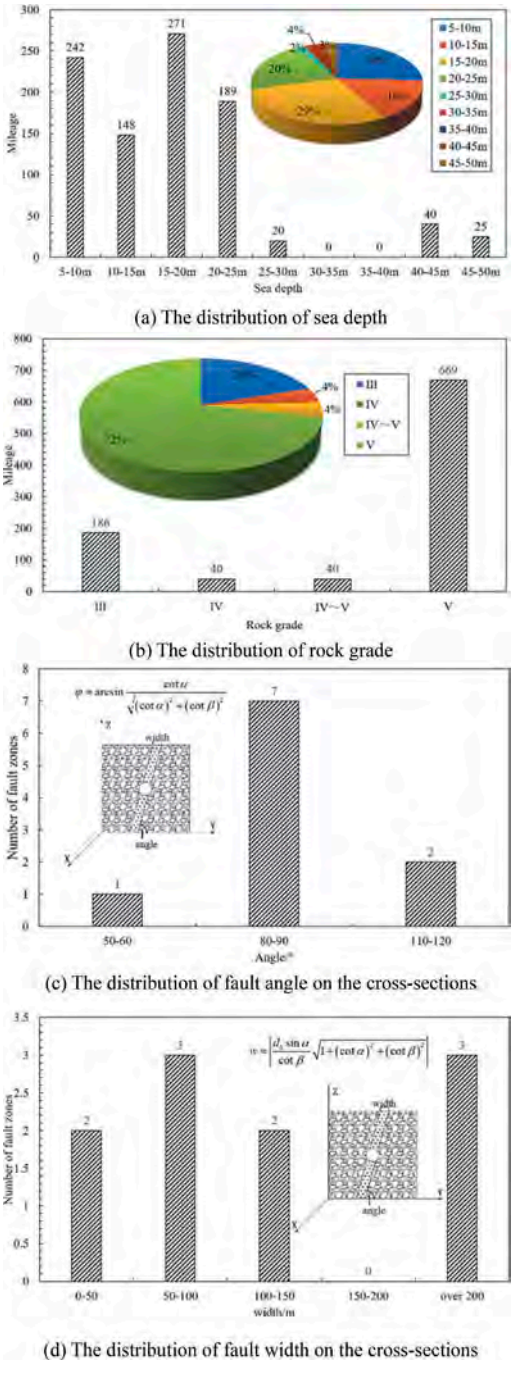

Figure 2. The distribution of four characteristics of fault zones.

3 DEFORMATION AND FORCE EVOLUTION LAW OF UNDERSEA TUNNEL CROSSING FAULT ZONE BASED ON 2D NUMERICAL SIMULATION

3.1 *Numerical model*

In this study, based on Hypermesh and FLAC 3D, a two-dimensional numerical model of the Qingdao Second Undersea Tunnel north line crossing the f10 fault zone (mileage NK8+400) was established (Figure 3). The model size is 200m×200m. Fixed supports are set at the bottom of the model, the normal displacement is constrained on four sides, and the upper plane is free. The bottom and four sides are set as impervious boundaries.

The rock mass and fracture zone are simulated by solid element with the Mohr-Coulomb mechanical constitutive model and the isotropic seepage fluid

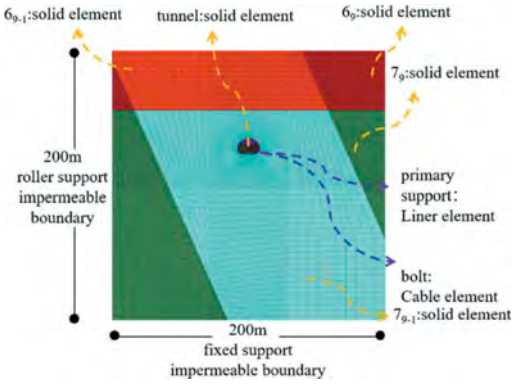

Figure 3. The 2D numerical model.

constitutive model. Liner unit and Cable unit were used to simulate the primary support and bolt, respectively. The parameters of rock are shown in Table 2, and the parameters of structural elements are shown in Table 3. Among them, the elastic modulus of steel arch is converted into the elastic modulus of concrete according to the proportion of their areas.

In order to consider the seepage of upper seawater during the tunnel excavation, the fluid-structure coupling model is used for calculation. In this model, displacement of monitoring points in the z-direction are arranged at the crown, shoulder, foot and invert of the tunnel. The xdirections are arranged at the wall of the tunnel.

3.2 *Model verification and result analysis*

The settlement of crown and shoulder and horizontal convergence in the calculated results are compared with the site construction monitoring data in the NK8 +400 mileage of the tunnel. The results are shown in Table 4.

As can be seen from the table, the results of monitoring items are relatively similar, and the maximum relative error is 4.17%, less than 5%, so it can be verified that the model has high reliability.

The computed cloud image of tunnel displacement in z-direction and x-direction and the construction step with maximum stress is shown in Figure 4 (The deformation is magnified by a factor of 100). It can be found that the entire section of the tunnel has shrunk. The position with the greatest displacement as well as the greatest settlement is the crown. The position with the greatest horizontal convergence is the wall. The maximum stress of the surrounding rock appears after the second excavation step. The minimum principal stress at the left shoulder is the largest, about -101.5kPa.

3.3 *Parameter analysis*

Respectively change the angle and width of fault zone crossed by tunnel to find out the variation trends of tunnel deformation with them, which is shown in Figure 5. The deformation of each typical part of the tunnel increases first and then decreases with the increase of the width of the fault zone. With the increase of fault zone angle, the displacements of

Table 3. The parameters of structural elements.

Parameter	Liner element	Cable element
Elastic modulus/GPa	35.26	206
Poisson's ratio	0.2	/
Cross-sectional area/m^2	/	2.53×10^{-4}
Tensile strength/MPa	/	400

Table 2. The parameters of rocks.

Parameter	6_9 Moderately weathered granite	7_9 Slightly weathered granite	6_{9-1} Medium-weathered crushed granite	7_{9-1} Slightly- weathered crushed granite
Elastic modulus/GPa	25	30	15	20
Poisson's ratio	0.35	0.3	0.45	0.4
Cohesion/kPa	500	700	100	200
Friction Angle/°	30	35	20	25
Tensile strength/MPa	0	0	0	0
Dry density /kg·m^{-3}	1530	1570	1550	1520
Porosity	0.01	0.005	0.04	0.02
Permeability coefficient /cm·s-1	3.47×10^{-6}	5.79×10^{-6}	2.31×10^{-4}	3.47×10^{-4}

Table 4. 2D model verification.

Monitoring item	Monitoring data/mm	Simulation result/mm	Absolute error/mm	Relative error/%
Crown settlement	-11.8	-12.0	0.2	1.69
Shoulder settlement(left)	-8.6	-8.5	0.1	1.16
Shoulder settlement(right)	-8.9	-8.7	0.2	2.25
horizontal convergence(left)	7.2	7.5	0.3	4.17
horizontal convergence(right)	-7.3	-7.6	0.3	4.11

crown, shoulder and wall gradually increase, while the displacements of foot and invert decrease slightly.

Respectively change the cohesion and friction angle of the fault zone (rock 79-1) crossed by tunnel to find out the variation trends of tunnel deformation with them, which is shown in Figure 6. With the increase of cohesion and friction angle of fault zone, the deformation of surrounding rock obviously decreases and then tends to be stable. The deformation values of the left and right shoulder, wall and foot of the tunnel are gradually close. Because the ratio of cohesion or friction angle between the fault zone and the surrounding rocks both sides is gradually close, the model is gradually close to the symmetric state in the calculation.

Respectively change the depth of seawater to find out the variation trends of deformation and the maximum internal force of the tunnel with it, which is shown in Figure 7. When the depth of seawater changes, the deformation mode of the tunnel crossing the fault zone does not change but still shrinks in the whole section. The displacement increases with the increase of sea depth. Among them, the invert rise is most affected by sea water depth change. The maximum internal force in each monitoring point of the section is stable after decreasing.

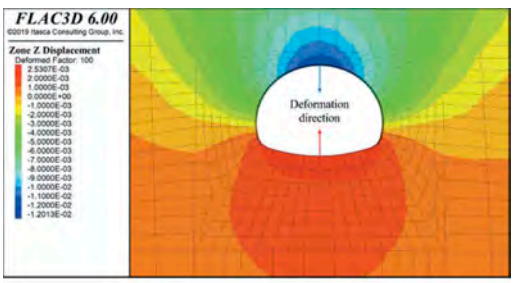

(a) Displacement in z direction

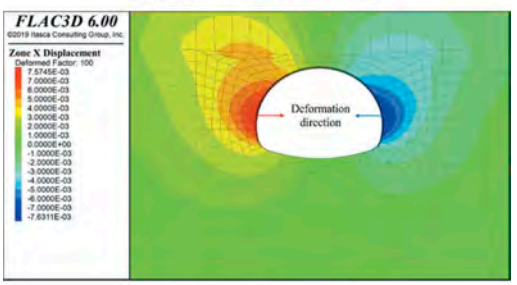

(b) Displacement in x direction

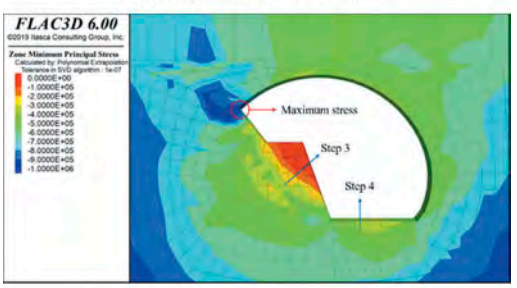

(c) Construction step with maximum stress

Figure 4. The cloud image of tunnel displacement and stress.

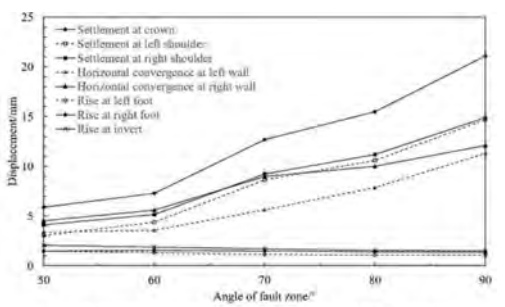

(a) Deformation variation with angle of fault zone

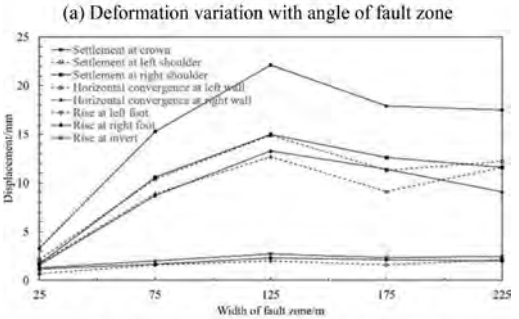

(b) Deformation variation with width of fault zone

Figure 5. Tunnel deformation variation with the shape of the fault.

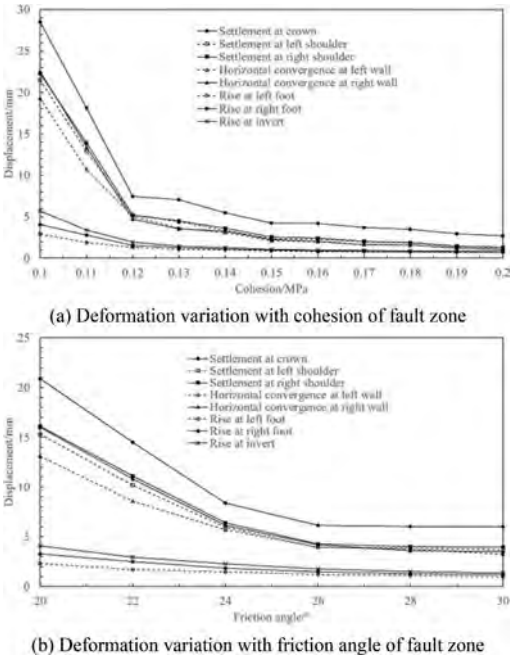

(a) Deformation variation with cohesion of fault zone

(b) Deformation variation with friction angle of fault zone

Figure 6. Tunnel deformation variation with parameters of fault.

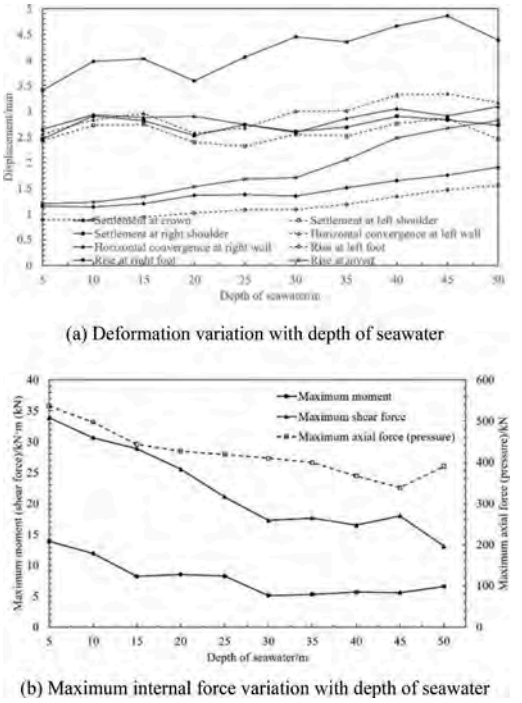

(a) Deformation variation with depth of seawater

(b) Maximum internal force variation with depth of seawater

Figure 7. The variation of tunnel deformation and maximum internal force with depth of seawater.

4 CONCLUSIONS

Based on the statistical analysis, numerical simulation and parameter analysis of Qingdao Second Undersea Tunnel crossing the fault zone, the following main conclusions are reached:

(1) 91% of the tunnel crossing fault zones have a seawater depth of less than 25m. 80% of the surrounding rock grade of the tunnel crossing fault zones is Ⅳ and Ⅴ. Most of the fault zones intersect with the tunnel at a high Angle. All fault zones cover the entire excavation range in the studied section.

(2) The entire section of the tunnel has shrunk. The position with the greatest displacement as well as the greatest settlement is the crown.

(3) The deformation of the tunnel increases first and then decreases with the increase of fault zone width. With the increase of fault zone angle, the displacements of crown, shoulder and wall gradually increase.

ACKNOWLEDGMENTS

The work presented in this study is supported by the Natural Science Foundation Committee Program of China (No. 52130805), Pujiang Talent support plan (No. 22PJD077) and the Research and consultation on comprehensive risk management of the second Jiaozhou Bay Tunnel project (No. ESJH-ZB-069).

REFERENCES

Abdollahi, M. S., Najafi, M., Bafghi, A. Y., et al, 2019. "A 3D numerical model to determine suitable reinforcement strategies for passing TBM through a fault zone, a case study: Safaroud water transmission tunnel, Iran". Tunnelling and Underground Space Technology, 88, 186–199.

Gao, C. L., Zhou, Z. Q., Yang, W. M., et al, 2019. "Model test and numerical simulation research of water leakage in operating tunnels passing through intersecting faults". Tunnelling and Underground Space Technology, 94, 103134.

Han, K. H., Wang, L., Su, D., et al, 2021. "An analytical model for face stability of tunnels traversing the fault fracture zone with high hydraulic pressure". Computers and Geotechnics, 140, 104467.

Kiani, M., Akhlaghi, T., Ghalandarzadeh, A., 2016. "Experimental modeling of segmental shallow tunnels in alluvial affected by normal faults". Tunnelling and Underground Space Technology, 51, 108–119.

Li, S. C., Zhang, J. W., Li, S. C., et al, 2007. "Displacement Convergence Method for Minimum Rock Cover above Submarine Tunnel". Rock and Soil Mechanics, 28(7), 1443–1447.

Li, S. C., Zhu, W. S., Chen, W. Z., et al, 2002. "Application of Elasto-plastic Large Displacement Finite Element Method to the Study of Deformation Prediction of Soft

Rock Tunnel". Chinese Journal of Rock Mechanics and Engineering, 21(4), 267–271.

Li, Z. Y., Huang, H. W., Zhou, M. L., et al, 2023. "Failure responses of rock tunnel faces during excavation through the fault-fracture zone". Underground Space, 10, 166–181.

Long, Y. X., 2020. Analysis of Construction Stability of Qingdao Metro Cross-sea Tunnel Crossing Fault Fracture Zone under Fluid-Solid Coupling Effect. Master Thesis. Shandong University of Science and Technology, Qingdao, Shandong, China.

Sabagh, M., Ghalandarzadeh, A., 2020. "Numerical modelings of continuous shallow tunnels subject to reverse faulting and its verification through a centrifuge". Computers and Geotechnics, 128, 103813.

Wang, K., Zhang, C. P., Wang, M. S., 2011. "Asymmetric Double-arch Subsea Tunneling-induced Ground Deformation Analysis". Rock and Soil Mechanics, 32 (9), 2771–2777.

Wang, Y., Huang, H. W., Li, S. C., 2007. "Risk Identification and Handling during Construction of Subsea Tunnel". Chinese Journal of Underground Space and Engineering. 3(7), 1261–1264.

Xu, Q. W., Cheng, P. P., Zhu, H. H., et al, 2016. "Experimental Study and Numerical Simulation on Progressive Failure Characteristics of the Fault-crossing Tunnel Surrounding Rock". Chinese Journal of Rock Mechanics and Engineering, 35(3), 433–445.

Yang, W. L., Xue, Y. D., Huang, H. W., 2015. "Numerical Simulation on Seepage of Jiaozhou Bay Subsea Tunnel in Fracture Zone". Tunnel Construction. 35(S2), 37–42.

Zaheri, M., Ranjbarnia, M., Dias, D., et al, 2020. "Performance of segmental and shotcrete linings in shallow tunnels crossing a transverse strike-slip faulting". Transportation Geotechnics, 23, 100333.

Zarei, H. R., Uromeihy, A., Sharifzadeh, M., 2011. "Evaluation of high local groundwater inflow to a rock tunnel by characterization of geological features". Tunnelling and Underground Space Technology, 26(2), 364–373.

Zhang, D. L., 2007. "Deformation Control Techniques of Unfavorable Geologic Bodies and Discontinuous Surfaces in Subsea Tunnel". Chinese Journal of Rock Mechanics and Engineering, 26(11), 2161–2169.

Tunnelling for a Better Life – Yan, Celestino, Thewes & Eberhardt (Eds)
© 2024 The Author(s), ISBN 978-1-032-80042-4
Open Access: www.taylorfrancis.com, CC BY-NC-ND 4.0 license

Research on surrounding rock by shallow tunnelling in Boulder-Cobble Mixed Formation: Instability characteristics and control strategies

Yiwen Qin*
Chang'an University, School of Highway, Xi'an, China

ABSTRACT: The construction of shallow tunnels has become increasingly challenging due to the complex geological conditions encountered, particularly in boulder-cobble mixed (BCM) formations found in river terraces. To understand the deformation characteristics of these formations, it is necessary to study the instability and failure evolution process of unlined tunnels in BCM formations. This research systematically investigates the failure evolution process and the variation laws of surrounding rock stress and displacement through a physical model test under 1g conditions. The study findings reveal a grouped pattern of movement in the collapsing movement. During the evolution process of instability, the surrounding rocks formed pressure arches multiple times, resulting in a clear development of staged deformation. The instability of the pressure arch zone leads to an expansion of the loose zone in the surrounding rocks, particularly in the tunnel vault area. To prevent the collapse of surrounding rocks effectively, it is suggested to control the stability of the first-formed pressure arch. Based on the instability evolution characteristics of the surrounding rock, strategies for preventing and controlling collapse are summarized and refined.

Keywords: Tunnel engineering, Boulder-Cobble Mixed formation, Progressive destruction, Pressure arch, Model test

1 INTRODUCTION

In recent years, the escalating demand for road construction in various topographical settings, including river terraces, floodplains, and piedmont areas, has given rise to increasingly intricate geological conditions during tunnel construction. This complexity is particularly pronounced when tunnels are being excavated in formations characterized by a mixture of boulders and cobbles, commonly referred to as boulder-cobble mixed (BCM) formations, often prevalent in river terraces. BCM formations consist primarily of boulders (particles exceeding 200 mm in diameter), pebbles (particles ranging from 20 to 200 mm in diameter), sand, gravel, and clay. Notably, giant particles (those exceeding 60 mm in diameter) comprise more than 50% of the entire formation, rendering it a composite material that exhibits its properties falling between rock and soil. Furthermore, the degree of cementation within the formation is notably poor. When exposed to water, fine particles are susceptible to erosion and loss, further compounding the challenges associated with tunnelling in BCM formations. Consequently, the process of tunnelling in BCM formations is fraught with difficulties, characterized by sluggish progress and elevated safety risks.

Several significant research endeavors have been undertaken to elucidate the key considerations for preventing and controlling tunnel accidents within such formations. Wang et al. (2013) investigated the deformation and stability of sand cobble strata underlying immersed tunnels. Cui et al. (2016) compiled an insightful summary regarding the issue of sludge management during the construction of shield tunnels within water-rich sandy cobble strata. In a study by Zhu et al. (2010), the progressive failure behavior of weak surrounding rock was examined, considering variables such as section size, groundwater influence, and the effects of blasting vibrations. Furthermore, Lai et al. (2016) delved into the realm of reinforcement testing for sleeve valve tubes within sandy cobble strata. Their work determined crucial grouting parameters for advancing curtain grouting during tunnel excavation. In a separate investigation, Zhang et al. (2015) conducted model tests for deep and shallow tunnels, confirming that deep tunnels generally do not reach the surface. In contrast, shallowly buried tunnels are prone to surface ground collapse. Another essential aspect He

*Corresponding author: qinyiwen@chd.edu.cn

DOI: 10.1201/9781003495505-110

et al. (2012) addressed involved the study of ground settlement patterns resulting from shield tunnelling in sandy cobble strata, incorporating field measurements and model testing. Additionally, Zhang et al. (2012) employed numerical analysis to estimate the impact of shield tunnelling within sandy cobble strata on tunnel alignment and the surrounding land surface. These studies collectively contribute to a comprehensive understanding of tunnel construction challenges and accident prevention in formations of this nature.

The above summary reveals several key observations: (1) Currently, research efforts related to tunnel collapses in BCM formations or sandy cobble strata primarily concentrate on treatment measures and causal analyses of accidents; (2) Investigations into the arching effect of tunnel surrounding rock heavily rely on numerical analysis methods, which may not comprehensively capture the entire process of surrounding rock deformation the tunnel (Kamata and Mashimo 2003); (3) Existing model tests have not systematically explored the formation and development of pressure arches during tunnel collapses and failures within BCM formations; (4) Importantly, the monitoring data from current tunnel construction operations highlight the significant impact of water on the stability of tunnel surrounding rock. Nevertheless, the influence of rainfall on the stability of tunnel surrounding rock is seldom addressed in existing research. To delve into the collapse process of tunnels in BCM formations, a similar simulation test in a 1g environment was conducted to investigate the evolution of collapses during tunnel excavation and the impact of rainfall on the stability of tunnel surrounding rock. This research seeks to uncover the variation patterns in stress and displacement fields during the tunnel failure process within BCM formations and propose key considerations for preventing and managing tunnel collapses under similar geological conditions.

2 PROJECT DESCRIPTION

A highway tunnel is situated about 500 meters west of Nianggai Village in Daxiang Township of Lhasa, China. The length of the tunnel is more than 500 m and the span of the tunnel is 13.06 m. The buried depth of the whole tunnel is 7-33 m, with an average of 20 m. The topography of tunnel area belongs to the river terrace. Geological survey report showed that formations of tunnel excavation are dense BCM formation and middle dense stratum. In BCM formation, the content of cobbles is more than 20%, the content of boulders is more than 40%, and the content of total giant particles is between 60% ~80%. The middle of the tunnel passes through the debris flow gully, in which there are streams and perennial flowing water, which recharge groundwater to BCM stratum on both sides. The permeability of the strata is strong, and the groundwater level is greatly affected by rainfall.

3 EXPERIMENT

Taking the framework-pore structure which is the most representative of BCM formation as an example, a similar simulation test in 1g was carried out to study on the evolution of collapse during tunnel excavation and the influence of rainfall on the stability of tunnel surrounding rock.

3.1 *Similarity theory*

The experiment used dimensional analysis which is based on Buckingham's π theorem (Buckingham 1914). The theorem appropriately describes a relationship between physical variables and fundamental dimensions. It is pointed out that any physical equations can be transformed into equations of dimensionless quantities (Russo et al. 2017). The physical variables that need to be considered in this experiment included: the parameters of geometry (L), stress (σ), strain (ε), displacement (δ), the Young's modulus (E), density (γ), Poisson's ratio (μ), cohesion (c) and internal friction angle (ϕ).

The similarity constant (C) is the ratio of the same physical quantity between the prototype and the model. Simple deformation of the relationship between the similarity constants obtained from the equilibrium equation, geometric equation and physical equation can establish the following similarity conditions:

$$C_\sigma = C_\gamma C_L \quad C_\delta = C_\varepsilon C_L \quad C_\sigma = C_c C_\mu \tag{1}$$

$$C_\varepsilon = 1 \quad C_\phi = 1 \quad C_\mu = 1 \tag{2}$$

Considering that the size of the whole model must be larger than the scope of the stress field of the surrounding rock readjusted after tunnel excavation, and considering the feasibility and economy of the test, the ratio of geometric 60 was finally chosen. At the same time, considering that the model is usually made of the same type of material as the prototype, the ratio of density 1 was chosen. The ratio of geometric and the ratio of density are substituted into formula group (1), so that the ratios of all physical quantities could be obtained. The ratios are shown below:

$$C_\varepsilon = C_\mu = C_\phi = 1 \tag{3}$$

$$C_E = C_\sigma = C_\delta = C_c = 60 \tag{4}$$

3.2 *Similar materials*

Considering that the mechanical properties of BCM surrounding rock differ greatly from rock or soil medium, which is mainly manifested large porosity, high deformation modulus, large internal friction angle and small cohesion. The deformation of surrounding rock is mainly caused by the moving between particles. Therefore, the key to achieve the simulation results is to satisfy the similarity of particle gradation between prototype and model. Based on the

typical particle size composition of tunnel surrounding rock in the geological prospecting data of the project, similar materials of BCM surrounding rock were prepared by mixing quartz sand with different mesh numbers, barite powder with different mesh numbers, vaseline and water. Geotechnical tests were carried out to determine the relevant parameters of different mix ratios, and the final selection of similar materials of BCM surrounding rock was 2-4 mesh quartz sand: 10-20 mesh quartz sand: 20-40 mesh quartz sand: 150 mesh barite powder: 600 mesh barite powder = 3.68: 3.59: 1: 1.08: 0.96. The physical parameters of prototype materials and similar materials measured by geotechnical tests are shown in Table 1.

Table 1. Physical parameters of BCM surrounding rock.

Parameter	Prototype	Model
Internal friction angle (°)	4700	40
Cohesion (kPa)	4800	39
Poisson ratio	4900	38
The Young's modulus (MPa)	5000	38

3.3 *Model equipment*

This test used a model box made of a tempered glass, and the sides were fixed with wooden boards. Its dimension was 1.5 m in length, 0.62 m in breadth, and 1.5 m in depth. The tunnel excavation hole was reserved in the middle and lower part of the glass. The measured physical quantities in this test mainly included the stress of surrounding rock and the internal deformation of surrounding rock. The stress measurement of surrounding rock adopted earth pressure cell, and the data acquisition adopted JM3813 type static strain gauge.

3.4 *Experiment design and procedures*

According to the actual project, the test simulated the excavation of the tunnel with a depth of 33 cm and a span of 22 cm. Firstly, the model box was filled with similar materials and making the formation fully consolidated under the action of gravity. Then the tunnel excavation was carried out. In BCM formation, the bench method has many advantages in construction convenience, construction progress and less disturbance, which is the first choice of tunnel excavation method (Lai et al. 2016). In this model test, the method of tunnel excavation was short bench method. The excavation height of the upper and lower bench was about 5 cm. Each excavation footage was 5 cm. The whole excavation process was kept at constant speed until the tunnel transfixion. After the surrounding rock was stabilized, the rainfall process was simulated by slowly adding water 30 kg to the surface of the model, and the amount of water added was about 5 kg each time.

To monitor the stress of surrounding rock during whole test process, a longitudinal measurement section was set up in the middle of the tunnel. On this section, several earth pressure cells were set up at the vault and side wall of the tunnel. The layout of measurement section and measuring points is shown in Figure 1.

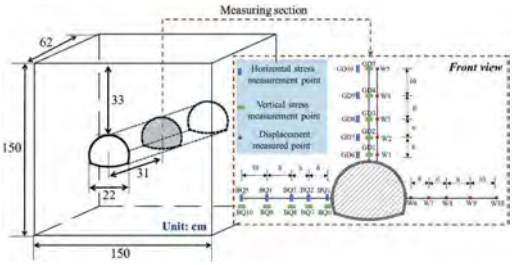

Figure 1. Sketch of measuring points for model test.

3.5 *Results and analysis*

3.5.1 *Analysis of shape characteristics of collapse arch*

As can be seen from Figure 2, three times of collapse occurred during the test, and each collapse formed the short-term stable collapse arches until the final ground collapse. In view of the fact that the shape of collapse body is the premise and foundation for determining the ultimate supporting force and collapse load, it is necessary to make a thorough analysis and study on it.

To study the shape of the collapse arches formed in the test process, the photographs of the short-term stable collapse arches were fitted respectively. The concrete steps are as follows: (1) Drawing scatter plots uniformly along the collapsed contour, and establishing a plane right-angle coordinate system with the vertex of collapse arch as the origin of the coordinate; (2) Measuring the coordinates of each point and using Origin software to fit the curves. The fitting curves of the collapse arches are shown in Figure 2.

Figure 2. The fitting curves of the collapse arches. a. The first collapse arch; b. The second collapse arch; c. The third collapse arch.

The fitting results showed that the fitting degree was above 0.85, which represented that the polynomial function selected was reasonable. Three fitting curves can be well described by the quadratic parabola ($y = ax^2 + bx$). With the enlargement of the collapse area, the absolute value of the parameter a was increasing and the absolute value of the parameter b

was decreasing. It can be seen that the collapse developed upward and tended to be symmetrical gradually. Table 2 showed the heights and spans of three collapse arches. It can be seen that the height of the collapse arch increased significantly until the ground collapse was formed; the span increased more obviously in the first two collapses, and it almost did not increase any more in the third. It showed that the collapse arch changed dynamically with the tunnel excavation and underwent a cyclic process of first formation, then destruction, formation again. From the point of view of treatment of collapse, strong support measures should be taken immediately after the first small-scale collapse, so as to control the height of the collapse within a small range, thereby reducing the load required for support and lining.

Table 2. The height and span of three collapse arches.

Condition	Height (cm)	Span (cm)
First collapse arch	9.22	12.75
Second collapse arch	21.86	17.62
Third collapse arch	28.15	17.93

3.5.2 *Variation law of surrounding rock stress*

Figure 3 depicted the change of stress in surrounding rock above the vault during tunnel excavation. The surrounding rock stress in the figure represented the changed value relative to the initial stress, not the absolute value of stress (Figure 4 was the same). The positive value indicated that the stress increased, and the negative value indicated that the stress decreased. It can be seen that before the tunnel was excavated to the measurement section, the vertical and horizontal stress of the surrounding rock above the vault increased slightly and the closer to the measurement section, the more obvious the increase was. This was due to the stress redistribution of the surrounding rock in front of the section to form the "beforehand arch", that was, the surrounding rock had already shown arching effect in front of the section. After tunnel excavation, the stress in surrounding rock above the vault decreased obviously, and the more close to the vault, the more obvious the stress decreased. The surrounding rock near the GD1 was completely loosened, resulting in the pressure gauge falling off. The stress of the outermost GD5 was almost zero during the whole excavation process and the other measuring points were negative, which represented that the disturbed area above the vault had a large area and had spread to the surface.

In the process of tunnel excavation, the horizontal stress of GD6 underwent two times changes of rising firstly and then falling. These two drastic changes of stress corresponded respectively to the time when the partial drop of blocks above the vault and the pressure gauge at the GD1 falling off. It demonstrated that it was theoretically feasible to predict the surrounding rock deformation by monitoring the stress changes inside the surrounding rock. The trends of GD7 and GD8 were basically the same, but the stress change of GD7 near the vault was larger. Research results (Zhu et al. 2010) had shown that the horizontal stress of surrounding rock decreases in the range of pressure arch, and the stress increases in the surrounding rock outside pressure arch due to the load borne by radial transmission. Therefore, the horizontal stress rising area of surrounding rock was taken as the range of pressure arch in this paper. Both the horizontal stress of GD9 and GD10 were close to or slightly greater than zero, which indicated that these two points belonged to the range of pressure arch and the internal boundary of the arch was at the position where the stress change was zero between GD9 and GD10.

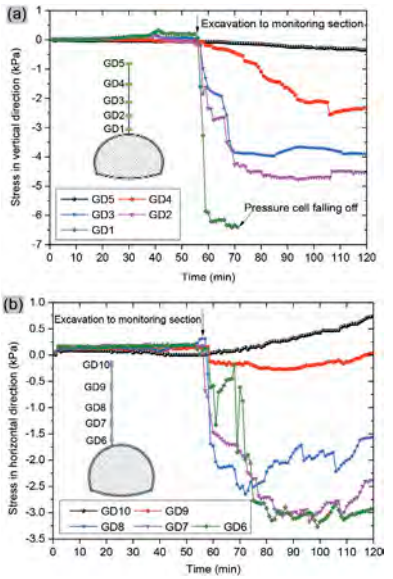

Figure 3. The change of stress in surrounding rock above the vault during tunnel excavation. a. Vertical stress; b. Horizontal stress.

Figure 4 illustrated the change of stress in surrounding rock of the side wall of the tunnel during tunnel excavation. It can be seen that before the tunnel was excavated to the measurement section, the vertical stress of each point on the survey line changed very little and the horizontal stress increased more significantly, which was consistent with the stress variation law of the surrounding rock above the vault. After tunnel excavation, only the vertical stress of BQ1 linear decreased and the vertical stresses of BQ2-BQ5 were not affected by excavation during the whole test process, which revealed that the disturbed area of the side wall of the tunnel was small. The horizontal stresses of BQ6-BQ8 close to the side wall of the tunnel increased

obviously, while BQ9 and BQ10 far from side wall of the tunnel were almost unaffected by the excavation. It was presumed that the BQ6-BQ8 belonged to the range of pressure arch and the horizontal stress of BQ7 increased most remarkably. To sum up we know the outer boundary of the arch was at the position where the stress change was zero between BQ8 and BQ9. The above analyses of the vertical and horizontal stress of surrounding rock revealed that the surrounding rock was in the order of disturbed area, inner of pressure arch, and initial stress area from inside to outside.

Figure 5 showed the change of stress in surrounding rock above the vault after adding water. The surrounding rock stress in the figure represented the changed value relative to stress after excavation stability (Figure 6 was the same), and excluded the data of GD1 which had been dropped. It can be seen that before the first collapse occurred, the vertical pressure of GD2-GD4 increased continuously to the peak value, while the vertical pressure of GD5 still decreased. The first collapse occurred shortly after the horizontal stress of GD6-GD8 increased to the peak value, which resulted in the pressure gauges at GD1, GD6 and GD7 falling off. Without taking no measures to deal with the situation after the first collapse, the vertical pressure of GD4 and GD5 continued to decrease and the horizontal pressure of GD8 and GD9 also decreased. The vertical stress of GD3 firstly decreased and then increased to the extreme value, and the second collapse occurred soon after the extreme value was reached. The collapse range was further expanded, which resulted in the pressure gauges at GD3, GD4, GD8 and GD9 falling off. The third collapse occurred in the process of cleaning up the falling body. It can be seen that the surrounding rock stress sharply increased before the first collapse, and decreased continuously during the development stage of the later collapse.

Figure 6 illustrated the change of stress in surrounding rock of the side wall of the tunnel after adding water. It can be seen that the vertical stress curves of BQ1 and BQ2 were like sine curve and the two curves changed successively during the whole collapse process. The change trend of BQ3 was basically the same as the change trend of BQ2 and BQ1, but the amplitude of the former was smaller. The vertical stress of BQ4 and BQ5 fluctuated near the X axis during the whole collapse process, which represented that these two points were basically not affected by collapse. When the vertical stress of BQ2 reached the maximum value, the first collapse occurred and then the second collapse occurred when the vertical stress of BQ1 and BQ2 reached the minimum value. At last, the third collapse occurred in the process of cleaning up the falling body. The horizontal stress of BQ6 increased all the time during the whole collapse process; the horizontal stress of BQ7 increased first and then decreased, and the maximum value of horizontal pressure was between the first collapse and the second collapse.

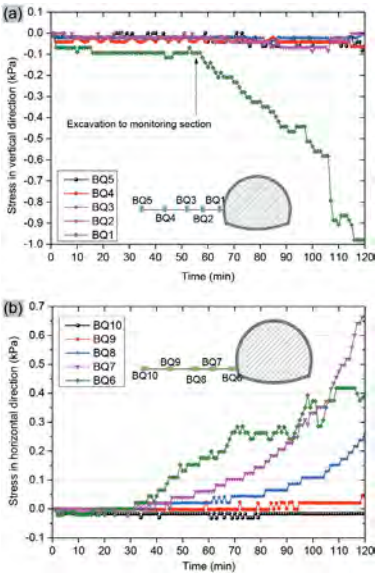

Figure 4. The change of stress in surrounding rock of the side wall of the tunnel during tunnel excavation. a. Vertical stress; b. Horizontal stress.

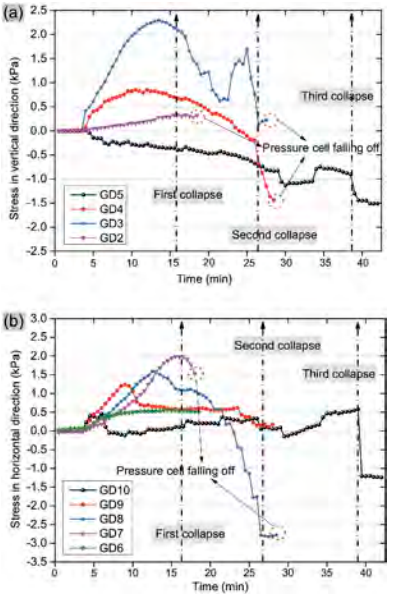

Figure 5. The change of stress in surrounding rock above the vault after adding water. a. Vertical stress; b. Horizontal stress.

The changes of horizontal stress of BQ8-BQ10 were very small, which demonstrated that these three points were basically in the initial stress area.

According to the test results, the development of the outer boundaries of the pressure arches and collapse arches were drawn, as shown in Figure 7. The failure behavior of the surrounding rock in the

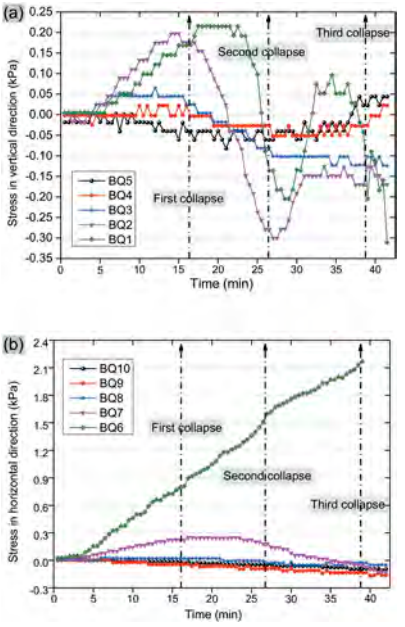

Figure 6. The change of stress in surrounding rock of the side wall of the tunnel after adding water. a. Vertical stress; b. Horizontal stress.

tunnel exhibited a progressive nature, mainly reflected in the formation of pressure arches and collapse arches during the local collapse of the surrounding rock above the tunnel vault and the subsequent collapse of the entire range. Both the internal pressure arch and the external collapse arch are load-bearing structures that can exert their compressive performance through self-stress adjustment (Guo and Zhou 2012; Chen et al. 2011). After forming the loose zone on the inner side of the tunnel, the arch structure is formed to bear the sharply increased load caused by the loosening of the surrounding rock. This effectively inhibits the deformation of the surrounding rock, and each stage of collapse ends with the formation of a collapse arch. The pressure arch expanded outward with the continuous expansion of the collapse area, and, in particular, the expansion at the vault was more significant than that at the sidewall. From the experimental results, the height of the pressure arch formed during the second time was expanded by 150% compared to the first time, while the span was only expanded by 25%.

4 DISCUSSION

4.1 *Failure mechanism of BCM surrounding rock*

The failures of BCM surrounding rock mass are mainly caused by the deformation incompatibility between framework grains and fine materials, which causes differential rotation between the two types of components. The yielding and failure in the interface

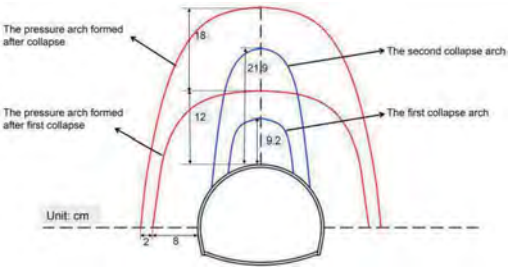

Figure 7. The development of the outer boundary of the arch and collapse arch in the process of collapse.

area gradually develop from local to overall failure, resulting in partial sliding of some framework grains relative to others along the yield interface. For the tunnel face, the failures of the surrounding rock are caused by the compression-shear and tensile failure of the surrounding rock above the vault, supplemented by the compression-shear failure of the surrounding rock around the sidewall. This is consistent with the test phenomena, i.e., the effect of the damage of the top surrounding rock is greater than that of the sidewall surrounding rock of an unlined tunnel in a BCM formation.

In addition, disturbing external factors, such as seepage and vibration, can accelerate the loosening and softening of the interface area, making it more susceptible to failure. Many scholars have conducted soil tests on samples composed of mixed particles with different water contents, and the results show that ϕ and c of the soil both decrease significantly as the water content increases (Qin et al. 2022b). When the formation is rich in water, the friction coefficient between particles and the bonding ability of the cementitious material decrease significantly compared with the dry state. In addition, the piping phenomenon may occur in the BCM formation under the action of groundwater, where the debris of medium and fine sand between large-sized cobbles and boulders will flow into the excavation face with the water, causing changes in the microstructure of the soil mass, such as the transformation from more compact framework-dense type soil mass to less stable framework-pore type soil mass. For shallow tunnel construction, it is essential to ensure a dry excavation environment (Fang et al. 2012). On the one hand, this can improve the working environment inside the tunnel, increase work efficiency, and, more importantly, it is an effective reinforcement measure for the BCM formation. In practical engineering, before the tunnel construction, the well-point dewatering can be carried out in sections with high groundwater (Qin et al. 2022a). This technology involves using a vacuum pump and wellpoints installed in a pattern around the construction site. The wellpoints create a low-pressure zone around them, and the vacuum pump draws water from the soil into the wellpoints, lowering the groundwater level below the construction working face as much

as possible to meet the need for dry construction. In addition, appropriate post-excavation grouting procedures during tunnel excavation can also effectively play a role in water blocking.

4.2 *Failure evolution process of the unlined tunnel under BCM formation*

It can be determined from the strength parameters of the BCM formation that ϕ was much weaker than c. A higher ϕ value increases the friction resistance due to soil particle contact (Terzaghi 1920). Therefore, in the absence of disturbance, an unlined tunnel in a BCM formation exhibits certain self-stability.

However, under an external disturbance (the action of gravity or hydrodynamic force), the local surrounding rock of the tunnel vault exhibits tensile failure, which is characterized by the continuous falling of particles; moreover, due to the compression-shear failure in the interior area, the falling particles may cause a large continuous piece of the surrounding rock to suddenly fall. With the adjustment of stress in the surrounding rock, the first pressure arch is formed on the surrounding rock above the tunnel vault, which greatly shares the load of the self-weight of the upper stratum and hinders the development of surrounding rock collapse. Its obvious feature is the formation of a short-term stable collapse arch. Therefore, in the early stage of collapse, the deformation of the surrounding rock will not be very rapid. The initial failure pattern is indicated by stage 1 shown in Figure 8. With the passage of time or continuous disturbance by external factors, the temporary equilibrium state in stage 1 is broken, and the collapse continues to develop upward. During the process of collapse development, the fracture surfaces in the surrounding rock gradually connect with each other, and the connected fracture surfaces lead to a larger range of collapse. During this process, the pressure arch initially formed in the surrounding rock begins to transfer upward. During the entire collapse process, the surrounding rock may experience the balance and instability process of the pressure arch many times, and the formation of each pressure arch has a certain hindering effect on the collapse of the BCM surrounding rock. The collapse of the surrounding rock at this stage exhibits obvious stage characteristics due to the action of the pressure arch, and the failure pattern is indicated by stage 2 shown in Figure 8. As the arch structure of the surrounding rock develops to the surface and gradually disappears, the collapse of the surrounding rock begins to develop rapidly. This failure pattern is indicated by stage 3 shown in Figure 8. Through the analysis of the entire collapse evolution process of the BCM surrounding rock, several characteristics can be extracted, which are crucial for selecting an appropriate tunnel support system.

a) Suddenness. Without any disturbance, the unlined tunnel segment in BCM formation can remain stable. However, this stability can be easily disrupted by external disturbances such as continuous excavation or rainfall, causing the surrounding rock above the tunnel vault to collapse suddenly. Although such formations exhibit high bearing capacity characteristics, their strength is prone to weakening due to natural loose features. Therefore, excavating the tunnel face directly without taking pre-support/pre-reinforcement measures is not recommended in actual tunnel construction.
b) Staging. During the collapse evolution of the surrounding rock, stress adjustments and transfers occur multiple times along the periphery of the tunnel profile, resulting in the formation of numerous pressure arches, making the collapse of the soil exhibit stage-wise characteristics. Each appearance of the arch structure has a certain inhibitory effect on the deformation development of the stratum. Still, the effect gradually weakens, manifested as the time for self-stabilization after each periodic collapse is gradually shortened. Therefore, controlling the stability of the first-formed pressure arch is the preferred measure by which to prevent tunnel collapse in BCM formations effectively.
c) Grouping. The collapse movement of the surrounding rock exhibits a grouping behavior characterized by a three-phase composite structure of "disturbed zone-pressure arch zone-initial stress zone." After the formation of the disturbed zone on the inner side of the tunnel, the external arch structure is immediately formed to bear the transferred soil pressure timely. Conversely, the instability of the pressure arch zone leads to the enlargement and extension of the disturbed zone soil, particularly in the vault area of the tunnel. Therefore, when small-scale soil collapses occur in tunnel construction, timely measures should be taken to reinforce the area and control the collapse range within the shallow disturbed zone to avoid further damage to the deep pressure arch zone and to trigger a large-scale collapse.

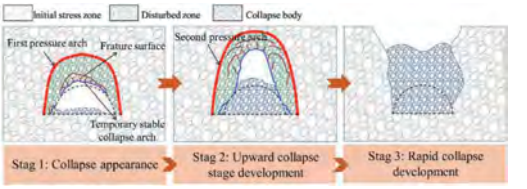

Figure 8. Failure evolution process of an unlined tunnel under a BCM formation.

4.3 *Insight into the optimized support strategy*

Choosing a suitable support structure system that matches the characteristics of strata deformation and failure is essential to control the collapse of the surrounding rock mass in tunnel engineering. The collapse of the surrounding rock mass in BCM exhibits

sudden, staged, and grouped features. To control the collapse of the surrounding rock mass, it is essential to promptly cut off the path of displacement and stress transmission during the collapse process. The pressure arch is a self-adjusting protection method formed during the surrounding rock mass deformation process. It can delay the deformation and damage of the BCM stratum in a short period and has a natural inhibitory effect on the development of surrounding rock deformation. Therefore, controlling the stability of the first-formed pressure arch is the preferred measure to prevent tunnel collapse in the BCM stratum. In practical tunnel construction, the stability control of the pressure arch is mainly achieved through two approaches (as shown in Figure 9). The first approach involves strengthening the supporting arch-feet to mobilize the surrounding rock's carrying capacity in the pressure arch area. The second approach involves limiting the development of arch height to help the loose surrounding rock bear the load.

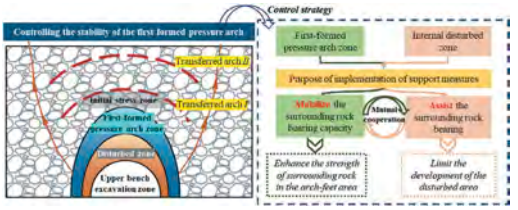

Figure 9. Control strategies for BCM surrounding rock collapse.

a) Enhance the strength of the supporting arch-feet. The soil arching effect describes the redistribution phenomenon of soil under shear stress, which mobilizes its shear strength and transfers the vertical load to the stable areas at the sides of the arch feet (Terzaghi, 1936). Researchers have found that the conditions for forming pressure arches include the development of shear stress in the soil and providing stable support at the arch feet (Guo and Zhou, 2012). For tunnels excavated by the sequential excavation method, the pressure arch formed in the surrounding rock is located around the tunnel crown profile, with a similar outer shape to the tunnel crown (Handy, 1985; Chen et al., 2011). It has been proven in many engineering practices that the instability of the arch structure is mainly caused by the failure of the tunnel excavation at the arch feet (Chen et al., 2013; Xiao et al., 2014). Hence, in tunnel construction in the BCM stratum, the stability of the surrounding rock at the arch-feet area should be the primary focus of control and monitoring. The tunnel support system should take appropriate measures to improve the bearing capacity of the surrounding rock at the arch-feet area, fully mobilizing the soil bearing capacity in the pressure arch zone.

b) Limit the development of arch height. Based on the grouping collapse characteristics of the surrounding rock, it can be inferred that the stability of the external pressure arch will gradually decrease as the loose zone of the surrounding rock inside expands. When the pressure arch zone becomes unstable, the loose zone of the surrounding rock will significantly expand outward. Therefore, for the tunnel construction in the BCM formation, appropriate pre-reinforcement or pre-support measures should be taken to assist the loose surrounding rock in bearing the load while minimizing disturbance to the surrounding rock caused by tunnel excavation, e.g., by avoiding intense construction disturbance activities, such as continuous drilling.

5 CONCLUDING REMARKS

(1) BCM formations are a common discontinuous medium consisting of high-strength framework grains such as boulders and cobbles, as well as low-strength filling materials such as sand and clay. Due to its significant heterogeneity, there is often incongruous deformation between the coarse and fine particles, resulting in yield failures in the interface regions between them. When tunnels are excavated, the surrounding rock in the vault area is subjected to both compressive-shear and tensile stresses simultaneously, making it more prone to failures than the sidewall area.

(2) Experimental results demonstrate that the unlined tunnel section in a BCM stratum is stable under normal conditions. Nonetheless, it can become unstable and collapse when subjected to external disturbances, such as continuous excavation or rainfall, causing the surrounding rock above the vault to loosen and collapse. The collapse motion of the surrounding rock follows a grouped movement pattern, which consists of three phases: the disturbed zone, pressure arch zone, and initial stress zone. Throughout the instability evolution process, pressure arches repeatedly form in the surrounding rock, leading to clearly staged deformation development.

(3) The instability of the pressure arch zone can lead to an increase and expansion of the loose zone, particularly in the tunnel vault area. To prevent tunnel collapse effectively in BCM formations, it is suggested that controlling the stability of the first-formed pressure arch is the preferred measure based on the deformation and failure characteristics of the surrounding rock. The main objective of support intervention is to mobilize the bearing capacity of the surrounding rock in the

pressure arch zone and enhance the bearing capacity of the loose zone by reinforcing the strength of the supporting arch-feet and limiting the arch height development.

ACKNOWLEDGMENTS

This research work was supported by the Fundamental Research Funds for the Central Universities, CHD (300102213706).

REFERENCES

Buckingham, E., 1914. "On Physically Similar Systems; Illustrations of the Use of Dimensional Equations." Phys. Rev. 4(4), 345–376.

Chen, C.N., Huang, W.Y., Tseng, C.T., 2011. "Stress redistribution and ground arch development during tunneling." Tunn. Undergr. Space Technol. 26 (1), 228–235.

Chen, R.P., Li, J., Kong, L.G., et al., 2013. "Experimental study on face instability of shield tunnel in sand." Tunn. Undergr. Space Technol. 33, 12–21.

Cui, K., Lin, W., 2016. "Muck Problems in Subway Shield Tunneling in Sandy Cobble Stratum." Pol. Marit. Res. 23(s1).

Fang, Q., Zhang, D.L., Wong L., 2012. "Shallow tunnelling method (STM) for subway station construction in soft ground." Tunn. Undergr. Space Technol. 29: 10–30.

Guo, P.J., Zhou, S.H., 2012. "Arch in granular materials as a free surface problem." Int. J. Numer. Anal. Meth. Geomech. 37(9): 1048–1065.

Handy, R.L., 1985. "The arch in soil arching." J. Geotech. Eng. 111(3), 302–318.

He, C., Feng, K., Fang, Y., et al., 2012. "Surface settlement caused by twin-parallel shield tunnelling in sandy cobble strata." Journal of Zhejiang University SCIENCE A. 13(11), 858–869.

Kamata, H., Mashimo, H., 2003. "Centrifuge model test of tunnel face reinforcement by bolting." Tunn. Undergr. Space Technol. 18(2-3), 205–212.

Lai, J.X., Feng, Z.H., Qiu, J.L., et al., 2016. "In Situ Test of Grouting Reinforcement for Water-Enriched Sandy Gravel Ground in River Floodplain." Adv. Mater. Sci. 2016, 1–12.

Qin, Y.W., Lai. J.X., Gao, G.Q., et al., 2022a. "Failure analysis and countermeasures of a tunnel constructed in loose granular stratum by shallow tunnelling method." Eng. Fail. Anal. 141: 106667.

Qin, Y.W., Qiu, J.L., Lai, J.X., et al., 2022b. "Seepage characteristics in loess strata subjected to single point water supply." J. Hydrol. 609: 127611.

Russo, L., Sorrentino, M., Polverino, P., et al., 2017. "Application of Buckingham π theorem for scaling-up oriented fast modelling of Proton Exchange Membrane Fuel Cell impedance." J. Power Sources. 353, 277–286.

Terzaghi, C., 1920. "New Facts About Surface-Friction." Phys. Rev. 16 (1), 54–61.

Terzaghi, K., 1936. Stress distribution in dry and in saturated sand above a yielding trap-door. In: Proceedings of First International Conference on Soil Mechanics and Foundation Engineering. Cambridge, 307–311.

Wang, Y., Sun, C.H., 2013. "Deformation Characteristics Research on Gravel Bed for Deep Buried Immerse Tunnel." Applied Mechanics and Materials. 353-356, 1480–1483.

Xiao, J.Z., Dai, F.C., Wei, Y.Q., et al., 2014. "Cracking mechanism of secondary lining for a shallow and asymmetrically-loaded tunnel in loose deposits." Tunn. Undergr. Space Technol. 43 (7), 232–240.

Zhang, C.P., Han, K.H., 2015. "Collapsed Shape of Shallow Unlined Tunnels Based on Functional Catastrophe Theory." Math. Probl. Eng. 2015(3), 1–13.

Zhang, Z.X., Zhang, H., Yan, J.Y., 2012. "A case study on the behavior of shield tunneling in sandy cobble ground." Environ. Earth Sci. 69(6), 1891-1900.

Zhu, H.H., Huang, F., Xu, Q.F., 2010. "Model test and numerical simulation for progressive failure of weak and fractured tunnel surrounding rock under different overburden depth." Chinese Journal of Rock Mechanics and Engineering. 29(6), 1113–1122. (in Chinese)

Tunnelling for a Better Life – Yan, Celestino, Thewes & Eberhardt (Eds)
© 2024 The Author(s), ISBN 978-1-032-80042-4
Open Access: www.taylorfrancis.com, CC BY-NC-ND 4.0 license

Practical approach for the control of surface settlements due to TBM tunnelling during excavation by following up of monitoring

Victor Rattia*
SENER Setepla Engenharia e Sistemas, São Paulo, Brazil

Hugo Rocha
Companhia do Metropolitano de São Paulo, São Paulo, Brazil

Andre Dantas
Instituto Federal de Educação, Ciência e Tecnologia de Goiás, Formosa, Brazil

Thiago Mendes
Instituto Federal de Educação, Ciência e Tecnologia de Goiás, Goiânia, Brazil
Universidade de Brasília, Brasília, Brazil

Andre Assis
Universidade de Brasília, Brasília, Brazil

ABSTRACT: Tunnel excavation with TBMs have turned into the favourite option for the construction of long tunnels to supply the demand for greater utilization of underground spaces, especially in urban areas. During TBM advancement, the face-stabilizing pressure is one of the most important factors for the proper controlling of ground movement as high face pressure often leads to surface upheaval whereas low face pressure might lead to collapse of the face and ultimately large surface settlement. Based on a recent semi-empirical formulation that describes the relation of the stress–strain behaviour of soils, the following paper is presented with the goal to provide an approach for the evaluation of surface settlement due to application of TBM face pressure, hence an aid tool for indicating tunnel face instability. Attention and alarm limits are also presented to consider uncertainties of geotechnical parameter of the groundmass. First, a brief presentation of the formulation for correlation of TBM face support pressure and the immediate surface settlement is given and then a procedure for continuous accompany of TBM excavation is provided as well as the bound limits. Finally, a case study of a tunnel construction for a metro system is presented here to offer a better understanding of the use of the present concept.

Keywords: Surface settlement, Face pressure, Tunnels & Tunnelling

1 INTRODUCTION

Nowadays the construction of tunnels in urban areas constitutes a good solution to meet the demands for new infrastructure and utility networks (i.e. water, gas, electricity, sewage, etc.) to the people that live in the cities. Two types of tunnels construction are majorly implemented in urban areas.

Tunnel boring machines (TBMs), compared with sequential tunnels, turn the most adopted tunnel construction method specially for the construction of long linear infrastructure assets and capability for minimizing the effects of ground surface movements.

No doubt the construction of tunnels by TBMs or sequential tunnels induce deformations on the groundmass that propagates into the surface in the form of settlements. These deformations can cause damages to nearby buildings, infrastructures or utility networks thus drawing the attention to the estimation of ground movement.

The settlement trough, in which is known this deformation, can be estimated by considering an empirical approach (Peck, 1969; Attewell and Woodman, 1982; New and O'Reilly, 1991; Celestino et al., 2000), analytical solution (Litwiniszyn, 1957; Loganathan and Poulos, 1998), numerical approaches (Lee and Rowe., 1990; Shin et al., 2002 and Fargnoli et al., 2015) or modelling test (Atkinson and Potts, 1977; Mair & Taylor, 1997; Meguid et al., 2008).

*Corresponding author: victor.rattia@sener.com.br

DOI: 10.1201/9781003495505-111

Regarding specifically the construction of tunnel with TBMs, Mair and Taylor (1997) stated that the most common procedures to minimise ground movement are based on methods to stabilise the tunnel face against groundmass instability by applying internal support pressure in the excavation chamber.

By considering the statements indicated above, the present paper is intended to offer an approach for estimation, during tunnelling, of tunnel face instability by the use of monitoring surface settlements in order to indicate in which manner groundmass behave ahead of the tunnel face.

The goal of this proposal is to provide an additional tool for decision aid in the establishment of a control of groundmass response during tunnel construction by the application of a formulation proposed by Rattia et al. (2022) which relates the maximum surface settlement with the applied support pressures that use an analogy with the hyperbolic behaviour of stress–strain curves of soils.

As an example of application of this method a step-by-step procedure is described and applied into two tunnels projects built with TBM: Extension of Line 1 to the new Fair of the Milan metro system and the Milan underground pass railway line in Italy, and the Bangkok MRTA project in Thailand.

2 MODELLING SURFACE SETTLEMENT

Tunnelling causes settlements at the surface due to changes in the state of stress of the groundmass around the excavation. Typical representation of this movement, in the transverse direction, was first introduced by Peck (1969) and later Attewell and Woodman (1982) by proposing an empirical model based on the Gaussian probability density function.

Regarding surface settlements due to TBM tunnelling, Atkinson (2007), based on centrifuge test results, observed that correlations between the surface settlement and the applied face support pressure could be obtained because low face pressure would cause large settlement and if a high face pressure is applied this would produce small surface settlement.

2.1 *The correlation approach for describing surface settlement due to TBM tunnelling*

Figure 1 shows a schematic representation of the behaviour of groundmass response due to TBM tunnelling observed by Atkinson (2007). During tunnelling, if the applied TBM support pressure (P) is equal to the estimated initial support pressure for tunnel-face stability (P_0), the surface settlement should be negligible. The initial portion of the settlement curve corresponds to predominantly elastic behaviour. The onset of plastic behaviour is identified as when the settlement curve approaches the asymptote given by P_{min} (the minimum applied TBM support pressure before face collapse may occur). Relatively larger settlements or even face collapse may occur when the applied TBM support pressure reaches P_{min}, which is not necessarily zero.

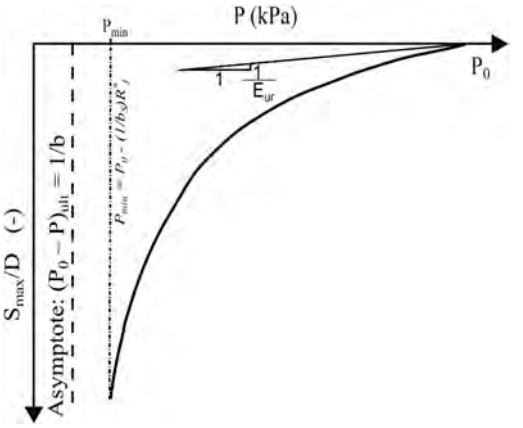

Figure 1. Settlement curve caused by tunnelling (Rattia et al., 2022).

According to Rattia et al. (2022), the behaviour can be mathematically expressed by a hyperbolic equation as follows:

$$\frac{S_{max}}{D} = \frac{a_s(P_0 - P)}{b_s(P_0 - P) - 1} \tag{1}$$

Where, S_{max} is the maximum surface settlement (mm), D is the tunnel diameter (mm), P is the applied TBM support pressure (kPa), P_0 is the estimated initial TBM support pressure for face stability (kPa), corresponding to null displacement, as and bs are best-fit parameters.

The value of P0, applied along the tunnel axis, may be estimated based on the limit equilibrium method (Anagnostou and Kovári, 1994, 1996) or on limit analysis approaches (Carranza-Torres, 2004; Davis et al., 1980), among other methods reviewed by Guglielmetti et al. (2008).

Also, according to Rattia et al. (2022), the values of best-fit parameters (a_s and b_s) are expressed, in terms of drained and undrained conditions, as:

$$a_s = 1/E'_{ur} \tag{2a}$$

$$a_s = 1/E_{ur} \tag{2b}$$

Where, E'_{ur} and E_{ur} are the unloading–reloading elastic moduli (kPa) for drained and undrained conditions, respectively.

$$b_s = \frac{1 + \sin\phi'}{2c'\cos\phi' + 2(P_0 - u_{w0})\sin\phi'} R_f^* \tag{3a}$$

$$b_s = \frac{1}{2S_u} R_f^* \tag{3b}$$

Where, c' is the effective cohesion (kPa), ϕ' is the effective friction angle (degrees), u_{w0} is the porewater pressure at the tunnel axis (kPa) and S_u is the undrained shear strength (kPa). $R_f^* = R_f/(C/D)$,

where R_f is the constant failure ratio proposed by Duncan and Chang (1970), which value is less than unity and is independent of confining pressure.

2.2 *Consideration of soil variability*

Kulhawy (1992) and Phoon and Kulhawy (1999a) explained that ground properties are subjected to uncertainties due to inherent ground variability, measurement error and transformation uncertainty. An appropriate description of these uncertainties is needed for the evaluation of geotechnical problems, especially when dealing with tunnelling projects due to groundmass variability results of scattered ground displacements.

To consider this situation, Rattia et al. (2022) proposed an expression based on the definition of a lower and upper bounds of the settlement curve as follows:

$$\left(\frac{S_{max}}{D}\right)_{upper\ bound} = \frac{a_{s90}(P_0 - P)}{b_{s90}(P_0 - P) - 1} \quad (4)$$

$$\left(\frac{S_{max}}{D}\right)_{lower\ bound} = \frac{a_{s10}(P_0 - P)}{b_{s10}(P_0 - P) - 1} \quad (5)$$

Where, a_{S90} and b_{S90} correspond to the 90th percentile and a_{S10} and b_{S10} correspond to the 10th percentile.

3 METHODOLOGICAL APPROACH

The proposed methodology is built upon a deterministic analysis of the variables for the computation of system performance variables. The output response of the system performance of the process is assumed to be represented by the maximum surface settlement (Smax) obtained from the model presented by Rattia et al. (2022).

Figure 2 shows proposed framework for assessment of tunnelling induced ground movement during TBM excavation. Three components are required to build an efficient model analysis of TBM performance to compare with the real surface settlement campaign. The first component is the estimation of the initial TBM face support pressure. The second component is model construction. The last component is the comparison of estimated model of surface settlement with the real surface settlements measure.

3.1 *Estimation of initial face support pressure – P_0*

To minimize the effects of tunnel construction with TBMs, especially in urban areas, a need for application of a support pressure is essential to maintain face stability. In this approach the TBM support pressure is called initial face support pressure (P_0) because constitute the first stage to initiate the representation of the model herein proposed.

As presented in Figure 2, first is necessary to collect information about the project, including the following: (i) site exploration data (e.g., quantification of soil layers and water level) for establishing input data such as material properties and model geometry and (ii) the type of tunnel excavation methods to be used (sequential or mechanized), which will indicate the expected type of ground movement.

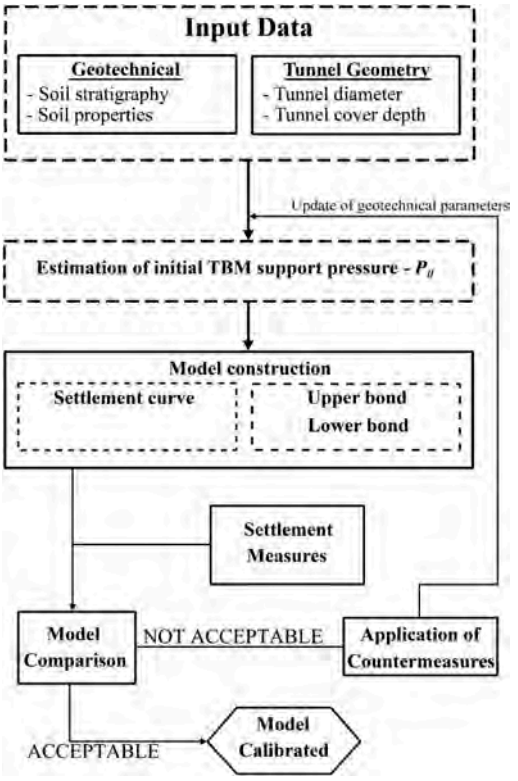

Figure 2. Proposed framework for accompanied of surface settlement.

To estimate the initial face support pressure, an extensive bibliography of methods exists and can be used in this approach. These are mostly based on limit equilibrium methods – LEM (Anagnostou and Kovári, 1994, 1996) or limit analysis (Carranza-Torres, 2004; Davis et al., 1980), known as analytical methods, and 2D or 3D numerical analysis also known as numerical methods. Guglielmetti et al. (2008) provided an extensive review of the analytical methods that could be used in the approach here proposed. As Numerical methods for the estimation of P_0 require a large computation effort, this type of method won't be considered.

3.2 *Model construction*

Once P_0 is estimated, either by using limit equilibrium method or limit analysis, the following procedure is to build the settlement curve according to Equation 1, as well as to represent in the model the upper and lower bounds of the settlement curve characterized by Equations 4 and 5.

3.3 *Model comparison*

In this last process a comparison of the surface settlement model with data regarding surface settlement is made. Two decisions are possible based on the analysis outcome:

i. The measured values of surface settlement are not within the limits foresee in the model and therefore not acceptable. An application of countermeasures is necessary: (*a*) e.g., update of input variables (geotechnical parameters) to adjust/ recalibrate the model if groundmass shows negligible deformation; and/or (*b*) ground treatment to assure face stability if groundmass shows potential mechanism of collapse.
ii. The measured values of surface settlement are within the limits foresee in the model and therefore acceptable. This means that the model is well calibrated according to ground mass properties showing agreement between the theoretical model and the observed values of surface settlement.

4 APPLICATION AND ANALYSIS OF THE PROPOSED MODEL

The present chapter is intended to show an example to illustrate the application of the proposed concept. The hyperbolic model (Equation 1) and the bound limits (Equations 4 and 5) were used to evaluate surface settlement as a function of support pressure.

This approach was applied to the Extension of Line 1 to the new Fair of the Milan metro system and the Milan underground pass railway line in Italy (Antiga and Chiorboli, 2009), and the Bangkok MRTA project in Thailand (Suwansawat and Einstein, 2006).

Table 1 summarizes the features of each case history collected from the literature. Basic input information regarding the tunnel geometry and the type of groundmass is indicated. Table 1 also presents the results of estimation of geotechnical parameters estimated based on Equations 2 and 3. The adopted values of R_f was of 0.8 and 0.9 for the sand and clay type soil mass, respectively. Values of P_0 were iteratively estimated by using the LEM until find a value that adequately represent the model with the data for each case history.

Figures 3 to 5 show the best-fit results for each case history using the equations presented by Rattia et al. (2022). A good agreement of the model with each case history data can be observed where values of R^2 were higher than 0.8.

Regarding soil variability representation, values of Coefficient of Variation (*CoV*), estimated through monitoring data, were used to estimate the upper and lower bounds. It can be observed that the *CoV*, on each case history, provided an adequate indicator for defining the soil variability limits that affect the development of surface settlement response due to TBM tunnelling.

In relation to geotechnical parameters, even though values of geotechnical parameters were not indicated by Antiga and Chiorboli (2009) and Suwansawat and Einstein (2006), different literature were consulted to allow a comparison with the data just obtained. Table 2 shows presents a summary of geotechnical parameters for the cities of Milan and Bangkok, used for the analysis of tunnelling projects different tunnelling projects performed in these cities.

As it is possible to observe from Table 1 and 2, a good agreement was achieved between the data estimated from the analysis of the case histories with the values collected from literature, indicating that the approach here presented could be used as a complementary tool for the analysis of surface settlements during TBM tunnelling.

Table 1. Best fit and geotechnical parameters estimated using the model presented by Rattia et al. (2022).

							Fitting parameters			Geotechnical parameters		
Reference	C (m)	D (m)	C/D	Type of soil	P_0 (kPa)	R_f*	$a_S D$	b_S	R^2	E'_{ur} (kPa)	c' (kPa)	φ' (kPa)
Project Line 1 Antiga and Chiorboli (2009)	15.00	6.60	2.27	Gravel and sand with a medium to high density	282	0.35	0.04680	0.00185	0.974	141026	0.34	30.50
Passante Ferroviario Antiga and Chiorboli (2009)	10.00	8.00	1.25	Gravel and sand with a medium to high density	254	0.64	0.05740	0.00330	0.950	139373	0.37	38.00
Bangkok MRTA project Suwansawat and Einstein (2006)	20.00	6.30	3.17	Stiff clay	180	0.28	0.14680	0.00255	0.813	42916	9.69	22.0

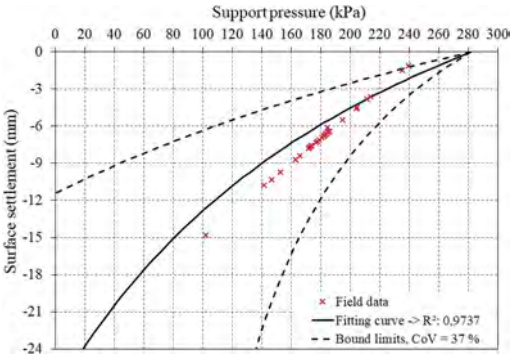

Figure 3. Upper and lower bounds of S_{max} of Line 1 project in Italy (after Antiga and Chiorboli, 2009).

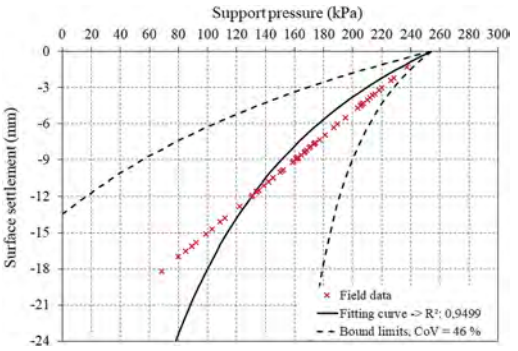

Figure 4. Upper and lower bounds of S_{max} of underground pass railway line project in Italy (after Antiga and Chiorboli, 2009).

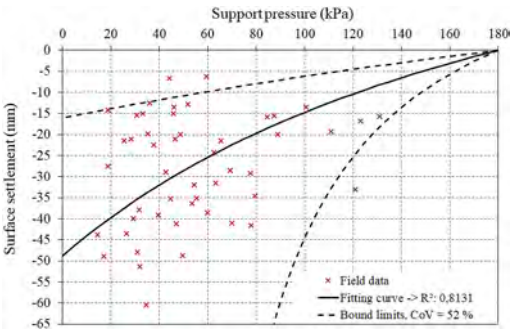

Figure 5. Upper and lower bounds of S_{max} of MRTA project in Thailand (after Suwansawat and Einstein, 2006).

5 CONCLUSIONS

The present paper was aimed to propose a practical approach for the control of TBM performance and groundmass influence through the estimation of surface settlement based on the applied TBM face support pressure during excavation.

The proposed approach is based on the formulation presented by Rattia et al. (2022), which also considers the inherent variability of soil properties through the definition of lower and upper bounds.

Three case studies, from previous published work in Italy and Thailand (Antiga and Chiorboli, 2009; and Suwansawat and Einstein, 2006), were presented to validate the approach here presented. It can be observed that the model adequately represented the groundmass behavior for each case study.

Furthermore, a reasonable estimation of geotechnical parameters from the data of each respective case study was obtained if compared with theoretical values also collected from others published works in Italy and Thailand, respectively (Fargnoli et al.,2015; and Surarak et al., 2012).

Finally, the authors believe that the proposed framework constitute a valuable tool in TBM tunnelling project because offers a procedure for recalibration of the settlement model as far as new monitoring and TBM face pressure data are incorporated enabling a real time information for the decision making.

Table 2. Published data of geotechnical parameters for the cities of Milan and Thailand.

Reference	Country	Type of soil	Geotechnical parameters E'_{ur} (kPa)	c' (kPa)	φ' (º)
Fargnoli et al. (2015)	Milan Italy	Gravelly sand	144000	0	33
Surarak et al. (2012)	Bangkok Thailand	Stiff clay	30000	11.5	28

ACKNOWLEDGMENTS

The authors recognized the importance of publication. Without this wouldn't be possible to have an overview of the concepts, variables, and approaches for analyzing tunnel face stability, ground movement and finally, to allow the development of new theories and approaches for solving tunneling problems. The authors hope that also this publication might contribute to the tunnelling industry as the publications did in this work.

The authors would also like to acknowledge the financial support of the Brazilian Research Agency – CNPq as well as the IFG (Instituto Federal de Goiás).

REFERENCES

Anagnostou, G. & Kovári, K. (1994). The face stability of slurry-shield-driven tunnels. Tunnelling and Underground Space Technology, 9 (2): 165–174.

Anagnostou, G. & Kovári, K. (1996). Face stability conditions with earth-pressurebalanced shields. Tunnelling and Underground Space Technology, 11 (2): 165–173.

Antiga A. and Chiorboli M. (2009). Tunnel face stability and settlement control using earth pressure balance

shield in cohesionless soil. Geotechnical Aspects of Underground Construction in Soft Ground – Ng, Huang & Liu (eds). Taylor & Francis Group, London, p.p. 365–371.

Atkinson JH and Potts DM (1977) Subsidence above shallow tunnels in soft ground. Journal of Geotechnical and Geoenvironmental Engineering 103(4): 307–325.

Atkinson J (2007) The Mechanics of Soils and Foundations. CRC Press, Boca Raton, FL, USA.

Attewell B and Woodman P (1982) Predicting the dynamics of ground settlement and its derivatives caused by tunnelling in soil. Ground Engineering 15(8): 13–22.

Carranza-Torres C (2004) Computation of Factor of Safety for Shallow Tunnels Using Caquot's Lower Bound Solution. Technical Report for Geodata S.p.A., Itasca Consulting Group, Minneapolis, MN, USA.

Celestino T, Gomes R and Bortolucci A (2000) Errors in ground distortions due to settlement trough adjustment. Tunnelling and Underground Space Technology 15(1): 97–100.

Davis EH, Gunn MJ, Mair RJ and Seneviratine HN (1980) The stability of shallow tunnels and underground openings in cohesive material. Géotechnique 30(4): 397–416.

Duncan JM and Chang CY (1970) Nonlinear analysis of stress and strain in soils. Journal of Soil Mechanics & Foundations Division 96(5): 1629–1653.

Fargnoli V, Gragnano C, Boldini D and Amorosi A (2015) 3D numerical modelling of soil–structure interaction during EPB tunnelling. Géotechnique 65(1): 23–37.

Guglielmetti V, Grasso P, Mahtab A and Xu S (eds) (2008) Mechanized Tunnelling in Urban Areas: Design Methodology and Construction Control. Taylor & Francis, London, UK

Kulhawy FH. (1992). On the evaluation of static soil properties. In: Stability and performance of slopes and embankments II. ASCE. p. 95–115.

Lee K and Rowe R (1990) Finite element modelling of the hree-dimensional ground deformations due to tunnelling in soft cohesive soils: part I – method of analysis. Computers and Geotechnics 10(2): 87–109

Litwiszyn J (1957) The theories and model research of movements of ground masses. In Proceedings of European Congress Ground Movement, University of Leeds, Leeds, UK, pp. 203–209.

Loganathan, N. & Poulos, H. G. (1998). Analytical Prediction for Tunneling-Induced Ground Movements in Clays. Journal of Geotechnical and Geoenvironmental Engineering, 124 (9): 846–856.

Mair R and Taylor R (1997) Theme lecture: bored tunnelling in the urban environment. In Proceedings of the 14th International Conference on Soil Mechanics and Foundation Engineering. CRC Press/ Balkema, Rotterdam, Netherlands, pp. 2353–2385.

Meguid M, Saada O, Nunes M and Mattar J (2008) Physical modelling of tunnels in soft ground: a review. Tunnelling and Underground Space Technology 23(2): 185–198

New, B.M. and O'Reilly, M.P., (1991). Tunnelling Induced Ground Movements; Predicting their Magnitude and Effects. In: Proceedings of the 4th International Conference on Ground Movements and Structures, Cardiff, invited paper, Springer, pp.671–697.

Peck RB (1969) Deep excavations and tunneling in soft ground. In Proceedings of the 7th International Conference on Soil Mechanics and Foundation Engineering, Mexico City, State of the Art Volume pp. 225–290.

Phoon, K.-K. & Kulhawy, F. H. (1999a). Characterization of geotechnical variability. Canadian Geotechnical Journal, 36 (4): 612–624.

Rattia V., Divall S., Gitirana G. and Assis P. (2022). Estimating settlements due to tunnel boring machine excavation. Proceedings of the Institution of Civil Engineers - Geotechnical Engineering. 1–12.

Shin, J. H., Potts, D. M. & Zdravkovic, L. (2002). Three-dimensional modelling of NATM tunnelling in decomposed granite soil. Géotechnique 52, No. 3, 187–200.

Surarak C., Likitlersuang S., Wanatowski D., Balasubramaniam D., Oh E. and Guan H. (2012). Stiffness and strength parameters for hardening soil model of soft and stiff Bangkok clays. Soils and Foundations 2012;52(4):682–697.

Suwansawat, S. & Einstein, H. H. (2006). Artificial neural networks for predicting the maximum surface settlement caused by EPB shield tunneling. Tunnelling and Underground Space Technology, 21 (2): 133–150.

Tunnelling for a Better Life – Yan, Celestino, Thewes & Eberhardt (Eds)
© 2024 The Author(s), ISBN 978-1-032-80042-4
Open Access: www.taylorfrancis.com, CC BY-NC-ND 4.0 license

Jet grouting soil improvement to excavate a tunnel under passing the A4 Milano-Venezia motorway for the extension of the line 1 of the Milan metro

M. Silvestri & D. Chirulli
De Sanctis Costruzioni S.p.A., Roma, Italy

A. Antiga* & P. Coppola
More Engineering s.r.l., Milano, Italy

ABSTRACT: The extension of the line 1 of the Milan Subway to the N-E outskirts of city entailed the execution of bored tunnels for a global length nearly 2 km in difficult geotechnical and hydrogeological context. The tunnels are built using conventional tunneling systems with partial and full face excavation. The excavation of the top section, above water level, of the tunnels requires the consolidation of the crown and of the face by sub-horizontal jet-grouting columns in order to obtain a band of consolidated soil suitable to guarantee a discharge arc. After the excavation of the top section the treatment of the lower part is done by injections that have to guarantee soil improvement and water tightness, then, the excavation of the lower section part happens. The work was found to be extremely complex for the presence of incoherent soil (sand and gravel) in an extremely variable hydrogeological context with water table level suddenly changing of some meters in a few months. In order to overcome these critical issues and assure greater safety and continuity of the works, the Contractor and its Consultant developed a detailed design proposal based on an observational approach, which considered several possible hydrogeological scenarios and staged excavations over small stretches This article presents the solutions adopted in terms of interventions (consolidation, excavation and lining) in correspondence of the route where the section underpasses the important infrastructure of the A4 motorway.

Keywords: Tunnelling, Jet Grouting, soil improvement, monitoring, incoherent soil

1 INTRODUCTION

The growing need for transport infrastructures has led to a stronger and stronger growth in the use of underground spaces in highly populated contexts.

The common presence of soils with poor mechanical characteristics, groundwater interfering with excavations and pre-existing structures has led to major improvements in the construction technologies, in the design techniques and in the construction materials. In these areas, that is in the cases in which the conditions of stability and water tightness of the excavation can be guaranteed only using important stabilization systems, there has been the exponential growth of the "mechanized" excavation systems, in particular in the equipment field with face stabilization systems (EPB Shield, Slurry Shield).

At the same time, despite the technological advances made in the field of soil consolidation and waterproofing systems, the "traditional" excavation systems have been relegated, to interventions of reduced extension, that is to the cases in which the road of the mechanized excavation is not economically reasonable.

Cases of urban excavation under difficult geotechnical conditions made with traditional excavation systems are increasingly rare.

An interesting experience of the application of the conventional tunneling systems with a full-face excavation with jet grouting consolidation soil is presented below; it relates to the realization of the extension of the line 1 of the Milan Subway in difficult geotechnical and hydrogeological context.

The work was found to be extremely complex for the presence of incoherent soil (sand and gravel) in an extremely variable hydrogeological context with water table level suddenly changing of some meters in a few months and limited overburden.

The undercrossing of the important A4 motorway in operation, completed the project framework.

*Corresponding author: a.antiga@more-engineering.it

DOI: 10.1201/9781003495505-112

2 GENERAL DESCRIPTION OF WORK

The project to extend line 1 of the metro from Sesto FS to Monza is part of a broader framework for strengthening the public transport system in the north of Milan.

It is aimed at ensuring a valid alternative to the strong private traffic currents coming from the Brianza and important road axes such as the A4 motorway and the SS n. 36 and at the same time, serves areas for which a strong urban development is expected.

Figure 1. Milan subway key map.

The extension of the M1 subway line in a northerly direction beyond the current Sesto FS terminus represents the most qualifying and functional element of the reorganization of the public system in the hinterland areas that most directly insist on the Milan-Monza route.

From this point of view, the extension of M1 plays a dual and important role: on the one hand, it guarantees interconnections at the local level between areas of future significant urbanization and, on the other, contributes to improving the interrelations between Milan and the most representative poles of the northern hinterland. The route covers the territories of the Municipalities of Sesto San Giovanni, Cinisello Balsamo and Monza.

The intervention extends for about 1800 meters and includes:

- 2 sections of cut-and-cover tunnel (total length: 300 m);
- 2 underground stations: Sesto Restellone and Cinisello-Monza;
- 4 bored tunnels (total length: 1207m);
- 5 shafts.

The route of the line in question intersects the planned extension of line 5 of the Milan Metro at the Cinisello-Monza station.

The amount of works is worth about 90.000.000 €.

The contract for the completion of construction works has been awarded in 2017 by De Sanctis Costruzioni S.p.A.

Contracting Authority: Metropolitana Milanese S.p.A. on behalf of the Milan Municipality.

In Figure 2 it is showed a key plan of the extension works.

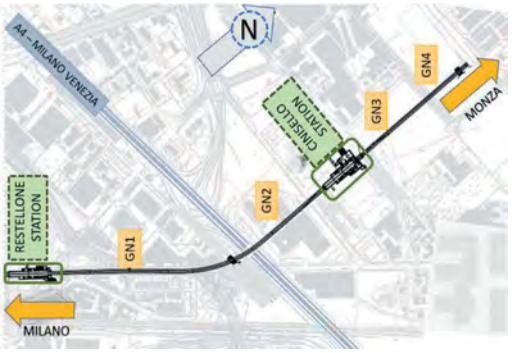

Figure 2. Key plan of the extension works.

3 THE UNDER PASSING OF THE A4 MOTORWAY

The route of the line in question intersects the A4 motorway from pk 13+769.49 to pk 13+846.97. In this section the tunnel is named "GN02". The overburden is approximately 15 m.

The A4 is a motorway which connects Turin and Trieste via Milan and Venice and passes north of Milan. is one of the most trafficked motorways of Italy with an ADT (Average Daily Traffic) of about 250.000 vehicles.

In this context it was important to limit the value of surface settlements. For this reason, as described below, a complex monitoring system had set up.

4 GEOLOGICAL AND GEOTECHNICAL FRAMEWORK

The subsoil of the Milan area consists of alluvial deposits within which different zones can be recognized located at increasing depths and with different granulometric characteristics.

In the area of our interest, located just north of the city, a well-known lithological unit is present up to a depth of about 40 meters; it consists of a gravel-sandy granular deposits with diffused pebbles and occasional silty-sandy layers. The intercalations of silty-sandy lenses are limited to a thickness of few meters. The mechanical characteristics of this unit are characterized by a zero cohesion value and a moderately high friction angle. The mechanical characteristics are essentially well-known and uniform in the whole area.

In detail, below the backfill soil, with an average thickness of 0.50 m, we can recognize two layers of interest for the works in question, up to the maximum depth of interest (40 m):

Formation SLG (Silty sand with gravel) (0.5÷6.0 m b.g.l.)
19 ÷ 20 kN/m3 unit weight
30 ÷ 33 ° friction angle
c' = 0 kPa drained cohesion

Formation GS (silty-sandy gravel) (6.0÷40.0 m b.g.l.):
20 kN/m3 unit weight
35 ÷ 38 ° friction angle
c' = 0 kPa drained cohesion

5 HYDROGEOLOGY FRAMEWORK

The main and crucial theme in defining the hydrogeological framework is the level of groundwater to be taken as a design reference: this determines in a decisive way the safety conditions, the costs and construction times.

The aquifer is characterized by high transmissivity and permeability values, equal to approximately 0,01 m²/s e a 0,001 m²/s. They determine its remarkable productivity, with specific flow values of (10÷25) l/s for lowering the aquifer level of one meter.

Over the last decades the trend of the piezometric level in the Milan area has been strongly influenced by the social evolution. The level of the groundwater has been known since the beginning of the 50s thanks to the piezoelectric map of the Province of Milan drawn up in 1958 and subsequently constantly updated. From the late 1970s, we began to see an upward shift in the piezometric levels in conjunction with an exceptional period of rainfall combined with a reduction in industrial water withdrawals due to the reduction in industrial activity. Since 1976, a cyclical (still ongoing), slow and progressive climb has begun, with approximately fifteen years cycles, due to the closure or relocation of numerous industries with consequent relocation of the water withdrawal points in areas far from the urban center. This hydrogeological context has been causing a negative interaction between groundwater and underground infrastructures for decades.

It conditions, in a significant way, the construction of all underground works in the Milan area. This is also due to the possible sudden variations (plurimetrical in one month) due to the high permeability and hydraulic transmission of the Milanese aquifer.

6 WORKS CHRONOLOGICAL HISTORY

6.1 *First public contract (2011)*

In 2011, the first Contract, for the L1 extension works, was awarded to a Joint Venture in a design-build contractual framework. Unfortunately, between the tender (2009) and the assignment of works (2011), the water table level increased for more than 4 m with a foreseeable increasing trend. Therefore, the Contractor had to deal with the actual recorded water table level. With the new water level configuration, the tunnel excavation was affected by significant water inflow. For this reason, the new design was characterized by important and massive ground improvement. The project was drafted and approved in 2011; tunnel excavation works began in 2012 after the excavation of the stations and shafts up to the excavation level of the bored tunnels.

6.2 *Works stop (2014-2017)*

When the works production had reached about 30% the financial difficulties of the JV Contractor, and the sudden further rise in the aquifer led to the termination of the contract at the end of 2014. The abandonment of the site, without the completion of the ground improvement treatments, followed the contract termination. This, combined with the endless increase of the water table, caused inexorably the flooding of the executed works (Figures 3, 4).

Figure 3. Flooding of the executed works.

In spring 2015, the groundwater level reached its peak, with a 5–6 m increase over year 2011 (year of the JV Detailed Design) values and 12–13 m increase over year 2008 (year of tender design final approval) values.

The period (2013-2015) was characterized by large fluctuations in the groundwater level. For all these reasons the Owner had to prepare an integration of the Final Design to reassign the works. The Owner also stated to insert in the new construction contract the obligation for the new contractor to develop the new Detailed Design considering the actual groundwater levels and its foreseeable trends (this was because after the peak of 2015 the levels of groundwater recorded show a downward trend).

6.3 *Second public contract (2017)*

According to the Italian law, in case of contractual termination of the awarded contractor, the works

Figure 4. Flooding of the executed works.

Contract can be entrusted to the second ranked company.

By this assumption the second ranked contractor manifested its availability for the completion of the work.

In June 2017 a new contract was signed between the Municipality of Milan (Owner, legally represented by Metropolitana Milanese S.p.A.) and De Sanctis Costruzioni S.p.A. (Contractor).

7 OBSERVATIONAL METHOD

An element that characterized the project was the strong variation in the groundwater level, which from 2012 to the present day has seen fluctuations first rising and then falling to approximately 4m (±4m).

All this considered, a technical table was opened which involved Client, Contractor and Designer to identify the design approach to be adopted in the Detailed Design.

In the light of the Client's Final Design, the contractual obligations and the actual variability of the hydrogeological hypotheses, the Contractor and his Consultant considered appropriate to study a proposal for a Detailed Design based on an Observational Method with the aim of reducing the risk in terms of time and cost of the project and increasing the safety factors of the tunnel works.

This was achieved by:

i. introducing a variability of the ground improvement interventions and of the execution phases;
ii. defining a rational and binding sequence of the work phases with well-defined activities to be completed in a well-determinate period;
iii. defining a realistic gradient increase of the water table level;
iv. using an "active monitoring system" during construction to combine the previous three points and adapt the design to the actual site conditions.

For further details, please refer to the article developed by the same themselves at WTC2020 (Iagulli G., Silvestri M., Messineo L., Antiga A.. An application of the Observational Method to deal with sudden water level changes: the 4 tunnels for the extension of the line 1 of the Milan subway. ITA-AITES World Tunnel Congress, WTC2020 and 46th General Assembly Kuala Lumpur Convention Centre, Malaysia 15-21 May 2020).

8 TECHNICAL SOLUTION FOR THE A4 UNDERPASS

The excavation of the GN02 tunnel was carried out between March and November 2022. Throughout this period, the groundwater level remained below the bottom excavation level. This condition, in accordance with the observational method, made it possible to advance with a full-face excavation.

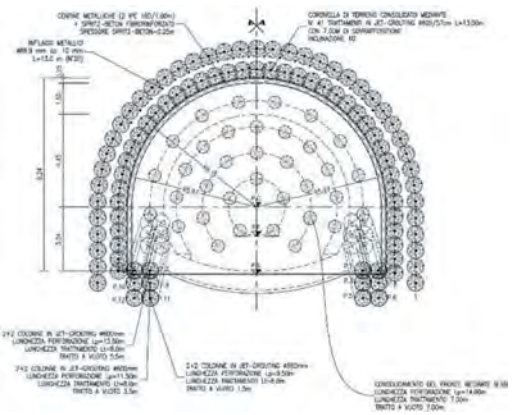

Figure 5. Cross section.

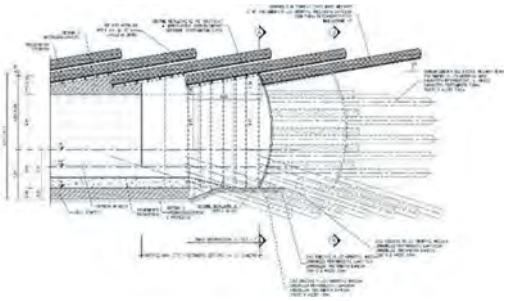

Figure 6. Longitudinal section.

For a typological section, the stabilization interventions and the executive phases are the following (figures 5, 6):

1. soil improvement intervention around the excavation section profile by means of sub-horizontal jet-grouting columns (800 mm) length 13.0 m (1);
2. face stabilization by sub-horizontal jet-grouting columns (600 mm) length 14.0 m (2);

3. temporary lining: steel ribs 2 IPE180/1.0 m + sprayed concrete (thk 0.25 m) reinforced with steel fibers; sprayed concrete (thk 0.10 m) reinforced with steel fibers in the excavation (3);
4. excavation of the face operating for segments (max length 6.0 m with single steps length 1.0 m);
5. inverted arch: reinforced concrete (thk 0.90 m);
6. internal lining: reinforced concrete (thk 0.50÷1.5 m.).

9 JET GROUTING

For the realization of the soil treatments with jet grouting columns at the contour and at the face, the single fluid system was used: in this system, the cement mixture acts as both the disintegrating fluid and the column constituent material.

The average operating parameters used for the construction of the columns are as follows:

- pressure 400 bar
- water cement ratio 1.0
- nozzles n.2, Ø3 mm
- rotation speed 15/20 rpm
- ascent speed 50 m/h
- flow rate 3 l/s
- Marsh viscosity 28 sec
- density 1.55 gr/cm^3

These parameters were fine-tuned by means of a specific test field carried out prior to the start of the works. In particular, the following tests were carried out:

- checks of the injection mixture (density, Marsh viscosity, preparation of test specimens for the verification of compressive strength at 7 days and 28 days);
- check on already completed columns (core drilling for compressive strength at 28 days) (Figure 7).

Figure 7. Treated soil samples.

According to the specifications, the required compressive strength of the consolidated soil had to be ≥5 MPa. The following table summarizes the results obtained. It can be seen that the value of the cylindrical compressive strength is much higher (minimum ≈30 MPa, maximum ≈40 MPa) than required.

Table 1. Laboratory test results on specimens.

	Dimension (mm)		Density	fc
Sample	Diameter	Height	kN/m^3	MPa
C1	94	94.3	24.17	30.99
C2	94	94.1	23.44	30.59
C3	94	94.3	24.29	37.59
C4	94	94.2	23.31	39.81

Figure 8. Consolidation of the tunnel face.

10 MONITORING SYSTEM

The GN02 tunnel undercuts the operating A4 motorway by approximately 50 m with a maximum overburden of 15 m. In this context, it was of great importance to control the deformations of the roadbed induced by excavation operations. For this reason, a complex monitoring system called 'OF Tunnel' was installed, derived from the patented 'OF System', devised by NTSG (New Tech System Generation; Rome, Italy), which also installed and operated it during the works. The system uses a very small set of fiber-optic sensors, allowing them to be installed inside the materials, making them fully

Figure 9. View from the A4 motorway (in red the underpass).

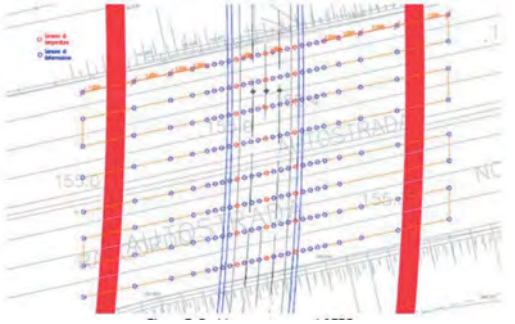

Figure 10. Optical sensor layout.

integrated with the object to be monitored. NTSG has developed a mathematical model, implemented in proprietary software, that calculates the values of the recorded parameters in real time using the data collected by the optical sensors. The 'OF' System has been patented in Italy and Europe.

In order to monitor subsidence, fiber-optic sensor arrays had been installed in cylindrical glass fibre RODs (GFRP) arranged as in Figures 10 and 11, one for each lane, 100m long, with 35 strain sensors and 3 temperature sensors for purging thermal effects.

The strain sensors were spaced 1m apart in the 16m centre (8m right and 8m left) above the subway for a total of 17 strain sensors. Outside the 16m excavation area, on each side were arranged in order 2 strain sensors spaced at 2m, 1 sensor at 3m, 5 sensors at 5m and finally 1 sensor at 10m, for a total of 9 sensors per side (18 in total in addition to the central 17). In total, each GFRP had 38 sensors, as three thermal sensors were associated with the deformation sensors, two at the ends of the GFRP and one in the centre, which were required to purge the data from thermal effects. In order to measure the deformation of the road surface, the GFRPs had been installed inside tracks approximately 10cm wide and at a depth such that they are approximately 10cm inside the road embankment. The connection between the GFRPs and the optical interrogator was via a multi-fiber link. The optical interrogator acquired the measurements taken by the sensors inside the GFRPs at a sampling rate of 1-100Hz and analyses the acquired data in real time.

Obviously, the system described was also sensitive to deformations of the infrastructure caused by vehicular traffic. However, the substantial difference between subsidence phenomena and deformations due to vehicular traffic lies in the time period that characterises them and in the type of deformation. The deformations to which the GFRP was subjected due to subsidence phenomena vary slowly over time and stabilise once the subsidence had settled, generating a permanent type of deformation. In the case of vehicle transit, the deformations were limited to a short time interval and of an elastic type. In order to calculate the actual deformations of the road surface due to ground subsidence, the deformations undergone by the GFRP were purged of the time effects circumscribed to short time intervals of an elastic type, so that only deformations that tended to increase in a stable manner over time (over slow time scales of long duration) were considered.

In addition, it had to be taken into account that asphalt changes its elasticity considerably due to temperature, generating different deformations on the substructure under the same load. In order to overcome problems of plastic deformations of the superstructure caused by the increase in exposure temperature, it was necessary to calibrate the behaviour of the superstructure at varying temperatures.

The system was equipped with a specific software that processes the data acquired by the sensors and sends it to an online computer platform that allows you to study against time the collected data, compare them with expected data, process predictive analyses, and configure alarm thresholds for absolute, relative and time values. The alarm thresholds entered were evaluated by means of numerical analyses described in the next section.

Figure 11. Array traces in the roadbed.

A typical visualization of the system on the roadbed is shown in Figure 12. The green dots at the sensors indicated that the measurement is below the alarm thresholds.

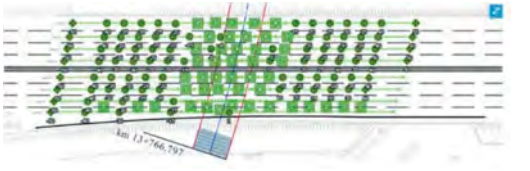

Figure 12. Status of sensors on the online platform.

11 NUMERICAL ANALYSIS

As mentioned in the previous section, the installed monitoring system required the evaluation of the expected subsidence values at the roadbed induced by the excavation of the tunnel.In particular, it had been necessary to evaluate the development of

subsidence as a function of the distance from the tunnel face from each individual sensor of the monitoring system. These values constituted the input of the Monitoring System described above.

The evaluation of the settlements and the study of the interaction of the structure (support and soil improvement interventions) with the soil and the aquifer, for the geotechnical and structural design of the excavation sections, had been conducted by means of a FEM analysis with the Plaxis calculation code. 3D analyzes were performed with simulation of the main construction phases (jet grouting face improvement, jet grouting soil improvement around the excavation, excavation, provisional lining, inverted arch, final lining).

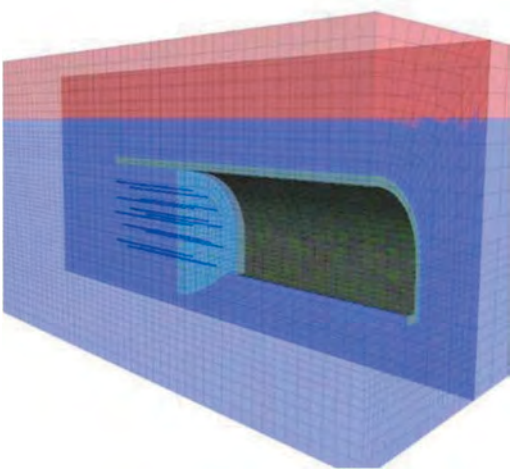

Figure 13. 3D FEM model.

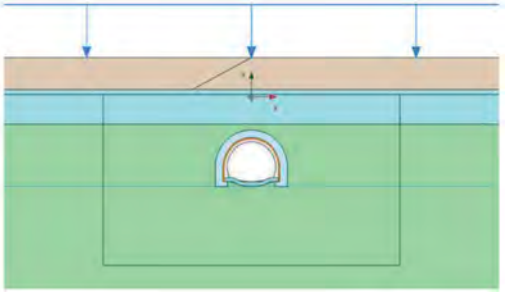

Figure 14. 2D FEM model.

These 3D analyzes allowed:

- the dimensioning of consolidations and the verification of the stability of the excavation conditions with reference to the conditions at the excavation face;
- determination of the expected deformation levels both tunnel face and tunnel cross section;
- the definition of the deconfinement curves for the calibration of 2D equivalent plane deformation models. In addition, 2D analyzes were carried out to determine the detailed design stresses on the structural elements.

In detail, from the three-dimensional modelling a series of matrices containing the values of the expected subsidence could be extracted, depending on the position of the excavation front, in the position of the individual sensors part of the eight arrays positioned on the roadbed.

The matrices had been implemented in the monitoring system platform. So proceeding, in each phase of work, the System was able to compare the value of the failure detected by the single sensor with that calculated, providing, in the event of exceeding the design limit, alert messages sent by the platform to all the actors involved in the work (building company, designer, concessionaire) by instant emails.

12 THE CONSTRUCTION PHASE

Prior to the commencement of excavation activities, an Emergency Management Plan had been implemented with the purpose of defining the operational procedures to be adopted with reference to the deformation behaviour detected, the monitoring system foreseen and with specific reference to the actions to be taken in the event of threshold values exceeding.

The threshold limit values for the parameters monitored defined the type of action to be implemented in order to identify and execute the necessary actions to prevent deformation phenomena detrimental to the functionality of the motorway infrastructure.

Figure 15. Construction phase.

Specifically, the following limit values were defined:

- of “warning and alarm” derived from the design analyses that modelled the effects of excavation in the surrounding mass in terms of expected deformations;

– of "immediate intervention" this value, superior to the design value, was provided directly by the motorway infrastructure concessionaire and set equal to 2 cm, considering it as a limit, beyond which, possible critical situations could arise for the operation and functionality of the motorway infrastructure.

During the course of the work, the data from the sensor monitoring system were constantly monitored and weekly monitoring reports were produced containing:

– processing of monitoring data acquired during the work week from the Sensor Monitoring System;
– the processing of monitoring data acquired during the work week from other conventional monitoring systems installed in the work area;
– the critical analysis of the values recorded by the monitoring systems according to the progress of the works;
– the punctual adaptation of the planned design solution for the consolidation, excavation and lining of the tunnel according to the data collected from monitoring.

The followed approach allowed to offer greater guarantees and reliability in terms of risk management related to the execution of the project (timing of the work and execution costs) both for the Client and for the Contractor.

Thanks to the presence of a capillary monitoring system, it was also possible to rationalise the quantities and the dimensioning of the ground improvement treatments with a significant economic optimisation of the works cost.

During the course of the works, no deformations were recorded on the roadbed such as to require the interruption of work or the slowing down of the operation of the motorway infrastructure.

Figure 16. Works completed.

The works were carried out regularly and on schedule, thus confirming the validity of the solutions adopted during the design phase.

The last excavation diaphragm was demolished on 8th December 2022 (Figure 16).

REFERENCES

Iagulli G., Silvestri M., Messineo L., Antiga A.. An application of the Observational Method to deal with sudden water level changes: the 4 tunnels for the extension of the line 1 of the Milan subway. ITA-AITES World Tunnel Congress, WTC2020 and 46th General Assembly Kuala Lumpur Convention Centre, Malaysia 15th-21st May 2020

Antiga A., Chiorboli M., De Luca U.. The potential for use of the Observational Method in tunnel lump-sum contracts. World Tunnel Congress 2019 Napoli (Italy). 22nd November 2022

Tunnelling for a Better Life – Yan, Celestino, Thewes & Eberhardt (Eds)
© 2024 The Author(s), ISBN 978-1-032-80042-4
Open Access: www.taylorfrancis.com, CC BY-NC-ND 4.0 license

Study on the mechanical behavior of the vertical pre-reinforcement

Yuto Tatebayashi* & Natsumi Tamura
Tokyo Metropolitan University, Hachioji, Japan

Tomohisa Amemiya
Ministry of Land, Infrastructure, Transport and Tourism, Tanabe, Japan

Kosuke Kawata & Nobuharu Isago
Tokyo Metropolitan University, Hachioji, Japan

ABSTRACT: The vertical pre-reinforcement bolt method is used to stabilize the ground above tunnels with shallow overburden to prevent ground surface subsidence and to stabilize slopes. However, it cannot be said to establish a quantitative design method for this application due to the variety of design concepts. In this paper, a study is conducted to examine quantitative characteristics by using model test and numerical analysis. Results shows the vertical pre-reinforcement method can improve the continuity of ground and decrease shear strain of ground by the distance of reinforcement. It also indicates the application leads to the change in the apparent rigidity of the ground. The relationship between the reinforcement conditions and the effect of this method was also clarified.

Keywords: Mountain tunnel, Auxiliary method, Vertical pre-reinforcement bolt, Model test, Numerical analysis

1 INTRODUCTION

General support member of the conventional tunneling method in mountain tunnel currently consists of shotcrete, rock bolts, and steel arched support. The confirmation of load-bearing capacity of surrounding ground is effectively brought by the stabilization of the groundmass for excavation. In recent years, due to the advantages of economical efficiency and flexibility of construction, auxiliary methods have been increasingly used in urban areas and shallow overburden where the ground strength is not sufficient for improving the safety of construction, as well as the efficiency.

Auxiliary method is a general one for the means of stabilizing tunnel, that is, the face stabilization, the constraint of ground surface settlement, the countermeasure against ground water and the protection of the surrounding environment. This makes it possible to apply the mountain construction method in conditions where the ground is poor and weak, such as fault zone or fracture zone in ground, urban area and shallow overburden area.

Vertical pre-reinforcement bolt method is thought as one of the auxiliary methods. This method reinforces the ground around tunnel by inserting bolts from the surface of scheduled excavation area and its surroundings. This method is expected to improve the safety of tunnel excavation, prevent ground surface settlement, and stabilize slopes above the tunnel.

In recent years in Japan, there have been several cases in which the method has been adopted with the objective of stabilizing the slope, especially at the portal zone, Suzuki et al. (1990) and Inoue et al. (1993), and there have been cases in which the method has been used in combination with other auxiliary methods such as forepoling and face shotcrete. In the design of pre-reinforcement bolt, the shear resistance is thought to increase by using it to maintain the stability of the slope behavior, which is not large in scale.

On the one hand, previous studies, such as Amemiya et al. (2022) and the experience of the past construction results have shown that the materials to reinforce are effective due to axial resistance, which prevents loosening of ground caused by tunnel excavation and stabilizes surrounding ground. In other words, unified design method has not yet been established due to the various approaches to design.

In this paper, the mechanism of this method is discussed and the influence of bolting conditions is examined in order to propose a quantitative and

*Corresponding author: yuto0224tate@gmail.com

DOI: 10.1201/9781003495505-113

rational design method for vertical pre-reinforcement bolt. Specifically, the changes in the fundamental behavior of the ground due to the application of the vertical pre-reinforcement bolts were examined by model test and numerical analysis for its application to actual tunnel construction.

2 RESEARCH METHODS

2.1 *Model tests*

In order to investigate the changes in the fundamental behavior of the ground due to the application of vertical pre-reinforcement bolts, model tests were conducted to simulate two types of tunnel excavation and bolting.

2.1.1 *Models and materials*

Figure 1 Shows the outline of the model test apparatus. It consists of a tunnel model, a load measurement system such as load cell and data logger, and a displacement measurement system with digital camera. Also the image analysis was done using the result of the picture to grasp the ground movement. Aluminum bar are used for the ground model and the chains with metal ball simulates the vertical pre-reinforcement bolts in Figure 1. The tunnel was acrylic model and its height and width was 100 mm. The tunnel diameter D could be defined 100 mm. Figure 2 shows the for excavation simulation, 5 PTFE sheets of 0.2-mm-thick and 17 PTFE sheets of 0.3-mm-thick were wrapped around the tunnel model. Totally 22 PTFE sheets are pulled out with every one sheet after piling up aluminum bars and setting the tunnel model. By extracting the sheet, aluminum bars around the tunnel move in direction to the tunnel center and the occurrence of displacement is regarded as tunnel excavation.

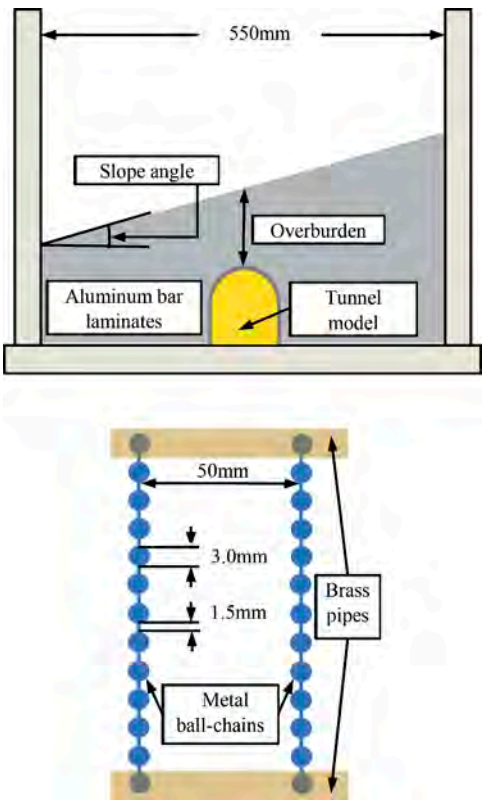

Figure 1. Outline of the model test apparatus.

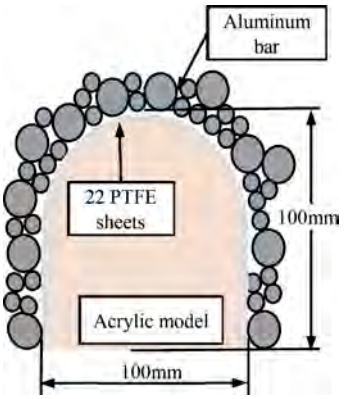

Figure 2. Simulation of tunnel excavation.

Table 1 shows the physical properties of the model tests. Previous studies with aluminum bar laminates as the ground indicate that aluminum bars of 1.6 mm and 3.0 mm in diameter with a weight mixture ratio of 3:2 results in an internal angle of friction of almost 30 degrees, which is close to sand's one, based on shear tests of the aluminum bar laminates (Murayama et al., 1969). The same diameter and mixing ratio were used because many experiments have been conducted using similar aluminum bar mixtures. Ball chains were used as reinforcement. The reinforcement was selected based on the following considerations: (1) if the bending rigidity of the reinforcement is too large, the two-dimensional experiment will not be able to reproduce the natural deformation behavior of the ground; (2) from the measurement results in the field, it is considered that the vertical pre-reinforcement bolts will be their effect by the axial force of the bolts (Shiroma et al., 2006). Therefore, it is reasonable to use materials for reinforcement in which axial forces are dominant in the ground; (3) metal ball chains have good friction with aluminum bars and high reproducibility due to no change in physical properties even after repeated use.

2.1.2 *Model test method*

Model test procedure is as follows. Firstly, the tunnel model wrapped with all of prepared PTFE sheets is placed on the centre. Using an acrylic plate,

Table 1. Characteristics of the ground material.

Material	Aluminium alloy
Length [mm]	100
Diameter [mm]	ϕ_1 =1.6, ϕ_2 =3.0
Weight ratio	ϕ_1:ϕ_2 = 3:2
Unit weight [kN/m^3]	21.4
Cohesion [kN/m^2]	0.00
Angle of internal friction [degree]	30

tensioned the metal ball-chains are fixed in place by hand. Aluminum bars are laid out from the bottom in 1cm thick increments. Markers for image analysis are placed every horizontal and vertical distance of 2cm centered in the tunnel, 30cm wide and high to the ground surface. They are placed every 2 cm on the ground surface. A cross-section of the ground is photographed each time the PTFE sheet is pulled out. The width of reinforcement was targeted in this study. Table 2 shows the case of the model test and the definition of placement situation in Figure 3.

Table 2. Case of the model test.

Case #	Reinforcement spacing[mm]	Reinforcement width
#A	No reinforcement	
#B	15	3.3D
#C		0.9D
#D		0.45D x 2 for sidewall

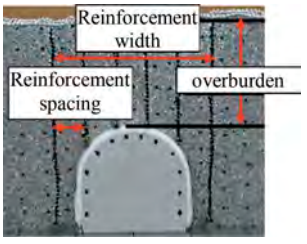

Figure 3. Definition of reinforcement placement in the model test.

2.2 *Numerical analysis*

Numerical analysis using finite difference method (Code: FLAC3D) was conducted where auxiliary construction methods are required.

2.2.1 *Numerical analysis models*

Figure 4 Shows the numerical analysis models. It includes the analysis area and the reinforcement condition. The ground category was assumed to be a poor one in Japanese technical standard, assuming portal zone where this method is often applied, and the ground was modeled using elastic-plastic model based on the Mohr-Coulomb failure criterion. The overburden is set to 1D (D:tunnel excavation width, 11.3 m) in all cases. In the case of a relatively shallow overburden, the analysis area was set to 2D from the side of the tunnel downward, 5D to the side, and 10D. The tunnel excavation method was assumed to be the full-section method with an auxiliary small bench, the length of 1m. The unit excavation length was also set at 1m. The temporary support such as shotcrete and so on was installed 1m behind the face. The lower half was excavated 3 m behind the upper face, and invert excavation was performed 3D behind the face. These excavation cycles were repeated until the tunnel reached 116 m in length, at which point the analysis was terminated.

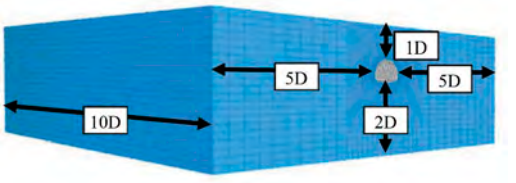

Figure 4. The numerical analysis model.

2.2.2 *Physical property values of the numerical analysis*

Table 3 shows the physical property values used in the analysis. For elasticity modulus and Poisson's ratio, the values used for modeling in poor ground category from the technical guideline shown by technical guideline of highway company, were used. For angle of internal friction and cohesion, values that have been shown to significantly reduce displacement of vertical pre-reinforcement bolts from previous studies were applied in this analysis. The tunnel section was based on Japanese highway standards, using the standard tunnel portal zone for a two-lane tunnel cross section as a reference. The tunnel supports were modeled using Shell elements as composite members with equivalent stiffnesses of shotcrete and steel arched support calculated.

Figure 5 Shows the conditions for bolting. Vertical pre-reinforcement bolts were modeled with beam elements, and properties were set using D32 rebar, which is frequently employed. Bolts were placed at equal intervals throughout the longitudinal section of the tunnel model.

2.2.3 *Analysis cases*

The analysis cases are shown in Table 4. The effectiveness of the application of the method and its effect on the behavior will be studied when the width and location of the concrete placement are different.

Table 3. The physical property values.

Model	Structural element	Elastic modulus	Poisson's ratio	Angle of internal friction	Cohesion
Ground	Solid	50 MPa	0.40	30 degrees	20 kPa
Tunnel support	Shell	8.90×10^3 MPa	0.20	-	-
Inverted arch	Shell	4.00×10^3 MPa	0.20	-	-
Reinforcing materials	Beam	2.05×10^5 MPa	0.30	-	-

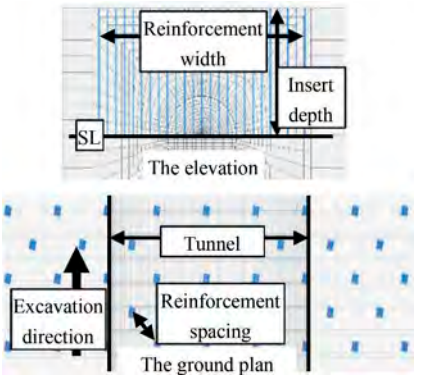

Figure 5. Placement of bolting in analysis.

Table 4. Analysis cases.

Case #-	Reinforcement spacing [m]	Reinforcement width[D]	Insert depth
#1	No reinforcement		
#2	2.0	3.0	To spring line from surface
#3		1.0	
#4		0.5D x 2 for sidewall	

3 RESULT

3.1 *Result of the model test*

The results of model tests are shown below. In model tests, each case was tested multiple times. Then, the ground surface settlement shown below is an average value of all experiments without clearly abnormal tendencies, as it was confirmed that there was little variation. The maximum shear strain in the ground is shown only for one representative case, because it is difficult to show the average value, and the trend of strain distribution is selected to be easy to understand.

3.1.1 *Maximum shear strain distribution*

Figure 6 Shows the maximum shear strain distribution for each case. In Case B, where the width of the tunnel was sufficiently larger than the excavation diameter, there was a change in the distribution of strain compared to Case A, where was fundamental case and no reinforcement, and Case C, where the width of the reinforcement was almost the same as the excavation diameter, the area of strain in the upper part of the tunnel became narrower.

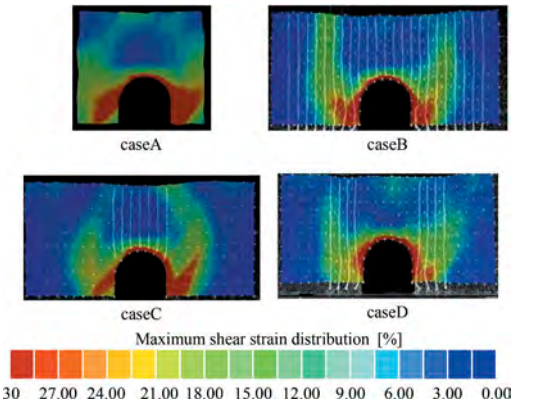

Figure 6. Result of maximum shear strain distribution from model test.

3.1.2 *Displacement vector*

Figure 7 Shows the displacement vectors in the ground for each case. For Case B and C, there was a change in distribution compared to Cases A. The distribution of displacements from the tunnel to the ground surface became more uniform. For Case D, the displacement in the upper part of the tunnel is not uniform. In this respect, the trend of the displacement distribution differs depending on the width of reinforcement.

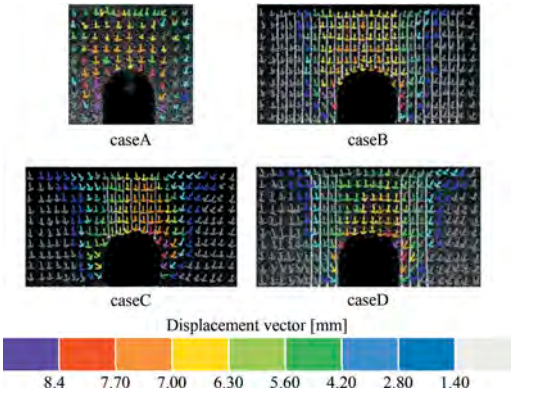

Figure 7. Result of displacement vector from model test.

3.2 *Result of the numerical analysis*

The results of the numerical analysis are shown below. In comparing the cases, the cross section in the center of the analytical model (at the 60 m depth point) was focused.

3.2.1 *Result of the ground surface settlement*

Figure 8 Shows the relationship between the distance from the center of the tunnel and the final settlement for each case. In all cases where the reinforcement was applied, the final subsidence of the ground surface decreased. The maximum reduction of ground surface subsidence by the method was 38% in Case B with a 3.0D casting width, 29% in Case C with a 1.0D casting width, and 6% in Case D without casting on the side of the tunnel, indicating that the displacement reduction effect was greater in Cases B and C with reinforcement above the tunnel.

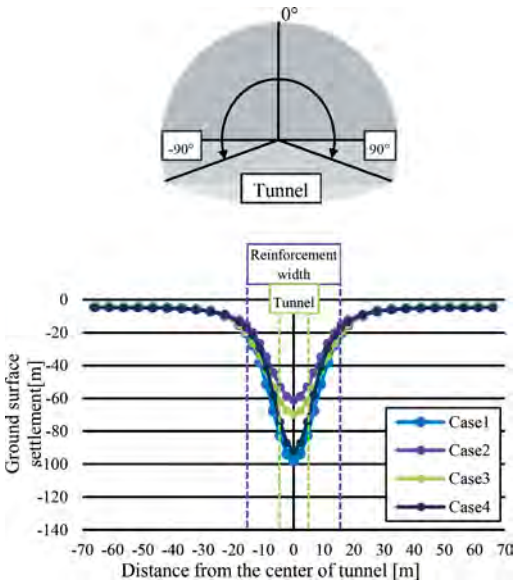

Figure 8. Result of ground surface settlement from analysis.

3.2.2 *Result of the bending moment in the tunnel support*

Figure 9 Shows the distribution of bending moments in the tunnel support in each case. For both installed widths, the bending moment of the support near the tunnel crown is reduced by the application of the reinforcement. There is little difference in the bending moment generated in the support structures between Case B and Case C. However, the distribution of bending moments in the case of casting only in the upper part of the tunnel is similar to that of the case in which vertical reinforcement is not applied. Furthermore, in the case of the sidewall, the bending moment increases from the shoulder to the spring line area.

4 DISCUSSION

4.1 *Model tests*

In Case C, where reinforcement bolt was placed only in the upper part of the tunnel, the extent to which the

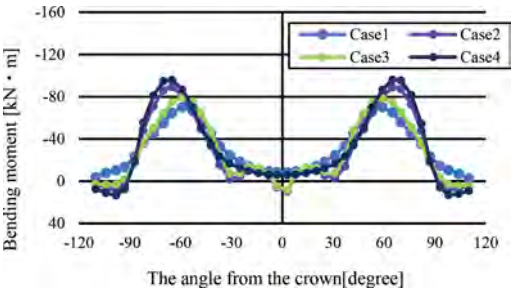

Figure 9. Result of the bending moment in the tunnel support.

ground is unified by the bolts is smaller, and only the upper part of the tunnel behaves as a single unit. Case D, in which bolts are not placed above the tunnel, is considered to indicate that the tunnel is not expected to be effective in integrating the ground above the tunnel.

When the bolts are placed only at the top of the tunnel, the ground above the tunnel can be integrated, but bolts on the sides of the tunnel are necessary to redistribute the stresses in the ground above the tunnel in a stable manner and improve the stability of the tunnel. However, when bolts are placed only on the sides of the tunnel, the stability of the ground around the tunnel is not expected to be improved. In other words, the vertical reinforcement bolt above the tunnel are considered to unify the ground, while the bolts at the sides of the tunnel are considered to be responsible for stress transmission.

4.2 *Numerical analysis*

Result of the numerical analysis indicates that the bolts above the tunnel mitigate stress changes in the ground and prevent loosening, and that the bolts on the sides of the tunnel transfer the load from the top of the tunnel to the ground and also mitigate stress changes in the ground. These results suggest that the bolts above the tunnel mitigate stress changes in the ground, thereby preventing shear failure of the ground and loosening of the ground due to tunnel excavation, and that the ground behaves as a single unit. It is also inferred that the lateral bolts transfer the load above the tunnel to the ground, resulting in a stable stress change in the ground with respect to the tunnel structure. This method enables stable tunnel excavation and suppresses ground deformation by mitigating stress changes in the ground through the use of vertical reinforcement. This method is expected to be effective in reducing ground surface subsidence and tunnel displacement.

5 CONCLUSION

By increasing the width of the pre-reinforcement bolting area, the area where deformation of the ground can be suppressed and also expanded horizontally, and a wider range of ground displacement suppression

effects can be expected. This method of construction mitigates the stress changes in the ground, and the ground tends to behave as a certain mass and shear strain is suppressed. This suggests that the application of this method makes the ground behave as a continuum and improves the apparent properties of the ground, and that a simple design using the numerical analysis is applicable to examine its effect by considering the installation of bolts in this method as a change in the apparent stiffness of the pile.

This study does not include an in-depth discussion of the whole physical properties of the ground. Therefore, further study is needed to determine the degree of improvement of the ground and the relationship between the physical properties of the applied ground and the effectiveness of this method and the conditions under which the ground is placed. In addition, the mechanical behavior of this method, including the relationship with the results of measurements at actual tunnel, should be clarified to realize a rational and quantitative design of this method.

REFERENCES

Amemiya T, Nagata T, Isago N, Kawata K, Shiroma H and Nishimura K Consideration of the mechanical behavior and the influence on ground of vertical pre-reinforcement Proceeding of the Eurock 2022- Rock and Fracture Mechanics in Rock Engineering and Mining No.1124 2022.

Inoue M, Koduki H, Tanaka Y Vertical Forepoling method at tunnel entrance of landsliding topography. Ishizuchi tunnel on Matsuyama expressway Journal of the Tunnel and Underground Vol.24 No.9 pp17–24 1993.9 (In Japanese).

Japan Society of Civil Engineers, 2009, Auxiliary method of mountain tunnelling, -2009- ed Asakura T, pp 1 and 232-235 (In Japanese).

Murayama S and Matsuoka H 1969 On the settlement of granular media caused by the local yielding in the media Proceedings of the Japan society of civil engineers' issue 172 pp 31–41 (In Japanese).

Ozaki M, Yamada H, Kawakita M, Magara M, Kobayashi Y Study for planning and effects of vertical forepoling bolt method on the slope with thin overburden Proceedings of tunnel engineering Jsce Vol.9 1999.11.

Shiroma H, Masuda M, Shinji M, Matsui M and Nishimura K 2006 A study on behavior of vertical pre-reinforced bolt bases on field measurement in the shallow tunnel Journal of Japan society of civil engineers vol 62 No.1 pp117–27 (In Japanese).

Suzuki R, Orii H, Vertical forepoling for construction of tunnel entrance of talus and land slide potentiality. Asuwayama tunnel on Fukui – Kawanishi line Journal of the Tunnel and Underground Vol.21 No.11 pp. 25–29 1990.11. (In Japanese).

Tunnelling for a Better Life – Yan, Celestino, Thewes & Eberhardt (Eds)
© 2024 The Author(s), ISBN 978-1-032-80042-4
Open Access: www.taylorfrancis.com, CC BY-NC-ND 4.0 license

Marble sludge in two-component grout applications

Carmine Todaro*, Andrea Carigi, Marilena Cardu & Daniele Peila
Politecnico di Torino, Turin, Italy

ABSTRACT: The two-component grout is currently the most used backfilling technology in shield tunnelling applications. The technology is widely used all around the world thanks to its versatility. In fact, by properly calibrating dosages and types of raw ingredients, the technical specifications proper of a certain construction site can be easily satisfied. In this work, an innovative two-component grout mix design is introduced, in which a marble sludge is added to component A of the two-component grout system as a new ingredient. The marble sludge, obtained during the cutting process of ornamental stones in marble quarries is commonly considered a waste, an environmental problem that must be correctly managed. The idea of the authors was, hence, to use the marble sludge as an ingredient in the two-component grout, by physically blocking it in the gelling reaction and making it permanently part of the backfilling material, confined between the bored medium and the lining extrados.

In this paper, a laboratory test campaign on the potential use of marble sludge in the two-component grout technology is reported. A standard two-component grout and the innovative one have been compared according to standardized testing protocols. Outcomes highlight that the innovative grout has similar properties compared to the standard one and that the addition of marble sludge does not worsen the grout's properties.

Keywords: two-component grout, backfilling, marble sludge, waste reduction

1 INTRODUCTION

At present times, the two-component grout is the most used backfilling technology in mechanised tunnelling, using shielded machines.

During the tunnel excavation and the machine advancement, a gap is continuously created from the difference in diameter between the head of the machine and the lining extrados. This gap is inevitable since this geometrical peculiarity is essential and allows for the assemblage of the segments in linings under the protection of the shield, as well as avoiding potential machine block due to convergence of the excavated medium.

This gap, commonly called annulus, has an order of magnitude of centimetres and is schematically shown in Figure 1.

Different technologies can be used for the complete filling of the annulus (Grasso et al., 2023) but two-component grout is undoubtedly the most popular all around the world, due to its aptitude for preventing and controlling surface settlements (Fargnoli et al., 2013). This feature is guaranteed by an almost instantaneous gelation of the grout: the material after the

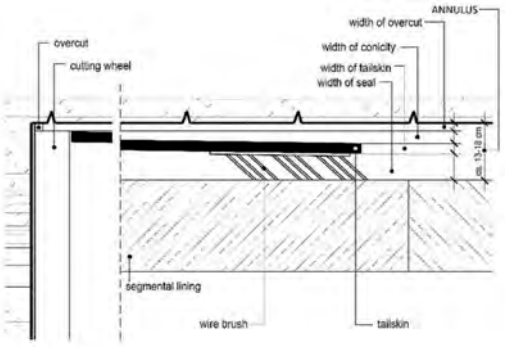

Figure 1. Annulus. Modified from thewes and budach (2009).

gelation starts immediately to improve its mechanical and elastic properties (Oggeri et al., 2021; Todaro and Pace, 2022).

The technology is based on two liquid components: the component A and the component B. The first is a cement-based material made up of cement, water,

*Corresponding author: carmine.todaro@polito.it

DOI: 10.1201/9781003495505-114

bentonite and retarding/fluidifying agent, while the second is commonly a solution of sodium silicate. Recently, new ingredients have been experimentally introduced to component A production such as, for example, fly ash, blast furnace slag, and industrial solid waste (André et al., 2022; Schulte-Schrepping and Breitenbücher, 2019; Song et al., 2020, Song et al., 2022).

These last studies were the starting point for this research, meaning that the idea to re-use something considered industrial waste was followed. In detail, the new ingredient selected to produce the component A has been the marble sludge, typical waste coming from the cutting process of ornamental stones. The choice was dictated by the nature of the marble sludge, composed mainly of calcium carbonate ($CaCO_3$) and directly available with a grain size distribution suitable for the proposed application. This material is produced in large amounts in marble quarries (Cobo-Ceacero et al., 2019): On average, for each cubic metre of marble exploited, 50-95 L of marble sludge is obtained. This material must be correctly managed, and the cost for its disposal significantly impacts the marble quarry business.

In this work, a preliminary test campaign is presented concerning the use of marble sludge powder as a raw ingredient for the production of component A. In the following paragraphs, the term "marble sludge" refers more specifically to the powder of marble, naturally produced during the cutting operation performed in a dry way (no water or other lubricants added).

Starting from a mix design typically used in construction sites for the two-component grout production, two different dosages of marble sludge have been tested to produce the grout. To verify the feasibility of using this new ingredient in the two-component grout technology, the component A properties, the reaction of gelation, and the hardened grout have been tested according to a standardised testing protocol (Todaro et al., 2019). The results of the grout prepared with the marble sludge have been compared to those of the reference mix.

2 THE ISSUE OF THE MARBLE SLUDGE

Considering the ornamental stone processing chain, the cutting operations are important since blocks of huge dimensions (m^3 of order of magnitude) are split into easily transportable slabs, suitable for further processing (Figure 2, left). Taking into account the Italian scenario, marble quarries are by far the most common, yet other types of ornamental stone quarries are also present on the national territory. For the reason of "abundance", authors have selected marble sludge as an experimental ingredient in this study (Figure 2, right).

Figure 2. Chain cutting machine used for splitting the marble blocks in slabs (on the left) and the marble sludge obtained during this cutting operation (on the right).

Considering only the Carrara marble basin, hundreds of thousands of tons of marble sludge are produced every year due to the huge production of blocks (about 900,000 tons/year) of one of the finest marbles in the world. This big production inevitably leads to big amounts of produced marble sludge. Additionally, the environmental problem associated with marble sludge disposal is challenging, especially in the area where quarries operate.

From this scenario, the authors' idea has been conceived, while considering the new big tunnel projects that are going to start in the next years in Italy according to the National Recovery and Resilience Plan funding: use the marble sludge in the backfilling phase in shielded mechanised tunnelling.

If, from one side, the environmental positive impact of "trapping" the marble sludge in a grout is practical, the calibration of the two-component grout mix design for using the marble sludge as an ingredient is a complex phase from the other side, considering the sensitive balance between compounds. The two mix designs presented have been calibrated not only to maximize the dosage of marble sludge but also to try to improve the mechanical performances of the obtained grout.

3 MATERIALS AND METHODS

The test campaign has been organised in two different parts: the first aimed to assess the properties of component A only and the gel time, while the second aimed to test the mechanical performance of the gelled grout at a short curing time. The short curing time is intended for no more than 3 hours after the casting. The procedure for preparing component A, for the sample casting and the used mix designs are reported in the following.

3.1 *Used materials*

To produce the two-component grout, Portland Cement type CEM I 52.5 R (CEN, 2011) was used. The accelerator, retarding/fluidifying agents, and

bentonite were provided by Mapei company. The marble sludge was instead provided by the "Rock cutting laboratory", part of the "Geomechanics and Geotecnology laboratory" of the Politecnico di Torino.

3.2 *Component a production and sample casting*

The component A production was carried out by using a laboratory stirrer, according to the procedure described in Todaro et al. (2019) and hereinafter shortly summarised in Table 1.

Table 1. Mixing procedure.

Phases	Impeller rotation speed (rpm)	Duration (min)
Start – only water	800	/
Bentonite mixing phase	2000	7
Marble sludge mixing phase	2000	if the marble sludge is added, the mixing time should be calibrated for obtaining a suitable mix
Cement mixing phase	2000	3
Mix of retarder/ fluidifying agent – End	2000	2

The mix designs used are reported in Table 2. Those where the marble sludge is used are "1M" and "2M", while "R" is the reference mix design. Dosages are expressed in kg/m^3.

Table 2. Mix designs.

Ingredient	1M	2M	R
Cement	230	230	230
Bentonite	30	30	30
Marble sludge	50	100	/
Water	834	816	853
Retarding/fluidifying agent	3.5	3.5	3.5
Accelerator	81	81	81

When component A was obtained, the sample casting was performed manually. The metered amount of components A and B were prepared in two different tanks, followed by quickly pouring component A inside the tank holding the component B, and later pouring all the grout into the empty tank, which led to the final step of emptying the grout (still liquid) into the sample moulds.

Used samples have dimensions in compliance with CEN (2016) (40*40*160 mm).

3.3 *Performed test*

The characterisation of component A, the reaction between components A and B, and the hardened grout at short curing time have been studied in accordance with the well-established, detailed procedure reported in Todaro et al. (2019). Briefly, the characterisation of component A was assessed by measuring the unit weight and the flow time on the fresh component A (i.e. within 10 minutes after the production) while the bleeding was assessed after 1, 3, and 24 hours after the component A production. The gelation of the grout obtained by turbulently mixing component A and component B has been assessed by measuring the gel time. Finally, the hardened grout has been characterised by assessing the surface compression strength (SCS) after 1 and 3 hours of curing.

3.3.1 *Unit weight*

The unit weight was assessed by using a mud balance (Figure 3), according to the standard ASTM D4380 (2020).

Figure 3. Mud balance used for the unit weight assessment. (Todaro et al., 2023).

3.3.2 *Flow time*

The flow time was assessed by using the Marsh funnel (Figure 4), in line with UNI 11152-13 (2005). This test provides indications on the viscosity of the tested material. The outcome of the test is the time spent by 1 L of mortar to flow through the funnel. The higher the viscosity of the mortar, the higher the flow time.

Figure 4. Marsh funnel used for the flow time assessment (Todaro et al., 2023).

3.3.3 *Bleeding*

The bleeding test allows the evaluation of the physical stability of component A. The test has been carried out according to UNI 11152-11 (2005). A standardised cylinder is filled with 1 L of component A, to which particles of cement tend to settle on the bottom of the cylinder due to the gravity force,, leaving a layer of water on the top of the surface. After a certain time, the volume of the segregated water is measured (V_w), and by computing the ratio on the whole volume of 1 L (V_t), the bleeding index is computed, expressed as a percentage according to equation (1):

$$Bleeding = \frac{V_w}{V_t}(\%) \quad (1)$$

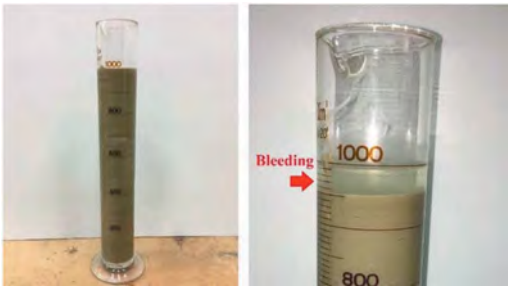

Figure 5. Bleeding assessment. (Todaro et al., 2023).

3.3.4 *Gel time*

The gel time has been assessed by following the experimental procedure proposed by Todaro et al. (2019) and used also by André et al. (2022). Once the quantities of components A and B are metered and prepared according to the mix design, component A is poured into component B; after that the whole material is quickly poured again in the empty tank and so on with subsequent series of pouring. The time recorded started when the first contact between components A and B occurred, and ended when the grout is not able to flow.

3.3.5 *Surface compression strength (SCS)*

The surface compression strength (SCS) has been assessed according to the procedure proposed by Todaro et al. (2020). A dynamometer was equipped with a flat circular bit having a surface of 177.9 mm^2 (A in equation 2) (Figure 6).

The test consists of the penetration of the bit orthogonally on the cast surface of the grout (previously cast in moulds with the shape in compliance to CEN (2016) and cured for 1 or 3 hours in a sealed environment) till a penetration of 5 mm is reached. The maximum force (F in equation 2) reached during the test is recorded. SCS is consequently computed according to equation (2) where F is expressed in N.

Figure 6. Dynamometer used for the surface compression strength assessment during the test. Todaro et al. (2020).

$$SCS = \frac{F}{A} \quad (2)$$

According to the reference standard, tests have been performed without demould samples. At least 6 tests were carried out for each assessment performed after 1 hour, while between 3 and 6 determinations were performed for testing after 3 hours of curing. The reason for a higher number of assessments at 1 hour of curing is related to the higher dispersion observed.

4 RESULTS

The obtained outcomes are summarised in Table 3.

Table 3. Used mix designs.

Mix design	1M	2M	S
Unit weight (kg/L)	1.20	1.27	1.17
Flow time (s)	36.0	38.0	34.5
Gel time (s)	7	4	8
SCS 1h (MPa)	0.38	0.45	0.41
SCS 3h (MPa)	1.65	1.71	1.62
Bleeding 1h (%)	0.3	0.0	/
Bleeding 3h (%)	0.68	0.00	1.04
Bleeding 24h (%)	3.10	2.40	2.09

5 DISCUSSION

Taking into account the unit weight, an increment of values is recognised for 1M and 2M compared to R. The higher weight for a fixed volume of the considered component A is due to the replacement of a certain amount of water with the marble sludge. However, values of 1.2-1.3 kg/L are typically

accepted in construction sites, therefore it can be stated that compliance has been respected.

On the other hand, a significant reduction in gel time was observed. If for 1M the reduction is only of 1 s (a time lapse consistent with the test error), the gel time of 2M is half of those of R. The value of 4 s is very short, hardly applicable in standard practices, and not commonly acceptable in construction sites. Probably, the gelation between components A and B is affected by the presence of the marble sludge that plays an active role as a further booster of the reaction.

Considering the flow time, a slow increase has been observed (about 4 % and 10 %, respectively for 1M and 2M) compared to the flow time of the mix R, but then again, these values are accepted in common practice.

Optimal results have been obtained for the bleeding test, despite the presence of the marble sludge and consequently the tendency of these particles to segregate (similarly to the concrete ones), bleeding values are lower than 1% after 3 hours and abundantly lower than 8% (the threshold commonly fixed for construction sites) after 1 day.

As for the strengths at short curing time, 2M seems to be more performant than R: values greater than about 10 % and 6 % compared to the reference mix design have been obtained for a curing time of 1 hour and 3 hours respectively. Differently, 1M exhibits similar results compared to R (for 1 hour of curing, the strength was lower than that of the reference mix).

6 CONCLUSIONS

This work describes a preliminary test campaign where marble sludge, a material considered as waste in the ornamental stone supply chain, is reused in a tunnelling application. The preliminary nature of the work is related to the used mix designs; in fact, starting from a real two-component grout mix, no variations on dosages of raw ingredients have been applied: only the water has been replaced by the marble sludge in a quantity dictated by the sludge dosages and the respective unit weights. This choice was dictated by the need to check the potential impact of the new ingredient on the two-component grout technology by monitoring the reference parameters and their "fluctuations" in presence of the new ingredient.

Despite this limitation, the results highlighted the concrete possibility of giving the marble sludge a noble use as an ingredient in the two-component grout technology, as backfilling in tunnelling applications. No breach has been actually identified, granted that the gel time could extend by increasing the dosage of the retarding/fluidifying agent. It is also important to note that an increment of the retarding/fluidifying agent could allow the increase of the marble sludge dosage that, according to the presented results, could turn into higher strength performances. In conclusion, the preliminary outcomes reported in this study highlight that the innovative grout has similar properties to the standard one and that adding marble sludge does not worsen the grout's properties.

Results presented in this paper should be considered as a first step of the research since further analyses on mechanical and elastic performance at long curing time should be carried out before transferring the technology to a pilot construction site.

The research is currently on-going.

ACKNOWLEDGMENTS

The authors want to thank Utt Mapei for chemical ingredients and Buzzi Unicem for cement.

FUNDING

This publication is part of the project NODES which has received funding from the MUR - M4C2 1.5 of PNRR funded by the European Union - NextGenerationEU (Grant agreement no. ECS00000036).

REFERENCES

André, L., Bacquié, C., Comin, G., Ploton, R., Achard, D., Frouin, L., Cyr, M., 2022. Improvement of two-component grouts by the use of ground granulated blast furnace slag. Tunn. Undergr. Sp. Tech. 122, 104369. https://doi.org/10.1016/j.tust.2022.104369.

ASTM D4380, 2020. Standard Test Method for Determining Density of Construction Slurries. American Society for Testing and Material International.

CEN. 2011, Cement. Composition, specifications and conformity criteria for common cements. EN 197-1:2011. European Committee for Standardization, Bruxelles (B).

CEN. 2016, Methods of testing cement - part 1: determination of strength. EN 196–1:2016. European Committee for Standardization, Bruxelles (B).

Cobo-Ceacero, C.J., Cotes-Palomino, M.T., Martínez-García, C., Moreno-Maroto, J. M., Uceda-Rodrìguez, M., 2019. Use of marble sludge waste in the manufacture of eco-friendly materials: applying the principles of the Circular Economy. Environ Sci Pollut Res 26, 35399–35410 (2019). https://doi.org/10.1007/s11356-019-05098-x

Fargnoli, V., Boldini, D., Amorosi, A., 2013. TBM tunnelling-induced settlements in coarse-grained soils: The case of the new Milan underground line 5. Tunn. Undergr. Sp. Tech. 38, 336–347. https://doi.org/10.1016/j.tust.2013.07.015.

Grasso, P., Lavagno, A., Brino, G., Cardu, M., Martinelli, D., Todaro, C., Carigi, A., Cotugno, G., Peila, D., Concilia, M., Bechter, S., Bringiotti, M., Nicastro, D., Manassero, V., Peinsitt, T., Santarelli, S., 2023. In: Bilotta, E., Casale, R., di Prisco, C.G., Miliziano, S., Peila, D., Pigorini, A., Pizzarotti, E.M. (Eds), Handbook on Tunnels and Underground Works: Volume 2: Construction – Methods, Equipments, Tools

and Materials. CRC Press, Boca Raton, London, New York, Leiden, pp. 11–216. DOI: 10.1201/9781003306467-2.

Oggeri, C., Oreste, P., Spagnoli, G., 2021. The influence of the two-component grout on the behaviour of a segmental lining in tunnelling. Tunn. Undergr. Sp. Tech. 109, 103750. https://doi.org/10.1016/j.tust.2020.103750.

Schulte-Schrepping, C., Breitenbücher, R., 2019. Two-component grouts with alkali-activated binders - Proceedings of the ITA-AITES World Tunnel Congress 2019, Naples (IT), May 3–9.

Song, W., Zhu, Z., Pu, S., Wan, Y., Huo, W., Peng, Y., 2022. Preparation and engineering properties of alkali-activated filling grouts for shield tunnel. Constr. Build. Mater. 314, 25620. https://doi.org/10.1016/j.conbuildmat.2021.125620.

Song, W., Zhu, Z., Pu, S., Wan, Y., Huo, W., Song, S., Zhang, J., Yao, K., Hu, L., 2020. Synthesis and characterisation of eco-friendly alkali-activated industrial solid waste-based two-component backfilling grouts for shield tunnelling. J. Clean. Prod. 266, 121974. https://doi.org/10.1016/j.jclepro.2020.121974.

Thewes, M., Budach, C., 2009. Grouting of the annular gap in shield tunneling – an important factor for minimisation of settlements and production performance - Proceedings of the ITA-AITES World Tunnel Congress 2009, May 23-28, Budapest (HU).

Todaro, C., Bongiorno, M., Carigi, A., Martinelli, D., 2020. Short term strength behavior of two-component backfilling in shield tunneling: comparison between standard penetrometer test results and UCS. Geoing. Ambient. Miner. 159 (1), 33–40.

Todaro, C., Martinelli, D., Boscaro, A., Carigi, A., Saltarin, S., Peila, D., 2022. Characteristics and testing of two-component grout in tunnelling applications, Geomechanics and Tunnelling. (2022) 1.

Todaro, C., Pace, F., 2022. Elastic properties of two-component grouts at short curing times: The role of bentonite, Tunn. Undergr. Space Technol. 130, 104756. https://doi.org/10.1016/j.tust.2022.104756.

Todaro, C., Peila, L., Luciani, A., Carigi, A., Martinelli, D., Boscaro, A., 2019. Two component backfilling in shield tunneling: laboratory procedure and results of a test campaign. In: Proceedings of the ITA WTC World Tunnel Congress 2019, Naples (IT), May 3–9. 10.1201/9780429424441-340

Todaro, C., Zanti, D., Carigi, A., Peila, D., 2023. The role of the bentonite in two-component grout: a comparative study. Tunn. Undergr. Sp. Tech. In Press.

UNI 11152-11, 2005. Sospensioni acquose per iniezioni a base di leganti idraulici - Caratteristiche e metodi di prova. Ente nazionale italiano di unificazione.

UNI 11152-13, 2005. Sospensioni acquose per iniezioni a base di leganti idraulici - Caratteristiche e metodi di prova. Ente nazionale italiano di unificazione.

Tunnelling for a Better Life – Yan, Celestino, Thewes & Eberhardt (Eds)
© 2024 The Author(s), ISBN 978-1-032-80042-4
Open Access: www.taylorfrancis.com, CC BY-NC-ND 4.0 license

Study of support design and construction results of unconsolidated in Aso Caldera

Teppei Tomita* & Tomohisa Ano
Eight-Japan Engineering Consultants Inc, Tokyo, Japan

Hisataka Nagamatsu
Kumamoto Office of River, MLIT, Japan

Hiroyuki Hirano
Shimizu Corporation, Kumamoto, Japan

Hiroto Tabata
Taisei Corporation, Kumamoto, Japan

ABSTRACT: Takimurozaka Tunnel is a 5.0 km long tunnel that passes through the Aso Caldera. As the design passed through low-intensity sections, high-standard support patterns and auxiliary methods were adopted using numerical analysis. The results of the study of two characteristic patterns are reported here.

Keywords: overburden, special ground, unconsolidated ground, analytical verification, Standard registration

1 INTRODUCTION

Mt. Aso is known for its large caldera and magnificent outer rim, which is one of the largest in the world. National Highway 57, which crosses the Aso Outer Rim from east to west, is an important route connecting Oita and Kumamoto prefectures (Figure 1). However, the topography and geology of the area make it susceptible to icing in winter and to disasters, making it an urgent issue to improve the roadability and traffic safety. In addition, the Takimurozaka road (L = 6.3 km) was planned because of the frequent occurrence of slope disasters due to recent extreme weather conditions, resulting in road closures for up to 40 days. The Aso Caldera in the proposed area is a huge caldera of about 320 km^2, measuring about 25 km from north to south and 18 km from east to west, formed by four eruptions between 270,000 and 90,000 years ago. The outer topography of the caldera is a plateau with a very gentle slope (1-3°) created by the Aso pyroclastic flow on the eastern side. On the west side, the old volcanic mountainside consists of slopes of about 10°, with pyroclastic flow plateaus bordering the outer caldera.

2 OUTLINE TUNNEL

When designing the tunnel, the route was carefully selected based on geological surveys, nearby construction results, and disaster history. As a result, the tunnel length is 4.8 km with a longitudinal gradient of 4%.

Figure 1. Plan location map (Aso Caldera).

The main tunnel is a large cross-section tunnel with an excavated cross-section of over 100 m2, and the evacuation tunnel is a small cross-section tunnel with an excavated cross-section of about 20 m^2. The

*Corresponding author: tomita-te@ej-hds.co.jp

DOI: 10.1201/9781003495505-115

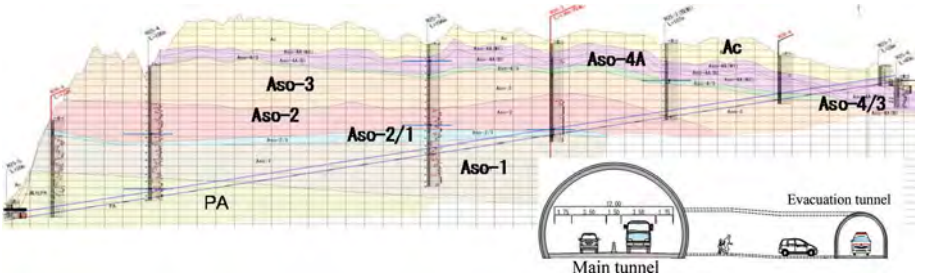

Figure 2. Geologic longitudinal section and tunnel cross-section.

geology of the tunnel is Quaternary pyroclastic flow deposits formed during the eruptive cycles of Aso Volcano. The geology is characterized by the fact that the hardness varies with the degree of fusion and that fragile pore sediments are distributed between the pyroclastic flow deposits formed during each eruptive cycle and are composed of pre-Aso volcanic rocks with uniaxial compressive strength of about 2.0N/mm^2 (tuffaceous hornblende), pyroclastic flow deposits (Aso-1 to Aso-4) and their pore sediments are distributed.

3 PROBLEM OF TUNNEL

3.1 *Overview of the geology of the Pre-Aso Volcanic Rocks (PA: Tuff breccia)*

The PA consists of pyroclastic rocks composed of pyroxene andesite lava and tuffaceous conglomerate that erupted about 85 years ago. The andesitic lava is relatively hard in rock fragments but is generally composed of tuffaceous conglomerate. The andesite lava has relatively hard rock fragments but is generally fractured and clumpy to flaky. The tuffaceous conglomerate consists of tuff containing fine pebbles and cobbles 10 to 30 cm in diameter. The matrix consists of well-consolidated clay to sandy soil.

3.2 *Overview of the geology near the Aso-4/3 pore deposits (Aso-4/3)*

It is distributed along the national highway between Aso-3 and Aso-4 at an elevation of about 760 m, but continuity is poor. The geology consists of volcanic ash and pumice fall deposits with thicknesses ranging from a few centimeters to tens of centimetres.

Photo 1. PA layer (tuff breccia) in outcrop No.1.

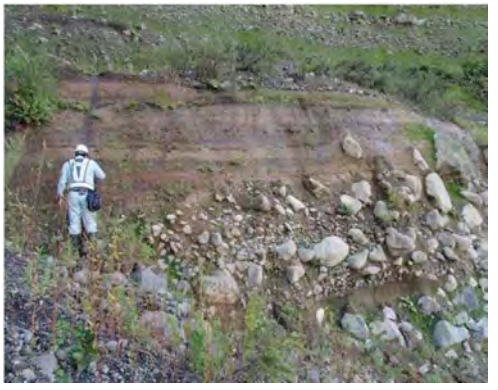

Photo 2. PA layer (tuff breccia) in outcrop No.2.

Table 1. List of geotechnical survey results.

Geological name	Core photo	Feature	N-value	Strength test		Deformation modulus
				Unconfined compression strength	Cohesion and internal friction angle	
Aso-4/3 Pore deposits		• The core is clay-like and crumbles easily under finger pressure. • Considered to be an impermeable to difficult-to-permeable layer. • Confirmed in holes H25-2 to H25-3.	5~9 (representative?)	Cheapple penetration test (Converted uniaxial compressive strength) 2,200(kN/m²) Unconfined compression strength (Block sampling) ●H26-4/3-1 48.5(kN/m²) ●H26-4/3-2 52.8(kN/m²) ●H26-4/3-3 42.3(kN/m²)	Otriaxial compression test(UU) (Block sampling) ●H26-4/3-1 C =17.6(kN/m²) φ =15.4° ●H26-4/3-2 C =24.6(kN/m²) φ =19.4° ●H26-4/3-3 C =18.1(kN/m²) φ =16.7°	Otriaxial compression test(UU) ●H26-4/3-1 E=4,133(kN/m²) ●H26-4/3-2 E=5,983(kN/m²) ●H26-4/3-3 E=5,303(kN/m²)
Pre-Aso Volcanic Rocks		• The core shape is mainly long cylindrical to rod-shaped cores. • The rock fragments are soft. • The core becomes shredded with dry and wet repetitions. • The boundary with the upper layer is weathered and the substrate becomes clay-like.	unweathered section (More than 200) weathering section 9~20 (representative?)	●H25-4hole 165.1~165.4m ●H25-4hole 180.5~180.8m ●H25-4hole 185.7~186.0m ●H25-5hole 16.35~16.65m ●H25-5hole 141~142m ●H25-5hole 124~127m ●H25-5hole 122.2~133.4m ●H26-4hole 122.6~122.8m 1,900(kN/m²) 160(kN/m²) 320(kN/m²) 1,716(kN/m²) 3,143(kN/m²) 2,944(kN/m²) 2,676(kN/m²) 4,888(kN/m²)	Otriaxial compression test(UU) ●H25-5hl 141~142m C =969(kN/m²) φ =25.9° ●H26-5hl 126~127m C =860(kN/m²) φ =30.3° ●H26-5hl 132.2~133.4m C =560(kN/m²) φ =35.9° ●H26-4hl 122.6~122.8m C =1150(kN/m2) φ =12.2°	OHorizontal loading test ●H26-4hole 100.5m (Tuff, gravel less than 5 cm) E=336,100(kN/m2) ●H26-4hole 77.5m (Tuff breccia, conglomerateMore than 10cm) E=307,800(kN/m2) Otriaxial compression test ●H26-5hole 141~142m

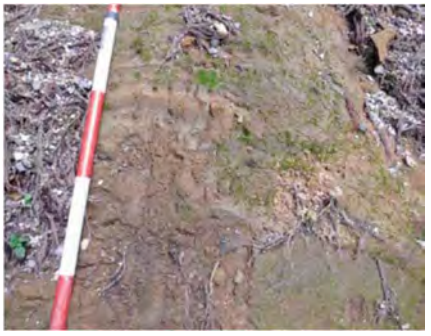

Photo 3. Aso-3/4 layer (Pore deposit) in outcrop.

Photo 4. Aso-4A layer(non-welded tuff) in outcrop.

3.3 *Summary of problems in each geology*

In the pre-Aso volcanic rocks (PA), the soil cover is 200 m, the unit volume weight is 21.1 kN/m^3, and the uniaxial strength is 3,000 kN/m^2, resulting in a strength ratio of 0.7. The Aso-4/3 pore deposit (hereinafter referred to as Aso-4/3) has a soil cover of 60 m, a unit volume weight of 16.7 kN/m^3, and a uniaxial strength of 50 kN/m^2, giving a strength ratio of 0.05. Since the soil strength ratio is less than 1 for both geological types, appropriate support structures and auxiliary construction methods were considered. Ground constants were calculated based on the results of triaxial compressive strength tests and horizontal load tests in the borehole at the site. The groundwater distribution in this tunnel was assumed to be such that Aso-1/2 is impermeable and there is little groundwater in the PA layer. The Aso-4/3 layer is also impermeable, and groundwater was assumed to be present above this layer, but no rainfall rise was observed in the groundwater monitoring wells.

4 ANALYTICAL STUDY OF SUPPORTING STRUCTURES FOR EACH FORMATION AT DESIGN

4.1 *Analytical study*

For the above-mentioned PA and Aso-4/3, appropriate support structures and countermeasures were investigated using analytical methods.

The countermeasures were studied using 2D and 3D numerical analysis. First, the tunnel portal support structure was confirmed, followed by the fore piling, long face bolt, high-strength support structure, early closure, and invert shape modification, in that order. The results, As shown in the table below, the Invert shape should be close to a circle, and for Aso-4/3, the area of the fore piling was set at 180 degrees. The evacuation shaft was also studied in the same way, and the support structure was determined.

Table 2. List of support patterns to be adopted.

		shotcrete	Rockbolt	Steel	Lining	Inverse shape	Auxiliary method
DI		20cm	6m@1m	H-150	40cm	-	-
PA	E-2	35cm	6m@1m	HH-200	40cm	Lower 1m	Fore piling(120°) Face bolt(@1.5m) early closure
Aso-4/3	E-3	25cm	-	HH-200	40cm	Lower 1m	Fore piling(180°) Face bolt(@1.5m) early closure

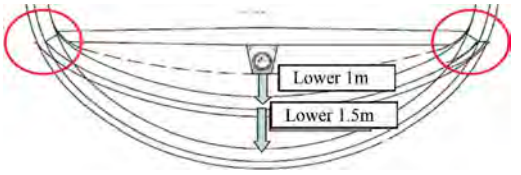

Figure 3. Invert shape change.

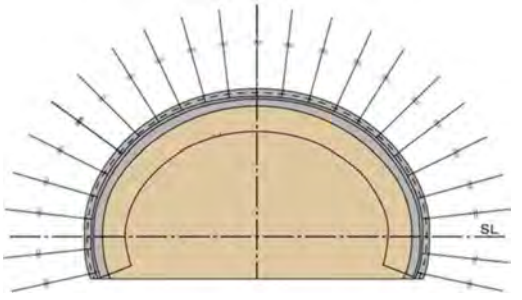

Figure 4. Normal support pattern.

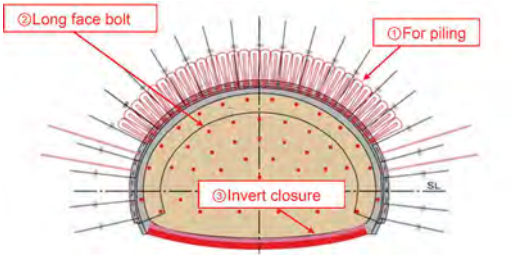

Figure 5. Special Support pattern of this tunnel (Auxiliary method).

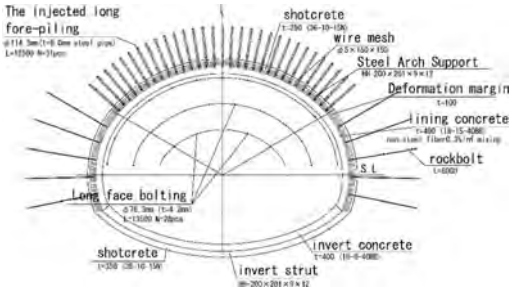

Figure 6. Support pattern of PA(Main tunnnel).

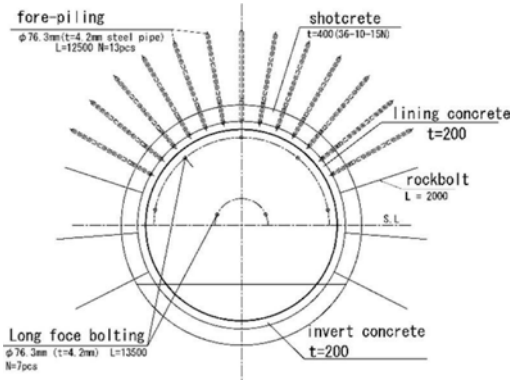

Figure 7. Support pattern of PA(Evacuation tunnel).

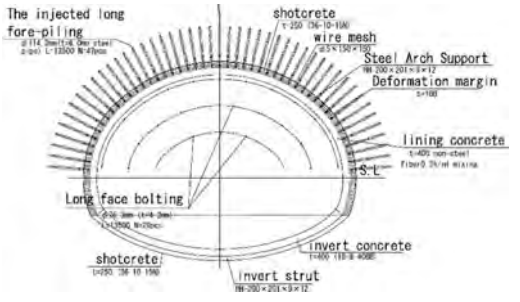

Figure 8. Support pattern of Aso-4/3A(Main tunnnel).

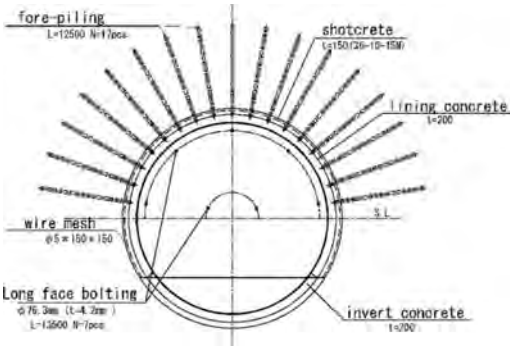

Figure 9. Support pattern of Aso-4/3(Evacuation tunnel).

4.2 *Considerations in the PA layer*

In the PA Formation, Aso-1 with high strength is distributed in the upper part, and the numerical analysis by FEM indicates that a complete soil cover is applied. As shown in Chapter3, the outcrops of the PA Formation are composed of alternating layers of tuff and tuff, and the strength of the tuff is high at the gravels and low only at the base of the tuff, so it is unlikely that only tuff will appear on the tunnel face. Therefore, it is unlikely that only tuff will occur on the tunnel face. Therefore, the extension of the ground classification at the time of design was set in the E pattern, where 20% of the PA layer is bad.

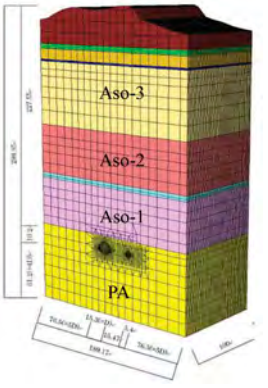

Figure 10. 2D analytical model in PA layer.

5 CONSTRUCTION RESULTS IN THE PA LAYER

5.1 *Results of main tunnel*

The results of the construction showed that the D I pattern was sufficient for the support structure. Pore volcanic ash (Aa) was distributed in some areas at the boundary between PA and upper Aso-1, and when this area appeared at the crown range, a fore-piling was required. The initial displacement speed of the A measurement (displacement of the upper half of the inner cavity) exceeded the control level II of D I of No201+5.0. The D II pattern was adopted, and the invert was early closure.

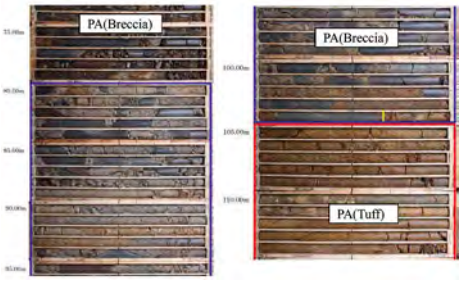

Photo 5. Core columnar view in PA.

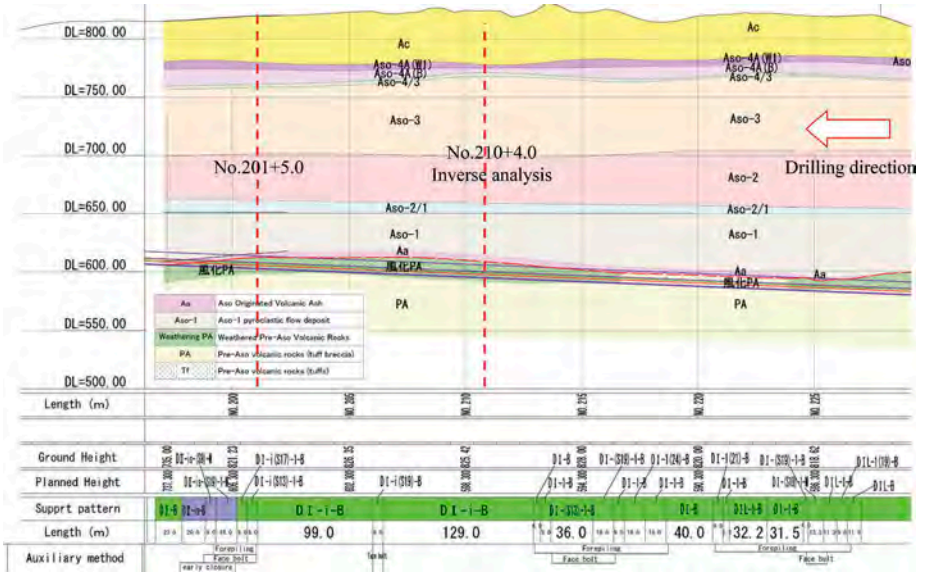

Figure 11. Geologic longitudinal section (after construction).

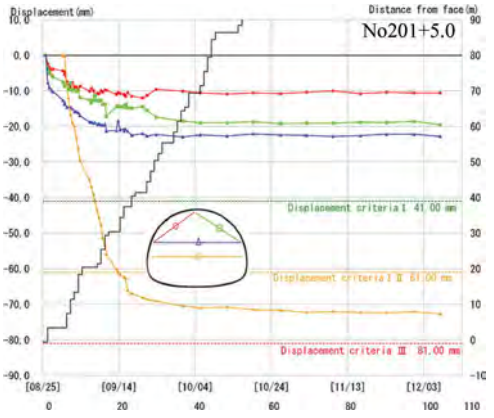

Figure 12. Displacement change with time.

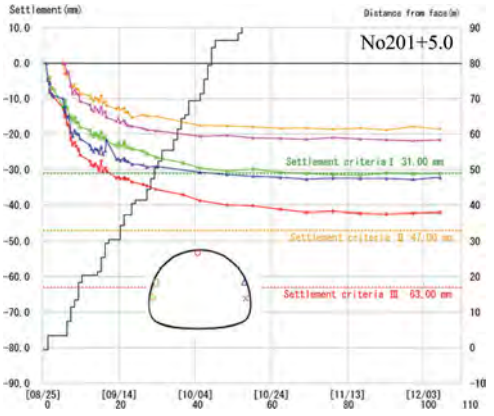

Figure 13. Settlement change with time.

Photo 6. Status of face (No.217).

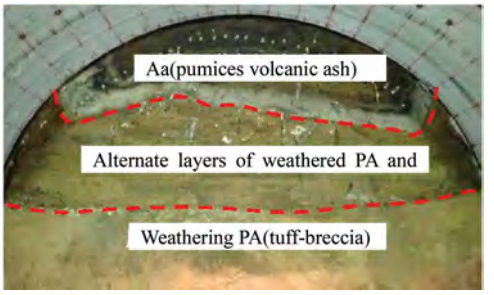

Photo 7. Status of face (No.199+10).

5.2 *Results of evacuation tunnel*

Similar to the main tunnel, DII (early closure) was used in areas where the initial displacement rate of the internal air displacement measurement was high and the displacement was contained. The DII pattern was used when the tuff was almost completely within the tunnel cross-section.

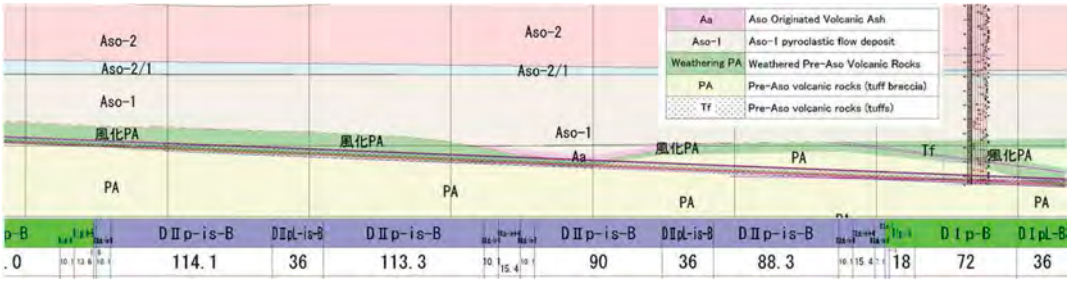

Figure 14. Geologic longitudinal section (after construction).

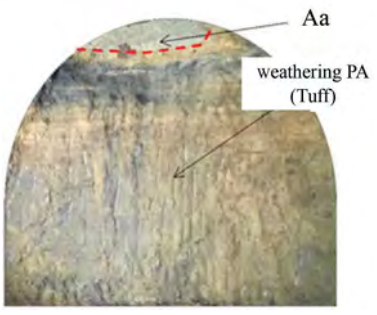

Photo 8. Status of face(1).

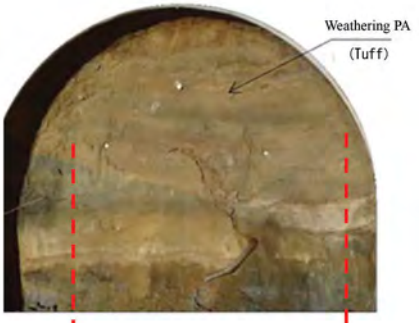

Photo 9. Status of face (2).

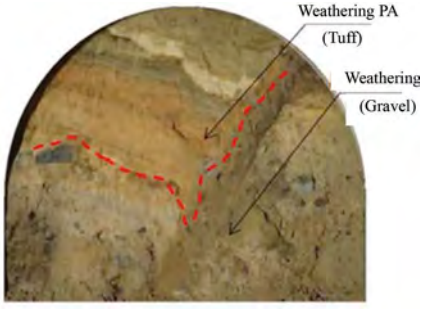

Photo 10. Status of face (3).

5.3 *Results of inverse analysis in the main well*

The deformation coefficients of the PA layer were calculated from the measurement results in the main shaft by performing an inverse analysis.

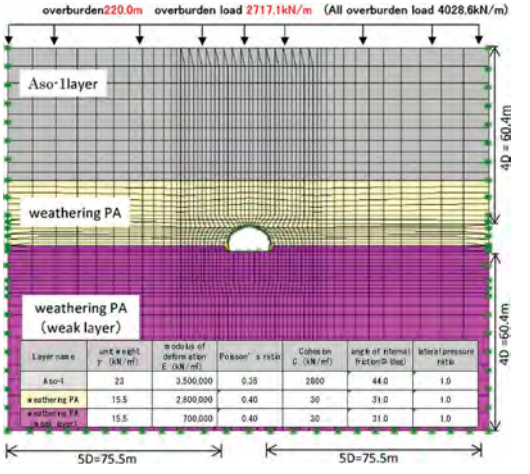

Figure 15. 2D Analysis model.

6 CONSTRUCTION RESULTS IN THE ASO-4/3 LAYER

6.1 *Organization of the main shaft*

Pattern E was adopted because displacement increased where Aso-4A(PF) pumice mixed gravel layer, Aso-4A(B) unconsolidated sand and gravel layer, and Aso-4/3 Pattern E was adopted because is placement increased where Aso-4A (B) unconsolidated sand and gravel layer and Aso-4/3 appeared. Leg piles were added in areas where the settlement trend did not subside.

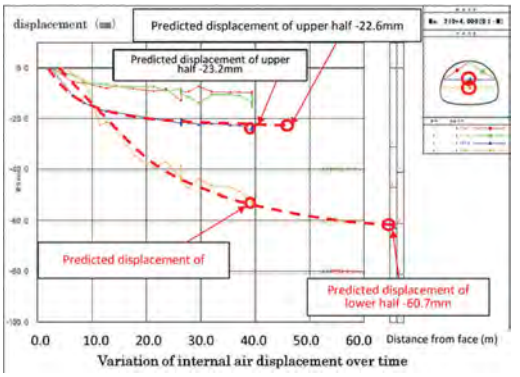

Figure 16. Approximate reproduced displacement.

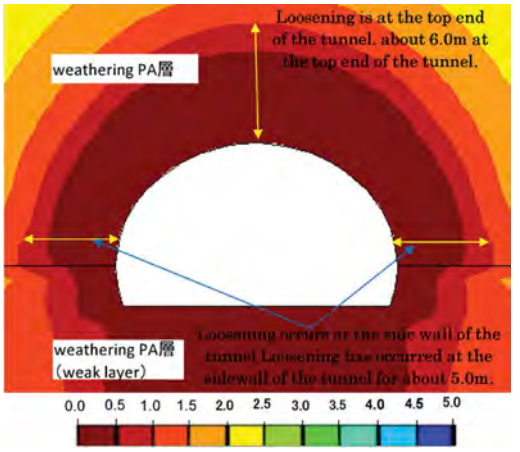

Figure 17. Loose area diagram.

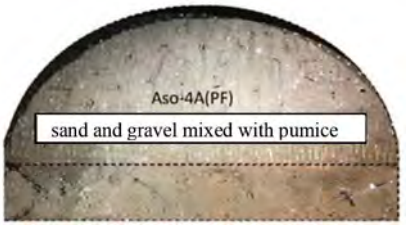

Photo 11. Status of face (TD408).

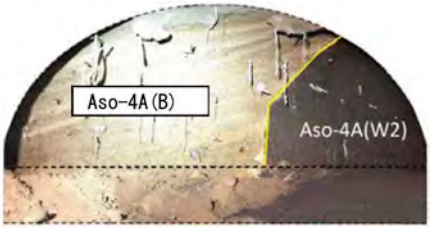

Photo 12. Status of face (TD488).

Photo 13. Status of face (TD608).

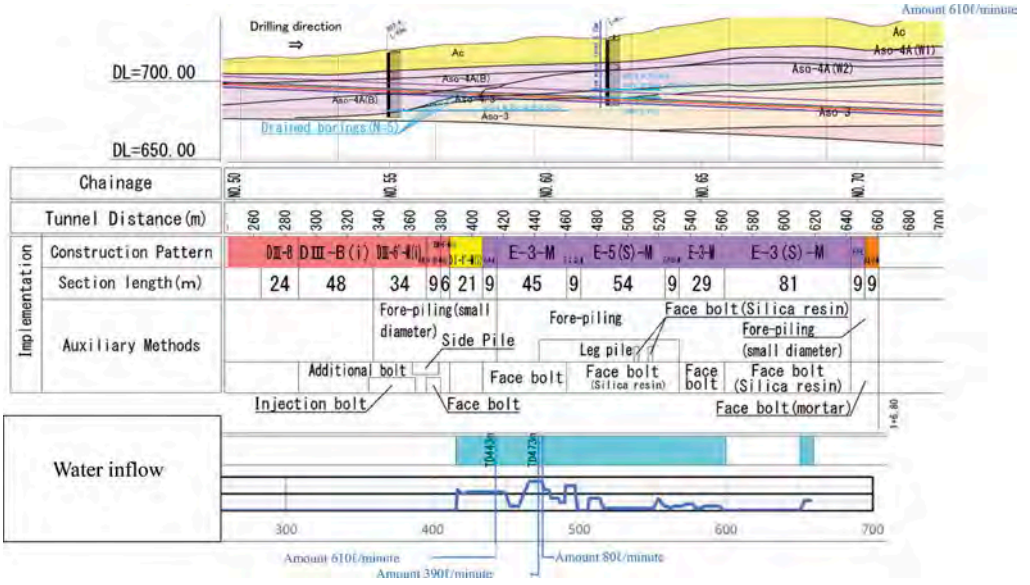

Figure 18. Longitudinal geologic section at Aso-4/3.

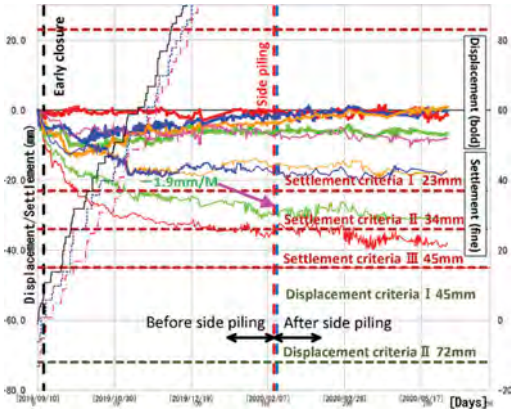

Figure 19. Measurement results Aso4A(PF).

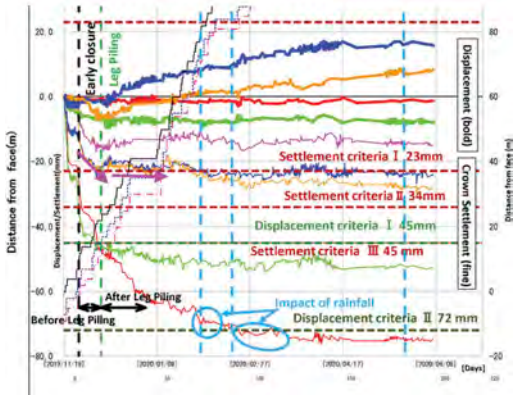

Figure 20. Measurement results Aso4A(B).

In addition, subsidence at the top of the tunnel, thought to be caused by rainfall in the previously constructed section, showed a tendency to re-sink. As a result of additional boring to analyse the cause, it was determined that the tunnel was constructed on a geological structure where a large amount of groundwater existed to the south of the main tunnel, and after rainfall, spring water collected like an underground river, causing the displacement due to water pressure. Therefore, a drainage bore was made to lower the groundwater. In addition, the tunnel lining was reinforced with steel bars to ensure that the water pressure would not cause problems even if groundwater were to affect the tunnel in the future.

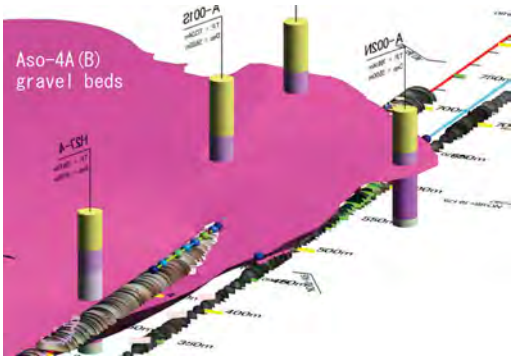

Figure 22. 3D geological model.

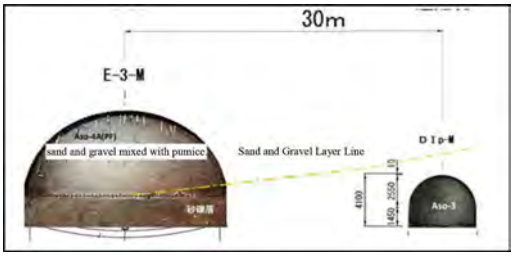

Figure 23. Geological transects.

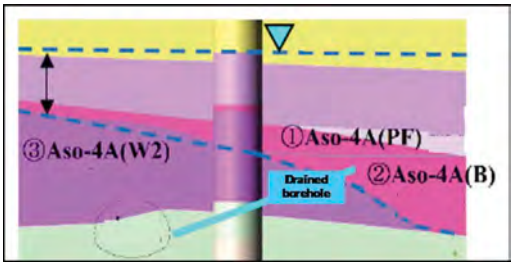

Figure 24. Drained borehole.

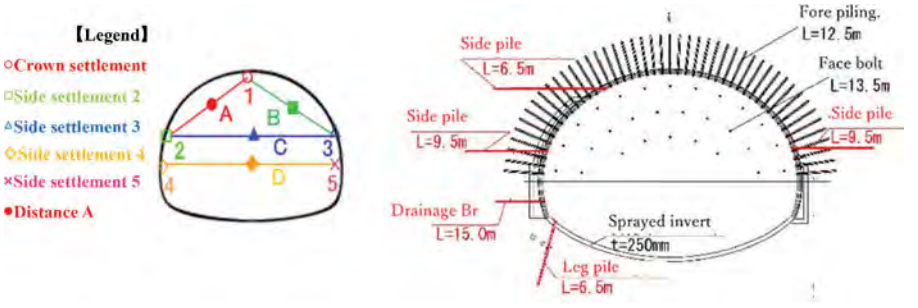

Figure 21. Additional measures in Aso-4/3.

6.2 *Results of measurement B*

In Aso-4/3, a preliminary analysis was performed and the following results were obtained. At that time, fore piling was designed at 180°, which is different from the normal range (120°), and the validity of the design was confirmed.

As a result, the shotcrete stress was approximately 9 N/mm^2 greater than the analytical value, while the steel arch stress was 225 N/mm^2 less. Since axial forces of approximately 1,000 kN were generated, it is assumed that flexural stress sharing also occurred in the shotcrete. It is concluded that the effect of 180-degree fore piling occurs.

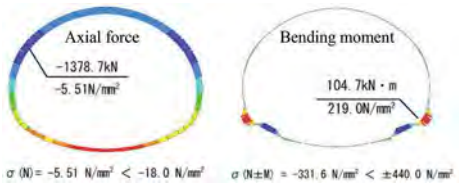

Figure 25. Shotcrete stress and steel arch stress during analysis.

7 CONCLUSION

The design and construction results are generally as expected. However, at the location of Aso-4/3, the top-end settlement has not converged and additional leg piles have been added; this phenomenon occurs when Aso-4/3 is below the invert, although the 3D analysis was performed to the extent that Aso-4/3 appears on the face. The Aso-4A(W) sand and gravel layer, which is worse than expected, appeared on the tunnel face, and it is believed that the top-end settlement did not converge because the geology was as bad as Aso-4/3, requiring auxiliary construction methods and early closure and because the bad layer continued in the lower part.

Future designs should pay special attention to the geological conditions at the boundary for risk management. For example, borings should be added, and the geology of the boundary area should be classified based on the assumption that the geology is poor.

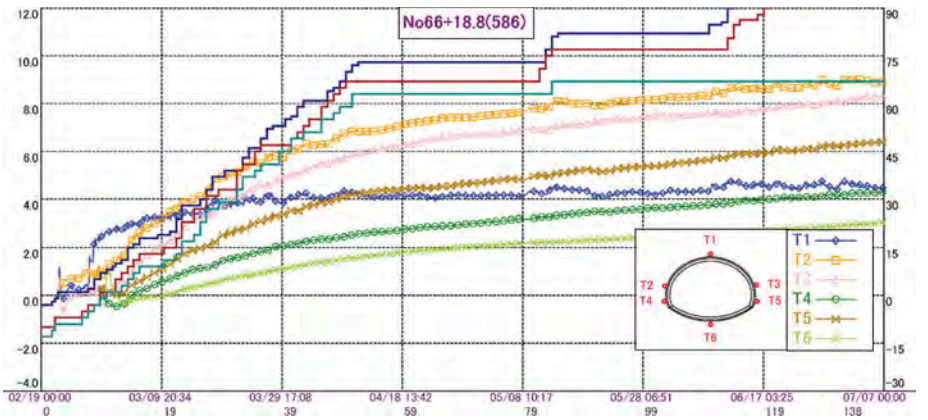

Figure 26. Shotcrete stress (B measurement).

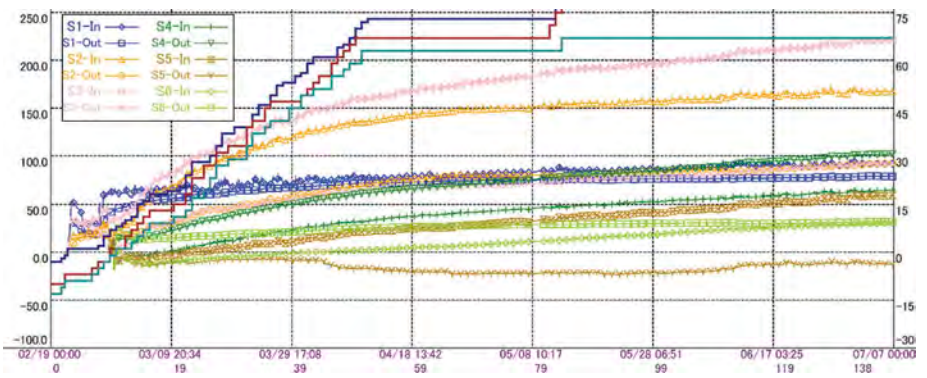

Figure 27. Steel stress (B measurement).

Tunnelling for a Better Life – Yan, Celestino, Thewes & Eberhardt (Eds)
© 2024 The Author(s), ISBN 978-1-032-80042-4
Open Access: www.taylorfrancis.com, CC BY-NC-ND 4.0 license

State of the art of soil conditioning technology for earth pressure balance shield tunnelling

Zeen Wan*, Shuchen Li, Shisen Zhao, Kai Qiu & Sihaowensong Hao
China University of Mining and Technology, Xuzhou, China

ABSTRACT: Shield has become the mainstream method for tunnel construction due to safety and high efficiency. However, due to the complex and changeable underground environment, the earth pressure balance shield (EPB) shield tunnelling faces many problems, such as mud cake and clogging in the clay strata, spewing in the water-rich sandy pebble strata, and tool wear in the hard strata. The above problems have seriously affected construction safety and efficiency, and soil conditioning technology is the key to solving them. To fully understand the state of the art of soil conditioning technology, this paper summarizes the relevant research at home and abroad through many literature reviews. The preconditions and causes of various problems are expounded and the current status and development history of the conditioning agents are summarized. The results show that there are many kinds of soil conditioning agents with uneven performances at present, lacking qualitative evaluation indexes and unified testing standards. The soil conditioning scheme shall be selected according to the strata characteristics. However, soil conditioning technology is mainly based on experience, and lacks scientific selection criteria. Finally, this paper proposes the soil conditioning technology based on the strata suitability combined with the latest research results, which can provide some theoretical guidance and reference value for shield tunnel construction.

Keywords: Earth pressure balance shield, Soil conditioning, Laboratory test, Strata suitability

1 INTRODUCTION

Recently, shield tunnelling has become the mainstream construction method for tunnel construction. It has a wide range of applicability in different geological conditions, high construction safety, and is suitable for the complex and ever-changing underground environment of cities (Liao et al., 2009; Dias and Kastner 2013; Herrenknecht et al., 2011; Wei et al., 2020). Due to the complex underground environment, varying soil conditions, and abundant groundwater in tunnel construction, EPB shield tunnelling faces many challenges, such as clogging, spewing, soil discharge detention, and abrasion (Li et al., 2014; Thewes 1999; Thewes and Hollmann 2016; Langmaack and Feng 2005; Langmaack and Lee 2016; Burbaum 2009; Gharahbagh et al., 2014), as shown in Figure1.

Soil conditioning is the most direct and efficient method to address the issues. The purpose of soil conditioning is to adjust the excavated soil in the tunnel face, spoil chamber and screw conveyor into a "plastic-flow state" (Peila 2014; Xiao et al., 2015; Mair et al., 2003; Merritt et al., 2003; Barbero et al., 2012). This aims to achieve smooth spoil discharge, maintain pressure balance, prevent adhesion and surging and ultimately achieve a gradual decrease in water and soil

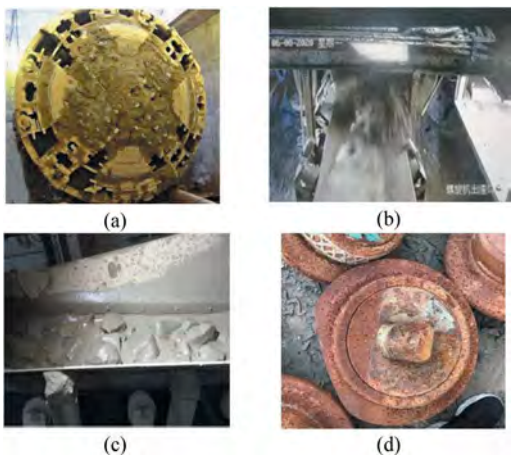

Figure 1. Challenges for EPB shield tunnelling: (a) clogging, (b) spewing, (c) soil discharge detention and (d) abrasion.

*Corresponding author: zeenwan@cumt.edu.cn

DOI: 10.1201/9781003495505-116

pressure along the spoil discharge direction (Xu et al., 2020; Maild 1995). A significant amount of research has been conducted on soil conditioning. This research has focused on different approaches for soil conditioning in various ground conditions, utilizing theoretical analysis, experimental studies, and numerical simulations. However, the current research on soil conditioning, both domestically and internationally, is often focused on addressing specific issues. There is a lack of systematic studies on ground adaptability for soil conditioning, and the field of soil conditioning lacks a unified set of standards and conditioning criteria.

This review aims to summarize the existing solutions and limitations for common challenges in soil conditioning. It will also provide an overview of commonly used soil conditioning agents and their technical parameters. Additionally, it will outline the experimental methods, indicators, and evaluation criteria for soil conditioning. After conducting a comprehensive literature review, soil conditioning techniques that are adapted to different ground conditions will be proposed. By gaining an understanding of the latest research developments in this field, this review will provide references and insights for future, more complex and in-depth research in the field of soil conditioning.

2 THE DEVELOPMENT OF SOIL CONDITIONING AGENTS

To achieve a plastic flow state in the excavated soil and meet the adaptability requirements of shield tunnelling, it is necessary to inject a certain number of chemical agents at the cutter head, the excavation chamber, and the screw conveyor. This helps to adjust the properties of the excavated soil to meet the requirements for efficient discharge, as shown in Figure 2. In addition to considering the adaptability to the ground conditions, it is also essential to research the properties of soil conditioning agents. As shown in Figure 3, the development of soil conditioning agents has evolved from simple water to a variety of additives. In the 1980s, Japan took the lead in using foaming agents as additives in shield tunnelling. Since then, this approach has gradually been adopted and promoted in various countries. In the 21st century, a system has emerged with foaming agents as the primary additive, supplemented by other additives.

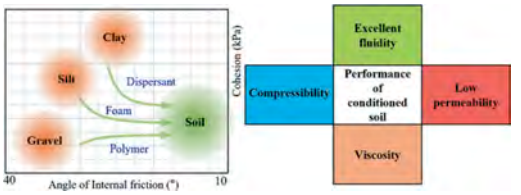

Figure 2. Purpose of soil conditioning.

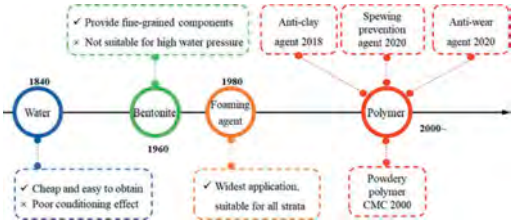

Figure 3. Development history of soil conditioning agents.

2.1 *Water and bentonite*

Water, as a low-cost and easily accessible additive, was initially used in soil conditioning. However, it has certain limitations, and its effectiveness is limited to specific ground conditions. Adding excessive amounts of water can affect the soil transportation on the conveyor belt. Bentonite slurry, commonly used in slurry pressure balance (SPB) shield tunnelling, is also widely applied as a soil conditioning agent in EPB shield tunnelling. Some scholars have conducted experiments on the conditioning of coarse-grained soil with bentonite (Mair et al., 2003; Maidl 1995; Williamson et al., 1999). After the hydration of clay minerals, such as montmorillonite, in bentonite, a hydrated compound is formed that exhibits viscosity, expansion, impermeability, and thixotropic properties. Bentonite can agglomerate the coarse particles of the soil, improve the impermeability of the soil mass, and prevent spewing. Bentonite is not suitable for all strata, and it often needs to be used in conjunction with other chemical agents. These may include foaming agents, anti-clay agents, polymers, and other additives.

2.2 *Foaming agents*

Foaming agents have the widest range of applications (Leinala et al., 2002). They can be used in fine-grained clay strata as well as in sandy and gravelly strata. Generally, foaming agents are diluted with water to a concentration of 2% to 3%. The diluted solution is then foamed through a foam-generating system and injected into the front of the cutter head, excavation chamber, and screw conveyor. This allows the injected foam to mix with the excavated soil, improving the flowability and plasticity of the excavated soil. Foaming agents are primarily composed of surfactants, water, and other additives. Regarding the mechanism of action of foaming agents, Leinala 2002 and Jancsecz 1999 have suggested that the main component surfactants consist of both hydrophobic chains and hydrophilic groups. Using electrostatic adsorption, the charged soil particles relate to water molecules, reducing the surface tension of water and preventing contact between clay particles. This enhances the plasticity and flowability of the soil. Common foaming agents are mostly anionic foaming agents. However, as shown in Figure 4, foaming agents with a combination of anionic and non-ionic

surfactants have a higher packing density, resulting in more stable foam (安井克豊 et al., 2014). They also have a longer half-life and are more favourable for mixing and contact with the soil, leading to better conditioning effects (Ross 1946).

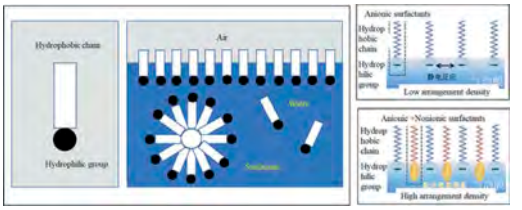

Figure 4. Surfactant molecules and foaming mechanism (Leinala 2002; Jancsecz 1999; 安井克豊 et al., 2014).

Researchers have conducted numerous studies on the foaming performance testing of foaming agents, ranging from qualitative observations to quantitative evaluations. Ross and Suzin 1985 initially proposed a visual assessment method for mechanically agitated foaming. Later, the Ross-Miles quantitative testing method was introduced in collaboration with Suzin. The foaming rate is evaluated based on the volume of generated bubbles, and the foam decay time is recorded as a stability evaluation indicator. Chen et al reviewed the experiments and indicators used to evaluate the foaming performance of foaming agents, both domestically and internationally. Through comparative analysis, they identified factors that affect foam stability. The half-life time (HT) is commonly used as a relatively intuitive and rapid evaluation indicator for foam stability. The foam half-life is defined as the time it takes for the foam to decay to half of its initial volume from the beginning of foaming (EFNARC, 2005). It is generally required that the HT of the foaming agent used should be greater than 5 minutes. A longer half-life of foam injection into the cutter head significantly increases the effective interaction time with the soil, which is beneficial for cutter head excavation and continuous muck removal. The HT of foam is influenced by factors such as the type of foaming agent, foaming agent concentration, foaming rate, and parameters of the foaming machine (Diego et al., 2019).

2.3 *Dispersants*

The high plasticity characteristics of clay strata are correlated with their mineral composition, porosity, and water content (Wu 2018; Kim et al., 2019; Liu et al., 2018). When the soil is predominantly composed of finer clay particles such as montmorillonite and kaolin, it exhibits higher cohesive strength. Macroscopically, it appears as larger cohesive soil masses and clay lumps, making it difficult for groundwater to infiltrate. During shield tunnelling excavation, the clay adheres to the cutter head tools, blocking the cutter head openings. Prolonged compression can lead to the formation of hardened clay cakes, which can adversely affect excavation efficiency (Wan et al., 2021). Dispersants can be classified as cationic, anionic, or non-ionic based on the charge carried by the surfactant. Currently, there are few types of dispersants used in shield tunnelling construction. The high-performance dispersant and polymer anti-adhesive agents were independently developed by our research group, both of which are anionic anti-adhesive agents. Because foaming agents have limited dispersing effects, dispersants are used as a new additive for preventing clay cake formation. The mechanism of dispersants is shown in Figure 5. Dispersants work by introducing high-density negative charges to the surface of clay aggregates, which can reduce the attractive forces between clay particle molecules and prevent the re-aggregation of separated clay particles. After dispersion, the clay particles or small clay aggregates are enveloped by the surfactants in the foaming agent, forming a barrier. The foam provides wrapping, support, and lubricating effects, facilitating the sliding of the clay aggregates against the metal surface. This promotes the transportation of excavated soil.

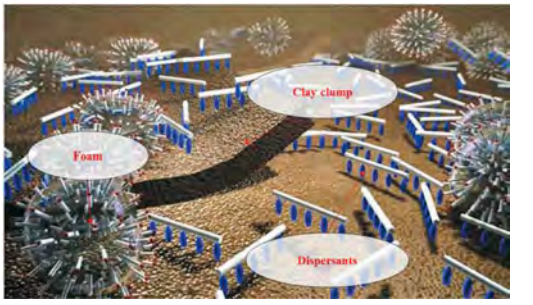

Figure 5. Schematic diagram of the mechanism of dispersants.

2.4 *Polymers*

During EPB shield tunnelling in permeable strata such as cobblestone and medium-coarse sand, there is a risk of spewing disasters when the groundwater is abundant and the water pressure is high. Ordinary foaming agents or bentonite alone cannot withstand high water pressure and prevent blowouts, as shown in Figure 6. Instead, polymers are required as effective additives for spewing prevention and they absorb free water by binding with water molecules. Soil-structured polymers adjust the soil properties and improve the soil's aggregation ability. They are suitable for the conditioning of coarse-grained soil (Mori 2016). Natural polymers such as starch, modified natural polymers such as carboxymethyl cellulose (CMC) and polyanionic cellulose (PAC), as well as synthetic polymers are used for soil conditioning (Milligan 2000).

A polymer produced from a single type of monomer is called a homopolymer, while a polymer produced from two or more different monomers is

called a copolymer. The higher the molecular weight of the polymer, the greater its aggregation effect, which can serve as an indicator to evaluate its performance. Many scholars have studied the use of common polymers as spewing prevention agents for shield tunnelling (Moss 1978; Moody 1992; Lyon 1999). They compared the advantages, disadvantages, and application methods of different types of polymers. Li et al., 2022 developed a high molecular weight polymer with a weight of 3.5 million and conducted transmission electron microscopy scanning experiments (TEM scanning) to demonstrate its chain-like aggregation structure. The mechanism of polymers is shown in Figure 7. The long chain structure of high molecular weight polymers allows them to adsorb and entangle soil particles of different sizes. The hydrophilic groups on the polymer chains form connections with water molecules, absorbing excess free water. Through the adsorption of polymer clusters, the different sizes of aggregates, fines, and water molecules are interconnected and aggregated, thereby improving the water resistance of the treated soil and reducing the likelihood of blowout accidents. The polymer adheres to the surface of soil particles, resulting in a significant increase in viscosity.

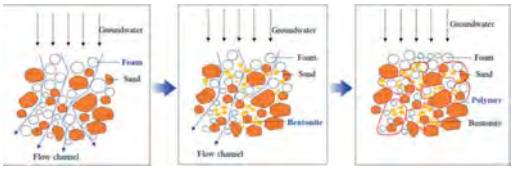

Figure 6. Principles of spewing prevention for different agents.

Figure 7. The action mechanism of polymers (Li et al., 2022).

2.5 *Anti-wear agents*

The wear of the cutter head, cutting tools, and screw conveyor for shield tunnelling in sand and gravel strata has been brought to the forefront. How to improve the service life of equipment is of great importance. Relevant scholars have explored various physical methods to protect the equipment, such as altering the material properties of the cutting tools to enhance their toughness to adjust the cutting parameters based on geological conditions to reduce tool wear (Zhang et al., 2013; Wei 2004). To reduce the frequency of tool replacement, another approach is to use additives to lubricate and protect the cutting tools, thereby reducing the contact area between the tools and the gravels. This helps to improve the wear resistance of the tools or mechanical equipment. The above-mentioned foam and bentonite also have certain lubricating properties, which can contribute to a certain degree of wear resistance. Furthermore, as a type of polymer, anti-wear agents can effectively reduce friction and wear, as shown in Figure 8. They can be injected into the cutter head and earth chamber along with the foam or bentonite slurry. During the soil conditioning process, they can cover the cutting tools and screw conveyor, providing lubrication and cooling to achieve the desired reduction in wear. In addition, its effect of reducing dust and clogging can also improve the service life of the cutting tool (Alber 2008; Li et al., 2019).

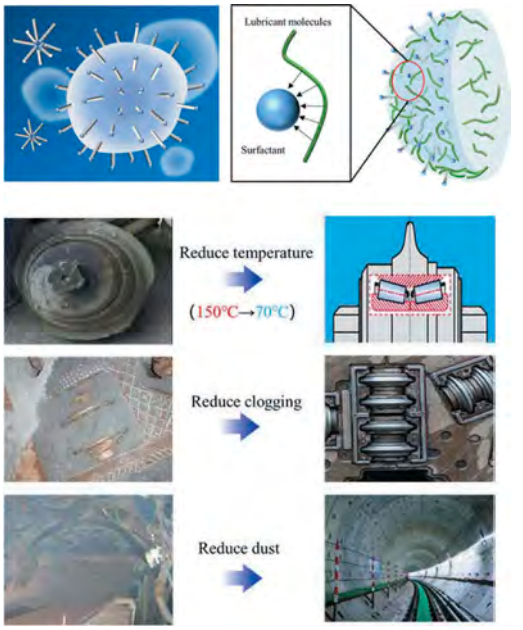

Figure 8. The action mechanism of anti-wear agents (Alber 2008; Li et al., 2019).

2.6 *A summary of the conditioning agents*

Based on the mechanisms and performance of the commonly used ground conditioning agents in shield tunnelling, each type of conditioning agent has its specific application range and is suitable for the conditioning of certain types of soil. Table 1 summarizes and categorizes the mechanisms of action, advantages, disadvantages, and applicable geological strata of various ground conditioning agents. Chemical soil conditioning agents have gradually become indispensable functional materials in soil balance shield tunnelling construction. For complex geological strata, a combination of different conditioning agents may be necessary. However, the selection process requires continual verification. Additionally, there are various types of conditioning agents available, with varying quality, thus necessitating standardized quality testing standards

Table 1. Summary and application scope of soil conditioning agents.

Agents	Effect	Advantage	Disadvantage	Strata
Water	Cooling, lubrication, and regulating water content	Cheap and convenient	Poor conditioning effect	Dry soil and rock
bentonite	Improving the workability and preventing spewing	High expansibility, supplementing fine-grained components	Poor treatment effect under high water pressure conditions	Coarse-grained strata
Foaming agents	Introducing gas to improve soil flow-plasticity	Lubrication, reduce adhesion, and improve soil fluidity	Easy to lose under high water pressure conditions	All strata
Dispersants	Reducing viscosity and dispersing	Solve clogging and mud cake issues	Dispersion takes a certain amount of time	High viscosity strata
Polymers	Agglomeration, reducing permeability, and preventing spewing	Capable of withstanding high-water pressure	Powdered polymers have poor solubility and are prone to clogging the pumping pipeline	Water-rich sandy strata
Anti-wear agents	Lubrication, clogging reduction, and cooling to protect the equipment	High effect of friction-reducing	Immature technology	Hard rock strata

3 APPLICATION OF SOIL CONDITIONING TECHNOLOGY

Due to the complexity of shield tunnelling construction strata, researchers have expanded the scope of soil conditioning from single sand and gravel or clay strata to include composite strata soil conditioning. In general, EPB shield tunnelling is suitable for excavating soil with a fine-grained content (>0.06 mm) exceeding 30%. Among them, clay-silt and silty-sand strata primarily composed of fine-grained soil are the most suitable strata for EPB shield tunnelling construction. These strata do not require any conditioning or simple water addition to meet the requirements of shield tunnelling excavation. As the coarse-grained content increases, the permeability also increases. In such cases, it is necessary to improve the water tightness of the soil by adding clay particles to supplement the fine-grained content. Currently, there is limited research on the adaptability of soil conditioning agents for various strata both domestically and internationally. More often, the conditioning schemes for specific strata are determined based on engineering experience. For instance, Langmaack and Feng 2005 proposed the adaptability range of soil conditioning agents based on long-term construction experience. Based on soil classification and particle size distribution, when dealing with finer-grained soils such as clay and silty soils, a combination of foaming agents and anti-stick agents is chosen for conditioning. This helps to prevent the formation of mud cakes on the cutter head and in the soil chamber. When the soil is silty or consists of fine sand, foaming agents can be used for conditioning alone to enhance the slurry discharge capacity. When the soil consists of medium-coarse sand and small-grained gravel, a combination of foaming agents and polymers can be used for conditioning to enhance soil impermeability and prevent surges. When dealing with large-grained gravel strata where fine-grained soil or other fine aggregates are lacking, it is necessary to add a certain amount of bentonite. In this case, the use of foaming agents and polymers in combination with bentonite can be applied for conditioning. This helps to prevent surges and provides lubrication for the cutting tools.

Soil classification and particle size distribution form the basis for selecting soil conditioning agents. The adaptability of various soil conditioning agents proposed by Langmaack is fuzzy, and they do not consider water pressure conditions. Therefore, based on engineering practices, Maild U 1995 proposed a range of strata adaptability for soil conditioning. It suggests that different soil conditioning agents have their own strata adaptability, which needs to be selected based on soil particle size distribution and water pressure conditions, as shown in Figure 9(a). When the particle size distribution curve is located in region A, the soil has a smaller particle size and a fine particle content of more than 30%. It mainly consists of impermeable soil. When the consistency index (Ic) ranges from 0.4 to 0.75, the soil exhibits good plasticity. In other cases, water, low-viscosity bentonite or polymers, and foam can be used for suitable conditioning. In region B, the permeability of the soil is greater than that of region A. During actual construction, when the permeability coefficient $k > 10^{-5}$ $m \cdot s^{-1}$ and the water pressure $p < 2$ bar, foam, polymer solutions, and fine-grained clay can be used for conditioning. When the soil particle size distribution curve is located in region C, the strata with water pressure below the groundwater level are not suitable for EPB shield tunnelling. Soil falls in region D mainly consist of coarse-grained soil particles. Due to their extremely high permeability, it is not possible to establish earth pressure balance during excavation.

Therefore, all soil conditioning methods are ineffective in this case. Budach and Thewes 2012 have made modifications to the suitability of Maild's soil strata through extensive experiments, as shown in Figure 10. If the particle distribution curve of the soil falls within range I and the fine-grained clay content is greater than 5%, a soil pressure balance shield tunnel using only foam as the ground conditioning agent is generally suitable for tunnel excavation below the groundwater level. For soil strata with particle size distribution curves falling within range II, effective conditioning can be achieved by using additional additives such as polymers or clay solutions. This can help meet the requirements for soil adaptability and facilitate the use of earthwork. These additives can alter the plastic flow behaviour of the soil, providing sufficient workability, compressibility, and low permeability. If the particle distribution curve of the soil falls within both range I and range II, then it is necessary to simultaneously meet the above requirements. If the soil grading curve falls within range III, and the soil meets the requirements of workability and compressibility after conditioning but fails to meet the requirement of a permeability coefficient $<10^{-5}$ m·s^{-1}, it is necessary to excavate above the groundwater level. If the particle size grading curve falls outside the range of I to III, it is necessary to reconsider whether to choose a soil-pressurized balanced shield machine for construction. The sand soil used in the test falls between regions I and II in terms of grading, and it requires the use of foaming agents alone or in combination with polymer, slurry, etc., for conditioning. Additionally, the water pressure should be less than 3 bar.

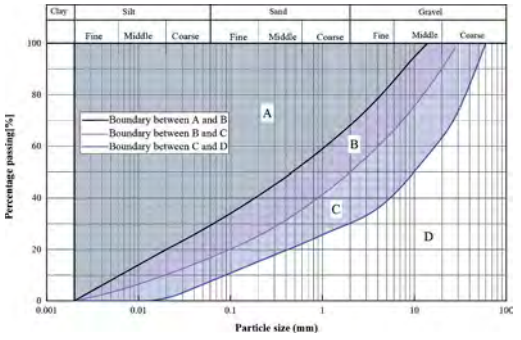

Figure 9. Soil conditioning based on engineering experience (Maild U 1995).

Although the above-mentioned study provides some guidance for soil conditioning construction, it still has certain limitations. For example, the actual crossing of strata by shield tunnelling is more complex, and the delineation between different types of soils is not clear. The occurrence of groundwater can vary significantly with the seasons. Therefore, to overcome the limitations of the current empirical-based soil conditioning schemes, our research team

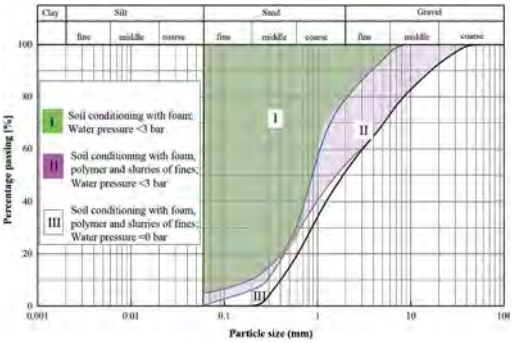

Figure 10. Soil conditioning based on tests (Budach and Thewes 2012).

has proposed a dynamic soil conditioning technology system based on extensive experiments and engineering validations (Li et al., 2019, 2022; Wan et al., 2021, 2022), as shown in Figure 11. Due to the varying factors considered in selecting soil conditioning schemes for different strata, the entire strata are divided into sandy strata, clay strata, and rock strata. For sandy strata, the soil permeability is the main consideration. Based on the permeability coefficient, the sandy strata are divided into generally permeable strata ($k < 10^{-4}$ m/s), highly permeable strata ($k = 10^{-2} \sim 10^{-4}$ m/s), and extremely highly permeable strata ($k > 10^{-2}$ m/s). Foaming agents, bentonite, and high-molecular-weight polymers are used in combination to reduce permeability and prevent water inflow. The specific selection of conditioning parameters depends on the permeability. For cohesive strata such as silty clay, and weathered mudstone, the cohesion of the soil should be the main consideration. The strata can be classified according to Ic as follows: soft (Ic < 0.5), medium soft (Ic = 0.5-0.75), medium hard (Ic = 0.75-1.00), and hard (Ic > 1.00). By combining dispersants and foaming agents, the clay particles can be dispersed effectively, achieving the effect of preventing clay cake formation. For rock strata, the division is primarily based on the abrasion coefficient (CAI) of the strata. The strata can be classified as follows: low abrasion (CAI<2.3), medium abrasion (CAI=2.3 -3.5), and high abrasion (CAI>3.5). Therefore, it is necessary to select foaming agents and abrasion-resistant agents for conditioning based on CAI. Shield tunnel construction involves complex and variable geological conditions, which often include composite strata instead of homogeneous ones throughout the entire cross-section. Therefore, it is necessary to take a comprehensive approach and consider the interactions between different strata. The proposed dynamic soil conditioning technology system still has certain shortcomings, mainly due to a lack of corresponding construction standards. In actual construction, it is still necessary to consider factors such as site-specific geological conditions, performance parameters of the soil conditioning agents, and the performance of the shield tunnelling machine.

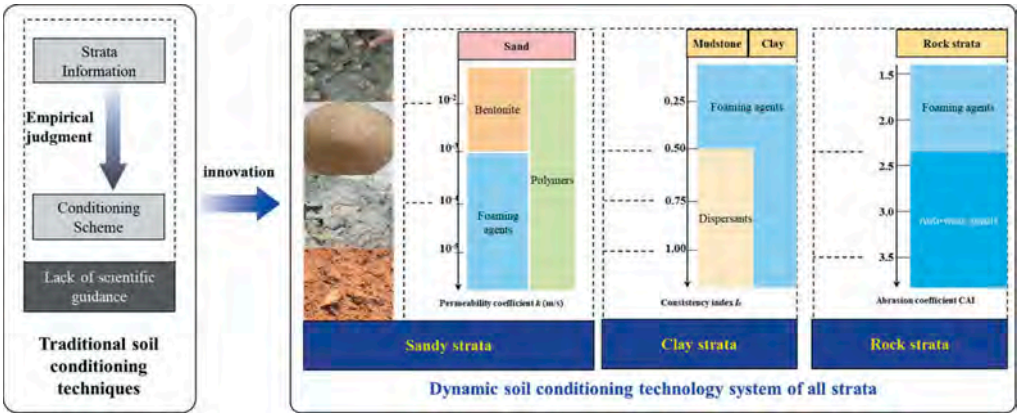

Figure 11. Dynamic soil conditioning technology system of all strata.

4 CONCLUSIONS

This article focuses on the safe and efficient tunnelling process of EPB shield tunnelling. Based on the characteristics of the traversed strata, the problems encountered in soil conditioning process are categorized into three main types: high cohesion strata with clay cake formation, water-rich strata with spewing, and hard rock strata leading to tool wear. The purpose of soil conditioning for EPB shield tunnelling is to transform the soil into a "flow-plasticity" state that can be accepted by the machine. The development history of soil conditioning agents, from none to various types available at present, has been summarized. The types and characteristics of these conditioning agents are outlined. Based on the application results of soil conditioning and the latest research achievements, a comprehensive strata-adaptive dynamic soil conditioning technology system is proposed. With the continuous development of shield tunnelling technology, soil conditioning techniques have also been evolving. However, there are still several areas of research that need to be explored:

(1) Soil conditioning agents have gradually become indispensable functional materials in shield tunnelling. However, the use of poor-quality conditioning agents can directly affect the safety and efficiency of tunnel construction. Currently, there is an urgent need to establish testing standards or protocols for conditioning agents.
(2) Due to the complexity of construction environments, shield tunnelling often involves traversing multiple layers of composite strata. Although this article proposes a comprehensive strata-adaptive dynamic soil conditioning technology system, it still requires a significant number of field experiments to validate its effectiveness.

ACKNOWLEDGMENTS

This work was supported by the National Natural Science Foundation of China (Grant No. 52308423), China Postdoctoral Science Foundation (Grant No. 2022M723402), and the Fundamental Research Funds for the Central Universities (Grant No. 2023QN1018).

REFERENCES

Alber, M., 2008. Stress dependency of the Cerchar abrasivity index (CAI) and its effects on wear of selected rock cutting tools. Tunnelling and Underground Space Technology. 23(4), 351–359.

Barbero, M., Peila, D., Picchio, A., et al,2012. Procedura sperimentale per la valutazione dell'effetto del condizionamento del terreno sull'abrasione degli utensili nello scavo con EPB. Geoingegneria Ambientale e Mineraria. 135(1), 13–19.

Budach, C., Thewes, M., 2012. New application ranges for EPB-shields in coarse-grained soils based on laboratory research. Proceedings of World Tunnel, Bangkok.

Burbaum, U., 2009. Adhäsion bindiger Böden an Werkstoffoberfächen vonTunnelvortriebsmaschinen. PhD Thesis. Dept. of Materials and Earth Sciences, Technische Universität Darmstadt.

Chen, Y., Zhang, X., Shang, Y., et al,2014. Measurement techniques of foam performance and influence factors of foam stability. China Mining Magazine. 23(S2), 230–234.

Dias, D., Kastner, R., 2013. Movements caused by the excavation of tunnels using face pressurized shields—Analysis of monitoring and numerical modelling results. Engineering Geology.152(1), 17–25.

Diego, S., Giorgio, V., Irene, B., et al,2019 . Classification of foam and foaming products for EPB mechanized tunnelling based on half-life time. Tunnelling and Underground Space Technology. 92, 103044.1–103044.6.

EFNARC, 2005. Specification and guidelines for the use of specialist products for mechanized tunnelling (TBM) in soft ground and hard rock. Recommendation of European Federation of Producers and Contractors of Specialist Products for Structures.

Gharahbagh, A. E., Rostami, J., Talebi, K., 2014. Experimental study of the effect of conditioning on abrasive wear and torque requirement of full face tunnelling machines. Tunnelling and Underground Space Technology, 41, 127–136.

Herrenknecht, M., Thewes, M., Budach, C., 2011. The development of earth pressure shields: from the

beginning to the present. Geomechanics and Tunnelling. 4(1), 11–35.
Jancsecz, S., Krause, R., Langmaack, L., 1999. Advantages of soil conditioning in shield tunnelling: experiences of LRTS Izmir. Proceedings of ITA-AITES World Tunnel Congress, pp. 865–875.
Kim, T., Kim, B., Le, K., et al,2019. Soil conditioning of weathered granite soil used for EPB shield TBM: A laboratory scale study. KSCE Journal of Civil Engineering. 23(4), 1829–1838.
Langmaack, L., Feng, Q., 2005. Soil conditioning for EPB machines: balance of functional and ecological properties. Proceedings of World Tunnel Congress and the 31st ITA General Assembly, Istanbul, Turkey: The International Tunnelling Association, pp. 729–735.
Langmaack, L., Lee K. F., 2016. Difficult ground conditions? Use the right chemicals! Chances–limits–requirements. Tunnelling and Underground Space Technology. 57, 112–121.
Leinala, T., Grabinsky, M., Klein, K., 2002. A review of soil conditioning agents for EPBM tunnelling. Proceedings of 17th Tunnelling Association of Canada Conference, Toronto, Canada,pp. 123–130.
Li, S., Wan, Z., Shang, J., et al,2019. Research progress of shield/TBM soil conditioning and tail sealing technology. Hazard Control in Tunnelling and Underground Engineering. 1(3), 14–21.
Li, S., Wan, Z., Zhao, S., et al,2022. Soil conditioning tests on sandy soil for earth pressure balance shield tunnelling and field applications. Tunnelling and underground space technology. 120(2), 10427.
Li, Z., Zhai, Z., Zhao, K., 2014. Causes of mud cake formation on cutter head of slurry shield and its control technology. Chinese Journal of Underground Space and Engineering. 10(S2), 1866–1871.
Liao, S., Liu, J., Wang, R., 2009. Shield tunnelling and environment protection in Shanghai soft ground. Tunnelling and Underground Space Technology. 24(4), 454–465.
Liu, P., Wang, S., Ge, L., et al,2018. Changes of Atterberg limits and electrochemical behaviors of clays with dispersants as conditioning agents for EPB shield tunnelling. Tunnelling and Underground Space Technology. 73, 244–251.
Lyon, J., 1999. Drilling fluids. No-dig International. 10(2), 20–25.
Maild, U., 1995. Erweiterung der Einsatzbereiche der Erddruckschilde durch Bodenkonditionierung mit Schaum. PhD Thesis. Ruhr-Universität Bochum.
Mair, R., Merritt, A., Borghi, X., et al,2003. Soil conditioning for clay soils. Tunnels and Tunnelling International. 35(4), 29–33.
Merritt, A., Borghi, F., Mair, R., 2003. Conditioning of clay soils for earth pressure balance tunnelling machines. Proceedings of Underground Construction. London: British Tunnelling Society, pp. 455–466.
Milligan, G. W. E., 2000. Lubrication and soil conditioning in tunnelling pipe jacking and micro-tunnelling: a state-of-the-art-review. London: Geotechnical Consulting Group.
Moody, G., 1992. The use of polyacrylamides in mineral processing. Minerals Engineering. 5(3-5), 479–492.
Mori, L., 2016. Advancing Understanding of the relationship between soil conditioning and earth pressure balance tunnel boring machine chamber and shield annulus behaviour. PhD Thesis. The Faculty and the Board of Trustees of the Colorado School of Mines, USA.
Moss, N., 1978. Theory of flocculation. Mine and Quarry Journal. 7(05), 57–61.
Peila, D., 2014. Soil conditioning for EPB shield tunnelling. KSCE Journal of Civil Engineering. 18(3), 831–836.
Ross, S., 1946. Foaming volume and foam stability. The Journal of Physical Chemistry. 50(5), 391–401.
Ross, S., Suzin, Y., 1985. Measurement of dynamic foam stability. Langmuir. 1(1), 145–149.
Thewes, M., 1999. Adhäsion von Tonböden beim Tunnelvortrieb mit Flüssigkteinsschilden. PhD Thesis. Institute of Soil Mechanics and Foundation Engineering
Thewes, M., Hollmann, F., 2016. Assessment of clay soils and clay-rich rock for clogging of TBMs. Tunnelling and Underground Space Technology. 57, 122–128.
Wan, Z., Li, S., Yuan, C., et al,2021. Soil conditioning for EPB shield tunnelling in silty clay and weathered mudstone. International Journal of Geomechanics. 21 (9), 06021020.
Wan, Z., Li. S., Zhao, S., et al,2022. Soil conditioning tests and screw conveyor spewing prevention technology of earth balance pressure shield tunneling in water-rich sandy stratum. China Civil Engineering Journal, 55(3): 83–93.
Wei, Y., Yang, Y., Tao, M., et al,2020. Earth pressure balance shield tunnelling in sandy gravel deposits: a case study of application of soil conditioning. Bulletin of Engineering Geology and the Environment. 79(9), 5013–5030.
Wei, Z., 2004. Analysis on tool consumption of hard rock tunnel boring machine. Tunnel Construction. 01, 52–55.
Williamson, G. E., Traylor, M. T., Higuchi, M., 1999. Soil conditioning for EPB shield tunnelling on the South Bay Ocean Outfall. Proceedings of RETC Rapid Excavation and Tunnelling Conference, Colorado, USA: Soc Min Engineers Aime, pp. 897–925.
Wu, Y. L., 2018. Investigation on foam stability and foam-conditioned soil properties under pressure in EPB TBM tunnelling. PhD Thesis. The Faculty and the Board of Trustee of the Colorado School of Mines, USA.
Xiao, C., Wang, S., Ye, Y., et al,2015. Study on soil conditioning technology for an EPB shield in an argillaceous siltstone formation. Modern Tunnelling Technology. 52 (05), 165–170.
Xu, Q., Zhang, L., Zhu, H., et al,2020. Laboratory tests on conditioning the sandy cobble soil for EPB shield tunnelling and its field application. Tunnelling and Underground Space Technology. 105, 103512.
Zhang, Z., Liu, P., Zhao, H., et al,2013. Research on material performance of TBM disk cutter rings. Research on Iron and Steel.41(01), 18–21+26.
安井克豊，松浦幸彦，佐藤研史，2014. 気泡シールド工事の環境負荷を従来の25分の1に低減: 堺石津シールド，平塚貯留シールド．トンネルと地下．45(10), 91–95.

Tunnelling for a Better Life – Yan, Celestino, Thewes & Eberhardt (Eds)
© 2024 The Author(s), ISBN 978-1-032-80042-4
Open Access: www.taylorfrancis.com, CC BY-NC-ND 4.0 license

Numerical prediction of tunnelling-induced displacement field in large and very shallow tunnels

Wenhui Yang*
School of Transportation, Southeast University, Nanjing, P.R. China
Department of Structural and Geotechnical Engineering, Sapienza University of Rome, Rome, Italy

Dingwen Zhang
School of Transportation, Southeast University, Nanjing, P.R. China

Daniela Boldini
Department of Chemical Engineering Materials Environment, Sapienza University of Rome, Rome, Italy

ABSTRACT: The application of a displacement field at the excavation boundary is a widely used and effective numerical technique to compute tunnelling-induced displacements. The principal assumption of this method is that the deformed tunnel shape is similar to the original one, i.e., circular, while its bottom remains fixed in its original position. In this paper, three-dimensional numerical analyses are described to propose a more suitable criterion for very shallow and large-diameter tunnels, characterized by two separated elliptical contraction shapes for the upper and lower parts of the tunnel section. Furthermore, quantitative description of the deformed pattern is provided, and the relationship of contraction and translation parameters with tunnel depth-to-diameter ratio is summarized and validated against monitoring data. The results show that the most appropriate deformation pattern for very shallow and large tunnels is characterized by an elliptical shape in the upper section and a circular shape in the lower part. The new approach provides a more realistic prediction of the surface displacement field if compared to that predicted by using the homothetic contraction of the tunnel section.

Keywords: Tunnel excavation, Displacement-controlled method, Large and shallow tunnel, Soil displacement, HSsmall model

1 INTRODUCTION

TBM-EPBs are often used in urban tunnel construction, generally resulting in very limited ground displacements. However, accurate prediction of excavation-induced movements is essential to avoid any damage of nearby surface and subsurface structures (Mair, 2008). Previous research has utilized various prediction methods, including empirical approaches (Peck, 1969), quasi-analytical solutions (Loganathan and Poulos, 1998), centrifuge experiments (Hagiwara et al., 1999) and numerical simulations (Nguyen et al., 2021; Yang et al., 2023. The displacement-controlled method (DCM) has proved to be an effective approach if the focus is on ground displacements rather than on structural forces in the tunnel lining (Boldini et al., 2018). When combined with advanced soil constitutive models, such as the Hardening Soil model with small-strain stiffness (HSsmall), very satisfactory results can be obtained also for small values of volume loss (Fargnoli et al., 2015). In this respect, the setting of a reasonable excavation boundary contraction pattern is of utmost importance (González and Sagaseta, 2001).

Different displacement pattern assumptions have been suggested in the past. Sagaseta (1987) proposed an isotropic convergence pattern towards the centre of the tunnel boundary. Cheng et al. (2007) introduced a widely adopted Circular DCM that accounts for both circular contraction and vertical translation of the tunnel boundary, as shown in Figure 1. It should be noted that this method was developed for subway tunnels, typically characterised by small diameters and large depths. It is based on the following assumptions: 1) the convergence is not uniform; 2) the deformed tunnel shape is similar to the

*Corresponding author: wenhui.yang@uniroma1.it

DOI: 10.1201/9781003495505-117

initial shape; 3) the convergence point is located between the converged tunnel centre and invert.

The Circular DCM has been successfully applied in predicting surface settlements induced by tunnelling in free-field conditions, as well as in studies of tunnel-structure interaction (Amorosi et al., 2014; Boldini et al., 2018). However, some researchers have pointed out that the tunnel excavation profiles are not always circular (Loganathan and Poulos, 1998; González and Sagaseta, 2001; Marshall et al., 2009). In practice, they are influenced by various factors, such as construction conditions, soil properties, anisotropic state of stress, etc… Considering non-uniform tunnel contraction, such as ovalization (Tamagnini et al., 2005), can contribute to more accurate predictive results. for shallow-buried large-diameter tunnels, for which larger stress and stiffness variations are expected with depth.

In this study, a series of numerical parametric analyses are conducted to investigate the influence of tunnel diameter and burial depth on the deformed tunnel profile especially for shallow-buried and large-diameter tunnels. Results show that as the depth to diameter ratio, *H/D*, decreases, the tunnel profile changes from a uniform circular contraction to a non-uniform contraction, with the upper part gradually assuming an elliptical shape. When *H/D* is less than 1.5, the profile stabilizes, exhibiting a contraction pattern with an elliptical shape of upper part and a circular shape of lower part. These numerical simulation findings have been validated using a real case study.

2 IMPACT OF TUNNEL DIAMETER AND AXIS DEPTH ON THE FINAL EXCAVATION BOUNDARY PROFILE

2.1 *Adopted methodology*

In practical constructions, the complexity of the engineering environment often makes very challenging the pre-installation of monitoring points for accurate deformation observation at the excavation face. Centrifuge experiments represent a feasible alternative, but they are typically associated to high costs and certain limitations in parameter

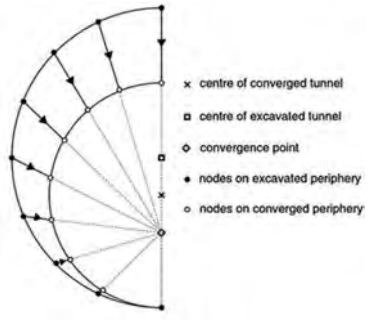

Figure 1. Commonly used circular DCM (modified from Cheng et al., 2007).

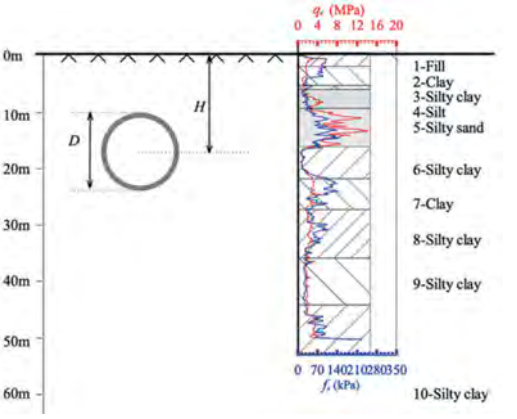

Figure 2. Geotechnical model at the tongjing road tunnel site.

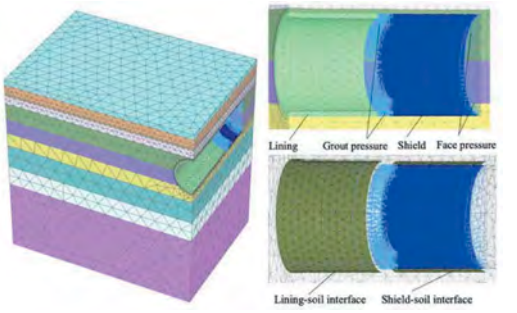

Figure 3. Numerical model.

settings. The finite element code Plaxis offers a viable solution to simulate the tunnel volume loss by assigning a contraction rate (C_{ref}) to the TBM shield, without pre-determining the final tunnel contraction pattern. The equilibrium state is reached during the iterative calculation process, and the final deformation profile is related to the stiffness of the surrounding soil (Plaxis, 2020). In this study, this method is adopted to obtain the final deformation profile of the tunnel.

2.2 *Description of the reference case*

The geotechnical model adopted in the numerical simulations refers to the Suzhou Tongjing road tunnel project. The soil profile at the construction area is shown in Figure 2. The soil is divided into 10 different layers, namely: 1- fill, 2- clay, 3- silty clay, 4- silt, 5- silty sand, 6- silty clay, 7- clay, 8- silty clay, 9- clay, and 10- silty clay. The TBM-EPB tunnel passes through layers 4- silt, 5- silty sand, 6- silty clay and 7- clay. The water table is at 1.5m below the ground surface and the pore pressure distribution is hydrostatic. During simulation of tunnel excavation, soil layers 1, 4, and 5 are set as drained, while other soil layers are set as undrained.

2.3 *Detail and validation of the finite element model*

In order to obtain a more accurate representation of the excavation boundary profile, a 3D step-by-step numerical tunnel excavation is implemented in Plaxis. This model incorporates detailed modelling of the TBM-EPB and the tunnel lining (Figure 3). Solid elements are used for the soil and the lining, while plate elements are employed to simulate the machine shield. Considering the symmetry of the model, only half model is created for numerical simulation. The finite element discretization consists of over 38411 elements. In the vicinity of the tunnel face, the mesh is refined to better handle significant stress and strain gradients in that region. Interaction surfaces are established between the tunnel lining and the soil, as well as between the shield machine and the soil (Figure 3). The face pressure and grouting pressure of shield follow a linear distribution with depth and are set equal to the total horizontal stress and total vertical stress at those locations, respectively.

The HSsmall constitutive law is adopted to get accurate numerical results. Table 1 and Table 2 shows the parameters of HSsmall model and the assumed values: all the values are calibrated on laboratory and in-situ tests data (Yang, 2023). The elastic model is used for the lining and the shield (the values of parameters are listed in Table 3). The construction process is modelled using a sequential excavation scheme (Fargnoli et al., 2015).

The tunnel diameter (13.2 m) and axis depth (16.7 m) also refer to very shallow and large Suzhou Tongjing road tunnel. C_{ref} is set equal to 0.45% based on field surface settlement monitoring results. The corresponding surface volume loss, $V_{l,s}$, results to be 0.48% using a Gaussian distribution curve with a width parameter K = 0.6 (Figure 4). It can be observed that the numerical calculation results are in good agreement with the semi-empirical and monitoring results, indicating the reliability and accuracy of the numerical model used in this study.

2.4 *Numerical results*

In order to investigate the influence of tunnel diameter and depth on the tunnel deformation profile, a series of parametric analyses are conducted, according to the tunnel characteristics listed in Table 4. The non-dimensional parameter H/D is used to analyse the combined effects of tunnel diameter and axis depth.

Figure 5 shows the impact of tunnel diameter on the tunnel deformation profile, having fixed the axis depth, H = 16.7 m, while Figure 6 that of the axis depth with a constant diameter, D = 13.2 m. In both cases, tunnel displacements are amplified by 100 times and normalized with respect to the tunnel radius. Results indicate that when H/D is relatively large, the tunnel profile appears to uniformly converge into a circular shape, which is consistent with the findings of Cheng et al. (2007). However, as H/D decreases, the tunnel profile gradually changes from a uniform circular contraction to non-uniform contraction. A notable feature is the gradual development

Table 1. Values of the Hssmall constitutive model parameters.

Parameters	1-Fill	2-Clay	3-Silty clay	4-Silt	5-Silty sand
γ_{dry} (kN/m^3)	15.2	15.7	14.6	15.3	15.7
γ_{sat} (kN/m^3)	19.6	20.0	19.2	19.6	19.9
OCR	1	3.47	2.67	1	1
c' (kPa)	0	11.4	9.1	0	0
φ' (°)	30.1	24.8	26.6	33.95	35.6
ψ' (°)	10.0	8.3	8.9	11.3	11.9
m	0.6	0.8	0.75	0.5	0.45
v_{ur}	0.25	0.2	0.2	0.25	0.25
G_0^{ref} (kPa)	96000	50000	55000	72000	102000
E_{ur}^{ref}/E_0^{ref}	0.2	0.3	0.3	0.2	0.2
E_0^{ref}(kPa)	240000	120000	132000	180000	255000
E_{ur}^{ref} (kPa)	48000	36000	39600	36000	51000
E_{50}^{ref} (kPa)	16000	12000	13200	12000	17000
E_{oed}^{ref} (kPa)	16000	12000	13200	12000	17000
$\gamma_{0.7}$	1e-4	2.1e-4	2.1e-4	1e-4	1e-4
p^{ref} (kPa)	100	100	100	100	100
K_0	0.50	0.98	0.86	0.44	0.42
K_0^{nc}	0.50	0.58	0.55	0.44	0.42
R_f	0.9	0.9	0.9	0.9	0.9
$\sigma_{tension}$	0	0	0	0	0
c_{inc} (kPa/m)	0	0	0	0	0

Table 2. Values of the hssmall constitutive model parameters.

Parameters	6-Silty clay	7-Clay	8-Silty clay	9-Silty clay	10-Silty clay
γ_{dry} (kN/m^3)	14.7	15.1	14.9	14.3	14.9
γ_{sat} (kN/m^3)	19.3	19.6	19.4	19.0	19.4
OCR	1.1	1.1	1.1	1.1	1.1
c' (kPa)	7.4	8.6	6.8	4.7	3.1
φ' (°)	27.4	27.6	27.1	27.9	29.1
ψ' (°)	9.1	9.2	9.0	9.3	9.7
m	0.7	0.8	0.8	0.75	0.75
v_{ur}	0.2	0.2	0.2	0.2	0.2
G_0^{ref} (kPa)	55000	95000	104000	85000	95000
E_{ur}^{ref}/E_0^{ref}	0.3	0.3	0.3	0.3	0.3
E_0^{ref}(kPa)	132000	228000	249600	204000	228000
E_{ur}^{ref} (kPa)	39600	68400	74880	61200	68400
E_{50}^{ref} (kPa)	13200	22800	24960	20400	22800
E_{oed}^{ref} (kPa)	13200	22800	24960	20400	22800
$\gamma_{0.7}$	2.1e-4	2.1e-4	2.1e-4	2.1e-4	2.1e-4
p^{ref} (kPa)	100	100	100	100	100
K_0	0.56	0.56	0.57	0.56	0.54
K_0^{nc}	0.54	0.54	0.54	0.53	0.51
R_f	0.9	0.9	0.9	0.9	0.9
$\sigma_{tension}$	0	0	0	0	0
c_{inc} (kPa/m)	0	0	0	0	0

Table 3. Values of the elastic model adopted for the shield and the lining.

Material	ρ (kg/m3)	E (GPa)	ν
Shield	24.7	200	0.2
Lining	2.7	35	0.2

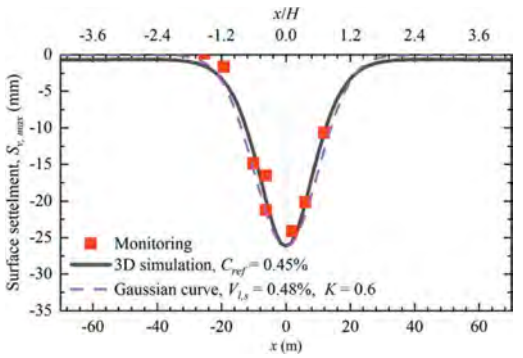

Figure 4. Comparison between numerical simulation results and monitoring data. the gaussian curve interpolating the settlement measurements is also shown.

Table 4. Investigated cases.

Variable	Parameters	Non-dimensional parameters
Tunnel diameter (D)	D = 4.4, 6.6, 8.8, 11, 13.2, 15.4, 17.6 m; H = 16.7 m	H/D = 3.8, 2.5, 1.9, 1.5, 1.3, 1.1, 0.9
Axis depth (H)	H = 15, 16.7, 20, 25, 30, 40, 50 m; D = 13.2 m	H/D = 1.1, 1.3, 1.5, 1.9, 2.3, 3.0, 3.8

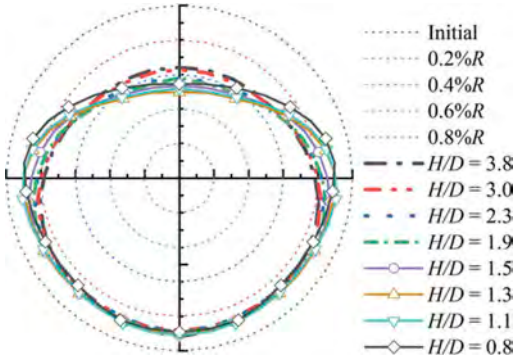

Figure 5. Final excavation boundary profile for different tunnel diameters and H = 16.7 m (scale: 1:100).

of an elliptical shape in the upper half of the tunnel profile, while the lower half remains mostly

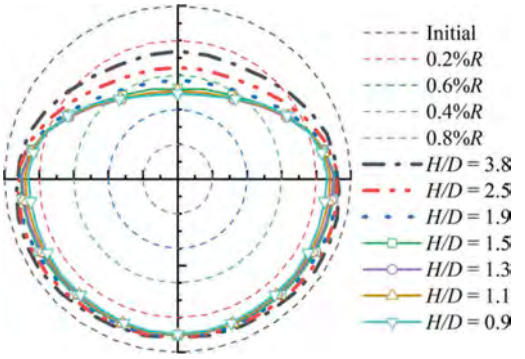

Figure 6. Final excavation boundary profile for different tunnel axis depths and D = 13.2 m (scale: 1:100).

unaffected by changes in H/D, maintaining a circular contraction. This observation is consistent with the results observed by Lueprasert et al. (2023). When H/D reaches 1.5, the profile shape stabilizes. These results indicate that the tunnel profile is strongly influenced by both tunnel diameter and axis depth and is closely related to H/D. The upper and lower parts of the tunnel can deform independently.

3 PARAMETERS DESCRIBING THE DEFORMATION PATTERN OF SHALLOW-BURIED AND LARGE-DIAMETERS TUNNEL

3.1 *The deformation pattern*

Based on the analysis mentioned above, a deformation pattern of shallow-buried and large-diameter tunnels is proposed, as illustrated in Figure 7. In these cases, the deformed tunnel profile exhibits an elliptical shape in the upper part and a circular shape in the lower part. For a more quantitative description of the deformed shape and its extension to more general cases, three variables are introduced: the ratio of the vertical and horizontal axis of the upper part - n_1, the ratio of the vertical and horizontal axis of the lower part - n_2, and the overall tunnel translation magnitude - β. A circular contraction corresponds to values of n_1 and n_2 equal to 1. β = 0 indicates no vertical translation, while β = 1 implies that the tunnel invert is translated to its initial position, i.e. that the tunnel is fixed at its bottom.

3.2 *The deformation parameters*

Figure 8, Figure 9, and Figure 10 illustrate the relationships between H/D and the tunnel profile deformation parameters n_1, n_2, β, respectively. As shown in Figure 8, when H/D<1.5, n_1 remains relatively stable at 0.9963 and when H/D>1.5, n_1 increases with H/D and is likely to reach 1.000 at H/D=5. As shown in Figure 9, n_2 is basically unaffected by the axis depth and tunnel diameter, with a stable value of 1.000, which means that the lower half tends to contract into a circular shape, as observed before. The bottom point

of the tunnel profile is not fixed at its original position but experiences a certain degree of uplift. Numerical simulations show that the overall tunnel translation rate β usually stabilizes at 0.10 (Figure 10).

In summary, for the shallow large tunnels (H/D<1.5), the convergence parameters of tunnel profile, n_1 and n_2 are taken as 0.9963 and 1.000 respectively. For deep or small tunnel (H/D>5), the values of n_1 and n_2 approach 1.000 and the tunnel profile can be considered to be circular. For other tunnel conditions (1.5 > H/D > 5), n_1 can be set between 0.9963 and 1.000. It should be noted that these two parameters should not be rounded, and at least four decimal places should be retained.

4 RESULT VALIDATION

To further validate the proposed deformation pattern and its parameters, a series of numerical simulations are conducted using a single-step excavation method to simulate tunnel excavation without considering the tunnel lining, as in Boldini et al. (2018). The prescribed displacements at the excavation boundary are determined using the parameters obtained in Section 3.2, i.e. n_1 = 0.9963, n_2 = 1, and β = 0.10. These displacements are then applied to the numerical simulation of the Tongjing road tunnel excavation.

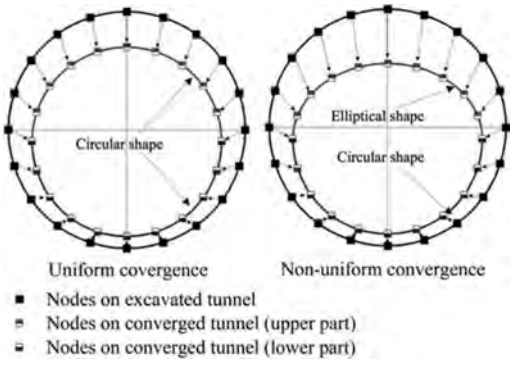

Figure 7. Schematic diagram of the displacement pattern.

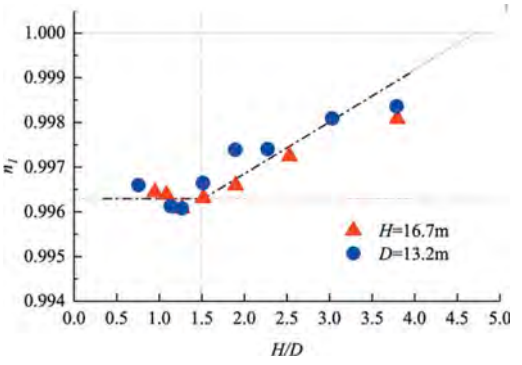

Figure 8. Relationship between n_1 and H/D.

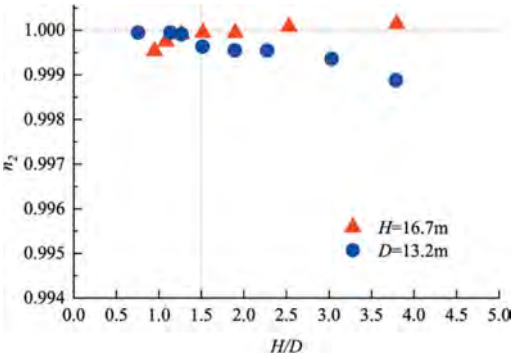

Figure 9. Relationship between n_2 and H/D.

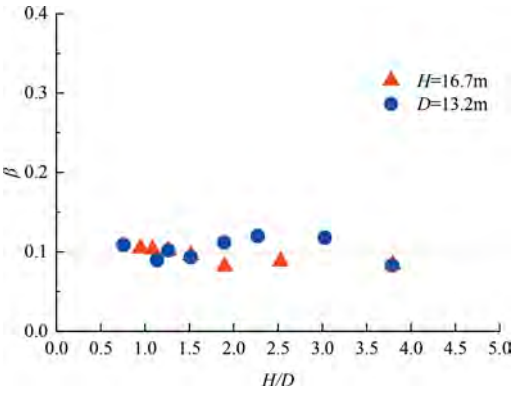

Figure 10. Relationship between β and H/D.

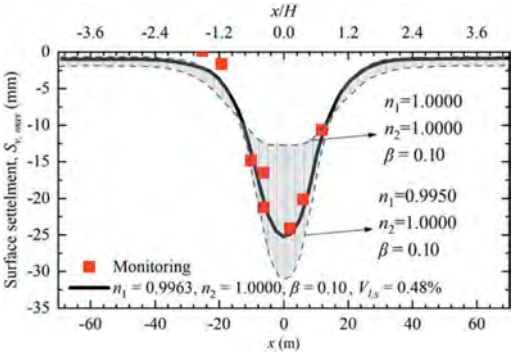

Figure 11. Comparison between the predicted surface settlement trough calculated with the bi-elliptical DCM and that with the circular DCM.

As shown in Figure 11, the implemented procedure successfully reproduces the ground settlement profile, showing an excellent agreement with monitoring data. This indicates that the proposed deformation assumptions are reasonable. Furthermore, Figure 11 also shows the predicted range of surface settlements for deformation parameters n_1 ranging from 0.9950 to 1.0000. It illustrates the significant

potential of the proposed deformation model, capable of predicting various settlement curves, with the non-uniform convergence mode offering a more realistic prediction of surface displacement compared to the circular tunnel convergence (n_1=1.0000).

5 CONCLUSIONS

Based on series of parameter analyses, this paper proposes an improved deformation pattern for very shallow and large tunnels, which considering independent deformations of the upper and lower tunnel sections. Furthermore, it introduces quantitative parameters to describe the tunnel deformation pattern and derives parameter values suitable for shallow and large-diameter tunnels for specific geotechnical conditions. The deformation assumptions and associated parameter values are validated by comparing the predicted surface displacement with monitoring data from a real case-history. Three key conclusions are obtained from this study:

(1) as *H/D* decreases, the tunnel profile gradually transitions from uniform circular contraction to non-uniform contraction and stabilizes when *H/D* reaches 1.5, with the upper part forming an ellipse and the lower part contracting into a circle;
(2) three variables, the ratio of the vertical and horizontal axis of the upper part and lower part - n_1 and n_2 - and the overall tunnel translation magnitude - β, can be used to describe the deformed tunnel shape. For shallow and large tunnels in the soil conditions described in this paper, n_1, n_2 and β are 0.9963, 1.0000 and 0.10, respectively;
(3) the proposed approach provides a more realistic prediction of the surface displacement field; as such, it has a significant potential of reproducing various settlement trough shapes caused by the excavation of large-diameter shallow-buried tunnels if compared to that predicted by adopting a circular tunnel contraction.

ACKNOWLEDGEMENTS

The authors are grateful for the financial support provided by the China Scholarship Council (CSC, No.202006090343).

REFERENCES

Amorosi, A., Boldini, D., De Felice, G., Malena, M., & Sebastianelli, M., 2014. Tunnelling-induced deformation and damage on historical masonry structures. Géotechnique, 64(2), 118–130.

Benz, T., 2007. Small-strain stiffness of soils and its numerical consequences, Ph.D. Thesis. University of Stuttgart, Stuttgart, Germany.

Boldini, D., Losacco, N., Bertolin, S., & Amorosi, A., 2018. Finite element modelling of tunnelling-induced displacements on framed structures. Tunnelling and underground space technology, 80, 222–231.

Cheng, C. Y., Dasari, G. R., Chow, Y. K., & Leung, C. F., 2007. Finite element analysis of tunnel–soil–pile interaction using displacement controlled model. Tunnelling and Underground Space Technology, 22(4), 450–466.

Fargnoli, V., Boldini, D., & Amorosi, A., 2015. Twin tunnel excavation in coarse grained soils: Observations and numerical back-predictions under free field conditions and in presence of a surface structure. Tunnelling and Underground Space Technology, 49, 454–469.

González, C., & Sagaseta, C., 2001. Patterns of soil deformations around tunnels. Application to the extension of Madrid Metro. Computers and Geotechnics, 28 (6-7), 445–468.

Hagiwara, T., Grant, R. J., Calvello, M., & Taylor, R. N., 1999. The effect of overlying strata on the distribution of ground movements induced by tunnelling in clay. Soils and Foundations, 39(3), 63–73.

Loganathan, N., & Poulos, H. G., 1998. Analytical prediction for tunneling-induced ground movements in clays. Journal of Geotechnical and geoenvironmental engineering, 124(9), 846–856.

Lueprasert, P., Jongpradist, P., Jongpradist, P., & Schweiger, H. F., 2023. Structural Responses of a Tunnel Lining Due to an Adjacent Loaded Pile. International Journal of Civil Engineering, 21(6), 1027–1043.

Mair, R. J., 2008. Tunnelling and geotechnics: new horizons. Géotechnique, 58(9), 695–736.

Marshall, A. M., Elkayam, I., & Klar, A. (2009, September). Ground behaviour above tunnels in sand-DEM simulations versus centrifuge test results. In Euro: Tun 2009, Proceedings of the 2nd International Conference on Computational Methods in Tunnelling, Bochum, Germany, pp. 9–11.

Nguyen, T. T., Do, N. A., Karasev, M. A., Kien, D. V., & Dias, D., 2021. Influence of tunnel shape on tunnel lining behaviour. Proceedings of the institution of civil engineers-geotechnical engineering, 174(4), 355–371.

Peck, B. B., 1969. Deep excavation and tunnelling in soft ground, State of the art volume. In 7th ICSMFE, Mexico City, Mexico, Vol. 4, pp. 225–290.

Plaxis, B., 2020. Plaxis 3D - Tutorial Manual. Connect Edition. V21.00,Delft, the Netherlands.

Sagaseta, C., 1987. Analysis of undrained soil deformation due to ground loss. Geotechnique, 37(3), 301–320.

Tamagnini, C., Miriano, C., Sellari, E., & Cipollone, N., 2005. Two-dimensional FE analysis of ground movements induced by shield tunnelling: the role of tunnel ovalization. Rivista Italiana di Geotecnica, 1, 11–33.

Yang, W., Boldini, D., & Zhang, D., 2023. Some observations on numerical modelling of tunnelling-induced soil movements by a displacement-controlled technique.In Proceedings 10th NUMGE 2023,London,UK.

Yang, W., 2023. Impact of a large-diameter shallow twin-tunnel excavation on adjacent high speed rail bridges and related protective measures. Ph.D. Thesis, University of Rome La Sapienza, Rome, Italy, Southeast University, Nanjing, P. R. China.

Tunnelling for a Better Life – Yan, Celestino, Thewes & Eberhardt (Eds)
© 2024 The Author(s), ISBN 978-1-032-80042-4
Open Access: www.taylorfrancis.com, CC BY-NC-ND 4.0 license

Stability numerical investigation of laminated and randomly discontinuous flat roof

Paraskevi Yiouta-Mitra* & Emmanouil Vougioukas
National Technical University of Athens, Greece

ABSTRACT: The behavior of laminated geological formations is governed by interbedding low tensile and shear strength which leads to separation and sliding respectively. These geological formations are commonly encountered in the construction of hydropower plants or in the mining industry for specific deposit types as well as in underground marble and limestone quarries. When the rock layers are internally discontinuous, their behavior significantly diverges from that of a beam succession. In this research, the behavior of multilayered randomly discontinuous with discrete fracture networks (DFN) roof in low overburden underground excavations is numerically investigated and compared to the behavior of sin-gle and multiple continuous or voussoir layers. A set of numerical analyses with the dis-crete element method are performed in UDEC and quantification of the multilayering ef-fect is produced for the unsupported discontinuous roof. The control of stresses and displacements by active reinforcement or passive support of the roof is of great interest. A second set of numerical analyses for the quantification of the reinforcement effects of pre-tensioned rockbolting and the passive support of shotcrete are also performed. Conclusions are drawn with respect to the degree of decrease of displacements magnitude in correlation to the support method. For continuous layers it is observed that the reinforcement of the roof reduces the vertical displacements to a lesser extent whereas for randomly fractured bedding layers, best support results are achieved by shotcrete.

Keywords: DFN, shotcrete, DEM, rockbolts, Simulation, voussoir

1 INTRODUCTION

The design of underground mines and caverns must consider geological, economical and safety aspects in the design stage. In mining, the case of tabular deposits is often the rea-son to select room and pillar or longwall mining methods. For the former, minimization of surface subsidence is paramount but with a simultaneous maximization of the recovery. Although pillars are the main support elements in a room and pillar scheme, their dimen-sioning must always be performed in conjunction with roof stability of chambers, espe-cially if retreat mining is to be performed afterwards. According to Ghasemi et al. (2012), the main parameters contributing to roof fall in room and pillar retreat mining involve, among thers, parameters such as the roof rock structure and quality and the panel width. Sherizadeh (2016) mentioned that different mechanisms can affect the stability of the roof and successful roof control can only be obtained if the failure mechanism is identified and understood properly. He performed a series of three dimensional distinct element analyses and concluded that the roof rock joint shear strength parameters have significant effect on the roof stability, whereas the rock-mass tensile strength had negligible effects.

Generally, in cases of excavations performed in horizontally stratified rock, a rectangular cross-section is the obvious economic selection. The structure of the roof rock has a con-siderable effect on the stability of the excavation and the choice of the support measures. The strata separate due to self-weight and deflect to the point of fracture, while at the same time the load is transferred to the supports of the roof, ie the abutments. The defor-mations of layered roof prior to collapse used to be greatly underestimated because frac-turing and transition to a voussoir roof was not considered. Bedding controls the strength of rock by defining beams or plates that span large openings. On the other hand, disconti-nuities define blocks of rock that may fall from the sides and roof of underground hard rock excavations. When the roof is in a fractured post-elastic state, the mechanisms of failure change to buckling, crushing and slip. Multi-layered buckling has been investigat-ed analytically (Yiouta-Mitra & Sofianos, 2018a), experimentally (Talesnic et al., 2007, Zhang et al., 2012) and numerically (e.g. Nomikos et al., 2002, He & Zhang, 2015, Yiouta-Mitra & Sofianos, 2018b, Abousleiman et al., 2020, Le and Oh, 2022).

The characterization of the discontinuities themselves, i.e. number of discontinuity sets, and for each

*Corresponding author: antipaxos@metal.ntua.gr

DOI: 10.1201/9781003495505-118

set, persistence, orientation spacing, location, shape and size plays an im-portant part in the evaluation of the mechanical behavior of the roof. In this research, a numerical discrete element scheme is used to explore the effects of multiple randomly fractured and multi-jointed layers in comparison to their continuous horizontally bedded and vertically fractured analogs and their response to reinforcement techniques. The DFN geometrical parameters are selected with a view to maintain as prominent mechanism of failure the discontinuous nature of hard rock underground roof.

2 NUMERICAL MODEL

The distinct element code UDEC is selected to model the behavior of the stratified roof of an underground opening. The basic validation of the models has been performed in a pre-vious numerical investigation (Yiouta-Mitra & Vougioukas, 2023) for the case of a single layer of limestone roof in gravitational field, comparing the results with the analytical so-lution for a fixed-end beam under its self-weight (Yiouta-Mitra & Sofianos, 2009). Three geometrical variables are considered in the current research; the number of layers, the number of vertical joints and the presence of a DFN with specific fractal characteristics to create a network at the project scale.

The model was partly of finer grid in the areas of interest for a better approach in rela-tion to the analytical solution. Indicative grid setups can be seen in Figure 1.

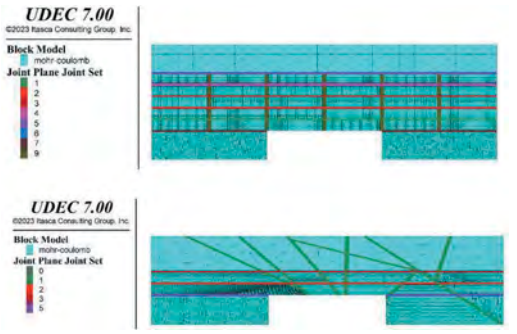

Figure 1. Indicative rockmass and discontinuities grid model setup for two cases: (a) 5-layer model with overburden and vertical joints at spacing 2.5 x the layer thickness (b) two-layer continuous model with DFN joints at project scale.

Simulations are performed for the case of continuous and cracked (vertical or random DFN discontinuities) stratified roofs, in limestone rock, shallow underground openings. Therefore the top boundary is free, while the side boundaries limit the horizontal dis-placements to simulate the far field. For a faster convergence of the model, fixed bounda-ries are applied at the bottom. Strong rock was considered so as to ensure that shear failure at the discontinuities would take precedence over the rock mass failure. The M-C failure criterion was prescribed for the discontinuities as well as the rock. The mechanical proper-ties are summarized in Table 1.

The bedding stiffness values are selected according to a wide range of bibliographic references (e.g. Bastola & Clugh, 2015) and the joint stiffness values are calculated according to Itasca (2022) for the specific numerical model parame-ters and the assumption of very stiff joints with no infilling material. As mentioned earlier, three geometrical parameters were varied in the models; the number of layers N was varied from 2 to 5, the crack spacing M was varied from 0.5 to 2m, giving ratios of crack spacing M to thickness t equal to 5;2.5;1.25;0.625 and the DFN was varied between 0 and 1, indicating existence or not.

The span was 4 m and the layer thickness 0.4m. For each roof case, the displacement of the excavation lower fiber was measured and the center point deflection monitored.

3 UNSUPPORTED ROOF RESULTS

3.1 *Two layers below massive rock overburden*

The numerical models with 2 layers amounted to six cases, a case of two continuous beams, four cases of a surplus of vertical crack sets spaced at sj/t = 5, 2.5, 1.25 and 0.625 and finally a case of a surplus of DFN. The deflections on a scanline at the lower fiber of the roof is depicted in Figure 2 for all cases. The lowest deflections were attained by the continuous beams while largest by the DFN case. It is clear that the random fracture net-work also produces unexpected and irregular patterns of deflections, contrary to a normally spaced discontinuity set. The effects of vertical joints spacing was found to be very small compared to the impact of the presence of a random project-scale fracture system. The numerical solution has provided a clear insight into the small differentiation between different vertical joints' spacing schemes, which is in accordance to the observations of previous research (Yiouta-Mitra & Sofianos, 2018).

Table 1. Mechanical properties of rock and discontinuities.

	c (MPa)	φ (deg.)	k_n (GPa/m)	k_s (GPa/m)	Density (g/cm^3)	G (GPa)	K (GPa)	E (GPa)
Rock	6.7	42			2.7	11.05	22.62	25.5
Bedding	0.1	30	10	1				
Joints	0	30	3700	370				

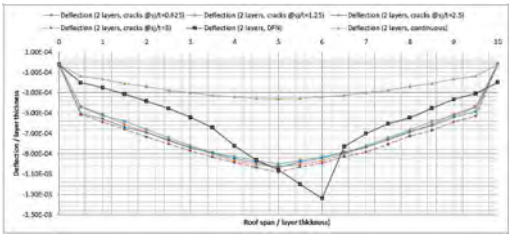

Figure 2. Scanline of displacements on immediate roof. The irregular curve corresponds to the random fracture network.

Figure 3 depicts the displacement vectors and the joint plane separation for the case of the DFN layered model. It becomes obvious that a wedge is formed around the center of the opening, which causes the irregularity in the deflections of the respective scanline in Figure 2.

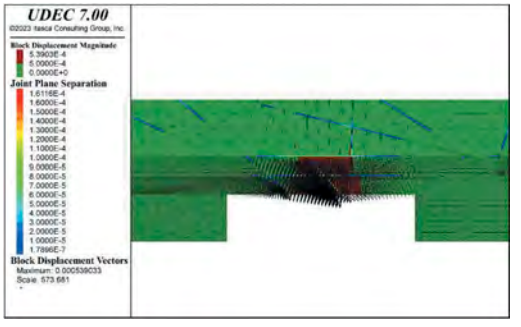

Figure 3. Roof deflections and crack separation for the DFN model with 2 layers.

3.2 *Five layers with and without overburden*

In this section two slightly different models were developed in order to detect the effects of the overburden in the case of shallow multi-layered excavations. It was interesting tonote the beneficial effects of the existence of the overburden, even as thin as the total of the layered imminent roof. Figure 4 contains the comparison of these cases, where it may be seen that both the randomly cracked roof as well as the sparsely spaced vertical joints' set depict deflections of similar magnitudes. In the case of no overburden over the five layers, the roof actually fails because it slides on the pre-existing cracks. The same happened with the randomly fractured roof but it has not been included in Figure 4 be-cause the displacement magnitudes far exceeded the other cases and would dwarf them. The multi-layered roof depicted larger deflection, as expected, compared to a roof of fewer layers. Another interesting observation in Figure 4, is to notice that when the vertical joints are more closely spaced, the deflections lessen. This is more obvious in the case with no overburden, otherwise, as noted in the previous paragraph, the effect of joint spacing on the immediate roof bending is less critical than other parameters. The formation of large blocks, equivalent to sparse but persistent jointing is the most detrimental to the stability of the flat jointed and layered roof.

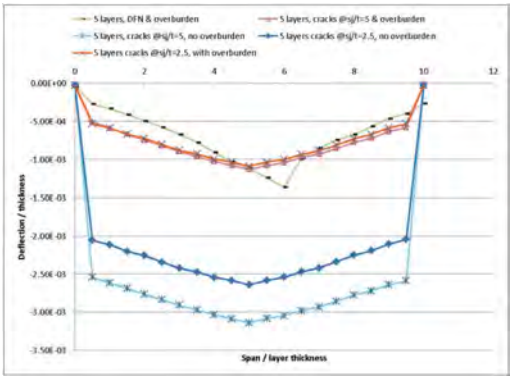

Figure 4. Effect of overburden on the stability of shallow layered roof.

The comparison between the behaviour of a combined vertical joints and randomly cracked multi-layered roof to the separate case has given better insight the mechanisms af-fecting the behaviour of blocky rockmass over rectangular openings. As can be seen in Figure 5, when there are no substantial vertical joints, the forming wedge is "trapped" be-tween the rotating sidewalls and all contact separations as well as roof deflections remain low (Figure 5a). In the case of the combination to a vertical joints set though (Figure 5b), despite their sparse distribution, sliding is enabled along their surfaces and since multiple layers are present, their weight overcomes the shear strength of the joints and the roof slides almost entirely vertically. Evidently, the wedge has detached since its displacement is in the order of magnitude of centimetres. Further, the area around the wedge has also displaced in the same order of magnitude, a difference order of magnitude of 2 with respect to the previous case. Similar observations are valid for the combinations of DFN combinations to smaller joint spacing.

4 SUPPORTED ROOF RESULTS

Specific cases of unsupported roof were selected to test the effectiveness of bolts and shotcrete support schemes with varying properties and layouts.

4.1 *Active bolts ideally simulated*

The roof of a layered underground opening is best reinforced with pre-tensioned bolts. The reinforcement

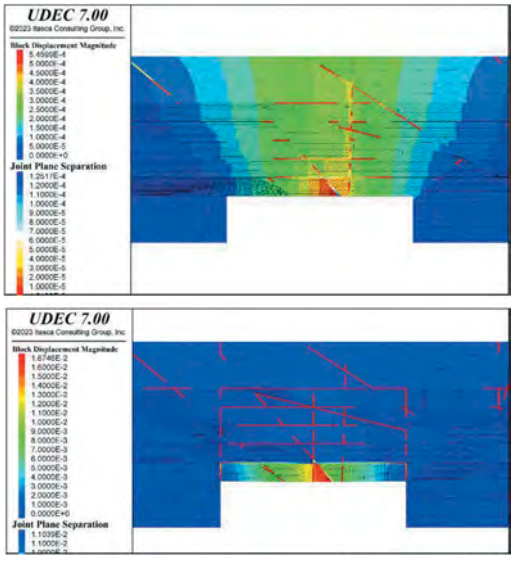

Figure 5. Response of five-layer roof (a) with DFN flat roof and (b) with DFN and vertical joints sparsely spaced at $s_j/t=5$.

aims at eliminating the separation of the lower layers by hindering the slipping between them. Thus, it forces individual continuous layers to function as a single solid roof. It has been verified that the response of the cracked roof is differentiated from that of the continuous layers. The active bolts are ideally simulated as concentrated compressive forces applied at the points of bolt installation.

For each case of multi-layered roof, the tightening of the layers with maximum required pretention $P_{b,\ max}$ = 141kPa is performed, on a 1x1m grid. The pre-tensioning force was calculated to prevent slip between the layers and was ideally simulated by applying a compressive force at the points of the bolt installation, such that would create shear strength equal to the shear stress of equation (1) at the level of the discontinuity:

$$P_b = \frac{\tau_{max}}{tan\varphi_j} \qquad (1)$$

where τ_{max} the maximum shear strain developed in the layers, i.e. shear stress that only depends on the roof span and φ_j the bedding friction angle.

The bolting pattern was varied between vertical and inclined bolts on the sides and the second one was the most effective 1x1 pattern. Figure 6 contains indicative results for the case of 2-layer and 4-layer roof for the two extreme cases of joint spacing, sj/t=5 and sj/t = 0.625 respectively. Similar support effects were recorded for all joint spacing layouts as can be seen in Table 2, were all cases are reported for the two-layer roof. The displacement reduction achieved was higher in the case of more sparsely jointed layered roof.

Table 2. Deflection reduction for two-layer roof with ideally pretensioned bolts.

Sj/t	5	2.5	1.25	0.25
Amelioration	51.74%	49.91%	45.59%	46.43%

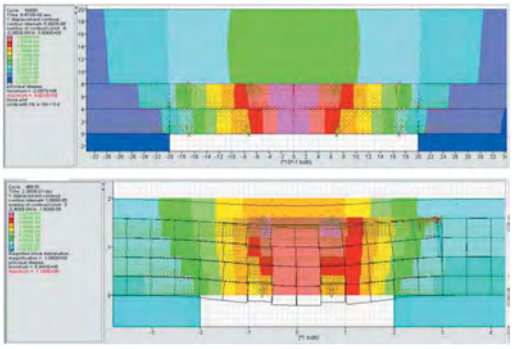

Figure 6. (a) Support with ideal vertical pretensioned bolts for 2-layer roof and (b) for 4-layer roof and side inclined bolt pattern.

4.2 *Shotcrete support*

Shotcrete is integrated into the excavation-support cycle of underground mines but also of many civil works. Its capacity is generally acting under four mechanisms, adhesion, direct shear, punching shear and flexure. These mechanisms are interdependent for their development. For example, if adhesion between the applied shotcrete and the rockmass is maintained, the failure will occur in direct shear. Otherwise, if it lost, flexural failure of the shotcrete layer will take place. In the specific case of layered and jointed hard rock formation of the current research, these four mechanisms are most applicable, since the rock mass failure is controlled by the orientation and shear strength of the discontinuities and not by overstressing. The large blocks are generally designed to be supported by rock bolts, it is mostly the smaller key blocks that shotcrete is called to support. The combination of rock bolts and shotcrete limits the kinematic freedom of unstable rock blocks and controls the unravelling of a blocky roof.

Thus, for the worst case scenario of five layers and the presence of a random fracture network, shotcrete was selected as appropriate support measure to be examined on its own. Four shotcrete schemes were applied. The first was standard shotcrete of 10 cm thickness, the second 20 cm and the third 15 cm but with practically unbreakable shotcrete-rock interface adhesion.

The varied properties of the shotcrete are depicted in Table 3. The difference between the four schemes is mainly the shotcrete thickness that has been varied from 10 to 20 cm. The adhesion role was also tested

and found to be quite significant in comparison. It is characteristic that Schemes 2 and 21 of shotcrete properties gave the highest roof reinforcement. Figure 7 contains the efficiency chart of all schemes as a percentage amelioration of the unsupported deflection of the roof.

Table 3. Properties of shotcrete in S.I. [N;m].

Scheme	1	2	21	3
Thickness	0.1	0.2	0.1	0.2
Normal coupling Stiffness	1E9	1E11	1E11	1E9
Shear coupling stiffness	1E9	1E11	1E11	1E9
Coupling cohesion	1E6	1E8	1E8	1E6
Coupling tension	1E6	1E8	1E8	1E6

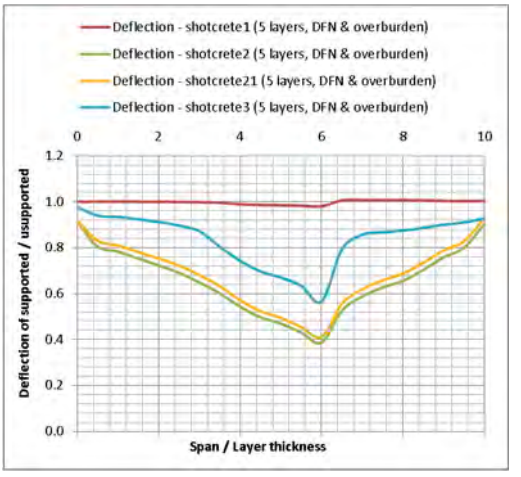

Figure 7. Percentage amelioration of deflection with shotcrete support for the randomly fractured layered roof.

Figure 8 depicts the supported flat roof and how the shotcrete, contrary to the rockbolts, creates a gradual, bending curve for the highly anisotropic randomly fractured roof. The shear forces in the shotcrete layer are maximized close to the protruding wedge that is formed in the middle of the roof. It is the point where failure is expected to take place for thinner layer or insufficient adhesion.

It must be noted that direct shear failure of the shotcrete will happen for a combined bolt and shotcrete application in the case of five layers with no overburden and vertical joints occurring at the abutments. This can be easily averted though, if the pattern of the bolts is the inclined one for the outer bolts and the loss of the shear strength of the joints is thus counteracted.

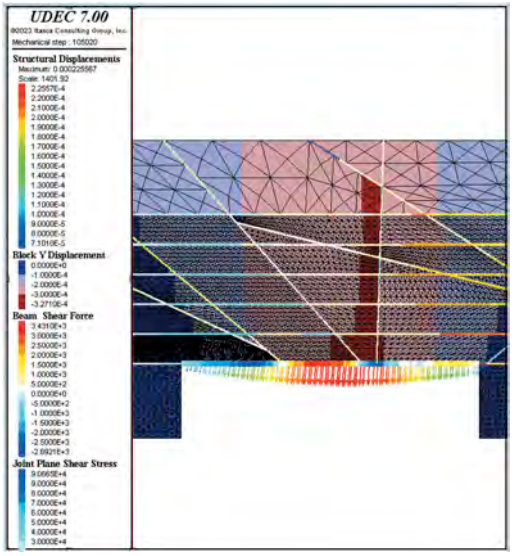

Figure 8. Shear forces and structural displacements of shotcrete for scheme 3.

5 CONCLUSIONS

A parametric numerical analysis has been conducted with a view to investigate the response of multi-jointed layered media to the bolt and shotcrete reinforcement technique as compared to randomly fractured layered media.

The varying parameters were geometric, while mechanical properties of rock and joints have been maintained at representative values for hard rocks in low overburden, low stiffness of bedding planes and stiff vertical joints. The numerical models were validated against analytical solutions for continuous and voussoir beam roof. The results of the numerical generalization to multiple multi-jointed layers has shown that the lowest cracked layer is of paramount importance to maintaining lower stresses and displacements to the upper layers. The response of the multiple stacked voussoir beams is different from that of the randomly fractured in that the roof is more likely to form unstable wedges of various sizes. Stabilisation by rock bolts is always a method that yields satisfactory results. Shotcrete was also found to function well so long as adhesion is satisfactory, usually around 0.5 – 1 MPa and sufficient thickness of shotcrete.

It is concluded that the reinforcement of the roof either by rockbolts, shotcrete or their combination, achieves the decrease of vertical displacements and abutment stresses, for blocky flat roof with systematic or random fracture patterns. Monitoring of the roof stresses and displacements is a good preventive measure for the case where change of the bolting pattern or shotcrete thickness is required due to structural changes of the roof.

ACKNOWLEDGMENTS

The authors would like to acknowledge the support of the Greek Tunnelling Society.

REFERENCES

Ebrahim Ghasemi, Mohammad Ataei, Kourosh Shahriar, Farhang Sereshki, Seyed Esmaeil Jalali, Ah-mad Ramazanzadeh, 2012. Assessment of roof fall risk during retreat mining in room and pillar coal mines, International Journal of Rock Mechanics and Mining Sciences, 54 (2012) 80–89.

Rami Abousleiman, Gabriel Walton, Sankhaneel Sinha, 2020. Understanding roof deformation mechan-ics and parametric sensitivities of coal mine entries using the discrete element method, International Journal of Mining Science and Technology, Volume 30, Issue 1, 2020, Pages 123–129.

Sherizadeh, Taghi, 2015. Assessment of Roof Stability in a Room and Pillar Coal Mine in the U.S. using Three-Dimensional Distinct Element Method. The University of Arizona.

Bastoia S & Chugh YP, 2015. Shear strength and stiffness of bedding planes and discontinuities in the immediate roof rocks overlying the no 6 coal seam in Illinois, 13th ISRM International Congress of Rock Mechanics, Montreal, Canada.

Nomikos P.P. & Sofianos A.I. & Tsoutrelis C.E., 2002. Structural response of vertically multi-jointed roof rock beams, International Journal of Rock Mechanics & Mining Sciences 39: 79–94.

Kim BH, Kaiser PK, Grasselli G, 2007. Influence of persistence on behaviour of fractured rock masses, Geological Society, London, Special Publications 2007; v. 284; p. 161–173.

Tien Dung Le, Joung Oh, 2022. Longwall face stability analysis from a discontinuum-Discrete Fracture Network modelling, Tunnelling and Underground Space Technology, Volume 124, 104480, ISSN 0886-7798, https://doi.org/10.1016/j.tust.2022.104480.

Yiouta-Mitra P., Sofianos A. I., 2018a, Multi-jointed stratified hard rock roof analysis and design, Int. J. Rock Mech. and Min. Sci. 106:96–108.

Yiouta-Mitra P. & Sofianos A.I., 2018b Multi-jointed voussoir beam analysis – Theory and implementation, 10th Asian Rock Mechanics Symposium, The ISRM International Symposium for 2018.

Itasca, 2022. Universal Distinct Element Code, Manual.

Shabanimashcool M, Li C., 2015. Analytical approaches for studying the stability of laminated roof strata. Int J Rock Mech Min Sci. 79: 99–108.

He L, Zhang QB., 2015. Numerical investigation of arching mechanism to underground excavation in jointed rock mass. Tunn Undergr Space Technol. 50: 54–67.

Zhang Z. X., Xu Y., Kulatilake P.H.S.W., Huang X., 2012. Physical model test and numerical analysis on the behavior of stratified rock masses during underground excavation, Int. J. Rock Mech. and Min. Sci., 49: 134–147.

Yiouta-Mitra, P., Sofianos, AI., 2009. Bolting requirements for non-jointed stratified rock roof. Proc. ISRM International Symposium SINOROCK2009 'Rock Characterization, Modeling and Engineering Design Methods', Hong Kong, 19-22 May, Paper No. 339, pp 649–653.

Tunnelling for a Better Life – Yan, Celestino, Thewes & Eberhardt (Eds)
© 2024 The Author(s), ISBN 978-1-032-80042-4
Open Access: www.taylorfrancis.com, CC BY-NC-ND 4.0 license

Responses of a shallow tunnel in liquefiable ground subject to multiple shakings

Jinghua Zhang*
Xi'an Jiaotong University, Xi'an, China
Tongji University, Shanghai, China

Emilio Bilotta
University of Naples Federico II, Naples, Italy

Yusheng Yang
Shanghai Construction No.4 (Group) Co., Ltd., Shanghai, China

Yong Yuan
Tongji University, Shanghai, China

ABSTRACT: This paper addresses the issue of the dynamic responses of a shallow tunnel in liquefiable ground subject to multiple shakings. The topic is of special importance, because earthquakes often strike the same geological location repeatedly in a short period. The current study is based on a centrifuge test of four consecutive shakings, where a rectangular tunnel is buried in saturated Hostun sand in plane-strain conditions. The OpenSees platform and the PM4Sand constitutive model are employed to replicate the experimental results, including the displacements, the pore pressures, and the accelerations of the soil-structure system. The validated numerical model is then reconfigured for more realistic resemblances to the boundary conditions of an actual engineering site. Further analysis is also performed, placing the emphasis on the uplift of the tunnel with different permeability coefficients of the ground.

Keywords: Liquefaction, Multiple-shakings, Numerical modelling, Soil-structure interaction

1 INTRODUCTION

It is very likely in a seismic event that the structures would experience a series of consecutive shakings in a short period of time. Since the dynamic behavior of the soil is usually stress-path dependent, the soil-structure interaction (SSI) would also differ because of the shaking histories of the excitation. The scenario to be studied in this paper is a shallow tunnel in liquefiable ground subject to multiple shakings. The OpenSees platform (Pacific Earthquake Engineering Research Center, 2021) and the PM4Sand constitutive model (Boulanger and Ziotopoulou, 2017) are employed to construct a plane-strain numerical model based on a centrifuge test of four consecutive shakings. The test-validated numerical soil-structure system is then reconfigured for more realistic resemblances to the boundary conditions of an actual engineering site, and further analysis is performed mainly regarding the uplift of the tunnel with different permeability coefficients of the ground.

2 THE CENTRIFUGE TEST

A series of centrifuge shaking table tests were conducted at the Schofield Centre, University of Cambridge by Miranda et al. (2023). Four physical models were prepared and tested, among which the first one is to be numerically simulated in this paper. An illustration of this centrifuge test model is shown in Figure 1. The centrifugal acceleration was 60*g*, so the scaling factor was 1: 60. The following descriptions and the numerical models are both of the prototype scale unless stated otherwise.

*Corresponding author: zhang.j@xjtu.edu.cn

DOI: 10.1201/9781003495505-119

As can be seen, a rectangular tunnel, made of aluminum sheets, was buried in saturated Hostun sand 5 m below the surface. A rigid container was adopted to allow displacement measurement by particle image velocimetry (PIV). Therefore, to mitigate the boundary effects of the container, two layers of absorbent material were attached to the sidewalls. After an initial equilibrium was reached during the swing-up, four shakings were fired consecutively. They were EQ1, EQ2, EQ3, and EQ4, whose accelerograms and Fourier spectra are shown in Figure 2. The intensities of the first three shakings are increased through the amplitudes, which are 0.06*g*, 0.11*g*, and 0.43*g*, respectively. The fourth shaking, however, has an amplitude of 0.45*g*, similar to that of EQ3, but it has five more full cycles in the waveform.

During the shakings, the acceleration responses, the vertical displacements, and the pore pressure data are registered by the sensors denoted as ACC#, PIV#, and PPT# in Figure 1, respectively.

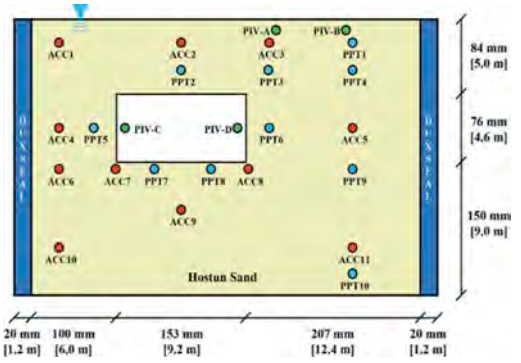

Figure 1. The centrifuge test model.

3 THE NUMERICAL SIMULATION

The numerical simulation of the centrifuge test is carried out employing the OpenSees platform. The finite element model is shown in Figure 3.

The majority of the model, i.e., the Hostun sand and the absorbent layers, are modelled by 2021 quadrilateral *u-p* coupled elements (McGann and Arduino, 2012). The nominal element size is 0.5 m. The constitutive model PM4Sand is used to capture the nonlinear behavior of the liquefiable Hostun sand, whose parameters are listed in Table 1. The detailed calibration process could be found in Zhang et al. (2023). The absorbent layers are considered elastic with a Young's modulus of 800 kPa, a Poisson's ratio of 0.46, and a mass density of 1.65 Mg/m^3 (Popescu and Prevost, 1993).

The tunnel lining is modelled by 54 elastic beam elements, defined around the interior of the rectangular hollow within the sand. The two translational degrees-of-freedom of the tunnel elements are equalled to those of the surrounding sand. Their material properties are a Yong's modulus of 7×10^7 kPa and a linear mass density of 15 Mg/m.

The computation takes two stages. The first stage is the application of the gravitational field. Sufficient step time is given for the soil-structure system to reach an initial equilibrium. In the second stage, the four consecutive shakings depicted in Figure 2 are inputted from the lateral sides and the base of the model. Although the duration of each shaking is shorter than 20 s, they are all given the step time of 200 s. Hence, stage two has 800 s in total.

As has been stated, the test data include the acceleration responses, the vertical displacements, and the pore pressures. The data of four key positions are compared with the numerical results in Figure 4. They are the acceleration responses by ACC7, the pore pressure data by PPT4, the settlement of the ground surface by PIV-B, and the average uplift of the tunnel by PIV-CD. The latter two are trivial in

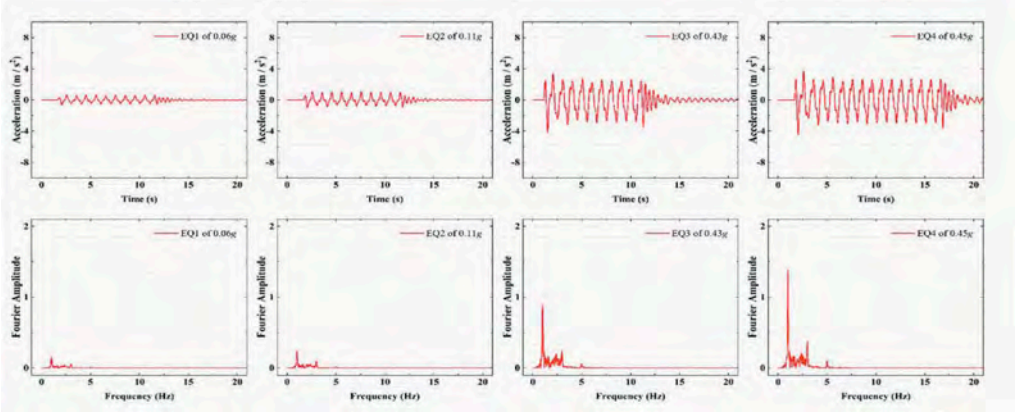

Figure 2. The input excitations.

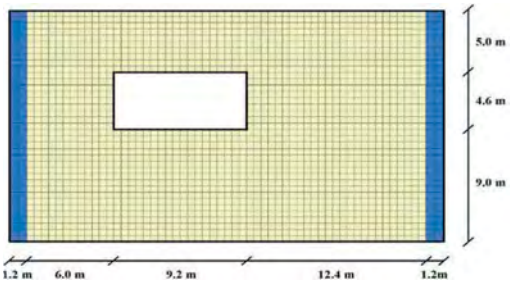

Figure 3. The finite element model.

the first two shakings, so they are absent in EQ1 and EQ2. Other than that, the centrifuge test data have been replicated by the numerical simulation with reasonable accuracy. Thus, the validity of the numerical simulation is verified.

Table 1. Constitutive parameters of the Hostun sand.

e_{max}: maximum void ratio	1.049
e_{min}: minimum void ratio	0.648
D_r: relative density	54 %
G_o: shear modulus constant	719
Q: critical state line parameter	8.4
R: critical state line parameter	0.78
ϕ'_{cv}: critical state effective friction angle	33.8°
v: Poisson's ratio	0.31
h_{po}: contraction rate parameter	0.07
ρ: mass density	1.96 Mg/m^3
k: permeability coefficient	6×10^{-4} m/s

4 THE NUMERICAL INVESTIGATION

The validated numerical soil-structure system is used for further investigation on the subject matter. However, for more realistic resemblances to the boundary conditions of an actual engineering site, it needs to be reconfigured. Firstly, the horizontal width of the liquefiable ground is extended to 100 m, which is more than 10 times the width of the tunnel. Then, the two absorbent layers are removed. Most importantly, differing from the boundary conditions of the rigid container, the seismic excitations are solely inputted from the base of the model. The two lateral sides are defined as periodical boundaries, which better represent the shearing deformations of the ground.

It has been noticed in a previous study that the rigid container could mitigate the effect of the input shakings (Zhang and Bilotta, 2023). Hence, to achieve a similar level of liquefaction to that of the Hostun sand in the centrifuge test, the original input excitations in Figure 2 are scaled by a factor of 0.35 in the reconfigured numerical model with the new boundary conditions.

The constitutive parameters in Table 1 are kept, except that the permeability coefficient ranges from 1×10^{-4} m/s to 1×10^{-3} m/s. Thus, a series of numerical simulations are computed, where the emphasis is placed on the variation of the permeability coefficient. The resulting changes are mainly discussed of the uplift of the tunnel and the pore pressure on the midpoint of the base slab, which are plotted in Figure 5.

The first two shakings, i.e., EQ1 and EQ2, are relatively light. In the centrifuge test, they were intended to increase the homogeneity of the Hostun sand and to probe the elastic characteristics of the soil-structure system. Their peak accelerations are smaller than 0.04g in the new simulations. Although there is some excess pore pressure accumulation, the Hostun sand does not reach full liquefaction. Hence, instead of floating up, the tunnel even exhibits some minor settlements.

The uplift of the tunnel only starts to manifest in the third shakings. Due to the greater amplitude of the input excitation, there is a sharp increment in the excess pore pressure. Before full liquefaction is reached by the Hostun sand, the uplift of the tunnel has already begun. There is a clear trend that smaller permeability of the sand would lead to larger uplift of the tunnel. In the case of $k = 1 \times 10^{-3}$ m/s, the tunnel exhibits significant settlements in the last shaking. This is in conformity with conventional perceptions, because sand of smaller permeability is easier to liquefy, and the accumulated excess pore pressure is harder to dissipate, thus sustaining a longer full liquefaction. Consequently, the Hostun sand would provide enough buoyant force for the tunnel to gradually overcome its self-weight and the resistance of the surrounding soil. This is clearly demonstrated by the pore pressure data in the last two shakings. The excess pore pressure of the green curve of $k = 1 \times 10^{-4}$ m/s is the last to dissipate, and the dissipation is also the slowest. Even in the first two lighter shakings, the excess pore pressure of the green curve exhibits an observable increment, while the others are almost flat. Interestingly, the differences between $k = 3 \times 10^{-4}$ m/s and $k = 1 \times 10^{-4}$ m/s are only seen on the pore pressures not on the uplifts of the tunnel in the third shaking. The differences in uplifts do not become significant until the last shaking. This could be related to the larger excess pore pressures of $k = 1 \times 10^{-4}$ m/s in the first two shakings. The sand of the smallest permeability coefficient is presumed to be more densified. Hence, the uplift of the tunnel in the following shaking is mitigated. However, in the last shaking, the prolonged input excitation amplifies the effect of limited drainage, resulting in a much greater uplift of the tunnel.

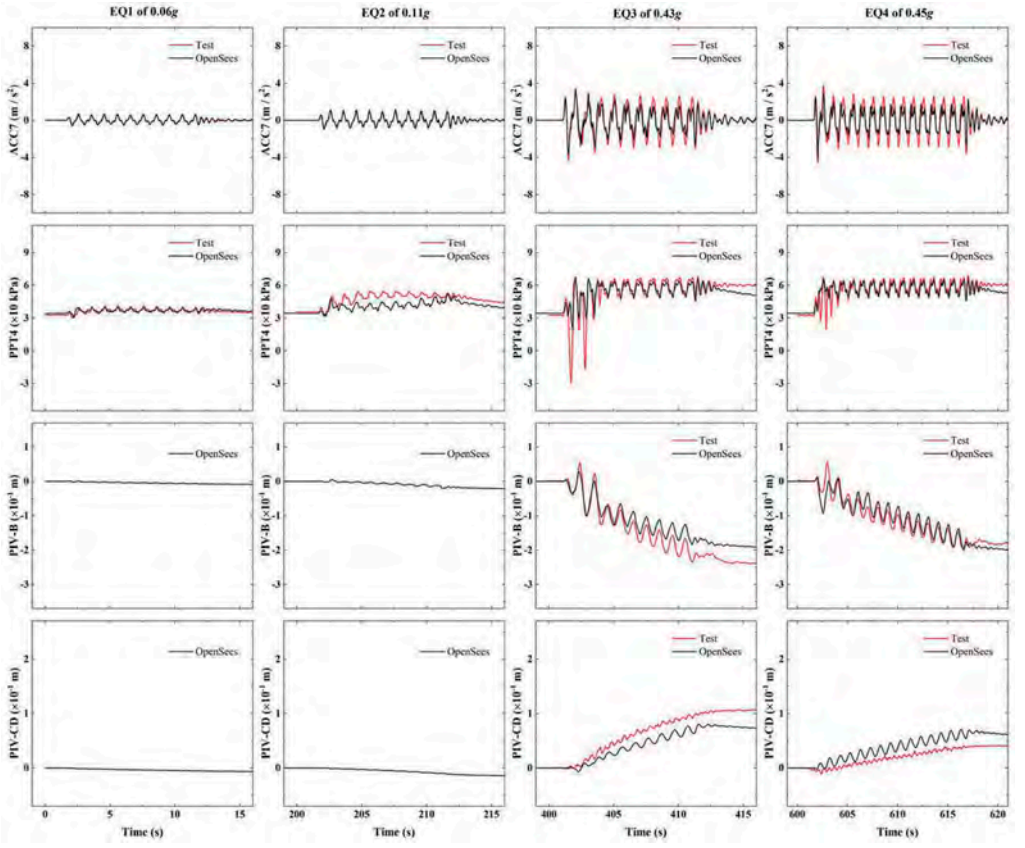

Figure 4. The comparison of the numerical results and the centrifuge test data.

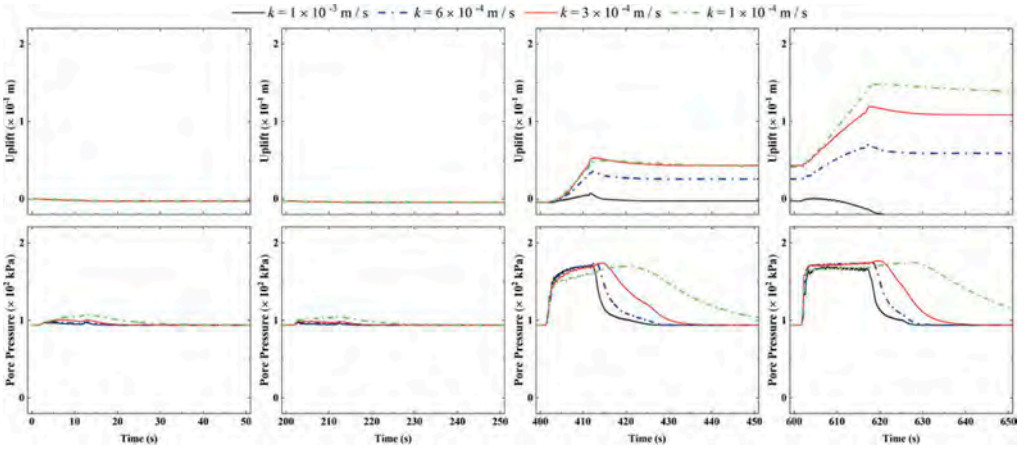

Figure 5. The uplift of the tunnel and the pore pressure on the midpoint of the base slab in the investigative numerical simulations.

5 CONCLUSIONS

Two-dimensional plane-strain numerical models are constructed employing the OpenSees platform and the PM4Sand constitutive model. The numerical simulation is validated against the data of a centrifuge shaking test.

The test-validated numerical soil-structure system is reconfigured for more realistic resemblances to the boundary conditions of an actual engineering site.

Further analysis is performed, placing the emphasis on the uplift of the tunnel with different permeability coefficients of the ground.

There is a clear trend that smaller permeability of the sand would lead to larger uplift of the tunnel. However, the exact responses of the tunnel are also dependent on the shaking histories of the excitation.

ACKNOWLEDGMENTS

The research was supported by the National Natural Science Foundation of China (52108383), the State Key Laboratory of Disaster Reduction in Civil Engineering (SLDRCE21-02), the Young Talent Fund of Xi'an Association for Science and Technology (959202313071), and the Shanghai Sailing Program (23YF1418600). The benchmark centrifuge tests are part of the project STILUS funded by the network SERA (Seismology and Earthquake Engineering Research Infrastructure Alliance for Europe, EC grant No. 730900). The authors wish to acknowledge the staff of the Schofield Centre at Cambridge University (UK), and its director Prof. Gopal Madabhushi.

REFERENCES

Boulanger, R.W., Ziotopoulou, K., 2017. PM4Sand (Version 3.1): A Sand Plasticity Model for Earthquake Engineering Applications. Davis, California, USA.

McGann, C.R., Arduino, P., 2012. Stabilized single-point 4 node quadrilateral element for dynamic analysis of fluid saturated porous media. Acta Geotechnica, 7, 297–311.

Miranda, G., Nappa, V., Bilotta, E., 2023. Physical modelling of the interaction between a tunnel and a building in a liquefying ground and its mitigation. Tunnelling and Underground Space Technology, 137, 105108.

Pacific Earthquake Engineering Research Center, 2021. OpenSees 3.3.0. https://opensees.berkeley.edu/

Popescu, R., Prevost, J.H., 1993. Centrifuge validation of a numerical model for dynamic soil liquefaction. Soil Dynamics and Earthquake Engineering, 12(2), 73–90.

Zhang, J.H., Bilotta, E., 2023. Numerical modelling of a shallow tunnel buried adjacent to a surface structure in liquefiable ground. In: Zdravkovic, L., Kontoe, S., Taborda D.M.G., Tsiampousi A. (Eds), Proceedings of the 10th European Conference on Numerical Methods in Geotechnical Engineering 2023. ISSMGE, London, UK.

Zhang, J.H., Bilotta, E., Madabhushi, G.S.P., et al, 2023. Numerical modelling of a tunnel adjacent to a surface structure in liquefiable ground. Géotechnique, online. http://dx.doi.org/10.1680/jgeot.22.00418.

Tunnelling for a Better Life – Yan, Celestino, Thewes & Eberhardt (Eds)
© 2024 The Author(s), ISBN 978-1-032-80042-4
Open Access: www.taylorfrancis.com, CC BY-NC-ND 4.0 license

Failure mechanism of reinforced faces and design method of advanced supports for tunnels excavated by the full-face mechanized method

Xiao Zhang*, Mingnian Wang & Li Yu
School of Civil Engineering, Southwest Jiaotong University, Chengdu, China
Key Laboratory of Traffic Tunnel Engineering Ministry of Education, Southwest Jiaotong University, Chengdu, China

ABSTRACT: The full-face mechanized method is one of the main development directions of the construction technology of tunnels excavated by the drilling and blasting method in China, and it is also the basis of intelligent construction technology of drilling and blasting tunnels. However, the significant increase of excavation area led to the reduction of tunnel face stability (especially in soft and fractured ground), which affect the popularization of the full-face mechanized method. Therefore, establishing the stability evaluation and control method for tunnel faces is the key issue to realize the full-face mechanized method in soft and fractured ground. To solve these issues, the model test and theoretical analysis methods are used to clarify the failure mechanism of tunnel face and reinforcing mechanism of advanced supports. First, the progressive failure mechanism and the failure mode of tunnel faces as well as the synergetic reinforcing mechanism of advanced supports are explored. Then, the calculation model and design method of the combined advanced support are established for tunnels excavated by the full-face mechanized method. The research results can provide theoretical support for the popularization of the full-face mechanized method.

Keywords: failure mechanism, tunnel face, pipe roof, face bolt, design of advanced supports

1 INTRODUCTION

The full-face mechanized method is one of the main development directions of the construction technology of tunnels excavated by the drilling and blasting method in China, and it is also the basis of intelligent construction technology of drilling and blasting tunnels. However, the significant increase of excavation area led to the reduction of tunnel face stability (especially in soft and fractured ground), which affect the popularization of the full-face mechanized method. Therefore, establishing the stability evaluation and control method for tunnel faces is the key issue to realize the full-face mechanized method in soft and fractured ground. Therefore, many advanced support techniques have been developed to provide safe excavation in conventional tunnelling, such as pipe roofing and face bolting (Lunardi, 2008). Many studies have been conducted to investigate the reinforcing mechanism of these techniques and the instability of the tunnel face.

Several authors have studied tunnel stability through numerical simulations (di Prisco et al., 2020; Li et al., 2015; Ng and Lee, 2002; Paternesi et al., 2017; Peila, 1994; Perazzelli and Anagnostou, 2013; Yoo, 2002; Yoo and Shin, 2003). The results show that pipe roofing and face bolting could reduce face extrusion, change the soil's stress condition ahead of the tunnel face, and effectively improve the face stability. Pipe roofing and face bolting has optimum parameters (including overlap length, density, and axial rigidity), maximizing the reinforcing effect. However, the soil stress redistribution due to pipe roofing and face bolting were rarely considered in these studies. Moreover, the simulation results were dependent on the adopted material models and the parameters and should be validated by other methods. Experimental studies (including n-g and 1-g tests) provided an effective way to validate the numerical models and explore the face instability mechanism.

Experimental tests have been conducted by several authors (Al Hallak et al., 2000; Calvello and Taylor, 1999; Chambon and Corte, 1994; Date et al., 2008; Di Prisco et al., 2018; Kamata and Mashimo, 2003; Takano et al., 2010; Yoo and Shin, 2003), and the reinforcing effect of pipe roofing and face bolting is intuitively shown. The results agree with those from numerical simulations, indicating that pipe roofing and face bolting can significantly reduce the face's extrusion and improve its stability. There is indeed an optimal reinforcement length beyond which improvements in the reinforcement effect are

*Corresponding author: xiao.zhang@swjtu.edu.cn

DOI: 10.1201/9781003495505-120

not apparent. The extent of the failure zone and the required support pressure to stabilize the tunnel face are reduced by this technique. However, the failure process of reinforced faces was not measured due to a lack of measurement techniques.

Theoretical studies have been carried out to efficiently analyse the reinforcement behaviours of face bolts and pipe roofs. There are mainly two kinds of theoretical analysis methods for assessing the stability of a reinforced tunnel face, including the limit analysis method and the limit equilibrium method. Oreste and Dias (Oreste and Dias, 2012), Anagnostou and Perazzelli (Anagnostou and Perazzelli, 2015) and Perazzelli and Anagnostou (Perazzelli and Anagnostou, 2017) proposed computational methods based on the limit equilibrium method, in which the failure surface in front of a tunnel face is assumed to be an inclined plane. Pan and Dias (Pan and Dias, 2017) and Qian et al.(Qian et al., 2019) analysed the safety factor of a reinforced tunnel face in combination with the upper-bound limit analysis method and the strength reduction technique. However, only one reinforcement measure is considered in these models. In practical engineering, face bolting and pipe roof techniques are usually comprehensively employed, but there is no theoretical model that considers the simultaneous effect of these two measures.

To address these issues, a series of model tests with different reinforcement parameters were conducted with a 31 cm diameter tunnel in this work. The model tests were performed by considering a dry granular material (dry sand). Based on the model test results, the failure mechanism of reinforced faces is revealed and a design method of advanced supports for tunnels excavated by the full-face mechanized method is proposed.

2 THE STRATEGY OF LABORATORY TEST

2.1 *Test instrument*

In a darkness room were the model tests performed. Using a non-invasive technique, particle image velocimetry (PIV), the ground's displacement was measured. A Nikon D610 digital camera (24 megapixels, 6016 px4016 px) and two 100 W spotlights were used to capture the images. These images were later post-processed by the PIV software PIVlab by Thielicke and Stamhuis (2014). In Figure 1(b) and (c), the internal dimensions of the box were 1.0 m ×0.6 m ×1.5 m, and the front wall was a 1.2 cm thick hardened glass. The inner and outer diameters of the half tunnel model made of a plexiglass half-cylinder were respectively 31 cm and 33 cm. A half-circle piston of the same material was employed to support the tunnel face, its thickness 2 cm and diameter 30.5 cm. The piston and a load cell were connected by a steel bar, and the load cell is connected by a threaded rod constrained by a threaded flange. Thus, the piston could be retracted by turning the handle to simulate the instability of the face. Moreover, as shown in Figure 1(b) and (d), a rectangular hole and a series of circular holes were respectively cut in the glass and drilled at the piston for bolt and pipe installation. The diameters of the holes at the piston and half-cylinder are respectively 4 mm and 5 mm, and the spacings between adjacent holes are respectively approximately 2 cm and 1 cm.

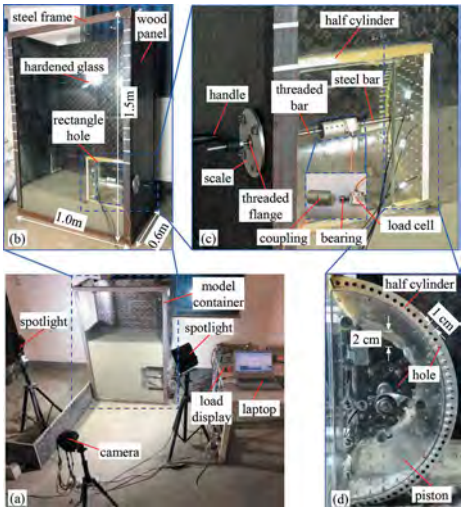

Figure 1. (a) Test instrument; (b) model container; (c) model tunnel and (d) piston and half-cylinder.

2.2 *Test materials*

Sand from the Minjiang River in Sichuan Province, China, was applied in this work. Figure 2 shows the grain size distribution. The sand is of medium density, namely the relative density being 0.58. A more detailed listing of the material properties is in Table 1.

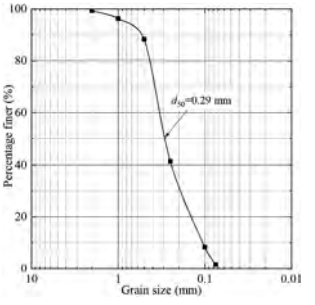

Figure 2. Grain size distribution of sand.

As shown in Figure 3, fibreglass bars 1.0 mm in diameter and 1.0 D (310 mm) in length were used as the bolting material. Additionally, to increase the friction between the bolt and soil, a layer of 0.2 mm–0.5 mm quartz sand was glued around the bolt with epoxy resin. The outer diameter of the bolt was approximately 3 mm. The elastic modulus E_b and tensile yield strength T_b of the bolt are 25 GPA and 581 MPa, respectively. The ABS pipe with outer

Table 1. Sand properties.

Parameters		Value	Parameters		Value
Unit weight	γ (kN/m^3)	15.8	Poisson's ratio	v_s	0.35
Relative density	D_r	0.58	Elastic modulus	E_s (MPa)	8.5
Friction angle	φ (°)	36	Water content	(%)	0.4
Cohesion	c (kPa)	0	Mean grain size	d_{50} (mm)	0.29
Dilatancy angle	Φ (°)	8.8			

diameter of 6mm, wall thickness of 1.5mm and length of 1.0 D (310 mm) were used as the pipe material, and the elastic modulus E_p is 2 GPa.

Figure 3. Reinforcement materials.

2.3 *Testing procedure*

In Figure 4(a), layers of 7.5 cm thickness were installed with a drop height of 10 cm. According to the layout of bolts in Figure 4 and diameter, bolts were installed through the rectangular hole and the circular holes layer by layer, and pipes were installed layer by layer through the circular holes at the half-cylinder. During the tests, the piston was slowly pulled out by turning the handle to control the collapse of the tunnel face. For face displacement $s \leq 1$ mm, 1 mm$<s<$3 mm and 3 mm$\leq s \leq$16 mm, the displacement increments were 1/24 mm, 1/8 mm and 1/4 mm, respectively. Besides, it is important to prevent any sand from entering the model tunnel. Therefore, the piston and a sponge-layer of 2mm thickness were pasted together and plastic foil was wrapped around the half-cylinder and piston, see Figure 4(b).

3 THE RESULTS OF MODEL TESTS

3.1 *Face failure process and pattern*

To assess the face failure process and pattern, the incremental shear strains of soil were analysed in this section. The shear strain concentration area can identify the shear bands.

In the unreinforced case, as shown in Figure 5(a), when s=1 mm the failure zone in front of the tunnel face was formed, initiated from the tunnel invert and the tunnel centre to the tunnel crown along the vertical direction. The sliding boundary of the failure zone consists of an arch line (upper failure zone) and a curved line (lower failure zone). At this moment the support pressure reached the limit support force (see Figure 5), which means that the peak strength of sand was mobilized, and the tunnel face was in the limit equilibrium state. With an increasing s, the upper failure zone gradually extended towards the ground surface. In this process, the support pressure gradually increased to the residual support pressure (see Figure 5), which was caused by an enlargement of the failure zone and the dilatancy of the sand. Finally, when s=15 mm, the upper failure zone reached the ground surface, and a chimney-like part (upper failure zone) and a wedge-like part (lower failure zone) could be distinguished. The failure angle θ is approximately 73°, and the extent of the failure zone in front of the face is approximately 0.29 D.

In the bolt reinforced case, as shown in Figure 6, the development progress and shape of the failure zone were similar to those of the unreinforced case, except that the extent of the failure zone was smaller and the sliding boundary was steeper. Specifically, the configuration of the failure zone was also a chimney-wedge-type mechanism, which indicates that the theoretical Horn model (Horn, 1961) is also applicable to the stability analysis of a reinforced tunnel face. The extent of the failure zone was approximately 0.22 D, the failure angle was approximately 78°. The results indicates that the stability of the tunnel face was increased by face bolting.

Figure 4. (a) Prepared ground, (b) pipes installation and (c) bolts installation.

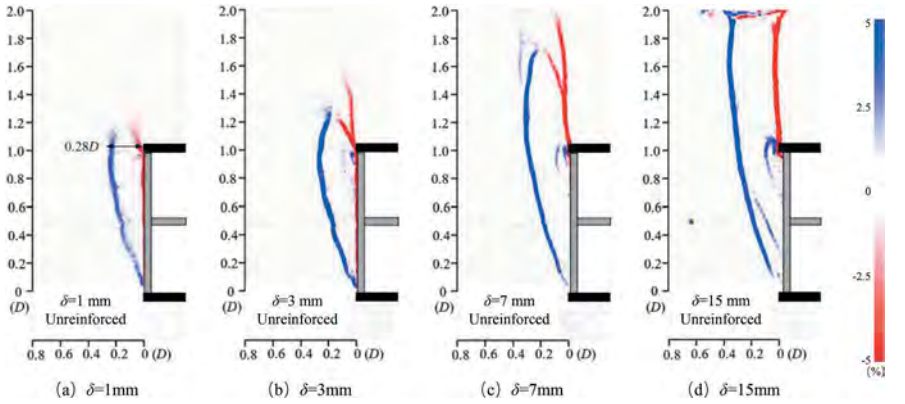

Figure 5. Incremental shear strains of soil for a unreinforced tunnel face.

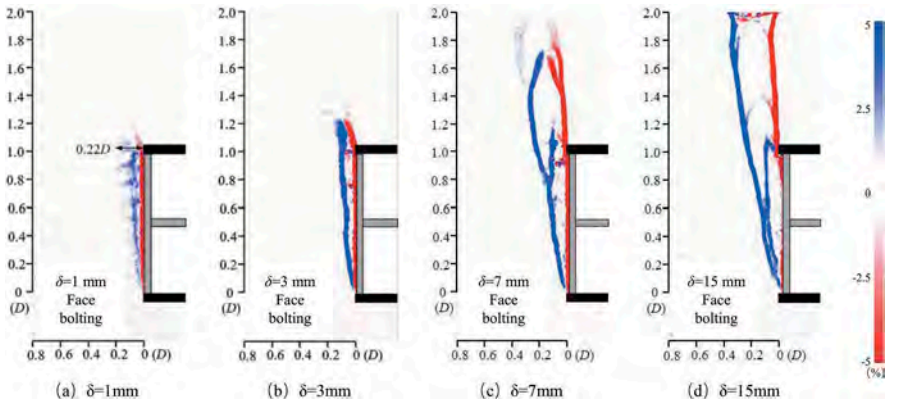

Figure 6. Incremental shear strains of soil for a bolt reinforced tunnel face.

In the bolt reinforced case, as shown in Figure 7, the development progress and shape of the failure zone were similar to those of the unreinforced case. Compared with the condition without reinforcement (see Figure 5), under the pipe roof reinforcement, only the failure surface appears in the soil in front of the tunnel face, while no obvious failure surface appears in the soil above the tunnel face, indicating that the pipe roof restricts the deformation of the soil above the tunnel face, reduces the soil pressure on the tunnel face, and improves the stability of the tunnel face. The instability range of surrounding rock in front of the palm face is 0.29 D, indicating that the pipe roof reinforcement has little effect on the failure range of the tunnel face, but can effectively reduce the failure range above the palm face, thus reducing the soil pressure.

3.2 *Reinforcing mechanism of pipe roofing and face bolting*

According to the model test results (see Figure 6), the force mode of a bolt reinforced tunnel face is shown in Figure 8. The bolt supporting force F_b increases the anti-sliding force F_2 and improves the stability of the tunnel face. The anchoring system of face bolt is composed of three parts, namely soil, grout and bolt. Therefore, there are five failure modes of face bolt in theory, namely: (1) Failure mode I, tensile failure of the bolt; (2) Failure mode II, shear failure of the bolt-grout interface in active area; (3) Failure mode III: shear failure of the soil-grout interface in active area; (4) Failure mode IV: shear failure of the bolt-grout interface in stable area; (5) Failure mode V: shear failure of the soil-grout interface in stable area. Therefore, the supporting force Fb of the face bolt should take the minimum bearing capacity corresponding to the five failure modes:

$$F_{\mathrm{b}} = \min(F_{\mathrm{I}}, F_{\mathrm{II}}, F_{\mathrm{III}}, F_{\mathrm{IV}}, F_{\mathrm{V}}) \tag{1}$$

where F_{I} is the ultimate bearing capacity of a face bolt under the I failure mode.

According to the model test results (see Figure 7), the force mode of a pipe roof reinforced tunnel face is shown in Figure 9. Due to the load transfer effect of the pipe roof, the soil pressure on the palm surface decreases from F_{q} to $\alpha_{\mathrm{p}}F_{\mathrm{q}}$ (α_{p} is the reduction coefficient of soil pressure, $0<\alpha_{\mathrm{p}}<1$), resulting in the decrease of the sliding force F_1. Therefore, the stability of the tunnel face is improved.

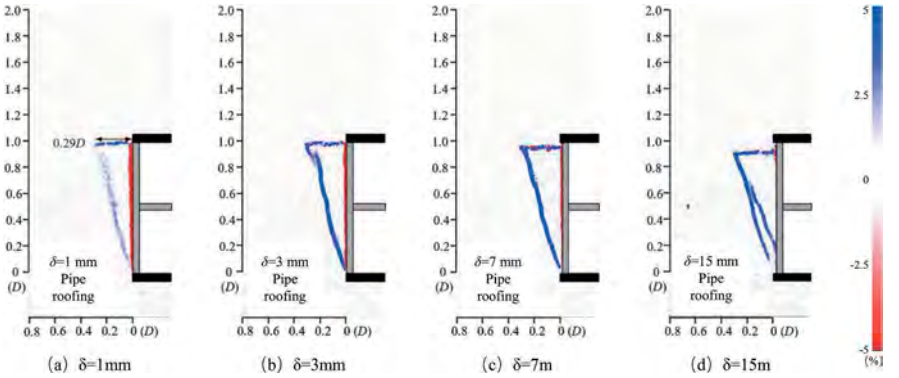

Figure 7. Incremental shear strains of soil for a pipe roof reinforced tunnel face.

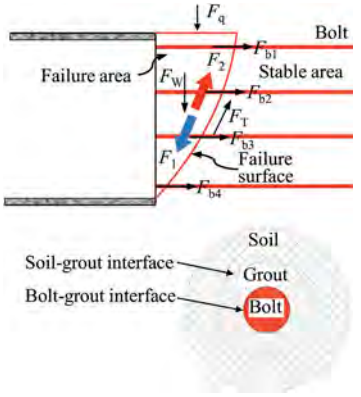

Figure 8. Force mode of a bolt reinforced tunnel.

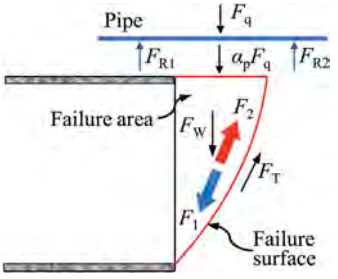

Figure 9. Force mode of a pipe roof reinforced tunnel.

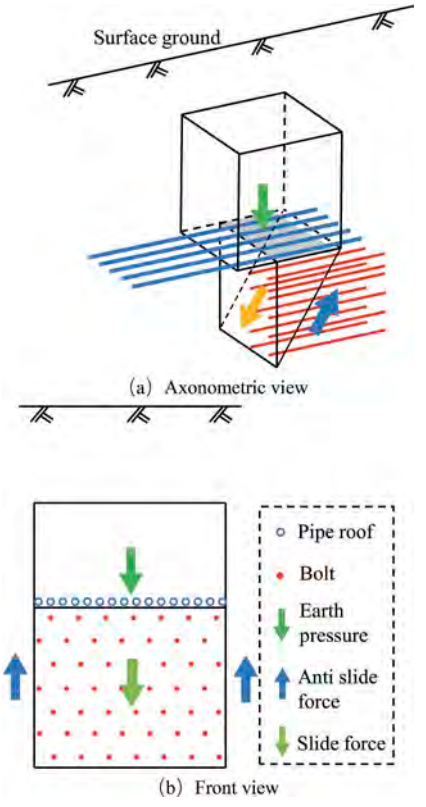

Figure 10. 3D tunnel face stability analysis model.

4 THE ESTABLISHMENT OF THEORETICAL MODEL

4.1 *Failure mechanism of a deep buried tunnel face*

For a deep buried tunnel face, the failure zone above the face is arched, and the failure surface in front of the face is linear or logarithmic spiral. The angle between the bottom of the failure surface and the horizontal direction is about $\pi/4+\varphi/2$ (φ is the friction angle of the ground). As shown in Figure 10, based on the classic prism-wedge model(Horn, 1961), a three-dimensional stability analysis model of the tunnel face is proposed, in which two kinds of advance support measures (pipe roofing and face bolting) are considered. The tunnel face is subjected to the earth pressure, sliding force and anti-sliding force (front and side).

4.2 *Stability analysis model for a tunnel face reinforced by advance support*

4.2.1 *Calculation method of stability coefficient K of tunnel face*

It is assumed that the ground is perfect rigid plastic material that meets Mohr–Coulomb strength

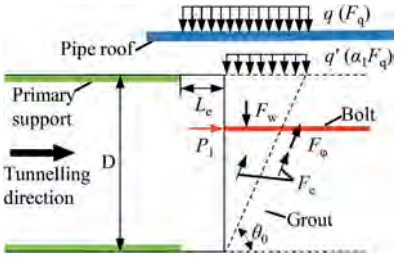

Figure 11. Force analysis of tunnel face.

criterion. As shown in Figure 11, the height and width of the tunnel face is D and B, respectively; the length of unsupported span is L_e. According to the force analysis of the tunnel face, the equation for the stability coefficient of the tunnel face is derived based on the limit equilibrium method as follows:

$$K = \frac{P_1 + \beta_1 F_c}{\beta_2 (F_w + \alpha_1 F_q)} + \beta_3 \geq [K] \tag{2}$$

$$F_c = \frac{cBD}{\sin\theta_0} + 2D^2 \cot\theta_0 \left[c + \lambda \left(\frac{2}{3} q + \frac{D\gamma}{3} \right) \tan\varphi \right] \tag{3}$$

$$F_w = \frac{D^2 B \gamma \cot\theta_0}{2} \tag{4}$$

$$F_q = qB(D\cot\theta_0 + L_e) \tag{5}$$

$$\beta_1 = \frac{1}{\sin\theta_0 \tan\varphi + \cos\theta_0} \tag{6}$$

$$\beta_2 = \frac{\sin\theta_0}{\sin\theta_0 \tan\varphi + \cos\theta_0} \tag{7}$$

$$\beta_3 = \frac{\cos\theta_0 \tan\varphi}{\sin\theta_0} \tag{8}$$

$$\theta_0 = \frac{\pi}{4} + \frac{\varphi}{2} \tag{9}$$

where K is the face stability coefficient; $[K]$ is the design stability coefficient of tunnel face, with the value of 1.15; F_c is the shear force on the failure surface; F_w is the weight of tunnel face; F_q is the vertical force exerted by the underlying ground; c is the cohesion of the ground; q is the earth pressure; γ is the bulk density of the ground; θ_0 is the failure angle of tunnel face; λ is the lateral pressure coefficient; β_1, β_2 and β_3 are the coefficients related to φ; P_1 is the support force of face bolt; α_1 is the load transfer coefficient of pipe roof.

4.2.2 *Calculation method of load transfer coefficient of pipe roof α_1*

According to the relationship between the overlapping length L_{plap} of the pipe roof and the disturbance length $Dcot\theta_0$ in front tunnel face, it can be divided into the following two conditions:

(1) $L_{plap} > Dcot\theta_0$, as shown in Figure 12 (a), the load on the tunnel face is the reaction force of the pipe roof;

(2) $L_{plap} \leq Dcot\theta_0$, as shown in Figure 12 (b), the load on the tunnel face within the overlapping length is the reaction force of the pipe roof, and that outside the overlapping length is the earth pressure.

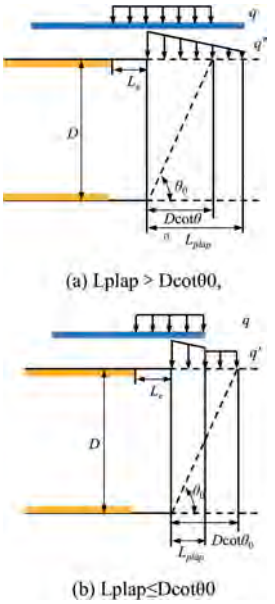

Figure 12. Force analysis of the tunnel face reinforced with pipe roof.

According to the ratio of the load on the tunnel face before and after pipe roofing, the formula of α_1 is obtained

$$\alpha_1 = \begin{cases} \dfrac{R_q}{S_p q(D\cot\theta_0 + L_e)} & L_{plap} \geq D\cot\theta_0 \\ \dfrac{R_q + S_p q\left(D\cot\theta_0 - L_{plap}\right)}{S_p q(D\cot\theta_0 + L_e)} & L_{plap} < D\cot\theta_0 \end{cases} \tag{10}$$

where R_q is the total reaction force of the pipe roof within the disturbance length, which can be calculated by elastic foundation beam theory (Selvadurai, 2013); S_p is the spacing of pipe roof.

4.2.3 *Calculation method of support force of face bolt P_1*

As shown in Figure 13, there are five failure modes of the fiberglass bolt on tunnel face(Anagnostou and Perazzelli, 2015): (1) tensile failure of the bolt; (2) shear failure of the bolt-grout interface in active area; (3) shear failure of the soil-grout interface in active area; (4) shear failure of the bolt-grout interface in stable area; (5) shear failure of the soil-grout interface in stable area.

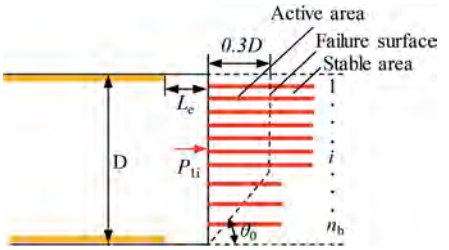

Figure 13. Force analysis of the tunnel face reinforced with bolt.

The calculation formula of the bolting force P_1 is as follows:

$$P_1 = \sum_{i=1}^{i=n_b} P_{1i} \tag{11}$$

$$P_{1i} = m_{bi} \times \min(P_{11i}\ P_{12i}\ P_{13i}\ P_{14i}\ P_{15i}) \tag{12}$$

$$P_{11i} = \frac{\pi d_b^2 f_b}{4} \tag{13}$$

$$P_{12i} = \pi d_b l_{Ii} f_t \left(2 + \frac{11.7 d_b}{l_{Ii}}\right) \tag{14}$$

$$P_{13i} = \pi d_h l_{Ii} \tau_m \tag{15}$$

$$P_{14i} = \pi d_b l_{IIi} f_t \left(2 + \frac{11.7 d_b}{l_{IIi}}\right) \tag{16}$$

$$P_{15i} = \pi d_h l_{IIi} \tau_m \tag{17}$$

where, P_{1i} is the bolting force of the i th row bolt; n_b is the number of bolt rows; P_{11i}, P_{12i}, P_{13i}, P_{14i} and P_{15i} is the bolting force of the i th row bolt corresponding to the five failure modes above; m_{bi} is the number of bolts in i th row; f_b is the tensile strength of bolt; d_b is the bolt diameter; f_t is the design value of the tensile strength of grout material; l_{Ii} is the anchorage length of the i th row bolt in the active area; l_{IIi} is the anchorage length of the i th row bolt in the stable area; d_h is the diameter of the anchor hole; τ_m is the shear strength of the grout-soil interface.

5 VERIFICATION

Based on the upper bound solution proposed by Leca and Dormieux (Leca and Dormieux, 1990), a safety factor analysis model of a tunnel face reinforced with an umbrella arch was established by Wang and Jia (Wang and Jia, 2009). To verify the accuracy of the proposed model, the calculation results are compared with those calculated by Wang and Jia (Wang and Jia, 2009). The values of k_g and k_s are assumed to be 40 MPa/m and 110 MPa/m, respectively. As shown in Figure 14, the safety factor increases with increasing cohesion, and the results of the two methods are in good agreement. The average difference between the results calculated by the proposed method and the limit analysis method is approximately 3.50%, and the maximum difference equals 8.68% at c=50 kPa.

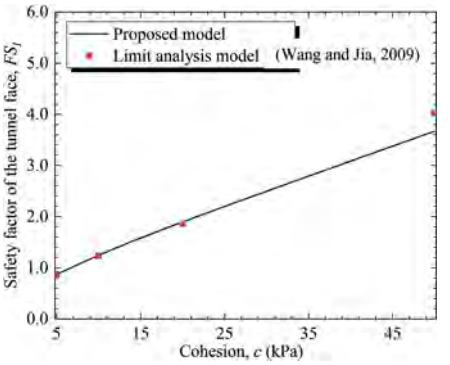

Figure 14. Comparison between the proposed model and the limit analysis method.

Pan and Dias (Pan and Dias, 2017) investigated the safety factor of a reinforced tunnel face by the numerical method and the limit analysis method. The safety factor is automatically calculated by the command for the strength reduction technique in FLAC^{3D}. To verify the accuracy of the proposed model, the calculation results are compared with those reported by Pan and Dias (Pan and Dias, 2017). As shown in Figure 15, the calculation results of the three methods have a similar trend in that the safety factor increases with the friction angle. Compared with the numerical method, the average differences in the results calculated by the proposed method and the limit analysis method equal 6.59% and 6.57%, and the maximum differences equal 10.79% and 14.45%, respectively.

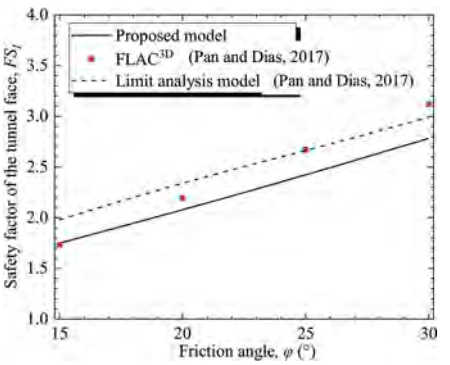

Figure 15. Comparison between the proposed model, FLAC^{3D} results and limit analysis method.

6 CONCLUSIONS

(1) The progressive failure mechanism and the failure mode of tunnel faces as well as the synergetic reinforcing mechanism of advanced supports are explored.

(2) A safety factor analysis model and a concise design flow for a reinforced tunnel face are established for the preliminary design of tunnels.
(3) The results calculated by the proposed model agree very well with those of the limit analysis methods and numerical software. For a tunnel face reinforced with an umbrella arch, the average difference between the safety factors of the proposed method and the limit analysis method is approximately 3.50%. For a tunnel face reinforced with face bolts, compared with the results from FLAC3D, the average difference of the proposed method equals 6.59%.

ACKNOWLEDGEMENT

The authors are grateful for the support from the National Natural Science Foundation of China (52208404 and 52378411).

REFERENCES

Al Hallak, R., Garnier, J., Leca, E., 2000. Experimental study of the stability of a tunnel face reinforced by bolts. Geotechnical aspects of underground construction in soft ground. Balkema, Rotterdam, 65-68.

Anagnostou, G., Perazzelli, P., 2015. Analysis method and design charts for bolt reinforcement of the tunnel face in cohesive-frictional soils. Tunnelling And Underground Space Technology 47, 162–181.

Calvello, M., Taylor, R., 1999. Centrifuge modelling of a pile-reinforced tunnel heading. Proc. of Geotechnical Aspect of Underground Construction in Soft Ground, Balkema, 313-318.

Chambon, P., Corte, J., 1994. Shallow tunnels in cohesionless soil: stability of tunnel face. Journal of Geotechnical Engineering 120, 1148–1165.

Date, K., Mair, R., Soga, K., 2008. Reinforcing effects of forepoling and facebolts in tunnelling, Proceedings of the 6th international symposium (IS-Shanghai 2008), pp. 635–641.

Di Prisco, C., Flessati, L., Frigerio, G., Castellanza, R., Caruso, M., Galli, A., Lunardi, P., 2018. Experimental investigation of the time-dependent response of unreinforced and reinforced tunnel faces in cohesive soils. Acta Geotechnica 13, 651–670.

Di Prisco, C., Flessati, L., Porta, D.J.A.g., 2020. Deep tunnel fronts in cohesive soils under undrained conditions: a displacement-based approach for the design of fibreglass reinforcements. 15, 1013–1030.

Horn, M., 1961. Horizontal earth pressure on perpendicular tunnel face, Hungarian National Conference of the Foundation Engineer Industry. Budapest:[sn], pp. 7–16.

Kamata, H., Mashimo, H., 2003. Centrifuge model test of tunnel face reinforcement by bolting. Tunnelling and Underground Space Technology 18, 205–212.

Leca, E., Dormieux, L., 1990. Upper and lower bound solutions for the face stability of shallow circular tunnels in frictional material. Geotechnique 40, 581–606.

Li, B., Hong, Y., Gao, B., Qi, T.Y., Wang, Z.Z., Zhou, J.M., 2015. Numerical parametric study on stability and deformation of tunnel face reinforced with face bolts. Tunnelling And Underground Space Technology 47, 73–80.

Lunardi, P., 2008. Design and construction of tunnels: Analysis of Controlled Deformations in Rock and Soils (ADECO-RS). Springer Science & Business Media.

Ng, C.W.W., Lee, G.T.K., 2002. A three-dimensional parametric study of the use of soil nails for stabilising tunnel faces. Computers And Geotechnics 29, 673–697.

Oreste, P.P., Dias, D., 2012. Stabilisation of the Excavation Face in Shallow Tunnels Using Fibreglass Dowels. Rock Mechanics And Rock Engineering 45, 499–517.

Pan, Q., Dias, D., 2017. Safety factor assessment of a tunnel face reinforced by horizontal dowels. Engineering Structures 142, 56–66.

Paternesi, A., Schweiger, H.F., Scarpelli, G., 2017. Numerical analyses of stability and deformation behavior of reinforced and unreinforced tunnel faces. Computers and Geotechnics 88, 256–266.

Peila, D., 1994. A theoretical study of reinforcement influence on the stability of a tunnel face. Geotechnical & Geological Engineering 12, 145–168.

Perazzelli, P., Anagnostou, G., 2013. Stress analysis of reinforced tunnel faces and comparison with the limit equilibrium method. Tunnelling and underground space technology 38, 87–98.

Perazzelli, P., Anagnostou, G., 2017. Analysis Method and Design Charts for Bolt Reinforcement of the Tunnel Face in Purely Cohesive Soils. Journal of Geotechnical and Geoenvironmental Engineering 143.

Qian, Z., Zou, J., Pan, Q., Dias, D., 2019. Safety factor calculations of a tunnel face reinforced with umbrella pipes: A comparison analysis. Engineering Structures 199, 109639.

Selvadurai, A.P., 2013. Elastic analysis of soil-foundation interaction. Elsevier.

Takano, D., Otani, J., Fukushige, S., Natagani, H., 2010. Investigation of interaction behavior between soil and face bolts using X-ray CT. ISTE London.

Thielicke, W., Stamhuis, E., 2014. PIVlab–towards user-friendly, affordable and accurate digital particle image velocimetry in MATLAB. Journal of open research software 2.

Wang, H., Jia, J., 2009. Face stability analysis of tunnel with pipe roof reinforcement based on limit analysis. Electronic Journal of Geotechnical Engineering 14, 1–15.

Yoo, C., 2002. Finite-element analysis of tunnel face reinforced by longitudinal pipes. Computers and Geotechnics 29, 73–94.

Yoo, C., Shin, H.K., 2003. Deformation behaviour of tunnel face reinforced with longitudinal pipes—laboratory and numerical investigation. Tunnelling and Underground Space Technology 18, 303–319.

Zhang, X., Wang, M., Li, J., Wang, Z., Tong, J., Liu, D., 2020. Safety factor analysis of a tunnel face with an unsupported span in cohesive-frictional soils. Computers and Geotechnics 117, 103221.

Tunnelling for a Better Life – Yan, Celestino, Thewes & Eberhardt (Eds)
© 2024 The Author(s), ISBN 978-1-032-80042-4
Open Access: www.taylorfrancis.com, CC BY-NC-ND 4.0 license

Key technologies and safety analysis of deep foundation pit construction in a sea area

Ziqiang Zhao* & Shanshan Gao
SGIDI Engineering Consulting (Group) Co., Ltd., Shanghai, China

ABSTRACT: The Shenzhen-Zhongshan Link used temporary cofferdams and artificial permanent land areas as the foundation platforms for deep foundation pit construction in a sea area, facing a series of complex engineering problems such as internal displacement of cofferdams, thick sand filling, thick sludge layers, and an ultra-close distance underpass of the Guangzhou-Shenzhen Coastal Expressway. Through key construction technologies such as foundation reinforcement treatment, casing drilling and grouting pile enclosure, earthwork layered excavation control, support servo automatic axial force compensation, and combined with information monitoring data results, the deformation patterns of the deep foundation pit support system at important construction nodes were analyzed. These verified that key construction technologies under complex sea conditions were crucial for ensuring the safety of deep foundation pit support systems and important buildings. Finally, the construction risks were successfully resolved.

Keywords: Sea area, Deep foundation pit, Deformation control, Monitoring and safety

1 INTRODUCTION

As an important cross-river channel connecting Shenzhen and Zhongshan, the Shenzhen-Zhongshan Link is about 30 kilometers from the Humen Bridge in the north and 38 kilometers from the Hong Kong-Zhuhai-Macao Bridge in the south. It integrates a tunnel, island, bridge and underwater workings, and is a national key project in the "China 13th Five-Year Plan" (Song Shenyou et al., 2020). Under complex marine environment conditions, the deep foundation pit engineering of the island tunnel is faced with a series of complex challenges. Firstly, a temporary cofferdam construction in the sea area is affected by long-term internal and external water pressure differences and ocean tidal power, which will continue to shift the cofferdam. The safety of the temporary cofferdam directly determines the safety of the deep foundation pit construction. Secondly, there are some poor formation conditions such as loose sand fill and creep of a thick silt layer, so it is very important to ensure the safety of the tunnel foundation pit, especially that running in close proximity to the bridge of the Guangzhou-Shenzhen Highway along the Pearl River. Thirdly, there is a deep silt layer along the expressway bridge. When the foundation reinforcement construction is carried out near the pier, the effective control of the extrusion deformation of the pier during the grouting process is crucial to protect the safety of the existing bridge in operation.

Three previous projects, the Wuhan East Lake Tunnel Project, which is the longest lake tunnel in China (Xu Shunping et al., 2013), the important cross river channel Ruyifang Tunnel Project in Guangzhou (Xu Jiangping, 2019), and the Boao Tunnel in Hangzhou (Gong Wei, 2019) have successfully applied the cofferdam system to solve the problem of open excavation foundation pit construction in water bodies. These provided a reference for the implementation of deep foundation pit engineering in the cofferdam construction section of the Shenzhen-Zhongshan Link. In recent years, there are more and more deep foundation pit projects adjacent to sensitive structures in urban construction. The application of an active servo system has solved the problem of excessive deformation caused by deep foundation pit enclosure structures to some extent (Zhao Ziqiang, 2017; Sun Jiuchun et al., 2019; Zhang Lingxi et al., 2023), and also provided a reference for the implementation of active servo systems in this project. Once again, the disturbance test of adjacent bridge piers during the construction of high-pressure rotary jet grouting piles (He Dawei et al., 2023) and the application practice of bridge pier correction engineering (Pan Zhenhua, 2016) provide

*Corresponding author: zhaoziqiang@sgidi.com

DOI: 10.1201/9781003495505-121

valuable experiences for predicting the potential deformation risks of reinforcement construction in advance. On the basis of existing engineering practice experience, this article analyzes and summarizes the key technologies of soft soil deep foundation pit engineering in the sea area.

2 KEY TECHNOLOGIES FOR DEEP FOUNDATION PIT CONSTRUCTION IN COFFERDAM CONSTRUCTION SECTION

2.1 *Temporary cofferdam and deep foundation pit*

In order to construct the foundation pit excavation working face in the deep-sea area, a temporary cofferdam is set up around the foundation pit, and then a land basin is formed by draining the seawater inside the cofferdam as the construction site for the deep foundation pit. The temporary cofferdam in the construction section has a perimeter of approximately 1393.4m, with a maximum width of approximately 116m on the west side and approximately 206m on the east side. The double-row steel sheet pile cofferdam type is adopted, and steel tie rods are used to connect the inner and outer rows of steel sheet piles. The width of the cofferdam is 10m, the elevation of the cofferdam body is+3.00m, and the top elevation of the outer row of steel sheet piles is+6.00m. To avoid scouring at the bottom of the slope, a rubble layer is set up on the upstream side of the cofferdam. A counter-pressure soil slope is set up on the downstream side of the cofferdam, and the slope surface is protected by concrete bags. The average elevation of the sea surface outside the temporary cofferdam is about+0.52m, and the elevation of the ground level inside the cofferdam is about -3.5m~-5.0m.

The foundation pit of the main tunnel in the cofferdam section is approximately 490m long, 46.20m~74.43m wide, and the excavation depth is approximately 13.21m~17.96m. The cofferdam section adopts two forms of foundation pit enclosure structures: 1-meter-thick underground diaphragm walls and steel pipe piles. The support forms are arranged in 3-4 layers of reinforced concrete support and steel support according to different depths. The typical profile of the temporary cofferdam and deep foundation pit in the construction section is shown in Figure 1.

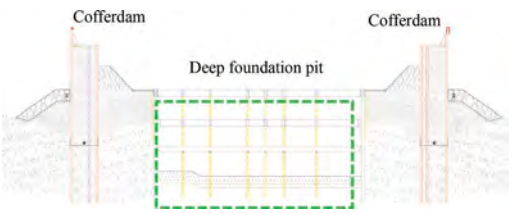

Figure 1. Typical profile of temporary cofferdam and deep foundation pit.

2.2 *Safety analysis of temporary cofferdam and deep foundation pit*

In the early stages of the project, in order to evaluate the safety of the temporary cofferdam and its embedded deep foundation pit in the cofferdam construction section, the general finite element analysis software ZSOIL was used to construct a typical profile model of the middle area of the cofferdam construction section. The excavation structure of the foundation pit and the deformation of the corresponding temporary cofferdam in the corresponding area were calculated under different excavation depth conditions. The numerical model after the completion of the foundation pit project is shown in Figure 2.

The numerical simulation analysis results in Figure 2 show that after the completion of the foundation pit project, the maximum horizontal displacement of the deep layer of the foundation pit enclosure structure is about 43mm, and the displacement of the top of the temporary cofferdam steel sheet pile towards the direction of the foundation pit is about 95mm. Both the temporary cofferdam and the foundation pit are in a safe and controllable state.

The results from the monitoring data for the points corresponding to those indicated in the numerical model in Figure 2, show a deep horizontal deformation curve for the foundation pit enclosure structure (Figure 3) and a similarly deep horizontal displacement deformation curve for the cofferdam structure (Figure 4).

The measured data curve in Figure 3 shows that after the completion of the tunnel foundation pit, the cumulative maximum horizontal displacement of the deep layer of the retaining structure is 56mm, and the maximum depth is located near the third foundation pit support. The measured data curve in Figure 4 shows that the cumulative maximum horizontal displacement of the deep layer of the temporary cofferdam is 93mm, with the maximum value located at the top of the cofferdam. The full measured data results during the process are reported in the article "Deformation Analysis of Marine Cofferdam and Embedded Deep Foundation Pit Engineering" (Liu Di et al., 2023). The numerical simulation results in Figure 2 above are seen to be consistent with the measured results in Figures 3 and 4, validating the correctness of the numerical simulation results in the early stage of the project, indicating that risk assessment through numerical simulation analysis is feasible in the early stage of the project. At present, the deep foundation pit project in the sea area has been successfully completed, and the deep foundation pit project and temporary cofferdam in the sea area have withstood the construction test, indicating that the plan of constructing temporary cofferdams for deep foundation pit construction in the sea area is safe and feasible.

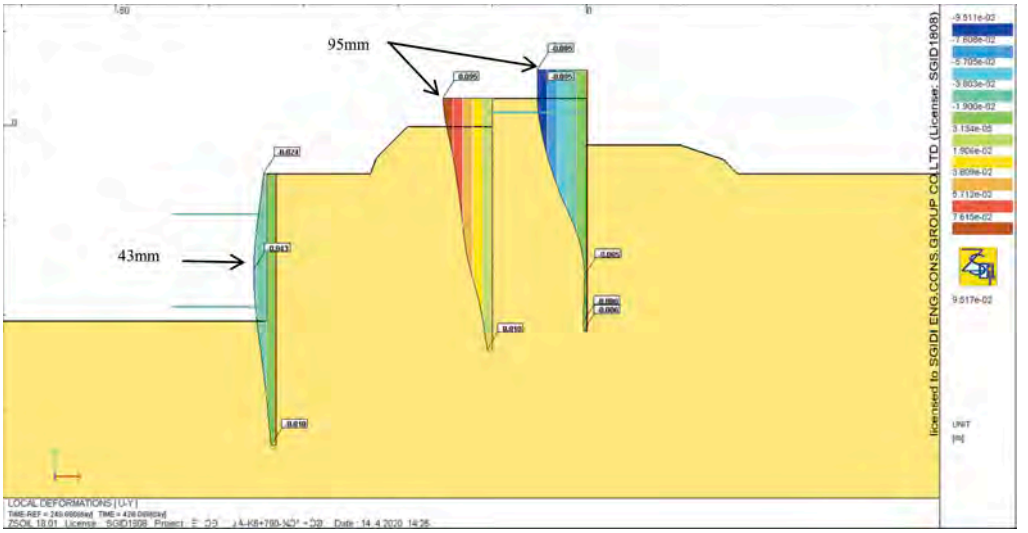

Figure 2. Numerical analysis results of temporary cofferdam and deep foundation pit.

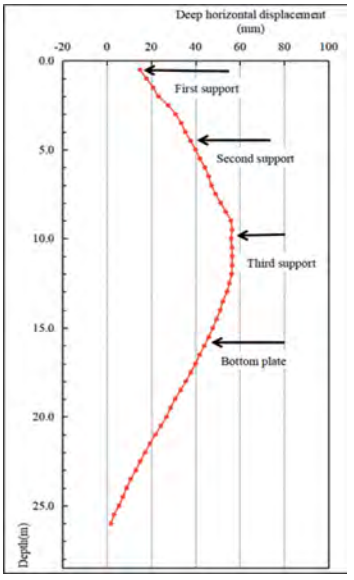

Figure 3. Measurement result of deep horizontal displacement of the deep foundation pit retaining structure.

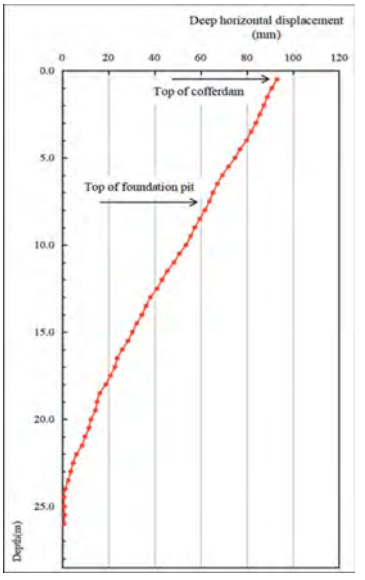

Figure 4. Measurement result of deep horizontal displacement of the temporary cofferdam.

3 DEFORMATION CONTROL TECHNOLOGY FOR FOUNDATION REINFORCEMENT ADJACENT TO THE HIGH-SPEED BRIDGE ALONG THE PEARL RIVER

3.1 *Foundation reinforcement treatment*

An artificial island area of approximately 353,800 square meters was formed in the sea area through manual sand filling. During the process of land reclamation, the deep sediment at the bottom of the sea area was consolidated using pre-load compaction combined with plastic drainage plates. The geological survey results showed that the strength of the sludge layer at the bottom of the island area made it difficult to meet the requirements for deformation control of the subsequent artificial island deep foundation pit excavation, which would have an impact on the safety of the foundation pit. Especially for the deep

foundation pit project on artificial islands that crosses the high-speed bridge along the Pearl River, deformation control is extremely strict. Taking the area where the F ramp tunnel foundation pit crosses the high-speed bridge along the Pearl River as an example, the thickness of the sludge layer in this area exceeds 14m. In order to enhance the soil strength in the passive area during the excavation process of the foundation pit, it is important to reduce the deformation of the foundation pit retaining structure towards the inside of the foundation pit, and control the displacement of the bridge piers caused by the deformation of the adjacent foundation pit retaining structure. This is done using high-pressure rotary jet grouting piles to reinforce the sludge layer in the foundation pit before excavation, and the reinforcement is carried out to the top surface of the fully weathered rock layer.

3.2 *Deformation control technology for reinforcement of foundation*

During the construction process of reinforcing the deep sludge layer of the foundation near the bridge pier area, the bridge piers are affected by grouting pressure compression, which can cause displacement towards the direction of compression. When the bridge pier continues to move too much in the same direction, it may lead to cracking and other defects of the bridge pier structure. In order to solve the problem of excessive deviation caused by foundation reinforcement construction on one side of the bridge pier, symmetrical tracking grouting is synchronously carried out on the opposite side of the bridge pier, which corrects the deviation of the bridge pier through the squeezing force generated by the opposite side foundation reinforcement. The result is that the total displacement of the bridge pier is within a controllable range. This process needs to be guided by precise pier deformation monitoring data for correction. The construction control site is shown in Figure 5, with reinforcement grouting equipment installed on the north and south sides of the bridge pier for symmetrical grouting.

Figure 5. Symmetrical reinforcement grouting construction on both sides of bridge piers.

Taking the reinforcement construction of the 50 # bridge pier foundation near the south side of the F ramp foundation pit as an example, the cumulative horizontal displacement curve of the two monitoring points of the 50 # bridge pier during the foundation reinforcement construction process is shown in Figure 6.

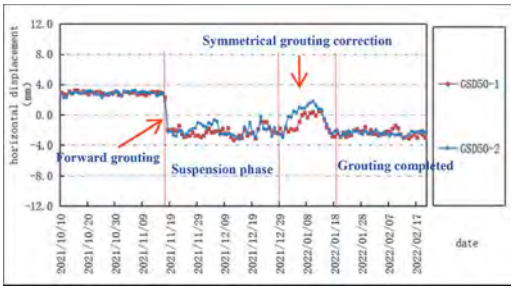

Figure 6. Duration curve of cumulative horizontal displacement of pier 50 #.

From the displacement duration curve of the bridge pier in Figure 6, it can be seen that during the initial stage of foundation reinforcement, the unilateral forward grouting construction caused significant compression deformation on the adjacent bridge pier, and the bridge pier produced a relatively significant displacement towards the south. At this time, the cumulative horizontal displacement change of the bridge pier exceeded 3mm, which is close to the warning value of the bridge pier deformation control. In order to prevent the continuous deformation of the bridge pier towards the south caused by the continued reinforcement construction, construction was suspended on site. After analyzing the reasons for the deformation of the bridge pier, construction measures were taken to add grouting equipment on the opposite side for symmetrical correction grouting. The displacement of the bridge pier was restored. Finally, the safety of the adjacent piers during the reinforcement treatment of the foundation pit was ensured.

4 DEFORMATION CONTROL TECHNOLOGY FOR DEEP FOUNDATION PIT EXCAVATION IN SENSITIVE DEFORMATION AREAS

4.1 *Support active servo system*

The Shenzhen-Zhongshan Link design includes 4 ramp tunnels and 1 main line tunnel on the east artificial island formed by sea reclamation, achieving connectivity with other highways. The tunnels on the island are all open excavation foundation pit projects. The deep foundation pits such as the main tunnel, F-ramp tunnel, and H-ramp tunnel are all adjacent to

the existing Guangzhou-Shenzhen Coastal Expressway. The foundation pit enclosure structure in the three underpass areas are about 0.6m~3.4m away from the bridge pier cap. During the excavation process of the foundation pit, the deformation control of the bridge pier is extremely strict. During the excavation process of the deep foundation pit, the steel support active servo system is used to compensate for the loss of support axial force, in order to reduce the deformation caused by the foundation pit enclosure structure, to ensure the safety of adjacent bridge piers. The active servo system consists of a control system (as shown in Figure 7) and a servo thruster (as shown in Figure 8). The servo thruster is mainly installed on top of the steel support and can automatically retract according to the oil pressure to compensate for the axial force of the steel support. The control system can automatically control the expansion and contraction of the servo thruster based on the changes in the support axis force, to compensate for the steel support axis force within a stable range. The active servo system mainly transmits the compensating axial force of the support system to the enclosure structure through the steel fence, and forms a large stress distribution in the contact area with the enclosure structure, which requires high strength of the enclosure structure. The retaining structure of the deep foundation pit near the underpass area adopts a locking steel pipe pile with a diameter of 1.40m, and a bored pile is embedded inside the steel pipe pile to enhance the stiffness of the retaining structure, in order to meet the requirements of stress intensity applied by the support active servo system.

Figure 7. Active servo control system.

Figure 8. Steel support active servo system.

4.2 *Analysis of deformation control in deep foundation pit excavation*

Taking the deep foundation pit of the east artificial island main tunnel crossing the high-speed bridge along the Pearl River as an example, this paper elaborates on the control effect of the active servo system in the deformation of the foundation pit enclosure structure. The horizontal distance between the outer side of the deep foundation pit enclosure structure in this area and the bridge pier cap is about 0.93m~1.83m, and the excavation depth is about 14.30m~15.51m. The enclosure structure adopts a lock buckle steel pipe pile with a diameter of 1.4m, and the steel pipe pile is embedded with drilled cast-in-place piles. The foundation pit is designed with four layers of support, with the first layer being concrete support and the second to fourth layers being steel support. The steel support is equipped with an active servo system. The typical profile of the deep foundation pit is shown in Figure 9.

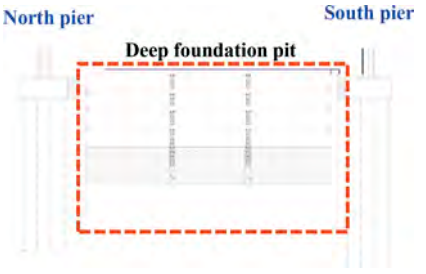

Figure 9. Profile of deep foundation pit crossing the high-speed bridge along Pearl River.

To understand the deformation of the retaining structure towards the inside of the deep foundation pit during excavation, one deep horizontal displacement monitoring hole is set up on both sides of the pit. At the same time, monitoring points for pier displacement are also set up on the pier columns on both sides of the bridge to understand the deformation of the pier during the entire excavation process of the foundation pit. Selecting the deep horizontal displacement monitoring hole data of the retaining structure on the north side of the foundation pit, the deep horizontal displacement change curves for key time nodes such as the installation of each support and the completion of the bottom plate and main structure of the tunnel, are shown in Figure 10.

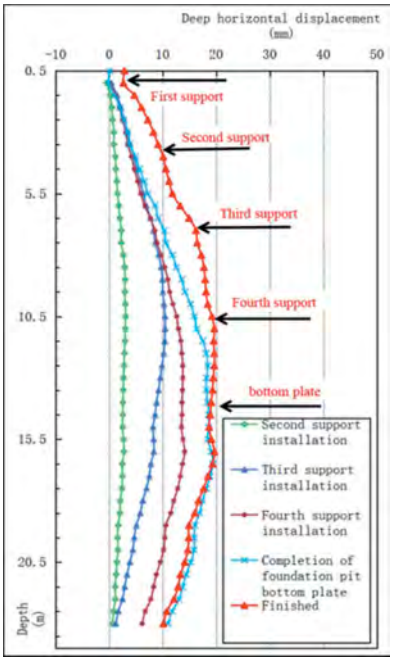

Figure 10. Key time nodes displacement curve of deep horizontal displacement of the north side envelope structure.

From the curve in Figure 10, it can be seen that during the excavation stage of the foundation pit, the deep horizontal displacement of the retaining structure continues to increase towards the direction of the foundation pit. As the excavation depth increases, the trend of displacement towards the pit becomes more obvious, and the cumulative maximum position depth also moves downward with the excavation surface. After the installation of the steel support active servo system is completed and the support axial force compensation is carried out, the deep horizontal displacement deformation trend above the support position is significantly suppressed. Through the active servo system, the deep horizontal displacement of the deep foundation pit enclosure structure is basically controlled within 2cm, which is about 40% less than the maximum deep horizontal displacement of the adjacent foundation pit enclosure structure without this technology.

The time-dependent deformation curve of the cumulative variation of the above deep horizontal displacement monitoring points at the depth of the first layer support to the fourth layer support position is shown in Figure 11.

From Figure 11, it can be seen that, firstly, during the excavation stage of the foundation pit, the deep horizontal displacement of the retaining structure shows a significant increasing trend. When the lower steel support servo system plays a role, the deep

Figure 11. Deep horizontal displacement duration curve of the retaining structure at the depth of each support position.

horizontal displacement increment of the retaining structure at the upper support position significantly decreases. The deformation increment of the retaining structure mainly occurs in the lower earthwork excavation area. Therefore, the deep foundation pit should be excavated in layers and the supporting system should be erected in time to effectively reduce the deformation of the enclosure structure. Secondly, the active servo system undergoes stress release before dismantling, during which the deep horizontal displacement of the retaining structure slightly increases. When the first reinforced concrete support is dismantled, the stress release is more concentrated, and there is a small sudden change in the upper part of the retaining structure, which then tends to stabilize.

Selecting the displacement monitoring points GSD53-2 and GSD54-2 on the south and north sides of the bridge piers respectively, and Figure 12 shows the cumulative value change duration curve of their foundation pit construction phase.

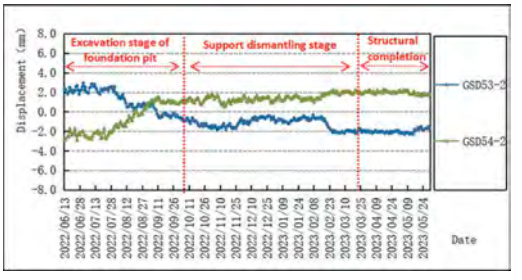

Figure 12. Pier displacement duration curve.

From Figure 12, it can be seen that during the excavation phase of the foundation pit, the bridge pier continues to move towards the foundation pit direction due to deformation of the foundation pit's retaining structure. However, after the completion of the excavation, the displacement of the bridge pier shows a significant reduction in its increasing trend. When the first layer of reinforced concrete supports are removed, the bridge pier displacement slightly increases with the sudden change of the retaining

structure, and then tends to stabilize. Finally, the cumulative horizontal deformation near the bridge pier is basically controlled at 2mm. Compared to the historical trend curves in Figures 11 and 12, it can be observed that the deformation trend of the bridge pier displacement is basically consistent with the deformation trend of the adjacent retaining structure. This indicates that the use of a steel support servo system can effectively control the deformation of adjacent bridge piers and ensure their safety.

5 CONCLUSIONS

Based on the engineering practice of solving construction problems, this article deeply analyzes the effectiveness and safety of the key technology application in response to the main issues facing the deep excavation project for the Shenzhen-Zhongshan Link, and draws the following conclusions:

(1) The scheme of constructing a deep excavation construction work platform through temporary cofferdams in the sea area is safe and feasible.
(2) When reinforcing the foundation in a thick sludge layer next to a bridge pier, a symmetric tracking grouting method was used on both sides of the bridge pier, combined with monitoring results of bridge pier displacement to dynamically correct the deviation, which effectively solved the problem of single-side extrusion deformation of the bridge pier.
(3) The active servo system can achieve dynamic compensation of steel support axial force, effectively solving the problem of excessive deformation of the deep foundation excavation retaining structure under ultra-close distance and ensuring the safety of adjacent bridge piers

REFERENCES

G Wei. 2019. Application of Sand-filled Membrane Bag and Double-layer Steel Sheet Pile in Large-scale Cofferdam Construction Under Marine Environment. Railway construction technology(08): 114–118.

H E Dawei, Y Jianhui, Z Kangrong, Z Shuai, W Yang. 2023. Indoor model tests on disturbance mechanism of adjacent high-speed railway piers caused by high-pressure jet grouting pile construction in soft soil area. Journal of Guilin University of Technology, 43(2): 245–251.

L Di, Z Ziqiang. 2023. Deformation Analysis of Cofferdam and Embedded Deep Foundation Excavation in Sea Area. Construction Technology, 52(6): 13–17.

P Zhenhua. 2016. Exploring on Rectification Technique for Pile Foundation of Simply-support Girder on Shanghai-Hangzhou Passenger Dedicated Railway. Railway Engineering(9): 38–42.

S Jiuchun, B Yanhui. 2019. Study on the Setting Method of Steel Supporting Axial Force Servo System for Subway Foundation Pit. Chinese Journal of Underground Space and Engineering, 15(S1): 195–204.

S P Xu, X S Dai, A Z Zhang, R H Jia, X B Xie. 2013. Mechanical analysis of double-layer Larsen steel sheet pile soil core composite cofferdam in Donghu Channel. Nanjing, Jiangsu, China: 6.

S Shenyou, C Weile, J Wenliang, X Fengyong, F U Baiyong. 2020. Key Technologies and Challenges of Shenzhong Link. Tunnel Construction, 40(1): 143–152.

X Jiangping, H Xueyang. 2019. Discussion on Calculation of Double-row Steel Sheet Pile Cofferdam for Immersed Tunnel. Guangdong architecture civil engineering, 26(02): 51–53.

Z Lingxi, Z Wenchao, Y Jing, L Luxian. 2023. Servo Control Analysis of Deep Foundation Excavation Deformation of Subway Station in Soft Soil. CONSTRUCTION TECHNOLOGY, 52(17): 55–60.

Z Ziqiang. 2017. Deformation Control Analysis of Steel Support Automatic Servo System in Deep Foundation Pit. Xiamen, Fujian, China: 6.

Tunnelling for a Better Life – Yan, Celestino, Thewes & Eberhardt (Eds)
© 2024 The Author(s), ISBN 978-1-032-80042-4
Open Access: www.taylorfrancis.com, CC BY-NC-ND 4.0 license

Data-driven stability analysis and uncertainty quantification of surrounding rock mass for tunnel

Hongbo Zhao* & Lin Zhang*
School of Civil Engineering and Geomatics, Shandong University of Technology, Zibo, China

ABSTRACT: Stability analysis is essential to the design, construction, and long-term safety operation of tunnel engineering. Numerical models have been widely applied to tunnel engineering. Meanwhile, uncertainty is a severe threat to tunnel stability analysis. However, numerical models are too time-consuming for large-scale projects, and conventional stability analysis cannot deal with uncertainty in practical tunnel engineering. This study developed a data-driven uncertainty quantification model to improve the efficiency of stability analysis and deal with uncertainty. A reduced-order model was utilized to construct the data-driven model and capture the mechanical and deformation properties of the surrounding rock mass in the tunnel. Probabilistic programming was adopted to evaluate and quantify the uncertainty of the surrounding rock mass during tunnel construction. A circular tunnel was used to verify and illustrate the developed method using an analytical and numerical solution. The results show that the uncertainty of surrounding rock mass could be quantified scientifically and that the developed method captures the mechanical mechanism under uncertainty. Then, the developed method was applied to practical tunnel engineering to demonstrate its performance. The results further proved that the developed method provides a scientific, helpful, and promising tool to characterize the properties and physical mechanism of the surrounding rock mass under uncertainty in the tunnel.

Keywords: Tunnel, Stability analysis, Data-driven model, Uncertainty quantification, Probabilistic programming

1 INTRODUCTION

Stability analysis of the surrounding rock mass is critical to the tunnel's design, construction, and operation. Meanwhile, uncertainty is an inherent property of the tunnel surrounding rock mass and directly impacts the stability analysis, safe construction, and the long-term safety of the tunnel. To scientifically evaluate the stability of the surrounding rock mass, various methods, such as analytical models, numerical models, machine learning, etc., have been developed in the past decades. The probabilistic method has also been developed to deal with the uncertainty. However, applying it to practical tunnel engineering is inaccessible due to repeated stability calculations during the traditional probabilistic analysis.

The analytical model has a rigid theory for stability analysis and can scientifically characterize the deformation and failure mechanism of surrounding rock mass. However, due to its many assumptions and conditions, the analytical model can only be applied to tunnels with simple geometric shapes and homogeneous rock formations. It is not easy to do practical tunnel engineering due to the complex geometric and geological conditions. Numerical models, such as the finite different method and finite element method, provide very accurate predictions of the mechanical behavior of geomaterials and the stability of geotechnical engineering structures (Jing & Hudson, 2002). However, a numerical model is too time-consuming in the practical tunnel. It hinders its application in practical tunnels, especially the analysis that requires a lot of calculation, such as back analysis and reliability analysis. The surrogated model provides an efficient model to approximate the response, such as deformation, strain, stress, etc., of tunnel surrounding rock mass (Fazio et al., 2017; Bozzano et al., 2012; Lv et al., 2017; Sun et al., 2018; Yu et al., 2007; Zhang & Yin, 2014; Zhao & Yin, 2009; Zhao & Yin, 2016). Various surrogated models have been developed to approximate the response of surrounding rock mass, such as deformation, safety factors, and support stress of

*Corresponding author: bxhbzhao@hotmail.com; hbzhao@sdut.edu.cn

DOI: 10.1201/9781003495505-122

supporting structures in tunnels. With the machine learning and artificial intelligence technology, various machine learning methods such as Artificial neural networks (ANN), support vector machine (SVM), relevant vector machine (RVM), etc., have been used to capture the complex, nonlinear relationship between the response of surrounding rock mass and their influence factors. However, these models did not characterize the physical mechanism of the tunnel deformation and failure.

Recent developments in data science provide an excellent way to reveal the mechanism behind data and deal with uncertainty (Lecun et al., 2015). Data sciences have been successfully applied in various fields (Veer & Bernards, 2008; Severson et al., 2019; Alipanahi et al., 2015; Huys et al., 2016; Markus et al., 2019). Recently, a reduced order model (ROM) was developed with some knowledge about the engineering structure under consideration. Uncertainty quantification has also been used in the engineering field. This study developed a ROM-based data-driven model and uncertainty quantification to capture the response of surrounding rock mass in a tunnel and deal with the uncertainty.

This study developed a data-driven stability analysis and uncertainty quantification model for tunnel engineering by combining numerical model, ROM, and uncertainty quantification. The remainder of this paper is organized as follows. Firstly, the ROM-based data-driven model is introduced in detail. Then, the basic idea, theory, and procedure of the developed model were presented briefly. In Section 4, the data-driven model was verified and illustrated by a circular tunnel and applied to a practical tunnel. Finally, results and conclusions are presented and discussed based on the study results.

2 DATA-DRIVEN MODEL AND UNCERTAINTY QUANTIFICATION

2.1 *ROM*

Recently, the ROM was developed to approximate the relationship between design variables and field variables in the engineering system. Generally, the ROM represented the field variables as follows (Audouze et al., 2009):

$$\tilde{u}^h(x,\theta) = \sum_{k=1}^{K} \beta_k(\theta)\varphi^k(x) + \tilde{g}(x,\theta) \quad (1)$$

$$\tilde{g}(x,\theta) = \begin{cases} g(x,\theta) & on\ \partial\Omega \\ 0 & elsewhere \end{cases} \quad (2)$$

where $\tilde{g}(x,\theta)$ is an extension of the boundary conditions in the whole domain. $\varphi^k(x)$ can be represented in the following equation.

$$\varphi^k(x) = \sum_{j=1}^{K} r_j^k w_j(x) \quad (3)$$

According to the ROM algorithm, a set of discrete solutions (snapshots) of a physical problem was obtained based on the experimental design and numerical model. Then, spatial Gram matrix Mx was generated in the following form.

$$M_{ij}^x = \left(w_i \cdot w_j\right),\ i,j = 1,2,\ldots,J \quad (4)$$

Where $w_j = u^h(\theta_j) - \tilde{g}(\theta_j), j = 1,2,\ldots,J$ $\left(w_i \cdot w_j\right)$ is the scalar product between w_i and w_j. The positive eigenvalues of $\mathbf{M}^{\mathrm{x}}$ are arranged in descending order.

$$\lambda_1 \geq \lambda_2 \geq \ldots \geq \lambda_J \geq 0 \quad (5)$$

The first K eigenfunctions $\varphi^k(x),\ k = 1,2,..K$ associated with the first K eigenvalues provide the orthogonal principal direction of snapshots. K can be determined by the following equation.

$$\frac{\sum_{i=1}^{K}\lambda_i}{\sum_{i=1}^{J}\lambda_i} > k \quad (6)$$

where k is the user-specified tolerance. In this study, k was taken to be 0.99999.

For any x_i, i = 1, 2,…I, and θ_j, j = 1, 2,…J, Equation 1 can be transferred to the following form.

$$\tilde{u}^h(x_i,\theta_j) = \sum_{k=1}^{K} \beta_k(\theta_j)\varphi^k(x_i) + \tilde{g}(x_i,\theta_j) \quad (7)$$

The unknown coefficient β can be obtained by solving the penalized minimization problem.

$$\min_{\beta_j \in R^K} \left\| u^{h,j} - \varphi\beta_j - \tilde{g}_j \right\|^2 + \mu \left\| \beta_j \right\|^2 \quad (8)$$

for which $\beta_j$can be obtained by solving the following normal equation:

$$\left(\varphi^T\varphi + \mu I_K\right)\beta_j = \varphi^T\left(u^{h,j} - \tilde{g}_j\right), j = 1,2,\ldots J \quad (9)$$

where μ is a small regularization parameter.

To unknown design variables θ and space variables x, the field variables can be obtained from the ROM model.

$$\tilde{u}^h(x,\theta) = \sum_{k=1}^{K} \beta_k(\theta)\varphi^k(x) + \tilde{g}(x,\theta) \quad (10)$$

where the coefficient $\beta_k(\theta)$ is expanded using the RBF as Equation (9):

$$\beta_k(\theta) = \sum_{j=1}^{J} \alpha_{jk}\psi\left(\frac{\left|\theta - \theta_j\right|}{\sigma}\right) \quad (11)$$

For any $\theta_{j'}$, $j' = 1,2,\ldots,J$, Equation (10) can be obtained based on Equation (9).

$$\sum_{j=1}^{J} \alpha_{jk} \psi\left(\frac{\left|\theta_{j'} - \theta_j\right|}{\sigma}\right) = \beta_{kj'} \tag{12}$$

where $\beta_{kj'}$ has been obtained using Equation (7). The above equations can be written in the compact form of Equation (11).

$$A\alpha_k = \beta_k \tag{13}$$

in which the unknown coefficient α_k can be solved using following equation.

$$\left(A^T A + \mu I_J\right)\alpha_k = A^T \beta_k,\ k = 1, 2, \ldots, K \tag{14}$$

2.2 *Uncertainty quantification*

Uncertainty quantification is a significant research field for engineering systems and was applied to computational fluid dynamics in 1986 (Guide, 1998). Monte Carlo simulation is commonly used with a precise algorithm for Uncertainty quantification (Hiriyur et al., 2011), but this approach requires significant computation times. Other Uncertainty quantification algorithms, among others, are polynomial chaos expansion, Karhunen-Loève expansion, and Bayesian methods. A new generation of Markov chain Monte Carlo (MCMC) sampling techniques, such as Hamilton Monte Carlo (Duane et al., 1987) and no-U-turn sampler, can be well adapted to high and complex posterior distributions, and many complex models can be applied without understanding fitting methods. PyMC3 is an open-source uncertainty quantification Python package (Salvatier et al., 2016). In this study, PyMC3 was adopted to deal with the uncertainty during the stability analysis of the tunnel.

3 DATA-DRIVEN STABILITY ANALYSIS AND UNCERTAINTY QUANTIFICATION FOR TUNNEL

This study developed a data-driven model to evaluate the stability of the tunnel by combining the numerical model and ROM. Then, PyMC3 was utilized to quantify the uncertainty during the stability analysis based on MCMC. The data-driven model was utilized to build the surrogated mode for stability analysis to improve the efficiency of uncertainty quantification.

3.1 *Data-driven surrogated model for tunnel stability analysis*

The physical model presents the nonlinear function mapping of the tunnel response and its influence factor. In this study, ROM-based data-driven was adopted to approximate the nonlinear. The data-driven model DD(X) can be defined in the following form.

$$DD(X) : R^N \rightarrow R^Q \tag{15}$$

$$\boldsymbol{Y} = DD(\boldsymbol{X}) \tag{16}$$

where $\boldsymbol{X} = (\boldsymbol{x}_1, \boldsymbol{x}_2, \ldots, \boldsymbol{x}_N)$, $\boldsymbol{x}_i (i = 1, 2, \ldots, N)$ denotes the design variables, which is the influence factors of tunnel response and $\boldsymbol{Y} = (y_1, y_2, \ldots, y_N)$ is a Q dimension vector of response field of tunnel.

In order to construct $DD(\boldsymbol{X})$, some snapshots need to be collected according to the ROM algorithm. This study used a numerical model and a Latin hypercube sampling method to generate snapshots.

3.2 *Uncertainty quantification*

To evaluate the uncertainty of stability analysis, PyMC3 was adopted to evaluate the response of the surrounding rock mass and their uncertainty based on the data-driven model. The predicting response u is presented in normally distributed observations, whose expected value is σu and is a nonlinear function of the uncertainty of the surrounding rock mass, which is approximated by the data-driven as follows.

$$u\tilde{N}\left(\mu_u, \sigma_u^2\right) \tag{17}$$

$$\mu_u = DD(X) \tag{18}$$

Uniform distribution $[X_l, X_u]$ was applied to the surrounding rock mass properties (X). X_l and X_u are the lower and upper bounds of X, respectively. According to the nature of tunnel engineering, other distributions, such as normal distribution, can also be selected based on the known information and knowledge.

$$XU(X_l, X_u) \tag{19}$$

PyMC3 is used to refine the above model, and the uncertainty of surrounding rock response based on a data-driven model is obtained.

3.3 *Procedure of the developed model*

This study utilized ROM, a data-driven model, to approximate the response of the tunnel surrounding rock mass and quantify the uncertainty by combining it with ROM, PyMC3, and a numerical model. PyMC3 is used to deal with the uncertainty based on MCMC. Data-driven improves efficiency with high accuracy. The procedure of the developed model is explained below (Figure 1).

Step 1: Collect the tunnel information and data such as the geological conditions, engineering scale, known parameters, numerical model and its boundary conditions, etc.

Step 2: Generate the sample points (snapshots) using LHS to compute the surrounding rock mass response at each sample point. Snapshots consist of the sample points and their response.

Step 3: Based on the snapshots, build the data-driven model to approximate the nonlinear function mapping of the response of the surrounding rock mass and its influence factors.

Step 4: Conduct the uncertainty quantification using PyMC3 based on MCMC.

Step 5: Obtain and quantify the uncertainty of the surrounding rock mass property and the corresponding response.

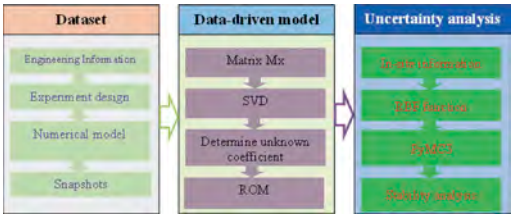

Figure 1. The flowchart of the developed method.

4 APPLICATION

4.1 *Numerical example (Zhao and Chen, 2021)*

This study utilized a circular tunnel with a radius of 1 meter to verify and illustrate the ROM-based data-driven model. The linearly elastic and perfect plastic was applied to the surrounding rock mass in the tunnel. The numerical model of the tunnel was calculated based on the Mohr-Coulomb criterion and associated flow rules in the plane strain conditions. The elastic model, Poisson's ratio, cohesion, and angle of rock mechanical parameters were 6.8 GPa, 0.2, 3.45 MPa, and 30°, respectively. The in-situ stress of the tunnel surrounding the rock mass is 30 MPa. According to the abovementioned procedure, a numerical model was used to build snapshots for ROM. Only a quarter of the tunnel was analyzed due to the symmetry (Figure 2). The numerical modeling included 900 elements and 1,822 nodes.

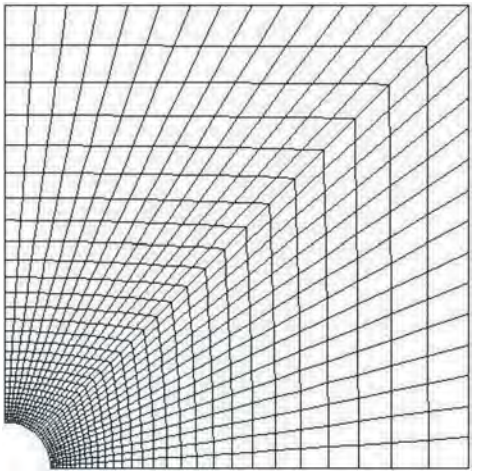

Figure 2. Numerical model for circular tunnel.

This study's design variables included the elastic modulus, Poisson's ratio, cohesion, friction angle, and geo-stress. Deformation and stress of the surrounding rock mass were the field variables. LHS was utilized to generate 50 sets of design variables. The FLAC3D model was used to calculate the corresponding field variables of each design variable. The snapshots consisted of the design variables and the field variables. The deformation and stress field could be obtained using the ROM-based data-driven model. The relative errors of horizontal deformation and stress are shown in Figure 3 and Figure 4, respectively. The maximum relative error of horizontal deformation was about

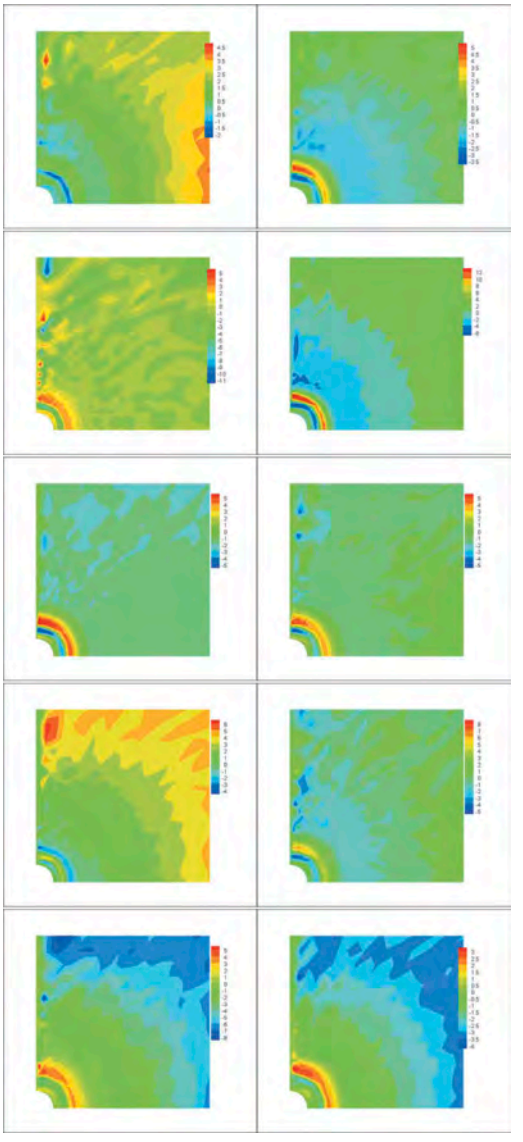

Figure 3. The relative error of horizontal deformation for snapshots.

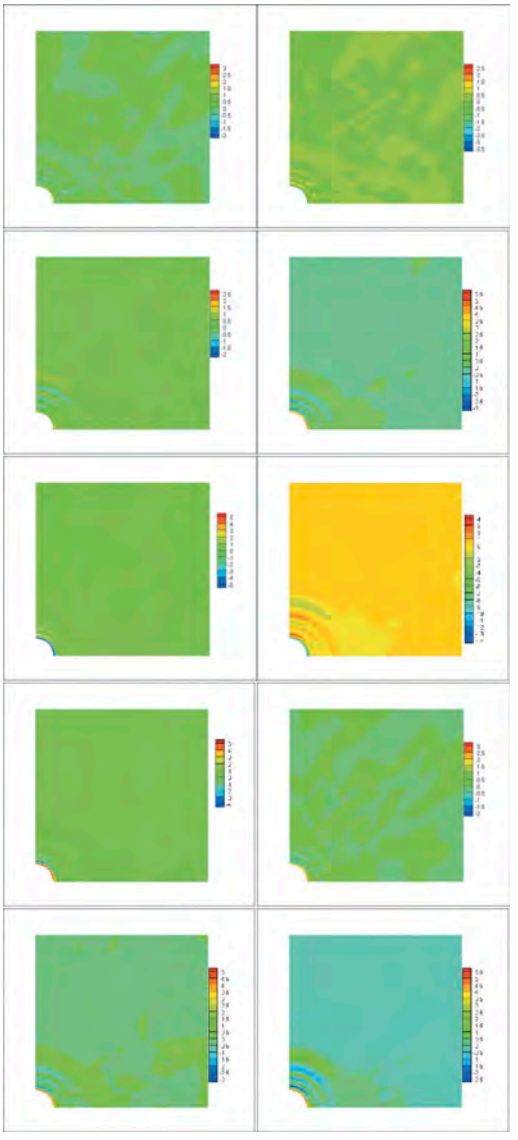

Figure 4. The relative error of horizontal stress for snapshots.

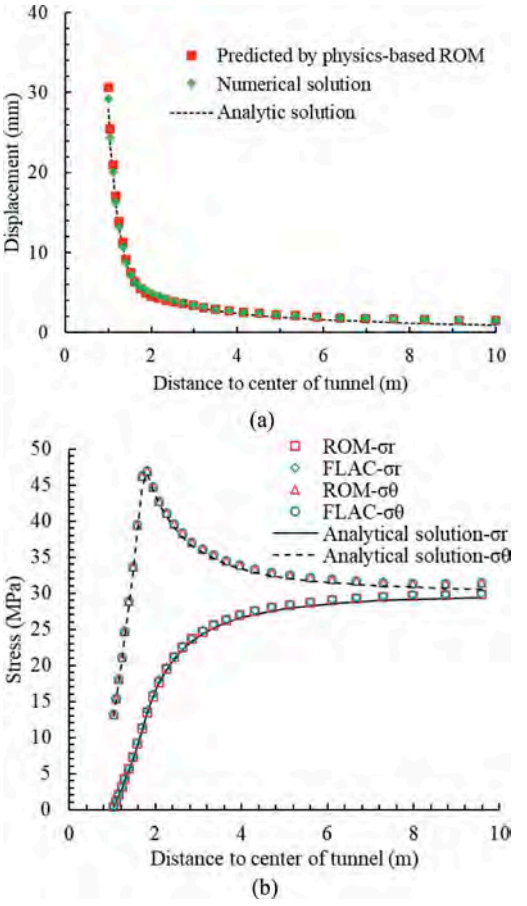

Figure 5. Comparisons of predicted deformation and stress of surrounding rock mass by data-driven model and other techniques. (a) Deformation (b) Stress.

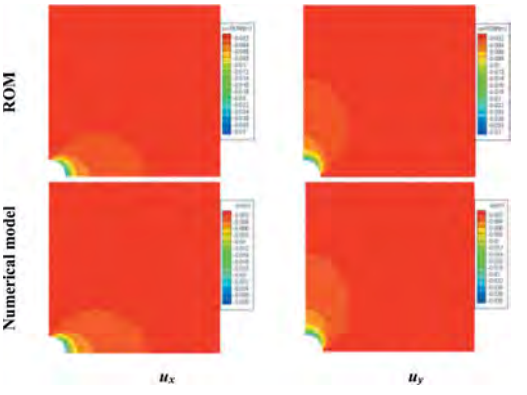

Figure 6. Comparison of the deformation field of a circular tunnel predicted using data-driven model and a numerical model.

12%, and the relative error was less than 10% for most snapshots. The maximum relative error of horizontal stress was about 7%, and the relative error was less than 5% for most snapshots. These results showed that the ROM model produced solutions that were in excellent agreement with those from numerical modeling. The results showed that the data-driven model can be selected as a surrogated model for approximating the deformation and stress field in the tunnel.

To further verify and illustrate the performance of the data-driven model, one case, which is different from the snapshots, was analyzed. The results were compared to the numerical and analytical models. Figure 5 shows the relationship between the deformation and stress in the different positions of the surrounding rock mass. It proved that the results agreed with the analytical and numerical solutions.

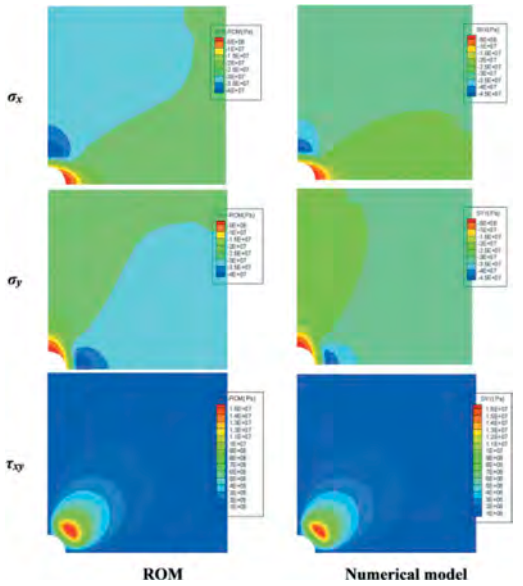

Figure 7. Comparison of the stress field of a circular tunnel predicted using the data-driven model and a numerical model.

Furthermore, the data-driven model captured the deformation and failure mechanism of the tunnel well.

The deformation and stress of the surrounding rock mass predicted by the data-driven models were compared with predictions from the numerical model in Figures 6 and 7. The deformation and stress field predicted by the data-driven were in excellent agreement with the predictions of the numerical model. It further showed that the data-driven model characterized the deformation and failure mechanism induced by tunnel excavation well.

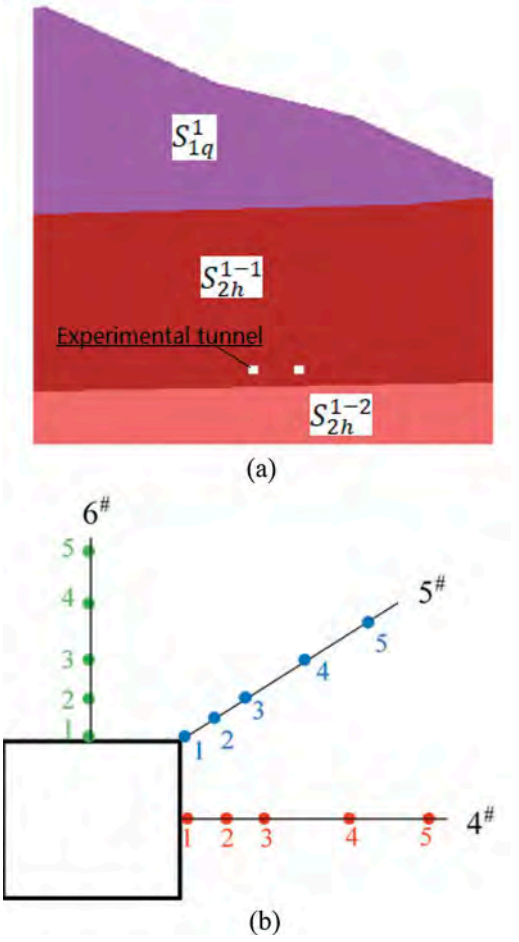

Figure 8. Goupitan tunnel (a)Geology profile, position of experimental tunnel; (b)The position of monitored borehole and point.

4.2 *Goupitan tunnel (Zhao et al., 2021)*

The Goupitan Hydropower Station, located in Wujiang, Guizhou Province, China, is a landmark electricity transmission project from west to east of the province. The preliminary design report of the project stated that the tailwater tunnel of the underground powerhouse on the right-hand bank and the construction diversion tunnel pass through a soft claystone rock mass. An experimental tunnel was excavated to investigate the rheological behavior of the claystone. The width, height, and buried depth of the tunnel were 2 m, 2 m, and 70 m, respectively. Some monitoring sites were set to observe the deformation of the surrounding rock during excavation. The tunnel is excavated through a rock layer S_{2h}^{1-2}; the S_{2h}^{1-1} stratum lies about 3 m below the tunnel, and layer S_{1q}^{1} lies 30 m above it (Figure 8a). A monitoring borehole $4^{\#}$–$6^{\#}$ was drilled at the 11.6 m position in the tunnel to the depth of 7 m, of which section $4^{\#}$ was horizontal, section $5^{\#}$ is inclined at 45°, and section $6^{\#}$ is vertical. Five monitoring points numbered 1 to 5 were located in the borehole at 0, 1, 2, 4, and 6 m, respectively ((Figure 8b)).

In this study, the efficiency was improved by using a surrogate model constructed by the data-driven model to replace the numerical model. In the present study, a uniform design was used to generate a set of 42 samples. Fast Lagrangian Analysis of Continua (FLAC) software was adopted to calculate the deformations of the surrounding rock mass. The width and maximum height of the model are both 100 m in the X- and Y-directions to minimize boundary effects. The boundary conditions were defined such that the Y-direction base and the left- and right-hand X-direction were fixed, and the top of the model was free. The average density of rock mass γ is 0.0265 MN·m^{-3}. This model assumed the upper S_{1q}^{1} rock mass to be elastic, with an elastic modulus of 28 GPa and Poisson's ratio of 0.25. Rock masses S_{2h}^{1-1} and S_{2h}^{1-2} were assumed to be Burgers material,

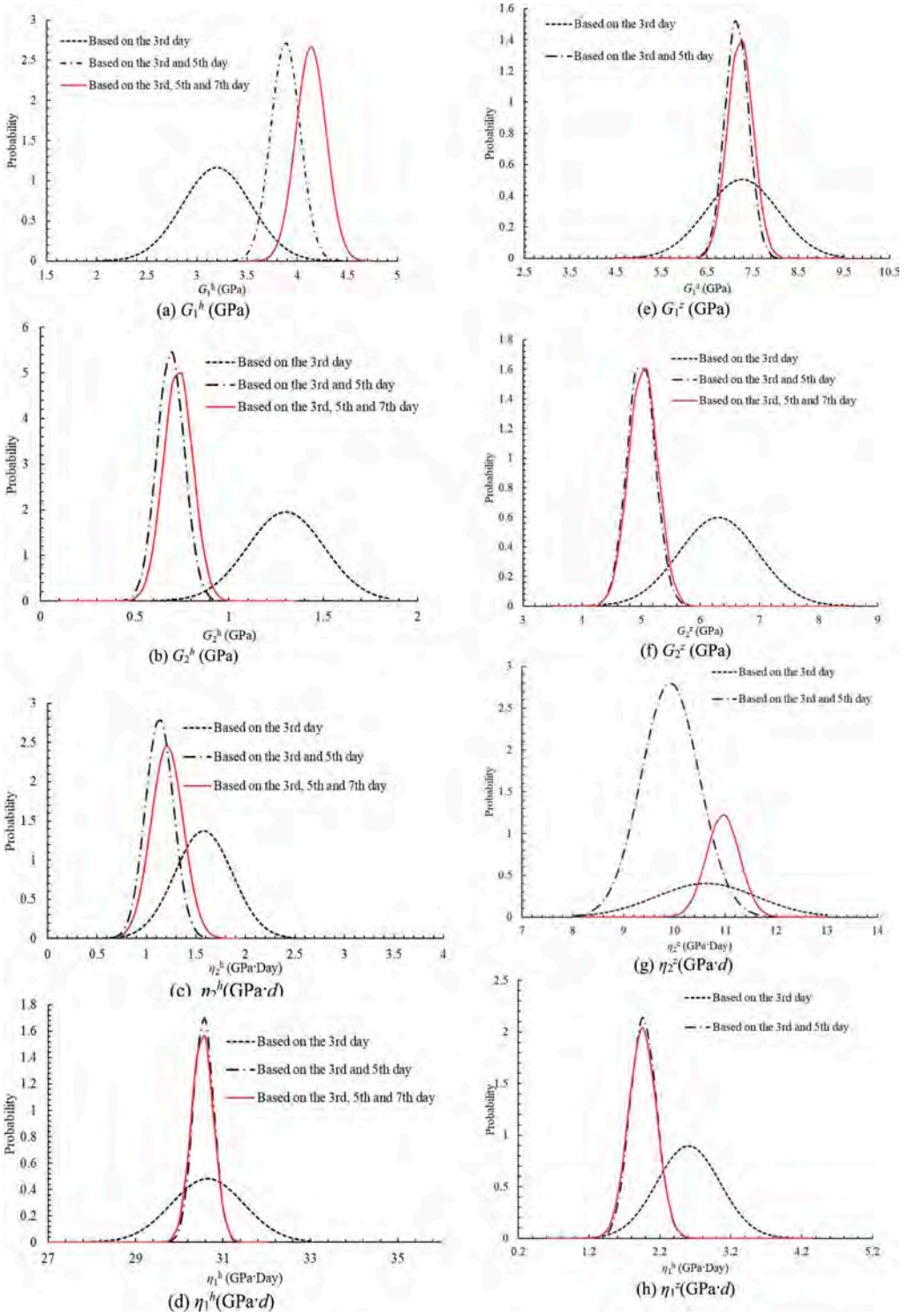

Figure 9. Obtained parameters and their uncertainty.

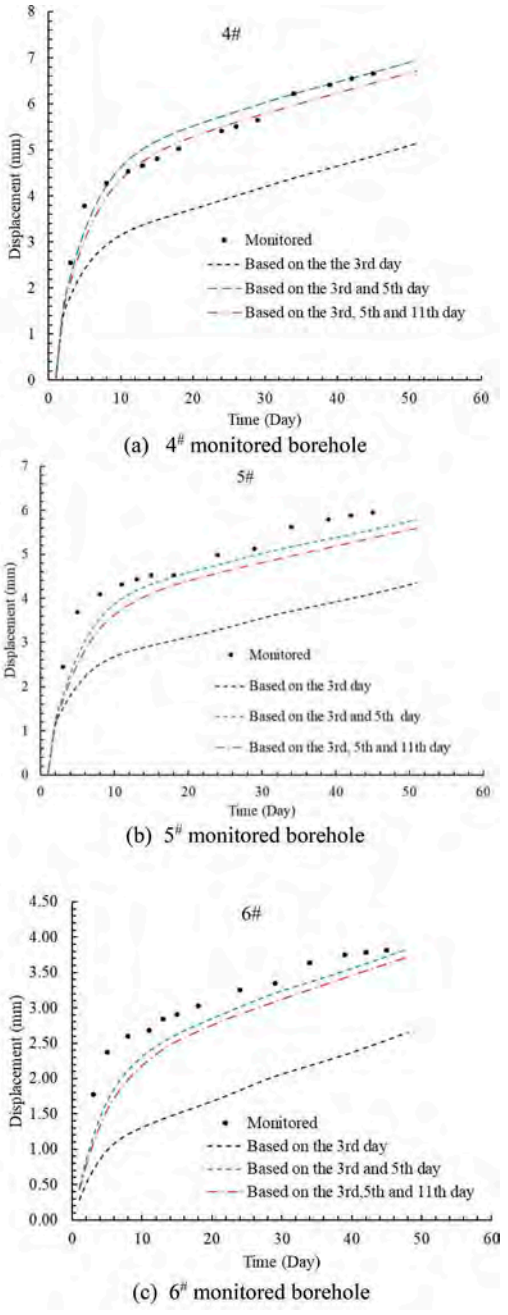

Figure 10. Comparison between monitored displacement and predicted using obtained parameters.

and their rheological properties were determined using the back analysis. Based on the displacement of the surrounding rock mass on days 3, 5, and 11 in the monitored boreholes $4^{\#}$ and $6^{\#}$, the rheological parameters of S_{2h}^{1-1} and S_{2h}^{1-2} and their uncertainties were quantified using MCMC (Figure 9). The deformation of the surrounding rock mass was investigated based on the rheological parameters of the Burgers model. The displacements of the monitored borehole were then predicted by a numerical model that used these rheological parameters. They are compared in Figure 10, in which it is evident that the predicted displacement approached the monitored displacement more closely with increasing time. It confirms that more monitored information helped determine the mechanical behavior of the rock mass. The predicted displacements for days 3 and 5 and days 3, 5, and 11 are in excellent agreement with the monitored values, showing that the obtained rheological parameters closely reflected the mechanical behavior of the rock mass surrounding the tunnel.

5 CONCLUSIONS

This study developed a data-driven model to evaluate and deal with the stability of the tunnel and its uncertainty. The results were in close agreement with the monitored data from the experimental tunnel, showing that the uncertainties inherent in the tunnel are reasonably evaluated using this approach, confirming that the data-driven model provides an efficient and effective scientific approach to stability and uncertainty analysis in the tunnel. The key findings of this work include:

(1) The data-driven model characterized well the complex and nonlinear function mapping relation between the response of tunnel surrounding rock mass and their influence factor. The data-driven model provides an excellent way to capture the deformation and failure law of the surrounding rock mass in the tunnel.
(2) The uncertainty quantification is a scientific and reasonable method to describe and analyze the uncertainty during tunnel excavation. The PyMC3 software package is a reliable tool for uncertainty quantification and is also helpful for other uncertainty analyses in rock mechanics and engineering.

REFERENCES

Alipanahi, B., Delong, A., Weirauch, M. T., Frey, B. J., 2015. Predicting the sequence specificities of DNA- and RNA-binding proteins by deep learning. Nature Biotechnology, 33, 831–838.

Audouze, C., Vuyst, F. D., Nair, P. B., 2009. Reduced-order modeling of parameterized PDEs using time-space-parameter principal component analysis. International Journal for Numerical Methods in Engineering, 80, 1025–1057.

Bozzano, F., Martino, S., Montagna, A., Prestininzi, A., 2012. Back analysis of a rock landslide to infer rheological parameters. Engineering Geology. 131-132, 45–56.

Duane, S., Kennedy, A.D., Pendleton, B.J., Roweth, D., 1987. Hybrid Monte Carlo. Physics Letters B. 195(2), 216–222.

Fazio, N.L., Perrotti, M., Lollino, P., Parise, M., Vattano, M., Madonia, G., Di Maggio, C., 2017. A three-dimensional back-analysis of the collapse of an

underground cavity in soft rocks. Engineering Geology. 228, 301–311.

Guide., 1998. Guide for the Verification and Validation of Computational Fluid Dynamics Simulations, AIAA G-077-1998(2002).

Hiriyur, B., Waisman, H., Deodatis, G., 2011. Uncertainty quantification in homogenization of heterogeneous microstructures modeled by XFEM. Int J Numer Meth Eng. 88(3), 257–278.

Huys, Q. J. M., Maia, T. V., Frank, M. J., 2016. Computational psychiatry as a bridge from neuroscience to clinical applications. Nature neuroscience,19(3), 404–413.

Jing, L., Hudson, J.A., 2002. Numerical methods in rock mechanics. International Journal of Rock Mechanics and Mining Sciences, 39(4), 409–427.

LeCun, Y., Bengio, Y., Hinton, G., 2015. Deep learning. Nature, 521, 436–444.

Lv, Q., Liu, Y., Yang Q., 2017. Stability analysis of earthquake-induced rock slope based on back analysis of shear strength parameters of rock mass. Engineering Geology. 228, 39–49.

Markus, R., Gustau, C., Biorn, S., et al. 2019. Deep learning and process understanding for data-driven earth system science. Nature, 566, 195–203.

Salvatier, J., Wiecki, T.V., Fonnesbeck, C., 2016. Probabilistic programming in Python using PyMC3. Peer Journal of computer sciences. 2, e55.

Severson, K. A., Attia, P. M., Jin, N., et al., 2019. Data-driven prediction of battery cycle life before capacity degradation. Nature energy, 4, 383–391.

Sun, Y., Jiang, Q., Yin, T., Zhou, C., 2018. A back-analysis method using an intelligent multi-objective optimization for predicting slope deformation induced by excavation. Engineering Geology. 239, 214–228.

Veer, L.J., Bernards, R., 2008. Enabling personalized cancer medicine through analysis of gene-expression patterns. Nature, 452, 564–570.

Yu, Y.Z., Zhang, B.Y., Yuan, H.N., 2007. An intelligent displacement back–analysis method for earth–rockfill dams. Computers and Geotechnics. 34, 423–434.

Zhao, H., Chen, B., Li, S., Li Z., Zhu, C., 2021. Updating models and the uncertainty of mechanical parameters for rock tunnels using Bayesian inference. Geoscience Frontiers, 12(5), 101198.

Zhao, H., Chen, B., 2021. Physics-based reduced order model for computational geomechanics. Geomechanics and Engineering, 27(4), 361–374.

Zhao, H., Li, S., Zang, X., Liu, X., Zhang, L., Ren, J., 2023. Uncertainty quantification of inverse analysis for geomaterials using probabilistic programming. Journal of Rock Mechanics and Geotechnical engineering. 2023, https://doi.org/10.1016/j.jrmge.2023.07.014.

Zhang, S., Yin, S., 2014. Determination of in situ stresses and elastic parameters from hydraulic fracturing tests by geomechanics modelling and soft computing. Journal of Petroleum Science and Engineering. 124. 484–492.

Zhao, H.B., Yin, S.D., 2009. Geomechanical parameters identification by particle swarm optimization and support vector machine. Applied Mathematics Modelling. 33, 3997–4012.

Zhao, H., Yin, S., 2016. Inverse analysis of geomechanical parameters by artificial bee colony algorithm and multi-output support vector machine. Inverse problems in science and engineering. 24, 1266–1281.

Tunnelling for a Better Life – Yan, Celestino, Thewes & Eberhardt (Eds)
© 2024 The Author(s), ISBN 978-1-032-80042-4
Open Access: www.taylorfrancis.com, CC BY-NC-ND 4.0 license

Study on settlement deformation of existing structures under ultra-large diameter shield tunnel*

Meitao Zou
Civil Engineering College of Tongji University, Shanghai, China

Cai LinZhen
Yunnan Yunlu Engineering Testing Co., Ltd

Xiongyao Xie
Civil Engineering College of Tongji University, Shanghai, China

ABSTRACT: In the tunnel subproject of the Caobao Road Expressway Project, the main body of the tunnel is planned to be constructed through using a 15m diameter slurry balance shield. The project shall make a way in between regions including Puhuitang, Haishangxin Village, and the Outer Ring Expressway, the complex surrounding environment is deemed to place obstacles to the underground passage of the shield. With references from actual practices of the Cao Bao Road Express New Construction Project underpassing the Hai Shang Xin Village and the Outer Ring Road Expressway, the presented work established a 3D elastic finite element analysis model using PLAXIS, simulations which returned a development pattern of housing and viaduct subsidence caused by shield construction during the shield crossing stage. In addition, different grouting pressures were simulated to study the effect of grouting on the ground building. The work shall provide insights into establishing feedback systems for deformation and reducing ecological impact in similar ultra-shield tunnel projects crossing ancient building complexes and railway throat areas.

Keywords: shield tunnel, numerical simulation, subsidence control, grout, PLAXIS

1 INTRODUCTION

Currently, underground space development technology has matured, with urban transportation mainly utilizing two forms: underground rail transportation and underground expressway transportation. In comparison to ground transportation and elevated roads, underground expressways alleviate traffic congestion and occupy less urban space, reducing the impact on the ecological environment.

Due to the urgency of developing underground spaces and constructing underground transport, scholars both at home and abroad have conducted extensive research on shield penetration through existing structures. They have reached comprehensive conclusions on the impact of shield excavation problems. The research methods used by the scholars mainly involve three approaches: model testing, numerical simulations, and on-site monitoring.

The similarity theory is primarily applied in establishing a shrinkage model for shield excavation through model testing. In a geotechnical centrifuge simulation of the shield construction process, Yang et al. (2021) obtained data on the surface railway settlement resulting from shield excavation. Nabizadeh and Mojtahedi (2021) also conducted model tests to explore the interaction between earthquake-induced fault deformation and soil deformation caused by shield tunnel excavation. Finite element numerical simulation is a prevalent approach for analyzing the deformation of the surrounding environment resulting from tunnel construction. Luo et al. (2020) developed a three-dimensional fluid-soil fully coupled mathematical model using FORTRAN through excavation of a finite element method to anticipate the ground settlement and pore water pressure changes induced by construction. Some scholars have integrated numerical simulation with other techniques to develop a thorough evaluation of shield excavation from various viewpoints. The frequently used ones include combining actual monitoring data with numerical simulation results.For instance, Hossain et al. (2016) conducted an objective analysis using elastic-plastic finite element numerical simulation, wherein they modified the pre-existing two-dimensional model to simulate the tunnel excavation process. They researched the impact of the tunnel excavation on existing buildings, existing tunnels, and the interaction of twin-tube tunnels. On the

*Corresponding author: 2232529@tongji.edu.cn

DOI: 10.1201/9781003495505-123

other hand, Sheng et al. (2019) examined the convergent displacement and damage characteristics of circular tunnels that were deeply buried through model experiments. They combined numerical simulation with a continuous numerical simulation to study the damage law of the tunnel perimeter rock. On-site monitoring employs a diverse array of tools, including 3D laser scanning (Ma & Zhao, 2019), Insar (Zhang et al., 2022), and other technologies, to track the deformation and settlement of buildings during construction and in existence. From the monitoring data collected, the precise and actual response of the tunnel excavation on the building can be determined.

According to scholarly research, numerical simulation has rapidly advanced in recent years, with its primary benefit being its systematic and three-dimensional dynamic analysis, making it well-suited for analyzing issues related to shield tunneling under complex geological conditions.

Based on the new construction of the underground expressway on Caobao Road in Shanghai, this thesis uses PLAXIS 3D geotechnical engineering finite element analysis software to establish a numerical simulation model. This model analyzes the settlement and deformation of ground structures throughout the entire process of the tunnel passing through Haishangxin village and S20 viaduct. The information gathered is based on theoretical analysis and numerical simulation, ensuring a comprehensive and objective evaluation of the project. Analyze the settlement variations in the building under various grouting pressures. Enhance construction techniques to diminish ground settlement, guarantee the safety and dependability of the underground building's shield tunnel, and propose solutions and references for future construction of similar large-scale shield tunnels.

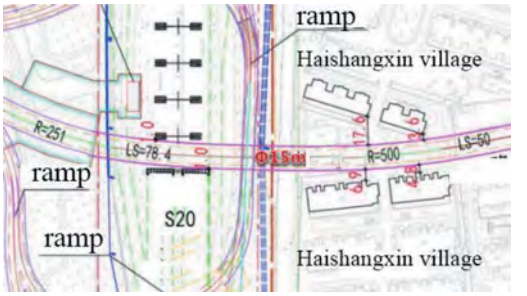

Figure 1. Modelled area: shield tunnel through Maritime Village and Outer Ring Road S20.

2 PROJECT OVERVIEW

2.1 *Background*

The new mainline expressway project on Caobao Road spans 7.18 kilometers, including a critical underground tunnel section stretching approximately 5.1 kilometers. Construction employs the mud-water balance shield machine. This study examines the impact on the surface structure during tunnel excavation either under or through the surface. The selected simulation area is illustrated in Figure 1. In this section, the Caobao Road Tunnel is only 3.6 meters away from Maritime New Village, while S20 elevated is only 1.0 meters away. Excavation of the tunnel is expected to have a significant impact on the surface structures.

2.2 *Tunnel structure*

The Caobao Road Tunnel's main line is composed of a single-bore shield that has a cross-section of "3 layers, two directions, 6 lanes". This is an exclusive thoroughfare for minibuses as illustrated in Figure 2. The shield is fashioned with a single-layer lining that has an outer diameter of 15m, an inner diameter of 13.7m, and a tube sheet thickness of 0.65m. And it adopts a ring width of 2m.

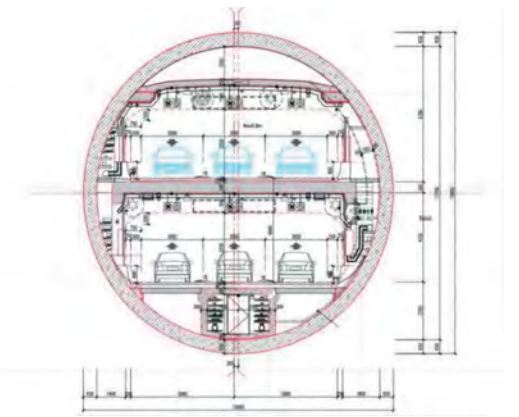

Figure 2. Cross-sectional structure of Caobao Road Tunnel.

2.3 *Geological condition*

Shanghai is situated in the lower course of the Yangtze River and is a prototypical deltaic sedimentary plain resulting from river influence. The soil layer within a depth of 40 meters comprises predominantly soft clay and sandy soil with a chalky texture. Shanghai is situated in the lower course of the Yangtze River and is a prototypical deltaic sedimentary plain resulting from river influence. The geological strata differ significantly across various districts, with a high groundwater table. The proposed area generally has a ground elevation of 4.0-5.5m. The underground diving level is buried at a depth of 1.4-3.3m, while the pressurized water is buried at a depth of 3.0-11.0m. The shallow area contains methane gas, quicksand phenomena, thick fill, bright and dark hills, and other undesirable geological conditions.

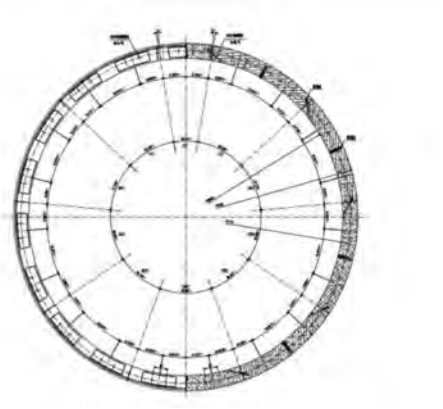

Figure 3. Cross-sectional structure of Caobao Road Tunnel.

3 NUMERICAL SIMULATION

The chosen finite element software for numerical simulation in this paper is PLAXIS 3D. PLAXIS 3D is particularly suitable for simulating the shield tunnel excavation process and is also effective in simulating shield tunnel construction steps. The software has numerous advantages in geometric modelling, structural modelling, and construction simulation which makes it widely used in the numerical simulation of shield tunnel boring construction.

3.1 *Numerical calculation model construction*

In order to streamline the simulation process and speed up computation time, the following assumptions have been incorporated into the numerical simulation of the shield tunnel as it penetrates existing ground structures:

(1) Assuming that the soil is a continuous, uniform, isotropic ideal elastic-plastic body, ignoring the inhomogeneity of the soil layer, and assuming that the soil layer is uniformly distributed as a horizontal layer, according to the research of Yang Min(1992), the modulus of elasticity of the Shanghai area should be taken to be 2.5-3.5 times of the compression modulus, and in the numerical simulation should be taken as a higher one, so it adopts 4 times for the simulation;
(2) Neglect the soil structure stress field, only consider the self-gravity stress field;
(3) The ground building is simplified, and the building is simplified as a beam-column structure, and the viaduct is simplified as a column-slab structure;
(4) Considering that the modulus of elasticity of reinforced concrete is much larger than that of soil, a linear elasticity model is used to simulate the shield tube sheet and beam-column plate, which is regarded as an elastic body;
(5) Considering the effect of shield tube sheet joints, the overall stiffness of the tube sheet is discounted according to the modified inertia method. In the cross section, the discount factor is usually 0.6~0.8 according to the experience, and this numerical simulation adopts 0.8 as the discount factor.
(6) The whole process of tunnel construction is simulated by using construction sequencing instead of the original continuous cycle construction process, and the construction process is simulated by changing the material type of the unit.

3.2 *Ontological modelling*

Shield excavation involves the interaction between soil and structure, and accurately simulating this relationship is crucial for successful modeling. The key lies in accurately simulating the interaction between the media.

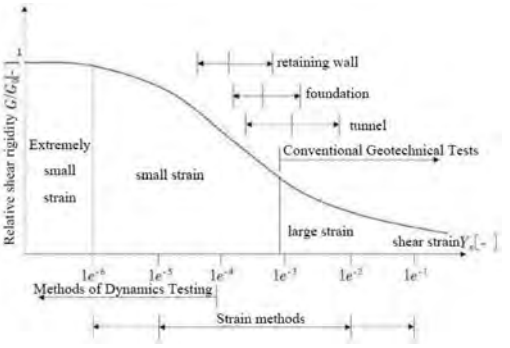

Figure 4. Geotechnical tests and geostructural stiffness versus strain plots.

From the relationship between strain and stiffness of typical soil in geotechnical tests and structures (Figure 4). This study, conducted with the use of standardized testing methods, aimed to determine the correlation between soil strain and stiffness under various loading conditions. The results showed a strong positive relationship between strain and stiffness, indicating that the stiffness of the soil increases as strain increases. These findings have significant implications for the design and construction of geotechnical structures, as well as for improving our understanding of soil mechanics. It appears that conventional geotechnical tests typically simulate model results under the influence of substantial strains. However, tunnels often exist between large and small strains. When considering the size of the actual shield structure and soil structure defects, it seems that the soil experiences significant strain. Moreover, MC model calculations generate more conservative and secure results in comparison to HSS/HS models, and they also feature a quicker calculation process. Therefore, the decision was taken to employ the MC model for simulation. The decision to employ the MC model for simulation was made due to its faster processing time.

The shield pipe sheet and ground building materials were simulated via a linear elasticity model founded on a generalized form, which employs Hooke's law. This model is based on Hooke's law, which states that stresses and strains change linearly when materials are stressed. The finite element simulation is founded on the subsequent fundamental equations:

$$\sigma = D\varepsilon$$

σ – stress component vector;
ε – vector of strain components;
D – the elasticity matrix.

3.3 *Material and construction parameters*

3.3.1 *Material parameters*

To achieve accurate simulation of actual engineering excavation, determination of soil-related parameters is crucial. Table 1 displays the relevant data for the selected soil parameters, as reported by the engineering geological investigation. The groundwater table is located 2.5m below the surface.

To more accurately simulate the on-site situation, the model size must be taken into account while also considering the scope of excavation and minimizing the impact of model boundaries. Additionally, careful control of calculation amounts is necessary. The numerical simulation model dimensions were established as follows: 100 meters for the soil and structure in the horizontal direction, 300 meters in the longitudinal direction (tunnel excavation direction), and 70 meters in the vertical direction for soil depth. Concrete strength for ground-level buildings was determined taking into account the actual construction age of the structure and used to calculate related parameters. Refer to Table 2 for building-related material parameters.

In addition, according to the design report, the parameters of the new construction of underground expressway on Caobao Road are taken as shown in Table 3.

According to the relevant formula of Peck's sinkhole in Figure 5 (Peck, 1969):

It is feasible to estimate the extent of the impact of tunnel excavation on the S20 outer ring viaduct.

$$i = \frac{Z}{\sqrt{2\pi}\tan\left(45 - \frac{\beta}{2}\right)^{\circ}}$$

Where:

i –Width coefficient of sinkhole, in m
Z – depth of the tunnel, in m
β – angle of internal friction of the ground around the tunnel

After calculating an effect range of 81.30 meters, a bridge length of 100 meters was chosen for analysis to ensure safety and reasonability.

The simulation focused on a residential building using a beam-column frame structure. A column-plate unit simulation was used to model the S20 elevated. Due to the bridge deck plate's stiffness being larger than the soil body, the stiffness of the bridge deck plate was set to a high value. The computational model displayed in Figure 6 presents the final outcome, with

Table 1. Table of soil structure and parameters.

Soil Layer No.	Elevation (m)	Volumetric weight (kN/m^3)	Density (kN/m^3)	Moisture content (1)	Cohesive forces (kPa)	The angle of internal friction (°)	modulus of compressibility (MPa)
Artificial landfill	2.3	20.00	20.17	—	22.00	18.20	0.75
Brownish-yellow silty clay	1.01	18.80	19.14	0.304	19.70	16.10	4.83
Grey silty clay	-2.14	18.70	19.06	0.299	2.60	29.40	9.22
Mucky silty clay	-4.83	17.40	17.72	0.427	11.70	15.60	2.98
Grey Mucky clay	-11.65	17.10	17.49	0.449	11.80	12.90	2.57
Grey sandy clay	-12.26	18.10	18.58	0.329	4.60	31.60	9.24
Grey clay	-21.38	17.70	18.19	0.370	14.30	15.20	11.07
Grey sandy silt	-30.38	17.80	18.43	0.338	15.90	17.20	4.08
Grey green silty clay	-33.22	19.60	20.12	0.227	47.50	16.60	7.53
Grey silty clay	-37.95	19.50	20.02	0.223	4.20	31.30	11.11
Grey silty clay mixed with silt	-38.48	19.60	20.02	0.237	48.30	17.00	7.98
Fight yellow - gray sandy sikt	-39.91	19.40	19.81	0.245	3.60	31.00	12.19
Fight yellow - gray silt	-58.08	19.60	—	—	2.80	33.20	15.22
Undrilled	—	19.50	—	—	2.90	34.60	16.43

Table 2. Table of soil structure and parameters.

Name	Unit type	Thickness (m)	Volumetric weight (kN/m^3)	Elastic modulus (MPa)	Poisson's ratio
Tunnel lining	physical unit	0.65	24.7	2.00×10^4	0.2
Residential Foundation	plate unit	0.40	24.35	2.20×10^4	0.2
S20viaduct slab	plate unit	0.50	24.7	2.20×10^4	0.2
S20viaduct bearing	plate unit	1.00	24.35	2.20×10^4	0.2
Viaduct columns	beam unit	0.65	24.7	2.06×10^4	
Building girders	beam unit	0.24	24.7	2.06×10^4	

Table 3. Table of construction parameters table.

Name	Detail	parameter
Tunnel	external diameter	15m
	internal diameter	13.7m
	Width of each ring of lining	2m
Haishangxin village presidential	Foundation size	10m×50m 10m×30m
	Floor height	3m
	Spacing of frame columns	4m
S20 Viaduct	height	15m
	widths	16m
	spacing of columns	5m
	distance between bridges	1m

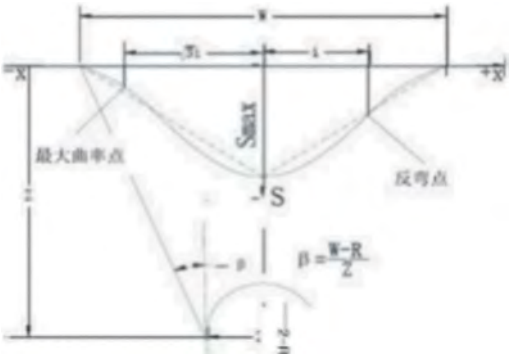

Figure 5. Schematic diagram of the calculation relationship of peck sinkhole.

boundary conditions set such that the surface is free, the bottom is fixed entirely, and the side is fixed normally.

3.4 *Tunnel construction simulation*

After constructing the soil and surface structure models and setting the tunnel model parameters, it is necessary to generate a finite element mesh to mesh the soil environment and surrounding

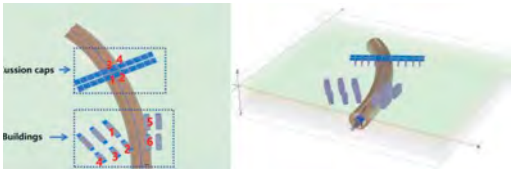

Figure 6. Calculation model of shield penetrating residential buildings and elevated structures. (Blue round tubes are tunnels, brown colour is negative interface)

structures. A pre-stage involves generating initial ground stress in the synchronous grouting simulation to construct the existing ground structure. The shield is first advanced 6 meters to indicate its proximity to the project site, after which the design for tunnel construction is initiated.

Initially, the excavation process involves freezing the soil layer within the shield machine's tunneling range, which is 15 meters in diameter, to indicate completion of the layer excavation. Then, activate the negative interface, plate activation (simulating the shield body location), and activate the shield loss cone shrinkage, with axial increment and 0% shrinkage at the shield's head. Finally, activate the working face pressure to proceed.

From the second stage of construction to the sixth, the loss of vertebrae contraction was altered in sequential increments of 0.1%, 0.2%, and so on, reaching 0.5% at the sixth stage (i.e., the final stage), and the loss pattern of the formation was changed to unity. This was done to account for the gradual contraction resulting from the progressive decrease in diameter during conical shield excavation and to stabilize the pressure at the excavation site.

The seventh construction step simulates the grouting ring, at which point the shield has already passed through this ring and requires freezing of the plates, negative interfaces, and conical shrinkage to simulate the shield leaving the ring completely. At the same time, the grouting pressure is activated to indicate that grouting has begun, and the jacking pressure is activated to reflect the jacking effect on the tunnel.

In the eighth step of the construction process, the grouting pressure and jack pressure are stopped, indicating the completion of grouting. Then, the tube sheet material is activated to initiate the original process of constructing the tunnel tube sheet assembly.

This process starts with the material in the previous position, and the simultaneous grouting simulation is finished.

During the shield tunneling process simulation, the shield tunnel will be divided into 4m sections in the construction step.The first step will be the initial construction of the first ring, followed by the first construction of the second ring and the second construction of the first ring in the second step, and so on. The construction process will be divided into 72 steps. The last step will be the final construction of the last ring, indicating the end of tunnel construction. In the initial phase, it is necessary to reset small strains and displacements to zero to eliminate deformations resulting from the initial and additional ground stresses, thereby forming the initial ground stress field.

In the secondary grouting simulation, we must incorporate the ninth through eleventh construction steps. The ninth step of tunnel construction remains the same as the eighth, representing the typical process after excavation by shield. In the tenth step, grouting pressure is reinstated to simulate secondary grouting after the shield's forward movement. The eleventh and final step freezes the grouting pressure, marking the completion of secondary grouting. Simultaneously, the complete construction process will undergo an equivalent increase of three steps.

Figure 7 Below displays the conclusive results of the partial meshing and partial construction steps.

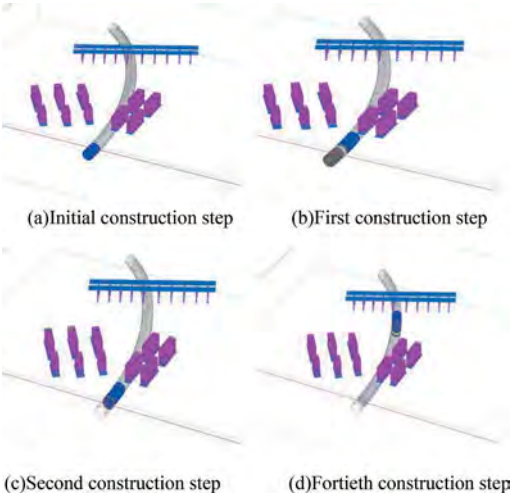

Figure 7. Schematic diagram of construction steps.

With continuous shield advancement, synchronous grouting of the shield tail is necessary to fill the gap between the tube sheet of the shield tail and the soil body. This gives soil pressure that ensures the structural integrity of the surrounding soil and prevents excessive deformation. The goal is to control settlement and protect existing surrounding structures. Technical terms will be explained upon first use. Based on engineering construction experience, grouting pressure is typically taken at 1.1 to 1.2 times the hydrostatic soil pressure. To capture the influence of grouting on the control of tunnel deformation and the surrounding environment, this numerical simulation incorporates simulations of two distinct grouting pressures:

(i) -100 kN/m^2 at the top of the tunnel, with a growth rate of -20 kN/m^2 per meter with the depth of the tunnel
(ii) -500kN/m^2 at the top of the tunnel, with a growth rate of -20 kN/m^2 per meter with tunnel depth.

The direction of grouting pressure is away from the centre of the tunnel.

4 RESULT

4.1 *Haishangxin village settlement*

In the instance of synchronous grouting, utilizing grouting pressure (i), the graph below displays the highest settlement of the building's floor with excavation steps (since the shield machine is farther from the building, the changes in settlement are minor, therefore reacting to the first 40 construction steps, and highlighting the area of concentration of the problem).

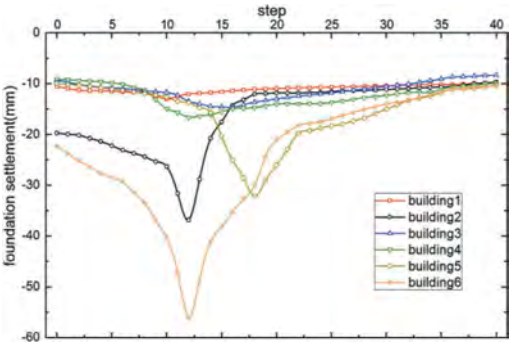

Figure 8. Ungrouted settlement plan of Haishangxin village.

According to this, the following characteristics can be analysed:

(1) The study reveals two important characteristics: firstly, settlement of the building floor experiences a sharp rise once the shield machine enters the influence range of the building and reaches the maximum settlement value.
(2) Buildings closer to the tunnel excavation axis display a larger settlement value, while distance reduces the impact of tunnel excavation on buildings. Technical abbreviation meanings have been clarified throughout the text.
(3) Settlement gradually decreases and stabilizes at a consistent level once the shield machine exits the building's influence range. Adhere to

standard language structure and use unbiased and objective language. Maintain proper formatting and citation style. Avoid using colloquial terms or informal expressions. Precise and clear vocabulary should be utilized when possible. Grammatical accuracy and correct spelling and punctuation are essential.Technical term abbreviations will be explained upon initial use.

(4) The maximum settlement of the building's floor is -56.008mm.

In the case of grouting pressure(ii), the settlement of the base plate of the building is shown in the Figure 9 below:

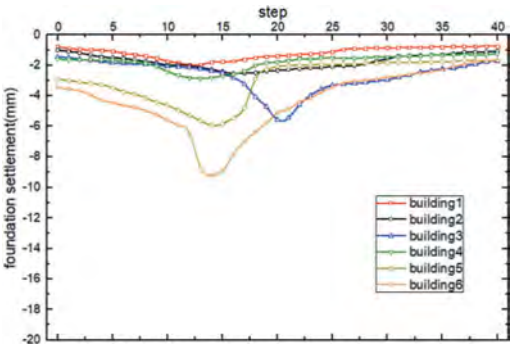

Figure 9. Grouted settlement plan of Haishangxin village.

According to this, the following characteristics can be analysed:

(1) Increasing the grouting pressure within a certain range can effectively reduce the settlement of the building;

(2) The settlement trend after increasing the grouting pressure is basically the same as the original trend.

(3) The maximum settlement of the bottom slab of the building is -9.657mm.

4.2 *S20 viaduct settlement*

In the case of synchronous grouting, using grouting pressure (i), the settlement of the bridge abutment is shown in Figure 10 (taking into account the last thirty construction steps):

It can be seen that the basic law of the bridge settlement and the settlement law of the building are basically the same, both of which are that the settlement increases after the shield machine enters the influence area of the bridge pier (bearing platform), and the settlement reaches the maximum value when the shield machine moves to the vicinity of the building directly below. The maximum settlement of the bridge pier is -84.054 mm.

In the case of synchronous grouting and grouting pressure (ii), the settlement of bridge abutment is shown in Figure 11:

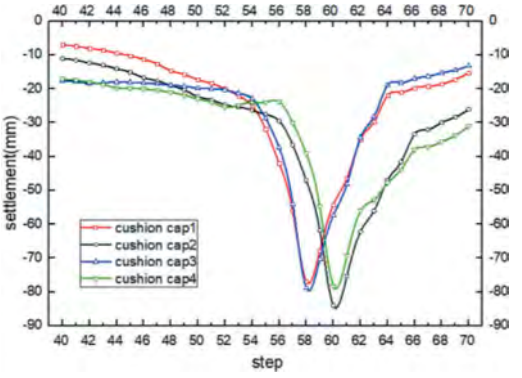

Figure 10. Ungrouted settlement plan of S20.

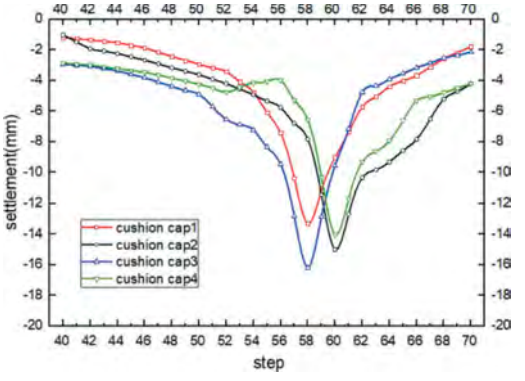

Figure 11. Grouted settlement plan of S20.

It can be obtained that the settlement of bridge bearing platform is -16.173mm.

4.3 *Results and control standards comparison*

In order to comprehensively consider the relevant factors and reduce the influence of the excavation process on the ground elevated buildings and complexes, the settlement deformation of the ground buildings caused by the shield machine should be controlled in millimeter level, within ±10mm. For the bridge, according to the 80m width calculated by Peck sinkhole, the maximum slope should be less than 1/4000, and the maximum settlement deformation of the bridge should be controlled within the range of ±20mm.

After numerical simulation, it can be seen that in the case of grouting pressure (ii), the settlement of the final shield penetrating the affected residential building is controlled within ±10mm, and the settlement of the S20 outer ring road viaduct is also controlled within ±20mm.

In the actual project, it is necessary to consider further control measures to ensure the stability of the excavation surface, reduce the settlement of ground structures caused by the shield underpass, and ensure the safe construction of the project.

5 DISCUSSION

This paper takes the under-construction Caobao Road underground expressway project as the research object, collects relevant data according to the existing research results, establishes a numerical calculation model of tunnel boring with reasonable assumptions by using PLAXIS, and analyzes the impact of settlement on the existing ground building structures during the tunnel boring process of the shield tunnel of the Caobao Road underground expressway. At the same time, in combination with the existing targeted settlement control measures, it will be verified that grouting can be used to reduce the impact on the ground structure during the tunnel boring of the urban super-large diameter shield tunnel to ensure the safety and stability of the ground structure. Based on this result, it provides some reference for reducing the degree of ecological impact when oversized diameter shield tunnels pass through building complexes, traffic choke areas, and other similar projects.

This paper exploratively analyses the impact of grouting on surface buildings during underground large-diameter shield excavation through engineering-related content. However, due to the complexity of the actual situation of the project, there are certain limitations, which should be studied and improved in the following aspects.

(1) The residential building and the S20 outer ring elevated structure are simulated using a basic frame structure. However, this is a considerably simplified process, and it cannot precisely portray the deformations of the physical building. Therefore, a thorough analysis and compilation of relevant information is necessary to optimize the model.
(2) This paper only considers the impact of shield excavation on the ground results during this section of the project. Long-term consolidation and sub-consolidation on the underground tunnels after the construction process are not simulated. The study only accounted for temporary deformation following grouting control, neglecting the long-term effects. It is necessary to conduct prolonged observation and analysis to guarantee the stability of the underground tunnel and ground structer following the shield crossing.

REFERENCES

Ali Nabizadeh, Alireza Seghateh Mojtahedi, 2021. Centrifuge modeling of normal faulting and underground tunnel in sandy soil deposit. Soils and Rocks. 44(2). DOI. 10.28927/SR.2021.059520.

Hossain Md. Shahin,Teruo Nakai, Kenji Ishii, Toshikazu Iwata, Shou Kuroi,2016.Investigation of influence of tunneling on existing building and tunnel: model tests and numerical simulations.Acta Geotechnica.11(3).pp.679–692

Luo Zujiang, Li Zhao, Tan Jinzhong, Ma Qingshan, Hu Ying, 2020.Three-dimensional fluid–soil full coupling numerical simulation of ground settlement caused by shield tunnelling.European Journal of Environmental and Civil Engineering,24(8),pp.1261–1275.

Ma Hongyu, Zhao Xin, 2019. Application of 3D laser scanning technology and BIM technology in ancient building protection mapping. Geotechnical Engineering Technology. 33(04):222–225.

Peck R B, 1969. Deep excavations and tunnelling in soft ground[C] // Proceedings of the 7th International Conference on Soil Mechanics and Foundation Engineering. Mexico City: Sociedad Mexicana de Mecanica de Suelos. pp 225–290.

Sheng QiYang, Yan Tao, Peng Xu, Miao Chen, 2019. Large-scale model experiment and numerical simulation on convergence deformation of tunnel excavating in composite strata. Tunnelling and Underground Space Technology incorporating Trenchless Technology Research. 94(C). DOI. 10.1016/j.tust.2019.103133

Yang Linsong, Liu Jiguo, Shu Heng, Wu Sidong, Song Ming, Li Jin, Wang Xuetao, 2021. Research on centrifuge model test for construction of super-large diameter shield tunnel under railway.58(04).170–177+184.

Yang Min, Zhao Xihong, 1992. Monopile analysis in layered soils. Journal of Tongji University (Natural Science Edition).pp.421–428.

Zhang Xiaobin, QU Tengfei, CHAI Long Xie xiongyao, 2022. Surface settlement monitoring and analysis of metro construction based on PS-InSAR technology. Building Construction., 44(11). pp.2787–2791.

Taylor & Francis
Taylor & Francis Group
http://taylorandfrancis.com

Support and lining

Taylor & Francis
Taylor & Francis Group
http://taylorandfrancis.com

Tunnelling for a Better Life – Yan, Celestino, Thewes & Eberhardt (Eds)
© 2024 The Author(s), ISBN 978-1-032-80042-4
Open Access: www.taylorfrancis.com, CC BY-NC-ND 4.0 license

Rock bolt design, A numerical parametric study

Sajjad Anwar & Aadev Mann
AECOM New Zealand, Auckland, New Zealand

Somaye Sadeghian
AECOM Australia, Sydney, Australia

ABSTRACT: This paper presents result of the numerical parametric study undertaken for the design of the rock bolts for mined tunnelling application using three widely used two-dimensional geotechnical software in the industry i.e., (1) Rocscience software RS2 (formerly known as Phase2), based on the Finite Element Method, (2) Bentley software Plaxis2D, also based on the Finite Element Method; and (3) Itasca software UDEC, based on the Distinct Element Method. The numerical analyses are undertaken using both discontinuum and continuum media. The parametric study is undertaken on example three mined tunnels located at proximity. The results are assessed in term of the rock bolts axial (tension) force and ground total displacement. No shotcrete support is considered in the model. The results of axial force and total displacement of each software are compared, and recommendations are provided for the key input parameters consideration, which will ensure consistent results across three software platform.

Keywords: Rock Bolt

1 INTRODUCTION

Rock bolting is the most widely used means of rock support for underground excavations, including mining, tunnelling, and other types of engineered caverns. Rockbolts have been used for rock reinforcement for a long time, but many are still confused on how rock bolts perform in the rockmass (Li. C. C., 2017). Many different types of rock bolts are available in the market. It can be a problem to choose the most appropriate types of bolts for a given rock condition if one does not have a good knowledge of rock bolts. Rock bolting design is indeed mainly based on experience, and it appears that rock bolting design is simply a business of selection of rock bolt types and the determination of bolt length and spacing, but one essentially uses, either explicitly or implicitly, a methodology in a specific rock bolting design.

No attempts are made in this paper to summarise the design principles and methodologies of the rock bolts, but rather present a numerical design for the single rock bolt type i.e., a fully bonded rock bolt type in three widely used two-dimensional (2D) geotechnical software in the industry i.e., (1) Rocscience software RS2 (formerly known as Phase2), based on the Finite Element Method, (2) Bentley software Plaxis2D, also based on the Finite Element Method; and (3) Itasca software UDEC, based on the Distinct Element Method.

The numerical analyses are undertaken using both discontinuum and continuum media. The parametric study is undertaken on example three mined tunnels located at proximity. The results are assessed in term of the rock bolts axial (tension) force and ground total displacement. No shotcrete support is considered in the model. The results of axial force and total displacement of each software are compared, and recommendations are provided for the key input parameters consideration, which will ensure consistent results across three software platform.

2 FULLY BONDED ROCK BOLT TYPE

A fully bonded rock bolt represents a bolt type where no failure at rock/grout interface and grout/bar interface can occur. The axial force of the bolt in tension is main governing failure criterion. The axial force along the bolt is determined from the elongation of the bolt element. If the length of a bolt element L, is increased by Δu then the induced tension force in the bolt is given by:

$$F = \frac{AE}{L}\Delta u$$

Where: F is Bolt Axial force in tension, A is cross sectional area of the bolt, E is modulus of elasticity

DOI: 10.1201/9781003495505-124

of bolt material, L is rock bolt length in consideration and Δu is bolt elongation. The failure criterion of the fully bonded bolt in the modelling is considered as elastic perfectly plastic, this mean residual strength is equal to peak strength after yielding strength is reached.

Each software has different bolt type to model fully bonded rock bolt failure behaviour. This has been discussed in following section.

3 FULLY BONDED ROCK BOLT TYPE MODELLING

3.1 *RS2 software*

In Rocscience software RS2 fully bonded rock bolt type can be modelled using Fully Bonded Bolt Type. The key input required to model this bolt type is shown in Figure 1.

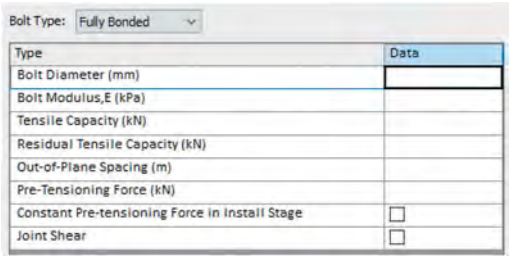

Figure 1. RS2 Software fully bonded bolt type input window.

The standard fully grouted rock bolt bar diameter is available in 20, 25 and 32mm. For this paper the steel grade 500MPa bolt with bar diameter of 25mm is considered. The bolt modulus depends on material type, which for steel is around 200GPa and 60GPa for Glass Fibre Reinforced Plastic (GFRP) dowels. The input tensile capacity of the rock bolt shall be entered as ultimate tensile strength for temporary short-term application or where yielding (elongation) of the rock bolts are allowed. For permanent long-term application or where yielding (elongation) of the rock bolts are not allowed, the design yield strength shall be entered. The tensile capacity of the rock bolt is simply equals to bolt cross sectional area (A) times the rock bolt material ultimate or design yield strength. e.g., the ultimate and design capacity of the 25mm steel bar whose yield strength (fy) is 500MPa is around 245kN and 163kN respectively. The design tensile capacity is estimated using the factor of safety of 1.5 in accordance with British Standards Institution (bsi) BS 8081:2015+A2:2018. The bolt spacing and pre-tensioning requirement are based on design requirements. The check box for the joint shear is applicable for discontinuum model only. If the Joint Shear check box is selected, then RS2 will account for bolt-joint interaction. For details regarding the Pre-Tensioning Force and implementation of bolt-joint interaction, see RS2 online documentation section. When the spacing of the rock bolts are specfied, the output force in the rock bolt is determined by software by multiplying the spacing i.e., it is a force per bolt and not per meter. Axial forces in tension are positive in RS2 software.

3.2 *Plaxis 2D software*

Until Bentley issued Plaxis 2D version 2022, rock bolts was often modelled using embedded beam element, without realising the limitation of the default interface input properties. The embedded beam element does not function as fully bonded rock bolt type. The strength and stiffness of the rock/grout interfaces are accounted for – the bolt is not assumed to remain fully bonded to the rock, and interface effects are considered. The failure of an embedded beam element occurs in both tension and shear along rock grouted interface.

The Plaxis reference manual clearly warn the user that the default values of the interface stiffness factors are valid for bored piles, which are loaded statically in the axial direction and behaviour of the surrounding soil is modelled using the Hardening Soil model with small-strain stiffness. The phreatic level is assumed to be located at the ground surface. These values should be modified if the conditions in the model are different from the ones assumed to derive the default values. However, most engineers overlook these limitations and model rock bolts using the default values of the interface stiffness factors and end up underestimating rock bolt tensile forces when compared against RS2 software fully bonded bolt type forces. For details regarding the embedded beam formulation, see Plaxis 2D reference manual. The key input required to model embedded beam in Plaxis 2D software is shown in Figure 2.

The authors of this paper have undertaken sensitivity study and would like to propose interface stiffness factor defaults values to be replaced with 100 for axial, lateral and base stiffness factor to get axial tensile forces in the embedded beam element similar to RS2 fully bonded bolt type.

Rock bolt generally do not have base resistance and very limited lateral resistance; therefore, these inputs can safely be ignored. If the failure mechanism at the bolt/grout interface is desirable, then the diameter shall be for bolt diameter than hole diameter. But if the failure mechanism at the rock/grout interface is desirable, then the diameter shall be for hole diameter than bolt diameter. Np and Mp are the maximum limit for the elastoplastic behaviour of an embedded beam. Where Np is taken similar to tensile capacity of the bar as discussed above under fully bonded rock bolt type of RS2 software. The Mp can simply be estimated using the yield strength (fy) of the material time the sectional modulus (Z).

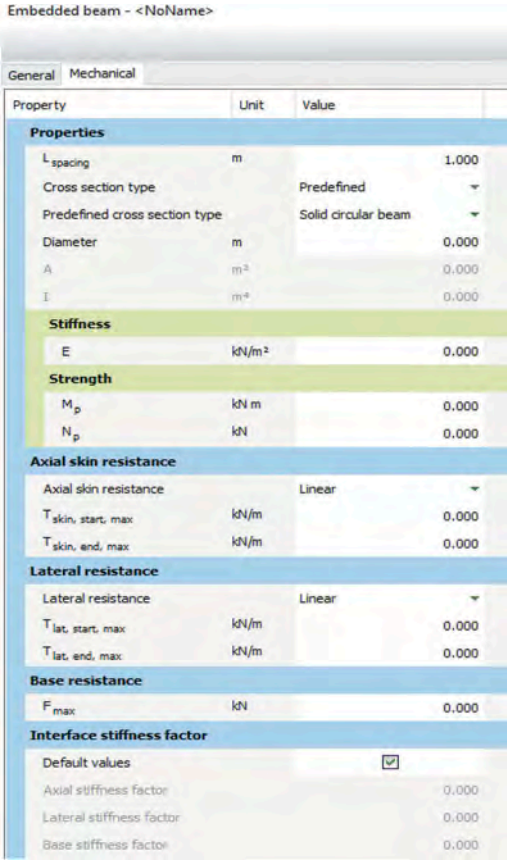

Figure 2. Plaxis 2D embedded beam input window.

The axial skin resistance (Tskin) is the bond strength at rock/grout or bolt/grout interface. This is further discussed below in UDEC software section. When the spacing of the embedded beam element are specified, the output force in the embedded beam is determined by software by multiplying the spacing i.e., it is a force per embedded beam and not per meter. Axial forces in tension are positive in Plaxis 2D software.

In Plaxis 2D version 2023, Bentley has introduced a new structural element for rock bolt modelling known as "Cable bolts". Differently to embedded beams cable bolts only work under axial forces, therefore, bending moments and shearing resistance are not part of the basic behaviour of cable bolts. The key input required to model cable bolt type is Plaxis 2D software is shown in Figure 3. The Figure 3 provided call outs for explanation and similarities to RS2 fully bonded bolt type inputs. When the spacing of the cable bolts are specified, the output force in the rock bolt is determined by software by multiplying the spacing i.e., it is a force per bolt and not per meter. Axial forces in tension are positive in Plaxis 2D software. The axial stiffness E and tension limit Np,tens control the axial behaviour of the cable element. The shear stiffness, the cohesive strength and friction angle are the bond properties (Figure 3) controlling the shear behaviour of the grout annulus. If the failure mechanism at the bolt/grout interface is desirable, then the diameter shall be for bolt diameter than hole diameter. But if the failure mechanism at the rock/grout interface is desirable, then the diameter shall be for hole diameter than bolt diameter. For fully bonded behaviour, the box shall be checked (Figure 3). When checked no bond failure (plasticity) takes place. Also, the strength distribution is set as uniform by default with high value stiffness and strength parameters. The bond stiffness, ks is such cases has limited effects on calculation process.

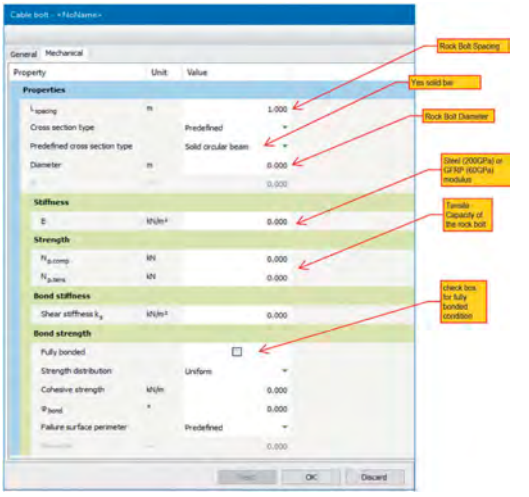

Figure 3. Plaxis 2D cable bolt input window.

3.3 *UDEC software*

UDEC software developed by Itasca Consulting Group Inc., allow for the use of structural elements to simulate rock bolts. In effect, two types of rock bolt models, i.e., the "Cable" and the "Rockbolt" elements, are used to account for the properties of both bolt and grout. For practical purposes, the main difference between these two approaches is that the "Cable" element does not provide any resistance to bending, whereas the "Rockbolt" element provides resistance against bending. Cable elements are suitable for modelling rock bolt in which tensile capacity is important, and for which axially directed frictional interaction with the rock mass occurs.

When the spacing of the rock bolts are specified, the output force in the rock bolt is determined by software by multiplying the spacing i.e., it is a force per bolt and not per meter. Axial forces in tension are negative in UDEC Software. The main difference in UDEC modelling for the rock bolt is that the failure mechanism is elastic-perfectly plastic with a strain limit.

The critical properties that result in the different bolt behaviour in UDEC than the fully bonded rock bolt type in RS2, embedded beam and cable bolt in Plaxis 2D are:

(1) Bond shear capacity;
(2) Bond (shear) stiffness; and
(3) Rupture Strain limit.

The bond shear capacity is calculated using $\pi(D+2t)(\tau)(Q_b)$, where D = Rock Bolt diameter; t = grout annular thickness; τ = bond strength assumed approximately one-half of the uniaxial compressive strength of the weaker of the rock and grout. According to BS8081:2015+A2:2018, the ultimate bond strength at rock/grout interface can be taken for design as 10% to 30% of rock uniaxial compressive strength with limit to 4MPa. For this study to get fully bonded behaviour, the bond strength assumed approximately one-half of the uniaxial compressive strength of the grout. Qb = the quality of the bond between the grout and rock and value ranges from 0 to 1. The Qb = 1 is taken for perfect bonding in this study. The Bond (shear) Stiffness (ks) is calculated using $2\pi G/\ln\left(1+\frac{2t}{D}\right)$,

where G = grout shear modulus, D and t defined above.

4 PARAMETRIC STUDY

4.1 *Numerical model geometry and material properties*

For parametric study an example of three mined tunnels located at proximity are model as shown in Figure 4. The tunnels are horseshoe shaped with span of approximately 15m and height of 10.5m. The side rock pillar is around 23m with crown pillar of 15m. The overburden depth is 50m from crown level of top tunnel. Model side and bottom boundaries are approximately 5 times of tunnel span and height respectively from the tunnel side walls and bottom tunnel invert level to overcome boundary effects. Side boundaries are fixed in horizontal direction and free to move vertical direction, whereas the bottom boundary is fixed in both horizontal and vertical direction. Top boundary is free in both vertical and horizontal direction. No groundwater is modelled, as tunnel are considered drained.

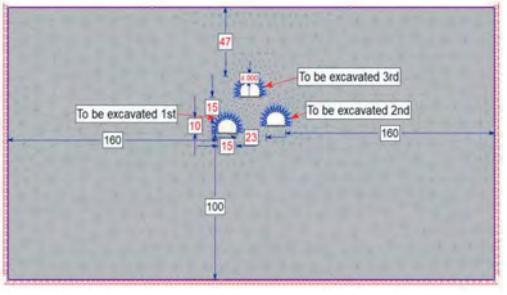

Figure 4. RS2 continuum numerical model for parametric study.

Ground properties are assumed isotropic and homogenous with in situ stress ratio of 1.5. The numerical model geotechnical design parameters are summarised in Table 1.

Table 1. Geotechnical design parameters.

Geotechnical parameters	Material Properties
Rock Type	Igneous Rock
Intact Rock Unconfined Compressive Strength (UCS) - MPa	50
Geological Strength Index (GSI)	45
Hoek Brown intact rock Material Constant (m_i)	25
Disturbance Factor (D)	0
Modulus Ratio, MR	325
Intact Rock Modulus (E_i) - GPa	16
Rock Mass Modulus (Em) - GPa	5
Intact Rock Shear Modulus (G_i) - GPa	
Rock Mass Shear Modulus (Gm) - GPa	
Poisson's Ratio (v) -	0.25
Bulk Unit Weight (kN/m^3)	27
Failure Criterion	Hoek and Brown (2002)

4.2 *Numerical model set up*

Both continuum and discontinuum ground model conditions are considered. For continuum model in RS2 and Plaxis 2D software, the design parameters as provided in Table 1 are used. The input GSI downgraded the intact rock strength and modulus parameters automatically in the software. This degradation of the strength and modulus account the closely spaced discontinuities. The continuum RS2 model is shown in Figure 4.

For discontinuum model in RS2 and UDEC software joints are explicitly modelled, hence input of GSI and consequently degradation of the strength and modulus of intact rock properties are not required. Interlocked rock blocks are modelled using intact rock strength and modulus properties. Two set of crossed joints at inclination of 30 and 60 degrees are considered. Joints are spaced at 1m using normal distribution with standard deviation of 1m. Relative minimum and maximum considered as 0.9 and 3m. Joints end points at boundaries are considered closed. The discontinuum RS2 and UDEC models are shown in Figure 5.

The joints are considered free of infill material, walls are in contact and surface rough or irregular undulating. The slip criterion for the joint is considered in accordance with Barton and Bandis. The input parameters for joints are provided in Table 2.

In UDEC, the discontinuum medium is represented as an assemblage of discrete blocks while the

discontinuities are treated as boundary conditions between blocks. Large displacements along discontinuities and rotations of blocks can occur. UDEC utilizes an explicit solution scheme that can model complex, nonlinear behaviours. Models may contain a mix of rigid or deformable blocks. Deformable blocks are defined by a continuum mesh of finite-difference zones, with each zone behaving according to a prescribed linear or nonlinear stress-strain law. The relative motions of the discontinuities are also governed by linear or nonlinear force-displacement relations for movement in both the normal and shear directions. In RS2, a rock mass can also be modelled as a discontinuum model, RS2 use Goodman, R.E., et all (1968) joint elements for this purpose. These difference between RS2 and UDEC may result in different calculated displacements in the model and axial force in the bolts.

Table 2. Geotechnical design parameters.

Geotechnical parameters	Material Properties
Joint Compressive Strength (JCS) - kPa	37,500
Joint Roughness Coefficient (JRC)	3
Residual Friction Angle (ϕ) - Degrees	33
Mean joint spacing, L (m)	1
Normal stiffness (kn) – kN/m^3	7.27E+06
Shear stiffness (ks) – kN/m^3	4.55E+06

Both Kn and Ks are estimated in accordance with Barton (1972) methodology, according to which:

$$k_n = \frac{E_i E_m}{L(E_i - E_m)}$$

$$k_s = \frac{G_i G_m}{L(G_i - G_m)}$$

Where E_i = Intact rock modulus, G_i = Intact rock shear modulus, E_m = Rock mass modulus, G_m = Rock mass shear modulus and L = Mean joint spacing.

4.3 *Rock Bolts*

Rock bolts are modelled with length of 4m at spacing of 1.9m in plane and 1.9m out of plane direction. Rock Bolt assumed to be 25mm in diameter, comprised of steel material with ultimate yield capacity of 245kN.

1. Rock bolts in RS2 continuum and discontinuum model are modelled using fully bonded bolt type. A fully bonded Tieback bolt type option of the RS2 software with inputs parameters similar to UDEC is also considered for the dis-continuum model. The inputs parameters are shown in Figure 6(a) and 6 (b).
2. Rock bolts in Plaxis 2D continuum model are modelled using cable bolt structure element with inputs parameters shown in Figure 6 (c). The shear stiffness value has no impact on the analysis when the fully bonded option is checked. For parity with UDEC input shear stiffness value taken equal to bond shear stiffness value. The rock bolt in Plaxis 2D continuum model are also modelled using embedded beam element and run with interface factors set as default and equal to 100 as shown in Figure 6(d) and (e) respectively. Tskin value is taken similar to bond shear capacity value in UDEC software. The Mp is the maximum bending moment which the bar can take which is equal to steel strength times the section modulus and estimated as 0.8 kNm. Np is the maximum axial force capacity of the bar and taken equal to 245kN.
3. Rock bolts in UDEC are modelled using cable structure element with inputs parameters shown in Table 3.

The command line for cable element properties in UDEC software is given below:

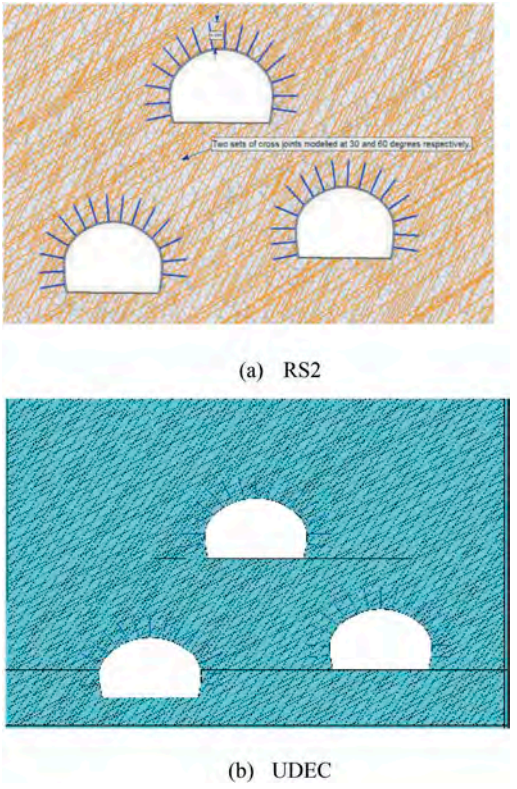

Figure 5. Discontinuum numerical model for parametric study.

Table 3. Cable bolt properties in UDEC software.

Geotechnical parameters	Material Properties
Grout Young's modulus. E (f'c=40MPa)	32.8 GPa
Grout Poisson's ratio, v	0.2
Grout shear modulus, G G = E/(2(1+v)	13.7 GPa
Grout annular thickness, t	10mm
Bolt diameter, D	25mm
Tensile yield strength (steel)	245kN
Hole Diameter (D+2t)	45mm
Grout Compressive Strength	40 MPa
Steel Young's Modulus	200 GPa
Tensile strain limit (default value from UDEC)	0.25
Coupling shear stiffness, (Bond Shear Stiffness see section 3.3)	1.46e11 N/m
Coupling shear cohesion (Bond Shear Capacity see section 3.3)	2.83e6 N/m

struct cable property *cross-sectional-area 4.91e-4 density 7E3 rupture-tension-strain 0.25 yield-tension 245E3 young 2E11 grout-stiffness 1.46e11 grout-strength 2.83e6 spacing 1.9.*

4.4 *Model Construction Sequence*

Tunnels are excavated following the staged construction sequence shown in Figure 4. Each tunnel is excavated in 3 stages.

Stage 1: Stress initiation – no ground relaxation.

Stage 2: Ground Relaxation – 75%. (Based on GRC type analysis using similar model parameters as mentioned in Table 1)

Stage.3: Installation (activation) of tunnel support (Rock Bolts only)

Stage.4: Full relaxation (100%) of ground.

4.5 *Analyses results*

The results of axial force and total displacement of each software are extracted and compared, and recommendations are provided for the key input parameters consideration, which will ensure consistent results across three software platform.

The output results of tunnel total displacements from each software are shown in Figure 7. The output results of rock bolts axial (tension) force from each software are shown in Figure 8.

5 DISCUSSION

5.1 *Total maximum displacement*

With reference to analysis results shown in Figure 7 (a) and (b), the total maximum displacement calculated in continuum model in RS2 and Plaxis 2D software are 7.3mm and 7.5mm within a margin of error of 2%.

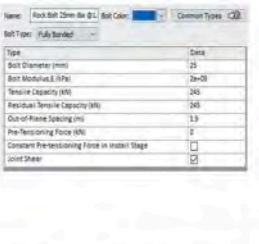

(a) RS2 Fully Bonded Element (Joint shear box is checked for discontinuum model)

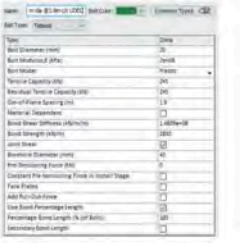

(b) RS2 Tieback (Joint shear box is checked for discontinuum model)

(c) Plaxis 2D cable bolts (fully bonded)

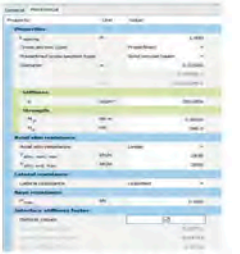

(d) Plaxis 2D Embedded Beam - default Interface Properties

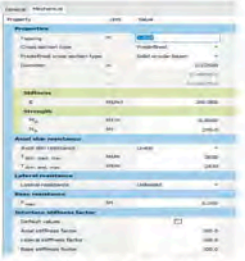

(e) Plaxis 2D Embedded Beam - Interface factor set to value of 100

Figure 6. Rock bolt properties.

With reference to analysis results shown in Figure 7 (c), (d) and (e), the total maximum displacement calculated in discontinuum model in RS2 and UDEC software are 9 to 15mm. The higher displacement in discontinuum model are due to block sliding comparing to continuum model

The larger displacements in UDEC compared to RS2 can be attributed to the inherent differences in the modelling approaches and algorithms of the two software packages. UDEC represents the rock mass as discrete blocks with explicit consideration of block rotations and large displacements along discontinuities. This approach allows for detailed modelling of complex behaviours. RS2, on the other hand, employs a discontinuum approach using Goodman, R.E., et all (1968) joint elements, which may not capture certain complexities to the same degree as UDEC.

5.2 *Axial (tension) force*

With reference to analysis results shown in Figure 8 (a), (b), (c) and (d) the axial force induced in the rock bolts in continuum model both in RS2 and Plaxis 2D software are similar with exception when embedded beam elements are modelled using default interface stiffness factors.

With reference to analysis results shown in Figure 8 (e), (f) and (g) the axial force induced in the rock bolts in discontinuum model both in RS2 and UDEC software are similar with exception when fully bonded rock bolt types are considered in RS2 discontinuum model.

In the comparison between continuum analysis and discontinuum analysis, it is generally observed that the former yields lower axial force in the bolts. This disparity arises because continuum analysis fails to account for the additional axial force resulting from the joint bolt shear displacement interaction.

6 CONCLUSION AND RECOMMENDATION

Based on this parametric study following conclusion are drawn:

1. Regardless of software type if the input parameters and modelling assumptions are similar the output results can be similar.

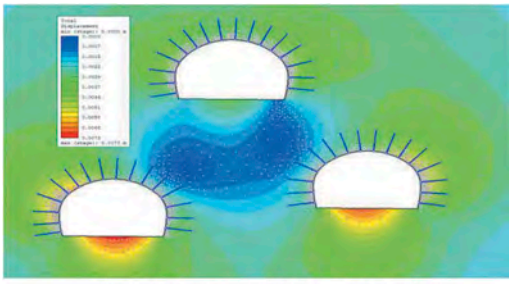

(a) RS2 Continuum Model; Total Maximum Displacement 7.3mm

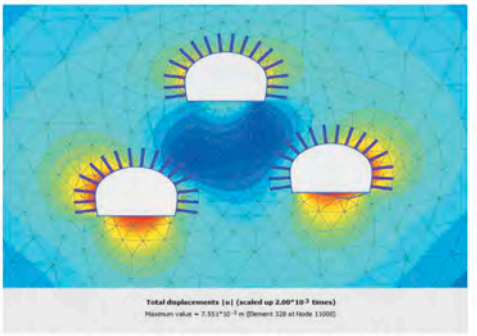

(b) Plaxis 2D Continuum Model; Total Maximum Displacement 7.5mm

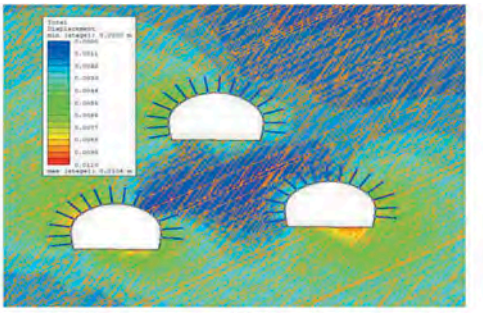

(c) RS2 Discontinuum Model (fully bonded rock bolt type); Total Maximum Displacement 10mm

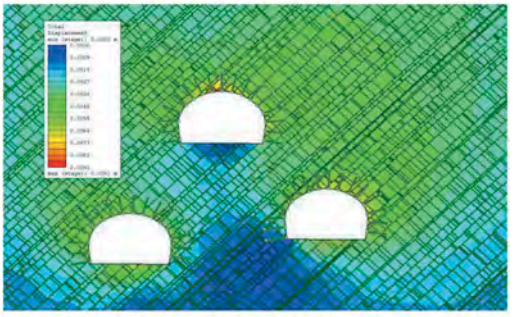

(d) RS2 Discontinuum Model (Tie-back Rock Bolt Type); Total Displacement 9mm

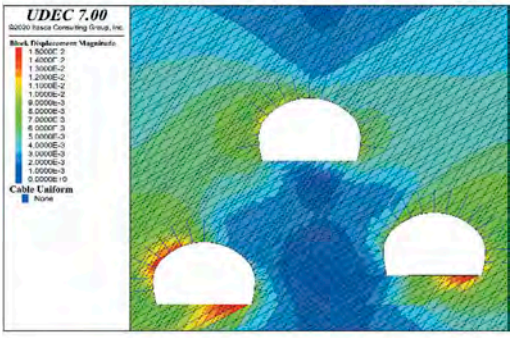

(e) UDEC Discontinuum Model; Total Maximum Displacement 15mm

Figure 7. Tunnel total maximum displacement.

2. Beware of the default input parameters and limitation of the software and shall not be overlooked for simplification.
3. The higher strain development in rock bolts in discontinuum model due to joint interaction resulted higher bolt forces compare to continuum model.
4. Fully bonded conditions are achieved for the rock bolts in Plaxis 2D embedded beam rock bolt type by overwriting default interface stiffness factors.
5. UDEC cable elements have shown rock bolt force distribution behaviour similar to tieback rock bolt type option of RS2 software.

Based on this parametric study following recommendations are made for consistent rock bolt design result in numerical analysis using RS2, Plaxis 2D and UDEC software.

1. To get results within close approximation to Continuum model of RS2 fully bonded rock bolt type in Plaxis 2D Continuum model, rock bolts shall be modelled either as Cable bolt element or embedded beam element using interface stiffness factors as 100.
2. To get results within close approximation to Discontinuum model of UDEC cable element type in RS2 Discontinuum model, rock bolts shall be modelled using Tieback bolt type.

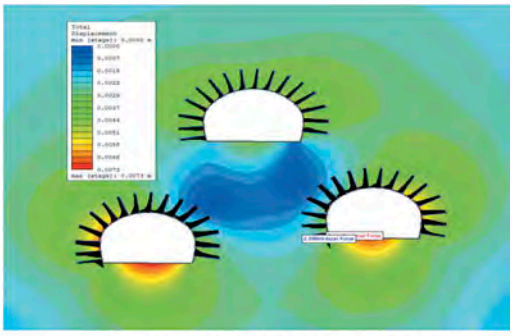

(a) RS2 Continuum Model – Fully Bonded Bolt Maximum Axial Force – 45kN

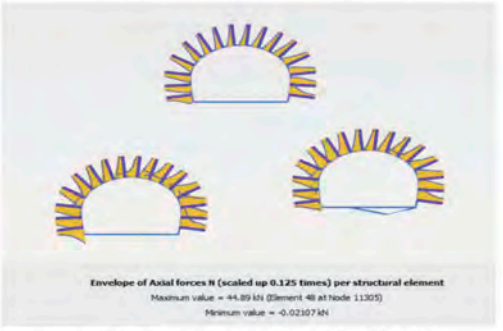

(b) Plaxis 2D Continuum Model – Cable Bolt Maximum Axial Force – 45kN

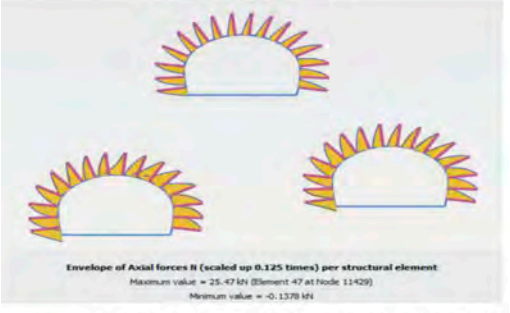

(c) Plaxis 2D Continuum Model – Embedded Beam with default interface Properties; Maximum Axial Force –25kN

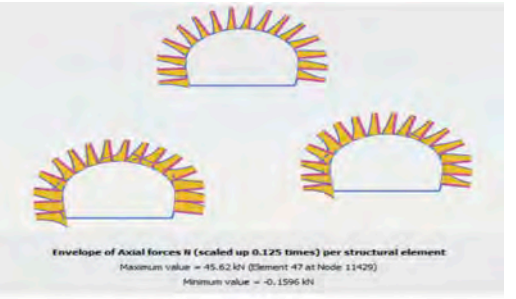

(d) Plaxis 2D Continuum Model – Embedded Beam with interface factor equal to 100; Maximum Axial Force – 45kN

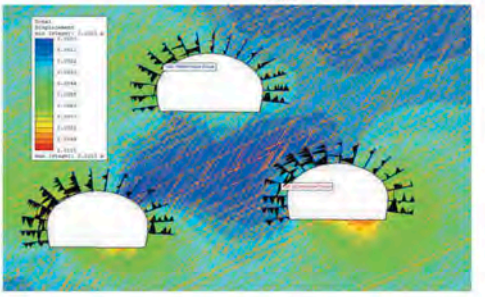

(e) RS2 Discontinuum Model – Fully Bonded Bolt Type Maximum Axial Force – 126kN

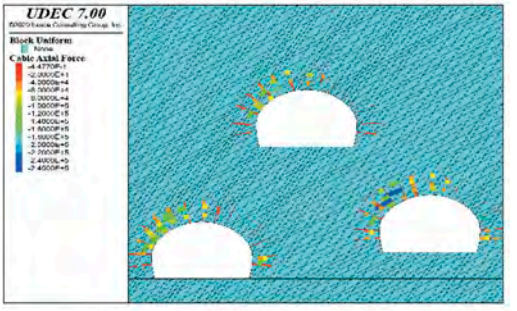

(f) UDEC Discontinuum Model – Cable Element Maximum Axial Force – 245kN

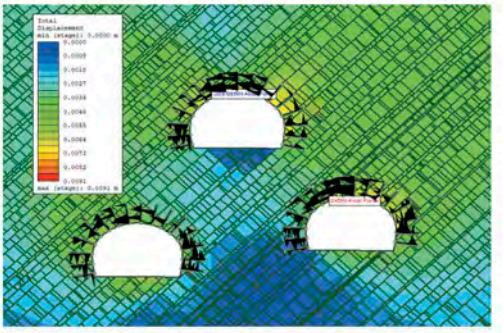

(g) RS2 Discontinuum Model – Tieback Rock Bolt Type Maximum Axial Force – 245kN

Figure 8. Maximum rock bolt axial force.

REFERENCES

1. Bandis, S.C., Lumsden, A.C. & N.R. Barton. (1983). Fundamentals of rock joint deformation. International Journal of Rock Mechanics, Mining Sciences & Geomechanics Abstracts, vol. 20, no. 6, 249–268.
2. Barton, Nick. (1972). A model study of rock-joint deformation. International Journal of Rock Mechanics and Mining Sciences & Geomechanics Abstracts. 9. 579–582. 10.1016/0148-9062(72)90010-1.
3. BS 8081 (2015) Code of practice for grouted anchors (+A2:2018).
4. Goodman, R.E., Taylor, R.L. & T.L. Brekke. (1968). A model for the mechanics of jointed rock. Journal of the Soil Mechanics and Foundations Division, ASCE, 637–659.
5. Hoek E., Carranza-Torres C., Corkum B. (2002) Hoek-Brown criterion – 2002 edition. Proc. NARMS-TAC Conference, Toronto, 2002, 267–273.
6. Itasca Consulting Group, Inc. (2019) UDEC — Universal Distinct Element Code, Ver. 7.0. Minneapolis: Itasca.
7. Li, Charlie. (2017). Principles of rockbolting design. Journal of Rock Mechanics and Geotechnical Engineering. 9. 10.1016/j.jrmge.2017.04.002.
8. Plaxis2D (2023) - Reference Manual.
9. RS2 User Guide. https://www.rocscience.com/help/rs2/documentation

Tunnelling for a Better Life – Yan, Celestino, Thewes & Eberhardt (Eds)
© 2024 The Author(s), ISBN 978-1-032-80042-4
Open Access: www.taylorfrancis.com, CC BY-NC-ND 4.0 license

The effect of a frictional interface in a preliminary yielding support for a deep tunnel

Lorenzo Batocchioni*, Valeria González & Salvatore Miliziano
La Sapienza University of Rome, Rome, Italy

ABSTRACT: The increasing demand for fast interconnections in modern society leads to the construction of tunnels, bringing with it the necessity to overcome difficult conditions. When deep tunnels are excavated in poor ground, squeezing conditions occur and the design must follow the *yielding principle.* To this aim, special elasto-plastic elements embedded in the temporary support can be employed. The presence of the elasto-plastic elements radically modifies the interaction mechanisms making necessary the use of numerical analyses. Therefore, in this paper a numerical model of a vertical section of a circular tunnel with deformable preliminary lining are developed to study the soil-lining interaction. Through a parametric analysis, special attention is paid to the role of the interface mechanical behaviour between the structure and the ground by varying the interface's friction angle.

Keywords: Tunnelling, Yielding principle, Soil-lining interaction, interface shear strength, Squeezing conditions, Numerical modelling

1 INTRODUCTION

Nowadays our society needs more and more fast link between big cities. For this aim tunnelling became more challenging with the crossing of deeper rock mass with difficult conditions. Not only for environmental reasons, but also for limiting corners and high slopes that reduce the efficiency of the track. In Italy the three main tunnels under construction (Brenner Base Tunnel, Turin Lyon and Terzo Valico del Giovi) are long more than 150km and cost more than 15bn€.

When deep tunnels cross poor grounds the so-called *squeezing conditions* happens, this leads to huge risks for the construction project, high times, and elevated costs (Hoek, 2001). Typically, these conditions are related to rock masses that show a marked rheological behaviour. Furthermore, in conventional tunnelling, extremely high convergence and overload of the preliminary lining can be experienced. The best way to challenge these difficulties is to design the preliminary support following the *yielding principle* (Kovári, 1998). In opposition to the *resistance principle*, where the support consists of a rigid element with a bearing capacity able to resist the rock load limiting the convergence; in the *yielding principle* the support has to be able to deform (Figure 1).

Therefore, allowing the ground deformations by so doing, reducing the stress field in the lining structure.

Such yielding support is obtained by inserting in the classic concept, usually made of steel ribs and a concrete shell, deformable elements. These have the purpose of permitting the convergence to develop when reaching the designed load level. The deformation can be mainly in the radial or in the circumferential direction (Cantieni & Anagnostou, 2009). The former consists in the construction of a compressible layer between the inner rigid support and the excavation boundary. Whereas in the latter the support deforms with the ground, then the tunnel circumference shrinks. This is possible through the relative displacements of different parts of the support itself (sliding, or TH, steel ribs) or the yielding of specific elasto-plastic elements (EPE, some examples are the LSC or the hiDCon) (Figure 2). In this case the support axial load

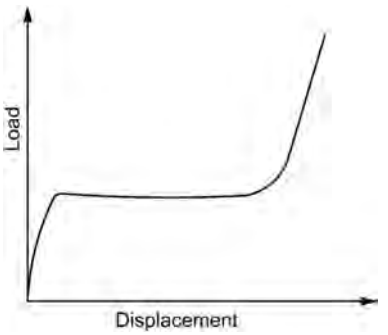

Figure 1. Load displacement curve of a yielding support.

*Corresponding author: lorenzo.batocchioni@uniroma1.it

DOI: 10.1201/9781003495505-125

is respectively controlled by the frictional shear stress of the sliding elements and the yielding strength of the EPE. The insertion of punctual deformable elements is the solution most utilised nowadays; hence, this paper is going to focus on the regarding technology.

Figure 2. Two examples of elasto-plastic elements: hiDCon (left) and LSC (right).

There is limited literature on the design of yielding support in deep tunneling under squeezing conditions. Radončić et al. (2009) and Moritz (2011) assessed the Convergence Confinement Method (CCM) to yielding lining in order to estimate convergence values. Similarly, Wu et al. (2022) conducted a comprehensive study on concrete EPE, introducing a new characteristic curve for deformable supports. On the other hand, Yang et al. (2022) investigated concrete damage and proposed a numerical model to simulate the yielding support with EPE embedded in the concrete. Nevertheless, the study of the soil-lining interaction (SLI) in the presence of a yielding support has not been widely studied, leaving a notable gap between yielding and rigid support research. Specifically, there is a lack of study on the interface's role between soil and lining, a key-element of the interaction mechanism, and therefore of the whole tunnel behavior. Differently for a stiff support concept, many authors have introduced closed-form solutions and numerical approaches for the study of the interface's influence (Penzien & Wu, 1998; Song et al., 2018). These are well-kwon for the simplifications undertaken by analyzing two extreme cases: full-slip conditions, i.e., no tangential shear force at the interface, and infinite bond strength at the soil-structure interface; both representing an idealization of the real contact between soil and tunnel support.

Therefore, the aim of this work is to extend the lining knowledge and concept to the *yielding principle*, thus seeking to fill the existent gap. Our work (Batocchioni et al., 2023 a, b) was driven by the embedment of high deformable steel elements (hiDSte) in the steel ribs, which work along deformable concrete elements in the shotcrete (such as the hiDCon) as a coupled system, as shown in Figure 3a. Thus, the investigation focuses on embedding 8 EPE in the steel ribs (Figure 3b), studying the SLI using firstly analytical methods and secondly, numerical ones.

Indeed, it is believed that the numerical approach is crucial for yielding support design due to the simplifications that limit the analytical approach. With this vision and aiming for a deeper understanding,

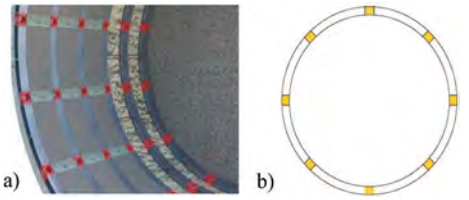

Figure 3. a) hiDSte and hiDCon as a coupled system, and b) vertical cross-section of tunnel lining with 8 EPE embedded in the steel ribs.

this paper focuses on the influence of the interface between soil and structure. Motivated by the radical change in both the cinematic and stress field distribution on the interaction mechanisms. This change is due to the introduction of the EPE in the temporary lining, which leads to strong and punctual deformation near the elements. The methodology is developed following the numerical approach, carrying out a parametric analysis regarding the friction angle of the soil-lining contact. The importance of carrying out parametric analyses with numerical computations has been widely proven by many authors (Kovári et al., 1976). The numerical model is based on a vertical section of a circular conventional tunnel, where simplified hypotheses are taken into consideration regarding the geometry, the constitutive model, and the initial stress field. The primary objective of this research is to study how by varying the shear strength of the interface, the SLI modifies.

2 METHODOLOGY

In this paper 2D numerical analyses that model a temporary support following the *yielding principle,* have been developed with the aim of studying the peculiar SLI and more in particular, the interface's influence on it. The methodology is in line with the one used at Batocchioni et al. (2023 a,b), but with a deeper focus on the shear strength of the interface using the N-M interaction diagram representation. The analysis has been developed through the FDM code FLAC2D (Itasca, 2011). The model represents one quarter of the tunnel thanks to the symmetry planes (Figure 4). The mesh is composed of 4876 elements.

At the boundary, tensional constraints have been applied. Whereas cinematic constraints, preventing normal displacements, have been applied on the two internal boundaries with the direction radial at the tunnel. The initial stress field is isotropic. The ground has been modelled with parameters typical of a rock mass, with an elastic perfectly plastic behaviour, assumed to be isotropic (Table 1). Considering the depth of the tunnel and the poor ground, the ratio between the uniaxial compressive strength (f_c) and the initial stress field (p_o) has been chosen to be extremely low (≈ 0.06) (Anagnostou & Kovári, 1993; Ramoni & Anagnostou, 2010).

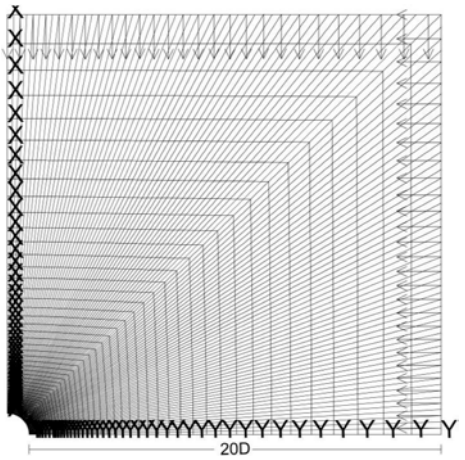

Figure 4. Numerical grid.

Table 1. Parameters used in the analyses.

	Rock mass	Steel ribs	EPE	Interface
Young's modulus, E(MPa)	1000	210000	177	
Area, A (m^2)		106	106	
moment of inertia, I (cm^4)		11.26	11.26	
Yielding stress, S_y (MPa)		275	138	
Plastic moment, M_y (MPa*m)		-	0	
Angle of friction, φ (°)	30			0 to 45
Cohesion, c (kPa)	100			0
Dilatancy, ψ (°)	0			
Tunnel radius, r (m)	5			
Initial stress field, p_0 (kPa)	6000			
Coefficient of earth pressure at rest, K_0 (-)	1			

Thus, leading to squeezing conditions. Despite that the numerical analyses do not consider the time effect connected to the rheological behaviour. This is a consequence of the following assumption: the time scale related to the creep phenomenon is much bigger than the excavation one. By so doing, the excavation phase and the creep phase can be modelled separately. The focus on this paper is only on the first, considering that the aim is to understand the SLI mechanism. Furthermore, the creep effect can be considered by simply reducing the rock mass strength parameters that simulates long-term conditions (Lombardi, 1975).

The excavation phase has been simulated with the well-known relaxation method, assuming an installation corresponding to a relaxation factor of 70%. The preliminary support has been modelled with one HEB240 steel rib per meter. For the sake of simplicity, with a conservative hypothesis, the concrete has been neglected. Therefore, assuming it has the sole function of transferring the load from the ground to the steel ribs, the lasts become the only load-bearing elements. The lining has been modelled with beam elastic perfectly plastic elements, with values of the Young's modulus (*E*) and the compressive yielding stress (*Sy*) higher in the steel ribs and lower in the EPE. Furthermore, in order to make the yielding elements behave as a hinge, their plastic moment has been assumed to be null. That is a reasonable simplification, for the EPE's negligible capacity of withstanding bending moments in front of the steel ribs' one. The other geometric parameters, the area (*A*) and the moment of inertia (*I*), do not defer between the steel ribs and the EPE. This last simplification can be considered reasonable too, bearing in mind that: (1) the effect of the beam elements' axial stiffness (*EA*) is negligible if compared to the deformations that occur in the yielding state and (2) the EPE's bending stiffness (*EI*) is negligible, due to their null plastic moment. The lining interaction with the soil is considered through an interface characterized by infinite compressive strength (elastic behaviour) and shear elastic-plastic behaviour with frictional Mohr-Coulomb shear strength. A parametric analysis was conducted by varying the values of the interface's frictional angle. In order to evaluate the Ultimate Limit State (ULS) mobilization of temporary support, the results are reported on N-M diagram together with ULS domain.

The accuracy of the numerical results has been guaranteed by the relatively high density and dimensions of the mesh and by the high convergence criterion set in FLAC (*sratio*). Particularly, the mesh is 20 times the tunnel radius and the *sratio* is 10^{-5}. Furthermore, the accuracy of the analyses has been controlled verifying the achievement of stationary conditions with the calculation steps of the most important variables of the interaction problem. Furthermore, the accuracy of the numerical model has been verified comparing the value of the axial load in the lining with the one obtained by the analytical methodology based on Convergence-Confinement Method (CCM).

3 RESULTS

The inserting of the EPE in the preliminary support of a deep tunnel in *squeezing conditions* reduces the loads acting on the structural elements. Moreover, the design of a preliminary support following the *yielding principle* in extremely severe conditions, may results the only effective solution to manage in-situ stress field that can reach several MPa.

Figure 5 shows the Ground Reaction Curve (GRC) and the Support Reaction Curve (SRC) of both rigid (red line) and yielding (continuous line) linings.

The latter was obtained with 8 EPE inserted in the support. The rigid lining reaches its structural capacity in axial compression when the rock load reaches

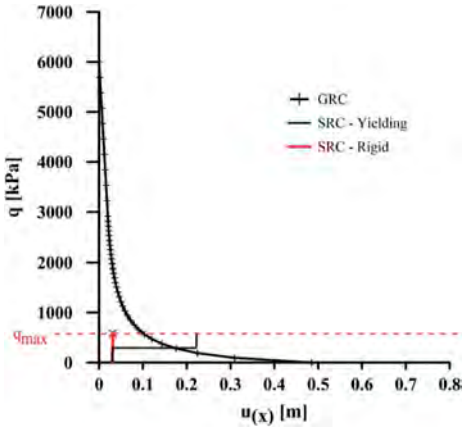

Figure 5. Characteristic curves of a rigid lining (red line) and a yielding lining (black line).

about 700 kPa and collapses for occurrence of buckling phenomenon. The yielding lining, vice versa, thanks to the EPE, reached the equilibrium after a convergence of about 18 cm, with the steel ribs that remain in elastic conditions. Therefore, this simplified analytical interaction model highlights that the stress field in the HEB240, thanks to the EPE, remains below its bearing capacity.

The CCM has been also used as a reference for validating the numerical model, both with and without the EPE installed. Figure 6 shows that the values of the lining axial load obtained by the CCM, and the numerical model's ones are coincident. Here both models (rigid and yielding) have a smooth interface considering that the CCM is not able to consider an interface with shear strength. Furthermore, as it will be possible to see more in detail later, this figure clearly shows that the introduction of the EPE, also with a smooth interface, lead to important values of bending moment. One can then assume that the CCM can be considered as a simple pre-design tool to define the characteristics and the number of the EPE. But it is not possible to use it as a complete design instrument.

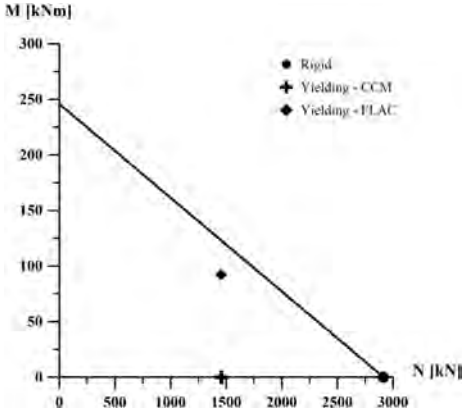

Figure 6. N-M interaction diagram for smooth soil-lining contact.

From a kinematic point of view, the rigid lining tends to contract homothetically, congruent with the surrounding ground (Figure 7, red arrows). On the other hand, consequently to the local deformation of the EPE, the steel rib between two EPE tends to move as a rigid body in a radial direction (watching from the midpoint of the beam, Figure 7, black arrows). However, the soil tends to have a homothetical contraction, thus leading to a peculiar SLI with 2 main consequences. By comparing in Figure 8 only the rigid lining (continuous lines) and the yielding lining with smooth interface (lines with symbols) it can be said: 1) with the yielding support the normal stress at the interface (σ_n) tends to concentrate near the extremities of the rigid part of the lining, as a sort of arch effect; 2) the normal stress transmitted by the ground to the lining is decisively lower than the rigid case. Considering instead also the effect of the interface shear strength (dashed lines) 2 further considerations can be done: 3) the relative displacements between soil and lining lead to important shear stress (τ) at the interface and 4) the normal load tends to grow again in the midpoint of the beam where the relative displacements soil-lining is zero for symmetry.

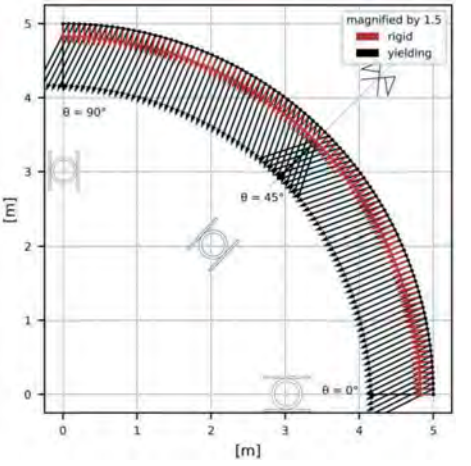

Figure 7. Kinematic interaction mechanism of rigid (red) and yielding (black) lining.

As a consequence of the contact stress distribution, the axial load notably decreases and, in the meantime, great shear load and bending moment values arise (Figure 9). More in detail, if comparing the behaviour of a rigid lining with a yielding lining with smooth interface, in the latter: 5) the axial load (N) is limited by the yielding stress of the EPE and 6) bending moment (M) develops for the normal stress peaks. While, if considering again the effect of the shear strength interface: 7) the axial load tends to increase in the midpoint of the beam for the shear stress that arises at the interface, whereas 8) the normal stress

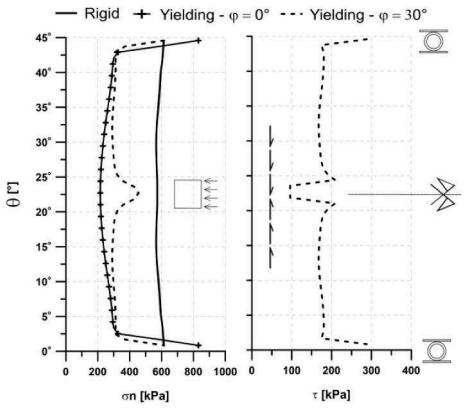

Figure 8. Interface variables: normal (σn) and shear (τ) stresses.

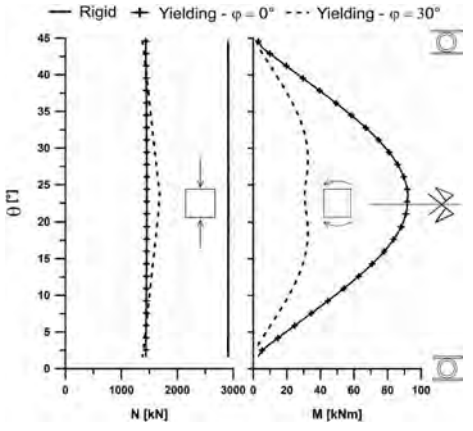

Figure 9. Structural variables: axial load (N), and bending moment (M).

concentration at the beam midpoint has a beneficial effect mitigating the bending moment values.

In line with the previous assumptions, i.e. with the rising value of the interface's friction angle, the maximum axial load increases and the maximum bending moment decreases, the authors find very interesting and useful to represent this trend on the N-M interaction diagram (Figure 10).

This graph clearly shows that the results fit in a linear relationship with a higher gradient than the one of the HEB240 N-M interaction domain. This means that as the friction angle of the contact between soil and lining increases, the severity of load acting on the support tends to reduce (structural beneficial effect). Furthermore, the parametric analysis shows that with the increment of the interface's friction angle, the EPE's axial closure reduces.

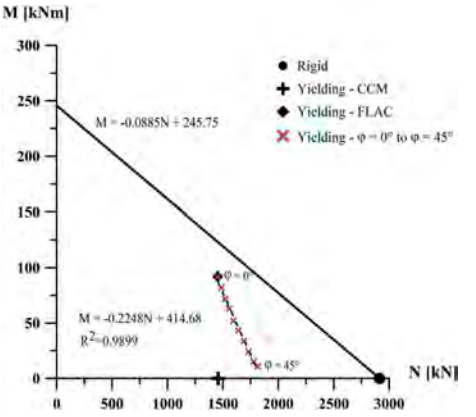

Figure 10. N-M interaction diagram with increasing interface's friction angle (φ from 0° to 45°).

In short, the friction of the contact between soil and lining can be seen as a dissipative device that helps the soil-lining system to support high load.

4 CONCLUSIONS

In the design of preliminary support, followed by the *yielding principle* in *squeezing conditions,* for the extreme rock loads, can be necessary the application of elasto-plastic elements embedded in the lining. These allow the development of the required convergence for sufficiently reducing the load acting on the lining.

In this paper specific 2D parametric numerical analyses have been developed with the aim of studying the soil-lining interaction mechanisms. Particular attention was given to the effects of the interface between soil and lining. The main outcomes can be summarised as follows:

- the insertion of the elasto-plastic elements in the rigid lining leads to an increase of the convergence with an important decrease of the axial load and the emergence of not negligible bending moment;
- the ability of the interface to develop a frictional strength has a beneficial effect on the behaviour of the support system;
- in the design of a yielding lining is of utmost importance the development of numerical analyses, whereas analytical simplified models, such as the Convergence-Confinement Method, should be used as a preliminary tool for preliminary design.

The results obtained by this work provide some relevant insight on the soil-lining interaction of the preliminary support following the *yielding principle*. These are useful to highlight the peculiar aspects of the interaction mechanism both from a kinematic and a static point of view and correctly develops the project.

ACKNOWLEDGMENTS

A deserved acknowledgement must be made to the Professor Kalman Kovári, that with his remarkable experience as well as goodness inspire this work.

REFERENCES

Anagnostou, G., Kovári, K., 1993. Significant parameters in elastoplastic analysis of underground openings. Journal of Geotechnical Engineering, 119(3), 401–419.

Batocchioni, L., Gonzalez, V., Miliziano, S., 2023. Soil-structure interaction of preliminary deformable lining for conventional tunnel in squeezing conditions using HiDSte elements. 2023 ISRM - Salzburg.

Batocchioni, L., Miliziano, S., Gonzalez, V., 2023. Effetti dell'introduzione di elementi elasto-plastici nel rivestimento preliminare di una galleria profonda in condizioni spingenti. XII IAGIG - Padova, 1–4.

Cantieni, L., & Anagnostou, G. (2009). The interaction between yielding supports and squeezing ground. Tunnelling and Underground Space Technology, 24(3), 309–322.

Hoek, E., 2001. Big tunnels in bad rock. Journal of Geotechnical and Geoenvironmental Engineering.

Itasca user manual, 2011. FLAC2D Version 7.0.

Kovári, K., Hagedorn, H., Fritz, P., 1976. Parametric Studies As a Design Aid in Tunnelling. 2nd International Conference on Numer Methods in Geomechanics, 2, 773–790.

Kovári, K., 1998. Tunneling in squeezing rock. Tunnel 5/98.

Lombardi, G., 1975. Qualche aspetto particolare della statica delle cavità sotterranee. Rivista Italiana di Geotecnica, 9, 187–206.

Moritz, B., 2011. Yielding elements–requirements, overview and comparison. Geomechanics and Tunnelling.

Penzien, J., & Wu, C.L., 1998. Stresses in linings of bored tunnels. Earthquake engineering & structural dynamics, 27: 283–300.

Radončić, N., Schubert, W., Moritz, B., 2009. Ductile support design. Geomechanics and Tunnelling.

Ramoni, M., Anagnostou, G., 2010. Thrust force requirements for TBMs in squeezing ground. Tunnelling and Underground Space Technology, 25(4), 433–455.

Song, F., Wang, H., & Jiang, M., 2018. Analytical solutions for lined circular tunnels in viscoelastic rock considering various interface conditions. Applied Mathematical Modelling, 55, 109–130.

Wu, K., Shao, Z., Sharifzadeh, M., Hong, S., Qin, S., 2022. Analytical computation of support characteristic curve for circumferential yielding lining in tunnel design. Journal of Rock Mechanics and Geotechnical Engineering.

Yang, K., Yan, Q., Shi, Z., Zhang, C., Ma, S., 2022. Numerical Study on the Mechanical Behavior of Shotcrete Lining with Yielding Support in Large Deformation Tunnel. Rock Mechanics and Rock Engineering.

Tunnelling for a Better Life – Yan, Celestino, Thewes & Eberhardt (Eds)
© 2024 The Author(s), ISBN 978-1-032-80042-4
Open Access: www.taylorfrancis.com, CC BY-NC-ND 4.0 license

Numerical calculation approach for the design of segmental tunnel lining equipped with inflatable O-ring sealing

Marco Bazzani* & Francesco De Santis
Systra SWS, Trento, Italy

Paolo Fantini
Systra SWS, Torino, Italy

Daniele Maturi
Systra SWS, Trento, Italy

Stefano Pesa
Systra SWS, Torino, Italy

ABSTRACT: This study proposes an effective FEM methodology for the analysis of the structural behaviour and performance of special tunnel lining concrete segment equipped with inflatable O-ring sealing devices, used to limit any potential water inflow within the annular gap. All relevant loading and boundary conditions are evaluated, both those expected during construction phases and during design life of the tunnel. Particular attention is given to the, not so frequently discussed, transient phase of the ring exiting the TBM tailshield and O-ring hose sequential inflation. In this scenario the ring is mainly supported by friction at circumferential joints and TBM rams forces.

The case study of a Double-Shield TBM adopting bi-component grout as backfilling material for the annular gap is presented. Within this framework the analysed rock tunnel has a maximum overburden of 130 m and segment equipped with O-ring sealing devices are installed every 200 rings.

Keywords: Segmental lining construction phases, FEM structural analysis, inflatable O-ring, water barrier

1 INTRODUCTION

Precast concrete segments are the standard technique for shielded TBM final lining and are object of accurate studies and numerical analysis in the design phase. In recent years the number of load cases analysed has increased in many countries, to inquire the lining behaviour under new and more detailed loading conditions.

This study presents the numerical calculation approach developed for the structural dimensioning of a special tunnel lining ring equipped with inflatable O-ring sealing.

After an introduction to this technique and construction sequences, the numerical model, its special load cases, and relevant results in terms of stresses are presented.

2 CHARACTERISTICS OF O-RING TUNNEL LINING

In recent projects, precast elements of segmental tunnel lining fit several cast in-situ accessories to limit any further on-site drilling. A special, and rather uncommon, type of equipment is the inflatable O-ring sealing installed at the extrados of segments (Figure 1).

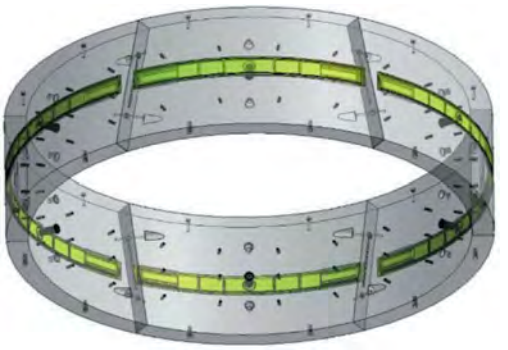

Figure 1. 3D view of segmental tunnel lining equipped with inflatable O-ring sealing system.

*Corresponding author: mbazzani@systra.com

DOI: 10.1201/9781003495505-126

2.1 *O-ring sealing equipment for precast segments*

2.1.1 *Fields of application*

The inflatable O-ring is a technical solution applied in the tunnel industry mainly for two purposes:

- Radial loading transfer:Hoses or bags installed at the extrados of steel ribs or segmental tunnel lining (in case of pea gravel backfilling) are inflated to transfer radial loading from the sound rock to the supporting structure and to guarantee their effective confinement.
- Longitudinal compartmentalization of fluids:Hoses or bags installed on break-in/out devices or at the extrados of segmental tunnel lining to create a barrier against the flow of liquids (grout, groundwater).

This paper presents the O-ring sealing solution applied to precast tunnel segments with the aim of providing a physical water barrier in the annular gap, additional to the bi-component grout injection.

2.1.2 *Adaptation of formwork and reinforcement*

To fulfil its scope without compromising the ring-building operations and the TBM advance, the inflatable bag is housed in a recess obtained at the extrados of the segments by inserting a plastic box in the formworks (Figure 3a).

This recess develops in the circumferential direction at the centre of the ring, locally reducing the thickness of the segments of about 5 cm. To avoid the interference with EPDM gasket, the recess is interrupted at 10 cm from the longitudinal joints. The shape of the inflated bag is studied to guarantee the water barrier over this concrete arch of 10+10 cm at the joint location. Not to affect the durability of the final lining, the steel reinforcement cages are shaped to guarantee the minimum concrete cover around the sealing system (Figure 3b).

2.1.3 *Accessories for O-ring device*

The plastic box adopted for creating the recess and housing the inflatable bag is completed with some accessories:

- Protection sheet on the top of the inflatable bag, to prevent any damages of the sealing system during prefabrication and transient stages.
- Hydro-swelling stripes to prevent water inflow at the interface between the plastic box and the concrete.
- Special socket accessible by the intrados of the segment, to perform the inflation of the O-ring device by cement grout injection (Figure 3).

2.2 *Construction sequence of the O-ring tunnel lining*

The peculiarities of ring assembly inside the shield and of tunnel lining completion are presented in this section. This study considers the Double-Shield mode for the TBM.

2.2.1 *Ring-building phase*

After removing the protection layer, segments are ready to be installed. The ring-building procedure is the same of standard rings. Particular attention must be paid to avoid bumps and to limit misalignments. The spear-bolts at longitudinal joint must be installed and fastened.

2.2.2 *Ring exiting the tailshield*

As TBM advances, the O-ring deflates and swipes outside the shield without colliding with tail brushes (Figure 4a).

Figure 2. Insertion of O-ring box inside formworks and reinforcement cage (source: Optimas).

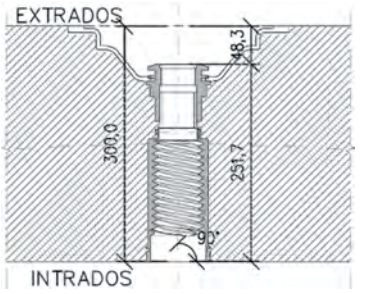

Figure 3. Detail of O-ring sealing system injection socket.

Backfilling injection is stopped on the standard ring before the O-ring guaranteeing an empty annular gap, necessary for the sealing bag inflation.

2.2.3 *O-ring inflation*

Once the O-ring has completely exited the tailshield, the TBM advancement is stopped, and the O-ring inflation can start (Figure 4b).

First, the inflatable bags are filled with a controlled-pressure cement grout injection (< 3 bar) performed segment by-segment, starting from the invert up to the crown.

Once the complete O-ring has been partially filled with cement grout, a second round of injection is performed to ensure the complete bag extension and the

radial loading of the O-ring. The pressure is limited to 5 bar to avoid local overloading on the tunnel lining. Spear-bolts at longitudinal joints guarantee sufficient shear resistance to sustain punctual loads produced by localized injection pressures.

2.2.4 *Completion of annular gap backfilling*

After the minimum required curing of the cement grout inside the inflatable bags, the TBM advance can restart, and, in parallel with it, the concurrent backfilling injection performed through the tail-shield. This operation must be performed avoiding excessive injection pressure (Figure 4c).

To seal the annular gap all around the O-ring and to provide a regular lateral support, secondary backfilling injections are performed upstream and eventually downstream of the inflated water barrier (Figure 4d).

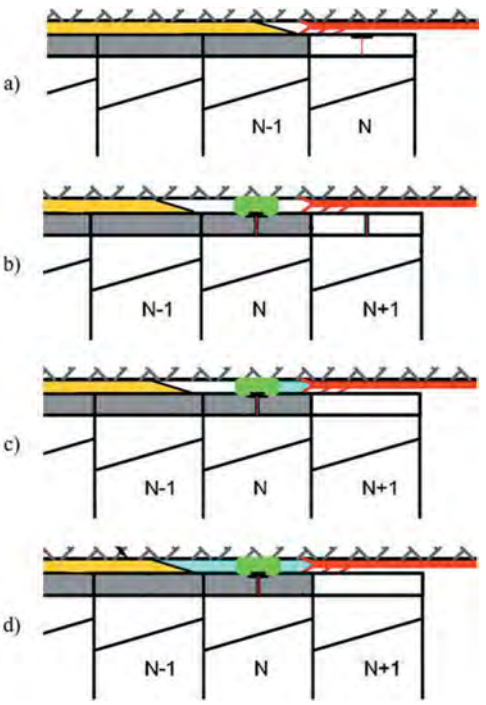

Figure 4. O-ring building and injection phases.

3 STRUCTURAL MODELLING OF O-RING TUNNEL LINING

A numerical study has been performed to simulate the structural behaviour of segments equipped with O-ring sealing devices.

A 3D FE model (Figure 5) has been developed using the software Strand7 (produced and distributed by Strand7 Ltd, Australia). A portion of the tunnel with a length equal to four consecutive rings (each made up of six segments) is implemented. The segments are modelled using 2D plate elements whose main characteristics are described hereafter:

- Dimensions: 0.14 x 0.15 m
- Thickness: 0.3 m
- Thickness at O-ring recess: 0.245 m (green)
- N° of plate elements per ring: 1728.

To consider the actual geometry of the tunnel, each ring is rotated of 30° compared to the previous one. The material behaviour of concrete has been considered as linear elastic.

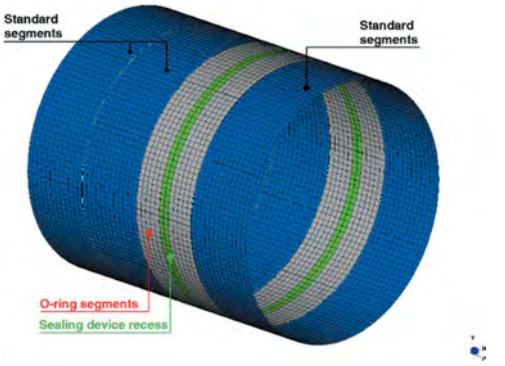

Figure 5. Overview of the adopted 3D model.

3.1 *Longitudinal joint behaviour assumptions*

Particular attention has been given to the modelling of longitudinal joints; the dimensions of the contact are 185mm x 1650mm (Figure 6).

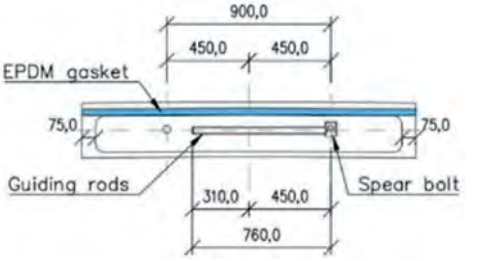

Figure 6. Contact area at longitudinal joints.

The surface of longitudinal joints is modelled adopting *point contact elements* with high axial stiffness acting only when subjected to compressive stresses. As shown in Figure 7, each *contact element* (red) is connected to the ring element *plate* by means of a series of *rigid links* (cyan).

The stiffness for each contact element in the joint has been considered as follows:

- Young's modulus of concrete: E_{cm}=39941 MPa
- Area of contact zone: A=3.05×105mm^2
- N° of joint links: n_1 = 13
- N° of elements per joint link: n_c = 18
- Reference length: L = 300 mm

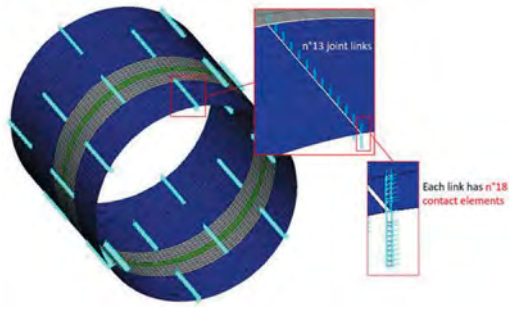

Figure 7. Detail of longitudinal joints modelling.

The reference length (L) has been set equal to thickness of the segmental lining. The overall stiffness of the longitudinal joint has been estimated as:

$$k_{TOT} = \frac{E_{cm}A}{L}$$

Hence, the specific stiffness for each contact element:

$$k_{i,FEM} = \frac{k_{TOT}}{n_1 \cdot n_c}$$

3.2 *Circumferential joint behaviour assumptions*

The contact zone between adjacent rings is characterized by the presence of five packers made of PP plastic material. Packers are modelled as *connection elements* whose behaviour has been defined considering the following parameters:

- Packer length: b_p=450mm
- Packer height: h_p=170mm
- Packer thickness t_p=2mm
- Area of each packer: A=7.65×104mm^2
- Young's modulus of packer: E=200 MPa
- N° of packers per joint np=5

The overall axial and tangential stiffness for each packer has been set equal to:

$$k_{p,Axial} = E_m \cdot A_p / t_p$$
$$k_{p,Tang} = 0.4 \cdot k_{p,Axial}$$

Considering n°=5 packer for each contact area, the overall coupling stiffness for each ring corresponds to:

$$K_{Axial} = n_{Segm} \cdot n_p \cdot k_{p,Axial}$$
$$K_{Tang} = n_{Segm} \cdot n_p \cdot k_{p,Tang}$$

From these values, the stiffness of each connection element included in the model has been defined dividing the stiffness of the ring joint contact area by the number of elements connecting one ring to the adjacent one (n_{cp} = 120 - Figure 8).

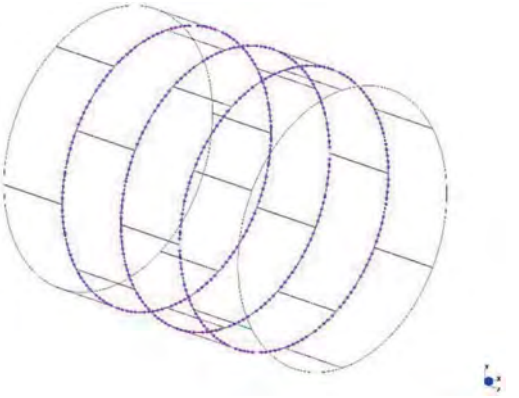

Figure 8. Connection element for friction coupling at ring joint.

3.3 *Connector behaviour assumptions*

Longitudinal connectors between rings have been modelled using *connection elements* (Figure 9).

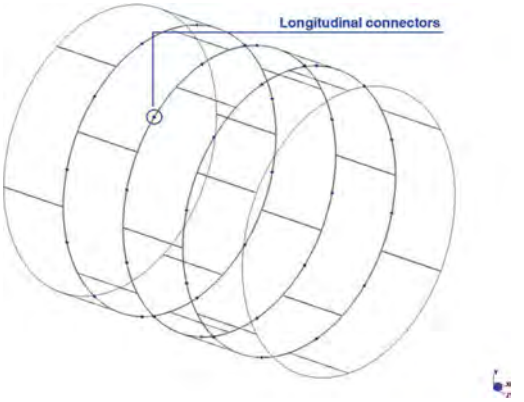

Figure 9. Connection element for longitudinal connectors.

To define the actual behaviour of longitudinal connectors, the *connection elements* have been provided with the constitutive law (shear force-displacement and pull-out force- displacement) provided by the connector supplier.

3.4 *Boundary conditions*

The rock-structure interaction has been considered by means of spring acting perpendicularly and tangentially to the lining surface. Radial springs have been considered with a non-linear behaviour, working only when in compression. Tangential bedding is coupled to radial one and they both deactivate simultaneously as the interface of the lining develops inwards displacement.

The stiffness of boundary springs has been evaluated in relation with rock and backfilling elastic modulus.

When bicomponent as backfilling material is applied, an extended approach is used based on a layered ground model. With this approach the annular gap and the surrounding ground are treated as an individual equivalent layer.

$$k_R = \frac{1}{\frac{d_{ag}}{E_{s,ag}} + \frac{d_{rm}}{E_{s,rm}}}$$

$$k_T = 0.4 \times k_{r,3h}$$

Where:

- k_R: radial bedding modulus [MPa/m]
- k_T: tangential bedding modulus [MPa/m]
- d_{ag}: average width of the annular gap [m]
- d_{rm}: influence depth of the rock mass [m]
- $E_{s,ag}$: constrained modulus of backfilled material [MPa]
- $E_{s,rm}$: constrained modulus of the rock mass [MPa]

According to bicomponent grout supplier, the following E-modulus – time law has been considered for the definition of the E values at the relevant time stages considered in the design of segments.

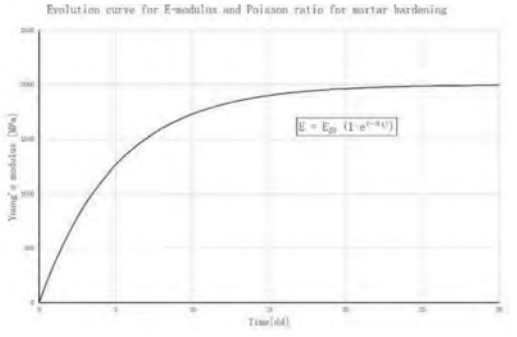

Figure 10. E-modulus-time law for bicomponent grout.

4 DESIGN SCENARIOS FOR O-RING TUNNEL LINING

O-ring tunnel segments follow a different installation procedure compared to the standard ones and the main differences are due to inflation sequence of the O-ring system. In fact, to allow proper expansion of the inflation bag, continuous injection of the bicomponent through the TBM shield must be temporarily stopped. In the time interval between stopping injection through the shield, and O-ring inflation, the O-ring is not supported by the rock mass as the annular gap is not filled.

The following paragraphs describe what are the boundary conditions and load assumptions considered to properly evaluate the expected structural behaviour of the O-ring segments at early stages.

It is noted that once the annular backfilling completion occurs, the behaviour of O-ring segments is practically comparable to the one expected for standard segments. The recess hosting the inflatable sealing shall in any case be considered when design verifications are carried out.

4.1 *External loads*

The design load and boundary conditions expected to occur during O-ring installation, mainly due to the TBM operational special sequence, are accompanied together with loads referred to the external environment in which the tunnel will be executed.

Here is a summary of the remaining external loads that have been considered for the design of the O-ring segments.

[G1] Self Weight

The self-weight of the structure is automatically applied by the software based on:

- Volume of elements
- Specific weight of concrete γ_C=25kN/m^3

[G2] Bi component

This load considers the weight of the bicomponent grout that will be injected within the annular gap between the tunnel ring and the external rock mass. This load is defined assuming:

- Specific weight of grout γ_G=12.6kN/m^3
- Annular gap thickness: t= 0.19m

The bicomponent self-wight has been applied as a vertical distributed load (Figure 11), varying linearly from a maximum value at the key of the ring, to a null value at level of tunnel longitudinal axis.

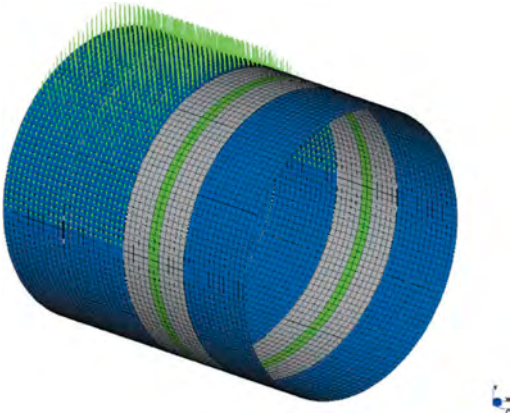

Figure 11. Bicomponent weight application.

[G3] Rock Wedge collapse

To simulate the effects of the geotechnical load expected in the region where the O-ring segments will be installed, it is assumed the weight of a triangular shaped rock wedge with a height equal to the

excavation diameter. The pressure due to wedge collapse has been calculated considering a specific weight of the rock equal to γ_R=27kN/m^3. The load has been applied to the FE model (Figure 12) throughout a distributed pressure with a triangular shape that has its peak at the key section in a way to generate a vertical force that is equal to the weight of the design rock wedge (F=973 kN).

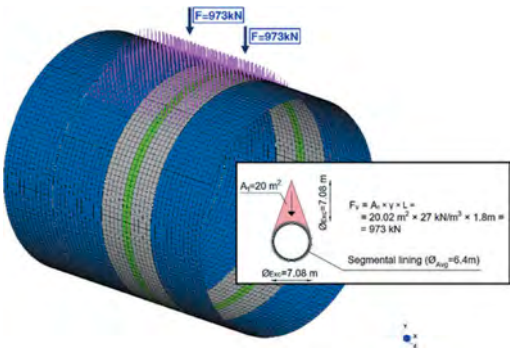

Figure 12. Rock wedge load calculation and application.

[Q01/a] Temperature Load

Winter and summer characteristic temperature loads have been defined considering two scenarios, both in permanent and transient conditions, varying the temperature of the rock mass between the values T_{Rock} = +4 - +12°C.

To define both uniform and variable temperature load, the initial value that defines the temperature of segments during installation has been set equal to T_0 =+10°C.

The temperature of the internal environment has been set instead equal to:

Summer	
Permanent	Construction
15	25
Winter	
Permanent	Construction
1	25

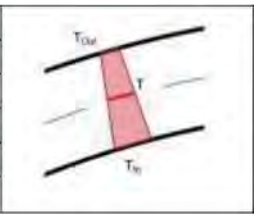

Figure 13. Temperature load.

4.2 *Ring exiting the tailshield*

Once the O-ring segment is about to exit the TBM shield, bi-component grout injection is stopped. At this stage, the annular gap is effectively filled only at the rings that precedes the O-ring. Most likely, also part of the annular gap at O-ring will be filled with grout, but on the safety side, it has been chosen to neglect the eventual partial bedding that will generate at O-ring.

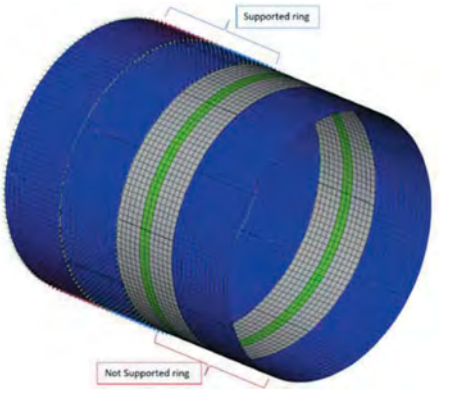

Hence, the following boundary conditions has been considered:

- Radial and tangential bedding at the two segments that precede the O-ring segment.
- Bedding stiffness is defined assuming the E modulus of the bi-component grout at t=3hr, E (t=3h)=50MPa. The associated stiffness is computed by implementing the formulation shown in §4.4.

Also TBM rams forces are considered by means of a distributed pressure acting at the ring joint of ring installed after O-ring segments still placed within TBM shield.

The value of this pressure is defined assuming that the TBM thrust is operating in double shield mode $F_{Nom,DS}$ = 8 MN.

Within this configuration (Figure 14), in addition to the structural self-weight, the possibility of a rock wedge acting right above the O-ring ring and the previously installed one is considered, while the bicomponent self-weight has been simulated as acting only on the rings that precedes the O-ring.

$$p = \frac{F_{Nom,DS}}{t \cdot Crf} = 1.32\,MPa$$

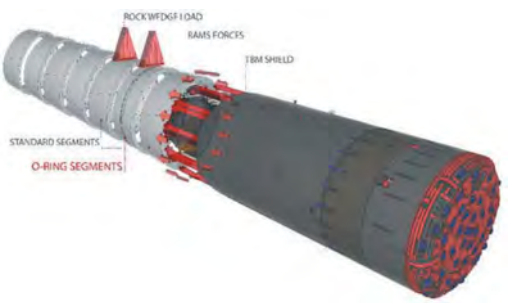

Figure 14. Overview of O-ring segments exiting TBM shield.

4.3 *O-ring inflation*

Once the O-ring segments have exited the TBM shield, the sealing device inflation takes places. In this stage the boundary conditions and the restrains applied to the model remain unvaried compared to the previous stage.

In addition to the boundary conditions and loads described in the previous paragraph, a radial pressure of 3bar is applied to the lower half of the ring to simulate the first step of the sealing device inflation.

The radial pressure is applied only to the central portion of the ring (Figure 15), where the sealing device will be located (≈300mm).

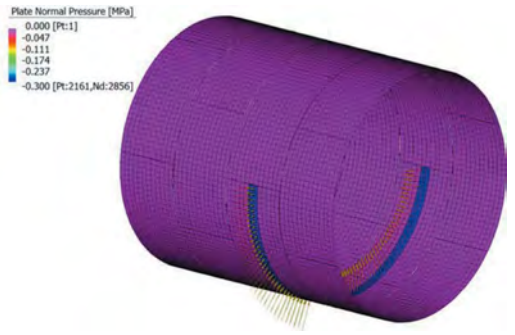

Figure 15. O-ring inflation 1st step.

The second step of the inflation sequence is modelled with a pressure applied to the entire area, all along the ring circumference, occupied by the sealing device (≈300mm), and the value is set equal to 5bar.

Also in this second and final step of the inflation sequence, the boundary conditions as well as the external loads remain unvaried compared to the ones illustrated in the previous paragraph.

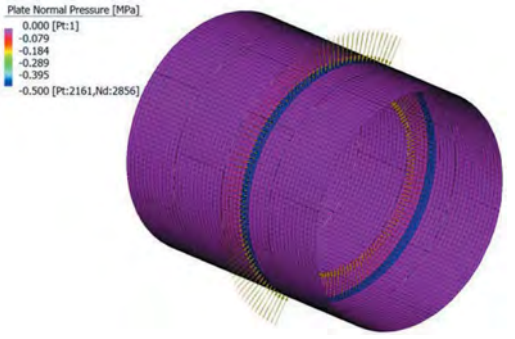

Figure 16. O-ring inflation 2nd step.

4.4 *Asymmetric water load during service phase*

Due to the water flow-limiting behaviour of the O-ring sealing device, it may occur that the water pressure acting at one side of the O-ring segment may differ from the value acting at the opposite side. Hence, this eventuality has been simulated by applying a differential water pressure to the FE model. The value of the differential water load has been estimated considering the maximum overburden level variation Δz that has been encountered within the distance at which to consecutive O-ring segments will be installed. The load is applied to the model considering the water pressure associated with the recorded overburden variation $w = \Delta z \times \gamma_w$ on the elements that precedes the sealing device, while no load is applied to the remaining portion of the model.

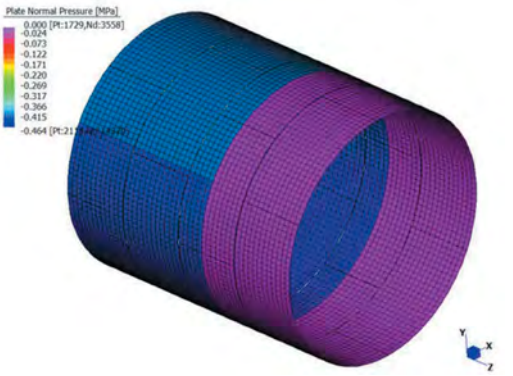

Figure 17. Asymmetric water load in service phase.

5 STRESS STATE IN O-RING TUNNEL LINING

Aim of this section is to describe what are the results obtained from the performed FE analysis.

It is noted that the scenario related to the O-ring exiting from the tailshield represents the decisive one with regards to the design amount of reinforcement. This is mainly due to the lack of confinement that occurs on the ring due to the void located within the annular gap. While on one side, the flexural request is very similar to the one registered in standard segments where radial bedding is active, the axial force registered within the ring is significantly lower, leading to a higher demand of reinforcement aimed at fulfilling all relevant sectional verifications.

The following Figure 18 and Figure 19 show the recorded contour of internal forces. It is noted that, due to the presence of the recess hosting the O-ring sealing, reinforcement design and verifications are carried out also with regards to the longitudinal direction (parallel to tunnel axis).

Once the inflation of sealing device takes place, when the inflation pressure (5bar) is acting on the entire ring, a significant increase of flexural demand is recorded in the longitudinal direction (yy) at the crown area, due to simultaneous presence of the inflation pressure and the rock wedge load.

These scenarios referred to the early stages during the ring installation phase are the decisive ones with

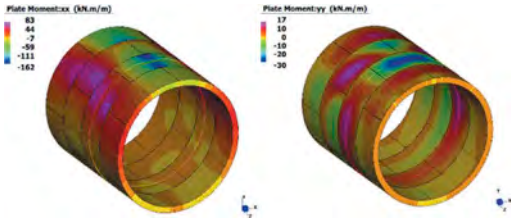

Figure 18. Contours of bending moment when O-ring segments exit the tailshield.

xx: circumferential direction.

yy: longitudinal direction.

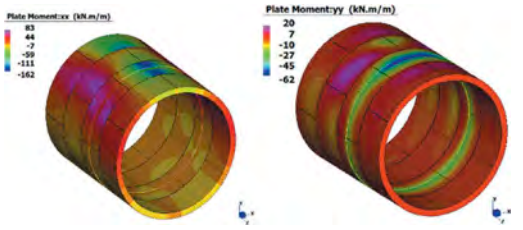

Figure 19. Contours of bending moment at the final step of the O-ring sealing inflation.

xx: circumferential direction.

yy: longitudinal direction.

regards to the reinforcement amount O-ring segments need to be provided with. The FE analysis results and the design verifications that have been carried out show that the critical section is in the key segment.

The M-N interaction domains shown in Figure 20 and Figure 21 referred to the O-ring section show the ULS verifications for the most critical investigated scenario.

The decisive case with regards to circumferential reinforcement is referred to the exit from the TBM shield. Once the inflation of the sealing device starts, the progressive increase of axial forces shifts the design M-N values towards the centre of the section M-N interaction domain, identifying a less demanding scenario. It is also observed that after the annular gap backfilling completion, mainly due to the stiffer support given by the surrounding environment, the recorded internal forces are again less demanding compared to the very early stages after ring assembly. The verification of the O-ring key section in ULS condition are shown in Figure 20, referring to circumferential direction (N_{xx} - M_{xx}).

With regards to the longitudinal direction (yy), the decisive scenario is recorded during the last inflation step, when the 5bar pressure is acting on the entire ring. The verification of the O-ring key section in ULS condition are shown in Figure 21, referring to circumferential direction (N_{yy} - M_{yy}).

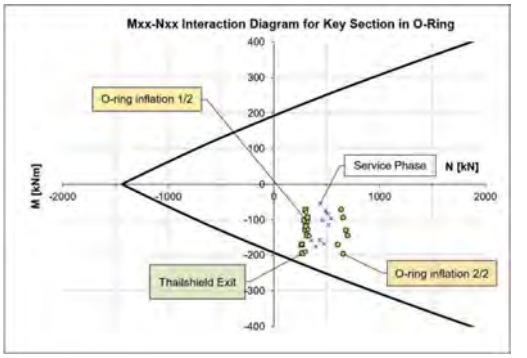

Figure 20. Verification of circumferential reinforcement.

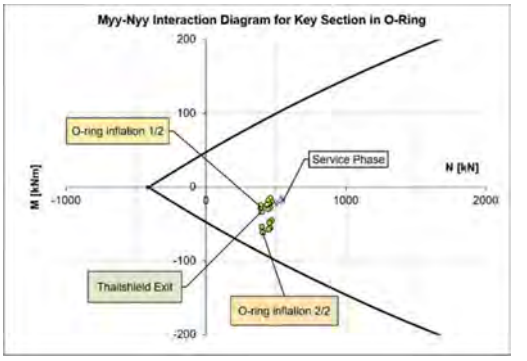

Figure 21. Verification of longitudinal reinforcement.

6 CONCLUSIONS

This article proposes a numerical modelling approach able to simulate the stress state acting within O-ring segments, which are assembled in a double shielded TBM.

Loads and constrain configurations have been implemented in the FEM model thanks to a meticulous study of the design scenarios, especially referring to the assembly sequences of rings equipped with O-ring type hydraulic sealing system.

The outcomes of the analyses show how these configurations are significantly critical and, in some cases, even dimensioning with regards to the design reinforcement.

REFERENCES

EN 1990, 2002. Eurocode: Basis of structural design.

EN 1992-1-1, 2004. Eurocode 2: Design of concrete structures - Part 1: General rules and rules for buildings.

AITES, 2019.Guidelines for the design of segmental tunnel linings.

DAUB, 2013. Recommendations for the design, production and installation of segmental rings.

Fib Bulletin n°83, 2017. Precast tunnel segments in fibre-reinforced concrete.

ACI 544.7R-16, 2016. Report on Design and Construction of Fiber-Reinforced Precast Concrete Tunnel Segments.

Lee, H. S., Kim, D. Y., 2006. Tunneling in Severe Groundwater Inflow Condition. Journal of the Korean Society of Geotechnical and Environmental Engineering. Vol. 7, No. 2, pp. 67–76.

Rahbar, A., Lees, D. J., Hosseini, A. H., Shahrokhi, Z., Wenner, D., 2017. The Design and Construction of Grouting against Water Ingress in the Headrace Tunnel for the Uma Oya Project, Sri Lanka. Proceedings of the World Tunnel Congress 2017 – Surface challenges – Underground solutions. Bergen, Norway.

Henzinger, M. R., 2019. Bedding of segmental linings at hard rock TBM tunnels. Doctoral thesis. Department of Civil Engineering Graz University of Technology.

Tunnelling for a Better Life – Yan, Celestino, Thewes & Eberhardt (Eds)
© 2024 The Author(s), ISBN 978-1-032-80042-4
Open Access: www.taylorfrancis.com, CC BY-NC-ND 4.0 license

The mechanism, functioning and installation of reinforced ribs of shotcrete in Norwegian Method of Tunnelling (NMT)

Rajinder Bhasin* & Mahdi Shabanimashcool
Norwegian Geotechnical Institute, Oslo, Norway

ABSTRACT: One of the key components of rock support in the Norwegian Method of Tunnelling (NMT) is the application of reinforced ribs of shotcrete (RRS) in tunnels. This basically comprises of six rebars with a center to center spacing of 10 cm mounted to rock bolts along the tunnel periphery and covered with sprayed concrete. During the last 25 years or so RRS has in many cases been installed in Norwegian tunnels instead of the in situ cast concrete arches (CCA) and heavy steel ribs. CCA was the common rock support in extremely and exceptionally poor rock masses when the rock mass quality Q was very low. RRS is in shape and support capacity similar to sprayed lattice girders but is more flexible in application because RRS is not prefabricated. In most cases RRS has been installed without any analysis of the support pressure or calculations of its capacity. RRS is considered to function as an active support which is in intimate contact with the rock mass and held in place through closely spaced rock bolts at 1m c/c spacing. It is envisaged that the bolts holding the RRS do not have any effect on load, shear force and bending moment distribution in RRS and that they only guarantee full contact of RRS with the rock mass. Thus, RRS functions as a liner element and behaves like a beam element which is in contact with the rock mass. This paper attempts to explain the mechanism of RRS and describe in detail its functioning & installation as a flexible rock support system. Some experimental and numerical results from literature on the behaviour of RRS are highlighted.

Keywords: Rock Support, Shotcrete, Reinforced Ribs of Shotcrete, Norwegian Tunnelling Method

1 INTRODUCTION

The Norwegian Method of Tunnelling (NMT) is a well-known underground construction technique that effectively minimizes the use of concrete and thereby contributes to reducing the production of CO_2 (Barton, 2017). NMT is emphasised by its single shell characteristics and differs from the conventional double shell New Austrian Tunnelling Method (NATM). In Norway alone more than 7000 kilometres of tunnels including hydropower, road and rail tunnels have been constructed using Norwegian Tunnelling Technology. The NMT method is considered safe, cost-effective & time saving. In addition to Norway, this tunnelling technology has been successfully adopted in various parts of the world including Korea, India and Sweden. This paper describes in general the design and installation of rock support according to NMT Principles. Emphasis is placed on reinforced ribs of shotcrete (RRS) which has revolutionized the installation of rock support in weak rock masses. RRS has for all practical purposes replaced cast concrete arches (CCA) and steel ribs in incompetent rock masses where the rock mass quality 'Q' characterised with the Q-system of rock mass classification is very poor to exceptionally poor (Barton et al, 1974, NGI 2017).

2 DOCUMENTATION AND OBSERVATIONS DURING UNDERGROUND EXCAVATION IN NMT

During underground excavation in Norwegian tunnels, it is very important to have a close visual inspection of the rock surface in the whole tunnel periphery before the rock is covered by sprayed concrete (NPRA, 2020). In addition to the visual observations, hammering with a scaling rod or a hammer will give important indications of deterioration of unstable rock giving particular sounds. Small cracks, invisible from the invert, can be observed with a closer look. It is important to have access to the face and crown by utilizing lifting equipment especially designed for this purpose. Rock mass stability is influenced by several parameters, but the following three factors are the most important as described in the Q-system of rock mass classification (see for e.g. NGI, 2017):

- Degree of jointing (block size): RQD/Jn
- Joint friction: Jr/Ja
- Stress: Jw/SRF

In hard rocks, deformations usually occur as shear displacements along joints. The friction along the joints will therefore be significant for rock mass

*Corresponding author: rkb@ngi.no

DOI: 10.1201/9781003495505-127

stability. Joint friction is dependent on joint roughness as well as thickness and type of mineral fillings. Very rough joints, joints with no filling or joints with only a thin, hard mineral filling will be favorable for stability. On the other hand, smooth joint surfaces and/or a thick filling of soft minerals will result in low friction and poor stability. In soft rocks where deformation is less dependent of joints, the joint friction factor is less significant.

The vertical stress in a rock mass commonly depends on the depth below the surface. However, tectonic stresses and anisotropic stresses due to topography can be more influential in some areas. This also applies for residual stresses inherent in some rock masses. Stability of the underground excavation will generally depend on the stress magnitude in relation to the rock strength. Moderate stresses are usually favorable for stability, and low stresses are often unfavorable. In rock masses intersected by zones of weak mineral fillings such as clay or crushed rock, the stress situation may vary considerably within relatively small areas. Experience from tunnel projects in Norway has shown that if the magnitude of the major principal stress approaches about 1/5 of the compressive strength of the rock, spalling (strain bursting) may occur (NPRA, 2020). When tangential stresses exceed the magnitude of the rock compressive strength, squeezing may occur. In other words, the anisotropy of the rock mass plays an important role when designing rock support.

2.1 *Application of Q-system to determine rock support*

Q-value and the six appurtenant parameter values give a description of the rock mass. Based on documented case histories a relation between the Q-value and the permanent support is found which can be used as a guide for the design of support in new underground projects. In addition to the rock mass quality (the Q-value) two other factors are decisive for the support design in underground openings and caverns. These factors are the safety requirements and the dimensions, i.e., the span or height of the underground opening. Generally, there will be an increasing need for support with increasing span and increasing wall height.

Safety requirements will depend on the use (purpose) of the excavation. A road tunnel or an underground powerhouse will need a higher level of safety than a water tunnel or a temporary excavation in a mine. To express safety requirements, a factor called ESR (Excavation Support Ratio) is used (Barton et al, 1974, NGI, 2017). A low ESR value indicates the need for a high level of safety while higher ESR values indicate that a lower level of safety requirement. The safety requirements and building traditions in each country may lead to different ESR-values than those given in a table in the Q-system.

The Q-value and the Equivalent dimension will be decisive for the permanent support design. In the support design chart shown in Figure 1, the Q-values are plotted along the horizontal axis and the Equivalent dimension along the vertical axis on the left-hand side. The support chart gives an average of the empirical data from examined cases. For a given combination of Q-value and Equivalent dimension, a given type of support has been used and the support chart has been divided into areas according to type of support. Note that the chart is not divided into definite support classes but shown as a continuous scale both for bolt spacing and thickness of sprayed concrete.

As the support chart is based on empirical data, it is able to function as a guideline for the design of permanent support in underground openings and caverns. The support chart indicates what type of support is used in terms of the center to center spacing for rock bolts and the thickness of sprayed concrete (shotcrete). It also indicates the energy absorption of the fibre reinforced sprayed concrete, as well as the bolt length and design of reinforced ribs of sprayed concrete. Support recommendations given in the chart are general. In especially difficult cases, an increase in the amount or type of support may be relevant.

The thickness of the sprayed concrete increases towards decreasing Q-values and increasing spans, and lines are drawn in the support chart indicating thicknesses. For positions between these lines the thicknesses will have an intermediate value. If deformation occurs, for instance caused by high stresses, reinforced concrete should be used in all categories.

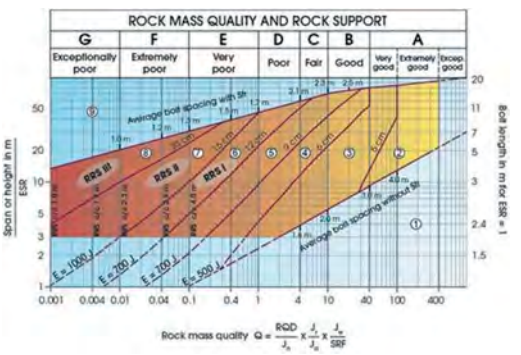

Figure 1. Rock mass quality Q related to the rock support requirements (NGI, 2017).

The length of the rock bolts depends on the span or wall height of the underground opening and to some degree on the rock mass quality. Recommendations for bolt lengths are given on the right-hand side of the diagram, but some evaluation is necessary. In unfavorable joint geometry, longer bolts than recommended in the diagram will be necessary, and there is also a general need for increasing bolt length by decreasing Q-value.

3 ROCK SUPPORT IN TUNNELS USING RRS

As mentioned in the previous section, rock support with reinforced ribs of sprayed shotcrete (RRS) arches has in many cases replaced the more traditional full cast concrete arches (CCA). This solution saves both time and costs. Reinforced ribs of shotcrete (RRS) must always be combined with bolts that are distributed throughout the arch. Normally, the distance between the installed bolts in the arch should be about 1.5 meters. The bolts should be long enough to be included as part of the rock support system. Figure 2 shows the principle of construction of RRS.

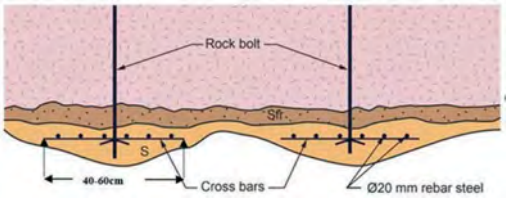

Figure 2. Principal of construction of RRS (NGI, 2017).

An important prerequisite for using RRS is proper workmanship and good quality control. When the sprayed concrete arches are subjected to heavy loads, the reinforcement will begin to act gradually as the deformations increase. The reinforcement in the arches should prevent further deformation. It is therefore important that the number of rebars in each section of RRS and the thickness and width of the sprayed arches are dimensioned in relation to the expected load on rock support. Normally, Ø20 mm rebars are used as they can be shaped according to the tunnel profile.

3.1 *Installation of RRS*

To ensure the best possible arch effect, the tunnel profile should be levelled with sprayed shotcrete. In poor rock conditions where RRS is to be installed, the theoretical profile is usually over excavated by around 30-60cm compared to the normally excavated profile. If necessary, scaling of rock is performed in a very careful manner. Normally a first layer of fibre reinforced shotcrete is sprayed up to a thickness of about 15-25 cm depending upon the rock mass quality followed by spraying a second layer of shotcrete without fibres to make the surface even for installation of rebars for RRS. The sprayed section must be at least 70 cm wide to accommodate the six rebars that shall be installed. In Norway it has been most common to use 6 pieces of 20 mm diameter rebars in each arch, mounted with crossbars of 40 cm to 60 cm (see Figure 2).

A crossbar is attached to the radial bolts, for example by drilling holes in the crossbar that is threaded onto the bolt and fastened with a screw and nut. The reinforcement is thus clamped behind the crosspiece, which can advantageously have notches or grooves for the rebar. Jointing of the rebars should be carried out with overlap behind the transverse irons. Figure 3 shows the installation of RRS near the face of a tunnel in the North of Norway. Note that the face of the tunnel is supported by shotcrete and bolts due to poor rock mass quality.

Figure 3. RRS installed close to the face of a tunnel where the tunnel face is also supported by bolts & shotcrete.

A fused construction of sprayed concrete arches can be constructed for increasing the capacity of RRS by mounting several rebars in several layers, increasing the thickness of the arcs and reducing the distance between the arches (NPRA, 2020). A third layer of shotcrete is then sprayed

without the fibres to cover the reinforcement. The total thickness of shotcrete including the second and third layer is approximately 30 cm.

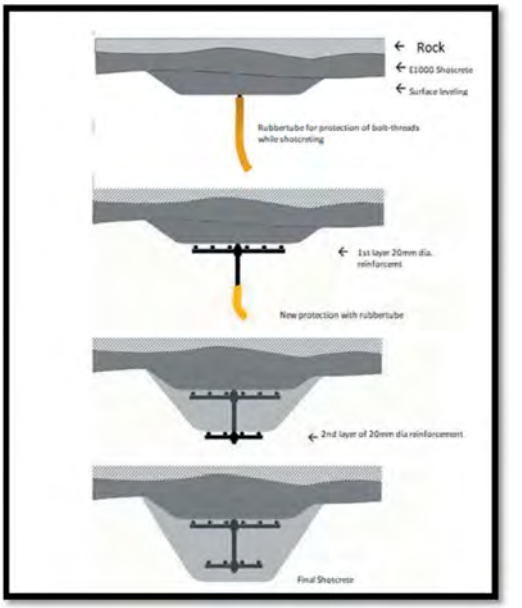

Figure 4. Mounting of rebars in several layers (double RRS) and radial bolts (Adapted from NPRA, 2020).

Figure 5 Shows the pipe umbrella roof system which was erected in a tunnel before installation of double RRS (see Figure 4) in very poor rock masses in the North of Norway. The pipe umbrella (12-15 meter in length) was implemented as pre-support to increase the stability of the tunnel and to decrease the risk of surface subsidence induced by tunnelling in the prevalent weak rock masses (disintegrated rock) at the section. The pipe roofing system consisted of 114 mm diameter pipes with a 3 m overlap. The working face of this tunnel was supported by supported by 32 mm dia. and 12 m long bolts which were sheared off after every excavation sequence and fastened with new bolt plates. The spacing of the RRS is about 1.5m along the length of the tunnel.

Figure 5. Pipe roofing prior to the installation of double RRS.

4 FUNCTIONING OF RRS

It is widely believed that RRS functions as an active support and is not passive in nature. This is due to the fact that RRS is in intimate contact with the rock mass and held in place through closely spaced rock bolts at 1.0-1.5m c/c spacing. It is envisaged that the bolts do not have any effect on load, shear force and bending moment distribution in RRS, they only guarantee full contact of RRS and rock mass. Keeping the above facts in mind, RRS will function as a liner element in this situation. This means that it will behave like a beam element which is in contact with the rock mass.

In most of the cases where RRS has been installed, it has served the purpose of supporting the rock mass. However, the exact bearing capacity and the behaviour of RRS under various loading conditions is still not well understood. Although RRS has been instrumented in a number of tunnels (see Figure6) to obtain information on the axial forces and strains in the rebars, the gathered data shows insignificant stresses and strains in RRS. This may be due to the fact that the instrumented sections did not have high overburden or that the rock support was overdesigned meaning that RRS was not necessary.

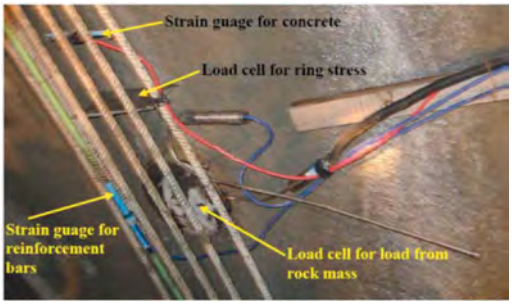

Figure 6. Instrumentation of RRS (photo: NGI).

Another reason why small loads and strains are recorded during instrumentation can be due to the fact that the location of rebars in RRS may not be appropriately located in the existing design cross-section (see Figure 2). It may be noticed that in the current design of RRS, as shown in Figure 2 the rebars are located in the outer side of the whole section comprising of the liner element. It is possible that this reinforcement should be placed in both the inner and outer part for better functioning. This issue has recently been investigated by researchers in South Korea which is described in the section underneath.

4 EXPERIMENTAL AND NUMERICAL STUDIES

Various researchers (e.g. Yu et al, 2016) have carried out experimental and numerical studies on studying the behaviour of RRS. Their results have indicated that placing the reinforcement bars at the bottom of the cross-section has no significant effect on improving the load-carrying capacity compared to a beam made of fibre reinforced shotcrete only.

The researchers performed numerical experiments on various types of shotcrete liners (see Figure 7). Prior to performing numerical analysis, they validated their numerical model with experiments results. The numerical model was implemented by OpenSees, which was developed by University of California to simulate the seismic response of structural and geotechnical systems.

In the numerical experiments it was shown that the peak load of the section B was slightly higher than that of A by approximately 1.5%. This means that reinforcing the rebar at the bottom of the cross-section has no significant effect on improving the load-carrying capacity. Compared with the post-peak load–displacements values, it is found that the supporting effect of C is superior to other cross sections.

Their overall results indicated that behaviors of the shotcrete lining based on the configuration of reinforcements show a significant difference. The maximum load-carrying capacity of the liner with doubly reinforced cross-section increases by

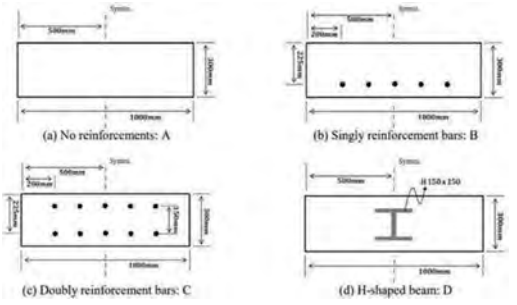

Figure 7. Cross-section of shotcrete liners, A: shotcrete only, B: singly reinforced bars, C: doubly reinforced bars, and D: H-shaped support (Yu et al, 2016).

10.21% when compared with the liner without reinforcements. Beyond the peak load, all the cases shown in could resist load softening (see Figure 8). Among them, however, the doubly reinforced cross-section shows the most supporting effects (in particular for the post-peak region) while the singly reinforced cross-section has almost no improvement. From the results of load-displacement curves, steel rebar type could be used as an alternative the previous steel reinforcement types such as H-shaped beam and lattice girder.

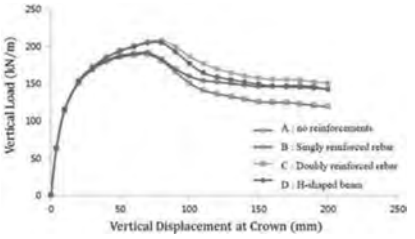

Figure 8. Load-displacement response of shotcrete with and without reinforcement (Yu et al, 2016).

What's important to remember is that the design of the structure is based on having the steel in the right place. Incorrect reinforcing steel placement can and has led to serious concrete structural failures. For example, lowering the top bars or raising the bottom bars by ½ inch more than that specified in a 6-inch-deep slab could reduce its load-carrying capacity by 20%.

Steel reinforcing bars and welded wire reinforcement should be positioned in the upper third of the slab thickness because shrinkage and temperature cracks originate at the surface of the slab. Cracks are wider at the surface and narrow with depth.

5 CONCLUSIONS

This paper has described one of the key components of the Norwegian Method of Tunnelling (NMT), which is the application of Reinforced Ribs of Shotcrete (RRS) as rock support in tunnels. RRS has practically replaced cost expensive cast concrete arches (CCA) and steel ribs as rock support in tunnels. One major advantage of RRS is that the reinforced ribs are in close contact with the rock mass and there is no gap or shadows formed between the final lining and the rock mass. This helps to avoid unwanted differential deformations around the periphery of the tunnel that may occur due to potential gaps between the final lining and the rock mass. Pre-spraying of shotcrete for immediate support helps to retain the self-bearing capacity or the inherent strength of the rock mass. In the cases where RRS are used, it is important to first utilise fibre reinforced sprayed concrete (Sfr) before applying a second smoothening layer of shotcrete without fibres. A guideline for use of RRS in relation to Q-values and equivalent dimension of the underground opening is given in the support chart of the Q-system (NGI, 2017).

ACKNOWLEDGMENTS

The authors acknowledge the support and literature utilised from the Norwegian Public Roads Administration (NPRA) and the Norwegian Tunnelling Society (NFF) for preparing this manuscript. The authors are also thankful to their colleague Dr. Pål Drevland Jacobsen for making arrangement for the tunnel site visit where double RRS were erected.

REFERENCES

Barton, N., R. Lien and J. Lunde, 1974, "Engineering classification of rock masses for the design of tunnel support", Rock Mechanics,Vol. 6, No. 4, pp. 189 236.

Barton, N., 2017 Minimizing the use of concrete in tunnels and caverns: comparing NATM and NMT. Innovative Infrastructure Solutions Volume 2 issue 1, Dec 2017, 2:52 DOI10.1007/s41062-017-0071-x

NFF, 2014. Norwegian Tunnelling Technology publication no. 23, Norwegian Tunnelling Society, Published online at NFF.no

NGI (2017). Using the Q-system. Rock mass classification and support design. Handbook by NGI and available at ww.ngi.no 54p.

NPRA (2020). Tunnel construction guidance handbook V520. Directorate of Public Roads (In Norwegian).

Yu, J., Kim, J., Kim, M., Kim, K. 2016. Numerical Study on Structural Behaviour of Arched Shotcrete Liner Reinforced with Steel Supports. International Journal of Latest Engineering Research and Applications (IJLERA) ISSN: 2455-7137, Vol. 01, Issue 07, October 2016, PP 48–54

Tunnelling for a Better Life – Yan, Celestino, Thewes & Eberhardt (Eds)
© 2024 The Author(s), ISBN 978-1-032-80042-4
Open Access: www.taylorfrancis.com, CC BY-NC-ND 4.0 license

Shotcrete structural behaviours as tunnel support in hard jointed rocks – Swedish state of the art

Yanting Chang*
Geton Consulting LTD, Stockholm, Sweden

Christian Höök
Sweco Sweden LTD, Gothenburg, Sweden

ABSTRACT: Shotcrete has been used as a tunnel support element in Sweden since 1960's. Intensive research work and engineering practise have been conducted. This paper presents the "state of the art" regarding the understanding of shotcrete structural behaviours, design guidelines and application requirements for underground engineering in Sweden.

Keywords: Shotcrete, Tunnel support, Structural behaviours, Jointed rocks

1 INTRODUCTION

Shotcrete has been used as tunnel support element in Sweden since 1960's and steel fibre reinforced shotcrete was introduced in the beginning of 1980's. Since 1980's comprehensive research works have been conducted to enhance the understanding of the shotcrete support mechanisms for jointed rocks. These studies have been aimed on shotcrete properties, mixing procedures, interactions between rock and shotcrete, long term durability, fire resistance etc. Based on the results of the research work, design guidelines and performance requirements including materials, mixing procedures, on-site testing, quality controls etc. have been developed for underground engineering structures.

This paper will present the major research results on shotcrete structural behaviours as well as the state of the art regarding design guidelines and requirements of shotcrete applications in Sweden.

2 SHOTCRETE STRUCTURAL BEHAVIOUR

Hard jointed rock conditions are often encountered in Sweden for constructions of underground structures, where rock blocks or loosening rock pieces are of major concerns. The load-bearing mechanism of a shotcrete layer applied to rock blocks has been studied, for example by Holmgren (1979, 1985) with punch load tests as shown in Figure 1. Three stages of support effects of a shotcrete layer under a punch load were identified (see Figure 2):

- Adhesion resistance,
- Bending resistance, and
- Membrane resistance.

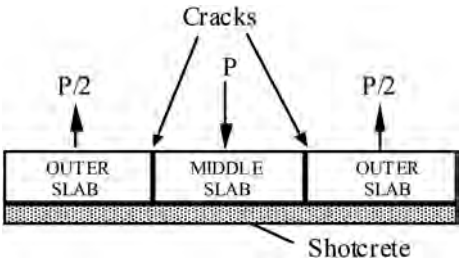

Figure 1. Set-up of the punch load test (after Holmgren, 1979).

The conducted studies in Sweden have resulted in the following significant findings:

- Shotcrete layers applied to jointed rock conditions have distinguished behaviours compared to shotcrete linings in soft rock conditions. For instance, adhesion between rock and shotcrete has essential importance for the shotcrete support functions in hard jointed rock conditions. As

*Corresponding author: yanting.chang@geton.se

DOI: 10.1201/9781003495505-128

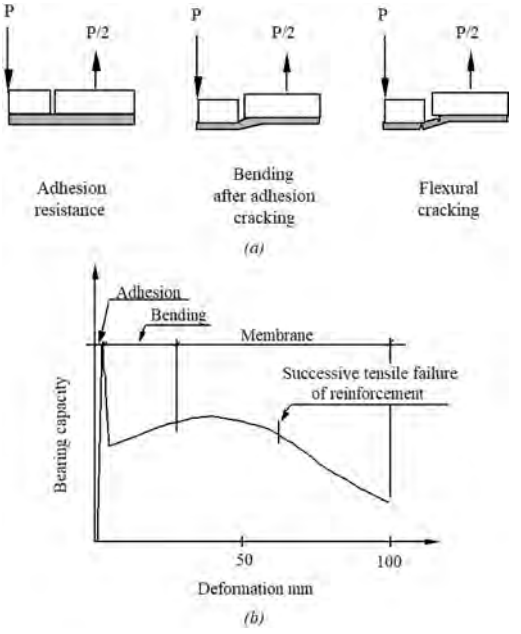

Figure 2. Failure modes of shotcrete subjected to block load (after Holmgren, 1979).

shown in Figure 2, the adhesion determines the maximum bearing capacity of the shotcrete layer,

- Steel fibres mixed in shotcrete have significant effects for bending and membrane resistances. Steel fibres will increase the residual flexural strength of shotcrete, making it ductile, which is essential for avoiding sudden failure of shotcrete,
- Hardening time of shotcrete shall be considered in rock excavation planning. If rock excavations resume short after shotcreting, the risk for damages in shotcrete because of early loadings will be relatively high (Chang, 1992, 1994; Ansell, 2019).
- Unevenness /irregularities of tunnel surfaces do not have adverse effects on the overall bearing capacities of shotcrete. In contrast, the unevenness /irregularities would enhance the overall bending capacity of shotcrete.

More details of the above findings are briefly presented as follows.

2.1 *Adhesion between rock and shotcrete*

Investigations of the adhesions for different rock types have been conducted during 1970's and 80′. The typical results for different rock types are shown in Table 1 (Hahn, 1983).

The investigation results show that the adhesion has significant variations depending largely on

- Rock types,
- Cleaning/washing of rock surfaces before shotcreting,
- Water leakages from rock surfaces,

Table 1. Typical results of adhesion with different rock types.

		Bond strength (MPa)	
Rock Type	Grain size	Smooth surface	Rough surface
Shale	Very fine grained	0.24	0.28
Lime stone-marlstone	Middle grained	1.49	1.89
Marble	Fine grained	1.38	1.52
Granite	Middle grained	1.04	1.40
Granite	Fine-middle grained	1.48	1.71

- Composition of shotcrete mixtures,
- Performance of shotcreting, e.g. angels and distances to rock surfaces.

The investigation results led to on-site quality controls by adhesion tests which are included in contractual documents for construction of underground structures.

2.2 *Steel fibres in shotcrete*

For investigating the effects of steel fibres, laboratory bending tests have been conducted and results show that the shotcrete bearing capacities in bending are largely dependent on the contents of steel fibres, see Figure 3. It is understandable that low fibre contents would cause low bending capacities, while too high fibre contents would lead to unsatisfactory blending the shotcrete mixtures, consequently poor bending capacities as well.

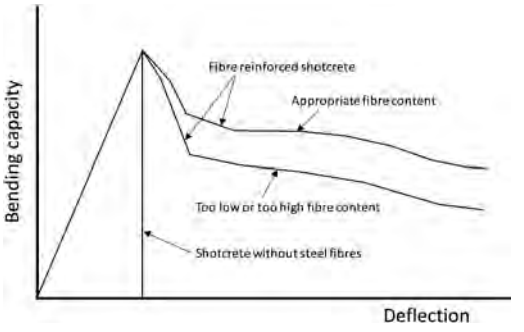

Figure 3. Steel fibre content and shotcrete bending capacity.

To ensure the required bearing capacities in underground structures, construction contractual documents include the clauses that pre-testing of flexural strengths shall be performed with different shotcrete mixtures and fibre contents. The approved shotcrete recipe including fibre contents shall not be

changed during construction phases without approval by the client.

2.3 *Effects of shotcrete hardening*

After shotcreting the shotcrete will be subjected to so called hardening process, i.e. the stiffness, strength and adhesion are increasing with time. Typical data collected from other countries for compressive strength and adhesion are shown in Figure 4 (Chang, 1994) and Figure 5 (Ansell, 2019). The factors to the strength variations are cement qualities, additive types and amounts, temperatures etc for the sample preparations.

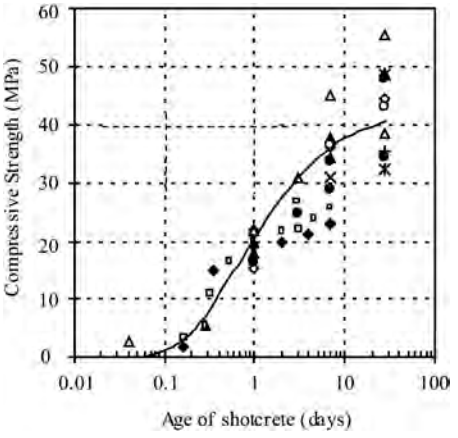

Figure 4. Development of compressive strength with time (based on data from literatures, Chang, 1994).

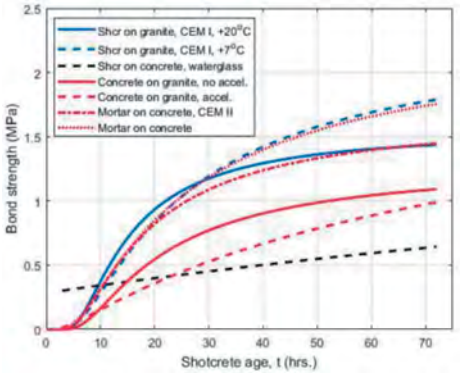

Figure 5. Development of adhesion strength with time (Ansell, 2019).

Blasting is the common method for rock excavations in Sweden and often performed nearby young shotcrete. Studies have been conducted to increase the knowledge on how the shotcrete is affected by the vibrations from blasting (Ansell, 2019).

These time-dependency phenomena have been taken into consideration in construction contractual documents. Under certain critical conditions, maximum allowed vibrations from blasting are specified, or mechanical excavation methods e.g. wire cutting or drill/ split are required.

2.4 *Effects of unevenness of rock surfaces*

All the theoretical calculation models for shotcrete layers are based on ideal dimensions and geometries. Questions have been raised about how the excavated tunnel surfaces with unevenness/irregularities affect the bearing capacity of shotcrete. Studies have been conducted to investigate the issues by laboratory model testing and numerical models (Chang, 1994; Chang et al 1995; Nilsson, 2003). The set-up of the laboratory models is shown in Figure 6.

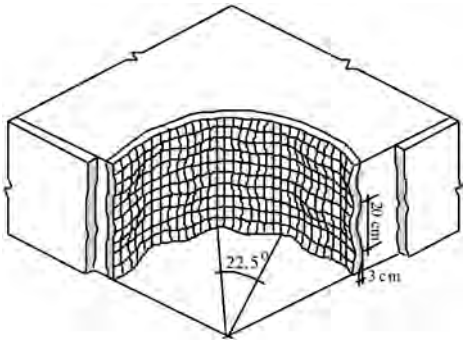

Figure 6. Set-up of the test model (Chang, 1994).

The major findings from the studies are:

- The unevenness/irregularities of the tunnel surface do not have significant adverse effects on the overall behaviour of the rock-shotcrete interactions. In contrast, the overall bearing capacity of shotcrete in bending is enhanced by the unevenness/irregularities of the tunnel surfaces,
- Observations from the model tests show that the apexes are the weak points of the shotcrete so that cracks often occur first at the apexes. It should be noticed that local cracks in the shotcrete are unfavorable to shotcrete durability. Therefore, bolts should be placed at the apexes to enhance the bond between shotcrete and the rock surface (see Figure 7). This could be achieved by site engineers purposely locating the positions of the bolts at the apexes of the tunnel surface.
- Placing more shotcrete at the recess may reduce local stress concentrations. However, covering over-breaks with shotcrete is very costly and has no significant improvement of shotcrete bearing capacity. It is more important to ensure that the shotcrete layer has sufficient thickness covering the apexes,

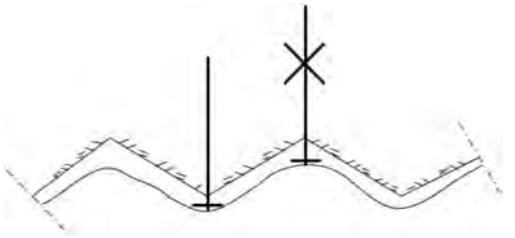

Figure 7. Suggested placement of rock bolts (Chang, 1994).

- The fact that the unevenness and irregularities of tunnel surfaces would cause local cracking in shotcrete reveal the importance of the residual strength of shotcrete for reducing risks of progressive tunnel failures. This also show the importance of the steel fibres in shotcrete.

3 DESIGN OF SHOTCRETE SUPPORT

Rock supports for underground structures in Sweden are divided into two categories:

- Typical rock supports,
- Special rock supports.

Typical rock supports apply for the following conditions:

- Tunnel span is less than 20 m,
- Rock cover/overburden is larger than ½ of tunnel span,
- Normal stress conditions, e.g. tunnel depth is less than 100m,
- Rock quality expressed by Q-index > 1,
- No buildings or structures that could be affected by the underground structure,
- Normal hydrogeological conditions where risks for high water leakage are judged being low.

Special rock supports and excavation methods are regularly adopted for conditions such as low rock covers, weakness zones with poor rock or high risk for considerable water leakages.

Design guidelines of rock supports for underground structures have been developed by the Swedish Transport Administration (Trafikverket, 2019), based on the engineering experiences and research results during the past decades. The simplified design process is shown in Figure 8. It would be distinguished that the employment of the observational method is an essential part of the rock support design process to be able to manage the uncertainties regarding rock mass properties, geological features such as fracture systems and hydrogeological conditions etc. The on-site observations include geological mappings (obligatory), identifying potential instable rock blocks (obligatory), deformation monitoring, stress monitoring, notices of water leakages etc. It is also worth to notice that risk management is involved throughout the whole process.

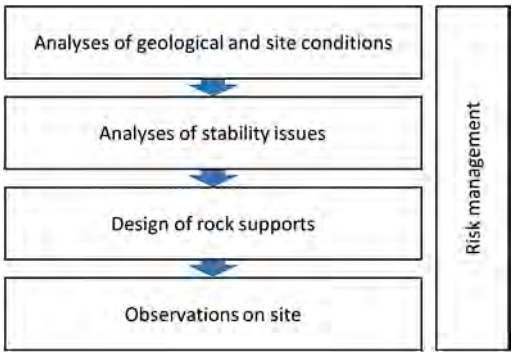

Figure 8. Simplified design process of rock supports (based on Trafikverket, 2019).

Geological conditions are investigated and commonly described in geological reports. Rock mass classifications are often carried out by using Q-index and RMR. One of the advantages with Q-index method is that rock supports can be estimated empirically, see Figure 9. Such empirical estimations are, however, often considered being on the safe side, which means that safety margins could be high, especially for hard jointed rock conditions. Another shortcoming of the empirical approaches is the lack of understanding for the interaction mechanisms between the shotcrete, bolts and rock mass.

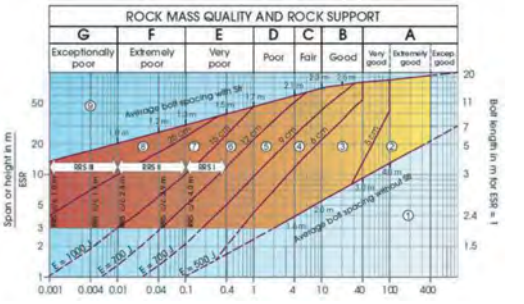

Figure 9. Estimation of rock supports based on Q-index (NGI, 2015).

For the jointed rock conditions in Sweden, the rock support design is, therefore, generally based on the design situations as given as follows.

- Conditions with good adhesion
- Conditions with no adhesion
- Weakness zones with or without swelling materials.

For these design situations, the support mechanisms of shotcrete are different. The design

methodology for the above conditions is briefly described as follows.

3.1 *Shotcrete support with good adhesion*

For jointed rock conditions with acceptable adhesion between rock and shotcrete, rock blocks could be stabilised by shotcrete combined with spot bolting. The bearing capacity of the shotcrete is determined by (Trafikverket, 2019):

$$B = \sigma_{adh} \cdot d \cdot L$$

Where, B is shotcrete bearing capacity (kN); σ_{adh} is adhesion (kPa); d is bearing width (m); L is circumference of the block base (m), see also Figure 10.

Please note that the bearing width d is dependent on the thickness of shotcrete and can be determined by Table 2.

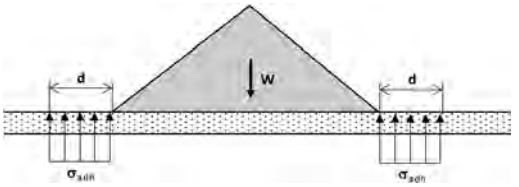

Figure 10. Design model for shotcrete support with adhesion (modified after Trafikverket, 2019).

Table 2. Shotcrete thickness and bearing width (Stille et al 1988).

Shotcrete thickness, tc (mm)	Bearing width, d (mm)
40	25
60	30
80	35

During the design phases, the block sizes could be estimated by statistical analyses of geological data, e.g. joint spacing and persistence.

During construction phases, geological mapping is obligatory in Sweden and rock blocks can be identified by the geologists. Spot bolting is performed when necessary.

3.2 *Shotcrete support without adhesion*

For conditions where adhesion between rock and shotcrete is judged being inefficient, shotcrete layer will be designed with consideration of interactions with rock bolts. The bending capacity at the first crack is considered as the origin of the bearing resistance of the shotcrete. The design model is shown in Figure 11.

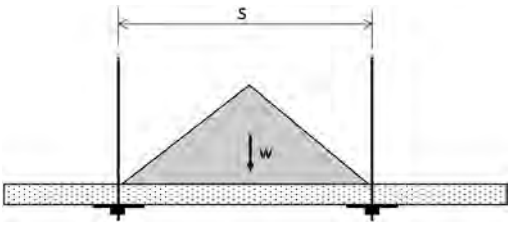

Figure 11. Design model for shotcrete support without adhesion (modified after Fredriksson, 1995).

The bending capacity of the shotcrete can be determined by

$$M_b = f_{max} \cdot t_c^2 / 6$$

Where M_b is the bending capacity (kN-m/m); f_{max} is the flexural strength at first crack (kPa); t_c is shotcrete thickness (m).

The bending moments in the shotcrete depend on the loads from the rock block and bolt spacing. An estimation of the maximum bending moment in shotcrete can be done by Figure 12.

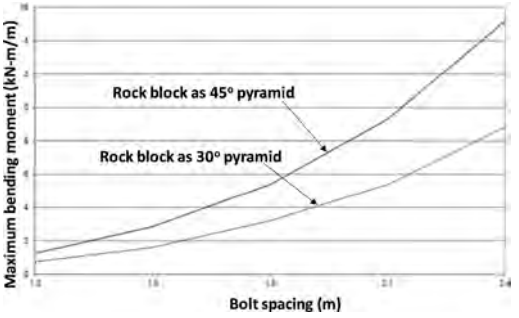

Figure 12. The maximum bending moment vs bolt spacing (modified after Fredriksson, 1995).

The design criterion is that the bending capacity M_b shall be higher than the bending moment cause by the rock block.

3.3 *Shotcrete support for weakness zones*

Weakness zones are often encountered, even in the hard and joined rock conditions. The support of weakness zones is often a combination of shotcrete together with rock bolts. The design model for rock support is shown in Figure 13.

The loads from the weakness zone can consist of two parts, see Figure 13:

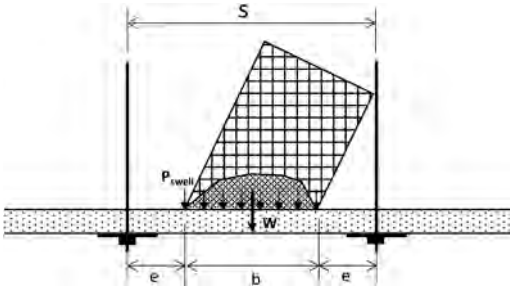

Figure 13. Support of weakness zone with shotcrete and bolts (modified after Holmgren, 1992).

- Weight of the losing material from the zone, W
- Swelling pressure from swelling minerals, p_{swell}.

The bending moment in the shotcrete can be determined by the theory of critical failure lines (Holmgren, 1992):

$$m = q\frac{S-2e}{4}\cdot\frac{S+2e}{4}$$

where m is the bending moment in shotcrete (kN-m/m); S is the bolt spacing (m); e is the distance from the bolts to the zone (m), q is the distributed load (kPa/m) on the shotcrete and is determined by

$$q = P_{swell} + \ W/\ b.$$

The bearing capacity of shotcrete determined by the formular in the previous section needs to be higher the bending moment given above.

4 MATERIAL AND SITE PERFORMANCE REQUIREMENTS

The following general material requirements apply for shotcrete support in underground structures, i.e. road and railway tunnels:

- Cement quality is chosen based groundwater chemical conditions, exposure classes and technical life length etc,
- Maximum aggregate size < 4 mm,
- Technical life length 120 years,
- Adhesion to rock > 0,5 MPa for normal rock conditions,
- Compressive strength >30 MPa,
- Steel fibres shall be used if no other types specified, fibre contents are regulated by the following requirements,
  - Maximum flexural strength 4 MPa in pure bending tests,
  - Residual flexural strength 3 MPa at 2 mm deflection in pure bending tests,
- Mixing components of shotcrete including water/cement ratio, aggregates, accelerators etc shall be approved by pre-testing and shall not be changed after approval.

For testing the shotcrete mechanical properties, the Euro codes SS-EN 14488-1:2005, SS-EN 14488-3:2006 and SS-EN 12504-1 are used.

The major requirements on shotcreting performance are given as follows:

- Shotcreting shall be performed by trained and certified personal,
- Shotcreting shall be performed with wet spraying methods,
- Shotcrete shall not be applied on rock surfaces with temperature below 5° C,
- Rock surface shall be cleaned by pressured water before shotcreting,
- Shotcreting shall only be performed after geological mapping.

5 CONCLUSIONS

Shotcrete has been successfully used in Sweden for underground structures for decades. The research work during the past decades have played important roles in understanding the support mechanisms using shotcrete in typical Swedish rock conditions. Design methods and guidelines have been developed based on the research work and practical experiences. Design of rock supports by considering the adhesions between rock and shotcrete is one of the significant characteristics of the Swedish method.

To reduce the environmental impacts caused by civil constructions, efforts are being made upon innovations of new materials and technologies for rock excavations and supports.

REFERENCES

ACI, 1982. Measurement of properties of fiber-reinforced concrete. ACI Manual of Concrete Practice, Part 5.

Andersson, G.L. and Poad, M.E., 1974. Early age strength properties of shotcrete, Use of Shotcrete for Underground Support. Proc. of Eng. Found. Conf., Easton, pp. 277–296.

Ansell, A., 2019. Guidelines for practical use when shotcreting close to blasting and vibrations in hard rock. Swedish Rock Engineering Research Foundation. Stockholm, Sweden, BeFo report 189.

Bryne, L.E., 2014. Investigation and development of material properties for shotcrete for hard joint rock tunnels. Swedish Rock Engineering Research Foundation. Stockholm, Sweden, BeFo report 133.

Chang, Y., 1992. Influence of early-age properties of shotcrete on tunnel construction sequences", Tech. Licentiate Thesis, Divsion of Soil and Rock Mechanics, Royal Institute of Technology, Stockholm, Sweden.

Chang, Y., 1994. "Influence of tunnel irregularities on shotcrete lining – A laboratory investigation", Report, the Division of Soil and Rock Mechanics, the Royal Institute of Technology, Stockholm, Sweden.

Chang, Y., 1994. Tunnel support with shotcrete in weak rock – A rock mechanics study. PhD Thesis. Royal Institute of Technology, Stockholm, Sweden.

Chang, Y., & Stille, H., 1995, Shotcrete as a tunnel linning – A laboratory study, 8th ISRM Congress, Tokyo, Japan.

Franzén, T., 1992. Shotcrete for Underground Support - A State of the art Report with Focus on Steel Fiber Reinforcement. Invited Lecture, Proc. of Rock Support in Mining and Underground Construction, Rotterdam, Canada.

Fredriksson, A., 1995. *Bergmekanik. Dimensionering av sprutbetong som ytförstärkning* (Desgin of shocrete as surface support). PM 1995-03-31, Swedish Railway Administration, Eastern Region.

Hahn, T., 1983. Adhesion of shotcrete to various types of rock surfaces. Swedish Rock Engineering Research Foundation. Stockholm, Sweden, Report 55.

Holmgren, J., 1979. Punch Loaded Shotcrete Linings on Hard Rock. Swedish Rock Engineering Research, SveBeFo, Stockholm, Sweden, Report No.7:2/79.

Holmgren, J., 1985. Bolt Anchored Steel Fibre Reinforced Shotcrete Linings. Swedish Rock Engineering Research, SveBeFo, Stockholm, Sweden, Report No.73:1/85.

Holmgren, J., 1992. *Bergförstärkning med sprutbetong* – Rock support with shotcrete. Vattenfall (State Power Company), Järfälla, Sweden.

NGI, 2015. Using the Q-system- Rock mass classification and support design. URL:www.ngi.no

Nilsson, U., 2003. Bearing capacity of fibre reinforced sprayed concrete anchored in rock, Swedish Rock Engineering Research Foundation. Stockholm, Sweden, BeFo report 64.

Saleh, I., 2017. Shotcrete and its properties – Experiences of shotcrete use in infrastuctures. Swedish Rock Engineering Research Foundation. Stockholm, BeFo report 154.

Sjölander, A., 2020. Structural behaviour of shotcrete in hard rock tunnels. Swedish Rock Engineering Research Foundation. Stockholm, Sweden, BeFo report 210.

Stille, H., Johansson, R. & Nord, G., 1988. Rock support and excavations under various conditions. Int. Symp. On Tunneling for Water Resources and Power Projects, NewDelhi, India.

Svensk Byggtjänst, 2020. AMA Anläggning - General material and performance description for construction work. Swedish Construction Services, Stockholm, Sweden.

Trafikverket, 2019. Design of rock structures *Projektering av bergkonstruktioner*. Swedish Transport Administration, Stockholm, Sweden, Publication number: 2019:062.

Tunnelling for a Better Life – Yan, Celestino, Thewes & Eberhardt (Eds)
© 2024 The Author(s), ISBN 978-1-032-80042-4
Open Access: www.taylorfrancis.com, CC BY-NC-ND 4.0 license

Study on the influence of cracks on mechanical behaviors of tunnel lining of high speed railway with a speed of 400 km/h

Peng Chen & Kai Liu
China Railway Southwest Research Institute Co., Ltd., Chengdu, China

Congwen Yan
China Railway Siyuan Survey and Design Institute Group Co., Ltd., Wuhan, China

ABSTRACT: In view of the current research status that most studies have not considered the influence of crack distribution patterns on lining structural stress, the ABAQUS finite element software and CDP model are used to study the influence laws of single crack, mesh cracks and radial cracks on the stress characteristics of high-speed railway tunnel lining structure. The main conclusions are as follows: (1) When the cracks are located at the crown, the influence on structural stress is the most obvious, and the crown cracks have the greatest influence on the tensile damage degree and deformation of the structure, and have little influence on the compressive bearing capacity of the structure;(2) Single longitudinal crack has the most obvious influence on the structural stress, and the tensile damage degree induced by non-penetrating cracks is positively correlated with the length and depth of cracks; (3) The tensile damage degree induced by mesh cracks is positively correlated with the length and width of crack distribution; (4) The tensile damage degree induced by radial cracks is negatively correlated with the area of regional center, and positively correlated with the number and length of cracks; (5) The larger the depth and range of cracks, the more obvious the increase of structural deformation. The 12m long and 0.9H deep longitudinal cracks on the vault can cause structural deformation to increase by more than 5 %.

Keywords: High-speed railway tunnel, Running speed of 400 km/h, Plastic damage, Cracks, Mechanical behaviour

1 INTRODUCTION

With the increase of operating mileage and life of high-speed railway tunnels, lining cracks often occurred, which have had different impacts on the safety and durability of tunnel structures[1~3].At present, China's high-speed railway tunnel at a speed of 400km/h is still in the research stage. With the speed boost of China railways, the requirements for tunnel section is higher and also the mechanical behaviors of tunnel structure become more complicated. As if the construction defects cause the lining cracks, it will bring more and more troubles to the safe operation of tunnels and so the research works on the structure mechanical behaviors of cracked linings are carried out in urgent need. For the high-speed railway tunnels at speed of 350km/h and below, the domestic and foreign experts have already commenced some corresponding research works[4~6]..

Taking the Beijing metro project as an example and based on the theory of concrete elastic-plastic damage, Xuan Liu [7] conducted the mechanical analysis of cracked linings. The analysis results show that the influence of vault crack is remarkable and the crack depth has the most significant impacts on the safety of lining structure.

Yujun Zhang[8] adopted the plane finite element model and the fracture mechanics theory to calculate and analyze the stability of different cracks at the secondary lining of tunnel. The main conclusions show that the depth and number of cracks have greater influence on the stability of cracks and fewer influence on crack width.

Yihong Zhang[9] established a cracked structure by using the finite element models and the contact elements, analyzed the changing law of the strength factors at the crack tip of lining with the crack characteristic parameters. The main conclusions show that the depth of lining crack has the most significant impacts on the safety of lining structure.

DOI: 10.1201/9781003495505-129

In summary, domestic and foreign experts have done extensive research works on the mechanical characteristics of cracked lining in tunnel and achieved the conclusions that the depth and number of cracks have had significant impacts on the stability of cracks. However, at present, most of the research works focus on the ordinary speed railway tunnel only and not yet consider the impacts of crack distribution patterns such as reticulated or radial cracks on the mechanical characteristics of lining structure. Therefore, this paper adopts ABAQUS finite element software and the concrete plastic damage model to study the impacts of different cracks such as single crack, reticulated crack or radial crack on the mechanical behaviors of lining structure of single or double line high-speed railway tunnels at a speed of 400km/h. It will provide a reference for the subsequent operation and maintenance decision of cracked lining in high-speed railway tunnel at a speed of 400km/h.

2 CONCRETE ELASTIC-PLASTIC DAMAGE MODEL

2.1 *Concrete damaged plasticity variable*

In order to describe the nonlinear mechanical behaviors of sensitive materials to damage like concrete under loading, this paper adopts the concrete damaged plasticity model (CDP model) in ABAQUS software to carry out research works [10, 11]. In the process of adoption, two assumptions are made as follows: ①the failure mode of concrete is assumed to be crushing or tensile cracking; ②concrete damage is assumed to be isotropic. Therefore, the plastic damage factor d is adopted to represent the reduction of material elastic modulus E due to damage and the plastic evolution equation is shown in equation (1).

$$\begin{cases} E = (1-d)E_0 \\ (1-d) = (1-s_t d_c)(1-s_c d_t) \end{cases} \quad (1)$$

Where, E_0 is the initial elastic modulus; s_t and s_c represent the state functions of tensile stress and compressive stress of concrete, respectively; d_t and d_c represent uni-axial tensile damage factor and uni-axial compressive damage factor, respectively.

2.2 *Stress-strain relationship and damage evolution equation of concrete*

In this paper, the stress-strain relationship of concrete in Code for Design of Concrete Structures (GB50010-2010) is recommended (as shown in Figures 1 and 2). Based on the assumption of strain equivalence, the damage evolution equation of concrete is obtained with reference to the research results of Zhenhai Guo[12].

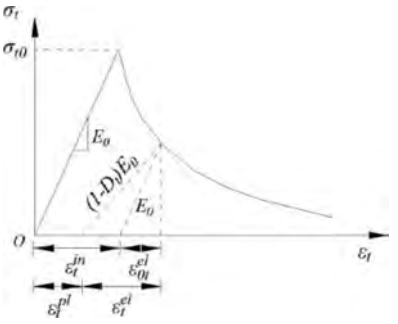

Figure 1. Uni-axial tensile stress-strain relationship of concrete.

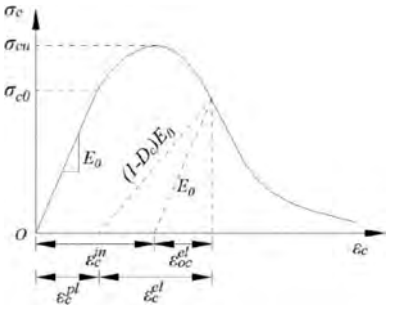

Figure 2. Uni-axial compressive stress-strain relationship of concrete.

According to the geometric relationships in Figures 1 and 2, the concrete damage evolution equation with taking the concrete elastic modulus E as the damage variable is obtained and shown in Equation (2).

$$d_k = \frac{(1-\beta_k)\varepsilon_k^{in} E_0}{(1-\beta_k)\varepsilon_k^{in} E_0 - \sigma_k} \quad (2)$$

Where, $d_k$represents the plasticity damage factor; k represents the damage type, k=t represents the pull-induced damage, k=c represents the compression-induced damage; ε_k^{in} represents the concrete inelastic strain; σ_k represents the value of concrete stress; β_k=$\varepsilon_k^{pl}/\varepsilon_k^{in}$ is the ratio of plastic strain vs. inelastic strain, while the 0.5~0.95 is taken under tension and the 0.35~0.7 is taken under compression; ε_k^{pl} is the plastic strain.

3 CALCULATION MODELS AND CONDITIONS

3.1 *Calculation model*

The finite element software ABAQUS is used to build a "load-structure" model and to study the mechanical behaviors of high-speed railway tunnel at a speed of 400km/h under the influences of different cracks. The longitudinal length of lining is 12m. The lining structure is simulated by C3D8R element and

the foundation spring is simulated by T3D2 element. According to the "Code for the Design of Railway Tunnels" (TB10003-2016), the vertical load of the single line tunnel within surrounding rocks of Class IV is 86.940kPa, the double line tunnel is 112.153kPa and the lateral pressure coefficient is 0.25. The load-bearing ratio of secondary lining within surrounding rocks of Class IV is 50%. The calculation model is shown in Figure 3. The cracks of lining are simulated by means of contact surface. Meanwhile, it is considered that the cracks do not transfer tensile stress and shear stress, but transfer compressive stress.

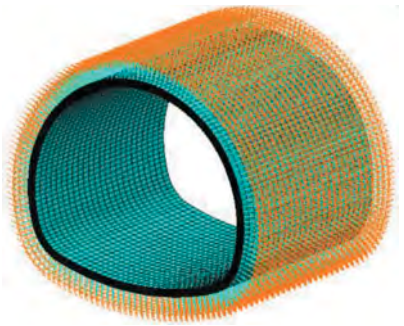

Figure 3. Finite element calculation model.

3.2 *Physical and mechanical parameters of materials*

According to the "Code for the Design of Railway Tunnels" (TB10003-2016), the parameter for the elastic foundation within surrounding rocks of Class IV is 350MPa/m. The concrete material is C35 and the standard values of tensile and compressive strengths are selected as the representative values of concrete strength. The physical and mechanical parameters are shown in Table 1. The bi-axial compressive strength is 1.16 times as much as the uni-axial compressive strength.

Table 1. Physical and mechanical parameters of concrete.

Class	γ(kN/m^3)	v	E_0(GPa)	f_{tk}(MPa)	f_{ck} (MPa)
C35	23	0.2	31.5	2.20	23.4

In Table 1, γ, v, E_0, f_{tk} and f_{ck} represent the concrete's weight, Poisson's ratio, initial elastic modulus, standard value of tensile strength and standard value of compressive strength, respectively.

3.3 *Calculation conditions*

In order to systematically explore the influences of single longitudinal crack, reticulated crack and radial crack on the mechanical behaviors of lining structure, the prepared calculation conditions are shown in Tables 2-4. Where, H represents the design thickness of lining structure.

Table 2. Calculation condition of single crack.

The Serial Numbers of Conditions	The angle between crack and tunnel alignment (°)	Length of crack (m)	Depth of Crack (m)	Locations	Remarks
1	/	/	/	/	No-crack
2~16	0	1, 3, 6, 9, 12	0.1H,0.5H,0.9H	Vault	/
17~18	30, 45	6	0.5H	Vault	/
19~27	0	6	0.1H,0.5H,0.9H	Haunch, Side wall, Foot of the wall	/
28~30	0	12	0.9H	Haunch, Side wall, Foot of the wall	/

Table 3. Calculation condition of reticulated cracks.

The Serial Numbers of Conditions	Length of reticulated cracks(m)	Width of reticulated cracks(m)	Crack spacing (cm)	Locations	Remarks
1	/	/	/	/	No-crack
2~4	0.5, 1, 1.5	0.5	25	Vault	The depth is 0.5H
5~7	0.5, 1, 1.5	1			
8~10	0.5, 1, 1.5	1.5			

Table 4. Calculation condition of radial cracks.

The Serial Numbers of Conditions	The area of radical cracks(m^2)	The numbers of cracks	Length of cracks(m)	Locations	Remarks
1	/	/		/	No-crack
2~4	0.25, 1, 4	3	3	Vault	
5~7	0.25, 1, 4	5	3	Vault	The depth is 0.5H
8~11	0.25	3, 5	4.5, 6	Vault	

4 ANALYSIS OF THE INFLUENCES OF CRACKS ON MECHANICAL BEHAVIORS IN SINGLE-LINE TUNNEL

4.1 *Single crack*

4.1.1 *Different locations*

The calculated results of single longitudinal crack conditions 1, 9, 20, 24 and 28 were selected separately for comparative analysis, so as to demonstrate the effects of crack locations on structure mechanical behaviors. The calculated results are shown in Table 5.

Table 5. Calculation results of single cracks at different locations.

conditions	Locations	S_1max (MPa)	S_3max (MPa)	Tensile damage	U_1 (mm)	U_2 (mm)
1	/	1.726	5.408	0.000	1.252	4.933
9	Vault	2.398	5.418	0.735	1.278	5.081
20	Haunch	1.726	5.408	0.000	1.253	4.934
24	Side wall	1.726	5.409	0.000	1.252	4.933
28	Foot of the wall	1.726	5.466	0.000	1.252	4.933

Where, S_{1max} and S_{3max} represent the maximum values of the first and third principal stresses of lining structure, respectively. U_1 represents the maximum value of unilateral horizontal convergence of lining structure and U_2 represents the maximum value of vertical displacement at vault.

As shown in Table 5, when the single longitudinal crack appears at vault, haunch, side wall or foot of the wall, the compression-induced damage degree of lining structure is 0 and the maximum value of the third principal stress is 5.408MPa~5.466MPa, which is far less than the design value of compressive strength of concrete C35. When the single longitudinal crack appears at vault, the Tensile damage degree of lining structure is 0.735 and the maximum value of the first principal stress of lining structure is 2.398MPa, which increases by 38.9% and the deformation of the structure increases slightly, compared with the no-crack condition. When the single longitudinal crack appears at haunch, side wall or foot of the wall, the Tensile damage factor of lining structure is 0 and the maximum value of the first principal stress of lining structure is 1.726MPa, which is the same as the no-crack condition. Therefore, the single longitudinal crack at vault has more significant influences on tensile properties of the structure, fewer influences on the compressive behaviors and slightly influences on the deformation, while the cracks in other locations hardly influence the mechanical behaviors of lining structure. As a result, the subsequent research will focus on the influence rules of the cracks at vault on tensile properties and deformation of lining structure.

4.1.2 *Depth and length of crack*

The influences of the depth and length of single longitudinal crack on mechanical behaviors of lining structure are analyzed by taking the calculated results of the Tensile damage degree, the unilateral horizontal displacement value of lining structure and the vertical displacement value of vault under conditions 2-16, as shown in Figures 4-6.

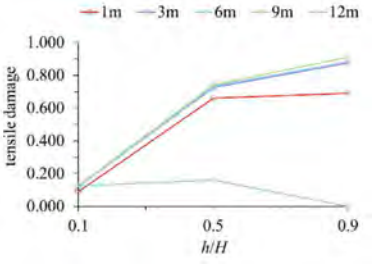

Figure 4. Tensile damage degree of lining structure with single longitudinal cracks.

As shown in Figure 4, when the crack does not penetrates through the primary lining (the length is less than 12m), the Tensile damage degree of the crack is positively correlated with the length and depth of crack, and the maximum Tensile damage degree is up to 0.910 with the increase of the length and depth of crack. When the crack penetrates through the primary lining (the length is 12m), the Tensile damage factor of the lining structure decreases

with the release of strain energy at the tip of lining crack. From the perspective of quantitative value, when the crack length is greater than 3m, the crack length does not have significant influences on the Tensile damage degree of lining structure, and the expansion of the crack is mainly controlled by crack depth.

Due to space limitation, only the calculation results of pull-induced damage under conditions 11, 12 and 13, respectively are introduced in this paper, as shown in Figure 5.

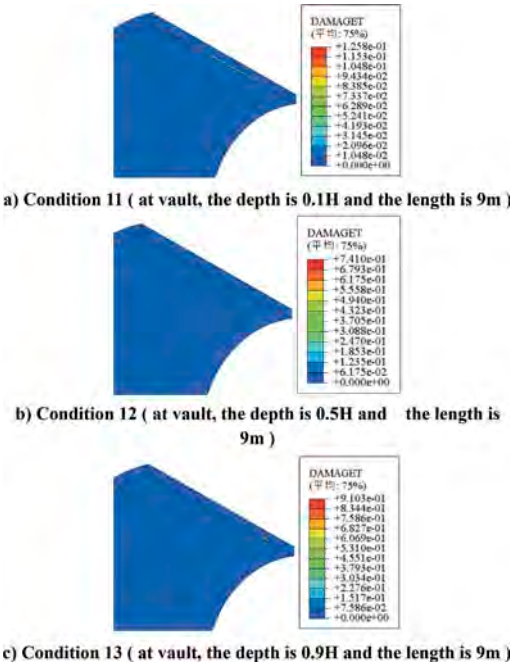

Figure 5. Tensile damage degree of vault with single crack.

As shown in Figure 5, when the crack depth is 0.1H, the crack expands along the direction of depth. When the crack depth is 0.5H and 0.9H, the crack expands along the direction of length. Therefore, the Tensile damage degree of lining structure is positively correlated with the crack depth. When the crack occurs shallowly, the crack expands along the direction of depth, and when the crack depth reaches a certain degree, the crack expands along the direction of length. Except for the condition of 12m-long crack, the variation trends of other cracks are identical to that of the 9m-long crack.

The calculation results of the maximum unilateral horizontal convergence of lining structure and the maximum settlement of vault under conditions 2-16 are shown in Figures 6 and 7.

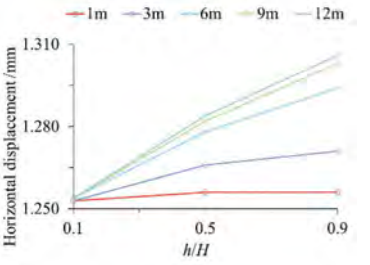

Figure 6. Maximum unilateral horizontal convergence of lining structure with single longitudinal crack.

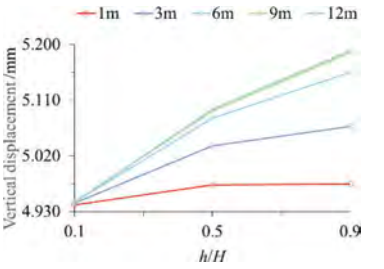

Figure 7. Maximum vertical displacement of vault with single longitudinal crack.

As shown in Figures 6 and 7, the maximum unilateral horizontal convergence of lining structure and the maximum vertical displacement of vault increase with increasing of the length and depth of cracks. When the crack length is 12m and the crack depth is 0.9H, the maximum horizontal displacement and the maximum vertical displacement of lining structure are 1.306mm and 5.190mm, respectively, which increased by 4.31% and 5.21%, compared with the no-crack condition.

4.1.3 *Crack strike angle*

The calculation results of conditions 9, 16 and 17 are selected, respectively to analyze the influences of different crack strike angles on the mechanical behaviors of lining structure.The calculation results of displacement behavior values of lining structure are shown in Figure 8.

The variation law of the maximum displacement along with the crack strike angle is shown in Figure 9. When the depth of the 6m-long crack at vault is 0.5H, the maximum displacement value slightly decreases with increasing of the crack longitudinal angle. When the angle reaches 30°and 45°, the vertical displacement decreases by 1.6% and 2.2%, and the horizontal displacement decreases by 1.2% and 2.0%, respectively.

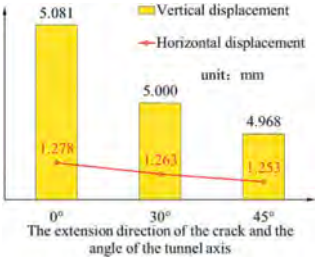

Figure 8. Displacements of lining structure under different crack strike angles.

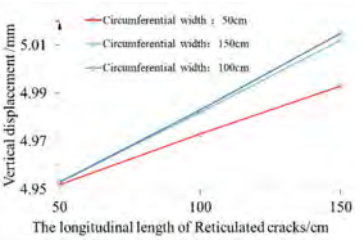

Figure 11. Maximum vault vertical displacement of lining structure with reticulated cracks.

According to the calculation results, when the crack strike angle reaches 30° and 45°, the Tensile damage degree of lining structure is 0. As shown in Figure 8, the influences of crack strike angles of 30° and 45° on lining deformation is less than that of longitudinal cracks, in which the unilateral horizontal convergence of lining structure decreases by 1.2% and 2.0%, and the vertical displacement of vault decreases by 1.6% and 2.2%, respectively. The larger the crack strike angle is, the smaller its influence on lining structure becomes.

4.2 *Reticulated crack*

The calculation results of the Tensile damage degree, the maximum unilateral horizontal convergence of lining structure and the maximum vertical displacement of vault under reticulated crack conditions of 1-10 are shown in Figures 9-11.

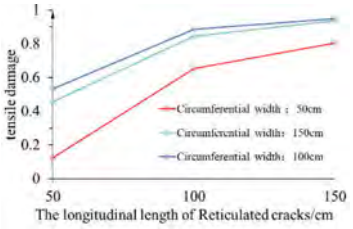

Figure 9. Tensile damage degree of lining structure with reticulated cracks.

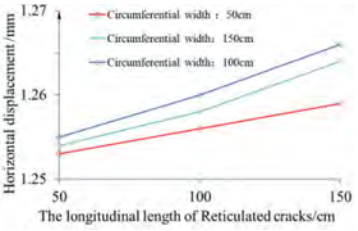

Figure 10. Maximum unilateral horizontal convergence of lining structure with reticulated cracks.

As shown in Figure 9,the Tensile damage degree of lining structure increases with the extension of the varying ranges of length and width of reticulated crack. When the length and width of reticulated crack are greater than 100cm, the maximum Tensile damage factor of lining structure will rapidly rise above 0.85, indicating that the crack has a development trend and propagates along with the alignment of tunnel.

As shown in Figures 10 and 11, the maximum horizontal convergence of lining structure and the maximum vertical displacement of vault are positively correlated with the length and width of reticulated cracks. When the length and width of reticulated crack increase up to 150cm, the maximum horizontal convergence of lining structure and the maximum vertical displacement of vault are 1.266mm and 5.015mm, which increase by 1.12% and 1.66%, compared with the no-crack condition. It indicates that the lining stiffness decreases accordingly.

4.3 *Radial crack*

4.3.1 *The area and number of crack central zone*

The calculation results of radial crack conditions 1 to 7 are selected, respectively to analyze the influences of the area of radial crack central zone and the number of cracks on the mechanical behaviors of lining structure. The calculation results are shown in Figures 12-14.

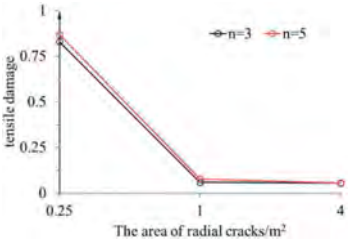

Figure 12. Tensile damage degree of lining structure with radial cracks of different areas.

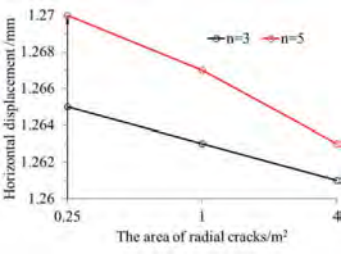

Figure 13. Maximum unilateral horizontal convergence of lining structure with radial cracks of different areas.

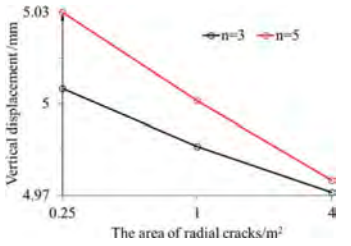

Figure 14. Maximum vault vertical displacement of lining structure with radial cracks of different areas.

As shown in Figure12, when the radiating area of crack ranges from 0 m^2 to 1 m^2, the pull-induced damage degree of lining structure decreases with increasing of the area of crack central zone; when the area of radial crack central zone is 0.25m^2, the pull-induced damage degree of lining structure is 0.869; when the area of radial crack central zone is above 1m^2, the pull-induced damage degree of lining structure is 0.078. It shows that the larger the area of radial crack central zone becomes, the less the possibility of crack propagation is.

As shown in Figures 13 and 14, the maximum unilateral horizontal convergence of lining structure and the maximum vertical displacement of vault decrease with increasing of the area of radial crack central zone and increase with rising of the number of cracks. When the number of cracks is 5 and the area of radial crack central zone is 0.25m^2, the maximum horizontal convergence of lining structure and the maximum vertical displacement of vault are 1.270mm and 5.030mm, which increase by 1.44% and 1.97%, compared with the no-crack condition. Thus, the lining stiffness is most significantly declined under this condition.

4.3.2 *The length and number of cracks*

The calculation results of the radial crack conditions 1, 2, 5 and 8~11 are selected respectively to analyze the influences of the degree of radial crack, the number of cracks on mechanical behaviors of lining structure and the calculation results are shown in Figures 15-17

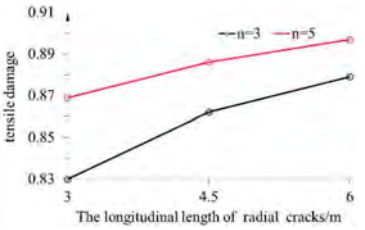

Figure 15. Tensile damage degree of lining structure with radial cracks of different lengths.

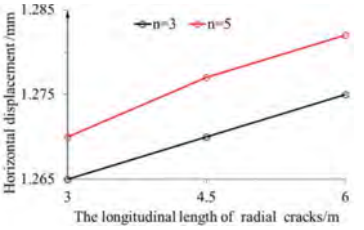

Figure 16. Maximum unilateral horizontal convergence of lining structure with radial cracks of different lengths.

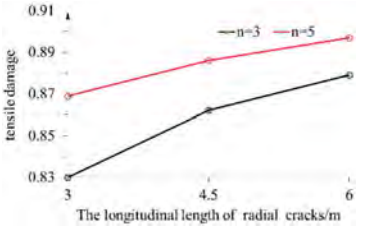

Figure 17. Maximum vertical displacement of vault with radial cracks of different lengths.

As shown in Figure15, the Tensile damage degree of lining increases with increasing of the number and length of radial cracks. When the length of crack is 6m long and its number is 5, the Tensile damage degree of lining structure is 0.897.

As shown in Figures 16 and 17, the maximum unilateral horizontal convergence of lining structure and the maximum vertical displacement of vault are positively correlated with the length and number of radial cracks. When the length of radial crack is 6m and its number is 5, the maximum unilateral horizontal convergence of lining structure and the maximum vertical displacement of vault are 1.282mm and 5.069mm, which increase by 2.40% and 2.76%, compared with the no-crack condition. It indicates that the lining stiffness decreases accordingly.

5 ANALYSIS OF THE INFLUENCES OF CRACK ON MECHANICAL BEHAVIORS OF DOUBLE-LINE TUNNEL

According to the analysis results of the influences of the crack on mechanical behaviors of double-line tunnel, the influence rule of each behavior parameter of single crack, reticulated crack and radial crack on the Tensile damage degree of lining structure, the maximum unilateral horizontal convergence of lining structure and the maximum vertical displacement of vault are consistent with those of single-line tunnel, but the degrees of influence are varying from each other. Only the calculation results of the most unfavorable conditions under each working condition are given, as shown in Table 6 to Figure 8.

As shown in Table 6, for single crack, under the most unfavorable working conditions of the depth and length of crack, the Tensile damage degree of lining structure is 0.947, and the maximum unilateral horizontal displacement of lining structure and the maximum vertical displacement of vault are 2.603mm and 9.660mm, which increase by 1.28% and 2.34%, compared with the no-crack condition. For the working condition of the most unfavorable crack strike angle, the Tensile damage degree of lining structure is 0.939, and the maximum unilateral horizontal displacement of lining structure and the maximum vertical displacement of vault are 2.593mm and 9.610mm, which increase by 0.89% and 1.81%, compared with the no-crack condition.

For the reticulated crack, the Tensile damage degree of lining structure is 0.979 under the condition of the most unfavorable length and width of crack, and the maximum unilateral horizontal displacement of lining structure and the maximum vertical displacement of vault are 2.582mm and 9.543mm, which increase by 0.47% and 1.10%, compared with the no-crack condition.

For the radial crack, under the most unfavorable conditions of the area and number of crack central zone, the Tensile damage degree of lining structure is 0.937, and the maximum unilateral horizontal displacement of lining structure and the maximum vertical displacement of vault are 2.593mm and 9.603mm, which increase by 0.89% and 1.74%, compared with the no-crack condition. Under the most unfavorable conditions of the length and number of cracks, the Tensile damage degree of lining structure is 0.950, and the maximum unilateral horizontal displacement of lining structure and the maximum vertical displacement of vault are 2.593mm and 9.603mm, which increase by 1.28% and 2.27%, compared with the no-crack condition.

The comparison with the single-line tunnel suggests the most unfavorable condition for all kinds of cracks, i.e., the Tensile damage degree of lining structure in double-line tunnel is generally greater than that of single-line tunnel, while the maximum unilateral horizontal displacement of lining structure and the maximum vertical displacement of the vault is smaller than that of single-line tunnel, indicating when the vault in single-line tunnel is cracked, the lining stiffness decreases more obviously than that of double-line tunnel, and when the vault in double-line tunnel is cracked, the crack propagates more easily than that of single-line tunnel.

6 CONCLUSIONS AND SUGGESTIONS

In this paper, a numerical simulation study is carried out on the influence rule of lining structure mechanical behaviors under the actions of single crack, reticulated crack and radial crack in the high-speed railway tunnel with a speed of 400km/h, or the single-line and double-line tunnels within Class IV surrounding rocks and plain concrete. The main conclusions are as follows:

(1) The influence of vault cracks on mechanical behaviors of lining structure is much greater than that of cracks at other locations. When the vault is cracked, the Tensile damage degree and deformation of lining structure will be affected, but the compression bearing behaviors of lining structure will be less affected.

Table 6. The most unfavorable situations of the influences of crack on mechanical behaviors of double-line tunnel.

Types of cracks	Influential factors	d_t	U_1 (mm)	U_2 (mm)	Remarks
No-crack	/	0	2.570	9.439	/
Single crack	Depth, length of crack	0.947	2.603	9.660	Length is 9m, depth is 0.9*H,* strike angle is 0°
	Crack strike angle	0.939	2.593	9.610	Length is 6m, depth is 0.5*H,* strike angle is 0°
Reticulated crack	Length, width of crack	0.979	2.582	9.543	Length is 150cm, width is 150cm
	The area and number of crack central zone	0.937	2.593	9.603	The area of crack central zone is 0.25m^2. the number of crack is 5, the length of crack is 3m
Radial crack	Length, number of crack	0.950	2.603	9.653	The area of crack central zone is 0.25m^2, the number of crack is 5, the length of crack is 6m

(2) The calculation results of the influences of cracks on lining structure in single-line and double-line tunnels show that the cracks at vault in single-line tunnel have more significant influences on lining stiffness, while the cracks at vault in double-line tunnel propagate more easily than that of single-line tunnel.

(3) The longitudinal crack has the most significant influences on the mechanical behaviors of lining structure; When the length of crack does not penetrate through the primary lining, the Tensile damage degree of lining structure increases with increasing of the length and depth of crack. When the length of crack is 9m and its depth is 0.9H, the Tensile damage degrees of lining structure in single-line or double-line tunnels are 0.910 and 0.947, respectively. When the length of crack is more than 3m, its extensibility is mainly controlled by the depth of crack. When the depth of crack is shallow (such as 0.1H), it mainly propagates along the direction of crack depth, and when the depth of crack reaches a certain degree (such as more than 0.5H), it mainly propagates along the direction of crack length.

(4) The Tensile damage degree of reticulated crack is positively correlated with the length and width of crack. When both the length and width of reticulated crack are 150cm, the Tensile damage degree of lining structure in single-line and double-line tunnels is 0.949 and 0.979, respectively, it develops longitudinally along the tunnel.

(5) The pull-induced damage degree of radial crack is negatively correlated with the area of crack central zone, and positively correlated with the number of cracks and the length of cracks. When the area of crack central zone is $0.25m^2$, the number of cracks is 5, and the length of cracks is 6m, the pull-induced damage degree of lining structure in single-line and double-line tunnels are 0.897 and 0.950, respectively.

(6) The greater the crack depth is, the wider the distribution range is and the more significant the influences on lining stiffness becomes. When the length of single crack is 12m and the depth is 0.9H, the maximum unilateral horizontal convergence of lining structure and the maximum vertical displacement of vault increase by 4.31% and 5.21%, respectively. When the depth of crack is 0.5H, the maximum unilateral horizontal convergence of lining structure and the maximum vertical displacement of vault increase less than 2.5% under the actions of all kinds of cracks.

In this paper, the influences of single crack, reticulated crack and radial crack on the mechanical behaviors of lining structure in single-line and double-line high-speed railway tunnels are studied and some study results are certainly achieved. However, there are still two shortcomings: one is that the influence rule of crack width on the mechanical behaviors of lining structure has not yet been considered; the other is that the study achievements about the influence rule of cracks on mechanical behaviors of lining structure has been inclined to be qualitative, and the quantitative study has not yet been fully realized. Therefore, the next study will further improve the integrity of indicators and the quantification of study results.

REFERENCES

[1] Yang Chengyong. Study on Cracks and Treatment Measures of High Speed Railway Tunnel lining[J]. Building Technique Development, 2017, 44(6): 53–54.

[2] Zhao Tiancheng. Discussion on Remediation Measures for Lining Defects of High-Speed Railway Tunnel[J]. Construction & Design for Project, 2020 (3): 101–103

[3] Chen Dongzhu. Study on Crack Disease of Tunnel Lining in High Speed Railway and Its Treatment Measures[D]. Central South University, 2012.

[4] Zhao Wei, Huang Rui, Zeng bin, et al. Multivariate Analysis on the Stability of Lining Cracks of Highway Tunnels[J]. Chinese Journal of Underground Space and Engineering, 2021, 17(S1): 419–425.

[5] Wang Wei, Deng Jun, Yin Juntao. Research on safety of lining structure in railway tunnel under spatial crack disease[J]. Journal of Safety Science and Technology, 2016, 12(01): 33–37.

[6] Wang Hualao, Liu Xuezeng, Li Ning, et al. Safety Evaluation Of Tunnel Lining With Longitudinal Cracks And Reinforcement Design[J]. Chinese Journal of Rock Mechanics And Engineering, 2010, 29 (S1): 2651–2656.

[7] Liu Xuan. Study on Influence of Cracking on Structure Safety of Subway Tunnels[D]. Beijing Jiaotong University,2018.

[8] Zhang Yujun, Li Zhiguo. 2D finite element analysis of bearing capacity of tunnel lining with cracks[J]. Rock and soil mechanics, 2005, 26(8): 1201–1206.

[9] Zhang Yihong. The Structural Safety Evaluation of Disease Tunnel Based on FiniteElement Method. Lanzhou Jiaotong University, 2013.

[10] Li Qingfu, Kuang Yihang, Guo Wei. CDP Model Parameters Calculation and Value Method Verification. Journal of Zhengzhou University(Engineering Science), 2021, 42(2): 43–48.

[11] Zhang Jing, Wang Qingyang, Hu Shouying. Parameters Verification of Concrete Damaged Plastic Model of ABAQUS. BUILDING STRUCTURE,2008,38 (8):127–130.

[12] Wang Xiyuan. Study on Mechanical Mechanism of Late-Short Anchor Assembly Structure of Repairing Cracked Lining based on Refined Simulation[D]. Southwest Jiaotong University,2018.

Tunnelling for a Better Life – Yan, Celestino, Thewes & Eberhardt (Eds)
© 2024 The Author(s), ISBN 978-1-032-80042-4
Open Access: www.taylorfrancis.com, CC BY-NC-ND 4.0 license

Design and verification of shear key support system for segmental lining openings at cross passages using non-linear finite element model

Jin Thai Chong*
Pini, Sydney, Australia

ABSTRACT: This paper presents the design and verification of a shear key support system for tunnel segmental lining openings at cross passages. During the construction of cross passages, temporary support is required to ensure the continuous transfer of hoop load within the segmental lining rings and maintain stability. Shear keys, along with other shear-transfer mechanisms, have been adopted as an alternative to traditional steel frames and lintel beams. The shear key system typically consists of steel circular hollow sections that are infilled with high-strength grout and installed at circumferential joints surrounding the openings. A non-linear finite element model is employed to determine the load transfer capacity of the shear key, analyze stresses in the adjacent segments, and verify the ultimate and service capacity of the system. The paper aims to present the efficiency and limitations of the shear key support system and promote the adoption of innovative support systems for cross passage construction, thereby contributing to the reliability and safety of tunnel structures.

Keywords: shear key support system, cross passages opening, temporary support, safety in design

1 INTRODUCTION

Cross passages are essential structures that facilitate not only maintenance and operational efficiency but also serve as crucial safety passage, providing emergency access, ventilation, and evacuation routes. However, constructing these passages poses technical and safety related challenges, especially when ensuring the stability of the tunnel lining around the openings during cross passage construction. Traditionally, steel frames and lintel beams have been used to provide temporary support during the construction of cross passages. While these methods have proven effective over the years, they often come with their own set of challenges, including increased costs, extended construction durations, safety issues related to the handling of heavy steel elements and potential disruptions to ongoing tunnelling operations. In recent years, the shear key system with combination of segment-embedded high performance bicone dowels has been adopted in several projects offering a promising alternative to traditional support methods. Comprising of steel circular hollow or reinforced cored sections filled with high-strength grout and positioned at circumferential joints around the openings, the shear key system promises to be an alternative that ensures the continuous transfer of hoop load within the tunnel lining rings, maintaining stability during cross passage construction. This paper seeks to present the design, verification, application, advantages, and limitations of the shear key support system. Furthermore, this paper recommends the design and verification processes with recognized standards, providing a comprehensive overview of the shear key system in the context of modern tunnel construction.

2 SHEAR KEY SYSTEM OVERVIEW

The excavation of the cross passages will require creating an opening in the segmental lining by removal of segments or cutting and removing portions thereof. Doing so breaks the continuous transfer of hoop load in the lining and requires a secondary thrust transfer system be installed to maintain stability in the system. Intercepting and transferring this hoop load away from the opening and into the adjacent rings is the key to creating a stable opening in a segmental lining. Aside from being designed to resist and transfer the forces within the cut rings to the adjacent rings, the support system must also limit deformations in the segmental liner to an acceptable level. For soft ground conditions, such as in clays or sands, high hoop loads may be expected on the tunnel lining. The traditional way to address the

*Corresponding author: jin.chong@pini.group

DOI: 10.1201/9781003495505-130

design of the openings under these high load conditions is to include a heavy propping system, often in the form of steel ring beams, vertical props, lintel beam, or combinations thereof. For openings where the loading is less than full overburden, or which are self-supporting, the propping system can be reduced or potentially eliminated with the application of shear key system with combination of segment-embedded high performance bicone dowels as shown in Figure 1.

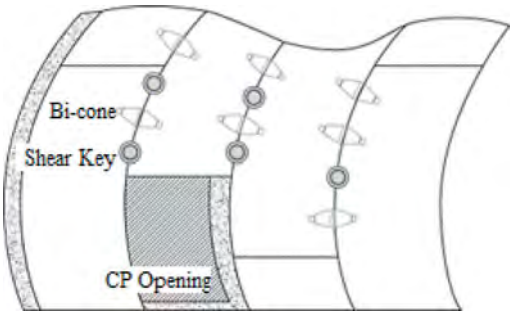

Figure 1. Illustration of bicone dowels and shear key system in circumferential joint.

The shear key system is typically compromised of cored hole reinforced with Steel Circular Hollow Sections (CHS) or vertical and spiral steel bars inside a cored hole. The core is infilled with high-strength grout, enhancing its bond with the surrounding concrete, and ensuring the effective transfer of stresses. The system is strategically positioned around the cross-passage openings between the ring-to-ring joint to ensure a uniform force distribution around the opening. According to research (Vladislav Mihaylov and Zenz, 2019), in comparison with plastic bicones dowel, the slip-free and stiff construction of shear keys means that the shear resistance can be mobilised without previous deformation, making it suitable for tunnels with expected high hoop load. Noteworthy applications include their use in cross passages in Aked Tunnel (Della Valle, Salas Monge and Savin, 2014), Wienerwald Tunnel, Perschling Tunnel and Pfänder Tunnel projects (Walter, Vladislav Mihaylov and Wagner, 2019). The use of shear keys has also been proposed for Follo Line as described by Ring and Johannes Gollegger (2019). The design principle of shear key system has also been referred to by Gehwolf et al. (2016).

3 DESIGN OF THE SHEAR KEY SYSTEM

This section describes the various considerations and recommendations that inform the shear key system design using CHS as shown in Figure 2.

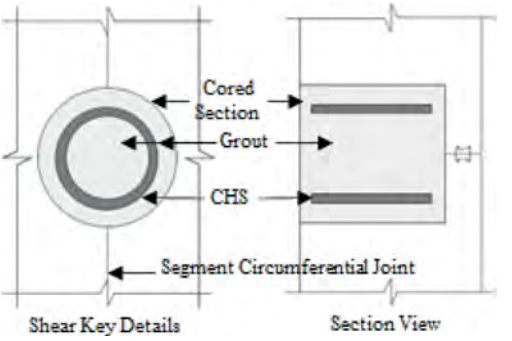

Figure 2. Shear key details.

3.1 *Sizing the Circular Hollow Section (CHS)*

The diameter of the CHS should align proportionally with the segment thickness. Generally, the CHS diameter could range between 0.5 to 0.75 times the segment thickness. This approach ensures that the CHS effectively carries shear loads while maintaining the segment's structural integrity. The CHS ought to possess an appropriate wall thickness to resist shear forces and bending moments. A thicker wall boosts shear resistance but also increases weight and cost. Selecting the steel grade for the CHS depends on anticipated loads and the desired safety factor. CHS sizing should facilitate easy installation, and it's crucial to ensure that sufficient grouting can envelop the CHS when placed in the cored hole. Additionally, the CHS should be positioned without hindrance to other structural elements such as reinforcement bars, dowels, or gaskets. This might involve adjustments to the CHS size or placement for compatibility.

3.2 *Cored hole size*

The cored hole diameter should be marginally larger than the CHS diameter to ensure a precise fit. Typically, an additional 40-50mm clearance around the CHS diameter is recommended. This allowance accommodates potential slight deviations during installation and provides space for grouting. The gap between the CHS and the cored hole facilitates the application of high-strength grout. This grout not only secures the CHS in position but also facilitates load transfer between the CHS and the adjacent concrete. It's essential to ensure that the gap is adequately wide for effective grouting while maintaining a strong bond between the CHS and the concrete.

3.3 *Depth of the shear key*

In practice, the depth usually spans from 0.5 to 0.6 times the segment thickness. This approach guarantees that the shear key engages a substantial part of the segment, effectively transferring the shear loads. A deeper shear key yields a broader surface for load transfer, dispersing shear stresses over a larger section

of the shear key. While deeper shear keys enhance load transfer, it's imperative to ensure that depth doesn't compromise the segment's structural integrity. A minimum concrete cover at the base of the shear key must be retained to sustain the segment's strength and durability in line with the project specific requirements.

3.4 *Spacing between two shear keys*

The spacing between shear keys is essential for effective load transfer. Typically, the center-to-center vertical spacing might range from 2 to 3 times the CHS diameter. Adequate spacing ensures even load distribution and reduces the risk of stress concentrations between adjacent shear keys. An FEA or truss model described by Gehwolf et al. (2016) as shown in Figure 3 can help to verify the chosen spacing and stress distribution, ensuring effective load transfer without causing stress concentrations or cracking of the concrete lining.

3.5 *Proposed design steps*

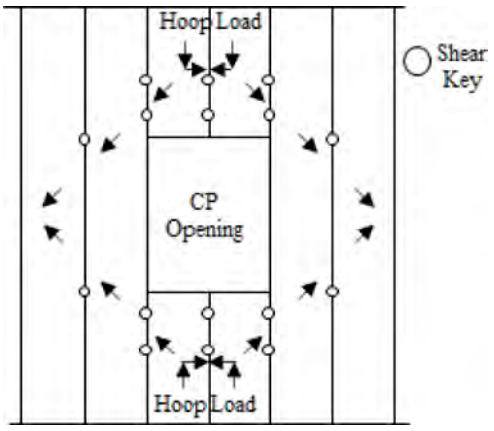

Figure 3. Shear key hoop load redistribution around the cross passage opening based on truss model.

The design and verification of the shear key system necessitate an integrated design approach, leveraging advanced computational tools and methodologies as summarized in the design and verification steps below.

1. Determine project requirements
   - Evaluate the need for a shear key system based on project specifications and requirements.
   - Assess the geological conditions and soil or rock stress near the intended cross passage location.
2. Determine optimum shear key arrangement
   - Analyse the segmental lining's structural behaviour and estimate complete lining hoop load.
   - Decide on the number of shear keys required around the cross passage opening considering the opening dimension and affected segment rings.
   - Consider the symmetrical arrangement around the cross passage opening using simplified truss model (Gehwolf et al., 2016).
   - Ensure positions avoid existing segment dowels, longitudinal segment joints, segment reinforcement (if any), and does not intersect the circumferential joint gasket.
   - Decide on the size of steel for the circular hollow sections (CHS) based on segment thickness, cored hole size, and the type of high-strength grout for infilling.
3. Verify Shear Key System Capacity on a single joint (2D Analysis)
   - Setup 2D axis symmetrical model of concrete with the proposed cored hole, CHS size, shear key spacing on a single joint.
   - Incorporate material properties, boundary conditions and anticipated hoop load to mobilize the shear key.
   - Evaluate the stresses developed on the concrete segment and the grout.
   - If stresses are excessive, return to Step 2. If not, proceed to Step 4.
4. Verify Overall System Capacity (3D Analysis)
   - Setup 3D FE Model of the tunnel lining with opening considering any segment bicone dowels and shear key with spring elements according to their actual position in the circumferential joint.
   - Simulate ground springs and impose loadings.
   - Assess the concrete segment's capacity to withstand all load cases and combinations.
   - Ensure that the shear forces are within the shear capacity of the shear key.
5. Refinement (if necessary)
   - If the design does not meet the requirements, return to the "Determine project requirements" or "Determine optimum shear key arrangement" steps and make necessary adjustments.
6. Finalize Design
7. Implementation & Monitoring
   - Monitor the performance of the shear key system during and after construction by verifying the expected ring deformation during lining opening and cross passage excavation against expected deformation informed by design.

4 CASE STUDY

4.1 *General description*

This case study involved partial removal of segments on two consecutive rings of a metro tunnel to give an

overview of the integrated design approach combining the 2D finite element and the 3D modelling techniques for design of tunnel opening with shear key system.

4.2 *Lining geometry*

The example described here concerns the construction of cross passage for connection between twin bored tunnels. The tunnel was excavated by an open-faced double shield TBM which allows safe installation of a universal segmental lining ring formed by 6 +0 precast pieces of steel fibre reinforced concrete (SFRC) segments . Each segment is provided with an all-round seal by elastomeric compression gasket which prevents groundwater entering the tunnel. The tunnel lining has an outer diameter of 6,690mm and an inner diameter of 6,170mm. The ring has been standardized to 1.7m wide. The thickness of lining is 260mm with a 28-day concrete strength of 50MPa. Table 1 shows the details of geometric characteristics of the precast concrete segmental lining.

Table 1. Geometric characteristics of the precast segmental lining.

Parameter	Value
Internal diameter	6,170mm
Lining thickness	260mm
No. of segment per ring	6+0
Ring width	1,700mm
Concrete strength	50 MPa
Ring connections	3 bicone dowels per segment

The opening on the lining was sized to provide a 5.2m high and 3.4m wide clear passageway for connection to the cross passage. This required partial removal of segments from two consecutive rings. The section of the tunnel where the opening to be formed is embedded in sandstone formation, with a total ground cover of approximately 50m above the tunnel crown.

4.3 *Shear key system description*

Openings have been designed considering the maximum expected ground loads from the segmental lining design, allowing for load relaxation arising from deformation of the opening rings. Zero groundwater pressure is assumed due to the installed temporary drainage and low permeability of the ground strata.

Combination of embedded bicone dowels and shear keys were adopted as cross passage opening support systems to accommodate both standard cross passages and cross passage with sump opening during temporary stage. The construction methodology assumed as part of analysis is that at each of the identified cross passage opening location, the steel pipe is installed inside 250mm diameter cored holes that are 150mm deep within the 260mm thick segment. The proposed 168 CHS (Grade 275) is installed and then grouted into the cored holes using non-shrink 60MPa grout. The cored hole location does not intersect the circle joint gasket so that water tightness of the ring is maintained in the long term.

The numbers and locations of the shear keys proposed are designed to allow optimum stress redistribution. There are total of 12 numbers of shear keys, 6 above the opening, and 6 below the opening. The shear key positions have been based on the avoidance of the existing bicone dowels as well as the longitudinal segment joints.

According to research (Walter, Vladislav Mihaylov and Wagner, 2019), it is expected that plastic bicone dowels to undergo a certain deformation in order to activate their effective shear resistance. Hence, when two or more load transfer elements are used, it is important to assess the load distribution to the relevant elements depending on the stiffness distribution. To address this, a 2D finite element model was used to verify and determine the load transfer mechanisms of the proposed shear key system across a joint, considering the anticipated lining hoop load. The shear key stiffness is then calibrated and adopted in the 3D model to assess the overall effect of opening to the segmental lining with the bicone dowel elements and ring to ring contact stiffness engaged. These models were crucial in studying load transfer mechanisms and assessing the capacity of the opened and adjacent rings to withstand force concentrations.

4.4 *2D Analysis*

Due to the complex load transfer system, a 2D non-linear finite element model using Strand7 has been utilised to determine the load transfer capacity of the shear key and to determine the stress concentrations, potential points of failure, and the overall behaviour of the shear key system. This model has also been used to check the load distribution between the 2 shear keys.

Material properties, such as material stress-strain curves, elasticity modulus, Poisson's ratio, and yield strength, are defined for concrete and grout materials for the compressive (crushing) and tensile (cracking) behaviour of the concrete material. These models have been run for both the service limit state (SLS) case to determine crack widths and the ultimate limit state (ULS) case to confirm the loading is within structural capacity. Different scenarios of axial forces due to earth pressures, groundwater pressures, and other external loads acting on the tunnel lining are applied on the plate element as edge pressures. For the 2D model, the curved segments were simplified as straight segments, considering that the straight segment will lead to conservative results as all shear load goes into the shear key whereas for

a curved segment model, some compressive load would be resisted by the boundary support on the external face of the segment. Only one half of the segment was modelled on each side of the shear key, and symmetric boundary conditions were provided on the plane of symmetry.

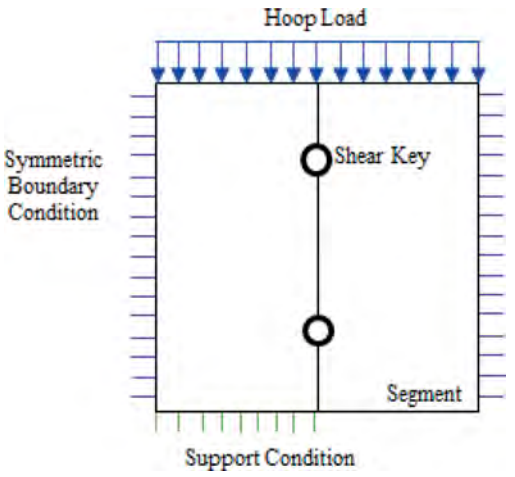

Figure 4. Shear key 2D modelling arrangement.

The segment-segment contact surface was modelled as frictionless, with a coefficient of friction set to zero. This assumption is consistent with research by Vladislav Mihaylov and Zenz (2019) to ensure that shear forces are exclusively transferred via the shear keys, eliminating any potential shear transfer through friction through segment-segment contact. The contact interface between the segments and the shear key system was defined using parameters from Eurocode 2. Based on a "very smooth" contact, a coefficient of friction of 0.5 was adopted for this interface, reflecting the inherent frictional resistance between the shear key and the segment.

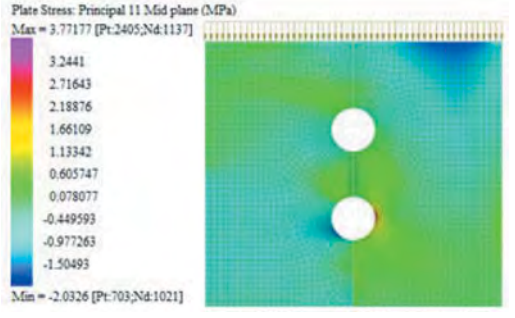

Figure 5. Concrete principal tensile stress (σ_{11}).

Design verification for both, concrete and grout elements, at ULS is done by checking the Major Principal (σ_{11}) stresses against the factored tensile design strength and Minor Principal (σ_{22}) stresses against the factored compressive design strength as calculated in accordance with relevant concrete design code or local standard. The design is considered adequate at ULS if the concrete stress does not exceed the design compressive or tensile strength. For the case study, the factored tensile design strength is taken as 3.33MPa for Grade 50 concrete, and 4MPa for the Grade 60 grout considering a material factor of 1.5. An example of a concrete segment principal tensile stress plot is shown in Figure 5, showing stress concentration at the bottom shear key region, as anticipated. At SLS, the concrete or grout is verified against the limiting tensile strain at cracking considering the project specific crack width limit. For this case study, tensile strain at crack width limit of 0.3mm gives 0.002 for the grout and 0.0012 for the segment. These are approximate values, and the actual tensile strength and modulus of elasticity can vary based on the specific mix design. It is recommended to refer to material test results or relevant local standards when available.

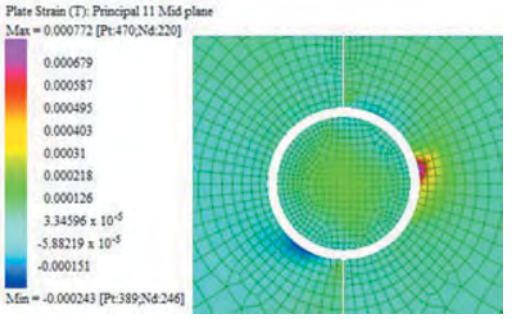

Figure 6. Grout and concrete principal strain (ε_{11}).

An example of a grout and concrete principal strain plot is shown in Figure 6. The study shows that the lower shear key, which is closer to the opening, carries 20 to 30% more shear load than the higher shear key. The analysis demonstrates that the first cracks appear in the concrete section near the bottom shear key closest to the opening. Tensile strains also indicate cracks in the middle part of the inner grout and in the outer grout. In the corners, strains show significantly higher values, indicating the gradual crushing failure of the segment as the applied hoop loads increase.

4.5 *3D Analysis*

The 3D model was then created to replicate the tunnel lining. Eight (8) monolithic rings comprised of a grid of quadrilateral shell elements have been considered in the analysis, which includes two (2) cut rings and three (3) adjacent rings either side. Radial

joints are considered by reducing the bending stiffness according to the Muir wood's formula (Wood, 1975). The ground medium was represented by radial springs. The stiffness of the radial springs was calculated using the linear load deformation relationship according to Duddeck & Erdmann (1985). Ground springs under tension were ignored and therefore no 'pulling' reaction was imposed on the segmental lining. The 3D model incorporated the opened and the adjacent fully enclosed rings in the temporary stage, without considering any support from the cross passage lining and the collar. Connection elements are used to simulate the behaviour of bicone dowels and shear keys with axial and shear stiffness. These connections are connected with compression only springs to allow separation to occur and to allow joint rotation. The magnitude of the shear force transferred by the shear elements is highly dependent on the stiffness of the shear key. While the non-linear modelled bicone dowels stiffness is typically determined from the shear force vs. displacement from the supplier's product data sheet, estimating the shear stiffness of a composite element like a shear key without a direct laboratory shear test can be a complex effort. The behaviour of a grouted CHS subjected to shear can be conceptually simplified to understand its shear strength and behaviour by isolating it into its individual components: the steel CHS and the grout. The shear strength of the steel can be derived from the steel's yield strength. Similarly, the shear strength of the grout often correlates with its compressive strength. For a fully bonded interface between steel and grout, a common assumption in grouted sections is that the combined shear strength of the composite can be conceptualized as a weighted average based on the area of each component. Displacement or deformation in shear is then related to the shear strain. For a given shear force, the induced shear stress on the grouted CHS can then be estimated. Using the relation between shear stress and shear strain, the displacement can be estimated by integrating the shear strain over the depth of the section. While these analytical models present an initial approach to understanding the behaviour, their limitations remain in simplifying complex interactions and potential non-linearities. As such, the use of these models is recommended in conjunction with experimental validation or advanced finite element simulations to ensure comprehensive insights, as recommended by Gehwolf et al. (2016). With the shear stiffness of the shear key calibrated, verification of the lining is performed considering load combinations and factors of safety in accordance with the national codes and standards. The design loads were applied directly on the tunnel lining under different load combinations. The resulting internal forces and moments from the 3D model were used to undertake the structural assessment for the lining and shear keys design.

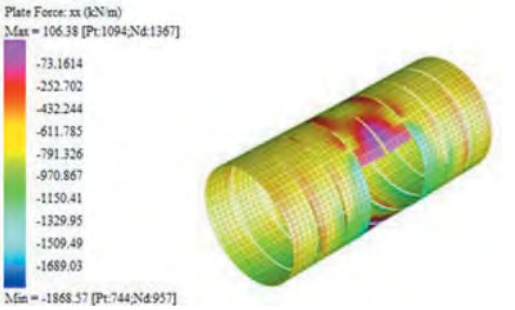

Figure 7. 3D Model hoop load distribution and deformation.

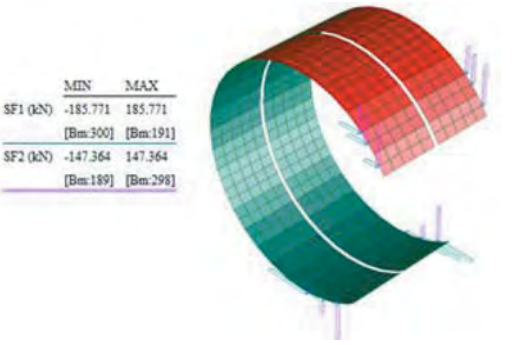

Figure 8. 3D Model shear forces of shear keys.

Figure 7 shows the full 3D model which was used for the design of the opening at the temporary stage during the cross-passage construction. The factored design load couples acting on the lining are checked against the Moment-Axial force envelope. In terms of serviceability, it is required that the ovalization produced under working loads be sufficiently relevant local standards, typically maximum distortion ratio of 2% and cracking, if any, be controlled with maximum crack width not exceeding the tolerable limits specified by the project requirement. The shear forces of each individual shear key are extracted from 3D models and verified against the total shear capacity of a shear key as shown in Figure 8.

The total shear capacity of the grouted CHS can be taken as the sum of the shear capacities of the steel and the grout assuming a perfect bond and interaction between the steel and the grout. Depending on the quality of the bond, the actual combined shear capacity might be less than the sum of the individual capacities. Hence, it is recommended to apply appropriate material factors based on relevant design codes or standards.

5 CONCLUSIONS

While FEM provides a detailed insight for the shear key system design and verification, it comes with

inherent assumptions, such as linear material behaviour in certain regions or simplifications in geometry. Recognizing and addressing these limitations is crucial for a holistic understanding of the results. Incorporating FEM into the design and analysis of the shear key system offers a detailed, comprehensive understanding of its behavior under various conditions. This method, combined with real-world validation and alignment with recognized standards, ensures that the system is both safe and efficient, meeting the demands of modern tunnel construction.

REFERENCES

Della Valle, N., Salas Monge, R. and Savin, E. (2014). Adoption of shear keys to provide stability to TBM tunnels segmental lining during cross passages construction: The example of Aked tunnel. In: Proceedings of the World Tunnel Congress 2014.

Duddeck, H. and Erdmann, J. (1985). On structural design models for tunnels in soft soil. Underground Space, 9.

Frodl, S. (2019). Support structures for segments at the construction of cross passages in different soil conditions. Geomechanics and Tunnelling, 12(1),pp.69–81. http://dx.doi.org/10.1002/geot.201800062.

Gehwolf, P., Walter, A., Galler, R. and Wagner, H. (2016). Shear tests on flexible shear dowels for use at cross passages with thin segmental linings/Scherversuche von flexiblen Scherdübeln für den Einsatz bei Querschlagsanschlägen mit schlanken Tübbingauskleidungen. Geomechanics and Tunnelling, 9(3). http://dx.doi.org/10.1002/geot.201600016.

Ring, B. and Johannes Gollegger (2019). Watertight segmental lining at drained cross passages under high water gradients. Geomechanics and Tunnelling, 12(1). http://dx.doi.org/10.1002/geot.201800064.

Vladislav Mihaylov and Zenz, R. (2019). Boßlertunnel – Anwendung von Schubdübeln bei den Sondertübbingen im Bereich der Verbindungsbauwerke. Geomechanics and Tunnelling, 12(1). http://dx.doi.org/10.1002/geot.201800067.

Walter, A., Vladislav Mihaylov and Wagner, H. (2019). Development of a guideline for cross passage junctions in segmental lined tunnels. Geomechanics and Tunnelling, 12(1),pp.19–32. http://dx.doi.org/10.1002/geot.201800065.

Wood, A.M.M. (1975). The circular tunnel in elastic ground. Géotechnique, 25(1),pp.115–127. http://dx.doi.org/10.1680/geot.1975.25.1.115

Tunnelling for a Better Life – Yan, Celestino, Thewes & Eberhardt (Eds)
© 2024 The Author(s), ISBN 978-1-032-80042-4
Open Access: www.taylorfrancis.com, CC BY-NC-ND 4.0 license

Environmental and economic advantages in using HPFRSCC in tunnelling

Massimo Coli*
Department of Earth Sciences, University of Florence, Firenze, Italy

Marco Francini
R & D Department, Unical S.p.A., Firenze, Italy

Lorenzo Martelli
European Investment Bank

Maurizio Tanzini
Pini Group, S.r.l., Italy

ABSTRACT: Concrete plays a key-role in tunnelling where it constitutes the final lining and represents one of the elements, which contributes to define the wideness of the opening in respect to the rock-mass behaviour. Concrete has a high carbon footprint, mainly due to the calcination reactions and the energy required for the production process, with a CO_2 emission of approximately 0,7 tons for Portland cement ton. International standards and regulation on sustainability and circular economy (CE) goals require the reduction of the carbon footprint to avoid increased prices rising and reach the carbon neutrality in 2050. Today, ready mixed High-Performance Fiber Reinforced Self Compacting Concrete (HPFRSCC) can be industrially available at the excavation face, ensuring a high degree of compactness and fully meet these needs. Its use is more environmental sustainable thanks to the use of low CO_2 cements and the substitution of part of the natural aggregates with recycled ones, recoverable from muck. HPFRSCC can reach strength up to 85-120 MPa, thus allowing a reduction in the thickness of the final lining, and consequently a reduced excavation diameter and of all the connected works. Here, we present a case history of a tunnel with 10 m of diameter where the classic 60 cm of final lining at 30-35 MPa had been replaced by HPFRSCC at 85 MPa, leads to a significant reduction of the diameter ensuring a higher durability and fire resistance. That implies a reduction in the volume to be excavated, with substantial costs-saving due to less time consuming and costly activities. For this goal, the focus of concrete qualification should switch from the concept of fixed mix to a product defined by its mechanical, durability and compatibility performances. The use of HPFRSCC for final lining increases tunnel durability, fire-resistance, and its environmental and financial sustainability and improve circular economy.

Keywords: Tunnelling, Concrete, Environment compatibility, Economic sustainability, Fibre reinforcement

1 INTRODUCTION

Tunnelling is a very expensive economic activity, a recent study of the EU Commission (EU, 2018a) fixed at about 35^{+}/-12 M€/km the cost of tunnelling, even if today it can also reach 40 M€/km. Most of the cost (50%) is for excavation work, lining weight at about 5% (WPI, 2012). Despite the diameter of the tunnel, it is interesting to consider the costs by m^3, which for conventional tunnel is about 230 €/m^3 and for base-tunnel around 330 €/m^3; the use of TBM can reduce this number by 1/3. Any topic that can reduce the excavation volume, and the muck, ensuring safety, technologies and loading gauge represents a significant chance for achieving costs reduction.

The thickness of the final lining, made in concrete, represents one of the elements that contribute to define the wideness of the excavation open in respect to the rock-mass behaviour saving the clear-section requirements.

Concrete has a high carbon footprint, which is mainly due to the calcination reactions and the

*Corresponding author: coli@unifi.it

DOI: 10.1201/9781003495505-131

energy required for the production process of the cement, with approximately 0.7 tons of CO_2 emission for ton of Portland cement.

In an economic balance, the environmental costs have to be also considered, and in particular the CO_2 emission that for concrete is planned to be drastically reduce for reaching the carbon neutrality in 2050 (Federbeton, 2020).

International standards and regulation on compatibility and circular economy (CE) goals require the reduction of the carbon footprint to avoid increased prices rising and reach the carbon neutrality in 2050.

The High Performance Fibres Reinforced Self Compacting Concrete (HPFRSCC) can give a response to this need.

2 THE HPFRSCC

Self-Compacting Concrete (SCC) can reach very high performance and durability.

The advanced formulation of the SCC is particularly open to the use of low-clinker cements, innovative additions, industrial by-products, recycled aggregates, including tunnelling muck; iIts formulation is based on a significant volume of cement +filler paste, which allows for very high fluidity with very low water/cement ratios.

SCC can be environmentally friendly, economical, very durable, successfully used in many types of construction. It can also enable for daring and innovative designs, both from a structural and architectural point of view.

The potential of ultra-performance and sustainable SCC is enormous. However, the use of large quantities of alternative materials and recycled aggregates (including those from muck) requires an adaptive formulation with expert use of admixtures, which must be ensured only by the competence of a qualified industrial manufacturer. This entails a fully performance-based prescription/control model, no longer based on compositional indications.

In an evolved vision, one should not look at the recipe of the concrete, but at the performance and properties that it guarantees. That implies a qualification process centred on the performance offered by a product with a proprietary and modifiable formulation, rather than on its fixed recipe.

This does not conflict with European standards, which provide for concrete with guaranteed performance (without recipe declaration), nor does it conflict with the qualification concept of Eurocode 7, which only provides for preliminary verification of the product's ability to satisfy the required performance. But above all, this fits perfectly with the natural approach of the specifier, who can focus on the pure performance necessary for the success of the project.

The addition of steel, carbon, basalt, or glass fibres can give considerable toughness to SCC, thus ensuring a new and important performance: ductility. The fibres, distributed homogeneously in the concrete mass, create a dense network of reinforcing elements capable of reducing post-cracking deformations (with hardening behaviour) and increasing fire resistance and durability.

To-day, ready-mixed High-Performance Fibre Reinforced Self Compacting Concrete (HPFRSCC) can be industrially prepared at the concrete batching plants on the construction site, and transported by concrete mixer trucks directly to the excavation face, thanks to the possibility of extending the workability maintenance time as desired by means the use of dedicated additives.

Ready-mixed HPFRSCC can reach strength over 100 MPa, thus allowing a reduction in the thickness of the final lining, and consequently a reduced excavation open and a gain in times and costs of all the connected works, allowing a more efficient work-cycle, with less equipment and labour.

Regarding the checks during construction, these can be limited to regular testing of the properties and performances guaranteed by the product, without any need to verify its compositional characteristics, for which it is often necessary to adopt rather questionable verification methods.

In tunnelling, the use of a low carbon footprint HPFRSSC, fosters the environmental compatibility (lower CO_2 emissions per m^3 of tunnel) of the entire work, increase the durability (longer operating life) and reduces the excavation sections (less m^3 = less earth work and less muck), being so cost-effective.

Furthermore, the possibility to use larger quantities of muck as aggregates (even fine ones and with low technical quality) implies less costs for muck transport and disposal, and less costs for supplying aggregates.

3 CASE HISTORY

In order to verify in the field the contribute that the use of HPFRSCC can give in reducing the final lining thickness, ensuring the same safety, and therefore gaining in the excavation open and all the others factors connected, some case history have been analysed. For having a comparison two cases, named A and B, have been analysed for a 12 m span highway tunnel with full face excavation by drill and blast methods.

Case history A refers to the excavation of a tunnel in a geological formation constituted by a Granitoids unit with a tunnel overburden of 600; case history B is related to the excavation in a complex sequence of conglomerates, sandstones and mudstones with an overburden of 800 m.

The adopted requirements for the lining of the tunnel (Figures 1–3) are as follows: (1) fully grouted rockbolts to stabilize the tunnel and a temporary lining made of fibre reinforced sprayed concrete 15 cm thick, for case A (section type Ab1) and steel ribs, spacing 1.0, embedded in shotcrete 25 cm thick, for case B (section type B0), sufficient to stabilize the tunnel during construction and until the

final lining is placed; (2) a drainage layer consisting of porous geotextile fabric, connected to drainage pipes in the final tunnel invert (3) a waterproof membrane to prevent water entering into the space behind the final concrete lining; (4) a cast in place concrete lining and invert capable of resisting loads imposed by the surrounding rock mass for both short and long term operation of the tunnel.

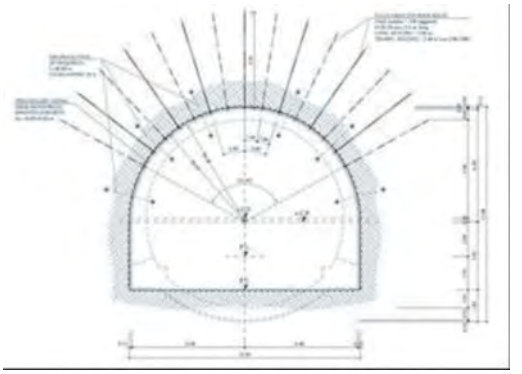

Figure 1. Tunnel excavation section type Ab1.

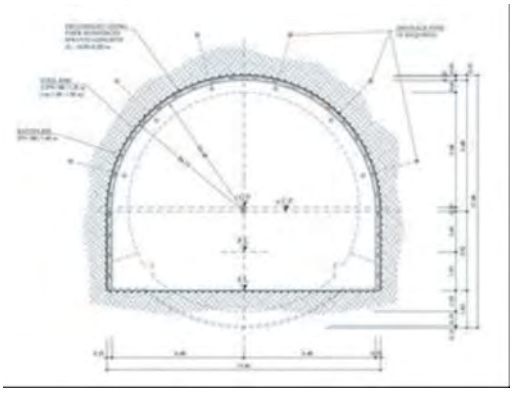

Figure 2. Tunnel excavation section type B0.

On the basis of geotechnical investigation and geomechanical characterization, the geomechanical parameters adopted for the numerical models have been defined (Table 1).

To analyse the positive effect of the use of HPFRSCC, in the dimensioning the tunnel lining support, some numerical plane strain analyses have been carried out using the 2D finite element programme Phase2 (©Rocscience, 1998 - 2001).

The numerical models implemented (Figure 4) non – linear, Mohr – Coulomb plasticity with a graded mesh of 6 – nodes triangular solid materials elements, and Timoshenko - beam elements with an elastic concrete material model.

To simulate the stress relief and 3D arching effects during excavation, a relaxation factor is applied to the

Figure 3. Construction of a complete tunnel lining consisting from right of: spritz-beton, a waterproof plastic membrane and a cast-in-place concrete final lining.

Table 1. Analyses input parameters.

	Depth m	γ kN/m^3	C MPa	ϕ°	E MPa	v	K_0
Case A	600	28	3.3	50	11,000	0.2	1
Case B	850	25	2.8	41	8,450	0.2	1

γ = Unit weight, c = cohesion, ϕ = friction angle, E = Young modulus, ν = Poisson's ratio, K_0 = lateral stress

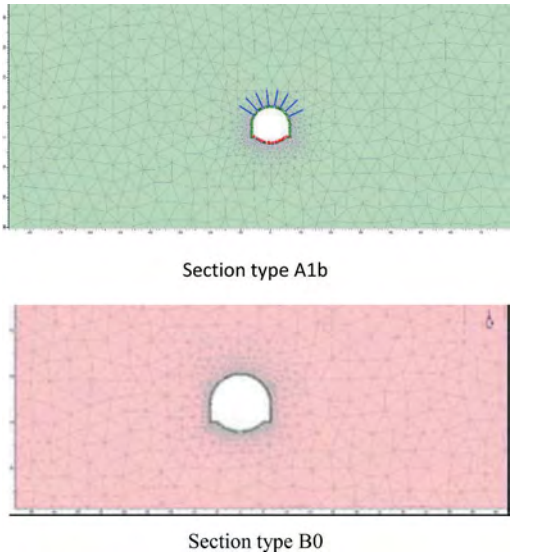

Figure 4. Part of the geometry and mesh of the two FE model.

rock mass in order to simulate the rock deformation prior to advance and installation of the lining at each excavation step (Vlachopoulos et al., 2009). This was realized through the stiffness reduction method, i.e. the rock within excavation zone is assigned lower elastic parameters (Young's modulus, Poisson's ratio) and the ground is allowed to deform to a new equilibrium before the lining installation.

The final step after the excavation and stabilization of the full tunnel profile is the installation of a final lining (Figure 5).

For both the section type, Ab1 and B0, the invert and vault final lining is made of cast concrete, respectively of 0.70 m and 0.60 m thick; the strength concrete class is C35/45, that is a cylinder characteristic strength equal to 28 MPa and a cube characteristic strength equal to 45 MPa.

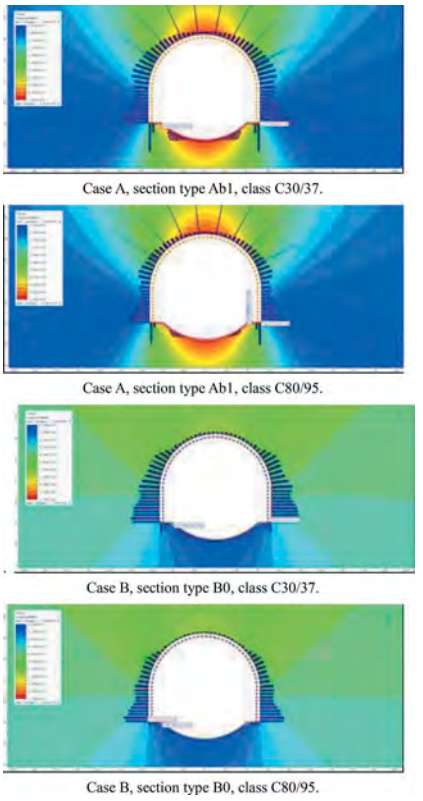

Figure 5. FEM results for the analysed configurations.

An additional numerical analysis has been carried out, for each section type, adopting HPFRSCC, characterized by a strength class C80/95, to evaluate the thickness reduction of the invert and vault final lining.

The results for the concrete strength properties C35/45 and C80/90 are presented in form of capacity limit curves, utilizing the support capacity diagrams proposed by Hoek et al. (2008), Kaiser (1985) and Sauer et al. (1994), (Figg.Figures 6–9).

For our purposes it is very important to have numerically verified the real technical feasibility of the premises.

4 DISCUSSION

From the analysis it results that the adoption of a HPFRSCC, with a value of the characteristic cylinder compressive strength equal to 80 MPa and a value of the characteristic cube compressive strength equal to 95 MPa, allow to halve the thickness of the final lining from 0.70 m to 0.35 m, for the invert, and from 0.6 to 0.3 m, for the vault.

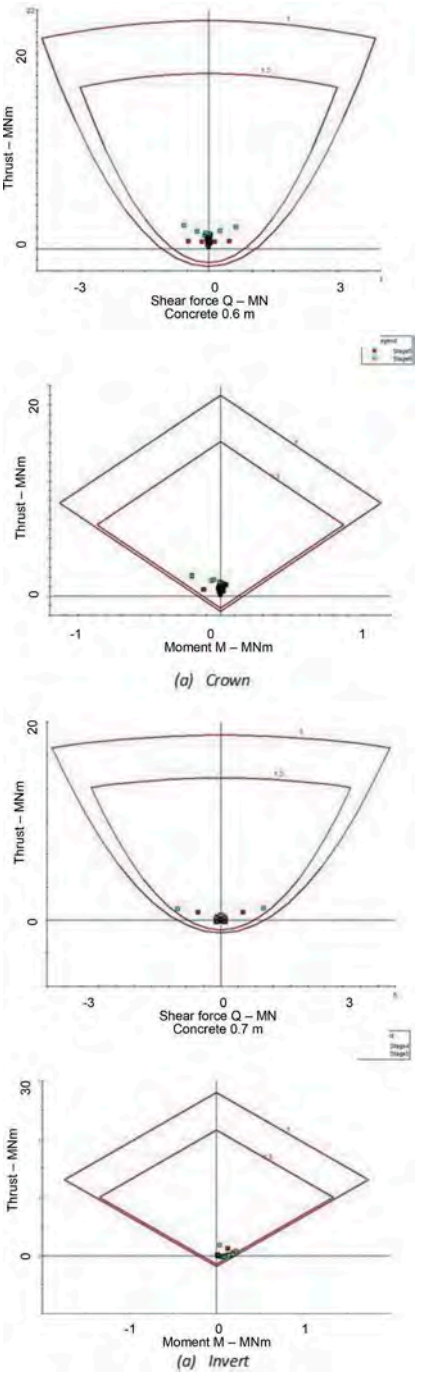

Figure 6. Case A (section type Ab1), FEM numerical analysis results, capacity limit curves/interaction diagrams for the final lining with a strength class equal to C30/37.

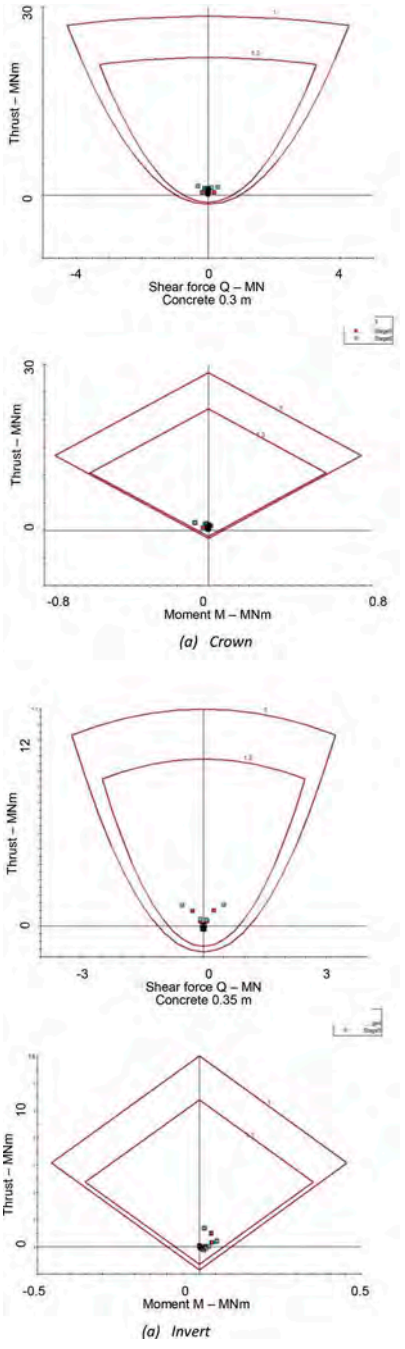

Figure 7. Case A (section type Ab1), FEM numerical analysis results, capacity limit curves/interaction diagrams for the final lining with a strength class equal to C80/95.

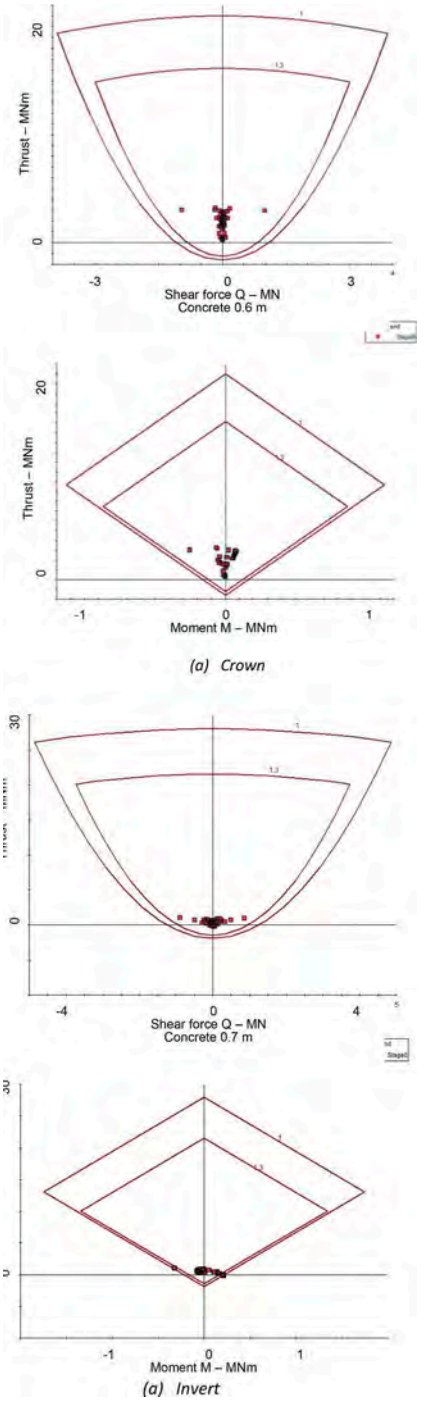

Figure 8. Case B (section type B0), FEM numerical analysis results, capacity limit curves/interaction diagrams for the final lining with a strength class equal to C30/37.

As stated in the introduction, a normal tunnels costs about 230 €/m^3 excavated, of which about 50% = 115 €/m^3 is for the excavation work and about 5% = 12 €/m^3 is for the lining.

From the above analysis it appears clear that the cost of the lining can be halved up to 6 €/m^3.

By the use of HPFRSCC, the excavation span, maintaining the clear open required, can be reduced by 35 cm in the invert and 30 cm in the vault, which corresponds to gain about 20 m^3 of excavation

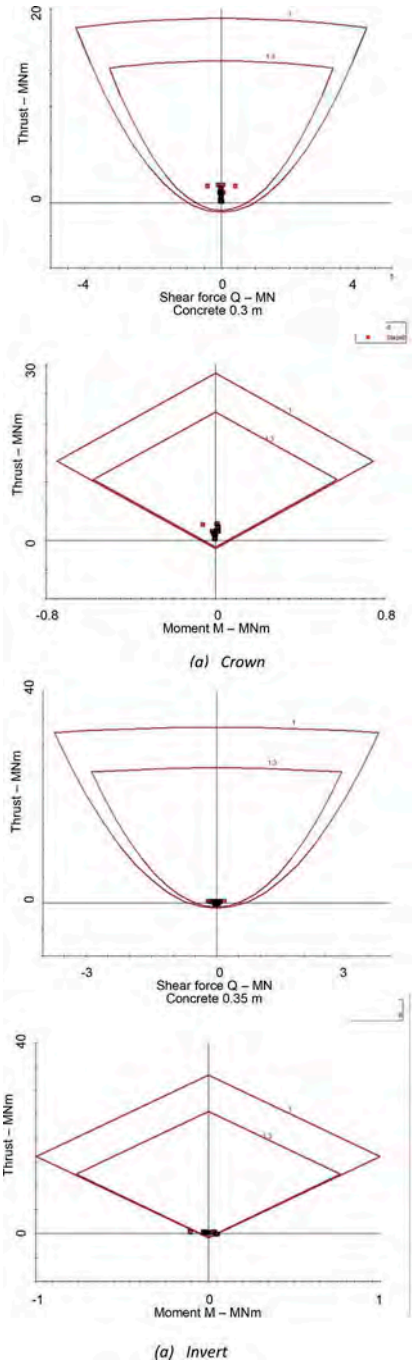

Figure 9. Case B (section type B0), FEM numerical analysis results, capacity limit curves/interaction diagrams for the final lining with a strength class equal to C80/95.

material for 1 m of a tunnel (= minus 20% from 113 m^3 to 90 m^3).

That corresponds into saving about 3,000 € for one m of tunnel (= minus 20%, from 13,000 €/m down to 10,350), or 3 M€ for km of a tunnel.

This solution is not only economic advantageous, but also environmentally friendly and compatible because reduces:

- the CO_2 emission related with cement furniture,
- the quantity of much produced and to be put on disposal,
- the trucks travels in need for supplying concrete and mucking, with the connected CO_2 emission and others pollutions,
- the conservation interventions,
- the total time to be planned for the execution,
- the final costs.

And increases:

- the production process,
- the lining resistance.
- the reuse of the muck in the same tunnel for concrete,
- the durability of the tunnel,
- the environmental compatibility of a design,
- the economic sustainability of a project.

HPFRSCC can easily substitute the use of reinforced concrete in tunnelling, largely boosting works and saving CO_2 emission that is estimated at about 1.85 ton of CO_2 for 1 ton of steel.

On more, instead that steel or carbon fibres it can be used basalt, or glass fibres, so farther reducing the carbon foot print.

5 DO NO SIGNIFICANT HARM – CIRCULAR ECONOMY

Considering EU funds, the REG. (EU) 2020/852 defines the criteria for determining whether an economic activity qualifies as environmentally sustainable for the purposes of establishing the degree to which an investment is environmentally sustainable, which is one of the conditions for eligibility of financing with EU funds and financial products. Two of the environmental objectives (art.9) is the transition to circular economy and climate change adaption. Having this type of sustainability criteria will contribute to steer the flow of capital towards sustainable investments; identify steps that financial institutions and supervisors should take to protect the financial system from sustainability risks (EU, 2018b).

With regards to the carbon footprint balance of a project, the use HPFRSCC lowers the CO_2 emissions decreasing: transport and concrete quantities.

Additionally, the use of HPFRSCC should help in increasing the energy efficiency by the use of less energy and less waste. Filling then some of the eligibility criteria for financing a project nowadays.

6 CONSIDERATIONS

The use of Fibres Reinforced Concrete began at the end of the 20th century (RILEM, 2003), and now is mature for a widespread use in tunnelling.

Because a tunnel project iter last up to 20 years it is now time to move design into the use of the HPFRSCC in order to have tunnelling on run by the half of this century, when the carbon neutrality must be reached.

That also help in elongating the Life Cycle Assessment (LCA) and having the Environmental Product Declaration (EPD) document as by EN 15804:2012+A1(ITB 2015).

Experiences in this way for saving CO_2 emissions, with the goal of contributing substantially in reaching carbon neutrality, have been already done for the segments of TBM tunnel (De Rivaz, 2022) and this goals is in the target of some Drill & Blast tunnel projects (Robinson, 2023; Holter et al., 2023), also coupled with sprayed waterproofing.

The use of HPFRSCC brings benefits in terms of costs reduction and increasing the necessary financial sustainability for the purposes of financing a specific underground investment project, and the application of sound and tested HPFRSCC can contribute in the fulfilling of sustainability criteria according to IFIs recommendations.

In order to mobilize additional funds and unlocking investments resulting in the private sector playing a larger role in the financing projects of this type and the achievement of the Sustainable Development Goals (SDGs), a diversification of construction products compatible with standards should be a priority.

7 CONCLUSIONS

The focus of this paper is to present, on the base of a case history, the real possibility of the use in tunnelling of the HPFRSCC, so saving times, costs and impacts while improves financial sustainability. Technology is ready, letting the HPFRSCC easily available at the tunnel face by concrete-mixer trucks with precast HPFRSCC (Figure10). The requirement for a performance-based model, is in compliance with EU technical codes and rules, and, furthermore, EU environmental requirements are targeted.

As summary, we have that for a Drill & Blast tunnel the use of HPFRSCC can reduce the total cost of the tunnel by about 10% (from 230 €/m^3 to 200 €/m^3) plus all the others connected savings as above quickly outlined. On this base, we can roughly estimate a total reduction of the tunnel cost from 230 €/m^3 down to 180 €/m^3 (= minus 20%) that for a classical tunnel the required section of about 113 m^2 now reduces to 90 m^2.

For a tunnel of 10 km, these numbers lowers the cost from around 260 M€ to 160 M€, so largely increasing financeability and environmental compatibility for a tunnelling project.

Therefore, the use of HPFRSCC can contribute in the success of an underground project by:

Figure 10. Furniture of the HPFRSCC at the tunnel face, ready-to-use, by means of concrete-mixer truck, is today possible.

– contributing to have a higher ratio Benefits/ Costs (BCR),
– contributing to have a reduced carbon footprint balance. These two points are nowadays key for supporting a sustainable development of an underground infrastructure.

The main output from the case history here presented is that the HPFRSCC is a challenge for tunnelling of the 21th century and its use must be the target of all the tunnel projects on run.

DISCLAIMER

The opinions expressed are personal and may not necessarily reflect the EIB Group position

REFERENCES

EU, 2018a. Assessment of unit costs (standard prices) of rail projects (CAPital EXpenditure). Luxembourg: Publications Office of the European Union, 2018. ISBN: 978-92-79-91813-1. doi: 10.2776/296711

EU, 2018b. Financing a Sustainable European Economy. Final Report 2018, by the High-Level Expert Group on Sustainable Finance. https://ec.europa.eu/info/publications/180131-sustainable-finance-report_en

Federbeton, 2020. La strategia di decarbonizzazione del settore del cemento. AITEC.

Hoek E., Carranza-Torres C., Diederichs M. & Corkum B., 2008. Integration of geotechnical and structural design in tunnelling. University of Minnesota 56th Annual Geotechnical Engineering Conference to be held in Minneapolis on 29 February 2008.

Holter K.G., Rossevold B.H. & Boyele K.M., 2023. New frontiers in SCL, Tunnelling J., April/May 2023, 32–38.

Kaiser P.K., 1985. Rational assessment of tunnel liner capacity. Proc. 5th Canadian Tunnelling Conference. Montreal.

ITB, 2015. EPD Environmental Product Degradation Type III. N.215.

RILEM, 2003. Reccomendadtions for design rules are available for steel fibre reinforced concrete. TC 162-TDF.

Rocscience, 2007. PHASE2. 2D finite element software. www.rocscience.com

Robinson N., 2023.Games changers. North American Tunnelling J., April/May 2023, 14–18.
WPI, 2012. Analysing international tunnel costs. Worcester Polytechnic Institute, AECOM, 96 pp.
Sauer G., Gall V. Bauer E & Dietmaier P., 1994. Design of tunnel concrete linings using limit capacity curves. in Computer Methods and Advances in Geomechanics, Eds.: Siriwardane & Zaman, Rotterdam, NL. 2621–2626.
Vlachopoulos N. & Diederichs M.S., 2009. Improved Longitudinal Displacement Profiles for Convergence Confinement Analysis of Deep Tunnels. Rock Mech Rock Engng (2009) 42: 131–146.

Tunnelling for a Better Life – Yan, Celestino, Thewes & Eberhardt (Eds)
© 2024 The Author(s), ISBN 978-1-032-80042-4
Open Access: www.taylorfrancis.com, CC BY-NC-ND 4.0 license

Structural and sustainability requirement with high performance fibre reinforced precast segment carbon counting example

Benoit de Rivaz*
NV Bekaert SA, Zwevegem, Belgium

ABSTRACT: Saving cost, reduced production time, improved handling, crack control and long-term durability, together with sustainability and carbon footprint reduction have driven the use of steel fiber as the predominant reinforcement for precast concrete segments worldwide the last 30 years. One of the aspects that are boosting the use of FRC in segmental linings is the introduction of guidelines for the design of FRC. In 2013, the fib presented the Model Code 2010 in which a specific part related to FRC is inserted. This document has sparked great interest in the tunnelling community and several documents consider Model Code 2010 as a reference. For this reason, fib Task Group1.4 "Tunnels" decided to create Working Party 1.4.1 on "Tunnels in Fibre-Reinforced Concrete". The Working Party prepared the present the fib bulletin 83 with the aim to support designer, clients and construction companies in introducing FRC in segmental lining tunnels referring to the indication of Model Code 2010. This paper will introduce the process to validate the material properties used for the design process according to fib bulletin 83 being considered as the reference basis for the design of FRC segmental lining and some recent detail carbon counting from international recent project.

Keywords: High performance steel fibre low carbon lining

1 INTRODUCTION

Underground space plays a vital role in sustainable urban planning as it provides a solution to the limited surface area available. In terms of transportation, underground networks enable efficient and rapid mass transit, helping alleviate congestion and reduce carbon emissions. Moreover, underground space is essential for the infrastructure required to sustain cities, such as dense networks of pipes for delivering fresh water and sewers for wastewater treatment. Additionally, it accommodates the extensive network of cables and service stations necessary for modern communication systems. By utilizing underground space, cities can optimize their resource management and minimize their environmental impact, contributing to a more sustainable urban future.

For a sustainable use of structural concrete, environmental and mechanical performances of concrete structures must have the same im-portance. By means of sufficiently high mechanical performances, the structural safety of a construction is ensured. In a tunnelling project, it is generally considered that 60% to 70% of embodied carbon is contained in the concrete linings of the shafts and tunnels. It is paramount, therefore that the tunnelling industry does its utmost to significantly reduce or eliminate its use of cement in all applications – segmental linings, in-situ linings, sprayed concrete, and annulus grouts. This is the reason why a great challenge for the coming years will be develop solution for low carbon lining. Mechanical excavated tunnels (tunnels excavated with a TBM – Tunnel Boring Machine) are more and more used in Civil Engineering. In these tunnels, the lining is made assembling precast segments used by the TBM as reacting elements in the excavation process. The use of Fibre-Reinforced Concrete (FRC) allows to reduce or eliminate the traditional reinforcement in the precast segment production. Over the last twenty years, the use of this technology has increased.

The use of Fibre Reinforced Concrete (FRC) allows several advantages, compared with traditional steel mesh or steel bar reinforcement according to fib bulletin 83 and all main recommendation published as:

Cracking control during construction phases.

- Higher impact resistance
- Durability advantages at final stage
- Reduction of costs

*Corresponding author: Benoit.DeRivaz@bekaert.com

DOI: 10.1201/9781003495505-132

- Sustainability advantages
- Boosting of the production process

Recent project has demonstrated that structural ductility, durability, and sustainability are going hand to hand. This holistic approach will be clearly a new booster for FRC tunnel lining. This paper will provide the start of the art on this issue, the key design principal and detail recent cases studies showing impact in carbon calculation saving in France, Middle East, and Australia.

2 SUSTAINABILITY & STRUCTURAL REQUIREMENT

For a sustainable use of structural concrete, environmental and mechanical performances of concrete structures must have the same importance. By means of sufficiently high mechanical performances, the structural safety of a construction is ensured. At the same time, a low environmental impact guarantees a sustainable development, which is, in accordance with the definition by the Brundtland Commission of the United Nations, a "development that "meets the needs of the present without compromising the ability of future generations to meet their own needs" (Brundtland Commission, 1987). FRC acts on the tensile behaviour of cracked concrete and imparts ductility to a fragile material. FRC's excellent properties which overcome cracking as well as its improved durability over reinforced concrete are why we continue to develop that material and explain its economic success. The Life Cycle Assessment (LCA) is a methodology for assessing environmental im-pacts associated with all the stages of the life cycle of a product or process. It quantifies a material impact on the environment over its entire existence, from extraction of the raw materials required for its production up to its end of life. This approach, combined with research into a low-carbon solution, will give new momentum to FRC.

3 BASIC FRC BEHAVIOUR

A minimum tensile (strength) strength > 2200 MPa is recommended for final ling application considering the performance required and concrete classes. The hooked ends ensure the desired fiber pull-out. This is the mechanism that generates the renowned concrete ductility and post-crack strength.

The tensile strength of a steel fiber has to increase in parallel with the strength of its anchorage. Only in this way can the fiber resist the forces acting upon it. Otherwise, it would snap, causing the concrete to become brittle. On the other hand, a stronger wire cannot be fully utilized with an ordinary anchor design. Therefore, the tensile strength of a fiber has to be perfectly aligned with its anchorage system and its diameter.

Wire ductility and concrete ductility are two different aspects. Dramix® 4D steel fibers create concrete ductility by the slow deformation of the hook during the pull-out process, and not by the ductility of the wire itself. The network provides by the fibre get a fundamental importance. Recommended diameter is 0.75mm and l/D= 80 to ensure a network > 10km/m3 with 40kg/m3. This network will play a key role in cracking control, structural ductility and allow low dispersion in the result.

Table 1. Influence of the l/D ratio on the network effect.

l/D	80/60	65/60	45/50
Length (mm)	60	60	50
Diameter (mm)	0.75	0.90	1.05
Aspect Ratio	80	65	45
Network (m/kg)	276	200	147

4 DESIGN PRINCIPAL

Model Code 2010 is the most comprehensive code on concrete structures. It covers their complete life cycle from conceptual design, dimensioning, construction, and conservation through to dismantlement. It is edited by fib Model Code 2010 was produced through the exceptional efforts of participants in 44 countries from five continents. The fib bulletin 83 document aims to support designers, contractors and clients with guidance for the use of steel fibre-reinforced concrete, known as FRC, in precast segmental lining tunnels constructed using tunnel boring machines (TBMs) The document is intended to complement the fib Model Code 2010 (MC2010), which presents a section on the design of FRC, with the Model Code 2010 being considered as the reference basis for the design of FRC segmental lining.

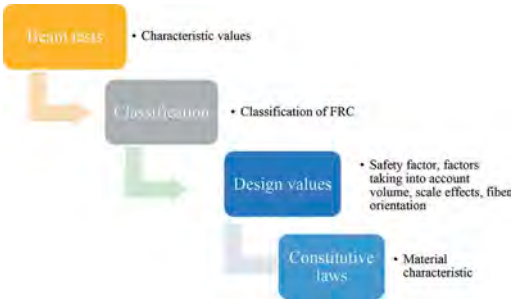

Figure 1. Illustrates the design process involved, from beam tests, classification, design values, and constitutive laws.

The tensile behaviour of the materials was characterized by performing bending tests on a notched beam. The tests were performed according to the EN 14651 European code, which is the reference standard for the CE label of steel and for ISO certification.

The compressive strength of the materials was measured by a testing cube with a side of 150 mm. For every cast made to produce every single segment, three beams were produced. In agreement with EN 14651, nominal strengths corresponding to four different crack mouth opening displacement (CMOD), namely 0.5, 1.5, 2.5 and 3.5 mm, were evaluated.

Figure 2 and 3 shows a typical result of the beam tests considering 40KG fibre type Dramix® 4D 80/60BGP with significant strength values. FL is peak force, fR1 and fR3 are the stresses related to CMODs equal to 0.5 and 2.5 mm respectively. These values are the reference ones for final lining design performed according to the fib Model Code 2010 prescriptions.

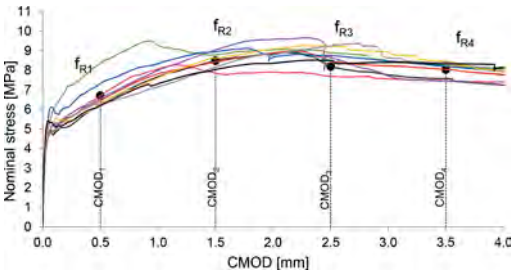

Figure 2. Curve Load -deflection of the beam bending tests according to EN 14651 (Roma University Report).

	f_L [Mpa]	f_{R1} [MPa]	f_{R2} [MPa]	f_{R3} [MPa]	f_{R4} [MPa]
Beam_01	4.68	6.70	7.86	7.69	7.47
Beam_02	4.90	6.28	8.49	8.20	7.58
Beam_03	4.78	6.45	8.41	8.42	8.04
Beam_04	5.15	6.56	9.04	8.64	7.44
Beam_05	5.72	7.33	8.95	8.75	8.19
Beam_06	5.03	6.27	8.60	9.23	8.45
Beam_07	5.63	7.75	10.2	8.99	8.54
Beam_08	4.60	6.28	8.16	9.25	8.40
Beam_09	5.43	6.18	8.03	8.50	8.33
Average	5.10	6.64	8.64	8.63	8.05
Characteristic	4.30	5.58	7.26	7.65	7.19

Figure 3. Results of the beam bending tests according to EN 14651 mean and characteristic value (Roma University Report).

To dimension a steel fiber-reinforced concrete segment, a reference test methodology needs to be adopted for the characterization of performance. In addition to the mechanical performance, various properties of the FRC can be specified.

Since brittleness must be avoided in structural behavior, fiber reinforcement can be used as substitution (even partially) of conventional reinforcement (at ULS), only if both the following relationships are fulfilled:

fR1k/ fLk > 0.4

fR3k/fR1k > 0.5

Where fLk is the characteristic value of the nominal strength, corresponding to the peak load (or the highest load value in the interval 0 – 0.05 mm), determined from the EN 14651 beam test. It is recommended to realize 12 beams per dosage and concrete mix formula.

If fibres are used as the only reinforcement for final lining, hardening post-crack behaviour at section level (beam test) allow immediately:

- Cracking control at SLS
- Structural ductility (ULS)

The Figure 3 shows the typical expected result considering FRC only as reinforcement. The performance class according to Model Code 2010 in this example is C40/50 5e FRC material, which means,

Fr1k> 5MPA.

Fr3k/fr1k> 1,3.

Indeed, materials with fR1k ranging from 4.0 MPa mini to 6.0 MPa are commonly used for precast tunnel segments without any bar reinforcement, combined with a fR3k/fR1k ratio in the ranges 1.1 < fR3k/fR1k < 1.3 or 1.3 < fR3k/fR1k < (class d and e respectively, according to the Model Code 2010 definition).

5 LOW CARBON PRECAST SEGMENTS CASE STUDIES

5.1 *Grand Paris*

The use of steel to replace all or a part of conventional reinforcement has been demonstrated to lower the embodied CO2 of the segmental lining. While it is possible to significantly reduce the embodied CO2 of a concrete mixture for segment production by replacing a portion of its cement content with alternative cementitious materials, there is little or no difference between the cementitious blends and contents required to produce fiber reinforced or conventionally reinforced concrete segments for tunnel linings.

Figure 6 shows an example reduction in CO2 emissions on a project made possible by modification of the concrete and further reduction by being able to replace the rebar with steel fibers in a dosage that satisfied all the design requirements. On a -per pound (kg) basis the embodied CO2 of conventional rebar and steel fibers is assumed the same. This is a generalization assuming the wire rod that the fiber is produced from, and the rebar have similar % recycled material content and similar steel production methods. In a precast segment the reduction in carbon footprint is due to the steel fibers being more efficient in reinforcing the element. In this example the elimination the combination of the right binder and steels fibre could conduct to a reduction 70%.

The recent project for the Grand Paris Linea 16.1 has shown the following:

- From the saving in the ratio of fibers compared with steel reinforcement bars, leading to

a significant reduction in CO2 emissions during transportation. If we compare 85kg/m3 for steel reinforcement bars with the 40kg/m3 for fibers, we get a saving on materials of more than 50%.

- By the benefit of better optimized loading for the fibers. 22 big bags of 1,100/kg per truck = 24.2 tons per load for the delivery of the fibers in comparison with 60 equivalent segments per truck = 17.85 T for the delivery of the concrete reinforcement bars.
- From the small diameter of the fibers which helps to further limit toxic emissions from the primary steel industry, due to primary coils which do not exceed 1 mm of wire diameter. The drawing technology is low emission.
- Fewer trucks on the road and optimized waste management in a large city like Paris is an important element to take into account. From an ecological point of view, the carbon balance is therefore very positive. In this respect, Bekaert has recently obtained its EPD (Environmental Product Declaration) Type III ITB certificate number 215/2021.
- The concrete chosen for the Line 16 Lot 1 fibre reinforced segments has a low carbon footprint of 170kg CO2 equivalent/m3 and reduces the carbon weight of the steel in the segments by 90kg equivalent CO2/m3 or nearly 11,000 tons equivalent CO2 per 10km.

Figure 4. Project jobsite Grand Paris - Photo Credit Eiffage Génie Civil.

In terms of concrete, there will be a before and after Grand Paris Express. Until now, to design the segments, we used reinforced concrete, that is to say concrete poured around cages of massive metal reinforcements.

The graph hereunder illustrates the main impact gain in term of carbon emission for typical Pre-cast segment ring used for a Metro tunnel.

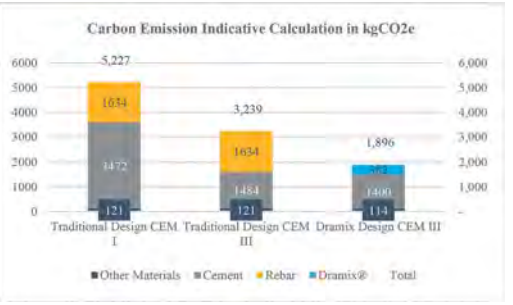

Figure 5. Typical Metro project, precast segment carbon emission counting.

This example (Figure 5) is based on the following assumption:

- Using a CEM III vs CEMI improves the CO2 score significantly.
- As we use 60% less reinforcement (100kg rebar vs 40 kg Dramix®) and also average rebar EPD is higher than Dramix® EPD, we end up with this difference with rein-forcement
- Using FRC allows thickness reduction by 2cm mini which results in additional savings in concrete.
- Thickness 38 cm

5.2 *Middle East Journey*

A paper by consultant COWI Denmark entitled 'Consultant's view of durable and sustainable concrete tunnel constructions in the Middle East" WTC 2018 Dubai provides this example how much CO2 emission saving was reached by replacing traditional concrete and steel-reinforced with steel fiber reinforcement and adding GBBS/FA to the concrete mix provides an example of reduction of concrete and further reduction by being able to replace the rebar with steel fibres in a dosage that satisfied all the design requirements.

This project as Doha Metro Green line has been designed with FRC using Dramix® fibre based on MC2010 to meet some specific condition:

- Very high chloride content: 10,000 - 50,000 mg/l
- High sulphate content: 100 – 5,500 mg/l
- High soil temperature: 28 - 32°C

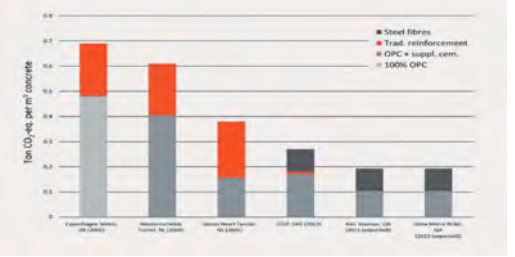

Figure 6. Evolution of Precast segment lining (Cowi/C. Edvarsen publication WTC 2018).

Main advantages

- Increased resistance to chloride-induced corrosion
- Eliminated risk of stray current-induced corrosion
- Easier production/handling
- Simplified segment precasting process

This return of experience in Middle East demonstrates that by using FRC increased resistance to chloride-induced corrosion and reduced carbon footprint. Durability and sustainability go hand in hand.

5.3 *The Montreal Metro Blue Line Extension Project*

The Montreal Metro Blue Line Extension Project consists of construction of 6 kilometres of tunnel, as well as five new underground stations. This represents a good example as well showing than durability and sustainability goes hand to hand. Indeed, the reduction in segment thickness achieved with fibers can be primarily attributed to the concrete cover requirements of 60-75 mm on both intrados and extrados rebar to ensure the durability against corrosion when designing according to Canadian code CSA A23.1:19 (2019). In contrast, when subjected to chloride exposure, corrosion in steel fiber reinforced concrete is limited to just a few millimeters from the surface, and nonetheless, does not lead to spalling cracks and is not regarded as a durability issue. CO2 savings in the segments is realized by replacing rebar with steel fibers as the quantity of steel required is 50% less per m3 of concrete with fibers. (40 kg/m3 vs 80 kg/m3) Additionally, the CO2 equivalent factor for rebar is reported to be 1.85 vs 0.88 for fibers. The fiber reinforced segments can be reduced in thickness due to no requirement for cover like rebar. This quantity of concrete savings also lowers the carbon footprint.

The owners' design engineer, AECOM, as part of a commitment to integrating sustainability best practices, performed a study utilizing the Envision framework to evaluate alternatives to achieve a most sustainable infrastructure project. Based on the results of this study the TBM bored tunnel sections will be lined with steel fiber reinforced precast concrete segments using low-carbon Supplementary Cementitious Materials (SCM) concrete.

In the TBM tunnel sections lined with pre-cast concrete segments, high performance Dramix® steel fiber 4D80/60BGP with a dosage of 40 kg/m3 is designed as standalone reinforcement.

See below table summarizing the results of the evaluation showing a reduction in total CO2 equivalent by nearly 50% using SFRC with an optimized SCM concrete mix design:

		Baseline Reinforced Concrete Mixture (OPC)			Moderate SCM Concrete Mixture with Fiber		
Mix Design Components	CO_{2eq} Factor	Mass (kg/m³)	CO_{2eq} (kg/m³)	% Replacement by Mass	Mass (kg/m³)	CO_{2eq} (kg/m³)	% Replacement by Mass
Portland Cement	0.92	475.0	437		348.8	319.1	
Slag	0.1466	0.0	-	0%	104.5	15.3	22%
Fly Ash	0.093	0.0	-	0%	0	0	0%
Silica Fume	0.014	0.0	-	0%	23.8	0.3	5%
Admixtures	1.67	4.5	7.5	1%	4.5	7.5	1%
Aggregate	0.06	1430	85.8		1430	85.8	
Steel bar	1.85	80.0	148.00		-	-	
Steel Fiber	0.88	-	-		40	36.4	
		Total	601		Total	387	

Figure 7. Embodied carbon in unit volume for the baseline and the optimized final mix designs.

	Ring width (m)	Tunnel Length (m)	D_{ex} (m)	D_{in} (m)	Ring Volume (m^3)	Total Concrete Volume (m^3)	CO_{2eq} (kg/m^3)	CO2eq Per 1 Linear Meter of Tunnel (ton)	Total CO_{2eq} (ton)
40 cm thick Segment-OPC	1.8	4066	9.4	8.6	20.4	46212	601	6.8	27,772
35 cm thick Segment-SCM	1.8	4066	9.3	8.6	17.7	40210	363	3.6	14,596

Figure 8. Calculation of total embodied carbon footprint of the PLB tunnel segmental lining for the baseline and the optimized final designs.

5.4 *The Forrestfield airport link*

"The Forrestfield airport link is a "design and construct" type of project; it will deliver an 8.5 km extension of the existing PTA urban rail network in Perth, Western Australia, connecting the Midland Line, just past Bayswater Station, to Forrestfield. The twin-bored tunnels will travel underneath the Swan River, Tonkin Highway and Perth Airport. The project will include three new stations; Redcliffe Station (located under-ground in Redcliffe), Airport Central Station (located underground at Perth Airport to service both domestic and international terminals) and Forrestfield Station. The tunnel excavation diameter is 7,100 mm; the segmental lining has an inside diameter of 6,170 mm, and thickness of segment is 300 mm with an average length of 1,600 mm".

The segmental lining was designed to meet the project's concrete requirements of 120-year service life with a minimum water/binder ratio of 0.35. This article draws its attention to the specific concrete mix design from the design up to the construction phases of the precast segmental linings.

Several trials were performed with cast concrete beams according to standard BS EN 14651 (single trial was made with #9 concrete beams) with 35 kg/.

The characteristic values of these results were more than the serviceability state 5.08 MPa at CMOD1 and 5.28 MPa at CMOD3. The results have confirmed the assumptions for the quantity reduction and the mix with 35 kg/m3 of Dramix® 4D 80/60BGP steel fibres content was adopted in project works.

Carbon Counting

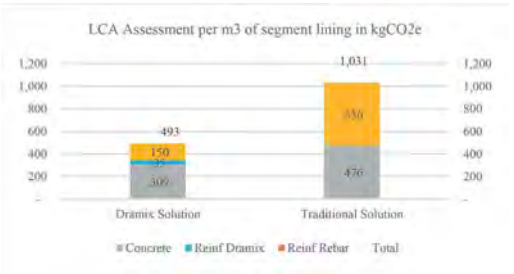

Figure 9. One Click LCA calculation.

6 EPD CERTIFICATE

An Environmental Product Declaration (EPD) is a document that transparently communicates the key environmental performance indicators of a product over its lifetime.

A third-party verification ensures that data relating to environmental aspects of Dramix® has been validated by an external organization.

This declaration is the Type III Environmental Product Declaration (EPD) based on EN 15804:2012 +A1 and verified according to ISO 14025 by an external auditor. It contains the in-formation on the impacts of the declared construction materials on the environment. Their aspects were verified by the independent body according to ISO 14025. Basically, a comparison or evaluation of EPD data is possible only if all the compared data were created according to EN 15804:2012+A1.

The environmental impact of Dramix® product (cradle to gate with options) is largely dependent on the energy intensive production of steel (half product) on which the manufacturer has only a limited influence. The carbon impact of steel production (Wire Rods) in the product stage A1 is as high as 85%. The impact of the production line largely depends on the amount of electricity consumed by manufacturing plant (0.34 kWh/kg of product). There are no significant emissions or environmental impacts in the A3 production processes alone (partly gas combustion). The production process itself does not have significant environmental impacts in the life cycle.

7 CONCLUSION

There has been a trend the last years that concrete tunnel linings have increased material consumption, cost, and environmental loads. Nowadays develop and/or improve tunnel construction methodology to choose the optimal tunnel lining, including environmental footprint and cost-effectiveness. Create required knowledge to produce final lining to meet new large infra-structure projects with modern demands to functionality incl. 100-year service life and environmental impact.

The use of steel fibre reinforced concrete will highly participate to meet low carbon lining by concrete consumption and steel reinforcement saving. If ductility and durability have been the key words the last 40 years, the sustainability will be the key driver for further FRC lining development in the coming years.

Indeed, new generation of binder combined with FRC allow new achievement:

- Provide excellent long-term durability performance exceeding that of Portland cement-based concretes.
- Excellent long-term durability performance exceeding that of Portland cement-based concretes. Extremely low embodied carbon footprint compared to conventional concretes on Port-land cements.
- Compared to reinforced concrete, fiber-reinforced concrete notably represents savings of around 5,000 tons of steel for 10 kilometers of tunnels (Typical Metro Tunnel).

We all believe that tunnels should use smart and sustainable construction materials. The future of tunnelling is choosing these materials today. High Performance steel fibre could play an important role in this final lining sustainable journey.

REFERENCES

A leap forward for SFRC segmental linings in France, April 2022. Tunnel Tech.

Allen, C., 2021. Low Carbon Concrete/rules of the thumb. T&T Journal.

Brundtland Commission, 1987. Our Common Future. Report of the World Commission on Environment and Development, 1987. United Nations World Commission on Environment and Development. Published as Annex to General Assembly document A/42/427.

Edvardsen, C. The consultant's view on service life design, WTC Congress, COWI A/S, Paral-lelvej.

EN 14651, 2005. Test Method for metallic fibre concrete. Measuring the flexural tensile strength.

FIB, 2010. Model Code 2010 – First complete Draft. Bulletin 55-56.

Forrestfield airport link project in Perth, Western Australia Precast concrete segmental lining. S.C. Scaffidi, Salini Im-pregilo S.p.A., Milano, Italia now e Build Spa &A. Anders, S. Porto & E. Torres SI-NRW JV, Redcliffe, Perth, Western Australia published in WTC2019.

ITB, 2015. EPD – Environmental Product Declaration Type III. No. 215.Precast tunnel segments in fibre reinforced concrete fib bulletin 83, October 2017.

Verya Nasri, Medhi Bakshi. Design and Construction of FRC Tunnel Segments in North America with Fiber-Enabled Carbon Footprint Reduction fib ACI 2023.

Tunnelling for a Better Life – Yan, Celestino, Thewes & Eberhardt (Eds)
© 2024 The Author(s), ISBN 978-1-032-80042-4
Open Access: www.taylorfrancis.com, CC BY-NC-ND 4.0 license

Research on reinforcement measures for soft plastic loess tunnel base

Qihua Deng*
Faculty of Architecture, Civil and Transportation Engineering, Beijing University of Technology, Beijing, China
China Railway 22 Bureau Group Co., Ltd., Beijing, China

ABSTRACT: The loess strata has characteristics such as collapsibility and structural sensitivity. Constructing tunnels in this formation can easily lead to excessive deformation of the initial supporting structures, especially causing cracking and heave disasters at the inverts position, which affects the safety during both the construction and operation periods. This article firstly analyzes the physical properties of soft plastic loess through indoor experiments. Secondly, specific reinforcement schemes are proposed based on the sleeve valve tube grouting reinforcement mechanism. Finally, the morphology, moisture content, strength, and range of influence of loess after grouting are analyzed through on-site monitoring data and core sampling analysis. The results indicate that the plasticity index and liquidity index of the loess samples are 12 and 0.55, respectively, with an average liquidity index greater than 0.50, indicating that the loess samples are in a soft-plastic state; The sleeve valve tube grouting reinforcement technique can effectively reduce the permeability and moisture content of the loess formation, as well as improve its unconfined compressive strength; The influence of the grouting process on the stress in the surrounding soil gradually decreases from near to far, and the maximum influence radius in the horizontal direction is 8.03 meters.

Keywords: Tunnelling, Soft plastic loess, Grouting reinforcement, Monitoring measurement

1 INTRODUCTION

Tunnels are an important means of transportation construction. With the increase in the number of tunnels, it is inevitable to encounter complex and adverse strata (Fu et al., 2022; Li et al., 2023), among which the loess strata has obvious structure, strong permeability, collapsibility, development of vertical joints, and other characteristics (Wei and Zhu, 2021; Zhang et al., 2018), which may cause construction risks such as water leakage, large deformation, falling blocks, and collapse in tunnel construction in this stratum, especially the risk of sudden instability caused by collapsibility (Liang et al., 2016). In addition, the disaster characteristics of loess may also lead to cracking and uplift of the arch structure, which will affect the later safe operation of the tunnel project (Liu et al., 2017).

During the construction of most loess tunnels, waterfall erosion, lateral erosion, headward erosion (Li et al., 2020), will occur due to surface water infiltration or groundwater erosion, which will lead to the decrease of surrounding rock strength, large deformation, loess collapse and other problems (Cheng et al., 2017; Sun et al., 2021), eventually leading to cracking and uplift disasters in the inverted arch. Based on the analysis of 27 loess tunnels, Sun (Sun et al., 2021) believes that the infiltration of surface water into the surrounding rock through joints and fissures will increase the water content of the loess and reduce the strength of the surrounding rock. The tunnel support structure bears more load, resulting in uplift and cracking disasters in the inverted arch. As the water content continues to increase, a saturated zone is formed at the bottom plate, which in turn affects the overall displacement of the tunnel (Li et al., 2022), and in severe cases will lead to tunnel collapse (Yan et al., 2022). Based on the deterioration mechanism of mechanical properties of loess surrounding rock under the action of surface water, Liu (Liu and Lai, 2020) used a multi-point independent loading test system for tunnel lining to analyze the deformation and cracking of lining structure. It was found that the development order of cracks in lining structure was type I initial cracks, L-type middle cracks and Y-type late cracks, and the types of cracks in lining were mostly concentrated in L-type. Li (Li et al., 2019) analyzed the stress state of the tunnel structure through a large-area immersion test on site. The results show that as the water content of the loess surrounding rock near the tunnel lining structure gradually increases, the inverted arch begins to produce upward

*Corresponding author: dqh18635489278@163.com

DOI: 10.1201/9781003495505-133

displacement. Therefore, a reinforcement method that can reduce the water content of loess and improve the overall strength of the stratum is needed. The grouting reinforcement method is to inject the solidified slurry into the stratum through a certain pressure and expand through the cracks in the soil to improve the overall physical and mechanical properties of the stratum (Lee et al., 2020). Grouting properties and grouting range are also different due to different formation conditions and actual construction control requirements (Wu et al., 2020). There is a loess fine grouting reinforcement scheme based on improving the physical and mechanical parameters of the slurry (Yang et al., 2020). Numerical manifold method is also used to simulate the whole process of grouting reinforcement, so as to analyze the influence of grouting reinforcement technology on the deformation of surrounding rock of deep tunnel caused by excavation (Xu et al., 2021). Some scholars analyzed the influence range of sleeve valve tube grouting reinforcement technology on improving the strength of surrounding rock of weak tunnel face by means of numerical simulation (Liu et al., 2019). At present, the research on sleeve valve tube grouting reinforcement technology mainly focuses on its slurry composition, casing material ratio, etc., and there are relatively few studies on the influence of reinforcement soil in the grouting process. In addition, most of the research methods used are laboratory tests and numerical simulations, while the loess strata are more sensitive to the structure, and field tests are needed to better reflect the grouting reinforcement effect.

In summary, this paper first analyzes the physical properties of soft plastic loess. Secondly, based on the grouting reinforcement mechanism of sleeve valve tube, a specific reinforcement scheme is proposed. Finally, the shape, water content, strength and grouting influence range of loess after grouting were analyzed by field monitoring data and core sampling. The research results of this paper have good theoretical significance and application value for the grouting reinforcement technology of loess tunnel basement.

2 PROJECT PROFILE

The total length of Shanggecun tunnel on Yinxi high-speed railway (Ganning section) is 6782.45 m (DK 207 + 517.55 ~ DK 214 + 300), the buried depth is 5.5 ~ 102 m, the length of grade IV surrounding rock is 2560 m, and the length of grade V surrounding rock is 4222.45 m. The tunnel position and profile are shown in Figure1. The strata in the tunnel site area are mainly Quaternary Middle Pleistocene aeolian clay loess, mainly hard plastic, and vertical joints are developed. Some sections of the tunnel body pass through the shallow buried slow slope, hard plastic loess and groundwater affected section, which has high construction risk and high safety risk. According to the drilling data and the survey of wells in the tableland, the groundwater level in the loess tableland is about 50 ~ 70m, and the thickness of the aquifer is 10 ~ 30m in the exploration depth. The area of loess tableland where the tunnel passes through is complete and open, and the groundwater occurrence condition in the center of loess tableland is relatively good, and the water level is shallow. In the deep section of the valley, the discharge conditions of surface water and groundwater are better, and the occurrence conditions of groundwater are relatively poor.

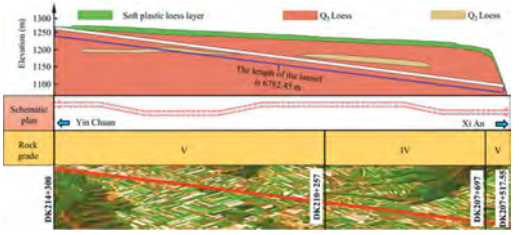

Figure 1. Tunnel location and geological profile.

3 DAMAGE STATUS

In the excavation process of Shanggecun Tunnel of Yinxi Railway (Ganning Section), the surface of the primary support structure is wet, and the phenomenon of water seepage (leakage) is more serious, which is dripping or linear outflow. The local section flows out in the form of strands along the tube roof drilling, and the arch foot is softened seriously. Settlement occurs at the vault, and cracking and uplift disasters occur at the inverted arch. After onsite investigation, the inverted arch parts of the DK210 + 600 ~ DK211 + 700 section of the tunnel have different degrees of cracking and uplift, as shown in Figure 2. The maximum crack width is 30 mm. At the same time, there is a more serious arch uplift disaster, and the amount of uplift is up to 30 cm. The inverted arch parts of the other sections have different degrees of cracking and uplift disasters. The cracks in the inverted arch are basically longitudinal cracks. In addition, the vault of the tunnel also has different degrees of subsidence.

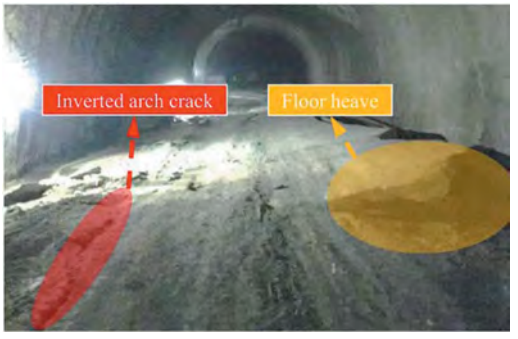

Figure 2. Tunnel location and geological profile.

4 PHYSICAL PROPERTIES OF SOFT PLASTIC LOESS

In order to reduce the disturbance to the undisturbed soil sample, the sample was sealed by the plastic film immediately after the sampling of the surrounding rock of the loess in the field, and then the sample was wrapped by the shock absorption foam, and sent to the laboratory within 24 hours. The indoor geotechnical tests such as density test, moisture content test and boundary moisture content test were carried out. The physical and mechanical parameters of the loess sample were obtained by statistical analysis as shown in Figure 3. In this experiment, the liquid limit and plastic limit of soil were measured by the combined measurement method of liquid and plastic limit. It can be seen from Figure 3 that the maximum water content of loess samples is 26.9 %, and the average water content is 26.1 %. The range of natural density is 1.94 ~ 1.98 g/cm^3, and the average natural density is 1.96 g/cm^3. The range of natural void ratio is 0.73 ~ 0.77, and the average natural void ratio is 0.75. The saturation of the sample is high, ranging from 91.90 % to 97.6 %, and the average saturation is 94.5 %. According to the average values of liquid limit and plastic limit of loess samples are 31.5 % and 19.5 % respectively, the plasticity index and liquid index can be calculated to be 12 and 0.55 respectively. The average liquid index is greater than 0.50, indicating that the loess sample is in a soft plastic state.

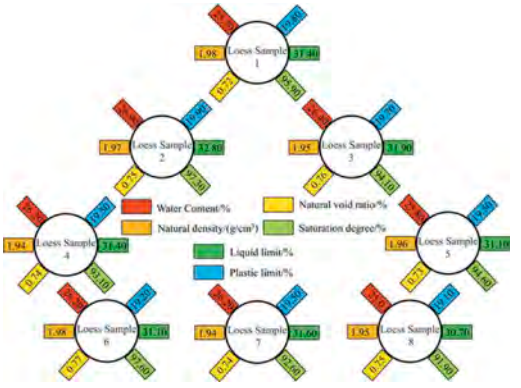

Figure 3. Tunnel location and geological profile.

5 SLEEVE VALVE TUBE GROUTING REINFORCEMENT MEASURES

5.1 *Reinforcement mechanism*

Splitting grouting is a dynamic grouting process in which the soil is compacted first and then split. It is grouted while the soil is split, so that the slurry can enter the soil after splitting and expand the reinforcement area. Sleeve valve tube grouting technology is an effective and economical soft soil foundation reinforcement method based on splitting grouting. First of all, the slurry enters the soil through the small hole on the sleeve valve tube, and produces a squeezing effect on the soil with a lower pressure. Secondly, with the continuous injection of slurry, the pressure of soil is increasing, and the squeezing effect of slurry on soil is gradually transformed into splitting effect. Finally, the slurry can flow in a wide range through the cracks in the soil after splitting, so as to complete the overall reinforcement of the foundation. The particles and pores of loess are small and dense. At the same time, the loess foundation also has collapsible characteristics. Therefore, when dealing with the soft plastic loess of the tunnel base, a simple, easy to implement, small space and economical soft foundation treatment method is usually needed. The sleeve valve tube grouting has the advantages of pre-buried casing, staggered peak construction and controlled grouting, which is very suitable for the treatment of loess foundation.

5.2 *Strengthening schemes*

The construction steps of sleeve valve tube grouting technology to reinforce the soft plastic loess tunnel base mainly include pre-embedded casing, drilling pressure tube, grouting and hole sealing treatment.

5.2.1 *Pre-embedded casing tube*

In the process of tunnel excavation, in order to prevent the collapse of surrounding rock, maintain the three-dimensional stress state of surrounding rock, and give full play to the self-bearing capacity of surrounding rock, it is necessary to construct the initial support structure in time. In this project, the initial support structure adopts the construction scheme of combining I-steel frame and shotcrete. The sleeve valve tube grouting needs to follow the excavation construction of the inverted arch. The construction period is long, which is not conducive to the timely closure of the initial support into a ring, and the risk is large. Therefore, Φ133 mm casing tube is reserved in the inverted arch and the filling layer. After the embedded casing tube is completed, the inverted arch and the filling surface can be poured. In the pouring process, it is necessary to protect the upper mouth of the casing tube to avoid the concrete falling into the casing tube and increase the difficulty of later drilling.

5.2.2 *Bore hole*

After the pouring of the inverted arch surface and the filling surface is completed, after the site is leveled, the drilling rig enters the field to drill in the reserved casing tube and drill to the design depth. The drilling position generally lags behind the construction of the secondary lining by 40 ~ 60 m. After the drilling is completed, the auxiliary drilling rig is used to press the plastic sleeve valve tube. Finally, according to the field test, the appropriate ratio of the casing material injection tube is determined, and the sleeve valve tube is sealed with the casing material.

5.2.3 *Grouting and hole sealing treatment*

After the backfilling of the inverted arch is completed and reaches the required strength, and the hole is sealed, the base sleeve valve tube grouting reinforcement is conducted. The grouting reinforcement profile is shown in Figure 4, with a transverse reinforcement range equal to the excavation width of the inverted arch and a vertical reinforcement range of 13 meters below the inverted arch. The grout holes are arranged in an equilateral triangle with sides of 1.5×1.5 meters, and the grout dispersion radius is 0.9 meters (as shown in Figure 5). The grouting material consists of P.O42.5 ordinary cement single liquid slurry mixed with a certain proportion of HPC admixture, with an admixture dosage of 15-20%, and a water-cement ratio of the slurry is 0.8:1. Φ76 mm steel sleeve valve tubes (with a thickness of 5 mm) are used for retrogressive grouting. Retrogressive layered grouting is achieved through the insertion of grouting core pipes and the use of grout plugs (layered length of 1-1.5 meters). When the grout plug is pressurized to 2.0 MPa with a hand pump, grouting begins. When the grouting process reaches a certain degree, the grouting is considered complete, and grouting can be carried out for other sleeve valve tubes. After grouting is completed, the floating slurry and loose debris inside the steel pipes should be promptly removed, and then filled and compacted with HoJa-53F micro-expansion grouting compound.

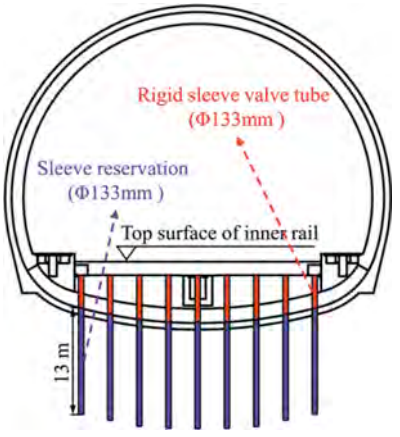

Figure 4. Grouting reinforcement range profile diagram.

5.3 *Result analysis*

5.3.1 *Core morphology*

After the completion of base grouting, a more intuitive analysis of the effectiveness of grouting can be achieved through core sampling from drilling (Mu et al., 2023). Therefore, after using sleeve valve tube grouting to reinforce the soft plastic loess at the base of Shangge Village Tunnel, core

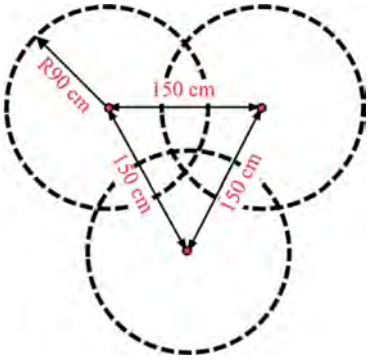

Figure 5. Grouting reinforcement diffusion range illustration.

samples were taken from the reinforced area to evaluate the application effect of sleeve valve tube grouting technology on soft plastic loess through the analysis of loess core samples. The morphology of loess core samples and drill holes before and after grouting is shown in Figure 6. Before grouting, a large amount of groundwater quickly infiltrated into the drill hole, indicating a high permeability of the soil. In addition, the surface of the loess core sample was water-rich, difficult to shape, and exhibited obvious characteristics of soft plastic loess. After the implementation of sleeve valve tube grouting reinforcement, there was no visible water in the drill hole, indicating a decrease in permeability compared to before grouting. Furthermore, there was no apparent water-rich morphology on the surface of the loess core sample, and the core sample exhibited better formation. Additionally, after grouting, cement mortar was observed in the cracks of the core sample, and compaction was observed in the cross-section, indicating good fracturing capability of sleeve valve tube grouting, which can effectively strengthen the soft plastic loess in a larger area of tunnel foundation. Therefore, the sleeve valve tube grouting reinforcement technology can reduce the permeability of soft plastic loess.

Figure 6. Loess core sample and borehole formations.

5.3.2 *Moisture content of core sample*

From the drilling and core sampling conducted before and after the grouting reinforcement, the water content of the yellow loess samples in the DK210+700, DK210+720, DK210+740, DK210 +760, DK210+780, and DK210+800 sections was measured through laboratory experiments, as shown in Figure 7. Prior to grouting reinforcement, the DK210+800 section had the highest water content in the yellow loess, reaching 34.4%. The DK210+700 section had the lowest water content, at 27.4%. The average water content of the six sections of yellow loess was 30.55%. After grouting reinforcement, under the splitting action of the grout, the soil mass was compacted, and pore water began to be expelled outward. The cracks in the soil mass were filled with grout, sealing off the groundwater supply lines. The water content of the yellow loess in all six sections showed varying degrees of decrease. Among them, the DK210+800 section had the highest reduction in water content, decreasing from 34.4% to 18.6%. The DK210+760 section had the smallest decrease, only about 1/5. The average water content of the six sections of yellow loess was 20.75%. Therefore, it indicates that sleeve valve grouting technology can effectively reduce the water content of soft plastic yellow loess.

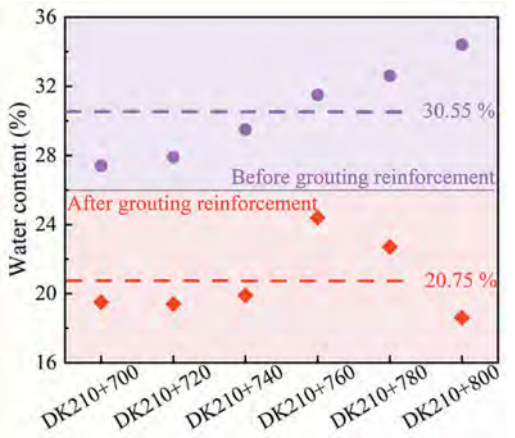

Figure 7. The water content of loess core sample.

5.3.3 *Core strength*

Before and after the grouting reinforcement, core samples were taken from the DK210+740 section by drilling. The core sampling range was 3.5 meters below the crown base. The 3.5-meter yellow loess core sample was divided into six sections, and each section was prepared into a cylindrical specimen with a diameter of 4.0 cm and a height of 8.0 cm for unconfined compressive strength testing. The steps for unconfined compressive strength testing were carried out according to the "Standard for Geotechnical Testing Methods"(GB/T 50123-2019, 2019). The unconfined compressive strength of the yellow loess core samples before and after grouting reinforcement is shown in Figure 8. Prior to grouting reinforcement, the maximum unconfined compressive strength within the range of 0-3.5 meters below the crown base in the DK210+740 section was 0.41 MPa. After grouting reinforcement, the unconfined compressive strength of the base yellow loess increased to varying degrees, with the highest increase being 0.16 MPa. Compared to the unreinforced state, the average unconfined compressive strength of the entire formation increased by 31.18% after reinforcement. Therefore, sleeve valve grouting technology can improve the strength of soft plastic yellow loess, reduce the load on tunnel support structures, and reduce the risk of deformation and cracking in support structures.

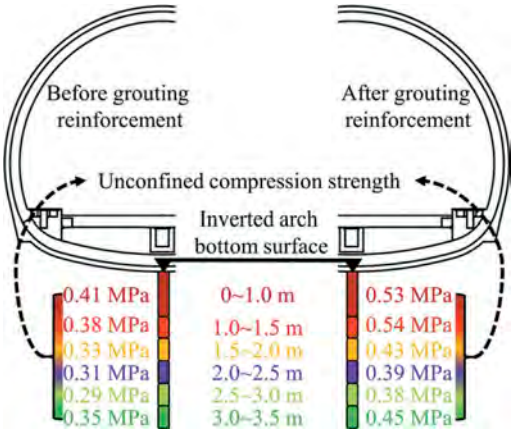

Figure 8. Unconfined compressive strength of loess core sample.

5.3.4 *Grouting influence range*

The advantage of sleeve valve grouting technology lies in its wide applicability, as it allows for continuous high-pressure fracturing grouting, enabling the formation of a large area of interconnected solidified grout within the soil. Therefore, the range of fracturing effects generated by sleeve valve grouting is crucial for reinforcing yellow loess formations. In this study, monitoring holes with pre-embedded soil pressure cells were set up around the grouting holes to monitor the stress increment in the soil during grouting. The arrangement of the monitoring holes is shown in Figure 9. Four monitoring holes were set up at distances from the grouting hole, with monitoring hole No.1 located at a distance of 1.5 m, monitoring hole No.2 at a distance of 4.0 m, and monitoring holes No.3 and No.4 at distances of 6.0 m and 7.5 m respectively. Each monitoring hole was equipped with a soil pressure cell at depths of 0 m, 2 m, and 4 m.

According to the data recorded by the soil pressure cells in the four monitoring holes, the stress increments in the soil at different depths during drilling or sleeve valve grouting can be obtained, as

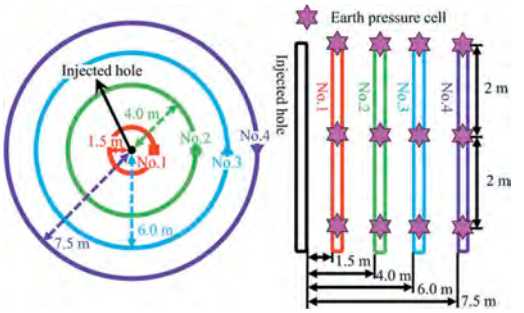

Figure 9. Layout schematic of monitoring stations.

shown in Figure 10. When the ungrouted borehole is formed, the yellow loess formation is in an undisturbed state, and the stress increments in each monitoring hole are all 0 kPa. After the grouting hole is drilled, in monitoring hole No.1, the stress increment in the soil increases from 21.31 kPa to 30.79 kPa with increasing depth; in monitoring hole No.2, the stress in the soil increases with increasing depth, reaching a maximum increment of 3.59 kPa; in monitoring hole No.3, the stress increment in the soil decreases with increasing depth, decreasing from 4.18 kPa to 1.24 kPa; in monitoring hole No.4, the stress increment in the soil decreases with increasing depth and reaches a minimum of only 0.2 kPa at a depth of 4 m. The stress increments in the soil in the four monitoring holes show two different trends with increasing depth. In monitoring holes No.1 and No.2, as the depth increases, the soil structure becomes stronger and the connection between the yellow loess particles becomes tighter, resulting in higher stress increments in the soil due to the drilling action. In monitoring holes No.3 and No.4, as the depth increases, more cracks appear in the soil, and the sensitivity to external forces decreases. When sleeve valve grouting is carried out after drilling, the stress increments in the soil in all monitoring holes decrease with increasing depth. The stress increment in monitoring hole No.1 decreases from 181.49 kPa to 81.93 kPa, in monitoring hole No.2 from 78.55 kPa to 35.19 kPa, in monitoring hole No.3 from 39.74 kPa to 22.48 kPa, and in monitoring hole No.4 from 31.86 kPa to 21.68 kPa. Sleeve valve grouting technology produces fracturing effects in the surrounding soil when grouting vertically, and then injects grout into the fractures to form grout veins. The grouting pressure is no longer simply transmitted vertically or horizontally but is transmitted along the weak structural planes of the soil that are subject to fracturing. In addition, as the distance between the monitoring hole and the grouting hole increases, the stress increment in the soil gradually decreases. Therefore, during sleeve valve grouting, the closer the monitoring hole is to the grouting hole, the more pronounced the fracturing effect will be.

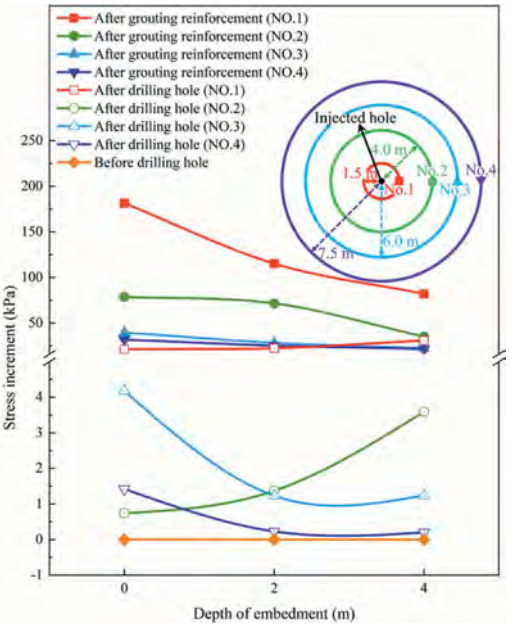

Figure 10. Stress increment of soil under sleeve valve tube grouting.

Based on the data recorded by the soil pressure cells after grouting, the influence range of horizontal grouting can be analyzed, as shown in Figure 11. Under different burial depths, the horizontal stress increments caused by grouting show a certain linear variation. By fitting the data, the following regression equations are obtained:

$$\sigma_0 = 202.88 - 25.26H_0 \; R^2 = 0.91 \quad (1)$$

$$\sigma_2 = 135.80 - 15.96H_2 \; R^2 = 0.96 \quad (2)$$

$$\sigma_4 = 88.40 - 10.12H_4 \; R^2 = 0.86 \quad (3)$$

In the equation,"σ_0" represents the soil stress increment at a burial depth of 0 m (kPa), "σ_2" represents the soil stress increment at a burial depth of 2 m (kPa), "σ_4" represents the soil stress increment at a burial depth of 4 m (kPa), "H_0" represents the horizontal distance at a burial depth of 0 m (m), "H_2" represents the horizontal distance at a burial depth of 2 m (m), and "H_4" represents the horizontal distance at a burial depth of 4 m (m).

From the regression equations (1), (2), and (3), it can be inferred that the horizontal influence range of the grouting hole at burial depths of 0 m, 2 m, and 4 m is 8.03 m, 8.50 m, and 8.73 m, respectively. Therefore, considering the worst-case scenario, the horizontal influence radius of the grouting hole is 8.03 m.

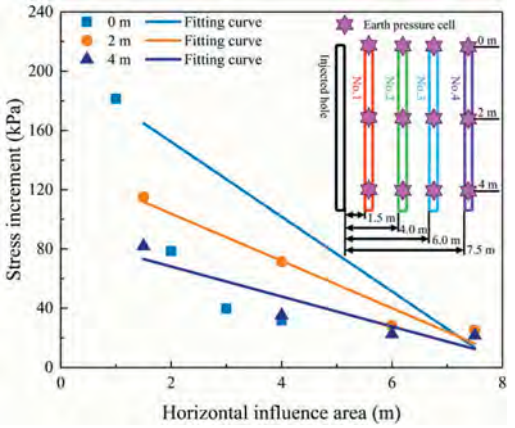

Figure 11. Influence range of horizontal grouting.

Through drilling core sampling before and after grouting with sleeve valve in the yellow loess layer, the morphology, water content, strength, and range of influence of the core samples were analyzed. The results show that the grouting reinforcement technology with sleeve valve can effectively reduce the water content of the yellow loess layer and improve the overall strength of the formation.

6 CONCLUSIONS

(1) Based on indoor experiments, the maximum water content of the loess sample is 26.9%, with an average water content of 26.1%. The natural density ranges from 1.94 to 1.98 g/cm3. The range of natural porosity is 0.73-0.77. The average values of liquid limit and plastic limit are 31.5% and 19.5% respectively. The plasticity index and liquidity index are 12 and 0.55 respectively. The loess sample is in a soft plastic state.

(2) After grouting reinforcement with sleeve valve tubes, the cracks in the loess formation are reduced, reducing the permeability of the soft plastic loess. The average water content is effectively controlled, decreasing from 30.55% to 20.75%. The unconfined compressive strength has been strengthened to some extent, with a maximum increase of 0.16 MPa.

(3) When grouting causes splitting in the soil, the stress in the surrounding soil near the grout begins to increase. The stress increment gradually decreases as the distance from the grout hole increases. The horizontal distance between the grout holes has an influencing radius of 8.03 m. These findings are important for evaluating the effectiveness of grouting reinforcement and determining grouting construction parameters.

ACKNOWLEDGMENTS

Thank you for the funding of the Science and Technology Research and Development Program of China Railway Corporation (2017G007-G)

REFERENCES

Cheng, X., Feng, H., Qi, S., Zhang, X., Liu, B., 2017. Dynamic Response of Curved Wall LTSLS Under the Interaction of Rainwater Seepage and Earthquake. Geotech Geol Eng 35, 903–914.

Fu, J., Li, H., Zhu, K., Chen, Y., Lei, Z., 2022. Study on Expansion Characteristics and Expansion Potential of Gypsum Rock. Geofluids 2022, 1–14.

GB/T 50123-2019, 2019. Standard for geotechnical testing method.

Lee, J.S., Sagong, M., Park, J., Choi, I.Y., 2020. Experimental analysis of penetration grouting in umbrella arch method for tunnel reinforcement. International Journal of Rock Mechanics and Mining Sciences 130, 104346.

Li, H., Fu, J., Chen, B., Zhang, X., Zhang, Z., Lang, L., 2023. Mechanical Properties of GFRP Bolts and Its Application in Tunnel Face Reinforcement. Materials 16, 2193.

Li, J., Shao, Shengjun, Shao, Shuai, 2019. Collapsible characteristics of loess tunnel site and their effects on tunnel structure. Tunnelling and Underground Space Technology 83, 509–519.

Li, Q., Liu, M., Yu, Y., 2022. Mechanical Behavior of Loess Tunnels Caused by Surface Water Joints Infiltration. Advances in Civil Engineering 2022, 1–22.

Li, X., Wang, L., Hong, B., Li, L., Liu, J., Lei, H., 2020. Erosion characteristics of loess tunnels on the Loess Plateau: A field investigation and experimental study. Earth Surf. Process. Landforms 45, 1945–1958.

Liang, Q., Li, J., Wu, X., Zhou, A., 2016. Anisotropy of Q2 loess in the Baijiapo Tunnel on the Lanyu Railway, China. Bull Eng Geol Environ 75, 109–124.

Liu, X., Wang, F., Huang, J., Wang, S., Zhang, Z., Nawnit, K., 2019. Grout diffusion in silty fine sand stratum with high groundwater level for tunnel construction. Tunnelling and Underground Space Technology 93, 103051.

Liu, Y., Lai, H., 2020. Experimental Study on Lining Cracking of Shallow Buried Loess Tunnel under the Simulation of Effect of Slide Surface Immersion. Applied Sciences 10, 6080.

Liu, Y., Lai, H., Xie, Y., Song, W., 2017. Cracks analysis of highway tunnel lining in flooded loess. Proceedings of the Institution of Civil Engineers - Geotechnical Engineering 170, 62–72.

Mu, W., Li, L., Zhang, Y., Yu, G., Ren, B., 2023. Failure Mechanism of Grouted Floor with Confined Aquifer Based on Mining-Induced Data. Rock Mech Rock Eng 56, 2897–2922.

Sun, W., Liang, Q., Qin, S., Yuan, Y., Zhang, T., 2021. Evaluation of groundwater effects on tunnel engineering in loess. Bull Eng Geol Environ 80, 1947–1962.

Wei, Z., Zhu, Y., 2021. Seepage in Water-Rich Loess Tunnel Excavating Process and Grouting Control Effect. Geofluids 2021, 1–13.

Wu, K., Cui, S., Liu, Y., Zhang, Q., Zhao, J., Zhang, Z., Han, Y., 2020. Study on the Mechanism of Grouting Under Different Tunnel Depth of Cross Passage. Geotech Geol Eng 38, 3291–3305.

Xu, X., Wu, Z., Sun, H., Weng, L., Chu, Z., Liu, Q., 2021. An extended numerical manifold method for simulation of grouting reinforcement in deep rock tunnels. Tunnelling and Underground Space Technology 115, 104020.

Yan, Q., Li, Y., Yuan, Y., 2022. Research on the Evolution Mechanism of Large Deformation of Expansive Loess Tunnel under Rainfall. Mathematical Problems in Engineering 2022, 1–10.

Yang, T., Zhang, J., Zhang, X., Zhang, Q., Yin, Z., 2020. Layered Grouting Technology Based on a Comprehensive Water-to-Cement Ratio for the Overlying Loess Stratum of Urban Shallow Tunnels. Advances in Civil Engineering 2020, 1–13.

Zhang, X.-L., Xue, Y.-G., Qiu, D.-H., Yang, W.-M., Su, M.-X., Li, Z.-Q., Zhou, B.-H., 2018. Multi-Index Classification Model for LoessDeposits Based on Rough Set and BPNeural Network. Pol. J. Environ. Stud. 28, 953–963.

Tunnelling for a Better Life – Yan, Celestino, Thewes & Eberhardt (Eds)
© 2024 The Author(s), ISBN 978-1-032-80042-4
Open Access: www.taylorfrancis.com, CC BY-NC-ND 4.0 license

Analytical solution to failure history of segment joint with inclined steel bolt

Xinping Dong* & Bingcan Du*
Zhengzhou University, Zhengzhou, China

Xiaoyang Chen*
China Construction Seventh Engineering Division Corp, Zhengzhou, China

ABSTRACT: In this paper, an explicit analytical formula is proposed for analyzing the failure history of a segment joint with inclined bolts as connecting element under high loading levels. By analyzing the full-scale test results, we have developed a non-linear interface model for the segment joint. Based on three assumptions, an explicit formula is derived using analytical methods. The explicit analytical expression consists of variables that have specific physical meaning. This allows us to determine the main factors that influence the rotation and ultimate bearing capacity of the segment joint, as well as the relationship between the mechanical behavior of the segment joint and these influencing factors. The mechanical behavior of the segment joint under high loading levels can be accurately described by the analytical formula. It is shown that: (1) The failure history of segment joints is subdivided into three stages: linear rotation, joint opening, and joint yielding; (2) The ultimate bearing capacity of segment joint is related to the axial force of segment joint, concrete compressive strength, joint dimensions; (3) For segment joint with inclined bolts, the ultimate bearing capacity of segment joint calculated by the analytical solution is in good agreement with that of the full-scale test performed for shied tunnels, such as Shanghai Yangtze River Tunnel. For joint with curved steel bolts, a correction method for the formula of ultimate bearing capacity is presented.

Keywords: segmental lining, segment joint, interface model, analytical formula

1 INTRODUCTION

Segmental tunnel lining is typically a prefabricated concrete structure composed of flat or box -type segments, with circumferential joints between rings and radial joints between segments. The mechanical behavior of radial joints (segment joints) has a significant impact on the deformation, internal force, failure behavior, and ultimate bearing capacity of the segmental lining as previously shown (Blom., 2002).

In the last 30 years, there has been a large amount of research on the mechanical behavior of segment joints. Several simplified models have been developed to describe their mechanical behavior, including the elastic-hinge (rotation spring) model as previously shown (ITA., 2000; GB 50157), beam model as previously shown (Cheng., 2010), contact algorithm model as previously shown (Su and He., 2007; He et al., 2005), and joint element model as previously shown (Molins and Arnau., 2011; Arnau and Molins., 2011; Zhu et al., 2000; Zhu et al., 2006). In the widely used rotation-spring model for segmental joints, the stress distribution and state at the contact surface between segments cannot be analyzed. This model is primarily used for elastic calculation, such as determining the deformation in service state of the lining system. The contact algorithm can be used to examine the opening and yielding state of a segment joint. However, the computation process and convergence checking based on the Finite Element Method (FEM) is cumbersome and costing-time.

In the field of lining failure behavior, the nonlinearity of the segment joint is a vital factor for describing the failure history of the lining system as previously shown (Blom., 2002). To describe the mechanical behavior of segment joints under high loading level, the analytical formula for the non-linear interface model of the segment joint is proposed and verified according to the measured data from the full-scale tests on segment joints conducted in China, and the FEM simulation on the segment joints in following

*Corresponding authors: dxp3000@163.com; dubc2000@163.com; 1471635300@qq.com

DOI: 10.1201/9781003495505-134

2 CONFIGURATION OF SEGMENT JOINT AND ITS NON-LINEAR INTERFACE MODEL

The connecting elements, such as curved steel bolts, reusable inclined steel bolts and straight steel bolts, are typically utilized in plain joints as previously shown (Liu and Hou., 1991). The study focuses on the segment joint connected by inclined steel bolts, as depicted in Figure 1.

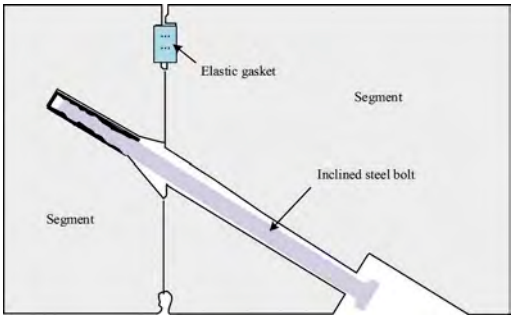

Figure 1. Segment joint with inclined steel bolt.

This type of connecting bolt is used in some crossing-river tunnels, such as the Shanghai Yangtze River Tunnel, the Nanjing Yangtze River Tunnel, the Shiziyang Ocean Tunnel, the Botlek Railway Tunnel in Netherlands, and metro section tunnels, such as, Nanjing Metro Line No. 10. There is no packing material between segment joints, resulting in the direct contact between the concrete segments in these joints.

The segment joint with the curved steel bolt is widely used in metro tunnels in China, as shown in Figure 2.

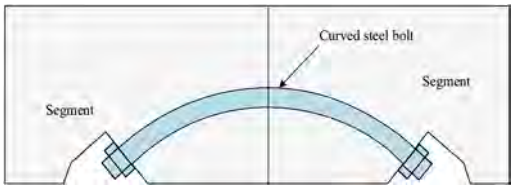

Figure 2. Segment joint with curved steel bolt.

To deal with the influence of the inclined steel bolts used in the 2nd Heinenoord tunnel, a series of full-scale tests were performed in Netherland as previously shown (Blom., 2002). Based on the tests results, it is concluded that the effect of inclined steel bolts on the rotation behavior and ultimate bearing capacity of segment joint is negligible. Therefore, the effect of inclined bolts can be disregarded in the failure history of segment joint as previously shown (Dong and Xie., 2013). For this type of segment joint, a non-linear interface element model can be applied, as indicated in Figure 3. The contact surface between segments is simulated using a surface spring with a non-tension gap element as previously shown (Arnau and Molins., 2011).

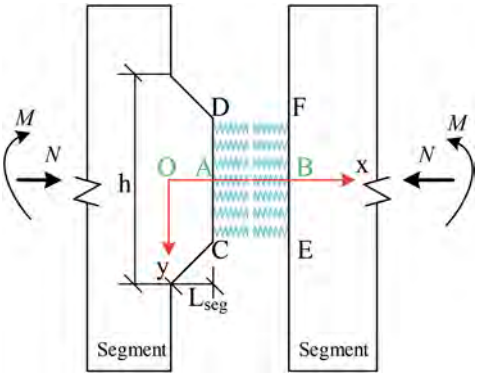

Figure 3. Non-linear interface model for segment joint.

3 ANALYTICAL SOLUTION TO THE NON-LINEAR MODEL OF THE SEGMENT JOINT

The non-linear model in Figure 3 can be solved using numerical methods, such as iteration methods or the FEM method. One of the disadvantages of the numerical method is that some important information about the mechanical properties of the segment joint is omitted, such as the essential dependence of the ultimate bearing capacity (UBC) on the parameters. In this study, certain assumptions are made on the non-linear model in order to derive explicit analytical expressions. According to the explicit formula, the failure characteristics of segment joints under high loading level and their causal factors, as well as the mapping relationships between the failure behavior and causal factors, could be understood more thoroughly and described more concisely.

3.1 *Assumptions on segment joint*

The coordinate system used in this paper is shown in Figure 3. Point O is the origin of coordinate system. The length of joint OA is L_{seg}, and h represents the height of segment joint. The line CD and EF represents the contact surface between segments.

Fundamental assumptions relating to the flexure of joint are as follows:

(1) Planar contact interface: the cross-section of the joint contact surface remains planar during joint rotation.
(2) No-tension between contact surfaces of joint: the normal stress at the contact surface is 0 when joint opening.
(3) Linear distribution of the normal stress between contact surfaces

Based on the aforementioned assumptions (3), the nonlinear stress distribution between contact interfaces, as shown in Figure 4, can be simplified.

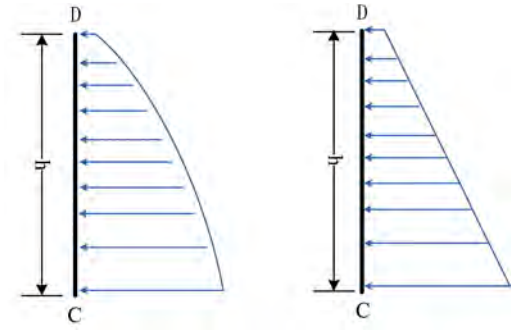

(a) Non-linear distribution (b) Simplified linear distribution

Figure 4. Distribution of normal contact stress.

It means that the contact normal stress on the interface surface CD and EF depends on the normal displacement and the constant k, as follows:

$$p = k \cdot d\ (y) \tag{1}$$

Where, p is the stress at y; $d(y)$ is the displacement at y; k is the normal contact stiffness of the contact surface. The value of k can be determined using the method proposed by Dong as previously shown (Dong and Xie., 2013).

3.2 *Stage I: Linear rotation of segment joint*

At stage I of linear rotation, the maximum normal stress p resulting from the bending moment M is less than the normal stress induced by the axial force N:

$$p \le \sigma_N = \frac{N}{A} = \frac{N}{bh} \tag{2}$$

Where, σ_N is the compression stress induced by axial force N; A represents the area of the segment joint, while b and h refer to the width and height of joint, respectively.

The rotation can be calculated according to the aforementioned assumption (1) and (3).

The rotation of section (OA) θ_{OA} resulting from the bending of beam OA is:

$$\theta_{OA} = \int_0^x \frac{1}{\rho} dx = \int_0^x \frac{M}{EI} dx = \frac{ML_{seg}}{EI} \tag{3}$$

Where, E is the Young's elastic modulus; I is the moment of inertia of area of segment joint; M is the bending moment applied to the segment joint.

The rotation between contact surface CD and EF resulted by the compression of surface spring is calculated as follows:

$$\theta_{AB} = \frac{\mathrm{M}}{k \int_0^h b \cdot y^2 dy} = \frac{M}{k \cdot I} \tag{4}$$

The total rotation of segment joint θ_{joint} is:

$$\theta_{\mathrm{joint}} = \theta_{OA} + \theta_{AB} = \frac{M}{kI} + \frac{ML_{seg}}{EI} \tag{5}$$

At the linear rotation stage I, the total normal stress can be considered as a direct superposition of the stresses generated by the axial force and bending moment respectively. The critical moment of joint opening can be calculated on according to Eq. (6)

$$M \le M_{\mathrm{t}} = \frac{N \cdot h}{6} \tag{6}$$

Where, M_t is the critical moment of joint opening.

3.3 *Stage II: Joint opening*

When the bending moment M continues to increase, and when $M > M_t$, according to the aforementioned assumption (2), the contact surfaces between joints start to separate. The distribution of the total normal stress in contact surface is shown in Figure 5.

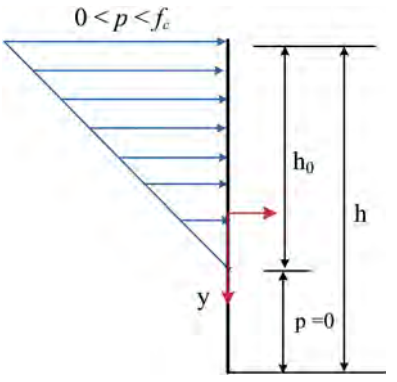

Figure 5. Distribution of contact stress at Stage II.

Where, h_0 is the effective height of the joint, which refers to the height of the joint's compression region. The normal stress in tension region is assumed to 0, according to the assumption (2).

Based on the normal stress distribution as shown in Figure 5, the equilibrium equations for internal force and bending moment can be obtained as follows:

$$N = \frac{pbh_0}{2} \tag{7}$$

$$M = N \cdot \left(\frac{h}{2} - \frac{h_0}{3}\right) \tag{8}$$

From Eq. (8):

$$h_0 = 3 \cdot \left(\frac{h}{2} - \frac{M}{N}\right) \tag{9}$$

The rotation θ_{AB} resulting from the surface spring is calculated as follows:

$$\theta_{AB} = \frac{2N}{9kb\left(\frac{h}{2} - \frac{M}{N}\right)^2} \tag{10}$$

The total rotation of segment joint at Stage II is:

$$\theta_{joint} = \frac{2N}{9kb\left(\frac{h}{2} - \frac{M}{N}\right)^2} + \frac{ML_{seg}}{EI} \tag{11}$$

3.4 *Stage III: Joint yielding*

With the increase of moment M, the effective height h_0 of the joint gradually decreases, while the stress p at the outer side gradually increases. When the stress p reaches the compressive strength f_c of the concrete, i.e.

$$\mathrm{p_{max}} = f_c \tag{12}$$

Where, f_c is the compressive strength of the segment concrete.

Then, the concrete begins to yield, and if moment M continues to increase, the yielding range at the interface surface gradually extends from the outer side to the inside. Assuming that the joint concrete is perfectly elastic-plastic material, the critical moment of joint yielding M_c, can be obtained as follows:

$$\mathrm{M}_c = N\left(\frac{h}{2} - \frac{2N}{3bf_c}\right) \tag{13}$$

Where, M_c is the critical moment of joint yielding.

When M increases to satisfy $M > M_c$, the joint cross-section rotation and the corresponding normal stress distribution are shown in Figure 6. In this figure, h_1 is the yielding height of joint, and h_0 is the effective height of the segment joint.

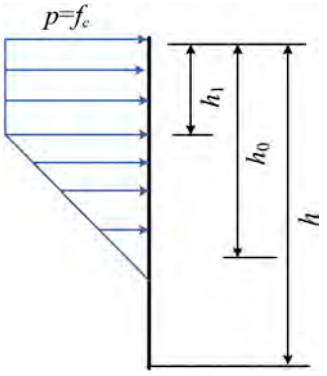

Figure 6. Distribution of contact stress at Stage III.

The ultimate bearing capacity of segment joint M_{lim} is:

$$M_{\mathrm{lim}} = \frac{-3N^2 + 3Nhf_c b}{6f_c b} \tag{14}$$

Where, M_{lim} is the ultimate bearing capacity (UBC) of segment joint.

The rotation caused by the surface spring at stage III is as follows:

$$\theta_{AB} = \frac{d}{h_0 - h_1} = \frac{f_c}{k(h_0 - h_1)} \tag{15}$$

The total rotation at stage III is:

$$\theta_{joint} = \frac{f_c}{k(h_0 - h_1)} + \frac{ML_{seg}}{EI} \tag{16}$$

Summarizing the Eqs. (5), (11), (16) gives:

$$\theta_{joint} = \begin{cases} \frac{M}{kI} + \frac{ML_{seg}}{EI} & M \le M_t \\ \frac{2N}{9kb\left(\frac{h}{2} - \frac{M}{N}\right)^2} + \frac{ML_{seg}}{EI} & M_t < M \le M_c \\ \frac{f_c}{k(h_0 - h_1)} + \frac{ML_{seg}}{EI} & M_c < M \le M_{\mathrm{lim}} \end{cases} \tag{17}$$

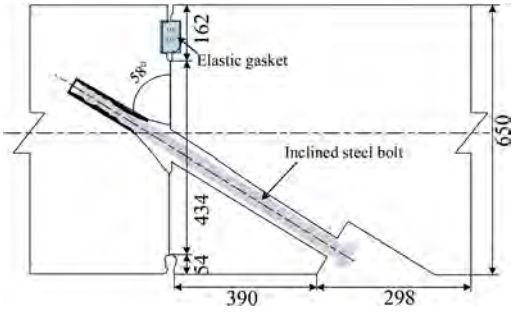

Figure 7. Joint dimensions (Unit: mm).

The length of segment joint is small, typically measured in millimeters, in engineering practice. Hence, the part of joint rotation $ML_{seg}/(EI)$ caused by the beam bending can be neglected. Moreover, when the external moment imposed on joint $M>M_c$ and the joint is in Stage III, the segment joint rapidly loses its bearing capacity. In other words, the failure history in Stage III is shorter. Therefore, the Eq. 17 can be simplified as follows:

$$\theta_{joint} = \left\{ \begin{matrix} \frac{M}{kI} & M \le M_t \\ \frac{2N}{9kb\left(\frac{h}{2} - \frac{M}{N}\right)^2} & M_t < M \le M_c \end{matrix} \right\} \tag{18}$$

The analytical solutions of Eqs. 18 and 14 for the failure history and ultimate bearing capacity of joint with the inclined steel bolt are verified against some full-scale tests in China in the following manner.

4 VERIFICATION OF ANALYTICAL FORMULA FOR THE NON-LINEAR INTERFACE MODEL OF JOINT

4.1 *Case 1: Shanghai Yangtze river tunnel*

The outer diameter and inner diameter of segmental lining are 15,000mm, 13,700mm, respectively. The height of the segment is 650mm and the width is 2000mm. The concrete strength is C60. The configuration of the segment joint is as shown in Figure 7 as previously shown (Chen et al., 2010). And the loading scheme is illustrated as shown in Figure 8.

The horizontal loading device is divided into axial force and longitudinal force. Eight 400-tons jacks are used to apply axial force, and the loading center is located on the centerline of the contact surface of the joint. The longitudinal force F is applied using pre-stressing ties. There are two vertical loading points, each located 700mm away from the centerline of the joint. Through a loading distribution beam, two 400-ton jacks are used to apply a line load to the segment, simulating the ground and water pressure, surcharge, and other loads.

Two loading cases include an axial force of N 1893 kN·m^{-1} for case 1 and 3333 kN·m^{-1} for case 2. In the loading process, the axial force is first applied to the transverse end of the segment and kept constant. Then, a vertical force 100 kN is applied per step in 10 steps.

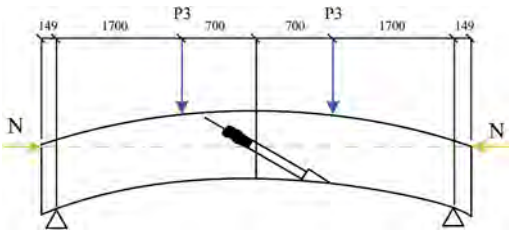

Figure 8. Schematic of loading methods.

Based on the dimensions and material, the ultimate bearing capacity of segment joint used in Shanghai Yangzi river tunnel can be calculated on according to Eq.14 and compared with that of the full-scale test, as shown in Table 1.

It can be seen that the ultimate bearing capacity calculated by the analytical solution agree well with that of the full-scale test, and the maximum error is less than 10%.

Based on the Eq. 18, the moment-rotation curve can be calculated and compared with the test results, as shown in Figure 9.

Table 1. Error of analytical solution.

Loading case	Axial force /kN/ ring	M_{lim} (test) /kN·m/ring	M_{lim} (Eq.14) /kN·m/ring	Error /%
Case 1	3786	790	758.8	3.95
Case 2	6666	1300	1211.3	6.82

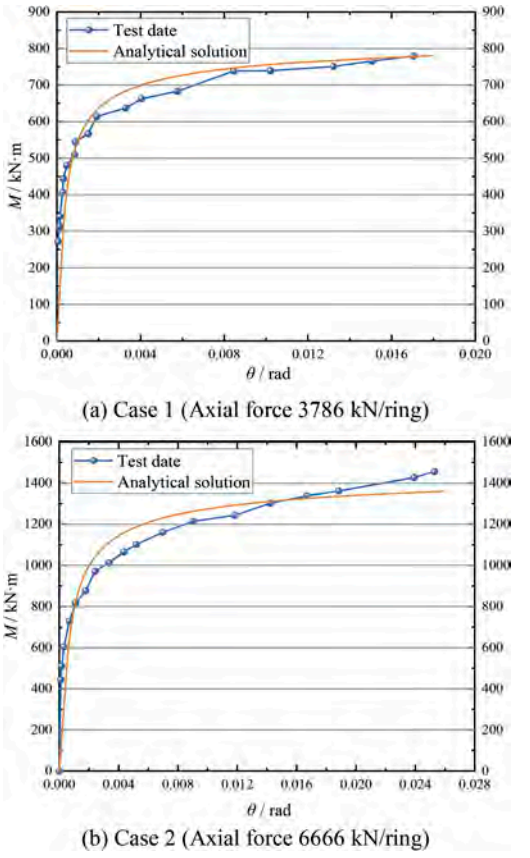

Figure 9. Rotation in joint, analytical results compared to experimental data.

As can be seen in Figure 9, the calculated joint rotation curves for two cases are in good agreement with those of the full-scale test.

4.2 *Case 2: Nanjing Yangtze river tunnel*

The dimensions and properties of the Nanjing Yangtze river tunnel is shown in Table 2.

The configuration of the segment joints is as shown in Figure 10.

The loading mode of the full-scale test on the mechanical performance of the segment joint subjected to the bending moment is shown in Figure 11. The axial force is the uniaxial compression load N, and the

Table 2. Parameters of the Nanjing Yangtze river tunnel.

Parameter	Value	Unit
Outer diameter	14.5	m
Inner diameter	13.3	m
Segment height	0.6	m
Segment width	2.0	m
Concrete compression strength	C60	
Number of segments per ring	9+keystone	
Connecting element	3 inclined bolts	
bolts grade	6.8 grade M36	

bending moment is $M = F{\cdot}a$, as shown in Figure 11 as previously shown (Liu et al., 2015; He et al., 2011)

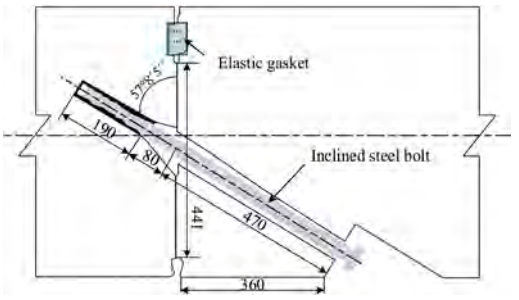

Figure 10. Joint dimensions (Unit: mm).

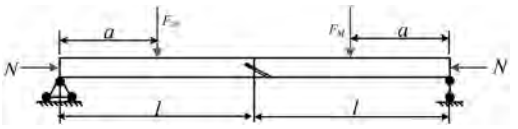

Figure 11. Schematic overview of loading method.

Hydraulic jacks are used as loading equipment. The horizontal axial force is generated by two 1500 kN jacks. The maximum axial force in the model test is 3000 kN, corresponding to a prototype value of 9000 kN; The bending moment is generated by two 1500kN jacks, and the maximum bending moment in the model test is 933.75 kN·m, corresponding to a prototype value of 2801 kN·m. The capacity of jacks meets the requirements of the failure test on segment joint.

Based on the internal forces in segmental lining of the Nanjing Yangtze River Tunnel, the axial force is applied from 3000kN to 8000kN, increasing by 1000kN per level. The loading procedure is as follows: first, a lower level horizontal load is applied, and then the vertical load is applied to produce the bending moment. The bending moment is applied gradually until the joint opening reaches approximately 2mm. Subsequently, the vertical loads are released. After the horizontal loads are increased to a higher level, the bending moment is applied again. According to Eq.18 and the properties of the full-scale test, the M-θ curves are calculated at axial force N =6049 kN, 7038 kN, 8027 kN. These curves are then compared to the M-θ curve of the full-scale test, as shown in Figure 12.

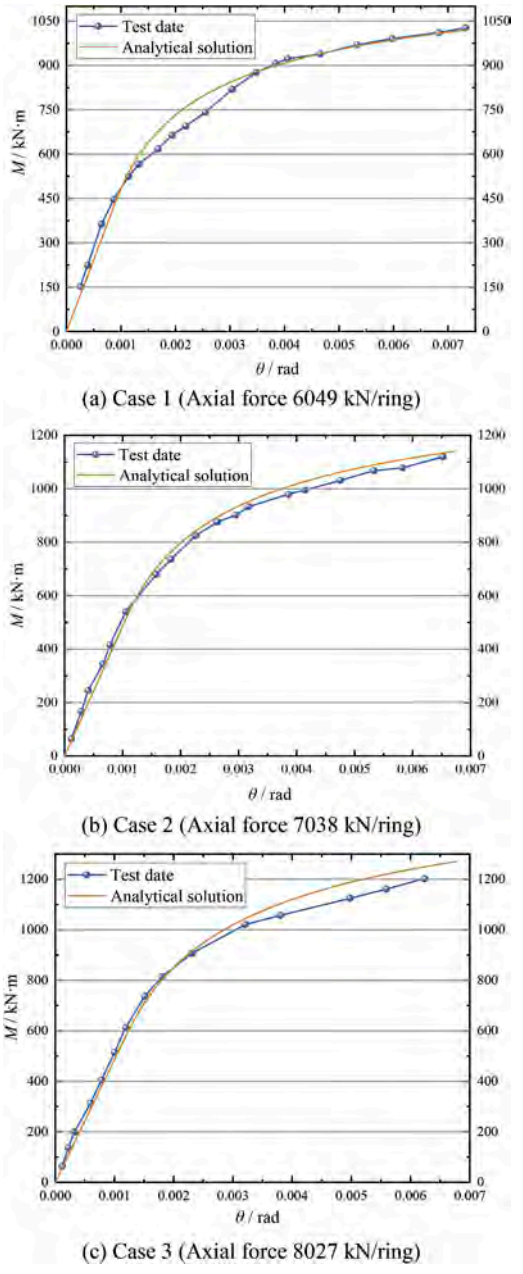

Figure 12. Rotation in joint, analytical results compared to experimental data.

As can be seen in Figure 12, the agreement between the calculated curves and the test curves on the Nanjing Yangtze River Tunnel is excellent.

For the three cases of the Nanjing Yangtze River Tunnel, the ultimate bearing capacity can be predicted more accurately using the aforementioned Eq. 14. The error rates are shown in Table 3

Table 3. Error of the analytical solution.

Loading case	Axial force/kN/ring	M_{lim} (test) /kN·m/ring	M_{lim} (Eq.14) /kN·m/ring	Error /%
1	6049	1063.3	1096.2	3.09
2	7038	1166.2	1230.2	5.49
3	8027	1264.6	1351.6	6.88

As shown in Table 3, the maximum error in the joint UBC is less than 7%.

4.3 *Case 3: Shenzhen metro tunnel*

The curved steel bolts are uses as connecting element in the segmental lining of tunnel located in Liyumen-Qianhaiwan section of Shenzhen Metro Line No.1. The outer diameter, inner diameter, and width of the ling system are 6m, 5.4m, 1.5m, respectively. The concrete strength grade of the segment is C50. Segments are connected with M24 curved steel bolts (with a mechanical performance grade of 8.8).

To address the diseases caused by neighboring construction, a full-scale test of a single ring is performed. There are 24 loading points (total number of jacks is 24×2 jacks) in the horizontal direction, and these 24 horizontal loading points are divided into 3 groups. The maximum load that can be supplied by a single jack is 1000kN, and the maximum stroke of a single jack is 300mm.

Lu as previously shown (Lu., 2019) utilized finite element software to simulate the loading history of the full-scale test. The comparison between the finite element calculation results and the full-scale test is illustrated in Figure 13.

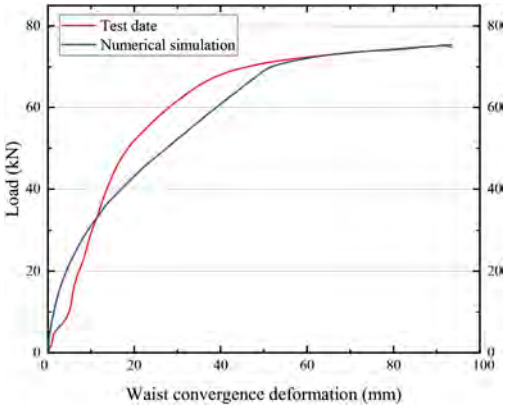

Figure 13. Convergence deformation at the springline, FEM results compared to the test data.

From the comparison, it can be observed that the numerical calculation of the FEM model closely matches the data from the full-scale test. It is evident that the simulation model of the segment joint can accurately simulate the mechanical behavior of the segment joint in the full-scale test.

Meanwhile, Lu as previously shown (Lu., 2019) used a FEM model of the segment joint to analyze the mechanical behavior of the joint under axial forces of 1000, 1500, and 1700 kN/ring, respectively.

Using Eq. 18 to analyze the FEM model by Lu, the moment-rotation curve is calculated and verified against the FEM results, as shown in Figure 14.

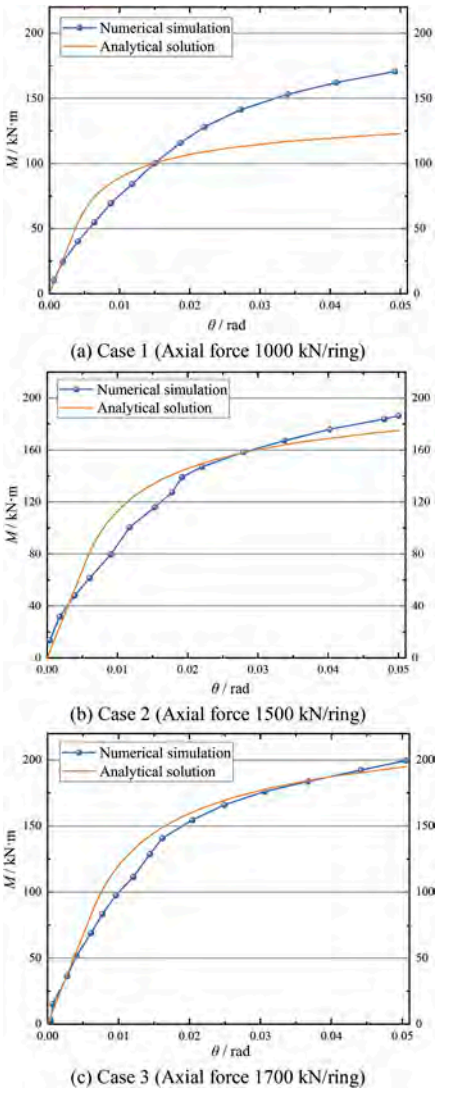

Figure 14. Rotation in joint, analytical results compared to experimental data.

From Figures 14(b) and (c), the calculated values for Case 2 and Case 3 are well-fitted to the simulation results, and the errors are shown in Table 4 for a rotation angle of 0.05 radians.

Table 4. Error of the analytical solution.

Loading case	Axial force/kN/ring	M_{lim} (FEM) / kN·m/ring	M_{lim} (Eq.14)/ kN·m/ring	Error (%)
1	1000	170.6	122.7	28.1
2	1500	186.4	175	6.11
3	1700	199.5	195	2.26

However, there is a significant difference between the calculated value of case 1 and the simulation results. This is due to the significant impact of the preload of the curved steel bolt at low axial forces. Therefore, the influence of the preloading generated by the curved bolts should be considered when the axial force is at lower levels. The solution is to multiply the axial forces by a correction factor greater than 1.0 when using the analytical model presented in this paper. And when the loaded axial force is at higher level, the preloading force becomes of minor importance, and the analytical solution model presented in this paper can be applied directly. After using the correction factor 1.4, the simulation results for case 1 are compared with the calculated values as shown in Figure 15.

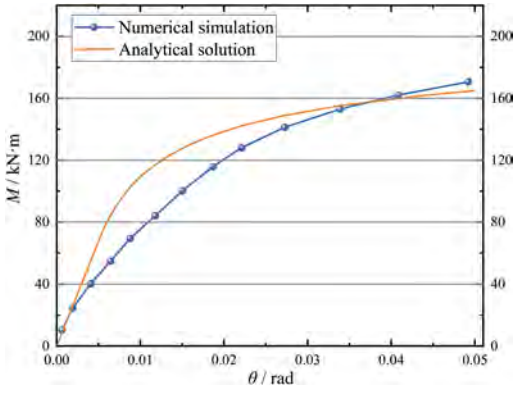

Figure 15. Rotation in joint, analytical results compared to experimental data.

As can be seen in Figure 15, the agreement for case 1 is very good after applying the correction factor. When the rotation angle is 0.05rad, the ultimate bearing capacity corresponding to the analytical model is 164.9 kN.m/ring, and the numerical model result is 170.6 kN.m/ring. The error in the ultimate bearing capacity is 3.34%.

5 CONCLUSION

(1) In failure history of a segment joint subjected to incremental moment with constant axial force, the mechanical behavior can be divided into three stages: linear rotation, joint opening, and joint yielding. When the bending moment exceeds the critical opening moment, the segment joint undergoes nonlinear opening and rotation. When the bending moment exceeds the critical yielding moment, the segment joint will enter Stage III and rapidly approach to its ultimate bearing state. The failure behavior and root cause of segment joints can be accurately described and interpreted by the analytical solution to the interface model presented in this paper.

(2) The explicit analytical equations for the ultimate bearing capacity of the segment joint are derived. According to the equation, the ultimate bearing capacity of the segment joint depends on several variables that have specific physical meaning. These variables include the axial force applied to the segment joint, the compressive strength of the concrete, and the dimensions of the joint. The formula can be used to predict the ultimate bearing capacity of segment joints.

(3) The analytical equations for the ultimate bearing capacity and M-θ curves have been validated using full-scale tests on segment joint with inclined steel bolts in the Shanghai Yangtze River Tunnel, and the Nanjing Yangtze River Tunnel. It demonstrates that, for the segment joint with inclined bolts, the analytical solution to interface model can accurately describe the mechanical behavior of the segment joints throughout the failure history. When neglecting the inclined bolt, the errors in the joint capacity in the Shanghai Yangtze River Tunnel are 3.95% and 6.82%, respectively. In the Nanjing Yangtze River Tunnel, the error are 3.09 %, 5.49 % and 6.88 %, respectively.

(4) The numerical model of a segment joint based on a full-scale test of a single ring with curved steel bolts, is selected as a case to verify the analytical solution. It demonstrates that, for the segment joint with curved steel bolts and at a loading level with higher axial force, the errors in the ultimate bearing capacity between the analytical solution and the FEM results are 6.11% and 2.26%, respectively. In the case of a segment joint subjected to a low axial force, the influence of the preloading caused by the curved bolts cannot be disregarded, and an adjustment factor for axial force can be incorporated into the analytical solution. After applying a correction factor of 1.4, the discrepancy between the adjusted analytical solution and

the numerical calculation is 3.34%. It shows that the analytical solution developed based on the segment joints with inclined steel bolts can be applied to the segment joints with curved steel bolts.

REFERENCES

Arnau, O., Molins, C., 2011. Experimental and analytical study of the structural response of segmental tunnel linings based on an in situ loading test. Part 2: Numerical simulation. Tunnelling and Underground Space Technology. 26, 778–788.

Beijing Urban Engineering Design & Research Institute, 2014. GB 50157—2013 Code for design of metro. China Architecture & Building Press. (in Chinese)

Blom, C.B.M., 2002. Design philosophy of concrete linings for tunnels in soft soils. PhD thesis. Dept of Civil Engineering and Geosciences, TU Delft, Netherlands.

Chen, Z.J., Yang, Z.H., Li, D.M., 2010. Experimental study on mechanical properties of longitudinal seam of Shanghai Changjiang shield tunnel. Underground Engineering and Tunnels. (4), 17–19. (in Chinese)

Cheng, X.H., 2010. Calculation Model of Shield Tunnel Segment with Joints Simulated by Beam Element. Chinese Journal of Underground Space and Engineering. 6 (5), 946–951. (in Chinese)

Dong, X.P., Xie, F.Z., 2013. Analytical solution of segment joint model for segmented tunnel lining. Chinese Journal of Underground Space and Engineering. 35(10), 1870–1875. (in Chinese)

He, C., Feng, K., Su, Z.X., 2011. Development and application of loading test system of prototype structure for underwater shield tunnel with large cross-section. Chinese Journal of Rock Mechanics and Engineering. 30(2), 254–266. (in Chinese)

He, C., Zeng, D.Y., Tang, Z.C., et al, 2005. Research on the segment joint design of river-crossing shield tunnels with large cross-section. Modern Tunnelling Technology. 42(6), 14–19. (in Chinese)

ITA, 2000. Guidelines for the design of shield tunnel lining. Tunnelling and Underground Space Technology. 15(3), 303–331.

Lan, X.P., Lu, L., Liu, L.H., 2009. Experimental Study on Mechanical Properties for Segment Joints of Super Tunnel Lining. Structural Engineers. 25(5),110–114. (in Chinese)

Liu, J.H., Hou, X.Y., 1991. Shield tunnel. Beijing: China Railway Press. (in Chinese)

Liu, S.J., Feng, K., He, C., et al, 2015. Study on the Bending mechanical model of segmental joint in shield tunnel with large cross-section. Engineering Mechanics. 32(12), 215–224. (in Chinese)

Lu, Y., 2019. Full-scale model test of shield tunnel segment and simulation analysis of circumferential joint. Master's thesis. China Academy of Railway Sciences, China. (in Chinese)

Molins, C., Arnau, O., 2011. Experimental and analytical study of the structural response of segmental tunnel linings based on an in situ loading test. Part 1: Test configuration and execution. Tunnelling and Underground Space Technology. 26, 764–777.

Su, Z.X., He, C., 2007. Shell-spring-contact model for shield tunnel segmental lining analysis and its application. Engineering Mechanics. 24(10), 131–136. (in Chinese)

Zhu, H.H., Cui, M.Y., Yang, J.S., 2000. Design model for shiel d lining segments and distribution of load. Chinese Journal of Geotechnical Engineering. 22(2), 190–194. (in Chinese)

Zhu, W., Huang Z.R., Liang J.H., 2006. Studies on shell-spring design model for segment of shield tunnels. Chinese Journal of Geotechnical Engineering. 28(8), 940–947. (in Chinese)

Tunnelling for a Better Life – Yan, Celestino, Thewes & Eberhardt (Eds)
© 2024 The Author(s), ISBN 978-1-032-80042-4
Open Access: www.taylorfrancis.com, CC BY-NC-ND 4.0 license

Numerical analysis of two deep circular shafts at a former gas works site on the London Power Tunnels Phase 2 scheme

Joseph Ellis*, Oliver Brown & Anna Simic
AECOM, Croydon, UK

Raj Kundan
HOCHTIEF-MURPHY Joint Venture - c/o J. Murphy & Sons Ltd., London, UK

John Coupland
Coupland Associates, Strathpeffer, Ross-shire, UK

ABSTRACT: London Power Tunnels (LPT) Phase 2 is a new purpose-built cable tunnel system which will replace the existing buried cable network in the south of London. This £1 billion National Grid scheme comprises 32.5km of 3m internal diameter deep underground tunnels and 8 shafts which will help keep Londoners connected to safe and reliable electricity supplies. The tunnels extend from Wimbledon in the West to Crayford in the East, reaching depths of up to 60m below ground level. At the New Cross site, a pair of circular shafts 41m and 36m deep, 15m and 10.5m diameter respectively, will receive cables from Circuits 1 and 2 of the new network of cable tunnels, whilst also providing permanent access and ventilation to the tunnels. Previous use of the site as a gas works has left a legacy of highly variable Made Ground to considerable depths, buried obstructions and ground contamination which required extensive remediation works. The paper will consider the design of the shaft linings, for which a system of secant piles, contiguous piles and underpinned precast concrete segmental linings, combined with fissure grouting of the Chalk, was chosen to cope with the challenging groundwater conditions. The design of the shaft linings was carried out using PLAXIS 3D numerical modelling with a three-dimensional zoned ground model based on ground investigation findings. The advanced analysis enabled a more sustainable and economical design to be produced than would have been possible with a uniform ground model. The interaction between adjacent shafts was also studied, which helped confirm that the contractor's proposed construction sequencing would be acceptable.

Keywords: London Power Tunnels, Shaft, Secant piled wall, Fissure grouting, Numerical analysis, Contaminated land

1 INTRODUCTION

London Power Tunnels (LPT) Phase 2 is a new purpose-built cable tunnel system which will replace the existing buried cable network in the south of London. This £1 billion National Grid scheme comprises 32.5km of 3m diameter deep underground tunnels and 8 shafts which will help keep Londoners connected to safe and reliable electricity supplies. Two new cable circuits will replace the existing 275kV Wimbledon to New Cross and New Cross to Hurst cable circuits. The new tunnels extend from Wimbledon in the West to Crayford in the East, constructed by tunnel boring machines (TBMs) in 5 tunnel drives with a precast concrete segmental lining and reaching depths of up to 60m below ground level. Shaft diameters vary between 9m and 15m depending on the requirements at each shaft location and are constructed by a variety of techniques including caisson sinking and underpinning with precast concrete segmental lining, sprayed concrete lining and secant piling. The shafts will later be covered by headhouses to provide access and ventilation for the tunnels. The scheme is currently under construction and due to be completed in 2027. HOCHTIEF-MURPHY Joint Venture are contracted to deliver the Package 2 Tunnels & Shafts and Package 5 Headhouses & M&E contracts on the scheme, and appointed AECOM as permanent works design partner.

*Corresponding author: joseph.ellis@aecom.com

DOI: 10.1201/9781003495505-135

The New Cross shafts site is located approximately 2km South of the River Thames, in the London Borough of Southwark. Works at the site comprise a pair of circular shafts 15m and 10.5m (reduced from 15m) in internal diameter, which serve as launch and service shafts for two Tunnel Boring Machines (TBMs) tunnelling towards King's Avenue in the West and Eltham in the East. The West shaft extends to a depth of 41m to top of base slab, allowing space for the High Angle Conveyor (HAC) to remove spoil from the shaft during tunnelling, while the East shaft is shallower at 36m depth. The shafts are connected by a Sprayed Concrete Lining (SCL) adit approximately 15m long, which serves as an access route between shafts during construction and in the permanent case.

2 SITE BACKGROUND

The New Cross shafts site is part of the former Old Kent Road gas works, opened in 1833 by the South Metropolitan Gas Company. At its largest in the late 1800s, the gas works included 13 gas holders, covering a total of 36 acres. Since its closure in 1953, the land has been gradually redeveloped for commercial use, including a large waste management facility and an existing National Grid substation. Today, only the Grade II listed gas holder No. 13 remains, which is located adjacent to the scheme site.

The scheme site occupies the footprint of three of these gas holders. While the above-ground structures have now been demolished, the below-ground legacy of the site is still very much present. This includes the buried gas holder foundations, significant depths of Made Ground and contaminated soils, all of which pose a risk to shaft construction at the site.

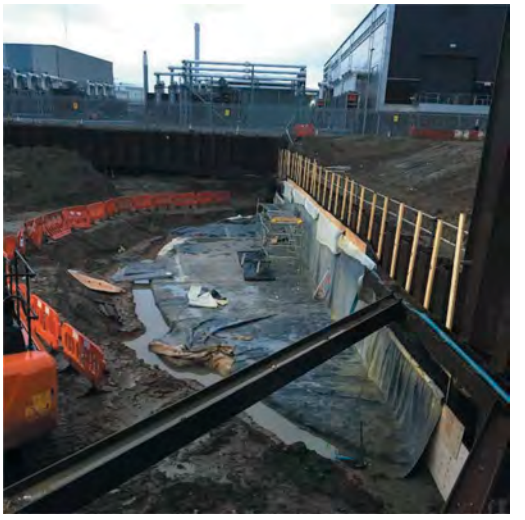

Figure 2. Enabling works cofferdam showing gasholder footprint prior to casting the protective capping slab (JSM Group, 2020).

2.1 *Enabling works*

The proposed location for the shafts was directly between two of the decommissioned gas holders. Whilst this was one of the few possibilities on a very constrained site, it resulted in very little clearance between the shafts and the existing gas holder foundations. This increased the risk of striking buried obstructions or releasing contamination during the sinking of the shafts. In order to mitigate this risk, an extensive programme of investigative and remedial works was carried out prior to construction by the enabling works contractor, JSM Group.

The enabling works included the excavation of a large cofferdam 48m long by 22m wide by 5m deep encompassing the footprint of the two shafts and part

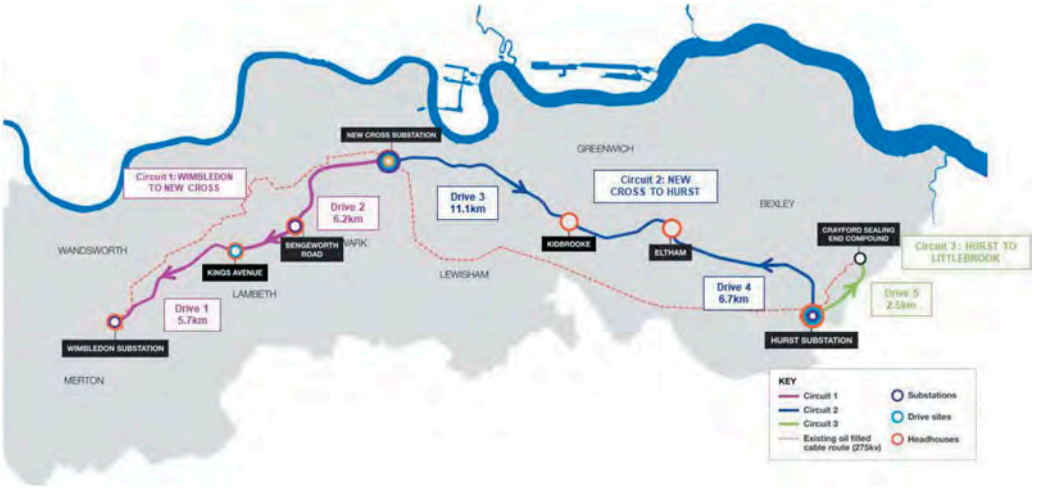

Figure 1. Tunnel route map showing the location of the New Cross Substation site.

of the footprint of one of the gas holders. During the works, the gas holder foundations were demolished down to the bottom level of the excavation, and the remaining foundations capped to contain any contaminated material. The capping consisted of a 300 mm thick concrete blinding layer, a Bentotex 30 geosynthetic clay liner and a 300mm thick concrete protection layer. The position of the remaining foundations was surveyed, which helped inform the choice of shaft position and diameter adopted in the detailed design stage. A number of boreholes were also drilled from the base of the excavation to provide a better understanding of the ground stratigraphy.

Upon completion of the remedial works, the cofferdam was initially backfilled with Class 2B and 2C site-won material (dry cohesive material and stony cohesive material). However, inclement weather conditions necessitated a switch to imported Type 1 granular fill material for the final layers of the backfill.

2.2 *Ground conditions*

The bedrock geology of the site comprises Thanet Sand Formation and Upper Chalk Formation, overlain by a combination of River Terrace Deposits and Made Ground to varying depths.

Such was the complexity of the ground stratigraphy due to historic activity, the site was divided into four different ground model zones for the purposes of the shaft design:

i. Zone 1: Area within the enabling works cofferdam but outside of the footprint of the area associated with the construction and backfill of the gasholder foundations.
ii. Zone 2: Area within the enabling works cofferdam and inside the footprint of the area associated with the construction and backfill of the gasholder foundations.
iii. Zone 3: Area outside the enabling works cofferdam and outside the footprint of the area associated with construction and backfill of the gasholder foundations
iv. Zone 4: Area outside the enabling works cofferdam but inside the footprint of the area associated with construction and backfill of the gasholder foundations.

The stratigraphy for each of these zones is summarised in Table 1, and the zoned areas illustrated in Figure 3.

Characteristic geotechnical parameters for each material are presented in Table 2. Limited ground investigation data was available for the Chalk, and therefore parameters were derived with reference to the guidance in CIRIA Report C574 (CIRIA, 2002) for the grade C2 to B2 material typically encountered at the site. The parameters have been derived such that the Chalk is represented as a continuum, as opposed to a material that is controlled by discrete discontinuities. Allowance was also made for creep of the Chalk, by adopting a 50% reduction in the long-term Young's modulus after Barthes et al (1994).

Table 1. Ground stratigraphy.

Strata	Depth of upper surface (m bgl)	Thickness (m)
Zone 1		
Engineered Fill	0.0	4.6
River Terrace Deposits	4.6	2.1
Thanet Formation	6.7	6.7
Upper Chalk	13.4	>30
Zone 2		
Engineered Fill	0.0	4.6
Made Ground	4.6	7.5
Made Ground – Puddle Clay	12.1	1.4
Upper Chalk	13.5	>30
Zone 3		
Made Ground	0.0	2.4 to 5.3
River Terrace Deposits	2.4 to 5.3	2.0 to 5.2
Thanet Formation	5.0 to 8.1	2.3 to 4.4
Upper Chalk	10 to 14.9	>30
Zone 4		
Made Ground	0.0	9.7 to 14.3
Upper Chalk	13.4	>33

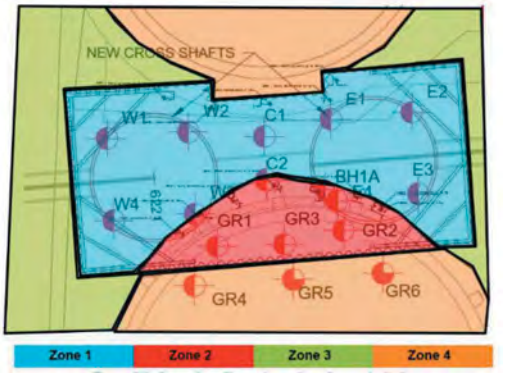

Figure 3. Ground stratigraphy zoning showing approximate position of shafts between the gas holders.

2.3 *Groundwater conditions*

Groundwater was found to be present in all strata at the site and was considered to be in hydraulic continuity between the upper aquifer (River Terrace Deposits) and lower aquifer (Thanet Sand and Chalk). Previous groundwater monitoring also identified perched groundwater within the Made Ground. Groundwater flow within the River Terrace Deposits and Thanet is facilitated by high intergranular permeability of these strata. Within the Chalk, intergranular permeability is lower and forms a much smaller proportion of the flow. Groundwater flow is instead facilitated by a network of fractures providing high secondary permeability.

Table 2. Characteristic geotechnical parameters.

Parameter	Units	FILL	MG	RTD
Bulk unit weight, γ_{bulk}	kN/m^3	20	17	18
Saturated unit weight, γ_{sat}	kN/m^3	21	18	19
Poisson's ratio, v	-	0.2	0.2	0.15
Coefficient of lateral earth pressure at rest, K_0	-	0.44 – 0.47	0.58	0.44 – 0.47
Undrained shear strength, c_u	kN/m^2	-	30	-
Drained cohesion, c'	kN/m^2	0	0	0
Friction angle (constant volume), φ_{cv}'	°	32	25	32
Friction angle (peak), φ_p'	°	34	-	34
Undrained stiffness, E_u[3,4]	MPa	-	12	-
Drained stiffness, E'[3,4]	MPa	20	9.5	25

Parameter	Units	TG	CH
Bulk unit weight, γ_{bulk}	kN/m^3	19	20
Saturated unit weight, γ_{sat}	kN/m^3	20	21
Poisson's ratio, v	-	0.2	0.25
Coefficient of lateral earth pressure at rest, K_0	-	0.7 – 1.5	0.5 – 1
Undrained shear strength, c_u	kN/m^2	-	-
Drained cohesion, c'	kN/m^2	0	20
Friction angle (constant volume), φ_{cv}'	°	32	35
Friction angle (peak), φ_p'	°	36	
Undrained stiffness, E_u	MPa	-	-
Drained stiffness, E'[1]	MPa	LoSt = 110 LgSt = 55	-
Rock mass modulus, E_{rm}[2]			ST = 800 LT = 400

1. LoSt = Low Strain (0.01% to 0.1%), LgSt = Large Strain (0.1% to 1.0%).
2. ST = Short-term, LT = Long-term

3 SHAFT DESIGN DEVELOPMENT

3.1 *Temporary ground support*

In order to manage the challenges of poor ground conditions, high groundwater pressures, spatial constraints between the existing gasholders and contamination risk during the construction phase, a solution was developed combining three components;

i. Secant piles and capping beam
ii. Contiguous piles
iii. Fissure grouting of the Chalk

The secant and contiguous piles were temporary in their function but remain incorporated in the works in the long-term. These three 'temporary' components worked together to enable the construction of a precast concrete segmental lining which provides permanent ground support and watertightness for the 120-year design life of each shaft. The segmental lining was excavated and constructed in 1m advances by underpinning, and therefore a robust solution that ensured the stability of the exposed soil face and the safety of the workforce was required.

For the shallower part of the shaft, up to 17m below ground level (bgl), where the ground was at greatest risk of instability, a secant piled wall was constructed, made up of 880mm diameter piles in a hard/firm arrangement. The primary function of the secant pile wall was to reduce groundwater infiltration, and therefore pile spacing was based on the maximum spacing needed to maintain contact between primary and secondary piles at the toe, including allowance for positioning and verticality tolerances. Typically, a secant pile wall also provides structural support to the ground and would require a closer pile spacing to ensure sufficiently large overlap between piles such that the contact stress does not exceed the concrete strength. However, given the use of precast segmental lining which was intended to act as the structural lining, this was not required at New Cross.

Below the secant piled wall, the bore of the secondary ('male') piles was extended to form a contiguous pile wall between 17 and 30m bgl. The contiguous piles were designed to act in conjunction with fissure grouting of the Chalk to reduce groundwater flows into the shaft. By incorporating contiguous piles, it was predicted that the average permeability of the ground surrounding the shaft would be reduced by an order of magnitude more than could be achieved with fissure grouting alone. The piles were installed by Murphy Ground Engineering using two rotary drill rigs to meet the schedule. Full depth temporary segmental casing was used both for soil support and to ensure the piles were drilled to an accuracy of 1:200 or better. At all times a positive water head was maintained within the casing.

Fissure grouting was performed by Spie Batignolles Fondations UK from the ground surface by drilling through the unreinforced primary piles. The grouting was carried out in two phases using Stage separated TaMs also known as MPSP (Multiple Packer Sleeved Pipe). The first phase was to drill and grout to a depth of up to 48m, both to grout between the contiguous piles on either side and provide the grout curtain below the piles. First phase grouting was carried out through every fourth primary pile and then through every second primary pile. The results of the first phase of grouting were then analysed to determine if the second phase, which was to drill through every first and third primary pile, would be to the toe level of the contiguous piles or would need to be taken to the same

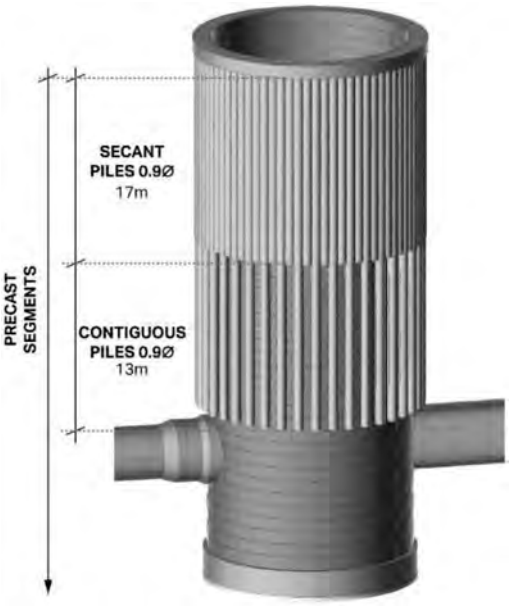

Figure 4. New Cross West Shaft 3D BIM model.

depth as the first phase. From this analysis it was considered prudent to drill and grout full depth at only four locations. On completion of the works and based on a 10% packer testing criterion the specified performance of 100% < 5×10^{-6} m/s and 95% < 1×10^{-6} m/s was shown to have been achieved.

3.2 *Permanent shaft lining*

The permanent shaft linings are comprised of a number of rings of precast concrete steel fibre reinforced segments supplied by FPMcCann. Each ring in the West shaft comprises 16 no. 350mm thick segments, whilst in the East shaft 14 no. 300mm thick segments make up each ring. The use of an off-the-shelf product brought with it benefits of tried and tested design details, whilst also ensuring that lead times were minimised.

The construction of the lining commenced at the top of the shaft, with the first ring being secured to the shaft capping beam with 400mm long dowels. The first ring was used as a shutter for the casting of the capping beam, which made it possible to install the dowels from the extrados face of the ring prior to casting the capping beam. The next advance of approx. 1.5m depth was then excavated and the following ring fixed to the rings above with vertical through-bolts integrated in the segment casting. Any void between each segment ring and the soil or secant piled wall was then filled with a cementitious grout to ensure that full frictional resistance would be mobilised at this interface.

EPDM gaskets fixed to the radial and circumferential joints ensure the watertightness of the shaft in the long-term.

3.3 *Tunnel portals*

Two openings were constructed in each of the shaft linings to provide a permanent access route between shafts and to facilitate the launch of the two TBMs. Two steel universal column sections ('needles'), with sizes up to 305x305x198, were fixed into the shaft segmental lining either side of each opening to enable the construction of the portals and SCL chambers. The needles provided a means for hoop force in the segmental lining to be transferred between segment rings through shear in the steel and carried over the crown and invert of the opening. Octagonal openings were formed in the segmental lining by stitch drilling, from which the excavation and spraying of the SCL chambers was undertaken. A reinforced concrete permanent portal was then cast around the openings to encapsulate the temporary needles and provide permanent ground support and water-tightness in the long-term.

3.4 *Base slab*

A cylindrical reinforced concrete base slab 2.0m and 1.5m thick was constructed in the West and East shaft, respectively. The base slabs feature a shear key extending beyond the extrados of the shaft segmental lining which provides additional resistance against uplift failure. Pressure relief wells were included in the base slabs to reduce groundwater pressures beneath the slab during construction, when the mass concrete infill necessary to resist uplift failure of the shaft had not yet been cast. The base slabs were designed to resist a nominal heave pressure of 10% of the effective overburden stress.

4 NUMERICAL ANALYSIS – MODEL DEFINITION

Design of the shaft was undertaken using advanced geotechnical finite element modelling in PLAXIS 2D and 3D. This approach made it possible to study a number of different aspects of the shaft design, including:

- Effects of the construction of each shaft on the adjacent shaft.
- Design forces occurring in the precast segmental lining and secant/contiguous piles.
- Design forces occurring in the shaft capping beam.
- Base heave pressures
- Shaft displacement

4.1 *Constitutive soil models*

The Mohr Coulomb constitutive model was adopted for all materials in the analysis. Whilst this constitutive model has various shortcomings, for instance it does not consider strain dependency of stiffness, it was considered the most appropriate model given the limited quantity of ground investigation data available.

All materials at the site are granular in nature and are therefore considered to exist in a drained state. This is with the exception of the Chalk within the fissure grouted zone which was assigned Undrained (A) parameters (strength and stiffness specified in terms of effective parameters, c' and ϕ) to simulate the short term stability ('stand up time') of vertical excavations.

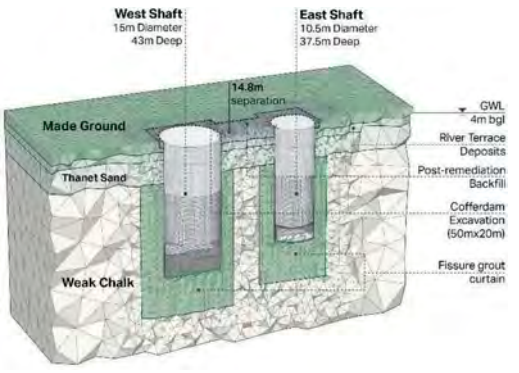

Figure 5. Cut-away view of PLAXIS 3D numerical model.

4.2 *Groundwater pressures*

All strata in the model were assigned a steady-state pore water pressure profile based on the maximum predicted groundwater level during the construction period, which was approximately 4m below ground level.

The effect of the fissure grouting of the was studied by first undertaking a SEEP/W analysis, in which the target permeability and width of the grouted zone was input to generate a prediction of the steady-state pore water pressures around the shaft. The output from SEEP/W formed the basis for the pore water pressures defined in PLAXIS, which were approximated by a gradient increasing from zero at the exposed shaft wall to the full hydrostatic pressure at a distance of 4m from the excavation face.

4.3 *Structural element properties*

The simulation of each structural element in the PLAXIS numerical model is described in the following sections. The construction of the SCL launch/connection adits and portals was not included in the model. Given the higher Young's modulus of the Chalk at this level, the construction of these adits was not anticipated to have significant effects on the shaft as a whole and hence these elements were designed using separate local numerical models.

4.3.1 *Secant piles*

The secant piled wall was modelled using linear elastic plate elements with equivalent properties to C32/40 grade concrete. Soil-structure interaction was defined with interface elements which limit the degree of shear force transmitted to two thirds of the soil strength.

According to L.Zdravkovic et al. (2005), any retaining wall is unlikely to be a continuous membrane along its perimeter, as it is made from number of vertical elements that are not fully connected in this direction. It is likely there will be joints between the piles and any vertical deviation of individual piles will also reduce the contact area between piles. This is particularly true at New Cross, where the wider pile spacing is likely to result in a small contact area between piles and a relatively low hoop-direction axial stiffness.

Two cases were therefore considered depending on which element the outputs would be used to design:

i. For secant pile design, the hoop direction stiffness of the plate element representing the piles was set to zero. This had the effect of maximising the bending moment in the vertical plane to give the most onerous case for the pile reinforcement design. The vertical stiffness considered only the reinforced secondary piles, as only these piles would be capable of resisting bending.
ii. For capping beam designs, the hoop-direction stiffness of the secant pile wall was modelled based on the calculated contact area between piles, assuming no deviation due to construction tolerances. This ensured that the share of hoop force between the secant piles and capping beam was realistic.

4.3.2 *Precast segmental lining*

The segmental lining was defined by linear elastic volume elements with stiffness properties equivalent to C45/55 concrete. Circumferential joints between rings were modelled explicitly using interface elements with a friction coefficient of 0.5. Radial joints were modelled using a reduced hoop direction bending stiffness after Muir Wood (1975).

4.3.3 *Base slab*

The base slab was modelled with linear elastic volume elements with interface elements to simulate the soil-structure interaction. It was found that the high stiffnesses of the base slab and the Chalk on which it was founded resulted in inaccuracies in the predicted contact stresses of the slab on the soil. More realistic results were obtained by adopting a reduced concrete stiffness during the base slab construction phase, which was then increased to the full value in subsequent construction phases.

4.4 *Construction sequence*

The construction of the shaft was modelled stage-by-stage in the numerical model. The key phases of the construction sequence are outlined in Table 3.

5 NUMERICAL ANALYSIS – RESULTS

5.1 *Shaft interaction*

One of the factors in choosing to adopt a three dimensional numerical analysis was the need to assess whether the construction of one shaft had an influence on the other. Displacements and total normal stresses on the West shaft lining were extracted for construction phases before and after the construction of the East shaft, as presented in Figures 6 and 7. Results are extracted at the point on the shaft closest to the adjacent shaft.

Change in horizontal total stress was predicted to be negligible, whilst change in displacement was predicted to be no more than 1mm.

Table 3. Construction sequence.

N°	Phase Name	Description
1	Initial phase	K_0 procedure to establish initial soil pressures. Maximum K_0 conditions applied.
2	Apply 75kPa surcharge	75kPa surcharge at ground surface representing construction loading
3	Construct secant piles	Activation of plate elements representing the secant piles
4	Construct capping beam	Cropping of piles, construction of capping beam and placing of backfill on top.
5	Underpinning	Excavate within secant piles in 1.5m advances and construct segmental lining by underpinning. When excavation enters the Chalk, apply pore pressure gradient at sides of excavation to represent fissure grouting.
6	Excavate and cast base slab	Excavate, install drainage blanket, blinding and cast base slab, represented with volume elements
7	Restore full hydrostatic pressure	Restore groundwater pressure in zone of fissure grouting
8	East shaft construction	Repeat steps 1 – 7 for East shaft
9	Cast mass concrete infill	Casting of C16/20 mass concrete infill to raise shaft invert levels to final tunnel invert level.

5.2 *Secant pile design forces*

The results of the PLAXIS 3D numerical modelling indicated that the forces occurring in the secant pile wall were heavily dependent on the ground stratigraphy in the immediate vicinity. As illustrated in Figure 6, the difference in strength and stiffness between the Made Ground and Chalk in Zone 2 created a 'fixed toe' condition which produced bending moments almost double those in Zone 1. For the purposes of pile design, the shafts were therefore divided into two regions

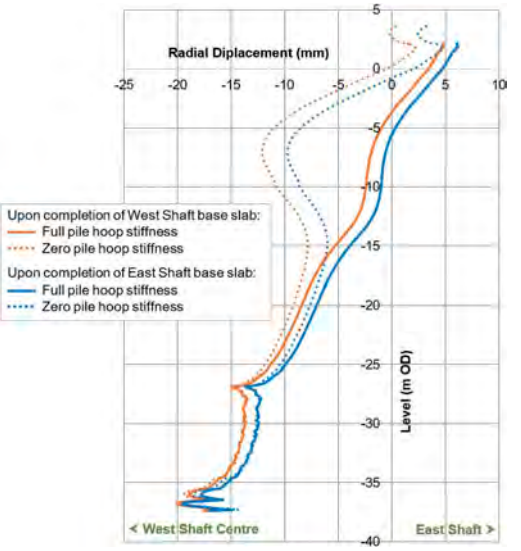

Figure 6. Displacement of West shaft lining before and after construction of the East shaft.

around their circumference – an area of low bending moment influenced by the Zone 1 ground conditions and an area of much higher bending moment influenced by the Zone 2 ground conditions. These regions formed the basis for the design of the secant piles with two different reinforcement typologies.

Agreement between the PLAXIS 2D and 3D models was found to be very good. This made it possible to streamline the process of designing the secant piles by using the 3D model to inform the extent of each type of reinforcement, and then using the 2D models within each zone to further refine the analysis. Within the 2D models, the sensitivity of the analysis to factors such as upper and lower bound secant pile hoop stiffness and the properties of the interface elements between the secant piles and segmental lining was studied.

6 CONCLUSIONS

The design and analysis of two deep circular shafts at the London Power Tunnels Phase 2 New Cross site has been carried out using the PLAXIS 2D and 3D numerical modelling packages. The analysis indicated that proposed design was feasible, and this was confirmed by successful construction of the design with minimal change to the overall concept.

The analysis was used to study the potential interaction between shafts with respect to stresses and displacements, which was found to be negligible. This can be attributed to the adoption of a secant piled wall for ground support, which minimised the relaxation of horizontal soil stress occurring between shafts during excavation. Additionally, compared to

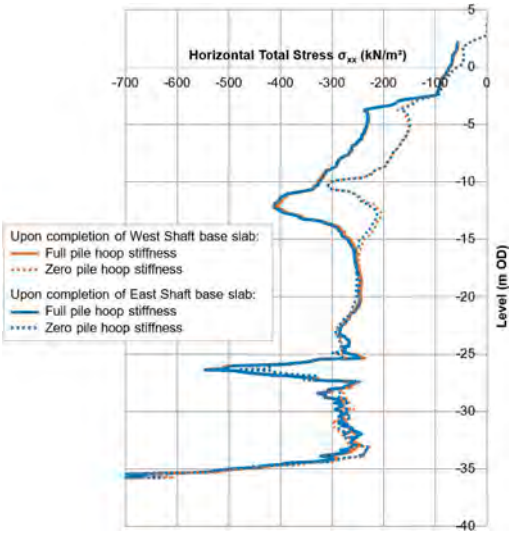

Figure 7. Horizontal total stress acting on West shaft lining before and after construction of the East shaft.

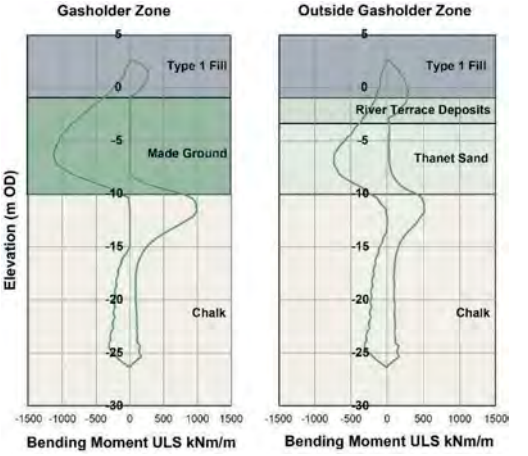

Figure 8. Bending Moment envelope for secant piles within and outside the gasholder zone (Zone 2).

the poor ground conditions in adjacent areas of the site, the ground between the shafts was comprised predominantly of virgin soil of relatively high strength and stiffness.

The outputs of the analysis have also been used to locally refine the pile reinforcement according to the varying ground conditions around the shaft perimeter. In doing this, a 25% reduction in steel reinforcement was achieved, as well as associated reductions in embodied carbon emissions.

The results highlight the importance of extensive ground investigation for shaft sites, particularly on brownfield sites with a long history of previous use. Localised areas of poor ground were found to have significant influence on the structural forces occurring in the shaft linings.

ACKNOWLEDGMENTS

The authors would like thank HOCHTIEF-MURPHY Joint Venture, National Grid and their engineering partners for their collaboration during the design process that resulted in this solution and for their permission to publish this paper.

REFERENCES

Barthes, H., Bordas, A., Bouillot, D., Buzon, M., Dumont, Ph., Fermin, J., Landry, J.-C., Larive, J.-P., Leblond, L., Morlot, J.-J., Szypura, L., Vanderbrouk, Ph. & Vielliard B. 1994. Proceedings of the Institution of Civil Engineers. The Channel Tunnel. Part 3: French Section, 102, 1–92.

CIRIA, 2002. Report C574: Engineering in Chalk. CIRIA, London, United Kingdom.

JSM Group, 2020. New Cross Remediation Works – Capping and Jet Grout Works. Unpublished.

Kundan, R., Daniele, S. & Martin, S., 2023. Challenges of delivering 32.5km of major tunnelling infrastructure in South London (UK), and the influences of an innovative "Enterprise". Tunnelling Association of Canada Conference 2023. Toronto, Canada. project delivery model

Muir Wood, A. M., 1975. The circular tunnel in elastic ground. Geotechnique, 25(1), pp. 115–127.

Zdravkovic, L., Potts, D. M. & St John, H. D., 2005, Modelling of 3D excavation in finite element analysis, Geotechnique 55, No. 7, pp. 497–513.

Tunnelling for a Better Life – Yan, Celestino, Thewes & Eberhardt (Eds)
© 2024 The Author(s), ISBN 978-1-032-80042-4
Open Access: www.taylorfrancis.com, CC BY-NC-ND 4.0 license

Comparative analysis of simplified solutions for the radial joint behaviour of segmental tunnel linings with finite element numerical modelling

Amin Emadi*
Senior Associate Engineer Tunnels, Sydney, Australia

Alexandre RA Gomes*
Chief Technical Principal Tunnels and Underground Works, Sydney, Australia

ABSTRACT: Tunnel segmental linings are composed by several individual precast concrete segments that are connected to each other through radial (longitudinal) and circumferential joints. The structural behaviour of the joints is an important aspect in the structural analysis of tunnel segmental linings. Because joints have more degrees of freedom and a reduced contact area with respect to the standard precast concrete segment thickness, stress concentration occur at the contact zones making them particular areas of concern regarding potential damage and failure. Currently, for typical load cases, the structural design of segmental tunnel linings is often based on simplified 2D rigid ring models with an equivalent reduced inertia (Muir-Wood model) to account for the presence of radial joints. However, for less standard and more asymmetric load and/or bedding conditions, a more detailed analysis of the lining behaviour is required to assess controlling failure mechanisms. This includes the explicit modelling of the radial joints in numerical models and the incorporation of consecutive rings and circumferential joints. Specifically for the radial joints, simplified methods such as Janssen or Bloom's approach based on torsional springs have been proposed. This paper presents a comparative analysis of these simplified methods used to model the radial joint behaviour with the results of a Finite Element Method (FEM) utilising a Concrete Damage Plasticity model (CDPM) which allow for a more detailed modelling of the concrete behaviour, including tensile and compressive damage initiations and evolutions, stiffness degradation and the material nonlinearity. Results indicate that the proposed simplified solutions are suitable for predicting maximum bending moments, but they may not accurately predict crack occurrence or verify serviceability requirements in case of significant joint rotation.

Keywords: Tunnelling, Radial joint, segmental tunnel, analytical approach, Concrete Damage Plasticity model

1 INTRODUCTION

Precast concrete segmental linings are interconnected by radial and circumferential joints, which play a critical role in the lining's structural behaviour. Understanding the behaviour of joints is essential for ensuring the stability and integrity of tunnel structures. Analytical approaches provide simplified solutions for assessing the behaviour of radial joints in segmental tunnel linings.

Jassen (1983) conducted a study on the performance of joints between adjacent parts of bridges. Building upon this work, Bloom et al. (2002) further refined the relationships by considering elastic-perfectly plastic behaviours for concrete. Tvede-Jensen et al. (2017) introduced the concept of the block compressive force of concrete as a parabola and made additional assumptions to enhance the existing relationships. The forementioned analytical approaches have been widely adopted by designers in various projects. The Japanese Society of Civil Engineering (JSCE) (2016) and the German Tunnelling Committee (ITA-AITES) (DAUB) (2013) have established specifications that utilize analytical approaches, specifically through use of beam spring models, to assess and verify the behaviour of radial joints.

Teachavorasinskun and Chub-uppakarn (2010) found that segmental joints have a significant influence on tunnel lining behaviour. They proposed a simplified method for evaluating the moment-carrying capacity of segmental tunnel liners using calibrated parameters from a true-scale model test. The study showed that jointed linings carry smaller maximum bending moments compared to non-jointed linings. This

*Corresponding author: amin.emadi@smec.com; alexandre.gomes@smec.com

DOI: 10.1201/9781003495505-136

reduction in bending moment, known as the moment reduction factor, can be determined based on angular joint stiffness and the number of lining segments.

Arnau and Molins (2011) utilized finite element analysis and experimental models to investigate stress distribution and displacement patterns within radial joints, providing valuable insights into their structural response. Yuelang et al. (2017) showed the mechanical behaviour of segmental joints is influenced by joint section details, loading conditions, and contact conditions between adjacent segments. The study's findings indicate that even a minor initial gap of 2 mm between segments has a notable impact on joint stiffness.

Full-scale tests and numerical analysis have been carried out to study the bending stiffness, joint opening variation, and failure characteristics of segmental joint structures for under-river shield tunnels by Williams (1982). Results show that the bending stiffness and joint opening behave significantly non-linearly, and concrete cracking and bolt breaking have been detected in the tests.

Caratelli et al. (2018) examined the behaviour of flat radial joints without connectors through full-scale experimental tests on fibre reinforced concrete elements. Tests involved inducing joint openings to simulate scenarios of high levels of ovalization of the lining. Results revealed the impact of concrete crushing and bursting phenomena on the joints.

X. Li et al. (2015) investigated the behaviour of longitudinal joints in shield tunnel operation. This research provides valuable insights and a progressive model for understanding and designing longitudinal joints in operational tunnels, considering factors like axial stress, bolt force, and concrete condition.

This paper presents a comparative analysis of these simplified methods used to model the radial joint behaviour with the results of a Finite Element Method (FEM) utilising a Concrete Damage Plasticity model (CDPM) which allow for a more detailed modelling of the concrete behaviour, including tensile and compressive damage initiations and evolutions, stiffness degradation and the material nonlinearity. Results from this comparison provide insights on the range of applicability of simplified methods for the structural analysis of segmental linings.

2 CDPM MATERIAL MODEL AND VERIFICATION

The CDPM finite element analysis (FEM), is used to simulate the behavior of the concrete. The stress-strain curve of the concrete assumed in the CPDM (FEM) model is shown in Figure 1. In the case of uniaxial tension, the stress-strain relationship in concrete follows a linear elastic pattern until it reaches the failure stress value σ_t. At this point, micro-cracking initiates within the material. Beyond the failure stress, the presence of micro-cracks is macroscopically represented by a softening stress-strain response, leading to localized strain within the concrete structure. When subject to uniaxial compression, the concrete's response remains linear until reaching the initial yield value σ_{c0}. In the plastic regime, the response typically exhibits stress hardening, followed by strain softening beyond the ultimate stress σ_{cu}. While this representation is somewhat simplified, it captures the primary characteristics of concrete's response.

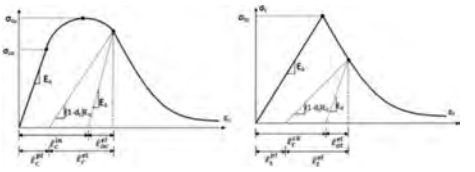

Figure 1. CDPM (FEM) - stress-strain diagram of concrete considering nonlinear behaviour in compression and tension.

The strain softening branch of the stress-strain curve is associated with the degradation of elastic stiffness, which is characterized by two damage variables: dt and dc. These variables range from zero to one and represent the degree of damage. The initial (undamaged) elastic stiffness of the material is denoted as E_0, while ε_c^{pl},ε_t^{pl},ε_c^{in} and ε_t^{in} represent the values of compressive plastic strain, tensile plastic strain, compressive inelastic strain, and tensile inelastic strain, respectively.

Liu et al. (2017) performed a comprehensive study on the behavior of joints in segmental tunnels using a full-scale ring test, as shown in Figure 2. Tested rings' outer and inner diameter were 6.2 m and 5.5 m, respectively. The segment thickness was 0.35 m, composed by C50 Concrete.

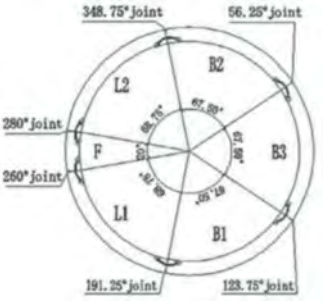

Figure 2. Segment layout of tested rings. (Liu et al., 2017).

For verification purpose, a radial joint at 348.75° was selected to exhibit joint closing behavior. Figure 3 illustrates the geometry of the model with the generated mesh.

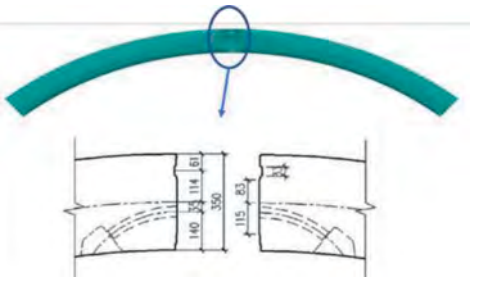

Figure 3. Geometry of the radial joint and finite element modelling using shell element (cpe4) meshing.

To assess the accuracy of the CPDM (FEM) model analysis to predict segment damage, the experiment by of Liu et al. 2017 was modelled in this study. For that, an axial load of 1400 kN was applied and the radial joint subjected to incremental joint rotation, until concrete failure was observed. Experimental results showed spalling of the segment extrados at the radial joint of the middle ring (see Figure 4).

Figure 4. Ultimate failure state of tested segment (Liu et al., 2017).

A similar behaviour was observed, in the CPDM (FEM) model, as indicated by the damage index of 0.9 shown in Figure 5, indicating concrete damage. This damage has the potential to propagate from the joint and extend beyond the segment's thickness along its surface, in alignment with the experimental findings.

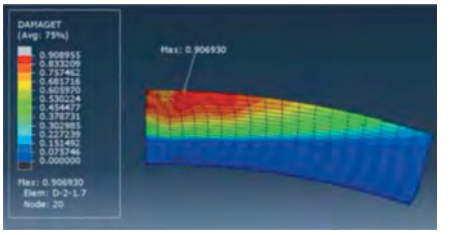

Figure 5. The damage Index in CDP FEM.

3 RADIAL JOINT MODELLING

3.1 *Geometry and material properties*

To compare the behaviour of the radial joint in the analytical approach with the CDPM (FEM) analysis, two adjacent segments were modelled, as shown in Figure 6.

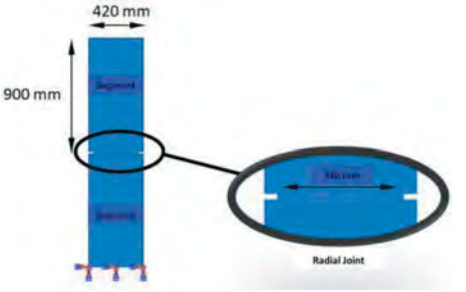

Figure 6. The geometry of the model and radial joint.

The thickness of the segments is 420mm and the radial joint contact area is 340mm. Parameters used in the model are presented in the table 1.

Table 1. Concrete properties for the CDPM analysis.

Density (kg/m3)	E (GPa)	Poisson ratio	compressive strength (MPa)	fbo / fco	K
2500	35.5	0.15	40	1.16	0.67

3.2 *Radial joint rotation*

In the analytical approach, the initial position of the joint is considered on the circular circumference at the ring radius. The deformation of the segment structure is calculated by analyzing the ring structure under the loads imposed on the tunnel. Assuming a change in shape from a circle to an ellipse and

Table 2. Equations for the radial joint in the analytical approach (Groeneweg, 2007).

	Closed	Opened	Plastic behavior
Rotation	$\phi = \frac{12M}{b\ell_t^2 E_c'}$	$\phi = \frac{8N}{9b\ell_t E_c' \left(\frac{2M}{N\ell_t}-1\right)^2}$	$\phi_{1,2} = \frac{\left(6N \pm \sqrt{21\,N^2+30Mf_c'b-15N\ell_t f_c'b}\right)\ell_t f_c'^2 b}{6\left(-2Mf_c'b+\ell_t Nf_c'b+N^2\right)E_c'}$
Rotational stiffness	$c_r = \frac{b\ell_t^2 E_c'}{12}$	$c_r = \frac{9b\ell_t E_c' M\left(\frac{2M}{N\ell_t}-1\right)^2}{8N}$	$c_{r1,2} = \frac{6\left(-2Mf_c'b+\ell_t Nf_c'b+N^2\right)ME_c'}{\left(6N \pm \sqrt{21\,N^2+30Mf_c'b-15N\ell_t f_c'b}\right)\ell_t f_c'^2 b}$
Maximum strain	$\varepsilon_{max} = \frac{\phi}{2} + \frac{N}{E_c' b\ell_t}$	$\varepsilon_{max} = \frac{-3\phi}{2}\left(\frac{2M}{N\ell_t}-1\right)$	$\varepsilon_{max} = \frac{f_c'\ell_t b+2NE_c'\phi}{2E_c f_c'\ell_t b}$
Maximum bending moment	n/a	$M_{max} = N\frac{\ell_t}{2}$	$M_{max} = N\frac{\ell_t}{2} + \frac{N^2}{2f_c'b}$

Where: lt = Height and width of the contact area, M = Bending moment, N = Normal ring axial load, b = width, Ec= module of elasticity, f'c= compressive strength of concrete, φ= Rotation in the joint, and Cr= rotational stiffness.

writing compatibility equations, the radial displacement of the joint is calculated. Table 2 provides a summary of the equations governing the rotational stiffness and reactions for all three situations in the analytical approach for closed joints, opened joints and concrete behaving plastic in joints (Groeneweg, 2007).

In the analytical approach, the contact length is determined by the rotation of two adjacent segments around a point. It is assumed that this rotation does not affect the normal ring axial load. Figure 7 illustrates the rotation of the joint obtained from the analytical approach equations considering two different normal ring axial load equivalent to 10%, and 70% of the sectional compressive capacity which is equal to $f_c' \times A$ where A is the gross area of the section.

The assumed geometry and material properties are identical to those used in the CPDM (FEM), as mentioned in section 3. The sectional compressive capacity is 1680 kN at 10%, increasing to 11,760 kN at 70% of the sectional compressive capacity. The simplified analytical approach fails to capture the fact that the two segments are not only rotating but also pushing against each other.

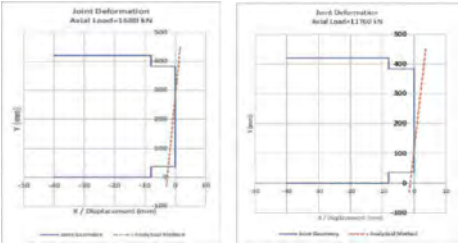

Figure 7. Radial joint opening in analytical approach and segments pushing against each other - CPDM (FEM model).

In the CPDM (FEM) model, the same axial loads as those assigned in the analytical approach are applied and the behavior of the joint is assessed for the gradual increase in the rotation of the two segments. The loading scheme of the model is shown in Figure 8.

Figure 8. Modelling of the rotation on radial joint.

A "hard contact" is generated as the two surfaces are compressed against each other. In the CPDM (FEM) model, the concept of "hard contact" is employed to define the interaction property in the normal direction of the adjacent segments. This modeling approach allows for the representation of the separation between two surfaces (Figure 9). It is worth noting that in the CPDM (FEM) model, the position of the normal force on the joint may vary due to rotation. Furthermore, the magnitude of the axial stress on the joint can be affected by both the modeling of the hard contact and by the anticipated rotation, which closely resembles practical conditions.

4 RESULT AND DISCUSSION

4.1 *Moment- rotation*

According to the analytical approach, as the flexural moment increases, the joint experiences three states:

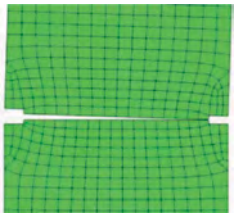

Figure 9. Separation between two surfaces at the radial joint.

(1) opening, (2) concrete yielding, and (3) concrete crushing.

Table 3 presents the corresponding rotations for each of these states, as derived from the analytical approach.

Table 3. Rotations (mrad) for Various Joint States.

	Axial load (kN)	
Joint states	N=1680	N=11760
Joint opens	0.28	1.96
Concrete yields	10.9	1.55
Concrete fails	53.4	7.62

Figure 10 Illustrates the relationship between the bending moment and the radial join rotation for different axial loads for both the analytical and the numerical models. Initially, when the joint is still closed, bending moments rapidly increase with rotation. As the joint starts to open, bending moment increases at a slower rate. In the third stage, concrete plastification occur, causing additional redution in the rate of increase of the bending moment with rotation.

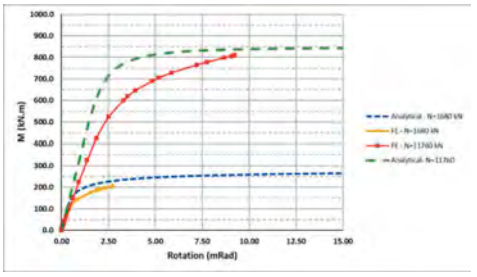

Figure 10. Bending moment – radial joint rotation relation: comparison between numerical and analytical models for various axial forces.

Based on Figure 10, the analytical approach shows good prediction capability with respect to maximum bending moments. However, there are some differences in the results between the two methods. The numerical method exhibits a slightly earlier transition from elastic to plastic behaviour compared to the analytical approach. This can be attributed to two factors. Firstly, the numerical analysis considers the effects of adjacent segments (hard contact approach), which results in forces being applied to the joint surface from the moment segment rotation initiates. This causes deformations to enter the non-elastic region more rapidly due to a reduced contact area. Secondly, the CDPM (FEM) considered in the numerical method provides a more accurate representation of nonlinear concrete behaviour, whereas the analytical approach assumes an elastic-perfectly plastic behaviour model.

It should be noted that due to the nonlinear behaviour and crack growth within the section, finite element models exhibit less rotational stiffness compared to the theoretical approach.

In the CPDM (FEM) model, the analysis may terminate or fail to converge due to the occurrence of tensional cracks. In contrast, the analytical approach does not impose a defined rotation limit, as the crack occurrence cannot be assessed in the analytical approach.

4.2 *Bursting stress*

Another significant finding is the comparison of bursting stress. Figure 11 illustrates a comparison between the bursting stress obtained from CPDM (FEM) analysis and the analytical approach, revealing a high level of accuracy in the analytical predictions, which is slightly on the conservative side. It is important to mention that in the CPDM (FEM) model, the evaluation of bursting is conducted at the location of the internal point load at joint, which dynamically changes with joint rotation. This implies that the bursting stress aligns well with the analytical approach at the specific point being compared. However, some discrepancies are observed if the evaluation is conducted for a section located closer to the outer side of the segment, as explained in the section 4.3.

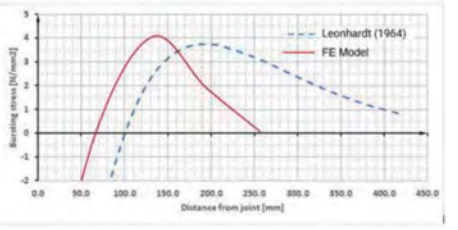

Figure 11. Bursting stress. comparison between numerical and analytical models.

It can be observed in both methods that the rotation of the Radial joint leads to the formation of tensile

cracks in the concrete. The mentioned observation is consistent with the findings presented in the next section regarding the expansion of tensile cracks at the stress concentration point within the contact zone. Despite both methods predicting the occurrence of cracks in the segment, the analytical method estimates the maximum tensile stress to happen at a distance of 190 mm from the edge of the segment, whereas the finite element method calculates the maximum tensile stress at a closer distance of 132 mm.

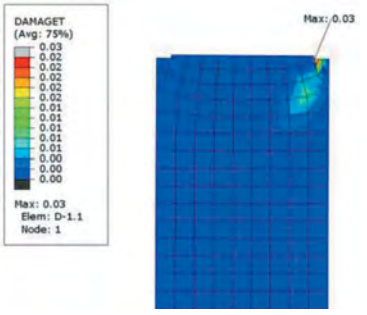

Figure 12. Occurrence of first crack for the model with axial load n = 11760 kn at m = 324.45 kn·m and rot = 1.38 mrad.

4.3 *Crack occurrence*

Cracking in concrete occurs when the tensile strain exceeds approximately 0.00011. In CPDM (FEM) analysis, concrete cracks are observed when the tensional damage index reaches around 0.1. Figure 12 illustrates the damage index at the onset of the first crack for the model subjected to an axial load of 11760 kN.

Based on Figure 12 and in comparison, to Table 3, it is evident that the occurrence of the first crack takes place at a significantly lower rotation than the threshold rotation determined by the analytical approach in Table 3.

Figure 13 Demonstrates a damage index of 0.9, indicating substantial damage, when the moment M reaches 201 kN·m for the section under an axial load of 1680 kN. Similarly, in Figure 14, a damage index of 0.9 is observed when the moment M reaches 808 kN·m for the section under an axial load of 11760 kN.

As shown in Figures 13 and 14, it is important consider the concentration of tensile stress within the segment, as they can lead to cracking and spalling of the segment, starting at the joint and extending beyond a distance greater than the thickness of the segment along its length.

While a satisfactory compliance between the CPDM (FEM) model and analytical approach is observed when evaluating the bursting stress at the section underneath the point load, a comprehensive comparison of the entire section reveals that the analytical method has limitations in predicting tensile stresses and induced cracks, whereas these phenomena can

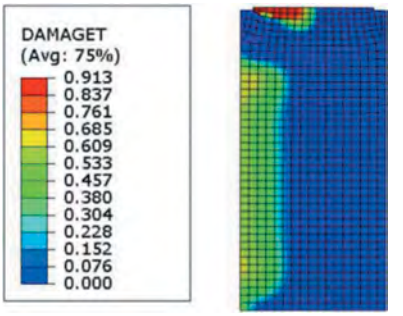

Figure 13. Damage index in cpdm for m = 200 kn·m in the model with n = 1680 kn.

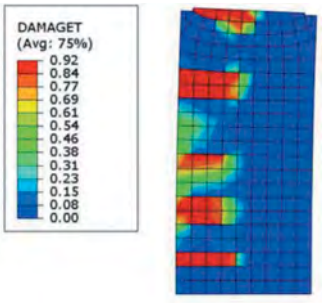

Figure 14. Damage index in cpdm for m = 808 kn·m in the model with n = 11760 kn.

be properly captured through the CPDM (FEM) model.

5 CONCLUSIONS

This paper presents a comparative analysis of the simplified analytical methods used to model the radial joint behaviour with the results of a Finite Element Method (FEM) using a Concrete Damage Plasticity Model (CDPM), which allow for a more detailed modelling of the concrete behaviour, including tensile and compressive damage initiation and evolution, stiffness degradation and the material nonlinearity. Results suggest that:

1. Both the CPDM (FEM) model and the analytical approach exhibit comparable and consistent bending rotation behaviour. This indicates that the analytical approach can be used with an acceptable level of accuracy.
2. Bursting forces induced by an equivalent concentrated load acting on the joint are similar for both the CPDM (FEM) model and the analytical approach.
3. The sole reliance on the analytical approach is insufficient for predicting crack occurrence beyond a certain magnitude of joint rotation.

Results underscore the importance of using numerical detailed modelling (such as CPDM FEM model) to assess cracking behaviour when large joint rotations are anticipated.

4. The region affected by tension crack has the potential to extend beyond the joint and expand over a distance greater than the thickness of the segment along its length.

While the analytical approach is often sufficiently accurate for practical use, it is important to establish the rotation limit beyond which the analytical approach's predictive accuracy in determining crack occurrence becomes inadequate. This limit may vary depending on factors such as material properties, geometry, and specific project constraints, including rotation resulting from building imperfections or structural deformations.

REFERENCES

Angelo, Caratelli., Alberto, Meda., Zila, Rinaldi., S., Giuliani-Leonardi., F., Renault. 2018. On the behaviour of radial joints in segmental tunnel linings. Tunnelling and Underground Space Technology, doi: 10.1016/J.TUST.2017.08.022

Arnau, O., & Molins, C. 2011. Experimental and analytical study of the structural response of segmental tunnel linings based on an in-situ loading test. Part 2: Numerical simulation. Tunnelling and Underground Space Technology, 26(6), 778–788.

Bloom, N. S., et al.2002. "Refinement of relationships to evaluate the behaviour of joints in segmental concrete structures." ACI Structural Journal, 99(2), 173–182.

German Tunnelling Committee. 2013. Recommendations for the design, production and installation of segmental rings. Technical report, Deutscher Ausschuss für unterirdisches Bauen e. V. (DAUB).

Groeneweg, T. 2007. Shield driven tunnels in ultra-high strength concrete: Reduction of the tunnel lining thickness. PhD diss., MSc Thesis, Delft University of Technology, The Netherlands.

Jassen, M. C. (1983). "Joints between adjacent parts of bridges." Journal of Structural Engineering, 109(2), 380–394.

Jin, Yuelang., Wenqi, Ding., Zhiguo, Yan., Kenichi, Soga., Zili, Li. 2017. Experimental investigation of the nonlinear behaviour of segmental joints in a water-conveyance tunnel. Tunnelling and Underground Space Technology, doi: 10.1016/J.TUST.2017.05.018

JSCE (Japan Society of Civil Engineers). 2016. Standard Specifications for Tunnelling–2016: Shield Tunnels. Tokyo, Japan: Japan Society of Civil Engineers.

Liu, X., Dong, Z., Bai, Y., & Zhu, Y. 2017. Investigation of the structural effect induced by stagger joints in segmental tunnel linings: First results from full-scale ring tests. Tunnelling and Underground Space Technology, 66, 1–18.

Teachavorasinskun, S., & Chub-uppakarn, T. 2010. Influence of segmental joints on tunnel lining. Tunnelling and Underground Space Technology, 25(4), 490–494.

Tvede-Jensen, T., et al.2017. "Enhanced analytical relationships for the behaviour of joints in segmental tunnel linings." Tunnelling and Underground Space Technology, 70, 20–29.

Williams, A. 1982. Radial Joints for Precast Segmental Tunnel Linings (No. Monograph).

Xiaojun, Li., Zhiguo, Yan., Zhen, Wang., Hehua, Zhu. 2015. Experimental and analytical study on longitudinal joint opening of concrete segmental lining. Tunnelling and Underground Space Technology, doi: 10.1016/J.TUST.2014.11.002

Tunnelling for a Better Life – Yan, Celestino, Thewes & Eberhardt (Eds)
© 2024 The Author(s), ISBN 978-1-032-80042-4
Open Access: www.taylorfrancis.com, CC BY-NC-ND 4.0 license

Steel lining support in headrace tunnel of Uma Oya Project, Sri Lanka

Ataollah Rahbar Farshbar*
Tunnelling Superintendent, Uma Oya Project, FARAB, Tehran, Iran

Ali Noorzad*
Faculty of Civil, Water and Environmental Engineering, Shahid Beheshti University, Tehran, Iran

P.V. Yuvaraju*
Mechanical Engineer, NDT and Painting QA/QC Inspector

B. Rejith Kumar*
Advanced NDT QA/QC Inspector

ABSTRACT: Uma Oya Multipurpose Development Project constructed in Sri Lanka. This project involves two Roller Concrete Core (RCC) dams, drill and blast link tunnel which connected two dams, 15.4 km mechanized headrace tunnel for transferring water to the top of a 618 m deep pressure shaft, underground powerhouse and turbine chamber and tailrace tunnel. During the boring in headrace tunnel, TBM faced a mud zone. The support for this system was concrete segment installation. Geotechnical studies confirm the clay and mud zone are surrounding this section. According to design of headrace tunnel as a pressurized water conveyance, another steel lining have been designed for this section.

Keywords: Uma Oya Project, Headrace Tunnel, Mechanized Tunnelling, Support, Mud Zone, Steel Lining

1 INTRODUCTION

The Uma Oya Multipurpose Development Project (UOMDP) is a water transfer, hydropower and irrigation project. The project extends partly into Badulla and Monaragala districts in the Uva province.

Bandarawela is the largest settlement within the project area, located halfway between the upstream and downstream ends of the scheme. The project will transfer long term an annual average water quantity of 145 MCM for irrigation purposes and will develop a head of more than 700 m for the generation of electricity in an underground power plant with a rated capacity of 120 MW.

Main Features of the Project:

- Two storage reservoirs at Puhulpola and Dyraaba in Welimada area
- Link or conveyance tunnel between the two reservoirs to transfer water from Puhulpola to Dyraaba reservoir
- Headrace tunnel to convey water from Dyraaba reservoirs to the power house
- Vertical pressure shaft at the end of the headrace tunnel and a surge shaft
- Underground power house and switchyard at Karandagolla
- Tailrace tunnel to convey water from the power house to downstream irrigation works

The salient features of the headrace tunnel (HRT):

- Elevation at intake (invert) - 960 m.a.s.l.
- Total Length - 15.4 km
- Tunnel slope - 0.01 and 0.002
- Excavation method – Double Shield Tunnel Boring Machine (DS-TBM)
- Excavation diameter - 4.3 m
- Design discharge - 19.5 m^3/s
- Flow conditions - Pressure flow

2 HEADRACE TUNNEL SUPPORT

This paper aims to review the steel lining support installation in headrace tunnel in Uma Oya Multipurpose Development Project. The excavation of the

*Corresponding author: ata.rahbar.f@gmail.com; a_noorzad@sbu.ac.ir; yuvaraju56@gmail.com; rejith.neduvakkattu@gmail.com

DOI: 10.1201/9781003495505-137

15.4 km long headrace tunnel started in March 2014 and breakthrough was on 2nd of October 2019. Two Double shield TBMs were used to mine the HRT to increase tunnel excavation advance rate and provide for higher quality tunnel lining. Headrace tunnel boring firstly started from the outlet side driving upwards and later 2nd TBM re-assembled from tail-race tunnel and started boring from HRT intake driving downwards (Rahbar et al., 2016).

There are design features separating this tunnel from other similar cases. First, this tunnel is a pressure tunnel, meaning that it will operate under hydraulic pressure in excess of 20 bars at the intake location with water up to 200 m water column. Second unique feature of HRT in the present project is various adverse geological conditions including hard abrasive rocks, undetected faults containing high pressure water and mud, as well as possibility of encountering karst.

Four different ground support types (TBM) have been selected for the HRT based on the anticipated ground conditions (Figure 1). They include the following:

- TBM 1: No support (invert segment only)
- TBM 2: Spot bolts where required (with invert segment)
- TBM 3: Systematic bolt pattern (with invert segment)
- TBM 4: Full ring segmental lining

Figure 1. Support in headrace tunnel.

Support type installation was based on the geological condition of the boring rock and for this reason, all the times there was a geologist with each shift on the TBM to check and control the face rock geological condition. After each stroke advance of TBM, the rock face geologically mapped and monitored through the cutter head manhole. Then the supervisors decided to install the full ring or shift from the full ring to invert only, or shotcrete and rock bolt support or reverse versa.

On December 24, 2014 during the upward boring from the outlet, a first significant water ingress occurred at the chainage 11+160 of the tunnel and the tunnel support type changed to the full ring. By the advance of boring, TBM faced to a completely weathered crushed zone and later mud zone which mixed with water ingress, flowed into the tunnel through the segmental lining holes. The chainage of the headrace tunnel in this section from the outlet to intake is CH. 12+287 to CH. 12+225, i.e. 62 m of headrace tunnel. Same as the other full ring area, pea gravel and grouting injection for this section have been examined which was not completely successful. Because the headrace tunnel is pressurized tunnel, and this zone contain mud and clay, finally it has been decided to design and install the steel lining support.

Ground water ingress was one of the great talented activities in headrace tunnel of Uma Oya project and achieved the lots of lessons learned from the deep underground geological condition in Sri Lanka (Rahbar et al., 2017, 2019 and 2022).

3 MUD ZONE SUPPORT DESIGN

Design indicates to use the S460 steel plates in 9.5 m-length/2 m-wide/30 mm-thickness. The design parameters were for:

- 3 m internal dimension,
- 14 bar internal pressure, and
- 20 bar external pressure.

According to the progress plan and the design specifications, 10 m out of 62 m design, revised for concrete lining from the waterway (means CH. 12 +287 to CH. 12+225). The steel lining installed on the other remaining parts of the crushed mud zone.

During the feasibility studies, there were some faults and crushed zones recognized in the headrace tunnel trace. Consequently, the designer has considered headrace tunnel alignment including three curves in 750 m radius and two slopes which is 1% for 9 km of tunnel from the intake and the remaining parts of the tunnel slope is 0.2 %.

First alignment bend starts from CH. 12+326 with 112 m length. So, the mud zone is located in the headrace tunnel bend area. According to the tunnelling surveying as-built and regarding the curve of tunnel, steel lining design in this section includes three bends.

The designed space between the steel lining and primary installed concrete segment is 30 cm which should be used for SCC back filling. Furthermore, a reducer as well as a final ring has been designed at the end of the steel lining. To conclude this section, total sums of the steel lining parts are as the following from CH. 12 + 235 to 12+287:

- 10 straight strakes which have been welded by two numbers of 2 m rolled pipes
- Three bend strake which have been welded of two no. of 2 m rolled and level adjusted pipes to prepare bend
- One reducer assembled in four parts in 1.1 m as a part of the steel transition and four parts welded at site
- One final ring assembled in two parts in 0.4 m as another part of the steel transition

The reducer and the final ring installed after the CH. 12+287. The other side of the support is the

concrete lining from CH. 12+235 to 12+225 and the concrete transition constructed from CH. 12+224.40 to 12+225 (Figure 2).

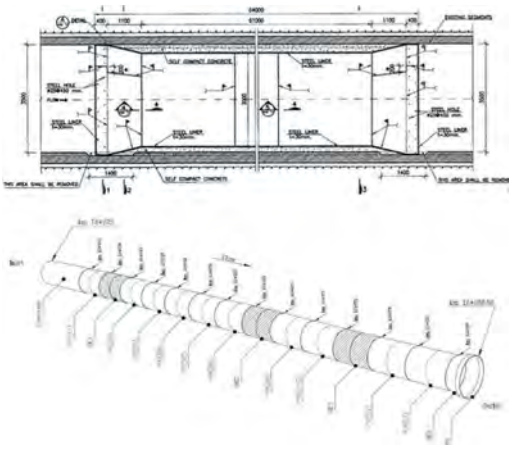

Figure 2. Steel Lining – Longitudinal section.

4 PROCESS AND CLASSIFICATION

The steel lining preparation in the rolling factory is as:

- Cutting the plates in the required length
- Rolling the plates
- Fit-up will be done to prepare the pipe for welding
- Welding the joint
- Back grinding and NDT will be followed
- Back welding
- NDT tests on the welded joints as QC protocols
- Grinding and repairs the welded joints, as required
- Repeat the NDT tests on the welded joints as QC protocol
- Fit-up two-welded pipes to each other to make one strake and above mentioned procedures will be followed for finalizing the strake
- Sand blast of each strake
- Painting in four layers by Hempel (1st- Hempadur Avant Guard Zinc, 2nd- Hempadur MIO, 3rd- Hempel's Brown and 4th- Hempel's Black)
- Boring holes for back filling in 11 cm diameter, will be welded, NDT and painting

The process of the rolling and welding is illustrated in Figures 3 and 4.

5 STEEL LINING INSTALLATION

As the welding and painting completed in the rolling factory, transporting the strakes needed a special trailer/flat car, which has been fabricated in the job site for this matter according to the heaviest load and maximum dimensions (Figure 5). During the transportation, some rolling wheels fixed on the steel lining to avoid any damage on the strakes.

Figure 3. Rolling the steel plates for steel lining support.

Figure 4. Welding process in rolling factory.

Due to the space limitation inside the tunnel, in addition to more than 3 km distance from the headrace tunnel portal, before starting the transportation all the steel segments assembled in the rolling factory (Figure 6). Moreover, the back strip belts fixed and welded on the joints.

For this reason, firstly all the rails, segmental inlays and booster jet fans removed from the tunnel. Later another jet fan installed near to the portal for blowing the air to the steel lining area. After delivery of all steel segments, welding of strakes inside the headrace tunnel started, and consequently it was required the dry condition for the process. In this section of the headrace tunnel the cumulative water leakage is 300 l/s. Therefore, before transporting the steel segments and starting the concrete lining, all

Figure 5. Special trailer.

Figure 6. Assembled steel lining.

the required water pumping and drainage systems delivered to the area and installed in the upstream of the steel lining section. Such that the procedure of the steel lining installation inside the headrace tunnel continued as below:

- Remove all the rails
- Remove jet fans
- Remove ventilation ducts
- Invert cleaning of the path
- Transport of all the pumps, pipes, connections and electrical drives
- Make a sump in the upstream
- Transport the steel segments
- Fit up the steel segments
- Installation of dewatering pipes and connect to the pumps
- Welding the strakes joints
- In parallel, start of the concrete lining
- NDT tests on the welded joints as QC protocols
- Grinding and repairs of welded joints, as required
- Repeat the NDT tests on the welded joints as QC protocol
- Painting
- Remove all the dewatering pipes
- Remove the sump
- Remove the pumps
- Cleaning the section

It should be noted that four numbers of 132 kW - 225 l/s water pumps (three active and one standby pumps) installed in the sump for dewatering while two pumps active simultaneously to fully dry the section with two lines of 16 inch poly ethylene pipes in 80 m length. The pipe lines installed in height of 1.5 m in the middle of the steel lining to proceed the welding and other activities (Figure 7). In all the shifts, one electrician was working in the sump area to looking after the pumps and operation.

6 WELDING METHOD

Type of filler used flux-core arc welding (FCAW), which is widely used in construction because of its portability and high welding speed. It is a flexible welding method, suitable for all welding positions, provided the welder uses the right filler material and flux composition.

- Process and classification of welding in rolling factory is:
- Process: FCAW
- Filler shielding gas: CO2
- Filler: ESAB 13.23, MG-51T, ESAB-81-Ni1-H4

Process and classification of welding inside the headrace tunnel is:

- Process: FCAW
- Filler shielding gas: CO2
- Filler: ESAB-81-Ni1-H4

7 STEEL LINING BACK FILLING

By completion of the steel lining welding and painting, back filling of the steel lining started through the designed holes in the steel lining. The diameter of this holes is 11 cm and seven holes bored in 8 m zig-zag spacing of steel lining strake. Also every 8 m a bulkhead fixed behind the steel lining for better solution in back filling (Figure 8).

Self-compacting concrete (SCC) mainly because of its self-compacting characteristics and strength. SCC is a highly flowable, non-segregating, special

Figure 7. Dewatering sump and lines.

concrete type that can settle into formworks, and encapsulates, heavily reinforced, narrow, and deep sections by means of its own weight. Mixing the class of SCC-30 concrete with non-tilting drum mixer inside the steel lining location.

After completion of the back filling, the caps welded and after QC tests, all the gaps and welded as well as damaged parts painted to the final layer.

During the preparation, transport, fit up, grinding, welding, QC tests, painting and demobilization from steel lining area, HSE officer was there to control the situation and the impacts. As welders using the gas and CO2 cylinders in small and narrow area under 2 lines of 16 inches pipes and supports. So, control of the PPE and the ventilation situation was very high requested and essential. For these reasons the First Aid boxes and all required extinguishers are keep in the working places as well as sump area.

8 CONCLUSION

Headrace tunnel of Uma Oya Multipurpose Development Project faced lots of the challenges during the construction from boring in very hard and abrasive rocks to the fractured and mud zone. This paper has

Figure 8. Back filling holes.

been focused on the steel lining design and execution in 62 m critically mud zone. During the mechanized excavation, concrete segmental lining installed in this section. Later exploratory drillings evidences that mud surrounded this section and as this tunnel would be a pressurized tunnel as well as the internal pressure in this section would be more than 10 bar, the consultant has reviewed the design and the second support based on the combination of the steel lining and concrete lining has been proposed. The steel lining details are summarized as below:

- 10 strakes in 4 m (jointing 2 pipes),
- Three bends in 4 m (jointing 2 pipes),
- One reducer,
- One final ring,
- Six welding machine,
- 350 litres of paints,

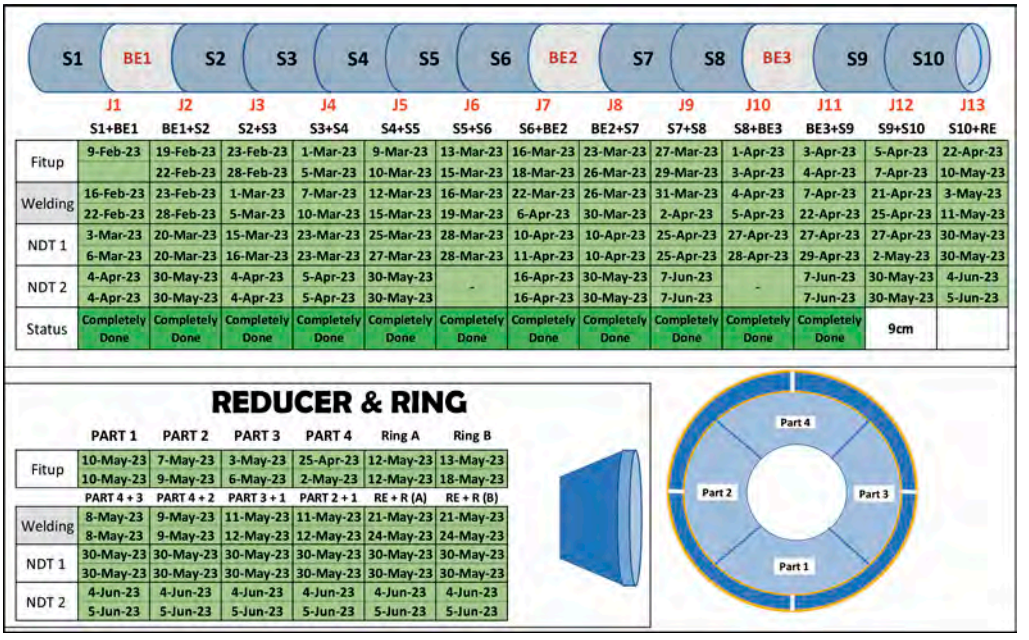

Figure 9. Steel lining time schedule.

- 60 litres of thinner,
- 1,500 m^2 area painted,
- 300 m NDT tests including 150 m UT and 150 m MT/PT in rolling factory,
- 140 m NDT tests including 150 m UT and 150 m MT/PT inside headrace tunnel.

After completion of the steel lining installation, fit up, welding and QC controls, back filling of the steel lining completed through the indicated holes. Final stage was to welding, NDT tests, any repair and painting this hole's caps. Delivery of first segment started on February 9, 2023 and the last NDT tests done on June 5, 2023 (Figure 9).

ACKNOWLEDGMENTS

Authors would like to acknowledge their gratitude to Ministry of Irrigation and Project Director Eng. D.C. S. Elakanda. Also authors would like to appreciate Project Manager Mr. Dezfouli, Executive Manager, Mr. Malekpour and colleagues at FARAB Company as well as subcontractor of Matris Company.

REFERENCES

Rahbar A., Rostami, J., 2016. Construction of Headrace Tunnel of Uma Oya Water Conveyance Project, Sri Lanka, Proceedings of the World Tunnelling Congress, San Francisco, USA.

Rahbar A., Lees, D.J., Hosseini A.H., Shahrokhi, Z., Wenner, D., 2017, The Design and Construction of Grouting against Water Ingress in the Headrace Tunnel for the Uma Oya Project, Sri Lanka, Proceedings of the World Tunnelling Congress, Bergen, Norway.

Rahbar A, Hosseini A.H., 2019, The Sealing of huge water ingress in headrace tunnel of Uma Oya Project, Sri Lanka, Proceedings of the World Tunnelling Congress, Naples, Italy.

Rahbar A, Noorzad, A., Ahmad Dezfouli, P., Mendis, Sh., 2022, Ground Water Control in Headrace Tunnel for the Uma Oya Project, Sri Lanka, Proceedings of the World Tunnelling Congress, Copenhagen, Denmark.

Tunnelling for a Better Life – Yan, Celestino, Thewes & Eberhardt (Eds)
© 2024 The Author(s), ISBN 978-1-032-80042-4
Open Access: www.taylorfrancis.com, CC BY-NC-ND 4.0 license

Durability of two-component backfill grout: An experimental study

Marta Di Felice & Anita Di Giulio*
GEEG, Geotechnical and Environmental Engineering Group, Rome, Italy

Nicola Valiante
Webuild S.p.A., Rozzano, Italy

ABSTRACT: Two-component grout is widely used in mechanized tunnelling to fill the annular gap behind the segmental lining. Besides the numerous advantages of this technology, it is well known that this type of mortar is subject to rapid degradation processes when exposed to air, even for short periods of time. This is not a concern under normal operating conditions, i.e. underground and often below the water table, but it may be detrimental to the quality of the backfilling in case part of the grout is temporarily exposed to air during the construction phases. In lack of dedicated standards, the purpose of this work is to share a laboratory experience on a topic that has not been fully addressed in the literature. The research activity presented in this paper was specifically designed to evaluate the effect of exposure to air and dry soil on a high-performance two-component mortar. The experimental study entailed the execution of visual inspections, UCS tests and mineralogical analyses on small and full-scale specimens subjected to specific exposure environments for an observation period of six months. The results show that, depending on the imposed conditions, there is a certain degree of decay of the mechanical properties but that they remain above those required by technical specifications.

Keywords: Tunnelling, TBM, Backfilling, Two-component grout, Laboratory test, Durability

1 INTRODUCTION

In TBM tunnelling, the use of two-component grout as backfilling material for the annular gap behind the segmental lining is experiencing a great diffusion, encouraging further technical and scientifical research on this topic. Several studies, among which Thewes and Budach (2009), Pelizza et al. (2010), Antunes (2012), Youn and Breitenbücher (2014), Mähner and Hausmann (2017) and Todaro et al. (2022), dealt with the mechanical characterization and the standardization of testing procedure for this material. On the other hand, there is little published knowledge on the long-term behaviour of two-component grout under site conditions as well as in the laboratory. Only recently a comprehensive work by Peila et al. (2015) provided some case histories and laboratory experience. Furthermore, on-site quality checks are generally not made public.

The long-term behaviour of the backfill as a component of the support system of the tunnel together with the lining is important not only in terms of safety and costs, but also to improve sustainability. Hence, its durability should be considered since the design phase.

Laboratory testing of two-component grout usually refers to standards made for concrete and single component mortars (for example UNI EN 11417-1:2012, UNI EN 13057, UNI EN 13295), which cannot be fully applied when the material is exposed to aggressive environments. The exposure conditions of the backfilling in fact are not comparable to those of the structural concrete and also several of those tests entail oven drying, which has proven to be detrimental for the integrity of the two-component grout.

For the backfilling grout, usually working in confined environments and below the water table, the exposure to aggressive environments during the tunnel life may be related to the characteristics of the groundwater (i.e. acid, rich of chlorides, sulphates) or to particular construction phases, during which the grout can be subjected to drying or low temperatures. In this context, it seems appropriate to define the experimental activity according to the conditions and needs of the specific project.

With the goal of sharing a laboratory experience focused of the long-term behaviour of the backfill, this work presents the study of the durability of the backfill grout carried out for the Inclined Pressure Shaft of Snowy 2.0 Project, carefully approached

*Corresponding author: anita.digiulio@geeg.it

DOI: 10.1201/9781003495505-138

starting from the design phase due to the special features of the backfilling required for this very challenging project (De Carli et. al (2022) and Di Giulio et al. (2023)).

The performance requirements were:

- unit weight>20 kN/m^3 or porosity<50%
- Unconfined Compressive Strength UCS≥15–20 MPa
- Young modulus E≥3.0–5.0 GPa
- Decay of UCS&E<20% after 10^6 loading/unloading cycles

The selection of a mix design able to meet these targets and its mechanical characterization was followed by a further experimental activity aimed at assessing the grout durability under specific site conditions; in fact, the project schedule involves a construction phase during which the drainages that cross both the lining and the backfill will be operational. These drainages will be necessary to discharge the external hydraulic load acting on the lining in a phase in which the tunnel will be dry but will probably put the backfill in contact with air for a few months. The object of the study was to verify if the two-component grout could withstand, without damage, this temporary phase.

2 MATERIALS AND METHODS

Two-component backfill grout consists of two fluids: a component A (binder, bentonite, water and a retarding agent) and a component B (accelerating additive, usually sodium silicate), which produce a gel within seconds from the moment they are mixed. The materials used and the mixing process significantly affect the behaviour of the grout, therefore, in the laboratory, particular attention was paid to the supply of the actual materials from the jobsite and to the mixing system, that was designed to simulate as closely as possible the injection system of the TBM. The durability of the grout was considered at an early design stage, with constrains on the binder and the filler to be used and on the porosity to be achieved.

The mix design reported in Table 1 (Di Giulio et al. 2023) was obtained after a trial phase aimed at finding a proper balance between the characteristics of the fresh and hardened grout, i.e. achieving high-performances while maintaining the component A fluid and stable enough to be pumped. The special features of this mix design with respect to common practice (Thewes and Budach 2009) are the use of a composite slag/cement binder, the low water/binder ratio (0.85), the reduced amount of bentonite, and, most importantly, the introduction of a superplasticizer to improve the workability and of a filler (silica flour) to impart structure. The component B was sodium silicate, which dosage is about 11% of the total weight of 1m^3 of grout.

Table 1. Mix design.

Binder (kg/m^3)	608
Filler (kg/m^3)	339
Water (kg/m^3)	518
Bentonite (kg/m^3)	2.8
Retarder (kg/m^3)	11.3
Superplasticizer (kg/m^3)	3.6
Accelerator (kg/m^3)	176

A series of laboratory tests was performed to measure the properties of the component A (viscosity at the Marsh' cone, density, gel time) and to verity the performance requirements on the hardened grout (unit weight, porosity, Unconfined Compressive Strength and elastic moduli). The unit weight and porosity were 16.5 kN/m^3 and 35%, respectively; the average UCS of the mortar was 36 MPa after 28 days and the average value of the Young's modulus was 10 GPa.

2.1 *Experimental program*

As already pointed out, the experimentation could not follow the existing standards for durability testing due to the peculiar features of two-component grout, so the study was carried out with a site-specific approach, dealing with expected conditions that could be detrimental for the grout integrity and performance on the long-term.

The experimentation lasted six months and consisted in the execution of UCS tests on samples cured in different environments, and in the preparation of a full-scale sample simulating the grout around a drainage hole, subjected to visual inspections, UCS tests and mineralogical analyses.

2.1.1 *Curing at controlled humidity*

The effect of a prolonged exposure to air was investigated on prismatic specimens, cured in water at constant temperature for about four months before the beginning of the tests. The samples were sealed in paraffin leaving free one of the bases, as shown in Figure 1, and then were kept at 25 °C in containers with relative humidity equal to 50%, 90% and 98%.

Temperature and humidity were monitored by a thermometer and a hygrometer for the entire test duration. After a first inspection, executed after two months of exposure, it was decided to continue the observation up to six months, exposing other samples (now six months old) to the worst conditions, i.e. 50% relative humidity. At the end of the fixed period of exposure the samples were subjected to visual inspection and UCS tests.

2.1.2 *Full-scale set-up: Simulation of the drainage hole*

A specific test set-up, illustrated in Figure 2, was developed with the aim of studying in the laboratory the potential degradation of the portion of grout surrounding the drains.

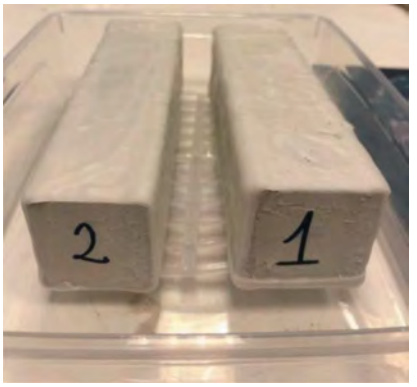

Figure 1. Prismatic specimen sealed in wax.

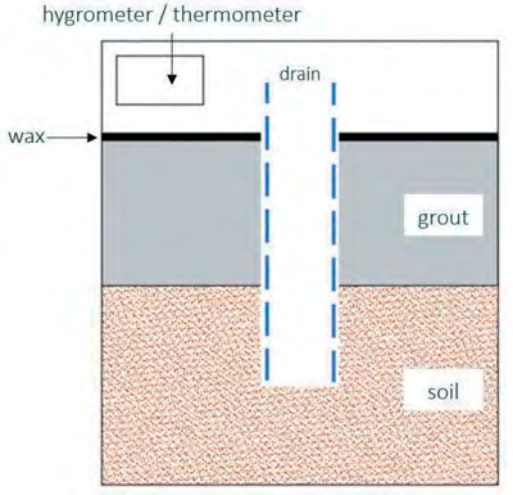

Figure 2. Scheme of the set-up for the simulation of the drainage.

A 40x40x18 cm block of grout was prepared leaving a PVC pipe (80 mm external diameter) in the centre. The grout was poured directly on a layer of sand, simulating the contact between backfill and rock mass, while the impermeable lining was simulated by a top layer made of wax. The casting of this full-scale sample (Figure 3) was the most challenging task of the experimentation, requiring the laboratory team to build a new system able to pour about 40 L of mixture in a continuous flow under 1 bar of pressure, which was much more complex than the system previously used and already discussed in De Carli et. al (2022).

After 40 days of curing in sealed conditions, the PVC pipe was extracted and replaced with a smaller slotted pipe, leaving a gap of about 2 mm between the hole wall and the external surface of the drain. The system thus made was then kept at a temperature of 25 °C and relative humidity, *hr*, of 70% for six months, during which visual inspection and UCS tests were performed at regular intervals.

Figure 3. Pictures of the full-scale set-up.

The value of relative humidity equal 70% was selected as the minimum among the available environmental measurements taken in another tunnel of the jobsite.

3 RESULTS

3.1 *Prismatic samples in unconfined environment*

As illustrated in Figure 4, which shows longitudinal sections of sawn prisms, the samples presented a dry/discolored external layer, while the inside appeared fresh.

Figure 4. Pictures of sections of samples sawn after exposure to air at different values of relative humidity, from the left: 50%, 90% and 98%.

The extent of the discolouration, localized at the exposed faces, is greater in the specimens exposed to lower humidity values (hr=50%), as could be expected. Beside the external discoloring, the exposure at hr=50% produced the formation of cracks propagating from the free base inwards.

The results of the UCS tests carried out on cubic samples sawn from the prisms are presented in Table 2 and Figure 5. It can be observed that the UCS of the control sample (cured in water for the same period) is about 36 MPa, congruent with the average UCS at 28 days of this mix, and that after two months of exposure all samples provided results comparable or above this value, in the range 34-45 MPa.

The thickness of the altered layer after two months was about 2 mm, but this did not translate in a deterioration of the performance, even for the samples kept at the lowest humidity.

Table 2. Results of UCS tests after exposure to air at hr=50%.

Curing conditions	Time of exposure (months)	Total age of samples (months)	UCS (MPa)
Standard	0	6	35.7
hr=50%	2	6	39.3*
hr=50%	2	6	45.2
hr=90%	2	6	33.8
hr=90%	2	6	40.6
hr=98%	2	6	43.6
hr=50%	6	12	51.6
hr=50%	6	12	29.7*
hr=50%	6	12	44.3
hr=50%	6	12	27.7*
hr=50%	6	12	42.5

*Sample including the exposed surface

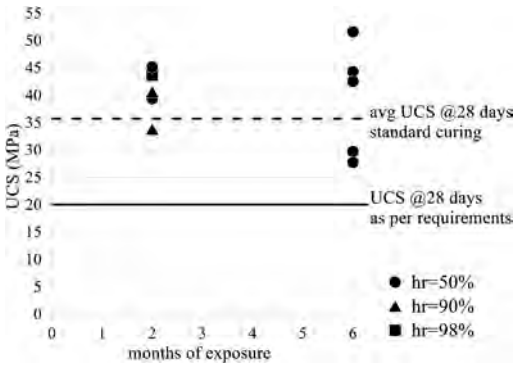

Figure 5. Results of UCS tests after two and six months of exposure to air at relative humidity = 50%.

As anticipated, once seen the cracks proceeding from the exposed face of the samples cured at hr=50%, it was decided to extend the observation period up to six months. The extent of the altered layer grew, producing measurable damages to the strength of the cubic samples containing the exposed surface; in fact, as it can be noted from Table 2 and Figure 5, the UCS values measured on the external portion of the prisms (28 and 30 MPa) are lower than the UCS measured on the internal portion of the same specimens (42-52 MPa).

A picture taken after the UCS test of a cubic sample containing the exposed face is shown in Figure 6. It's worth noting that the test was conducted putting the altered surface parallel to the vertical axis in order to have regular surfaces on which apply the load. Of course, this could have an influence on the results.

3.2 *Full-scale sample with drainage crossing*

The block of grout was inspected after one, three and six months of exposure to air at 25 °C and humidity 70%.

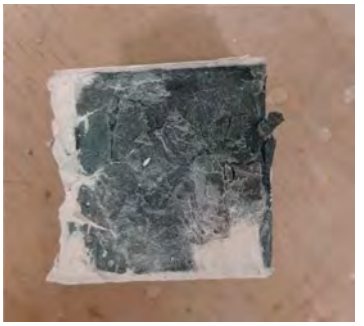

Figure 6. Broken sample with an exposed surface.

Figure 7 shows the microscopic enlargements of the portion of grout immediately around the drainage hole, taken at the first and last visual inspections.

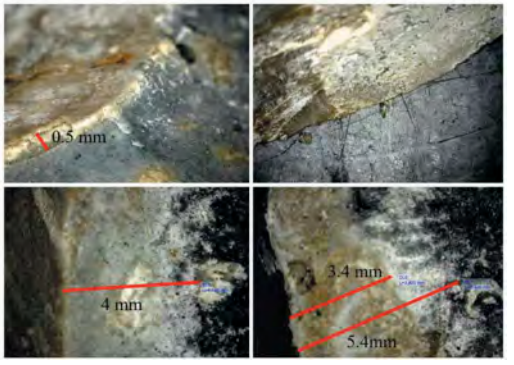

Figure 7. Enlargements of the layer of grout exposed to air within the drainage, after 1 month (above) and 6 months (below).

The boundary between altered and "fresh" grout can be easily spotted by colour, so it was possible to measure its progress over the time. After one month, the thickness of the altered layer was less than 1 mm, about 0.2 – 0.5 mm, after 3 months it was about 3-4 mm, after six months it was between 4 and 6 mm.

During the first and last inspection, portion of the block near the drainage hole were sawn to obtain cubic samples for UCS tests. The results are reported in Table 4 and Figure 8.

Table 3. UCS tests on samples retrieved from the block.

Time of exposure (months)	Density (Mg/m3)	UCS (MPa)
1	1.66	36.7
1	1.70	29.5
1	1.64	28.1
6	1.68	29.9
6	1.68	22.3
6	1.59	26.2
6	1.70	28.6

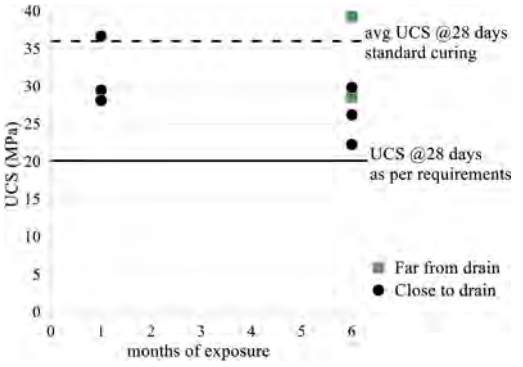

Figure 8. UCS values after 1 and 6 months of exposure.

The measured UCS values, even if always higher than the threshold of 20 MPa set by performance requirements, are generally below the average UCS expected for this mix design at 28 days. This difference may be due to the preparation of the block, which entailed the injection of a huge volume of grout in a single step and a dry, even if sealed, curing. These conditions made the formation of joints and small defects in the block practically unavoidable. Also, the presence of these joints made quite difficult the preparation of cubic samples from the block (from which the modest number of tests that could be executed).

The result show that a reduction of strength due to the exposure to air can be detected comparing the UCS values obtained at different inspections. In fact, after six months of exposure, the samples closer to the hole had an average UCS of 26 MPa, about 17% lower than that of the samples taken close to the hole after one month (31 MPa). Also, visual inspection allowed to observe that the failure of these samples occurred along pre-existing surfaces, while samples retrieved beyond a layer of about 10 cm from the drainage hole provided higher UCS values and appeared fresh after the tests, as shown in Figure 9.

Figure 9. Pictures of samples retrieved from the full-scale block. On the left a sample taken far from the drainage hole, on the right one taken close to it.

3.3 *Mineralogical analyses*

Portions of the block were subjected to mineralogical (DRX - X-ray diffraction) and petrographic analyses to understand the process of alteration that the grout experiences when exposed to air.

Table 4 synthetizes the results of DRX analyses carried out at three and six months on altered and fresh portions of grout.

Table 4. Results of mineralogical analyses.

	3 months		6 months	
Phases	Fresh	Altered	Fresh	Altered
Quartz	27	27	27	26
Calcite	8	9	10	10
Gypsum	1	1	1	1
Vatherite	-	24	-	23
Aragonite	-	4	-	2
Ettringite	3	-	3	-
Smectite	-	-	-	-
Alite/belite	0	-	2	-
Portlandite	-	-	-	-
Amorphous	60	35-40	57	38

It can be noted that the recognized phases are practically the same, with a significant part of the samples composed by not-crystalline phases and quartz (the filler), compounds contained by the clinker as gypsum, calcium silicates (alite/belite) and other hydration products. The altered layer contains more vaterite, a meta-stable form of calcite, at the expenses of the amorphous phase.

Figure 10. Detail of the passage between altered and fresh grout (yellow line). The porosity is shown in the red circles.

The petrographic study highlights the separation between the white and dark layers already observed at a macroscopic level, sometimes gradual and sometimes neat, the latter associated with a higher porosity. The porosity consists mainly of spherical voids presumably due to air entrapped during mixing, but also from narrow cracks probably due to shrinkage (Figure 10).

The altered portion is characterized by a predominantly micritic matrix typical of carbonation due to reaction with the CO_2 in the air.

4 CONCLUSIONS

The study here presented was carried out to investigate the long-term behaviour of the backfilling grout of the IPS of the Snowy 2.0 project, following

a site-specific approach. The experimentation was aimed at evaluating the effects of the exposure to air and low humidity on two-component grout. The experimental activity was developed to simulate specific and severe environmental conditions, in lack of dedicated standards, and involved prismatic samples as well as a full-scale set-up, simulating a portion of grout around a drainage hole.

At the end of an observation period of six months, the following conclusions can be drawn:

- the alteration that the two-component grout undergoes when exposed to air at low humidity is caused by carbonation phenomena and, in this high-performance mix, proceeds from the external surface inwards at an average rate less than 1 mm/month measured on the full scale sample;
- cubic samples obtained from sealed prisms with one free face in contact with air, at relative humidity equal to 50%, provided UCS values in the range 42-52 MPa measured far from the exposed surface, and lower values (28 and 30 MPa) when containing the altered layer;
- in the full-scale sample, the alteration proceeding from the exposed surface (4-6 mm) and the formation of cracks due to the casting procedure, volume of the block and dry curing, produced a reduction of the strength in the layer of grout immediately surrounding the hole. This reduction was observed comparing average UCS values obtained after one and six months of exposure, which are about 31 and 26 MPa, respectively;
- in the full-scale sample, the grout resulted substantially unaffected, in terms of strength and aspect, beyond a layer of about 10 cm from the exposed surface.

ACKNOWLEDGMENTS

The authors would like to thank Snowy Hydro Ltd and Future Generation Joint Venture for promoting and supporting the development of these studies.

The authors would like to thank the laboratory ANALITICA S.a.s. for the mineralogical analyses and the valuable knowledge made available to interpret them.

REFERENCES

Antunes, P., 2012. Testing procedures for two-component annulus grouts. North American Tunnelling proceedings, 14–22.

De Carli, G., Valiante, N., Mancinelli, L. Sebastiani, D., 2022. High performance TBM Backfill grout. Proceedings of the ITA-AITES World Tunnel Congress 2022, Copenhagen (Denmark).

Di Giulio, A., Di Felice, M., Valiante, N., De Carli, G., 2023. Single and two-component grout as high-performance backfilling materials. Proceedings of the ITA-AITES World Tunnel Congress 2023, Athens (Greece).

Mähner, D., Hausmann, M. 2017. New Development of an Annular Gap Mortar for Mechanized Tunnelling. In AFTES International Congress 2017, Paris (FR), 13-16 November 2017.

Peila D., Chieregato A., Martinelli D., Salazar Onate C., Shah R., Boscaro A., Dal Negro E., Picchio A. (2015). Long term behavior of two component back-fill grout mix used in full face mechanized tunneling. GEAM. GEOINGEGNERIA AMBIENTALE E MINERARIA, vol. 144 n. 1, pp. 57–63. - ISSN 1121-9041.

Pelizza, S., Peila, D., Borio, L., Dal Negro E., Schulkins, R., Boscaro A. 2010. Analysis of the performance of two-component back-filling grout in tunnel boring machines. Proceedings of the ITA World Tunnel Congress 2010, Vancouver (CA), May 14–20.

Thewes, M., Budach, C. 2009. Grouting of the annular gap in shield tunneling – an important factor for minimization of settlements and production performance. Proceedings of the ITA-AITES WTC.

Todaro, C., Martinelli, D., Boscaro, A., Carigi, A., Saltarin, S., Peila, D., 2022. Characteristics and testing of two-component grout in tunnelling applications. Geomechanics and Tunnelling, 15: 121–131. https://doi.org/10.1002/geot.202100019

Youn, B. Y., Breitenbücher, R., 2014. Influencing parameters of the grout mix on the properties of annular gap grouts in mechanized tunneling. Tunnelling and underground space technology, 43, 290–299. https://doi.org/10.1016/j.tust.2014.05.021

Tunnelling for a Better Life – Yan, Celestino, Thewes & Eberhardt (Eds)
© 2024 The Author(s), ISBN 978-1-032-80042-4
Open Access: www.taylorfrancis.com, CC BY-NC-ND 4.0 license

Tangential resistance between primary and secondary lining with PVC waterproofing sheet membrane

Luigi Forlingieri
Arup, Milan, Italy

Carmen Hu & Mirko Morosi*
Arup, London, UK

Angelica Zanichelli
Arup, Milan, Italy

ABSTRACT: Urban areas have continuing growing demand for mobility, and as such a great interest is being taken in underground construction. Sprayed Concrete Lining (SCL) is a well-established method for large diameter tunnel construction throughout the UK and the world, sometimes referred to as NATM (New Austrian Tunnelling Method). A SCL tunnel usually consists of a primary and a secondary lining. The primary lining is often adopted to support the ground loading during construction, usually assuming full degradation in long term condition. Subsequently, a drainage layer or waterproofing layer will be installed depending on the type of tunnel. The secondary lining will be constructed in the final stage. Depending on the groundwater table and permeability of the ground, tunnel watertightness becomes one of the most critical aspects of tunnel design. When a waterproofing membrane is required, a specific "sandwich" configuration between the primary and secondary lining is used. The common approach is to neglect any of the tangential frictional resistance provided at the interface between the waterproofing sheet membrane and the permanent lining due to its smoothness and a number of factors which could influence the predicted behaviour.

The tangential resistance is a product of the interaction between the primary lining, the loading conditions and the interface friction of the PVC membrane. This paper summarises the key findings of introducing a friction interface between the primary and secondary lining as part of the permanent lining design, thereby, leading to re-distribution of the stresses across the lining interface, and directly assessing the impact on the lining response, and an optimisation of the tunnel geometry. The application of friction interface is a complex interaction, and recommendations will be made in this paper to inform future designers of permanent linings.

Keywords: waterproof membrane, friction resistance, sprayed concrete lining, tangential spring

1 INTRODUCTION

Urban areas have continuing growing demand for mobility and, as such, there is great interest in underground space utilisation and underground construction. Sprayed Concrete Lining (SCL) is a well-established method for large diameter tunnel construction throughout the UK, sometimes referred to as NATM (New Austrian Tunnelling Method). SCL is one of the most common methods of construction, due to its adaptability to different tunnel geometry/size and ground conditions.

A SCL tunnel usually consists of a primary and a secondary lining. The primary lining is often adopted to support the ground loading during construction, usually assuming full degradation in long term condition. Subsequently, a drainage layer or waterproofing layer is installed depending on the type of tunnel. The secondary lining, generally cast in-situ, is constructed in the final stage.

Depending on the groundwater table and permeability of the ground, tunnel watertightness becomes one of the most critical aspects of tunnel design. When a waterproofing membrane is required, a specific "sandwich" configuration between the primary and secondary lining is used.

It is clear that friction resistance at the interface between the primary and secondary lining can impact

*Corresponding author: mirko.morosi@arup.com

DOI: 10.1201/9781003495505-139

the structural design of the secondary lining. With better understanding of the interface resistance, better design of the secondary lining there is the opportunity to optimise lining thickness and reinforcement.

2 OBJECTIVE

The general approach is to neglect any of the friction resistance provided at the interface between the waterproofing sheet membrane and the secondary lining due to its smoothness and the difficulties in the definition of all the factors that are needed to predict the correct behaviour.

Although the benefit of introducing friction resistance is clear, this value is extremely difficult to define and depends, amongst others, on factors such as the undulation (roughness) of the primary lining, installation method, gaps due to concrete shrinkage and the presence of infill grouting between the waterproofing membrane and the secondary lining.

The paper aims to define the impact of friction resistance at the interface on the global behaviour (e.g. internal stresses, lining deformation) of the secondary lining, and provide an insight for secondary lining design which is more representative of the actual behaviour.

In this paper, different loading conditions and friction coefficients between primary and secondary lining are considered to evaluate the variability of the lining system.

3 NUMERICAL MODELLING

3.1 *Geometry*

A typical lining layout is modelled using numerical software LS-DYNA. A 2D view of the plane strain model is shown in Figure 1. A thin portion of the lining – 0.5m deep with 4 volume mesh elements in the depth of the lining is modelled.

The external height of the tunnel is 11.40m, and it is 12.87m wide at the springline. The primary lining thickness is modelled as 375mm. The secondary lining is 350mm thick, whereas the invert is modelled with a variable thickness (max. 1560mm).

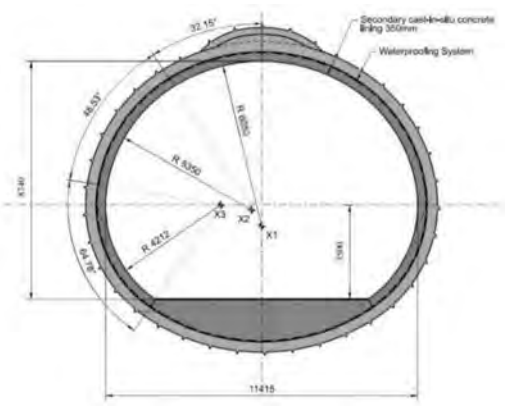

Figure 1. 2D view of the geometry of the tunnel.

3.2 *Tunnel lining interface*

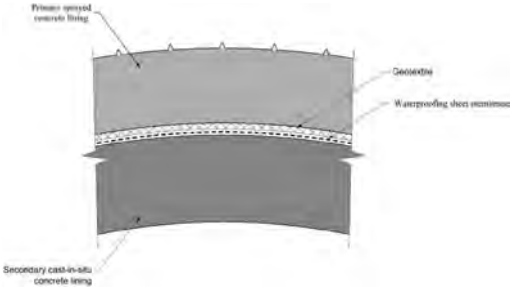

Figure 2. Detailed interface between primary and secondary lining.

The concrete linings and the soil are modelled with solid 3D constant stress elements defined by 8 nodes, called solid elements in LS-DYNA. A typical mesh of 0.2x0.2m is used for the soil, while approximately 0.1x0.1m mesh is used for the linings, to have 3 elements with a total 0.5m out-of-plane thickness.

The interaction between the soil and the primary lining and between the primary and secondary linings are modelled in LS-DYNA with a penalty based contact elements (*AUTOMATIC_SURFACE_TO_SURFACE), in which numerical springs are defined at the linings interface to prevent penetration of one of the linings into the other. Whenever a slave node attempts to penetrate the master surface, a reaction force is generated. The magnitude of the force acting at the slave node is proportional to the penetration depth achieved by the slave nodes and to the lowest stiffness of the two mediums in contact. Reaction forces at the master surface side are generated by equilibrium. Both normal (F_N) and friction penalty forces (F_f) are generated, with the latter assigned as $F_f = m \times F_N$, where m is the friction coefficient.

Different friction coefficients are set between primary and secondary lining, to investigate the effects of this parameter to the response of the system.

In absence of dedicated lab tests, a value of the friction coefficient between primary and secondary linings of 0.15 is adopted in the base model, assuming the following shear friction values for each interface:

- Primary lining (rough) to geotextile of 0.6
- Geotextile to PVC membrane of 0.25
- PVC membrane to secondary lining (smooth) of 0.45.

The friction coefficient at the tunnel crown is always set to 0.0, under the assumption that the secondary lining would settle under its-own self-weight due to gravity.

The typical friction coefficient between soil and concrete is between 0.6 to 1.0. An average value of 0.8 is adopted for all the models.

3.3 *Materials*

Concrete C32/40 and C40/50 properties are used for primary and secondary lining, respectively. The elastic modulus of the primary lining is reduced with respect to the value reported in the Eurocode to account for early strength development. The design values of compressive and tensile capacity used in the model are similar to typical design situation. Concrete mechanical properties are detailed in Table 1. The ground medium is modelled as linear elastic material, adopting the properties detailed in Table 2.

Table 1. Concrete elements properties.

Element	E_{cm} [GPa]	f_{ck} [MPa]	f_{cd} [MPa]	f_{ctd} [MPa]
Primary lining	17	32	18.13	1.41
Secondary lining	30	40	22.67	1.64

Table 2. Ground medium properties.

Element	ρ [kN/m^3]	E [MPa]	υ [-]
Soil	20	500	0.3

Concrete is modelled with a smeared crack model, implemented for the 8-node single integration point solid elements, based on the Ottosen plasticity model (*MAT_WINFRITH_CONCRETE). As it is a material model with solid elements, it allows the capture of in-plane/out-of-plane through thickness tension, compression, bending, shear as well as concrete cracking in tension, crushing in compression, tension stiffening and compression softening. This model considers the effects of confinement effect in the compressive strength calculation of concrete.

3.4 *Boundary conditions*

The model is built assuming a plane-strain condition. All the nodes are restrained in the Y direction and supported in the Z direction, both sides of the model are restrained in the X direction.

Initial vertical stresses are used to initialise the horizontal stresses on the soil, using *INITIAL_STRESS_DEPTH. For the main model, a factor k, which is defined as the ratio between the total horizontal stress and the total vertical stress ($\sigma_{hor}/\sigma_{vert}$), of 1.5 is used. Different k values are considered as sensitivities (see Section 3.6). In this study only symmetrical loading condition is considered.

3.5 *Construction stages*

The model is analysed in typical NATM construction sequences as described in Table 3.

Table 3. Construction stages.

Stage	Time (s)	Description
1 – Initial Phase	0	Initial stress application
2 – Primary Lining Installation	0 to 1	Primary lining activation with gravity loading at 0.5s.
3 – Secondary Lining Installation	1 to 1.5	Secondary lining installation
4 – Primary Lining Degradation	1.5 to 2	Primary lining degradation (*LOAD_STIFFEN_PART) 50% of its initial stiffness
5 – Final stage	2 to 2.5	End of Analysis

This model adopted a "*creep*" deformation (50% elastic modulus reduction) for the primary lining during its degradation, after which the applied loading resisted by this layer is partially transferred to the secondary lining.

The simulation of the applied loading is consistent with this modelling approach, where soil and water pressure are applied at the soil-to-primary lining interface in form of total stresses.

3.6 *Models scenarios*

To analyse the effects of friction between the primary and secondary lining in typical tunnel lining configuration, different models are created. These models differ in terms of parameters: k values and friction coefficient between primary and secondary lining.

Table 4. Models developed for the study.

Model name	k	μ (Primary to Secondary)
Base model (M1)	1.5	0.15
Model 2 (M2)	1	0.15
Model 3 (M3)	0.5	0.15
Model 4 (M4)	1.5	0.0
Model 5 (M5)	1.5	0.3
Model 6 (M6)	0.5	0.0

4 RESULTS

In the following sections, the key LS-DYNA model results are presented and discussed. The base model is the one described in detail in Section 3, whereas all the sensitivity analyses are carried out with different design parameters as described in Section 3.6, to investigate how different model inputs affect the tunnel lining behaviour in term of internal forces and deformed shape.

Model results are shown at six cross sections of interest, for both the primary and secondary lining. The locations of interest are indicated in Figure 3.

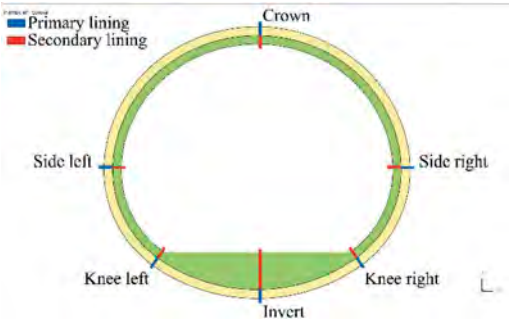

Figure 3. LS-DYNA model cross sections location.

4.1 *Influence of stress initialisation (k=1.5 vs. k=0.5)*

Before investigating the influence of the friction coefficient at the primary to secondary lining interface, preliminary findings from the comparison between different stress initialisation (k=0.5 vs. k=1.0 vs. k=1.5) are provided.

Figure 4 illustrates the deformed shapes of the primary lining for the three modelling scenarios at the end of Stage 5 (t = 2.5s). It is evident that different k values leads to different deformed shapes and generates active and passive soil pressure at different locations around the lining. The secondary lining final deformation is the result of two contributions. The first contribution is the deformation occurring due to its own self-weight, and it develops during the secondary lining installation (Stage 3). The initial shape of the secondary lining is governed by the deflections occurred in the primary lining during Stage 1 and 2, that are functions of the k values, see Figure 4. Between 1.0s and 1.5s (Stage 3), the secondary lining deformation is driven by the gravity loading, and it is characterised by crown inward deformation with a gap created between the primary and secondary linings, side walls outward deflections and invert settlement (outward deflection). The second contribution of the secondary lining deformation occurs during Stage 4 (onset at 1.5s), and it is the result of the primary lining degradation. In this phase, a fraction of the soil stress applied at the soil-to-primary lining interface is transferred at the primary-to-secondary lining interface, as induced by the primary lining degradation. During Stage 4, a general inwards deformation of the two linings is observed. Larger deformations occur in the primary lining across the crown area due to the presence of the gap which was created during Stage 3. Inward deformations are captured at the side walls and invert, whereas only limited deformations are observed at the knees section of the lining, where the secondary lining invert slab constrains the primary lining deflection.

These behaviours are detailed in Figure 5, which shows the primary and secondary lining deflections at the end of the analysis (Stage 5), representing the deformations measured from Stage 3, see a) and b),

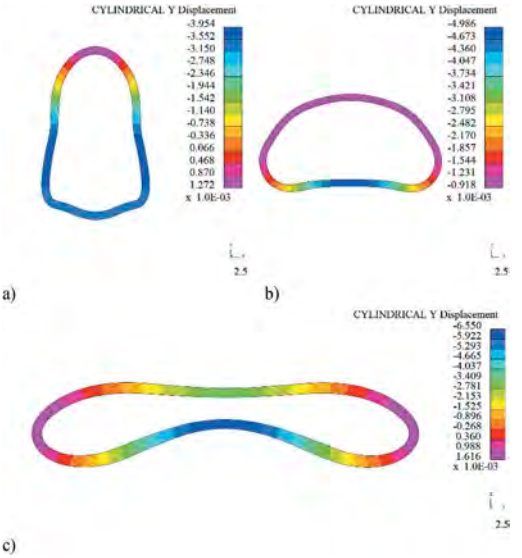

Figure 4. Primary lining deformed shape of the three models [m]: a) M1 (k=1.5), b) M2 (k=1.0) and c) M3 (k=0.5). Magnification factor = 1000.

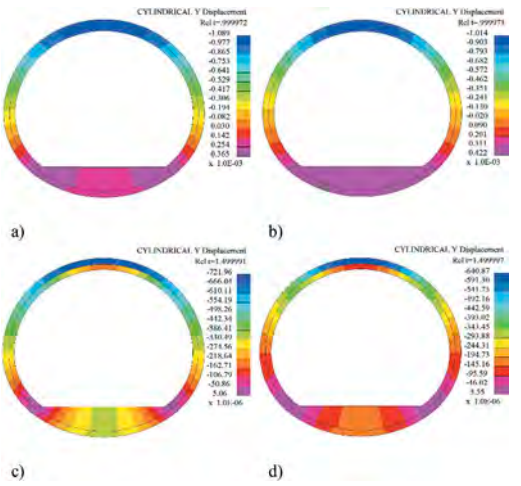

Figure 5. Primary and secondary lining radial deflections [m] at end of Stage 5. Deflections relative to Stage 3 for a) k=1.5 (M1) vs. b) k=0.5 (M3). Deflections relative to Stage 4 for c) k=1.5 vs. d) k=0.5.

and the deformations measured from Stage 4, see c) and d), for k =1.5 and k=0.5, respectively. Positive deflections represent outward deflections, negative inward deflections.

Despite a significantly different initial deformed shapes, the numerical findings suggest that the lining deformation after the secondary lining installation is practically not influenced by the k value and consequent initial primary lining deflected shape, see a) vs. b) from Figure 5.

Table 5. Normal stress between soil and primary lining at t=1.0s (& t=2.5s).

Model	Crown [kPa]	Shoulder [kPa]	Side W. [kPa]	Knee [kPa]	Invert [kPa]
M1	330 (300)	330 (310)	400 (380)	470 (510)	360 (330)
M3	135 (120)	220 (205)	350 (330)	300 (320)	170 (170)

Table 6. Normal stresses and stress ratio at primary lining to secondary lining interface at t=2.5s.

Model	Crown [kPa]	Shoulder [kPa]	Side W. [kPa]	Knee [kPa]	Invert [kPa]
M1	110	120	170	260	150
Stress ratio	(110/ 260=) 42%	(120/ 260=) 46%	(170/ 260=) 65%	(260/ 260=) 100%	(150/ 260=) 58%
M3	60	75	110	160	80
Stress ratio	(60/ 160=) 38%	(75/ 160=) 47%	(110/ 160=) 69%	(160/ 160=) 100%	(80/ 160=) 50%

These findings are also supported by the radial stress results provided by performed simulations.

Table 5 summarises the normal stresses at the interface between the soil and the primary lining, where the stresses are extracted at the beginning of Stage 3 (t=1.0s) and at the end of the analysis (t=2.5s). The latter values are detailed within parentheses. It can be observed how the soil pressure is almost constant throughout the analysis's stages, i.e. no significant increase of normal stress at t=1.0s and t=2.5s.

Table 6 details the final normal stress build-up at the primary to secondary lining interface. Despite different magnitudes, by comparing the stress profile developed at the secondary lining profile for M1 and M3 (k=1.5 vs. k=0.5) it can be observed that for both models the largest stresses develop at the knee level.

Moreover, it can be noted that the ratio between the stress at knee level and the stress at the other locations of interest are similar between M1 and M3, see normalised stresses illustrated in Table 6.

These results show that the primary lining deformation is predominately influenced by the stress initialisation (k value), while the secondary lining deformation is not significantly affected by the primary lining pre-imposed deformation. However, the secondary lining internal forces are affected by the k value.

The correlation between the friction resistance and the force development in secondary lining is discussed in the following sections.

4.2 *Influence of friction coefficients for k=1.5 models*

This section details the comparison between Base Model (M1) and Models 4 (M4) and 5 (M5).

During the secondary lining gravity loading development (Stage 3), the secondary lining undergoes a vertical shortening (shortening of the crown-to-invert distance), whilst developing only very small outward deflections at the sidewalls. The analysis shows that the smaller the friction coefficient, the larger the secondary lining vertical shortening is. Up to this modelling stage, there is negligible influence of the friction coefficient to the secondary lining internal force development, except for the invert results, which show relatively smaller axial force with corresponding larger bending moment development for increasing friction coefficient. Possible interpretation of this mechanism is that a friction resistance partially reduces the axial force induced by gravity loading, while inducing internal bending moment due to friction tangential stresses developed at the lining interface.

More significant influence offered by the friction coefficient is shown at the following stage (Stage 4), triggered by the primary lining degradation, which unfold between 1.5s and 2.0s. Further evidence is that the larger vertical deflections occur for increasing friction coefficient, while larger vertical shortening is measured for decreasing friction coefficient, with maximum shortening observed for M5 (μ=0.0). Larger horizontal shortening is also observer for smaller friction coefficient (μ=0.0).

Figure 6 and Figure 7 show the development of axial force and bending moment at the crown and invert of the primary and secondary lining, while Figure 8 and Figure 9 show the development of axial force and bending moment at the side walls of the primary and secondary lining.[1]

The key observation is the opposite trend for the secondary lining axial force developed at the crown and side walls, which increases with decreasing friction coefficient throughout Stage 4, whilst the secondary lining axial force at the invert increases with increasing friction coefficient. The same trend is observed for the bending moment at the invert level, not at the side wall, while negligible bending moments develops at the crown.

4.3 *Influence of friction coefficients for k=0.5 models*

This section details the comparison between Model 3 (M3) and Models 6 (M6).

During Stage 3 phase (1.0s to 1.5s), same trends observed for k=1.5 models (see 4.2) are here observed for k=0.5 (e.g. same friction coefficient influence on the axial force and bending moment

1 Bending moment sign convention depends on the cut-section local axes: positive bending moments are associated to inwards deflection at the right-side wall and invert, while positive bending moments are associated to outwards deflection at the left-side wall and crown.

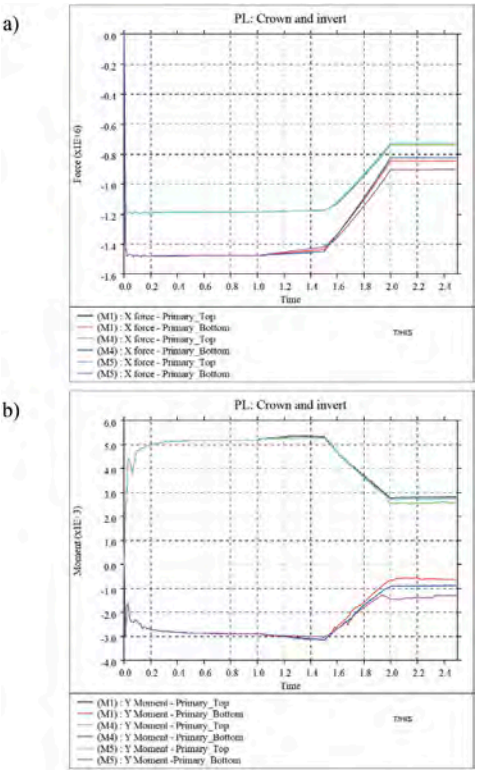

Figure 6. Comparison between M1 (μ=0.15), M4 (μ=0.3) and M5 (μ=0.0): primary lining crown (top) and invert (bottom) a) axial force [N] and b) bending moment [Nm].

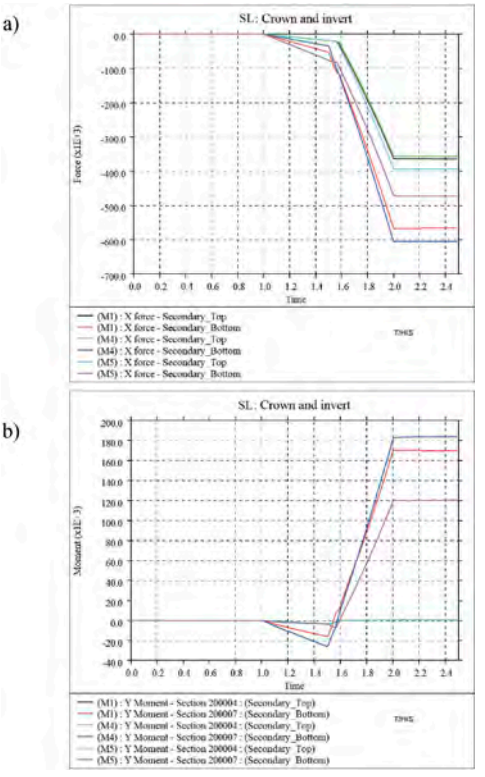

Figure 7. Comparison between M1 (μ=0.15), M4 (μ=0.3) and M5 (μ=0.0): secondary lining crown (top) and invert (bottom) a) axial force [N] and b) bending moment [Nm].

developing at the invert level). This is explained by observing that the lining deflections measured for k=1.5 and k=0.5 between 1.0s to 1.5s are essentially the same, see 4.1. Therefore, in the following, discussion is focused on the results from Stage 4.

In this stage, smaller internal forces variations are generated due to friction coefficient when compared with k=1.5 results. A possible interpretation is that smaller radial stresses are transferred to the secondary lining at the final stages (Stage 4 and Stage 5), see

Table 6, which in turn induce smaller friction stresses.

Regarding the influence of the friction coefficients at the side walls and invert, it shows a opposite trend of what observed for k=1.5 scenario.

Figure 10 and Figure 11 show the development of axial force and bending moment at the crown and invert of the primary and secondary lining. Figure 12 and Figure 13 show the development of axial force and bending moment at the side walls of the primary and secondary lining.

For k=0.5 models, with increasing friction coefficient results in an increase of the axial force at the secondary lining side walls, while at the invert level the larger axial secondary lining forces occur with the lower friction coefficient. The bending moment development follows the same trend both for the invert and the side walls, as it was measured with opposite outcomes for k=1.5, see 4.2.

A possible interpretation of this trend is that an outward primary lining deformation prior to the secondary lining installation, as occurs at the side walls for k=0.5 and invert for k=1.5, might facilitate and enhance the bonding between the primary lining and the secondary lining at Stage 4, during which a general inward deflection of both linings has been observed.

At the crown sector, same dependence on the friction coefficient is confirmed for the axial force development, as shown by k=1.5 results, with larger secondary lining axial force measured for smaller friction coefficient.

Further considerations of observed response behaviour are provided as follows.

5 DISCUSSIONS

Performed analyses show that, while the tunnel deformation is primarily influenced by the initial primary lining deformation, which is driven by the stress initialisation (k factor), a more significant

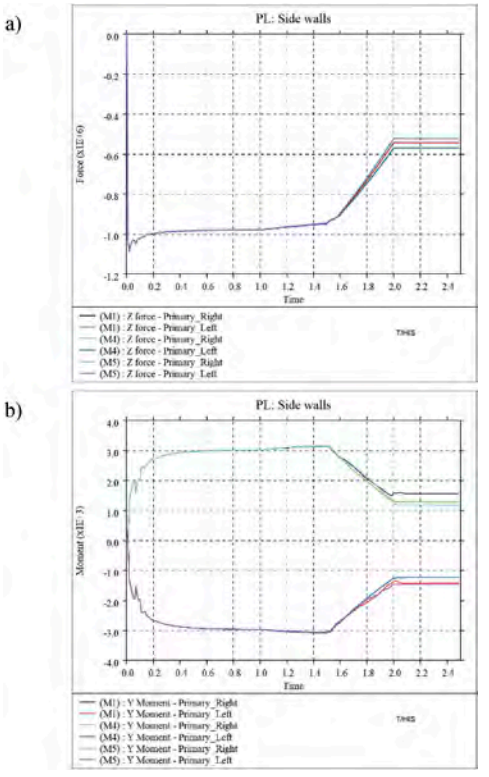

Figure 8. Comparison between M1 (μ=0.15), M4 (μ=0.3) and M5 (μ=0.0): primary lining side walls a) axial force [N] and b) bending moment [Nm].

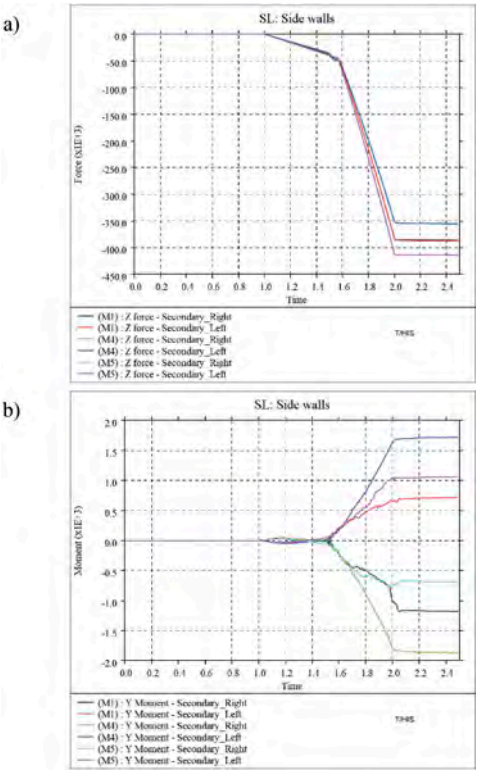

Figure 9. Comparison between M1 (μ=0.15), M4 (μ=0.3) and M5 (μ=0.0): secondary lining side walls a) axial force [N] and b) bending moment [Nm].

internal force development at the secondary lining only starts with the primary lining degradation.

The secondary lining deformation is influenced by the friction stresses developed at the interface with the lining. These friction stresses are a result of normal stresses experienced by the lining and the relative tangential deformations between the lining and the contact surface.

Further additional complexity to this mechanism is the different combinations of primary and secondary lining curvatures, achieved prior to and during the final stage (Stage 4), in the same sectors.

The following analogies are found via developed numerical investigations:

1. Tunnel sectors where the largest axial force is measured in the primary lining at the end of Stage 2 (at side walls for k=0.5 and at invert for k=1.5) are the same sectors where the axial force and bending moment are larger with higher friction coefficient in the secondary lining at the end of Stage 5.
2. For the same section of linings (side walls for k=0.5 and invert for k=1.5) the largest compressive strain is developed at the primary lining. This is observed during the degradation stage.
3. The initial deformation of the side walls for k=0.5 and invert for k=1.5 is an outward deformation, where passive pressure of the surrounded soil is engaged. Larger axial compressive stresses are developed at the primary lining near face, as induced by outward curvature.
4. During the primary lining degradation, the line-of-thrust of the primary lining axial force moves towards the primary lining centreline, reflecting a decrease of the axial force eccentricity, both across side walls for k=0.5 and across the invert for k=1.5. In terms of deflections, in both sectors (side walls for k=0.5 and invert for k=1.5), the primary lining curvature reduces, while deforming towards the secondary lining.

On the contrary, for both k=0.5 and k=1.5, the axial force at the crown decreases with increasing friction coefficient. This response shows that it is not directly correlated to the friction coefficient for two reasons: firstly, following a conservative approach, no friction coefficient is assigned to the sector where a gap is generated due to secondary lining gravity deformations; secondly this gap is closing while the lining degradation occurs. Consistent with the observed trend, negligible bending moments develop

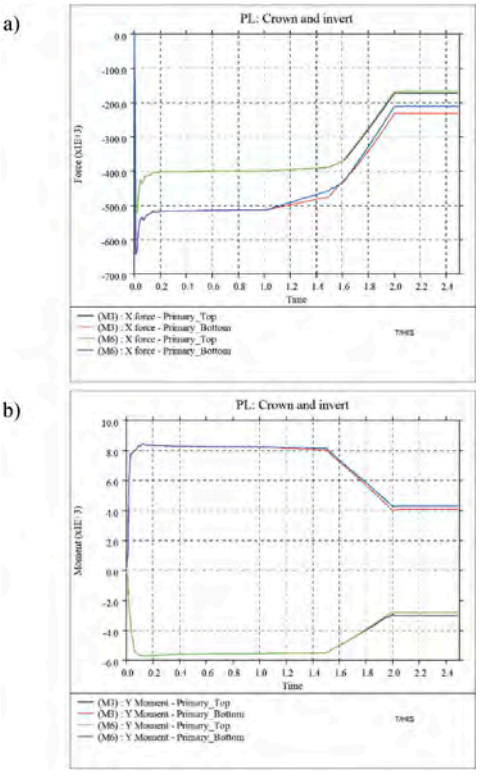

Figure 10. Comparison between M3 (μ=0.15) and M6 (μ=0.0): primary lining crown (top) and invert (bottom) a) axial force [N] and b) bending moment [Nm].

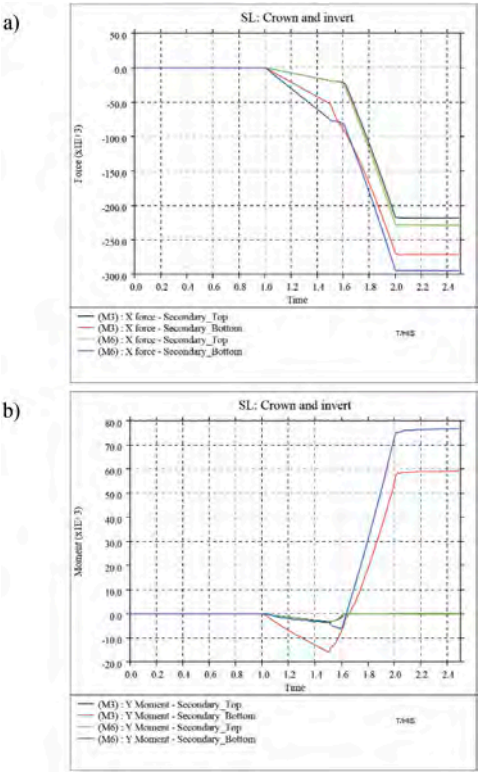

Figure 11. Comparison between M3 (μ=0.15) and M6 (μ=0.0): secondary lining crown (top) and invert (bottom) a) axial force [N] and b) bending moment [Nm].

across the secondary lining crown, which is indicative of an arch-type response.

Knee levels findings have been found to be an exception from what stated by analogies 2 & 4, for k=0.5 and for both k=1.5 and k=0.5, respectively. This can be explained by the lining geometry, with the secondary lining invert modelled with flat top-face. For this reason, the tunnel is highly restrained at the knee levels, therefore, the deformed shape is "locked-in". This contributes to a different response behaviour at the tunnel knee levels, where our numerical investigations have shown the largest soil stress transfer to the secondary lining.

6 CONCLUSIONS

The objective of this research is to investigate different factors affecting the secondary lining response, with primary focus on the influence of the friction resistance. The magnitude of this friction resistance is shown to be one of the key factors influencing behaviour and stress distribution.

The following can be concluded based on the following assumptions:

- Total stress is applied at the soil to primary lining interface throughout the construction sequence, with no seepage considerations.
- Secondary lining with flat invert.
- Plain strain and symmetrical soil stress loading is applied.

For tunnel secondary lining design, it is often understood that neglecting the friction coefficient would have result in the largest axial forces with minimal bending moment, and therefore a conservative approach. However, this may not be the case based on our results comparing k=1.5 and k=0.5.

At the invert, for a k=1.5 scenario, increased axial forces and bending moment are expected to develop with an increase of friction, which is opposite, despite smaller variation, to what has been observed for k=0.5 scenario. The design of tunnel lining requires the consideration of variable axial force and its associated bending moment capacity; therefore, it is not always conservative approach of neglecting the friction coefficient. At the sidewalls, the analyses outcome proves the common approach of neglecting the friction coefficient being conservative for condition of k =1.5. Whereas it may be conservative for k=0.5 scenario, given the beneficial trend of the axial force

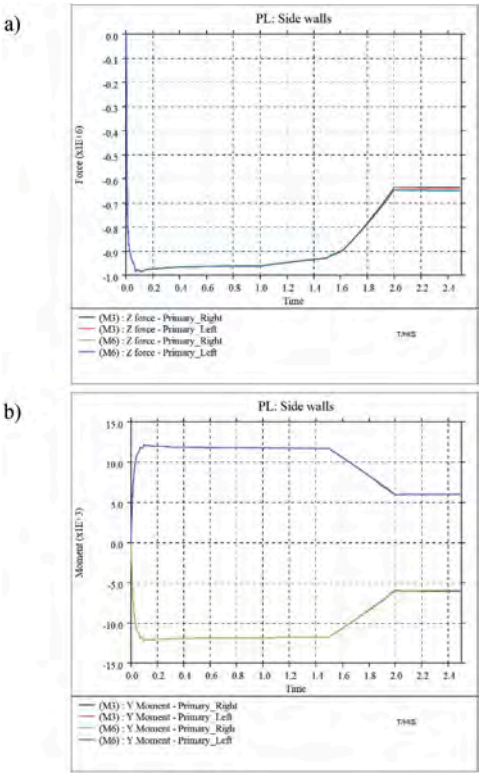

Figure 12. Comparison between M3 (μ=0.15) and M6 (μ=0.0): primary lining side walls a) axial force [N] and b) bending moment [Nm].

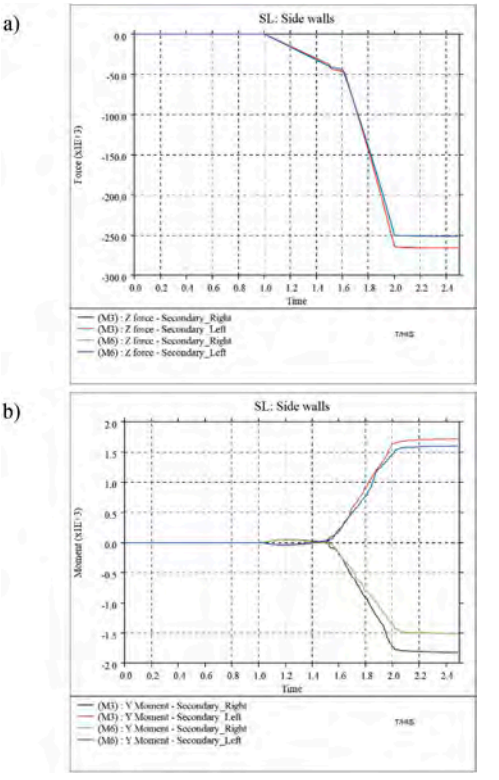

Figure 13. Comparison between M3 (μ=0.15) and M6 (μ=0.0): secondary lining side walls a) axial force [N] and b) bending moment [Nm].

and minimum variations of the associated bending moment.

At the crown, the analyses outcome proves the common approach of neglecting the friction coefficient being always conservative, provided zero friction is adopted.

In conclusion, numerical findings show a not univocal interpretation of the impact of the friction coefficient, with its influence closely correlated with the stress initialisation (k values). Therefore, the application of the friction coefficient between the primary and secondary lining may not always be conservative.

REFERENCES

LS-DYNA ® Keyword User's manual volume I. (2021). www.lstc.com

LS-DYNA ® Keyword User's manual volume II-Material models. (2021). www.lstc.com

LS-DYNA ® Keyword User's manual volume II- Multi-Physics Solvers. (2021). www.lstc.com

Formazin, J. C. Batereau. The shear strength behaviour of certain materials on the surface of geotextiles. International Society for Soil Mechanics and Geotechnical Engineering, 5/C/2. https://www.issmge.org/publications/online-library

Tunnelling for a Better Life – Yan, Celestino, Thewes & Eberhardt (Eds)
© 2024 The Author(s), ISBN 978-1-032-80042-4
Open Access: www.taylorfrancis.com, CC BY-NC-ND 4.0 license

Carbon reduction in conventional tunnelling by advanced design

Angelos Gakis
Dr. Sauer & Partners, Salzburg, Austria

Petr Salak*
Dr. Sauer & Partners, Tel Aviv, Israel

Franz Wilhelmstoetter
Dr. Sauer & Partners, Herndon, VA, USA

ABSTRACT: The escalating annual extraction of materials from the Earth's crust, highlights the urgency for more sustainable construction practices. The construction industry is responsible for approximately 50-60% of global material consumption and 37% of CO_2 emissions. Embracing eco-friendly, low-carbon materials aligns with UN Sustainable Development Goals.

Tunnelling projects contribute to sustainable, long service-life infrastructure with minimal disruption. Projects like high-speed rails and metro/LRT lines provide low-emission transportation whereas hydro-power projects, provide more sustainable energy sources. However, the construction of such projects is still associated with substantial emissions.

The assessment of the environmental impact should start at the early stages of the design, and when selecting the optimal construction method, as this can potentially lead to significant reduction of carbon emissions. A collaboration among stakeholders is also fundamental. Overcoming challenges involves incentivizing eco-friendly practices from project inception. However, developing carbon-efficient designs often encounters obstacles in codes and standards.

As regards the materials, instead of setting unrealistic targets to eliminate steel and concrete, which are integral to underground construction, the use low emission materials and relying on local resources, recycling and reusing material from excavation should be promoted.

The most direct way to lower the carbon emissions is to reduce the actual required material quantities. The focus of this article is on how the use of advanced design tools and concepts can support this target. Case studies, such as the Eglinton Crosstown LRT in Toronto and Bank Station Capacity Upgrade in London, showcase the environmental benefits of such advanced design approaches.

Keywords: Tunnelling, Conventional Tunnelling, Finite Elements, Carbon Reduction

1 INTRODUCTION

The annual extraction of materials from the Earth's crust is on a continuous rise, with current projections reaching 186 billion tons by the year 2030—a staggering twofold increase from the 2015 levels (Sobek, 2022). A significant contributor to this surge is the construction industry, accounting for approximately 50-60% of global material consumption and contributing to 37% of total CO_2 emissions (Spyridis & Bergmeister, 2023). At the same time, the rapid pace of urbanization adds buildings equivalent in size to the city of Paris every five days, heightening the sector's environmental impact.

Encouraging sustainable construction practices, prioritizing low-carbon concrete and eco-friendly materials aligns with broader sustainability goals outlined in the United Nations Sustainable Development Goals (https://sdgs.un.org/goals), particularly Goal 9 (Industry, Innovation, and Infrastructure) and Goal 13 (Climate Action). The UNEP's report, developed in collaboration with the Yale Center for Ecosystems + Architecture within the Global Alliance for Buildings and Construction, emphasizes the need for innovative cooperation models to decarbonize building materials

*Corresponding author: petr.salak@dr-sauer.com

DOI: 10.1201/9781003495505-140

(United Nations 2023). Three over-arching strategies are identified: i) avoiding unnecessary extraction and production, ii) transitioning to regenerative materials, and iii) enhancing the decarbonization of conventional materials. Implementing these strategies collectively holds the key to a more sustainable built environment, aligning with global climate objectives.

Tunnelling projects are providing infrastructure with long service life and minimum disruption to the environment. Projects like high-speed rails and metro/LRT lines not only aim to improve the quality of life but also mitigate environmental impacts by offering alternative, low-emission means of transportation. Similarly, hydro-power projects, where tunnelling plays a significant role, contribute to the generation of more sustainable forms of energy. However, tunnel construction is not innocent when it comes to associated emissions.

The environmental impact assessment and planning of tunnelling projects can commence as early as the feasibility and concept design stages, where strategic and influential decisions are made, such as the selection of the construction methods, followed by the detailed design phase, where support elements can be optimized through advanced and innovative design concepts. Engineers possess the necessary tools to significantly minimize the usage of concrete and steel.

2 OPTIMAL CONSTRUCTION METHOD SELECTION

Some of the largest infrastructure projects in urban environment involve metro or light rail transit systems, where tunnelling is used to create long, linear running tunnels and, in many instances underground stations. A recent example is the Crossrail project in London, featuring 21 km of twin running tunnels and the construction of 5 out of the 7 new underground stations using conventional tunnelling means. Underground construction can utilise various construction methods, in many cases predetermined in the project contracts.

While country-specific preferences exist, long running tunnel sections in uniform geological conditions are typically well-suited for tunnel boring machines (TBMs), which demonstrate impressive advance rates. On the other hand, tunnels in highly variable geology, significant overburden, numerous intersections, and changing geometries are better suited for excavation via conventional means. Running tunnels excavated via TBM nowadays feature a single-pass-lining compared to conventionally excavated tunnels that often involve a two-pass-lining, comprising an initial (temporary) shotcrete liner followed by cast-in-place final (permanent) liner. Combined/composite linings design approaches, where the initial tunnel lining also provides some permanent load-bearing function, are becoming more common in conventional tunnelling, reducing the overall lining thickness and material quantities.

For the construction of underground stations in urban rail projects, the most common excavation techniques are cut-and-cover and conventional tunnelling. Although inherently different, both methods can create large underground spaces necessary for accommodating trains, platforms, vertical circulation, systems, and ventilation. From a structural point of view, a rectangular cut-and-cover box carries loads in bending and shear compared to a round or ovoid tunnel shape which carries loads predominately in compression. This simple fact makes a big difference from a carbon footprint point of view as bending moments and shear forces often require thick wall and slab thicknesses with heavy reinforcement.

The Eglinton Crosstown LRT project in Toronto, Canada (Figure 1) provided an opportunity to compare fully designed cut-and-cover with mined stations. Steel and concrete quantities were assessed for excavation support, and the permanent liner for a typical station with platform and crossover sections. In this comparison, a cut-and-cover station required approximately eight times as much steel and one and a half times as much concrete for excavation and support, while for the permanent liner, it required about 19 times as much steel and one and a half times as much concrete compared to a mined station.

Achieving meaningful carbon reduction in any tunnelling project demands a comprehensive approach to lowering CO_2 emissions, the primary contributor to man-made global warming. In the instances of different construction methods mentioned above, the decision for the optimal method is typically driven by cost and schedule criteria, which may not always align with the method having the least environmental impact. Therefore, an optimal solution should consider environmental impact alongside cost and schedule considerations.

Figure 1. Underground station Cavern (Eglinton LRT project, Toronto).

3 A COLLABORATIVE APPROACH

Reducing construction emissions calls for an early involvement and collaboration of all relevant parties: the public, owners, designers, suppliers, and contractors. The current paradigm, where project owners award projects mainly on lowest price criteria, sets a basis where the designers produce fast and inefficient designs using simple analytical methods to align with cost considerations. The contractors naturally seek the fastest and lowest cost solution, which potentially contributes the highest environmental impact.

The current paradigm, where project owners award projects mainly on lowest price criteria, makes it likely more challenging to consider environmentally friendly solutions.

While the contractor undoubtedly plays a key role in reducing the carbon footprint of a tunnelling project, the owner and their designer must lay the groundwork from the onset of the project. The opportunities to reduce the carbon footprint of a tunnelling project during the design phase can be substantial and come at a comparatively small cost.

In essence, the necessity to reduce CO_2 emissions must become a fundamental project requirement incentivizing environmentally friendly practices. To design structures which are pushing the limits in efficiency, carbon reduction and constructability, the designer needs time to deploy advanced and innovative design techniques. The efforts and complexities on the design side will increase compared to the common practice to achieve these goals.

One reoccurring obstacle to the development of carbon efficient tunnel designs lies in prescribed codes and standards. The absence of dedicated structural design codes for tunnelling, particularly in conventional tunnelling, often compels owners and designers to resort to general structural building codes. These codes typically require minimum reinforcement quantities based on gross concrete area, leading to excessive quantities of rebar in cases such as tunnel or cavern inverts, where structurally such quantities may not be required. Choosing applicable project codes and standards wisely can have a significant impact on reducing the carbon footprint.

4 MATERIALS

Arguably, the two most important materials in underground construction are steel and concrete, each possessing unique characteristics such as durability, strength, ductility, that make them highly desirable for construction.

However, both materials come with a considerable environmental cost, demanding significant energy input and consequently contributing to a substantial carbon footprint. On average, one ton of steel emits approximately 1.85 tons of CO_2, while one cubic meter of concrete emits about 0.35 tons of CO_2. To put these values in perspective, the steel industry alone contributes 8% of global CO_2 emissions and 23% of global energy consumption. In 2019, global cement production reached 4.1 billion tons, contributing to 6% of global CO_2 emissions and 7% of global energy consumption.

Despite ongoing efforts to reduce CO_2 emissions in the production of both materials, these remain significant and require substantial amounts of energy (approximately 55% of cement CO_2 emissions are process related).

In regular concrete, it is possible to reduce concrete emissions by adding fly ash, silica fume, slag, limestone, pozzolana, however, this is not as easy with sprayed concrete due to the fast strength gain requirements that makes the reduction or substitution of cement more complicated.

Fiber reinforced concrete or shotcrete is also common in tunnelling. Although fibres can provide significant time and safety benefits, their incorporation does not necessarily translate into reduced material quantities when compared to traditional rebar reinforcement. To illustrate, if a 5m inner diameter tunnel with 20cm lining is to be reinforced with either minimum rebar reinforcement 0.2% of the gross concrete area or with a nominal 30kgr/m^3 of steel fibres, rebar reinforcement results in 50kgr of steel per tunnel meter while steel fibres in 100kgr.

The carbon reduction in tunnelling requires therefore a more elaborate approach aided by advanced design, that focuses on reducing the overall size of excavation and support requirements (lining thickness, tunnel size, reinforcement quantities) or even using unreinforced linings where applicable. Furthermore, the use of low-emission materials, relying on local sources, recycling, and reusing of excavation materials are key elements in delivering environmentally friendly projects.

5 ADVANCED DESIGN

Design plays a crucial role in reducing steel and concrete quantities. Each ton of material saved through advanced design not only translates to a reduction in CO_2 emissions during production, transportation to the project site, and installation, and considering the full life cycle even during demolition and recycling. Nonetheless, as outlined in the previous sections, an appropriate project framework is required to incentivise, enable, or even force the designers to focus their efforts on material savings.

Few important aspects related to tunnelling are described in the following sections.

5.1 *Advanced material models/design methods*

Numerical analysis methods provide the most advanced means of simulation of engineering problems. In tunnelling, it is imperative to consider the

behaviour of both soil/rock medium, and of the tunnel support elements as well as the interaction between them. The selection of the appropriate constitutive model for geomaterials and concrete/steel is not straight forward. In many cases, advanced soil models are used in combination with linear elastic concrete models yielding unrealistic results. Another important aspect is the level of detail included in the numerical analysis, related to both the geometrical aspects as well as the staged construction. The effects of each of these parameters need to be optimized with regards to the objective of the analysis and the computational effort. Additionally, a model is only good if it can be interpreted. Therefore, the engineer is encouraged to rely on tools he is experienced with and can derive useful results from. As an example of advanced simulation, Figure 2 shows the calibration of the concrete damaged plasticity (CDP) model used in Abaqus against the ASTM C1550 flexural strength test. CDP is an advanced model for concrete, yet simple to define and interpret, which assumes tensile cracking and compressive crushing mechanisms, with the uniaxial compressive and tensile responses characterised by damaged plasticity (Lubliner et al 1989). Calibrating a concrete model such as CDP against experimental results provides greater confidence in the outcomes of the finite element (FE) analysis and supports optimised designs.

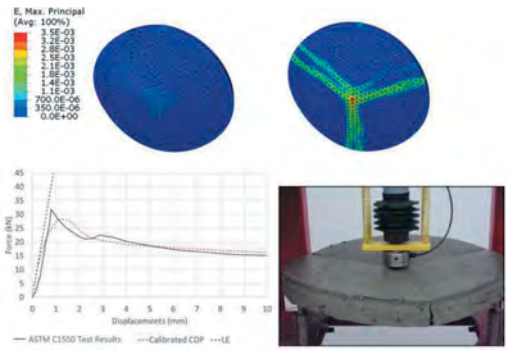

Figure 2. Top – Maximum principal strains at the bottom of a test panel at 2mm deflection (left – linear elastic and right CDP). Bottom – calibration of experimental results from round panels using the linear elastic (LE) and the CDP models.

5.2 *Shape optimisation*

The cross-section of a tunnel is one of the most influential factors affecting the performance under given loading conditions. Although the minimum size and the main geometrical aspects are typically related to the required spaceproofing envelope, this can be further optimized to provide the best fit to the exerted stresses. Gakis et al. (2019) assessed the performance of 7 separate cross-sections (Figure 3) with the same cross-sectional area of 50m^2 and variable height over width aspect ratio, in a probabilistic scenario varying the main soil properties (elastic modulus, shear strength and K_0) as well as the elastic modulus of the lining. The study concluded that the optimization of the tunnel shape can provide notable savings in terms of lining design and increase the overall structural safety.

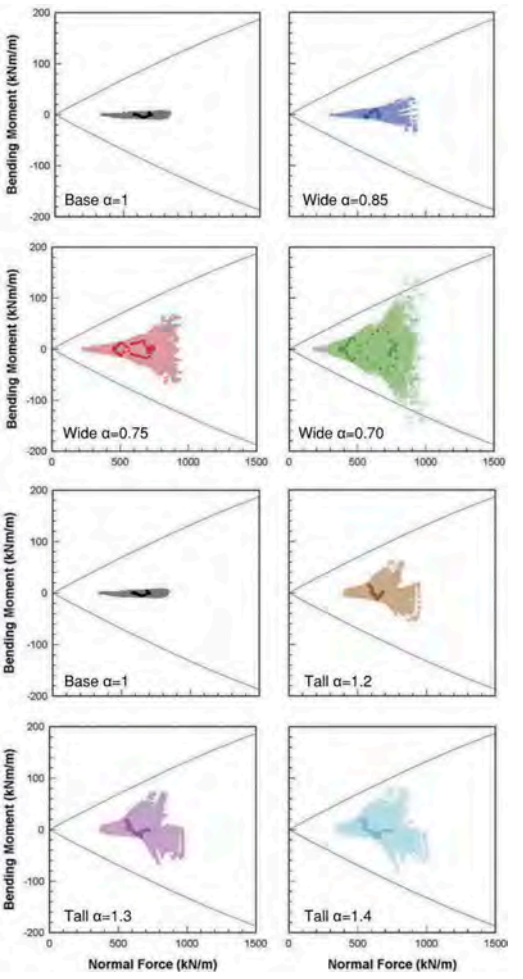

Figure 3. Interaction diagrams for the analysed sections with variable aspect ratio (α) of height over width (Gakis et al. 2019).

5.3 *Openings*

Multiple openings in tunnel linings are common in mined stations for the formation of tunnel intersections. These openings result in redistribution of the lining stresses that can potentially be carried by the existing tunnel support or may require additional measures such as the implementation of additional reinforcement or thicker concrete linings. To identify with confidence the capacity of the lining following an opening, it is important to use non-linear concrete models in 3D finite element analysis. Figure 4

illustrates the importance of using advanced models also for the tunnel lining (Gakis & Salak 2016). The use of the CDP model with careful examination of the post-peak behaviour, allowed the design of this complex intersection relying purely on steel fibre reinforced shotcrete, without any additional thickening or reinforcement.

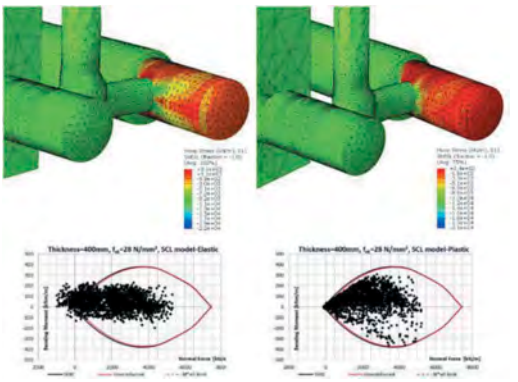

Figure 4. Hoop lining stresses and interaction diagrams of a linear elastic concrete model (left) compared to a concrete damaged plasticity model (right) (Gakis & Salak 2016).

5.4 *Combined/composite linings*

In various past projects, shotcrete linings have been assumed to be of insufficient quality to serve an extended service life due to the application of shotcrete with alkaline accelerators that reduce the long-term strength or due to inconsistent quality and poor compaction. This double shell approach, where initial and final linings are assumed to act independently, inevitably results in thicker overall linings and as such higher material quantities.

The load sharing in tunnel linings is however a reality, one that the designer must exploit in order to produce more economical and environmentally friendly designs. This is further supported by the advancements in shotcrete technology such as automated and mechanized spraying, improved mix designs, alkali-free accelerators, stringent quality control processes and improved profile control result in a product similar to a well compacted poured concrete.

The type of load sharing depends on several factors, with a deciding one being the interface between the two lining layers. If a sheet waterproofing membrane is used, it is assumed that shear stresses are not transferred between the linings (Combined Linings). With spray on membranes, an increased adhesion can be expected and therefore a part of the shear stresses is assumed to be transferred, with the overall support acting as a Composite Lining.

A basic requirement for the design of combined or composite linings is the use of advanced numerical modelling with special focus on the simulation of the interface between the two support layers.

6 CASE STUDIES

6.1 *Eglinton crosstown LRT, Toronto*

Three mined stations of Eglinton Crosstown LRT, two of which included also long crossovers with a total length of 1km, were excavated in glacial deposits encountering highly permeable soft ground units with high water tables. The project requirements specified a double shell approach for the mined elements with the initial linings serving only as temporary supports.

The 18.7m wide by 15m high Platform Caverns were constructed from the previously excavated Cross-Cut tunnels (15.6m wide by 18.2m high) as shown in Figure 5 for one of the mined stations (Avenue).

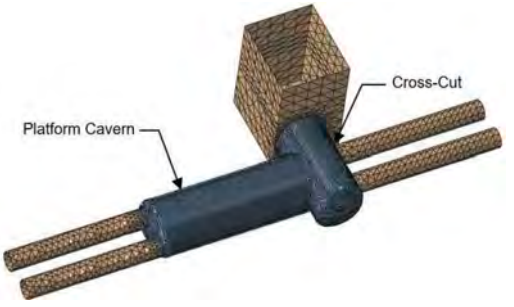

Figure 5. 3D FE model east part of Avenue station.

In order to design these rather complex intersections which introduced sizeable openings into the Cross-Cut tunnels (Figure 6), 3D soil-structure interaction FE analyses using Abaqus were executed. The analyses included the actual excavation and support steps and utilised an advanced Hardening Mohr-Coulomb material for the soil and the CDP model for the linings. The CDP model, which was calibrated against experimental data from the project, allowed capturing the stress redistribution during the formation of the openings in the initial linings and resulted in no additional reinforcement or thickening requirements. The same approach was used in the design of the final linings optimising the reinforcement requirements.

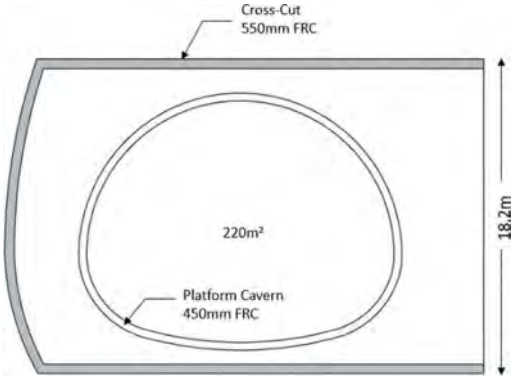

Figure 6. Section along the Cross-Cut tunnels indicating the openings for the Platform Caverns.

As a result, the overall steel savings through the optimised design, compared to a standard design with linear elastic models considered for the linings (SEM standard in Figure 7), were approximately 1,960 tons of steel or 3,670 tons of CO_2.

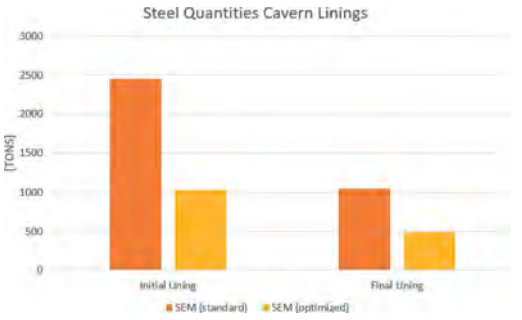

Figure 7. Comparison of steel quantities in the mined Caverns of the Eglinton Crosstown LRT between the optimised and a standard design.

Furthermore, after gaining experience from the excavation of the main station Caverns and with the agreement of the project owner, a combined lining approach was implemented in areas where no bar reinforcement was required, i.e., where the Cavern linings were not subjected to high bending forces due to connections of internal structures or nearby intersections of different underground structures.

The final linings following the combined lining approach were executed with fibre-reinforced poured concrete throughout the tunnel section.

The waterproofing system consisted of compartmentalized PVC membrane with grids of water barriers (sectioning system) and arrays of grout pipes to allow grouting of the gap between primary and secondary lining which will establish the watertightness of tunnel lining and ensure transmission of contact forces between both linings.

To account for some degradation of shotcrete in direct contact with soil, the initial lining was divided into two shells: a 100 mm thick sacrificial layer and a 350 mm thick, durable initial shotcrete lining (Figure 8). The 350 mm thick final lining for long-term performance was also sub-divided into two shells: a 300 mm thick long-term poured concrete lining and a 50 mm thick layer to account for the fire damage on the intrados of combined lining (following a heat-transfer analysis).

The numerical simulation was executed with Abaqus using 1m long 3D models to enable advanced simulation of the contact between the various elements (Figure 9). The waterproofing membrane was modelled with a frictionless tensile contact to prevent shear stress and a hard normal contact allowing transfer of normal forces and separation between the linings. The initial and final linings were simulated with shell elements and the poured invert was modelled with continuum elements tied to the final lining. The steps of the analysis were the following:

1. Geostatic step establishing in-situ stresses.
2. Excavation and installation of the initial lining taking full-short term loads.
3. Installation of the final lining on the deformed mesh of the initial lining and activation of the pore water pressures acting on the extrados of the final lining.
4. De-activation of the 100mm sacrificial layer of the initial lining.
5. Application of zero tensile strength at the location of the initial lining construction joints (sidewalls and temporary invert connections to outer lining), to investigate the effect of rebar corrosion.
6. Reduction of strength/stiffness of the initial lining to simulate long-term creep effects.
7. De-activation of the 50mm fire damage layer of the final lining.
8. Reduction of strength/stiffness of the final lining to simulate long-term creep effects.

Additionally, the final lining was checked against the contact grouting pressures and against self-weight at 1-day strength.

Indicative results for the final lining at stage 8 are shown in Figure 10.

As a result of the combined lining approach, the thickness of the final linings was reduced from the nominal 500mm (double-shell approach) to 350mm.

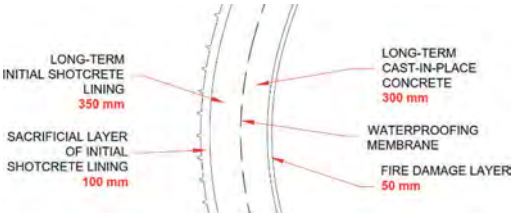

Figure 8. Thickness of linings used in FEA.

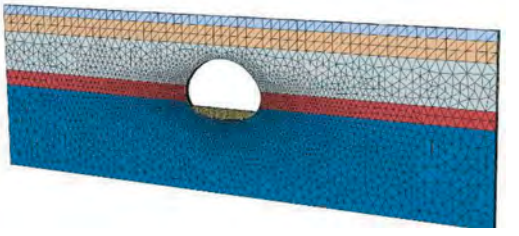

Figure 9. Combined lining FE Mesh.

6.2 *Bank station capacity upgrade, London*

The Bank station upgrade project involved among others the excavation of multiple new sprayed concrete tunnels in the stiff London clay deposits, aimed to increase the capacity of this busy transportation

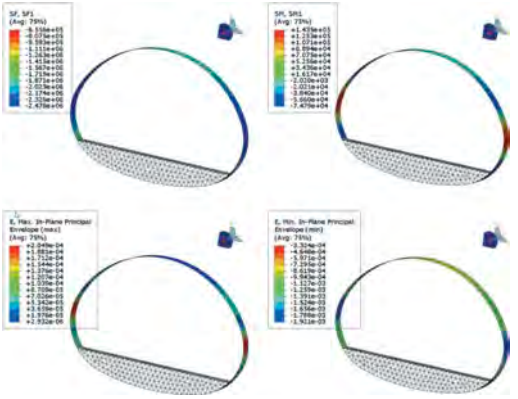

Figure 10. FEA results - final lining at creep step. SF – axial hoop force (N), SM – bending moment in hoop direction (Nm), E-max – maximum strain and E-min – minimum strain.

hub. An overview of the FE models deployed for the design of the new tunnels is shown in Figure 11.

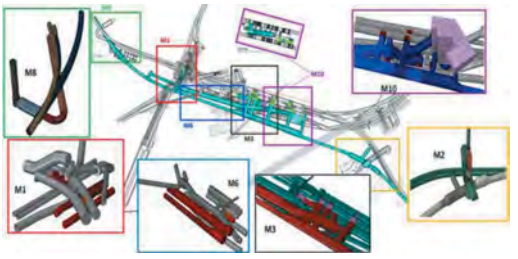

Figure 11. Overview of models for the new sprayed concrete tunnels at Bank station upgrade (Nasekhian & Spyridis 2017).

The tunnel lining system was double shell with both primary and secondary linings considered part of the permanent structure. The minimum thickness of the secondary lining was set to 150mm to allow all fixings to be installed preventing penetration of the membrane.

Between the two linings, a double bonded spray-on waterproofing layer was applied. The detailed composition is shown in Figure 12.

The designed distinguished between the short-term (5 years) and the long-term (120 years) periods. The load sharing between the two linings was defined by numerical analyses. The CDP material model was used for both linings to account for the non-behaviour, assuming conservatively a linear-elastic behaviour under compression and realistic behaviour under tension accounting for the residual flexural capacity of the fibre reinforced shotcrete.

During the short-term steps, the excavation and installation of the primary lining was simulated under undrained conditions. In the long-term steps, the secondary lining was installed, and the water pressures were applied assuming effective stress parameters.

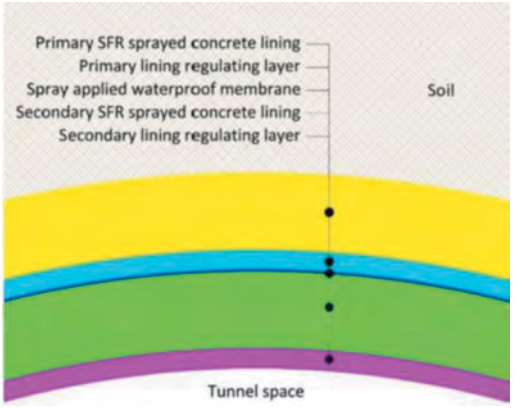

Figure 12. Sprayed concrete lining composition at Bank station upgrade project (Nasekhian & Feiersinger 2019).

The results of the combined lining approach at Bank, led to an optimisation of the lining thickness and to significant savings in excavation volumes and shotcrete quantities (up to 50% reduction of the thickness of the secondary lining) as well as in overall construction time.

7 CONCLUSIONS

Tunnelling projects, despite providing infrastructure with long service life and supporting low emission transportation and sustainable energy projects, still contribute significantly to the CO_2 emissions of the construction industry. Immediate action is required to lower the impact to the environment and provide more sustainable infrastructure. This means that the tunnelling industry needs to rethink the way its operating by incorporating the environmental impact on several aspects of tunnelling projects.

The selection of the optimal construction method, for example between TBM or conventional tunnelling for longer tunnels or cut and cover versus conventional tunnelling for deep stations, needs to consider among others the environmental impact.

A collaborative approach involving all stakeholders is deemed essential for reducing construction emissions. Contrary to the current common practice of awarding projects based on the lowest price, there is an imminent need for establishing carbon reduction as a fundamental project requirement during the early design phases. Similarly, the project codes and standards need to be chosen carefully as they may have significant impact on reducing the carbon footprint of a tunnelling project.

Steel and concrete, the main materials used in tunnelling, carry a significant 'environmental cost'. Using low emission materials and focusing on local resources, recycling, and reusing the excavation material play an important role. Focusing on reducing the actual material quantities by minimising excavation and support element size through

advanced design is imperative. This is aided by the implementation of advanced material models in numerical analyses, also for the support elements. For the optimisation of the tunnel shape, probabilistic analyses can be used to derive the minimum excavation volume thus providing significant material savings. Considering the permanent action of the initial tunnel lining in combined/composite lining concepts is also pivotal in reducing the overall lining thickness.

Case studies from the Eglinton Crosstown LRT project and the Bank Station Capacity Upgrade underscore the tangible benefits of advanced design, including substantial material savings and overall construction time.

In conclusion, the article presents a compelling case for reshaping tunnelling practices to align with sustainability goals. Through innovative construction methods, collaborative, and the integration of advanced design principles, the tunnelling industry can contribute to global efforts aimed at achieving a more sustainable built environment.

REFERENCES

Gakis, A., Kalogeraki, C. and Spyridis, P., 2019. Risk-based tunnel design utilizing probabilistic two-dimensional finite element analyses. In Tunnels and Underground Cities. Engineering and Innovation Meet Archaeology, Architecture and Art (pp. 2129–2138). CRC Press.

Gakis, A. & Salak, P. (2016). Efficient design of openings in SCL tunnels. Tunnels and Tunnelling International, October 2016, pp. 41–46.

Laubbichler, J., Schwind, T., Gakis, A., Sanz, A. and Soto, F., 2021. Advanced design of large cavern intersections in soft ground without conventional bar reinforcement. Geomechanics and Tunnelling, 14(4), pp.367–376.

Lubliner, J., Oliver, J., Oller, S., and O˜nate, E., 1989. A plastic-damage model for concrete. Int. J. Solid. Struct., 25(3), 299–326.

Nasekhian, A. and Feiersinger, A., 2019. SCL optimisation at Bank–A combined lining approach. London: Tunnels and Tunnelling (April 2019), pp.27–32.

Nasekhian, A. and Spyridis, P., 2017. Finite Element modelling for the London Underground Bank Station Capacity Upgrade SCL design and deep tube tunnels assessment. In EURO: TUN 2017: Proceedings of the IV International Conference on Computational Methods in Tunneling and Subsurface Engineering (pp. 637–644). Studia Universitätsverlag, Innsbruck, Austria.

Spyridis, P. and Bergmeister, K., 2023. Optimizing the climate impact of tunnel structures by advanced numerical simulations. In Expanding Underground-Knowledge and Passion to Make a Positive Impact on the World (pp. 967–975). CRC Press.

Sobek, W. (2022). Non nobis - about building in the future (volume 1) Stuttgart: avedition.

United Nations Environment Programme, & Yale Center for Ecosystems + Architecture (2023). Building Materials and the Climate: Constructing a New Future. https://wedocs.unep.org/20.500.11822/43293

Tunnelling for a Better Life – Yan, Celestino, Thewes & Eberhardt (Eds)
© 2024 The Author(s), ISBN 978-1-032-80042-4
Open Access: www.taylorfrancis.com, CC BY-NC-ND 4.0 license

Advanced joint non-linear design analysis and verification of the arched cut and cover tunnels at High Speed 2 project (UK)

Nayef Al Haddid*, Sotiris Psomas & Mengxiao Li
COWI UK Ltd, London, UK

ABSTRACT: Conventional rectangular cut-and-cover tunnel linings, although tried and tested, present an inefficient solution to load dissipation. This design often leads to either limitations in height of backfill or over-sized tunnel sections wasting time, materials and contributing unnecessary carbon to the environment. In the High Speed 2 project arched cut-and-cover tunnels have been adopted and bring about several benefits by addressing a few of the problems rectangular linings encounter. At the same time, they introduce a controlled-mechanism (frictional knuckle-joint) in the arch that enables the designer to create a break in the tensile stress load path, reducing moments via limiting the length of development, while simultaneously maintaining stabilizing axial forces. In this Paper the non-linear finite-element analysis of frictional knuckle-joints in a twin-arch concrete lining, illustrates the behaviour of these joints and highlight important modelling considerations; with focus on contact modelling, joint articulation, local stresses and bursting at the joints. This Paper aims to share the findings of the advanced non-linear finite element analysis of knuckle-joints and their verification as well as to demonstrate the benefits of utilizing such type of construction in cut-and-cover tunnels for Rail infrastructure.

Keywords: Tunnelling, TBM, Performance prediction, Simulation, Friction joint, Contact, Sensitivity analysis

1 INTRODUCTION

The High Speed 2 (HS2) is Britain's new high speed rail line running between London and Birmingham. Forming parts of the route will be six green tunnels, three of which are cut-and-cover tunnels, and two of those are twin horseshoe tunnels; each horseshoe is formed from a precast concrete side wall and roof segments, and a common precast concrete central wall segment.

The precast segments are fabricated off-site in 2.49 m wide modules. These are later delivered to site for installation. The wall segments are landed and levelled first, followed by the roof segments. The roof and wall segments make contact via 'dry' concrete-to-concrete knuckle joints. An in-situ RC invert base slab is then cast which ties the bottom of the precast walls together. The in-situ slab is monolithic with the precast components, achieved via reinforcement continuity through a loop-to-loop rebar connection. The completed structure is then back-filled in a balanced, controlled manner. The final tunnel height and breadth are approximately 9.5m and 20.0 m respectively. All concrete is strength class C50/60 with steel grade 500B reinforcement.

This paper will mainly focus on the analysis of the tunnel lining, using the LUSAS finite element analysis software, with explicit modelling of the knuckle-joints utilising contact elements, to accurately capture the joint behaviour, and its effect on the global structural behaviour of the lining.

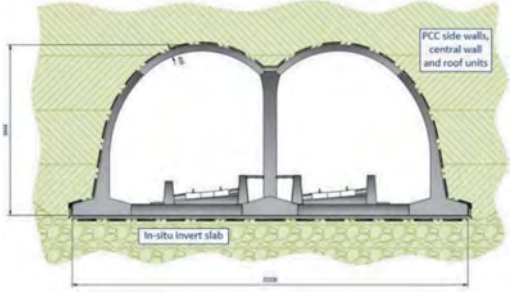

Figure 1. Diagram showing lining structure.

*Corresponding author: n.alhaddid@gmail.com

DOI: 10.1201/9781003495505-141

2 THE JOINT

The knuckle-joint utilised in the precast segments is made of up of two parts, the convex part of on the roof unit and the concave part on the wall units.

Figure 2. Geometry of the convex and concave parts of the joint.

As Figure 2 shows, the central section of both parts of the joint are formed by circular arches of different radii, that taper off towards the lining extrados. The intrados is capped with a relief zone that allows a 15mm gap, at perfect installation.

Joints in tunnel linings have been extensively researched and various paradigms developed to address their effects. Those paradigms have ranged from closed-formsolutions, such as *Muir-Wood (1975)*, to joint idealization approaches such as *Duddeck and Erdmann (1985)* to more advanced uses of rotational springs in beam and shell models to account for joint non-linearity, such as *Leonhardt and Reimann (1965)*, *Janssen (1983)*, *Blom (2002)* and most recently *Tvede-Jensen et al. (2017)*.

However, the primary assumption of a flat contact face between the considered segments limits the use of those models in applications where curved contact faces are utilised. Other sources for predicting contact areas and stresses, such as those presented in Roark's Formulas for Stress and Strain, are based on linear-elastic materials in geometrically linear scenarios. As such explicit modelling of the knuckle-joint was necessary to fully understand the structural behaviour of the joint itself and cascading effects on the rest of the lining.

3 SCOPE

This paper aims to demonstrate the merits and concerns of a an arch with two pin joints. The paper will also investigate the effects of the following attributes on the curved joint behaviour, in hopes of providing insights to future designer and modellers:

- Mesh size
- Contact stiffness
- Friction coefficient
- Modelling reinforcement

The metrics used to quantify the effects of the above factors on local joint behaviour and global lining behaviour will include, local metrics:

- Peak contact axial stress: the peak axial stress within the contact width, in MPa.
- Peak contact shear stress: the peak shear stress within the contact width, in MPa.
- Contact width: the width of contact established, in mm.
- Contact penetration: the amount of inter-penetration between the contact elements, in mm.
- Bursting force in the lining: the bursting force generated within the roof and wall units, in kN.
- Joint rotation: the total joint rotation, i.e. the difference between the wall joint rotation and the roof joint rotation, in degrees.

and global metrics:

- Axial force: axial force at various points of interest, in kN.
- Bending moment: bending moment at various points of interest, in kN.
- Shear force: shear force at various points of interest, in kN.

Metrics will only be discussed where there are notable observations. The points of interest for the global effects are shown on Figure 3.

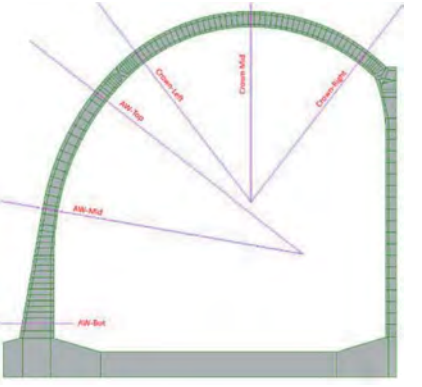

Figure 3. Points of interest for the calculation of the global effects; AW: Arch wall.

4 THE MODEL

4.1 *Geometry*

The analysis consist of half-space 2D plane-strain finite element model, with symmetry supports along the line of symmetry, to limit the size of the model, as shown in Figure 4.

The actual reinforcement arrangement in the crown and wall units was accurately modelled, with limited rationalization to control element shapes. The plane-strain elements were assigned a breadth of 1000mm (into the page).

The roof unit thickness is 400mm, with arch wall unit beginning at 400mm until mid-height where it begins to increase reaching a thickness of 894mm at the base. The footings of the arch wall and central wall start at a thickness of 1000mm and reduce to the thickness of the invert slab, which is 650mm. The thickness

Figure 4. LUSAS 2D plane-strain model showing modelled reinforcement and line of symmetry.

of the central wall is 550mm and flares to form a concave joint on each side.

4.2 *Elements*

Plane-stress continuum plate elements were used for the model, those elements are 4-noded quads with two degrees of freedom at each node. While these nodes cannot capture curvature (would require quadratic elements at the expense of model run times), at fine mesh conditions and appropriate use, they are capable of approximating curves. The model was meshed to ensure fine mesh density and aspect ratios near 1 in the vicinity of the joints, with elements size ranging between 15mm – 25mm. To optimize run times the mesh size increase gradually moving away from the joints and less scrutiny is applied regarding aspect ratios.

4.3 *Materials*

Linear-elastic concrete properties, shown in Table 1, were applied to the majority of the model except for the joints, where a smeared multi-crack non-linear concrete material model was used to avoid development on unrealistic stresses, properties shown in Table 2. The steel reinforcement was assigned linear-elastic steel properties, summarised in.

Table 1. Linear-elastic concrete material.

Elastic Modulus	37 GPa
Poisson's ratio	0.20
Unit density	2.50 tonnes/m³

Table 2. Smeared multi-crack non-linear concrete material.

Initial elastic Modulus	37 GPa
Poisson's ratio	0.20
Unit density	2.50 tonnes/m³
Uniaxial Characteristic Compressive Strength	50 MPa
Uniaxial Characteristic Tensile Strength	3 MPa
Strain at peak compressive strength	0.0022
Fracture energy per unit area	0.1516

Table 3. Linear-elastic steel material.

Elastic Modulus	210 GPa
Poisson's ratio	0.20
Unit density	7.849 tonnes/m³

4.4 *The contact elements*

The contact elements are modelled using 'slidelines' in LUSAS, these elements allow for the modelling of smooth contact, frictional contact, fully tied (rigid connection) and sliding only contact. The contact element formulation is simplistic, focussing on detecting and monitoring contact throughout the analysis via a double-pass approach between parent and child bodies/surfaces. When contact is detected, interaction forces are introduced to prevent penetration between surfaces/bodies.

The contact stiffness is calculated using the following equation, based on the averaged material and geometric properties of the elements adjacent to the contact node:

$$\varepsilon_i = S_{fac,i}\frac{k_i l_i}{2t_i} \quad (1)$$

where ε_i is the contact stiffness at node i, $S_{fac,i}$ is the stiffness scale factor, k_i is the bulk modulus, l_i and t_i are the element length and thickness respectively.

The stiffness scale factor is made accessible to the user to modify the contact stiffness and indirectly affect contact widths, stresses, and penetrations.

The relevant properties made accessible to the user are the parent element stiffness factor, child element stiffness factor, coulomb friction coefficient and a means to control the zone around each node where the contact search occurs.

4.5 *Supports*

The support regime adopted for the analysis was simple, 17kN/m² compression-only spring were applied to the base of the tunnel, and fixed horizontal springs applied along the vertical line of symmetry running through the centre of the central wall.

4.6 *Loads*

The loads considered in the analysis were also simplified in self-weight applied via a vertical acceleration of 9.81 m/s^2, and the weight of the backfill, applied via a variation with depth from finished ground level (24m above formation level – 14.m above crown level). The bulk unit wight of backfill adopted was 20 kN/m^3. No factors were applied to the loads.

5 DOUBLE PIN JOINT ARCH ANALYSIS

By analysing three models of the double arch lining with; no joint, pin joint and a frictional knuckle-joint (the design), it was observed that no change occurred to axial or shear performance of the lining whereas the arch wall experiences significant reduction in bending moment. This can be seen in, showing over 80% drop in the moment at the middle of the arch wall and over 33% at the top, with only a 7.8% increase at the base of the wall where moment is already critical and therefore designed for.

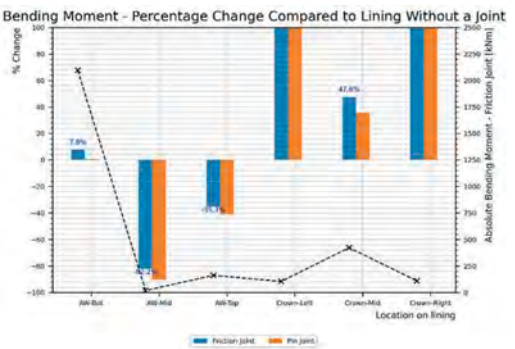

Figure 5. Percentage change in bending moment for the frictional joint and pin joint linings compared to the no joint lining model. Bars portray the percentage change and the line plot shows the bending moment for the frictional joint model.

However, by introducing the joints, the roof unit experiences higher bending forces at its centre due to the increased displacement/rotation and subsequent alteration of the line of thrust within the lining.

6 FINDINGS

6.1 *Mesh size*

The local mesh size at the joint was varied to investigate the effects of mesh size on joint behaviour; the adopted values were 5mm, 10mm, 15mm, 20mm and 25mm.

The mesh size analysis shows that the contact width is sensitive to the mesh discretization adopted, specifically at higher loads. Figure 7 shows that:

1. At lower loads, the difference between the contact width on the concave and convex parts is large. this difference reduces at higher loads.

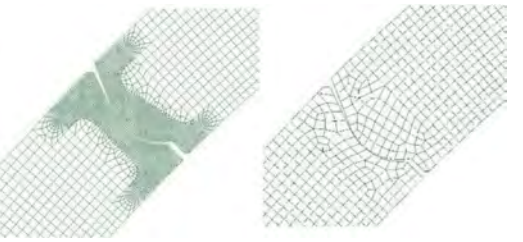

Figure 6. (a) 5mm mesh size (b) 25mm mesh size.

2. Finer mesh discretization shows significantly better agreement between the contact widths registered by the contact elements on the concave and convex parts of the joint, specifically for 5mm and 10mm meshes.
3. The concave part of the joint (wall) tends to underestimate the contact width while the convex part (crown) tends to overestimate the contact width; increasingly divergent with coarser meshes.

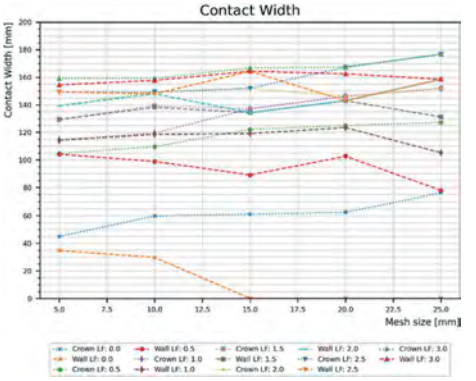

Figure 7. Variation of contact width with mesh size; where a load factor of 0.0 represents self-weight.

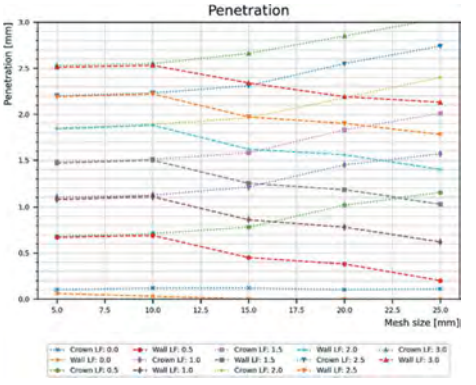

Figure 8. Variation of inter-surface penetration with mesh size; where a load factor of 0.0 represents self-weight.

The inter-penetration between the surfaces in Figure 8, shows similar results, where meshes

coarser than 10mm show increasing divergence in the value of penetration in the convex and concave parts, about the seemingly real value identified in finer meshes (5mm and 10mm).

The peak axial stress at the contact point, shown in Figure 9, shows that at 5mm and 25mm mesh sizes exhibit a higher contact stress than the 10mm, 15mm or the 20mm. This appears to be due to random alignment of nodes at different mesh discretization near the point of initial contact; as shown in Figure 10.

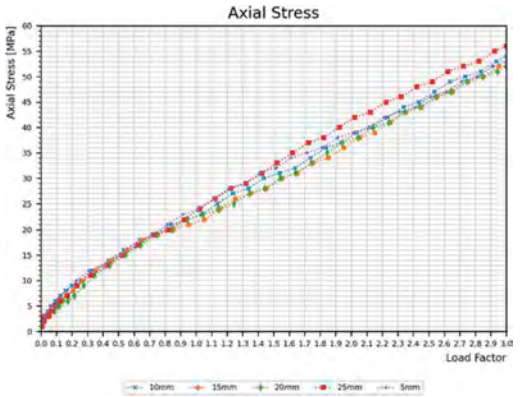

Figure 9. Variation of peak axial contact stress against increasing load factor, for the various mesh sizes.

While peak stresses may not be of any design importance they may cause convergence issues, specifically when using non-linear materials within the model.

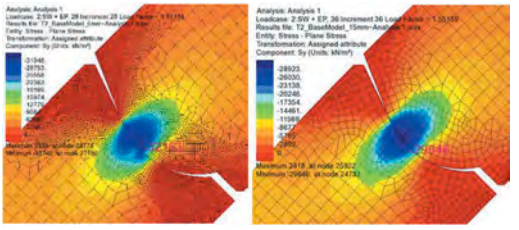

Figure 10. Axial stress at joint at load factor 1.5 in kPa; (a) 5mm mesh (b) 15mm mesh.

6.2 *Contact stiffness*

Naturally, when increasing the contact stiffness we see a linear increase in peak stress at contact, this conforms to Eq. (1) above.

More interestingly, increasing the contact stiffness past 1.0 does not seem to have a significant effect on increasing bursting forces observed in the crown or wall, with the highest increases occurring at the higher load factors, with a maximum increase of 8% when doubling contact stiffness at Crown-LF:3.0 in Figure 12. However, halving contact stiffness leads to a 15% reduction in bursting force in the wall, for the same case.

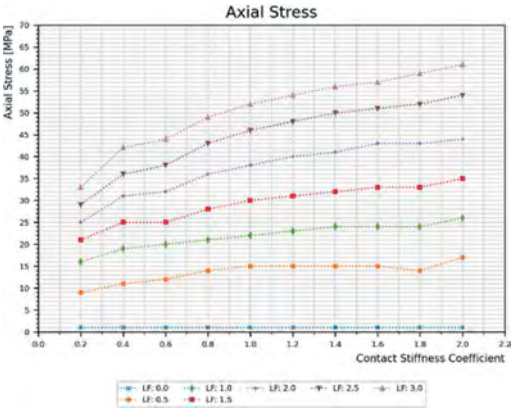

Figure 11. Variation of peak axial stress at contact with contact stiffness, where a load factor of 0.0 represents self-weight.

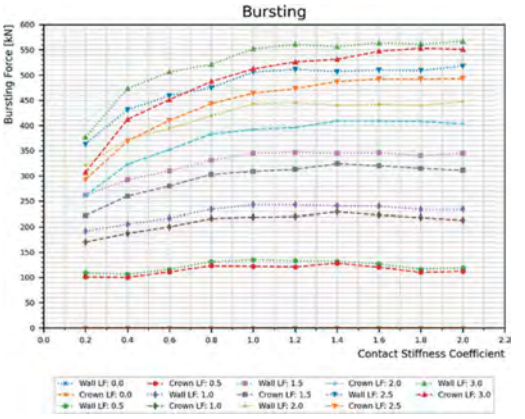

Figure 12. Variation of bursting forces in the wall and crown, with contact stiffness, where a load factor of 0.0 represents self-weight.

The unsymmetric response to altering contact stiffness can be explained by observing the change in contact width.

Figure 13 shows the inversely proportional relationship between contact stiffness and contact width, plateauing after 1.0-1.2 contact stiffness factor. This explains why reducing contact stiffness has a significant observable effect on bursting forces, while increasing them is substantially less effective.

Bursting forces increase with reducing contact width, as the gradient of stress dispersal is steeper requiring higher stabilising radial stresses to satisfy local equilibrium.

Naturally the same inverse proportionality can be observed when inspecting the penetration results.

An indirect effect of increasing the contact stiffness is increasing the shear stresses observed at the joint. Figure 15, shows shear stress increasing by 30% for LF: 2.0 when doubling the contact stiffness factor from 1.0 to 2.0. This effect is less pronounced

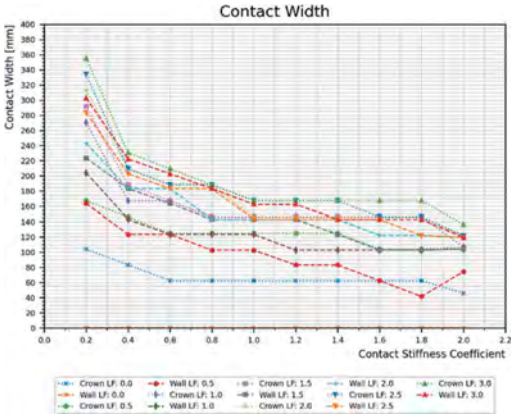

Figure 13. Variation of contact width with contact stiffness, where a load factor of 0.0 represents self-weight.

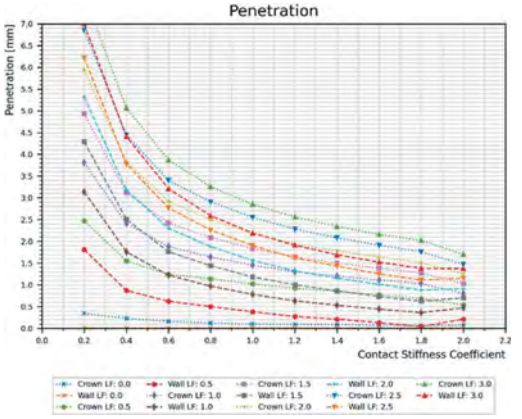

Figure 14. Variation of penetration with contact stiffness, where a load factor of 0.0 represents self-weight.

at lower load factors, with LF: 1.5 only showing a 10% increase when undergoing the same change.

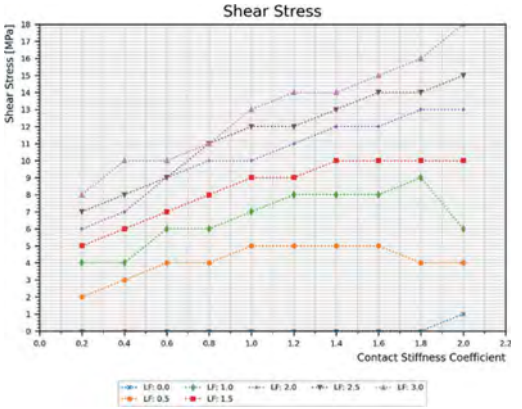

Figure 15. Variation of peak shear stresses at the contact, with contact stiffness, where a load factor of 0.0 represents self-weight.

Lastly, increasing contact stiffness has been observed to slightly reduce the joint rotation, this is likely due to higher axial stresses translating to higher frictional forces, the effect is not significant.

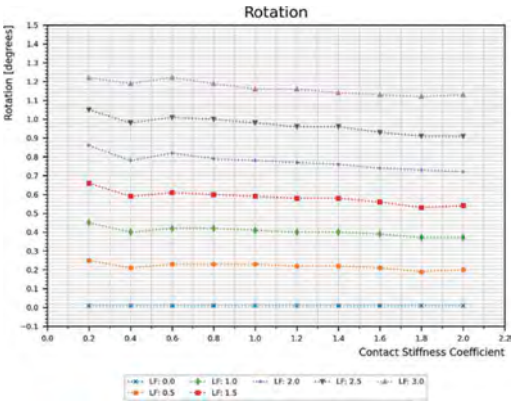

Figure 16. Variation of joint rotation with contact stiffness, where a load factor of 0.0 represents self-weight.

6.3 *Friction coefficient*

One important aspect of any contact element when considering non-smooth contact, is the friction coefficient as it is the main variable affecting the tangential contact properties.

As is anticipated, increasing the coefficient of friction leads to an increase in rotational stiffness and therefore lower rotation. At 1.5 load factor the joint rotation is 8.3% lower for a 0.7 coefficient than a 0.2 coefficient.

The opposite trend can be observed in the peak shear stress near the contact where an increase in the friction coefficient leads to an increase in the peak shear stress. This trend is observed up to a load factor of 2.5x full backfill, above which lower coefficients show higher shear stresses, likely due to the higher rotation altering the stress field.

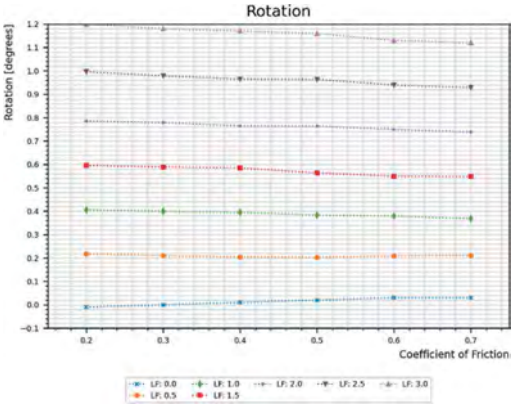

Figure 17. Variation of joint angle with coefficient of friction, where a load factor of 0.0 represents self-weight.

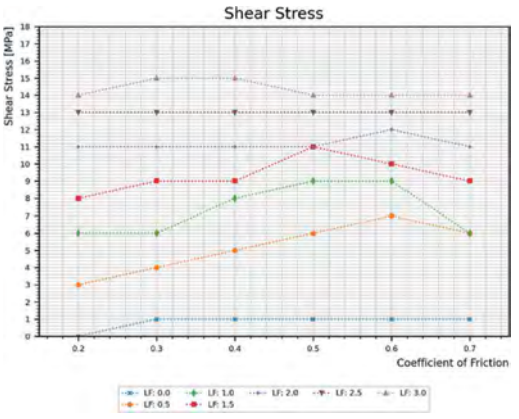

Figure 18. Variation of peak shear stress with coefficient of friction, where a load factor of 0.0 represents self-weight.

Similarly, the increased rotational stiffness constraining the joint rotation leads to higher peak axial stresses. Figure 19 shows an increase between 15% and 20% for most load factors.

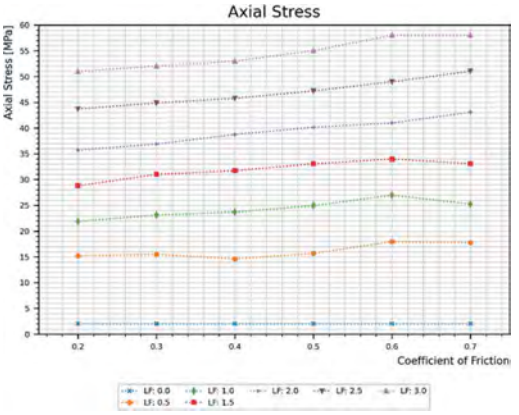

Figure 19. Variation of peak axial stress with coefficient of friction, where a load factor of 0.0 represents self-weight.

As the joint rotation becomes more restricted with higher friction coefficients, the joint becomes less able to rotate towards a more stable configuration. A more stable configuration would be categorized as one which maximises contact width and reduces contact eccentricity by centring the line of thrust.

Figure 20 shows the reduction in contact width with increasing friction coefficients. At a load factor of 1.0 we see a reduction of 11.5% in contact width between a 0.2 and 0.7 coefficient of friction.

The penetration increases slightly but not significantly as is expected, matching the increase in peak axial stress, while the bursting forces in the wall and the crown are seemingly unaffected by the friction coefficient.

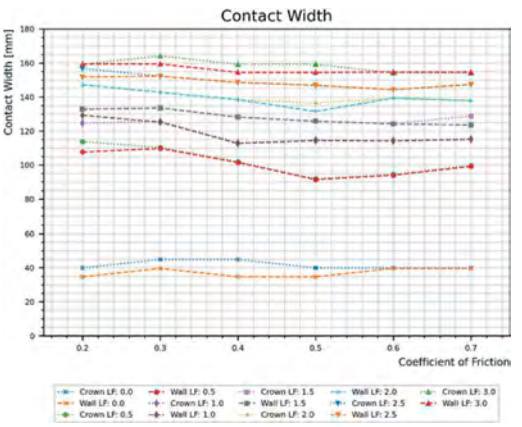

Figure 20. Variation of contact width with coefficient of friction, where a load factor of 0.0 represents self-weight.

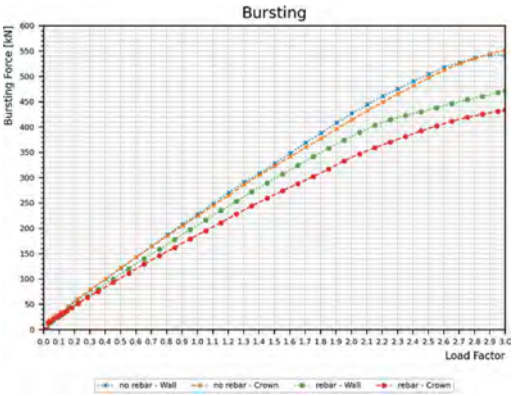

Figure 21. Variation of bursting forces with load comparing results for the model with reinforcement modelled and the one without.

6.4 *Reinforcement*

Modelling reinforcement has shown no significant impact on peak stresses at contact, contact width or contact penetration; indicating that contact properties are agnostic towards the presence of reinforcement, particularly the lack of effect on axial stiffness of the contact.

However, the bursting forces and the joint rotation have shown clear effects. Figures 21 and 22 show that modelling the reinforcement has limited the tensile bursting stresses and therefore more accurately captured a lower bursting force.

Another observation is the bigger difference between the bursting force in the crown and the wall, where the model with no reinforcement shows little difference. This is due to the differing quantity of reinforcement between the crown and the wall near the joint.

Figure 23 shows another benefit of modelling reinforcement; where the model with reinforcement shows lower joint rotation, due to increased stiffness of

the wall and crown units, compared to the model without the reinforcement. This leads to more precise displacements, especially where the structure is heavily loaded (i.e. at high load factors) or heavily reinforced.

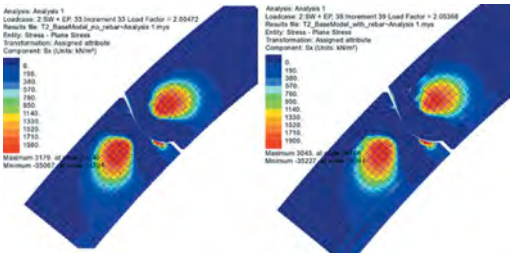

Figure 22. Radial (Bursting) tensile stresses at joint at load factor 2.0 in kPa; (a) without reinforcement (b) with reinforcement.

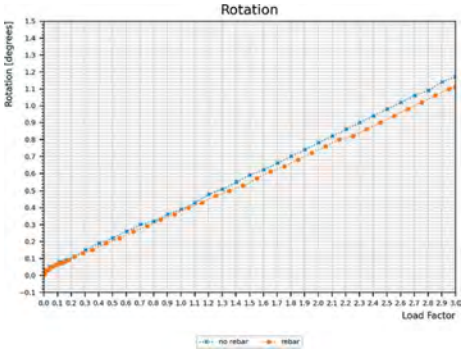

Figure 23. Variation of joint rotation with load comparing results for the model with reinforcement modelled and the one without.

7 VERIFICATIONS

The structural verifications of the tunnel lining were focussed on designing for the following:

1. Shear and moment transfer at the loop-to-loop connections.
2. Crushing and bursting at the knuckle joints.
3. General section capacity checks, particularly at the base of the arch walls.

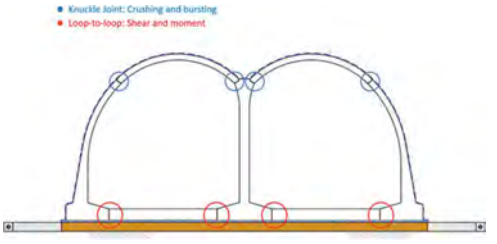

Figure 24. Showing specific points of interest for design considerations.

For more detail on the design development, construction, sustainability and other challenges refer to *Smith and Psomas (2023)*. The fire design and testing were detailed in *Psomas et al. (2023)* and the calibration between finite element analysis and physical testing for joint behaviour has been covered in *Li et al. (2024)*.

8 CONCLUSIONS

This paper presented an overview of the twin-arch tunnel design used for the green tunnels on HS2, focussing on the finite element modelling aspects of the knuckle-joint and subsequent effects on the design. The particular focus was on mesh size, contact friction coefficient, contact stiffness and modelling of reinforcement.

Regarding mesh size, mesh sensitivity analysis has been shown to be crucial as mesh size will dictate the sensitivity of the contact elements, with coarser meshes ove-estimating contact width, causing stress concentrations and convergence issues as well as showing disparity between stresses observed at wither side of the joint.

Similarly, the stiffness of the contact elements significantly impact the local stress field at the joint by altering contact width and penetrations. It was observed that increasing the contact stiffness past that of the parent geometries has less of an effect than reducing stiffness. Primarily, the contact stiffness should be calibrated so as not to underestimate the bursting forces generated while not leading to artificially high stresses.

The friction coefficient analysis highlighted the impact on the joint articulation, with increased friction reducing joint rotation and leading to shorter contact widths and higher axial and shear stresses.

Finally, the effect of modelling reinforcement showed the significant influence the reinforcement has on constraining radial tensile stresses, leading to more accurate bursting forces, as well as increasing the stiffness of the units and reducing joint rotation observed.

ACKNOWLEDGMENTS

The Authors would like to thank HS2 and EKFB Green tunnels Team for permission to publish and their support respectively.

REFERENCES

Blom, C.B.M., 2004. Design philosophy of concrete linings for tunnels in soft soils.

Duddeck, H. and Erdmann, J., 1985. Structural design models for tunnels in soft soil. *Underground Space; (United States)*, *9*.

Janssen, P., 1983. Tragverhalten von Tunnelausbauten mit Gelenktübbings. PhD thesis Technische Universität Braunschweig.

Leonhardt, F., Reimann, H., 1965. Betongelenke. Versuchbericht, Vorschläge zur Bemessung und konstruktiven Ausbildung. Deutscher Ausschuss für Stahlbeton DAfStb, Heft 175.

Li, M., Psomas, S. and Al-Haddid, N., 2024. Validation of Joint Non-Linear Numerical Analysis with Large Scale Physical Testing for Arched Cut and Cover Tunnels at HS2 Project (UK). In *Tunnelling for a Better Life*. CRC Press.

Psomas, S., Al-Haddid, N. and Monckton, H., 2023. Fire design analysis for the Green Tunnels at High Speed 2 project (UK). In *Expanding Underground-Knowledge and Passion to Make a Positive Impact on the World* (pp. 861–869). CRC Press.

Smith, E. and Psomas, S., 2023. Innovative and sustainable twin arch solution for High Speed Two Green Tunnels. In *High Speed Two (HS2): Infrastructure Design and Construction (Volume 3)* (pp. 187–202). ICE Publishing.

Tvede-Jensen, B., Faurschou, M. and Kasper, T., 2017. A modelling approach for joint rotations of segmental concrete tunnel linings. *Tunnelling and Underground Space Technology*, *67*, pp.61–67.

Wood, A.M., 1975. The circular tunnel in elastic ground. *Geotechnique*, *25*(1), pp.115–127.

Tunnelling for a Better Life – Yan, Celestino, Thewes & Eberhardt (Eds)
© 2024 The Author(s), ISBN 978-1-032-80042-4
Open Access: www.taylorfrancis.com, CC BY-NC-ND 4.0 license

The stiffness of circular joints and its effect on the deformation of the tunnel segmental lining along the longitudinal direction

Xin Han*
School of Highway, Chang'an University, Xi'an, China
Department of Environment, Land and Infrastructure Engineering (DIATI), Politecnico di Torino, Turin, Italy

Fei Ye
School of Highway, Chang'an University, Xi'an, China

Pierpaolo Oreste
Department of Environment, Land and Infrastructure Engineering (DIATI), Politecnico di Torino, Turin, Italy

ABSTRACT: When analysing the damage phenomenon (crack, seepage, et al.) of a segmental lining during tunnel construction, its movement and deformation along the longitudinal direction is a critical aspect to be studied. Since the segmental lining is assembled by segments and using connecting bolts, there are many joints in the lining, which are the weak part of the lining and have an obvious deformation under the application of construction loads. This paper focuses on the circular joint which has a great influence on the segmental lining deformation along the longitudinal direction. Firstly, the evaluation methods of the bending stiffness and shear stiffness of a circular joint are developed; and then, based on the interaction between the connecting bolt and its hole, the methods for the evaluation of the shear stiffness of a single bolt and the one of the whole circular joint are proposed; finally, the segmental lining deformation along the longitudinal direction is analysed and the main factors are discussed.

Keywords: Tunnel segmental lining, Circular joint, Shear Stiffness, Bending Stiffness, lining behaviour in the longitudinal direction, Connecting Bolts, Bolt/Bolt hole interaction, Finite Element Method (FEM), Numerical Methods

1 INTRODUCTION

Segmental lining is widely used to support the surrounding ground when the tunnel boring machines (TBM) is adopted for the tunnel construction. Since the segmental lining consists of segments and connecting bolts, there are many joints that influence its behaviour. During the construction of the tunnel, the crack and seepage can be observed inside the lining (Gong et al., 2020; Lu, 2020), and the uplift movement of the segmental lining is a common phenomenon (Zhou and Ji, 2014).

In order to understand the reasons of the crack and seepage inside the lining, the segmental lining deformations along the longitudinal direction are widely studied using numerical models and analytical solutions (Chen et al., 2018; Cheng et al., 2021). Regarding this type of analysis, the influence of the circular joints is fundamental. Shiba et al. (1988) proposed the equation for the joint bending stiffness. Li et al. (2019) carried out a laboratory test to evaluate the joint stiffness under the application of a normal forces and moment. Cheng et al. (2021) suggested the general solution for the segmental lining deformation. Based on laboratory test, researchers (Guo et al., 2023a; Guo et al., 2023b; Liu et al., 2018) tested the bending and shear deformation of joints in the detailed; they further explained the nonlinear behaviour of the joint due to the nonlinear properties of the constituent materials.

In this paper the methods used to determine the variable joint bending and shear stiffnesses of the circular joints are introduced. Furthermore, a FEM model is developed to calculate the segmental lining deformation along the longitudinal direction and an iterative procedure is proposed in order to correctly consider the variable joint stiffness values. Using the proposed

*Corresponding author: hanxin@chd.edu.cn

DOI: 10.1201/9781003495505-142

method, deformations of rings and joints can be evaluated separately, and the nonlinear deformation of the tunnel segmental lining can be researched.

2 STIFFNESS OF THE CIRCULAR JOINT

When the tunnel segmental lining has a deformation along the longitudinal direction, the stiffness of the circular joints shows a nonlinear behaviour with the increase of the joint deformation. The methods adopted to calculate the bending and the shear stiffnesses of the circular joints are discussed in this section.

2.1 *Bending stiffness*

The bending stiffness of a circular joint is affected by the state of the joint, which can be described by the location of the neutral axis: it can be represented by the angle φ introduced by Shiba et al. (1988) and is determined by the existing normal force and the applied moment. There are two kinds of circular joint states: open and closed. When the joint is closed, the segments are connected each other, and the bending stiffness of the joint is the same of the lining segment. The limit moment M_{lim} of the circular joint before opening can be determined by the normal force N with the following equation:

$$M_{lim} = \frac{N \cdot I}{A \cdot R_e} \tag{1}$$

where I is the inertia moment of the ring cross-section, A and R_e are the cross-sectional area and the external radius of the ring, respectively.

When the joint is open, the bending stiffness of the joint show a nonlinear behaviour. The influence of the moment and of the normal force can be represented by a parameter λ,

$$\lambda = \frac{N \cdot (D_e - t)}{4 \cdot M} \tag{2}$$

where D_e is the external diameter of the tunnel, t is the thickness of the lining.

The equivalent bending stiffness $(EI)_{eq}$ of the joint can be obtained by the following equation (Han et al., 2023a):

$$(EI)_{eq} = \left[K_{com} \cdot \left(\frac{\pi}{2} - \varphi - \sin\varphi \cdot \cos\varphi\right) + K_{ten} \cdot \left(\frac{\pi}{2} + \varphi + \sin\varphi \cdot \cos\varphi\right)\right] \cdot \frac{(D_e - t)^3 \cdot t}{16} \cdot L_{b,p} \tag{3}$$

where $L_{b,p}$ is the projection length of the bolt, and K_{ten} are the tensile stiffness and compression stiffness of the joint:

$$\begin{cases} K_{com} = \frac{2 \cdot E_{con}}{L_{b,p}} \\ K_{ten} = \frac{2 \cdot E_b}{l_b} \cdot \frac{n \cdot A_b}{A} \end{cases} \tag{4}$$

where E_{con} is the elastic modulus of concrete, E_b is the elastic modulus of the bolt steel, l_b is the length of the bolt, n is the number of connecting bolts in the circular joint and A_b is the cross-sectional area of the connecting bolt.

In Equation 3, when the normal force is equal to 0, the angle φ can be obtained by the following simplified equation:

$$\varphi + cot\varphi = \pi \cdot \left(\frac{1}{2} + \frac{K_{ten}}{K_{com} - K_{ten}}\right) \tag{5}$$

When the normal force is larger than 0, the angle φ can be derived on the basis of Equation 2:

$$\lambda = \frac{2 \cdot m \cdot (\cos\varphi + \varphi \cdot \sin\varphi) - \pi \cdot \sin\varphi}{-2 \cdot m \cdot (\varphi + \cos\varphi \cdot \sin\varphi) + \pi} \tag{6}$$

where m can be determined by K_{com} and K_{ten}:

$$m = \frac{K_{com} - K_{ten}}{K_{com} + K_{ten}} \tag{7}$$

Furthermore, the equivalent bending stiffness of the joint also can be rewritten with the ratio between the equivalent bending stiffness of the joint and the one of the segmental lining ring:

$$(EI)_{eq} = \mathrm{JBSE}_{Boltz} \cdot E_{con} \cdot I \tag{8}$$

where JBSE_{Boltz} is the joint bending stiffness efficiency based on the Boltzmann function; it is equal to the ratio of the bending stiffnesses between the joint and the ring, and it can be considered as a modifying parameter of the bending stiffness of the lining ring.

JBSE_{Boltz} is a function of the λ parameter:

$$\mathrm{JBSE}_{Boltz} = \frac{(A_1 - A_2) \cdot \alpha}{1 + \mathrm{e}^{(\lambda - \lambda_0)/q}} + A_2 + \Delta \tag{9}$$

where A_1, A_2, λ_0 and k are the basic parameters, α and Δ are the modified parameters. The detailed derivation of these parameters can be found in the reference (Han et al., 2023c):

A_1 is the lower value of the modified parameter JBSE_{Boltz}, which can be obtained by Equation 3 and Equation 4 when the normal force is equal to 0;

A_2 is the upper value of JBSE_{Boltz} which is equal to 1;

λ_0 is the specific value of λ when JBSE_{Boltz} is equal to $(A_1 + A_2)/2$, where the equivalent bending stiffness of the joint $(EI)_{eq}$ can be obtained by Equation 5, the angle φ can be derived by Equation 3, and λ_0 can be calculated by Equation 6;

q is a constant value, and can be obtained by the following equation:

$$q = \frac{A_2 - A_1}{4 \cdot \mathrm{JBSE}'} \tag{10}$$

where JBSE'is the slope of the centre point (λ_0, (A_1 +A_2)/2), which can be obtained by two adjacent points with a tiny increase $\Delta\lambda$, where the ordinate value of $JBSE_{Boltz}$ can be obtained on the abscissa value and $\lambda_0 + \Delta\lambda$ based on Equation 3, Equation 5 and Equation 8;

α and Δ are the modified parameters and can be obtained by the following equations:

$$\alpha = \frac{\left(1 + e^{(1-\lambda_0)/k}\right) \cdot \left(1 + e^{(-\lambda_0)/k}\right)}{e^{(1-\lambda_0)/k} - e^{(-\lambda_0)/k}} \tag{11}$$

$$\Delta = -\frac{(A_1 - A_2) \cdot \alpha}{1 + e^{(1-\lambda_0)/k}} \tag{12}$$

Based on Equation 3 and Equation 8, the equivalent bending stiffness of the joint can be calculated separately. The results are shown in Figure 1 referring to a well-known case of a shield tunnel (Zhou and Ji, 2014), and the results by the two methods show a very good consistence.

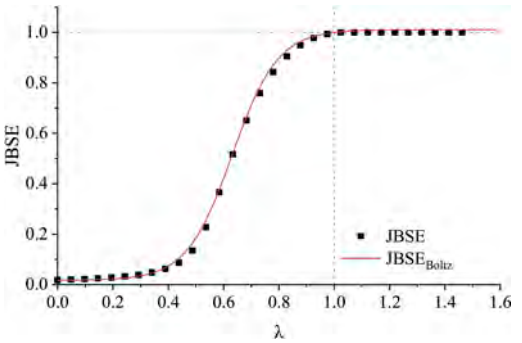

Figure 1. The trend of the joint bending stiffness based on the Equation 3 and Equation 8 calculation for a well-known case of a shield tunnel (Han et al., 2023c; Zhou and Ji, 2014).

2.2 *Shear stiffness*

The shear stiffness of a joint is influenced by the relative displacement of segments. Since the connecting bolts are installed along the circular joint, the inclination angle of the bolts varies with the location of the bolts on the circular joint. The shear stiffnesses of a single bolt and of the whole circular joint are here discussed separately.

2.2.1 *Shear stiffness of a single connecting bolt*

Based on the Timoshenko theory, the equivalent shear stiffness of a joint $(k \cdot G \cdot A)_{eq}$ is equal to the ratio between the shear force V_{total} applied on the joint and the corresponding relative displacement v_{seg} together with the projection length of the connecting bolt L_{bp}.

$$(k.G.A)_{eq} = \frac{V_{total}}{v_{seg}} .L_{bp} \tag{13}$$

When the segments have a relative displacement along the joint Δv_{seg}, the ratio between the increasement of the applied shear force ΔV_{total} and the corresponding relative displacement can be defined as shear stiffness K_{eq}:

$$K_{eq} = \frac{\Delta V_{total}}{\Delta v_{seg}} \tag{14}$$

where the applied shear force on the joint ΔV_{total} is equal to the shear force of the bolt on the cross section along the joint.

Furthermore, considering the inclination angle of the connecting bolt, the equivalent shear stiffness of the joint is the combination of the joint-bolt tensile stiffness and the joint-bolt shear stiffness when only the bolt is considered during the shear deformation (Han et al., 2023d):

$$K_{eq} = K_{eq,Q} \cdot \cos^2(\alpha) + K_{eq,N} \cdot \sin^2(\alpha) \tag{15}$$

where $K_{eq,Q}$ is the joint-bolt shear stiffness and $K_{eq,N}$ is the joint-bolt tensile stiffness, when the bolt is perpendicular to the plane of the joint; α is an inclination angle of the connecting bolt.

Based on the relative displacement direction and the tensile state of the bolt, there are two basic models for the joint shear deformation: the tensile model and the no tensile one, because there is no constraint on the bolt head when the bolt is compressed along the axial direction.

When the joint deformation follows the no tensile model, the shear stiffness K_{eq} can be obtained by the shear stiffness of the joint:

$$K_{eq} = K_{eq,Q} \cdot \cos^2(\alpha) \tag{16}$$

Based on the results of Han et al. (2023d), the joint-bolt tensile stiffness has a constant value (the green line in Figure 2), and the joint-bolt shear stiffness has a nonlinear trend varying the relative displacement between the segments (the blue lines in the figure).

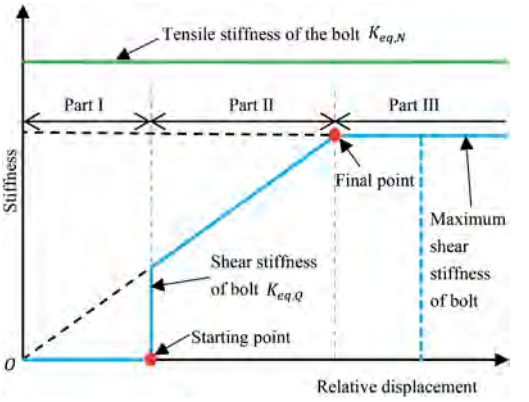

Figure 2. The joint-bolt tensile stiffness and the shear stiffness when the bolt is perpendicular to the plane of the joint (after Han et al., 2023d).

The tensile stiffness of the joint can be obtained by the following equation:

$$K_{eq,N} = \frac{1}{\frac{\coth(\rho \cdot l_{thread})}{E_b \cdot A_b \cdot \rho} + \frac{l_{shank}}{E_b \cdot A_b} + \frac{1}{K_{x,o}}} \tag{17}$$

where l_{thread} is the length of the thread part of the bolt which is installed inside a concrete bolt hole, l_{shank} is the length of the shank part of the bolt. Parameter ρ can be obtained by the following equation:

$$\rho^2 = \frac{\beta_c \cdot \pi \cdot d_b}{E_b \cdot A_b} \tag{18}$$

where β_c is the concrete foundation shear modulus, d_b is the diameter of the bolt. $K_{x,o}$ represents the compressive stiffness of the concrete surface under the application of the washer of the bolt head.

$$K_{x,o} = k_c \cdot \frac{\pi}{4} \cdot \left(d_{washer}^2 - d_h^2\right) \tag{19}$$

where d_{washer} and d_h are the diameter of the washer and the bolt hole, respectively; k_c is the concrete foundation compressive modulus. The parameters k_c and β_c can be determined by laboratory tests and are discussed in the references (Han et al., 2023b).

The shear stiffness of the joint has three parts, and also includes three key parameters: a maximum shear stiffness, locations of a starting point and of a final point. The maximum value of the shear stiffness can be obtained by the following equation:

$$K_{eq,Q,max} = 2 \cdot E_b \cdot I_b \cdot \beta^3 \cdot |\eta| \tag{20}$$

where I_b is the moment of inertia of the bolt cross-section, η and β are two parameter; β depends on the concrete foundation compression modulus:

$$\beta = \sqrt[4]{\frac{k_c \cdot d_b \cdot 1000}{4 \cdot E_b \cdot I_b}} \tag{21}$$

the η parameter depends on the bolt length and on β: the detailed derivation of them can be seen in Han et al., 2023d.

The location of the starting point can be obtained by the following equation:

$$L_{start} = \frac{d_{max,h,l} - d_b}{2} \cdot \frac{l_{shank}^3}{l_{bolt,l}^2 \cdot \left(3 \cdot l_{shank} - 2 \cdot l_{bolt,l}\right)} \cdot \frac{1}{\cos(\alpha)} \tag{22}$$

The location of the final point is equal to the sum of the length of part I and part II.

$$L_{final} = L_{start} + L_{partII} \cdot \frac{1}{\cos(\alpha)} \tag{23}$$

where $L_{part_{II}}$ is the length of part II:

$$L_{PartII} = \frac{2}{K_{eq,Q}} \cdot \frac{15 \cdot E_b \cdot I_b}{4 \cdot l_{bolt,rs}^3 + 10 \cdot E_b \cdot I_b \cdot \delta \cdot l_{bolt,rs} - 10 \cdot E_b \cdot I_b \cdot \beta \cdot l_{bolt,rs}^2} \cdot \frac{d_{max,h,r} - d_b}{2} \tag{24}$$

where $d_{max,h,l}$, $d_{max,h,r}$, $l_{bolt,l}$ and $l_{bolt,rs}$ are geometrical parameters of the bolt, δ and ω are the middle parameters which can be found in the reference (Han et al., 2023d), where the segment connected with the bolt head is the left one.

The representation of the connecting bolts in the cross section of the segmental lining rings is shown in Figure 3. The green rectangle is the first ring and the white one is the second installed segmental ring. The angle ϑ represents the location of each connecting bolt in the cross section.

The bolts have different angles with the circular joint. The equivalent inclination angle γ is used to represent the angle of the bolt axis with the displacement vector of the lining segment.

2.2.2 *Shear stiffness of a circular joint*

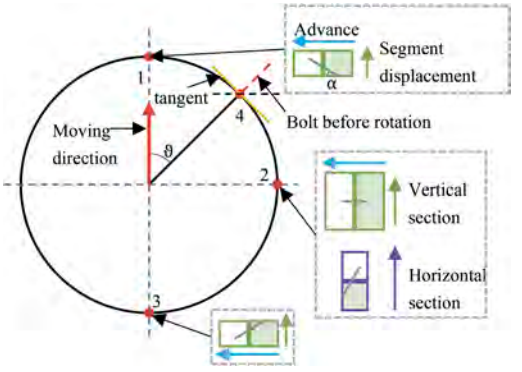

Figure 3. Different axial directions of the bolts in the cross section (after Han et al. (2023d)).

The angle γ of the considered bolt with the location ϑ can be determined by the following equation:

$$\gamma = \arcsin(\sin\alpha \cdot \cos\vartheta) \tag{25}$$

where α is the inclination angle of the bolt at point 1 as shown in Figure 3, ϑ represents the location of the considered bolt in the cross section ($\vartheta \in [0,\ \pi]$).

When $\gamma > 0$, the joint-bolt tensile stiffness can be ignored, and the joint-bolt shear stiffness can be obtained by Equation 16, where the angle α is replaced by γ. When $\gamma \leq 0$, the shear stiffness of the joint can be calculated using Equation 15 by replacing α with γ. Finally, the shear stiffness of the circular joint can be obtained by the summation of the shear stiffness K_{eq} of all the bolts in the lining cross section.

Table 1. The assumed material parameters.

Bolt steel Elastic modulus (GPa)	Bolt Steel Poisson's ratio	Concrete Elastic modulus (GPa)	Concrete Poisson's ratio	Concrete foundation compression modulus (MPa/mm)	Concrete foundation shear modulus (MPa/mm)
206	0.3	35.5	0.2	74.87	10.10

Table 2. The geometrical parameters of the bolting system.

Bolt diameter (m)	Diameter of gasket (m)	Inclination angle of the bolt (°)	Length of the bolt on the left segment (m)	Length of the bolt on the right segment (shank part + thread one) (m, m)	Max and min hole diameter on the left segment (mm, mm)	Max hole diameter (mm)
0.03	0.07	30	0.282	0.06 + 0.19	36, 40	60

The calculated results of the shear stiffness of each bolt are shown in Figure 4 and the one of the whole circular joint with the increase of the relative displacement is shown in Figure 5, where the joint is connected by 19 bolts. The assumed material parameters of the bolt steel and concrete are listed in Table 1 and the structural parameters are listed in Table 2.

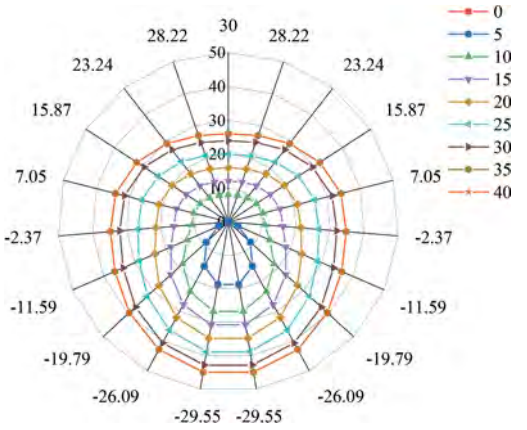

Figure 4. The distribution of the shear stiffnesses on the joint connected by 19 bolts.

From Figure 4, the shear stiffness of all the bolts on the circular joint shows a uniform distribution: the value of the shear stiffness of the joint increases from the top to the bottom. With the increase of the relative displacements of the segments, the shear stiffness of each bolt increases correspondingly. Based on Figure 5, the shear stiffness of the circular joint shows a similar trend with the one of the single bolt, where the minimum shear stiffness of the joint is determined by the joint-bolt tensile stiffnesses of all the bolts.

Based on Equation 13, the shear stiffness of the circular joint can be determined based on the relative displacement of the segments together with the projection length.

The distribution of the shear stiffness on the circular joint is uneven as shown in Figure 4: there are different start points and final points for each bolt varying the equivalent inclination angle γ based on Equation 22, Equation 23 and Equation 25. Considering the uniform distribution of the bolts on the circular joint, a virtual bolt at the location $\vartheta = 45°$ is used to represent the shear stiffness of the circular joint together with the number of bolts. Therefore, the shear stiffness can be derived by Equation 15:

$$\begin{cases} K_N & v_{seg} < L_{s,\vartheta=45°} \\ K_N + K_Q \cdot \frac{v_{seg}}{L_{f,\vartheta=45°}} & L_{s,\vartheta=45°} \le v_{seg} < L_{f,\vartheta=45°} \\ K_N + K_Q & v_{seg} \ge L_{f,\vartheta=45°} \end{cases} \tag{26}$$

where n is the number of bolts on the circular joint, $L_{s,\vartheta=45°}$ and $L_{f,\vartheta=45°}$ are the start point and the finial point when the equivalent inclination angle is equal to $\gamma_{\vartheta=45°}$ at location $\vartheta = 45°$ (Equation 25):

$$\begin{cases} K_N = K_{eq,N} \cdot \sin^2(\gamma_{\vartheta=45°}) \cdot \frac{n}{2} \\ K_Q = K_{eq,Q,max} \cdot \cos^2(\gamma_{\vartheta=45°}) \cdot n \end{cases} \tag{27}$$

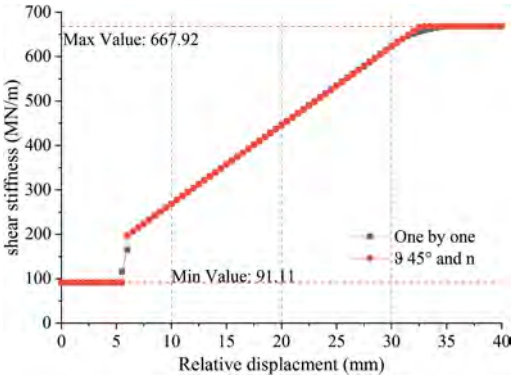

Figure 5. The shear stiffness of a circular joint connected by 19 bolts varying the relative displacements.

Based on Equation 26, the shear stiffness of the circular joint is also shown in Figure 5: a good consistence between the two curves can be seen and Equation 26 can be used to calculate the equivalent shear stiffness of a circular joint.

Based on Equation 13, the equivalent shear stiffness of the joint $(k \cdot G \cdot A)_{eq}$ can be obtained as:

$$(k \cdot G \cdot A)_{eq} = \begin{cases} K_N \cdot L_{bp} & v_{seg} < L_{s,\vartheta=45^\circ} \\ K_N \cdot L_{s,\vartheta=45^\circ} + \left(K_N + K_Q \frac{L_{s,\vartheta=45^\circ} + v_{seg}}{2 \cdot L_{f,\vartheta=45^\circ}}\right) \cdot \left(v_{seg} - L_{s,\vartheta=45^\circ}\right) \cdot L_{bp} & L_{s,\vartheta=45^\circ} \le v_{seg} < L_{f,\vartheta=45^\circ} \\ \frac{K_N \cdot L_{s,\vartheta=45^\circ} + \left(K_N + K_Q \frac{L_{s,\vartheta=45^\circ} + L_{f,\vartheta=45^\circ}}{2 \cdot L_{f,\vartheta=45^\circ}}\right) \cdot \left(L_{f,\vartheta=45^\circ} - L_{s,\vartheta=45^\circ}\right) + \left(K_N + K_Q\right) \cdot \left(v_{seg} - L_{f,\vartheta=45^\circ}\right)}{v_{seg}} \cdot L_{bp} & v_{seg} \ge L_{f,\vartheta=45^\circ} \end{cases} \quad (28)$$

On the basis of Figure 1 and Figure 5, both of the bending stiffness and shear stiffness of a circular joint show a nonlinear behaviour with the relative displacement of the segments on the joint. Considering a nonlinear behaviour of the circular joint, the segmental lining deformation along the longitudinal direction is discussed on the next section.

3 SEGMENTAL LINING DEFORMATION

3.1 *FEM model of segmental lining deformation*

During the construction of a tunnel using the Tunnel Boring Machines (TBMs), the applied forces on the segmental lining can be divided into two classes: the loads along the axial direction of the tunnel, and the ones on the cross section of the tunnel, perpendicular to the axial direction. The forces on the cross section are produced by the slurry (the filling material) and the ground surrounding the tunnel; the mechanical behaviour of the slurry change over time, and the state of the slurry transforms slowly from a liquid state to solid one. When the slurry is in the liquid state, there are great buoyancy forces acting on the segmental lining; the buoyancy effect of the slurry decreases with the hardening phase (Fu et al., 2023). The slurry presence in the model is considered with a fluid zone and a solid one separately (Figure 6). Due to strong constraints by the tail brush inside the TBM tail, a fixed constraint is applied on the first node of the model. For the forces applied along the axial direction of the tunnel, the friction between the lining and the surrounding ground is ignored, and the normal force (axial force in the longitudinal direction) acting on the segmental lining is equal to the applied normal force by the hydraulic jacks: these forces can affect the bending stiffness of the circular joint on the basis of Figure 1.

Based on the Timoshenko theory, a FEM model is adopted to analyse the lining deformation along the longitudinal direction: it represents both the segmental lining rings and circular joints using standard elements and joint elements as shown in Figure 6. With the FEM model, the behaviours of joints and rings can be separately analysed considering the nonlinear behaviour of joints as previously introduced.

On the FEM model (Figure 6), the external forces on each node $[F]$ are equal to the global stiffness matrix $[K]$ multiplied by the corresponding nodal displacements $[S]$:

$$[K] \cdot [S] = [F] \quad (29)$$

The global stiffness matrix can be obtained by composing the local stiffness matrices on each element:

$$[K] = \begin{bmatrix} k_{1,a} & k_{1,b} & 0 & \cdots & 0 & 0 \\ k_{1,c} & k_{1,d} + k_{2,a} & k_{2,b} & \cdots & 0 & 0 \\ 0 & k_{2,c} & k_{2,d} + k_{3,a} & \cdots & 0 & 0 \\ \vdots & \vdots & \vdots & \ddots & 0 & 0 \\ 0 & 0 & 0 & \cdots & k_{n-1,d} + k_{n,a} & k_{n,b} \\ 0 & 0 & 0 & \cdots & k_{n,c} & k_{n,d} \end{bmatrix} \quad (30)$$

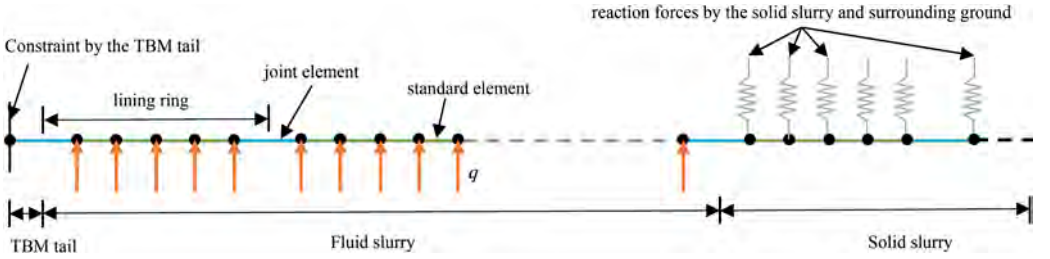

Figure 6. The numerical elements of the segmental lining model with the applied constraints (after Han et al., 2023c).

where the terms of the stiffness matrix depend on the element stiffness matrix:

$$[k_E]_i = \begin{bmatrix} k_{i,a} & k_{i,b} \\ k_{i,c} & k_{i,d} \end{bmatrix} = \frac{EI}{l^3} \begin{bmatrix} \frac{12}{1+\Phi} & \frac{6l}{1+\Phi} & -\frac{12}{1+\Phi} & \frac{6l}{1+\Phi} \\ \frac{6l}{1+\Phi} & \frac{4+\Phi}{1+\Phi} l^2 & -\frac{6l}{1+\Phi} & \frac{2-\Phi}{1+\Phi} l^2 \\ -\frac{12}{1+\Phi} & -\frac{6l}{1+\Phi} & \frac{12}{1+\Phi} & -\frac{6l}{1+\Phi} \\ \frac{6l}{1+\Phi} & \frac{2-\Phi}{1+\Phi} l^2 & -\frac{6l}{1+\Phi} & \frac{4+\Phi}{1+\Phi} l^2 \end{bmatrix} \tag{31}$$

where Φ is the ratio between the bending stiffness (EI) and shear stiffness (kGA) of elements based on Timoshenko theory:

$$\Phi = \frac{12 \cdot (EI)}{(kGA) \cdot l^2} \tag{32}$$

For the standard element, the bending stiffness and shear stiffness depend on the material of the segmental ring (concrete),, $(kGA) = (k \cdot G_{con} \cdot A)$, k is the shear coefficient based on the Timoshenko theory.

For the joint element, the bending stiffness (EI) can be determined based on Figure 1 and the shear stiffness (kGA) depends on Figure 5 with the relative displacement of segments.

Before the hardening of the slurry, the state of slurry is liquid. The length of the liquid zone is determined by the speed of the TBM excavation v and by the hardening time of slurry t_0:

$$d = v \cdot t_0 \tag{33}$$

The buoyancy force can be quickly evaluated with the Archimedes' principle based on the specific weight of the slurry γ_{sl} and of the concrete ring γ_{con}:

$$q = \gamma_{sl} \cdot \frac{\pi}{4} \cdot D_e^2 - \gamma_{con} \cdot \frac{\pi}{4} \cdot \left[D_e^2 - (D_e - 2t)^2 \right] \tag{34}$$

In the FEM model, the influence of the solid slurry and of the surrounding ground can be considered by adding a series of additional springs connected to the nodes in the global stiffness matrix [K] along the main diagonal (Oreste, 2007). The additional terms can be obtained by the following equation:

$$[k_w]_{i,a} = \begin{bmatrix} k_w \cdot l_{av,i} & 0 \\ 0 & 0 \end{bmatrix} \tag{35}$$

where $l_{av,i}$ is the average length of the elements around the node i, and k_w is the spring stiffness considering the stiffness of the solid slurry and of the ground; it can be determined by the following equation (Han et al., 2023c):

$$k_w = \gamma_G \cdot (50 \cdot h_0 - 6.25\pi \cdot D_e) \tag{36}$$

where γ_G is the bulk density of the ground, h_0 is the depth of the tunnel axis from the ground surface.

Based on Equation 8 and Equation 28, the bending stiffness of the joint depends on the bending moment and on the normal force acting on the joint; the shear stiffness of the joint depends on the relative displacement of segments on the joint. An iterative procedure needs to be adopted to analyse the deformations of the segmental lining along the longitudinal direction.

The FEM model can be calculated on the basis of the following procedure:

Step 1: calculating the moment M_0 and the relative displacement v_0 of each joint considering JBSE equal to 1 and the shear stiffness of the joint at its maximum value;

Step 2: based on Equation 8 and Equation 28, calculating the new bending stiffness and the shear stiffness of each joint, and also the new moment M_1 and the relative displacement v_1; furthermore, the new average value of the moment between M_0 and M_1, and the relative displacement $\overline{v_1}$ can be obtained;

Step 3: calculating the new bending stiffness and new shear stiffness by Equation 8 and Equation 28, and also the moment M_i and the relative displacement v_i, where $i = 2,\ 3,\ 4 \ldots$.

Step 4: comparing the new moment M_i and relative displacement v_i with the corresponding average values $\overline{M_{i-1}}$ and $\overline{v_{i-1}}$; when the biggest differences of the moments and the relative displacements are larger than a specific value, the average value $\overline{M_i}$ and $\overline{v_i}$ can be obtained and substituted into the step 3 and so on; otherwise, finishing the iterative procedure.

3.2 *The influence of the circular joint stiffnesses*

Based on the developed FEM model, the segmental lining deformation along the longitudinal direction can be obtained for a real case, with an external diameter of the tunnel of 8.5m, a thickness of the lining of 0.4m and a length of the ring 1.6m. The densities of the slurry and of the segmental lining are 1938kg/m^3 and 2500kg/m^3, respectively; the density of the ground is 1800kg/m^3 and the depth of the tunnel from ground surface is 15m. The assumed advancing speed of the TBM is 0.5m/h, and the hardening time of the slurry is 15h. The material and structural parameters of the connecting bolt and of the bolt hole is the same as Table 1 and Table 2. The JBSE and the shear stiffness of the joints along the longitudinal direction are shown in Figure 7 and Figure 8.

From Figure 7, the normal force has a significant influence on the joint bending stiffness. When the normal force is equal to 0, the joint has a low bending stiffness. With the increase of the normal force, the bending stiffness of the joint also increases. However, the distribution of the bending stiffness is not uniform, and the joints close to the fluid slurry zone have low stiffness values. When the normal force is larger than 5MN, only the first joints have a lower bending stiffness than the rings; most of the bending stiffness values of joints are close to the one of the ring.

Based on Figure 8, the shear stiffnesses decrease from the first joint within the fluid slurry zone, and the

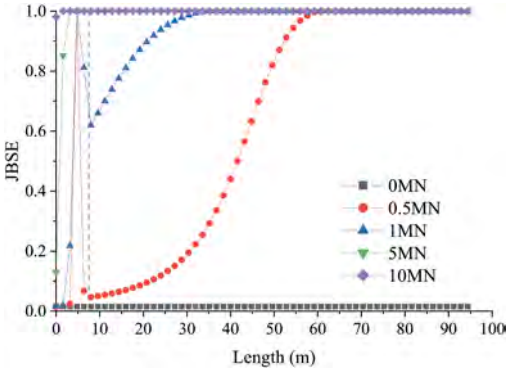

Figure 7. The JBSE value of the joint along the longitudinal direction, for different values of normal forces.

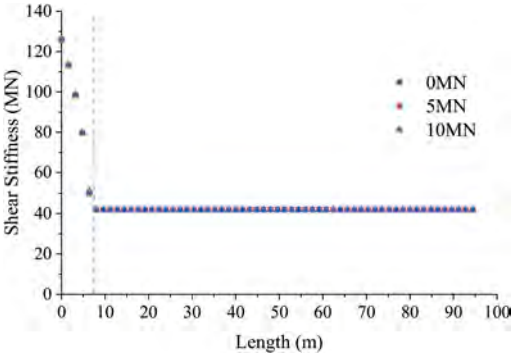

Figure 8. The shear stiffness of the circular joint along the longitudinal direction, for different values of normal forces.

values keep as a constant in the solid slurry zone; the normal force has no effect on the shear stiffness. Therefore, the thrust force has a slight influence on the vertical displacements of the segmental lining, while influencing the bending deformation; the fluid slurry zone has a significant effect on the uplift displacement. The influence of the length of the fluid slurry zone is shown in Figure 9 and Figure 10, where the hardening times of slurry are taken 1h, 5h, 10h and 15h separately.

In Figure 9 the joints show a significant displacement than rings: it means that the uplift displacement of segmental linings is caused by the relative displacements of joints in the fluid slurry zone. In Figure 9 the hardening time of the slurry has a significant influence on the vertical displacements of segmental lining. When the hardening time of the slurry is reduced, the buoyancy phenomenon in the liquid slurry decreases (Figure 10): it causes a reduction of the relative displacement of the first joint as shown in Figure 9.

The density of the slurry is another factor affecting the buoyancy phenomenon. The vertical displacement of the segmental lining along the longitudinal direction is shown in Figure 11 with different slurry densities.

From Figure 11, the vertical displacements of the segmental lining along the longitudinal direction

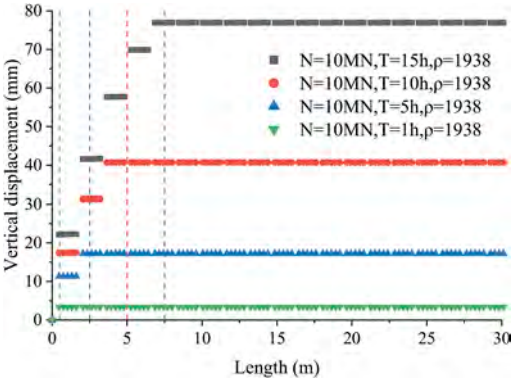

Figure 9. Vertical displacements of the segmental lining for different slurry hardening times varying the distance from the TBM tail.

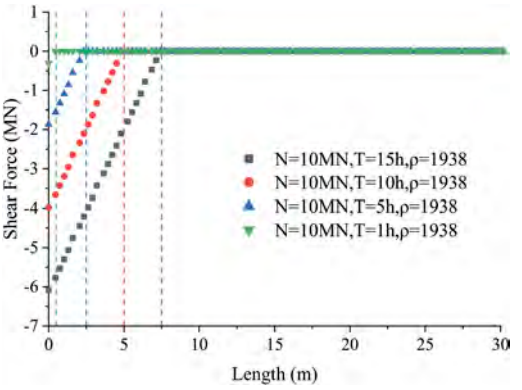

Figure 10. The shear forces on the segmental lining for different slurry hardening times varying the distance from the TBM tail.

decrease with the decrease of the slurry density in the fluid slurry zone. The reduction of the vertical displacement increases when the density of the slurry varies from 1600 to 1200kg/m^3 and from 1200 to 800kg/m^3.

Based on the results of Figure 9 and Figure 11, reducing the hardening time and the density of the slurry is a useful technique to decrease the uplift displacement of the tunnel lining.

4 CONCLUSIONS

Focusing on the nonlinear behaviour of segmental lining joints, calculation methods for the bending stiffness and shear stiffness of circular joints are discussed, and the effect of the slurry presence on the segmental lining deformation along the longitudinal direction is analysed.

1. The bending stiffness of joints is discussed, and the a calculation method is developed. The bending stiffness of joints is determined by the normal forces and the moment applied on the joint: the

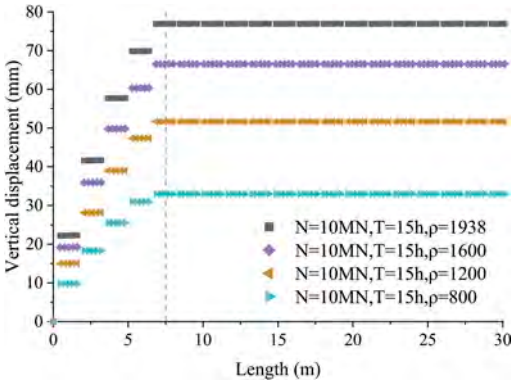

Figure 11. Vertical displacements of the segmental lining with different slurry densities varying the distance from the TBM tail.

value of the bending stiffness decreases with the increase of the moment.

2. A simplified method for the evaluation of the joint shear stiffness with a single bolt is developed. Considering that the shear stiffnesses of inclined bolts are not uniform, the equation of the shear stiffness of a circular joint is proposed. Based on the calculated results of the shear stiffness, the joint shear stiffness increases with the relative displacement of the joint.
3. Considering the nonlinear behaviour of joints, a FEM model based on the Timoshenko beam theory is introduced and an iterative procedure is adopted to calculate the segmental lining deformation along the longitudinal direction. The FEM model can successfully evaluate the deformation of the rings and the joint separately.
4. Based on the calculated results, the normal force shows an obvious influence on the bending stiffness of joints, but no effect on their shear stiffness. The vertical displacements of the lining are mainly influenced by the relative displacements of the joints. Furthermore, decreasing the hardening time and the density of the slurry the vertical displacements of the segmental lining can be reduced.

ACKNOWLEDGMENTS

This study was financially supported by the Fundamental Research Funds for the Central Universities, CHD (Grant No. 300102212702), and this support is gratefully acknowledged. The first author also would like to appreciate the scholarship from China Scholarship Council (Grant No. 202106560030) for his study in Politecnico di Torino.

REFERENCES

Chen, R.P., Meng, F.Y., Ye, Y.H., Liu, Y., 2018. Numerical simulation of the uplift behavior of shield tunnel during construction stage. Soils Found. 58, 370–381.

Cheng, H.Z., Chen, R.P., Wu, H.N., Meng, F.Y., Yi, Y.L., 2021. General solutions for the longitudinal deformation of shield tunnels with multiple discontinuities in strata. Tunn. Undergr. Space Technol. 107.

Fu, Y., Mei, C., Chen, X., Li, W., Yu, B., Li, X., Wang, B., Wang, S., 2023. The time-dependent grout buoyancy behavior based on cement hydration mechanism. Cem. Concr. Res. 166.

Gong, C., Yang, J., Fu, J., 2020. Characteristics and Influencing Factors of Segment Cracking of Large-Diameter River-Crossing Shield Tunnelling in Composite Rock Strata. Modern Tunnelling Technology 57, 30–42.

Guo, W., Feng, K., Zhou, Y., Lu, X., Qi, M., He, C., Xiao, M., 2023a. Experimental and numerical investigation on the shear behavior and damage mechanism of segmental joint under compression-shear load. Tunn. Undergr. Space Technol. 139.

Guo, W., Feng, K., Zhou, Y., Yang, W., Lu, X., Xiao, M., He, C., 2023b. Full-scale test and numerical modeling on deformation and damage behavior of segmental joints under ultimate compression-bending load. Eng. Struct. 279.

Han, X., Oreste, P., Ye, F., 2023a. The buoyancy of the tunnel segmental lining in the surrounding filling material and its effects on the concrete stress state. Geotech. Geol. Eng. 41, 741–758.

Han, X., Oreste, P., Ye, F., 2023b. The contribution of the bolting system to the shear stiffness of circumferential joints in tunnel segmental linings. Comput. Geotech. 162, 1–21.

Han, X., Oreste, P., Ye, F., 2023c. The important role of stiffnesses values of circular joints on the stress state developed in the tunnel segmental lining. Geomech. Geophys. Geo-Energy Geo-Resour. 9, 1–32.

Han, X., Oreste, P., Ye, F., 2023d. The influence of the nonlinear behaviour of connecting bolts on the shear stiffness of circular joints in a tunnel segmental lining, Submitted to Journal.

Li, X., Zhou, X., Hong, B., Zhu, H., 2019. Experimental and analytical study on longitudinal bending behavior of shield tunnel subjected to longitudinal axial forces. Tunn. Undergr. Space Technol. 86, 128–137.

Liu, X., Dong, Z.B., Song, W., Bai, Y., 2018. Investigation of the structural effect induced by stagger joints in segmental tunnel linings: Direct insight from mechanical behaviors of longitudinal and circumferential joints. Tunn. Undergr. Space Technol. 71, 271–291.

Lu, D., 2020. Analysis on mechanical characteristics and cracking pehnomena of segment structure for shield tunnel during construction period. Southwest Jiaotong University.

Oreste, P., 2007. A numerical approach to the hyperstatic reaction method for the dimensioning of tunnel supports. Tunn. Undergr. Space Technol. 22, 185–205.

Shiba, Y., Kawashima, K., Obinata, N., Kano, T., 1988. An evaluation method of longitudinal stiffness of shield tunnel linings for application to seismic response analyses. J. Jpn. Soc. Civ. Eng, 319–327.

Zhou, S.H., Ji, C., 2014. Tunnel segment uplift model of earth pressure balance shield in soft soils during subway tunnel construction. Int. J. Rail Transp. 2, 221–238.

Tunnelling for a Better Life – Yan, Celestino, Thewes & Eberhardt (Eds)
© 2024 The Author(s), ISBN 978-1-032-80042-4
Open Access: www.taylorfrancis.com, CC BY-NC-ND 4.0 license

Comparison of structural load-bearing performance between precast and cast-in-place permanent linings

Koki Kikuchi*, Atsushi Kusaka & Yu Koizumi
Public Works Research Institute, Tsukuba, Japan

Toshi Watanabe
PCL Association, Tokyo, Japan

Yoshitomo Tatsumi
Toda Corporation, Tokyo, Japan

ABSTRACT: In Japan, road tunnels are commonly constructed using conventional tunneling methods. For tunnel cross-sections with an internal width of approximately 10 m, the standard specification includes the application of 30 cm thick unreinforced concrete using the cast-in-place method for the permanent lining. Cast-in-place unreinforced concrete has been established as a standard specification owing to its affordability and consistent quality assurance. Recently, precast permanent linings have been considered to accelerate construction and enhance quality under specific condition. However, in terms of load-bearing performance, the effects of the joint structure, joint location, and number of joints between precast slabs on the failure mechanism and structural capacity of the lining have not been fully clarified. Accordingly, evaluating these effects at the design stage is difficult. In this study, we conducted full-scale lining loading tests using two types of precast permanent linings with different joint structures and an unreinforced concrete permanent lining. In the experiment, we considered the failure mechanism and load-bearing capacity of the precast permanent lining compared with those of the cast-in-place unreinforced concrete permanent lining.

Keywords: Tunnelling, Cast-in-place unreinforced concrete lining, precast concrete lining, load-bearing capacity, full-scale load testing

1 INTRODUCTION

In Japan, road tunnels are commonly constructed using conventional tunneling methods. According to the Technical Standards of Road Tunnel and its Explanation (For Structure) (2003), cast-in-place unreinforced concrete with a design thickness of 30 cm is commonly applied in sections with an inner width of approximately 10 m and where no external forces other than self-weight are expected. These specifications were not determined through performance assessments but have become assumed standards for typical sections for two-lane road tunnels based on past construction records and the cost-effectiveness and consistent quality of unreinforced concrete. In tunnels in which construction satisfying the above specifications has been conducted in standard sections, instances of significant deterioration in structural stability during the operational period are extremely rare. Therefore, despite not being determined through performance assessments, specifications for conventional lining work can ensure the load-bearing capacity and other performance criteria.

Recently, precast lining work in some cases in Japan has been one of the factors considered to improve the speed of construction. However, the adoption of precast lining work in mountain tunnels in Japan is very rare, and the impact of joint structures, joint positions, and the number of joints between precast sections on the failure mechanism and structural strength of the lining has not been fully elucidated.

In this study, we conducted large-scale loading tests using two types of precast lining work with different joint structures to understand the mechanical properties of precast lining work, including load-bearing capacity and failure mechanisms, in comparison with conventional lining work.

2 OUTLINE OF THE LINING STRUCTURE

2.1 *Case 1 Cast-in-place reinforced lining*

Figure 1 shows an overview of the full-scale specimen as previously reported (Ishimura et al., 2017). The specimen had a plain cross-section with no joints

*Corresponding author: kikuchi-k573ck@pwri.go.jp

DOI: 10.1201/9781003495505-143

or changes in lining thickness. The lining thickness was 300 mm, and the outer diameter was 9700 mm. The design uniaxial compressive strength (UCS) of the concrete was 18 N/mm². A typical lining used in Japanese road tunnels was assumed in this case.

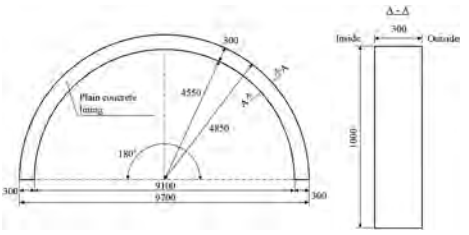

Figure 1. Overview of specimen (case1).

2.2 *Case 2 precast lining consisting of two pieces*

Figure 2 shows an overview of the full-scale specimen as previously reported (Fujiwara et al., 2023). It consisted of two symmetrical pieces with one joint at the crown. The lining thicknesses were 140 mm for the general section, 200 mm for the joint, and 196 mm for the foot section. The outer diameter remained constant at 9480 mm.

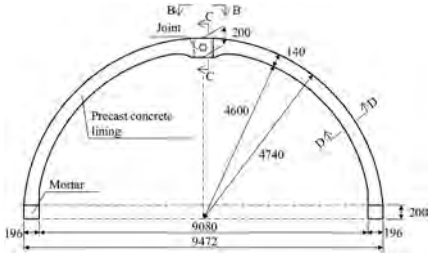

Figure 2. Overview of specimen (case2).

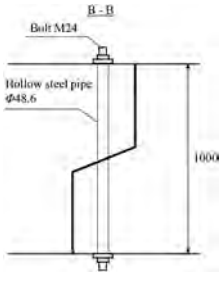

Figure 3. Joint structure (case2).

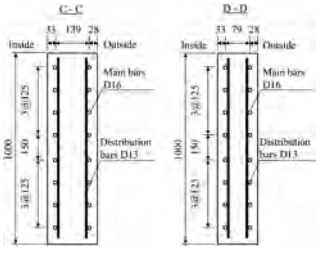

Figure 4. Reinforcement arrangement (case2).

Figure 3 shows the joint structure as previously reported (Tatsumi et al., 2023). The joints were connected to the plates and nuts using M24 bolts from the ends, whereas the right and left pieces were interlocked. The connecting hole for the bolt insertion was fabricated from a φ48.6 mm SD345 hollow steel pipe. The tightening torque was 100 Nm and the initial state of the structure was similar to a pin with a small rotational spring value. A rubber plate 5 mm thick was placed on the contact surface of the piece.

Figure 4 shows the reinforcement arrangement. The designed UCS of the concrete was 60 N/mm². The main reinforcement consisted of eight SD345-D16 bars on the interior and exterior surfaces, and the SD345-D13 bars were placed inside the main reinforcement at a pitch of approximately 250 mm. The joints were thickened on the inside surface by approximately 85° to 95°, and the main bars on the inside were straight members without curvature. The legs were cast with a no-shrink mortar and a designed UCS of 80 N/mm² after the specimens were installed to avoid weak areas owing to differences in the UCS.

2.3 *Case 3 precast lining consisting of three pieces*

Figure 5 presents an overview of the full-scale specimens. It consisted of three pieces with joints at 20° and 110°. The designed lining thickness was 170 mm.

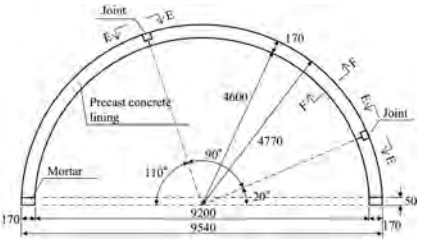

Figure 5. Overview of specimen (case3).

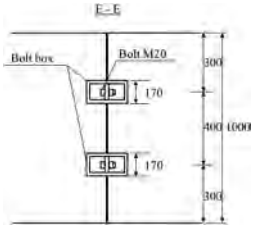

Figure 6. Joint structure (case3).

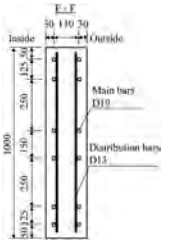

Figure 7. Reinforcement arrangement (case3).

Figure 6 shows a schematic of the joints. The joints were bolted together using M20 bolts at two points on the outer surface of the specimen. Each specimen was fastened with an axial force of approximately 20 kN. The contact surfaces of the frame were smooth.

Figure 7 shows the reinforcement arrangement. The designed UCS of the concrete was 40 N/mm². The main reinforcement consisted of six SD345-D19 bars on the inside and outside surfaces, and the SD345-D13 bars were placed inside the main reinforcement at

a pitch of approximately 250 mm. For the legs, a no-shrink mortar with a designed UCS of 80 N/mm² was placed after the specimens were installed to avoid weak areas owing to the UCS differences.

3 OUTLINE OF THE EXPERIMENT

3.1 *Outline*

Figure 8 shows a schematic of the test equipment. This full-scale equipment could load a specimen of the same size as the general section of a two-lane road tunnel in Japan. Seventeen hydraulic jacks with a loading capacity of 2000 kN were installed on the reaction wall at a 10° pitch. Each jack was capable of load, displacement, and springing control. The springing control maintained a constant spring and could simulate arbitrary ground reaction forces.

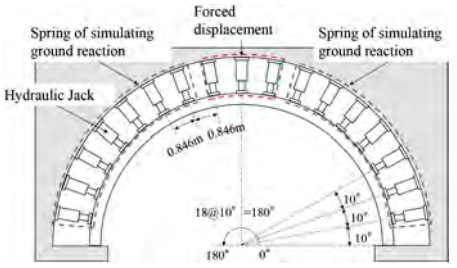

Figure 8. Overview of test equipment.

In the experiments, the loading type was designed to simulate the passive earth pressure acting on the crown under conditions in which a sufficient ground reaction force could be applied. First, as a preliminary loading, the loading jacks were loaded in stages of up to 40 kN/jack under full jack load control to ensure the stability of the equipment and specimen by maintaining close contact between the loading jacks and specimen and a constant hydraulic pressure. Each specimen was subjected to an axial force equivalent to its weight. Subsequently, the 80°, 90°, and 100° jacks were forced to displace the specimen to the inside by 0.5, 0.8, and 0.5 mm at a loading rate of 1–2 mm/min per step as the main loading. The jacks, except the loading jacks, were spring-loaded, and the spring constant was set to 400 kN/mm. According to Specifications for Highway Bridges: Part IV Substructures (2017), this provides a ground deformation coefficient of approximately 500 MN/m².

During the experiment, we measured the reaction force and stroke of each jack, circumferential strain on the interior and exterior surfaces of the specimen, circumferential strain of the main reinforcement approximately the joints, and the amount of joint opening. In addition, the cracks on the specimen surface were visually observed and recorded between loading steps.

In addition, we simultaneously prepared cylindrical test specimens while casting the full-scale test specimen. The properties of the concrete obtained through uniaxial compression tests conducted on the day of load testing are listed in Table 1. The average values for each piece of the precast lining are shown.

Table 1. Properties of concrete.

		CASE1Cast-in-place unreinforced lining	CASE2Two-piece precast lining	CASE3Three-piece precast lining
UCS	(N/mm^2)	25.4	70.4	68.3
Tensile Strength	(N/mm^2)	2.0	3.9	3.9
Young's Modulus	(kN/mm^2)	19.3	36.3	36.5
Poisson's Ratio	-	0.15	0.20	0.19

3.2 *Calculation method of M-θ for joints*

A schematic of the measurement conditions near the joint is shown in Figure 9. The rotation angle θ of the joint was calculated using the measurement results of the gap width installed on the upper and lower surfaces of the joint according to Design Standards for Railway Structures and Commentary (Shield Tunnel) (2022).

The bending moment (M) of the joint was first calculated by determining the bending strain from the strain measurements of the inner and outer main bars near the joint, both to the left and right of the center of the joint. Subsequently, the second moment of the area of the equivalent section about the axis at the center of the section (h/2) was calculated using the Young's modulus ratio (n). These values were used to calculate M of each structural element, which was then averaged to estimate the bending moment of the joint.

However, because we did not consider the softening of the Young's modulus, the calculated bending moment may have been larger than the actual value when the nonlinear range was reached. Additionally, under the assumption of plane-stress conditions, the value became approximate when the deformation or failure of the section increased such that the assumption of plane-stress conditions no longer held. Note that both the rotation angle and bending moment were calculated using the initial values set at the initial step of the applied load.

3.3 *Evaluation method for the load-bearing performance of lining*

To assess the load-bearing capacity and failure mechanisms of the linings, we focused on two distinct aspects: local damage, such as tensile cracking

and compressive failure, and the ultimate limit state at which the entire lining becomes destabilized.

Regarding the local damage, we examined the variations observed on the surface of the lining, such as cracks and crushing, and focused on the applied load values at which these occurred, locations of damage initiation, and number of affected areas. For the overall structural destabilization, we defined the maximum load as the load-bearing capacity of the entire lining structure and used it to evaluate the load-bearing capacity.

4 EXPERIMENTAL RESULTS

4.1 *Case 1 Cast-in-place unreinforced lining*

Figure 10 shows the relationship between the applied load (the total of three load jacks) and crown displacement (post-unloading steps are omitted). As the displacement increased, the applied load increased linearly. Tensile cracking initially occurred on the inner surface at the top and then on the outer surface of the shoulder at relatively low load levels. Subsequently, compressive failure occurred in reverse order, beginning with the outer surface at the top and then the inner surface of the shoulder, reaching an overall load-bearing capacity of approximately 2400 kN.

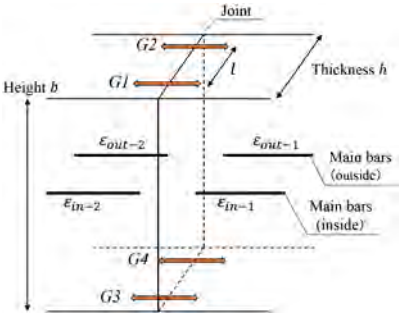

Figure 9. Schematic diagram of the measurement.

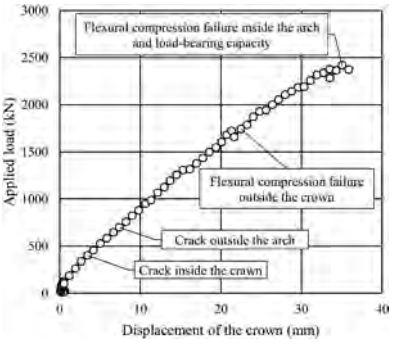

Figure 10. Load–displacement curve.

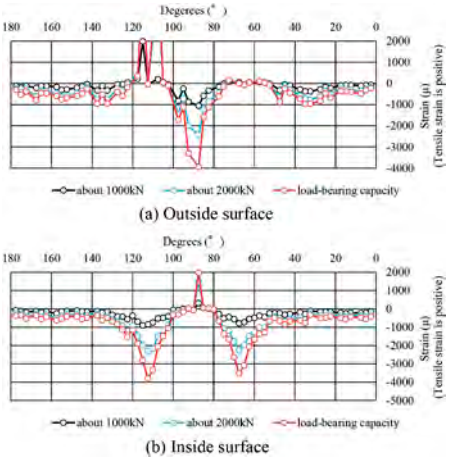

Figure 11. Strain distribution.

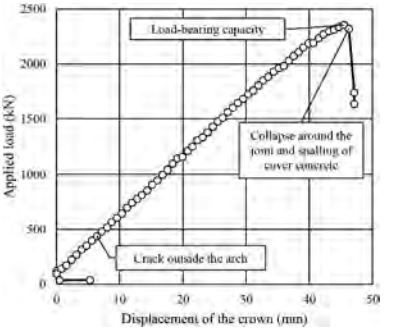

Figure 12. Load–displacement curve.

Figure 11 shows the circumferential strain distributions on the inner and outer surfaces when reaching approximately 1000 and 2000 kN, respectively, and the overall load-bearing capacity. At the crown, both the concrete and main reinforcement were in a state of full cross-sectional compression. On the outer surface at the crown and the inner surface of the shoulder, compressive strains of approximately -3000μ to -4000μ were observed, whereas tensile strains were observed on the opposite sides, and all other sections were in a state of full compression. Thus, we inferred that the axial forces developed uniformly and bending moments occurred at the crown and shoulder sections, leading to bending compressive failure and ultimately resulting in the attainment of the overall load-bearing capacity of the structure.

4.2 *Case 2 Two-piece precast lining*

Figure 12 shows the relationship between the applied load (the total of three load jacks) and crown displacement (post-unloading steps are omitted). As the displacement increased, the applied load increased linearly. Tensile cracking occurred on the outer

shoulder surface at approximately 500 kN, after which no significant damage was observed. At approximately 2400 kN, the load-bearing capacity was reached, spalling occurred near the crown surface, and the displacement gauge fell off. Shortly thereafter, cracks resembling compression were observed on the inner surface at approximately 85°–95°, accompanied by spalling of the lining surface, resulting in a decrease in load.

Figure 13 shows the condition near the crown after unloading, and Figure 14 shows the condition of the main reinforcement. Cracks resembling compression cracks were observed on both the inner and outer surfaces near the crown, along with spalling. On the upper surface, cracks with a width of approximately 10 mm developed horizontally from the center of the steel pipe, with the concrete covering the inner side detached. When the detached concrete was removed from the inner surface of the test specimen, we confirmed that the main reinforcement near 90°–95° had deformed inwardly into a convex shape.

Figure 15 shows the M-θ curve in the joint area. As the load increased, the stiffness approached its maximum value, and a significant increase in the slope occurred at approximately 35 mrad. This was considered to be due to the closure of the gaps between the contact surfaces at approximately 35 mrad, along with the increased transmission of axial forces and bending moments caused by the structure. After the onset of crushing and spalling near the joint, the reliability of the measured values decreased, and we considered them as reference values because of their unloading-induced behavior.

(a) Inside the crown (b) Outside the crown

Figure 13. Condition of the failure joint.

Figure 14. Condition of the main reinforcement failure.

Figures 16 and 17 show the circumferential strain distribution in the concrete and main reinforcement at approximately 1000 and 2000 kN

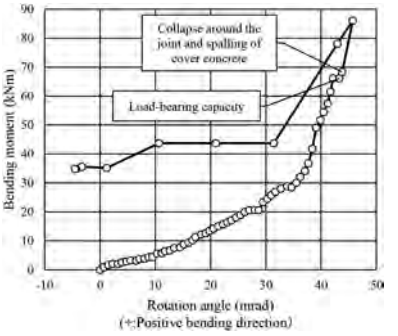

Figure 15. Moment–rotation curve.

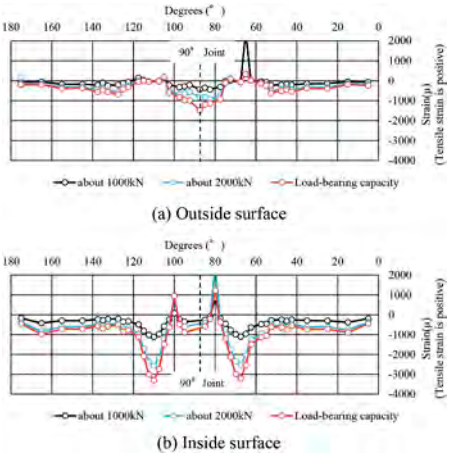

Figure 16. Strain distribution.

and the load-bearing capacity. At the crown section, both the concrete and main reinforcement were in a state of full cross-sectional compression. In the shoulder section, bending compression occurred with tensile strain on the outer surface and compressive strain on the inner surface. In sections other than the crown and shoulder, both the inner and outer surfaces exhibited small compressive strains, indicating complete compression. On the outer surface of the concrete, a significant tensile strain was measured at approximately 1000 kN. However, it decreased in subsequent steps owing to the stress relief caused by the occurrence of cracks approximately the strain gauge. Additionally, the yield strain calculated from separate tensile tests of the steel reinforcement was approximately 1900μ, suggesting that the steel reinforcement had not reached the yield point according to the strain measurements inside the test specimen.

From the above observations, we can infer that the axial compression forces developed uniformly in the test specimen with the application of load, and bending moments occurred in the shoulder section.

Near the crown, the lining remained in a state of full compression with minimal bending moments, eventually resulting in the compression failure of the concrete near the crown and spalling of the steel reinforcement owing to deformation; thus, the overall load-bearing capacity was attained. Compared with the cast-in-place unreinforced lining in Case 1, the following common points were identified:

- The load-bearing capacity was approximately similar.
- Near the shoulder section, axial forces and bending moments were generated, resulting in bending compression, whereas from the foot to the shoulder, small axial compression forces were generated, resulting in full compression.

However, differences were also noted:

- In the two-piece precast lining, the overall load-bearing capacity was reached through buckling of the main reinforcement and spalling of the covered concrete near the crown joint. However, note that the shoulder section also experienced strains close to the ultimate strain, suggesting it was in a state approaching cross-sectional failure.

4.3 *Case 3 Three-piece precast lining*

Figure 18 depicts the relationship between the applied load (total of three load jacks) and crown displacement. The load–displacement relationship was approximately linear but exhibited two peaks: approximately 2550 kN (the first peak) at approximately 37 mm of displacement and 2600 kN (the second peak) at approximately 46 mm of displacement. At relatively low loads, tensile cracking occurred on the inner surface of the crown and outer surface of the shoulder at 70°. From approximately 2300 kN to the first peak, cracks were observed in the concrete, indicative of compressive failure on the inner surface of the shoulder at 110° and spalling.

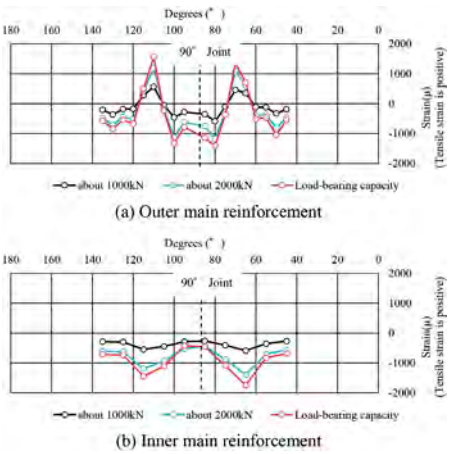

Figure 17. Strain distribution.

Near the second peak, spalling of the covered concrete on the outer surface at 110°, buckling of the main reinforcement, and spalling of the inner concrete surface occurred, resulting in a decrease in the load.

Figure 19 shows the conditions near the shoulder after unloading. The outermost main reinforcement deformed near 115° with spalling of the covered concrete. While deformation of the inner side reinforcement was not observed, spalling of the covered concrete was evident. Furthermore, cracks considered to be caused by compression were detected on the outer surface of the crown, which were not visible during the experiment because of the load plate.

Figure 20 shows the M-θ curve in the joint area. For the joint at 110°, changes in slope occurred at approximately -4 and -12 mrad. Up to approximately -4 mrad, was considered to be due to axial force introduction and the fitting of the test equipment to the test specimen. A constant negative bending moment slope was observed up to approximately -12 mrad. However, beyond this point, it remained relatively constant at approximately -20 mrad. The step at approximately -12 mrad coincided with the step in which signs of crushing were observed on the inner surface near 110°. In other words, the behavior of the joint was considered to change owing to cross-sectional failure. Beyond this point, the reliability of the measured values decreased, possibly because of the partial spalling of the bottom displacement gauge near the first peak; thus, we considered them as reference values.

For the 20° joint, the deformation was considered to be small. Compared with the 110° joint, the bending moment was approximately 1/2, the rotation angle was approximately 1/10, and the joint was under full compression.

Figures 21 and 22 show the circumferential strain distributions in the concrete and main reinforcement at approximately 1000, 2550 (first peak), and 2600 kN (second peak). Please note that, because of the positioning of strain gauges, values from certain locations that could not be accurately obtained have been omitted. The strain in the outer surface of the concrete near 110° exhibited a slight tensile strain up to the first peak but transitioned to compression at the second peak, indicating full cross-sectional compression. At 20°, both the concrete and main reinforcements were in a state of full compression. The inner surface of the concrete at 90° exhibited almost no strain, but the main reinforcement exceeded its yield point under tension. Numerous longitudinal tensile cracks on the concrete surface from the early stages suggested a decrease in strain owing to the stress relief caused by concrete surface cracking.

At 70°, both the concrete and main reinforcement were in a state of bending compression. Except for the crown and shoulder sections, all other sections exhibited full compression.

From these observations, we inferred that with the application of the load, the axial compression forces developed consistently throughout the test specimen. In the joint area near 110°, bending compression was

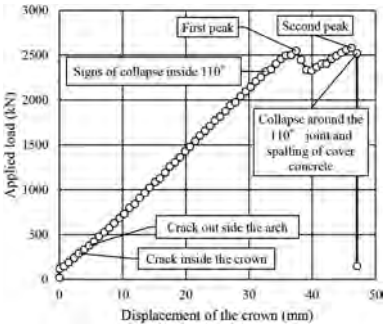

Figure 18. Load–displacement curve.

(b) Outside at the 110° joint (b) Inside at the 110°joint

Figure 19. Condition of the failure joint.

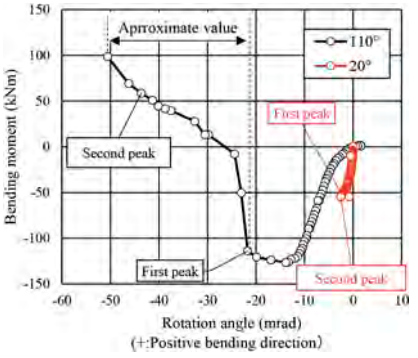

Figure 20. Moment–rotation curve.

observed until the first peak, followed by full compression. Ultimately, the concrete compression failure and deformation of the steel reinforcement resulted in spalling, causing structural instability. However, deformation may have occurred in weak areas at locations where the load plate served as a fulcrum and did not provide support, which may not be the case in scenarios with the anticipated ground reactions.

Compared with the cast-in-place unreinforced lining in Case 1, the following common points were identified:

- The load-bearing capacity was approximately similar.

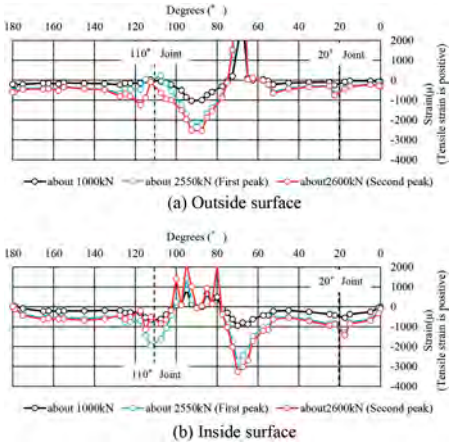

Figure 21. Strain distribution.

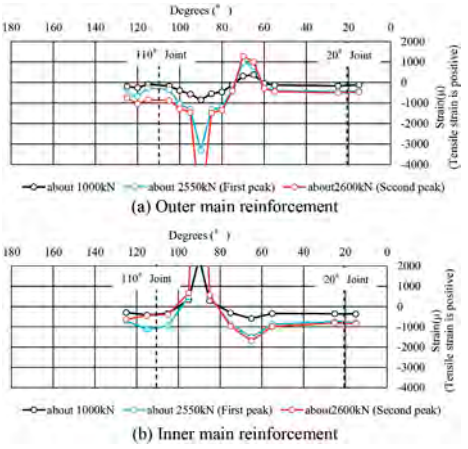

Figure 22. Strain distribution.

- Axial forces and bending moments were generated at the crown and shoulder sections until the first peak with bending compression, whereas small axial compression forces were generated from the foot to the shoulder, resulting in full compression.
- A decrease in load owing to bending compression failure occurred at the crown and shoulder sections (represented by the first peak).

However, the following differences were also noted:

- The three-piece precast lining exhibited two peaks in the load.
- The second peak was determined by the buckling of the main reinforcement and the spalling of the covered concrete near the joint area at 110°.

4.4 *Consideration of the failure mechanism*

In the cast-in-place unreinforced lining, under relatively small loads, tension cracks appeared on the inner surface of the crown and outer surface of the shoulder. Subsequently, section failure occurred on the outer surface of the crown and inner surface of the shoulder, ultimately affecting the overall load-bearing capacity of the structure. Both axial forces and bending moments were generated in the crown and shoulder regions, resulting in flexural-compressive failure. The final load-bearing capacity was approximately 2400 kN.

Although the presence or absence of tensile cracks in the precast lining varied depending on the joint position, it exhibited failure mechanisms similar to those of cast-in-place unreinforced linings. The final load-bearing capacity of the entire structure was approximately 2400–2600 kN, which was equivalent to that of a cast-in-place unreinforced lining. However, unlike the cast-in-place unreinforced lining, where the load decreased shortly after the flexural–compressive failure in the shoulder region of the concrete, in the precast lining near the joints, both rebar buckling and spalling of the cover concrete caused a reduction in load. The failure patterns observed in these cases closely resembled the seismic damage in reinforced concrete bridge piers (Figure 23), and we speculated that they shared a similar mechanism. Based on the Specifications for Highway Bridges: Part V Seismic Design (2017), for reinforced-concrete bridge piers, a method for investigating the failure mechanism was established by comparing the axial force exerted on the reinforcing bars with the resistance of the cover concrete, as shown in Figure 24 (Maekawa et al., 2003). We are currently exploring an investigative approach for assessing the spalling of cover concrete and buckling of reinforcing bars observed in precast linings. The following were the estimated failure mechanisms of the precast lining:

Stage 1: In both experiments, the joint structures were relatively resistant to the generation of bending moments compared with the general section of the specimen. Consequently, the influence of the axial forces became significant, resulting in a state of full cross-sectional compression.

Figure 23. Seismic damage (Hanshin Expressway Management Engineering Center et al., 2020).

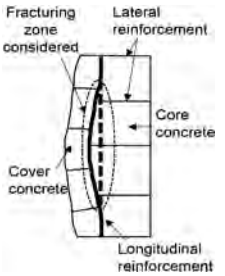

Figure 24. Failure mechanism.

Stage 2-1: For the two-piece precast lining, the joint section (90°) was displaced inward as a load was applied. The main reinforcement on the inner surface of the crown, which initially had a straight configuration, gradually deformed inward owing to the influence of bending moments. This deformation resulted in the development of axial compression forces.

Stage 2-2: For the three-piece precast lining, as the load was applied, the curvature of the main reinforcement in the joint section (110°) increased. After the first peak, the lining reached a state of full compression and axial compression forces developed in the steel reinforcement.

Stage 3: The force exerted by the deformed main reinforcement on the convex side pushing against the covered concrete exceeds the resistance of the covered concrete and causes it to spall.

Stage 4: With a reduction in the effective cross-sectional area, both the buckling of the steel reinforcement and the compressive failure of the concrete on the opposite side occurred almost simultaneously.

The phenomena in Stages 3 and 4 significantly affect the overall load-bearing capacity of the structure and are considered critical for determining the limit state of the lining.

5 CONCLUSION

In this study, we conducted full-scale load tests on two types of precast concrete linings with different joint structures and compared them with the cast-in-place unreinforced lining commonly used in Japan. Thus, we assessed the mechanical performance, including the load-bearing capacity and failure mechanisms. The following are the conclusions of this study:

- Under conditions where a ground reaction force of approximately 500 MPa can be expected around the perimeter, in the assumed loading scenario considering the uplift loads, the load-bearing capacities of the two-piece precast and three-piece precast linings used in this study were approximately comparable to that of the cast-in-place unreinforced lining. Furthermore, we confirmed that the axial forces and bending moments in the crown and shoulder areas followed a failure mechanism similar to that of a cast-in-place unreinforced lining.
- The joints of the two types of precast lining exhibited different results in terms of their maximum rotational angles and M-θ slopes due to differences in their structures and positions. However, we observed that M and θ were approximately proportional, and the joint area tended to fail almost simultaneously with the load-bearing capacity of the lining.
- The bending moments of the precast lining joints were reduced, resulting in an overall state of compression. As a result, compressive forces dominated the main reinforcement with curvature, resulting in

deformation and forces that pushed out the cover concrete. This phenomenon exceeded the resistance of the cover concrete and caused spalling.

- The spalling of the cover concrete significantly affected the load-bearing capacity of the entire structure under the experimental conditions and for the targeted precast linings.

In the lining design, from a stress calculation perspective, placing the main reinforcement away from the centroid is advantageous. However, when the cover concrete is thin and compressive action occurs from the convex side to the inner side, cover concrete spalling may occur. On the side facing the ground, resistance can be expected owing to the ground; however, on the inner side, the resistance may not be reliable. Therefore, the inspection method proposed in this paper for the inner side design should be considered when setting member cross-sections.

Generally, the rotational spring constant increases with the introduction of axial compressive forces. Therefore, the M-θ curve obtained in this study may not be applicable under certain loading conditions for the same joint configuration.

Future research will involve numerical analysis to reproduce the failure mechanisms and investigate inspection methods related to the spalling of cover concrete considering axial compressive forces.

REFERENCES

Fujiwara S., Natsume T., Kojima K., Watanabe T., Koizumi Y., Kikuchi K., 2023. Evaluation of load-bearing capacity of precast lining plate on full-scale loading tests. Japan Society of Civil Engineers 2023 Annual Meeting, III-187. (in Japanese)

Hanshin Expressway Management Engineering Center, 1997. From Earthquake to Recovery [Photo Book], p.192.

Ishimura T., Isago N., Kusaka A., 2017. Experimental Study on the Reinforcement Effect of Carbon Fiber Sheets Fixed with Steel Materials in Tunnels. Japan Society of Civil Engineers 2017 Annual Meeting, III-383. (in Japanese)

Japan Road Association, 2003. Technical standard of road tunnel and its explanation (for structure), pp.125–128. (in Japanese)

Japan Road Association, 2017. Specifications for Highway Bridges Part IV Substructures, pp.187–190. (in Japanese)

Japan Road Association, 2017. Specifications for Highway Bridges Part V Seismic Design, pp.177–190. (in Japanese)

Maekawa K., Pimanmas A., Okamura H., 2003. Nonlinear Mechanics of Reinforced Concrete, CRC Press, Boca Raton, United States, p.708.

Railway Technical Research Institute, 2022. Design Standards for Railway Structures and Commentary (Shield tunnel), pp.222–225. (in Japanese)

Tatsumi Y., Imamura S., Yamamoto S., Morita T., Dahara T., Taniguchi T., Koizumi Y., Kikuchi K. Experimental Study on Load-Bearing Capacity of Three Section Type Precast Lining. Japan Society of Civil Engineers 2023 Annual Meeting, III-186. (in Japanese)

Tunnelling for a Better Life – Yan, Celestino, Thewes & Eberhardt (Eds)
© 2024 The Author(s), ISBN 978-1-032-80042-4
Open Access: www.taylorfrancis.com, CC BY-NC-ND 4.0 license

Development and application of highly adaptable lining equipment for complex tunnels with variable sections

Jinshu Liu*
China Railway Construction Heavy Industry Corporation Limited, Changsha, China

ABSTRACT: Aiming at the requirements from the complex construction scenarios and working conditions of tunnels with variable sections such as alternating large and small sections, right-angle turns and small entrances, a brand-new highly adaptable lining equipment is developed to solve the problems of existing tunnel lining equipment such as low assembly efficiency, long transition period, and high labor intensity. By studying the method for rapid assembly of trolley formwork, the mode is changed from the installation of fragmented small formwork to the overall installation of pre-assembled large modules, and auxiliary installation devices as module lifting mechanism are innovatively designed, so as to realize the automatic lifting in narrow spaces in tunnel. The equipment, in fabricated gantry structure, is equipped with automatic rail feeding device and traversing mechanism to realize automatic rail feeding in tunnels with alternation of variable sections and right-angle turns in tunnel, thus effectively shortening the transition time in tunnel. As compared with traditional construction equipment, the assembly cycle is shortened from 15 days to 7 days, and the number of constructors is decreased from 10 to 6.

Keywords: rapid assembly, lifting mechanism, automatic rail feeding, right-angle turns in tunnel

1 INTRODUCTION

In recent years, the tunnel construction in China has developed rapidly. As an important part of tunnel construction, secondary lining directly affects the stability of tunnel structure and traffic safety. The secondary lining construction has gone through the stages of manual formwork erection, manual formwork setting up, fully hydraulic lining trolley and intelligent lining trolley. The first lining trolley was introduced in China as early as 1978, and was initially applied to Dayaoshan Tunnel of Beijing-Guangzhou Railway. At present, lining trolley has been widely used in the construction of national key projects such as railways, highways and hydraulic engineering [1]~[4].

The digitalization and automation of lining is a hot topic in current study. The experts and scholars as well as benchmarking enterprises in China have carried out a large number of studies. Dong Wanlong et al [5] studied the trolley positioning technology to solve the walking problem in small-radius curved tunnels; Wang Baiquan [6] studied the control system of intelligent trolley to effectively realize automatic control and real-time monitoring of pouring process; Ji Haidong et al [7] developed a new digital lining trolley for pressurized pouring tunnel, realizing the mold grouting, high-frequency vibration and digital control.

Aiming at the problem of obvious change in section size in the process of tunnel construction, Liu Yunzhu [8] designed a lining trolley for tunnels with variable sections to adapt to 5 different tunnel sections; Ren Wenbin [9] designed a lining trolley for variable sections of super-large section tunnels, which can meet the adaptive design of sections in 14.5 m to 25 m; Li Feng [10] studied the key elements of design and manufacture of lining trolley for variable sections, and achieved good economic benefits; Xue Jiangsong et al [11] focused on the influence of formwork connection hinge points on the change of trolley sections in combination with the characteristics of variable sections of Lanzhou-Chongqing Railway.

The current research mainly focuses on the intelligent design of lining trolley for railway and highway tunnels and the adaptive design of large-section tunnels with variable sections. The existing lining trolley cannot meet the special needs in tunnel construction such as narrow spaces, varied section shapes and many right-angle turning branches. Therefore, it is urgent to design a highly adaptable lining equipment

*Corresponding author: liujinshu@crchi.com

DOI: 10.1201/9781003495505-144

for the lining of complex tunnels with variable sections to solve the problems existing tunnel lining equipment such as low assembly efficiency, long transition period and high labor intensity.

2 OVERALL DESIGN OF HIGHLY ADAPTABLE LINING EQUIPMENT

2.1 *Structural composition and parameter design of highly adaptable lining equipment*

In order to meet the needs of secondary lining operation for special tunnels with variable complex small sections, a brand-new lining equipment with high adaptability is developed, which is capable of adapting to tunnels with variable sections and has the functions of crossing small-section tunnels and right-angle turns. Its main structures include traveling system, gantry assembly, formwork assembly and auxiliary installation device, as shown in Figure 1, with the performance parameters as shown in Table 1.

Figure 1. Structure diagram of highly adaptable lining Equipment.

Table 1. Performance parameters of highly adaptable lining equipment.

S/N	Parameter	Technical Indicator
1	Adaptable section size 1	Clear span: 5.5 m; arch camber height: 4.5 m
2	Adaptable section size 2	Clear span: 6 m; arch camber height: 5 m
3	Section type	1/4 arch
3	Lining thickness	350mm
4	Single covering length	6m+6m
5	Top formwork removal stroke	200mm
6	Travel drive	Track-type traveling, gradeability ≥ 6%
7	Deformation of side formwork	≤2mm
8	Deformation of top formwork	≤1mm

2.2 *Traveling system*

The traveling system device is the power unit for movement of the whole vehicle, consisting of active traveling box, driven traveling box, traversing mechanism and track. The traveling motor realized the traveling by driving the chain to rotate the running wheel through a reducer, where a sprocket and a drum are connected outside the output shaft of the reducer. During traveling, the bottom oil cylinder jacks up the whole machine, the track is suspended, the wire rope is pulled by the drum to automatically drive the track to move forward; then the bottom oil cylinder is retracted, and the whole machine is lowered onto the track to realize the forward positioning of the whole machine. In order to meet the requirements of covering tunnel sections with different track elevations, heightening joints are set above the running box and below the traversing device in the traveling system.

2.3 *Gantry assembly*

The gantry assembly is the main supporting structural member of the formwork, bearing the mass of concrete and formwork during pouring. In order to ensure a rapid transition in tunnel, the gantry assembly is designed as split type and consists of two symmetrical 6 m unit modules, each of which can be separately assembled into a trolley in 6 m long. During a transition, by splitting the gantry, the trolley in 12 m long can be split into two symmetrical trolleys in 6 m long each.

In order to meet the requirements of internal traffic space, the gantry is equipped with a swing-type rotating cross brace, which realizes rapid swing and connection through the swing pin shaft and self-locking lead screw mechanism and supports stress. In the covering, the cross brace rotates to the middle position and the screw rod rotates tightly to bear the lateral pressure transmitted by the formwork on both sides to ensure the rigidity of the overall structure. After covering, it rotates to both sides to make the middle passage open to traffic. Due to the rotational structure of the cross brace, the operation load is small and safe. The section passage space is ≥ 3.3m wide and ≥ 4.2m high.

2.4 *Formwork assembly*

The formwork assembly is the working face of trolley, mainly consisting of dome assembly, lateral formwork and blocking system. A modular design concept is adopted for the formwork assembly, where both the side formwork and top formwork are of modular design. Different formwork module combinations can be selected during installation to meet the construction requirements of different sections, as shown in Figure 2 and Figure 3.

The dome assembly consists of 10 sets of top modules, each 1.2 m wide. In order to meet the construction requirements of the following 2 sections, as

shown in Table 2. The top formwork is designed as flexible formwork, which can be deformed according to the radian of the framework. Universal formwork units can be used for dome with different spans to realize convenient span construction.

Table 2. Performance parameters of highly adaptable lining equipment.

Specification of dome	Section 1	Section 2
Span/mm	5500	6000
Radius/mm	3437	3750
Springing height/mm	4500	5000

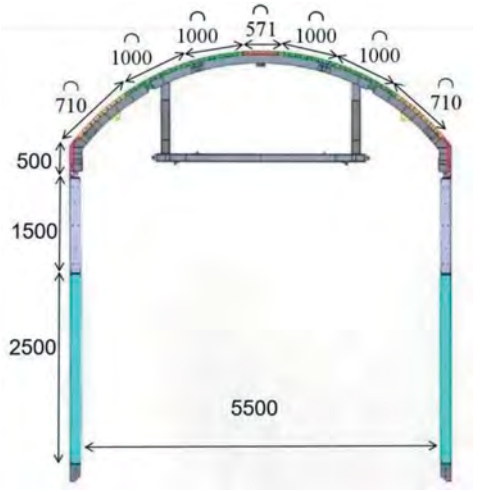

Figure 2. Structural diagram of formwork assembly in 5.5m trolley.

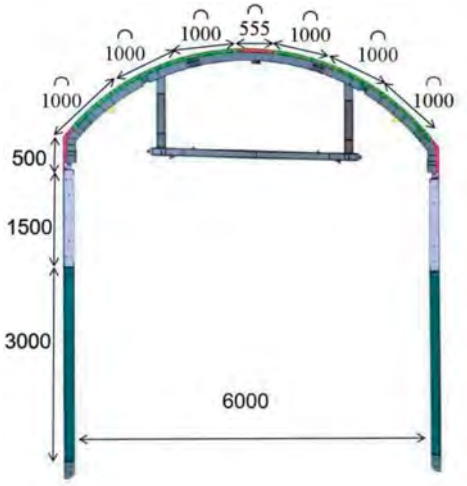

Figure 3. Structural diagram of formwork assembly in 6m trolley.

The lateral formwork assembly consists of 10 sets of lateral formwork modules, each with a width of 1.2 m. Each set of lateral formwork is assembled by two or more pieces of lateral formwork. A single piece of lateral formwork has the height of 1.5 m, 2.5 m, 3 m etc. They are combined according to different springing heights to realize the design of 5.5m and 6m springing heights. The combination of formwork in 1.5 m and 2.5 m high can meet the springing height of 4m, and the combination of formwork in 1.5 m and 3 m high can meet the springing height of 5 m. The formwork combinations for the two sections are shown as Figures 2 and 3.

2.5 *Auxiliary installation devices*

In-tunnel auxiliary installation devices include top formwork lifting mechanism and lateral formwork lifting mechanism. The top formwork lifting mechanism consists of winch, pulley block, sliding track, sliding support and lifting platform. Under the action of the winch, the pulley block drives the sliding support to rise and fall on the sliding track through the steel wire rope, thus driving the lifting platform to rise and fall. The top formwork assembly can be lifted from the ground to above the gantry through this lifting mechanism; the lateral formwork lifting mechanism consists of winch, sliding support and sliding track. The sliding track is installed on the top of the gantry, while the winch is installed on the sliding support and can move forward and backward along the sliding track. When lifting the lateral formwork, the winch wire rope bypasses the pulley of the dome framework to lift the side formwork upward. They can effectively improve the automation in tunnels with narrow sections.

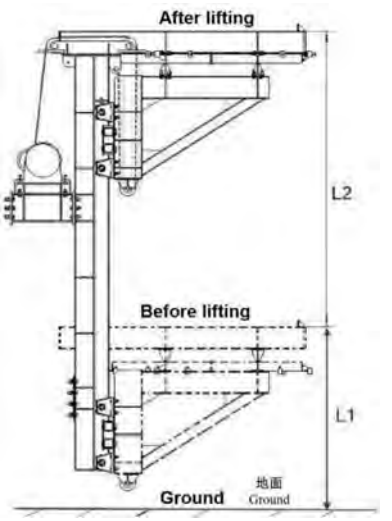

Figure 4. Schematic diagram of lifting in tunnel.

3 STRUCTURAL ANALYSIS OF HIGHLY ADAPTABLE LINING EQUIPMENT

3.1 *Determination of boundary conditions*

The trolley mainly bears the lateral pressure of concrete, the dead weight of concrete and the dead weight of structure. Of them, the top formwork bears the dead weight of concrete and structure, which is mainly directly connected to the section, and the side formwork mainly bears the lateral pressure of concrete. As shown in Figure 5.

3.2 *Lateral formwork pressure*

The lateral pressure of concrete acting on the formwork is increased with the pouring height of concrete. Where the pouring height reaches a certain critical value, the lateral pressure will no longer be increased. At this time, the lateral pressure is the maximum lateral pressure, as shown in Figure 6.

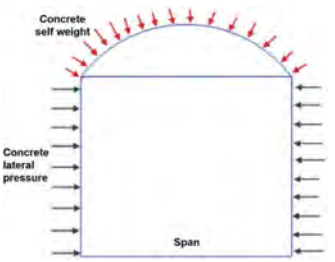

Figure 5. Schematic diagram of trolley stress.

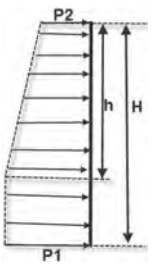

Figure 6. Schematic diagram of lateral formwork pressure.

$$P_0 = \min\begin{cases} 0.22\gamma_c t_0 \beta_1 \beta_2 v^{\frac{1}{2}} \\ \gamma_c H \end{cases} \quad (1)$$

Where

p_0 —Lateral pressure of newly poured concrete on the formwork, in KN/m2

γ_c —Gravity density of concrete, in 25KN/m3

t_0 —Initial setting time of newly poured concrete, taken as 5h

β_1 —Correction coefficient of admixture influence, taken as 1

β_2 —Influence coefficient of concrete slump, taken as 1.15

v —Concrete pouring speed, in m/h

H —Total height from the position for the calculation of lateral pressure to the top surface of newly poured concrete

A - Concrete pouring area

In consideration of the concrete impact load and the concrete pouring speed, a safety factor of 1.2 is taken, and the lateral pressure of concrete is calculated as follows:

$$P_1 = 1.2P_0 \quad (2)$$

Thus the effective head height is calculated h_c

$$h_c = \frac{P_1}{\gamma_c} \quad (3)$$

The lateral formwork load is mainly subject to the concrete pressure, as shown in Figure 6, with its load calculation formula as below:

$$\mathrm{F} = \mathrm{AP} \quad (4)$$

The lateral pressure of concrete at the upper section of lateral formwork is calculated first, the load on which section is variable.

For section $^{\mathrm{h}}$,

$$F_1 = (P_1 + P_2)/2 \times (h \times w) \quad (5)$$

For section H-h, the lateral pressure is unchanged and subject to a load as below:

$$F_2 = P_1 \times (H - h) \times W \quad (6)$$

In conclusion, the total lateral formwork load is calculated as below.

$$F = F_1 + F_2 \quad (7)$$

3.3 *Finite element analysis*

In addition to their own gravity, the vault and lateral formwork bear uniformly distributed loads, and the bottom of the model releases the degrees of freedom in the span direction. The trolley is made of material Q345, with the material parameters as shown in Table 3.

The load of formwork is determined according to Section 3.1. In consideration of the dead weight and concrete weight, the formwork system is calculated with finite element calculation software, with the calculation results as shown in Figures 7, 8 and 9. The stress of the gantry assembly bears the reaction force of the formwork system and the dead weight of the gantry assembly. The reaction force of the formwork is extracted to analyze the stress of the gantry, with the calculation results as shown in Figures 10 and 11.

Table 3. Design of Q345 material parameters.

S/N	Parameter	Value
1	Density ρ/(t/mm3)	7.85e-9
2	Elastic modulus E (MPa)	2.1e5
3	Poisson's ratio μ	0.3
4	Yield strength σs (MPa)	345
5	Allowable stress for weld: 0.8*σs/(MPa)	276

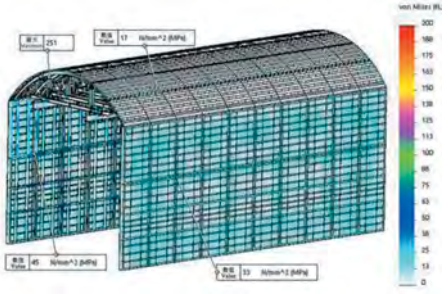

Figure 7. Stress nephogram for finite element analysis of formwork assembly.

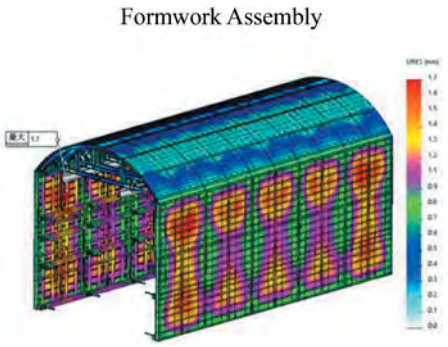

Figure 8. Displacement nephogram for finite element analysis of formwork assembly.

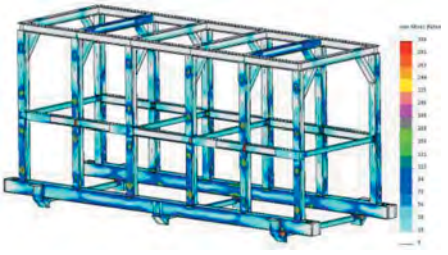

Figure 9. Displacement nephogram for finite element analysis of dome assembly.

The overall maximum stress of the formwork assembly model is 251 MPa, with the overall stress below 45 MPa. The local concentrated stress of the gantry assembly is 230 MPa, with the overall stress

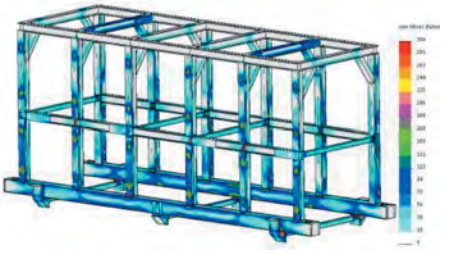

Figure 10. Stress nephogram for finite element analysis of gantry assembly.

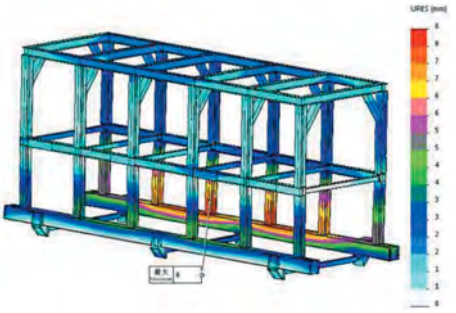

Figure 11. Displacement nephogram for finite element analysis of formwork assembly.

lower than 150 MPa. The maximum deformation of lateral formwork, top formwork and gantry is 1.7m, 0.9mm and 8mm respectively, meeting the design requirements.

4 RAPID INSTALLATION AND VERIFICATION OF HIGHLY ADAPTABLE LINING EQUIPMENT

4.1 *Quick installation method*

4.1.1 *Modular installation*

In order to improve the trolley installation efficiency, a method for overall installation of pre-assembled large modules is developed, wherein the top formwork is divided into 10 unit modules, and each single module is assembled on the ground to form the dome module. The dome module is lifted to the top of the gantry by the top formwork lifting mechanism, and then pulled to the set position to complete the assembly and connection of 10 top formwork modules in turn, as shown in Figure 12.

After the top formwork is installed, it is necessary to connect the lateral formwork with the shoulder of the top formwork. The top formwork unit is designed with a lateral formwork winch, which can quickly complete the connection between the lateral formwork and the shoulder of the top formwork with manual assistance, greatly improving the installation efficiency and reducing the intensity of manual operations.

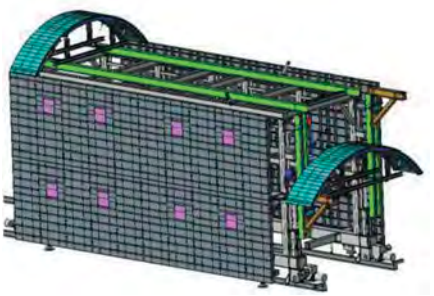

Figure 12. Schematic diagram of trolley installation process.

4.1.2 *Trolley formwork removal*

The formwork removal process is shown in Figure 13. After the completion of pouring, the plugging, foot formwork, lead screw and bottom corner cross beam are removed to control the shrinkage of lateral formwork and shoulder formwork cylinder, so that the removal of lateral formwork is completed. The jacking oil cylinder of the gantry is controlled to shrink, and the dome is lowered, so that the formwork removal of the dome is completed. The maximum stripping stroke of lateral formwork is 200mm, and the maximum stripping stroke of top formwork is 170mm.

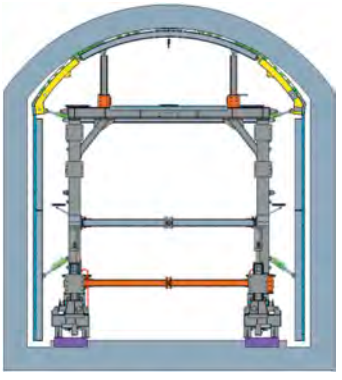

Figure 13. Schematic diagram of formwork removal process of trolley.

4.1.3 *Small-radius right-angle turns*

A trolley in 12 m long is divided into two trolleys in 6 m long each, and each single trolley can independently turn in a tunnel for walking and covering construction. Before a turning, the lifting mechanism, walking platform, block and other related components are removed. When turning, the trolley in 6 m long first travels to the middle of an intersection and turns through reverse actions of the traversing devices at both ends of the trolley, where a 90° turn is completed by about 57 actions with the single cycle turning angle of 1.6°. The second trolley in 6 m long, after completing a turn in the same way, is connected with the first trolley and is combined into a trolley in 12 m for covering construction in situ. The small-radius right-angle turning process is shown as Figure 14 and Figure 15.

Figure 14. Schematic diagram of trolley splitting.

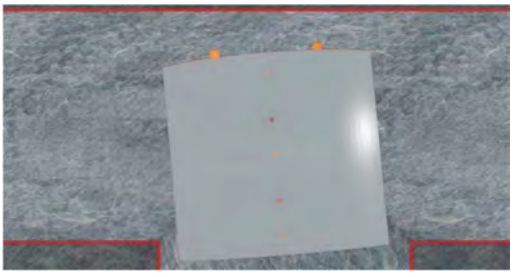

Figure 15. Schematic diagram of a right-angle turning in tunnel by a 6m trolley.

4.2 *Engineering verification*

The equipment was applied for the first time in a construction site, with good construction results achieved, and has now been popularized to many construction sites. As compared with ordinary trolley, the number of installers is decreased from 10~12 to 6~8, the installation time is shortened from 15 days to 7 days. The on-site installation of a trolley is shown as Figure 11. The installation time of each component in the 6-person team is shown as Table 4.

Figure 16. Schematic diagram of trolley installation.

Table 4. Statistics of installation time for each component.

S/N	Component installed	Ordinary trolley	Highly adaptable lining equipment
1	Track, traveling mechanism and lower longitudinal beam	1	0.5
2	Gantry and connecting beam	1	0.5
3	Lifting mechanism and lateral shifting mechanism	1	0.25
4	Lateral formwork cleaning and lateral formwork lead screw	4	1
5	Top formwork skeleton	5	0.5
6	Lateral formwork		
7	Adjustment of clearance and dislocation of top formwork	2	2
8	Installation of vibrating system	0	0.5
9	Action debugging and trolley positioning	1	0.5
10	Total	15	5.75

5 CONCLUSIONS

It has been verified that the highly adaptable lining equipment can effectively meet the requirements from the complex construction scenarios and working conditions of tunnels with variable sections such as alternating large and small sections, right-angle turns and small entrances.

By designing the combination of flexible formwork and modules, two different tunnel sections in 5.5 m and 6 m can be realized, which only requires replacing two sets of top formwork and one set of lateral formwork, thus ensuring the economy of lining construction.

The dome module is pre-assembled on ground and lifted to the top of the gantry in groups to realize an overall modular installation of the structure, effectively reducing the material cleaning and transportation time, and greatly improving the installation efficiency of lining equipment in narrow tunnels.

The development of automatic auxiliary installation devices effectively solves the challenge of rapid lifting in narrow spaces. Only loaders are required to assist in installing the gantry for the trolley installation in tunnel, and no other auxiliary equipment is needed, reducing the manual labor intensity, decreasing the number of installers and saving the installation time.

Aiming at the challenge of small-radius right-angle turning of complete vehicles at T-shaped and cross-shaped tunnel intersections, a trolley in 12 m long is designed into two trolleys in 6 m each that can be quickly split and merged. Each section is iteratively deflected by a traversing mechanism to quickly realize right-angle turning in narrow spaces. During a transition, there is no need to disassemble the whole machine device, and it can quickly pass through complex sections, solving the problem of long transition period of traditional lining trolley, realizing automatic track feeding and right-angle turning in tunnels with alternation of variable sections, and effectively shortening the transition time in tunnel.

REFERENCES

[1] Ma Jun. "High-performance Concrete Lining Reinforcement Technology for Culvert Lateral Top Arch in Alpine Environment." Advances in Science and Technology in Water Resources 33.6 (2013): 4.

[2] Xie Hongrui. "Brief Analysis on the Application of Steel Formwork Trolley in Coal Mine Inclined Shafts" Architectural Engineering Technology and Design 000.007(2015):1877–1878.

[3] Chen Bin, Zuo Yanzhi. Summary of Application Technology of Formwork Trolley for Secondary Lining of CB Intake Tunnel [J]. Architectural Engineering Technology and Design, 2015, 000 (007):159–159.

[4] Song Xiaoqiang. Analysis on Applications of Automatic Lining Trolley in Highway Tunnel Construction [J]. China Plant Engineering, 2023(1):246–249.

[5] Dong Wanlong, Bai Shouxing, Li Yantao. Positioning Control Technology of Formwork Trolley for Secondary Lining in Undercut Tunnels with Small-radius Curve [J]. Architecture Technology, 2022(009):053.

[6] Wang Baiquan. Research and Application of New-type Intelligent Lining Trolly Construction Automatic Control System [J]. Tunnel Construction (Chinese and English), 2019.

[7] Ji Haidong, Liu Zaizheng, Zhang Haitao. Research and Application of New-type Digital Lining Trolley for Pressurized Pouring Tunnel [J]. Tunnel Construction (Chinese and English), 2018, 38(8): 7.

[8] Liu Yunzhu. "Design of Lining Trolley for Laojianshan Tunnel with Variable Sections" Railway Construction Technology, 12(2016):5.

[9] Ren Wenbin. "Design and Application of Lining Trolley for Variable Sections of Super-large Section Tunnels" Railway Construction Technology (2021).

[10] Li Feng. "Design and Application of Steel Formwork Lining Trolley for Variable Sections" Hebei Enterprise 25.007 (2009):82–83.

[11] Xue Jiangsong, Xie Weiyan. Design and Application of Lining Formwork Trolley for Single-track Tunnels with Variable Sections on Lanzhou-Chongqing Railway [J]. Academic Journal of Xinyang Normal University: Natural Science Board, 2011, 24(1):4.

Tunnelling for a Better Life – Yan, Celestino, Thewes & Eberhardt (Eds)
© 2024 The Author(s), ISBN 978-1-032-80042-4
Open Access: www.taylorfrancis.com, CC BY-NC-ND 4.0 license

Mechanism of anchor cable in super-span tunnel and its design method

Jianyou Liu* & Gang Lu
China Railway Engineering Design Consulting Group Co., Ltd., Beijing, China

Yong Zhao
Sichuan Tibet Railway Co., Ltd. Tibet, China

Shaoshuai Shi
China Railway Economic and Planning Research Institute Co., Ltd., Beijing, China

ABSTRACT: The maximum excavation span of the Badaling long-span tunnel on the Beijing-Zhangjiakou Railway is 32.7m. The initial support force is mainly provided by prestressed anchorage cable, prestressed anchor, and s shotcrete. Combined with the anchor cable arching effect, suspension effect, confining pressure effect, and span reduction effect, the mechanism of anchor cable action in the Badaling long-span tunnel is analyzed, and the safety factor is obtained. Based on the bearing arch theory, a method for designing the supporting structure of a "one injection and double anchor" tunnel is proposed. The results show that the prestressed anchorage cable can provide effective anchoring force before the load-bearing arch is completed and reduce the displacement of the vault. The calculated displacement of the vault is 0.3mm; Under the suspension and arching action of prestressed anchorage cables, the Badaling long-span tunnel has been verified to have safety factors of 2.5, 8.83and 4.62respectively; Put forward the design method of "one injection and double anchor" support structure, the support effect is effectively guaranteed, and the safety reserve is high. The research method provides a reference for the design of tunnel supporting structure.

Keywords: Super large span tunnel, Prestressed anchorage cable, Load-bearing arch, Mechanism of action, Support design

1 INTRODUCTION

Anchor rods (cables) have been widely used in tunnel engineering and have become an important component of anchor spray support. Due to the complexity of the anchor rod anchoring system medium and the diversity of anchor rod forms, there is no unified theory on the mechanism of anchor rod anchoring. At home and abroad, the mechanism of bolt action is studied from the following two aspects. The first aspect is based on the load transfer mechanism of bolt, especially the bond stress distribution and load transfer mechanism between bolt and grouting body, grouting body and surrounding rock. On the other hand, the mechanism of bolt action is studied from the reinforcement effect of anchorage body.

Starting from the engineering practice, it is not the ultimate goal to obtain the maximum anchoring force by the load transfer mechanism of the anchor rod. While ensuring the safety of the project, striving to be economical and rapid is the primary goal in engineering practice. Effective and reasonable use of anchoring force in engineering, that is, from the perspective of reinforcement effect to study the mechanism of bolt action.

Predecessors have put forward the theory of bolt suspension, composite beam and composite arch. Dong put forward and discussed the theory of loose circle support, the classification method of loose circle surrounding rock and bolt-shotcrete support. After a lot of measurement work, Freeman put forward the theory of bolt center point and expounded the concepts of pull-out section and anchorage section of full-length bonded bolt. Zou studied the

*Corresponding author: liujianyou2008@qq.com

DOI: 10.1201/9781003495505-145

working mechanism of bolt in different rocks and discussed the influence mechanism of mechanical parameters of different rock masses through simulated block test. Through indoor test and theoretical analysis, Hou studied the strengthening effect of bolt support on the peak strength and residual strength of rock in the anchorage range, and analyzed the control degree of anchorage body on the plastic zone and fracture zone of surrounding rock.

Based on the Badaling large-span tunnel, this paper analyzes the mechanism of prestressed anchor cable in super-large-span tunnel, and puts forward the safety factor of Badaling large-span tunnel under suspension and arching. Based on the theory of tunnel bearing arch, the design method of super large section tunnel with ‘ one spray double anchor ‘ as the main supporting structure system is established. The research method provides a reference for the design of anchor cable support for super-large-span tunnels.

2 SUPPORTING SYSTEM OF SUPER-LARGE-SPAN TUNNEL

The ‘Code for Design of Railway Tunnels’ (TB10003-2016) defines the tunnel span classification, and defines the tunnel with an excavation span greater than 14 m as a super-large-span tunnel, but there is no classification for super-large spans. Here we define the tunnel with a span greater than 18 m as a super-large-span tunnel. In the railway industry, super-large-span tunnels are mainly used in railway tunnels or underground stations with three or more lines.

There are two main design ideas of tunnel support system:

(1) Rigid support system based on secondary lining. This kind of support system takes the secondary lining concrete as the main bearing structure, emphasizes the bearing role of the secondary lining, and ignores the role of primary support such as shotcrete and bolt. Because the bolt is a hidden project, the construction quality is difficult to detect, and the construction effect is difficult to evaluate. Therefore, in the actual construction of tunnels in China, the designed bolt is often not implemented, resulting in most of the tunnels in China mainly relying on the support of the secondary lining.

(2) Flexible support system based on bolting and shotcreting. This kind of support system uses shotcrete, anchor, anchor cable, grouting and other means to reinforce the surrounding rock, and forms a surrounding rock bearing arch around the tunnel to bear the main load of the tunnel. The supporting system makes full use of the self-bearing effect of surrounding rock, and emphasizes the role of anchor rod in the design and construction process.

For medium and small span tunnels, the rigid support system based on secondary lining can meet the requirements of tunnel stability. However, for super-large-span tunnels over 18 m, the bending moment caused by the weight of the secondary lining itself is very large, and the actual bearing effect is very small. If the rigid support system based on the secondary lining is still used, the designed secondary lining structure will be very thick, resulting in huge engineering waste.

Therefore, in the super-large-span tunnel of Badaling Great Wall Station of Beijing-Zhangjiakou High-speed Railway, we propose a new support structure system for super-large-span tunnels with 32.7 m grade V surrounding rock-prestressed anchor mesh shotcrete shell self-bearing support structure. The main support measures of the support system are as follows:

(1) Steel frame: Φ22 grid steel frame 150 × 160mm, spacing 0.8m;
(2) Shotcrete: 35cm thick;
(3) Ordinary anchor: mortar anchor with a diameter of 25 mm and a length of 6 m, with a circumferential spacing of 2.4 m and a longitudinal spacing of 0.8 m, is used to reinforce the surface surrounding rock;
(4) Prestressed anchor bolt: 32mm in diameter, 11m long prestressed anchor bolt, circumferential spacing of 1.2m, longitudinal spacing of 0.8m, tension design value of 100kN, used to reinforce shallow surrounding rock;
(5) Prestressed anchor cable: anchor cable length of 25 m, ring, longitudinal spacing of 2.4 m, prestressed design value of 700kN and 1000kN, used to reinforce deep surrounding rock;
(6) Secondary lining: 60 cm thick molded reinforced concrete lining structure, the main reinforcement is HRB500 steel bar with a diameter of 28 mm and a spacing of 20 mm, as a safety reserve.

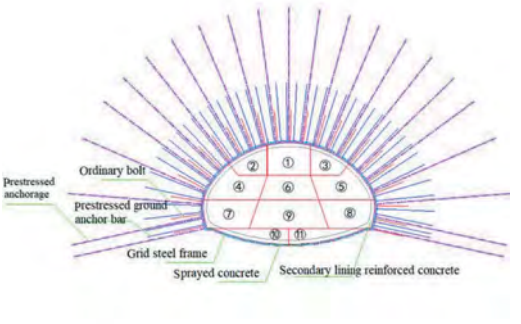

Figure 1. Supporting system of super-large-span tunnel.

3 THE ACTION MECHANISM OF ANCHOR CABLE IN SUPER-LARGE SPAN TUNNEL

The action mechanism of anchor cable in super-long-span tunnel includes: suspension effect, span reduction effect, confining pressure effect and arching effect.

3.1 *Suspension effect of anchor cable*

In the super-large span tunnel, the suspension effect of the anchor cable is mainly manifested in two aspects: the suspension effect on the bearing arch of the surrounding rock and the suspension effect on the unstable block.

(1) Suspending effect on bearing arch of surrounding rock

In the super-long-span tunnel, the reinforcement effect of ordinary mortar anchor and prestressed anchor will form a bearing arch of surrounding rock around the tunnel. However, this bearing arch can only play a bearing role after the excavation of the tunnel is completed and the construction of the anchors of each arch ring is completed. This is similar to the segment of the shield tunnel. Only after the segment is completely assembled to form a closed loop, the segment can play a bearing role.

The arch rings excavated in the super-long-span tunnel are equivalent to the segments of the shield tunnel. The construction process of the ordinary anchor bolt and the prestressed anchor bolt is equivalent to the production process of the segments, and the role of the prestressed anchor cable is to suspend the arch rings before each arch ring is arched to stabilize each arch ring, as shown in Figure 1. Therefore, the prestress F_1 of the anchor cable should be greater than the weight of each arch ring, that is:

$$F_1 = \frac{G_1}{n} \tag{1}$$

Where, G_1 is the weight of arch ring; n is the number of anchor cables on the arch ring.

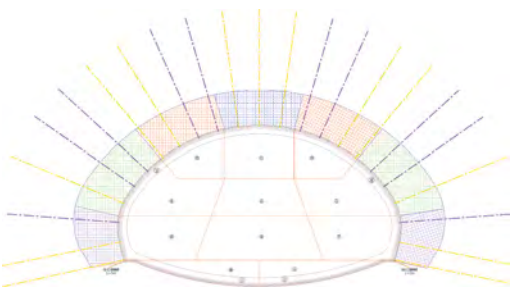

Figure 2. Suspension effect of prestressed anchor cable.

(2) The suspension effect on unstable blocks

The unstable block of tunnel surrounding rock is a possible sliding block formed by the cutting of structural planes such as joints and cracks in surrounding rock. The larger the span of the tunnel, the larger the scale of the unstable block that may be formed, and the smaller the stability coefficient of the block. At this time, the role of the anchor cable is to ensure that the unstable block does not slide during the tunnel excavation through the suspension effect. Therefore, the prestress F2 of the anchor cable can be calculated according to the following formula:

$$F_2 = \frac{G_2 - Q_2}{n_2} \tag{2}$$

Where, G_2 is the weight of unstable block; Q_2 is the frictional resistance of the structural plane to prevent the block from sliding down; n_2 is the number of anchor cables acting on unstable blocks.

3.2 *Span reduction effect of anchor cable*

The prestressed anchor cable is equivalent to increasing the elastic support on the tunnel surface, and the prestress of the anchor cable is equivalent to the support reaction force. Taking the surrounding rock in a certain range around the tunnel as an arch member to bear the load of surrounding rock, a series of anchor cables can be regarded as a series of supports. The span of the bearing arch of the surrounding rock of the super-long-span tunnel will be reduced from the span L_0 of the tunnel to the spacing L_1 of the adjacent anchor cables, and the stress system of the long-span tunnel will be transformed into a multi-support continuous beam. The span reduction effect of anchor cable can effectively reduce the stress and deformation of rock strata and improve the bearing capacity of surrounding rock bearing arch.

The load structure model can be used to calculate the influence of the span reduction effect of the anchor cable on the deformation and stress of the bearing arch, as shown in Figure 3. The bearing arch of surrounding rock formed by ordinary anchor bolt and prestressed anchor bolt is taken as the concentrated load of simply supported arch beam structure. Under the action of vertical load q, horizontal load kq and prestress F_3 of anchor cable, the settlement s of bearing arch vault is affected by the following parameters:

$$s = f_1(q, k, F_3, L, H, E_m) \tag{3}$$

Where, q is the vertical load; k is the horizontal load coefficient; F_3 is the anchor cable prestress; L is the tunnel span; H is the height of the tunnel; E_m is the deformation modulus of the bearing arch rock mass.

The above calculation model can also be used to calculate the anchor cable prestress F_3 required to meet the requirements of vault settlement control.

In addition, during the excavation of super-large-span tunnels, various temporary vertical and horizontal supports are often used to divide the super-large-span tunnels into several small-section tunnels for construction, such as CD, CRD, double-sided drift method and other conventional construction methods. Due to the influence of temporary support, large machinery is difficult to unfold, resulting in a significant reduction in the construction efficiency of super-large-span tunnels.

The span reduction effect of anchor cable can replace the temporary support structures such as middle partition wall and temporary cross brace of these conventional construction methods. By adopting anchor cable support and canceling temporary support, the mechanized excavation of large section of super large span tunnel can be realized, and the safety and work efficiency can be improved.

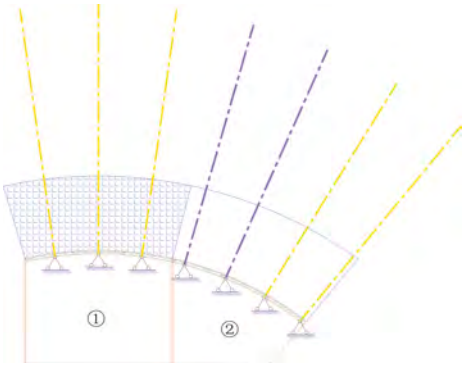

Figure 3. Span reduction effect of anchor cable in large span tunnel.

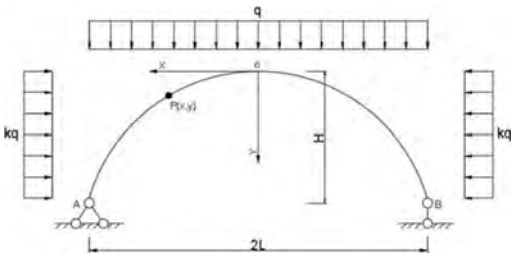

Figure 4. Computation module.

3.3 *The confining pressure effect of anchor cable*

The prestress of the anchor cable acts on the surface of the tunnel surrounding rock, so that the tunnel bearing arch changes from a two-way stress state to a three-way stress state. The prestress of the anchor cable provides a confining pressure for the tunnel bearing arch, thereby improving the compressive strength of the rock mass in the bearing arch and also improving the bearing capacity of the bearing arch.

The confining pressure σ_3 of the tunnel wall includes the prestress of the anchor cable F_4, the prestress of the anchor bolt F_b, the support force p_s of the grille steel frame and the shotcrete, and the support force p_c of the secondary lining concrete.

$$\sigma_3 = \frac{F_4}{s_1 \cdot s_2} + \frac{F_b}{s_{b1} \cdot s_{b2}} + p_s + p_c \qquad (4)$$

Where, F_4 is the prestress of prestressed anchor cable; s_1 and s_2 are the ring and longitudinal spacing of the anchor cable respectively; F_b is the prestressing force of the bolt; s_{b1} and s_{b2} are the ring and longitudinal spacing of the bolt, respectively.

The compressive strength σ_m of rock mass can be calculated according to the following formula.

$$\sigma_m = \sigma_3[\tan(\frac{\pi}{4} + \frac{\varphi_r}{2})]^2 + 2C_r \cdot \tan(\frac{\pi}{4} + \frac{\varphi_r}{2}) \qquad (5)$$

Where, σ_m is the compressive strength of the rock mass in the bearing arch; C_r is the cohesion of rock mass; φ_r is the internal friction angle of rock mass.

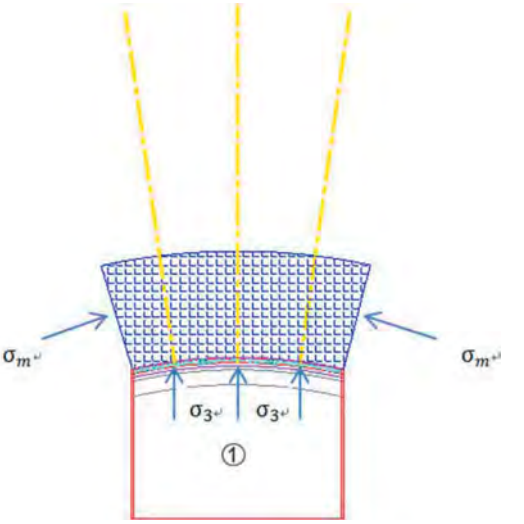

Figure 5. The confining pressure effect of anchor cable.

3.4 *Improvement effect of anchor cable*

The improvement effect of anchor cable on surrounding rock is mainly reflected in the following four aspects:

(1) The anchor cable connects the rock blocks in the bearing arch together, which improves the integrity of the rock mass in the bearing arch.
(2) The prestress of the anchor cable can make the joint fissure of the rock mass close, increase the normal stress on the joint surface, and improve the shear strength of the structural surface.
(3) The grouting during the construction of the anchor cable will fill the gap of the rock mass, thus improving the cohesion and internal friction angle of the structural plane.
(4) When the structural plane slides through the anchor cable, the anchor cable grouting body and the anchor cable steel strand need to be cut off, so as to improve the cohesion C_r and internal friction angle φ_r of the rock mass in the bearing arch, and improve the compressive strengthσ_m of the rock mass in the bearing arch. As shown in (6).

$$\sigma_m = \sigma_3\left[\tan\left(\frac{\pi}{4}+\frac{\varphi_r}{2}\right)\right]^2 + 2\left[C_r + \frac{\sin\varphi}{s_1 s_2} f_v A_s + f_{cv} A_{cs}\right]\tan\left(\frac{\pi}{4}+\frac{\varphi_r}{2}\right) \quad (6)$$

Where, A_s is the cross-sectional area of anchor cable steel strand; A_{cs} is the cross-sectional area of anchor cable grouting body; f_v is the shear strength of steel strand; f_{cv} is the shear of grouting body; φ is the angle between anchor cable and structural plane.

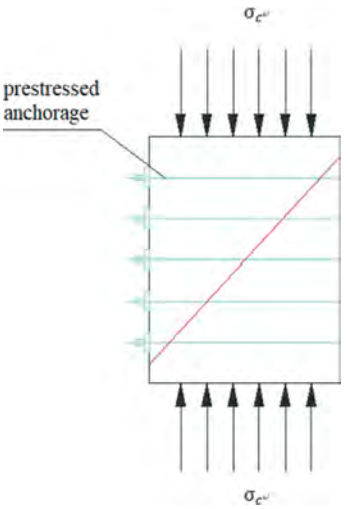

Figure 6. Improvement effect of anchor cable.

3.5 *Arching effect of anchor cable*

After all the construction of the anchor cable is completed, the tension at both ends of the anchor cable diffuses according to the stress diffusion line of 45 °, and a larger bearing arch is formed around the tunnel. The thickness d_b of the bearing arch can be calculated according to the following formula.

$$d_b = L_f - 0.5\frac{r+L_f}{r}s_1 \quad (7)$$

Where, L_f is the length of the free section of the anchor cable; s_1 is the circumferential spacing of the anchor cable; r is the curvature radius of the tunnel wall.

Assuming that the vertical load outside the arch of the anchor cable is q, the horizontal load is kq, the tunnel span is L, and the tunnel height is H, the axial force R of the bearing arch is:

$$R = \frac{kq(H+d_b)}{2} + \frac{q(L+d_b)^2}{8(H+d_b)} \quad (8)$$

The safety factor of the bearing arch$K$is:

$$K = \frac{\sigma_m \cdot d_b}{R} = \frac{8\sigma_m \cdot d_b(H+d_b)}{4kq(H+d_b)^2 + q(L+d_b)^2} \quad (9)$$

According to formula (7), the bearing arch thickness d_b required to meet the safety factor K of the bearing arch can be calculated, and the length of the free section of the anchor cable can be calculated according to formula (5).

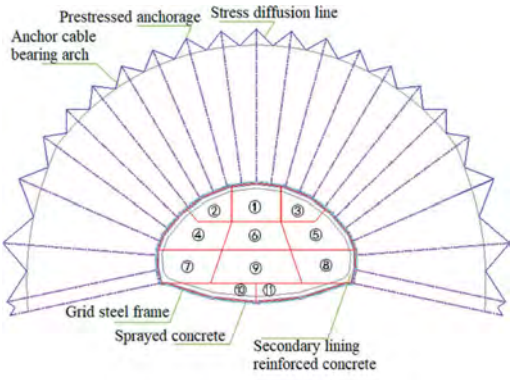

Figure 7. Arching effect of anchor cable.

4 DESIGN METHOD OF PRESTRESSED ANCHOR CABLE

The design of anchor cable mainly includes the design of anchor cable prestress, spacing, length (free section length and anchorage section length) and other parameters, as well as the design of anchor cable structure.

4.1 *Design of pre-stressing force of anchor cable*

According to the action mechanism of anchor cable in super-large span tunnel, the design of anchor cable tension must meet the following requirements:

In order to ensure the stability of the surrounding rock of the tunnel during the construction process, the prestress F_d of the anchor cable should be greater than the prestress F_1 and F_2 required for the suspension effect of the anchor cable, refer to formulas (1) and (2).

$$F_d > \max(F_1, F_2) \quad (10)$$

The design of prestressed anchor cable in the large span section of Badaling tunnel is based on the theory of prestressed anchor bearing arch. The thickness of bearing arch is determined by combining the three hinged arch model and the design parameters of prestressed anchor bolt. The compressive strength of rock mass in bearing arch is calculated by the method of 'one spray double anchor', and the safety

factor is used to verify the safety and reliability of supporting structure design.

4.2 *Prestressed anchor cable supporting theory*

The pre-stressed anchor cable support technology is developed on the basis of the pre-stressed technology. The in-depth study of the anchoring technology improves the theoretical system of the pre-stressed anchor cable support. Bolt support theory has suspension theory, bearing arch theory, surrounding rock loose circle theory, composite beam theory, etc., among which only suspension theory and bearing arch theory can provide support design parameters. The load-bearing arch theory is suitable for relatively thick layered rock strata, and the load-bearing arch with certain strength is formed within the anchorage range of the anchor cable. Therefore, the bearing arch theory of prestressed anchor cable is used as the theoretical basis for the support design of Badaling large-span transition section tunnel.

Table 1. Design parameters of prestressed anchor cable tension for large-span tunnel of Badaling underground station.

Anchor cable tension design	5 core anchor cable	7 core anchor cable	Explanation
Design reference value / kN	300	400	According to the requirements of surrounding rock stability control, the minimum tension of anchor cable needs to be provided. When it is less than this value, it is necessary to make up the anchor cable or take other alternative measures. The minimum allowable value of anchor cable monitoring.
Design tension value /kN	490	700	Locking value of anchor cable tension construction
Design target value /kN (Tension design value)	700	1000	After the excavation of the tunnel is completed, the expected target value of the anchor cable tension when the surrounding rock deformation is stable is determined according to the deformation of the surrounding rock and the stress characteristics of the anchor cable. When the anchor cable is detected, the detection standard is 1.2 times of the value.
Design limit value/kN	1040	1450	The ultimate tension value of the anchor cable used in the design of the anchor cable is 80 % of the anti-pulling force of the anchor cable. The maximum allowable value of anchor cable monitoring.
Pullout strength of anchor cable / kN	1302	1822	The maximum tension value provided by the anchor cable is the minimum value of the holding force between the steel strand and the grouting body, the cohesion between the grouting body and the surrounding rock, and the tensile strength of the steel strand.

Note: (1) When the anchor cable is detected, the detection standard is 1.2 times of the design target value of the anchor cable tension; (2) When anchor cable monitoring, anchor cable tension measured value should be greater than the design reference value, less than the design limit value.

4.3 *Three-hinged arch model*

As shown in Figure 4, it is assumed that the section of the prestressed anchor reinforced bearing arch structure is a three-hinged arch, the vertical load is q, the horizontal load is kq, and k is the ratio of horizontal stress to vertical stress. The vault O is taken as the origin, the arch height is H, the arch span is L, P (x, y) is any point on the left half arch, OP is taken as the detachment body, and the bearing arch is assumed to be a reasonable arch axis. The arch side wall can be obtained, and the vault axial force is:

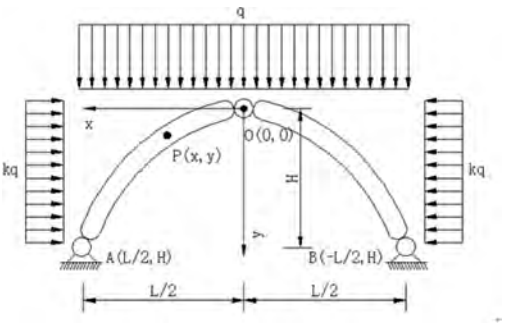

Figure 8. Three hinged arch stress model.

$$R_{sidewall}=\sqrt{\left(\frac{qL^2}{8H}-\frac{kqH}{2}\right)^2+\left(\frac{qH}{2}\right)^2} \quad (11)$$

$$R_{vault}=\frac{kqH}{2}+\frac{qL^2}{8H} \quad (12)$$

4.4 *The joint action of one anchor and two sprays*

Under the combined action of prestressed anchor bolt, prestressed anchor cable and shotcrete, the formula of confining pressure strength is:

$$\sigma_3=P_b+P_a+P_S \quad (13)$$

$$[\sigma_c]=\sigma_3.\tan^2\left(45^\circ+\frac{\phi_g}{2}\right)+2C_g.\tan\left(45^\circ+\frac{\phi_g}{2}\right) \quad (14)$$

Where, P_b is the pre-stressed anchor support force (kpa); P_a is the supporting force of prestressed anchor cable (kpa); P_s is the shotcrete support force (kpa).

σ_c is the compressive strength of rock mass in the bearing arch; C_g is the cohesion (kpa) of medium-hard rock or soft rock after grouting improvement; ϕ_g is the internal friction angle of medium hard rock or soft rock after grouting improvement.

According to the joint support effect of one anchor and double spray, the safety factor is checked to judge the support effect of prestressed anchor cable design parameters.

$$d_b=L_1-0.5\frac{r+L_1}{r}s_1-0.5s_1 \quad (15)$$

$$K_{sidewall}=\frac{[\sigma_c]\cdot d_b}{R_{sidewall}} \quad (16)$$

$$K_{vault}=\frac{[\sigma_c]\cdot d_b}{R_{vault}} \quad (17)$$

Where, $K_{sidewall}$is the safety factor of the side wall; K_{vault} is the safety factor of the vault; d_b is the thickness of the bearing arch; $L_1$is the length of the free end of the prestressed anchor; s_1 is the circumferential spacing of the anchor; r is the radius of curvature of the tunnel wall.

The safety factor of the primary support structure of the prestressed anchor cable under different stresses is shown in the following figure:

According to the settlement results, the safety factor 1.15 is taken as the critical value, that is, when the prestress of the anchor cable is attenuated to 400 kN, the safety factor of the initial support structure is 1.15, and the prestress of the anchor

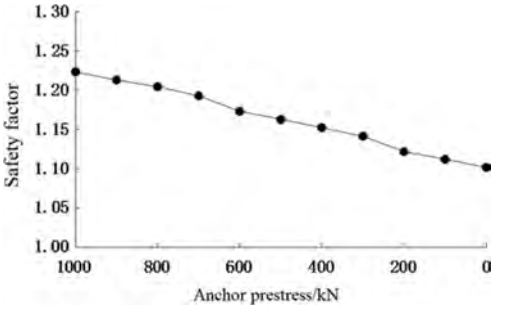

Figure 9. The safety factor curve of primary support structure under different stress of anchor cable.

cable 400 kN is the minimum prestress of the anchor cable detection. Therefore, in the actual construction, when the anchor cable prestress is less than 400 kN, other engineering measures need to be taken to make up for the loss of anchor cable prestress. When the anchor cable prestress is greater than 400 kN, it can be considered that the anchor cable structure is effective, and other engineering measures are not considered. The design parameters of anchor cable prestress are shown in Table 2.

Table 2. Design parameters of anchor cable prestress.

Anchor prestress	Prestress value/kN	Safety factor
Minimum	400	1.15
Stretch locking value	700	1.19
Design value	1000	1.22

5 CONCLUSIONS

Through the analysis of the mechanism of anchor cable in Badaling large-span tunnel, the arching effect, suspension effect, span reduction effect and confining pressure effect of anchor cable on large-span tunnel are studied. Based on the bearing arch theory, a design method suitable for super-long-span tunnels with ‘ one spray and two anchors ‘ as the main supporting structure system is established, and the following main conclusions are obtained:

(1) The prestressed anchor cable can effectively provide the anchoring force, reduce the vault displacement and improve the mechanical parameters of the surrounding rock before the bearing arch is not closed. After the prestressed anchor cable is completed, the vault displacement is calculated to be 0.3mm.
(2) The supporting effect of prestressed anchor cable in Badaling large-span tunnel is effectively guaranteed. Under the action of prestressed anchor cable suspension and arch formation, the safety factors of Badaling large-span tunnel are verified to be 2.5,8.83 and 4.62 respectively.

(3) Based on the bearing arch theory, the design method of " one spray double anchor " support structure is proposed. Considering the safety factor of the primary support structure, the safety and reliability of the prestressed anchor cable are proved.

REFERENCES

Chen L. H., Lin, Zhi, Li X. P., 2011. Study on efficacy of systematic anchor bolts in highway tunnels [J]. Rock and Soil Mechanics. (06): 248–253. (Chinese)

Dong F. T., Song H. W., Guo Z. H., et al, 1994. Support theory of roadway surrounding rock loosening ring. Journal of China Coal Society. (01): 21–32. (Chinese)

Freeman. T. J., 1978. The behavior of fully-bonded rock bolts in the fielder experimental tunnel. Tunnels and Tunnelling. 7:37–40.

Fu, Q., Ms. X., 2007. The reduced span mechanism of rock bolt and application in the deep long-span roadway. China Mining Magaine. (05): 64-65+68. (Chinese)

Gu, Y., 2011. Research on prestressed anchor cable support technology for the tunnel with large deformation. Master Thesis. Xi'an University of Science and Technology, Shaanxi, Xi'an, China. (Chinese)

Hou C. J., Gou P. F.,2000. Research on strengthening mechanism of surrounding rock with bolt support in roadway. Chinese Journal of Rock Mechanics and Engineering. 19 (3): 342–342. (Chinese)

Ming, J., Shan, Q., Yan R. F., 2014. Study on supporting technology for roadways of soft rock mass in natural caving method. Journal of Mining and Safety Engineering. 31 (01): 34–40. (Chinese)

Pan, R., 2002.Application of bolt combination arch theory in coal lane. Journal of Mining and Safety Engineering. 2002, 19 (2): 57–58. (Chinese)

Zhang L. W., 2002. Wang Ren. Research on status quo of anchorage theory of rock and soil. Rock and Soil Mechanics. (05): 627–631. (Chinese)

Zhu X. G., 2006. The reinforcement mechanics of fully grouted rock bolt in underground engineering. PhD Thesis. Dalian University of Technology, Liaoning, Dalian, China. (Chinese)

Zou Z. H., Wang Z. L., 1993.Working mechanism of anchor rods in different rock masses. Chinese Journal of Geotechnical Engineering. (6). (Chinese)

Tunnelling for a Better Life – Yan, Celestino, Thewes & Eberhardt (Eds)
© 2024 The Author(s), ISBN 978-1-032-80042-4
Open Access: www.taylorfrancis.com, CC BY-NC-ND 4.0 license

Using orthogonal flexible support structure to deal with large deformation of soft surrounding rock tunnel: A case study

Yang Liu*
Key Laboratory of Transportation Tunnel Engineering, Ministry of Education, School of Civil Engineering, Southwest Jiaotong University, Chengdu, China

Wenge Qiu
Key Laboratory of Transportation Tunnel Engineering, Ministry of Education, School of Civil Engineering, Southwest Jiaotong University, Chengdu, China
Chengdu Tianyou Tunnelkey Co, Ltd, Chengdu, China

ABSTRACT: High stiffness supporting structure is difficult to cope with the large deformation problem of soft surrounding rock tunnel effectively, safely, and economically. This paper presents a kind of orthogonal flexible support structure (OFSS) for soft surrounding rock tunnels, which has the advantages of low damping, large travel, and high compressibility. Field application results show that: 1) the OFSS gives full play to the role of absorbing surrounding rock deformation and releasing surrounding rock pressure; 2) The OFSS ensures the tunnel safety limit, no spalling of concrete, steel frame yield phenomenon; 3) The OFSS has obvious advantages in construction safety and economy. The research results provide a new idea and method for the treatment of large deformation of similar soft surrounding rock tunnels, which is of great engineering and theoretical value.

Keywords: Soft rock tunnel, Large deformation, Energy principle , Orthogonal flexible support structure, Case study

1 INTRODUCTION

When the tunnel passes through the high ground stress and weak surrounding rock strata in the western region of China, it is very easy to produce serious large deformation disasters, which will not only lead to the damage and intrusion of the supporting structure, increase the safety risk, but also lead to the repeated input of supporting materials, the soaring construction cost and the delay of the construction period (Wang et al., 2012; Chen et al., 2017; Yang et al., 2017; Li et al., 2018; Kang et al., 2022; Zhang et al., 2023). The new Languang railway has a total length of 492km and a tunnel length of 343km, among which the tunnels containing soft rocks such as carbonaceous slate and carbonaceous phyllite, such as the Muzaling tunnel et al., have a total length of 83km. Under the influence of high ground stress and strong geological structure, serious large deformation of weak surrounding rock occurred in tunnel construction, with the maximum radial deformation reaching meter level, resulting in deformation and destruction of supporting structure, which greatly increased the construction safety risk, delayed construction progress, and increased construction cost (Zou et al., 2010; Sun et al., 2012; Wu et al., 2013; Zhao et al., 2014; He et al., 2014; Huang et al., 2014; Wu et al., 2014; Huang et al., 2016; Li et al., 2017). The newly built Lixiang railway is located in the fault zone formed by the collision and accumulation of the Eurasian plate and the Indian Ocean plate. The Zhongyi tunnel et al., along the line, are subjected to the intense compression action of large-scale geological structures, resulting in great tectonic stress, crushing, and metamorphism of surrounding rock and joint fissure development. During construction, large deformation of weak surrounding rock occurred continuously, with the maximum horizontal convergence deformation of 87cm on one side and the maximum uplift of the bottom plate reaching meter-level, resulting in deformation, damage, and erosion of the initial supporting structure, which required multiple disassembly and replacement, seriously affecting normal construction

*Corresponding author: liuyangtunnel@my.swjtu.edu.cn

DOI: 10.1201/9781003495505-146

safety and construction schedule (Li et al., 2018; Yan et al., 2019a, b; Deng et al., 2020; Gan et al., 2020; Li et al., 2021; Li et al., 2022). Therefore, large deformation of weak surrounding rock will be one of the key technical problems plaguing tunnel construction in western China (Cheng et al., 1997; Wang et al., 2008; Wang et al., 2010; Sun et al., 2015; Chang et al., 2015).

Through a large number of tunnel construction practices, we have accumulated a wealth of experience in dealing with large deformation of soft surrounding rock tunnels, but there has been no breakthrough in the study of weak surrounding rock tunnel support design theory and supporting construction methods. The problem of large deformation is encountered in the construction of soft surrounding rock tunnels, and the construction site is always difficult and slow in the process of "implementation-destruction-disassembly" of the cyclic supporting structure, resulting in a serious delay in the construction period, eventually becoming the key control problem of the whole tunnel and even the whole line. The reasons are as follows:

First, theoretical research on tunnel support design of weak surrounding rock is seriously backward. The current tunnel design specifications still regard the theory of loose pressure based on collapse arch as the guiding principle for tunnel design and construction. However, this is different from the pressure mechanism generated by the plastic deformation extrusion support structure of weak surrounding rock in large deformation tunnels. Moreover, it is inconsistent with the surrounding rock pressure distribution law obtained from the field measurements of a large number of tunnel projects with large deformation of the weak surrounding rock. In addition, the large eccentric tensile failure mode of supporting structure under loose load also runs counter to the small eccentric compressive shear failure mode shown in a large number of tunnel projects with weak surrounding rock (Qiu et al., 2017).

Second, the weak surrounding rock tunnel support design concept is backward. At present, when encountering the phenomenon of large deformation in the weak surrounding rock tunnel in China, the mainstream support design concept is "early support and strong support".

A large number of weak surrounding rock tunnel engineering cases shows that "early support and strong support" often cannot effectively solve the problem of large deformation. The final stable state of the tunnel comes from the full release of surrounding rock pressure after repeated disassembly of damaged supporting structures. After accumulating a lot of experience in soft rock large deformation tunnels, people gradually realize the correctness and necessity of the support design concept which is different from "early support and strong support" and allows the surrounding rock to produce a certain deformation to release the surrounding rock pressure.

Based on the principle of energy, this paper carries out the design and field application of the orthogonal limit energy dissipation support system based on the large deformation control project of a weak surrounding rock tunnel in western China. The research results will provide new ideas, new theories, and new methods for the design and construction of tunnel support with similar weak surrounding rock and large deformation, which has great engineering and theoretical significance.

2 CASE BACKGROUND

The tunnel in this paper is located in Aba County, Aba Prefecture, Sichuan Province (Figure 1), which is a one-way two-lane highway tunnel. The strike of the tunnel is 124°, the length is 5564m, and it is a very long tunnel with a maximum buried depth of 357m.

Figure 1. Tunnel site.

2.1 *Geological condition*

The tunnel is located in the mountainous plateau, and the mountain spreads from south to north. Geological data show that the strata of the tunnel are interbedded with strong-medium weathering metamorphic sandstone and slate, and the main mineral components are quartz, feldspar, and mica. Due to the influence of regional structure and fracture, the surrounding rock exposed by actual excavation is easily weathered and broken to form sheet rocks or cuttings, showing typical phyllite characteristics, with soft lithology, easy slime and softening in water, expansion, and creep, and extremely poor engineering geological conditions. The maximum main stress of the tunnel measured by the hydraulic fracturing method is 11.15MPa. The surrounding rock exposed by excavation is shown in Figure 2.

2.2 *Large deformation status*

The initial support design of the tunnel is a Z5d composite lining of V-class surrounding rock. 50m after construction, due to the serious deformation and damage of the initial support, the support design was changed to Da composite lining.

To more accurately grasp the deformation and failure status of the tunnel, this paper used the three-

Figure 2. The surrounding rock exposed by excavation.

dimensional laser scanning technology to carry out the initial support deformation monitoring for section DK75+157~DK75+167 of Da composite lining.

The monitoring results are shown in Figure 3. Cool colors mean that the deformation has not exceeded the limit, whereas warm colors mean that the deformation has exceeded the limit. As shown in Figure 3, varying degrees of invasion have been generated throughout the monitoring section. Among them, the invasion at the left waistband is the most serious, exceeding 60cm, while the invasion at the right waistband is relatively light, generally ranging from 0~30cm. The deformation of the initial support has entered a state of slow convergence.

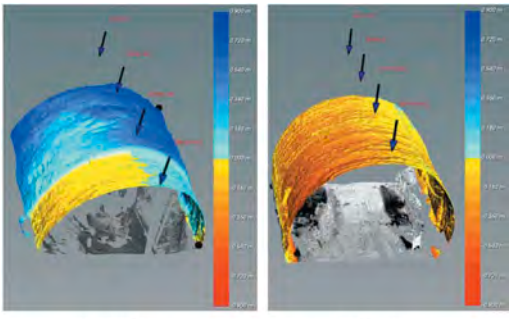

a) Initial state b) Final state

Figure 3. The deformation monitoring result.

The deformation and failure status of the initial support observed on-site is shown in Figure 4.

The deformation and failure rule of the initial support shows that the support structure has compressive shear failure under the deformation pressure of the surrounding rock.

a) Longitudinal cracking b) Shotcrete spalling

c) Steel arch buckling

d) Full circumferential invasion

Figure 4. The deformation and failure status of the initial support.

3 ORTHOGONAL FLEXIBLE SUPPORT SYSTEM

3.1 *Energy type support principle*

The energy released by a large deformation tunnel is constant from the excavation to the final stable state. The basic equation is given below:

$$W = F \times S \tag{1}$$

Where W is work, F is force and S is displacement. Eq. (1) shows that, when the W is constant, there are infinite solutions for F and S. The strength design concept uses the support structure with high-stiffness to provide strong supporting resistance. The deformation of the surrounding rock is small, and the internal force of the support structure is huge. Commonly used concrete and steel arches are high-stiffness support structures. Even if its thickness and stiffness are increased, it is difficult to suppress the deformation of surrounding rock in the high-situ stress soft rock stratum. On the contrary, the flexible support concept uses a support structure with low

stiffness and high deformability to absorb the deformation of the surrounding rock and release the pressure of the surrounding rock. Figure 5 shows the support process with two different support concepts.

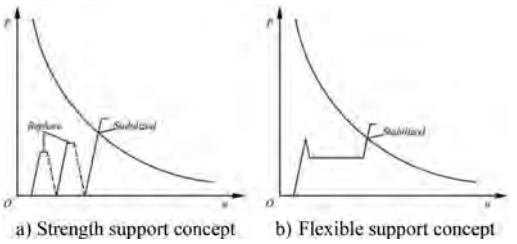

Figure 5. The working process of two support concepts in dealing with the large deformation of the tunnel.

3.2 *Field application*

According to the results of initial support deformation monitoring in Chapter 2, the orthogonal flexible support design of a large deformation tunnel is carried out by further utilizing the deformation pressure variation characteristics of the surrounding rock, as shown in Figure 6.

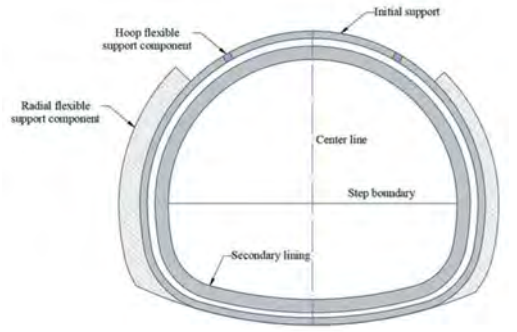

Figure 6. OFSS.

The main support parameters of the OFSS are as follows:

1) Single-layer initial support, I22b steel frame, spacing 60cm;
2) The hoop flexible support components are installed at the left and right arches of the steel frame (30°), with a height of 30cm, and are connected by bolts;
3) The radial flexible support components are arranged between the steel frame and the surrounding rock (Arch waist to corner), with a thickness of 80cm on the left and 50cm on the right;
4) Using C25 shotcrete, thickness 26cm.

The on-site construction process is shown in Figure 7.

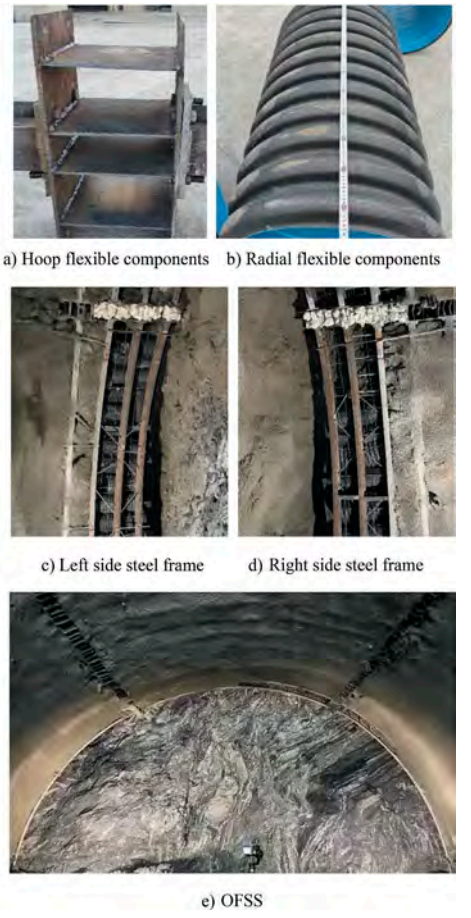

Figure 7. Construction process of OFSS.

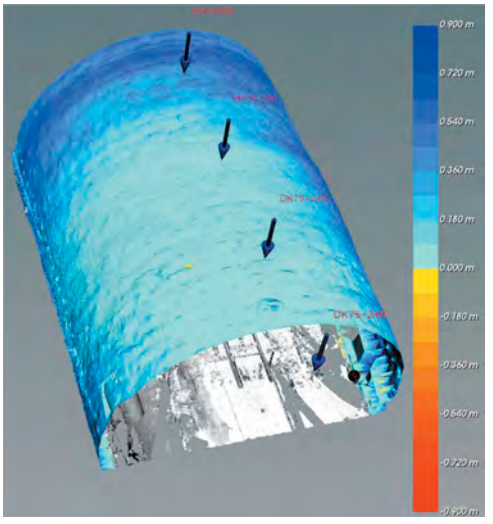

Figure 8. Deformation monitoring result.

The large deformation treatment effect of the orthogonal flexible supporting structure is shown in Figure 8.

Figure 8 shows that no invasion occurs in the whole test section of the OFSS. Further, the typical section is selected to investigate the deformation convergence of each key point, the result is shown in Figure 9.

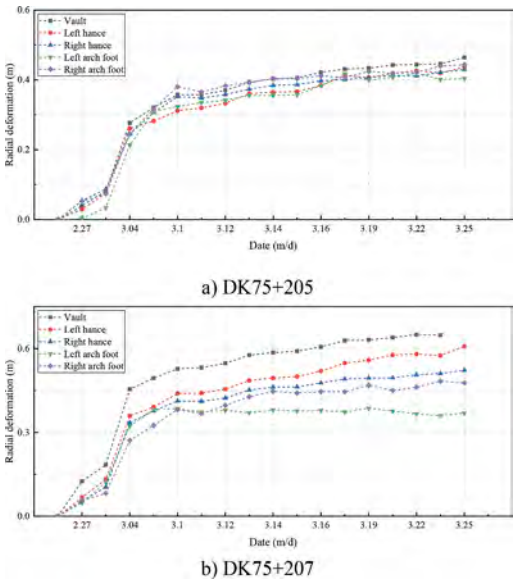

Figure 9. Deformation convergence of typical section.

Figure 10 Shows that key points of the typical section have entered a state of slow convergence.

4 CONCLUSIONS

Aiming at the difficult problem of large deformation treatment of high in-site stress and soft rock tunnels, this study proposes an OFSS based on the energy principle. The related study results are as follows:

1) The deformation pressure of surrounding rock acts on the initial support of the large deformation tunnel, rather than the loose load formed by the collapsing rock mass of the arch.
2) The OFSS which acts on both the hoop and radial direction of the tunnel is proposed.
3) The OFSS effectively solves the problem of large deformation support of soft rock tunnels and has important engineering and theoretical value.

REFERENCES

Kang Yongshui, Geng Zhi, Liu Quansheng, Liu Bin, Zhu Yuanguang. Research progress of large deformation disaster control techniques and methods of soft rock in China [J]. Rock and Soil Mechanics,2022,43 (08):2035–2059.

Wang Hongfeng, Zhong Zuliang. Large deformation disaster and its treatment in ultra-shallow buried loess tunnel with large bias pressure separation [J]. Chinese Journal of Underground Space and Engineering,2012,8 (S2):1841–1845.

Chen Y. Research on dynamic risk assessment and support decision of tunnel large deformation disaster [D]. Chengdu University of Technology,2017.

Li Yongbing. Discussion on prevention and treatment of large deformation disaster of surrounding rock of tunnel [J]. Western Exploration Engineering,2018,30 (04):189–192.

Zhang Dingli, Sun Zhenyu, Tao Weiming. Characteristics and active control methods of large deformation disaster in tunnel surrounding rock [J]. Railway Standard Design,2023,67(01):1–9.

Yang Shengqi. Mechanism and anchoring control technology of large deformation hazard of surrounding rock structure in deep high-stress soft rock roadway. Jiangsu Province, China University of Mining and Technology,2017-12–01.

Zhao Fushan. Large deformation control technology of soft rock with high ground stress in Liangshui Tunnel of Lan-Yu Railway [J]. Tunnel Construction,2014,34 (06):546–553.

Zou Chong, Wang Chaopeng, Zhang Wenxin, Gao Pan. Experimental study on stress control of carbonized SLATE section in Muzailing Tunnel of Lanzhou-Chongqing Railway [J]. Tunnel Construction,2010,30(02):120–124.

He Chunbao, Shu Lihong. Deformation mechanism and construction control of soft rock tunnel with high ground stress in Lan-Yu Railway [J]. Journal of Railway Engineering,2014(05):68–73.

Sun Shaofeng. Characteristics and large deformation control technology of soft rock tunnel in Lan-Yu Railway [J]. Modern Tunnel Technology,2012,49(03):125–130.

Wu Guangming, Liu Zhichun, Wu Xiaohui. Large deformation control technology of soft rock in Liangshui Tunnel of Lan-Yu Railway [J]. Railway Standard Design,2013(12):82–86.

Huang Mingli, Zhao Jianming, Tan Zhongsheng, Li Yanzong. Analysis of deformation force characteristics of lining-surrounding rock structural system in Ling-ridge section of Muzailing Tunnel on Lanzhou-Chongqing Railway [J]. Modern Tunnel Technology,2016,53 (06):89–99+107.

Li Yanzong, You Xianming, Zhao Shuang. Study on deformation control scheme of high ground stress soft rock tunnel through section: A case study of Muzhailing Tunnel on Lanzhou-Chongqing Railway [J]. Tunnel Construction,2017,37(09):1146–1152.

Huang Xinmei. Experimental research on double-layer support and Double-layer lining of the tunnel [D]. Chang'an University, 2014.

Wu Mingjian. Research on soft rock excavation and support technology of Liangshui Tunnel on Lan-Yu Railway [D]. Southwest Jiaotong University,2014.

Yan Hongjiang, Deng Zhigang. Large deformation control technology of soft rock with high ground stress in Zhongyi Tunnel of Lixiang Railway [J]. Journal of Water Resources and Architectural Engineering,2019,17 (01):67–72.

Yan Hongjiang, Liu Chengyu, Deng Zhigang, Luo Honglin. Mechanical mechanism of large

deformation in initial support of Zhongyi tunnel of Lixiang Railway [J]. Journal of Water Resources and Architectural Engineering,2019,17(05):168–173+180.

Deng Zhigang. Inverse calculation of ground stress in large deformation tunnel based on relative deformation: A case study of Zhongyi Tunnel of Lixiang Railway [J]. Tunnel Construction (Chinese and English),2020,40 (S1):194–201.

Li Guimin, Guo Yongfa, Zhao Haiyan. Key Technology of Design and Construction of Prestressed Resin Anchor Rod for Zhongyi Tunnel of Lixiang Railway [J]. China Railway,2021(02):17–26.

Li Guimin. Construction control technology of large deformation section of Lixiang Railway basalt tunnel [J]. Tunnel Construction (Chinese & English),2018,38(S1):167–174.

Li Guimin, Guo Yongfa, Ding Wenyun. Cracking treatment of large deformation basalt tunnel lining of Lixiang Railway [J]. China Railway,2022(12):106–113.

Gan Jianbin. Application of anchor rod in soft rock large-deformation construction of Lixiang Railway tunnel [J]. Anhui Architecture, 2019,27(11):169–170.

Cheng Hua, Sun Jun. Numerical analysis of nonlinear large deformation in the mechanical mechanism of composite tunnel lining with weak surrounding rock [J]. Chinese Journal of Rock Mechanics and Engineering,1997 (04):34–43.

Sun Jun, Pan Xiaoming, Wang Yong. Study on nonlinear rheological mechanics characteristics and anchoring mechanism of large compressive deformation of soft surrounding rock in tunnel [J]. Tunnel Construction,2015,35(10):969–980.

Wang Shudong. Research on large deformation control technology of soft surrounding rock of tunnel in complex ground stress zone [D]. Beijing Jiaotong University,2010.

Wang Shudong, Liu Kaiyun. Intelligent prediction method of large deformation in soft surrounding rock construction of long tunnel [J]. China Railway Science,2008 (02):82–87.

Chang Lijun. Comprehensive construction technology of large deformation tunnel in the soft surrounding rock of high-speed railway [J]. Railway Construction Technology,2015(02):51–54+57.

Qiu Wenge, Li Bingtian, Tian Mingjie, et al.Analysis of stress mode of tunnel initial support based on field measurement [J]. Tunnel Construction (Chinese & English),2017,37(12):1508–1517.

Tunnelling for a Better Life – Yan, Celestino, Thewes & Eberhardt (Eds)
© 2024 The Author(s), ISBN 978-1-032-80042-4
Open Access: www.taylorfrancis.com, CC BY-NC-ND 4.0 license

Study on railway tunnel lining anti-crack surface reinforcement strengthening and design method

Zhiqiang Liu* & Xiaofei Xing
China Railway Southwest Research Institute Co., Ltd., Chengdu, China

Lun Gong
School of Civil Engineering of Southwest Jiaotong University, Chengdu, China

ABSTRACT: In order to avoid excessive reinforcement of cracks in plain concrete lining and ensure the stability after crack treatment and reinforcement, this paper proposes a reinforcement measure of protective covering rebars for tunnel lining cracks, and verifies its design method effectiveness. The main conclusions include: (1) a reinforcement measure of protective covering rebars is proposed, and the applicable environmental conditions of protective covering rebars are determined; (2) The reinforcement measure of protective covering rebars is only applicable to reinforcing crack with depth less than 0.5*H*; (3) The design process and checking calculation method of reinforcement of protective covering rebars have been put forward; (4) The protective covering rebars can avoid the tensile stress concentration at the crack tip, and play a role in strengthening the structure and restraining the crack development; (5) The case shows that after reinforcement, the safety factor of lining increases from 1.23 to 4.66, and the safety factor of protective covering rebars is 29.79, indicating that the reinforcement of protective covering rebars is effective.

Keywords: Railway tunnels, Cracks, Protective covering rebar, Design method

1 INTRODUCTION

With prolonged service life of tunnels, lining cracking has become one of the major problems that impact safe operation of tunnels [1~3]. The foreign and domestic experts have conducted research into conditioning of cracked lining.

Taking the Beijing metro project as an example and based on the theory of concrete elastic-plastic damage, Xuan Liu [7] conducted the mechanical analysis of cracked linings. The analysis results show that the influence of vault crack is remarkable and the crack depth has the most significant impacts on the safety of lining structure.

For example, Wang Hualao et al. [4] have calculated the lining safety factor of the Anji Tunnel under the effect of longitudinal crack, and proposed the method of plastering mortar to strengthen the cracked plain concrete whose safety factor meets the standards; for the plain concrete that does not meet the standards, I20a@550m+ reinforcing mesh + shotcrete are used for strengthening.

indicate that the W steel belt + reinforcing mesh + shotcrete will allow the safety factor of cracked structure to increase from 0.92 to 2.69, and lap rockbolt grouting will allow the safety factor of structure to increase from 0.97 to 2.51, thus meeting the standard requirements.

In addition to the aforesaid methods, there are other common crack conditioning techniques such as concrete bushing, corrugated plate bushing, partial replacement and overall replacement[7~11], and these techniques have been well proven. In practical strengthening design, however, some designers have raised two questions. First, for the defective crack in plain concrete lining, will bushing and replacement result in waste of resources? Second, for a crack that is repaired by plastering or grouting, if the grouting quality is poor or any environmental action causes the lining stress to change, will the crack further propagate? To address these questions, this paper proposes a surface reinforcement strengthening method and its design, to hopefully provide reference and help in improving the effectiveness of conditioning of cracked railway tunnel lining.

*Corresponding author: liuzhiqiang06@163.com

DOI: 10.1201/9781003495505-147

2 ANALYSIS OF SURFACE REINFORCEMENT STRUCTURE AND ITS APPLICATION CONDITIONS

2.1 *Surface reinforcement structure*

Surface reinforcement should preferably be used together with mortar cover and jointed with the lining structure by using anchor bolts, so as to create a member with consistent stress. The structural composition is shown in Figure 3.

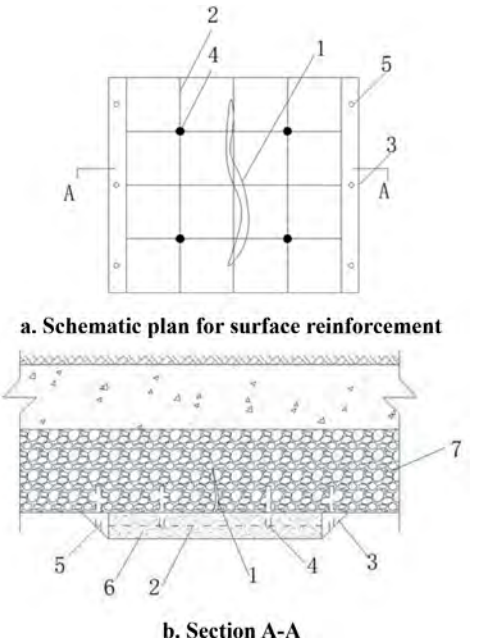

Figure 1. Schematic diagram for surface reinforcement structure. (1 - crack; 2 - surface steel bar; 3 - side retaining structure; 4 - reinforcement anchor bolt; 5 - retaining anchor bolt hole; 6 - mortar cover; 7 - lining).

As shown in Figure 3, surface reinforcement is mainly composed of 4 parts, i.e. surface steel bar, side retaining structure, reinforcement anchor bolt and mortar cover. The surface steel bar is the main stress-bearing member and is meant to control crack opening. The side retaining structure and reinforcement anchor bolt are meant to fasten the surface reinforcing mesh, connect the surface reinforcement and lining and allow the surface reinforcement and lining to share the stress. The waterproofing mortar is mainly meant to prevent rusting and maintain durability of surface reinforcement. Surface reinforcement strengthening steps: (1) Clean the lining base surface, apply interface treating agent, and increase base surface bond strength; (2) Use reinforcement anchor bolt to fasten the surface reinforcing mesh composed of the surface steel bars; (3) Fasten and strengthen the side retaining structure; (4) Apply the surface mortar, and form the surface reinforcement structure

2.2 *Analysis of application conditions of surface reinforcement*

Surface reinforcement is designed to inhibit surface crack propagation and thus achieve crack conditioning. This paper mainly probes into how surface reinforcement will strengthen plain concrete lining. Therefore, surface reinforcement does not play a significant role in improving compressive strength, shear strength and permeation resistance of the structure. If the surrounding rock in the segment to be strengthened has noticeable adverse geological conditions such as flowing deformation or degradation, the stress mode of lining will significantly deviate from the "Code", and also from the empirical perspective, the lining should be strengthened overall, so strengthening by surface reinforcement is deemed unsuitable in this condition. If strengthening by surface reinforcement is required, the ambient conditions, lining structure and crack defect of the to-be-strengthened segment must meet the following requirements: (1) The ambient strata have no flowing deformation, degradation or adverse geological phenomena; (2) The crack has no concomitant defect of water leakage; (3) Under the load pattern specified by the "Code", the compressive strength and shear strength of the structure must meet the relevant requirements; (5) The to-be-strengthened segment has no other defects; (4) There is only a single crack that has no tendency of propagation.

2.3 *Analysis of depth threshold of crack in strengthening by surface reinforcement*

Based on previous experience, if the ambient environmental conditions of the tunnel do not include landslide, soft foundation base, differential settlement or goaf and the load of surrounding rock is loose load or deformation load, the lining stress is dominated by "pressure—bending". Therefore, if the stress condition is not complex, the depth of crack shows certain pattern. For a plain concrete structure, the engineering experience indicates that the surrounding rock grade is I~IV. This paper mainly examines the pattern of lining crack depth under the load pattern of Grade III and IV surrounding rock. The lining section is from a two-line tunnel of a high-speed railway with design speed 400km/h. The height of the tunnel is 10.98m, its width 14.06m and sectional area 118.80m^2. The concrete strength of the lining is C35, its ultimate tensile strength 2.4MPa and its ultimate compressive strength 26.0MPa. Lining thickness is 45cm. The lateral pressure coefficient is 0 and 0.3 respectively. The calculated structural crack distribution and third principal stress (S3) are shown in Figure 2 and Figure 3 (q in the figure is the vertical surrounding rock pressure).

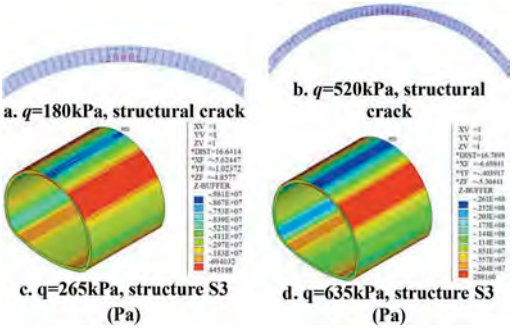

Figure 2. Lateral pressure coefficient 0, simulated and calculated lining crack.

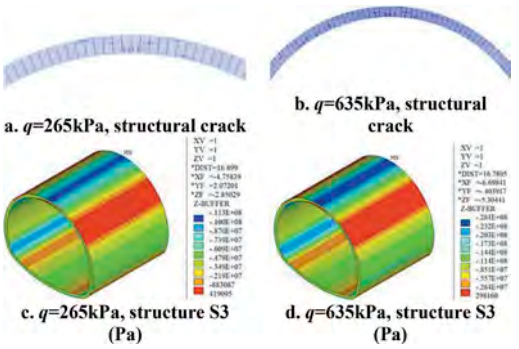

Figure 3. Lateral pressure coefficient 0.3, simulated and calculated lining crack.

As shown in Figure 2 and Figure 3, if the lateral pressure coefficient is 0 and 0.3, the crack-inducing load of the structure is 180kPa and 265kPa, the corresponding crack depth is 0.5*H* and 0.4*H*, the compressive stress of the structure in this case is 9.81MPa and 11.3MPa, and the compressive safety factor is 2.65 and 2.30. The worst case deviates from Clause 2.4 of the "Code" by less than 5%, so it is deemed that the compressive strength of lining still has a certain safety margin. If the load is 520kPa and 635kPa, the minimum principal stress of the structure reaches the ultimate strength and a plastic hinge is formed at the crack, so it is deemed that the structure reaches the ultimate limit state. In this case, the crack depth is 0.6*H* and 0.5*H*, and the crack depth propagation is insignificant.

Therefore, if the compressive strength of the structure meets the design requirements, the crack depth usually does not exceed 0.5*H*, so surface reinforcement is only suitable for strengthening at a single crack with depth ≤0.5*H*. (Note: *H* is lining thickness).

3 STUDY ON SURFACE REINFORCEMENT STRENGTHENING DESIGN METHOD

3.1 *Surface reinforcement strengthening design process*

Surface reinforcement strengthening design is done in 3 steps. Step 1 is to determine the application conditions of surface reinforcement. Step 2 is to select proper surface reinforcement parameters and analyze the stress on the post-strengthening cracked lining. Step 3 is checking calculation of the post-strengthening lining strength and surface reinforcement strength. Surface reinforcement strengthening design process is shown in Figure 4.

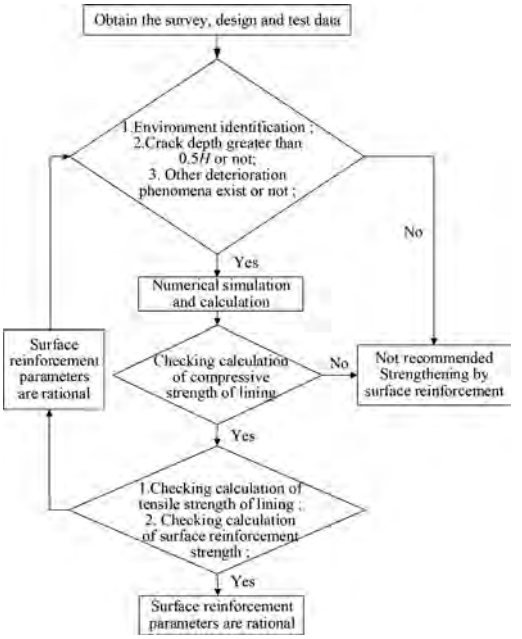

Figure 4. Surface reinforcement strengthening design process.

In the calculation, the ambient conditions of the to-be-strengthened segment must meet the requirements of 2.2. In numerical simulation and calculation, the load types of the lining must be determined based on the burial depth, surrounding rock grade and geotechnical properties of the to-be-strengthened segment. If deformation pressure is dominant, the "stratum—structure" method should be used to calculate the structural effect. If loose pressure is dominant, the "load—structure" method should be used to calculate the structural effect. Crack should be simulated by using the contact surface. With consideration of the physical properties of crack and the safety issue, it is deemed that the crack should have the following properties: (1) When exposed to axial tension, the crack is split without transferring the axial tension, and the residual tensile strength of the crack is not taken into account; (2) When exposed to axial compression, the crack is closed without transferring the axial compression, but the two interfaces of the crack do not intrude into each other; (3) Without consideration of the tangential bond strength and coefficient of friction of the crack interfaces, the interfaces are deemed to be smooth.

Surface reinforcement should preferably be used together with crack grouting to strengthen the lining, but it is hard to guarantee the effectiveness of crack grouting. For the sake of safety and easy construction, the design should take account of the following: (1) The surface reinforcement should have uniform longitudinal and circumferential spacing; (2) Checking calculation of the strengthening effectiveness of surface reinforcement can be done without considering the strengthening effect of crack grouting and mortar cover; (3) Surface reinforcement simulation can be done by using the shell element or link element, and the surface reinforcement and lining are connected at the anchor bolt and side retaining structure; (4) If surface reinforcement simulation is done by using the shell element, the equivalent thickness of the surface reinforcement model should be calculated by using the principle of equivalent axial stiffness.

3.2 *Checking calculation of strengthening effectiveness of surface reinforcement*

(1) Checking calculation of surface reinforcement strength To evaluate how surface reinforcement will strengthen cracked lining, it is necessary to conduct checking calculation of surface reinforcement strength and post-strengthening lining strength.

If surface reinforcement simulation is done by using the shell element, the maximum tensile stress σ_{hmj} and maximum compressive stress σ'_{hmj} of the surface reinforcement can be directly extracted. If surface reinforcement simulation is done by using the link element, the maximum axial tension N_{hmj} and axial compression N'_{hmj} of the surface reinforcement can be extracted. The axial force is divided by the surface reinforcement area A_{s}, to obtain the maximum tensile stress σ_{hmj} and maximum compressive stress σ'_{hmj}. The safety factor of surface reinforcement is calculated by Equation (1).

$$K_{\mathrm{hmj}}=\min(R_{\mathrm{s}}/\sigma_{\mathrm{hmj}}, R_{\mathrm{s}}/\sigma'_{\mathrm{hmj}}) \tag{1}$$

Where: R_s is the ultimate strength of surface reinforcement. According to the *Code for Design of Railway Tunnel* (“the Code”), the safety factor of surface reinforcement is ≥2.0.

(2) Checking calculation of lining strength

Checking calculation is done with the least favorable cross-section for compressive strength and tensile strength of lining. The main process: First calculate axial force N and bending moment M by using the axial stress of the nodes in the least favorable cross-section, and then calculate the tensile safety factor K and compressive safety factor K'.

The effective cross section axis of lining is used as the central axis of second moment of area of section, the axial force N_i of cross section i is calculated by Equation (2) and bending moment M_i is calculated by Equation (3).

$$N_i=\frac{1}{2}\sum_{j=1}^{n-1}[(\sigma_j^i+\sigma_{j+1}^i)\cdot S_{j,j+1}^i]\cdot l_z \tag{2}$$

$$M_i=\frac{1}{2}\sum_{j=1}^{n-1}\{[(\sigma_j^i+\sigma_{j+1}^i)\cdot S_{j,j+1}^i]\cdot l_z\cdot t_a\} \tag{3}$$

Where: n is the number of nodes in the cross section i; j is the node j in cross section. When the cross section is at the crack, the starting point of j is at the crack tip node. When the cross section is not at the crack, the starting point of j is at the free face node of the lining. The node number increases progressively from the lining free face to the surrounding rock side. σ_j^i, σ_{j+1}^i The axial stress corresponding to i cross section and j node. It is negative if pointed towards the cross section and positive if away from the cross section. $S_{j,j+1}^i$ The Euclidean space distance at j node and j+1 node. In the global coordinate system of the model, if the coordinate of j node is (x_j,y_j), the coordinate of j+1 node is (x_{i+1},y_{i+1}), then

$$S_{j,j+1}^i=\sqrt{(x_{j+1}-x_j)^2+(y_{j+1}-y_j)^2} \tag{4}$$

Where l_z is the longitudinal dimension, which is 1m in the calculation. t_a is the t axis coordinate value of the point of action of resultant force of trapezoidal load from j node to j+1 node, and is calculated by Equation (5), where t_j^i is the t axis coordinate value of j node.

$$t_a=\frac{S_{j,j+1}^i}{3}\cdot\frac{\sigma_j^i+2\sigma_{j+1}^i}{\sigma_j^i+\sigma_{j+1}^i}+t_j^i \tag{5}$$

After the bending moment and axial force of the lining at the least favorable cross-section are obtained, the tensile safety factor K and compressive safety factor K'_i of the lining post strengthening are calculated by Equations (6) and (7).

$$K_i=\varphi\frac{1.75R_1bh}{\frac{6M_i}{h}-N_i} \tag{6}$$

$$K'_i=\frac{\varphi R_{\mathrm{a}}bh}{N_i} \tag{7}$$

Where: R_1 is the tensile strength of concrete, R_a is the compressive strength of concrete, and φ is the longitudinal bending coefficient of concrete member, which can be selected or calculated as per “the Code”; b is the breadth of section of member, and h is the effective depth of section of member. According to “the Code”,

the tensile safety factor of the structure should be ≥3.6 and compressive safety factor ≥2.4.

4 DEMONSTRATION OF SURFACE REINFORCEMENT EFFECTIVENESS AND CASE ANALYSIS

(1) Analysis of strengthening effectiveness of surface reinforcement

The tunnel section of a two-line tunnel of a high-speed railway with design speed 400km/h is used here, where the tunnel crown length is 6m and the depth of the longitudinal crack is 0.5*H*. The strength grade of concrete is C35, the φ12mm@50mm×50mm surface reinforcement is used for strengthening, and the steel reinforcement grade is HRB400. The surrounding rock grade in the to-be-strengthened segment is IV, and the load bearing proportion of the secondary lining is 50%; The vertical load on the structure is 77kPa and is loose load; The lateral pressure coefficient is 0.15. The finite element software is used to create the "load-structure" model for analysis, where the longitudinal dimension of the model is 12m. The physical and mechanical parameters of the material are selected according to "the Code". The calculated first principal stress (S1) of the structure before and after strengthening is shown in Figure 5.

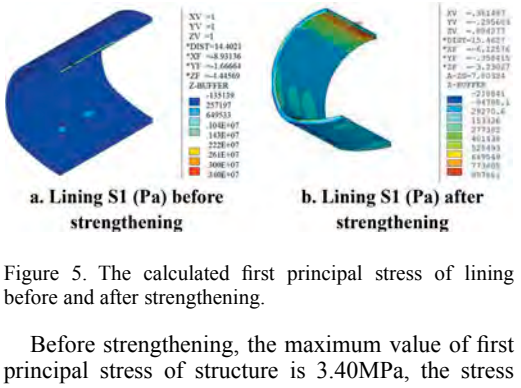

Figure 5. The calculated first principal stress of lining before and after strengthening.

Before strengthening, the maximum value of first principal stress of structure is 3.40MPa, the stress appears at the crack tip, and stress concentration happens. After strengthening, the first principal stress of structure is reduced to 0.90MPa, and it appears at the lining surface at the end of the crack in the lengthwise direction.

Therefore, surface reinforcement will reduce the tensile stress of structure, prevent tensile stress concentration at the crack tip and thus strengthen the structure and inhibit crack propagation.

(2) Checking calculation of surface reinforcement strength

The calculated first principal stress (S1) and third principal stress (S3) of surface reinforcement structure are shown in Figure 6.

As seen in Figure 6, the maximum value of first principal stress of surface reinforcement is 14.3MPa and that of third principal stress 0.024Pa. This

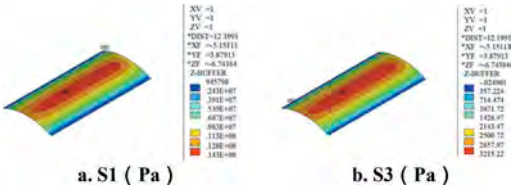

Figure 6. Calculated stress of surface reinforcement.

indicates that the surface reinforcement is mainly exposed to tensile stress. The design strength of HRB400 bar is R_g=400MPa. In calculation by Equation (1), the safety factor of surface reinforcement is $K_{hmj} = 27.97 > 2.4$, so the surface reinforcement has enough strength.

(3) Checking calculation of lining strength

The axial stress of the nodes at the least favorable cross-section before and after strengthening is extracted and calculation is done by using Eqs. (2) and (3). Before strengthening, the bending moment at the least favorable cross-section is 33.88kN·m and the axial force 138.38kN; After strengthening, the bending moment at the least favorable cross-section is 69.36kN·m and the axial force 519.75kN.

Calculation is done by using Eqs. (6) and (7). The calculated safety factor of structure before and after strengthening is shown in Table 1.

Table 1. Calculated safety factor of structure before and after strengthening.

Case	Bending moment (kN·m)	Axial force (kN)	*K*	*K*'	Strength Checking calculation
Before strengthening	33.88	276.75	1.23	284.06	Unqualified
After strengthening	69.36	519.75	4.66	11.02	Qualified

As shown in Table 1, the lining structure was dominated by tensile stress before and after strengthening. Before strengthening, the safety factor of structure is 1.23<3.6, which fails to conform to "the Code". After strengthening, the safety factor of structure is 4.66>3.6, which conforms to "the Code". Therefore, the φ12mm@50mm×50mm surface reinforcement will effectively strengthen the longitudinal crack with 6m length and 0.5*H* depth at the crown.

5 CONCLUSIONS AND PROSPECTS

To prevent over-strengthening at surface crack in railway tunnel and ensure sufficient stability of crack after strengthening, this paper proposes a surface reinforcement strengthening method and its design method for the purpose of lining surface crack conditioning, and demonstrates the effectiveness of this method. Main conclusions:

(1) A surface reinforcement strengthening method is proposed that consists of 4 parts including surface steel bar, side retaining structure, reinforcement anchor bolt and mortar cover. The environmental conditions that support application of surface reinforcement are defined.
(2) Under the load pattern specified by "the Code", if the compressive strength of the lining meets the design requirements, the crack depth usually does not exceed 0.5*H*, so surface reinforcement is only suitable for strengthening at a single crack with depth < 0.5*H*.
(3) The surface reinforcement strengthening design process and checking calculation method are devised. As proven, the surface reinforcement will prevent tensile stress concentration at the crack tip and thus strengthen the structure and inhibit crack propagation.
(4) When the φ12mm@50mm×50mm surface reinforcement is used to strengthen the crack with 6m length and 0.5*H* depth at the crown, the safety factor of structure increases from 1.23 to 4.66 and that of the surface reinforcement is 27.97. After strengthening, the structural strength conforms to "the Code".

This paper has examined the strengthening effectiveness of surface reinforcement in plain concrete crack conditioning, and verifies the effectiveness of surface reinforcement in crack conditioning. For high-speed railway tunnel, however, the stability of surface reinforcement under the action of train induced wind has not been investigated, so this will be further investigated in future research.

REFERENCES

[1] Li Changshu. Research on Distribution and Safety Evaluation in Lining Split of High Speed Railway Tunnel Based on Statistical Analysis[D]. Beijing: Beijing Jiaotong University, 2018.
[2] Wang Wei, Deng Jun, Yin Juntao. Research on safety of lining structure in railway tunnel under spatial crack disease[J]. Journal of Safety Science and Technology, 2016, 12(1):33–37.
[3] Li Wei, Yang Dan, Li Qing. Analysis on the Influence of Concrete Structure Cracks on the Durability of High-speed Railway Tunnel Lining[J]. Modern Tunnelling Technology, 2020, 57(z1):273–276.
[4] Wang Hualao, Liu Xuezeng, Li Ning, Et Al. Safety Evaluation of Tunnel Lining With Longitudinal Cracks and Reinforcement Design[J]. Chinese Journal of Rock Mechanics and Engineering, 2010, 29(Z1): 2651–2656.
[5] Yu Jingwen, Gong Lun, Xu Zichao, et al. Analysis of Stress State of Assembly Structure for Rapid Repair of Lining Cracking in Traffic Tunnels[J]. Subgrade Engineering, 2017(4):123–127.
[6] Chen Jiang, Yang Junsheng, Cao Nengxue, et al. Study on crack remediation and reinforcement of lining in railway tunnel[J]. Journal of Safety Science and Technology, 2014, 10(9):134–139.
[7] Su Chenhong, An Nannan, Wang Zhifeng. Study on crack remediation and reinforcement of lining in railway tunnel[J]. Journal of Architecture and Civil Engineering, 2020, 37(5):203–213.
[8] Fu Bingxian, Ma Weibin, Zou Wenhao, et al. Key Technologies for Lining Structure Design and Application of Corrugated Plate of Railway Tunnel Lining[J]. Railway Engineering,2021,61 (10):1–6, 17.
[9] Yu Hongqin, Qi Jun, Liu Huairong. Study on Causes to and Treatment of Concrete Cracking of the Secondary Lining of Qilianshan Tunnel [J].Modern Tunnelling Technology, 2021, 58(1):217–222.
[10] Shao Donghua. Study on Defect Correction Technology for Tunnel Lining in High-speed Rail Line[J]. Railway Construction Technology, 2019(z1):113–117.
[11] Wang Zhijie, Xu Haiyan, Zhou Ping, et al. Study on the Treatment of Lining Defects of Highway Tunnel[J]. Railway Standard Design, 2017, 61(10): 125–132.

Tunnelling for a Better Life – Yan, Celestino, Thewes & Eberhardt (Eds)
© 2024 The Author(s), ISBN 978-1-032-80042-4
Open Access: www.taylorfrancis.com, CC BY-NC-ND 4.0 license

An innovative primary support system of steel shotcrete composite structure in the tunnel

Junfu Lu & Minhao Li*
State Key Laboratory of Geohazard Prevention and Geoenvironmental Protection, Chengdu University of Technology, China

ABSTRACT: Steel arch-shotcrete support structure is widely used in tunnel primary support because of its advantages of timely support, flexible operation and superior seismic performance. However, with the development of traffic construction in China's western region, high-ground stress soft rock tunnels continue to appear during tunnel construction. Due to the complex geological structure, climatic and hydrological environment and stratigraphic and lithologic conditions, tunnels often pass through difficult geological environments such as high seismic intensity, high geological disaster risk, high tectonic stress, weak surrounding rock fracture zone and fault fracture zone. The supporting structure often bears large deformation pressure. Due to the large difference in mechanical properties between steel and shotcrete, the bonding ability between the two contact interfaces cannot resist shear stress, and relative slip occurs between steel and concrete. With the increase of relative slip, the shotcrete cracks and peels off, the steel arch is twisted, the structure loses the ability of collaborative deformation, and the overall instability of the supporting structure is destroyed. In this study, combined with theoretical analysis and numerical simulation, a steel-sprayed concrete composite structure tunnel initial support system composed of longitudinal connectors, stud shear connectors and U-shaped steel bars is proposed to improve the tunnel initial support system under external loads. The ability to resist deformation, overall bearing capacity, integrity and safety provide a reference for tunnel engineering design.

Keywords: Complex geology, Tunnel supporting, Steel and concrete, composite structure

1 INTRODUCTION

With the advantages of timely support, flexible operation and superior seismic performance, the steel arch-sprayed concrete support structure is widely used in the initial support of tunnels (Chiorean CG et al.,2017; Ding et al.,2018). Under complex geological conditions such as high ground stress, weak surrounding rock and groundwater, the supporting structure often bears large surrounding rock loads. Due to the large difference in mechanical properties between steel and shotcrete, the bonding ability between the two contact interfaces cannot resist shear stress, and relative slip occurs between steel and concrete. With the increase of relative slip, the shotcrete cracks and peels off, the arch is distorted, the overall bearing capacity of the supporting structure decreases sharply, the structure loses its synergistic deformation ability, and the surrounding rock is unstable and destroyed (Ghorbani M., 2020; Zhang et al., 2021).

Given the above-mentioned engineering difficulties, the research team in the tunnel field has proposed a variety of solutions from different perspectives.

Liu et al (2021) showed that the support method of double HK200b-type steel sets combined with large-diameter foot reinforcement bolts (FRB) and deep invert could effectively control the large deformation of the casing tunnel. Steel-concrete composite support (SCCS) was proposed by Wang et al (2021) to improve the support of loess tunnels. Based on the similarity theory, the mechanical behaviour of π-type SCCS arch under symmetric and asymmetric bias conditions without grouting was studied by a large-scale ring model test. Huang et al (2018) developed a new type of concrete-filled steel tube reinforcement support structure. This support is composed of a seamless steel tube bent to conform to the cross-section of the roadway and filled with concrete. The long-term large-scale deformation of deep roadways can be effectively controlled by using the support system of CSTS combined with

*Corresponding author: liminhao@stu.cdut.edu.cn

DOI: 10.1201/9781003495505-148

anchor cable. Xu et al (2017) designed a new type of grid steel frame-core tube support system. The outside of the structure is composed of flexible steel grilles and granular structural members. The inside of the structure is composed of steel core tubes. The units are connected by connecting steel plates with rubber pads. Steel core tube and steel sleeve connection A support system with square steel confined concrete (SQCC) was proposed by Wang et al (2016,2018), and the pure bending indoor test and numerical test of square steel confined concrete jointless members, flange joint members and casing joint members were carried out. Through field reference, the deformation of the surrounding rock is well controlled. Some researchers (Li et al.,2020; Liu et al.,2021) used concrete-filled steel tubular (CFST) support as a solution to the problem of large deformation of tunnels. The passive support method with high support resistance, such as concrete-filled steel tubular support and U-shaped steel, is used to form a passive support ring to assist or mobilize the surrounding rock of the roadway to exert its bearing capacity.

Although experts have proposed a variety of solutions, there are still many defects. For example, the additional materials will greatly increase the cost of the project, the complex support system will greatly extend the construction period, and the applicability of some new structures is not strong.

Based on the above challenges, a new type of initial support system for tunnel steel reinforced concrete composite structure is designed. This paper first introduces the design and function principle of the new support system. Then, the stress characteristics of traditional support and combined support are compared and analyzed by numerical simulation to verify the superiority of the new combined structure.

Through the use of this structure, the stiffness of the initial support structure of the tunnel can be increased, the cooperative deformation ability between the structures in the initial support system can be enhanced, the bearing capacity and deformation resistance of the initial support structure can be improved, to solve the problem of deformation and failure of the initial support structure due to the excessive in-situ stress in the tunnel.

2 DESIGN OF SUPPORTING SYSTEM

2.1 *Introduction of supporting system*

In this paper, a primary support system of tunnel shotcrete composite structure composed of three steel arches, longitudinal connection plate, stud shear connectors, U-shaped arches and shotcrete is taken as the research object, which is referred to as the primary support system of tunnel SRSC (Steel Reinforced Shotcrete) composite structure. The schematics of each structural member are shown in Figure 1.

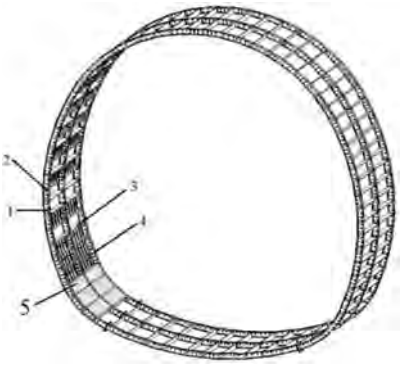

Figure 1. Schematic of SRSC composite structure support system (1-steel arch, 2-stud, 3- longitudinal connection plate, 4- U-shaped steel, 5-Shotcrete).

Table 1. The structural functions of the primary support system of SRSC composite structure.

Structure	Function	Components
Steel arch	The section steel provides strong support resistance to withstand the pressure of surrounding rock in a short time	Section steel, bolts and flanges
Stud shear connector	The stud ensures that the steel and concrete form a whole and co-stress and coordinate the deformation of the steel mesh	Stud
Longitudinal connection plate	Strengthen the longitudinal stability of the support system	L-shaped panels, bolts, diaphragms
U-shaped steel	Reinforced support system ring stability, improves the bearing capacity	U-shaped steel, steel wire
Shotcrete	closed exposed rock surface, to prevent surface weathering	Shotcrete

Table 1 and shows the structural functions and details of the initial support system of the SRSC composite structure.

It can be seen from the table that the tunnel SRSC composite structure support system makes up for some of the functional deficiencies in the traditional support form. Firstly, the longitudinal connection is arranged between each steel arch to make the primary support structure of the tunnel have good stability along the longitudinal direction. Each steel is connected to make it a support system to jointly deform. Each steel arch improves the interaction between steel and shotcrete by arranging stud shear connectors at the web. The ability to increase the stability of the support structure in the circumferential direction and increase the bearing capacity of the support system by arranging circumferential U-shaped steel bars.

2.2 *Design principle*

2.2.1 *Steel and shotcrete*

The overall stiffness of the steel arch is large, and the small deformation under the load can better control the deformation of the surrounding rock. It can provide a large early support stiffness and can bear the main surrounding rock deformation pressure of the overall support system. The steel arch can be combined with diaphragm, stud shear, steel bar and shotcrete in time to form a combined support of composite structure so that the support structure becomes a whole with good adaptability to the section, which enhances the effectiveness of the combined support of composite structure and has good stress conditions. In the SRSC system, the spacing of steel arches and the type of steel arches should be determined according to the actual situation of the tunnel engineering site. For the convenience of erection, each steel arch is generally divided into 2~6 sections, and the joint stiffness is guaranteed. The number of sections should be adapted to the size of the section and the excavation method.

In the early stage of deformation, shotcrete plays a bonding resistance role. The bonding failure depends on the mineral composition of the surrounding rock surface and the thickness of the spray layer. The bonding resistance effect mainly depends on the quality of the surrounding rock (the mineral composition of the surrounding rock surface) and its surface cleanliness and increases with the increase of the thickness of the spray layer to a certain extent. The thickness of shotcrete should be compatible with the height of the steel arch section. The shotcrete protective layer directly between the steel frame and the surrounding rock should not be less than 40 mm, and the concrete protective layer on the free side should not be less than 20 mm.

2.2.2 *Stud connection*

In the tunnel SRSC composite structure support system, the stud shear members are arranged in parallel on the inner and outer sides of each steel arch web with a certain spacing, aiming to enhance the cooperative working ability with shotcrete and the bearing capacity of the structure. The design and layout of the stud shear parts in the SRSC composite support system of the tunnel are shown in Figure 2 below.

The stud shear connector is subjected to complex stresses such as tension, shear and bending of concrete and steel during the stress process. When the load is applied to the component, the component moves, and the studs also move in the same direction. The shear force is mainly transmitted to the surrounding concrete through the root of the stud. When the external load is transmitted to the root of the stud through the weld, local pressure is generated in the concrete at the root, and a large deformation is generated, so that the whole stud tends to rotate in the direction of the bending moment, and the rotation of the stud is constrained by the concrete at the top cap. As the load continues to increase, the studs are damaged.

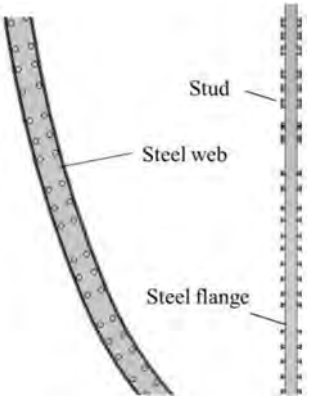

Figure 2. SRSC composite structure supporting system of stud shear connector layout.

2.2.3 *Longitudinal connection plate and U-shaped steel bar*

In the SRSC composite structure support system, the longitudinal connection plate provides lateral support. Through the diaphragm, the steel arches can be connected to form a structural system. The diaphragm can effectively enhance the lateral stiffness of the system and coordinate the overall deformation of the support structure. The diaphragm in the SRSC composite structure support system is composed of L-shaped panelling, hexagonal bolts, and steel plates. The schematic diagram of each structural member is shown in Figure 3 below.

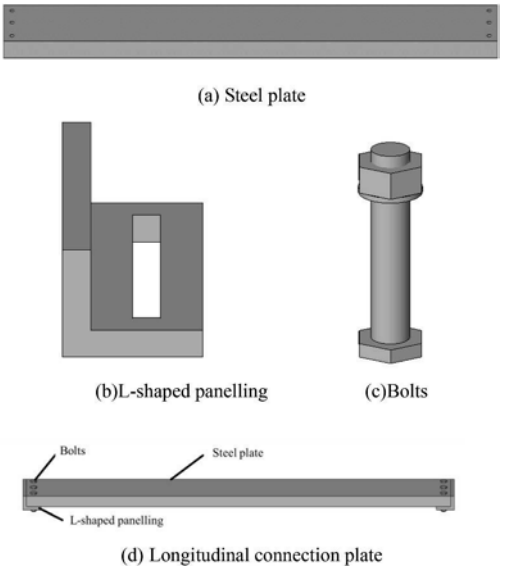

Figure 3. The composition of the longitudinal connection plate.

The role of the longitudinal connection plate and U-shaped steel bar in the tunnel SRSC composite structure support system is to strengthen the ability of cooperative work between steel arches and control the stability of the support system in the longitudinal and circumferential directions and the ability to combine with concrete. The layout of the longitudinal connection plate in the support system is shown in Figure 4

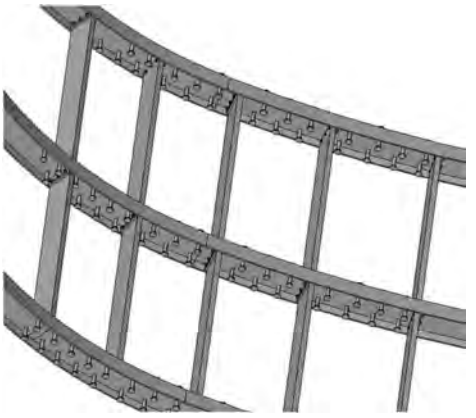

Figure 4. The layout of the longitudinal connection plate.

For the design of the steel bar in the initial support system of the SRSC composite structure, the U-shaped steel is bent. The arc of the vertical straight section of the U-shaped steel bar is roughly the same as that of the upper and lower diaphragms of the corresponding tunnel. If the U-shaped steel bar is arranged at the edge of the straight wall of the initial support of the tunnel, the bending arc is not considered. The U-shaped steel bar is shown in Figure 5.

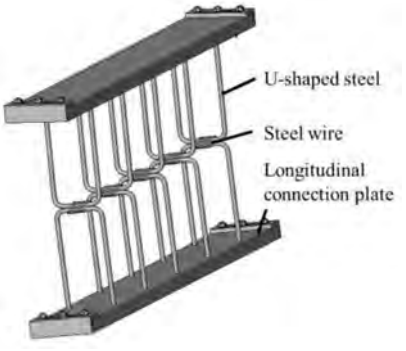

Figure 5. U-shaped steel composition diagram.

After the diaphragm is installed between the steel arches, U-shaped steel bars are welded at a certain distance between the lower and upper parts of the diaphragm by welding, as shown in Figure 5 above. The U-shaped steel bars are arranged along the longitudinal direction of the tunnel, as shown in Figure 6.

From Figure 6, the welded U-shaped steel bar at the lower part of the upper diaphragm intersects the straight section of the middle part of the welded U-shaped steel bar at the upper part of the lower diaphragm. The height of the upper and lower U-shaped steel bars should be the same as that of the adjacent two diaphragms. The intersection part is tied with steel wire.

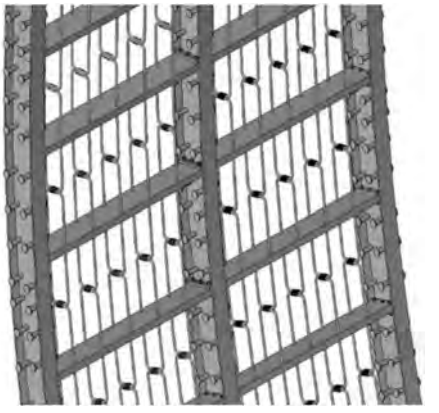

Figure 6. Layout diagram of U-shaped steel in steel arch.

The role of U-shaped steel bars is to improve the stability of the support system in the ring, strengthen the bonding ability with shotcrete, and increase the bearing capacity of the support system.

3 NUMERICAL COMPARISON EXPERIMENT

In this section, the failure modes, ultimate bearing capacity, failure and stress deformation characteristics of SRSC composite structure support system and traditional support from under bending state are analysed by numerical test. To compare the failure modes and mechanical characteristics of two different tunnel support forms under a bending state, the feasibility and support effect of the SRSC composite structure support form are verified.

3.1 *Modelling and parameter selection*

Modelling establishment: In this paper, for the particularity and complexity of the structure, the eight-node hexahedral reduction integral element (C3D8R) in the solid element is used for the steel arch, diaphragm, stud, concrete and fixed end, and the three-dimensional truss two-node complete integral element (T3D2) is used for the steel bar element, only considering the tension or pressure.

The concrete plastic damage (CDP) model is selected for shotcrete, which can reflect the development behaviour of cracks, the change of damage degree and the process of tensile softening during the failure process of materials.

Figure 7. Numerical calculation model.

The double oblique line model is used for the constitutive model of the steel and the stud. The average bond stress-relative slip relationship between the interfaces can be simulated by the cohesive behaviour in the interaction properties. The model of the structure is shown in the Figure 7.

Regarding the interface contact of each component, the Boolean operation is used to combine each steel arch with diaphragms and studs. Secondly, the interface between the steel bar and the diaphragm is constrained by the Tie and Coupling Constraint. Steel arches (with studs), diaphragms, studs and steel bars are embedded in the concrete solid element by Embedded.

Parameter select: The support component sizes and mechanical parameters are shown in Table 2.

Table 2. Component design parameters.

Support component	Type	Size /mm
Steel arch	I16	160×88×6
Stud	Q345	63×7
Diaphragm	Q345	140×1000
Steel bar	φ20	-
Shotcrete	C30	-

The specific physical and mechanical parameters are shown in Table 3. The concrete is C30.

Table 3. Steel material performance parameters.

	Elastic modulus E/ GPa	Poisson's ratio μ	Yielding Strength f_y/ MPa	Ultimate strength f_b/ MPa
Steel arch	205	0.3	345	510
Diaphragm	205	0.3	345	510
Stud	198	0.3	345	510
Steel bar	210	0.3	370	-

3.2 *Result analysis*

3.2.1 Comparative analysis of bearing capacity

Figure 8 shows the bearing capacity of the two supporting forms. It can be seen from the figure that in the initial stage of loading, the stress of the two support forms increases linearly with the load. With the increase of load, the two supporting forms of steel arch have entered the plastic stage one after another. When q = 0.12 MPa, the yield stress of the SRSC steel arch is 33 % higher than that of the traditional supporting arch, q = 0.66 MPa. The arch of the SRSC supporting system reaches the ultimate stress state, and the ultimate bearing capacity of the SRSC supporting system is 153 % higher than that of the traditional supporting system.

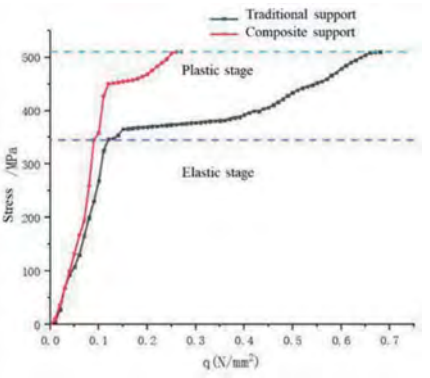

Figure 8. Stress load comparison curve.

Therefore, the SRSC supporting system has a greater ability to bear the load. The traditional steel arch has greater structural stress under the same load, and the structure is more likely to reach yield and ultimate load, which leads to the loss of bearing capacity of the support system. In the plastic development stage, the plastic yield development speed of the steel arch in the traditional support form is much larger than that in the SRSC support structure system. The stiffness of the SRSC support system is greater. The internal force of the steel arch under the same load also shows that the diaphragm, studs and

steel bars in the SRSC support form optimize the overall stress mode of the structure and increase the bearing capacity of the support system.

3.2.2 *Comparative analysis of vertical displacement*
Figure 9 describes the pattern and difference of vertical displacement change between the two support systems under different loads.

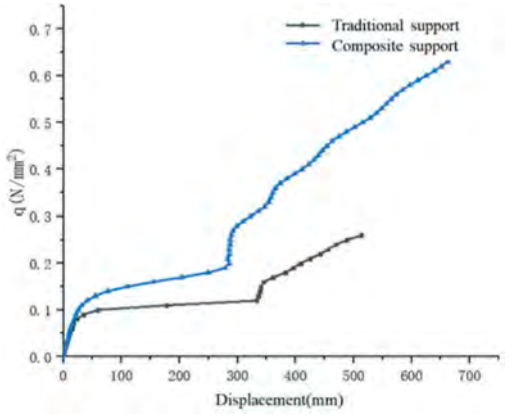

Figure 9. Load vertical displacement comparison curve.

When q = 0.09 MPa, the maximum displacement of the traditional support form begins to enter the plastic stage is 34.5 mm, and the maximum displacement of the SRSC support system is 21 mm. The displacement of the traditional support form increases by 1.64 times under the same load. It can be concluded that the traditional support form enters the plastic yield stage earlier than the SRSC system, and the SRSC support system has a stronger ability to resist deformation. When the support form enters the plastic yield stage, when q = 0.12MPa, the SRSC support system begins to enter the plastic stage. At this time, the maximum displacement is 40mm, and the traditional support form has produced a large displacement deformation. The maximum displacement of the traditional support form is 332mm. Compared with the SRSC support system, the traditional deformation is increased by 8.3 times. When the traditional support form arch reaches the ultimate stress (q = 0.26MPa), the maximum displacement deformation of the steel arch is 513.4mm, and the maximum displacement deformation of the SRSC support system is 289.3mm. The displacement of the traditional support form is increased by 1.77 times. Therefore, it can be seen that the stiffness of the SRSC system is larger, and the effect of restraining the deformation of the support system is more obvious. Under the same load, the displacement of the SRSC support system is smaller.

3.2.3 *Comparative analysis of lateral displacement*
Figure 10 shows the lateral displacement deformation of the two supporting systems under the same load.

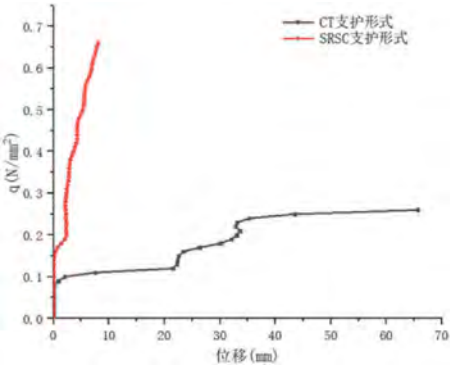

Figure 10. Load lateral displacement comparison curve.

It can be seen from Figure 10 that under the same load, the lateral displacement deformation of the SRSC supporting system is much smaller than that of the traditional supporting structure. Before 0.09 MPa, the growth curve of load and deformation of the traditional supporting structure in the elastic stage is a straight line, and the lateral displacement is basically within 0.04 mm. With the increase in load, the traditional supporting arch reaches the yield stress and enters the plastic deformation stage. The supporting capacity and supporting effect of the supporting form begin to decrease, and the curve begins to show obvious nonlinearity. The SRSC supporting system has almost no lateral deformation before q = 0.16 MPa. With the increase in load, the concrete failure and the structural members in the supporting structure reach the yield stress failure, and the slope of the load-displacement curve becomes larger. When the concrete is destroyed, the load-displacement curve increases linearly. In short, the diaphragm and each component in the SRSC support system can effectively control the lateral deformation of the support form, make the lateral deformation of the support form develop more smoothly, and have better stability and deformation control ability in the lateral direction of the support system.

3.2.4 *Comparative analysis of failure characteristics*
Figure 11 shows the failure characteristics of the two different support systems.

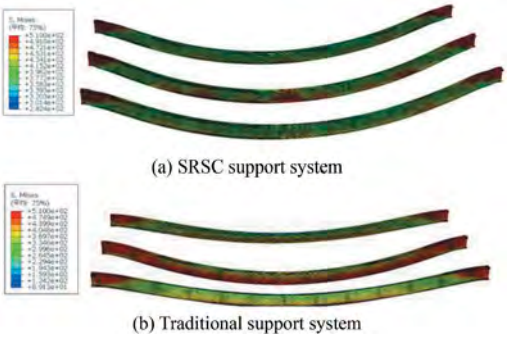

Figure 11. The deformation characteristics of different support forms.

It can be seen from Figure 11 that there are some differences between the two kinds of support failure modes. The failure mode of the SRSC support system is that the three steel arches are mainly buckling along the loading direction, and the lateral steel arches have no obvious lateral torsional buckling along the out-of-plane. The failure mode of the traditional support form is that three pieces of steel are locally bent along the loading direction, and the lateral steel arch is distorted and buckled due to insufficient lateral support. It shows that the overall stability of the SRSC support system is better in the bending state, and the three steel arches can coordinate the deformation. The arch steel will not work alone due to excessive load, failing the support structure.

4 CONCLUSIONS

(1) Compared with the traditional support form, the yield load of SRSC support is increased by 33 %, and the flexural ultimate bearing capacity is increased by 153 %. It can be seen that the SRSC support system has greater rigidity. The diaphragm, studs and steel bars in the support system optimize the overall stress mode of the structure, and the ductility is better. The SRSC support form has a greater ability to withstand loads and can provide stronger support capacity and greater bearing capacity.

(2) The SRSC support system has smaller bending deformation in the vertical and lateral directions. When the traditional support form is destroyed, the vertical deformation and lateral deformation of the traditional support form are 1.77 times and 29.98 times that of the SRSC support system, respectively. The diaphragm and each structural member in the SRSC support system have a significant effect on the displacement deformation of the support structure, and the support system shows excellent ductility.

(3) In the tunnel SRSC composite structure support system, the steel arch has enough lateral support, and the failure mode is mainly the overall buckling along the loading direction. The three steel arches are coordinated and deformed, and the lateral steel arch does not have obvious distortional buckling. The overall stability of the support system is better.

(4) Through the use of this structure, the stiffness of the initial support structure of the tunnel can be increased, the cooperative deformation ability between the structures in the initial support system can be enhanced, and the bearing capacity and deformation resistance of the initial support structure can be improved, to solve the problem of deformation and failure caused by the excessive in-situ stress of the initial support structure in the tunnel.

ACKNOWLEDGEMENTS

This research was supported by the National Natural Science Foundation of China (Grant No. 51978088) and the State Key Laboratory of Geohazard Prevention and Geoenvironment Protection Independent Research Project (Grant No. SKLGP2021Z007).

REFERENCES

Chiorean CG, Buru SM, 2017. Practical nonlinear inelastic analysis method of composite steel-concrete beams with partial composite action. Eng Struct. 134, 74–106.

Ding, FX., Liu, J., Liu, XM., et al, 2018. Experimental investigation on hysteretic behaviour of simply supported steel-concrete composite beam. J Constr Steel Res. 144, 153–65.

Ghorbani, M., Shahriar, K., Sharifzadeh, M., 2020. A critical review of the developments of rock support systems in high-stress ground conditions. International journal of. Min Sci Technol. 30(5), 555–72.

Huang, W.P., Yuan, Q., Tan, Y.L., et al., 2018. An innovative support technology employing a concrete-filled steel tubular structure for a 1000-m-deep roadway in a high in situ stress field. Tunn. Undergr. Space Technol. 73, 26–36.

Li, W.T., Yang, N., Mei, Y.C., et al 2020. Experimental investigation of the compression-bending property of the casing joints in a concrete-filled steel tubular supporting arch for tunnel engineering. Tunn. Undergr. Space Technol. 96. https://doi.org/10.1016/j.tust.2019.103184.

Liu, D.J., Zuo, J.P., Wang, J., et al, 2020. Large deformation mechanism and concrete-filled steel tubular support control technology of soft rock roadway-A case study. Eng. Fail. Anal. 116. https://doi.org/10.1016/j.engfailanal.2020.104721.

Liu, W., Chen, J., Luo, Y. et al.,2021. Deformation Behaviors and Mechanical Mechanisms of Double Primary Linings for Large-Span Tunnels in Squeezing Rock: A Case Study. Rock Mech Rock Eng 54, 2291–2310.

Wang, Q., Jiang, B., Li, S.C., et al, 2016. Experimental studies on the mechanical properties and deformation & failure mechanism of U-type confined concrete arch centring. Tunn. Undergr. Space Technol. 51, 20–29.

Wang, Q., Jiang, B., Pan, R., et al., 2018. The failure mechanism of surrounding rock with high stress and confined concrete support system. Int. J. Rock Mech. Min. Sci. 102, 89–100.

Wang, Z.C., Xie, Y., Lai, J.X., et al., 2021. Designing an innovative support system in loess tunnel. Geomech. Eng. 24 (3), 253–266.

Xu, F., Li, S.C., Zhang, Q.Q., et al., 2017 A new type support structure introduction and its contrast study with traditional support structure used in tunnel construction. Tunn. Undergr. Space Technol.63, 171–182.

Zheng, YC., He, SY., Yu, Y., et al, 2021. Characteristics, challenges and countermeasures of giant karst cave: a case study of Yujingshan tunnel in high-speed railway. Tunn Undergr Space Technol. 114. https://doi.org/10.1016/j.tust.2021.103988

Tunnelling for a Better Life – Yan, Celestino, Thewes & Eberhardt (Eds)
© 2024 The Author(s), ISBN 978-1-032-80042-4
Open Access: www.taylorfrancis.com, CC BY-NC-ND 4.0 license

Stress analysis of high geothermal tunnel lining structures considering different cooling measures

Mingrui Luo*, Zuobing Yuan, Lintao Fan, Liangliang Tao & Yanhua Zeng
State Key of Laboratory of Intelligent Geotechnics and Tunnelling, Chengdu, China
School of Civil Engineering, Southwest Jiaotong University, Chengdu, China

ABSTRACT: Laying insulation and ventilation are usually used as cooling measures in high geothermal tunnels, and laying cooling tubes in the lining structure part as a new cooling measure, the research on the cooling process and effect of cooling tubes on the lining structure is still lacking. Therefore, in order to study the effect of different cooling measures on the internal force of the supporting structure of high geothermal tunnel, this paper establishes an indoor test platform for the force of lining structure of high geothermal tunnel, and carries out the test of cooling measures. The results show that: ventilation and cooling pipe can effectively reduce the influence of surrounding rock on lining temperature; the cooling effect of GHEs is better than that of ventilation; in the process of cooling, the circumferential stress borne by the lining is mainly tensile stress; the coupled effect of ventilation and cooling pipe can reduce the lining temperature faster; the flow rate of the cooling pipe is in the range of 0.4m/s~0.6 m/s, and the cooling effect is better with the wind speed in the range of 1~2m/s.

Keywords: High geothermal tunnel, Laboratory test, GHEs, Ventilation, Stress

1 INTRODUCTION

In recent years, large and deep tunnels have been built, and the problem of warm and hot water in the highlands has arisen(Chen et al., 2021; Lin et al., 2022; Yan et al., 2019; Zeng et al., 2020a; Zhang et al., 2021). High ground temperatures during tunnel construction are not only hazardous to workers and reduce equipment productivity, but the long-term effects can weaken the structure of the tunnel lining, making it extremely difficult to complete the project safely(Gao et al., 2017; Liu et al., 2019; Tang et al., 2016). Therefore, research on high temperature tunnel construction has been a focus of attention.

Typically, high geothermal tunnels are cooled through ventilation(Fan et al., 2017; Tao et al., 2022a; Tao et al., 2022b; Zeng et al., 2020b; Zhou et al., 2016; Zhou et al., 2021). Tan et al. (Tan et al., 2014) investigated the effect of different wind speeds and insulation layers on the cooling effect of tunnels. Liu et al. (Liu et al., 2016) investigated the temperature stress variation characteristics of lining structures. Another cooling method is the use of the application of ground heat exchangers (GHEs). GHEs can take advantage of the high heat capacity properties of the material and are therefore widely used for geothermal energy extraction and utilization(Adam and Markiewicz, 2009; Brandl, 2006; Zhang et al., 2016a; Zhang et al., 2014; Zhang et al., 2016b). At present, energy foundation, energy geotextile(Lee et al., 2012) and other technologies have been developed Ventilation does not only have a significant impact on the perimeter heat transfer loop, but also on the GHEs.(Bidarmaghz and Narsilio, 2018).

Currently, ventilation to lower the temperature of the surrounding rock has been intensively researched by modelling experiments, theoretical calculations, and numerical simulations. The findings of previous research indicate that GHEs concentrate stress in the lining, primarily in the circumferential direction. However, the majority of existing studies concentrate on the cooling effect of ventilation on tunnels and the thermal performance of geothermal heaters. There are few studies that take into account lining stresses under the synergistic effect of ventilation and GHEs, and even fewer studies that conduct pertinent indoor tests.

Consequently, in order to better understand how various cooling techniques affect lining stresses. In this work, a test platform was developed to investigate various GHEs flow rates and ventilation wind speeds. To analyse the impacts of various cooling measures on lining temperature and the characteristics of lining stress variations, cooling tests with only ventilation, solely GHE activation, and the coupling of the two were conducted. The results can serve as a benchmark for high-temperature geothermal tunnel projects.

*Corresponding author: romery@163.com

DOI: 10.1201/9781003495505-149

2 LABORATORY TEST

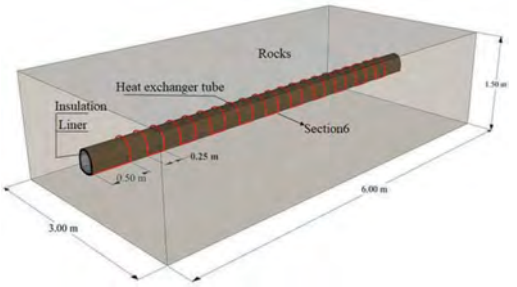

Figure 1. Schematic diagram of test platform.

A stainless-steel box with measurements of 6 m by 3 m by 1.5 m serves as the model test chamber. To provide thermal and moisture insulation boundaries, the box's long sides were surrounded by 5 cm thick insulation boards made of rubber-plastic and water-repellent rock wool. The model tunnel had a cross section that was 30 cm broad, 33 cm high, and 2 cm thick. Steel wire mesh and CGM general-purpose high-strength non-shrink grout are used to line the tunnel, while rubber-plastic material serves as the thermal insulation layer. The ratio of similarity is 1:30.

PERT pipes having an outside diameter of 16 mm and a thickness of 0.015 mm are used by the GHEs. With a total pipe length of 23 m, the cooling pipes' beginning and last rings were installed at either end of the tunnel at a distance of 25 cm.

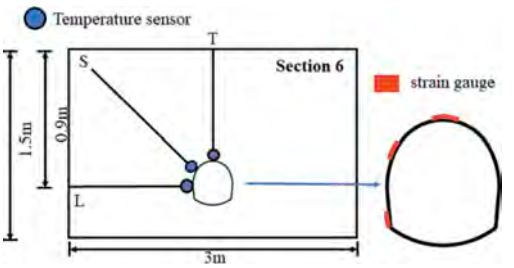

Figure 2. Schematic diagram of sensor deployment at cross section No. 6.

The thermal insulation layer was placed in front of the heat pipes, which were fitted with flow meters and throttling valves to regulate the flow rate. To guarantee that the temperature of the water entering into the test chamber is always consistent, the fluid in the heat exchanger tubes exits the test chamber and enters the circulating thermostat system. At the entrance and outlet of the heat exchange tubing lines, flow meters and type K thermocouples are attached.

Three test portions were separated by 150 cm in the test chamber. Air temperature sensors were positioned in the tunnel, and 20 K-type thermocouples were dispersed throughout the enclosure in three different directions in each segment. Sensors in each direction are laid out at irregular spacing.

To take a peek at h different cooling measures on lining stresses. The flow rates inside the tubes of the GHEs used in this investigation were set to 0.4 m/s, 0.6 m/s, and 0.8 m/s. Full cross-section uniform ventilation was used for ventilation, with air velocities of 0, 1, 2, and 3 m/s.

Table 1. Experimental program of different cooling measures.

Test No.	Flow velocity (m/s)	Wind speed (m/s)
1	-	1
2	-	2
3	-	3
4	0.4	-
5	0.6	-
6	0.8	-
7	0.4	1
8	0.4	2
9	0.4	3

3 RESULTS AND DISCUSSION

From the three kinds of working conditions, namely, ventilation only, GHEs only, GHEs and ventilation coupling effect, 1 group of working conditions is selected respectively, and the temperature field of surrounding rock and the temperature field of tunnel lining are obtained along the direction of tunnel depth when the test is carried out for 48 h. The temperature field of the surrounding rock and the temperature field of the tunnel lining are distributed according to the temperature boundary. It can be seen that the test platform can be basically divided into three sections according to the distribution of temperature field, the inlet section (L1~L3) and the outlet section (L9~L11) are more obviously affected by the temperature boundary, and the high-temperature smooth section (L3~L9) can better simulate the high geothermal

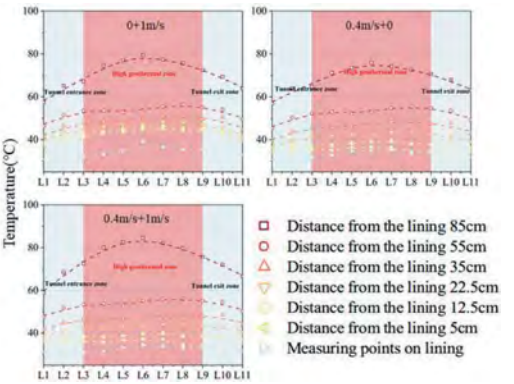

Figure 3. Temperature field distribution of the test platform along the tunnel depth direction during 48h of the test.

tunnel of the actual project. Therefore, in the subsequent analysis, the L6 section is selected for analysis.

3.1 *Ventilation-only conditions*

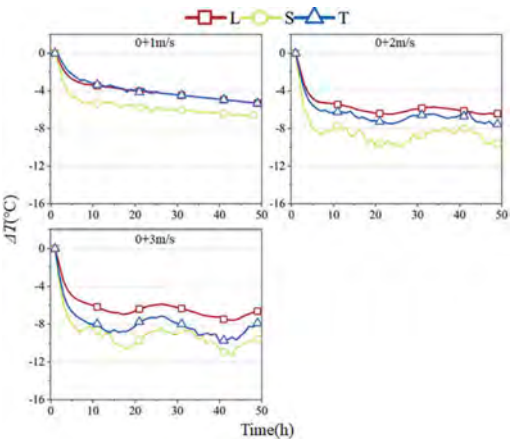

Figure 4. Diagram of temperature changes in the lined girdle, footing, and vault for ventilation-only.

Figure 4 depicts the temperature variation at various lining structure sites when just ventilation is used. With a wind speed of 1 m/s, the cooling amount at the arch's foot and vault is nearly equal—it is 80.15% of the cooling amount at the arch's waist. When the wind speed reaches 2 m/s, the temperature drop at the arch top and the arch foot varies, with the temperature reduction at the arch foot being 12.17% smaller than that at the arch top and equal to 66.85% of the temperature reduction at the arch waist. The cooling amount of the working condition with wind speed of 2 m/s increased at all places compared with the working condition with wind speed of 1 m/s. Among them, the largest increase in temperature reduction at the arch waist is 31.00%; the smallest increase in temperature reduction at the foot of the arch is 17.26%; and the increase in temperature reduction at the arch top is 29.42%. When the wind speed reaches 3m/s, the cooling amount of the arch foot is 84.23% of the cooling amount of the arch top and 69.29% of the cooling amount of the arch waist. Comparing the results of the working conditions with wind speed of 3m/s and wind speed of 2m/s, the growth of temperature reduction at each position is within 0~4.35%.

It can be seen that at different wind speeds, the temperature reduction at the foot of the arch, the waist of the arch and the top of the arch increased with the test. Among them, the fastest cooling and the largest amount of cooling was observed at the arch waist, and the slowest cooling and the smallest amount of cooling was observed at the foot of the arch. This is due to the wind flow and lining surface convection heat transfer, and convection heat transfer coefficient and the shape of the heat transfer surface and other factors related to the arch waist at the heat transfer surface is the flattest, so the fastest cooling speed, and the cooling amount is also the largest.

With the increase of wind speed, the temperature at the foot of the arch and the top of the arch gradually appeared to be different, and the cooling amount and cooling speed of each position also gradually increased, but when the wind speed exceeded 2m/s, this change was no longer significant. And with the increase of wind speed, the fluctuation of lining temperature is also gradually significant. This is because the convective heat transfer coefficient is determined by the Nusselt number, and the Nusselt number is positively correlated with the flow rate, so the larger the wind speed, the larger the convective heat transfer coefficient and the larger the cooling rate. And the heat of the lining structure comes from the surrounding rock, and the heat replenishment capacity of the surrounding rock is limited. Therefore, when the wind speed reaches 2m/s, the heat transfer between air-lining-surrounding rock has reached equilibrium, and continuing to increase the wind speed does not reduce the lining temperature.

As seen from Figure 5, the stress development law of the lining is basically consistent with the temperature change law. In the working condition of wind speed 1m/s, the stress at the foot of the arch and the arch top is basically the same, which is about 59.35% of the stress at the arch waist. When the wind speed reaches 2m/s, the stresses at the vault and the foot of the arch do not increase with the elevation of cooling, the stress at the vault is 91.98% of the stress at the vault in the case of wind speed 1m/s, the stress at the foot of the arch is almost unchanged, and the stress at the arch waist is elevated by 10.11%. When the wind speed reaches 3m/s, the stress at the arch is elevated by 31.29%, the stress at the arch waist is elevated by 22.56%, and the stress at the footing is elevated by 13.46%. The stresses in the lining are dominated by tensile stresses, which is due to the fact that the ventilation continuously extracts heat from the lining, leading to a decrease in the lining temperature, and thus the cold contraction of the concrete produce's stresses dominated by tensile stresses.

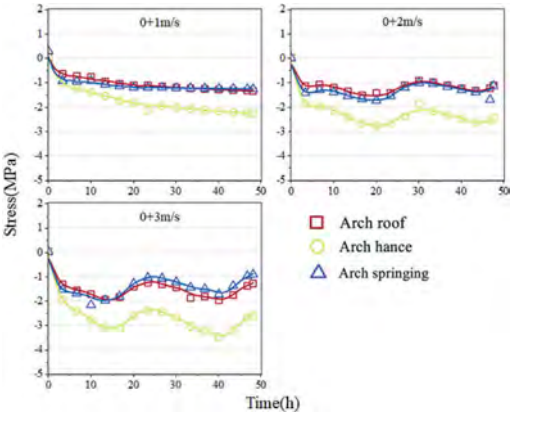

Figure 5. Diagram of stress changes in the arch waist, foot of the arch, and vault of the lining when ventilated-only.

Compared with the temperature development law, it can be seen that the stresses in the footing and vault of the lining are almost the same when the wind speed is 2m/s or less, and the growth of the stresses is less affected by the wind speed. When the wind speed reaches 3m/s, the stress at the vault is about 82.79% of the stress at the top of the arch. The stress at the arch waist has been higher than the other two locations, and the growth rate of stress increases with the increase of wind speed. This is due to the fact that the tunnel is subjected to the joint action of the surrounding rock pressure and stress, under the action of the surrounding rock pressure, the compressive stress is mainly distributed in the arch top and the foot of the arch, and the tensile stress mainly appears at the arch waist. And the results of the stresses show that at all locations of the lining, the stresses are tensile stresses. Therefore, the tensile stress at the top of the arch and the foot of the arch is relatively small compared to the stress at the arch waist.

3.2 *GHEs-only conditions*

As shown in Figure 6, the effect of GHEs on lining temperature is significantly greater than that of ventilation. In the case of GHEs flow rate of 0.4m/s, the cooling of the arch footing is 81.29% of the cooling of the arch waist and 66.26% of the cooling of the arch top. In the case of GHEs with a flow rate of 0.6 m/s, compared with the case with a flow rate of 0.4 m/s, there is not much change in the cooling amount of each position, and the change is basically within 12%. When the flow velocity of the GHEs increased to 0.8 m/s, the cooling amount at each position decreased, and the decrease was between 25 and 29%. This indicates that the cooling effect is basically the same when the flow velocity is within 0.4m/s to 0.6m/s. When the flow velocity is greater than 0.6m/s, the cooling effect instead decreases. This is because the cooling effect of GHEs on the lining is heat conduction, which is faster than convection heat transfer. When the flow rate in the GHEs is low, the cooling effect of the GHEs is more stable, when the flow rate is greater than 0.6m/s, the liquid in the pipe of the GHEs heats up faster, so when reaching section 6, the water temperature is already higher, and therefore the cooling effect on the lining is weakened.

From Figure 7, it can be seen that in the case of running GHEs only, the stress development pattern of the arch waist, footing and vault of the lining is basically the same as that of the ventilated-only case, but in the values are basically smaller than that at the ventilated-only case, the stresses at each position of the lining. In the case of GHEs with a flow velocity of 0.4 m/s, the difference in stress between the vault and the footing is small, and the stress at the vault is only 33.45% of that at the arch waist. When the flow velocity reaches 0.6m/s, the stress at the vault increases by 45.61%, the stress out of the arch

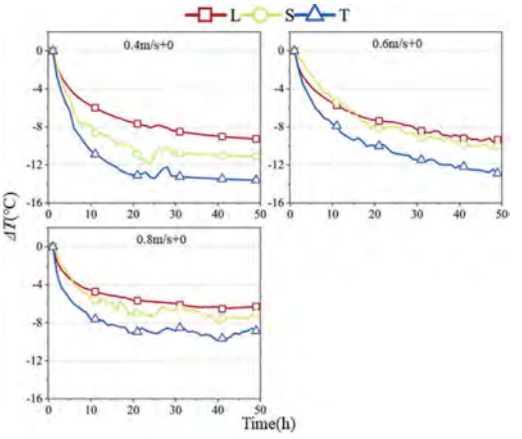

Figure 6. Temperature variation of the lining's arch waist, arch foot, and arch top when only GHEs are activated.

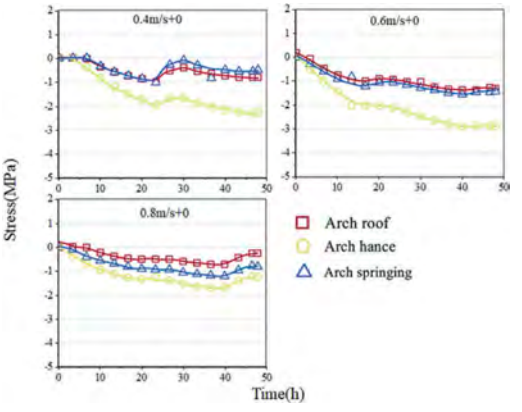

Figure 7. Diagram of stress changes in the arch waist, foot of the arch, and vault of the lining when only the GHEs are activated.

increases by 24.39%, and the stress at the arch waist increases by 68.55%. When the flow rate reaches 0.8m/s, the stresses at each place start to decrease instead, and the maximum decrease can reach 57.04%. Combined with Figure 6, it can be seen that the stress change of the lining has a highly sensitive correlation with the operating parameters of the GHEs. When the flow rate of GHEs is 0.6m/s, the stress at the arch waist can reach 2.79MPa, but it is still smaller than the stress at the arch waist in the case of wind speed of 3m/s.

3.3 *Coupling of GHEs and ventilation*

Figure 8 shows the temperature variation at various locations of the lining when GHEs and ventilation are coupled. It can be seen that the temperatures at the arch waist and arch top of the lining are closer. Compared with the case of ventilation only, the increase of temperature reduction in the coupled

case is from 21.63 to 51.80%; compared with the case of GHEs only, the temperature reduction in the coupled case decreases at the vault in the case of GHEs flow rate of 0.4m/s + wind speed of 1m/s, and in the rest of the cases and locations, the increase of temperature reduction in the coupled case is from 2.43 to 47.73%.

Compared with the case of GHEs flow rate of 0.4 m/s + wind speed of 1 m/s, the temperature reduction at the foot of the arch is improved by 15.28%, at the arch waist by 8.46%, and at the vault by 15.71% in the GHEs flow rate of 0.4 m/s + wind speed of 2 m/s case. When the wind speed increased to 3m/s, the cooling amount at each location of the lining basically no longer changed. This indicates that the working condition of GHEs flow rate of 0.4m/s + wind speed of 2m/s has reached the heat exchange equilibrium state of GHEs-air-surrounding rock.

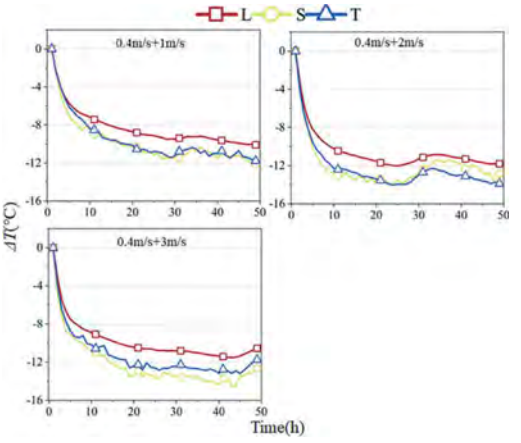

Figure 8. Temperature variations of the lining's girdle, footing, and vault when GHEs and ventilation are coupled to cool the lining.

As shown in Figure 8, in the case of GHEs flow rate of 0.4m/s + wind speed of 1m/s, compared with the case of only activating the GHEs flow rate of 0.4m/s, the stress at the soffit is reduced by 143.67%, while the stress at the soffit is elevated by 27.18%, and at the foot of the soffit is almost the same. Compared to the case of only ventilating the wind speed of 1m/s, the stress at the soffit was reduced by 28.10%, while the stress at the gable waist was elevated by 32.23%, and at the foot of the soffit was elevated by 64.20%. When the wind speed increased to 2 m/s, the stresses at all locations were elevated from 17.11% to 34.22% compared to the conditions with only ventilation or only GHEs activated. When the wind speed increases to 3m/s, the stress at each position increases and decreases at different positions compared with the conditions of ventilation only or GHEs only activation.

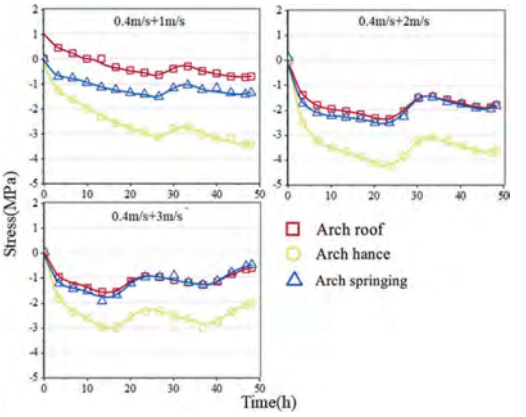

Figure 9. Stress changes in the arch waist, arch foot, and arch top of the lining for GHEs and ventilation coupled with cooling.

It can be seen that in the case of coupled cooling with GHEs and ventilation, there is a difference between the stresses at the vault and the foot of the arch when the wind speed is 1~2 m/s; after the wind speed exceeds 2 m/s, the stresses at the vault and the foot of the arch are almost the same.

Overall, the coupled cooling of ventilation and GHEs will achieve more desirable results when the purpose is cooling. The reasonable range of flow rate is 0.4~0.6m/s and wind speed are 1~2m/s. However, the ensuing stresses are also the largest, and the tensile stress at the arch waist in the GHEs flow rate of 0.4m/s + wind speed of 2m/s can be up to 3.60MPa, whereas the standard value of axial tensile strength of the standard C80 moulded concrete is only 3.11MPa. The tensile strength of the CGM concrete used in this study is more than 6MPa and therefore was not damaged. However, in the actual project, the concrete for high geothermal tunnel lining needs to be specially designed.

3.4 *Comparison of lining stresses before and after cooling down*

Heating of the perimeter rock and lining was required to bring them to a high ground temperature environment first before cooling measures could be carried out. The lining temperature increased from room temperature of 23°C to 45°C during this period. The lining increased in volume due to thermal expansion, but additional compressive stresses were created in the lining due to the confinement of the surrounding rock, the variation curve of which is shown in Figure 10. It can be found that the temperature stresses in the arch top, arch waist and arch footing are all 0 when they are not heated, and the lining stresses in the three places are gradually increasing with the increase of temperature. Among them, the increase of the arch waist is the largest, and its maximum value reaches 4.9 MPa; while the difference between the arch top and arch foot stress is not big, the arch top

stress is slightly smaller than the arch foot, and the two change trends are similar, and the maximum values are 1.8 MPa and 2.4 MPa, respectively.

Through the combination of heat exchanger and ventilation cooling measures, the stress on the lining is converted from relative compression to relative tension, which effectively reduces the increase of lining stress caused by high ground temperature. It can be concluded that the combination of heat exchanger and ventilation can effectively reduce the heat damage caused by high ground temperature in the actual project.

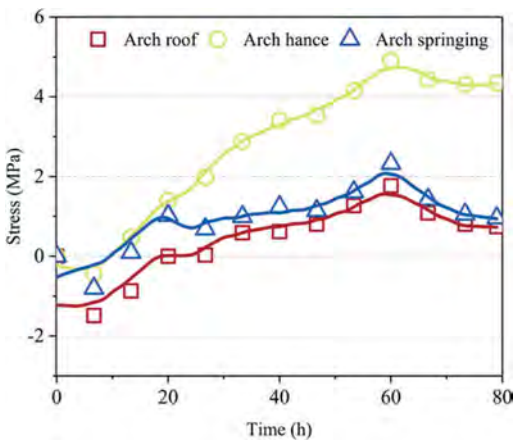

Figure 10. Graph of lining stress with increasing temperature.

4 CONCLUSIONS

(1) Conclusions should state concisely the most important propositions of the paper as well as the author's views of the practical implications of the results.
(2) During the implementation of the cooling measures, both the cooling process and the form of stress development in the lining were exponential. With the increase of operation time, the rate of change of temperature and the rate of change of strain both decrease gradually.
(3) Heat exchange is a dynamic process, the lining temperature change will show certain fluctuations, and the cooling effect of ventilation is greatly influenced by the air temperature. The fluctuation of temperature will affect the lining stress.
(4) There are differences in lining stresses at different locations. In the case of ventilation only, the cooling at the arch waist is the largest; in the case of activating GHEs only, the cooling at the arch top is the largest; and in the case of coupled cooling by GHEs and ventilation, the cooling at the arch waist and arch top is the largest.
(5) Under the effect of different cooling measures, the stress of the lining is dominated by tensile stress, which are all manifested as the maximum stress at the arch waist, which can reach 3.6 MPa, and the effect of this additional stress on the structural stress needs to be considered in the structural design.
(6) The lining stress decreases with running time, while the circumferential stress at the nodes under the radial path increases with running time and eventually stabilizes.

ACKNOWLEDGMENTS

We thank Prof. Qixiang Yan for his guidance and sponsorship of this study. We would like to thank Senior Engineer Xiaoling Cao and Associate Professor Liangliang Sun for their guidance of this study.

The authors gratefully acknowledge the financial support of the National Natural Science Foundation of China No. 52178394, No. U21A20152).

REFERENCES

Adam, D., Markiewicz, R., 2009. Energy from earth-coupled structures, foundations, tunnels and sewers. Géotechnique 59, 229–236.

Bidarmaghz, A., Narsilio, G.A., 2018. Heat exchange mechanisms in energy tunnel systems. Geomechanics for Energy and the Environment 16, 83–95.

Brandl, H., 2006. Energy foundations and other thermo-active ground structures. Géotechnique 56, 81–122.

Chen, Q., Zhang, H., Zhu, Y., Chen, S., Ran, G., 2021. Study on distributions of airflow velocity and convective heat transfer coefficient characterizing duct ventilation in a construction tunnel. Building and Environment 188, 107464.

Fan, Lei, Zeng, Yanhua, Liu, Kelin, Zhou, Xiaohan, 2017. Tunnel temperature fields analysis under the couple effect of convection-conduction in cold regions. Applied Thermal Engineering

Gao, X., Wu, H., Zhang, Z., Cao, X., Sun, L., Yu], N., 2017. Coupled cooling method and application of latent heat thermal energy storage combined with pre-cooling of envelope: Method and model development. Energy.

Lee, C., Park, S., Won, J., Jeoung, J., Sohn, B., Choi, H., 2012. Evaluation of thermal performance of energy textile installed in Tunnel. Renewable Energy 42, 11–22.

Lin, M., Zhou, P., Jiang, Y., Zhou, F., Lin, J., Wang, Z., 2022. Numerical investigation on comprehensive control system of cooling and heat insulation for high geothermal tunnel: A case study on the highway tunnel with the highest temperature in China. International Journal of Thermal Sciences 173, 107385.

Liu, P., Cui, S.G., Li, Z.H., Xu, X.F., Guo, C., 2019. Influence of surrounding rock temperature on mechanical property and pore structure of concrete for shotcrete use in a hot-dry environment of high-temperature geothermal tunnel. Construction and Building Materials 207, 329–337.

Liu, W.V., Apel, D.B., Bindiganavile, V.S., 2016. Cylindrical models of heat flow and thermo-elastic stresses in underground tunnels. International Journal of Numerical Methods for Heat Fluid Flow.

Tan, X., Chen, W., Yang, D., Dai, Y., Wu, G., Yang, J., Yu, H., Tian, H., Zhao, W., 2014. Study on the influence of airflow on the temperature of the surrounding rock in a cold region tunnel and its application to insulation layer design. Applied Thermal Engineering 67, 320–334.

Tang, Y., Xu, G., Lian, J., Su, H., Qu, C., 2016. Effect of temperature and humidity on the adhesion strength and damage mechanism of shotcrete-surrounded rock. Construction Building Materials.

Tao, L.L., Ren, X.C., Zhao, D.X., Zeng, Y.H., Zhou, X. H., 2022a. Numerical study on effect of natural wind and piston wind on anti-freezing length of tunnels with high geo-temperature in cold region. INTERNATIONAL JOURNAL OF THERMAL SCIENCES 172.

Tao, L.L., Zhou, X.H., Tian, X.Y., Ye, X.Q., Zeng, Y.H., Liu, X.R., 2022b. Study on the temperatures of railway tunnel side ditches in high-latitude cold regions based on the effects of wind. CASE STUDIES IN THERMAL ENGINEERING 30.

Yan, J., He, C., Zeng, Y., Wang, B., Zhang, J., 2019. Cooling Technology and Effect Analysis for High Geothermal Tunnel on Sichuan-Tibet Railway. Zhongguo Tiedao Kexue/China Railway Science 40, 53–62.

Zeng, Y., Tao, L., Ye, X., Zhou, X., Fang, Y., Fan, L., Liu, X., Yang, Z., 2020a. Temperature reduction for extra-long railway tunnel with high geotemperature by longitudinal ventilation. Tunnelling and Underground Space Technology 99, 103381.

Zeng, Y., Tao, L., Ye, X., Zhou, X., Fang, Y., Fan, L., Liu, X., Yang, Z., 2020b. Temperature reduction for extra-long railway tunnel with high geotemperature by longitudinal ventilation. Tunnelling and Underground Space Technology 99.

Zhang, G., Cao, Z., Wang, W., Mei, X., Zhao, X., Shen, S., Na, T., 2021. Field test and numerical investigation on thermal environment of tunnel with air layer structure. Building and Environment 203, 108105.

Zhang, G., Guo, Y., Zhou, Y., Ye, M., Chen, R., Zhang, H., Yang, J., Chen, J., Zhang, M., Lian, Y., Liu, C., 2016a. Experimental study on the thermal performance of tunnel lining GHE under groundwater flow. Applied Thermal Engineering 106, 784–795.

Zhang, G., Xia, C., Yang, Y., Sun, M., Zou, Y., 2014. Experimental study on the thermal performance of tunnel lining ground heat exchangers. Energy and Buildings 77, 149–157.

Zhang, G., Xia, C., Zhao, X., Zhou, S., 2016b. Effect of ventilation on the thermal performance of tunnel lining GHEs. Applied Thermal Engineering 93, 416–424.

Zhou, X., Zeng, Y., Fan, L., 2016. Temperature field analysis of a cold-region railway tunnel considering mechanical and train-induced ventilation effects. Applied Thermal Engineering, 114–124.

Zhou, X.H., Ren, X.C.A., Ye, X.Q., Tao, L.L., Zeng, Y.H., Liu, X.R., 2021. Temperature field and anti-freezing system for cold-region tunnels through rock with high geotemperatures. TUNNELLING AND UNDERGROUND SPACE TECHNOLOGY 111.

Tunnelling for a Better Life – Yan, Celestino, Thewes & Eberhardt (Eds)
© 2024 The Author(s), ISBN 978-1-032-80042-4
Open Access: www.taylorfrancis.com, CC BY-NC-ND 4.0 license

Thrust jack loading of large diameter precast segmental tunnel lining

M.A. Mooney & H. Zheng
Center for Underground, Colorado School of Mines

C. Naito, S. Quiel & Z. Ouyang
Department of Civil and Environmental Engineering, Lehigh University

ABSTRACT: This paper presents the results of thrust jack load testing on large diameter tunnel lining segments, and associated comparison to design procedures used worldwide to assess thrust jack bursting stresses. Large diameter tunnels constructed via shield tunnel boring machines are increasingly being adopted worldwide for roadway and metro projects. When tunnels reach such large diameters, thrust jack loading often becomes a critical governing load case. Thrust jack loading induces radial and tangential bursting stresses, as well as spalling stresses, that can damage the lining. An experimental study was performed to examine induced stresses in 13 m diameter, 45 cm thick steel fiber reinforced concrete (SFRC) and hybrid SFRC + rebar segments. From experiments, radial bursting stress governed sfrc thrust jack failure while transverse bursting stress governed hybrid failure. Transverse bursting stress occurs near mid-segment depth while radial bursting stress occurs (within SFRC) within one-half of segment thickness. The german tunneling society guidelines provide a good estimation of radial and transverse bursting stress capacity if the observed burst depth is used. Aci code simplified formulae and the iyengar approach overestimated the bursting stress of SFRC.

1 INTRODUCTION

Large diameter (13 m and greater) segmental lining systems are increasingly being adopted for highway and transit tunnels worldwide. The design of large diameter segmental lining is notably different from the far more common 6-7 m diameter segment lining systems. As detailed in Mooney et al. 2020, a number of critical aspects are quite different for large diameter lining, including segment joint rotational stiffness, slenderness ratio, and whole ring behavior with 10-12 joints compared to the 5-6 joints of most metro-size tunnels. One major difference is in the thrust jack loading imparted to segments during construction (Figure 1). TBM thrust capacity generally grows with the excavated area created by the TBM. The thrust jacks transfer the thrust through the bearing area of the lining's leading edge. While the lining bearing area for thrust force grows with tunnel diameter D, total TBM thrust grows with D^2. AS D reaches 13 m and greater, TBM thrust force can become the governing and difficult load case to design for.

With the critical thrust jack load case, many segmental lining projects have been designed with a steel fiber reinforced concrete (SFRC) and hybrid SFRC + rebar to accommodate the bursting stresses predicted by design procedures (Tiberti et al. 2015; Conforti et al. 2019). Design procedures for thrust jack loading are recommended by ACI-544.7R-16, German Tunneling Committee (2013), and others. To evaluate segment capacity under the estimated thrust force, different design methods are available, including simplified equations (ACI 318-14, German Tunneling Committee, 2013), analytical approaches (Iyengar 1962) and computational modeling. The paper describes the results of full-scale thrust jack experiments performed to better understand the actual performance of SFRC and hybrid SFRC + RC segments subjected to thrust jack loading. A comparison of observed response with design code predicted response is made.

2 DESIGN PROCEDURES

Thrust jack force spreads over the leading edge of the liner segment, inducing radial and transverse (circumferential) tensile stresses that eventually diminish at some distance away from the load pad. The state of practice in bursting stress design analysis is summarized in ACI 544.7R-16, recommending the use of (a) ACI 318 simplified equations; (b) German tunneling committee (2014) equations; (c) Iyengar (1962) diagram analysis; and/or (d) finite element analysis. The simplified equations to estimate the bursting force T_{burst} and depth d_{burst} where T_{burst} occurs are provided by ACI 318 (Equation 1) and the German tunneling committee (Equation 2).

DOI: 10.1201/9781003495505-150

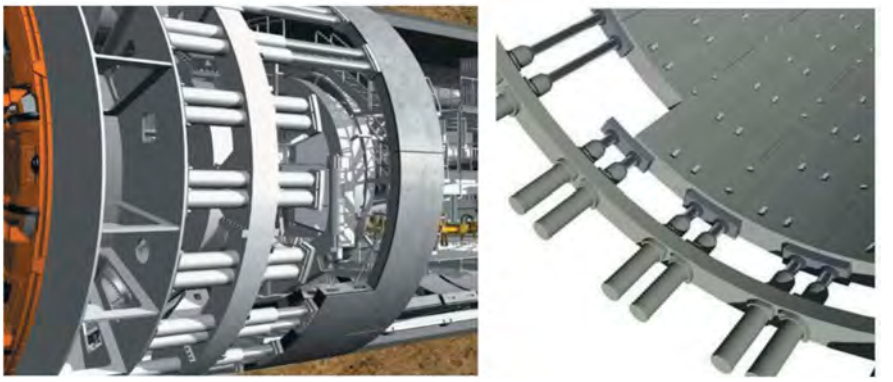

Figure 1. Illustration of TBM thrust jacking loads applied to ring end/bearing area of most recently installed segments. (left: Herrenknecht, 2015, right: Groeneweg 2007).

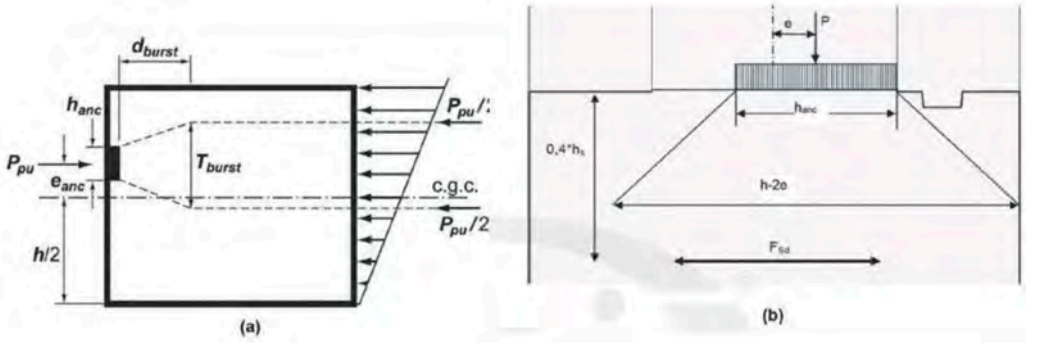

Figure 2. Bursting force estimation via simplified equations recommended by (a) ACI 318-14. and (b) the German tunneling committee.

Figure 2 illustrates the pertinent parameters wherein Figure 2a from ACI 318 conveys more of a post-tensioning beam girder application while Figure 2b from the German Tunneling committee more directly conveys thrust jack load application across a portion of the thickness of the segment.

$$T_{burst} = 0.25F_{jack}\left(1 - \frac{h_{anc}}{h}\right); d_{burst} = 0.5(h - 2e_{enc}) \quad (1)$$

$$T_{burst} = 0.25F_{jack}\left(1 - \frac{h_{anc}}{h - 2e_{enc}}\right); d_{burst} = 0.4(h - 2e_{enc}) \quad (2)$$

Equations are provided in ACI 544.7R-16 to calculate the maximum radial (r) and transverse (t) bursting stresses based on T_{burst} and d_{burst}. The maximum bursting stress developed in the radial ($\sigma_{p,r}$) and transverse ($\sigma_{p,t}$) directions are given in Equations 3 and 4, where key terms are illustrated in Figure 3.

$$\sigma_{p,r} = \frac{T_{burst}}{\phi a_l d_{burst}} \quad (3)$$

$$\sigma_{p,t} = \frac{T_{burst}}{\phi h_{anc} d_{burst}} \quad (4)$$

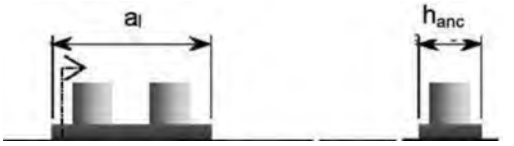

Figure 3. Thrust load pad geometry terms incorporated into ACI 544.7R-16 bursting stress calculations. a_l is the length of the load pad in the transverse (circumferential) direction while h_{anc} is the load pad dimension in the radial direction.

The treatment of radial bursting stress is clear from the ACI equations in that d_{burst} is defined at a depth equal to 0.4-0.5 of the segment thickness h. However, ACI uses the same d_{burst} term for transverse bursting stress, suggesting that the maximum tensile stress in the transverse direction occurs close to the load pad at

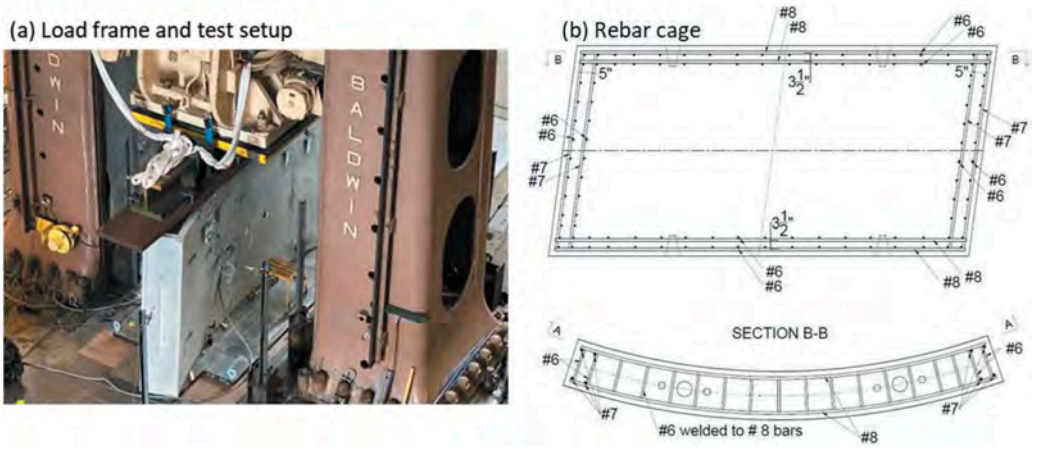

Figure 4. (a) 22 MN capacity load frame and test setup at Lehigh University; (b) steel rebar used in hybrid segment. notation used for the bars: #*d* where *d* = diameter in number of one-eight inch increments.

a similar depth as the radial maximum bursting stress. This will be examined later in the paper based on experimental results.

Estimated bursting tensile stresses were determined using the ACI 318 and DAUB simplified method, as well as by using the Iyengar method (for radial bursting stress) using the following inputs: l = 4.06 m, $t = h$ = 450 mm, l_p = 1.6 m, t_p = 275 mm, e_t= 760 mm, and e_r = 0. Two pairs of jacks are assembled symmetrically on one segment.

3 THRUST JACK LOAD EXPERIMENTAL TESTING

3.1 *Load frame and segment setup*

A cooperative experimental program was performed by Colorado School of Mines and Lehigh University to test 450 mm thick segments from a 13 m diameter tunnel project in Virginia, USA. The segments were tested in Lehigh University's Fritz Laboratory using a 22 MN (5000 kip) capacity Baldwin universal testing machine (Figure 4a). Two steel reinforcement designs were adopted: (1) SFRC and (2) hybrid SFRC + conventional rebar, i.e., SFRC + RC. The detailed design of the RC is shown in Figure 4b. The reinforcement bars have 50 mm clear cover from the segment surface. The strength of steel reinforcement bars is approximately 410 MPa.

The SFRC mix was prepared with cementitious content of 445 kg/m^3 and a w/c ratio of 0.35. 4D Bekaert steel fiber was used. The fiber content was 38.5 kg/m^3 with 61 mm length, 7.5 mm diameter and 80 aspect ratio for each fiber. The average 28 day compressive strength was 65 MPa. The average 28 day split tensile strength was 7.4 MPa. Crack mouth opening displacement tests were also performed according to EN 14651 procedure, and the peak flexural strength is 1030 psi. The inverted tensile strength was estimated to be 5.44 MPa. The average elastic modulus is 30.9 GPa obtained from compressive tests on SFRC samples. Therefore, the tensile strain limit was estimated to be 180 με.

Extensive instrumentation was used to characterize behavior during loading, including displacement transducers, strain gauges, load cells and distributed fiber optic sensors (DFOS), the detailed discussion of which is beyond the scope of this paper.

3.2 *SFRC test results*

Thrust jack loading of SFRC segments revealed a clear radial bursting stress failure at an approximate thrust jack load magnitude of 4400 kip (Figure 5). Long before this abrupt failure, the segment exhibited intrados and extrados cracking with crack widths summarized per load level in Figure 6. The longitudinal cracking shown in Figure 6 is caused by transverse bursting stresses. Early onset cracking due to radial bursting stress is not visible on the extrados and intrados as these cracks would run in the transverse direction. It is reasonable to assume that such cracking did also occur well before the ultimate failure at 4400 kip.

Radial and transverse strain behavior was recorded by internal strain gages embedded at multiple depths below the load pad. Measured radial strains reached the tensile strength/strain limit of 180 με at a depth of 9-10 in. below the load pad. This is consistent with the ACI 318 prediction of 0.5 times the segment thickness, assuming no eccentric loading. The radial strains reached the tensile strength limit at a thrust jack load level of 3500 kip, which is notably lower than the 4400 kip ultimate failure in Figure 5. Measured transverse strain reached 180 με at a depth of 38-40 in. below the load pad (Figure 6).

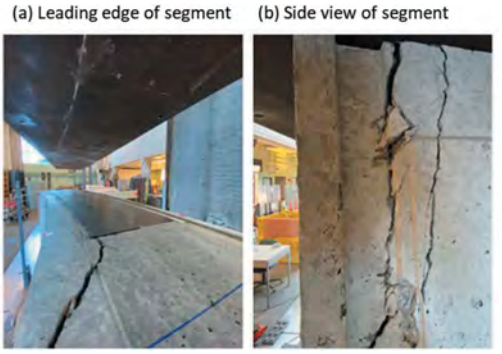

Figure 5. (a) Leading edge where radial bursting stress induced cracking is clear; (b) side of the segment where radial bursting stresses (left to right) exceeded the tensile capacity of the SFRC.

This depth d_{burst} of transverse strain is clearly different from radial d_{burst} that is not captured or conveyed in design codes. The transverse limit strain reached 180 με at a thrust jack load of 4000 kip. This level is consistent with persistent crack widths ≥ 0.008 in, the maximum level of crack width that is typically prescribed in tunnel lining design (e.g., AASHTO 2017). Summarizing results, the SFRC segment reached radial bursting stress ultimate limit state at $d_{burst,r}$ = 9-10 in. at thrust jack load of approximately 3500 kip, followed by transverse bursting stress ultimate limit state at $d_{burst,t}$ = 38-40 in. at a thrust jack load of approximately 4000 kip.

3.3 *Hybrid SFRC + RC test results*

The hybrid SFRC + RC segment was loaded to 5000 kip thrust jack load without the visible abrupt radial bursting stress failure that the SFRC segment experienced. The 5000 kip capacity of the test rig prevented loading the hybrid segment further. The measured internal radial strains at depths = 9-10 in. below the load pad remained at or below 180 με. The perimeter rebar in the radial direction (Figure 4b) is located in this vicinity and therefore is supporting this tensile stress. As shown in Figure 7, longitudinal cracking emerges at 4000 kip thrust jack loading. These are due to transverse bursting stresses. The measured transverse strains within the segment reach 180 με at 4000 kip a mid depth of the segment, i.e., 40 in. In this area, there is no rebar to provide tensile capacity. This demonstrates that the 'light' rebar cage with perimeter reinforcement provides important radial bursting stress capacity but this essentially shifts the governing ultimate limit state to transverse bursting stress failure. Collectively, the SFRC-only transverse bursting stress capacity is not much more than the radial bursting stress capacity. Therefore, the benefit of a perimeter rebar cage insofar, as improving bursting stress capacity, is limited. It is worth mentioning that when a full ring of

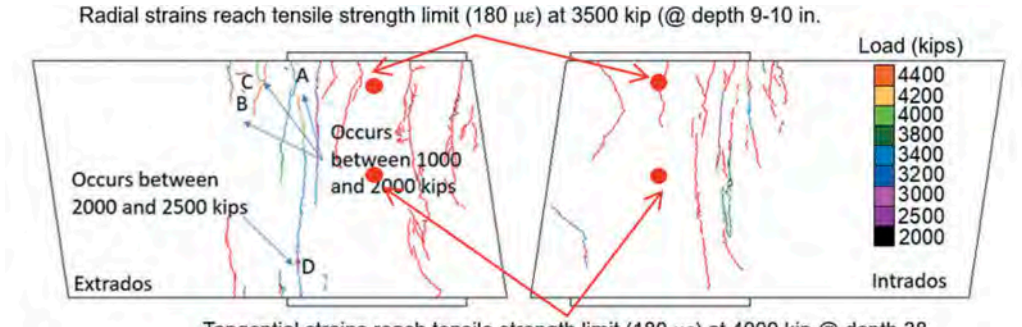

Test 3 Intrados Crack Width (in.)								Test 3 Extrados Crack Width (in.)								
Load (millions of pounds)	A	B	C	D	E	F	G	A	B	C	D	E	F	G	H	I
1.0																
2.0								0.004	0.002	0.004						
2.5	0.002							0.004	0.003	0.006	0.009					
3.0	0.004	0.002	0.004					0.004	0.004	0.007	0.009	0.006				
3.4	0.006	0.002	0.006	0.004	0.004		0.004	0.004	0.004	0.007	0.009	0.007	0.007			
3.8	0.009	0.003	0.006	0.006	0.004	0.004	0.004	0.004	0.004	0.007	0.010	0.007	0.007	0.004	0.006	
4.0	0.009	0.004	0.006	0.006	0.004	0.004	0.004	0.004	0.004	0.007	0.025	0.010	0.007	0.004	0.006	
4.2	0.009	0.004	0.006	0.006	0.007	0.004	0.004	0.004	0.004	0.007	0.030	0.012	0.020	0.004	0.007	
4.3	0.010	0.006	0.006	0.006	0.007	0.004	0.004	0.007	0.006	0.009	0.032	0.012	0.020	0.006	0.009	0.007

Figure 6. Crack width records during loading as well as locations of maximum observed bursting stresses.

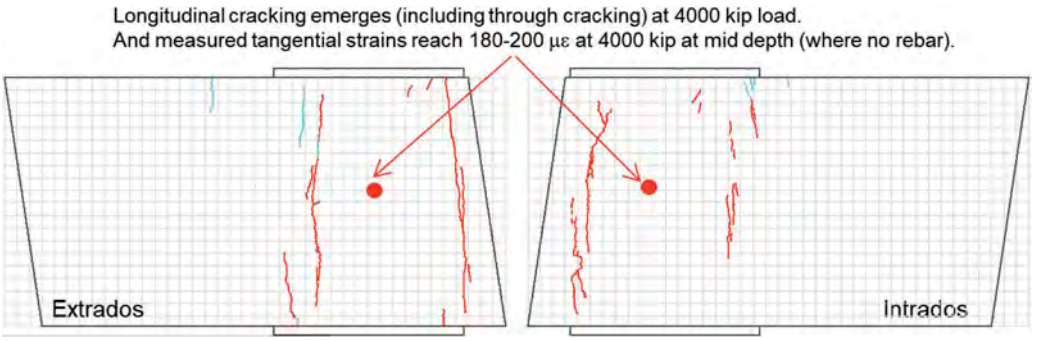

Figure 7. Hybrid segment crack width records and locations of maximum observed bursting stresses.

segments is installed, adjacent segments provide beneficial confinement in the transverse (circumferential) direction, while there remains no confinement in the radial direction. This circumferential direction confinement likely boosts the transverse bursting stress capacity. However, there are cases, such as in continuous tunneling, where thrust jack loading is imparted to segments before the full ring is installed.

4 COMPARISON WITH DESIGN PROCEDURES

The results from SFRC testing are directly compared with design code procedures. Using the geometry of the tested SFRC segment, the reasonable assumption of no eccentricity, and the assumed SFRC tensile strength = 790 psi, ACI 318, German Tunneling Society (DAUB), and Iyengar diagram based capacities are summarized in Table 1. Radial bursting stress is the controlling bursting mode by approximately 20%. DAUB is more conservative than ACI 318, while Iyengar's estimation is less conservative. For transverse bursting stress capacity, we take the liberty to use $d_{burst,t}$ = 38-40 in. in the equations. The use of $d_{burst,r}$ would lead to much higher transverse bursting stress capacities.

The observed results from SFRC testing are summarized in Table 2. Major visible radial bursting failure occurred at 4400 kip. Per crack width criteria of 0.008 in., transverse bursting failure occurred at 3800 kip while radial bursting failure is not determinable per cracking because the resulting circumferential cracks are internal and not observable on the intrados and extrados faces. Per tensile strain limit, radial bursting occurred at a thrust jack load of 3500 kip while transverse bursting occurred at a thrust jack loading of 4000 kip.

Comparing the observed behavior with design equations, we observe that ACI 318 radial bursting matches the observed major failure and DAUB matches the results from tensile strain measurements. The Iyengar diagram seems too conservative in radial bursting stress capacity. DAUB estimation is more in line with the observed transverse bursting stress failure load based on both crack width and tensile strain limit, assuming the use of $d_{burst,t}$ in the estimation. It

Table 1. Ultimate thrust jack load capacity (no partial safety factors; SFRC tensile strength = 790 psi).

Method	Radial	Transverse	Notes
ACI 318	4500 kip	5400 kip*	Radial governs
DAUB	3700 kip	4300 kip*	Radial governs; DAUB more conservative than ACI;
Iyengar Diagrams	5300 kip	NA	Predicts highest capacity; not applicable for transverse.

*using $d_{burst,t} >> d_{burst,r}$. Tangential capacity much higher if using $d_{burst,t} = d_{burst,r}$

Table 2. Observed radial and transverse bursting stress failure in SFRC testing.

Failure criteria	Radial	Transverse	Notes
Major (collapse) failure	4400 kip		Clear radial bursting stress failure near load pad.
Cracking/crack width	Not observable	3800 kip	Cracking due to radial bursting stress is internal and runs circumferential; not observable on intrados or extrados.
Tensile strain limit (180 με)	3500 kip	4000 kip	Shows radial governs but tangential is significant and at mid segment depth unlike radial immediately below pad.

is worth noting that the number of experimental tests is very limited, and these results should be verified with further testing, additional diameters, etc.

5 CONCLUSIONS

Full scale thrust jack load testing on 13 m diameter SFRC and SFRC + RC segments revealed that: (a) radial bursting stress governs SFRC thrust jack failure; (b) maximum radial bursting stress occurs at a distance equal to one-half of the segment thickness; (c) maximum transverse bursting stress occurs at a distance of one-half the segment length; (d) that perimeter rebar improves radial bursting stress capacity shifting the governing condition to transverse bursting stress at mid-depth of the specimen. A comparison with multiple design methodologies shows: (a) good radial bursting stress prediction by DAUB; (b) slight overestimation of radial bursting stress capacity by ACI 318 and significant overestimation by Iyengar; and (c) good transverse bursting stress prediction by DAUB if the actual $d_{burst,t}$ of segment mid-depth is used; and (d) significant overestimation of transverse bursting stress capacity by ACI 318. All design code calculations should be clarified to differentiate between depth of maximum bursting stresses in radial vs. transverse directions. The results presented here are based on very limited testing. Further testing is warranted to both confirm findings and to further enhance understanding of this critical load case for large diameter segmental lining.

ACKNOWLEDGEMENTS

The authors wish to acknowledge the funding support provided by the US Federal Highway Administration as well as the overall project management of WSP.

REFERENCES

ACI 318-14: Building Code Requirements for Structural Concrete and Commentary, ACI Committee 318, 2014.

ACI 544-7R-16: Report on Design and Construction of Fiber- Reinforced Precast Concrete Tunnel Segments, ACI Committee 544, 2016.

Conforti, A., Trabucchi, I., Tiberti, G., Plizzari, G. A., Caratelli, A., & Meda, A. (2019). Precast tunnel segments for metro tunnel lining: A hybrid reinforcement solution using macro-synthetic fibers. *Engineering Structures*, *199*, 109628.

German Tunneling Committee, 2013, Lining Segment Design: Recommendations for the Design, Production, and Installation of Segmental Rings, Taschebuch für den Tunnelbau, Ernst und Sohn, Berlin, pp. 17–121.

Groeneweg, T., 2007, "Shield Driven Tunnels in Ultra High Strength Concrete: Reduction of the Tunnel Lining Thickness", MSc Thesis, Delft University of Technology, The Netherlands.

Iyengar, K. T., 1962, Two-Dimensional Theories of Anchorage Zone Stresses in Post-Tensioned Beams, ACI Journal Proceedings, V. 59, No. 10, pp. 1443–1466.

Mooney, M., Epel, T., Wilson, A., Zheng, H., & Nitschke, A. (2020). Experimental Behavior of Large Diameter Segmental Lining Systems: A Review, *Proc. North American Tunneling Conference 2020*.

Plizzari, G. A., & Tiberti, G. (2006). Steel fibers as reinforcement for precast tunnel segments. *Tunnelling and Underground Space Technology*, *21*(3), 438–439.

Tiberti, G., Conforti, A., & Plizzari, G. A. (2015). Precast segments under TBM hydraulic jacks: Experimental investigation on the local splitting behavior. *Tunnelling and Underground Space Technology*, *50*, 438–450.

Ouyang, Z., Zheng, H., Patmanidis, C., Naito, C., Quiel, S., Mooney, M. (2023). Full-Scale Testing of Precast Tunnel Lining Segments Under Thrust Jack Loading: Design Limits and Ultimate Response, Tunnelling and Underground Space Technology, 2023, https://doi.org/10.1016/j.tust.2023.105446.

Tunnelling for a Better Life – Yan, Celestino, Thewes & Eberhardt (Eds)
© 2024 The Author(s), ISBN 978-1-032-80042-4
Open Access: www.taylorfrancis.com, CC BY-NC-ND 4.0 license

Computational approaches towards segmental linings with a reduced environmental impact

Gerrit E. Neu, Vladislav Gudžulić & Günther Meschke*
Ruhr University Bochum, Bochum, Germany

ABSTRACT: With ever-rising environmental concerns, designing more sustainable concrete structures is vital. One approach is to improve the methods of designing structures with less material consumption. Steel Fiber Reinforced Concrete (SFRC) in conjunction with smart design hybrid concepts shows great potential for material savings and improved durability of segmented tunnel linings. This paper focuses on the model-based design of SFRC structures, with the aim of analysing the effect of fibre choice and orientation on the structural behaviour and to investigate hybrid design concepts, characterized by a combination of high-performance steel fibre concrete in highly stressed zones and conventional SFRC in interior zones of the segment. The contribution presents advanced approaches for the serviceability assessment and non-linear design of SFRC segmental tunnel linings. The proposed Multi-Level FRC model is able to derive the post-cracking response of SFRC from the actual fibre properties instead of indirectly from bending tests and therefore allows for the explicit assessment of SFRC mixture parameters and fibre orientation on the structural performance. This contribution compares the performance of conventional, fibre reinforced concrete segments and hybrid designs subjected to tunnelling related loading cases and demonstrates how advanced numerical models, in conjunction with robust optimization and uncertainty models, and smart hybrid designs can be utilized to generate less vulnerable and more economical SFRC structural designs with a reduced environmental impact. Finally, a user-friendly design tool for SFRC tunnel linings, utilizing Artificial Neural Networks trained by virtual data, is presented.

Keywords: SFRC, Discrete crack models, Optimization, Uncertainty modelling, Reliability, Segmental tunnel lining

1 INTRODUCTION

Concrete is one of the most used materials globally, with an estimated yearly consumption of around 30 billion tons and continuously increasing demand (Monteiro et al., 2017). The construction industry began with a range of initiatives and innovations aimed at the sustainable use of resources within the construction sector. The environmental impact of the construction can be either reduced by the usage of materials with better sustainability characteristics (e.g. reduction of the cement content, cement-free binding agents, recycled aggregates) or by improving the structural and lifetime performance of concrete (e.g. ultra- and high-performance concretes, the addition of micro and macro fibres, carbon concrete composites), thus reducing consumption.

Segmental tunnel linings as used in mechanized tunnelling are traditionally designed and constructed using pre-cast reinforced concrete (RC) lining segments. Driven by durability considerations, recent developments in the tunnelling industry are, however, changing this paradigm, as Steel Fiber-Reinforced Concrete (SFRC) is becoming more widely used worldwide (see De la Fuente et al. (2012), grand Paris express - Metro Line 16-1, Doha Metro, etc.). Since the reinforcement scheme of SFRC segments is characterized by diffusely distributed steel fibres, they provide reinforcement in the entire segment, especially at segment extremities in which traditional reinforcement bars cannot be placed due to minimum concrete cover requirements. Furthermore, the absent minimum concrete cover requirements result in an earlier activation of the reinforcement effect in FRC and a potential slimming of the components. Steel fibres also substantially reduce concrete spalling at vulnerable locations, such as at the segment corners or in the vicinity of the jack loading platens, which results in increased robustness of the lining system (Bakshi and Nasri, 2017). Furthermore, the crack bridging capabilities of SFRC offer superior

*Corresponding author: guenther.meschke@rub.de

DOI: 10.1201/9781003495505-151

crack width control in comparison to RC. Another, benefit of SFRC linings is that steel fibre reinforcement can significantly contribute to reduced costs in production and transport.

A disadvantage of fibre-reinforced concrete (FRC) is the overall scatter in terms of the post-cracking behaviour due to the varying fibre orientation and distribution, which depends on the concrete casting process and the geometry of the component. This complicates the design of FRC structural members due to the need for conservative assumptions regarding the residual strength of cracked FRC.

The objective of the presented work is to develop novel fibre-reinforced segmental lining concepts to reduce the environmental impact and the costs of mechanized tunnelling projects through the use of sophisticated numerical methods for structural design. In order to do so, a simulation approach capable of predicting the structural response of segmental linings subjected to tunnelling-related loads is presented, which can as well capture the post-cracking behaviour of FRC and its scatter (Section 2). This computational model is then used to evaluate fibre-based reinforcement concepts and compare their structural performance with conventional reinforcement schemes to demonstrate their suitability for tunnel segments subjected to thrust jack loads (Section 3). Finally, the proposed modelling techniques in conjunction with optimization algorithms and uncertainty modelling are used to derive hybrid fibre-reinforced segment designs with a reduced environmental and economic impact, while the required level of safety is ensured through the probabilistic safety concept (Section 4). This highlights the potential reduction in concrete volume and steel amount by applying nonlinear FE models in conjunction with methods of optimization to the structural design procedure.

2 COMPUTATIONAL MODEL FOR RC AND SFRC

The design of FRC structures according to guideline-based approaches (e.g. fib model code 2010) is based on local verifications, for which the external stress resultants are determined by linear-elastic models and the resistance of a material point or cross-section is estimated through assumptions regarding the stress distributions in a cracked cross-section. In order to conduct a model-based analysis of a FRC structures to provide an assessment of the load-bearing capacity, the crack formation and the failure process, non-linear numerical models accounting for the post-cracking behaviour of FRC has to be used.

2.1 *Multi-level FRC model*

The basis of the modelling approach is discrete crack representation using zero-thickness cohesive interface elements (IEs). Zero-thickness interface elements are inserted between the solid finite elements in the part of the domain where cracking is expected (Figure 1, top). All material nonlinearities due to cracking are modelled by the cohesive-frictional traction-separation relationship of the interface elements (Figure 1, bottom), while the bulk elements are assumed to behave as a linear elastic material. The material behaviour of the IEs is modified to account for post crack SFRC behaviour using a traction-separation law as proposed by Zhan et al. (2016). The traction-separation (t-w) law describes the post- and pre-cracking strength of SFRC as a function of crack opening and is derived using a multi-level fibre pull-out model. At the level of a single fibre, a semi-analytical model for the pull-out of steel fibres (Zhan and Meschke, 2014) is used to obtain the pull-out response of fibres with arbitrary inclinations relative to a crack surface and embedment lengths based on the concrete and fibre properties. On the crack scale, the crack bridging stress (t-w law) is obtained by homogenizing the response of multiple fibres crossing the crack, while accounting for the distributions of fibre orientations and embedment lengths. Therefore, the multi-level FRC model allows to directly assess the influence of the individual fibre type and the fibre

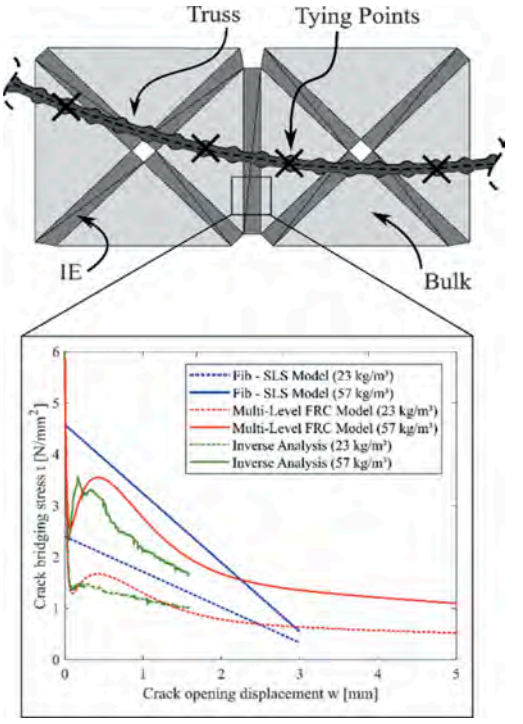

Figure 1. Top: Placement of interface elements (IE) between the regular finite elements (Bulk) and indication of the tying scheme for the consideration of rebars. Bottom: Comparison of the traction-separation laws determined by the multi-level FRC model (red) for SFRCs with 23 and 57 kg/m^3 of steel fibres with stress-crack opening laws derived from bending tests by inverse analysis (green) and the fib model code 2010 (blue).

cocktail on the structural behaviour. For more details and validations see Gudžulić et al. (2020) and G.E. Neu et al. (2022). It should be noted that also arbitrary stress-crack opening relationships can be used (e.g. the stress-crack opening relationships proposed in the fib model code 2010 for modelling the tensile behaviour of SFRC at SLS and ULS).

In order to account for reinforcement bars, rebars are modelled as linear trusses and coupled with the concrete matrix using a constraint condition between control points located on the rebar elements and their respective projection points within the elements in which they are embedded (Gall, 2018). The constraint condition includes the bond-slip mechanism as provided in the fib model code 2010.

2.2 *PC and SFRC material properties*

In this article, the structural response of different segment designs is evaluated which can be either consists of SFRC, RC or combinations of these materials. The inputs for the material model are taken from a multi-level validation campaign (Gudžulić et al., 2020). For the concrete, a Young's modulus E_c of 39 976 N/mm², a tensile strength f_t of 6.0 N/mm² and a mode I fracture energy G_f of 0.136 N/mm was determined. The experimental campaign included fibre pull-out tests of Dramix 3D 55/60 and Dramix 3D 65/60 hooked-end steel fibres at different embedment lengths and orientations. After the successful validation of the model at the fibre level, the traction-separation laws were derived and used for numerical analyses of 3-point bending tests with different contents (23, 57 and 115 kg/m^3) of Dramix 3D 65/60 fibres. The resulting stress-crack opening laws predicted by the Multi-Level FRC model are shown in Figure 1 (bottom) for a fibre content of 23 kg/m³ (red dotted line) and 57 kg/m³ Dramix 3D 65/60 fibres (red line). In addition, the linear stress-crack opening relationships for SLS calculations in accordance with the fib model code 2010 (blue lines) and based on an inverse analysis (Amin et al., 2015 - green lines) were derived from the experimental results of the bending tests and shown for comparison. For simulations on the structural scale, the traction-separation laws are incorporated in the numerical FE model using interface elements (Figure 1, top).

3 STRUCTURAL ANALYSIS OF RC AND SFRC SEGMENTS

The jack pressure applied to the segmental linings during tunnel advancement is resulting in potential critical stresses and therefore can lead to cracking between the jack pads and within the segment. In order to evaluate the suitability of different reinforcement schemes for tunnel lining segments and highlight their benefits as well as drawbacks, the structural response in terms of load-bearing capacity and serviceability performance is investigated and compared for the thrust jack loading case. For this comparison, the properties and conditions of a reference tunnel project are used as a basis for the analysis.

3.1 *Segment designs and model description*

To compare a conventional and a fibre-reinforced segment, the concrete and fibre properties from the multi-level validation campaign described in Section 2.2 are used. The conventional reinforcement layout (Φ10-10 + additional rebars in high stressed regions) was derived by using conventional design procedures according to EN 1992 (2005), German tunnelling Committee DAUB (2013) & DB RIL 853 (1998) and is shown in Figure 2 (bottom).

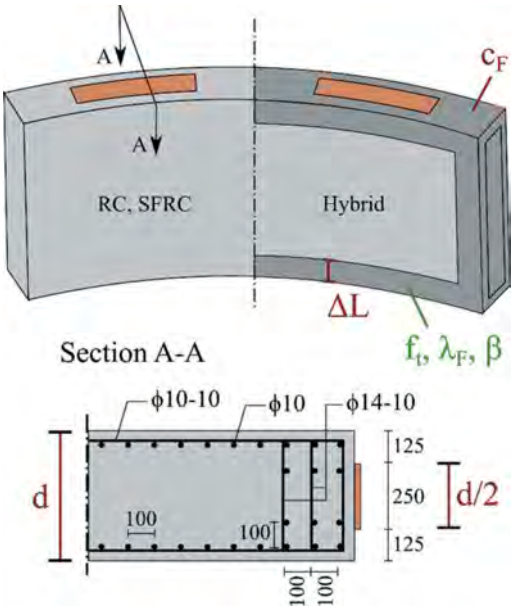

Figure 2. Top: Segment geometry of the reference tunnel project with a inner radius of 4.8 m and a 7+0 segmentation. Bottom: The reinforcement scheme of the RC segment at the thrust jack application region.

All rebars are represented by linear truss elements with an elastic-plastic material law using the Von-Mises yield criterion and linear hardening. An elasticity modulus of 200 000 N/mm^2, a yield strength of 550 N/mm^2 and an isotropic hardening modulus of 1977.53 N/mm^2 for all rebars are assumed. The bond-slip behaviour is incorporated according to fib model code 1990. The SFRC segment is reinforced by 57 kg/m3 Dramix 3D 65/60 hooked-end steel fibres, which results in a similar overall steel amount per segment (SFRC ≈ 258 kg/segment vs RC ≈ 260 kg/segment). In addition, the concept of hybrid fibre-reinforced segment designs is adopted (Plückelmann and Breitenbücher, 2020), which is characterized by different SFRC layers placed according to the level of structural stresses. Here, the high stressed

regions around the jack pads and the longitudinal joint are reinforced by a 200 mm wide layer (ΔL) containing 57 kg/m^3 Dramix 3D 65/60 hooked-end steel fibres (Figure 2, top) while in the remaining segment a fibre content of 23 kg/m^3 is used (post-cracking behaviour according to Figure 1, bottom). The overall steel amount can therefore be reduced to 146 kg/segment, which is a reduction of around 57% when compared to the standard SFRC segment.

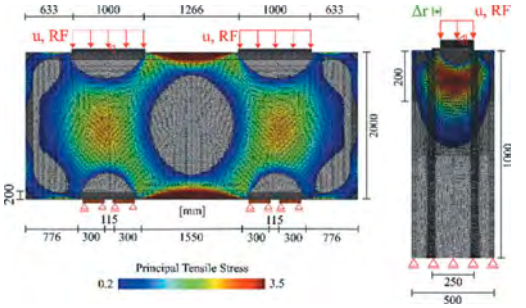

Figure 3. Geometry, boundary conditions, mesh and distribution of the principal tensile stresses of the plane segment model (left) and the partial area loading model (right).

Plane FE models analogous to the design models for the thrust jack loading case in engineering practice are used for a comparison of the investigated reinforcement schemes. The geometry, boundary conditions, mesh and the distribution of principal tensile stresses in the elastic regime are shown in Figure 3. The models represent different cuts through the segment. The partial area loading model (analogue to the strut & tie models in engineering practice - Figure 3, right) is used to analyse the bursting stress underneath the thrust jack pads, which are not covered in the plane stress model (Figure 3, left). In general, the partial area loading model (Figure 3, right) is decisive for the load-bearing capacity of a segment subjected to thrust jack loading while the plane stress segment model (Figure 3, left) is employed to check, if the derived design can prevent the occurrence of critical cracks between the thrust jack pads.

3.2 *Results: Plane stress segment model*

In terms of the force-displacement behaviour (Figure 4, top), the RC segment has the greatest load-bearing capacity (25.63 MN) followed by the SFRC (24.38 MN) and the hybrid segment (22.74 MN).

For an applied displacement of around 0.86 mm (F ≈ 8.95 MN), the first cracks (Figure 5) between the jack pads are initiated at all investigated reinforcement schemes and further propagate with increasing loading. At a displacement of around 1.5 mm (F ≈ 16 MN), bursting cracks in the middle of the segment are initiated and their propagation results in a further increase of the maximum separation (see plateau at

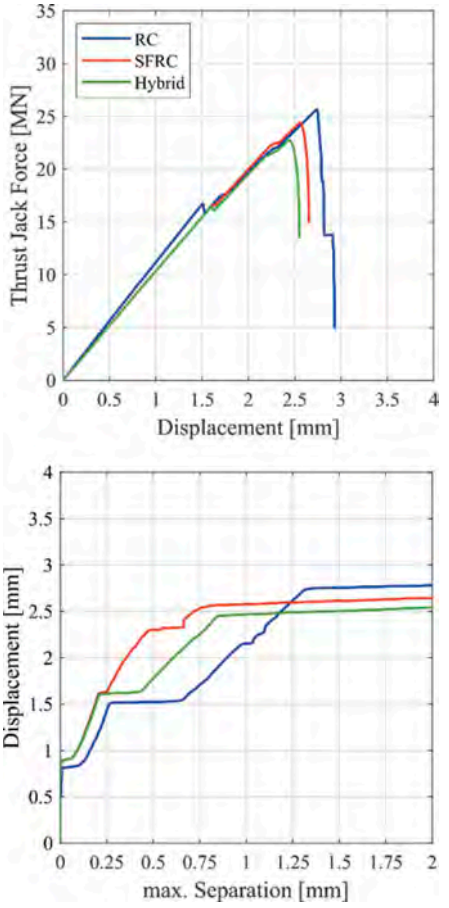

Figure 4. Plane segment model: Force-displacement curves (top) as well as the relationships between the applied displacement and the maximum crack width (bottom) for all investigated reinforcement schemes.

a displacement of 1.5 mm in Figure 4, bottom) as well as a minor drop and change in stiffness of the force-displacement curves (Figure 4, top). Failure occurs due to damages around the load and support plates (diagonal cracks & cone formation) at an applied displacement of approx. 2.5 mm, characterized by major crack openings (> 1 mm) and a plateau in the displacement-separation curves (Figure 4, bottom).

The crack patterns at an applied displacement of 2.4 mm of the RC, SFRC and hybrid reinforced segments are shown in Figure 5. While the conventional reinforcement results in the formation of multiple cracks between the jack plates (Figure 5, top), the fibre-reinforced segments still provide a better crack width limitation (compare curves up to a displacement of 1.5 mm in Figure 4, bottom). In order to provide a reinforcement effect, the crack has to cross the reinforcement layer. The concrete cover restrictions delay the activation, because the crack need to propagate towards the rebar and therefore

further opens at the concrete surface. Overall, the fibre-reinforced segments provide better crack width limitation capabilities due to providing reinforcement everywhere in the segment, especially regarding the bursting cracks initiated in the middle of the segment (Figure 5). The hybrid segment performs equivalent to the full FRC segment up to a displacement of around 1.5mm (F ≈ 15MN), because all cracks developed inside the strengthening layer. When cracks initiate and propagate towards the weaker reinforced regions of the hybrid segment at increased load, a decreased crack width control is observed (Figure 4, bottom).

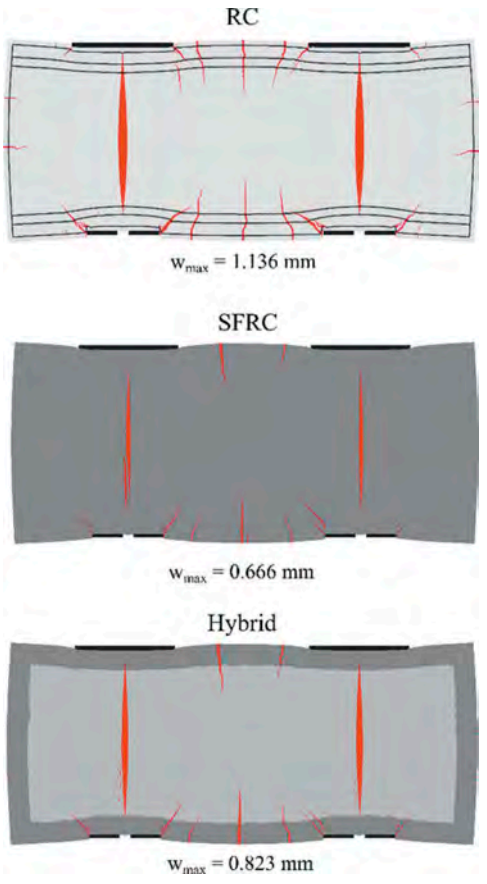

Figure 5. Plane segment model: Crack patterns of the RC, SFRC and hybrid segment and the corresponding maximum separation at an applied displacement of 2.4 mm (magnification 75x).

3.3 *Results: Partial area loading model*

In contrast to the plane stress segment model, an overall decreased load-bearing capacity and a superior performance of the fibre-reinforced segments can be observed (SFRC: 24.25 MN, Hybrid: 22.08 MN and RC: 19.71 MN). While the fibre-reinforced specimens fail due to the formation of a wedge underneath the jack pad, the RC segment fail due to the propagation of the bursting crack through the whole specimen (Figure 6, bottom).

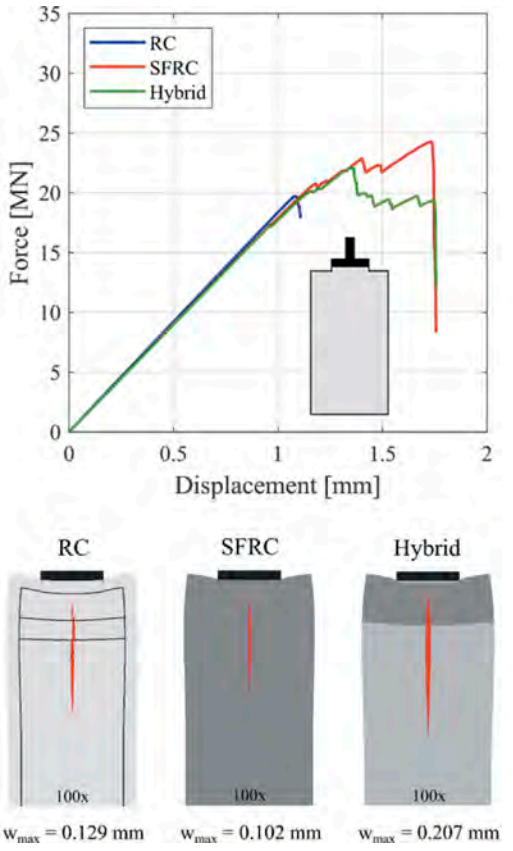

Figure 6. Top: Partial area loading model: Force-displacement curves for all investigated reinforcement schemes. Bottom: Crack patterns including the maximum separation value at an applied displacement of 1.089 mm. The RC specimen fails to a propagation of the bursting crack up to the bottom, whereas the fibre-reinforced specimen fail due to a wedge formation underneath the jack pad.

At an applied displacement of 0.94 mm (F ≈ 17 MN), the splitting crack is initiated and propagates in vertical direction (Figure 6, bottom). For the RC specimen, the splitting cracks initiate at the rebar layer and the rebars can immediately prevent a further crack opening and propagation. The rebars begin to yield at an applied displacement of 1.07 mm, which results in a propagation of the splitting crack towards the bottom of the specimen and consequently the failure of the specimen. In the fibre-reinforced specimen, the fibres provide a sufficient crack bridging resistance after a certain propagation of the splitting crack. At a displacement of 1.36 mm (Hybrid) and 1.43 mm (SFRC), the shear strength of the concrete is exceeded, and the wedge formation is initiated, which results in a drop of the force-displacement curve (Figure 6, top).

In comparison to the SFRC specimen, the hybrid fibre reinforcement provide less residual strength and therefore a softening in the structural response (Figure 6, top) in conjunction with a faster crack opening occurs (Figure 6, bottom). Figure 6 (bottom) shows the crack pattern of the RC, SFRC and a hybrid specimen at an applied displacement of 1.089 mm, which represents the structural response shortly before the yielding of the rebars in the RC specimen. The RC and SFRC specimen show a similar performance in terms of the maximum crack opening, but the bursting crack already propagated towards the bottom and therefore the fibre reinforcement will be more effective upon further loading due to the absence of rebars. In contrast to the SFRC specimen, a higher maximum crack opening can be observed for the hybrid specimen due to the propagation of the bursting crack outside the stronger reinforced layer.

4 RELIABILITY-BASED DESIGN OPTIMIZATION

For the example presented in this section, the Multi-Level FRC model, along with optimization algorithms and uncertainty models, is utilized to design a hybrid fibre reinforced tunnel lining segment subjected to thrust jack loads. The optimization-based design is carried out on the basis of the reference tunnel project presented in Section 3, for which the maximum thrust jack force of the tunnel boring machine F_{design} is specified as 5600 kN. The to-be-designed hybrid fibre reinforced segment consists of two SFRC layers (Figure 2, top), whose required thickness d as well as the fibre content c_F and width ΔL of the strengthening SFRC layer is determined by solving an optimization task under consideration of uncertainties. As reinforcement for the core zone, a FRC with a fibre content of 25 kg/m^3 is applied. In order to design the lining segment subjected to thrust jack forces, the two FE models used in Section 3 (see Figure 3) are employed in the optimization task.

4.1 *Objective and input of the optimization problem*

The optimization task is formulated to minimize the design variables (segment thickness d, the fibre content c_F and the width ΔL of the strengthening SFRC layer) while material uncertainties (fibre orientation λ_F, tensile concrete strength f_t and shear strength β) and imperfections (thrust jack eccentricity Δr – see Figure 3, right) are considered. It should be noted, that in this optimization problem the objective function to be minimized is specified as a weighted sum of the design variables d (80%), ΔL(10%) and c_F (10%), so that the minimum is at the constraint limit state defined by the four inequality constraints applied to both FE models. All constraints are formulated in terms of accepted failure probabilities to account for the scatter through the considered a priori uncertain parameters and therefore providing a robust segment design (for the load bearing capacity $P_{f,ULS} = 10^{-5}$ and for the crack width control $P_{f,SLS} = 0.067$). For the failure criteria, the load bearing capacity F_{max} should be larger than the maximum thrust jack force $F_{design} = 5600$ kN and, in order to ensure a sufficient serviceability performance, the crack width between the thrust jack pads is restricted to 0.1 mm. Due to the computational effort involved in solving an optimization task under uncertainty, Feed-forward Artificial Neural Networks (ANNs) with two hidden layers are used as surrogate models. The ANNs for both structural models are trained with back propagation using results of 1800 FE calculations each (design of experiment generated by Latin Hypercube). A detailed description of the optimization task, uncertain variables and the probability constrains can be found in G.E. Neu et al. (2022).

4.2 *Optimized segment design & constraint limit state*

Due to the formulation of the optimization task, the minimum of the objective function will be on the constraint limit state (CLS), which divides the design space into feasible as well as unfeasible regions and is defined by inequality constraints. Three different strategies for optimizing a segmental lining are investigated:

- **Reference:** The optimization task as described in Section 4.1 is solved to design a hybrid SFRC segment using a conventional C40/50 concrete. The concrete tensile strength is modelled as a lognormal distributed random variable ($\mu = 1.24$, $\sigma = 0.18$). The compressive strength f_c (EN 1992, 2005), the elasticity modulus E_c (EN 1992, 2005) and the mode I fracture energy G_f (fib model code 1990) are assumed to be fully correlated with the lognormal distributed concrete tensile strength.
- **High-Performance:** This scenario should investigate how the use of a better performing concrete could further minimize the segment thickness. Therefore, the concrete tensile strength is modelled as a lognormal distributed random with the parameters $\mu = 1.51$ and $\sigma = 0.18$ (corresponds to C70/85).
- **Recycled:** In contrast, the use of a more environmentally friendly concrete (i.e. using recycled aggregates or modified cement paste) can lead to a lower concrete strength. Investigations in Kang et al. (2012) showed that the use of 50% recycled concrete aggregates lowered the measured tensile strength by 18%. This strength reduction is applied by adopting the concrete tensile strength distribution parameters $\mu = 1.04$ and $\sigma = 0.18$.

Due to the monotonic behaviour of all considered intervals, the CLS of the before-mentioned strategies are evaluated for a single realization of the intervals ($\Delta r = 40$mm, $\beta = 5.0$, $\lambda_F = 0.35$). More information regarding the uncertainty modelling, the parameter

ranges and different realizations can be found in G. E. Neu et al. (2022).

As can be seen in Figure 7, the segment thickness d and the fibre content c_F are dominating the shape of the constraint limit states for each case, whereas the cap width ΔL has only a minor influence. When only using the minimum fibre content of 25 kg/m^3, a segment thickness of d ≈ 435 mm ('high performance'), d ≈ 450 mm ('reference') and d ≈ 465 mm ('recycling') will lead to feasible designs. An increase of the fibre content up to 40 kg/m^3 enables a reduction of the segment thickness to d ≈ 400 mm for the reference case. However, by further increasing the fibre content, only small reductions of the segment thickness can be achieved. The width of the SFRC cap ΔL is the least sensitive design variable. If a certain width is provided (tensile stresses occur within the strengthening SFRC layer), only small improvements with increasing cap width ΔL can be obtained (see 'reference' case at higher fibre contents c_F in Figure 7).

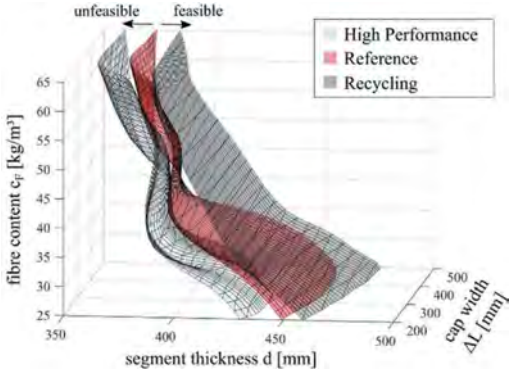

Figure 7. Constraint limit states in the design space for the 'reference', the 'high performance' and the 'recycling' case.

Finally, the evaluation of the objective function is performed for all cases and the optimum of each individual objective $R_{1,2,3}$ as well as the resulting design variables are summarized in Table 1.

Table 1. Design variables for each individual objective $R_{1,2,3}$ employed in the multi-objective optimization task for the investigated cases (results are rounded off).

	R1	R2	R3	d [mm]	ΔL [mm]	c_F [kg/m³]
Reference	372	200	25	402	200	41
High Performance	358	200	25	391	200	38
Recycling	384	200	25	426	200	36

The optimization results in a 402 mm thick segment with a 200 mm wide SFRC cap containing 41 kg/m³ of fibres for the reference case. When compared to the conventional RC segment design (Figure 2, bottom), the steel content is reduced by 59% (106 vs 260 kg/segment) and the concrete volume is reduced by 20% (3.61 vs 4.53 m³/segment). The use of a better performing concrete can further reduce the segment thickness (3.2 vs. 3.61 m³/segment). while a similar steel content in comparison to the reference case can be achieved (92 vs 106 kg/segment). As an alternative, the use of concrete with recycled aggregates still leads to a segment design with a lower concrete volume (3.83 vs 4.53 m³/segment) and a reduced steel content (108 vs. 260 kg/segment) in comparison to the conventional RC design.

4.3 *Design tool for SFRC and hybrid segments*

As part of the model development for the design of hybrid reinforced segments using the Multi-level FRC model in combination with optimization algorithms, neural networks were derived that can predict crack width and load-bearing capacity as a function of segment thickness, fibre content, fibre orientation, and concrete strength (Section 4.1 and G.E. Neu et al. (2022)). These ANNs were implemented in a software-based design tool with a suitable graphical user interface to assist engineers in the design of fibre reinforced segment and to provide a straightforward access to the prediction models presented within this article (Figure 8).

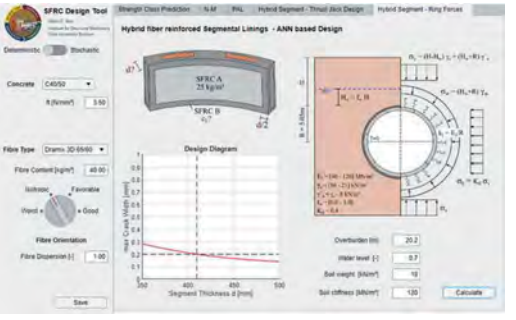

Figure 8. ANN-based design tool of hybrid fibre-reinforced segmental linings.

5 CONCLUSIONS

The results presented in this paper demonstrate the role of advanced numerical modelling approaches in the design of more sustainable fibre-reinforced concrete structures. The presented multi-level FRC model was used to compare the structural performance in terms of load-bearing capacity (ULS) and crack development (SLS) of conventional and fibre reinforced segments subjected to thrust jack loadings. It was shown that SFRC segments offer a better crack

width control and provide a comparable load-bearing capacity in comparison to RC segments with an equivalent steel content. In addition, the concept of hybrid fibre reinforced segments (placement of different SFRC layers according to the level of structural stresses) was investigated and showed to be able to reduce the overall steel content significantly.

As application case, a reliability-based optimization for the design of fibre-reinforced segmental tunnel linings subjected to thrust jack forces has been performed. A segment design is derived, consuming up to 20 % less concrete and reducing the steel content by 59 % as compared to a conventional RC design. Using high-performance concrete, a further reduction can be achieved (steel content -13 %, concrete volume -11 %), while the use of recycled concrete has been shown to be an environmentally friendly alternative (58 % less steel content and a 15% lower concrete volume in comparison to a conventional RC segment design).

ACKNOWLEDGMENTS

Financial support was provided by the German Research Foundation (DFG) in the framework of project B2 of the Collaborative Research Center SFB 837 Interaction modeling in mechanized tunnelling (Project no.: 77309832). This support is gratefully acknowledged.

REFERENCES

Amin, A., Foster, S., Muttoni, A., 2015. Derivation of the σ-w relationship for SFRC from prism bending tests. Structural Concrete, 93–105.

Bakshi, M., Nasri, V., 2017. Design of Fiber-Reinforced Tunnel Segmental Lining According to New ACI Report. In Canadian Society for Civil Engineering Annual Conference 2016: Resilient Infrastructure. Canadian Society for Civil Engineering (CSCE).

DB Ril 853, 1998. Richtlinie 853: Eisenbahntunnel planen, bauen und instandhalten. Deutsche Bahn. Technical report.

De la Fuente, A., Pujadas, P., Blanco, A., Aguado, A., 2012. Experiences in Barcelona with the use of fibres in segmental linings. Tunnelling and Underground Space Technology 27, 60–71.

European Comittee for Standardisation, 2005. EN 1992 - Eurocode 2: Design of concrete structures.

Gall, V. E., 2018. Numerical Investigation of Hybrid Segmental Lining Response to Mechanized Tunneling Induced Loadings. Ph. D. thesis, Ruhr University Bochum.

German tunnelling committee (DAUB), 2013. Recommendations for the design, production and installation of segmental rings. Technical report. Deutscher Ausschuss für unterirdisches Bauen e. V. (DAUB).

Gudžulić, V., Neu, G.E.,Gebuhr, G., Anders, S., Meschke, G., 2020. Numerisches Mehrebenen-Modell für Stahlfaserbeton: Von der Faser- zur Strukturebene. Beton und Stahlbetonbau, 115(2), 146–157.

International federation for structural concrete (fib), 2013. Fib Model Code for Concrete Structures 2010, Ernst & Sohn.

International federation for structural concrete (fib), 1993. Fib Model Code for Concrete Structures 1990.

Kang, T., Kim, W., Kwak, Y.-K., Hong, S.-G., 2012. The Choice of Recycled Concrete Aggregates for Flexural Members. IABSE Congress Report, 18(21), 726–731.

Monteiro, P. J., Miller, S. A., Horvath, A, 2017. Towards sustainable concrete. Nature materials, 16(7), 698–699.

Neu, G.E., Edler, P., Freitag, S., Gudžulić, V., Meschke, G., 2022. Reliability based optimization of steel-fibre segmental tunnel linings subjected to thrust jack loadings. Engineering Structures.

Plückelmann, S., Breitenbücher, R., 2020. Hybrid lining segments–bearing and fracture behavior of longitudinal joints. In Tunnels and Underground Cities: Engineering and Innovation meet Archaeology, Architecture and Art, pp. 2881–2890. CRC Press.

Zhan, Y., Meschke, G, 2014. Analytical model for the pull-out behavior of straight and hooked-end steel fibers. Journal of Engineering Mechanics, 140(12), 04014091.

Zhan, Y., Meschke, G, 2016. Multilevel computational model for failure analysis of steel-fiber–reinforced concrete structures. Journal of Engineering Mechanics, 142 (11), 04016090.

Tunnelling for a Better Life – Yan, Celestino, Thewes & Eberhardt (Eds)
© 2024 The Author(s), ISBN 978-1-032-80042-4
Open Access: www.taylorfrancis.com, CC BY-NC-ND 4.0 license

Snowy 2.0 - Support design for intersections between access tunnel and caverns

Xuan-Phu Nguyen*
Tractebel Engineering, Lyon, France

Pier-Luigi Tonioni, Aï-Na Blaise & Reza Taherzadeh
Tractebel Engineering, Gennevilliers, France

Davide Galli
Future Generation Joint Venture, Cooma, Australia

Giancarlo Cardone
Snowy Hydro Limited, Cooma, Australia

ABSTRACT: This paper aims to present the design of the reinforcement required for the segmental liner of a TBM tunnel crossed by large caverns at great depth. Indeed, when a TBM tunnel is intersected by subsequent excavations, there is a significant risk of overloading the liner, especially for large excavations, in a highly stressed jointed rockmass of low/medium strength. Such situation is the case of the intersections between the Main Access Tunnel (MAT) and the two caverns of the 2200 MW pumped hydro-power Snowy 2.0 in Australia. In addition, the construction planning is characterised by multiple strict logistical constrains. To address these conditions and constraints, a combination of measures is implemented. Sliding steel ribs are employed to provide support to the precast concrete lining segments. Temporary and permanent rockbolts are also used for temporary and permanent support, and an observational approach is adopted to monitor and adapt to the changing conditions during construction. Numerical analyses are performed on discontinuous models using 3DEC and Unwedge software. On one hand, 3DEC models are used to simulate the behaviour of the jointed rock mass and the support system, enabling the evaluation of concrete segment damage evolution. Moreover, the excavation sections and planning of the cavern are adjusted so as to be aligned with the general schedule and logistical constraints while assuring MAT01 liner stability. On the other hand, Unwedge models are carried out to design definitive rockbolts based on rock block stability analysis. Some in situ measurement from the observational methods are compared with numerical results, according to the observational method.

Keywords: Concrete segment, Sliding steel rib, Discontinuous, Numerical modelling, Observational method

1 INTRODUCTION

Snowy 2.0 is a 2200 MW pumped-storage hydropower, currently under construction, extended from the Snowy Mountain Scheme in the southeastern Australia, linking two existing reservoirs, Tantangara and Talbingo, through a 720 m depth Power Station Complex (PSC) by 27 km tunnels (Figure 1). The PSC consists of two caverns – the Machine Hall (MH) for six generation units and the Transformer Hall (TH) - connected by six busbar galleries and six draft tube tunnels.

The PSC is accessed, during the construction phase and permanently, by the Main Access Tunnel (MAT01) and the Egress, Cable and Ventilation Tunnel (ECVT01), from which drill and blast (D&B) tunnels are realised for the construction of the caverns. MAT01 and ECVT01 are both excavated by TBM and supported with pre-cast reinforced concrete

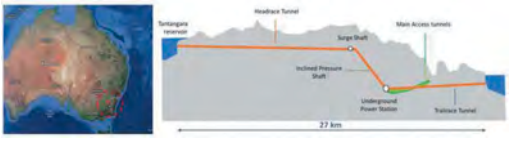

Figure 1. Snowy 2.0 – Project location (left) and alignment (right) Ref: Snowyhydro.com.au.

*Corresponding author: xuan-phu.nguyen@tractebel.engie.com

DOI: 10.1201/9781003495505-152

segmental lining. During construction, MAT01 is excavated first and serves as the main access to the PSC and its surrounding tunnels. It is the only lined tunnel that crosses the two caverns.

Due to planning considerations, the circulation inside MAT01 must be maintained as long as possible, even during the excavation of the overlying upper levels of the caverns. It follows that any issue at the intersections between MAT01 and the two caverns would induce the construction of the whole PSC halted. Therefore, these intersections represent a critical point in the detailed design of the project, requiring a robust design methodology.

2 GEOLOGICAL SETTING

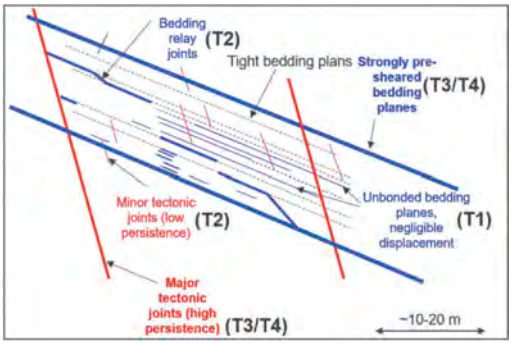

Figure 2. Structural model of the rockmass.

The project area is situated within the south-eastern portion of the Lachlan Orogen (Fold Belt) of New South Wales, which comprises a suite of early Palaeozoic Era (550-350 Ma) sedimentary, igneous, and metamorphic rocks that have developed during several orogenic periods. The PSC is in the Ravine Beds Formation, under 600 – 720 m depth. The formation consists of thick sequences of indurated siltstone (70%) and interbedded/interlaminated sandstone with conglomerate (30%). The joint pattern around the PSC consists of bedding and tectonic joints (Figure 2) that are classified in:

- Minor joints T1 and T2 are in-between pre-sheared joints, dominantly bedding joints, undergoing negligible tectonic displacements.
- Major joints T3 and T4 are pre-sheared joints, considered as the main weakness planes in the rockmass. Their main characteristics are presented in Table 1, and dip-direction indicated in Figure 2. One observes that both jointsets dip in the direction from TH to MH.

Rockmass geomechanical characteristics being relatively heterogeneous, a "central" case is considered for the present study:

- For an equivalent homogeneous medium: *UCS* = 58 MPa and *GSI* = 72;

Table 1. Major joint-sets T3/T4 characteristics.

Parameter	Bedding joints	Tectonic joints
Dip (°)	35	75
Dip-direction (°)	75	125
Spacing (m)	10	20
Friction angle (°)	30	
Cohesion (MPa)	0	

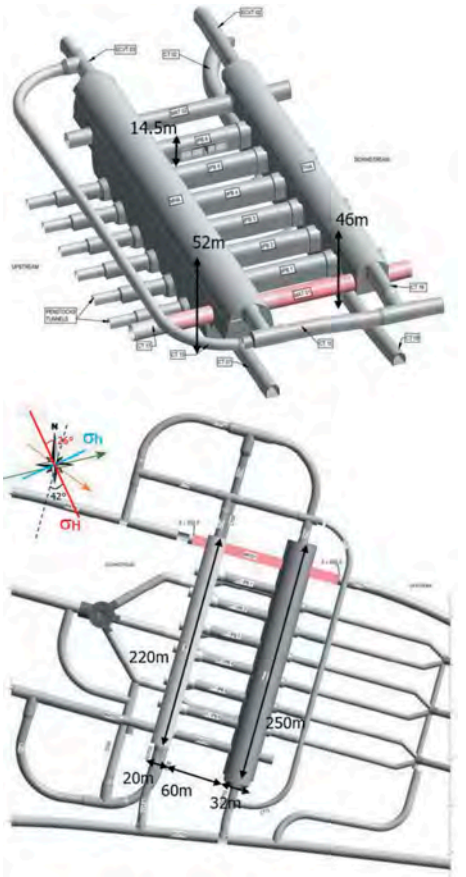

Figure 3. Perspective (top) and plan (bottom) views of the PSC with MAT01 highlighted in red. Orientations of horizontal principal stresses σ_h and σ_H, major bedding (green) and tectonic (orange) joint-set dip-direction are marked.

- For discontinuous medium cut by the major joints (T3/4) into blocks in which are lumped the minor joints, the rock blocks (matrix) are characterised by: *UCS* = 58 MPa and *GSI* = 78. In other words, the absence of major joints increases *GSI* from 72 to 78.

Vertical stresses at the PSC are practically lithostatic with a unit weight of 27 kN/m^3, the value at the middle of the caverns being σ_v = 19 MPa.

Horizontal stresses are strongly anisotropic, the minor and major principal component ratios are respectively K_h = 1.5 and K_H = 2.3, i.e. σ_h = 28.5 and σ_H = 43.7 MPa (orientations indicated in Figure 3). Rockmass permeability being extremely low, all the calculations are carried out in total stress.

3 DESIGN METHODOLOGY

MAT01 is excavated with a single shield 11 m diameter TBM and supported by 38 cm thick pre-cast reinforced concrete segmental lining (Table 2). Generally, lined tunnel is expected to be overloaded at intersections with subsequent excavations around which stress concentration is induced by deconfinement (see §4.2), resulting in concrete segment damage due to excessive compression stresses and/or ring collapse due to ovalisation (see §4.3) and its inherent discontinuity. The larger the subsequent excavation and the higher the in situ stresses, the more important the tunnel lining overloaded.

Table 2. MAT01 main dimensions.

Parameter	Symbol	Unit	Value
Boring diameter	ϕ_{exc}	m	11.08
Annular gap	δ_{gap}	cm	21
Internal ring diameter	R_i	m	9.90
External ring diameter	R_e	m	10.66
Segment thickness	t_{ring}	m	0.38
Concrete strength	f'_{ck}	MPa	50
Ring width	L_{ring}	m	2.00

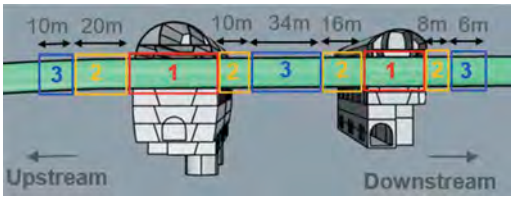

Figure 4. Lining damages zoning around MAT01 – caverns intersections. Cavern excavation benching is shown.

Accordingly, around the MAT01 - caverns intersections, lining damage was foreseen and was firstly evaluated in terms of extensions depending on the construction sequence (see §4.3). Indeed, MAT01 lining in the PSC was sub-divided into 3 zones, as sketched in Figure 4:

- Zones 1 - inside the 2 caverns: The most critical phase occurs at the excavation of the caverns crowns, giving rise to lining vertical ovalisation.
- Zones 2 - beside the caverns sidewalls: They are characterised by lining horizontal ovalisation induced by vertical stress concentration beside the caverns.
- Zones 3 - outside of zones 2: These zones are less affected by the excavation of the PSC, but the failure risks are not totally discarded.

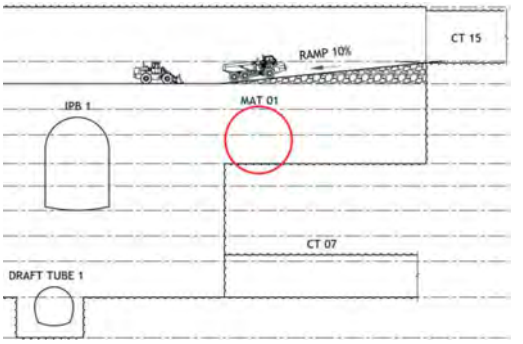

Figure 5. Excavation and traffics in the cavern and in MAT.

Table 3. Sliding steel rib characteristics.

Parameter	Unit	Value
Grade	-	+QT630
Section	-	TH44
Density	Gg/m^3	0.00785
Young modulus	MPa	2x105
Poisson ratio	-	0.2
Cross sectional area	m^2	5.57x10-3
Bending inertia	m^4	1.243x10-5
Elastic section modulus	m^3	1.65x10-4
Yield point	MPa	630
Tensile strength	MPa	790
Limit axial forces	MN	0.5
Limit axial stress	MPa	90 (15% σ_y)

Additional support along these extensions must have been installed before damage occurring. On one hand, the additional support must retain the damaged concrete segments, the overlying rock and the traffic load related to circulation inside the vaults of the caverns which are under construction (Figure 5). On the other hand, for zones 2 & 3 beside and outside the caverns, it must also be able to receive further loading induced by rockmass convergences during the excavation of the lower parts of the PSC. Thus, additional support must follow the "yielding principle", while assuring enough resistance. Considering the multiple logistic constraints, sliding steel ribs were chosen as the main additional support. These are made of top-hat cross-section steel profiles (Thyssen-Heintzmann - TH) with friction connecting loops that allow the ring of ribs to accommodate larger displacements with limited sliding resistance. The sliding limit force and the spacing were designed according to the "resistance principle", capable to withstand the weight of the

overlying rocks and the traffic load in the cavern. They are estimated with a local continuous model, using FLAC3D software, in which the rock is represented with residual properties. The sliding limit force being estimated at 500 kN/m, the section TH44 was chosen, the spacing is 1 m, allowing to have 2 ribs per each lining ring (2 m long).

After the PSC construction, all the steel ribs must be dismantled so as MAT01 space-proofing can be satisfied. Damaged lining rings, expected in zones 2 and maybe part of zones 3, must also be dismantled. The final extensions of liner dismantling will be decided based on monitoring data, according to the observational method. Special attention was given to the lining dismantling procedure (see §5) as they are expected to be strongly stressed.

After damaged liner dismantling, a definitive support system, consisting of rockbolts and shotcrete, will be realised. These elements are designed based on the stability of local rock blocks/wedges formed from geological joints and excavation surfaces. This design is carried out using Unwedge software.

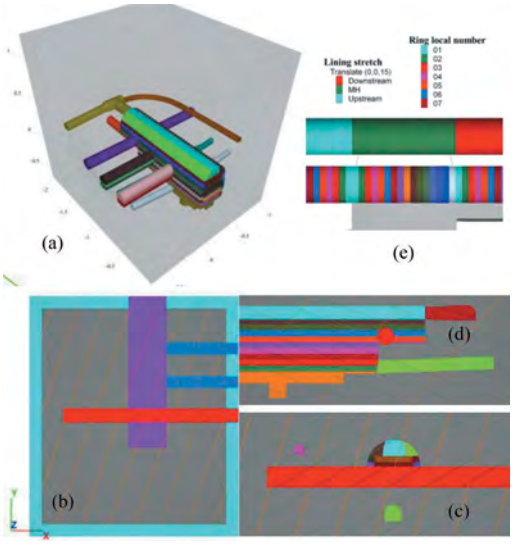

Figure 6. 3DEC model for MAT01-MH intersection: a) model limits (unit of 100m); b) horizontal cut-plane at MAT01 axis level; c) and d) vertical cut-planes along MAT01 and MH axes; e) lining ring enumeration.

4 STRUCTURAL INTEGRITY OF THE SEGMENTAL LINING AND SLIDING STEEL RIBS

4.1 *Numerical models*

Discontinuous models are built using 3DEC software where major bedding and tectonic joint sets (see §2) are explicitly represented. Figure 6 shows the extension of a local model focused on the MAT01-MH intersection, with all the excavation divisions following the initial phasing. Bedding joints are shown to be more horizontal than tectonic joints, and thus expected to have larger impact on MAT01 lining. Moreover, as both joint sets dip towards the upstream (TH towards MH), overload on MAT01 lining is expected to be more pronounced on the upstream side than on the downstream side of MH.

Rock blocks are represented by an elastic perfectly plastic model with a bi-linear Mohr-Coulomb criteria fitted to the Hoek-Brown criterion. Similar models fitting the Barton-Bandis failure criterion are adopted for joints. Main characteristics of rock blocks and joints are shown in §2.

MAT01 lining is represented by shell-type structural elements called "liner" in 3DEC, which are linearly elastic (without failure) and resist to membrane and bending actions. Liner and rock excavation surface interaction is modelled using interface elements whose parameters are estimated from annular gap backfill material properties: Young's modulus E_{bf} = 1 GPa, uniaxial compression strength UCS_{bf} = 2 MPa, and thickness t_{bf} = 21.5 cm. The interface normal stiffness can be estimated as $k_n = E_{bf}/t_{bf}$ = 1/0.215 = 4.65 GPa/m. The interface normal tensile resistance is null and compressive resistance is infinite, meaning that liner nodes can be detached from the rock excavation surface but cannot penetrate into the rockmass. In the shear direction, without data, we assume that the interface shear stiffness is equal to the normal stiffness $k_s = k_n$. Assuming a friction angle of ϕ_{bf} = 30°, the corresponding cohesion is c_{bf} = 0.58 MPa. In fact, the numerical interface between liner and rock excavation surface represents the backfill material and its two interfaces with the rock excavation surface and the concrete lining extrados. As the concrete lining surface is relatively smooth, the liner – rock excavation surface shear resistance in the model would be smaller than the annular backfill shear resistance. As a friction angle of 30° is already relatively small, for the numerical liner-rock interface, we consider a friction angle of 30° and a null cohesion as the reference parameters. A liner-rock interface shear-directional cohesion of 0.58 MPa has also been considered for parametric study.

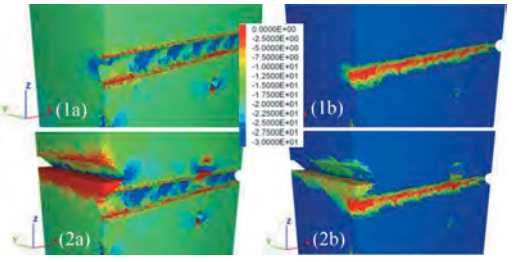

Figure 7. Vertical σ_{zz} (a) and horizontal σ_{yy} (b) stress contours after MAT01 (1) and caverns crown (2) excavations.

Effect of longitudinal joints between segments in each lining ring on its bending inertia is accounted for using Muir Wood (1975)'s formulae. In the MAT01 axis, separation between rings is explicitly represented,

with enumeration shown in Figure 6e. However, no direct interaction between adjacent rings is modelled.

4.2 *Rockmass behaviour*

Figure 7 exhibits stress concentrations after excavations of MAT01 (1) and after MH stage-1 (2): vertical stresses are concentrated by the excavation sides, horizontal stresses, above and below. The rock slab in-between MH stage-1 and MAT01 experiences significant stress releases: from 15-30 MPa to 0-5 MPa in the vertical direction (figures a), and from over 30 MPa to 0-10 MPa in horizontal plan (figure b). These rock blocks are totally plasticised. That's why we used rockmass residual properties when estimating necessary sliding limit force (see §3).

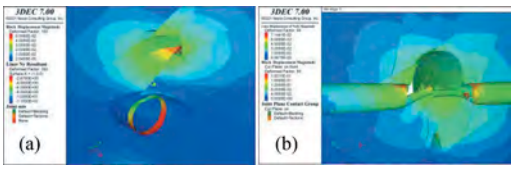

Figure 8. Rock displacement around MH-MAT01 intersection after CHT (a) and complete PSC (b) excavations.

In presence of a bedding joint intersecting the zone in-between MAT01 and the stage-1 of the cavern, convergences towards the cavern excavation enhance shear displacement on this joint (Figure 8a), giving rise to local overload concentration on MAT01 lining due to subsidence of the lower rock block. At the end of all the PSC excavations (Figure 8b), displacements on the cavern wall are about 10 cm, rock bedding layers clearly bend towards the caverns, and MAT01 lining rings in zones 2 (beside the caverns) horizontally ovalised. This excavation induced displacement fashion is typical for anisotropic rock masses and largely reported in literature (Sainsbury and Sainsbury, 2017).

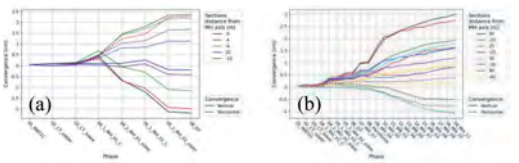

Figure 9. Evolutions of MAT01 convergences at sections inside (a) and outside (b) MH. Negative values indicate extensions.

MAT01 ovalisation can also be observed with convergences at different sections (Figure 9). Note that negative values indicate divergences. Outside the caverns (Figure 9b), lining ring ovalisation is horizontal and diminishes with increasing distance from the caverns sidewalls. In zones 3 which are relatively far from the caverns, some convergences are still considerable, larger than 1% of the tunnel diameter. Inside the cavern (Figure 9a), ovalisation is mainly vertical and varies depending on the relative position of the considered section to bedding joints and to the overlying excavation in the caverns.

4.3 *Lining integrity evaluation*

By "damage" we refer to the state of efforts at a point on the liner that does not verify ULS following AS5100.5:2017. Figure 10a presents the lining effort verification against the strength envelope on *M-N* diagram for the stretch on MH downstream. The first five rings exhibit significant effort exceedance from the envelope. To visualise the location of the exceeding points, we introduce the strength ratio which is the ratio between the distance E_{ed} from the centre of the strength envelope to a given effort point and the corresponding distance E_{lim} from the centre to the envelope: $SR = E_{ed}/E_{lim}$. Accordingly, $SR \geq 1$ indicates that the efforts exceed the resistance envelope, while $SR < 1$, the efforts are inside the resistance envelope. Based on lining *SR* (Figure 10b), and its evolution with the excavation of the PSC, extensions of zones 2 are delimited for each excavation phase. Accordingly, deadlines for sliding steel ribs installation and excavation sections in the caverns can be adjusted vs logistic constraints. Besides, the *SR* contour shows that MAT01 lining damage on the upstream side is farther than in the downstream side, which confirms the expected effect of bedding joint orientation (see §2).

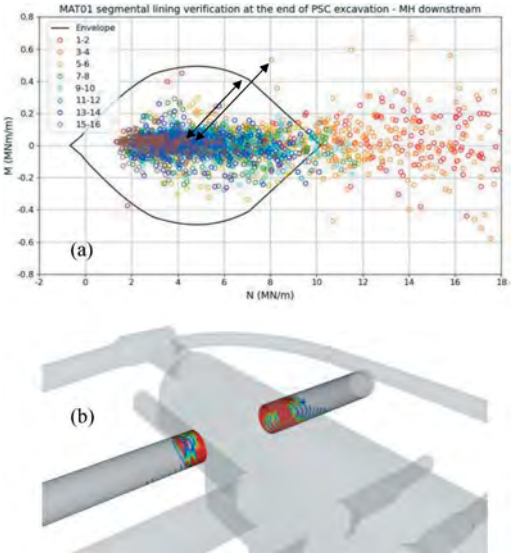

Figure 10. Lining verification after MH excavation: (a) effort points coloured following ring enumeration vs ULS envelope, and (b) strength ratio $SR > 1$ contour.

In zones 3, some slight and local exceedances of the strength envelope can be observed. In addition, in the case of higher cohesion $c_{bf} = 0.58$ MPa between the liner and the surrounding rockmass (see §4.1),

some tensile forces appear in crown and invert of the liner. As MAT01 is situated near the border of the PSC (see Figure 2), the PSC excavation induced rock displacement is not symmetric around MAT01, but toward the PSC centre. Figure 11 shows that, with higher shear strength on the rock-liner interface, this rock displacement pattern generates tensile axial forces on the crown and the invert of the liner. Note that in the numerical model, the lining rings are represented by continuous and elastic shell-type structural elements, while they are made up from discrete segments. Calculated tensile forces in a lining ring mean that the ring presents the risk of instability due to loosing contacts between segments on longitudinal joints. Thus, concrete segments in zones 3 are supported with rockbolts (two CT26WR L = 6 m per segment). In zones 1, due to delayed sliding steel rib installation for logistic constraints, similar rockbolt support applies prior to excavation of the Central Heading Tunnel (CHT) in the crown of the caverns (see Figure 13).

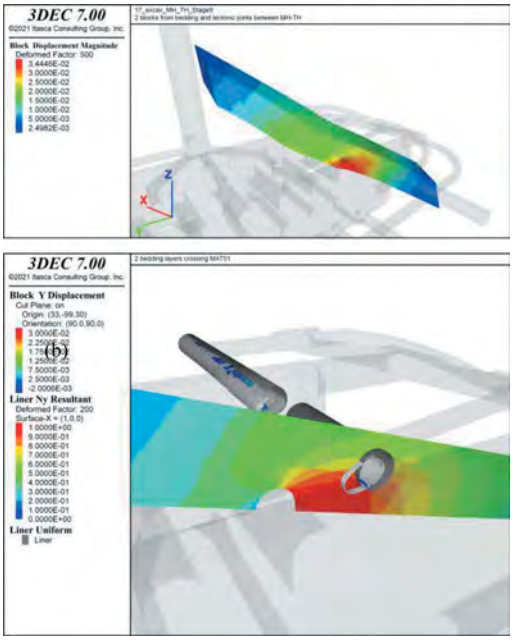

Figure 11. Interaction between two rock blocks crossing MAT01 in zone 3, between the two caverns and beside IPB-1, cut by three bedding joints and two tectonic joints, and the liner. (a) Perspective view of the blocks total displacement. (b) Bocks horizontal displacement on a cross-section, liner tensile force contour in exaggerated deformation and its initial geometry.

4.4 *Sliding steel ribs verification*

Steel ribs are verified for material resistance on cross-section according to AS4100:1998. As steel ribs are fixed in the tunnel axis direction on concrete lining intrados, or braced between each other by longitudinal strutting tubes, steel structure stability, such as buckling, are not verified. For material resistance verification, the most critical measure for each cross-section is the von Mises equivalent stress σ_g resulting from combined bending moment M, axial N and shear V forces (Hirt and Bez, 1994). We introduce the strength ratio for each cross-section as the ratio between design values of the maximal equivalent and yield stresses $SR = \sigma_{gd}/f_{yd}$. Without bending moment and shear force, the sliding limit force only corresponds to a SR = 20%.

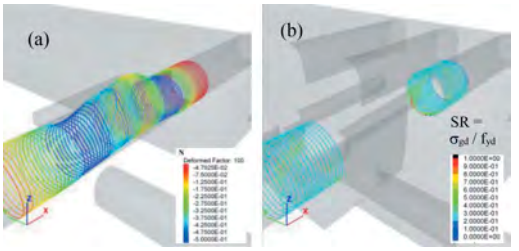

Figure 12. Steel rib axial force just before breakthrough into MAT01 (a) and strength ratio SR at the end of all PSC excavations (b).

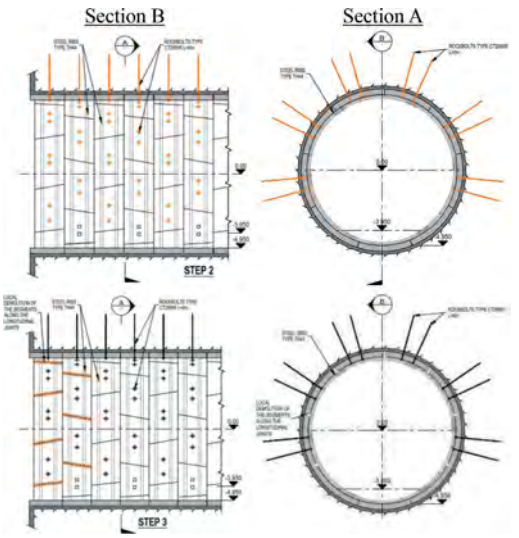

Figure 13. Concrete segment stabilisation with rockbolts (STEP 2) and ring stress release by local demolition along longitudinal joints (STEP 3).

Figure 12a shows steel rib axial forces just before the breakthrough into MAT01. One observes that the sliding limit force is reached in sections below the cavern excavation sidewall, while outside the cavern and in the middle of the stretch inside the cavern, they are far below. All strength ratios $SR < 1$. At the end of PSC excavation, steel ribs slide on over 10 m from the sidewalls of the caverns, but strength ratios are mainly below 1, except for some closest ribs that are intersected by bedding joints (Figure 12b).

5 LINER DISMANTLING AND DEFINITIVE SUPPORT

As shown in §4.3, concrete segments in zones 2 are expected to be significantly damaged, and shall be dismantled, allowing the definitive rock support based on rockbolts and shotcrete to be installed. Nevertheless, due to logistic constraints, the dismantling of the segments in zones 2 will be postponed after the completion of the caverns excavation, during which they will be temporarily supported by provisional sliding steel ribs. The final effective dismantling extension will be decided based on monitoring data.

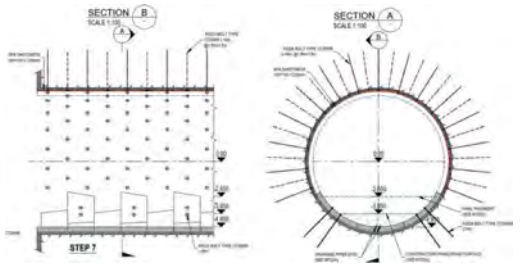

Figure 14. Definitive support replacing damaged concrete segments.

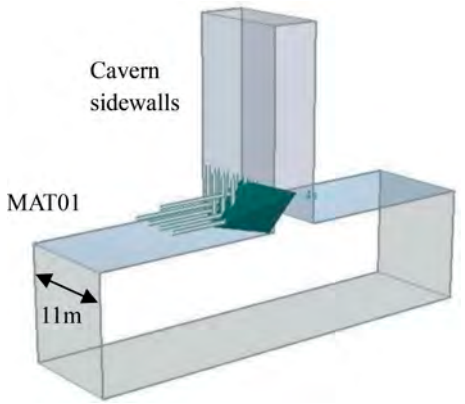

Figure 15. Unwedge model for a rock block situated on the MAT01 crown and adjacent to a cavern side wall with definitive support.

The most critical point upon dismantling concrete segments in zones 2 at the end of the PSC excavation is that they have been significantly stressed due to rockmass convergence. Thus, to ensure maximal safety, the following principles applies:

- Stabilisation of each segment to be dismantled with two rockbolts type CT26WR, L = 6 m (Figure 13 – STEP 2).
- De-stressing of the ring by punctual demolition of the segments before the removal of the temporary steel ribs (Figure 13 – STEP 3). The concrete segment and the retained rock wedges by the rockbolts are verified using Unwedge software.
- Dismantling is to be carried out in small areas, maximum at a time two rings (4 m round length) and in an angular opening < 90° (1/4 circle). During the transient between segments removal and permanent rockbolt installation, the rockmass stability will be assured by a primary 100 mm shotcrete having f'_c > 1 MPa and the two rockbolts on each segment deprived of the plate. Rock wedge stability is accordingly verified using Unwedge software.

Definitive support consists of another 100 mm secondary shotcrete (200 mm in total) and rockbolts CT26WR with L = 6 m, @1.5mx1.5m (Figure 14). Rock wedge stability is verified with these support elements using Unwedge software (Figure 15). For this analysis, all the jointsets (see Figure 2) are considered in different combination. In addition to the weight of the wedges, ground water pressure and seismic loading are also considered. All the safety factors are larger than unity, indicating that rock wedge stability verification is attaint.

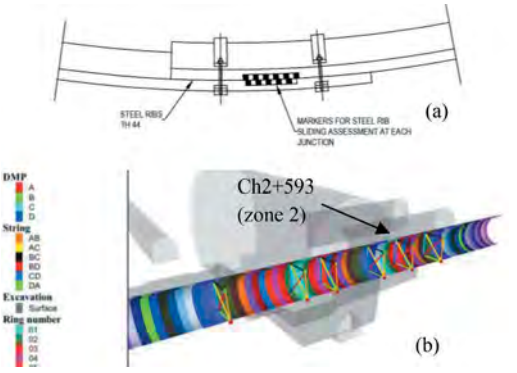

Figure 16. Markers for steel ribs sliding measurement (a); DMP and strain gauges measured sections (b).

Figure 17. Central Heading Tunnel excavated in MH (a); Sliding steel rib installation in MAT01 (b).

6 MONITORING VS NUMERICAL RESULTS

The MAT01 stretch in the PSC, as identified in Figures 3 and 4, must be extensively monitored during construction. In addition to geological mapping, the monitoring system consists in:

- concrete lining rings: displacement/convergences using DMP (Displacement monitoring point) and stresses using strain gauges on steel rebars;
- sliding steel ribs: stresses using strain gauges and relative sliding displacement (Figure 16a);
- temporary rockbolts: axial force using load cells;
- joint shear displacement: video inspection via borescope camera.

Currently, MAT01 as well as surrounding construction tunnels for the PSC have been finished. The excavation of the PSC has been started with the CHT in both caverns (Figure 17a. The lower part of all the sliding steel rib has been installed in MAT01 (Figure 17b).

Some preliminary monitoring data, mainly in terms of lining rings DMP displacements and stress is provided. The allocations of the measured sections and the DMP positions on each section are shown in Figure 16b. For each measured section/ring, convergences following six directions ("string") as shown in the figure are provided. Also, a lining ring being composed of nine segments, each segment is measured with a couple of strain gauges installed on its intrados and extrados rebars (Figure 18).

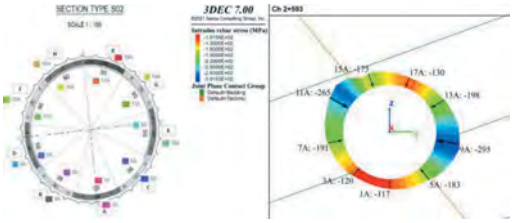

Figure 18. Implementation of strain gauges on a concrete segmental ring and example of corresponding numerical results.

Figures 19a exhibits DMP convergence on the lining ring at chainage 2+593 (marked in Figure 17) on zone 2 next the MH downstream sidewall. The current phase, namely "04_1_MH_01_C" for CHT of MH excavation stage-1, is marked by blue line. Corresponding monitored data is plotted in Figures 19b as temporal evolution. The period during which the CHT excavation front is above MAT01 is marked with blue rectangle. Both numerical and monitored results indicated small displacement by the current phase.

Similar presentation for stresses on the same lining ring is exhibited in Figure 20. Again, both numerical and monitored results indicate relatively small stress by the current phase. More significant values for DMP convergences and stress are expected after caverns crown side slashing from the CHTs which is planned for the next couple of months.

7 CONCLUSIONS

Support design for the intersections between the Main Access Tunnel MAT01 and the two caverns of the Australian Snowy 2.0 pumped-storage hydropower, as part of the Power Station Complex (PSC) detail design, has been described. It consists in a principal access to the whole PSC during construction as well as in the service phase. Excavated by TBM and lined with pre-cast concrete segments, MAT01 directly crosses the two caverns of large dimensions, and surrounded by several construction tunnels and galleries, at some 700 m depth in a medium strength and jointed rockmass. To accommodate these significant excavation volumes and to meet multiple construction planning and organisation constraints, sliding steel ribs and rockbolts are used to support damaged concrete segments during construction, coupled with an observation method. At the end of the PSC excavation, sliding steel ribs and damaged lining rings will be dismantled and replaced by a definitive support composed of shotcrete and rockbolts.

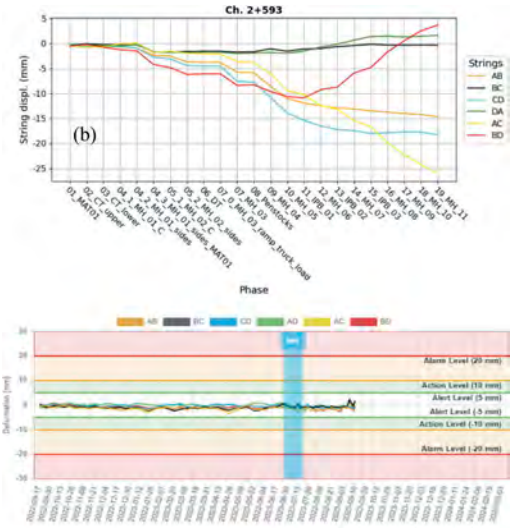

Figure 19. Numerical (a) and monitored (b) DMP displacements at ch. 2+593.

Numerical analyses have been performed on discontinuous models where major tectonic and bedding joints are explicitly represented. The results showed considerable and anisotropic rock convergences toward the two caverns, accompanied by joint shear displacements, and bending of rock bedding layers. Based on these results, MAT01 lining in the PSC was sub-divided into 3 zones – inside the cavern, adjacent to the caverns sidewalls and farther, called zones 1, 2 and 3 respectively – of different rock mass – liner interactions, logistic constraints, thus support method and planning. The extensions of these stretches depend on their positions relative to the caverns and

the bedding joint dip-direction: longer extension for the upstream side (toward which bedding layer dips) and for the larger cavern (MH). The results also showed that sliding steel ribs are effective in accommodating large tunnel convergences in a highly stressed rockmass. Only a few ribs next to the cavern sidewalls fail at intersection with bedding joints experiencing large shear displacements. Definitive support replacing dismantled lining rings is also satisfactorily verified based on rock wedge stability.

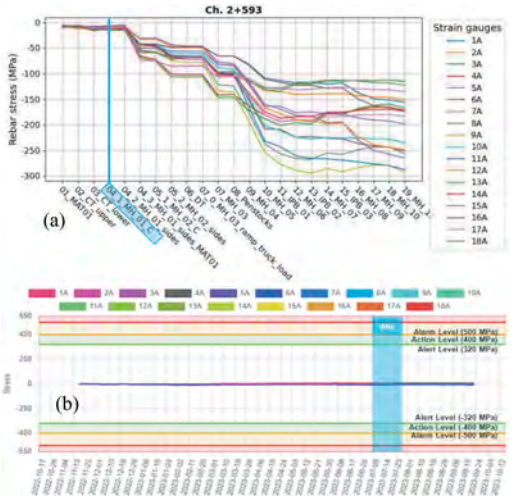

Figure 20. Numerical (a) and monitored (b) stresses on steel rebars at ch.2+593.

The excavation of the PSC has been started and currently at the excavation of the Central Heading Tunnels (CHTs) in the caverns crown. Numerical and monitored results are in good agreement so far, both indicating negligible convergences and stresses in the liner. However, larger values are expected just after the side slashing from the CHTs, and naturally during the excavation of the lower part in the caverns.

ACKNOWLEDGMENTS

The authors would like to acknowledge all the peers from Tractebel who contributed to the design of the Snowy 2.0 Power Station Complex over the years. Fruitful discussions with Snowy Hydro Ltd and Future Generation Joint Venture are also acknowledged.

REFERENCES

AS 5100.5, 2017. Bridge design - Concrete. Australian Standard.

AS 4100, 1998. Steel structures. Australian Standard.

Hirt, M.A., Bez, R., 1994. Construction métallique - Notions fondamentales et méthode de dimensionnement. In: Traité de Génie Civil de l'Ecole Polytechnique Fédérale de Lausanne.

Muir Wood A.M., 1975. The circular tunnel in elastic ground. Géotechnique, n°25(1), 115–127.

Sainsbury, B.L., Sainsbury, D.P., 2017. "Practical Use of the Ubiquitous-Joint Constitutive Model for the Simulation of Anisotropic Rock Masses". Rock Mechanics and Rock Engineering 50(6), 1507–28.

Tunnelling for a Better Life – Yan, Celestino, Thewes & Eberhardt (Eds)
© 2024 The Author(s), ISBN 978-1-032-80042-4
Open Access: www.taylorfrancis.com, CC BY-NC-ND 4.0 license

Research on high-quality and high-durability of tunnel lining by mixing volcanic glass powder

Mitsugu Nomura*
CTI Engineering International Co., Ltd., Tokyo, Japan

Satoshi Tomoto
CTI Engineering Co., Ltd., Tokyo, Japan

Takayoshi Shiina & Noriyuki Mitsui
Nishimatsu Construction Co., Ltd., Tokyo, Japan

Susumu Yoshida
Civil Engineering Research Institute for Cold Region, Sapporo, Japan

Daishin Hanaoka
Kanazawa Institute of Technology, Kanazawa, Japan

ABSTRACT: In this study, cores were sampled from several locations in the arches of the lining concrete of a road tunnel that was no longer in use to confirm the state of cracking damage at the casting end and to confirm the decline in concrete quality at the casting end by focusing on the distribution of the coarse aggregate. In this project, we conducted a series of fundamental experiments to investigate the feasibility of using volcanic glass powder, a pozzolanic material, as a concrete admixture to increase the resistance to material separation during casting and to moisture and salt penetration after curing, thereby realizing high-quality, highly durable lining concrete. The lining concrete using volcanic glass powder has been put to practical use through experiments from basic testing to construction.

Keywords: lining concrete, long-term quality, casting, volcanic glass powder, deterioration, admixture

1 INTRODUCTION

Concrete lining of road tunnels was constructed using slide arch-centres, and until the 1970s, concrete was placed by conveyor feeding or by pulling out pipes at the arch crown. Since the 1970s, however, the standard method has been to use a concrete pump to press-in concrete through a single spout per span.

The characteristic feature of this concrete placing method is that the concrete flows from the top of the arch- centre to the shoulder and fills the arch-centre. Fresh concrete flowing over a typical arch-centre length of L=10.5 m is prone to material separation and bleeding due to the prior flow of cement paste in addition to the settling of coarse aggregate.

In this study, one of the causes of the failure is considered to be the method of placing concrete in the arch crown. As a method to improve it from the material aspect, we devised the use of volcanic glass powder as an admixture to increase the resistance to material separation.

2 PROBLEMS WITH TUNNELS IN JAPAN

Japan has approximately 11,000 road tunnels, 5,000 railway tunnels and 44 pumped storage power plants, over 4,700km hydro tunnels in Japan. Most railway tunnels were constructed in 1920-1990, and most road tunnels were constructed after 1960 as Figure 1.

The average age of railway tunnels is 66 years, and over 100 years are 12% of the total. Furthermore, many road tunnels reaching 30-50 years of in-service are increasing.

2.1 *Increased maintenance due to aging road tunnels*

Road administrators in Japan have inspected and repaired underground structures including tunnels under their responsibility in accordance with the related laws and standards. However, their maintenance cost has been increasing as they are after construction.

*Corresponding author: nomura.mitsugu@ctii.co.jp

DOI: 10.1201/9781003495505-153

To improve this situation, institutionalization requires the development of long-term repair plans for all road assets as a maintenance management program based on appropriate asset management theory, and to ensure efficient budget execution.

On the other hand, many new road tunnels are being constructed to improve regional networks and reduce disaster risks. Efforts are required to reduce the future maintenance costs of these new road tunnels.

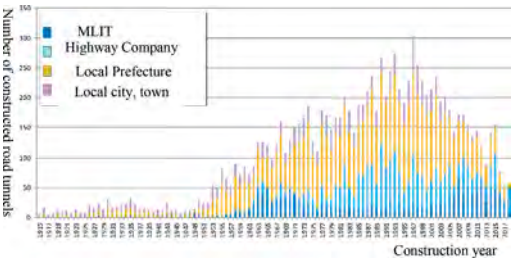

Figure 1. Number of constructed tunnels of road (MLIT annual report). MLIT; Ministry of Land, Infrastructure Transport and Tourism

2.2 *Initiatives in the infrastructure sector efforts toward carbon neutrality*

Japan's greenhouse gas (GHG) emissions from the infrastructure sector, including both direct and indirect emissions by the industry, account for about0.7% of total emissions. In contrast, GHG emissions from construction sites, including the supply chain for construction materials and construction-related cargo, account for about 10% of total emissions. Steel and cement emit a large amount of construction materials during production, and the cement industry accounts for 8% of the world's CO_2 emissions.

The tunnel is shotcrete and concrete lined, and the TBM makes extensive use of cement in the segments, so there is a strong need to reduce GHG emissions during the construction phase.

3 CHARACTERISTICS AND EXPECTED EFFECTS OF VOLCANIC GLASS POWDER

Concrete using industrial by-products such as coal ash (fly ash) and blast furnace slag powder has so far been put to practical use. In October 2020, the Japanese government announced the "2050 Carbon Neutral Declaration," setting a concrete goal to realize a decarbonized society and reduce greenhouse gas emissions to virtually zero by 2050. In line with this, the Japanese government has set a specific goal of achieving a decarbonized society and virtually eliminating greenhouse gas emissions by 2050. In line with this, the future of coal-fired power plants for a decarbonized society is still being determined globally and there is concern that there will not be a stable supply of those industrial by-products.

3.1 *Volcanic glass powder*

In Japan, a volcanic country, volcanic sediments (natural pozzolanic materials) are distributed and buried, and their utilization is expected, and JIS A6209 (Volcanic glass powder for concrete) was established in 2020. Regarding volcanic glass powder concrete, Tomoyose et al. studied the effects of powder degree and replacement ratio on strength development, and the proponents improving durability and strength properties.

After the volcanic ash is mined, it is crushed using a roll crusher, classified using a cyclone, and the particle size is adjusted to produce the product. Volcanic

Table 1. Basic properties of volcanic glass powder.

Item	Component(%)								Density (g/m³)	Specific surface area		Activity index	
	Silicon dioxide	Aluminum oxide	Magnesium oxide	Sulfur trioxide	Free calcium oxide	Chloride ion	Ignition loss	Moisture		BET method (cm²/g)	Blaine value (cm²/g)	7 days age	28 days age
Category Ⅰ (JIS)	70.0 or more	15.0 or less	5.0 or less	3.0 or less	1.0 or less	0.10 or less	4.0 or less	3.0 or less	2.25~2.40	80000 or more	-	100 ore more	105 or more
Category Ⅱ (JIS)										40000 or more		95 or more	100 or more
Category Ⅲ (JIS)										10000 or more		90 or more	95 or more
Fine powder A	71.2	12	0.4	0.11	0.1 or less	0.002	1.2	0.1	2.36	186020	6000	97	103
Fine powder B	70.5	12	0.4	0.26	0.1 or less	0.002	1.3	0.3	2.32	430310	14000	98	104

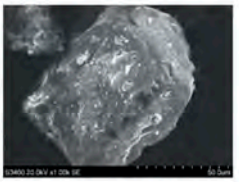

Volcanic glass fine powder A

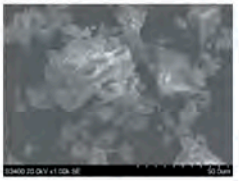

Volcanic glass fine powder B

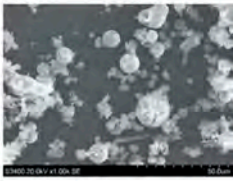

Classifying fly ash (Brain value 4400)

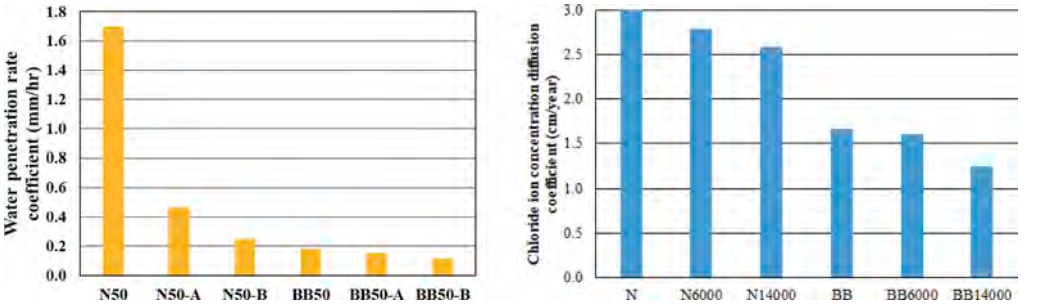

Figure 2. Surface penetration inhibition effect of volcanic glass powder.

glass powder with a large specific surface area has good reactivity and strength development. As for the use of volcanic sediments as construction materials, there have been several reports on the use of Shirasu from Kagoshima Prefecture and volcanic sediments from Hokkaido as concrete admixtures, but the advanced use and diffusion of volcanic sediments existing in various regions of Japan are still far from progressing.

3.2 *Basic properties of volcanic glass powder*

First, it is necessary to understand that volcanic glass powder is derived from volcanoes near the mining area, and that its properties and characteristics vary depending on the place of origin. This study uses commercialized volcanic glass powder from Fukushima Prefecture, Japan.

Two types of BET specific surface areas, 186 020 cm^2/g and 430 310 cm^2/g, which are equivalent to JIS Category I as Table I, are available for this product. The strength and durability of both types were checked to determine the difference in effect due to the difference in specific surface area.

Araki et al. shows Figures 2 as the results of the water penetration test for the N-50 and BB-formulations and shows the moisture penetration rate coefficients obtained from the moisture penetration tests.

The addition of volcanic glass powder suppressed moisture penetration in both the N and BB formulations.

The comparison of moisture penetration rate coefficients shows that N50-B suppresses moisture penetration more than N50-A. This indicates the pozzolanic reaction of the volcanic glass powder formed the dense microstructure.

Here, the durability of lining concrete, which is not a load-bearing structure, is discussed. Deterioration of reinforced concrete is generally understood to be corrosion of the reinforcing steel or loss of integrity with the concrete as neutralization progresses from the surface due to water or gas penetration and reaches the reinforcing steel.

Although there is some evidence that the development of neutralization does not affect the strength of concrete, the risk of debonding should be increased because the material bond in the concrete is considered to have decreased. Based on this hypothesis, suppressing surface penetration of water and gases in unreinforced concrete lining should improve durability and a longer service life.

Table 2. Efficiency of volcanic glass powder.

Item	Physical properties confirmed
Bleeding test	In the case of ordinary Portland cement blends, the amount of bleeding in concrete with volcanic glass powder is about half that without, regardless of the difference in BET specific surface area.
Compression strength test	An increase in strength was observed from the 7days curing compared to the no-additive blend.
surface permeability test	Torrent's proposed method and criteria were used to evaluate the denseness of the concrete surface layer. The permeability of the concrete specimens was evaluated using a five-level grading system, and no data corresponding to the "extremely poor" and "poor" categories were identified. This indicates that the addition of volcanic glass powder reduces the air permeability and increases the denseness of the concrete.
moisture penetration test	The addition of volcanic glass powder suppressed water penetration, and the effect of suppression of water penetration was remarkable in the N blend.
Salt barrier test	The effect of the addition of volcanic glass powder was confirmed, and the effect was remarkable.

The results of bleeding tests were also improved by mixing the volcanic glass powder, and it was considered that the concrete placing method to tunnel arches suppressed quality deterioration due to material separation.

3.3 *Example of application of volcanic glass powder*

Since volcanic glass powder has already been commercialized as a concrete admixture, the types of structures used here will be summarized.

3.3.1 *Design architecture and water pool*

In Japan, design architecture that makes the most of the texture of materials is widespread, and concrete is often used as a finish. Volcanic glass powder has been used for more than 20 years because it improves the workability of fresh concrete, resulting in a beautiful finish without uneven colour. Currently, most of the volcanic glass powder commercialized in Japan is consumed in this field.

Its use in the water pool has been empirically used to improve the waterproofing quality of the frame before waterproofing coating is applied by taking advantage of the reduced permeability of the cast-in-place concrete.

Figure 3. Application examples for public buildings.

3.3.2 *Port structures and structures subject to salt damage*

Concrete structures that are washed by salty seawater or exposed to flying salt accelerate neutralization and are prone to deterioration from the surface. Concrete structures placed in the sea have no coating or other means to block salt penetration, so volcanic glass powder, which is dense and highly effective in inhibiting salt penetration, is often mixed into the concrete.

In the case of the Abashiri Port facility in Hokkaido, the use of volcanic glass powder in some parts of the facility was contrasted with the non-use case.

It was reported that after 30 years of construction, surface deterioration became apparent in the unused portions, but the dense surface quality was maintained in the portions where volcanic glass powder was applied.

Figure 4. Application examples for port structure and tide embankment.

3.3.3 *Tunnel lining and underground structures*

Tunnel linings are cast in arches using a blow-up method, which often causes filling problems when using reinforced concrete structures, so volcanic glass powder is sometimes mixed in to ensure fluidity in the formwork and resistance to material separation.

In addition, when a tunnel lining is planned with a water-tight structure to prevent groundwater infiltration after completion, volcanic glass powder is sometimes mixed as an elemental structure of the water barrier to improve water penetration resistance.

In addition, there are other cases of application to concrete segments of TBMs. Concrete segments are subjected to uneven pressure during assembly and excavation, which can cause cracks and chips in the concrete. In addition, the influence of neighboring structures may cause new stresses in the segment structure after completion. Particularly in road projects, TBMs with large cross-sections are often installed in parallel, and the concrete segments of the preceding TBM are subjected to partial stress overload due to the proximity of the following TBM, which can cause cracking and other problems. Volcanic glass powder may be mixed into the concrete to densify the material voids in the concrete and prevent cracking.

Figure 5. Application examples for tunnel structure, waterproof section.

Figure 6. Application examples for tunnel structure, RC concrete entrance.

Figure 7. Concrete segment for road tunnel TBM.

4 APPLICABILITY TEST OF VOLCANIC GLASS POWDER TO TUNNEL LINING CONCRETE

Nomura et al. studied the terms of the performance requirements for road tunnels, it has been determined that the concrete lining should not cause damage to users due to scouring or spalling, that it should minimize user disturbance due to repair or inspection restrictions, that is, it should resist deterioration, and that there should be no leakage or cracking that would cause discomfort or uneasiness to users. It is also desirable that there be no leakage or cracking that would cause discomfort or uneasiness to users, and that there be no large repair scars or other damage inside the tunnel.

To improve the durability of lining concrete, it is necessary to improve the homogeneity of the concrete at the casting stage to prevent defects at the gable end, which is considered to be one of the causes of scour and spalling, and to improve the surface quality to prevent deterioration factors from penetrating the surface of the concrete. The surface quality of the concrete should be improved to prevent deterioration factors from penetrating through the surface of the concrete.

Therefore, in this study, we confirmed the existence of the hypothesized damage condition at the edge of the lining and confirmed the improvement effect of the homogeneity and surface property of concrete using volcanic glass powder by simulation tests using a mock-up formwork and construction tests in an actual tunnel.

4.1 *Potential defects in lining concrete*

When tunnel lining concrete is soundly inspected, anomalies such as a muddy sound can be detected when the concrete seems to sound visually on the surface but has latent structural defects such as swelling or internal cracks.

In this study, based on past inspection records and field investigations, we attempted to identify areas where deformation had occurred in the gable ends of road tunnels that were no longer in service, and to remove concrete from the deformed areas to observe potential defects.

4.1.1 *Sampling test results*

The sampling was conducted at a section where there was no evidence of deformation due to external forces and little leakage. In this span, longitudinal cracks of 0.4 mm to 0.6 mm and several transverse cracks were observed, as shown in Figure 8, which were probably caused by drying shrinkage. No surface cracks were observed at the sampling points.

As shown in Figure 9, the deformation is characterized by shallow layered internal cracks at 2 cm to 5 cm in depth. The crack edges have not reached the surface and have barely fallen off. The reasons for the occurrence of such cracks include tension caused by the adhesion of gable and lap formwork during resetting, and compression caused by formwork torsion due to uneven jacking down. In addition, the authors believe that because concrete flows and is cast in the gable end far from the concrete spout, the concrete becomes brittle due to material separation. If insufficient compaction occurs, this may lead to cracking on the surface and interior due to age-related deterioration.

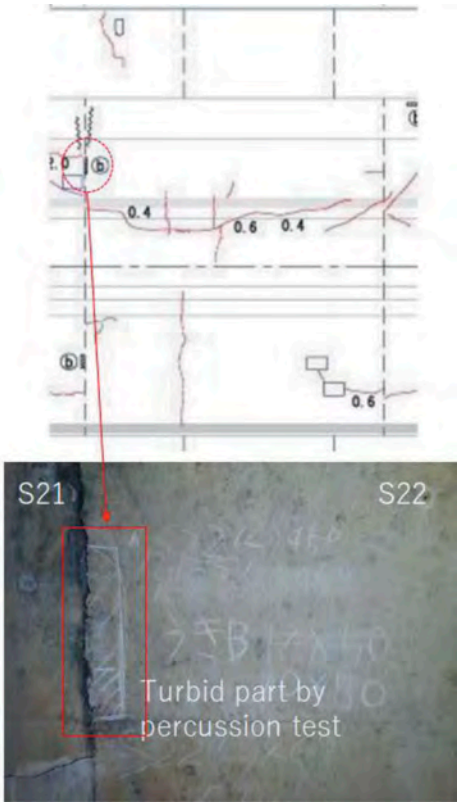

Figure 8. Condition of sampling test point.

4.1.2 *Homogeneity degradation due to concrete placement method*

Since the 1970s, the standard method of lining road tunnels has been to press-fit concrete into the arch crown using a concrete pump at one spout per span. With this method, it is possible to compact the concrete up to the shoulder section by using a vibrator

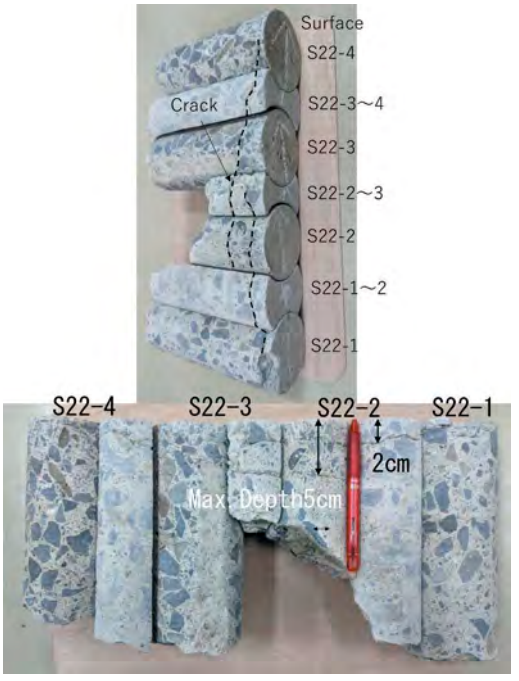

Figure 9. Damage condition of the turbinate by percussion inspection.

through an inspection window installed in the slide centre. However, compacting the arch crown section was difficult because the concrete had to be left to flow and fill up to the gable section. Although improved compaction methods such as formwork vibrators and pull-out vibrators are used nowadays, the method of placing arch crowns has not essentially changed.

Figure 10 shows the construction status of the gable end of the sidewall. The cement paste and bleeding water that have separated from the material can be observed, and the same phenomenon is thought to be occurring at the arch crown where the compaction status cannot be confirmed.

Figure 11 shows the construction status of the gable end of the sidewall. The cement paste and bleeding water that have separated from the material can be observed, and the same phenomenon is thought to be occurring at the arch crown where the compaction status cannot be confirmed.

Therefore, it is possible that coarse aggregate does not reach the gable end far from the casting entrance due to material separation, that the quality of the concrete may not be ensured, and that the bleeding water may not be discharged sufficiently. Although concrete is placed continuously, placement interruptions will inevitably occur due to the changeover of concrete mixer trucks and piping setups. In such cases, the rod vibrator cannot be used to compact the area where the placing is resumed, which may result in a layered boundary surface. Although those in charge of construction have long recognized this problem, there have been few cases in which actual tunnels have been sampled and verified. In this study, core samples were obtained from the shoulders, and observations focused on the distribution of coarse aggregate.

Figure 10. Situation inside the tunnel centre during placement of concrete for tunnel lining.

Figures 11 shows observations focusing on the coarse aggregate distribution of cores taken from the area sampled in this tunnel (span number S5) and from an area within the same span that was determined to be sound by scrutiny and sounding. The coarse aggregate density in the gable end was lower than that in the centre of the span, confirming that material separation had occurred during concrete placement, as observed by the core appearance.

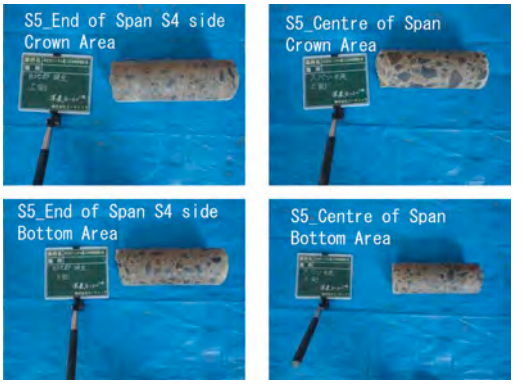

Figure 11. Core condition of end of span area and centre area.

4.2 *Simulated construction test*

In order to determine the mix design of concrete to be used for the construction test, test mixing was conducted on actual equipment and a simulated construction test was conducted using a mock-up formwork. The reason for observing changes in fresh performance over time here is that Tomoyose et al.

reported that the addition of volcanic glass fine powder, which has a large specific surface area after pulverization, to concrete can significantly reduce mortar flow.

4.2.1 *Factory slump test*

Figure 12 shows the change over time of the slump test (JIS A1101:2020) after 45 minutes and 90 minutes of mixing of the determined formulation in the actual test mixing. The slump volume, which was 23 cm immediately after mixing, became 20 cm at 45 minutes and 16 cm at 90 minutes after the slump test. Since it was confirmed that the amount of slump decreased in a relatively short time, it was decided to confirm whether workability could be ensured in the execution by a flowability test using a mock-up formwork.

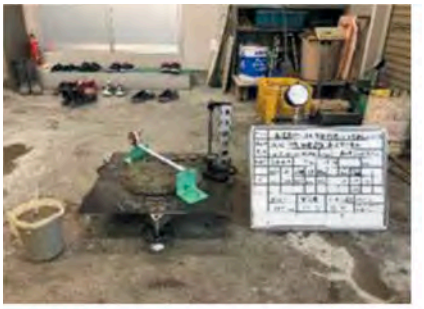

a) 23 cm immediately after mixing

b) 20 cm 45 minutes after mixing

c) 16 cm 90 minutes after mixing

Figure 12. Factory slump test (JIS A1101:2020).

4.2.2 *Flowability test*

Figure 13 shows the dimensions and structure of the mock-up formwork. The front surface is an acrylic panel to observe concrete flow, and the pipe length for concrete pumping is 30 m, the same as that in the tunnel pit. The method of placing the concrete into the formwork was free-fall from a height of 1.5 m above the edge of the formwork.

First, pumping was interrupted when concrete was placed to a height of 1.0 m at the placement position, and the flow condition was recorded. Then, a rod vibrator was inserted at 1.5 m intervals for 10 s to compact the concrete, and the flow was recorded. The same procedure was repeated every 50 cm, and the top edge was finished and cured at the end.

Figure 13. Flowability test (Field).

4.3 *Practice tests*

After evaluation of the simulated test, it was determined that there were no problems with flowability in the formwork and material separation resistance. The test was conducted as part of the normal construction process, and except for a change in the concrete, the construction was carried out as usual.

4.3.1 *Applicable formulations for implementation testing*

(1) 24-15-40N in Table 3 is the mix used in the specifications at the time of ordering the lining concrete for the subject works (σ28=18N/mm^2 or more, minimum unit cement content 270kg/m^3). (2) 27-18-20N is the current mix used by the contractor for the actual lining to improve workability and surface quality. (3) 27-18-20N (VGP) is an improved mix with volcanic glass powder. The volcanic glass powder used in Formulation (3) is Type B (BET specific surface area: 430 310 cm^2/g) as shown in Table 1 as a result of laboratory test mixing as described.

4.3.2 *Placing of concrete*

Concrete was placed using a concrete pump with a pipe length of L=30 m, as in the case of placing concrete for a normal span. Practice tests were conducted for three spans using the 27-18-20N (VGP) mix (3), and no problems were observed in any of them.

In parallel with the concrete placement, concrete flowing through the arch at the end was sampled to confirm the amount of coarse aggregate by quantitative sampling, and it was confirmed that the coarse aggregate was sufficiently transported to the gable end in the construction test.

Table 3. Applicable formulations of volcanic glass powder concrete for lining.

	B					
	W/B (%)	s/a (%)	C	VGP	1) AE water reducer	2)AE water reducer
(1)24-15-40N	56.7	47.5	279		2.79	
(2)27-18-20N	53.6	50.4	327		3.27	
(3)27-18-20N(VGP)	53.6	51.9	312	15		5.89

C: Ordinary Portland cement, VGP: Volcanic glass powder (density 2.30 g/cm3, Blaine specific surface area 14000 cm^2/g)
1) AE water reducer(Standard), 2)AE water reducer(High performance)

Figure 14. Practice test (construction site).

4.4 *Surface quality of lining concrete after improvement*

4.4.1 *Evaluation of surface quality*

The surface quality was evaluated approximately two months after construction. Surface water absorption tests were conducted using the SWAT (Surface Water Absorption Test) method at the three locations shown in Figure 15 on the existing concrete side.

The average values of three tests conducted using (3) were collected and compared with (2) on Figure 16.

In both formulations, the surface water absorption rate coefficient was considered good at some of the gable ends, but all other areas were evaluated as general.

In the case of (2), the surface water absorption coefficient tended to be higher on the existing side, while in (3), the coefficient tended to be higher in the gable section.

Figure 17 shows the surface air permeability at each measurement point as a result of the surface air permeability test. In this test, the results showed that (2) was evaluated as inferior and (3) was evaluated as general, and that the addition of the volcanic glass powder slightly improved the results.

Figure 15. Location of surface water absorption test and surface air permeability measurement.

4.4.2 *Quality surface water absorption speed*

Surface water absorption tests were conducted using the SWAT method. The test result of (2), which does not include volcanic glass powder, is poor at the Joint and tends to improve toward the End of Span, while the test result of (3) is stable throughout the entire Span length. In particular, it is important to note that the surface quality of the Shoulder, which is prone to problems, is stable.

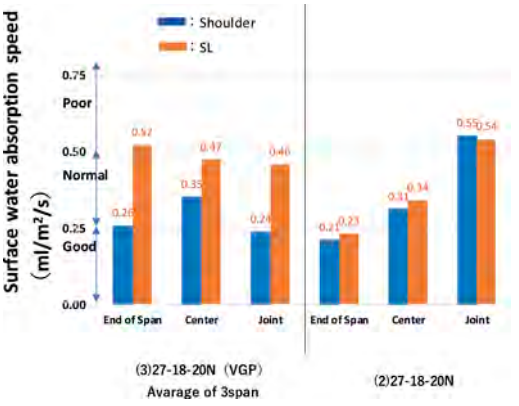

Figure 16. Surface water absorption test results (SWAT test).

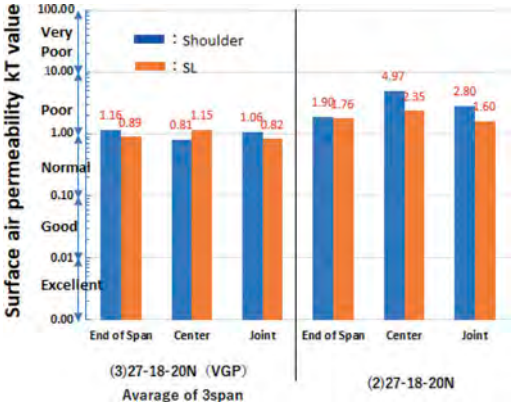

Figure 17. Surface air permeability test results (TORRENT test).

4.4.3 *Surface air permeability*

Surface air permeability tests were conducted using the TORRENT Test Method. The TORRENT Test is considered to represent the resistance to carbon dioxide gas infiltration from the concrete surface, and therefore, (3) is considered to be the most effective method for improving the surface quality of concrete. (3) may also increase the long-term resistance to neutralization compared to (2).

5 CONCLUSION

The effects of adding fine powder materials on concrete to improve workability and durability have been known, but it was confirmed that similar effects can be expected for volcanic glass powder and that it can be applied to tunnel lining concrete.

The addition of volcanic glass powder to the concrete lining increased the resistance to material separation and, with sufficient curing, contributed to the improvement of surface quality such as densification. In the mock-up construction tests, the addition of volcanic glass powder to the concrete lining increased the resistance to material separation and, with sufficient curing, contributed to the improvement of surface quality such as densification. In addition, in the execution test, it was confirmed that the coarse aggregate could be transported to the gable end and the homogeneity of the concrete was improved.

REFERENCES

Araki. T, Nomura. M et al., 2022 The strength and durability of concrete with the addition of volcanic glass fine powder, Proceedings of the Japan Concrete Institute, Vol. 44, No.1.

Hayashi. K., Hosoda. A., 2013 Fundamental Study on Evaluation Method of Covercrete Quality of Concrete Structures by Surface Water Absorption Test, Japanese Journal of JSCE, E2, Vol.69, No.1, pp.82–97.Ministry of Land, Infrastructure, Transport and Tourism Tohoku Regional Development Bureau, 2021 Guide for ensuring the quality of concrete structures (draft) (for tunnel lining concrete).

Nomura. M, Tomoto. S et al., 2016 Research of tunnel append-age conservation monitoring system with mems technology, Tunnel Engineering of the Japan Society of Civil Engineers, Vol.71, No.3, p.l_63-l_79.

Shiina.T, Sato.K et al., 2012 Effects of concrete casting methods on the quality and fill ability of tunnel lining, The construction technology research of The Japan Society of Civil Engineers, pp.7–14.

Saito.T, Meguro.M et al., 2020 Effect of construction factors on surface deterioration of the crown of lining concrete, Tunnel Engineering of the Japan Society of Civil Engineers, Vol.76, No.1, pp.99–111.

Tomoyose.A, Noguchi.T et al., 2018 A basic property and influence on fluidity of volcanic glass powder and clay friction, Cement Science and Concrete Technology, Vol.72, No.1, pp.438–445.

Torrent.R.T 1992 A two-chamber vacuum call for measuring the coefficient of permeability to air of the concrete cover on site, Material and Structures, 25, pp.358–365.

Ueda.H, Matsuda.Y et al., 2004 Deterioration of tunnel lining concrete, Proceedings of the Japan Concrete Institute, Vol.26, No.1, pp.759–764.

Tunnelling for a Better Life – Yan, Celestino, Thewes & Eberhardt (Eds)
© 2024 The Author(s), ISBN 978-1-032-80042-4
Open Access: www.taylorfrancis.com, CC BY-NC-ND 4.0 license

Achieving high load-bearing capacity linings in sprayed concrete and segmental linings with high-performance steel fibres

David Oliveira*
Aurecon, Brisbane, Australia
University of Wollongong, Wollongong, Australia

ABSTRACT: The design of fibre-reinforced concrete structures must follow the design principles concerning limit state similar to those adopted for conventionally reinforced concrete. However, the use of linear elastic analysis or conventional yield line theory may, in many cases, underestimate the benefits of the fibres to provide greater load-bearing capacity, particularly when high-performance steel fibres are adopted. This paper will present two case studies of real tunnel projects where the use of non-linear modelling of steel fibre-reinforced concrete elements coupled with physical testing provided significant benefits in the design and construction of tunnel lining. The first case focuses on the design of thin tunnelling linings using rock-bolted shotcrete linings. In this case, the non-linear modelling coupled with full-scale field tests demonstrated load-bearing capacities up to 3-5x greater than conventional design methods. The second case presents the design of a segment lining and the effects of fibre reinforcement on longitudinal joints' bursting and splitting capacity under rotation. In this case, non-linear modelling coupled with laboratory testing on large-scale segment joint samples demonstrated that conventional reinforcement would be unnecessary, whereas analysis with linear-elastic theory indicated otherwise..

Keywords: high capacity fibre reinforcement, sprayed concrete lining, TBM segments, non-linear stress

1 INTRODUCTION

Concrete is a material that is strong in compression but weak in tension and with a brittle behaviour under typical unconfined applications. As a result, steel reinforcement bars are traditionally used to enhance these two weaknesses by carrying the tensile forces after the concrete has cracked in structural applications, consequently providing ductility to the system. In conventionally reinforced concrete, the tensile strain of the concrete at cracking is much lower than the yield strain of the steel bars, which results in concrete cracking before any significant load is transferred to the steel. As a result, steel reinforcement also needs to limit the crack widths under specified levels for serviceability and aesthetic purposes but, most importantly, durability.

The use of fibres in concrete aims to achieve the same principles, i.e. to provide post-crack tensile and flexural capacity and crack-width control. However, unlike reinforcing bars, fibres are distributed in the volume of concrete. Hence, the distance between fibres is much smaller than the spacing between conventional bars, and the result is no longer a system with two materials but one composite material. Such understanding is essential as it has implications for design. Conventional design methods of reinforced concrete may not always capture the full benefits of fibre-reinforced concrete (FRC), as will be discussed in this paper.

A key advantage of using FRC is reducing construction time compared to the traditional single or double layers of conventional reinforcing bars or welded wire mesh. Heavy construction equipment for lifting and placing reinforcing bar cages is eliminated since the FRC can be directly pumped or sprayed. As a result, large-scale tunnel projects may save several weeks. Jobsite simplifications also improve safety as reducing labour-intensive tasks reduces the personnel involved and their exposure to working at heights.

However, due to concrete workability requirements whilst fresh and adequate distribution of fibres during mixing, it is vital to understand that there are practical limits to the amount of steel that can be included in a concrete mix. Therefore, the structural capacity is unlikely the same as that achieved with

*Corresponding author: david.a.oliveira@aurecongroup.com

DOI: 10.1201/9781003495505-154

conventionally reinforced concrete. In contrast to the capacity limit, contractors and designers are always looking for savings associated with member sizes (thickness of linings), thus concrete volume, which higher capacities can facilitate. Reduced concrete volumes will also directly impact formwork costs of cast-in-situ linings, time of concreting and cost and risks associated with transporting TBM segments.

Therefore, reducing tunnel lining thicknesses provides significant cost-savings and sustainability benefits, and to meet the market demands, suppliers have developed high-performance fibres engineered to achieve higher strength, stiffness, and heat or chemical resistance in particular applications.

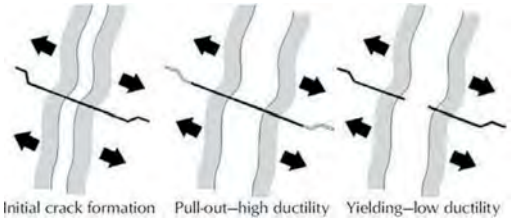

Figure 1. Example of figure and figure caption.

High-performance fibres aim to address two fibre-reinforcement mechanisms: fibre pull-out and fibre yielding/rupture (Figure 1). A good fibre-concrete bond is essential for developing post-cracking tensile capacity across the crack. High ductility FRC is obtained when fibres are pulled out across cracks in a controlled manner without significant yield or rupture.

However, it is essential to understand the difference between ductility and toughness. Ductility is the ability of the material to develop relatively large deformations before rupturing. Conversely, toughness is the material's resistance to these large deformations, which combines ductility and capacity. In most design cases, high toughness is the target, and the fibre yield capacity must be compatible with the pull-out capacity to achieve high toughness. For this reason, developing high-performance fibres involves improvements in both pull-out and yield strength.

Figure 2 presents two examples of steel fibres used in shotcrete applications in Australia. The left-hand side is a traditional end-hooked steel fibre commonly used in tunnelling applications. The right-hand side is a high-performance version with "double" end hooks for better development of strength, particularly at low deformation and smaller crack widths (≤ 0.5 mm). As seen, the improvement in pull-out capacity is followed by an increase in tensile strength from 1345 MPa to 1850 MPa. The high-performance steel fibre presented in Figure 2 is an improvement of an older but similar double-end hooked fibre version of the same supplier with a different aspect ratio and length (Dramix 4D 65/60BG). An increase in tensile strength from 1500 MPa to 1850 MPa was necessary to reduce the yielding of the fibres and achieve higher "toughness" values at crack widths exceeding 3 mm, i.e. at ultimate limit state, and when the smaller diameter version (65/35) was used with concretes with average compressive strengths, fcm, greater than 50 MPa.

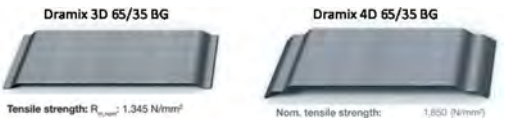

Figure 2. Examples of end-hooked steel fibres: (a) more traditional fibre on the left-hand side; (b) high-performance "double-end-hooked" fibre on the right-hand side.

With high-capacity steel fibres in the market, there is a natural desire to take advantage of their availability in design by potentially reducing tunnel lining thickness or replacing conventional steel bar reinforcement where possible due to the abovementioned advantages. Such a design reduces construction costs and can provide more sustainable solutions with a lower carbon footprint by reducing the volume of concrete used and the quantity of steel.

This paper presents two case studies of tunnel projects in Australia where high-performance steel fibres were adopted in design and verified by testing with significant project benefits. The first case refers to a shotcrete application, whilst the second is a precast segmental lining design.

2 SPRAYED CONCRETE APPLICATION

At the start of construction of the Westconnex motorway project in Sydney, the New M4 and M8 tunnels included in their shotcrete specification an intention to achieve a high-performance Fibre-Reinforced Shotcrete (FRS). This intention was expressed via the specification of relatively high design values for residual flexural strengths at SLS and ULS, respectively, fr1 = 3.5 MPa and fr4 = 3.0MPa following BS 14651. These values could be considered relatively common practice in cast-in-situ applications at the time of construction of these projects using longer and larger diameter fibres but, to the author's knowledge, less common in sprayed concrete, i.e., shotcrete, where shorter fibres with smaller diameters are generally preferred due to workability.

These projects adopted the steel fibre shown on the left-hand side of Figure 2 in their mix design with a fibre count of 40-45 kg/m3 and a 40 MPa concrete strength. The performance during production indicated that the specified values of fr1 = 3.5 MPa and fr4 = 3.0 MPa were achieved only in terms of average values, i.e. not as 95% characteristic, and resulted in approximately 50% of non-conformances that had to be addressed via the project's NCR process.

The M4-M8 Link Tunnels were the next project to be constructed as part of the Westconnex motorway. Despite the unsuccessful previous attempt, this project took on the challenge of achieving the above high performance since the residual flexural strength values of the New M4 and M8 tunnels were incorporated into the project's Scope of Works and Technical Criteria (SWTC).

The design team then recommended using the high-performance fibre shown on the right-hand side of Figure 2 as the world's first shotcrete application with such fibres, which was taken forward by construction and procurement teams, resulting in a shotcrete mix design that performed as intended during construction, i.e. with characteristic values of fr1k = 3.5 MPa and fr4k = 3.0MPa and a minimal number of non-conformances. Following the successful mix design, the next question was: how to leverage such a high-performance steel fibre-reinforced shotcrete (SFRS) in tunnel lining design?

An investigation on how to push the boundaries of the flexural capacity of thin, rock-bolted shotcrete linings led the design team to consider compressive membrane action (CMA) in the structural performance of the tunnel linings. Non-linear stress analysis investigations during the detailed design stage provided confidence that such an approach could provide linings with a capacity many times greater than conventionally predicted in the past with either deterministic methods, such as Barret and Mccreath (1995) or yield line theory.

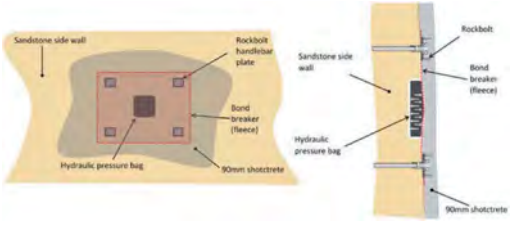

Figure 3. Schematic of large-scale field testing on shotcrete lining.

The design team proposed large-scale field tests of the as-constructed shotcrete linings with a 90 mm thickness to confirm such significant benefits following a verification assisted by testing (fib, 2013). A schematic of the test, using hydraulic bags to load the shotcrete lining to failure, is depicted in Figure 3, with some shown photos in Figure 4. Further details are presented in Bernard et al. (2022).

The test results are presented in Figure 5 against the predictions of a numerical back-analysis conducted after the tests. The back analysis followed the same methodology described in Bernard et al. (2022) but now has the actual rock bolt plate geometry embedded into the shotcrete, modelled as presented by Oliveira and Kozak (2021).

Figure 4. Photos of the large-scale field testing on shotcrete lining.

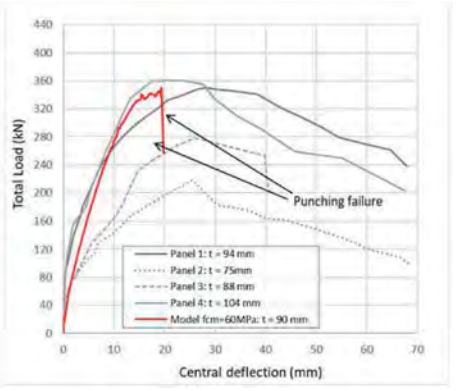

Figure 5. Large-scale field test results with numerical back-analysis.

All four test panels indicated load capacity approximately 4-5 times greater than that predicted by conventional methods used in previous projects, about 65 kN for a 90 mm thick lining. In addition, visual inspections of the failed panels during testing and the numerical back-analysis model confirmed that the capacity of the 90 mm thick lining was mainly limited by the pull-out capacity or punching shear failure of the rock bolts, as shown in Figure 6, also highlighted by the yielding of the handlebars. Once the four rockbolts plates forming the shotcrete panel failed (pulled out), the shotcrete lining would span further to the neighbouring rockbolts. As a result, the ductility seen in Figure 5 post-peak results from the enhanced flexural capacity provided by the high-performance steel fibres, tolerating the significant increase in the span for the lining panels. In contrast, the numerical back-analysis model shows a brittle failure upon rockbolt pull-out as the model only considers one-quarter of the geometry with planes of symmetry assumed at the four sides of the model, meaning that all neighbouring bolts also fail. Nevertheless, the numerical back-analysis confirmed that lining capacity was limited by the punching shear of the bolts rather than a flexural failure of the lining.

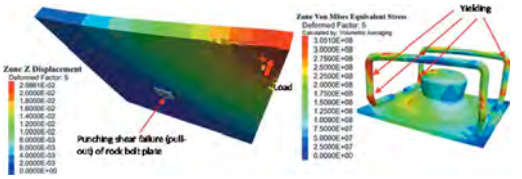

Figure 6. Numerical back-analysis of one-quarter of the panel.

The above application of high-performance steel fibres in shotcrete allowed a reduction of approximately 15% in tunnel lining thickness.

The second case study presented in this paper refers to the design of TBM segment joints for a metro project in Sydney, as discussed below.

3 BURSTING/SPLITTING CAPACITY FOR TBM SEGMENTS

The design action effects, essentially bending moments and axial forces, acting on segmental lining need to be transferred between segments in a ring via the performance of their joints, particularly the longitudinal or radial joints. These actions are transferred by simple compression, where the applicable eccentricity induces a joint rotation due to the bending moments acting in the segment bodies or any additional distortions from geometrical ring build imperfections.

The immediate failure mechanism associated with joint compression is a simple bearing crushing failure. However, this simple compression and its associated deformed shape generates tension at a certain depth.

The typical design of longitudinal joints often involves analysing the applicable elastic stresses acting in the potential bursting zone within the disturbed region (D-region) either with numerical analysis or based on an approximate solution proposed by Iyengar (1962). Suppose the maximum tensile stress in the D-region is estimated to be lower than the design splitting strength of the FRC segment, which is the peak tensile splitting strength reduced by a safety factor. In that case, the design is deemed satisfactory without further reinforcement requirements based on the assumption that the risk of cracking initiation parallel to the applied load is mitigated and that the fibre reinforcement controls any minor preexisting cracking. On the other hand, if the maximum tensile strength is exceeded, additional checks assuming the residual tensile strength of the FRC are required or that extra conventional bar reinforcement is added.

If the residual tensile capacity of the FRC is to be used in the design without bar reinforcement, analysis of joints with concentrated loads will often follow the classic strut-and-tie model proposed by Leonhardt and Mönnig (1973). The diffusion of transverse stresses is assumed to develop within the D-region, which is assumed to be limited to the segment thickness (h) or the effective thickness ('h-2e'). The tensile transverse stresses are uniformly distributed over a length of 0.8h, while compression is distributed along 0.2h, as depicted in Figure 7.

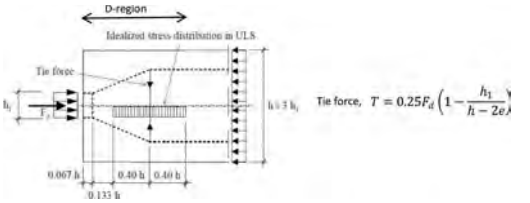

Figure 7. Strut and tie model to design partially loaded areas (DafStb, 2010).

Design analysis for a section of the Sydney Metro approaching depths of 90 m and with high groundwater pressures indicated that the longitudinal joints of the 260 mm thick segments (with a joint length of 130 mm) could experience axial forces of up to 4000 kN/m at ULS, i.e. already factored up, with an eccentricity of up to 30 mm (Figure 8) including geometrical ring build imperfections. This load can be applied as an equivalent rectangular stress block with a length of 50 mm.

Figure 8. Critical joint load case for segmental lining design.

A tie force T = 750 kN/m can be estimated based on the equation presented in Figure 8, taking Fd = 4000 kN/m, h_1 = 50 mm, h = 260 mm and e = 30 mm. The design capacity, R, to resist such tensile force is estimated by multiplying the tensile residual strength of the FRC over the length of 0.8(h-2e) and factored down by a typical reduction factor of 0.6. The design capacity was estimated as R = 151 kN/m based on a typical residual tensile strength of 1.575 Mpa for an associated fr_1 = 3.5 MPa for FRC mixes using the Dramix 4D 80/60 BG fibre (tensile strength of 1800 MPa).

The above-estimated design capacity is significantly below the design tie force, indicating a splitting failure that would, in principle, require extra bar reinforcement. However, there is a significant drawback in the assumption presented above. The assumed D-region is based on elastic solutions that ignore the beneficial effects of fibre reinforcement in allowing the development of crack propagation in a controlled manner, thus likely significantly increasing the depth of the D-region. As a result, the design team adopted the following steps to investigate the actual capacity of an FRC segment:

- Increase the residual tensile capacity of segments by using high-performance steel fibres. The

previously used Dramix 4D 80/60 BG fibre, with a tensile strength of 1800 MPa, was replaced by the newer Dramix 4D 80/60 BGP with a tensile strength of 2200 MPa. The concrete mix design targeted an fck = 66 MPa with fr1 > 4 MPa and fr4 > 4 MPa, achieved without any increase in fibre count compared to the previous fibre type.

- The design would be based on non-linear stress analysis to more accurately estimate crack propagation and strength development resulting from fibre reinforcement. It is important to note that the Model Code 2010 (fib, 2013), Sections 7.2.2.4.4 and 7.11, and the AS 5100.5, Section 2.3.6, recommend that the mean values of the material characteristics be considered in such analysis.
- The design would also follow the verification assisted by testing principles described in section 7.12 of the Model Code 2010 (fib, 2013) based on a combination with the non-linear model previously described. Verification assisted by testing is the procedure where loading tests on a limited series of representative specimens are used to determine the response of structural members or systems. The verification assisted by testing aims to obtain design values for the parameters governing the response of structural members and systems under specified load conditions for a certain limit state, in this case, splitting/bursting failure.

3.1 *Non-linear stress analysis*

A smeared crack constitutive model was adopted in the commercial software ATENA to model both the splitting and crushing of concrete. The plasticity model for crushing is based on the triaxial failure surface of Menetrey and Willam (1995).

The entire model can also be described with respect to the equivalent uniaxial stress-strain law as depicted in Figure 9a with the compression behaviour before the peak following the Model Code Clause 7.2.3.1.3 (fib, 2013).

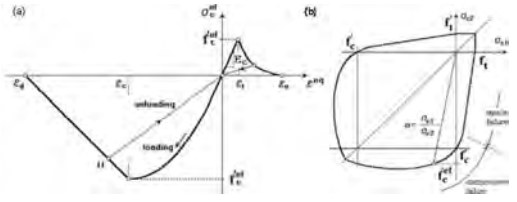

Figure 9. Concrete model: (a) Uniaxial stress-strain law (fib, 2013); (b) Biaxial failure function (after Kupfer, 1969).

The effects of biaxial enhancement are considered based on the relationship presented by Kupfer et al. (1969), illustrated in Figure 9b.

The above model was adjusted in the tensile zone to follow the constitutive tensile law proposed by the Model Code 2010 (fib, 2013), as shown in Figure 10.

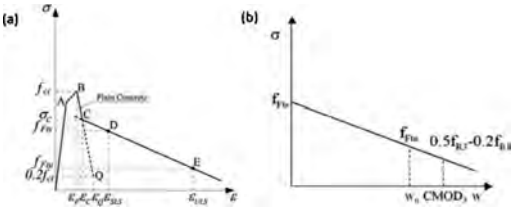

Figure 10. (a) Tensile constitutive law from Model Code 2010 (fib, 2013); (b) corresponding crack width definitions.

The mix design pre-production testing indicated a value of fcm = 75 MPa for the proposed fck = 66 MPa, also confirmed during production testing. The residual flexural tensile strengths previously discussed were converted to equivalent residual uniaxial tensile strength by the equivalent stress block factors of 0.45 and 0.37, respectively. The peak uniaxial tensile strength was adopted based on the targeted characteristic value estimated by equations provided by the Model Code 2010, resulting in a value of fctk = 3.2MPa, noting that this underestimates the actual tensile strength considering a specified tensile splitting strength of 5 MPa for the mix. The Young Modulus was adopted as E = 37800 MPa.

Two partial segments with 750 mm length each were modelled to represent the combined bending effects of the segments and the joint. The joint includes the guide rod pocket of 32 mm diameter and gasket and caulking grooves of 65 mm length each. Considering that the segment depth is 260 mm, the contact length left for the longitudinal joints is 130 mm, of which 32 mm is the guide rod diameter/pocket. Contact elements were used between the segments with applied zero bond, i.e. zero tensile strength.

To achieve failure, i.e. collapse, the load is applied at an eccentricity of 30 mm on one side of the model, employing an applied displacement that is incrementally increased to induce joint rotation.

Figure 11 presents the minor principal stresses, i.e. compressive stresses, developed at a joint rotation of 11.57 mrad. As observed, the stresses are distributed over the entire contact length on one side of the guide rod and approximately 15 mm on the other side, which, if converted to an equivalent uniformly distributed load, could be conservatively assumed to act only on one side of the rod, i.e. with a = 50 mm. The maximum crack width observed was approximately 0.6 mm with no signs of a wedge failure formation, i.e. punching shear of the stress block.

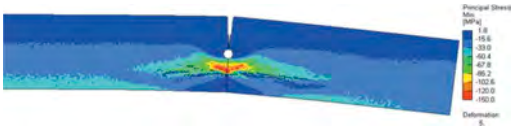

Figure 11. Minor principal stress (compression) distribution at peak capacity with a maximum observed crack width of approximately 0.5 mm.

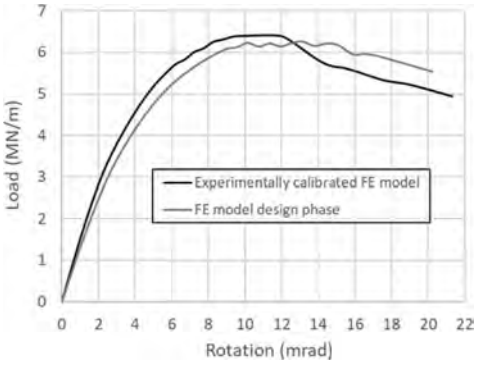

Figure 12. Model results for load-rotation performance.

Figure 12 shows the load rotation behaviour of the FRC joint with a peak resistance of approximately 6250 kN/m. A design resistance of 3810 kN/m is estimated if a reduction factor of 0.6 is applied to the predicted peak resistance. Considering that it is only approximately 6% lower than the ULS load, i.e. already factored up, this capacity can be deemed acceptable if verified by testing due to increased confidence in the predictions.

3.2 *Verification assisted by testing*

Three specimens representative of the segment joints were tested for failure under concentrated loads to verify the above predictions of bursting and splitting. The joint samples were square columns with 260 mm x 260 mm x 650 mm dimensions and cast with the same concrete mix design adopted for the segments. The top section of the columns was formed to have the same geometry as the segment longitudinal joints. The layout of the tests is depicted in Figure 13.

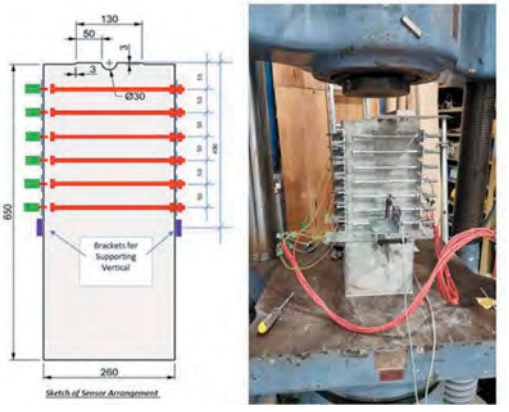

Figure 13. Testing configuration.

LVDT sensors were connected to one side of the samples and positioned against reference arms glued to the other side of the specimen (Figure 13 LHS) at several depths to monitor the lateral expansion and, consequently, the crack widths.

The specimens were loaded over the entire available joint area on one side of the guide rod, over a length of 50 mm (Figure 14). This configuration represents an eccentricity of 40 mm, which is more severe than the case previously discussed and, therefore, considered conservative for verification purposes.

Figure 14 presents the test results against a numerical back-analysis of the tests to calibrate the FRC parameters. Unfortunately, the compression machine used in the testing was not servo-displacement controlled, and, therefore, it could not capture the post-peak behaviour accurately, as the testing increments were based on loads and not displacement. Nevertheless, the most relevant phase of the tests up to peak resistance was adequately captured and could be used compared against model predictions. Post-peak performance could also be qualitatively assessed by comparing the cracking patterns observed in the samples and those observed in the numerical model (Figure 14 RHS).

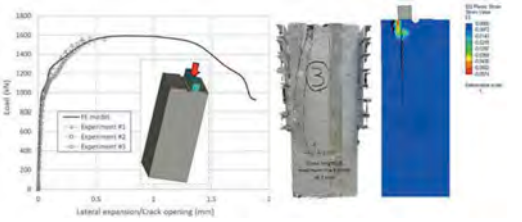

Figure 14. Experimental testing results versus numerical back-analysis: (LHS) load versus crack width curves; (RHS) comparison of cracking pattern between physical samples and numerical model.

As observed above, the back-analysis model represented the experimental results with a high degree of agreement regarding loads, crack widths and length. It should be noted, however, that the model stopped at a crack width of 1.9 mm while the tests had crack widths up to 7 mm. An important observation of the verification tests is the cracks' development length and, therefore, the D-region depth. In all tests, the average length corresponded to approximately 2 to 2.7 times the effective thickness of 180 mm (i.e. 260-2x40). This observation confirmed the previous hypotheses that a D-region limited to 0.8(h-2e) is over-conservative and cannot adequately capture the benefit of the fibres.

Based on the test results alone, it could be estimated that a 1 m joint length would provide an ultimate capacity of 1600 kN x 1000 mm/260 mm = 6150 kN/m. However, as highlighted above, these tests imposed a higher eccentricity and are therefore conservative as the joint experiences more significant rotations.

The material parameters adopted in the segment joint design analyses were recalibrated based on the

current numerical back-analysis results as a final design check. The analysis discussed in the previous section was then re-run. Figure 13 presented the experimentally recalibrated curve with marginally higher predicted capacity, i.e. 6350 kN/m instead of the previous 6250 kN/m, indicating a good quality Class-A prediction during the design phase.

Based on the above, enough confidence was gained with the non-linear analysis and verification assisted by testing to confirm that extra bar reinforcement was not required. This result provided reasonable savings in costs and carbon footprint and benefits to the pre-cast yard not having to deal with joint ladder reinforcement, thus slightly improving the casting program.

4 CONCLUSIONS

With high-performance steel fibres available in the market, there are significant opportunities for designers to provide cost-effective solutions by reducing tunnel lining thickness and/or replacing conventional steel bar reinforcement where possible. FRC solutions can reduce construction costs and provide more sustainable solutions due to a lower carbon footprint associated with the reduced volume of concrete and the quantity of steel. In addition, large-scale tunnel projects may save several weeks in their program by removing the tasks associated with lifting and placing reinforcement cages, as the FRC can be directly pumped or sprayed. Jobsite simplifications also improve safety as reducing labour-intensive tasks reduces the personnel involved and their exposure to working at heights.

However, conventional design methods may not always fully or adequately represent the behaviour of FRC, limiting the benefits of such a solution. Non-linear stress modelling coupled with verification assisted by testing via large-scale field tests or large-scale laboratory tests may provide a valuable method to understand the problems at hand better and achieve the desired cost-effective solutions, as illustrated by the two case studies presented in this paper.

ACKNOWLEDGMENTS

The author would like to acknowledge the contribution of a few organisations that participated in one form or another in the work presented here. Without their support, this work would not have existed. These organisations are the Acciona Buygues Samsung JV, the Accional Ferrovial JV and Mahaffey Testing.

REFERENCES

Barrett, S. V. L. and McCreath, D. R. (1995). Shotcrete Support Design in Blocky Ground: Towards a Deterministic Approach. Tunnelling and Underground Space Technology, Volume 10(1), pp. 79–89.

Bernard, E. S. (2008). Embrittlement of Fiber-Reinforced Shotcrete. Shotcrete, V. 10, No. 3, Summer 2008, pp. 16–21.

Bernard, E. S., Oliveira, D. A. F, Forrest, B. H. (2022). In situ flexural failure of unbonded fibre reinforced shotcrete linings in response to point loading. Tunnelling and Underground Space Technology 119 (2022) 104235.

DafStb (2010). DAfStb-Guideline—steel fibre reinforced concrete, pp. 48. Berlin, Germany (German version).

fib (2013). fib Model Code for Concrete Structures 2010. Lausanne.

fibHarding, A. (2022). Tunnel segmental lining design Course Notes. IngeOexpert. https://ingeoexpert.com/en/courses-online/tunnel-segmental-lining-design-course/

Iyengar, K. T. (1962). Two-Dimensional Theories of Anchorage Zone Stresses in Post-Tensioned Beams. ACI Journal Proceedings, V. 59, No. 10, Oct., pp. 1443–1466.

H. Kupfer, H. K. Hilsdorf and H. Rusch (1969). Behavior of Concrete under Biaxial Stresses. ACI Materials Journal, Vol. 66, pp. 656–666.

Leonhardt F, Mönnig E.(1973) Vorlesungen uber Massivbau. Casos Especiais de Dimensionamento de Estruturas de Concreto Armado - Volume 2 - Portuguese Brazilian Edition, Publisher: Interciência (1978).

Menetrey, P. & Willam, K.J. 1995. Triaxial Failure Criterion for Concrete and its Generalization. ACI Structural Journal. 1995;92:311–8

Oliveira D. and Kozak P., 2021. A Review of the Behaviour of Domed Rock Bolt Plates and their Use in Sydney Tunnelling". Australian Geomechanics 56 (3), pp 73–84.

Tunnelling for a Better Life – Yan, Celestino, Thewes & Eberhardt (Eds)
© 2024 The Author(s), ISBN 978-1-032-80042-4
Open Access: www.taylorfrancis.com, CC BY-NC-ND 4.0 license

EN 14488-3 notched panel versus EN 14651 notched beam testing for pre-construction trial conformance testing of Sprayed Concrete Linings (SCL)

Chris Peaston
Peaston Concrete Consultancy, Nottingham, UK

Benoit De Rivaz*
NV Bekaert SA, Zwevegem, Belgium

ABSTRACT: In 2011 EFNARC introduced a notched panel test as a potentially equivalent alternative to the EN 14651 notched beam method of deriving flexural strength parameters consistent with limit state design to fib MC 2010. In 2022 EN 14487 and EN 14488-5, the relevant European Standards for Sprayed Concrete, were updated to reference the alternate methodologies. This paper applies Analysis of Variance methods to the results of prior laboratory-based investigations of cast and sprayed concrete undertaken to support the equivalence the alternate methodologies. This shows statistically significant differences in the alternate flexural strength parameters, contrary to the prerequisite requirement for consistent MC2010 performance classification. Full-scale sprayed concrete pre-construction trials were conducted using three different Bekaert Dramix® steel fibres and a macro synthetic fibre in both a contemporary CEM I and a CEM IIIB basic mix, which is being developed for potential use on the UK's HS2 project and achieves an embodied carbon reduction of 60%. In notched panel tests the steel fibres achieved a minimum MC2010 2c performance classification with the macro synthetic fibre achieving 1c classification. In the case of the commonly used Dramix® 4D 65/35BG fibre, alternate notched panel and beam tests showed the anticipated higher beam f_L strengths to have a statistically significantly difference. Nonetheless residual flexural tensile strength parameters were statistically identical and led to consistent MC2020 ductility classification. In any event notched panel f_L determination is likely to be conservative and, given the less brittle failure, MC2010 crack control classification is likely to better represent the in-situ material performance. The improved consistency in a full-scale trial supports the adoption of the alternate notched panel methodology, confirms the potential to achieve the MC2010 3c performance classification with high performance steel fibres, and has the potential for more efficient fibre proportioning leading to further carbon savings.

Keywords: Fibre reinforced concrete, Residual flexural strength, Performance classification, Embodied carbon, Sustainability

1 INTRODUCTION

EN 14487-1:2022, the European Standard for sprayed concrete, prescribes differing ways of specifying and measuring the ductility of sprayed fibre reinforced concrete (SFRC). These include an EN 14488-5 energy absorption test, used in empirical design methodologies, and an EN 14488-3 flexural tensile strength test, in which residual strengths are determined using notched beam specimens in accordance with EN 14651 consistent with limit state design to fib MC 2010.

In 2011 EFNARC introduced a notched panel test, based on the EN 14488-5 energy absorption test specimen, as a geometrically analogous alternative to the EN 14651 notched beam methodology, thereby potentially providing equivalent residual flexural tensile strengths. It was suggested that the notched panel test had several advantages, including using a test specimen that better represents the material in the real structure, with potentially reduced variability. This is particularly relevant to sprayed concretes where the production of suitable test specimens otherwise typically involves sawing beams from a larger test panel.

In 2022 EN 14488-3 was updated to include a residual flexural tensile strength test based on the original EFNARC (2011) proposal and EN 14487-1 was amended to include reference to the alternate notched specimen methodologies for residual flexural tensile strength determination.

This paper reports the results of a series of spraying trials using combinations of two different basic

*Corresponding author: Benoit.DeRivaz@bekaert.com

DOI: 10.1201/9781003495505-155

mixes and four fibres in which notched panel and beam test derived flexural tensile strength parameters were compared to examine the equivalence of the alternate tests, consider the difference in their variability, and determine the consequences for pre-construction trial conformance.

SFRC for tunnelling works are typically CEM I rich mixes with consequent relatively high embodied carbon. The spraying trials were undertaken alongside an ongoing project successfully demonstrating the potential to deliver a sprayed concrete using a CEM IIIB cement (Goodier et al., 2022), with a 60% reduction in embodied carbon, and the opportunity was taken to spray a range of fibres in a typical contemporary CEM I and alternate CEM IIIB basic mixes.

2 BACKGROUND

The equivalence of the notched panel and beam methodologies was supported by investigations comparing the results of specimens cast from the same concrete in the respective standard tests, originally coordinated by Meda (2018), and published by De Rivaz et al. (2019). In this investigation a total of six different mixes was compared by considering the ratios of the limit of proportionality (LOP) strength (f_L) and the four residual flexural tensile strengths (f_{R1}, f_{R2}, f_{R3} and f_{R4}) determined using the alternate test methods. The means of the ratios of each parameter across the six mixes were found to be close to unity.

These observations were particularly valid for three of the six mixes using the same Bekaert "Dramix®" 4D 65/35BG fibre type and dosage, which at 25 kg/m^3 was said to be typical of a SFRC, with the typically higher values returned in the panel test being attributed to the larger fracture surface. A comparison of coefficients of variation (CoV) also showed that those for the panel tests were typically markedly lower. This led to the conclusion that the panel test appeared to be suitable for characterising SFRC.

Similar investigations comparing specimens prepared from individual sprayed concrete mixes have also been undertaken (Gagnon and Jolin, 2019). In this case the Dramix® 4D 65/35BG fibre type was used at dosages of 30 and 50 kg/m^3 in C30/37 and C50/60 strength basic mixes to give a total of four combinations of fibre and concrete mix type.

In-situ fibre contents were not determined, although a subsequent investigation (Darveau and Jolin, 2021) repeated the 30 kg/m^3 C50/60 combination in a nominally identical basic mix and measured the in-situ fibre content as 22.9 kg/m^3. This represents fibre losses of 24% and leads to a similar in-situ fibre content to the 25 kg/m^3 used in the previous investigation using cast fibre concretes. The Darveau and Jolin (2021) investigation confirmed that in cast and sprayed concretes with nominally identical in-situ fibre contents, SFRC performance is improved due to preferential fibre alignment.

A Gagnon and Jolin (2019) comparison of the ratios of the five individual flexural tensile strength parameters showed the panel test generally returning higher values than the beam test, consistent with the observations of the previous investigation on cast concretes, with ratios close to unity for f_L, highest at low crack widths and reducing with increasing crack width to near to unity at f_{R4}. A comparison of coefficients of variation once again showed typically lower variability in the panel test determined parameters.

These observations were also explained by the larger fracture surface, in combination with better load distribution across the fracture area, leading to the conclusion that the slightly higher strengths returned in the panel tests were not problematic and the test had the potential to be an appropriate alternative for the evaluation of SFRC.

In the knowledge of the investigations outlined above, the forthcoming amendments to the relevant European standards, and to encourage innovation with the potential for more efficient design, the first Author had previously written the alternate notched panel methodology into the construction specification for pre-construction trial qualification of sprayed concrete for the linings (SCL) in the southern section (S1/S2) of the UK's High Speed Two (HS2) project (HS2, 2020).

A prerequisite requirement of the HS2 S1/S2 SCL specification was an appropriate pre-construction trial correlation of notched panel with notched beam test parameters although, on closer examination, and despite the contemporaneous supporting evidence summarised above, the prior investigations lack the necessary equivalence to ensure the consistent application of MC2010 based FRC performance classification criteria when assessing conformance.

The present investigation started by applying analysis of variance (ANOVA) techniques, which compare the respective within group and inter group variance, to pairs of equivalent panel and beam test derived flexural tensile strength parameters in the prior Gagnon and Jolin (2019) investigation. There are five such parameters for each test and four combinations of basic mix and fibre type giving twenty pairs of data. Of these data pairs only eight, five of which came from the same mix, were found to come from the same populations with less than a 5% chance of an incorrect judgement.

In one of the four mixes none of the five pairs of flexural tensile strength data from the two notched test types were found to come from the same population and, while the "c" class performance for the ratio f_{R3k}/f_{R1k}, i.e. $0.9 < f_{R3k}/f_{R1k} < 1.1$, in which the "c" relates to the ductility of the FRC, was consistently achieved for both panels and beams from each of the four mixes, the MC2010 classification of FRC performance was only consistent between panels and beams in one instance.

In Figures 1 and 2 the results for the two mixes using a 30.0 kg/m^3 fibre dosage are respectively presented and show the mean values for each of the

flexural tensile strength parameters, along with standard deviation error bars, and their characteristic values calculated using a log normal distribution appropriate to EN 1990 procedures for an unknown population mean.

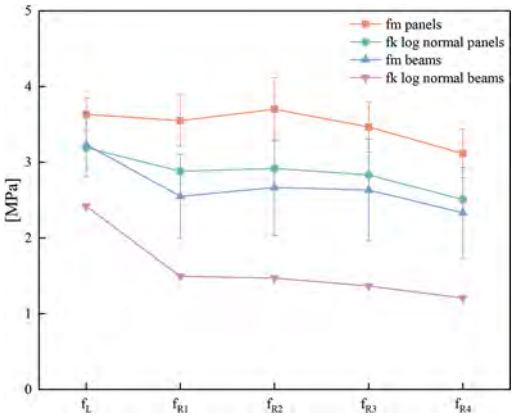

Figure 1. Gagnon And Jolin (2019) 30.0 kg/m^3 C30/37 mix beam and panel mean and characteristic flexural tensile strengths.

In the 30.0 kg/m^3 C30/37 mix (Figure 1) only the f_L values were demonstrated to come from the same population and performance classification in accordance with MC2010 was respectively 2.5c for panels and 1c for beams. The higher variability and relative brittleness in the beam failure is illustrated by the respective f_{R1k}/f_{Lk} values, which relate to crack control performance, of 0.90 and 0.62.

On the other hand, in the 30.0 kg/m^3 C50/60 mix (Figure 2) all five pairs of flexural tensile strength parameters were shown to come from the same respective populations and, in combination with the higher strength matrix, lead to a consistent 3c MC2010 classification. In this case the respective

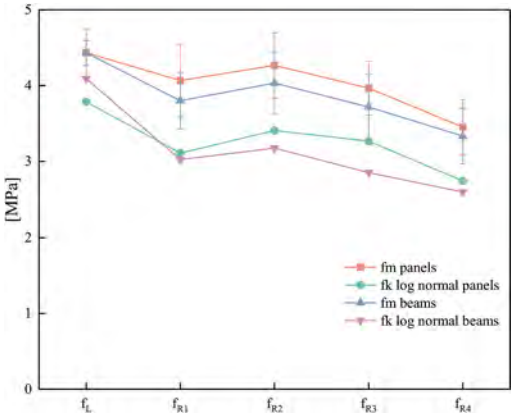

Figure 2. Gagnon And Jolin (2019) 30.0 kg/m^3 C50/60 mix beam and panel mean and characteristic flexural tensile strengths.

panel and beam f_{R1k}/f_{Lk} values were 0.82 and 0.74 and are much as might be anticipated with the beam test expected to yield higher f_L, given the smaller fracture surface, and panel test expected to yield higher residual flexural tensile strengths given the more even load distribution over a larger fracture surface.

Nonetheless the results for the 50.0 kg/m^3 fibre dosage, which might have been expected to give more similar performance given the typically more ductile failure at higher fibre dosage, were also inconsistent. Overall these results failed to achieve the prerequisite requirement that panel test results should lead to comparable or correlative MC2010, or indeed EN 14487-1(2022), performance classification as the equivalent beam tests and suggest, either that the assumption of equivalence is flawed, or that there was a significant difference in either the preparation and/or testing of the respective panel and beam test specimens in the proceeding work.

Against this background the opportunity was taken to conduct further trials using the two different basic mixes identified in Section 1 above and four fibre types, including the Dramix® 4D 65/35BG fibre which was the subject of the previous work, in the equivalent of a full-scale pre-construction trial.

3 SPRAYING TRIALS

The principal aim of the spraying trial was to obtain data for the notched panel test and for this reason 6 No. 600 mm x 600 mm by 100 mm non-absorbent plywood backed test sample panels were sprayed for each of the total of eight combinations of fibre type and basic mix.

The first of the two sprayed concrete mixes trialled was based on a contemporary liquid accelerated CEM I mix design and the second was based on a powder accelerated 70% ground granulated blast furnace slag (GGBS) mix (CEM IIIB) being developed for potential use on the HS2 project. Mix details are given in Table 1 and show that the mixes were nominally identical except for the cement type and admixture combination.

Table 1. CEM 1 and CEM IIIB mix designs.

	CEM I (kg/m^3)	CEM IIIB (kg/m^3)
CEM I	480	144
GGBS	0	336
4/10 aggregate	510	510
0/4 aggregate	1160	1160
Steel Fibres	40	40
Accelerator	38.4	33.6
Superplasticiser	4.50	3.50
Viscosity	1.0	1.50
Water	192	192

The spraying trials took place in the period April to June 2023 and were conducted at the premises of Shotcrete Services Ltd (SSL) in a purpose-built, although unheated, mock tunnel section. Sprayed concrete basic mix batching, including fibre addition, was undertaken at the adjacent third-party quality assurance accredited premises of SSL sister company Wealden Concrete. The batching and spraying work was therefore entirely under the control of one organisation.

The CEM I mixes were sprayed using a Meyco Suprema sprayed concrete pump with integral accelerating admixture dosing and an Oruga spraying manipulator. The CEM IIIB mixes were sprayed using a Turbosol TB30 sprayed concrete pump, powder accelerator dosing equipment and the same manipulator. Typically, 2 m^3 of material was batched for each trial, with fibres manually weighed and dosed directly into the truck mixer hopper.

Dramix® 4D 65/35BG, 3D 80/30BGP and 4D 90/50BG hooked end drawn wire steel fibres were sprayed at a dosage of 40 kg/m^3 along with a Synmix HP35 macro synthetic fibre at a dosage of 7 kg/m^3. In the case of each of the two mixes sprayed with the commonly used Dramix® 4D 65/35BG fibre, two additional test panels were sprayed. These were respectively 1200 mm x 1200 mm x 150 mm, from which notched beam specimens were cut to allow a comparison with the notched panel test data, and 1200 mm x 600 mm x 150 mm, from which cores were taken for compressive strength and in-situ fibre content determination. In these cases the basic mix was also sampled for cube compression testing and flow tests were conducted. All test panels were screeded flat to aid test specimen preparation.

Pumping delivery rates and accelerating admixture dosages were recorded, along with concrete basic mix and ambient temperatures. The hardened panels were covered in wet hessian, left to cure in the mock tunnel overnight and were either cored or rough sawn in the following days to produce the required test sample pieces.

Cube specimens were cured at the batch plant in accordance with standard quality procedures and the relevant panels were cored by SSL to produce the necessary core test sample pieces prior to shipping to Loughborough University where the compressive strength testing and fibre content determination work was conducted in its Civil Engineering laboratory. All core compression testing was undertaken at the university except for the 24 hr cores, which for logistical reasons were tested by an SSL appointed test house. The 1 and 3–day cores were tested in the as received condition with subsequent cores tested in the saturated condition.

The bending test sample panels were shipped to Bekaert's laboratory in Belgium where 28–day notched panel and beam testing, including the preparation of the specimens, was undertaken with the samples air cured in ambient laboratory conditions. 28–day sawn cube compression testing was also undertaken by Bekaert on samples of the two mixes sprayed with the Dramix® 4D 35/65BG fibre. These were cut from the notched beam test specimens immediately after testing.

4 STRENGTH DEVELOPMENT

The basic mix cubes were tested in groups of three at 7 and 28 days and returned respective means of 35.3 MPa and 34.9 MPa for the CEM I mix and 30.3 MPa and 35.7 MPa for the CEM IIIB mix.

The principal method of assessing the strength development of the sprayed material was by core compression testing in accordance with BS EN 12390-3. 6 No. cores were tested at 1, 3, 7 and 28 days, with 3 No. cores cut both parallel and perpendicular to the direction of spraying. In the case of the CEM IIIB mix it was not possible to test the 1-day cores and testing was delayed by several days.

All cores were ground to achieve the specified 1:1 length:diameter ratio and density tests were also undertaken in accordance with BS EN 12390-7. The 1 and 3-day densities were determined in the as-received condition, with all other cores being stored under water after receipt and prior to testing, and density determined in the saturated condition. Nonetheless the 3 and 7-day specimens were received at the laboratory just in time and the prior temperature control was not recorded. All core volumes were determined from the measured dimensions rather than by water displacement.

Apart from the CEM I mix 1-day strengths, there was little difference in the mean of the two subgroups of cores at each age. The statistical significance of the difference between the CEM I 1-day parallel and perpendicular cores was examined by ANOVA. This led to the conclusion that, with less than a 1% probability of being incorrect, the groups of core results came from different populations.

Nonetheless, by inspection confirmed by further ANOVA, there was no significant difference in the means of any of the other subgroups of cores at each age for either basic mix, which were therefore subsequently treated as belonging to the same populations. The data presented in the results below, is therefore based on a statistical analysis of all 6 No. cores tested at each age.

The 28-day sawn cube tests returned respective mean results of 31.3 MPa and 31.8 MPa for the CEM I and CEM IIIB mixes, corroborating the respective 28-day mean core strengths of 30.1 MPa and 33.1 MPa. In Figure 3 the core compression strength development with age is plotted and shows that the CEM IIIB core strength was consistently greater than the CEM I core strength with the 28-day cube strength consistent with the core strength in each case.

The compressive strengths were all lower than expected and the basic mix cubes failed to meet the anticipated C32/40 strength class suggesting that the concrete was of a slightly lower strength. There were

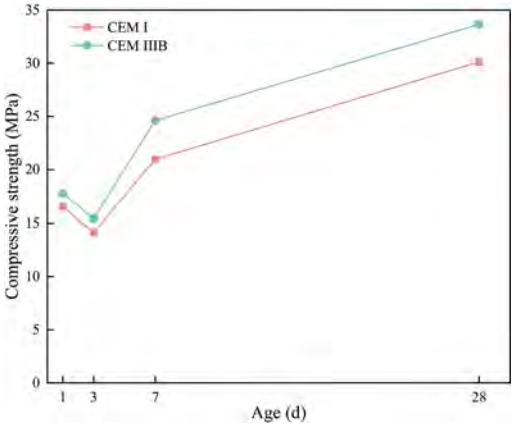

Figure 3. Core compressive strength development.

some anomalies in the 24-hour and 7–day strength development, which might be explained by the varying and uncontrolled curing regimes, although by 28–days the in-situ cores and cubes strengths were consistent albeit slightly lower than the base mix cube strengths.

5 FIBRE CONTENT AND REBOUND

Fibre contents were determined for all 6 No. cubes and 18 No. core specimens tested at Loughborough University from the Dramix® 4D 65/35BG fibre CEM I mix and from 3 No. cubes and 9 No. cores for the corresponding CEM IIIB mix. These returned respective mean values of 35.1 kg/m^3 and 24.4 kg/m^3 for the CEM I mix and 37.8 kg/m^3 and 22.4 kg/m^3 for the CEM IIIB mix. An ANOVA on the in-situ fibre content samples indicated a statistically significant difference in the in-situ fibre contents with a 5% chance of an incorrect judgement.

The basic mix cube fibre contents were a little lower than the 40 kg/m^3 dosage rate, which was attributed to the relatively small sample size and inevitable losses during the fibre extraction process. The in-situ fibre content determinations may be subject to similar errors, although indicate respective fibre rebound losses of up to 39% and 44%. These are high in comparison with the 24% determined in Section 2 from the Darveau and Jolin (2021) investigation and are at the high end of the range reported elsewhere (Kaufman et al., 2013), although led to broadly comparable in-situ fibre contents.

6 FLEXURAL TENSILE STRENGTH

Notched panel tests were conducted in groups of six from each of the eight mix combinations. The result of one test on a Dramix® 3D 80/30BGP fibre CEM I panel was discarded due to an unusual crack pattern. Seven notched beam test specimens were prepared from each of the relevant test panels for the two Dramix® 4D 65/35BG fibre mixes.

The mean, sample standard deviation and CoV were calculated for each group of test results. Characteristic values for flexural tensile strength parameters were also calculated using a log normal distribution and performance classified in accordance with MC2010 consistent with the treatment of the Darveau and Jolin (2021) data in Section 2. The mean and characteristic values for the CEM I and CEM IIIB mixes are respectively shown in Figures 4 - 7.

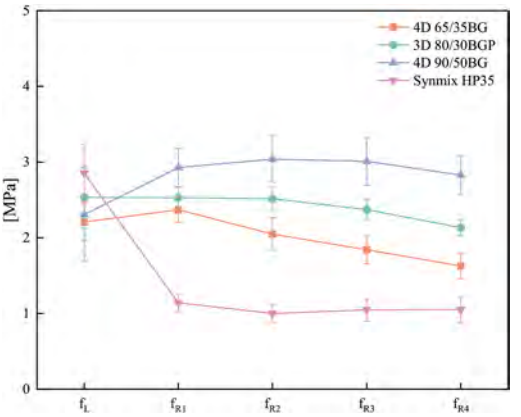

Figure 4. CEM I mix mean flexural tensile strengths.

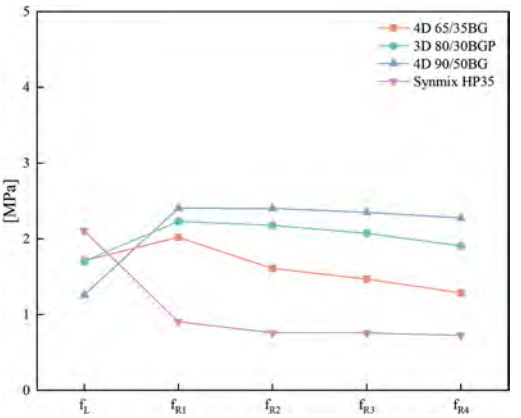

Figure 5. CEM I mix characteristic flexural tensile strengths.

For the notched panel tests this showed that all the Dramix® steel fibres used in this investigation achieved at least a minimum 2b performance class ($0.7 < f_{R3k}/f_{R1k} < 0.9$), and a minimum f_{R1k}/f_{Lk} value of 0.9.

In the CEM I mixes some of the better performing fibres achieved the 2c classification and, despite the statistically significant lower in-situ fibre content, in the slightly stronger CEM IIIB mixes, the Dramix® 3D 80/30BGP fibre achieved the 3c classification.

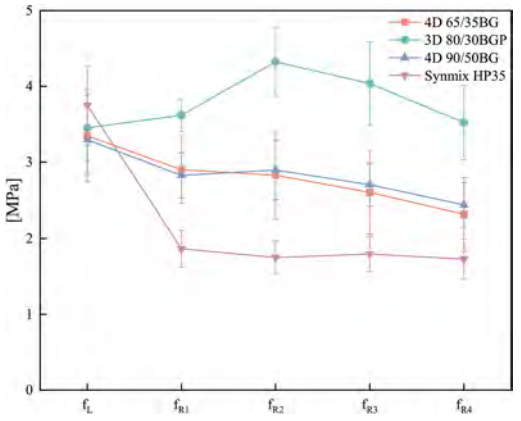

Figure 6. CEM IIIB mix mean flexural tensile strengths.

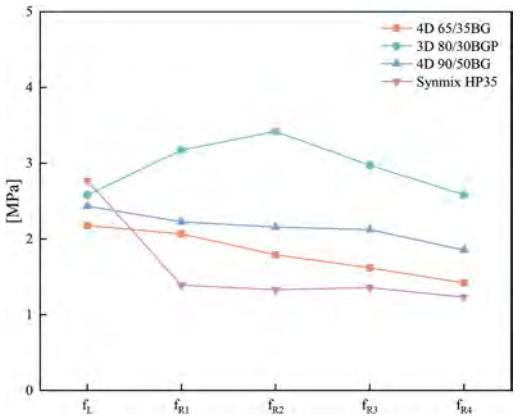

Figure 7. CEM IIIB mix characteristic flexural tensile strengths.

Steel fibre performance classified in this way, which accounts for the variability of individual groups of results, was therefore broadly similar in the two mixes.

In the CEM I series CoV for f_L were in the range 11 – 27% and were significantly higher than those for the residual flexural tensile strength parameters, which had a maximum value of 11%. In the CEM IIIB series the f_L CoV was in the range 13 – 18% and the variability of the residual strength parameters was typically greater than for the CEM I mixes, with CoVs in the range 6 - 21%.

The two macro synthetic fibre mixes had similar mean f_L and f_L variability to the steel fibres mixes in the respective basic mix series, which is as expected since the fibres have little effect on the matrix tensile cracking strength. Nonetheless a significantly more brittle failure is illustrated by the respective CEM I and CEM IIIB mix f_{L1k}/f_{Lk} values which were 0.43 and 0.5. The variability of the residual strengths was also comparable to that of the steel fibres mixes and the ductility ratio also respectively achieved the "b" and "c" classification. Nonetheless, this is at a significantly reduced overall performance level compared with the steel fibres, with the brittle failure leading to relatively low f_{R1k} values and a maximum 1c performance class.

Figures 8 and 9 respectively show the mean and characteristic flexural strength parameters for the CEM I and CEM IIIB mixes. ANOVA testing of f_L and residual strength parameters for the two Dramix® 4D 65/35BG fibre mixes shows that there was a statistically significant difference between f_L strength in panel and beam tests in both mixes. The beam f_L was higher and can be explained by the smaller fracture surface. Except for f_{R4} in the CEM IIIB mix, the residual flexural strengths showed no statistically significant difference, which is helpful since these are being used to classify performance according to MC2010.

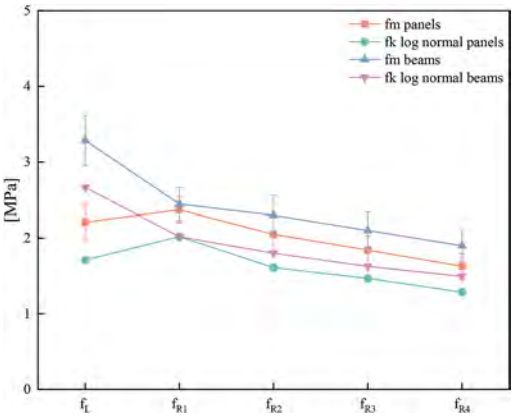

Figure 8. CEM I mix mean and characteristic flexural tensile strengths.

The higher f_L strength and more brittle drop from f_L to f_{R1} in the beam tests, which can also be explained by the smaller fracture surface, was reflected in the lower f_{R1k}/f_{Lk} ratio, which in some cases only just exceeded the minimum 0.4 requirement. In the CEM I series the 2b classification was unaffected, although the greater variability of the CEM IIIB series led to a 1.5c classification. Some care is therefore required in interpreting the results, although this may be a result of greater variability in the lower embodied carbon CEM IIIB production process, which was still being developed and used prototype equipment.

The results in this relatively small comparison were therefore as might be anticipated. The smaller fracture surface explains the higher beam f_L strength, and a less brittle fracture resulting from the improved load distribution in the larger panel fracture surface leading to nominally identical residual flexural strength performance and MC2010 ductility classification. The difference in panel and beam f_L was statically significant, although suggests that a panel test derived result is conservative while the

classification of crack control and ductility in the larger specimen is more representative of likely in-situ performance.

The prior Darveau and Jolin (2021) investigation indicated the potential to achieve MC2012 3c performance in a C30/37 concrete, albeit that the panel and beam test results were inconsistent. The current testing programme suggests improved consistency in a full-scale pre-construction trial and will be continued to confirm the potential to achieve equivalent and consistent panel and beam MC2010 performance of a minimum 3c classification using high performance steel fibres.

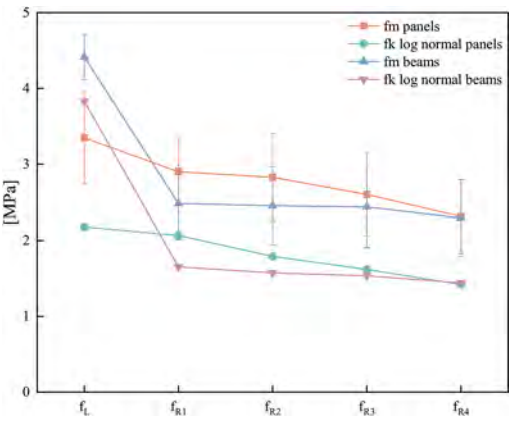

Figure 9. CEM IIIB mix mean and characteristic flexural tensile strengths.

7 CONCLUSIONS

Analysis of variance (ANOVA) examination of prior laboratory-based investigations supporting the equivalence of the EN 14651 notched beam and EN 14488–3 notched panel tests showed statistically significant differences in flexural strength parameters leading to inconsistent MC2010 performance classification.

A full-scale pre-construction trial in which Dramix® 4D 65/35BG, 3D 80/30BGP and 4D 90/50BG hooked end drawn wire steel fibres, and a Synmix HP35 fibre were each sprayed in two different basic mixes, achieved a minimum MC2010 2c performance classification for the steel fibres, although the more brittle macro synthetic sprayed fibre reinforced concrete (SFRC) performance led to a 1c classification.

Notched panel and beam tests in the two 4D 65/35BG mixes showed statistically significant differences in f_L strengths, although residual flexural tensile strength parameters were statistically identical and led to consistent MC2020 ductility classification. Notched panel f_L determination is likely to be conservative and, given the less brittle failure, MC2010 crack control classification is likely to better represent the in-situ material performance.

Reduced notched panel test residual flexural tensile strength variability leads to smaller margins when conformance is based on characteristic strengths consistent with limit state design. This may lead to more efficient sprayed concrete mix design, including a reduction in the fibre volume required to achieve conformance. Pre-construction trial costs are likely to be increased although, depending on the size of the project, subsequent savings in the material costs may lead to overall savings.

In any event the improved design efficiency leads to a reduction in embodied carbon in a conformant Sprayed Concrete Lining (SCL) and, once the increasing and frequently mandatory costs of carbon offsetting are included, overall cost savings may be realised.

ACKNOWLEDGMENTS

The Authors would like to acknowledge the contributions of collaborators Stuart Manning of Shotcrete Services Limited, Professor Chris Goodier and PhD students Zhi Hu and Umer Jadoon of Loughborough University, John Reddy of Ecocem and Michael Sataya of Arup and supporters at HS2 Ltd's Innovation Team and HS2 Main Works Civils Contractor, Skanska Costain STRABAG Joint Venture.

REFERENCES

Darveau, J., Jolin, M., 2021. Three Point Bending Test on Square Panel with Notch on Sprayed and Cast Specimens (3PBT on Square Panel) – Dramix 4D 65/35 BG. Report for Bekaert Underground Solutions, CRIB, Laval University.

De Rivaz, B., et al., 2019. Fibre reinforced spray concrete performance criteria: Comparison between EN14651 and EFNARC three-point bending test on square panel with notch. Tunnels and Underground Cities: Engineering and Innovation meet Archaeology, Architecture and Art. Eds, Peila, Viggiani & Celestino. Taylor & Francis Group. London.

EFNARC 2011. Testing Sprayed Concrete. EFNARC Three Point Bending Test on Square Panel with Notch. Flexural tensile strength of fibre concrete on sprayed test specimen.

EN 12390-3. BS EN 12390-3: Testing hardened concrete. Compressive strength of test specimens. London: British Standards Institution.

EN 14487-1. BS EN 14487-1: Sprayed concrete - Part 1: Definitions, specifications and conformity. London: British Standards Institution.

EN 14488-3. BS EN 14488-3: Testing sprayed concrete. Flexural strengths (first peak, ultimate and residual) of fibre reinforced beam specimens. London: British Standards Institution.

EN 14488-5. BS EN 14488-5: Testing sprayed concrete. Determination of energy absorption capacity of fibre reinforced slab specimens. London: British Standards Institution.

EN 14651. BS EN 14651: Test method for metallic fibre concrete — Measuring the flexural tensile strength

(limit of proportionality (LOP), residual). London: British Standards Institution.
EN 1990. BS EN 1990: Eurocode: Basis of structural design. London: British Standards Institution.
fib MC 2010. Model Code for Concrete Structures 2010. Ernst & Sohn.
Gagnon, A., Jolin, M., 2019. Three Point Bending Test on Notched Beam (EN 14651) and Notched Square Panel (E3PBT). Report for Bekaert-Maccaferri Underground Solutions, CRIB, Laval University.
Goodier, C., Peaston, C., Reddy, J., Manning, S., and Sataya, M., 2022. Low Carbon Sprayed Concrete, HS2 Innovation Discovery Report.
HS2 SCL Specification 2020 1MC03 Main Works - Contract Lot S1. Specification - Sprayed Concrete Linings - S1 and S2. Document no.: 1MC03-SCJ_SDH-TN-SPE-S000-000001.
Kaufman, J., Frech, K., Schuetz, P., and Munch B., 2013. Rebound and orientation of fibers in wet sprayed concrete applications. Construction and Building Materials, Vol 49, pp 15–22.
Meda, A., 2018. Comparison Between EN14651 EFNARC three point Bending Test. Report for Bekaert-Maccaferri Underground Solutions, University of Rome Tor Vergata.

Tunnelling for a Better Life – Yan, Celestino, Thewes & Eberhardt (Eds)
© 2024 The Author(s), ISBN 978-1-032-80042-4
Open Access: www.taylorfrancis.com, CC BY-NC-ND 4.0 license

Tunnel lining design in hard rock conditions. application of observation method. A case study of a large-scale tunnel cavern for underground train station

Martin Petkov*
Tyrens Group AB, Stockholm, Sweden
University of Architecture, Civil Engineering and Geodesy (UACEG), Sofia, Bulgaria

Pia Hansson
Tyrens Group AB, Stockholm, Sweden
Tyrens Sverige AB, Stockholm, Sweden

Johan Pilbacka
Tyrens Sverige AB, Stockholm, Sweden

ABSTRACT: Two mutually exclusive approaches - one that adheres to the requirements of the Eurocode system and the requirements for concrete reinforced concrete structures (with reinforcement bars, wire meshes, lattice girders, etc.) and the other that is also applicable with the Eurocode system - will be presented for designing tunnel rock support - an observational technique using fibre-reinforced shotcrete and rock anchors to apply flexible rock support in hard rock.

An underground section with exceptionally large cross-section dimensions is used as a case study. The width and height are 45 m and 15 m, respectively, with a net cross-section of more than 500 square meters.

Tunnel is built in hard rock conditions with three major discontinuities systems (joint systems). Geological conditions are rated from Poor to Fair - Q index 1 to 4.

Along with the outcomes of observations made during execution and predictions made using potential ways to estimate and forecast the behaviour, a comparison of rock reinforcement solutions obtained using the various methods will also be provided.

Using empirical analysis, the NGI Q system will be used to calculate the necessary rock support measures.

According to theoretical models that take into account the elastic behaviour of concrete with the limit stress approach, analysis is being done to calculate the thickness of steel fibre-reinforced shotcrete and the capacity of the lining to absorb bending moments in combination with rock anchors.

Using the distinct element approach, numerical analysis was performed to determine the displacements in characteristic spots and to determine the stability of the rock mass and rock reinforcement (rock anchors).

Limit equilibrium method local block/wedge analysis for rock block stability.

Calculating the limit values for the displacements using a software for tracking the displacements, their convergence, and their attenuation.

A proposal for the development of the topic will be given.

Keywords: Rock support, Fibre reinforced tunnel lining, Observation method

1 INTRODUCTION

The application of sprayed concrete (shotcrete) tunnel linings with reinforcement (bars or fibre) and rock bolts is the most common method of reinforcing an underground structure - tunnels and caverns. In parallel with the development of sprayed concrete applications, tunnelling has evolved and tunnels are constructed in a wide range of geotechnical conditions, from soft soils to hard rock. Despite the strong development of technologies, materials and methods for tunnel performance, some questions regarding the theoretical basis of the applied design methods are still insufficiently substantiated.

*Corresponding author: marto@abv.bg

DOI: 10.1201/9781003495505-156

2 REGULATORY REQUIREMENTS

Structures, such as buildings, must adhere to the European System for the Design of Structures - Eurocode. This requires meeting the guidelines outlined in EN 1990 to 1999 and their associated national annexes and parameters. Precision in adherence to these standards is essential for designing sound structures. In the Eurocode system, the limit state method with partial safety factors and two boundary conditions is specified, including safety (load carrying capacity) and serviceability control (deformation). The safety of building structures is controlled by the computed values of the actions. Eurocode 7: Geotechnical Design stipulates the need to verify that boundary conditions for the geotechnical aspect of the structure are not surpassed.

Alongside the application of Eurocodes in tunnel practice, numerous other methodologies and models are available for the design of tunnel linings. These alternatives differ significantly from the requirements of EN 1992-1-1:2004. Eurocode 2: Design of concrete structures - Part 1-1: General rules and rules for buildings and EN 1992-2:2005. Eurocode 2: Design of concrete structures - Part 2: Concrete bridges - Design and detailing rules in terms of design principles. However, they are founded on observation and analysis, i.e. the observation method, of previously constructed tunnels. The NGI Q system (Barton N. Using the Q-system. Rock mass classification and support design. Handbook.) serves as an example of one such method. The methodology was developed between 1971 and 1974 and has since undergone numerous updates in line with advancements in technology and materials for tunnel construction. Drawing on the extensive experience gained from over 2000 tunnel construction examples, the methodology has been refined to ensure its effectiveness and efficiency. The approach is employed for rocky soil masses and is founded on the principle of comparable experience - definite established data for a particular soil base and structure predicted to exhibit similar geotechnical behaviour to previously constructed structures.

3 JUSTIFICATION FOR APPLYING A DESIGN SOLUTION

As per Section 2 of EN1997-1:2004. Eurocode 7: Geotechnical design, limit states may be verified using one or several methods including: calculation - analytical method; numerical modelling, failure criteria; adoption of prescribed measures - empirical method, classification system, experience; experimental models and testing; observation methods used in this study include in-situ monitoring and special geological observations. Construction measures employed consisted of exploration, pre-injection procedures, and special excavation procedures.

It is noteworthy that the aforementioned methods are permissible for geotechnical structures and design, but they are not delineated for reinforced concrete structures.

Hoek, E. et al. (1999) outlines a methodology for assessing rock mass behaviour and design. It summarises the potential problems related to discontinuities in the rock mass, which include loosening, rock wedge/block failure, spalling, and collapse. Empirical and analytical approaches are suitable to design tunnel reinforcement that is adapted to the conditions. The predictability of low rock mass strength versus rock mass stresses involving overloading and subsequent occurrences of buckling, rupture, defoliation, cracking, plastic deformation or swelling of the rock array, can be achieved through analytical or empirical methods, or through observation of the rock mass condition. Analytical methods and design measures are applicable in adverse conditions such as weathering, swelling, alteration zones, fracturing, or significant water pressure.

4 DESCRIPTION OF THE CASE

The examined tunnel is a part of the Gothenburg-based Underground Railway Station. Its cross section widens in a cone-like shape, gradually increasing from 30.15 m at the eastern end to 44.77 m. Alongside this, the height of the cross-section also increases from 11.20 m to 15.00 m due to the widening of its profile. In the centre of the cross-section, there are vertical, monolithic reinforced concrete columns and a longitudinal reinforced concrete beam which serve to partially take the rock pressure.

Initially, a tunnel lining solution was proposed that included shotcrete with a thickness of over 250 mm, four-bars lattice girder at spacing of 1.5 m, a double welded reinforcing steel mesh, and system rock bolts. Owing to the considerable cross-sectional dimensions, a staged approach is necessary, beginning with the excavation of three pilot tunnels (as shown by number 1 on Figure 2), followed by the application of the first layer of sprayed concrete, the construction of reinforced concrete structures, including columns and longitudinal central beam (as shown by 3 on Figure 2), before finally fully excavating the profile and removing the temporary rock columns (as indicated by 4 on Figure 2).

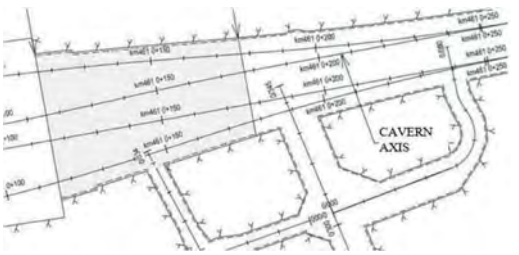

Figure 1. Layout of East Station.

The sprayed concrete and the longitudinal cast in place beam are rigidly connected to transfer axial and shear forces, as well as bending moments, from the tunnel lining to the monolithic beam.

In this section, the rock cover varies in size, but it is never less than 12.5 m, which is more than half the width of the cross-section from the wall to the colonnade.

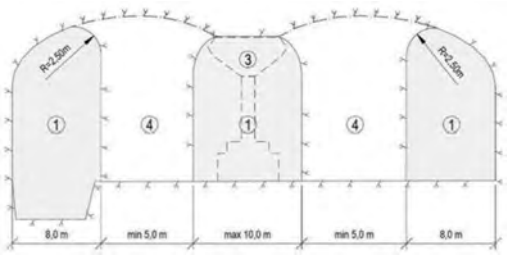

Figure 2. Layout of East Station.

Structural forces within the tunnel lining were calculated via a spatial Finite Element Method, continue model built using geotechnical design software.

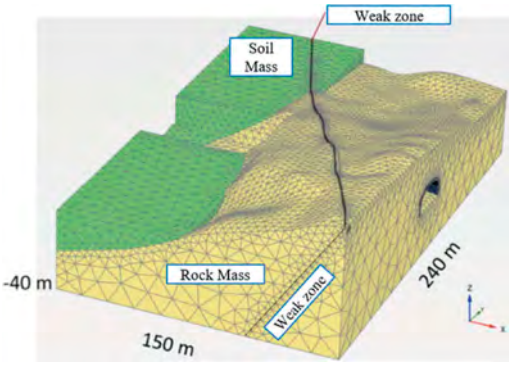

Figure 3. Continuous FEM model of East Station.

The rock mass in the model was defined as continuous and follows parameters based on Mohr-Coloumb theory, with a cohesion of c=1.80 MPa, an internal friction angle of 50˚, a modulus of elasticity of 23.7 GPa, a Poisson's ratio of 0.25, and a tensile strength of 0.62 MPa.

FEM analyses were conducted for various stress state cases of the rock mass, and the results were summarized. Using the limit state method as per Eurocode 2 requirements, dimensional checks were carried out. The dimensional checks conducted on the tunnel structure in 10.0 m lengthwise strips revealed that sections reinforced with Q335 type welded mesh and four-bars steel lattice girder, consisting of 8 mm diameter bars spaced at 150 mm centres, have the requisite capacity for shear forces in the radial direction. However, application of transverse shear reinforcement (stirrups) is also necessary for larger sections.

An unforeseen and irrational outcome of the numerical model is the discovery of significant tensile forces, as well as numerous local concentrations, in the longitudinal direction of the structure that are greater than those in the radial direction. High shear forces are also present. The large tensile and longitudinal forces in the tunnel lining, which can exceed 2.0 MN of tension, necessitated a significant amount of longitudinal reinforcement. For instance, 32 mm diameter bars were laid over a 100 mm distance since it was not feasible to apply welded steel mesh. Additionally, in the area of the rock mass that is weak, there are further peaks of shear forces which amplify the results. As a result, there is a need for an increased cross section.

The findings were assessed according to previous experiences at comparable locations, with the Gjøvik Olympic Cavern Hall, Norway serving as the reference site, in comparison to the data outlined in Barton el. al. (2015). Following the comparative analysis, it was discovered that the Gjøvik Olympic Cavern Hall project implemented significantly fewer rock anchors and steel fibre reinforced sprayed concrete, with larger cross-section dimensions, under nearly identical conditions and devoid of a colonnade in the middle of the vault. After over 30 years of successful operation at the analogue site, this conclusion indicates a need to reassess the design method used and seek a more appropriate solution. However, it is important to ensure that the solution satisfies safety and serviceability requirements.

5 NEW DESIGN SOLUTION

The basis of the new design solution involves evaluating potential failure mechanisms and redefining the primary load-bearing element. The design solution recognises the rock mass and its characteristic of dilution surrounding the openings, which produces compressive arches throughout the tunnel section, as the principal load-bearing element. Its capacity further increases with the substantial horizontal compressive stresses that are typical for this section. After concluding that the rock mass (geotechnical structure) was the principal load-bearing element, plans were made to reinforce it, rather than reinforcing the concrete. The core of the proposed approach is 'rock mass reinforcement'. It was predicted that a failure mechanism could arise from the creation of one or more wedges in the tunnel arch caused by gravity in the newly proposed design. In order to obtain stable and durable tunnel strengthening, decide on alarm levels for the displacements, and determine initial response measures if the behaviour of the array differs significantly from that predicted, necessary analyses and controls have been determined for this mechanism. To demonstrate that the composite set of tunnel bracing measures can achieve rock mass stability, the following analyses were conducted:

An empirical analysis was conducted to determine the required rock bolting measures. The analysis was conducted in adherence with NGI Q-system guidelines. Numerical modelling was implemented to determine the thickness of reinforced steel structural fibre sprayed concrete, as well as to assess rock mass stability, rock reinforcement with rock anchors, and displacement at characteristic points for alarm/critical levels. Stability of rock blocks was assessed through local block analysis using the limit equilibrium method.

5.1 *Empirical analysis*

Based on implementation experience, it is worth noting that the use of the NGI Q-system results in solutions that are more conservative than those obtained through analytical methods. This means that the NGI Q-system inherently incorporates certainty, for instance, in accounting for variations in performance quality.

The vertical red lines depicted in Figure 4 demonstrate the anticipated rock conditions range, with the red horizontal line displaying the planned tunnel width of 22.5 m. This width represents only 50% of the actual tunnel width, as a central colonnade of monolithic reinforced concrete columns has been included specifically to withstand mountain pressures. When the blue line is crossed, the system is suggested to be paired with another analysis method, such as a numerical model. Notably, the sprayed concrete thicknesses of t ≤120 mm are considerably smaller than the original solution of t = 250 mm, while maintaining the same length and rock anchor distribution.

At Q=1 conditions, it is necessary to add 400 mm thick sprayed concrete ribs consisting of two rows, each with six reinforcing bars of 16 and 20 mm in diameter. The ribs must be installed over a distance of 4.0 m.

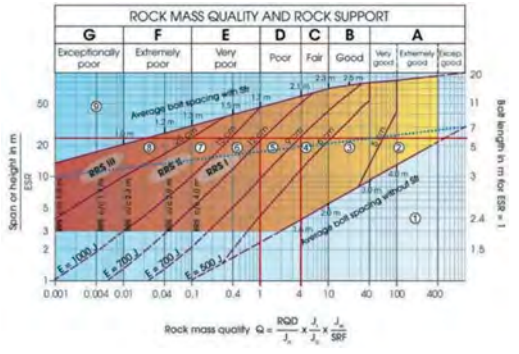

Figure 4. Empirical diagram for rock support/ reinforcement with intervals based on anticipated rock conditions, NGI Q system.

Due to technological constraints, a revised solution was developed for a rock revetment that can be applied across a range of expected rock conditions. The new solution was designed with conservative specifications to ensure its effectiveness. Verification of the fastening according to the revised solution was conducted through further analysis to confirm its sufficiency. Further analysis is also necessary as the connection with the colonnade in the middle of the tunnel is complex, and there is a need to consider load absorption and transfer from mountain rock compression on the monolithic columns, which is crucial for ensuring safety and stability.

5.2 *Analysis of fibre reinforced sprayed concrete*

According to Barrett and McCreath, el. al. (1995), there exist six probable failure modes of shotcrete when employed for tunnel strengthening in robust rock mass having block cracks. These modes include adhesion, flexure, shear, punching, compression, and tension. The distinct models are displayed in Figure 5. There may be other failure patterns and combinations apart from the listed six; however, observations on accomplished processes indicates that the aforementioned six are responsible for over 90% of the failures.

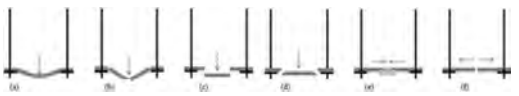

Figure 5. Fracture models of sprayed concrete have been studied. Observations of falling rock wedges indicate that failure in shotcrete is caused by inadequate adhesion (a), bending (b), shear (c), punching (d), compression (f), and tension (f).

The empirical analyses conducted verify that the proposed method, involving a system anchorage applied at a distance of 1.5 m in both directions, along with fiber reinforced sprayed concrete of a 15 cm thickness, effectively prevents the formation of secondary wedges between the rock anchors. A four-step analytical analysis procedure was carried out, in line with the recommended guidelines of Swedish Road authority regulation: Projektering av bergkonstruktioner.

Verification of the adequacy of adhesion between the fiber reinforced shotcrete and the rock mass is a crucial aspect. The wedge is unconstrained by the anchors, and its adhesion to the shotcrete is examined thoroughly. In this study, a pyramidal rock wedge is formed between two rock anchors, as shown in Figure 6.

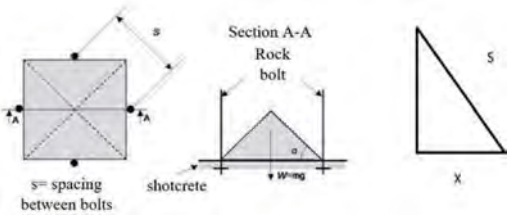

Figure 6. A rock wedge forms between rock anchors as part of the system anchorage, which helps disperse loading and reinforces shotcrete.

Assuming good adhesion between the dispersed reinforced sprayed concrete and the rock mass, it is recommended to use the following equation:

$$W_d \leq \frac{\sigma_{adk}.\delta_m.O_m}{\gamma_C} \rightarrow \sigma_{adk} = \frac{W_d.\gamma_C}{\delta_m.O_m} \quad (1)$$

$$W_k = m.g \quad (2)$$

$$W_d = W_k.\gamma_d.\gamma_{G;dst} \quad (3)$$

Where, W_d is Design dead weight of the rock wedge, W_k is characteristic dead weight of the rock wedge σ_{adk} is the characteristic value for adhesion between rock wedge and shotcrete, δ_m is the load bearing height of shotcrete, O_m is the rock wedge/ shotcrete load bearing perimeter, γ_C is partial factor for shotcrete, γ_d is the factor of safety, m is the mass of rock wedge, g is the gravity acceleration.

The analysis is conducted based on prerequisites related to the bond strength (adhesion), load magnitude, and anchor from the system rock reinforcement spacing. The size and weight of the rock wedge are determined for varying distances between the anchors at 30 and 45 degrees inclination within the rock mass. The required adhesion value is then calculated, and a bond strength exceeding 0.5 MPa (for solid rock mass) is deemed satisfactory.

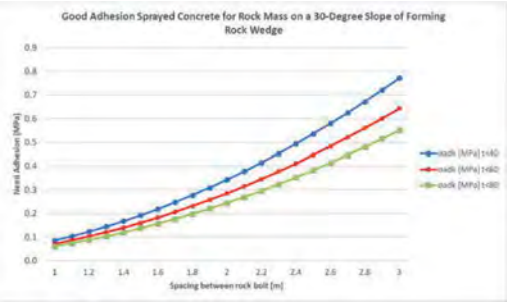

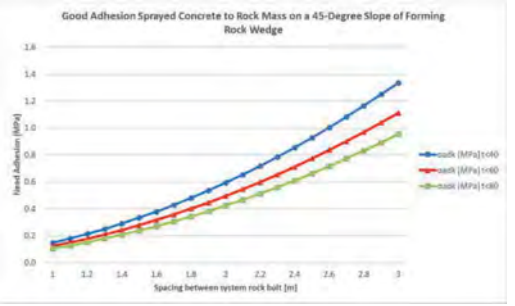

The second check is conducted for cases where there is poor bond or high rock mass cracking. In such situations, it is assumed that dispersed reinforced concrete absorbs the actions by bending and absorbing bending moments, and that shotcrete is anchored with rock anchors. The flexural tensile strength determines the bending moment capacity of the dispersed reinforced sprayed concrete. For a reinforced concrete section that has not yet experienced cracks, this stress value represents its tensile strength.

The bending moment capacity of dispersed reinforced sprayed concrete can be determined by assuming that it is greater than or equal to the characteristic maximum bending moment capacity of the material.

$$M_d \leq \frac{f_{flcrk}.t_c^2}{\gamma_C.6} \rightarrow t_c = \sqrt{\frac{M_d.\gamma_C.6}{f_{flcrk}}} \quad (4)$$

$$M_d = M_k.\gamma_d.\gamma_{G;dst} \quad (5)$$

Where, f_{flcrk} is characteristic value of the tensile strength of concrete until the formation of a first crack, t_c is thickness of dispersed reinforced sprayed concrete, M_d design bending moment.

The maximum design bending moment's magnitude is reliant on the slack zone's size that loads the liner between the anchors. The maximum moment can occur either in the middle of the zone/field under consideration or at the attachment points - such as rock bolts and, more specifically, steel plates of anchors. Beam or plate theory can be useful in determining the potential moment.

The analysis involved calculating the characteristic value of the bending moment at varying distances between the rock anchors, as well as determining the size of the loosened zone, at two angles - 30 and 45 degrees. Following the analysis, the results were charted, and the required thickness of the lining and characteristic value of the maximum bending moment were computed.

The adequacy of the section to resist buckling of a pyramid-shaped rock wedge that forms between rock anchors must be evaluated.

$$W_d \leq \frac{\tau_{bk}.t_c.O_m}{\gamma_C} \rightarrow t_c = \frac{W_d.\gamma_C}{\tau_{bk}.O_m} \quad (6)$$

$$W_d = W_k.\gamma_d.\gamma_{G;dst} \quad (7)$$

Where, τ_{bk} is characteristic shear strength of shotcrete.

The ultimate assessment is to determine the extent of penetration through the anchor support plates, given the presence of low adhesion situations.

$$W_d \leq \frac{\tau_{bk}.\pi.t_c.(2b + t_c)}{\gamma_C} \quad (8)$$

For verification purposes, a graph is formulated demonstrating the necessary thickness of shotcrete, in

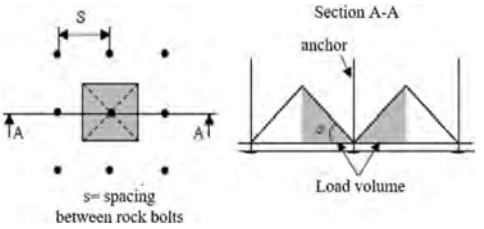

Figure 7. Load on anchor plate.

relation to varying distances between rock anchors, under the influence of loads caused by a rock wedge created at either a 30 or 45-degree angle.

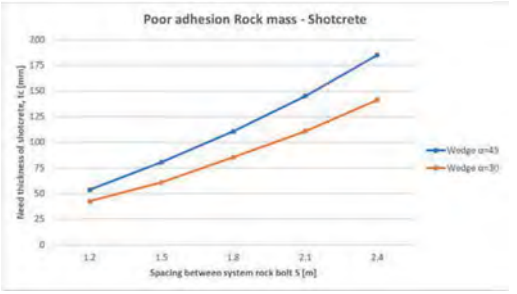

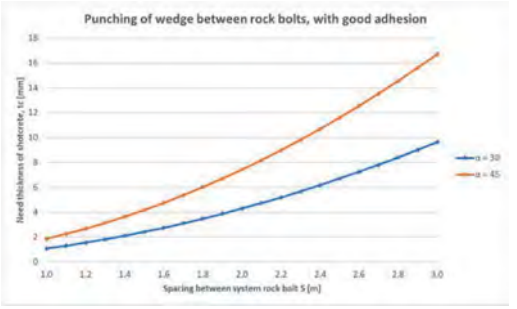

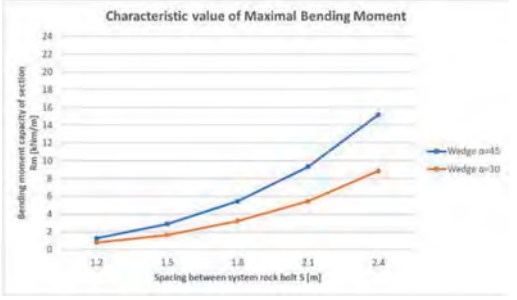

5.3 *Check for a gravity-loaded arch*

In cases of insufficient rock coverage, where the rock mass is unable to withstand the pressures and arches generated during tunnel construction, or when the rock mass has low strength, it becomes essential to use dispersed reinforced sprayed concrete to fully absorb the mountain pressures. In this instance, the geometry of the tunnel roof is analysed to ensure that only compressive stresses arise in the section and that they are transmitted to the surrounding walls. The equations stated by Holmgren, J. el. al. (1992) and Stille, H., Holmberg, M., Nord, G., el. al (1989), can be utilised to initially calculate the necessary thickness of the sprayed concrete.

$$t_c = \frac{2.B.W_k.\gamma_d.\gamma_{G;dst}}{6.3.\left(\frac{f_{ck}}{\gamma_k}.\alpha_{cc}\right)}.\sqrt{1+\frac{B^2}{10.f^2}} \tag{9}$$

$$t_c = \frac{B.W_k.\gamma_d.\gamma_{G;dst}}{2.\left(\frac{f_{ck}}{\gamma_k}.\alpha_{cc}\right)}.\sqrt{1+\left(\frac{\mathrm{B}}{4.\mathrm{f}}\right)^2} \tag{10}$$

$$t_c = \frac{B.q}{2.f_{cd}}.\sqrt{1+\left(\frac{\mathrm{B}}{4.\mathrm{f}}\right)^2} \tag{11}$$

$$f = \frac{B}{2}.tg\left(45-\frac{\varphi}{2}\right) \tag{12}$$

$$f = B.\sqrt{\frac{q_v}{8.q_h}} \tag{13}$$

Where, t_c is thickness of shotcrete, f is collapse arch height determined according to equation 12 and 13, f_{cd} is design compression strength of shotcrete,f_{ck} is characteristic compression strength of shotcrete, B is the width of tunnel section, W_k is characteristic value of rock mass action, q_v, q_h is the value of vertical or horizontal rock mass load, perpendicular to tunnel axis.

5.4 *Numerical analysis*

Numerical analysis is performed using the UDEC/ Itasca software to assess the effectiveness of rock support and the stability of the tunnel. The analysis is conducted in two typical locations - the standard section and at the lowest point of rock coverage (12.5 m).

The discrete element method (DEM) is based on the laws of motion that govern solid bodies and the interaction between them. It relies on dividing the time period during which solid bodies move into a certain number of computational intervals. The technique is valuable in simulating the disintegration of cohesive forms, e.g. a solid rock formation, comprised of distinct parts (i.e. the separate rock segments defined by the main fissure systems in the mountain), as it allows for the portrayal of the behaviour of the fragmented rock masses in the vicinity of the tunnel and the acquisition of the estimates for potential movements.

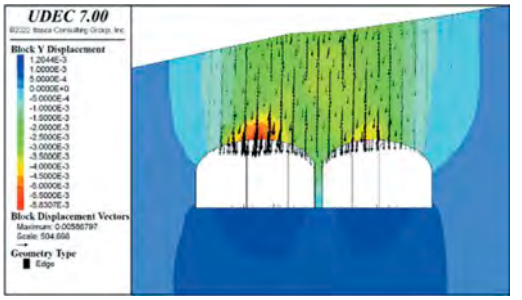

Figure 8. Analysis results for section A-A. Vertical displacements in the rock mass under gravitational stress.

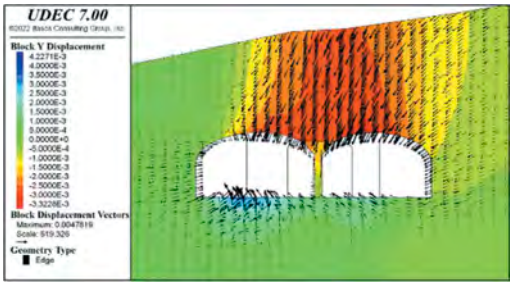

Figure 9. Analysis results for section A-A. Vertical displacements in the rock mass under high horizontal stress.

The analysis revealed a displacement of 9.3 mm in the tunnel profile's arch. The forces in the rock anchors did not surpass 130 kN and remain within the allowable limits for the chosen anchor type – rock bolt, featuring an anchor and epoxy anti-corrosion coating (PC bolt M27) at 214 kN. Furthermore, the study included an examination of the rock mass displacements, sliding, and crack opening. The maximum displacements observed are slips up to 5mm, and the maximum opening value of cracks is up to 2.7mm. Both phenomena were realized in different, localized sections around the tunnel.

Based on the analyses conducted and the results obtained using the Discrete Element Method, it can be concluded that both sections are stable, even without dispersed reinforced lining. Furthermore, the selected number, distribution, and length of rock anchors are adequate for achieving a new equilibrium state in the array.

It is essential to establish a solid connection between the rock mass and the concrete columns to restrict rock mass displacements during final excavation phases, i.e. removal of temporary rock columns. A comparison of results was conducted based on the initial stressed state of the massif, i.e. gravitational and high horizontal. It can be inferred that the gravity condition plays a crucial role in determining the required rock anchorage. The initial horizontal stresses within the massif positively impact the stability of the rock formation surrounding the tunnel profile by creating arcs of compressed rock.

5.6 *Block analysis*

To identify the largest single block resulting from the mutual intersection of main fracture systems and determine the corresponding geotechnical indicators describing the state of the cracks, rock wedge block analysis was performed using the limit equilibrium method. This analysis aims to trace the failure mechanism arising from rock wedge formation in the tunnel arch. The geotechnical indicators were determined during mapping of completed works and geological surveys. The analysis assumes zero cohesion in the cracks and only rock anchors for rock anchorage. Dispersed reinforced shotcrete is not considered due to increased safety factors. The rock mass is assumed to be drained and not affected by underground water pressure.

Rocscience UnWedge software was used to analyse excavations of underground tunnels intersected with fracture systems. The stability has been assessed by calculating the safety factor of tetrahedral rock wedges formed around the perimeter of the block and the contour of the tunnel.

To analyze the tunnel profile, three distinct models have been employed: the Left Tunnel, which refers to the part located to the left of the colonnade; the Right Tunnel, which pertains to the section located on the right side of the colonnade; and a full profile, with the colonnade excluded from the center. The complete profile model outlines the scenario in which the monolithic strengthened concrete columns and the rock mass fail to establish a close connection.

The design tensile and shear capacity of rock reinforcement, specifically rock anchors, are incorporated in the model.

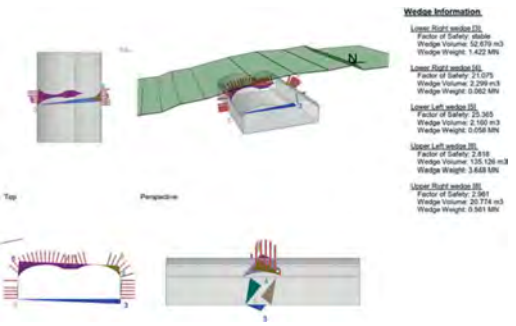

Figure 10. Block analysis results for full profile, without concrete pillars.

6 SUMMARY OF RESULTS

Since the inception of the new project solution, the following outcomes have been realized:

A. The structural thickness of the fiber-reinforced lining, composed of sprayed concrete with steel

fibers, has been successfully reduced by more than 50%.

B. The necessity for the application of bar reinforcement, steel reinforcing lattice girders, or welded steel reinforcing meshes has been entirely obviated. Except the quantities benefits this also leads to streamlined technological and cyclical operations for the excavation of the tunnel, presenting a significant advantage over the initial solution.
C. The absence of steel rebars eliminates the need to fill over excavated material during the blasting process, as there is no requirement for strict adherence to the tunnel contour based on the theoretical profile dictated by steel rebars. This is halving the volume of shotcrete.
D. This method enables a prompt implementation process and improves site safety.
E. This is a sustainable solution from an environmental perspective.

7 CONCLUDING REMARKS AND FINDINGS

When formulating designs for underground infrastructures, the analysis must initiate by identifying potential failure and accident mechanisms. This scrutiny, necessitate supplementary checks or using of alternative methodologies compared to widely accepted practices.

Designing tunnels in hard rock conditions based solely on normative requirements for conventional buildings and bridges is not practicable. Aspects, such as the interaction between the rock mass and the structure, together with other factors not encompassed in the initial sections of Eurocode, must be taken into consideration.

Advisable is to employ normative documents, such as Eurocode 1992, only subsequent to a thorough evaluation of the resultant solution, especially in the context of hard rock formations. Basing the design on Eurocode system results in significant alteration to the reinforced concrete elements and a concomitant underestimation of the geotechnical conditions and associated dangers. For instance, the creation of rock wedges can go unnoticed in models of a continuous environment, causing a lack of appropriate systemic measures.

Essential is to identify and address such phenomena in order to implement effective solutions. The regulation and assessment of a diverse range of software products should be based on the specific assignment and geotechnical circumstances. The standard protocol entails calibration of the model after conducting a risk analysis and allowing specialists, experienced in similar projects, to handle the process.

Results should be subjected to diligent examination, ensuring their dependability and validity through alternative available approaches if deemed necessary. The assumed modeling technique, models of the soil array, and the consideration of "disturbances in the array" have the potential to yield nonsensical outcomes that can substantially over or underestimate specific parameters. For instance, deformations may arise as a result of such occurrences.

In high-stiffness models, incorporating rigid constructions results in significant oversizing of tunnel linings, rendering them unsafe, impractical, or uneconomical. This is due to the intricate technological processes and work operations involved in hazardous environments, such as unreinforced arrays and work at height.

Hence, a comprehensive appraisal of the necessity and repercussions of utilising reinforced concrete structures for tunnel linings is fundamental before initiating the implementation process.

To ensure the successful implementation of the dispersion-reinforced tunnel lining method, it is crucial to position the anchor plates on the last bearing layer of sprayed concrete. This is a vital requirement, often overlooked during execution.

It is necessary to carry out frequent displacement monitoring and periodic assessments of them to ensure adherence to the anticipated values specified in the project.

ACKNOWLEDGMENTS

We would like to express our heartfelt gratitude to Swedish Traffic organization (Trafikverket) that allowed result and findings to be published and shared with readers.

REFERENCES

Barton, N., 2022. Using the Q-system. Rock mass classification and support design. Handbook.

EN 1992-1-1:2004. Eurocode 2: Design of concrete structures - Part 1-1: General rules and rules for buildings.

EN 1992–2:2005. Eurocode 2: Design of concrete structures - Part 2: Concrete bridges - Design and detailing rules.

EN1997-1:2004. Eurocode 7: Geotechnical design - Part 1: General rules.

Hoek, E., 1999. Putting numbers to geology – an engineer's viewpoint. Published in the Quarterly Journal of Engineering Geology, 32(1): 1–19.

Barton, N.,2015. Forty Years with the Q-system – Lessons and Developments. //Nick Barton and Associates.

Barrett, S.V.L., McCreath, D.R. Shotcrete support design in blocky ground: towards a deterministic approach. //Tunnelling and Underground Space Technology, 1995 10 (1): 78–99.

Projektering av bergkonstruktioner. Rapport. Trafikverket. Publikationsnummer 2019: 062, ISBN: 978–91–7725–412–6

Holmgren, J., 1992. Bergförstärkning med sprutbetong. Vattenfall. ISBN 91-7186-298–6

Stille, H., Holmberg, M., Nord, G., 1989. Support of weak rock with grouted bolts and shotcrete. //Int. J. Rock Mech. Min. Sci. & Geomech. Abstr., 26 (1): 99–113.

Tunnelling for a Better Life – Yan, Celestino, Thewes & Eberhardt (Eds)
© 2024 The Author(s), ISBN 978-1-032-80042-4
Open Access: www.taylorfrancis.com, CC BY-NC-ND 4.0 license

Risk assessment and large diameter segmental lining design in swelling ground

Sergio Sánchez*
AECOM. Enterprise Capabilities Europe, Madrid, Spain

Michael Mains
AECOM, Vancouver, Canada

Carlos Álvarez
AECOM. Enterprise Capabilities Europe, Madrid, Spain

Emeline Barrouillet
AECOM, P. City, Panama

Carlos Garrido & Mikel Ferreres
AECOM. Enterprise Capabilities Europe, Madrid, Spain

ABSTRACT: Extensive record of tunnels excavated according with the SEM approach in swelling ground exists for both clayey soils and rocks and sulphated rock masses. However, there is less experience in shield tunnels bored under pressurized conditions (E.P.B. and slurry shields) where the impact is supposed to be lower due to the limited stress relief and navigation under saturated conditions. This paper includes the studies conducted for the risk assessment done for a large diameter TBM tunnel designed under complex geological environment which comprised mixed ground and face conditions including swelling soils and clayey soft rocks. The study also describes the approach adopted and impact on the design of the segmental lining of the tunnel planned also in a context of high regional seismicity. The design of this lining included a detailed parametric study performed to handle the existing uncertainties related with ground characterization, potential deconfinement and complex geological configurations.

Keywords: Tunnelling, TBM, Swelling, Shield, Volcanics and sedimentary rocks, Segmental lining

1 INTRODUCTION

During the detailed design of the segmental lining of a large TBM tunnel in Central America, large swelling potential of residual soils and soft sedimentary rocks was confirmed in formations which also included volcanic units.

Although the swelling phenomenon was detected and expected to be significant, difficulties during site investigation made it particularly challenging to characterize the swelling behaviour to the level needed for design. This combined with the complexity of swelling behaviour around pressurized TBMs, and the fact that no previous underground structures have been built in the rock formations under analysis, led the designers to adopt a risk based design approach.

In addition to site and laboratory testing, an analysis of state of the art of swelling analyses for similar lithologies and pressurized TBM tunnels was conducted.

This paper summarizes the risk analyses carried out as well as the final design approach for lining subjected to both significant swelling and earthquake loads combined.

2 A LITERATURE REVIEW ON SWELLING IN TUNNELLING PROJECTS

There is a large number of references for swelling in tunnels, due to its potential for considerable cost overruns and damage to the lining. For example, problems associated with swelling in the tunnels crossing the Jura Mountains and Baden-Wütemberg region in Central Europe have been studied, due to the presence of sulphate-clay rocks with the presence of gypsum (CaSO4-2H2O) and anhydrite (CaSO4), often associated with the presence of Keuper facies (Bustcher et al., 2016)

*Corresponding author: sergio.sanchez@aecom.com

DOI: 10.1201/9781003495505-157

Recently Ramon (2014), developed a thesis for analysing and describing the swelling mechanisms of Tertiary sulphated claystones in Spain based on observations from well-known tunnels, bridges and embankments where heave induced by gypsum crystal growth in rocks and compacted soils containing sulphates.

However, there are fewer cases involving tunnels in volcanic rocks or pressurized TBMs. Carter et al. (2010) compiled a number of cases of hydroelectric tunnels excavated in the Andean formations of central Chile, where volcanic-sedimentary rocks are prevalent. The study performed analyses on the evolution of swelling behaviour of rocks containing clay minerals (specifically the smectite group -e.g., montmorillonite, nontronite, rectorite etc.) backed by a robust laboratory campaign consisting of free swell, confined Huder Amberg, null tests (on intact rock samples and on powder samples), scanning electron microscopy (SEM) detailed petrography, and X-ray diffraction. Carter et al. (2010) generally identified Oligocene-Miocene age rocks composed of andesitic/dacitic lava flows, volcaniclastic andesitic breccias, and sedimentary epiclastic rocks related with the Coya Machali formation as the most problematic rock types with respect to swelling.

However despite the extensive work carried out, exact swell-mineralogy relationships are still not clear. A meaningful guide for the development of sampling and lab testing was nevertheless established and contributes towards a better understanding of the mechanisms that may impact lining design.

Similar lab tests were carried out by Piaggio (2017) and supplemented by cyclic and triaxial testing, again on Andean volcanic rocks containing clay minerals. Swelling pressure tests with powdered rock show that swelling tended to be very dependent on the initial conditions like compaction load. Triaxial tests proved to be helpful in order to set up an analytical relationship to apply in a numerical model regarding the volumetric strains due to swelling.

The difficulty of obtaining representative samples of the rock mass, as well as the importance of the preparation of the samples to be tested and its influence on the results obtained in the laboratory tests is analyzed by Nielsen (2021). The tested samples taken from tunnels with expansivity problems related to fault zones in granites and metasandstones, with presence of swelling clay minerals.

It is clear that the swelling mechanism in fault zones and in volcanics/volcano-sedimentary rocks is complex and not yet fully understood. Therefore, consideration of the order of magnitude of the swelling pressures observed in other projects around the world and in a variety of geological environments is necessary to understand whether analytical models reflect reality. Several cases of swelling in tunneling projects have been summarized in Figure 1.

Notably few examples of swelling exist for TBM tunnels. Some examples of TBM projects in Jurassic formations of Central Europe have been reported by Kovari, (2014); Wittke et al, (2017) & Grossauer et al (2019), although most cases treat open face TBMs rather than closed face pressurized TBMs. Of particular interest is the Third Belchen tunnel tube for which Ziegler et al. (2022) provided a detailed discussion to understand swelling behavior based on instrumented sections records.

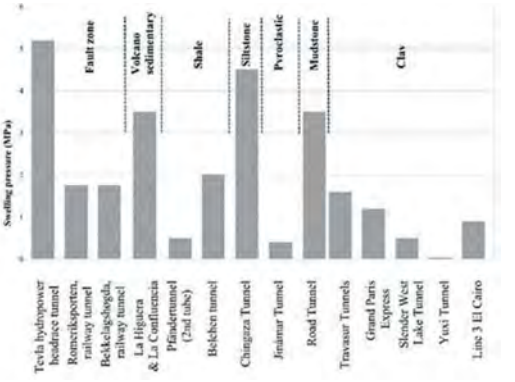

Figure 1. Sweeling pressure of swelling rocks and soils at tunnelling projects.

Interesting experience has been recorded in the non sulphated Ontario Shale. Several references of smaller diameter TBMs are available (Lo et al. 2005, Cushing et al. 2016, Dimillo et al. 2016). However these again only treat open faced rock TBMs and the studies mostly focus on the time-dependency of the loads. This experience has also been applied to Sydney's shale bedrock (Dadfar et al. 2023) for the design of segmental linings.

Only a few references are available for closed faced pressurized TBMs. Ashraf (2006) described the use of 2D numerical models for the design of the segmental lining for the El Cairo Metro Line 2 tunnel which excavated soils with clay minerals. More detailed analysis, also for El Cairo Metro, is provided by Lecomte et al. (2014), who described the characterization work done to obtain representative parameters of the hard and high plasticity clay affected by Line 3 Phase 2. Swelling was expected to be triggered by changes in pore pressures due to the stress release generated by tunnel excavation.

The Slender West Lake tunnel in China (Wang et al. 2016) is another case of closed face TBM in swelling clay where instrumented sections with pressure cells and strain gauges were installed to investigate the distribution and magnitude of swelling loads.

3 SWELLING MECHANISM AND ITS SIMULATION

In clayey rocks, the swelling mechanism can a combination of osmotic flow between clay

minerals resulting on an increase in the distance between them, and the hydration with/ incorporation of water between the silicate layers of the mineral.

For the initiation of this mechanism, different conditions must be accomplished (Lo, 2005):

- A stress release and corresponding hange in pore pressure;
- The presence of water;
- and a salt concentration gradient between the soil/ rock pores and the ambient fluid

For both sulphated rocks and clays, Grob's swelling law which considers logarithmic relationship between swelling strains and axial stress in the direction of swelling is generally accepted. This is consistent with the reduction of swelling deformations when a confining pressure is imposed, and the reduction of the swelling pressures when the swell deformation is allowed:

$$\varepsilon_i^{q(t=\infty)} = -k_{qi} \cdot log_{10}\left(\frac{\sigma_i}{\sigma_{q0i}}\right) \qquad (1)$$

Where $\varepsilon_i^{q(t=\infty)}$ is the final swelling strain, k_{qi} is the swelling parameter, σ_i the axial stress and σ_{q0i} the maximum swelling pressure.

This relationship was subsequently developed as to 2D and 3D for numerical analyses (Anagnostou, 1993, Wittke et al, 1998), which later incorporated the effect of seepage flow (Agnanostou 1992, 1993; Wittke, 2003) and the possibility of simulating the swelling rate over the time (Wahlen et al, 2009).

In sulphated rocks, further developments allowed for the chemical coupling and temperature effects for the simulation of gypsum crystal growth (Alonso et al, 2008; Ramon, 2014).

A specific constitutive model was developed for the commercial software PLAXIS which was developed by Benz (2010) and Schädlich (2013) and it is based in the previous work developed by Wittke and Anagnostou. This model is used for the swelling calculations presented later in this paper.

4 EXAMPLE OF SEGMENTAL LINING DESIGN IN SWELLING ROCK

4.1 *Complex geological conditions*

During the design of Ø12m ID TBM tunnel in Central America, high swelling potential was detected in both the soft residual overburden soils and tertiary rocks (siltstone, mudstone & carbonaceous mudstone) which would eventually host the tunnel. Swelling was determined as a governing load case for 2.3 km of the alignment and initial laboratory test suggested swelling pressures significantly higher than anything the design team could find in the available literature. Further, the project is located in a region of very high seismicity. The initial attempts to design the segmental lining for the combined effects of a worst-case swelling scenario and high seismic forces proved cost prohibitive. This triggered the need a risk-based approach to determining the impact of swelling on the lining design. The following provides some context to the subsurface conditions of this design example.

Table 1. Index and mechanical parameters of the swelling potential soils.

	γ_{ap} (kN/m^3)	Fines (%)	P.I.	Su (kPa)	E' (MPa)
Silty mud	16.0	70	29	11	2
Residual soil	19.0-19.5	50-75	30	65-170	13-30

Table 2. Index and mechanical parameters of the swelling potential soils.

	γ (kN/m^3)	σ_{ci} (MPa)	E_m (MPa)
Mudstone	21.5	1.6	200
Silstone	22.0	3.0	80-575

The potential for swelling was first detected by weathering potential characterized by Slake Durability Index. Figure 2 shows the SDI compared the content of phyllosilicates in the swelling prone rock units.

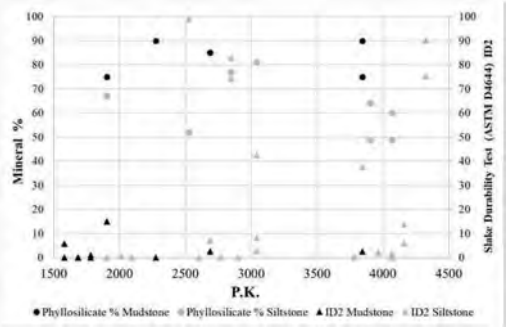

Figure 2. Mineralogy, clay content and SDI.

The swelling prone rock units contain clay in the range of 30 to 65%; with smectite contents in the range 40 to 80%. Some samples had smectite reaching as high as 90%.

For the specific characterization of swelling behavior, null pressure and free swelling tests were performed in accordance with ASTM D 4546-08 & ASTM D 3877. Huder-Amberg tests were also performed and yielded results

which suggested swell pressure far in excess of the ASTM test results and significantly higher than anything the design team could find in the literature. This made it much more difficult to accurately characterize the swelling behavior from a design standpoint.

After consideration of all testing results and a thorough review of the literature, it was determined that the Huder-Amberg tests were yielding erroneous results, likely resulting from poor sample handling and preservation and, possibly, due to the stress path typical of this test and maybe inappropriate for these soft rocks. Ultimately, a free swelling of a 3% and a null pressure close to 500 kPa were accepted as the probable maximum limits based on ASTM testing.

4.2 *Swelling loads in codes and standards*

Swelling is identified in many design codes as a geological hazard and/or load case that must be incorporated into the design. However, guidance on how to do so is notably light. AASHTO LRFDTUN (2017) for example defines swelling as something that needs to be evaluated but it don't provide load factors nor does it clearly state in which load combinations it should be featured.

FHWA-NHI-10-034 (2009) (Technical Manual for Design and Construction of Road Tunnels — Civil Elements. 2009) and FHWA-HIF-20-035 (2020) (Precast concrete segmental liners for large diameter road tunnels) both similarly treat swelling in the same way as other particular ground loading cases (such as squeezing ground, rock wedge load, creeping ground, etc..), that is as a specific type of ground classification which generates earth pressure. The former appears to suggest that swelling be treated as a ground load and thus subject to standard earth pressure load factors, however the latter identifies swelling as a "transient load" suggesting it have some other undefined load factor.

Other internationally recognized design guides such as the British tunnelling Society's (BTS) "Tunnel design guide" which explicitly states "Where swelling is unavoidable, the linings should be designed specifically for the stress-dependent portion of volume change".

Therefore it is interpreted by the authors that the code intent is generally to treat swelling as an earth pressure (in other words a pressure on the lining exerted by earth – regardless of the mechanism generating it). Thus, a load factor of 1.35 as defined for earth pressures in the AASHTO (2017) is assumed to be the appropriate way to handle swelling in the LRFD context.

4.3 *Design approach used for the segmental lining*

In theory, the use of pressurized slurry TBM excavation should mitigate the degree of swelling compared to typical open face TBM or conventionally mined excavation. The pressure in the excavation chamber maintains some degree of confinement around the excavation perimeter which limits the changes in stress which trigger swelling. Further, the slurry (or conditioned muck) in the excavation chamber preserves the saturated state of the ground, limiting the change in moisture content of the ground during excavation.

Although these two mechanisms should limit the degree to which swelling is triggered, changes in stress around the excavation perimeter are unavoidable and the pressure state in the excavation chamber can become more difficult to control in mixed face conditions. Even the use of quick hardening two-component grouts cannot fully confine the ground after excavation. In addition, hyperbaric interventions, issues with the backfill grouting injections or defects in the grouted annulus cannot be ignored and would all have a detrimental effect on swelling.

In the reference case discussed herein, the high weathering potential of the swelling prone rocks suggests a high potential of developing new cracks or modification of the existing joints/discontinuities allowing water ingress. These considerations led the design team to conclude that swelling remains one of the critical load cases despite the use of a pressurized TBM for excavation.

For the design of the reference Ø12.0m ID segmental lining, the selection of the swelling parameters was critical. Not only was there no other recorded experience of swelling in the region, but the laboratory data suggest highly varying results depending on the type of test performed as previously discussed. Thus, the design process began with a sensitivity analysis where the impact on the tunnel lining of different scenarios consisting of maximum swelling strain and null pressure were evaluated. The upper and lower limits of the analysis were defined by both the lab testing results and characteristic values seen in the literature. All calculations were carried out using the finite element software PLAXIS where the swelling mechanism was modelled using the purpose designed "Swelling Rock Model" constitutive model. This approach avoided complex coupled constitutive models with large number of input parameters difficult to obtain in such heterogenous geological conditions. Ultimately, it was determined that the swelling law be defined by a maximum swelling strain ($\varepsilon_i^{q(t=\infty)}$) of 5% and a maximum swelling pressure of 1 MPa, placing this project on the upper end of swelling loads. Figure 3 shows the proposed swelling law as envelope of the existing laboratory data.

These limits were selected in order to envelope all of the ASTM swell test results and provide a sufficient buffer to account for the risk of higher swelling see in the literature. Further, the swell strain and null pressure selected was not too penalizing since the finite element calculation was based on a "coupled" analysis where the volumetric strain is only based on the change of stress rather than the total value of stress (in other words, volumetric strain is only impacted by the slope of the blue line in Figure 3.

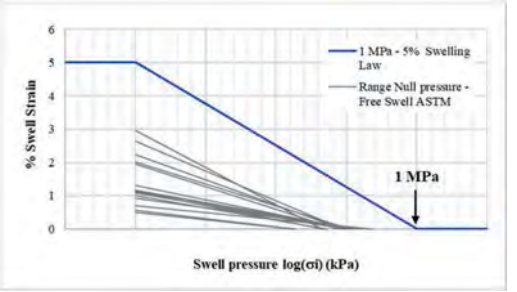

Figure 3. Swelling Law proposed after lab testing analysis and risk analysis.

Once the constitutive model was defined, a total of 14 sections were analyzed considering a range of geometrical, phreatic and geological conditions. The 4 most critical sections were selected for additional 2D dynamic models to ensure that lining was capable of handling the combined effect of swelling and earthquake. These dynamic calculations were run for 3 different time histories equivalent to imposing ground motions with a PGA of 1.06·g.

Despite the combined effect of high swelling loads and significant earthquake, the lining was able to be optimized to a 500mm thickness.

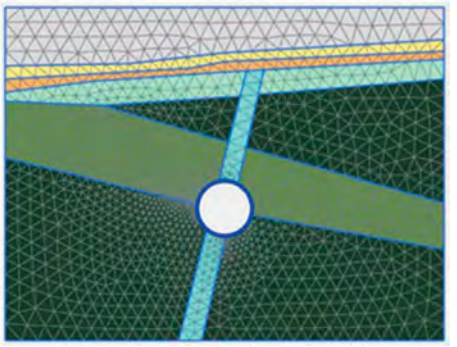

Figure 4. Example of numerical model simulating mixed face conditions in swelling ground.

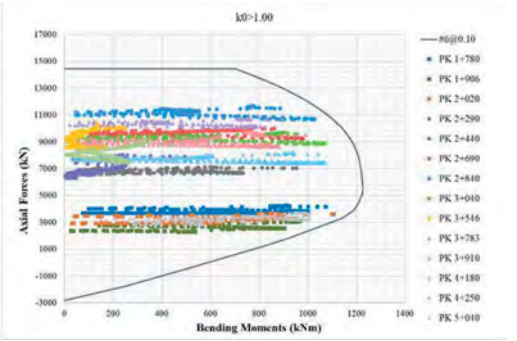

Figure 5. Verification of M-N loads at the analysed swelling prone sections.

4.4 *Impact of swelling during operation*

The internal structures of the example project were very sensitive to differential settlements. Thus, it was critical to understand how swelling deformations imposed on the lining would dissipate along the length of the tunnel. Since the swelling mechanism in pressurized TBM tunnels is not well understood, the design of the lining had to account for localized swelling impacting the internal structures in the longitudinal direction in addition to the full swell condition discussed in the previous section.

The total and differential swelling deformations imposed on the lining is a direct function of the length of tunnel over which the swelling occurs, and since it is impossible to know the length of the swelling zone, another sensitivity analysis had to be carried out.

Based on the numerous 2D models carried out for the lining, the design understood well what the potential magnitude of displacement the invert of the tunnel would experience under different swelling scenarios. However, these models fail to capture the tridimensional behaviour of the lining.

Subsequently, these 2D plane strain models were used to calibrate equivalent loads to be used to model swelling in a 3D finite difference model using the software FLAC 3D 7.00.

The 3D model was iterated such that swelling load was applied at progressively longer lengths of the tunnel. The results of each model were combined to investigate the changes in total and differential displacements of the tunnel invert as a function of the number of segmental rings carrying a swelling load. This exercise was carried twice. The first analysis covered the 'green field' condition, aimed at analysis how the tunnel behaves midway between stations. The second sensitivity analysis, addressed the issue of swelling activated close to a fixed point; equivalent to a 'station boundary condition'.

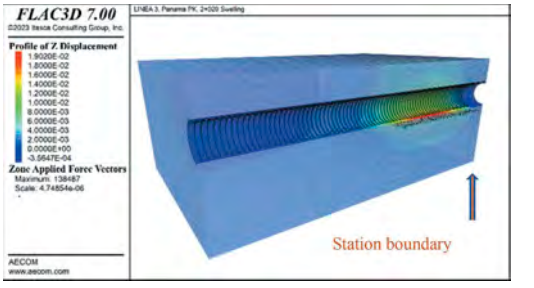

Figure 6. 3D numerical model for sensitive analysis of swelling triggered close to a station boundary.

The first analysis demonstrated that the highest angular distortions were more or less located at the edges of the applied swelling load. The second analysis (shown in Figure 7), illustrates that the presence of a station or shaft wall produces lower total displacements but higher (more critical) angular displacements.

5 CONCLUSIONS

The mechanisms related to swelling in the context of pressurized slurry TBM tunnelling is not well understood yet.

Although there are extensive records of SEM/ NATM tunnels impacted by swelling, limited references exist for pressurized EPB/Slurry TBMs. This paper provides a brief overview of the relevant literature and discusses how the uncertainties regarding swelling can be handled in design. Specifically, an example of lining design for a large diameter tunnel excavated by slurry shield in non sulphated swelling rocks is provided. Specifically, it is argued that the risks and uncertainties around swelling loads can be managed by a detailed program of numerical analyses based on lab testing and industry published experience from other projects.

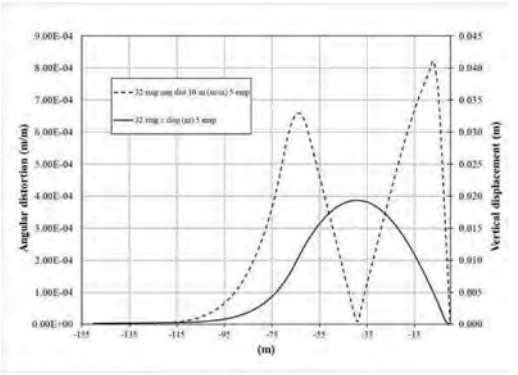

Figure 7. Analysis in terms of angular distortion of the potential swelling impact close to a station boundary.

For segmental lining design, extensive 2D PLAXIS models were useful to capture the mixed ground conditions of the project. The "Swelling Rock Model" was used to incorporate lab data and evaluate the sensitivity of the lining to different swelling parameters.

Greater accuracy needed to predict potential heave during operation was obtained by using 3D models simulating the rings and their longitudinal behaviour.

REFERENCES

AASHTO LRFDTUN. Road Tunnel Design and Construction Guide Specification. 2017

Alonso EE, Olivella S (2008) Modelling tunnel performance in expansive gypsum claystone. 12th International Conference on Computer Methods and Advances in Geomechanics, Goa 2008, pp 891–910

Anagnostou, G. (1993). A model for swelling rock in tunnelling. Rock Mechanics and Rock Engineering 26 (4), 307–331.

Butscher, C., Mutschler, T. & Blum, P., 2016. Swelling of Clay-Sulfate Rocks: A Review of Processes and Controls. In Rock Mechanics and Rock Engineering, vol. 49. Trans Tech Publications, Springer-Verlag GmbH, Austria, pp. 1533–1549.

Bjorge Brattli, Einar Broch, Stability problems in water tunnels caused by expandable minerals. Swelling pressure measurements and mineralogical analysis. Engineering Geology 39. 1995. pp. 151–169.

Carter, T.G., Castro, S.O., Carvalho, J.L., Hattersley, D., Wood, K. Tunnelling Issues of Chilean Tertiary Volcaniclastic Rocks. Proc. MIR 2010. XIII Ciclo di conferenze di Meccanica ed Ingegneria delle Rocce, Torino, Nov., 2010 pp. 215–236.

Cushing, A.; Hurt, J.; Carvalho, J. Time-Dependent Deformations of Excavations and Tunnels in the Greater Toronto Area. Proceedings of the World Tunnel Congress 2016.

DiMillo, T. et al. Development of a grout mix to be used as annular fill behind pre-cast concrete segments installed in tunnel with time dependent deformation character. TAC Annual Conference. 2016.

FHWA-NHI-10-034. Technical Manual for Design and Construction of Road Tunnels — Civil Elements. 2009.

FHWA-HIF-20-035. Precast Concrete Segmental Liners for Large Diameter Road Tunnels. Literature Survey and Synthesis. 2020)

Grossauer, K.; Carrera, E.; Schmid, W.; Zieger. Tunnel design and construction in swelling ground with lowoverburden and hydrothermal ground water conditions. Proceedings of the World Tunnel Congress 2019.

Jianxiu Wang, Jiaxing Liu, Xiaotian Liu, Yunhua Jiang, and Xuezeng Liu. In-site Experiments on the Swelling Characteristics of a Shield Tunnel in Expansive Clay: A Case Study. Korean Society of Civil Engineers, Journal of Civil Engineering. 2016.

Kovári, K.; Vogelhube, M. Empirical Basis for the Design of Tunnel Linings in Swelling Rock containing Anhydrite. Proceedings of the World Tunnel Congress 2014

Lecomte, B., Giuliani-Leonardi, S., Eymery, R., Serratrice, J.F.. Management of unexpected swelling clay on Cairo Metro line 3 Phase 2. Proceedings of the World Tunnel Congress 2014 – Tunnels for a better Life. Foz do Iguaçu, Brazil

Lo, K. Y; Mici, S. Evaluation Of Swelling Properties Of Shales For The Design Of Underground Structures. Geotechnical Research Centre. Faculty of Engineering The University of Western Ontario. Research Report GEOT-10-05. 2005.

Martin Ziegler, Arash Alimardani Lavasan, Simon Loew. Stress evolution around a TBM tunnel in swelling clay shale over four years after excavation. Tunnelling and Underground Space Technology 128. 2022.

Nilsen, B., Lama, R.D., 2021. Challenges and Some Recommendations Related to Estimation of in-situ Swelling Pressure of Gouge Materials. In: J. Sulem (Ed.), Rock Mechanics and Rock Engineering, vol. 54. Trans Tech Publications, Springer-Verlag GmbH, Austria, pp. 5141–5147.

Pérez-Romero, J., Oteo, C.S. de la Fuente, P. Design and optimization of the lining of a tunnel in the presence of expansive clay levels. Tunnelling and Underground Space Technology 22. 2006. pp. 10–22

Piaggio, G., Schönborn, Barla, M., 2017. Swelling Rocks Investigation on Hydro Tunnels – A Comprehensive Characterization based on Laboratory Tests and Constitutive Models. Proceedings of the World Tunnel Congress 2017, pp. 236–237.

PLAXIS Manual. Swelling Rock model.

Schädlich, B. (2013). Internal report: Swelling Rock model. Technical University Graz.

Ramon A (2014) Expansion mechanisms in sulphated rocks and soils. PhD thesis, Universitat Politècnica de Catalunya, Barcelona

Wahlen R, Wittke W (2009) Kalibrierung der felsmechanischen Kennwerte für Tunnelbauten in quellfähigem Gebirge (Calibration of the rock mechanical parameters for tunnels in swelling rock). Geotechnik 32:226–233

Wittke, W., Wittke, M.; Erichsen, C.; Wittke-Schmitt, B.; Wittke-Gattermann, P.; Schmitt, D. AJRM as basis for design and construction of more than 70 km of tunnels of the Railway Project Stuttgart-Ulm. Geomechanics and Tunnelling 10 (2017), No. 2.

Wittke-Gattermann, P. & Wittke, M. (2004) Computation of Strains and Pressures for Tunnels in Swelling Rocks. Proc. ITA 2004 E14, 1–9.

Tunnelling for a Better Life – Yan, Celestino, Thewes & Eberhardt (Eds)
© 2024 The Author(s), ISBN 978-1-032-80042-4
Open Access: www.taylorfrancis.com, CC BY-NC-ND 4.0 license

The numerical analysis for the segments floating mechanism of the large-diameter shield tunnel in the Rich Water Strata

Zhou Shi, Jin-Feng Xu & Xiong-Yao Xie
Key Laboratory of Geotechnical and Underground Engineering, Ministry of Education, Tongji University, Shanghai, China
Department of Geotechnical Engineering, College of Civil Engineering, Tongji University, Shanghai, China

ABSTRACT: In order to explore the segment floating mechanism of large-diameter shield tunnel in complex strata with abundant water near the sea and take corresponding control measures, this study, based on the Fuzhou Binhai Express Metro project, established a numerical calculation model considering the multi-factor coupling effect of shield machines, segments, slurry, and strata, and analyzed the interaction mode for slurry and segment, and segment floating mechanism under different slurry pressure distribution forms. The results show that: As the slurry pressure at the lower part of the tunnel segment increases, the floating displacement of each tunnel segment will correspondingly increase. At the same time, the floating displacement of the right and lower sides of each tunnel segment is relatively large, while the floating displacement of the upper and left sides is relatively small. The overall structure presents a torsional elliptical state of compression from the diagonal to the center of the segment. The change in the distribution form of slurry pressure has the greatest impact on the floating displacement of the first tunnel segment behind the shield tail, and the change in the distribution form of slurry pressure has a significant impact on the floating displacement difference between the upper and lower positions of the tunnel segment, while the impact on both sides is relatively small. The misalignment between adjacent segments gradually increases with the increase of slurry pressure at the bottom of the segment. The closer it is to the shield tail, the greater the misalignment between adjacent segments. Moreover, the change in slurry pressure distribution at the bottom of the segment has the greatest impact on the misalignment between adjacent segments near the shield tail. As the slurry pressure at the lower part of the segment increases, the growth rates of upper and lower misalignment are 200% and 142.8%, respectively. When the slurry pressure on the upper part of the segment is high, the overall axial force and bending moment at various parts of the tunnel segment are small, and the distribution range of negative bending moments on the upper part of the segment and the value of negative axial force on the lower part are small.

Keywords: Shield tunnel, Segment Floating, Numerical model, Slurry pressure, Segment misalignment

1 INTRODUCTION

During the construction of large-diameter shield tunneling in the soft and water rich strata near the sea, due to the influence of seawater environment, the groundwater head is high and the formation buoyancy is large, which makes it difficult for conventional synchronous grouting mortar to solidify quickly in humid environments. In addition, the bearing capacity of the weak strata is small, so it is unable to effectively constrain the deformation and displacement of the lining segments that detach from the shield tail. Moreover, due to the prolonged flow of the slurry behind the wall, the slurry often accumulates and fills at the bottom of the lining segment due to uneven diffusion under gravity and construction disturbances [1,2]. Under the action of formation buoyancy and uneven distribution of slurry pressure, the lining segment often experiences significant floating and misalignment, resulting in a significant deviation between the shape of the tunnel section and the design axis, which exceeds the specification requirements[3,4].

During shield tunnel construction, the engineering problem of uneven distribution of slurry pressure on the lining segment causing the segment floating has attracted widespread attention from scholars. Some progress has been made in field and indoor experiments, theory, and model calculations. However,

DOI: 10.1201/9781003495505-158

comprehensive analysis shows that during shield tunnel construction, the shield machine, lining segments, slurry, and strata are in a complex interaction state, which causes the segment floating to be influenced by multiple coupling factors [5,6]. In previous studies on slurry and tube theory and numerical calculation models, most of researchers simplified the effects of other factors while analyzing the interaction between the structures. In engineering practice, the deflection and compression effect of the shield machine on the segment and the uneven pressure of the support shoes in each zone of the jack can have an impact on the interaction state of the slurry segment. The overly simplified numerical model and theoretical assumptions in previous studies have caused significant differences between the analysis results and engineering practice [7,8]. Therefore, when constructing the numerical model, the complex coupling effect of the shield machine-lining segment- slurry-strata should be fully considered, to comprehensively evaluate the mutual influence between various components in the model.

Based on the Fuzhou Binhai Express Metro project, this study analyzes the interaction between the slurry and the lining segments during large-diameter shield tunneling construction in the water rich areas near the sea by numerical calculation. Based on the specific construction mode in engineering practice, establish a numerical calculation model for the multi factor coupling effect of shield machine-lining segment-slurry-strata. Through calculation and analysis, the interaction mode between slurry and lining segments under different forms of slurry pressure distribution and the segment floating law are explored, in order to reveal the segment floating mechanism of lining segments in the complex strata environment of rich water near the sea and propose reasonable engineering disposal measures.

2 NUMERICAL CALCULATION AND ANALYSIS OF SEGMENTS FLOATING

2.1 *Overview of engineering geology*

The outer diameter and inner diameter of a shield tunnel segment on the Fuzhou Binhai Expressway are 8.3m and 7.5m respectively. The starting and ending mileage of the left line is ZDK54 +354.106~ZDK58+622.528, with a length of 4246.399 meters. The left line has a total of 2360 linings. The shield tunnel section line is mainly laid along (near) the coastline and is mainly located in alluvial plains, coastal plains, and sea land interaction plains. The strata traversed by shield tunneling are complex and variable, involving (including mud) fine sand, (including mud) silty clay, silt, and muddy soil. The soft soil and water rich conditions make the assembled lining segments bear a significant water buoyancy effect. Under complex geological conditions, the deviation of shield machine posture results in the lining segments being in a biased state during the assembly process. At the same time, complex geological conditions lead to uneven diffusion of slurry and mud backflow, which causes obvious floating floating after the lining segments are assembled and detached from the shield tail. The horizontal and vertical posture of the lining segments is poor, as shown in Figure 1.

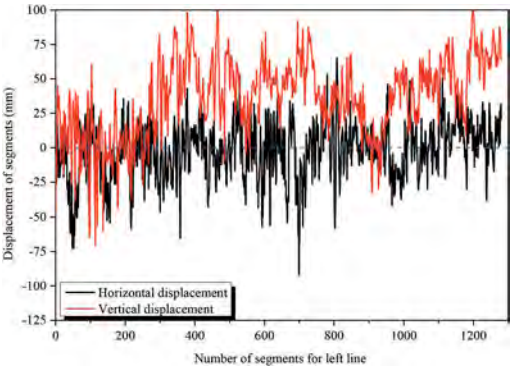

Figure 1. Horizontal and vertical attitude deviation of segments.

From Figure 1, it can be observed that during the excavation of the shield tunneling in the rich water layer near the sea, the assembled segments have significant deviations in both the horizontal and vertical directions compared to the design axis. Compared to the horizontal difference, the vertical difference value of the segments is larger and the fluctuation is more obvious. According to the statistical results of the first 1280 rings of lining segments, the overall vertical displacement of the lining segment ranges from -75mm to 100mm, with approximately 77% of the lining segments experiencing positive floating displacement. In the range of 900 to 1280 rings, the floating displacement of the lining segment shows a corresponding increasing trend with the ring number, and the correlation coefficient between the two reaches 0.72.

2.2 *Numerical model and boundary condition*

Based on the actual interaction mode between the shield machine and the lining segment during field engineering practice, this study established a numerical calculation model for the interaction between the shield machine, the lining segment, the slurry, and the strata, as shown in Figure 2.

2.2.1 *Components contact mode settings*

The adjacent lining segments at the joint are connected by bolts in blocks. After the lining segments are assembled, the pre tightening force quickly applied firmly connects the bolts and the lining segments. The bolts and the lining segments deform

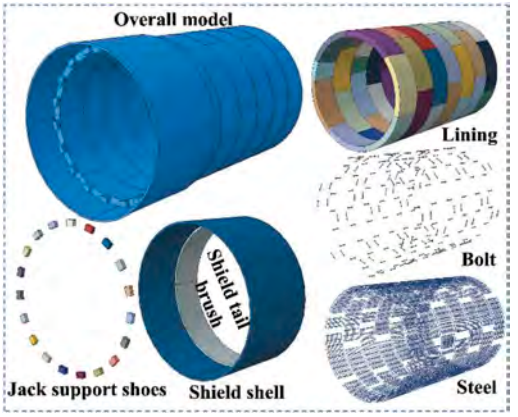

Figure 2. Numerical model of interaction for shield machine-segment-slurry-soil.

harmoniously and bear the force together. At the same time, the steel bars in the lining segments are poured together with the concrete structure, firmly connected to each other and cannot slide. Therefore, in this numerical model, the bolts and steel bars are combined with the lining segments in an embedded interaction form to meet the coordination and unity of the interaction modes between each other. The continuous transmission of mechanics and deformation modes between adjacent segments is achieved through the interaction between interfaces. Not only normal stress is transmitted between adjacent interfaces, but there is also a significant tangential force. The frictional interaction between segments and waterproof rubber pads is simulated using the Coulomb friction model.

2.2.2 *Thrust setting of shield machine jack*

The geological conditions in the rich water area near the sea are complex, and there is often the posture deviation and forward tilting of the shield during the tunnel construction. The deviation in posture between the shield machine and the lining segment causes each group of jack support shoes to not be in the same plane, and there is a significant difference in the thrust and cylinder stroke of each group of jack. In this numerical model, the non-uniformity of the thrust of each group of jack should be considered, and 19 sets of support shoes should be simulated using solid units. The normal interaction between the support shoe and the lining segment is simulated through hard contact, and the tangential interaction is achieved through Coulomb friction model.

2.2.3 *Shield machine and shield tail brush*

In this numerical model, a shield shell and shield tail brush model were established. The deviation of the rear cylinder of the shield machine was simulated by the up and down rotation of the shield shell model, and the deflection effect of the shield machine was simulated by the circumferential rotation of the shield shell, in order to objectively and truly characterize the interaction between the shield machine and the lining segment. According to the field monitoring results of segment floating, the impact range of shield machine construction is revealed. In this numerical analysis model, the segment is set as 7 rings, with the segment that is about to detach from the shield tail being defined as the second ring, and the segment in the first ring behind the shield tail being defined as the third ring. In the model in this study, a whole structure was used to simulate the shield tail brush. The thickness of the shield tail brush model is the width of the pores between the shield shell and the lining segment. The model length is based on the actual length of the tail brush, and the structural properties are set based on the relevant parameters of the steel wire.

2.2.4 *Slurry pressure and load distribution form*

Engineering practice has shown that the floating of the lining segment mainly occurs during a period of time after detachment from the shield tail. At this time, the slurry on the outer wall of the lining segment is still in a flowing state, and the lining segment floating in the slurry is mainly affected by the static buoyancy and dynamic slurry pressure of the surrounding liquid slurry. The displacement of the lining segment is not limited and is in an floating state. Therefore, the main reasons for the floating of the lining segment in the complex environment of rich water near the sea are the dynamic slurry pressure and the aforementioned shield tail compression effect. The grouting system behind the shield tunneling machine wall is composed of 6 grouting holes, with 2 grouting holes arranged at equal intervals in the upper, middle, and lower parts. During the grouting process behind the wall, the slurry gushes out from the grouting holes. Correspondingly, different mechanical interaction modes can be divided into the following five types as a whole, as shown in Figure 3.

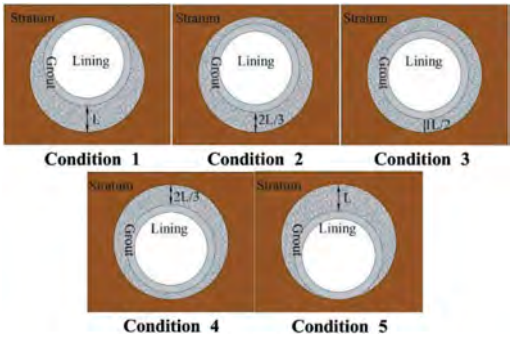

Figure 3. Relative positions of slurry and segments under different working conditions.

During the slurry solidification, the slurry will gradually penetrate into the soil, and the slurry pressure will dissipate accordingly. At the same time, the groundwater content in the water rich strata near the sea is rich, and the slurry is further diluted. Therefore, the slurry pressure will continue to decrease. When the slurry solidifies, the slurry pressure will dissipate to 0, which acts as the contact medium between the soil layer and the lining segment and transfers the soil pressure to the lining segment. The slurry pressure on the outer wall of the segment that has just emerged from the shield tail is the highest, and gradually decreases to 0 along the longitudinal direction of the tunnel. At the position where the slurry pressure is 0, the external load on the segment structure is equal to the soil pressure. The shield machine is subjected to external earth pressure, and the first lining segment located in the shield tail only bears the thrust of the jack, while the second lining segment bears the compression of the tail. The segments of the 3rd and 6th rings not only bear external soil pressure, but also linearly reduced slurry pressure. The segments of the 7th ring bear external normal soil pressure, and the longitudinal distribution of engineering loads in the numerical model is shown in Figure 4.

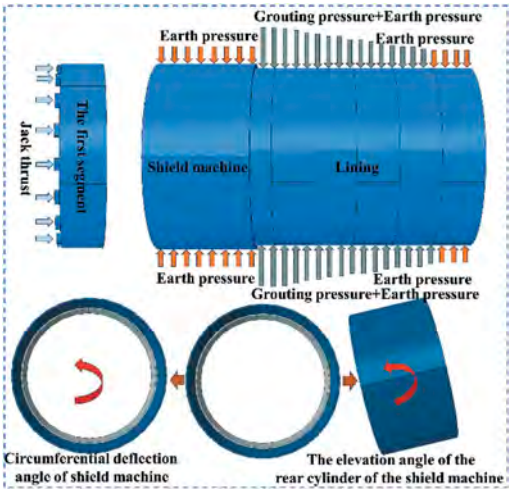

Figure 4. Engineering load distribution and action mode.

Based on the relative position relationship between the slurry and the lining segment in Figure 4 above, combined with field engineering practice and real-time slurry pressure data of shield machines, and referring to the dynamic slurry pressure calculation method applied to the lining segment in most unfavorable distribution state of slurry (i.e. when the strata water content is relatively high, the permeability of the slurry in the formation is low, and the slurry diffusion method is compaction grouting, with most of the slurry mainly accumulating in the lower part of the lining segment) in reference [7]. This study set up a total of five calculation conditions, and the load magnitude and parameter distribution of each component of the model under different calculation conditions are shown in Table 1.

Table 1. Load magnitude and calculation parameters of each component under different working conditions.

Part	Weight/kg•m^{-3}	Elastic modulus / Gpa	Poisson's ratio	Yield stress / MPa	Yield strain
Shell	7850	210	0.1	640/800	0/0.021
Shield tail brush	7850	70	0.28	302/455	0/0.0754
Lining	2500	36.4	0.2	25.3/84.5	0/0.1
Bolt	7850	210	0.1	640/800	0/0.021
Steel	7850	210	0.1	302/455	0/0.0754
Jack	7850	210	0.1	640/800	0/0.021
Jack thrust F1	Jack thrust F2	Jack thrust F3	Jack thrust F4	Jack thrust F5	Jack thrust F6
2.3MPa	2.5MPa	2.4MPa	2.6MPa	2.3MPa	2.7MPa
Condition 1	Condition 2	Condition 3	Condition 4	Condition 5	
upper part 0.05MPa	upper part 0.1MPa	upper part 0.15MPa	upper part 0.2MPa	upper part 0.25MPa	
lower part 0.25MPa	lower part 0.2MPa	lower part 0.15MPa	lower part 0.1MPa	lower part 0.05MPa	

2.3 *Analysis of calculation results*

2.3.1 *Floating displacement of lining segment*

The working condition 1 in this numerical calculation is based on the field engineering practice. After the segment is assembled, the floating displacement of the third lining segment is obtained through field measurement. After the numerical calculation, the floating displacement of the segment in the numerical model is compared with the field measurement results, as shown in Figure 5.

From Figure 5, it can be seen that under different working conditions, the second and third lining segments both have larger floating displacement on the right and lower sides of the segment, while the floating displacement on the upper and left sides is smaller, which is mainly because in the field engineering practice, when the shield shell produces a rear cylinder pitch angle, the entire shield shell also undergoes circumferential deflection along the design axis. In this study, the shield shell is circumferential counterclockwise deflection. Driven by frictional contact between the shield shell and the second lining segment, the assembled and connected lining segments will also experience

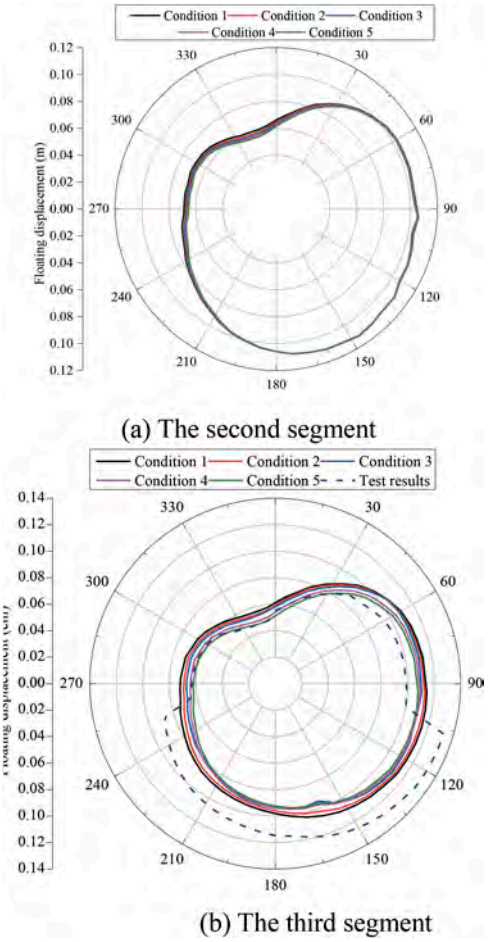

Figure 5. Distribution of numerical calculation results for floating displacement at various positions of segments.

corresponding deflection, and the external slurry of the second and third lining segments has not reached a solidification state at this time, which cannot limit the deflection of the segments. Therefore, the right side of these two lining segments will also deflect upward, resulting in significant vertical floating displacement. The vertical floating displacement of the left and upper parts of the lining segment will be limited by the circumferential deflection of the shield shell. At the same time, it can be observed that the vertical floating displacement of the second lining segment is greater than that of the third lining segment under different working conditions. As the slurry pressure at the lower part of the segment increases, the vertical floating displacement of the second and third lining segments will correspondingly increase. The overall structure of the segment shows a deformation state of squeezing from the center of the segment in the lower right and upper left directions. The overall pattern of the field segment floating test results and numerical calculation analysis results is in good agreement, with an average error of 17.3%. Therefore, it can be concluded that the numerical calculation model and related boundary condition settings in this study have good engineering applicability.

2.3.2 *Comparative analysis of lining segment floating and misalignment results*

Engineering practice has shown that after the completion of segment assembly and detachment of the shield tail, complex floating and staggered structures occurred within the longitudinal and transverse ranges. In order to verify the engineering applicability of the numerical model in this study, the distribution of floating and staggered structures in the numerical model was compared and analyzed with the statistical results of the sensitive parts of the segments in engineering practice, as shown in Figure 6.

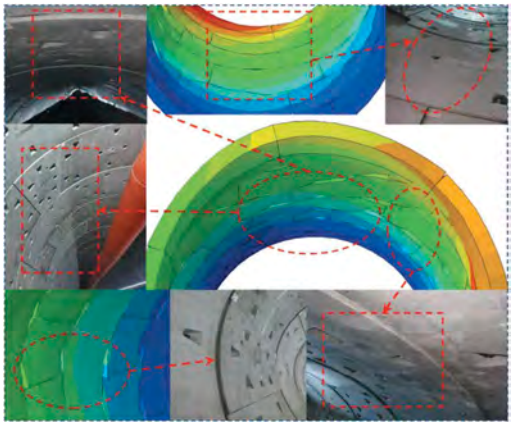

Figure 6. Comparison of numerical calculation and engineering practice for segments floating.

From Figure 6, it can be seen that after the field lining segments were assembled and detached from the shield tail, the apparent floating displacement occurs in every lining segments, and the difference in floating displacement between each lining segment led to the occurrence of a stepped staggered platform between the adjacent segments. That is, along the longitudinal direction of the tunnel, the N +1 lining segment floated floatings relative to the N ring lining segment, which is more evident in the upper and lower parts of the lining segment. At the same time, under the coupling effect of factors such as the longitudinal and circumferential deflection of the shield machine compared to the design axis, uneven distribution of slurry pressure, and bolt dragging between the adjacent lining segments, the forces acting on each lining segment are extremely uneven within the spatial range, resulting in elliptical

deformation of the segment structure with different shapes, leading to significant segments misalignment and joint opening. The complex external load action modes and distribution states within the spatial range have led to varying degrees of compression and stretching between the various blocks within the segment structure. As the smallest and most irregularly shaped block in the entire lining segment, K block bears complex loads from other blocks during the assembly process, and is often difficult to be in the standard design position during the final installation process. The uneven distribution of external forces can easily cause K blocks to undergo extrusion deformation towards the interior of the tunnel after assembly. The numerical simulation calculation results indicate that under external loads and boundary conditions that are consistent with actual engineering, the proposed numerical calculation model with multi coupling factor in this study can effectively present typical floating displacement and dislocation phenomena such as stepped misalignment at the top and bottom of lining segments, lateral wall ring misalignment, and K-block extrusion in field engineering. From this, it can be concluded that the numerical calculation model in this study has good engineering applicability.

2.3.3 *Misalignment and internal force distribution*

The above calculation results of the vertical floating displacement of the segments indicate that during the construction of a large diameter shield tunnel, due to the complexity of construction factors and slurry distribution, there are significant differences in the vertical floating displacement between different segments along tunnel. The spatial variation of the floating displacement between adjacent segments can lead to the occurrence of adjacent misalignment. Field engineering practice and numerical calculation results indicate that the values of adjacent misalignment between the upper and lower parts of adjacent segments are often larger compared to other parts, and they are most susceptible to changes in the distribution form of slurry pressure. This study obtained four adjacent misalignment between the 2nd and 6th rings from numerical calculation results, as shown in Figure 7.

From Figure 7, it can be seen that along the tunnel, the adjacent misalignment at the upper position and the adjacent misalignment at the lower position gradually increase with the increase of the slurry pressure at the bottom of the segment. The closer to the shield tail, the greater the adjacent misalignment between adjacent segments, and the misalignment between rings 2 and 3 is the largest. From the comparative analysis of adjacent misalignment under different slurry pressures, it can be concluded that the different distribution forms of slurry pressure in the lower part of the lining segment have the greatest impact on the adjacent misalignment near the shield tail between segments 2 and 3. As the lower slurry pressure increases, the upper adjacent misalignment of segments 2 and 3 increases from 5mm to 15mm, and the lower adjacent misalignment

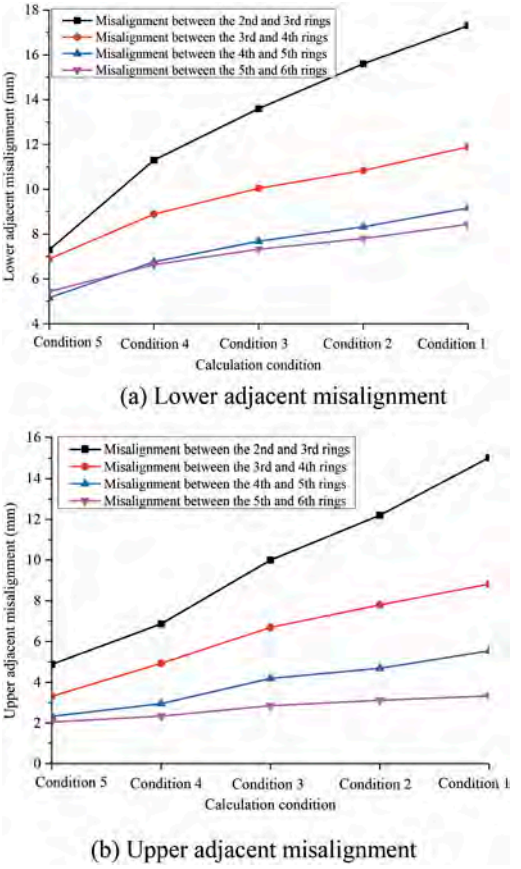

Figure 7. Analysis of misalignment between adjacent segment under different working conditions.

increases from 7mm to 17mm, with growth rates of 200% and 142.8%, respectively. Among them, in condition 5, the upper and lower adjacent misalignment of the lining segment are relatively small. In comparison, the difference in the distribution of slurry pressure at the lower part of the segment has the smallest impact on the adjacent misalignment between rings 5 and 6. As the lower slurry pressure increases, the adjacent misalignment at the lower and upper parts of rings 5 and 6 increases by 3mm and 1mm, respectively.

The above calculation results indicate that the change in the distribution form of external slurry pressure has the greatest impact on the spatial distribution characteristics of the floating displacement and longitudinal misalignment of the third lining segment. The overall asymmetric deformation of the segment structure can cause extremely uneven internal force distribution. Therefore, this study obtained the bending moment and axial force of the third lining segment along the circumferential direction of various parts under different working conditions, as shown in Figure 8.

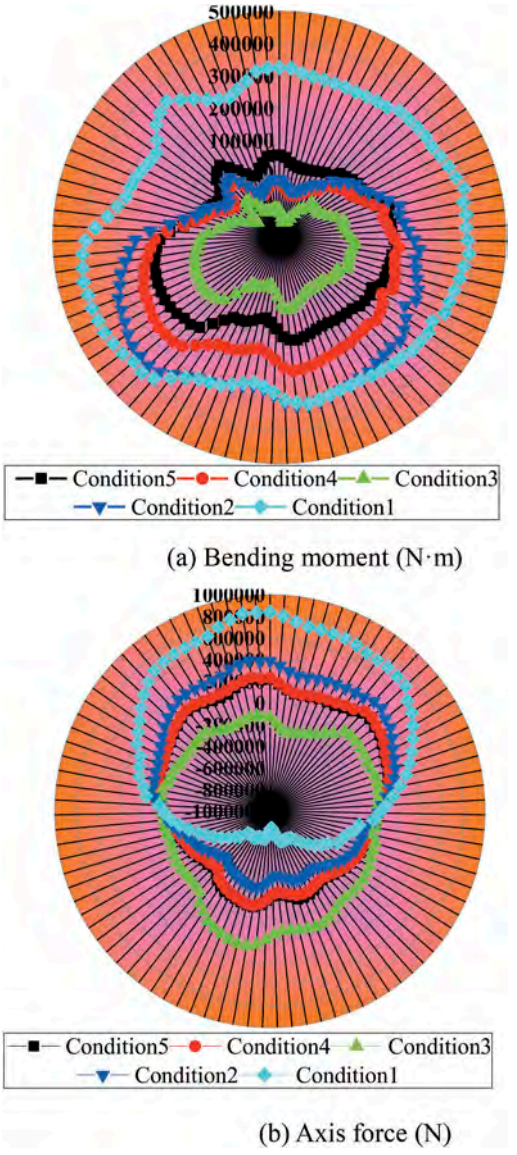

Figure 8. Bending moment and axial force distribution of the third segment under different working conditions.

As shown in Figure 8, the change in the distribution of external slurry pressure on the segment will have a significant impact on the axial force and bending moment distribution of the third lining segment structure. For Condition 1 and Condition 2, when the slurry pressure at the bottom of the lining segment is high, there is a significant bending deformation at the bottom of the lining segment structure, resulting in a larger bending moment at the lower part of the structure. At the same time, in Condition 2, there is a negative bending moment at the local position of the upper part of the lining segment, which shows a deformation trend of opening outward, which can easily cause tensile cracks on the outer wall of the lining segment, and the outward opening of the joint, further leads to the pouring of groundwater from the outer wall into the lining segments and tunnels, resulting in overall structural leakage. At the same time, from the distribution of axial force, it can be found that compared to other working conditions, there is a significant negative axial force in the lower structure of the lining segments in working conditions 1 and 2, that is, there is a significant tensile stress distributed in the lining segments, and the lower part of the structure is prone to tensile failure. When the external slurry pressure distribution of the lining segment is relatively uniform in Condition 3, the bending moment and axial force values of each part of the lining segment structure are generally small. In this case, when the lining segment floats upward as a whole, the distribution range of negative bending moment and negative axial force values on the upper part of the lining segment is large, that is, there are many parts of the structure that open outward and produce tensile deformation. These parts are sensitive areas for tensile cracks to occur outside the structure, and groundwater outside the lining segment is prone to seeping into the concrete inside the segment. For conditions 4 and 5, compared to conditions 1 and 2, the axial force and bending moment at various locations of the segment structure are generally smaller, and the distribution range of negative bending moment at the upper part and the value of negative axial force at the lower part of the segment are smaller. Therefore, the possibility of structural joint opening and tensile cracks occurring on the outer wall of the segment is higher. It can be concluded that the larger slurry pressure at the upper part of the segment structure can significantly reduce the floating displacement of the segment structure while also improving the structural stress, reducing tunnel leakage disasters caused by the outward opening of segment joints and the development of tensile cracks on the outer wall. At the same time, it can be observed that there is not a significant difference in axial force between the various parts of the segment structure in Condition 4 and Condition 5, but the bending moment values in each part of the segment structure in Condition 5 are smaller and the overall distribution is more uniform. From the distribution of adjacent misalignment under different working conditions mentioned above, it can be observed that compared with Condition 4, the adjacent misalignment at the upper and lower parts of the 2nd and 3rd lining segments in Condition 5 is smaller, and the pulling effect between the bolts and segments between the 2nd lining segments is weakened. Therefore, the bending deformation of the lining segment is small, and the overall bending moment of the lining segment structure is relatively small.

Based on the above analysis, it can be found that changes in the distribution form of slurry pressure

can lead to significant changes in the magnitude and distribution form of the floating displacement of the shield tail and the adjacent misalignment. During the synchronous grouting process of the shield tunnel, the slurry with lower consistency has greater fluidity. Under the influence of factors such as gravity and construction disturbance, the slurry on the upper part of the segment will slide and accumulate along the outer side of the segment to the bottom of the segment, and the slow initial setting speed of the slurry causes the slurry to be in a liquid flow state for a long time. As the upper slurry gradually slides down, a large amount of liquid mortar in a flowing state accumulates in the lower part of the lining segment, resulting in a significant floating force on the lining segment. At this time, the amount of slurry in the upper part of the lining segment decreases, causing a sharp decrease in the downward slurry force. The floating displacement occurs in the lining segment structure in liquid slurry due to the large difference in slurry pressure between the lower and upper parts of the segment, resulting in adjacent misalignment due to the difference in slurry pressure. The segments closest to the shield shell (the 2nd and 3rd rings in this calculation model) are surrounded by the newly injected and most flowable slurry. Therefore, the slurry at the bottom of the segment has the highest buoyancy force. The above calculation results indicate that the larger slurry pressure at the bottom of the segment can cause significant adjacent misalignment between the 2nd and 3rd lining segments. At the same time, it is also easy to cause tension cracks on the outer wall of the lining segment and the outward opening of the joints, thereby increasing the risk of groundwater pouring into the lining segment to corrode steel bars and leak diseases. When the slurry pressure on the upper part of the lining segment is greater than that on the lower part of the lining segment, the control effect of lining segment misalignment is the best. Therefore, during the shield tunneling process, the slurry on the outer wall of the lining segment located at the shield tail and just detached from the shield tail should be quickly condensed, to prevent the upper part of the lining segment from sliding and accumulating slurry at the bottom of the tunnel, and during the synchronous grouting process behind the wall, the amount of grouting at the upper part of the lining segment should be appropriately increased to generate greater slurry pressure, effectively preventing the occurrence of floating of the lining segment structure.

3 CONCLUSIONS

This study established a numerical calculation model for the multi factor coupling effect of shield machine-lining segment-slurry-stratum, and analyzed and explored the interaction mode of slurry-lining segment and the floating law of lining segments under different slurry pressure distribution forms. The main research conclusions are as follows:

(1) As the slurry pressure at the lower part of the segment increases, the vertical floating displacement of each lining segment will correspondingly increase. At the same time, the counterclockwise circumferential deflection effect of the shield machine will cause larger floating displacement on the right and lower sides of each lining segment, while smaller floating displacement on the upper and left sides. The overall structure of the segment presents a torsional elliptical state of compression from the diagonal to the center of the segment. Compared with the lining segment in the shield tail, the change in the distribution form of slurry pressure has the greatest impact on the floating displacement of the first lining segment behind the shield tail. The change in the distribution form of external slurry pressure has a greater impact on the floating displacement difference between the upper and lower positions of the segment, while the impact on both sides is relatively small.
(2) The misalignment between adjacent segments along tunnel gradually increases with the increase of slurry pressure at the bottom of the segment. The closer the segment is to the shield tail, the greater the misalignment between adjacent segments. The change in the distribution of slurry pressure at the bottom of the segment has the greatest impact on the misalignment between adjacent two segments near the shield tail. As the lower slurry pressure increases, the increase in misalignment between the upper and lower segments is 200% and 142.8%, respectively. When the slurry pressure on the upper part of the segment is high, the overall axial force and bending moment at various parts of the segment structure are small, and the distribution range of negative bending moments on the upper part of the segment and the value of negative axial force on the lower part are small.

ACKNOWLEDGEMENTS

This work was supported by the National Key R&D Program of China under grant 2019YFC0605100 and 2019YFC0605103; the National Nature Science Funds of China under grant 51978431, and 52038008; and the Science and Technology Project of the Department of Transport of Yunnan Province China (Yunnan Transportion Science and Education [2021] No.7). The authors gratefully acknowledge their financial support.

REFERENCES

[1] Huai Rong-guo, Huang Si-yuan, Zhong Xiao-chun, et al. Development and Engineering Application of

Novel Synchronous Double-Component Grouting behind Shield Segment [J]. Tunnel Construction, 2022, 42 (09): 1521–1528. (in Chinese)
[2] Tielin Chen, Tiezheng Pang, Yong Zhao, et al. Numerical simulation of slurry fracturing during shield tunnelling, Tunnelling and Underground Space Technology, 2018, 74: 153–166.
[3] Zhu Wei, Lu Kai-jun, Xing Hui-tang, et al. Experimental Study of "Time-controlling Cement Mortar" in Backfill Grouting of Shield Tunnel [J]. Tunnel Construction, 2022,42 (05): 784–790. (in Chinese)
[4] Yu Qun-zhou, Sun Le-sheng, Zhou Cheng, et al. Control of Floating Segment of Shield Tunneling in Water-rich Hard Rock Stratum [J]. Journal of Civil Engineering and Management, 2022, 39 (01): 61–67. (in Chinese)
[5] Fu Yan-bin, Mei Chao, Bian Yue-wei, et al. Analytical Solution and Application of Large-diameter Shield Segment Uplift Considering the Filling Rate of Grouting [J]. China Journal of Highway and Transport, 2022,35 (11): 171–179. (in Chinese)
[6] Xiao Ming-qing, Feng Kun, Zhang Yi, et al. Analysis of Segment Dislocation Caused by Grout Buoyancy during Synchronous Grouting of Shield Tunnels [J]. Tunnel Construction, 2021,41 (12): 2048–2057. (in Chinese)
[7] Wang Dao-yuan, Yuan Jin-xiu, Zhu Zheng-guo, et al. Theoretical solution of longitudinal floating movement of underwater shield tunnel and its application [J]. Rock Soil mechanics, 2014, 35 (11): 3079–3085. (in Chinese)
[8] Zhang Jian, Jin Jun-jie, Feng Tu-gen, et al. Optimization of mixture ratio of muck grout by earth pressure balance shield machine [J]. Chinese Journal of Geotechnical Engineering, 2023,45 (04): 748–757. (in Chinese)

Tunnelling for a Better Life – Yan, Celestino, Thewes & Eberhardt (Eds)
© 2024 The Author(s), ISBN 978-1-032-80042-4
Open Access: www.taylorfrancis.com, CC BY-NC-ND 4.0 license

Analysis of composite shell lining based on laminated theory

Wen Shuyi*
China Railway Academy Co., Ltd

ABSTRACT: Spraying waterproof membrane can make the shotcrete and membrane have a composite effect. However, at present, there is no design guidance and reference literature on the structure analysis of composite shell lining. Using laboratory testing methods, a comparative test was conducted on four point beams bending toughness and energy absorption for structures with and without waterproof membrane. The equivalent thickness of the sandwich structure was calculated based on the flexural strength or deflection reduction ratio . And based on the laminated theory, the equivalent thickness theory was derived, and the rationality of the experimental results was verified through examples; At the same time, it was found that the key factors affecting the equivalent thickness of the laminated are the shear strength of the sprayed waterproofing, the thickness of the sprayed waterproofing, and the equivalent diameter of the tunnel etc through the laminated theoretical formula. The greater the shear stiffness of the sprayed membrane, the thinner the thickness of the sprayed membrane, the thinner the equivalent thickness . It was found that the method used in this article can determine the equivalent thickness, with small dispersion and high degree of fit, and can provide guidance for design company.

Keywords: composite shell lining, laminated theory, sprayed membrane

1 INTRODUCTION

The waterproofing of double shell lining tunnels is achieved by installing prefabricated sheet membrane, which are installed between the primary lining (outer) and the secondary lining (inner). The sheet membrane serves as a separation layer or sliding layer between the lining. However, in tunnels with complex geometric shapes, it is difficult for sheet membrane to closely adhere to the excavation contour, and due to damage or excessive stretching caused by a large number of welds, steel reinforcement installation, and poor installation of secondary concrete lining, the waterproof board often leaks.

When using spray waterproofing with high double-sided bonding strength combined with permanent sprayed concrete as the first and second layers of sprayed concrete, due to the composite behavior between the two layers, the first and second layers of sprayed concrete can be considered as a single composite structure, i.e. composite shell lining [1].

As a relatively new lining structure, composite shell lining tunnels are less commonly used domestically and internationally, such as the Crossrail and London Underground Bank Station renovation and upgrading projects. Although the International Tunneling Association released the "ITAtech Design Guidance For Spray Applied Waterproofing Membranes" in 2013 to guide and standardize the application of this technology, it did not provide a clear calculation method for the stress on the lining structure[2], and there is a lack of measured parameter data. In order to solve this problem, the theory of laminated glass in other industries was mainly used in the early stage. Reference[3] is a specification for laminated glass, which provides an algorithm for calculating the equivalent thickness of laminated glass. However, compared to concrete, the material properties are different, and no theoretical derivation or analysis is provided. Bennison[4] studied the mechanical properties of laminated glass and indicated that performance can be improved by combining rigid, structural, non PVB interlayers with modern glass processing methods; However, there has been no research on concrete structures and laminated structures with sprayed membrane. Liu Runquan[5] conducted in-depth research on the bending theory of composite sandwich beams and calculated the bending stress and deflection of sandwich beams using analytical methods, but did not obtain the equivalent thickness and bending moment distribution. Reference[6] studies the stress state and potential failure mechanisms of spray membrane

*Corresponding author: 359418435@qq.com

DOI: 10.1201/9781003495505-159

interfaces, as well as membrane testing methods. Some scholars also explore through numerical simulation methods. Reference[7] used contact surface elements and other forms to simulate the spray membrane, but the setting parameters of the contact surface were mainly based on some assumptions, and the calculation results of different engineering examples varied greatly. Reference[8] combines drained and undrained conditions to numerical analyze axial force, bending moment, and stress of each layer sprayed concrete under six different second layer thickness conditions of 50mm~300mm. In recent years, some research work has tested simulated components of tunnel lining structures containing spray membrane from an experimental perspective. References [9-10]: Aecom Corporation in the UK, in collaboration with Warwick University, conducted spray panel tests on composite shell lining under soft soil conditions, and conducted cyclic tensile and shear tests on the core for analysis. Reference[11,12] conducted laboratory tests on sandwich beams and obtained load-deflection curves, which also proved that there is a high degree of composite effect at spray membrane interface. The University of Cambridge has produced a compression bending test beam containing a spray membrane layer, and tested the stress and strain changes of each section of the specimens during the loading process. A preliminary study was conducted on the mechanical properties of the specimens[13]. Chinese scholars have also conducted research on its load-bearing mechanism, material characteristics, and structural design. Zhou Ping[14] used experimental methods to analyze the stress characteristics of multi-layer lining structures under interlayer action. Previous studies have found that each layer of multi-layer sprayed concrete has a radial anti slip effect. When they form a composite lining, they can form an overall load-bearing structure. Jiang Yajun et al. [15] established numerical calculation models for double shell lining, composite shell lining, and single shell lining based on the mechanical and interface parameters of the sprayed membrane measured through experiments, and conducted internal force analysis of the composite lining. Jiang Yajun et al. [16] investigated the shear failure mechanism and mechanical properties of the interlayer interface of the double-sided bonded tunnel lining structure, and obtained relevant parameters based on the Mohr Coulomb constitutive model, which can serve as a basis for judging the failure of the contact surface of the double-sided bonded tunnel spray membrane lining. Deng Yisan [17] quantitatively measured the integrity of structures with strong interlayer bonding, but did not establish a mechanical relationship between the external load and the various composite layers.

This article obtains the equivalent thickness of the sandwich spraying membrane structure through laboratory experiments, and proposes a composite shell lining analysis method based on the Laminated theory for verification.

2 RESIDUAL STRENGTH TEST

2.1 *Test purpose*

In order to obtain the equivalent thickness of the composite shell lining, the bending toughness is tested using the four point bending method in accordance with the "Technical Specification for Application of Sprayed Concrete". By comparing the bending strength and residual bending strength of the small beam with and without sprayed membrane, the equivalent thickness of the interlayer structure is obtained. It is determined that the equivalent thickness can be calculated in the analysis to comprehensively consider the influence of sprayed membrane interlayer shear.

2.2 *Test method*

The cross-section of the small beam is 150 × 150 × 550mm, the bending toughness is tested using the "SANS" mechanical universal testing machine produced by Meters Industrial Equipment Company, with a loading rate of 0.15mm/min. The deflection change at the center of the beam is tested using a specially designed fixture to fix the sensor. During the testing process, a pair of telescopic displacement sensors and a combination of telescopic and clamp displacement sensors are used on both sides of the beam sample (mutual verification of accuracy), Used to test the deflection of the beam under compression, the installation form of the test is shown in Figure 1.

Figure 1. Beam specimen and deflection test sensors.

2.3 *Result analysis*

Conduct bending toughness testing on the beam specimen, with BASF Master345 sprayed membrane in the middle,both layers are synthetic fiber concrete. The stress-strain curves is shown in Figure 2. The bending strength and residual bending strength under various working conditions are shown in Table 1.

For synthetic fiber concrete, the proportion of flexural strength incorporating BASF sprayed membrane to the flexural strength without sprayed membrane is 62%, and the proportion of residual flexural strength incorporating BASF sprayed membrane to the residual flexural strength without sprayed membrane is 72%, 55%, 64%, and 87%, respectively. The

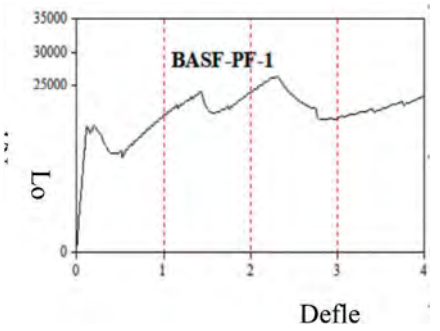

Figure 2. Load-deflection curve of concrete beam.

Table 1. Shotcrete (residual) bending moment in each layer.

Item	BASF-PF	BASF-SF	PF	SF
Bending strength	2.98 (62%)	3.26 (56%)	4.82	5.86
Residual strength (deflection 0.5mm)	2.12 (72%)	2.5 (62%)	2.94	4.02
Residual strength (deflection 1mm)	2.03 (55%)	2.7 (74%)	3.68	3.65
Residual strength (deflection 2mm)	2.59 (64%)	3.04 (84%)	4.07	3.60
Residual strength (deflection 4mm)	3.15 (87%)	3.26 (96%)	3.64	3.41

comprehensive judgment ratio is 68%. For steel fiber reinforced concrete, the proportion of flexural strength incorporating BASF sprayed membrane to the flexural strength without sprayed membrane is 56%, and the proportion of residual flexural strength incorporating BASF sprayed membrane to the residual flexural strength without sprayed membrane is 62%, 74%, 84%, and 96%, respectively. Based on comprehensive judgment, the proportion is 74%. Due to the formula for flexural strength being $f_c = \frac{PL}{bd^2}$, the deflection at the midpoint of the span is $y(\frac{l}{2}) = \frac{46Pl^2}{108bd^3}$. Therefore, in the case where the deflection of sandwich beams is equivalent to that of homogeneous beams, if the load or flexural strength accounts for 68%, the section height is determined $\sqrt[3]{0.68} \times 150mm = 0.88 \times 150mm = 132mm$. Similarly, the equivalent thickness of steel fiber reinforced concrete sandwich beams is determined by the section height $\sqrt[3]{0.74} \times 150\text{mm} = 0.90 \times 150mm = 136mm$.

3 ENERGY ABSORPTION TEST

3.1 *Test purpose*

The energy absorption of circular plates refers to the "Standard for Testing Methods of Fiber Reinforced Concrete" (CECS13-2009). By comparing the energy absorption values without and with sprayed membrane, the equivalent thickness of the sandwich structure is obtained. It is determined that the equivalent thickness can be calculated in the analysis to comprehensively consider the influence of interlayer shear.

3.2 *Test method*

The stress-strain curve of a circular plate under central compression is tested through three point support and central point loading. The deflection value is the displacement of the central compression point of the circular plate, and the loading rate is controlled to 4.0 mm/min according to the regulations. Based on the stress-strain curve of each specimen, the energy absorption values of the specimen under compression to the following characteristic deflection points of 5mm, 10mm, 20mm, and 40mm are calculated through integration.

In the experiment, both steel fiber reinforced concrete and plain concrete follow the normal testing method, where the bottom and top surfaces of the sample during molding serve as the lower support and upper compression surfaces, to ensure uniform stress on the sample. The installation form of the experiment is shown in Figure 3.

Figure 3. Energy absorption specimen.

3.3 *Result analysis*

Perform energy absorption testing on the plate specimen, with BASF sprayed membrane in the middle of steel fiber reinforced concrete in both layers. The load/energy absorption value deflection curve is shown in Figure 4, and the energy absorption values for various working conditions are shown in Table 2.

For steel fiber reinforced concrete, the proportion of energy absorption value incorporating BASF sprayed membrane at 5mm, 10mm, 20mm, and 40mm to the energy absorption value without sprayed membrane is 100%, 90%, 84%, and 84%,

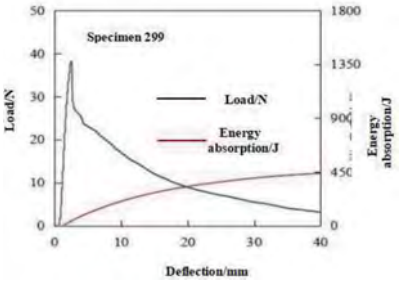

Figure 4. Load-deflection curve of concrete beam.

Table 2. Shotcrete energy absorption values.

Item	Peak load/ KN	Energy absorption/J			
		5mm	10mm	20mm	40mm
Steel fiber shotcrete	39	104	221	374	509
Steel fiber shotcrete+Master345 +Steel fiber shotcrete	35 (90%)	105 (100%)	198 (90%)	316 (84%)	427 (84%)

respectively, and the comprehensive judgment proportion is 90%; The peak load also accounts for 90%. Due to the deflection of the midpoint of the plate $\delta = \frac{q \times r^4}{64E \times h}$, with a peak load ratio of 90% for 40mm deflection, the equivalent thickness of the sandwich plate also accounts for 90%, which means that if the equivalent thickness of the cross-sectional is 90% × 75mm=67.5mm.

4 LAMINATED THEORY

4.1 *Laminated theory analysis*

Composite shell lining uses the same material (i.e. concrete) for two layers, and uses bonding material (i.e. spray membrane) between the concrete layers to make sandwich beams. Using the deflection (δ_{eq}) of the composite shell lining to be equal to that (δ_{mean}) of the homogeneous lining, based on the principle of equivalent deflection of a simply supported beam, the overall equivalent thickness of the composite shell lining is estimated. The sandwich simply supported beam is shown in Figure 5.

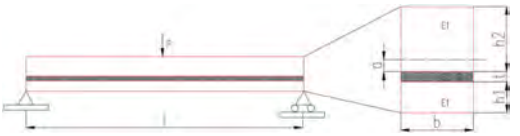

Figure 5. Laminated simply supported beam.

The key parameters considered in the solution are the thickness and elastic modulus of the main material layer, as well as the shear stiffness of the sprayed membrane. The specific formula is as follows :

$$\delta_{eq} = \frac{Pl^3}{48(EI)_{eq}} + \frac{Pl}{4(AQ)_{eq}} \tag{1}$$

$$\delta_{mean} = \frac{Pl^3}{48E_1 I_{eq}} \tag{2}$$

Based on the principle of deflection equivalence, it is inferred that :

$$I_{eq} = \frac{1}{E_1\left[\frac{12}{(AQ)_{eq}l^2} + \frac{1}{(EI)_{eq}}\right]} \tag{3}$$

$$h_{eq} = \sqrt[3]{\frac{12}{E_1\left[\frac{12}{(AQ)_{eq}l^2} + \frac{1}{(EI)_{eq}}\right]}} \tag{4}$$

$$(EI)_{eq} = \frac{E_1 h_1^3}{12} + E_1 h_1\left(\frac{h_1}{2} - a\right)^2 + \frac{E_2 t^3}{12} + E_2 t\left(\frac{t}{2} + a\right)^2 + \frac{E_1 h_2^3}{12} + E_1 h_2\left(\frac{h_2}{2} + t + a\right)^2 \tag{5}$$

Considering the thickness of sprayed membrane t is thinner, after simplification and organization

$$(EI)_{eq} = E_1\left[\frac{h_1^3}{12} + \frac{h_1^3}{12} + \left(h_2^2 - h_1^2 + 2th_2\right)a + (h_1 + h_2)a^2 + t^2 h_2 + th_2^2\right] \tag{6}$$

$$(AQ)_{eq} = \frac{G\left(t + \frac{h_1}{2} + \frac{h_2}{2}\right)^2}{t} \tag{7}$$

Substitute formulas (4) and (5) into formula (3) and simplify them to obtain the overall equivalent thickness of composite shell lining:

$$h_{eq} = \sqrt[3]{\frac{12}{E_1\left[\frac{12t}{G \times B \times l^2} + \frac{1}{E_1[C \times a \times D \times a^2 + F]}\right]}} \tag{8}$$

Wherein,

$$a = \frac{\frac{h_2^2}{2} + t\left(\frac{t}{2} + h_2\right)^2 + h_1\left(\frac{h_1}{2} + t + h_2\right)}{h_1 + t + h_2} - t - h_2 \tag{9}$$

$$B = \left(t + \frac{h_1}{2} + \frac{h_2}{2}\right)^2 \tag{10}$$

$$C = h_2^2 - h_1^2 + 2th_2 \tag{11}$$

$$D = h_1 + h_2 \tag{12}$$

$$F = \frac{h_1^3}{12} + \frac{h_1^3}{12} + t^2 h_2 + th_2^2 \tag{13}$$

In the formula, δ_{eq} is the deflection of composite shell lining, δ_{mean} is the deflection of the homogeneous lining, P is the concentrated load, a represents the distance from the upper edge of the sprayed membrane layer to the centroid of the composite shell lining, ℓ is the span of the beam (ℓ is approximately equal to the arc length between the plastic points of the tunnel), h_1 is the thickness of the first sprayed concrete, h_2 is the thickness of the second sprayed concrete, t is the thickness of the sprayed membrane layer, and E_1 is the elastic modulus of the sprayed concrete, E_2 is the elastic modulus of sprayed membrane, G is the shear modulus of sprayed membrane, $(EI)_{eq}$ represents the overall stiffness of composite shell lining, and $(AQ)_{eq}$ represents the shear stiffness of composite shell lining. Based on the principle of equal disturbance mentioned above, an equivalent thickness is easy to calculate (considering the influence of sprayed membrane shear in the equivalent thickness).

4.2 *Key influencing factors of equivalent thickness*

According to section 4.1, the curve shown in Figure 6 can be generated, and the relative relationship between the equivalent thickness and the shear modulus of sprayed membrane, the thickness of sprayed membrane can be obtained.

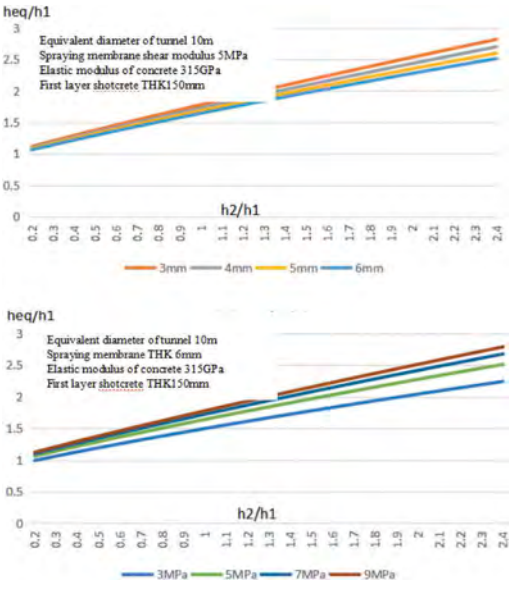

Figure 6. Laminate theory design chart.

From the above figure, it can be seen that when the shear modulus of sprayed membrane remains unchanged, the thicker the sprayed membrane thickness, the smaller the corresponding equivalent thickness; Under the condition that the thickness of sprayed membrane remains unchanged, the greater the shear stiffness and shear resistance of sprayed membrane, the stronger the corresponding equivalent thickness.

4.3 *Example research*

Taking a composite shell lining project as an example, when the thickness of the first layer of sprayed concrete is 150mm, corresponding to the thickness of the second layer of 150mm, 100mm, and 50mm, the equivalent thickness heq of the homogeneous body is calculated. The theoretical analysis and calculation results are detailed in Table 3. For example, when the first layer thickness of sprayed concrete is 150mm, the second layer thickness of sprayed concrete is 100mm, and the spraying membrane layer with a thickness of 6mm jointly form a composite shell lining, the composite shell lining provides the same stiffness as the 233mm homogeneous lining.

The bending toughness test was only conducted on the first layer of concrete and the second layer of concrete with a thickness of 75mm. In this case, the equivalent thickness of the composite shell lining structure accounts for 88% to 90% of the homogeneous structure, approximately 89%; For the cases where the thickness of the second layer is 100mm and 50mm respectively, an approximate value of 89% will be taken, and further experimental research will be conducted in the next stage. According to the deflection formula in the energy absorption test, it can be inferred that the equivalent thickness of sandwich structures accounts for 90% of homogeneous structures. The equivalent thickness obtained from the experiment is shown in Table 3.

Table 3. Equivalent thickness of CSL.

Item	h1=150mm h2=150mm	h1=150mm h2=100mm	h1=150mm h2=50mm
Equivalent thickness of Residual strength test h_{eq}	267mm (89%)	223mm (89%)	178mm (89%)
Equivalent thickness of energy absorption test h_{eq}	270mm (90%)	225mm (90%)	180mm (90%)
Equivalent thickness of Laminated Theory h_{eq}	274mm (91%)	233mm (93%)	190mm (95%)

From the analysis in the above table, considering the influence of interlayer shear, the difference between the equivalent thickness obtained by the on-site test method and the equivalent thickness obtained by theoretical method is small, and the consistency is high, which proves the correctness of the theoretical calculation of the equivalent thickness of the interlayer. However, due to the lack of strain gauges attached to the first and second layers of concrete in laboratory tests,

it is not possible to determine the bending moment distribution of the two layers of concrete. Further research on bending moment distribution will be conducted in conjunction with other interlayer energy absorption tests.

5 CONCLUSIONS

There is currently no detailed design guidance for the efficient design of composite shell lining tunnels. Sprayed membrane has good bonding strength and shear strength. The equivalent thickness of the sandwich structure was obtained through laboratory experiments, and its rationality was verified through laminated theory, which can provide theoretical guidance for design. The conclusion is as follows:

(1) The equivalent thickness of the sandwich structure with spray membrane was calculated using the bending toughness of the small beam and the energy absorption test of the disk, and verified using the laminated theory analysis method. The obtained equivalent thickness has a good discrete type and a high degree of fit, indicating that the method of using the deflection equivalent laminated theory is feasible.

(2) The proportion of equivalent thickness obtained through bending toughness test is 88%~90%, and the proportion obtained through energy absorption test is 90%. Both tests produce load-deflection curves, indicating that the two method are essentially the same. Similar projects can choose either method for testing in the future.

(3) Obtain the relative relationship between the equivalent thickness of the interlayer and the shear modulus of spray membrane, as well as the thickness of spray membrane. The larger the shear modulus, the smaller the spray membrane thickness, resulting in a larger equivalent thickness.

REFERENCES

[1] Alun Thomas.Sprayed Concrete Lined Tunnels Second Edition.2022.

[2] ITAtech Activity Group Lining and Waterproofing. ITA tech design guidance for spray-applied waterproofing membranes[R]. Geneva: ITA, 2013.

[3] Draft european standard pren 13474, glass in building-design of glass panes, part 1:general basis of design. January 1999.

[4] Bennison SJ, Qin M H, Davies P S . High-performance laminated glass for structurally efficient glazing[J]. innovative light, 2008.

[5] Liu Runquan, Shi Yong, Zhu Xi, et al.Calculating method investigation and theoretic analysis of sandwich beams at bending [J]. Fiberglass/Composite Materials, 2006 (6): 4

[6] Su J. Stress status of sprayed waterproofing membrane under groundwater pressure within composite SCL tunnels[J]. Expanding Underground, 2023, 3 (2):1003–1011.

[7] Bloodworth A, Su J. Numerical analysis and capacity evaluation of composite sprayed concrete lined tunnels[J]. Underground Space, 2018, 3(2):87–108.

[8] Su J, Bloodworth A. Utilizing composite action to achieve lining thickness efficiency for sprayed concrete lined (SCL) tunnels[C]// World Tunnel Congress 2016. 2016.

[9] Su J, Bloodworth A G, Haig B. Experimental investigation into the interface properties of composite concrete lined structures[C]// World Tunnel Congress. 2013.

[10] Jiang, Bloodworth, Alan. Interface parameters of composite sprayed concrete linings in soft ground with spray-applied waterproofing.[J]. Tunneling & Underground Space Technology, 2016, 59:170–182.

[11] Su J, Bloodworth A. Experimental and numerical investigation of composite action in composite shell linings[C]/ / 7th International Symposium on Sprayed Concrete. 2014.

[12] Su J, Bloodworth A.Numerical calibration of mechanical behaviour of composite shell tunnel linings[J].Tunnelling and Underground Space Technology, 2018, 76 (JUN.):107–120.DOI:10.1016/j.tust.2018.03.011.

[13] Nakashima M, Hammreb AL, Thewes M,etal.Mechanical behaviour of a sprayed concrete liningisolated by a sprayed waterproofing membrane [J].Tunnelling and Underground Space Technology, 2015,47: 143.

[14] Zhou Ping, Wang Zhijie, Lei Feiya, et al.Experimental study on mechanical behavior of single-layer lining of steel fiber reinforced concrete tunnel considering interlayer effect [J]. Journal of Civil Engineering, 2019.

[15] Jiang Yajun, He Bin, Zhao Jumei, et al.Study on Mechanical Properties of Tunnel Lining Structure with Spray-applied Waterproofing Membrane [J]. Modern Tunnel Technology, 2022 (001): 059.

[16] Jiang Yajun, Zhao Jumei, He Yudi, et al.Mechanical Characteristics of Interface Between Layers of Double-Sided Adhesive Spray-Applied Membrane Waterproof Tunnel Lining [J]. Tunnel Construction (in Chinese and English), 2023.

[17] Deng Yisan, Li Gang, Zhang Jianwei, et al Study on composite surface of waterproof single-layer lining by tests [J] Journal of Railway Science and Engineering, 2022 (003): 019.

[18] Li Deming, Wen Shuyi, Zhang Jianwei, et al Performance Test and Engineering Application of Macro-polyolefin Fiber Reinforced Shotcrete Used as Single-shell Lining [J] Modern Tunnel Technology, 2021.

[19] Wen Shuyi, Yan Jinxiu, Zheng Bo. The Application of Tam Seal800 Spray Waterproofing in Chengdu Metro Tunnel [C]//The 2019 Academic Annual Meeting of the Chinese Civil Engineering Society. [2023-10-19]

Tunnelling for a Better Life – Yan, Celestino, Thewes & Eberhardt (Eds)
© 2024 The Author(s), ISBN 978-1-032-80042-4
Open Access: www.taylorfrancis.com, CC BY-NC-ND 4.0 license

Singapore's land transport authority: 25 years of sprayed concrete lining tunnelling

Alvin Sim, Kin Boon Chang, Massimo Marotta*, Chee Keong Poh & Mohd Mohiadeen
Land Transport Authority, Singapore

ABSTRACT: Since 1995, Singapore's Land Transport Authority (LTA) has been developing the expansion of the underground rail and road transport systems within the Island City. The development of the Singapore MRT network system has relied predominantly on the use of Tunnel Boring Machines to ensure rapid and safe construction of the running tunnels. Other than for the construction of Cross Passages connecting the twin bored tunnels, Sprayed Concrete Lining have been extensively used during the construction the MRT network to solve technical challenges as to facilitate underpinning or removal of obstruction prior to bored tunnelling. SCL has also been used for critical undercrossing as the preferred trenchless method as well for the construction of TBM launching chambers, linkways, and more. The paper describes several case studies starting from 1999 till recent.

Keywords: Tunnelling, Sprayed Concrete Lining, SCL

1 INTRODUCTION

The MRT Corporation, now Land Transport Authority, was established on 14th October 1983. The construction of the first line (North South Line) of the Singapore Mass Rap-id Transport system started in October 1993. By January 1988, the construction was completed for Phase I and Phase II. The initial opening of the first 6 km of the North South Line from Yio Chu Kang to Toa Payoh happened on the 7th of November 1987 and by 12 December 1987 the section between Novena to Outram Park was also opened to public.

The rest of the line opened in staged until completion in July 1990. Among the various tunnelling methods, mined tunnels using Sprayed Concrete Lining (SCL) was used in some of the contracts.

The photo in Figure 1 shows one of the first SCL tunnelling in Singapore, excavated through the Fort Canning boulders bed. The soldier piles and lagging temporary support for Raffles Place Station can be seen at the end of the tunnel.

Generally, the use of SCL for MRT tunnelling has been for the construction of the numerous cross passages connecting at regular intervals the twin MRT running tunnels, in compliance with the Fire Safety in Rapid Transit System.

The cross passages have a typical excavation section of around 16-18 m^2. Over 100 cross passages have been constructed to date.

Figure 1. One of the first SCL tunnels for the North-East Line.

SCL has also been used for the construction of TBM launching chambers, where the TBM shield is assembled within the chamber thus reducing the size required for the launching shaft.

In addition, SCL has also been used as a trenchless solution for the construction of short section of running tunnels, or to solve construction challenges such as underpinning, advance tunnels for removal of obstructions prior to TBM drive, pedestrian underpasses, etc.

*Corresponding author: marotta_massimo@lta.gov.sg

DOI: 10.1201/9781003495505-160

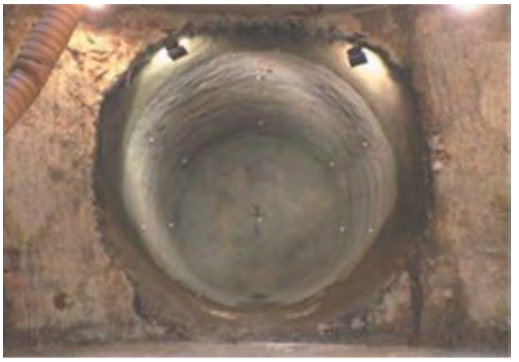

Figure 2. TBM Launching Chamber by SCL.

Most of the SCL tunnelling in Singapore has been challenging in relation to varying and complex geological conditions, the urban context, the necessity of maintaining limited induced deformation and a challenging construction environment.

The next paragraphs will include several case studies of SCL application in the past 25 years.

2 DTSS ADVANCE TUNNEL (1999)

Singapore implemented a Deep Tunnel Sewerage System (DTSS) project as the long-term solution to meet future needs in wastewater collection, treatment and disposal through the 21st century. Under the first phase of this project, 70km of tunnels of diameters varying from 3.3m to 7.2m were constructed between 2001 and 2005 using Earth Pressure Balance (EPB) boring machines. During the early planning stage (1997) the Ministry of Environment (NEA) analysed the possible interference and impact of tunnelling underneath the future operational North-East Line MRT.

Anticipating the additional constraints that could be imposed under the rail protection Act, NEA and the LTA jointly developed plans which included the construction of an advance tunnel using SCL through which the future DTSS TBM could safely undercross the NEL MRT tunnels. The construction of the SCL advance tunnel was then included as part of the Land Transport Authority NEL Contract 705, which also includede the construction of two stations and twin bored tunnels 1.7 km in length.

As described in Barraclough et al. (2004) the work commenced with the construction of an access shaft, 31.5 in depth with an internal diameter of 4.8m, followed by the excavation of a 20m long Adit with cross section of 13 m^2. The 40 m length main tunnel, with a cross section of 56 to 59 m^2, was constructed using heading/bench & invert with a round length from 0.8 to 1 meter for the heading, and 1.6 to 2.4 meters for bench/invert. The tunnel is located within cemented Old Alluvium (OA), The SCL design considered the additional stresses during NEL tunnelling.

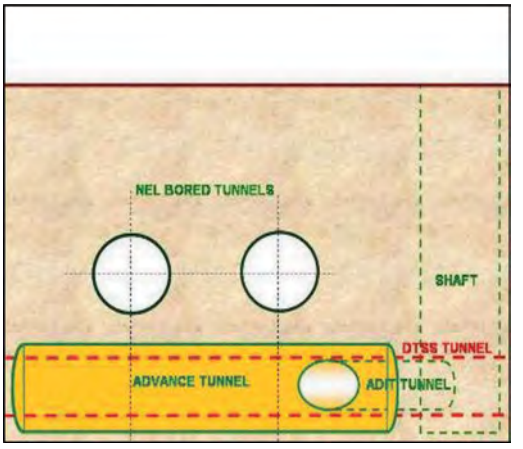

Figure 3. Advance tunnel for DTSS tunnel to bore trough.

To avoid the need of a steel cradle and launch frame within the advance tunnel, the contractor proposed to backfill the advance tunnel with foamed grout. In April 2002, the EPB TBM passed through the backfilled advance tunnel at a rate of approximately 15 m per 24 hours. The TBM stopped in the inspection chamber for nine days to allow remedial work to be carried out on the cutterhead. The total operation, breaking into the advance tunnel end wall, moving through, stopping for the remedial work, and then breaking out of the opposite less than originally programmed.

3 OVERRUN TUNNELS UNDER ORCHARD ROAD (2005)

The construction of Contract 825, the first phase of the Circle Line (CCL1), required 110m long twin overrun tunnels to be constructed to the west of Dhoby Ghaut station directly under Orchard Road, (Singapore's main shopping road), near to The Istana; the President's residence.

The only available access to construct the tunnels was through the partially complete Dhoby Ghaut interchange station, which was being further developed to add a third line to an already busy interchange station. Consequently, all access was through the shell of a structurally complete station, awaiting electrical and mechanical fit out, and was therefore limited to a small opening in the roof slab. This spatially limited access placed severe constraints on the construction approach that could be used, leaving SCL as the only

viable option. The drive commenced in completely-to-highly weathered mudstone and siltstone, known locally as S4 Jurong and proceeds into the S2 Jurong, with a moderately to slightly weathered grade.

Due to variability of the ground and the proximity of settlement sensitive structures, the initial scheme consisted of an advance pilot tunnel followed by enlargement to the final heading section.

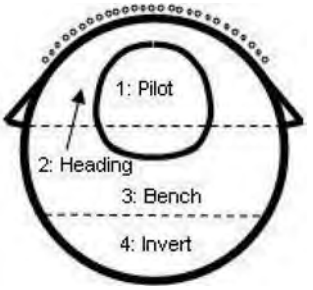

Figure 4. Excavation scheme with Pilot Tunnel.

This scheme was used for around half of the drive then changed to heading/bench/invert once the geological conditions were confirmed satisfactory.

The support design, for the 39 m2 cross section tunnel, included a 250 to 350 mm shotcrete with 2 layers of wire mesh and lattice girders. Forepoling were used every second advance as additional heading support measure.

To minimise settlements, a total number of 14 recharge wells were installed along the tunnel alignment. Despite this effort, localized higher settlements (up to a max of 80-100mm) have been recorded on surface. The settlement of the existing MRT station was however within the acceptable level with a maximum-recorded settlement of 7mm.

4 ADVANCE TUNNELS UNDER SERANGOON STN (2006)

Circle Line 3 Contract 852 included a twin tunnel from Serangoon to Bartley station, undercrossing the operational North-East Line (NEL) Serangoon station with low cover ranging from 0.6m to 1.5m in soft ground conditions. Two temporary SCL advance tunnels were built to clear a total number of 42 temporary steel piles (21 for each bound), left in place during the construction of Serangoon station which would obstruct the Tunnel Boring Machine (TBM) drives. The SCL tunnel were backfilled before TBM boring through.

As described in Pearce et al (2006), during the construction of the outer tunnel considerable water inflow of about 500L/min was encountered about 8m away from the existing station during the drilling

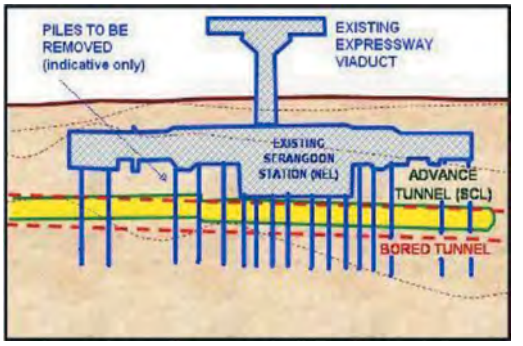

Figure 5. Longitudinal profile of advance tunnel.

operation for the installation of forepoles. Instrumentation recorded an immediate drawdown in groundwater table and a corresponding immediate settlement of 8mm in the NEL structures and the elevated expressway located directly above the station.

Figure 6. High water ingress during excavation.

The settlement and the risk for further settlements, caused concerns. Consequently, all works were temporarily stopped to allow for a careful review of the original design and construction methodology. Due to the presence of the backfill shallow cover to the tunnel crown and the a water head of over 20m, the work resumed with the following measures:

- Vertical jet grouting of the first backfill band from road surface as pre-treatment to eliminate crown failure and water ingress into the excavation below.
- Horizontal grouting, with 10 numbers of horizontal pipes drilled from within each tunnel beneath the station base slab. Grout was injected in stages of 600mm through the non-return valves fitted along the pipe sleeve using expandable packers.
- Systematic use of block grouting beyond the tunnel face.
- Systematic installation of pipe roof canopy.

Figure 7. Pipe roof canopy installation.

The settlements of the station after restarting the excavation using the described method have been kept to a further 6mm only. The advance tunnels construction, pile removal & backfilling were completed in April 2006 without interruption to train service and road traffic. The two TBMs had successfully negotiated past the NEL station in July 2006, maintaining the settlements of the stations within the pre-determined review level.

5 KTM RAILWAY UNDERPINNING (2006)

During construction of the Circle Line 4 Contract 855 underpinning works were required for the piled foundations of an existing retaining wall and bridge abutment in the east side of the intersection between Commonwealth Avenue West and North Buona Vista Road. A total number of 19 H piles would have been within the slurry TBM bored tunnel inner drive. The bridge overpasses the Malaysian state KTM railway, linking Singapore to Malaysia.

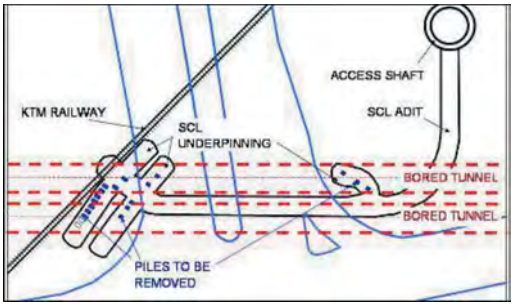

Figure 8. Plan view of the temporary SCL tunnel/shaft.

An 18 m deep access shaft was constructed, followed by a 72 long Adit tunnel, from which the 3 underpinning tunnels were then excavated in Jurong formation. The SCL supports were designed with a shotcrete shell of 200-250mm in thickness, with 2 layers of wire mesh and lattice girders generally spaced at 1m.

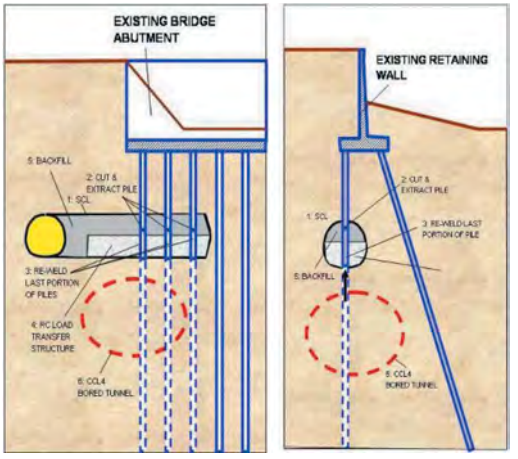

Figure 9. Section indicating the piles to be removed.

The removal of sections of H piles was carried out in the following the sequence:

1) Mined tunnel excavation, exposing the piles to be removed.
2) Casting of the Reinforced Concrete spread footing with a box out around the pile.
3) Installation of 2 hydraulic jacks at the sides of the piles to be extracted.
4) Cut the portion of H piles within the SCL tunnel
5) Extract the H piles in section of 1.5m long.
6) Reconnect H piles and repeat steps 2 to 5 for each pile.
7) Complete casting the transfer beam
8) Backfill of upper half of the SCL tunnel with foamed concrete.

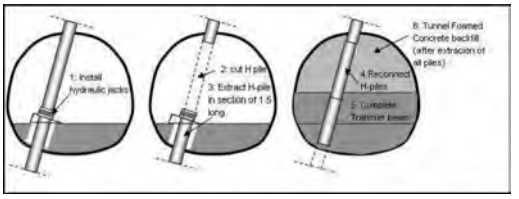

Figure 10. Sequence of piles removal.

The KTM underpinning and piles removal was successfully completed in September 2006 and the TBM tunnels successfully undercrossed the KTM railway in April 2007 with no deformation/impacts on the structure affected by the underpinning.

6 CIRCLE LINE 4 - AYA MINED TUNNELS (2007)

During the construction of the Circle Line Stage 4 and 5 Contract 855, mined tunnels were proposed for

a section of about 70m where cut and cover section was not feasible due to the proximity of the critical utilities such as high voltage electrical cables, gas pipes and telecommunication cables. The mined tunnels section consists of two tunnels undercrossing a busy four-lane two-way roadway (the Ayer Rajah Avenue). The twin tunnels, with an average overburden of 10m, pass through challenging residual soil and highly weathered sandstone and siltstone with distinct discontinuities. The design and construction of the mined tunnels been carried out in a manner that will not cause excessive movement to the utilities and the roadway.

The entire 70m of both inner and outer bound tunnels were divided into four modules each. The length of each module varies from 14m to 21m.

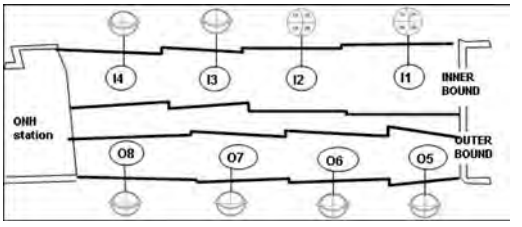

Figure 11. AYA Tunnels excavation modules.

To accommodate a branching railway switch track, two of the modules in the inner bound tunnel (Modules I1 and I2) were larger resulting in a max 100 m2 cross section. Those modules were constructed adopting side drift methodology and the typical modules adopting conventional top heading, bench and invert construction methodology. The excavation was supported by pipe roof, shotcrete and steel arch girders. The length of pipe roofing ranged from 21 m to a maximum of 27 m in length with a lapping of 6 m.

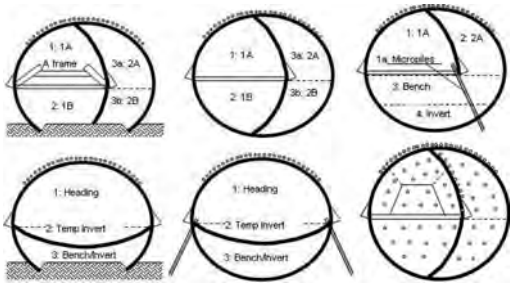

Figure 12. Excavation & Support schemes for different modules.

As the twin tunnels were located very close to each other, the narrowest section resulted in a soil pillar of about 0.5m at the narrowest point. For the execution of the Pipe Roof canopy, pull drilling method has been used, where the pipe roofing steel pipes are used as casing and progressively installed during the drilling, thus minimizing the risk of settlement due to drilled hole instability. A sacrificial pilot bit allowed retrieval of the drilling string after completion of each pipe.

The improvement the soil in between adjacent pipes was done double packer grouting through non-return valves. Face nailing has been extensively used during all the stages of excavation. The execution of face nailing solved localized instability problems and acted as a confinement at the face to reduce pre-deformations.

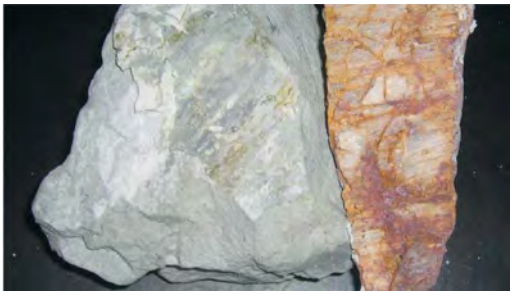

Figure 13. Slickensides observed in Jurong Formation rock.

Despite a systematic use of face nailing, some local instability still occurred, mainly due to the narrow spacing of discontinuities and separation planes. This was addressed by increasing the number of face nails installed at the tunnel face (around 1 number/square meter).

7 DTL1 – C905 (2010)

The Downtown Line Stage 1 (DTL1) is a 4.3km underground rail transit system with seven MRT stations. It runs from Chinatown Station, the new downtown Marina Bay Financial Centre, Integrated Resort, Promenade Station and Bugis Station. Contract C905 consists of two stacked TBM tunnels each for the CCL extension line and DTL 1 line. The TBMs were launched from two independent temporary shafts. In addition, there are two twin connection tunnels to the existing Promenade station. Of those, three of the connection tunnels have been excavated using the Sprayed Concrete Lining method (SCL), while the other one using Earth Pressure Tunnel Boring.

7.1 *SCL Tunnels under operational MRT*

The two Downtown Line connection tunnels are vertically stacked and underpass the existing Circle Line tunnels which became revenue operational on the 17th of April 2010.

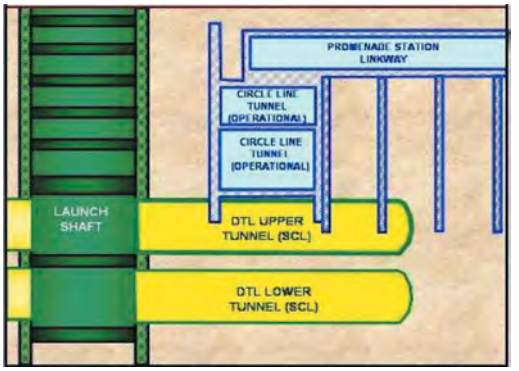

Figure 14. Longitudinal profile of tunnels undercrossing live MRT.

The upper tunnel required localized breaking out of the existing operational tunnel diaphragm wall and linkway piles during the excavation. As a result, a much thicker temporary lining was used for the upper tunnel, comprising of a double layer of shotcrete and 2 lattice arches of a total SCL thickness of 550mm. The geological conditions are of competent Old Alluvium. Nevertheless, tunnelling process was strictly controlled to minimize settlement and vibration to the operational tunnels.

Figure 15. Demolition of CCL tunnel DWall during tunnelling.

While mining undercrossing the CCL tunnels, an extensive monitoring regime of the live tracks was implemented. Monitoring was executed in real time with the use of Automated Total Station. The actual movement to the track due to the excavation of mined tunnel.

7.2 *SCL Tunnels under Formula 1 Circuit*

The CCL lower tunnel connects the launch shaft to the existing operational Promenade Station wall. The tunnel length is 90 m with an average overburden of 20m. Originally designed at tender as cut & cover tunnel, it was then proposed by the

Figure 16. Extensive monitoring of the live CCL tunnels.

Contractor to adopt a trenchless method following the announcement that public road above the tunnel alignment would become part of the Formula 1 race track. The tunnel excavation diameter is 7.15 m with a support system comprising lattice girders, wire mesh and shotcrete. Forepolings (d.25mm, L = 4m) were used along with length and spacing depending on the geology. Where surface access permitted ground treatment, jet grouting (JGP) was used to stabilise the tunnel heading in poorer ground condition, however this could not be done for the section directly below the F1 track. The excavation commenced on 13 August 2009 and by a month later it was temporarily stopped when the face was at the edge of the F1 track along Raffles Boulevard.

Figure 17. Tunnel excavation on hold prior to F1 race in 2009.

The tunnel face was strengthened with additional shotcrete and monitoring was installed to check any eventual face movement. The F1 criteria for any surface deformation (in term of differential settlements) are in fact quite stringent, with a maximum allowable differential settlement of 3mm over 4 meters. The excavation restarted after the F1 event and was completed in April 2010.

8 DTL 2: SCL UNDER THE NORTH-EAST LINE (2013)

Construction of Downtown Line 2 C921 required two x 60 meters long SCL tunnels constructed just 2 meters below the operational North-East Line tunnels and few meters below an existing underpass. The tunnels pass through the Fort Canning Boulders Bed formation. The construction scheme included the installation of pipe roofing canopy.

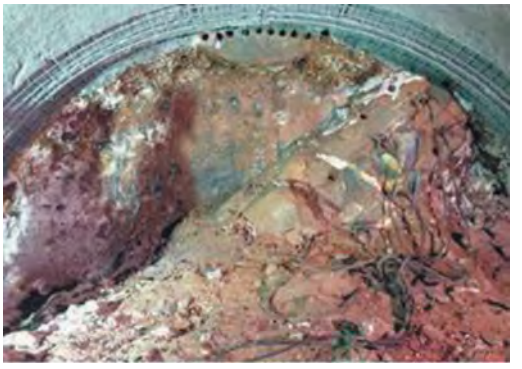

Figure 18. Tunnel face in Fort Canning Boulders Bed.

9 CRIPPLE SIDING & VENTILATION PASSAGES (2014)

Construction of Downtown Line 3 C927 required a Cripple Sided tunnel is located in between the two bored tunnels driven from Bedok Town Park Station (BDTP).

The length of the tunnel is about 170m and the tunnel is connected to the Expo drive bored tunnel by 5nos of ventilation passage and the drive 2 by 1no of cross passage.

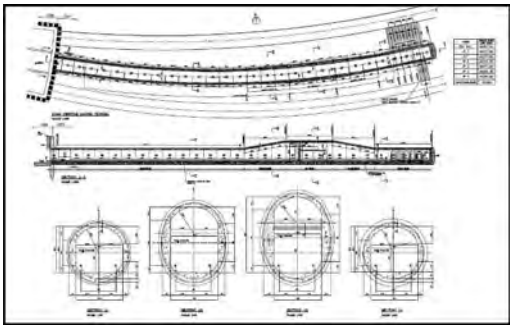

Figure 19. Plan, Profile and Sections of Cripple siding tunnel.

Geological conditions were predominantly competent Old Alluvium soil with SPT-N value over 100. Overburden ranges from 20.5m to 25.5m in depth. Heading excavation was carried out first, for the entire length of the tunnel 170m maintaining the constant heading height in all three circular, transition and oval sections. The typical advance length of the heading excavation ranged from 1m to 1.4m. Typical temporary lining design was 300mm thick shotcrete lining of shotcrete grade C30 with two layers of wire mesh and lattice girder. The tunnel geometry consists of a standard section and a higher section or "ventilation section" to facilitate the installation of ventilation equipment.

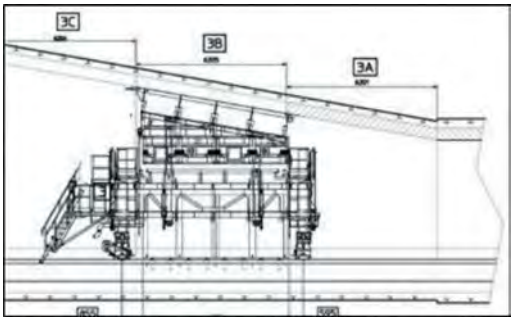

Figure 20. Variable formwork set up for transition profile.

A special CIFA hydraulic formwork was manufactured with the ability to be adapted, on site, for a total of 10 configurations (8 configurations for the 2 transitions, 1 configuration for the standard section, and 1 configuration for the ventilation section). The 6m formwork was designed for a single stage casting of sidewall and crown, improving productivity, and reducing the number of Construction Joints.

Additionally, 5 contiguous ventilation passage (VP) were constructed between the cripple siding tunnel and the expo bound bored tunnel.

Figure 21. Waterproofing and completed tunnel lining.

10 DOWNTOWN LINE 3 –ENTRANCE LINKWAY (2014)

During the project, the Contractor proposed a change in the construction method of the subway from Bedok Reservoir Station (BDR) to Entrance B.

Figure 22. The five completed ventilation passages.

The original design required a jacking shaft (1), for interlocking pipe-jacking method, which is part of the Entrance B. To mitigate a programme delay, delinking the linkway construction from the Entrance B construction, the Contractor proposed to use SCL tunnel with umbrella pipe-roofing method, carried out from the station side.

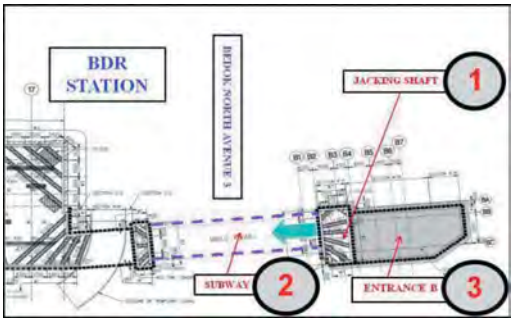

Figure 23. Original sequence using pipe roof by jacking.

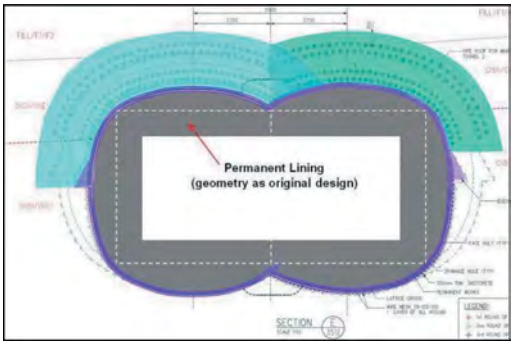

Figure 24. SCL double drift maintaining the permanent lining.

The reason for two SCL drifts is due to the shallow tunnel overburden, which would not allow executing with a single circular tunnel around the full permanent lining box.

The excavation is particularly challenging due to the poor geological conditions (OA(C)/OA(D)/ OA(E)/Fluvial F1 and F2, and due to the presence of a 1200 mm diameter water pipe (steel pipe) just 1.0 m above the tunnel crown.

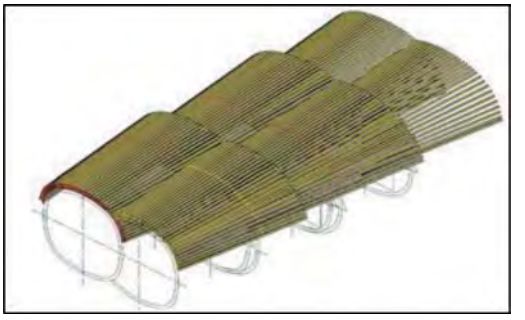

Figure 25. Pipe roofing canopy for both drifts.

The excavation was completed on the 24th of October 2014. Nearly 10 months were taken for the completion of drift 1 excavation, with a productivity of 1.2m/week including pipe roofing, while drift 2 took 6.5 months. Permanent lining took 5 months for drift 1 and drift 2.

Figure 26. Pipe roofing by horizontal drilling rig.

Productivity of Drift 1 excavation was 1.2m advance/week.

11 T213 MINED TUNNELS (2017)

11.1 *Three arches tunnel in rock*

The 3-Arches tunnels were constructed to connect the Station box with the Cut and Cover tunnel, accommodating a cripple siding tunnel in between the two MRT bounds.

Drill & Blast, Drill & Split or Mechanical Excavation were used for the various rock conditions.

Figure 27. The 3-Arches tunnel in rock during permanent lining.

11.2 *Two arches tunnel in soil*

The 2-Arch tunnels were constructed to connect the Cut and Cover tunnel with the bored tunnel, accommodating the transition to the cripple siding tunnel in between the two MRT bounds. Multi-drift excavation method, with use of pipe roofing and face nailing, was used to excavate the tunnels in weathered rock. Due to mix face conditions, hybrid support system was utilised locally, comprising of soft ground supports and hard rock support such as rock bolts. Drill and split method was used in mix face to break the rock to minimise any disturbance to soil portion.

Figure 28. A partial stage of the 2-Arches tunnel excavation.

12 T226 MINED TUNNELS - GROUND FREEZING (2018)

The Thomson East-Coast line T226 construction required stacked mined tunnels 44 m in length, undercrossing the live MRT. The geology consists of weak ground types of Marine Clay, Estuarine Clay and the weaker layers of Old Alluvium (OA).

Ground freezing was used to prevent the flow of water ingress during SCL tunnel excavation, with the formation of two rows of continuous ice walls (Chua et al, 2018).

With the aid of ground freezing, controlled excavation, and stringent monitoring regime, the SCL tunnel excavation was successfully completed with no impact to the live MRT

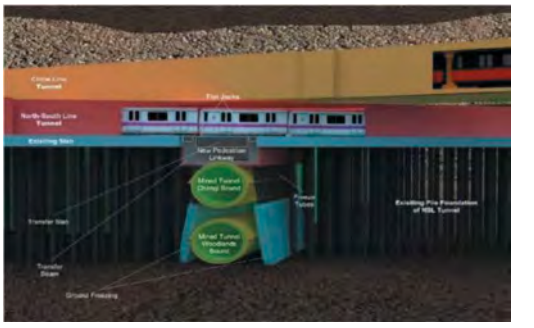

Figure 29. SCL tunnels undercrossing live MRT lines.

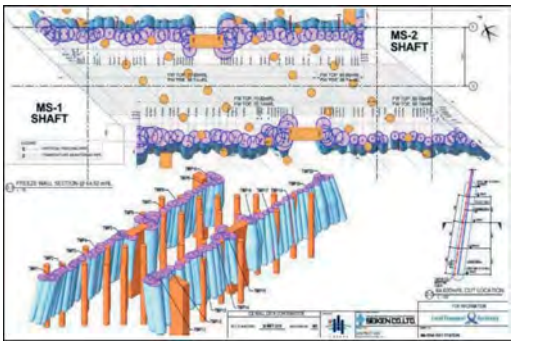

Figure 30. Model of the live monitoring of Ice Wall.

13 CONCLUSION

From the first applications using traditional techniques and methodology, to the recent complex applications using multi drift method or ground freezing, SCL tunnelling has been a key engineering solution to the many challenges which are typical of tunnelling in an urban environment.

SCL tunnelling has been widely used as trenchless solutions, to facilitate removal of obstruction prior to TBM tunnelling, and it has been widely used for the construction of Cross Passages, TBM Launching Chambers and shafts. Due to the complex and variable geological conditions, various excavation and support methods have been adopted, such as multi drift, side drift, advance pilot tunnel and conventional sequential method, in combination with the use of pre supporting/improvement techniques SCL is a very versatile and adaptable tunnel method, which, if designed and applied correctly, can be utilized to solve a multitude of construction problems in an urbanized environment.

REFERENCES

Barraclough, B., O'Carrol, J. and Mcchesney, S.A. (2004). Safe passage of TBM under new NEL tunnels, using

a foam grout backfilled advance tunnel. Proceeding of WTC 2004, Singapore - Underground Space for Sustainable Urban Development, pp. 22–27.

Chua, T.S., Lew. M., Hashida, K., Tada, H., Takeda, S., Marican, S. and Nair, R.S., (2018) "Ground freezing for the design and construction of SC tunnels underneath Marina Bay Station, Singapore". Proceeding of Underground Singapore 2018. Singapore.

Ganeshan, V. Ow, C.N., Marotta, M., Yoshimitsu, A., and Jee, Y.Y. (2006) "Grouting and its application in Tunneling", Proceeding of the International conference on Deep Excavation, 2006, Singapore.

Knight Hassel, C.K., Rosser, H.B and Eng, W.C. (2001), "Difficult Ground Conditions Encountered During Construction of a Cross Passage in Old Alluvium", Underground Singapore 2001, pp. 24–31.

Lee, G. S. and Chia, K.S. (2010) "Long Tunnel Drives in Circle Line Stage 4" Proceedings of the World Urban Transit Conference 2010 (WUTC 2010), Singapore, pp. 393.

Lim, J., Muthu Kumarasamy, D., Marotta, M. (2017) "Latest development in Horizontal Grouting for Cross Passages in Thomson-East Coast Line C1-C2." TUCSS Hulme Prize Competition paper.

Marotta, M, (2013) "Singapore`s Land Transport Authority: 15 years of innovative use of sprayed concrete lining". Proceeding of Singapore International Transport Conference and Exhibition - SITCE 2013. Singapore.

Mohiadeen, M., Marotta, M. (2018) "Construction of a 170m long cripple sided tunnel using Variable Geometry Hydraulic formwork in DTL 3, C927" Proceeding of Underground Singapore 2018. Singapore.

Nair, R.S., Seutscher M.S., Tham K.S. and Mcchesney S. A. (2000), "Construction of an advance tunnel for the Deep Tunnel Sewerage System (DTSS) using sprayed concrete lining" Proceeding of Tunnels and Underground Structures 2000, pp. 227–234.

Osborne, N.H., Sigl, O and Ming, A.W. (2006). "Design and Construction of SCL Tunnels under Orchard Road", Proceeding International conference on Deep Excavation, 2006, Singapore.

Ow, C.N, and Koh, C.T. (2006). "Construction of Rail Tunnels using Sprayed Concrete Lining for Circle Line Stage 4, Singapore", Proceeding of the International Symposium on Underground excavation & tunneling, 2006, Bangkok, Thailand.

Pearce, B.M., Ow, C.N., Lee Y.K. and Y.K. Wong, Y.K. (2006) "Construction of Advance Tunnel under Serangoon MRT Station to facilitate the Removal of Steel Pipes" International Symposium on Underground excavation & tunneling, 2006, Bangkok, Thailand, pp. 161–170.

Pearce B.M., Ow, C.N., Lim, K.K., Wong, Y.K., and Lee, Y.K., (2006) "Tunneling under the operational North East Line Serangoon MRT Station" Proceeding of the International conference on Deep Excavation, 2006, Singapore.

Pearce, B.M., Koh, C.T., Tong, S.Y. and Marotta, M. (2006) "SCL challenge under AYA", Tunnels & Tunnelling International, April 2006, pp 32–35.

Pearce, B.M., Poh, C.K., Marotta, M, and Lee, C.L. (2011) Downtown Line 1, Contract C905 – Stacked tunnelling under Formula 1. Proceeding of the World WTC 2011, Stockholm, Sweden.

Sigl, O., and Rieker, K. (2001) "Singapore soft Ground – Playground for TBM, off-limits for the NATM" Rock and Soil Engineering, Vol.5, pp.204–212.

Sigl, O, and Lin, J.J. (2011) Design and construction of NATM/SCL tunnel under an operating MRT tunnel for DTL1 Contract 905" Proceeding of Underground Singapore 2011, Singapore.

Sim, Z.R. (2019) "Application of Ground Freezing for Mined Tunnel in T226 Marina Bay Station". TUCSS Hulme Prize Competition paper. Singapore.

Tong, S.Y., Stadelmann, R, Mann, C.R, Tang, S.K., Marotta, M, Joshi, M.C., Singhal, V, and Ow, C.N. (2008) Design and construction of mined tunnels in challenging site conditions. Proceeding of World Tunnelling Congress 2008. Agra. Vol. 2, pp. 1220–1229.

Tong, S.Y., Marotta, M, Joshi, M.C., Ow, C.N., Singhal, V, Stadelmann, R, and Tang, S.K. (2008) "Design and construction of twin mined tunnels in residual soil", Proceeding of the International conference on Deep Excavation, 2008, Singapore.

Tong, M.S.Y., Stadelmann, R, Tiang, K.L., Tang, S.K., Singhal, V, and Ow, C.N. (2009) "Interaction between twin tunnels at close proximity and under shallow overburden in urbanized area. Proceeding of World Tunnelling Congress 2009 - Safe Tunnelling for the City and for the Environment.

Williams, I., Osborne, N., and Aw, E.T., (1999) Recent Large –diameter tunnel construction in Singapore using Sprayed Concrete Linings" Tunnelling and Underground Space Technology, Vol. 14, pp 527–538.

Yi, K.H., and Tong, S.Y.M. (2014), "Ground Movement Behavior from Cross Passage Mining in Hard Rock and Very High Permeable Residual Soil", Underground Singapore 2014.

Yi, K.H., and Tong, M.S.Y. (2015) "Construction experiences from cross passage in very hard rock and blasting works near segmental lining. Proceeding of World Tunnelling Congress 2015, Dubrovnik.

Yi, K.H., and Tong, M.S.Y. (2016) "Cross Passage Mining in Highly Permeable and Soft Ground". Proceeding of the 15th Asian Regional Conference on Soil Mechanics and Geotechnical Engineering. Fukuoka.

Tunnelling for a Better Life – Yan, Celestino, Thewes & Eberhardt (Eds)
© 2024 The Author(s), ISBN 978-1-032-80042-4
Open Access: www.taylorfrancis.com, CC BY-NC-ND 4.0 license

Design of precast bolted universal segmental tunnel lining for the London Power Tunnels phase 2 scheme

Anna Simic*, Oliver Brown & Joseph Ellis
AECOM, Croydon, UK

ABSTRACT: London Power Tunnels (LPT) Phase 2 is a new purpose-built cable tunnel system which will replace the existing buried cable network in the south of London. This £1 billion National Grid scheme comprises 32.5km of 3m internal diameter deep underground tunnels and 8 shafts which will help keep Londoners connected to safe and reliable electricity supplies. The tunnels extend from Wimbledon in the West to Crayford in the East, reaching depths of up to 60m below ground level.

This paper introduces the design of the bolted universal segmental tunnel lining which will house the three new cable circuits. The paper presents the design for four different Tunnel Boring Machine (TBM) tunnel drives by addressing the ground through which the tunnel is built, and the numerical analysis adopted for the lining design. The tunnel route travels through the full stratigraphy of the London Basin, which includes overconsolidated clays, sands and chalk. Extensive parametric studies for different parameters including surface surcharge, groundwater pressures, coefficient of earth pressure at rest (K0), and degree of stress relaxation have been conducted using PLAXIS 2D to identify the most onerous design scenarios. Loads arising from primary and secondary grouting, gantry wheel loads, the cable installation monorail system and cable brackets were also considered in the analyses. The analyses were supported by closed-form calculations to verify ram forces, bolt capacity, gasket performance and the effects of ring build tolerances. These analyses gave the designer confidence that the tunnel lining will be able to resist the ground, groundwater, construction and long-term loading.

Keywords: Tunnelling, Numerical analysis, Simulation, Tunnel Boring Machine (TBM)

1 INTRODUCTION

London Power Tunnels (LPT) Phase 2 is a new purpose-built cable tunnel system which will replace the existing buried cable network in the south of London. This £1 billion National Grid scheme comprises 32.5km of 3m internal diameter deep underground tunnels and 8 shafts which will help keep Londoners connected to safe and reliable electricity supplies. The project will replace three existing high voltage transmission cable circuits from Wimbledon to New Cross, New Cross to Hurst and Hurst to Crayford. The new tunnels extend from Wimbledon in the West to Crayford in the East, constructed by Tunnel Boring Machines (TBMs) in 5 tunnel drives with a precast concrete segmental lining and reaching depths of up to 60m below ground level. Shaft diameters vary between 9m and 15m and are constructed by a variety of techniques including caisson sinking and underpinning with precast concrete segmental lining, sprayed concrete lining and secant piling. The shafts will be covered by headhouses to provide access and ventilation for the tunnels. The scheme is currently under construction and due to be completed in 2027. HOCHTIEF-MURPHY Joint Venture are contracted to deliver the Package 2 Tunnels & Shafts and Package 5 Headhouses & M&E contracts on the scheme, and appointed AECOM as permanent works design partner.

This paper presents the design of the bolted universal segmental tunnel lining which is utilised in four of the five tunnel drives and will house two of three new cable circuits.

It will cover the design of four TBM tunnel drives by addressing the ground through which the tunnel is built, and the numerical analysis adopted for the lining design. The four tunnel drives are as follows:

- Drive 2: New Cross to Kings Avenue (via Bengeworth) – 6.3km – TBM Edith
- Drive 3: New Cross to Eltham (via Kidbrooke) – 11.1km – TBM Grace

*Corresponding author: anna.simic@aecom.com

DOI: 10.1201/9781003495505-161

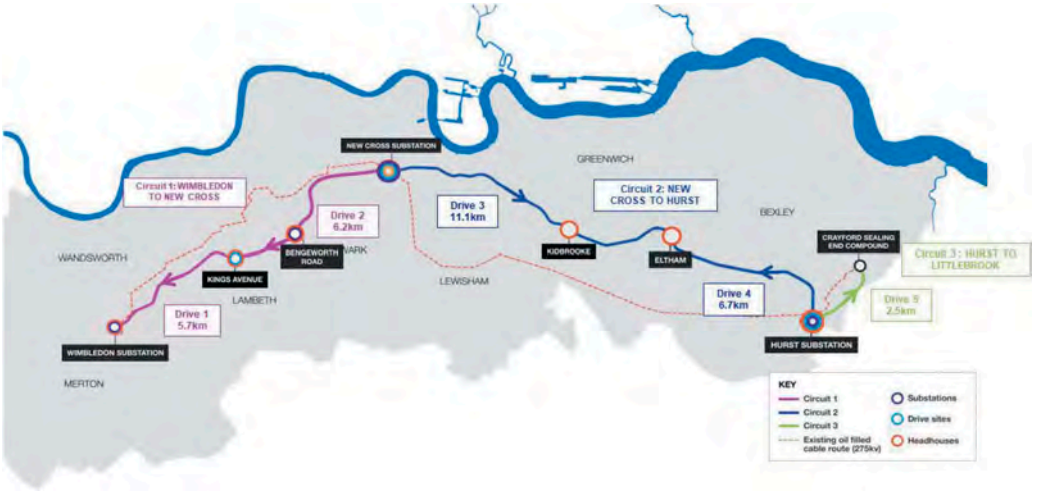

Figure 1. Scheme overview.

- Drive 4: Hurst to Eltham – 6.7km – TBM Christine
- Drive 5: Hurst to Crayford – 2.5km – TBM Christine (relaunched following refurbishment and modifications after the Hurst to Eltham drive)

The tunnel route travels through the full stratigraphy of the London Basin, which includes overconsolidated clays, sands and chalk. Extensive parametric studies for different parameters including surface surcharge, groundwater pressures, coefficient of earth pressure at rest (K0), and degree of stress relaxation have been conducted using PLAXIS 2D to identify the most onerous design scenarios. Loads arising from primary and secondary grouting, gantry wheel loads, the cable installation monorail system and cable brackets were also considered in the analyses. The analyses were supported by closed-form calculations to verify ram forces, bolt capacity, gasket performance and the effects of ring build tolerances.

2 ELEMENTS OF THE TUNNEL

2.1 *Segments*

The tunnel lining is formed of steel fibre reinforced precast concrete segmental rings. A universal ring system was adopted where both circumferential faces of the ring are inclined to the tunnel axis. This ring taper is split between the two circumferential faces to enable the tunnel drive to follow the design alignment through rotation of the segmental ring. Each ring has six tapered segments. The geometry of the ring is shown in Figure 2 with a ring length on tunnel centreline of 1.2m. The internal radius is Ri = 1500mm, the thickness of the segment is Ts = 180mm and the depth of extrados and intrados groove is dext = 60mm and dint = 24mm, respectively. The set of angle for an ordinary segment is θo = 60°, for a top segment is θt =69° and for the key segment is θk =51°.

2.2 *Circumferential joints*

High durability plastic dowels were used as the connection device between segments on the circumferential joint. Two dowels per segment was adopted. The use of dowels permits rapid erection of segments and reduced cycle times. The dowels also allow a self-centring function during erection and ensure a close control over stepping between adjacent rings. The dowels were designed so that their design tensile capacity is sufficient to retain the compression in the circumferential joint gaskets when fully compressed on release of the TBM shove rams. The shear capacity of the dowels was also checked to be able to withstand the maximum torque capacity of the TBM.

2.3 *Radial joints*

Steel bolts were used to secure the radial joints. All bolts and cast-in sockets are a single assembly and of proprietary design. The bolts were designed to have sufficient tensile capacity to retain the compression in the radial joint gaskets when fully compressed on release from the segment erector. Bolting in the radial joints is only required during segment ring assembly and so must be kept in place 100m back from the tunnel excavation face and if adverse local ground conditions are encountered.

2.4 *Gaskets*

The segmental tunnel lining has to resist external water pressures of up to 6 bar, limiting water ingress/egress to a negligible amount. The seal is

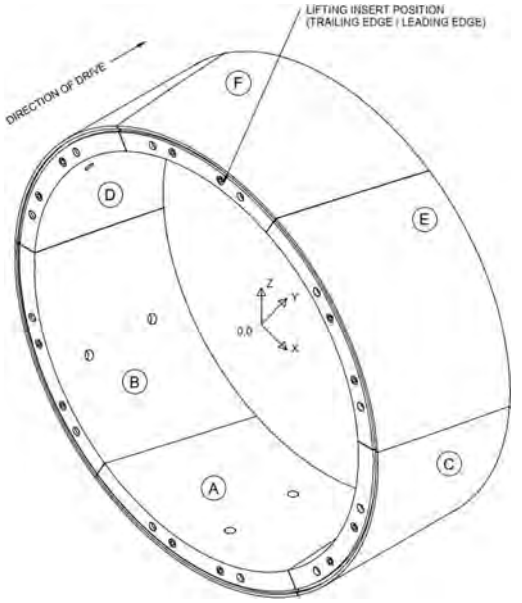

Figure 2. Universal lining segment arrangement.

Figure 3. TBM edith being lowered into new cross shaft.

created by the inclusion of cast-in gaskets in all segments made of ethylene propylene diene monomer (EPDM). The gaskets are supplied as a continuous loop with the joints formed to the correct angles for each type of segment. Further the joint formation has been designed to minimise the additional rubber material forming the joint to avoid hard spots in the gaskets. The gaskets were pressure tested to 10 bar pressure with 10mm offset and a 4mm gap between bearing surfaces in a rig to model a cruciform joint arrangement.

2.5 *Reinforcement*

All segments contain steel fibre reinforcement, with additional traditional rebar reinforcement cages incorporated in specific locations. The bar reinforced rings are to be used to construct the first 16 rings and the last 16 rings of each drive and where an increased robustness of tunnel lining is required.

3 EXCAVATION AND SUPPORT METHODS

The tunnel will be excavated and constructed using an Earth Pressure Balance (EPB) TBM.

The cutting head diameter is 3636mm, providing a 10.4m^2 total cutting face area. Behind the cutting head, the shield has a length of 11.6m and a diameter of 3600mm. This difference in radius between the cut radius and the diameter of the tail skin creates an annulus of 18mm allowing ground deformation and settlements to occur. During the excavation, the TBM applies a face pressure to balance the forces within the ground and to control the ground deformation and settlements. The pressure is applied by regulating the volume of spoil in the plenum and by rams, which allow the TBM to advance. As the TBM advances, after the erection of the ring, the 138mm annulus between the excavation diameter and the external diameter of the lining is grouted through the tail skin.

4 GROUND AND GROUNDWATER CONDITIONS

4.1 *Geology*

The geology present along the tunnel alignment is presented in Figure 4 and Table 1.

4.2 *Groundwater conditions*

There are typically two main aquifers in Greater London. Groundwater is present in the surface superficial deposits of Alluvium and the River Terrace Deposits where present, supported by the underlying, low permeability London Clay. This is typically referred to as the ‘upper aquifer’. In the vicinity of the River Thames, in the central section of the LPT Phase 2 alignment, the upper aquifer is likely to be tidally influenced by the River Thames.

Groundwater is also present in discrete granular units in the upper section of the Lambeth Group, in particular in the Channel Sands and in permeable layers within the London Clay and the Harwich Formation (the basal layer of the London Clay). The water bearing layers of these strata are referred to as the ‘intermediate aquifer’. These water bearing layers within these strata vary significantly in

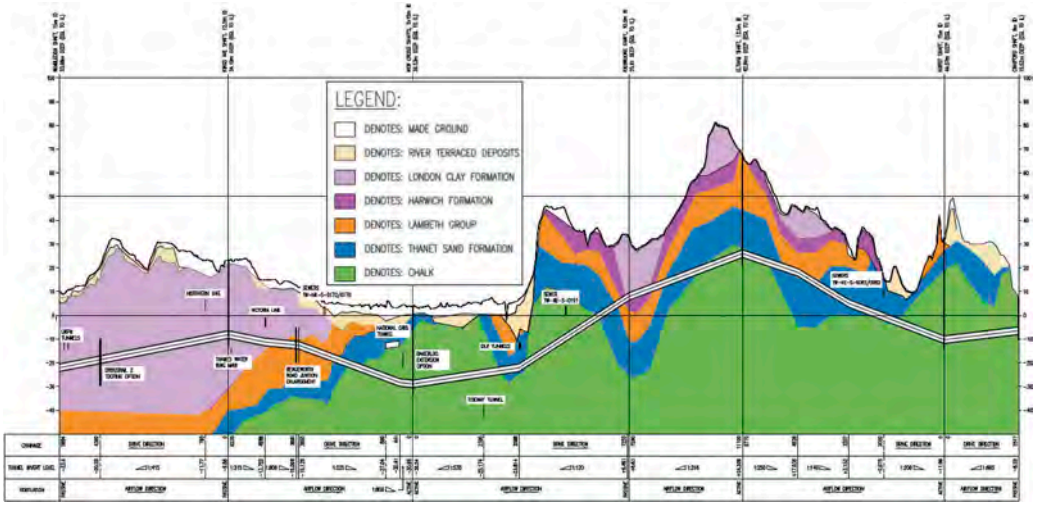

Figure 4. LPT phase 2 geotechnical overview (national grid/WSP, 2019).

Table 1. Geology along the tunnel alignment.

Era	Period	Epoch	Formation/ Strata		Composition	Depositional Environment
Cenozoic	Quaternary	Anthropocene	Made Ground		Highly variable. Hard-standing and granular soils of particle sizes varying from clay to cobble and more rarely boulder with fragments of brick and concrete etc. May contain some contaminated or hazardous materials dependent upon former land uses.	Anthropogenic activity.
		Holocene	Alluvium		Predominantly sand, silt and clay with localised peat and organic matter.	Overbank deposits of flooding fluvial systems.
		Pleistocene/ Holocene	River Terrace Deposits		Predominantly gravel and sand, with localized clay beds and lenses.	Fluvial floodplain.
	Paleogene	Eocene	Thames Group	London Clay	Brown, and blue grey clay, locally silty and with silt and fine sand layers.	Deepwater marine.
				Harwich	Glauconitic, sandy clay and silt with shells and shell fragments.	Intermediate depth marine.
		Paleogene	Lambeth Group	Woolwich	Clay, locally laminated and locally with abundant shell fragments. Contains sand filled channels.	Marginal marine, estuarine and deltaic.
				Reading	Mottled clay with sand filled channels.	
				Upnor	Calcareous gravely sand.	
			Thanet Group	Thanet Sands	Fine sand.	Shallow marine.
				Bullhead Beds	Locally clayey fine sand with abundant cobbles of rounded flint.	
Mesozoic	Cretaceous		Chalk (Newhaven)		Calcareous white limestone (chalk).	Shallow to intermediate depth warm marine.

thickness and in their lateral extent across the LPT Phase 2 alignment.

The main water-bearing sequence below the LPT Phase 2 alignment is known as the 'lower aquifer' and comprises the Chalk, the overlying Thanet Sand Formation and the granular Upnor Formation, which is the basal unit of the Lambeth Group. Silt and clay bands may be present in the lower part of the Thanet Sand and may reduce the vertical flow, thus impeding hydraulic continuity within the lower aquifer. Groundwater flow in the Chalk is predominantly via fractures which facilitates rapid flow due to the high secondary permeability. The Chalk matrix has a much smaller contribution to groundwater flow due to the lower intergranular permeability.

In the western end of the route, where the London Clay is present at shallow depths with a variable but significant thickness, the groundwater in the lower aquifer below the route alignment in this section is confined under pressure by the overlying low permeability units. In vicinity of the New Cross shaft site and along the majority of the tunnel alignment towards the Hurst shaft site to the east, the overlying Lambeth Group and the London Clay are either absent or present in sections. Where the overlying low permeability units are absent, in these sections, the lower aquifer is unconfined with groundwater potentially present at shallow levels. The eastern end is directly underlain by the unconfined lower aquifer with the Chalk surface present at shallow depths beneath layers of superficial deposits of River Terrace Deposits and Alluvium. The groundwater in the lower aquifer in this area is shallow and is likely to be in hydraulic continuity with the overlying superficial deposits with potential tidal influence where the route alignment is close to the River Thames.

A review of the EA publication for the groundwater levels in the Chalk Aquifer in the London Basin between 2000 and 2018 indicates that the groundwater level in the lower aquifer varies from approximately -2 m OD to -13 m OD in the western end, -8 m OD to -2 m OD in the central area and +15 m AOD to +10 m AOD in the eastern end of the alignment. The groundwater regime in the western and central areas of the LPT Phase 2 alignment are likely to be affected by the geological faults present in this area where up to four faults have been mapped. The faults include the Rotherhithe Fault, the Streatham fault, the Greenwich fault. Several solution features and deneholes have also been identified in the vicinity of the Hurst shaft site. These features have the potential to modify groundwater flows locally, particularly if they extend below the groundwater level.

5 LOAD COMBINATIONS

The design of the segmental tunnel primary lining was based on combinations of the following load cases:

Table 2. Load cases.

Primary grouting pressure	The greater of: Total stress + 50kPa or Groundwater pressure +50kPa,
Secondary grouting pressure	Applied as a localised triangular load equal to the groundwater pressure + 50kPa at crown, shoulder or axis.
Monorail load	Loading applied at the tunnel crown from cable installation using the monorail system: i) Cable pulling SW=25kN F_y=7kN F_z=4kN, F_x=20 ii) Laying off cable SW=25kN F_y=4kN F_z=1kN iii) Cable sagging SW=25kN F_y=4kN F_z=2kN
Cable bracket loading	Pull-out force acting on the lining: i) Permanent load (22kN) ii) Accidental short-circuit load (40kN)
Allowance for future development or construction surcharge	75kPa surcharge applied at the ground surface covering either: i) The full model width ii) Half the model width

SW = self-weight, F_y = vertical, F_z = horizonal, F_x = longitudinal

All load combinations were simulated for upper and lower bound geotechnical parameters (c, c_u, φ, E), minimum and maximum earth pressure coefficient ($K0_{min}$, $K0_{max}$), and minimum and maximum groundwater level (WL_{min} and WL_{max}).

Temporary handling and stacking loads, TBM ram forces and the effects of steps, lips and ring build tolerances were considered using separate empirical and closed-form calculations not covered in this paper.

Figure 5. Example of completed tunnel lining with cable brackets installed.

6 NUMERICAL ANALYSIS

6.1 *PLAXIS analysis*

Structural forces and displacements in the precast segmental tunnel lining for each combination of

ground conditions were evaluated using PLAXIS 2D plane strain numerical modelling. The Finite Element Method allows a comprehensive analysis of soil-structure interaction to be carried out which considers the tunnel construction sequence and loads applied to the lining in both the short and long-term.

Loading applied to the tunnel lining in the PLAXIS model includes the primary and secondary grouting pressures, ground surface surcharges, cable bracket loading (including loads imposed by a short-circuit event), as well as the load from the monorail.

6.1.1 *Constitutive soil models*

Due to the limited ground investigation and laboratory testing data available, the Mohr-Coulomb constitutive model has been adopted, which assumes the stress-strain relationship to be linear elastic-perfectly plastic. Prior to yielding, the gradient of the stress-strain curve is defined as the Young's modulus of the soil (E'). When the stress state reaches exceeds the failure criterion, the ground exhibits a perfectly-plastic behaviour. An increase in soil stiffness with depth has been modelled. However, the model does not account for stress dependency or stress-path dependency of the stiffness. Nor does it distinguish between large stiffness at small strains and reduced stiffness at engineering strain levels. Therefore, the stiffness parameters were specified in accordance with the dominant strain levels associated with TBM tunnel construction, considered to be 0.1 – 1%.

Strata were assigned a drainage type of drained or undrained, depending on the material type (granular or cohesive) and whether short or long-term conditions apply. Where a material is considered to behave in an undrained manner, it was modelled with the undrained (A) drainage type, which enables undrained behaviour to be modelled using an effective stress analysis with effective stiffness and effective strength parameters (c', ϕ'). With this drainage type, PLAXIS automatically adds the stiffness of the water to the stiffness matrix to distinguish between effective stresses and (excess) pore pressures. Steady state pore pressures were generated based on the phreatic levels specified for each stratum.

6.1.2 *Ground model and ground relaxation*

The stress relief or relaxation of the ground and three-dimensional arching effect due to shaft or tunnel advancement can be simulated in two-dimensional models using the stress reduction method, often referred to as the β- or λ-method. Initial stresses P_0 acting around the location where the tunnel is to be constructed are divided into a part λP_0 that is applied to the unsupported tunnel opening and a part $(1-\lambda)P_0$ that is applied to the supported tunnel, where P_0 is the in situ stress. To apply this in a PLAXIS two-dimensional analysis, one can use the staged construction option with a reduced ultimate level of ΣMStage. The ΣMStage parameter defines the degree of equilibrium achieved in a construction phase, which progresses from zero at the start of the construction phase (forces out of equilibrium) to unity at the end (full equilibrium reached).

Stress relaxation, λ, was first calculated for each geological stratum using the expression for an isotropic elastic medium after Panet (1979) and for an isotropic elastic-plastic medium after Panet (1995). The PLAXIS 2D plane strain analysis was then calibrated to match the predicted radial displacement and volume loss from these closed form solutions. This is performed in the model by de-activating the soil elements within the tunnel and running the analysis to the required value of ΣMStage to reach the target displacement.

Table 3 summarises the minimum and maximum values of stress relaxation for each soil type. Due to the similar ranges of values for each soil type, an overall minimum and maximum value of 30% and 62% will be adopted for all materials in the 2D finite element (FE) analysis, respectively.

Table 3. Values of PLAXIS ΣMStage parameter corresponding to the elastic (Panet, 1979) and elastic-plastic (Panet, 1995) solutions for ground relaxation for each soil type.

	ΣMStage Parameter	
Material	Elastic	Elastic-Plastic
London Clay Formation	0.30	0.59
Harwich Formation (Cohesive)	0.31	0.62
Harwich Formation (Granular)	0.34	0.62
Lambeth Group (Granular)	0.35	0.59
Lambeth Group (Cohesive)	0.31	0.54
Thanet Formation	0.35	0.59
Chalk	0.34	0.50
Adopted value for design (upper and lower bound for all materials)	0.30	0.62

6.1.3 *Modelling of the tunnel lining*

The precast segmental tunnel lining was modelled in PLAXIS 2D using two-dimensional plate elements with isotropic stiffness properties equivalent to concrete grade C50/60. Radial joints were not modelled explicity, but instead represented by reducing the flexural stiffness of the lining according to the approach proposed by Muir Wood (1975). This approach considers a reduced second moment of area based on the number of joints, as given by Equation 1.

$$I_e = I_j + I_s\left(\frac{4}{n_s}\right)^2 \quad (1)$$

Where, I_e is equivalent second moment of area; I_j is second moment area of the joint (m^4); I_s is second moment area of the segment (m^4); n_s is number of segments in a ring (including key).

Interface elements were applied to the extrados of the tunnel lining to simulate soil-structure interaction by limiting the degree of shear force transferred.

6.2 *LUSAS analysis*

A separate LUSAS analysis was also prepared to assess the structural behaviour of the tunnel lining due to either eccentric loads or concentrated loads such as gantry wheel loading. This model includes a more detailed simulation of the radial joints in the tunnel lining and therefore is able to more accurately assess the localised effects of large, concentrated loads on these joints.

6.2.1 *Modelling of the tunnel lining*

The tunnel lining was modelled using a two-dimensional bedded beam analysis. The bedded-beam spring model describes the tunnel lining as a series of beams of rectangular cross-section connected to a series of radial and tangential springs, representing the interaction between the lining and the ground. The springs are allocated with a stiffness, which is dependent on the Young's modulus and the Poisson's ratio of the ground and the radius of the tunnel. The stiffness of the support springs will be based on Duddeck & Erdmann (1985).

$$k = \frac{E_c\ (1-\upsilon)}{R(1-2\upsilon)(1+\upsilon)} \qquad (2)$$

Where, k is radial spring stiffness (kN/m^3), E_c is Young's Modulus of the continuum (kN/m^2); υ is poisson's ratio; R is tunnel radius (m).

The radial spring stiffness is modelled in LUSAS as a lift-off spring to ensure that they only work in compression.

In the longitudinal direction, the trailing edge of each ring is connected to the previous rings and therefore the nodes are fixed in the longitudinal direction.

Hinges (pinned end connections) between beam elements were used to represent the bolted connection between the segments in each ring. As the location of the segmental joints will rotate as the tunnel lining is constructed, the gantry wheel loadings could be positioned in numerous configurations in relation to the joints. In order to ensure the most onerous loading scenario is considered, the tunnel lining was checked for each wheel loading type positioned close to a segmental joint, as well as in the centre of the segment.

7 RESULTS OF NUMERICAL ANALYSIS

The results of the PLAXIS 2D analysis for each tunnel section, for upper and lower bound soil parameters, is presented in Figure 6 and Figure 7.

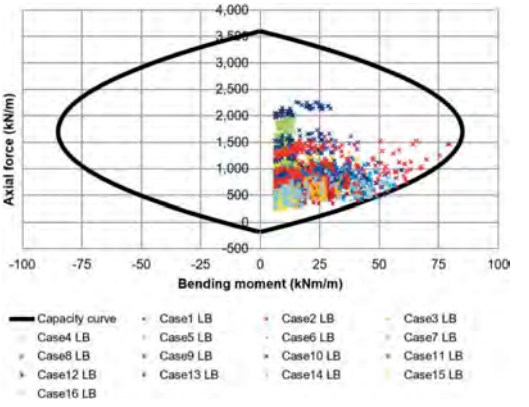

Figure 6. Lining forces extracted from PLAXIS 2D model (lower bound geotechnical parameters).

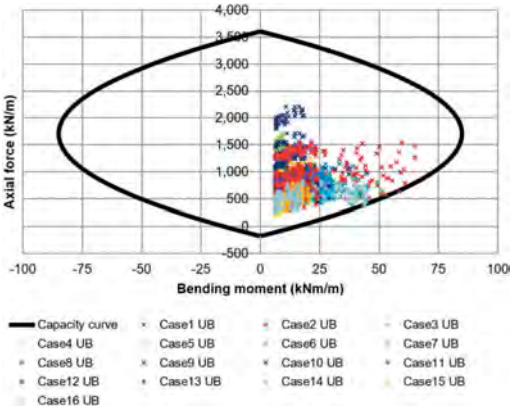

Figure 7. Lining forces extracted from PLAXIS 2D model (upper bound geotechnical parameters).

8 CONCLUSIONS

The purpose of the analyses described in this paper was to assess the behaviour of the precast segmental lining under all loading conditions.

The results of the FE models were corroborated by additional empirical and closed form calculations.

These analyses gave the designer confidence that the tunnel lining will be able to resist the ground, groundwater, construction and long-term loading.

ACKNOWLEDGMENTS

The authors would like to thank the contractor HOCHTIEF-MURPHY Joint Venture, National Grid and their engineering partners for their collaboration during the design and construction process and for their support with this paper.

REFERENCES

Anon (2003). Final recommendation of RILEM TC 162-TDF: Test and design methods for steel fibre reinforced concrete sigma-epsilon-design method. Materials and Structures, 36(262), pp.560–567.

Bamforth, P.B (2007). C660 Early-age thermal crack control in concrete, London, CIRIA.

British Tunnelling Society & Institution of Civil Engineers, (1997). Model specification for tunnelling, London: Thomas Telford.

Duddeck & Erdmann, (1983). Structural design models for tunnels: Tunnelling 82, proceedings of the 3rd international symposium, Brighton, 7–11 June 1982, P83–91. Publ London: IMM, 1982. International Journal of Rock Mechanics and Mining Sciences and Geomechanics Abstracts, 20 (1), p.A15.

Environment Agency (2018). Management of the London Basin Chalk Aquifer, Status Report - 2018, EA.

Fédération Internationale du Béton (2013). fib model code for concrete structures 2010. Berlin, Ernst & Sohn.

Guyon, Y. (1974). End block reinforcement and reinforcement cages in the anchor zones, Limit-state Design of Prestressed Concrete, Volume 2.

Muir Wood, A. M. (1975). The circular tunnel in elastic ground. Géotechnique, 25(1), pp.115–127.

Muir Wood, A. M. (1976). Discussion: The circular tunnel in elastic ground. Géotechnique, 26(1), pp.231–237.

Panet, M. (1979). Les déformations différées dans les ouvrages souterrains. Fourth Int. Congr. on Rock Mechanics. Montreux, vol.3, Balkema, Rotterdam I, 291–301.

Panet, M. and Guenot, A. (1983). Analysis of convergence behind the face of a tunnel: Tunnelling 82, proceedings of the 3rd international symposium, Brighton, 7–11 June 1982, P197–204. Publ London: IMM, 1982. International Journal of Rock Mechanics and Mining Sciences and Geomechanics Abstracts, 20 (1), p.A16.

The Concrete Society (2007), TR 63 Guidance for the Design of Steel-Fibre-Reinforced Concrete.

ITA Working Group 2 – Research (2019). Guidelines for the Design of Segmental Tunnel Linings.

Kundan, R., Daniele, S. and Martin, S. (2023). Challenges of delivering 32.5km of major tunnelling infrastructure in South London (UK), and the influences of an innovative “Enterprise” project delivery model. Proceedings of the Tunnelling Association of Canada (TAC) 2023 Conference.

Tunnelling for a Better Life – Yan, Celestino, Thewes & Eberhardt (Eds)
© 2024 The Author(s), ISBN 978-1-032-80042-4
Open Access: www.taylorfrancis.com, CC BY-NC-ND 4.0 license

Value engineering of concrete mix to save 230 tonnes of steel fibre for the west section of the Thames Tideway Tunnel

Jiang Su*
AtkinsRealis, Epsom, UK

Sagar Sheth
Ramboll, London, UK

Annie Ellison & Chris Barret
BMB, London, UK

ABSTRACT: The Thames Tideway Tunnel is the biggest infrastructure project the UK water industry has undertaken since its privatisation in 1989. The 25km-long tunnel is split into the West, Central and East contracts. The West contract is approximately 7km long from Acton to Carnwath Road in West London. The 7 km-long, 7.2m internal diameter main sewer tunnel was originally designed as a precast segmental lining tunnel with cast in-situ concrete secondary lining using 40km/m^3 steel fibre to achieve both mechanical performance and durability in 120 years of design life. BAM Nuttall, Morgan Sindall, Balfour Beatty Joint Venture (BMB) is the contractor on the Tideway West section. Before starting the main tunnel secondary lining construction, BMB initiated an exercise to value engineer the original secondary lining concrete mix. As the Category 3 checker for the main sewer tunnel, Ramboll has supported client BMB in its pursuit. Working in collaboration with the main tunnel designer, Ramboll helped develop a testing regime for a new mix which reduces the quantity of steel fibre from 40kg/m^3 down to 35kg/m^3. This has involved undertaking a large-scale beam testing programme to verify the new mix to understand its pre-crack and post-crack behaviour based on the monitoring results from traditional strain gauges and leading-edge digital imaging correlation techniques. With close collaboration with the contractor and the main tunnel designer, Ramboll guided the back-analysis of the beam test results and concluded that the new concrete mix performed as well as the previous one. The works have been carried out in conjunction with Tideway, which has subsequently approved using the new mix with the lower fibre content. The new concrete mix has saved up to 230 tonnes of steel fibres for the 7 km-long west section of the main tunnel, bringing significant environmental and financial benefits.

Keywords: Thames Tideway Tunnel, Secondary Lining, Steel fibres, Value engineering

1 INTRODUCTION

London, a major global city, is still relying on a combined sewerage system, which was designed by Sir Joseph Bazalgette and constructed in the 1860s. This system that captures both rainwater runoff and sewage has a design capacity of four million people. As London's population grew to eight million by 2012, the sewerage system could not cope with the volume of the combined sewage overflows (CSOs), leading to increasingly frequent overflows to the river Thames. These discharges have to be reduced to improve the ecology of the river Thames and comply with the EU's Wastewater Treatment Directive (EU, 1991).

The overall Tideway scheme is a significant new combined sewage storage and transfer system that will help protect the river Thames by tackling the problem of overflows from the capital's ageing sewers. The Main Tunnel, a major component of the system, will run from Acton in West London to Abbey Mills Pumping Station in East London. It will intercept, store, and convey the flows from the most polluting CSOs, which currently discharge directly into the river. The flow will then run to the Beckton Sewage Treatment Works via the Lee Tunnel (Jewell

*Corresponding author: Jiang.su@atkinsrealis.com

DOI: 10.1201/9781003495505-162

& O'Connor, 2012), the construction of which was already completed in January 2016 (Ashenden & Garrett, 2016).

There are three Main Works contracts for the scheme: West, Central and East. BAM Nuttall, Morgan Sindall, Balfour Beatty Joint Venture (BMB) Joint Venture is responsible for the delivery of the West Main Works contract. This contract covers all works between Acton in West London and Carnwath Road in the east, approximately 7km in length (Figure 1). The tunnel designer is Morgan Sindall Engineering Solutions (MSES), and the Category III check is performed by Ramboll UK.

Figure 1. Thames Tideway and Lee Tunnel Route and Sites (Courtesy of Tideway).

As the west section main tunnel is constructed exclusively in London Clay, an earth pressure balanced (EPB) tunnel boring machine was used. The external and internal diameter of the main tunnel primary lining is 7.8m and 7.1m, respectively. The main tunnel primary lining is formed from steel fibre-reinforced precast concrete segmental rings. The external and internal diameter of the main tunnel secondary lining is 7.1m and 6.5m, respectively. The main tunnel secondary lining is formed from steel fibre-reinforced cast in-situ concrete.

The primary lining has been designed to be able to resist all the long-term external ground and groundwater pressure, plus any future surcharge loads as specified in the project design requirements. The secondary lining is designed to resist the internal water pressure with the confinement from the primary lining and surrounding ground. The secondary lining is also designed for long-term durability purposes as the sewage water is corrosive in nature.

2 LINING DESIGN AND VALUE ENGINEERING

2.1 *Secondary lining critical load case*

The main tunnel secondary lining design was considered very challenging. The reasons are explained in detail below. When the main tunnel primary lining is constructed, all the short-term external ground load and groundwater pressure will be applied to the primary lining. With the perfect circular shape of the main tunnel, little bending moment will be generated in the primary lining. Hence, the whole primary lining cross-section will be in compression. When the secondary lining is installed, it will not take any short-term external ground load or groundwater pressure. The early-age thermal and shrinkage effect of the secondary lining will lead to the secondary lining contracting in volume slightly, potentially leaving a gap between the primary lining intrados and the secondary lining extrados. This gap will then be filled back with no-shrink grout to ensure good contact between the two layers of lining and form a composite lining with full composite action, which will provide a greater overall capacity to any external or internal loads. It should be noted that the secondary lining, despite being incorporated into the composite lining system, is at a stress-free status. As the tunnel is constructed in London Clay, long-term consolidation ground and long-term water pressure will be applied to the extrados of the primary lining at a later stage. These additional external loads will be shared between the primary and the secondary linings according to the relative axial stiffness ratio between the two linings. Therefore, a small magnitude of axial compression and bending will be generated in the secondary lining to resist the external load, as shown in Figure 2 (a). The darker and lighter blue colour in the primary and secondary linings represents greater and less axial compression, respectively.

The most challenging load case for the secondary lining is when the internal surcharge pressure is applied to the intrados of the secondary lining. This simulates an extreme rainfall or flooding scenario in which the whole Thames Tideway tunnels are fully stored with stormwater with a water head from the tunnel level up to the ground level. Under this load case, the composite lining will resist the internal water pressure, which results in axial tension being generated in the tunnel linings. This axial tension is not a design challenge for the primary lining because its magnitude, which was determined by the maximum water head, is less than the axial compression induced by the external ground load and groundwater pressure. In comparison, this axial tension is a significant design challenge for the secondary lining because the magnitude of the axial tension is usually greater than the axial compression generated under the effect of long-term consolidation loads. Hence, the secondary lining needs to be designed under a full tension stress status while still satisfying the stringent maximum crack width requirements to ensure its long-term durability. The lining stress status of this stage is shown in Figure 2 (b), with the light blue and red colours representing reduced axial compression and tension in the primary and secondary linings, respectively.

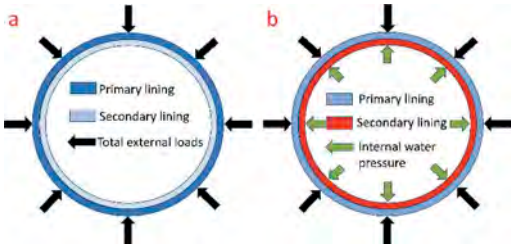

Figure 2. Lining stress status under external load only (a) and under both internal and external loads (b).

2.2 *Strain-hardening behaviour of concrete lining*

With the understanding of the critical load case for the secondary lining, the next step was to decide what types of reinforcement should be used in the secondary lining to resist the axial tension in the lining in the most efficient way. Steel fibres were selected as the main reinforcement in the concrete secondary lining as they could provide sufficient post-crack ductility, crack width control and reduced concerns about the impact of sewage water-induced corrosion on the reinforcement.

Bekaert's Dramix steel fibres are the most widely used ones in the UK tunnelling market. It has three main types of steel fibres, each with different tensile strength, number of hooks, length and aspect ratios, suiting different types of applications. While Dramix 3D has mostly been used for the sprayed concrete lining application, the Dramix 4D and 5D have been used more in the precast and cast in-situ concrete lining (De Rivas, 2020). From a structural performance perspective, the concrete reinforced by the Dramix 3D steel fibres usually demonstrates a strain-softening behaviour, whilst those reinforced by the Dramix 5D steel fibres usually demonstrate a strain-hardening behaviour, as shown in Figure 3 below. The visual difference between the two types of behaviour is that a single crack is usually formed under a typical 3-point or 4-point bending test for the former, whilst multiple cracks are usually formed for the latter, which could result in reduced crack width when compared with the scenario when a single crack is developed. Typical sprayed concrete lining using Dramix 3D steel fibres under a 4-point bending test showing a single crack with increased crack width under increasing external loading can be found in Su and Bloodworth (2018).

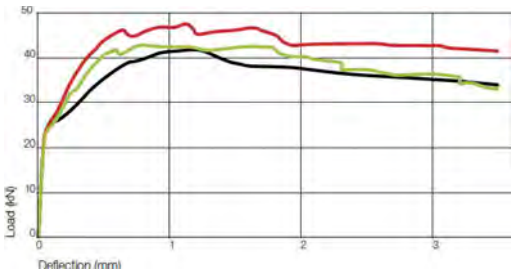

Figure 3. Performance of steel fibre reinforced concrete (SFRC) using Dramix 5D steel fibre (Bekaert, 2018).

2.3 *Value engineering of the secondary lining*

The main tunnel designer, MSES, was also the tunnel designer for the Lee Tunnel project, which adopted the same lining configuration as the Tideway West Contract but was constructed at a much deeper level (Psomas et al., 2014). The designer was trying to replicate the successful design and construction experience from the Lee Tunnel to the Tideway West Contract by utilising the beneficial effects of multiple cracking modes by using high-performance steel fibre-reinforced concrete to satisfy the project's stringent crack width limit for the tunnel secondary lining when under internal surge pressure. For the Lee Tunnel project, a 40kg/m^3 dosage of Bekaert Dramix 5D 6560BG was used for the main tunnel secondary lining. The adoption of this concrete mix was verified through large four-point beam laboratory tests undertaken at the Building Research Establishment (BRE). The test results were rigorously reviewed and verified prior to the construction (Psomas, 2020). With past successful experience, the same dosage of steel fibre was proposed for the Thames Tideway West main tunnel secondary lining.

Prior to the construction of the tunnel's secondary lining, BMB undertook a comprehensive value engineering exercise with the objectives of reducing the construction cost, programme, and embodied carbon. One of the potential value engineering options is to reduce the steel fibre dosage from 40kg/m^3 to 35kg/m^3 in the secondary lining without compromising its performance under the critical internal surge pressure loading condition. Hence, a value engineering investigation of this potential option was proposed and carried out in the following stages.

This value engineering comprises testing of five large 35kg/m^3 dosages of SFRC beams under a 4-point bending test configuration. The performance of the beams was monitored using strain gauges, potentiometers, and digital image correlation (DIC). These results were compared with the test results from the Lee Tunnel project large beams, which used 40kg/m^3 steel fibres in the same concrete mix and under the same 4-point bending test configuration. The objective of this test is to prove that this new Tideway West Contract proposed 35kg/m^3 concrete mix will perform at an equivalent or better than the previous 40kg/m^3 concrete mix adopted in the Lee Tunnel project.

The first author of this paper previously worked as the technical director of the Category III checker. He was commissioned by the Contractor BMB as a special adviser to witness the large beam tests, analyse the beam test results against the previous Lee Tunnel beam results, and produce evidence documents to convince senior technical leads from both

the Contractor BMB and the Thames Tideway to adopt this new concrete mix with reduced quantity of steel fibres. This paper describes this process.

This paper will first describe the large BRE beam tests, followed by a qualitative and quantitative comparison between the new and previous concrete mix in the aspects of (1) load-deflection, (2) load-strain, and (3) crack spacing and crack width. A conclusion is drawn in the end.

3 BRE BEAM TESTS

3.1 *Beams production, transportation and storage*

A laboratory testing program was devised to validate the performance characteristics of a 35 kg/m³ SFRC beam. Five large-scale beams, each weighing approximately 4 tonnes, were cast by Tideway West, and subsequently transported to the Structural Test Laboratory at BRE (Building Research Establishment) for testing.

The five specimens consisted of three SFRC beams, one hybrid composition integrating both steel fibres and steel bars reinforcement, and one entirely unreinforced beam. All specimens shared common dimensions, measuring 5400 mm in length, 1000 mm in width, and 300 mm in depth. The samples were cast as slabs on a release membrane to ensure a smooth bottom surface. The sides of the beams had a matt texture consistent in appearance with the use of a conventional steel or timber shutter and release agent. Furthermore, to mitigate the risk of damage during transportation, the beams were positioned on one of their long edges, resembling deep beams.

On arrival at BRE's Structural Test Laboratory, the samples were unloaded carefully and placed in a temporary storage position still oriented as deep beams, as shown in Figure 4. Lifting points were cast into each side of the samples, and suitable lifting links were supplied for use during the delivery and testing by Tideway West. After completion of the delivery, the three fibre-reinforced samples and the single conventionally reinforced sample were carefully rolled over such that the bottom surface at the time of casting was now the upper surface of each of the samples. The fifth unreinforced sample was not rotated until some space had been created by the testing of the earlier samples. All these efforts were made to avoid any potential damage to the beams, which in turn would affect the performance of the beams in the tests.

Figure 4. Beam samples unloaded and stored on edge.

3.2 *Beams test configurations*

Inverted four-point flexural tests were conducted on all five beam samples. Each sample was securely restrained at both ends, and loads were incrementally applied at the third span positions until structural failure was observed. To provide context, it is worth noting that the most closely related small-scale laboratory test, BS EN 14488-3, is typically performed on sprayed concrete beams with dimensions approximately one-tenth the size of the tests detailed in this study.

Figure 5 illustrates the specific dimensions and support configurations employed in the beam tests. Load application was facilitated through pairs of hydraulic cylinders with a capacity of 250 kN at each third-span position. These cylinders had a maximum potential displacement of 200 mm. At each loading point, the two cylinders were coordinated via a common loading bar measuring 1200 mm in length, featuring a curved contact surface with a nominal radius of 50 mm. Similar curved contact surfaces were utilized at the locations of end restraints. All four cylinders were interconnected through a manifold and length-matched pipework. The force exerted by each hydraulic jack was quantified using a 100 kN load cell. Three of these load cells were integrated into the data logging system, while the remaining one was connected to a digital readout unit, offering real-time monitoring of applied forces.

To assess vertical movement during testing, linear variable differential transformers (LVDTs) were strategically positioned at the loading points, at the centre span, and at the supports. Figure 6 schematically represents the arrangement of hydraulic rams and potentiometers. Additionally, Figure 7 provides a photographic depiction of the beam test setup.

Figure 5. Dimension of loading and supports for beam tests.

3.3 *Strain monitoring*

Direct contact strain measurements were conducted employing demountable transport research laboratory pattern vibrating wire strain gauges. These strain gauges featured a nominal gauge length of 140 mm. A total of 14 pairs of gauge

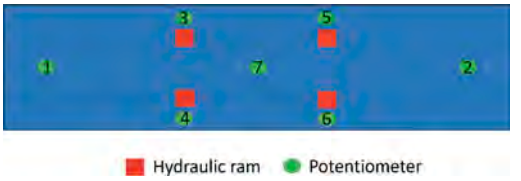

Figure 6. Positions of hydraulic rams and potentiometers.

Figure 7. Laboratory beam test set-up.

targets were arranged along the centreline of the specimen, establishing a measurement zone spanning from the mid-span section of the tension face of the beam to a point extending beyond the loading positions at the third-span locations, as depicted in Figure 5. The cumulative length encompassed by the strain gauges equated to 1950 mm. Additionally, a single pair of gauge targets was affixed to the compression surface of the beam at its mid-span position. The secure attachment of all gauge mounting targets was ensured through the use of a polyester resin-based filler applied to a clean and dust-free surface of the samples. The strain gauges were interconnected with a DataTaker 615 logger. The resulting data were stored within the logger for subsequent download and in-depth analysis following the conclusion of the test.

3.4 *Digital image correlation*

The Digital Image Correlation (DIC) monitoring of the test beams was conducted by the National Physical Laboratory (NPL). To capture high-resolution images, three cameras were strategically positioned at the front, back, top and perpendicular to the specimen face under investigation. Lighting conditions were carefully managed, utilizing a combination of work lights provided by BRE and laboratory lighting to ensure optimal image quality.

The camera solution utilised a resolution of 8256x5504 pixels, recorded in the NEF format, and compressed to 12-bit depth to accommodate the acquisition of a sufficient number of images. Image acquisition occurred at intervals of 0.5 seconds, utilizing three synchronized cameras, each with internal clocks set to less than 0.3 seconds for precise coordination. An intervalometer setting was utilized to guarantee synchronization across all images. Furthermore, the front camera also captured a load indicator, providing a load timestamp for the datasets. The configuration of the DIC system is illustrated in Figure 8.

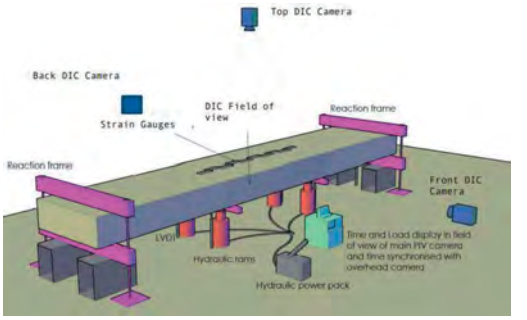

Figure 8. DIC arrangement for beam tests.

4 VALIDATION OF THE TEST RESULTS

This section compares the test results between the new concrete mix with 35kg/m^3 steel fibres and the previous one with 40kg/m^3 steel fibres. To ease the comparison, the SFRC beams using 35kg/m^3 concrete mix will be referred to as the new beams, whilst those using 40kg/m^3 concrete mix will be referred to as the previous beams. All other constituent materials are the same. Selected test results are presented and compared in the following aspects:

1. Load-displacement results
2. Load-strain results
3. Crack spacing results
4. Crack width results

4.1 *Load-displacement results*

As the load-displacement curves for the three new SFRC beams (beams no.1-3) are very similar, only the beam no.2 curve is presented here in Figure 9. Certain strain-hardening behaviour was observed, from the first crack load (approx. 100kN) to the peak load (approx. 135kN), followed by a strain-softening behaviour. The post-peak stress displacement was developed asymmetrically. This depends on which side of the beam will first develop a big crack.

Figure 10 shows the load-displacement curve for the hybrid beam (no.4). For the hybrid beam, a similar level of first cracking load around 100kN was observed. A much greater level of strain-hardening behaviour was observed, which led to a peak load of up to 400kN. This is much greater than the SFRC

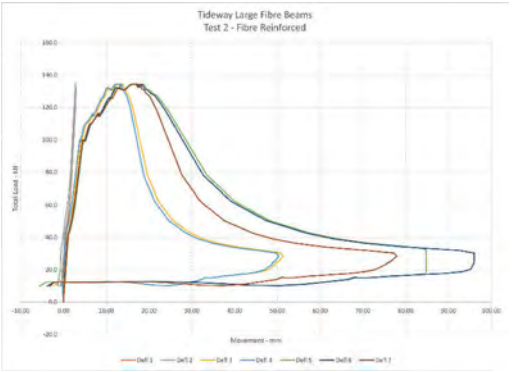

Figure 9. Load-displacement curve for new beam no.2.

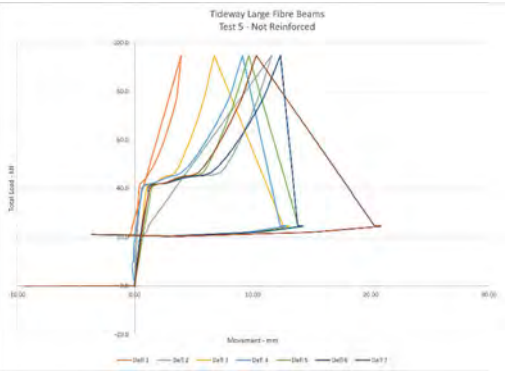

Figure 11. Load-displacement curve for plain concrete beam no.5.

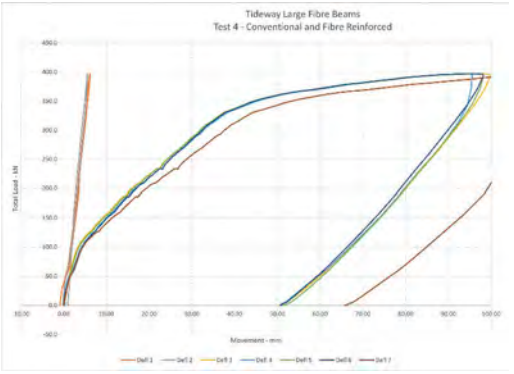

Figure 10. Load-displacement curve for hybrid beam no.4.

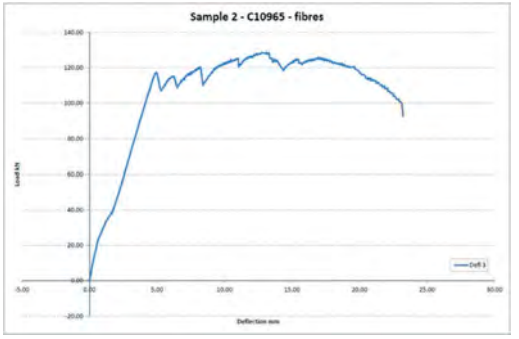

Figure 12. Load-displacement curve for a previous beams.

beam, which only has a peak stress of around 135kN. Figure 11 shows the load-displacement curve for the plain concrete beam (no.5). As expected, a brittle behaviour was observed with a slightly lower pre-crack peak load around 95kN. No ductility was observed.

A typical load-displacement curve for the previous SFRC beam is shown in Figure 12. When comparing to the new beam no.2 curve in Figure 7, the following interim conclusions can be drawn: (1) For the first crack loading, the previous beam is 20% higher than the new concrete mix (120kN vs 100kN). (2) For the peak loadings, the previous and new beams are similar, around 135kN. (3) Both previous and new beams have demonstrated similar and sufficient ductility at a moderate displacement range (i.e., up to 15-20mm displacement). It should be noted that the critical load case for the Tideway West main tunnel secondary lining is the serviceability limit state (SLS) lining crack width check under a full internal surge water loading scenario. Hence, the main focus on the load-displacement curve is on the small and moderate displacement range.

4.2 *Load-strain results*

This section presents the strain-displacement results for the selected new beam No.2 and compares them with the results from the selected old beams.

Figure 13 shows the strain-time curve in a logger cycle (i.e., time) sequence for strain gauges at the non-crack positions. It can be observed that the strain develops linearly up to the peak strain and then retains a slightly reduced level of strain for a certain period while the beam displacement is still developing. This is a clear demonstration of the ductility of the concrete beam, with steel fibres at the cracking position still providing residual tensile strength.

Figure 14 shows detailed load-strain displacement curves. It can be seen that the peak load occurs between 120-140kN with a corresponding strain between 100-110 με. After peak load, load suddenly drops with slightly increased strain between 110-120 με. Maximum strain up to the end of the loading testing stage is around 135 με. Strain-hardening behaviour is observed at the residual strain stage.

Figures 15 and 16 show the strain-time curve for previous beams. It can be seen that the first crack occurs when strain reaches between 150-190 με. Residual strain ranges from 120 to 180 με.

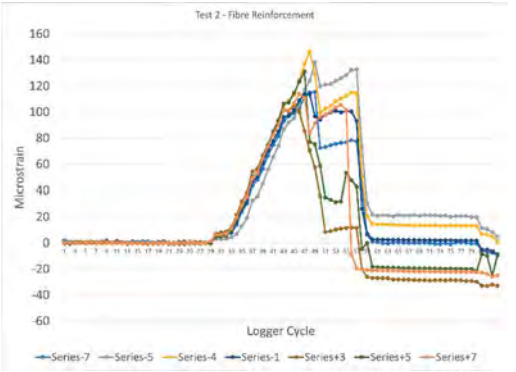

Figure 13. Strain-time curve for new beam no.2.

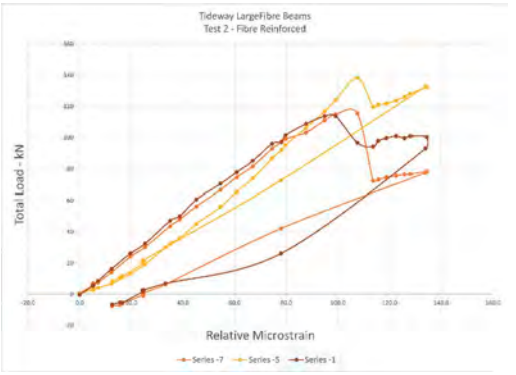

Figure 14. Strain-displacement curve for new beam no.2.

Figure 17 shows the strain-time curve for strains at cracking positions for the new mix beam no.2. Much greater strain levels, between 2000-4500 με, were observed. This is similar to that observed for previous beams, the results of which are not presented here due to space limit.

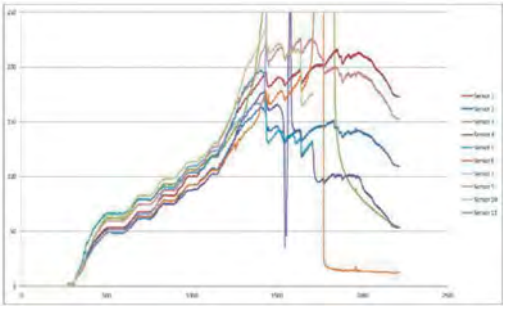

Figure 15. Strain-displacement curve for previous beams.

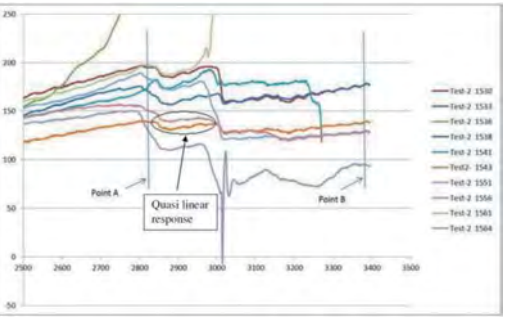

Figure 16. Strain-displacement curve for previous beams.

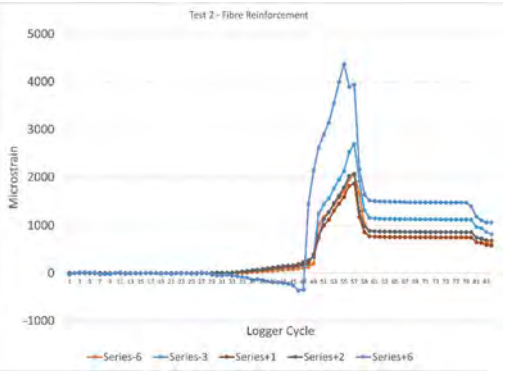

Figure 17. Strain-displacement curve for new beam no. 2 at cracks.

4.3 *Crack spacing results*

This section presents the crack spacing results from both manual observation and digital imagining correlation (DIC).

Figure 18 shows manual crack spacing measurement in the laboratory right after the completion of the test for new beam no.2. Crack depth was also marked in red. It was concluded that visible crack spacing is between 250-400mm. Figure 19 shows crack spacing for one previous beam, which ranges between 170mm and 530mm, indicating a higher variation.

Figure 20 shows the DIC crack spacing results, ranging from 80mm to 370mm. Based on Figure 9, the right-hand side beam first developed a bigger crack. Hence, the crack spacing on the right-hand side of the beam is more representative. It can be found all crack spacing on the right-hand side of the centreline of the beam is less than 300mm.

4.4 *Crack with results*

This section presents the crack width results from both the new SFRC beam no.2 and the selected beam results with the previous concrete mix.

Figure 18. Manual crack spacing measurement on new beam no.2.

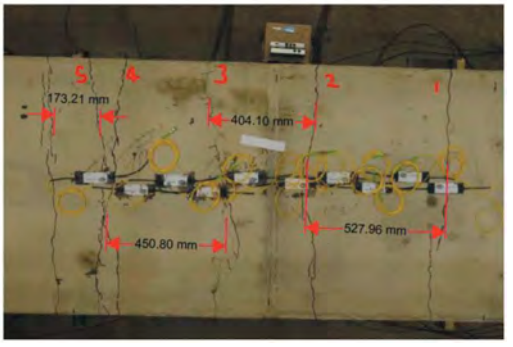

Figure 19. Manual crack spacing measurement on previous beam.

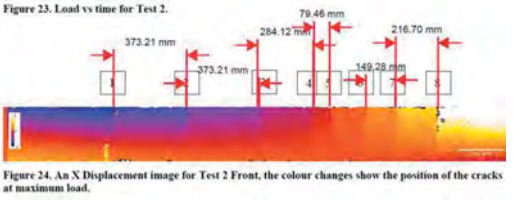

Figure 20. DIC crack spacing measurement on new beam no.2.

Figure 21 shows that the maximum crack width at the level of 15mm below the beam top surface was around 0.3mm when the beam was under a peak load of 134.4kN. The blue line and the green lines at the level 50mm below the top beam surface, both show a value around 0.5mm, are treated as outliers because these values don't follow the crack development pattern, which should have a bigger crack width closer to the tension surface (i.e., top beam surface) and gradually reduces with the increasing depth.

Figure 22 shows typical crack width results for a beam using the previous concrete mix. A red line was drawn to identify the maximum crack under the same loading of 134.5kN. It shows the maximum crack width for this beam is around 0.35mm and between 0.3-0.6mm for other beams using the previous concrete mix. In comparison, the maximum crack width for the beams using the new concrete mix shows higher consistency, all ranging around 0.3mm.

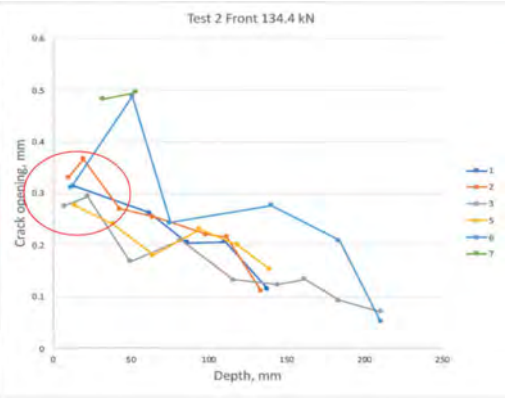

Figure 21. Crack width for new SFRC beam no.2.

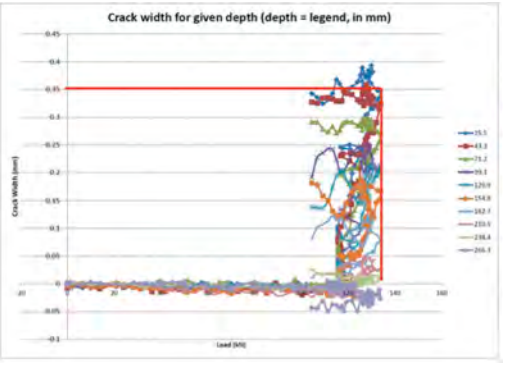

Figure 22. Crack width for selected beams using the previous concrete mix.

5 CONCLUSIONS

This large BRE beam test results have significant implications on the understanding of the performance of the SFRC lining, in both mechanical behaviour and the design approach.

Traditionally, 40kg/m3 steel fibres have been used as a default dosage for SFRC mix. This BRE beams test used the same concrete mix with a slightly reduced 35kg/m3 steel fibre dosage. Their performance under the same testing regime was compared like for like. The comparison shows that the new 35kg/m3 steel fibre concrete mix performs at least at the equivalent level as the 40kg/m3 steel fibre concrete mix under the applicable small displacement range.

From a designer's perspective, it is evident from the load-displacement and load-strain curves, that

a strain-hardening post-cracking behaviour was observed in all SFRC beam test results. This provides confidence in the adoption of the multiple cracking modes for the tunnel lining design.

These test results also inform the industry of a key design assumption for calculating the maximum design crack width, which is that the crack spacing is equivalent to the lining thickness. With the use of DIC technology, this design assumption has been verified and can be used in predicting the maximum crack width when the tunnel's secondary lining is under internal surge pressure.

In addition to that, the DIC crack depth results also show that the crack is developing in a linear pattern and propagating from the lining surface into the concrete lining. Hence, a linear relationship in terms of the crack width at different depths is also a valid assumption.

With the combined effects of the above factors as well as the close collaboration between the contractor, designer and the Category III checker, this new concrete mix with 35kg/m3 steel fibre dosage has been used, and the tunnel secondary lining design based on this concrete mix has also passed the rigorous Category III checking process. This has led to a saving of 230 tonnes of steel fibres for a 7km long Thames Tideway West main tunnel, achieving significant savings on construction cost and embodied carbon without compromising the tunnel lining's structural and durability performance. In addition, the case study presented in this paper can be used as a reference for future similar value engineering exercises on the use of SRFC tunnel linings.

ACKNOWLEDGEMENTS

The authors would like to take this opportunity to thank the contribution made by BRE and NPL, as well as the people involved in this study from the BMB and MSES. The authors would also like to thank the approval from Tideway for the publication of this paper.

REFERENCES

Psomas, S., Eddie, C.M., Sutherden, R. and Matta, M., 2014. SFRC for cast-in-place (CIP) permanent linings: Thames Tideway Lee Tunnel Project in East London, UK. In: 2nd Eastern European Tunnelling Conference, Athens. 2014.

Psomas, S., 2020. Service limit state design for pressurised steel fibre reinforced concrete tunnel linings. Tunnels and Underground Cities: Engineering and Innovation Meet Archaeology, Architecture and Art: Volume 6: Innovation in Underground Engineering, Materials and Equipment-Part 2, pp.2898–2908.

De Rivaz, B., 2020. Twenty years of FRC tunnel final lining: lessons learnt, design proposal and new development. Tunnels and Underground Cities: Engineering and Innovation Meet Archaeology, Architecture and Art: Volume 5: Innovation in Underground Engineering, Materials and Equipment-Part 1, pp.2026–2034.

Bekaert., 2018. The new and ultimate Dramix Range – Dramix 5D technical brochure.

Su, J., Bloodworth, A., 2018. Numerical calibration of mechanical behaviour of composite shell tunnel linings. Tunnelling and Underground Space Technology, 76, 107–120.

Tunnelling for a Better Life – Yan, Celestino, Thewes & Eberhardt (Eds)
© 2024 The Author(s), ISBN 978-1-032-80042-4
Open Access: www.taylorfrancis.com, CC BY-NC-ND 4.0 license

Dynamic response characteristics of ultra-shallow buried metro station structures under surface vibration load

Lianjin Tao
The Key Laboratory of Urban Security and Disaster Engineering, Ministry of Education, Beijing University of Technology, Beijing, China

Lijia Deng*
Beijing University of Technology, Beijing, China

Yu Zhang
Beijing University of Civil Engineering and Architecture, Beijing, China

Zhibo Jia
Beijing University of Technology, Beijing, China

ABSTRACT: With the rapid development of urban transportation construction, numerous engineering projects involving the construction of new roads crossing established underground railway lines have emerged. The vibratory compaction of road surfaces has a significant impact on the structural integrity of subway stations to some extent. In the context of the crossing of Road 5 with the established shallow-buried subway station, numerical simulation methods were employed to study the dynamic response characteristics of the shallow-buried subway station under the action of surface vibration loads. Furthermore, sensitivity analysis was conducted on factors such as vibration frequency and excitation force. The research results indicate that under the influence of surface vibration loads, the acceleration response of the station's structure exhibits a trend of attenuation from top to bottom and from the center towards both sides, specifically: top plate > middle plate > side walls > bottom plate. As the vibration frequency increases, the acceleration response of the station's structure gradually intensifies. Based on the aforementioned research findings, it is recommended that the optimal construction parameters for vibratory compaction of the roadbed above this shallow-buried subway entail a vibration frequency of 28-33Hz and an excitation force ranging from 150-300kN.

Keywords: ultra-shallow buried metro station, adjacent construction, surface vibration load, structural dynamic response

1 INTRODUCTION

With the rapid advancement of urban transportation infrastructure, a plethora of engineering instances has emerged where new road construction intersects established underground railway tunnels. In the construction of such contemporary urban roads, there is a preference for the application of asphalt mixtures as protective layers. This is done to mitigate the direct abrasion of the roadbed caused by vehicular wheels, while simultaneously distributing the vehicular loads, thus providing a smooth and slip-resistant road surface for vehicular travel. In our nation, it is generally to utilize vibratory compactors for the dynamic compaction of roadbeds. The compaction of road surfaces by vibrating road rollers constitutes a dynamic process. When a vibratory roller is acted on the road surface, it can be considered as a surface vibration load (Peng A. P et al., 2019). The construction of new roads crossing established underground stations, in our country, presents significant technical challenges and a multitude of uncertainties. Inadequate control measures during the construction process not only jeopardize the smooth operation of subway vehicles but also pose a substantial risk to the safety of traffic. Hence, the impact of vibrating road rollers during construction above established underground railway tunnels warrants particular attention concerning subway structural

*Corresponding author: dlj2540306792@outlook.com

DOI: 10.1201/9781003495505-163

integrity. Precisely elucidating the dynamic response characteristics of super-shallow buried subway station structures under the influence of surface vibration loads holds practical significance.

Many scholars employ various methodologies, including field research, theoretical analysis, numerical simulations, and model experiments, to research the characteristics of structural dynamic response under surface vibration loads. Lai, J et al. (2016) showed that surface vibration loads can affect subway tunnels in the range of approximately 14 m depth of burial. The genesis of surface vibration loads primarily stems from vehicular-induced vibrations, explosive detonations, and vibrations generated during road construction; Yi, H et al.(2019) conducted an analysis using numerical simulations and model experiments to explore the enduring impact of surface vibration loads on the cumulative deformation and dynamic response characteristics of subway tunnel linings. Their research demonstrates that tunnels situated beneath high-speed rail lines exhibit the phenomenon of cumulative deformation under the prolonged influence of vibration loads. This underscores the imperative need to account for the effects of vibration loads in engineering design (Zhang, X et al., 2021); CAO Z.G et al. (2018) have pioneered the provision of analytical solutions for the dynamic response of tunnels under the influence of surface moving loads. They have undertaken a comprehensive examination of the underground tunnel vibration issue induced by surface traffic loads, considering varying load speeds, positions, lining structures, and tunnel depths; Jin, ZY et al. (2021) have conducted an analysis of the long-term vehicular-induced vibrations on the mechanical behavior and waterproofing performance of prefabricated underground passages; Xu, Ret al. (2023) employing on-site explosive vibration monitoring, has researched surface vibration velocities and instantaneous energy obtained from various blasting schemes. This study highlights the significant impact of tunnel depth on surface vibrations; Peng, A.P et al. (2019) through a combination of field experiments and numerical simulations, have undertaken an analysis of the dynamic response of concrete beam bridges with varying cross-sectional designs under the vibratory compaction of asphalt road surfaces on the bridge decks. Currently, there is a limited body of research regarding the dynamic interaction between roller-induced vibrational loads and subterranean structures. Hence, there is a compelling need to embark on a mechanistic exploration of the effects of surface vibration loads generated by roller operations on the dynamic interaction with the foundation and underground structures. This entails considering factors such as ground load frequency and excitation force to more accurately assess the vibrational response of subterranean structures induced by surface vibration loads.

Therefore, in the context of the Road 5's close proximity crossing with the Beijing Daxing International Airport line, this paper undertakes an analysis of the impact of various roller models on structural safety and examines the influence of surface vibration loads generated at different frequencies on the vibrational response of subway station main structures.

2 THEORETICAL ANALYSIS OF VIBRATORY COMPACTION

2.1 *Dynamics model of the vibration system of roller*

When a vibratory road roller compacts the roadbed, the compacted layer experiences a dynamic force, the magnitude of which is contingent upon mechanical parameters such as the vibration wheel's frequency, amplitude, static weight, and excitation force. Due to the inherently complex and stochastic nature of vibratory road roller compaction, the vibrational forces exerted by the vibration wheel on the compacted layer are simplified for analysis purposes. The operational mechanism of the vibratory road roller involves the rolling wheel utilizing its own gravity to press down, while the rear wheel (the vibration wheel) carries out the compaction operation. The force exerted by the rolling wheel on the construction material can be regarded as a constant force in motion:

$$P_1 = G_1 \tag{1}$$

G_1 is the gravitational force of the rolling wheel in kilonewtons (kN).

During the operation of a vibratory road roller, the centrifugal force generated by the rotation of the eccentric block within the vibration wheel results in highly efficient and continuous vibrational impacts on the compacted layer. The force exerted by the vibration wheel on the roadbed is approximately equal to the sum of the vibration wheel's weight and the excitation force:

$$P_2 = G_2 + F \tag{2}$$

G_2 is the gravitational force of the vibration wheel (kN)

F is the force exerted by the circular vibrational motion of the vibration wheel on the ground (kN)

The centrifugal force is generated by the rotation of the eccentric block

$$F_0 = M_e\omega^2$$

M_e represents the eccentric distance of the eccentric block (kN·m);ω is the vibration frequency (rad/s)

The force exerted by the circular vibrational motion of the vibration wheel on the ground is the

vertical component of the centrifugal force produced by the rotating eccentric block, denoted as F_0;

$$F = F_0 \sin \omega\ t \tag{3}$$

Typically, the excitation force F_0 of the vibration wheel is about 2-3 times greater than the weight of the vibration wheel itself. When a road roller is laying pavement, the vibrational force of the vibration wheel on the road surface can be expressed as follows:

$$P_2 = \begin{cases} G + F_0 \sin \omega\ t & P_2 > 0 \\ 0 & P_2 \leq 0 \end{cases} \tag{4}$$

During the compaction process with the vibrating steel wheel, assuming the contact surface of the compacted material is rectangular, measuring 0.2×1.8m (as shown in Figure 2); Analyze the dynamic response of the station structure under the vibrational load of the road roller, assuming a uniform distribution of contact stress. Substituting the formulas for Zhi et al. (2003) into equations (1) and (4) yields:

$$p_1 = \frac{13G_1}{WL} \tag{5}$$

$$P_2 = \begin{cases} \frac{13(G+F_0 \sin \omega t)}{WL} & F > 0 \\ 0 & F \leq 0 \end{cases} \tag{6}$$

W is the diameter of the vibration wheel (mm)
L is the width of the vibration wheel (mm)

Utilize the ABAQUS DLOAD subroutine to compute the load applied to the compacted road surface by the vibratory road roller, as described by formula (6).

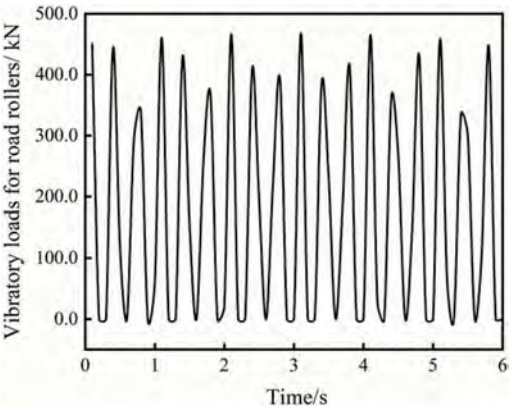

Figure 1. Vibratory roller vibration load time histoty curve.

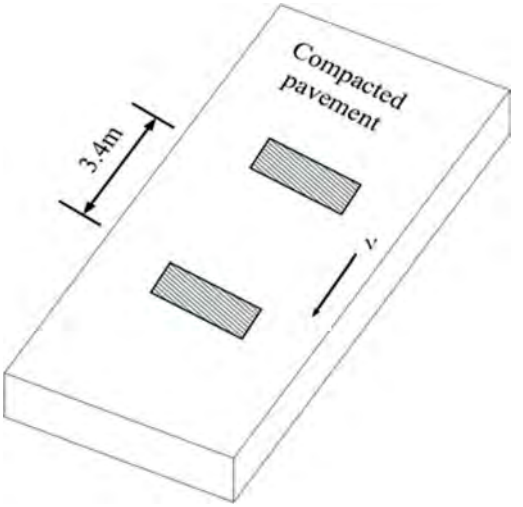

Figure 2. The pavement is subjected to uniform vibration loads diagram.

3 NUMERICAL MODELLING

3.1 *Relative position of structures*

According to the planning needs of urban development, the construction of the soil roadbed of planning Road 5 above the established Daxing International Airport Line is carried out using vibratory roller compacting to improve operational efficiency. The construction section of which the interval is K35 +475.232-K35+495.232 is in parallel with the main structure of the metro station, as shown in Figure 3; the vibratory roller compacts the first layer of soil 2m away from the station top plate, and the width of the main structure of the station is 30m, and the height is 16m.

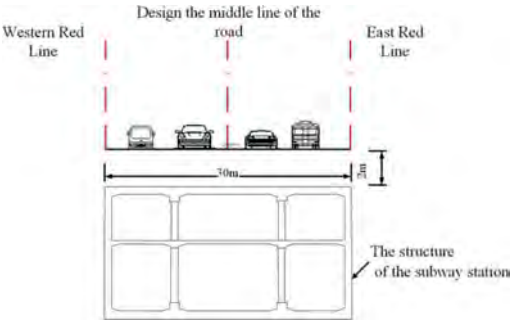

Figure 3. Longitudinal section of the station along the established Daxing International Airport line.

3.2 *Calculation parameters*

The center columns of the established Daxing International Airport Line are C50 reinforced concrete; the

wall, slab, and beam structures are C40 reinforced concrete. The stratum distribution in the calculation model is from top to bottom: miscellaneous fill, powdery clay, silt, fine sand, and pebbles. The parameters of the physical and mechanical properties of each soil layer and structure are shown in Table 1. The modulus of elasticity and Poisson's ratio of the soil layer are taken as kinetic parameters according to the wave velocity test of the ground investigation data.

3.3 *Calculation model*

In this paper, ABAQUS finite element analysis software is used to carry out numerical simulation research on the influence of the vibration load of the roller on the overburdened soil of an ultra-shallow buried underground station. According to the above relative position relationship between the new construction and the established construction, the numerical calculation model is established as shown in Figure 4. When the ratio of the dimension of the foundation plane to the dimension of the structure plane is greater than 5, the results of the dynamic calculation tend to be stable, and the influence of the lateral boundaries can be ignored (Huai-feng et al., 2016). Considering the calculation time and the storage capacity of the computer, the Z-axis length of the calculation model in this paper is 20m for the 3-span structure, and the width of the X-axis is taken as 4 times the length of the station, which is 120m; the vertical direction (Y-axis) is taken as 50m up to the pebble layer, and the embedment at the top plate of the station is 2 m. To satisfy the requirements of the accuracy of power calculations, it is desirable to take the mesh size within 1/8~1/10 of the wavelength of the highest frequency; the enclosing rock and the reinforced concrete structure solid cell simulation is adopted, and Mohr-Coulomb criterion and plastic damage model are used respectively.

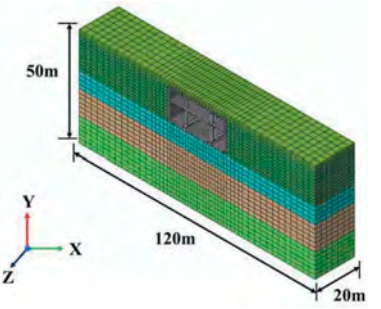

Figure 4. Finite element calculation model.

4 VIBRATION RESPONSE ANALYSIS

4.1 *Description of the calculation*

To ensure the continuous deformation resistance and load-bearing capacity of the station's main structure during the construction of the road surface with a vibratory road roller, an analysis was conducted under the vibrational effects of three different models of road rollers at a vibration frequency of 33Hz and a speed of 10km/h. The analysis focused on the vibrational velocity and vertical deformation of the station's main structure. Table 2 presents the operational parameters of various models of vibratory road rollers. Figure 5 and Table 3 depict the maximum deformations and maximum vibrational velocities of the station's main structure under the influence of different models of road rollers. The XS202 road roller model exhibits a maximum vertical deformation of -3.521mm, while the YZ18 road roller model displays a maximum vertical deformation of -3.168mm, both of which do not meet the safety control values for rail transit structures.

Table 1. Physico-mechanical parameters of surrounding rock and structures.

Objects	Name	Thickness/m	Density/ ($kg \cdot m^{-3}$)	Elastic modulus/ MPa	Poisson's Ratio	Cohesion/ kPa	Friction angle/(°)
Soil Layer	Miscellaneous fill	2.0	2090	47	0.40	17.0	17.0
	Powdery clay	16.0	1980	125	0.38	23.0	12.0
	Silt	8.0	1960	223	0.36	20.7	27.6
	Fine sand	12.0	1900	346	0.35	0.0	28.0
	Pebble	12.0	2000	568	0.33	0.0	35.0
The Main Structure of the Subway Station	Sidewall	0.9	2500	32500	0.20	-	-
	Top plate	0.9	2500	32500	0.20	-	-
	Floor	0.4	2500	32500	0.20	-	-
	Bottom floor	1.0	2500	32500	0.20	-	-
	Roof beam	1.8	2500	32500	0.20	-	-
	Floor beam	0.9	2500	32500	0.20	-	-
	Bottom beam	2.0	2500	32500	0.20	-	-
	Pillar	0.8×1.0	2500	34500	0.20	-	-

Conversely, the YZ16JC road roller model records a maximum vertical deformation of -1.578mm, with a main structure vibrational velocity of 2.26 cm/s. The main structure of the station did not show any deformation that threatened structural safety and thus complies with regulatory requirements.

Table 2. Working parameters of the vibratory roller.

Number	Vibrating Wheel Weight (kg)	Roller Weight (kg)	Vibration Frequency (Hz)	Excitation Force (kN)
XS202	13500	6500	28/33	370/255
YZ18	12000	6000	33/38	328/220
YZ16JC	7700	8300	28/33/38	300/150

In light of the calculations and the project context mentioned above, the choice has been made to employ the YZ16JC road roller for the road surface construction above the station's main structure.

4.2 *Effect of vibration frequency on the station structure*

The compaction efficiency of a vibratory roller depends mainly on the operating frequency of its vibrating wheel. Consequently, the operational frequency of the roller significantly impacts the reliability of the station's main structure and the compaction quality of the asphalt pavement. Furthermore, the dynamic response of various underground structural components and the attenuation characteristics of different vibrational frequencies have consistently remained focal points and challenges in research. Therefore, this study, in conjunction with the YZ16JC roller, which features three distinct operational frequencies: 28Hz, 33Hz, and 38Hz, analyzes the influence patterns of different frequencies on the vibration characteristics of the station's main structure. The sensor placement across various sections of the station's main structure is illustrated in Figure 6. The top, middle, and bottom plates monitor vertical responses, while Sidewalls monitor lateral structural response.

Under the influence of surface vibration loads, the distribution of peak accelerations at various measurement points on the station's main structure at different frequencies is shown in Figure 7. Simultaneously, the classification of measurement points is done based on different sections, and the peak accelerations for each section are summarized, as presented in Table 4.

From Figure 7, it is discernible that the acceleration response of the station's main structure exhibits a fundamentally symmetrical distribution, with

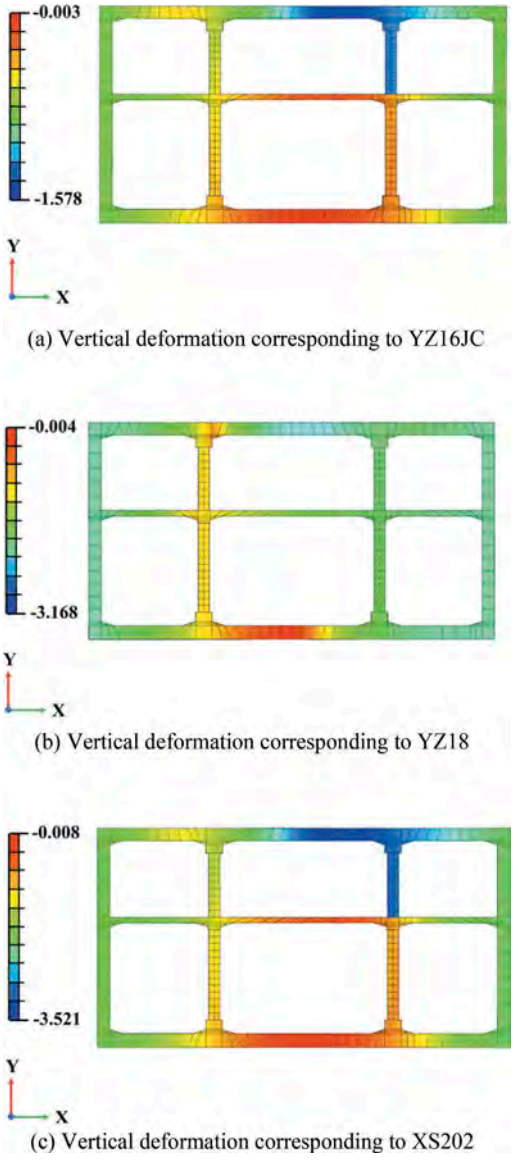

Figure 5. Deformation of the main structure of the station according to different rollers.

Table 3. Deformation and vibration speed of our main structure when getting off different rollers.

Number	Vertical Displacement (mm)	Vertical Speed (cm/s)	Position
XS202	-3.521	3.098	Roof Span Center
YZ18	-3.168	2.781	Roof Span Center
YZ16JC	-1.578	2.262	Roof Span Center

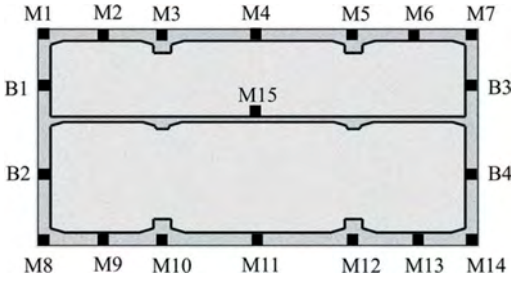

Figure 6. Diagram of measurement point layout.

a decreasing trend in the vertical direction from top to bottom and in the lateral direction from inner to outer. Specifically, the order of magnitude is as follows: top plate > middle plate > side walls > bottom plate. In other words, the closer the measurement point is to the vibration source, the greater the dynamic response, with a maximum peak acceleration of 1.239 m/s² (at *f*=38Hz). At the same frequency, there is a substantial difference of approximately 0.652 m/s² between the maximum peak accelerations observed at the top plate and the bottom plate measurement points. As the frequency increases, the peak accelerations at all measurement points gradually increase from 0.533 m/s² to 1.239 m/s². Furthermore, under the vibration frequencies of 33Hz and 38Hz, the peak accelerations at each measurement point are respectively 35% and 126% higher than those observed at 28Hz. Notably, the maximum peak accelerations for both the top plate and the bottom plate occur at the mid-span.

As depicted in Figure 8, with the increase in frequency, the peak accelerations at various sections of the station's main structure witness a rise. The most significant increase in peak acceleration occurs when transitioning from 33Hz to 38Hz. Specifically, as the frequency shifts from 28Hz to 33Hz, there is an average increase of 24.75% in peak acceleration across all sections. When moving from 33Hz to 38Hz, this average increase in peak acceleration rises to 43.86%. Overall, it is evident that the vibrational response of the top plate is more significantly influenced by frequency, exhibiting a greater attenuation magnitude compared to other sections. The attenuation amount for peak acceleration on the top plate is 0.706 m/s², with an attenuation rate of 56.9%.

To elucidate the temporal variations in acceleration responses of the subway station's main structure during the operation of the upward vibratory roller, the peak acceleration measurement points for frequencies of 33Hz and 38Hz. The resulting acceleration time history curves for these points are presented in Figure 9.

From Figure 9, it is evident that the acceleration responses at various measurement points on the station's main structure exhibit pronounced periodic

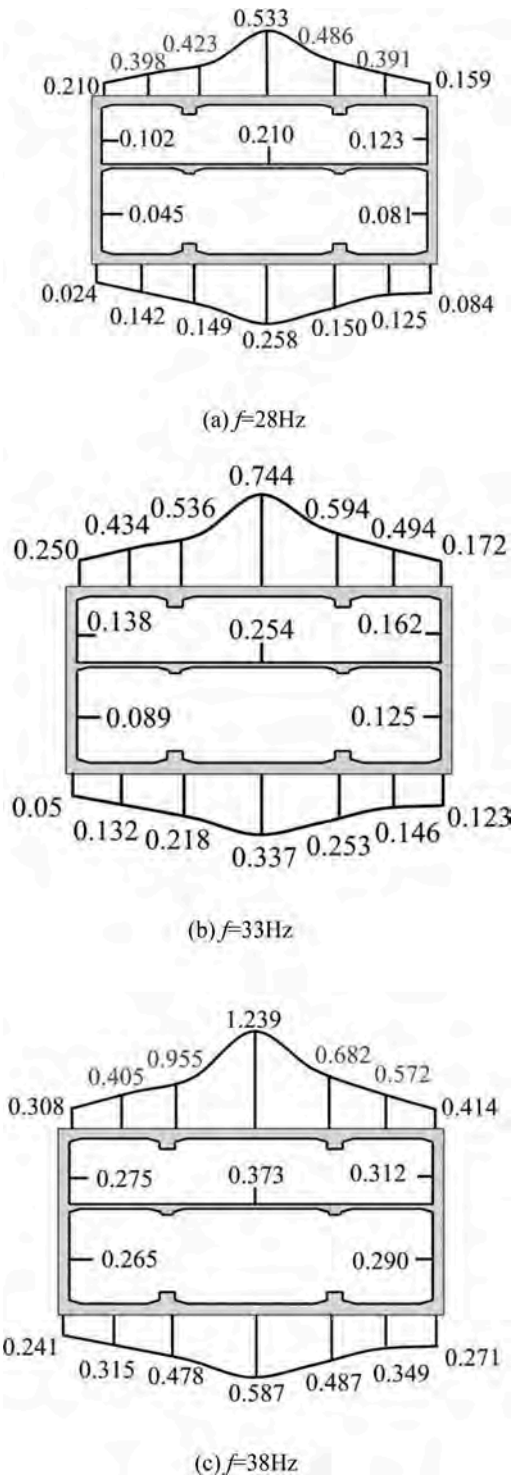

Figure 7. Peak acceleration distribution of station main structure measurement points according to different frequencies (m/s^2).

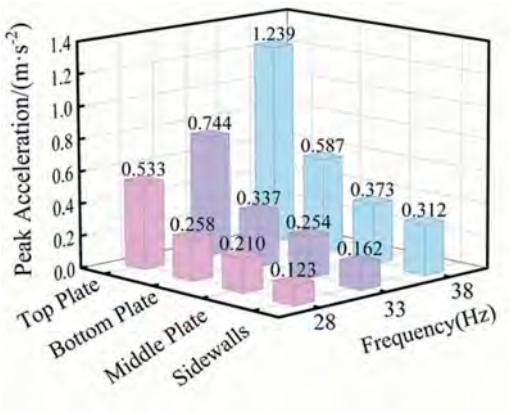

Figure 8. Change pattern of peak acceleration with frequency for each part of the station's main structure.

Table 4. Peak acceleration of each part of the main structure of the station at different frequencies.

	Peak Acceleration/(m·s^{-2})			
Frequency	Top Plate	Middle Plate	Bottom Plate	SideWalls
28	0.533	0.210	0.258	0.123
33	0.744	0.337	0.337	0.162
38	1.239	0.587	0.587	0.312

variations at different frequencies, with the amplitude of each cycle not remaining constant. Furthermore, Figure 9 also illustrates that changes in frequency scarcely affect the temporal patterns of structural vibration responses, and only influence the magnitude of the response intensity.

5 CONCLUSIONS

This study employs numerical simulation techniques within the context of the crossing of Road 5 with the established Daxing International Airport Line. It investigates and analyzes the dynamic responses of road surface structures during construction by different vibratory rollers with varying excitation forces, and frequencies. The primary conclusions are as follows:

(1) In the case of the engineering project involving the crossing of Road 5 with the existing shallow-buried subway station, to ensure the continuous deformability and load-bearing capacity of the station's main structure, it is advisable to employ the YZ16JC vibratory roller for construction. With an increase in the frequency of the station's main structure, the peak acceleration at each measurement point increases by 24.75%. Although the deformation of the

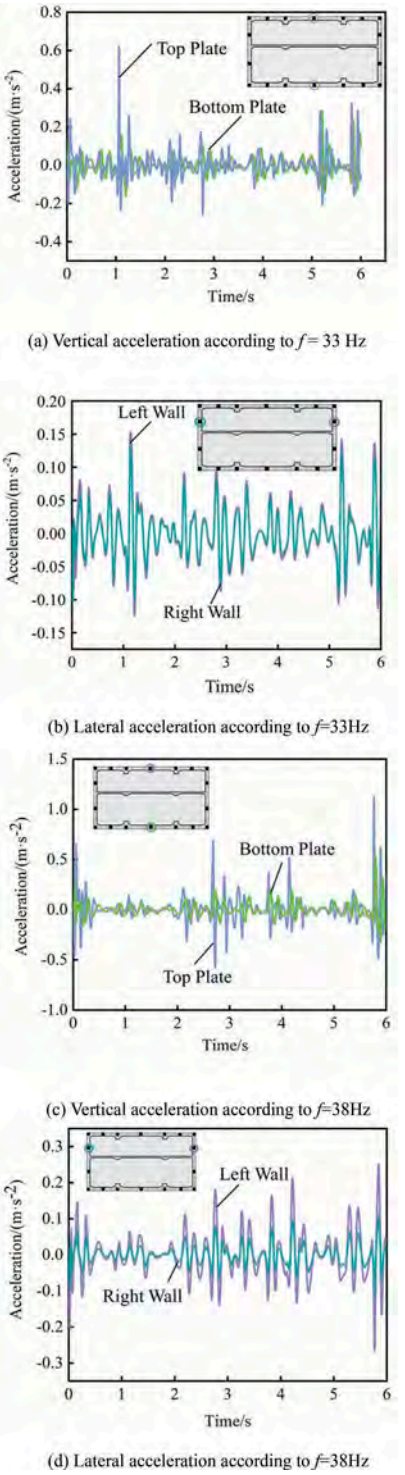

Figure 9. Time history curves of measurement points recording peak acceleration in each part of the main structure of the station.

station's main structure does not exceed the allowable limit, it exceeds the safety warning value for rail transit. Therefore, it is not recommended to use high-frequency rollers (even though high frequencies can enhance the compaction height of asphalt pavement). Additionally, monitoring of the Daxing International Airport Line section and track structure is warranted.

(2) The amplitude response of acceleration in the station's main structure is as follows: top plate > middle plate > side walls > bottom plate. This indicates a vertical attenuation from top to bottom and a lateral attenuation from the center towards both sides, with a maximum difference in peak values of approximately 111.073%.

(3) Frequency variations have almost no impact on the peak distribution in the time domain and the temporal patterns of the structure. At different frequencies, the measurement points for recording peak accelerations on the station's main structure's top plate are consistently located at the mid-span of the top plate, and each measurement point exhibits consistent periodic variations in the time history curve.

REFERENCES

Cao, C. G., Tang, H., Yuan, Z. H., Cai, Y. Q., Zhang, L. G., & Liu, Y. P., 2019. Evaluation study of vibration induced by surface traffic loads in adjacent shallow buried tunnels. Journal of Rock Mechanics and Engineering, 38(8), 1696–1706.

CAO Zhigang, SUN Si, YUAN Zhonghao, et al., 2018. Analytical investigation of dynamic impact of moving surface loadson underground tunnel[J]. Chinese Journal of Geotechnical Engineering, 2018, 40(12): 2262–2273.

Huai-feng, W. A. N. G., Meng-lin, L. O. U., & Ru-lin, Z., 2016. Determining Rayleigh damping parameters for time history analysis of soil layers with deep deposit. Chinese Journal of Geotechnical Engineering, 38(3), 468–476.

Jin, Z., Qi, T., & Liang, X., 2021. Evaluation of the structural and waterproof performance of a precast and assembly underpass under long-term surface dynamic loads. Tunnelling and Underground Space Technology, 115, 104047.

Lai, J., Wang, K., Qiu, J., Niu, F., Wang, J., & Chen, J., 2016. Vibration response characteristics of the cross tunnel structure. Shock and Vibration, 2016.

Peng, A. P., Dan, H. C., & Yang, D., 2019. Experiment and numerical simulation of the dynamic response of bridges under vibratory compaction of bridge deck asphalt pavement. Mathematical Problems in Engineering, 2019.

Peng, Anping; Li, Liang., 2019. Comparative test and numerical analysis of dynamic response of bridge under vibration load and moving load. Journal of Railway Science and Engineering (09), 2256–2264. doi:10.19713/j.cnki.43-1423/u.2019.09.017.

Xu, R., Zhang, J., Wu, B., & Zhang, F. L., 2023. Vibration Reduction and Explosion Control Investigation for an Ultra-Shallow Buried Tunnel under Crossing Buildings Based on HHT Analysis. Sensors, 23(17), 7589.

X.-L. Zhi, X.-X. Jiang, and A.-M. Sha, 2003. "Pavement subbase course stress by vibrating compaction on course," Journal of Chang'an University (Natural Science Edition), vol.23, no.3, pp. 33–36.

Yi, H., Qi, T., Qian, W., Lei, B., Pu, B., Yu, Y, & Li, Z., 2019. Influence of long-term dynamic load induced by high-speed trains on the accumulative deformation of shallow buried tunnel linings. Tunnelling and Underground Space Technology, 84, 166–176.

Ye, S., Zhao, Z., & Wang, D., 2021. Deformation analysis and safety assessment of existing metro tunnels affected by excavation of a foundation pit. Underground Space, 6(4), 421–431.

Zhang, X., Zhou, S., He, C., Di, H., & Si, J., 2021. Experimental investigation on train-induced vibration of the ground railway embankment and under-crossing subway tunnels. Transportation Geotechnics, 26, 100422.

Tunnelling for a Better Life – Yan, Celestino, Thewes & Eberhardt (Eds)
© 2024 The Author(s), ISBN 978-1-032-80042-4
Open Access: www.taylorfrancis.com, CC BY-NC-ND 4.0 license

Mechanical response and fault-resistant design of urban shallow subway tunnel under normal fault

Lianjin Tao
The Key Laboratory of Urban Security and Disaster Engineering, Ministry of Education, Beijing University of Technology, Beijing, China

Jiangong Liu*, Zhigang Wang & Ming Shi
Beijing University of Technology, Beijing, China

ABSTRACT: Based on the Taiyuan subway tunnel project crossing through an active fault zone, this paper utilizes ABAQUS software to construct a three-dimensional refined model. The model aims to investigate the mechanical behaviour and fault-resistant design methods of urban shallow subway tunnels that cross normal faults. Using numerical simulation and mathematical induction, the study explores the impact of two primary factors, namely fault dip angle and fault displacement, on the mechanical response and damage degree of the subway tunnel structure. In addition, ellipticity is employed to unveil the spatial deformation characteristics of the tunnel cross-section. The findings indicate that due to normal fault dislocation, the lining structure deflects at a specific angle to adjust to the fault's forced displacement. This results in local segments of the structure becoming de-hollowed and out of sync with the soil layer's movement. Secondly, the hanging wall's damage area and stress-strain exceed that of the footwall by several times. Thirdly, the tunnel deformation's maximum position depends on the fault dislocation's location. The implementation of segmental lining mitigation measures notably diminishes the detrimental impact of fault displacement, ultimately leading to a reduction in both the magnitude of destruction and the affected area of the tunnel structure.

Keywords: Active fracture, Numerical simulation, Parametric analysis, Disaster prevention and mitigation

1 INTRODUCTION

Many urban areas in China are situated in seismic zones with high intensities and a widespread distribution of rupture zones. Examples of such cities include Beijing, Urumqi, Taiyuan, and others. In response to the demands of economic and social objectives, the route design of tunnel structures with linear characteristics will inevitably traverse the active fault zones. Given the significance of active fracture damage severity and the necessity for tunnel structure construction, acquiring a profound comprehension of fracture zone damage mechanisms and design methods in urban shallow underground tunnel structures is crucial for maintaining tunnel infrastructure and ensuring public safety.

Extensive research has been conducted by scholars worldwide on the harm process of the soil layer above, the mechanics and harm process of the tunnel construction, and the development of fault resistance for fault displacement. With regard to the damage of the overlying soil body, Cole and Lade (1984) found, through experiments on sandy soil, that the shape and location of the damage surface of the surface fault are determined by the depth of the soil body, expansion angle, and the fault dip angle. Liu (2004) concluded, through model experiments, that when the damage surface propagates to the surface, the ratio of the vertical displacement to the thickness of the soil body ranges from 4% to 8%, which is independent of the fault dip angle. Liu et al. (2005) investigated the horizontal and vertical displacement of bedrock through centrifuge experiments and found that the impact of vertical displacement of bedrock on the overlying sediment is greater than that of horizontal displacement. Guo et al. (2002) employed finite element calculations to demonstrate that, under equal fault dislocation, reversed faults have the greatest destructive effect on the overlying sediment layer, followed by normal faults, and strike-slip faults have the least destructive

*Corresponding author: 1492319496@qq.com

DOI: 10.1201/9781003495505-164

effect. Regarding the damage mechanisms of tunnel structures crossing active faults, Liu et al. (2013, 2014a, b) undertook an analysis of the stresses and distribution of damage in tunnel structures, considering different fault displacements. Additionally, they carried out extensive investigations into circumferential and longitudinal strains, in addition to the pressures from surrounding rock. Zhong et al. (2020) also explored this subject in their research, where numerical simulations were carried out to examine fault movement, tunnel-fault intersection angles, and the mechanical characteristics of the rock surrounding the tunnel through numerical parameter analyses. Following the strike-slip fault's action, damage indicators were used to evaluate the extent of the tunnel's damage. Regarding the fracture-resistant design of cross-fault tunnel structures, Jiang et al. (2011) examined the articulated design and overcuts design, and proposed techniques for computing section length and stiffness at the section. Moreover, Tao et al. (2022) utilized numerical analysis and model tests to derive the analytical solution for the longitudinal direction of the tunnel structure when under the action of the fault. Lastly, An et al. (2021) contributed to this research topic. and Wang et al. (2023) discovered varying mitigation effects of flexible joints at different locations, identifying fault displacement surface position as the optimal location for achieving maximum mitigation of tunnel damage.

In summary, there are still deficiencies in the mechanical response of city shallow subway tunnels that cross active fault zones. Based on the Taiyuan Subway Line 1 project, this paper examines an interval tunnel that crosses the active fault zone in Jiaocheng. A three-dimensional refinement model of the tunnel-fault is established using ABAQUS to investigate the mechanical response of the tunnel lining and the disaster mechanism of the change of inclination and displacement when the normal fault is in action. At the same time, it has been confirmed that the segmental lining has a mitigating effect, which provides valuable reference points for the relevant engineering design.

2 PROJECT OVERVIEW

The dissertation centres on the initial phase of Taiyuan City's Urban Rail Transit Line 1 scheme, a subterranean transport network spanning 28.737 km, encompassing 24 subways all arranged in an "L" configuration. The $F_{1\text{-}1}$ and $F_{1\text{-}2}$ Jiaocheng fault zones are traversed by the Line 1 Phase I plan as determined through ground investigative data, superficial seismic interpretation findings, and joint profile analysis between Jinyang Road station and Xiaojingyu station illustrated in Figure 1. The tunnel covering is 9 m thick and cuts orthogonally across the Jiaocheng fault. In urban metro tunnels, the overburden ratio H/D falls between 0.6 and 1.5 for shallow tunnels (Wang, 2006).

Figure 1. Layout of station interval and distribution of active fault zones in Jiaocheng.

3 MODELLING AND PARAMETER SELECTION

3.1 *Numerical model establishment*

Based on the engineering data, we constructed a refined three-dimensional fault tunnel model which can be seen in Figure 2. To enhance the accuracy of our calculations, we ensured that the model's length is 120m, width is 30m, height is 35m and the overburden thickness is 9m, while also eliminating any influence from boundary effects. The soil layer along the z-axis is gridded at intervals of 2m while the tunnel structure is gridded at intervals of 1m. The circular tunnel is divided into 48 grids around its perimeter. The tunnel lining measures 6m in outer diameter, 5.2m in inner diameter, and 0.4m in thickness. To consider the apparent mechanical response of the structure during the fault displacement process, a finer grid is used in the 15m vicinity surrounding the tunnel. The model's side and bottom surfaces are normally restrained surfaces, while the

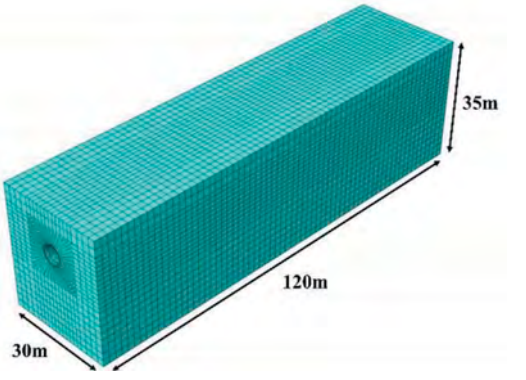

Figure 2. Three-dimensional nonlinear numerical model.

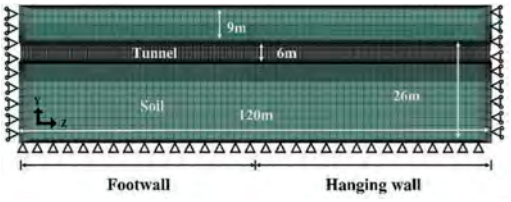

Figure 3. Three-dimensional numerical model section.

top surface is free, as illustrated in Figure 3. The normal contact surface between the fault and the tunnel employs hard contact, while the tangential contact surface employs coulomb friction with a friction coefficient of 0.3.

3.2 *Model material parameters*

C3D8R elements were implemented in ABAQUS software to replicate the fault and tunnel geometry. The soil material is presumed to be elastic-plastic in adherence to the Mohr-Coulomb criterion. The soil and lining structure parameters are displayed in Table 1. The C40 tunnel lining was employed, while the Concrete Plastic Damage Model (CDP) was applied to investigate the concrete's damage characteristics such as compression cracking and tension under the effect of displacement. Table 2 provides some damage parameters of the concrete.

Table 1. Soil and lining parameters.

Type of material	Density ($kg \cdot m^{-3}$)	Modulus of Elasticity/ MPa	Poisson's Ratio	Internal friction angle(°)
Lining parameters	2400	24150	0.2	22
Soil	2010	13.6	0.33	18

Table 2. Partial damage parameters for concrete.

Stress/ MPa	Inelastic strain	Stress Damage Factor	Stress/ MPa	Crack Strain	Tension damage Factor
14.9	0	0	2.41	0	0
19.3	0.0001	0.0738	1.89	0.00002	0.1288
26.2	0.00048	0.2098	1.63	0.00007	0.3491
24.8	0.0013	0.3926	1.26	0.00011	0.4879
21.3	0.00189	0.4933	0.95	0.00016	0.6116
17.9	0.00247	0.573	0.81	0.0002	0.6646
13.1	0.00374	0.6951	0.52	0.00035	0.7964
10.5	0.00444	0.7396	0.37	0.00051	0.8511
7.4	0.00644	0.8204	0.3	0.00073	0.8921
6.1	0.00742	0.8448	0.26	0.00081	0.9002

3.3 *Calculation analysis*

Due to the complexity of the lining-soil contact relationship in the actual project, we simplify the model as follows: (1) The tunnel structure in the model is horizontal. (2) The tunnel structure assumes a circular cross-section. (3) Each unit in the model is assumed to be isotropic.

Numerical simulation procedure: (1) Calculate initial soil stress equilibrium by applying normal constraints to the bottom and sides of the 3D model and gravity loads, as illustrated in Figure 4(a). (2) Apply fault displacement. Release the lower and lateral boundary constraints of the hanging wall, and implement a uniform and consistent displacement load in the direction of the fault displacement. The boundary constraints of the footwall should remain unchanged to imitate the downward movement of the hanging wall, illustrated in Figure 4(b). Taking into account only the impact of fault displacement, it has been determined that the influence of speed on the outcomes can be disregarded as long as the displacement is limited to 0.02mm during the simulation.

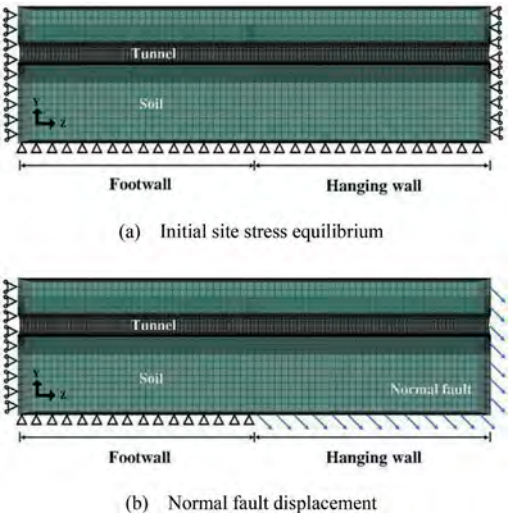

Figure 4. Procedures of numerical simulation.

The study employs the control variable method to investigate the influence of fault dip angle and fault displacement on the tunnel structure. Table 3 illustrates the varying working conditions.

4 RESULTS

4.1 *Analysis of fault dip angles*

The tunnel ellipticity expresses the cross-sectional deformation of the tunnel, and it can be calculated as follows (GB 50446-2017):

$$T = 2^{*}(a - b) \div D \quad (1)$$

Table 3. The calculation conditions of the numerical models.

Fault dip (°)	Vertical dislocation volume/m	Horizontal dislocation volume/m	Fault dip (°)	Vertical dislocation volume/m	Horizontal dislocation volume/m
30	0.225	0.13	45	0.13	0.13
45	0.13	0.13	45	0.33	0.33
60	0.075	0.13	45	0.56	0.56
75	0.035	0.13	45	0.75	0.75

Where, T is the ellipticity; a is the long half-axis of the tunnel(m); b is the short half-axis of the tunnel(m); D is the radius of the tunnel(m). In order to calculate the ellipticity of the tunnel under the effect of the normal fault, the vertical displacement difference c at the bottom of the tunnel vault and the horizontal displacement difference d at the left and right supply waists of the tunnel are extracted, and then the ellipticity of the tunnel can be obtained from Equation (1):

$$T=(c+d)\div D \tag{2}$$

Figure 5 shows the ellipticity distribution curves of the tunnel structure in the axial direction for various fault dip angles. It can be observed that maximum values of ellipticity for fault dip angles of α=30°, α=45°, α=60° and α=75° are 7.72‰, 4.69‰, 3.72‰, and 1.69‰ respectively. It is worth noting that for a dip angle of 30°, the maximum ellipticity exceeds 55.4% of the required limit of 5‰ set by the acceptance specification for shield tunnels. The ellipticity gradually reduces with increasing fault dip angle, while the location of maximum deformation in the tunnel section remains unaffected by fault dip angle.

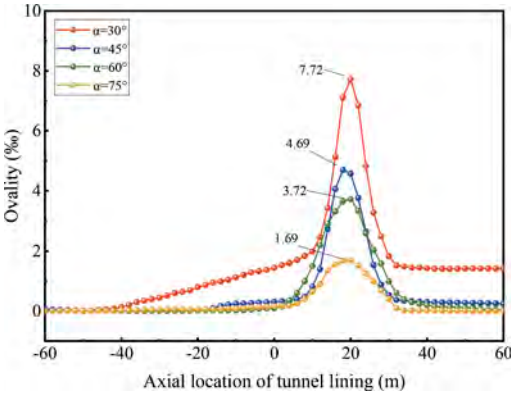

Figure 5. Ellipticity distribution of lining at different fault dip angles.

The plastic and shear strain cloud diagrams of the tunnel under various fault dip angles are illustrated in Figure 6. Additionally, Figure 7 displays the plastic damage factor cloud diagrams. From Figure 8, it can be observed that the largest values of plastic strain under the four operating conditions of α=30°, α=45°, α=60°, α=75° are 6080με, 3931με, 4378με and 2291με respectively. Additionally, the largest values of intra-annular shear strain under the four conditions are 6893με, 3126με, 2285με and 2264με. It is evident that the values of plastic damage and annular shear strain decrease significantly with an increase in fault dip angle.

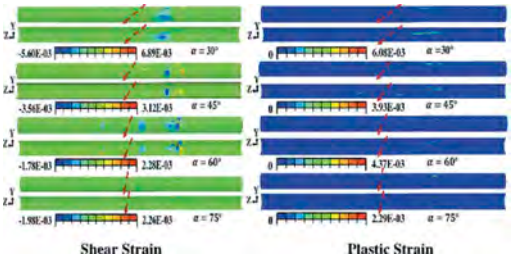

Figure 6. Cloud of shear strain and plastic strain indicators for tunnels with different fault dip angles.

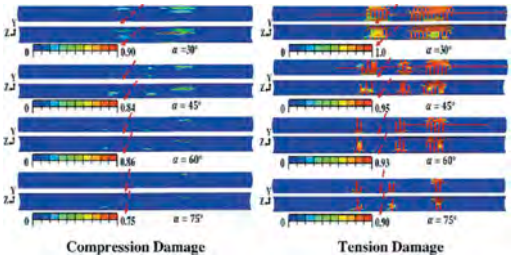

Figure 7. Cloud of compression damage and tension damage indicators for tunnels with different fault dip angles.

Figure 9 displays the tension damage factors that were calculated for different working conditions. The maximum tension damage factor is 1.0, reached when α=30°, whereas the other tension damage factors are 0.95, 0.93 and 0.9 respectively. Additionally, the tunnel structure contributes maximum compressive

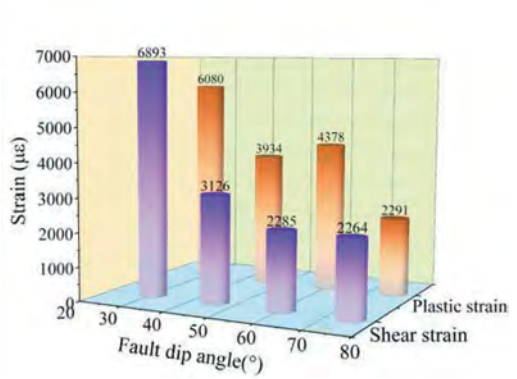

Figure 8. Comparison of damage indicators of lining structures for different fault dip angles.

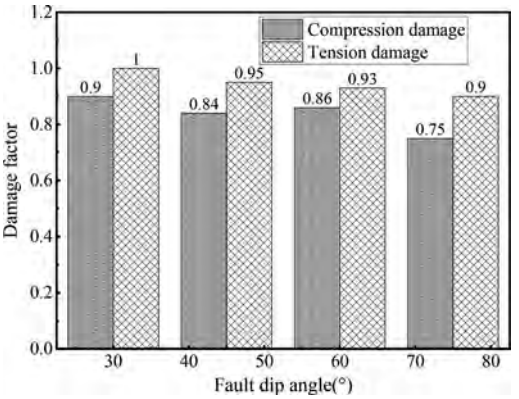

Figure 9. Comparison of volume indicators of lining structures for different fault dip angles.

damage factors of 0.9, 0.84, 0.86, and 0.75 respectively. The extent of the maximum tension damage experienced by the tunnel structure decreases as the fault dip angle increases and the area of damage reduces significantly (Figure 7).

Based on the above analysis, it is evident that the lining structure sustains varying degrees of damage at different fault dip angles. The degree of damage to the structure was assessed using four qualitative indicators, namely plastic strain, shear strain, section ellipticity, and tunnel damage factor. The degree of damage to the tunnel is highest at the dip angle of α=30° when there is a fixed amount of vertical displacement. As the dip angle increases, the damage to the tunnel decreases gradually.

4.2 *Analysis of fault displacements*

The axial distribution curves of ellipticity for the tunnel structure, under different fault displacements, are depicted in Figure 10. It is observed that the values of maximum ellipticity for four different

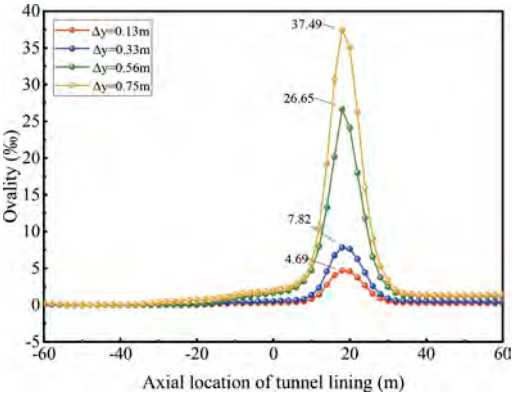

Figure 10. Ellipticity distribution of the lining at different fault displacements.

conditions of vertical displacements Δy=0.13m, Δy=0.33m, Δy=0.56 and Δy=0.75m, are 37.49‰, 26.65‰, 7.82‰, and 4.68‰, respectively. The first three conditions surpassed the maximum ellipticity limit of 5‰ mandated by the shield tunnel acceptance specification by 6.5-fold, 4.3-fold, and 0.6-fold, correspondingly. Consequently, the tunnel went beyond the permitted value of cross-sectional deformation during fault displacement, leading to damage. Additionally, the tunnel section's ellipticity amplifies with a higher degree of vertical displacement and is far greater than the variation ascribed to the fault dip angle. The level of fault dislocation remains unaffected by the location of maximum deformation within the tunnel section.

The plastic and shear strain of the tunnel caused by different fault displacements are displayed in Figure 11, along with the plastic damage factor presented in Figure 12. Based on the findings presented in Figure 13, the maximum values of plastic strain were 1545με, 4066με, 4935με, and 6078με for the four working conditions of Δy=0.13m, Δy=0.33m, Δy=0.56m, and Δy=0.75m. The maximum values of shear strain were 3934με, 11600με, 23870με, and 28160με respectively under four conditions. It is evident that as the displacement increases, the plastic damage and annular shear strain of the tunnel also increase significantly.

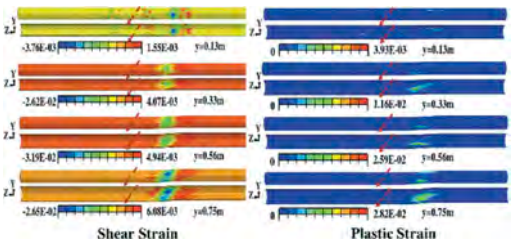

Figure 11. Cloud of shear strain and plastic strain indicators for tunnels with different fault displacements.

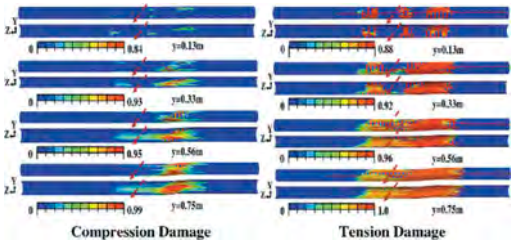

Figure 12. Cloud of compression damage and tension damage indicators for tunnels with different fault displacements.

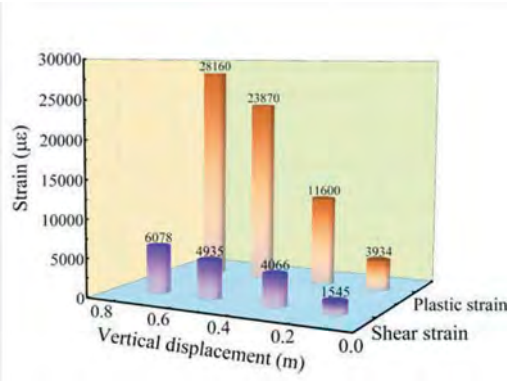

Figure 13. Comparison of damage indicators of lining structures for different fault displacements.

Figure 14 displays the computed tension and compression damage factors for various working conditions. The maximum value of the compression damage factor is 0.99 at Δy=0.75 m, while the remaining tensile damage factors are 0.95, 0.93, and 0.84. Meanwhile, the tunnel structure exhibits maximum tension damage factors of 0.88, 0.92, 0.96, and 1.0, respectively. As the level of displacement becomes greater, there is a corresponding increase in the maximum level of tension damage experienced by the tunnel structure, and the resulting damage spreads across a broad range (Figure 12).

The above analyses indicate varying levels of damage to the lining structure caused by different amounts of displacement. The degree of damage was evaluated using four factors-plastic strain, shear strain, section ellipticity, and tunnel damage factor. Displacement is a crucial factor in tunnel lining damage as it directly impacts the circumferential shear strain of the tunnel structure and the deformation of the tunnel interface. The extent of displacement is a determining factor in the resulting damage.

4.3 *Mitigation effects of segmental lining*

After installing flexible joints, the normal fault caused a 0.2m vertical displacement and 0.035m horizontal displacement. Figure 15 illustrates the damage indices

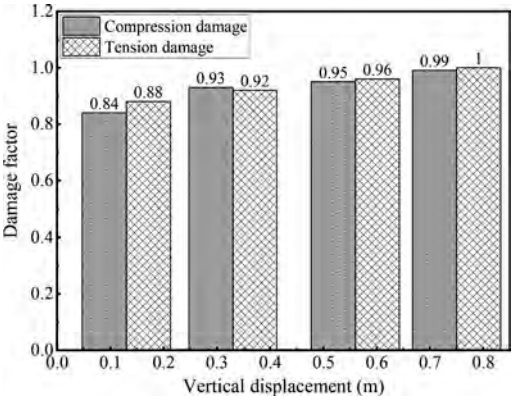

Figure 14. Comparison of volume indicators of lining structures for different fault displacements.

of the lining structure. A comparative analysis was conducted on the structural damage of the lining structure with and without flexible joints, specifically in terms of the maximum damage index value and range. In comparison to Figure 16, the lining structure's maximum plastic strain value is 2.05×10^{-3}, which is 50.96% lower after the installation of flexible joints. Consequently, the plastic strain damage area is significantly reduced and concentrated mainly in the vicinity of the flexible joint. Compared to the readings presented in Figure 16, the maximum damage factor for tensile stress incurred by the concrete structures with flexible joints was 0.88, whilst the corresponding figure for structures without flexible joints was significantly higher at 0.94. Furthermore, the damage area resulting from such stress was significantly more contained in the former. Meanwhile, the maximum level of shear stress experienced by the rings was 1.18×10^{-3}, indicating a reduction of 47.79% when compared to the other measurements. The greatest instances of tension damage, compression damage, and intra-ring shear strain in the lining structure happen near the flexible joints and fault displacement within the section lining. The scrutiny indicates that the installation of flexible joints contributes to a better adaptation of the

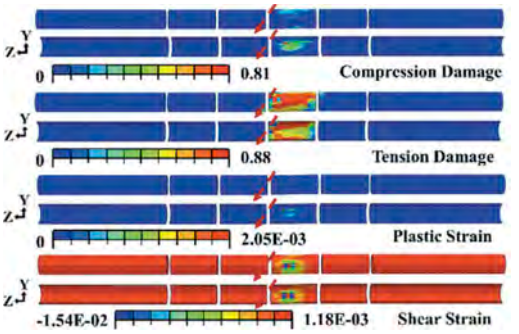

Figure 15. Cloud of strain and volume indicators for segmental lined tunnels.

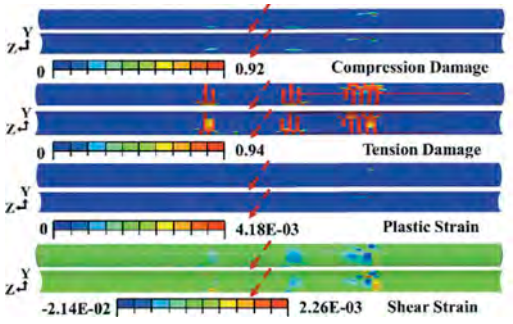

Figure 16. Cloud of strain and volume indicators for tunnels without segmental lining.

lining structure towards the fault-induced deformation and a more effective reduction of structural damage caused by fault displacement.

5 CONCLUSIONS

The paper utilizes the Taiyuan Subway Line 1 Project's interval tunnel, which crosses the Jiaocheng fault zone, to create a refined 3D model that simulates the normal fault dislocation. Through the analysis of two critical variables, fault dip angle and fault displacement, the study extracts the mechanical response and catastrophic mechanism of the tunnel construction under various influencing factors. Structural damage degree is evaluated using three aspects: tunnel cross-section ellipticity, tunnel maximum tension and compression damage factor, and tunnel structure strain. Furthermore, the mitigation effect of segmental lining is investigated based on the maximum tension and compression damage factor, and structure strain. The primary conclusions are as follows:

(1) The deformation of the cross-section of the tunnel decreases as the fault dip angle increases. However, when the fault dip angle is 30°, the largest deformation generated by the tunnel cross-section occurs and the deformation decreases from the dislocation position towards both ends. The vertical fault displacement is a key influence on the tunnel section deformation. The position of maximum tunnel cross-section deformation is not influenced by fault dip angle or displacement, but is instead determined by the fault misalignment position.

(2) Normal fault results in an evident upper disk effect. The emergence of a local dehiscence section between the lining structure and soil layer causes slight strain in the lower disk. The upper disk displays maximum values of circumferential shear strain and plastic strain, as depicted in the cloud diagram. Furthermore, the damage volume of the upper disk exceeds that of the lower disk.

(3) Implementing measures to mitigate segmental lining, such as reducing the plastic strain and shear strain of the tunnel structure under normal fault, leads to a decrease in the degree and scope of tension and compression damage. This leads to an improvement of the tunnel structure's damage from large-area to localized lining section, visibly enhancing fault-resistant performance in subway tunnels through faults.

REFERENCES

An S, Tao L J, Han X C, et al, 2021. Application of two-level design method on subway tunnel crossing active fault: a case study on Urumqi subway tunnel intersected by reverse fault dislocation[J]. Bulletin of engineering geology and the environment, 80:3871–3884.

Code for Construction and Acceptance of shield tunnel (GB 50446-2017) [S]. Beijing: China Architecture and Architecture Press.

Cole J R, D A, Lade P V, 1984. Influence zones in alluvium over dip-slip faults[J], Journal of Geotechnical Engineering, 110(5):599–615.

Guo E D, Shao G B, 2002. Seismic fracture response analysis method of covered soil layer site [J]. Earthquake Engineering and Engineering Vibration, 22(5): 122–126.

Jiang S P, Lin Z, 2011. Shaking table model test study of tunnel through fault [J]. Rock and Soil Mechanics, 32(09):2709–2713.

Liu S H, Dong JX, Xu GM, 2005. Engineering effects of underground faults on overlying soils of different soil qualities [J]. Chinese Journal of Rock Mechanics and Engineering,24(11):1868–1874.

Liu X Z, 2004. Experimental study on propagation of active fault failure in soil [J]. Chinese Journal of Geotechnical Engineering, 26(3):425–427.

Liu X Z, Wang X L, Lin L L, 2013. Model test study on the influence of viscous slip dislocation of normal fault with 75° dip Angle on highway tunnel [J]. Chinese Journal of Rock Mechanics and Engineering,32(08):1714–1720.

Liu X Z, Wang X L, Lin L L, 2014. Experimental analysis of influence of 45° dip normal fault stick-slip dislocation on tunnel [J]. Journal of Tongji University (Natural Science Edition), 42(01):44–50.

Liu X Z, Wang X L, Lin L L, 2014. Experimental study on the influence of 60° dip normal fault stick-slip dislocation on mountain tunnel [J]. Journal of Civil Engineering, 47(02):121–128.

Tao L J, Wang Z G, Shi C, et al, 2022. Analytical solution for longitudinal response of pipeline structure under fault dislocation based on pasternak foundation model [J]. Chinese Journal of Geotechnical Engineering, 44 (09): 1577–1586.

Wang M S, 2006. Key points of underground excavation in tunnel engineering [J]. Tunnel Construction, 2006 (05):16–27.

Wang Z G, Tao L J, Shi C, et al, 2023. Study on the mechanical behavior of utility tunnel structure considering flexible joints under reverse fault dislocation [J]. Journal of Railway Science and Engineering, 20(06):1–12.

Zhong Z L, Wang Z, Zhao M, et al. 2020. Structural damage assessment of mountain tunnels in fault fracture zone subjected to multiple strike-slip fault movement[J]. Tunnelling and Underground Space Technology, 104.

Tunnelling for a Better Life – Yan, Celestino, Thewes & Eberhardt (Eds)
© 2024 The Author(s), ISBN 978-1-032-80042-4
Open Access: www.taylorfrancis.com, CC BY-NC-ND 4.0 license

Analytical solution for longitudinal response of cross-fault mountain tunnels based on foundation beam model

Lianjin Tao, Mingyang Qiu*, Haixiang Zhang, Zhibo Jia & Cheng Shi
The Key Laboratory of Urban Security and Disaster Engineering, Ministry of Education, Beijing University of Technology, Beijing, China
Beijing Key Laboratory of Earthquake Engineering and Structural Retrofit, Beijing University of Technology, Beijing, China

ABSTRACT: Tunnel crossing active fault is a common issue in mountain tunnels. Researching the analytical solutions for the longitudinal response of tunnels under fault dislocation is of great importance for disaster prevention in mountain tunnels. This paper summarizes the mechanical models for analytical solutions of longitudinal responses in tunnels crossing faults, compares the characteristics and applicable conditions of various foundation beam models, analyzes the key factors affecting the accuracy of the analytical solutions of foundation beam models, and finally proposes a general model for calculating longitudinal deformation in foundation beams. The results show that the current analytical solution models for foundation beams crossing faults seldom consider factors such as the form of fault sliding, tunnel joint methods, and external forces on tunnels. The general foundation beam model can introduce new parameters without changing the algorithm and enhance the efficiency of displacement analysis. This study provides guidance for subsequent displacement prediction and disaster prevention in mountain tunnels crossing active faults.

Keywords: Fault Dislocation, Mountain Tunnel, General Foundation Beam Model, Analytical Solution, Key Influencing Factors

1 INTRODUCTION

With the implementation of 'the Belt and Road', the construction of tunnel projects in the high-intensity areas of Southwest China is increasing. These projects inevitably cross active fault zones. Consequently, numerous scholars have conducted extensive research on the longitudinal dynamic response of tunnels under fault displacement. These researches include theoretical analysis, numerical methods, and model experiment simulations. Most of them analyse the shear dislocation effects caused by fault displacement on tunnels, specifically the longitudinal deformations and internal forces. This is crucial to prevent excessive deformation of tunnels, which can lead to leakage or longitudinal tensile damage, ensuring the safe operation of tunnels. As a verification and supplement to numerical methods, analytical solutions directly reflect the mechanisms of core parameters in function form and calculate the equivalent models quickly in the preliminary design of tunnels.

The analysis of underground pipelines crossing active faults has developed into a complete system. In 1975, Newmark et al (Newmark et al., 1975) first proposed the small deformation analysis method of shallowly buried pipelines under fault displacement, considering that fault displacement only causes axial deformation of the pipeline, but did not take into account the bending deformation of the pipeline. Kennedy (Kennedy., 1977) expanded the research of Newmark, treating the pipeline as a cable with only tensile stiffness but no bending stiffness under bending deformation, and then he studied the impact of single curvature large deformation bending beams on pipelines under fault displacement. This simplified method of longitudinal structure was widely used in strike-slip and normal faults for many years. Based on Kennedy's work, Wang et al (Wang et al., 1985) considered the bending stiffness of pipelines. Both Kennedy and Wang used a single curvature model to study the mechanical response of buried pipelines to strike-slip fault displacement, but they overestimated the effect of soil resistance on bending strain. Based on the simplified methods of pipelines, many scholars began to use the foundation beam model to study the analytical solution for tunnels crossing faults.

*Corresponding author: qiumy0417@163.com

DOI: 10.1201/9781003495505-165

Considering the fault zone width had an impact on tunnel structural internal forces and deformations, some scholars (liu et al., 2020; Yu et al., 2023; Tao et al., 2022) proposed an analytical solution for the longitudinal response of tunnels under active fault displacement based on the Pasternak two-parameter foundation beam model. Li et al (Li et al., 2023) considered the influence of horizontal friction, simplifying shield tunnels as Timoshenko beams in Vlasov two-parameter foundation. Integrating this model into the analytical framework, he examined the response patterns of existing shield tunnels to fault displacement, highlighting the significant influence of factors such as the vertical distance between tunnel and fault, fault fracture zone width, and structural longitudinal bending stiffness on the tunnel's maximum longitudinal internal force. Zhao (Zhao., 2019) simplified the tunnel as a shear beam on homogeneous elastic surrounding rock, deriving the tunnel's longitudinal response analytically through Green's function method. His research particularly focuses on comparing the effects of fault fracture zone length and surrounding rock's elastic resistance coefficient on the dynamic response of tunnel lining structures. Luo (Luo., 2023) simplified the tunnel as an Euler-Bernoulli beam, assessing the impact of fault dip angle and tunnel-fault intersection angle on the tunnel's mechanical response. Adaptations and additions to the foundation beam model parameters for varying geological conditions have been made to more accurately describe the tunnel's longitudinal mechanical response. However, many studies had idealized assumptions about the geological and dynamic characteristics of faults, along with fault sliding forms, tunnel joint methods, and external forces on tunnels, leading to less precise and efficient calculations and analyses of tunnel internal forces and deformations. As research progresses, more parameters will be incorporated into the foundation beam model. Therefore, establishing a universal model calculation approach and adjusting the influencing parameters based on this model to rapidly and accurately obtain the foundation beam's dynamic response is an imperative issue to be addressed.

This paper will first conclude and analyse the research progress of theoretical analytical solutions for longitudinal responses in tunnels crossing faults. Subsequently, it will comprehensively analyse factors affecting the accuracy of analytical solutions and propose a universal approach for calculating these solutions. Finally, the paper will summarize the characteristics and future development directions of research on longitudinal analytical solutions for tunnels crossing faults.

2 THE ANALYTICAL MODEL FOR LONGITUDINAL DEFORMATION OF TUNNEL

Current research on analytical models for the mechanical response of pipelines crossing faults is extensive (Wang et al., 2011), with the elastic foundation beam model being a commonly used mechanical model. Wang et al. (Wang et al., 1985) first divided the pipeline into four segments, as shown in Figure 1. The AC segment, a high-curvature area, was bisected by the fault trace at point B into AB and BC sections. Within this area, the pipeline was considered as a beam undergoing large single-curvature deformation, while the pipeline outside this high-curvature area (A'A, CC') were treated as elastic foundation beams. Based on the continuity requirements between adjacent sections, it was able to calculate the bending moment at the junctions of the large deformation beam and its adjacent elastic beams. Karamitros et al. (Karamitros et al., 2006) referred to the elastic plate theory and Wang's segmentation of pipelines and treated pipelines as elastic beams in the fault zone. The remaining areas were considered as semi-infinite elastic foundation beams. Their calculations took into account the bending stiffness of the pipeline cross-section, as well as the axial and lateral interactions between soil and pipeline. This approach was used to study the influence of curvature on axial strain, enabling a more precise determination of maximum strain.

The segmentation approach for pipelines initially assumes a high-curvature area. The shear force, bending moment, and rotation outside this high-curvature area are calculated using the foundation beam theory. Subsequently, iterative solutions within the high-curvature zone are conducted using boundary continuity conditions, aiming to identify the most adverse combination of axial and bending strains. Finally, based on the balance between externally applied axial forces and the internal stresses developed on the pipeline's cross-section, the maximum strain of the pipeline is calculated. This method significantly improves the precision of analytical predictions for pipelines crossing faults and provides convenience for researchers to consider the interaction between the surrounding rock and tunnel.

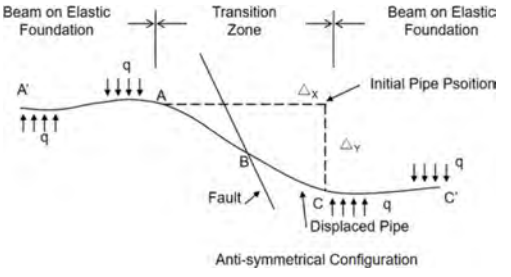

Figure 1. Pipeline analysis model proposed by Wang and Yeh.

Based on existing underground pipeline mechanical models, scholars had gradually applied the foundation beam model to the longitudinal stress analysis of tunnels crossing faults. The segmentation approach for cross-fault pipelines and tunnels differs as follows: (1) Cross-fault tunnels take into account

the width of the fault fracture zone, using this as a boundary condition to differentiate between fault and non-fault areas; (2) Compared to pipelines, tunnels have greater stiffness, and their deformations under fault displacement can be considered small, suitable for calculation using the elastic foundation beam model; (3) The joint forms in tunnels are more complex. Liu et al. (Liu et al., 2020), based on the Karamitros et al. model, factored in the thickness of the fault fracture zone, dividing the tunnel under fault displacement into three regions as shown in Figure 2. They were the displacement affected zone, the transitional influence zone, and the non-influenced zone, the tunnel in each zone as an elastic foundation beam. Many studies of the seismic response analytical solutions for tunnels crossing faults, had generally simplified the cross-fault tunnel model into three areas: the hanging wall, the fault zone, and the footwall. This segmentation approach no longer considers the intermediate fault zone as a single elastic beam, but rather takes into account the interaction between the tunnel and surrounding rock. Using foundation beam theory for all areas, it enables a more straightforward and rapid calculation of the impact of fault displacement on the tunnel's longitudinal mechanical response.

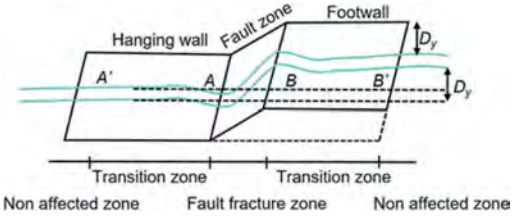

Figure 2. Tunnel analysis model proposed by Liu.

3 THE KEY FACTORS IN ANALYTICAL SOLUTION

Currently, analytical solutions mainly develop around the elastic foundation beam model. In this model, the tunnel structure is treated as a simplified beam, and the surrounding rock is regarded as a simplified foundation. The fault displacement is imposed on the soil or rock layer in forms such as concentrated, distributed, or harmonic vibration, and introduced into the analytical solution as an external load. Factors like the shear effects of the beam, the choice of foundation model, and the ground reaction coefficient are crucial in influencing the accuracy of the analytical solution.

3.1 *The type of beam*

The concept of longitudinal analytical solutions for tunnels posits that shield tunnels can be longitudinally equated to a beam. This idea was first proposed and extensively researched by Shiba Y et al. (Shiba Y et al., 1988). Based on the theory of longitudinal structure-soil interaction in tunnels, shield tunnels are typically simplified as Euler-Bernoulli beams and Timoshenko beams. These two types of beams are commonly used to describe the deformations of tunnels caused by fault displacements. The Euler-Bernoulli beam considers only bending deformations and does not account for shear effects. In its force analysis, line segments perpendicular to the beam's axis before deformation remain perpendicular and unchanged in length after deformation. Timoshenko et al. (Timoshenko et al., 1921) expanded on the Euler-Bernoulli beam by incorporating shear deformations, proposing that after deformation, the sections are no longer perpendicular to the neutral axis. The action of shear forces creates a shear angle in the beam, as shown in Table 1.

Some scholars considered the real stress-strain state during tunnel fault displacement, had incorporated the effects of tunnel segmentation and joints in their theoretical analyses. Yu et al based on the Pasternak two-parameter foundation beam theory, derived an analytical solution for the longitudinal seismic response of tunnels with segmented flexible joints crossing faults. Li et al considered the impact of plastic deformation of annular joint connections on the longitudinal mechanical response of tunnels, simplifying the tunnel as a Timoshenko beam on Vlasov two-parameter foundation. He found that the mechanical response characteristics calculated by the analytical model were consistent with those obtained from model experiments and numerical calculations. Yan et al. (Yan et al., 2022) proposed elastic and viscoelastic foundation beam models to analyze the seismic response of cross-fault tunnels with flexible joints. Geng et al. (Geng et al., 2021) established a longitudinal calculation model for cross-fault shield tunnels considering the nonlinear contact effects of annular joints. For tunnels crossing faults, incorporating joints as a flexible adaptation to surrounding rock deformations is an effective seismic mitigation measure. Thus, introducing joint design into the foundation beam model, simplifying the tunnel as short beams of finite length suitable for the shear deformation of Timoshenko beams, can better simulate the actual conditions of tunnel displacement damage.

3.2 *The type of foundation beam*

The foundation beam model takes into account the interaction between the tunnel and the surrounding rock. The commonly used foundation beam models in cross-fault tunnels can be broadly categorized into two types based on whether they consider damping effects: elastic and viscoelastic. The elastic foundation beam includes the Winkler model, the two-parameter model, and the three-parameter model; the viscoelastic foundation models include the Maxwell model, Kelvin model, etc.

3.2.1 *Elastic foundation beam*

In 1867, Winkler proposed an idealized soil parameter model, the Winkler model, which assumes that the stress at any point on the foundation is directly

Table 1. The difference between Euler-Bemoulli beam and Timoshenko beam.

Type	Euler-Bemoulli beam	Timoshenko beam
Deformation characteristics	1. No shear strain; 2. The cross-section remains perpendicular to the neutral axis after deformation	1. Shear strain; 2. The cross-section does not remains perpendicular to the neutral axis after deformation
Force Analysis	Only one variable v: Vertical displacement γ: Rotation angle caused by shear deformation	Two variables v, γ
scope of application	Very long beams and thin plates.	Short beams and thick plates.
basic formula	$\theta=\frac{dv}{dx}$	$\theta=\frac{dv}{dx}-\gamma$
Sketch Map	Euler-Bemoulli beam: 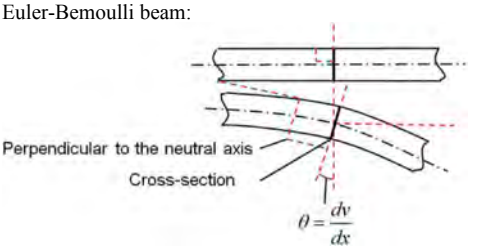 Timoshenko beam: 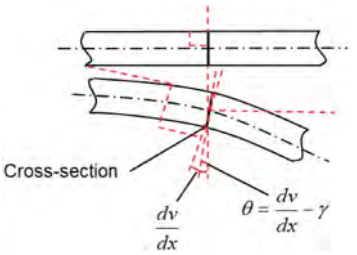 	

proportional to the settlement of the foundation at that point. In 1954, Pasternak et al. (Pasternak et al., 1954) further expanded on the Winkler foundation model, incorporating shear effects and proposing the two-parameter Pasternak foundation beam model. In the same year, Kenney et al. (Kenney et al., 1954) showed a critical load velocity that significantly alters the response of the beam. In 1965, Kerr et al. (Kerr et al., 1965) introduced a new three-parameter foundation beam model. In 1966, Vlasov et al. (Vlasov et al., 1966) introduced a stochastic parameter γ to describe the vertical displacement distribution of an elastic foundation, proposing a modified Vlasov two-parameter foundation beam model.

Although the Winkler elastic foundation beam model involves fewer parameters, it is widely applied in industrial, agricultural, and civil building foundations, including the simulation of underground pipelines and surrounding rocks, making it the most extensively used and easily understood pipeline analytical solution model. Li et al. (Li et al., 2023) used the Winkler elastic foundation beam model to construct elastic foundation beam elements based on analytical functions. In studies of the mechanical response of cross-fault tunnels, the two-parameter foundation beam model is more common. Compared to the Winkler elastic foundation beam, it also considers the effect of shear. Luo et al. (Lou et al., 2016) used the two-parameter elastic foundation beam model and the Timoshenko beam model to construct finite elements, suggesting that the beam base model elements are not suitable for calculations of the Pasternak elastic foundation Timoshenko beam under non-uniform load. The three-parameter foundation beam model no longer views the foundation as a single-property soil but considers the impact of different soil layers on the analytical solution, which is widely applied in the study of the impact of nearby construction on tunnels (Han et al., 2023; Feng et al., 2022). The more parameters a foundation beam model has, the more complex the calculations, but the more precise the results. Therefore, when calculating the longitudinal mechanical response of tunnels, the foundation beam model should be selected flexibly according to different external environmental conditions.

3.2.2 *Viscoelastic foundation beam model*

Elastic foundation beams do not account for damping factors present in practical engineering. Many scholars have gradually recognized the impact of foundation viscosity on the vibrational characteristics of foundation beams, leading to the development of

research on viscoelastic foundation beams. In 1994, Huang et al. (Huang et al., 1994) studied the dynamic response of viscoelastic Winkler foundation beams. Calim et al. (Calim et al., 2009) investigated the dynamic response of viscoelastic Pasternak foundation beams under pulse excitation using integral transforms. Fu et al. (Fu et al., 2020) considered a Timoshenko beam on a viscoelastic Pasternak foundation and studied the beam's transverse free vibration characteristics. The mechanical behavior of real foundations strongly depends on the properties of the soil, often exhibiting creep phenomena and demonstrating rheological behavior that is time- and frequency-dependent. Therefore, considering the viscoelasticity of the foundation can better reflect the coupling between the foundation and the beam.

In research on tunnels crossing faults, Yan et al. considered the impact of shear deformations and used a Kelvin viscoelastic foundation to simulate the interaction between surrounding rock and tunnel. He derived an analytical expression for the longitudinal seismic steady-state response of tunnels crossing faults. Compared to the Kelvin model, the standard solid model or the Zener model has a stronger ability to describe creep and relaxation behavior, better reflecting the mechanical behavior of viscoelastic solids. Moreover, natural faults typically exhibit segmentation in their average displacement rates and sliding modes (referred to as creep slip and viscous slip), with few cases of uniform overall sliding. However, whether it is creep slip or viscous slip displacement, the displacement caused by such scenarios in tunnels crossing faults is considered as a known condition. There is still room for improvement in process simulation.

4 THE APPROACH OF GENERAL MODEL CALCULATION

When calculating the longitudinal mechanical response of tunnels crossing faults, different foundation beam models are selected based on varying condition parameters and the desired level of detail, with more parameters making the solution process more complex. To facilitate easier computation and parameter introduction, this paper summarizes the deflection control equations of various models and provides a general calculation approach for quickly and conveniently obtaining the dynamic response analysis of foundation beams.

Based on the fundamental principles of elasticity and starting from the analysis of infinitesimal beam segments, the deflection control differential equation for the beam on the foundation is derived by introducing parameters considered during force analysis. This facilitates the analysis of the internal forces of foundation beams in different fault zones. Referring to the cross-fault diagram mentioned earlier, and taking the Pasternak foundation beam as an example, the internal forces of the beam are analyzed in segments. Parameters are introduced in 4.1 and 4.2, as detailed below:

4.1 *The balance equation of tunnel*

$$EI\frac{d^4\omega}{dx^4} + p(x)b = q(x) \tag{1}$$

Where, $p(x)$ is the reaction force generated beneath the tunnel; $q(x)$ is the external load applied to the tunnel; $\omega$is represents deflection; b is the tunnel width.

When using the Winkler foundation beam, $p(x) = k\omega$

When using the Pasternak two-parameter foundation beam:

$$p(x) = k\omega - G_p b\frac{d^2\omega}{dx^2}$$

4.2 *The control equation of beam's deflection*

For an Euler-Bernoulli beam:

$$EI\frac{d^4\omega}{dx^4} + kb\omega - G_p b\frac{d^2\omega}{dx^2} = q(x) \tag{2}$$

For a Timoshenko beam:

$$\left(1+\frac{bG_p\mu}{GA}\right)EI\frac{d^4\omega}{dx^4}+kb\omega-\left(\frac{bk\mu}{GA}+\frac{bG_p}{EI}\right)EI\frac{d^2\omega}{dx^2}=q(x) \tag{3}$$

Where, $\frac{bG_p\mu}{GA}$ is represents the beam's shear stiffness; G_p is the foundation's shear stiffness; k is foundation reaction.

4.3 *Simplification of the differential equation*

$$\omega^{(4)} - 4\lambda^2\rho\omega'' + 4\lambda^4\omega = \frac{q(x)}{EI} \tag{4}$$

Where, $\lambda = \sqrt[4]{\frac{kb}{4EI}}, \rho = \frac{G\lambda^2}{k}$

4.4 *General solution for the deflection equation*

$$\begin{aligned}\omega = {} & e^{\alpha x}(c1\cos\beta x + c2\sin\beta x)\\ & +e^{-\alpha x}(c3\cos\beta x + c4\sin\beta x)\end{aligned} \tag{5}$$

Where $\alpha = \lambda\sqrt{1+\rho}, \beta = \lambda\sqrt{1-\rho}$

4.5 *Depending on zone to establish general solution*

Assuming the fault displacement amount is y, and based on the segmentation diagram in Figure 2.

when the active fault boundary $x \to -\infty, \omega \to 0$,; when the active fault boundary $x \to +\infty, \omega \to 0$,

Therefore, the simplified formula for each zone as follows:

$$\begin{cases} \omega_1 = e^{\alpha_1 x}(A_1\cos\beta_1 x + A_2\sin\beta_1 x) & x<0 \\ \omega_2 = e^{\alpha_2 x}(A_5\cos\beta_2 x + A_6\sin\beta_2 x) + \\ e^{-\alpha_2 x}(A_7\cos\beta_2 x + A_8\sin\beta_2 x) - y & 0\le x\le d \\ \omega_3 = e^{-\alpha_3 x}(A_{11}\cos\beta_3 x + A_{12}\sin\beta_3 x) & x\ge d \end{cases} \tag{6}$$

Where, A_1、A_2、A_5、A_6、A_7、A_8、A_{11}、A_{12} are undetermined coefficients.

4.6 *Establishing boundary constraint equations*

The deflection, angle of rotation, bending moment, and shear force of the tunnel structure at points A and B must satisfy continuity requirements, resulting in 8 boundary constraint equations:

$$\begin{cases} \omega_1|x=0=\omega_2|x=0 \\ \omega'_1|x=0=\omega'_2|x=0 \\ -EI\omega''_1|x=0=-EI\omega''_2|x=0 \\ -EI\omega'''_1|x=0=-EI\omega'''_2|x=0 \end{cases} \tag{7}$$

$$\begin{cases} \omega_2|x=d=\omega_3|x=d \\ \omega'_2|x=d=\omega'_3|x=d \\ -EI\omega''_2|x=d=-EI\omega''_3|x=d \\ -EI\omega'''_2|x=d=-EI\omega'''_3|x=d \end{cases} \tag{8}$$

Establishing Boundary Constraint Equations to Solve for Undetermined Coefficients.

4.7 *Differentiation of the deflection curves*

Further differentiation of the deflection curves yields the angle of rotation θ, bending moment M, and shear force Q in different affected zones of the tunnel:

$$\theta=\begin{cases} \omega'_1 \; x<0 \\ \omega'_2 \;\; 0\le x\le d \\ \omega'_3 \; x\ge d \end{cases} \tag{9}$$

$$M=\begin{cases} -EI\omega''_1 \; x<0 \\ -EI\omega''_2 \;\; 0\le x\le d \\ -EI\omega''_3 \; x\ge d \end{cases} \tag{10}$$

$$Q=\begin{cases} -EI\omega'''_1 \; x<0 \\ -EI\omega'''_2 \;\; 0\le x\le d \\ -EI\omega'''_3 \; x\ge d \end{cases} \tag{11}$$

5 CONCLUSIONS

This paper discusses the research progress of analytical solutions for the longitudinal response of tunnels crossing active faults, analysing factors that affect the accuracy of the analytical solution models and providing a general calculation approach for analytical solutions. The following conclusions can be drawn:

(1) According to analyse the development of mechanical response models for tunnels crossing faults, it is observed that the foundation beam model for cross-fault tunnels adequately considers the impact of the fault fracture zone. The segmentation of tunnels with the width of the fracture zone as a boundary condition for establishing constraint equations further enhances the precision of the analytical solution. Compared to the stiffness of pipelines, the stiffness of tunnels is greater, allowing tunnel deformations to be considered as minor under fault displacement, and the use of elastic foundation beams enables rapid calculation of tunnel deformation.

(2) Most theoretical solutions for tunnels crossing faults use the elastic foundation beam model. Existing models have shortcomings in reflecting the geological characteristics of active faults and the dynamic properties of viscous sliding. Factors such as fault displacement rate, horizontal friction resistance, and segment joint forms are seldom involved in overall analytical solutions. The researches should fully consider the impact of these factors on the analytical solution for tunnels crossing faults to improve the accuracy of fault displacement calculations.

(3) A general elastic foundation beam model for solving the longitudinal response of tunnels crossing active faults is proposed. The genera model can modify parameters according to external conditions, addressing the issue of excessive parameters and complex solving processes in cross-fault foundation beam models. The model lays the foundation for constructing analytical elements, ultimately enhancing the efficiency and accuracy of deformation calculations.

REFERENCES

ACY, ACH BJT, et al. Active length of a continuous pipe or tunnel subjected to reverse faulting[J].Soil Dynamics and Earthquake Engineering, 148[2023-10-27].

Calim F F. Dynamic analysis of beams on viscoelastic foundation[J]. European Journal of Mechanics, 2009, 28(3):469–476.

Chiou Y J, Chi S Y, Chang H Y .A Study on Buried Pipeline Response to Fault Movement[J]. Journal of Pressure Vessel Technology, 1994, 116:1(1):36–41.

Element For Beam on Winkler Elastic Foundation Based on Analytical Trial Function[J]. Engineering Mechanics, 2015, 32(3): 66–72.

Feng Guohui, Chen Guangzai, Zhang Di.,et al. Analytical solution on uplift deflection of underlying existing tunnel induced by foundation pit excavation[J/OL].Journal of Railway Science and Engineering:1–11[2023-10-30].

Feng Guohui, Xu Changjie, Zheng Mingwang.,et al. Deformation response analysis on existing tunnel caused by shield tunneling underlying considering axial internal force [J]. Journal of Southeast University (Natural Science Edition), 2022, 52(03):523–529.

Fu Yanyan, Yu Yunyan. Analytical solution to transverse free vibration characteristics of a simply supported Timoshenko beam on viscoelastic Pasternak foundation [J]. Journal of Vibration and Shock, 2020, 39(19):32–38.

Geng Ping, Chen Pingliang, Chen Changjian, etal. Longitudinal Analysis Model of Shield Tunnel Considering Contact Nolinearity and Its Application.Journal Of Tongji University(Natural Science).

Han ShouCheng, Zheng Kanglong, Wang Xianming.,et al. Simplified Algorithm for the Influence of Shield Tunnel Construction on Existing Pipeline Deformation Based on Kerr Foundation Model[J].Water Resources Engineering Design, 2023(12):73–75.

Huang, w., and Zou, Y., The dynamic response of a viscoelastic Winkler foundation-supported elastic beam impacted by a low velocity [J]. Computers & Structures, Vol. 52, No. 3, 1994, pp. 431~436.

Karamitros D K, Bouckovalas G D, Kouretzis G P .Stress analysis of buried steel pipelines at strike-slip fault crossings[J].Elsevier, 2007(3).

Kennedy RP, Chow AW, Williamson RA. Fault movement effects on buried oil pipeline. Transport Eng [J] ASCE 1977;103:617–33.

Kenney, J., Steady state vibrations of beam on elastic subgrade for moving loads [J]. Journal of Applied Mechanics, ASME, Vol. 21, No. 4, 1954, pp. 359~364.

Kerr, A.D., A study of a new foundation model [J]. Acta Mechanica, Vol. 1, No. 2, 1965, pp. 135~147.

Li hanyuan, Li xinggao, Liuyang., et.al. Longitudinal stress and deformation characteristics of shield tunnel crossing active fault [J].Journal of Zhejiang University (Engineering Science), 2023, 57(02):340–352.

Li Xiao,Luo Shuang,Cao Qiongqiong, etal. General model construction and feasibility analysis for deflection equation of elastic foundation beam [J].Journal of TongJi University [2023-10-27].

LIU Guozhao,QIAO Yafei., et al. An analytical solution of longitudinal response of tunnels under dislocation of active fault [J].RockandSoilMechanics, 2020, 41 (03):923–932.

Luo Shuang. Development of Pasternak elastic foundation beam element based on analytical shape function [D]. Beijing: China Agricultural University, 2016.

Luo Xun, Wang Mingnian, Yu Li., et.al. Calculation Model of Three-dimensional Mechanical Response of a Tunnel Under UnevenDislocation of Oblique-slip Fault [J]. Modern Tunnelling Technology, 2023, 60(04):86-94 +146.

Newmark NM, Hall WJ. Pipeline design to resist large fault displacement. In: Proceedings of the US National Conference on Earthquake Engineering. Ann Arbor: University of Michigan; 1975. p. 416–25.

Ni P, Mangalathu S . Simplified evaluation of pipe strains crossing a normal fault through the dissipated energy method[J]. Engineering Structures, 2018, 167:393–406.

Pasternak, P.L., On a new method of analysis of an elastic foundation by means of two foundation constants. Gosttd. Izdat. Literaturi po Stroit. i Arhitekture, Moskow. 1954.

Shiba Y, Kawashima K, Obinata N,et al. An evaluation method of longitudinal stiffness of shield tunnel linings for application to seismic response analyses.[J].Doboku Gakkai Ronbunshu, 1988(398):319–327.

Tao Lianjin, Wang Zhigang, Chi Cheng., et al. Analytical solution for longitudinal response of pipeline structure under fault dislocation based on Pasternak foundation model[J].Chinese Journal of Geotechnical Engineering, 2022, 44(09):1577-1586+1-2.

Timoshenko P S P LXVl, On the correction for shear of the differential equation for transverse vibrations of prismatic bars[J]. Philosophical Magazine, 1921, 41 (245):744–746.

Valsamis A I, Bouckovalas G D .Analytical methodology for the verification of buried steel pipelines with flexible joints crossing strike-slip faults[J]. Soil Dynamics and Earthquake Engineering, 2020, 138(11):106280.

Vlasov, V.Z., and Leont'ev, N.N., Beams, plates and shells on elastic foundations,1961 (English translation by Israel program for scientific translation, Jerusalem, 1966.

Wang Bing, Li Xing, Zhou Jin., et.al. An Improved Analytical Method of Buried Steel Pipeline Response Under Strike-slip Fault Movement [J]. Engineering Mechanics, 2011, 28(12):51–58.

Wang LRL, Yeh Y. A refined seismic analysis and design of buried pipeline for fault movement. Earthquake Engineering Structure Dynamics, 1985;13:75–96.

YAN Gao-ming, ZHAO Bo-ming, WANG Zi-jun, et al. Simplified analytical solution for responses of fault-crossing tunnels with flexible joints under fault movement [J]. Structures, 2022, 45: 984–998.

Yan Gaoming, Zhao Boming.,et al. Analytical Solution for Longitudinal Seismic Responses of Fault-crossing Tunnels [J]. Journal of Vibration and Shock, 2022, 41(13):228–238.

Yu Haitao, Yuan Yong, Zhang Zhongjie., et al. Application of Response Displacement Method on Seismic Design of a Complex Underground Structure[J]. Chinese Journal of Underground Space and Engineering, 2011, 7(5): 857–862.

Zhao Jianfeng. Research on dynamic response of cross-fault tunnel based on Shear beam model[D]. Southwest Jiaotong University, 2019.

Tunnelling for a Better Life – Yan, Celestino, Thewes & Eberhardt (Eds)
© 2024 The Author(s), ISBN 978-1-032-80042-4
Open Access: www.taylorfrancis.com, CC BY-NC-ND 4.0 license

Experimental study on mechanical properties of grouted π-type SCCS arch

Zhichao Wang* & Wei Li
School of Highway, Chang'an University, Xi'an, China

Yuancheng Cai
School of Highway, Chang'an University, Xi'an, China
China Water Resources Beifang Investigation, Design and Research Co., Ltd., Tianjin, China

ABSTRACT: The excavation process of large cross-section highway traffic tunnels causes significant disturbance, making it difficult to control the deformation of the surroundings. After the application of traditional support, there are often insufficient strength, buckling instability of the support structure arch, and engineering diseases such as primary support falling and intrusion. Steel-concrete composite support (SCCS) is a promoting type of support with high strength and good stability, which can provide a viable solution for the support problem in loess tunnels, however, the research on the bearing capacity of grouted π-type SCCS arch in loess highway tunnels is not sufficient. This paper conducted a large-scale ring model test to investigate the mechanical behaviour of the grouted π-type SCCS arch under typical surrounding loess pressure. The failure pattern, ultimate bearing capacity, the progressive deformation and strain development were presented via the model test. It is concluded that the ultimate bearing capacity of grouted π-type SCCS arch was 195.44 kN, and its failure presented a symmetrical deformation pattern, shaping with arch crown and arch shoulder converging inward and arch foot expanding outward, and it underwent coordinated radial deformation which was resulting that the deformation at the shoulder and foot was the most pronounced. The result is providing reliable theoretical guidance for further on-site applications.

Keywords: Tunnel engineering, model test, π-type SCCS arch, Mechanical characteristics

1 INTRODUCTION

The steel-concrete composite structure fully utilizes the characteristics and performance of steel and concrete through the interaction between materials, which has advantages such as high load-bearing capacity and high stiffness. It is gradually promoted and applied as the support form in tunnel engineering (Wang et al., 2018; Wang et al., 2020; Li et al., 2015). When the tunnel is constructed in weak and fractured strata, loose soil strata and high stress strata, the case including the excessive deformation of surroundings and failure of support structures will be encountered frequently, the steel-concrete composite structure can be fully reflected the principle of strong support in the construction, which play a good supporting effect. It has good practical application significance and research value. (Wang et al. 2017; Jiang, 2016; Wang et al. 2021).

The essence of the tunnel support structure lies in protecting the bearing capacity of the surroundings and maintaining its three-dimensional stress state before being disturbed(Zhu et al. 2022;Gong et al, 2023;Gu et al, 2022). The support function of steel-concrete composite structure in tunnel construction stage is often reflected in two aspects: (1) The installation stage of the steel frame, a reasonable cross-section of the steel frame should be constructed as soon as possible to play a bearing role, achieving convenient construction and simplifying the construction process, reducing the generation of loose loads by the surroundings. (2) The pouring stage of the core concrete, the advantages of the materials are fully utilized through combined action to achieve collaborative work effects. Numerous scholars have developed different composite structures as skeleton arch structures for tunnel support based on different tunnel conditions, and have conducted in-depth research on its combined effect of bearing performance via theoretical derivation, experimental research, and on-site application. Li et al. (2016) proposed a three-dimensional constrained concrete support system for the deformation of surrounding rock in deep underground engineering, studied the mechanical performance and failure mechanism of the support system, and verified the rationality of the

*Corresponding author: wangzc@chd.edu.cn

DOI: 10.1201/9781003495505-166

support system through theoretical calculations and loading tests. Wang et al. (2021) used a large-scale mechanical testing system for traffic tunnel support structures to conduct large-scale mechanical performance comparison tests on composite I-steel arches, composite confined concrete arches, and single confined concrete arches, and proposed engineering suggestions for the application of confined concrete support systems in traffic tunnels. Sun et al. (2023) conducted pure bending indoor tests on steel tube concrete support structures considering the bond slip characteristics of arch concrete, and conducted in-depth analysis of the mechanical response of the components under bending moments. Wang et al. (2019) studied the failure mechanism and mechanical properties of confined concrete arches through a full-scale mechanical testing system, and obtained a formula for calculating the bearing capacity of confined concrete arches. Jiang et al. (2023) studied the mechanical properties of constrained concrete arches with different cross-sectional shapes under different load modes and cross-sectional parameters using a large-scale support structure loading system.. Wang et al. (2020) used a large cross-section tunnel constrained concrete composite arch mechanical test system to study the overall bearing capacity and deformation mechanism of the composite arch, and conducted on-site applications based on the research results. Huang et al. (2018) applied the steel tube concrete support system in deep tunnels, fully demonstrating the obvious advantages of high bearing capacity and good stability of steel concrete composite support.

The above research has achieved many important results, but there are few reports on the bearing capacity of steel-concrete composite arch frame under the pressure from loess tunnel. Although Wang et al. (2021) developed π-type SCCS support system suitable for loess tunnel construction, and investigated the bearing capacity of the π-type SCCS arch without grouted via experiment. However, the failure characteristic and the bearing capacity of grouted π-type SCCS arch remains necessary to explore, where it is acting the load from surrounding loess.

This paper designed the large-scale ring model test for a grouted π-type SCCS arch based on the principle of similarity. Firstly, the grouting performance parameters were determined by conducting concrete ratio tests and compressive strength tests, and model specimens were made subsequently. Then, it is gradually loading until the specimen failed, the deformation, strain development patterns, and failure characteristic modes of the support structure were obtained by simulating the pressure of the surrounding of loess. The result is providing reliable theoretical guidance for further on-site applications.

2 TEST MATERIAL AND SPECIMEN PROCESSING

2.1 *Law of similarity*

Based on the general law of similarity, the similarity of model test can be deduced by the following equation.

$$\frac{\sigma}{E} = f(\frac{P}{El^2}, \frac{\gamma l}{E}, \mu) \tag{1}$$

Where, stress σ is correlated with the elastic modulus E, buck density γ, Poisson's ratio μ, load P, and geometric dimension l. Depending on the dimension of the model, the reduced scale is defined to $C = 10$, Prototypes and models use the same materials and the gravity is ignored. The similar relationship between prototype and model experiments is shown in Table 1. Herein, "m" represents model and "p" represents prototype.

2.2 *Material used for modeling*

For satisfying the requirements of the scale experiment, the grouted concrete for model test should keep flow ability and compressive strength during being packed into the hollow π type SCCS arch. The experimental material was a mixture of cement, fly ash, sand, stone (d<5 mm), water, expander, and water reducer (rate of 25%) in a weight ratio of 310:80:770:1108:162:31.2:3.9 (kg/m^3), and with an age of 28 days. The properties of trial concrete are described in Table 2.

2.3 *Specimen processing*

(1) Arch frame fabrication. the π-type SCCS arch was prefabricated with model scale.

Table 1. Similarity ratio of main physical parameters.

Item	Geometric dimension l	Stress σ	Young's modulus E	Area load Q	Poisson's ratio u	Strain ε
similarity relation	$C_l = \frac{l_p}{l_m}$	$C_\sigma = \frac{\sigma_p}{\sigma_m}$	$C_E = \frac{E_p}{E_m}$	$C_Q = \frac{Q_p}{Q_m}$	$C_\mu = \frac{\mu_p}{\mu_m}$	$C_\varepsilon = \frac{\varepsilon_p}{\varepsilon_m}$
Similarity's ratio	10	1	1	1	1	1

Table 2. The compressive strength of the tested concrete.

Test number	Compressive strength (MPa)
1	48.4
2	46.9
3	44.5
Average value	46.6

(2) Welded line Sealing. Before grouting the core concrete, the welded line needed to be polished and then coated with transparent glass adhesive to seal the welds to prevent slurry loss during the grouting process.
(3) Cut the grouting hole. The grouting hole should be cut in the top of the complete specimen and it was also should be polished the opening to prevent cutting of workers.
(4) Grouting preparation. The specimen was fixed the on the concrete vibration table and adjusted its position to keep horizontal, which is to prevent the slurry from not flowing and not being dense.
(5) Grouting core concrete. Poured the prepared concrete into the hollow arch frame, and used steel rods for vibration to fully flow the slurry
(6) Concrete maintenance. Sealed the injection port with plastic film to prevent water loss. Sprayed water mist on the grouting port every 3 hours to ensure the humidity and curing conditions of the concrete.

3 EXPERIMENT METHOD

3.1 *Test apparatus*

The laboratory test apparatus is shown in Figure 1. which has such characters: (1) the control system manages fifteen loading cylinders to accurately achieve the expected load, and each loading cylinder worked independently with a loading stroke of 230 mm, rated pressure of 10 MPa, loading accuracy of 0.175 kPa, and a minimum loading speed of 90 s/mm. (2) The pressure sensor measures the pressure in real-time and transmitted the data to the control system.

3.2 *Loading pattern and observation design*

One loading pattern of symmetrical loads in the spandrel was applied for reproducing the tunnels that undergo the typical surrounding loess pressure, which is summarized by the literature (Wang et al., 2023). The specific monitoring instrument layout plan is shown in Figure 2.

3.3 *Test method*

The flowchart of the scale experiment is described in Figure 3. The experiment adopted graded level for

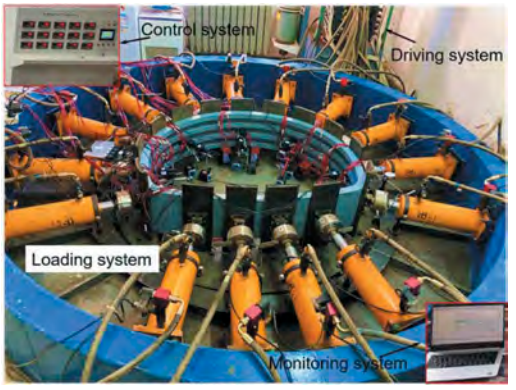

Figure 1. Test loading system.

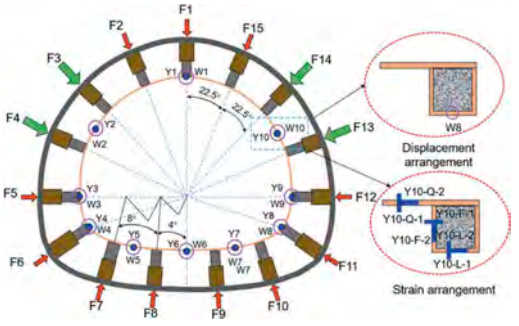

Figure 2. Monitoring instrument layout plan.

loading, the preload setting should not exceed 2% of the ultimate load, and the formal loading should begin after 5 minutes of holding pressure. The formal loading was set as one level every 0.5 kN, the loading rate was set to 0.05 mm/s, and the holding time was set to 5 minutes. Except the oil cylinders of F7-F10 as the passive carrying cylinders, which provided the reaction, each loading level ensured synchronous for each oil cylinder, maintaining a 2:1 loading ratio between F3, F4, F13, and F14 oil cylinders and other loading cylinders. The test was stopped until the specimen was loaded to the point of destruction.

4 TEST RESULTS

(1) Overall failure mode

The deformation of the specimen continued to increase with increasing load. When the load of the single oil cylinder continued to increase to 16 kN, the internal weld nodes of the arch foot collapsed, causing local wrinkles and bulges. At the same time, the arch bottom gradually converged inward and undergoes bending deformation. However, the overall integrity of the arch frame was good and can continue to bear the load. When the load increased to 22 kN, there was a large area of paint peeling and wrinkling damage at the arch foot. Through out the cracks, it

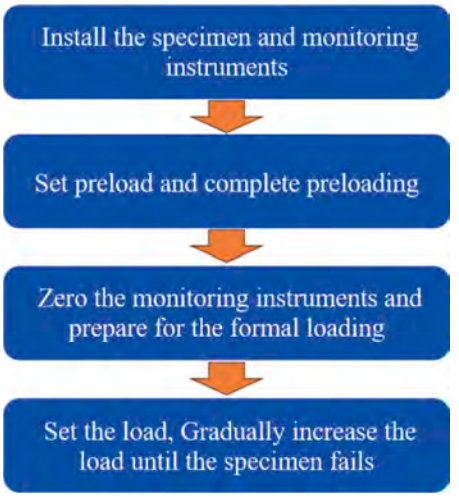

Figure 3. Loading test process.

can be clearly seen that the core concrete was broken, and the arch frame was unstable and damaged. The damage basically follows a symmetrical distribution, as shown in Figure 4.

(2) Displacement variation characteristics

Figure 5 shows the load displacement relationship curve of the single oil cylinder in the key parts of the arch frame. It can be found that the load of F3-4 and F13-14 was twice that of other active loading cylinders, and the loading synchronization of each cylinder was good, meeting the preset load conditions of the test. Until the time was reaching 4813s, the load displacement curve of each oil cylinder (as shown in Figure 6) showed a turning point, and the total load borne by the arch began to decrease. At this point, the ultimate bearing capacity was 195.44 kN. It is worth noting that as a key part of transmitting the upper load, the arch foot generated local stress concentration, which resulted in the load of F6 and F11 cylinders being much greater than that of other cylinders.

At the end of the loading test, the maximum positive displacement of the arch was at the arch shoulder (31.87 mm), and the maximum negative displacement occurred at the left arch foot (-15.23 mm). This is because after applying double the load on the symmetrical arch shoulder, resulting in coordinated radial deformation and transmitting the force to the lower part. The arch foot was located in the stress concentration area, with the maximum force, resulting in outward extrusion deformation, negative displacement, and accompanied by local wrinkles and buckling.

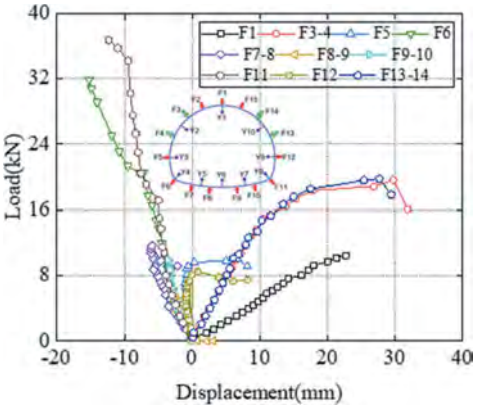

Figure 5. Load displacement curve.

(3) Strain variation characteristics

According to Figure 7, the strain distribution at the same position of the arch showed a symmetrical development trend. The average strain of Y1 measuring point was 2065 με, the strain of Y1 was 1.809 times greater than the elastic–plastic threshold strain. The maximum strain was the circumferential strain of the lower flange, which was -5776 με.

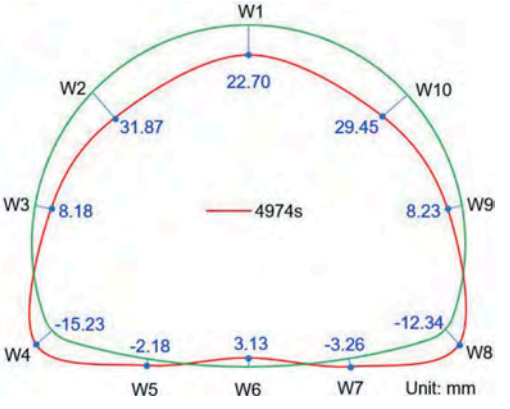

Figure 4. Overall failure of arch frame.

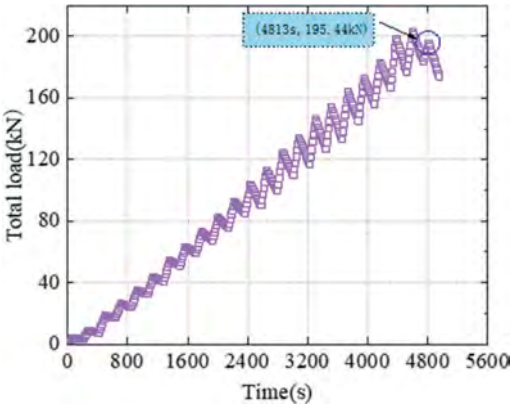

Figure 6. Total load time curve.

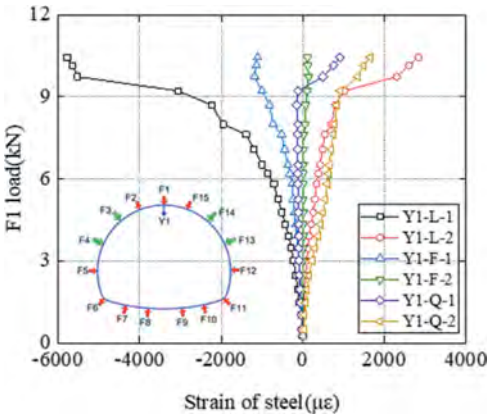

Figure 7. Strain of steel arch frame at Y1 measurement point.

5 CONCLUSION

This paper was based on the principle of similarity to create a 1:10 large scale model test for investigated the mechanical property of the grouted π-type SCCS arch, and conducted failure tests using a large underground engineering loading platform. The test was under the pressure of loess surroundings simulated by applied the symmetrical biased loads. It was focus on the tunnel support with its failure form, strain and displacement development law, and bearing capacity. The following conclusions are drawn in this article:

(1) The grouted π-type SCCS arch exhibited a symmetrical deformation pattern with the shape of "the crown and shoulder converging inward, and arch foot expanding outward".
(2) The ultimate bearing capacity of the grouted π-type SCCS arch was 195.44 kN, and the steel section showed the highest stress on the lower flange.
(3) The grouted π-type SCCS arch underwent coordinated radial deformation and it is resulting that the deformation at the shoulder and foot was most pronounced, the stress concentration and buckling of the foot were damage-prone areas which should strengthen the bearing design.

ACKNOWLEDGEMENT

This study was supported by the National Natural Science Foundation of China (Grant No. 52008028) and the Fundamental Research Funds for the Central Universities, CHD (Grant No. 300102212204).

REFERENCES

Gong F.Q, Wu W.X, Li T.B, et al., 2023. Simulation experimental study of spalling failure of surrounding rock of rectangular tunnel of deep hard rock. Rock and Soil Mechanics, 40(6):2085–2098.

Gu L.J, Feng X.T, Kong R, et al, 2022. Excavation Stress Path Induced Fracturing Mechanism of Hard Rocki Deep Tunnel. Rock Mechanics and Rock Engineering, 56 (3):1779–1806.

Huang W.P, Yuan Q, Tan Y.L, et al, 2018. An innovative support technology employing a concrete-filled steel tubular structure for a 1000-m-deep roadway in a high in situ stress field. Tunnelling and Underground Space Technology, 73:26–36.

Jiang B, Xin Z, Zhang X, et al, 2023.Mechanical properties and influence mechanism of confined concrete arches in high-stress tunnels. International Journal of Mining Science and Technology, 33(7):829–841.

Jiang B, 2016. Control Mechanism and Application of Confined Concrete for Super Large Section Tunnel on Weak Surrounding Rock. Jinan: Shandong University. (in Chinese)

Li S.C, Wang Q, Wang H.T, et al., 2015. Model test study on surrounding rock deformationand failure mechanisms of deep roadways with thick top coal. Tunnel Underground Space Technology, 47:52–63.

Li S.C, Wang, Q, Jiang, B, et al, 2016. Modeling and experimental study of mechanical properties of confinedconcrete arch in complicated deep underground engineering. International Journal of Geomechanics, 17(6), 04016137.

Sun H.B, Zhang J.L, Yang H.X, et al,2023. A Study on the Bearing Characteristics of Composite Concrete-filled Steel Tube Support Structure in Tunnels. Modern Tunnelling Technology, 60(2): 103–114. (in Chinese)

Wang Q, Jiang B, Pan R, et al, 2018. Failure mechanism of surrounding rock with high stress and confined concrete support system. International Journal of Rock Mechanics and Mining Sciences, 102:89–100.

Wang Q, Pan R, Jiang B, et al, 2017. Study on failure mechanism of roadway with soft rock in deep coal mine and confined concrete support system. Engineering Failure Analysis, 81: 155–177.

Wang Q, Luan Y.C, Jiang, B, et al, 2019. Mechanical behaviour analysis and support system field experiment of confined concrete arches. Journal of Central South University, 26(04):970–983.

Wang Q, Xu S, Jiang B, et al, 2020. Research progress of confined concrete support theory and technology for underground engineering. Journal of China Coal Society, 45(08):2760–2776. (in Chinese)

Wang Q, Xiao Y.C, Jiang, B, et al, 2021. Research and Application of High Strength Confined Concrete Arch in Traffic Tunnel. China Journal of Highway and Transport, 34(09):263–272.

Wang Q.B., Xin Z.X., Jiang, B., et al, 2020. Comparative experimental study on mechanical mechanism of combined arches in large section tunnels. Tunnelling and Underground Space Technology, 99: 1–11.

Wang Z.C, Cai Y.C, Xie Y.L, et al, 2023. Laboratory study on mechanical behavior of hollow π-type steel–concrete composite support in loess tunnel, Tunnelling and Underground Space Technology, 141(2023)105280.

Wang Z.C, Du K, Xie, Y.L, et al, 2021. Buckling analysis of an innovative type of steel-concrete composite support in tunnels. Journal of Constructional Steel Research, 179, 106503.

Wang Z.C, Su X.L, Lai H.P, et al, 2021. Conception and evaluation of a novel type of support in loess tunnels. Journal of Performance of Constructed Facilities, 35(1), 04020144.

Zhu Z.G, Fang Z.C, Xu F, 2022. Model test study on the rock mass deformation law of a soft rocktunnel under different ground stresses. Frontiers in Earth Science, 10.962445.

Tunnelling for a Better Life – Yan, Celestino, Thewes & Eberhardt (Eds)
© 2024 The Author(s), ISBN 978-1-032-80042-4
Open Access: www.taylorfrancis.com, CC BY-NC-ND 4.0 license

Study on deformation joint width of mining tunnel under the operation of a normal fault

Qi Wang*
School of Mechanics and Aerospace Engineering, Southwest Jiaotong University, Chengdu, Sichuan, China
School of Civil Engineering, Southwest Jiaotong University, Chengdu, Sichuan, China

Dingwei He, Junbo Chen & Ping Geng
School of Civil Engineering, Southwest Jiaotong University, Chengdu, Sichuan, China

Huoming Shen
School of Mechanics and Aerospace Engineering, Southwest Jiaotong University, Chengdu, Sichuan, China

ABSTRACT: Tunnel is frequently necessary to cross the active fault zone due to the constraints of geological conditions and route design. In this study, a three-dimensional finite element model of large-scale tunnel crossing normal fault is created based on the second underwater tunnel project in Jiaozhou Bay, Qingdao. The width of the deformation joint is the primary element that influence the deformation and stress of the tunnel. The findings indicate that when the width of the deformation joint is between 0.1 m and 0.2 m, it may effectively reduce the abrupt change of the staggered platform at the intersection of the tunnel and the fault zone, and there are no overt benefits or drawbacks. The first principal stress distribution pattern in the cross-section of a tunnel follows the sequence of Hance <Invert < Arch foot < Spandrel < Crown.

Keywords: Mining tunnel, Normal fault, Fault dislocation, Anti-fault measures, Joint width

1 INTRODUCTION

The vast territory of China has a complex and diverse geography. Localized tectonic plates are shifting, and numerous active faults may be seen everywhere. China is presently constructing its transportation infrastructure quickly thanks to the traffic power plan idea, and the advancement of line traffic engineering will usher in a new peak hour. The active fault zone will have to be crossed by several mining tunnels[1-2].

A type of geological risk with fault structural features is active fault dislocation. The upper and lower plates move in relation to one another as a result of the fault dislocation, which creates complicated spatial three-dimensional deformation and stress characteristics. The tunnel will encroach on the limit, fracture, experience severe deformation, and potentially collapse as a result of the fault's displacement. Numerous instances have demonstrated that the cross-fault tunnel has resulted in significant damage as a result of fault dislocation[3]. For instance, the Longdongzi tunnel[4, 5] in the Longmenshan fault zone was severely damaged in the 2008 Wenchuan earthquake, with damage including the slope collapse at the right line's exit, rockfall at the left line's entrance section, cracking at the left line portal's end wall, circumferential staggered platform damage, secondary lining collapse at the upper side wall, top arch, and more. As an example, the Shigangba diversion tunnel in the active Chelongpu fault region had a shearing slip in the 1999 ChiChi earthquake with a numerical dislocation of 4 m and a horizontal dislocation of 3 m [6].

The mechanical reaction of cross-fault tunnels to fault dislocation is now being researched both domestically and internationally. Through the use of model tests, Liu et al. [7, 8] investigated the mechanical reaction of the tunnel under various dip angle reverse fault conditions. Through the use of a numerical model using the finite difference technique, Zhao [9] investigated the stress and deformation law of tunnel lining under the influence of reverse fault dislocation and described the failure form of tunnel lining. By developing a comprehensive mechanical model of the buried pipeline-soil, Jin & Li[10] examined the pipeline's buckling stability under the influence of a thrust fault. Karamitros[11] estimates the stress distribution properties of subterranean pipelines

*Corresponding author: qiwang@swjtu.edu.cn

DOI: 10.1201/9781003495505-167

under the influence of fault dislocation through theoretical analysis. When it comes to fortification techniques for navigating an active fault tunnel, it is common practice to increase the lining section, shorten segment length, install shear joints, and other strategies[12]. For the Wushaoling Tunnel spanning the F7 active fault, Liang et al. [13] conducted the extended section design with a reserved displacement of 100 years. In order to strengthen the structural toughness of the tunnel and pass through active faults, Yang [14] suggests applying high toughness cement-based composite (ECC) to the weak spot of the tunnel lining and to a mountain tunnel. Russo[15] uses the Bolu tunnel in Turkey as an example and discusses geometric deformation and load distribution.

As can be observed, the research mentioned above findings provide a valuable point of reference for investigating the mechanical response and failure mechanism of cross-fault tunnels under the influence of fault dislocation. They also establish a framework for the investigation of cross-fault tunnel fortification techniques. However, various areas, different structures, and different types of active faults have extremely diverse impacts on tunnels because of the periodic dislocation of these faults. Thus, the second underwater tunnel in Jiaozhou Bay, Qingdao, is used as an engineering example in this work. The tunnel that crosses the active fault using the mining approach is simulated using the finite element method. A comparison is made between the sensitivity of the tunnel construction to deformation joint width. Technical reserves for engineering construction are provided by studying the tunnel's deformation and stress characteristics.

2 NUMERICAL MODELS AND ASSUMPTIONS

2.1 *Project overview*

Shibei District of Qingdao City and Huangdao District are connected by the second underwater tunnel over Jiaozhou Bay in Qingdao. The entire tunnel is 17.48 km long, of which 14.36 km is the main line tunnel. Drilling and blasting and the shield method are the combined construction schemes used in this tunnel (Figure 1). The entire tunnel is situated in the North China fault block area, where the fault structure is developed, according to the geological survey report of the engineering site and the seismic safety evaluation report of the site. The tunnel in the drilling and blasting section in the sea area primarily passes through the Cangkou fault.

The Cangkou Fault is located on the eastern margin of the Jiaoliao-Taihang Uplift in the North China Craton. The Muping-Jimo Fault Zone's southern region has a significant Late Pleistocene active fault that is distinguished by its normal fault characteristics. The fault dips to the northwest (NW), trends northeast (NE), and generally has a rather straight track. The severe dip angle of the fault is typically between 70° and 88°, with occasional local variations between 60° and 80°. The abrupt displacement in a century is predicted to be 0.49 m, and the typical fault fracture zone width is 50 m. The second underwater tunnel's mining portion will cross the southern part of the Cangkou fault in Jiaozhou Bay in Qingdao at an angle of roughly 80 degrees, which will have a significant impact on the project.

In order to examine the impact of width of deformation joints on the anti-dislocation performance of the tunnel, this research investigates the dynamic response of a mining tunnel with different width of deformation joints under the action of a normal fault dislocation.

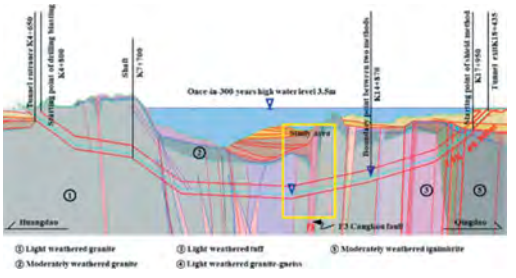

Figure 1. Schematic diagram of tunnel engineering profile.

Table 1. Physical and mechanical parameters of strata.

Geotechnical Terminology	Specific Gravity (kN/m^3)	Elastic modulus (MPa)	Poisson's ratio	Cohesion (kPa)	Internal friction angle (°)
Silt	16.5	6	0.45	10	8
Fine-grained clay	19.2	15	0.35	24	16
Medium weathered granite	25.5	15000	0.3	1000	45
moderately weathered orthogneiss	26	12000	0.3	500	35
fault zone	25	200	0.4	150	23
Fragmented rock	25.5	7000	0.28	700	37

Table 2. Numerical model parameters.

	Length	Width	Height	
Stratigraphic model (m)	360	105	130	
Hoof-shaped tunnel structure (m)	Length	Span	Height	
	360	16.33	13.22	
Fault	Width	Dip Angle	Dislocation	
	50m	75°	49cm	
	Concrete grade	Elastic modulus	Density	Poisson's ratio
Tunnel	C40	32.5 GPa	2500 kg/m^3	0.2

2.2 *Model parameters and boundary conditions*

A three-dimensional finite element calculation model is created in the finite element program ABAQUS[16] in accordance with the particular engineering geology and mining technique tunnel section, as illustrated in Figure 2. The model's overall dimensions are length×width×height=360 m×105 m×130 m, with a tunnel depth of 80 m. The Cangkou fault zone has a width of 50 m, a dip angle of 75 degrees, and a tunnel construction that traverses an active fault. The tunnel and soil layer are in a coulomb friction contact, the normal direction is in a hard contact, and the tangential friction coefficient is 0.8[17-18]. The model's upper surface is considered to be a free surface, the remaining lower portion is subject to normal fixed restrictions, and the lower surface of the upper plate of the model is subject to a vertical displacement of 49 cm in order to replicate the normal fault dislocation. The Mohr-Coulomb constitutive is adopted by the surrounding rock, whereas the isotropic elastic constitutive is adopted by the deformation joints and the tunnel. Table 1 displays the physical and mechanical properties of the formation as per the engineering geological survey report. The main structure of the tunnel is made of C40 concrete, and the tunnel deformation joints are considered to be flexible materials. The elastic modulus is 325 MPa (0.01×E_C40), and the density is 1.12×10^3 kg/m^3. Model parameters are listed in Table 2.

2.3 *Calculated cases*

Two different joint width are merged, as shown in Figure 3. With 0.1 and 0.2 m of width for vertical joint. Of these, the vertical deformation joint is perpendicular to the tunnel axis. The specific cases are shown in Table 3.

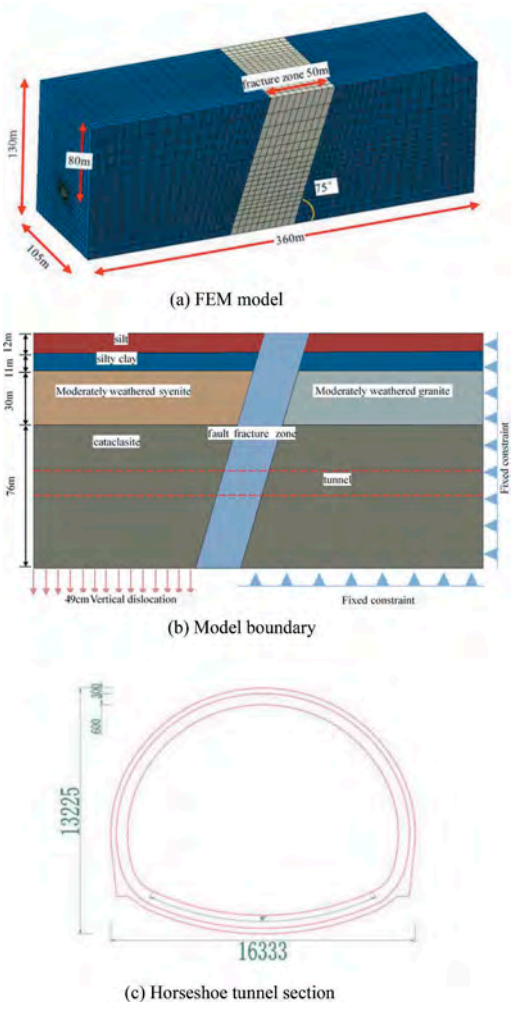

Figure 2. Schematic diagram of calculation model.

3 RESULTS

3.1 *Effect of deformation joint width*

It is discovered that the fault table amount of each section is essentially the same, which is restricted to the space, after the fault table amount of the cross section with the deformation joint width of 0.1 m and 0.2 m is extracted, respectively. As seen in Figure 4, it only provides the incorrect table quantity for the vertical joint. The distribution law is comparable, the peak value of the incorrect tables under the width of the two types of deformation joints is not significantly different, and the rapid

Table 3. Design cases of deformation joint.

Case	Burial depth (m)	Modulation length (m)	Expansion joint form	Joint width (m)
1	80	12	Vertical tunnel axis	0.1
2	80	12	Vertical tunnel axis	0.2

change of the incorrect platform happens at the deformation joint's location. It is important to note that for vertical seams, the amount of fault of two deformed joints surpasses 2 cm when the width of deformable joint is 0.1 m. However, only one deformation joint has more incorrect platforms at the arch waist than 2 cm when the deformation joint's width is 0.2 m. It demonstrates that a wider deformation joint within a suitable range helps to enhance the deformation performance of the tunnel that through the fault.

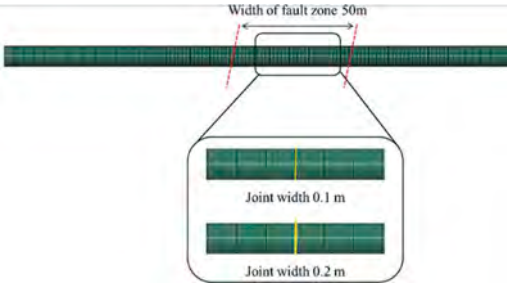

Figure 3. Schematic diagram of calculation cases.

3.2 *Deformation distribution*

The maximum amount of incorrect platform among the five tunnel monitoring locations is determined by comparing the deformation and the amount of incorrect platform for each type of deformation joint, as indicated in Table 4. The extreme value of the incorrect platform at the tunnel's arch waist is often much greater than its values at the other four measuring places, suggesting that the shear failure there is the strongest. Additionally, the quantity of staggered abutment in the tunnel is decreasing from the arch waist to the arch crown and inverted arch, suggesting that the deformation of the staggered abutment is centered at the arch waist and progressively extends to the higher and lower sides.

When comparing the breadth of deformation joints, there is no discernible difference between 0.1 m and 0.2 m, although there are fewer deformation joints under 0.2 m that have displacement of more than 3 cm at the arch waist. It is evident that when it comes to enhancing the deformation performance of the tunnel that crosses the active fault zone, the case of 0.2 m performs better than the case of 0.1 m. Under cases of 0.1 m and 0.2 m, the width of the deformation joint has no discernible influence, and it is not seen that the deformation of the tunnel grows considerably as the width of the deformation joint increases. The displacement of the tunnel abutment at the junction and fault zone is very minor. The dislocation deformation will be somewhat lessened when the deformation joint width is 0.2 m.

Table 4. Extreme value of dislocation of tunnel structure under different joint width (cm).

Location	Case 1	Case 2
Cown	2.085	1.357
Spandrel	2.237	1.918
Wist	2.253	2.178
Arch foot	2.106	1.473
Invert	2.140	1.189

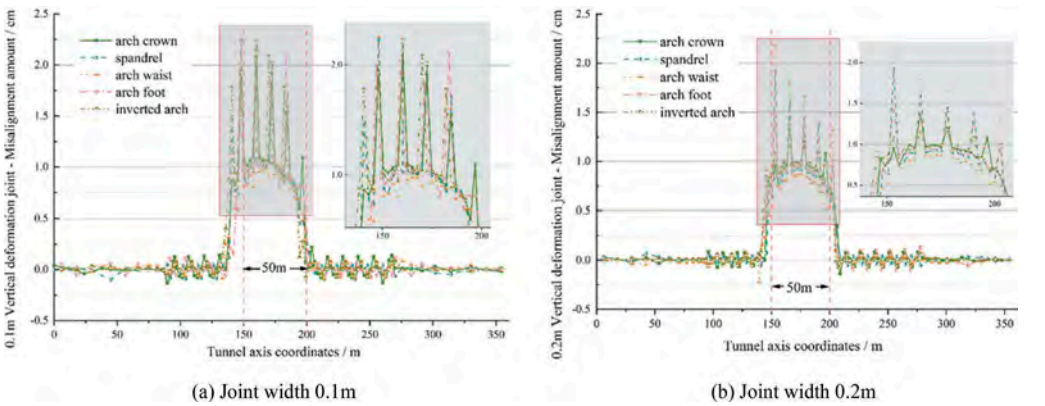

Figure 4. The amount of vertical deformation joints of tunnel with different width of deformation joints.

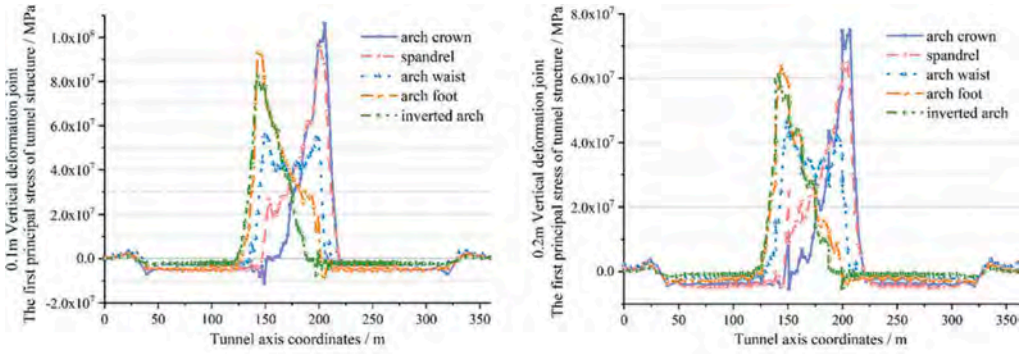

(a) Joint width 0.1m (b) Joint width 0.2m

Figure 5. Stress distribution of tunnels with different deformation joint widths.

3.3 *Stress distribution*

The first principal stress of the cross section of the tunnel structure is extracted as shown in Figure 5. From a numerical perspective, the highest main stress of the tunnel with a 0.1 m deformation joint is 107.0 MPa, whereas the maximum principal stress with a 0.2 m deformation joint is 75.69 MPa, representing a drop of 29.26%. This is due to the breadth of the deformation joint. Tunnel stress dramatically reduces with increasing deformation joint width, and the broader deformation joint may effectively mitigate the effects of active faults on the tunnel.

Regarding the two cases, the law of arch waist < inverted arch < arch foot < arch shoulder < vault applies to the initial primary stress of each segment of the tunnel cross section. The first primary stress at the inverted arch, arch foot, arch shoulder, and vault is shown by the longitudinal distribution as a single peak, whereas the arch waist displays a double peak. The peaks are all situated near the fault plane, suggesting that the fault displacement causes visible stress at the lower wall tunnel's vault and shoulder as well as the upper wall tunnel's inverted arch and arch foot. There is clear stretching of the lining on the upper and lower fault planes at the arch waist.

4 CONCLUSIONS

The following conclusions are made for the peculiar normal fault dislocation form of the Jiaozhou Bay Second Submarine Tunnel Project in this research based on the finite element analysis of the anti-normal fault dislocation and taking into account the impact of width of deformation joints:

(1) The 49-cm displacement of the normal fault clearly caused deformation in the tunnel. Furthermore, the locations of the deformation joints in the fault zone and the intersection of the fault plane with the upper and lower walls are where the majority of the fault platforms are found. As one moves away from the fault line, the misalignment rapidly diminishes and the deformation fluctuation is contained to a radius of about 10 m beyond the fault plane. The vertical seam may deform by approximately 1 cm.

(2) The law of arch waist<inverted arch<arch foot<arch shoulder<vault is the first principal stress distribution of the tunnel cross section, according to research and analysis of the stress characteristics of the tunnel lining. This is because fault dislocation-induced earth pressure acts on various areas of the tunnel.

REFERENCES

[1] Anastasopoulos I & Gazetas G, 2007. Foundation-structure systems over a rupturing normal fault: Part I. Observations after the Kocaeli 1999 earthquake. Bulletin of Earthquake Engineering, 5(3), 253–275.

[2] Wang Q, Geng P, Li P S, et al., 2023. Failure analysis and dislocation-resistant design parameters of mining tunnel under normal faulting. Engineering Failure Analysis, 143, 106902.

[3] Yang X F, Li Y Q, Wu J G, 2022. Analysis on deformation failure and prevention of surrounding rock in fault structural zone of a deep-buried tunnel on an expressway. Journal of Highway and Transportation Research and Development, 39 (06),103-110+118.

[4] Gao B, Wang Z H, Yuan S, et al., 2009. Earthquake damage of highway tunnel in Wenchuan earthquake. Journal of southwest Jiaotong University, 44 (03),336-341+374.

[5] Wang Q, Geng P, Chen J B, He C, 2023. Dynamic discrimination method of seismic damage in tunnel portal based on improved wavelet packet transform coupled with Hilbert-Huang transform. Mechanical Systems and Signal Processing, 188, 110023.

[6] Xin C L, 2015. Aseismic and damping measures research for fault-crossing tunnel structures based on seismic damage mechanism. PhD Thesis. Southwest Jiaotong University, Chengdu, China.

[7] Liu X Z, Wang X L, Lin L L, 2013. Model test study on the influence of 75 ° dip normal fault stick slip dislocation on Highway Tunnel. Journal of Rock Mechanics and Engineering, 32(08),1714–1720.

[8] Liu X Z, Liu J D, Li X F, et al., 2015. Experimental study on anti-dislocation effect of reverse fault articulated tunnel lining. Journal of Rock Mechanics and Engineering, 34 (10), 2083–2090.
[9] Zhao B P, 2018. Study on the impact of inverse fault misalignment on highway tunnels. Highway, 63(11), 329–332.
[10] Jin L, Li H J, 2011. Buckling analysis of buried pipeline under thrust fault. Engineering Mechanics, 28 (12), 98–104.
[11] Karamitros D K, Bouckovalas G D, Kouretzis G P, 2007. Stress analysis of buried steel pipelines at strike-slip fault crossings. Soil Dynamics and Earthquake Engineering, 27(3), 200–211.
[12] Caulfield J, Kieffer S, Tsztoo D F, Cain B, 2005. Seismic design measures for the retrofit of the Claremont. RETC Proceeings Calif, USA.
[13] Liang W H, Li G L., 2004. Scheme design of Wushaoling extra long tunnel. Modern Tunnel Technology, (02), 1–7.
[14] Yang X X, Ren Z H, Wen J C, et al, 2022. Analysis of mechanical response of mountain ridge tunnel lining structure under positive fault misalignment. Highway, 67(04), 378–385.
[15] Russo M, Germani G, Amberg W, 2002. Design and construction of large tunnel through active faults: a recent application. International Conference of Tunnelling & Underground Space Use, 16–8.
[16] Smith M, 2009. ABAQUS/Standard User's Manual, Version 6.9.
[17] Zhao W S, He X Z, Chen W Z, et al, 2012. Seismic response analysis method and engineering application of shield tunnel. Geotechnical Mechanics, 33 (08), 2415–2421.
[18] Parsons T, Stein R S, Simpson R W, et al., 1999. Stress sensitivity of fault seismicity- A comparison between limited-offset oblique and major strike-slip faults. Journal of Geophysical Research Atmospheres, 104202(10), 183–220.

Tunnelling for a Better Life – Yan, Celestino, Thewes & Eberhardt (Eds)
© 2024 The Author(s), ISBN 978-1-032-80042-4
Open Access: www.taylorfrancis.com, CC BY-NC-ND 4.0 license

Analysis of issues in the theory and calculation methods of composite lining for hard rock tunnels

Ning Wang & Xiangjun Yang
China Railway Academy Co., Ltd., Chengdu

ABSTRACT: Currently, in the design of tunnels for highways and railways in China, the use of composite lining or segmental lining for support is more prevalent, with very few instances of employing single-layer lining as a support method. For hard rock tunnels, the surrounding rock itself possesses inherent stability. However, adhering to conventional Chinese design methods necessitates the use of composite lining, leading to significant material waste, low construction efficiency, and slow project progress. Through literature review and theoretical analysis, this paper addresses the current design situation and existing regulations. It provides insights into the methods and analyses employed in the current theoretical framework for composite lining in China, focusing on rock classification methods, surrounding rock pressure, and lining structure calculations. The paper identifies the irrationalities in the existing theory and design methods for hard rock composite lining in China and offers recommendations for improving the design of lining structures in hard rock tunnels in China.

Keywords: Hard Rock, Surrounding Rock Analysis, Lining Design, Problem Analysis

1 INTRODUCTION

Since the establishment of the People's Republic of China in 1949, the country's infrastructure was in dire need of development. The nation embarked on railway construction projects, with railways such as Chengdu-Chongqing, Tianjin-Lanzhou, and Baoji-Chengdu successively commencing construction. With the introduction of advanced foreign concepts, the construction of the 14.295-km Dayaoshan Extra-Long Tunnel, designed and constructed using the New Austrian Tunneling Method (NATM), began smoothly, marking a rapid development in China's railway tunnel construction technology[1]. Through continuous research exploration and the summarization of design and construction experiences, several tunnels such as Nanling Tunnel, Liupanshan Tunnel, and Yuntai Mountain Tunnel were successively completed[2].In 1988, the former Ministry of Railways compiled the Guidelines for the New Austrian Tunneling Method in Railway Tunnels[3], signaling the transition of China's railway tunnel construction from traditional mining methods to the "New Austrian Tunneling Method." Since the beginning of the 21st century, data indicates that by the end of 2021, the total number of operational railway tunnels reached 17,532, with a total length of 21,055 kilometers. Among them, 734 new operational railway tunnels were added, contributing 1,425 kilometers to the total length. Additionally, there are 23,268 road tunnels with a cumulative length of 24,698.9 kilometers, including 1,952 new operational road tunnels spanning 2,699.6 kilometers[4]. China has truly become a tunneling powerhouse.After more than 40 years of rapid development, China's tunnel construction technology has achieved significant technological innovations in theoretical research, special soils, shield tunneling, and other aspects[5].

In the process of rapid development, some issues arise. Through researching the construction of hard rock tunnels both domestically and internationally, it is observed that in China, the use of single-layer lining as a permanent support method is relatively rare, and its widespread application is far less than in foreign countries[6]. Compared to composite lining, single-layer lining has various advantages such as simplified procedures, rapid construction, and economic feasibility. Foreign practices have also demonstrated that single-layer lining can meet durability requirements. However, in the field of hard rock, its extensive use has not been widely explored in China[7]. To investigate this issue, we start by examining the current status of tunnel design in Chinese railways and highways, contrasting it with the design concepts and methods used in hydraulic tunnels. We analyze the shortcomings in the existing analysis and design of hard rock tunnel surrounding rock from the perspective of commonly used standards and methods in engineering design.

Hard rock primarily refers to grade I to III surrounding rocks with uniaxial compressive strength greater than 30 MPa.

DOI: 10.1201/9781003495505-168

2 DEFINITION AND CHARACTERISTICS OF HARD ROCK

The tunnel structure is located within the surrounding rock, and its structural integrity, stability, and the surrounding rock are closely interrelated. Different types of surrounding rock correspond to different forms of damage[8]. Wang Tao[9] believes that accurately assessing the quality of tunnel surrounding rock and providing a rational tunnel design scheme are the foundation for ensuring construction safety. Designers need to conduct in-depth analyses of the deformation and failure patterns of surrounding rock during tunnel construction, and provide timely and accurate scientific evaluations of the stability of tunnel surrounding rock to ensure construction safety and personnel safety[10]. Therefore, when investigating the surrounding rock and design issues of hard rock tunnels, it is necessary to first summarize and analyze the relevant conditions based on domestic rock analysis.

The determination of the hardness of rocks can be done through various methods, including uniaxial saturated compressive strength determination, Young's modulus determination, and point load testing. Different standards have subtle differences in the definition of hard rock, but mainly rely on qualitative and quantitative criteria. Standard for Engineering Classification of Rock Mass (GBT50218-2014)[11], Code for Design of Railway Tunnel (TB 10003-2016)[12], Specifications for Design of Highway Tunnels (JTG 3370.1-2018)[13], Code for Geotechnical Investigations of Urban Rail Transit (GB 50307-2012) [14], and Code for Hydropower Engineering Geological Investigation (GB 50287-2016)[15], each standard classifies hard rock as follows:

For quantitative classification of hard rock, domestic standards universally use saturated uniaxial compressive strength (fr) for determination. The standards generally consider fr > 30MPa as hard rock, and fr ≤ 30MPa as soft rock.Therefore, when conducting the analysis, this criterion serves as the basis for the assessment.

3 ROCK MASS CLASSIFICATION

The foundation of tunnel design in China relies on rock mass classification, where different rock mass grades have a decisive impact on the choice of tunnel support methods and support parameters. Therefore, it is essential to conduct a research analysis of the relevant regulations on rock mass classification in various domestic industry standards.

3.1 *Relevant regulations in standards*

(1) Relevant provisions of theStandard for Engineering Classification of Rock Mass (GBT50218-2014) and Highway Tunnel Design Code(JTG 3370.1-2018) are as follows:

Both standards have similar requirements for rock mass classification, employing both qualitative and quantitative methods. During engineering classification, it is necessary to consider both qualitative and quantitative classifications, mutually validating each other to obtain a more accurate rock mass classification.

The qualitative characteristics of the rock mass's basic quality are determined by two factors: rock hardness and rock integrity. The combination of these factors allows for a qualitative classification of the rock mass's basic quality, as detailed in Table 1.

The quantitative division of rock mass basic quality adopts a comprehensive index method composed of multiple parameters. Two quantitative indicators, the rock saturated uniaxial compressive strength (R_c) and the rock mass integrity index (K_v), are used as parameters to calculate the rock mass basic quality index (BQ). This index serves as the quantitative basis for classification. The basic quality index, formed by and, can be expressed in various mathematical forms, with popular methods including the product-quotient method and the sum-difference method.

The standard employs stepwise regression, stepwise discrimination, and other methods to establish and validate the calculation formula for the basic quality index (BQ), which belongs to the sum-difference model. The calculation model considers and as factors, with BQ as the dependent variable. Through regression comparison, a binary linear regression formula with two specified conditions is selected. During application, coefficients are adjusted based on engineering practicalities. The final result is an existing formula with good rationality, as shown in Equation 1.

$$BQ = 100 + 3R_c + 250K_v \quad (1)$$

When conducting detailed classification of rock mass quality, if there is the presence of groundwater,

Table 1. Rock basic quality qualitative classification.

	Intact	Slightly Intact	Moderately Fractured	Fractured	Extremely Fractured
Hard Rock	I	II	III	IV	V
Moderately Hard Rock	II	III	IV	IV	V
Moderately Soft Rock	III	IV	IV	V	V
Soft Rock	IV	IV	V	V	V
Extremely Soft Rock	V	V	V	V	V

the stability of the rock mass is influenced by structural planes, and there exists a set of controlling factors, and the engineering rock mass exhibits three initial stress states characterized by the strength-to-stress ratio, it is necessary to adjust the rock mass basic quality index (BQ) accordingly, as detailed in Equation 2. The rock mass classification is then determined based on the modified engineering rock mass quality index obtained.

$$[BQ] = BQ - 100(K_1 + K_2 + K_3) \quad (2)$$

In the equation:

[BQ]-the underground engineering rock mass quality index.

K_1-the correction coefficient for the influence of groundwater in underground engineering.

K_2-the correction coefficient for the influence of the main structural orientation in underground engineering.

K_3-the correction coefficient for the influence of the initial stress state.

(2) Relevant provisions of the Code for Design of Railway Tunnel (TB 10003-2016) are as follows:

The Railway Design Code align with Table 1 in the classification of rock mass quality. However, their classification is more detailed, not only categorizing based on the hardness and integrity of the surrounding rock but also relying on qualitative assistance from engineering geological features, structural characteristics, and the intact state after surrounding rock excavation. Additionally, quantitative rock mass classification is performed using the elastic longitudinal wave velocity of the surrounding rock.

(3) Relevant provisions of the Code for Hydropower Engineering Geological Investigation (GB 50287-2016) are as follows:

Three indicators, namely rock strength, rock integrity, and rock structure type, serve as the basis for preliminary classification. The quantitative rock mass classification primarily adopts the Hydropower Classification (HC) method[16]. This method uses the total score of five factors – rock strength (A), rock integrity (B), structural plane condition (C), groundwater (D), and main structural orientation (E) – to control the stability of the surrounding rock, as indicated in Equation 3. The rock mass strength-to-stress ratio (S) is used as the limiting criterion, and the determination table is provided in Table 2.

$$T = A + B + C + D + E \quad (3)$$

In addition to the classification specified in this code, the Geological Investigation Code for Hydropower Engineering stipulates that the classification of rock mass in large-span underground chambers should also undergo comprehensive evaluation based on other relevant national standards. Furthermore, international commonly used rock mass classifications, such as the Q system classification, can be used for comparison.

Table 2. Basic quality classification table for rock mass in hydraulic engineering.

Rock Mass Category	Total Evaluation Score (T)	Rock Mass Strength-to-Stress Ratio (S)
I	T>85	>4
II	85≥T>65	>4
III	65≥T>45	>2
IV	45≥T>25	>2
V	T≤25	-

3.2 *Summary and problem analysis*

(1) The engineering rock mass classification standard belongs to the second-level general standard of national standards[11]. It is applicable to rock engineering in various departments and industries, covering different types of rock engineering such as mines, tunnels, waterworks, railways, and highway tunnels, as well as various underground chamber projects like underground factories, mining areas, and underground warehouses. Code for Design of Railway Tunnel, Specifications for Design of Highway Tunnels, Code for Geotechnical Investigations of Urban Rail Transit, and Code for Hydropower Engineering Geological Investigation serve as technical standards for their respective industries.

The engineering rock mass classification standard and the rock mass classification provisions for hard rock in railway tunnels and highway tunnels are essentially consistent. They mainly use the BQ method for rock mass classification, supplemented by qualitative judgments for final determination.

In contrast, the hydropower industry, as outlined in the mentioned code, uses the HC method for classification, with additional correction based on the rock mass strength-to-stress ratio. It is noteworthy that, for the first time, the code suggests that the rock mass in large-span underground chambers in hydropower engineering can be compared using internationally recognized rock mass classifications such as the Q system classification.

(2) The BQ method, HC method, and Q system method have classification indicators as shown in Table 3. All three rock mass classification methods incorporate rock strength, rock integrity, groundwater, and initial stress state indicators into the classification factors. Among them, the Q system method and HC method consider structural plane condition indicators, while the BQ method considers the relationship between structural planes and the tunnel axis.

The BQ method for rock mass classification employs two main indicators as control factors, supplemented by other factors for result correction. Similar to the Q-system, the BQ method relies on the sum and difference method for calculation. The main indicators in the BQ method

Table 3. Classification parameter indicators for rock mass classification methods.

Classification Parameter Indicators		Q System Method	HC Method	BQ Method
The primary indicators	Rock Strength	SRF	A, Rb	Rc
	Rock Integrity	RQD, Jn	B, Kv	Kv, Jv
	Groundwater	Jw	D	K_1
	Initial Stress State	SRF	S	K_3
	Structural Plane Condition	Jr, Ja	C/E	-
	Relationship Between Structural Plane and Tunnel Axis	-	-	K_2

are chosen for their convenience and efficiency, but the wide range of values for various correction parameters places a high demand on the experiential knowledge of geological and design personnel[17].

In the BQ method, the compressive strength of the rock mass (R_c) holds a disproportionately significant weight in the BQ value. This overemphasis on compressive strength limits the application of the BQ method in hard rock tunnels under high stress conditions. According to Wang Guangde's research[16], the BQ method demonstrates the lowest correlation with actual rock mass categories in hard rock tunnels compared to the RMR, Q-system, and the hydropower sector's HC classification method. Chen Lixiang[18]conducted regression analysis on the correlation between BQ method rock mass classification and Q-system rock mass classification based on actual engineering geological conditions. The obtained relationship curve has a correlation coefficient of 0.788, indicating a relatively weak correlation between BQ values and Q values.

The HC method for rock mass classification determines classifications based on five main factors. Among these factors, rock strength, rock mass integrity, and structural plane conditions have a significant impact on the results, while the influence of groundwater and structural plane orientation is relatively minor[19]. Wang Tao et al.[20], through literature research, found a high degree of consistency between the HC method and the Q system in assessing rock mass quality. They conducted regression analysis on a large amount of data from the literature, establishing a relationship equation between HC values and Q values with a correlation coefficient of 0.866. This indicates a significant correlation between the HC method and the Q system in evaluating rock mass quality.

The Q-system rock mass classification employs six basic parameters for classification determination. It comprehensively considers geological factors, and its calculation formula is clear. It utilizes a product calculation method and is applicable under various stress conditions. It is mostly suitable for formations of medium to hard rock and is less suitable for soft or weak formations.

(3) Based on the above, the BQ classification method widely used in most domestic industries demonstrates better applicability in the field of soft rock, while its application in the field of hard rock is less satisfactory. It is recommended that, in the future, for the surrounding rock analysis of hard rock caverns, the HC method used in hydraulic tunnels or the adoption of the Q classification method from foreign sources be considered for rock mass classification.

4 SURROUNDING ROCK PRESSURE

The determination of surrounding rock pressure is a prerequisite for tunnel design and a fundamental research topic in the field of tunnel engineering[21]. The rational determination of tunnel surrounding rock pressure not only ensures the safety of the design but also influences its economic feasibility. In the design specifications for railway and highway tunnels in China, provisions are made for surrounding rock pressure. The specifications for the surrounding rock pressure of rock caverns in urban rail projects are implemented according to the standards of railway tunnel design specifications. This article only presents normative clauses related to the surrounding rock pressure of hard rock caverns, limited by space constraints, and does not list all related regulations.

4.1 *Relevant specification provisions*

(1) The Code for Design of Railway Tunnel (TB10003-2016) adopts the calculation formula for the surrounding rock pressure of deep-buried tunnels as shown in Equation 4:

$$q = 0.45 \times 2^{S-1} \times \gamma w \tag{4}$$

In the equation:
q-the vertically distributed pressure;
S-the rock mass classification;
R-the rock mass density;
W-the width influence coefficient, $w = 1 + i(B - 5)$;
B-the tunnel width;
i-The rate of change of surrounding rock pressure for each additional 1 meter:when B < 5m, i is set to 0.2; when B > 5 m, iis set to 0.1.

(2) In the Specifications for Design of Highway Tunnels (JTG3370.1-2018), the formula for calculating surrounding rock pressure is stipulated to be the same as Equation 4, but with slight adjustments to the width correction coefficient i.

(3) In the Guidelines for Design of Highway Tunnel (JTGT D70-2010), the calculation of surrounding rock pressure is specified as follows:

➢ The loose rock pressure is the sum of the pressure acting on all tunnel support structures. When calculating internal forces for initial support or secondary lining, an appropriate method should be employed for load distribution to determine the corresponding calculated load for the support layer.

➢ For shallow-buried tunnels, only the loose rock pressure should be considered. For deep-buried tunnels, not only should the loose rock pressure be taken into account, but also the deformation pressure of the surrounding rock. For continuous arch tunnels and tunnels with small clearances, the deformation pressure may be omitted.

➢ The vertical surrounding rock pressure in deep-buried tunnels can be calculated using the Prandtl formula or a method similar to Equation 4. The horizontal surrounding rock pressure aligns with the specifications in both railway tunnel design codes and highway tunnel design codes.

(4) In the Code for Hydropower Engineering Geological Investigation (NB_T 10391-2020), the calculation of surrounding rock pressure and in-situ stress should comply with the relevant provisions of the current industry standard Load Standards for Hydraulic Structures (GB/T 51394-2020). The relevant provisions of Load Standards for Hydraulic Structures are as follows:

➢ For surrounding rock with good self-stabilizing conditions and stable deformations after excavation, the surrounding rock pressure may be omitted in the design of permanent support structures.

➢ When measures such as anchor spraying support or steel frame support are taken during the excavation process, resulting in the basic stability of the surrounding rock, the design should consider minimal or no impact of surrounding rock pressure on permanent support structures.

➢ For blocky, medium-thick to thick-layered structures of surrounding rock, the standard value of surrounding rock pressure can be determined based on the gravitational effects of unstable rock blocks within the surrounding rock.

➢ For thin-layered and fragmented, loose structures of surrounding rock, the loosened portion of uniformly distributed surrounding rock pressure is recognized as 0.2 to 0.3 times the excavation width of the tunnel.

➢ For shallow-buried tunnels where a stable arch cannot be formed, the standard value of surrounding rock pressure should be calculated based on the gravitational effects of the overlying rock mass on the tunnel arch, with adjustments made according to the construction measures adopted.

4.2 *Summary and problem analysis*

Comparing the various specifications regarding the regulations on surrounding rock pressure leads to the following conclusions:

(1) The methods used for calculating surrounding rock pressure differ among the specifications. The methods for calculating surrounding rock pressure in highway and railway tunnel design specifications are generally consistent. However, the highway tunnel design guidelines sometimes apply the Prandtl theory to calculate surrounding rock pressure. This can result in significant differences in the calculated surrounding rock pressure compared to that obtained from highway tunnel design specifications, significantly impacting structural design.

(2) The existing formulas for calculating surrounding rock pressure in railway and highway tunnel design specifications are based on statistical data from 127 single-track tunnels with 417 construction collapse data, including the Chengkun and Guikun railways. These formulas assume that the self-weight of the collapsed rock mass acts entirely on the lining structure, using the self-weight of the collapsed rock and soil as the basis for surrounding rock pressure[22]. For rock tunnels, there is a critical block effect, and the instability of a critical block can trigger a chain reaction, leading to collapse. However, if the critical block is stabilized through methods such as shotcrete or anchor reinforcement, the surrounding rock pressure on the lining structure is much less than the self-weight of the collapsed rock mass statistically obtained. This results in calculated surrounding rock pressure values for hard rock tunnels being much higher than the actual values, affecting the economic feasibility of lining structure design.

(3) The design specifications for hydraulic tunnels differ significantly from those for railway, highway, and subway tunnels. Hydraulic tunnels do not use collapse statistical formulas for calculating surrounding rock pressure in hard rock caverns. Instead, they employ different methods based on the specific nature of the surrounding rock. In completely stable caverns, surrounding rock pressure may be disregarded. For locally unstable caverns, only the pressure from locally unstable blocks is considered. For thin-layered and fragmented, loose structures of surrounding rock, the surrounding rock pressure is approximately 0.2 to 0.3 times the width of the tunnel excavation. Under conventional spans, the calculated surrounding rock pressure is less than that specified in railway, highway, and urban rail regulations.

(4) Zhu Hehua[23] simulated the damage to surrounding rock at different depths and found that with increasing depth, the damaged area of the surrounding rock gradually expanded, leading to an increase in collapse load. The statistical

formulas for deep-buried rock pressure in railway and highway tunnels ignore the influence of depth, significantly impacting the calculated results of surrounding rock pressure.

5 LINING STRUCTURE DESIGN

5.1 *Relevant regulations of specifications*

(1) The relevant provisions of the Code for Design of Railway Tunnel (TB10003-2016) are as follows:

➢ For the initial support of shotcrete lining and composite lining, design parameters can be determined by the engineering analogy method. During construction, corrections should be made through monitoring and measurement. For tunnels with complex geology, large spans, multiple lines, and special requirements, in addition to using the engineering analogy method, numerical methods or approximate methods should be combined for analysis and determination.

➢ When calculating composite lining, the initial support should be calculated based on the main load-bearing structure. The secondary lining in Class I to III surrounding rock can be considered as a safety reserve, while in Class IV to VI surrounding rock and specific conditions, it is advisable to design according to the load-bearing structure.

➢ Composite lining is recommended for tunnels, and load-structure models should be used for lining calculations. When using the load-structure method to calculate the internal forces and deformations of tunnel lining, the constraining effect of surrounding rock on lining deformation, such as elastic reaction force, should be considered. The magnitude and distribution of elastic reaction force can be determined by using local deformation theory based on factors such as lining structure type, backfill condition, and the deformation characteristics of surrounding rock.

➢ The design parameters for initial support and secondary lining should be determined by engineering analogy and theoretical analysis based on tunnel rock classification, rock structure characteristics, and ground stress conditions.

➢ The lining of tunnel sections in dark tunnels and open-cut sections should be checked for section strength at the damage stage. Different safety factors should be used in the calculations for different load combinations that the structure is subjected to.

(2) The relevant provisions of the Specifications for Design of Highway Tunnels (JTG 3370.1-2018) are as follows:

➢ Highway tunnels should be equipped with lining, and the selection of shotcrete lining, integral lining, or composite lining should be based on tunnel rock grade, construction conditions, and usage requirements. Composite lining is recommended for expressways, first-level highways, and second-level highways.

➢ The type of lining structure and support parameters should be determined through comprehensive analysis using engineering analogy and structural calculations based on usage requirements, rock grade, engineering geology and hydrogeological conditions, tunnel burial depth, structural load characteristics, and in consideration of surrounding engineering environment, support methods, and construction methods.

➢ For the design of composite lining, engineering analogy can be used, and theoretical analysis may be applied if necessary.

➢ The initial support of composite lining should primarily be designed using the engineering analogy method. When necessary, support parameters can be determined by the stratum-structure method, and separate verifications should be conducted for usage and construction stages.

➢ The secondary lining of composite lining should be primarily calculated using the load-structure method, taking into account the influence of factors such as elastic resistance.

➢ When both the secondary lining and initial support of composite lining jointly bear the surrounding rock pressure and other external loads, the stratum-structure method can be used to calculate internal forces and deformations. Verification can also be carried out using the load-structure method.

(3) The relevant provisions of the Code for Hydraulic Tunnel Design (NB_T 10391-2020) are as follows:

➢ For Class I and Class II surrounding rock, tunnels with excavation diameters (tunnel width) less than 5 m may not require support. For diameters between 5 m and 10 m, it is advisable to use shotcrete support, and for tunnels larger than 10 m, anchor spraying support is recommended. In the presence of locally unstable blocks, random anchor rods or bundled anchor rods should be used for reinforcement.

➢ Class III surrounding rock is suitable for mesh anchor spraying support; Class IV surrounding rock is suitable for reinforced concrete lining. Depending on the tunnel scale and geological conditions, combined support methods such as anchor spraying, mesh support, or steel support can also be used after analysis. Class V surrounding rock should undergo reinforced concrete or other permanent lining.

➢ The design of unsupported and anchor spraying support should be determined using the engineering analogy method. For high-pressure or important projects with concrete-lined tunnels, finite element analysis of seepage and load-carrying structures is recommended. The thickness and reinforcement of the lining can be comprehensively determined based on calculation results, engineering analogy, and structural requirements.

➢ The structure of hydraulic tunnels should be designed based on persistent conditions, transient conditions, and accidental conditions.

5.2 *Summary and problem analysis*

Comparing the relevant provisions of different specifications regarding lining structure design, the following conclusions can be drawn:

(1) Railway, highway tunnel design codes, and hydraulic tunnel design codes generally use the engineering analogy method for initial support design, placing a significant emphasis on the experience of the design personnel.
(2) Both railway and highway tunnel design codes propose that the secondary lining can be calculated using the load-structure method for internal forces and deformations. However, they do not explicitly specify the proportion of surrounding rock pressure shared by the secondary lining. Additionally, the codes do not clearly define the proportion of reserves when the secondary lining serves as a safety reserve. In practical design, due to the challenging assurance of the construction quality of initial support, often the entire surrounding rock load is considered as a safety reserve.
(3) The construction quality and durability of shotcrete are challenging to ensure. In the selection of lining structure forms, both railway and highway tunnel design codes generally recommend using composite lining. The railway tunnel code specifies that mining method tunnels should adopt composite lining support structures, and the highway tunnel design code clearly recommends composite lining for specific grades of highways.
(4) The hydraulic tunnel code explicitly specifies the support forms for different rock classes. For Class I and II rock, anchor spraying support is recommended; Class III rock is suitable for mesh anchor spraying support, and Class IV and V rock are suggested for reinforced concrete lining.
(5) In railway and highway tunnel codes, the commonly used load-structure method tends to separate the analysis of initial support and secondary lining, deviating from the actual situation.
(6) The hydraulic tunnel design code recommends using finite element analysis (stratum-structure method) for lining structure analysis, which better considers the overall coordination among surrounding rock, initial support, and secondary lining.

6 CONCLUSION

This paper, starting from the current state of railway and highway tunnel design in China, compares the design concepts and methods of hydraulic tunnels. It analyzes the shortcomings in the classification of hard rock tunnel surrounding rock, surrounding rock pressure, and lining design from the perspective of commonly used standards and methods in engineering design. The following conclusions are drawn:

(1) Surrounding Rock Classification: Railway and highway tunnels mainly use a combination of qualitative and quantitative methods for surrounding rock classification. The BQ method is employed for quantitative analysis, relying on two main indicators as control factors and supplemented by other factors for result correction. The BQ method is convenient and fast, but its application in hard rock tunnels with high ground stress is greatly restricted due to the excessive weight given to rock compressive strength () in the BQ values. The BQ method shows the lowest agreement rate with actual surrounding rock categories in hard rock tunnels. It is recommended to make relevant corrections to the BQ method in the analysis of hard rock tunnels, improving its applicability to hard rock caverns.
(2) Surrounding Rock Pressure: Different specifications use varying methods for calculating surrounding rock pressure, leading to significant differences in the results. For hard rock tunnels, their self-supporting capability is strong, and according to related studies, surrounding rock pressure is related to tunnel depth. The empirical formulas for surrounding rock pressure used in railway and highway tunnel construction statistics do not consider depth factors and are overly conservative compared to actual situations. It is suggested to abandon existing empirical formulas for hard rock tunnels, analyze surrounding rock pressure based on rock grade and self-supporting capability, and pay attention to the treatment of locally unstable blocks.
(3) Lining Structure Design: The railway and highway tunnel design codes do not prescribe suitable lining support forms based on rock type, often recommending composite lining. In structural calculations, the load-structure model is employed without considering the coordination of surrounding rock, initial support, and secondary lining as a whole, leading to differences from actual conditions. During load distribution, the specifications do not explicitly specify the magnitude of loads, resulting in designs often considering the entire surrounding rock pressure. It is suggested that for hard rock tunnels, appropriate support forms should be adopted, and structural calculations should consider the coordinated forces of surrounding rock and lining structures, emphasizing the stabilizing effect of initial support on surrounding rock.
(4) Hydraulic tunnels have large tunnel dimensions and significant variations, often located in well-rocked chambers with strict water treatment requirements. Their design concepts

and methods differ significantly from railway and highway tunnel design specifications. However, hydraulic tunnels have a deep understanding of hard rock properties, and in the classification of surrounding rock, surrounding rock pressure, and lining structure design, they handle hard rock economically and ensure safety through industry validation. It is recommended that in the railway and highway tunnel design process, relevant design concepts and methods from hydraulic tunnels can be selectively absorbed and borrowed, balancing safety and economy in hard rock tunnel design.

The use of shotcrete as a permanent structure in the European region has a long history. Currently, many engineering cases in China also use shotcrete as a permanent lining structure for hard rock tunnels. With the development of shotcrete technology, factors such as shotcrete quality and durability that impact the development of single-layer lining structures will be overcome. Hard rock tunnels are expected to experience comprehensive development in theory, design, construction, materials, etc., ushering in the flourishing development of single-layer lining structures for hard rock tunnels.

REFERENCES

[1] Tian Siming, Wang Wei, Yang Changyu, et al. 40 Years of Development and Prospects of China's Railway Tunnels [J]. Tunnel Construction (Chinese-English), 2021, 41(11): 1903.

[2] Liu Hui, et al. Technical History of Tunnels and Underground Engineering in China [M]. Beijing: Beijing Jiaotong University Press, 2021.

[3] Wang Xiaoliang, et al. Guidelines for the New Austrian Method in Railway Tunnels [M]. Beijing: China Railway Publishing House, 1988.

[4] China Industrial Research Network. In-Depth Research Report on the Current Situation and Future Investment in China's Tunnel Construction Industry (2023-2030) [Z], 2023.

[5] Zhao Yong, et al. Theory and Methods of Tunnel Design [M]. Beijing: People's Communications Press Co., Ltd., 2019.

[6] Chen Bing. Design and Engineering Reliability Research of Single-Layer Lining for Tunnels [D]. Southwest Jiaotong University, 2008.

[7] Chen Libao, Gong Yanfeng, Qiu Wenge, et al. Design of Some Key Issues in Single-Layer Lining [J]. Modern Tunnel Technology, 2009, 46(03): 38–42.

[8] Liu Shaofeng. Calculation Method of Safety Coefficient and Failure Probability for Initial Lining of Rock Tunnels [D]. Hunan University, 2017.

[9] Wang Tao. Research and Engineering Application of Subgrade Classification Method for Weak Surrounding Rock in Hydraulic Tunnels [D]. Kunming University of Science and Technology, 2023.

[10] Xi Boqi. Research on Deformation of Surrounding Rock and Stability of Support Structure in Soft Rock Tunnels [D]. Lanzhou Jiaotong University, 2023.

[11] GB/T 50218-2014, Standard for Engineering Rock Mass Classification [S]. Beijing: China Planning Press, 2014.

[12] TB 10003-2016, Code for Design of Railway Tunnels [S]. Beijing: China Railway Publishing House, 2016.

[13] JTG 3370.1-2018, Code for Design of Highway Tunnels [S]. Beijing: People's Communications Press Co., Ltd., 2018.

[14] GB 50307-2012, Code for Geotechnical Investigation of Urban Rail Transit Engineering [S]. Beijing: China Planning Press, 2012.

[15] GB 50287-2016, Code for Geological Investigation of Hydropower Engineering [S]. Beijing: China Planning Press, 2016.

[16] Wang Guangde. Research on Rock Mass Classification under Complex Conditions [D]. Chengdu: College of Environmental and Civil Engineering, Chengdu University of Technology, 2006.

[17] Yang Xianquan. Comparison and Engineering Practice of National Standard BQ and Norwegian Q Values for Rock Tunnel Classification [A] Proceedings of the 2020 National Civil Engineering Construction Technology Exchange Conference (Volume I) [C]. Construction Technology Magazine, Construction Technology Editorial Department, 2020: 5.

[18] Chen Lixiang, Chen Shougen, Tu Peng, He Tao. Study on the Relationship between Q Value Method, RMR Method, and BQ Method in Rock Mass Classification of Underground Caverns [J]. Subgrade Engineering, 2017, (06): 107–112.

[19] Tang Zhiqiang, Zhang Ruichao, Wang Lei, et al. Application Research of Modified Hydroelectric HC Method in Surrounding Rock Classification of Underground Plant Chambers [J]. Geological Disaster and Environmental Protection, 2022, 33(02): 86–91.

[20] Wang Tao, Wu Shunchuan, Pu Shijiang, Kui Gai, Sun Junlong, Wang Rui, Ren Zijian. Study on Correlation and Support Comparison of Rock Engineering Geological Classification and Q Classification in Hydraulic Engineering [J]. Journal of Kunming University of Science and Technology (Natural Science Edition), 2023, 48(02):64-72+86.

[21] Sun Jun, Hou Xueyuan. Underground Structure [M]. Beijing: Science Press, 1987.

[22] Xiao Mingqing. Safety Coefficient Method for Overall Lining Structure Design of Tunnels [M]. Beijing: People's Communications Press Co., Ltd., 2020.

[23] Zhu Hehua, Huang Feng, Xu Qianwei. Progressive Failure Test and Numerical Simulation of Surrounding Rock in Deep-buried Soft and Fragmented Tunnel [J]. Journal of Rock Mechanics and Engineering, 2010, 29(06): 1113–1122.

Tunnelling for a Better Life – Yan, Celestino, Thewes & Eberhardt (Eds)
© 2024 The Author(s), ISBN 978-1-032-80042-4
Open Access: www.taylorfrancis.com, CC BY-NC-ND 4.0 license

Analysis of mechanical behavior and engineering suggestions for double-arch tunnel without middle drift

Chenyang Wang
College of Earth Science, Chengdu University of Technology, Chengdu, China

Dan Zhang
Sichuan Highway and Bridge Construction Group Co Ltd, Chengdu, China

Yusheng Li
College of Earth Science, Chengdu University of Technology, Chengdu, China

ABSTRACT: The construction method of double-arch tunnel without middle drift has complex interaction between surrounding rock and supporting lining, which needs to be explored. Based on the engineering background of the Xisujiao No.2 Tunnel of the Yijin Expressway, a three-dimensional numerical simulation method was used to establish a finite element model of the unexcavated middle tunnel connected arch tunnel. The excavation and support processes of the tunnel were simulated, and the mechanical responses and displacement change laws of the surrounding rock, support structures, etc. were obtained at various construction stages. Optimization analysis was also conducted. The results show that the excavation and support of the later tunnel will increase the deformation and stress of the earlier tunnel. As the excavation progresses, there is a significant stress concentration phenomenon in the supporting structure, and tunnel partition wall is the part that bears the largest force. The stress on the tunnel secondary lining structure in the first tunnel is significantly uneven, In order to address these issues, appropriate measures need to be taken.

Keywords: Arch tunnel, Numerical simulation, displacement, stress

1 INTRODUCTION

Traditional methods such as central pilot tunneling or three-guide tunneling in the construction process of continuous arch tunnels present issues such as complex construction procedures, long construction period, and high costs. Moreover, they can lead to significant disturbance to surrounding rocks and poor waterproofing effect, severely impacting the construction efficiency and quality of continuous arch tunnels. Therefore, the search for an efficient, fast, and cost-effective construction method has become an important research direction in the field of tunnel construction. In this regard, the construction of continuous arch tunnels without a central pilot tunnel has been studied by scholars. It utilizes a structural system composed of continuous arch frames and prefabricated segments, enabling simultaneous excavation and lining of the tunnel, which saves the excavation and support of the central pilot tunnel, thereby reducing construction costs and time.

Existing studies on double-arch tunnels have mainly focused on the mechanical behavior analysis of central pilot tunnel excavation. Wang (2020) developed a mechanical testing system for large-section combined arches in continuous arch tunnels and conducted comparative experiments on restrained concrete arches and traditional I-shaped steel arches. They proposed a novel technique for restrained concrete arch support that effectively controls the deformation of large-section tunnel surrounding rock. Bo Min (2020) employed a combined approach of numerical simulation and model testing to analyze the influence of different cavity sizes on the crack characteristics, deformation response, and stress state of tunnel linings, revealing the mechanism of lining cracking caused by cavities. Cheng et al. (2023) combined distributed fiber optic monitoring, inversion analysis methods, and finite element simulation capable of reflecting concrete cracking behavior to obtain and analyze various information on deformation, internal forces, and cracking of linings during the construction process of continuous arch tunnels.

As a result, double-arch tunnel without middle drift has fundamentally different force forms and construction procedures compared to the middle drift tunnel construction method. Therefore, it is not

DOI: 10.1201/9781003495505-169

appropriate to simply apply the experience from middle drift construction to the construction of double-arch tunnels without it. In terms of on-site monitoring, Zeng et al.(2019) examined the example of the Bailongpo Tunnel on the Wuyi Expressway in Yunnan Province and analyzed the technical difficulties encountered in the construction process of continuous arch tunnels without a central pilot tunnel, such as ensuring the stability of the middle partition wall and protecting the preceding tunnel structure. Li et al. (2022) analyzed the mechanical behavior of tunnels under different excavation methods using finite element numerical simulation and found that the method of continuous arch tunnel construction without a central pilot tunnel has strong feasibility and applicability in shallow and weak strata. Regarding theoretical calculations, Jiang et al. (2023) investigated the impact of existing support structures in the preceding tunnel and the construction of the subsequent tunnel on loosened loads, proposed a calculation formula based on the Pusch theory, and conducted comparative analysis in conjunction with on-site monitoring data from the Manla Tunnel. Although these studies provide some guidance for engineering practices of continuous arch tunnels without a central pilot tunnel, further research is still required on the mechanical behavior analysis and construction process improvement of such tunnels.

In the construction method of continuous arch tunnels without a central pilot tunnel, the excavation of the intervening rock pillar will inevitably affect the distribution of secondary stress. The unexcavated subsequent tunnel plays a crucial supportive role for the adjacent side and surrounding rock around the preceding tunnel. Compared to segmented tunnels, tunnels with smaller clearances, or central pilot tunnel advanced construction, the distribution area, spatial pattern, and variation characteristics of the loose ground pressure zone in continuous arch tunnels without a central pilot tunnel are significantly different. Hence, it is necessary to conduct numerical simulations to determine the deformation of surrounding rocks and the force parameters of the support system. By thoroughly exploring the characteristics and mechanical behavior of continuous arch tunnels without a central pilot tunnel, a better understanding of their engineering performance can be achieved, enabling the optimization of construction plans and ensuring the safety and reliability of tunnel engineering. This study aims to provide technical support and reference for tunnel engineering construction and holds significant engineering application value.

2 ENGINEERING GEOLOGICAL CONDITIONS

The West Su Jiao No. 2 Tunnel is generally oriented in a north-south direction. The designed entrance and exit mileposts for the left lane are ZK80+488 to ZK82+311.5, with a tunnel length of approximately 1823.5m and a maximum depth of 300m. For the right lane, the designed entrance and exit mileposts are K80+500 to K82+322, with a tunnel length of approximately 1822m and a maximum depth of 320m.As shown in Figure 1, it mainly traverses the Lower Cambrian strata such as the Canglangpu Formation and the Longwang Temple Formation. The lithology of the tunnel surrounding rocks mainly includes dolomitic limestone, fine sandstone, siltstone, and argillaceous siltstone. The rock types are complex, with significant variations in hardness, uneven layer thickness, and poor interlayer bonding. The integrity of the rock mass is fragmented, and local intense joint zones are developed due to significant structural influences. The eastern side of the tunnel exit is adjacent to the Yewladda River. The shallow surface of the slope is mainly covered with boulders and gravel, with a few steep cliffs and rock exposures at steep slopes. The surface vegetation mostly consists of weeds and low shrubs.

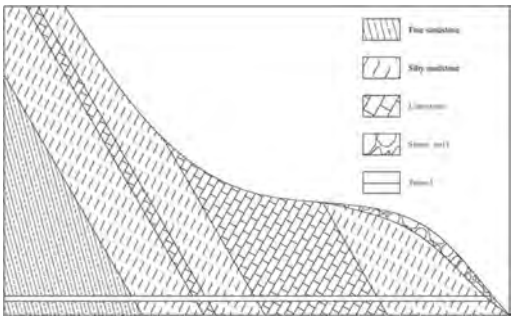

Figure 1. Tunnel geological conditions.

The main tunnel body falls within Grade Ⅳ, with well-developed joint structures in the fragmented rock mass, including thick-layered structures and intercalated fractured structures. The stability of the surrounding rocks is poor, and phenomena such as collapse and falling blocks are prone to occur in the crown of the tunnel. The stability of the sidewall rock mass is also poor, with a potential for collapse. Grade Ⅴ surrounding rocks are relatively low in proportion and are mainly present at the tunnel entrance and exit sections, as well as in the Lower Cambrian Longwang Temple Formation, where gypsum layers exist. The integrity of the rock mass is fragmented to fractured, and the stability of the surrounding rocks is poor. Significant deformation occurs in localized soft rock and fractured zones after excavation and requires enhanced support. The crown is susceptible to collapse and falling blocks, and the stability of the sidewall rock mass is poor.

3 NUMERICAL SIMULATION

3.1 *Assumption conditions*

The traditional method of constructing middle drift tunnel has achieved good practical results, with

certain economic benefits. It has advantages such as strong adaptability and mature technology. However, it also has prominent issues such as complex procedures, large temporary support requirements, excessive material waste, and significant disturbance to the surrounding rock.

The method of double-arch tunnel without middle drift has advantages over the traditional method in terms of simpler procedures, shorter construction period, lower cost, and less disturbance to the surrounding rock. It is suitable for the construction of large-span continuous arch tunnels and has been increasingly favored by scholars and companies in recent years. Specifically, this method eliminates the excavation of a central pilot tunnel and adopts controlled excavation of the leading tunnel together with the downward stepping of the intermediate partition wall. Advanced support and systematic anchoring are used in the deformed pressure zone and loosened pressure zone above the intermediate partition wall. Then, a prefabricated steel arch or lattice arch is placed in the empty position of the intermediate partition wall to form a closed loop. After completing the secondary lining support of the leading tunnel, the excavation of the trailing tunnel is carried out.

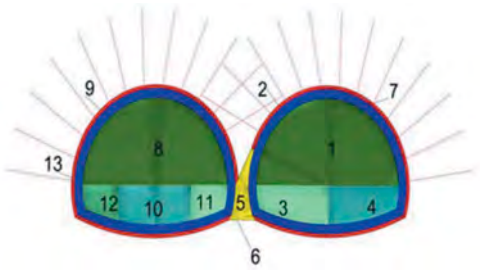

Figure 2. Construction sequence diagram.

The simulated continuous arch tunnel in this study adopts the construction method without a central pilot tunnel. The right-side tunnel (leading tunnel) is excavated using a benching method. After completing the upper bench excavation, the lower bench is excavated in two stages, with the part near the central partition wall excavated first, and the remaining part excavated last. While the left tunnel (trailing tunnel) is excavated in multiple controlled blasts. In this simulation, the thickness of the partition wall is 600mm.The construction sequence is illustrated in Figure 2, where the numbers in the figure correspond to the construction steps described in Table 1.

3.2 *Computation model*

The simulation of working conditions should be kept as consistent as possible with the actual situation. However, due to the complexity of the actual construction process, it is susceptible to various influencing factors. Therefore, appropriate simplifications

Table 1. Construction sequence.

Right line		Left line	
number	process	number	process
1	Excavation of upper bench	8	Excavation of upper bench
2	Primary support	9	Primary support
3	Excavate the left side of the lower bench	10	Excavate the middle part of the lower bench
4	Excavate the right side of the lower bench	11	Excavate the right side of the lower bench
5	Excavate the middle partition wall	12	Excavate the left side of the lower bench
6	Supporting the middle partition wall	13	Secondary lining
7	Secondary lining		

can be made during the simulation process to reduce computational complexity while emphasizing key aspects of the research problem. The model's upper surface is a free boundary, and normal velocity constraints are applied to all other surfaces except the upper one. The tunnel surrounding rock employs a Mohr-Coulomb constitutive model, while initial support, intermediate partition walls, and secondary lining all utilize elastic constitutive models. Solid elements are used to simulate the rock, initial shotcrete, secondary lining, and intermediate partition walls. Cable elements are employed for anchor rods, and shell elements with equivalent stiffness transformation are used to simulate steel frames and longitudinal connecting reinforcement. The physical parameters of relevant materials are listed in Table 2.

Table 2. Material parameters.

Material	Density	Poisson	Young	cohesion	Friction
Rock	2.64	0.40	1.2	0.15	25
Primary support	25	0.25	20		
Secondary lining	25	0.2	30		

4 ANALYSIS OF CALCULATION RESULTS

4.1 *Displacement analysis*

The deformation pattern of the surrounding rock during tunnel excavation is shown in Figure 3. The displacement of the monitoring point is shown in Figure 4. After the excavation of the upper step in the right line, the displacement of the right line's crown and invert rapidly increases, and within a certain range, it tends to stabilize. The maximum

displacement of the crown is 6.32mm, and the maximum displacement of the invert is 9.32mm. The crown and invert of the left line exhibit a slight downward trend and gradually reach an equilibrium state. This indicates that during the upper step excavation, the right line experienced significant disturbance, while the deformation of the surrounding rock in the left line was minor. During the excavation of the lower step in the right line, the displacement of the crown and invert in the left line remains relatively unchanged, indicating that the left line remains stable. The displacement of the crown in the right line also remains constant, indicating effective support during the upper step excavation. However, the displacement of the invert in the right line continues to increase, reaching 10.15mm, suggesting a significant impact from the lower step excavation on the invert of the right line.

During the upper step excavation in the left line, significant subsidence occurred in both the crown and invert of the right line. The crown subsided by 3.6mm, and the invert subsided by 0.7mm, indicating that the upper step excavation in the left line caused certain interference to the right line. The invert of the left line rose by 11mm, while the crown subsided by 6.3mm, and these changes occurred rapidly. This suggests that the upper step excavation in the left line caused significant disturbance to the left line itself. When excavating the lower step in the left line, apart from slight uplift observed in the invert of the left line, the displacement of other monitoring points remained relatively unchanged, indicating that the surrounding rock had reached a relatively stable state at this point.

According to the figure, it can be observed that the displacement of the surrounding rock at the arch crown and arch bottom is most significant during the section formation stage (i.e., the stage of upper bench excavation), with the highest rate of change. The influence of lower bench excavation stage on the displacement of the surrounding rock is relatively small. Therefore, it is crucial to select a reasonable initial support method and carry out timely construction of

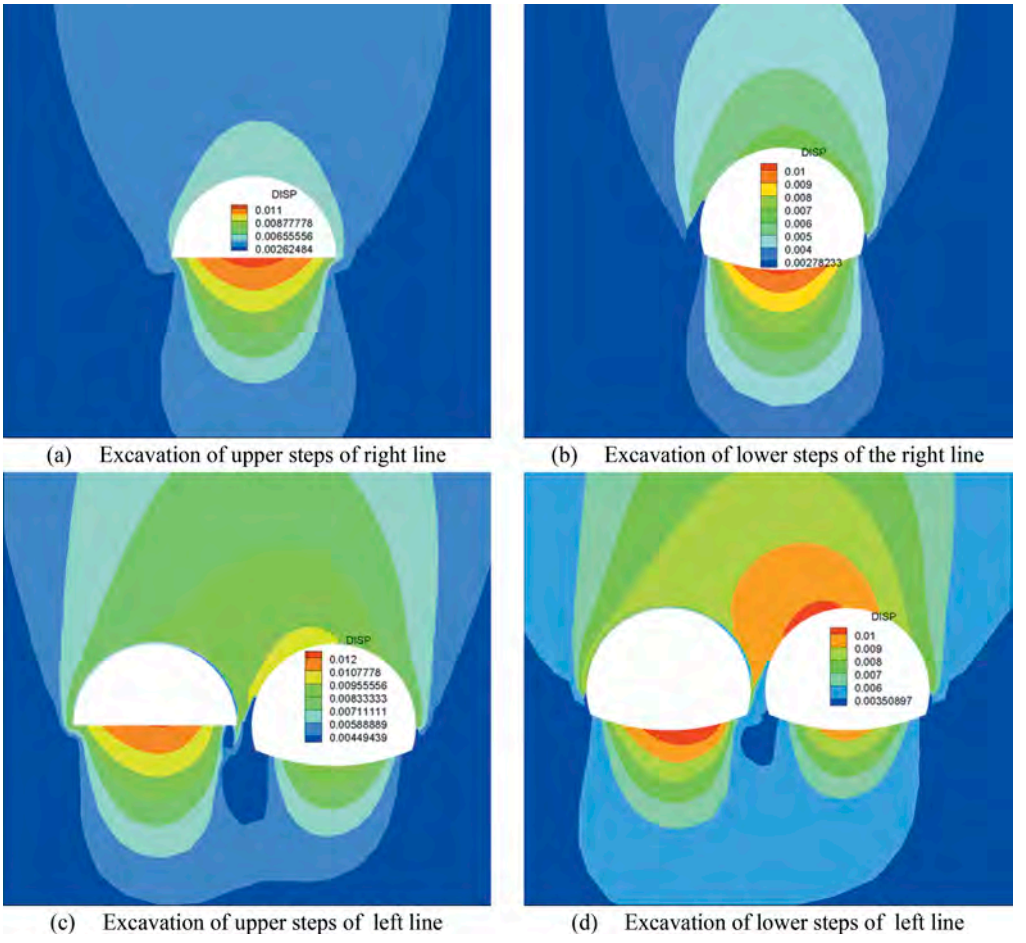

(a) Excavation of upper steps of right line (b) Excavation of lower steps of the right line

(c) Excavation of upper steps of left line (d) Excavation of lower steps of left line

Figure 3. Cloud diagram of rock displacement.

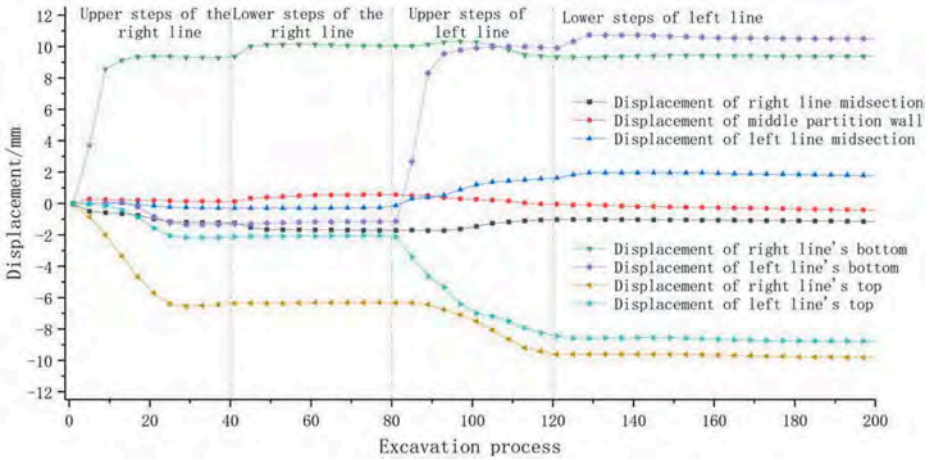

Figure 4. Displacement of tunnel surrounding rock.

the initial support to ensure the safety and stability of the tunnel. When the surrounding rock reaches a stable equilibrium state, the maximum settlement at the arch crown of the right tunnel is 9.8 mm, and the maximum uplift at the arch bottom is 9.4 mm. The maximum settlement at the arch crown of the left tunnel is 8.8 mm, and the maximum uplift at the arch bottom is 10.5 mm. After the construction of the double-arch tunnel without middle drift, the vertical displacement magnitudes of the arch crowns and arch bottoms in the left and right tunnels are basically consistent. However, it should be noted that during the excavation of the left tunnel, the right tunnel has already completed the secondary lining construction, and a significant settlement phenomenon occurred at the arch crown of the right tunnel when the left tunnel was excavated in the upper bench stage. This may lead to cracking or damage in the secondary lining of the right tunnel's arch crown. Therefore, during the excavation of the left tunnel, it is necessary to strengthen monitoring and inspection of the arch crown of the right tunnel, and promptly identify and address any potential issues.

With the excavation of the tunnel, the monitoring points at the arch crowns of both the left and right tunnels move towards the excavation face, causing loosening and deformation of the surrounding rock. During the excavation of the lower bench in the right tunnel, significant movement of the surrounding rock is observed at the location of the partition wall, which is mainly caused by the displacement resulting from the re-construction of the partition wall. Since the partition wall is constructed only during the excavation of the lower bench in the right tunnel, it experiences uneven pressure from the surrounding rock on both sides during the construction process, resulting in deformation and displacement of the partition wall. To reduce the displacement of the partition wall, it is necessary to minimize the construction time of the partition wall and adopt a rational primary support method.

During the excavation of the left tunnel, significant displacement is often observed at the arch crown monitoring points in the right tunnel, indicating that the excavation of the left tunnel has an impact on the surrounding rock of the right tunnel. Due to the distance between the left and right tunnels, the excavation of the left tunnel exerts lateral pressure on the surrounding rock of the right tunnel, resulting in displacement at the arch crown of the right tunnel. To control the displacement of the arch crown in the right tunnel, it is necessary to strengthen the monitoring of the right tunnel's arch crown during actual construction and promptly implement reinforcement measures.

It is worth noting that after the excavation of the left tunnel, the rate of displacement change at the monitoring points is significantly higher than during the excavation of the right tunnel. This indicates that the left tunnel is more significantly affected, and there may be more complex deformation and damage to the surrounding rock. Therefore, in actual tunnel engineering, special attention should be given to the deformation and damage conditions at different parts of the tunnel in order to implement corresponding support and reinforcement measures, ensuring the safe and stable operation of the tunnel.

4.2 *Stress analysis*

4.2.1 *Analysis of surrounding rock stress*

As shown in Figure 5, with the excavation of the tunnel, the originally stable surrounding rock is disrupted, and the rock undergoes deformation to reach a new stable state. However, the support system hinders this deformation process, resulting in stress concentration. After the completion of the excavation of the right tunnel, the stress distribution in the surrounding rock gradually stabilizes. At this point, the stress in the surrounding rock is mainly concentrated at the

tunnel's arch position, while the stress distribution in the top surrounding rock of the tunnel is relatively small and uniform. The stress in the middle of the surrounding rock is lower, but stress concentration phenomena also occur.

With the completion of the left line excavation, the stress in the surrounding rock redistributes. Stress mainly concentrates at the positions of the arch feet of both tunnels and the position of the middle partition wall. This phenomenon occurs because the excavation of the left line disrupts the originally concentrated stress in the rock mass, and the surrounding rock undergoes stress readjustment to achieve a new stable state. At this point, the stress distribution on the top surrounding rock of the tunnel becomes relatively uniform and lower, indicating that during excavation, the stress on the tunnel's top is relatively low, and the rock deformation is more influenced by gravity. The horizontal stress during excavation is mainly transmitted through the tunnel's sidewalls rather than its top. The stress contour maps showing the change in rock stress after excavation also reveal that the impact of tunnel excavation on the surrounding rock decreases with increasing distance from the tunnel.

4.2.2 *Analysis of secondary lining stress*

According to the analysis results from Figure 6, the stress distribution of the secondary lining structure in the right tunnel exhibits notable non-uniformity. This is particularly evident in areas such as the arch bottom, arch top, and corners of the tunnel walls, where stresses are relatively high and both tensile and compressive stresses are present. Notably, there is a pronounced tensile stress at the left side of the arch

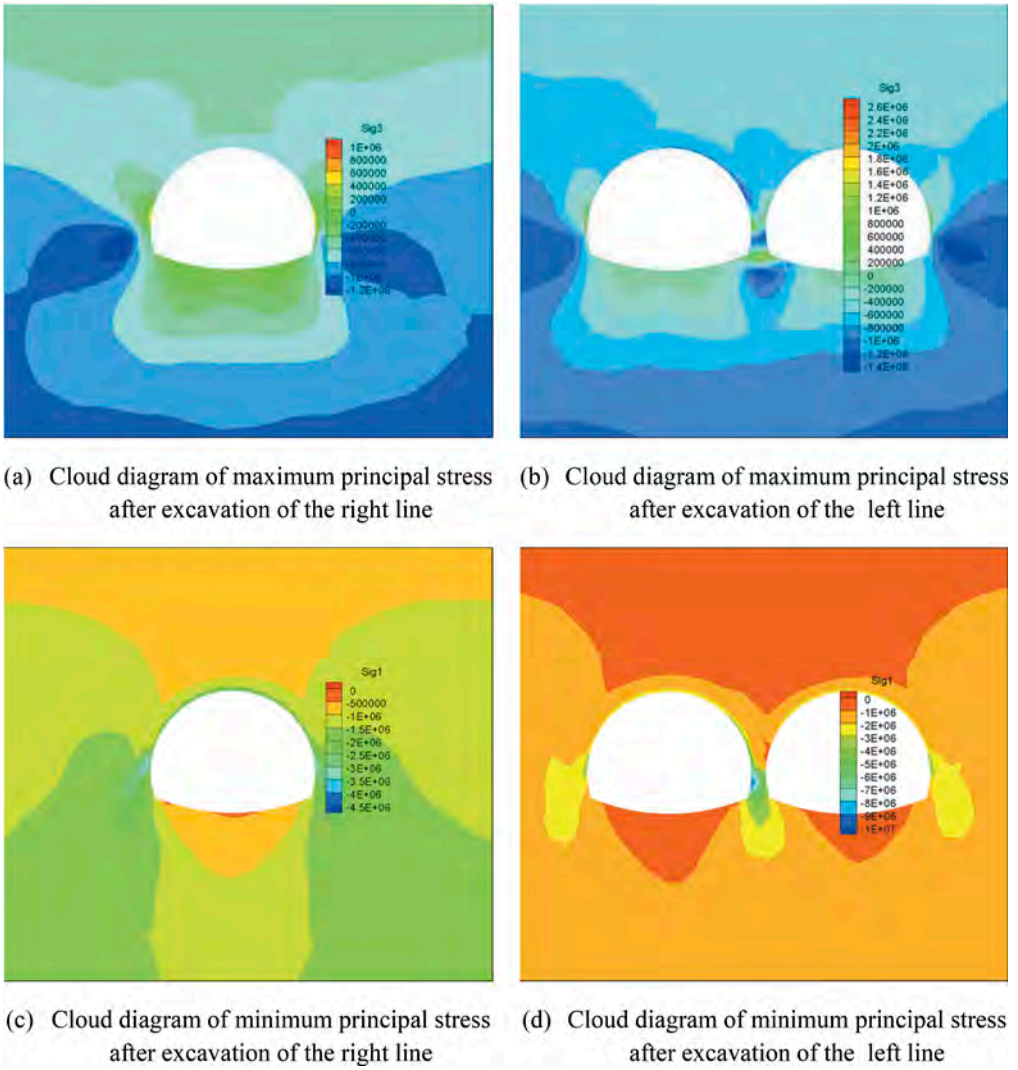

(a) Cloud diagram of maximum principal stress after excavation of the right line

(b) Cloud diagram of maximum principal stress after excavation of the left line

(c) Cloud diagram of minimum principal stress after excavation of the right line

(d) Cloud diagram of minimum principal stress after excavation of the left line

Figure 5. Cloud diagram of rock stress.

bottom, reaching up to 1.27 MPa, which might lead to cracking. Additionally, a significant tensile stress of 1.1 MPa is observed at the left side of the arch top, warranting enhanced monitoring and maintenance. While there is some localized accumulation of compressive stress at the corners of the right tunnel's walls, it is relatively minor and not sufficient to cause damage.

In contrast, the stress distribution of the secondary lining structure in the left tunnel is more uniform, with stress values at various locations falling within reasonable ranges. Only a slight stress concentration is present at the right corner of the tunnel's wall, which does not affect the structural safety.

Comparatively, the analysis reveals that the secondary lining structure in the right tunnel experiences pronounced stress concentration, which could potentially lead to structural damage or instability. Therefore, in practical construction, appropriate support measures, such as reinforcement or additional structural elements, are necessary to ensure the stability and safety of the secondary lining structure. Simultaneously, further research and analysis on the stress distribution patterns of the secondary lining structure are needed to provide more scientifically and rationally designed solutions for actual construction.

4.2.3 *Analysis of in the partition wall stress.*
Analyzing the stress variation pattern of the central partition wall. According to Figure 7, it can be observed that the stress distribution on the central partition wall is relatively concentrated, and the stress values fluctuate within a certain range. This indicates that the central partition wall undergoes relatively small stress variations during the construction process, exhibiting good stability.

In the figures, the maximum tensile stress on the central partition wall is 2.6 MPa, and the maximum

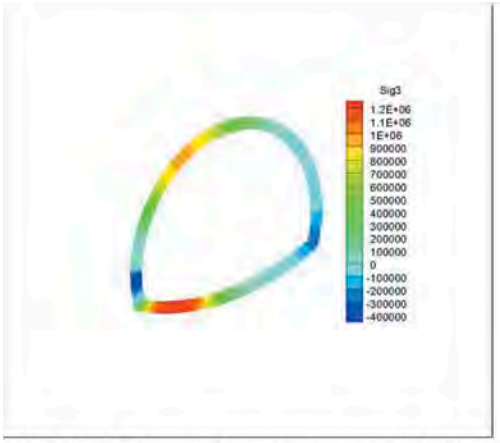

(a) Cloud diagram of maximum principal stress in the right line secondary lining

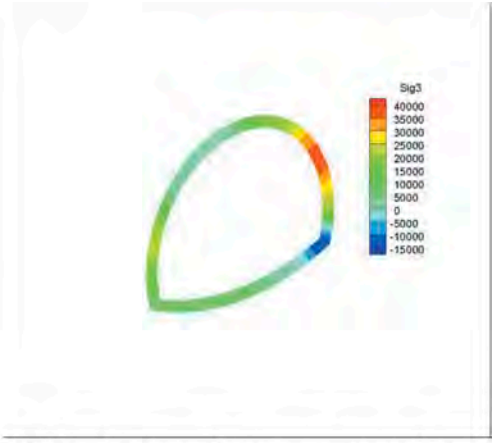

(b) Cloud diagram of maximum principal stress in the left line secondary lining

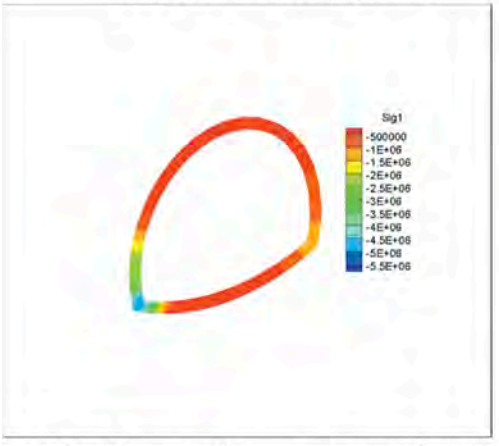

(c) Cloud diagram of minimum principal stress in the right line secondary lining

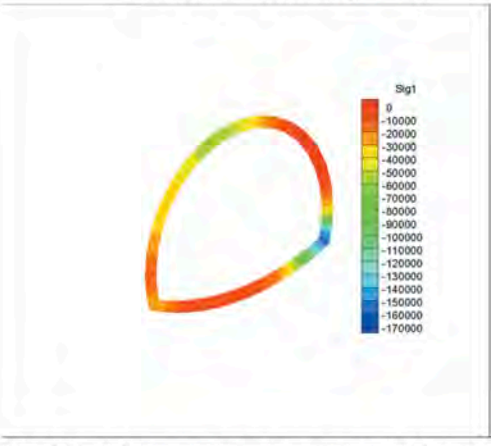

(d) Cloud diagram of minimum principal stress in the left line secondary lining

Figure 6. Cloud diagram of secondary lining stress.

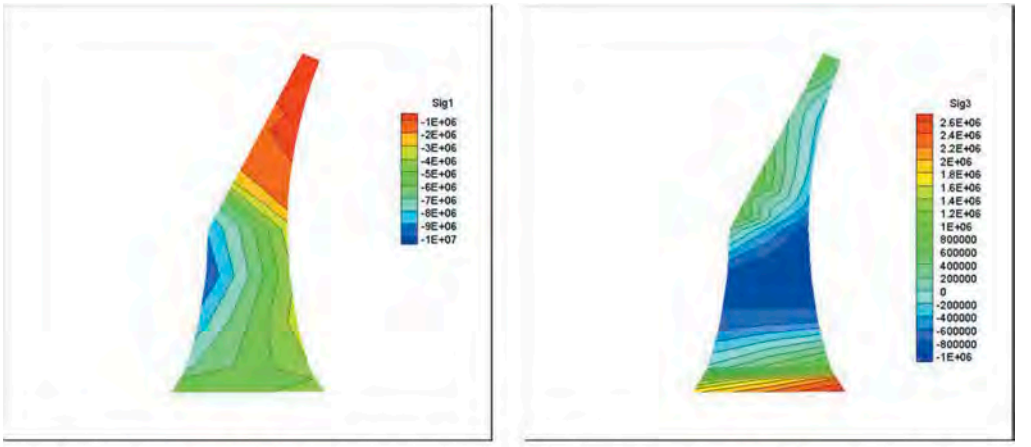

(a) Cloud diagram of minimum principal stress in the partition wall

(b) Cloud diagram of minimum principal stress in the partition wall

Figure 7. Cloud diagram of partition wall stress.

compressive stress is 10 MPa, with the maximum tensile stress located at the lower right end of the wall and the maximum compressive stress on the left side. This may imply that, due to high tensile stress, the lower part of the wall is more prone to cracking or deformation. Moreover, during usage, the stress on the central partition wall may change due to variations in tunnel environment and geological conditions. To enhance the safety and stability of the wall during usage, appropriate measures can be taken to reinforce the central partition wall, reducing stress concentration at the lower part of the wall, such as increasing wall thickness, using high-strength materials, or installing additional reinforcement structures.

4.3 *Conclusion*

1. The stress distribution in the surrounding rock is dynamic and changes as the excavation process progresses. Stress concentration mainly occurs at the crown, intermediate wall, and corners of the tunnel. The intermediate wall experiences the highest stress and requires reinforcement with steel mesh and improved foundation. The construction of secondary lining and the excavation of adjacent tunnels also affect the stress distribution in the surrounding rock.
2. The secondary lining structure exhibits significant stress concentration in certain areas, especially in advance tunnels, which can lead to cracking or damage. Therefore, it is necessary to implement appropriate support measures, such as strengthening support or installing reinforcement structures, to ensure the stability and safety of the secondary lining structure.
3. When the left and right tunnels overlap, it is important to pay attention to protecting the structure of the leading tunnel and timely pour the secondary lining for the arch and walls. This helps to improve the overall stiffness and load-bearing capacity of the continuous arch tunnel.
4. The displacement and stress of the surrounding rock and support structures are primarily influenced by the excavation of the upper bench, while the impact of excavation of the lower bench is relatively smaller on them.

5 OPTIMIZED CONSTRUCTION PROCESS

In the construction of consecutive tunnels, the secondary lining of the leading tunnel lags behind the tunnel excavation, and when constructing the following tunnel, the fact that the secondary lining of the leading tunnel has not reached the specified age must be taken into account. In this situation, the excavation of the following tunnel will exert significant vibration effects on the secondary lining of the leading tunnel, leading to disturbance and deformation of the surrounding rock, and resulting in stress concentration in the already poured secondary lining of the leading tunnel, which can even lead to cracking. In the construction of double-arch tunnels under this circumstance, it is necessary to develop a reasonable construction plan to ensure that the secondary lining of the leading tunnel reaches the specified age as soon as possible, and to take effective measures to minimize the impact of the excavation of the following tunnel on the secondary lining of the leading tunnel. For instance, controlling the excavation progress and the amount of explosives used in blasting can be implemented during the construction of the following tunnel to avoid excessive vibration effects. Furthermore, it is essential to precisely control the construction sequence and timing during the process of bench installation and inverted

arch construction, ensuring a uniform stress distribution during the construction process and avoiding stress concentration phenomena. Therefore, the pouring of the secondary lining in the leading tunnel and the excavation of the following tunnel must be carefully coordinated.

The construction environment of double-arch tunnels is typically challenging, and the complexity and variability of geological conditions are significant difficulties in construction. Especially when adopting the method of double-arch tunnel without middle drift, risks such as ground stress release, rock burst, and roof collapse caused by rock excavation need to be addressed. Therefore, before construction, it is necessary to conduct thorough investigation and analysis of the geological conditions in order to develop a reasonable construction plan and appropriate measures to address the challenges.

The method of double-arch tunnel without middle drift in continuous arch tunnels has significant advantages compared to traditional construction methods. However, this method requires the use of advanced construction techniques, and it is necessary to ensure the smooth progress of the construction face during the construction process while maintaining the overall stability of the tunnel structure. Therefore, before construction, it is necessary to thoroughly debug and inspect the equipment, as well as develop detailed construction plans and implement safety management.

During the construction process, it is necessary to tightly control the tunnel excavation, support, drainage, and other aspects. Real-time monitoring and control of parameters such as tunnel displacement and stress are also required to ensure the overall stability and safety of the tunnel. Additionally, the management and maintenance of the construction site are essential aspects of construction process control.

Finally, in the construction of double-arch tunnel without middle drift, it is required to immediately carry out support work after excavation, and the pouring of the intermediate partition wall should closely follow the excavation face. This places high demands on construction organization and coordination abilities. This method has a certain range of adaptability to surrounding rock conditions but is not suitable for special geological conditions, such as large cross-sections, great depths, significant lateral pressures, or abundant joint and crack formations. Additionally, this method lacks sufficient construction experience and data support, and it carries certain risks and uncertainties. It requires continuous summarization and improvement through practical engineering projects.

REFERENCES

Bo Min, et al, 2020. Cracking performance of asymmetric double-arch tunnels due to the voids behind linings. Thin-Walled Structures. 154:0263–8231

Cheng, X.H., Zhao, Z.Z., 2023. Research progress on lining cracking and mechanical behavior during the construction of double arch tunnels. Engineering Mechanics. 40 (05): 1–19

Ding, Y., Wang, J., Xu, G.W., 2019. Numerical simulation analysis of the stability of surrounding rock in layered rock tunnels. Journal of Chengdu University of Technology (Natural Science Edition). 46 (03): 363–372

Gao, H.J., He, P., Chen, Z., 2020. Research on the calculation method of process load for deep buried asymmetric multi-arch tunnels. Journal of Geotechnical Engineering. 42: 1059–1066

Guo, J.J, Zhang, G.H., Chu, C., 2022. Safety assessment of ancient buildings under large-span multi-arch tunnels. Journal of Chongqing Jiaotong University (Natural Science Edition). 41 (08): 53–57

Jiang, C.Y., Tang, H., Deng, Q., et al, 2023. Study on the calculation method of surrounding rock pressure in deep buried multi arch tunnels without central guide. Journal of Central South University (Natural Science Edition). 54 (03): 1168–11177

Lai, J.X., et al, 2006. Discussion on Construction Technology of Multiple Arch Tunnel without Middle Guide Tunnel. Railway Architecture. 04: 34-35+43

Li, Z.H., et al, 2010. Key Technologies for Design and Construction of Highway Double Arch Tunnel. Beijing, People's Communications Publishing House.

Li, Z.H., Tong, Y., Chen, S.W., et al, 2022. Comparative study on the construction methods of double arch tunnels in shallow and weak strata with or without a central guide tunnel. Modern Tunnelling Technology. 59 (S1): 59–73

Tunnelling for a Better Life – Yan, Celestino, Thewes & Eberhardt (Eds)
© 2024 The Author(s), ISBN 978-1-032-80042-4
Open Access: www.taylorfrancis.com, CC BY-NC-ND 4.0 license

A mechanical analysis model for tunnels crossing active fault zones

Mingnian Wang, Xiao Zhang* & Li Yu
School of Civil Engineering, Southwest Jiaotong University, Chengdu, China
Key Laboratory of Traffic Tunnel Engineering Ministry of Education, Southwest Jiaotong University, Chengdu, China

ABSTRACT: Tunnels that cross active fault zones will inevitably be damaged, and a proper mechanical analysis model is an effective tool for tunnel design. Generally, there are three types of active faults, i.e., strike-slip, dip-slip (normal and reverse) and oblique-slip (normal and reverse strike-slip) faults. However, there is no mechanical analysis model that suitable for all types of active faults. In this work, a mechanical analysis model for tunnels crossing active fault zones is proposed, which is applicable to different kinds of active faults. To be specific, a prediction method of stratum displacement under different types of faults is proposed by using a mathematical statistical analysis of field measured data; then, the calculation method of longitudinal tunnel displacements and forces is established based on the beam-spring model; finally, the analysis model of tunnel cross-section displacement and forces is presented based on the deformation-structure method. Additionally, the calculation results obtained from the proposed model agree well with those from model tests and numerical simulations under the action of strike-slip, dip-slip and oblique-slip faults. The proposed model improves the existing analytical models in terms of accuracy and applicability, and it is valuable for fast, economic, and reliable analysis and design of tunnels crossing active faults.

Keywords: Active faults, Tunnel engineering, Coseismic-slip, Mechanical analysis

1 INTRODUCTION

Affected by intense tectonic activity, numerous faults are distributed worldwide due to the interaction between different tectonic plates, such as the East African Great Rift Valley, San Andreas Fault, and Hayward Fault. Consequently, many tunnels must cross these active faults to meet route planning requirements. However, the dislocation resulting from earthquakes when a tunnel crosses an active fault can cause irreversible damage, including cracking, substantial deformation, and even structural collapse. Consequently, the seismic impact of active faults on tunnels has garnered significant attention among researchers and practitioners alike.

A series of model tests (Baziar et al., 2014; Burridge et al., 1989; Cai et al., 2019) and numerical simulations (Ranjbarnia et al., 2020; Sabagh and Ghalandarzadeh, 2020; Zhao et al., 2019) have been conducted to investigate the tunnel response under faulting. The results show that the tunnel is subjected to a combination of tensile (compressive), bending and shearing, and experiences an elongated 'S'-shaped deformation along the tunnel axial; the tunnel internal forces increase with the increase of fault displacement, stratum stiffness and tunnel stiffness; under the action of fault zone displacement, the tunnel will be severely damaged, especially near the fault zone, where tunnel collapse and cracking may occur.

However, the numerical simulation of a tunnel crossing an active fault zone takes several hours even in a high-performance computer, which is not applicable to engineering design. Therefore, a series of analytical models have been proposed for the mechanical response analysis of a tunnel or pipeline under the action of faulting. Newmark and Hall (Newmark and Hall, 1975) firstly proposed a cable-like model for a pipeline under a strike-slip fault without considering the contribution of lateral stratum resistance. Kennedy (Kennedy et al., 1977) extended this model by considering stratum resistance, but the pipeline′s flexural stiffness is still not considered. Later, Wang and Yeh (Wang and Yeh, 1985) partitioned the pipeline into four segments to compensate the limitation of the cable-like models in neglecting the contribution of pipeline′s flexural stiffness. After that, this model is

*Corresponding author: xiao.zhang@swjtu.edu.cn

DOI: 10.1201/9781003495505-170

improved and developed by many authors (Hu et al., 2022; Karamitros et al., 2007; Karamitros et al., 2011; Talebi and Kiyono, 2021; Trifonov and Cherniy, 2010; Wang and Wang, 1995) and some shortcomings have been overcome. Despite the ongoing improvements and development of analytical models, they are not without shortcomings. These include:

(1) The existing models for analyzing faulting in tunnels tend to oversimplify the permanent fault displacement by treating it as a constant value, which avoids the need for solving complex equations. However, the permanent fault displacement resulting from faulting is actually nonlinear, and this simplification does not reflect the true nature of the phenomenon.
(2) Different fault types show different mechanical characteristics, in which the normal fault is in tension, the reverse fault is in compression, the strike-slip fault is in shear, and the oblique-slip fault is in combined state. However, the current analytical models for assessing the interaction between tunnels and faults do not fully take into account these distinct mechanical characteristics. As a result, there is a need for a comprehensive analytical model that can be applied to all types of active faults.

To this end, this paper presents a novel approach for predicting the stratum coseismic-slip and tunnel response under fault dislocation. The proposed method is highly accurate, and is applicable to all types of active faults.

2 PREDICTION METHOD OF STRATUM COSEISMIC-SLIP

2.1 *Statistical analysis of stratum coseismic-slip characteristics*

For the sake of enabling further analysis, the coordinate system Oxyz is established to lie along the fault plane. Specifically, the horizontal (x-axis) aligns parallel to the fault plane, the longitudinal (y-axis) aligns perpendicular to the fault plane, and the vertical (z-axis) aligns perpendicular to the horizontal plane, as illustrated in Figure 2.

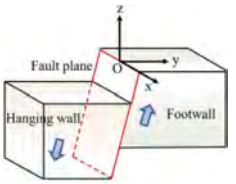

Figure 1. 3D coordinate system.

2.1.1 *Statistics of stratum coseismic-slip curve*

A total of 45 stratum coseismic-slip curves were measured, primarily originating from the Taxkorgan, Yutian, Wenchuan, and West Kunlun Mountain earthquakes(Chenxia et al., 2011; Guihua et al., 2008; Guihua et al., 2009a; Guihua et al., 2022; GuiHua et al., 2009b; Wen-qiao et al., 2011; Xiwei et al., 2010; Xiwei et al., 2002; XIwei et al., 2008; Yong et al., 2008; Z et al., 2021), encompassing normal fault, reverse fault, and right-lateral strike-slip fault, as presented in Figure 3. These curves exhibit an "S" type configuration, with a prevalent trend of larger coseismic-slip near the fault plane. Moreover, the dislocation decreases gradually to convergence as the distance from the fault increases. The curve's shape is predominantly determined by the two parameters of the coseismic-slip's maximum value and range.

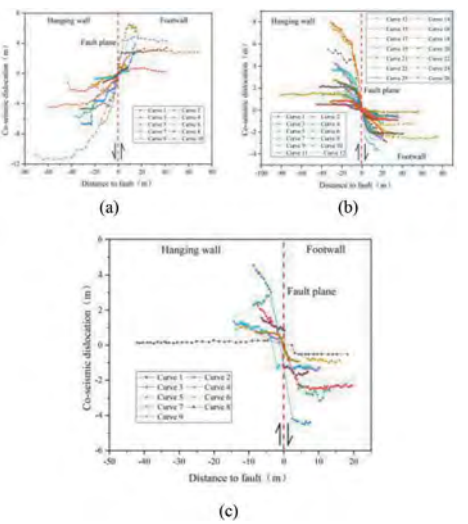

Figure 2. Measured stratum coseismic-slip curves: (a) normal fault, (b) reverse right-lateral strike-slip fault (vertical direction), (c) reverse right-lateral strike-slip fault (horizontal direction).

2.1.2 *Normalization of stratum coseismic-slip curve*

Based on the observation that coseismic-slip is maximal at the fault plane and gradually declines on either side, the measured stratum coseismic-slip curve is shifted accordingly. Additionally, due to the distinct geographical locations and topography of each curve, the data is discrete, and normalization is carried out using the influencing factors of curve shape. For design convenience, coseismic-slip curves of the hanging wall and footwall are normalized separately, while the coseismic-slip's range and maximum value i and u_{max} are defined as depicted in Figure 4. Furthermore, to validate the precision of the proposed method for predicting coseismic-slip, a randomly selected curve for each fault type is excluded from normalization processing and fitting analysis, and solely employed for verification purposes.

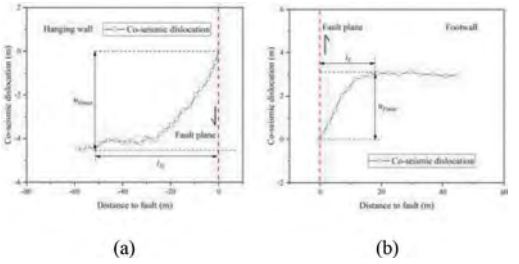

Figure 3. Schematic diagram of normalization index: (a) hanging wall, (b) footwall.

The normalization index is employed to normalize both the co-seismic stratum dislocation u and fault distance y:

$$\bar{u}_H = \frac{u_H}{u_{H\max}} \tag{1}$$

$$\bar{u}_F = \frac{u_F}{u_{F\max}} \tag{2}$$

$$\bar{y}_H = \frac{y}{i_H} \tag{3}$$

$$\bar{y}_F = \frac{y}{i_F} \tag{4}$$

where $\bar{u}_H$ and $\bar{u}_F$ are the normalized stratum coseismic-slip of the hanging wall and footwall respectively; u_H and u_F are the original stratum coseismic-slip of the hanging wall and footwall respectively; $\bar{y}_H$ and $\bar{y}_F$ are the normalized fault distance of the hanging wall and footwall respectively; y is the original fault distance.

Upon normalization of the stratum coseismic-slip curve, the largest coseismic-slip is observed at the fault plane. As fault distance increases, coseismic-slip gradually reduces, eventually reaching a minimum value beyond the deformation range, and then remaining relatively constant. This is demonstrated in Figure 5.

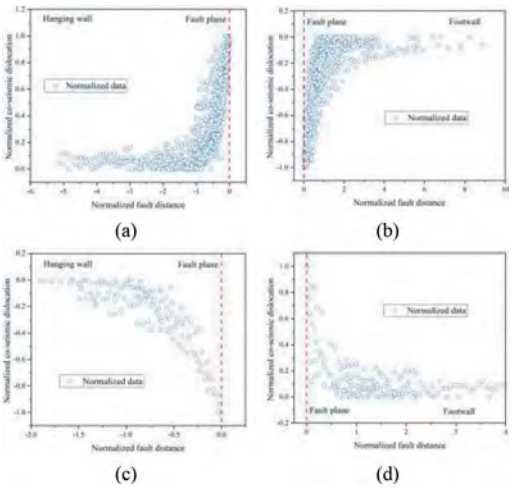

Figure 4. Normalized stratum coseismic-slip data: (a) vertical direction (hanging wall), (b) vertical direction (footwall), (c) horizontal direction (hanging wall), (d) horizontal direction (footwall).

2.2 *Fitting analysis of stratum coseismic-slip range*

To develop a comprehensive method for predicting the stratum coseismic-slip applicable to various fault types, it is necessary to account for the direction of the coseismic-slip based on the nature of the fault. For establishing a consistent approach for data analysis, positive values of the coseismic-slip data for normal and reverse faults are unified as the vertical direction data, whereas positive values of the coseismic-slip data for left-lateral and right-lateral strike-slip faults are unified as the horizontal direction data. The subsequent analysis is based on the established three-dimensional coordinate system.

2.2.1 *Fitting analysis of vertical coseismic-slip range*

The fitting analysis is conducted based on the positive values of the vertical coseismic-slip range of both the hanging wall and the footwall, as presented in Figure 6. The goodness of fit is 0.82, and the calculation formulas are established as follows:

$$i_{\mathrm{Hz}} = 11.09 u_{Hz\max}^{0.44} \tag{5}$$

$$\mathrm{i}_{Fz} = 11.09 u_{Fz\max}^{0.44} \tag{6}$$

where i_{Hz} and i_{Fz} are the coseismic-slip range of the hanging wall and the footwall in the vertical direction respectively; u_{Hzmax} and u_{FZmax} are the maximum coseismic-slip of the hanging wall and the footwall in the vertical direction respectively, which can be obtained according to the earthquake safety evaluation.

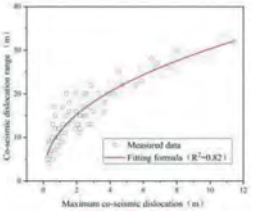

Figure 5. Vertical coseismic-slip range fitting diagram.

2.2.2 *Fitting analysis of horizontal coseismic-slip range*

Analogously, a fitting analysis is performed based on the range data of horizontal coseismic-slip, as presented in Figure 7. The goodness of fit is 0.85, and the resulting calculation formulas are as follows:

$$i_{Hx} = 5.04u_{Hx\max}^{0.24} \tag{7}$$

$$i_{Fx} = 5.04u_{Fx\max}^{0.24} \tag{8}$$

where i_{Hx} and i_{Fx} are the coseismic-slip range of the hanging wall and the footwall in the horizontal direction respectively; u_{Hxmax} and u_{FXmax} are the maximum coseismic-slip of the hanging wall and the footwall in the horizontal direction respectively, which can be obtained according to the earthquake safety evaluation.

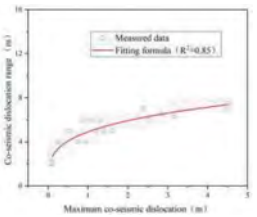

Figure 6. Horizontal coseismic-slip range fitting diagram.

2.3 *Fitting analysis of stratum coseismic-slip*

Based on the influence factors and deformation characteristics of the stratum coseismic-slip curve, the fitting principles are guided by several criteria. Firstly, the fitting curve should attain the maximum coseismic-slip. Secondly, the fitting curve should accurately represent the deformation range. Thirdly, the fitting curve must exhibit the maximum coseismic-slip on the fault plane and decrease gradually towards both sides. Finally, the goodness of fit of the fitting curve should be maximized.

2.3.1 *Fitting analysis of vertical coseismic-slip*

(1) Hanging wall.

Using the normalized coseismic-slip data of the hanging wall in the vertical direction as a basis, this study selected four functional forms, including linear, exponential, peck, and power function, for fitting analysis. The results of the fitting analysis are presented in Table 1 and Figure 8.

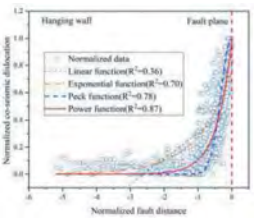

Figure 7. Normalized data fitting of hanging wall in vertical direction.

The fitting curve of the linear and exponential functions fails to attain the maximum coseismic-slip, displays low goodness of fitting, and fails to converge. In contrast, the fitting curve of the peck function and power function successfully reaches the maximum coseismic-slip, conforms to the deformation characteristics of the measured curve, and shows high goodness of fitting. Consequently, the subsequent fitting analysis focuses on the peck and power functions. The power function exhibits a goodness of fit of 0.87, while the peck function displays a goodness of fit of 0.78. Therefore, the calculation formula of the normalized coseismic-slip of the hanging wall in the vertical direction selects the power function fitting formula.

Table 1. Comparison of fitting functions.

Serial number	Functional form	Fitting formula	Goodness of fitting
1	Linear function	$\bar{u}_{Hz} = 0.49 + 0.19\bar{y}_H$	0.36
2	Exponential function	$\bar{u}_{Hz} = e^{\bar{y}_H - 0.28}$	0.70
3	Peck function	$\bar{u}_{Hz} = e^{\frac{-\bar{y}_H^2}{0.19}}$	0.78
4	Power function	$\bar{u}_{Hz} = 0.99 * 9.28^{\bar{y}_H}$	0.87

$$\bar{u}_{Hz} = 0.99 * 9.28^{\bar{y}_H} \tag{9}$$

A conversion process is carried out to obtain the actual calculation formula of coseismic-slip for the hanging wall in the vertical direction:

$$u_{Hz} = \varphi_1 u_{Hz\max}(0.99 * 9.28^{\frac{y}{i_{Hz}}}) \tag{10}$$

where φ_1 is the fault type judgment coefficient, 1 for normal fault and -1 for reverse fault.

(2) Footwall

The normalized coseismic-slip data of the footwall in the vertical direction was subjected to fitting analysis, as shown in Figure 9. Among the different function forms, the power function exhibited the highest goodness of fit at 0.85. Hence, the power function was selected to determine the calculation formula of the footwall coseismic-slip in the vertical direction:

$$\bar{u}_{Fz} = -0.99 * 0.16^{\bar{y}_F} \tag{11}$$

$$u_{Fz} = \varphi_1 u_{Fz\max}(-0.99 * 0.16^{\frac{y}{i_{Fz}}}) \tag{12}$$

2.3.2 Fitting analysis of horizontal coseismic-slip

The normalized coseismic-slip data of both the hanging wall and footwall in the horizontal direction underwent fitting analysis, as depicted in Figure 10. The power function fitting curve yielded a high goodness of fit of 0.97 and 0.95 for the hanging wall and footwall, respectively. Thus, it was selected as the calculation formula for the horizontal coseismic-slip:

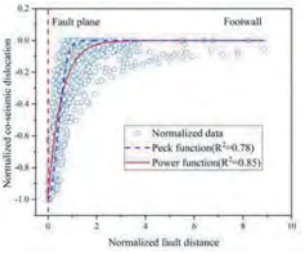

Figure 8. Normalized data fitting of footwall in vertical direction.

$$\bar{u}_{Hx} = -0.99 * 10.49^{\bar{y}_H} \tag{13}$$

$$u_{Hx} = \varphi_2 u_{Hx\max}(-0.99 * 10.49^{\frac{y}{l_{Hx}}}) \tag{14}$$

$$\bar{u}_{Fx} = 0.99 * 0.03^{\bar{y}_F} \tag{15}$$

$$u_{Fx} = \varphi_2 u_{Fx\max}(0.99 * 0.03^{\frac{y}{l_{Fx}}}) \tag{16}$$

where φ_2 is the fault type judgment coefficient, 1 for right-lateral strike-slip fault and -1 for left-lateral strike-slip fault.

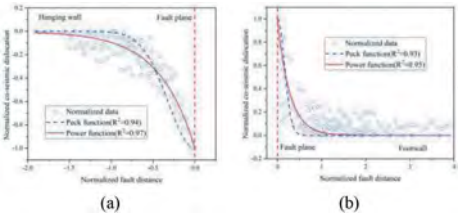

Figure 9. Normalized data fitting in horizontal direction: (a) hanging wall; (b) footwall.

2.3.3 *Fitting analysis of longitudinal coseismic-slip*
After the dislocation of the active fault, the coseismic-slip data measured in the vertical and horizontal directions are typically more detailed than that of the longitudinal coseismic-slip data. The latter is challenging to measure and as such, the available longitudinal data is often limited. However, the longitudinal data can be inferred based on parameters such as the fault type and fault dip angle, as shown in Table 2.

It can be seen that the relationship between the longitudinal coseismic-slip and the vertical coseismic-slip of an active fault can be expressed as the tangent value of the fault dip angle:

$$u_y = \frac{u_z}{\tan\alpha} \tag{17}$$

Hence, considering that normal faults are mainly subjected to tension in the longitudinal direction while reverse faults are mainly subjected to compression, the formula for predicting the longitudinal coseismic-slip is derived as:

$$u_{Hy} = \frac{u_{Hz}}{\tan\alpha} = \varphi_1 \frac{-u_{Hz\max}(0.99 * 9.28^{\frac{y}{l_{Hz}}})}{\tan\alpha} \tag{18}$$

$$u_{Fy} = \frac{u_{Fz}}{\tan\alpha} = \varphi_1 \frac{u_{Fz\max}(-0.99 * 0.16^{\frac{y}{l_{Fz}}})}{\tan\alpha} \tag{19}$$

where α is the fault dip angle.

3 ANALYSIS OF TUNNEL RESPONSES UNDER FAULT DISLOCATION

3.1 *Analysis of the longitudinal tunnel coseismic-slip*

The coseismic-slip data of tunnels crossing active faults are often scarce due to various factors, such as topographic conditions, survey difficulties, and safety concerns. A commonly accepted assumption is that the resistance of the tunnel, being a long and linear structure, can be neglected in the face of stratum deformation, which is in turn assumed to be equivalent to the deformation of the tunnel structure(Kawashima, Kazuhiko, 1994). In the scenario where a tunnel intersects an active fault, the coseismic-slip of the tunnel is equal to that of the stratum when the tunnel is perpendicular to the fault. However, in actual engineering, it is common for the tunnel to intersect the fault at an intersection angle, as illustrated in Figure 14 (a). In such a case, the coseismic-slip of the tunnel can be obtained by considering the geometric relationship between the tunnel and the stratum, as depicted in Figure 14 (b):

Table 2. Coseismic-slip parameters of wenchuan earthquake (Xibin et al., 2013).

Observation point	Horizontal coseismic-slip (m)	Vertical coseismic-slip (m)	Fault dip angle (°)	Longitudinal coseismic-slip (m)
Xiaoyudong West	2.15	1.36	37	1.84
Xiaoyudong East	2.71	1.51	32	2.44
Qingping	2.58	3.70	61	2.01
Bailu middle school	1.63	2.00	51	1.63

$$u_{T-z} = u_z \tag{20}$$

$$u_{T-x} = u_y \cos\beta + u_x \sin\beta \tag{21}$$

$$u_{T-y} = u_y \sin\beta - u_x \cos\beta \tag{22}$$

Namely:

$$u_{T-Hz} = \varphi_1 u_{Hz\max}(0.99 * 9.28^{\frac{y_T}{i_{T-Hz}}}) \tag{23}$$

$$u_{T-F_Z} = \varphi_1 u_{Fz\max}(-0.99 * 0.16^{\frac{y_T}{i_{T-Fz}}}) \tag{24}$$

$$u_{T-Hx} = \varphi_1 \frac{-u_{Hz\max}\cos\beta(0.99 * 9.28^{\frac{y_T}{i_{T-Hz}}})}{\tan\alpha} + \varphi_2 u_{Hx\max}\sin\beta(-0.99 * 10.49^{\frac{y_T}{i_{T-Hx}}}) \tag{25}$$

$$u_{T-Fx} = \varphi_1 \frac{u_{Fz\max}\cos\beta(-0.99 * 0.16^{\frac{y_T}{i_{T-Fz}}})}{\tan\alpha} + \varphi_2 u_{Fx\max}\sin\beta(0.99 * 0.03^{\frac{y_T}{i_{T-Fx}}}) \tag{26}$$

$$u_{T-Hy} = \varphi_1 \frac{-u_{Hz\max}\sin\beta(0.99 * 9.28^{\frac{y_T}{i_{T-Hz}}})}{\tan\alpha} - \varphi_2 u_{Hx\max}\cos\beta(-0.99 * 10.49^{\frac{y_T}{i_{T-Hx}}}) \tag{27}$$

$$u_{T-Fy} = \varphi_1 \frac{u_{Fz\max}\sin\beta(-0.99 * 0.16^{\frac{y_T}{i_{T-Fz}}})}{\tan\alpha} - \varphi_2 u_{Fx\max}\cos\beta(0.99 * 0.03^{\frac{y_T}{i_{T-Fx}}}) \tag{28}$$

where u_{T-Hz}, u_{T-Fz}, u_{T-Hx}, u_{T-Fx}, u_{T-Hy}, and u_{T-Fy} are the tunnel coseismic-slip; β is the intersection angle; y_T is the distance from a point on the tunnel to the fault plane, $y_T = \frac{y}{\sin\beta}$; i_{T-Hz}, i_{T-Fz}, i_{T-Hx}, and i_{T-Fx} are the coseismic-slip range of tunnels crossing active faults, $i_T = \frac{i}{\sin\beta}$.

3.2 *Analysis of the tunnel cross-section coseismic-slip*

In any cross section of the tunnel (the fault distance at the center of the tunnel is y_0), n feature points are taken along the perimeter of the tunnel, i.e., $N_1(x_1,y_1,z_1)\ldots N_i(x_i,y_i,z_i)\ldots N_n(x_n,y_n,z_n)$, as shown in Figure 11.

According to the geometric relationship in Figure 10, the calculation formula of fault distance y_i of point N_i (x_i, y_i, z_i) is obtained as follows:

$$y_i = y_0 - z_i \cot\alpha + x_i \cos\beta_t \tag{29}$$

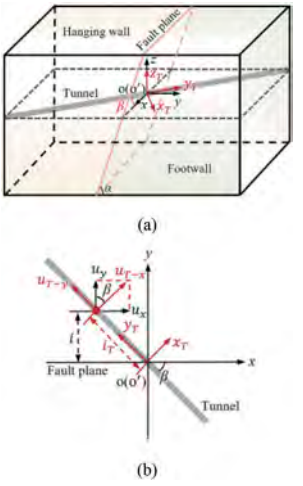

Figure 10. (a)intersection angle; (b) geometric relationship.

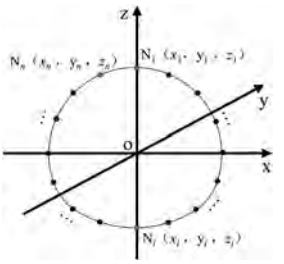

Figure 11. Schematic diagram of tunnel cross section feature points.

The deformation u'_i ($u'_{x,i}$, $u'_{z,i}$) of point N_i can be obtained by substituting fault distance y_i into the tunnel deformation calculation formula in Section 3.1.

3.3 *Calculation method of the longitudinal tunnel response*

Once the vertical, horizontal, and longitudinal coseismic-slip u_{T-z}, u_{T-x}, and u_{T-y} of the tunnel are acquired (see Section 3.1), the Euler-Bernoulli beam theory can beutilized to determine the longitudinal axial force N, bending moment M, and shear force V:

$$N = EA\frac{du_{T-y}(y_T)}{d(y_T)} \tag{30}$$

$$M_x = -EI\frac{d^2u_{T-x}(y_T)}{d(y_T)^2} \tag{31}$$

$$V_x = -EI\frac{d^3u_{T-x}(y_T)}{d(y_T)^3} \tag{32}$$

$$M_z = -EI\frac{d^2u_{T-z}(y_T)}{d(y_T)^2} \tag{33}$$

$$V_z = -EI\frac{d^3 u_{T-z}(y_T)}{d(y_T)^3} \tag{34}$$

Namely:

$$N = EA[\varphi_1 \frac{B_1 \sin\beta \ln(C_1)}{D_1 \tan\alpha} F_1 * C_1^{\frac{y_T}{D_1}} - \varphi_2 \frac{B_2 \cos\beta \ln(C_2)}{D_2} F_2 * C_2^{\frac{y_T}{D_2}}] \tag{35}$$

$$M_x = -EI[\varphi_1 \frac{B_1 \cos\beta \ln^2(C_1)}{{D_1}^2 \tan\alpha} F_1 * C_1^{\frac{y_T}{D_1}} + \varphi_2 \frac{B_2 \sin\beta \ln^2(C_2)}{{D_2}^2} F_2 * C_2^{\frac{y_T}{D_2}}] \tag{36}$$

$$V_x = -EI[\varphi_1 \frac{B_1 \cos\beta \ln^3(C_1)}{{D_1}^3 \tan\alpha} F_1 * C_1^{\frac{y_T}{D_1}} + \varphi_2 \frac{B_2 \sin\beta \ln^3(C_2)}{{D_2}^3} F_2 * C_2^{\frac{y_T}{D_2}}] \tag{37}$$

$$M_z = -EI\varphi_1 \frac{B_3 \ln^2(C_3)}{{D_3}^2} F_3 * C_3^{\frac{y_T}{D_3}} \tag{38}$$

$$V_z = -EI\varphi_1 \frac{B_3 \ln^3(C_3)}{{D_3}^3} F_3 * C_3^{\frac{y_T}{D_3}} \tag{39}$$

$$M = \sqrt{M_z^2 + M_x^2} \tag{40}$$

$$V = \sqrt{V_z^2 + V_x^2} \tag{41}$$

where B_n, C_n, D_n, and F_n are the calculation parameter s, n=1, 2, 3, specific values are shown as Table 3; E is the equivalent elastic modulus of the tunnel; A is the tunnel section area; I is the tunnel moment of inertia.

Table 3. Calculation parameters value.

		Calculation parameters			
Value of n		B_n	C_n	D_n	F_n
n=1 (N)	Hanging wall	$-u_{Hz\max}$	9.28	i_{T-Hz}	0.99
	Footwall	$u_{Fz\max}$	0.16	i_{T-Fz}	-0.99
n=2 (M_x,V_x)	Hanging wall	$u_{Hx\max}$	10.49	i_{T-Hx}	-0.99
	Footwall	$u_{Fx\max}$	0.03	i_{T-Fx}	0.99
n=3 (M_z,V_z)	Hanging wall	$u_{Hz\max}$	9.28	i_{T-Hz}	0.99
	Footwall	$u_{Fz\max}$	0.16	i_{T-Fz}	-0.99

3.4 *Calculation method of the tunnel cross-section response*

The deformation of n nodes of support structure is calculated by the method of cross section deformation of tunnel through active fault zone, see Section 3.2. Then, after loading the deformation into the model shown in Figure, the internal force of the tunnel cross-section can be obtained.

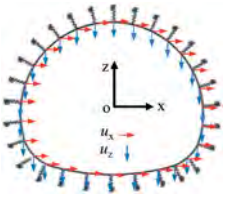

Figure 12. Internal force calculation model of tunnel cross section.

4 VERIFICATION

To verify the internal force calculation method of tunnels crossing active faults, a finite element model is established using the Midas GTS NX 2022 software. In the model, the tunnel is simulated using beam elements with an element length of 0.5 m to ensure precise calculations. A tunnel with a total length of 100 m, an external diameter D of 15 m, and a thickness t of 0.7 m is modeled for the analysis. The material used for the tunnel is C35 reinforced concrete with an elastic Young's modulus of 32.5 GPa and Poisson's ratio of 0.2.

Due to its prevalence and complexity in practical engineering, the oblique-slip fault is often the focus of seismic hazard analyses. In this study, the analysis model utilizes a normal left-lateral strike-slip fault with a dip angle α of 76° and an intersection angle β of 80°. The coseismic-slip is 1m in both the vertical and horizontal directions, with 0.5m occurring in the hanging wall and 0.5m occurring in the footwall. To ensure appropriate boundary conditions, the coseismic-slip of the analysis case is specified to the boundary nodes. Figure 15 displays the relevant details of the boundary conditions.

Figure 16 to Figure 18 depict the axial force, bending moments, and shear forces of the tunnel. The analytical results are represented by solid lines while the finite element method (FEM) results are represented by symbols. The theoretical model displays remarkable agreement with the FEM-based analysis.

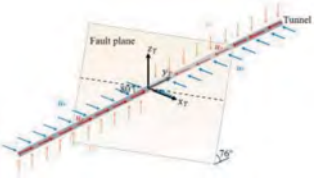

Figure 13. Boundary conditions.

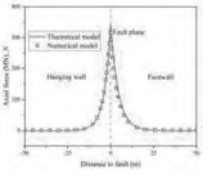

Figure 14. Axial force.

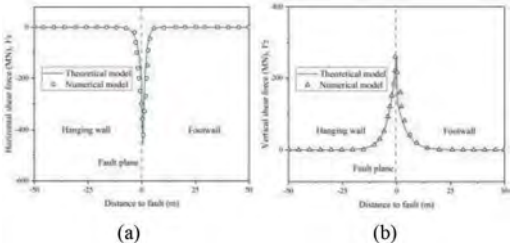

Figure 15. Shear force: (a) *Vx*; (b) *Vz*.

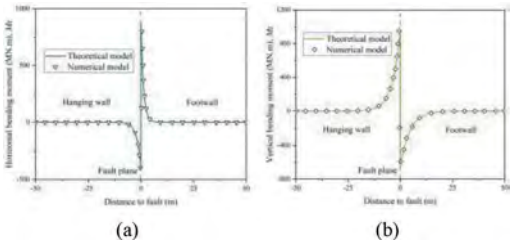

Figure 16. Bending moment: (a) *Mx*; (b) *Mz*.

5 CONCLUSIONS

This study presents a novel approach for predicting the stratum coseismic-slip and tunnel response under fault dislocation. The main findings of this research can be summarized as follows:

(1) The coseismic-slip of active faults exhibits an "S" shape, with the maximum coseismic-slip occurring at the fault plane and decreasing gradually as the fault distance increases. The form of the coseismic-slip curve is primarily affected by the range and maximum value of the coseismic-slip.

(2) By conducting mathematical statistical analysis, the prediction method of the vertical and horizontal coseismic-slip range of active faults is fitted. The theoretical calculation values exhibit excellent agreement with the measured values, which can serve as a useful reference for determining the engineering fortification range crossing or near the active fault.

(3) In view of the crucial parameters such as the coseismic-slip range and maximum, a prediction method for the stratum coseismic-slip is formulated. The derived theoretical values exhibit excellent agreement with the empirical measurements. The proposed approach is universally applicable for all types of faults and offers high computational accuracy and efficiency.

(4) Based on the prediction method for stratum coseismic-slip, the calculation method is developed to determine the coseismic-slip and response of tunnels. The results obtained from the proposed method demonstrate excellent quantitative agreement with the corresponding finite element analysis results.

ACKNOWLEDGEMENT

The authors are grateful for the support from the National Natural Science Foundation of China (52378411 and 52208404).

REFERENCES

Baziar, M.H., Nabizadeh, A., Lee, C.J., Hung, W.Y., 2014. Centrifuge modeling of interaction between reverse faulting and tunnel. Soil Dynamics and Earthquake Engineering 65, 151–164.

Burridge, P.B., Scott, R.F., Hall, J.F., 1989. Centrifuge study of faulting effects on tunnel. Journal of geotechnical engineering 115, 949–967.

Cai, Q., Peng, J., Ng, C.W., Shi, J., Chen, X., 2019. Centrifuge and numerical modelling of tunnel intersected by normal fault rupture in sand. Computers and Geotechnics 111, 137–146.

Chenxia, L., Xiwei, X., Xueze, W., Rongzhang, Z., Guihua, C., Hu, Y., Yanfen, A., Xiang, G., 2011. Rupture segmentation and slip partitioning of the mideastern part of the Kunlun Fault, north Tibetan Plateau. Science China Earth Sciences. 41(09), 1295–1310.

Guihua, C., Feng, L., Rongzhang, Z., Xiwei, X., Guihua, Y., Xuze, W., Yanfen, A., Chenxia, L., 2008. SEVERAL ISSUES IN THE QUANTITATIVE ANALYSIS OF CO-SEISMIC SURFACE RUPTURE PRODUCED BY REVERSE FAULTS: A CASE STUDY FROM THE 2008 WENCHUAN EARTHOUAKE. SEISMOLOGY AND GEOLOGY 03, 674–682.

Guihua, C., Xiwei, X., Guihua, Y., Yanfen, A., Renmao, Y., Tingting, G., Xiang, G., Hu, Y., Xibin, T., 2009a. Coseismic slip and slip partitioning of multi-faults during the M 8.0 2008 Wenchuan earthquake. CHINESE JOURNAL OF GEOPHYSICS 52(05), 1384–1394.

Guihua, C., Zhongwu, L., Xiwei, X., Haoyue, S., Guanghao, H., Peng, G., Peng, S., Zhaode, Y., Tao, L., 2022. Co-seismic surface deformation and late Quaternary accumulated displacement along the seismogenic fault of the 2021 Madoi M7.4 earthquake and their implications for regional tectonics. CHINESE JOURNAL OF GEOPHYSICS 65(08), 2984–3005.

GuiHua, Y., XiWei, X., GuiHua, C., 2009b. Relationship between the localization of earthquake surface ruptures and building damages associated with the Wenchuan 8.0 earthquake. CHINESE JOURNAL OF GEOPHYSICS 52 (12), 3027–3041.

Hu, Z., Ren, X., Wang, Q., Wang, R., Pan, R., 2022. Analytical method for the mechanical response of buried pipeline under the action of strike-slip faulting. Underground Space 7, 268–277.

Karamitros, D.K., Bouckovalas, G.D., Kouretzis, G.P., 2007. Stress analysis of buried steel pipelines at strike-slip fault crossings. Soil Dynamics and Earthquake Engineering 27, 200–211.

Karamitros, D.K., Bouckovalas, G.D., Kouretzis, G.P., Gkesouli, V., 2011. An analytical method for strength verification of buried steel pipelines at normal fault crossings. Soil Dynamics and Earthquake Engineering 31, 1452–1464.

Kawashima, Kazuhiko, 1994. Seismic design of underground structures. Japan: Kashima Publishing House.

Kennedy, R.P., Williamson, R.A., Chow, A.M., 1977. Fault movement effects on buried oil pipeline. Transportation Engineering Journal of ASCE 103, 617–633.

Newmark, N.M., Hall, W.J., 1975. Pipeline design to resist large fault displacement, Proceedings of US national conference on earthquake engineering. Ann Arbor, MI, pp. 416–425.

Ranjbarnia, M., Zaheri, M., Dias, D., 2020. Three-dimensional finite difference analysis of shallow sprayed concrete tunnels crossing a reverse fault or a normal fault: A parametric study. Frontiers of Structural and Civil Engineering 14, 998–1011.

Sabagh, M., Ghalandarzadeh, A., 2020. Numerical modelings of continuous shallow tunnels subject to reverse faulting and its verification through a centrifuge. Computers and Geotechnics 128, 103813.

Talebi, F., Kiyono, J., 2021. A refined nonlinear analytical method for buried pipelines crossing strike-slip faults. Earthquake Engineering & Structural Dynamics 50, 2915–2938.

Trifonov, O.V., Cherniy, V.P., 2010. A semi-analytical approach to a nonlinear stress–strain analysis of buried steel pipelines crossing active faults. Soil Dynamics and Earthquake Engineering 30, 1298–1308.

Wang, L.J., Wang, L.R., 1995. Buried pipelines in large fault movements. American Society of Civil Engineers, New York, NY (United States).

Wang, L.R.L., Yeh, Y.H., 1985. A refined seismic analysis and design of buried pipeline for fault movement. Earthquake engineering & structural dynamics 13, 75–96.

Wen-qiao, L., Jie, C., Zhao-de, Y., Ming-da, H., Li Tao, Song, Y., Xiao-dong, Y., 2011. COSEISMIC SURFACE RUPTURES OF MULTI SEGMENTS AND SEISMOGENIC FAULT OF THE TASHKORGAN EARTHQUAKE IN PAMIR. SEISMOLOGY AND GEOLOGY 33(02), 260–276.

Xibin, T., Renmao, Y., Xiwei, X., Guihua, C., Chungpai, C., 2013. CO-SEISMIC RUPTURE AND DISPLACEMENT IN THE XIAOYUDONG AREA PRODUCED BY THE 2008 WENCHUAN EARTHQUAKE,CHINA,AND ITS MECHANISM. SEISMOLOGY AND GEOLOGY 35(02), 247–260.

Xiwei, X., Guihua, C., Guihua, Y., Xijie, S., Xibin, T., Lichun, C., Jianbao, S., Yugao, C., Wenshan, C., Shuping, Z., Kang, L., 2010. Reevaluation of surface rupture parameters of the 5· 12 Wenchuan earthquake and its tectonic implication for Tibetan uplift. CHINESE JOURNAL OF GEOPHYSICS 53(10), 2321–2336.

Xiwei, X., Guihua, Y., Wentao, M., Yongkang, R., Guihua, C., Zhujun, H., Lanfeng, Z., 2002. EVIDENCE AND METHODS FOR DETERMINING THE SAFETY DISTANCE FROM THE POTENTIAL EARTHQUAKE SURFACE RUPTURE ON ACTIVE FAULT. SEISMOLOGY AND GEOLOGY 24(04), 470–483.

XIwei, X., Xueze, W., Jianqing, Y., Baoqi, M., Jie, C., Rongjun, Z., Honglin, H., Qinjian, T., Yunlin, H., Zhicai, W., Zhaomin, S., Xijie, F., Guihua, Y., Lichun, C., Guihua, C., Shene, Y., Rongkang, R., Xiguang, L., Chenxia, L., Yanfen, A., 2008. THE Ms 8.0 WENCHUAN EARTHQUAKE SURFACERUPTURES AND ITS SEISMOGENIC STRUCTURE. SEISMOLOGY AND GEOLOGY 03, 597–629.

Yong, L., Rongjun, Z., Densmore, A.L., Liang, Y., Richardson, N., Shunli, D., A. Ellis, M., Yi, Z., Yulin, H., Hao, C., Baocheng, Q., Bolin, M., 2008. Surface Rupture and Deformation of the Yingxiu-Beichuan Fault by the Wenchuan Earthquake. ACTA GEOLOGICA SINCA 82 (12), 1688–1706.

Z, Y., J, L.-Z., X, L., J, X., W, Y., L, H., T, L., 2021. Detailed mapping of the surface rupture of the 12 February 2014 Yutian M s 7.3 earthquake, Altyn Tagh fault, Xinjiang, China. Science China Earth Sciences 64(1), 127–147.

Zhao, K., Chen, W., Yang, D., Zhao, W., Wang, S., Song, W., 2019. Mechanical tests and engineering applicability of fibre plastic concrete used in tunnel design in active fault zones. Tunnelling and Underground Space Technology 88, 200–208.

Tunnelling for a Better Life – Yan, Celestino, Thewes & Eberhardt (Eds)
© 2024 The Author(s), ISBN 978-1-032-80042-4
Open Access: www.taylorfrancis.com, CC BY-NC-ND 4.0 license

Study on mechanical characteristics of a DDCI connection structure for longitudinal joints

Mingqing Xiao, Junwei Chen & Guangqiao Xue
China Railway Siyuan Survey and Design Group Co., Ltd, Wuhan, China
NATIONAL-LOCALJonit Engineering Research Center of Underwater Tunnelling Technology, Wuhan, China

Zhiguo Yan
State Key Laboratory for Disaster Reduction in Civil Engineering Tongji University, Shanghai, China
Department of Geotechnical Engineering, Tongji University, Shanghai, China

Shaofeng Wang
China Railway Siyuan Survey and Design Group Co., Ltd, Wuhan, China
NATIONAL-LOCALJonit Engineering Research Center of Underwater Tunnelling Technology, Wuhan, China

ABSTRACT: In order to solve the large deformation problem of Haitai Yangtze River tunnel and improve the stiffness of longitudinal joint, a DDCI connection structure for longitudinal joint is proposed in this paper. By using the numerical software ABAQUS, the DDCI connection structure model was established, and the tensile and shear characteristics of the structure were studied. According to the numerical results, the influence of the form, size and material of the component on the mechanical characteristics of DDCI connection structure was analysed, and the optimization scheme of DDCI connection structure is proposed, which provides a reference for related engineering applications.

Keywords: DDCI connection structure, Longitudinal joints, Mechanical characteristics Tunnelling

1 INTRODUCTION

The Haitai Yangtze River tunnel is a cross-river tunnel connecting Haimen and Taicang with a total length of 11.2km, which is an important infrastructure construction project. Due to the fact that the tunnel is located under water, the tunnel confronts the challenge of large structural deformation, which means higher requirements to the joints. It is well known that the joint structure type is greatly significant in the design of shield tunnel structure, which should not only consider the surrounding geological conditions, load and waterproof requirements, but also the construction convenience, economic rationality, construction period pressure, maintenance difficulty and other factors.

Currently, most of the longitudinal joints of the existing shield tunnel segments are bolted, which can be caught in a dilemma when it comes to the tunnel with large diameter. If single-row bolts are used, the corresponding longitudinal joint stiffness is small and the structural deformation is large, which is not conducive to the structural safety. Otherwise, if double-row bolts are used, the large hand holes will greatly weaken the force section of segment structure, thus reducing the bearing capacity of the structure and affecting the structural safety. Moreover, the hand holes can reduce the suction force of the vacuum sucker used in the assembly of lining segments, which pose threat to construction safety. In order to avoid the adverse influence of hand holes and achieve rapid assembly, the present scheme adopts the quick connection method with embedded parts, mostly relating to CT-type connection. However, the female joints of CT-type connection method are generally hollow embedded components, which causes great reduction on the thickness of the segments and also requires extremely high fabrication accuracy and construction accuracy. In addition, the existing quick connection method can potentially affect the waterproof safety for changing the conventional segment assembly method.

In view of the technical problems such as that the existing conventional inclined bolts cannot meet the deformation requirements of the shield tunnel, the construction difficulty and poor waterproof safety of CT-type connection, as is shown in Figure 1, this paper proposes a new longitudinal segment joint,

DOI: 10.1201/9781003495505-171

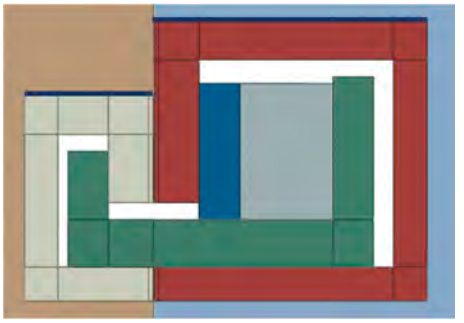

Figure 1. Section view of DDCI connection.

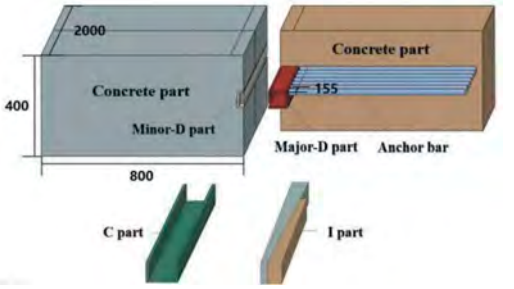

Figure 2. DDCI connection of longitudinal segments.

DDCI connection, which can realize multi-point connection without hand holes. By combining this connection and the traditional inclined bolts in the longitudinal joints of lining segments, the relative sliding of the joint surface can be reduced during assembly and meanwhile the impairment of concrete section can be avoided. Also, the waterproof safety can be ensured with DDCI connection. The following sections will analyse the mechanical response of the new DDCI connection structure by numerical simulation method, and propose the optimized structure design.

2 MODEL EXPERIMENT

This study intends to carry out systematic scientific research on the mechanical behaviour of DDCI longitudinal joints connection through numerical calculation by ABAQUS, including the optimization of the form, material and geometric size of the DDCI connection.

2.1 *Numerical model*

The numerical model of DDCI connection is composed of concrete blocks, major-D part, minor-D part, C part, I part and anchor bar, as shown in the Figure 2. The major-D part and the minor-D part which are embedded in two adjacent concrete blocks respectively are connected to the concrete by anchor steel bars. The length of the concrete block is 800mm, the thickness is 400mm, and the width is 2000mm. The diameter of the anchor steel bar is 25mm, and the spacing is 155mm. Other values of form and size vary in the DDCI studies. For materials, the segments are made of concrete of C60 and the anchor bar is designed as HRB500. The model is calculated using an eight-node linear hexahedron element.

In order to investigate the influence of different forms, sizes and materials on the mechanical properties of DDCI connections, a number of working conditions were designed by numerical experiments. To fasten DDCI connection and provide preload, two types of I parts are studied, which can be named as form A and form B. As is shown in Figure 3, form A consists of a steel rod and a sleeve, of which the outer side is designed with evenly distributed barbs, and the angle between the barbs and the sleeve is 45 degrees. When the A-form I part is inserted into the gap between the major-D part and the C part, the presence of barbs render the I part an expansion force, thus fixing the DDCI connection. Form B includes two wedge members of different lengths. The longer wedge member is firstly inserted into the gap between the major-D part and the C part during assembly, and then the shorter wedge member is inserted. The deeper the wedge inserted, the greater the preload provided.

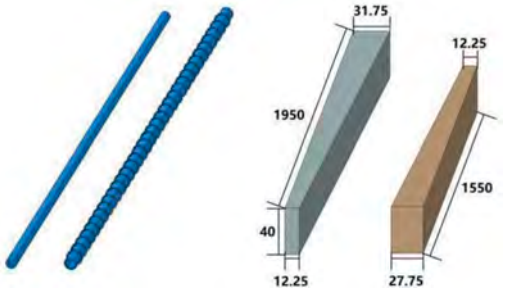

Figure 3. I parts of DDCI: form A (left); form B (right).

In terms of size, in order to acquire better mechanical properties of DDCI connection, the study changes the size of C part and D part. The thickness of the C part is set as 8mm and 10mm, the thickness of the D part is set as 8mm, 10mm and 12mm, and the length of the cantilever end of minor-D part is set as 14mm and 42mm respectively. In summary, considering the influence of size, four groups of working conditions are designed as is shown in Figure 4.

Obviously, the materials of the structure have a significant influence on its mechanical response, so the effects of different materials are also taken into consideration in the study. For D part and C part, the test uses a variety of steel types, including Q690, Q550 and Q345, and the size scheme of C10-D12-14 is adopted in the experiment. For I part, the materials of the sleeve in form A and wedge members in form B are deigned experimentally using polyamide and polytetrafluoroethylene. To sum up all above, the working conditions are listed in Table 1.

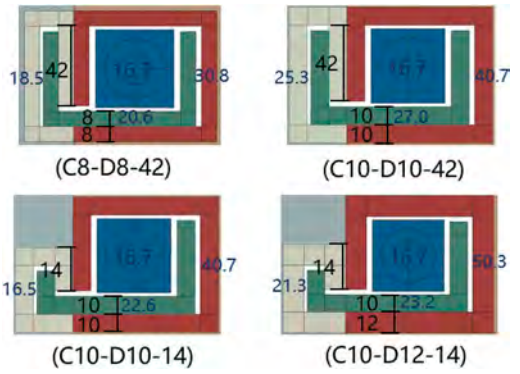

Figure 4. Four working conditions of different sizes.

Table 1. Working conditions of DDCI model.

	I part	C part and D part
1	Form A - polyamide	C10-D10-42-Q550
2	Form A- polytetrafluoroethylene	C10-D10-42-Q550
3	Form B - polyamide	C10-D10-42-Q550
4	Form B- polytetrafluoroethylene	C10-D10-42-Q550
5	Form A- polytetrafluoroethylene	C8-D8-42-Q550
6	Form A- polytetrafluoroethylene	C10-D10-14-Q550
7	Form A- polytetrafluoroethylene	C10-D12-14-Q550
8	Form B - polyamide	C10-D12-14-Q690
9	Form B - polyamide	C10-D12-14-Q550
10	Form B - polyamide	C10-D12-14-Q345

In the study of all working conditions, the tensile behaviour of concrete segment joints is used as evaluation criteria. In the model shown in Figure 5, the vertical and horizontal displacement of the left concrete block is limited, and the vertical displacement of the right concrete block is limited. Meanwhile, the tensile forces are applied at two ends of the concrete blocks equally. In order to study the stiffness of DDCI connection, the opening of concrete segments during the increase of the tensile force is an important observation value.

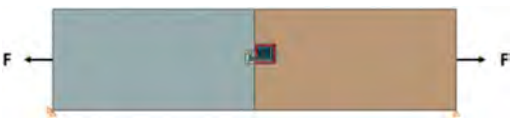

Figure 5. Tensile experiment on DDCI numerical model.

2.2 *Physical model*

To verify the results of the numerical simulation, the study also supplemented some physical experiments on DDCI connection. In the experiment shown in Figure 6, two T-shape rectangular concrete blocks were poured with fiber concrete labeled C60, of which the optimized DDCI connection obtained by numerical simulation was installed in the middle. Besides, the anchor bars of D parts and the reinforcement cage in the concrete are designed according to the actual scheme of the Haitai Yangtze River Tunnel. In physical experiments, hydraulic jacks are used to exert tension on concrete blocks and pull rod displacement gauges are used to measure the opening of concrete segments under different tensile forces, so as to evaluate the stiffness of DDCI connection.

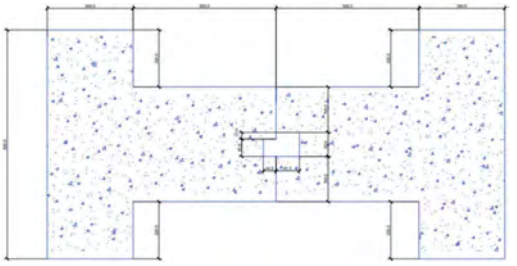

Figure 6. Tensile experiment on DDCI physical model.

3 DISCUSSION

Through numerical simulation and validation of physical experiments, a deep understanding of DDCI connection is acquired. In this section, the influence of form, size and material on the DDCI connection will be discussed in order to obtain the optimal structural solutions.

3.1 *Influence of form*

In terms of form, the influence of form A and form B on DDCI connection stiffness was both analysed by numerical simulation. For form A, the length of the barbs was changed to 18mm and 45mm respectively. As is shown in Figure 7, the results show that when the segment opening is 4mm, the tensile force borne by DDCI connection with 18mm barb is about 0.5MN, while the tensile force borne by DDCI connection with 45mm barb is about 0.7MN. However, the stiffness of form A is significantly lower than that of the inclined bolt connection.

For form B, the study modified the jacking force of the wedge member to 0 and 100kN. As is shown in Figure 8, the results show that when the segment opening reaches 4mm, the tensile force borne by DDCI connection is about 2.7MN and the stiffness of the connection with jacking force of 100kN is slightly higher than that without jacking force. On the whole, DDCI connection of form B has a better effect, of which the stiffness is greatly improved compared with the inclined bolt connection.

3.2 *Influence of size*

In order to test the influence of size, four working conditions were studied, where the dimensions of D part and C part were designed differently, including the thickness and the length of the cantilever

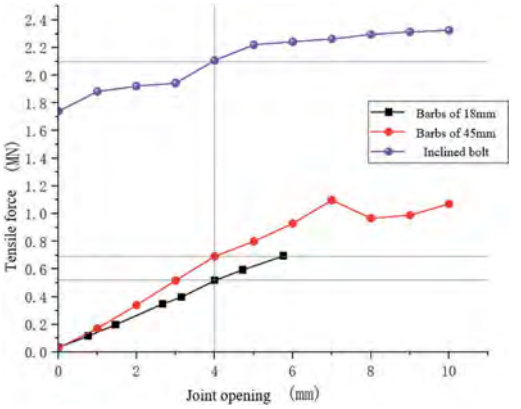

Figure 7. Tension-opening curve of DDCI of form A.

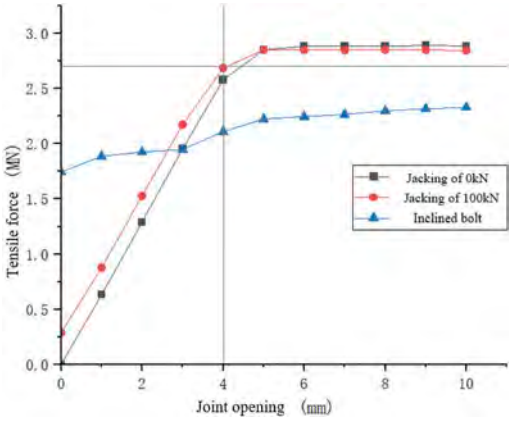

Figure 8. Tension-opening curve of DDCI of form B.

end. According to the size of the DDCI connection, the four working conditions are named as C8-D8-42, C10-D10-42, C10-D10-14 and C10-D12-14, which is shown in Figure 4. To clarify with C10-D12-14, it represents that the thickness of C part is 10mm, the thickness of C part is 12mm and the cantilever end length of minor-D part is 14mm.

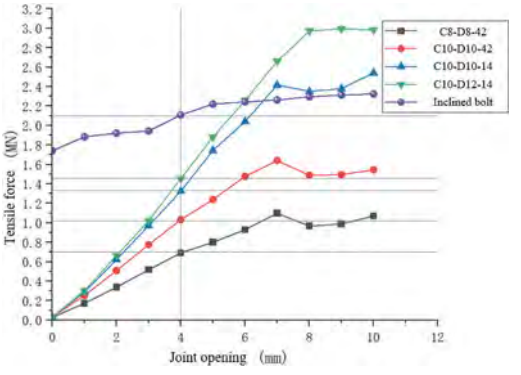

Figure 9. Tension-opening curve of DDCI of different sizes.

The experimental results are shown in the Figure 9, from which it can be found that the overall stiffness of DDCI connection with minor-D part of short cantilever end is obviously larger than that of DDCI connection with minor-D part of long cantilever end. The stiffness of DDCI connection of C10-D12-14 is the highest, of which the tensile force is over 1.4MN when the joint opening is 4mm. Also, the raise in the thickness of DDCI may lead to the increase in the stiffness of connection. As a consequence, the connection of C8-D8-42 has the lowest stiffness because of its long cantilever end and small thickness. Moreover, with the gradual increase of the joint opening, the stiffness differences in different working conditions will become more obvious. Confronted with large structural deformation, the stiffness of DDCI connections of C10-D10-14 and C10-D12-14 is even larger than that of the connection with inclined bolts.

3.3 *Influence of material*

Numerical simulation experiment shows that different materials can lead to different mechanical behaviours of DDCI connection. The I part is designed with polyamide and polytetrafluoroethylene. However, considering the effect of practical engineering and material property, it is well believed that the use of polytetrafluoroethylene for sleeve of form A and polyamide for wedge members of form B is the most appropriate scheme.

For the materials of D part and C part, the numerical simulation experiment is carried out for an insightful analysis, where steel of Q690, Q550 and Q345 are involved. The results are shown in Figure 10, from which it can be concluded that when the joint opening is less than 3mm, the different types of steel have little influence on the stiffness. Nevertheless, when the joint opening reaches 4mm, the stiffness of the working conditions with Q690 and Q550 is slightly higher than that of the working condition with Q345. With the gradual change of the joint opening, the stiffness of the condition with Q345

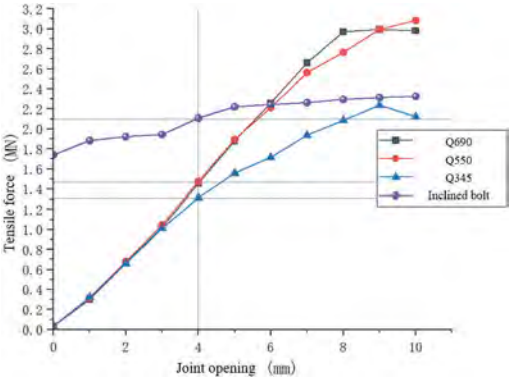

Figure 10. Tension-opening curve of DDCI of different materials.

is obviously the worst, but the stiffness of working conditions with Q550 and Q690 are just similar. Taking the construction economy into consideration, Q550 is the best choice for D part and C part due to its comparably better effect and low price.

3.4 *Validation of physical experiment*

The optimum DDCI connection scheme was obtained by the numerical experiments, including wedge members made of polyamide material as I part. The dimensions of D part and C part are determined according to the working condition C10-D12-14, which are made of Q550 steel. Following the design above, test blocks were poured and DDCI connection was installed to perform physical experiments in order to verify the results of the numerical simulation. The T-shaped concrete blocks were placed vertically and the hydraulic jacks were fixed to the concrete with the steel frame, which is shown in Figure 11.

Figure 11. Physical experiment of DDCI connection.

The displacement meters are arranged on the two surfaces of the segment joint to measure the value of opening at both ends and the middle of the surfaces. Several strain gages are installed inside the concrete to measure the mechanical behaviour of the anchor bars of major-D part and minor-D part. In the physical experiment, in order to test the tensile properties of DDCI connection, the computer-controlled hydraulic jacks applied load to the structure step by step according to the loading scheme shown in Table 2.

The outer surface of the concrete segment is denoted as plane A and the inner surface is denoted as plane B. The measuring points of the joint opening from one end to the other end are denoted as 1, 2 and 3 respectively. Therefore, the six displacement meters can be named as A1, A2, A3 and B1, B2, B3. Similar to the numerical simulation, the change in the opening of the segment joint as the tensile force increased was recorded, of which the results are shown in the Figure 12.

Table 2. Loading scheme.

Step	Load/kN	Time/min
1	120	preload
2	240	5
3	360	5
4	480	5
5	600	5
6	720	5
7	840	5
8	960	5
9	1080	5
10	1200	5
11	-	10

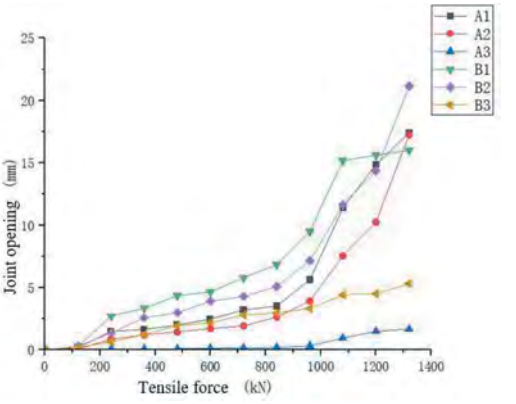

Figure 12. Tension-opening curve of DDCI in physical experiment.

The results show that when the average joint opening is 4mm, the tensile force that the concrete segments can withstand is about 1MN, which is slightly smaller than the numerical simulation results. However, considering the influence of test site factors, the reduction of stiffness is permissible. In terms of mechanical behaviour, the results of numerical simulation are basically verified by the physical experiments.

4 CONCLUSIONS

In order to investigate the mechanical properties of DDCI connection, a great number of numerical simulation and physical experiments have been carried out so far. Based on the analysis results, some important conclusions concerning DDCI connection can be drawn as follows:

(1) The feasibility of DDCI connection is verified by the experiments. Through a special mold and pouring method, major-D part and minor-D part can be fixed in the concrete segments with anchor bars, which make them work together. With the jacking device, C part and I part can be

smoothly installed into the gap of D parts, through which a certain preload will be provided.

(2) The optimum design of DDCI connection is given by the discussions above. The form of I part is determined as form B, which includes two wedge members of different length. The dimension plan of C part and D parts is determined according to the working condition of C10-D12-14, which means the thickness of C part is 10mm, the thickness of D part is 12mm and the length of the cantilever end of minor-D part is 14mm. Considering the requirements of construction economy and structural mechanics, the material of I part is designed as polyamide and the material of C part and D parts is designed as steel of Q550.

(3) The strength and stiffness of the DDCI connection is proved by the experiments. Although the results of physical experiments are not as good as that of numerical simulation, the strength and stiffness of DDCI connection can meet the structural requirements of Haitai Yangtze River Tunnel. Combined with inclined bolts, DDCI connection can effectively reduce the large deformation of tunnel structure.

ACKNOWLEDGMENTS

The great support for this work of 'Study on structural mechanical behaviour test and numerical simulation of DDCI new connection for longitudinal joints of lining segments in Haitai Yangtze River Tunnel project' is appreciated.

REFERENCES

ASTM D2938-95, 1995. Standard test method of unconfined compressive strength of intact rock core specimens. ASTM International, West Conshohocken, PA, USA.

Cairns, R.B., 1965. Infrared spectroscopic studies of solid oxygen. PhD Thesis. University of California, Berkeley, CA, USA.

Guo, R., He, C., Su Z. X., et al, 2011. "Study of shearing mechanical properties of segment joints of shield tunnels. Mode. Tunn. Tech. 48(4), 72–77.

Holt, R.M., Kenter, C.J., 1992. Laboratory simulation of core damage induced by stress release. In: Tillerson, J. R., Waversik, W.R. (Eds.), Rock Mechanics – Proceedings of the 33rd U.S. Symposium on Rock Mechanics (USRMS). A.A. Balkema, Rotterdam, Netherlands, pp. 959–968.

Levinsky, N.G., 1977. Fluid and electrolytes. In: Thorn, G. W., Adams, R.D., Braunwald, E. (Eds.), Harrison's Principles of Internal Medicine, 8th ed. McGraw-Hill, New York, NY, USA, pp. 364–375.

Vutukuri, V.S., Lama, R.D., 1978. Dynamic elastic constants of rocks. In: Lama, R.D., Vutukuri, V.S. (Eds.), Handbook on Mechanical Properties of Rocks, vol. II. Trans Tech Publications, Clausthal-ZellerfieL, Germany, pp. 236–237.

Tunnelling for a Better Life – Yan, Celestino, Thewes & Eberhardt (Eds)
© 2024 The Author(s), ISBN 978-1-032-80042-4
Open Access: www.taylorfrancis.com, CC BY-NC-ND 4.0 license

Research on support parameters of the second Jiaozhou Bay Subsea tunnel based on the total safety factor method

Mingqing Xiao, Wenhao Sun, Libao Chen & Linsen Jin
China Railway Siyuan Survey and Design Group CO., LTD, Wuhan, China

ABSTRACT: Although China has gained some experience in submarine tunnel construction, there are still some theoretical unclear areas in the design of support structures for drilling and blasting method tunnels, such as the exact role and load-bearing capacity of primary support during construction and operation. Therefore, the design of primary support is generally based on empirical analogy method. This research article proposed support parameters for the Second Jiaozhou Bay subsea tunnel based on empirical analogy, then conducted quantitative analysis of support parameters such as anchor rod length, anchor rod spacing, and shotcrete thickness by total safety factor method. The results indicate that the support structure design parameters based on empirical analogy have a larger overall safety factor and optimization space. The bearing arch effect of the surrounding rock and anchor rock is significant, and the length increase of the anchor rod has a significant effect on the safety factor improvement, especially for the III-level surrounding rock. Under the condition of unchanged or slightly increased safety factor, properly increasing the length and spacing of anchor rods can significantly reduce the anchor rod quantity. Economic and technical comparison analysis results show that the support parameter optimized by the method of total safety factor has significant economical advantages.

Keywords: Drilling and Blasting Method, Total Safety Factor Method, Support Parameter, Subsea Tunnel

1 INTRODUCTION

With the development of the national economy, the demand for cross-sea transportation is increasing. Cross-sea transportation can be achieved through bridges and tunnels. Submarine tunnels are increasingly showing their superiority due to advantages such as being unaffected by typhoons, minimal environmental impact, and no interference with shipping. In recent years, during the selection process of different cross-sea transportation schemes, tunnel schemes often become the preferred choice.

The main factors that influence the selection of tunnel lining structure types and the design of support parameters include the type of tunnel usage, engineering geological and hydrogeological conditions, and construction methods. For deep-buried submarine tunnels, the external water pressure is high, and circular lining structures are suitable for fully sealed tunnels. Tunnel Boring Machines (TBMs) are suitable for circular lining structures, while drilling and blasting methods are suitable for various lining structure types.

Composite lining is commonly used in transportation tunnels. Many scholars at home and abroad have conducted in-depth research on the calculation methods of initial support for composite lining, proposing methods such as engineering analogy, characteristic curve method, formation-structure method, and limit analysis-based formation-structure method. However, there is a lack of clear load values and safety factor calculations. In the calculation of secondary lining, the load-structure method is generally used. Due to the different calculation methods used for initial support and secondary lining, it is difficult to evaluate the overall safety of the composite lining structure as a whole. To address this issue, Xiao Mingqing et al. established a method for designing the total safety factor of composite lining tunnels and used this method to analyze the safety of railway tunnels. They also conducted research on controversial issues such as the role of anchor rods, tunnel load-bearing structure, and optimization of support parameters.

2 ENGINEERING BACKGROUND

The Jiaozhou Bay Second Subsea Tunnel is located within the city limits of Qingdao on the Shandong Peninsula, between the existing Jiaozhou Bay Tunnel and Jiaozhou Bay Bridge. Once completed, it will serve as an important link between the West Coast New Area and the main urban area of Qingdao on the East Coast.

The Qingdao Jiaozhou Bay Second Subsea Tunnel project is a bi-directional 6-lane urban expressway with a design speed of 80km/h. The total length of the project is approximately 17.5km, with the tunnel section

DOI: 10.1201/9781003495505-172

accounting for 14.37km. The underwater section is approximately 10km long. The tunnel layout consists of two main tunnels and a central service tunnel, making it the largest and longest underwater tunnel in China upon completion. The construction method for this project combines drilling and blasting, shield tunneling, and open-cut methods. The drilling and blasting section of the tunnel is 9,427m long, while the shield tunneling section is 3,253m long.

Figure 1. General plan layout diagram of the tunnel.

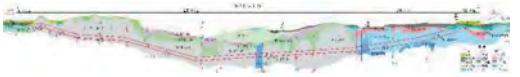

Figure 2. Cross-sectional illustration of the tunnel.

3 SUPPORT PARAMETERS BASED ON EMPIRICAL ANALOGY METHOD

Considering that the Jiaozhou Bay Second Subsea Tunnel has a much greater burial depth compared to the Jiaozhou Bay Tunnel, Xiamen Xiang'an Tunnel, and Haicang Tunnel, the support parameters for the Jiaozhou Bay Second Subsea Tunnel were preliminarily determined through the empirical analogy method based on the design and construction experiences of the aforementioned projects. The support parameters for the subsea section are shown in Table 1.

Table 1. Support parameters for the jiaozhou bay second subsea tunnel based on empirical analogy method.

Lining Type		Type III	TypeIV	Type V
Rock Grade		III2	IV2	V2
Initial Support	Anchor	ϕ22 multiple corrosion-resistant anchors for arch, L=3.5m, spacing 1.2×1.2m	ϕ22 multiple corrosion-resistant anchors for arch wall, L=3.5m, spacing 1.0×1.0m	ϕ22 multiple corrosion-resistant anchors for arch wall, L=4.0m, spacing 0.75×1.0m
	Steel Mesh	Local, ϕ8	ϕ8, 20×20cm	ϕ8, 15×15cm
	Shotcrete	C35 10cm	C35 28cm	C35 26cm
	Steel Frame	--	22H170 grid, spacing 1.0m	25H220 grid, spacing 0.5m
Secondary Lining	Arch, Wall	C50, 50cm※	65cm※	70cm※
	Inverted Arch	--	80cm※	90cm※
	Reinforcement	22mm @150mm	25mm @150mm	28mm @150mm

Note: The "※" in the secondary lining thickness represents C50 reinforced concrete lining; without "※" represents C50 plain concrete lining; Shotcrete: plain concrete is CF45 steel fiber reinforced concrete.

4 SUPPORT PARAMETERS BASED ON TOTAL SAFETY FACTOR METHOD

4.1 *Total safety factor method*

This method focuses on the tunnel approaching or reaching the failure stage and integrates the geological-structural method with the load-structural method. It establishes a unified approach to evaluate and calculate the safety of tunnel support structures by organically integrating the rock mass, loads, and support structures.

The calculation of rock pressure is based on the "design value of rock pressure." Considering that tunnel rock pressure varies with multiple factors such as support parameters, timing of support installation, and characteristics of support materials, the design of hypothetical support force is obtained to simultaneously meet the safety and economic requirements of tunnel support structures when the tunnel approaches or reaches the failure stage.

In the calculation of support structures, the tunnel support structure is divided into three layers: the rock-bearing arch, the shotcrete layer (including steel frames), and the secondary lining. The safety factors of the rock-bearing arch, shotcrete layer, and secondary lining are calculated separately. The lower limit of the total safety factor of the support structure can be approximately calculated using the following formulas:

Construction phase (without secondary lining):

$$\mathrm{Kc} = \eta \mathrm{K1} + \mathrm{K2} \tag{1}$$

Operation phase: When using durable anchor rods,

$$\mathrm{Kop} = \eta \mathrm{K1} + \xi \mathrm{K2} + \mathrm{K3} \tag{2}$$

When using non-durable anchor rods,

$$\mathrm{Kop} = \xi \mathrm{K2} + \mathrm{K3} \tag{3}$$

Where, K1, K2, and K3 represent the safety factors of the rock-bearing arch, shotcrete layer, and secondary lining when subjected to the design value of rock pressure. η is the modification coefficient for the safety factor of the rock-bearing arch, and ξ is the adjustment coefficient for the bearing capacity of the shotcrete layer.

4.2 *Safety verification of support parameters using empirical analogy method*

The rock mass parameters refer to the 《Feasibility Stage Survey Report of the Second Subsea Tunnel in Qingdao》 and the 《Highway Tunnel Design Code》 (JTG 3370.1-2018). The recommended lower 1/3 quantile values of rock mass level parameters are shown in Table 2.

Based on the selected types of lining (Type III-V) using the empirical analogy method, the results show that the safety factors of initial support and secondary lining of each type of lining can meet the

Table 2. Physical and mechanical parameters of rock mass levels.

Rock Mass Level	III	IV	V
Density (kN/m3)	25.17	23.17	18.83
Elastic Resistance Coefficient Ke (MPa/m)	733.33	300	133.33
Deformation Modulus E (GPa)	10.67	2.87	1.00
Poisson's Ratio	0.28	0.33	0.43
Internal Friction Angle φ (°)	42.67	31.00	22.33
Cohesion c (MPa)	0.97	0.37	0.10

requirements. The construction phase total safety factor Kc ranges from 3.80 to 8.80, meeting the minimum safety factor requirement of 1.8. The operation phase total safety factor Kop ranges from 9.72 to 28.90, meeting the minimum safety factor requirement of 3.6. Overall, the safety factors of the support parameters are relatively high, indicating significant potential for optimization.

4.3 *Research on support parameters using the total safety factor method*

4.3.1 *Research plan for initial support parameters*

In the design of composite lining structures, there are three different design concepts based on the different functions of initial support and secondary lining: the first concept treats the initial support as a temporary structure and the secondary lining as the load-bearing main body; the second concept treats the initial support as the load-bearing main body and the secondary lining as either a safety reserve or for bearing minimal loads; the third concept treats both as load-bearing main bodies. Different design concepts result in different support parameters.

From the perspective of initial support, there are three possible structural schemes for initial support (for ease of explanation, regardless of whether the shotcrete contains steel mesh or steel frame, it is simply referred to as the "shotcrete layer"):

(1) Structure without systematic anchor support, where the initial support mainly consists of the shotcrete layer, without systematic anchor support, only local anchors are installed to prevent spalling.
(2) Combined support of shotcrete and anchor, where the initial support consists of both the shotcrete layer and systematic anchors.
(3) Anchor-dominated support structure, where the rock pressure is entirely borne by systematic anchors, and the local loose load between anchors is borne by the shotcrete layer, with a minimum structural thickness of 8cm.

In summary, this study first divides the initial support schemes into three categories based on their load-bearing roles, and then further divides each category into three research schemes based on different combinations of anchors and shotcrete. The specific schemes are shown in Table 3.

Table 3. Classification of research schemes for initial support design parameters.

	Role of Initial Support	Combination of Anchors and Shotcrete	Remarks
1	Scheme 1: Initial support bears only construction	Subscheme 1-1: Without systematic anchors	Common anchors
2	phase load; secondary lining bears all rock	Subscheme 1-2: Anchor-dominated	
3	pressure and water pressure during operation	Subscheme 1-3: Combined anchor and shotcrete	
4	Scheme 2: Initial support and secondary lining bear the	Subscheme 2-1: Without systematic anchors	Durable anchors
5	load together, with secondary lining bearing	Subscheme 2-2: Anchor-dominated	
6	all water pressure	Subscheme 2-3: Combined anchor and shotcrete	
7	Scheme 3: Initial support serves as the load-bearing main	Subscheme 3-1: Without systematic anchors	Durable anchors
8	body, with secondary lining bearing only	Subscheme 3-2: Anchor-dominated	
9	water pressure	Subscheme 3-3: Combined anchor and shotcrete	

4.3.2 *Preliminary determination and optimization principles of initial support parameters*

There are many strength grades for shotcrete and secondary lining concrete in initial support. In order to reduce the computational workload, this study adopts a uniform strength grade of C35 for shotcrete based on similar engineering experience and durability design requirements.

The minimum construction requirement for shotcrete thickness is 8cm, and the minimum construction requirement for secondary lining thickness is 35cm (based on the minimum value of secondary lining thickness in the design specifications for three-lane tunnels in highway tunnels).

The anchor rods are all Φ22 anchor rods, with a minimum length of 2.5m. The length is selected within the range of 2.5m to 5.0m, and for specific conditions, 6.0m and 7.0m long anchor rods are used for calculation. The spacing between anchor rods is not greater than half the length of the anchor rod.

Referring to the research results of "Calculation and Research on Support Parameters of High-Speed Railway Tunnels" (Xiao M. Q., et al), the recommended values for the safety factor of initial support are as follows: for Scheme 1 and Scheme 2, the total safety factor Kc during the construction phase

should be greater than or equal to 2.1, and for Scheme 3, the total safety factor Kc during the construction phase should be greater than or equal to 3.0.

4.3.3 *Preliminary support parameter design scheme comparative analysis*

4.3.3.1 Scheme 1

(1) Scheme 1-1 (Without Systematic Anchors)

Based on the minimum thickness of the shotcrete layer of 8cm, with a thickness increment of 2cm, multiple schemes were developed for rock grades III-V, and the initial support safety factors for each scheme are shown in the table below.

Table 4. Calculation results for scheme 1-1.

	Rock Grade	Shotcrete Thickness (cm)	Total Safety Factor Kc
1	III	8	1.24
2		10	1.94
3		12	2.32
4		14	2.69
5		16	3.06
6		18	3.42
7	IV	12	1.44
8		14	1.68
9		16	1.91
10		18	2.14
11		20	2.37
12		22	2.59
13	V	20	1.46
14		22	1.60
15		24	1.74
16		28	2.01
17		30	2.15
18		32	2.29
19		8	1.24

From Table 3.3-2, it can be observed that when considering only the load-bearing capacity during the construction phase and without installing anchors, the minimum shotcrete thickness required for rock grades III-V is 12cm, 18cm, and 30cm, respectively, to meet the requirement of the initial support safety factor Kc≥2.1 during the construction phase. Increasing the thickness of the shotcrete improves the safety factor to some extent, but the effect is not significant. Therefore, for rock grades IV and V, it is not economical to rely solely on shotcrete to increase the safety factor.

(2) Scheme 1-2 (Anchor as Dominant Support)

In the anchor-dominant support scheme, the minimum shotcrete thickness of 8 cm was chosen for rock grades III-V based on construction requirements. Then, various support schemes were proposed based on different anchor rod lengths and spacing.

From Table 5, it can be seen that when considering only the construction phase load in the initial support,

Table 5. Calculation results for scheme 1-2.

	Rock Grade	Shotcrete Thickness (cm)	Anchor Rod Length (m)	Anchor Rod Spacing (m)	Total Safety Factor Kc
1	III	8	2.5	1.0×1.0	7.49
2		8	2.5	1.2×1.2	7.00
3		8	3.0	1.5×1.5	7.61
4		8	4.0	2.0×2.0	8.95
5	IV	8	3.5	1.5×1.5	2.83
6		8	4.0	2.0×2.0	2.92
7		8	4.5	2.0×2.0	3.16
8		8	5.0	2.5×2.5	3.26
9	V	8	4.5	1.0×1.0	1.91
10		8	5.0	1.0×1.0	2.07
11		8	6.0	1.0×1.0	2.37
12		8	7.0	0.8×0.8	2.26

for rock grade III with good rock properties and strong arch bearing capacity of the anchor rock, the overall safety factor is larger. Additionally, increasing the length of the anchor rod significantly improves the safety factor. For rock grade IV, anchor rods with a length of 3.5m and spacing of 1.5m, or a length of 4.0m and spacing of 2.0m, can meet the requirement of the total safety factor Kc≥2.1 during the construction phase. For rock grade V, when the shotcrete thickness is 8cm and the anchor is the dominant support, anchor rods with a length of 6.0m or above are required to meet the requirement of the total safety factor Kc≥2.1 during the construction phase. However, the overall safety factor is relatively small, and the short length and spacing of the anchor rods result in a longer construction period and inconvenience in construction.

(3) Scheme 1-3 (Anchor-Spray Combination Support)

In this scheme, the initial support needs to bear the load together with the anchor rock arch and the shotcrete. The overall safety factor of the initial support is obtained by adding the safety factors of the shotcrete and the anchor rod. In the anchor-spray combination support, there are various combinations. Based on the results of Scheme 1-1 and Scheme 1-2, it can be concluded that for rock grades III, IV, and V, when the shotcrete thickness exceeds 12 cm, 18 cm, and 30 cm respectively, the total safety factor during the construction phase can be met. By considering different combinations of shotcrete thickness, anchor rod length, and spacing, the following design schemes are proposed, and the safety factors of the shotcrete, anchor rock arch, and anchor-spray combination are calculated as shown in the table below.

From the table above, it can be seen that rock grade III has a relatively high overall safety factor. For rock grades IV and V, if the shotcrete thickness required for the steel frame is not considered, a shotcrete thickness of 12 cm with anchor rods of

Table 6. Calculation results for scheme 1-3.

	Rock Grade	Shotcrete Thickness (cm)	Anchor Rod Length (m)	Anchor Rod Spacing (m)	Safety Factor		
					Shotcrete	Anchor Rock Arch	Anchor-Spray Combination
1	III	8	3.0	1.5×1.5	1.24	6.37	7.61
2		10	3.5	2.0×2.0	1.94	7.30	8.83
3		10	4.0	2.0×2.0	1.94	8.56	10.5
4	IV	12	4.0	1.5×1.5	1.44	2.43	3.87
5		14	4.0	1.5×1.5	1.68	2.54	4.22
6		16	4.5	2.0×2.0	1.91	2.72	4.63
7	V	20	4.0	1.0×1.0	1.45	1.27	2.72
8		24	4.0	1.0×1.0	1.74	1.36	3.10
9		26	5.0	1.5×1.5	1.88	1.36	3.24
10		28	5.0	2.0×2.0	2.01	1.26	3.27

length 4.0m and spacing 1.5m can meet the safety factor requirement during the construction phase for rock grade IV. Similarly, for rock grade V, a shotcrete thickness of 20 cm with anchor rods of length 4.0m and spacing 1.0m can meet the safety factor requirement during the construction phase. Considering the overall cost, the anchor-spray combination scheme provides a higher safety factor for the initial support compared to the scheme without a systematic anchor rod or the anchor-dominant support scheme.

4.3.3.2 Scheme 2

Schemes 1 and 2 both involve the normal operation of ordinary anchor rods and durable anchor rods during the construction phase, representing the same working conditions. The difference lies in the failure of ordinary anchor rods during the operational phase. Scheme 1 requires a stronger secondary lining to maintain the safety factor during the operational phase compared to Scheme 2. Therefore, the safety factor calculation for the initial support is not listed here. Please refer to Section 3.3.3.1 for details on Scheme 1.

4.3.3.3 Scheme 3

In this scheme, the initial support is considered as the main bearing body. Therefore, in this section, rock grades III-V are calculated with the safety factor based on the initial support bearing 100% of the rock pressure, without considering the contribution of the secondary lining to the bearing. For cases where the shotcrete serves as a permanent support structure, steel fiber reinforced concrete or steel frame reinforcement is used, providing good ductility, and the total safety factor is considered not less than 3.0.

(1) Scheme 3-1 (No Systematic Anchor Rods)

From Table 7, it can be seen that when the initial support is considered as the main bearing body without using anchor rods, the minimum shotcrete thickness required for rock grades III-V to meet the total safety factor Kc≥3.0 is 16cm, 26cm, and 38cm, respectively.

Table 7. Calculation results for scheme 3-1.

	Rock Grade	Shotcrete Thickness (cm)	Total Safety Factor Kc
1	III	14	2.69
2		16	3.06
3		18	3.42
4	IV	24	2.83
5		26	3.07
6		28	3.31
7	V	36	2.89
8		38	3.01
9		40	3.13

(2) Scheme 3-2 (Anchor-Dominant Support)

For rock grades III-IV, the shotcrete thickness is taken as the minimum construction requirement of 8cm. For rock grade V, based on preliminary calculations, when the shotcrete thickness is between 8cm and 18cm, the required anchor rod length or diameter is too large, exceeding the range of materials commonly used in construction. Therefore, the minimum shotcrete thickness is taken as 20cm. Various support schemes are proposed based on different anchor rod lengths and spacing, and the results of the safety factor calculations for each scheme can be found in Table 8.

From Table 8, it can be seen that when the initial support is considered as the main bearing body, for rock grade III (with an 8cm shotcrete thickness), configuring a shotcrete thickness according to the minimum length of 3.0m for anchor rods and anchor rod spacing less than 1.5m, the total safety factor for the initial support is 7.61, meeting the requirements for the total safety factor. For rock grade IV (with an 8cm shotcrete thickness), selecting anchor rods with a length of 3.5m and spacing of 1.0m can satisfy the requirement of a total safety factor Kc≥3.0 during the construction phase. For rock grade V (with a 20cm shotcrete thickness), selecting anchor rods

Table 8. Calculation results for scheme 3-2.

	Rock Grade	Shotcrete Thickness (cm)	Anchor Rod Length (m)	Anchor Rod Spacing (m)	Safety Factor		
					Shotcrete	Anchor Rock Arch	Anchor-Spray Combination
1	III	8	3.0	1.5×1.5	1.24	6.37	7.61
2		8	3.5	1.5×1.5	1.24	7.33	8.57
3		8	4.0	2.0×2.0	1.24	7.71	8.95
4	IV	8	3.5	1.0×1.0	0.97	2.21	3.18
5		8	4.0	1.2×1.2	0.97	2.30	3.27
6		8	4.5	1.5×1.5	0.97	2.37	3.34
7		8	5.0	2.0×2.0	0.97	2.41	3.38
8	V	20	4.0	1.0×1.0	1.45	1.27	2.72
9		20	5.0	1.0×1.0	1.45	1.57	3.02
10		20	6.0	1.2×1.2	1.45	1.96	3.06
11		20	7.0	1.5×1.5	1.45	1.62	3.07

with a length of 5m and spacing of 1.0m can meet the requirement of a total safety factor Kc≥3.0, but the safety factors for rock grades IV and V are relatively low.

(3) Scheme 3-3 (Anchor and Shotcrete Combination Support)

The calculations for Scheme 3-1 indicate that for rock grades III-V, when the shotcrete thickness is greater than 16cm, 26cm, and 38cm respectively, the requirement of a total safety factor greater than 3.0 can be met without setting anchor rods. In the anchor and shotcrete combination scheme, different combinations of shotcrete thickness, anchor rod length, and spacing are proposed (considering the use of steel frames for rock grades IV and V, with minimum shotcrete thicknesses of 20cm and 24cm respectively). The calculated safety factors for shotcrete, anchor-rock arch bearing, and the combination are shown in the following table.

From the table above, it can be seen that rock grade III generally has higher safety factors. For rock grade IV, considering the use of steel frames and a required shotcrete thickness of 20cm, selecting anchor rods with a length of 4.0m and spacing of 1.5m can meet the safety factor requirements during the construction phase. For rock grade V, with a shotcrete thickness of 24cm, selecting anchor rods with a length of 4.5m and spacing of 1.2m can meet the safety factor requirements during the construction phase. When the initial support is considered as the main bearing body, taking into account the quantity of shotcrete and anchor rod works and assuming comparable overall costs, the anchor and shotcrete combination scheme provides higher safety factors for the initial support compared to the scheme without systematic anchor rods or the anchor-dominant scheme.

4.3.4 *Study on secondary lining parameters*

The initial support structure of the tunnel needs to bear all the additional loads released during excavation. It is the main body of the support system and integrates with the surrounding rock, essentially assisting in bearing the load of the surrounding rock. The secondary lining structure is usually considered as a safety reserve, but due to its inherent stiffness, it will share part of the load with the initial support after construction.

Table 9. Calculation results for scheme 3-3.

	Rock Grade	Shotcrete Thickness (cm)	Anchor Rod Length (m)	Anchor Rod Spacing (m)	Safety Factor		
					Shotcrete	Anchor Rock Arch	Anchor-Spray Combination
1	III	8	3.5	1.5×1.5	1.24	7.33	8.57
2		10	4.0	2.0×2.0	1.94	8.26	10.20
3		12	4.0	2.5×2.5	2.32	8.20	10.52
4	IV	20	4.0	1.5×1.5	2.37	2.87	5.24
5		22	4.5	1.5×1.5	2.59	3.13	5.72
6		24	4.5	2.0×2.0	2.83	3.04	5.87
7	V	24	4.5	1.2×1.2	1.74	1.34	3.08
8		26	5.0	1.5×1.5	1.88	1.36	3.24
9		28	5.0	2.0×2.0	2.01	1.26	3.27

For the rock section of grade III in this project, the surrounding rock is self-stable, so the load borne by the secondary lining structure is relatively smaller compared to the rock sections of grade IV and V. Based on empirical analogies, reinforcing bars may not be necessary for the secondary lining in the grade III rock section, while for the grade IV and V rock sections, reinforced concrete structures are considered. The strength grade of the secondary lining concrete is selected as C50 for reinforced concrete and C40 for plain concrete or steel fiber reinforced concrete.

4.3.4.1 Grade III Rock

The minimum structural requirement for the secondary lining thickness is 35cm. Based on empirical analogies, the determined thickness for the secondary lining is 50cm. Considering that the secondary lining in this project needs to withstand certain water pressure, a comparative study was conducted for three thicknesses: 40cm, 45cm, and 50cm. The analysis results are as follows:

Table 10. Analysis results of secondary lining for grade III rock section.

	Lining Thickness (cm)	Safety Factor K3	Total Safety Factor Kop
1	40	9.86	27.41
2	45	10.63	28.39
3	50	9.31	29.76

From the table above, it can be seen that the calculated overall safety factors are all greater than 27, meeting the requirement of not less than 3.6. Therefore, the thickness of the secondary lining for the grade III rock section is determined as 40cm.

4.3.4.2 Grade IV Rock

Based on empirical analogies, the determined thickness for the arch wall of the grade IV rock section is 70cm. Since the load on the secondary lining in the grade IV rock section is greater than that in the grade III rock section, the thickness of the secondary lining for the grade IV rock section is compared based on the grade III rock section.

Table 11. Analysis results of secondary lining for grade IV rock section.

	Lining Thickness (cm)	Reinforcement Details	Crack Width (mm)	Safety Factor K3
1	40	‖ 25@100	0.21	7.91
2	50	‖ 25@100	0.16	10.34
3	60	‖ 25@100	0.136	12.74
4	70	‖ 25@100	0.116	15.13

Therefore, the thickness of the arch wall for the grade IV rock section is determined as 50cm.

4.3.4.3 Grade V Rock

Following the same approach as mentioned above, the thickness of the secondary lining for the grade V rock section is considered as 55cm, with reinforcement details of ‖ 28@100.

4.3.5 *Calculation of secondary lining under water pressure*

For the above-mentioned secondary lining schemes, the safety factors obtained when subjected to a water head pressure of 20m are shown in the table below:

Table 12. Safety factors of secondary lining under water pressure.

Rock Grade	III	IV	V
Safety Factor K3	10.42	6.00	5.22

For the grade III rock section, plain concrete is used, and the calculated safety factor is 10.42, meeting the safety factor requirement of not less than 3.6. For the secondary lining from grade IV to grade III rock section, reinforced concrete structures are used, and the calculated safety factors are 6.00 and 5.22, respectively, both meeting the safety factor requirement of not less than 3.0.

4.3.6 *Recommended support parameter scheme*

Based on the total safety factor method, the recommended support parameter scheme for the second submarine tunnel is shown in the table below:

4.4 *Comparison analysis of design results between empirical analogy method and total safety factor method*

4.4.1 *Safety factor comparison*

The safety factors for the lining types determined by the empirical analogy method and the total safety factor method are shown in the table below:

From the above table, it can be seen that the safety factors of the support parameters determined by both methods meet the requirements. However, the safety factors corresponding to the support parameters determined by the total safety factor method are slightly lower than those determined by the empirical analogy method. This indicates that the total safety factor method provides a more detailed analysis of the components of the support system, and the design results are more economical while meeting the specified safety factor conditions.

Table 13. Support parameter table for the second submarine tunnel based on the total safety factor method.

Lining Type		Type III	Type IV	Type V
Rock Grade		III2	IV2	V2
Initial Support	Anchor	φ22 multiple corrosion-resistant anchors for arch, L=4.0m, spacing 2.0×2.0m	φ22 multiple corrosion-resistant anchors for arch wall, L=4.5m, spacing 2.0×2.0m	φ22 multiple corrosion-resistant anchors for arch wall, L=5.0m, spacing 1.5×1.5m
	Steel Mesh	–	φ8, 20×20cm	φ8, 20×20cm
	Shotcrete	C35 10cm	C35 22cm	C35 26cm
	Steel Frame	–	φ22H160 grid, spacing 1.0m	工20a Steel frame with spacing of 0.75m
Second-ary Lining	Arch, Wall	CF45, 40cm	50cm※	55cm※
	Inverted Arch	–	60cm※	65cm※
	Reinforcement	–	‖ 25mm @100mm	‖ 28mm @100mm

Table14. Safety factor comparison for each lining type.

		Empirical Analogy Method			Total Safety Factor Method		
Lining Type		Type III	Type IV	Type V	Type III	Type IV	Type V
Rock-Load Arch	Reduction Coefficient η_1	1.00	0.68	0.35	1.00	0.81	0.45
	Construction Phase K_{1c}	7.64	3.19	1.37	8.27	3.09	1.36
	Reduction Coefficient η_2	1.00	1.00	0.76	1.00	1.00	1.00
	Operation Phase K_{1op}	16.11	4.23	1.37	16.42	5.03	1.61
Shotcrete	Reduction Coefficient ξ	1.00	1.00	1.00	1.00	1.00	1.00
	Safety Factor K_2	1.16	3.19	2.43	1.94	2.59	1.88
Secondary Lining	Safety Factor K_3	11.63	6.95	5.92	10.42	6.00	5.22
Initial Support (Total)	Construction Phase K_c	8.80	6.38	3.80	10.21	5.68	3.24
Total	Operation Phase K_{op}	28.90	14.37	9.72	28.78	13.62	8.71

Table 15. Comparison of major engineering quantities for each lining type.

	Empirical Analogy Method			Total Safety Factor Method			
Lining Type	Type III	Type IV	Type V	Type III	Type IV	Type V	Unit Price Indicators (CNY)
Excavation (m3)	131.5	171.38	174.70	127.1	161.40	165.58	340.22
Initial Support Shotcrete (m3)	4.25	13.66	14.68	2.86	10.48	12.41	1351.80
Steel Fiber (kg)	–	–	–	128.7	–	–	7.96
Steel Mesh (t)	–	0.123	124.17	–	0.119	120.45	9.06
Anchors (m)	72.92	105	168	29	32.63	68.35	103.76
Secondary Lining Concrete (m3)	14.75	29.91	32.21	11.89	23.1	25.35	1567.91
Longitudinal Reinforcement (t)	1.110	2.243	2.823	–	3.33	4.19	9062.41
Project Cost (10,000 yuan)	9.12	15.60	17.39	6.98	13.99	15.90	/

4.4.2 *Comparison of major engineering quantities*

The calculated meter quantities of major engineering works for the lining types determined by the empirical analogy method and the total safety factor method were compared, and combined with the unit price indicators of the project budget, the quantity and cost comparison are shown in the table below:

From the above table, it can be seen that compared to the support parameters determined by the empirical analogy method, the support parameters recommended by the total safety factor method are significantly more cost-effective. For Grade III lining (corresponding to Grade III rock), the project cost is reduced by approximately 23.5%. For Grade IV lining (corresponding to Grade IV rock), the project cost is reduced by approximately 10.32%. For Grade V lining (corresponding to Grade V rock), the project cost is reduced by approximately 8.6%.

5 CONCLUSION

The support structure design parameters determined by the empirical analogy method generally have a large safety factor, indicating room for optimization.

The rock-load arch effect of each rock grade is significant, and increasing the anchor length has a noticeable effect on increasing the safety factor, especially for Grade III rock.

By appropriately increasing the anchor length and spacing while keeping the safety factor unchanged or slightly increased, the number of anchor works can be greatly reduced.

Economic and technical comparative analysis results show that the optimized support parameter design results based on the total safety factor method are significantly more cost-effective.

REFERENCES

Cai M. F., He M. C. Liu D. Y., 2002. Rock mechanics and engineering[M]. Beijing: Science Press.

Editorial Department of China Journal of Highway and Transport, 2015. Review on China's Tunnel Engineering Research:2015. China Journal of Highway and Transport, 28(05),1–65.

Editorial Department of China Journal of Highway and Transport, 2022. Review on China' S Traffic Tunnel Engineering Research: 2022. China Journal of Highway and Transport, 35(04):1–40.

Guan B. S., 2003. Key points of tunnel design[M]. Beijing: China Communications Press.

Xiao M. Q., 2019. Exploration on the Several Problems of Tunnel Design with the Total Safety Factor Method. Journal of Railway Engineering Society, 36 (01):65–69.

Xiao M. Q., 2020. Design of Railway Tunnel Support Structure Based on Overall Safety Factor Method. China Railway, (12):82–88.

Xiao M. Q., Chen L. B., Xu C., et al, 2018. Calculation Study of Support Parameters of High-speed Railway Tunnel. Tunnel Construction, 38(03):406–413.

Xiao M. Q., Xu C., 2019. Modification and Application of Design Method for Total Safety Factor of Composite Lining Tunnel. Tunnel Construction, 39(03):421–429.

Xiao M. Q., Xu C., 2019. Research on the Representative Value of Deep Buried Tunnel Surrounding Rock Pressure Based on Total Safety Factor Method. Journal of Railway Engineering Society, 36(02):64–69.

Zhang C. Y., Wang S. T., Wang L. S., et al, 1997. Principles of Engineering Geological Analysis [M]. Beijing: Geological Publishing House.

Zheng Y. R., Zhu H. H., Fang Z. C., et al, 2012. The stability analysis and design theory of surrounding rock of underground engineering [M]. Beijing: Chin a Communications Press.

Tunnelling for a Better Life – Yan, Celestino, Thewes & Eberhardt (Eds)
© 2024 The Author(s), ISBN 978-1-032-80042-4
Open Access: www.taylorfrancis.com, CC BY-NC-ND 4.0 license

Research on the airproof performance of shield tunnel segment sealing gasket based on laser surface microstructure

Mingqing Xiao, Guangqiao Xue & Junwei Chen
China Railway Siyuan Survey and Design Group Co., Ltd, Wuhan, China
NATIONAL-LOCAL Joint Engineering Research Center of Underwater Tunnelling Technology, Wuhan, China

Chaoyong Zhang
Huazhong University of Science and Technology, Wuhan, China

Shaofeng Wang
China Railway Siyuan Survey and Design Group Co., Ltd, Wuhan, China
NATIONAL-LOCAL Joint Engineering Research Center of Underwater Tunnelling Technology, Wuhan, China

ABSTRACT: At Present, the research on the joint sealing performance of the shield tunnel segment mainly focuses on joint waterproof performance. However, many shield tunnels pass through methane gas strata. Gases and liquids having different physical properties lead to different leakage characteristics. Therefore, it is necessary to research the joint airproof performance of the shield tunnel segment. In this article, we set up an experimental platform to test the joint airproof performance and use a picosecond laser to construct microstructures on the surface of the EPDM sealing gasket. We observe the microstructures of the gasket surface processed with different laser powers, scanning speeds and scanning spacings by microscope and analyze the relationship between the hydrophilic property and the airproof performance of the gasket. It is found that using lasers to construct microstructures on the gasket surface effectively improves the airproof performance of the gasket.

Keywords: shield tunnel, segment joint, picosecond laser, surface microstructure, gas leakage

1 INTRODUCTION

Many researchers have researched the microstructure and sealing properties, especially the hydrophilic and hydrophobic properties and surface wettability. Sizhu Wu[1] discussed femtosecond laser processing of various microstructures and summarized the results of femtosecond laser fabrication of infiltrating surfaces. Xiqin HE[2] researched the laser processing of micropores and microcolumns. Maolin Zhou[3] researched superwetting surfaces. Guangfei Wang[4] researched super-hydrophobic fabrication methods of silicone rubber materials and summarized them to provide an overview of the up-to-date research state and progress in detail. Xue Bai[5] used a femtosecond laser to create a microgroove array structure and obtained an anisotropic and super-hydrophobicity surface. Guoqiang Li[6] processed metal surfaces to obtain a variety of surface structures by combining the femtosecond laser micro/nano machining technology and the bionic design principles. Mingqing XIAO[7] proposed that the contact surface of the gasket is uneven and has tiny leakage holes; its waterproof ability is controlled by the maximum contact stress of the contact surface and the flow resistance of the tiny holes between the contact surface. Improving the evenness of the contact surfaces can reduce the number and size of tiny holes, and it is also a critical factor in strengthening the waterproof ability. Wenqi DING[8] carried out a series of test sets and evaluated the joint waterproof performance of the shield tunnel in the Nanjing Weisan Rd.

From the above research, it can be seen that many researchers have extensively researched the preparation of sealing gasket surfaces with special wetting properties using different methods and techniques. However, the research on the joint sealing performance of the shield tunnel segment mainly focuses on joint waterproof performance. The research on the airproof performance of the microstructure of the gasket surface is relatively limited. In this article, we use a picosecond laser to construct microstructures on the surface of the EPDM gasket, set up an experimental platform to test its airproof performance, research the

DOI: 10.1201/9781003495505-173

effect of different gasket surface microstructures on airproof performance, verify constructing microstructures on the gasket surface can improve its airproof performance.

2 AIRPROOF PERFORMANCE OF THE GASKET SURFACE MICROSTRUCTURE

2.1 *Experimental platform*

The experimental uses an ultrashort pulsed laser manufactured by EdgeWave Germany, model PX200-3-GFH, which has a maximum power of 100W, a wavelength of 1064nm and a maximum repetition frequency of 2MHz. Figure 1(a) shows a schematic diagram of the laser system. Figure 1(b) shows the tested EPDM gasket. It has an outer shape of 70mm by 70mm, an inner shape of 46mm by 46mm, a thickness of 8mm and a chamfer radius of 6.5mm. Before using the laser to construct the gasket surface microstructure, the gasket requires to be ultrasonically cleaned for 15 minutes in anhydrous ethanol and deionized water. Afterwards, take it out, air-dried naturally, and place it in sample bags for later use. The experimental platform consists of a 6MPa pressure gauge, a three-way valve, and two flanges to secure the gasket, as shown in Figure 1(c).

When testing the airproof performance of the gasket, place two similarly treated gaskets inside the two flanges and then fix the gasket and the flange with chloroprene rubber adhesive, and wait for 90 minutes. After stood for 90 minutes, assembling and tightening the flanges, maintaining a compression gap of 8mm, inputting air pressure between the two flanges by using an inflation pump and recording the breakdown pressure of the gasket from the pressure gauge.

2.2 *Results of airproof performance experimental*

While testing the airproof performance of the gasket surface micro-structure, try to exclude interference factors such as environmental temperature, external air pressure, and the dryness of the gasket surface. Each group of parameters conducts three replicate experiments and averages the results. For groups with differing results, additional experiments are needed to ensure the relative accuracy of the experimental results. The results are shown in Table 1.

3 ANALYSIS OF TEST RESULTS

3.1 *Analysis of surface microstructure and airproof performance*

The surface microstructure of the gasket is photographed using a microscope, and a three-dimensional map and a height distribution map of its surface microstructure are generated using VK analysis software.

Figure 2(a) shows the smooth control group surface with no microgroove array structure. Only some shallow microgroove arrays appear when using 9.85W laser power to process the gasket surface, as shown in Figure 2(b). There is no prominent microstructure. It might be due to the lower laser power, resulting in less energy being delivered to the surface per unit time, causing most of the surface not to be processed or completely processed. When the laser power is increased to 13.25W, as shown in Figure 2(c), the surface receives more energy per unit of time, and as a result, the surface forms a uniform and neat microstructure. Due to the laser scanning spacing of 60μm, the observed surface consists of microgroove arrays with a spacing of 60μm. When the laser power is further increased to 16.2W, as shown in Figure 2(d),

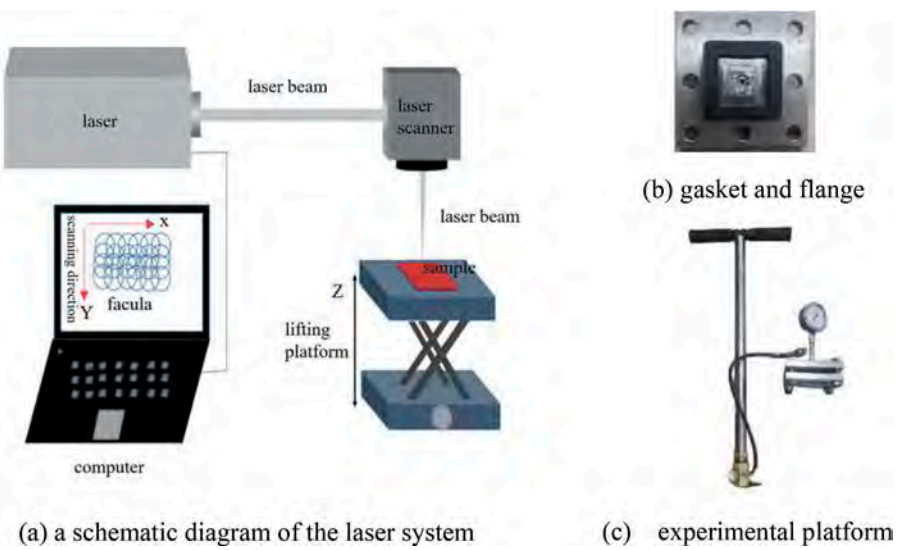

Figure 1. Airproof performance experimental platform.

Table 1. Experimental record sheet of airproof performance.

number	frequency/KHz	power/W	speed/ m/s	spacing/ μm	airproof performance/MPa	note
1	800	9.85	1	60	3.3	
2	800	13.25	1	60	3.5	
3	800	16.2	1	60	3.2	
4	800	9.85	0.5	60	3.5	
5	800	13.25	0.5	60	3.5	
6	800	16.2	0.5	60	3.8	
7	800	16.2	0.3	40	3.2	
8	800	16.2	0.5	40	2.9	
9	800	16.2	1	40	2.9	
10	800	16.2	2	40	2.9	
11	800	13.25	0.5	40	3.2	
12	800	13.25	0.3	40	3.1	
13	800	9.85	0.5	80	3.3	
14	800	13.25	0.5	80	3.7	
15	800	16.2	0.5	80	3.6	
16	800	16.2	0.5	100	3.6	
17	-	-	-	-	2.9	control group

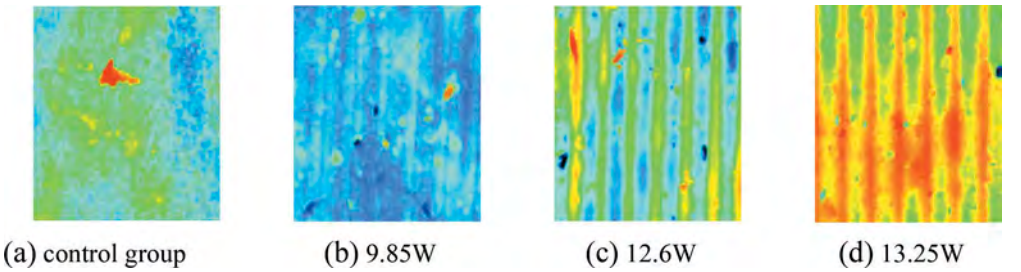

Figure 2. Three-dimensional micrographs at different powers.

the laser power is relatively high, the surface absorbs the most energy per unit time, and a series of processes such as melting, vaporization, and reformation occur more completely. This results in more pronounced and uniform microstructures. The height of the microgroove arrays increases slightly.

Figure 3 shows that as the scanning speed increases from 0.3m/s to 2m/s, the surface of all samples has linearly arranged microgroove arrays. When scanning at a lower speed of 0.3m/s, the surface absorbs more energy per unit time and more of the base material was removed from the surface. This leads to the maximum height of the microgroove arrays, as shown in Figure 3(a). However, there are some imperfections in the microgroove array, and its height is uneven, which can affect the airproof performance. When the scanning speed is increased to 0.5m/s, the microgroove arrays are neatly arranged at a consistent height, with a high average height, as shown in Figure 3(b), and the airproof performance is improved. When the laser scanning speed is further increased to 1m/s, less energy is applied to the material surface per unit time, resulting in a smaller microgroove array height, as shown in Figure 3(c). When the scanning speed reaches the maximum of 2m/s, laser processing is faster but less complete, resulting in the least pronounced groove structures with the lowest height, as shown in Figure 3(d).

As can be seen from Figure 4(a), when the scanning spacing is 40 μm, due to the small scanning spacing, the laser repeatedly processes the same position, which will lead to dense groups of microgroove arrays on the surface or even the phenomenon of squeezing each other and the degree of neatness is inferior to that of the surface of the scanning spacing of 60 μm. The airproof performance is relatively poor, which is also confirmed by the experiment results. In addition, the airproof performance of the test experiment with scanning spacing of 80μm and 100 μm is also good so that the scanning spacing can be appropriately larger.

3.2 *Analysis of contact angle and airproof performance*

Take the control group and the first to the sixth test group samples, and measure the surface contact angle with a JC2000 instrument. During the test,

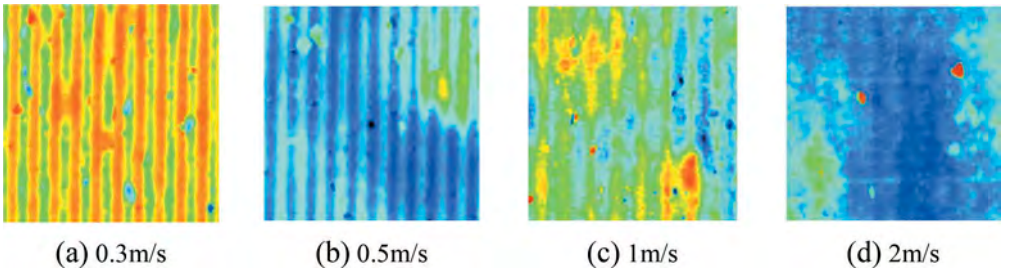

Figure 3. Three-dimensional micrographs at different scanning speed.

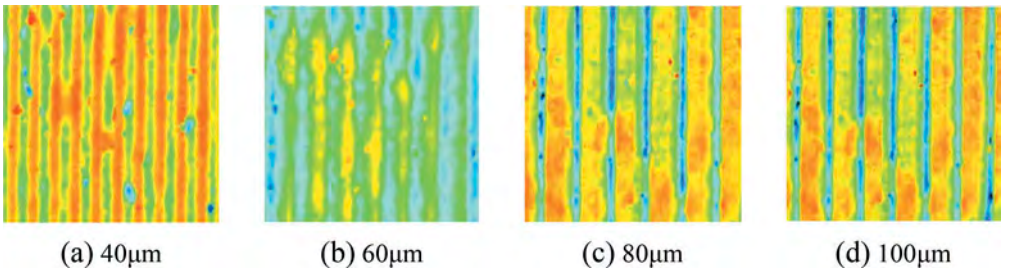

Figure 4. Three-dimensional micrographs at different scanning spacing.

place the sample, drop the deionized water droplets onto the sample surface, and control the volume of each drop to be at eight μL. Using a camera to capture and shoot the image of the sample surface, analyze its contact angle microscopic image by the software Drop Mete and measure the size of the contact angle by the software ImageJ. The contact angle and airproof performance for each group are shown in Figure 5.

Figure 6 compares the airproof performance and contact angle for each group. It is obvious that the contact angle is the largest in the control group, about 89º, while smaller in the other groups, from 30 º to 75 º. In addition, all the other groups improved airproof performance compared to the control group. The first, second, fourth, and sixth groups show more remarkable improvement because their contact angles are smaller, and the third and fifth groups show more

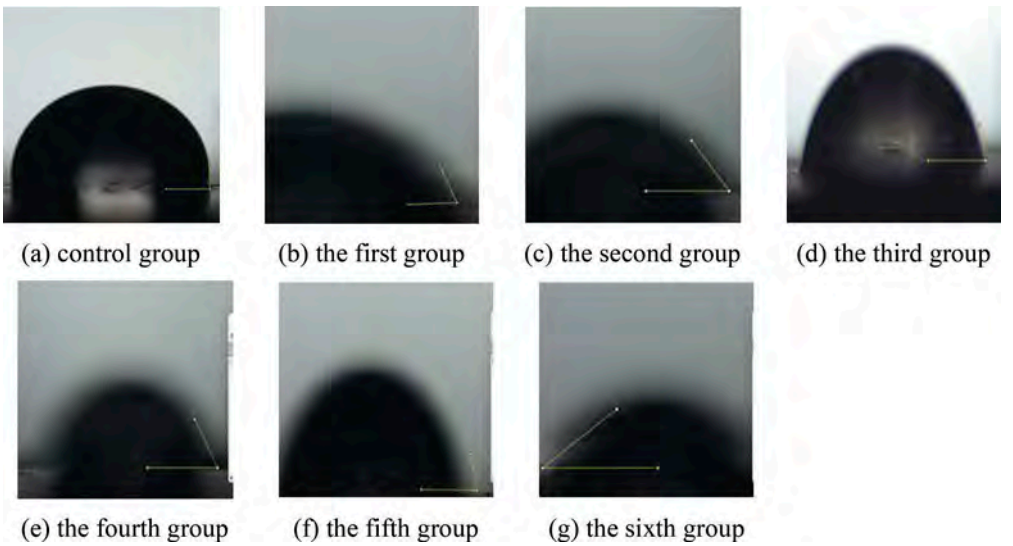

Figure 5. Contact angle comparison diagram.

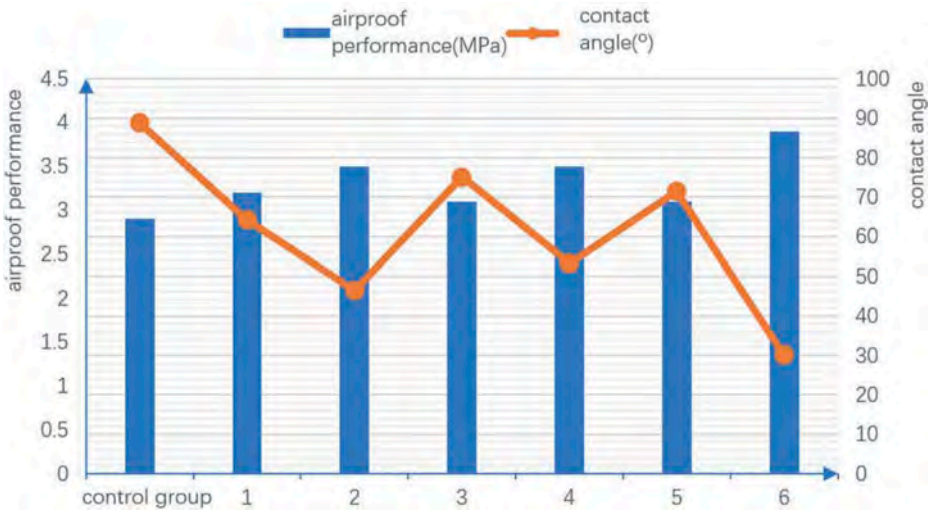

Figure 6. Comparison of the airproof performance and contact angle for each group.

remarkable improvement because of their larger contact angles. In particular, the sixth group, which has the best airproof performance, use a laser power of 16.2 W, a scanning speed of 0.5 m/s, and a scanning spacing of 60 μm to form a neat and uniform microgroove array structure. Its contact angle reaches a minimum of 30 °, and its airproof performance improves by about 30% compared to the control group.

It can be said that the contact angle of the gasket is smaller after laser processing, and with the increase of laser power, the contact angle tends to become smaller. At the same time, the smaller the contact angle is, the better the airproof performance is.

3.3 *The experiment of airproof performance of the gasket surface microstructure*

The experimental platform consists of three steel templates, two L-shaped and one square-shaped steel template. When assembled, these three steel templates form a T-shaped joint, as shown in Figure 7. The laser parameters for the gasket surface are given in section 3.3.2. The gasket was compressed to an opening of 8 mm, under 15 mm offset, firstly, and connected to an air pressure loading device at one end and to an airproof performance test device, Air pressure it until 2MPa. At this time, the air pressure between the two sealing gaskets should be recorded every day. The

Figure 7. Platform of airproof test.

Table 2. The air pressure results between the two sealing gaskets (MPa).

Gasket Type \ Days(day)	1	5	10	15	20	25	30	35	40	45
gasket 1 (unprocessed)	2	1.38	0.94	0.73	0.59	0.5	0.43	0.37	0.32	0.29
gasket 2 (processed)	2	1.73	1.53	1.34	1.18	1.05	0.94	0.86	0.82	0.80
gasket 3 (processed)	2	1.74	1.54	1.36	1.19	1.07	0.96	0.87	0.84	0.81

whole experiment was divided into three groups. The first group used an unprocessed sealing gasket, while the gaskets of the second and third groups were processed. Each group of experiments was recorded for 45 days, and Table 2 shows the air pressure results between the two sealing gaskets for each five days. From the table, we can see that the residual air pressure of the laser-processed gasket is 0.80Mpa. It is much larger than the unprocessed gasket, which is 0.29Mpa, verifying the effectiveness of constructing microstructures on the gasket surface in enhancing its airproof performance.

4 CONCLUSIONS

In this article, we use a picosecond laser to construct microstructures on the surface of the sealing gasket and set up an experimental platform to test airproof performance. We analyze the effects of laser power, scanning speed, and scanning spacing on the airproof performance of the gasket as well as the hydrophilic properties of the gasket surface after being processed with a picosecond laser. The gasket surfaces with uniform and appropriately sized microstructures have extraordinary airproof performance. The main conclusions are as follows:(1) When the gasket surface is not processed by laser, its hydrophilic property is poor, and the contact angle between the drop and the surface is almost at right angles. (2) The airproof performance of the gasket is improved after its surface is processed by laser. (3) The better the hydrophilic property of the gasket surface, the better the airproof performance. In the future, we will continue to research the correlation between the laser processing parameters and the hydrophilic properties of the gasket surface in order to obtain a better gasket surface.

REFERENCES

[1] Sizhu Wu, Xiaodong Lv, Chuanzong LI, et al. Advances in the Preparation of Functional Surfaces with Special Wettability by Femtosecond Laser Ablation(lnvited)[J]. Acta Photonica Sinica, 2021, 50 (06): 23–45. (in Chinese)

[2] Xiqin He, Xinglin Tong, Xuzhi Chen, et al. Advances in laser micromachining of inverted cone microarray[J]. Laser Journal, 2021, 42(01): 7–10. (in Chinese)

[3] Maolin Zhou, Xuyao He, Xingyu Wu, et al. Self-pumping and scalable fog collector with diode-like micro-hole arrays inspired by natural asymmetric wettability[J]. Applied Materials Today,2020, 21, 100851.

[4] Guangfei Wang, Anling Li, Wen Zhao, et al. A Review on Fabrication Methods and Research Progress of Superhydrophobic Silicone Rubber Materials[J]. Advanced Materials Interfaces, 2021, 8, 2001460.

[5] Xue Bai, Qing Yang, Yao Fang, et al. Anisotropic, adhesion-switchable, and thermal-responsive superhydrophobicity on the femtosecond laser-structured shape-memory polymer for droplet manipulation[J]. Chemical Engineering Journal, 2020, 400 (prepublish).

[6] Guoqiang Li. Bionic Functional Structure by Femtosecond Laser Micro/nanofabrication Technologies[D]. University of Science and Technology of China, 2015. (in Chinese)

[7] Mingqing XIAO, Guangqiao XUE, Yuan ZHONG, et al. Experimental Research on the Waterproof of Double Gaskets in Segment Joint of Shield Tunnel[J]. Journal of Railway Engineering Society, 2021(2): 80–85. (in Chinese)

[8] Wenqi DING, Chenjie GONG, Khalid M. Mosalam, et al. Development and application of the integrated sealant test apparatus for sealing gaskets in tunnel segmental joints[J]. Tunnelling and Underground Space Technology incorporating Trenchless Technology Research, 2017, 63:54–68.

Tunnelling for a Better Life – Yan, Celestino, Thewes & Eberhardt (Eds)
© 2024 The Author(s), ISBN 978-1-032-80042-4
Open Access: www.taylorfrancis.com, CC BY-NC-ND 4.0 license

Research on the application of marine engineering mass concrete with anti-cracking agent

Biao Xie*, Wen Xu & Yu Jiang Wang
Southeast University, Nanjing, China
State Key Laboratory of High Performance Civil Engineering Material, Jiangsu Sobute New Materials Co., Ltd, Nanjing, China

Jian Zhang
State Key Laboratory of High Performance Civil Engineering Material, Jiangsu Sobute New Materials Co., Ltd, Nanjing, China

Wenliang Jin & Jian Liu
Shen-Zhong Link Administration Center, Zhongshan, China

ABSTRACT: In order to prevent the cracking of marine engineering mass concrete, and the water seepage deterioration of the structure is caused. The double-control technology (temperature and expansion deformation control of concrete) with anti-cracking agent is used instead of the cooling water pipe to control concrete crack. The mixing ratio is low cement dosage, high content mineral admixture and 8% anti-cracking agent. The anti-crack agent can reduce the heat release rate of early hydration and compensate shrinkage of concrete in the temperature drop stage. At the same time, the work performance, mechanical properties and durability of the concrete are excellent. After the calculation and analysis of cracking risk through finite element sumulation, when the length of the anti-cracking concrete is poured within 20m, the cracking risk value is less than 0.7, and the concrete will not crack, meet design and construction requirements.

Keywords: marine, mass marine concrete, anti-cracking agent, crack control

1 PREFACE

Once the problem of cracking occurs in Marine mass concrete, the erosion of seawater will accelerate the deterioration of reinforced concrete. In the world, the crack control of Marine mass concrete is mainly based on temperature control of concrete, which is to restrain the formation of concrete temperature cracks by reducing the concrete entering temperature, the peak temperature of concrete, and the temperature difference of concrete inside and outside. However, a large number of engineering cases show that in some structures with strong constraints and shrinking, even if extremely strict temperature control measures are carried out, concrete cracking still exists, and the existence of cracks will lead to the deterioration of the concrete in Marine engineering, which is unfavorable to the stability of the concrete structure.

Concrete cracking is a complex multi-factor coupling process. In the crack control design of mass concrete, researchers usually only consider the shrinkage cracking caused by temperature drop, but the actual process is often much more complicated. The cracking of concrete can be summarized as that when the shrinkage of concrete is constrained (both internal and external constraints), the tensile stress generated is greater than the ultimate tensile strength of concrete. The strain deformation of concrete is an important parameter for concrete cracking. Of course, the driving forces causing strain deformation of concrete include temperature stress, dry shrinkage deformation, self-shrinkage, etc. For some parts with large volumes and large constraints, shrinkage deformation is superimposed on each other, and simple temperature control measures are often difficult to achieve the purpose of cracking control of the concrete.

Through the research, the anti-crack agent developed by special technology can effectively delay the hydration heat release and compensate for the concrete shrinkage in the whole process by reducing the

*Corresponding author: 517472351@qq.com

DOI: 10.1201/9781003495505-174

early hydration heat release rate of the cementing material and the dual control technical means of the whole process compensation of concrete shrinkage in stages, to achieve the purpose of concrete crack control. In general, it can simplify the temperature control measures (no cooling water pipe is arranged), speed up the construction progress, and reduce the project cost, which has great significance for the crack control construction of mass concrete.

2 TEST

2.1 *Raw materials*

The test raw materials are shown in Table 1.

Table 1. Concrete mix ratio (kg/m³).

Raw material	Index
Cement	P·II 42.5 cement
Sand	Medium sand of Ganjiang II area with fineness modulus of 2.6, with mud content less than 2.0%
Gravel	5~25mm continuous gradation, good grain shape, hard texture, the linear expansion coefficient of small clean gravel
Fly ash	Grade I fly ash, in line with the requirements of "fly ash used in cement and concrete" (GB/T1596-2005) Class F I requirements
Mineral powder	Tangshan S95 grade slag powder, the specific surface area is not more than 500 m³/kg
Water reducing agent	Jiangsu Subote reduced high-performance polycarboxylic acid water reducing agent (water reducing rate of 26.3%, solid content of 20%, the amount of mixing is calculated by solution)
Anti-cracking agent	The anti-cracking agent (HME-V) developed by Jiangsu Subote New Materials Co., Ltd. is composed of calcium oxide, lightly-burned magnesium oxide and hydration heat control material
Mixing water	tap water

2.2 *Concrete design*

This project is a tunnel side wall structure in the Marine environment, the thickness of the side wall is up to 1.5m, and the length of a single pouring is 20m, which is a typical large-scale concrete for Marine engineering. Because the side wall structure is poured on the bottom plate, the side wall will be constrained by the finished bottom plate during the temperature drop stage, resulting in the stress concentration of the side wall. As a result, concrete is prone to cracking.

In view of the above situation, the design strength of the concrete structure is $C_{28d}45$, $C_{56d}50$, the design principle of the concrete mix ratio is low temperature rise, and has a certain degree of expansion, with shrinkage compensation. by adding anti-cracking agent, on the one hand, the hydration temperature rise inhibitor is used to reduce the heat release rate and temperature rise in the cement hydration acceleration period. On the other hand, based on the characteristics of the deformation process of the solid structure, the expansion components (calcium oxide and magnesium oxide) with different expansion characteristics are used to realize the compensation shrinkage in stages and the whole process.

The actual mix ratio shall be reasonably designed with reference to the design principles of Specification for mix proportion design of ordinary concrete (JGJ 55-2011)and the requirements of Standard for Construction of Mass Concrete(GB 50496-2018)and Specification for Concrete Construction of port and Waterway Engineering(JTS 202-2-2011).After comprehensive consideration, the concrete mix ratio is shown in Table 2.

Table 2. Concrete mix ratio (kg/m³).

number	cement	fly ash	slag	HME-V	sand	gravel	Water	water reducing agent
1#	189	105	126	0	769	1063	143	appropriate amount
2#	189	105	92	34	769	1063	143	

3 TEST RESULTS AND ANALYSIS

3.1 *Effect of anti-cracking agent on dosage of water-reducing agent and strength of concrete*

The anti-cracking agent of Jiangsu Subody New Materials Co., Ltd. is added to replace 8% of the cementing material (instead of 34kg/m³ mineral powder), the water-binder ratio of concrete is 0.34, and the dosage of the water-reducing agent is calculated as a percentage of the total cementing material. The specific dosage is determined according to the slump of the concrete mix is 200mm, and the dosage of other materials is unchanged. The mixing performance of concrete is shown in Table 3.

Table 3. Concrete performance (kg/m³).

number	HME-V/%	slump/mm	water reducing agent/%	Compressive strength/MPa		
				7d	28d	56d
1#	/	200	1.0	48.7	59.8	63.4
2#	8.0	200	1.15	43.5	57.6	65.1

Comparing the mix ratio of 1# (ordinary concrete) and 2# (crack-resistant concrete), it can be seen that to maintain the same concrete fluidity after the

addition of crack -resistant agent, the amount of water reducing agent will slightly increase, which may be due to the adsorption effect of crack resistant agent on water reducing agent, but this can be adjusted by the amount of water reducing agent, but the overall effect on the workability of concrete is little. It can be seen from the strength data that the strength of 1# and 2# both meet the strength design requirements. The strength of 7d and 28d of the group with anti-cracking agent 2# is slightly lower than that of the group without anti-cracking agent, but the strength of 56d is higher than that of the comparison group. This is because the anti-cracking agent can delay the hydration heat release rate of cement on the premise of ensuring the total heat release is unchanged, so the early compressive strength of 2# concrete is lower than 1#, but with the increase of age, the compressive strength of 2# group 56d concrete gradually catches up.

3.2 *Effect of anti-cracking agent on chloride ion permeability coefficient of concrete*

In addition to the cracking damage caused by temperature drop and self-shrinkage of Marine concrete, the deterioration damage caused by chloride ion erosion of concrete reinforcement also needs attention. The chloride ion permeability coefficient is an important parameter that directly reflects the resistance of concrete to chloride ion permeability. The test results of the chloride ion permeability coefficient based on the Standard of Test methods for long-term Performance and Durability of ordinary Concrete(GB/T50082-2009) RCM method are shown in Table 4.

Table 4. Results of the chloride ion permeability coefficient test.

number	HME-V/%	Chlorine permeability/10^{-12}cm/s
1#	0	2.9
2#	8%	1.8

As shown in Table 3, the chloride ion permeability coefficient of concrete is reduced after the anti-cracking agent is added, indicating that the anti-cracking agent can improve the chloride ion permeability resistance of concrete. This is mainly due to the expansion of the anti-cracking agent role can influence the structure of the aggregate and cement mortar surface structure, the structure of hardened cement paste pore, improve the concrete slurry aperture distribution, reduce the straight hole, thus reducing the porosity of concrete structure compactness, thus improve the resistance to chloride ion permeability of concrete for Marine (harbor) engineering were, prevent the chloride ion erosion damage of reinforced concrete.

3.3 *Regulation of hydration heat of anti-cracking agent*

The lower the adiabatic temperature rise of concrete, the smaller the temperature drop range in the temperature drop process, and smaller the temperature stress on the concrete itself, which is beneficial to the improvement of the anti-crack performance of the overall structure. This project delays the hydration rate of cement through the hydration regulation effect of anti-cracking agent, so that the heat release of the cementing material can be released in a longer period. At the same time, the heat dissipation performance of the open surface of the structure can finally reduce the maximum temperature peak value of the solid engineering structure, to reduce the risk of structural cracking.

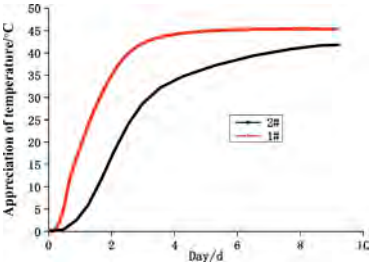

Figure 1. Results of adiabatic temperature rise test.

In order to compare the control effect of hydration heat of anti-cracking agent, the adiabatic temperature rise test of 1# and 2# concrete was carried out. As can be seen from Figure 1, the adiabatic temperature appreciation of 2# concrete at different stages is significantly lower than that of 1# concrete, and the statistical value of specific characteristic temperature rise is shown in Table 5. Through the data, it is found that the anti-cracking agent has a significant effect on the regulation of cement hydration and heat release. In 3d, the adiabatic temperature rise of 1# concrete is 42.16°C, while the adiabatic temperature rise of 2# concrete is only 28.56°C. The anti-cracking agent greatly delayed the hydration heat release rate of early cement. At 9d, the adiabatic temperature appreciation of 1# concrete was 45.35°C, while the adiabatic temperature appreciation of 2# concrete was 42.24. According to the analysis in Figure 1, the adiabatic temperature appreciation of 1# concrete was flat, while the adiabatic temperature appreciation of 2# concrete still had a certain upward trend. The hydration regulation effect of anti-cracking agent is only to prolong the heat release process but has little effect on the final total heat release, which is also in line with the development law of slightly decreasing strength in the early stage and gradually catching up with strength in the later stage as shown in Table 3.

Table 5. Characteristic adiabatic temperature rise of concrete (/°C).

	Characteristic value of temperature /°C					
number	1d	2d	3d	5d	7d	9d
1#	18.76	34.94	42.16	44.87	45.34	45.35
2#	4.22	17.41	28.56	37.48	40.05	42.24

3.4 *Effect of anti-cracking agent on the regulation of expansion process of Marine concrete*

The actual construction conditions are complex, the temperature field of concrete is changing, and the deformation performance tested under constant temperature laboratory conditions is quite different from that of solid. Therefore, to study the strain deformation law of offshore concrete in solid structures, the temperature variable deformation law of 1# concrete and 2# concrete was tested by simulating the actual temperature field. The anti-cracking agent was mixed with 8% and other materials remained unchanged.The temperature variable deformation results of concrete are shown in Figures 2-4.

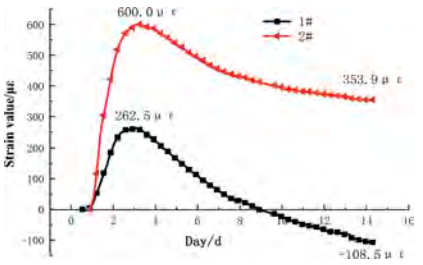

Figure 2. Temperature change deformation test results.

As shown in Figure 2, under the condition of temperature change, the concrete strain increases first and then decreases, and the maximum deformation occurs at the temperature peak of 3d, where the maximum strain value of concrete 1# is 262.5με, while the maximum strain value of concrete 2# is 600.0με, indicating that concrete doped with anti-crack agent expands 337.5με more than ordinary concrete at the temperature rise stage. During the expansion of the early temperature rise stage, the concrete structure will produce pre-compressive stress when constrained, and this part of the compressive stress will be stored in the structure, which is beneficial to resist the shrinkage deformation in the later temperature drop stage. After the temperature peak of concrete, the temperature of concrete began to decrease, and the strain value of concrete also decreased. At 14d, the strain of ordinary concrete was negative -108.5με and the stress state of concrete was tensile stress, while the strain of crack-resistant concrete was still positive 353.9με.

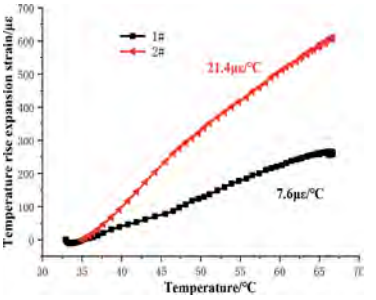

Figure 3. Temperature rise deformation test results.

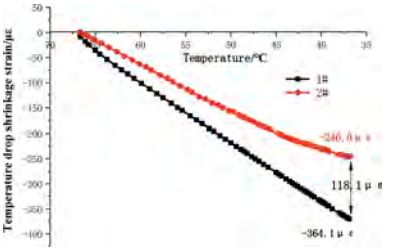

Figure 4. Temperature drop deformation test results.

In the control of the expansion process, the expansion performance not only plays in the temperature rise stage but also needs to play the ability of continuous expansion in the temperature drop stage to compensate for the shrinkage deformation of concrete in the temperature drop stage. According to Figures 3 and 4, the temperature rise and temperature fall processes were analyzed in stages. We found that the unit temperature deformation values of ordinary concrete and crack-resistant concrete were 7.6με/°C and 21.4με/°C respectively in the temperature rise stage (Figure 3), indicating that the anti-crack agent had begun to play an expansion role in the temperature rise stage. At the same time, in the temperature drop stage, the temperature peak point is zero. Figure 4 shows that the final shrinkage values of ordinary concrete and crack-resistant concrete are -364.1με and -246.0με, respectively, indicating that the crack-resistant concrete is still undergoing shrinkage compensation in the shrinkage stage, and the compensated shrinkage strain value reaches 118.1με, which is in line with the expectation and is beneficial to crack control.

3.5 *Finite element software simulation and analysis*

Combined with the above concrete mix ratio data and the engineering entity structure, due to the high temperature in summer, the risk of cracking is generally large, so the mix ratio of 1# concrete and 2# concrete are simulated and calculated respectively under the summer construction conditions, the mold temperature is 32°C, and the cracking risk coefficient is calculated respectively according to the section length.

$$\eta = \sigma(t)/f_t(t)$$

Where σ(t) is the maximum tensile stress of concrete at time t, and is the tensile strength of concrete at f_t(t) time t. According to the Technical Specification for Thermal Cracking Control of Mass Concrete of Port and Waterway Engineering (JTS 202-1-2010), the evaluation criteria for concrete cracking risk are as follows: It is generally believed that concrete will crack when it is $\eta > 1.0$; Considering the fluctuation of material properties, it is considered that concrete has a greater risk of cracking when $0.7 < \eta < 1.0$; When the value is less than 0.7, the concrete will not crack basically.The finite element calculation model of the risk coefficient of pouring length cracking is shown in Figure 5, and the calculation results are shown in Figure 6.

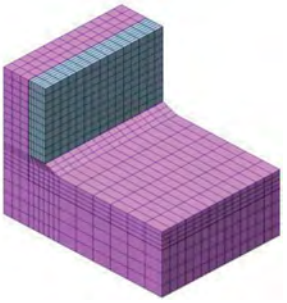

Figure 5. Finite element modeling.

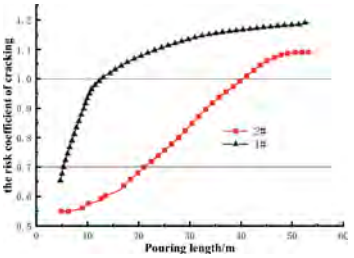

Figure 6. Simulation result.

According to the calculation results in Figure 5, the cracking risk of anti-cracking concrete under the same pouring conditions is lower. According to the calculation, when the length is less than 20m, the cracking risk coefficient is less than 0.7, and the length of one-time pouring is much higher than that of ordinary concrete, which has obvious crack control advantages.As shown in Figure 7, the side wall of the 20cm tunnel was poured at one time, and no cracking was found after observation after mold removal.

Figure 7. Construction diagram of side wall.

4 CONCLUSIONS

The experiment shows that the anti-cracking concrete has excellent performance in terms of working performance, adiabatic temperature rise and deformation, and the analysis and calculation of the side wall structure combined with the simulation calculation method show that the cracking risk coefficient of the concrete with anti-cracking agent can be reduced, and the side wall will not crack basically, which provides valuable experience for crack control of such large-scale concrete in Marine engineering, Summarise as follows:

(1) The addition of anti-cracking agent will slightly increase the amount of water-reducing agent, which can be solved by increasing the amount of water-reducing agent, which has basically no impact on the working performance of concrete. The anti-cracking agent will slightly reduce the 28d strength, but the 56d strength gradually overtakes the ordinary concrete.
(2) The anti-crack agent has the dual control function of temperature and expansion field, can reduce the early hydration rate and adiabatic temperature appreciation of concrete, and can compensate the deformation in the temperature drop stage, and the compensation shrinkage value is 118.1με, which has a significant effect on inhibiting the later shrinkage cracking of concrete.
(3) According to the simulation calculation, the cracking risk coefficient of concrete with anti-cracking agent is less than 0.7, and the side wall will not crack basically, and the scheme meets the requirements of construction design when the single pouring length is 20m and the casting mold temperature is 32°C.

ACKNOWLEDGMENTS

The authors would like to acknowledge the research support by the Key Field R & D Program of Guangdong Province (Grant No.: 2019B111106002).

REFERENCES

Tian, Q., Wang, Y.J., Zhang, S.Z., et al, 2014. Anti-cracking Technology for Side-wall Structure Based on Dualregulation of Temperature Field and Expansion History. China Concrete and Cement Products. China, (05), 20–24.

Li, H., Tian, Q., et al, 2016. Cracking risk analysis of concrete during construction period for shiplock. Port & Waterway Engineering. China,(07), 147-153+157.

Yu, Y.M., Li, L., et al, 2019. Crack control technology of side wall mass concrete inrail transit engineering. China Harbour Engineering. China,39(10), 17–20.

Xu, W., Zhang, S.S., Li, J. T., 2019. Research on key technology of concrete crack control for ultra-high cable tower structure. China concrete and cement products. China,(07), 84–87.

Yan, Y.P., Shan, H.Y., et al, 2012. Mechanism analysis and life prediction of chloride ion impermeability of Marine concrete mixed with mineral admixtures. Highway. China,(01), 148–152.

Zhao, R.X., 2018. Experimental study on chloride ion permeability of marine concrete. New building materials. China,45(06), 37–39.

Fang, L.Z., 2016. Research And Application On Gentle Volumeexpansion Concrete With Dual Source Of Calciumand Magnesium.. China.

Tang, M.Y.,2016. Effects of Light-Burned MgO Expansive Agent on Durability of Hydraulic Concrete. Jiangsu architecture. China,(04), 101–104.

Shang, R.C., 2017. Experiment on the influence of MgO expansion agent on durability of hydraulic concrete in cold area. Jiangsu concrete. China,(04), 91-94+98.

JGJ 55, 2011. Specification for mix proportion design of ordinary concrete. China Academy of Building Sciences, Beijing,China.

GB 50496, 2018. Standard for Construction of Mass Concrete. MCC Building Research Institute Limited, Beijing,China.

JTS 202, 2011. Specification for Concrete Construction of port and Waterway Engineering, Beijing,China.

JTS 202-1, 2010. Technical Specification for Thermal Cracking Control of Mass Concrete of Port and Waterway Engineering. CCCC Wuhan Harbor Engineering Design and Research Institute Co., LTD, Beijing,China.

GB/T50082,2009.Standard of Test methods for long-term Performance and Durability of ordinary Concrete. China Academy of Building Sciences, Beijing,China.

Tunnelling for a Better Life – Yan, Celestino, Thewes & Eberhardt (Eds)
© 2024 The Author(s), ISBN 978-1-032-80042-4
Open Access: www.taylorfrancis.com, CC BY-NC-ND 4.0 license

Development and application of wall-climbing grinding robot for tunnel lining steel formwork

Ke Yan*
China Railway Construction Heavy Industry Corporation Limited, Changsha, China

ABSTRACT: In order to solve the problems of high safety risk, high labor intensity and low operation efficiency when manually grinding the steel formwork for tunnel lining, an integrated, lightweight and modular design method is adopted to develop a wall-climbing grinding robot with small size, light total weight, convenient disassembly and assembly, which can be suitable for narrow working conditions of tunnel lining. The self-adaptive intelligent operation of the robot in tunnel lining formwork with different curvature radius is realized by flexible grinding mechanism, dual ranging sensor and difference algorithm. A static model is created to analyze the stress of main frame and verify the reliability of robot structure. Finally, the robot has been verified in practical engineering applications. By adjusting the parameters such as grinding speed, working walking speed, wire brush press amount and wire brush diameter, the grinding efficiency is improved to 5~6 times of manual operation efficiency, effectively solving a series of problems existing in manual maintenance of secondary lining trolley.

Keywords: wall-climbing robot, tunnel lining, self-adaptive, industrial verification

1 INTRODUCTION

In the tunnel drilling and blasting construction, the secondary lining trolley is the most core construction equipment to ensure the secondary lining operation. In order to ensure the lining quality of the tunnel surface, it is required that the steel formwork surface shall be polished and oiled once within a limited operation time after each lining by the lining trolley.

The existing operation is mainly completed by manually holding the angle grinder. For the upper end of side formwork and lower end of top formwork of lining trolley, manual direct operation is impossible. It is necessary to set up a temporary walking platform between the outer side of steel formwork surface and the tunnel surface through the lining grouting window to help workers complete the whole formwork grinding operation. When manual grinding is carried out in the tunnel, the working space between the steel formwork and the tunnel lining surface is narrow, with high operation intensity and inconvenient operation. In addition, to control the operation time, multiple workers need to cross-operate on the temporary walking platform synchronously, which has a high safety risk and causes great physical damage to operators when dust is generated during operation. Therefore, there is an urgent need to develop a device to meet the needs of mechanized grinding for secondary lining trolley [1, 2, 3].

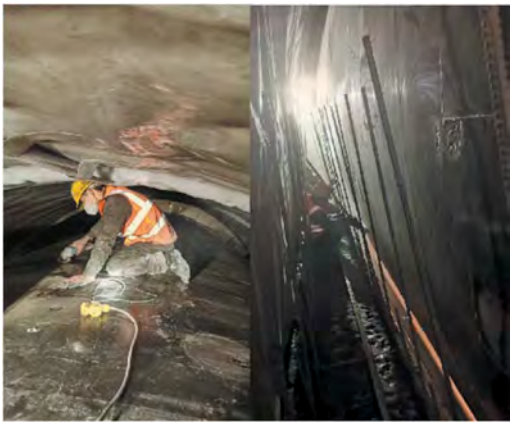

Figure 1. Manual grinding of secondary lining trolley in tunnel.

At present, a number of wall-climbing robots have been developed at home and abroad, which are mostly used in large-scale wall cleaning, inspection, spraying and other operation scenarios, such as petrochemical storage tank maintenance, ship maintenance, wind power operation and maintenance and building cleaning. In the above application scenarios, the operation space is large and the field of vision is good. In order to improve the operation efficiency,

*Corresponding author: yanke@crchi.com

DOI: 10.1201/9781003495505-175

most robots are equipped with large operation modules, resulting in a large overall size and heavy weight. The construction trajectory is controlled visually, but this design idea is not suitable for the narrow operating environment of tunnel lining [4, 5].

In order to solve the problem that the existing wall-climbing robot is large in size and unsuitable for tunnel working conditions, this paper develops a wall-climbing grinding robot with small size, light total weight, convenient disassembly and assembly, which can be suitable for narrow working conditions of tunnel lining.

2 DESIGN OF ROBOT BODY

In this paper, the wall-climbing robot adopts an integrated, lightweight and modular design. It can be operated by a single person to realize the grinding operation of secondary lining trolley. Meanwhile, the automatic operation of products is realized by using the difference guidance of ranging sensor, which solves the problem of low construction efficiency in visual operation.

As shown in Figure 2, the overall structure of the robot consists of an adsorption walking module, an electric control module and an operation module. The robot body structure includes adsorption walking module and electric control module, which have the functions of adsorption, walking, automatic guidance and convenient replacement of operation modules.

Figure 2. Wall-climbing grinding robot.

2.1 *Design of adsorption walking module*

In order to ensure the normal operation of the robot in narrow working conditions, it is necessary to carry out integrated and lightweight design on the adsorption walking module.

When the working surface of wall-climbing robot is made of magnetic material, permanent magnet adsorption is often selected. This method has simple structure and reliable adsorption, which is widely used in petrochemical industry, shipbuilding and other scenarios. The steel formwork of secondary lining trolley is made of magnetic material and has the conditions for magnetic adsorption. In this paper, multi-point arrangement, direct adsorption and indirect adsorption are adopted to ensure the stable adsorption of the robot.

The walking modes of wall-climbing robot usually include wheeled, crawler type and foot type. Among them, the crawler type walking module has strong load capacity but slow movement speed; the foot type walking module has strong obstacle crossing ability but poor movement ability [6, 7]. The wheeled walking module has fast movement speed, flexible steering and certain load capacity. In order to ensure the operation efficiency and reliability, this paper adopts the wheeled walking mode.

2.1.1 *Selection of permanent magnet material*

With reference to mature products on the market, NdFeB material is selected as the raw material of magnet assembly. It has strong magnetic performance, large coercive force parameters and a wide operating temperature range. The specific grade of NdFeB is N42, and its parameters are shown in Table 1. Although there are materials with higher grades such as N50 and N52, their maximum operating temperature is only 60°C. Considering the extreme high temperatures that may be faced by field operations, it is a better choice to sacrifice some magnetic attraction force to ensure the stable operation of stable magnet assembly [8].

Table 1. Parameters and performance of N42 NdFeB.

Parameter	Value
Residual magnetic induction intensity	12.8-13.2Kgs
Intrinsic coercive force	≥12Koe
Maximum magnetic product energy	318-342kJ/m3
Operating temperature	≤80°C

2.1.2 *Design of adsorption walking module*

The adsorption drive module wheel is composed of magnet, magnet housing, rubber wheel and drive motor. In order to ensure the magnetic attraction force of the chassis, the magnet is made into a circular ring as part of the drive wheel to ensure that the distance between the magnet and the working surface is small and stable as much as possible. The outer side of the magnet is wrapped by a housing, which is knurled to improve anti-skid performance.

When the magnet contacts with the working surface, since the outer diameter of the magnet housing is slightly smaller than that of the rubber wheel, under the action of magnetic attraction force, the rubber wheel is deformed and fully contacts with the adsorbed surface. The magnetic rubber wheel structure effectively controls the gap between the magnet and the adsorbed surface, so that the adsorption assembly can provide stable magnetic attraction force. In addition, the rubber wheel is deformed due to magnetic force and fully contacts with the adsorbed surface to improve the stable force of friction with magnet housing.

As shown in Figure 3, the rubber wheel is arranged adjacent to the magnet, so that the adsorption force of the magnet is close to the action point of the supporting force of drive wheel, effectively controlling the arm of force between them. In addition to bearing the weight of the robot body, the frame of the adsorption walking module does not need to bear the additional loads brought by magnetic attraction force. This structure is conducive to the lightweight design of adsorption walking module.

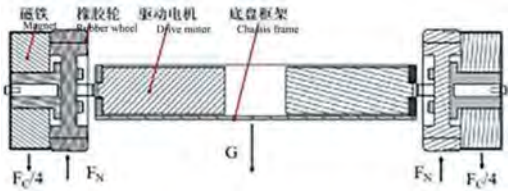

Figure 3. Stress analysis of adsorption walking module.

2.2 *Stress analysis*

When the robot works on the secondary lining trolley, there are three extreme working conditions: 1) downward sliding during facade movement; 2) overturning of the robot around its lower end during facade operation; 3) insufficient driving force during plane movement [9, 10].

As shown in Figure 4, when the wall-climbing robot is stationary at the vertical position of the lining trolley formwork, it is necessary to check two extreme working conditions: facade sliding and facade overturning.

2.2.1 *Downward sliding*

In order to ensure that the vertical adsorption of the wall-climbing robot is stable and does not slide down, its static friction force shall be greater than the gravity of the robot. The formula is as follows:

$$F_c = 2(F_{N1} + F_{N2}) + F_n$$
$$G \leq 2\mu(F_1 + F_2)$$

Where: F_1 is the static friction force between the front driving wheel and the working surface, and F_2 is the friction force between the rear driving wheel and the working surface. F_n is the pre-tightening force of wire brush after compression deformation. F_{N1} and F_{N2} are the supporting forces of front and rear driving wheels respectively. G is the gravity of robot, and F_C is the magnetic attraction force of adsorption module.

2.2.2 *Longitudinal overturning*

When the robot operation module is located above the chassis, there will be a risk of longitudinal overturning around the contact point Q at the lower end of the robot during facade running.

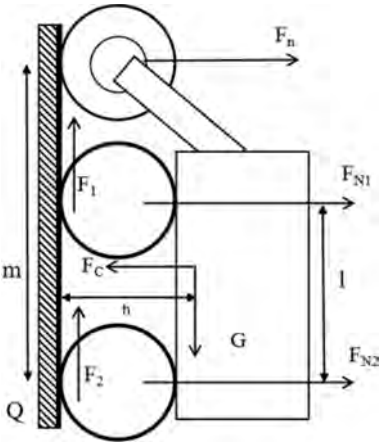

Figure 4. Analysis of facade stress on robot.

$$\Sigma M_Q = 0$$
$$F_C \cdot \frac{l}{2} - Gh - 2F_{N1}l - F_n m \geq 0$$

In order to ensure that the robot does not overturn and there is a certain safety margin, Among them, safety factor k=1.5, friction coefficient μ=0.5, total weight of robot G=460N, distance from center of gravity of robot to operation 94mm, wheel base between front and rear driving wheels l=365mm, pre-tightening force of wire brush Fn=100N, wheel base between wire brush and rear driving wheel m=555mm, the adsorption force F_C required by the adsorption module is ≥1200N.

2.2.3 *Plane drive*

In order to ensure that the robot can run normally on the top of the secondary lining trolley, it is necessary to ensure that the driving force is greater than the static friction force of the chassis. The formula is as follows:

$$F_f = \mu(mg + F_c)$$
$$\mathrm{T} = F_f \cdot r$$

The radius of the driving wheel is r=40mm, and there are 4 drive motors in total for the robot body, so the torque T of a single drive motor is ≥5N▪m.

2.3 *Automatic orientation*

When grinding is carried out in the tunnel, it is not conducive to visual control of robot operation due to narrow environment and large height difference of temporary walking platform. In order to improve the grinding efficiency, reduce the labor intensity of operators and ensure their construction safety, the operation mode of automatic guidance is better than visual control.

Due to the narrow space, dark light, poor communication signal, heavy dust during operation and no obvious characteristics of the working surface for reference in tunnel construction by drilling and blasting method, there are obvious limitations in technical methods such as electromagnetic induction, optical detection, ultrasonic detection and coordinate detection under this working condition. This paper designs an automatic guidance technology suitable for tunnel lining.

2.3.1 *Guidance technology analysis*

For electromagnetic induction/optical detection technology, it is necessary to pre-lay magnetic tapes/nails or colored ribbons with stable reflectivity in the working environment, fix the traveling route of the robot, and carry electromagnetic sensor or photoelectric sensor on the robot. This method has high reliability, but it has a high requirement for flatness of working surface and large transformation of the working surface. There are many undulations on the lining window surface of the secondary lining trolley, and the walking surface is the working surface. It is necessary to polish and oil the working surface, which has the risk of damaging the reference elements. More importantly, both technologies need to transform the steel formwork surface of the secondary lining trolley, which is not conducive to on-site construction and cost control.

Ultrasonic detection uses wall or similar object to locate and guide the reflected signal of ultrasonic waves. It is not necessary to set the datum plane, controlling the guidance cost. However, during the secondary lining of tunnel, the working space is narrow and the steel formwork has no obvious characteristics, so it cannot be positioned and guided by the existing environment;

There are two methods for image recognition technology. One is to use CCD system to dynamically design the image information of the environment around the path and compare it with the image database information of the environment around the proposed operating path, so as to make decisions on subsequent operating paths. However, in practical application, there are problems such as poor real-time performance and difficulty in establishing the environment information section of operating path. The second is the image identification method of identification line, which is implemented by identifying the guide line on the path required for the robot, dynamically taking the image of identification line with a CCD system, and judging the travel deviation of the robot to determine the subsequent movement path [11, 12]. It is difficult to implement this method for the radial transformation of secondary trolley.

2.3.2 *Ranging difference guidance*

In this paper, the combination of laser detection technology and inertial navigation technology is used to realize automatic guidance operation under the working condition of secondary lining trolley for tunnel.

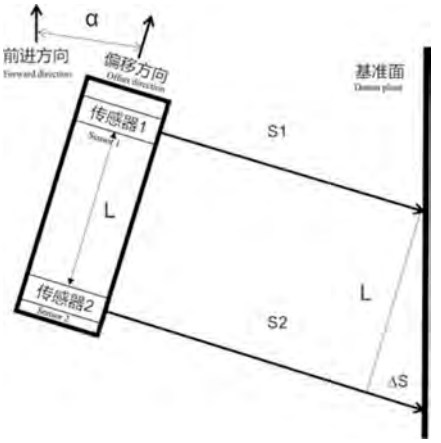

Figure 5. Schematic diagram of ranging difference guidance.

As shown in Figure 5, the distances from the two laser ranging sensors arranged in parallel to the datum plane are S_1 and S_2 respectively. When the walking path of the wall-climbing robot does not deflect, $S_1=S_2$; On the contrary, when there is an obstacle on the wall surface, the wall surface is bent or the wall-climbing robot slips, the walking path of the wall-climbing robot deviates from the movement direction of the robot, and the difference between the distances from the two laser ranging sensors to the datum plane is ΔS. The deflection angle $\alpha = \arctan(\Delta S/L)$ of the wall-climbing robot is calculated by using a trigonometric function, By detecting the deflection angle in real time, the difference algorithm is used to control the speed of left and right side wheels, so that S1=S2 and the robot can walk straight. Where, L is the distance between light outlets of two laser sensors.

By using the lane change point set on the datum plane, the ranging sensor detects a sudden change in distance and triggers the lane change program. The inertial navigation module reads the yaw angle of the robot in real time to control the steering of the robot and complete the lane change action. Through datum plane positioning, the laser ranging sensor can calibrate the absolute position of the robot from the datum plane during operation. After lane change is completed, it shall be ensured that the robot does not repeat grinding and miss the required operation area.

3 DESIGN OF OPERATION MODULE

The operation module mainly has the functions of grinding and dust collection. In this paper, the grinding and dust collection modules are effectively integrated. Meanwhile, other operation modules can be expanded through the quick-change assembly interface of the robot body (as shown in Figure 6).

Figure 6. Quick change diagram of operation module of wall-climbing robot.

3.1 *Design of grinding and dust collection module*

According to the grinding requirements of steel formwork, there are many commonly used methods such as high-pressure water, laser, sandblasting and mechanical grinding. High-pressure water has the problems such as easy re-rusting, need to set up high-pressure pumping station, water supply and drainage; the investment in laser grinding equipment is large, and the cables will reduce the flexibility of equipment. Shot blasting and polishing have great environmental pollution [13].

The above grinding methods have poor applicability to the narrow working environment of tunnel. The mechanical grinding is simple in structure, has high operation efficiency and little disturbance to the environment, and can effectively meet the grinding requirements of steel formwork.

The grinding module consists of base, quick-change assembly, self-adaptive adjustment assembly, grinding motor, transmission assembly and wire brush. Among them, the self-adaptive adjustment assembly consists of adjusting nut, disc spring, guide rod, damper and positioning wheel.

Grinding operation in tunnel will generate a large amount of dust, which has a great impact on the health of operators. In order to control dust and purify the working environment, it is necessary to design a dust collection module. The dust collection module is mainly composed of centrifugal fan, filter (built-in filter element), dust cover, etc. In order to ensure the service life of centrifugal fan, the filter is installed between the centrifugal fan and the integrated housing so that filtered clean air enters the fan space.

3.2 *Stress analysis of wire brush*

In order to clarify the influencing factors of grinding effect, calculate the theoretical load of wire brush, guide the adjustment of grinding operation parameters and complete the selection of grinding motor, the stress of wire brush is analyzed.

As shown in Figure 7, the steel wires are symmetrically distributed left and right. For convenience of calculation, the included angle from the contact surface to the disengagement of wire brush is defined as $2\theta_{max}$, the number of steel wires within this range is 2n, and the maximum cutting depth is d_{max}. The $i(1 \le i \le n)$steel wire on either side of the yaxis within this range is taken as the research object, and its cutting depth is d_i $(0 \le d_i \le d_{max})$, and the included angle with the yaxis is θ_i $(0 \le \theta_i \le \theta_{max})$[14].

The analysis is as follows:

1) The included angle $2\theta_{max}$within the contact range increases with the increase of press amounta_e:

$$2\theta_{max} = \arccos((1 - a_e)/1)$$

The number of contact steel wires increases in equal proportion with the increase of the angle within the contact range, that is, the steel wires are evenly distributed on the wire brush:

$$\frac{n_0}{\theta_{max0}} = \frac{n_1}{\theta_{max1}}$$

2) Maximum cutting depth $d_{max}$is defined as a function which increases with the press amounta_e:

$$d_{max} = f(a_e)$$

According to the test situation, a directly proportional relationship is temporarily taken here, wheres is the proportionality coefficient:

$$f(a_e) = s \cdot a_e$$

3) It is assumed that the maximum cutting depthd_{max} and included angle $\theta_{max}$are nequally divided by nsteel wire on either side within the contact range:

$$d_i = \frac{i}{n} d_{max}, \ (1 \le i \le n)$$

$$\theta_i = \frac{n - i}{n} \theta_{max}, \ (1 \le i \le n)$$

To sum up, the calculation is as follows:
Contact normal forceF_n:

$$F_n = \frac{4}{3} E^* \sqrt{\frac{d_f}{2} d_i^3} = \frac{4}{3} E^* \sqrt{\frac{d_f}{2} \left(\frac{i}{n} \cdot s \cdot a_e \right)^3}$$

$$\frac{1}{E^*} = \frac{1 - v_e^2}{E_e} + \frac{1 - v_s^2}{E_s}$$

Where, $E^*$is the Young modulus of contact, and E_e,V_e,E_s,v_s are the Young modulus and Poisson's ratio of steel wire and steel formwork respectively. The corresponding relationship between the calculated press amount and the torque and grinding power is shown in Table 3:

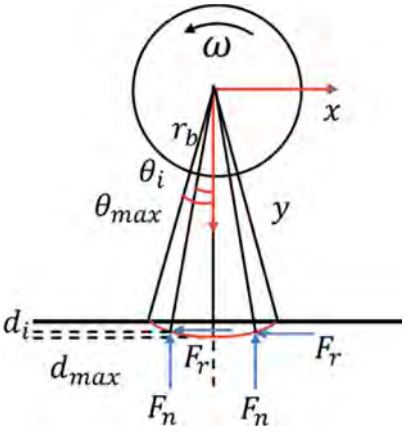

Figure 7. Stress diagram of wire brush.

Table 2. Stress analysis parameters of wire brush.

Parameter	Value	Parameter	Value
Poisson's ratio of wire brush v_e	0.277	Poisson's ratio of workpiece v_s	0.3
Young modulus of wire brush E_e	207	Young modulus of workpiece E_s	206
Diameter of steel wire d_f	0.3 mm	Friction coefficient μ	0.1
Radius of wire brush l	45 mm	Coefficient of cutting depth s	13.75
Rotation speed	1000 rpm	Number of steel wires 2n	35

Table 3. Load parameters of wire brush.

Press amounta_e(mm)	3	4	4.5	5	6
TorqueT(N · m)	1.7	3.1	3.8	4.6	6.5
PowerP_1(W)	179	327	401	485	684

3.3 *Self-adaptive adjustment*

Due to the discontinuous variable curvature of some steel formworks for secondary lining trolley, the grinding mechanism should have a certain adaptive ability to the curved surface. In order to realize the constant force contact between the wire brush and the working surface and ensure the grinding effect, the design mode of disc spring + damper is adopted to achieve stable contact and constant force grinding between the grinding module and the steel formwork surface.

The positioning wheel is adjusted to the height of the wire brush under the preset press amount (i.e. the maximum deformation of the wire brush) to ensure that the wire brush fully contacts with the working surface under the action of disc spring pressure. The grinding down force corresponding to different press amount is calculated according to the stress model of wire brush, and the position of the adjusting nut is adjusted with reference to the load-deformation curve until the pretightening force of the disc spring is greater than the normal force of the wire brush.

When the curvature of the working surface changes, the positioning wheel is under the action of disc spring pressure. It is closely attached to the working surface. Since the position of positioning wheel is relatively fixed to the wire brush and the pretightening force of the disc spring is greater than the normal force corresponding to the deformation of the wire brush, it can ensured that the outer diameter of the wire brush is in close contact with the working surface and the press amount remains unchanged, thus realizing constant force grinding by the wire brush.

4 SIMULATION ANALYSIS AND ENGINEERING TEST

4.1 *Simulation analysis*

4.1.1 *Stress analysis of main frame*

The main frame of the robot consists of an adsorption walking module chassis and an operation module base. The electric control module is integrated in the electrical cabinet and installed on the adsorption walking module chassis, and the operation module base is connected with the adsorption walking module chassis through quick-change assembly. According to the preliminary scheme selection, the single magnetic attraction force of the magnetic wheel is 300N. In order to further ensure the adsorption effect, a prefabricated auxiliary magnetic device is additionally installed in the center of the chassis, with a single magnetic attraction force of 300N and a total of 600N. The normal force F_n for grinding of wire brush is rounded to 100N.

The chassis frame is made of Q345B, and the operation module frame is made of aluminum alloy 6061-T6. There are 6 simulation conditions in total, as shown in Table 4:

Table 4. List of stress calculation conditions for robot frame.

S/N	Operation status	Magnet assembly
1	Horizontal grinding	Additional installation of auxiliary magnetic device
2	Facade grinding	Additional installation of auxiliary magnetic device
3	Facade grinding and obstacle crossing	Additional installation of auxiliary magnetic device
4	Horizontal grinding and obstacle crossing	Additional installation of auxiliary magnetic device
5	Facade grinding and obstacle crossing	No additional installation of auxiliary magnetic device
6	Horizontal grinding and obstacle crossing	No additional installation of auxiliary magnetic device

Among them, the stress/displacement concentration is most obvious under working condition 3 (as shown in Figure 8) and working condition 4 (as shown in Figure 9).

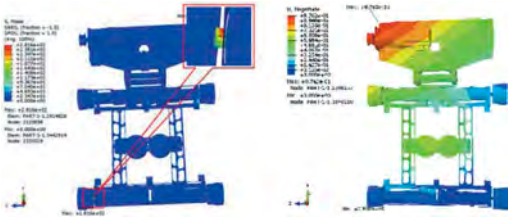

Figure 8. Stress/Displacement Nephogram of robot frame under working condition 3.

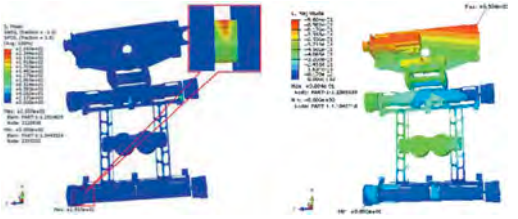

Figure 9. Stress/displacement Nephogram of robot frame under working condition 4.

The simulation results show that the stress of the frame structure is less than the maximum allowable stress of the material under various working conditions, and the overall structure of the robot is reliable. It is necessary to optimize the structure in the stress concentration area. See Table 5 for specific parameters.

Table 5. Statistics and analysis of robot frame simulation results.

S/N	Maximum displacement/mm	Maximum stress/MPa	Safety margin
1	0.477	116.2	66%
2	1.237	114.5	67%
3	0.976	281.6	18%
4	0.98	255.7	26%
5	0.848	192.7	44%
6	0.985	157.3	54%

Note: 1) For Q345B material, the allowable stress is taken as 345 MPa; for aluminum alloy 6061-T6 material, the allowable stress is taken as 315 MPa. Through communication with the Designer, the safety factor has been uniformly considered in the calculation improvement provided by it.2) Safety margin = (allowable stress-calculated stress)/ allowable stress × 100%

4.1.2 *Operation analysis of dust collection module*

In order to discuss the rationality of dust collection module, this paper analyzes it with simulation software. As shown in Figure 10, when the dust cover and the working surface form a confined space, for the dust in an area between the dust cover and the wire brush, under the negative pressure generated by the centrifugal fan, the dust near the air inlet of the filter can quickly enter the filter to complete filtration, but the dust far away from the air inlet flows slowly or cannot move to the air inlet.

According to the results of simulation analysis, in the design of dust collection module, it is necessary to keep an effective confined space between the dust cover and the working surface during dust collection operation, and compress the space between the wire brush and the dust cover as much as possible. In addition, in order to improve the mobility of dust and ensure the dust collection effect, the wire brush is in close contact with the working surface, so that the dust has a certain initial kinetic energy under the action of wire brush, thus ensuring the operation efficiency of dust collection module.

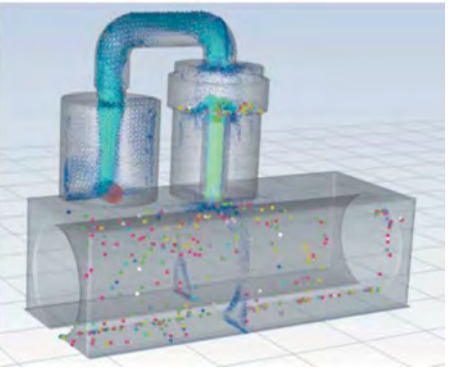

Figure 10. Simulation analysis diagram of dust collection module.

4.2 *Industrial verification*

According to the actual operation requirements of drilling and blasting construction, the robot body and operation module are tested on the secondary lining construction site of tunnel. Through on-site practical operation, the wall-climbing robot body can stably walk and automatically operate on the working surface of the secondary lining trolley, and the operation module can effectively realize grinding and dust collection operations. By optimizing the grinding operation parameters, the operation effect and operation effect of the product are further improved.

4.2.1 *Operation function verification of robot*

The robot is absorbed onto the secondary lining trolley, and then it is controlled to complete forward/backward, left-handed rotation, right-handed rotation and other functions in the side formwork and top formwork through the remote controller. After the datum plane is arranged, the robot can carry out automatic operation according to a predetermined

trajectory. When the battery is low and the ranging sensor exceeds the limit, the buzzer will give an alarm; when the battery is insufficient, the robot stops working and automatically returns. The grinding/dust collection module is installed through the quick-change assembly. The grinding module can effectively remove the attached concrete and better adapt to the curvature change of the working surface to ensure the grinding operation effect. The dust collection module can effectively control the flying dust.

4.2.2 *Operation effect test of robot*

As shown in Figure 11, the wall-climbing grinding robot can effectively remove the concrete attached after secondary lining.

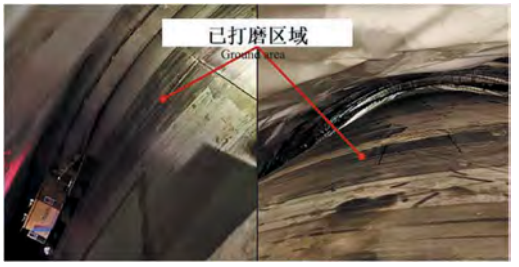

Figure 11. On-site operation effect of wall-climbing robot.

Combined with the stress model of wire brush, relevant variables are adjusted to test the operation effect. The main parameters are grinding speed, working walking speed, wire brush press amount and wire brush diameter.

1) The test results show that the higher the grinding speed, the slower the walking speed and the greater the press amount of the wire brush, the better the grinding effect (as shown in Figure 12).
2) For floating rust and attached concrete on the grinding surface layer, the wire brush with a wire diameter of 0.15 mm has the best operation effect and efficiency; for grinding of severe corrosion, the wire brush with a wire diameter of 0.3 mm has the best operation effect and efficiency; for grinding of set concrete, the wire brush with a wire diameter of 0.5 mm has the best operation effect and efficiency.

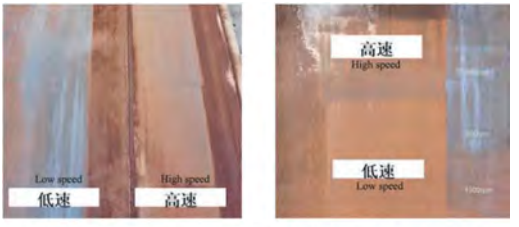

a) Different walking speeds b) Different grinding speeds

Figure 12. Operation effect after adjustment of grinding parameters.

4.2.3 *Mechanical operation efficiency test*

For different grinding objects such as attached concrete, floating rust, severe corrosion and set concrete, adjusting appropriate grinding parameters can effectively improve the grinding efficiency. According to the actual test, when the robot designed in this paper is used for grinding Grade C rust, the derusting grade can reach St2 (as shown in Figure 13), and the operation efficiency is 5~6 times that of manual grinding (as shown in Figure 14).

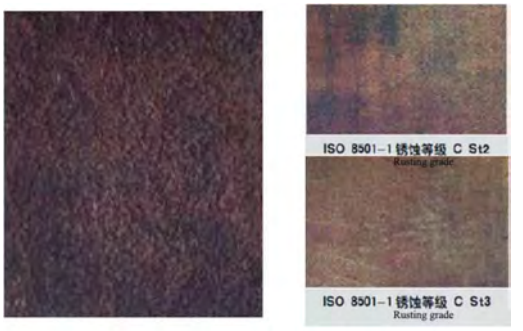

a) Rust grade C b) Derusting grade

Figure 13. Steel plate derusting standard.

Figure 14. Comparison between manual operation and robot operation.

4.2.4 *Summary of robot industrial verification*

Through industrial verification, the robot can meet the grinding operation requirements of secondary lining trolley, effectively reducing labor intensity, controlling operation risk and improving grinding efficiency. Meanwhile, during the test, it is also found that the robot has facade turning sliding and uneven grinding effect in some areas. For the facade sliding problem, we will consider solving it from the aspects of turning algorithm control and magnetic optimization; for the uneven grinding effect, we will consider solving it from the self-adaptive adjustment structure and other aspects.

5 CONCLUSION

(1) In view of the problem that the wall-climbing grinding robot is not suitable for narrow working conditions of tunnel secondary lining, this paper proposes an integrated, lightweight and modular wall-climbing grinding robot for rust removal and oiling. The robot is designed with adjacent magnetic drive assemblies, which ensures the stability of magnetic attraction and driving performance of the robot body and realizes continuous operation on the steel formwork surface of the secondary lining trolley.

(2) Combined with the overall stress of the wall-climbing robot, this paper calculates the working conditions of facade sliding, overturning and insufficient plane driving force of the robot. Based on the operation requirements of secondary lining trolley, the type selection design of magnet assembly and driving assembly is completed. The structural performance of the chassis frame is checked by statics simulation, and the trial-manufactured robot realizes stable operation.

(3) Based on the existing guidance technology, this paper proposes a guidance method with dual ranging sensor and difference algorithm to realize intelligent operation of robot. By setting up a datum plane on the secondary lining trolley, the robot realizes real-time linear deviation correction, fixed-point lane change and path planning on the working surface.

(4) By establishing the mechanical model of wire brush grinding, the corresponding relationship between the deformation of wire brush and the power of grinding motor is obtained. The self-adaptive grinding mechanism is designed. It has been verified by test that the wire brush can better adapt to the curvature change of the working surface and ensure the grinding effect. The grinding effect and efficiency are further optimized by adjusting the parameters such as grinding speed, working walking speed and wire brush press amount.

REFERENCES

[1] International Conference on Computer, Control and Robotics (ICCCR). Shanghai,China: IEEE, 2021: 60–65.

[2] Zhao Junyou, Zhang Yaning, Bi Xiaodong, Yan Chengxin, Dong Yafei. Optimization Design of Magnetic Adsorption Structure and Performance Test of Wall-climbing Robot for Sand Blasting and Rust Removal [J]. Journal of China University of Petroleum (Edition of Natural Sciences), 2020, 44(04): 94–99.

[3] Yan Chenfei, Sun Zhenguo, Zhang Wenzeng, Chen Qiang. Optimization Design of Combined Permanent Magnetic Adsorption Device with Variable Magnetization Direction Unit [J]. Transactions of China Electrotechnical Society, 2016, 31 (03):188–194.

[4] Zhang Xuejian, Liu Chunhui, Yu Zhuqing. Research and Development of Boiler Water Wall Wear Detection Robot [J]. Mechanical Design and Research, 2018, 34(1):1–4+7.

[5] Wang Jiafeng, Yu Zhuqing, Lv Xue. Design and Optimization of Adsorption Structure for Storage Tank Wall Climbing Robot [J]. Automation & Instrumentation, 2022, 37 (9): 36–41+56.

[6] Ross B, Bares J, Fromme C., A Semi-Autonomous Robot for Stripping Paint from Large Vessels[J]. The International Journal of Robotics Research, 2003, 22 (7-8):617–626.

[7] Nguyen S T, La H M. A climbing robot for steel bridge inspection[J]. Journal of Intelligent & Robotic Systems, 2021, 102(4): 1–21.

[8] Hou Jiarui, Wan Yi, Sun Lixin. Design and Analysis of Adsorption Structure of Wind Power Tower Wall-climbing Robot [J]. Mechanical & Electrical Engineering, 2018, 35 (9): 939–943.

[9] Zhao Z, Tao Y, Wang J, et al.The multi-objective optimization design for the magnetic adsorption unit of wall-climbing robot[J]. Journal of Mechanical Science and Technology, 2022, 36(1): 305–316.

[10] Xinrui L, Denghui G, Yuan C. Design and optimization of the magnetic adsorption mechanism of a pipeline-climbing robot[J]. Journal of Mechanical Science and Technology, 2021, 35(11): 5161–5171.

[11] Eckart Uhlmann, and Christian Sommerfeld. Dynamic contact analysis of abrasive filaments with a discrete system[J]. Advances in Abrasive Technology, 2017, 3-6:626–634.

[12] Du Xiaoyu, Yang Pei, Zhang Minglu. Design and Analysis of Wall-climbing Robot with Modular Operation [J]. Mechanical Science and Technology for Aerospace Engineering, 2023, 41.

[13] Wang Jingxin, Guo Yanbao, Zhang Zheng, Wang Bin. Mechanical Analysis and Magnetic Adsorption Structure Optimization Design of Crawler Type Wall-climbing Robot [J]. Artificial Intelligence and Robotics Research, 2023, 38 (4): 70–75.

[14] Xu Y, He K, Zhao W L, et al. A novel design of a wall-climbing robot and experimental study on magnetic wheels[C]//2021

Tunnelling for a Better Life – Yan, Celestino, Thewes & Eberhardt (Eds)
© 2024 The Author(s), ISBN 978-1-032-80042-4
Open Access: www.taylorfrancis.com, CC BY-NC-ND 4.0 license

Retrospective analysis of the design and manufacture of a case of steel fibre reinforced segmental lining in view of the actual behaviour of some rings on site

Zhuangzhi Yang* & Zonghua Gu
CRTG, China Railway Tunnel Group, Guangzhou, China

Patricio García de Haro
Tunnelconsult Engineering S.L., Barcelona, Spain

ABSTRACT: Steel fibre reinforced concrete is increasingly being used as a construction material in ring-shaped tunnels excavated by TBM. This paper examines a real case of the use of steel fibre reinforced concrete for segmental lining, where some segments, once produced, showed a different behaviour than expected. The breakage of some of them and the appearance of cracks in others required a thorough review of all the stages in the life cycle of the segments up to their final placement in the tunnel. The detailed design of the segments is being reviewed, as well as the manufacturing process, the handling and transport of the segments and the assembly of the rings.

Keywords: Steel fibre reinforced concrete (SFRC), precast segmental lining, manufacturing, behaviour, breakage, cracks, EPB

1 INTRODUCTION

This paper discusses a 2.5 km-long and 7.2 m outer diameter underground structure that was excavated and built by one of CRTG's own EPB machines.

The structure is intended to be used as a utility gallery. The tunnel has a rectilinear layout. In terms of the longitudinal profile, halfway along the alignment is the location of the maximum overburden of about 18 m, while at both entrances is the minimum overburden of about 7.0 m. The tunnel has a gradient of up to 2.50 %. The utility gallery is situated in the Middle East and was built three years ago.

While erecting and assembling the rings for tunnel construction, the SFRC segments demonstrated decreased strength, leading to the development of cracks and partial or complete breakage of the segments. The first cracks already appeared in the assembly of blind rings.

Given this scenario, it was necessary to conduct a comprehensive investigation on the life cycle of the segments, from the design to their placement inside the tunnel. This also required repairing a significant number of segments, both before and after installed. Similarly, a considerable number of segments had to be discarded during construction.

It should be noted that in this project, the segments were supplied by the client, while CRTG was only responsible for excavating the tunnel and assembling the rings. Finally, CRTG was also contracted to carry out the necessary repairs to the rings.

The following figures illustrate some of the various segments that broke during construction, without being limiting. Otherwise, they would not have been the subject of analysis, but mere incidents of work.

In total, more than 1,600 rings of 1,500 mm length (about 9,600 segments) were produced in six and a half months.

Taking into account the days of downtime (due to breakdowns, maintenance, waiting for materials, availability of storage space, etc.) the average production was about 7.5 rings per day. In total there were 55 days of downtime, and excluding these, the average daily production was 10 rings/day. The maximum ring production reached was 19 rings per day.

During the production of the rings, while some segments were rejected, others had to be repaired due to defects. For this purpose, the defective

*Corresponding author: yang.zhuangzhi@crtg.cn

DOI: 10.1201/9781003495505-176

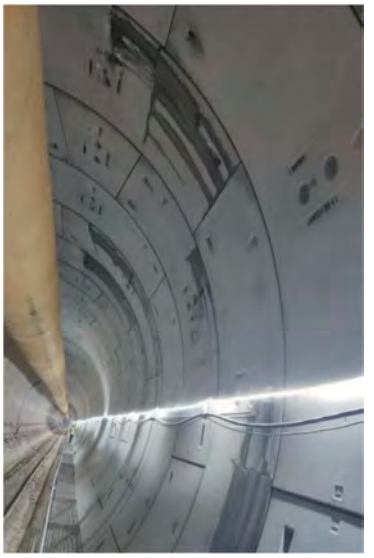

Figure 1. General view of the utility gallery during construction.

Figure 2. Detail of a SFRC segment that broke in half during installation.

Figure 3. Detail of another halved SFRC segment (both pieces).

segments were divided into three categories: "Minor defect", "Major defect" and "Rejected".

A total of 800 defective segments (8.5% of production) were recorded before transferring to the tunnel. 110 were rejected because of severe cracks, while 680 could be repaired. Of the latter, 590 segments were affected by minor cracks. The main defect was minor cracks in the area of bolt holes and sockets, less than 0.20 mm wide. When such cracks reached one of the surfaces, they became larger cracks and their width increased. If the width was greater than 0.30 mm, the segment was rejected. Micro-cracking occurred in the centre of sockets and bolt holes area due to the temperature difference between day and night and the moulds not being properly covered during curing.

Figure 4. Detail of crack traversing the entire segment face before and after repair.

2 PRECAST SEGMENTAL LINING

The segmental lining consists of a ring with an internal diameter of 6500 mm, which is 350 mm thick and 1500 mm in length. The ring, commonly known as the universal type, has a 5+1 configuration, taper of ±20 mm, straight joints between segments (excluding key and counter keys), and bolts in both longitudinal (segment to segment) and circumferential (ring to ring) joints. The keystone is inclined at an angle of 20.5º.

The segmental lining was designed with a service life of 100 years, which is a typical duration for this type of structure. The utility gallery is situated in a hot and humid environment with high concentrations of chlorides and sulphates in the soil and groundwater.

Class C50/60 concrete (in accordance with EN 206-1:2013) was required for the precast segmental lining. A triple-bend cement type with reduced Portland cement content that can react with sulphates was identified for producing Class C50/60 concrete.

Among the permitted combinations, the triple mix was specified as OPC (35%) + GGBS (60%) + MS (5%), i.e. Portland cement, ground granulate blast furnace slag and micro silica. The water/cement ratio was restricted to a maximum of 0.40. Moreover, the minimum cementitious material content was prescribed as 380 kg/m^3.

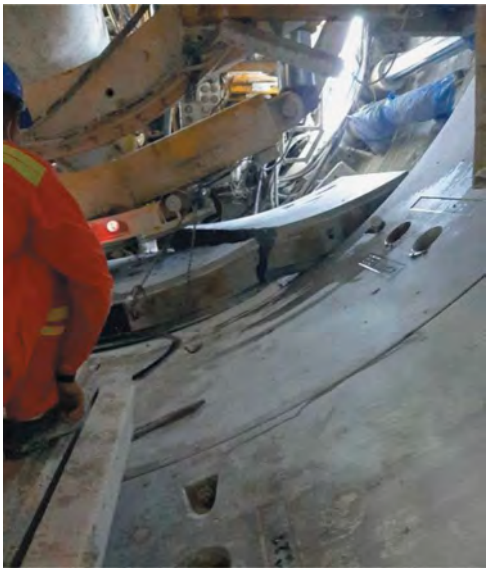

Figure 5. SFRC segment broken during ring assembly.

Figure 6. A different view of the broken segment shown in the previous figure.

The concrete mix included SIKA Viscocrete-TS100, a superplasticizer specifically developed for high performance concrete, as well as for precast tunnels segments and steel fibre reinforced concrete (SFRC).

The designer of the ring specified the use of steel fibres to replace steel reinforcing bars in order to minimize the risk of corrosion. This was because "*the corroding element is removed by the use of steel fibres"*. He also stated that "*the use of SFRC is also considered because of the demonstrated increase in ductility (strain-softening behaviour when tested in bending) in relation to unreinforced concrete and the effective elimination of spalling damage, as well as the ability to control drying shrinkage cracking*". However, despite the previous misinformed statement, the SFRC adopted had a strain-hardening behaviour, with better post-cracking behaviour and ductility than a strain-softening mixture.

HE++90/60 fibres were used. The main characteristics of the fibres were: diameter of 0.90 mm, a length of 60 mm, an aspect ratio (L/D) of 67, a wire tensile strength of 1900 N/mm^2 and a number of fibres per kg of 3200. A steel fibre dosage of 40 kg/m^3 of concrete was established.

A 1.5 kg/m^3 of polypropylene (PP) fibre was added to the concrete mix as a protective measure against thermal instability in the event of exposure to accidental fire (concrete spalling).

The following figures show some of the most commonly found defects in the tunnel segmental lining:

Figure 7. Cracking after the bolt tightening into its pocket.

All these unforeseen defects accelerate the degradation process of the structure over time.

2.1 *Durability strategy during the design phase*

The design for durability was based on the "Deem-to satisfy design approach" and "Avoidance of deterioration design approach", as outlined in the Model Code for Service Life Design by the International Federation for Structural Concrete (The fib). This approach focuses on adhering to standards/codes and using non-reactive materials to completely prevent corrosion from occurring.

The durability design considered the ground and groundwater conditions obtained from the project-

Figure 8. Crack during the installation of the next ring segments due to the thrust of the TBM jacks.

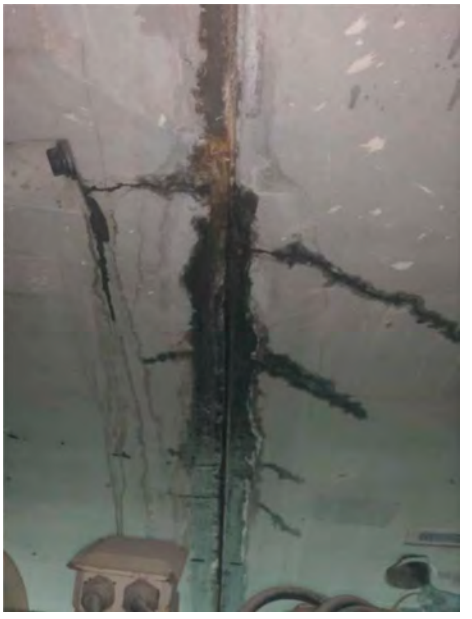

Figure 9. Cracks in the area of the bolt insert (on the upper left) and in the circumferential joint in both segments.

specific ground investigation. The appropriate parameters were then determined for the precast segmental lining to ensure minimum maintenance of the tunnel structure during its expected lifetime.

Since the tunnel was expected to remain permanently submerged, the outer face would be exposed to long-term contact with high levels of chlorides in water. Therefore, an "Aggressive" type of exposure was chosen.

The main deterioration mechanisms that could affect the long-term durability of the tunnel were thought to be chloride-induced corrosion and sulphate attacks, although other mechanisms may also contribute.

To provide corrosion protection under such severe environmental conditions, the crack width of the

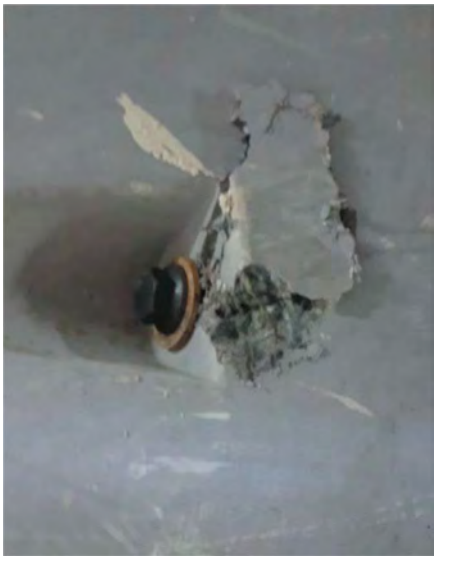

Figure 10. Pocket side-face blowout after installation of the bolt.

precast segments was restricted to 0.2 mm. When the crack width is limited to this value, water that seeps through it has the potential to dissolve calcium hydroxide from the cement matrix. As a result, when the dissolved calcium hydroxide comes in contact with the atmosphere and reacts with carbon dioxide, it forms calcium carbonate, which may seal the crack.

According to the determined exposure classes and considering a concrete of C50/60, the concrete covers were set to 60 mm in the extrados surface (X3) and 70 mm in the inner and joint surfaces (X5) for the conventionally reinforced rings in singular areas on the tunnel alignment.

3 CASTING STAGES

This section briefly describes the steps involved in casting, from preparation of the moulds to stacking. Before the concrete was poured, the moulds were oiled and the socket areas were greased. The concrete was transported from the batching plant to the moulds by a truck mixer rather than a conveyor system. The use of the truck mixer system resulted in cold joints in some segments as the concrete was not poured continuously. The addition of steel fibres to the concrete mix was done manually as the plant did not have the required automatic dosing system. Vibration was carried out by a supervisor manually controlling the equipment. Once the pour was complete, the external surface was quickly cleaned and smoothened by hand. In spite of that, in order to ensure the consistent quality of the concrete produced and used on the project, both the concrete plant and the casting yard responsible for the

production of concrete and precast segments had an accredited ISO9001 quality assurance system and operating procedures.

In order to shorten time to reach minimum strength of demoulding, steam curing system was used. Once casting and covering process was over, moulds were taken to the steam curing for 10-12 hours to reach early strength level (which is 18 MPa) for demoulding.

Under no circumstances was the maximum temperature of the concrete segments allowed to exceed 70°C. To this end, thermocouple temperature sensors were used on a representative number of segments during the concrete curing process to monitor the actual temperature.

If compressive strength test requirements were fulfilled, segments were ready for demoulding. An important consideration at this point is to complete the covering process as soon as possible. Late covering causes an increase in the micro cracking percentage of the segments.

The steam curing system was used to reduce the time required to achieve the minimum demoulding strength, set at 18 MPa (cylindrical). By doing so, the concrete reached 18 MPa early strength in 8-10 hours, but the demoulding was carried out at the cubic strength value instead of the cylindrical, which is in fact about 15 MPa. The average early strength value for demoulding was 23.7 MPa (in cubic specimen). The demoulding equipment was a mobile 3-pad vacuum lifter.

During production, the segments were stored in the production hall in a concave position. All sides and the outer surface of the segments were then inspected in the same production hall. If the segments received initial approval, they were sent to the turning machine to be turned into the convex position. The segments were turned into the convex position using special equipment, one by one and after 3 days of casting.

After inspection on the internal face and approval of the repair works (if necessary), the segments were initially stacked separately for 7 days to allow the concrete to reach stacking capacity. After these 7 days, a maximum of four regular segments were stacked in their final position in the stack-yard, while the key segments were stacked separately. Transfer from the plant to the site took place a minimum of 14 days after casting.

Deliveries were planned by loading a complete ring onto a trailer and the quantities delivered were agreed on the basis of instructions from the site and the progress of the TBM, as the storage capacity on site was not very large. The average delivery was about 6.5 rings per day for almost seven months.

Taking into account that the 7-day laboratory test results 'met' the minimum strength capacity required for the concrete, a 13-day period was considered sufficient for delivery to site. The distance between the precast plant and the construction site was 75 km and the delivery of a ring took approximately one and a half hours.

4 TESTS AND INVESTIGATIONS PERFORMED BEFORE AND FOLLOWING THE SEGMENT RUPTURES

Tests were carried out on fresh concrete during the segment production phase.

In addition, following the defects observed in the rings and the first broken segments during assembly in the tunnel, tests were also carried out on cast segments, using two split segments.

4.1 *Fresh concrete tests during the casting process*

The fresh concrete was tested for unconfined compressive strength. Two samples for each mix (one mix is for three to four segments) to check early strength and three samples per production shift to check 7 days and 28 days were prepared.

The 7-day compressive test results were between 55-72 MPa for the cubic specimens and the 28-day results were between 70-80 MPa also for the cubic specimens. In terms of early strength, the compressive strength results vary somewhat, ranging from 18 to 28 MPa (cubic specimens).

The fresh concrete was also tested for flexural strength in groups of three specimens at 7 and 28 days according to the established test schedule. The minimum values required at 28 days were: $f_{r1k} > 4$ MPa, $f_{r1k}/f_{Lk} > 0.4$ and $f_{r3k}/f_{r1k} > 1.10$. All these requirements were met. However, tensile strength values obtained at age 7 days were not reported.

Finally, fibre washout tests were carried out on fresh concrete. Steel fibres washout tests were done three times a week on two different samples to check how much steel fibre the segments contained per m^3. The results were between 38 kg – 44 kg per m^3.

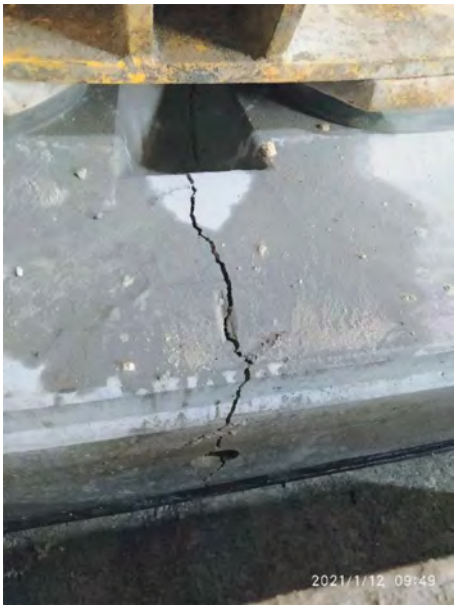

Figure 11. Crack that occurred when the segment was to be installed.

Figure 12. A view of the crack above, across the face of the circumferential joint.

4.2 *Tests on split segments*

On the other hand, the tests on the cast segments used two of the split segments.

These tests on the first segment consisted of seven core samples recovered with a Hilti machine from the segment in the presumably weakest areas. Of these, three were for fibre distribution tests, two were for uniaxial compressive strength tests and the remaining two were for tensile strength tests.

Nine core samples were taken from the second cast segment and tested as follows: five for fibre distribution, two for compressive strength and two more for tensile strength.

Figure 13. View of a segment split along the minor axis of the piece. The brown stain on the left is dirt from when it fell.

The average compressive strength values obtained were 58 MPa for one of the segments and 69 MPa for the other (all values in cylindrical specimen). For the indirect tensile tests, the values ranged from 4.7 to 7 MPa, with the minimum required by the designer being 2.6 MPa. However, 2.6 MPa was the design tensile strength of the mixture, namely the characteristic strength f_{R1k} affected by the partial factor for concrete γ_c=1.5. The requirement should have been established much higher. Fibre distribution tests were in line with requirements.

Figure 14. View of the other half of the SFRC split segment shown above, seen from the lifting sockets.

Figure 15. Detail of the concrete mass with fibres from the same splitting surface.

Figure 16. View of the positions where the cores were obtained for testing in one of the split SFRC segments.

4.3 *Full scale tests*

When using SFRC-based precast segmental linings, two types of full-scale segment tests are required to verify the design:

– Flexural test: aims to simulate the behaviour of the segment mainly under transient loading conditions. It allows the crack load, the load at the maximum design crack width and the ultimate load to be determined.

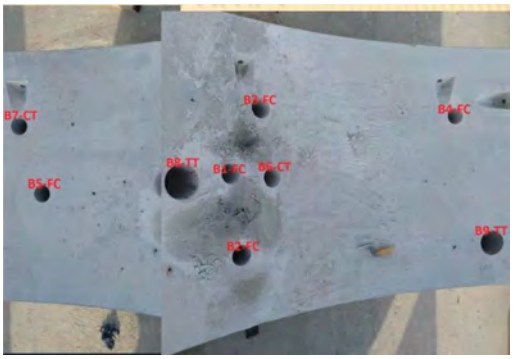

Figure 17. View of the positions where the cores were obtained in the other split SFRC segment under test.

– Point load test: representative of the thrust load condition of the TBM. Allows verification of shear loads. Also allows for verification of burst and burst loads and measurement of crack width.

A minimum of two segments should be tested for each type of test. The problem is that although full-scale testing is highly recommended, it requires suitable testing facilities, which are not available everywhere. For the same reason, these tests could not be performed in the present case.

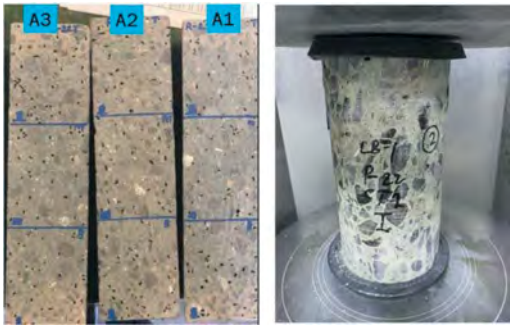

Figure 18. View of some samples obtained from a split segment and its division for fibre distribution tests (left). Compressive strength test of one of the cores obtained from a split segment (right).

5 REVIEW OF THE DESIGN AND CALCULATION PHASE OF SFRC RINGS

After reviewing the manufacturing process of the segments and analysing their mechanical strength, it can be concluded that although the manufacturing process was not the most technologically advanced, the results of the strength tests carried out on specimens obtained from damaged segments met the project requirements. In concluding this, it should be noted that there is an important scale and shape factor between the laboratory specimens tested and the segments. In the light of these results, it was decided to revise the design of the rings.

The design process of the rings presents inaccuracies and some errors of importance. Firstly, the ULS load combinations considered scenarios of current groundwater conditions (ULS1), a seismic event (ULS2), high and low groundwater situation (ULS3 and ULS4) and secondary grouting (ULS5). However, despite stating that all combinations follow the prescriptions in Eurocode 2, only ULS1 load combination had the applicable factors of 1.35 for permanent loads and 1.5 for transient loads. The other four combinations were treated as "accidental combinations" with all factors set to 1.0.

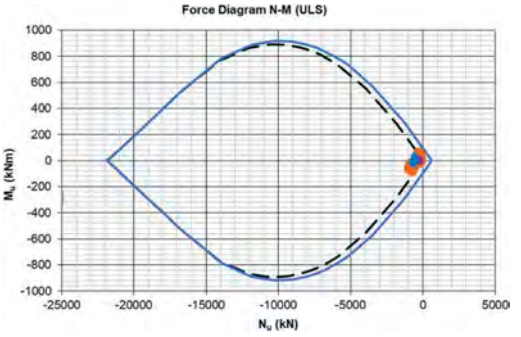

Figure 19. N-M diagram for ULS2 to ULS5.

This procedure is fine for ULS2 and ULS5 (as prescribed by the ITA), but combinations ULS3 and ULS4 should have been treated as regular ULS combinations.

When observing the N-M diagrams obtained from load combinations ULS2 to ULS5 it can be seen that the sectional capacity is quite close to the limit in many cases. It should be also taken into account that the relevant partial factor for concrete is γ_c=1.2 for accidental load combinations. This design approach has a lower safety margin compared to "true" ULS combinations and may lead to potentially unconservative designs.

Secondly, another fact to take into consideration is the fact that cracking control was not performed. The designer states that the cracking moment is larger than the bending moment is SLS combinations, and therefore the crack width check is not required. However, conventionally reinforced concrete is provided with minimum reinforcement areas, which is deployed in order to ensure that the member ultimate strength is larger than the cracking moment and to avoid brittle failure after the cross-section develops a crack. In this particular case, the SFRC segments had a cracking moment M_{cr}=125.6 m·kN and a design ultimate strength M_u=89.8 m·kN. Given the post-cracking behaviour of the segment it may be advisable to perform crack control checks and consider cracked sections even if the segment should be uncracked in ideal conditions, especially in structures difficult to repair and with low structural redundancy.

Thirdly, the estimation of the tensile stresses developed at the joints due to TBM thrust is correct and

performed according to the ITA provisions, but the tensile stress values obtained are checked against the wrong parameter. Indeed, the joint bursting and spalling due to TBM ram shoe thrust are checks performed in ULS since it is the breaking of the segment that is being analysed. Instead of studying this phenomenon as a ULS scenario, the designer compares the tensile stresses obtained to f_{ctm} as if it were a SLS check and states that "SLS conditions are verified". This assumption allows the designer to compare the maximum tensile spalling stress obtained in the circumferential joint (equal to 4.0 MPa) with the mean tensile strength of the concrete of 4.1 MPa.

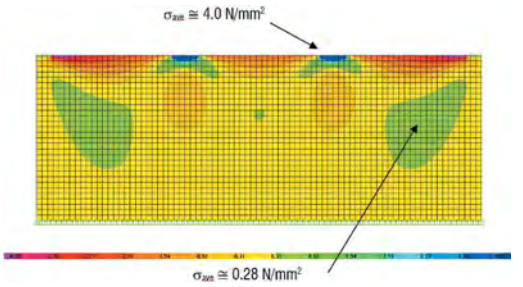

Figure 20. Average spalling stresses due to TBM thrust.

However, this assumption serves only to ensure that about half of the segments will crack if the foreseen load is applied. The tensile strength that should have been used is the design residual strength of the SFRC f_{Ftud} = 0.98 MPa which is much lower.

The adoption of the design residual strength could have entailed a change in the solution such as the possible adoption of a perimetral reinforcement in order to comply with the ULS requirements. Also, through-thickness bursting stresses were checked in the same manner with tensile stress values substantially higher than the design residual strength.

Fourthly, the temporary stages of the segments were studied, which included demoulding, first stacking (2 segments per stack at age 7 days), storage (a whole ring per stack at age 28 days) and transportation (at 28 days). In spite of these clear stages the segments must follow, after 7 days of age the segments were stacked in stacks of 4, which was not foreseen in the initial design.

Finally, the seismic action was introduced as a racking deformation that distorts the circular geometry of the lining. The said deformation was not introduced accurately in the Plaxis software and the internal forces obtained may be incorrect.

6 FINAL INSPECTION AND NECESSARY REPAIRS TO SFRC SEGMENTS

After completion, the tunnel was inspected to determine what repairs were needed.

During this supervision work, several types of pathology were found in the rings. These were: dry cracks, cracks with leakage, leakage in the joints, leakage through the secondary grouting sockets, broken edges and corners. More specifically, 45% of the rings were found to have pathologies.

The repairs consisted of epoxy resin injection for crack leaks (230 cases), smoothing filler for dry cracks (642 cases), cementitious sealing in the case of grouting socket leaks (118 cases) and PU injections for joints leaks (79 cases). The number of broken edges and corners to be repaired was nine.

Needless to say, only the defects on the intrados of the lining could be repaired. Those on the extrados remain unaddressed and unknown.

In addition, to ensure the correct stability of the lining, gap filling with secondary grouting was performed in all rings.

Figure 21. A cracked segment is repaired by injections.

7 CONCLUSIONS AND RECOMMENDATIONS

The case of a precast concrete and steel fibre segmental lining for a 6.50 m internal diameter utility tunnel, where the segments did not perform as expected, has been reviewed.

After analysing the various stages in the life cycle of the segments up to their final installation in the tunnel, it can be concluded that the detailed design phase and fabrication stages are critical in the use of this technology.

Steel fibre rings should only be used where the ground and the loads allow. The designer must have a high level of knowledge of the strength of the SFRC material and the ground of the tunnel alignment must be very well characterised in order to avoid errors in the calculations. The numerical models developed must be accurate and load combinations shall have the appropriate load combination factors.

Crack control should always be performed even if the bending moment in SLS is smaller than the cracking moment of the section, especially when the design ultimate bending strength is substantially smaller than M_{cr} and the structure is difficult to repair and presents limited structural redundancy. The catastrophic consequences of a collapse in a tunnel should be taken into consideration in the design phase, and all sections should be checked in SLS as cracked sections and no damage to the

segments should be allowed during TBM ram thrust or any other scenario.

As stated in di Prisco, M. et al., "*Fibre reinforcement is suitable for structures where diffused stresses are present. In structures with both localised and diffused stresses, which is the usual case, it is better to base the reinforcement on a combination of rebars and fibre reinforcement*".

Steel fibre rings should never be used on the assumption that the tunnel will behave as a perfect arch subject only to axial forces. In addition to the nature of the ground, which must have suitable geomechanical characteristics, the thrust of the TBM may dictate the design of the segments, which is a very important localised load that is best resisted by means of conventional rebars. The design of the rings must be appropriate to each circumstance.

Steel fibres are not a universal solution (as some designers think) and therefore do not work in all cases as presented. In most cases, only rings with conventional reinforcement based on steel rebars will be suitable; in other cases, it may be necessary to combine steel fibres with conventional reinforcement in the joints in order to withstand the stresses to which the ring is subjected during assembly or in temporary stages, the bending stresses caused by the actions of handling, transport and other transient loads. In the smallest number of cases (small segments, low stresses, etc.) and after proper and truthful design, the segments may be steel fibre-based only. This is very important and should be taken into account in the design.

The designer must be completely independent of time, economic or commercial considerations in his decision to use steel fibres in the project of the tunnel.

REFERENCES

ACI 544.7R-16, 2016. Report on design and construction of fiber-reinforced precast concrete tunnel segments. ACI Committee 544, American Concrete Institute, Farmington Hills, MI 48331, USA. ISBN: 978–0–87031–948–8.

Castrogiovanni, G. et al., 2019. Steel fibre reinforced concrete for segmental lining – crack mitigation measures at design phase. In book: Tunnels and Underground Cities: Engineering and Innovation meet Archaeology, Architecture and Art, pp.1889–1897. Proceedings of the WTC 2019 ITA-AITES World Tunnel Congress (WTC 2019), May 3–9, 2019, Naples, Italy. CRC Press, London, UK. ISBN 9780429424441.

CEB-FIP, 2017. Fib Bulletin 83. Precast tunnel segments in fibre-reinforced concrete. State of the art report. ISBN 978-2-88394-123–6.

CEB-FIP, 2013. Model Code for concrete structures 2010. Design code. Ernst & Sohn. Berlin, Germany. ISBN: 978–3–433–03061–5.

ITAtech, 2016. Guidance for precast fibre reinforced concrete segments – Vol. 1: Design Aspects. Report no. 7, ISBN: 978–2–9701013–2–1.

Di Prisco, M. et al, Fibre-reinforced concrete in fib Model Code 2010: principles, models and test validation. Structural Concrete 14 (2013) No. 4.

Tunnelling for a Better Life – Yan, Celestino, Thewes & Eberhardt (Eds)
© 2024 The Author(s), ISBN 978-1-032-80042-4
Open Access: www.taylorfrancis.com, CC BY-NC-ND 4.0 license

Robustness evaluation on non-circular segmental tunnel linings: Case study on quasi-rectangular shield tunnel

Yuhang Ye
College of Civil Engineering, Tongji University, Shanghai, P.R. China
Guangzhou Metro Design Research Institute Co. Ltd., Guangzhou, P.R. China

Zhen Liu* & Xian Liu
College of Civil Engineering, Tongji University, Shanghai, P.R. China

ABSTRACT: As effective alternatives for underground construction in high density urban area, non-circular shield tunnels often face more challenges in complex surrounding environment due to their non-circular cross-sections. In order to provide theoretical guidance for the non-circular tunnels under design and service period, this paper proposes a robustness evaluation method for non-circular shield tunnels. This method is based on macro-level nonlinear structural modelling and prototype structural experiment. The elastoplastic failure process of the structure is revealed and discussed. The energy-based robustness evaluation method is proposed considering the development of structural plasticity. The robustness evaluation of the non-circular shield tunnels could then be carried out. In this study, Quasi-rectangular shield tunnel (QRST) is taken as an example for robustness evaluation. The research shows that the proposed method can effectively evaluate structural robustness of non-circular tunnels with different parameters. Considering key structural parameters such as reinforcement and bolt positions, the optimization direction of non-circular tunnels is discussed based on the robustness evaluation method. The research will lay the foundation for future application of non-circular shield tunnels.

Keywords: non-circular tunnel, energy-based robustness evaluation, Quasi-rectangular tunnel, structural optimization, bolt position

1 INTRODUCTION

During the operation period, tunnels will always face various unexpected circumstances, such as top overburden (Liu et al., 2018a), lateral unloading (Liu et al., 2016), surrounding construction (Jin et al., 2018), material deterioration (Zhang et al., 2022), etc. Therefore, for both circular and non-circular tunnel structures, an accurate prediction of the failure characteristics and robust performance of the structures under different unexpected circumstances are rather important. Relevant studies can bring an insight into how to evaluate structural performance and provide theoretical guidance for the design and maintenance of tunnels (Yuan et al., 2012).

Conducting structural failure tests is an effective way to explore the failure process of the structure and evaluate its mechanical properties at the same time. He et al. (2014) used a comprehensive loading system for the staggered assembly tunnel structure of the Shiziyang Tunnel, and explored the failure mechanism of the structure. Based on the load-bearing process, the effective stiffness coefficient and residual bearing capacity coefficient were used to evaluate the structural performance during the failure process (Zhang et al., 2019). Liu et al. (2016) studied the mechanical behavior and failure process of the continuously jointed segmental tunnel linings under unexpected conditions of top overburden and side unloading, and defined a structural bearing capacity safety factor to evaluate the structural robustness.

Since structural failure tests are one-time and expensive, in recent years, many macroscopic nonlinear numerical models are established to simulate the structural failure process and evaluate the robust performance of the structure under unexpected conditions. Zhao et al. (2017) established a nonlinear analysis model based on the beam and rigid-plate spring model to simulate the failure process of the structure. Chen et al. (2020)

*Corresponding author: 1hugospace@tongji.edu.cn

DOI: 10.1201/9781003495505-177

established a refined three-dimensional numerical model, verified it with full-scale tests, and analyzed the failure mechanism and failure process of the structure. The failure process of the structure under top unloading conditions were also investigated (Wu et al., 2022). Liu et al. (2022a; 2022b) established nonlinear macro-level models and carried out an explanation of the failure mechanism of RC and FRC tunnels with staggered joints. The robustness of the structure with different structural parameters are also evaluated.

Since robustness evaluation based solely on structural failure test has limitations such as insufficient monitoring methods and accidental graded loading. Existing robustness evaluations often focus on some load or deformation indicators, and do not consider the relationship between the load and deformation in the whole field. Therefore, in this study, a tunnel structure robustness evaluation process is proposed. Taking a Quasi-rectangular shield tunnel (QRST) as an example, full-scale structural tests are first carried out and referenced. A nonlinear macro-level structural model is then established and validated by the test. Then the robustness evaluation method of the structure is carried out, providing guidance for practical engineering applications.

2 NONLINEAR BEHAVIOR OF QRST

2.1 *Full-scale failure test of tunnel structure*

Considering the increasingly intensive urban underground space, non-circular shield tunnels with high space utilization (such as DOT tunnels and QRST tunnels) will be more and more widely utilized. The QRST shield boring machine uses three cutterheads for full-section cutting during tunnel excavation (Liu et al., 2018c). Till now, QRST tunnels have been successfully utilized in many cities such as Ningbo and Hangzhou, China.

QRST tunnel lining has an outside dimension of 11.5m × 6.937m. The thickness and width of the segment are 0.45m and 1.2m, respectively. The thickness and width of the interior column are 0.35m and 0.7m, respectively. A typical cross-section of the QRST lining is shown in Figure 1. The tunnel is composed of ten blocks and an interior column (LZ). Ten blocks include two T-shape block (T1 and T2), three standard blocks (B1, B2 and B3), three C blocks (C1, C2 and C3), a contiguous block (L), and a key block (F).

Liu et al. (2018a) carried out a full-scale failure test for a QRST specimen. By simulating the tunnel structure subjected to a top loading overburden condition, the weak parts and ultimate bearing performance of the structure are revealed. A photo of the test is shown in Figure 2. 30 loading points are exerted on the structure, which are divided into three groups of P1 (8 loading points), P2 (10 loading points), and P3 (12 loading points). The details of the test loading procedure are introduced by Liu et al. (2018a).

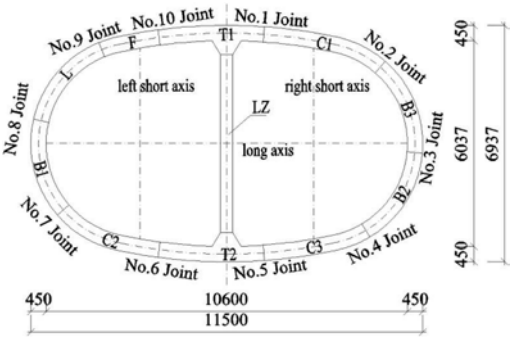

Figure 1. Schematic diagram of QRST.

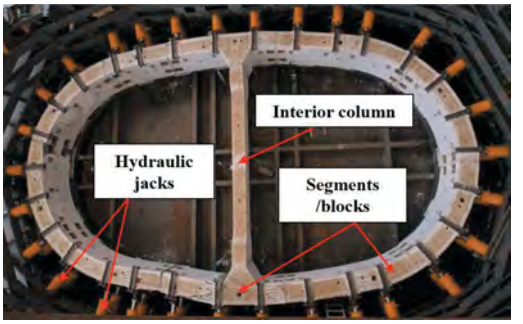

Figure 2. Photo of full-scale test.

2.2 *Nonlinear macro-level model*

A macro-level nonlinear FEM model of QRST structure is built by LS-DYNA [LS-DYNA, 2007], which is possible to simulate material and geometric nonlinearity of the structure. For the material nonlinearity, the elasto-plastic constitutive relationship is given to the concrete, rebar and bolt in the model, in order to simulate the actual nonlinear bearing situation. For the geometric nonlinearity, the influence of the large structural deformation and the large rotation of the joint on the bearing mechanism of the whole structure is considered. An assumption is made that the degrees of freedom (DOF) are only in plane.

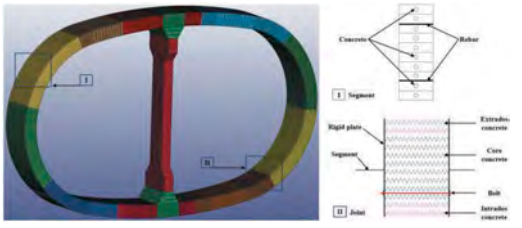

Figure 3. Illustration of nonlinear model.

As shown in Figure 3, the segment is simulated using a thick shell element, and the concrete and steel reinforcement are simulated in layers, all based on the results of the material properties test and Code for

Design of Concrete Structures in China (GB 50010-2010). The joints are simulated by rigid-plate-spring (RPS) model. Among the rigid plates, a number of zero-length nonlinear compression spring elements (concrete) and a nonlinear tension spring element (bolt) are used to simulate the actual compression-bending behavior of the longitudinal joint.

2.3 *Comparison of test and model*

The calculation results of the nonlinear macro-level model are compared with the results of the full-scale structural test to verify the numerical model. The structural convergence deformation of the long-axis and two short-axes, and the opening deformation of the longitudinal joints are selected to make comparisons, as shown in Figure 4 and Figure 5, respectively.

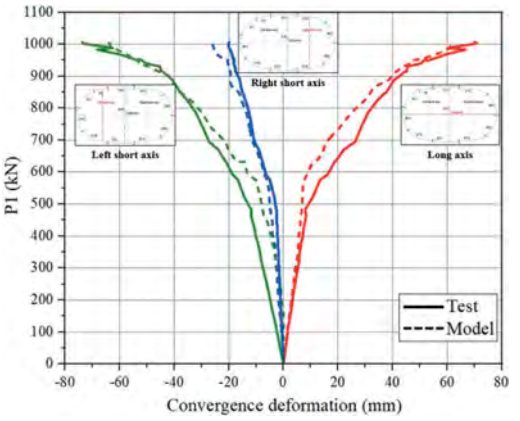

Figure 4. Comparison on convergence deformation of long axis and short axes between the test and the numerical model.

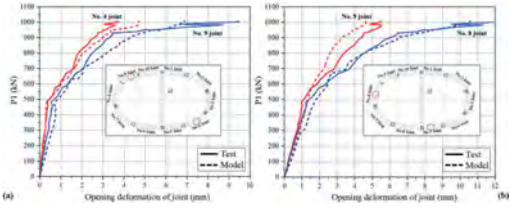

Figure 5. Comparison on opening deformations of joints (a) No. 4 and No. 9 joints (b) No.5 and No.8 joints.

The comparison results show that the nonlinear macro-level model fully captures the multi-stage behavior of the QRST structure. According to the convergence deformation development of the structure in Figure 4, it can be concluded that the structural deformation goes through three main stages of elasticity, elastoplasticity and plastic instability in sequence. The comparisons suggest that the nonlinear macro-level model can be used as a tool for analyzing the ultimate bearing capacity and failure process of the non-circular tunnel like QRST.

2.4 *Failure mechanism of QRST*

Based on the experiment campaign and the numerical model, the failure mechanism of QRST structure can be summarized. In the first elastic stage, the structure behaves linearly. When P1 reaches about 500-600 kN, the cracks induced by bending moment appear at many cross-sections of the segment, leading to the first significant decrease in the overall bearing stiffness of the structure. After entering the elastioplastic stage, the cracks on the compression side of different joints and the bolt yielded phenomenon appear sequentially, which gradually decreased the overall stiffness of the structure. It should be noted that the reinforcement of segment at T2 block near No.6 joint is also yielded. Here the plastic hinge emerges characterized by above mentioned phenomenon of joint and reinforcement. It can be found that during the failure process, plastic hinges appear at No.8 joint, No.6 joint, No.3 joint, No.5 joint, and T2 block sequentially. Along with the appearance of these plastic hinges, the internal forces of the structure are redistributed, the overall stiffness of the structure decreases, and the structural deformation continues to develop. Eventually, when the segment of T2 block near No. 6 joint is damaged subjected to bending moment and shear force, characterized by concrete spalling and hoop stirrup broken, the structure finally loses the bearing capacity and enters instability stage, leading to structural failure.

3 ROBUSTNESS EVALUATION METHOD

For tunnel structures, since different load distribution modes lead to different structural failure paths, the definition of structural robustness index using only load or deformation will not be comprehensive enough. Therefore, the evaluation of structural robustness index should be performed from the energy perspective. For the QRST structure in this study, the external load of the structure in the test is 30 point loads, and thus the external work of the structure, i.e., the internal work, can be obtained by using formula (1).

$$E_n = \sum_{i=1}^{30} \int_0^{\delta_{n,i}} F_i(\delta) d\delta \tag{1}$$

where E_n is the current calculated external work. i varies from 1 to 30. $\delta_{n,i}$ is the current displacement of the corresponding point load. $F_i(\delta)$ is the force function with respect to displacement δ of the corresponding point load.

According to formula (1), the external work of the structure is obtained through the numerical model. The external work of the structure under the design state (SLS), the state corresponding to the emergence of the first plastic hinge point, and the state corresponding to the emergence of four plastic hinges on one side of the structure, are summarized in Table 1. The ductility index and reserve index are used to

Table 1. External work and robustness indices of specimen at different states.

State	External work (J)
Design state (SLS)	2125
Emergence of first plastic hinge (Plasticity point)	23500
Emergence of four plastic hinges (Instability point)	393157
Ductility index	12.47
Reserve index	137.96

characterize the robustness performance of the structure, respectively. Where the ductility index is the ratio of the external force work at the instability point to the external force work at the plasticity point, while the reserve index is the ratio of the external force work at the instability point to the external force work at the SLS point, as listed in Table 1.

4 INVESTIGATION ON KEY STRUCTURAL PARAMETERS

For investigating the influence of key structural parameters like reinforcement and bolt position, two more cases are analyzed, to explore the optimization direction of the QRST structure. Compared with the original structure, the segment reinforcement of the second tunnel structure is increased because the designed buried depth is increased. Compared with the second structure, the bolt position of the third structure is adjusted. Here, according to the nature of positive and negative moments of the joints, the bolts are moved 50mm from the original position to the moment tension side of the joints, see Table 2. Following the same process, Zhang et al. and Liu et al. carried out relevant studies from the joint and structure levels, respectively (Zhang et al., 2021; Liu et al., 2018b).

Table 2. Differences between three structures.

State	Reinforcement ratio	Bolt position (to internal surface)	
		Positive moment joint	Negative moment joint
First structure	1.51%	200mm	200mm
Second structure	2.36%	200mm	200mm
Third structure	2.36%	150mm	250mm

The established numerical model is also compared with the structural test, in which the convergence deformation is selected to make a comparison, as shown in Figure 6, validating the applicability of the proposed model. Using the robustness indices proposed in the previous section, the three different structures are compared and the summarized results are presented in Table 3.

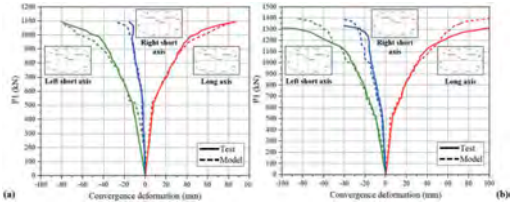

Figure 6. Comparison on structural convergence deformations between the test and the numerical model (a) Second structure (b) Third structure.

Table 3. External work and robustness indices of three structures.

No	First structure	Second structure	Third structure
External work (J)			
SLS	2125	5396	5332
Plasticity point	23500	23600	34111
Instability point	90778	99263	162633
Robustness indices			
Ductility index	3.86	4.21	4.77
Reserve index	42.72	18.40	30.50

Based on comparison of the external work and robustness indices between the first and the second structures. It can be found that, since the designed buried depth of the structure rises substantially with the reinforcement, the energy corresponding to the SLS point also rises. However, since the first plasticity point always occurs at joints, the increase of reinforcement has little effect on the energy of the plasticity point. Since the instability point of the structure is also governed by the segment subjected to bending moment, the elevation of reinforcement somewhat enhances the energy at the instability point. From the view of structural robustness, although the increase of reinforcement enhances the ductility of the structure to some extent, it drastically reduces the safety reserve of the structure, which is uneconomical for the structure.

Comparison of the second and third structures shows that the optimization of the bolt position, has little effect on the SLS point, however substantially affects the structural performance in the elasto-plastic stage. Since the structural test is a single-ring test, the performance of the structure is mainly determined by the joints. The optimization of the bolt position effectively improves the bending capacity of the longitudinal joints (Zhang et al., 2021), thus delays the emergence of the plastic hinges. The energy of the plasticity point and the instability point of the structure are improved, and the robustness indices also increase significantly. Compared with the first ring, the safety reserve of the third ring is still low,

indicating that the parameters of the joint and segment are still not in the optimal design, which point out the direction for future structural optimization.

5 CONCLUSIONS

In this study, a nonlinear macro-level model is established based on the full-scale failure test of the QRST. An energy-based robustness evaluation method is proposed. The optimization direction of the structure is also discussed based on test results and simulation results of three QRST structures with different segment reinforcement ratio and bolt positions. The following conclusions are drawn:

(1) The proposed nonlinear macro-level model for QRST is established, and the model has a good accordance with the full-scale tests of structures with different parameters.
(2) The energy-based robustness performance of the non-circular tunnel structure is more comprehensive.
(3) The enhancement of reinforcement has less effect on the robustness of the structure, and the optimization of bolt position has a significant effect on the robustness of the structure.
(4) The optimization of the structure should take into account the parameters of both reinforcement and bolt, which should be optimized in a better proportion to maintain high ductility and safety reserves of the structure.

REFERENCES

Chen R P, Chen S, Wu H N, et al. Investigation on deformation behavior and failure mechanism of a segmental ring in shield tunnels based on elaborate numerical simulation[J]. Engineering Failure Analysis, 2020, 117: 104960.

GB 50010-2010. Code for Design of Concrete Structures. Beijing: China Architecture & Building Press; 2010 (in Chinese).

He Chuan, Feng Kun, Yan Qixiang. Prototype test study on mechanical characteristics of segmental lining structure of underwater railway shield tunnel[J]. Engineering Sciences, 2014,12(02):65–74.

Liu X, Bai Y, Yuan Y, et al. Experimental investigation of the ultimate bearing capacity of continuously jointed segmental tunnel linings[J]. Structure and Infrastructure Engineering, 2016, 12(10): 1364–1379.

Liu X, Ye Y, Liu Z, et al. Mechanical behavior of Quasi-rectangular segmental tunnel linings: First results from full-scale ring tests[J]. Tunnelling and Underground Space Technology, 2018, 71: 440–453.

Liu X, Liu Z, Ye Y, et al. Mechanical behavior of quasi-rectangular segmental tunnel linings: Further insights from full-scale ring tests[J]. Tunnelling and Underground Space Technology, 2018, 79: 304–318.

Liu X, Liu Z, Yuan Y, et al. Quasi-Rectangular Shield Tunneling Technology in the Ningbo Rail Transit Project-[M]//High Tech Concrete: Where Technology and Engineering Meet. Springer, Cham, 2018: 2765–2773.

Liu X, Sun Q, Song W, et al. Numerical modeling and parametric study of hybrid fiber-rebar reinforced concrete tunnel linings[J]. Engineering Structures, 2022, 251: 113565.

Liu X, Zhang Y, Bao Y, et al. Investigation of the structural effect induced by stagger joints in segmental tunnel linings: Numerical explanation via macro-level structural modeling[J]. Tunnelling and Underground Space Technology, 2022, 120: 104284.

LS-DYNA (2007), LS-DYNA Keyword User's Manual, Livemore Software Technology Corporation, California, USA.

Wu H N, Chen S, Chen R P, et al. Deformation behaviors and failure mechanism of segmental RC lining under unloading condition[J]. Tunnelling and Underground Space Technology, 2022, 130: 104687.

Zhang L, Feng K, Gou C, et al. Failure tests and bearing performance of prototype segmental linings of shield tunnel under high water pressure[J]. Tunnelling and Underground Space Technology, 2019, 92: 103053.

Zhang W, De Corte W, Liu X, et al. Optimization Study on Longitudinal Joints in Quasi-Rectangular Shield Tunnels[J]. Applied Sciences, 2021, 11(2): 573.

Zhao H, Liu X, Bao Y, et al. Nonlinear simulation of tunnel linings with a simplified numerical modelling[J]. Structural engineering and mechanics: An international journal, 2017, 61(5): 593–603.

Tunnelling for a Better Life – Yan, Celestino, Thewes & Eberhardt (Eds)
© 2024 The Author(s), ISBN 978-1-032-80042-4
Open Access: www.taylorfrancis.com, CC BY-NC-ND 4.0 license

The effect of polypropylene fiber on the strength and crack propagation of foam concrete

Ruibo Yin*, Qiang Li, Xianglong Zeng & Wei Qiao
School of Highway, Chang'an University, Xi'an, Shaanxi, China

ABSTRACT: Aiming at the foamed lightweight soil used in tunnel engineering, polypropylene fiber was used for modification treatment, and the influence of polypropylene fiber on foamed concrete was studied. The benchmark mixure ratio was obtained through trial test. Based on the benchmark mixure ratio, the wet weight, flow value and compressive test of foamed concrete with different the fiber ratios were carried out. SEM test was carried out to analyze the microstructure and explore the law of crack propagation. The results show that the fiber ratio has little effect on the wet weight, and the flow value decreases with the increase of the fiber ratio. When the water: cement: foam = 1:2.00:0.06 and the fiber ratio is 0.75%, the 7d unconfined compressive strength of fiber foamed concrete is the highest. The fiber foamed concrete produces short cracks under compression, and the cracks expand and connect until they are destroyed. Increasing the fiber ratio can reduce the number of cracks. When the fiber ratio reaches 1.5%, more cracks are generated locally. The microstructure analysis confirmed that the polypropylene fiber can be closely bonded to the foam concrete, and the fiber limits the cracking of the surrounding pores through the bonding force, thereby preventing the extension of the through pores and inhibiting the crack propagation.

Keywords: Fiber foamed concrete, Polypropylene fiber, 7d unconfined compressive strength, Crack propagation, Microstructure

1 INTRODUCTION

With the in-depth study of foamed lightweight soil, it has been widely used in many construction projects in recent years. Foamed lightweight soil in engineering applications mainly uses cement as a cementitious material, also known as foam concrete. Foamed concrete has been applied in frozen soil construction section, shock absorption layer and tunnel portal backfill in tunnel engineering due to its excellent thermal insulation characteristics and lightweight and high-strength porous structure.

A series of mechanical properties tests on foamed concrete were carried out by (Zhang et al., 2018). Based on the test results, the constitutive model of the material was established. According to the Galongla tunnel, the influence of different factors on the damping effect of the tunnel was explored. The uniaxial and triaxial tests on foam concrete were carried out by (Chen et al., 2011), which proved that foam concrete can be used as a reserved deformation layer material for tunnels. Based on the deep-buried soft rock tunnel of Yiba Expressway, the influence of foam concrete on its long-term stability was studied. Li (Li et al., 2022) explored the factors affecting the strength of foam concrete filled with natural gas tunnels. (Su et al., 2016a, b, 2017) focused on the influence of wet density, curing age and cyclic loading and unloading on the mechanical properties of foamed lightweight concrete, and studied the influencing factors of its pouring effect. (Zhao et al., 2017a, b) carried out a detailed study on the influence of polypropylene fiber and alkali-resistant glass fiber on the mechanical properties of foamed lightweight concrete. (Qiu et al., 2019) analyzed the variation of unconfined compressive strength of foamed lightweight concrete under different mixure ratios from the perspective of microstructure by scanning electron microscopy. (Hu et al., 2019) carried out a detailed study on the mechanical properties of fiber foam lightweight concrete and its dynamic characteristics used in the transition section of road and bridge. (Li et al., 2013) realized the surface modification of polypropylene fiber by acrylic acid chemical grafting method, explored the mechanical properties of modified polypropylene fiber foam concrete, and analyzed the effect of modified fiber on pore structure and plastic shrinkage cracking. (Ma et al., 2012) studied the effect of apparent density and polypropylene fiber on the performance of foam concrete. This paper focuses on the influence of polypropylene fiber on the wet weight, fluidity and

*Corresponding author: 2021121122@chd.edu.cn

DOI: 10.1201/9781003495505-178

compressive strength of foam concrete. The influence of reinforcement on the performance of fiber foamed concrete is analyzed from the macro and micro perspectives, and the crack propagation law of compression failure is explored.

The strength of foamed concrete is mainly due to cement hardening, so the failure of foamed concrete soil tends to brittle failure after reaching the ultimate load. Only relying on internal pores to achieve strength ductility has little effect, and the strength ductility of the material is poor. This feature is a more prominent defect in the application of foamed concrete engineering. The addition of fiber materials can significantly improve the defects of brittle failure of foamed lightweight soil and improve the strength ductility of foamed concrete materials.

2 TEST MATERIAL SELECTION AND MIX DESIGN

The test raw materials of fiber foamed concrete mainly include water, cement, foam and fiber materials. The cement is ordinary Portland cement P. O.42.5 cement, the foaming agent is high concentration QW-100 cement foaming agent, and the fiber material is polypropylene short fiber. The specific information of each raw material is shown in Table 1.

Table 1. Test raw materials.

Testing material	Water	Cement	Blowing agent	Fiber material
Tupe	Tapwater	P. O.42.5 Cement	QW-100 Cement foaming agent	Polypropylene fiber(13.5mm)

3 THE BENCHMARK MIX PROPORTION DESIGN

The concept of fiber ratio is defined as the mass percentage of fiber material,that is, the fiber ratio= [(Quality of fiber material)/(Quality of foam concrete)]×100%.Compared with the quality of foam concrete, the quality of polypropylene fiber is very small, and the influence on the overall mixure ratio is relatively small. Therefore, the benchmark mixure ratio of foam concrete is preliminarily determined. On the basis of the benchmark mixure ratio, the effects of different fiber ratios on the wet weight, flow value and 7d unconfined compressive strength of foam concrete are studied.

3.1 *Trial mix design calculation*

Taking 1000kg/m^3 as the design wet density, the benchmark mixure ratio test was carried out. The water-cement ratio was used as the benchmark variable, and the foam blending amount was 3.0% of the cement mixing amount. The mixure ratio of the trial test was designed and calculated according to the specification. The specific trial mixure ratio is shown in Table 2.

Table 2. Trial mix proportion of foamed concrete.

Materials Water cement ratio	Water(kg)	Cement(kg)	Foam(kg)
1:1.60	226.59	362.54	10.88
1:1.65	222.26	366.73	11.00
1:1.70	254.45	432.56	12.98
1:1.75	249.78	437.12	13.11
1:1.80	280.31	504.56	15.14
1:1.85	275.34	509.38	15.28
1:1.90	287.45	546.16	16.38
1:1.95	315.77	615.75	18.47
1:2.00	326.80	653.60	19.61
1:2.05	321.39	658.85	19.76
1:2.10	316.16	663.93	19.92

3.2 *Trial test*

3.2.1 *Wet weight test*

According to the Technical Specification for Design and Construction of Cast-in-place Foamed Light Soil Subgrade (TJG F10 01-2011), the wet weight of the foamed concrete should be controlled at 5~11kN/m^3, and the wet weight test should be carried out one by one for all the trial mixure ratios. The wet weight test results of foamed lightweight soil are shown in the figure.

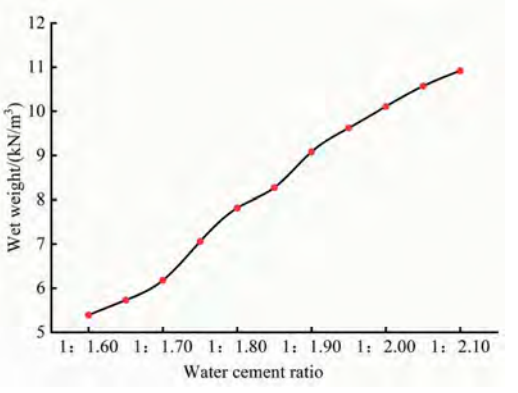

Figure 1. Water cement ratio-wet weight curve of foamed concrete.

The correlation between the wet weight of foamed concrete and the water-cement ratio is significant, and

the wet weight gradually increases with the decrease of water-cement ratio. This is because the density of cement is significantly greater than the density of water, and the wet weight of foam concrete increases with the increase of the proportion of cement in the mixing material.

It can be seen from the figure that when the water-cement ratio reaches 1:2.00, the wet density reaches 10kN/m^3, that is, the wet density reaches 1000kN/m^3. Therefore, when the water-cement ratio reaches 1:2.00~1:2.10, the mixure ratio meets the design wet density requirements.

3.2.2 *Flow value test*

The fluidity of foamed concrete in actual construction is a key indicator, which is measured by testing its flow value. According to the Technical Specification for Design and Construction of Cast-in-place Foamed Light Soil Subgrade (TJG F1001-2011), the flow value of foam concrete should be controlled at 160~190mm. The flow value test results are shown in the figure.

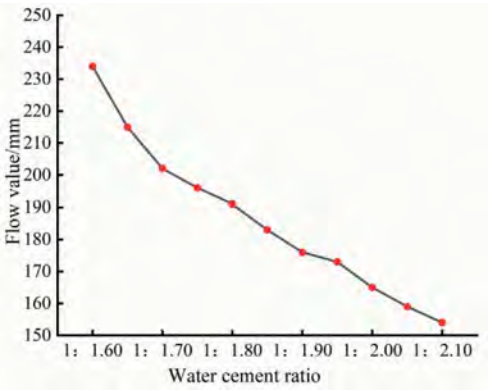

Figure 2. Water cement ratio-flow value curve of foamed concrete.

The fluidity of foam concrete is mainly affected by the proportion of mixing water. The larger the water cement ratio is, the higher the proportion of mixing water is, the stronger the fluidity is, and the larger the flow value is. The flow value test curve can significantly reflect that the flow value decreases significantly with the decrease of water-cement ratio, and when the water-cement ratio is less than 1:1.70, the flow value reduce rate decreases significantly. From the flow value curve, it can be seen that the water-cement ratio in the range of 1:1.85~1:2.00 meets the requirements of the flow value range recommended by the specification.

3.2.3 *Water absorption test*

Water absorption refers to the ability of the material to absorb water in the soaking state, which is usually expressed by mass water absorption. There are a large number of pores in foam concrete, which may be used as channels for water flow, and the influence of water on engineering facilities is very significant, so it is necessary to test its water absorption.

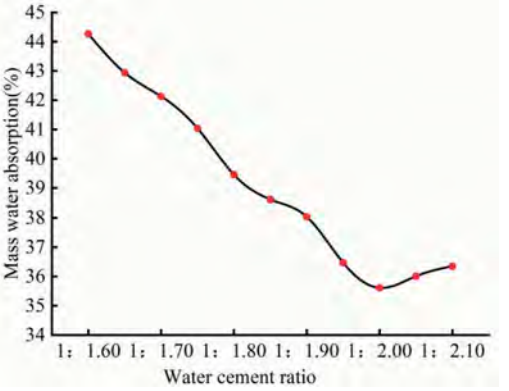

Figure 3. Water cement ratio- mass water absorption curve of foamed concrete.

The mass water absorption rate of foamed concrete decreases with the increase of cement ratio, and the water absorption rate is stable at about 36% when the water cement ratio is less than 1:1.95. When the water-cement ratio reaches 1:2.00, the corresponding mass water absorption rate is the smallest.

3.2.4 *7d unconfined compressive strength test*

Compressive strength is an important index to reflect the bearing capacity of materials. The bearing capacity of foam concrete is measured by unconfined compressive strength index. According to the Technical Specification for Design and Construction of Cast-in-place Foamed Light Soil Subgrade (TJG F10 01-2011), the 7d unconfined compressive strength test of foam concrete was carried out, and the sample was made by 100 × 100 × 100mm standard test mold.

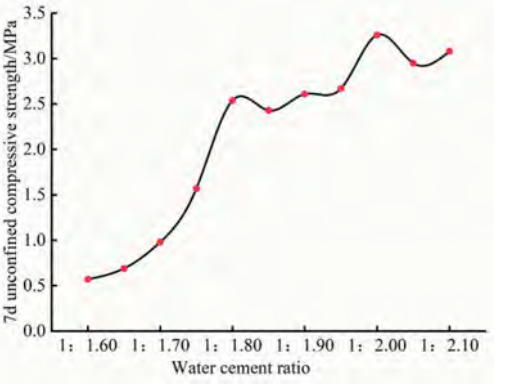

Figure 4. Water cement ratio-7d unconfined compressive strength curve of foamed concrete.

When the water-cement ratio is greater than 1:1.80, the growth rate of unconfined compressive strength increases significantly with the decrease of water-cement ratio. When the water-cement ratio reaches 1:1.80, the unconfined compressive strength increases steadily with the decrease of water-cement ratio, and the compressive strength is the highest when the water-cement ratio is 1:2.00.

Based on all the test results, water: cement: foam = 1:2.00:0.06 was selected as the benchmark mixure ratio of fiber foamed concrete to carry out subsequent tests.

4 STUDY ON BASIC PHYSICAL PROPERTIES OF FIBER FOAMED CONCRETE

The fiber material is polypropylene bundle short fiber, which has high temperature resistance, high tensile strength and good chemical stability, and can be closely bonded with foam concrete. The diameter of polypropylene fiber used in the experiment is micron grade, and the fiber length is 13.5 mm, and the fiber tow itself does not have adhesion and has good dispersibility. The fiber ratio of the test ranged from 0.00% to 1.50% and was divided into 7 grades.

4.1 *Effect of fiber on wet weight and fluidity*

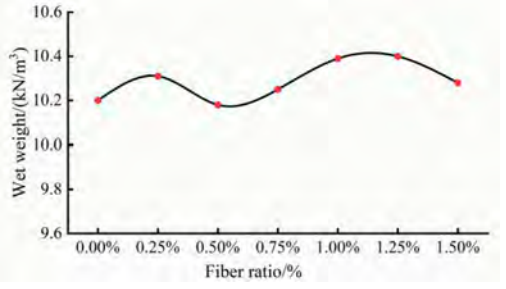

Figure 5. Fiber ratio-wet weight curve of fiber foamed concrete.

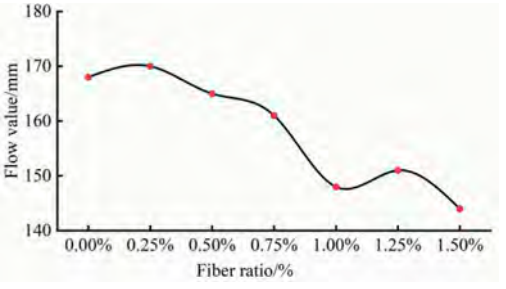

Figure 6. Fiber ratio-flow value curve of fiber foamed concrete.

The fiber ratio has little effect on the wet weight of fiber foamed concrete, and its wet weight is basically stable at 10.3 kN/m^3. The flow value is significantly affected by the fiber ratio. The higher the fiber ratio, the more polypropylene fibers are dispersed inside the fiber foamed concrete, and the flow of the foam concrete is greatly inhibited.

Through the test of two basic physical performance indexes of wet weight and flow value, combined with the test data, it can be seen that the fiber reinforcement effect has no effect on the wet weight, and has a great influence on the fluidity.

4.2 *Effect of fiber on compression resistance*

4.2.1 *Compressive strength under different fiber ratios*

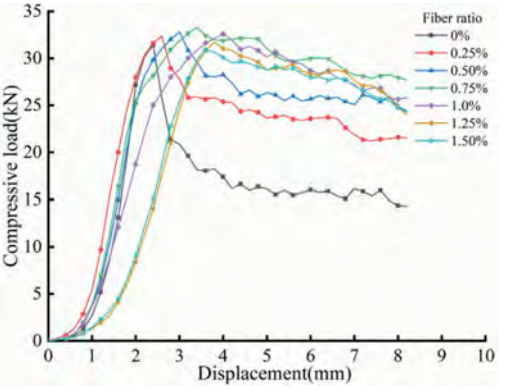

Figure 7. Compressive load versus displacement curve of fiber foamed concrete.

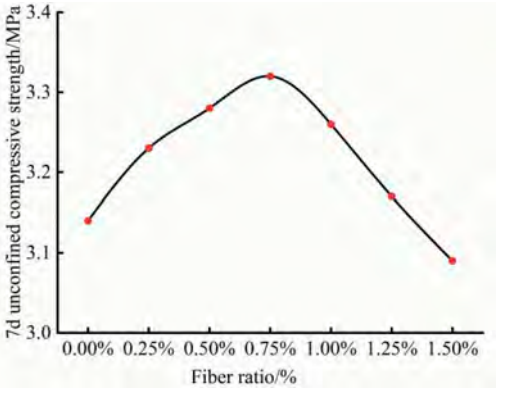

Figure 8. 7d unconfined compressive strength versus fiber ratio curve of fiber foamed concrete.

After the compressive load of non-fiber foamed concrete reaches the maximum value, the load drops sharply, and the compressive failure type tends to

brittle failure. With the increase of fiber ratio, the plastic characteristics of fiber foamed concrete are more obvious, and the compressive load gradually decreases after reaching the peak value, which proves that polypropylene fiber significantly improves the strength ductility of fiber foamed concrete, and the improvement effect is the best when the fiber ratio is 0.75%. With the increase of fiber ratio, the 7d unconfined compressive strength of fiber foamed concrete increases first and then decreases gradually, and reaches the maximum when the fiber ratio is 0.75%, so the best fiber ratio is 0.75%.

4.2.2 *Comparison of compressive failure cracks*

Figure 9. Non-fiber(a) and fiber(b) foamed concrete.

The compressive failure of foamed concrete produces penetrating cracks, and the small fragments at the cracks fall off directly. After reaching the peak value, the strength drops sharply and the residual strength is low. Most of the fiber foamed concrete cracks do not penetrate the whole specimen, and most of the small particles at the cracks are not directly detached due to the internal fiber traction. The integrity is strong, and the strength gradually decreases after reaching the ultimate compressive strength, and the residual strength is high.

Figure 10. Crack propagation of fiber foamed concrete.

Compared with the cracks that directly penetrate the whole specimen produced by the compression of non-fiber foamed concrete, the fiber foamed lightweight soil produces short cracks in the compression, and then the short cracks are connected until the compression is destroyed. This is because the expansion and extension of the cracks are limited by the internal fibers.

4.2.3 *Research and analysis of compression crack propagation under different fiber ratios*

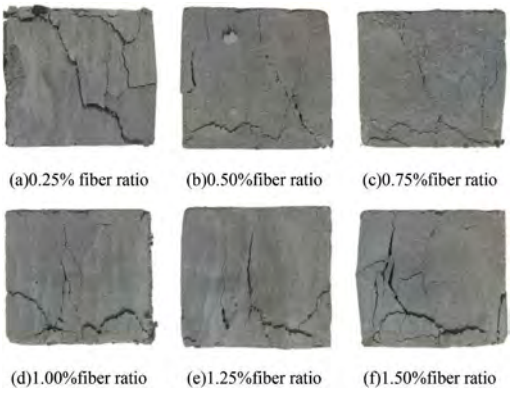

Figure 11. Crack propagation in compression failure of specimens with different fiber ratios.

When the fiber ratio is 0.25%, the fiber foamed concrete is compressed to produce penetrating cracks. This is due to the low fiber ratio, the internal fiber content is less, the crack propagation inhibition is limited, and the cracks are gradually connected to form cracks throughout the whole. With the increase of fiber ratio, the length and number of cracks produced by compression decrease significantly, and the development of cracks is limited, and no penetrating cracks are produced during compression failure. When the fiber ratio is increased to 1.5%, the effect of fiber on the expansion of compressive cracks is significantly reduced. During the process of compression and fracture, bulging deformation occurs along the side edge, while the fiber still has a traction effect on the cracked fragments, preventing the specimen from being crushed, so that it still has a certain residual strength.

When the fiber ratio is too high, there are a large number of fibers inside, and the fiber spacing is significantly reduced. The distribution direction of the fibers will be significantly affected by the distribution direction of the surrounding fibers, which makes the number of fibers distributed in different directions uneven, and the inhibition effect on crack propagation is significantly reduced. When there are too many internal fibers, local agglomeration of fibers will occur. The fiber agglomeration part will affect the crystal distribution produced by the hydration reaction of foam concrete, and then affects local strength and produces weak parts. The combined effect of the two factors makes the high fiber ratio foamed concrete produce more cracks under

pressure, and the fiber has a poor effect on inhibiting the crack propagation and the compressive strength is low.

From the 7d unconfined compressive strength curve and compressive crack propagation of foam concrete with different fiber ratios, it can be seen that the fiber reinforcement effect has a very significant effect on the 7d unconfined compressive strength, and the polypropylene fiber material with higher tensile strength improves the compressive strength by inhibiting the propagation and extension of cracks during compression.

5 STUDY ON THE MICROSTRUCTURE

For the specimens before and after the compression failure of fiber foamed concrete with a fiber ratio of 0.75%, SEM electron microscope scanning experiments were carried out to observe the microstructure of fiber foamed concrete and conduct qualitative description analysis.

5.1 *Before compressive failure*

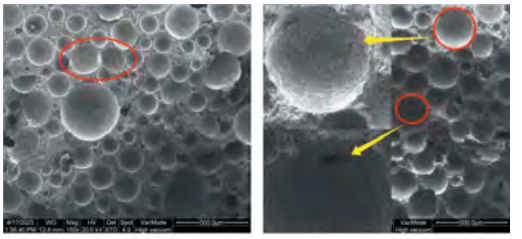

(a) (b)

Figure 12. Pores of fiber foamed concrete.

There are a large number of pores in foam concrete, among which the largest number are independent pores of different sizes, and there are interconnected pores. Most of the inner walls of the pores are smooth, but there are still very small pores, and holes will appear in the pore walls of a few larger pores.

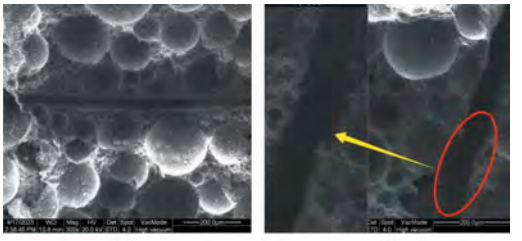

(a) (b)

Figure 13. The combination of fiber and foam concrete.

Polypropylene fiber and foam concrete can be closely bonded together, and the bonding interface is relatively complete and dense, which can give full play to the bonding force of cement cementitious materials in foam concrete.

5.2 *After compressive failure*

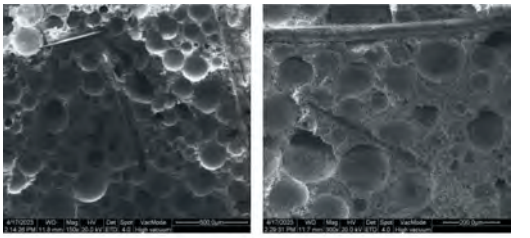

(a) (b)

Figure 14. Microstructure of fiber foamed concrete.

In the process of compression failure of fiber foamed concrete, the larger pores are connected with each other, forming a continuously expanding crack, while the smaller pores can still maintain relatively intact. Due to the bonding force between the polypropylene fiber and the foam concrete and its excellent tensile properties, the internal polypropylene fiber limits the cracking of the surrounding pores, prevents the further development of the connected pores, and significantly inhibits the expansion and extension of the cracks. The bonding interface between fiber and foam concrete changes from dense to loose and rough.

6 CONCLUSIONS

In this paper, by adding polypropylene fiber to foam concrete, the mix ratio and strength performance of the material are studied, and the crack propagation law of compression failure is analyzed by combining macro and micro analysis. The following conclusions are obtained:

1) Taking the water-cement ratio as a variable, based on the design wet density of 1000kg/m^3, the foam concrete trial test was carried out, and the benchmark mixure ratio with the lowest mass water absorption and the highest unconfined compressive strength was obtained, that is, water: cement: foam is 1:2.00:0.06.
2) Using polypropylene fiber as fiber material, through the wet weight and flow value test, it is concluded that the fiber ratio has no effect on the wet weight, and has a great influence on the flow value. When the fiber ratio is less than 0.25%, it has little effect on the fluidity. When it is higher than 0.25%, the fluidity decreases significantly with the increase of the fiber ratio.

3) The fiber reinforcement effect of polypropylene fiber can improve the 7d unconfined compressive strength of foam concrete. When the fiber ratio is 0.75%, the improvement effect is the largest, and the fiber reinforcement effect makes the strength of foam concrete gradually decrease after reaching the ultimate compressive strength.
4) The compression failure of non-fiber foamed concrete directly produces through cracks, while the fiber foamed concrete first produces short cracks in the compression process, and then the cracks extend to each other until the failure. When the fiber ratio is higher than 0.50%, the compression failure no longer forms through cracks. After the fiber ratio reaches 1.5%, due to the high fiber content, the fiber spacing is significantly reduced, and the fiber distribution direction is greatly affected by the fiber spacing, which makes the fiber 's inhibition effect on crack propagation worse. At the same time, there is a local fiber agglomeration phenomenon, which affects the local strength, and then makes the fiber foamed concrete produce more cracks locally when it is damaged by compression, and a large number of fibers still have the effect of delaying the further development of damage, avoiding the crushing of the specimen and maintaining its integrity.
5) Through the SEM electron microscope scanning experiment on the samples before and after compression failure, it is further confirmed from the microstructure level that polypropylene fiber and foam concrete can be closely bonded. The compression of fiber foamed concrete makes the internal large pores crack and extend into cracks. The internal fibers rely on the bonding force to prevent the surrounding pores from cracking, prevent the further development of the penetrating pores, and then inhibit the expansion of the cracks.
6) Through the above conclusions, it is confirmed that the fiber foam concrete effectively overcomes the disadvantages of brittle failure and poor strength ductility of foam concrete, and is expected to be more widely used in tunnel construction and other projects.

REFERENCES

Chen Weizhong, Tian Hongming, Yang Fudong, etc. Study on the influence of foam concrete reserved deformation layer on the long-term stability of deep buried soft rock tunnel [J]. Geotechnical mechanics, 2011,32 (09): 2577–2583.DOI: 10.16285/j.rsm.2011.09.042.

Hu Wenhan. Study on Dynamic Characteristics of fiber Foamed Lightweight Concrete Road-Bridge Transition Section [J].Subgrade Engineering, 2019, No.203 (02): 105–109.DOI: 10.13379/j.issn.1003-8825.2019.02.21.

Li Chunbao, Cong Ziqin, Guan Di, etc. Study on influencing factors of compressive strength of foam concrete filled in natural gas tunnel [J].Concrete, 2022 (07): 183–187.

Li Qijin, Li Guozhong, Du Chuanwei. Effect of modified polypropylene fiber on properties of foamed cement [J]. Journal of Composites, 2013,30 (03): 14–20.DOI: 10.13801/j.cnki.fhclxb.2013.03.001.

Ma Yiping, Li Guoyou, Yang Lixiang etc. Effect of apparent density and polypropylene fiber on shrinkage cracking of foamed concrete [J].Materials, 2012,26 (06): 121–125.

Qiu Youqiang, Li Yongliang, Liu Yaofu etc. Study on the microstructure and strength characteristics of foamed lightweight soil [J].China-foreign highway, 2019,39 (01): 215–217.DOI: 10.14048/j.issn.1671-2579.2019.01.044.

Su Qian, Jiang Ruixue, Zhao Wenhui, etc. Influencing factors and mechanism analysis of pouring effect of foamed lightweight concrete [J].Railway building, 2017,57 (08): 143–145 + 150.

Su Qian, Zhao Wenhui, Wang Yawei, etc. Experimental Study on Mechanical Properties of Foamed Lightweight Concrete [J]. Railway Building, 2016, No.506 (04): 144–148.

Su Qian, Zhao Wenhui, Wang Yawei etc. Experimental study on uniaxial cyclic loading and unloading of foamed lightweight concrete [J].Railway standard design, 2016,60 (08): 21–25.DOI: 10.13238/j.issn.1004-2954.2016.08.005.

Wang Wubin, Zhao Wenhui, Su Qian etc. Experimental Study on Mechanical Properties of Polypropylene Fiber Reinforced Foamed Lightweight Concrete [J]. Railway Building, 2017, No.516 (02): 146–150.

Zhao Wenhui, Su Qian, Li Ting, etc. Experimental study on mechanical properties of glass fiber reinforced foamed lightweight concrete [J].Industrial building, 2017,47 (09): 110-114 + 80. DOI: 10.13204/j.gyjz201709022.

Zhao Wusheng, Chen Weizhong, Ma Shaosen, etc. Damping mechanism of foam concrete tunnel damping layer [J].Geotechnical mechanics, 2018,39 (03): 1027–1036. DOI: 10.16285/j.rsm.2016.0507.

Tunnelling for a Better Life – Yan, Celestino, Thewes & Eberhardt (Eds)
© 2024 The Author(s), ISBN 978-1-032-80042-4
Open Access: www.taylorfrancis.com, CC BY-NC-ND 4.0 license

Research on construction technology of drilling and blasting tunnel based on load adjustment control technology

Guogang Ying*
Ningbo Langda Engineering Technology Co., Ltd, Ningbo, China
Ningbo Tech University, Ningbo, China

Rongjun Zheng, Yapeng Xing & Weimin Chen
Ningbo Langda Engineering Technology Co., Ltd, Ningbo, China

ABSTRACT: In response to problems such as cracking, block falling, local buckling and water leakage, tunnel load adjustment control technology has been introduced. Based on the ChangAoNong tunnel, the application of load adjustment control technology in the drilling and blasting tunnel was analysed. The results show that the application effect of load adjustment control technology in three-lane widening and four-lane tunnel is obvious, which can significantly optimize the structural force of the initial branch, improve the rationality of the internal force on the tunnel support structure, and greatly reduce the influence of bias voltage. The load adjustment control technology can greatly enhance the safety of the primary support and secondary lining, and provide a new technical direction for tunnel design optimization. Based on the regulation and control of the internal force of the tunnel lining, the optimization of the lining design parameters is realized, the consumption of labour, material and machinery in the process of tunnel construction is reduced, so as to reduce the carbon emissions in the physicochemical stage of tunnel engineering.

Keywords: load adjustment control technology, Internal force optimization, structural safety, disease prevention and control, carbon emission

1 INTRODUCTION

The stress of tunnel support structure is complex and difficult to predict, and the structural stability is poor, which is prone to lining cracking, block falling, local buckling and water leakage, structure instability and other problems(Chen, J.X., et al., 2018, Hu, C.F., et al., 2018). The essential reason for the above diseases lies in the incongruity of deformation between surrounding rock and supporting structure, and the dominant performance is that the stress distribution of supporting structure under external load is unreasonable. Therefore, it is of great practical significance to optimize the stress distribution of tunnel support structure.

With the development of modern tunnel technology, the theoretical system based on stress control is becoming more and more mature(Xu, R.X., 2000, Huang, H.Y., et al., 2019, Qiu, W.G., et al., 2017, Tian, M.J., et al., 2018). Zhang, D.L., et al. (2019) established the collaborative optimization design method of tunnel support structure system from the essence of the interaction between tunnel surrounding rock and support structure. Peng, L.M., et al. (2001) established the optimization calculation model of tunnel reinforced concrete lining structure by applying the basic theory of inequality constrained optimization in Lagrange multiplier method. Liu, Y.H. (2002) introduced the simple complex optimization method in the structural optimization theory, and established the optimization design model of highway tunnel lining section. There are many scholars(Yang, H.X., 2022, An, H.G., 2003, Huang, D.W., et al., 2018) have optimized the design parameters of tunnel support structure from multiple angles based on the big data analysis method.

Under the support of many theoretical research results, a large number of new tunnel support structures continue to appear(LI, X.F., et al., 2017, Wang, B., et al., 2023, Sun, J., et al., 2021, Dong, B., et al., 2021). Among them, the resistance limiting and energy dissipation support structure developed by

*Corresponding author: guogangying@nbt.edu.cn

DOI: 10.1201/9781003495505-179

Dai, J., et al. (2022), the graded yield support structure developed by Dong, J.H., et al., the buffer layer yield support structure developed by Tian, Y., et al. (2020) and the circumferential yield support structure developed by Lei, S.X., et al. (2020) have achieved good results in application engineering.

Different from the above structures, the load adjustment control technology combines the stress control theory and prestress technology, which can not only adjust the stress distribution of the tunnel initial support structure(Ma, K., et al., 2022), but also control the deformation state of the tunnel structure, so as to effectively reduce the peak bending moment and nonuniformity of the tunnel lining. Based on the ChangAoNong tunnel, this paper introduces the principle and construction method of the load adjustment control system, analyses the application of the load regulation control system in the tunnel engineering construction, and verifies the internal force regulation effect of the primary support and secondary lining structure.

2 DESIGN OF LOAD ADJUSTMENT CONTROL SYSTEM

2.1 *Principle of load adjustment control system*

The load adjustment control of tunnel is divided into two stages: load adjustment and deformation control, in which load adjustment is the basis of deformation control. Load adjustment is to enhance the load adjustment ability of the arch by installing multiple load adjusters on the steel arch of the initial support, realize the long-distance transfer of the load on the arch, and make the internal force of the steel arch become clear and controllable. Deformation control is to make the steel frame produce camber by applying specific preload, so as to basically offset the linear change of the steel frame under the surrounding rock pressure, stabilize it in a linear state close to zero stress, make the steel arch in the full section compression state, and greatly reduce the peak bending moment and nonuniformity of the primary support structure.(Ying, G.G., et al., 2023).

2.2 *Composition of load adjustment control system*

The tunnel load adjustment control system consists of two parts: load adjuster and load applicator (Figure 1).

2.2.1 *Load adjusters*

The load adjuster is divided into main unit and over excavation unit. The main unit is composed of top plate, adjusting screw, adjusting nut, ejector rod, outer sleeve, piston, oil cylinder, high-strength oil pipe connecting hole, positioning hole and anchor bolt (Figure 2). The over excavation unit is composed of extended screw rod and extended nut (Figure 3).

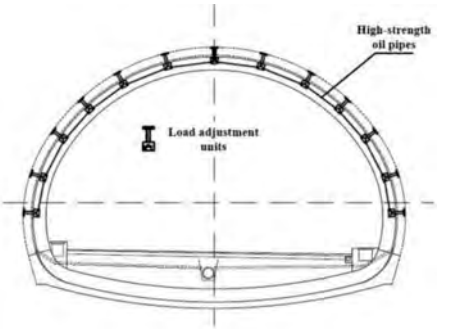

Figure 1. Load adjustment control system.

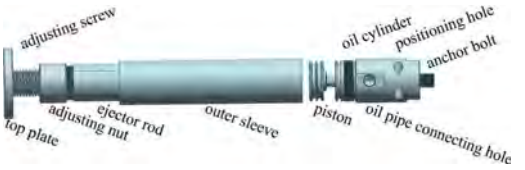

Figure 2. Main unit.

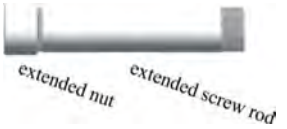

Figure 3. Over excavation unit.

The load adjuster needs to be connected in series with high-strength oil pipes. Considering the high oil pressure in the hydraulic system, the high-strength oil pipe needs to use high-pressure steel wire braided hose. The hose is designed with five layers, consisting of a liquid resistant inner adhesive layer and an intermediate adhesive layer, two layers of steel wire braided and an outer adhesive layer with excellent corrosion resistance, as shown in Figure 4.

Figure 4. High-strength oil pipes.

After the installation of the hydraulic system, it is necessary to install the high-pressure ball valve as the interface of the hydraulic system to facilitate the subsequent pressurization adjustment.

Figure 5. High-pressure ball valve.

2.2.2 *Load applicator*
The load applicators include a high-pressure oil pump for oil delivery and a high-pressure oil gauge for control.

Figure 6. Portable high-pressure oil pump.

Figure 7. High-pressure oil gauge.

Considering the site construction conditions, portable high-pressure oil pump (Figure 6) is required. The maximum oil storage capacity of the oil pumps is not less than 2000cc, and the maximum pressurized load is not less than 70MPa. During oil filling, it is necessary to connect the high-pressure oil gauge (Figure 7) to accurately control the oil pressure in the hydraulic system.

2.3 *Construction technology of load adjustment control system*

The tunnel load adjustment control system can be installed synchronously with the steel frame. Generally, the installation of the system can be completed before the construction of the shotcrete, which will not affect the excavation progress of the tunnel. The main construction process is as follows:

2.3.1 *Installing load adjuster*
Installation of adjustment unit after the erection of the steel frame, the load adjuster can be connected by welding or bolts, and the two adjacent adjustment units are installed alternately in front of and behind the steel arch frame (Figure 8).

Figure 8. Installing load adjuster.

Figure 9. Connecting high-strength oil pipes.

After the load adjuster is installed, rotate the adjusting nut to ensure that the top plate is close to the surrounding rock. If the tunnel is over excavated seriously, it is necessary to add a Over excavation unit. After all adjustment units are installed in place, connect them in series with high-strength oil pipes (Figure 9), pressurize them with oil pumps, exhaust the air in the oil circuit, and check the leakage of the oil circuit.

2.3.2 *Pressurization process*
According to the principle of the load adjustment control system, the pressurization process of the regulation system needs to be carried out twice. The oil pressure in the hydraulic system must be loaded to 5MPa through the oil pump 1-2 days after the completion of the initial support shotcrete construction, so as to form a regulating layer between the surrounding rock and the initial support structure.

The secondary pressurization is carried out after the steel arch is closed. At this time, the oil pressure needs to be applied to the design value, so that the steel arch has pre deformation.

Figure 10. Pressurization process.

2.3.3 *Bolt anchorage*

Before the construction of secondary lining, lock the piston with anchor bolt. At this time, the load adjustment stage of the load adjustment control system is over, and the prestressed provider is transferred from the hydraulic system to the anchor bolt to ensure the continuous existence of prestress.

3 ENGINEERING APPLICATION CASE ANALYSIS

In order to verify the influence of the load adjustment control system on the tunnel support structure, field comparative tests were carried out at zk18 +460~zk18+480 section of the left line of ChangAoNong tunnel, in which zk18+460~zk18+470 were the regulation section and zk18+470~zk18+480 were the comparison section.

3.1 *Project overview*

ChangAoNong tunnel is a three-lane widened tunnel with small clear distance. The bedrock at the tunnel site is granite.

The joints are developed or relatively developed. The joints are mainly closed and lack of water. The left line of the tunnel has a total length of 885m, grade V surrounding rock is 717m, and the proportion of grade V surrounding rock is 81.02%. The right line of the tunnel has a total length of 880m, grade V surrounding rock is 613m, and the proportion of grade V surrounding rock is 69.66%. The outline of the tunnel is shown in Figure 11.

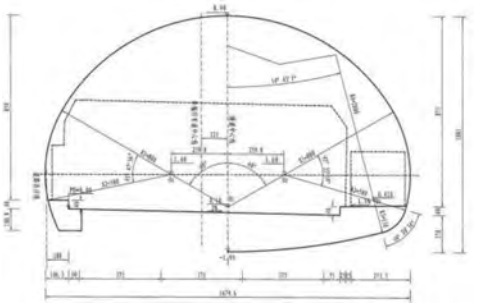

Figure 11. Outline design drawing of the tunnel.

3.2 *Design of load adjustment control system*

According to the design concept introduced above, the load adjustment control system of ChangAoNong tunnel is designed. Considering that the regulating load is closely related to the surrounding rock pressure of the tunnel, a proportional relationship is established between the vertical surrounding rock pressure and the regulating load of the arch wall, arch abutment and arch crown, and is named as the internal force control coefficient. Through the finite element software, the reduction of the bending moment of the tunnel vault under different internal force control coefficients is calculated. The results are shown in Table 1, and the adjustment of the bending moment is shown in Figure 12.

Table 1. Reduction of arch crown bending moment.

Internal force control coefficient	Moment reduction
1.0:1.2:0.6:0 (scheme I)	Over 90%
1.0:1.0:0.5:0 (scheme II)	Over 70%
1.0:0.8:0.4:0 (scheme III)	Over 50%

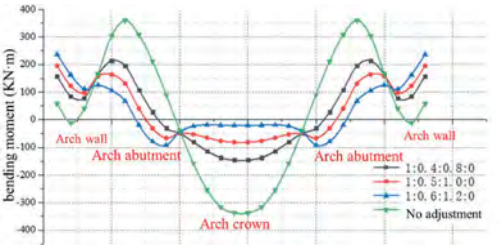

Figure 12. Comparison of bending moment distribution.

Considering the economy of the scheme, the internal force control coefficient in scheme II is adopted for the load adjustment control system applied in ChangAoNong tunnel, and the bending moment reduction is expected to reach more than 70%. The tunnel secondary lining is optimized based on the adjusted bending moment, and the design structure is shown in Table 2.

Compared with the design of the section of the comparison section, the load adjustment device is installed in the primary support structure of the adjusting section, and the concrete thickness of the secondary lining arch ring is reduced by 10cm.

3.3 *Application effect analysis*

In order to analyse the application of load adjustment control system in ChangAoNong tunnel, monitoring sections were set up at zk18+465 and zk18+478 sections to monitor the internal force of tunnel structure.

Table 2. Lining design of experimental section.

Section	initial support					Secondary lining	
	advanced support	bolt	Shotcrete	Steel arch	Load Adjusting unit	arch ring	inverted arch
Adjusting section	Φ42×5mm advanced small pipe	Φ22-5 hollow grouting anchor rod	31cm C25 shotcrete	I25a section steel, spacing 0.75m	15, evenly divided by arch ring	55cm C40 reinforced concrete	65cm C40 reinforced concrete
Contrast section	Φ42×5mm advanced small pipe	Φ22-5 hollow grouting anchor rod	31cm C25 shotcrete	I25a section steel, spacing 0.75m	/	65cm C40 reinforced concrete	65cm C40 reinforced concrete

3.3.1 *Bending moment adjustment effect of initial support*

According to the action mechanism of the tunnel, combined with the design parameters of the tunnel structure and the strain monitoring data, the bending moment of the tunnel structure can be calculated. Take zk18+478 section as the contrast section, and compare it with zk18+465 section of the adjusting section. The bending moment distribution is shown in Figure 13:

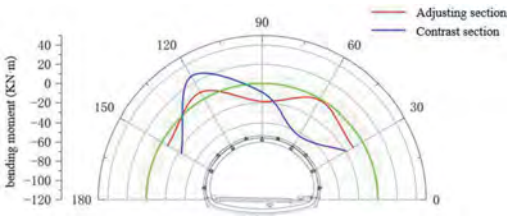

Figure 13. Distribution of tunnel bending moments.

Observe the change of bending moment at each measuring point of the structure and draw an image. The change of tunnel bending moment is shown in the Figure 14.

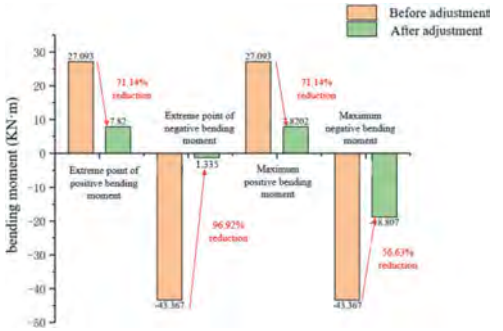

Figure 14. Diagram of extreme changes in tunnel bending moment.

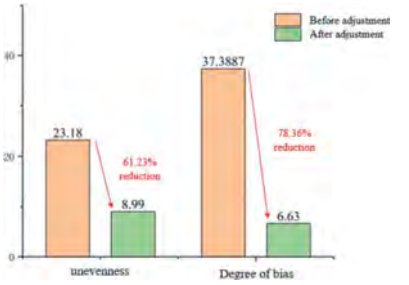

Figure 15. Diagram of tunnel moment distribution change.

According to Figure 14, the bending moment at the extreme point of the original positive bending moment decreased from 27.093KN·m to 7.82KN·m, a decrease of 71.14%, and the bending moment at the extreme point of the original negative bending moment decreased from -43.367KN·m to -1.335KN·m, a decrease of 96.92%. The position of the maximum positive bending moment remained unchanged, and the size decreased from 27.093KN·m to 7.82KN·m, a decrease of 71.14%. The position of the maximum negative bending moment shifted from the right arch waist to the arch crown, and the size decreased from -43.367KN·m to -18.807KN·m, a decrease of 56.63%. It can be seen that after the application of the load regulation system, the load acting on the structure has been transferred and the stress has been redistributed. According to the goal, the rationality of the bending moment distribution has been significantly improved.

According to Figure 15, the unevenness of bending moment before and after adjustment is reduced by 61.23%, and the bias of bending moment is relieved by 78.36%. It can be seen that after the application of the load regulation system, the stress concentration phenomenon of the structure is obviously improved, and the influence of load bias on the structure is basically eliminated

3.3.2 *Safety of secondary lining*

Since the secondary lining of the regulation section is optimized according to the design, it is necessary

to check the safety factor of the lining of this section. According to the field measured data and the calculation method in the specification, the safety factors of the secondary lining in the comparison section and the secondary lining with the load adjustment control system before and after optimization are calculated respectively, and the calculation results are shown in Figure 16.

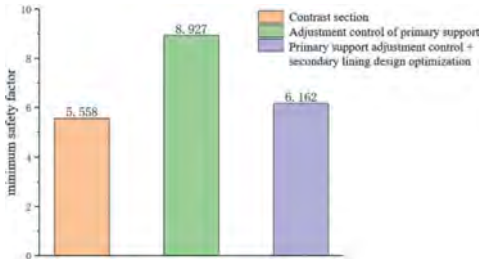

Figure 16. Tunnel second lining safety factor.

The safety factor of the secondary lining of the regulation control section was increased from 5.558 to 8.927, indicating that the application of the load adjustment control system can greatly enhance the safety of the secondary lining. After the application of the optimal design, the thickness of the secondary lining is reduced by 10cm, and the safety factor of the secondary lining is reduced from 8.927 to 6.162, which is still about 11% higher than the safety factor of 5.558 before adjustment, which shows that the optimal design of the secondary lining is reasonable from the perspective of safety.

3.3.3 *Analysis of emission reduction effect*

The manufacturing, transportation and installation of the load adjustment control system will bring additional carbon emissions to the tunnel construction, and the optimal design of the secondary lining can effectively reduce the carbon dioxide emissions during the tunnel construction stage. In order to clarify the emission reduction effect of the load adjustment control system, it is necessary to calculate the carbon emissions of the two schemes respectively.

In this study, the tunnel construction steps are divided into 12 construction results, including advanced small conduit, surrounding rock excavation, anchor rod, reinforcement mesh, steel arch, load adjustment device, connecting reinforcement, anchor rod, shotcrete, secondary lining reinforcement, inverted arch concrete, and arch wall concrete. The carbon emissions generated in each construction result can be divided into four parts: building material production, building material transportation, construction machinery and equipment, and construction personnel. According to the *JTG/T 3832-2018 highway engineering budget quota* and the calculation table of the quantities of ChangAoNong tunnel, the construction results are converted into the carbon emissions of materials and machinery shifts for calculation and summary. The calculation results are shown in Figure 17:

It can be seen from Figure 17 that the carbon emissions generated by the construction results of surrounding rock excavation, steel arch frame, shotcrete, secondary lining reinforcement and arch wall concrete decreased by 719.6 kg CO_{2eq}, 1306.0 kg CO_{2eq}, 982.0 kg CO_{2eq}, 2772.4 kg CO_{2eq} and 6281.4 kg CO_{2eq} respectively. The installation of load regulating device increased the carbon emissions by 2968.5 kg CO_{2eq} in the physicochemical phase of the project, and the other steps had no significant impact. To sum up, the application of the load adjustment control system has reduced the carbon emissions of the ChangAoNong tunnel project in the physicochemical phase by 9092.9 kg CO_{2eq}, i.e., 909.29 kg CO_{2eq} /m.

4 CONCLUSIONS

According to the application of load adjustment control system in ChangAoNong tunnel in this study, the following four conclusions can be summarized:

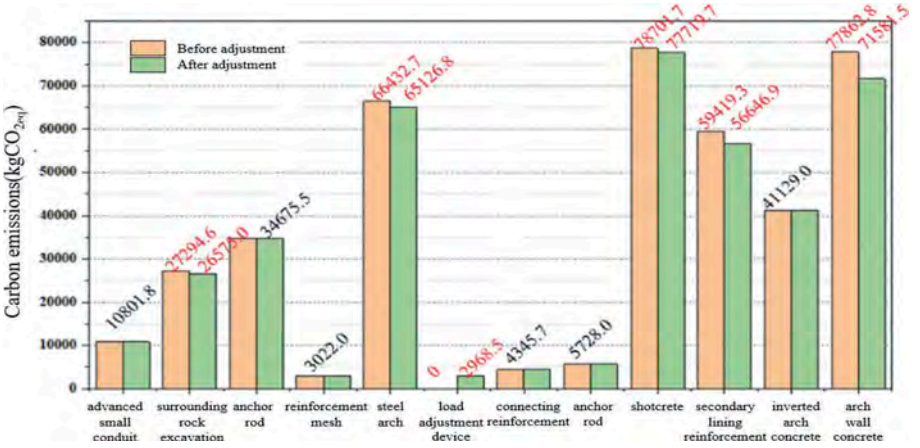

Figure 17. Calculation results of engineering carbon emissions in the test section.

1. The main function of the load adjustment control system is to adjust the surrounding rock pressure of the tunnel initial support structure, control and reduce the peak bending moment and unevenness of the tunnel lining, so as to realize the optimization of the tunnel lining structure design. The engineering verification shows that the application effect is obvious in three-lane widening and four-lane tunnel.
2. The application of the load adjustment control system reduced the maximum positive and negative bending moment of the primary support by 71.14% and 96.92%, the unevenness of bending moment by 61.23%, and the bias degree by 78.36%, which shows that the load adjustment control system can significantly optimize the structural stress of the primary support, improve the rationality of the internal force of the tunnel structure, and greatly alleviate the bias effect.
3. According to the monitoring results of ChangAo-Nong tunnel, after the adjustment and optimization of the primary support stress, the minimum safety factor of the secondary lining is still slightly greater than that of the secondary lining in the comparison section after the thickness is reduced, which verifies the rationality and scientificity of the secondary lining optimization method, and provides a new technical direction for the safety and economy of tunnel design optimization.
4. Based on the adjustment and control of the internal force of the tunnel lining, the optimization of the lining design parameters is realized, which can reduce the material and energy consumption in the process of tunnel construction, and reduce the carbon emission of the tunnel in the physico-chemical phase by about 909.29kg CO_{2eq}/m, which provides a new technical direction for the green and low-carbon tunnel design optimization.

REFERENCES

Chen, J.X., Luo, Y.B., & Wan, L., 2018. "Current Status and Challenges of Research on Super Long Span Highway Tunnels. Road Machinery & Construction Mechanization. (1), 36–44.

Hu, C.F., & Xing, L.M., 2018. "Approximate analysis of reasonable arch axis under multi-source loads. Journal of East China Jiaotong University. 35(2), 46–55.

Xu, R.X. 2000. "Research on nonlinear analysis and optimization design of underground structure. Hohai University, Nanjing.

Huang, H.Y., Qiu, W.G., & Huang, H., 2019. "Research on initial support optimization of stone railway tunnel. Journal of Railway Science and Engineering. 16(1), 152–161.

Qiu, W.G., Sun, K.G., & Wang, L.C., 2017. "Optimization of initial support of large section tunnel based on surrounding rock stability. China Civil Engineering Journal. 50(S2), 8–13.

Tian, M.J., Qiu, W.G., & Zhu, W., 2018. "Analysis of construction measurement information and optimization of initial support of single-track railway tunnel. Railway Construction. 58(11), 78–82.

Zhang, D.L., Sun, Z.Y., & Hou, Y.J., 2019. "Tunnel support structure system and its synergistic effect. Chinese Journal of Theoretical and Applied Mechanics. 51(02), 577–593.

Peng, L.M., Shi, C.H., & Liu, X.B., 2001. "Optimal design model and application of tunnel reinforced concrete structure. China Journal of Highway and Transport. 14(2), 71–74.

Liu, Y.H. 2002. "Research on cross-section optimization selection and reliability analysis of high-grade highway tunnel support structure. Hunan University, Changsha.

Yang, H.X. 2022. "Theory and analysis method of optimal design modeling of the whole process of underground cavern. Hohai University, Nanjing.

An, H.G., 2003. "Research on comprehensive integrated intelligent method for stability and optimization of large cavern group. Chinese Journal of Rock Mechanics and Engineering. 22(10), 1760–1760.

Huang, D.W., Feng, Q.S., & Liu, K.F., 2018. "Optimal design analysis of metro shield tunnel cross-section based on bending moment minimization. Journal of the China Railway Society. 40(9), 159–166.

Li, X.F., Wang, C.B., & Wang, H.J., 2017. "Experimental study on bearing characteristics of U-shaped steel closed shrinkable steel frame. Journal of Zhejiang University (Engineering Science). 51(12), 2355–2364.

Wang, B., Yu, W., & Zi, X., 2023. "Discussion on the Rationality of Different Support Modes for Large Deformation Tunnels in Soft Rock: Taking the Muzhailing Highway Tunnel as an Example. Tunnel construction. 43(01), 36–47.

Sun, J., Jiang, Y., & Wang, B., 2021. "Research on Nonlinear Rheological Properties of Squeeze Type Large Deformation of Soft Rock Tunnel with High Ground Stress and Engineering Renovation with Yield Support. Tunnel construction. 41(10), 1627–1633.

Dong, B., Yang, J.J., & Yin, H.B., 2021. "Analysis of the yielding performance of steel arch joints in tunnels. Tunnel construction. 41(09), 1524–1529.

Dai, J., Yang, X., & Wang, J.J., 2022. "Application of limited resistance and energy dissipation support in large deformation double track railway tunnels. Tunnel and Underground Engineering Disaster Prevention and Control. 4(04), 41–51.

Dong, J.H., Xu, B., & Wu, X.L., "Analysis of mechanical characteristics of graded yielding support structure in soft rock tunnel with high ground stress. Journal of China Highway Engineering.

Tian, Y., Chen, W.Z., & Tian, H.M., 2020. "Research on buffer layer yielding support design considering the weakening of soft rock strength and time effect. Geotechnical Mechanics. 41(S1), 237–245.

Lei, S.X., & Zhao, W., 2020. "Research on the mechanism of large deformation circumferential yielding support in soft rock tunnels. Geotechnical Mechanics. 41(03), 1039–1047.

Ma, K., Chen, L.-P., & Fang, Q., 2022. "Research on the Stress Characteristics of Initial Tunnel Supports Based on Active Load Adjustment. Appl. Sci. 12(14), 7214.

Ying, G.G., Zheng, R.J., & Li, X.J. 2023. "Research on the Application of Load Adjustment Control Technology in Super Large Section Tunnels. Paper presented at the World Transport convention.

Tunnelling for a Better Life – Yan, Celestino, Thewes & Eberhardt (Eds)
© 2024 The Author(s), ISBN 978-1-032-80042-4
Open Access: www.taylorfrancis.com, CC BY-NC-ND 4.0 license

Construction and applicability of using double supports in a large overburden ground conditions as a countermeasure to suppress displacements

Simin Zhai*, Devini Abeyawardena, Hidekazu Aoki & Sadatoshi Ohmori
Penta-Ocean Construction Co., LTD, Tokyo, Japan

Nobuharu Isago
Department of Civil and Environmental Engineering, Tokyo Metropolitan University

ABSTRACT: In mountain tunnel constructions, there is a concern that the large overburden at vulnerable fault zones may cause deformations due to the large ground load, leading to an instability of the tunnel structure. In such cases, to ensure stable excavation and support construction, a rigid multiple support structure that can withstand the load can be used. Another method is the drift advancing tunnel construction method that can be used to release initial stresses in the ground before constructing the main tunnel support. In the Aokuzuretōge Tunnel, a two-lane road tunnel, the total length is 4,998m while the maximum overburden is 610m. The geology of the Nagano side of the tunnel is mainly mylonite, a metamorphic rock, and the area around the fault is soft. In this construction section, the problematic large overburden section was only about 100m long. Although, the implementation of the drift advancing tunnel construction method was considered as a countermeasure, since this method required separate procurement of machinery to construct the drift, it was believed to be disadvantageous in terms of the cost and the construction period. Therefore, we adopted the double-support construction method, which is still very rarely used in Japan. In addition, ultra-high-strength sprayed concrete with a design standard strength of 54 N/mm2 was applied to the section with the largest overburden to ensure the stability of the tunnel. This paper describes the design concept and construction results of the countermeasures that were taken to reduce the displacement due to the large overburden.

Keywords: Large Overburden, Double Supports, Ultra-high-strength sprayed concrete, Mountain Tunnels

1 INTRODUCTION

The Sanen-Nanshin Expressway starts the Chuo Expressway from Iida City in Nagano Prefecture to Inasa-cho in Shizuoka Prefecture, a high-standard arterial road of approximately 100km in length. The Aokuzuretōge Tunnel is a two-lane road tunnel totaling 4,998m located on the border of Nagano Prefecture and Shizuoka Prefecture in this Expressway.

The tunnel is located about 500m west of the Median Tectonic Line. Based on the excavation of the previous investigation shafts, the main geological feature is thought to be mottled mylonite, a fault rock has undergone plastic flow under high temperature, pressure, and dynamic metamorphism.

The Nagano construction side of the tunnel is 2,854m, and the excavation began in April 2019 (Figure 1, Table 1). The displacement and deformation

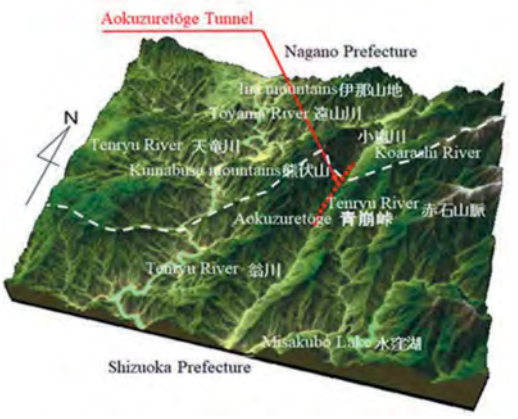

Figure 1. Tunnel location map.

*Corresponding author: shibin.taku@mail.penta-ocean.co.jp

DOI: 10.1201/9781003495505-180

Table 1. Construction outline.

Name of construction	Sanen Nanshin Expressway Kogarashi Tunnel Main Mine Construction
Orderer	Ministry of Land, Infrastructure, Transport and Tourism Chubu Regional Development Bureau, Japan
Contractor	Penta-Ocean Construction Co., Ltd., Japan Nagoya Branch
Construction site	Minamishinano, Iida City, Nagano Prefecture, Japan
Length of construction section	2,854m from the Nagano side mouth of the 4,998m
Inner cross section	63m^2 (standard part at the time of completion)
Excavation cross section	124m^2 (shoring pattern EdI-aF)
Construction period	August 9, 2018 to November 30, 2024
Construction method	NATM (Full Face Method With Auxiliary Bench Cut)
Excavation method	Blasting excavation (sliding: tire method)

after excavation of about 2730m from the start were relatively small since the geology was mainly composed of mottled mylonite, and the tunnel stability was ensured with the DI Support Pattern.

However, after the excavation distance of 2,730m, which passed the hypothetical fault F15, the displacement and deformation increased after the tunnel excavation. Cracking of the shotcrete, buckling of the steel arch supports, deformation of the rock bolt plates, and bolt breakages were confirmed (Figure 2).

The overburden of the section from 2,730m excavation distance on the Nagano construction side to 2,854m at the end of the construction area increased sharply from 530m to 610m. Based on this, it was determined that a support structure and a construction method that can withstand extremely large ground loads would be necessary for Subsequent tunnel excavation, and a study was conducted. As a result, it was decided to apply double supports using ultra-high-strength shotcrete with a design strength of 54 N/mm^2 for the section and to apply a tunnel shape close to a perfect circle.

This paper reports the process of application of double support using ultra-high-strength shotcrete in this section and the construction results.

2 GEOGRAPHY AND GEOLOGICAL OVERVIEW

2.1 *Topography overview*

Figure 3 shows the geological profile of the Nagano construction side of the Aokuzuretōge Tunnel. This tunnel is planned in a steep mountainous area with an altitude of about 590m to 1,260m. The overburden is 1.5D (D is the tunnel excavation diameter) at about 31m from the Nagano Side entrance and beyond that point, the overburden increases as the tunnel is excavated.

In the section approximately 440m from the tunnel entrance at the Nagano construction side to the construction zone boundary, it was impossible to apply standard supports based on the design method because the overburden is over 500m. The maximum is 610m on the Nagano construction side, about 58m from the boundary of the construction area (Japan Road Association, 2023).

2.2 *Geological overview*

As a result of the investigation pit excavation conducted prior to the excavation of the main pit (Motoki et al., 2020), the geology mainly was patchy mylonite found in the section of about 2,600m from the tunnel entrance on the Nagano construction side. The displacement and deformation after excavation of the survey pit were relatively small because the patchy mylonite was relatively stiff.

However, it was confirmed that the fine-grained mylonite and muddy mylonite were distributed in the section after 2,600m, which was far away from the tunnel entrance on the Nagano construction side, and the displacement and deformation after tunnel excavation increased. In addition, since the displacement and deformation after excavation will continue for an extended period in the evacuation tunnels, the cross-sectional shape is made close to a perfect circle, and double support is applied.

Figure 2. Deformation situation of the support which occurred.

3 DEFORMATION HISTORY OF SUPPORT MEMBERS

From the Nagano construction side entrance to around 2,740m, the support pattern DI-b shown in Figure 4 was applied except for the support pattern DIII at the

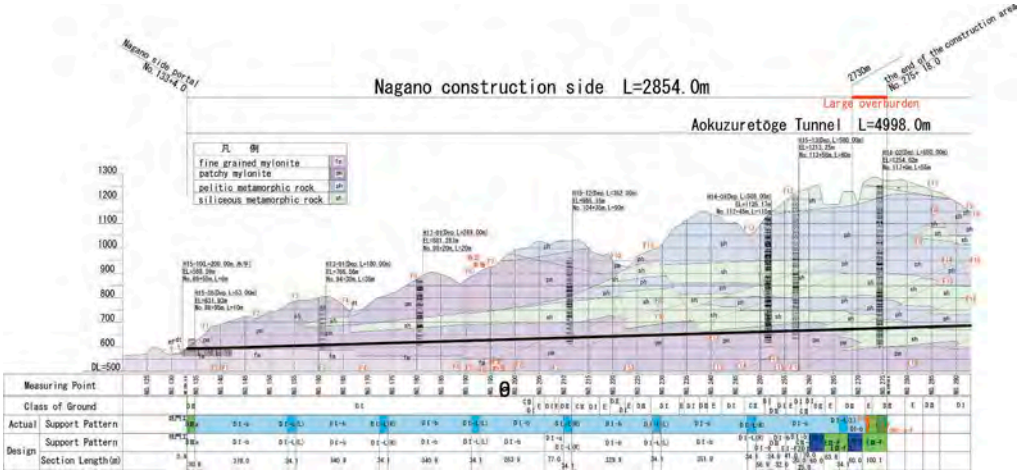

Figure 3. Geological profile.

tunnel entrance. In this section, the convergence and crown settlement were comparatively small, about 1 to 2 cm at maximum, and a convergence tendency was confirmed at a distance of 2D from the tunnel face.

However, after passing through F15, shown in Figure 3, the rock types that appeared at the tunnel face included black shale. Cracks in the shotcrete and steel cracks appeared at the top of the tunnel, and the steel arch support buckled, as shown in Figure 2. In addition, the deformation of the plate of the rock bolt and its breakage was confirmed in the rock bolt on the side wall. For this reason, in the section where the deformation occurred, additional rock bolts were installed, and additional shotcrete with a thickness of 10 cm was applied to ensure the stability of the tunnel and the safety of construction.

4 EXAMINATION OF TUNNEL STRUCTURE AND CONSTRUCTION METHOD

4.1 *Mechanism of deformation generation*

Figure 5 shows the convergence and crown settlement measurement results in the section where the support deformation occurred. This figure shows that both the convergence and crown settlement were increased, and the displacement and deformation trend of the shotcrete increased to the face distance of 20m (about 1.0D). In particular, the displacement and deformation rates are significant, and the convergence is larger than the crown settlement after the tunnel excavation.

From the above, in this deformed section, the deformation of the supporting element occurred due to displacement and deformation at an early stage about the distance of 4m to the tunnel. These results coincided with the time when underground observation confirmed the deformation.

From these results, it was considered that the deformation occurred in the support member due to displacement and deformation in the early stage after excavation when the strength of the shotcrete was not sufficiently developed.

4.2 *Consideration of countermeasures*

From the tunnel observation and measurement results, it was considered that deformation occurred

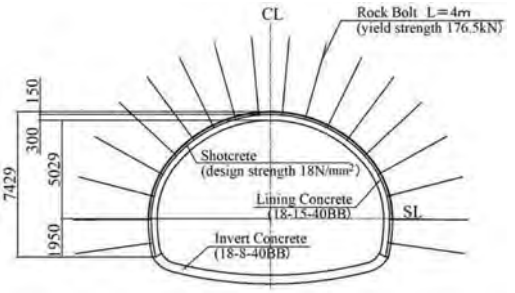

Figure 4. Support Pattern DI-b.

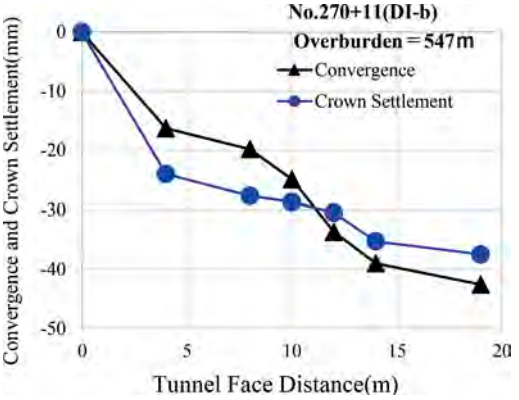

Figure 5. Measurement results of displacement and deformation in the deformation occurrence section.

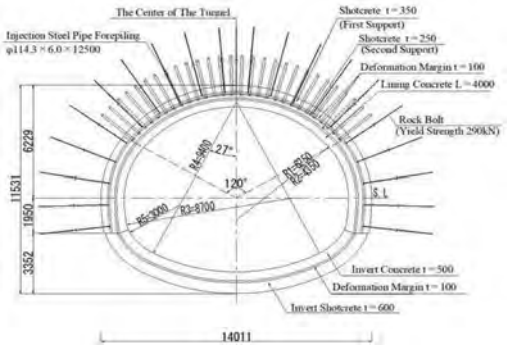

Figure 6. Considered support structure.

in the steel arch support and the shotcrete at a face distance of about 4m. As shown in Figure 2, the shotcrete at the top of the tunnel has cracks in the longitudinal direction, and it is thought that horizontal displacement and deformation are the causes of deformation.

In many cases, early closure using supportive inverts effectively suppresses horizontal displacement and deformation (Susumu et al., 2019). However, considering that deformation occurs at a face distance of 4 m in this tunnel, it is necessary to complete closing at a face distance of 3 m or less. It was considered difficult to apply the method because closing the full cross-section face of about 124m^2 near the face needs to include the operating range of the construction machine, and it was challenging to ensure the safety of the work. Based on the above about the support structure behind the deformation-occurring section, the use of a high-rigidity support structure based on the construction results of the adjacent Shizuoka construction section was examined.

Specifically, the double support structure shown in Figure 6 was adopted. For the top heading and bench, high-strength steel HH-200 (ss540) was used for the high-arch support, and high-strength shotcrete with a design strength of 36 N/mm^2 was used. At that time, the shotcrete thickness of the first support was set at 35 cm, and the shotcrete thickness of the second support was set at 25 cm. As for the rock bolts, only the first support was applied, and high-strength bolts with a yield strength of 290kN for a length of 4 m were applied.

As for the shape of the invert, the tunnel's center was 1m deeper than the usual cross-section so that the radius was reduced, and the high-strength steel HH-200 (ss540) invert supports were used for the early closure. At that time, high-strength shotcrete with a design strength of 36N/mm^2 shall be applied for the shotcrete of the invert, and the thickness shall be 60cm, equivalent to the total thickness of the primary and second support in the top heading and bench. However, to ensure the construction's safety, the closing distance was approximately 6 to 8 m from the top heading face.

In addition, for the 40m section from No.273+18 to No.275+18, which has the maximum overburden, it is assumed that the initial stress of the ground will increase further, therefore ultra-high strength shotcrete with a design strength of 54N/mm^2 was applied (Hazama Ando Corporation, 2023).

5 EFFECTS OF COUNTERMEASURES

After the deformation occurred, countermeasures were considered, materials such as steel arch support were procured, and double-supported tunnel excavation was resumed.

First, an auxiliary construction method, the injection Steel pipe forepiling, shown in Figure 6, was constructed. The top heading was excavated using blasting and installing the first support. After that, the bench was excavated, and the first support was installed. The second support was installed 6-7m behind the top heading face, and early closure was performed by inverting the support about 10m behind.

5.1 *Displacement and deformation*

Figures 8(a) and (b) show the convergence and crown settlement measurement results at No.273 +05, where the overburden is 609m. In the figure, initial values are set at the time of the first and second support construction and arranged by the tunnel face distance.

In addition, this figure also shows the convergence and crown settlement in the section where ultra-high strength shotcrete was applied, which will be described later.

This figure confirmed that both the convergence and crown settlement increased during the period from the construction of the first support to the construction of the second support. In particular, a comparatively large value of about 90mm was obtained for the convergence, but no deformation

Figure 7. Construction status of double support section.

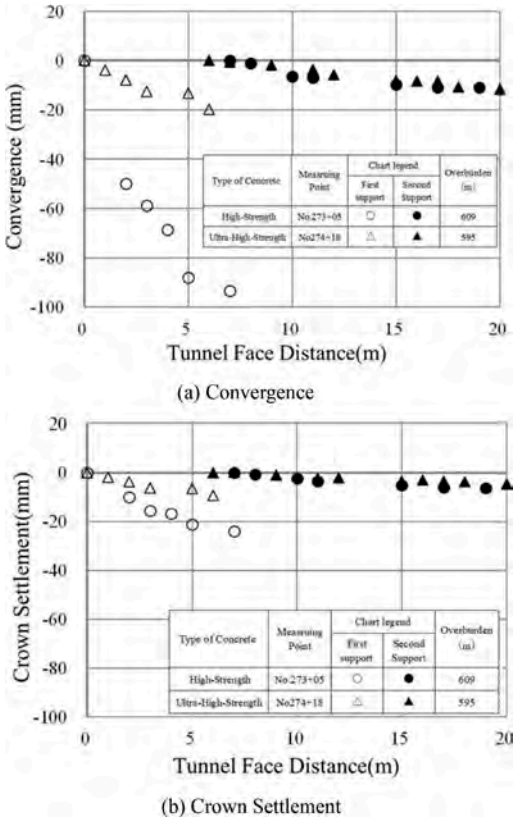

Figure 8. Measurement results of the convergence and crown settlement.

was confirmed in the shotcrete, steel arch supports, and rock bolts.

After that, it was found that by installing the second support, both the convergence and crown settlement were reduced to about 10mm, and the rate of increase in displacement and deformation also decreased.

Therefore, the first support with high-strength concrete, high tensile steel arch support, and high-strength rock was not found to cause any deformations in the supports because the material strength increased along with the stiffness of the support. Although displacement and deformation could not be sufficiently controlled at the first support stage, secondary support and early closure with supported inverts ensured that subsequent displacements and deformations were controlled.

5.2 *Effects of ultra-high-strength shotcrete*

In the 40m section from No.273+18 to No.275+18, which is the construction zone boundary, the maximum overburden is 610m, so the ultra-high strength shotcrete with a design strength of 54N/mm^2 was applied. In this case, ordinary high-strength shotcrete was used for the steel arch support. The thickness of the shotcrete was 35cm for the first support and 25cm for the second support. The same high-strength bolts were also applied to the rock bolts.

Figures 8(a) and (b) show the convergence and crown settlement when ultra-high-strength shotcrete is applied compared to the case when normal high-strength shotcrete is applied.

This figure shows that the application of ultra-high-strength shotcrete can reduce the convergence and crown settlement at the construction stage of the first support to approximately 1/6 to 1/3. On the other hand, there was no significant difference in the convergence and crown settlement after the construction of the second support.

Based on the above, when the double support structure is applied, the displacement and deformation of the tunnel after the construction of the first support are not significantly different from those of the standard single support. However, it was found that the displacement and deformation after the construction of the second support were small and stabilized in an early stage. In addition, although the application of ultra-high-strength shotcrete can suppress the displacement and deformation after the construction of the first support, it is considered that there is no significant difference in the suppression effect of the displacement and deformation after the construction of the second support.

6 VERIFICATION OF EFFECTIVENESS

Numerical analysis was conducted to verify the effect of double supports applied in the Nagano section of the Aokuzuretōge Tunnel.

6.1 *Analysis method*

The effect of the applied double support was verified using numerical analysis. The analysis code used for verification was FLAC3D by the finite difference method. The ground was assumed to be an elastoplastic body according to the Mohr-Coulomb failure criteria, and the support members were assumed to be a composite shell by the steel arch supports and shotcrete.

The support effect of the rock bolts was sufficiently small and therefore, that it was not considered to model and did not consider the auxiliary construction method.

6.2 *Analysis model and input physical property values*

Figure 9 shows the analytical model, and Table 2 shows the input physical property values of the ground and supports.

Based on the *Tunnel Numerical Analysis Manual* of the Japan Highway Public Corporation Test Research Institute (Nihon Doro Kodan Research Institute, 2002), the analysis area was set to 60m to the

left and 70m to the right of the tunnel's center and 120m to the longitudinal direction. The area below the invert was about 3.75D (D: tunnel excavation diameter) of 45m, and the overburden was 500m (about 40D). In order to reproduce the maximum overburden of 610m, a distributed load of 2.7×10^2kN/m^2 was applied in the initial ground analysis.

Among the input physical property values used in the analysis, the ground's modulus of elasticity was assumed to reproduce the displacement and deformation in the support pattern DI, where deformation occurred in this tunnel.

Regarding the modulus of elasticity of the shotcrete at the stage of tunnel excavation, the value of general construction steel was used in the research results of Tsuchiya (1985). In addition, the second support was constructed when the tunnel face distance was 8 m, changing the composite shell's elastic modulus from the first support to the second support.

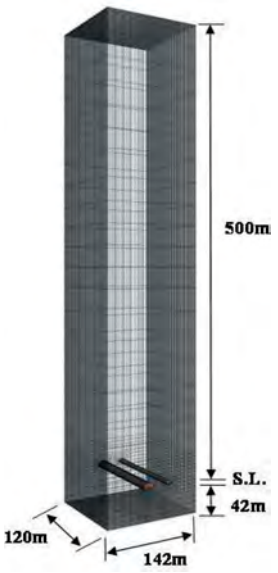

Figure 9. Analysis model.

6.3 *Analysis result*

Figure 10(a) and (b) compare the analysis results and measurement results when double support using high-strength shotcrete with a design strength of 36N/m^2 is applied. Figure 11(a) and (b) compare the analysis and measurement results when applying ultra-high-strength shotcrete with a design strength of 54N/m^2.

In this context, (a) is the convergence, and (b) is the crown settlement. The horizontal axis is the tunnel face distance, while the vertical axis represents convergence and crown settlement.

However, from Figure 10, the convergence in (a) shows that the measurement results greatly exceeded the analysis results at the first support stage. At the stage of the second support in (a) and the crown settlement shown in (b) at the stage of the first support and the second support, the analysis and measurement results were in general agreement. From this, the numerical analysis could not reproduce the significant convergence immediately after constructing the first support. However, the convergence at the second support stage and crown settlement at the first and second support stages can be reproduced by changing the rigidity of the first and second support.

Figure 11(a) and (b) show that analysis results and measurement results of the convergence and crown settlement when the double support structure with ultra-high strength shotcrete was used generally agreed with each other. In addition, compared with the double support using high-strength shotcrete with a design standard strength of 36N/mm2 shown in Figure 10(a) and (b), the measurements using ultra-high-strength shotcrete suppresses the amount of convergence and crown settlement.

Table 2. Physical property values for numerical analysis.

Ground condition	Element	Elasto-plastic solid		
	Elastic modulus E (N/m^2)	3.0×10^9		
	Unit volume weight γ (kN/m^3)	27		
	Poisson Ration ν	0.48		
	Adhesive force c (N/m^2)	3.0×10^6		
	Internal friction angle φ (deg.)	50		
Support members	Construction order of main tunnel	1st	2nd	Inv. Support
	Element	Rigid shell	Rigid shell	Rigid shell
	Type of steel support	HH-200	HH-200	HH-200
	Thickness of sprayed concrete (mm)	350	250	600
	Compressive strength of sprayed concrete (N/mm^2)	36(54)	36(54)	36(54)
	Elastic modulus E_s (kN/m^2)	$9.63\times10^6(1.26\times10^7)$	$1.02\times10^7(1.31\times10^7)$	$8.12\times10^6(1.11\times10^7)$

():Ultra high strength sprayed concrete

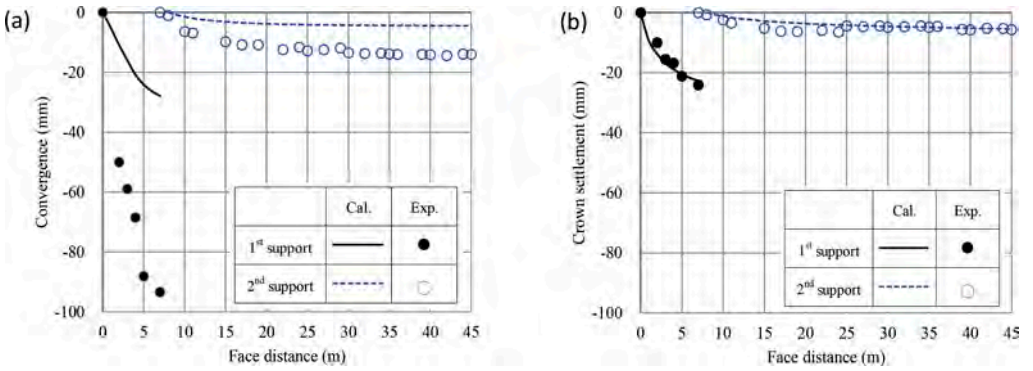

Figure 10. Comparison of measurement results and analysis results (shotcrete with a design strength of 36N/mm^2).

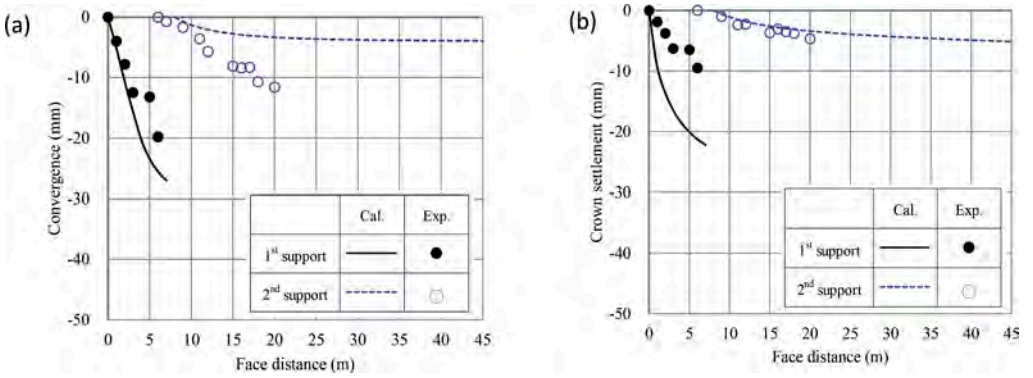

Figure 11. Comparison of measurement results and analysis results (shotcrete with a design strength of 54N/mm^2).

7 CONCLUSION

In the construction section on the Nagano side of the Aokuzuretōge Tunnel, a large ground load caused deformation of the support members, so double support was applied to the 76m section from No.272+02 to the boundary of the construction section. At that time, ultra-high-strength shotcrete with a design strength of 54N/mm2 was used instead of the standard high-strength shotcrete for the section from No. 273+18 to the boundary of the construction zone, where the overburden was particularly large.

As a result, there was no deformation of the support after excavation, and it was considered that the stability of the tunnel was secured. In addition, applying ultra-high strength shotcrete when double support is applied under construction conditions with significant overburden, displacement and deformation after tunnel excavation can be suppressed. The effect of suppressing this displacement and deformation was also confirmed by numerical analysis in which the rigidities of the primary and second support composite shells were changed.

REFERENCES

Hazama Ando Corporation: First Application of Ultra High Strength Shotcrete in Mountain Tunnel Construction, 2023, https://www.ad-hzm.co.jp/info/2023/20230410.php

Japan Road Association: Technical standards for road tunnels (structure)・commentary, pp.125–127, 2003.

Motoki Baba, Tomoaki Sakurai, Shigeru Ishikawa, Takaaki Koide: Challenging complex geology along the median tectonic line with 3D computerized construction, Tunnel and Underground, Vol.51, No.10, pp.31–40, 2020.

Nihon Doro Kodan Research Institute: Technical Document Guide for Analytical Design of Urban NATM Tunnels 2002.

Susumu Yuba, Yoshihiro Morikawa, Masanao Aizawa, Sadatoshi Oomori: Overcoming the fragile Nichinan Group using the central advanced pilot shaft, Tunnel and Underground, Vol.50, No.1, pp.7–14, 2019.

Takashi Tsuchiya: Studies on the parameters and grounds for the tunnel design program, Journal of JSCE 364/III-4, pp.31–40,1985.

Tunnelling for a Better Life – Yan, Celestino, Thewes & Eberhardt (Eds)
© 2024 The Author(s), ISBN 978-1-032-80042-4
Open Access: www.taylorfrancis.com, CC BY-NC-ND 4.0 license

Mechanical evolution mechanism of primary support under steel arch frame corrosion in subsea tunnel

Yiteng Zhang*
China Railway Economic and Planning Research Institute, Beijing, China
School of Civil Engineering, Southwest Jiaotong University, Chengdu, China

Siming Tian
China Railway Economic and Planning Research Institute, Beijing, China
School of Qilu Transportation, Shandong University, Jinan, China

Mingnian Wang & Li Yu
School of Civil Engineering, Southwest Jiaotong University, Chengdu, China

ABSTRACT: In the subsea tunnel built by drilling and blasting method, the section steel frame of primary support is corroded by long-term ions, and the bearing capacity and degradation mechanism of the primary support after corrosion are the key to long-term safety evaluation of the tunnel. Based on the stress characteristic state of a subsea tunnel, eccentric concrete components with section steel frame were constructed. First, eccentric concrete components with steel frame sections that had varying rates of corrosion were obtained using an electric acceleration test. A handmade counterforce mechanism was then used to enhance eccentric loading. This paper investigates the bearing capacity and law of failure form of corroded primary support that vary with the eccentricity distance and corrosion rate. It also determines the critical corrosion rate for the primary support with section steel frame that satisfies the plane cross-section assumption. Ultimately, the evolution process of the primary support's mechanical deterioration under the section steel frame's corrosion influence was uncovered using numerical simulation. This attenuation of primary support bearing capacity was caused by the following factors: the geometric and mechanical parameters of the section steel frame, which contributed between 32.69% and 37.75%; the attenuation of concrete mechanical parameters, which contributed between 18.36% and 20.8%; and the bond-slip degradation, which contributed between 43.09% and 46.58%.

Keywords: Subsea tunnel, Primary support, Section steel frame corrosion, Corrosion degradation test, Mechanical evolution mechanism

1 INTRODUCTION

A tunnel is an underground structure with a complicated operating environment and surrounding geological conditions. The operation safety of the tunnel is gravely threatened by a number of degradation characteristics that will undoubtedly arise with longer operating times. These characteristics include lining cracking, water leakage, block failure in extreme circumstances, tunnel floor uplift or slurry rising, etc (Liu et al., 2021). This is because the materials of the tunnel support structure, like steel and concrete, are deteriorating to varying degrees, and the surrounding rock of the tunnel has deteriorated because of its own geological conditions, groundwater conditions, or construction factors.

The environment within subsea tunnels is more special than that of ordinary tunnels; saltwater has a high concentration of ions such as sulfate (SO_4^{2-}) and chloride (Cl^-), and high water pressure encourages ion transport (Jin et al., 2013; Wang et al., 2019). The steel in the supporting structure system is easily depassivated and corroded by ion erosion, resulting in the weakening of its mechanical parameters and the degradation of the bond strength (Zhang et al., 2022), which ultimately has an impact on the tunnel's supporting structure system bearing capacity and safety. The subsea tunnel designed based on NATM theory often has poor surrounding rock conditions in the section with section steel frame, where the primary support will bear a large load. The section steel frame's corrosion not only

*Corresponding author: zytzytlvzq@163.com

DOI: 10.1201/9781003495505-181

causes the corrosion expansive force but also breaks down the bond between the section steel frame and the shotcrete, allowing slippage to occur. Because the section steel frame and the shotcrete are unable to work together, the bearing capacity of the primary support is significantly reduced. The decay law and degradation mechanism of the primary support bearing capacity after the section steel frame corrosion have become the key to the long-term safety evaluation of operational tunnels.

Based on the stress characteristics of the primary support at a particular site, and taking into consideration two factors: the loading eccentricity and the corrosion rate of the section steel frame, twelve sets of section steel frame concrete eccentric components were made in order to reflect the influence of corrosion on the bearing capacity of section steel frame corrosion from a macro perspective. Different eccentricity was taken into consideration to load the components after performing accelerated electrolytic corrosion experiments to determine different corrosion rates. The failure form and bearing capacity of the primary support with corrosion rate and eccentricity were investigated, and the critical corrosion rate of primary support with section steel frame that meets the plane cross-section assumption has been obtained. Finally, the decay of geometrical and mechanical parameters of steel frame corrosion, the decay of mechanical parameters of concrete caused by corrosion expansion, and the degradation of bond-slip between section steel frame and concrete caused by corrosion respectively contribute to the decay of primary supporting capacity is revealed.

2 TEST METHOD FOR CORROSION DEGRADATION OF SECTION STEEL FRAME IN PRIMARY SUPPORT

2.1 *The methods of loading and ion-accelerated corrosion*

The primary support structure is a ring shape in practice, and the idea of "straight instead of curved" is adopted to simulate the stress characteristics of the primary support (Feng et al., 2021), and straight beams with equal sections are selected to replace the primary support curved beam members to carry out research on the characteristics of the primary support bearing capacity under erosion environment indoors (Figure 1). Since the primary support is an eccentric compression member, the test will be equipped with a bull leg under the straight beam to achieve eccentric loading (Figure 2).

Affected by water pressure and drainage methods, the primary support of the subsea tunnel is immersed in seawater, so the primary support components are eroded by chloride ions everywhere., which has the characteristics of global corrosion and deterioration. Consequently, in order to imitate the project's real circumstances, the primary support members in this

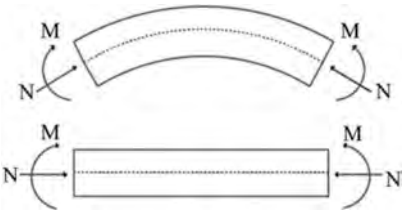

Figure 1. Schematic diagram of "straight instead of curved" equivalence principle.

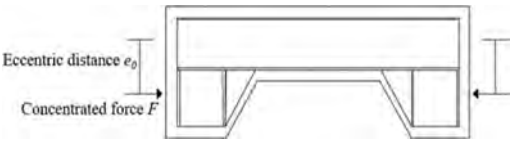

Figure 2. Eccentric loading form.

test were completely immersed in NaCl solution, and then the section steel frames in the primary support were corroded by electrical acceleration test.

2.2 *Deterioration test device and measuring system*

Using the weathering capsule trough portion of a subsea highway tunnel as an example, the primary support section was made of NO. 22b I-shaped steel, and the concrete was made of C25 shotcrete with a 32cm thickness. Therefore, the cross-section width b and height h of the columns of eccentric members were determined to be 32cm×32cm, and the bull legs of the members were employed for test loading, as shown in Figure 3.

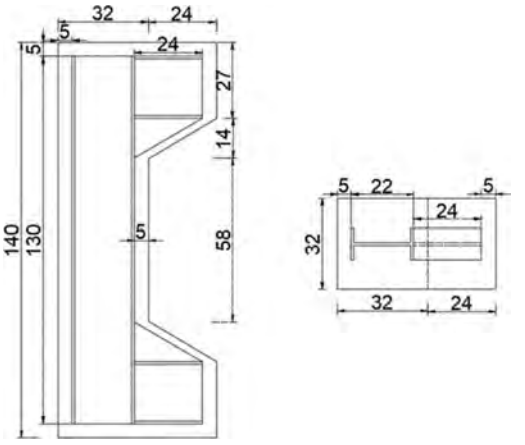

Figure 3. Dimensions of the specimen (unit: cm).

The experiment constructed a total of 12 steel reinforced concrete eccentric compression components, primarily examining the effects of varying eccentricity and corrosion rate on the eccentric components' bearing capacities. The test conditions are shown in Table 1.

Table 1. Eccentric member test conditions.

Specimen number	Eccentricity	Target corrosion rate/%
B-1-1	6.4cm (Relative eccentricity *e*=0.2)	0
B-1-2		3
B-1-3		6
B-1-4		9
B-2-1	11.2cm (Relative eccentricity *e*=0.35)	0
B-2-2		3
B-2-3		6
B-2-4		9
B-3-1	16cm (Relative eccentricity *e*=0.5)	0
B-3-2		3
B-3-3		6
B-3-4		9

The main steps involved in producing eccentric compression components are cutting I-shaped steel, welding brackets, pasting and waterproofing I-shaped steel strain gauges, making molds, injecting I-shaped steel and connecting wires, pouring concrete, demoulding components, curing, and forming, etc. The formed components are shown in Figure 4.

Figure 4. Eccentric member.

2.2.1 *Electric accelerated corrosion test*

This test uses an electric accelerated corrosion test method, which is based on Faraday's law (Hou et al., 2019), to accelerate the corrosion of I-shaped steel. This accelerated electrolysis test mainly adopts an electrolytic cell composed of DC power supply, wire, 5% NaCl solution, stainless steel, steel pipe frame, tarpaulin and wooden pad, as shown in Figure 5.

Test steps: Prepare a 5% concentration NaCl solution in the electrolytic cell, immerse the component in it for more than 7 days, and allow the salt water to slowly penetrate into the interior of the component, in contact with the I-shaped steel inside; Connect the electrolysis circuit according to Figure 5, turn on the power, adjust the current, and control the current to 1A; Maintain a constant flow and turn the power on at the target time that was initially intended and determined using Faraday's principle..

2.2.2 *Loading device*

n the test, the static loading method was used, and a homemade reaction frame (Figure 6) was

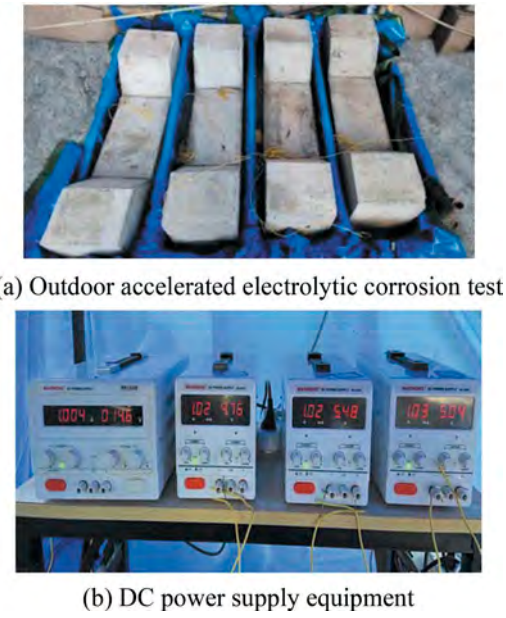

(a) Outdoor accelerated electrolytic corrosion test

(b) DC power supply equipment

Figure 5. Electric accelerated corrosion test.

employed. Its internal dimensions were 2.5m long × 1.5m wide.

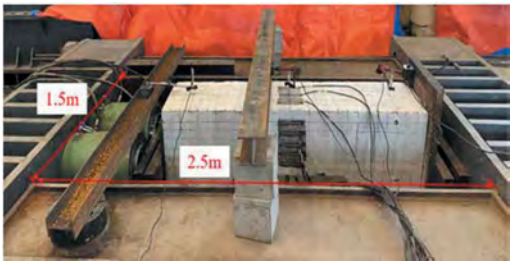

Figure 6. Homemade counterforce frame device.

2.2.3 *Measuring system*

The majority of the tests involve deformation tests of eccentric compression components and strain tests on I-shaped steel and concrete surfaces.

(1) Strain testing of I-shaped steel
Strain gauges are pasted on both sides of the web and flange of the I-shaped steel, and the arrangement of measuring points is shown in Figure 7. The number of I-shaped steel strain gauges is shown in Figure 8. The A and C sides are the flange side of the I-shaped steel, and the B and D sides are the web side of the I-shaped steel.

(2) Strain testing of concrete surface
Thirteen concrete surface strain test sites in total are positioned at the eccentric compression member's mid-span location; five monitoring points are situated on surfaces ② and ③, and three monitoring points are situated on surface ①. The location of strain measurement points on the concrete surface is shown in Figure 9.

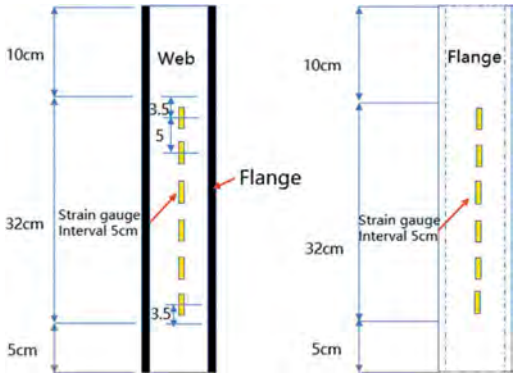

Figure 7. Measurement point for I-shaped steel strain.

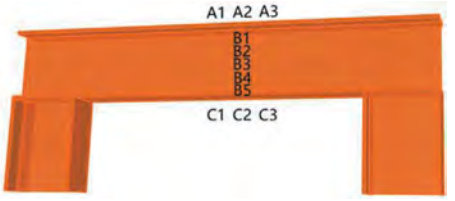

Figure 8. Schematic diagram of I-shaped steel strain gauge pasting position.

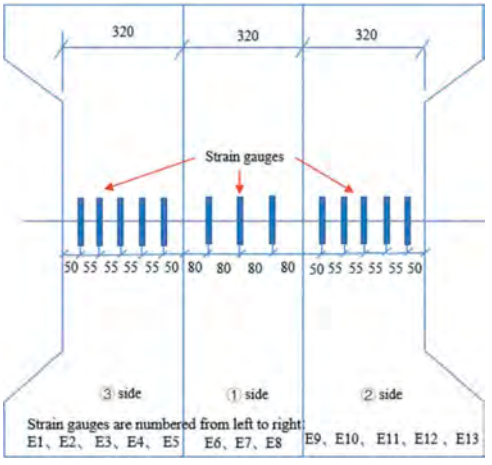

Figure 9. Measurement points for concrete surface strain.

(3) Deformation test of eccentric compression components

Each eccentrically compressed component is equipped with 4 displacement test points. Two displacement meters, ① and ②, are respectively arranged on the compression and tension sides of the span. Two displacement meters, ③ and ④, are symmetrically arranged on both ends of the tension side. The specific arrangement of displacement test points is shown in Figure 10.

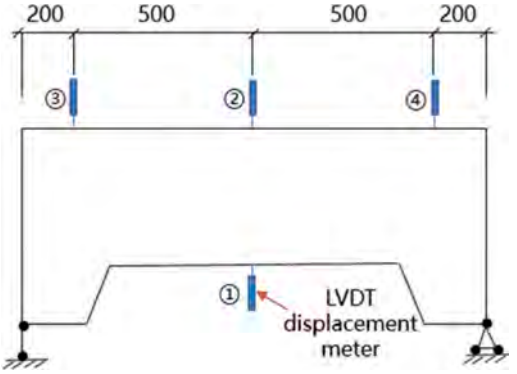

Figure 10. Displacement meter layout measuring point.

3 MECHANICAL EVOLUTION OF PRIMARY SUPPORT UNDER SECTION STEEL FRAME CORROSION

3.1 *Failure mode of primary support with corroded section steel frame*

The loading failure of steel reinforced concrete eccentric members has experienced elastic, concrete cracking, crack development, concrete spalling in compression zone, steel bending and other stress processes, but the failure process is different, and the influence of eccentricity plays a dominant role.

3.1.1 *Failure mode when relative eccentricity* e=*0.2*

When the relative eccentricity *e*=0.2, the failure process of specimens with different corrosion rates is roughly the same: when the initial load is less than the initial cracking load, both concrete and steel are in the elastic stage, and at this time, the deflection and strain values are small and the development trend is slow; When the load is about 45% -50% of the ultimate load, there is a slight cracking sound inside the specimen, and in the specimen's center control section, a first longitudinal discontinuous fine cracking emerges. As the load increases, the longitudinal crack gradually widens and extends. When the load reaches about 95% of the ultimate load, the section steel flange in the compression zone begins to yield, longitudinal cracks and deflections increase sharply, and the concrete begins to peel off. When the load reaches the ultimate load, the section steel undergoes compression buckling, and the concrete at the longitudinal crack of the concrete component collapses. Lateral cracks also occur on the smaller side of the compression zone. The typical failure of B-1-4 components is shown in Figure 11.

3.1.2 *Failure mode when relative eccentricity* e=*0.35*

For the test component with relative eccentricity *e*=0.35, the component is in the elastic stage before cracking. When the load reaches about 45% of the ultimate load, several transverse cracks appear in the

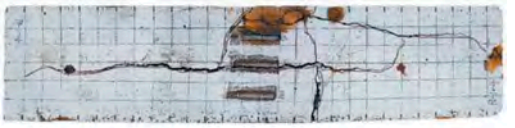

(a) The failure mode of the A-side

(b) The failure mode of the B-side

(c) The failure mode of the C-side

(d) The failure mode of the D-side

Figure 11. Typical failure mode of B-1-4 member.

(a) The failure mode of the A-side

(b) The failure mode of the B-side

(c) The failure mode of the C-side

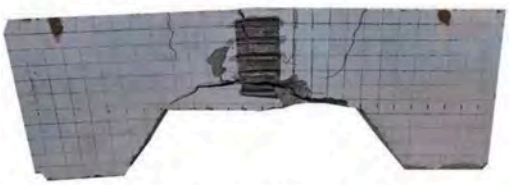

(d) The failure mode of the D-side

Figure 12. Typical failure mode of B-2-4 member.

central control section of concrete. With the further increase of the load, the width of the transverse crack of the central section increases, and the transverse crack of the surrounding section also begins to appear. When the load is increased to about 98% of the ultimate load, the compression side of the I-shaped steel flange side yields. When loading to the ultimate load, the flange side of the I-shaped steel in the tension zone yields, the tensile crack of concrete intensifies, and the deflection increases sharply. Finally, the concrete in the compression zone of the central section of the specimen collapses and falls off, and the I-shaped steel appears buckling phenomenon, which is the failure of large eccentric compression. Typical failure of B-2-4 components is shown in Figure 12.

3.1.3 *Failure mode when relative eccentricity e=0.50*

For the test component with relative eccentricity e=0.5, the component is in the elastic stage before cracking. When loading to about 25% of the ultimate load, several transverse cracks appear in the central section of concrete. With the further increase of the load, the width of the tension transverse crack of the central section increases, and several transverse tension cracks begin to appear in the surrounding section. When the load is increased to about 85% of the ultimate load, the flange of the I-shaped steel on the tension side yields, and the crack at the central section widens abruptly. When loading to the ultimate load, the I-shaped steel flange on the compression side yields, the tensile crack of concrete intensifies, and the deflection increases sharply. Finally, the concrete in the compression zone of the central section of the specimen collapses and falls off, and the I-shaped steel appears buckling phenomenon, which is the failure of large eccentric compression. Typical damage of B-3-4 components is shown in Figure 13.

3.2 *Influence of corrosion on primary support capacity*

The test primarily recorded three characteristic values: the ultimate load, the residual load, and the cracking load. Table 2 displays the recording results.

When the eccentricity is fixed, the relationship curves between different corrosion rates and the bearing capacity of the component can be obtained, as shown in Figure 14.

The load characteristic values fall almost linearly as the corrosion rate increases (from 0% to 9%) while the eccentricity remains constant. The

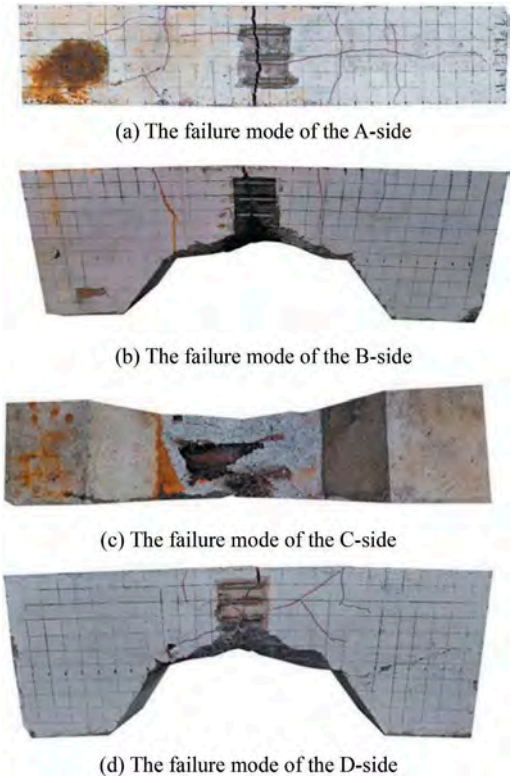

Figure 13. Typical failure mode of B-3-4 member.

reduction in the cracking load is from 27.8% to 33.9%, the reduction in the ultimate load is from 23.9% to 26.7%, and the reduction in the residual load is from 32.8% to 34.0% when the corrosion rate is between 0% and 9%. The synergistic effect between the two is reduced as a result of corrosion destroying the bond between I-shaped steel and concrete. The load shared by I-shaped steel decreases with increasing corrosion degree, lowering the bearing capacity of core concrete.

3.3 *Influence of corrosion on primary support deformation*

Based on the mechanical analysis, the component's central control section has the highest internal force and deflection, making it the most dangerous section. The test component's deflection curve varies with load as seen in Figure 15. The only deflection of the component before the ultimate load is attained, limited by the test techniques.

When the eccentricity is constant, the component's ultimate deflection rises as the corrosion rate increases. The rationale is that more corrosion means a higher rust expansion force produced by the I-shaped steel within the specimen, resulting in the more severe initial defects of the specimen. At the same time, the bond between I-shaped steel and concrete weakens, resulting in poor coordinated deformation. Under the combined action, the stiffness of the component decreases. When the corrosion rate is constant, the component's ultimate deflection rises as the eccentricity increases. The rationale is that the specimen's tensile component proportion increases with eccentricity, and the deflection at the centre section increases correspondingly.

3.4 *Plane cross-section assumption analysis*

Due to the slip caused by the interface bond degradation between corroded section steel and concrete, the section of steel and concrete does not meet the plane cross-section assumption. The critical corrosion rate of different eccentric components meeting the assumption of plain section is obtained by comparing the strain distribution of central section steel and concrete in the loading test. Figure 16 shows the strain of I-shaped steel and concrete at the central section, where the applied load is 50% of the ultimate load (i.e. 50%P_u).

When the relative eccentricity is e=0.20 (small eccentric member) and the corrosion rate of I-shaped steel $\rho \leq 3\%$, the strain distribution difference

Table 2. Load characteristic values of eccentric members.

Specimen number	Relative eccentricity e	Corrosion rate/%	Cracking load /kN	Ultimate load /kN	Residual load /kN
B-1-1	0.20	0	1371	2688	1439
B-1-2		3	1211	2522	1271
B-1-3		6	1091	2321	1145
B-1-4		9	920	2045	966
B-2-1	0.35	0	865	1765	908
B-2-2		3	776	1650	814
B-2-3		6	680	1512	714
B-2-4		9	571	1328	600
B-3-1	0.50	0	617	1542	648
B-3-2		3	542	1425	596
B-3-3		6	488	1318	536
B-3-4		9	407	1130	468

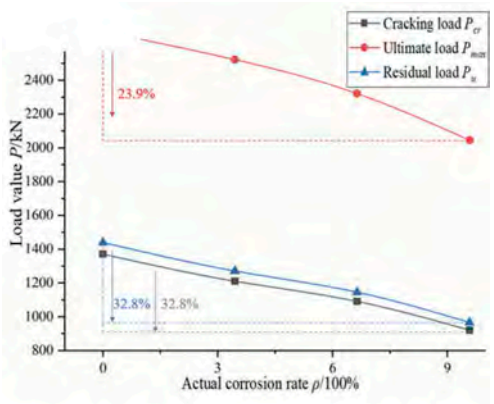

(a) Relative eccentricity e=0.2

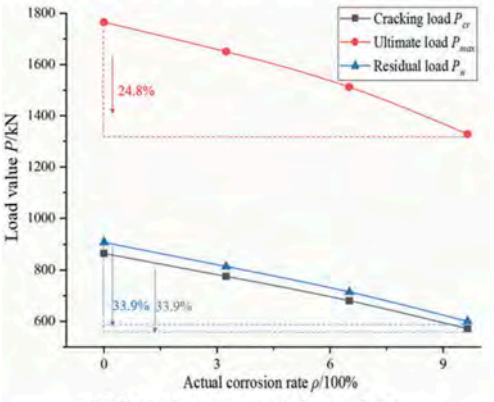

(b) Relative eccentricity e=0.35

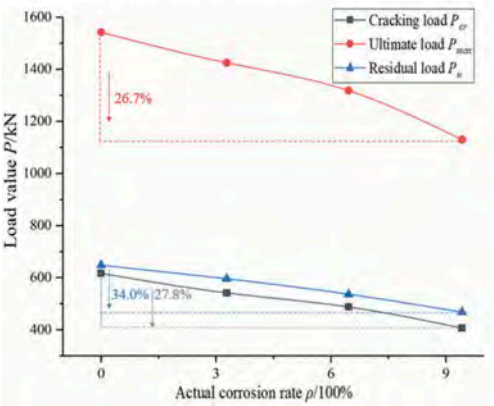

(c) Relative eccentricity e=0.5

Figure 14. Relationship between load characteristic value and corrosion rate.

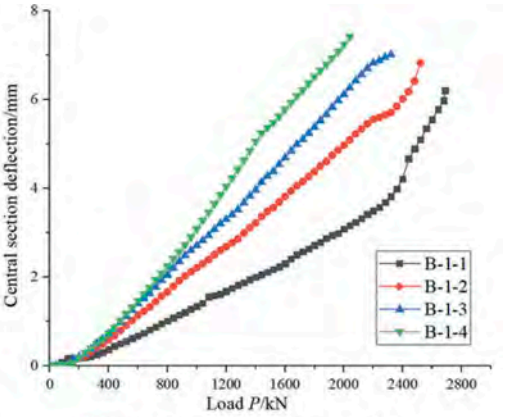

(a) Relative eccentricity e=0.2

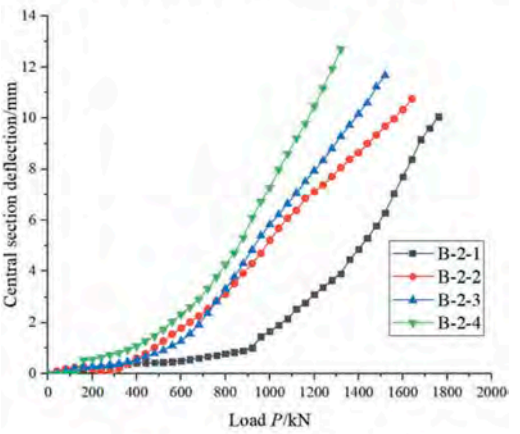

(b) Relative eccentricity e=0.35

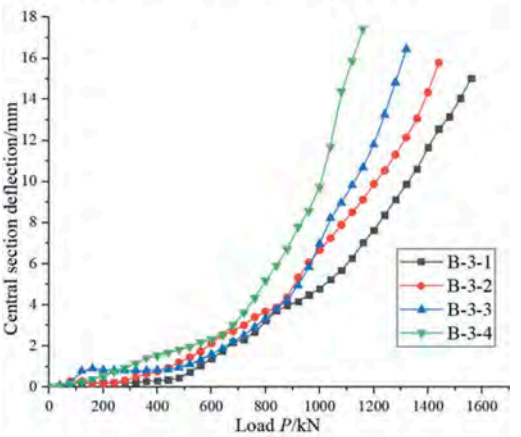

(c) Relative eccentricity e=0.5

Figure 15. Load-deflection curve.

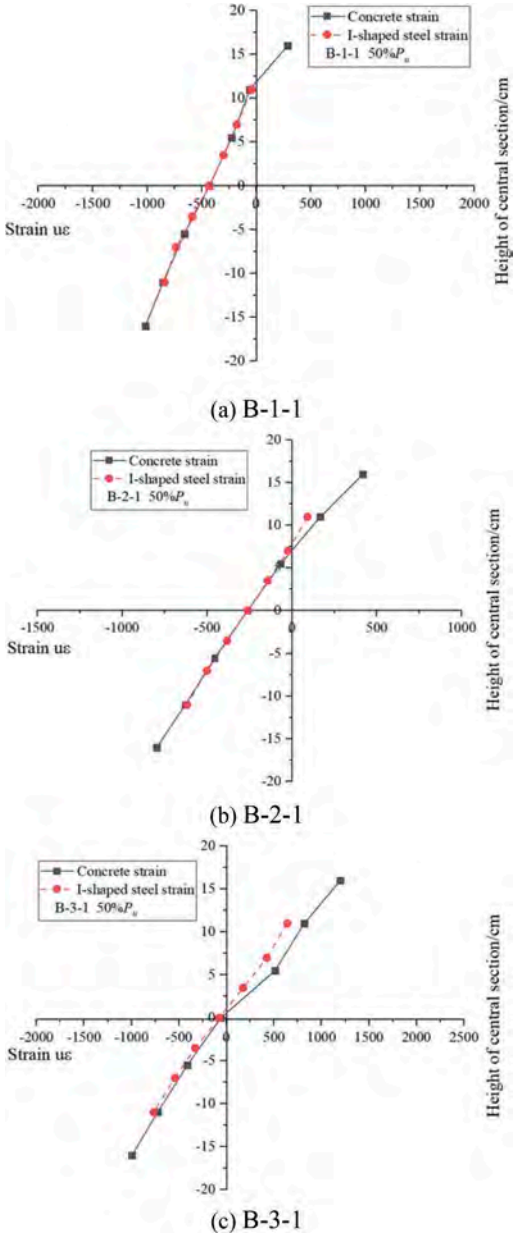

Figure 16. Strain distribution of I-shaped steel and concrete (Only part).

between I-steel and concrete is small, and the cross-section strain conforms to the plane cross-section assumption. When the relative eccentricity is e=0.20 (small eccentric member) and the corrosion rate ρ>3%, the strain distribution between I-shaped steel and concrete is different, and the cross-section strain does not conform to the plane cross-section assumption. When the relative eccentricity is e=0.35 and 0.50 (large eccentric members), the external load reaches 50%P_u, the strain distribution between the I-shaped steel and the concrete is quite different from the beginning, and the cross-section strain does not conform to the plane cross-section assumption.

4 DECAY MECHANISM OF PRIMARY SUPPORT BEARING CAPACITY

The decrease of geometry and mechanical parameters of the section steel frame under corrosion, the decrease of concrete mechanical parameters caused by rust expansion, and the degradation of the bond between the section steel frame and concrete caused by corrosion will directly lead to the attenuation of the primary supporting capacity. In order to reflect the influence of the three factors on the bearing capacity attenuation, the finite element ANSYS numerical simulation method is used here to analyze the contribution of each factor to the bearing capacity attenuation. The final ANSYS model is shown in Figure 17.

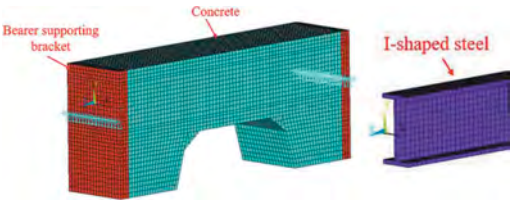

Figure 17. Numerical calculation model of the eccentric member.

By studying the impact of each of the three factors on bearing capacity, as shown in Figure 18 .The contribution rate of geometric and mechanical parameters of the section steel frame caused by corrosion to the primary support bearing capacity attenuation is 32.69%~37.75%, the contribution rate of concrete mechanical parameters attenuation caused by rust expansion is 18.36%~20.8%, and the contribution rate of bond slip degradation between the section steel frame and concrete caused by corrosion is 43.09%~46.58%. The degradation of bond slip between the three has the greatest contribution to the attenuation of bearing capacity, while the degradation of concrete parameters caused by rust expansion has the smallest contribution to the attenuation of bearing capacity. In practical engineering, to prevent a significant decrease in the primary support bearing capacity due to bond slip degradation, connectors can be installed between the section steel frame and concrete to enhance the bond between the section steel frame and concrete.

5 CONCLUSIONS

Firstly, the primary support of section steel frame with different corrosion rates was obtained through

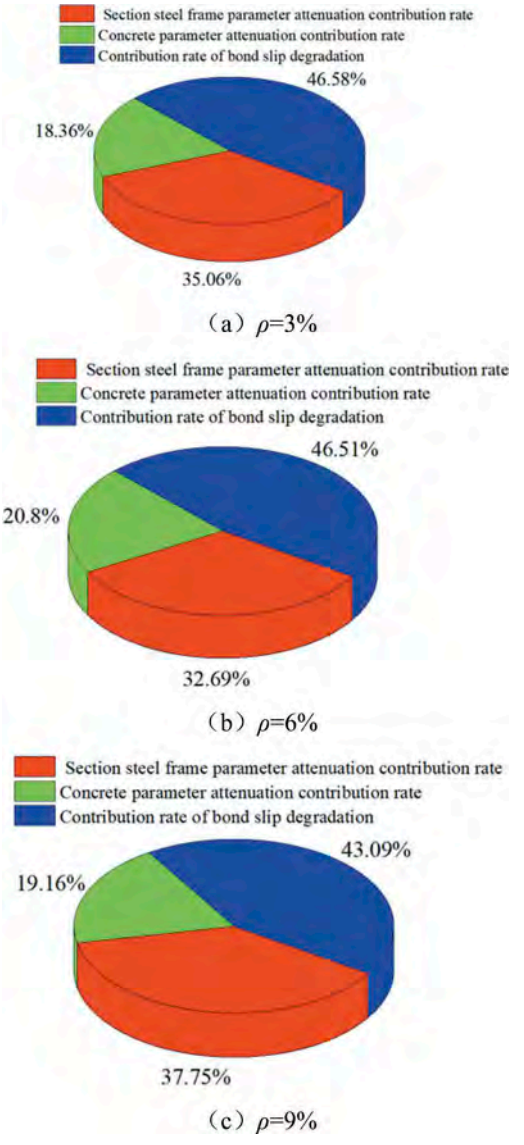

Figure 18. Percentage contribution of primary support bearing capacity decay.

electric acceleration testing, and then the mechanical degradation law of the primary support with corroded section steel frames was obtained through eccentric loading. Finally, numerical simulation was used to reveal the mechanism of corrosion on bearing capacity attenuation. The following conclusions could be drawn.

(1) When the corrosion rate of the section steel frame is 0%~9%, the failure mode characteristics of the primary support during corrosion are mainly determined by the eccentricity. The small eccentricity failure sign is concrete crushing, and the large eccentricity failure sign is the steel yield failure under tension.
(2) When the corrosion rate ranges from 0% to 9%, the reduction in cracking load ranges from 27.8% to 33.9%, the reduction in ultimate load ranges from 23.9% to 26.7%, and the reduction in residual load ranges from 32.8% to 34.0%.
(3) Based on the strain development law of concrete and I-shaped steel in eccentric component tests, the critical corrosion rate of the primary support of the section steel frame meeting the plane cross-section assumption was obtained.
(4) The contribution rate of geometric and mechanical parameters of the section steel frame caused by corrosion to the primary support bearing capacity attenuation is 32.69%~37.75%, the contribution rate of concrete mechanical parameters attenuation caused by rust expansion is 18.36% ~20.8%, and the contribution rate of bond slip degradation between the section steel frame and concrete caused by corrosion is 43.09% ~46.58%.

ACKNOWLEDGMENTS

This research was funded by the National Natural Science
Foundation of China (Grant No. 52308417).

REFERENCES

Feng, K., Yang, R., Geng, J., Cao, X., He, C., Yang, W., Zhang, H., 2021. Experimental investigation of mechanical-performance deterioration of HFRC segment under combined effect of sustained loading and chloride-induced corrosion. Tunnelling And Underground Space Technology 114.

Hou, L., Guo, S., Zhou, B., Chen, D., Aslani, F., 2019. Bond-slip behaviour of corroded reinforcement and ultra-high toughness cementitious composite in flexural members. Construction And Building Materials 196, 185–194.

Jin, Z.-q., Zhao, T.-j., Gao, S., Hou, B.-r., 2013. Chloride ion penetration into concrete under hydraulic pressure. Journal Of Central South University 20, 3723–3728.

Liu, D., Zhong, F., Huang, H., Zuo, J., Xue, Y., Zhang, D., 2021. Present Status and Development Trend of Diagnosis and Treatment of Tunnel Lining Diseases. China Journal of Highway and Transport 34, 178–199.

Wang, J., Niu, D., Wang, Y., He, H., Liang, X., 2019. Chloride diffusion of shotcrete lining structure subjected to nitric acid, salt-frost degradation, and bending stress in marine environment. Cement & Concrete Composites 104.

Zhang, Y., Wang, M., Yu, L., Guo, X., Wang, Z., Li, C., 2022. Experimental and numerical research on the influence of steel arch frame corrosion on security of supporting system in subsea tunnel. Tunnelling And Underground Space Technology 120.

Tunnelling for a Better Life – Yan, Celestino, Thewes & Eberhardt (Eds)
© 2024 The Author(s), ISBN 978-1-032-80042-4
Open Access: www.taylorfrancis.com, CC BY-NC-ND 4.0 license

Effect of excavation on the pipe roof deformation under the action of the pipe roof-beam support system

Wen Zhao, Qian Bai* & Dongli Pi
School of Resources and Civil Engineering, Northeastern University, Shenyang, China

ABSTRACT: The pipe roof method can significantly reduce the deformation resulting from excavation and is widely used in the construction of underground spaces. Based on Shifu Road station of Shenyang Metro Line 4, this paper studies a new support system for constructing ultra-shallow buried subway stations, named pipe roof - beam support system. Firstly, the influence of large section excavation on pipe roof deformation under different parameters such as beam spacing, transverse span, burial depth and steel pipe diameter was analysed by numerical simulation. Then, according to the linear regression model, the effect degree of the key parameters on the pipe roof deformation was investigated. Finally, based on the elastic foundation beam theory, a calculation model of pipe roof deformation was established and compared with the numerical simulation results. The results show that: The pipe roof deformation due to excavation is linearly increasing in relation to the beam spacing and exponentially increasing in relation to the transverse span. Increasing the diameter of the steel pipe can effectively reduce the pipe roof deformation due to the increased beam spacing. The influence on the pipe roof deformation is in descending order of magnitude: transverse span, beam spacing, steel pipe diameter and burial depth. The results of the pipe roof deformation at different pipe diameters calculated according to the Pasternak double-parameter elastic foundation beam theory are in good agreement with the numerical simulation results.

Keywords: Subway station, Pipe roof method, Excavation, Pipe roof deformation, Numerical simulation, Theoretical model

1 INTRODUCTION

Subway is generally in the prosperous area, with the continuous development of underground space, the environment of underground engineering is increasingly complex, which is difficult to construct using double-side heading method, pile-beam-arch method and other traditional tunnelling method, and it is difficult to ensure the safety of construction (Fang et al., 2011). To reduce the surface settlement caused by the excavation construction of subway station, a pipe-roof method is increasingly popular to use (Xie et al., 2019; Lunardi, 1990). To solve the problem, low bearing capacity and flexural stiffness, of traditional pipe-roof structure, the steel tube slab (STS) method (Jia et al., 2018; 2020; Lu et al., 2023) and the small pipe-roof-beam method (Bai et al., 2023) were proposed, which are successful in minimizing the soil disturbance caused by the excavation construction of subway station.

Jin et al. (2011) explored the surface settlement mechanism and structural forces of the NTR method under different construction conditions using a combination of numerical simulation and site monitoring, and investigated the damage mode and flexural performance of the rib-beam structure of the NTR pipe-roof structure through laboratory tests.

Lu et al. (2022a) studied the deformation characteristics of SSCP structure by numerical simulation, and analysed the effect of parameters such as longitudinal spacing of steel support, size of transverse steel support and vertical steel support on the deformation of steel support and surface settlement, and obtained the optimal parameter combination of steel support for SSCP structure. Subsequently, the wall thickness and chord height ratio of a single steel pipe in the pipe-roof structure were studied, and it was concluded that the change of wall thickness and chord height ratio had significantly impact on the bearing capacity of the pipe-roof structure (Lu et al., 2022b).

*Corresponding author: baiqianneu@163.com

DOI: 10.1201/9781003495505-182

Jia et al. (2019) conducted laboratory tests and numerical simulation to study the bending performance and damage mode of STS structure, and the results showed that the STS method can improve the transverse stiffness of the pipe-roof structure. Subsequently, the surface settlement mechanism caused by STS structure deformation using a combination of numerical and monitoring investigation, indicating that the STS structure as a kind of pre-support system has significant advantages.

In summary, many investigations have conducted on the support mechanism of pipe-roof, soil deformation caused by excavation under pipe-roof support. However, the diameter of the steel pipe for the new pipe-roof structure has not yet been systematically studied. Steel pipe is an important component of the pipe-roof structure, and its diameter can affect the mechanical properties of the structure and the surface settlement. Hence, it is critical for the design and construction of pipe-roof to determine the relationship between steel pipe diameter and other parameters. It has an important practical significance of guidance that study effect of different steel pipe diameter on the structural deformation mechanism, summarize the deformation characteristics of the main structure and surrounding soil with different pipe-roof diameters and different parameters, and a reasonable choice of the pipe diameter of the pipe roof structure.

2 NUMERICAL SIMULATION MODELING

In the practical construction of tunnel engineering, the deformation control standards for the pipe-roof-beam structure are extremely strict. Therefore, researching the deformation characteristics of the pipe-roof-beam structure is of significant importance. In this investigation, a three-dimensional numerical model was established using Midas GTS NX software. Based on previous finite element models, a numerical analysis model of the pipe-roof -beam structure under soil pressure is calibrated, using the same material properties, element types, component contact forms, and meshing methods. To emphasize the variable of steel pipe diameter, simplifications are made to the overall station structure and excavation method. The side piles are simplified as diaphragm walls following the principle of equivalent stiffness, while considering the case without temporary support. The deformation patterns of station excavation under the most unfavorable conditions are studied, and the soil excavation method employs the benching tunnelling method. Along the longitudinal direction of the steel pipe, the analysis is conducted over one span of the pipe-roof-beam structure. A schematic representation of the finite element model of the pipe-roof-span structure is shown in Figure 1. Subsequently, the research investigates the influence of different beam spacing, transverse span, burial depth, and other parameters on the deformation performance of the pipe-roof-beam structure with varying steel pipe diameters.

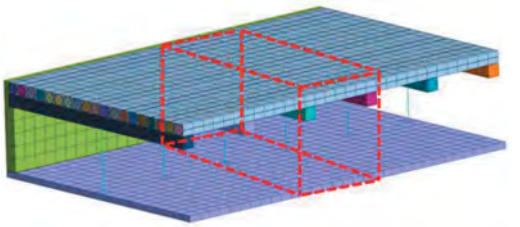

Figure 1. Schematic diagram of finite element model of the pipe-roof structure.

2.1 *Calculation basic assumptions*

(1) Surface settlement caused by pipe-roof construction can be controlled through grouting between the pipes to achieve zero settlement or controlled pre-uplift before excavation. Therefore, this paper's simulation did not take into account surface settlement caused by pipe jacking.
(2) The subway station has undergone dewatering treatment of the surrounding soil prior to construction. Hence, the impact of groundwater is not considered.
(3) In underground engineering simulations, the majority of soil models use the Mohr-Coulomb model. However, the traditional Mohr-Coulomb model does not consider the impact of the soil's second principal stress yield conditions and neglects the effects of soil unloading, resulting in significant disparities between simulation results and reality. To ensure the accuracy of numerical simulations, this paper employs the Modified Mohr-Coulomb constitutive solid element model to better simulate the soil unloading process. Soil calculations are conducted using the Modified Mohr-Coulomb constitutive model, assuming homogeneity and isotropy within the same soil.
(4) The structures, including pipe-roof, station linings, beams, columns, and slabs, are treated as homogeneous and isotropic materials and are modeled using an elastic constitutive model.

2.2 *Parameter selection*

The primary geological stratum on the project site consists predominantly of sandy soil. Based on geological conditions, it is known that only a small amount of miscellaneous fill soil exists at the top of the stratum. The pipe-roof structure as a whole is situated within the sandy soil stratum, and the physical and mechanical properties of these sandy soil layers are very similar. Therefore, the stratum is simplified to homogeneous sandy soil for analysis in the model. Detailed structural parameters can be found in Table 1.

Table 1. Indexes of stratum mechanics parameters.

soil	γ/ kN·m^{-3}	c/ kPa	φ/ °	E/ MPa	Eu/ MPa	μ
medium-coarse sand	20	2	34	31.6	252.8	0.25

Notes: γ is volumetric weight; c is cohesive forces; φ is internal friction angle; E is Elastic Modulus; Eu is unloading modulus; μ is Poisson ratio.

The subway station primarily consists of a composite structure composed of arches, beams, side walls, and steel columns to collectively bear loads. In order to better describe the deformation characteristics and mechanical properties of each structural component, solid elements were employed to simulate the arches, beams, bottom slab, side walls, and grouting between arches, while beam elements were used to simulate the intermediate columns. The beam elements are considered isotropic and yield-free linear elastic materials, approximated as ideal elastic bodies. It is assumed that the vertical displacements between the soil and intermediate columns were negligible. The main structural parameters were determined based on the actual engineering design data and the 'Code for Design of Concrete Structures' (GB50010-2010, 2010). Specific values for the main structural components are provided in Table 2.

Table 2. Parameters of structural materials.

Components	γ/kN·m^{-3}	E/MPa	u
Pipe-roof	30.0	61000	0.25
Bottom slab	25.0	40000	0.20
Beams	26.0	45000	0.20
Side walls	30.0	61000	0.25
Intermediate columns	25.0	69000	0.25
Grouting between arches	20.0	500	0.30
Second lining	24.0	20000	0.20

2.3 *Network segmentation*

Using the Midas GTS NX finite element analysis software, a three-dimensional finite element model was constructed for nonlinear construction stage analysis, as depicted in Figure 2. According to the Saint-Venant principle (Xia, 2021), the stress and strain resulting from tunnelling polit excavation only affect the region within a maximum excavation span of 3 to 5 times the polit's centerline distance. Along this boundary, it is assumed that the displacements caused by excavation were negligible. To minimize the influence of boundary constraints on the calculation results, the model dimensions were set as follows: 140 m in the horizontal direction, 75 m in the vertical direction, and one span length in the longitudinal excavation direction. In the model, the positive X-axis pointed horizontally to the right, the positive Y-axis was aligned with the station excavation direction, and the positive Z-axis extended vertically upward from the ground.

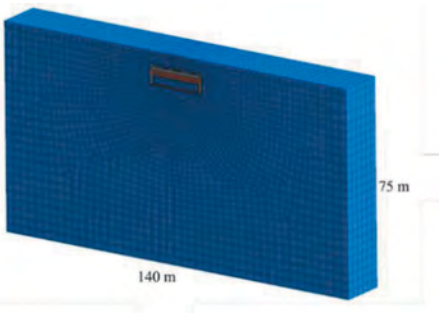

Figure 2. Schematic diagram of finite element calculation model.

3 EFFECT OF PARAMETERS ON PIPE-ROOF DEFORMATION

3.1 *Steel pipe diameter*

To analyze the deformation of the pipe-roof in a cross-support system with steel pipes of different diameters within various ranges, seven different steel pipe diameters were selected for investigation: 300, 600, 900, 1200, 1500, 1800, and 2100 mm. The remaining computational parameters were as follows: beam spacing (L) is 8 m, transverse span (S) is 20 m, and the burial depth of the overlying soil (H) is 5 m.

Figure 3 illustrates the lateral deformation curves of the station's pipe-roof structure after excavation with different diameter steel pipe support. It can be obtained that under varying steel pipe diameters, the deformation trend of the pipe-roof structure is fundamentally consistent. The overall arch structure exhibits a sinking tendency, and the deformation curve closely approximates a parabolic shape. Deformation values on both sides of the pipe-roof structure are relatively small, gradually increasing as they approach the midpoint, where they reach their maximum values. Simultaneously, the end sections of the pipe-roof structures with different steel pipe diameters show a slightly larger deformation value than 0 mm, indicating an upward deformation at the ends. This can be attributed to the upward support exerted by the side walls at the ends of the pipe-roof structure. The deformation values at the mid-span of the pipe-roof decrease as the steel pipe diameter increases. For steel pipe diameters ranging from 300 mm to 2100 mm, the corresponding maximum deformation values of the arch structure are 19.5 mm, 14.1 mm, 11.8 mm, 11.2 mm, 10.2 mm, 9.7 mm, and 8.5 mm, respectively. Compared to

a steel pipe diameter of 300 mm, increasing the steel pipe diameter from 600 mm to 2100 mm results in a reduction of 27.7%, 39.5%, 42.6%, 47.7%, 50.3%, and 56.4% in the maximum pipe-roof deformation values. The increase in steel pipe diameter leads to an increase in the pipe-roof structure's flexural stiffness, subsequently reducing the deformation values. Thus, it can be concluded that within the range of different steel pipe diameters for the pipe-roof, the variation in steel pipe diameter significantly influences the maximum pipe-roof deformation values.

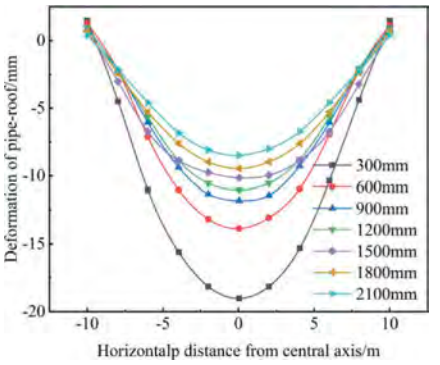

Figure 3. Deformation curve of pipe-roof in the cross section of station span.

3.2 *Spacing between beams*

The vertical deformation values at the mid-span position of the 900 mm diameter pipe-roof structure were extracted under five different beam spacing conditions, as depicted in Figure 4. It can be observed that under varying beam spacing, the deformation trend of the pipe-roof structure remains largely consistent. The pipe-roof structure, as a whole, exhibits a sinking trend, with the deformation curve closely resembling a parabolic shape. Deformation values at both sides of the pipe-roof structure are relatively small, gradually increasing as they approach the mid-span position, where they reach their maximum values. Simultaneously, the end sections of the pipe-roof structures with different beam spacing exhibit identical deformation values, slightly greater than 0 mm, indicating upward deformation at the ends. This is attributed to the upward support exerted by the side walls at the ends of the pipe-roof structure. The deformation values at the mid-span of the pipe-roof increase with an increase in beam spacing. The corresponding maximum deformation values of the pipe-roof structure are 11.8 mm, 18.8 mm, 31.3 mm, 47.4 mm, and 61.8 mm for beam spacings of 4 m, 8 m, 12 m, 16 m, and 20 m, respectively. For each 4 m increase in beam spacing, the maximum pipe-roof deformation values increase by 7.0 mm, 12.5 mm, 16.1 mm, and 14.4 mm, with growth rates of 59.3%, 66.5%, 51.4%, and 30.4%, respectively. From a beam spacing of 6 m to 24 m, the difference in maximum deformation values is 50.0 mm, with a growth rate of 423.7%. Increasing beam spacing similarly leads to a significant increase in arch structure deformation.

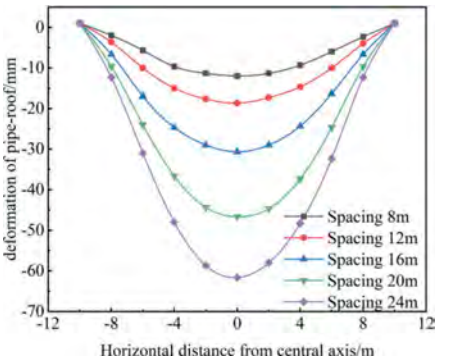

Figure 4. Deformation curves of 900 mm diameter pipe-roof structure under different beam spacing.

3.3 *Transverse span*

Taking the 900 mm diameter pipe-roof structure as an example, the extracted vertical deformation values at the mid-span position of the pipe-roof structure are shown in Figure 5 under five different transverse span conditions. It can be obtained that under varying transverse spans, the deformation trend of the pipe-roof structure remains fundamentally consistent. The pipe-roof structure, as a whole, exhibits a sinking trend, and the deformation curve closely approximates a 'bowl' shaped parabola. Deformation values at both sides of the pipe-roof structure are close to 0 mm. As one moves from the sides towards the mid-span position, the deformation values gradually increase and reach their maximum at the mid-span. The mid-span pipe-roof deformation values increase with an increase in transverse span. The corresponding maximum deformation values of the pipe-roof structure are 11.8 mm, 21.0 mm, 31.8 mm, 44.3 mm, and 56.5 mm for transverse spans of 20 m, 22.5 m, 25 m, 27.5 m, and 30 m, respectively. When the transverse span increases from 20 m to 30 m, with each 2.5 m increment, the maximum pipe-roof deformation values increase by 9.2 mm, 10.8 mm, 12.5 mm, and 12.3 mm, with growth rates of 77.9%, 51.4%, 39.3%, and 27.8%, respectively. While the pipe-roof deformation gradually increases with larger transverse spans, the growth rates progressively decrease. The difference in maximum deformation values for the pipe-roof structure's transverse spans from 20 m to 30 m is 44.7 mm, with a growth rate of 378.8%. Therefore, an increase in the transverse span of the pipe-roof structure similarly leads to a significant increase in pipe-roof structure deformation.

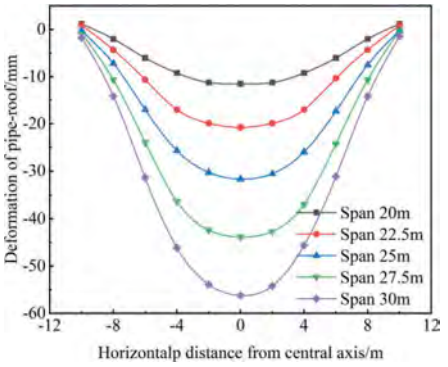

Figure 5. Surface settlement curve of 900 mm diameter pipe curtain at different lateral spans.

3.4 *Soil burial depth*

Taking the 900 mm diameter pipe-roof structure as an example, the extracted vertical deformation values at the mid-span position of the pipe-roof structure under five different burial depth conditions are shown in Figure 6. It can be observed that under varying burial depths, the deformation trend of the pipe-roof structure remains fundamentally consistent. The pipe-roof structure, as a whole, exhibits a sinking trend, and the deformation curve closely approximates a 'bowl' shaped parabola. As one moves from the sides towards the mid-span position, the deformation values of the pipe-roof structure gradually increase and reach their maximum at the mid-span. The mid-span pipe-roof deformation values increase with an increase in burial depth. When the burial depth increases from 3 m to 11 m, with each 2 m increment, the growth rates of pipe-roof deformation are 77.96%, 51.42%, 39.30%, and 27.53%, respectively. As burial depth increases, the growth rate of pipe-roof deformation gradually decreases. Therefore, it can be concluded that burial depth has a relatively minor impact on pipe-roof deformation.

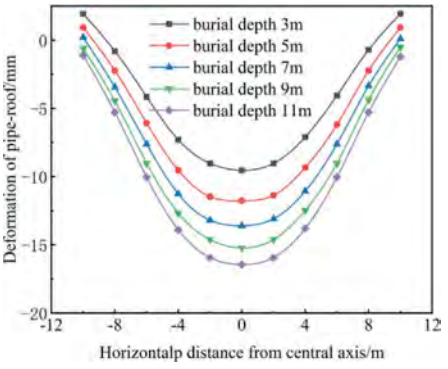

Figure 6. Deformation curve of 900 mm diameter pipe curtain under different burial depth of soil.

4 EFFECT MAGNITUDE

To investigate the pipe-roof deformation caused by soil excavation under pipe-roof structure support, a multivariate linear regression analysis was conducted using SPSS software. In this analysis, the pipe-roof diameter was treated as the independent variable, while three factors, namely beam spacing, transverse span, and burial depth, were set as independent variables. The pipe-roof deformation was defined as the dependent variable.

4.1 *Steel pipe diameter and beam spacing*

From Figures 7 and 8, it can be obtained that the histogram of pipe-roof deformation exhibits an overall favorable pattern of normal distribution. In the cumulative probability plot of standardized residuals, the residuals closely adhere to the vicinity of the straight line, indicating a pronounced adherence to the normal distribution pattern.

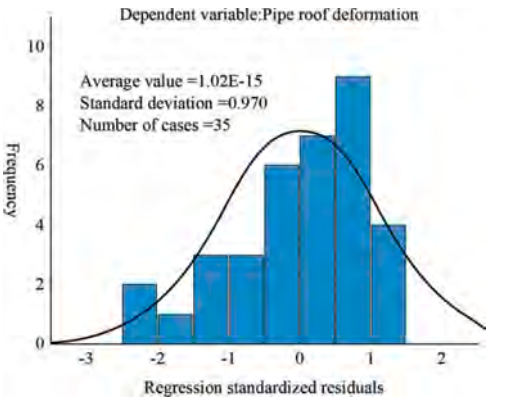

Figure 7. Histogram of surface settlement residuals for pipe-roof structures.

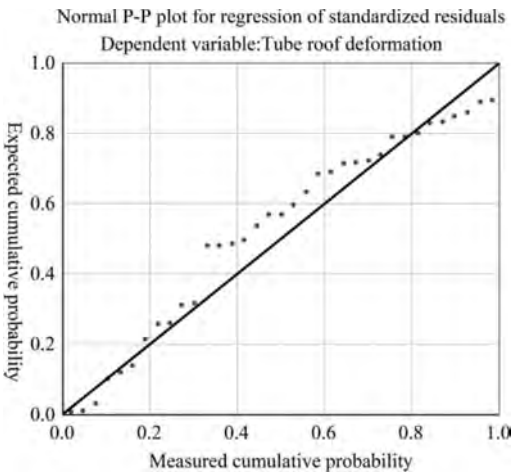

Figure 8. Cumulative probability map of standardized residuals of surface settlement of pipe-roof structures.

4.2 *Steel pipe diameter and transverse span*

Figures 9 and 10 reveal that the histogram of pipe-roof deformation generally follows a well-defined pattern of normal distribution. In the cumulative probability plot of standardized residuals, the residuals closely align with the vicinity of the straight line, indicating a clear adherence to the normal distribution pattern.

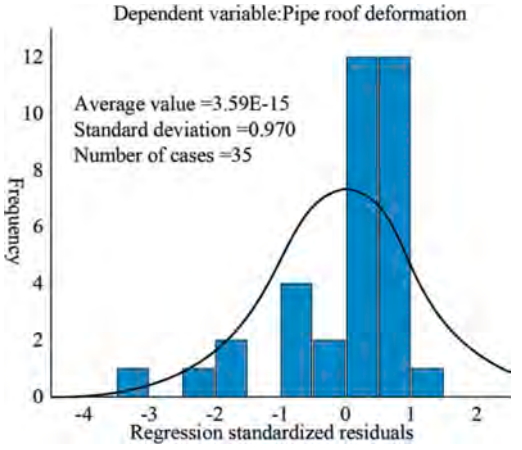

Figure 9. Histogram of surface settlement residuals for pipe-roof structures.

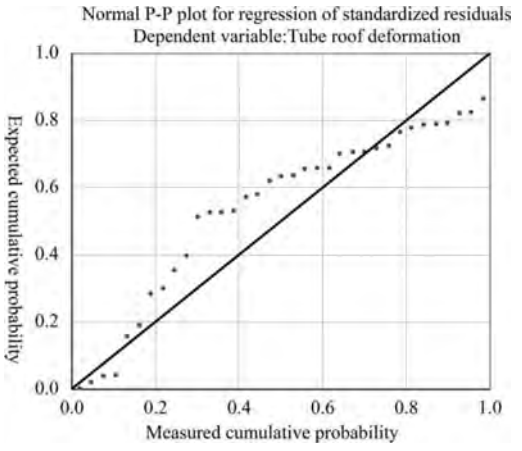

Figure 10. Cumulative probability map of standardized residuals of surface settlement of pipe-roof structures.

4.3 *Steel pipe diameter and soil burial depth*

Figures 11 and 12 illustrate that the histogram of pipe-roof deformation generally exhibits a strong pattern of normal distribution. In the cumulative probability plot of standardized residuals, the residuals closely adhere to the vicinity of the straight line, indicating a clear adherence to the normal distribution pattern.

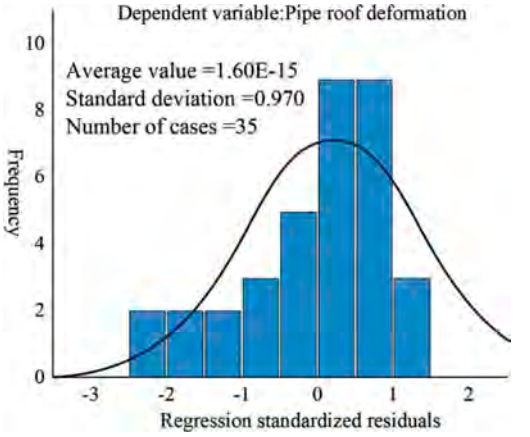

Figure 11. Histogram of surface settlement residuals for pipe-roof structures.

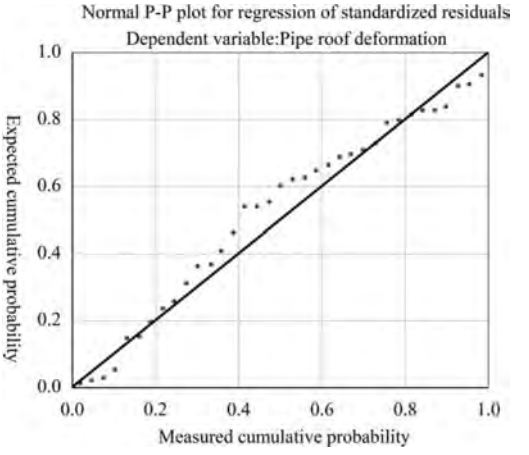

Figure 12. Cumulative probability map of standardized residuals of surface settlement of pipe-roof structures.

Through multivariate linear regression analysis conducted in SPSS software, a high level of fit was obtained for the relationship between pipe-roof deformation caused by soil excavation under pipe-roof structure support with different steel pipe diameters and parameters such as beam spacing, transverse span, and burial depth. This demonstrates a strong linear relationship between pipe-roof deformation and these parameters. A regression equation for burial depth was derived from the software analysis. Additionally, the overall frequency histogram of standardized residuals exhibits a favorable pattern of normal distribution, and in the cumulative probability plot of standardized residuals, the residuals are predominantly distributed near the straight line, confirming the accuracy of the regression equation. Based on the magnitude of the absolute values of the standardized regression coefficients, the influence magnitude on pipe-roof

deformation can be ranked as follows: transverse span > beam spacing > steel pipe diameter > burial depth. Therefore, the parameter with the greatest impact on pipe-roof deformation displacement is the transverse span of the pipe-roof structure, followed by beam spacing, then steel pipe diameter, and the parameter with the least impact is burial depth.

5 CALCULATION MODEL OF DEFORMATION

Based on the Pasternak elastic foundation beam theory, this study focuses on single steel pipe concrete structures used in pipe-roof construction. It aims to establish deformation calculation model for these structures and analyze the excavation-induced deformation patterns under various steel pipe diameters.

The Pasternak elastic foundation beam model assumes the presence of a shear layer between the foundation and the beam, where the shear layer can only undergo lateral shear deformation (Liu, 2021). This introduces interacting shear forces between independent springs to mitigate foundation discontinuities [67]. Based on the Pasternak elastic foundation beam theory, this study focuses on single steel pipe concrete structures within pipe-roof construction, with its simplified model shown in Figure 13.

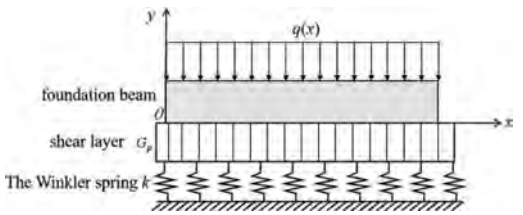

Figure 13. Schematic diagram of the Pasternak calculation model.

This paper employs a semi-infinite elastic foundation beam analysis for the mechanical model of the pipe-roof. The construction of the pipe-roof's mechanical model during the excavation of the tunnel is illustrated in Figure 14.

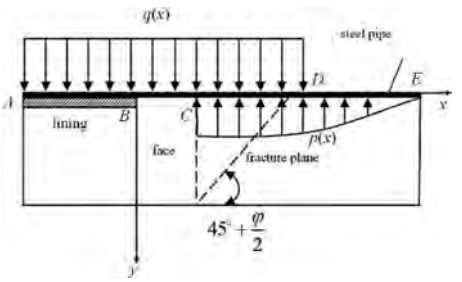

Figure 14. Pasternak-based two-parameter elastic foundation beam tunnel construction pipe-roof force calculation diagram.

5.1 *Governing differential equations*

Under the action of the soil pressure $q(x)$ from the soil, the relationship between the foundation reaction $p(x)$ and the displacement $\omega(x)$ in the Pasternak dual-parameter elastic foundation beam model is expressed as follows:

$$p(x) = k\omega(x) - G_p \frac{d^2\omega(x)}{dx^2} \tag{1}$$

where k is coefficient of subgrade reaction, and G_p is the shear modulus of the foundation, associated with the foundation's shear deformation.

When the overburden pressure $q(x) = q_0$ and the foundation reaction $p(x) = 0$ in section BC, the governing equation for section BC is:

$$EI\frac{d\omega^4(x)}{dx^4} = b_0 q_0 \tag{2}$$

When the overburden pressure $q(x) = q_0$ and the foundation reaction is given by equation (1) in section CD, the governing equation for section CD is:

$$EI\frac{d\omega^4(x)}{dx^4} - G_p b^* \frac{d\omega^2(x)}{dx^2} + kb^*\omega(x) = b_0 q_0 \tag{3}$$

When the overburden pressure $q(x) = 0$ and the foundation reaction is given by equation (1) in section DE, the governing equation for section DE is:

$$EI\frac{d\omega^4(x)}{dx^4} - G_p b^* \frac{d\omega^2(x)}{dx^2} + kb^*\omega(x) = 0 \tag{4}$$

where b^* represents the equivalent width of the beam, and b_0 is the width of the elastic foundation beam, i.e., the steel pipe diameter.

$$b^* = b_0 + \left(G_p/k\right)^{1/2} \tag{5}$$

5.2 *Solution of the governing differential equations*

The solution to the governing equation for section BC is:

$$\omega_1(x) = \frac{b_0 q_0}{24EI}x^4 + A_1x^3 + A_2x^2 + A_3x + A_4 \tag{6}$$

The solution to the governing equation for section CD is:

$$\begin{gathered}\omega_2(x) = e^{\alpha x}(B_1\cos\beta x + B_2\sin\beta x) + \\ e^{-\alpha x}(B_3\cos\beta x + B_4\sin\beta x) + \\ \frac{q_0}{kb^*}\left[1 - ch\beta(x-s-d)\cos\beta(x-s-d)\right]\end{gathered} \tag{7}$$

The solution to the governing equation for section DE is:

$$\omega_3(x) = e^{\alpha x}(B_1 \cos \beta x + B_2 \sin \beta x) + e^{-\alpha x}(B_3 \cos \beta x + B_4 \sin \beta x) \quad (8)$$

5.3 *Deformation of pipe-roof with different diameters*

The maximum pipe-roof deformations were extracted for steel pipe diameters of 300 mm, 600 mm, 900 mm, 1200 mm, 1500 mm, 1800 mm, and 2100 mm in numerical simulations, and these values were compared with the theoretical calculations as shown in Figure 15. Overall, the two approaches yield relatively close pipe-roof deformation results. It is worth noting that the deformations calculated based on the Pasternak model theory are consistently greater than the numerical simulation results, indicating a conservative tendency in the theoretical formulas proposed in this study.

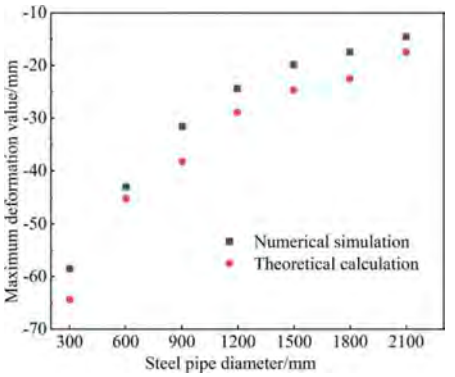

Figure 15. Comparison of theoretical and numerical simulation values of pipe-roof deformation.

The comparative results between theoretical calculations and numerical simulations for different steel pipe diameters are presented in Table 3. After computation, it is observed that the average error between theoretical calculations and numerical simulations for various steel pipe diameters is 18.95%. Thus, there is a good consistency between the theoretical calculations and numerical simulation results. The reason for the theoretical calculations yielding larger pipe-roof deformation values compared to numerical simulations can be attributed to the actual dense arrangement of steel pipes, which results in a favorable synergistic effect between the pipes, effectively restraining soil deformation and relaxation. In contrast, the calculations only consider the stress on individual steel pipes without considering the combined effects between them, leading to larger deformation values.

6 CONCLUSIONS

This study investigated the effect of parameters including beam spacing, transverse span of pipe-roof structure and burial depth on the deformation mechanism of pipe-roof structure is through numerical simulation. Subsequently, the deformation calculation model of pipe-roof structure with different diameters is established, as well as the influence of different parameters on the selection of reasonable diameter of steel pipe was explored. The following conclusions are drawn:

(1) The pipe-roof structure and beams are arranged crosswise to bear the upper load together, which effectively control the surface settlement. The diameter of the steel pipe has a significant effect on the deformation characteristics of the pipe-roof structure. The trend of surface settlement groove is to gradually gather to the center of the surface, which is constant with pipe-roof deformation, showing a "basin"-shaped settlement curve.
(2) The maximum value of pipe-roof deformation has a linear relationship with the spacing of beams, and the increasing pipe-roof deformation due to the increase of spacing of beams can be effectively reduced by increasing the diameter of steel pipes; the maximum value of pipe-roof deformation has an exponential relationship with the transverse span.
(3) The regression equations regarding the pipe-roof deformation between the steel pipe diameter and the parameters of beam spacing, transverse span, and burial depth, respectively, were obtained, and the accuracy of the regression equations was verified by standardized residual frequency histograms.
(4) The deformation calculation model of pipe-roof structure of different diameters based on Pasternak's elastic foundation beam theory is obtained, and the theoretical calculated values are in good agreement with the numerical simulation results, with an average error of 18.95%.

ACKNOWLEDGMENTS

The research described in this paper was supported by the National Science Foundation of China (No. 51878127).

Table 3. Comparison of theoretical calculation and numerical simulation results under different steel pipe diameters.

Steel pipe diameter (mm)	300	600	900	1200	1500	1800	2100
Theoretical results (mm)	64.33	45.21	38.15	28.79	24.56	22.41	17.25
Simulation results (mm)	58.5	42.9	31.3	24.2	19.6	17.1	14.3
Average error	9.89%	5.43%	21.88%	19.02%	25.31%	30.67%	20.46%

REFERENCES

Bai, Q., Zhang, Y., Zhao, W., et al, 2023. Construction of subway station using the small pipe roof-beam method: A case study of Shifu Road station in Shenyang. Tunn. Undergr. Sp. Tech. 135, 105000.

Fang, Q., Zhang, D., Wong, L.N.Y., 2011. Environmental risk management for a cross interchange subway station construction in China. Tunn. Undergr. Sp. Tech. 26(6): 750–763.

GB 50010-2010, 2010b. Code for design of concrete structures, China Building Industry Press, Beijing. (In Chinese).

Jia, P.J., Zhao, W., Chen, Y., et al, 2018. A case study on the application of the steel tube slab structure in construction of a subway station. Appl. Sci. 8(9), 1437–1447.

Jia, P., Zhao, W., Guan, Y., et al. 2019. Experimental study on the flexural behavior of steel tube slab composite beams and key parameters optimization. Adv. Struct. Eng. 22(11), 2476–2489.

Jia, P.J., Zhao, W., Khoshghalb, A., et al, 2020. A new model top redict ground surface settlement induced by jacked pipes with flanges. Tunn. Undergr. Sp. Tech. 98 (12), 103–330.

Jin, C.F., Yan, S., Niu, P., 2011. Local Buckling Analysis for Large Diameter Underground Jacked Steel Tubes under External Load. Key Engineering Materials. Trans Tech Publications Ltd. 501–504.

Liu, X.Y., 2021. Mechanical response and evaluation of pile foundation under the influence of tunnel construction in water-rich stratum. Beijing Jiaotong University, Beijing, China. (In Chinese).

Lu, B., Dong, J., Zhao, W., et al, 2022a. Novel pipe-roof method for a super shallow buried and large-span metro underground station. Undergr. Space. 7(1), 134–150.

Lu, B., Zhao, W., Du, X., et al, 2022b. Analysis of Ultimate Bearing Capacity and Parameters of Steel Support Cutting Pipe Roofing Structure. Transport. Res. Rec. 2676 (4), 348–36.

Lu, B., Jia, P., Zhao, W., et al, 2023. Longitudinal mechanical force mechanism and structural design of steel tube slab structures. Tunn. Undergr. Sp. Tech. 132, 104883.

Lunardi P.J., 1990. The cellular arch method; technical solution for the construction of the Milan railway's Venezia station. Tunn. Undergr. Sp. Tech. 5(4), 351–356.

Xia X.Z., 2021. Inverse analysis of tunnel surrounding rock based on DE-BP neural network and research of support parameters. Dalian University of Technology, Dalian, Liaoning, China. (In Chinese).

Xie, X., Zhao, M., Shahrour, I., 2019. Experimental study of the behavior of rectangular excavations supported by a pipe roof. Appl. Sci. 9(10), 2082.

Tunnelling for a Better Life – Yan, Celestino, Thewes & Eberhardt (Eds)
© 2024 The Author(s), ISBN 978-1-032-80042-4
Open Access: www.taylorfrancis.com, CC BY-NC-ND 4.0 license

Study on horizontal earth pressure of segment considering the influence of backfill grouting pressure

Jian-ling Zhong* & Xiao-chun Zhong
School of Civil Engineering and Transportation, Hohai University, Nanjing, Jiangsu, China

Yong-zhou Jian & Fu-dong Li
CCCC-SHB Fourth Engineering Co., Ltd., Luoyang, Henan, China

ABSTRACT: The reasonable application of backfill grouting pressure is very important for the design of tunnel lining and the control of surface settlement. In order to explore the influence of grouting pressure on the earth pressure of segment, the model test of earth pressure of segment considering the effect of backfill grouting was carried out. On this basis, a numerical analysis model considering the influence of grouting pressure was established, and the distribution law of earth pressure of segment under different grouting pressure and different buried depth was obtained. The results show that: 1) The distribution rules of numerical simulation and model test results are basically the same. With the increase of burial depth, the more uniform the earth pressure distribution of the whole circumferential segment is. 2) the vertical earth pressure and horizontal earth pressure acting on the segment show a parabola distribution of large in the middle and small on both sides. 3) The grouting pressure has a significant effect on the earth pressure of the segment, but has little influence on the ground reation and the coefficient of ground reation. The earth pressure of the segment increases linearly with the increase of grouting pressure. 4) When the buried depth of the tunnel is shallow, the lateral earth pressure coefficient is suggested to be 0.07-0.13 higher than the coefficient of erath pressure at rest. When the buried depth is deeper, the lateral earth pressure coefficient is suggested to be 0.1-0.2 higher than the coefficient of erath pressure at rest.

Keywords: shield tunnel, backfill grouting, horizontal earth pressure, lateral earth pressure coefficient, ground reation

1 INTRODUCTION

Shield tunneling method has become the mainstream construction method of shield tunnel construction because of its advantages of convenient construction, little impact on the surrounding environment, safety and efficiency (Hong and Feng, 2020; Editorial department of china journal of highway and transport, 2022; Zhu and Chen, 2001). Backwall grouting is an important means to control the surface settlement during shield tunneling, and the grouting quality after the wall is determined by the grouting quantity and grouting pressure. Too large or too small grouting pressure will affect the ground around the tunnel, and affect the force of the segment to a certain extent.

Attention has been paid to the influence of backfill grouting of shield tail segment on the earth pressure. Many scholars have carried out theoretical analysis and model tests. Koyama et al (1998,2003) studied the effect of backfill grouting on the earth pressure of tunnel segment through model test. The results show that when the grouting pressure is low, the earth pressure is low and uniformly distributed, and when the grouting pressure is high, the earth pressure on the segment is high and uneven. Liu et al (2020) studied the effect of grouting on the surrounding ground and the filling process of grouting through small-scale model tests. The results show that the distribution of grouting pressure in the space at the tail of the shield is uneven, and the earth pressure of the segment is more sensitive to the quantity of grouting than the suspension and start-up of the grouting operation. Qin et al (2004) based on the pressure filtration diffusion mode of backfill grouting put forward by fractal theory, considered that the segment pressure increases linearly with the increase of grouting pressure. Ye et al (2009) draw the same conclusion.

*Corresponding author: Jian-ling Zhong 2073969912@qq.com

DOI: 10.1201/9781003495505-183

In the field measurement studies, Bezuijen et al (2004) studied and analyzed the field monitoring data of backfill grouting pressure of Sophia tunnel, and considered that the grouting pressure has an effect on the earth pressure of the segment during construction, and the earth pressure acting on the segment after the final setting of the slurry is mainly water pressure. Li et al (2014, 2022) is based on a large number of field measured earth pressure, which shows that the backfill grouting pressure has an obvious effect on the earth pressure of the segment, and the smaller grouting pressure is beneficial to the long-term stability of the earth pressure acting on the segment. Wang and Hao (2018) by collecting the measured data of 52 typical earth pressure monitoring sections of 35 shield tunnels, the results show that the earth pressure on the segment is uniformly distributed along the circumferential direction, and the lateral earth pressure coefficient ranges from 0.5-2.3. Hashimoto et al (2006) collates and analyzes the field measured data of the earth pressure of the shield tunnel segment, and thinks that in the soft clay stratum, the grouting pressure has little influence on the segment earth pressure, in the hard clay stratum, the earth pressure is mainly affected by the grouting pressure, and in the sand stratum, the distribution of the segment earth pressure considering the grouting pressure is relatively uniform.

In the numerical simulations, Zhu et al (2000) through finite element analysis, the grouting pressure has a great influence on the internal force of the segment, and when the grouting pressure is unevenly distributed, the simulated earth pressure of the segment is closer to the measured value. Kaspere and Meschke (2006) through finite element analysis, the grouting pressure has a great influence on the internal force of the segment, and when the grouting pressure is unevenly distributed, the simulated earth pressure of the segment is closer to the measured value. Wei (2007) obtained the distribution and pattern of the earth pressure in different construction stages by numerical simulation, and the top vertical earth pressure is greater than the horizontal diameter. Ji (2004) used a variable rigid body to simulate the change of slurry properties with time in shield tunnel construction, and the effects of slurry thickness, soil properties, segment stiffness and tunnel buried depth on the earth pressure of the segment are analyzed. the results show that the earth pressure on the segment increases gradually with the construction process, and the deeper the tunnel is buried, the more uniform the earth pressure acting on the segment is.

From the above research, it can be seen that the research on the earth pressure of the segment considering the grouting pressure is mainly on the magnitude, distribution pattern and surrounding stratum deformation. There are few detailed studies on the vertical earth pressure, horizontal earth pressure, ground reation and the variation of lateral earth pressure coefficient of the tunnel under the action of grouting pressure. Therefore, this paper carries out the segment earth pressure model test under the influence of backfill grouting. Based on this, establishes a numerical analysis model considering the influence of backfill grouting pressure, in order to obtain the variation law of earth pressure on the segment under different burial depth and different grouting pressure.

2 ESTABLISHMENT OF NUMERICAL MODEL

2.1 *Numerical model establishment and material parameters determination*

Establish 3D finite element model with size of 60 m×40 m×1 m (length×height×width). The buried depth of shield tunnel is 6 m (15 m), the outer diameter of the segment is 6 m, and the segment thickness is 0.3 m. Due to it is difficult to quantify the grouting layer respectively, it is equivalent to a homogeneous and equal thickness layer, and the main component of the equivalent circle zone is a mixture of soil and slurry, and its elastic modulus and Poisson's ratio are between soil and slurry (Zhang et al, 2002), The thickness is 0.2 m. The values of the finite element model parameters are shown in Table 1.

Mohr Coulomb is used in soil. The tunnel lining and grout layer are simulated by linear elasticity. The tunnel lining is simulated by shell element and its elastic modulus is reduced to a certain extent. The horizontal displacement constraint is applied on the left and right sides of the model, and the vertical displacement constraint is imposed on the bottom.

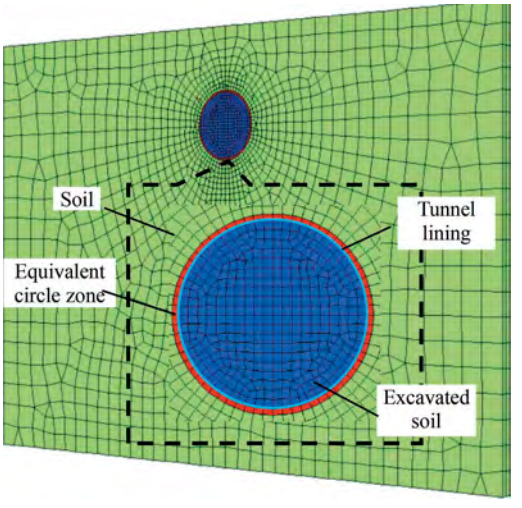

Figure 1. Finite element model of shield tail backfill grouting.

Table 1. Finite element calculation parameter.

Materials \ Properties	Density γ(kN/m^3)	Young's modulus E(MPa)	Shear modulus G(MPa)	Bulk modulus K(MPa)	Poisson's ratio v	Friction angle φ (°)	Cohesion c(kPa)	Coefficient of earth pressure at rest K_0
Soil	19.00	-	11.54	25.00	0.30	20	22	0.5
Tunnel lining	25.00	2.58E4	-	-	0.167	-	-	-
Equivalent circle zone	21.00	-	1.67	2.22	0.30	-	-	-

2.2 *Model condition setting and simulation steps*

In this paper, the effects of different grouting pressures on the earth pressure of segments under 6 m and 15 m burial depths are considered. The grouting pressure is considered according to the uneven distribution, as shown in Figure 2, the pressure gradient is 15 kPa/m, and the grouting pressure mentioned below refers to the pressure value at the top. The grouting pressure of 6 m buried depth is 50 kPa, 70 kPa, 90 kPa, 110 kPa, 130 kPa, 150 kPa. The grouting pressure of 15 m buried depth is 220 kPa, 240 kPa, 260 kPa, 280 kPa, 300 kPa, 320 kPa and 340 kPa respectively.

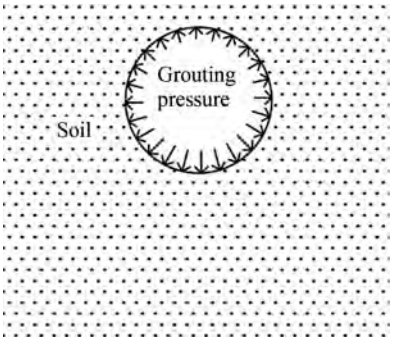

Figure 2. Grouting pressure distribution pattern.

After establishing the finite element model with appropriate parameters, the numerical simulation steps are as follows:

(a) Initial ground stress balance: calculate the gravity stress balance to complete the formation of the initial ground stress field.
(b) Tunnel excavation: kill the soil element, shell element, grouting and other soil element in the range of the core cylinder of tunnel excavation, and apply grouting pressure.
(c) Backfill grouting construction: release the grouting pressure, activate the grouting layer and shell unit, and set the material parameters to complete the segment and grouting operation.
(d) Calculation of shield tunnel construction.
(e) Data collation and analysis.

2.3 *Validation of the numerical model for its effectiveness*

In the numerical simulation process, medium equivalent circle zone parameter reduction, boundary condition setting and load step setting have a great influence on the numerical calculation results. Therefor the accuracy of the numerical calculation results should be verified.

In the early stage, the test equipment was developed and the indoor model test was carried out (Zhong et al, 2023). The influence of construction factors such as different buried depth, different backfill grouting density, segment attitude and grouting filling rate on the segment earth pressure of shield tunnel. The schematic diagram of the test device is shown in Figure 3. The test device is composed of pressure supply system, construction simulation system, data acquisition system and grouting system. The tunnel lining is simulated by plexiglass with outer diameter of 15 cm, inner diameter of 14 cm and thickness of 0.5 cm with a density of 1.18 g/cm3. The elastic modulus is 2300 MPa, and the Poisson's ratio is about 0.2. In the tank, the layered filled sand simulation formation, the density of sand is 1.59 g/cm3, The elastic modulus is 30 MPa, the internal friction angle is measured at 32.1° according to the straight shear test, and the cohesive force is 0. The earth pressure of the segment is collected by setting 8 groups of strain miniature earth pressure gauges equidistant from the circumferential direction of the plexiglass segment.

Establish a numerical model with the same size and the same material parameters as the model test done in the previous stage. Mohr Coulomb is used for the soil, the tunnel and grout layers are calculated by linear elasticity. The equivalent circle zone parameters are same as the Table 1. The boundary condition setting is the same as section 1.1. The finite element model is shown in Figure 4, and the calculation results of the comparison are shown in Figure 5.

From the comparison of earth pressure results, the distribution law of numerical simulation and model test results is basically the same. The deviation of the two results is 4.88%, and the erath pressure distribution of the whole peripheral segment is relatively uniform. It is considered that the simplified analysis method calculated in this paper is feasible.

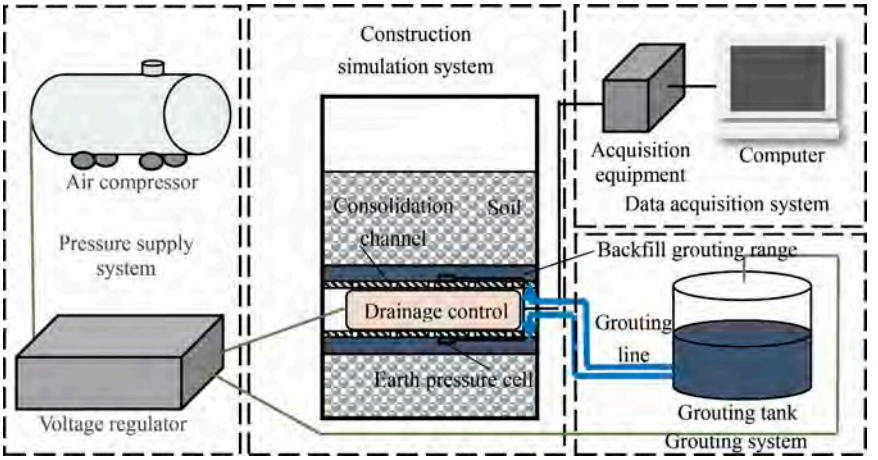

Figure 3. Simplified diagram of laboratory model test device.

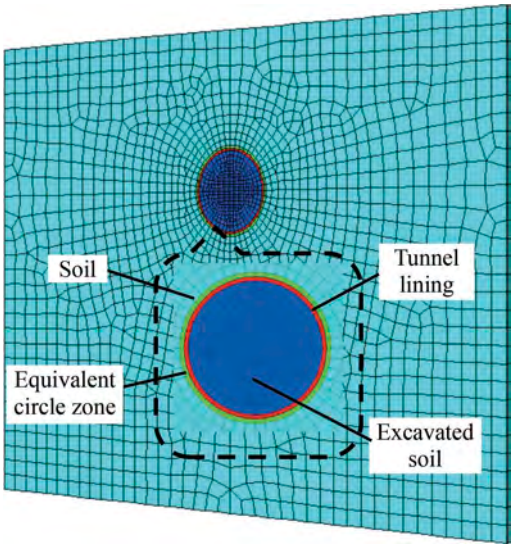

Figure 4. Finite element model of shield tail backfill grouting in laboratory test.

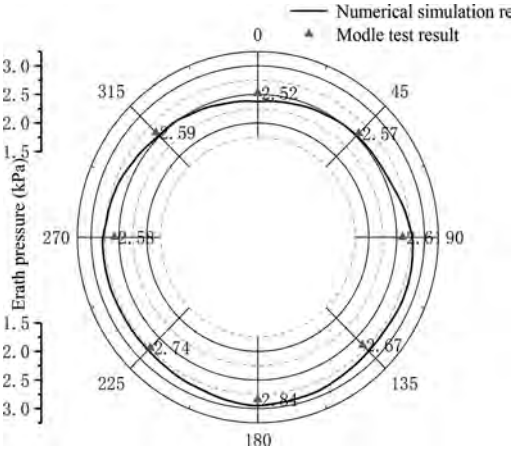

Figure 5. Comparison of earth pressure results.

3 ANALYSIS OF EARTH PRESSURE DISTRIBUTION

According to the modified routine method, in addition to the vertical earth pressure on the segment structure, the difference between the horizontal earth pressure and the vertical erath pressure will also determine the force bending moment in the segment. This paper mainly discusses the horizontal earth pressure and ground reation of the segment to provide reference for the segment structure design.

In the numerical calculation, the stiffness of the tunnel segment is increased by 1000 times, at this time, the elliptic deformation of the segment can be ignored, and the horizontal earth pressure of the segment will no longer include the ground reation. The magnitude and distribution range of the ground reation can be obtained by subtracting the horizontal earth pressure including the ground reation and the horizontal earth pressure excluding the ground reation. Figure 6 shows the numerical calculation of the earth pressure distribution pattern of the segment when the buried depth is 6 m and the grouting pressure is 110kPa.

As can be seen from Figure 6, the vertical earth pressure of the segment is parabolic distribution, which the earth pressure at the top and bottom of the segment is large and small on both sides. This is related to the deformation of the stratum, that is, the relative dislocation of the soil particles. The greater the relative dislocation of the soil particles, the more obvious the decrease of the earth pressure. The relative dislocation of soil particles in

the spandrel is the largest, and the relative dislocation of soil particles in the crown is the smallest, thus forming a parabolic distribution of large in the middle and small at both ends (Zhong et al, 2006).

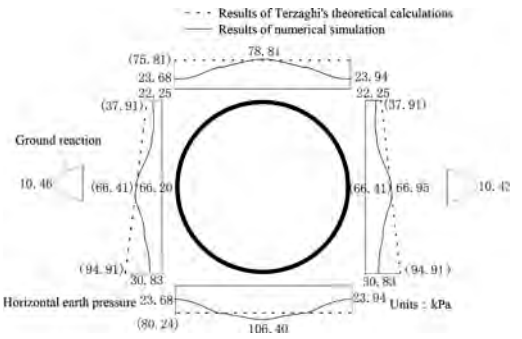

Figure 6. The earth pressure distribution of the segment.

The horizontal earth pressure distribution of the segment is not strictly trapezoidal distribution, but a approximate parabolic distribution. This is because the shield tunneling ring and complete the backfill grouting, slurry is consolidated under the surrounding rock pressure. The initial stress state of the soil layer is that the vertical earth pressure is greater than the horizontal earth pressure, that is, the vertical consolidation deformation of the tunnel is larger than the horizontal consolidation deformation, as shown in Figure 7. Vertical relaxation degree is greater than the horizontal, until the earth pressure is relatively close. From the above analysis, it can be seen that the soil mass at the spandrel is relatively large, and the final performance is that the earth pressure at the spandrel is close to or reaches the active earth pressure state, while the earth pressure at the arch waist changes less. The above analysis results can be obtained from literature (Zheng et al, 2013). According to the resulting tunnel failure mode, the tunnel plastic failure surface is shown in Figure 8. In addition to the arch forming a pressure arch, the horizontal direction also forms an obvious pressure arch.

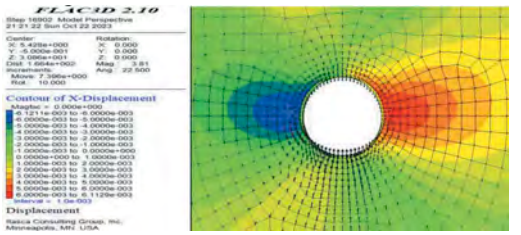

Figure 7. Vector diagram of soil deformation around tunnel.

(a) Destruction of shallow buried tunnel

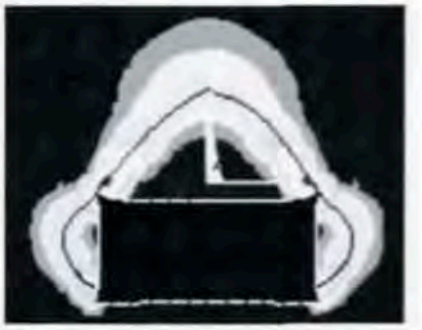

(b) Destruction of deep buried tunnel

Figure 8. Numerical simulation of tunnel failure surface.

4 EFFECT OF GROUTING PRESSURE ON EARTH PRESSURE

4.1 *Earth pressure of segment*

The distribution of earth pressure of segments under two buried depths is shown in Figure 9. Where p represents the backfill grouting pressure (the same below). Where p = 50 kPa ~ 70 kPa is under 6 m buried depth, and p = 220 kPa ~ 340 kPa is 15 m buried depth. It can be seen from Figure 8 that the ratio of earth pressure to crown earth pressure at each position of the segment is between 0.78 and 1.46 at 6 m depth, and between 0.96 and 1.27 at 15 m depth. That is, the distribution of earth pressure acting on the segment tends to be more uniform when the buried depth of the tunnel is deeper.

Under 6 m buried depth, the Terzaghi loose earth pressure of the tunnel crown is 75.81 kPa, and the 15 m buried depth is 147.13 kPa. It can be seen from Figure 10 that with the increase of grouting pressure, the earth pressure at each position of the segment increases linearly, and the earth pressure on the tunnel crown gradually exceeds the Terzaghi loose earth pressure. This is because the increase of grouting pressure can effectively reduce the surface settlement, and the loose deformation of the soil around the tunnel decreases, then the earth pressure acting on the segment gradually changes to the overburden soil weight.

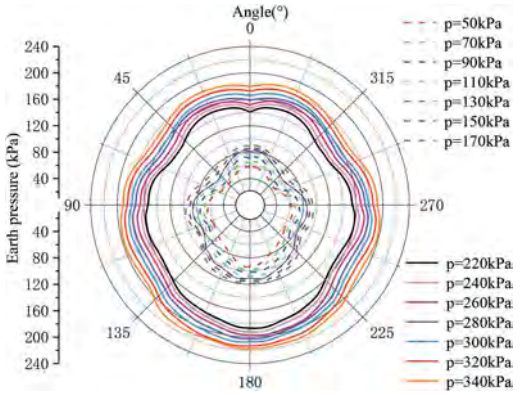

Figure 9. Distribution of segment earth pressure under different grouting pressure in 6 m and 15 m buried depth.

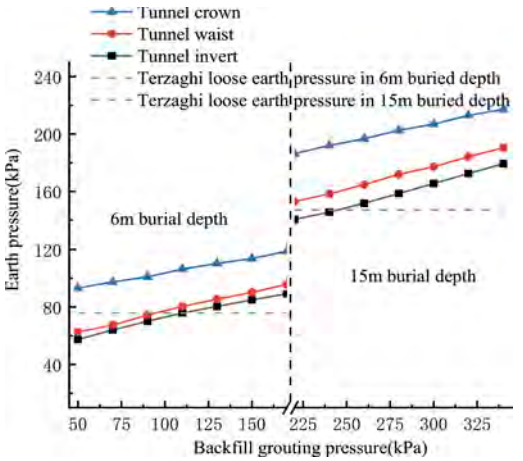

Figure 10. Variation of earth pressure at each position of segment.

During shield construction, the grouting pressure not only affects the pressure on the lining segment, which is also an important aspect of surface settlement. According to Figure 11, when the tunnel buried depth is shallow, the grouting pressure increases and the surface settlement deformation is more sensitive. When the grouting pressure fluctuates the overburden weight by 20 kPa, the ground deformation is controlled within 10 mm. Excessive grouting pressure will lead to surface uplift. When the tunnel is deep, the grouting pressure has less influence on the ground deformation. When the grouting pressure is greater than the weight of the overburden, the ground deformation can meet the settlement requirements of 10 mm.

4.2 *Lateral earth pressure coefficient*

The lateral earth pressure coefficients at each position on the side of the segment can be calculated by obtaining the horizontal earth pressure and vertical

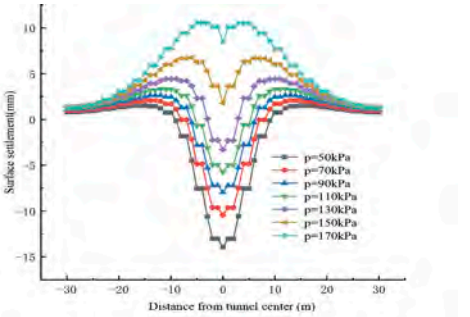

(a) Surface settlement under different grouting pressures at 6 m buried depth

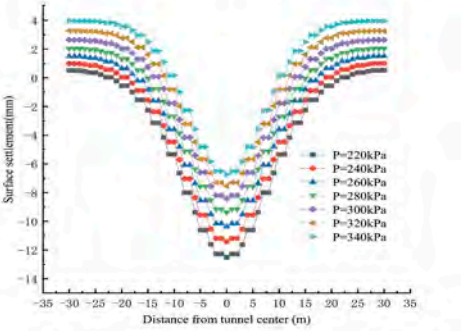

(b) Surface settlement under different grouting pressures at 15 m buried depth

Figure 11. Surface settlement under different burial depths and different grouting pressures.

earth pressure of the segment. As can be seen from Figure 12, in the two cases of deep burial and shallow burial, the grouting pressure basically has no effect on the lateral earth pressure coefficient, and the lateral earth pressure coefficient varies around the coefficient of earth pressure at rest, ranging from 0.28 to 2.98, which is similar to the conclusion that the lateral earth pressure coefficient measured by Wang and Hao (2018). According to the deformation state of the soil around the tunnel, the change of lateral earth pressure coefficient can be divided into two areas: when $K<K_0$ is the I zone. The horizontal dislocation deformation of the soil particles at the spandrel is larger but the vertical dislocation deformation is small, so that the decrease of the lateral earth pressure is much larger than that of the vertical earth pressure, so the lateral earth pressure coefficient is smaller than the coefficient of earth pressure at rest. when $K_0 < K$ is the II zone The horizontal dislocation deformation of soil particles is small but the vertical dislocation deformation is large. So the decrease of vertical earth pressure is much larger than that of horizontal earth pressure, and the coefficient of lateral earth pressure of segment is larger than that earth pressure at rest, and the maximum is 2.98.

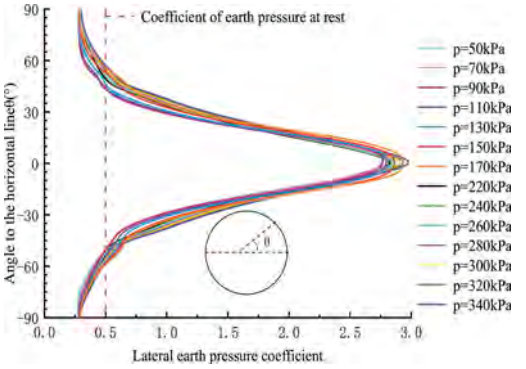

Figure 12. Effect of different grouting pressures on lateral earth pressure coefficient of segment under two kinds of burial depth.

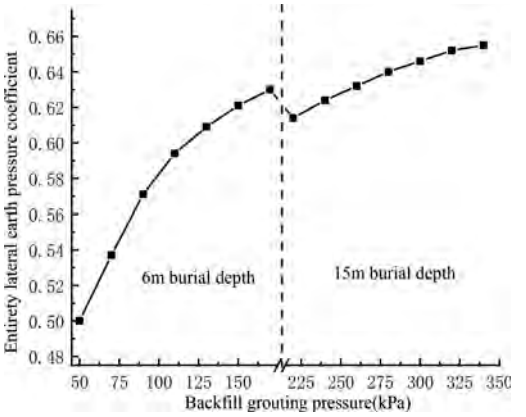

Figure 13. Variation of overall lateral earth pressure coefficient of segment under different burial depth and grouting pressures.

By comparing the sum of the horizontal earth pressure acting on the segment to the sum of the vertical earth pressure, the lateral earth pressure coefficient of the segment ring can be obtained. It can be seen that the lateral earth pressure coefficient of the whole segment is larger than the initial coefficient of erath pressure at rest(0.5). At 6 m buried depth, the entirety lateral earth pressure coefficient varies greatly under different grouting pressure, and when the grouting pressure increases from 50kPa to 170kPa, the entirety lateral earth pressure coefficient increases by 0.13. However, when the buried depth is 15 m, the change of grouting pressure has little influence on the entirety lateral earth pressure coefficient, which is maintained at about 0.6, and the variation range is not more than 0.1.

When the buried depth of the tunnel is shallow, the coefficient of lateral earth pressure is suggest 0.07-0.13 higher than that of coefficient of earth pressure at rest. When the buried depth of tunnel is deeper, it is suggested that the coefficient of lateral earth pressure is 0.1-0.2 higher than earth pressure at rest. This is consistent with the conclusion drawn by Han (2017) that the actual lateral earth pressure coefficient of the segment considering the effect of synchronous grouting at the shield tail is 0.1-0.2 higher than the recommended value of geological prospecting.

4.3 *Ground reation and the coefficient of ground reaction*

Deep buried or shallow buried grouting pressure has little influence on the ground reation and the coefficient of ground reation. When the tunnel buried depth is certain, the ground reation decreases with the increase of grouting pressure, and the coefficient of ground reation increases with the increase of grouting pressure. Although the grouting pressure increases and the earth pressure on the segment also increases, the overall distribution of the earth pressure on the segment is uniform, so the deformation of the segment under the uniform pressure is small, resulting in the reverse ground reaction caused by the displacement of the segment to the soil.

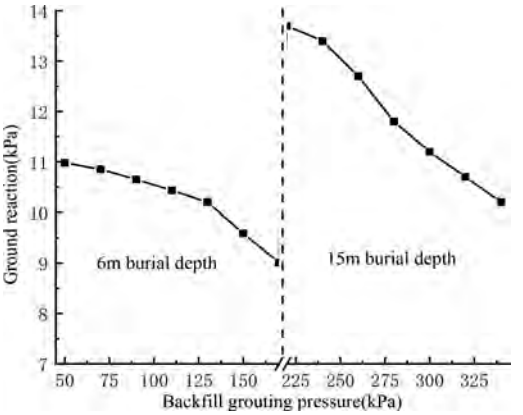

Figure 14. Change of ground reation under different grouting pressures.

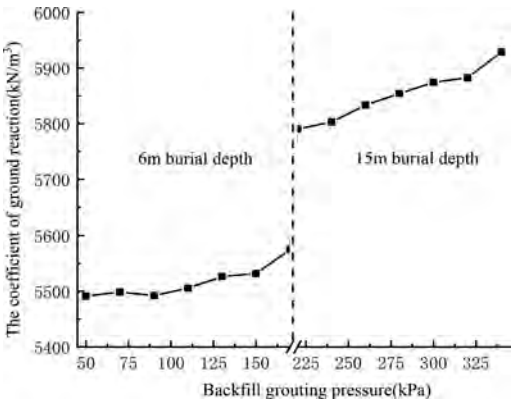

Figure 15. Change of the coefficient of ground reation under different grouting pressures.

5 CONCLUSION

From the above study, the following conclusions can be obtained:

(1) The influence of the backfill grouting pressure on the segment earth pressure simulated by the equivalent circle zone method based on the concept of gap parameters is basically consistent with the results of the previous model test, which shows that the simplified analysis method calculated in this paper is feasible.
(2) Considering the influence of backfill grouting, the vertical earth pressure and horizontal earth pressure of the segment show a parabola distribution of large in the middle and small on both sides.
(3) The earth pressure of the segment increases linearly with the increase of grouting pressure, and with the depth of the tunnel, the earth pressure acting on the segment is more uniform.
(4) The lateral earth pressure coefficient varies around the coefficient of earth pressure at rest, ranging from 0.28 to 2.98. When the buried depth of the tunnel is shallow, the lateral earth pressure coefficient is suggested to be 0.07-0.13 higher than the coefficient of erath pressure at rest. When the buried depth is deeper, the lateral earth pressure coefficient is suggested to be 0.1-0.2 higher than the coefficient of erath pressure at rest.
(5) The grouting pressure has little influence on the ground reation and the coefficient of ground reation.

ACKNOWLEDGMENTS

The research was conducted with funding provided by the National Science Foundation of China (Grant No. 52178387 and No. 51678217).

REFERENCES

Hong, K. R., Feng, H. H., 2020, Development trends and views of highway tunnels in china over the past decade. China Journal of Highway and Transport, 33(12), 62–76.

Editorial department of china journal of highway and transport, 2022, Review on China's traffic tunnel engineering research:2022. China Journal of Highway and Transport, 35(04), 1–40.

Zhu, W., Chen R. J., 2001, Current status and prospects of shield tunnel construction technology (lecture3)—the basic principle of shield tunnel and its appli-cation in China. Geotechnical Engineering World, 4(11), 19-21 +65-66

Sato, Y., Koyama, Y., Okano, N., 1998, Back-fill grouting model test for shield tunnel. Quarterly R eports of RTRI, 39(1), 35–39. Japan.

Koyama, Y., 2003, Present status and technology of shield tunneling method in Japan. Tunnelling and Underground Space Technology, 18(2/3), 145–159. Japan.

Liu, C., Li, J., Zhang, Z.,et al, 2020, Model tests on tail-grouting process during URUP shield tunneling in soft soil. Tunnelling and Underground Space Technology, 103

Qin, N., Ye, F., Han, X. B., et al, 2021, Pressure filtration diffusion model of shield tunnel back-filled grout-ing based on fractal theory. Journal of Central South University (Science and Technology), 52 (12), 4484–4491

Ye, F., Zhu, H. H., He, C., 2009, Back-filled grouts diffusion model and its pressure to segments of shield tunnel. Rock and Soil Mechanics, 30(05), 1307–1312.

Bezuijen, A., Talmon, A. M., Kaalberg, F. J., et al, 2004, Field measurements of grout pressures during tunnelling of the sophia rail tunnel. Soils and Foundations, 44(1), 39–48. Netherlands.

Li, X., Zhou, S. H., Wang, P. X., et al, 2014, Study of distribution law of earth pressure acting on shield tunnel lining based on insitu data. Rock and Soil Mechanics, 35(S2), 453–459.

Li, X., Zhang, Y. S., Geng, A. P., et al, 2022, Field measurement analysis of large diameter shield tunnel structure. Journal of Underground Space and Engineering, 18 (01), 297–304.

Wang, D. Y., Hao, S. H., 2018, Distribution laws of earth pressure acting on a shield tunnel based on measured data. Modern Tunnelling Technology, 55(03), 46–53

Hashimoto, T., Brinkman, J., Konda, T., et al, 2006, Simultaneous backfill grouting pressure development in construction phase and in the long-term. Tunnelling and UndergroundSpace Technology, 19(4-5), 01–107. Japan.

Zhu, H.H., Ding, W. Q, Li, X. J., 2000, Construction simulation for the mechanical behavior of shield tunnel and its application. China Civil Engineering Journal, 33(03), 98–103.

Kasper, T., Meschke, G., 2006, On the influence of face pressure,grouting pressure and design in soft ground tunnelling. Tunnelling and Underground Space Technology, 21(2), 160–171. Germany.

Wei, K. L., 2007, Sudy on the law of the ground-settlementand earth pressure change of sheild tunneling in shenzhen metro. Chinese Journal of Underground Space and Engineering, 3(01), 35–39.

Ji, Y. P., 2004, Study of stratum displacement and earth pressureconsidering construction program of shield tunnel. PhD Thesis, Hohai unoversity.

Zhang, Y., Yin, Z. Z., Xu, Y. F., 2002, Analysis on three-dimensional ground surface deformations due to shield tunne.Chinese Journal of Rock Mechanics and Engineering, 21(03), 388–392.

Zhong, X. C., Zhong, J. L., Yu, L. C., et al, 2023, Model test of shield segment earth pressure considering the influence of shield tail grouting. Chinese Journal of Underground Space and Engineering, 19(Suup.), 201–208.

Zhong, X. C., Zhu, W., 2006, Back analysis of soil pressure acting on shield lining segment. Rock and Soil Mechanics, 27(10), 1743–1748.

Zheng Y. R., Wang, Y. F., 2013, Evolution of rock mass pressure theory and researches on tunnel failure mechanism. Tunnel Construction, 33(06), 423–430.

Han, L. 2017, Construction loads and earth pressures on large shield tunnel lining with unconventional overburden. PhD Thesis, Shanghai: Shanghai Jiao Tong University.

Tunnelling for a Better Life – Yan, Celestino, Thewes & Eberhardt (Eds)
© 2024 The Author(s), ISBN 978-1-032-80042-4
Open Access: www.taylorfrancis.com, CC BY-NC-ND 4.0 license

Impact of base rock deterioration on the mechanical characteristics of loess-expansive mudstone tunnel lining structure

Haoyan Zhu*
School of Highway, Chang'an University, Xi'an, China

ABSTRACT: In order to study the stress characteristics and displacement deformation law of the secondary lining structure of the loess-expansive mudstone binary structure tunnel under the expansion and softening of the surrounding rock of the tunnel basement, the nonlinear finite element numerical simulation method was used to carry out different degrees of deterioration of the basement under different water contents. The influence of the secondary lining structure of the tunnel with different thicknesses of loess and mudstone (i.e., different spatial position relationships) was analyzed to obtain the variation law of the displacement of the surrounding rock of the tunnel and the stress and strain characteristics of the secondary lining structure of the tunnel. The results show that with the increase of the water content of the surrounding rock of the tunnel (that is, the degree of deterioration is deepened), the vault settlement and the tunnel bottom uplift of the tunnel lining structure show an increasing trend, and the degree of deterioration has little effect on the vault settlement and has a great influence on the tunnel bottom uplift. When there is loess layer in the overlying surrounding rock, the maximum principal stress distribution of the secondary lining structure unit shows a large change in the force at the arch waist, and the value increases with the deepening of the deterioration, while the minimum principal stress changes more obviously at the inverted arch. The vault settlement of the lining and the uplift of the tunnel bottom decrease slightly with the decrease of the thickness of the overlying loess layer, but the growth rate is consistent. The research results can provide a theoretical reference for the deterioration mechanism of tunnel lining structure performance under variable loads during the operation period of loess-expansive mudstone dual structure tunnel.

Keywords: Highway tunnel, Expansive mudstone, Surrounding rock softening, Supporting structure, Numerical simulation

1 INTRODUCTION

Mudstone is a special geological body between soil and rock mass. Its engineering properties are extremely complex and changeable. Water expansion and disintegration are the main engineering geological characteristics of mudstone (Um et al., 2009; Gautam et al., 2016). The argillaceous rock series is widely distributed in China and the world (Guangzhi, 2018; Lichuan et al., 2014). Among the many diseases that occur in tunnels in mudstone areas, the inverted arch floor heave is particularly significant, which even seriously affects the stability of tunnel structure and the comfort and safety of driving. The inverted arch floor heave of mudstone tunnel brings great trouble to the construction and research of engineering. The surrounding rock of inverted arch base may produce mechanical effects such as expansion, softening and rheology due to the change of groundwater storage environment, which is an important cause of inverted arch floor heave disease (Xiong et al., 2020).

There are many factors that cause the uplift of the tunnel bottom and the mechanism is extremely complicated. The failure of the tunnel inverted arch floor heave is related to geological structure, geological environment, load conditions, type design and construction quality, and the failure forms of the tunnel floor heave are also different (Mingqing et al., 2019; Zeng et al., 2014). Erfeng et al. (2013) described the engineering geological characteristics of Liangjiashan mudstone by classifying and geochemical analysis of the mudstone of Liangjiashan tunnel in Tianshui. Through the field monitoring and numerical simulation of the surrounding rock pressure of the mudstone flint, Qinpeng et al. (2016) showed that the mudstone was softened after saturation and caused uneven stress, resulting in obvious uplift failure of the inverted arch. Through monitoring measurement and numerical simulation, Dongdong et al. (2016) discussed the mechanical properties of the inverted arch of the tunnel after the soft flow of mudstone in water.

*Corresponding author: zhuhaoyan068@gmail.com

DOI: 10.1201/9781003495505-184

At present, the expansion pressure of the basement surrounding rock is equivalent to the uniform load in the design of the tunnel structure (Wilson, 1980; Chuntan et al., 2019), and the influence of the change of the water content of the basement surrounding rock on the stress of the tunnel and the floor heave of the inverted arch is not well considered, especially the simulation of the expansion and softening process caused by different water content. Therefore, it is particularly important to study the stress of the mudstone tunnel and the deformation and failure mechanism of the inverted arch under the action of basement expansion and softening. In view of this, based on the equivalent relationship of expansion theory caused by temperature deformation and humidity change, ABAQUS thermal plate is introduced, and the volume expansion caused by mudstone material heating is used to equivalent the volume expansion caused by mudstone water absorption. The analysis of base swelling effect is carried out to study the influence of swelling characteristics on the stress of tunnel structure and inverted arch deformation under different water content conditions, so as to provide theoretical basis for the deterioration mechanism of tunnel lining structure performance under variable load during operation period of tunnel in loess-mudstone area.

2 NUMERICAL SIMULATION OF SURROUNDING ROCK DETERIORATION OF TUNNEL BASE

2.1 *Establishment of the model*

According to the Saint Venant Principle, the actual influence width of surrounding rock stress redistribution after tunnel excavation is generally 3-5 times the distance around the center of the cavern. The change of surrounding rock stress at 3 times the excavation width is generally not more than 10 %, and the change of surrounding rock stress at 5 times the excavation width is generally not more than 3 %. Therefore, in order to reduce the influence of tunnel excavation and the simulation of expansion and softening of surrounding rock on the boundary effect, the left, right and lower sides of the cross-section size of the model are selected about 4 times the diameter of the excavation section. The established soil layer calculation model includes 247464 grids. The C3D8R hexahedral element is selected for the surrounding rock, the primary support and the secondary lining. The finite element mesh extracted from the finite element software is shown (Figure 1). In this paper, the initial support of the model adopts C25 shotcrete with a thickness of 0.28 m, and the secondary lining adopts C30 concrete with a thickness of 0.5 m. The tunnel section is 80 km/h highway tunnel standard section, the tunnel span is 12.76 m, and the height is 10.36 m. The thickness of the overlying soil on the top of the tunnel is 40 m (the overlying loess layer is reduced from 30 m to 0 along the excavation direction, and the thickness of the mudstone layer is increased from 10 m to 40). The distance between the tunnel arch bottom and the lower boundary is 37.64 m. The cross-sectional size of the model is 90 × 90 m, the longitudinal length along the tunnel axis is 24 m, and the excavation footage is 2 m. The ABAQUS model change method is used to complete the excavation and lining arrangement of the tunnel, and then the field variables are used to control the change of the surrounding rock parameters of the base, and the influence of the water expansion and softening of the expansive mudstone of the tunnel base on the tunnel structure is simulated.

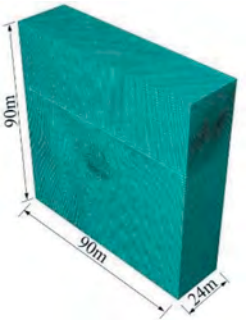

Figure 1. The ABAQUS model of the tunnel.

There are contacts between the tunnel surrounding rock and the primary support, the primary support and the secondary lining. By defining the contact surface, the deformation coordination between the various structures of the model can be ensured. The contact surfaces are set between the tunnel surrounding rock and the primary support, and between the primary support and the secondary lining, so that the effective combination of the surrounding rock, the primary support and the secondary lining together constitute a relatively coordinated bearing body. The bottom interface of the formation calculation model is set with fixed constraints. The left, right, front and rear interfaces of the model are set with normal constraints, and the upper interface is free constraint.

2.2 *Basic assumptions of the model*

In the actual tunnel construction, due to the complex and changeable geological conditions, numerical simulation is difficult to simulate the actual engineering conditions. Therefore, this paper combines the relevant data to simplify the numerical simulation. The assumptions are as follows:(1) Assuming that the surrounding rock is isotropic, uniform and continuous material; (2) The natural stress field of surrounding rock only considers the effect of self-weight stress, and does not consider the complex stress such as tectonic stress which is difficult to be

expressed by formula; (3) The change of stress and strain of surrounding rock is always in the elastic-plastic range. The numerical simulation adopts Mohr-Coulomb yield criterion, and the numerical simulation of supporting structure material adopts linear elastic constitutive relation; (4) The stress and strain of the simplified humidity field are linear elastic relationship. The water absorption and expansion thermodynamic model of surrounding rock is isotropic heat conduction model. It is assumed that the specific heat, thermal conductivity and thermal expansion coefficient of the surrounding rock material do not change with temperature; (5) The material parameters of the primary support, secondary lining and excavation part of the tunnel are not affected by the change of temperature field. The interface between the primary support and the surrounding rock is adiabatic boundary, that is, the expansion only occurs in the surrounding rock, and the model boundary is adiabatic boundary.

2.3 *Theoretical basis of temperature field simulation humidity field*

From a macro perspective, the expansion process of expansive mudstone is the volume expansion of surrounding rock caused by the change of water content. By controlling the water content, the stress-strain and displacement changes of tunnel lining structure caused by expansive mudstone can be reflected. The built-in temperature field program of ABAQUS software changes the temperature change field controlled by heat conduction by controlling the temperature conditions, and then analyzes the stress change of the component. According to the basic theory of humidity stress field, the conversion formula of temperature expansion coefficient and humidity expansion coefficient is deduced, and the expansion effect of mudstone after water absorption is realized by temperature analogy method. Therefore, this paper uses ABAQUS built-in temperature field to simulate the expansion of expansive mudstone.

When the water content of mudstone is less than the saturated water content, the flow differential equation can be simplified as follows:

$$\frac{\partial}{\partial x}\left(k_x\frac{\partial u}{\partial x}\right)+\frac{\partial}{\partial y}\left(k_y\frac{\partial u}{\partial y}\right)+\frac{\partial}{\partial z}\left(k_z\frac{\partial u}{\partial z}\right)=C_w\frac{\partial u}{\partial t} \quad (1)$$

Where, k_x, k_y, k_z are the permeability coefficient (m/d); u is the head value of matric suction (m). $u = -u_w/(\rho_w g)$, where u_w is the matric suction (Pa); ρ_w is the density of water (kg/m^3). t is time (d); C_w is the specific water bulk density (1/m), which indicates the change value of the water content of the mudstone when the matrix suction of the unit volume mudstone changes by a unit head.

The heat conduction differential equation of the material is as follows:

$$\frac{\partial}{\partial x}\left(\lambda_x\frac{\partial T}{\partial x}\right)+\frac{\partial}{\partial y}\left(\lambda_y\frac{\partial T}{\partial y}\right)+\frac{\partial}{\partial z}\left(\lambda_z\frac{\partial T}{\partial z}\right)=\rho C_v\frac{\partial T}{\partial t} \quad (2)$$

Where, λ_x, λ_y, λ_z are thermal conductivity (W/(kg·°C)); t is temperature (°C); ρ is material density (kg/m^3); C_v represents the specific heat capacity (J/(kg·°C)).

Comparing the above unsaturated flow differential equation with the heat conduction differential equation, it is found that the two are basically the same in form. Therefore, the corresponding parameters in the seepage differential equation and the heat conduction equation can be exchanged. It is considered that solving the temperature field T parameter is to solve the matrix suction u of the expansive mudstone in the humidity field, so that the volume change of water in the unit volume mudstone can be calculated as $\Delta w = C_w \Delta u$. The strain increment caused by temperature change and the strain increment caused by humidity change are as follows:

$$\Delta\varepsilon_T = \alpha\Delta T \quad (3)$$

$$\Delta\varepsilon_w = \beta\Delta w \quad (4)$$

Where, α and β are temperature expansion coefficient and humidity expansion coefficient respectively. Let the above two formulas be equal, then:

$$\alpha = \frac{\beta\Delta w}{\Delta T} = \frac{\beta C_w \Delta u}{\Delta T} \quad (5)$$

Based on the above theory and formula analysis, the differential equation of expansive mudstone seepage problem is similar to the differential equation of heat conduction of temperature field material in mathematical expression. Through equivalent conversion, the seepage field of surrounding rock can be simulated by means of temperature field. Therefore, the volume expansion caused by water absorption of expansive mudstone can be approximated as the volume expansion caused by temperature change of mudstone material for equivalent conversion.

2.4 *Model parameters*

According to the specification, combined with the grade V surrounding rock of a mudstone tunnel and the geological survey data of similar projects, the physical and mechanical parameters of the model surrounding rock and supporting structure are given in Table 1.

According to the description of the basic theory of expansion in the previous section, the indoor test of mudstone and the reference, the following parameters are obtained: the initial water content is 12%, the void ratio e is 0.65, and the relative density G_s of mudstone is 2.71. It is assumed that the water content of mudstone in the surrounding rock of the project is 24%. According to the relationship between expansion force and temperature in numerical calculation: $\Delta P_s = 3\alpha K \Delta T$ (ΔP_s, K are the expansion force

Table 1. Physical and mechanical parameters of model materials.

Material	Density/ (kg/m^3)	Elastic Modulus/ GPa	Poisson Ratio	Cohesion/ kPa	Internal Friction Angle
Loess	1820	0.15	0.39	32	26
Mudstone	2200	1.30	0.35	260	30
Initial Support	2400	28.00	0.20		
Secondary Lining	2360	30.00	0.20		

increment and bulk modulus of mudstone respectively). The temperature field is used to simulate the humidity field. At this time, the change of water content can be expressed as $C_w \Delta T(1 + e)/G_s$, and the water content can be calculated according to the following formula:

$$w = \frac{C_w \Delta T(1+e)}{G_s} + w_0 \tag{6}$$

Fredlund et al. (1993) used the laboratory test to obtain the value of C_w is about 0.0846m^{-1}. The initial moisture content of mudstone is 12 % humidified to different moisture contents. The initial moisture content corresponds to T_1 = 0, and the final moisture content corresponds to temperature T_2 = 2.330 °C. The thermal calculation parameters of mudstone with different water content are calculated, as shown in the following Table 2.

Table 2. Thermal parameters of mudstone under different water content conditions.

Water Content/%	Temperature Expansion Coefficient $\alpha/10^{-5}$	Temperature Load ΔT/°C
12		0 ~ 2.330
16	2.0	0 ~ 2.330
20	3.9	0 ~ 2.330
24	8.5	0 ~ 2.330

Table 3. Physical and mechanical parameters of softened mudstone.

Softening Grade	Density/ (kg/m^3)	Elastic Modulus/ GPa	Poisson Ratio	Cohesion/ kPa	Internal Friction Angle
Not	2200	1.30	0.35	260	30
Weak	2020	0.90	0.35	100	28
Moderate	1930	0.35	0.35	50	26
Strong	1840	0.13	0.35	25	22

Aydan summarized the material parameters of Tertiary soft rock such as a large number of mudstone, and obtained the empirical relationship between the unit weight, Poisson 's ratio, elastic modulus and internal friction angle of mudstone and the uniaxial compressive strength, and calculated the parameters of mudstone after softening. After calculation, the physical and mechanical parameters of softened mudstone are listed in the following Table 3.

2.5 *Simulation condition setting of tunnel surrounding rock expansion and softening*

In order to better simulate the influence of water expansion and softening of surrounding rock on the tunnel during the operation of the tunnel, the excavation simulation of the three-dimensional dynamic construction stage of the tunnel is considered first. Expansive mudstone is a V-level weak surrounding rock, and the step-by-step excavation method is generally used to achieve the purpose of controlling stress and deformation. In this paper, the three-step method is used to construct the tunnel. The excavation footage of the tunnel is unified to 2m, the initial support is delayed by 2m, and the second lining is constructed after the end of the initial support. In this way, the displacement, deformation and stress distribution characteristics after excavation and support can be obtained. Then, based on the predefined field and temperature variable field in ABAQUS to control the change of surrounding rock parameters, the finite element analysis of expansion and softening simulation under different water content of surrounding rock is carried out, and the mechanical properties of tunnel structure caused by volume expansion and softening of surrounding rock are calculated. The deterioration area set in this paper is the 2m depth area at the bottom of the tunnel, which is the expansion and deterioration area of surrounding rock.

3 ANALYSIS OF CALCULATION RESULTS OF EXPANSION AND SOFTENING OF SURROUNDING ROCK AT TUNNEL BASE

3.1 *Analysis of surrounding rock displacement*

In order to compare and analyze the vertical displacement of surrounding rock with the change of excavation cloth, the curves of vault settlement and tunnel bottom uplift of monitoring sections (A, B, C, D) at 1m, 8m, 16m and 24m during tunnel excavation are drawn, as shown in the Figures 2 and 3.

It can be seen from the figure that in the tunnel excavation stage, the vault settlement value and the tunnel bottom uplift value are in the order of 1m to 24m from large to small. The main reason is that the vertical displacement of the surrounding rock has different degrees of influence with the excavation process. At the same time, in the expansion and softening stage of the substrate, the displacement value also increases with the increase of the water content in the substrate deterioration area (that is, the degree of deterioration deepens).

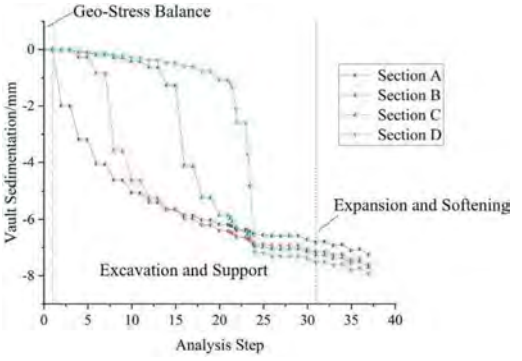

Figure 2. The curve of vault sedimentation with analysis step.

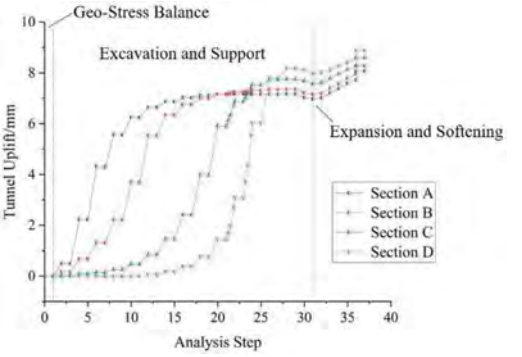

Figure 3. The curve of tunnel uplift with analysis step.

The vertical displacement cloud diagram of the whole tunnel model after construction and under the action of strong deterioration is shown in the Figures 4 and 5.

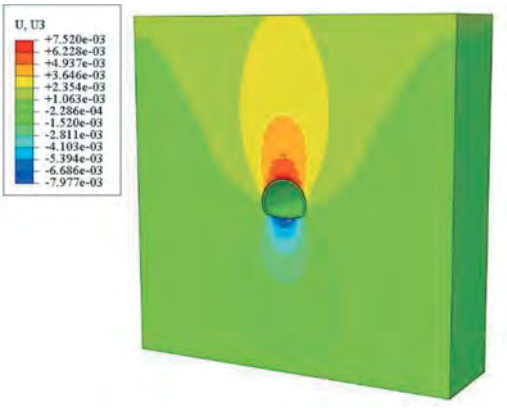

Figure 4. Undeteriorated vertical displacement after tunnel construction.

In order to analyze the change of displacement distribution of tunnel surrounding rock under the condition of different degrees of base deterioration, the vertical displacement values of representative nodes

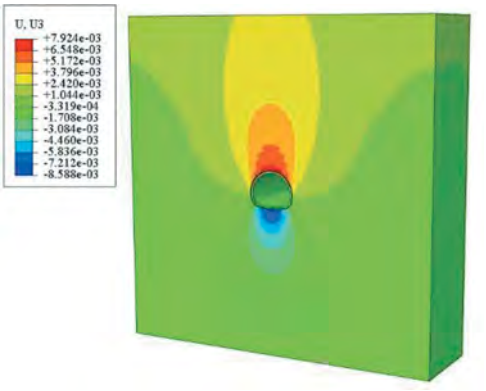

Figure 5. Vertical displacement of tunnel base under strong deterioration of surrounding rock.

of four sections of lining vault and arch bottom are extracted, and the vertical displacement values of vault settlement and arch bottom uplift of four different monitoring sections are drawn. The relationship curves between water content and expansion and softening stages are shown in the Figures 6 and 7.

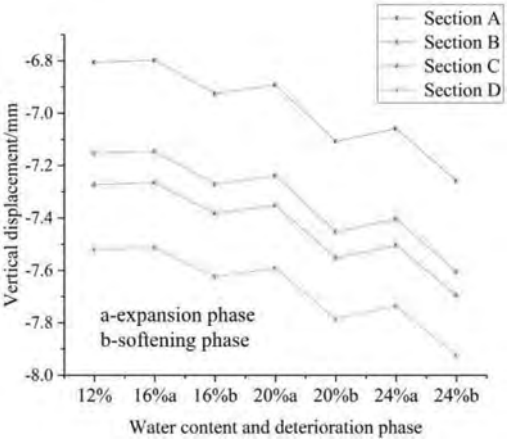

Figure 6. The relationship curve between vault sedimentation and water content.

It can be seen from the figure that under the action of expansion and softening of the basement surrounding rock, the maximum settlement value and uplift value appear in the monitoring section D of the inverted arch surrounding rock. The maximum settlement value of the tunnel vault is 7.92 mm, and the change after construction is 5.37%. The maximum uplift value of the inverted arch bottom is 8.88 mm, and the change after construction is 7.66%. The arch bottom heave increases with the increase of the water content of the basement surrounding rock and the process of gradual expansion and softening. With the increase of water content, the settlement value of the vault decreases slightly under the action of each level of expansion, and increases continuously under the

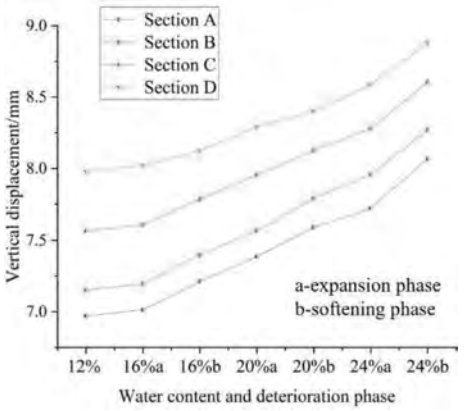

Figure 7. The relationship curve between tunnel uplift and water content.

action of each level of softening. It can be seen that the water absorption and expansion of the surrounding rock at the bottom of the tunnel can have a certain inhibitory effect on the settlement of the tunnel vault.

3.2 *Lining stress analysis*

The section of the secondary lining support structure at section A is taken for analysis. The maximum principal stress and minimum principal stress cloud diagram of the lining support structure under the strong deterioration of the basement surrounding rock are shown in the Figures 8 and 9.

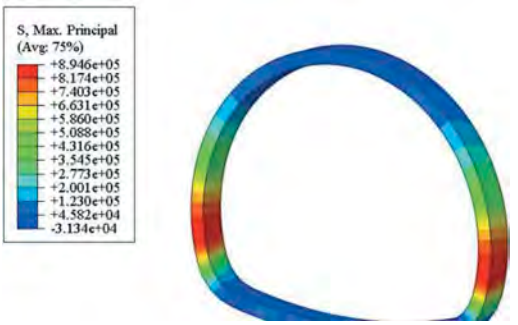

Figure 8. The maximum principal stress cloud diagram of strong deterioration surrounding rock lining structure.

In order to analyze the variation of the maximum and minimum principal stress distribution of the tunnel secondary lining along the circumferential direction, the maximum and minimum principal stress distribution curves of the tunnel lining unit under different water content conditions are drawn, as shown in the Figures 10 and 11.

From the diagram, it can be seen that after the tunnel excavation is completed, with the increase of the water content of the surrounding rock, the

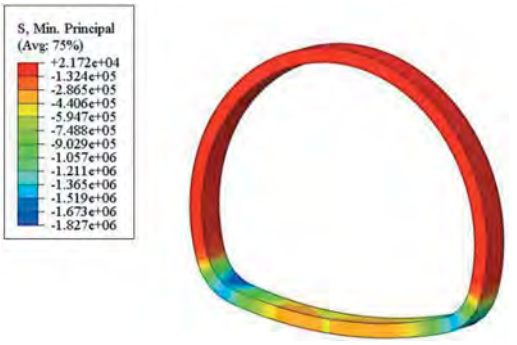

Figure 9. The minimum principal stress cloud diagram of strong deterioration surrounding rock lining structure.

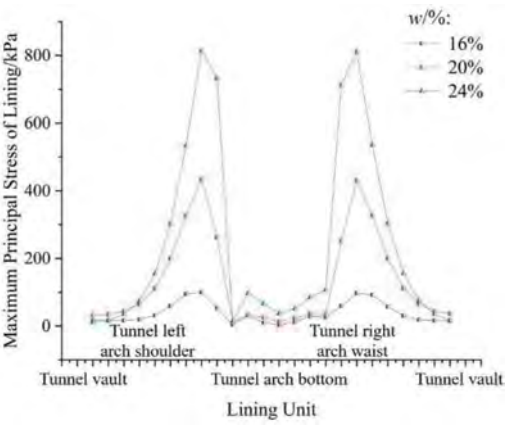

Figure 10. The variation curve of maximum principal stress of lining.

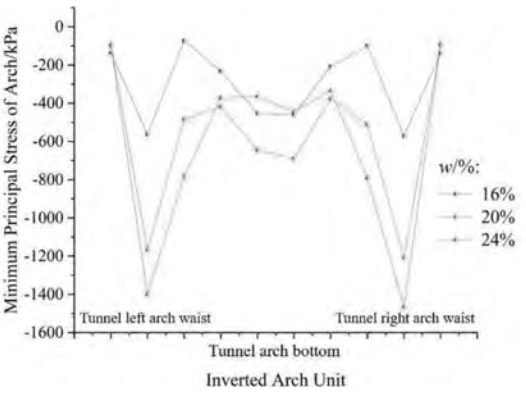

Figure 11. The minimum principal stress change curve of inverted arch.

maximum principal stress at the inverted arch position gradually becomes larger, and the stress concentration phenomenon occurs at the arch waist. The minimum principal stress of the ring unit of the inverted arch lining is negative, that is, the compressive stress. The

compressive stress of the inverted arch unit increases with the increase of water content. The minimum principal stress at the arch bottom is relatively larger than that at the vault, and the stress concentration occurs at the arch foot.

The stress variation curve of the inverted arch is basically axisymmetric. The maximum principal stress σ_1 of the inverted arch is positive, the minimum principal stress σ_3 is negative, and the absolute value of σ_3 is greater than σ_1. With the increase of water content, that is, the deepening of mudstone expansion and softening, the maximum principal stress at the arch waist and the minimum principal stress at the arch foot show an increasing trend. The problem of concrete cracking caused by excessive tensile stress at the arch bottom of the tunnel invert should be considered emphatically.

4 CONCLUSIONS

Based on the temperature field simulation humidity field theory of ABAQUS and the softening effect theory of surrounding rock, this paper analyzes the influence of different expansion and softening effects on the stress and deformation of loess-mudstone tunnel lining structure through numerical simulation. The following conclusions are obtained:

(1) With the increase of the water content of the surrounding rock of the basement, the uplift of the arch bottom and the settlement of the vault increase continuously. The expansion effect has little effect on the settlement of the vault, while the softening effect has a relatively large effect on the settlement of the vault. The water absorption expansion of the surrounding rock at the bottom of the tunnel can have a certain inhibitory effect on the settlement of the tunnel vault.

(2) With the enhancement of the deterioration of the basement surrounding rock, the maximum principal stress and the minimum principal stress of the inverted arch waist and the arch foot show an increasing trend. The concrete tensile deformation and failure caused by the excessive tensile stress at the inverted arch position of the tunnel should be considered.

(3) The range of the deterioration area of the basement surrounding rock, the stress and deformation of the tunnel lining structure at the top of the tunnel section and the deterioration of the surrounding rock on the left and right sides should be further considered, and the stability of the lining structure under different surrounding rock deterioration can be completely analyzed.

REFERENCES

Um, Jeong-Gi, Shin, Mikyoung, 2009. Variations of physico-mechanical properties of the cretaceous mudstone in haman, gyeongnam due to freeze-thaw weathering. TUNNEL AND UNDERGROUND SPACE, 19(2), 146–157.

Gautam T p, Shakoor A, 2016. Comparing the slaking of clay-bearing rocks under laboratory conditions to slaking under natural climatic conditions. Rock Mechanics and Rock Engineering, 49, 19–31.

Guangzhi X, 2018. Discussion on design and construction improvement measures based on current typical diseases of railway tunnel lining. Tunnel Construction, 38(9), 1416–1422

Lichuan W, Xiaowen X, Hui L, et al, 2014. Analysis on causes for and renovation of floor structure of a high-speed railway tunnel located in slightly-dipping interbedded rock mass. Tunnel Construction, 14(1), 53–61.

Xiong Y l, Liang Q g, Wang B, et al 2020. Research status and key scientific issues of inverted arch heave deformation in mudstone tunnels of high-speed railway. Journal of Lanzhou University, 39(4), 25–33.

Mingqing D u, Wang X, Zhang Y, et al, 2019. In-situ monitoring and analysis of tunnel floor heave process. Engineering Failure Analysis, 109, 104323.

Zeng Z y, Xu B s, Hu S q, et al, 2014. Numerical analysis of tunnel liner failure mechanism in expansive soil considering water-increased state. Rock and Soil Mechanics, 35(3), 871–880.

Erfeng O, Qingguo L, Dewen L, et al, 2013. A study of geochemistry of tertiary mudstone in tianshui—a case study of liangjiashan tunnel. Advances in Earth ence, 28(3), 106–114.

Qingpeng Z, Qingguo L, Bowen M, et al, 2016. Test study on the mechanical characteristics of mudstone tunnel on baoji-lanzhou pdl. Journal of Railway Science and Engineering, 13(11), 2133–2141.

Dongdong D, Qingguo L, Shanchang X u, et al, 2016. Test study on the mechanical characteristics of tunnel invert on softening mudstone section. Journal of Railway Science and Engineering, 13(10), 2001–2008.

Wilson A h, 1980. Method of estimating the closure and strength of lining required in drivages surrounded by a yield zone. International Journal of Rock Mechanics & Mining Sciences & Geomechanics Abstracts, 17(6), 349–355.

Chuntan F, Qingguo L, Dongdong D, 2019. Stress characteristics and deformation law of inverted arch of large section loess tunnel. Journal of University of Jinan (Science and Technology), 33(2), 107–114.

Fredlund D g, Rahardjo H, 1993. Soil mechanics for unsaturated soils. New York: Wiley-Interscience Publication, 97–99.

Taylor & Francis
Taylor & Francis Group
http://taylorandfrancis.com

Conventional tunnelling

Taylor & Francis
Taylor & Francis Group
http://taylorandfrancis.com

Tunnelling for a Better Life – Yan, Celestino, Thewes & Eberhardt (Eds)
© 2024 The Author(s), ISBN 978-1-032-80042-4
Open Access: www.taylorfrancis.com, CC BY-NC-ND 4.0 license

Crystalline silica exposure in tunnel construction: Identifying barriers to safe practices

Frederick Anlimah* & Vinod Gopaldasani
University of Wollongong, Wollongong, Australia
Centre for Occupational, Public and Environmental Research in Safety and Health (COPERSH), Wollongong, Australia

Catherine MacPhail
University of Wollongong, Wollongong, Australia

Brian Davies
University of Wollongong, Wollongong, Australia
Centre for Occupational, Public and Environmental Research in Safety and Health (COPERSH), Wollongong, Australia

ABSTRACT: The construction industry, particularly tunnel construction, exposes workers to respirable crystalline silica (RCS), which can cause incurable illnesses such as silicosis and lung cancer. Despite a range of control measures being implemented, these measures do not completely remove the potential risk of RCS. This research aimed to identify the barriers and challenges hindering the implementation of effective controls and the adoption of safe work practices to protect workers from RCS exposure in tunnelling. A mixed-method approach was employed for this research. Tunnel construction workers were observed, surveyed and interviewed to gauge their knowledge and attitudes and understand their challenges in reducing RCS exposure. The preliminary analysis of the data reveals a diverse array of sociotechnical factors interacting to influence RCS exposure. It is noteworthy that participants consistently emphasised the project as the most exemplary one they have been involved in, although there is room for improvement. Although there is a notable proficiency in understanding RCS exposure and management in tunnelling, there appears to be a noticeable deficiency in perceived contentment regarding dust control. Several factors were identified as interacting to prevent the effective management of dust. These include perceived time pressure, absence of on-tool dust controls for some equipment, and low risk perceptions among workers, and inadequate enforcement of controls. Moreover, participants highlighted communication and heat-related challenges as hindrances to the continuous wearing of respirators. This research highlights the need for a paradigm shift in tunnel construction to address the barriers associated with RCS exposure reduction. It emphasises the importance of collaboration among various stakeholders, advocating for more effective controls, enforcement strategies and enhanced worker education through knowledge sharing.

Keywords: Tunnelling, Dust Control, Challenges, RCS, Silicosis

1 INTRODUCTION

Tunnelling, or the creation of underground passages or openings, supports water, sewer, and utility systems and significantly helps to move thousands of people through road and railway lines to reduce congestion and create more connected communities. In Australia, tunnels are being constructed in Melbourne, Brisbane, and Sydney, like other major cities worldwide. For example, the Metro Tunnel project, led by the Victorian Government (2023), is actively constructing twin 9km rails that will have five new underground stations, connecting Sunbury in the west to Cranbourne/ Pakenham in the southeast of Melbourne.

Several tunnelling projects must be completed to achieve these train services. Completing these tunnelling projects involves excavation, material removal and boring or cutting through different rock formations that contain quartz (ATS 2018; WHSQ 2013). The process of tunnelling through quartz-bearing rocks produces dust containing harmful tiny particles known as crystalline silica within the dust, exposing workers to respirable crystalline silica (RCS) if left uncontrolled (Bakke et al. 2014).

Although several interventions like foam (Guo et al. 2019), air curtains (Cai et al. 2020), press-in ventilation (Guo et al. 2020) and water misting (Sun et al. 2023) are available, hazardous exposure to RCS is still an

*Corresponding author: faka857@uowmail.edu.au

DOI: 10.1201/9781003495505-185

ongoing risk in tunnelling (Leite et al. 2023; WHSQ 2013). These exposures may lead to silicosis (Leung et al. 2012) and other illnesses like lung cancer (IARC 1997), chronic obstructive pulmonary disease (Rushton 2007) and kidney disease (Vupputuri et al. 2012).

Given these risks, examining tunnelling operations to gain a deeper understanding of the practices and challenges related to dust controls has become essential. Previous studies investigating workplace dust control practices have predominantly focused on construction rather than tunnelling.

Research on tunnelling dust control practices, include a survey conducted among Australian Institute of Occupational Hygienists that identified challenges hindering exposure reduction. These challenges include a lack of management commitment, financial constraints, employer prioritization of other concerns over worker health protection, over-reliance on personal protective equipment, and a lack of knowledge-sharing (Cole et al. 2023). Cole (2016) also identified best practices across several countries rather than challenges faced by workers and management in using dust control measures.

In construction, a study by Xing et al. (2018) identified practices employed by the Chinese government to reduce dust emissions on construction sites. The practices were categorised into technological, economic, supervisory, organisational, and assessment-based measures. They further noted that the government is more inclined to use technologies and organisational measures to encourage dust exposure reduction. Similarly, Zuo et al. (2017) found that construction site managers with personal experience in dust pollution employed by companies committed to dust control or working for larger firms tended to demonstrate greater awareness of dust exposure consequences, potentially resulting in increased self-responsibility for controlling dust. Kaluarachchi et al. (2021) revealed that workers' awareness of dust pollution consequences and their sense of responsibility positively affected personal norms, subsequently influencing their behaviour in dust control management.

Beyond the construction sector, a study by Haas et al. (2016) noted that US miners paid more attention to RCS exposure and silicosis risks when they first started working. However, this vigilance waned as they became more comfortable with their job responsibilities. This decrease in attention does not appear to be related to knowledge, as Sifanu et al. (2023) discovered that knowledge does not significantly influence the attitudes and behaviours required to reduce respirable dust exposure among copper miners. Furthermore, Utuk and Atulomah (2023) also observed that negative attitudes towards dust control exist even among workers with adequate knowledge of exposure risk in a cement factory.

When these factors are considered alongside the limited protection provided by engineered dust controls, even when they are highly efficient (Anlimah et al. 2023), work practices and associated barriers contribute to RCS overexposure reported in the literature (Leite et al. 2023). Therefore, the current study seeks to contribute to the body of knowledge by providing evidence of the practices and challenges associated with effective dust control in tunnelling.

2 METHOD

A mixed research approach involving an online survey, site observations and interviews was adopted for the study.

2.1 *Data collection instrument*

A customised version of the Safety Attitudes Questionnaire (SAQ) developed by Sexton et al. (2006) was utilised to understand the knowledge and attitudes related to dust control in tunnelling. The SAQ has been used in various medical facilities in the USA, Sweden and Cyprus, as reported by Al Malki et al. (2018) and Alayed et al. (2014) and is suitable for understanding the safety attitudes of workers.

The lead author initiated the modified questionnaire, which the co-authors reviewed independently. Necessary revisions were discussed and implemented. Subsequently, professionals from the tunnelling industry assessed the questionnaire for its suitability. The questionnaire evaluated five domains: teamwork climate, awareness and control of dust, dust control satisfaction, stress recognition and working conditions. Table 1 highlights the number of items under each domain.

Table 1. The five domains evaluated by the questionnaire.

Scale	Definition	N° of Items
Team Climate	Quality of collaboration among workers to control dust	6
Awareness and control of dust	Creation of awareness about the risk and control measures for RCS	10
Dust control satisfaction	Positivity about dust control practices	5
Stress recognition	Acknowledgement of how excessive dust impacts work performance	3
Work condition	Perceived quality of dust control practices and logistical support, including staffing and equipment	5

In addition to the survey, semi-structured interviews were conducted to delve deeper into the knowledge, attitudes, and challenges associated with managing dust on the project. Site observations were conducted during multiple site visits between August 2022 and September 2023.

2.2 *Study sites*

The research was conducted at a tunnelling project managed by a principal contractor in Australia. Various dust-generating tools and equipment were utilised on

the project including excavators, rock hammers, rock saws, surface miners and roadheaders. The roadheaders were used to excavate crossover caverns. The tunnels are being bored by two double-shield, hard rock tunnel boring machines (TBM), which were launched at the dive site and will be retrieved later at the extraction site.

2.3 *Participant selection*

Employees at each site were informed about the purpose and goals of the study during their weekly toolbox meetings. Those interested in participating accessed the online study by scanning a QR code. Follow-up interactions took place throughout the four-week survey period. Interviews were conducted after the survey had concluded and occurred face-to-face for each participant, except for two, where it was conducted online. One author conducted the interviews. All interviews were recorded with consent.

2.4 *Data analysis*

Data were analysed using Jamovi (2023) computer statistical software package for MacBook (version 2.3.19). Demographic information was presented through frequencies and percentages. Calculations of the sub-domain values in the survey were based on the instructions of Sexton et al. (2006) with minor adjustments due to the use of a 4-point Likert scale. To convert scores to a 100-point scale, 100/3 was used instead of the original 25. Respondents with a mean score of 75 or higher on the 100-point scale were classified as having a positive attitude towards a specific domain. Interview responses were thematically analysed in NVivo.

2.5 *Ethical consideration*

The research protocol received approval from the Human Research Ethics Committee of the University of Wollongong (Protocol Number: 2021/280).

3 RESULTS

3.1 *Demographic information*

The survey included 174 employees who were either frontline workers or leaders such as leading hands, engineers, supervisors, safety advisors, superintendents and managers. Participants were from diverse age groups and work backgrounds. Respondents were relatively young to middle-aged workers. The largest age group was 25 to 34 years, comprising 49% (n = 85) of the participants, while the smallest group (n = 2; 1%) consisted of workers over 54 years, as shown in Figure 1.

Survey respondents brought diverse work experiences across various industries to the study. About 29% (n = 50) had 11 to 20 years of experience, followed by 25% (n = 43) with 6 to 10 years and 16% (n = 27) with 3 to 5 years. However, most participants had limited experience in tunnelling projects, with participants with less than a year of experience accounting for 32% (n = 56) of the sample, as highlighted in Figure 2.

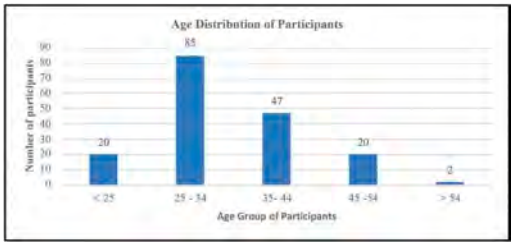

Figure 1. Age distribution of respondents.

Figure 2. Work experience of participants.

Furthermore, 54% (n = 94) of the participants held no supervisory role, while the remaining 46% (n = 80) did. Among the 40 employees interviewed, 40% (n = 16) were workers, whereas 60% (n = 24) held supervisory roles.

3.2 *Reliability assessment*

The overall Cronbach's alpha value for the survey was 0.912, with a mean of 3.27 (SD = 0.352), while that of the five domains was between 0.761 and 0.895. The questionnaire therefore had high internal consistency.

3.3 *Factor structure and multi-level modelling*

A five-factor confirmatory factor analysis was conducted to evaluate the tool's validity by comparing it against observed data. The fit of the final model, which retained 29 items, was generally satisfactory: $\chi 2(619) = 367$, $p < 0.001$; CFI = 0.92; TLI = 0.0911; RMSEA = 0.0628; SRMR = 0.0701. Factor

estimates are detailed in Table 2 (all estimates are $p < 0.05$ except values marked with *).

Table 2. Factor estimates for the attitudes domain.

	Team Climate	RCS Awareness	Dust control satisfaction	Stress recognition	Work condition
Team Climate	1.000	0.380	0.873	0.175	0.847
Awareness and control of dust		1.000	0.242	0.402	0.391
Dust control satisfaction			1.000	0.107*	0.872
Stress recognition				1.000	0.143*
Work condition					1.000

An independent samples T-test revealed no statistically significant difference in employment levels (supervisor or not) across domains. Similarly, an ANOVA analysis showed no significant differences in attitudes based on age, work or tunnelling experience ($p > 0.05$). Further analysis illustrates interrelationships among the domains, with Teamwork significantly linked to Awareness and Control of Dust ($r = 0.284$, $p < 0.001$) and Dust Control Satisfaction ($r = 0.786$, $p < 0.001$). For additional correlations, refer to Table 3 below.

Table 3. Correlation matrix for dust control attitude. (r = Pearson's r and p = p-value).

		Teamwork	Awareness and Control of Dust	Dust Control Satisfaction	Stress Recognition	Work Condition	Age	Experience in Tunnelling	Supervisor or not
Teamwork		—							
Awareness and Control	r	0.284	—						
	p	< .001	—						
Dust Control Satisfaction	r	0.786	0.130	—					
	p	< .001	0.008	—					
Stress Recognition	r	0.124	0.315	0.055	—				
	p	0.101	< .001	0.474	—				
Work Conditions	r	0.732	0.298	0.812	0.071	—			
	p	< .001	< .001	< .001	0.353	—			
Age	r	0.003	- 0.014	0.004	- 0.097	0.085	—		
	p	0.963	0.818	0.955	0.207	0.153	—		
Experience in Tunnelling	r	- 0.099	0.139	- 0.141	0.14	- 0.108	0.596	—	
	p	0.193	0.067	0.063	0.066	0.156	< .001	—	
Supervisor or not	r	0.069	- 0.07	0.085	- 0.131	0.02	- 0.114	- 0.201	—
	p	0.365	0.355	0.268	0.085	0.699	0.134	0.004	—

3.4 *Attitudes towards dust control*

A positive domain score of 76 for Awareness and Control of Dust demonstrates a good attitude towards efforts to raise awareness about RCS exposure and control. However, similar positive attitudes are not observed in the other domains. The results suggest that excessive dust impacts the work output of workers, evidenced by the negative score of 60 for Stress Recognition, as illustrated in Figure 3.

93% of participants positively perceive that they receive adequate information regarding the impacts and effects of dust, as well as strategies for reducing dust levels. Site observations align with these findings, supporting awareness creation and implementation of various dust control measures, including on-tool water spray systems, the establishment of exclusion zones, sprinklers around the work area and ventilation systems.

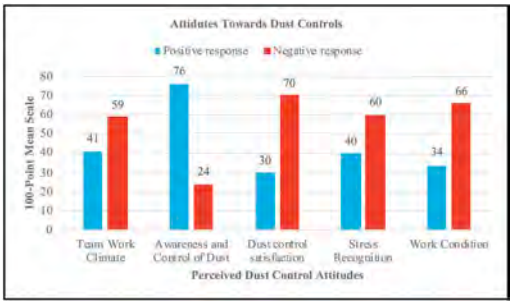

Figure 3. Attitudes towards dust control.

Additionally, the project is required to adhere to strict client RCS exposure control requirements. This includes specific measures such as the prohibition of dry sweeping and the use of handheld water sprays to control dust. Moreover, the client has representatives on the project to monitor compliance. A third-party conducts monthly monitoring of personal RCS exposure. In case of recorded overexposures, thorough investigations are conducted to determine the root cause. The outcomes of these personal exposure monitoring efforts are displayed on notice boards and communicated during toolbox meetings. Furthermore, matters concerning dust exposure are actively discussed in safety committee meetings.

These efforts may be a contributing factor to many interviewed participants quick to point out that when compared to other tunnelling projects they have worked on, the research site stood out as one of the best in dust control.

3.5 *Dust control challenges*

3.5.1 *Technical and operational factors*

However, when dust control is inadequate, or there is no engineered control for an activity, workers may adopt unauthorised methods to minimise their exposure. For example, while dust-generating tools like hammers, twin headers, and rock saws have on-tool controls, applying these measures to equipment such as an excavator with a bucket for scraping the floor or a dozer for stripping proves challenging. In such circumstances, there is reliance on water sprinklers installed above ground around the work area or air-assisted water spray systems. While these controls reduce dust, installing irrigation-type sprinklers with a spray distance between 5 - 30m raises concerns about understanding factors influencing dust control.

Additionally, factors like wind, space restrictions and vehicle (equipment) movement limit the effective use of air-assisted spray mist. Consequently,

workers sometimes resort to handheld dust suppressions, although the practice is prohibited on the project. Similarly, in the TBM tunnel, where outby workers deal with residual dust, management has experimented with different approaches, such as consulting experts and testing sprinkler systems. However, because they have not identified a fully effective solution, workers use water hoses to clean their work areas.

Furthermore, the challenge of ensuring that ventilation systems adequately remove dust is also encountered when excavating with a roadheader, especially when transitioning between different phases of excavation.

Participants highlighted multiple reasons for non-compliance with dust control measures at the worker level. This includes the type of activity, time factor, laziness and indifference on the part of workers.

3.5.2 *Organisational factors*

Inadequate enforcement compounds challenges faced in exposure reduction, evidenced by some observed hammer drilling activities that did not use any on-tool extraction. Also, using prohibited dust control methods, such as handheld dust suppression in some situations, lends to the theme.

3.5.3 *Challenges with the use of respirators*

Compliance issues are not restricted to engineering controls but are also associated with using respirators or dust masks.

Three types of respirators are used on the project: the P2-rated mask, half face mask (rubber mask) and one brand of powered air purifying respirator (PAPR). While it is mandatory for every worker to wear a respirator before entering the work area, the continuous use of respirators poses a challenge. Reasons cited for frequently removing masks include discomfort caused by hot weather conditions, the need to drink water, wipe their face or communicate with others.

In a restricted work environment with multiple activities and several vehicle movements, communication among the work teams is important for worker safety and discussions about the work process. However, workers often find it necessary to compromise their respiratory protection to have these conversations. While participants acknowledged the challenge of speaking in the P2 mask, the difficulty was more severe with the half-face mask and the PAPR. However, participants noted that the PAPR used on the project was more comfortable than the P2 and half-face mask.

In addition to these challenges, there is resistance among some workers to comply with the shaving requirement for the use of P2 and half-face masks despite the provision of shaving tools in some washrooms. The main reason is rooted in personal lifestyle choices.

Presently, only a specific group of workers on the project receives PAPR, which does not require a clean-shaven face. Most participants advocated for the use of only the PAPR on the project. Irrespective of these challenges with the continuous use of mask, participants rate compliance as high.

3.5.4 *Dust risk perception*

These compliance related issues were mainly attributed to the low dust-risk perception of workers, as the severity of dust-related problems is not immediate. Moreover, dust has only recently emerged as a significant concern for workers, possibly heightened by the nationwide awareness of RCS exposure in the engineered benchtop industry (SafeWork SA 2023).

The project's reliance on construction contractors, who may typically operate in environments with less strict dust control measures, further contributes to a lack of awareness of dust control requirements and compliance. This low dust risk perception makes some workers complacent, especially when they do not see dust in the work area.

3.5.5 *Addressing dust control challenges*

Across the participants, a strong consensus was the need for more education, particularly emphasising the consequences of RCS exposure. This can be done by using silicosis patients to share their experiences or having medical professionals and experienced tunnellers share their knowledge.

Furthermore, participants stressed the importance of enhanced collaboration between tunnel clients, government entities, and regulatory bodies to reduce dust exposure. Regular visits by regulators were advocated to ensure compliance. To enhance collaboration, they recommended the establishment of a dedicated learning team to champion research efforts to find effective solutions and share best practices across Australian tunnelling projects.

Participants also believed that having competent professionals or more hygienists among the work teams to help translate the dust control and ventilation plans into practice would enhance dust control practices.

One participant proposed a solution to address concerns about cost optimisation potentially affecting dust controls. The participant suggested that the cost for dust control should be predetermined and fixed for all bidding firms to eliminate variability and ensure a consistent commitment to effective dust control measures across tunnelling projects.

4 DISCUSSION

The study employed a survey, site observations, and interviews to understand practices and challenges in reducing RCS exposure during tunnelling. The results indicate the survey effectively identifies dust control knowledge and attitudes among tunnellers, allowing for detailed exploration through interviews. Positive factor loadings in the survey's five domains suggest a favourable relationship between observed variables and respective latent factors. The generally satisfactory

fit model of the survey indicates further scale refinement would result in stronger factor loadings and a better fitting model.

The study emphasised a positive attitude toward Awareness and Control of Dust on the project, while other domains mainly received negative ratings. The score for Dust Control Satisfaction as shown in Figure 3 demonstrate there is room for improvement in reducing dust exposure on the project despite participants praising the project's dust control measures when compared to their previous experiences. The negative ratings may be due to instances where the supervisory team had to step in to stop the dust generating activity to rectify the cause. Positive correlations between Teamwork and Awareness and Control of Dust, and between Teamwork and Dust Control Satisfaction, suggest opportunities for practical interventions. Improving one domain is likely to influence the others positively.

Some of the challenges faced in tunnelling are similar to ones faced in general construction such as cost, inadequate risk perception of dust, and worker attitudes (Abas et al. 2021). The study findings are consistent with the results of Utuk and Atulomah (2023) that negative attitudes towards dust control exist even among workers with adequate knowledge of exposure risk. Additionally, findings about heat affecting compliance for dust masks in underground tunnels align with ATS (2018). Thus, their recommendation for a "worker respite station" in tunnelling where workers can cool down or have a drink is highly seconded.

The study further indicates that when workers perceive controls as inadequate, they prioritise alternative approaches to complete the job, even if unsafe. This highlights that workers focus on getting the job done rather than prioritising safety. Hence, when assigning tasks, supervisors should emphasise the necessary dust controls. Additionally, interactions among work teams can adopt coaching conversations, as explained by Long (2021).

Calls for collaboration are consistent with the current cooperation between industry and Australian regulators termed the Air Quality Working Group (AQWG) (ATS 2020). The partnership has led to the publication of several reference materials to help improve occupational health outcomes, including RCS exposure reduction.

The need for increased education is highlighted by limited formal academic education specific to tunnelling, unlike mining. These efforts will enhance engineers' understanding of factors influencing the effectiveness of dust controls in the design of work activities. Moreover, the decade-old guide for tunnelling in Australia (SWA 2013) lacks comprehensive information on dust control, although it is understood to be under review by the collaborative working group.

The insights from the study highlight the complexities of implementing dust control measures and the need for ongoing attention to equipment, employee compliance, and the dynamic nature of tunnelling. Addressing these challenges requires effective collaboration, equipment design, training, and enforcement of controls.

Limitations to consider when interpreting the study results include that although the sample size aligns with qualitative research methods and objectives (Dworkin 2012), it is crucial to note that these findings may not represent all tunnelling projects in Australia or globally. Additionally, the results presented are based on a preliminary research data analysis.

5 CONCLUSIONS

This research aimed to identify the barriers and challenges hindering the implementation of adequate controls and the adoption of safe work practices to protect workers from RCS exposure in tunnelling. It demonstrates the feasibility of reliably and meaningfully measuring tunnellers' dust control knowledge and attitudes. The study reveals a complex interplay of organisational, operational, technical, environmental and individual factors influencing dust exposure on tunnelling sites. Furthermore, the study highlights that despite advancements in dust control in tunnelling, continued improvement requires collaboration, strict enforcement, technological advances in dust control, and enhanced respiratory protection.

The study demonstrates that the level of knowledge and attitudes towards dust control in tunnelling can be measured. The study supports the recommendation to standardise the cost aspect of dust control for all bidding firms, thereby eliminating variability and ensuring a consistent commitment to dust control from tunnelling companies. It advocates for stricter enforcement of standards, urging tunnelling clients and governments to allocate funds for research addressing identified gaps and facilitating opportunities for sharing best practices among tunnel contractors. Knowledge sharing should include experiences from experienced tunnellers, medical professionals, and silicosis-diagnosed patients with workers to help raise workers' risk perception. Furthermore, the study calls for more focused formal studies on tunnelling dust control.

There is a need for focused research to address identified gaps, such as the absence of on-tool controls for excavators or dozers. Solutions for eliminating residual dust in tunnels merit increased research attention, including improvements in communication when using respirators.

ACKNOWLEDGEMENTS

This research constituted an independent study in the Centre of Occupational Public and Environmental Research in Safety and Health (COPERSH) supported by a doctoral scholarship funded by the Occupational Safety and Health Research Alliance (OSHRA). Gratitude goes to Leanne Treadwell for her feedback on the interview questions and reading through the manuscript.

REFERENCES

Abas, N, Ali, MM & Abas, N 2021, 'Masonry Dust Risk Control Practices and the Barriers to the Adoption of Engineering Controls in Reducing Risk due to Dust Exposure in Masonry Work', in IOP Conference Series: Materials Science and Engineering, vol. 1200, p. 012026.

Al Malki, A, Endacott, R & Innes, K 2018, 'Health professional perspectives of patient safety issues in intensive care units in Saudi Arabia', *Journal of Nursing Management*, vol. 26, no. 2, pp. 209–18.

Alayed, AS, Lööf, H & Johansson, U-B 2014, 'Saudi Arabian ICU safety culture and nurses' attitudes', *International Journal of Health Care Quality Assurance*, vol. 27, no. 7, pp. 581–93.

Anlimah, F, Gopaldasani, V, MacPhail, C & Davies, B 2023, 'A systematic review of the effectiveness of dust control measures adopted to reduce workplace exposure', *Environmental Science and Pollution Research*, vol. 30, no. 19, pp. 54407–28.

ATS 2018, 'Good practice to control silica dust exposure during NSW tunnel construction: Air quality working group information package Part 2 of 12′, Available at https://www.ats.org.au/resources/working-group-papers/ .Accessed on 23 November 2023.

ATS 2020,*NSW Air Quality Working Group*, viewed 20 December 2023, Available at https://www.ats.org.au/resources/working-group-papers/. Accessed on 23 November 2023.

Bakke, B, Ulvestad, B, Thomassen, Y, Woldbæk, T & Ellingsen, DG 2014, 'Characterization of occupational exposure to air contaminants in modern tunnelling operations', *Annals of occupational hygiene*, vol. 58, no. 7, pp. 818–29.

Cai, P, Nie, W, Liu, Z, Xiu, Z, Peng, H, Du, T & Yang, B 2020, 'Study on the air curtain dust control technology with a dust purifying fan for fully mechanized mining face', *Powder Technology*, vol. 374, pp. 507–21.

Cole, K 2016, 'Investigating best practice to prevent illness and disease in tunnel construction workers'.

Cole, K, Glass, D, Bence, T, Pisaniello, D, Knott, P, Rowett, S & Johnson, S 2023, 'Prevention of the Occupational Silicosis Epidemic in Australia: What Do Those Who Assess Workplace Health Risk Think Should Be Done Now?', *Ann Work Expo Health*, vol. 67, no. 2, pp. 281–7.

Dworkin, SL 2012, *Sample size policy for qualitative studies using in-depth interviews*, Springer, 0004–0002.

Guo, L, Nie, W, Yin, S, Liu, Q, Hua, Y, Cheng, L, Cai, X, Xiu, Z & Du, T 2020, 'The dust diffusion modeling and determination of optimal airflow rate for removing the dust generated during mine tunneling', *Building and Environment*, vol. 178, p. 106846.

Guo, Q, Ren, W & Shi, J 2019, 'Foam for coal dust suppression during underground coal mine tunneling', *Tunnelling and Underground Space Technology*, vol. 89, pp. 170–8.

Haas, EJ, Willmer, D & Cecala, AB 2016, 'Formative research to reduce mine worker respirable silica dust exposure: a feasibility study to integrate technology into behavioral interventions', *Pilot Feasibility Stud*, vol. 2.

IARC 1997, *IARC Monographs on the evaluation of carcinogenic risks to human*, Available at http://monographs.iarc.fr/ENG/Classification/index.php. Accessed on 14 August 2023

Kaluarachchi, M, Waidyasekara, A, Rameezdeen, R & Chileshe, N 2021, 'Mitigating dust pollution from construction activities: A behavioural control perspective', *Sustainability (Switzerland)*, vol. 13, no. 16.

Leite, M, Nordby, K-C, Skare, Ø, Ulvestad, B, Ellingsen, DG, Dahl, K, Johansen, T & Petter Skaugset, N 2023, 'Exposure to Particulate Matter and Respirable Crystalline Silica in Tunnel Construction Workers Using Tunnel Boring Machines', *Annals of Work Exposures and Health*, vol. 67, no. 5, pp. 584–95.

Leung, CC, Yu, ITS & Chen, W 2012, 'Silicosis', *The Lancet*, vol. 379, no. 9830, pp. 2008–18.

Long, I 2021, *Essentials of Safety: Maintaining the Balance*, CRC Press.

Rushton, L 2007, 'Chronic obstructive pulmonary disease and occupational exposure to silica', *Reviews on environmental health*, vol. 22, no. 4, pp. 255–72.

Safe Work Australia 2013,*Guide for Tunnelling Work*, Available at http://www.safeworkaustralia.gov.au/system/files/documents/1702/guide-tunnelling.pdf Accessed on 15October 2023.

SafeWork SA 2023, *Safety campaign to target silica exposure in workplaces*, Available at https://www.safework.sa.gov.au/news-and-alerts/news/news/2023/safety-campaign-to-target-silica-exposure-in-workplaces. Accessed on 14 October 2023.

Sexton, JB, Helmreich, RL, Neilands, TB, Rowan, K, Vella, K, Boyden, J, Roberts, PR & Thomas, EJ 2006, 'The Safety Attitudes Questionnaire: psychometric properties, benchmarking data, and emerging research', *Bmc Health Services Research*, vol. 6.

Sifanu, M, Taylor, TK, Kalebaila, KK, Hayumbu, P, Nabiwa, L & Linde, SJ 2023, 'Knowledge, Attitude, Behavior Practices and Compliance of Workers Exposed to Respirable Dust in a Zambian Copper Mine', *International Journal of Environmental Research and Public Health*, vol. 20, no. 18, p. 6785.

Sun, H, Liu, Y, Jiang, T, Liu, T & Liu, D 2023, 'Application of dust control method based on water medium humidification in tunnel drilling and blasting construction environment', *Building and Environment*, p. 110111.

The Jamovi Project (2023). *Jamovi* (version 2.3.19) [Computer Software]. Available at https://www.jamovi.org. Accessed on 13 June 2022.

Utuk, UU & Atulomah, N 2023, 'Knowledge, Attitude, Perception and Health-Seeking Behaviour Regarding Occupational-Risk of Cement-Dust Exposure Among Lafarge Workers in Ewekoro Ogun State, Nigeria'.

Victorian Government 2023, *Metro Tunnel Project*, Available at https://bigbuild.vic.gov.au/projects/metro-tunnel. Accesed on 23 November 2023 2023

Vupputuri, S, Parks, CG, Nylander-French, LA, Owen-Smith, A, Hogan, SL & Sandler, DP 2012, 'Occupational silica exposure and chronic kidney disease', *Renal Failure*, vol. 34, no. 1, pp. 40–6.

WHSQ 2013, *Occupational dust and silica conditions in some Queensland construction and related industries*, Accessed on 14 August 2023.

Xing, J, Ye, K, Zuo, J & Jiang, W 2018, 'Control Dust Pollution on Construction Sites: What Governments Do in China?', *Sustainability*, vol. 10, no. 8.

Zuo, J, Rameezdeen, R, Hagger, M, Zhou, Z & Ding, Z 2017, 'Dust pollution control on construction sites: Awareness and self-responsibility of managers', *Journal of Cleaner Production*, vol. 166, pp. 312–20.

Tunnelling for a Better Life – Yan, Celestino, Thewes & Eberhardt (Eds)
© 2024 The Author(s), ISBN 978-1-032-80042-4
Open Access: www.taylorfrancis.com, CC BY-NC-ND 4.0 license

Design and construction optimisation of the Karanga-a-Hape Station mined tunnels and bored tunnel cross passages on the City Rail Link project

Vinnothan Balakumarasingham*
Aurecon (formerly Link Alliance & Tonkin and Taylor), Auckland, New Zealand

Pierre Daudibertières* & Emmanuel Chatoux
Vinci Construction Grands Projets, Nanterre, France

Wataru Okada
WSP, Auckland, New Zealand

ABSTRACT: The City Rail Link (CRL) is a major railway construction project underway in Auckland, New Zealand. The project includes the design and construction of two underground rail stations, the redevelopment of an existing surface rail station, two new rail tunnels and the connection to an existing line. This paper presents the design and construction optimisation of the Karanga-a-Hape Station Mined Tunnels and the Bored Tunnel Cross passages on the project. Karanga-a-Hape Station is a 32m-deep mined underground, twin platform station with four cross passages along the bored tunnel alignment. An overview of the design of the elements is presented with particular focus on the construction optimisation of the secondary linings during detailed design, the programme and implications for methods. The secondary lining formwork selection process is described along with formwork systems and shape optimisation. Lessons learnt from design and construction are presented along with future opportunities for optimisation.

Keywords: Tunnelling, Secondary Lining, Tunnel Formworks

1 INTRODUCTION

1.1 *Project overview*

The City Rail Link (CRL) is New Zealand's largest transport infrastructure project ever to be constructed. CRL is a 3.45km twin-tunnel underground rail link up to 42 metres below the city centre transforming the downtown Waitematā Station (Britomart) into a two-way through-station that better connects the city's rail network.

It includes a redeveloped Maungawhau Station, where the CRL connects with the North Auckland (Western Line) and new underground stations - one midtown underneath Albert Street called Te Waihorotiu Station and Karanga-a-Hape Station just off Karangahape Road with entrances at both Mercury Lane and Beresford Square.

The Link Alliance is delivering the main works including three new stations, twin tunnels, rail systems and work at the existing Waitemata Station (Britomart) to accommodate the new rail connection. Link Alliance comprises City Rail Link Limited, Vinci Construction Grands Projets, Downer NZ Ltd, Soletanche Bachy International NZ Limited, WSP (NZ) Limited, AECOM New Zealand Limited and Tonkin + Taylor Limited[1].

Figure 1. City Rail Link contract C3 alignment and station.

1.2 *Karanga-a-Hape station tunnels*

Karanga-a-Hape Station is a 32m-deep mined underground, twin platform station. A temporary access

*Corresponding author: Pierre.daudibertieres@vinci-construction.com; Vinno.Bala@aurecongroup.com

DOI: 10.1201/9781003495505-186

shaft was constructed halfway along the Adit 1 alignment (Figure 2) and served as the only access and egress point during the construction of both the primary and secondary linings.

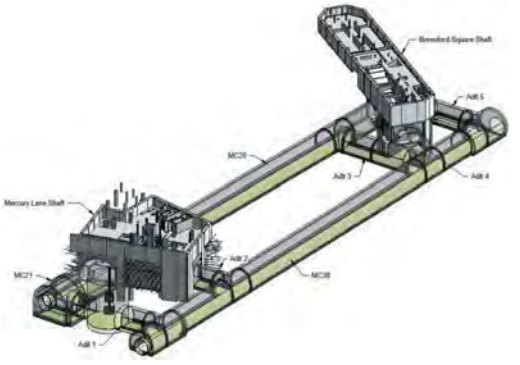

Figure 2. Station shaft and tunnels layout.

The tunnels were excavated through the East Coast Bays Formation, a sandstone that varies from very weak to strong interbedded layers across the project alignment. However, there were channelised sandstones present at Karanga-a- Hape along with a possible fault that contained a broken zone.

The tunnels were constructed with road headers and the primary lining comprised shotcrete followed by a geotextile and a PVC sheet waterproofing membrane.

The secondary lining sections varied to account for ventilation requirements. The secondary lining sections were split into platform tunnel (PT) and adit (AD) sections.

Corbels are present in all the PT sections but were optioneered out of the AD sections to aid formwork construction and operation in the smaller cross sections.

All tunnel profiles are effectively at grade except for Adit 1 which has a 6.9% slope. Section geometry, thicknesses and profile lengths are presented in Table 1.

Table 1. Secondary lining profile summary.

Tunnel Section	Profile (length)	Width x Height at intrados	Max thickness
Platform tunnel MC30	PT-1 (186m)	9.0m x 7.9m	400 mm
Platform Sub-Zone MC31	PT-2 (20m)	10.3m x 7.9m	550 mm
Platform Sub-Zone MC32	PT-2 (8m) PT-4 (13m)	10.3m x 7.9m 10.9m x 9.0m	550 mm 800 mm
Platform tunnel MC20	PT-1 (123m)	9.0m x 7.9m	400 mm
Platform Sub-Zone MC21	PT-5 (32m)	13.4m x 9.6m	900 mm
Adit 1	AD-2 (30m)	7.9m x 6.7m	350 mm
Adit 2	AD-1 (12m)	7.9m x 7.2m	350 mm
Adit 3	AD-1 (32m)	7.9m x 7.2m	350 mm
Adit 4	AD-3 (21m)	10.3m x 6.7m	400 mm
Adit 5	AD-2 (27m)	7.9m x 6.7m	350 mm

2 KARANGA-A-HAPE TUNNEL SECONDARY LINING DESIGN

2.1 *Design team organisation*

The design team comprised both local and international based firms to leverage both local geological expertise and broader metro and large span tunnel design experience.

2.2 *Lining design*

2.2.1 *Design philosophy*

The detailed design was based on an unreinforced drained tunnel with reinforcement only provided at the corbels and the junctions with the adits. The design itself was carried out by long established methods such as the use of bedded beam models documented extensively in published literature.

2.2.2 *Early contractor input*

The alliance delivery model facilitated early contractor input with regular co-ordination between the contractor's methods team and the designers. Specifically, the design was able to facilitate the preferred formwork transition strategy (4.2.1). The tunnel geometry was frozen early in the detailed design to facilitate procurement discussions with formwork suppliers.

2.3 *Lessons learnt*

The reinforcement detailing was carried out by the steel supplier based on detailed design intent drawings. The drawings and schedules were checked by project engineers and the designer's representative on site but there were inevitable issues with the supplier interpreting the design intent drawings. As such, in house production of the construction drawings and schedules would have led to the removal of an additional quality assurance process and potentially reduced lead times for reinforcement supply.

The transitions between platform tunnels and the sub-zones (MC30 to MC31) necessitated two

formwork transformations for relatively short sections. Each transformation took 2 to 3 weeks and was both logistically and labour intensive. As such, the need for shorter unique sections could be reappraised for similar projects in the future where there is safe scope for an extended larger initial excavation for the primary lining.

The design of the interfaces with the headwalls were initially based on concrete-to-concrete bearing connections with the secondary lining. However, during construction it became apparent that this was not possible at the largest section (MC32- PT-4). The secondary lining had to be built before the headwall was completed and it would not be possible to safely install a stop end along the circumferential face of the

Figure 3. Headwall stitched to secondary lining.

tunnel. As such, a stitch detail was provided to connect the headwall to the secondary lining (Figure 3).

3 CONSTRUCTION

3.1 *Concrete mix design and performance*

3.1.1 *Concrete mix specifications*

The main concrete design requirements were as follows:

- Compressive strength at 28d: 40MPa
- Flexural tensile strength at 28d: 3.8MPa
- Drying shrinkage at 56d under 1000 µstrain
- Maximum W/C ratio of 0.45
- Fire resistance to the RABT-ZTV (car) curve
- Minimum of 20% of Pulverised Fly Ash (PFA) in the binder, to satisfy the project's minimum cementitious replacement targets (no other cementitious replacement materials – such as ground granulated blast furnace slags, metakaolins etc.- were available in New Zealand during the CRL construction
- Maximum core temperature of hardening concrete: 75°C
- Maximum temperature differential between core and skin during concrete hardening following an evolutive criterion depending on concrete maturity, as per CIRIA C766
- 10MPa at formwork striking time

In addition, the mix design needed to satisfy the following constructability requirements:

- 100m pumpability
- Slumpflow of 500mm +/-50mm with workability retention of 3h

It was decided to proceed with a flowable mix rather than a self-compacting mix, in order to increase its robustness and limit quality issues linked to batching variability. Vibration was provided with skin vibrators fixed to the formwork (Figure 8). The fire resistance was provided by the inclusion of polypropylene microfibres. 6mm long, and 18µm diameter fibres were selected. The fibre content was optimized to 0.9kg/m3 following a series of furnace tests on 1200x1200mm concrete panels.

Two mixes were used:

- Mix A: 40MPa concrete with 30% PFA
- Mix B: 40MPa concrete with 40% PFA, designed to limit detrimental thermal effects on larger section pours

3.1.2 *Strength and temperature predictive modelling, and implementation of site-based maturity strength and temperature controls*

To refine striking times and optimize construction cycles, and to remain in control of thermal issues such as early age cracking and delayed ettringite formation, we implemented a program of thermo-numerical predictive calculations and site based concrete maturity controls.

Determining the correct striking times was paramount for the large pours of unreinforced concrete, to avoid detrimental cracking, and meet programme targets.

We performed semi-adiabatic calorimetry tests as per the EN 196-9 (2010) test methods on the proposed binders, to determine their heat release properties. Along with general constituents' properties, formwork and shotcrete thermal exchange properties, and sample-based calibration, this allowed us to build an accurate thermo-numerical model to study and predict strength gain, and temperature developments in the structures, depending on fresh concrete and ambient temperatures.

This work drew on over 15 years' experience of the Alliance partners, including several PhDs and extensive site implementation, on thermo-numerical calculations for concrete structures.

This was used to determine which mix to use based on the lining thickness, and current temperature conditions, and when to strike the forms.

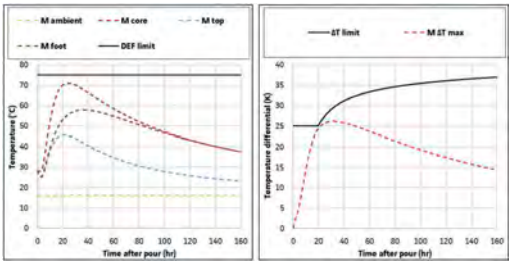

Figure 4. Expected temperature and differential within 0.9m thick section with Mix A in spring.

Table 1 shows the predicted striking times at 10MPa, along with maximal authorized fresh concrete temperature to prevent thermal issues, for various lining thicknesses poured with Mix A:

Table 2. Mix A pouring guidelines.

Tunnel final lining thickness	Max allowed concrete temperature at delivery	Expected time (from the end of pour) to achieve 10 MPa within the tunnel lining
≤700mm	32°c	13 hours
>700mm ≤900mm	28°c	15 hours
>900mm ≤1100mm	23°c	17 hours

These results were compiled in a thermal study report shared with the construction teams and used as a planning tool for the pours on site.

For the actual construction phase a maturity calculation tool was built, based on a preliminary equivalent age/strength calibration phase. The construction teams were trained to use the tool, which would allow them to determine their striking time.

Initial monitoring of the pours was implemented with thermocouples placed at the core and at 50-100mm of the surface, to control peak core temperature and temperature differential, and to determine surface concrete strength for striking with the maturity tool.

After validation of the predictive modelling for core temperature and temperature differential, only surface temperature was monitored on subsequent pours for the site teams to determine exact striking time at 10MPa, to enable construction cycles optimizations.

The maturity tool formulas calibration was verified every 6 months by crushing cylinders kept at specific temperatures, at various ages.

3.2 *Tunnel formworks*

The construction of the Karanga-a-Hape station tunnels secondary lining necessitated the use of four different sets of formwork. Different types of formwork were specified depending on the geometrical and logistical constraints as well as the number of pours and performance expected in the different tunnel sections. These four sets are summarised in Table 2 and described in the following sections.

Table 3. Summary of formworks sets.

Tunnel Section	Description	No.	Manufacturer
Platforms MC20 & MC30	Pre-stressed full section	1 unit + 3 junctions.	Tunnel Formworks International
Platform MC21	Crown	1 unit + 1 junction.	Liando Tianjin
Adits A1, A2, A3 & A5	Separated Crown and Sidewalls	2 sets	Liando Tianjin
Adit A4	Separated Crown and Sidewalls	1 set + 1 junction.	Liando Tianjin

3.2.1 *Platforms formwork*

A single formwork system was designed to build all the platform tunnels and adapt to the 3 different sections existing along the alignment. This was only possible due to the early involvement of the construction team in the design process which allowed the tunnel sections geometry to be refined so to optimise the need for formworks.

The basic principle was to keep the geometry of the sidewalls unchanged and to extend the section by inserting straight extension pieces in the crown (Figure 5).

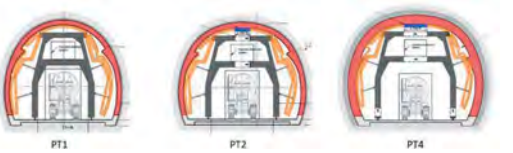

Figure 5. Platform tunnel sections.

The key elements which had to be considered were:

- The total length of the formwork: This was dictated by the width of the junctions with the connection adits as the junction must be poured in one go. This meant the initial 10m maximum pour length considered in the design had to be increased to 11.5m.
- The interface with the headwalls: This meant the whole gantry system had to sit within the extent

of the formwork and the end access platforms had to be easily removable.

- The assembly constraints: The maximum size and weight that can be transported to site, lifted down the shaft, transferred to and from the assembly location and lifted in place had to be determined early in the formwork design process.
- The transformation methodology: The design of the system had to take into account all the temporary stages so the assembly was stable throughout the transformation process. Due consideration also had to be given to the size and weight of the elements in relation to the space and handling constraints at the time of their installation and removal. The elements involved in a transition are shown in Figure 6 and Figure 7
- The minimum traffic gauge: The minimum gauge through the gantry to allow site traffic and services.
- The position of the concrete ports and vibrators: The concrete windows and ports were spaced so to ensure the maximum concrete drop would not exceed 2.0m (Figure 8). The compressed air vibrators were placed according to their radius of influence and the thickness of the lining.
- The desired performance: Since the main formwork was due to build approximatively 350lm of tunnel lining in 33no. bays, the cycle time required to strike, tram and reset the system was of prime importance to achieve the construction programme. To make this process as efficient as possible, all the movements were operated hydraulically. This included:

  – Bogies on rails
  – Hydraulic legs for vertical adjustment
  – Horizontal rams for horizontal of the whole form structure on the gantry
  – Hydraulic rams to operate the corbel shutters
  – Hydraulic props to operate the side skins
  – Hydraulic pins to lock the props in place
  – Pre-stressing jacks at the end of the props

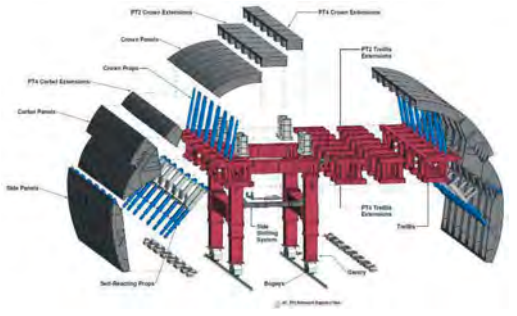

Figure 6. Platform tunnel formwork exploded view.

Figure 7. PT form during transition (central section about to be inserted).

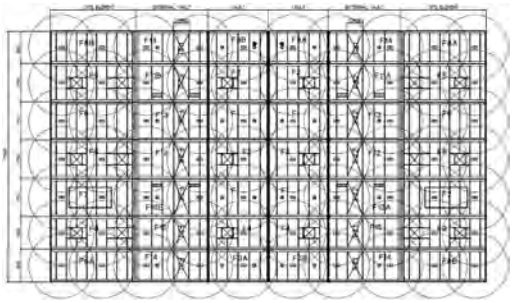

Figure 8. Developed view of skin vibrators and windows.

3.2.2 *Junctions formworks*

The formworks add-on required to form the junction of the main tunnels with connection adits were included into the same scope to ensure the best compatibility of the systems. Although efforts were made to standardise the junctions as much as possible, the different section types and levels meant that 3 junction formwork types were required to build the five junctions (Figure 9).

3.2.3 *MC21 cavern formwork*

The formwork of the MC21 cavern was developed giving attention to the same consideration as described in 3.2.1, however the solution was very different as the constraints were different. The main differences were:

- **The length of the cavern:** The cavern was only 33m long and took only 3 pours and did not need any reconfiguration. This meant the design was kept as basic and economic as possible with no hydraulics involved. All the skin movements were operated manually using turnbuckle props.

Figure 9. Junction formwork.

This resulted in longer cycle times during construction but was balanced by the reduced assembly and commissioning time required.

- **The assembly constraints:** Due to the large 14m wide section of the cavern to be built, the space available for the assembly was less of a constraint, meaning larger individual elements could be handled which sped up the assembly.

Figure 10. MC21 formwork.

3.2.4 *Adits formworks*

The station comprises 5 connection adit tunnels (Figure 11), relatively short in length and with some distinct features such as junctions and corners (Table 4).

During the design phase, the section profiles AD1 and AD2 were optimised so they use the same radii and only differed in height. This allowed the development of a set of formworks which could be used in 4 of the 5 adits. However, it was not possible to rationalise the section of Adit A4 and so a specific set of formworks had to be procured for this location.

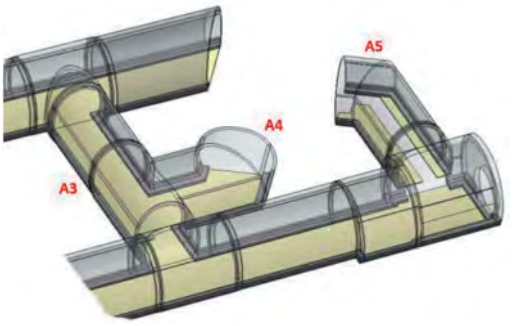

Figure 11.3D. View of adit A3, A4 and A5.

Table 4. Summary of tunnel adits sections.

Adit	Section	Length	Unique feature (s)
A1	AD2	34m	-
A2	AD1	11m	-
A3	AD2	30m	Junction with A4
A4	AD3	15m	Corner and junction with. A3
A5	AD2	20m	Corner

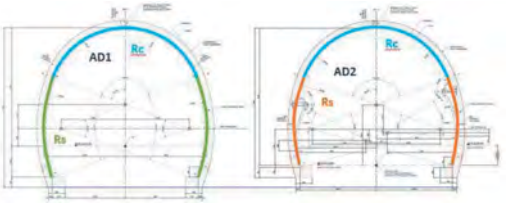

Figure 12. Adit sections AD1 and AD2 geometry.

The key elements considered during the procurement of the adit formworks were:

- **Mobility:** Since the adits were relatively short, it was identified that an important part of the effort would be spent in assembling, transferring and transforming the formwork elements.
- **Repeatability:** The formworks' design aimed at reusing the same parts as much as possible, minimising the need for special single use pieces.
- **Durability:** The system had to be simple and robust so it could be used for a number of pours over several months with minimum maintenance.

With these considerations in mind, it was decided to use steel formwork and to split the pours between sidewalls and crowns, resulting in smaller formwork elements that could be pre-assembled at the surface and transferred between adits.

The sidewalls were cast in 4m-long bays using 2m-long modules connected. The reaction frame allowed the skin to tilt to adjust to the different tunnel profiles. Two specific corner pieces were designed to build the corner in Adit A5.

Figure 13. 4m Sidewall Formwork.

Figure14. Sidewall formwork reconfigured in inner (top) and outer (bottom) corners using insert pieces.

Figure15. Junction between adits A3 and A4.

For the crown, two 5m-long formworks were procured. They featured a hydraulically operated gantry which allowed tramming as well as vertical and lateral adjustments.

The two modules were designed with a triangular removable section which allowed the system to be reconfigured in a corner setup with minimal need to extra components as shown on Figure 7. All the skin pieces were reused and only a few specific supporting beams had to manufactured. These removable sections were broken down into small elements to help with the handling in constrained spaces during the reconfigurations.

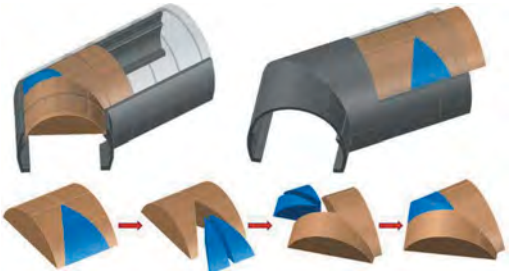

Figure 16. Crown formwork reconfiguration.

A dedicated set of formworks were developed for adit A4 following the same principle. Junction add-ons were also designed to build the junction between adits A3 and A4.

Figure 17. Adit A4 Crown formwork skin during manufacture with corner and junction piece.

4 CROSS-PASSAGES DESIGN

4.1 *Primary and secondary lining design*

The primary lining comprised a 125mm shotcrete shell (sprayed in two passes) and the secondary

Figure 18. Adit A4.

lining was a 300mm thick traditional concrete section. Similar, to the typical cross sections away from the junction in the station tunnels both layers were designed as unreinforced concrete sections using well documented methods.

4.2 *Collar design*

A relative innovation in the collar design and construction was the removal of the need to temporarily support the cross passage openings with lintels. This was achieved by reinforcing the first stage concrete in front of the cross passages and anchoring it to the bored tunnel segments.

Figure 19. Reinforcement for first stage concrete and cross passage opening without lintel.

5 CROSS-PASSAGES CONSTRUCTION

An overview of the cross passage construction sequence is as follows:

1. Probe drilling
2. Saw cutting the segments
3. Removing the segments
4. Excavating in 2m steps
5. Shotcreting
6. Secondary lining pour
7. Collar reinforcement placement
8. Collar pour.

The collars were fixed at 90 degrees from the bored tunnel intrados and the secondary lining formwork only allowed for perpendicular stop ends. As such, additional concrete sections were required between the collar and the secondary lining to fill the gap (Figure 20). The collar formwork and stop ends could comfortably be adjusted to create the angles created (Figure 7).

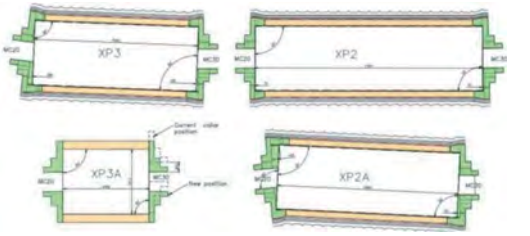

Figure 20. Collar and secondary lining arrangement.

Figure 21. Collar form meeting cast secondary lining section.

6 CONCLUSIONS

Early contractor involvement during the detailed design of the secondary linings facilitated a formwork selection process that sped up construction. This was mainly due to formwork that could be enlarged on site to form different profiles. Whilst the adaptation of formwork on site can be logistically and labour intensive it is preferable to having bespoke formwork for each tunnel profile.

The use of BIM to produce 3D sequencing drawings was commonplace on this project and was

a valuable tool in conveying construction methods to everyone involved in the operations.

Cross passage openings are typically formed with lintels above and below the opening and jambs either side. This typically involves lifting and fixing steel sections in a confined working environment. However, reinforcing the first stage concrete in front of the cross passages removes this risk. Moreover, in this instance a separate team could carry out this task whilst the mining team was utilised elsewhere.

ACKNOWLEDGMENTS

The authors would like to thank the Link Alliance for the permission to submit this paper.

REFERENCES

[i] https://www.cityraillink.co.nz/.

Tunnelling for a Better Life – Yan, Celestino, Thewes & Eberhardt (Eds)
© 2024 The Author(s), ISBN 978-1-032-80042-4
Open Access: www.taylorfrancis.com, CC BY-NC-ND 4.0 license

Experiences during tunnelling in extreme ground conditions in the Himalayas - Excavation of Rohtang Tunnel, India

Radek Bernard*
SG-Geotechnika a.s., Prague, The Czech Republic

ABSTRACT: The 9,02 km long, single tube, two-lane bi-directional Rohtang Highway Tunnel through the Himalayas was finally opened on the October 2020. It was constructed at an elevation near 3.100 m above the sea level. This tunnel, which is still one of the longest highway tunnel of the World at such altitude, is also known by its complex and challenging geotechnical conditions, which unfortunately caused significant delays for the completion of the construction. Finally construction works takes approx. 10 years from the start of 2010 till the end - autumn 2020. Rohtang tunnel shortens the Manali–Leh Highway (NH 21) by about 50 km and should provide a route between Himachal Pradesh State and the union territories in Jammu and Kashmir over the whole year in the future, once further tunnels on this route will be completed.

Keywords: Drill & Blast, long tunnel, high overburden

1 INTRODUCTION

The Rohtang Tunnel (after opening new name added – The Atal Tunnel) is a highway tunnel located in the eastern part of Himalayas in the North Indian state of Himachal Pradesh. The tunnel was excavated from both directions by the Drill and Blast method with application of the NATM philosophy. From the South Portal, near to Manali, practically all-round year and from the North Portal, between Sissu and Khoksar (Lahaul & Spiti Valley) only approx. half year (summer season).

The project was constructed by FIDIC principles according to the Red book. The Contract was awarded to a joint venture of AFCONS, an Indian construction company and STRABAG (Austria). The design of the tunnel was provided by a Design Consultant SMEC International (Australia) and proof checked by a joint venture of 3G (Austria) and VAYAMTECH (India). Construction supervision was ensured by a joint venture of D2 Consult International (Austria) and ICT-PEMS (India) acting as an Engineer. Author of this article worked at this organization as a Leader of supervision party that time. The Rohtang tunnel is single tube as shown at Figure 1, with two 4 m wide bi-directional lanes, walkways and emergency egress channel located below the road structure 3,6 m wide and 2.25 m high precast escape channel, which connects both portal areas is accessible every 500 m through a stairs in niches.

The tunnel is horseshoe shaped with completed regular cross section of 75.9 m^2, and increased at the section of Seri Nallah fault zone constructed with deep invert (587.5 m long). Separated smoke duct is located at tunnel crown area allowing emergency ventilation. The tunnel lining is double shell with intermediate waterproofing membrane installed only in Seri Nallah section. The rest of the tunnel is sealed within construction joints by swelling tapes. Groundwater is collected by longitudinal drainage pipes. Primary support consists of shotcrete lining with wire meshes and lattice girders or steel fibre-reinforced shotcrete lining with lattice girders (in technological classes I. to III. without lattice girders). Self-drilling and/or Swellex rock bolts were used for radial rock bolting, spiles in the crown area as required. Final lining was made of cast-in-situ plain concrete, except Seri Nallah section and locations around large niches, where reinforced concrete was used.

1.1 *Basic features of the project*

Basic features of the project you can see on Table 1.

2 GEOLOGICAL SITUATION

The Rohtang tunnel is located in Higher Himalaya and about 100 km south of Indus Suture Zone (Indus

*Corresponding author: radek.bernard@geotechnika.cz

DOI: 10.1201/9781003495505-187

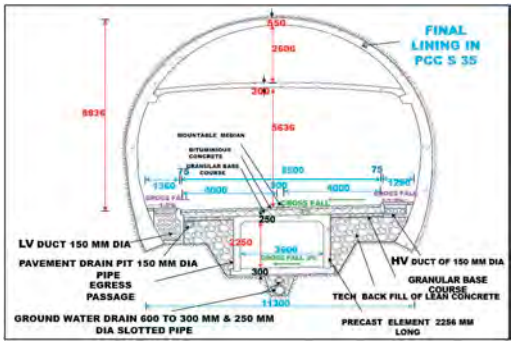

Figure1. Cross section of Rohtang highway tunnel.

Table 1. Main characteristics of the project.

Part of the Tunnel	Characteristic
Invert elevation at SP	3.060 m asl.
Invert elevation at NP	3.085 m asl.
Regular cross sectional area	75.9 m^2
General slope	0.5%, ascending from both portals
Finished dimension	Approx. 12 m wide at tunnel road level
Tunnel shape	Modified horse shoe
Concrete final lining	Cast in situ concrete
Smoke duct	At tunnel crown, above carriageway
Drainage system	Collect seepage water on side walls
Roadway	8 m wide with two lanes (1 m walkway)

Tsangpo Ophiolite belt). The project is situated in Rohtang Axial zone, which has a NW-SE trend, which divides the drainage system of Chandra river in the north and river Beas in the south with following tectonic features. The major tectonic feature separate the Lahaul-Spiti segment of the Spiti-Zanskar basin from the Tandi basin and also the Chamba-Bhadarwah basin and represents crystalline core with doubly plunging disposition.

This zone has the elements of mantled gneiss exhibiting anataxis and migmatization and underlies the Infra cambrian sediments. The overlying sedimentary sequence and its metamorphosed basal part are welded to the crystalline basement and it forms the root zone area of the Salkhala Nappe. The area is always covered by snow on the top with valleys and valley slopes having thick cover of vegetation. Seri Nalla is a significant stream which crosses the alignment and joins Beas Kund nala at about 1.8 km downstream of the South portal site. The general drainage pattern of the area encompassing the project site is sub-parallel and is structurally controlled. The South and North portal of tunnels are at elevation 3060 m and 3085 m respectively. The general srike of foliation of these folded and faulted mountains is NW-SE. In general the average trend of dip direction and amount of foliation of these rocks is 220/350° along with three major joints and one random joint. The main lithological rock units are Phyllitic quartzite, Quartzitic Phyllite, Migmatitic gneiss, Phyllites and Biotite Mica Schist. Geological profile is shown at Figure 2.

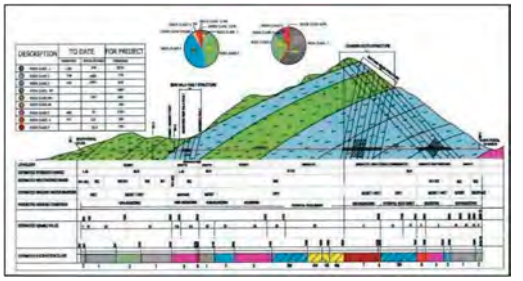

Figure 2. Longitudinal geological profile from design.

In general, the average trend of dip direction is 220° and plunge of foliation of these rocks is 350° along with three dominant joints planes and one random joint plane. Maximum overburden of the tunnel reaches 1860 m near chainage 6+000. The most complex and complicated geological condition was found in Seri Nallah fault zone within chainage 1+900 to 2+450 with maximum overburden 300 m located under small river valley as written above. The tunnel drive of Rohtang Tunnel was divided by design into six segments, based on the overburden depth primarily for the support system, see Table 2.

Table 2. Classification of tunnel based on overburden depth.

Segment	Overburden Depth (m)
I	0 to 300
II	301 to 600
III	601 to 900
IV	901 to 1.200
V	1.201 to 1.500
VI	> 1.500

3 TUNNELLING WORKS

The tunnel was excavated with horizontal excavation sequence. Tunnel face was divided into top heading and bench. To reach breakthrough of the tunnel as soon as possible, the highest priority was given to the top heading excavation. Therefore, in case of any machinery or labour reduction, all available resources were shifted to the top heading face, even at the cost of interruption benching works. That is why bench was excavated after breakthrough more than 1 km behind the top heading from both directions. Taking

into account the total length of almost 9 km accessible only from two portals, it was clear that proper planning and organization of all tunnelling works together with effective logistic was a key factor for construction schedule of the tunnel. Construction sit on the South portal you can see on the next Figure 3.

Figure 3. Rohtang's construction site at the South portal – more than 3000 m above the see.

That means independent working areas for all tunnelling main works throughout the tunnel, which included top heading excavation, half sided bench excavation, main tunnel drainage and concreting of base slab, concreting of first kicker (lower part of final lining slightly above the road level), installation of pre-cast emergency egress structure, concreting of second kicker and backfilling works up to the road level, installation of cable ducts and concreting of walkways, concreting of final arch lining, reinforcement and concreting of ventilation slab. In addition, there were other independent works on tunnel niches and on both tunnel portals. Construction of road structure and E&M works had to be completed afterwards. The Rohtang tunnel breakthrough was finally reached after 7 years from beginning of works on 15th of October 2017, directly at chainage 5+000 m. Breakthrough of the top heading brought many advantages for the rest of tunnelling works, especially with respect to a considerable length of the tunnel and limited access to the North portal. Firstly, all north portal works became accessible through the tunnel from south, which enabled in case of need direct material supply from large construction site near the South portal. It must be noted that south portal was more accessible and less affected by weather/climate condition than north portal. This logistic connection was successfully used mainly during winter period when operation of north portal construction site was significantly limited. It means breakthrough finally enabled to continue concreting works in full swing during winter period. On the other hand, considerable increasing of the traffic inside the tunnel was disturbing the rest of tunnelling works, mainly in Seri Nallah fault zone and benching stretches. Very positive impact to the all construction steps had the fact, that after the breakthrough natural tunnel ventilation was created, so all tunnel ventilation ducts could be removed. It enabled start of all re-profiling works and further excavation works in Seri Nallah fault zone, where huge ventilation ducts occupied almost all cross section. Moreover, due to natural ventilation, temperature inside the tunnel dropped from 36°C at the tunnel face to nearly natural temperature from outside.

3.1 *Tunnel excavation from South Portal in detail*

Tunnel construction from the South portal started by top heading excavation in August 2010, using mentioned Drill and Blast method. Top heading excavation had more than 1.000 m advance to bench at the beginning. Predominantly quarzitic schists with bands of phyllitic quartzites and phyllites with occasional seams of carbonaceous phyllites were encountered till chainage 1+900 during the first 18 months. No major problems occurred during initial drive from the South portal to Ch. 1+900, except for minor dripping of water and occasional wedge failures, which were easily managed by the Contractor. When tunnel excavation reached approx. Ch. 1+900, adverse shear zone, consisting of clay with minor rectangular fragments of quarzitic schists, charged with water was encountered 10° oblique to the tunnel axis from western side of excavated face at beginning of year 2012. Initial water inflow of 2 – 2.5 l/s was recorded. The fact of that shear, later very big fault zone called Seri Nallah, was confirmed for several hundred meters. The Q value of rock excavated determination was only around 0.5 indicating "Very Poor" rock condition. Accordingly, the rock support was immediately changed from more favourable rock classes to RC 6, later to RC 7 (the worst designed RC). You can see in Table 3 how Q values were divided and proposed RC at this project according design.

Table 3. Classification of tunnel based on Q value according design.

Serial No.	Condition	In situ "Q" - value	Excavation RC
1.	Good	> 10	1
2.	Fair	4 – 10	2
3.	Poor	1 – 4	3
4.	Very Poor	0.4 - 1	4
5.	Very Poor	0.1 – 0.4	5
6.	Exceptionally Poor	0.001 – 0.01	6 or 7

From Ch. 1+911 to Ch. 1+918 large deformation of primary support system was observed. Within 24 hours significant cracks were developed in the shotcrete of the primary lining, widths between 50 mm

and 300 mm were noticed. Deformations of primary lining also sharply increased and exceeded the amount of 500 mm. Immediately necessary measures were taken to prevent the collapse of the primary lining. From Ch. 1+904 to Ch. 2+049, the encountered rock condition featured highly jointed and sheared variously weathered quarzitic phyllites with a number of shear seams along and across the bedding planes. With ongoing excavation, geology slowly changed along the tunnel profile from rock to highly fractured, loose rock, (nearly soil condition). Rock condition changed from RC 1 with Q value ~ 20 (as determined/predicted in the tender document) to RC 6 (or 7) with Q value distinctly less than 1.

As already mentioned, the most difficult part of south drive was overcoming of the Seri Nallah fault zone with many large water inflows and frequent ingresses of loose river borne material inside the tunnel. Several types of remedial actions were implemented: dewatering pipes installation, single and multistage grouting using rock bolts, sequential excavation with top heading division into small panels and immediate support using shotcrete, wire meshes and rock bolts, single/double pipe roofing, temporary invert of top heading. Pilot tunnel and PU grouting were also used with no success. A total of 42 pipe roof umbrellas with single or double rows and length with 9, 12 or 15 m were installed within the Seri Nallah fault zone. These pipe roof umbrellas had dia firstly 87 mm, then only 114 mm. In April 2012, at Ch. 2+049, a sudden heavy inflow of water was observed at the centre of the face. The initial discharge was estimated with approx. 5 l/s and during the coming four hours, water inflow increased to 30 l/s that time. That rapid increase of water flow was then followed by a blowout of material from the crown area. The washed out material consisted of pieces of rock, rectangular in shape ranging in size from 1 to 5 cm. This washout resulted in the formation of a cavity/loose zone on right side of the crown of tunnel profile. The volume of slurry washed out was estimated with up to 300 m^3. As per the predictions of the geological studies and reports of the project should most probably have crossed the Seri Nallah Fault Zone near Ch. 2+200. However, these predictions also indicated that extensions of the fault zone could be expected. And further that due to the very shallow dipping angle of geological formations and the fault zone itself, earlier influence on the tunnel construction could be assumed. The surface study of the geological features and their correlations with geological features encountered at tunnel level (Ch. 2+049) indicated that this problem was not related only to the Seri Nallah fault, but was reflected especially due to another lineament crossing the tunnel alignment at this location. This statement is also in agreement with the fact that as per studies undertaken earlier, the Seri Nallah fault is the contact between quarzitic/phyllitic schist and the magmatic rocks. The Seri Nalla itself is one of the minor tributaries of Beas River, which is joined by several other small perennial cross drainages in the vicinity of the tunnel alignment at the surface. After stabilisation of the tunnel face, another major blowout occurred during tunnel construction at Ch. 2+076 on 7th September of 2012. Crushed material mixed with water and slurry of about 1.000 m^3 filled the tunnel from the crown area, creating another cavity/loose zone. The geological profile of that section indicated that the surrounding rock massif was heterogeneous in nature and mainly consisting of alternating bands of moderately to thinly jointed with a number of shear zones varying in thickness from 0.1 to 2 m. To stabilise the area, contact and cavity grouting was executed at Ch. 2+048 to Ch. 2+071 with 6 m long self-drilling rock bolts around the tunnel periphery (between 10 to 2 o´clock). The total grout consume was about 135 tons. After tunnel face stabilization, core drilling was carried out by using a diamond core drilling machine (4 boreholes 15 to 30 m long). Interpretation of core drilling indicated that the zone of dilated rock mass was created above the tunnel by the intersection of shear zone, which together with the high amount of water resulted by flowing conditions of the rock material. No major cavity was found during that investigation. After passing the tunnel section between Ch. 2+049 to Ch. 2+085 with heavy support by double pipe roof umbrellas, tunnelling conditions continued to be still difficult. Construction of the upcoming 406 m tunnel meters (between Ch. 2 +049 and Ch. 2+455) took more than 3 and half years. The presence of this weak and water bearing Seri Nala zone in highly sheared rock resulted in the formation of dilated material zone above the crown of the tunnel, which was slowly shifting to the left side the further tunnel excavation continued. In summer 2014 water inflow to tunnel profile increased approx. to 85 l/s and beginning of year 2015 the total water inflow reached 100 l/s, resulting in a lot of material wash out occurred at the tunnel face, which had to be solved by mentioned remedy actions. Also, a change of material composition was noticed. The highly fractured and shared material that was encountered in the beginning of the Seri Nallah stretch slowly gave way to so called river borne material (RBM), at least partially rounded rock fragments of different origin not necessarily related to the rock at/ or close to the tunnel face. Figure 4 shows the situation at Ch. 2+390. That day huge volume of loose material with water came to the tunnel by excavation from left side of the Top heading.

To stabilise the crown area and left side firstly 76 mm dia, then 89 mm dia pipe roofing were carried out, which unfortunately could not undertake the load of disturbed rock massif and it failed. Then 114 mm dia pipe roofing installed and it has also failed at some pipe roof stretches. Finally double layer skin to skin pipe roof 114 mm dia, 15 m long perforated pipes, including 76 mm dia drainage pipes up to length 24 m were installed at critical area from Ch. 2+413 till Ch. 2+445 as shown on the Figure 5. Perforated pipes were of course used for

Figure 4. Material wash out at top heading in ch. 2+390 dated 30/08/2014.

optimal grouting procedures of surrounding massif. The highest inflow 102 l/s of water was observed from Ch. 2+403 onwards till passing the Seri Nalla Fault Zone. At the start of the year 2016 regular rock massif was finally encountered.

Figure 5. Installation of double pipe roof umbrella with dia 114 mm at the stretch of 2+413 to 2+445.

3.2 *Tunnel excaviation from North Portal in detail*

Tunnel excavation from North Portal (NP) was found much different compared to the South. The overburden was much higher and tunnel drive went through hard rock formation for the most part of that stretch. Weather conditions allowed working during procedure max. 6 to 7 months per year, depending on the snowfall. North drive included rock bursting and squeezing condition during excavation with overburden reaching almost 1.9 km, caused large convergences over 20 cm and extensive cracks of primary lining. Due to delayed release of rock mass stress, convergences were decreasing very slowly till stabilization of profile usually more than 100 m behind the tunnel face. Proper timing of rock bolting was very important as well. Additional rock bolting (Swellex) perpendicular to the rock foliation was regularly used immediately after application first layer of primary lining to reduce convergences. Primary lining showed significantly cracking, while excavating through subhorizontally laid migmatite gneisses with alternate bands of thinly foliated mica schist, dipping in tunnel drive direction with high overburden. Slots as one optional solution were used at this part of the project. The reason was that shotcrete cracking in the primary lining developed behind the tunnel face of the Top Heading with a delay of approx. 10-15 m in the crown, between 12 o'clock and 1 o'clock position. The monitoring profiles were stabilized approx. 100 to130 m behind the tunnel face. To overcome the difficult stress conditions, mentioned slots were predominantly used with positive reaction of the primary lining. Slots are actually gaps of a primary lining with width of approx. 50 cm, with only 1 layer of wire mesh and thin layer of shotcrete. This tool enabled the rock mass to release stress by allowing deformations through closing of the gap and preventing damages of the primary lining. Having slots to get stress release had nevertheless negative effect on lattice girders, which were kinked and have distorted the integrity of the shotcrete shell. Consequently, the shotcrete shell got also cracking accordingly same time. Such negative effect accompanied by an increased deformation behavior of the primary lining was usually eliminated by using another tool of our Himalayan tunneling. So, when above mentioned slots did not ensure sufficient primary lining, the Engineer instructed to use lining stress controllers (LSC), which could ensure the shotcrete shell integrity, but it was more expensive instrument. One row of the Slot in the primary ling located approximately at 1 o'clock is shown on Figure 6. Successful utilization of two rows LSC under overburden about 1.800 m can be seen at Figure 7.

According to Table 3, tunnelling condition were usually classified as "Fair" or "Poor" there and the rock formations composed of high grade of metamorphic migmatite. The variation of migmatite

Figure 6. One row of slot in the primary lining behind tunnel face of the top heading, NP at July of 2017.

Figure 7. Two rows of LSC, then 1 row of LSC close to tunnel face of top heading, NP at July of 2015.

includes micaceous gneiss, magmatic schist or phyllites with a significant proportion of quartzite.

Following chart on Figure 8 summarizes yearly progress of top heading excavation from both portals till the breakthrough. After 10 years of hard-won progress, the completed tunnel was opened to the traffic on 3rd October of 2020. The South Portal of the tunnel one day prior opening can be seen on Figure 9.

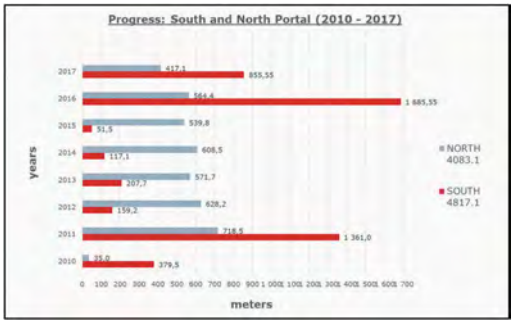

Figure 8. Top heading excavation yearly progress.

Figure 9. The South Portal of the Atal tunnel, one day prior official opening.

4 CONCLUSIONS

The young Himalayan Mountains with their complex geology and such geotechnical conditions do always hold surprises during tunnel construction. From the examples of Rohtang Tunnel shown in this article, it is clear that not only careful and as detailed as possible geological investigations are required prior and during the execution of the project, but the same also needs to be done with concentrated attention of all parties involved in the project, namely Contractor, Engineer, Designer and Client. Only combined efforts throughout all different project stages (Feasibility study, Design, Execution and Implementation) will provide the necessary flexibility of the construction process that allows instant and immediate reaction to changing geological and geotechnical conditions. The all parties of this project are definitely happy that Rohtang/Atal Tunnel was finally opened approx.. after 10 years in the Autumn 2020. The following fact added a certain prestige and uniqueness to this project. In conclusion, the author can note with great pleasure and pride that this project was awarded in the category "Outstanding Large Project of the Year" on the global conference of the international organization FIDIC, held in Geneva from 11th to 13th September of 2022.

ACKNOWLEDGMENTS

The author thanks to the Employer and especially to the client for possibility to work on such challenging project in Himalaya and also thanks for consent to publish this article at international congress - WTC.

REFERENCES

Bernard, R., Döllmann, O., Kunc, L. „Experiences by excavation of Rohtang highway tunnel in Himalayas near Manali". In Proceedings/Book of Abstract, 13th International Conference, Underground Construction Prague 2016, pp. 24.

Bhandari, R.C., Jangade, B.D., Saini, S. Choudhary, B. Kumar, Saleira Wesley. „Geological Investigation for Tunnel Projects and their Impact on Cost and Schedule Related to Project Construction with Special Reference to Highway Tunnels in Himalayas". 4th Indian Rock Conference, Indorock - 2013, 29-31 May 2013, pp. 214–225.

Rites (1996). „Feasibility Study Highway of highway tunnel across Himalayan Ranges", Manali, Himachal Pradesh, Phase II Main Report, Vol-I., 1996.

Bernard, R., Ertl, H. „Tunnelling in Extreme Ground Condition – Execution of Rohtang Highway Tunnel in The Himalayas". In Proceedings of BRO Seminar, Challenges in planning, investigation, design and construction of highway tunnels in Himalayan region. New Delhi, India, 2nd to 3rd Nov. 2017.

Korejčík, J., Bernard, R., Mitrenga, P., Ertl, H., Chauhan, S. „Rohtang Highway Tunnel, NATM Experience in Himalayas", In Proceedings/Book of Abstract, 14th International Conference, Underground Construction Prague 2019, pp.27.

Bernard, R. „Experiences during Tunnelling in Extreme Ground Conditions in The Himalayas – Excavation of Rohtang Tunnel, India", Czech technical magazine „ Tunnel" No. 4/2022, ISSN 1211-0728, pp. 4–13.

Tunnelling for a Better Life – Yan, Celestino, Thewes & Eberhardt (Eds)
© 2024 The Author(s), ISBN 978-1-032-80042-4
Open Access: www.taylorfrancis.com, CC BY-NC-ND 4.0 license

The impact of ramp width on tunnel face stability during ramp excavation

Qi Chen* & Ying Cui
Yokohama National University, Yokohama, Japan

ABSTRACT: When excavating a tunnel using the short bench cut method of NATM, the top heading of the tunnel cross-section is excavated first; then, the bench simultaneously follows several to tens of meters behind. A ramp is maintained to access the top heading from the bench. Tunnel failure has been reported during ramp excavation, with the unsterilized side wall of the ramp being considered one of the contributing factors. Additionally, the width of the ramp is a significant factor that influences the stability of the tunnel face. Hence, a comprehensive investigation into the influence of the ramp excavation on the stability of the tunnel and the surrounding ground, as well as the impact of ramp width, was conducted through a combination of two-dimensional experiments and corresponding DEM analysis.

An experimental setup involving an aluminum laminate apparatus was employed to visually observe the response of the surrounding ground during tunnel excavation. A semi-circular acrylic cylinder was used to simulate the support for the top section of the tunnel. The excavation was modeled by directly removing the aluminum rods. After maintaining the unchanged conditions following the excavation of the top heading, the ramp was excavated with various widths to investigate their effects on the ground and the support system. Furthermore, corresponding DEM analysis was conducted to investigate the mechanisms underlying the results obtained from the model experiment.

Both experimental and analytical results indicate that the failure mode during ramp excavation is recognized as the bearing capacity failure due to the loosening of the surrounding ground with the ramp excavation. Further, this result indicates significant deformation occurring at a shallower depth for a wider ramp compared to other cases.

Keywords: Tunnelling, NATM, Ramp excavation, Simulation

1 INTRODUCTION

Various tunneling techniques presently employed encompass conventional mining methods, the New Austrian Tunnelling Method (NATM) (Takasaki, 1996), the tunnel boring machine (TBM) method, and the cut-and-cover method. The selection of a specific tunneling method is contingent upon diverse factors, including the thickness and strength of the surrounding rock, groundwater conditions, and construction constraints. In the context of mountainous highway construction, the unpredictable presence of unidentified obstacles and intricate geological conditions frequently necessitate prompt adjustments during excavation. Mining methods are commonly utilized in mountain tunnel excavation owing to their ability to provide real-time geological information from the excavation surface. Moreover, the New Austrian Tunnel Mining (NATM) method, categorized as a mining method, leverages the mechanical properties of the soil to withstand external soil pressures. This methodology facilitates the implementation of suitable excavation and support techniques, presenting substantial economic advantages. Consequently, the widespread adoption of the NATM method is observed in tunnel construction projects situated in mountainous regions.

In mountain tunnels constructed using the NATM method, the step excavation technique is commonly employed for both excavation and tunnel support. This method entails dividing the tunnel into upper and lower sections, which are systematically excavated in stages, creating a distinct separation known as a "bench." In scenarios where the surrounding rock exhibits considerable strength, a longer step length may be utilized to facilitate the operation of construction machinery. However, challenges arise during the excavation of the upper section, particularly when encountering loose soil, leading to the generation of earth pressure (Akutagawa et al., 1998). This pressure can induce deformation and settling of the tunnel support structure. Consequently, when confronted with weak rock strength or expansive soils, it is preferable to adopt shorter step lengths. This approach aids in minimizing the risk of tunnel support

*Corresponding author: chen-qi-yp@ynu.jp

DOI: 10.1201/9781003495505-188

deformation, particularly in the upper section of the tunnel (Nakano et al., 2010). To address the transportation of excavated soil and waste materials from the upper section and facilitate the movement of construction machinery, a connecting passage or ramp is typically excavated between the upper and lower sections. Notably, instances of tunnel collapse or support damage in the ramp section are prevalent in tunnel construction, as evidenced in the construction of the Hokuriku Shinkansen, as reported by JRTT (2017).

The influence of the width of the ramp connecting the upper and lower sections on tunnel support remains unclear. Therefore, gaining a comprehensive understanding of the impact of ramp construction and its width on geological conditions and support is imperative for designing an appropriate tunnel excavation method.

In this study, two-dimensional simulation experiments were carried out for upper excavation and ramp excavation of a specific soil section with short steps in a tunnel using aluminum bar aggregate and an acrylic tunnel lining model. Discrete element numerical simulations were also used. The aim was to investigate the effect of ramp excavation on tunnel support and geological conditions, as well as the effect of ramp width. Regarding established studies, many researchers have conducted simulation experiments on excavated tunnels in soft, unconsolidated strata.

Murayama et al. (1971) conducted trapdoor experiments using laminated aluminum rods to explain and discuss the arching effect of tunnel earth pressure. Kikumoto (2005) also conducted trapdoor experiments using laminated aluminum rods. They found that the earth pressure acting on the tunnel support foot (around the trapdoor) converged to a constant value after excavation.

Adachi et al. (1985) buried a variable-diameter metal cylinder in layered aluminum bars and gradually reduced its diameter to simulate ground loosening during tunnel excavation. They investigated the effect of ramp excavation, which couldn't be simulated by trapdoor experiments. They addressed the drawback of trapdoor experiments, where the discontinuous contact point with the fixed plate becomes a singularity. Their conclusions were as follows: the loosening zone develops rapidly above the upper edge and eventually extends below the spring line. The loosening zone reaches the surface when the soil cover is shallow but decreases as the soil cover increases.

Sakurai et al. (1994) reproduced the soil loosening phenomenon by placing an airbag in stacked aluminum rods and reducing the pressure inside the airbag. They assumed the pressure inside the air pocket to be the minimum support pressure required to sustain the mountain's deformation, and they measured the loosening load. They elucidated the discontinuous surface of the stacked aluminum rods where abrupt changes occurred inside.

In Koike's experiment (2020), a semicircular tunnel lining model was embedded in stacked aluminum rods with a hollow interior of the support, and a small number of aluminum rods were withdrawn from the ground below the lining model to obtain ground settlement and deformation of the support structure. The following conclusions were drawn from the experiment: a) Continuous removal of aluminum rods in the ramp results in the formation of a slip line between the support foot and the excavation position, leading to tunnel settlement. b) Among different excavation widths, wider excavation is more likely to cause settlement than narrower excavation.

This study delves into a spectrum of ground behaviors, extending from upper excavation to ramp excavation, a subject hitherto unexplored in the existing literature. Diverging from Koike's research, our study incorporates a novel approach to upper-section excavation, integrating the burial and removal of aluminum rods within the support structure. Furthermore, in alignment with insights from prior research, this study interprets soil damage around the tunnel as a discontinuity problem. Consequently, we employ the Discrete Element Method (DEM) for numerical analysis, recognizing its suitability for simulating model tests in this context.

2 MODEL TEST

2.1 *Laboratory model test*

In this study, experiments were conducted utilizing a model featuring a half-cylinder buried within laminated aluminum rods. The primary objective was to elucidate the behaviors of the ground in two distinct phases: the excavation of the upper section of the tunnel and the subsequent excavation of the ramp. Notably, this research delves into the discussion of the influence of the ramp's width, maintaining consistent testing conditions across all cases during the upper-section excavation phase.

2.1.1 *Soil particles for surrounding ground*

This experiment simulates the tunnel excavation in loose sandy soil. Aluminum rods have a close density with sand soil. The length of the aluminum rods is 50 mm, and they were piled up to create a ground with a two-dimensional plane strain state. Two types of aluminum rods with diameters of 1.6 mm and 3.0 mm were combined in a 3:2 weight ratio and compacted to maintain a constant density across the entire area.

The unit weight of the aluminum rod laminate area was set to 21 kN/m^3, referring to the previous research that used the same aluminum rods (Kikumoto, 2005).

2.1.2 *Lining model*

Figure 1 illustrates a schematic diagram of the acrylic lining model employed in this experiment. The front of the lining model is marked with colors to facilitate the measurement of the deformation of the lining. Load cells were positioned within the foot recesses to measure the vertical loads exerted on the individual support foot of the lining.

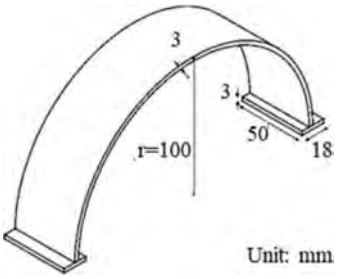

Figure 1. Schematic view of the lining model.

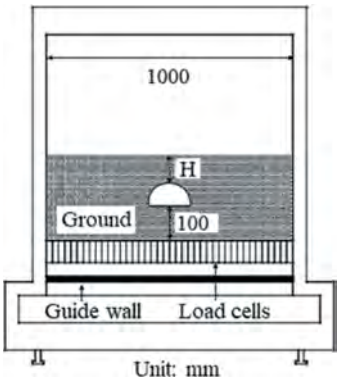

Figure 2. Two-dimensional trapdoor apparatus.

2.1.3 *Experimental setup*

Figure 2 represents an overview of the experimental setup. The base comprises 40 aluminum blocks, each 24.5 mm wide, arranged at 0.5 mm intervals. Ball bearings between adjacent blocks minimize vertical friction from block collapse. Load cells attached to the bottom of each aluminum block measure the vertical load. A tripod-mounted video camera captures images of tunnel and ground behavior during excavation.

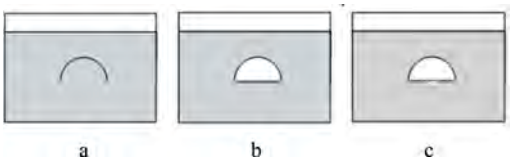

Figure 3. Experiment process.

2.1.4 *Experiment procedure*

Figure 3 illustrates the experimental process. Initial values of foot load and bottom load are measured before loading. To achieve the specified unit weight, the required weight of aluminum rods per 50 mm stacking is calculated, and the specimen is leveled and compacted after each 50 mm stacking. After reaching a model foundation height of 100 mm, the acrylic lining model is placed, ensuring that both foot of the lining model are at the same height. Accumulation continues until the depth of aluminum rods covering the upper part of the lining model reaches 200 mm, the same as one time the diameter of tunnel lining, as shown in Figure 3a. Table 1 shows the parameters of the model ground and aluminium rods.

Table 1. Aluminum bars' particle parameter.

Porosity	Density of particles [kg/m³]	PSD(diameter)
0.22	2700	1.6mm:3mm = 3:2

The excavation process is modeled by removing the aluminum rods manually. Figure 3b shows the condition after the top section excavation. The top-section excavation involves removing aluminum rods from the top edge to simulate the excavation process, ensuring the inner surface of the model remains consistently horizontal. For every 40 grams of aluminum rod removed in the initial half of the excavation, ground load, and foot load are measured and documented through photography.

During ramp excavation, as depicted in Figure 3c, a photograph is taken for every 5 grams of aluminum rod removal, and bottom load and foot load measurements are conducted until the lining model's foot settles approximately 20 mm from its initial position. Despite settlement causing deformation in the width of the excavation ramp, the aluminum rod removal area is maintained within the pre-deformation width for the duration of the experiment.

To study the effect of ramp width in the lower section of the tunnel, experiments were conducted using the three conditions shown in Figure 4. All experimental conditions were kept consistent in the upper half until the end of the excavation. The experiments were grouped as follows in Table 2. During the excavation process, the ground bottom and foot load are collected for each step.

Table 2. Experiment cases.

Ramp with	0.1D (20mm)	0.2 D (40mm)	0.5 D (100mm)
H=D	Case 1	Case 2	Case 3

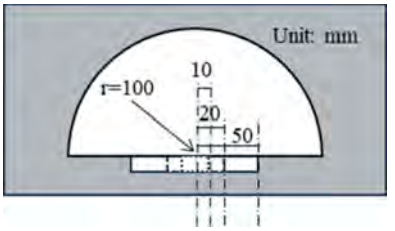

Figure 4. Ramp excavation.

2.2 *Outline of the DEM simulation*

This study incorporates DEM to analyze the various behaviors of soil particles and tunnel models due to ramp excavation.

2.2.1 *Simulation process*

The DEM resolution process aligns with the model test, as illustrated in Figure 5. Initially, a soil body with the tunnel model is generated, and subsequent excavation is performed by removing particles. Excavation simulations are conducted separately for various ramp widths. Table 3 provides an overview of the simulation groupings for DEM. Unlike the experiment, the DEM simulations do not use a single removal of weight. For upper excavation, the process is divided into four steps, as depicted in Figure 5a, involving the removal of particles from the interior of the tunnel at 15%, 40%, 67.5%, and 100%. Ramp excavation, as shown in Figure 5b for DEM case 1, involves removing particles within a limited width of the interior tunnel surface at the end of the upper excavation, within a depth range of 0.5 cm, 1 cm, 1.5 cm, and so forth. In DEM case 2 and DEM case 3, particles within a limited width and depth range are removed in increments of 0.3 cm, 0.6 cm, 0.9 cm, and so on.

Table 3. Simulations condition varies.

Ramp width	0.1D (20mm)	0.2D (40mm)	0.5D (100mm)
No cohesion	Dem case1	Dem case2	Dem case3
Cohesion:17kPa	-	Dem case4	-

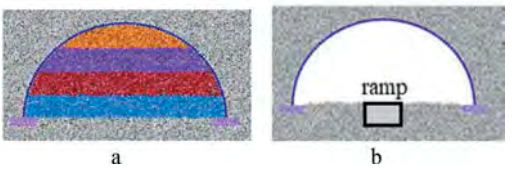

Figure 5. DEM simulation process.

Since the DEM depends on the parameters of the particles, it is necessary to calibrate the parameters of the two unintelligible materials. (Itasca, 2019)

2.2.2 *Soil particle parameter*

For calibrating soil particle parameters. In this study, a fitted biaxial compression experiment was used for calibration. The sketch of the experiment is shown in Figure 6 below. The biaxial compression experiment was carried out using an aluminum rod with a peripheral pressure of 19.6 Kpa and simulated. After several trials and errors, the parameters are shown in Table 4, and the fitting results as stress ratio (σ1/σ3) and void ratio are shown in Figure 7.

Table 4. Bi-axial simulation parameters.

Normal stiffness [N/m]	Shear stiffness [N/m]	Friction coefficient	Rolling resistance Friction coefficient	Angel of internal friction [°]
2×10^7	2×10^7	0.2	0.2	29

(e=0.18, g=9.8N/m, ρ=2700kg/m³)

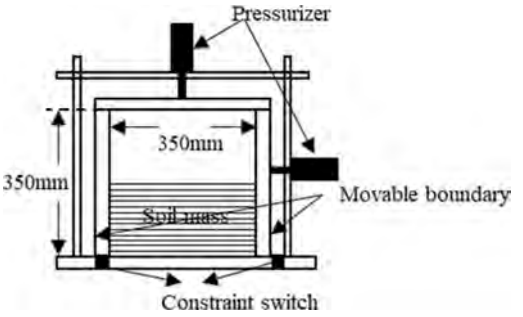

Figure 6. Bi-axial compression test equipment sketch.

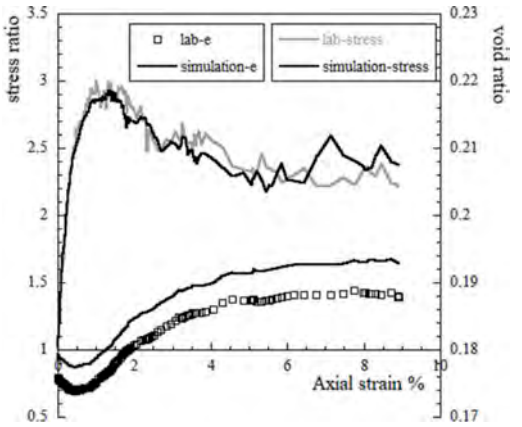

Figure 7. Bi-axial compression test results comparison.

2.2.3 *Lining particle parameters*

Regarding the calibration of the tunnel model parameters, the cantilever beam compression and bending experiments and their simulations, as well as the uniaxial compression test simulations, were used. The sketch of the cantilever beam compression experiment is shown in Figure 8a, and the bending experiment and its numerical simulation were performed on an acrylic plate with the parameters shown in Table 5. The simulation of the uniaxial compression experiment is shown in Figure 8b, and the parameters are shown in Table 6. The results obtained after coupling these two experiments and simulations are shown in Table 7, Figure 9, and Figure 10. The difference in the results of the uniaxial compression test in 10 is neglected

because of the small stresses in this experiment and the fact that the axial direction of the tunnel model is mainly considered for force transfer rather than deformation.

Table 5. Parameter of cantilever test.

Particle rad [mm]	1.5
Accumulation thickness [mm]	3
Approximate density [kg/m³]	1350
Acting force [N]	2.5

Table 6. Parameter of uniaxial compression test.

Height [mm]	9
Width [mm]	3
Axial strain	5‰

Table 7. Common Parameters.

Normal stiffness [N/m]	10^{11}
Shear stiffness [N/m]	7.5×10^{10}
Parallel pond normal stiffness [N/m]	10^{11}
Parallel pond shear stiffness [N/m]	7.5×10^{10}
Friction coefficient	0.5
internal friction Angle [°]	50

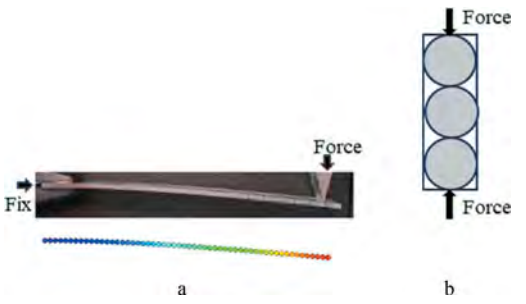

Figure 8. Cantilever test for lining model.

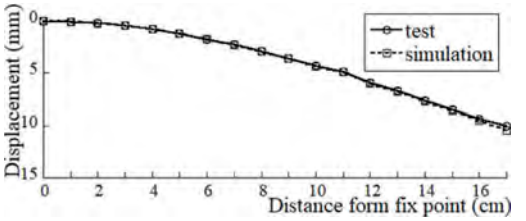

Figure 9. Cantilever test results.

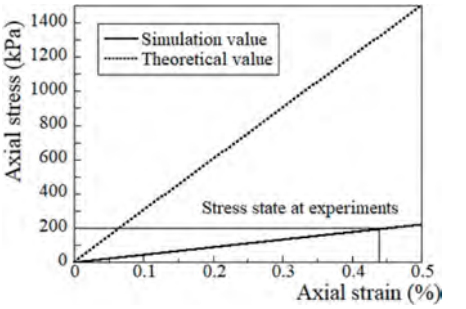

Figure 10. Uniaxial compression test results.

3 RESULTS AND DISCUSSION

3.1 *Verification of the simulation results for 4 cm width*

3.1.1 *Upper-section excavation*

Since there is no variable in the upper excavation of each group, all the experimental results in this study should theoretically behave the same way at the end of the upper excavation. In the DEM, since there is no variable in the numerical simulation, only one set of results of the upper excavation process is taken for comparison with the experimental results. Figure 11 shows the stresses on the tunnel footing as the upper excavation proceeds.

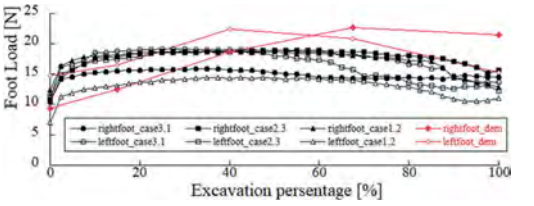

Figure 11. Foot-load during upper excavation.

It can be seen from the figure:

a) In the experiment and simulation, although the initial particle distribution is different, resulting in different forces on the left and right feet of the tunnel model, the initial average force on the left and right feet is the same.
b) In both experiments and simulations, the force acting on the feet of the tunnel model increases and then decreases as the excavation proceeds.
c) In the experiments, the average force acting on the tunnel feet before and after the upper excavation did not change significantly, reproducing the conclusion of Kikumoto (2005).
d) In the simulation, the force acting on the foot after the end of the upper excavation is relatively large compared with the experiment, which may be due to the uneven distribution of particles in the numerical simulation.

During the upper excavation, the experimental case2 and numerical simulation results showed a slight foot settlement, as shown in Figure 12. This may be due to the uneven distribution of particles.

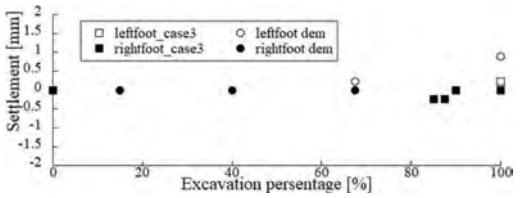

Figure 12. Foot settlement during upper excavation.

3.1.2 *Ramp excavation*

Figures 13 and 14 below show the force on the foot of the tunnel model during the excavation of a ramp with a width of 4cm and the variation o the settlement of the tunnel foot with the depth of excavation, respectively.

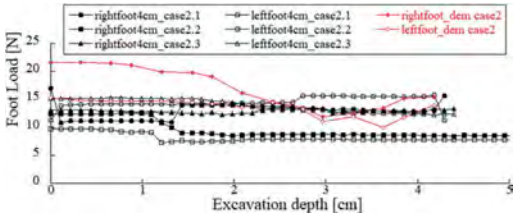

Figure 13. Foot load during ramp excavation [case2(4cm)].

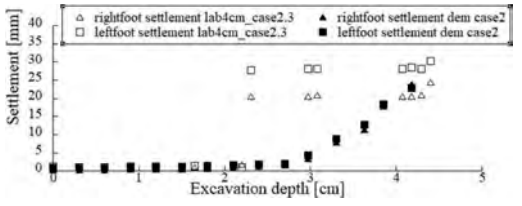

Figure 14. Foot settlement during ramp excavation [case2 (4cm)].

The following tendency can be seen in the figure:

a) Transient settlement damage occurred in the experiment when the excavation was up to 2.3 cm, and there was a sudden change in the force on the foot when the settlement occurred. Whereas in the numerical simulation, the settlement occurred with continuity. But the final settlement is consistent.
b) Although the force on the foot changes when settlement occurs, it remains stable overall.

3.1.3 *Discussion*

The results of the DEM simulations are specifically analyzed in the next section. Figure 15 below shows the forced settlement at the toe of the tunnel and the change in porosity of the particles below the toe of the tunnel during the tunnel ramp excavation. The porosity increased before the tunnel settlement occurred. The extent of porosity monitoring is shown in Figure 16. Figure 17 shows the contact force distribution of the soil around the tunnel at different stages. Considering the conclusions above, the damage mechanism of tunnel settlement can be concluded: due to the excavation of the inclined shaft, the porosity of the loose soil at the bottom of the tunnel increases, leading to a decrease in the supporting force (Terzaghi, 1943), and the development of a shear zone at the foot of the tunnel support eventually leads to damage.

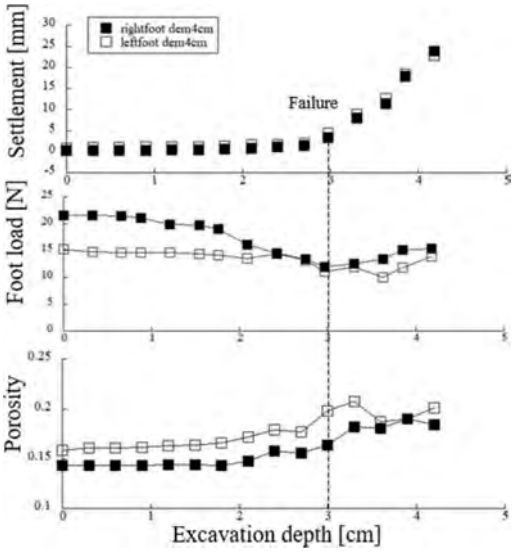

Figure 15. DEM results discussion of DEM case2.

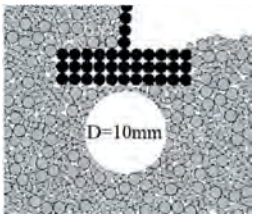

Figure 16. Porosity analysis area.

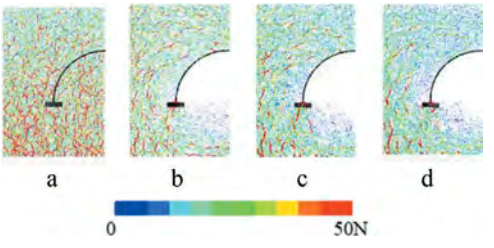

Figure 17. Progress of the contact force (width 4 cm) a. initial sate, b. after upper-section excavation, c. before failure, d. after failure.

3.2 *Effect of ramp width*

Figure 18 shows the changes in forces on the foot of the tunnel model, settlement, and porosity of the soil underneath it as excavation proceeds for each ramp width in the DEM numerical simulation result.

Table 8. Contact force for various width.

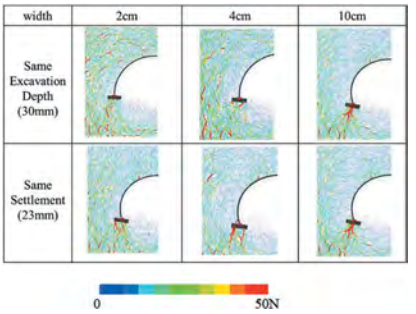

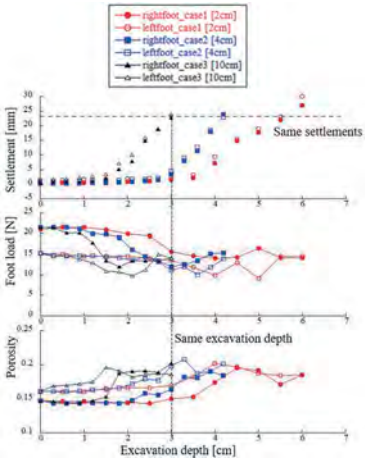

Figure 18. DEM results for various ramp width.

It is clear from the figure that the wider the ramp, the smaller the excavation depth. Table 8 compares the soil contact forces for the same excavation depth (30mm) and the same lining settlement (23 mm). It can be found that:

a) For the same depth of excavation as 30mm. Although settlement damage to the soil occurred in both the ramp width 4 cm and 10 cm excavation conditions, there was no significant reduction in contact force after damage occurred in the ramp width 4 cm case.
b) For the same lining settlement as 23mm, there was no significant difference in the force chain of each case.

4 CONCLUSIONS

The following conclusions were obtained in this study.

a) The suitability of the DEM for the ramp excavation issue was verified. The DEM analysis effectively simulated the ground failure patterns, enabling a clear observation of settlement and soil loosening caused by ramp excavation.
b) The mechanism of ground failure during ramp excavation was elucidated. Throughout the excavation process, the load acting on the foot of the tunnel support remained relatively constant. However, constraints between soil particles decreased, leading to increased porosity and, subsequently, reduced bearing capacity.
c) The influence of the excavation width of the ramp on excavation stability was investigated. Both experimental and numerical simulation results supported the finding that the larger the excavation width, the shallower the soil layer that can be excavated, corroborating findings from Koike's experiment (2020). Additionally, the DEM analysis indicated that, under the conditions of this study, there is minimal variation in the contact force distribution within the ground after damage, regardless of different ramp widths.

REFERENCES

Hidekuni Takasaki. et al., 1996. Appraisal of NATM as methodology and prospective subjects in tunnelling. Proceedings of the Japan Society of Civil Engineers. No.547/III-36, pp.243–pp.248.

Shinichi Akutagawa, Tsutomu Kitani, Yasunori Abe and Shunsuke Sakurai., 1998. A consideration on tunnel pressure derived from the Terzaghi's formula based on an equilibrium assumption in a limit state. Proceedings of tunnel engineering, JSCE, No.8, pp.95–pp.99.

NakanoKiyoto, 2010. Analysis of behaviour of early-closed tunnel and its current practice. Proceedings of tunnel engineering, JSCE, No.20, pp.151–pp.162.

JRTT., 2017. Press Conference on the Hokuriku Shinkansen and Kakihara Tunnel Cave-in Accident. Japan.

Sakura Murayama. et al., 1971. Earth pressure on tunnels in sandy ground. Proceedings of the Japan Society of Civil Engineers. Volume 1971, Issue 187, pp. 95–pp.108.

Mamoru Kikumoto. 2005. Study on the Mechanism of Earth Pressure Generation around Tunnel Periphery Ground. PhD Thesis. Kyoto University, Kyoto, Japan.

Toshihisa Adachi. et al., 1985. Experimental study on thin flexible tunnel support system. Doboku Gakkai Ronbunshu, Volume 1985, Issue 358, pp.47–pp.52.

Shunsuke Sakurai, et al., 1994. Model tests on deformation and loosening pressure of shallow tunnel. Doboku Gakkai Ronbunshu, No.487, III-26, pp.271–pp.274.

Konan Koike., 2020. Experimental study of the behavior of small earth-covered tunnels with aluminum bar laminates during excavation of the lower half of the tunnel. Master Thesis. Kyoto University, Kyoto, Japan.

ITASCA. 2019. PFC 6.0 Documentation. State of Minnesota, USA.

Karl Terzaghi., 1943. Theoretical Soil Mechanics. Wiley and Sons. New York, USA.

Tunnelling for a Better Life – Yan, Celestino, Thewes & Eberhardt (Eds)
© 2024 The Author(s), ISBN 978-1-032-80042-4
Open Access: www.taylorfrancis.com, CC BY-NC-ND 4.0 license

Deep underground mined cavern excavations in Auckland city centre, New Zealand

Thomas Cheung*, Wataru Okada & Shu Fan Chau
City Rail Link, Link Alliance, Auckland, New Zealand

ABSTRACT: This paper presents the application of the latest technology in tunnel engineering during the detailed design process and construction of Karanga-a-Hape (KHP) Station for the City Rail Link (CRL),the largest transport infrastructure project in New Zealand. KHP Station is the deepest mined underground station in the Auckland city centre. This is the first time a deep station has been excavated in East Coast Bays Formation (ECBF). Comprehensive ground investigation has been carried out and the data used to assist engineering geologists and geotechnical engineers to interpret and build up a comprehensive 3D ground model for efficient planning, design and construction.

Building Information Modelling (BIM) is mandatory for both temporary support and permanent structure designs in this project. The proposed primary supports are designed based on the 2D analysis and empirical formula and are optimized by using 3D analysis, particularly at the junction and tunnel-shaft interface. The process helps the tunnel engineers to understand the overall picture of the studied area and to predict the impacts to the stakeholders. The tunnel excavation was started from the temporary access shaft in September 2020. The tunnel deformation and ground movement has been kept well under control with no adverse impacts on the nearby structures. In mid 2023, the mined section has been fully lined with permanent concrete and successfully handed over to the rail systems and track team.

Keywords: Tunnelling, Mined Excavation, BIM, Polypropylene Fibre Reinforced Shotcrete (PFRS), City Rail Link

1 INTRODUCTION

The City Rail Link (CRL) Project in Auckland is the largest transport infrastructure project ever in New Zealand (NZ) and will help Auckland cater for the demands of population growth over the next 30 years.

The C3 (main stations and tunnels) contract is the largest of all the CRL contract packages. It consists of the construction of a 3.5 km long twin rail tunnel underneath Auckland's city centre, between Waitematā Station (Britomart) and Maungawhau Station (Figure 1 and Figure 2). Two new architecturally-designed stations with underground platforms will be built on Albert Street – Te Waihorotiu Station (entrances at Victoria Street and Wellesley Street) and Karangahape Road – Karanga-a-Hape (KHP) Station (entrances at Mercury Lane and Beresford Square) – providing new transport connections.

The reference design is undertaken by a Principal Technical Advisor (PTA) consortium led by Aurecon and including Jasmax, Grimshaw, Mott MacDonald, Golder, and Arup.

In July 2019 City Rail Link Limited signed a contract for the C3 works with Link Alliance, comprising City Rail Link Ltd (CRLL), Vinci Construction Grands Projets S.A.S., Downer NZ Ltd, Soletanche Bachy International NZ Limited, WSP (NZ) Limited, AECOM NZ Limited and Tonkin + Taylor Limited. The client, construction contractors and design firms all work together and share their expertise to deliver the Project. The alliance model promotes innovation and flexibility and helps achieve value for money.

Karanga-a-Hape Station is a 32m-deep mined underground, twin platform station, with access shafts, platforms, lifts, escalators, and equipment rooms housing station, tunnel services, and plants. The entrances of the station are from both Mercury Lane and Beresford Square. It will be the deepest station of the CRL project (Figure 3).

2 KARANGA-A-HAPE STATION DESCRIPTION

Karanga-a-Hape Station comprises two station shafts, one at Mercury Lane and one at Beresford Square, platform tunnels and five connection adits. The twoplatform

*Corresponding author: thomas.cheung@linkalliance.co.nz

DOI: 10.1201/9781003495505-189

Figure 1. Plan of CRL's alignment.

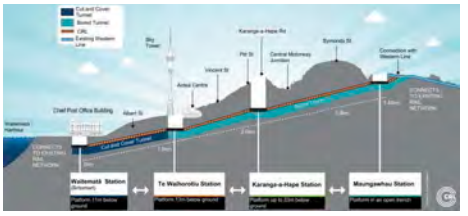

Figure 2. Section of CRL's alignment.

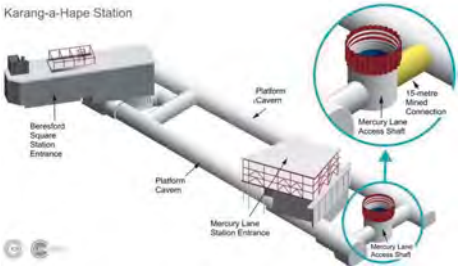

Figure 3. KHP station at construction stage.

tunnels (MC20 and MC30) and adits have been mined using sequential excavation method (SEM).

The total length of mined platform tunnels (MC20 and MC30) is about 219m and 228m respectively, with an active platform length of 203m to accommodate nine-car trains at the station.

Two stub tunnels each 10.2m long are assigned at the northern end of the station to facilitate the re-launch of the Tunnel Boring Machine (TBM).

The general tunnel layout of the station is shown in Figure 4. The excavated span is from 7m to about 13m and the diagonal span can be up to about 20m at the connection between platform tunnel and adit tunnel to facilitate different construction stages. The tunnel construction sequence requires that the TBM is able to transit through the platform tunnels (MC30 and later MC20) from the south to north. For the MC30 platform tunnel, the transit occurs with only primary lining installed whereas for MC20 the transit occurs after installation of secondary (permanent) lining. Within 21m at each end of the platform tunnels, the cavern profiles are widened. The widening is required to allow sufficient length for the TBM transit alignment to shift towards the middle of the station and clear the walls of the typical section.

Figure 4. General tunnel layout of Karanga-a-Hape Station.

3 APPLICATION OF BUILDING INFORMATION MODELLING (BIM) IN DESIGN

BIM is a process focused on the development, usage, and transference of a digital information model to improve the design, construction, and operations of a project.

The objective of BIM in CRL is to achieve a single source of truth and long-term cost savings through the following BIM benefits:

- Single source of truth: To improve collaboration and reduce errors.
- Data interoperability: To improve project delivery and collaboration.
- Visualization: To improve safety and reduce risk in design and construction by clash analysis and 3D coordination of integrated disciplines.
- Integrate asset data: To increase collaboration between different parties in Link Alliance and quick access to accurate information.

The application of BIM in Project and Operational and Maintenance (O&M) lifecycle management helps to form and enhance the whole lifecycle management in CRL.

The BIM modellers extract the latest information from the 3D model (Figure 5) for the tunnel engineer to use in their design modelling and analysis. In addition, clash analysis is carried out for each submission to ensure that the conflicts between each design parties have been solved.

Figure 5. Isometric view in BIM of KHP station.

4 APPLICATION OF 3D GEOLOGICAL MODEL IN DESIGN

Extensive existing boreholes data available from Auckland Council records and a total of more than 195 specific CRL boreholes confirmed the geological conditions along the CRL alignment. In-situ tests, including dilatometer and pressuremeter testing, and televiewer surveys of structure, were undertaken along with a comprehensive suite of laboratory tests to determine geotechnical design parameters.

3D geological model was created by CRLL by using Leapfrog Works software. Link Alliance has developed this model and mapped a combination of geological and geological units. Boreholes and corresponding data drilled after starting of the Project are also uploaded for use (Figure 6).

Using the geotechnical digital transformation, the engineers and geologists can easily access the data from a single source and review all the data in 3D view (Figure 7 and Figure 8). The geological section along the tunnel is much easier to be generated, which enhance the work efficiency.

Figure 6. Geotechnical database soilcloud.

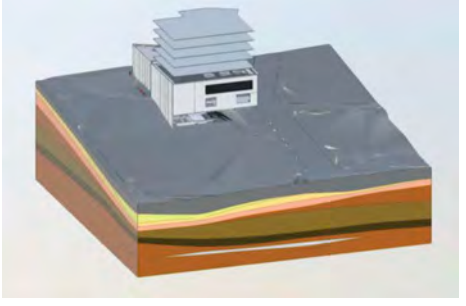

Figure 7. 3D geological model imported into BIM.

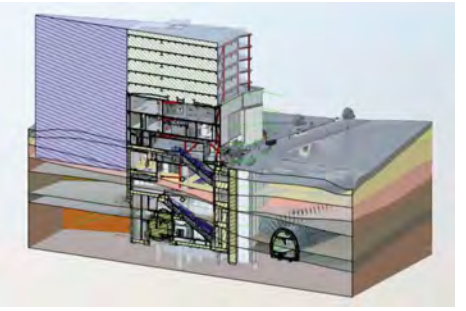

Figure 8. Cross section in BIM (Combined Model).

5 GEOLOGY AT KARANGA-A-HAPE STATION

The station area extends from Mercury Plaza to Beresford Square. Fill is generally 1 to 2m thick but is up to 4m thick at the south of the ridge crest at Karangahape Road and is mostly comprised of pavements with granular sub-grades.

Local deposits of Pleistocene age Tauranga Group Alluvium (TA) infill the heads of paleo-tributary gullies.

A variable thickness of weathered well-cemented, moderately strong sandstone, East Coast Bays Formation (ECBF). Bedding in this layer is horizontal or sub-horizontal. The unit drops in level from the north to south of the station. A narrow fault zone is inferred to be intersected in the vicinity of the Mercury Lane Shaft.

Tunnel excavation is predominately within massive EUs3 and EUg3 (slightly to unweathered weak to moderately strong ECBF, the unit is also referred as "channelized sandstone") materials. The Unconfined Compressive Strength (UCS) is about 10 to 25 MPa with a Geological Strength Index (GSI) of 60 to 85. On top of EU3 is the slightly to unweathered very weak ECBF (EU2) with, an UCS of about 1 to 3 MPa and a GSI of 55 to 80 and highly to moderately weathered ECBF (EW). The general geological profile along the MC30 platform tunnel is presented in Figure 9. It is found that the rockhead level is less than a tunnel diameter at some locations with broken rock masses across the station (Figure 10).

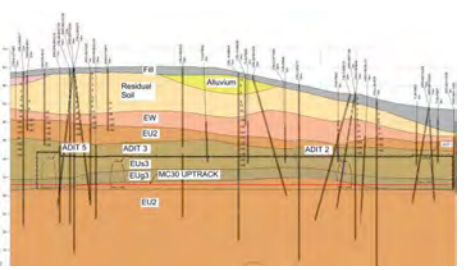

Figure 9. General geological section along MC30 platform tunnel.

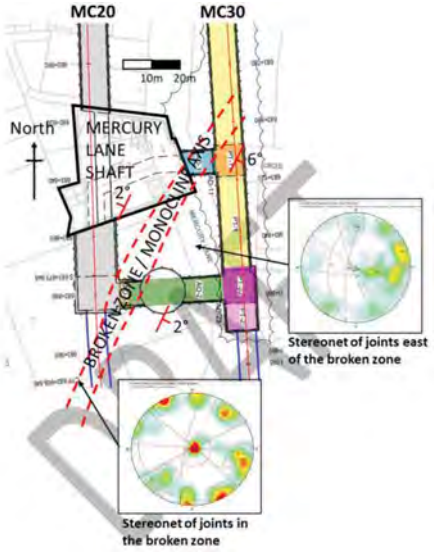

Figure 10. Anticipated broken rock masses across KHP station.

6 TUNNELLING DESIGN

6.1 *Ground relaxation of tunnelling*

Numerical analyses are carried out to confirm the ground reaction curves (GRCs) to assess the three-dimensional nature of an advancing tunnel face using two-dimensional methods. The adopted theory is the Convergence Confinement Method (AFTES, 2001 and Almog et al, 2015). The GRCs are plotted using numerical models to determine the degree of ground relaxation and load on tunnel lining from an empirical relationship and longitudinal deformation profile (LDP).

6.2 *Numerical analysis*

Finite Element Method (FEM) analysis using PLAXIS 2D (Figure 11) and 3D (Figure 12) have been carried out, taking into account the tunnel geometry (shape, span, height), geological conditions, shotcrete stiffness development, and temporary support requirements with existing building loadings and shaft excavation. A steady-state seepage analysis has been also undertaken to determine groundwater pressure distribution in the ground.

Although the modelling technology is advanced, the analytical methods developed by past experience in the tunnelling industry are still invaluable. For example, the proposed advance length is first verified from the empirical ground stand-up time, within which the ground is able to stand prior to application of the primary support system. An advance length assessment has been carried out using the methodology provided in Lee and Schubert (2008) and Lauffer's chart ('Lauffer, H. (1988)).

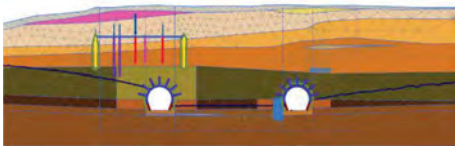

Figure 11. PLAXIS 2D analysis at KHP.

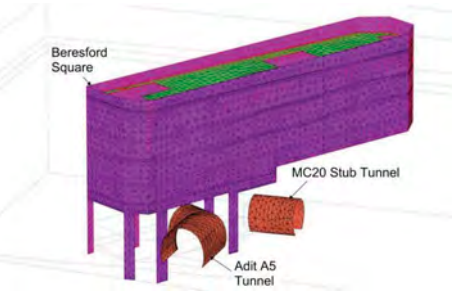

Figure 12. PLAXIS 3D analysis at beresford square shaft and Adit A5 & MC20 stub tunnels.

6.3 *Optimisation of design*

To increase the efficiency of construction, the tunnelling design has been further optimized after obtaining more site data from the excavation.

The initial design has considered the effects of joints to the excavation and proposed primary supports based on boreholes logs, photos, and televiewers. The data is limited by the borehole spacing, drilling direction, and drillhole size. The geological mapping records obtained from the excavated tunnel section (Figure 13) have been referenced to update the RS2 analysis modelling to reflect the actual site conditions (Figure 14) and to optimize the design (Figure 15).

For example, the original primary support design at MC30 Subzone 31 junction consists of split heading and a temporary central wall due to uncertainty of rock cover, which introduces construction complexity (Figure 14). Removal of the central wall and lapping of mesh may result in longer construction time and potential quality issues. The new boreholes have confirmed over the junction the EUs3 thickness at the junction is about 1.2 m to 1.5 m, and the overall rock cover (EU2 & EU3) is about 4.0 m in total, which is roughly half of the tunnel span. All data is reassessed in the 3D model (Figure 16) and cross-checked with the 2D model. The analysis has demonstrated that split heading excavation is not required and full-face top heading excavation is technically feasible. The excavation of this portion had been successfully completed in late 2020 (Figure 17). The accumulated ground settlement at MC30 Subzone 31 junction is about 2.8 mm to 5.0 mm which is well under the limit (i.e. 21 mm).

Figure 13. Geological mapping.

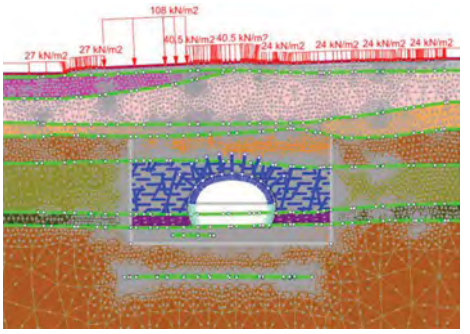

Figure 14. RS2 analysis at KHP.

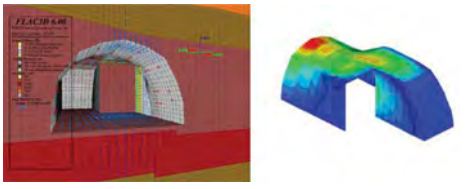

Figure 15. FLAC3D analysis at KHP (Split Top Heading Excavation).

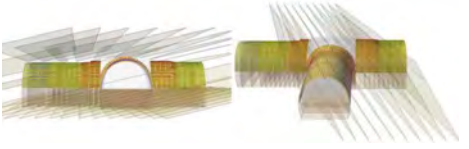

Figure 16. RS3 analysis at KHP (Full Top Heading Excavation).

7 TUNNEL CONSTRUCTION

Top heading and bench excavation sequence were adopted for the Karanga-a-Hape Station platform tunnels and adits. The tunnel was excavated in a full-width top-heading along the tunnels. Rock dowels and Polypropylene Fibre Reinforced Shotcrete (PFRS) with the full thickness of the primary support arch built up in layers were applied for the top-heading. The bench of the tunnel excavated afterwards.

Excavator was used for all excavation with the operator's cabin under supported ground conditions. All tunnels were constructed without any personnel entry under unsupported ground conditions at all times. For the installation of rock bolts, an automated carousel bolter was used. First, a safety shotcrete layer was applied within the same shift and at the end of each excavation advance to protect the excavation surface against deterioration and prevented localised slabbing failures. Temporary support rock bolts were subsequently installed, and a second layer of shotcrete was then applied. Upon completion of the excavation, the temporary support was installed, and remote shotcreting was adopted by using the shotcrete robot.

Figure 17. Excavation at KHP Adit A1.

Figure 18. TBM breakthrough at KHP station MC30 cavern.

Figure 19. TBM in the KHP MC30 mined stub tunnel.

The mined excavation at MC30 was completed successfully before the first TBM broke into the cavern on 17 Oct 2021 (Figure 18) and TBM was then relaunched in the mined stub tunnel (Figure 19).

The second TBM transition was also completed in July of 2022 as shown in Figure 20.

Figure 20. TBM transition in KHP MC20 mined tunnel with permanent lining.

Figure 21. A zephir rail vehicle delivering tracks for installation at Karanga-a-Hape Station.

8 CONCLUSIONS

With the advanced technology in digitalization and modelling, the tunnel excavation and primary support can be studied in detail and results can be graphically presented. Optimization on the design can be carried out by adopting the latest site excavation and mapping information.

For the overall performance of mined tunnel excavation at Karanga-a-Hape Station, the ground movements are kept under well control and there are no adverse effects on the nearby structures. The permanent lining of KHP Station has been completed by the time of preparing this conference paper (Figure 21).

ACKNOWLEDGMENTS

The paper is published with the permission of the City Rail Link Limited and Link Alliance for which the authors would like to gratefully acknowledge. The design and construction of the project is currently undertaken by Link Alliance.

REFERENCES

AFTES (French Tunnelling and Underground Space Association) (2001) “Recommendation on the Convergence-confinement Method”.

B Gaudin, D Burke, M Bartilucci and L Kumar (2021) “Integrated BIM approach for New Zealand’s largest railway project”. Proceedings of Australasian Tunnelling Conference, ATS 2020+1, pp754–775.

City Rail Link (CRL) Official Site (N.D.) from https://www.cityraillink.co.nz/.

E Almog, M Mangione and G. Cachia (2015) “Ground relaxation in segmental lining design using the convergence-confinement method”. Proceeding of the Underground Design and Construction Conference 2015, Hong Kong, The Institute of Materials, Minerals and Mining (IOM3), Hong Kong Branch, pp335–345.

K Howard and C J Howard (2021) “Future proofed tunnels at Karang-ā-hape Road Station”. Proceedings of Australasian Tunnelling Conference, ATS 2020+1, pp965–970.

T Ireland, P Kirk and S Eratne (2021) “Competitive Alliance procurement process for a major underground railway – City Rail Link, Auckland”. Proceedings of Australasian Tunnelling Conference, ATS 2020+1, pp380–392.

Y Z Lee, and W schubert (2008) “Determination of the Round Length for Tunnel Excavation in Weak Rock”. Tunnelling and Underground Space Technology 23 (2008), pp221–231.

Tunnelling for a Better Life – Yan, Celestino, Thewes & Eberhardt (Eds)
© 2024 The Author(s), ISBN 978-1-032-80042-4
Open Access: www.taylorfrancis.com, CC BY-NC-ND 4.0 license

Construction of Girgaon Station of Mumbai metro line – 3, a combination of cut & cover and conventional tunnelling and mix of social and technical challenges in congested urban environment

S.G. Dalvi*
Sr. Deputy General Manager, Mumbai Metro Rail Corporation Ltd., Mumbai, India

Ravi Ranjan Kumar
Executive Director (Civil), Mumbai Metro Rail Corporation Ltd., Mumbai, India

S.K. Gupta
Director Projects, Mumbai Metro Rail Corporation Ltd., Mumbai

Ashish Rawat
Construction Manager/Geotech, Hindustan Construction Company Ltd, Mumbai

ABSTRACT: Girgaon station lies amidst residential and commercial establishments in congested bustling downtown marketplace in Mumbai, India. Construction of this station, one of the 26 underground stations on the 33.5 Km long Colaba-Bandra-Seepz (Line 3), has been an engineering feat. There were 139 buildings in the Zone of Influence of Station Box. Fourteen building housing 560 PAPs were demolished to make space for station. Critical buildings were supported and repaired prior to construction. Impacts on day-to-day life were handled with care and consultations. Pre-Construction Building Condition Survey, Instrumentation and Monitoring and structural audit reports helped in alleviating apprehensions during construction. PAPs will be rehabilitated later in-situ to preserve their lively-hood and social fabric under a unique rehabilitation scheme. Steel decking was provided for space and traffic management plans. Acquisition of land and rehabilitation of PAPs in the congested Girgaon locality was a major influencing factor in project execution. This was handled with public consultations and special policies by the State Government for Rehabilitation and Resettlement. Station plans were modified to accommodate these requirements. The station is now 71 % complete. The paper will delve into these technical, social, and logical challenges successfully dealt in construction of this station as a case study of undertaking a mega urban project in a socially responsive manner.

Keywords: cut & cover, conventional tunnelling, social and technical challenges

1 INTRODUCTION

As cities grow and expand, the demand for efficient transportation systems becomes increasingly critical. Tunnels offer an effective solution for providing underground transportation infrastructure, but the implementation of tunnelling projects in congested urban areas presents numerous challenges. Traditional tunnelling methods, such as the Cut & Cover technique, can cause significant disruption to the urban fabric, affecting businesses, communities, and the environment. On the other hand, Conventional Tunnelling techniques may be more suitable for sensitive urban areas but come with their own set of social and technical challenges.

As urbanization continues to intensify, cities face increasing challenges in expanding and upgrading their transportation infrastructure to meet the demands of a growing population. Tunnelling plays a crucial role in addressing this urbanization with limited problems posed to the residents in terms of limited space, environmental concerns, and social implications. By analysing case studies, best practices, and lessons learned, this study aims to provide insights into effective strategies for mitigating the adverse effects of tunnelling and cut & cover

*Corresponding author: shantaram.dalvi@mmrcl.com

DOI: 10.1201/9781003495505-190

excavations on urban communities while ensuring efficient and sustainable project outcomes.

Mumbai Metro line-3 is a 33.5 km long underground corridor running along Colaba – Bandra - Seepz. The dense and historic urban environment of Mumbai on the narrow north-south peninsular region, necessitated for underground alignment of this metro line. Line-3 is the first underground metro line for Mumbai as the current public transport system are overcrowded and the road transport network is congested. To decongest the existing public transport and increase mobility across the region, Mumbai Metro Line-3 was planned as an underground metro. The corridor is marked with 27 key stations out of which 26 will be underground and only 1 station is at grade. This project is twin tunnel project with adequate cross passages throughout the network. Mumbai Metro Line-3 (MML-3) project joins South Mumbai and Central Mumbai and has several interchanges with Indian Railways Suburban network and Mumbai Metro Line-1.

MML-3 Project has a standard gauge (1435 mm) and maximum permissible speed is 85 km/h. There are 8 coaches rolling stock for each train with a total passenger capacity of 2406 and axle load of each coach is kept at 17 Tons. Length of one metro train will be 22.60 m. Power supply for metro trains will be through the overhead 25 kV AC traction supply and the propulsion system will be a 3-phase drive system.

Integration of Line 3 will provide a faster, effective, dependable mode of public transport and will also become a key factor in increasing public transit usage reducing the carbon footprints. As planned, construction of underground metro rail corridor is carried out using Tunnel Boring Machines (TBM's), Conventional tunnel excavation and Cut & Cover station boxes. This paper presents a mix of social and technical challenges in congested Urban Environment during Construction of Girgaon Station of Mumbai Metro Line – 3, through a combination of cut & cover and conventional tunnelling.

2 GIRGAON STATION - LOCATION

The upcoming Girgaon Metro Station is located in a densely inhabited locality in old Mumbai. Building structures under which the tunnel passes and in the vicinity of the cut and cover station box are mostly dilapidated. The narrow streets are congested with heavy traffic at all times. The location of the station was decided, basis the social importance of the place with places of worship and business avenues in the vicinity.

Land acquisition, dilapidated structures in the zone of influence, traffic congestion due to limited space availability, adverse mixed geological conditions and water ingress due to proximity to the sea were the primary challenges which were overcome efficiently, some prior to start of construction works and some during the course of construction of this station box.

Figure 1. Location of Girgaon Metro Station.

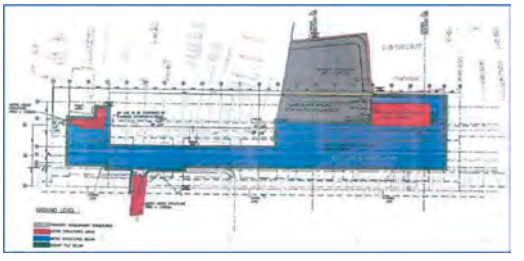

Figure 2. Redevelopment plan of Girgaon Metro Station.

This paper details the measures undertaken and at times the changes adopted to overcome these social and technical challenges and the successful completion of the Girgaon metro Station.

3 CHALLENGES IN GIRGAON METRO STATION CONSTRUCTION

3.1 *Land acquisition*

Land Acquisition was a major challenge from the very inception of the project, this being the most densely populated area with a high congestion of the structures

and no open tracts of land available. Structures were identified to be demolished for in-situ rehabilitation (Figure 2) of PAP's (Project Affected Persons).The displaced residents would be reinstated in the reconstructed buildings at the same location after the completion of the station.

A series of public hearings were conducted firstly to explain the importance of the upcoming Metro Station in the area and finally to convince them for the land to be acquired and their rehabilitation and settlement. In the process the Rehabilitation schemes were also explained. Coordination was done between various Government bodies to verify the Ownership and tenancy rights of the displaced residents.

Despite a number of public hearings and other in-situ redevelopment plans developed, a minor section of the residents/owners remained unconvinced for the urban development of the area and denied handing over the structures for the works to start. This accounted for a delay in the start of the cut and cover excavation works for the station.

As a consequence of the refusal of land, a general re-sizing of the station box was done to accommodate the station in the available space. The original layout and the modified layout are depicted in Figure 2.

Figure 3. Original & modified layout of Girgaon Metro Station.

Girgaon Station had a reduction in length after tender stage, length was reduced to 244.675 m from 289.6 m. Reduction in length was undertaken to mitigate impacts of delay in land acquisitions and space constraints at site. The profile of land change extensively as alternative land was made available by the authorities instead of initially conceived land plans. This resulted into modification in construction methods. Further, extensive R&R and property development works were planned in the available land pocket, with a component of the works overlapping the underground station structure. Structural provisions of these R&R and PD works, as well as space planning within station area had to be suitably changed to accommodate structure needs of multi-storeyed R&R and PD structure above ground.

3.2 *Dilapidated structures in the zone of influence*

Details of the Damage Category assigned to structures in the Zone of Influence of the Girgaon Station Box excavation are shown in Table 1 as below:

Out of a total of 140 structures in the Zone of Influence (ZOI) of the Girgaon Station Box, 35 structures were in a dilapidated condition. It was of prime importance to minimize construction induced settlements in order to prevent the loss of property and life. Stringent measures in consultation with the Detailed Design Engineer, General Consultant and the Client were adopted in terms of supporting the dilapidated structures, structural repairs and monitoring of all the structures in the ZOI.

Prior to the start of the TBM mining operations under these structures, a detailed Building Condition Survey was undertaken and structural Audits for critical structures undertaken upon the Damage Classification. Structural repairs and supports were provided to the structures as per the recommendations of the Structural Audit Reports.

Instrumentation and Monitoring formed an integral part of the project. Structures were monitored for tilt, cracks, vibration and settlement. Real-Time monitoring was carried out during the TBM mining as well as during the station excavation through conventional tunnelling.

Precautionary measures were in place in case some settlements were noticed.

3.3 *Congestion due to Limited Space Availability*

Girgaon Metro station is planned on the Jagannath Shankar Seth Road (JSS); located on the central verge along 12 m wide road. The station is about

Table 1. Damage category assigned to structures in ZOI.

Station/ Tunnel	Total No of Structures within ZOI	Heritage Structures	NOCReceived (Structures Surveyed)	Damage Category						Structural Audit Completed	NOC Refused (Structures Not Surveyed)
				Very Severe	Severe	Moderate	Slight	Very Slight	Negligible		
Girgaon Station Phase-1 (0 to 25m)											
Station	80	1	76	0	20	39	17	0	0	18	4
Girgaon Station Phase-2 (26 to 50m)											
Station	59		53	4	11	26	10	2	0	3	6

0.73 km away from the Kalbadevi Metro station. The entry and exit of the station are planned on both sides of the road. This station is being built in one of the busiest and densely populated residential areas of South Mumbai.

Girgaon is one of the very congested and populous locations in this stretch of MML3 Project. Due to the limited availability of land, part of the Station box was designed under the existing road and to manage the traffic congestion, steel decking was placed for uninterrupted traffic movement.

An efficient traffic management was put to place and the lane was transformed to a one way lane. Traffic Marshals manned the major junctions for managing a smooth flow of traffic.

Excavation for the cut and cover station box commenced with space constraints at the surface with limited heavy equipment and at times specialized equipment to cater to the limited space available. Consequent to the excavation up to the base slab, widening of the bored tunnel was taken up through conventional means. Special temporary openings to accommodate the muck transport from the tunnel widening were made use of. Construction sequencing of the cut and cover station box modified and re-modified at times due to space constraints and in order to ease workability at Girgaon station. Same is explained in the series of Figures below:

Once the casting of the base slab up to desired level was accomplished, walls up to the Mezzanine slab were casted and subsequently the mezzanine slab. Widening of the bored tunnel was taken up immediately upon casting of the mezzanine slab. Since the excavation could not be done by blasting, mechanical breaking of the rock was proceeded with which was another cause of the prolonged excavation regime.

Following are the models for the Girgaon station from the Building Information Modelling Software (BIM).

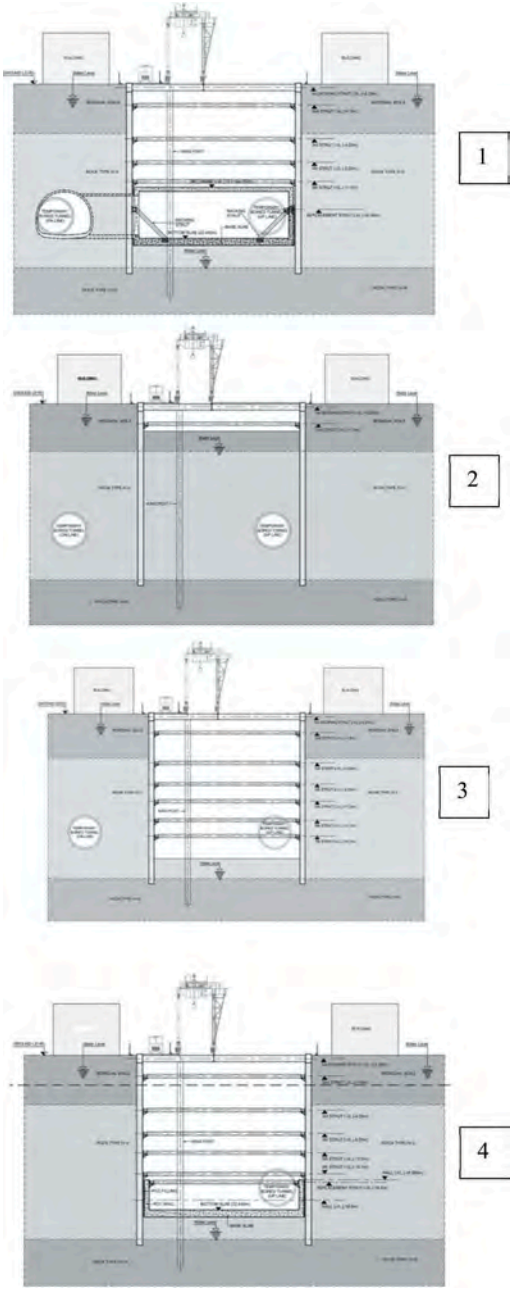

Figure 4. Stages of construction for cut & cover at Girgaon.

3.4 *Adverse geological conditions – mixed ground*

Figure 6 is a representation of the Geological Profile of Girgaon Station. As is evident, it represents a mixed geology of hard and soft Breccia in general and a small patch of hard, compact, fresh Basalt. This patch of Basalt extended from the up line tunnel to the right portion of the Station Box and pinched out prior to reaching the down Line tunnel.

The secant piles drilled prior to the start of excavation of the station box could not be socketed into the hard and compact basalt which posed problems of water ingress and excavation when the excavation reached that particular level. Corrective measures in the form of raker piles were taken up which resulted in delay in excavation works. Mechanical breaking of this hard basalt was also challenging since blasting could not be taken up in the midst of this densely populated location.

3.5 *Water ingress - Girgaon station in close proximity to sea*

The Girgaon Station is placed in close proximity to the sea (Figure 7) with a very high ground water table. Excavation started with all precautionary measures in place for anticipated high water ingress into the excavation.

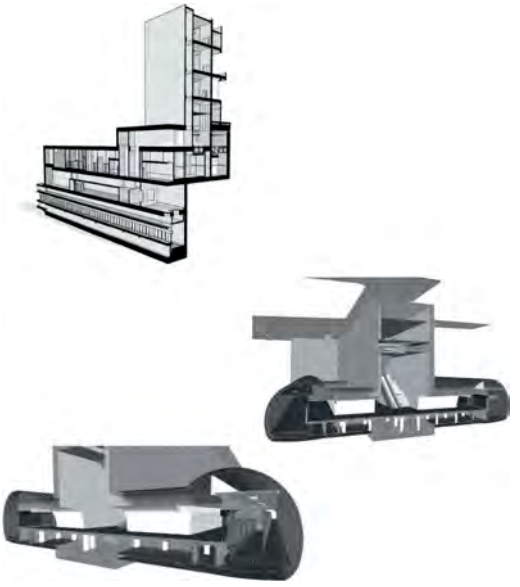

Figure 5. BIM model for Girgaon station.

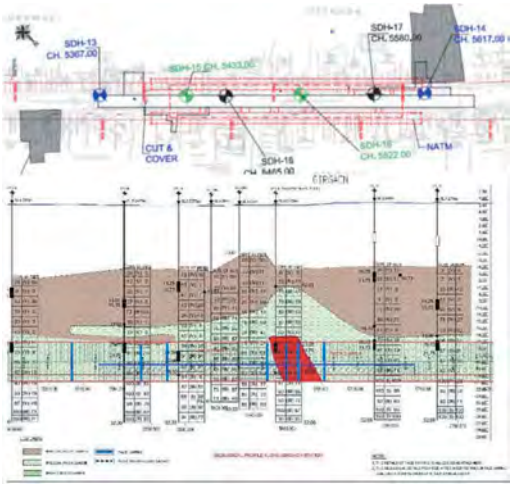

Figure 6. Geological profile of Girgaon.

Figure 7. Location of Girgaon Station in close proximity to the sea.

High water ingress was observed at a number of places during the excavation of the station box which was overcome by grouting measures. The materials used for grouting the walls of the station box were Cement, Sodium Silicate and in extreme cases Polyurethane Grout (both single and double component). No major incidents of settlements in the Zone of Influence were reported barring a few minor ones which were taken up on priority and amicable solutions were provided.

4 INSTRUMENTATION & MONITORING

Extensive Instrumentation and Monitoring regime was enforced for all the structures in the Zone of Influence of Girgaon Station to counter any unforeseen situations during the course of the excavation. Monitoring was carried out for Vibration levels, settlement, cracks and tilt. Real-time monitoring for 3-D deflections in buildings across the alignment through prisms was also carried out. Water levels in existing wells and additionally installed Standpipes were monitored throughout the stretch on a daily basis and with increased frequency of monitoring when the need arose in case of any noted abnormal changes in readings.

The data collected from the instruments was thoroughly analysed at different levels by the Instrumentation Engineers, by detailed design consultants and finally by the General Consultants and a final report formulated and circulated on a daily, weekly and monthly basis. No major adverse effects in the form of settlement, draw down of ground water table or tilting of structures were evident barring a few minor settlements to the tune of 6 to 8mm.

5 SIGNIFICANT ADVANTAGES

1. The station construction work was converted into cut & cover which made construction work easier than the previously proposed conventional method.
2. A portion of work got shifted off-road and reduced inconvenience to the public by appropriate segregation of pedestrian and vehicle movement.
3. Station box shortened by approximately 60m which reduced the scope of secant pile and assisted in the early completion of piling activity.
4. Reassessment in station box size eliminated the construction of secant pile work in front of one of the dilapidated structures of concern.
5. Width of concourse got significantly increased as a result and ease the movement of passengers facilitated for operation of Line-3.
6. Fruitful utilization of land pockets above ground to meet the integration requirements of metro station and property redevelopment in accordance with the approved plan.

7. Ancillary building occupies one compact location and rest of the area made available for redevelopment of property for rehabilitation of PAP's.
8. During an emergency, a greater number of evacuation routes shall be available to the public.

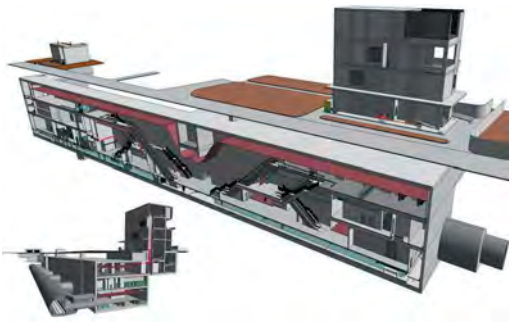

Girgaon Metro Station – 3D Model

9. Tunnel ventilation system and fan room will be ideally located on wide cut and cover box closer to the platform end.

6 CONCLUSION

Despite all odds and what seemed to be a gigantic task, excavation for the Girgaon Metro Station was accomplished with efficacy. Assessment of all work fronts were made at different levels on priority and timely interventions for appropriate and adequate changes wherever required were adapted for a successful and timely completion of various activities at Girgaon Metro Station.

Construction activities, in one of Mumbai's busiest market places with limited space and congested streets amidst a dense network of dilapidated structures was completed in the face of adversity through sheer grit, determination and adaptation to the latest technical knowhow in the construction industry.

Tunnelling for a Better Life – Yan, Celestino, Thewes & Eberhardt (Eds)
© 2024 The Author(s), ISBN 978-1-032-80042-4
Open Access: www.taylorfrancis.com, CC BY-NC-ND 4.0 license

Challenges in the conventional tunnel mixed-face execution

Thiago de Sá Lima*
Construtora Aterpa, F\lorianópolis-SC, Brazil

Bruno Scodeler
Maffei Engenharia, São Paulo-SP, Brazil

Eloi Palma Filho
DNIT, Brasília-DF, Brazil

ABSTRACT: The construction of tunnels by the sequential method (NATM, SEM, SCL) has as one of its fundamental principles, the contribution of the massif that surrounds the executed section, through the redistribution of tensions in the excavated region (arching), which, added to the treatment applied in the work area, it keeps the displacements in balance, enabling underground construction. Predicting the behavior of tunnels excavated in heterogeneous masses is additionally difficult, since the heterogeneity of materials can occur in an incalculable number of directions, formats, positions in the section, dimensions and type of formation. Sections excavated in this region, usually called Mixed Section, have a robust treatment, closer to the treatments adopted for sections in Soil, which in theory would be the worst case scenario. For the project contractor, the uncertainties regarding the deadline and cost of the work increase as, even with robust sounding campaigns, there remains a possibility of significant variation in these sections in relation to the theoretical compartmentalization of the project. This variation has a very large impact on project costs and deadlines, as well as on the acquisition of construction insurance. Taking as a basis the tunnels executed in the Florianópolis ring road, the transition sections between the soil regions at the entrances of the tunnels and the rock region inside the mountain, a large proportion of tunnels excavated in heterogeneous environments is shown, the so-called mixed classes, with the most diverse characteristics possible. Of the 6.700 m excavated, around 1.100 m (14%) took place in mixed-class massif regions. This article aims to report the difficulties in the conception, design and execution of tunnels excavated in mixed classes, as well as the view of contractors for work of this nature, considering the execution of the 4 (four) tunnels, which took place between Jan/21 and Oct/23.

Keywords: Tunnelling, NATM; SCL, Mixed-face, Tunnel Design, Ring road

1 INTRODUCTION

The Florianópolis Road Ring is a new road section that is being implemented in compliance with the obligations set out in the road concession contract signed by Autopista Litoral Sul. Its main objective is to divert long-distance traffic distance from the metropolitan region of Greater Florianópolis, in the south of Brazil, South America.

The route passes through municipalities of Governador Celso Ramos, Biguaçu, São José and Palhoça. The project presented refers to part of the South Section, specifically between the Km 220+396 and Km 228+310, which foresees the construction of 4 double tunnels. (ANTT, 2018).

Figure 1. Florianopolis ring road location. ANTT, 2018.

The tunnels are situated along the ring road, as showed in Figure 2.

*Corresponding author: thiagora22@hotmail.com

DOI: 10.1201/9781003495505-191

Figure 2. Tunnel along of Florianopolis road ring. Miyazato, 2023.

2 MIXED SECTION - DEFINITION

Tunnel excavation using the sequential method (NATM, SEM, SCL), has as its principle, taking advantage of the natural behavior of homogeneous masses, in the redistribution of tensions when excavated, seeking balance with the smallest possible displacement.

In general, mixed sections are present in the transition range between homogeneous masses, which naturally forms a heterogeneous region. Considering the layout of the tunnel, the formation found in the excavated section and its surroundings, will go through an incalculable range of compositions, making it impossible to characterize each one of them in the project, nor to predict construction methodologies and customized treatments for each situation, causing difficulties from the conception from the project until its execution.

By characteristic, definitions of mixed sections bring inaccuracy, with impacts on the project, economic viability and execution. Example of idealized mixed section is showed in Figure 3.

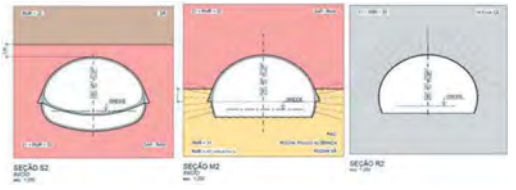

Figure 3. Mixed section, in center, an intermediate situation between soil (left) and rock (right). Source: Authors.

And these mixed sections, found as the excavation progresses, also raise concerns about the stability of the excavation front. As highlighted by LUNARDI, 2008, the stability of the face plays a fundamental role in maintaining tunnel deformations at acceptable levels, and for the short and long-term stability of the excavation. It is in the face (or transition) zone that the design engineer must intervene to regulate and control the deformation response.

Furthermore, mixed-face conditions, if not properly characterized in advance, can lead to contractual impasses (Attewell, 1995, p. 32), overriding issues inherent to the design or execution technique.

Mixed face situations, as highlighted by Rodriguez Ortiz, 2006, p. 121, based on a series of occurrences in Spanish road tunnel works, bring with them a probable incidence of unwanted overbreaks, which is an example of both a technical and economic problem.

2.1 *Difficulties*

After defining the best route for a tunnel, be it for adduction, road, rail or for any other purpose, the next step is to estimate a theoretical geological compartmentation throughout the future construction.

This compartmentalization will be the basis for a project that must be created within a search for economic and executive viability. As what is sought is safety, in addition to precision in the demand for construction and financial resources for the project, depending on the length of the mixed section stretches, this search becomes an exercise almost in futurology.

Even if the investigations are of good quality, the behavior of the mass/structure set in mixed-class regions is difficult to be precise. The risk of geological accidents and/or costs due to unforeseen variations become a point of attention in the project, often leading to changes in layout or unfeasibility of construction.

2.1.1 *From the tunnel designer's point of view*

The construction of tunnels in mixed sections involves additional risks compared to tunnels entirely in soil or rock.

In a mixed tunnel with soil on the roof and/or in a considerable part of the excavation section, the main precautions related to a tunnel built entirely in soil are necessary, such as controlled advancement and the need for treatments for roof and/or front stability.

However, there is an additional stage in the excavation cycle of a mixed face tunnel similar to a rock tunnel, which is the fire blasting stage. Carrying out rock blasting with explosives in mixed tunnels, in addition to the fact that productivity is affected, by adding an additional step to the cycle (compared to the soil tunnel), brings a new risk, which is a greater difficulty in controlling advance distance.

If the blast generates greater progress than expected, the actions (and efforts) in the temporary support systems will be greater (and consequently the risks). On the other hand, if the blast operation does not remove enough to install a steel ribs at the design spacing, it is usually decided to install the steel ribs at a lower spacing (in favor of safety), which impacts productivity.

For the design of a mixed section, a more unfavorable condition is generally accepted in terms of efforts in the coating, in which there is a predominance of soil in most of the section and with the rocky top in the lower part of the section (Figure 4a).

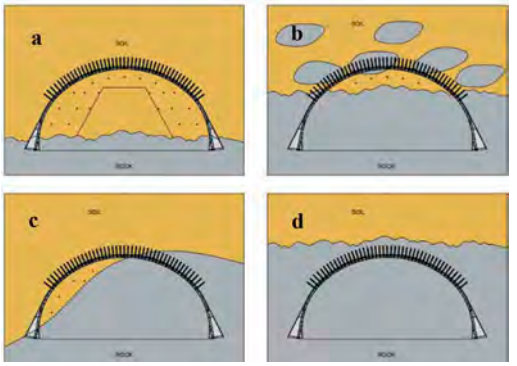

Figure 4. Mixed section, idealized condition, and other possibilities. Source: Authors.

The section idealized for design, however, has a limited occurrence in terms of extension. In practice, until there is complete certainty about the rock cover conditions of a tunnel, sufficient for greater advances to be made and tie rods to be used (usual solution for rock tunnels), the mixed section is used, which is much closer to a tunnel in the ground than a tunnel in rock.

Thus, the mixed section can be used in the most diverse interface conditions between soil and rock, some of which are shown in Figure 4b, c and d.

Certain conditions, despite not being the most unfavorable from the point of view of sizing the support and/or covering, are terrible in terms of execution, such as 2b, c and d.

Scenarios containing transition zones on the roof (2b), in which the behavior is closer to the soil behavior, but containing little altered rock blocks (boulders) bring difficulty both in the execution of treatments (forepoling and nailing) and in the controlled dismantling of the rocky part, as shown in Figure 5.

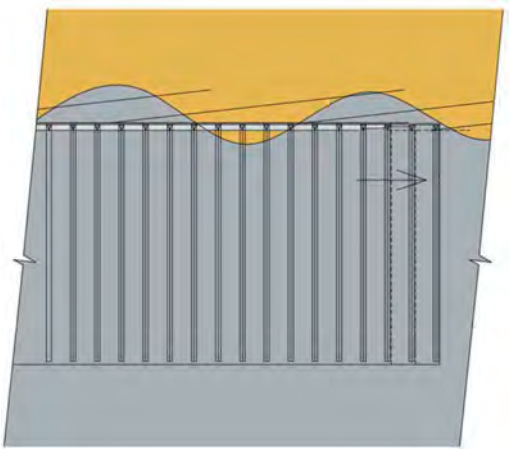

Figure 5. Forepoling and Nailling in mixed section with longitudinal variation of the rock. Source: Authors.

Even an excavation front completely in rock may not be favourable in terms of execution, as for example in the case of a small rock cover, or one that has a large longitudinal variation, where the treatment alternately intercept soil and rock along the perforations. In this condition, the tunnel is constantly susceptible to intersecting soil at the excavation front. It is common for accidents to occur when the reduction and/or removal of treatments (filling) is anticipated due to the presence of rock on the excavated face.

Faced with the uncertainty and risks involving excavations in these conditions, the designer normally opts for conservative solutions, maintaining the roof treatment (albeit in smaller quantities) and support closer to a ground tunnel, with the use of steel ribs and short advances (~ 1m).

These two scenarios in particular, when they occur over large areas, tend to have a significant negative impact on the progress of the construction.

2.1.2 *From the project financier's point of view*

Underground constructions such as tunnels are considered expensive and usually adopted as a last solution among other engineering role of possibilities.

Part of this scenario is due to the difficulty related to predict the real costs of a tunnel that may have significant variations in the geological conditions.

Although a good investigation campaign is important and necessary, depending on the massif peculiarities, much uncertainty related to proportion between soil, rock and mixed tunnels extensions remains for the construction phase, which will – inevitably – raise economic and deadline risks.

Hence, the viability of a tunnel often will be granted by the length of the tunnel that will require a mixed face solution. The economic contingency necessary to cover a significative variation of mixed class might be extremally high compared to the cost of the project.

The Project Financier has the challenge to format the best contractual model for this kind of project, in a way that it is financially safe and attractive for constructors. The main question in this aspect is to supply safety to the constructors that unpredicted variations in the project will not have a financial impact in the contract. Even in cases where the is expected to have a geological uncertainty, having a good project design and a qualified constructor reduce the chance of the variation of costs when facing these uncertainties.

2.1.3 *From the contractor's point of view*

When contracting the execution of a project, the contractor specializing in underground excavations will mobilize the best composition of resources (Equipment and Labor), considering the approved schedule, based on construction processes and with appropriate costs.

For excavations and supports in regions generally characterized by the homogenous presence of soil, resources will be dimensioned with a focus on pre-supports such as forepolings, CCPh, pre-injections, face nailing, sub-horizontal drains, among others. The progress of excavation is carried out conventionally

with cutters, mechanized and manual breakers, as well as conventional excavators themselves.

When it comes to excavations in rock masses, the resources are different. It focuses on an adjusted cycle of rock drilling, use of explosives, cleaning of detonated material and supports defined in the project.

Considering the general characteristics of excavation in soil or rock, some resources are coincident, but with significant adjustments in their quantity and functionality.

When it comes to the execution of tunnels in mixed sections, pre-support resources tend to be used for excavation in soil and also those for excavation and support in rock. Productivity is, in general, lower than that of excavations in competent soil, but with demand for a varied line of resources with a high degree of unproductivity.

From the transition from a tunnel excavated completely in the ground, to a classification for rock, depending on the types and levels of weathering suffered, there is an incalculable variety of soil/rock compositions "faced".

The photos shown in Figure 6 are of the evolution of a mass over the course of a week of progress, in Tunnel 1 of the Florianópolis road contour, the Tunnel with the largest presence of mixed sections in the project. This evolution exemplifies how vast the portfolio of resources and expertise must be to maintain the productivity and safety of the project. The four sections illustrated in the photos were mapped as a mixed section, however under very different conditions.

Figure 6. Mixed faces with different aspects, in the same tunnel and same week. Source: Authors.

Figure 7. Different locations where mixed face support was applied in the same tunnel. Source: Authors.

In the Figure 7, another set of photos, in the same tunnel.

The presence of rock in the lower, upper or lateral portion of the section brings many differences in the construction sequence and risks to workers. Furthermore, tools are generally sized for best performance in rock or soil; Hybrid tools tend to bring greater cost and unproductivity.

As they are regions of contact between materials, they tend to have a greater presence of water, creating more difficulty for the executor. Masses with the presence of water, when exposed during excavation, tend to be carried by infiltrations and behave with a shorter stand-up time of the excavated material. Hence the demand for a consistent contingency plan.

As these are regions with a higher risk of geological accidents, the technical teams that define which project section to use tend to be more conservative, naturally leading to an increase in the section considered a mixed section.

The Figure 8 demonstrates, based on the drilling reports, the proportion of soil/rock in the mixed class excavation region in Tunnel 1, on the Florianópolis ring road. For safe execution, the presence of a multidisciplinary team and technical support capable of identifying the best construction sequences, using the best equipment and tool resources, is essential.

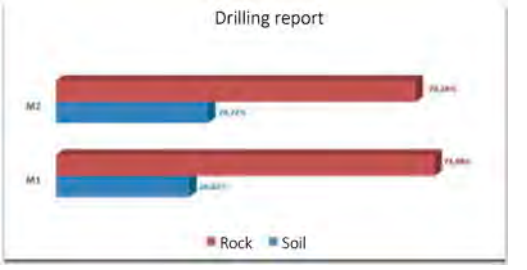

Figure 8. Drilling reports, Florianopolis ring road Tunnel 1. Source: Authors.

2.1.4 *Data from Florianópolis Ring Road*

The Florianópolis Ring Road were built in the Granite massif. Of the 4 (four) tunnels built, two of them had a very short soil-to-rock transition, thus contributing to the accuracy of expected costs and deadlines. On the other hand, tunnels 1 and 2, present in

Table 1. Tunnels data (extensions).

	Soil	Mixed	Rock
Foreseen	515.23	1,438.08	5,130.71
Realized	917.02	1,045.20	5,121.79
Difference	+ 401.79	- 392.88	−8.92

the massif of the Pedra Branca region, had extensive mixed class portions.

The consequence of the greater presence of mixed classes were variations in cost and time, as shown in the Table 1.

4 CONCLUSIONS

The execution of conventional tunnels in mixed-face zones requires a high level of attention, due to their technical and economic sensitivity. Projects must pay special attention to these sectors, in order to predict, in the best possible way, the condition that will be found on site, in terms of behavior and extent. The builder, in turn, must foresee countermeasures for the executive phase, if the extent and behavior of the mixed-face zone are worse than the initial prediction.

In the works on the Florianópolis Road Ring, the mixed-face zones were found to have smaller extensions under construction than the project forecast.

ACKNOWLEDGMENTS

The authors would like to thank the owner of the work, Concessionária Arteris, the constructor, Consórcio Aterpa-J. Dantas, and the design companies, Maffei Engenharia and CJC Engenharia.

REFERENCES

ANTT. 2018. Projeto Executivo do Contorno Rodoviário de Florianópolis-SC (*in Portuguese*). Brasília, DF.

Attewell, P. B. 1995. Tunnelling Contracts and Site Investigation. CRC Press.

Lunardi, P. 2008. Design and Construction of Tunnels: Analysis of controlled deformation in rocks and soils (ADECO-RS). Springer.

Miyazato, C. K. 2023. Incorporação das obras dos túneis no contrato de concessão (*in Portuguese*). Presentation made at Simpósio de Túneis Rodoviários. Florianópolis-SC.

Rodríguez Ortiz, J. M. 2006. Geomechanical problems in recent Spanish tunnels. In Geotechnical Risks in Rock Tunnels – Campos e Matos, Ribeiro e Sousa, Kleberger & Lopes Pinto (eds). Taylor & Francis Group, London, ISBN 0 415 40005 8.

Tunnelling for a Better Life – Yan, Celestino, Thewes & Eberhardt (Eds)
© 2024 The Author(s), ISBN 978-1-032-80042-4
Open Access: www.taylorfrancis.com, CC BY-NC-ND 4.0 license

Research on key technologies for the construction of extra long tunnels on green roads in karst peak cluster areas

Zhiming Dong*
CHELBI Engineering Consultants.INC, Beijing, China

Baode Guo
HUABANG Construction Group., Lanzhou, China

Yuanfu Zhou
Chongqing Jiaotong University, Chongqing, China

Mengyan
Institute of Karst Geology, China Geological Survey, Guilin, China

Shaochuan Xing
CHELBI Engineering Consultants.INC, Beijing, China

ABSTRACT: Taking the Siding Extra Long Tunnel, the longest highway tunnel in Guangxi, China, as the engineering background, the key technology research for the construction of green highway extra long tunnels in karst peak cluster areas was carried out. BIM technology was applied to analyze the light environment of tunnel portal buildings such as sunlight analysis and glare analysis, and a hollow-bamboo-cut tunnel portal structure was proposed; In response to the geological characteristics of tunnels in karst peak cluster landform areas, a joint detection technology of "single hole radar-cross hole radar-hole surface radar" geological advance prediction has been developed, forming a method for predicting and treating karst caves in extra long highway tunnels in karst peak cluster areas; We have developed a water stop that combines drainage and anti karst crystallization functions, and proposed a treatment structure for water and mud inrush and arch top karst cavities in highway tunnels in karst peak cluster areas. The research results have ensured the safety and quality of tunnel construction, saved construction time, created direct economic benefits of 36.75 million RMB, improved the quality of tunnel engineering, reflected the concept of green highway construction, and achieved significant economic and social benefits.

Keywords: Green Highway Tunnel, Karst peak clusters, Hollow hole portal, Portal light environment, BIM technology, Borehole geophysical exploration, Anti crystallization drainage facilities

1 INTRODUCTION

By end of 2022, there are 24850 highway tunnels with a length of 26.7843 million linear meters totally nationwide in China. In 2022, an increase of 1582 highway tunnels with a total length of 2.0854 million linear meters totally. Among them, there are 1752 extra long tunnels with a length of 7.9511 million linear meters totally, and 6715 long tunnels with a length of 11.7282 million linear meters totally[1]. China has become the country with the largest number of highway tunnels and the fastest growing tunnel scale in the world. The mainstream trend of tunnel engineering technology development is moving towards safer, more economical, greener, and more artistic directions[2].

The distribution of karst areas in China is extensive, with three contiguous areas of special poverty concentrated in karst areas. The transportation construction in karst areas is significant for poverty alleviation and transportation power. The karst peak cluster area is widely distributed in Yunnan, Guizhou, Sichuan, Chongqing, southwestern part of Hunan, northern part of Guangdong and other areas. Its unique geological structure has formed many scenic spots such as Guilin mountains and rivers,

*Corresponding author: 11607775@qq.com

DOI: 10.1201/9781003495505-192

however, it also brings new challenges to tunnel construction.

The tunnel portal is not only the "face" of tunnel, but also the "throat" of tunnel. The "black hole" and "white hole" effects at the tunnel portal area have a great impact on driving safety. A large amount of research has been conducted domestically and internationally on the impact of the lighting environment and portal type at the tunnel portal. The differences and measured values of the brightness outside the tunnel between the bamboo-cut portal and end-wall portal types are explained in the detailed design rules for highway tunnel lighting[3], however, the separation between the civil design of tunnel portal and the design of light environment is a common phenomenon. How to comprehensively consider the coupling of tunnel opening geography, terrain, geological conditions and the design of light environment, fully apply new technologies such as BIM, and create tunnel portal buildings with beautiful landscapes, low energy consumption, and safe driving is an important manifestation of actively practicing the development concept of "green highways".

2 RESEARCH ON THE DESIGN OF LIGHT ENVIRONMENT AT THE PORTAL OF GREEN HIGHWAY TUNNEL

2.1 *Characteristics of light environment at tunnel portal*

Highway tunnel is an extremely special road traffic operating environment, characterized by significant differences in the light environment inside and outside the tunnel, and low brightness levels in the middle section. Entering the tunnel, adapting from a bright environment to a dark environment is dark adaptation; Drive out of the tunnel and adjust from a dark environment to a bright environment is light adaptation. The visual adaptation curve is shown in Figure 1. According to research on the light environment and physiological effects to light[4], the visual requirements for driving at tunnel entrances are not only brightness, but also transition time, color temperature, etc., especially in the portal section. At the same time, the tunnel portal section is located at the junction of light and dark adaptation, and there are also optical issues such as glare and stroboscopic effects.

2.2 *BIM simulation analysis of tunnel luminance*

The application of BIM technology in tunnel engineering is receiving increasing attention. This project has established a Revit-Dynamo-Excel modeling solution to digitize and program tunnel BIM models. At the same time, Insight 360 is used to achieve functions such as sunlight analysis, interactive sunlight path simulation, and glare analysis[5]-[6].

Creating three types of tunnel portal (end-wall, bamboo-cut, and hollow-bamboo-cut) simulation models by Revit software, as shown in Figures 2-4.

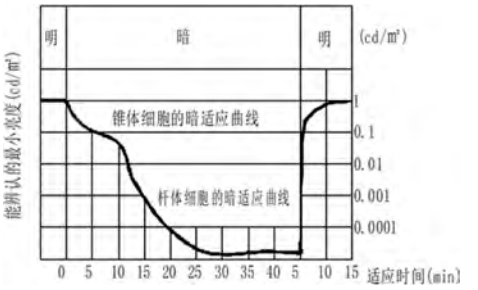

Figure 1. Visual adaptation curve.

Figure 2. End-wall portal tunnel simulation model.

Figure 3. Cut-bamboo portal tunnel simulation model.

Figure 4. Hollow-cut-bamboo portal tunnel simulation model.

The Revit Insight 360 Sunlight Factor Analysis type was selected, which used the Sunlight Factor (DF) sky model. In the field of architecture, daylight factor refers to the percentage ratio of the internal and external luminance levels of a building (structure) under CIE full overcast sky conditions, expressed as:

$$DF = (E_i/E_0) \times 100\% \quad (1)$$

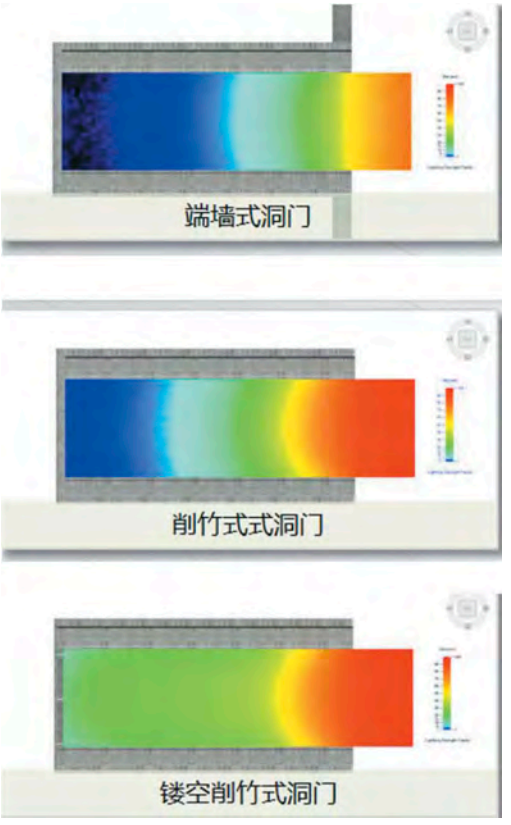

Figure 5. Comparison of solar factor distribution scale in different portal types.

Among them, Ei is the sunlight illuminance value at a certain point on the indoor analysis plane, and Eo is the illuminance value on the outdoor unobstructed horizontal plane at the same time.

The variation law of sunlight factor in the simulation analysis of three types of tunnel portal is shown in Figure 5.

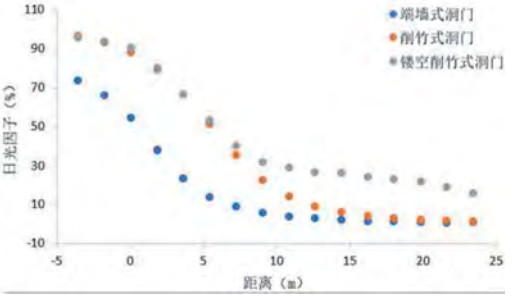

Figure 6. Comparison of daylight factor simulation results of different portal types.

The operating conditions and BIM simulation analysis results of different portal structure types indicate that the changes in road surface illumination inside the hollow-bamboo-cut portal tunnel are smoother, and the transition of the lighting environment is more humanized, which can effectively improve the driver's visual comfort and have a good dimming effect.

2.3 *BIM simulation analysis of tunnel glare*

The generation of solar glare is not only related to the height and position of the sun, but also to the geographical location of the tunnel, the direction of the tunnel, and the direction of vehicle travel. Through observation, it was found that the direct glare generated by the sun has the greatest impact on the driver. It usually occurs during the early morning when the sun has just risen and the evening when the sun gradually sets. The glare generated during other periods is indirect glare or refracted and reflected light.

In order to study the distribution characteristics of sunlight glare at tunnel exits with different directions, four typical directions of east, west, south, and north were selected. In Revit, models were created for the east exit (for eastbound vehicles driving out), west exit (for westbound vehicles driving out), south exit (for southbound vehicles driving out), and north exit (for northbound vehicles driving out). Revit software integrates interactive sun path tools that support visualizing sunlight. In addition to any specified geographic location, it can also be used to create solar studies at any time, studying the impact of natural light and shadows on the internal and external aspects of a project.

To evaluate the distribution characteristics of solar glare at tunnel exits with different orientations throughout the year, four representative dates in astronomy were selected, namely the spring equinox (March 20th), summer solstice (June 21st), autumn equinox (September 23rd), and winter solstice (December 21st). The spring equinox, summer solstice, autumn equinox, and winter solstice are the four solar terms that reflect the return movement of direct sunlight. Based on the BIM model, a roaming tool was used to simulate the process of vehicles driving out of the tunnel exit from four different directions. The distribution of sunlight glare at the tunnel exit from different directions was obtained at the spring equinox, summer solstice, autumn equinox, and winter solstice. The results are shown in Figure 7. When the sun appears in the driver's field of view simulated by the camera, it indicates the occurrence of solar glare.

Figure 7. Simulation of sunlight glare in east portal.

The solar glare at the east exit occurs in the morning, without considering the obstruction of surrounding objects. The sunrise time is considered as the start time of the solar glare, and the end time of the glare can be obtained through Revit simulation. The distribution of solar glare at the east exit is shown in Table 1. The maximum glare duration at the east exit of the tunnel occurs at the summer solstice, which is 2 hours and 17 minutes, but there is no significant difference in glare duration compared to the spring and autumn equinoxes, The minimum duration of glare occurs during the winter solstice.

Table 1. Distribution time and duration of solar glare at the east portal.

Date	Glare Starting Time	Glare Ending Time	Glare duration
Spring Equinox (March 20th)	06:51	09:05	2h 14min
Summer Solstice (June 21st)	06:03	08:20	2h 17min
Autumn Equinox (Sep 23rd)	06:35	08:50	2h 15min
Winter solstice (December 21st)	07:23	08:30	1h 7min

The sunlight glare at the west exit occurs in the evening, and the distribution time and duration pattern were similar to those at the east exit.

Based on the BIM model simulation, it was found through roaming analysis that there will be no sunlight glare at the south and north exit.

The simulation of glare and lighting environment at the exit of different tunnel portal types are shown in Figure 8 below.

By simulating and comparing the light environment of different tunnel exit types, and using the environmental diagram method[7] for calculation, the driver's view brightness at a distance of 48.66m from the tunnel exit was increased by 70.76% compared to the end-wall tunnel portal exit. The use of hollow-bamboo-cut tunnel portal achieved a humanized transition of brightness inside and outside the tunnel, increasing the driver's visual brightness at the tunnel exit section. Due to the adaptation of human vision to changes in the brightness of the tunnel entrance, The driver's resistance to solar glare is enhanced, which can effectively prevent glare and improve driving safety.

(1)End-wall Portal

(2)Bamboo-cut Portal

(3) Hollow-bamboo-cut Portal

Figure 8. Light environment simulation diagram in different portal types.

3 RESEARCH ON GEOLOGICAL PREDICTION TECHNIQUES IN KARST PEAK CLUSTER AREAS

3.1 *Geological characteristics of karst peak cluster areas*

From the process of occurrence, development, and evolution, karst peak cluster landforms belong to the middle age of the development process of karst landforms. Further development of peak clusters can form peak forests and isolated peak landforms. The hydrological system within the peak cluster depression can be summarized as a binary structure, lacking a river water system on the surface and only forming a surface karst system; Underground caves and pipelines often form a dense underground drainage network system.

The tunnel engineering in karst peak cluster areas has problems and characteristics such as large depth fluctuations, long tunnel length, strong karst development, and high risk of water and mud inrush in tunnels.

3.2 *Advance prediction technology of drilling radar*

Drilling radar is a geophysical method in the well that emits high-frequency electromagnetic waves into the stratum, utilizing the propagation characteristics of electromagnetic waves in the stratum to obtain stratum information and interpret unfavorable geological bodies underground. It has high resolution and a large detection range. There are three measurement methods for drilling radar: single hole reflection measurement, cross hole measurement, and hole to ground measurement. In order to verify the effectiveness of the drilling radar method in advanced geological prediction of tunnels, this project adopted a combination of single hole, cross hole, and hole ground methods, and conducted experimental work relying on tunnel engineering.

The geological advance prediction method for tunnels has been developed for karst peak cluster landform areas based on advanced drilling, drilling radar, and ground radar technology, which combines "single hole-cross hole-hole surface" and "three hole combination". The method has been verified through exploration in the Siding extra long tunnel, and the prediction results are very consistent with actual exploration, improving the accuracy of advance prediction, overcoming the shortcomings of single hole's unable to locate karst and multiple holes' affecting construction duration.

Figure 9. Photos of drilling radar on-site testing.

3.3 *BIM simulation analysis of tunnel water inflow*

Prediction of water inflow in karst tunnels is a prerequisite and foundation for tunnel design and construction. At present, the method of tunnel water inflow prediction includes rainfall infiltration method, groundwater dynamics method, groundwater runoff modulus method, and depression infiltration method. BIM technology plays a significant role in improving the accuracy of tunnel water inflow by improving the calculation of catchment area using rainfall infiltration method and determining the location of water inflow.

Figure 10. Technical process of "three hole combination method".

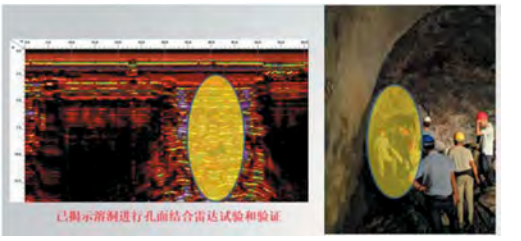

Figure 11. Test and verification of aperture surface combined with radar.

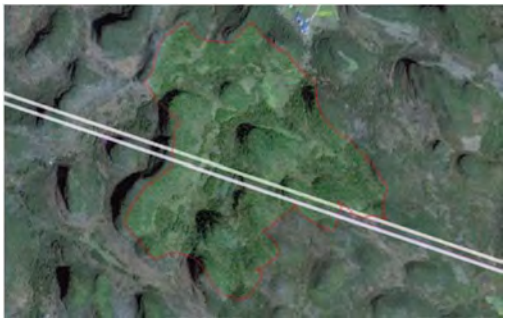

Figure 12. Watershed analysis (red lines indicate regional boundaries).

The achievements of civil engineering 3D design and a series of functions of Map 3D have been expanded and achieved by Civil 3D effectively, which can handle geographic information, planning, and engineering decision-making. Building a BIM model by using Civil 3D can quickly perform watershed analysis and water drop analysis.

Creating terrain surfaces and conducting watershed and surface runoff analysis through Civil 3D, combined with hydro-geological and engineering geological analysis, possible development channels and directions of underground karst can be effectively inferred, providing reference and reference for karst prediction during tunnel construction in karst areas.

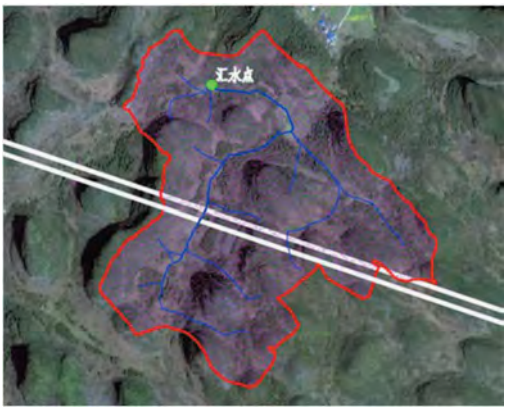

Figure 13. Water drop analysis (blue line indicates the direction of the drop).

Figure 14. Underground runoff path and direction of surface water collection in watershed depressions.

4 RESEARCH ON TUNNEL STRUCTURE AND WATERPROOF & DRAINAGE TECHNOLOGY IN KARST PEAK CLUSTER AREAS

4.1 *Hydrological characteristics of karst peak cluster areas*

The vertical zoning of groundwater hydrodynamics in karst peak cluster areas can be divided into four zones: vertical infiltration zone, seasonal alternation zone, saturated zone, and slow flow zone. Vertical infiltration zone refers to the zone above the groundwater level during the rainy season; The seasonal alternation zone refers to the zone between the groundwater levels during the high and low water periods; The saturated zone refers to the zone between the groundwater level during the dry season and the local erosion drainage benchmark.

Due to the large terrain fluctuations in karst peak areas and the long length of tunnels, a tunnel may cross multiple vertical zones of groundwater hydrodynamic forces in a longitudinal direction. The tunnel faces a great risk of mud and water inrush. In addition to the pressure of surrounding rock, the tunnel structure also needs to withstand complex and variable groundwater pressure.

The lithology of the karst peak cluster area is mostly composed of soluble rock masses such as limestone and dolomite. The surrounding rock is severely corroded, and the groundwater hardness is relatively high. Crystallization is very common in the tunnel drainage system, with prominent crystal blockage at construction joints. And the construction joint is the weak point of tunnel waterproofing and drainage, and the difficulty of construction quality control. Once the waterproof and drainage facilities in the tunnel fail, it is easy to form seepage, water gushing, and water curtains, seriously affecting driving safety.

Figure 15. Water curtain disease formed at construction joints.

4.2 *Optimization of tunnel support structure in gushing water section*

The design of general anti water pressure lining mainly involves increasing the thickness of the tunnel secondary lining and improving the compressive capacity of the tunnel section to bear groundwater loads. Based on the research and analysis of vertical zoning of groundwater in karst peak cluster areas, a double-layer initial support system was proposed for tunnels located in the vertical infiltration zone to seasonal alternation zone. The parameters of the tunnel support system were optimized, and grouting+double-layer initial support system was adopted to achieve drainage limit conditions. The bearing capacity of the initial support was increased and part of the water pressure was borne, the thickness of the secondary lining was reduced, the cost of template trolley transformation was saved, the construction difficulty was reduced, the construction period was accelerated.

4.3 *Research and application of anti crystallization waterstop*

In response to the widespread problem of crystallization in the drainage system of tunnels in karst peak cluster areas, a waterstop with both drainage and anti crystallization functions has been developed and applied to tunnel construction joints and settlement joints.

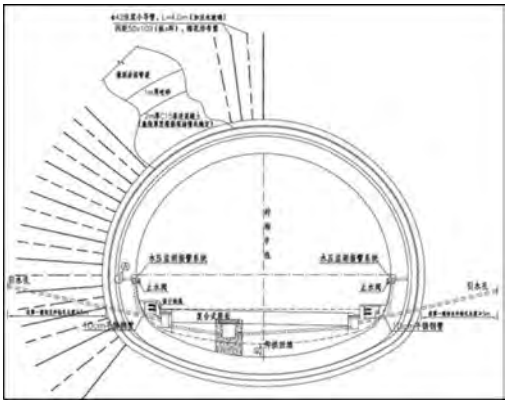

Figure 16. Optimization section of tunnel support structure in gushing water section.

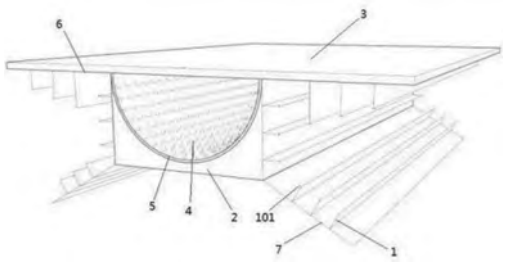

Figure 17. Waterstop with drainage and anti crystallization functions.

The application of waterstop with drainage and anti crystallization functions prevents crystallization blockage in the drainage channel, ensures smooth drainage of the channel, reduces water pressure on the tunnel structure, improves the durability of drainage waterstop, and enriches the types of tunnel waterstop.

5 ENGINEERING APPLICATION ANALYSIS

5.1 *Overview of tunnel*

The Siding Extra Long Tunnel, located in the Guilin-Liucheng Highway in Guangxi, was completed and opened in December 2021. It was the longest highway tunnel in Guangxi at that time.

Figure 18. Photos of siding extra long tunnel.

The starting and ending chainage of the left tunnel were ZK61+220~ZK66+860, with a length of 5640m. The starting and ending chainage of the right tunnel were K61+192~K66+839, with a length of 5647m. The maximum burial depth of the tunnel was about 301m. The construction clearance of a single tunnel was 11.0m×5.0m (width×High). The azimuth angle of the entrance direction of the tunnel axis was about 262°(8° due east by south), the azimuth angle of the tunnel body section was about 289°, and the azimuth angle of the exit direction is about 282° (12° due west by north). The left and right entrance and exit doors are all equipped with new hollow-bamboo-cut type portals.

5.2 *Analysis of social and economic benefits*

New technologies and products such as the light environment design technology for green highway tunnel portal, hollow-bamboo-cut portal, drilling geological radar prediction technology in karst peak cluster areas, BIM simulation analysis technology for tunnel water inflow, and waterstop with drainage and anti crystallization functions have been successfully applied to the Siding extra long tunnel. The landscape effect of the tunnel portal has been improved by the key technology, especially, the “white hole” and “black hole” effects of the tunnel portal have been effectively solved, glare has been effectively prevented, the driving comfort and safety of the tunnel portal have been improved, and the energy consumption of tunnel lighting has been reduced, saving 75.1 tons of energy conversion standard coal annually.BIM technology has been used to simulate and predict tunnel water inflow. advanced geological prediction methods such as single hole reflection measurement, cross hole measurement, and hole ground measurement have been proposed to evaluate and analyze the environmental impact of tunnels in karst peak cluster areas. The concept and construction method of “connecting first, prevention, drainage, blockage, and interception combined, adapting to local conditions, protecting ecology, and comprehensive management” have been proposed. The construction methods for tunnel disaster prevention and ecological protection in karst peak cluster landform areas have been formed. The new type of waterstop with drainage and anti crystallization functions can be applied to tunnel construction joints and settlement joints. It’s functions such as waterproofing, drainage, and anti crystallization, effectively solving the problems of water leakage in tunnel construction joints and settlement joints, as well as crystal blockage of drainage facilities. According to calculations, a direct economic benefit of 36.75 million RMB has been created, the quality of tunnel engineering has been improved, and the concept of green highway construction were reflected. The economic and social benefits are very significant.

6 CONCLUSION

Through theoretical analysis, simulation, on-site testing, and engineering applications, a systematic study was conducted on the key technologies for the construction of extra long green highway tunnels in karst peak cluster areas.Based on the above, the main achievements and conclusions can be drawn as follows:

(1) BIM technology has been applied to the study and analysis of the light environment of tunnel portal for the first time, such as sunlight analysis and glare analysis. Innovative proposals has been made for the structural type of hollow-bamboo-cut portal, and the construction process and method of hollow-bamboo-cut portal has been formed
(2) Based on the geological characteristics of tunnels in karst peak cluster landform areas, BIM technology has been applied to establish a prediction method for tunnel water inflow, and a joint detection technology of "single hole radar-cross hole radar-hole surface radar" geological advance prediction has been developed
(3) A waterstop, combined drainage and anti karst crystallization functions,has been developed. The problems of water leakage from tunnel construction joints and settlement joints, and crystal blockage of drainage facilities have been effectively solved

The research results of this article have been promoted and applied to multiple highway projects in China. However, further research is needed to address issues such as the construction of tunnel clusters, and the impact on water environment during tunnel operation in karst peak cluster areas.

REFERENCES

[1] Ministry of transport. Statistical bulletin on the development of transportation industry in 2022[R]. Beijing: Ministry of transport, 2023.
[2] YAN Jinxiu. Development trends in world tunneling technology: Safe, economical, green and artistic[J]. Tunnel Construction, 2021, 41(5): 693.
[3] Ministry of transport. Guidelines for Design of Lighting of Highway Tunnels:JTG/T D70/2-01 –2014[S]. Beijing: China Communications Press Co.,Ltd., 2014.
[4] Liu Yingying, Lin Liyong, Xu Jingfeng. Study on Photobiomobulation of Tunnel Lighting [J]. LIGHT & LIGHTING, 2009, 33 (4): 13
[5] DONG Zhiming, GUO Baode, XU Zeqi, ZHANG Xiaoqin, CAO Jiantao. Research and Application of Light Environment of Highway Tunnel Portal Based on BIM Technology[J]. Tunnel Construction, 2021, 41(S2): 144–150.
[6] Cao Jiantao, Wng Lei, Xu Zeqi, Dong Zhiming. Research and application of BIM modeling method for lining structure of mountain tunnel[J]. HIGHWAY, 2020, (08): 386–389.
[7] Dong Zhiming. Study on the influence of portal form of highway tunnel on the brightness of exit section[J]. HIGHWAY, 2014, (08): 296–299.

Tunnelling for a Better Life – Yan, Celestino, Thewes & Eberhardt (Eds)
© 2024 The Author(s), ISBN 978-1-032-80042-4
Open Access: www.taylorfrancis.com, CC BY-NC-ND 4.0 license

Challenges and lessons learned from 100 km of major hydropower tunnels in Bhutan

Tashi Dorji*
Druk Green Power Corporation, Thimphu, Bhutan

Dean Brox
Dean Brox Consulting, Vancouver, Canada

Sonam Wangdi
Druk Green Power Corporation, Thimphu, Bhutan

ABSTRACT: Bhutan is a small mountainous kingdom located in the eastern part of the Himalayas between China in the north and India in the east, west and south. There exist several major rivers throughout Bhutan that provide excellent opportunities for hydropower development that have been constructed since the 1980's. To date, more than 100 km of long (6-23 km) and medium to large size (6-12 m) low pressure headrace tunnels have been constructed by traditional drill and blast methods via multiple adits along the tunnel alignments and finished with concrete linings. The headrace tunnels have been constructed within both the Lesser and Greater Himalaya geological environments where challenging geotechnical conditions have been experienced including major geological faults with running ground and collapses, large volume and high-pressure groundwater inflows, appreciable overbreak, abrasive rock conditions, and in some cases the need to re-align the tunnel. Traditional and innovative mitigation measures including pre-support forepoling, sequential excavation, and pre-drainage have been successfully implemented to allow the completion of the headrace tunnels and operations of the multiple hydropower plants.

Keywords: Lessons Learned, long tunnels, drill and, blast excavation, hydropower

1 INTRODUCTION

Bhutan is a small mountainous kingdom of less than 40,000 km^2 and about 750,000 inhabitants and located in the eastern part of the Himalayas between China in the north and India in the east, west and south. There exist several major rivers throughout Bhutan where excellent opportunities for hydropower development have been completed since 1985 with glacial meltwater from the northern part and relatively high precipitation especially during the monsoon season. To date, more than 100 km of long (6-23 km) and medium to large size (6-12 m) low pressure headrace tunnels (HRTs) have been constructed by traditional drill and blast methods via multiple adits along the tunnel alignments and finished with concrete linings. Despite the headrace tunnels being sited within the lower Himalaya geological environment, challenging geotechnical conditions have been experienced including major geological faults with running ground, large volume and high-pressure groundwater inflows, appreciable overbreak, abrasive rock conditions, and in some cases the need to re-align the tunnel. Traditional and innovative mitigation measures have been successfully implemented to allow the completion of the headrace tunnels and operations of the multiple hydropower plants. Significant associated underground excavations have also been constructed in Bhutan as part of these hydropower projects including large powerhouse caverns and long pressure and surge shafts. Figure 1 presents a typical large and steep valley where hydropower projects have been planned and constructed in Bhutan.

2 PAST, RECENT AND CURRENT PROJECTS

Table 1 presents the past and recently completed major tunnels along with current major tunnels. All of the hydropower tunnels in Bhutan can be recognized as major tunnels as part of large hydropower developments with installed generation capacities varying from 120 MW to 1200 MW. One of the

*Corresponding author: t.dorjee2167@drukgreen.bt

DOI: 10.1201/9781003495505-193

projects is currently in construction and two of the projects have experienced exceptional circumstances that has prevented them from being commissioned and these unique challenges are discussed later.

Figure 1. Major valley for hydropower tunnels.

Table 1. Summary of hydropower tunnels in Bhutan.

Project	COD	Capacity MW	Length km	Size m
Chhukha	1986	336	6.5	5
Tala	2007	1020	23	6.8
Dagachhu	2015	126	7.7	4.4
Punatsangchhu 1	2027	1200	9	10
Punatsangchhu 2	2024	1020	8.5	11
Mangdechhu	2019	720	13.5	6.5
Nikachhu	2023	129	9	4.5
Kholongchhu	2027	600	15.8	5.7

COD = Commercial Operation Date

3 DESIGN AND CONSTRUCTION APPROACH

3.1 *Tunnel design*

All of the tunnels have been designed as high elevation, low gradient pressure tunnels aligned subparallel to the major valleys that typically transect multiple cross valleys. Horseshoe, circular, and D-shaped cross-sectional geometry has been adopted with full (100%) concrete linings for long-term low maintenance hydropower operations.

Limited geotechnical investigations were completed at most projects given the very difficult access along the steep terrain and densely vegetated topography. Geotechnical drilling was typically limited to the dam and powerhouse locations with only short holes along the tunnel alignments that was sometime supplemented with geophysical surveys. Exploration adits were typically excavated at most dams and powerhouses that provided good insight into the main bedrock types as well as for in situ testing of rock mass deformability. Table 2 presents a summary of the key investigations completed for the tunnels.

Table 2. Summary of Key Investigations for the Tunnels.

Project	Total Drilling, m	Drift Length, m
Chhukha	?	?
Tala	?	580
Dagachhu	980	N/A
Punatsangchhu 1	1129	550
Punatsangchhu 2	1640	N/A
Mangdechhu	638	452
Nikachhu	1946	727
Kholongchhu	1420	808

3.2 *Tunnel construction*

Traditional drill and blast methods have been used for the construction of all of the hydropower tunnels to date using multiple adits parallel to valley with individual camps and spoil sites at each adit location. The smaller size tunnels, typically less than 6.8 m have been excavated full face while the larger tunnels were excavated by top heading and bench stages. Some of the major tunnels have experienced significant geological overbreak during construction given the highly fractured nature of the bedrock at some projects. Traditional components of rock support including pattern rock bolts, mesh, shotcrete, and steel ribs with forepoling/spiling for adverse geological occurrences (AGO's) formed the various tunnel support classes that were evaluated based on face mapping after each blast. Most of the construction adits were sealed with concrete plugs following completion but at least two (2) adits were completed with hydraulic pressure doors for future access and inspections. Finally, most of the tunnels were constructed under design-build (EPC) type of contracts, with the most recent including a Geotechnical Baseline Report (GBR) for risk sharing of the encountered geotechnical conditions. The increasing number of future major tunnelling projects in Bhutan with long and deep tunnels with challenging access and increasing environmental impacts has led to the scope for the consideration for the use of tunnel boring machines (TBMs) as has been recently and successfully used in neighbouring Nepal and again being used in India. The construction of several of the major tunnels in Bhutan have resulted in contractual disputes. Bonaventura et al. (2015) have reported that 55% of claims associated with long and major tunnels in Bhutan have been due to differing site conditions (with 49% due to adverse geotechnical conditions) which have resulted in appreciable delays in the completion of construction for dispute resolution.

4 ENCOUNTERED GEOTECHNICAL CONDITIONS

4.1 *Regional and local geology*

The majority of the major hydropower tunnels constructed to date in Bhutan have been sited within the Lower Himalayan geological region where the bedrock formations have been only subjected to very limited distortion and tilting unlike that associated with the central and upper Himalayan geological regions. Typically, bedrock formations include mixtures of gneiss, phyllite, mica-schist and quartzite of variable rock mass quality and degree of fracturing. The quartzite bedrock is particularly very strong with rock strengths varying from 250 MPa to 350 MPa. Figure 2 presents a typical example of a major outcrop of quartzite in Bhutan. Major shear zones of low quality and non-durable phyllite are often intermixed within the more competent and durable quartzite.

Figure 2. Major outcrop of quartzite.

4.2 *Groundwater conditions*

All of the tunnel alignments are aligned sub-parallel to major valleys with elevated topography and with the significant groundwater recharge from annual monsoon rains there is appreciable groundwater resources in the project areas. Extensive permeability testing has been performed as part of geotechnical investigations for dam sites that has indicated Lugeon values generally ranging from Lu=1 to Lu=10 for shallow depths to 100 m and Lugeon values generally less than Lu=3 for depths greater than 200 m. Large groundwater inflows have been experienced during the excavation of most of the HRT's with short-term dissipation of inflows. Major and continuous inflows of more than 125 l/s at Nikachhu HRT.

4.3 *In situ stresses*

Hydro-fracturing testing has been typically carried out at the powerhouse locations primarily for the evaluation of low in situ stresses for steel lining design of the pressure shaft. Hydro-fracturing testing results can however also offer insight into the possible maximum in situ stresses for the powerhouse cavern stability and rock support requirements. The powerhouse caverns and pressure shafts of most of the hydropower projects in Bhutan have been sited at the intersection of a main valley and that of a cross valley where a topographic "nose" exists with limited lateral cover. These areas are commonly associated with low confining in situ stresses or are de-stressed as a result of intersection geological faults associated with the topographic valleys. Multiple geotechnical drillholes have been completed as part of the powerhouse cavern and pressure shaft designs and hydro-fracturing testing have been performed at varying depths of such drillholes to provide multiple testing results and greater confidence in the prevailing in situ stresses in these important project areas.

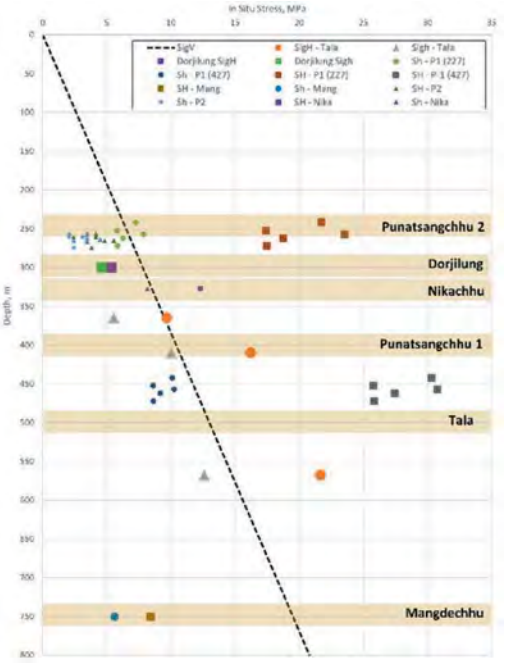

Figure 3. Hydrofracturing testing results at powerhouses.

Figure 3 presents the results from several campaigns of hydro-fracturing testing at the powerhouse and pressure shaft sites of various projects in Bhutan.

5 MAJOR HYDROPOWER TUNNELS

5.1 *Chhukha*

The Chhukha hydropower project that included a 6.5 km, 5 m HRT was the first major project constructed in Bhutan starting in 1979, and with the commissioning of the plant in 1986. Madhavan et al,

(1987) and Shukla (2016) report that during the excavation of the downstream section of the D-shaped HRT a saturated sand seam was unexpectedly intersected after 565 m that resulted in a sudden in-rush up to 50 m^3/s of flowing ground with failure of steel rib support and fatalities and a delay of six months before construction resumed with a re-aligned section. Subsequent drilling investigations confirmed the presence of a deep slide area above the tunnel of water saturated fluvial terrace deposits with very limited cover. No probe drilling ahead of the tunnel face was performed during excavation and this represented a key technical shortcoming. Unwatered inspections of the Chhukha tunnel were performed in 2011 and again in 2021 using a remote operated vehicle (ROV) and no signs of any form of distress were observed of the concrete lining after a total of 35 years of operations.

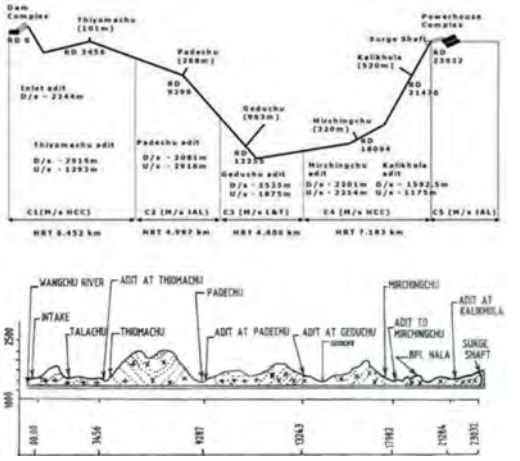

Figure 4. Layout and re-alignment for tala headrace tunnel.

5.2 *Tala*

The construction of the Tala hydroelectric project commenced in late 1997 and the construction of the HRT was completed in November 2004 with the first generating unit commissioned in 2006 and with the final unit commissioned in 2007. The 23 km long HRT was constructed as a 6.8 m internal diameter of horseshoe-shape using traditional drill and blast methods from a total of 5 adits with 11 working faces with a layout as presented in the plan and profile layout of Figure 4. The maximum cover along the HRT was about 1000 m. The alignment of the HRT includes six (6) bends. The total length of HRT was divided into four packages as indicated in Figure 4. Package C-1 comprised of 6.5 km length of initial reach of HRT from desilting chambers side. Package C-2 consisted of 5.0 km length of HRT. Package C-3 comprised of 4.4 km length of HRT. Package C-4 with a length of 7.2 km was the most typical package with regards to the difficult tunnelling conditions.

Construction of the HRT was delayed by approximately one year due to challenging geological conditions with nearly 30% of the geological conditions classified as poor to very poor and there were large variations in the originally anticipated rock mass conditions as per the contract and as actually encountered rock mass conditions in the HRT excavation (Singh and Khazanchi, 2010). For the HRT, 75% was expected to be excavated through class I to class III (very good to fair tunnelling medium) and 25% in class IV and in class V (poor to very poor tunnelling medium). However, about 27% of tunnel length was excavated in class III and 74 % was excavated in class IV, V, VI and in exceptionally poor tunnelling conditions.

Table 3 presents the summary of the originally anticipated geotechnical conditions versus the actual geotechnical conditions and the increase if poorer conditions of a total of 48%. It is particularly noted from Dev et al. (2013) that concrete grade M15A20 was used as backfilling between the steel arch ribs for tunnel support classes IV, V, and VI for the poorest of geotechnical conditions and that the internal diameter of the HRT was reduced to 6.5 m along these sections. Very difficult tunnelling conditions were experienced at a shear zone downstream of the Mirchingchu adit where the HRT was re-aligned under deep cover over a length of about 1190 m and special tunnel support was installed. Despite this a major failure of the high-capacity support occurred as shown in Figure 5.

Table 3. Anticipated and actual geotechnical conditions.

Rock Class	Anticipated %	Actual %	Increase %
1	0%	0%	
2	6%	0%	
3	69%	27%	
4	21%	41%	20%
5	4%	21%	17%
6	0%	6%	6%
7-AGO	0%	5%	5%
Totals	100%	100%	48%

Finally, the Tala tunnel experienced problems after 13 years of operations with the loss of appreciable pieces of concrete lining along a 35 m section along the upstream section as a result of ongoing instability as squeezing due to insufficient support at this section that was aligned sub-parallel to a major lineament and cross valley creek. The instability was detected and identified from an unwatered inspection in 2021 using a remotely operated vehicle (ROV) and repairs of this section were performed over a 3-month period in 2022 (Brox et al, 2023).

5.3 *Dagachhu*

The construction of the 7.7 km HRT for the Dagachhu hydropower project commenced in 2009 and was commissioned in 2015. The HRT was constructed through

Figure 5. Failure of high-capacity tunnel support.

a mixed sequence of gneiss and mica-schist with a maximum cover of about 630 m. The tunnel transected two main valleys where open aerial pipeline bridge sections were constructed of lengths 600 m and 100 m. The rate of progress of excavation with initial support was limited due to the poor encountered conditions and generally ranged from 1.25 m/day to 1.5 m/day and rate of progress of the final concrete lining generally ranged from 3 m/day to 6 m/day. Groundwater inflows were generally very limited below 1 l/s but with only five locations of elevated inflows from of 3 l/s to 11 l/s. Figure 6 presents the longitudinal and statistical distributions of installed tunnel support for northern 4 km section of the tunnel that indicates that mainly Classes 2 and 3 were installed. Minor squeezing conditions were experienced during construction under the maximum cover section over a length of 640 m with cracking of the initial support shotcrete and minor buckling of the lattice girders that required the installation of additional initial support comprising mesh reinforcement followed by a final concrete lining that required an additional 2.5 months.

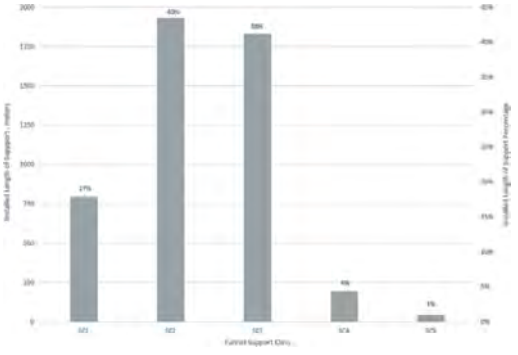

Figure 6. Distribution of installed tunnel support.

The Dagachhu HRT experienced some very challenging conditions along the northern low cover section whereby a 15 m high cavity formed during excavation with flowing ground and high groundwater inflows. Pipe umbrella support had to be installed along this section without blasting and excavation by excavator only of suspected geological fault materials as presented in Figure 7. A portion of this section of the HRT resulted in misalignment and in order to provide an acceptable final lining solution a 160 m long section of steel lining was required to be installed.

Figure 7. Pipe umbrella support in Dagachhu HRT.

5.4 *Punatsangchhu 1*

The Punatsangchhu 1 headrace tunnel was the first large size (10 m) tunnel constructed using top heading and bench methods from December 2009 to December 2012 and was completed under two contracts for the upstream 7.5 km and the downstream 1.5 km and using only two intermediate access adits. The 9 km HRT parallels the left bank of the valley under a maximum cover of 500 m. The achieved progress of excavation was consistent with what was planned as 65 m of top heading in 25 days for an average of about 2.6 m/day and about 60 m of benching in 5 days for an average of about 12 m/day. There were no good quality rock conditions anticipated along the HRT and the installed distribution of tunnel support was Class 3 (52%), Class 4 without ribs (37%), Class 4 with ribs (10%), and Class 5 (< 1%).

While preparing for the casting of the kerb concrete along a 105 m upstream section of the HRT, movement in the 250 mm steel rib supports occurred that resulted in the significant dislodging of steel ribs and the detachment of large rock blocks. At this location it was observed that a thick clay shear zone was present and was highly saturated that caused the instability as shown in Figure 8.

5.5 *Punatsangchhu 2*

The 8.6 km Punatsangchhu 2 HRT was the second largest size (11 m) tunnel constructed using top heading and bench methods and was contracted in 2 packages, included excavation utilizing two intermediate access adits, and was constructed from late 2012 to October 2018. At the time, it was the largest HRT constructed in Asia.

Figure 9 illustrates the HRT. The HRT parallels the right bank of the valley under a maximum cover of about 560 m.

Figure 8. Dislodging of Steel Ribs at Shear Zone.

The maximum cover along the alignment was 580 m. Average progress rate of excavation for the top heading was 3.3 m/day, and 6.9 m/day for benching. Difficulties were encountered along both access adits due to the intersection of major shar zones necessitating re-alignments of the access adits to the intersection of the main HRT. Rock support comprised a series of classes from a minimum pattern rock bolts of 6 m length through to 250 mm steel ribs with variable spacings from 400 mm to 750 mm with 125 mm shotcrete. While an average or typical overbreak of 1.5 m was realized, which represents an appreciable amount for backfilling, there were a limited number of locations for major overbreak as much as 12-14 m occurred that was associated with the intersection of very poor conditions and where more than 1100 bags of concrete was backfilled.

Figure 9. Top heading and Benching in Punatsangchuu 2.

A major collapse occurred during the excavation of intermediate adit 2 and the junction with the main tunnel whereby a low dipping shear zone was intersected. Despite the installation of high-capacity support of steel ribs, rock bolts, fibre-reinforced shotcrete with forepoling and channels to support the crown from detachment as a precautionary measure, several large blocks became dislodged and caused distortion of the installed support as shown in Figure 10.

In addition to challenges with the excavation of the HRT, a major collapse occurred in the powerhouse. On March 3, 2016, a massive roof fall of approximately 100,000 m^3 occurred in the downstream surge gallery (cavern) which halted the operations in the major caverns and required additional strengthening measures.

Figure 10. Distortion of high-capacity tunnel.

The collapse extended up to 100 m upwards into the overlying deep overburden above the powerhouse. Prior to concluding anything on the treatment measures for the muck dislodged into the cavern and the cavity formed over the crown of the downstream surge chamber, there was a strong need to determine the extent of the resulting cavity. Even to understand the influence of cavity formation on the adjacent transformer cavern, the cavity needed to be delineated. Therefore, the project client adopted several techniques to decipher the shape and dimensions of the cavity including, cavity monitoring surveying, geophysical, cross-hole tomography seismic surveys, borehole scanning, and exploratory drilling. In 2022, a major stabilization program was initiated with the backfilling of cavern, placement of reinforced concrete walls, and the installation of nearly 20,000 m of 100-ton tie-back strand anchors (Roberti, 2023).

5.6 *Mangdechhu*

The construction of the 13.5 HRT of the 720 MW Mangdechhu project parallels the left bank of the Mangdechhu valley commenced in early 2012 and was completed in 63 months using five (5) intermediate access adits. The maximum cover along the HRT was about 900 m. A design change completed during the early stage of the HRT was the size of the intermediate access adits from 6.5 m to 7.5 m to better facilitate ventilation, services, and mucking as requested by the contractor. The distribution of anticipated and actual tunnel classes is presented in Table 4 which indicates a minor increase in poorer than expected ground in comparison to the construction of other HRT's.

In addition, tunnel excavation experienced challenges with a major fallout at the intersection of Adit 3 and the HRT as depicted in the graphic of Figure 11.

Finally, squeezing conditions with buckling of steel ribs occurred with deformation as much as 560 mm along an upstream section of the HRT with mica schists, quartzitic schists and quartz biotite gneiss

under a cover varying from 750 m to 1000 m as presented in Figure 12. In addition, post-excavation slabbing due to dilation to a depth of 1.5 m.

Table 4. Anticipated and actual tunnel classes.

Rock Class	Anticipated %	Actual %	Increase %
1	0%	0%	
2	25%	6%	
3	50%	71%	21%
4	20%	22%	2%
5	5%	1%	
6	0%	0%	
7-AGO	0%	0%	
Totals	100%	100%	23%

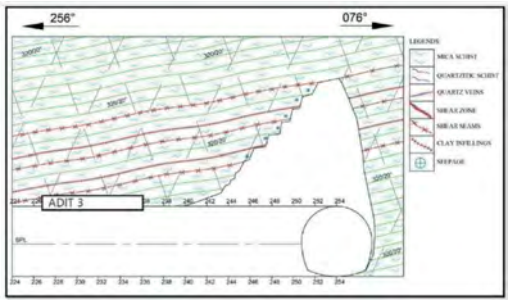

Figure 11. Major fallout of ground at intersection of HRT.

Figure 12. Squeezing conditions and buckling of steel ribs.

5.7 *Nikachhu*

The 9 km HRT for the Nikachhu power plant is the most recently completed major tunnel and was constructed using four (4) intermediate access adits through mixed rock conditions of mica schist, quartzitic schist and quartz biotite gneiss. Tunnel excavation experienced multiple challenges including the intersection of large unstable wedges, major shear zones with squeezing conditions with a maximum convergence of over 550 mm, slabbing and rockbursting under high cover section of 700 m to 1000 m and large groundwater inflows up to 125 l/s as presented in Figure 13. Mitigation for some of these challenges included stress relief holes were provided for release of stresses, split heading excavation with top heading and benching, and curved invert struts for the squeezing conditions poor rock mass.

After the completion of the project, the Nikachhu hydropower plant will provide additional water to the Mangdechhu Hydropower Plant (MHP) to enhance power generation during lean seasons as the water discharged from its tailrace tunnel is spilled directly into the dam of Mangdechhu.

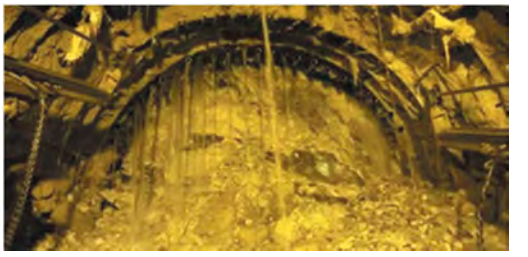

Figure 13. Very Large groundwater inflows.

5.8 *Kholongchhu*

The 15.8 km HRT for the Kholongchhu hydropower plant started construction in April 2021 utilizing six (6) intermediate access adits. The HRT parallels the right bank of the north-south oriented valley and the maximum cover along tunnel is about 560 m and there exist two cross valleys where the minimum cover is less than about 75 m and 45 m where steel lining sections will be required as part of the design to prevent leakage during operations. A total of eleven (11) lineaments have been identified to transect the HRT with 2 described as minor, 4 as intermediate, and 5 as major lineaments. Most of lineaments are oriented mainly

Figure 14. Adit construction at Kholongchhu.

north-easterly but the major lineaments are oriented east-west and southeasterly. The main rock types anticipated to be encountered during construction are gneiss with bands of quartzites, amphibolites, schist and intrusions of porphyritic granite of variable thickness. The anticipated distribution of tunnel classes has been estimated to be Class 2 (8%), Class 3 (77%), Class 4 (8%), and Class 5 (7%). The construction of the project is on hold since mid-2022 due to restructuring of the project ownership and is expected to resume construction by the end of 2023. Since April 2021 until mid-2022, some progress in development of HRT portals have been made as shown in Figure 14.

5.9 *Future tunnel – Dorjilung*

A major new tunnel is currently planned as part of Dorjilung hydropower project and comprises a 15 km, 11 m size tunnel aligned sub-parallel to the Kirichhu valley in eastern Bhutan. Maximum cover along the tunnel is about 800 m over a relatively short section and about a 500 m length of cover over 500 m. The geology along the tunnel alignment comprises mainly very strong but closely spaced fractured quartzite (~70%) and phyllites (~30%).

The tunnel alignment passes below two major valleys with cover of about 100 m and where geological faults or fractured zones are anticipated and where steel lining sections will be required unless re-aligned. Drill and blast methods of excavation with a total of 6 intermediate adits represent the base case for studies to date. The highly fractured nature of the quartzite has been recognized as a key risk for excessive overbreak, even for top heading and bench stages of excavation given previous limited controlled drilling and blasting practices where significant overbreak was experienced.

Accordingly, this tunnel is the first major tunnel in Bhutan where the use of a tunnel boring machine (TBM) is being contemplated. Based on a preliminary schedule comparison there is a possible 18-month savings with the use of a TBM with concurrent pre-cast concrete segmental lining. The use of a TBM is considered to be technically viable for this tunnel regarding the geotechnical conditions and key environmental advantages of the TBM option are available power from a nearby hydropower plant located immediately downstream as well as the elimination of the multiple intermediate access adits and the associated logistics of camps, spoil sites and traffic. Accordingly, the TBM option will be further evaluated holistically in terms of logistics, overall project timeline, cost-benefit to the project and risks associated with the use of a TBM for the site-specific geotechnical conditions of the HRT.

6 UNIQUE CHALLENGES OF OTHER COMPONENTS

The hydropower projects in Bhutan have experienced unique challenges associated with other major components of the projects which has prevented the commissioning of some of the projects. A major landslide is present along the right bank at the Punatsangchhu 1 project preventing the construction of the dam. A significant collapse has occurred within the downstream surge cavern of the Punatsangchhu 2 project which is under rehabilitation. At Tala there has been the ongoing failure of rock bolts in the powerhouse after several years of operations.

7 KEY CHALLENGES AND LESSONS LEARNED

The following challenges and key lessons learned from the past 100 km of hydropower tunnels in Bhutan are:

- Unanticipated adverse geotechnical conditions were encountered that caused appreciable delays in the absence of comprehensive geotechnical investigations;
- Large instabilities have generally been experienced with the construction of large size tunnels;
- Greater attempts are to be made for deep geotechnical drillholes along all long and deep headrace tunnels as well for all key components such as surge and pressure shafts;
- Greater geotechnical testing should be conducted especially for very strong and abrasive bedrock;
- Improved evaluation of main lineaments along the tunnel alignments and their geological characterization;
- Detailed geotechnical models are required to be developed for main project components based on improved investigations to be attempted despite the challenging mountainous terrain;
- Improved estimates should be developed for anticipated groundwater inflows;
- Geotechnical Baseline Reports (GBRs) should be prepared in accordance with the format and content of the ASCE guidelines for all new major tunnels to attempt to limit claims and avoid confusion of presenting factual and interpretative geotechnical information that should be contained in their respective reports (GIR and GDR);
- Improved practices to be included in technical specifications for controlled drilling and blasting possibly with computerized jumbos to limit overbreak, and;
- The option of tunnel boring machines (TBMs) in conjunction with pre-cast concrete segmental linings should be thoroughly evaluated and considered for construction of new major tunnels subject to acceptable geotechnical conditions and logistical requirements.

REFERENCES

Bonaventura H., Hadikusumo, W., and Tobgay, S., 2015. Construction Claim Types and Causes for a Large-Scale

Hydropower Project in Bhutan, Journal of Construction in Developing Countries, 20(1), 49–63.

Brox, D., Wangdi. S., and Namgyal, D. 2023. Correlation of ROV Observations with Actual Damage in the Tala Headrace Tunnel, World Tunnel Congress, Athens, Greece.

Dev, H., Singh, R., and Sengupta, C. K. 2013. Rock Supports and Geological Appraisal for Head Race Tunnel of Tala Hydroelectric Project, Bhutan. Indian Society for Rock Mechanics and Tunneling Journal, Vol 19., No.1.

Madhavan, K., Parasuraman, M.P., and Sood. P.K. 1987. Rock Failure near Face IV of the Chhukha Power Tunnel, ISRM Congress, Montreal.

Shukla, M. 2016. Practices in Planning, Design and Construction of Head Race Tunnel of a Hydroelectric Project. ICCCGE 2016: 18th International Conference on Civil, Construction and Geological Engineering held in Toronto, Canada during June, 13-14, 2016. This paper was also able to find a position in the international conference of Dams and Hydropower held at Laos in May 2016.

Singh, R., and Khazanchi, R.N. 2010. Time and Cost Aspects of Tunnel Construction in Different Rock Mass Condition, Indian Society for Rock Mechanics and Tunneling Journal, Vol 16., No.2.

Roberti, P., Mishra, A.K., Pielmeier, M., and Bandi, V. 2023.Stabilization of a collapsed rock mass and installation of 100 tons permanent strand anchors at the Punatsangchhu-II Hydroelectric Project, Bhutan. World Tunnel Congress, Athens.

Tunnelling for a Better Life – Yan, Celestino, Thewes & Eberhardt (Eds)
© 2024 The Author(s), ISBN 978-1-032-80042-4
Open Access: www.taylorfrancis.com, CC BY-NC-ND 4.0 license

Design and construction considerations for cross passages in Bangkok subsoil

Ochok Duangsano*
Geotechnical & Foundation Engineering Co., Ltd, Bangkok, Thailand

Aphichat Sramoon
TEAM Construction Management Co., Ltd., Bangkok, Thailand

Auttakit Asanprakit & Arthit Chayaroon
Geotechnical & Foundation Engineering Co., Ltd, Bangkok, Thailand

Noppadol Phienwej
Asian Institute Technology, Bangkok, Thailand

ABSTRACT: The design and construction of underground cross passages are one of the challenging tasks in soft ground tunnelling in urban areas. According to the construction of MRT Orange Line (East Section) Project in Bangkok, two cross passages between an intervention shaft and a segmental tunnel lining are designed and constructed to serves emergency egress for commuters and ventilation purpose. The application of New Austrian Tunnelling Method for tunnel construction is employed for cross passages. Special measures of ground improvement by jet grouting and pre-support techniques are employed prior to excavation. In addition, the application of special segments for bored tunnel and the use of temporary steel ring to support the opened ring of the bored tunnel are utilized to effectively enhance safety and stability. This paper presents an introduction to the project, specific site constraints and requirements on the design and construction. It also provides the design process and key considerations on the construction of cross passages work which contribute to the successful implementation of the tunnelling works.

Keywords: Tunnelling, Cross passage, Primary lining, NATM, Final lining

1 INTRODUCTION

In the last few decades, the expansion of congested urban areas has rapidly increased the demand for underground structures, particularly metro tunnels. Owning to a tunnelling work, it is undeniable that a design and construction of cross passages are considered to be one of the most challenging tasks for tunnelling in soft ground conditions. This is due to the complicated construction sequence and high proportion of ground-structure interaction. It also involves difficult technical challenges in supporting the tunnel face, excavation profile, and existing bored tunnel lining (Kuyt, 2015).

The MRT Orange Line (East Section) project – Contract E2, an intervention shaft is designed to be typically positioned at every 750 m between two underground stations along the tunnel alignment to provide a means of emergency escape and ventilation system in accordance with NFPA 130. Due to restrictions of the construction area, a top – down construction by using diaphragm walls for an intervention shaft 14 (IVS14) to cover the tunnel is restricted in very dense areas. Thus, a cross passage is proposed to tackle this issue as shown in Figure 1.

Three aspects of cross passage design and construction generally require structural and geotechnical considerations including excavation and support installation of primary lining, support of running bored tunnel during construction, and permanent lining of the cross passage.

A primary support typically involves a shotcrete lining, also known as a sprayed concrete lining, with additional reinforcements as required. Excavation and support installation of the primary lining play an essential role in maintain stability and controlling the level of ground movements which is particularly in

*Corresponding author: ochok_d@gfe.co.th

DOI: 10.1201/9781003495505-194

urban areas. During the excavation and opening for cross passage, the forces in tunnel lining can be distributed and transferred to the adjacent fully enclosed tunnel rings (Lee and Choi, 2014). Consequently, support of bored tunnel is required to transfer of the excessive loads from tunnel lining and mitigate lining ovalization resulted from tunnel opening and mined adit excavation. The final lining is the main permanent structural support element of cross passages which include cast-in-place reinforced concrete, connecting concrete collar and waterproofing system.

In this paper, the design methodology and construction of the cross passage for the MRT Orange Line Project is presented.

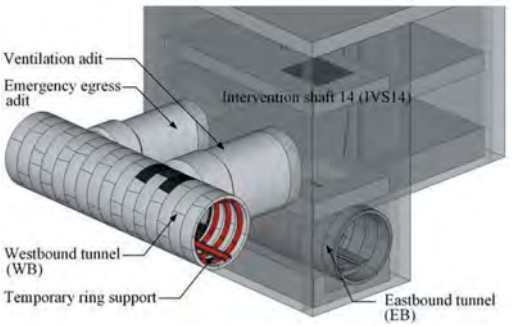

Figure 1. IVS14 and cross passage.

2 PROJECT DESCRIPTION

Mass Rapid Transit Authority of Thailand (MRTA) has implemented the MRT Orange Line (East section) project to proceed a comprehensive rail system in Bangkok, Thailand. CKST Joint Venture is awarded to carry out the design and construction. AGATE consortium is commissioned by CKST as their designer for this contract. The MRT Orange Line Project – Contract E2 has four underground stations, three intervention shafts and 3.68 km of twin bored tunnels. In this contract, a cross passage connected between the intervention shaft no.14 (IVS14) and Westbound (WB) tunnel is required to serve two primary purposes namely, ventilation works and emergency egress work. A longitudinal section of cross passage is shown in Figure 2.

2.1 *Geological conditions*

The geological condition of Bangkok subsoil is relatively uniform throughout the area. The uppermost 2.0 m thick layer is the fill material, which is underlain by an 8.0 to 15.0 m thick of soft clay layer. A medium stiff clay layer is found at a depth of approximately 10.0 m from the surface with a thickness of about 2.0 to 3.0 m. Below this layer is 1st stiff clay in which the thickness is about 6.0 to 10.0 m. The 1st sand layer is generally found at a depth of 25 to 30 m. The piezometric pressure head observed during the construction is about 13 m below the ground surface level.

The cross passage is designed to be positioned in the firm soil stratum of the 1st stiff layer and to avoid groundwater issues as depicted in Figure 3. Depth of ground surface level to the springline of tunnel is approximately 17 m.

3 CROSS PASSAGE SYSTEMS

Two adit tunnels connected between IVS14 and the WB tunnel are required to provide a ventilation purpose and evacuation of passengers. The requirement of minimum dimensions for ventilation adit tunnel is 3.9 m high and 3.4 m wide, whereas egress tunnel is required for 2.1 m high and 2.4 m wide. Figure 4 shows a typical section of adit tunnel where the total

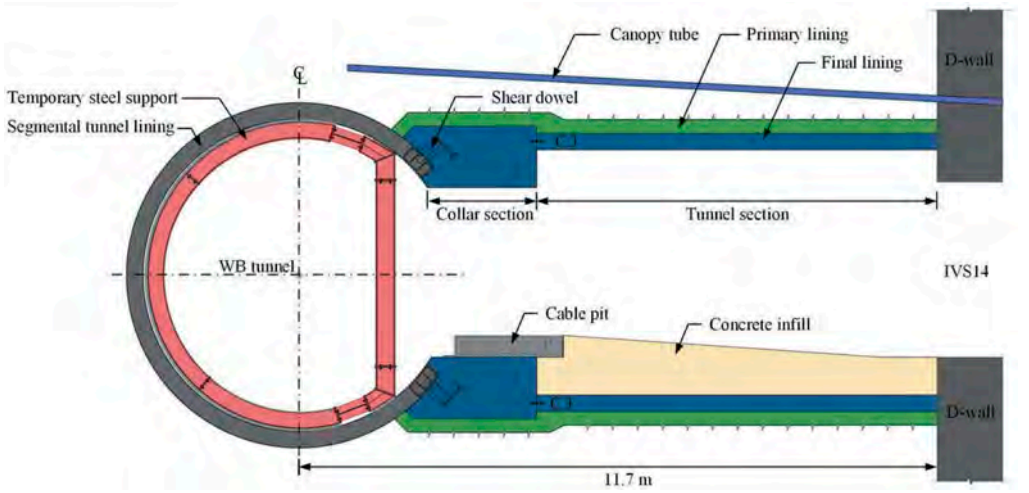

Figure 2. Typical longitudinal section of cross passage.

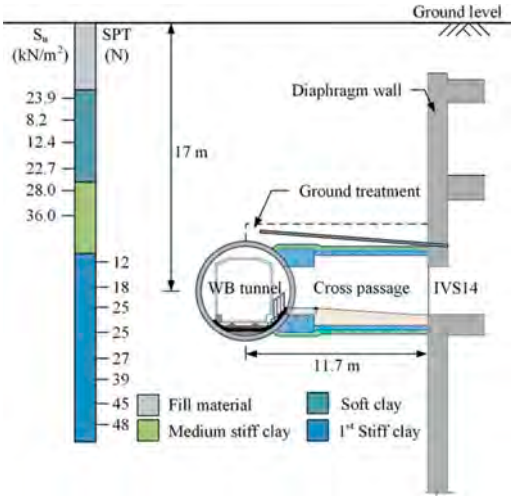

Figure 3. Soil profile and cross passage position.

excavation area of ventilation adit and egress adit are 27.91 m^2 and 21.74 m^2, respectively. Main components of this structural system are described in the following sections.

3.1 *Ground improvement*

In the area of the cross passage, the WB tunnel connected to the adit tunnels is partially situated in the medium stiff clay and 1st stiff clay layers. To stabilize the surrounding ground during construction of cross passages and opening of the bored tunnel as well as to mitigate the potential impacts on the existing structures, ground improvement is proposed to be applied by jet grouting techniques. The minimum required strength of the ground improvement in the medium stiff clay layer is 1.0 MPa.

3.2 *Pre-support*

Canopy tubes, also known as a pipe roof method, are adopted as pre-support to be installed ahead of the tunnel face to improve the tunnel stability, stand-up time of the ground, and to allow safe excavation. A perforated steel pipe is 12 m long with an outer diameter of 114.3 mm and a wall thickness of 5.6 mm. The steel grade of the pipe is SS400 which is equivalent to a yield strength of 245 MPa.

The pipes are designed as longitudinal beams carrying the imposed load from surrounding grounds. The pipe span is taken as 1.5 times the length of the round length (John and Mattle, 2003). The section properties of the pipe are used in conjunction with the induced bending moment to calculate the maximum stress in the pipe.

3.3 *Primary lining*

The primary lining or shotcrete lining is typically designed to sustain the ground loads, controls the deformations during tunnel construction, secures safe working conditions, and provide support until the final lining is completely installed. The primary lining of cross passages involves a shotcrete lining in combination with wire mesh and lattice girder.

3.3.1 *Shotcrete*

Shotcrete is applied as the primary support to provide the stability of the tunnel excavation. Shotcrete lining is designed to be 250 mm thick with a minimum compressive strength of 25 MPa at 28-day strength. The early strength development of shotcrete has to conform to Class J2 according to the Austrian Guideline for Sprayed Concrete.

3.3.2 *Wire mesh*

Welded wire mesh of 6 mm diameter bars at 100 mm spacing in both circumferential and longitudinal directions is applied into two layers. This material is used to strengthen the structural capacity of the shotcrete lining.

3.3.3 *Lattice girders*

Lattice Girders are installed in conjunction with shotcrete to provide immediate support and to maintain the designed shape of the tunnel excavation. A three-bar type (G105-25-32) of lattice girders with steel grade GR.75 equivalent to s yield strength of 520 MPa is proposed to be installed at every 1.0 m spacing.

3.3.4 *Excavation sequence*

Excavation sequence is a major influence on the stability of mined adit tunnel and ground movements in a soft ground condition. For the excavation of mined adit tunnels, the New Austrian Tunnelling method (NATM) also referred as Sequential Excavation method (SEM) is proposed to be applied for tunnel construction. The concept of NATM in soft ground is to provide the immediate tunnel support by closing the invert quickly to prevent the excessive ground movements (Mostafa et al., 2013).

Tunnel excavation is designed to sequentially perform into three stages; top heading, bench and invert as illustrated in Figure 5. A round length of 1.0 m is typically utilized for top heading and bench, whereas 2.0 m is employed for invert excavation.

In addition, further criteria are considered for the design and construction of cross passages as follows:

- The cross-sectional profile should be as smooth as poosible in order to prevent stress concentration.
- Ring closure of the invert should be done behind the tunnel face as quickly as possible to create a load support ring.
- A 50 mm thick flashcrete layer is installed at the face and covered all other exposed ground surface immediately after completion of each excavation round.
- Elephant's foot was also provided at the bottom of the top heading to increase its stability.

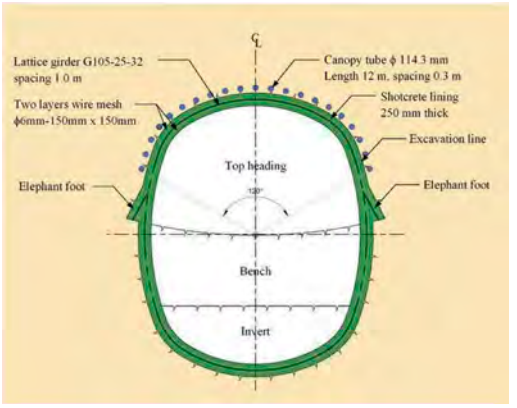

Figure 4. Typical cross section of primary lining.

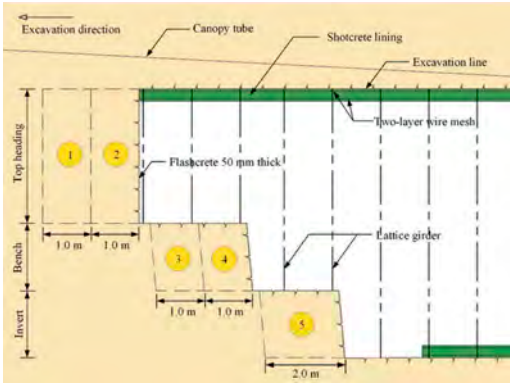

Figure 5. Excavation sequence for adit tunnels.

3.3.5 *Analysis of primary lining*

A two-dimensional (2D) finite element (FE) software RS2 by Rocscience is utilised for the analyses and simulation of ground conditions, loads acting on the primary lining, ground responses to the tunnel excavation and structural forces induced in the lining. The bottom boundary of the FE mesh was assigned at a depth of 50 m below the ground surface, while a width of the model was 100 m. For the displacement boundary a fixed constraint was applied only for the modelling bottom, whereas the movement was restrained in the horizontal direction for the two side boundaries. The boundary of ground surface was set as a free displacement in all directions. The FE simulation of the NATM tunnel is represented in Figure 6.

The primary lining was simulated as beam elements for both ventilation tunnel and emergency egress tunnel. In finite element stability analyses of mined tunnel, an equivalent stiffness is generally assigned to the shotcrete lining to account for hardening during application of the load as well as creep and shrinkage. Consequently, a modulus of E = 15,000 GPa is applied as the equivalent of the primary lining according to John and Mattle (2003). Soils are modelled as an elastic-plastic material using the Mohr-Coulomb failure criteria.

The simulation for the primary lining design utilises a multi-staged modeling approach. An initial stage describing the in-situ stress state of the soil prior to tunnelling. The modeling stages are established to assess the individual construction stages. Top heading excavation is modelled by reduction the stress within the excavation area to simulate the excavation and prior to installation of the support and it is followed by support installation. The modelling sequence is concluded with bench and invert excavation and installation of the shotcrete lining. The amount of relaxation to be applied is derived from the ground reaction curve (GRC) corresponding to the longitudinal displacement profile (LDP) of tunnel excavation. The LDP can be generated by using axis-symmetrical analysis as shown in Figure 7.

The shotcrete lining is checked for its integrity. The capacity of the shotcrete lining is determined in accordance with BS8110.

3.4 *Support systems for opening*

In accordance with the requirements of the project, where openings are to be formed in the running tunnel lining, temporary internal support to the running tunnel shall be provided. These supports shall adequately restrain the lining such that, on completion of the cross passage and removal of the temporary supports.

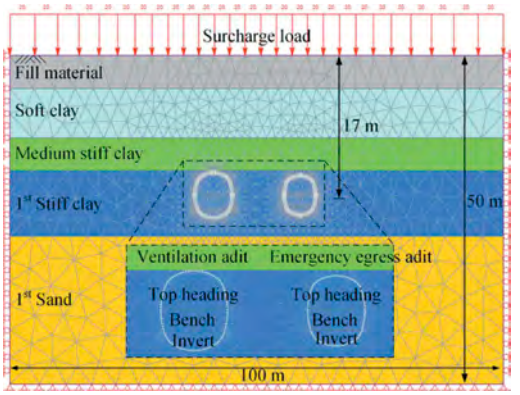

Figure 6. 2D Finite element analysis.

3.4.1 *Bored tunnel and steel segments*

A precast concrete structure is utilised for twin bored tunnel. The internal diameter of precast concrete tunnel lining is 5.7 m with a thickness of 0.3 m. The width of the segment is 1.4 m. Each tunnel consists of three ordinary segments, two countered key segments, and one key segment (5+1).

To allow for openings at the cross passage, five rings are partially replaced by steel segments. The removeable fabricated steel segments are installed at

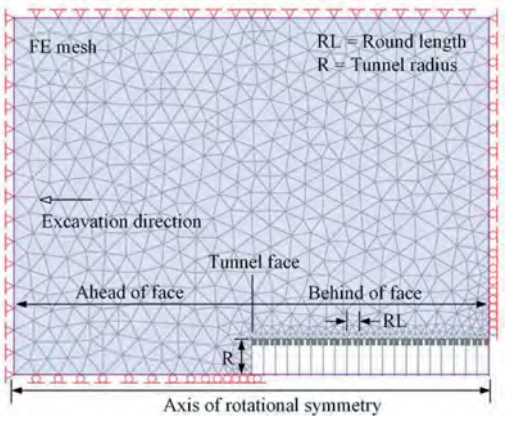

Figure 7. Axisymmetric analysis.

the opening areas for ventilation tunnel and emergency egress tunnel as illustrated in Figure 8.

3.4.2 *Temporary ring support*

A temporary internal support system of full moon type is utilised as presented in Figure 9. This system is capable in dealing with the heavier loads, which provides support for a full 360 degrees of the tunnel. The structural steel frame consists of a series of rigid ring beam, vertical steel props and cross beams to potentially support the opened tunnel rings and transferred the loads around the opening. A gap between the temporary ring support and the segments are filled by non-shink grout with equivalent strength of concrete so that the loads can effectively transfer between two structures.

3.4.3 *Analysis of temporary steel support*

According to the requirement of the project specification, the maximum allowable deflection on radius of the running tunnel is 15 mm. A three-dimensional finite element analysis by using Plaxis3D is preliminary employed to investigate the effects of adit tunnels excavation on the TBM tunnel. As a results, it is found that 16 rings of the tunnel lining are

Figure 8. Steel segments for opening.

Figure 9. Temporary steel support.

necessarily to be required to mitigate large ovallisation and overstress of the structural system.

A structural system of 3D shell spring model constitutes 16 rings of the tunnel lining associated with a temporary steel support were then taken into consideration. The tunnel linings are modelled as curved beam elements defined by the cross-sectional properties. The inner steel ring is modelled as curved beam element whereas column and longitudinal beam are modelled by straight beam element. Connection between the tunnel linings and the inner steel rings is simulated by radial springs. Coupling between adjacent rings is simulated by shear springs. Interaction between ground and the lining is modeled by springs in radial and tangential directions. For more detailed information about the analysis procedure and related results, it can be found in the previous study (Jayasiri et al., 2022).

3.5 *Final lining*

In this project, the permanent lining followed the same oval shape profile as the primary lining as shown in

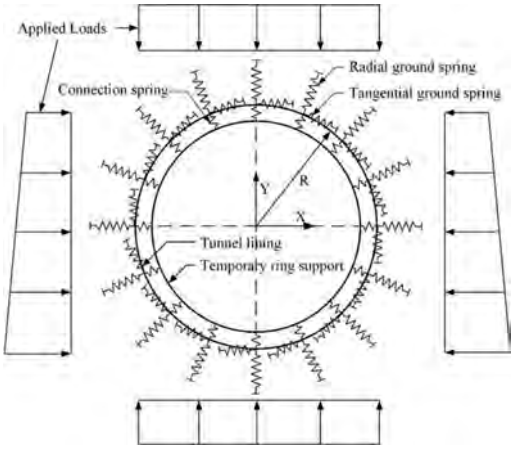

Figure 10. Idealized simulation of shell spring model.

Figure 11. This shape generally requires less excavation area, thickness of final lining and quantity of reinforcements. Once the excavation of adit tunnels was completed and temporary steel supports inside the bored tunnel are still active, a permanent reinforced concrete lining is then constructed so that the loads from the segmental tunnel are able to transfer to this stiffed section after removal of the steel ring supports.

The junction was designed to fully support the running tunnel lining at the opening together with the ground and groundwater loads on the junction itself and maintained the specified watertightness of the tunnels. The final lining was also analysed using the finite element code RS2. For these analyses the following loads on the final lining were taken into account: full overburden pressure, different water pressures with groundwater at current level and surface level and a surcharge load of 50 kPa. The concrete collar section was also designed to carry the entire loads from the surrounding soils as well as the loads transferred from segmental tunnel lining at the opening areas. It should be noted that the primary shotcrete lining was assumed to be fully degradable in the long-term condition, thus the property of shotcrete material was not taken into account in the simulation of permanent tunnel lining.

Characteristic concrete cube strength at 28-day of 40 MPa and a steel grade of SD50 (yield strength = 490 MPa) were employed for the construction of the permanent lining. A concrete cover to all reinforcement types of 50 mm was proposed for the final lining subject to the requirements of the exposure condition and 4-hour fire resistance. To transfer a load from segmental lining to the collar section, shear dowels are installed.

The structural capacity in terms of Ultimate Limit State (ULS) of the final lining is determined in accordance with BS8110. Furthermore, verification of Serviceability Limit State (SLS) is performed to satisfy the allowable crack width of 0.3 mm for the final lining.

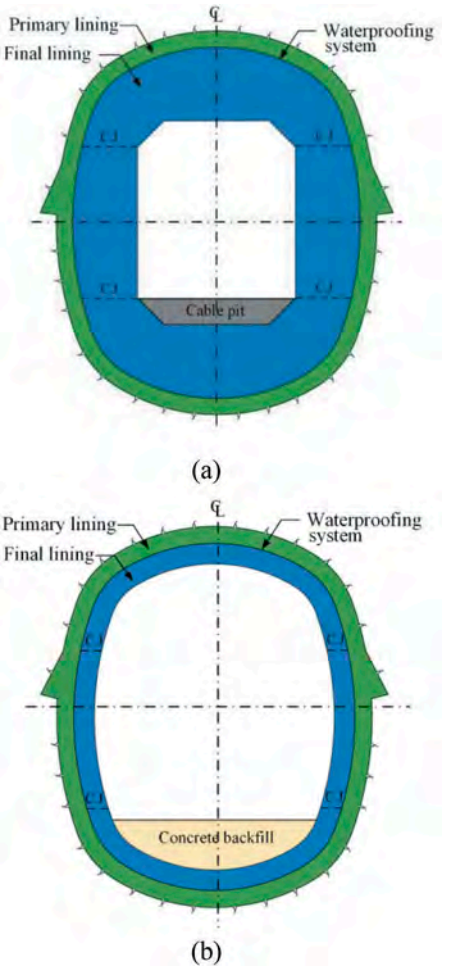

Figure 11. Final lining profiles; (a) collar section, (b) tunnel section.

4 CONSTRUCTION

This section aims to briefly present the construction sequences of the cross passage to connect between the running tunnel and IVS14. Work sequences can be described as follows:

- Construct and complete IVS14.
- Carry out ground improvement at the medium stiff clay layer.
- Excavate and construct WB tunnel. In this project, an earth pressure balance shield machine is employed to tunnel lining conduction.
- Install the temporary steel support within the WB tunnel prior to mined adit excavation.
- Verify geological condition and effectiveness of ground treatment. Both vertical and horizontal probes are conducted in this stage.
- Install pre-support using a drill rig. For each adit tunnel, 16 steel pipes are provided.
- After completion of the canopy tubes installation, demolish the diaphragm wall.
- Commence excavation and support installation of the emergency egress adit tunnel. A sequential excavation is carried out.
- During excavation of mined adit, instrumentation and monitoring is frequently conducted to observe the responses of the running tunnel, existing structures as well as the shotcrete lining.
- When the excavation reaches to the WB tunnel and support installation is completed, steel segments are then removed to allow for opening.
- Excavate and complete the primary lining of ventilation tunnel as well as remove steel segments.
- Prepare reinforcement work for the final lining. The concrete collar is cast at the site. The tunnel section is subsequently constructed to complete final lining. A waterproofing system is provided between two linings and at every construction joint.
- Remove the temporary steel support inside the WB tunnel.

Figure 12. Illustration of cross passage construction.

- Reinstate the diaphragm wall and complete cross passage work.

5 INSTRUMENTATION AND MONITORING

Instrumentation and monitoring of ground displacements and structural movements play an important role in underground construction, particularly cross passages in urban areas. The results from measurement can be used to verify and alert both the designer and the contractor in order to prevent the potential impacts in terms of structural integrity and serviceability.

In general, geotechnical instruments are proposed to be installed, which consist of ground surface settlement markers and an inclinometer as shown in Figure 13. The purpose of surface settlement points is to determine movements of the ground surface during the excavation of cross passages. An inclinometer is installed to observe a lateral movement of the surrounding soils.

To ensure safety and serviceability of the adjacent existing structures, tilt meters and target prisms are used to measure inclination and movements in three axes. The control values are typically set based on the allowable movements and distortion that have no adverse impacts on the structures.

In addition, it is important to check the potential effects on the running tunnel during the excavation of NATM tunnels and the stage of tunnel opening. A series of target prisms are implemented in order to monitor the allowable lining deflection.

Convergence monitoring is also conducted to monitor the primary lining deflection of mined adit tunnels. Tunnel displacement results need to be evaluated in every sequence of tunnel excavation.

5.1 *Ground surface settlement*

Monitoring data of ground surface settlements over the tunnel alignment after the excavation and primary support installation of cross passage is plotted in Figure 14. The maximum ground displacement of 11.28 mm is observed after completion of the emergency egress tunnel. It is obviously evident that a larger ground movement

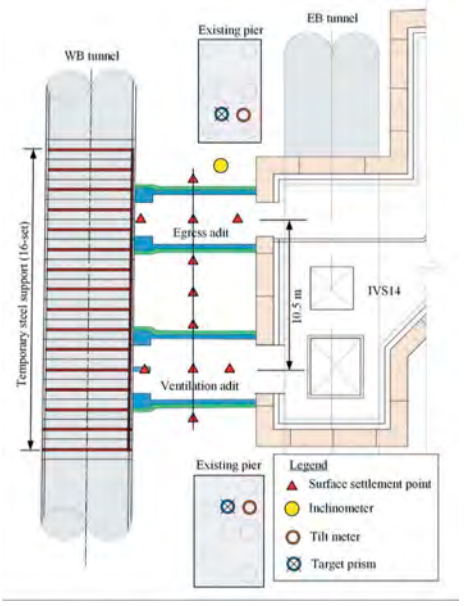

Figure 13. Layout of instrumentation.

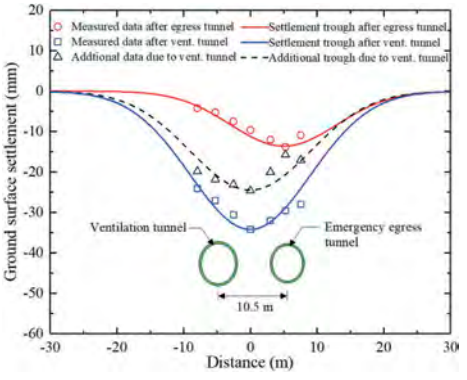

Figure 14. Ground surface settlement.

is induced by excavation of the ventilation tunnel in which 35 mm is recorded as the maximum value.

5.2 *Lateral movement*

Figure 15 shows results of soil displacement in horizontal direction subjected to the advancement of two adit tunnels. As can be seen in the graph, the inward movement of about 5 mm after excavation of the egress tunnel is recorded. This movement continues

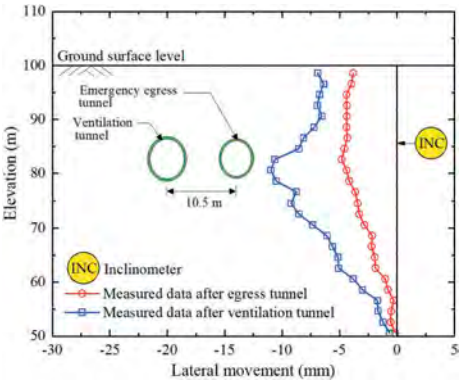

Figure 15. Lateral soil movement.

to significantly increase to 12 mm at the tunnel after the advancement of ventilation tunnel. It is found that large inward displacements commonly appear at the tunnel sprinline and sharply decrease below the level of tunnel position.

6 CONCLUSIONS

Successful cross passage through soft ground in an urban environment can be achieved efficiently and safely using the approach as provided in this article. The success depends on careful consideration of all condition such as ground conditions, geotechnical conditions, groundwater, existing structures, planning, construction work, and ensure that a robust design properly reflects these conditions. A properly design of excavation and support system of the primary lining is the key to mitigating potential risks during excavation and is crucial to ensure minimal ground movements that could damage structures. Careful consideration of site conditions and implementation of a temporary steel support for the running TBM tunnel allow construction of cross passage to proceed with safety. Instrumentation and monitoring system is also a key factor in geotechnical works which can contribute to a successful construction project.

ACKNOWLEDGEMENT

The authors would like to appreciate Mass Rapid Transit Authority of Thailand (MRTA), CKST Joint Venture and Right Tunnelling for their valuable project data.

REFERENCES

Kuyt, J., 2015. Observed loading behavior during cross passage construction: Brisbane Airport Link Project.

Proceedings of the 19th International Conference on Soil Mechanics and Geotechnical Engineering. Seoul, South Korea, pp. 959–968.

John, M., and Mattle, B., 2002. Design of tube umbrella. Magazine of the Czech Tunnelling Committee and Slovak Tunnelling Association. Vol.3, pp. 4–11.

John, M., and Mattle, B., 2003. Factors of shotcrete lining design. Tunnels & Tunneling International. Vol.35(10), pp. 42–44.

Jayasiri, N., Chao, K. C., Phienwej, N., Duangsano, O., and Asanprakit, A., 2022. Design and analysis of tunnel cross-passage openings: 3D finite element analysis versus 3D shell-spring approach. Innovative Infrastructure Solutions 7(3). Vol.3, pp. 4–11.

Lee, T. H., and Choi, T. C., 2017. Numerical analysis of cross passage openings for TBM tunnels. Proceedings of 19th International Conference on Soil mechanics and Geotechnical Engineering. Seoul, pp. 1173–1719.

Mostafa, S., Farshad, K., Masoud, G., and Shahab, Y., 2013. Design of sequential excavation method for large span urban tunnels in soft ground – Niayesh tunnel. Tunnelling and Underground Space Technology. 35(7), pp. 178–188.

NFPA 130. Standard for fixed guide-way transit and passenger rail systems. National Fire protection Agency. 2017.

Tunnelling for a Better Life – Yan, Celestino, Thewes & Eberhardt (Eds)
© 2024 The Author(s), ISBN 978-1-032-80042-4
Open Access: www.taylorfrancis.com, CC BY-NC-ND 4.0 license

Construction of underground rail tunnel above deep tunnel sewerage system

Hock Mun Fong, Qiufang Li* & C. Veeresh
Land Transport Authority, Singapore

ABSTRACT: Contract T313 consists of the construction of the underground Xilin Station and Cut and Cover tunnel with a total length of approximately 1,150m. The tunnel configuration is complex with multiple tunnel cells at different levels consisting of Downtown Line and Thomson East Coast Line main lines and reception tracks into the new East Coast Integrated Depot. The west end of Cut and Cover site is bounded by two canals at grade, i.e. 22.5m wide Sungei Ketapang and 45m wide Sungei Bedok, and an existing Deep Tunnel Sewerage System (DTSS) tunnel undercrossing 6m below the tunnel base slab. The excavation is approximately 64m wide and 26m deep, which poses a challenge to DTSS tunnel. The existence of thick soft marine clay with fluvial sand layers adds to the construction risks, as there is concern of blowout and excessive water ingress during the construction. To mitigate any impact to DTSS tunnel, design and construction is planned such that movement on the DTSS are maintained within the allowable limits by closely monitoring the various instruments installed in and around the site. This paper presents the details of various mitigation measures adopted and lessons learned during the excavation works above the DTSS tunnel.

Keywords: Underground construction, DTSS, Fluvial sand, Mitigation measures

1 INTRODUCTION

Contract T313 is part of East Coast stretch of the Thomson-East Coast Line (TEL) for Singapore Mass Rapid Transit (MRT) System. It is a complex contract comprising the construction of Xilin Station and 4.5 km of multiple cell cut and cover tunnels. Long cut and cover construction has been subdivided into various zones of different complexities to facilitate the construction. Cut and Cover tunnel Zone 9A is sandwiched between the existing Sungei Bedok Canal and Sungei Ketapang Canal on the surface and a Deep Tunnel Sewerage System (DTSS) buried underground (Figure 1a and 1b). Sungei Bedok and Sungei Ketapang canals are U shape concrete structures with a depth of 6m, and a width of 45m and 22.5m respectively. DTSS is a deep tunnel located 6m below the proposed Cut and cover tunnel and this tunnel is constructed with a segmental lining and consists of an internal in-situ concrete lining with an internal diameter of 6m. Cut and cover tunnel at Zone 9A is a 60m wide section comprising of 8 distinctive cells to accommodate train tracks for 2 reception tracks each for Down Town Line (DTL) and TEL. Construction of proposed cut and cover tunnel just above the DTSS tunnel and below the intersecting canals poses many challenges for design and construction. This paper presents the details of design considerations, construction challenges and various mitigation measures implemented during the excavation works.

2 DESIGN DEVELOPMENT

2.1 *Ground conditions*

The site is predominantly underlain by Quaternary deposits of Kallang Formation (KF) overlying Old Alluvium (OA). From soil investigation, the site typically consists of 9m of man-made superficial Fill, which overlies about 27m thick recent sedimentary deposit of Kallang Formation (KF). KF comprises of geological members of Marine Clay (M), Fluvial Sand and Clay (F1 & F2). OA layers below KF are of varying degrees of weathering. Competent OA strata is generally founded at 36m below ground level at this location.

2.2 *Design concept*

Two canals on the surface are temporarily diverted outside the tunnel footprint (Figure 2). The Earth Retaining and Stabilising Structure (ERSS) for cut and cover tunnel utilises diaphragm wall with temporary strutting

*Corresponding author: Li_qiufang@lta.gov.sg

DOI: 10.1201/9781003495505-195

Figure 1a. Site layout plan.

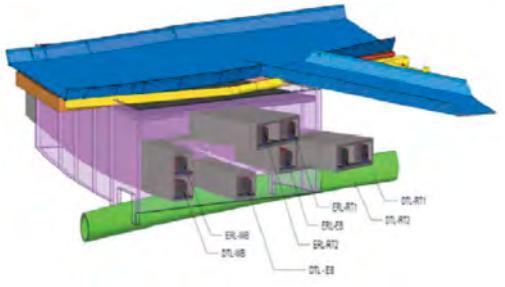

Figure 1b. Zone 9A construction above DTSS.

system. The strutted excavation is designed within perimeter diaphragm walls penetrating to about 70m depth, i.e. to about 40m below FEL. Due to the DTSS tunnel protection requirement, the diaphragm walls have to be terminated at 3m above DTSS tunnel. To facilitate the stage-by-stage construction, a cut-off diaphragm wall with T panels has been constructed parallel to the DTSS tunnel. To minimise heaval or upward movement of DTSS tunnel, mitigation measures such as 3m layer of ground improvement (GI) by Deep Soil Mixing (DSM) below the base slab is designed. This GI will provide resistance against upheaving of base during excavation works. To further minimise the heaving, a sequential compartmentalised excavation and casting sequence is designed (Figure 3).

Figure 2. Canal diversion.

2.3 *Design optimisation*

While excavation works progressing on adjacent zone to zone 9A, a few incidents of water ingress at diaphragm wall joints were encountered. These incidents have led to the concerns on the 3m of GI's

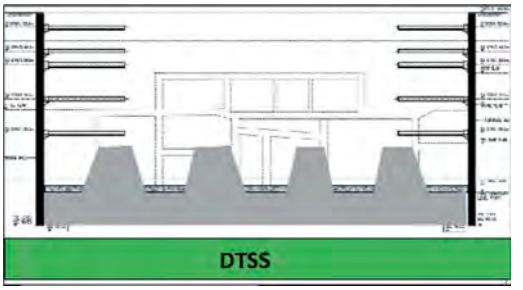

Figure 3. Zone 9A ERSS and excavation sequence.

effectiveness around the DTSS tunnel, main reason for this concern being the presence of the F1 sands in the area where the DTSS tunnel passes through and blowout of the excavation base may occur due to high water pressures. This would damage the DTSS tunnel and cause lowering of the groundwater pressure in the surrounding area with consequential settlement. Hydrogeological studies have been carried out to review the overall system effectiveness. As a result a progressive groundwater control strategy is formulated as follows:

- Low pressure grouting of F1 sand around the DTSS tunnel to reduce the flow from zones of high permeability through the base of the excavation.
- Provision of passive relief wells in the grouted F1 sand and in the OA in case the treated layers are not effective in reducing the permeability.
- Provision of active abstraction wells in F1 sand in the area inside and outside the excavation. These wells would be activated to reduce groundwater pressure and flow in the event that instrumentation results indicate more than 2m of water head above the excavation level at each stage of excavation.

2.4 *Instrumentation and monitoring*

Comprehensive instrument and monitoring is implemented inside and outside tunnel excavation to verify the design prediction, groundwater pressure in particular. This consists of the monitoring of the ground

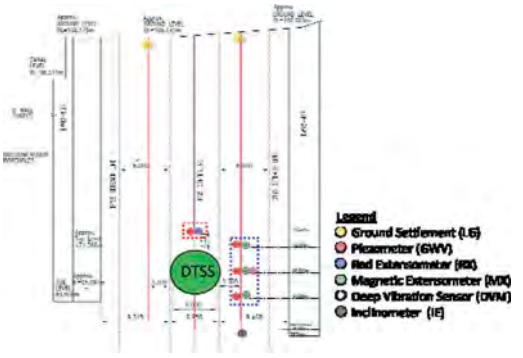

Figure 4. Instrumentation.

and subterranean movement by settlement marker, inclinometer and extensometer, and pore water pressure changes by piezometers. The detailed arrangement of instrumentation is shown in Figure 4.

3 CONSTRUCTION

3.1 *Diaphragm wall*

3.1.1 *Diaphragm wall installation*

The cut-off diaphragm wall maintains a 6m lateral clearance from DTSS and embeds more than 40m into competent OA soil. T shape panels are constructed by BC40 trench cutter machine. T shaped panel is prone to trench collapse, especially at connection corner while excavation in weak ground even with the stabilising fluid. To mitigate the risk, ground improvement by DSM is implemented encompassing the perimeter of trench to strengthen the ground before diaphragm wall trenching (Figure 5a, 5b and 5c). With this provision, the verticality of trench also improved.

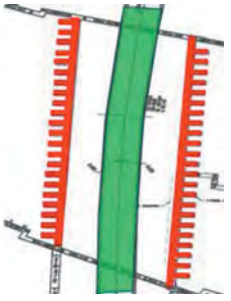

Figure 5a. Dwall panel layout.

Depending on the actual ground conditions encountered, the diaphragm wall penetration ranges between 70m to 85m below ground. The diaphragm wall panel is heavily reinforced with a maximum rebar cage weight of 120ton. The two section of cage is connected to ensure it function as a monolithic structure. This warrants a tandem lifting by 2 nos. of 180ton crane, during which stitching bars are inserted for the connection.

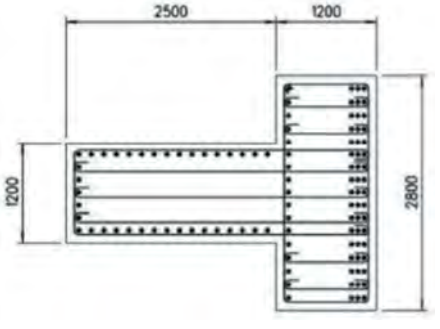

Figure 5b. T shaped Dwall rebar arrangement.

Figure 5c. Dwall cage tandem lifting.

3.1.2 *Water ingress*

The Dwall joints have provision of water stop to prevent the water ingress through the joints, further grouting is carried out at the joint where fluid sand layers exist. Despite of the provision, several water ingress incidents occurred. Notably at the most severe case adjacent to Zone 9A, water with fluvial sand gushed in at a rapid rate of approximately $2m^3$/min into excavation (Figure 6). The leak source is immediately covered with sand bags inside excavation while remedial works outside excavation are carried out to grout the flow path. Learning from these incidents, the termination level of water stop for the Dwall joint has been increased to embed into the impermeable soil. The incidents have given a timely warning on the high possibility of groundwater pressure in the F1 sand for excavation above the DTSS tunnel, where there is a gap in the cut-off wall due to existence of tunnel.

Figure 6. Water ingress.

3.2 *Struts*

Five (5) layers of temporary steel strutting are used to support the excavation. A truss system with hanging king posts is deployed to provide support and restraint to the long span of struts, as it is not possible to install king posts in the proximity to the DTSS (Figure 7).

Figure 7. Strus and truss.

3.3 *Low pressure permeation grouting around DTSS*

In addition to the GI layer using DSM below the base slab, low pressure permeation grouting (LPPG) is carried out as close as 0.5m away from DTSS (Figure 8) as an additional mitigation measure. LPPG is required to achieve a permeability of no more than $1x10^{-7}$ m/s to ensure its effectiveness in minimizing the groundwater flow in.

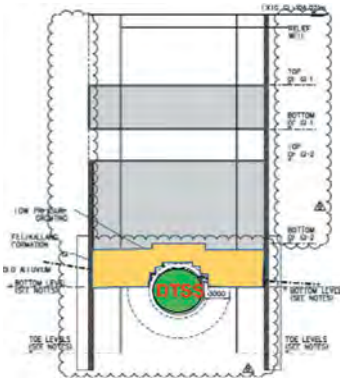

Figure 8. Section of grouting.

3.3.1 *Trial LPPG*

A field trial grouting prior to the production grouting is carried out to prove the suitability of the method and grouting materials. TAM grouting is employed with a grout diameter of 1.3m and 1m spacing. The grouting pressure is maintained at max of 10 bar and flow rate is 2-20l/min. Grouting material adopts majorly cement grouts with the chemical grouts at the perimeter. The mix ratio of the grouting material is shown in Table 1 and Table 2. Permeability test by falling head method is conducted prior to and after the grouting. It is found k value for post-grouting location achieve 10^{-8} m/s, a reduction in permeability of at least 2 orders of magnitude.

Table 1. Mix ratio for cement grout.

Water (l)	Cement (kg)	Total volume (m^3)
760	760	1

Table 2. Mix ratio for chemical grout.

Solution A (1 m^3)		Solution B (1 m^3)	
Cement	760kg	Sodium silicate	400l
Water	760l	Water	600l

3.3.2 *Production LPPG*

The close proximity of the drilling works to DTSS requires a tight control of the verticality of drilling operation as well as precise level monitoring. Furthermore, a plastic bit instead of metal bit is used for drilling within 3m clearance of DTSS to eliminate the risk of damage of DTSS tunnel by puncturing the structure (Figure 9). The grouting sequence is planned in a manner that presents the least risk to the DTSS tunnel. Generally, grouting starts from center, i.e. closest to DTSS, and moves towards diaphragm wall. This sequence allows the grout injected in final stage going towards the diaphragm wall rather than the DTSS tunnel, relieving the high forces on existing tunnel.

Figure 9. Plastic drilling bit.

3.3.3 *LPPG performance*

Falling head permeability tests are carried out at selected grouted column and the result shows the k value is in the range of 10^{-8} m/s. Furthermore, pumping tests are conducted to assess the effectiveness of the improved ground and also to evaluate the extent of water drawdown and details are presented in subsequent sections.

3.4 *Groundwater control system*

A grouting program resulting in uniform reduction of groundwater flow in the F1 sand will effectively safeguard the DTSS tunnel, while the lack of uniformity of the treatment can result in local channels of groundwater flow that will be difficult to detect prior to excavation. It is for this reason that the pumping wells are installed and ready for activation should actual groundwater flow during excavation indicates concerns about basal instability (Figure 10).

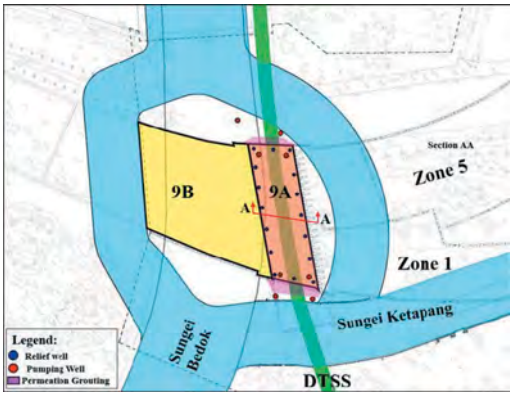

Figure 10. Layout plan of wells.

3.4.1 *Passive relief well*

A total of 16 nos. of passive relief wells evenly spreading inside the excavation zone are installed. The passive wells are installed with 150mm diameter borehole to a depth equivalent to 2m above the diaphragm wall toe, a 50mm diameter perforated pipe extend from the F1 layer to the base of well provided. These passive wells will relieve any water present in untreated zones below the base and in addition prevent high pressures build up below the base.

3.4.2 *Pumping test*

Three numbers of pumping tests are conducted to investigate the hydrogeological conditions to assist in the design of the appropriate groundwater control scheme, as well as validation of the efficacy of LPPG. Each test involves a single pumping well and five observation wells installed with piezometers and standpipes. During the test, water is abstracted from the aquifer with measurements of the groundwater response from within the F1 aquifer being taken at the observation wells. An equipment test is carried out before the pumping test to determine the range of abstraction rate for the submersible pump, which is capable to pump up to 0.5l/s to 5l/s (Figure 11). The test is undertaken in accordance with BS EN22282-4:2012 and comprises three types of test namely Step Discharge Test, Constant Discharge Test and Recovery Test.

Figure 11. Abstraction pump.

In view of the site constraints, first pumping test is carried out outside excavation on the northern side prior to completion of LPPG. The test indicates that the aquifer is connected across a significant distance under the canal. However, the level of drawdown observed is very limited, suggesting that the F1 in this area is well recharged by surrounding aquifers and water bodies. Second pumping test is conducted within excavation after LPPG completed. All the piezo tips inside the observation wells show no response when the groundwater level within the pumping well maintains 10m below original level during equilibrium state, suggesting the grouting in the specific area is effective. Third pumping test is undertaken immediately outside the southern grouted zone outside the excavation. The majority of the surrounding observation wells indicate a clear connection with the pumping well drawdown, suggesting the grouting does not appear to be fully effective and areas of high permeability still exist. As a result, another round of grouting at the outer perimeter is carried out.

3.4.3 *Active pumping well installation*

In total, 8 nos. of active wells were installed on the northern and southern end, comprising of 2 nos. outside excavation and 2 nos. inside excavation for each case. The active pumping wells are installed with a borehole diameter of 300mm terminating at DTSS invert level, i.e. 66mRL and a 150mm diameter PVC perforated pipe is installed from 80mRL and 67mRL.

3.4.4 *Functioning test*

Tests are undertaken to check that the active well pumps are functioning correctly, and the auto cut-off /cut-in are working. All eight active wells are tested simultaneously for 4 hours to simulate the actual conditions. The proposed pumping rate is between 1-25l/min inside excavation and 40-150l/min outside excavation. From these tests, water drawdown in the wells is noted in the range of 12m to 20m, indicating the pump and associated system are functioning as per the requirements. However, very limited response is observed in nearby piezometers, partially due to low permeability of grouted zone and short duration of test. These wells are regularly checked for clogging up. All active wells on the south are activated when excavation reached S4 strut level, i.e. 91.5mRL, and the other 4 active wells on the north are activated when excavation reached S5 strut level, i.e.86.5mRL.

3.4.5 *Change in excavation sequence*

Taking into consideration of the performance of excavation and ground water response from piezometers, the construction sequence from S5 level to formation level is proposed for optimisation. The initial proposal requires a 9-section compartmentalized excavation and slab construction, which takes considerable time and also requires several joints in base slab. As

actual performance is better than anticipated, it is proposed to optimise excavation sequence. Upper 4m is excavated in one stage and remaining 4m depth is in 3 compartments starting from centre towards both ends. Three compartments will expose smaller area when approaching formation level, to check the ground condition and instrumentation readings to gain more assurance prior to full excavation (Figure 12). During excavation, conservative review level of 2m water head above the excavation level is set as limit to stop the works.

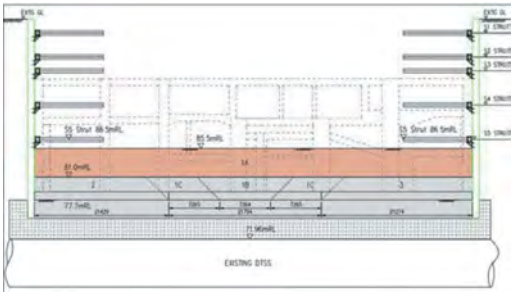

Figure 12. Revised construction sequence.

The flow of passive wells records around 36m^3/day (from 9 wells) with the bulk volume from one single well on the south (Figure 13). The active wells abstract around 30m^3/day mostly from the 2 internal wells on the south. When one of the piezometers reading slightly breaches the suspension level, additional 5nos. of passive relief wells are installed in between the wells that see high water flow. At the last stage of excavation, these large wells are converted into active wells by setting up pumps inside to actively drain the water. The measure has shown an immediate effect by bringing down the piezometric pressure. In general, excavation zone is dry and piezometric level dropped in tandem with excavation progress and remained below the target level (Figure 14). Works are carried out 24hrs period and it took around 45 days from the last stage excavation to the successful casting of base slab for entire zone 9A above DTSS tunnel.

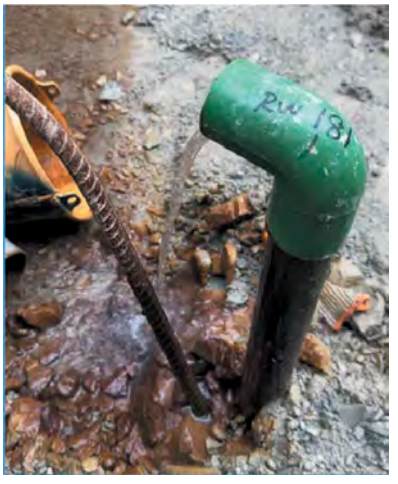

Figure 13. Outflow from relief well.

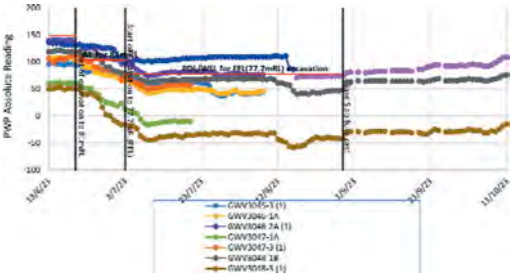

Figure 14. Piezo readings in response to excavation.

4 CONCLUSIONS

The strategy of employing ground treatment in F1 together with dewatering system proves its effectiveness in the control of ground movement and groundwater pressure. This strategy, which is implemented prior to excavation, rather than as a contingency to remedy blowout when occurs, reduces the significant excavation risk. Close monitoring and analysis of instrument response that leads to prompt intervention where necessary also plays a major part in the success of the execution of the works.

ACKNOWLEDGMENTS

We greatly appreciate the contributions from LTA project team, design team, contractors, consultants, hydrogeologist, International Panel of Advisors and PUB for their meticulous advice, planning, design, monitoring and implementation of the works in completing zone 9A excavation safely and successfully.

REFERENCES

BS EN ISO 22282-4: 2012. Geotechnical investigation and testing – Geohydraulic testing – Part 4: Pumping tests.

Tunnelling for a Better Life – Yan, Celestino, Thewes & Eberhardt (Eds)
© 2024 The Author(s), ISBN 978-1-032-80042-4
Open Access: www.taylorfrancis.com, CC BY-NC-ND 4.0 license

A study of merits and demerits of steel decking verses concrete decking for traffic management and construction logistics during construction of underground metro stations for Colaba-bandra-seepz (line 3) in Mumbai, India

Subodh Kumar Gupta*
Director (Projects), MMRCL Mumbai

Ravi Ranjan Kumar*
Executive Director (Civil), MMRCL, Mumbai

Datta Binnar*
Senior Deputy General Manager, MMRCL

Sunil Vishwakarma*
Head planning Mumbai Metro Rail Corp. Ltd, CEC-ITD-Tata JV

ABSTRACT: Mumbai Metro Rail Corporation Ltd is implementing Colaba-Bandra-SEEPZ (Line 3), a 33.5 Km fully underground metro rail project, in Mumbai, India. With a population of more than 23 million the Mumbai Metropolitan region is the 9th most populated region in the World. Alignment of Line 3 is substantially in old and historic part of the city, with a topography of a narrow land mass and sea/ creek on three sides.

There are 26 underground stations out of which 23 stations are being constructed below arterial/sub-arterial roads. Buildings are at the edge of the footpaths with little or no offsets. These footpaths are also narrow. As a result, extensive amount of temporary decking had to be installed for managing traffic movements and construction logistics.

Two types of temporary decking have been used in the works, concrete decking at 3 stations and steel decking at the remaining 20 stations. Use of these two types of decking has flagged interesting outcome. Steel decking were easy to install and dismantle but costlier on upfront cost of construction. These would have a good scrap value or could be reused. Concrete decking was economical on upfront cost but required more time for construction and had limited salvage value. It also involved breaking and disposal of debris.

The economics of construction of decking is only one aspect as there are environmental and social implications of either of these two types of decking. There are implications for the safety of buildings around the construction site also.

After using both types of decking interesting statistics have been collected which could be of guidance to authorities and contractors for future projects in urban areas requiring decking. This paper would delve into the merits and demerits of these two types of decking using real time data collected during construction of works.

Keywords: Mumbai Metro Line 3, Underground stations, Cut & Cover, NATM, bottom-up, Traffic Management, steel decking, concrete decking, construction cost, construction time, urban environment, merits, demerits

1 INTRODUCTION

Mumbai city, financial capital of India has witnessed very rapid growth in population and employment and invite to mass rapid transit system to reduce the congestion on roads and existing overcrowded sub-urban railway system. It connects, Bandra-Kurla Complex, both Domestic and International Airport as well as SEEPZ area in Andheri (E). Projects civil work is divided in to 7 packages to facilitate smooth

*Corresponding author: subodh.gupta@mmrcl.com; raviranjan.kumar@mmrcl.com; datta.binnar@mmrcl.com; sunilkumar-vis@tataprojects.com

DOI: 10.1201/9781003495505-196

construction and to ensure timely completion. As Mumbai is densely populated city with very little space available for development, Metro line 3 is planned fully underground and most stations are planned below the roads. After detailed Geotechnical investigation, building foundation study, tunnel alignment was finalized.

2 STATION PLANNING

Station planning for Mumbai Metro Line-3 was preceded by a technical review of the station locations.

1. Adequacy of road width where cut & cover construction is proposed.
2. Availability of land for cut & cover access shafts, where NATM construction is proposed.
3. Availability, adequacy, and suitability of land earmarked for street level facilities such as entrance structures, ventilation shafts and the ancillary building.
4. Availability of worksites at station box ends to allow launching/ retrieving of TBMs and removal of muck from the tunnels.

With the above general considerations, the underground station typology in Mumbai metro line 3 used two different methods: Cut & Cover and Partly Cut & Cover, Partly NATM (New Austrian Tunnelling Method) Hybrid method.

3 CONSTRUCTION METHODOLOGY OF THE METRO STATIONS

3.1 *Cut & Cover station – bottom-up construction*

(i) Site clearance, temporary, Traffic diversion, utility diversion etc
(ii) Installation of retaining wall of continuous secant piles
(iii) Installation of king post, construction/installation of traffic decking, supporting of major utilities below decking.
(iv) Excavation from top to bottom, installation of steel struts/walers soil anchors at subsequent level, rock anchoring as required.
(v) Construction of base slab, platform, OTE
(vi) Construction of station structure, concourse slab, roof slab, Entry /Exit
(vii) Waterproofing, Backfilling, Dismantling/removal of decking, reinstatement of utility, roads footpath, street Furniture etc.

3.2 *Partly cut & cover, partly NATM/hybrid method*

(i) TBM is driving through the Station area first (use of sacrificial segments, logging of the TBM tunnel face in respect to sub-soil and groundwater conditions).

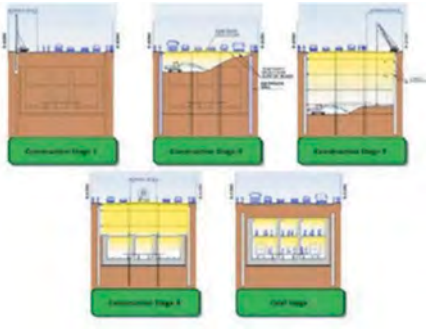

Figure 1. Typical construction sequence of bottom-up method.

(ii) Excavation of the station box down to proposed formation level.
(iii) Ground conditions will be observed and logged during Station box excavation.
(iv) Stabilizing the portal structure of 6.0m wide cross passage for start-up situation
(v) Excavation of the cross passages (top heading) from the station box towards the TBM tunnel
(vi) Dismantling of sacrificial TBM segments, enlargement of TBM tunnel to form top heading portion of platform NATM Tunnel
(vii) Excavation of the cross passages (invert) from the station box towards the TBM tunnel
(viii) Dismantling of sacrificial TBM segments, enlargement of TBM tunnel to form complete platform tunnel.

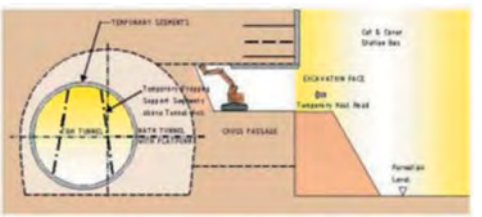

Figure 2. Typical construction sequence of Hybrid station.

4 NECESSITY OF DECKING AND SELECTION OF DECKING

Underground Metro stations are planned below the existing Arterial /sub arterial road and traffic junction. 20 are being constructed below roads out of which 13 are cut and cover methods, and 7 hybrid method partly cut and cover and partly NATM stations with bottom-up construction methodology. As roads traffic in Mumbai city cannot be closed or blocked, Decking is very essential and mainly used for movement of traffic (one Lane south bound + one Lane North bound) and to facilitate as construction platform for construction logistic, labour restroom etc. Decking is also used to

support major utilities like wate supply, sewer line, Gas pipeline, Communication and electric cables etc.

For station construction by Cut & Cover method, Hybrid Method, following scenario emerge for traffic management.

Scenario A: Complete closure of traffic – no decking required – Not possible in Mumbai.

Scenario B: On a bi-directional roads one directional traffic diverted to alternate road.

Scenario C: On bi-directional roads, partial traffic is diverted to alternate routes while one + one lane maintained on available reduced carriage way width.

4.1 *Selection of decking*

MMRC/Civil contractor of respective packages have opted the decking methodology considering the following factors:

i) Traffic management as per traffic rules and regulations
ii) Ease of construction, Fabrication/ construction time schedule, availability of resources
iii) Site condition, location, Environmental and Social aspects,
iv) Stability of adjoining existing structures, underground major utilities.
v) cost of installation/Construction and dismantling after-construction works.
vi) Recycle, reuse, scarp value, Debris disposal, Considering the above factors, most civil work package contractor had preferred steel decking except partly concrete decking in package 3 and package 4.

Details of decking used in Metro Line-3 are summarized in Table 1.

Table 1. Types of decking used in Mumbai metro line–3.

	Station Names		
Contract & Contractor-JV	Cut & Cover	C&C/ NATM	Type of decking
UGC-01 L&T-STEC -JV	1. Cuffe Parade 2. Vidhan Bhavan 3. Churchgate	Hutatma Chowk	Steel decking
UGC-02 HCC-MMS - JV	CST	1. Kalbadevi 2. Girgaon 3. Grant Road	Steel decking
UGC-03 Soma Dogus– JV	1. Mumbai Central 2.Mahalakshmi 3. Science Museum 4.Acharya Atre Chowk 5. Worli	–	Steel decking RCC decking
UGC-04 CEC-ITD Cem-TPL-JV	1. Siddhi Vinayak 2. Dadar	Sitaladevi	Steel decking RCC decking
UGC-05 J. Kumar-CRTG-JV	1. Dharavi, 2. B.K.C. 3. Vidyanagari	Santacruz	Steel decking
UGC-06 J. Kumar-CRTG-JV	1. CSIA Domestic Airport 2. Sahar Road 3. CSIA International Airport	—	—
UGC-07 L&T STEC -JV	1. MIDC 2. SEEPZ	Marol Naka	Steel decking

4.2 *Design of decking*

4.2.1 *Steel decking*

Steel decking is designed for 70R loading as per IRC-6 specifications and IS-800 2007.

Station size is 26m x 250m.(approx.). Traffic decking is supported on secant pile capping beam and on king post pile. The grids for the decking were designed as per available steel sections.

Design consists of:

1. Steel members spanning between capping beam and king post.
2. The king post column is built up 4-legged circular hollow section. At places RCC piles also as constructed to form the king post.
3. King post are planned in a way as to not interfere with station columns, logistic and material, equipment movement and generally at a spacing of 10-12m.
4. Longitudinal main beams are placed over the king post, which support the transverse beams supported on RC capping beam and longitudinal main beam.
5. Longitudinal beam section as built-up UB/UC and IS beams.
6. Over the main beam secondary beam were placed to form a diagrid system, these secondary beams are UB /UC and IS sections.
7. Secondary beams support the prefabricated decking panels of size varying from 1200 x 1200 to 2000 x 2000,
8. The decking panel is fabricated by forming a frame of IS beams with channel and angle with Chequered plate of 8mm to 10 mm.
9. Decking panel is fitted with neoprene rubber bearing pads to minimise vibrations and noise.
10. Joints are filled with rubber packing.
11. Speed breakers were installed to limit traffic speed to 20 km/hr.
12. Crash barriers were conservatively designed to prevent any mishaps as decking was planned over station deep excavation.

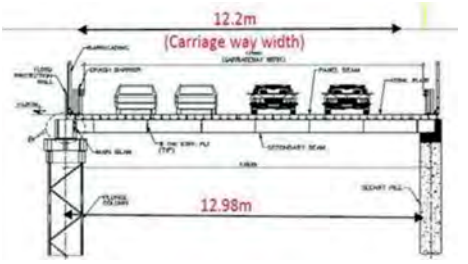

Figure 3. Typical steel decking arrangement.

4.2.2 *Concrete decking*

Like the steel decking at certain stations RCC deck slab were installed. Due to the congested area of the station location and issues of movement of crane required installation of steel sections it was prudent to provide RCC desking. The loading conformed to IRC loading. To facilitate TBM activity, de-mucking activity, retrieval of TBM cutouts were provided to ensure smooth Station construction and smooth traffic movement. The framing plan for the decking comprises of the following.

1. On one side of the decking RCC capping was taken advantage of for forming the main beam.
2. RCC plunge columns were cast as bored cast in situ piles at a spacing of 10-12 m and over the king post columns RCC main beam was cast.
3. The transverse main beam and secondary beam at suitable spacing along with the deck slab was cast in place for a the RCC decking system.
4. Major utility supporting with steel brackets like 1450mm twin water lines, gas pipelines, dry utilities like MTNL, BEST, many OFC cables, etc.

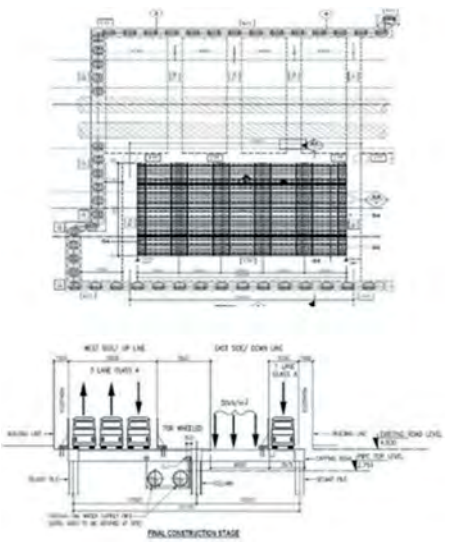

Figure 4. Typical concrete decking arrangement.

5 CONSTRUCTION METHODOLOGY AND CONSTRUCTION TIME OF DECKING

5.1 *Steel decking*

Steel decking is constructed in panels of grid of approximately 11m x13m panel, sequence of Steel decking construction is broadly involves following steps.

1. Site clearance, utility shifting, Fabrication of girder, U beam ISMB as per required size, specification in casting yard-10 days
2. Temporary Diversion of Traffic, installation of Main Beam, Secondary Beam, Girder Installation of – ISMB, fixing of chequered plate, Bearing Pad, ramblers, speed breakers etc.- 3 days
3. Supporting Major Utilities Beneath the decking

Figure 5. Steel decking installation in progress.

Overall speed of construction of steel decking was observed to be about 150 m^2 /day.

Figure 6. Construction of RCC decking.

Table 2. Construction cost of RCC decking and steel decking/m^2.

Items (Unit)	Concrete Decking			Structural Steel Decking		
	Quantity	Rate (INR)	Cost (INR)	Quantity	Rate (INR)	Cost (INR)
Concrete (Cum)	0.56	10000	5600	0.1	9000	900
Steel TMT (MT)	0.07	50000	3500	0.012	50000	600
Structural Steel including fabrication. (MT)				0.5	80000	40000
Total construction cost.			**9100**			**41500**
Dismantling (Cum)	0.56	4000/m^2	4000		1000/m^2	1000
Scrap value (MT)	Nil			0.1 (@20%) Of used material.	-30000	-3000
Reuse of material				0.4 (@ 80 % of used material))	60000	-24000
Disposal cost	7000/10 m^3-40 km lead		700			Nil
Net cost/m^2			**14920**			**15500**

5.2 *Concrete decking*

RCC decking is constructed in following step: (10 m Length)

1. Site clearance, below ground utility shifting-7 days
2. Construction of Caping beam over the secant pile wall-4 days.
3. Excavation till beam and PCC level -4 days
4. Shuttering and Rebar work for the beams (@ 4 m c/c)Concreting of beams – 4 days
5. Shuttering, Rebar work and concreting of deck slab-4 days.
6. Curing of deck slab, Beam -7days

Total construction time of 10m concrete decking was @ 30 days and overall speed was about 20-25m^2/day.

The construction cost of steel decking is around 4 times higher than Concrete decking. Initial investment is high cashflow is blocked for construction period of around 6 years. However, its it can be reused at another site after dismantling. It has good scrap value after dismantling. As concrete decking requires high cost and more time dismantling. So net cost of concrete and steel is almost equal at the completion stage.

6 SUITABILITY OF DECKING FOR URBAN ENVIRONMENT

6.1 *Traffic management and logistic management*

Mumbai City development spanning from South to North both sides surrounded by Arabian Sea. City road network is loaded with heavy traffic and road width are very narrow. Most of the arterial road and sub-arterial roads are catering heavy traffic during peak hours. Closure or blocking of roads is a very tedious job leads to further traffic congestion and inconvenience to locals and travellers. So, it is very necessary to keep the traffic movement smoothly while development of any infrastructure projects like, bridges, metro, roads, etc. Most of the metro stations of Line 3 are planned on the major arterial roads. While preparing traffic management plan it was planned that 1 north + 1 south bound traffic will be kept open for traffic and balance area of the right of ways will be used for construction of metro as partial or complete closure of road is not possible for long time, expeditious method of decking is need of the city. Steel decking is speedy activity and can be completed within short time span. However, concrete decking is time consuming activity including curing of concrete time.

Keeping this into consideration 16 stations was constructed using temporary steel decking and where area was densely populated, partial or complete closure of the road was possible with the diversion of traffic on the alternate roads, concrete decking was adopted.

6.2 *Ambient air quality monitoring & noise level*

The Noise Pollution (Regulation and control) Rules, 2000 provides for ambient air quality standards in respect of noise for various categories of urban area for daytime and nighttime in terms of dB(A) Leq. It is observed by the base line monitoring conducted by MMRC before the construction activities of MML-3 the noise values are already exceeding the prescribe standards as per Noise Rules, 2000. Base line levels observed at Cuffe pared are 69.0-73.5 dB(A) in daytime and 59.8-62.3 dB(A) in nighttime. The noise values observed at Churchgate are 70.5-76.0 dB(A) in daytime and 60.8-63.7 dB(A) in

Figure 7. Traffic management at dadar station.

nighttime. The values near Mahim (St. Xavier's College) are 64.3-69.4 dB(A) in daytime and 54.5-60.0 dB(A) during nighttime. The base line noise levels are already exceeding the permissible standards of noise pollution control rules, for residential zone. This clearly shows the contribution of noise values from other sectors like transport, commercial activities and construction activities other than metro rail construction activities.

While designing the steel decking, bearing pads was introduced below decking panel to absorb vibrations, reduce impact noise generation. Traffic movement speed was restricted to 20 km/hr with suitable arrangement of speed breakers /rumbles strips at certain interval as a traffic calming measures. Damaged bearing pads were replaced on time to time, corroded, broken welded joints, of chequered plate, structural member were repaired from time-to-time periodic maintenance to avoid noise generation during traffic movement.

Ambient noise level monitoring at Steel decking site and concrete decking of similar nature of traffic and surroundings site are as presented following table.

Steel decking panels are very noisy during movement of construction machinery /heavy vehicles. More noise was observed on sites of steel decking during traffic movement. Many complaints were received in Mahalaxmi, Giragaon, Kalbadevi, Cuffe Parade residential areas.

Whereas no complaints of noise was logged at Sitaladevi, Dadar, Worli, where RCC decking was used.

6.3 *Logistic management*

As most of the stations are planned on roads with densely populated urban area, there is little space available as work area to facilitate logistic management. RCC Decking constructed at Dadar and Sitaladevi has facilitated space for logistic to support station construction like storage of material, Heavy machinery movement, parking etc., without causing much noise and vibration**.**

6.4 *Stability of adjoining buildings/structures, supported utilities*

UGC-04 package chosen RCC decking for traffic movement, logistic management and to support two 1450mm water line. To avoid any jerk to it as traffic speed was restricted 20 Km/hr. not much vibration was observed. For ensuring safety of buildings/struc-

Figure 8. Supporting of 1450 mm water pipeline below rcc decking at sitaladevi station.

Table 3. Ambient Noise level (December 2019).

	Steel decking			Concrete decking	
Station	Day time 6.00am-10.00 pm (db.)	Night- time 10.00 pm -6.00 am (db)	Station	Day time 6.00am-10.00 pm (db.)	Night- time 10.00 pm -6.00 am (db.)
Mumbai Central	55-110.1	48.00- 89.2	Dadar	51.6-110.7	46.00-82.7

tures in influence zone, instrumentation and monitoring system was installed on buildings, water pipelines. The precise level markers, bi-reflex 3D optical targets, crack meters, tilt plates, ground settlement marker, vibrometer were used. The real time monitoring system were also installed on the old, dilapidated buildings and has been monitored at regular intervals during tunnelling, piling, NATM excavations, etc.

Major Utilities are also protected with suitable rubber pads and suitable protective measures as approved by concerned utility owner.

Both watermains was successfully supported without any damage during entire project duration while traffic and logistic movement on deck.

7 REMOVAL/DISMANTLING OF DECKING

7.1 *Steel decking*

(i) Utility supported on decking is reinstated on compacted soil or permanent pedestal constructed from roof slab.
(ii) Removal of decking panels
(iii) Removal of secondary beam with Crane
(iv) Uninstallation /Removal of main beam with crane

Figure 9. Steel decking dismantling.

7.2 *Concrete decking*

After completion of work, backfilling of soil, concrete decking dismantling is very tedious task involves stagewise and time-consuming process.

1. Utility supported on decking is reinstated on compacted soil or permanent pedestal constructed from roof slab.
2. cutting/breaking of decking slab in panels using pavement cutter
3. RCC beams breaking using diamond wire rope cutter.
4. Concrete deck cutting average speed of is only 45-50 sqm/ day.
5. This involves debris generation and creates noise and dust. Noise and dust generation is mitigated with the help of water jet.
6. Debris are taken to casting yard /open space, debris are broken in small pieces, after recovery of TMT rebar scrap, debris are disposed in designated dumping site /backfilling area.

Figure 10. Breaking of RCC decking.

8 MERITS AND DEMERITS OF RCC DECKING V/S STEEL DECKING

After due deliberation of Decking used in Mumbai Metro Line 3 station construction in urban environment, merits and demerits of RCC decking and Steel decking are summarized in table given below.

Table 4. Comparison of steel & RCC decking.

Sr. No.	Construction Parameter	RCC Decking	Steel Decking
1	Construction Time	Required 30 days to complete one panel Including curing time, average speed of construction is 20–25 sqm/day.	Requires skilled manpower, Fabrication, Secant piles, capping beams is a independent & parallel activity, speedy installation, @ 150/m^2 (approx.)/day.
2	Construction/ installation Cost	INR 10,000 to 12,000/m2	INR 40,000-45,000/m^2, Net cost INR 14000-15000/m2 Considering 80 % reuse and 20% scrap.
3	Dismantling Time and cost	45-50 m^2/ day and activity is a tedious, cumbersome & time consuming. Dismantling is additional cost approx. Rs.5000/m^2	Speedy activity 450-500 m^2/day; dismantling cost is negligible i.e., Rs. 1500/m^2
4	Suitability for Urban Environment Noise, Vibration	Slow progress, Require closure of roads & alternate routes during construction, inconvenience to traffic due to prolonged construction and curing time. Routine and Smooth Traffic Movement. Negligible noise Minimal environment issue due to noise and dust.	Speedy construction, Noise issues can be suitably mitigated. High Noise, Vibration due to Traffic impact on steel plate joints
5 (a)	Reuse, Recycle, Scrap Value	Reuse is nil, retrieve the Re-bar for scrap is also a costly and time-consuming activity, Requires machinery time and space, thus the effective recovery and scrap value is negligible.	80% of the material can be reused with very negligible waste. 20 % scrap has good resale value @30-35% of market price.
5(b)	Debris Generation	Very High volume of debris generation requires space of breaking, High noise and dust during breaking. Debris disposal around 40-50 km from city involves high transportation cost as well as environment issues. Rs. 7000/10 m^3 per truck.	No debris generation, environment friendly.
6	Water Leakage/ Dewatering Cost, construction ease.	Watertight structure, no effect on work during monsoon: de-mucking and logistic lowering activity needs to plan as per the fixed openings.	Water Leakage through joints, affects work progress during monsoon. Flexibility of opening during excavation, speedy de-mucking and construction as per requirement.

9 CONCLUSION

Based on the above study it can concluded that Steel decking is techno-economical feasible than the RCC decking for the Urban environment. Steel decking affects traffic movement for shorter time as well as road and utility reinstatement is a faster as it requires lesser time for removal/dismantling. As there is no debris or dust generation and it can be reused and recycled, it is environment friendly option.

However, initial investment in steel decking is high and net cost at completion stage is at-par with RCC decking. It is also observed that steel decking causes noise during traffic movement, logistic handling, specially during nighttime which is inconvenience to surrounding urban environment. Noise generation can be mitigated to some extent with bituminous coating over steel decking and installing noise barrier in urban area. RCC decking is feasible in Environment sensitive zones of urban area and cater specific need of project, utility support and working area for logistic management. It requires more construction time, dismantling time which prolongs overall construction time and affect traffic management, road and utility reinstatement. Initial cost is low as compared to steel decking, however, RCC deck breaking is costly, time-consuming activity, generates debris. Handling and disposal of debris in urban environment is challenging task.

REFERENCES

1. Indian Road Congress -06: Standard Specifications and Code of Practice for Roads Bridges, Section-II, Loads and Stresses – 2014,
2. Indian Road Congress -21: Standard Specifications and Code of Practice for Roads Bridges (Section-III) Cement Concrete (Plain and Reinforced)-2000
3. IS 456: Indian Standard Plain and Reinforced Cement Concrete Code of Practice – 2007
4. IS 800: Indian Standard General Construction in Steel – Code of Practice – 2007

Tunnelling for a Better Life – Yan, Celestino, Thewes & Eberhardt (Eds)
© 2024 The Author(s), ISBN 978-1-032-80042-4
Open Access: www.taylorfrancis.com, CC BY-NC-ND 4.0 license

Automatic blasting design and construction system optimized for geological conditions

Ryo Hemmi*, Yasuo Ide & Kousuke Kakimi
Shimizu Corporation, Chuo-ku, Tokyo, Japan

Toshiya Shizawa
Furukawa Rock Drill Co.,Ltd., Chiyoda-ku, Tokyo, Japan

Fumika Ito
ENZAN KOUBOU CO., Ltd., Kamigyo-ku, Kyoto, Japan

ABSTRACT: In the blasting excavation method for conventional tunnel projects, the stability of the tunnel, excavation cycle time, and construction cost are significantly affected by the fact that if the blasting pattern implemented is suitable for the geological conditions, there is little deviation between the tunnel excavation shape after blasting and the planned excavation line, and overbreak are minimal. One of the parameters that significantly affects the geological conditions is the rock mass strength of the tunnel face; therefore, it is important to design blasting patterns that vary the drilling position, number of holes, and amount of explosive charge according to the strength. The developed automatic blasting design and construction system evaluates the rock mass strength of the tunnel face based on the drilling energy collected when drilling the previous cycle's charging holes using the fully automated tunneling jumbo. Based on the results, the system automatically de-signs blasting patterns by varying drilling positions, the number of holes, and amount of explosive charge. Furthermore, by simulating the drilling sequence in advance using drilling software, the designed blasting pattern can be automatically loaded into the jumbo from the system, and the charging holes can be drilled automatically in the shortest possible time without interference between the individual booms. The results of application tests of this system in highway tunneling project in Japan showed a 41.4% reduction in overbreak of tunnel during excavation and a 7% reduction in the basic unit of explosives consumption compared to before applying the system, and the system contributed to the formation of a smooth tunnel cross-section.

Keywords: Automated, Mechanized, Blasting Excavation, Fully Automated Tunneling Jumbo

1 INTRODUCTION

In conventional tunneling projects, blasting excavation result in overbreak, where more rock is excavated than required for the designed cross-section, and as well as underbreak, where insufficient rock is excavated (Figure 1). Large quantities of these increase labor and material expenses for tasks such as mucking, scaling, and shotcreting, which result in longer excavation cycles and higher construction costs. Furthermore, especially significant overbreak can cause extensive damage to the rock mass surroundings, enlarging the loosened zone and ultimately reducing the durability and quality of the tunnel. Hence, it is critical to improve the accuracy of blasting excavation and reduce such occurrences.

To improve the accuracy of blasting excavation, it is crucial to have a thorough comprehension of the geological conditions. Subsequently, a suitable blasting pattern should be designed by choosing the right number and locations of holes, as well as an appropriate charge that matches these specific conditions.

The design of blasting patterns in Japan has traditionally depended on the expertise and intuition of skilled operators. However, this approach lacks a quantitative basis in numerical data, and as such, cannot be reproduced, making it difficult to apply to future automation and mechanization developments.

Therefore, the new system has been developed to automatically design of optimal blasting patterns utilizing quantitative geotechnical data. The system uses drilling energy data, which is correlated with rock strength, a critical factor that significantly impacts geological conditions. Furthermore, by linking the system with a fully automated tunneling jumbo equipped with a machine control system, we have developed an

*Corresponding author: r_hemmi@shimz.co.jp

DOI: 10.1201/9781003495505-197

Automatic Blasting Design and Construction System for Optimized Blasting that automates everything from blasting pattern design to charge hole drilling, although the system is operated under limited conditions. This paper shows an overview of the system and the achievements and challenges encountered during its implementation in highway tunneling project in Japan.

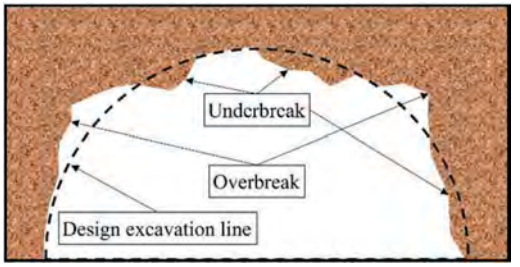

Figure 1. Tunnel forms of overbreak and underbreak after blasting excavation.

2 AUTOMATIC BLASTING DESIGN AND CONSTRUCTION SYSTEM FOR OPTIMIZED BLASTING

2.1 *System workflow*

The System workflow shows Figure 2. Phases ① to ③ are the design phase of the blasting pattern, and phases ④ to ⑦ are construction phase.

Firstly, during the design phase, the drilling energy is acquired from the previous excavation. This energy

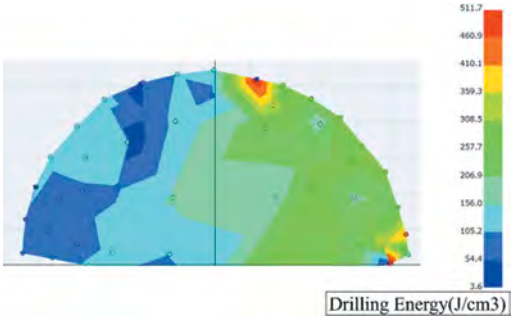

Figure 3. Contour maps.

represents the calculated energy required by the tunneling jumbo to drill through the face surface, determined using hydraulic pressure data acquired from the jumbo. This parameter correlates with the strength of the rock mass. The system analyses this parameter to determine the distribution of hard and soft areas on the tunnel face, creating a contour map (Figure 3). The drilling energy is also utilized to design a blasting pattern, which are produced as zone maps.

Meanwhile, during the construction phase, a new drill plan is formulated based on the designed blasting pattern. Following this, a simulation is conducted to examine interference between the booms. Drifter settings are adjusted accordingly and the jumbo drills automatically. The drilling energy generated during automatic drilling is then utilized to design the blasting pattern for the next drilling.

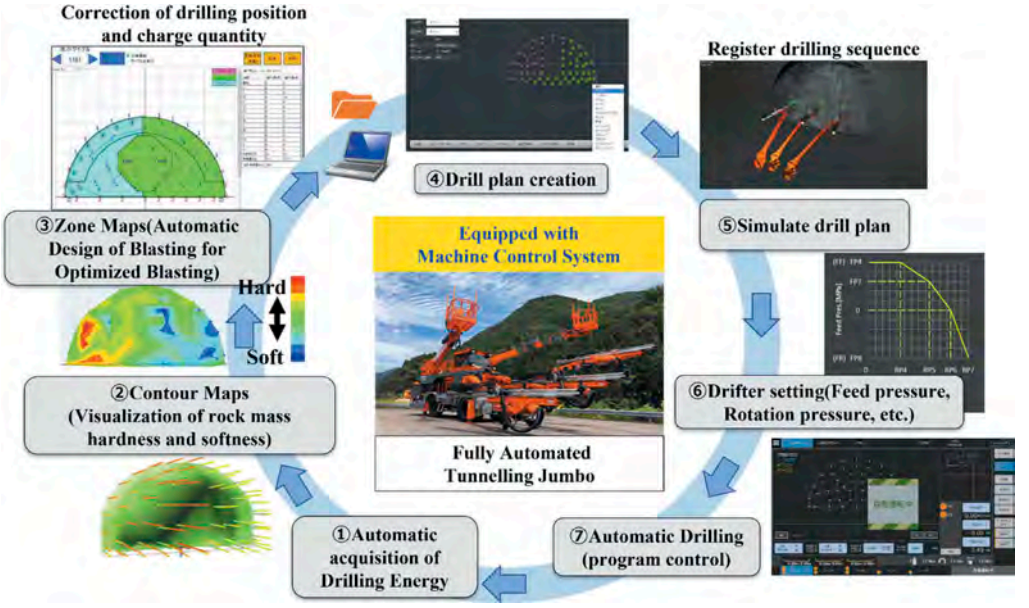

Figure 2. Workflow of automatic blasting design and construction system for optimized blasting.

2.2 *Automatic design of optimal blasting patterns*

Within the system, blasting patterns are designed by dividing the tunnel face into five sections to account for its heterogeneity of the face. The first section is situated in the center of the face, playing a crucial role in maintaining blasting quality and forming the free face. The second and third sections, positioned on the right and left shoulders of the face, significantly impact overbreak and underbreak during drilling and blasting. The lower right and left areas constitute the final two sections. The optimal blasting pattern is then selected for each of the divided sections, and the blasting pattern for the entire face is designed by combining the selected patterns. The optimal pattern for each area is determined based on the hardness and softness of the rock mass as determined by the average drilling energy value within the section. Based on prior experience, a "poor rock pattern" (light blue) is identified as 150 J/cm^3 or less, a "fair rock pattern" (yellowish green) is classified as 150 J/cm^3 to 300 J/cm^3, a "strong rock pattern" (pink) is defined as 300 J/cm^3 or more, and the blasting pattern appropriate is automatically selected from the three levels of blasting patterns (Figure 4). Different blasting patterns are established for the standard rock mass classification in Japan (CI, CII, and DI), the system selects the most appropriate blasting pattern for the next construction from a pool of 243 patterns (5 sections to the power of 3) based on the rock classifications (Figure 5). Each blasting pattern is assigned a specific file name and is stored in a shared folder within the system.

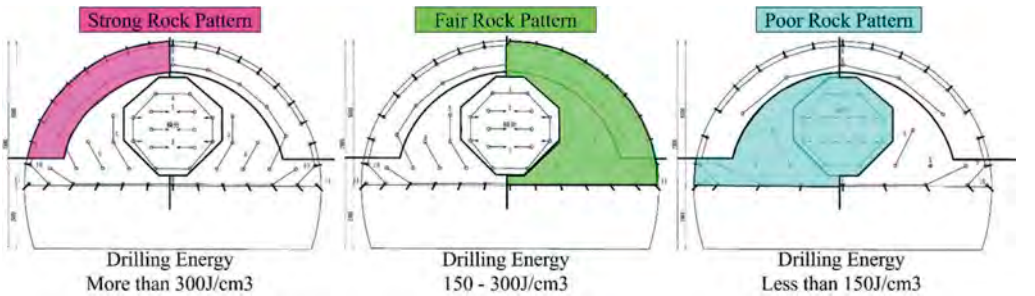

Figure 4. Criteria blasting pattern (examples when the rock class classification is DI).

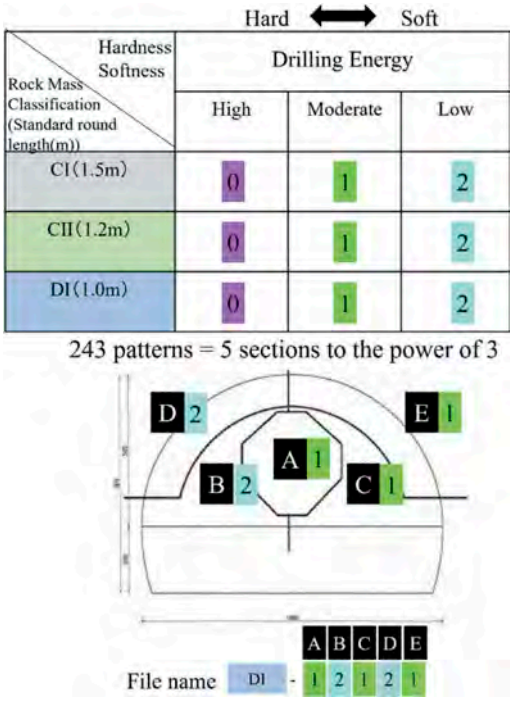

Figure 5. Method of designing blasting patterns.

2.3 *Automatic construction*

Once a blasting pattern has been designed, the tunneling jumbo with the system automatically reads the shared folders in the system when the machine starts and creates a drill plan corresponding to the designed blasting pattern from the stored file names. After the blasting pattern design is completed, the tunneling jumbo with the system automatically reads the shared folders in the system when the machine is started and creates a drill plan corresponding to the designed blasting pattern from the saved file names.

At this time, if the drill plan's drilling sequence is simulated before, then the jumbo can drill automatically without any human intervention. Currently, manual input simulates drilling, but the implementation of automatic input is underway to enable future automation.

2.4 *Improve the efficiency of explosives management and loading operations*

The designed blasting patterns are presented as zone maps (Figure 6). After the system analysis is finished, the zone maps are automatically distributed to the personnel's tablets and PCs for sharing. Additionally, contour maps demonstrating the rock mass hardness and

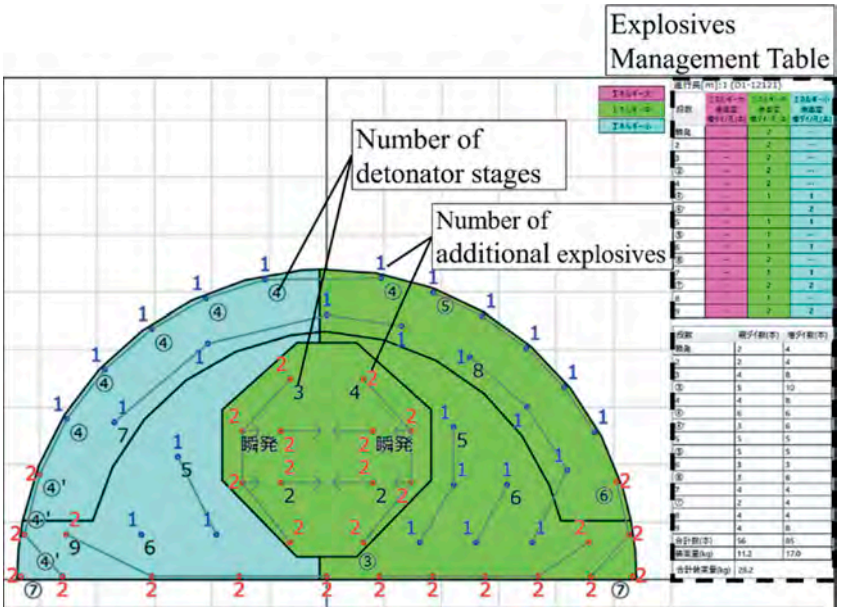

Figure 6. Zone Map(Automatically designed optimal blasting pattern).

softness are sent at this juncture. By comparing the zone and contour maps with the evaluation of the rock mass determined by tunnel face mapping, the responsible individual can review the drilling energy thresholds (Figures 7 and 8). This assessment can aid in the design of optimal blasting patterns that accurately capture changes in the geological condition. The zone maps display the quantity of charge utilized in the blasting pattern, together with the amount of detonating explosives, detonator steps, and additional explosives to be charged in individual holes. This information can improve the effectiveness of explosives preparation for handling operators, optimize the loading operations for tunnel workers, and facilitate the automation of explosives management. these data are instrumental in improving overall efficiency in blasting work.

Figure 7. Conformation of the rock mass condition using the contour map.

Figure 8. Confirmation of pattern by the zone map.

3 IMPLEMENTATION AT A TUNNELING PROJECT

3.1 *The project overview*

The Maki Tunnel Project is a two-way highway tunneling project currently under construction in Toyama Prefecture, Japan. It spans 1,578 meters in length and was the site of a system demonstration test. The geological formations predominantly comprise rhyolite and rhyolitic pyroclastic rock and feature intermittent andesite intrusions. Based on the laboratory rock tests conducted during the design phase, it was found that the unweathered rock has a uniaxial compressive strength of 132 N/mm^2, while the weathered rock has a uniaxial compressive strength of 18.4 N/mm^2. The examined section

showed the widespread distribution of greenish grey to blackish-grey rhyolite, and in some areas weathered and altered rock mass to a brownish-brown color (Figures 9 and 10). Discontinuities in the bedrock were partially developed and intercalated with clay. The rock mass classification for this section was D I. Based on tunnel face mappings, the range of rating varied from 36.75 to 38.0 points, with nearly identical geological conditions.

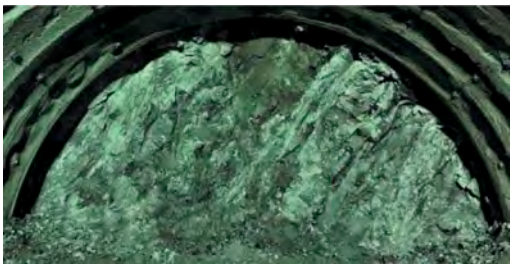

Figure 9. Tunnel face of the section where the test was conducted.

Figure 10. Completion status of loading.

3.2 *Evaluation method*

The Digital Finished Shape Surveying method (Sasajima et al., 2020), utilizing 3D-Lazaer Scanstation P40 cyclone tunnel, was employed to measure the extent of overbreak and underbreak before and after the system's application. The method's measured accuracy is ±5 mm. Within one excavation length (DI:1.00 m), the point clouds within an area of every 10 degrees of arc and every 10 cm of depth of the tunnel excavation wall face were averaged, and the underbreak were defined as those inside the design section and the overbreak as those outside the design section. The efficacy of the Automatic Blasting Design and Construction System for Optimized Blasting was assessed through this method.

3.3 *Effects of system implementation*

3.3.1 *Improve blasting excavation accuracy*

Before implementation of the system, the average underbreak measured 3.87 cm, with the average overbreak of 16.87 cm. Following implementation of the system, the average underbreak measured 1.19 cm and the average overbreak measured 9.89 cm. These results indicate a reduction of 69.3% in overbreak and a reduction of 41.4% in underbreak. Consequently, the excavation surface achieved a smoother finish (Figure 11). The explosives consumption intensity decreased by 7% after the implementation of the system, as the post-application value was 0.40 kg/m^3 while the pre-application average was 0.43 kg/m^3.

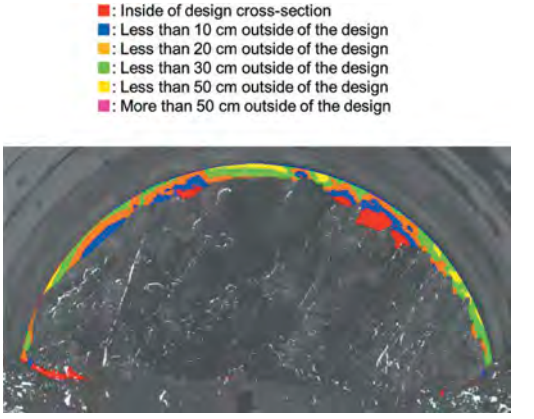

Figure 11. The result of finished shape survey on the tunnel excavation surface.

3.3.2 *Effect of cycle time reduction*

The application of the system has also proven effective in reducing the excavation cycle. The new automated design has eradicated the requirement for time-consuming blasting pattern Drill plan creations. Additionally, automated drilling has improved drilling speed and efficiency, resulting in a reduction of drilling time by 16% (from 37 minutes, standard time (East Nippon Expressway Company Limited, et al., 2022), to 31 minutes) compared to the standard method. The time needed to load explosives was reduced by 23% (standard time: 30 minutes → 23 minutes) by optimizing the process of explosive loaded, compared to the standard method.

3.4 *Improvements for better system operation.*

The system accounts for the rock mass variability and devises blasting patterns by dividing the tunnel face into five sections. This enables accurate design based on actual geological characteristics. However, it cannot take into consideration instances of localized hard rocks like hard rock veins or large boulders. Improvements to the system that allow blasting patterns to be designed for more localized hard and soft parts of the rock mass, such as additional charging holes when the drilling energy is locally high, should be considered.

Additionally, rock fallout resulting from key-blocks may occur on the tunnel face. As the face where the fallout occurred is not flat, the excavation length of charge holes need adjustment according to the excavation results. Improvements of system are necessary to measure excavation conditions utilizing a 3D scanner and lidar, and to adjust the designed blasting pattern based on the obtained data.

4 SUMMARY

A new, Automatic Blasting Design and Construction System for Optimized Blasting has been developed, which automates the blasting pattern design and drilling of charge holes to improve accuracy in conventional tunneling. The following findings were obtained as a result.

(1) The system analyses drilling energy as a quantitative indicator, assesses the rock mass's hardness and softness in each of the five sections where the tunnel face is divided, and automatically designs blasting patterns based on the evaluation results. The introduction of this system has resulted in a reduction in the overbreak and the underbreak when compared to the pre-system introduction period. Moreover, the amount of explosives used has decreased, and excessive damage to the rock mass has been eliminated.
(2) The implementation of the system has optimized the drilling and charging processes, resulting in a notable decrease in cycle time in contrast to standard methods.
(3) To achieve more precise blasting that aligns with the actual geological conditions, the system needs improvement to create blasting patterns that can adapt to local rock mass variations. It is also imperative to enhance the system to adjust the blasting pattern in accordance with the tunneling excavation progress of the previous cycle.

ACKNOWLEDGMENTS

The authors express their gratitude to Central Nippon Expressway Company Limited Kanazawa Branch, Toyama Expressway Office Tokai-Hokuriku Expressway 4-lane promotion room, Yoshiteru Goto, Hiroki Kuriyagawa, Kosuke Tanimura, Ken Ogasawara, and Takahiro Sakai for their valuable cooperation during the testing at the Maki Tunnel project. They also extend their thanks to Takahashi Yasuhiro of JAPEX CORPORATION for designing the criteria blasting pattern, and to Dr. Dohta Awaji, Al Adzam Shah bin Azman and Zhiyuan Tang for their meticulous proofreading of this paper.

REFERENCES

K. Sasajima, T. Tsukiji, A. Kimura, K. Tanimura, 2020. Trial of 3D Laser Scanner in Finished Shape Surveys in Low-Strength Ground-the Susami-Kusimoto Road, the Nisiki Tunnel-. Tunnels and Underground, Vol.51, No.5, pp.47–55

East Nippon Expressway Company Limited, Central Nippon Expressway Company Limited and West Nippon Expressway Company Limited, 2022. Estimation Standards for Civil Engineering Works, 2022 Edition.

Tunnelling for a Better Life – Yan, Celestino, Thewes & Eberhardt (Eds)
© 2024 The Author(s), ISBN 978-1-032-80042-4
Open Access: www.taylorfrancis.com, CC BY-NC-ND 4.0 license

Effect of focusing tube geometry and abrasive flow rate on rock drilling width

Hyun-Joong Hwang*
Department of Civil and Environmental Engineering, Korea Advanced Institute of Science and Technology (KAIST), Daejeon, Republic of Korea

Yohan Cha
Disposal Performance Demonstration R&D Division, Korea Atomic Energy Research Institute (KAERI), Daejeon, Republic of Korea

Jin Kim, Changhee Park & Gye-Chun Cho
Department of Civil and Environmental Engineering, Korea Advanced Institute of Science and Technology (KAIST), Daejeon, Republic of Korea

ABSTRACT: The necessity for underground space development has recently emerged due to overcrowding and the lack of space in downtown areas. Meanwhile, many civil complaints occur due to noise and vibration during rock excavation to create underground spaces in downtown areas. Rock excavation using abrasive waterjet is characterized by low noise and low vibration and has the advantage of resolving these civil complaints. In addition, it does not generate heat during rock excavation, so it does not form a heat-affected zone. It does not transmit mechanical stress to the surrounding ground, so it has the advantage that an excavation damaged zone does not occur. To achieve effective rock excavation, a significant excavation depth is required, necessitating the provision of an appropriate excavation width. The excavation width is related to the dispersion of the jet, and various parameters of the abrasive waterjet system affect jet dispersion. In this study, we experimentally observed the variation in rock drilling width by controlling the focusing tube geometry and abrasive flow rate in an abrasive waterjet system, and based on these observations, we analyzed the dispersion of the jet. The findings of this study contribute to the field of rock excavation techniques by providing a systematic method for estimating excavation width with an abrasive waterjet. Accurately predicting and controlling excavation width enables operators to optimize operations and make informed decisions regarding equipment setup, resulting in more successful excavation outcomes.

Keywords: Abrasive waterjet, Rock excavation, Drilling width, Focusing tube geometry, Abrasive flow rate

1 INTRODUCTION

Waterjet technology is a technology that uses high-pressure water to remove target materials. Waterjet technology is a low-noise, low-vibration method that can solve civil complaints from nearby residents (e.g., construction delays and interruptions) caused by noise and vibration during rock excavation construction in urban areas. Meanwhile, various previous studies on rock drilling and cutting using waterjet technology have been conducted to date (Summers, 1992; Summers, 1995). In the case of high-strength rock, excavation using only water is inefficient, and to solve this problem, abrasive waterjet technology, which sprays a mixture of water and abrasives, has begun to be used (Hashish, 1989; Momber and Kovacevic, 1998; Karakurt et al. al., 2012). The basic abrasive waterjet mechanism is as follows (Figure 1). High-pressure water generated through a hydraulic pump passes through a tiny diameter orifice and is converted into high-speed water. This high-velocity water mixes with the abrasive in the mixing chamber and transfers momentum to the abrasive. In this process, the abrasive is accelerated and gains kinetic energy (Momber, 1998; Roth et al., 2005; Cha et al., 2019). The water and abrasive mixture passes through a focusing tube, gains a straight direction, and is sprayed into the air.

*Corresponding author: hyunjoong@kaist.ac.kr

DOI: 10.1201/9781003495505-198

The distance between the end of the focusing tube and the target material is called the standoff distance, and while passing through it, the jet partially disperses and removes the target material.

Meanwhile, when rock drilling using abrasive waterjet technology, a wide drilling width must first be constructed for deep drilling. When drilling is performed by fixing the waterjet nozzle at the initial position, there is a limit to forming a deep drilling depth. Therefore, when rock drilling is performed by inserting a waterjet nozzle into the hole using a wide drilling width, it is possible to form an effective drilling depth. Drilling width is affected by various parameters such as standoff distance, abrasive flow rate, water pump pressure, and focusing tube geometry (Oh and Cho, 2014). In this study, experiments were conducted on focusing tube geometry (i.e., diameter and length), water flow rate, and abrasive flow rate among various parameters that affect drilling width. Rock drilling width was observed according to focusing tube diameter, focusing tube length, water flow rate, and abrasive flow rate, and the influence of each parameter was analyzed.

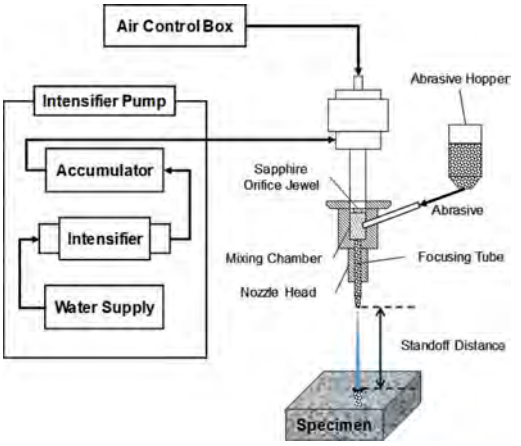

Figure 1. Schematic diagram of abrasive waterjet (Hwang et al., 2019).

2 EXPERIMENTAL PROGRAM

A drilling experiment using an abrasive waterjet was conducted using granite, which is commonly found at construction sites in the Republic of Korea, as the target material. The physical properties of granite are summarized in Table 1. The abrasive used was garnet, which is commonly used in industry. Garnet is a material with a high hardness of 7.5–8.5 Mohs scale, and in this experiment, the experiment was performed with particles with a size of approximately 0.18 μm. Additionally, the abrasive waterjet system used an intensifier-type pump; details are summarized in Table 2.

This drilling experiment sought to observe the influence of four parameters (i.e., focusing tube diameter, focusing tube length, water flow rate, and abrasive flow rate) on the drilling width of granite. To observe the influence of focusing tube diameter (D_f), two focusing tube diameters of 0.76 and 1.02 mm were applied. To observe the effect of focusing tube length (L_f), an experiment was performed using three focusing tube lengths of 76.2, 101.6, and 152.4 mm. Additionally, to analyze the effect of water flow rate (*WFR*), two orifice diameters (D_O) of 0.254 and 0.33 mm were used under the same water pump pressure condition of 320 MPa. At this time, an experiment was performed using the water flow rates of 28.3 and 50.0 ml/s as variables. Lastly, to observe the effect of abrasive flow rate (*AFR*) on drilling width, a granite drilling test was performed at four abrasive flow rates of 5.6, 7.5, 11.1, and 15.0 g/s. In all experimental conditions, the standoff distance, defined as the distance between the abrasive waterjet system and the target material, was applied equally at 100 mm. Additionally, the water pump pressure of 320 MPa was applied equally to all experiments. Details of the parameters applied in the experiment are summarized in Table 3.

Table 1. Granite properties.

Density/ (kg/m^3)	2650
Specific gravity/ (-)	2.65
Porosity/ (%)	0.68
Absorption/ (%)	0.25
Uniaxial compressive strength/ (MPa)	212
Young's modulus/ (GPa)	55.7
ISRM classification	Very strong rock

Table 2. Specifications of waterjet pump.

Pump type	Power/ (HP)	Max. water pressure/ (MPa)	Max. water flow rate/ (ml/s)
Intensifier pump	50	412	100

Table 3. Experiment cases and details.

Water pump pressure/ (MPa)	320
Standoff distance/ (mm)	100
Focusing tube diameter/ (mm)	Effect of focusing tube diameter (L_f = 76.2 mm, D_O = 0.254 mm) 0.76, 1.02
Focusing tube length/ (mm)	Effect of focusing tube length (D_f = 1.02 mm, D_O = 0.33 mm) 76.2, 101.6, 152.4
Water flow rate/ (ml/s)	Effect of water flow rate (L_f = 76.2 mm, D_f = 1.02 mm) 28.3, 50.0
Abrasive flow rate/ (g/s)	Effect of abrasive flow rate (D_f = 1.02 mm, D_O = 0.33 mm) 5.6, 7.5, 11.1, 15.0

3 RESULTS AND DISCUSSION

The results of a granite drilling experiment using an abrasive waterjet system analyzed in detail how parameters such as focusing tube geometry (i.e., diameter and length), water flow rate, and abrasive flow rate affect drilling width. In order to observe the influence of each parameter clearly, all parameters except the corresponding parameter were strictly controlled.

3.1 *Effect of focusing tube diameter*

Figure 2 clearly shows the effect of focusing tube diameter on drilling width. In all abrasive flow rate conditions, the larger the focusing tube diameter, the larger the drilling width was. Physical reasons can explain these results. This is because the larger the diameter of the focusing tube, the wider the jet spreads when sprayed into the air. Specifically, the larger the focusing tube diameter, the wider the cross-sectional area of the end exposed to the air, so the jet is dispersed more widely. Also, a larger focusing tube diameter means the space inside the focusing tube is wider. This relatively reduces the number of collisions of abrasive particles with the inner wall of the focusing tube due to the large internal space and reduces interference between abrasive particles. Therefore, the larger the focusing tube diameter, the more energy the abrasive has, and when sprayed with air, it is widely dispersed to form a large drilling width. In addition, it was observed that a similar drilling width was formed despite the focusing tube diameter being different under a specific abrasive flow rate condition (i.e., *AFR* = 7.5 g/s). This shows an optimal condition between focusing tube diameter and abrasive flow rate.

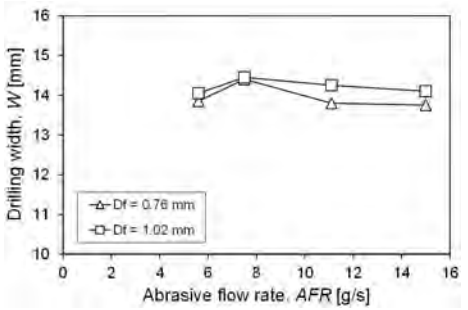

Figure 2. Effect of focusing tube diameter on the drilling width.

3.2 *Effect of focusing tube length*

Figure 3 shows the effect of focusing tube length on drilling width. The drilling width decreased in all abrasive flow rate conditions as the focusing tube length became longer. This is related to the time the abrasive particles stay inside the focusing tube. The longer the focusing tube length, the longer the abrasive particles stay and move inside the focusing tube. Staying inside the focusing tube for a long time relatively increases the number of collisions of abrasive particles with the inner wall and increases interference between abrasive particles. In this process, the abrasive particles lose some of their energy and form a straight line with the water, aligning the flow. In other words, the longer the focusing tube length, the longer the abrasive particles stay inside the focusing tube, losing some energy due to collision and interference, and are aligned with water in a straight flow, reducing the drilling width. Conversely, if the focusing tube length is too short, the jet does not travel in a straight line, so it can be sprayed widely when sprayed into the air. Therefore, when rock drilling using an abrasive water jet, it is important to determine an appropriate focusing tube depending on the purpose.

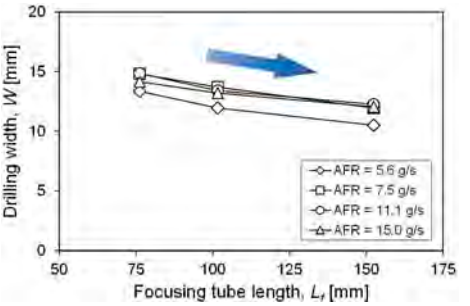

Figure 3. Effect of focusing tube length on the drilling width.

3.3 *Effect of water flow rate*

The effect of water flow rate on granite drilling width was observed in Figure 4. Overall, under abrasive flow rate conditions, the larger the water flow rate, the larger the drilling width was. This is related to the momentum of water, which is the initial energy of the abrasive waterjet system. Water gains energy and gains momentum through a hydraulic pump and orifice. Additionally, water transfers momentum in the process of mixing with the abrasive, and as a result, the abrasive gains momentum and accelerates. All of these processes are the basic mechanisms of an abrasive waterjet system.

Meanwhile, in the same abrasive waterjet system, as the water flow rate increases, the relative momentum of the water also increases. Therefore, if the initial energy of the water is high, relatively more momentum can be transferred to the abrasive particles, forming a wider drilling width. However, under certain abrasive flow rate conditions (i.e., *AFR* = 5.6 g/s), a wider drilling width was observed despite the low water flow rate. This suggests that an optimal condition exists between water flow rate and abrasive flow rate, and an in-depth understanding of the optimization of parameters is necessary.

3.4 *Effect of abrasive flow rate*

Figure 4 clearly shows the effect of abrasive flow rate on drilling width. In all focusing tube length conditions, as the abrasive flow rate increased, the drilling width tended to increase and then decrease. This

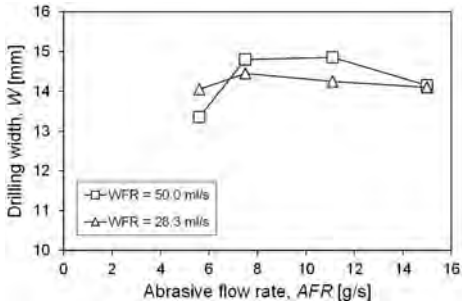

Figure 4. Effect of water flow rate on the drilling width.

means that there is an optimal condition for abrasive flow rate for drilling width. When the focusing tube length was 76.2, 101.6, and 152.4 mm, the optimal abrasive flow rate representing the maximum drilling width was analyzed to be 11.1, 7.5, and 11.1 g/s, respectively. Through this, it can be predicted that the optimal abrasive flow rate for granite drilling width under the same standoff distance condition exists within the range of approximately 8.0–11.0 g/s. In an abrasive waterjet system, the optimal abrasive flow rate is an important factor in field application as abrasive accounts for a significant portion of the total operating cost. When a certain amount of abrasive material is added, the abrasive accelerates, and during movement, frequent collisions and interference between abrasive particles occur, resulting in relatively large energy loss. Therefore, in order to create an effective drilling width, it is efficient to use an abrasive flow rate of 8.0–11.0 g/s.

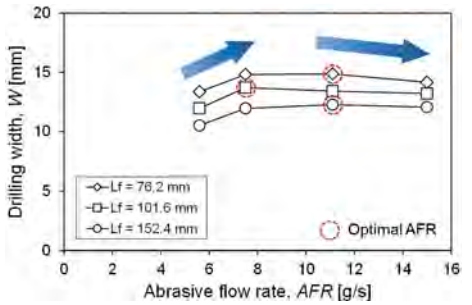

Figure 5. Effect of abrasive flow rate on the drilling width.

4 CONCLUSIONS

In this study, a granite drilling experiment was performed using abrasive waterjet technology. Drilling width according to focusing tube diameter, focusing tube length, water flow rate, and abrasive flow rate was observed and analyzed. The drilling experiment results are summarized as follows:

- The larger the focusing tube diameter, the larger the rock drilling width was. This is because the cross-sectional area at the end of the focusing tube is larger, so the jet is absolutely wide when sprayed into the air.
- Drilling width decreased as the focusing tube length became longer. This is because the longer the focusing tube length, the longer the abrasive particles stay inside, resulting in some energy loss due to collision and interference.
- Water flow rate is the initial energy of the abrasive waterjet system, and the larger the water flow rate, the wider the drilling width was observed. This is because the abrasive is accelerated and sprayed by receiving momentum from water with relatively high energy.
- As the abrasive flow rate increased, the drilling width increased and then decreased. Optimal abrasive flow rate ranges from approximately 8.0–11.0 g/s.

ACKNOWLEDGMENTS

This work was supported by a grant (RS-2023-00245334) funded by Korea of Ministry of Land, Infrastructure and Transport (MOLIT).

REFERENCES

Cha, Y., Oh, T. M., Cho, G. C. (2019). “Waterjet erosion model for rock-like material considering properties of abrasive and target materials.” Applied Sciences, 9(20), 4234.

Hashish, M. (1989). “A model for abrasive-waterjet (AWJ) machining.” J. Eng. Mater. Technol., 111(2), pp. 154–162.

Hwang, H. J., Cha, Y., Oh, T. M., Cho, G. C. (2019). “Effect of standoff distance and abrasive flow rate on the removal volume for AWJ rock drilling.” In ASEM19. International Association of Structural engineering and mechanics.

Karakurt, I., Aydin, G., Aydiner, K. (2012), “An experimental study on the depth of cut of granite in abrasive waterjet cutting.” Mater. Manuf. Process., 27, pp. 538–544.

Momber, A. (1998). “The kinetic energy of wear particles generated by abrasive–water-jet erosion.” J. Mater. Process Technol. 83, pp. 121–126.

Momber, A. W., & Kovacevic, R. (1998). Principles of abrasive water jet machining. Springer Science & Business Media.

Oh, T.M., Cho, G.C. (2014), “Characterization of effective parameters in abrasive waterjet rock cutting.” Rock. Mech. Rock. Eng., 47(2), pp. 745–756.

Roth, P., Looser, H., Heiniger, K., Bühler, S., 2005. Determination of abrasive particle velocity using laser-induced fluorescence and particle tracking methods in abrasive water jets. In Proceedings of the 2005 WJTA Conference and Exposition, Houston, TX, USA, pp. 21–23.

Summers, D.A. (1992), Hydraulic mining: jet-assisted cutting. In: Hartman HL (ed) SME mining engineering handbook, 2nd edn., Society for Mining, Metallurgy, and Exploration Inc., California, pp. 1918–1929.

Summers, D.A. (1995), Waterjetting technology, E & FN Spon, London.

Tunnelling for a Better Life – Yan, Celestino, Thewes & Eberhardt (Eds)
© 2024 The Author(s), ISBN 978-1-032-80042-4
Open Access: www.taylorfrancis.com, CC BY-NC-ND 4.0 license

Development of advanced tunnel blasting and shotcrete as automated tunnel construction system

Keita Iwano*
Kajima Corporation, Gifu, Japan
Kajima Corporation, Tokyo, Japan

Takahiro Aoyagi & Takafumi Yamagishi
Kajima Corporation, Tokyo, Japan

Takashi Mega
Kajima Corporation, Gifu, Japan
Kajima Corporation, Tokyo, Japan

Takaaki Inuzuka
Kajima Corporation, Tokyo, Japan

ABSTRACT: A lot of manual operations are still inevitable at the tunnel face where's always in danger for rock collapse, and manpower saving and keeping safety there is most important issues. Therefore, advanced automatic operation technology has been studied to replace manual operations The next-generation construction system with automated machinery called A^{4}CSEL (Automated, Autonomous, Advanced, Accelerated Construction system for Safety, Efficiency and Liability) is promoted for 6 main steps of tunnel excavation. In this paper, two steps of them, blasting and shotcrete, are picked up. Blasting conventionally have been implicitly modelled only by tunnel workers with enough experience. Therefore, the theoretical evaluation formula for optimum blasting needs to be constructed with several factors that affect blasting result. Then, the optimum blast planning system is developed based on that formula and can be used by even inexperienced planner. According to the site trials, this system clarified to reduce the amount of overbreak and operation time. Shotcrete is quite difficult for its automation because sufficient skills for nozzle manipulation is required. In order to shift it to advanced operation, the automated shotcrete machine has been developed, and its nozzle manipulation system based on the optimum plan is also integrated. Based on the tests in mock-up tunnel, this system can spray the concrete with high accuracy of thickness, and also reduce the amount of rebound. These two steps of them are sure to reach in certain level for current tunnel site. It is sure that this automated construction system can improve the productivity, safety and manpower saving. In the near future, the A^{4}CSEL for Tunnel will be introduced to the many sites in Japan.

Keywords: Tunnel construction, Automation, Mechanization, Blasting, Shotcrete

1 INTRODUCTION

For construction industry in Japan, the skilled labour shortage, a lot of accidents, and low productivity have been significant issues for a long time. Therefore, epoch-making construction system is extremely required to achieve the goals such as the manpower saving, safety and high productivity. Authors are promoting the A^{4}CSEL (quad-accel:Automated/Autonomous/Advanced/Accelerated Construction system for Safety, Efficiency and Liability), a next-generation construction system with automated construction machinery. The key issues to make this system work well is not only introducing automated machines but also the structuring effective scheme in which the machine's operation data is analysed and operating procedure is improved. This new construction system has been applied at dam site for the first time and is also applied for tunnel construction (A^{4}CSEL for Tunnel) In this paper, productive blasting (drilling and charging) and shotcreting are picked up among other steps in tunnel construction cycle.

2 CONCEPT FOR AUTOMATED TUNNEL CONSTRUCTION

As shown in Figure1, mountain tunnel construction mainly consists of 6 steps and repeats them by each

*Corresponding author: iwanokeita@kajima.com

DOI: 10.1201/9781003495505-199

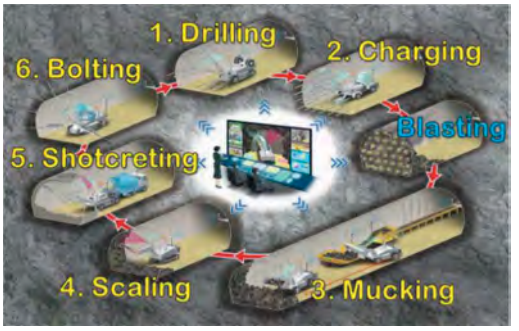

Figure 1. The concept of A^{4}CSEL for Tunnel.

1 to 1.5m advance. In Japan, tunnel construction is currently taken place by 5 skilled workers per party, and 24hours operation by 2 parties for day and night shift. They are quite versatile, and excavation advance rate depends on their skill and experience. Recently, they are getting aged and there are still few newcomers due to the negative image of risky

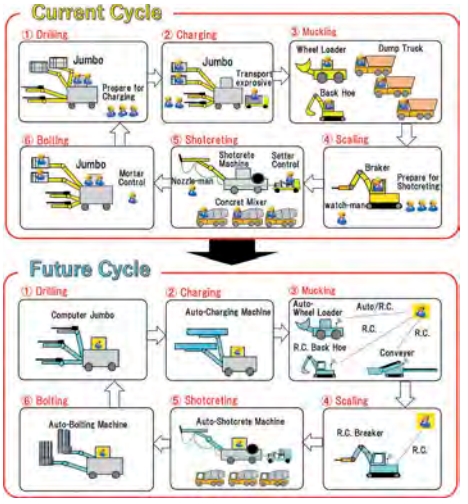

Figure 2. Image of current and future tunnel excavation cycle.

Picture 1. Mock-up tunnel.

Picture 2. Kamioka real-size test tunnel.

and hard work. Now that, time of drastic change is around the corner.

Authors are applying the A^{4}CSEL, a next-generation construction system, to the tunnel construction field. The concept of A^{4}CSEL for tunnel is shown in Figure 1. As for 6-step cycle from drilling to bolting, once automated machines are fully prepared, A^{4}CSEL for tunnel makes it possible to realize the productive construction with one-man operation either on the machine or in the remote-control room (Figure 2). So far, the process of A^{4}CSEL for tunnel is advancing with step by step from mock-up tunnel site (Picture 1) to the real-size test tunnel site(Picture 2).

3 THE OPTIMUM BLAST PLANNING

3.1 *Overview of optimum blast planning*

Blasting consists of drilling and charging. Conventionally, its plan had been implicitly made based on veteran worker's experience.In order to accomplish the optimum blasting using automated machine and digital data, cycling the positive loop shown in Figure 3 is essential, these are:

a. Implementing blasting (drilling and charging) according to the optimum plan and digitalizing the data for next blast.
b. Visualizing the blast data and analysing it to adjust next blast plan.
c. According to the analysis, improving the blast plan via automated planning system.

The key points to make this loop work well are as follows:

- Need to establish the blast evaluation formula in order not to rely on the veteran worker's experience and to be able to judge the blast results by anyone who hasn't been engaged in blasting at all.
- Need to establish the blast planning system that integrates the blast evaluation formula for being able to automatically analyse the blast result and improve its plan.

Figure 3. The positive loop for optimum blasting.

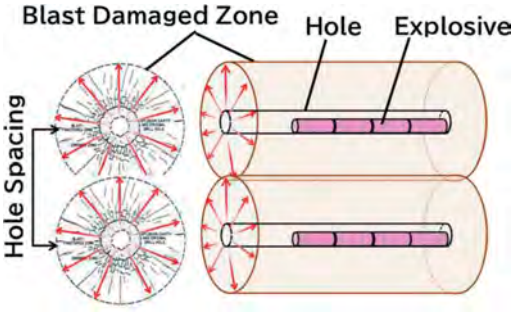

Figure 5. The concept for blast damaged zone.

3.1.1 *Blast evaluation formula*

In order to judge the blast design and its result effectively and evenly, authors have organized the blast evaluation formula based on theoretical solution. In general, there seems to be 3 factors that mostly influence the blast result, these are, rock property (rock strength, fractures, etc.), drilling property (drill diameter, length, etc.), charging property (types of explosives, explosives charge per hole, etc.) Based on these 3 factors mentioned above, blast evaluation formula can calculate the effective blast damaged zone for the rock around the specific blast hole (Figure 4. Figure 5). Validity of this formula had been confirmed at mine tunnel. Through the drilling test in the real-size test tunnel, this formula has been adjusted to be able to normalize the rock strength parameters that don't depend on the Jumbo manufacturer, drifter, and drill setting parameters such as percussion pressure and thrust pressure.

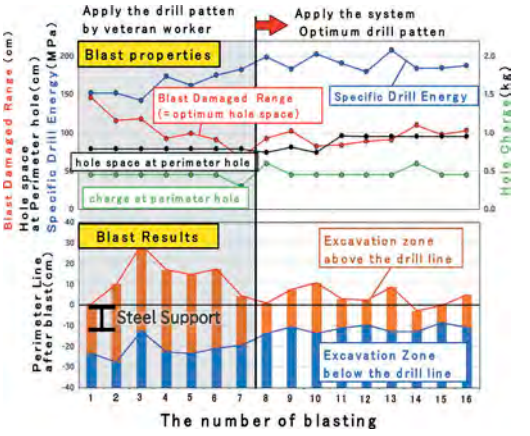

Figure 6. Blast visualization system chart.

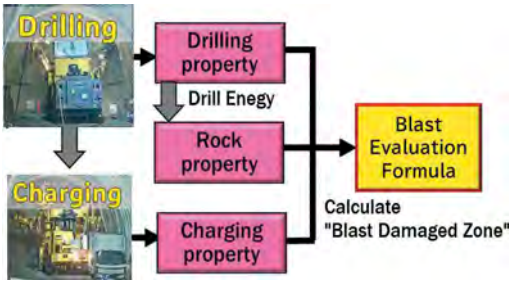

Figure 4. Calculation Flow to Blast damaged zone.

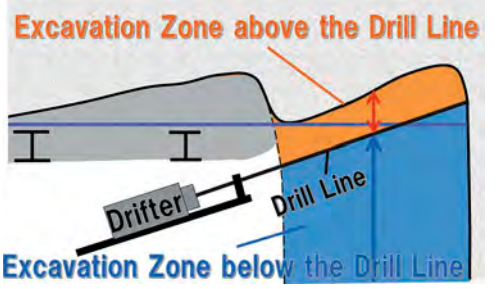

Figure 7. Excavated zone in tunnel perimeter.

3.1.2 *Blast visualized system*

Because blasting has been conducted against natural rock, the blast result always contains some sort of dispersion. In order to grab the blast result tendency and evaluate the validity of blast plan from it, the concept of statistics has to be considered.Therefore, authors created the blast visualized system in which both blasting properties and their result in last 20 to 30 blasts are shown in one chart and its tendency is quite easy to grasp for users. As shown in Figure 6, visualized chart is separated into top and bottom in this system. The blast properties are plotted in top and, the blast results are in bottom. Blast properties in top of the chart are such as specific drill energy (rock strength), blast damaged range (optimum hole space), hole space at perimeter, charge at perimeter hole. Blast results in bottom of the chart are excavation zone either above (orange) or below (blue) the drilling line. As shown in Figure7, these separated excavation zones (orange and blue zone) are respectively calculated based on the drilling line data and scanned tunnel profile data after blasting. By showing excavation zone separately like this, the essential reason of having the redundant overbreak can be clarified and the adjustment for next blast plan becomes effective.

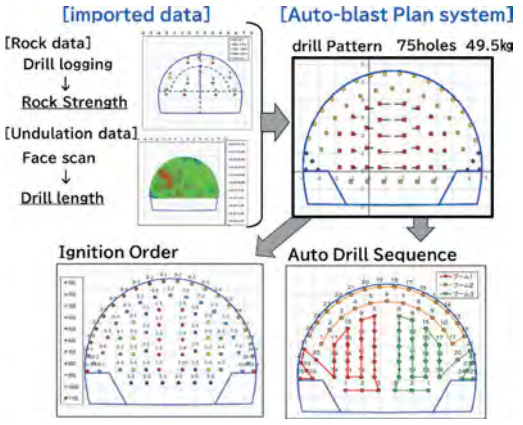

Figure 8. Automated blast planning system.

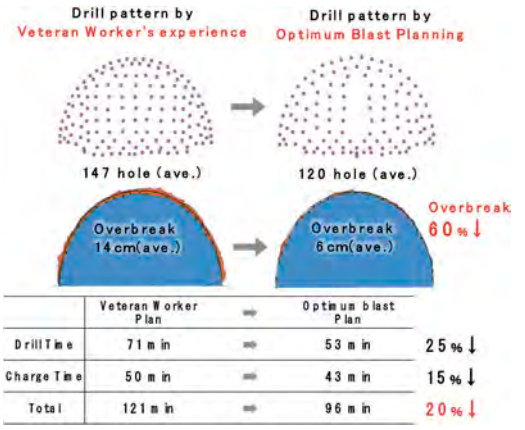

Figure 9. Comparison for blast productivity.

3.1.3 *Automated blast planning system*

The automated blast planning system in which blast evaluation formula has been integrated can produce the optimum drilling pattern and its charging plan. In the system, as an input data, previously obtained rock data and tunnel face undulation data are imported. At first, tunnel face is separated into several zones and then, based on the undulation data, the appropriate drilling length and amount of charge per hole are calculated respectively in each zone. After that, with imported rock data, the optimum hole spacing for each zone is calculated via blast evaluation formula. Once previous blast data are obtained, the whole procedure mentioned above can be automatically conducted.

After the automatic drilling pattern is produced, the manual pattern adjustment is possible if necessary. In the system, the hole ignition order and drilling sequence for automatic drilling via computer jumbo can be designed. This system also supports input/output data for different jumbo manufacturers.

3.2 *Application to tunnel site*

The Optimum blast planning system (blast visualized system and automated blast planning system) is applied to on-going tunnel construction site. As shown in Figure 6, at first the blast plans are conventionally designed by veteran worker even though the computer jumbo and scanner are ready for use, then from No.8 blasting in the Figure 6, the optimum blast planning system has applied. Especially, in the blast optimizing process, hole space at perimeter (black dot line in top chart in Figure 6) is adjusted to minimize the difference between the black dot line and red dot line (blast damaged range; optimum hole space).Since the optimum blast planning system has applied, the productivity of blasting work was found to be significantly improved, such as reduction of drilling time by 25%, charging time by 15%. Totally, the combined time of them reduced by 20%, and the average overbreak also reduced by 60% compared to the blasting designed by experienced workers. Blasting is the first step of the tunnel construction cycle and tends to contribute the productivity for subsequent steps such as mucking and shotcrete. Therefore, controlling the blasting performance by this system is quite meaningful.

4 THE AUTOMATED SHOTCRETE

4.1 *Overview of automated shotcrete*

The automated shotcrete system is thought to be quite difficult because it requires not only automated machines but also sufficient nozzle operation that must work in accordance with surface condition. In order to make the system be more productive which means shorter operation time and lower spray rebound, it must integrate the optimum shotcrete planning that are flexibly designed according to the surface roughness and necessary spray thickness for each spray zone. The key issues for developing the automated shotcrete system are as follows (Figure 10):

- Machine motion control
- Shotcrete thickness measurement
- Shotcrete operation planning

4.2 *Machine motion control*

Conventionally, shotcrete machines are operated by manual operators called nozzle-man via remote controller while they are keeping visual check of the sprayed shape.

Machine motion control is that conventional machine is fully reconstructed by being attached several sensors in order to make it possible to work according to automatic shotcrete planning (Figure 11). These sensors such as telescopic motion and rotary angle are attached with all booms, arms, and nozzles as shown in Figure 12 to be able to digitally communicate with proportional control valves and main control unit. Especially, the swing angle and swing speed sensors are required high precision and resolution because their abilities such as response lag might directly affect the concrete sprayed shape.

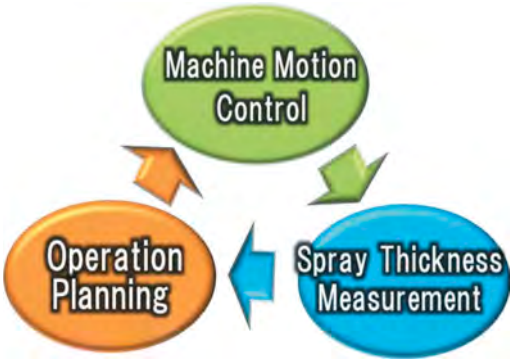

Figure 10. Key elements for automated shotcrete system.

4.3 *Shotcrete thickness measurement*

3D scanner is mounted in front of the automated shotcrete machine shown in Figure 13 and is applied to grasp the surface shape and roughness on face and wall before or between shotcrete spraying. Before the shotcrete spraying starts, the scanning results enable users to calculate the necessary amount of concrete and to give the appropriate order to the concrete plant. Between spraying the concrete such as the time of altering the concrete mixier truck, the scanning results make it possible to confirm the surface shape as the original plan and to adjust its plan if necessary. The 3D scanning system takes only within one minute from starting scanning to showing the result and has automatic shut cover to protect from heavy dust while spraying shotcrete.

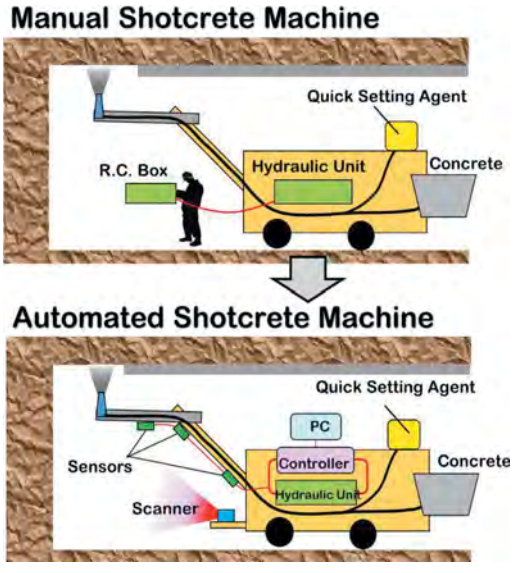

Figure 11. Manual and automated shotcrete machines.

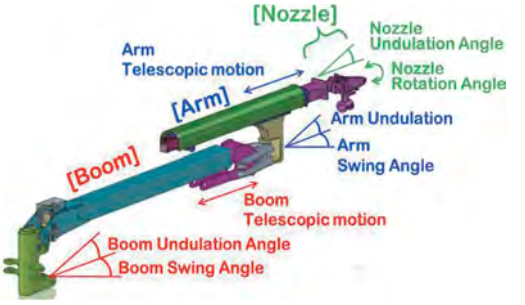

Figure 12. Movable part in shotcrete machine.

4.4 *Shotcrete operation planning*

Shotcrete operation planning is to make nozzle-work sequence and give it to automated shotcrete machine. The nozzle-work sequence is automatically calculated based on surface shape and the fundamental nozzle-work movements that has previously organized through the studies in mock-up tunnel. Therefore, the shotcrete operation planning does not follow the veteran's nozzle-work as a teaching data but is able to give the optimum combination of fundamental nozzle-work movements which enables shortest operation time and lowest spray rebound with maximum concrete pumping rate. The shotcrete operation planning is divided into three modes such as face spray, wall spray, and steel support spray as shown in Figure 14.

Figure 13. 3D scanner mounted on the shotcrete machine.

4.4.1 *Fundamental nozzle-work stereotype at mock-up tunnel*

The mock-up tunnel is temporally constructed to implement the fundamental parametric study for shotcrete in which how several parameters affect the spray performance is examined. Through these studies, fundamental nozzle-work movements are established in which final sprayed width and thickness can be numerically estimated from several combinations

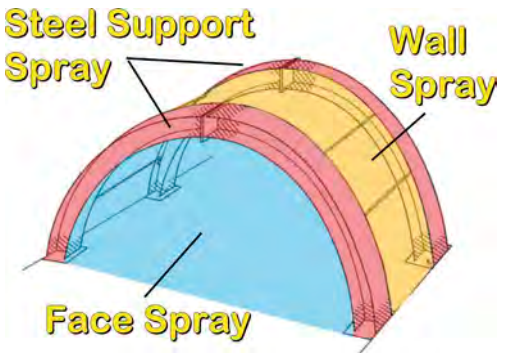

Figure 14. Three nozzle-work modes in automated shotcrete.

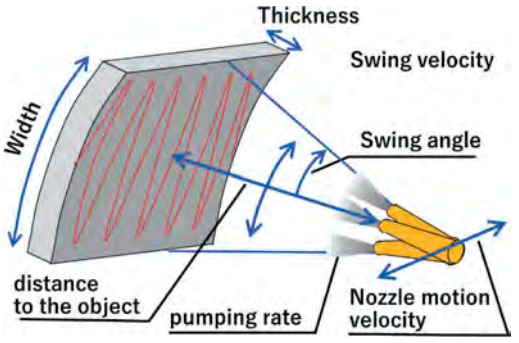

Figure 15. Parameters that affects the spray performance.

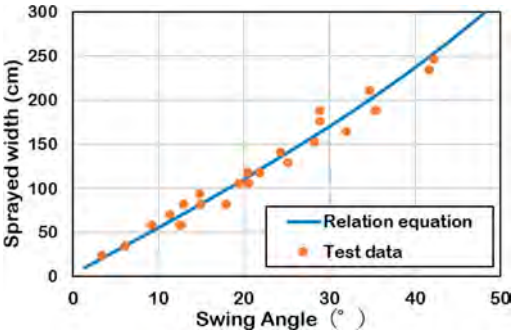

Figure 16. Relation between sprayed width and swing angle.

of parameters. As shown in Figure 15, these parameters are such as the spray distance to the object, swing angle, swing velocity, nozzle motion velocity, concrete pumping rate. The parametric studies clarify the relation between each pair of parameters, such as sprayed width and swing angle shown in Figure 16.

4.4.2 *Automated shotcrete trial at real-size test tunnel*

Kamioka test tunnel is also constructed as a real-size test site to confirm the automated shotcrete

Figure 17. Face spraying by automated shotcrete.

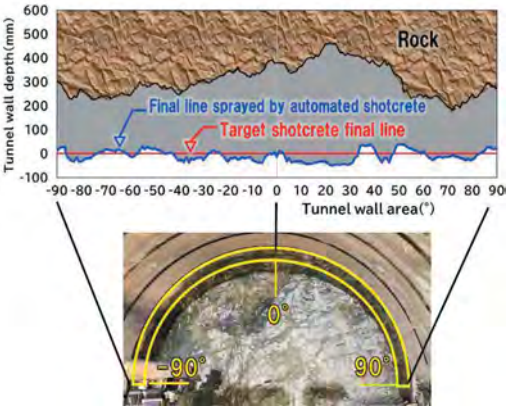

Figure 18. Shotcrete thickness accuracy in wall spray model.

performance in the realistic situation such as rough surface made by blasting.

For in-situ surface roughness, the shotcrete operation planning is implemented in which the surface is divided into several zones according to the necessary spray thickness, and then nozzle-work sequence for each zone is determined based on the combination of fundamental nozzle-work movements. Figure 17 is the face spray mode by automated shotcrete machine. Figure 18 shows the thickness accuracy of shotcrete in wall spray mode in which the final surface is

within few cm accuracies to target final line.

5 CONCLUSIONS

In order to overcome several urgent problems for current tunnel excavation in Japan, new construction system called A^{4}CSEL is under development. In this paper, two steps of tunnel excavation cycle, epoch-making blasting and shotcreting are introduced. The key points for them to be truly productive and

optimum is not only producing automated machines but also structuring effective scheme and planning for these machines. Now other steps of tunnel cycle are also under development in Kamioka test tunnel and in the near future the A^{4}CSEL for tunnel will be introduced to the many sites in Japan.

REFERENCES

Satoru Miura, Shigeru Mutaguchi, Keita Iwano, 2020."Productivity improvement with automation technology in tunnel construction -Shotcrete automation-". Journal of Civil Engineering, Vol.61, No.1, pp96–99.

Satoru Miura, 2021."Application for A^{4}CSEL next-generation construction system". Journal of Civil Engineering, Vol.62, No.1, pp120–123.

Takaaki Inuzuka, Keita Iwano, et.al, 2019. "The Automatic shotcrete system of tunnel". 74th JSCE Annual Meeting, VI–1080.

Takaaki Inuzuka, Keita Iwano, et.al, 2020. "The Automatic shotcrete system of tunnel (2nd Report)". 75th JSCE Annual Meeting, VI–433

Keita Iwano, Yasunari Tezuka, 2021. "Highly productive tunnel blasting based on automated operation and its data analysis". 76th JSCE Annual Meeting, VI–676.

Takaaki Inuzuka, Shigeru Mutaguchi, et.al, 2023. "The Automatic shotcrete system of tunnel (3rd Report)". 77th JSCE Annual Meeting, VI–930.

Tunnelling for a Better Life – Yan, Celestino, Thewes & Eberhardt (Eds)
© 2024 The Author(s), ISBN 978-1-032-80042-4
Open Access: www.taylorfrancis.com, CC BY-NC-ND 4.0 license

Unforeseen excavation of mixed face soil conditions in a hard rock drill and blast road tunnel

Pål Drevland Jakobsen*
The Norwegian Geotechnical Institute (NGI), Norway

Helle Nilsen
LNS, Risøyhamny, Norway

Alf Kristian Lund
The Norwegian Geotechnical Institute (NGI), Norway

ABSTRACT: The Bergåsen road tunnel located in the northern Norway was pre-investigated and planned to be a 2 km hard rock tunnel through marble and granites. After approximately 600 m tunnelling with conventional drill and blast, the tunnel entered a mixed face soil zone of 70 m length. The mixed face soil consist of an over consolidated clay moraine and a inhomogeneous weathered rock material. The clay moraine has shear strength from 250 – 1200 kPa dependent on the triaxial load conditions, while the weathered rock material's shear strength is from 50 kPa and up to the megapascal range. As the tunnelling entered the unforeseen soil zone, the tunnelling was stopped for almost 4 months in order to carry out additional pre-investigations and revisions of the tunnel design. The basics of the tunnel design are use of reinforced sprayed concrete arches with pipe umbrella bolts for the temporary support. The main aim of this paper is to present results and experiences from the pre-investigations and design, as well as tunnelling speed with unit times and lessons learned from the actual construction of the pipe-umbrella reinforcement, double reinforced sprayed concrete arches, excavation with scaling hammer and road header excavator. The paper also presents details about the temporary support system which is double reinforced sprayed concrete arches (RRSII). The selection of of RRSII over more commonly used lattice girders is mainly due to the additional design and production time of lattice girders compared to RRSII.

Keywords: Tunnelling, soft ground, sprayed concrete ribs, support

1 INTRODUCTION

December 2022 the tunnelling contractor Leonhard Nilsen & sønner (LNS) entered in a partly soil tunnel face during the excavation of the Bergåsen road tunnel close to Mosjøen in Norway. From the pre-investigations of the Bergåsen tunnel it was foreseen a weakness zone in this area of 5 to 10 m length at the tunnel level. In reality the zone consisted of an approximately 70 m long zone of clay moraine material and weathered and disintegrated rock. From mid-january 2023 a pre-investigation scheme started, in parallel with a design study for excavation and temporary tunnel support.

The selected method comprises:

- relative short excavation rounds of 1.5 – 2.0 m under the support of spiling and pipe umbrella bolts.
- drainage holes in the tunnel face to avoid pore pressure, and to control potential erosion
- grouted face bolts with plates
- 10 cm reinforced sprayed concrete, mainly to show potential cracking and to support workers close to the face for potential smaller instabilities
- Monitoring of displacements with inclinometers above the tunnel roof
- Use of reinforced sprayed concrete ribs in a semi-circular tunnel cross-section.

Norwegian tunnelling is main experience derives from hard rock tunnelling (NFF 2022). However, the soil conditions experienced in Bergåsen has similarities to the Joberg tunnel excavated in 2015-2016 (Aagaard et al. 2017). Some of the experiences from the Joberg tunnel was utilised in the design of the Bergåsen tunnel.

*Corresponding author: pal.jakobsen@ngi.no

DOI: 10.1201/9781003495505-200

Figure 1. Map of Norway, red pin show approximate location of the tunnel. (from www.norgeskart.no).

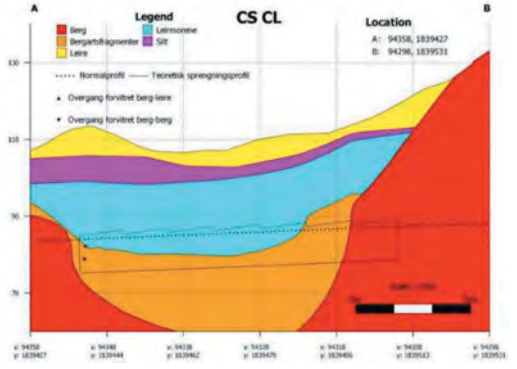

Figure 2. Geotechnical model of the soil stratas along the soil zone in Bergåsen tunnel. Red legend shows massive rock of marble and granites, cyan colour is clay moraine and brown colour is weathered and disintegrated rock.

2 INVESTIGATIONS CARRIED OUT PRIOR TO THE SOIL TUNNELLING

From mid-January to mid-February 5 core-drilling holes was drilled from the tunnel face through the soil zone. 2 of the core holes were drilled with conventional rock core drilling equipment, with low core recovery percentage. Conventional rock core drilling equipment is more easy available in Norway, and was selected to get a certain measure of the soil zone length. The remaining 3 core holes from the tunnel face was drilled with a triple tube with drilling fluids and a core-catcher setup. From the surface it was drilled 3 core holes vertically to establish knowledge of the various soil stratas above the tunnel. These holes has also been utilized for pore-pressure measurements and monitoring during the tunnelling. Data from pre-investigation drillings, as well as laboratory testing of cores resulted in the following geotechnical model of the soil zone.
The laboratory testing comprised:

- Water content
- Sieve curves
- Mineralogy
- Swelling pressure and free-swelling
- Triaxial tests for determining cohesion and friction angle

The laboratory testing indicated the following average values for the soil materials.

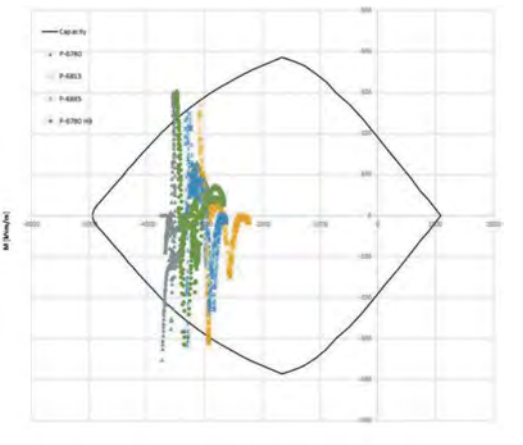

Figure 3. Moment-Axial load plot for various tunnel chanages compared to the capacity envelope of reinforced sprayed concrete ribs used for temporary support. The points outside the envelope originates from a sharp edge between the wall and semi-circular tunnel floor in the numerical model.

Table 1. Interpreted average values for clay moraine and weathered rock. The low frictional angle from weathered rock is due to challenges in obtaining reliable cores for laboratory testing.

Material	γ kN/m^3	m -	Eoed Ref MPa	c' kPa	φ' degrees	Ψ Degrees
Clay moraine	23.8	0.85	100	26	33	1.5
Weathered rock	20.8	0.77	49	42	23	0.4

From the tender stage of the tunnel, it was 7 total sounding drillings from the surface close to the soil zone. The data obtained from the total sounding drillings were interpreted as poor weathered rock mass. All the total sounding drillings ended above the

tunnel level, with the wrong conclusion of showing rock mass above the tunnel profile.

The geotechnical model and laboratory test results (Table 1) was utilized in a Plaxis numerical model for analyses of face-stability during excavation, settlements over time as well as loads on the support, for the temporary construction including support and excavation. During the excavation of the tunnel, Hoek-Brown failure criteria was used to describe the properties of the weathered rock material (Marinos and Hoek 2000), and the interpreted values in Table 1 for weathered rock was abandoned.

3 DESIGN AND EXPERIENCES FROM EXCAVATION AND TEMPORARY TUNNEL SUPPORT

3.1 *Design*

Figure 5 Shows the basic design of the tunnel with pipe umbrellas. The cross-section area at the start of each pipe bolt is 87.9 m^2 increasing to 112 m^2 at the end of one screen. The length of the heading arch is between 22.4 and 26.6 m length.

The design of temporary tunnel support and excavation of the tunnel were based on cyclic rounds comprising the

following activities:

1. Removal of sprayed concrete from the face/parts of the face
2. Excavation with a scaling hammer or rotating drum, and surveying
3. Application of 8-10 cm sprayed concrete with fibres classified as E1000 according to SVV N500 (NPRA 2022) in both face, roof, walls and surveying
4. Installation of grouted radial bolts for support and construction of the reinforced sprayed concrete ribs
5. Construction of reinforcement in the sprayed concrete ribs and surveying
6. Spraying of RRS2 and surveying
7. New excavation round.

3.2 *Observations and risk mitigation during excavation*

A daily meeting was arranged by the designer NGI with representatives from the contractor and the tunnel owner. The daily meeting assessed the following aspects:

- Water leakages and potential erosion of the tunnel face
- Instabilities at the face during excavation
- Instabilities between the spiling bolts/pipe-umbrella bolts
- Instabilities under the spiling bolts/pipe
- Deformation/displacements in the RRS2
- Visual observation of cracks in the sprayed concrete
- Visual observations of the tunnel floor with special focus on transition from wall to floor
- Instabilities behind the tunnel face.

Based on these aspects together with pore pressure measurements, displacements in the soil every day was graded with "caution level" 0, 1 or 2. Based on these assessment a total of 13 defined counter measures were available at site, where red coloured bullet points was not utilized during construction:

1. Reduce the excavation area
2. Reduce the excavation length
3. Grout leakage in/ahead of the tunnel face

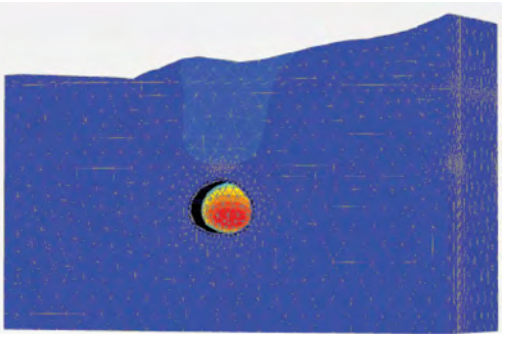

Figure 4. Example of Plaxis 3d interpretation of face stability of fullface excavation.

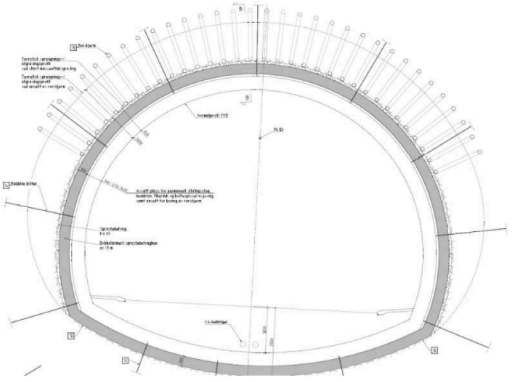

Figure 5. Basic design of tunnel cross-section with pipe umbrellas.The sprayed concrete ribs are around the tunnel cross-sectionincluding the floor.

4. Drill drainage holes in the tunnel face and around the tunnel face
5. Inrease bolt lengths
6. Change bolt spacing
7. Apply spiling bolts in lower parts of the tunnel walls
8. Utilize bolts between the reinforced sprayed concrete ribs
9. Drain water away from the tunnel face floor
10. Utilize sprayed concrete in the tunnel floor

11. Utilize coarse rock material to keep the tunnel floor
12. Pre-investigations (probe drilling with measurement while drilling (MWD) or core drilling
13. Install RRS2 between the already installed RRS2.

For point 1 and 2 the tencency during construction was to increase the excavation length from 1.5 to 2.0 m, and in some cases even up to 2.5 m. For the total of 45 rounds of excavations only 4 rounds utilized divided cross-section. The first round utilized 4 divisions, the second and third round 2 divisions and the 22nd round was divided due to instabilities at the tunnel face.

3.3 *Spiling bolts and pipe umbrella*

For the initial 12 m of the soil zone spiling bolts with 32 mm diameter was utilized ahead of the tunnel face. The reasons for utilizing these spiling bolts are that delivery time of the more rugged pipe umbrella bolts are long, as well as the tunnel cross-section was to small to install the pipe umbrella bolts from the start of the unforeseen soil zone. After the excavation of the initial zone with spiling bolts, Ø114 mm top hammer pipe umbrella bolts with thickness 8 mm was utilized as shown in Figure 4. A total of 5 pipe umbrella screens of 15 m was used, each containing 34 pipe bolts. Each screen had a 3-4 m overlap. The precision of screen 2 to 5 was very good, and within cm deviation for the whole 12 m screen, while the first screen had deviations in the dm scale. The initial pipe umbrella screen's deviation demanded cutting and removal of 5 of the 34 pipe bolts during excavation. Pipe umbrella #1 was carried out in 115 hours, while pipe umbrella #2 to #5 had an average time consumption of 60 hours, which shows the conctractor improvement on capacity and learning.

3.4 *Excavation*

The excavation was carried out with a scaling hammer mounted on excavator. Some of the rounds were excavated by a rotating drum head. In the softest material the drum head was efficient and secured an even excavation, while in parts containing lower degree of weathering and blocks the drum head was to weak.

The first 10 rounds was based on the excavator operator's skill and pure observations during the excavation. In some cases, this approach exceeded the planned excavation length of 1.5 m, and also caused some minor overbreak and underbreak in areas without spiling bolts. In order to comply with this deviation, a scanner was mounted on a pick up continuously scanning and showing real-time estimations to the excavator operator where to excavate. Experiences with the scaling hammer are:

- Efficient (4-6 hours of scaling for one full face of 1.5 m which is equal to 150-180 solid m^3
- Sufficient power to remove the sprayed concrete on the tunnel face prior to the excavation, as well as blocks and rock with less degree of weathering
- Quality of contour and the face was poorer compared to the drum head.

Experiences with the drum head are:

- Smooth contour in the tunnel walls and roof towards the pipe umbrella system
- Less efficient than the scaling hammer, and in some cases up to 10 hours excavation in cases with blocks and less degree of weathering in the tunnel face.

Figure 6. Excavation with drum head. The left part of the tunnel face is supported by sprayed concrete, and the right part shows theweathered rock (brown material) and clay moraine (grey materialon top).

3.5 *Sprayed concrete*

Immediate after each excavation round, sprayed concrete has been applied to the exposed geo surfaces. The base-case thickness of sprayed concrete has been 8 cm. The concrete fulfilled the Norwegian public road administration R761 criteria for "E1000 sprayed concrete" with fibre. (NPRA 2018). The strength development of the sprayed concrete has been in accordance with (Norsk Betongforening, 2021), for a sprayed concrete "J2+", meaning that 0.6 MPa strength should be fulfilled after 60 minutes after spraying. In order to achieve this development of strength the concrete was heatet from the concrete fabric (approximately 60 minutes drive from the construction site).

For the spraying of RRS2 there has not been set any regulations on strength development for the concrete, but site-tests to achieve a good sprayability was carried out.

3.6 *Reinforced sprayed concrete Ribs (RRS2)*

To support the pipe umbrella and to enable a load bearing element around the tunnel profile, double reinforced sprayed concrete arches (RRSII) was constructed during tunnelling. The c/c distance between each RRSII was 1.5 m for the first 50 m of the soil zone. For the last 25 m the c/c distance was increased to 2.0 m due to knowledge about displacement, experience on excavation and confidence in the design and contractor quality performance.

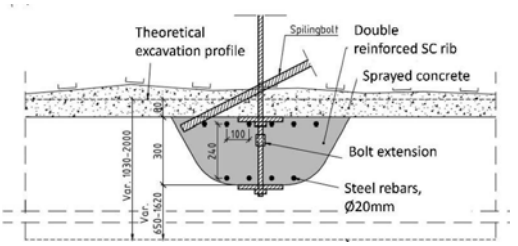

Figure 7. Design of RRS2 for temporary rock support The ribs are constructed around the whole tunnel cross-section including the floor.

Figure 8. Rebars of RRSII prior to application of sprayed concrete.

For the long term monitoring of loads and displacement in RRS2 it has been installed fibre optic cables in 3 ribs. The fibre optics follows the circumference is attached to the reinforcement bars inside the sprayed concrete rib, enabling micro-strain measurements along the the tunnel walls, roof and floor. The monitoring will be a part of the complete tunnel's ITS system, and can be used for future measurements of possible deformations.

3.6 *Displacements during and after excavation*

Prior to the excavation, a sub-horizontal extensometer was installed over tunnel roof. Continuous measurements on displacement were recorded and used as a verification of the tunnel stability, with special attention to the unsupported area from the last RRSII and the tunnel face. The inclinometer measurements show that displacement starts approx. 10 m (one tunnel diameter), similar to experiences in deep hard rock tunnels (Vlachopolus 2009), in front of the tunnel face, with approximately 5-6 mm vertical displacement in the tunnel roof prior to excavation. Additional 10-15 mm displacement occurs during the excavation of the face prior to the construction and hardening of the intital layer of sprayed concrete and RRSII.

Installation of prisms for measuring displacement and convergence on every 2nd RRSII were installed during the excavation. The maximum displacement on RRSII are 14 mm in one single point. The average displacement measured on RRSII are in the range of 5-7 mm. The total vertical deformation is 25-30 mm.

In order to measure potential long term displacement due to soil consolidation over time, it has been installed fibre optic cables in 3 of the RRSII. This enable to measure micro-strains over time, in order to detect potential deformations in the temporary support.

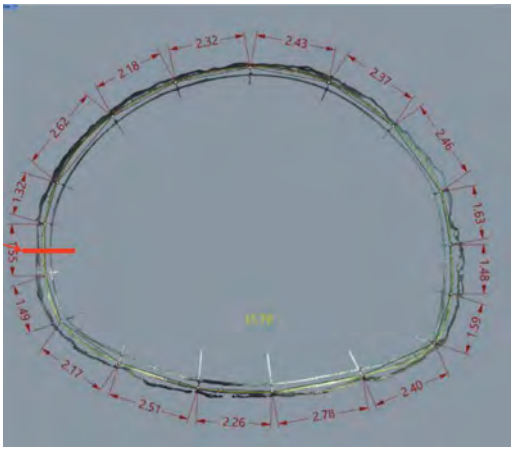

Figure 9. Scan of excavation profile reinforcment prior to sprayed concrete and fibre optic cable entrance (red line).

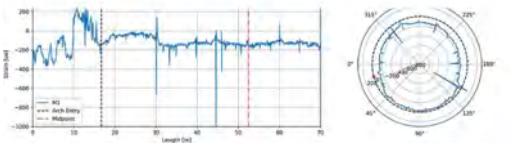

Figure 10. Example plot of measured micro-strain in one RRSII.

4 COST AND TIME CONSUMPTION

A rough distribution of the additional cost for tunnelling through the soil zone is presented in Figure 11. The additional cost includes chronologically redesign work, pre-investigations, additional temporary support (e.g. concrete, reinforcement for RRS2, pipe umbrella bolts, grout material), waiting time (the contractor production was halted by 3-4 months), cost affiliated with reduced tunnelling capacity, the normal production rate in hard rock of Bergåsen tunnel is 70-80 m/week, while the performance in the soil zone was approximately 1 m per day as an gross average for the 75 m long zone. The total additional cost for the soil zone is in the range of 150 to 200 MNOK.

Table 2 shows the average tunnelling performance between the pipe umbrella installation, and that the average tunnelling performance had a capacity of 16.5 hours per meter.

Figure 11. Rough distribution of cost for various activities related to excavation of the unforeseen soil zone.

Table 2. Average production time between pipe umbrella installations.

Chainage from	Chainage to	Hours/m
6773	6784.5	21
6784.5	6796	26.7
6796	6808	15
6808	6820	13.4
6820	6832	14.8
6832	6846	10.4

The net time consumption per excavation round is presented in Table 3. One excavation round, of 1.5 to 2.0 m, was typically carried out in 20-30 hours including the installation time of pipe umbrellas.

Table 3. Activities and corresponding net average usage of time per excavation round.

Activity	Time (hours)	Remarks
Excavation	7	Varied from 3 – 15 hours dependent on excavability.
Initial spraying of concrete	3	Varied from 2-4 hours
Bolting	5	Varied from 2 – 10 hours dependent on bolt-hole stability
Installation of rebars in RRS2	3	Varied from 2.5 – 10 hours
Spraying of RRS2	3	Varied from 2-4 hours
Installation of face bolts	5	Only installed every 8 to 12 m of the tunnel. Approximately 0.5-1.0 hours per round
Adjustment of face bolts	0.5	Cutting and installation of new bolt plate after each exc. round
Drilling of drainage holes	0.5	
Unforeseen issues		Cutting of pipe bolts,

5 CONCLUSIVE REMARKS

The unforeseen soil zone at Bergåsen tunnel was successfully excavated by July 2023. The pre-investigations at the tunnel face halted the tunnelling for approximately one month, while the design and approval from the client and third party control took nearly three months. The actual excavation and temporary support of the zone was carried out in 100 days without any major incidents. Two tunnel workers was reported with minor injuries not causing long absence injuries. The quality of e.g. pipe umbrella and sprayed concrete application improved day by day improving both the quality and capacity of the tunnelling method throughout the work.

ACKNOWLEDGMENTS

The Authors would like to show their gratitude to the tunnel owner, Statens vegvesen for the cooperation during the excavation and allowing to publish the experiences in this paper, as well as Bent Aaagaard for sharing insights from the Joberget tunnel in quite similar ground conditions.

REFERENCES

Aagaard, B., Gylland, A.S., Schubert, P., Løne, B., 2017. The Joberg tunnel. Successful tunnelling in moraine. Proceedings of theWorld Tunnel Congress 2017.

Maidl, U., Handbook of Tunnel Engineering II. Basics and Additional Services and Constuctrion. Bochum, Ernst&-Sohn 2013.

Marinos, P., Hoek, E., 2000. GSI: A geologically friendly tool for rock mass strength estimation. Melbourne, GeoENG 2000.

N500, Vegtunneler 2022. Norwegian regulations for road tunnels, published the Norwegian Roads Administration. In Norwegian only.

Norsk Betongforening, Publication 7. Sprayed concrete for rock support. 2022. In Norwegian only.

Norsk forening for fjellsprengningsteknikk (NFF). Tunnel production statistics, available on https://nff.no/publikasjoner/tall-og-statistikk/. 2022.

R761: 2018. Prosesskode 1 Standard beskrivelse for vegkontrakter. Norwegian Public Roads Administation. In Norwegian only.

Vlachopoulos, M.D.N., 2009. Improved Longitudinal Displacement Profiles for Convergence Confinement Analyses of Deep Tunnels. Rock Mechanics and Rock Engineering, 2009.

Tunnelling for a Better Life – Yan, Celestino, Thewes & Eberhardt (Eds)
© 2024 The Author(s), ISBN 978-1-032-80042-4
Open Access: www.taylorfrancis.com, CC BY-NC-ND 4.0 license

Evaluation of removable time of tunnel lining formworks using surface wave techniques

Kengo Kato*, Chitose Kuroda & Noriyuki Utagawa
SATO KOGYO CO., LTD., Tsukuba, Japan

Kentaro Ohno
Tokyo Metropolitan University, Hachioji, Japan

ABSTRACT: The removable time of tunnel lining formworks was evaluated using surface wave techniques. Our findings are as follows: (1) *Stiffness evaluation*: The change in the stiffness of early-age lining concrete can be assessed by measuring the propagation of surface wave, and the Rayleigh wave (R-wave) velocity is estimated using the Spectral Analysis of Surface Waves method. (2) *Unconfined Compressive Strength (UCS) Evaluation*: UCS can be determined based on the R-wave velocity. To achieve this, the R-wave velocity is converted to the primary wave (P-wave) velocity using a dynamic Poisson's ratio, and the results from test specimen result (i.e., the relationship between P-wave velocity and UCS) are utilized. It is crucial to measure a time-dependent dynamic Poisson's ratio to ensure accuracy. (3) *Measurement system requirements*: We have provided the necessary requirements for the measurement system based on the test results.

Keywords: Removable time, lining formworks, Surface waves, Concrete Surface wave techniques

1 INTRODUCTION

Assessing the removable time of tunnel lining formworks holds significant importance in the management of concrete quality during tunnel construction. Removable time primarily hinges on the unconfined compressive strength (UCS) of the lining concrete, as specified in JSCE 2016 guidelines (JSCE 2016). It is crucial to directly measure the properties of the lining concrete because the strength development of early-age concrete is influenced by the curing environment.

The main objective of this study is to determine the removable time of tunnel lining formworks through the application of surface wave techniques. Initially, an overview of the Spectral Analysis of Surface Waves (SASW) method and the conversion process from Rayleigh wave (R-wave) velocity to primary wave (P-wave) velocity is provided. Subsequently, the proposed evaluation procedure is outlined. The experimental techniques and findings from the full-scale experiment are elaborated upon and discussed in detail. Finally, we furnish the necessary system requirements to ensure the accurate implementation of these measurements.

2 BACKGROUNDS

It is assumed that stresses exerted on the lining concrete by surrounding rocks and mountains are adequately relieved during the concrete casting process, following method like NATM (New Austrian Tunnelling Method). In this context, the self-weight of a lining is the primary factor considered when determining the removable time of the lining formworks. Under these conditions, the typically required UCS falls within the range of 2 to 4 MPa, and this strength is typically achieved within approximately 24 hours of concrete placement, as specified in JSCE 2016 guidelines (JSCE 2016).

The commonly employed method for assessing the UCS of lining concrete is to use test specimen data prepared with the same concrete material and mix as the lining concrete. This approach is favored because it allows for easy UCS determination, although there is no guarantee that the UCS of the lining concrete is identical to that of the test specimens. To address this limitation, several methods have been proposed, including the concrete thermal behavior-based method (e.g., Harrison 1995) and the ultrasonic wave amplitude-based method (*Tobichima Corp*). These

*Corresponding author: kengo.kato@satokogyo.co.jp

DOI: 10.1201/9781003495505-201

methods predict the UCS based on material-specific relationships established through test specimens and lining concrete but may require additional equipment.

The utilization of elastic waves represents a widely accepted method for monitoring the evolution of concrete specimen properties. Numerous studies have demonstrated that dynamic Poisson's ratio and dynamic Young's modulus are sensitive to concrete age and generally register higher values compared to static ratios (e.g., FHWA 2006). Although a few studies have proposed prediction models for time-dependent Poisson's ratio (e.g., FHWA HIPERPAV software), the practical application of such models requires validation through in situ measurements.

In the late 1950s and early 1960s, Jones (1958) pioneered the use of surface waves to determine the thickness and elastic stiffness of pavement slabs and the underlying layers. In the early 1980s, researchers developed a surface wave technique involving an impactor and established a relationship between wavelength and velocity, giving birth to the "Spectral Analysis of Surface Waves" (SASW) method. Given the wide recognition and acceptance of the SASW method, it has been adopted in concrete engineering applications. For instance, Cho (2006) employed the SASW method to assess the compressive strength of single-layer high-strength concrete slabs. Kim et al. (2014) used the SASW method to evaluate primary wave velocities (P-wave) and found the impact echo method effective in determining concrete thickness and defect locations.

To the best of our knowledge, the SASW method has primarily been employed for measuring the properties of hardened concrete in concrete engineering fields. Its application to early-age concrete is currently limited, possibly due to challenges such as (1) difficulty in measuring surface wave propagation through formworks and (2) considerations of heat of hydration, thermal behavior, and drying shrinkage during the hardening process, which are critical for long-term durability.

Our research endeavors revolve around two key objectives: (1) assessing the stiffness evolution of early-age lining concrete beneath the lining formworks by employing impact techniques and (2) evaluating the unconfined compressive strength (UCS), a critical parameter for the removal of tunnel lining formworks, based on R-wave velocities. To accomplish this, we utilize data from test specimens to establish the relationship between P-wave velocity and UCS. Additionally, we employ wave propagation theory to convert R-wave velocity into P-wave velocity.

3 THEORETICAL BASIS

3.1 *Spectral Analysis of Surface Waves (SASW)*

Nazarian and Stokoe (1985) and Nazarian and Stokoe (1986) provide the practical and theoretical basis for the SASW (Spectral Analysis of Surface Waves) method. In the SASW method, a transient stress pulse is generated through impact, and the resulting R-wave propagates exclusively within the top layer of the layered system. Richart et al. (1970) established the theory of surface wave propagation, demonstrating that the depth to which the wave travels depend on the depth-to-wavelength ratio. Wavelength is governed by the ratio of phase velocity to frequency, which means that the investigation depth can be controlled by selecting frequency ranges induced by impact.

Phase velocities are computed by measuring the time it takes for a component frequency to travel between two accelerometers. The speed of a component frequency, $V_{R(f)}$, can be determined given that the distance, L, between the two accelerometers is known: The relationship can be expressed as:

$$V_{R(f)} = \frac{L}{\Delta t_f} \tag{1}$$

where $V_{R(f)}$ is the R-wave velocity for a given frequency, L is the distance between two accelerometers, and f is the frequency. The travel time between accelerometers for each frequency can be calculated using the following equation:

$$\Delta t_{(f)} = \frac{\phi_{(f)}}{360 \cdot f} \tag{2}$$

where $\varphi_{(f)}$ is the phase difference in degrees for a given frequency. The wavelength, λ_f, corresponding to a component frequency can be determined using the following equation.

$$\lambda_{(f)} = \frac{V_{R(f)}}{f} \tag{3}$$

The cross-power spectrum is a complex function that can be represented with real and imaginary components. In practice, the phase of the cross-power spectrum is used to determine the travel time (Nazarian and Stokoe 1986). The cross-power spectrum is calculated using the following equation.

$$G_{xy} = S_y(f) \cdot S_x^*(f) \tag{4}$$

Where G_{xy} is the cross-power spectrum, S_y is the linear spectrum of the output, and S^*_x is the complex conjugate of the linear spectrum of input motion. These equations describe the fundamental principles and calculations involved in determining phase velocities and other parameters using the SASW method.

3.2 *Conversion of R-wave velocities to P-wave velocities*

Richart et al. (1970) established the relationship between the P-wave velocity and R-wave velocity and introduced a conversion equation that connects to the R-wave velocity to the P-wave velocity, incorporating the dynamic Poisson's ratio. The conversion equation is detailed as follows:

$$\frac{V_R}{V_P} = \alpha \cdot K_R \tag{5}$$

where V_p is the P-wave velocity and α and K_R are functions of the dynamic Poisson's ratio, can be calculated using the following equations:

$$\alpha = \sqrt{\frac{1-2\nu}{2-2\nu}} \tag{6}$$

$$K_{R_s}^6 - 8K_{R_s}^4 + \left(24 - 16\alpha^2\right)K_{R_s}^2 + 16\left(\alpha^2 - 1\right) = 0 \tag{7}$$

Furthermore, *HIPERPAV* offers a time-dependent dynamic Poisson's ratio curve as expressed below.

$$\nu_{dynamic} = -a \cdot \ln(t + 1.1) + 0.425 \tag{8}$$

where t is the concrete age in hours and a is a fitting parameter with *HIPERPAV* using $a = 0.05$. It's essential to note that Eq. 7 is empirical and developed based on a specific concrete type and curing environment. Consequently, its application to all concrete types is open to discussion, a point that will be addressed later in the discussion. These equations collectively describe the relationship between P-wave and R-wave velocities, considering the dynamic Poisson's ratio, and the time-dependent behavior of the dynamic Poisson's ratio as provided by *HIPERPAV.*

4 EVALUATION FLOW

Figure 1 outlines the proposed evaluation process for determining the removable time of tunnel lining formworks.

1. *Test Specimen Preparation*: Test specimens made from the same material and concrete mix as the lining concrete are prepared. Measurements are taken for the Unconfined Compressive Strength (UCS), P-wave velocity, and S-wave velocity of test specimens.
2. *UCS-P-Wave Velocity Relationship*: A relationship between UCS and P-wave velocity is developed based on the data obtained from the test specimens.

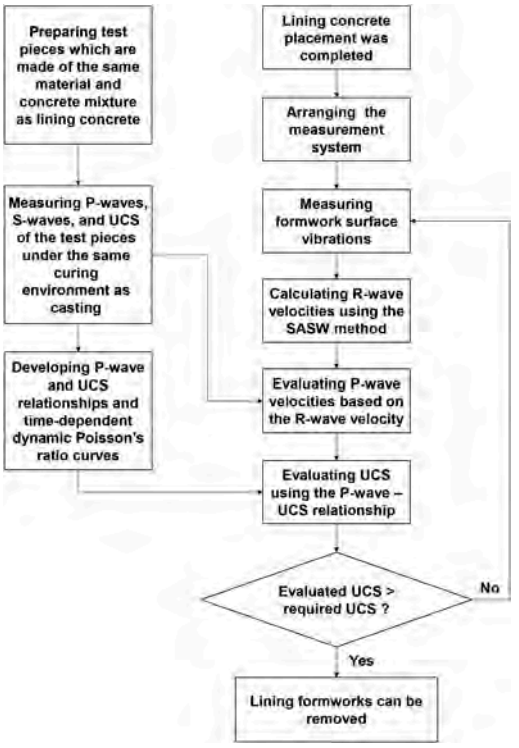

Figure 1. The proposed evaluation process for determining the removable time of tunnel lining formworks.

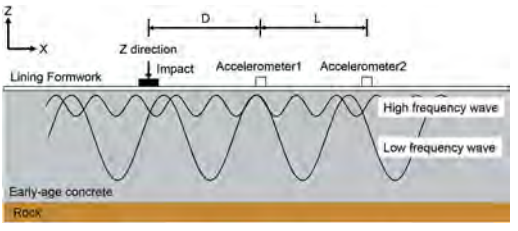

Figure 2. The measurement system configuration.

3. *Dynamic Poisson's Ratio Calculation*: Using the P-wave and S-wave velocities, a dynamic Poisson's ratio is calculated, and a time-dependent dynamic Poisson's ratio curve is established. These relationships are essential for the evaluation of UCS and P-wave velocity of the lining concrete.
4. *Impact on Lining Formwork*: The surface of the lining formwork is impacted using an impulse hammer, either during or after the concrete placement process. Vibrations resulting from this impact are recorded using two accelerometers mounted on the formwork surface.
5. *R-Wave Velocity Calculation*: Early-age lining concrete's R-wave velocities are calculated using the SASW (Spectral Analysis of Surface Waves) method.

6. *Conversion to P-Wave Velocities*: The R-wave velocities are then converted to P-wave velocities using the equation described in Eq. 7.
7. *UCS Evaluation*: Finally, the UCS of the early-age lining concrete is evaluated based on the data collected from the test specimens.

To implement this evaluation methodology, several assumptions are made:

1. *Homogeneous Properties*: It is assumed that the properties of early-age lining concrete are homogeneous, meaning they are consistent throughout the material.
2. *Equivalence to Test Specimens*: The physical properties of early-age concrete, including strength and stiffness, are assumed to be equivalent to those of the test specimens.
3. *Stability of Lining Formwork*: The lining formwork is assumed to remain stable and stationary during and after the impact, implying that it is sufficiently heavy and won't shift due to the impact.

These assumptions provide the basis for the proposed methodology, and the accuracy of the results will depend on how well these assumptions hold in practice.

5 TEST METHODS

Figure 2 illustrates the configuration of the measurement system used in this study, providing an overview of the equipment.

- Accelerometers: Two triaxial accelerometers (Model: 356B21, *PCB Piezotronics, Inc*) were employed. These accelerometers had a measurement range of 4.9 g and different frequency ranges depending on the direction: 10,000 Hz in the y and z directions and 7,000 Hz in the x direction. They were mounted on the formwork surface to monitor vibrations.
- Data Logger: The NI-9234 data logger from National Instruments Corp was used for data recording. It featured a sampling rate of 50 kHz/s/ch (50,000 samples per second per channel) and a measurement range of -5 V to +5 V.
- Impulse Hammer: An impulse hammer with a hammer mass of 0.16 kg (Model 086C04, *PCB Piezotronics, Inc*.) was utilized to generate elastic waves. These waves propagated through the formwork and the placed concrete to be measured by the accelerometers.
- Distances and Thicknesses: The setup included specific distances: the distance (L) between the accelerometers was set to 500 mm, and the distance (D) between the impact location and the accelerometer was set to 500, 1,000, and 1,500 mm.

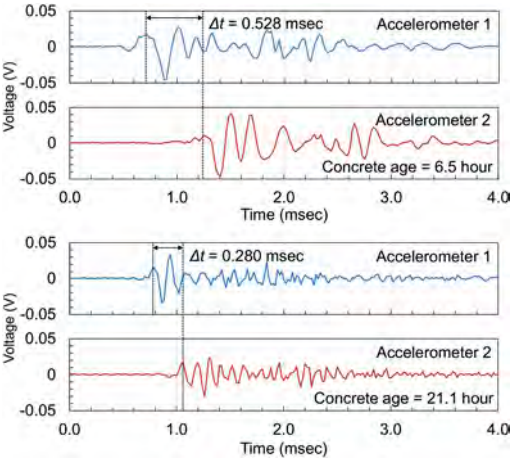

Figure 3. The acceleration responses recorded at the concrete age of 6.5 and 21.1 hours.

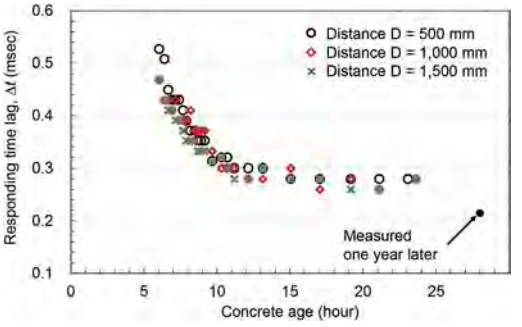

Figure 4. The responding time lag,Δt.

The accelerometers were mounted in proximity to the injection hole, and the impact commenced 6.5 hours after the initiation of concrete casting. During the initial 3.0 hours, impacts occurred every 15 minutes. Subsequently, the frequency of impacts was adjusted to every 30 minutes for the 3.0 to 6.0-hour period, every 1 hour for the 6.0 to 15.0-hour period, and every 2 hours for the 15.0 to 21.0-hour period. For each measurement, the formwork surface was impacted five times, and the results were averaged.

6 RESULTS

The methodology was applied during a full-scale tunnel lining experiment conducted in July 2022, involving the use of self-compacting concrete (SCC) cast through an injection hole. The concrete placement took approximately 3 hours. The thickness of the lining concrete was 400 mm, while the thickness of the formwork plate was 6.0 mm.

Figure 3 shows the examples of acceleration responses in the z-direction (i.e., perpendicular to

formwork surface) shown in Figure 2 recorded at 6.5 hours and 21.1 hours from the beginning of casting. The response time lag, Δt, was observed to decrease as time progressed, with a value of 0.528 msec at 6.5 hours and 0.280 msec at 21.1 hours. Figure 4 shows the response time lag, Δt, over the concrete age. The data indicated a consistent reduction in response time lag with increasing concrete age, regardless of the distance between accelerometers. It suggests that the wave propagation speed increased as the concrete aged. The lining concrete surface was directly impacted one year later, and surface vibrations were recorded. The response time lag, Δt, at this point was 0.215 msec, indicating that the wave propagation was faster than those recorded within 24 hours after placement.

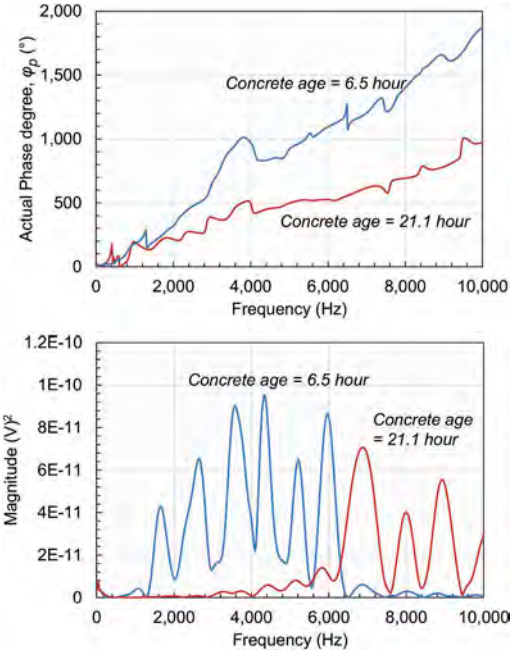

Figure 5. The actual phase angle and magnitude of cross power spectrum.

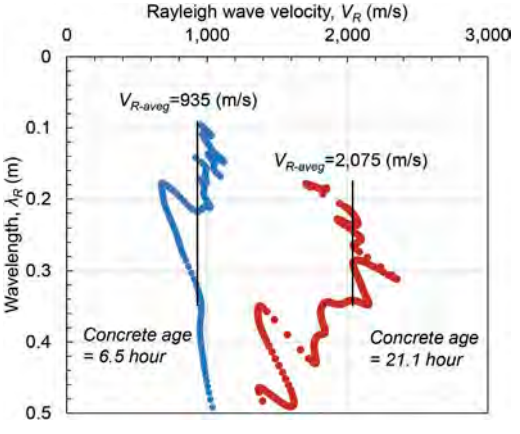

Figure 6. $\lambda_{(f)} - V_{R(f)}$ relationship at the concrete age of 6.5 and 21.1 hours.

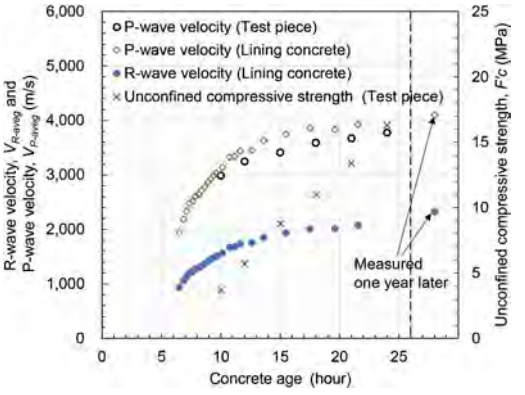

Figure 7. The comparisons of the V_R, V_P , and $F'c$.

The R-wave velocity was calculated using the SASW method. Figure 5 shows the examples of the magnitude and actual phase angle, φ_p, of the cross-power spectrum at concrete ages of 6.5 and 21.1 hours. The dominant frequency was 3,670 to 5,950 Hz at the concrete age of 6.5 hours and 6,970 to 9,010 Hz at the concrete age of 21.1 hours, showing that the dominant frequency shift ed from low to high frequency ranges as concrete aged. Below approximately 1,800 Hz, the actual phase angle, φ_p remained relatively consistent with frequency. However, at a concrete age of 6.5 hours, its value was observed to be larger than that at 21.1 hours, highlighting distinctions related to concrete age. Figure 6 shows the relationship between $\lambda_{(f)}$ and $V_{R(f)}$. The averaged $V_{R\text{-}aveg}$ for $\lambda_{(f)}$ was less than 0.35 m was 935 m/s at 6.5 hours and 2,075 m/s at 21.1 hours, highlighting a significant increase in $V_{R\text{-}aveg}$ with concrete age. Notably, pronounced differences in $V_{R(f)}$ were observed when $\lambda_{(f)}$ was less than the lining concrete thickness (0.4 m).

Figure 7 shows the R-wave and P-wave velocities of the early-age lining concrete. To mitigate scattering in cases where $\lambda_{(f)}$ exceeded 0.40 m (equivalent to the lining concrete thickness), we calculated the $V_{R\text{-}aveg}$ for cases where $\lambda_{(f)}$ was less than 0.35 m (approximately 0.85 × lining concrete thickness). The average $V_{R\text{-}aveg}$ was 935 m/s at 6.5 hours, 1,482 m/s at 9.4 hours, and 2,075 m/s at 21.1 hours, indicating a consistent increase in $V_{R\text{-}aveg}$ with the age of the concrete. Furthermore, the $V_{P\text{-}aveg}$ was 1,947 m/s at 6.5 hours, 2,988 m/s at 9.4 hours and 3,922 m/s at 21.1 hours, indicating an increasing trend in $V_{P\text{-}aveg}$ as the concrete aged. The data revealed that the $V_{P\text{-}aveg}$ of the early-age lining concrete was overestimated by 5 - 10 % compared to that of the test specimens.

The V_P of the test specimen was measured using the A1410 Pulsar (*ACS, Acoustic control systems*),

a device that records the velocity of ultrasonic waves traveling on the material's surface. The V_P was 2,987 m/s at 10 hours and 3,776 m/s at 24 hours. These results indicate a consistent increase in V_P with the concrete age. Furthermore, the V_P of the lining concrete was also measured one year later, registering at 4,150 m/s. This suggests that the V_P reached 91 % of its maximum value within the initial 24 hours. Additionally, The UCS was determined in accordance with JIS A 1108. The USC measured 3.69 MPa at 10.0 hours and increased to 16.3 MPa at 24 hours. This demonstrates a progressive increase in USC with concrete age. In addition, we also conducted measurements of the 28-day UCS for cored samples, which yielded an average value of approximately 60 MPa (Kato et al. 2022). Consequently, the UCS reached around 27 % of the maximum within the initial 24 hours.

Figure 8 illustrates the relationship between the V_P and USC for the test specimen. Assuming a required UCS is 4.0 MPa, the removal of the lining formwork can be considered when the $V_{P\text{-}aveg}$ of the lining early-age concrete surpasses approximately 3,000 m/s.

7 DISCUSSIONS

The dynamic Poisson's ratio of the lining concrete was back-calculated based on the P-wave velocity of the test specimens. Figure 9 compares these values with those from Eq. 7. The back-calculated dynamic Poisson's ratio ranged 0.287 to 0.214 and exhibited a decreasing trend with the concrete age, with values smaller than those in Eq. 7. These discrepancies resulted in an overestimation of the $V_{P\text{-}aveg}$ for early-age lining concrete, as depicted in Figure 7. Regressive analysis indicates that a fitting parameter of a = 0.066 provides the most accurate estimate in this context. The field test was conducted in the summer season, and our data indicated that the SCC began to harden rapidly. This led to the emergence of a distinct time-dependent Poisson's curve. As a result, we strongly recommend the development of a time-dependent dynamic Poisson's ratio curve under the same curing environment as the construction site.

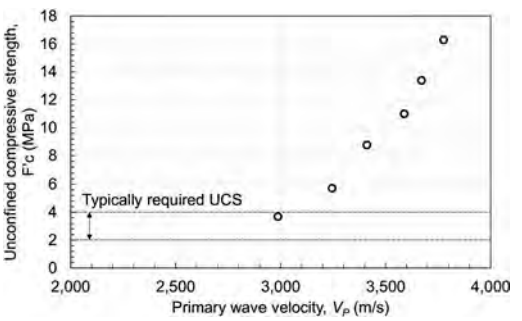

Figure 8. The relationship between V_P and $F'c$ of the test piece.

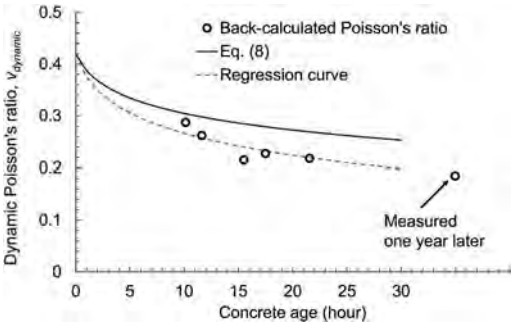

Figure 9. The back-calculated poisson's ratio.

8 MEASUREMENT SYSTEM REQUIREMENTS

1) Accelerometers

The SASW method relies on vibrations recorded in the vertical direction, making one-dimensional accelerometers suitable for measurements. Furthermore, as depicted in Figure 5, the dominant frequency of formwork surface vibrations resulting from the impact falls below 10,000 Hz. However, it's important to note that the frequency range that accelerometers can effectively measure depends on their mounting methods. When accelerometers are mounted using magnets and adhesives, their actual measurement range is reduced, typically by approximately 70% of the maximum capacity, according to information from the seller (personal communication). Consequently, to meet the required frequency range, accelerometers should be capable of measuring frequencies exceeding 15,000 Hz.

2) Data loggers

In general, to ensure measurement accuracy, sampling rates should exceed 10 times the target measurement ranges. As illustrated in Figure 7, the $V_{R\text{-aveg}}$ of the hardened concrete is approximately 2,300 m/s. With a distance of L = 500 mm, the propagation duration of R-waves is approximately 0.2 msec, resulting in a corresponding sampling frequency of 50 kHz. However, it's important to consider the space, L, when determining the sampling rate. As indicated in Eq. 9, space L is calculated as a function of wavelength. Based on the measurements, the wavelength should be smaller than 0.85 times the lining thickness. For instance, in the experimental case, the space L should exceed 100 mm, necessitating a corresponding sampling frequency of 250 kHz. Therefore, it is advisable to determine the sampling frequency of data loggers while taking space L into account.

3) Hammers

In Japan, the standard lining concrete thickness is typically 300 mm (JASCE 2022). As indicated in Figure 7, the $V_{R\text{-}aveg}$ of early-age lining concrete within 24 hours falls within the range of approximately 900 – 2,100 m/s. In line with Eq. 2, it is essential that impacts produce waves encompassing frequencies of 3,600 – 8,400 Hz to ensure accurate evaluations. As demonstrated in Figure 5, the impulse hammer utilized in this study meets this requirement.

4) Spaces between accelerometers

According to Heisey et al. (1981), for accurate measurements in geotechnical engineering fields, it is advisable to maintain a space, L, between accelerometers that is both less than two wavelengths and greater than one-third of a wavelength.

$$\frac{1}{3}\lambda_R \leq L \leq 2\lambda_R \tag{9}$$

The results indicate that the wavelength should ideally be less than 0.85 times the lining thickness. Therefore, for a lining thickness of 300 mm, the recommended range for space, L, falls between 85 - 510 mm.

5) Spaces between impacts and accelerometers

Sanchez-Salinero demonstrated that an optimal space between impacts and accelerometers can be represented as D/L = 1.0 (Sanchez-Salinero 1987). However, as depicted in Figure 4, the response time lag was not significantly affected by the D/L ratio ranging from 1.0 to 3.0. Therefore, we recommend that the space, D, should adhere to the following criterion.

$$1.0 \leq \frac{D}{L} \leq 3.0 \tag{10}$$

9 CONCLUSIONS

We have developed an impact method to determine the removable time of tunnel lining formworks. This method is straightforward and easily applicable in practice. Our key findings are summarized below:

1) The evolution of the R-wave velocity in early-age lining concrete can be assessed using the SASW method. P-wave velocities can also be determined by converting the R-wave velocity with a dynamic Poisson's ratio.
2) The Unconfined Compressive Strength (UCS) can be estimated based on R-wave velocities. To ensure precision, it is essential to measure a time-dependent dynamic Poisson's ratio.
3) Detailed measurement system requirements are provided based on our test results.

REFERENCES

Cho, Y. S. 2006. Non-destructive testing of high strength concrete using spectral analysis of surface waves. NDT & E International, Volume 36, Issue 4, June 2003, pp. 229–235.

Federal highway administration (FHWA). 2006. Integrated materials and construction practices for concrete pavement: a state-of-the-practice manual, FHWA publication No. HIF-07-004, December 2006, pp. 326.

Harrison, T. A. 1995. Formwork striking times – criteria, prediction and methods of assessment. Construction industry research and information association, CIRIA Report 136, pp 70.

Heisey, J. S., Stokoe, K. H., II, Hudson, W. R., and Meyer, A. H. 1982. Determination of in situ shear wave velocities from Spectral Analysis of Surface Waves. Research report 256-2, Center for Transportation Research, The University of Texas at Austin, 277 pp.

Japanese Association of Civil Engineering (JSCE). 2016. Standard Specification for Tunneling-2016.

Jones, R. 1958. In situ measurement of the dynamic properties of soil by vibration methods. Geotechnique, Vol. III, No. 1.

Kato, K., Koyama, H., Hiromitsu, T., Fujiwara, S., Kuroda, C., Utagawa, N., Ono, T., Uno, Y. 2022. Automation of tunnel lining construction with Self-Compacting Concrete: full-scale experiment and numerical simulation. World Tunnel Congress 2022, DOI: 10.1201/9781003348030-293.

Kim, G., In, CW., Kim, J. Y., Kurtis, K. E., and Jacobs, L. 2014. Air-coupled detection of nonlinear Rayleigh surface waves in concrete—Application to microcracking detection. NDT & E International, Volume 67, October 2014, pp. 64–70.

Nazarian, S., and Stokoe, K. H., II. 1985. In situ determination of elastic moduli of pavement systems by Spectral-Analysis-of-Surface-Waves method (Practical Aspects). Research report 3681-IF. Center for Transportation Research, The University of Texas at Austin, 1985.

Nazarian, S., and Stokoe, K. H., II. 1986. In situ determination of elastic moduli of pavement systems by Spectral-Analysis-of-Surface-Waves method (Theoretical Aspects). Research report 3681-IF. Center for Transportation Research, The University of Texas at Austin, 1986.

Sanchez-Salinero, I. 1987. Analytical investigation of seismic methods used for engineering applications. Ph.-D. dissertation. University of Texas at Austin.

Sue, J. C., Sanchez-Salinero, I, Roesset, J. M., and Hudson, W. R. 1986. Investigation of variables affecting in situ determination of elastic moduli of pavement systems by surface wave method. Report 437-3F. Center for Transportation Research, The University of Texas at Austin, November 1986.

Tunnelling for a Better Life – Yan, Celestino, Thewes & Eberhardt (Eds)
© 2024 The Author(s), ISBN 978-1-032-80042-4
Open Access: www.taylorfrancis.com, CC BY-NC-ND 4.0 license

Construction of desilting chambers and connecting tunnels for Vishnugad Pipalkoti He Project (444MW) in adverse geological conditions and very remote location - A case study

Rakesh Kumar Khali*
Vice President Operations-Tunnel & UG Works, G R Infraprojects Limited, Delhi, India

ABSTRACT: Vishnugad Pipalkoti HE Project is one of the major ongoing Project in the state of Uttarakhand, Chamoli District. This has been designed to generate 444MW by harnessing hydro power potential of mighty Alaknanda River. Three Desilting Chambers each with a size of 390 m (L) x 16 m (W) x 21.5m (H) designed to eliminate suspended sediments from the water conductor- system and minimize the entry of sediments to power-house and to ensure the safety and longevity of the turbines and other under- water parts. Construction of these closely spaced chambers and connecting tunnels posed numerous challenges due to Difficult rock condition, difficult terrain, and complex layout arrangements.

Author wants to highlight the planning process, construction methodology, innovations adopted, construction of access roads and connecting tunnels, non-availability of space for infrastructure, mitigation measures, execution challenges faced, and on the spot, solution adopted at this remote site. Also wants to share the successful experience of construction of this prestigious project with the field engineers.

Keywords: Conventional Tunnelling

1 INTRODUCTION

Vishnugad Pipalkoti HEP with the installed capacity of 444 MW is one of the major ongoing Hydro Electric Projects envisaged to harness the huge potentials of river Alaknanda. The Project shall utilize about 240 m of water head of the Alaknanda River, available in a stretch from Helong in Upstream to Birahi in Downstream. It is a Run- of- the River (ROR) scheme using a diurnal storage. The annual energy generation from the project is estimated to be about 1813 MU.

The Main components of the project are as below:

- Concrete Gravity Dam of 65 m heigh with four under- sluices for passing 8004 cumecs of flood discharge.
- Three Power Intakes followed by 03 Desilting chambers each with a size of 390 m (L) x 16 m (W) x 21.5 m (H).
- One Head- Race- Tunnel of 8.8 m finished dia and
- 13.5 Km length, to be bored with the TBM and DBM methods.
- An underground Machine Hall sizing 146 m (L) x
- 20.3 m (W) x 50 m (H).
- An underground Transformer Hall measuring 142 m (L) x 16 m (W) x 24.5 m (H).
- An underground Surge tank measuring 120 m (L) x 16 m (W) x 35 m (H)
- One Tail Race Tunnel of 8.8 m finished dia and
- 3.07 Km length.

3D view of the Desilting chambers of the Project is shown below and its location is shown as Figure 1:

2 DESILTING CHAMBERS

Main feature of Vishnugad Pipalkoti Project are its Desilting Chambers and associated tunnels. Construction of the Desilting Chamber Complex and its associated tunnels for the Vishnugad Pipalkoti HE Project, was carried out from 2014 to 2023, involved excavation of three major Chambers, each of a size like that of a typical cavern of an underground power station, (Figure 1). The Chamber layouts and associated tunnel works, which were principally sized and dimensioned for silt control purposes, were designed by the approved designer for Tehri Hydro Development Corporation Limited (THDCIL), a PSU of the Government of India. As such the layouts of the tunnels and chambers were optimized principally from a hydraulic- viewpoint, with rock- mechanics aspects, considered of

*Corresponding author: rakesh.khali@grinfra.com

DOI: 10.1201/9781003495505-202

secondary importance only. However, in the steep Himalayan topography of the site, steeply dipping geology (phyllites, gneisses and schists) dominated rock conditions, making excavating and reinforcing the Chambers and Intake structures as a challenging task. From the contractor's perspective the main Chamber constructability issues were wall and crown control, pillar reinforcement and excavation sequencing, whereas for the Chamber Intakes, rock-slide stability was of highest concern. Figure 1 shows the Desilting Scheme and location map.

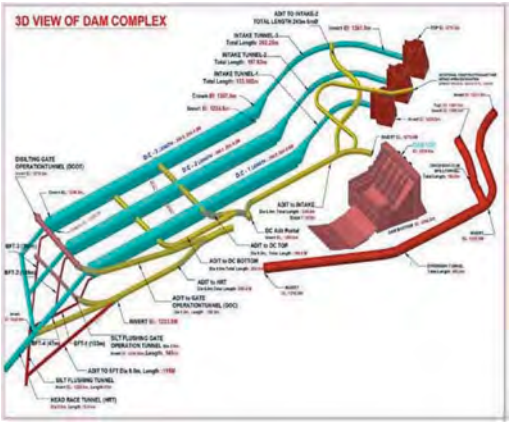

Figure 1. Project desilting scheme and location map.

2.1 *Desilting arrangements*

The desilting of water is proposed to be done in three underground desilting chambers of 390m length and 16m width x 21.5m high. The design discharge through each chamber is 76.29m3/sec + 20% for silt flushing, that is equal to total discharge of 91.53m3/sec. The velocity through the chamber has been kept about 0.35m/sec and smooth flow without turbulence is considered to obtain 90% efficiency for removal of silt particles of size 0.2mm and above.

The shape of the desilting chamber was provided in such a manner that the sediment could easily pass into the flushing ducts at the bottom by sliding over hopper bottom. Sufficient number of holes were provided in the slab at the bottom of hopper portion to pass the flushing water- deposited silt into the ducts.

For maintenance of the sediment chambers periodically, two platforms were provided on either side, just above the hopper. The platforms are of 1.5m width and duly provided with holes to pass the silt deposited on them. Access to the chamber is provided at the top of the chambers themselves on the sides through adits and shafts. From the top up to the platform ladders have been provided to descend.

Water flowing out of all the three sediment chambers is collected into one tunnel at the end, and it becomes head race tunnel to feed water into the power house. A gate is provided at the end of each sediment chamber, so that individual chambers can be emptied after closing of the gates on either side for maintenance purposes. The gates are operated from a common gate chamber tunnel provided at EL. 1270m. The flushing gates are also operated from the same gate chamber. The intake gates are capable of partial opening so that discharge into the sediment chamber can be controlled and regulated. The silt chamber gates shall remain fully opened or fully closed and used only for maintenance of silt-chambers.

The flushing ducts in each sediment chamber is provided with a gate to regulate the flushing discharge during monsoon and non-monsoon season. During monsoon season continuous discharge is allowed through flushing ducts. During non-monsoon, silt is less in water and hence intermittent flushing is done and thus maximum quantity of water available is utilized for power generation. Therefore, flushing gates shall be capable of partial opening also.

The silt laden water from each flushing duct is collected in one D shaped silt flushing tunnel of size 3.6m x 4m to flush the discharge 45.8m3/sec. The length of silt flushing tunnel is 680m. The design velocity through the silt flushing tunnel is 3.18m/sec.

3 GEOLOGY OF THE PROJECT AREA

The project area forming a part of Alaknanda valley exposes rocks belonging to Garhwal Group and Central Himalayan Crystalline and are composed mainly of calc arenaceous rocks with basic intrusive and migmatite bodies, whereas around Helong low to medium grade metamorphic rocks are exposed. The rocks of 'Carbonate Suite of Chamoli' of 'Garhwal Group' occur between Chinka and Helong and also contain the major magnesite bodies of this region. Generally, the magnesite deposits are restricted to the non- siliceous horizons of dolostones and show a distinct structural control. Pipalkoti Anticline (double plunging anticline) is a regional fold between Birahi and Helong, representing the western continuation of anticlinorium of Tejam.

All the project components are in between Birahi and Helong. The rocks occurring at the dam and Desilting Chamber site are quartzites and along most of the length of the tunnel alignment are, quartzite with biotite schist, interbedded and interbanded with grey slates and dolomites/limestone. Grey thinly bedded slates with minor interbeds of limestone, dolomitic limestone with subordinate grey slates, grey pyritous shale/slates, thinly bedded dolomitic limestones, grey slate/phyllite, white siliceous dolomite with magnesite and talc schist are a common presence. Light grey dolomite with stromatolitic structures, interbedded quartzite phyllite and dolomite, all belong to Garhwal Group. However at the powerhouse site rocks occurring are the calcareous shale and dolomitic limestone/dolomite, while along TRT dolomitic limestone, meta basics, augen

gneisses and schist. The rocks overall are very complexly folded and faulted. The rocks of the area can be categorized into four formations viz. Pipalkoti Formation, Chinka Formation, Gulabkoti Formation and Helong Formation.

3.1 *Intakes and desilting chambers*

Three numbers intake structure rectangular shape have been proposed on the right bank of the river Alaknanda upstream of the diversion structure. Three numbers of intake tunnels designed as 6m modified horse shoe are proposed on the right bank of the river Alaknanda.

So far as the hot water springs are concerned the same will not create any problem for accommodating Desilting chambers in the right bank as confirmed from the geological investigation. From the available space it is observed that putting the desilting basins downstream of the dam axis in the right bank of the river is the right choice based on the geological investigation carried out. Three numbers of desilting chambers of size 320m (L) x 16m (W) & 21.5m (H) are proposed on the right bank to ran over sediment particles of size 0.2 mm and above.

This hole is located at the 20 m U/S of dam axis in the desilting chamber area. The vertical hole has proved Overburden up to 9 m depth (El, 1318.93 m) below which bed rock consisting of mainly fine grained grayish white- quartzite with a biotite chlorite schist band between 12.45-14.0 m has been met up to drilled depth of 110.3 m (EL. 1208.73 m). The overburden consists of boulders and pebble of quartzite in a sandy matrix. Thin shear zone has been recorded from 49.50-49.70 m, 57.47-57.65 m, 78.50-78.70 and 91.70-92.40. The percentage core recovery ranges from 80 to 100 percent while the RQD varies from 10 to 100 percent.

4 METHODOLOGY

The excavation and concreting of De-Silting Chambers was done in following steps for all three De-Silting Chambers. The step of Top ramp and Bottom ramp removal and plugging of Adits has to follow completion of activities in DC-3, DC-2 and DC-1 scheduled from Top and Bottom Adit.

After extension of Adits into De-Silting Chamber, junction treatment was done as per good for construction drawings, only then the activities of De-Silting Chamber started.

4.1 *Excavation of Adit to De-Silting Chamber Top & Bottom*

Excavation was done by drill blast method, using Two Boom Hydraulic Drill Jumbo for drilling, excavator PC-200 or equivalent and 10T/ 18T dumper for mucking, Two Boom Hydraulic Drill Jumbo for rock bolting and Shotcreting equipment with robo arm (Cifa/ Normat or equivalent) for shotcreting. Generated muck was disposed to the nearest dumping yard from Adit to DC top.

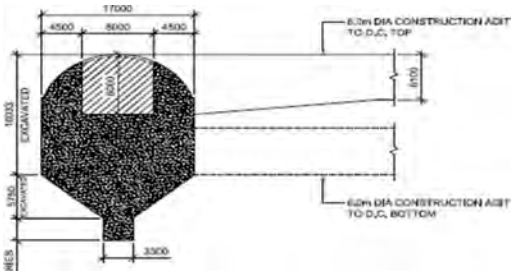

Figure 2. Cross section of Adit to Desilting Chamber top.

4.2 *Excavation of Pilot tunnel and side slashing inside De-Silting Chamber*

Excavation of pilot tunnel 8m x 8m, D-shape was carried out in both Up-Stream and Down-Stream directions after extension of Top adit into DC by drill & blast method. Drilling & charging activity was carried out with the help of Two Boom Hydraulic Drill Jumbo.

Scaling was done after blasting and de-fuming to avoid any incident by removing any visible fallout rock mass. Scaling was done with excavator PC-200 or equivalent or manually with the help of crowbar.

As soon as scaling is completed, geological mapping of the face and crown was done and 3-D log to be maintained from time to time.

Initial layer of sealing SFRS to be applied if required to support the rock mass after blasting. Shotcreting was done with the help of shotcrete machine with robo arm and 4Cum/ 6Cum Transit mixers available at site.

Mucking activity was carried out with the help of Side dump loader CLG 856 or equivalent and 10T/ 18T dumpers. Generated muck was disposed to the nearest dumping yard from Adit to DC top.

Permanent cement grouted rock bolts of 25 dia and 6m/ 8m with c/c spacing as per rock class was done after mucking is completed.

Permanent SFRS shotcreting as per rock class was carried out after rock bolting activity. Shotcreting was done with the help of shotcrete machine with robo arm.

After excavation of 390m long pilot tunnel, slashing works to be carried out in the same sequence as explained above for pilot tunnel.

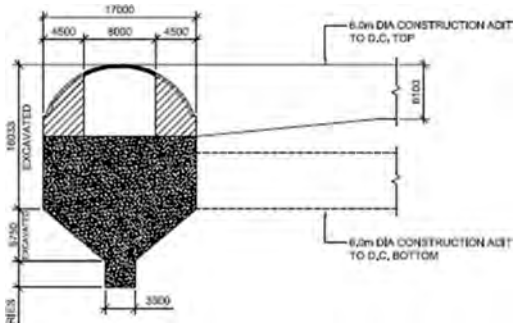

Figure 3. Cross section of desilting chamber showing pilot and arch slashing.

4.3 *Drilling & blasting of 1st bench of 2.5m*

Activity comprises of only drilling & blasting of 1st bench to provide platform for concreting works of 1st beam and wall portion. Drilling was carried out with the help of ROC-203. Ramp was prepared in a gradient of 1:10.

Drilling & blasting then carried out in both directions from Adit to DC Top. Drilling was done with the help of ROC-203. after leaving 6m from either sides of Adit to DC top for turning and smooth movement of traffic.

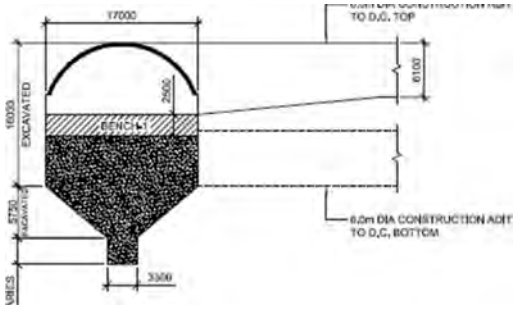

Figure 4. Cross section shows the excavation of 1st bench.

4.4 *Muck removal after drilling & blasting of 1st Bench*

Mucking activity was carried out with the help of Side dump loader CLG 856 or equivalent and 10T/ 18T dumpers. Generated muck was disposed to the nearest dumping yard from Adit to DC top.

Permanent cement grouted rock bolts of 32dia and 6m/ 8m with c/c spacing as per rock class was done after mucking is completed.

Permanent SFRS shotcreting as per rock class then carried out after rock bolting activity. Shotcreting was done with the help of shotcrete machine with robo arm.

Muck removal was done from Adit to De-Silting Chamber Top.

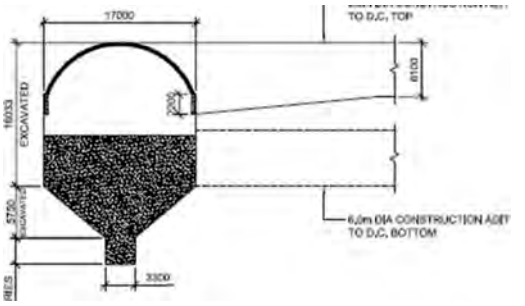

Figure 5. Show the arrangement of mucking for 1st bench.

4.5 *Drilling & blasting of 2nd bench of 2.5m*

Activity comprises of only drilling & blasting of 2nd bench to provide platform for concreting works of 1st beam and wall portion. Drilling was done with the help of ROC-203. Ramp was prepared in a gradient of 1:10.

Sand bags were used to cover the blasting area to avoid damage in wall concrete due to fly rocks.

Muck removal and permanent rock supports was done as explained in Section 7.2.5 after concreting of 2nd lift of side walls.

Muck removal was done from Adit to De-Silting Chamber Top.

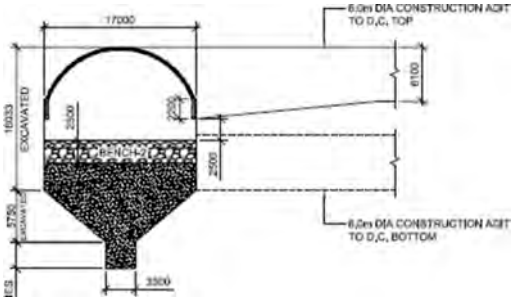

Figure 6. Cross section shows the excavation of 2nd bench.

4.6 *Drilling & blasting of 3rd and 4th bench up to hopper top*

Activity comprises of only drilling & blasting of 3rd bench to provide platform for concreting works of wall portion. Drilling was done with the help of ROC-203. Ramp to be prepared in a gradient of 1:10.

Muck removal and permanent rock supports was done as explained in Section 4.5 after concreting of 3rd lift of 2.5m explained in Section 4.9.

Muck removal was done from Adit to De-Silting Chamber Top.

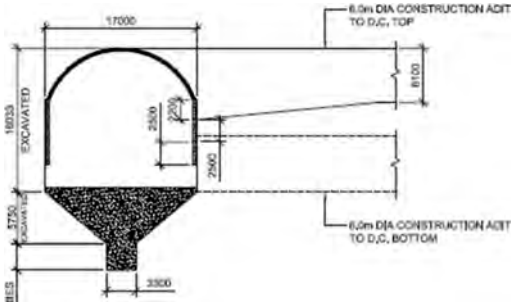

Figure 7. Cross section shows the excavation up to 3rd bench.

4.7 *Concreting of the desilting chamber up to the 4th bench of 10m*

Reinforcement fixing for the beam and wall portion up to a height of 10 m was accomplished in a single operation using 5m shutters. The reinforcement fixing for the 10 m height was carried out manually using staging and scaffolding. To prevent sagging of the reinforcement, anchor bolts were inserted according to the design specifications before concreting.

The concreting of the beam and wall was executed with the assistance of standard shuttering plates with a height of 10 m and length of 5m. The concrete was compacted using mechanical vibrators. The grade of concrete used was as per the design, with a specification of M25, and the maximum size of the aggregate used was 40mm. Contact grout holes, as specified in the design, were provided by inserting PVC pipes during concreting.

Concreting was done by a concrete pump and 6Cum Transit mixers. The concrete was supplied through Adit to DC Top from the nearest batching plant located at the dam site. Sandbags were placed under the wall portion to prevent slurry leakage, and reinforcement bars were curtailed inside for further tying down.

Proper treatment was applied at construction joints before resuming the work. The junction between the crown shotcrete and wall concrete was filled with SFRS to rest on the concrete wall.

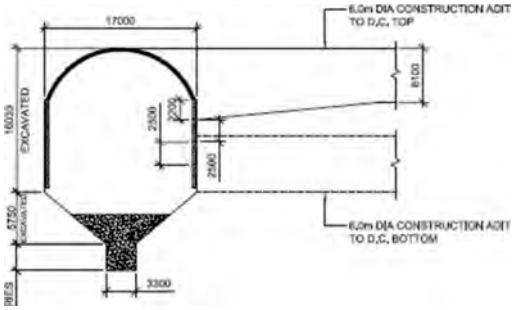

Figure 8. Shows the wall concreting of desilting chamber.

4.8 *Excavation of 5th bench of 2.75m*

Sequence of execution is same as explained earlier was followed. Muck removal was done from Adit to De-Silting Chamber Bottom.

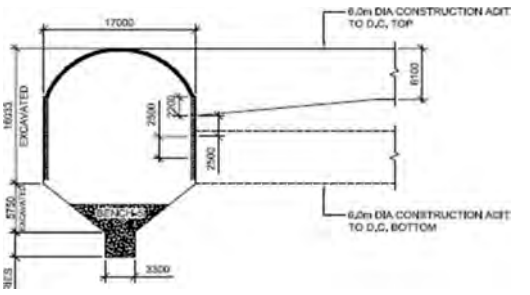

Figure 9. Shows the excavation of 5th bench.

4.9 *Excavation of construction adit to flushing trench up to DC, excavation of 2nd Ramp and Trench*

Construction adit (Adit to Flushing Trench) interconnecting all three DC's was done to facilitate for excavation and concreting works of part wall and trench portion which shall be plugged after completion of DC works instead of enlarging all BFT's for excavation and concreting purpose which resulted excess cost. Sequencing of works is explained below considering this construction adit in place.

Excavation of Adit to Flushing Trench up to DC was completed to provide passage for further activities inside DC.

Excavation of Adit was done from Silt Flushing Tunnel (SFT) towards DC. Adit was excavated in a minimum dimension of 4m D-shaped for effective and smooth working and was plugged with concrete after completion of works in DC.

The junctions with trenches were flared for getting required turning radius for equipments to move inside DC; same was backfilled with concrete and will become a part of plug structure.

Excavation sequence is same as for any tunnel by Drill Blast Method (DBM)

a) Drilling b) Charging & Blasting c) De-fuming d) Scaling & Mapping e) Initial sealing Shotcrete or SFRS (if required) f) Final Rock support

Excavation of 2nd Ramp was carried out by drill & blast method. Drilling was done with the help of ROC-203.

Completion of Excavation of Adit to Flushing Trench from SFT was ensured before excavation of ramp and below ramp portion for mucking purpose.

Drilling & blasting of Trench area then carried out. Drilling was done with ROC-203. Ramp was prepared in a gradient of 1:10.

Muck removal and permanent rock supports was done as per the requirement.

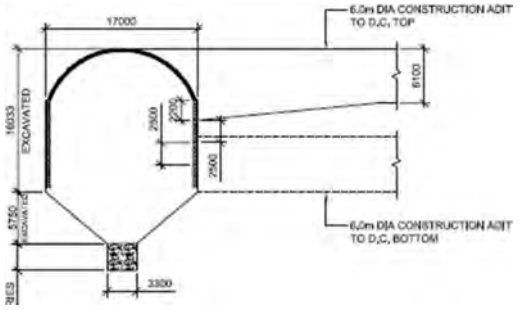

Figure 10. Shows the completed excavation.

4.10 *Concreting of hopper portion and Trench*

Concreting of hopper portion was done only after excavation of DC up to trench level.

Concreting method is same as done for walls except for the shutter used with gantry traveller. Concrete was supplied from Adit to Flushing Trench. Shutter length considered is 6m.

Concreting of trench was done after concreting of hopper portion and gantry removal with the help of traditional shuttering.

Concrete then supplied through Adit to Flushing Trench from nearest Batching plant located at dam site.

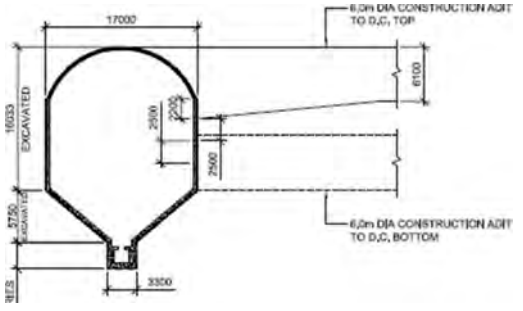

Figure 11. Shows the concreting of hopper and trench.

5 EQUIPMENT USED

Most modern equipment's were used for excavation and concreting of various stages oDC-1.2 &3 as explained below:

5.1 *Pilot excavation and arch slashing*

Two Boom Hydraulic Drill Jumbo: 1no
Side Dump Loader CLG 856 or equivalent: 1no
Excavator PC-200 or equivalent: 1no
Shotcrete machine 30m3/hr: 1no
Dumpers 18T: 5nos
Transit Mixers 4Cum: 6nos

5.2 *Benching*

ROC 203 or equivalent: 2
Excavator PC-300/200:2nos
Shotcrete machine 30m3/hr: 1no
Dumpers 18T: 5nos
Transit Mixers 4Cum: 6nos

5.3 *Concreting*

Transit Mixers 6Cum: 6nos
Batching Plant 60m3/hr: 1no

6 SAFETY PRECAUTIONS: RISK HAZARD ASSESSMENT

All safety measures to be followed as per the standard Safety Management Plan.

Operator & supporting labour staff shall put on necessary PPE's during the work at heights as proposed.

During excavation, the excavated profile shall be cut in specified shape and dimensions with designed rock support methods to ensure safe working area.

Scaffolds of proper type shall be provided for all work that cannot be done from the ground or from part of a permanent structure or from ladder or other available means of support and safe means of access shall be provided to every place at which workers are required to work.

All working platforms, gangways and runs from which workers are liable to fall more than 2 meters shall be

a) Of adequate width depending upon the type of work done and closely boarded, planked or plated. For platforms, the width shall not be less than 60cms. For gangways or runs are used for passage or materials the width shall not be less than 60 cms.
b) Provided with suitable guardrails of adequate strength to height of 1 meter above the working surface and toe-boards of at least 20cms in height to prevent fall of persons, materials or tools.
c) In addition to the above listed precautionary and safety measure. Certain IS codes for safety norms enlisted below should also be strictly followed:

Table 1. Shows the safety codes referred during execution.

Sr. No.	IS Code Description	IS Code
1	Safety Code for Excavation Works	IS : 3764
2	Safety code for blasting & related drilling operations	IS : 4081
3	Safety code for working with construction machinery	IS : 7293
4	Code of practice for safety colors and safety signs	IS : 9457

7 DIFFICULTIES IN CONSTRUCTION

During execution lot of problems faced by the working team. Some of the major problems are highlight here below:

7.1 *Managerial difficulties in streamlining the VPHEP:*

While talking so much of poor geology as a major challenge to the underground work, we often tend to overlook many other extraneous factors which cause serious delay in execution of the project. Coupled with it stand up the hostile local populace and remote location of site.

The VPHEP was planned to commission by 2025 but been inordinately delayed. Local people have posed lot of problems to the project authorities and contractors: viz, non- transfer of land required for the project even after drawing 75% of the payment as compensation and raising issues related to employment and petty construction-contracts. Authorities have assured employment to local people and given them a chance to work in the project on the basis of their qualifications. After getting the job they more than often formed a union in connivance with local leaders and collected hostile- rabble-rousers and disrupted the smooth functioning of the company authorities and district administration. Instead of silently working on the posts allotted to the local workers, they engage in protest marches and sometimes in pilfering construction material too. The company has lodged several FIR's in this matter and has also removed some hostile staff from the project. Project activities are seriously hampered due to local disturbances and continuous strikes, for more than a month at a stretch. As a result, in 7 year only 14% work of the project was completed.

Finally, the work started at this site but still the project is moving ahead with the re scheduled dates. It looks from the speed picked up now work will be completed soon with support of authorities.

Dam site at Helong is stands at a remote location near Joshimath where the Project components like diversion tunnel, desilting chambers, silt flushing tunnels, part HRT and intake structures which are the starting points of the project, could not be made functional because authorities faced lot of problem due to non- cooperative attitude of local people. Alternative ways were explored by the management and, in some cases, paid an extra amount to carry on the works. Several cases of manhandling with engineers and staff working at site. Such cases were given legal cognizance reported thereof.

Finally we restored the work sequence by doing efforts and educating people with help of district administration.

The blockade of National Highway especially during the monsoon, made the situation worst: supply chain management was severely affected. As a result, construction material like cement, steel, structural steel could not reach the site on time. Storage facilities were limited for want of flat land available in the region. Lack of diesel storage also created hurdles and further delayed the execution of the project. Internal road links passing through the acquired land of the locals were also laid seizure upon by the so-called owners who continue demanding undue compensation. It also delayed the project schedule.

Construction of Char Dham project, a govt project, was started to widen the roads and to give good accessibility to pilgrims. The project also created interruptions during its implementation which was further complicated by the huge rush of vehicles during the yatra season.

Covid -19 also gave a big setback to the project. All movements were stopped by govt Nakas at different places even for human movement documents were demanded,at every nakka, for vehicles carrying construction materials. This severely delayed the project.

Transportation of big equipment was hit the most. Equipment's were transferred in various consignments to the site after strengthening the weak bridges and dismantling big equipment's in pieces and then reassembling at the site. This was a major exercise which directly caused enormous delay in mobilization of equipment's to the site. Lot of innovative thinking was given to identify safe routes for the equipment's to reach the site. Finally, with the help and cooperation of local authorities we could mobilize the site but huge wastage of time did take place.

7.2 *Problem in vertical wall concreting in desilting chamber and innovative solution adopted.*

Vertical wall concreting was critical activity and very time consuming, to overcome this 10m shutter was introduced and 5m length of vertical wall was done at a time on each wall by providing 2 shutters in each chamber. This proved to be a successful innovation and concreting was done in a faster way.

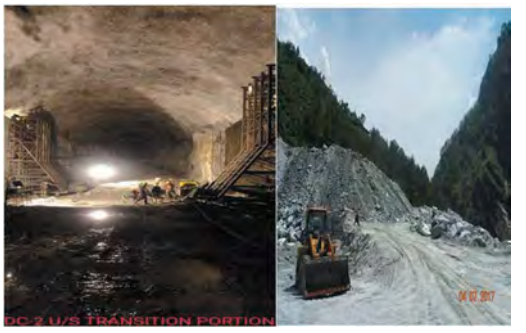

Figure 12. Shows the shutters used on both sides of Desilting chamber and view of dumping yard.

7.3 *Non availability of Dumping Yard*

Dumping space at dam site was limited and after continuous dumping the space got occupied fully. By providing gabion walls to some extent the space was increased but that also was not sufficient. Then with

the consent of THDCIL some local land was taken on lease for dumping at a distance within 7-8km and this arrangement worked well and work was done in a faster way.

8 CONCLUSIONS

The scheme, the considerably big in India at 444 MW, will generate power after completion with the Desilting Complex Chamber excavations and ancillary tunnels providing their designed role.

Despite so many problems requiring significant engineering input, the Desilting Complex, comprising three Chambers 390m long, 16m wide, approximately 21.5m high has been completed to the original hydraulically designed shapes. Execution of the final works has not been without challenges however, and the final arrangements have only been accomplished through the cooperation and integration of important ideas put forward by many parties, and then engineered to detailed design level only as part of the construction works. The overall final arrangements now comprise several support elements not foreseen in the original tender design drawings and by introducing in-house innovation at project level, this was the key of success to complete these important structures.

ACKNOWLEDGMENTS

Author is thankful to THDCIL for giving this opportunity to execute the job and all kind of support extended during execution of this prestigious project.

REFERENCES

1. DPR of Vishnugad Pipakoti Hydro Electric Project'.
2. Rock mass classification and support design- NGI, OSLO, June 2022.
3. Tunnelling in week rock Elsevier Geo engineering book series vol.5, Elsevier, Amsterdam (2006)
4. Underground excavation in rock, E.Hoek & E.T. Brown.
5. Geotechnical Engineering Office, Civil Engineering Department, The Hong Kong,- Geoguide 4, Guide to Cavern Engineering.
6. Xiao Liu, Peng Yan, Ming Chen, Sheng Luo- Wuhan University, China- Optimization analysis of excavation procedure design of underground powerhouse under high in-situ stress in China.
7. Design and construction aspects of desilting chamber of Teesta-III, B.K.Ojha, Project director, Navayuga Engineering co Pvt. Ltd.

Tunnelling for a Better Life – Yan, Celestino, Thewes & Eberhardt (Eds)
© 2024 The Author(s), ISBN 978-1-032-80042-4
Open Access: www.taylorfrancis.com, CC BY-NC-ND 4.0 license

Construction of Tunnel T-49A on Dharam – Qazigund section of Udhampur-Srinagar-Baramulla New BG railway line project in highly adverse geological conditions- A case study

Rakesh Kumar Khali*
Vice President Operations-Tunnel & UG Works, G R Infraprojects Limited, Delhi, India

Sharanappa Yalal*
Cluster Head, J&K, Hindustan Construction Company Limited, Mumbai, India

ABSTRACT: A number of challenging tunnelling projects are under construction across the length and breadth of the country to connecting significant but remote places to rest of the country. With a serious intent to ease the day –to-day life of the people of Jammu and Kashmir and to connect them through railway network to the world outside the valley, it has become necessary to create a passage through the mountains therein. The Indian Railways decided to connect the people of this beatific valley all through the weathers. Hence the most economic rail linking project officially known as Udhampur Srinagar Baramulla Rail Link Project (USBRL). The whole track passes through an insurmountably adverse Himalayan Geology, keeping in view the fact that 70% of the track is covered by series of tunnels between Udhampur and Qazigund. The length of tunnels between Udhampur to Qazigund ranges between few hundred meters to 12.78 kms. The first longest length of the Tunnel is 11.20km. The Pir Panjal Tunnel (T-80) has already been commissioned in 2013 and is fully operational on date. Another longest railway tunnel in the series of this project is T-49, having a length of 12.78km surpassing the length of the previously built longest tunnel, i.e., T-80 Tunnel. Considering the construction difficulties, approach and time bound project, Tunnel T-49 has been split into two projects- T-49A measuring 5100m and T-49B covering a distance of 7700m. Hereunder we will discuss the T-49A project.

The project - which is in the advance stage of construction, has been christianed as Tunnel Package T-49A, forms an important part of Prestigious Udhampur Srinagar Baramulla New BG Rail Line Project in the Union Territory of Jammu and Kashmir.

The Twin tunnels, i.e., "the Main" and the "Escape tunnels" of 5.1 Km length each, horse shoe shaped, with 7.12m and 4.5m finished dia respectively, are to be bored through NATM through a fragile geology where surprises confront our engineers day in and day out .

The authors wants to highlight the details of the planning process, execution challenges, innovations done, introduction of additional adits, simultaneous working of various activities and extremely poor road conditions faced where supply- chain- management was the key to success. Being the project of national importance this stretch was tunnelled within the time schedule. This successful experience will be helpful for all the field engineers who are working day and night in different part of the country and abroad.

1 OUTLINES OF THE PROJECT

Tunnel T-49 is the longest Railway tunnel in USBRL Project having a length of 12.78 Kms, divided into 2 parts viz T-49A and T-49B.

Here, we will discuss T49A Project which consists of two major rail bridges 2 and 3, summer station-yards, combining the 5100m main tunnel & 5205ms long Escape Tunnel. Both tunnels are intersect each other by cross passages at every 375m. The T-49 tunnel will connect the two-railway stations, namely Sumber in the south and Arpinchala on the North. The Main Tunnel starts from chainage 111500 and ends at 116600.

The project is located around 200Km from Jammu, in the Ramban district of State of Jammu and Kashmir. It can be approached through NH44 up to Ramban, and from Ramban to Harog, 30kms, through the State highway. From Harog to the site, it is connected through a very difficult 20km long hilly road. All access roads are slide- prone and frequently blocked due to rain fall. Figure 1&2 shows the site location maps.

*Corresponding author: rakesh.khali@grinfra.com; sharanappa.yalal@hccindia.com

DOI: 10.1201/9781003495505-203

Figure 1. Location map.

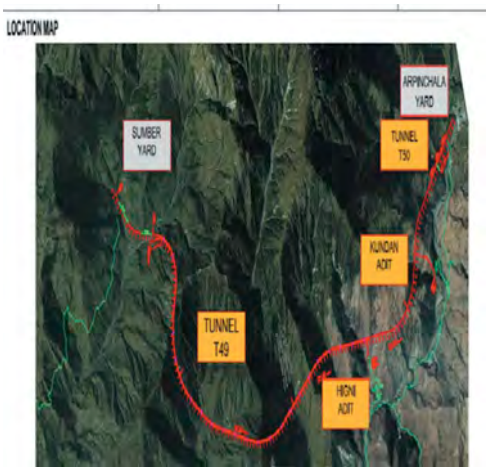

Figure 2. Site location map.

2 GEOLOGY

Regional Geology within the current project area consisting of three major geological formations (FRM) can be distinguished in general: the Ramban FRM, the Salkhala FRM and the Ramsu FRM. The Dumgali FRM can be mapped too, but its appearance is rather scarce. The main tectonic feature within the project area is the Main Central Thrust (MCT), which crosses the alignment close to the Sumber Nala.

2.1 *Geology along the alignment*

The individual rock types of the above described geological formations are characterized below, based on the current knowledge and the current state of geological investigations within the project area.

2.1.1 *Phyllites*

Phyllites are widespread and common project area. They occur in almost every formation. Their texture is manyfold: near the portal T49-P1, the Phyllites are mapped as massive rock - body (Figure 3). But in general, the schistosity planes are thinly laminated and the jointing is closely spaced. Hence the rock mass is strongly fractured (Figure 2). Generally its colour varies between light brown to grey, but at times, also with a darker brown; in combination with other

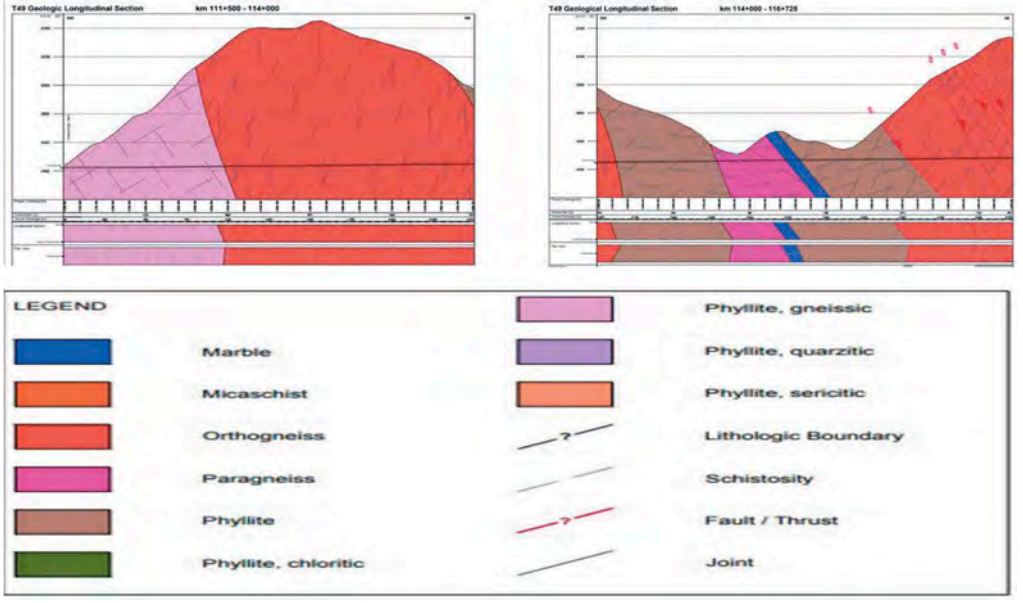

Figure 3. Geological L Section of T49.

minerals also greenish and greyish. The Phyllites sometimes show open joints up to 10 cm wide, but as a whole below 0.5 cms. The schistosity- -planes display in general a high persistency; hence they are mechanically active. The schistosity planes are predominately dipping into 355° - 50° with a dipping angle of about 40°. The joint orientation shows generally a NW to W striking, but with a few exceptions.

2.1.2 *Orthogneiss*
Orthogneiss within the current project area is located mainly along the ridges which build the topographic boundaries of the Urnihal catchment. This Orthogneiss is generally massive, the foliations and joints display a wide spacing of up to 200 cm.

2.1.3 *Paragneiss*
Paragneiss, apart from Phyllite, is the most dominant rock type in the project area and occurs within the entire Salkhala FRM. The Paragneiss is interbedded within the Phyllites, because of their common sedimentary origin. The dip direction of the Paragneiss is almost entirely NE, with dips between 40 and 70°

2.1.4 *Micaschists*
Micaschists are much less common in the current project as the Phyllites and Paragneisses are. They have been mapped around the Urnihal Nala at its orographic right-hand flank. The schistosity displays a thin thickness of approx. 6-20 cms.

2.2 *Regional- scale tectonic features*

2.2.1 *Main Central Thrust (MCT)*
The MCT runs through the project area. Although its direct morphological impact is marginal, its influence on the structural inventory and, therefore, on the geotechnical behaviour of the rock mass in the project area is of paramount significance. The MCT follows a northward -incline from the confluence of the Sumber Nala and the Anchah Nala, along the northern slopes of the Sumber Nala over a flat top at Sinkhli (Figure 10); and, thereafter, continues through a small valley lying in north of the settlement called Duda in the Bishelari River valley. Somewhere near Digdol, the MCT enters the mountains on the other side of the Bishelari River. Within the current project area, the MCT crosses the alignment only once at bridge BR-3. In the literature concerned, a strict NW-SE orientation is annotated to the MCT, but it appears, that the MCT regionally follows a more differentiated pattern.

2.2.2 *Pir Panjal Thrust (PPT)*
The PPT thrust is inter-bedded between the MCT in the north and the Main Boundary Thrust (MBT) in the south. The PPT is easily detectable by using aerial photographs, as it defines the northern boundary between a brighter rock- type in the south and a darker one in the north, the latter in most of the cases, is a Phyllite. The rock, south of the PPT, is mainly a volcanic basalt and other sediments of the so-called Panjal traps. For the current project, the fault is not relevant because it crosses the alignment south of the project area.

2.2.3 *Main Boundary Thrust (MBT)*
The MBT is the best detectable in the topography. It follows the Chenab River from Peerah to the area around Dharamkund. At Dharamkund, it leaves the Chenab valley and continues along the Chinji Nala. From thereon, the MBT continues all along this valley unto the settlement of Damni in the Ans River valley, farther in the West. This thrust separates the upper Dharamsala (Murree) formations in the footwall from the Panjal traps **in the hangings**. This thrust describes a horizontal overthrust of approx. 100 kms. Its morphologic significance is very prominent.

2.2.4 *Seismicity*
The proximity of young thrust planes like the Main Central Thrust (MCT), indicates that the project area is located within a tectonically high active area in the past and also probably so in the future. The largest recorded earthquakes in the region show Richter magnitudes of up to 6 which means, that the intensity may also rise to 7, even if no record of such an event exists. The project is defined to be located within the Seismic Zone V, as per the IS: 1893-7

3 CONSTRUCTION SEQUENCE

The Tunnel -construction moves in a sequential manner which involves

1. Excavation 2. Primary Support 3. Geotechnical Monitoring 4. Water Proofing of tunnel, 5. Final Lining 6. Second Stage concreting and conduit fixing

As per the current worldwide practice, sequence from 3 to 6 are mostly common, but as far as the sequence A & B are concerned, methods of excavation and primary support vary largely depending upon the site conditions.

Ground Behavior Type	Classification Method	Ground type	Relevant Parameters: Orientation of mechanically relevant foliations (boundary, moderate, unfavorable)			t/s (below 100 m, 100 - 300 m, up to 1000 m)			Mountain water inflow (no, yes)		stress tolerance (low, high)		Size of jointed rock body (<20 cm, 20-200 cm, >200cm)			Abrasivity (low, medium, high)		
GBT 01	RMR	GTs 02, 03, 09	x			<1	<1	<1	x			x		x	x			
GBT 02		GTs 01, 06, 07	x	x		>1	>1	>1	x		x			x			x	x
GBT 03		GTs 04, 05, 08	x		x	>1	>1	>1	x		x		x		x	x	x	
GBT 04		GTs 10		x	x	>1	>1	>1		x	x		x			x		
GBT 05	Abrasivity	GTs 02, 03, 07, 09	x			<1	<1	<1	x		x	x		x	x		x	x
GBT 06		GTs 01, 05, 06	x	x		<1	>1	>1	x		x		x	x			x	
GBT 07		GTs 04, 08, 10		x	x	>1	>1	>1	x	x	x		x			x		
GBT 08	Overburden Stresses to rock massif strength	GTs 02, 03, 09	x			<1	<1	<1	x			x		x	x			x
GBT 09		GT 01, 06, 07	x	x		<1	<1	>1	x		x	x	x	x			x	x
GBT 10		GT 05, 08		x	x	<1	>1	>1	x		x			x		x	x	
GBT 11		GTs 04, 10		x	x	>1	>1	>1	x	x	x		x	x		x		

Figure 4. Ground behavior type.

OVERBURDEN	low		high		low		high	
WATER	none to little		none to little		little to moderate		little to moderate	
SCENARIO	optimistic	pessimistic	optimistic	pessimistic	optimistic	pessimistic	optimistic	pessimistic
GBT								
GBT 1, 5, 8,	SC 1	SC 2	SC 2	SC 3	SC 3	SC 4	SC 3	SC 4
GBT 4	SC 4	SC 5	SC 5	SC 5	SC 5	SC 6 L	SC 5	SC 6 L
GBT 2,3,6,9,	SC 2	SC4	SC4	SC4	SC 3	SC 4	SC 5	SC 5
GBT 7, 10,	SC 4	SC 5	SC4	SC 5 SQ	SC 5	SC 5 SQ	SC 5	SC 5 SQ
GBT 11	SC 4	SC 5	SC4	SC 5	SC 5	SC 5 SQ	SC 5 SQ	SC 6 SQ

Figure 5. Ground behavior type and support classes.

3.1 *Excavation*

Excavation of tunnel is based on the ground types, ground behavior type and finally selection of support type. Before excavation of tunnel face ground types, ground behavior type is characterized by detailed geo-mechanical study at tunnel face and at the project site and geotechnical design is established for selection of support type (Figures 5 & 6)

3.1.1 *Support classes*

Following support classes are encountered at the project-

Normal drill-and-blast method was adopted to excavate in support class SC2, SC3 and SC4. Wedge-cut blasting pattern was adopted here to fragment the rock mass into the desired size. For supporting class SC5 and SC6, special techniques were adopted to excavate the rock mass without disturbing the equilibrium of the surrounding rock mass, a process hereafter discussed in Para 8.

3.1.2 *Primary support*

Based on the support-classes, the supports have been designed to stabilize the excavated tunnel.

Typical support measures have been shown in the following Figures 6,7, 8, 9, and 10

Table 1. Support classes of T49A (%).

Support Class T49A (%)	
Support Class	Actual
SC1	0.00
SC2	53.20
SC3	29.61
SC4	13.26
SC5	2.30
SC6	1.63
SC4SQ	0.00
SC5SQ	0.00
SC6SQ	0.00

3.1.3 *Adverse geological conditions*

Tunnelling through Himalayan region is always a challenge and our team faced many of them during the execution of T49A. Excavation through support classes SC1, SC2, SC3 and SC4 were almost easier to cross through but in support classes SC5 and SC6 were very challenging. A number of thick- to- very thick, very weak and unstable shear zones were confronted (Table 01) where the mining team struggled day and night, and finally crossed effectively through the challenging zones without wasting a single day– no minor or major injury sustained, no mining equipment damaged .

As mentioned in para **7.1.1 SC5 and SC 6 encountered were 3.93% i.e. 200.43m**

Very loose and unstable strata were encountered as shown in the table no 2:

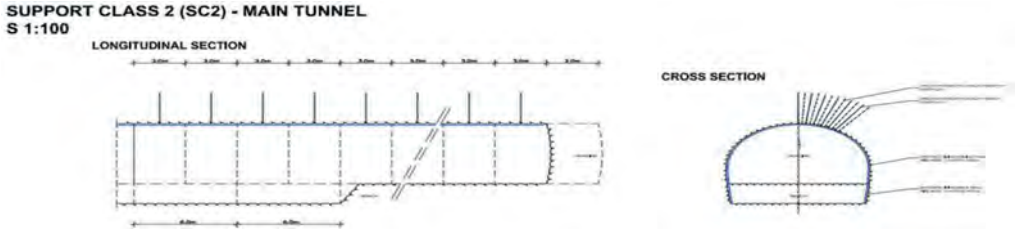

Figure 6. Support measures SC2.

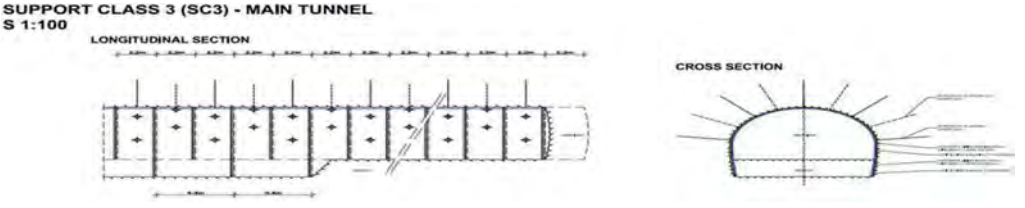

Figure 7. Support Measures SC3.

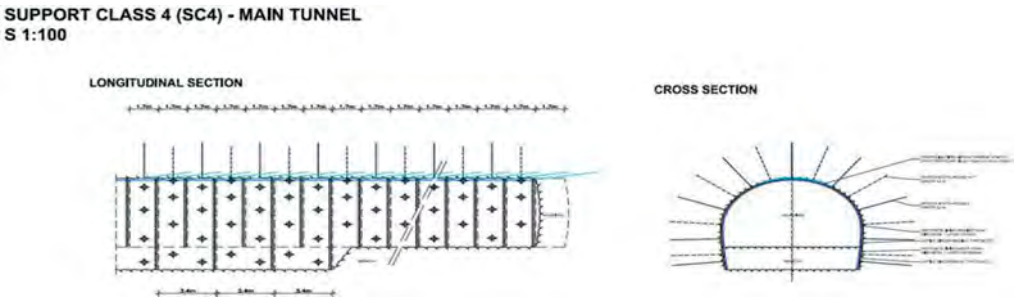

Figure 8. Support Measures SC4.

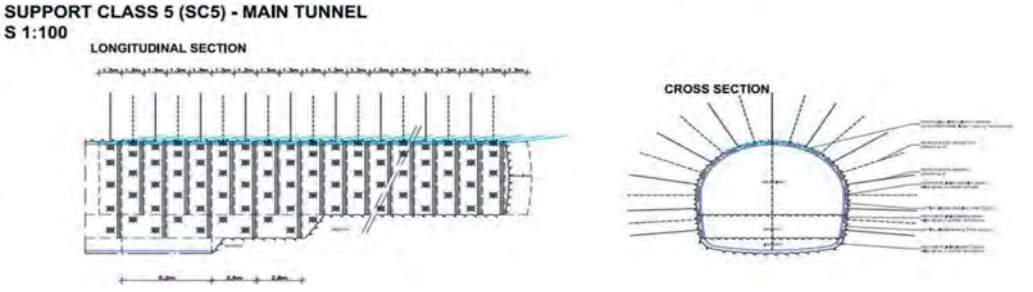

Figure 9. Support Measures SC5.

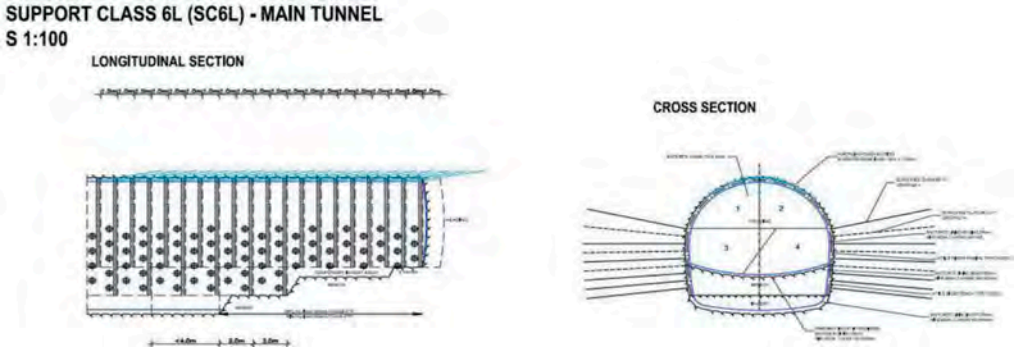

Figure 10. Support Measures SC6.

Table 2. Summarized length of loose strata in the main tunnel T49A.

S. No.	From tunnel Meter	To tunnel Meter	Unit	Length
1	3445	3504	m	59
2	3742	3774	m	32
3	3915	3921	m	6
4	3958	3981	m	23
5	4003	4029	m	26
6	4092	4098	m	6
7	Total		m	152

As shown in Figure 11, sequential excavation of top heading, benching and invert excavation was adopted to tackle the adverse geological conditions:

Figure 11. Excavation in adverse geological conditions.

3.1.4 *Top heading excavation*

1. Sealing shotcrete with SFRS
2. Excavation of the left Crown and installation of lattice girder followed by wire-mesh fixing and shotcrete.
3. Excavation of the right Crown and installation of the lattice Girder, followed by wiremesh fixing and shotcrete
4. Installation of 12m long (27nos)76mm dia fully grouted pipe roof
5. Repeating the sequence no 1 and 2 till excavation of 8m length **with leaving Support core body** (Figure 12)
6. Removal of Partial Support- Core body and installation of rock bolts.
7. Repeating the sequence no 01 to 06 for further advancements.

3.1.5 *Benching excavation*

1. left wall and installation of lattice Girder followed by wiremesh fixing and shotcrete
2. Excavation right wall and installation of lattice Girder followed by wiremesh fixing and shotcrete
3. Installation of fully grouted rock bolts
4. Repeating sequence no 01 to 03 for further advancements.

3.1.6 *Invert excavation*

After stabilization of tunnel and after monitoring its geotechnical instrumentation data, when no deformation located, invert excavation of 2m length was carried out with full primary support and the excavation cycle repeated till crossing the loose and unstable ground.

4 CHARGING & BLASTING

The charging pattern followed for excavation was in accordance with the norms of wedge- cut and the drilling and blasting patterns. The only modification made in charging was: two numbers of primers were used in cut holes. Owing to the presence of phyllite and quarzitic phyllite rock, pow-der factor was also moderately used.

It varied from 1.0 to 1.5 kg/m3, depending upon the rock strata encountered. Power gel 80% explosives with non-electrical delay detonators were used with cortex.

5 CYCLE- TIME AND SEQUENCE

Sequence of boring cycle time in different rock class is as under –

As explained earlier, drilling was done with Atlas Copco- -make Boomer at the Main Tunnel and With Tam Rock Make- boomer at the Escape Tunnel.

6 LINING OF TUNNEL

The entire portion of the tunnel was concrete –lined, and the weak portion was covered with RCC lining. The concrete lining was done by using shuttering gantries of 12m lengths with CIFA hydraulics and shutter vibrators mounted on gantry shutters. The

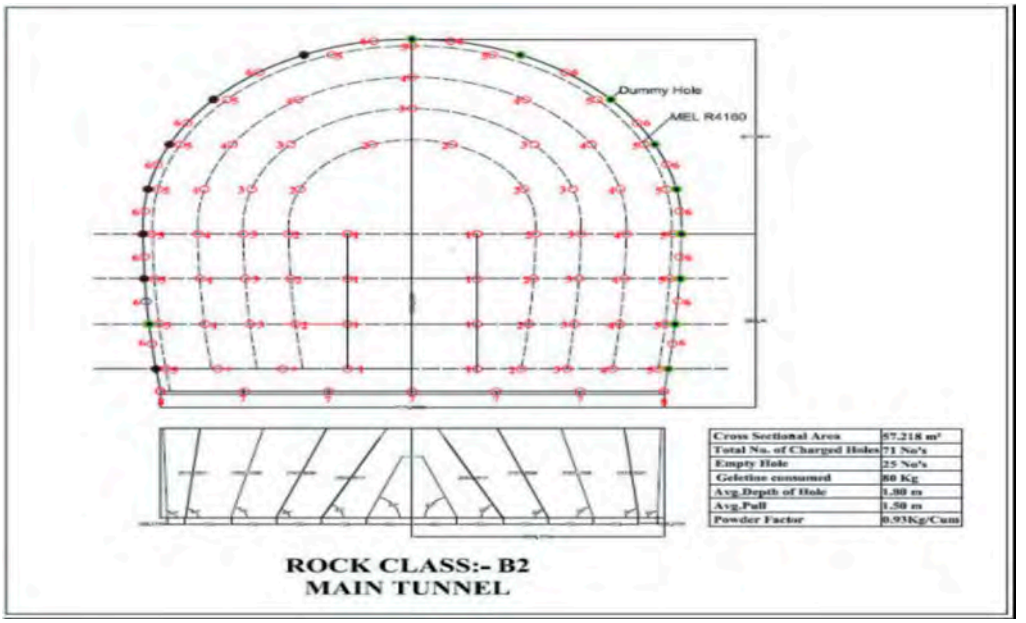

Figure 12. Blasting patterns used for the main and escape tunnels.

Table 3. Time cycle for different rock classes main tunnel T48, J &K.

Activity	Rock Class B1	B2	C1
Time in Minutes			
Profile Marking	15	0	0
Face drilling	130	60	30
Charging Explosive and Blasting	75	50	45
Defuming	20	15	15
Mucking	180	120	45
Chipping & loose Scaling	30	30	30
Survey	15	15	15
Face Sealing	30	30	30
Wire mesh Fixing	0	45	30
Lattice girder Fixing	0	60	60
Shotcrete	75	60	60
Rock Bolting	120	75	45
Fore Poling/Pipe roofing	0	0	80
Miscellaneous works	30	30	30
Total Time (Minutes)	720	590	515
Total Time (Hours)	12.0	9.8	8.6
Advancement (m)	3.5	1.5	1

Figure 13. Rocket Boomer in operation at the main Tunnel.

gantry was movable on rails. Concrete placing was done by using BP 1800 concrete pumps.

After completion of the primary support and after stabilization of the area, a final support with concrete lining, both with reinforcement and without reinforcement depending upon the rock classes, was done successfully. It included the following steps-

(a) Erection of gantry
(b) Preparation of the bed and PCC (M15) concrete for Kerb beam.
(c) Placing of a perforated 250mm dia. Pvc pipe.
(d) No fine concrete over the Pvc pipe.
(e) Erection of **form work**.
(f) Fixing of geotextile.
(g) Fixing of water proofing membrane
(h) Reinforcement of Kerb beam.
(i) Concrete of Kerb beam
(j) Reinforcement of the crown and wall (in RC B, B2, C1, C2, C2b and D)

Figure 14. Tam rock boomer in operation at escape tunnel.

(k) Mobilization of auto- movable gantry.
(l) Final checking and survey.
(m) Pouring of concrete (M30A20) 300mm to 400mm depending upon the rock class.

7 DIFFICULTIES IN CONSTRUCTION

7.1 *Poor ventilation, fault zones encountered and innovation done by introduction of a new Adit*

Since the Tunnel had to be bored from one face for a length of 5.1Km, after crossing 2.5 km, it had become impossible to maintain proper ventilation inside the tunnel, even after lot of efforts. Somehow, we could reach up to 3.2Km in the Main Tunnel and Escape tunnel. Also the fault zones were encountered while advancing creating operational problems. Disadvantage at this 5.1Km long face was a result of the poor geology throughout the advancement of the initial length, as water seepage from the crown was travelling along the tunnel- alignment. The Fault zone was encountered at several places where heavy seepage occurred. As a result, the work of the whole face came to a standstill at one point of time. Heading- benching method was adopted with the NATM, followed by a 76dia pipe roofing and grouting. One set of pipe roofing of 10m advance contains 27nos of pipes with self-drilling bits. To consolidate the area, various SD anchors were provided to stabilise the roof and the side, followed by lattice girder and shotcreting. Also, it was felt to introduce a new ADIT to mitigate a 5.1km length of single- face to provide an additional 2 faces. This decision brought about a turn around and we could complete the excavation on time. The author wants to highlight this innovation for the information of fellow engineers as explicated below:

This Tunnel (T-49A) was awarded in 2013 December for execution of a 5.1 Kms twin -tunnelling with a single face. As per the standard tunnelling methods, we could take up the mining only with one face covering about 2.5 KM. Doing 5.1 Km long mining

Figure 15. Concrete lining arrangements.

with one face is difficult and maintaining safety and environmental parameters were very much difficult. Maintaining good ventilation inside the tunnel for boring such a long tunnel, is not possible by adopting any random methodology as per the tunnelling guidelines. In addition to the ventilation, maintaining supply -chain for tunnelling activities and for hauling excavated muck from the face to the dumping yard is also one of the major challenges in such conditions.

It is pertinent to mention that the contract was awarded without provisions of any intermittent Adit to divide the tunnelling into two zones. In order to overcome the challenge, the Project team successfully coordinated with the client consultant and convinced him for reviewing the provision of an additional Adit. As a result, the client agreed upon and approved our proposal for taking up an additional Adit at the tunnel chainage, 3650m, from the South Portal.

The location of the Adit was decided considering the favourable geology and the minimum length to be excavated for the Adit. For this, the detailed investigation was conducted to finalize the location and, after delibirations, the length of Adit was finalised as 310 m. The working team completed the entire Adit length within 4 months, including portal development from the starting point. The excavation diameter of the Adit was kept the same as that of the tunnel, i.e., 7.15 m finished diameter.

With the introduction of the new Adit, we successfully completed about 1.8 Kms tunnelling through the new Adit. The detailed diagram showing the mining done by the Adit is shown below:

Figure 16. Pictorial view of T-49A Tunnels and new Adit.

With this new innovation, the following favourable advantages were achieved as detailed below:

- Maintained good air quality inside the tunnel to keep hazard free atmosphere in the tunnel which is the prime requirement of excavation.
- Ensured reduction in the cycle time and maintained speedy progress.
- Reduction in construction cost by reducing the lead for hauling the muck and other construction materials.
- Ensured an accident-free construction site by reducing the existing lead inside the tunnel by diverting vehicle through the newly constructed Adit.
- Diverted heavy seepage of water through the newly constructed Adit and ensured a dry tunnel for (3650 m) construction of the second stage construction works.
- Imparting an overall support to the construction activities inside the tunnel to executing the works parallely and reducing the construction period.

The innovative idea of introducing an additional Adit not only facilitated the smooth and quality construction but also saved the overall construction period of the Project to about minimum 20 months.

7.2 *Project roads*

The project is linked through 150 km long Jammu-Srinagar National highway up to Ramban, and thereafter through a 50 km long Ramban Gool State Highway. From the State highway, the Sumber and Kohli sites are connected through a very rough and earthen 25 km long hilly road. The Dharam site is further connected through a 15 km long rough, undulating hilly, and earthen project-approach road. The National Highway traffic is badly affected during the winters and the rains. Mostly, one way traffic is permitted over more than four months in a year. As a result, the transportation of construction materials, diesel, and other essential material supplies is heavily affected, further escalating the cost. Moreover, the project approach roads are very slide prone as the road remains blocked due to mass movement of hill slope debris most of the time.

As the approach road to the site is in hilly region, the maintenance is very difficult. Initially, we mobilised our equipments to this site via Reasi, as only

Figure 17. Photo: Condition of project approach road at different locations during rainfall.

one bally bridge was available to cross the Chenab River at Dharamkund and the same was not capable to take more than 15 tons of load. Later on, a steel girder bridge was constructed for 70R loading. Still, we were able to mobilise the heavy equipment's to our site as per and requirement. This resulted in a loss of more than six-month work time. During the monsoon, the road would be washed away at several

places and also get blocked because of the landslides. The reason was the sinking tendency of various stretches which stand already detached from the mountain slope. Not only a considerable time was lost due to poor roads, but a few accidents also occurred during construction. We suffered a setback due to the break in the supply chain stopping the work for many months altogether. The same was restored by putting manifold all efforts, equipments, and manpower. Apart from the blockage, the gradient is very steep and the bends are very sharp. As a result, only six-wheel vehicles with a limited load can travel through.

During the rainy season, the life becomes very miserable and even survival becomes a challenge. It becomes clear from the above photographs that the workforce engaged at the project site is fighting with nature for survival.

7.3 *Muck management*

The major activity taken up during construction of the tunnel is disposal of excavated material or spoils. This material, if disposed off into nearby water bodies, insidiously increases water turbidity, thereby causing adverse effect on aquatic flora and fauna. For the success of any underground project, muck dumping yards are the key facility. Therefore, at every location, a separate dumping yard was required to accommodate the huge quantity of excavated tunnel muck. As this area is undulating and there is steep slope, a limited land for muck disposal is available. There are no approach roads either. Due to unavailability of the dumping area and the approach road at all location, adverse effect on the progress was recorded. Over the time, a land for the dumping yard was acquired near the Portal identified and the negotiations were initiated.

To acquire this land from the local inhabitants on lease, the clients and district administration were liasoned. Stability was ensured at steeper locations by properly protecting the same in benches, providing base drainage and surface protection against erosion. The excavated material was also tested at reputed labs for reutilization as coarse and fine aggregates. The left-out material was used for developing the job facilities, playgrounds, and other project infrastructures.

7.4 *Non-availability of power*

Construction power was not available for execution of the job. DG sets of 5.5MW capacity were deployed at all three locations for power production. Possibility was explored for grid power in close coordination with the power department; and, as a result, we got grid power at all locations. This way mitigated to get rid of the costliest captive DG power.

7.5 *Nonavailability of area for Infrastructure*

No space was available for infrastructure at the site. Benches were made on the hill with the help of dozer and the slopes were protected with the help of gabions and shotcrete. The foundations were made at different work fronts for installing batching plant, compressors, transformers, etc. Extra efforts were required for initial mobilization.

8 CONCLUSION

1. Most of the problems in the Himalayan tunnelling can be attributed to the lack of knowledge of the geology ahead of the face. These problems have resulted in loss of time and costs overrun, which eventually deprives the country of the project benefits. It is essential that detailed exploration of the work must be carried out before the start. The exploration ahead of face should be undertaken on a continuous basis.
2. Selection of proper equipment's is significant for the speedy and successful completion of a Project.
3. NATM Technology is the best and safe in soft ground conditions and is recommended to be implemented widely at different Himalayan location for infrastructure projects.
4. Proper construction planning of each activity of this railway Tunnel paved way for faster construction.
5. Timely decision of introducing new Adit paved the way for faster construction and ensured better ventilation of the 5.1 km long twin tunnels.
6. Teamwork, proper co-ordination/co-operation, and dedication of our engineers have been the formulae to bring the project into proper shape snd achieving this success.

ACKNOWLEDGEMENTS

The authors are thankful to Northern Railways and IRCON International for their support and cooperation during the execution of the works.

REFERENCES

1. Proceedings of WTC'2015, WTC'2016.
2. Proceedings of Tunnelling Asia-2015, 2017, 2019, 2022.

Tunnelling for a Better Life – Yan, Celestino, Thewes & Eberhardt (Eds)
© 2024 The Author(s), ISBN 978-1-032-80042-4
Open Access: www.taylorfrancis.com, CC BY-NC-ND 4.0 license

Construction of a new tunnel in proximity to an in-service tunnel by implementing measures to control blasting vibration and ground displacement

Yasunori Kobayashi*, Takaaki Ishii & Tadahiro Koma
West Nippon Expressway Co., Ltd, Osaka, Japan

Kiyoto Nakano
Nippon Expressway Research Institute Co., Ltd, Tokyo, Japan

Yusuke Kinomura
Obayashi Corporation, Tokyo, Japan

ABSTRACT: The Myojinsan Tunnel Phase II line of the Matsuyama Expressway is a two-lane road tunnel construction project with a length of 2,545 m and an excavated cross-sectional area of 75 m^2. By establishing a new parallel line to the expressway in service, it is expected to alleviate traffic congestion and serve as an alternative road in the event of a disaster. The service line is an important route for local life and economic activities, and it was essential to secure local lifelines, so it was necessary to minimize road closures and road restrictions associated with the construction. This tunnel has a varied and complex geology influenced by the Median Tectonic Line. The end portal side was a blasting excavation section mainly made up of hard andesite, while the start portal side was a mechanical excavation section mainly made up of unstable landslide deposits. Because of the proximity to the in-service tunnel, a major challenge was to control the impact of blasting vibration and ground displacement. In blasting vibration countermeasures, we established a blasting vibration monitoring system, and mitigated the impact on the in-service tunnel by adopting split blasting based on blasting vibration predictions. As countermeasures against the displacement of the unstable ground, we controlled the ground displacement and mitigated the impact on the in-service tunnel by installing landslide restraint piles from outside the tunnel, steel pipe forepiling and long face bolts from inside the tunnel, as well as by adopting top heading temporary invert with shotcrete. By implementing these various measures and taking safety into consideration, we have successfully completed the construction work.

Keywords: proximity construction, Phase II tunnel, in-service tunnel, blasting vibration predictions, Median Tectonic Line, landslide ground

1 INTRODUCTION

Construction work is conducted on an approx. 6.3km section between Iyo and Uchiko Ikazaki interchanges to expand the Matsuyama Expressway to a four-lane highway as illustrated in Figure 1. The excavation work of the Myojinsan tunnel began in May 2019.

The Myojinsan tunnel was 2,545m long, and the excavation area of the tunnel reached 75 m^2. The construction site is parallel to the Matsuyama Express way currently in service, thus passing through Myojinsan mountain with an altitude of 634m. The construction was difficult due to the complicated geological structure with variations influenced by the Median Tectonic Line as well as the neighboring construction parallel to the in-service line. Under such a condition, excavation could have both dynamic and static impacts on the in-service line, so it was crucial to understand the behaviour during construction. On the other hand, the in-service line had to minimize road closures and road restrictions due to construction to ensure human flow and logistics. Hence, the inspection and monitoring of in-service line during construction of Phase II line was also limited in time and duration. This paper reports on the measures taken to reduce the

* Corresponding author: y.kobayashi.ac@w-nexco.co.jp

DOI: 10.1201/9781003495505-204

Figure 1. Location of construction work.

impact on the in-service line, management methods and the results of these measures, which were issues in the construction of Myojinsan tunnel as previously reported by Ishii et al. (2022, 2023).

2 CONSTRUCTION OVERVIEW

A summary of the construction wrok is given in Tabel 1.

Table 1. Construction Overview.

Construction Name	Matsuyama Expressway Myojinsan tunnel construction	
Contractee	West Nippon Expressway Company Ltd. (Shikoku Branch)	
Construction Period	Apr 6th 2018 - Jan 29th 2023 (1,760 days)	
Overview	Construction extension: 4,073mTunnel extension: 2,545m	
	Major material:	concrete: 22,300㎥
		Reinforcing steel: 134 t
		Rock bolt: 21,300 pieces
		Steel support: 1,470 units

3 OVERVIEW OF TOPOGRAPHY AND GEOLOGY

Figure 2 Is the geological longitudinal section. The geological structure of the tunnel can be divided into two major sections, that is, the blasting excavation section mainly made up of hard andesite and the mechanical excavation section mainly made up of unstable landslide deposits. The paper is going to cover the details in both sections.

3.1 *Blasting excavation section*

80% of the tunnel is made up of andesite thus extremely hard with an unconfined compressive strength of 100 MPa and a high elastic wave velocity of up to 5 km/s despite the existence of columnar joints as shown in Figure 3.

Figure 3. Face conditions of andesite.

The support patterns at the time of design were mainly the B or the C type with some D type. Blasting excavation was adopted as an efficient excavation method. Figure 4 shows the representative support pattern in the blasting excavation section.

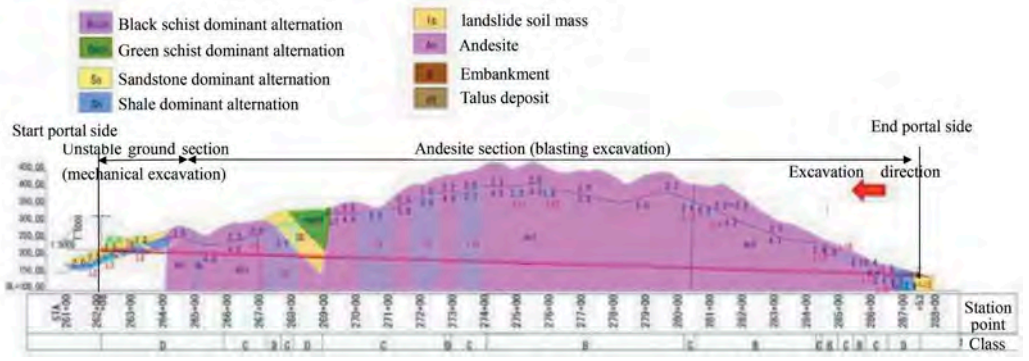

Figure 2. Geological longitudinal section.

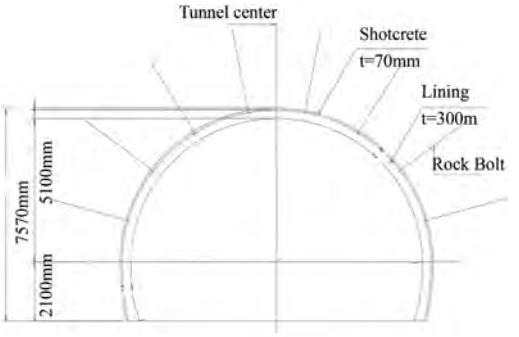

Figure 4. Support pattern in blasting excavation section.

3.2 *Mechanical excavation section*

As shown on the left side of Figure 2, the 250m section at the start portal side was affected by the Median Tectonic Line and consisted of landslide deposits as shown in Figure 5. The geological structure is Izumi Group shale dominant alternation with a low elastic wave velocity of 1.5 km/s, and the most unstable areas were soft enough to allow breaker excavation and were interbedded with a thin layer of clay. Mechanical excavation was adopted to minimize the impact on the landslides.

Figure 5. Face conditions of landslide deposits.

4 CONTROL OF BLASTING VIBRATION IMPACTS

4.1 *Blasting vibration issues in hard rock ground*

The distance between the Phase II line tunnel and the in-service line was as close as about 3D at the tunnel center distance relative to the tunnel excavation outer diameter D. The construction was carried out in an indirect influence area where loads, displacement, and deformation could affect the existing tunnel. Furthermore, the in-service line, which has been in service for about two decades since construction, had cracks in some sections of the tunnel lining according to the prior management inspection records. There were sections that were in the preventive maintenance stage, a condition in which no functional problems had occurred, but it is desirable to take measures from the viewpoint of preventive maintenance. Therefore, it was necessary to study the impacts of blasting vibration on the lining of the in-service line.

Vibration velocity meters were installed before the excavation at two points, TD (Tunneling Distance) 350m and 650m, during the night closure of the in-service line, which was executed twice a year. The impacts on the in-service tunnel were then monitored on a steady basis. The allowable vibration velocity was set at 2-4 cm/sec for each soundness classification of the existing tunnel (East, Central and West Nippon Express Company Limited, 2020). To minimize the impact on the in-service line from the viewpoint of the unevenness of the ground and the safety of the in-service line, the control standard value was set to the V=2.0cm/sec, which is applied in the AA judgment, the most severe of all, “immediate repair is required”.

4.2 *Blasting vibration control*

4.2.1 *Monitor system for the in-service line*

In general, the explosive amount increases in proportion to the unconfined compressive strength of the site, so blasting vibration also tends to increase accordingly. Especially in hard rock ground, the maximum amount of explosives per stage (hereafter referred to as “simultaneous explosive amount”) was thought to be around 10 kg at which could result enormous blasting vibrations. Moreover, although the explosive amount for each blast is reviewed based on the actual result of the previous blast, an excessive amount might still be used for the improvement of the excavation cycle. Test blasting thus became necessary in the pursuit of the optimal explosive amount to minimize the blasting vibration.

The test blasting provided useful data for the calculation of the maximum simultaneous explosive amount that does not exceed the control standard value of blasting vibration and the minimum amount required for excavation. The tunnel consists of highly variable geology, which also plays a major role in the propagation of blasting vibrations. Hence, test blasting was carried out whenever the support pattern was changed or the degree of the weathering of the ground and fracture spacing were changed.

Since the purpose is to reduce the vibration at the in-service line, the blasting vibration V’ was measured at the measuring point of surveillance walkway on the in-service line side, the same location as the blasting point, as shown in Figure 6. The value V’

was then converted to blasting vibration Vc at the control point. The above conversion from the measurement points to control points was based on equation (1). Measuring instruments were permanently installed on the in-service line side even during non-test blasting, and the vibrations were daily monitored.

$$V_c = V' \sqrt{(D_L / D_L')} \quad (1)$$

D_L: Distance between the blasting point and the measuring point (=36.0m)

D_L': Distance between the blasting point and the control point (=27.0m)

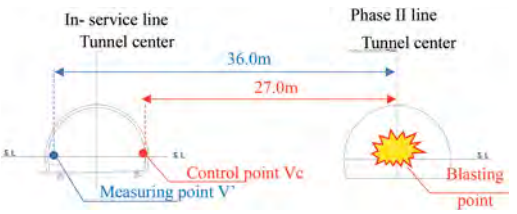

Figure 6. Arrangement of vibration measuring point.

4.2.2 *Reduction of simultaneous explosive amount*

The results of the test blasting in the hard rock ground proved that the simultaneous explosive amount must be suppressed to meet the control standard value. A common countermeasure is the usage of detonators to provide a time delay between blastings, such as MSDS detonator, nonelectric delay detonator with fuse, and electronic detonator (Oshima et al., 2014), but split blasting using a sequential blasting machine is also an applicable option. Considering the construction conditions, the split blasting was adopted as the least expensive method that can suppress the vibration caused by blasting on the in-service line. As illustrated in Figure 7, the split blasting is a method of reducing the simultaneous explosive amount by dividing the tunnel face blasting into blocks.

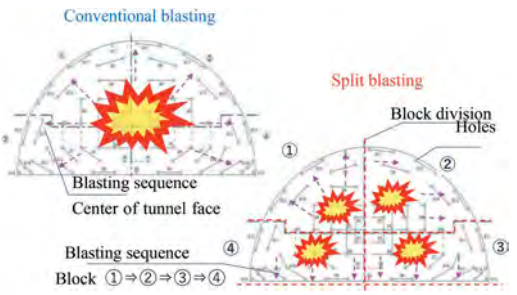

Figure 7. Split blasting using sequential blasting machine.

4.3 *Result of countermeasures*

The K value was calculated from the blasting vibration obtained by the test blasting, and the maximum simultaneous explosive amount W_{max} at which the control standard value of V = 2.0cm/s occurs was calculated using equation (2).

$$W_{max} = \sqrt[1/0.75]{V \times D_L^2 / K} \quad (2)$$

K: The value obtained in the test blasting

The assumption is that the blasting vibration can be suppressed to less than 2.0cm/sec if the simultaneous explosive amount is below W_{max} Figure 8 shows the relationship among W_{max} (the maximum simultaneous explosive amount based on equation (2)), W (the actual simultaneous explosive amount when using split blasting), and W_c (the estimated simultaneous explosive amount based on equation (3) when conventional blasting is used).

$$W = W_c / n \ \therefore \ W_c = W \times n \quad (3)$$

n: number of divisions

No countermeasures were required at TD=100m and TD=1500m as the simultaneous explosive amount used at the site was small compared to W_{max}. In the other sections, the simultaneous explosive amount was reduced by using split blasting, which allowed blasting without the simultaneous explosive amount exceeding W_{max}. Figure 9 shows a comparison of the vibration velocity when using split blasting and conventional blasting. Although the allowable vibration velocity exceeded in most cases with the conventional blasting, the use of split blasting allowed excavation below the allowable vibration velocity. Figure 10 is an example of the results from the measuring instrument installed permanently in the lining of in-service line at TD = 650m. It clearly indicates that the blasting vibration did not exceed the set allowable vibration velocity of 2.0cm/sec. Thus, by calculating the K value from the test blasting and controlling the simultaneous explosive amount by split blasting, the blasting vibration could be suppressed to the allowable vibration velocity of 2.0cm/sec.

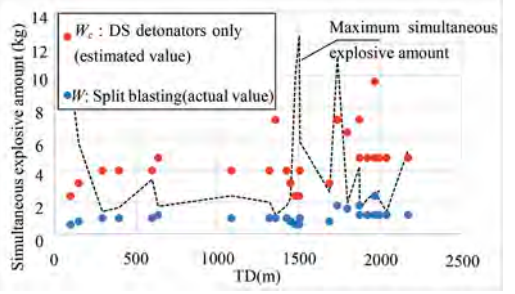

Figure 8. Comparison of simultaneous explosive amount.

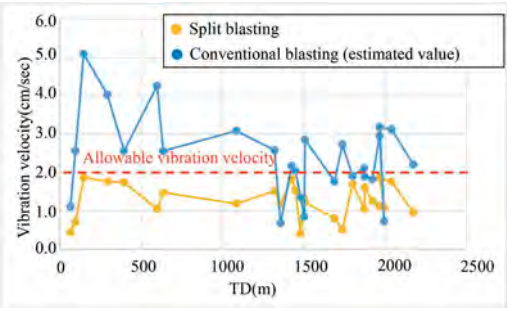

Figure 9. Comparison of vibration velocity.

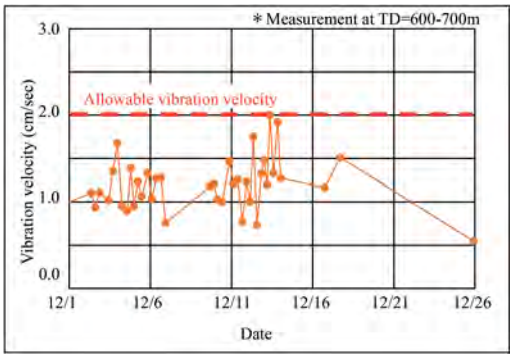

Figure 10. Vibration velocity on the in-service line.

5 DISPLACEMENT CONTROL OF LANDSLIDE DEPOSITS

5.1 *Challenges in Phase II line construction*

In the mechanical excavation section, there was a landslide ground affected by the Median Tectonic Line. The landslide is characterized by seven landslide blocks divided into A to E, which are in a folded position, blocks E and F are the largest landslides with 120 m long and 100m wide in the main line direction. Figure 11 shows an overview of the landslide ground. Therefore, landslide countermeasures were studied during the construction of the in-service line, and countermeasure works were carried out from the inside of the tunnel as well as from the surface directly above the tunnel. From the surface, construction was carried out using vertical prereinforcements and restraint piles.

The landslide control works are shown in Figure 12, where landslide control work shown in red was conducted during the Phase II line, and other colours were conducted during the in-service line. Countermeasures were also carried out from inside the tunnel by different kinds of auxiliary methods such as pipe forepiling. On the other hand, it was recorded that during the construction of the in-service line landslide sliding was observed on the surface area, and a maximum of 250mm of both

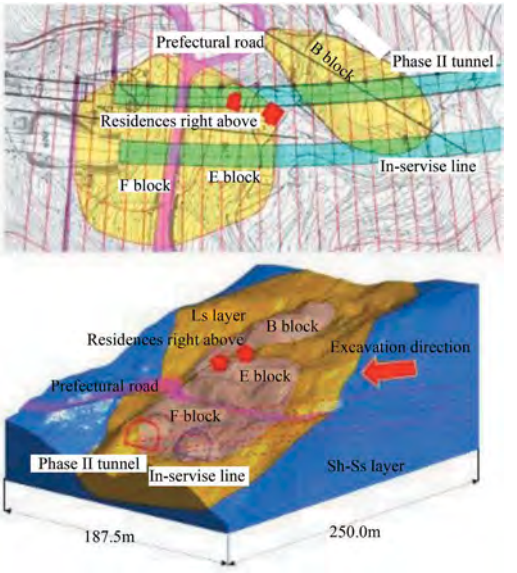

Figure 11. Overview of landslide ground.

crown settlement and convergence occurred during excavation of the in-service tunnel, and both crown settlement and convergence generally remained above 100mm in other sections. Furthermore, since the excavation of the in-service tunnel had some impact on the ground surface, we have continued to monitor the landslide even after the construction of the in-service line was completed and the landslide was confirmed to be under control. In the construction of the Phase II line, it was necessary to prevent the landslide from sliding and to control the impact on the ground surface and the in-service line because there were two residences and a prefectural road in the affected area.

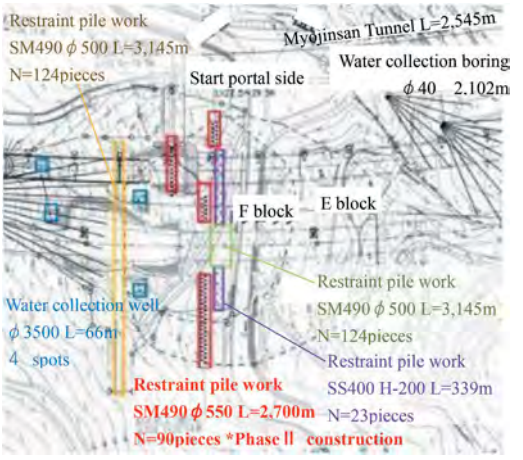

Figure 12. Overview of landslide control works.

5.2 *Landslide prevention work and measurement work*

Prior to the construction of the Phase II line, a landslide study committee organised by academics and others was held to discuss the countermeasure works. As a result, a plan was recommended to complete the landslide restraint piles before the tunnel face reached blocks E and F, where there was concern about the impact of tunnel excavation.

It was therefore decided to take measures to drive a total of 90 steel pipe piles with a length of 30m and a diameter of 550mm for the restraint piles around the start portal side of the Phase II line as shown in Figure 12. To monitor the surface displacement due to landslide sliding and tunnel excavation, several measurement items have been set up as shown in Table 2, including TS (total station) automatic 3D measurement. A large monitor was installed in the site office for real-time monitoring of various measurement results and early detection of abnormalities. An environment that facilitates the prompt identification of signs of abnormality has been created by using a system, which clearly indicates measurement graphs and always updates them automatically. In the system, numerical data were displayed in different colours and visualized so that abnormal values could be recognised immediately.

Table 2. Measurement Items.

	Measurement Item	No. of measured cross-sections /points
In-service tunnel measurement	Lining concrete stress	9
	Convergence/Crown settlement	9
	Temperature in the tunnel	9
	Vibration velocity	2
Measurement B	Crack displacement	4
	Radial displacement of surrounding ground	3
	Shotcrete stress	3
	Steel supports stress	3
Other measurements	Prior crown settlement ahead of face	27
	3D ground surface settlement	111
	Residence inclination	10

5.3 *Displacement control measures in tunnel*

Early closure of this section was planned by the full-face method with auxiliary bench cut in mechanical excavation. The early closure is highly effective in reducing displacement as the section is closed in the immediate vicinity of the face and has a good track record (Sato et al., 2015, Awaji et al., 2016, Toyama et al., 2018). However, the in-service line construction records showed that face collapse and sudden water inflow had occurred during the excavation, and it was considered that the in-service line and landslides might be affected due to the tunnel excavation. Therefore, it was considered difficult to cope with rapid changes in the face conditions in the case of large division of heading, where the bench is excavated just below the top heading face.

As a result, long bench cut method excavation was brought into the plan since it can respond flexibly to various ground conditions based on the behaviour of the ground during the top heading excavation. However, as the long bench cut method has a longer closure distance and a smaller displacement control effect compared to early closure, temporary closure with top heading temporary invert in the immediate vicinity of the face was also adopted in combination. Hence, a temporary closure immediately after the top heading excavation, as in the excavation procedure shown in Figure 13, was considered to both cope with sudden changes in ground conditions and to control displacement.

Auxiliary methods were also studied as countermeasures to stabilise the face and to control surface settlement. Six patterns of auxiliary methods, including the initial design, were studied as well as the economics of these method. As a result, it was decided to adopt the L=12.5m, 180°steel pipe forepiling and long face bolt shown in Figure 14 as the most rational auxiliary method, taking into account the impact on the in-service line.

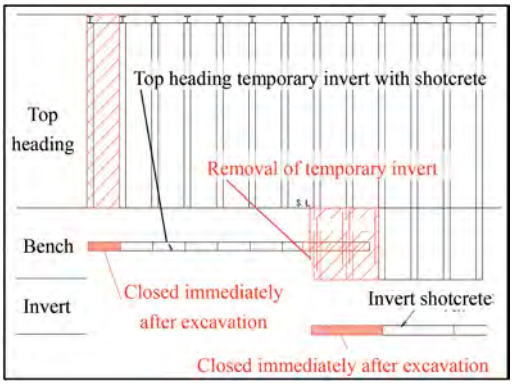

Figure 13. Excavation procedure.

5.4 *Revising the management standard values*

A pre-measurement period of approximately 20 months without the influence of Phase II line excavation was used to study the influence of temperature and other factors on the measurement of the in-service line. The measurement results are shown in Figure 15. The stress increment in the lining showed a correlation with temperature, with seasonal fluctuations increasing and exceeding the control standard

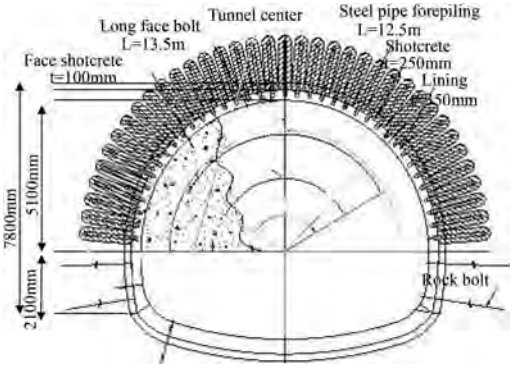

Figure 14. Support pattern in mechanical excavation.

value even during the periods when there was no effect of excavation. In particular, the lining stress varied widely from a minimum of -1.5 to a maximum of 1.1N/mm^2 depending on the season. In addition, two-dimensional FEM analysis during design assumed that the stresses at the inner edge of the in-service line lining were on the tensile side, but the measurement results during the actual construction indicated a compressive tendency and different deformation modes. The control standard values for the displacement measurement of the Phase II line at the planning stage were determined from the stability of the ground around the Phase II line, that is, the critical strain of the ground, and were managed independently of the in-service line, as there was no relationship with the in-service line. Therefore, based on the actual measurement results, the following procedure was adopted to eliminate external factors such as seasonal fluctuations and to revise the control values for the lining stress increment of the in-service line and the displacement measurement of the Phase II line, which have a mutual relationship.

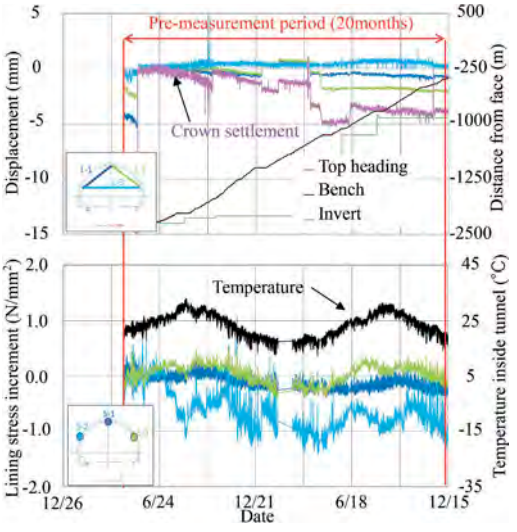

Figure 15. Measurements during pre-measurement period.

From the pre-measurement results, seasonal fluctuations were eliminated as far as possible and the amount of change due to the effect of excavation was extracted. In other words, the position where the excavation of the Phase II line starts to affect the in-service line was set at 30m (about twice the tunnel diameter) before the measurement position, the lining stress at this time was set as the initial value, and the control standard value for the lining stress increment on the in-service line was re-established. To find a relationship between the in-service line and the Phase II line, a control standard values were set with the feedback from the measurement results. First, to understand the relationship between the displacement measurement results of the Phase II line and the lining stress increment of the in-service line, we focused on the changes in both as the face progresses, as shown in Figure 16. Figure 17 shows a scatter diagram with the convergence, crown settlement and foot settlement on the horizontal axis and the lining stress increment at the in-service line on the vertical axis. A linear correlation with some variations can be observed. The displacement at which the lining stress increment at the in-service line reaches the control standard value (compressive stress, -5.40N/mm^2 as specified by East, Central and West Nippon Express Company Limited (2020)), was then determined from the linear approximation and re-established as the control standard value for the displacement measurement.

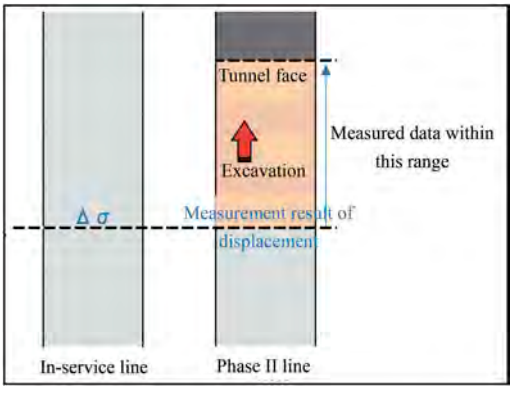

Figure 16. Lining stress increment and displacement.

5.5 *Results of countermeasure works*

Figure 18 indicates the results of displacement measurements of the Phase II line. Overall, the crown settlement tended to be greater than the convergence. Particularly, the final settlement of 67mm was relatively large at the right shoulder of the tunnel. However, the displacements tend to converge around 20 days after the bench excavation and invert shotcrete. The displacement converges after about 2D (twice the tunnel diameter), which is similar to the trend of

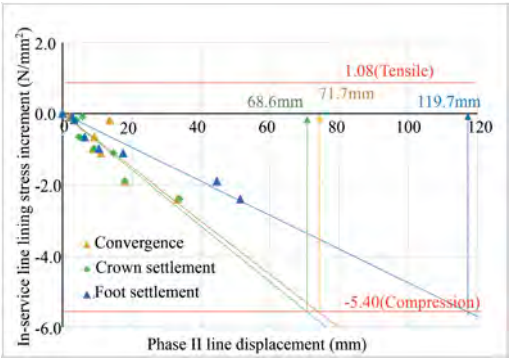

Figure 17. Phase II displacement and lining stress.

convergence in the in-service line shown in Figure 19. It means if the displacement on the Phase II line side can be suppressed and converged earlier, the impact on the in-service line side will also be reduced.

At TD = 2,370m, the final settlement reached 129mm, the largest amount for the entire tunnel line, which exceeded the control standard value Level III. In this section, as the ground conditions gradually deteriorated, the convergence was small, but there was a tendency towards increased foot settlement and a higher displacement rate during the top heading excavation. Considering that a large displacement of 250 mm had occurred in this section during the construction of the in-service line, additional horizontal rock bolts were urgently installed to control the settlement. On the other hand, as shown in Figure 19, the measured values of the in-service line indicated only small changes with respect to the control standard value confirming that the impact was small. No new deformations were found in the crack displacement gauges of the lining installed in the same section, and the same was true in the visual inspections.

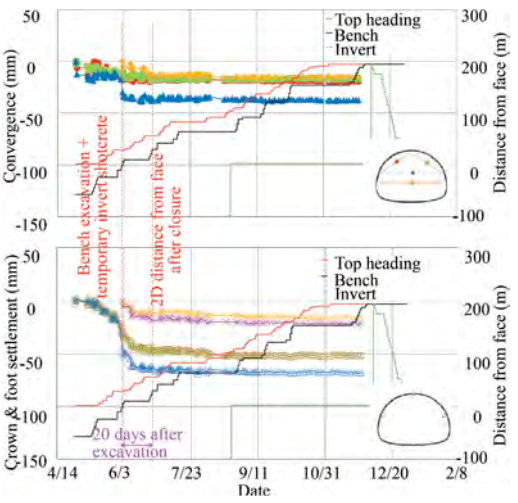

Figure 18. Displacement of Phase II line.

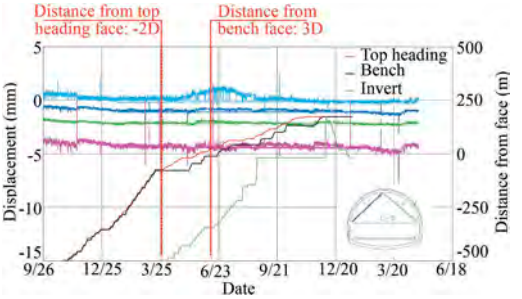

Figure 19. Convergence of in-service line.

6 CONCLUSIONS

In the blasting excavation section, the impact on the in-service line was significantly reduced by determining the K value through test blasting, setting the maximum simultaneous explosive amount, and adopting the split blasting with a sequential blasting machine. Generally, the calculation of K value is often based on the results of one or a few times of test blasting. However, as this tunnel is a case of blasting in close proximity to the in-service line, it was considered important to capture the impacts of blasting vibrations for each change in ground conditions, and the maximum simultaneous explosive amount was determined with a high degree of accuracy.

Also, preliminary studies have been conducted in the mechanical excavation section right from the beginning, considering the geological risks in the landslide ground. Although the construction was in close proximity to the in-service tunnel, there was a wealth of geotechnical information available, such as previous construction records, compared to newly constructed tunnels. This information could be used comprehensively and reflected in the safety of the Phase II line construction. The results of the various measurements could be fed back to the construction quickly and appropriately. In recent years, with technological innovations in auxiliary methods, early closure, which can reduce the closure time as much as possible, has become mainstream where displacement control and the influence on surrounding ground are concerned. However, in the case of landslide weak ground, it is crucial to be able to respond quickly to the risk of face collapse as the ground changes, and the excavation method adopted in this project has demonstrated its superiority.

Besides, although it is commonly recognized that the top heading temporary closures is effective in controlling displacement, there have been many reported cases of sudden displacement occurring when the temporary closure is removed in landslide ground similar to this tunnel, and this concern was also raised at the study stage. For this reason, the frequency and point of displacement measurements were increased, and second opinions from geological experts were used to determine the class of ground.

On the other hand, although the maximum displacements that occurred during the removal of temporary closure were 50 mm of settlement and 30mm of convergence, the displacements converged after the primary invert was completed.

The tunnel was constructed safely and reasonably by using a management method based on the initial values set and the actual measurement result. As similar issues in close proximity construction are expected to increase in the future, it would be great if the newly studied methods in this paper could be taken as a reference. Still, depending on the condition of the ground and the lining of the in-service line, further measuring instruments could be added, but if the number of items to be managed increases, it may instead become more difficult to assess the condition of the ground and the lining. A comprehensive study of the reliability and reasonability of the measurements needs to be carried out.

REFERENCES

Awaji, D., Isago, N., Kusaka, A., Kawata, K., 2016. Performance Requirement of Immediate Ring Closure Method for Difficult Ground Conditions in Conventional Tunneling. ITA-AITES World Tunnel Congress 2016, pp. 640–649.

East, Central and West Nippon Expressway Company Limited, 2020. Design outline volume 3 Tunnel preservation edition (6) Tunnel Proximity Constructions, 3-4, 3-7. (In Japanese)

Ishii, T., Watanabe, H., Ito, A., Kinomura, Y., 2022. Proposal of management method of in-service tunnel using blasting vibration prediction and lining stress increments. Tunnels and Underground, 53(9), pp. 17–28. (In Japanese)

Ishii, T., Watanabe, H., Ito, A., Kinomura, Y., 2023. Penetrating the landslide area adjacent to the Median Tectonic Line with various measures from inside and outside the tunnel. Tunnels and Underground, 54(7), pp. 47–56. (In Japanese)

Oshima, K., Kato, Y., Ito, T., Kurokawa, N., 2014. Construction of Twin Tunnels Directly Above an Existing Tunnel. 8th Asian Rock Mechanics Symposium, pp. 1011–1020.

Sato, J., Maeda, T., Kimura, A., kusumoto, F., 2015. Tunnel Designed with Early Ring Closure in Squeezing Ground. ITA-AITES World Tunnel Congress 2015.

Toyama, M., Tokutomi, Y., Kobayashi, H., 2018. Measure for heaving of roadbed in squeezing ground – Kyushu Shinkansen Nishikyushu line Tawarazaka tunnel -. ITA-AITES World Tunnel Congress 2018, pp. 1577–1587.

Tunnelling for a Better Life – Yan, Celestino, Thewes & Eberhardt (Eds)
© 2024 The Author(s), ISBN 978-1-032-80042-4
Open Access: www.taylorfrancis.com, CC BY-NC-ND 4.0 license

Cross passage tunnel excavation by core cutting machine (Stitching) and hydraulic rock splitters in hard rock at Mumbai Metro Station Line-03 (Aqua Line)

Ashish Kumar Saw*
PG student in Tunnel, MIT World Peace University, Pune, India

Sandeep Potnis
Head, School of Tunnel Engineering, MIT world Peace University, Pune, India

Charuhas M. Jadhav
Executive Director Civil, Mumbai metro line3, India

Mainak Roy
Chief Resident Engineer Mumbai metro line3_UGC07, India

ABSTRACT: lots of soft & hard ground tunnels, including metro tunnels, railways tunnels and road tunnels, have been constructed in many cities in an India. Nearly all tunnels have cross passages between two tubes. In soft ground area, cross passages could be built in many kinds of methods, such as, cut-and-cover, mining methods and combined method and in hard rock will be excavated with traditional mining techniques including use of excavators, rock hammers and splitters, drilling & blasting, drilling & chiseling and stitch coring with rock splitter, shot creating and rock bolting. Cross passage tunnel in Metro Line-3 of Mumbai is a sequentially excavated (SEM) by core cutting with help of rock splitter, more than 10m long tunnel in volcanic breccia rock with 15m2 excavation area which accommodates 6.35m O.D of pre cast segment lining. Twin tube TBM tunnels. Continue excavation process with using advanced methodology and equipment rather than the normal excavation methodology by pneumatic hand breaker. The methodology has be followed for construction of cross passages in MML-03 UGC07.

Keywords: Cross passage, Core cutting machine (Stitching), Conventional Excavation, SEM/NATM, Surface settlement, Underground metro, ground behavior

1 INTRODUCTION

Mumbai Metro Line – 3 (Aqua Line), also known as Colaba–Bandra-SEEPZ line, is a part of the metro system presently under construction in Mumbai, India. Mumbai is the financial capital of India and Mumbai Metropolitan Region Limited (MMRL) is one of the fastest growing metropolitan regions in India. The major challenge in the region today is to provide connectivity and drive growth by providing adequate inputs in infrastructure that will improve the quality of life of the residents. The Metro model has been recognized as an efficient, economically viable and environment-friendly mass transport system to improve the overall traffic and transportation scenario in Mumbai. Currently Mumbai Metro Line 3 (CBS 33.5 km: Colaba - Bandra - SEEPZ) is being implemented by MMRC (Mumbai Metro Rail Corporation). When completed, the 33.5-km fully underground corridor will be the first underground metro line in Mumbai and will cater to 1.75 million passengers daily with a frequency of 3-4 minutes, ferrying more than 2500 passengers at a time. Line-3 is expected to reduce road congestion and have a significant sustainable environmental impact on CO^2 emissions and fuel consumption as well as. Underground Stations at Marol Naka, MIDC, SEEPZ and associated tunnels on CBS (Contract No. UGC 07 awarded to L&T & STEC JV) by MMRC. L&T & STEC JV has appointed AMBERG-STUP JV as Consultants for the design of the project.

Main tunnels consist of twin tube configuration of 5.8 meters internal diameter each, excavated using an Earth Pressure Balance (EPB) Machine of 6.66 meters boring diameter. A total of 42 Tunnel Boring

*Corresponding author: ashishsaw25288@gmail.com

DOI: 10.1201/9781003495505-205

Machine (TBM) breakthroughs by 17 TBM machine in entire length.

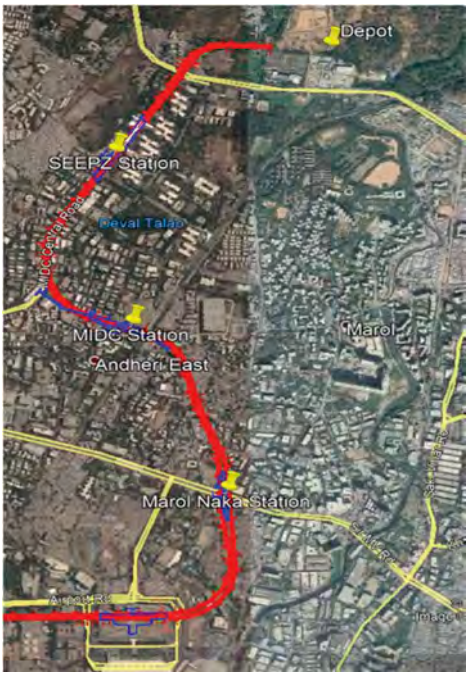

2 PURPOSE

Cross passage are designed to allow final evacuation from train cab to track bed. The exit from the tunnel is through the track bed between the two rails of the track, from where passengers must enter a protected cross-passage (complying with the provisions of NFPA 130:2010) which shall be located one at each point station the end of the platform where the emergency exit staircase is located or 244 m (maximum distance) from the portal access point. Access is available from the tunnel to street level and to the exit station through a tunnel portal. In long tunnel sections (tunnels between two consecutive stations) where there is a mid-ventilation shaft, to ensure the presence of only one train in the ventilation section, an emergency stairway leading to road level is to be provided within the shaft and located within 2 hours of a protected cross way. The cross-passages of the tunnel will be protected with jet fans to prevent the entry of smoke when the doors are opened.

3 ALIGMENT AND LAYOUT PLAN OF TBM AND CROSS PASSAGE TUNNEL

Cross passage in between TBM tunnel from CSIA to RAMP at UGC07 under Mumbai Metro Line – 3 (Aqua Line).

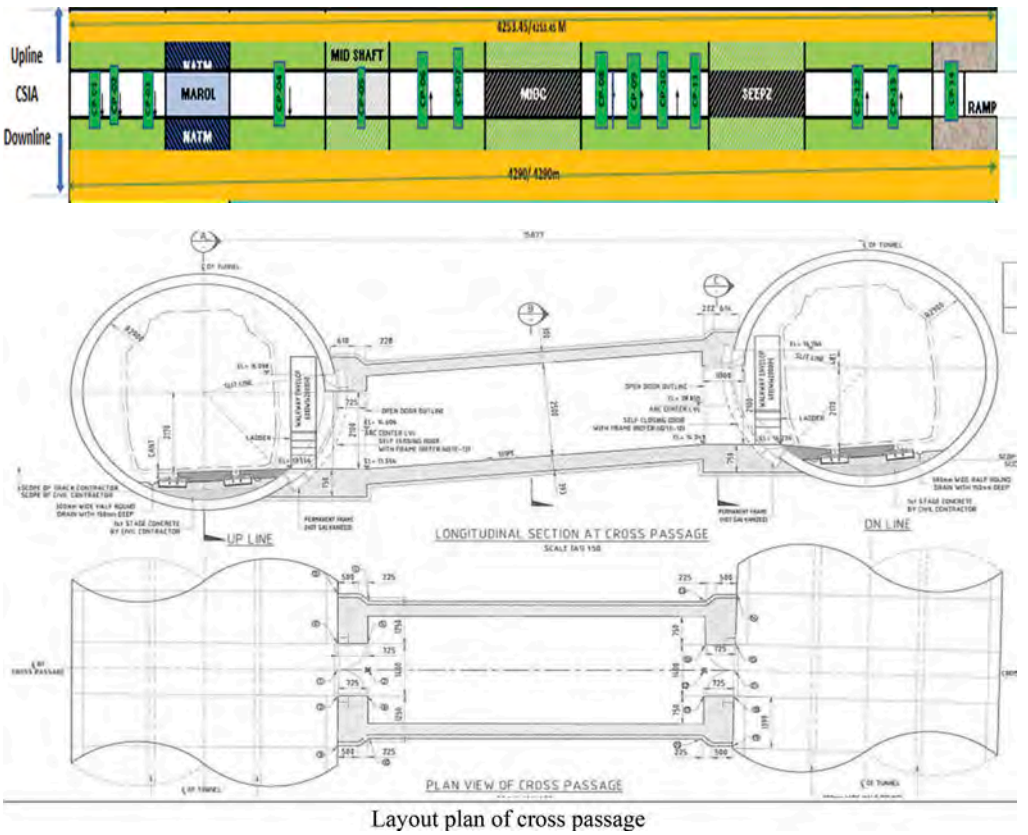

Layout plan of cross passage

4 COSTRUCTION METHODS OF CROSS PASSAGE IN METRO TUNNEL

The construction of cross passage is most important to participate in metro construction. If any process encounters improper operation, the overall construction safety of the cross passage will be affected, resulting in the tunnel body being the main risk.

4.1 *Temporary bracing support system to carry out the work of cross passages*

Bracing systems generally consist of ring girders (and cross beams /tie beams which are connected by means of bolted and welded connections. To reduce the deformation of the lining due to cross passage openings, a third ring beam is included with the cross beam. The design assumed that the steel ring beam was placed in close contact with the tunnel segmental lining. Therefore, it is important that the gap between the lining and the steel support is filled Suitable material to avoid excessive deformation. The analysis is performed using the structural analysis program STAAD Pro V8i. The structure is modeled as a 3D space structure frame. Steel rings are installed in the springs depending on the modulus of elasticity of the soil

4.2 *Ground behavior*

The ground behavior is evaluated for the full cross sectional area without considering any modifications including the excavation method or sequence and support or other auxiliary measures.

Influencing factors are considered for the evaluation of the Ground Behavior:

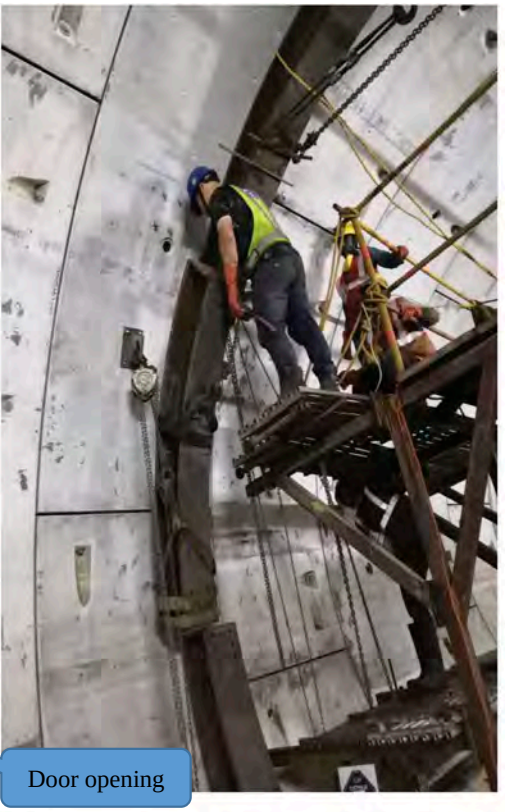

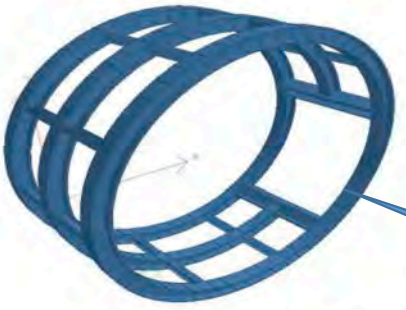

3D schematic View of Temporary Bracing

Bending Moment Envelope - ULS

Shear Force Envelope - ULS

- Ground Type (GT)
- Virgin stress conditions
- Shape and size of the underground structure (final shape and size)
- Position of underground structure in relation to surface or existing structures
- Boundaries between different ground types
- Ground water, seepage force, hydraulic head

The support design need to cater to take care of the predicted ground behavior. To initiate the design, an empirical approach is used to understand support requirement to stabilize the cavity. Support derived from empirical method is used as input for numerical modelling.

The maximum unsupported span of 2.5m for rock class III is on higher side as compared to the size of cross passage, so maximum unsupported span is limited to 1.5m for rock class III. The minimum length, L of rock bolts has been estimated from the excavation width B and the Excavation Support Ratio ESR as per Barton et al (1980):

L= 2+ (0.15 x B)/ESR

From the above formula, minimum length, L of rock bolts has been determined to be 2.5 m for cross passages. The above length of rock bolts may be optimized based on numerical modelling and radius of plastic zone at around the tunnel. Shotcrete with steel fibers is also recommended to prevent spalling. Initial layer of shotcrete is to be provided on a necessary manner before spalling is occurred. Based on Grimstad and Barton (1993)'s chart provided in figure below, primary support system can be derived on an initial basis as given below.

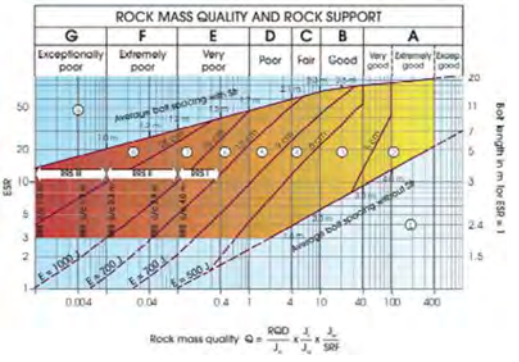

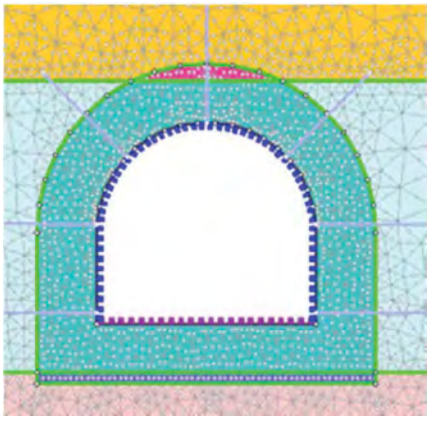

Excavation of Cross Passage, application of internal pressure and application of disturbed rock mass around excavation periphery.

5 EXCAVATION METHODS OF CROSS PASSAGE IN METRO TUNNEL

Excavation of cross passage will start from the completed tunnel. The concept of excavation in rock or soft ground will be based on partial excavation, which is divided into two stages, heading and bench/inverted excavation. excavation by heading and benching method will be safer and better in terms of performance.

5.1 *Above spring level Excavation by Core cutting machine (5 Kw) and Hydraulic Rock splitters (4 Kw)*

Excavation will be done in two parts as heading & benching and it shall be followed only higher grade of rock which RMR value has 75 to 100 Mpa. Above the spring level (SPL) it means semicircular portion is known as heading and remaining lower portion is benching below the SPL. Heading portion will be limited to arch portion only, cannot be extended below to arch portion in any case. This

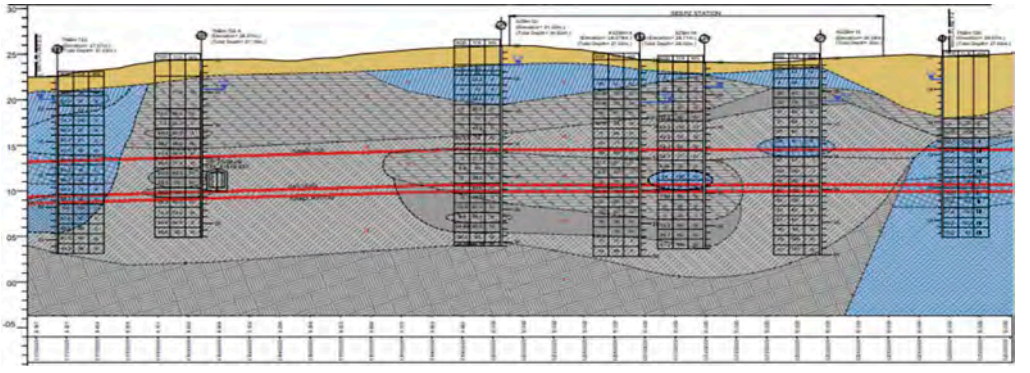

heading portion shall be excavated by peripheral coring, rock splitting, handheld breakers and excavator mounted breakers only. Length of each cycle of excavation along the axis of the cross passage shall be limited to less than 1.0 meter. Once the excavation completed for full 1.0m length final dressing & trimming to the required profile shall be done manually.

Then arch stabilization shall be done by fixing wire mesh and applying dry shotcrete i.e., primary lining as per approved designs, drawings and geological report of RESS (Required excavation supporting system).

After drilling 100 mm-200 mm diameter, 800 to 1000 mm long core holes as shown in figure (2) and (3) above, rock splitters are placed inside such holes to split or break the rock. Will go Once the rock splitting/breaking is done, the rock pieces will be further broken by excavator breaker or pneumatic hand breaker, To ensure that pieces of dirt can be picked up manually.

After achieving two rounds of heading excavation, benching excavation will be done either by excavator installed rock breaker or core cutting machine depending on the quality of the rock. Before going for further benching works, ensure that all necessary rock supports are provided as per the drawing and recommendation of the geologist. To produce less impact throughout the rock profile, the benching would be divided into sections by drilling some holes vertically. The complete sequence is detailed as shown below.

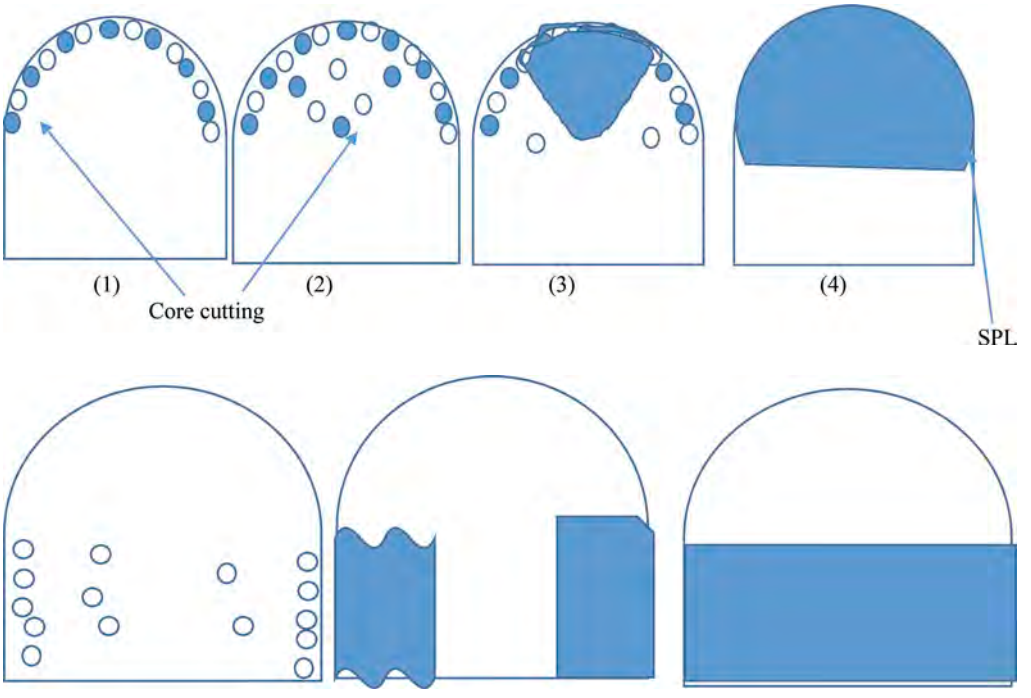

6 CONCLUSIONS

The construction activities of cross passage should be taken up to start construction of permanent structural works in TBM shaft at the earliest. TBM separated from shaft. Therefore, a circular vertical shaft was established between the two main tunnels from the ground surface level and then horizontal cross passages were made under the shafts to connect both the tunnels so that Cross passage are designed to allow final evacuation from train cab to track bed.

Professional work of all parties involved and cooperation based on trust and mutual appreciation are key factors in the success of the project.

ACKNOWLEDGMENTS

The authors would like to thank to MMRCL, MAPLE General Consultancy & AECOM India and Mr. Charuhas M. Jadhav (Executive Director (Civil) MML3), Mr. Mainak roy (CRE UGC07) for their ongoing support and permission to publish information about the project in this paper.

REFERENCES

Hsiung, B. C. B. and Chuay, H. Y. (2006). Geotechnical Risk Assessment and Performance-Based Evaluation of a Deep Excavation in the Kaohsiung MRT System Project, TAIPEI2006 International Symposium on New Generation Design Codes for Geotechnical Engineering Practice, Taipei, Taiwan.

Z.H. Huang, X.D. Hu, J.Y. Wang, H.B. Lin and R.Z. Yu. 2008. "Key techniques in cross passage construction of Shanghai Yangtze River Tunnel by artificial ground freezing method," The Shanghai Yangtze River Tunnel – Theory, Design and Construction, Complimentary Special Issue to The Sixth International Symposium on Geotechnical Aspects of Underground Construction in Soft Ground, Shanghai, pp. 205–210.

F. Qiu and X.D. Hu. 2006. "3D Visualization Analysis of the Frozen Soil Curtain for the Cross-Passage Construction in Tunnels," Proc. 2nd National Symposium on Geotechnical Engineering, Science Press, Beijing, 79–83. (in Chinese)

Hoek E., Carranza – Torres C. (2002). Hoek – Brown failure criterion, Edition 1, In: Proc. NARMS-TAC Conference, Toronto, 1, 267–273.

Oreste P. P. (2003). A procedure for determining the reaction curve of shotcrete lining considering transient conditions. Rock Mechanics and Rock Engineering, 36, 209–236.

Tunnelling for a Better Life – Yan, Celestino, Thewes & Eberhardt (Eds)
© 2024 The Author(s), ISBN 978-1-032-80042-4
Open Access: www.taylorfrancis.com, CC BY-NC-ND 4.0 license

Test and research on load spectrum of tunnel drill jumbo

Xin Liu*
China Railway Construction Heavy Industry Corporation Limited, Changsha, China

ABSTRACT: The drill jumbo is an excavation equipment widely used in tunnel drilling and blasting works. To better ensure the reliability of the whole life cycle of the equipment, establishing a scientific and reasonable fatigue strength theory and safety assessment system is the key to the stable operation of the equipment. Combined with the construction experience of drilling and blasting method, this paper collects the load spectrum of reliability test for a certain type of drill jumbo, studies the load collection method and load spectrum compiling method, develops the load spectrum database, introduces the load spectrum acquisition method integrating various parameters such as stress, torque and rotation speed, and forms a complete process of load spectrum data pre-processing, editing and compiling by using measured data, so as to provide accurate and simplified data for the study of load spectrum of drill jumbo. It also provides important technical support for the fatigue damage analysis and life prediction of equipment components under pavement random load spectrum based on fatigue damage theory, as well as the fatigue durability research of drive system.

Keywords: drill jumbo, drive system, load spectrum, fatigue life analysis

1 INTRODUCTION

During construction, the drill jumbo will bear random loads caused by road roughness. Such random loads usually cause cumulative fatigue damage to components of the drive system of the drill jumbo. To ensure that the trolley drive system components do not suffer fatigue damage during their service life, it is necessary to carry out fatigue strength analysis on the trolley drive system components. Many scholars have studied the load spectrum of equipment in different fields, but there is relatively little research on the load spectrum of drive system under complex working conditions of drill jumbo. The main research focuses on the theoretical strength analysis and fatigue life of work boom. Song Yingpeng [1] simulated the fatigue life of the boom of drill jumbo under extreme working conditions, and calculated the fatigue life to provide a reference for the boom design of similar equipment.; [2] Wu Nan carried out modal and fatigue analysis on the feed beam of drill jumbo based on SolidWorks Simulation Module, obtained relevant natural frequency and service life data, and proposed improvement measures.; [3] Wang Yansheng studied the relationship between average stress and fatigue limit of telescopic boom material of drill jumbo during tension-tension or tension-compression fatigue test, and estimated the stress fatigue life formula of telescopic boom material under different conditions of frequency according to equivalent theoretical fatigue limit and stress fatigue life.

2 STRUCTURE ANALYSIS OF DRIVE SYSTEM

The drive system structure of a drill jumbo is shown in Figure 1. In the actual operation of the drill jumbo drive system, the drive shaft inputs power to the front rigid drive axle and the rear steering drive axle to drive the wheels to realize the traveling of the drill jumbo. The axle not only bears the weight of the whole vehicle, but also needs to withstand the impact caused by uneven road surface during driving. It is functionally both a bearing part and a force drive part. It is the most critical and complex drive component in the drive system. Its frequent cumulative fatigue damage caused by alternating loads will cause fatigue failure of the axle housing. Therefore, the drive system is the most ideal test object for road load spectrum collection and also the key to fatigue reliability research of the drive system.

*Corresponding author: liuxin@crchi.com

DOI: 10.1201/9781003495505-206

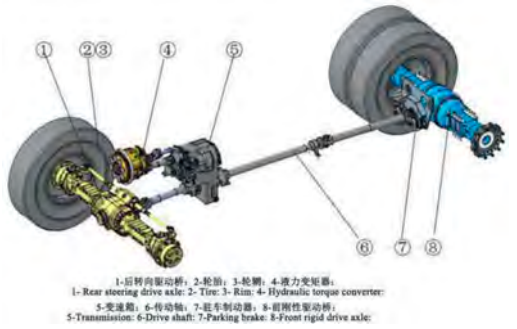

Figure 1. Structure diagram of drive system of a certain type of drill jumbo.

3 AXLE SIMULATION ANALYSIS

3.1 *Load simulation analysis*

The finite element analysis software Abaqus should be used to simulate and analyze the drive axle housing. According to the running characteristics of this type of trolley and the axle load, the stress condition of the axle housing can be simplified into the following three load conditions: tangential force Fx when the trolley runs and brakes, lateral force Fy when the trolley travels on the side slope, and vertical force Fz of vehicle weight when the trolley travels. The axle housing is loaded and analyzed under the one-way load condition in Table 1. For example, as shown in Figure 2, the tangential force Fx loading is the same, but the lateral force Fy is limited by the test of axle housing structure form. It is considered to decompose it equivalently into lateral tensile pressure along the axle housing axis and bending moment along the upper and lower surfaces of the axle housing for load analysis. The load response sensitivity analysis is shown in Figure 3. According to the stress results of measuring points in Table 2, the selected area has obvious stress and strain responses, the change gradient is less than 10%, and the stress does not exceed the yield limit, which is an ideal test area. Accordingly, the positions of measuring points for real vehicle load test will be determined. At the same time, according to the load magnitude, it can be seen that the maximum contribution load is vertical force Fz. Based on the basic factor of vertical force Fz, the composite load contribution analysis of lateral force Fy and vertical force Fz under the working conditions in Table 3 is carried out. According to the stress results of measuring points in Table 3, the composite load of tangential force Fx and vertical force Fz has a great impact on the axle housing, with a load contribution rate of 31.7%; the lateral bending moment Fmy decomposed by the lateral force Fy has a great impact on the axle housing, and the load contribution rate is 74.9%; the contribution rate of lateral tension Fyl decomposed by lateral force Fy to the axle housing is 3.7%, which has little influence and can therefore be ignored. It can be seen from the comprehensive analysis that when the trolley is running on a side slope, the lateral bending moment Fmy and vertical force Fz decomposed by the lateral force Fy are both acting on the upper and lower surfaces of the axle housing. The load test is carried out on the real vehicle against the vertical force Fz, and the tangential force Fx and lateral force Fy are characterized compoundly by the tested vertical force Fz.

Figure 2. Schematic diagram for application of vertical load (Fz).

Table 1. One-way load condition of axle housing.

	Load condition	Applied load/N
Condition 1	Tangential force Fx	12.8×10^4
Condition 2	Lateral force Fy	12.1×10^4
Condition 3	Vertical force Fz	40.2×10^4

4 AXLE ROAD LOAD SPECTRUM DATA ACQUISITION

4.1 *Setting of load test conditions*

The working conditions of the trolley in actual operation will be random, which are mainly reflected in the construction site, road conditions and driver's driving habits. It is necessary to determine a certain representative industrial test site. After investigation and analysis of typical operation conditions on the construction site, a mountainous tunnel construction site will be selected. Combined with jumbo operation conditions and on-site road conditions, the test conditions will be determined as shown in Figure 5 below, and the reference mileage and driving speed of the test section are shown in Table 5.

4.2 *Acquisition of load spectrum*

The expression form of load spectrum involves many parameters, mainly including force, moment, acceleration, displacement, torque, strain, velocity, etc. According to the load spectrum test requirements of the drill jumbo, strain gauges are used to collect the strain of key parts of the axle housing, torque strain gauges are used to collect the strain of the drive shaft, and wireless speed sensors are used to collect the rotation speed of the drive shaft.

Sensor pasting is shown in Figure 6. The above various sensor signals are connected to a multi-channel data acquisition instrument, and all channels should be synchronized by the acquisition software

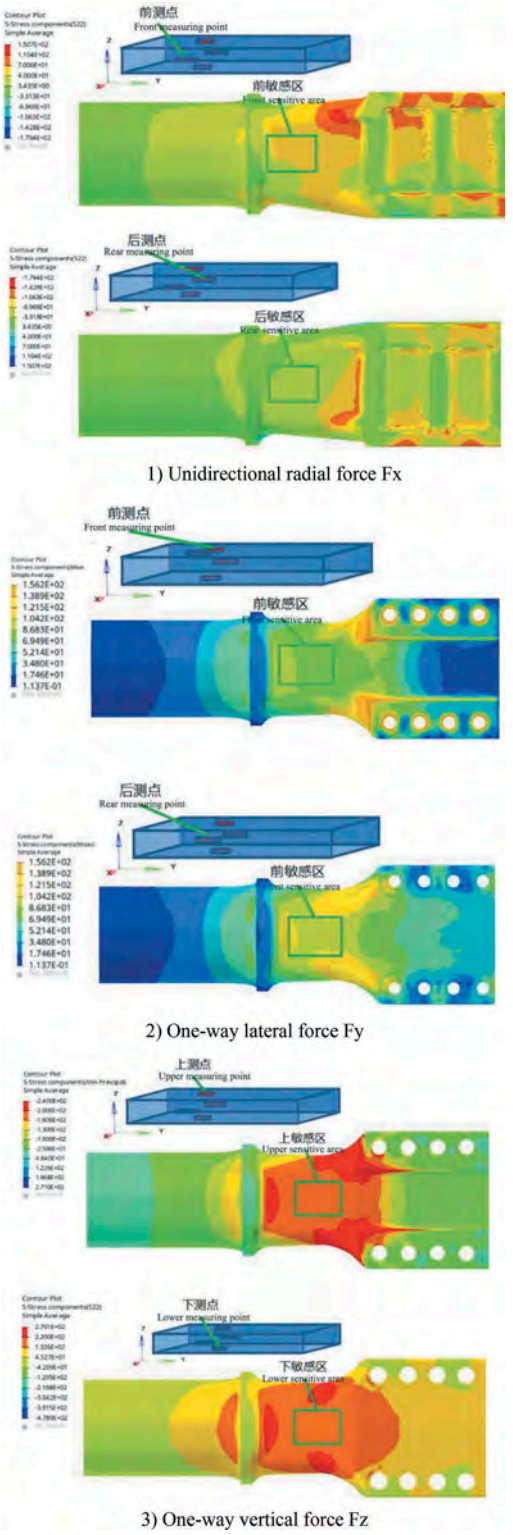

Figure 3. Simulation nephogram of axle housing load sensitive area.

according to time domain to collect various data at the same time. The acquisition scheme and device and equipment are shown in Figure 7.

4.3 *Load calibration*

The axle housing load calibration is to paste strain gauges on the tested parts, assemble bridges, output voltage signals, use a calibration loading table as shown in Figure 8 to load the axle housing, apply vertical force Fz from small to large to the axle housing, measure the corresponding output strain value of the strain gauges, and obtain the values of test strain and external load. The static torsion test bench is used to obtain the values of torque and strain for the drive shaft. The load test scheme and equipment are shown in Figure 7. The acquisition device is a dynamic signal testing, analysis and acquisition instrument. The axle housing can send the half-bridge circuit output signals of single direct strain gauge set, and the drive shaft can send the full-bridge circuit output signals of torque gauge set. The calibration results are shown in Table 6. It can be seen from the data results that the calibration test has good linearity, and the correlation coefficients after calibration data fitting are all above 0.95, indicating high calibration fit accuracy. The results are accurate and reliable, meeting the requirements.

5 PREPROCESSING OF LOAD SPECTRUM DATA

The original load-time history of jumbo test has certain randomness, which is difficult to be directly applied in engineering. It is usually necessary to remove singular values, trend terms, filter and denoise the original data, then compile the required load spectrum according to the actual conditions, and at the same time, it can also carry out frequency spectrum analysis on the data to study the regularity of the load spectrum.

5.1 *Zero drift processing*

Usually, due to device heating, strain gauge pasting deviation, structural residual stress and other reasons, the initial output signal of the dynamic acquisition instrument has a “drift phenomenon” that is not zero. The piecewise linear zero drift hypothesis can be used for signal processing. The measured signal is processed in M sections to obtain the mean value of each section of signal S_1~S_5, and the zero drift in each section is A~E. The average solution point values are A(0,0)B(M, (S1+S2)/2), C(2M, (S2+S3)/2), D(3M, (S3+S4)/2), E(4M, (S4+S5)/2) and F(5M, S6+(S6-S5)/2), The zero drift value of each segment is subtracted point by point from the measured signal amplitude to obtain the load signal after eliminating

Table 2. Simulation analysis results of one-way load sensitive area of axle housing.

	Measuring point	Micro strain	Stress/MPa	Maximum stress	Stress difference
Condition 1	Front measuring point	324.2	68.1MPa	179.4MPa	12.9MPa
	Rear measuring point	-262.9	-55.2MPa		
Condition 2	Upper measuring point	511.9	107.5MPa	156.2MPa	8.9MPa
	Lower measuring point	-469.5	-98.6MPa		
Condition 3	Upper measuring point	826.2	-173.5MPa	270.1MPa	15.7MPa
	Lower measuring point	-901	189.2MPa		

Table 3. Multi-directional load conditions of axle housing.

	Load condition	Applied load/N
Condition 4	Vertical force Fz + tangential force Fx	$40.2\times10^4+12.8\times10^4$
Condition 5	Vertical force Fz + lateral bending moment Fmy (14°)	$40.2\times10^4+8.5\times10^7$
Condition 6	Vertical force Fz+lateral bending moment My (14°)+lateral tension Fyl	$40.2\times10^4+8.5\times10^7+12.1\times10^4$

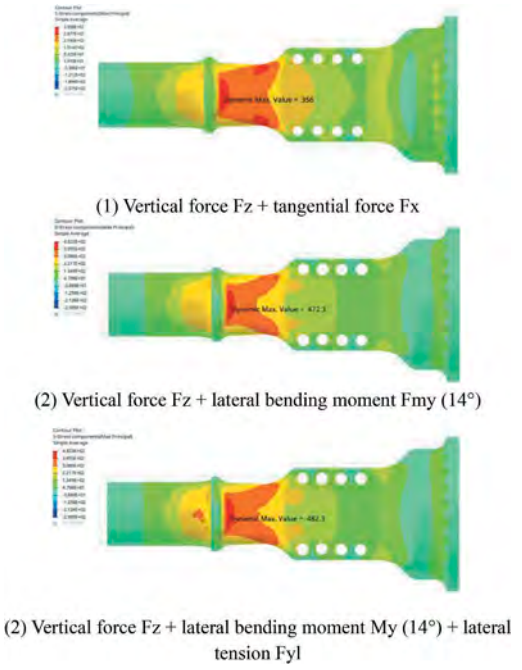

(1) Vertical force Fz + tangential force Fx

(2) Vertical force Fz + lateral bending moment Fmy (14°)

(2) Vertical force Fz + lateral bending moment My (14°) + lateral tension Fyl

Figure 4. Simulation nephogram of axle housing load contribution.

Table 4. Simulation analysis results of multi-directional loads on axle housing.

	Contributed load	Maximum stress	Contribution
Condition 4	Tangential force Fx	355.8MPa	31.7%
Condition 5	Lateral bending moment Fmy (14°)	472.3MPa	74.9%
Condition 6	Lateral tension Fyl	482.3MPa	78.6%

a) Curved slope

b) Pothole road

c) Road inside tunnel

d) Inverted trestle

Figure 5. Test condition diagram.

Table 5. Test mileage and running speed.

S/N	Road conditions	Chainage/m	Test speed km/h
1	Curved slope	200	5-8
2	Pothole road	500	5-8
3	Road inside tunnel	1000	12-15
4	Inverted trestle	50	3-5

the zero drift value, as shown in Figure 9. During the test of this jumbo, the method of removing zero drift by software should be selected to complete the true recovery of strain signal.

a) Axle housing strain gauge b) Drive shaft torque strain gauge c) Drive shaft speed sensor

Figure 6. Schematic diagram of senser installation position.

Figure 7. Schematic diagram of acquisition system construction.

Figure 8. Loading platform for load calibration.

Table 6. Load calibration results.

S/N	Member	Load parameters	Fitting equation	Correlation coefficient
1	Drive shaft	Torque load	y=11.0553x-5.25-6	R^2=0.9856
2	Axle housing	Vertical load	y=15.422x +31.176	R^2=0.9802

5.2 *Removal of trend items*

Trend items often cause the test signal to deviate from the baseline. When there is an obvious trend item in the signal that has not been eliminated, distortion will occur during correlation analysis and power spectral density analysis. The trend item is fitted by least square method, and then the trend item will be removed by subtracting the trend item from the original data.

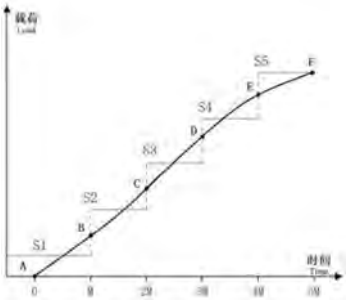

Figure 9. Segmented zero drift processing method.

The load data obtained from the test is $\{x_k\}(k=1,2,3\cdot\cdot,n)$, and the test data fitting is carried out by an m-order polynomial, then:

$$\hat{x_k} = a_0 + a_1 k + a_2 k^2 + \cdots + a_m k^m = \sum_{j=0}^{m} a_j k^j$$
$$k = 1, 2, 3, \cdots, n \quad (1)$$

Based on the principle of least squares, the coefficients to be determined for each order of the function are confirmed so that the sum of squares of errors between the function and discrete data is minimized, namely: $\hat{x}_k k = 1, 2, 3, \cdots n\hat{x}_k x_k$

$$E(a) = \sum_{k=1}^{n} (\hat{x}_k - x_k)^2 = \sum_{k=1}^{n} \left[\sum_{j=0}^{m} a_j k^j - x_k \right]^2 \quad (2)$$

$E(a)$The conditions for the existence of extreme values are:

$$\frac{\partial E}{\partial a_1} = 2 \sum_{k=1}^{n} k^i \left(\sum_{j=0}^{m} a_j k^j - x_k \right)^2, k = 1, 2, 3, \cdots, n \quad (3)$$

For each partial derivative, an m+1-member linear system of equations is produced: a_i

$$\sum_{k=1}^{n} \sum_{j=0}^{n} a_j k^{j+i} - \sum_{j=0}^{n} x_k k^i = 0 \quad (4)$$
$$k = 1, 2, 3, \cdots, m$$

The m+1 linear equations are solved to obtain m+1 undetermined coefficients. $a_j(j = 1, 2, 3, \cdots, m)$

In the above equations, m is the order of the set polynomial, and its value range is 0≤j≤m.

1) When m=0, the trend term is a constant, including:

$$\sum_{k=1}^{n} a_0 k^0 - \sum_{k=1}^{n} x_b k^0 = 0 \quad (5)$$

It is solved as follows:

$$\hat{x}_k = a_0 = \frac{1}{n}\sum_{k=1}^{n} x_k \tag{6}$$

It can be easily obtained from Formula (6) that when m=0, the trend term in the signal is an arithmetic mean value of the signal data and a constant. At this time, the calculation formula for eliminating the constant trend term is:

$$y_k = x_k - \hat{x}_k = x_k - a_0, k = 1, 2, 3 \cdots, n \tag{7}$$

2) When m=1, the trend term is linear, including:

$$\begin{cases} \sum_{k=1}^{n} a_0 k^0 + \sum_{k=1}^{n} a_1 k - \sum_{k=1}^{n} x_k k^0 = 0 \\ \sum_{k=1}^{n} a_0 k + \sum_{k=1}^{n} a_1 k^2 - \sum_{k=1}^{n} x_k k = 0 \end{cases} \tag{8}$$

It is solved as follows:

$$\begin{cases} a_0 = \frac{2(2n+1)\sum_{k=1}^{n} x_k - 6\sum_{k=1}^{n} x_k k}{(n-1)} \\ a_1 = \frac{12\sum_{k=1}^{n} x_k k - 6(n-1)\sum_{k=1}^{n} x_k}{n(n-1)(n+1)} \end{cases} \tag{9}$$

$$y_k = x_k - \hat{x}_k = x_k - (a_0 - a_1 k)$$

$\hat{x}_k = a_0 + a_1 k$, the calculation formula for eliminating trend terms is:

$$y_k = x_k - \hat{x}_k = x_k - (a_0 - a_1 k) \quad k = 1, 2, 3 \cdots, n \tag{10}$$

The analysis of the collected data shows that most of the data trend terms are linear, mostly primary and a few quadratic. Therefore, m=2 is selected to carry out polynomial elimination processing on the test signal. On the basis of the principle of least squares method, the trend term of axle housing strain signals with significant trend terms is eliminated. The trend term elimination results are shown in Figure 10.

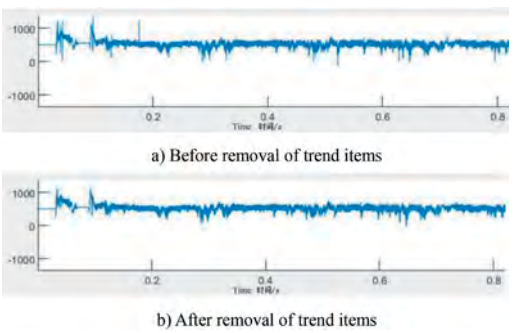

Figure 10. Elimination results of torque trend terms for front drive shaft.

5.3 *Filtering and noise reduction*

Noise, as an interference item to be avoided in the load spectrum signal, should be eliminated. The locality of non-stationary signals within a single cycle in time domain is an important characteristic of vehicle load spectrum signals. According to the principle of Fourier transforming, the corresponding program is compiled in MATLAB. Through the spectrum analysis of the signal before filtering of the front drive shaft, it can be known that the working frequency of the trolley is mainly concentrated within 5 Hz, so low-pass filtering can be used to remove high-frequency interference signals. Figure 11 is a comparison diagram of signals before and after drive shaft filtering under curved slope working condition. It can be seen from the figure that selecting Babbitt low-pass filter can achieve the effect of removing interference signals without obvious changes in signals before and after the filtering.

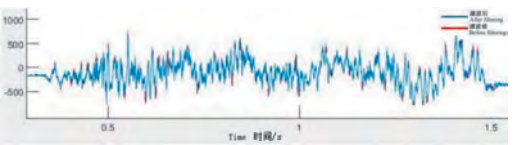

Figure 11. Signal diagram of front drive shaft before and after torque filtering.

5.4 *Inspection and elimination of singular values*

In the acquisition of load signals, the load-time history measured by sensors will usually lead to abrupt changes in test data due to computer test systems or human errors, so there will be some anomalies in the acquired signals. These abnormal peak points are also called singular values. The existence of singular values will affect the accuracy of data processing and cause relatively big errors in fatigue life, so they must be identified and eliminated during preprocessing of load signals. The common methods include amplitude threshold method, gradient threshold method, standard deviation method and “6” gradient method. According to the characteristics of the test data, the “6” gradient method is used to remove abnormal peak points. $\sigma\,\sigma$

In the "6" gradient method, it is believed that the gradient obtained by differentiating the original data at equal time intervals approximately obeys the normal distribution N(). According to the "6" principle, most of the positive values are located in (), and the probability of value taking within this range can reach 99.74%. It is generally believed that the situation of not taking values within this range will hardly occur in a test. Therefore, for a group of data, = 1, 2, 3 ⋯, n, calculate the mean and standard deviation as: $\sigma\,\mu$, $\sigma^2\sigma$ $\mu - 3\sigma$, $\mu + 3\sigma\{X_i\}$ $i\mu\,\sigma$

$$\mu = \frac{1}{n}\sum_{i=1}^{n} \mu_i \tag{11}$$

$$\sigma = \sqrt{\frac{1}{n-1}\sum_{i=1}^{n}(\mu_i - \mu)} \qquad (12)$$

By setting a gradient threshold and comparing it with the difference between the gradient mean value and the variance of the gradient, if the difference is greater than the gradient threshold of the variance, it will be recognized as a singular peak. The signal curve of the front axle before and after abnormal points elimination is shown in Figure 12.

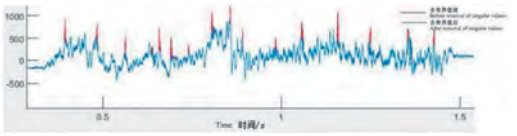

Figure 12. Signal comparison of rear drive shaft before and after singular value removal.

5.5 *"Principle of valley-peak extraction*

In the process of trolley acquisition and test, to ensure the authenticity and integrity of the acquired data, the sampling frequency is usually set very high. The initial acquisition frequency of this trolley is set to 50 Hz, which will lead to a particularly large amount of collected data. Only by signal compression, editing and counting can truly useful random signals be obtained.

The inflection point of the time-domain signal is a key point constituting the load cycle, but the non-inflection point in the time-domain signal does not affect the fatigue damage result. The waveform of the signal after valley-peak extraction is basically the same as that of the original signal, and the sequence of the original signals is not changed. See Figure 13 below for the comparative analysis of arbitrarily selected front axle loads.

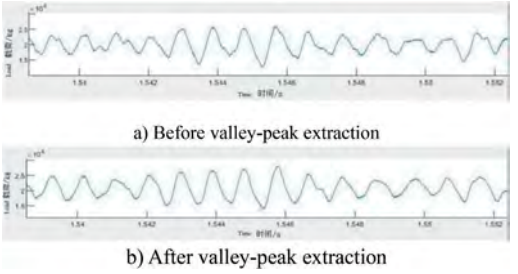

a) Before valley-peak extraction

b) After valley-peak extraction

Figure 13. Signal diagram before and after load Valley-peak Extraction of Front Axle.

6 PREPARATION OF LOAD SPECTRUM DATA

The jumbo test is characterized by harsh road conditions, strong comprehensiveness of operating conditions and strong randomness of loads. However, for each road condition, its load characteristics still have a certain regular trend. The load-time history of each working condition after removal of zero drift, trend term, filtering and noise reduction, singular value inspection and elimination is shown in the following Figure 14.

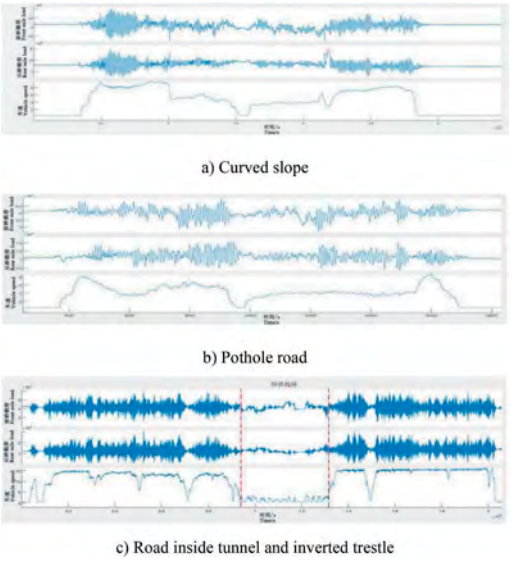

a) Curved slope

b) Pothole road

c) Road inside tunnel and inverted trestle

Figure 14. Load-time history diagram under various working conditions.

7 CONCLUSIONS

This paper puts forward a load test scheme of the drive system combined with the load characteristics of the drive system, drilling operation conditions and actual use by users. The load tests under different road conditions during actual operation should be carried out to reproduce the loads of the jumbo in actual use.

By removing zero drift, trend item, filtering and noise reduction, singular value inspection and elimination and other data processing links of load test data, the load time history diagram under various working conditions will be compiled.

Through the test load time history diagram, it provides important load data for subsequent fatigue damage analysis and life prediction of equipment components under pavement random load spectrum based on the fatigue damage theory.

REFERENCES

[1] Song Yingpeng, Guan Huisheng, Ge Wenchang, Zhou Yao. 2017. *Simulation of Boom Fatigue Life of AXERA_T1 Drill Jumbo under 5 Working Conditions* [J]. Mine Machinery, 45 (12): 14–17.

[2] Wu Nan, Sun Zhaopeng. 2021. *Modal and Fatigue Analysis of Feed Beam Based on SolidWorks Rock Jumbo* [J]. Coal Machinery, 41(10):84–86.
[3] Wang Yansheng, Wang Huiping, Yang Junsen, Lin Gang. *Study on Fatigue Life of Telescopic Boom Materials for Drill Jumbo* [J]. Tunnel Construction, 24(4):5–6.
[4] Jin Hongjie, Zang Liguo, Li Yaowei 2022. *Research and Application of Load Spectrum Compilation Technology for Vehicle Chassis Test* [J]. Journal of Chongqing University of Technology, 36(12):256–264.
[5] Wan Jiuyuan, Zhang Qiang, Huang Jinjian et al. 2017. *Research on Key Technologies of Load Spectrum Test for Loader Drive System* [J]. Engineering Machinery, 2017,48(9):33–38.
[6] Yang Ping, Zou Xihong. 2021. *Compilation Method of Enhanced Load Spectrum Based on Road Simulation Test* [J]. China Journal of Mechanical Engineering, 19(5): 419–424.
[7] Dong Guojiang, Yan Feng, Han Jie. 2021. *Method and Research on Load Spectrum Extraction of Vehicle Suspension Components* [J]. Journal of Vibration and Shock, 40(2):103–110.
[8] Wang Chunshan, Wang Xi, Yang Guangxue et al. 2018. *Railway Train Load Spectrum and Its Application* [M]. China Railway Publishing House.
[9] Wan Yipin. 2021. *Load Spectrum of Loader Working Device and Its Application* [M]. Xidian University Press.
[10] Liu Yongcheng. 2011. *Load Test and Treatment of Wheel Loader Drive System* [J]. Construction Machinery and Mechanization, 28 (8): 83–85.
[11] Liu Yongcheng. 2010. *Load Spectrum Measurement and Smooth Processing of Loader Drive System Based on Real Environment* [J]. Mine Machinery, 38 (19):49–52.
[12] Liu Yanlong, 2015. *Dynamic Load Spectrum Extraction and Bench Test Load Spectrum Compilation of Automotive Drive System* [D]. Chongqing: Chongqing University of Technology.
[13] Mariusz K. Preliminary secection of road sectionsfor high-mobility wheeled vehicle testing under provinggroung condition [J]. Applied Sciences. 2022, 12:3513.
[14] Yu Jin, Liang Jian, He Liqiang, Tu Xudong, 2022. *Study on the Application of Three-arm Drill Jumboin Tunnel Excavation Construction* [J]. Bridge and Tunnel Engineering, 11(5)123–125.

Tunnelling for a Better Life – Yan, Celestino, Thewes & Eberhardt (Eds)
© 2024 The Author(s), ISBN 978-1-032-80042-4
Open Access: www.taylorfrancis.com, CC BY-NC-ND 4.0 license

Experimental study of step method construction in soft and broken surrounding rock section of super-long and large section tunnels

Yuanming Liu*, Yiqian Wang, Ting Zhu, Miaoliang Tian & Qingzhi Cheng
College of Civil Engineering, Guizhou University, Guiyang, China

ABSTRACT: The construction method of long and big section soft and broken surrounding rock tunnels has a significant impact on the construction period.The double-sided methods, CRD methods and CD methods are slow in construction speed and not conducive to mechanized construction. The step method has the characteristics of simple process, fast construction, timely support, and high mechanization. To meet the requirements for the construction period of ultra long tunnels, the step method should be selected for construction under safe conditions. At present, there are the following shortcomings in the research on the construction of weak and fractured tunnels using the step method: 1) The variation law of tunnel arch settlement with step height is not yet clear; 2) The optimal step height method has not been established yet. A tunnel bench method construction model test was conducted based on the Tongzi Tunnel to analyze the influence of bench height on tunnel arch settlement, surrounding rock pressure, and internal force of tunnel support. Research has shown that as the excavation height of the upper step increases, the settlement of the tunnel arch increases, and the maximum settlement of the arch is reached when the height of the upper step is 0.5H (H is the tunnel height). The excavation height of the middle step should not exceed 0.4H. The optimized construction industrial parameters are as follows: 0.45H for the upper step, 0.35H for the middle step, and 0.2H for the lower step; The length of bench should be 4-6 meters.On site construction monitoring shows that when the tunnel adopts the three-step method in the V-level surrounding rock, the settlement displacement of the tunnel vault and the convergence displacement of the arch waist are both within the control range, and the construction efficiency is high and safe.

Keywords: Weak and broken surrounding rock, Construction methods, Model test; Bench method, Parameter optimization

1 INTRODUCTION

In recent years, along with the rapid development of Chinese expressway, the tunnels in China are getting longer and longer, with larger spans and more complex geological conditions for crossing. Chinese tunnel construction level is getting higher and higher, and the construction machinery and equipment are getting more and more advanced. But the tunnels whose length are more than 10,000 meters, still faces the problem of tight schedule. Especially, the tunnel construction method has a significant impact on the construction period of large-span tunnels with weak and fractured surrounding rocks. CD method, CRD method and double sides heading method inevitably lead to slow construction schedule and low economic efficiency (Cui 2010, Gu and Huang, 2014, Li et al, 2018, Wang et al, 2018, Wei et al, 2011, Zhang et al, 2013). However, the step method has the characteristics of simple process, fast construction, timely support, and high mechanization.

In China, many tunnels with soft and weak surrounding rocks have been successfully constructed by the step method. Xin Guo simulated the three-step method which was used Ping'an Tunnel, and the results showed that the step method was beneficial to the stability of the surrounding rock (Xian, 2016). The three-step method was used instead of double sides heading method in V-class surrounding rock section of the Dawangding Tunnel, which was completed 10 months earlier than the original schedule and saved construction costs (Liu and Xie, 2010). The step method instead of the double sides heading method, also,improved the construction progress of V-class surrounding rock section of Qihaoling Tunnel (Chen 2008). Lu Dewen conducted a test on the construction of Liangjiashan Tunnel's V-class surrounding rock section using the three-step method, which showed that the tunnel deformation and lining structure stresses were in a safe condition (Lu et al, 2018). Lin Minxing proposed that the construction of highway tunnels with class V surrounding rock can be completed faster by using the step method than the CD method, which shortens the construction period and saves the construction cost (Lin 2018).

*Corresponding author: liuym_2021@163.com

DOI: 10.1201/9781003495505-207

In order to further promote the efficient construction technology of soft and broken surrounding rock tunnel, the step method construction should be optimized. Several scholars have carried out research on optimization of construction parameters for the step method. Song Shuguang and others studied the mechanical effect law of the construction process of the step method in liangshui tunnel of the Lanzhou-Yuzhou Railway with soft and crushed perimeter rock, and concluded that the height of the step was optimal at the maximum width of the program (Song et al, 2011). Zou Chenglu found than the settlement of the vault increased as the height of the step method increased from 0.55H to 0.75H. It was considered that the optimum height of the step was 0.65H (Zou et al, 2013a, Zou et al, 2013b). Deng Tao studied the Zhongtiaoshan Tunnel of the Menghua Railway and optimized the length and height of the steps. When Step length was controlled in 4.8m~ 6.4m, the structural stress was the most favorable. Increasing the height of the upper step can reduce the deformation of the tunnel, but it was not the higher the better. It was more appropriate that the height of the upper step was controlled in 0.5H~ 0.7H (H refers to the height of the tunnel, the same below) (Deng et al, 2017). Liu Zhaowei found the arch settlement decreased when the step height of Duanjiaping Tunnel of Menghua Railway was from 0.2H to 0.5H, but the value of arch settlement was very close. The step height which was 0.3H~0.5H was good for controlling tunnel deformation (Liu and Li, 2017).

To sum up,there are still deficiencies in the optimization of step height, mainly in: 1) there are contradictions in tunnel vault settlement change law and step height; 2) a number of optimal step heights were proposed, but they are very different; 3) the research was mostly based on numerical simulation, and very few studies on modeling tests or field test validation (Wangle 2004, Xu et al, 2018).

Tongzi Tunnel which was the key project of Chongzun Expansion Project (in Guizhou), is the first longest tunnel under construction in karst area and the first longest tunnel under construction in Guizhou Province. It is separated two-way six-vehicle oversized sectional tunnel, traversing through karsts, faults, coal seams and other adverse geological conditions, with amaximum depth of 639m and length of 10,500m. About 19.0% of its length is in class III surrounding rock, and about 70.5% is in class IV surrounding rock, and about 10.5% is in class V surrounding rock. In order to meet the schedule requirements, there is an urgent need to optimize the construction method of the weak and broken perimeter rock section.

This paper carries out the construction model test of the step method in the soft and broken surrounding rock section of Tongzi Tunnel, analyzes the influence of the step height on the settlement of the tunnel vault, the pressure of the surrounding rock and the internal force of the tunnel support, and researches the optimal step height of the step method for the construction of tunnels through the weak and broken zone.

2 TUNNEL CONSTRUCTION MODEL TEST PLAN

2.1 *Model test benches*

The section ZK44+665~ ZK44+645 of Tongzi Tunnel was took as a typical section. The section of the enclosing rock level V, medium weathering tuff sandwiched between mudstone, rock quality is softer, the overall enclosing rock is more broken. As shown in Figure 1, the tunnel lining of Tongzi Tunnel is a composite tunnel lining with V-class surrounding rock. The tunnel lining is a composite lining with the span of 17.4m and the height of 11.85m.

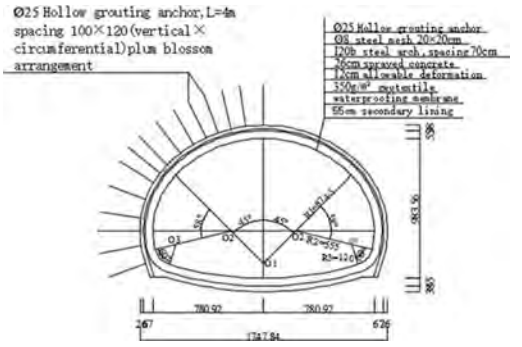

Figure 1. Composite lining drawing.

As shown in Figure 2, the tunnel model test rack is designed according to a 1:50 similarity ratio. The front of the test rack consists of square steel tubes and tempered glass and acrylic panels. The sides are composed of steel plates and square steel. The internal dimensions of the tunnel model test stand are 2m wide, 0.8m deep and 1.2m high. The modeled tunnel is 0.237m in height and 0.348m in width.

Figure 2. Tunnel model test bench diagram.

2.2 *Tunnel surrounding rock materials*

Similar material ratios were used with the mass ratio barite powder: quartz sand: petroleum jelly = 600:420:80. The test specimens for mechanical properties of similar materials are shown in Figure 3.

Figure 3. Sample.

Determination of cohesion and angle of internal friction of materials using fully automated triaxial instrument. The physical-physical-mechanical properties of the surrounding rock of the prototype tunnel and the similar materials of the model tests are shown in Table 1.

Table 1. Physical and mechanical properties.

Surrounding rock level	Severek N/m³	Deformation modulus / GPa	Poisson's ratio/μ	Internal friction horn /φ°	Cohesion/ MPa
prototype	21.0	<1.3	0.40	26	0.05
model	21.0	0.026		24	0.04

2.3 *Tunnel surrounding rock pressure test method*

As shown in Figure 4, a pressure box was pre-built within the simulated tunnel envelope to test the pressure variations in the tunnel envelope. Tunnel perimeter rock pressure was measured using a DH3181-2 static strain tester.

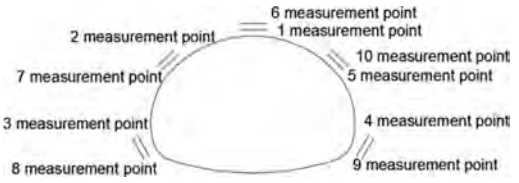

Figure 4. Arrangement of surrounding rock pressure measuring points.

2.4 *Supporting materials*

In modeling tests, gypsum simulation and thin metal shell simulation are usually used for the simulation materials of initial support. In this test, 0.5mm post thin steel plate was used to simulate the initial tunnel support.

As shown in Figure 5, applying strain gauges to the simulated support surface can test the support deformation and then calculate the internal force of the tunnel support. Support deformation was measured using a DH3181-2 static strain tester.

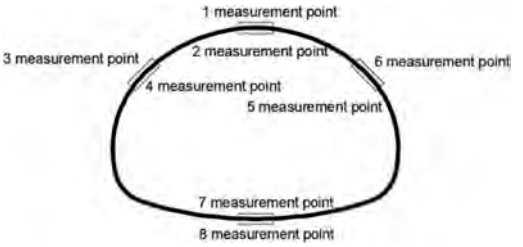

Figure 5. Measurement point arrangement.

Due to the small internal space of the model test tunnel and the small value of the vault settlement, the measurement of the tunnel vault settlement is difficult and no suitable measurement method has been reported.

This test cleverly uses the percentage meter to measure the settlement of the arch of the model test tunnel, which is a good solution to this problem. A schematic diagram of the percentage meter arrangement is shown in Figure 6(a). The percentile meter used for the model test is shown in Figure 6(b). The accuracy of the meter is 0.01 mm. The model test is set up to measure the section: 0+20 cm.

Figure 6. Schematic diagram of the layout of the dial indicator.

After simulating the surrounding rock is filled, the model test first stood for 24 hours, then excavated work.

3 ANALYSIS OF THE BENCH METHOD CONSTRUCTION

3.1 *Bench excavation program*

The height of the step method construction steps should meet the space requirements for mechanical

excavation. The construction plan for the step method is shown in Table 2, with the height of the upper step increased from 0.4H to 0.6H.

Table 2. Step height.

	Model test tunnels			Prototype tunnels/m		
Programs	Up	Middle	Down	Up	Middle	Down
Program One	0.4H	0.4H	0.2H	4.74	4.74	2.37
Program Two	0.45H	0.35H	0.2H	5.33	4.15	2.37
Program Three	0.50H	0.4H	0.1H	5.93	4.74	1.19
Program Four	0.55H	0.35H	0.1H	6.52	4.15	1.19
Program Five	0.60H	0.3H	0.1H	7.11	3.56	1.19

Tunnel step method excavation process is shown in Figure 7. According to the step overrun 10cm (i.e., the upper step overrun the middle step 10cm, the middle step overrun the lower step 10cm), each step of the excavation footing 10cm. The length of the model test tunnel is 80cm, according to each cycle of footage is 10cm, a total of 8 cycles, need 24 steps to complete the tunnel excavation.

Taking excavation program 2 as an example, the morphology of the various stages of construction, such as upper step excavation, upper step excavation, lower step excavation, upper penetration, and lower penetration, is shown in Figure 8.

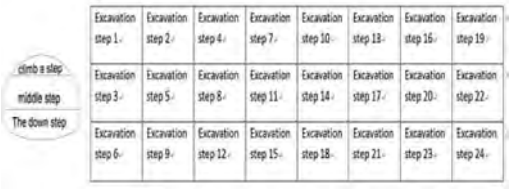

Figure 7. Schematic diagram of excavation.

3.2 *Analysis of arch settlement*

The tunnel vault settlement curves for the five scenarios are shown in Figure 9, and the tunnel vault settlement for each key process is shown in Table 3. The relationship between the final vault settlement values and step heights for the five scenarios is shown in Figure 10.

As shown in Table 3, after the excavation of the upper step of scheme 1 (step 4), the top of the arch sinks 0.075mm, after the excavation of the middle step (step 8), the top of the arch sinks 0.655mm, after the excavation of the lower step (step 12), the top of the arch sinks 0.935mm, after the upper part

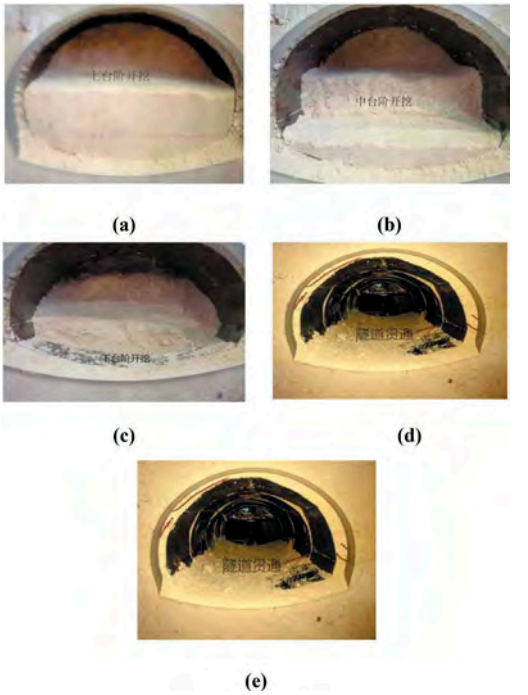

Figure 8. Construction process and form of bench method.
(a) Upper bench excavation (b) Middle bench excavation
(c) Lower bench excavation (d) Upper penetration
(e) Lower penetration

of the test section passes through (step 19), the top of the arch sinks 1.405mm, and after the lower part of the test section passes through (step 24), the bottom part of the arch sinks 1.405mm. the other schemes are so similar. The other scenarios were similar.

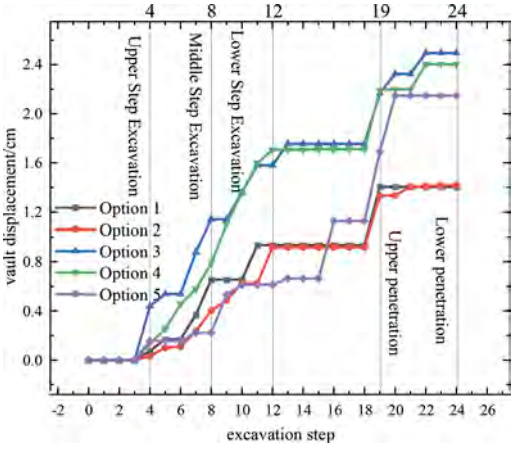

Figure 9. Settlement displacement diagram of arch crown.

Table 3. Settlement displacement of arch crown unit: mm.

Name of program	Upper bench excavation Step 4	Middle bench excavation Step 8	Lower bench excavation Step 12	Upper penetration Step 19	Lower penetration Step 24
Program One	0.075	0.655	0.935	1.405	1.405
Program Two	0.032	0.404	0.918	1.333	1.417
Program Three	0.440	1.141	1.581	2.166	2.495
Program Four	0.132	0.786	1.707	2.191	2.402
Program Five	0.157	0.223	0.612	1.691	2.147

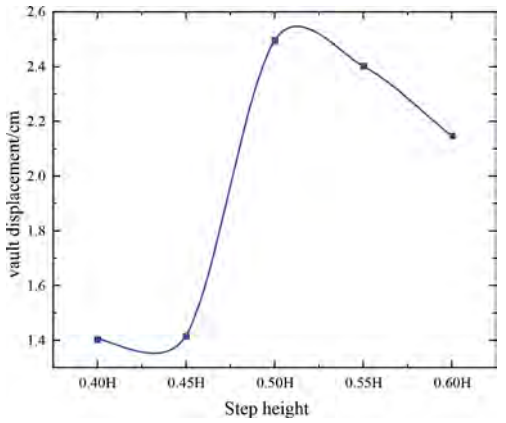

Figure 10. Settlement displacement of arch crown in key construction steps.

From Figures 9, 10 and Table 3:

(1) From 0.4H to 0.50H, the vault settlement increases with the step height. From 0.50H to 0.60H, the settlement of the vault decreases with the increase of the step height. When the height of the upper step is 0.5H, the maximum settlement of the vault is 2.495mm.
(2) When the upper step height of 0.4H→0.45H, the vault settlement increased by 6.4%; when the upper step height increased to 0.5H, the vault settlement increased by 87% compared to 0.4H.
(3) From the viewpoint of arch settlement, the average arch settlement of tunnel arch of Option 1 and Option 2 is lower than that of Option 3, Option 4 and Option 5, which is a better excavation plan.

It can be seen that when the three-step method is used in the construction of the tunnel in the weak and broken surrounding rock section, the height of the upper step should not be more than half of the total height of the tunnel excavation, while the middle step of the excavation height is smaller for the stability of the tunnel, the more favorable. Of course, the height of the middle step excavation should also meet the minimum space requirement for construction machinery. The lower step excavation has basically no effect on the settlement of the tunnel vault.

3.3 *Surrounding rock pressure*

The perimeter rock pressures after excavation for Scenarios I to V are shown in Table 4, Table 5, Figures 11 and 12.

Table 4. 0+20cm section perimeter rock pressure/kPa.

Position	Program One	Program Two	Program Three	Program Four	Program Five
Left arch foot	37	38	45	46	47
Left arch shoulder	28	29	41	41	38
Vaulting	2	2	3	2	2
Right arch shoulder	22	24	45	42	36
Right arch foot	41	39	48	47	45

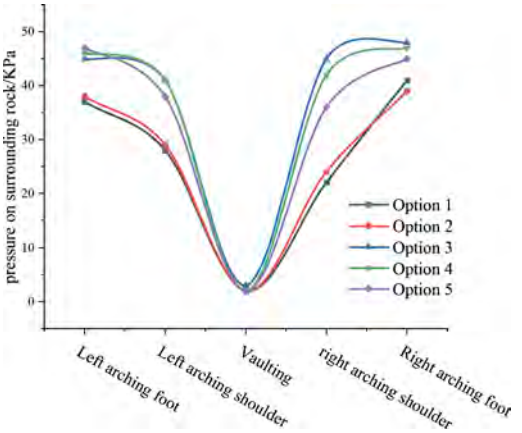

Figure 11. 0+20cm section perimeter rock pressure.

The following conclusions can be drawn from Figure 11.

(1) the pressure of the surrounding rock at the vault is the smallest, which is about 2 kPa or so. It shows that the closer to the critical surface, the smaller the surrounding rock stress in the radial direction of the tunnel. meanwhile, the radial surrounding rock pressure is maximum at the foot of the arch.

(2) The pressure on the surrounding rock caused by different excavation schemes is also different. Option 3 has the highest surrounding rock pressure, indicating that the tunnel is most unfavorably stressed when Option 3 is adopted. Option 1 has the least stress in the surrounding rock of the tunnel.
(3) As the excavation height of the upper step increases, the stress value of the tunnel surrounding rock increases, but when the excavation height of the upper step exceeds 0.5H, the stress value of the surrounding rock decreases instead. If the height of the upper step of Option 3 is 0.6H, the maximum value of perimeter rock pressure occurs at the foot of the arch as 48kPa, and the maximum value of surrounding rock stress of Option 1 occurs at the foot of the arch as 41kPa, which is reduced by 7kPa in comparison.

Table 5. 0+40cm section perimeter rock pressure/kPa.

Position	Program One	Program Two	Program Three	Program Four	Program Five
Left arch foot	27	27	35	35	34
Left arched shoulder	35	36	46	50	45
Vaulting	17	19	29	27	20
Right Arch Shoulder	35	36	46	51	40
Right arch foot	26	26	33	33	35

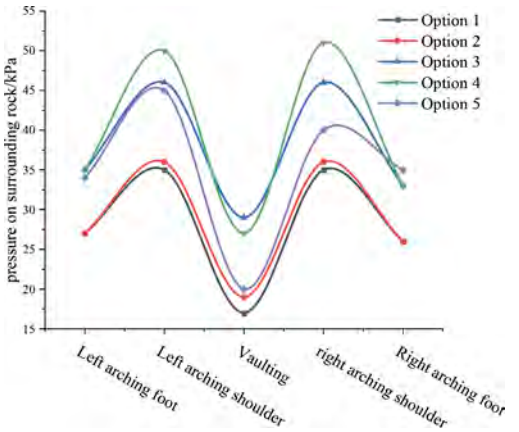

Figure 12. 0+40cm section perimeter rock pressure.

The following conclusions can be seen in Figure 12:

(1) The pressure of surrounding rock at each position shows that the pressure of surrounding rock at the arch shoulder is the largest, the pressure of surrounding rock at the foot of the arch is the second largest, and the pressure of surrounding rock at the top of the arch is the smallest. Taking Scheme 1 as an example, the peripheral rock pressure of the left and right arch shoulders is 35kPa and 35kPa, the peripheral rock pressure of the left and right arch footings is 27kPa and 26kPa, and the peripheral rock pressure of the arch top is 17kPa.
(2) As the step height increases from 0.4H to 0.55H, the pressure of the surrounding rock at each location tends to increase. Taking the left arch foot perimeter rock pressure as an example, the perimeter rock pressure is 27kPa, 27kPa, 35kPa, 35kPa at step heights of 0.4H, 0.45H, 0.50H, and 0.55H, respectively; When increasing from 0.5H to 0.6H, the peripheral rock at each position except the right arch foot shows a decreasing trend. Take the right arch shoulder surrounding rock pressure as an example, when the step height is 0.55H and 0.60H, the surrounding rock pressure is 51kPa and 40kPa respectively.

Comparing Figures 11 and 12, as the tunnel is excavated, the pressure of the perimeter rock at the top of the arch and the arch shoulder increases, and the pressure of the perimeter rock at the foot of the arch decreases. It indicates that the pressure of the surrounding rock is shifted to the deeper part except the foot of the arch. From the first layer position, the pressure of surrounding rock at the top of the arch is the smallest, the pressure of surrounding rock at the shoulder of the arch is larger, and the pressure of surrounding rock at the foot of the arch is the largest. Pay attention to the foot of the arch support measures during construction.

3.4 *Internal force of lining*

The axial force of the support for each scheme option is shown in Figure 14 and Table 6, and the bending moment values are shown in Figure 13 and Table 7.

From Figures 12 and 13, and Tables 6 and 7, the following conclusions can be seen.

(1) The lining axial forces of the scenarios are relatively close to each other, indicating that the step excavation height has a small effect on the lining axial forces. As the height of the upper step increases, the value of lining bending moment increases, with the maximum bending moment in Scenarios III and IV. The point of minimum value of bending moment occurs at the bottom of the arch and maximum value occurs at the arch waist.
(2) The left and right arch girdle axial forces are larger, and the arch top and bottom axial forces are smaller. Step height 0.4H increases to 0.5H, axial force in each part increases. Step height 0.5H increases to 0.6H, and the axial force in

each part decreases. Take the left arch waist axial force as an example, when the step height is 0.4H, 0.45H, 0.5H, the axial force is 3.3N, 3.65kN, 3.81kN respectively; when the step height is 0.5H, 0.55H, 0.6H, the axial force is 3.81kN, 3.50kN, 2.4kN respectively.

(3) The left and right arch waist bending moments are larger, and the arch top and bottom bending moments are smaller. Step height 0.4H increases to 0.55H, bending moment increases in all parts. Step height 0.55H increases to 0.6H, and the bending moment decreases in each part. Still take the left arch waist bending moment as an example, when the step height is 0.4H, 0.45H, 0.5H, 0.55H, the bending moment is 5.2 N-m, 15.8 N-m, 31.1 N-m, 32.0 N-m respectively; when the step height is 0.55H, 0.6H, the bending moment is 32.0 N-m, 22.3 N-m respectively.

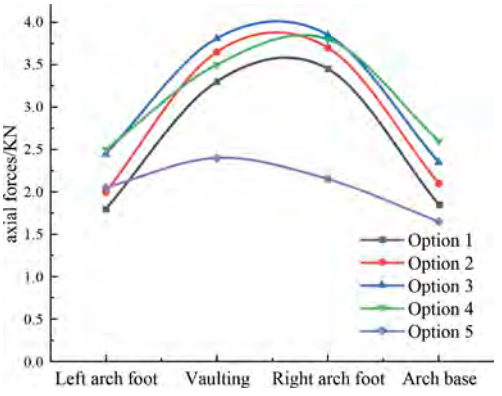

Figure 13. Axial force.

Table 6. Axial force unit: kN.

Position	Program One	Program Two	Program Three	Program Four	Program Five
Left arch foot	1.80	2.00	2.45	2.50	2.05
Vaulting	3.30	3.65	3.81	3.50	2.40
Right arch foot	3.45	3.70	3.85	3.80	2.15
Arch base	1.85	2.10	2.35	2.60	1.65

3.5 *Optimization of construction parameters of bench method*

When the height and length of the steps was chosen, the force and deformation are not the only limiting conditions. when analyzed from the aspects of construction interference, operational efficiency and equipment arrangement, but the efficiency of

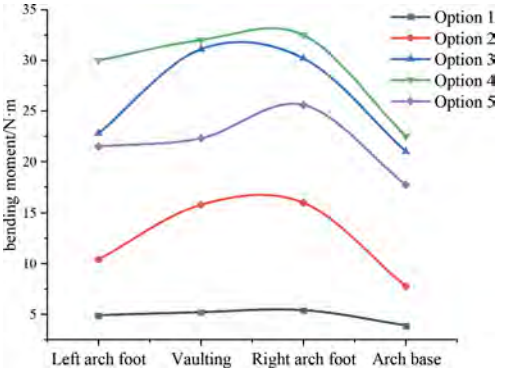

Figure 14. Bending moment.

Table 7. Bending moment unit: N·m.

Position	Program One	Program Two	Program Three	Program Four	Program Five
Left arch foot	4.9	10.4	22.8	30.0	21.5
Vaulting	5.2	15.8	31.1	32.0	22.3
Right arch foot	5.4	16.0	30.2	32.5	25.6
Arch base	3.9	7.75	21.0	22.5	17.7

construction and convenience issues are also the key factors in controlling the dimensions of the steps.

From the point of view of deformation and mechanics, the length and height of the steps are adapted to a wider range, so when determining the parameters of the steps, more consideration can be given to the construction machinery as well as the convenience of manual operation and construction efficiency.

(1) The length of the upper step can be controlled within 6 m to better control the deformation of the tunnel, and the mechanical operation is convenient, but should not be less than 4 m; the length of the middle step is mainly to consider the drilling operation space requirements.

(2) taking into account the construction workspace, blasting machinery pick ballast efficiency and other factors, the length of the upper step is appropriate for 4 to 6 m, the length of the middle step is appropriate for 3 to 5 m. The length of the middle step is appropriate for 3 to 5 m.

(3) The upper step mainly considers the excavator picks the ballast and the wet spraying manipulator operation efficiency, the step height is determined as 3.5~5.5m, uses the simple pedestal construction; The middle and lower steps (with up-arches) are assisted by climbing ladders, and the height of the steps should not be too high in consideration of the convenience of manual drilling and arch stand operation.

To summarize, when the tunnel class V perimeter rock section is excavated by the three-step method, the following conclusions can be drawn from the analysis of three aspects: vault settlement, perimeter rock stress and lining force:

1) As the excavation height of the upper step increases, the settlement of the tunnel vault increases and reaches the maximum value of the vault settlement when the height of the upper step is 0.5H.
2) The height of the center step excavation also has an effect on the internal force of the tunnel. The excavation height of the center step should not exceed 0.4H.
3) The lower step excavation has basically no effect on the tunnel surrounding rock.

If Tongzi Tunnel V perimeter rock section using three-step method of excavation, it is recommended that the construction industry parameters are as follows:

Step height: upper step 0.45H, middle step 0.35H, lower step 0.2H.

4 SUMMARY

Tunnel similarity modeling work was carried out for the soft and broken surrounding rock section of Tongzi Tunnel, and its main contents and related conclusions are as follows:

1. Compared with the double sidewall guide pit method and CD method, the construction efficiency can be improved by using the three-step method. Under certain conditions, the use of three-step method in the soft and broken section of Tongzi Tunnel can accelerate the construction progress under the premise of ensuring safety.
2. Tongzi Tunnel V perimeter rock section using three-step method of excavation, the optimized step height used in practice, the specific construction parameters are as follows: the upper step 0.45H, the middle step 0.35H, the lower step 0.2H, effectively controlling the deformation of the surrounding rock.
3. Comprehensive consideration of construction workspace, blasting machinery pick ballast efficiency and other factors, and ultimately determine the three-step method of the steps suitable for rubbing and length, the length of the upper step is appropriate for 4 ~ 6m, the length of the middle step is appropriate for 3 ~ 5m.

FUNDING

This work was supported by the Science and Technology Planning Project of Guizhou Province (the Qiankehe major special project [2018] 3011, the Qiankehe Basic Project ZK [2022] General Project 082, and the Qiankehe Basic Project [2019] No. 1057), the Guiyang Metro Line 3 Phase I Engineering Research Project (Project No. GD3-FW-YJ-05-2020-13-ZB), and the Regional First-class Discipline Construction Project in Guizhou Province (QYNYL [2017] 0013).

REFERENCES

Chen, L.B., 2008. Application of three step method in soft surrounding rock of mountain tunnel on Passenger Dedicated Line [J]. Journal of Railway Engineering. (12): 72–74

Cui, X.P., 2010.Comparison and improvement of CRD method and three bench seven step excavation method[J]. Tunnel Construction, 30 (2): 131-134+ 178.

Deng, T., Liu, D.G., Cai, M.J., et al,2017. Optimization analysis of geometric parameters of bench method used in Zhongtiaoshan Tunnel[J].Tunnel Construction, 37 (12):1550–1556.

Gu, S.C., Huang, R.B.,2014. Influence of CRD method and bench method construction on surrounding rock deformation of metro tunnel [J].Journal of Architectural Science and Engineering,31 (01):111–119.

Li, B.P., Han, J.J., Gao, S.M., 2015. Comparative analysis of CRD method and positive bench method in shallow buried section of xishipo tunnel [J].Journal of Xi'an University of Technology, 35(02):135–141.

Liu, Z.W., Li, J., 2018. Application of bench method (with inver-ted arch) one-time excavation construction technology in soft rock tunnel [J]. Tunnel Construction, 38 (02):287–294.

Liu, Y.H., Xie, S.L., 2010. Application of three step method in Dawangding tunnel construction[J]. Highway Traffic Technology, (12):101–104.

Lu, D.W., Liang, Q.G., Ou E.M., 2018. Experimental study on surrounding rock pressure of Expressway mudstone tunnel [J]. Journal of Underground Space and Engineering, 2012,8 (06): 1178-1184+1200.

Lin, M.X., 2018.Application of three bench method and middle partition heading method in highway tunnel construction [J]. Jiangxi Building Materials. (1):142–143.

Song, S.G., Li S.C., Li L.P., et al, 2011. Study on Rules of Mechanical Effect in Process of Construction of Super-large Cross-section Tunnel in Weak and Broken Surrounding Rock Excavated by Bench Method [J]. Tunnel Construction,31 (sup.1):170–175.

Wang, C.H., Zhang, A.J., Fan, X.F., et al, 2018.Numerical experimental study on surrounding rock control mechanism of super largesection tunnel constructed by upper and lower bench method and CRD method[J]. Highway, 63 (05):313–317.

Wang, S.P., 2004. Simulation test of tunnel with broken surrounding rock. PhD Thesis. University of Zhejiang, Hang Zhou,China.

Wei, B.X., Tang, H.X., Chen, Y., 2011. Effect comparison and numerical analysis of CRD method and upper and lower bench method in tunnel excavation [J]. China Highway, 31 (04): 192–196.

Zhang, W., 2013. Comparison and selec-tion of construction feasibility between CRD method and three bench method for Shallow Metro Tunnel[J]. Journal of Nanyang Institute of Technology, 5(06):92–95.

Zou, C.L., Shen, Y. S., Jin, Z.Z., 2013a. Optimization analysis of geome-tric parameters of bench method construction of large section tunnel in soft and broken surrounding rock [J]. Highway Engineering,38 (02):27-31+35.

Zou, C.L., Shen, Y. S., Jin, Z.Z., 2013b. Experimental study on the proportion of similar materials of V-grade surrounding rock of tunnel based on orthogonal design [J]. Subgrade Engineering, (03): 6–9.

Xian, G. 2016. Comparative study on construction of soft rock tunnelby bench method and full section(including inverted arch) method–taking Ping'an tunnel of Chengdu-Lanzhou Railway as an example [J]. Tunnel Construction, 36 (11): 1302–1309.

Xu, Q. W., Wang, W.X., Sun, Z.L.,2018. Model test study on surrounding rock failure characteristics of shallow buried red bed weak tunnel [J]. Chinese Journal of Geo-technical Engineering, 40((sup.1): 37–41.

Tunnelling for a Better Life – Yan, Celestino, Thewes & Eberhardt (Eds)
© 2024 The Author(s), ISBN 978-1-032-80042-4
Open Access: www.taylorfrancis.com, CC BY-NC-ND 4.0 license

Innovative practice of mechanized and intelligent construction technology for railway mountain tunnel drilling and blasting method

Ke Liu
China Railway Eryuan Engineering Group Co. Ltd., Chengdu, China
CREEC (Chengdu) Survey, Design and Research Co. Ltd., Chengdu, China

Yu Yu
China Railway Eryuan Engineering Group Co. Ltd., Chengdu, China

Yajun Li & Xiongwei Liu
China Railway Eryuan Engineering Group Co. Ltd., Chengdu, China
CREEC (Chengdu) Survey, Design and Research Co. Ltd., Chengdu, China

ABSTRACT: In order to implement the national high-quality development goal and further improve the level of railway tunnel construction technology, during the construction of Zhengzhou-Wanzhou high-speed railway, we have carried out experimental research on tunnel drilling and blasting mechanization construction technology, forming fundamental innovative achievements in intelligent construction technologies such as mechanized full-section construction method, high-performance active support technology, and intelligent equipment cluster. On this basis, by integrating the new generation of intelligent information perception technology, neural network algorithms, machine self-identification and self-learning technology, research on intelligent construction technology for the main construction processes of tunnel drilling and blasting method is carried out, trying to illustrate innovative achievements such as intelligent advanced geological prediction, intelligent identification and classification system for surrounding rock, intelligent optimization system for support parameters, intelligent construction system for excavation and support, and intelligent control and detection system for tunnel quality; furthermore, taking the change design as an example, this paper elaborates on the application of intelligent construction technology in the construction process of Zhengzhou-Wanzhou high-speed railway tunnel, and preliminarily establishes an intelligent tunnel drilling and blasting method construction system with certain intelligent characteristics.

Keywords: Mountain tunnel, Intelligence, Active support, Deformation pressure, MWD, Change design

1 INTRODUCTION

With the rapid development of technology and information technology, significant progress has been made in the research and application of new generation cutting-edge information and communication technologies such as industrial internet, Internet of Things, artificial intelligence, big data, cloud computing, image/video recognition, and 5G, which greatly improves industrial production efficiency and rapidly penetrates into the field of engineering construction, promoting industry transformation and development.

The scale of transportation engineering construction in the western region of China is gradually expanding, and mountain tunnels are developing towards the "four super" directions of "super long, super deep, super large, and super complex". At the same time, they are gradually entering extremely harsh environmental areas such as extremely frigid, high-altitude, high-intensity earthquake zones, etc. The longest railway tunnel currently under construction in China has exceeded 40km [1]. Existing engineering practices [2] have once again proven that the drilling and blasting method is still the most reliable, mature, adaptable, and widely used tunnel excavation method. However, due to the prominent extreme adverse geological problems such as high rock temperature, high heat, extremely high stress, deep

DOI: 10.1201/9781003495505-208

active faults, and ultra-high water pressure, the use of drilling and blasting method in tunnel construction faces unprecedented challenges. The only way is to replace people with machines, reduce man or even become unmanned. However, tunnel engineering faces a series of problems such as the complexity of the construction process, the randomness and fuzziness of rock mass changes, the adaptability of support materials and support systems, the safety and economy of engineering construction, etc., which drive the development of intelligent construction technology integrating mechanization and digitization /informationization to achieve construction goals.

Currently, some scholars have conducted research on intelligent tunnel construction technology. Guo Weishe[3] elaborated the main problems and development prospects faced by TBM intelligent construction method; Wang Tongjun[4] studied the intelligent construction technology system of railway tunnels from a management perspective; Ma Weibin[5] conducted research on intelligent construction technology for prefabricated and assembled tunnels using drilling and blasting methods; Wang Zhijian[6-8] conducted research on the use of mechanized, information-based, and intelligent construction technologies for railway tunnels; Liu Feixiang[9] and others have developed a series of complete sets of equipment with intelligent features for extremely complex environments on high plateaus. The intelligent construction of tunnels is currently in the exploration and development stage. Due to the complex process of drilling and blasting method, there are still few research results on the use of drilling and blasting method for multi process construction of mountain tunnels. There are few discussions on intelligent construction methods with high reliability and high implementation based on the multi-process construction characteristics of drilling and blasting method for tunnel. The full-process mechanization and intelligent construction technology of drilling and blasting method is still under active exploration and research.

In recent years, in the construction process of complex mountainous railway projects such as Sichuan-Qinghai,and Zhengzhou-Wanzhou, we have actively explored and studied the large-scale mechanized construction technology in drilling and blasting method, achieved rich results and practical experience, and gradually promoted it to the construction of the Sichuan-Tibet Railway. Especially represented by Zhengzhou-Wanzhou High Speed Railway, from 2018 to present, under the approval of China State Railway Group Co., Ltd, research has been carried out on the mechanized and intelligent construction technology of high-speed railway mountain tunnels using drilling and blasting methods. Some of the achievements have been preliminarily applied. Based on the research and practice of intelligent design and construction technology for the Zhengzhou-Wanzhou high-speed railway tunnel, this article elaborates on the foundation and key technologies of intelligent tunnel construction during the design and construction stages of the drilling and blasting method.

2 URGENCY OF RESEARCH ON INTELLIGENT CONSTRUCTION USING DRILLING AND BLASTING METHOD

Looking at the current situation of railway engineering construction in China, the level of intelligent construction in bridges, tracks, and other areas is relatively high. However, the level of large-scale mechanization in tunnel construction, especially in mountain tunnels, is still very low. The level of intelligence is even lower, and it has become a shortcoming that restricts the development of railways. The drilling and blasting method for mountain tunnels involves multiple construction processes, complex work processes, and uncontrollable factors. In addition, the construction environment is poor and the construction risks are high. Against the backdrop of the younger generation's increasing unwillingness to choose tunnel construction as a high-risk work, the demand for mechanized and intelligent tunnel construction is increasing. Taking the project department of a section of the Zhengzhou-Wanzhou high-speed railway as an example, there were approximately 1935 participants. The distribution of each age group is shown in Table 1. Among them, the proportion of workers aged 40-60 who are truly engaged in frontline operations is as high as 62%! The aging of the workers conducting construction of tunnels using drilling and blasting methods is obvious, and the proportion is continuing to expand. Therefore, the current research on intelligent construction technology for the entire process of tunnel drilling and blasting is extremely urgent.

Table 1. Age statistics of personnel in a project department of Zhengzhou-Wanzhou high-speed railway.

age	Below 20	20~30	30~40	40~50	50~60	Above 60	Total
Number	6	160	494	645	561	69	1935
Proportion (%)	0.3	8.3	25.5	33.3	29.0	3.6	100.0

3 BASIC TECHNOLOGY OF INTELLIGENT CONSTRUCTION OF MOUNTAIN TUNNEL DRILLING AND BLASTING METHOD

The intelligent construction of mountain tunnels is based on mechanized construction technology, which includes intelligent construction equipment covering various processes, simplified mechanized construction methods suitable for large-scale equipment operations, and high-performance active support technology for tunnels that provide construction safety and structural support for mechanized methods. All three are indispensable.

3.1 *Intelligent construction equipment*

Intelligent equipment is an important foundation for the construction of drilling and blasting methods. Cutting-edge technologies are comprehensively utilized such as intelligent sensing, image recognition, artificial intelligence, and the Internet of Things to overcome core technologies of intelligent equipment such as high-precision measurement and positioning, machine automatic control, and data standardization interaction in tunnels. Matching software and hardware are also developed and intelligent upgrading of 9 sets of equipment for the main construction process are conducted, covering the main equipment for four major work areas, i.e., advance support, drilling and blasting excavation, initial support and secondary lining. Details are shown in Table 2.

3.2 *Mechanized full-section construction method*[10]

The mechanized full-section method is a construction technique that utilizes large machinery to excavate and shape the designed section in one go (see Figure 1 and Figure 2). It includes variations such as the full-section method (without invert), full-section method (with invert), and micro step method.

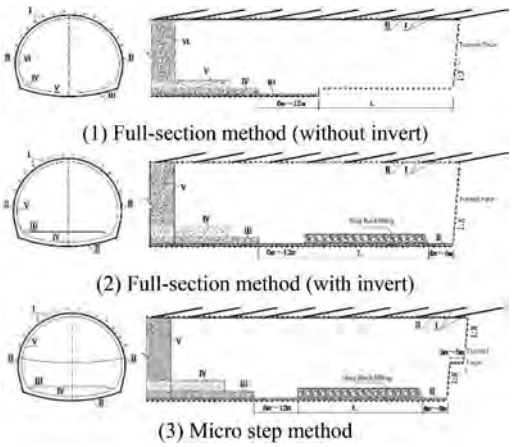

Figure 1. Construction process of full-section mechanized method.

Table 2. Intelligent construction equipment for drilling and blasting method.

Work area	Name of equipment	Main function	Sketch map
Advance support	Intelligent grouting jumbo	Automatic measurement, slurry production, mixing, grouting, and cleaning; remote pumping; automatically generating grouting logs; data exchange	
Drilling and blasting excavation	Intelligent rock drillin jumbo	Intelligent positioning; automatic drilling; remote control; intelligent surrounding rock classification; automatically generating drilling logs; data sharing	
	Intelligent rock bolting jumbo	Intelligent positioning; integrated intelligent construction of anchor rod including drilling, injection, and anchoring; generating anchor rod construction logs; data sharing	
Initial support	Intelligent lagging jack installation jumbo	Remote control; 3D reconstruction of contours; intelligent precise positioning; assembly trajectory planning; Automatically generating assembly logs	
	Intelligent wet shotcreting jumbo	Intelligent positioning; automatic shotcreting; automatically calculating the shotcreting volume; remote control; Automatically generating shotcreting logs; data exchange	
	Intelligent waterproof board laying jumbo	Automatic installation of waterproof boards; automatically calculating the amount of waterproof board and evaluating its looseness; automatically generating laying logs	
Secondary lining.	Intelligent lining jumbo	Pressurized pouring, and automatic vibration; real time liquid level display, temperature monitoring, pressure monitoring; automatically generating lining logs; data exchange	
	Intelligent maintenance jumbo	Constant temperature and humidity maintenance, real-time monitoring of constant humidity; automatically generating maintenance logs	

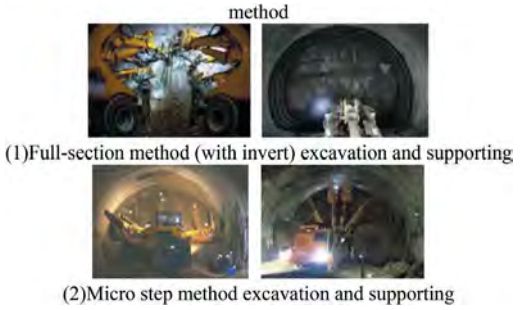

Figure 2. Full-section mechanized construction.

The mechanized full-section method is characterized by full ring excavation and overall support. One variation, the micro step method, involves excavating the section with a stepped face, typically with a step length of 3-5m. The upper step is excavated to a height of 1/2 to 2/3 of the section height, while simultaneous excavation and support are carried out for both upper and lower steps, including the invert. For more details about the scope of application of the mechanized full-section method, please refer to Tables 3.

Efforts are made to ensure the stability and safety during excavation. In hard rock areas, a specific slope rate can be applied to enhance the stability of the tunnel face. This helps prevent potential instability issues. In soft rock areas, an alternative approach involves designing the excavation face as a spherical curved surface. This design mitigates stress concentration and improves the stress flow distribution around the face. The spherical tunnel face offers advantages over an upright face, particularly in areas where the stress exerted on the face exceeds the strength of the rock. By adopting a spherical tunnel face, the longitudinal extrusion displacement of the tunnel face can be effectively controlled.

3.3 *High-performance active support technology* [10]

3.3.1 *Active forepoling technology for tunnel face*

The mechanized full-section method requires a much larger excavation area compared to the multi-step method. This increased scale has negative implications for the overall stability of the tunnel face under similar geological conditions. In order to address this challenge, an active forepoling system is designed to actively control the pre-deformation of the rock ahead of the tunnel face. This support system includes various components such as shotcrete, grouting small ducts, grouting pipe sheds, anchor rods, and pre-grouting. The objective of the active forepoling system is to reduce the pressure exerted by the rock on the potential sliding area of the tunnel face or enhance the mechanical properties of the rock. The applicability of this support system depends on the specific categories of tunnel face stability, as indicated in Table 4.

3.3.2 *Active support of tunnel body*

To address the issue of rapid and excessive early deformation in mechanized full-section construction tunnels, a new active support system has been

Table 4. Application of forepoling technology for tunnel face.

Construction method Tunnel face stability	Full-section method	Micro step method
Stability (LS)	①Local shotcrete on the tunnel face	—
Temporary stabilization (TS)	①Local shotcrete on the tunnel face ②Advance pipe shed (small duct) or tunnel face anchor rod	①Local shotcrete on the tunnel face ②Advance pipe shed (small duct) or tunnel face anchor rod
Unstability (US)	—	①Local or full shotcrete on the tunnel face ②Advance pipe shed or tunnel face anchor rod or tunnel face pre grouting ③Combination of advanced pipe shed and anchor rod on the tunnel face, and pre grouting on the palm surface ④Other measures

Table 3. Application of mechanized full-section construction.

Rock Category Construction method	II	III	IV General sections	IV Other sections	V General sections	V Other sections
Full-section method(without inverted arch)	○	○	○	△	—	—
Full-section method (with inverted arch)	△	△	△	○	△	—
Micro step method	—	—	—	△	○	○

implemented. This system incorporates anchor rods, high-performance shotcrete, and high-strength full-ring steel frames, as shown in Figure 3 and Figure 4. It takes advantage of the properties of the support component materials and structures while leveraging the efficiency of large-scale equipment. It intervenes and improves the bearing conditions of the rock before excavation or provides rapid support inside or outside the rock after excavation. By implementing primary support and early closure, a collaborative "rock-support" bearing system is established. This system actively enhances the mechanical parameters of the rock by providing timely and effective support force, protecting the surrounding rock, and utilizing the inherent stability of the rock. At the same time, it restricts rock deformation and constrains the deformation load on the rock, thereby reducing the burden on the support structure. This comprehensive approach ensures the safety of tunnel construction and structure while achieving reliable and cost-effective tunnel support.

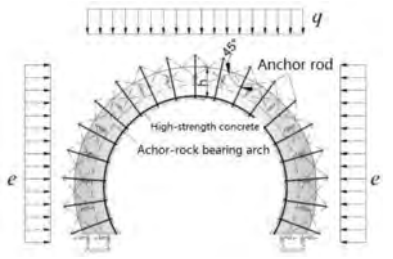

Figure 3. High-performance active bearing system.

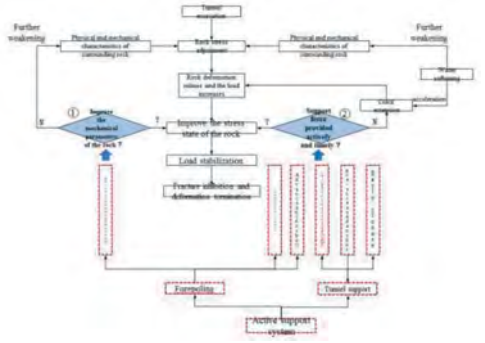

Figure 4. Principle and roadmap of high-performance active bearing system.

4 KEY TECHNOLOGIES FOR INTELLIGENT CONSTRUCTION OF MOUNTAIN TUNNEL DRILLING AND BLASTING

Intelligent construction methods for tunnel drilling and blasting are built upon full-process mechanized construction and incorporate cutting-edge technologies such as intelligent perception, artificial intelligence algorithms, and machine self-recognition and self-learning capabilities. These technologies enable information perception, interconnection, processing, and decision-making regarding various aspects of tunnel construction, including rock conditions, support systems, equipment, personnel, and materials. The aim is to achieve safe, reliable, green, and efficient tunnel construction across survey and design, construction, quality control, and construction management stages. In general, the intelligent construction technology of tunnel drilling and blasting includes intelligent geological prediction, intelligent rock identification, intelligent design of support parameters, intelligent construction of excavation and support, intelligent construction quality control, etc.

4.1 *Intelligent geological prediction*

Intelligent geological prediction technology combines traditional drilling methods with Measurement While Drilling (MWD)[11] (Figure 5) and artificial intelligence. During drilling, integrated sensors in drilling rigs and anchor rod rigs collect real-time data on drilling direction, formation characteristics, and drilling parameters. This data is then analyzed to create a visual geological cloud map where hardness and completeness of different rocks are shown in different colours, displaying rock strength and crack development, and predicting the geological structure ahead of the tunnel face. The technology enables real-time, visual, accurate, automatic and well-informed geological prediction, improving the accuracy of predictions and providing a basis for intelligent support parameter design. Parameters such as propulsion speed, impact pressure, propulsion pressure, rotary pressure, water pressure, and water flow rate are measured during advance long drilling, borehole deepening, bolt drilling and other drilling process. The geological cloud map can be visualized

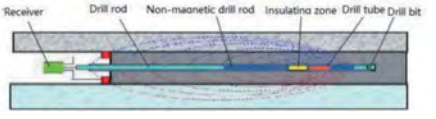

Figure 5. Principle and structure of electromagnetic wave wireless measurement while drilling.

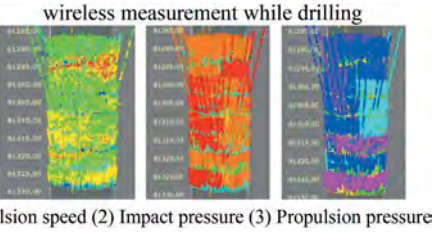

Figure 6. Geological cloud maps with independent expression of drilling parameters.

Table 5. Geological cloud map colour analysis table.

Colour	Blue	Cyan	Green	Yellow	Orange	Red
Labelled advance velocity values	less than -40	-40 ~ -20	-20 ~ 10	10 ~ 20	20 ~ 40	more than 40
Rock strength gradient	high		medium		low	

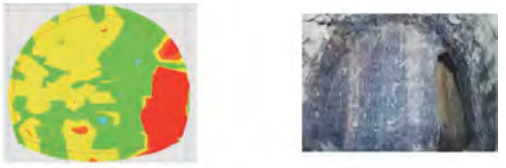

(1) geological cloud map (2) karst cave

Figure 7. MWD technology forecasting DK451+150 karst cave at Gaojiaping Tunnel.

separately based on drilling parameters or through assigning weights to each indicator. Please refer to Table 5 and Figure 6 for more details.

In the Gaojiaping Tunnel on the Zhengzhou-Chongqing High-speed Railway (Figure 7), the geological cloud map at DK451+147 (tunnel portal) indicates uniform rock strength at the tunnel face, which is consistent with the excavated rock. However, in the lower cycle at DK451+148-+150, the geological cloud map of the boreholes shows a sudden change to red near the right wall in front of the tunnel face, indicating a predicted sharp decrease in rock strength. This is attributed to the extensive development of karst in the tunnel. Additional advanced drilling techniques were employed, and after excavation, a karst cave extending 5m along the tunnel's axial direction was discovered in this area.

4.2 *Intelligent identification of surrounding rock*

When applying drilling and blasting construction method, surrounding rock can be quantitatively classified, wholly or partial, by a variety of indicators, and there are many classification methods. The commonly used methods in the world are RMR method [12], Q method [13], GSI method [14], RMI method [15], BQ method [16] and hydropower system HC method [17]. Generally, BQ method is applicable for traffic tunnels, and local optimization is carried out according to the characteristics of tunnels. As proposed by the Standard for Classification of Engineering Rock Mass (GB/T50218), classification of surrounding rock should be determined by comprehensive comparison of various classification methods, but there are many problems in practical application: 1) different methods differ in adaptability, resulting in inconsistent classification results, or even differ greatly, so there is a large deviation between the classification results and the actual situation; 2) some evaluation indexes and values of most classification methods depend on the subjective judgment of geological professionals, which are uncontrollable and rely on their work experience and identification skills, so the classification results may be unreliable; 3) when a key indicator is difficult to obtain due to objective conditions, the method cannot be implemented. In general, the reason for the above problems is that most of the core indicators of surrounding rock classification methods pay too much attention to the physical parameters of surrounding rock, but in fact it is difficult to truly realize the rapid, interference-free and reliable value of core parameters.

4.2.1 *Intelligent classification of surrounding rock*

Use intelligent drilling jumbo to collect thousands of samples of drilling parameters of tunnel faces with different lithology and different rock grades. Through analysis, it was found that there was a certain correlation between the drilling parameters and the rock grade: there was a monotonic correlation between the rock grade and six drilling parameters, which provided the possibility and feasibility of using the drilling parameters to classify the surrounding rock. The scatter diagram of some drilling parameters and rock grade is shown in Figure 8.

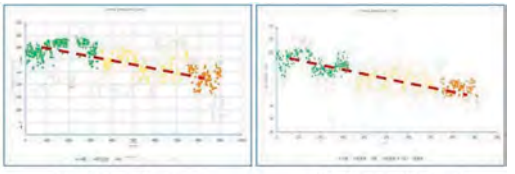

(1) Strike Pressure (2) Propel Pressure

Figure 8. Scatter diagram of relationship between drilling parameters and rock grade.

There are two kinds of intelligent classification methods of surrounding rock based on drilling parameters: ① direct classification, that is, collecting enough drilling parameters of tunnel face by drilling jumbo and forming a one-to-one sample library based on the classification results of surrounding rock based on the current standard, based on which

the machine model of "drilling parameters - surrounding rock grade" is established, and the accuracy is gradually improved through autonomous learning of machine and the continuously improved sample library, so as to realize the intelligent classification of surrounding rock;②Indirect classification means that enough drilling parameters and rock classification indexes (including rock hardness, rock integrity and groundwater development) are collected by the drilling jumbo to form a one-to-one sample library, based on which the machine model of "drilling parameters - classification indexes" is established, and then the accuracy is gradually improved through autonomous learning and the continuously improved sample library, so as to indirectly realize the intelligent classification of surrounding rock. The main difference between the two methods is the intelligent acquisition of classification index, such as the technologies of real-time acquisition of rock strength and the intelligent acquisition of rock integrity.

There are many factors affecting the grade of surrounding rock, which belongs to a typical highly nonlinear problem. It is difficult to determine the relationship between drilling parameters and the grade of surrounding rock with traditional statistical analysis methods. However, with the support of big data samples and machine learning, a strong nonlinear fitting ability can be formed, with the characteristics of continuous learning and optimization, which can solve the problem of highly nonlinear fitting. Based on machine learning theory, five kinds of intelligent classification models for surrounding rock tunnel face (i.e.,①support vector machine (SVM) model, ②particle swarm optimization support vector machine (PSO-SVM) model, ③erro back propagation (BP) model, ④genetic algorithm neural network (GA-BP) model, □forward neural network (RBF) model) are established. By comparison, the accuracy of SVM and BP models is higher, and the overall accuracy is 86.8% and 86.9% respectively. Its model structure is shown in Figure 9.

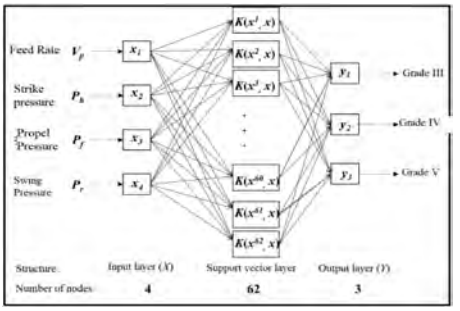

Figure 9. SVM model structure.

The intelligent classification model of surrounding rock tunnel face is adopted to realize the intelligent classification of grid area of tunnel face, which is realized in four steps, as shown in Figure 10-Figure 12.

①Tunnel face zoning: the tunnel face is divided into grids based on the distribution characteristics of boreholes. Each zone must contain at least one borehole.The grid size of the zone is 2m. Taking the tunnel face with a line spacing of 5m at a speed of 350km/h as an example, it can be divided into 6 rows and 6 columns, a total of 34 zones.

②Surrounding rock classification while drilling: call the intelligent classification model of surrounding rock when drilling with the trolley, and classify the surrounding rock at the borehole in real time and dynamically according to the drilling parameters.

③Regional classification of surrounding rock of tunnel face: according to the classification results of surrounding rock while drilling, the classification of surrounding rock of boreholes in each zone is mathematically averaged to determine the rock grade of each zone and realize the regional classification of surrounding rock of tunnel face.

④Comprehensive classification of surrounding rock of tunnel face: the grid weight value of each zone of tunnel face is proposed (see Table 6), and the classification results of each zone are weighted average, and finally the overall rock grade of tunnel face is obtained. The overall weight parameters are determined according to the principle of arch crown>side wall>inverted arch> the middle part.

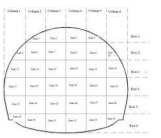

Figure 10. Grid zoning of tunnel face.

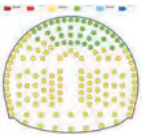

Figure 11. Classification of surrounding rock of blast hole in tunnel face.

Figure 12. Classification of surrounding rock in tunnel face grid zone.

Table 6. Weight value of tunnel face zoning.

Zone	Zone number	Single zone weight value	Total weight value
Arch crown	Zones of 1, 2, 3, 4, 5, 6, 7, 8, 9, 10	0.049	0.49
Sidewall	Zones of 11, 12, 15, 16, 17, 18, 21, 22, 23, 24, 27, 28	0.03	0.36
Invert arch	Zones of 13, 14, 19, 20, 25, 26	0.015	0.09
Middle part	Zones of 29, 30, 31, 32, 33, 34	0.01	0.06

4.2.2 *Intelligent prediction of surrounding rock classification*

Based on the characteristics of lateral zoning and vertical stratification of the surrounding rock of the tunnel face, and the revealed intelligent classification of the surrounding rock of multiple tunnel faces, the spatial mapping relationship of the surrounding rock grade of the tunnel face along the longitudinal direction is established, so that the surrounding rock grade in a certain range in front of the tunnel face can be automatically and dynamically predicted, and then the surrounding rock in front of the tunnel face can be comprehensively predicted in real time by combining the prediction information of advance drilling, geophysical prospecting and the surrounding rock prediction information at the survey stage, see Figure 13.

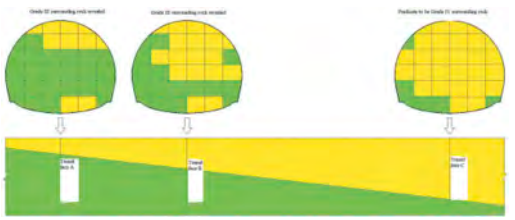

Figure 13. Intelligent prediction of tunnel surrounding rock.

4.3 *Intelligent optimization of support parameters*

4.3.1 *Intelligent design of support parameters*

The intelligent design of support parameters is an important part of the intelligent construction of tunnel. It is followed by intelligent construction process of excavation and support based on the intelligent identification of surrounding rock, including the support parameter database, intelligent matching and recommendation of support parameters, intelligent verification and optimization of support parameters, etc.

(1) Support parameter database: collect general reference drawings of tunnels with different designers, different speeds, single and double lines, and deep and shallow buried tunnels, and use Oracle11g to establish a database with characteristic information, including seven functional objects: tables, queries, forms, reports, pages, macros, and modules. The database contains 255 sets of design parameters, including advance support, reinforcement of tunnel face, primary support, and secondary lining parameters.

(2) Intelligent matching and recommendation of support parameters: it is carried out by using intelligent searching of database to match feature information of database feature parameters and parameters such as line design speed, surrounding rock grade, single and double line, buried depth, etc.

(3) Intelligent verification and optimization of support parameters: in order to facilitate the quantitative verification and optimization of the advance support parameters of tunnel face and support parameters of tunnel body, the advance support design method based on the limit equilibrium theory and the high performance active support design method based on the deformation pressure theory are used to optimize the preliminary support parameters of the system.

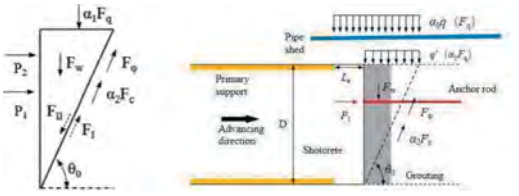

Figure 14. Quantitative design model of advance support of tunnel face.

According to the model figure [10] in Figure 14, with reference to the safety factor of slope stability, the calculation stability factor K of the tunnel face is introduced, and the calculation formula that can quantify the stability of the tunnel face is derived by using the limit equilibrium method:

$$K = \frac{P_1 + P_2 + \beta_1 \alpha_2 F_c}{\beta_2 (F_w + \alpha_1 F_q)} + \beta_3 \qquad \text{(Formula 1)}$$

$$\beta_1 = \frac{1}{\sin\theta_0 \tan\varphi + \cos\theta_0} \qquad \text{(Formula 2)}$$

$$\beta_2 = \frac{\sin\theta_0}{\sin\theta_0 \tan\varphi + \cos\theta_0} \qquad \text{(Formula 3)}$$

$$\beta_3 = \frac{\cos\theta_0 \tan\varphi}{\sin\theta_0} \qquad \text{(Formula 4)}$$

Where P_1 is the shotcrete support force of the tunnel face, P_2 is the bolt support force of the tunnel face, $\boldsymbol{\alpha_1}$ is the rock pressure reduction coefficient of the tunnel face advance pipe shed, $\boldsymbol{\alpha_2}$ is the cohesion increasing coefficient of grouting in the tunnel face. The stability coefficient K of the tunnel face is calculated through the trial calculation of the support parameters continuously and automatically adjusted by the system until $K \geq [k]$. The stability coefficient [K] of tunnel face design is taken as [K]=1.15 according to *Technical Code for Rock Bolt and Shotcrete Support Engineering* (GB 50068). The optimization design process is shown in Figure 15 below.

As shown in Figure 16, the parameters of primary support and secondary lining are optimized according to the calculation formula of surrounding rock deformation pressure derived from large-scale test. The optimized calculation of vertical and horizontal deformation pressures of surrounding rock shall consider the grade of surrounding rock and the BQ value of the basic quality index of surrounding rock.

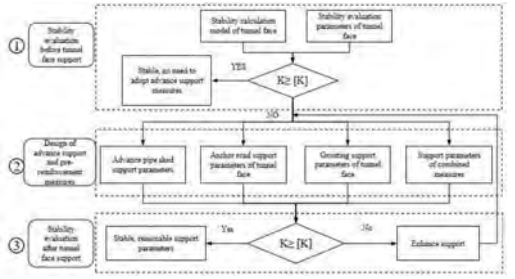

Figure 15. Design process of quantitative advanced support parameters for tunnel face.

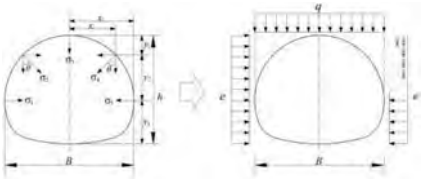

Figure 16. Schematic diagram of deformation pressure calculation of deep buried tunnel.

Here is the expression[10] for vertical value q and horizontal value e of deformation pressure derived from factors such as unit weight of surrounding rockγ, surrounding rock grade s and tunnel span B:

$$q = 0.33\gamma \cdot w \cdot e^{0.6s} \quad \text{(Formula 5)}$$

$$e = \lambda q \quad \text{(Formula 6)}$$

Where, s is the grade of surrounding rock, $h = 0.33w \cdot e^{0.6s}$is the calculated height of equivalent deformation pressure, and $w = 0.2 + 0.1B$ is the correction factor of tunnel span, λ Is the lateral pressure coefficient. The value of grade III surrounding rock is not greater than 0.25, the value of grade IV is among 0.25~0.5, and the value of grade V is among 0.5~1.0.

Here is the expressions of vertical value q and horizontal value e of deformation pressure derived from factors of the unit weight of surrounding rock γ, the basic quality index BQ of rock mass, the tunnel span B and other factors:

$$q = 0.33\gamma(0.2 + 0.1B)e^{-0.006BQ+4.2} \quad \text{(Formula 7)}$$

$$e = 2.7e^{-0.0066BQ}q \quad \text{(Formula 8)}$$

Where, BQ is the basic quality index of rock mass, which is calculated and determined according to *Standard for Engineering Classification of Rock Mass (*GB/T 50218).

Considering the structural safety and cost, the maximum value of the safety factor of the optimized support system shall be twice the minimum value, and shall be controlled according to Table 7.

Table 7. Safety factor control table of intelligent optimization design.

Category of supporting structure	Section tension/ compression control type	Maximum value	Minimum value
Advance support of tunnel face	/	2.3	1.15
Primary support with profile steel	Pull	3.6	1.8
	Press	3.06	1.53
Primary support without profile steel	Pull	5.4	2.7
	Press	3.6	1.8
Reinforced concrete lining	Pull	4.8	2.4
	Press	4.0	2.0
Plain concrete lining	Pull	7.2	3.6
	Press	4.8	2.4

4.3.2 *Visual expression of support parameters*

To make support system visible, and reflect the progress of the support system in the construction process, the lightweight BIM Technology based on parametric and procedural modeling with the advantages of visualization, coordination, simulation and graphing, is adopted to solve the problems of difficult to modeling and integration, high cost, large volume and high requirements for equipment and operators, which commonly exists in the traditional BIM Technology, and realize the dynamic simulation of the construction process of the support system, see Figure 17.

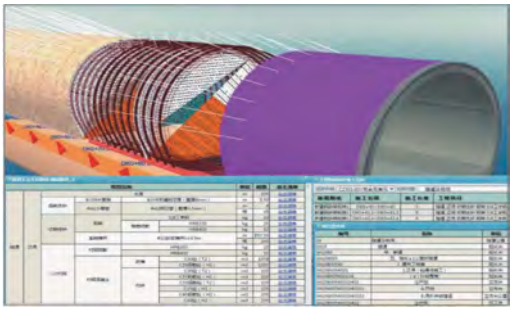

Figure 17. Visual expression of design and construction.

4.4 *Intelligent construction of excavation and support*

Intelligent excavation and support is the core part of intelligent construction of tunnel drilling and blasting. Its essence is that it can only be equipped with the process of execution of construction orders, real-time data acquisition and real-time feedback. According to the operation requirements of the main processes, the high-efficiency and high-quality construction operations are realized by giving the main construction equipment highly intelligent functions.

4.4.1 *Environmental perception of intelligent equipment*

The intelligent perception of construction equipment on the construction process and environment is the basic and core element of the whole intelligent construction system, the source and basis of all data, and is equivalent to the "eyes" and "ears" of the whole system. A series of intelligent equipment such as rock drilling jumbo, concrete wet spraying jumbo and concrete lining jumbo, is used to real-time collect and precept ambient temperature, pressure, speed, acceleration, angle, displacement, voltage and structure length, width, thickness and flatness. Various airborne sensors automatically collect process information during the construction of intelligent equipment to form construction logs, and realize the real-time dynamic perception of different sources and types of information through analysis, such as information of drilling parameter, tunnel contour (excavation contour, support contour, lining contour, etc.), support construction, lining pouring and equipment real-time status, provides basic data support for intelligent identification and classification of surrounding rock, intelligent optimization of support parameters and intelligent control of construction quality, as shown in Figure 18.

Figure 18. Dynamic environment perception by intelligent equipment.

4.4.2 *Mutual recognition of intelligent equipment cluster*

Because the tunnel construction process is relatively complex, there are many types of equipment with different functions, the construction data acquisition communication protocols of different processes are different, and the types, formats and storage forms of intelligent sensing data are also different. Therefore, it is necessary to integrate and establish the interactive method of unified multi-source and heterogeneous data, clarify the unified interactive system between tunnel geological data, support data, construction data, quality data and equipment perception data, establish a IOT system on construction site with high reliability and low delay, build information data interaction and conversion interfaces for intelligent equipment cluster, and realize the interconnection and mutual recognition of data, making each equipment cluster an important part of the intelligent construction system chain to identify each other, rather than an independent individual, as shown in Figure 20.

4.4.3 *Remote cooperative control of intelligent equipment cluster*

The tunnel construction environment for drilling and blasting is poor, and there may be adverse geological risks. Remote control center can be developed through remote control technology to realize the safe and efficient construction of the main process of the tunnel with fewer or no people. By real-time collecting image information and equipment status information of tunnel excavation and support, based on 4G, 5G and WiFi networks and other communication means and information interaction units, with the help of online high-definition video, and through in-depth analysis of the control center, machine instructions are formed to manipulate the equipment to automatically carry out drilling, charging, spraying, moving, positioning, scanning, pouring and other operations, greatly reducing the number of operators in harsh construction environment, and realizing back-end operation by equipment and remote measurement and video monitoring, to reduce the construction risk in practical, as shown in Figure 19. According to the requirements of construction process, function levels and positioning of equipment, movable remote control or indoor fixed remote cooperative control center (Figure 20) can be used to realize centralized monitoring and remote command of various equipment for tunnel construction.

Figure 19. Schematic diagram of remote cooperative control of intelligent equipment cluster.

Figure 20. Type of remote cooperative control center.

4.5 *Intelligent control of construction quality*

According to the construction quality evaluation index of the main process of drilling and blasting method, evaluate whether the construction is implemented to the extent to meet the design parameters, such as control of overbreak and underbreak, support thickness, support flatness, reinforcement cover thickness, reinforcement spacing, lining thickness, etc. Its core is to preliminarily realize the process control of construction quality through the accurate operation of

intelligent equipment, and obtain the quality parameters of engineering entities through the intelligent sensing elements after the completion of construction, to form the quality parameter detection database, compare the key parameters with the evaluation standards specified in relevant specifications, obtain the construction quality evaluation results, and put forward engineering countermeasures to realize the final control of construction quality. The quality inspection mainly relies on high-precision laser scanning technology, which has the following functions: ①High-precision and fast scanning of excavation contour, accurately detect overbreak and underbreak, evaluate the excavation quality by comparing with the design contour, and estimating the quantities of supporting structures; ②Before and after the completion of shotcrete, the 3D contour is reconstructed quickly with high precision, so as to evaluate whether the thickness and flatness of shotcrete meet the requirements, and the material loss and shotcrete construction quality; ③Before and after the construction of secondary lining, the deformation of surrounding rock and primary support, as well as the construction quality of the main structure of lining, are evaluated by high-precision reconstruction of 3D contour, the spacing of lining reinforcement and the thickness of protective layer, as shown in Figure 21.

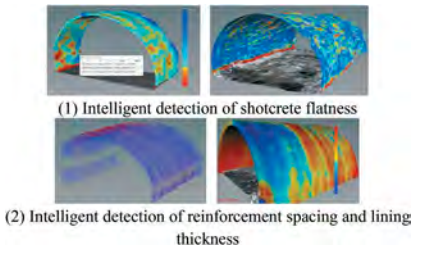

Figure 21. Schematic diagram of intelligent control of construction quality.

5 CASE STUDY OF INTELLIGENT CONSTRUCTION OF MOUNTAIN TUNNEL BY DRILLING AND BLASTING METHOD

Tunnels in Hubei section of Zhengzhou-Wanzhou HSR took the above technology as core intelligent development program, established the intelligent construction collaborative management platform to coordinate the implementation of the whole process of intelligent construction technology, and solve a series of challenges in the implementation of intelligent construction technology, and guided the design, construction and construction management of works in practice. Taking the design change as an example, since it involves the rights and responsibilities of all parties involved in the construction, it is of strict logical relevance; In traditional way, design change needs to be completed jointly by all parties involved in the construction on site, featured complex, many data, long cycle, and heavy workload. So the traditional way cannot meet the requirements of high standards and high requirements for railway construction management. Therefore, a intelligent process of design change was developed to automatically compare the rock grade of the tunnel face obtained from the intelligent classification and identification of surrounding rock, digital imaging of the tunnel face, advanced drilling and other multi-source geological information with the original design. The design change process would be started if the above two were inconsistent, and the parties involved in the construction would put forward their opinions online and form minutes, and the intelligent optimization of support parameters would be synchronously started, and relatively optimal design parameters would be recommended and finally confirmed by the person in charge of the design unit. The changed design parameters were distributed to each equipment cluster to complete the construction in the form of data that could be identified by the construction equipment. In this way, the efficiency of design change based on clear rights and responsibilities was improved by implementing the design change process with fewer people and no one on site, as shown in Figure 22 below.

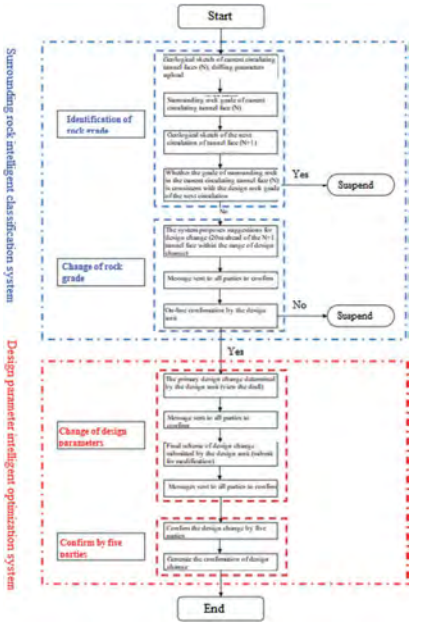

Figure 22. Overall flow chart of intelligent design change.

6 CONCLUSIONS AND OUTLOOK

6.1 *Conclusions*

(1) Driven by the development direction of cutting-edge technologies in the world and major national development strategies, it is an urgent

need to integrate new technologies such as artificial intelligence, big data, cloud computing and robots into the construction process of tunnels.

(2) As the demand of the drilling and blasting method for the number and quality of construction personnel is gradually increasing, the intelligent level and degree of construction equipment need to be gradually improved, the range and accuracy of intelligent perception of equipment for the environment and surrounding rock still need to be improved, and the function integration of intelligent equipment and the collaborative ability between equipment clusters still need to be strengthened.

(3) Although the traditional surrounding rock classification reflects the actual physical characteristics of the surrounding rock itself based on the physical and mechanical parameters such as rock strength, rock integrity and groundwater state, it is relatively difficult to obtain parameters quickly, so is difficult to adapt to the intelligent demand. While the technical path, which indirectly reflects and evaluates the surrounding rock quality based on real-time dynamic feedback, and combines with artificial intelligence, big data and machine learning, will gradually become the research focus of intelligent drilling and blasting method.

(4) With the extensive application of intelligent construction technology, the essential theory and design method of tunnels using large-scale equipment will be gradually improved to adapt to new construction technology, such as surrounding rock deformation pressure theory, accurate and quantitative design method of three-dimensional advanced support of tunnel face, design method of high-performance active support system, etc.

6.2 *Outlook*

Chatgpt[18], the natural language processing tool driven by generative AI technology, has profoundly changed people's cognition of the application of AI technology. AI technology has been developed to the extent to cause social change. However, the research and application of intelligent construction technology of tunnel drilling and blasting in the field of infrastructure still remain in the initial stage, and various technical paths and implementation methods are quite different, so it is necessary to continue to invest in and intensify on research and development efforts. In the future, with the improvement of perception and accuracy of equipment, the iteration and evolution of artificial intelligence algorithms, the improvement of machine recognition and learning ability, and the improvement of the essential theory of tunnel engineering, the highly-intelligent design and construction of the whole unmanned process of drilling and blasting based on complex and multi-process operation will become a reality in the foreseeable future.

REFERENCES

[1] Zhang Yu. Study on Hydrogeological Conditions and Route Optimization of Yigong Tunnel of Sichuan-Tibet Railway [D]. Chengdu University of Technology, 2021.

[2] Wang Yafeng, Zeng Jing, Jiang Jiayun. Construction Technology of Open TBM in Gaoligongshan Tunnel Crossing a High-Pressure Water-Rich Weak-Fracture Altered Structural Belt [J]. Tunnel Construction, 2021,41(3):449.

[3] Guo Weishe, Hong Kairong, Gao Pan, et al. Status quo and prospects of tunnel intelligent construction in China[J]. Tunnel Construction, 2023, 43(4):549.

[4] Wang Tongjun. Railway tunnel construction methods evolution in China and intelligent construction system and prospects[J]. China Railway, 2020 (3):1.

[5] Ma Weibin, Wang Zhiwei. Research on prefabrication and assembly of railway tunnels excavated using drilling-and-blasting and prospects of intelligent construction[J]. Tunnel Construction, 2022, 42 (7):1119.

[6] Wang Zhijian. Status and prospect of intelligent construction technology of tunnel of Zhengzhou-Wanzhou high-speed railway[J]. Tunnel Construction, 2021, 41(11):1877.

[7] Wang Zhijian. Innovative Practices of Intelligent Tunnel Construction Technology for Zhengzhou-Wanzhou Railway [J]. China railway, 2020 (12):10–19.

[8] Wang Zhijian. The Construction Technology of Large Cross-sectional Tunnel in Zhengzhou-Wanzhou High-speed Railway with Safety and Rapid Standardization[M]. Beijing: China Communications Press, 2020.

[9] Liu Feixiang, Ji Haidong, Xiao Zhenghang. Complete set of equipment technology system for drill-and-blast tunnel construction in Sichuan-Tibet railway[J]. Tunnel Construction, 2021, 41(8):1281.

[10] Liu Ke. Key design technology for largecross-section mechanized construction of mountainous tunnels[J]. Tunnel Construction, 2022, 42(4):703.

[11] Su Yinao, Dou Xxiurong. Measurement while drilling, log-ging while drilling and logging tools [J]. Petroleum Drilling and Production Technology, 2005, 27 (1):78–82, 89.

[12] Bieniawskiz. Engineering classification of jointed rock masses[J]. Civil Engineering in SouthAfrica, 1973, 15(12): 335.

[13] Barton N, Lien R, Lunde J. Engineering classification of rock masses for the design of tunnel support[J]. RockMechanics, 1974, 6(4):189.

[14] Sonmez H, Ulusay R. Modifications to the geological strength index (GSI) and their applicability to stability of slops[J]. International Journal of Rock Mechanics and Mining Sciences, 1999, 36(6):743.

[15] Palmström A. RMi: arock mass characterization system for rock engineering purposes[D]. Norway: University of Oslo, 1995.

[16] Standard for engineering classification of rock mass: GB/T 50218-2014[S]. Beijing: China Planning Press, 2014.

[17] Code for hydropower engineering geological investigetion:GB50287-2006[S]. Beijing:ChinaPlanning Press, 2008.

[18] Lei Lei. The Challenge of ChatGPT to the Subjectivity of Legal Persons[J]. Law Science, 2023(09):3–15.

Tunnelling for a Better Life – Yan, Celestino, Thewes & Eberhardt (Eds)
© 2024 The Author(s), ISBN 978-1-032-80042-4
Open Access: www.taylorfrancis.com, CC BY-NC-ND 4.0 license

The Brenner Base Tunnel: An overview of the excavation types used in the project

David Marini* & Giuseppe Venditti
BBT SE, Bolzano, Italy

David Unteregger & Romed Insam
BBT SE, Innsbruck, Austria

Roberta Marazzo
BBT SE, Bolzano, Italy

ABSTRACT: To date, the Brenner Base Tunnel project has completed more than 160 km of tunnels, including 60 km of the main tunnels. The latter include large stretches excavated using machines, but D&B as well, with low and high overburdens. Double and single shield TBMs are the favoured choice for the excavation of the main tunnels, as they allow the laying of prefabricated segments. For the excavation through important fault zones, but also in particular geological, geotechnical and hydrogeological conditions, more conventional excavation methods were selected, including drill and blast, hammers and excavators, preventive consolidation by jet-grouting, cut and cover, and artificial tunnels as well as ground freezing. And it was precisely the freezing method that proved to be a winning choice when it came to excavating under the Isarco river, also with a view to respecting the environment.

Keywords: Brenner Base Tunnel, ground freezing, TBM

1 BRENNER BASE TUNNEL PROJECT

1.1 *Introduction*

The Brenner Base Tunnel is a flat railway tunnel that connects two States and is the central part of the new Munich-Verona railway corridor, along the extended Scandinavian-Mediterranean corridor within the European TEN-T transport network. It stretches between Innsbruck (Austria) and Fortezza (Italy) for a total length of 64 km including the Innsbruck bypass) and will be the longest underground railway link in the world.

The main benefits of the project include the shift of freight and passenger traffic to rail, eliminating traffic congestion, to the benefit of people and the environment, greater safety from natural hazards and a significant reduction in journey times. Today, travelling by train from Fortezza to Innsbruck takes 80 minutes for passenger traffic and 105 for freight traffic, while in the future, when the tunnel is completed, it will take 25 and 35 minutes respectively.

1.2 *Progress of the works*

In September 2023, the Brenner Base Tunnel (BBT) reached approximately 70 per cent of excavation progress corresponding to 160 km of a tunnel system that altogether includes almost 230 km distributed among main tubes, exploratory tunnel and other service and/or logistics tunnels (see Figure 1).

Along the entire corridor covered by the BBT project, there are four main lots in progress. Work on the following construction lots is in progress (see Figure 2):

- H21 “Sill Gorge”
- H41 “Sill gorge – Pfons”
- H53 “Pfons – Brenner”
- H61 “Mules 2-3”
- H71 “Isarco river underpass”

In lot H41, the TBM “Lilia” started excavating the main east tube from Ahrental towards South on 2 May 2023. The TBM, with its diameter of 10.4 m, will complete the approximately 8.1-kilometre-long

*Corresponding author: david.marini@bbt-se.com

DOI: 10.1201/9781003495505-209

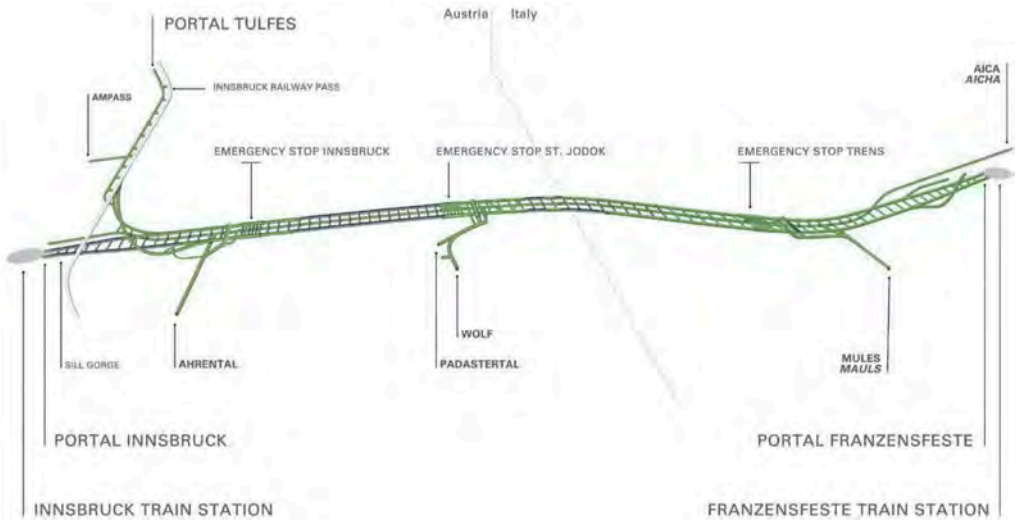

Figure 1. 3D plan of the Brenner Base Tunnel with construction progress.

tunnel section to reach the town of Navis where it will meet up with the tunnel excavated as part of lot H53. The assembly of the TBM "Ida", which will similarly excavate the west main tube, is currently in progress. On 4 April 2023, the last construction lot of the BBT as well as one of the longest of the entire base tunnel was awarded, namely the H53 Pfons-Brenner contract. Construction work on this lot started in May 2023. In Italy, construction is ongoing on the construction lots H61 Mules 2-3.

The excavation and lining activities of the Isarco river underpass lot were completed in August 2023 in accordance with the scheduled contractual deadlines and costs; the landscaping and renaturation of the external areas continue. TBM "Virginia" in the Mules 2-3 lot excavated a total of 14.2 km of the east main tunnel and completed its journey to the Brenner Pass on 30 March 2023. The lot has reached an overall progress of 91 per cent and work is in progress on the final lining in the emergency stop (see Figure 3), the access tunnel to the emergency stop and the cross passages, as well as the last kilometres of TBM excavation in the west main tunnel.

The excavation of the emergency stop in Trens, in lot H61 'Mules 2-3′ was completed in April 2022, with the exception of the opening of the diaphragms in the ventilation tunnels to the east main tunnels, which was postponed for logistical reasons.

2 CONSTRUCTION LOTS

The civil engineering works of the Brenner Base Tunnel are divided into several construction lots, of which seven main lots have been completed (considering the main railway tunnels, the exploratory tunnel as well as the access tunnels), two has been completed in 2023 and four are under construction (see Figure 2).

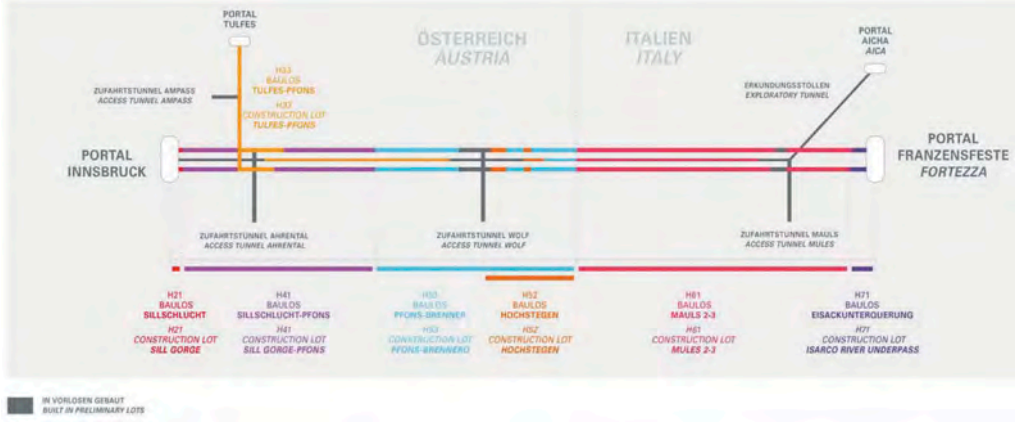

Figure 2. Overview of main construction lots underground works.

Figure 3. Photo central tunnel Emergency stop and cross passages.

Figure 4. TBM cutter head, construction lot Mules 2-3.

3 EXCAVATION METHODS

3.1 *Introduction*

Depending on the geological, geotechnical and hydrogeological conditions of the rock mass, the geometric constraints and the scheduling of the activities, roughly 50% of the excavation work will be excavated with TBMs, 50% using drilling and blasting as well as mechanical digger. The choice was made to use shielded TBMs, as they allow the precast tubbing ring lining to be placed immediately behind the TBM, thus guaranteeing a high degree of safety during execution, and at the same time the creation of a ring that under normal conditions serves as the final lining.

3.2 *Mechanised excavation*

Depending on the performance requirements and the main purposes identified, mechanised excavation involves the use of double shield, single shield and open TBMs.

In Italy, a 24.5 km section of the exploratory tunnel was excavated with a double shield TBM, whereas the Austrian section involved the excavation of 16.5 km of the exploratory tunnel with the use of an open TBM.

The TBM excavation of the main tunnels involves the use of prefabricated segments with high performance characteristics in both Italy and Austria. This required the use of double and/or single shield TBMs.

In Italy, more than 25 km of main tunnels were excavated with double shield TBMs, with an excavation diameter of 10.7m, a length of approx. 205m and a weight of approx. 2,400t (see Figure 4).

When fully operational, each individual TBM requires a nominal capacity of 4,200 kW (12x350 kW) and a main cylinder thrust force of 95,000 kN, corresponding to 9,500 t. The forces at play are impressive and require not only a high quality of the materials used, but above all highly complex and properly designed systems.

The peculiarity of the main tunnels is the application of a lining made of tubbing rings, despite the great excavation depth. This tubbing ring lining, for excavations in Italy, is 45 cm thick and is made up of 6 +1 elements plus a base arch in reinforced concrete with an average length of 1.75 m. It uses a double sealing system. The ring laid down in the project is a universal size, and by rotating it around its axis it is possible to stagger the longitudinal joints between the segments and to follow the altitude/plane profile and the deviations of the route. The tunnel complex uses a system drained externally from the tubbing ring by 20-25 cm pea- gravel and internally by a groundwater collection system, consisting of openings at the base of the ring and two micro-fissured collectors placed next to the base element. The water flows into the collectors and is then conveyed to the cross passages identified for vertical discharge to the exploratory tunnel along which it flows to its respective outlets at Aica on the south side and at the Sill Gorge on the north side. The peak of the main tunnels is located at the state border.

In May 2021, TBM 1072 achieved record excavation production by exceeding a monthly production of 860m, corresponding to an average daily production for that month of 30.71m/day.

In the H41 construction lot Sill Gorge-Pfons, two single shield machines with an effective drilling diameter of 10.4 m have been used to drive the main tunnel tubes from Ahrental southward, starting in May and June 2023, respectively and excavating stretches of approx. 8.1 km and 8.4 km. The two TBM with backup structure are each approx. 160 m long and weigh approx. 2,420 tons. The total engine power of each TBM is 4,550 kW (13x350 kW). In total, the TBMs used have 18 double presses and thus a total of 36 thrust cylinders. The installed nominal thrust is 128,000 kN each at an operating pressure of 300 bar and the maximum jacking force is approx. 183,000 kN at 500 bar.

The tubbing ring system to be used is a single-sealed and bolted universal ring system with a tubbing ring thickness of 40 cm and a ring conicity of 40 mm. The ring pitch is 6+0 in accordance with the requirements of the tender, and the ring width is 1.95 m (see Figure 5).

The ring pitch in question consists of four rhomboid tubbing rings (tubbing rings B1, B2, C1 and C2) and two trapezoidal tubbing rings (tubbing rings A and K).

Figure 5. Tubbing ring lining in construction lot H41.

The width of the ring gap varies between 28 cm in the crown and 25 cm in the base slab. In order to take into account the drainage effect of the tunnel tube, the ring bedding, where the geological conditions permit, is usually carried out with pea gravel, which is injected and compacted in some areas if necessary, and a mortar bed or pearl gravel - mortar mixture in the base slab.

Ordinary, additional and special measures have been defined for mechanical excavation with TBMs, which include additional mechanical equipment and technical measures in order to be able to react to critical excavation situations and to avoid long-term excavation interruptions.

In planning the mechanical TBM excavations, the findings from driving the exploratory tunnel, which was completed with an open TBM in the period between October 2015 and July 2020 as part of the H33 Tulfes-Pfons construction lot, were considered in their entirety.

3.3 *Excavation with conventional methods*

3.3.1 *Drill and blast excavation*

Some sections of the Brenner Base Tunnel are characterised by changes in the geometry of the excavation sections and different lengths, thus requiring a drill & blast excavation with consolidation of the tunnel by means of radial anchors, welded mesh mats and shotcrete and, where necessary, supplemented with ribs, forepoling and consolidation of the excavation front. In Austria the methodological approach is to excavate tunnels usually with a partial section, in Italy full-section excavation is preferred, the partial section is also applied to sections larger than 10m in diameter (e.g. TBM assembly chambers) and under special conditions.

3.3.2 *Excavation in fault zones*

The fault zone of the Periadriatic Seam (located approximately at km 46+800 to km 47+600) at the point of tectonic contact between the European Plate and the African Plate was also excavated using mechanical diggers, requiring major geognostic investigation in advance and special consolidation measures. The data clearly show that the rock mass with cachyrites, cataclasites and tonalitic mylonites is significantly less resistant to deformation as compared to “healthy” rock (granite and tonalite), thus causing more deformation with subsequent ample plasticisation around the cavity itself. Furthermore, intensely fractured rock was found in stretches along the route, due to tectonic activity (see Figure 6).

Parametrisation had shown the need to include rock face consolidation measures which in some cases would still not succeed in reducing convergence at the rock face to acceptable levels.

Figure 6. Excavation front in the fault zone of the Periadriatic Seam.

For this reason, a controlled deformation of the cavity to be modulated based on the maximum expected deformation has been applied as starting solution. In the execution phase, the observational method combined with careful monitoring identified strongly asymmetric behaviour with significant deformations along the tunnel axis and somewhat lesser deformations along the radial. These conditions led to the choice of a rigid lining to consolidate the cavity, combined with rock face consolidation that limited the deformations along the tunnel axis to an acceptable level.

During the works, in-depth monitoring was performed with extensometers at the front, convergence measurements, strain gauge and load cells mounted on the ribs, bolts and radial multi-base extensometers.

In the Austrian section, the Hochstegen fault zone, a water-bearing and therefore hydrogeologically very challenging tunnel section, is located at km 29+500 to km 30+200. Geologically, the zone lies in a heterogeneous lithological sequence between the Bündner schists of the Glockner nappe in the north and the central gneiss in the south. Worth mentioning in this respect is the eponymous Hochstegen marble and the Rauhwacke zone lying to the north of it. With overburdens of 600 m to 800 m, transient water

inflows of 150 l/sec/10 m and pressures of up to 80bar were predicted here. The situation was further complicated by the fact that a Natura 2000 site and important groundwater resources for the region lie above the hydrogeologically sensitive section. Therefore, very restrictive construction measures (injections, sealing, etc.) were prescribed by the authorities for this section. The major challenge is that the groundwater level at the surface must not be lowered by more than 30 cm as a result of the tunnelling activities. To ensure this, massive and time-consuming injection campaigns were tendered to ensure a largely sealed excavation that prevents a lowering of the groundwater level (see Figure 7).

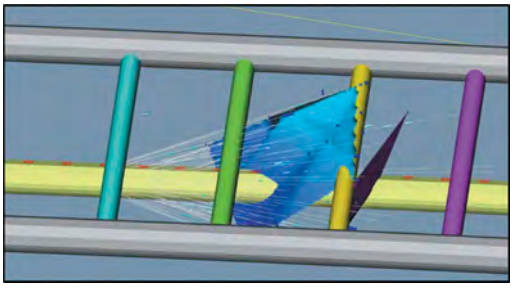

Figure 7. 3D model of the injections from the exploratory tunnel.

In particular, the high-water pressures of up to 80 bar meant that the injection campaigns and injection screens had to be very tightly meshed and carried out in several rings in order to seal the tunnel as much as possible.

Currently, the injection and excavation work are being carried out as a preliminary measure in the exploratory tunnel, and it has been possible to avoid any significant water inflows in the excavated areas of the Rauhwacke zone and the Hochstegen marble (see Figure 8). The findings from the exploratory tunnel will be subsequently incorporated into the excavation of the main tunnel tubes, so that they can be optimized.

Figure 8. Injection work in the Hochstegen fault zone.

3.3.3 *Innovative Jet Grouting technology in alluvial soils*

For the tunnel stretches excavated in the valley floor area north of the Isarco River, which were not accessible from the surface due to the high overburdens, subhorizontal advance pre-consolidation with Quick Set Jet Grouting technology was used injections (see Figure 9).

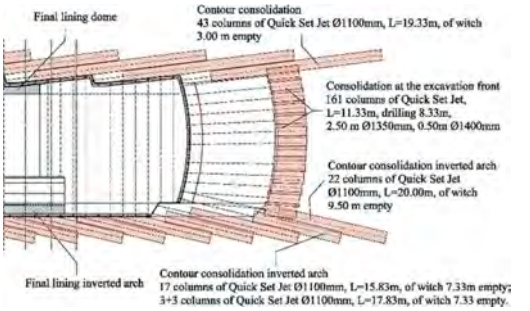

Figure 9. Longitudinal excavation profile with QSJG®.

The QSJG® technology, thanks to the use of special setting accelerators conveyed in the jet-injection phase through independent circuits within the drill rods, which allowed the cement mixture and setting accelerator to mix only downstream of the injection nozzle, created columnar jet-grouting treatments even in the presence of significant hydraulic head (up to 30m from the keystone) without the need for preliminary waterproofing injections.

The use of a specific hydraulic preventer also prevented the column from being emptied by counteracting the high hydrostatic pressures involved, and also allowed the installation of special plugs to seal the consolidated column. By employing appropriate injection parameters, it was possible to carry out columnar treatments with a diameter of up to 1,400 mm, larger than those carried out with traditional methods (see Figure 10).

Figure 10. Excavation with QSJG® method.

The transition between the debris and the rock substrate inevitably involves mixed excavation fronts, i.e. partially occupied by debris and partially by medium fractured and altered rock.

A technical solution was also provided for these transition sections, proposing QSJG® interventions in the debris sector, and interventions called Roto Injection Controlled Parameters (RICP), for the altered and fractured rock sector.

The technique, as compared to the QSJG® technology, consists of injecting a more permeating mixture with reduced energy, partly using the same equipment as the QSJG®.

The aim was to cement the fine debris that fills the fractures and discontinuities in the rock mass which had been intercepted and brought into contact with the cavity, for a sufficient distance to prevent the flow of water in the rock mass around the excavation, interrupting the communication between the various fractures and discontinuities and guaranteeing the impermeability of the rock sector as requested by the design.

A single injection treatment using the RICP technique has an influence radius of approximately 90 cm, comparable to a treatment using traditional valve injection. A further feature of the implemented technical solution was the possibility of carrying out the two consolidation techniques, RICP in the rock section and QSJG® in the debris section, in separate but continuous phases, and above all within the same hole, for all those treatments that were necessary in the transition areas between rock and debris (see Figure 11).

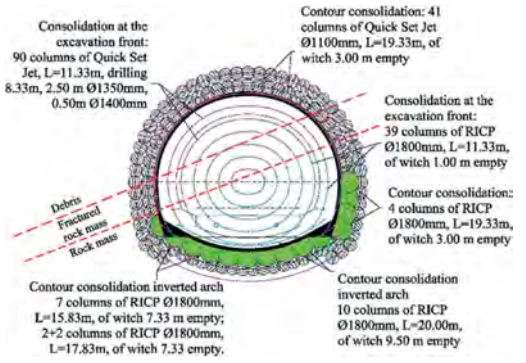

Figure 11. Excavation cross-section with RICP.

For the excavation of the tunnel stretches in the areas of the Isarco River valley floor, which are completely surrounded by groundwater debris and landslide material, large-diameter (2000 mm) vertical bifluid jet grouting treatments were carried out to create a ring of consolidated soil around the tunnel cavity (Figure 12), varying in thickness between 3.00 and 4.50 m depending on the type of excavation section and position (dome or inverted arch).

In order to allow the realisation of compartmentalised excavation "fields", the construction of baffles of consolidated soil was planned, again by means of columnar jet-grouting treatments; the individual excavation fields were no longer than 15 m and the length depended on the excavation geometries. A plug of approximately 3.5 m thickness was planned at the cross-section changes: the partition is positioned astride the cross-section change. If the distances between one section change and the next were greater than 15 m, a further internal partition was provided, in this case 2.0 m thick, i.e. a row of interpenetrating Jet Grouting treatments.

The excavation, following this consolidation technique, was carried out full-section without groundwater drainage.

3.3.4 *Ground freezing technology*

The Isarco river underpass was built by means of four tunnels, driven with full-section excavation from shafts placed laterally to the riverbed, after consolidation works were carried out using artificial soil freezing technology in order to obtain a reduction in the speed of the underground water flows (Figure 12).

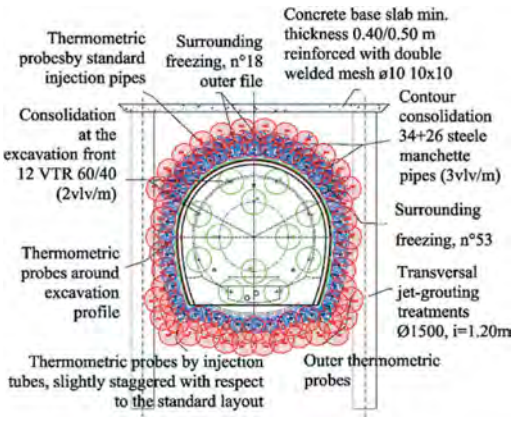

Figure 12. Excavation section type and jet grouting consolidation.

The freezing of the ground was carried out by means of the so-called 'mixed method':

- Phase one - liquid nitrogen freezing (open or direct circuit) during which the compressed liquid nitrogen, at a temperature of -196°C, is conveyed from 4 storage silos of 50,000 litres/each to the two portals at the entrance to the tunnels inside special insulated pipes. Once the refrigerant fluid reaches the distribution portals - outside the perimeter of the tunnel to be excavated - it is conveyed into coaxial stainless steel pipes, called 'freezing probes', subtracting heat from the ground and dispersing it into the atmosphere in the form of gas through suitable venting chimneys located at the top of the shafts. In this phase, an ice wall is formed around the area to be excavated with the geometric characteristics and temperatures in the design;

- Phase two - brine maintenance (closed or indirect circuit), during which this calcium chloride solution is circulated within a closed circuit by means of sending pumps from a refrigeration plant, consisting of 3 chillers of 240 kW each, one of which is a backup, and sent inside the same freezing probes already used in the liquid nitrogen freezing phase at a temperature of between -30 °C and -35 °C. The brine removes heat from the ground by heating up and returns to the refrigeration system where it is cooled again and fed back into the circuit. This allows the ice shell formed in the first freezing phase to be preserved, without significantly increasing its size.

The second phase remained active and after verifying that the design requirements had been met, the excavation phases began (see Figure 13).

Figure 13. Consolidation section of the Isarco underpass.

Thanks to this technique, which is both safe and eco-compatible as no products are injected or dispersed into the ground, it was possible to safely excavate the four tunnel sections under the Isarco River in an environmentally friendly way, managing to avoid temporarily re-routing the river and subsequently returning it to its natural bed.3.2 xxx

3.3.5 *Cut-and-cover method*

Coming from the Innsbruck railway station, the Sill Gorge construction lot is the connection to the Brenner Base Tunnel. The route leads through the upstream Silltal tunnel, which is approx. 130 m long, before crossing the river Sill to reach the main portal of the Brenner Base Tunnel.

The Sill-valley tunnel passes through the foot of Mount Isel, with primarily blocky flow debris; only in the central area with the highest overburden, was the first appearance of the bedrock from the geological explorations expected.

After extensive variant studies, tunnelling using cut and cover was finally selected, requiring a slope cut of up to 45 m in height. Based on the geological prognosis, the slope cut was secured with bolted shotcrete and 2 anchor beams with tensioned braided anchors. Due to the highly fissured boulders found during the works, it became necessary to reinforce the consolidation of the slope cut by adapting and trengthening the nailing and tie-back anchors (now with 5 anchor beams).

The execution of the cut was successful, the construction of the concrete structure for the Sill-valley tunnel is ongoing (see Figure 14). Finally, the Sill-valley tunnel will be covered, landscaped and renaturalized as a recreational area for the city of Innsbruck.

Figure 14. Cut-and-cover method in construction.

4 CONCLUSIONS

The tunnel system of the Brenner Base Tunnel - due to the diversity of rock masses to be crossed, the different geometries required (main tunnels, access tunnels, passages, chambers, etc.) and a subdivision into construction lots with logistical and time constraints - requires a multiplicity of excavation methods: these methods are described in this article, considering the experience gained in the excavation more than 160 km of tunnels.

ACKNOWLEDGMENTS

We would like to express our sincere thanks to BBT SE CEOs Gilberto Cardola and Martin Gradnitzer, both for their willingness to share the technical experience of the Project and their support of our active participation in international events in our sector.

REFERENCES

[1] John, M., Reiter, F., Skuk, S. & Venturini, G. BBT-Symposium (2007) – Geotechnische Aspekte für den Bau des Brenner Basis Tunnels.

[2] Marini D., Venditti G., 2022; The excavation of the Brenner Base Tunnel where the Eurasian and Adriatic tectonic plates collide; Expanding Underground - Knowledge and Passion to Make a Positive Impact on the World, pp. 1346–1356: ISBN 978-1-003-34803–0

[3] Marini D., Venditti G., 2023; The excavation of the Brenner Base Tunnel where the Eurasian and Adriatic tectonic plates collide; Expanding Underground - Knowledge and Passion to Make a Positive Impact on the World, pp. 720–725; ISBN 978-1-003-34803-0

[4] Marottoli A., Marazzo R., Vecchione G., 2022; Tecnica del congelamento per la galleria più lunga al mondo; Quarry and Construction 3/2022, pp. 78–89

[5] Skuk S., Egger H., Conti U. M., Renghi D., Barnabei E., Toro, M. Fornari M., Spaziani A, Voza A., 2022: Challenging 14.2 km stretch of the Exploratory Tunnel completed by DS-TBM – Geological - Geotechnical experiences at the italian's lot Mules 2-3. Gallerie e Grandi Opere Sotterranee, vol. 144: 45–54.

Tunnelling for a Better Life – Yan, Celestino, Thewes & Eberhardt (Eds)
© 2024 The Author(s), ISBN 978-1-032-80042-4
Open Access: www.taylorfrancis.com, CC BY-NC-ND 4.0 license

Key construction technologies for high-speed railway tunnels that with shallow buried depth and gentle slope in loess platform

Weijun Mi*
China Railway Academy Co., Ltd, Chengdu, China
Lanzhou University, Lanzhou, China
Northwest Research Institute Co., Ltd of CREC, Lanzhou, China
Qinghai Province Key Laboratory of Permafrost and Environmental Engineering, Golmud, China

Yingsheng Wang
China Railway Academy Co., Ltd, Chengdu, China

Huyuan Zhang
Lanzhou University, Lanzhou, China

Xueyun Miao
China Railway Academy Co., Ltd, Chengdu, China
Northwest Research Institute Co., Ltd of CREC, Lanzhou, China
Qinghai Province Key Laboratory of Permafrost and Environmental Engineering, Golmud, China

Junping Zhang
China Railway Academy Co., Ltd, Chengdu, China

Manyin Zhang
Lanzhou University, Lanzhou, China

ABSTRACT: In loess platform the special genesis has shaped the complex groundwater occurrence conditions and special surrounding rock conditions. When a high speed railway tunnel has to cross the loess platform in the form of shallow depth and gentle slope, it faces technical difficulties caused by many factors such as gentle slope with long distance, and poor stability of the surrounding rock. Taking into consideration the engineering geological characteristics in loess platform, this paper studies the relationship between the critical buried depth and space, the change law of water content of the surrounding rock, the overall mechanical behaviors and deformation characteristics of the tunnels with shallow buried depth and gentle slope in loess tableland areas. The classification formula and correction factor for the critical overburden depth are derived in terms of the tunnels with shallow buried depth and gentle slope in loess tableland areas, and the spatio-temporal variation rules and the key change time points of water content of the surrounding rock are determined. The comprehensive subgrade treatment measures, pre-grouting measures to improve the strength of the surrounding rock, and key control measures for roof ripping construction are proposed for the tunnels with shallow buried depth and gentle slope in loess platform.

Keywords: Loess platform, Shallow buried depth and gentle slope, Tunnel construction, Key technology

1 INTRODUCTION

Since the beginning of the new century, the transportation industry has developed rapidly[1], and a large number of railway trunk lines, branch lines and special lines have been built in the loess area[2], among which the Yinxi high-speed railway is an important part of the national "eight vertical and eight horizontal" high-speed railway network[3].

Domestic and foreign experts and scholars have conducted a large number of field test studies on the shallow burial problem in the construction of loess

Fund Project: Science and Technology Research and Development Program of China Railway Corporation (2017G007-G)
*Corresponding author: mwj0806@126.com

DOI: 10.1201/9781003495505-210

tunnel. Combined with theoretical analysis, systematic studies have been conducted on the boundary of deep and shallow burial, surrounding rock pressure, the interaction mechanism between the initial support and surrounding rock, and reasonable initial support in loess tunnel[4] ~ [7].

Li Guoliang, Jin Baocheng, Shao Shengjun, Wang Zaiguang, Mi Weijun et al.[8] ~ [12], relying on the construction of Zhengzhou-Xi'an and Baoji-Lanzhou high-speed railway, the applicability of large section loess tunnel construction method is studied experimentally,and the deformation and stress characteristics of the surrounding rock and supporting system of the step method are proved, which provides a basis for solving the key technology of the construction of large section loess tunnel.

Wang Mingnian et al.[13], [14] investigated and studied the relationship between surface cracks and buried depth in 12 tunnels of Zhengzhou-Xi'an high-speed railway, and conducted in-depth research on the deep and shallow buried boundary of super-large cross-section in loess tunnels, and drew the dividing line of deep and shallow buried.

The Loess Tunnel Engineering, edited by Zhao Yong, Li Guoliang, Yu Yu et al.[15], summarized the history and current situation of loess tunnel construction, and pointed out the existing technical problems and development direction of loess tunnel construction.The calculation method of the boundary between deep and shallow loess tunnel and the design load of loess surrounding rock are determined. The construction technology of basement treatment of collapsible loess tunnel is introduced based on engineering examples.

According to the existing research results, our country has accumulated a lot of tunnel construction experience in the loess region. Especially in recent years, domestic scholars have done a lot of related research work for the new high-speed railway, Such as Zhengzhou-Xi'an high-speed railway, Lanzhou-Xinjiang high-speed railway, Baoji-Lanzhou high-speed railway and Lanzhou-Chongqing high-speed railway.

There are 22 tunnels crossing the loess platform in Gan-ning section of Yinchuan-Xi'an high-speed railway, with a total length of 84.18km, accounting for 57.53% of the total length of the whole line. Due to the regional differences in origin, particle composition and engineering characteristics of loess age, Yinchuan-Xi'an high-speed railway still faces many technical problems in loess tunnels when it is built in Loess platform.

Especially when the tunnel passes through the shallow buried and slow slope section in the loess platform, there are obvious differences in the vertical and horizontal topography, the thickness of the loess layer and the engineering characteristics of the tunnel. The main problems to be solved are as follows: (1)the definition of deep and shallow buried tunnels in the loess Tableland; (2)Changes of water content of surrounding rock and key control time points of construction changes; (3)Deformation mechanism and control measures of surrounding rock in shallow and slow slope section; (4)Suitable base treatment method.

2 CHARACTERISTICS OF SHALLOW BURIED AND SLOW SLOPE TUNNEL IN LOESS PLATFORM

2.1 *Engineering geological characteristics of loess platform*

As a part of the Ordos Platform, Ganning Loess Plateau is based on the Mesozoic palaeo-geomorphic basin, and has formed the typical Quaternary Early Pleistocene(Q_1) and Middle Pleistocene(Q_2) deep protogenetic loess in the long deposition of 2 ~ 3 million years. In the Late Pleistocene period (Q_3), affected by the geological tectonic movement, the platform rose intermittently in the region, and was gradually cut up by the tractive erosion of rainwater collection, rivers, floods, etc., forming the geomorphic unit of the loess latform today.

Figure 1. Topography and geomorphology map along Yinxi high-speed Railway.

Between Ning Xian County and Huan Xian County is the typical latform unit of Dongzhi Loess platform. the surface is gentle, open, flat and continuous, covering about 700 square kilometers, it spans the four counties and districts of Qingyang City. It is the largest loess latform with the thickest soil layer and the best preserved Loess latform, and is called "the first Loess latform in the world". The elevation of surface on Dongzhi loess platform is 1237 ~ 1442m, the elevation of the bottom of the Loess latform is 980 ~ 1112m, and the relative elevation difference is 257 ~ 330m.

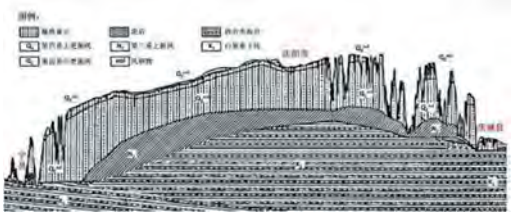

Figure 2. Geological profile of Dongzhi loess platform.

As shown in Figure 2, the bottom layer is Upper Neogene mudstone or sandstone, on which there is large thickness of Middle Pleistocene loess of Quaternary system (Q2eol), and the top layer is shallow Upper Pleistocene loess (Q3eol). In the gully area of the margin of the loess platform, there are 5 ~ 6m thick landslide accumulation loess and alluvial loess on the surface. The loess in Dongzhi platform has typical characteristics of aeolian loess, with no obvious bedding, high clay content and vertical joint development. In addition, affected by local topographic characteristics, it also has engineering characteristics such as high water content and poor self-stability. Geotechnical parameters are shown in Table 1.

Table 1. Geotechnical parameters of surrounding rock in loess platform.

stratum	Upper Pleistocene clay loess of the Quaternary system (Q_3^{eol})	Middle Pleistocene in the fourth system Clay loess (Q_2^{eol})	
thickness /m	10.0~25.0	150.0~190.0	
Void ratio/e	0.75~0.98	0.65~0.78	
Liquid index /I_l	-0.30~0.22	0.22~0.57	
Plasticity index /I_p	10.91~12.20	10.94~12.41	
Coefficient of collapse /δ_s	0.016~0.060	0.000~0.008	
density /g/cm^3	1.63~1.91	1.88~1.91	1.96~1.97
Moisture content /%	14.3~21.6	21.3~22.9	25.5~26.0
Relation to water level	above	above	below

2.2 *Shallow buried and slow slope characteristics of tunnels in loess platform*

The length of DK182+493 ~ DK280+200 section of Yinxi high-speed railway crosses the Dongzhi loess platform is 97.71km, and the DK207+517.55 ~ DK214 +300 section of Shangge-cun tunnel has a total length of 6782.45m, which passes through the loess platform. The maximum buried depth of Shangge-cun tunnel is 102m, the exit is located at surface, and the minimum buried depth is about 5.5m. The longitudinal slope of the tunnel is 25‰, and the buried depth of the exit section, DK211+376 ~ DK214+300,is less than 50m, and 2924m is in the shallow buried section, accounting for 43.11% of the total line length. As shown in Figure 3.

Section DK254+200 ~ DK259+006.36 of Yima Tunnel, with a total length of 4806.36m,enter Dongzhi Loess platform in a downward direction. The maximum buried depth of Yima tunnel is about 122m, the entrance is located at surface, and the minimum buried depth is about 3m. The longitudinal slope,DK254+200 ~ DK254+900,at the entrance of the tunnel is 22.5‰ and the longitudinal slope, DK259+900 ~ DK259+006.36,is 25‰. The buried

Figure 3. Route diagram of Yinxi high-speed railway crossing Loess platform.

depth, DK254+200 ~ DK255+975,at the entrance is less than 50m, and 1775m is in the shallow buried section. It accounts for 36.93% of the total line length.

3 CRITICAL BURIED DEPTH OF SHALLOW BURIED DEPTH AND GENTLE SLOPE TUNNEL IN LOESS PLATFORM

3.1 *Comparison between the calculation of the standard formula of critical depth and the actual buried depth*

The Technical Specification for Railway Loess Tunnel (Q/CR 9511-2014) stipulates that the depth of the loess tunnel is 1.4 ~ 2.1 (H+B); New loess (Q_3, Q_4) tunnel deep and shallow buried depth h_c can be upper limit 1.8 ~ 2.1 (H+B); Old loess (Q_1, Q_2) tunnel depth h_c can be lower limit 1.4 ~ 1.7 (H+B).

According to the survey and design data, the excavation height H and width B of the excavated section of Yinxi high-speed railway tunnel are 12.09m and 15.1m respectively. The tunnels in the Loess Tableland are located in the Upper Pleiocene clay loess (Q_3^{eol}) and the Middle Pleiocene clay loess (Q_2^{eol}) of the Quaternary system, among which the DK214+116 ~ DK214+300 tunnels in Shangge-cun are located in the Upper Pleiocene clay loess (Q_3^{eol}). The upper part of DK213+842 ~ DK214+116 is located in Upper Pleistocene clay loess (Q_3^{eol}) of Quaternary system, and the lower part is located in Middle Pleistocene clay loess (Q_2^{eol}) of Quaternary system. Section DK211+000 ~ DK213+842 of Shangge-cun Tunnel and section DK255+440 ~ DK256+281 of Yima Tunnel are located in Q_2^{eol} of Middle Pleistocene system.

According to the Technical Specification for Railway Loess Tunnel (Q/CR 9511-2014), the depth h_c of the deep and shallow buried depth of the tunnel on the Loess Plateau is as follows:

1) In the Upper Pleiocene clay loess (Q_3^{eol}) stratum, the depth of DK214+116 ~ DK214+300 section of Shangge-cun Tunnel is h_c= 48.94 ~ 57.10m;
2) In the Middle Pleistocene clay loess (Q_2^{eol}) stratum of the Fourth system, the deep and shallow buried depth of Shangge-cun Tunnel DK211+000 ~ DK213+842 and Yima Tunnel DK255+440 ~ DK256+281 is h_c=38.09 ~ 46.22m.

The loess platform is flat and open, the stratum soil is uniform and the stratum line is straight. There is no flowing water on the surface, the underground water depth is 50 ~ 70m, and the aquifer thickness is 10 ~ 30m in the exploration depth. The groundwater type is mainly Quaternary unconsolidated layer pore diving, which has both the general characteristics of unconsolidated layer pore diving and the hydraulic properties of fissure water. It is mainly distributed in the top part, and the aquifer is mainly Middle Pleistocene loess.

The pore water recharge of the quaternary loose layer in the tunnel area is mainly vertical infiltration of atmospheric precipitation and lateral and downward infiltration of surface water. According to the actual situation on site, Shangge Village tunnel DK210 +884.1 ~ DK210+958.45, tunnel buried depth of 61m, affected by groundwater, tunnel positive hole is located in the soft plastic clay loess layer (Q_2^{eol}), as a V-level surrounding rock, normal tunnel excavation still has an impact on the surface deformation. The soil at the top of the tunnel is difficult to form a natural arch, which is still under the influence of construction. The actual buried depth of the tunnel is obviously greater than the critical depth calculated by the standard, as shown in Table 2. Therefore, according to the actual situation, it is necessary to modify the depth h_c of the tunnel in Loess Yuan.

3.2 *Correction of the formula of critical depth about tunnel which with shallow buried depth and gentle slope in loess platform*

Different from the shallow buried tunnel in loess beam and Loess hill of geomorphic units, the tunnel running through loess platform has certain deviation between the calculated and measured critical depth h_c due to the influence of groundwater and high water content, which needs to be verified and corrected by calculation, simulation and measured values.

1) Derivation of the calculation formula of critical depth h_c for deep and shallow buried tunnels in loess platform

According to the code, the surrounding rock pressure of shallow buried loess tunnel mainly consists of vertical surrounding rock pressure and horizontal surrounding rock pressure, and the vertical surrounding rock pressure directly affects the buried depth of loess tunnel.

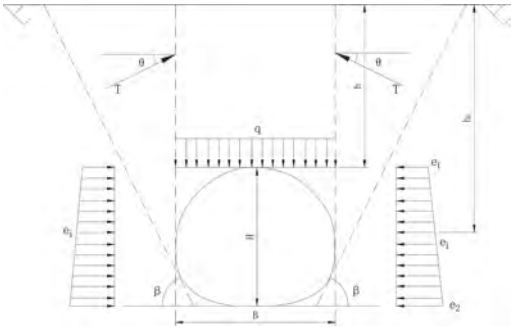

Figure 4. Schematic diagram of surrounding rock pressure in shallow buried loess tunnel.

As shown in Figure 4, the calculation formula of vertical surrounding rock pressure is as follows:

$$q = \gamma h - \frac{\lambda \gamma h^2 tan\theta}{B} \tag{3.1}$$

the formula:γ——Surrounding rock weight, kN/m^3;

h ——Tunnel depth, m;

λ ——Pressure coefficient of tunnel surrounding rock, $\lambda = \frac{tan\beta - tan\emptyset_c}{tan\beta(1+tan\beta(tan\emptyset_c - tan\theta)+tan\emptyset_c tan\theta)}$;

θ ——The friction Angle between the two sides of the roof soil column is generally selected according to the experience value of the Design Code for Railway Tunnels, as shown in Table 3;

$\emptyset_c$ ——The friction Angle of surrounding rock and the values of each soil layer in Shangge-cun tunnel and Yima tunnel are shown in Table 4;

β ——Rupture Angle at maximum thrust,

$tan\beta = tan\emptyset_c + \sqrt{\frac{(tan^2\emptyset_c+1)\ tan\emptyset_c}{tan\emptyset_c - tan\theta}}$

2) Determination of correction factor k of critical depth h_c for deep and shallow buried tunnels in loess platform

By substituting all parameters into equation (3.1), the calculation values of the depth and shallow buried depth h_c of the tunnel in Loess platform when it passes

Table 2. Calculation value and actual buried depth of some tunnel sections in loess platform.

				The vault is buried deep /m	
Tunnel name	Paragraph mileage	Surface characteristics	Stratigraphic lithology	Calculated buried depth	Actual buried depth
Shangge-cun tunnel	DK213+872~DK213+994	Slight fluctuation	Q_3 Clay loess	48.94~57.10	5.6~9.0
	DK213+845~DK213+860	Gentle terrain	Q_3 Clay loess	48.94~57.10	12.8~13.1
	DK210+884~DK210+958	Gentle terrain	Q_3、Q_2 Clay loess	38.09~46.22	60.9~59.5
	DK210+050~DK210+175	Gentle terrain	Q_3、Q_2 Clay loess	38.09~46.22	71.1~72.5
Yima tunnel	DK255+440~DK255+450	Gentle terrain	Q_3、Q_2 Clay loess	38.09~46.22	35.4~35.6
	DK256+260~DK256+281	Large fluctuation	Q_3、Q_2 Clay loess	38.09~46.22	52.1~58.6

through the Upper Pleistocene clay loess (Q_3^{eol3}) formation, the middle Pleistocene clay loess (Q_3^{eol3}) formation and the Upper Pleistocene sandy loess (Q_3^{eol3}) formation are shown in Table 5.

Table 3. Statistical table of θ values of surrounding rock at all levels.

The level of surrounding rock	I, II, III	IV	V	VI
θThe values	$0.9\phi_c$	$0.7\phi_c$~$0.9\phi_c$	$0.5\phi_c$~$0.7\phi_c$	$0.3\phi_c$~$0.5\phi_c$

Table 4. Statistical table of friction Angle of surrounding rock of shallow buried depth and gentle slope tunnel in loess platform.

Tunnel name	Stratigraphic age	Stratigraphic origin	Soil layer name	Mean friction Angle φ/°
Shangge-cun tunnel	Q_3	eol	Clay loess	20.57~23.68
	Q_2	eol	Clay loess	18.60~22.73
Yima tunnel	Q_3	eol	Clay loess	28.64~32.30
	Q_2	eol	Clay loess	18.60~20.21

As can be seen from Figure 4 and formula (3.1), the surrounding rock pressure of the shallow buried loess tunnel is closely related to the depth and width of the tunnel in addition to the weight of the surrounding rock, the coefficient of surrounding rock side pressure, the friction Angle on both sides of the roof and soil column, the friction Angle of surrounding rock, and the fracture Angle of the surrounding rock, etc. In addition, the surrounding rock pressure q is a quadratic function of the tunnel buried depth h. When the surrounding rock pressure reaches a maximum value, the surrounding rock pressure will be reduced to a maximum value. The corresponding buried depth of the tunnel is h_c.

The partial derivative is calculated on the left and right sides of equation (3.1), that is, when $\frac{\partial q}{\partial h}=0$, the tunnel buried depth obtained is h_c, the depth of deep and shallow buried boundary of loess tunnel.

$$h_c=\frac{B}{2\lambda tan\theta} \tag{3.2}$$

2) The correction factor k of the critical depth h_c buried in the tunnel in loess platform is determined

By substituting each parameter into equation (3.2), the calculation value of the depth and shallow buried depth h_c of the tunnel in Loess platform can be obtained when it passes through the Upper Pleistocene clay loess (Q_3^{eol3}) formation, the middle Pleistocene clay loess (Q_3^{eol3}) formation and the Upper Pleistocene sandy loess (Q_3^{eol3}) formation.

The critical depth calculated by the empirical formula h_c is obviously less than the actual buried depth when part or all of the tunnel is located in the groundwater table due to the special landform and engineering geological characteristics of the Loess platform. In this case, the critical depth h_c calculated by equation (3.2) is close to the actual buried depth. When part of the tunnel is located in the water table, the actual buried depth of the tunnel is 49.4 ~ 58.1m, and the calculated critical depth is 56.68 ~ 58.84m. The actual buried depth is 0.87 ~ 0.99 times of the calculated value. When the tunnel is completely below the groundwater level, the actual buried depth of the tunnel is 60.9 ~ 68.0m, the calculated critical depth is 59.53 ~ 60.70m, and the actual buried depth is 1.02 ~ 1.12 times of the calculated value.

Therefore, the determination of critical depth h_c for deep and shallow tunnels in Loess platform can be divided into three cases: above groundwater level, partly in groundwater and below groundwater level.

(1)Determination of the critical depth h_c for deep and shallow burial when the tunnel is located above the groundwater level.According to the empirical formula h_c, the upper limit of the depth h_c of the new loess (Q_3, Q_4) tunnel can be 1.8 ~ 2.1 (H+B). Old loess (Q_1, Q_2) tunnel depth and shallow buried boundary depth h_c recommended lower limit 1.4 ~ 1.7 (H+B);

(2)Determining the critical depth h_c of the deep and shallow buried in the water table of the tunnel part. According to the formula, $h_c=\frac{B}{2\lambda tan\theta}\ k$, k is 0.87 ~ 0.99.

(3) To determine the critical depth h_c for the deep and shallow burial of the tunnel below the groundwater level, h_c=$kh_c=\frac{B}{2\lambda tan\theta}$, k is derived from the formula, and k is 1.02 ~ 1.12.

Based on the above correction, the critical depth of the tunnel in the Loess platform is 48.9 ~ 58.6m when it is located above the groundwater level, 57.6-60.2 m when part of the tunnel is located in the groundwater, and 61.0 ~ 62.3m when all of the tunnel is located in the groundwater. Therefore, the starting and ending mileage of the shallow buried section of Shangge-cun Tunnel of Yinxi High-Speed Railway is DK210+050 ~ 214+000, and the length is 3950m, which is 58.24% of the total length of the tunnel (the original calculated length is 2924m/ 43.11%). The starting and ending mileage of the shallow buried section of Yima Tunnel is DK254+320 ~ DK256+737, and the length is 2417m, which is 50.21% of the total length of the tunnel (the original calculated length is 1775m/36.93%), which accords with the original calculation results.

4 VARIATION LAW OF MOISTURE CONTENT IN SURROUNDING ROCK OF SHALLOW BURIED DEPTH AND GENTLE SLOPE TUNNEL IN LOESS PLATFORM

4.1 *On-site layout of test components*

According to the characteristics of engineering geology and hydrogeology iin loess platform and the characteristics of tunnel excavation, representative sections DK256+280, DK255+443 and DK211+493 of Yima Tunnel and Shangge-cun tunnel were selected to study the variation rule of surrounding rock water content.

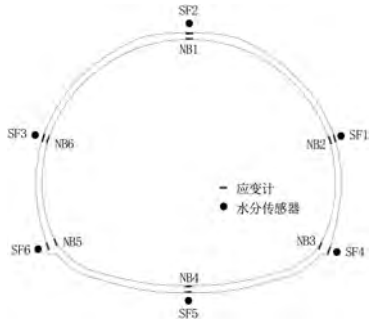

Figure 5. Layout of full-section test components.

In the whole section, 6 groups of moisture sensors are arranged in the surrounding rock at the position of arch top, left arch waist, right arch waist, left arch foot, right arch foot and arch bottom, as shown in Figure 5.

4.2 *Change law of water content of all surrounding rocks in groundwater*

Figure 6 shows the variation curve of water content at monitoring points of DK256+280 section of Yima Tunnel. When the tunnel vault is located below the groundwater level, the variation of surrounding rock water content has a certain correlation with the construction process.

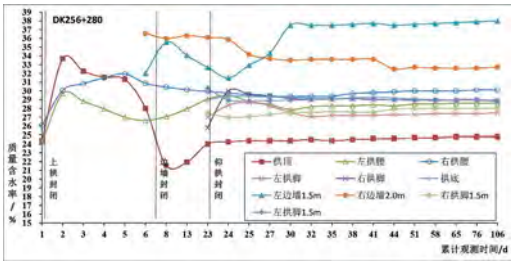

Figure 6. Variation curve of water content at monitoring points of DK256+280 section.

Because the tunnel is located in groundwater, the water content is high, among which the water content in the left and right side walls is greater than 32%, the water content in the left and right surrounding rock is 28.1 ~ 29.9%, the water content of the center of the surrounding rock is 25.9%, the water content of the surrounding rock at the lower step is basically less than 30%, and the surrounding rock soil is basically in a soft plastic state. Due to the disturbance of the original soil by excavation, the downward migration of water from the upper arch, the water content at the bottom of the arch and the right arch foot is larger, with an average value of 27.5 ~ 29.1%. Under the influence of groundwater on the tunnel vault, the water content of surrounding rock on the upper step takes longer to reach stability after 28d, while that on the lower step reaches basic stability after 3-9d.

4.3 *Change law of moisture content of surrounding rock, when part surrounding rock in groundwater*

Figure 7 shows the aging curve of water content of surrounding rock in section DK255+443 of Yima tunnel. In the past 2 months after the excavation of the face of the monitored section, the water content of surrounding rock basically shows a two-stage change law of "gradually increasing first and then leveling off", namely "increasing period" and "stable period".

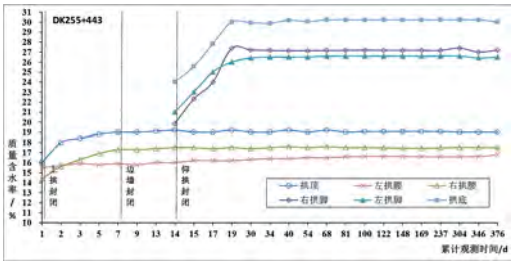

Figure 7. Variation of water content at monitoring points of DK255+443 section.

The water content in the surrounding rocks at the arch roof and the arch waist increased gradually from the initial 16% to 16.6% ~ 19% and then stabilized, with an increase of 1.1% ~ 3.1%. The water content in the surrounding rock at the arch foot and the center of the arch bottom gradually increased from the initial 20% ~ 24% to 26.6% ~ 30.2% and then stabilized, with an increase of 5.6% ~ 7.3%. The growth period is basically within 7 days, and the water content of surrounding rock fluctuates in a small range during the stable period.

4.4 *Change law of moisture content of surrounding rock, when the surrounding rock above groundwater*

Figure 8 shows the field test results of water content in surrounding rock of DK211+493 section at the Shangge Village Tunnel.

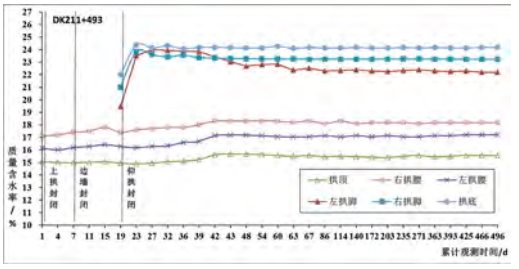

Figure 8. Variation of water content at monitoring points of DK211+493 section.

The water content in surrounding rock represented by this section of tunnel shows certain regularity in time and space. n terms of space, the water content in

surrounding rock varies from 15% to 18.5% at the arch roof and arch waist, and from 22.3% to 24.4% at the invert and arch foot. In terms of time, the initial water content in surrounding rock at the arch foot and the center of the arch bottom increases in a small range, and basically remains unchanged with the initial water content, and only fluctuates in a small range, with the change range generally ranging from 0.3% to 0.8%.

5 KEY CONTROL MEASURES IN THE TUNNEL CONSTRUCTION PROCESS

5.1 *Control measures for comprehensive treatment about foundation of loess tunnel*

Affected by the special landform and geological conditions of loess platform, the exit section of Shanggecun Tunnel and the entrance section of Yima Tunnel of Yinxi high-speed Railway are both located in collapsional loess layer. According to the foundation treatment principle of shallow buried and gentle slope section of tunnel in loess area, and compared with the foundation treatment method of loess tunnel, replacement filling method and compact-pile method are selected as the foundation treatment methods suitable for the shallow buried section of tunnel of Yinxi high-speed railway in loess platform.

1) Comprehensive treatment measures for foundation replacement in the exit section of shallow buried and gentle slope section of tunnel.

According to the survey data, at the junction of light and dark at the exit of Shangge-cun Tunnel, the loess layer under the foundation does not have collapsibility that between DK214+000 and DK214 +150, while the loess layer under the foundation that between DK214+150 and DK214+300 has collapsibility, the thickness is 0.0~2.6m.

In order to ensure the stability of open cave foundation and make the foundation treatment have continuity at the intersection of light and dark, the replacement is used to treat the foundation in DK214 +000 ~ DK214+300 sections of all open cave. The thickness of the replacement section is 1.0m, the replacement material is the mixture of lime and soil, and the compaction coefficient is 0.95.

For the excavation section of the shallow buried depth and gentle slope tunnel, when the tunnel base is Q2 clay loess, the foundation bearing capacity is significantly increased by 1.69 ~ 2.37 times after the treatment of the replacement measures with the mixture of lime and soil, and the allowable bearing capacity and the ultimate bearing capacity of the ash filling layer are more than 790kPa and 7.7MPa, respectively. This fully shows that the method of using replacement with the mixture of lime and soil to improve the basement bearing capacity of the shallow buried section of tunnel in Dongzhi loess platform.

2) compaction treatment of foundation at section in entrance of tunnel which is shallow buried depth and gentle slope.

The thickness of the collapsible loess layer under DK254+200 ~ DK254+399 section at the entrance of Yima tunnel is 0.0 ~ 4.9m, and the collapsible loess layer between DK254+399 section and DK254 +570 section at the entrance of the dark cave is not collapsible. DK254+200 ~ DK254+375 section used compaction pile with the mixture of lime and soil in the basement treatment.

The compaction pile is arranged in a triangular plane, with a diameter of 0.4m, a pile length of 7.0m, and a pile spacing of 0.8m. The top of the pile is equipped with mat of the mixture with lime and soil, and the material of the compaction pile body is 10% cement improved soil.

In the range of compaction depth, the collapsibility coefficient δs of soil that between piles ranges from 0.000 to 0.009, which is less than the limit value of 0.015. The average compaction coefficient ηd of soil between piles ranges from 0.91 to 0.96, which is greater than the limit value of 0.90. Pile compaction coefficient λc is 0.97 ~ 0.99, not less than the limit value of 0.97. The unconfined compressive strength qu of the pile is 1176 ~ 1252kPa, which is greater than the limit value of 1000kPa.

The load test curve of composite foundation is basically a progressive smooth curve. The bearing capacity of composite foundation in the test area of No. I, II and III cement-soil compaction piles is 335kPa, 345kPa and 355kPa, respectively, which are all greater than the design value requirements of 215kPa.

5.2 *The control of compaction with hydraulic high frequency vibration*

Hydraulic high frequency compaction treatment device is mainly composed of base parts, hydraulic exciter, fixture hydraulic cylinder, clip, hole forming device and other components. When hydraulic high frequency vibration compaction is used, the hole formation time of 6m depth is 118 seconds. Construction vibration monitoring shows that the maximum vibration wave velocity occurs within 0 ~ 2m below the base surface, all of which are less than the range of the safe construction control wave velocity of the loess tunnel, and the farther away from the compaction hole, the smaller the vibration wave velocity, and the deeper the working surface from the ground, the greater the attenuation range of vibration wave velocity.

When the diameter of the high frequency vibration compaction pile is D=300mm and the spacing is 600mm or 750mm, the soil collapsibility between the piles is completely eliminated, the average compaction coefficients η_d are 0.91 and 0.94, respectively, are greater than 0.9, and the minimum compaction coefficients ηdmin are 0.89 and 0.93, respectively, are greater than 0.88. Meet the requirements of 《Technical Regulations for Foundation Treatment of Railway Engineering》 (TB 10106-2010, J 1078-2010). When the pile

spacing is 900mm, the minimum densification coefficient η_{dmin} is 0.88, and the average densification coefficient η_d is 0.89, which is less than the standard limit of 0.90. Therefore, when hydraulic high-frequency vibration compaction is used to treat collapsibility loess layer and the hole spacing is S=2.5D=750mm, the compaction effect of foundation soil is the best. In engineering application, the pile spacing can be controlled at 800mm according to the actual field test.

5.3 *Control measures for surface grouting to change surrounding rock characteristics*

1) Surface grouting design

The average buried depth of DK213+880 ~ DK213+900 in Shangge-cun Tunnel is 6.76m, and the surface has a depression about 3.86m in length. The cracks appear on the surface of the tunnel at DK213+882. In order to ensure the safety of excavation, the treatment of vertical grouting with rigid sleeve valve tube on the surface.

The transverse range of grouting reinforcement is 5m on both sides of the tunnel excavation contour line, the vertical direction is 3m below the vault to 5m above the vault, and the invert bottom to 5m above the vault.

2) Effect analysis of grouting measures

The surrounding rock in the grouting area was experimented with indoor geotechnical tests, and the changes of main physical and mechanical parameters before and after grouting were obtained, as shown in Figure 9.

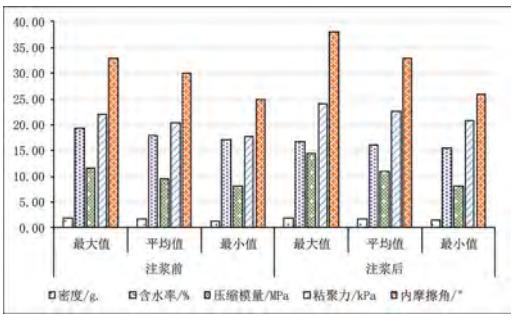

Figure 9. Comparison of mechanical parameters of surrounding rock in adjacent sections before and after grouting.

As can be seen from Figure 9, the main physical and mechanical parameters of surrounding rock have improved after grouting, the average water content of surrounding rock has decreased from 18% to 16%, and the maximum, minimum and average values of compression modulus, cohesion and other parameters have increased to varying degrees, with their respective average values increasing by about 10% ~ 35%. It shows that the slurry and soil combination formed after surface grouting directly increases the compactness of surrounding rock itself, improves the strength of surrounding rock as a whole, and significantly improves the stability of surrounding rock.

5.4 *Control measures for roof ripping about inclined shaft of soft plastic loess tunnel*

1) Technical scheme of key control measures for roof ripping

In the construction of shallow buried tunnels in loess platform, the roof ripping of soft plastic loess tunnels is related to tunnel support and deformation. There is an obvious arch molding area at the intersection, if the strength of structure about intersection support is insufficient, the arch pressure is over-developed, and the surrounding rock will appear settlement, deformation and cracking, and then produce the "closed door" collapse accident in the roof ripping section. Therefore, it is necessary to strengthen the measures of closed-loop support at the inclined shaft lining and intersection, control the excavation process strictly, reserve enough deformation subsidence, strengthen the strict monitoring of the process and improve early warning before the implementation of the roof ripping.

In order to quickly complete the closure of the support system in the cross section of inclined shaft and positive tunnel, based on the experimental study of the key construction technology of the soft plastic loess inclined shaft in the shallow buried section, the beam of steel frame with landing gate type in the positive hole of the intersection section is added, and the technology of the tunnel with advanced support and strengthening support are optimized.

In the monitoring measurement, the main contents are the sinking of arch in inclined shaft, the settling of portal frame, the sinking of vault in the lifting section and the change of headroom. There are 8 observation sections with a longitudinal spacing of 5m, which are arranged in the arch of the strengthening section and the positive hole of the lifting section about the inclined shaft respectively. There are 5 observation points in each section.

2) Effect analysis of key control measures for roof ripping

Figure 10 is the curve with time history about the cumulative settlement of the arch top in inclined shaft No. 1, and Figure 11 is the curve with time history about the cumulative settlement of the arch top at large mileage section in inclined shaft No. 1.

It can be seen from Figure 10 and Figure 11 that: (1) The maximum cumulative Settlement deformation of the arch top at the intersection of inclined shaft and positive hole is 15mm, and the maximum cumulative displacement value of headroom change is 5.4mm. (2) The maximum cumulative settlement value of the gantry at the intersection is 47.3mm, which appears at the section measurement point GD00. (3)The maximum cumulative settlement value of the positive tunnel after the initial support is

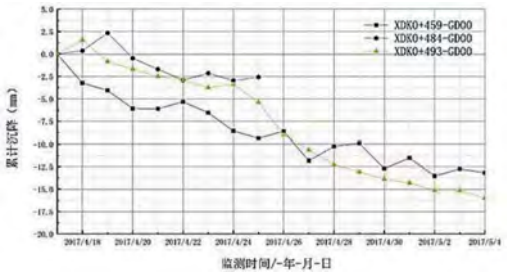

Figure 10. The curve with time history about the cumulative settlement of the arch top in inclined shaft.

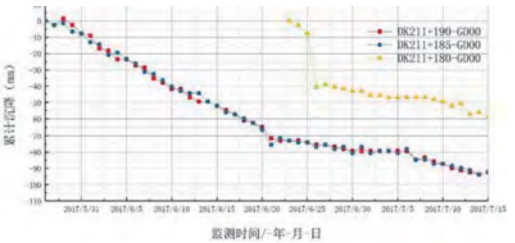

Figure 11. The curve with time history about the cumulative settlement of the arch top at large mileage section in inclined shaft.

97.6mm, and the maximum cumulative displacement value of intersection headroom change is 49.07mm.

It can be seen from the above analysis that with the excavation of the straight holel at the intersection of inclined shaft, the surrounding rock will produce plastic deformation, and the settlement of the tunnel arch will gradually increase during the excavation of the middle and lower steps. The settlement deformation tends to be stable after the inclined shaft cross gate frame is closed into a ring by compressive composite lining.

6 CONCLUSIONS

1) Based on the analysis of engineering geology and hydraulic characteristics of Dongzhi loess platform, combined with the analysis of the buried depth, longitudinal slope and length of Shangge-cun Tunnel and Yima tunnel respectively, the tunnel whose longitudinal slope is greater than 10‰ and buried depth is less than 50m is defined as a shallow buried depth and gentle slope tunnel in Loess platform.
2) Based on the characteristics of groundwater level in loess platform, experiment in lab and field, the load calculation method of large-section tunnel in soft plastic loess stratum is proposed, and the corresponding load distribution model of surrounding rock is determined. For the condition that part or all of the tunnels in the Loess platform are located in groundwater, the correction formula of the critical burial depth is derived as $h_c k$, and the classification range of the coefficient k value is limited (0.91 ~ 0.98 for part of the tunnels in groundwater, 1.0 ~ 1.09 for all the tunnels in groundwater).
3) According to the changes of water content about surrounding rock in different strata of tunnels in Loess Plateau, the variation trends of time and space is “increasing period” and “stabilizing period” of water content with time were obtained, and the increasing period of water content about surrounding rock in different lithologies was determined to be 10 ~ 15 days.
4) When treating the basement of the shallow buried depth and gentle slope section in the loess platform, factors such as the layering position and thickness of collapsible loess layer, collapsible grade and extent of loess under the tunnel basement, foundation treatment method and treatment depth should be considered in combination with the engineering geological characteristics of loess. Accordingly, comprehensive treatment measures such as replacement and precompression,impact compaction pile treatment, and high frequency vibration controllable compaction treatment with hydraulic should be adopted.During the construction ofthe shallow buried depth and gentle slope section of loess tunnel, the physical and mechanical parameters of surrounding rock are significantly improved after the prevention and control measures of changing the characteristics of surrounding rock by advance grouting, with an average increase of 10% ~ 35%, which improves the strength and overall stability of surrounding rock.
5) After the special measures of roof ripping in inclined shaft, the maximum cumulative settlement value of arch top is 15mm at the intersection of initial support about strengthening section of inclined shaft, and the maximum cumulative displacement value of headroom change at intersection is 5.4mm; The maximum cumulative settlement value of the cross-port door frame is 47.3mm; The maximum cumulative settlement value of the initial support of the positive tunnel is 97.6mm,and the maximum cumulative displacement value of intersection clearance is 49.07mm. The settlement deformation tends to be stable after the inclined shaft cross gate frame is closed into a ring by compressive composite lining.

REFERENCES

[1] Zhang Hui, Wei Dongming. Achievements, Challenges and paths of high-quality development of the Belt and Road Initiative to promote high-level opening-up [J/OL]. Journal of lanzhou university (social science edition), 2023 (05): 13 to 26 [2023-10-28]. https://doi.org/10.13885/j.issn.1000-2804.2023.05.002.

[2] Tian Siming, Wang Wei, Yang Changyu, et al. Development and prospect of Railway Tunnels in China in the past 40 years [J]. Tunnel Construction (Chinese and English), 2021, 41(11):1903–1930.

[3] Meng Xianglian, Xia Wanyun, Zhou Fujun et al. Analysis and study on engineering characteristics of loess in Dongzhi Yuan Area of Yinxi High-Speed Railway [J]. Journal of Railway Engineering, 2016, 33(12): 24-28+52.
[4] Zhao Zhanchang, Xie Yongli. Some problems in structural design and construction of Loess highway tunnel [J]. Modern Tunnel Technology, 2008, 45(06): 56-60+81.
[5] Yu Li, Wang Zhuhong, Zhang Yiteng et al. Analysis of influence of soil-rock boundary height on safety of initial support structure in shallow buried loess tunnel [J]., 57 modern tunnel technology, 2020 (02): 104–109. The DOI: 10.13807/j.carol carroll nki determined by MTT. 2020.02.015.
[6] Wang Next Year, Dong Yucang, Yu Li. Elastic-plastic analytical solution of surrounding rock of loess tunnel based on bilinear strength criterion [J]. China Railway Science, 2019, 40(06):68–77.
[7] Yu Li, Lu Cheng, Duan Ruyu et al. Calculation method of surrounding rock pressure in shallow loess tunnel [J]. China Railway Science, 2019, 40(04):69–76.
[8] Li Guoliang, Jin Baocheng, Shao Shengjun, Wang Zaiguang, Mi Weijun, Baolankezhuan Loess tunnel foundation collapse deformation evaluation and treatment of key technologies. Gansu Province, Lanxin Railway Ganqing Co., LTD., 2020-12-02.
[9] Shao Shengjun, Li Jun, Li Guoliang et al. In-situ immersion test of large thickness collapsible loess tunnel [J]. Chinese Journal of Geotechnical Engineering, 2018, 40(08):1395–1404.
[10] Wang Zhengming, Key technology of high-speed railway construction in collapsible loess area. Shaanxi Province, China Railway First Survey and Design Institute Group Co., LTD., 2016-01-01.
[11] Mi Weijun, Jia Jun, Jia Yan, et al. Study on static compaction treatment of loess tunnel foundation in Baolankezhuan [J]. Journal of Railway Engineering, 2015, 32 (11): 98-101+119.
[12] Mi Weijun, Jia Yan. Study on Mechanical characteristics of lateral static compaction of Loess Foundation [J]. Journal of Railway Engineering, 2016, 1:16–51.
[13] WANG Tinext Year, Guo Jun, Luo Lusen et al. High-speed rail buried depth of loess tunnel boundary depth study [J]. Rock and soil mechanics, 2010, 31 (4): 1157–1162. The DOI: 10.16285/smj.r.2010.04.012.
[14] Guo Jun, Wang Yingnian. Study on engineering characteristics of large section loess tunnel [J]. Highway Transportation Technology, 2009 (06):96–101.
[15] Zhao Yong, Li Guoliang, Yu Yu, et al. Loess Tunnel Project [M]. Beijing: China Railway Press, 2011

Tunnelling for a Better Life – Yan, Celestino, Thewes & Eberhardt (Eds)
© 2024 The Author(s), ISBN 978-1-032-80042-4
Open Access: www.taylorfrancis.com, CC BY-NC-ND 4.0 license

Construction procedures of the tunnel for the extension works of Madrid Metro Line 3 from Villaverde Alto to El Casar

Miguel Núñez
Doctor Civil Engineer, General Manager of Collective Transport Infrastructures of Community of Madrid, Spain

Jesús Zurdo
Civil Engineer, General Direction of Collective Transport Infrastructures of Community of Madrid, Spain

ABSTRACT: The extension of Line 3 of the Madrid Metro to El Casar includes the construction work of the infrastructure necessary for operation, including the execution of the double-track underground section that, starting from the current end of the tunnel in Villaverde, will reach El Casar. allowing the connection with the Line 12 station (Metrosur) and the Cercanías Line C3 station, in Getafe. Among these works, the construction of a new station and 2,600 m of tunnel is currently being carried out. Given the compactness of the materials present in this section, with the presence of crystallized gypsum in a considerable proportion, part of said tunnel is being carried out with the Madrid Sequential Excavation Method (MSEM). This construction procedure is based on systems widely used in areas with materials that are more similar to those found in this section. The system uses flexible support through the application of shotcrete on the contour of the excavation and the collaboration of perimeter metal trusses. This type of procedure is favored by the layout of the tunnel, far from buildings and, above all, by the nature of the terrain, which has high compactness and resistance, which allows this method to be used without reducing the level of safety or causing any damage. to nearby structures. The performance achieved after applying this procedure are 3 - 4 passes per day (1m each), carrying out work on the fronts 24 hours a day from Monday to Friday and concreting the invert on the weekend, which represents a monthly advance of about 60-80 m per front.

Keywords: underground, Tunnel, Construction methods

1 INTRODUCTION

The construction works for the extension of the Madrid Metro Line 3 to El Casar are made up of a double track underground section that, starting from the current end of the tunnel in Villaverde, will reach the height of the Suburban C3 line and Metrosur El Casar stations in Getafe, with which it will interconnect. For this, a new station and 2600 m of tunnel are being constructed.

The tunnel is being constructed using three construction procedures depending on various factors, among which can be highlighted depth, geological-geotechnical characteristics of the excavated ground, construction performance, works safety, etc.

These procedures are the:

1. Cut and cover method

Figure 1. Typical cross section cut and cover method.

DOI: 10.1201/9781003495505-211

2. Belgian or Traditional Madrid Method

Figure 2. Section type traditional madrid method.

3. Madrid Sequential excavation Method

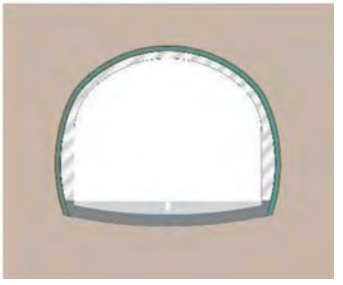

Figure 3. Section type madrid sequential excavation method.

2 CUT AND COVER TUNNEL CONSTRUCTION

If the tunnel grade level is at a shallow depth, a cut-and-cover tunnel is constructed between diaphragm walls, as it is not advisable to bore a tunnel with small overburden depth. This is the case of the section that will access the future line 3 station at El Casar, and the end-of-line for shunting after the station. At some 200 m from the start of the works, a complex geological section was detected in which materials of anthropogenic origin are overlaid, which are alluvial material with water flow, altered green clays, other clays and gypsums. To cross these materials with a mined tunnel would require prior treatment of the ground, therefore it was considered safer to cross them using the cut-and-cover method between diaphragm walls with a prior cutting of the ground.

The construction procedure consists of the digging of two side trenchs in which are installed diaphragm walls on which a reinforced concrete slab will be constructed that will form the tunnel roof. This slab can either be build on the levelled ground between the crowning of the retaining walls and, after its hardening, the excavation can be started below the slab or open-cut excavation carried out between the walls, floor slabs then constructed, and the excavation covered with a roof and the original ground surface replaced. Both approaches are used for the tunnel for the extension of Line 3 to El Casar: the first allows the replacement of the surface to be progressed while the tunnel is executed underneath, while the second is necessary at excavation machinery entrances where temporary ramps are form from the outer surface.

The construction sequence in the case of covering before excavating the tunnel consists of the following phases:

Preparation of the work platform.

Figure 4. Phase 1 cut and cover.

Construction of guide stub walls and the retaining walls.

Figure 5. Phase 2 cut and cover.

Excavation and preparation of the ground at the cover slab support level.

Figure 6. Phase 3 cut and cover.

Positioning of rebar and concreting of the cover slab.

Figure 7. Phase 4 cut and cover.

Replacement of the ground over the slab (this can be done at any convenient time).

Figure 8. Phase 5 cut and cover.

Excavation of the tunnel down to the strut level. Connection of the retaining walls with struts, steel reinforcement and concreting of the strut waler beam.

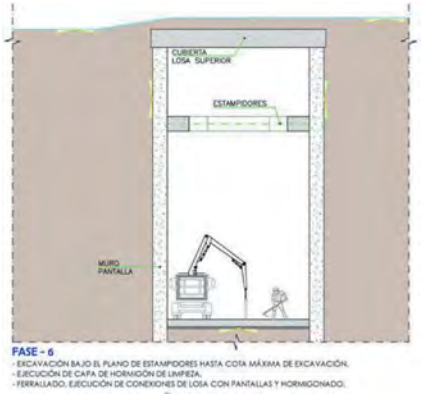

Figure 9. Phase 6 cut and cover.

Excavation under the struts to the bottom level. Laying of lean concrete. Construction of slab connections with retaining walls, steel reinforcement and concreting.

Construction of the Track Superstructure. Installation of the catenary, installations and finishes.

Figure 10. Phase 7 and 8 cut and cover.

3 BELGIAN OR TRADITIONAL MADRID METHOD

This method is widely used in the construction of metro tunnels in Madrid, as it adapts well to the nature of the ground and due to the high level of safety that is achieved during excavation as the size of the open front is minimised at all times. A disadvantage is that the excavation has to be carried out by manual means, and the number of skilled workers that it requires given that performances of some 40 m per month are usually obtained with three shifts made up of 12 workers per shift, therefore several fronts must be opened in order to meet reasonable works execution times. The above is true for the coarse and fine sands found in a large part of Madrid's terrain. However, the ground crossed by the tunnel for the Line 3 Extension to El Casar belongs to the tertiary basin of Madrid, where very compact clays are present with gypsum and even gypsum rock which provide very unfavourable excavation conditions for the work with this construction methodology as very low performance is achieved due to the ground hardness that must be dig with jackhammers.

The excavations are carried out in four phases that are executed successively:

Heading or excavation of the vault.

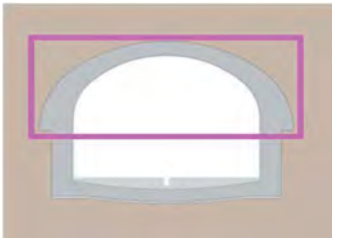

Figure 11. Phase 1 traditional madrid method.

The excavation starts with a small gallery in the crown, called the top heading, of the order of 1 metre in width and 2.5 metres in length that is continuously shored up with underpinned timber boards to stabilize the excavation. The excavation of the front then continues by laterally widening the gallery with passes of a similar size, so that the alteration of the ground is minimal in each pass. When the complete width is excavated, formwork is put in place and the tunnel vault is concreted.

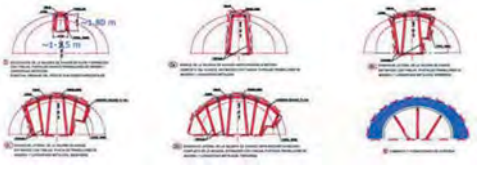

Figure 12. Construction sequence.

Given the aforesaid adverse conditions for excavation in ground formed by compact clays or directly in gypsum rock, an adaptation of the Traditional Madrid Method was proposed involving extending the length of pass from 2.5 to 3 m and avoiding

shoring, taking advantage of the fact that the ground remained stable with discontinuous support.

With this method, as fewer props are required, the front can be accessed with small machinery but that has better performance than the manual method, thus achieving a certain improvement in the cycle time.

Figure 13. Heading front with a combination of manual means and small machinery.

Central area bench excavation.

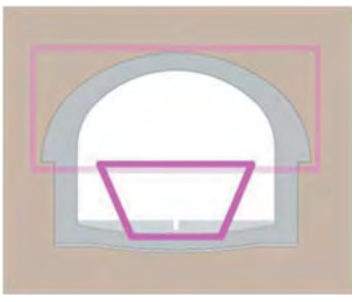

Figure 14. Phase 2 traditional madrid method.

The lower central part of the excavation is excavated several rings behind the completed inverted vault (at some 15 to 20 m from the front) in such a way that the mass concrete vault is not undercut. Due to the size of the chamber to be excavated and the height to the roof, a backhoe is used.

Figure 15. Bench excavation and transition ramp to the heading front.

Side walls (Hastiales).

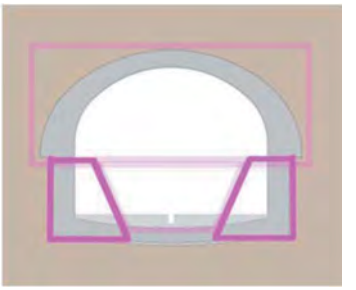

Figure 16. Phase 3 traditional madrid method.

After the bench excavation, the side walls are executed in a staggered way. The length of the side wall pass is 2.5 m (3 m), identical to that of a heading pass, but offset by 1.25 (1.5m) and without excavating facing passes so that an inverted vault ring is never completely undercut, and it is always supported either on unexcavated ground or on a previously executed side wall.

Figure 17. Excavation of a wall trench.

Invert.

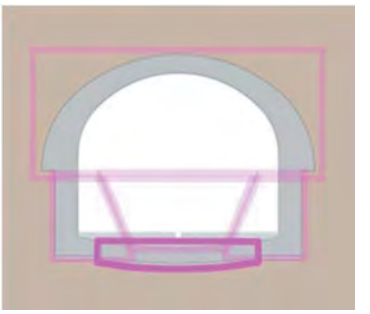

Figure 18. Phase 4 traditional madrid method.

Finally, invert of the tunnel is excavated and concreted, which closes the structural ring which makes up the complete section. Usually, it is executed in sections of some 20 m in length in order to complete the work at weekends.

Figure 19. Refining the excavation of the inverted vault bed assist with a stencil.

As a complement to the excavation and construction of the lining-support, slurry is injected into the backfill in order to close possible gaps between the concrete lining and the ground, whether caused by the loss of temporary shoring of the excavation or because an air bubble was trapped during concreting.

4 MADRID SEQUENTIAL EXCAVATION METHOD

The compactness of the materials excavated in the mined tunnel for the extension of the Madrid L3 to El Casar, made up of compact clays with gypsum in variable proportions and gypsums with hard clays over a large part of its layout, has complicated the construction by the Traditional Madrid Method due to the hardness of the materials whose excavation by the applicable means (pneumatic jackhammers or low-power machines due to space limitations) does not provide reasonable performance making it impractical to complete the tunnel within a reasonable timeframe. Consequently, an excavation method was proposed whose excavation front would have a larger opening and thus provide the opportunity to use excavation machinery of sufficient power to break up the front material more effectively and would allow an excavation rate compatible with the works schedule.

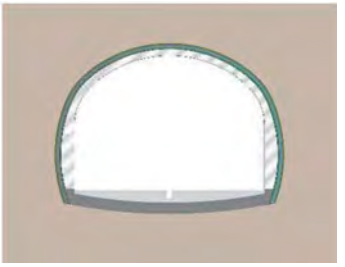

Figure 20. Section type of madrid sequential method.

The excavation procedure for this work has been called the "Madrid Sequential Method" (MSM) in reference to similar excavation systems based on the construction of a flexible support by the application of a certain thickness of concrete sprayed on the excavation contour (together with other reinforcement elements).These types of procedures are not usual in urban environments given the greater deformability that the support allows and lower stability of the excavation front when they are used in soils. Nevertheless, it is considered that the tunnel layout, away from buildings, and the nature of the ground, which is not rocky and has high compactnesses and resistances, allows this procedure to be used without detriment to the safety level or affecting nearby structures.

The elements that make up the support in the MSM are:

- Sprayed concrete, HP-30/F/12/IIa+Qc.
- Polypropylene reinforcement fibre of the sprayed concrete dosed at 3 kg/m³.
- Trusses with HEB 140 profile spaced at 1 m.
- Front sealing with sprayed concrete for protection against the weather at weekends or during prolonged stoppages.

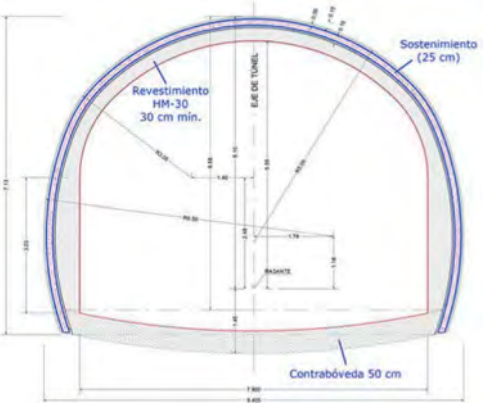

Figure 21. Elements of support.

The section is excavated in a single phase, the complete section except the lower part of the invert, with a 1 m pass (it has been checked that the open front is almost completely stable).

When the excavation is finished, a 6 cm layer of sprayed concrete reinforced with polypropylene fibre is wet-gunned by a robot. Then, a truss is put in place against the sealing formed from an HEB-140 profile that will be embedded in another layer of sprayed fibre-reinforced concrete of 19 cm thickness. So that the truss is not forced into the base of the excavated ground when it comes under load, it is supported on metal base plates. The next pass starts when the above process is complete.

Figure 22. Excavation the complete section.

Figure 23. Detail of elements that make up the support.

Figure 24. Colocation of HEB 140 profile.

At the end of the week, the inverted vault section corresponding to the previously executed support is concreted, thus closing the structural ring.

Although deformations of the supports are monitored in all the other methods, in the MSM it is essential to carry out an exhaustive monitoring of the closing of the excavation and the support by means of convergences, because, as the support is more flexible, it will deform until it reaches equilibrium with the ground pressure. In the case of there being heterogeneity in the ground not considered in the calculation, this would be shown in the increase of deformation above that envisaged, and the support can be suitably reinforced to solve a possible problem. Thus, a convergence reading section is put in place every 20 m to collect data every day at the start in order to verify the slowing down of the deformation and the stabilisation of the excavation.

Figure 25. Sprayed concrete.

Figure 26. Front sealing.

Figure 27. Tape extensometer.

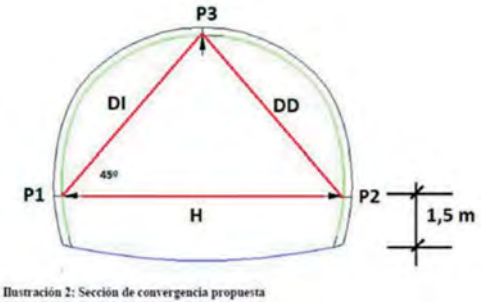

Figure 28. Convergence section.

Figure 29. Convergence reading.

Example of convergence graph showing a trend towards stabilization of measurement.

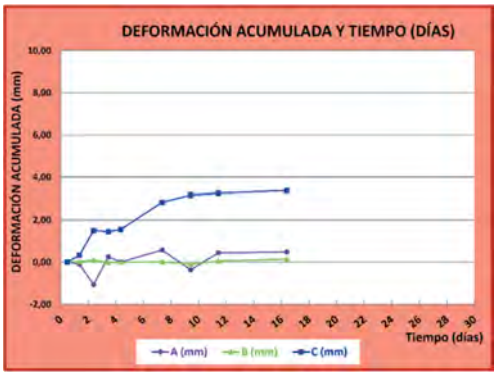

Figure 30. Example of convergence graph with a trend toward stabilisation of the measurements.

The performances obtained are 3 to 4 passes per day and front with support work at 24 hours per day from Monday to Friday and concreting of the inverted vault at the weekend, which equates to monthly progress of around 50 m per front. The support and inverted vault described allow a stable excavation in itself.

Nevertheless, a non-structural HM-30 mass concrete lining is constructed (but also strong and, therefore, redundant) which will smooth the irregularity of the sprayed concrete surface, thus matching the finish of the rest of the tunnel, without complicating hanging systems for the energy conduits and tunnel installations. It will be constructed by means of a moving formwork carriage in 10 to 15 m sections as soon as there is sufficient distance with respect to the front and its interior contour will be coincident with that of the tunnel support constructed by the Traditional Madrid Method.

Figure 31. Finished section.

Tunnelling for a Better Life – Yan, Celestino, Thewes & Eberhardt (Eds)
© 2024 The Author(s), ISBN 978-1-032-80042-4
Open Access: www.taylorfrancis.com, CC BY-NC-ND 4.0 license

Deformation failure characteristics and control measures of shallow loess tunnel of water-rich stratum: A case study

Kunjie Tang* & Junling Qiu
School of Highway, Chang'an University, China

ABSTRACT: With the acceleration of tunnel construction, it is inevitable to cross the collapsible loess region. The engineering properties of loess are very poor in the water-rich environment. Additionally, if the buried depth is shallow, the load bearing capacity is further weakened, which can increase the difficulty of tunnel construction. Therefore, this paper provides a case study on the Pangwan Tunnel based on a geological survey, numerical simulation, and on-site monitoring. The failure characteristics of the studied area under the original support scheme are analyzed in detail, and the extreme deformation mechanism is discussed combining the geological conditions and surrounding rock properties. The results show that there are five main reasons resulting in the extreme deformation of the Pangwan Tunnel, which are: abundant groundwater, low strength of surrounding rock, disintegration of loess after water immersion, depth of tunnel is shallow. Then, the corresponding countermeasures are proposed, which are advance drainage, large arch foot and foot-lock bolt, sealing tunnel face and grouting timely, as well as advance pipe shed and small pipe grouting. Finally, from the feedbacks of field application results, extreme deformation of the Pangwan Tunnel is effectively controlled. This work can provide some helpful guidance for similar projects.

Keywords: Shallow loess tunnel, Water-rich, Extreme deformation failure, Countermeasures

1 INTRODUCTION

In recent years, China experienced a fast expansion of its highway network. As the network advances to the northwestern part of China, it is inevitable for some highway routes to pass through China's Loess Plateau (Qiu et al., 2020a). Because of the unique structure and complex engineering properties of loess, the diversity of engineering problems is unprecedented during construction of loess tunnel (Qiu et al., 2018). Especially, tunnel is built in water-rich loess stratum, surrounding rock strength decreases rapidly, and it's going to be silted with poor stability after excavation, that in-turn results in extreme deformation of surrounding rock and by extension damage the supporting structure. For example, during the Shangge Village tunnel (Hong et al., 2021a) passes the soft-plastic loess stratum, distresses including falling blocks and a deformed steel arch were observed during tunnel construction (Figure1a). Meanwhile, seepage water is observed on the tunnelling face and water catchments in the middle and lower benches (Figure 1b). Currently, Pangwan Tunnel is a key project in the Loess Plateau of China, which connects Fu-Yin Highway and Qinglan Highway. It is different from other loess tunnels in that the Pangwan Tunnel inevitably passes through the water-rich loess stratum due to restricted route schemes. Entrance of the tunnel is extremely disadvantageous due to geological conditions and brings great difficulties and challenges to construction.

Extreme deformation of loess tunnels is always a puzzling problem, which causes safety issues and decreases construction quality. Aiming at this problem, many scholars have conducted research. Xue et al. used the Delphi-extension model to study the deformation characteristics in loess ground. Influencing factors on deformation were analyzed through mining statistical data by rough set (Xue et al., 2018). Taking the loess tunnel with large section of Lanzhou-Chongqing Railway as the research object, Hu et al. found that the vault subsidence weakened slowly, while the side wall horizontal displacement weakened quickly, and the horizontal convergence was generally less than the vault subsidence. Meanwhile they suggested that the appropriate reserved length of core soil is 2R/3 (R is the tunnel conversion radius), which can

*Corresponding author: tangkunjie@chd.edu.cn

DOI: 10.1201/9781003495505-212

effectively control the longitudinal deformation of surrounding rock (Hu et al., 2012). Zhao et al. systematically summarized the engineering problems of HSR tunnels constructed in loess ground. They found that the displacement of the tunnel in loess ground was highly relevant to the engineering properties of loess (Zhao et al., 2018). Based on Dayoushan loess tunnel, Lai et al. proposed that the final deformation of the tunnel can be predicted by exponential function through field test and research and gave the reserved deformation of vault and side wall respectively (Lai et al., 2015).

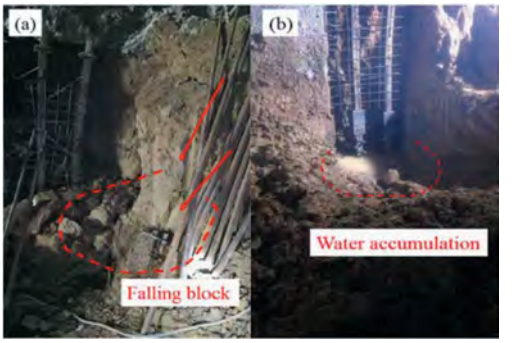

Figure 1. Distresses during tunnel construction (a: Falling block, b: Water accumulation at the tunnel toes).

Moreover, as the engineering properties of loess are greatly affected by water environment, more research results have shown that the tunnel can occur severe deformation during construction in water-rich loess (Qiu et al., 2020b; Weng et al., 2019, 2021). Li et al. carried out large-scale field immersion tests on loess ground with an existing tunnel. The results show that surface water could infiltrate into the invert arch of the tunnel, causing extreme deformation of loess near tunnel arch crown (Li et al., 2019). Cui et al. investigated the deformation characteristics of surrounding rock under different loess states and proposed the reasonable reserved deformation amount of tunnel under different loess states (Cui et al., 2021). Hong et al. studied deformation characteristics of soft-plastic loess tunnel by carrying out a series of in situ measurements and numerical simulations (Hong et al., 2021a, 2021b). The results indicated that when the tunnel is totally embedded in the soft-plastic loess, the radial displacement values above the wall waists undergo dominant deformation, while the radial displacement of wall feet is smaller. To control surrounding rock deformation, they proposed to use advanced drainage in combination with advanced small pipe grouting.

Although some exceedingly valuable experience and lessons of tunnelling in loess stratum have been documented in the literature, there have been limited studies focused on shallow water-rich loess tunnel. Due to the lack of experience and awareness, serious engineering accidents occurs during construction, which seriously endangers the safety of construction personnel and tunnel construction equipment (Jefferson et al., 2004; Derbyshire et al., 2011). To further explore the deformation characteristics of shallow water-rich loess tunnel, taking Pangwan Tunnel as a case study, this paper records the deformation process of surrounding rock through on-site monitoring, analyzes the mechanism of extreme deformation, and put forward corresponding countermeasures. The results are found to be effective based on the analysis for the on-site monitoring, which can guide in the construction of the Pangwan Tunnel. Additionally, the results of the paper create a value-set of references for similar projects.

2 PANGWAN TUNNEL OVERVIEW

2.1 *Project description*

Pangwan Tunnel is a key control project in the connection line between Fu-Yin Highway and Qinglan Highway. It is located in Xiji County, Guyuan City, which is in the Loess Plateau of Ningxia Region, as shown in Figure 2. A design structure of two unidirectional bores and four lanes, a construction clearance width of 13.36 *m*, a construction clearance height of 10.76 *m* and a speed of 80 *km/h* are adopted by Pangwan Tunnel. The lengths of the left and right lines are 1558 *m* and 1605 *m* respectively, the maximum burial depths are 169 *m* and 157 *m* respectively. The surrounding rock above class Ⅴ accounts for more than75.3%. The tunnel entrance is located on the gentle slope of the valley, with a topographic gradient of about 2°.

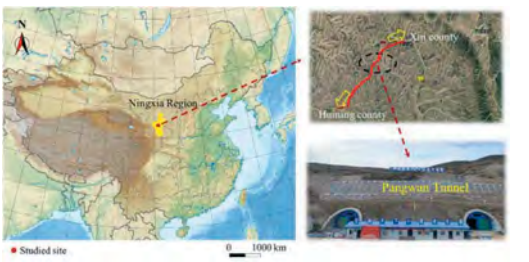

Figure 2. Tunnel location.

2.2 *Geological conditions*

Pangwan Tunnel is located in the central area of loess plateau, rugged terrain, ravines and soil are collapsible loess. The geological structure of the tunnel region belongs to the fold area of the Kunlun Qinling geosyncline. The northeast tunnel region is the corridor transition zone (Liupanshan complex anticline), and the southwest region is the Geosyncline Caledonian fold belt. The elevation of the ridge ranges from 1960 *m* to 2140 *m*, and the relative elevation difference is about

180 *m*. It declines from south to north, and the topography undulates greatly. The tunnel entrance with a topographic gradient of about 2°. Pangwan Tunnel geological conditions are shown in Figure 3.

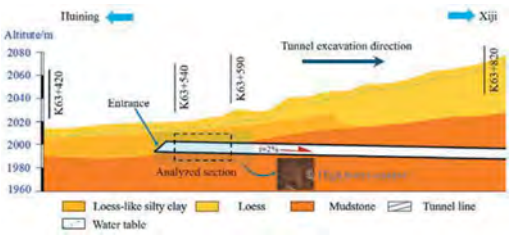

Figure 3. Pangwan tunnel geological conditions.

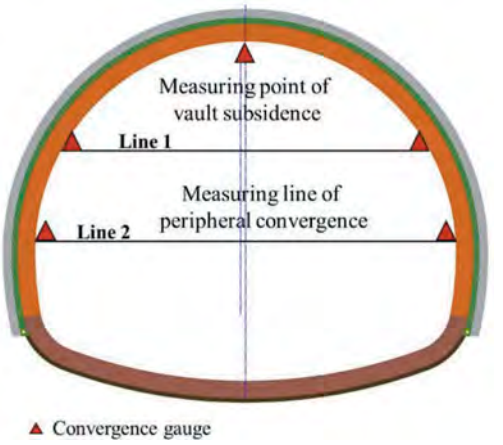

Figure 4. Layout of deformation measurement.

According to the engineering geological survey and drilling, the surrounding rock of the study area (ZK63+540 ~ ZK63+590) is mainly composed of loess-like silty clay and loess, with underlying sandy mudstone. The physical and mechanical parameters of surrounding rock are shown in Table 1.

3 DEFORMATION FAILURE CHARACTERISTICS AND MECHANISM

3.1 *On-site monitoring*

Because the entrance section of Pangwan Tunnel (ZK63+540 ~ ZK63+590) is Ⅴ class surrounding rock, the stability is poor. Therefore, this section is selected as research section and carried out on-site monitoring. A test section is arranged every 5m and the test contents include tunnel vault subsidence and horizontal convergence. The test data are selected when the measuring points reading remain stable. The layout of measuring points is shown in Figure 4.

3.2 *Results analysis*

Typical sections ZK63+571 and ZK63+577 of the left line are selected for analysis, and the typical time-displacement curves of the surrounding rock are shown in Figure 5.

The maximum vault subsidence of ZK63 + 571 and ZK63 + 577 sections are 263.8 *mm* and 253.2 *mm* respectively, and the maximum horizontal convergence are 108 *mm* and 81.6 *mm*. Extreme deformation occurs during construction of shallow water-rich loess tunnel. Additionally, in some seriously deformed areas, initial support damage or even large-scale collapse occurs during the on-site monitoring.

In ZK63+571 section, extreme deformation occurs in the vault within 1-5 days after excavation. After the excavation of the upper step, the vault subsidence reaches 85.1 mm, achieving 32.3% deformation. The horizontal convergence reaches 30 *mm*, achieving 27.8% deformation. When the lower step excavation is completed, the vault subsidence reaches 191.8mm, achieving 72.7% deformation; and the horizontal convergence reaches 74.5 *mm*, achieving 68.9% deformation. After the inverted arch is poured, the vault subsidence and horizontal convergence reach 254.1 mm and 99.6 *mm*, achieving 96.3% and 92.2% of the deformation, respectively.

In addition, it can be seen from Figure 5 that the deformation trend of surrounding rock in the two selected sections is almost the same, and the two typical sections show three stages of rapid deformation development, continuous deformation development and stable deformation. (1) Rapid development stage of deformation: the tunnel is in the initial stage of excavation, the surrounding rock is disturbed, and the stress of surrounding rock is released. The initial support may be delayed, so the deformation rate and deformation amount of surrounding rock increase continuously, and the maximum deformation rate

Table 1. Surrounding rock physical and mechanical parameters.

Surrounding rock type	Density $\gamma(kN/m^3)$	Poisson ratioμ	Friction angle $\varphi(°)$	Elastic modulus $E(MPa)$	Cohesion $k(kPa)$
Loess-like silty clay	18.5	0.32	25	8.5	28
Loess	18.7	0.35	20	9	30
Sandy mudstone	25×10^3	0.38	32	1.36×10^3	447

occurs at this stage. Therefore, advance support should be strengthened at this stage to improve the strength of surrounding rock. (2) Sustainable development stage: the subsidence and convergence rate of surrounding rock decrease obviously due to the effect of initial support and the formation of plastic zone. However, the vault subsidence and horizontal convergence continue to increase, so the disturbance of surrounding rock should be reduced as much as possible to realize the deformation stability of surrounding rock. (3) Deformation stability stage: the inverted arch of the tunnel is completed, which increases the support reaction and enhances the stability of the tunnel. The deformation rate is very small and the tunnel deformation tends to be stable.

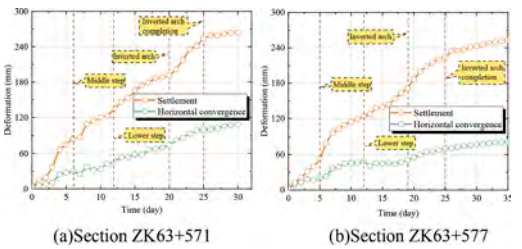

Figure 5. The time-displacement curves of surrounding rock.

3.3 *Deformation and failure characteristics*

3.3.1 *Extreme deformation*

From the monitoring results, the surrounding rock shows extreme deformation. The maximum vault subsidence of ZK63+571 and ZK63+577 sections are determined to be 263.8 *mm* and 253.2 *mm*, with maximum horizontal convergence of 108 and 81.6 *mm*, respectively.

3.3.2 *Fast deformation rate*

The deformation rate of Pangwan Tunnel initial support is large, and the subsidence rate of the vault increases suddenly in two stages. (1) Rapid deformation occurs within 1-5 days after excavation, and the maximum deformation rate of ZK63+571 section vault reaches 30.18 *mm/d*. (2) During the excavation of the middle step stage, due to more water at the arch foot of the upper step, the loess disintegrated under water immersion, which can cause the loess at arch foot seriously soften and the bearing capacity decrease sharply. Meanwhile, the excavation of the middle step causes the increase of the subsidence rate of the vault. The maximum deformation rate of ZK63+577 section at this stage reach 26.2 *mm/d*, far exceeding the stability standard stipulated by The New Austrian Tunneling Method (the deformation rate is less than 0.2 *mm/d*), and the support system is difficult to stabilize.

3.3.3 *Ground cracks*

As shown in Figure 6 (a), cracks appear on the ground. Affected by the construction method and stratum, after the excavation of ZK63 + 540 ~ ZK63 + 590 section, cracks of different degrees appear on the ground. The width of the cracks is 8 ~ 20 *mm*, and the distance between the two cracks is 23 ~ 32 *m*.

3.3.4 *Varied failure types*

According to tunnel monitoring data and site conditions, the tunnel surrounding rock deformation area damage is more serious. Affected by the water-rich environment, the stability of loess is very poor. When excavating the upper step to the vicinity of ZK63+566 section, the steel frame is ready to be arranged, cracks suddenly appear on the initial spray surface of the lower step, about 1.5 *cm* wide. Subsequently, cracks also appear on the initial spray surface above the middle step, about 2 *cm* wide, and several cracks appear at the position above the upper step. The soil above and in front of the excavation surface collapses suddenly (Figure 6 (b)).

The initial support structure suffers great damage after the collapse. A large range of cracks appear on the vault and side wall (Figure 6 (c) and (d)), with a maximum width of 0.5 *cm*. Meanwhile, the sprayed concrete around falls off and some I-steel arches are exposed.

In the process of tunnel excavation, the tunnel face seepage and serious accumulation water at arch foot, making the surrounding rock flow plastic. The loess at the arch foot softens seriously, and the bearing capacity decreases sharply, leading to the arch foot failure and the severe vault subsidence. The steel arch of the vault seriously intrudes into the secondary lining boundary (Figure 6 (e)).

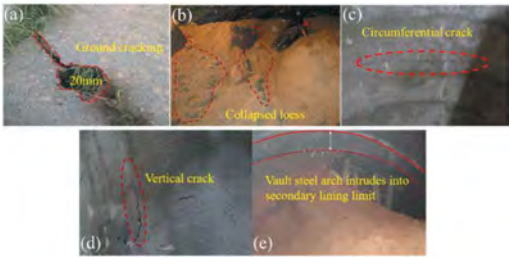

Figure 6. Deformation characteristics of tunnel surrounding rock (a: ground cracking, b: partial collapse, c: circumferential crack, d: vertical crack, e: vault subsidence).

3.4 *Extreme deformation mechanism*

According to the geological conditions and surrounding rock properties, it is concluded that the main reasons for the deformation and failure of the Pangwan Tunnel are as follows:

3.4.1 *Low strength of surrounding rock*

The surrounding rock strength of Pangwan Tunnel is low, and the surrounding rock above class V accounts for more than 75%. Joint fissures are developed relatively. Meanwhile, the groundwater is enriched in the ZK63+540 ~ ZK63+590 sections, with high water content. Through laboratory tests, pressure-deformation curve tests of loess soil samples with different moisture content are carried out (Figure 7). As shown in Figure 7, the deformation coefficient (ratio of compression to soil sample height) increases gradually with the increase of water content, which will reduce the strength of surrounding rock, produce extreme deformation as well as bring many difficulties to construction.

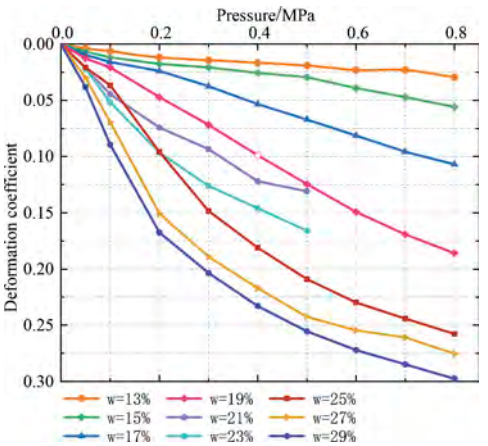

Figure 7. Pressure-deformation curve of loess samples.

3.4.2 *Abundant groundwater*

Studies have shown that loess is a metastable sediment with unconsolidated vertical joints (Li et al., 2019; Dušan et al., 2014). Loess behaves like a brittle material with high strength when dry, while after it is immersed in water, the bonding materials of loess break up, and the strength decreases dramatically (Graziani et al., 2012; Houston et al., 1988; He et al., 2020).

Both surface underground water is abundant in the entrance section of tunnel (Figure 8). The water-rich section of the tunnel is at the boundary between silty clay and mudstone. Due to the development of joints, coupled with the strong permeability of clay, mudstone permeability is poor, so that groundwater accumulates here. The maximum water content of loess-like silty clay in ZK63 +540~ZK63+590 sections is 31.3%, average water content is 23%~25%. The liquid limit index of the soil samples reaches 1.24 partially, presenting fluid plastic state, and the average is 0.86, presenting soft plastic state.

Figure 8. Inverted arch water accumulation and tunnel face seepage water.

3.4.3 *Disintegration*

The disintegration of loess is one of the main factors causing extreme deformation. The strength and mechanical properties of loess are especially affected by water (Xu et al., 2020; Sun et al., 2021). In the water-rich environment, the collapsibility of loess is relatively weak, mainly manifested as disintegration (Zhang et al., 2015). Under the action of water, the change of matric suction in loess makes water infiltrate into soil rapidly through pores, and then increases pore water pressure, promoting the chemical dissolution reaction between mineral cement and water in loess particles (Wang et al., 2019; Li et al., 2019). Moreover, the matric suction of soil decreases with the increase of water content, which weakens the interconnecting force between soil particles and reduces the strength of soil. Disintegration occurs when the bonding strength between soil particles is insufficient. Because of the disintegration of loess, the self-stability of surrounding rock decreases greatly after excavation, and engineering diseases such as vault collapse frequently occur. The process of loess disintegration is shown in Figure 9.

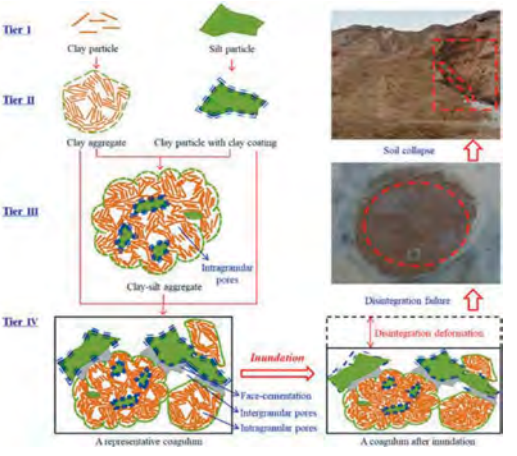

Figure 9. Conceptual model of loess disintegration mechanism.

3.4.4 *Shallow buried depth*

Affected by the excavation disturbance, the surrounding rock pressure appears redistribution. Due to stress release and excavation of soil, stress concentration area and stress unbalance area are formed in the vault,

and gradually spread from the inner strata to the ground (Shao et al., 2021). The wedge shape with sliding tendency is gradually formed in the shallow stratum, having the trend of sliding towards the inside tunnel face. Failure surface is formed when the tensile stress or shear stress of the sliding surface exceeds the shear strength of the soil. The whole wedge collapses along the sliding face and forms obvious longitudinal cracks on the ground.

In addition, the surrounding rock pressure at the top of shallow loess tunnel is mainly vertical pressure, and the lateral pressure is very small (Soranzo et al., 2015; Liu et al., 2020). With the tunnel expansion, the stress state of loose zone soil and the weight of overlying soil will change. When advance reinforcement or initial support system cannot maintain the coordinated deformation and balance, forming bearing arch is difficult. The soil sinks rapidly along the middle line of the tunnel, which intensifies the development of ground cracks. The formation mechanism of ground cracks is show in Figure 10.

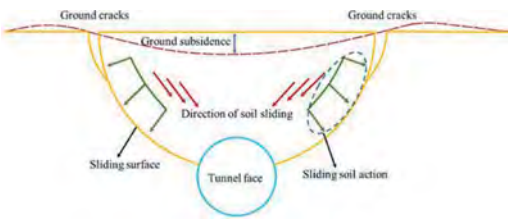

Figure 10. Formation mechanism of ground cracks.

4 COUNTERMEASURES FOR DEFORMATION FAILURE

4.1 *Countermeasures*

When the tunnel is constructed in shallow water-rich loess stratum, it is easy to cause the initial support failure, the tunnel face instability and the vault collapse due to the low strength of the surrounding rock. This not only affects the project progress and construction quality, but also causes a great threat to the safety of construction personnel (Lai et al., 2018; Wang et al., 2021). Therefore, it is very important to control the extreme deformation of shallow water-rich loess stratum for tunnel construction. Through the analysis of various conditions, the probability of extreme deformation of surrounding rock increases when the overall stiffness of initial support is not enough, the construction of invert and lining are not timely, as well as the construction methods are improper. Aiming at the extreme deformation characteristics of tunnel in shallow water-rich loess stratum, the construction countermeasures are put forward as follows.

4.1.1 *Advance drainage*

After excavation of soft plastic loess, water seepage occurs on the tunnel face, and a catchment area is formed at the bottom of the side wall. The permeation of water causes the transformation of the loess from soft plastic state to flow plastic state. The softening and strength reduction of soil caused by water migration are the main reasons for extreme deformation, so drainage measures should be taken. Hong et al. adopted a combination of advance drainage and small pipe grouting to lower the groundwater level below the excavation contour, transforming the surrounding rock from soft plastic state to hard plastic state (Hong et al., 2021a). The deformation of surrounding rock is reduced and the construction of tunnel is guaranteed.

According to the excavation method characteristics, a temporary drainage ditch is set at the corner of each step, as shown in Figure 11 (a). Drain water from side wall and tunnel face timely to prevent water accumulation at the base, side wall and arch foot.

4.1.2 *Large arch foot and foot-lock bolt*

When the tunnel is constructed by step method, the subsidence of vault can be effectively controlled by expanding the arch foot in soft surrounding rock (Li et al., 2012). For the case of large subsidence of Pangwan Tunnel vault, the way of enlarging arch foot at the junction of upper and lower steps is adopted, as shown in Figure 11 (d). The enlarged arch foot is beneficial to reduce the support subsidence caused by the soaked-softening soil of the arch foot. Furthermore, it plays an important role in supporting the vault structure during the middle step excavation. The loess at the arch foot presents flow plastic state under water immersion. If the accumulated water is not drained away in time, the bearing capacity will drop sharply. Therefore, the drainage of accumulated water needs to be completed before erecting the arch frame.

Additionally, 4~6 *m* long *Φ*89 large foot-lock bolts are applied to the arch waist and arch feet for reinforcement (Figure 11 (b) and (c)). U-shaped steel bars are used to weld the anchor pipes to stabilize surrounding rock deformation.

4.1.3 *Sealing tunnel face and grouting timely*

After the tunnel face is exposed to air for 1~1.5 *h* in water-rich section, the water drips along the tunnel face, which is easy to form accumulated water at the foot of the wall and arch foot. In this process, the tunnel face is sealed as early as possible. 3~5 *cm* concrete should be sprayed immediately after the excavation of the arc guide pit (Figure 11 (e)) to prevent soil stripping caused by long-term exposure and water seepage in the tunnel face. In addition, the information about tunnel collapse can be obtained by observing whether there are cracks on the concrete surface.

According to the laboratory test results, the tunnel face of soft plastic loess is drum out type, which is an unstable state. Except for the shotcrete sealing of the tunnel face, the effect of grouting on the tunnel face to control the tunnel face stability is also obvious.

4.1.4 *Advance pipe shed and small pipe grouting*

Pre-supporting within 120° of the vault, forming a pre-support system with the steel frame, is an

economical and effective support method for large-section loess tunnels (Shin et al., 2008). In the shallow water-rich section of Pangwan Tunnel, long pipe shed and small pipe supplementary grouting are adopted for advance support (Figure 11 (f)). The specific parameter is 12 *m* *Φ*89 long pipe shed, longitudinal interval 6m layout. The length of 5m and the longitudinal spacing of 2 *m* *Φ*42 small grouting pipes are arranged between the long pipe sheds. This Advance support system is suitable for the stratum with unstable tunnel face, especially the water-rich stratum. The long pipe sheds have large stiffness and long support distance as well as the small conduits laid between them can limit the collapse of the soil under the pipe shed.

Figure 11. Site control countermeasures (a: arch foot drainage ditch; b, c: application of foot-lock bolt; d: application of large arch foot; e: seal of tunnel face; f: advance pipe shed and small pipe grouting).

4.2 *Verification of the countermeasures*

Surrounding rock deformation is an important basis to measure the stability of surrounding rock. Figure 12 shows the time-displacement curves of surrounding rock at the sections ZK63+571 and ZK63+577 after treatment. The maximum horizontal convergence of the two sections is 120.1 *mm* and 113.2 *mm*, respectively, and the maximum vault subsidence is 36.5 *mm* and 32.9 *mm*, respectively. The maximum deformation rate is 15 *mm/d*. Moreover, during the excavation of inverted arch, the subsidence rate increases. Before the inverted arch is conducted, the two sections achieve 94.2% and 97.8% deformation respectively. In water-rich loess tunnel, the subsidence can be effectively controlled by sealing the tunnel face and pouring the inverted arch timely after the excavation.

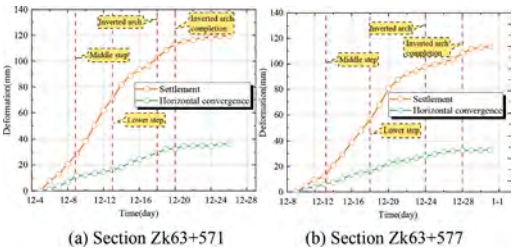

Figure 12. Time-displacement curve of surrounding rock after treatment.

Therefore, after the implementation of countermeasures, the surrounding rock deformation control has achieved good results. Not only the deformation rate of surrounding rock is reduced, but also the total deformation is greatly reduced, which ensures the quality and safety of tunnel construction.

5 CONCLUSIONS

To explore and study the deformation characteristics of shallow water-rich loess tunnel, a case study involving a shallow water-rich loess tunnel is provided and studied in terms of the extreme deformation characteristics, influencing factors and effective countermeasures. The rationality and effectiveness of the countermeasures are verified by tunnel on-site monitoring and numerical simulation. The successful experience of this case can provide a meaningful reference to similar projects in the future, and based on the experience, the following conclusions can be drawn:

(1) Loess is widely distributed in Nanjun region of Ningxia province. Especially in the shallow water-rich sections, various potential geological disasters may occur during construction. The soft surface formed by the joints in the shallow loess stratum is easy to form ground craks during the excavation. Coupled with the surrounding rock deterioration caused by groundwater, the strength is significantly reduced, which makes the surrounding rock reach plastic yield, resulting in extreme deformation and even local collapse. The deformation of Pangwan Tunnel is characterized by severe vault subsidence, cracking of initial support, failure of arch foot and partial collapse of surrounding rock. The maximum displacement and deformation speed of the studied tunnel region are 263.8 *mm* and 30.18 *mm/ d*, respectively.

(2) The deformation that occurred in the shallow water-rich section is remarkable, as an extreme deformation and rate. The extreme deformation is mainly caused by the abundant groundwater and the loess's special properties after water immersion. Meanwhile, the shallow depth of the tunnel and unreasonable support scheme also plays an important role in intensifying deformation of the surrounding rock.

(3) The proposed countermeasures mainly include the following: advance drainage; large arch foot and foot-lock bolt; sealing tunnel face and grouting timely; advance pipe shed and small pipe grouting. After conducting the countermeasures, the maximum deformation significantly reduces, which is approximately 45.5% of deformation before treatment. Specifically, the maximum horizontal convergence and vault subsidence are 36.5 *mm* and 120.1 *mm*, respectively. The achieved results confirmed that the proposed countermeasures can remarkably decrease the displacement amount as well as the speed of deformation, verifying the effectiveness of the proposed countermeasures based on the geological characteristics.

ACKNOWLEDGMENTS

The authors gratefully acknowledge the Construction Science and Technology Project of Xi'an (No. SZJJ2019-23), the Project on Social Development of Shaanxi Provincial Science and Technology Department (Grant No. 2021SF-513), the National Natural Science Foundation of China (No. 51978066).

REFERENCES

Graziani, A., Boldini, D., 2012. Remarks on axisymmetric modeling of deep tunnels in argillaceous formations. Tunnelling and Underground Space Technology. 28, 70–79.

Dušan, B., Zoran, B., Čebašek, V., et al, 2014. Characterisation of collapsing loess by seismic dilatometer. Engineering Geology. 181,180–189.

Cui, G.Y., Ma, J.F., Wang, D.Y., et al, 2021. A large 3D laboratory test on the deformation characteristic of shallow loess tunnel under different plastic states. Bulletin of Engineering Geology and the Environment. 80, 7577–7590.

Derbyshire, E., 2011. Geological hazards in loess terrain, with particular reference to the loess regions of China. Earth-Science Reviews. 54, 231–260.

Soranzo, E., Tamagnini, R., Wu, W., 2015. Face stability of shallow tunnels in partially saturated soil: centrifuge testing and numerical analysis. Géotechnique. 65(6), 454–467.

Hong, Q.Y., Lai, H.P., Liu, Y.Y., et al, 2021a. Deformation control method of a large cross-section tunnel overlaid by a soft-plastic loess layer: a case study, Bulletin of Engineering Geology and the Environment. 80, 4717–4730.

Hu, S.M., Zhang, D.L., Guo, T., et al, 2012. Analysis on deformation characteristics of large-section loess tunnel. Journal of the China Railway Society. 34, 117–122.

Hong, Q.Y., Lai, H.P., Liu, Y.Y., et al, 2021b. A case study on deformation characteristics of a large cross-section tunnel passing through a soft-plastic layer with different spatial locations. Arabian Journal of Geosciences. 14, 272.

He, S.Y., Wang, X.L., Fan, H.B., et al, 2020. The study on loess liquefaction in China: a systematic review. Natural Hazards. 103, 1639–1669.

Jefferson, I.F., Mavlyanova, N., O'Hara-Dhand, K., 2004. The engineering geology of loess ground: 15 tasks for investigators-the Mavlyanov programme of loess research. Engineering Geology. 74, 33–37.

Lai, J.X., Fan, H.B., Lai, H.P., 2015. In-situ monitoring and analysis of tunnel deformation law in weak loess. Rock and Soil Mechanics. 36(7), 2003-+.

Li, W., Zhang, C., Zhang, D., et al, 2022. Face stability of shield tunnels considering a kinematically admissible velocity field of soil arching. Journal of Rock Mechanics and Geotechnical Engineering.14(2), 505–526.

Li, J., Shao, S.J., Shao, S., et al, 2019. Collapsible characteristics of loess tunnel site and their effects on tunnel structure. Tunnelling and Underground Space Technology. 83, 509–519.

Li, X.A., Wang, L., Yan, Y.L., et al, 2019. Experimental study on the disintegration of loess in the Loess Plateau of China. Bulletin of Engineering Geology and the Environment. 78, 4907–4918.

Li, P., Xie, W.L., Pak, R.Y., et al, 2019. Microstructural evolution of loess soils from the Loess Plateau of China. Catena. 173, 276–288.

Liu, D.P., Zhang, D.L., Fang, Q., et al, 2020. Displacement characteristics of shallow-buried large-section loess tunnel with different types of pre-supports: A case study of new badaling tunnel. Applied Sciences. 10, 195.

Lai, J.X., Wang, X.L., Qiu, J.L., et al, 2018. Extreme deformation characteristics and countermeasures for a tunnel in difficult grounds in southern Shaanxi, China. Environmental Earth Sciences. 77, 1–14.

Li, W.J., Sun, M.L., Zhu, Y.Q., et al, 2012. Arch springing stability and its control techniques during construction of tunnels with weak surrounding rocks by bench cut method. Chinese Journal of Rock Mechanics and Engineering. 31, 2729–2737.

Qiu, J.L., Wang, X.L., Lai, J.X., et al, 2018. Response characteristics and preventions for seismic subsidence of loess in Northwest China. Natural Hazards. 1909-1935.

Qiu, J.L., Lu, Y.Q., Lai, J.X., et al, 2020a. Failure behavior investigation of loess metro tunnel under local-high-pressure water environment. Engineering Failure Analysis. 115, 104631.

Qiu, J.L., Lu, Y.Q., Lai, J.X., et al, 2020b. Experimental study on the effect of water gushing on loess metro tunnel. Environmental Earth Sciences. 79, 261.

Sun, W., Liang, Q.G., Qin, S.H., et al, 2021. Evaluation of groundwater effects on tunnel engineering in loess. Bulletin of Engineering Geology and the Environment. 80, 1947-1962.

Houston, S.L., Houston, W.N., Spadola, D.J. 1988. Prediction of field collapse of soils due to wetting. Engineering Geology. 114, 40–58.

Tu, S., Li, W., Zhang, C., et al, 2023. Effect of inclined layered soils on face stability in shield tunneling based on limit analysis. Tunn. Undergr. Space Technol. 131, 104773.

Weng, X.L., Sun, Y.F., Zhang, Y.W., et al, 2019. Physical modeling of wetting-induced collapse of shield tunneling in loess strata. Tunnelling and Underground Space Technology. 90, 208–219.

Weng, X.L., Zhou, R.M., Rao, W., et al, 2021. Research on subway shield tunnel induced by local water immersion of collapsible loess. Natural. Hazards. 108, 1197–1219.

Wang, J.D., Gu, T.F., Zhang, M.S., et al, 2019. Experimental study of loess disintegration characteristics. Earth Surface Processes and Landforms. 44, 1317–1329.

Wang, K., Xu, S.S., Zhong, Y.J., et al, 2021. Deformation failure characteristics of weathered sandstone strata tunnel: A case study. Engineering Failure Analysis. 127.

Xu, P.P., Zhang, Q.Y., Qian, H., et al, 2020. Investigation into microscopic mechanisms of anisotropic saturated permeability of undisturbed Q 2 loess. Environmental Earth Sciences. 79, 412.

Xue, Y.G., Zhang, X.L., Li, S.C., et al, 2018. Analysis of factors influencing tunnel deformation in loess deposits by data mining: a deformation prediction model. Engineering Geology. 232, 94–103.

Zhang, A.J., 2015. Study on deformation control of the tunnel in saturated soft loess area.

Zhao, Y., He, H.W., Li, P.F., 2018. Key techniques for the construction of highspeed railway large-section loess tunnels. Engineering. 4, 254–259.

Tunnelling for a Better Life – Yan, Celestino, Thewes & Eberhardt (Eds)
© 2024 The Author(s), ISBN 978-1-032-80042-4
Open Access: www.taylorfrancis.com, CC BY-NC-ND 4.0 license

Impacts of the February 2023 Kahramanmaraş, Turkey earthquakes on outlet works in rock formations

Pelin Uygur, Özgür Öztürk, Erol Dumlu* & Fatih Çalışkan
General Directorate of State Hydraulic Works, Dams and HEPP Department, Ankara, Turkey

ABSTRACT: On February 6, 2023, two earthquakes of moment magnitude (Mw) of 7.7 and 7.6 occurred in Kahramanmaraş-Turkey. The earthquakes had a widespread impact, affecting 11 provinces across Turkey and resulting in the occurrence of numerous aftershocks. In response to these earthquakes, engineering teams under the General Directorate of State Hydraulic Works were mobilized to assess the potential effects on nearly 140 dams. Outlet works are usually constructed in rock formations in State Hydraulic Works' applications for dams. Consequently, seismic loads have historically been overlooked during structural analyses. Post-earthquake inspections revealed minor damages to the outlet works attributed to ground shaking, thus supporting the assumption for seismic loads. This paper aims to provide an overview of the conditions of the inspected structures, the geological characteristics of the sites, and the seismic data collected in the wake of these seismic events.

Keywords: Outlet works, tunnels, conduits, earthquake, case studies

1 INTRODUCTION

On February 6, 2023, two earthquakes of moment magnitude (Mw) of 7.7 and 7.6 occurred in Kahramanmaraş-Turkey. The earthquakes had a widespread impact, affecting 11 provinces across Turkey and resulting in the occurrence of numerous aftershocks. In response to these earthquakes, engineering teams under the General Directorate of State Hydraulic Works were mobilized to assess the potential effects on nearly 140 dams.

This paper focuses on the outlet works of inspected dams, which are underground structures. These subterranean constructions exhibited remarkable resilience during the earthquakes, with minimal to no damage. Consequently, case studies presented were chosen based on the extent of damage observed in the dam bodies.

Underground structures had long been assumed to be sustainable against earthquake effects. Dawding and Rozen (1978) presented 71 cases of rock tunnels and formed relationships between damage levels and peak ground parameters. Although classified damage levels did not account for geological conditions or the presence of lining, they stated that there was no damage in both lined and unlined tunnels up to a surface acceleration of 0.19 g. Owen and Scholl (1981) collected data from 127 underground structures and introduced deformation modes of tunnels resulting from seismic waves. Hashash et al. (2001) discussed a detailed seismic design approach for underground structures.

Wang et al. (2001) assessed the damage inflicted by Taiwan Chi-Chi Earthquake on mountain tunnels. 57 tunnels, 49 of which are damaged, were investigated, damage patterns were classified, and possible influences of tunnel damage such as eathquake intensity, condition of surrounding ground and seismic capacity of the tunnel were evaluated.

Yashiro et al. (2007) generated a profile of historical damage to mountain tunnels in Japan. They also provided retrofit measures such as additional ground support along with repairing and strengthening of lining.

Li (2011) studied the impacts of Wenchuan earthquake on mountain tunnels. His study explored various factors influencing damage, including epicentral distance, seismic wave propagation direction, fault zones, and the bedrock-overburden contact plane.

Jaramillo (2017) presented several case studies involving rock tunnels constructed using different methods. He highlighted the significance of lining presence and adequate ground support in mitigating tunnel damage.

*Corresponding author: eroldumlu@dsi.gov.tr

DOI: 10.1201/9781003495505-213

2 BRIEF DESCRIPTION OF KAHRAMANMARAŞ EARTHQUAKES

Turkey is encircled by two prominent fault zones, which predominantly affect the Anatolian Plate, covering a substantial portion of the country's surface. The North Anatolian Fault (NAF), spanning approximately 1200 km, stretches across the northern region of Turkey, serving as the boundary between the Arabian and Eurasian plates. NAF is notorious for its high seismic activity, having generated major earthquakes with moment magnitudes reaching as high as 7.9. Adjacently, the East Anatolian Fault (EAF), extending 580 km, bridges the gap between the Arabian and Anatolian Plates, connecting to the eastern terminus of the NAF. Together, NAF and EAF accommodate the westward motion of the Anatolian Plate. Both faults are classified as transform faults, characterized by their significant seismic activity.

On February 6, 2023, two major earthquakes occurred in Kahramanmaraş-Turkey within a span of 9 hours. Both seismic events were located along the East Anatolian Fault, exhibiting a left-lateral strike-slip fault mechanism.

At 04:17 (01:17 GMT), an earthquake of Mw 7.7 and focal depth of 8.6 km (AFAD, Disaster, and Emergency Management Presidency) struck Pazarcık Kahramanmaraş-Türkiye, rupturing Narlı, Erkenek, Pazarcık and Amanos fault segments. The earthquake induced nearly 300 km long surface rupture and significant surface displacement up to 7 m. The maximum recorded peak ground acceleration (PGA) attributed to this earthquake was 1.23 g.

Subsequently, a Mw 7.6 earthquake happened at 13:24 (10:24 GMT) at Elbistan-Kahramanmaraş- Türkiye with a focal depth of 7.0 km (AFAD). Çardak and Doğanşehir fault zones were activated, resulting in a total rupture length of 160 km. This earthquake led to substantial surface displacement, reaching up to 8 m, with a maximum recorded PGA of 0.65 g. Figure 1 displays the earthquake epicentre locations and finite faults, sourced from USGS database.

Succesive earthquakes impacted 11 cities across Turkey, resulting in a devastating toll. Over 50,000 lives were lost, with an additional 115,000 individuals suffering injuries. Approximately 40,000 buildings collapsed as a result of these events. Furthermore, the earthquakes inflicted damage on infrastructure, and ground failure (liquefaction, landslides, rockfalls etc.) is observed in numerous instances.

3 CASE STUDIES

In this study, the selection of tunnel/conduit cases for outlet works was based on the extent of damage to the dam body. The primary focus of this study is on the outlet works of the most severely damaged dams among the 140 dams examined by the State Hydraulic Works. Figure 2 illustrates the locations of the dam sites featured as case studies in this paper.

Figure 1. Epicenters and finite faults of Kahramanmaraş Eartquakes.

The tunnels and conduits originally served as diversions during the dams' construction phase. However, during the water retention phase, they were converted into outlet works by directing the flow through steel pipes via a plug. During our inspections, it was not possible to access the upstream part of the plug, so our examination was limited to the downstream part of outlet works.

Figure 2. Location of the dam sites.

In the State Hydraulic Works' practice, tunnels are constructed with reinforced concrete lining, support systems are implemented, and both backfill grouting and pressure grouting are carried out. Additionally, these outlet works have a minimum of 25 meters of overburden above them and both the tunnels and conduits are constructed within or on top of rock formations. Furthermore, it is important to note that tunnels presented herein were constructed via drill and blast method, where as cut and cover method was applied for the conduits.

The values of peak ground acceleration (PGA) and peak ground velocity (PGV) obtained from the instrumented stations are sourced from both USGS and AFAD databases. The USGS database is utilized for establishing the contours of PGA and PGV.

3.1 *Sultansuyu Dam*

Sultansuyu Dam is an earthfill embankment dam, operating since 1994 in city of Malatya for irrigation purposes. Dam body has a 53 m hydraulic height and a 60 m structural height. There are two outlet works on each embankment: a conduit on the left abutment and a tunnel on the right.

The circular tunnel has a 4.5 m internal diameter (ID) and 0.5 m lining thickness with 28 m maximum overburden height. Hydraulic section of the conduit is 3.6 m wide horseshoe shape with a modified horseshoe outline and 0.8 m lining thickness. Maximum fill height above the conduit is 22 m.

The bedrock of the dam site is identified as the Beylerderesi Formation, composed of loosely consolidated sandstone-conglomerate-claystone alternation. It is classified as poor rock with an RMR value of 40.

The Elbistan Earthquake (Mw 7.6) had a higher impact on the dam site, with the epicenter located 82 km away and the ruptured fault, 15 km away. The site falls within close proximity to the 0.20 g PGA contour and between PGV contours of 20 cm/s and 50 cm/s. The nearest monitoring station, situated 7.4 km away, recorded a PGA of 0.476 g and a PGV of 35 cm/s during the earthquake. Reservoir elevation at the time of the event was 8 meters below the dam crest.

Subsequent inspections carried out after the earthquake revealed the presence of cracks along the dam crest, extending a total length of 400 m and reaching depths of 2.5 to 3.0 m (Figure 3). Outlet works also sustained some slight damage as minor cracks (Figure 4). Detailed studies are carried out in order to rehabilitate the dam body and appurtenant structures.

Figure 3. Cracks along the dam crest.

Figure 4. Minor cracks observed in the lining.

3.2 *Arıklıkaş Dam*

Arıklıkaş Dam has been operating since 1998 in the city of Osmaniye for irrigation purposes. It is a homogeneous eartfill embankment dam and its hydraulic height and structural height are 24.50 m and 32.50 m, respectively. Active conservation capacity of the reservoir is 1.67 hm^3.

Outlet works are carried out via a reinforced concrete coated steel pipe with an ID 0.6 m and a -0.3 m lining thickness. Maximum fill height above the conduit is 20 m.

Geologically, the site is situated on tertiary-aged flysch composed of claystone-siltstone-sandstone-sandy limestone-marn alternations, which reach the surface on both abutments. 18 m thick alluvium is found on the riverbed.

Pazarcık Earthquake had a higher impact on the dam site, which is 14,5 km away from the ruptured fault and 45 km away from the epicenter. The site is positioned between the PGA contours of 0.20 g and 0.50 g and the PGV contours ranging from 20 cm/s to 50 cm/sec. The nearest station, situated 20 km away from the site, recorded a PGA of 0.715 g and a PGV of 119.2 cm/sec during the event.

Subsequent assessments following the earthquakes revealed wide-span splits along the dam crest (Figure 5), and openings in the upstream riprap parallel to the dam axis (Figure 6). Additionally, there was an elevation loss at the crest and horizontal movement toward the upstream.

As the conduit is full of water and located beneath the dam body, the structural condition could not be directly observed. However, the water conveyance capacity remains stable, and no outflow has been detected at the upstream part of the energy dissipator. These findings provide positive indications that there is no risk of collapse or breakage in the pipe.

3.3 *Gömükan Dam*

Gömükan Dam and Irrigation Project comprises Gömükan Dam, two main water conveyance lines,

Figure 5. Wide-span splits along the dam crest.

Figure 6. Openings in the upstream riprap.

and an irrigation network. The project's water transport infrastructure includes a 3080 m long open channel conveyance line that commences downstream of the dam and connects with a 2400 m long conveyance tunnel.

Gömükan Dam is being constructed as a concrete face rockfill dam with a 73.70 m hydraulic height. Diversion is carried out through a 260 m long circular tunnel, followed by a 225 m long conduit. Both of these structures feature an inner diameter of 3.50 m and are equipped with a 0.35 m thick reinforced concrete liner. The conduit initiates downstream of the dam body and has 2.0 meters of backfill above it. The tunnel, on the other hand, exhibits a maximum overburden height of 53 meters.

The conveyance tunnel is also under construction. At the time of the earthquakes, excavation works and installation of ground support were being executed. The tunnel is designed with an ID of 3.00 m, a -0.35 m thick reinforced concrete liner, and a maximum overburden height of 100 meters.

The geological composition at the dam site is characterized by sediments of igneous rocks within the ophiolite complex. Bedrock is mainly limestone and serpentinite blocks together with siliceous shale, with marn bands composed of sanstone, conglomerate, and claystone alternations. The geological classification for the tunnel indicates that it is situated in a weak rock environment, with an RMR value of 30. The conveyance tunnel is also surrounded by the ophiolite complex, featuring similar properties.

Pazarcık Earthquake had a higher impact on the project components. Given the proximity of the dam site and the conveyance tunnel, both were subjected to a similar range of ground motion parameters. The distances from the dam site to the epicenter and ruptured fault are 120 km and 11.5 km, respectively. The dam site falls within the PGA contours of 0.20 g to 0.50 g and PGV contours ranging from 20 cm/s to 50 cm/s. The nearest station, located 17 km away from the site, recorded a PGA of 0.477 g and a PGV of 45.5 cm/sec during the event.

Subsequent to the earthquakes, the diversion facilities of the dam continued to operate without any signs of damage. On the other hand, conveyance tunnel has suffered damages such as disintegration of shotcrete and wiremesh (Figure 7), deformed steel ribs on the side wall (Figure 8), rockfalls at the not yet supported sections (Figure 9), and heave of the bottom shotcrete support (Figure 10).

3.4 *Tahtaköprü Dam*

Tahtaköprü Dam, which has been in operation since 1975, is situated in the city of Hatay, Turkey, and is designed for irrigation purposes. The project was recently revised, and dam crest elevation was raised by 9 m in order to expand irrigation areas and generate hydroelectric power. It is an earthfill embankment dam with a hydraulic height of 44.50 m and an active conservation capacity of 327 hm^3. There is a diversion tunnel, which was also used in the

Figure 7. Disintegration of shotcrete and wiremesh.

Figure 8. Deformed steel ribs on the side wall.

Figure 9. Rockfalls.

Figure 10. Heave of the bottom shotcrete support.

retrofit, with an internal diameter (ID) of 4.0 m and a lining thickness of 0.35 m. Outlet works are carried out by a 3.2 m ID reinforced concrete coated steel pipe with a 1.0 m thick lining. Maximum fill height above the conduit is approximately 30 m and overburden height above the tunnel reaches up to 45 m.

Bed rock formation on the site primarily consists of peridotite, with a few meters of mildly weathered zone on the surface but hard and intact on deeper levels.

Ground motion parameters and spatial properties for Pazarcık Earthquake (Mw 7.7) are presented here since there are no records available for Elbistan Earthquake (Mw 7.6) at the nearest station, which is 0.12 km away from the dam. Additionally, distances from epicenter and ruptured fault of the Pazarcık Earthquake are significantly shorter, with an epicentral distance of 50 kilometers and a distance from the ruptured fault to the dam of 11.5 kilometers. Dam site is located between peak ground acceleration (PGA) contours of 0.20 g and 0.50 g, peak ground velocity (PGV) is more than 50 cm/sec. Maximum PGA and PGV reported at the nearest station are 0.26 g and 60 cm/sec respectively.

At the time of the event, reservoir storage was about 18% of the active storage. No damage has been observed for the dam and appurtanent structures due to Pazarcık Earthquake. In addition to the good quality of the foundation for the conduit and surrounding rock for the tunnel, it should be noted that the retrofit project included a reevaluation of the dynamic response of the dam. This reassessment led to the adoption of a maximum design earthquake (MDE) with a PGA of 0.44 g for the design process.

3.5 *Yarseli Dam*

Yarseli Dam, located in southern Turkey on the Beyazçay River, was constructed for irrigation and was completed between 1985 and 1989. Dam body stands at a height of 42 m and impounds up to 55 million m^3 of water. A diversion conduit with an ID of 2.80 m was constructed beneath the dam under an overburden thickness of 28 m.

Our technical team conducted an inspection of this dam, which is closer to the Pazarcık- Earthquake, compared to the Elbistan Earthquake. Closest distance to the ruptured fault is 16.5 km. PGA reported from the nearest station, located 11 km away from the dam site, is measured at 0.544 g with a PGV of 53.5 cm/s. The dam is situated between PGA contours of 0.20 g and 0.50 g, with PGV exceeding 50 cm/sec.

Following the occurence of these two significant earthquakes, a thorough inspection of the dam revealed the presence of two primary cracks on the crest, with depths varying between 0.6 and 1.25 m and widths ranging from 0.02 to 0.15 m (Figure 11).

Meanwhile, the inspection included the conduit, which was subjected to ground shaking. There were only minor cracks in the conduit lining constructed beneath the dam.

Figure 11. Primary cracks on the crest.

3.6 *Reyhanlı Dam*

Reyhanlı Dam, with a height of 25.20 m, is designed as a clay core zoned dam for irrigation and flood control in the city of Hatay, Turkey. Remarkably, it holds the record for the longest crest in the country, stretching over an impressive 9.3 km. The dam's reservoir is replenished with redirected floodwaters from the Karasu and Afrin Rivers during the winter season. The construction of this significant dam was successfully completed on a silty clay foundation between 2018 and 2019, despite the geological constraints. As part of this project, two conduits were engineered, featuring an inner diameter of 3.50 m and a 1.00 m lining, all situated under an overburden depth of 23.5 m.

Regarding seismic considerations, Reyhanlı Dam is situated 105 km away from the epicenter of Pazarcık Earthquake, with a proximity of only 29.5 km to the ruptured fault. In contrast, Elbistan Earthquake had a lesser impact on the dam due to its greater distance from the dam site, which is 192 km from the epicenter to the site. PGA and PGV, recorded at the nearest station which is 11.4 km away, were measured 0.226 g and 29.1 cm/s, respectively. Dam site is situated between PGA contours of 0.20 g and 0.50 g and PGV contours of 20 cm/s and 50 cm/s.

Our team has observed that there were deep cracks on the dam crest, some of which extend to a depth of 1.8 m and a subsidence of up to 0.5 m (Figure 12).

Furthermore, there were cracks ranging from 1 to 1.5 cm at the joints of the conduit within this project (Figure 13). Disruption and cracks were also noted in the penstock support concrete (Figure 14). Detailed studies are being conducted for the rehabilitation of the dam body and its associated structures.

Figure 12 . Deep cracks on the dam crest.

Figure 13. Cracks in the lining of the conduit.

3.7 *Kartalkaya Dam*

The Kartalkaya Dam, constructed between 1965 and 1972 on the Aksu River in Kahramanmaraş serves the purpose of providing irrigation and drinking water. This 56 m high dam is a clay core zoned dam with a water retention capacity of 195 hm^3. Furthermore, a tunnel with an inner diameter of 5 m and a lining thickness of 0.40 m was constructed with an overburden of approximately 101.50 m, primarily comprising the geological formations of karker and serpentine.

In the context of seismic events, the Kartalkaya Dam was situated in relatively close proximity to the fault line that ruptured during the Pazarcık Earthquake, at a distance of approximately 5 km. Since the epicenter of Elbistan Earthquake is further away from the dam site, Kartalkaya Dam experienced a more significant impact from the Pazarcık Earthquake. PGA and PGV recorded at the 11.5 km away nearest station is measured 0.76 g and 104.8 cm/s, respectively. USGS contours confirmed a PGA exceeding 0.50 g and a PGV exceeding 50 cm/s.

Figure 14. Cracks in the penstock support concrete.

According to our team's inspection reports, the majority of damage cases were concentrated at the crest of the dam body, specifically in the form of cracks and undulations resulting from settlement (Figure 15). Additionally, it is important to note that no damage attributable to earthquakes was observed within the tunnel.

Figure 15. Cracks and openings on the crest of the dam body.

3.8 *Kalecik Dam*

Kalecik Dam is a clay core rockfill dam, located in Osmaniye, on the Beyazçay River, which is one of the tributaries of the Ceyhan River. It was constructed between 1983 and 1985 for irrigation purposes. The 77 m high dam from the river bed was constructed onto the geology of weathered diabase. The tunnel, with a diameter of 3.00 m and a lining thickness of 0.30 m, was designed to accommodate 95 m of overburden.

Pazarcık Earthquake had a substantial impact on the dam site due to its close proximity to the ruptured fault, being only 18 km, although it was located about 50 km from the epicenter of the earthquake. PGA and PGV recorded at the nearest instrumented station, which is situated 21.5 km from the dam site, were measured 0.715 g and 119.2 cm/s, respectively. Furthermore, it's worth noting that the dam site falls within the range of PGA contours, with values ranging between 0.20 g and 0.50 g, as well as PGV contours, with values ranging from 20 cm/s to 50 cm/s.

Figure 16. Longitudinal cracks and subsidence on the dam crest.

Following a comprehensive inspection of the dam, the engineering team observed subsidence of up to 1.5 m and the presence of longitudinal cracks along the crest (Figure 16). However, it's important to note that there was no damage detected within the tunnel or penstock during this inspection.

4 CONCLUSIONS

In the case studies section, we provide information about the analyzed tunnels/conduits. This includes essential data such as the distance of the tunnels from the epicenter, PGA and PGV contours, PGA and PGV values measured from the nearest station, and the distance to the ruptured faults following two earthquakes. When evaluating the peak acceleration values measured from the nearest stations, we observed a range of low to high acceleration values. Additionally, the distances to the ruptured faults were relatively short in some of the cases.

However, despite these challenging conditions, minimal damage occurred in a few structures, and most of them remained undamaged.

We believe that the absence of damage resulting from ground shaking can be attributed to several factors. These include the fact that the tunnels were lined, appropriate support systems were implemented during the construction phase, they were situated within rock formations, backfill grouting and pressure grouting were applied effectively, and there was sufficient cover thickness above them. Furthermore, it is important to note that outlet works presented here have relatively smaller openings in comparison to highway tunnels.

REFERENCES

AFAD (Disaster, and Emergency Management Presidency). 2023. 06 Şubat 2023 Pazarcık-Elbistan Kahramanmaraş (Mw: 7.7 – Mw: 7.6) Depremleri Raporu. (https://deprem.afad.gov.tr/assets/pdf/Kahramanmara%C5%9F%20Depremi%20%20Raporu_02.06.2023.pdf)

AFAD (Disaster, and Emergency Management Presidency), 2023. Deprem Kataloğu. 06- 02-202304:17:32, Pazarcık (Kahramanmaraş) Mw 7.7. (https://deprem.afad.gov.tr/event-detail/408326)

AFAD (Disaster, and Emergency Management Presidency), 2023. Deprem Kataloğu. 06- 02-202310:24:47, Elbistan (Kahramanmaraş) Mw 7.6. (https://deprem.afad.gov.tr/event-detail/408491)

Bieniawski, Z.T., 1989. Engineering rock mass classifications. New York: Wiley.

Dowding, C. H., Rozen, A., 1978. Damage to rock tunnels for earthquake shaking. Journal of the Geotechnical Engineering Division, ASCE 104 (GT2), pp. 175–191.

Gokceoglu, C., 2023, 6 February 2023 Kahramanmaraş – Türkiye Earthquakes: A General Overvıew. The International Archives of the Photogrammetry, Remote Sensing and Spatial Information Sciences, Volume XLVIII-M-1-2023 39th International Symposium on Remote Sensing of Environment (ISRSE-39) "From Human Needs to SDGs", 24–28 April 2023, Antalya, Türkiye.

Hashash, Y. M. A., Hook, J. J., Schmidt, B., Yao, J. I. C., 2001. Seismic design and analysis of underground structures. Tunneling and Underground Space Technology, 16, pp. 247–293.

Jaramillo, C. A., 2017. Impact of seismic design on tunnels in rock – Case histories. Underground Space 2, pp. 106–114

Li, T., 2011. Damage to mountain tunnels related to the Wenchuan earthquake and some suggestions for aseismic tunnel construction. Bulletin of Engineering Geology and the Environment (2012), pp. 297–308.

Middle East Technical University, Preliminary Reconnaissance Report on February 6, 2023 Kahramanmaraş-Pazarcık Mw= 7.7 and Elbistan Mw= 7.6, Kahramanmaraş-Türkiye Earthquakes, Earthquake Engineering Research Center, Report No: METU/EERC 2023-01.

Owen, G.N., Scholl, R.E., 1981. Earthquake engineering of large underground structures. Report no. FHWA/RD-80/195. Federal Highway Administration and National Science Foundation.

U.S. Geological Survey, 2023, Mw 7.5 - Elbistan earthquake, Kahramanmaras earthquake sequence. (https://earthquake.usgs.gov/earthquakes/eventpage/us6000jlqa/executive).

U.S. Geological Survey, 2023, Mw 7.8 - Pazarcik earthquake, Kahramanmaras earthquake sequence. (https://earthquake.usgs.gov/earthquakes/eventpage/us6000jllz/executive).

Wang, W. L., Wang, T. T., Su, J. J., Lin, C. H., Seng, C. R., Huang, T.H., 2001. Assessment of damages in mountain tunnels due to the Taiwan Chi-Chi Earthquake. Tunnelling and Underground Space Technology 16, pp. 133–150.

Yashiro, K., Kojima, Y., Shimizu, M., 2007. Historical earthquake damage to tunnels in Japan and case studies of railway tunnels in the 2004 Niigataken-Chuetsu earthquake, Quarterly Report of RTRI, Vol. 48, No. 3, pp. 136–141.

Tunnelling for a Better Life – Yan, Celestino, Thewes & Eberhardt (Eds)
© 2024 The Author(s), ISBN 978-1-032-80042-4
Open Access: www.taylorfrancis.com, CC BY-NC-ND 4.0 license

Research and development support for the construction of the big circle line on the example of the line's intersection with the existing facilities of the Moscow metro

V.V. Viazovoi, R.A. Evtushenko, D.S. Konyukhov & D.S. Petunina*
JSC «Mosinzhproekt», Moscow, Russia

ABSTRACT: In March 2023, the Big Circle Line of the Moscow Metro, the largest project of the Russian metro construction and one of the largest in the world, was fully commissioned. The project envisaged the construction of 28 new stations and the complete reconstruction of 3, the creation of 47 interchanges, including perspective ones, of which 19 were radial lines of the existing underground. A special construction task was to ensure safety of passenger traffic on the existing metro lines. Special measures were developed for each case of intersection or adjunction to the existing underground lines, taking into account the projected impact of construction and installation works, technical condition of facilities, construction methods and engineering and geological conditions at the site. Among the most difficult construction sections were: the interchange at the Sokolniki station of the Sokolnicheskaya line, the very first line of the Moscow Metro, which is a monument of architecture. In order to construct the adjacency of the station under construction to the operating station, soils were consolidated against the walls of the operating station; interchange at Pechatniki station on Lyublinsko-Dmitrovskaya line, a semi-underground station combined with the Nischenka river collector and built in the floodplain of the Moskva River in very difficult geological conditions; Maryina Roshcha station, which is being constructed using a drilling and blasting method directly beneath present Maryina Roscha station on the Lublinsko-Dmitrovskaya line, one of the deepest stations of the Moscow Metro. The drill and blast tunnelling method was used to accelerate, including directly under the operating station, calculations were made, and the necessary measures were arranged to ensure the safety and comfort of passenger traffic. Given the complexity of the engineering and geological conditions in Moscow and the dense urban development including not only surface facilities but also the existing underground network, the described experience will be interesting for further development of underground space in large metropolitan areas.

Keywords: Tunnelling, TBM, Drill and blast tunnelling method, Metro, Underground space, Geotechnical monitoring

1 INTRODUCTION

In March 2023, the Big Circle Line of the Moscow Metro, the most ambitious Russian metro construction project and one of the largest in the world, was put into full operation.

The project envisaged the construction of 28 new stations built from scratch and 3 completely reconstructed stations, 47 interchanges, including future ones, of which 19 were on the radial lines of the existing metro.

A special task of construction was to ensure the safety of passenger traffic on the existing metro lines. Special measures were developed for each case of crossing or adjoining the existing metro lines, taking into account the predicted impact of construction, technical condition of the structures, construction methods and engineering and geological conditions of construction.

The construction of the Big Circle Line provided a great and unique experience of construction in the conditions of the existing metro. The following construction sections were among the most challenging:

- a transfer point at Sokolniki station of the Sokolnicheskaya line, the very first line of the Moscow Metro. This station is an architectural monument. A geotechnical monitoring system was organised during the construction of the interchange tunnels. Soil consolidation close to the walls of the existing

*Corresponding author: petuninads@mosinzhproekt.ru

DOI: 10.1201/9781003495505-214

station was carried out to ensure that the station under construction adjoins the existing station;
- interchange at Pechatniki station of the Lublinsko-Dmitrovskaya line, a semi-subterranean station combined with the Nishenka River collector and built in the floodplain of the Moscow River in very difficult geological conditions. A two-track tunnel was excavated under the existing station, traffic on the existing section was closed, and simultaneously with the excavation, preparations were made for the construction of the interchange hub: repair of the track structure and dismantling of the station cover slabs;
- Maryina Roshcha station, which is being built using a drilling and blasting method directly under the Lublinsko-Dmitrovskaya line station of the same name – one of the deepest stations of the Moscow Metro. In order to accelerate the works using the above method, calculations were made, and the necessary measures were taken to ensure the safety and comfort of passenger traffic.

Taking into account the complexity of engineering and geological conditions of Moscow and dense urban development, including not only surface facilities, but also the existing underground network, the adopted experience is of interest for the development of underground space of large megacities.

2 CONSTRUCTION OF THE BIG CIRCLE LINE TUNNELS UNDER SOKOLNIKI STATION

Sokolniki station of the Sokolnicheskaya line is one of the first stations of the Moscow Metro – it was from this station that the first underground train with passengers departed on 15 May 1935. The station design is three-bay, columned, shallow. It became a template for the construction of stations of the open method of works (Figure 1).

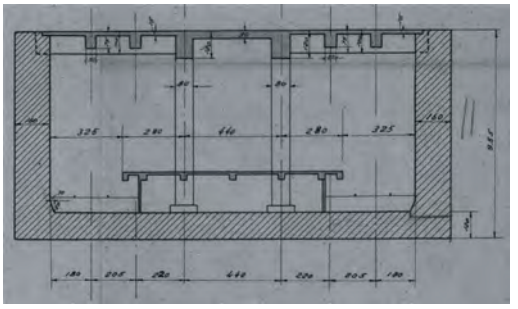

Figure 1. Construction of sokolniki station – the first station of the first line of the Moscow metro. drawing of 1933.

The station lobby consists of several parts: underground with a ticket office, intermediate and elevated.

The intervening soils are bulk soils represented by tight-plastic loams and sands with loam and clay interlayers, with construction debris; fine, dusty water-saturated sand with pressure water at the base of the station structure.

The route of the Big Circle Line ran at an angle of about 74° under the structures of Sokolniki station in clay, limestone and marl. The tunnel lining at the crossing section is high-precision precast reinforced concrete, 6 m in diameter. The crossing tunnels were driven by 'Herrenknecht' tunnel boring mechanised complexes (TBM).

In the course of the survey works, it was revealed that Sokolniki station has a deformation joint at the section falling within the zone of influence of the construction of the Big Circle Line tunnels, from which water drainage is organised.

Numerical modelling of the possible impact of construction on Sokolniki station was performed, taking into account the technical condition of the station and its lobby, as well as the design and condition of the expansion joint. The possibility of mutually independent displacements of the station structures in the area of the joint location was taken into account. The results of the modelling studies are given in Table 1.

Since such settlement values could lead to the occurrence of ledges in the settlement joint zone, damage to the station waterproofing, changes in the longitudinal profile of the tracks and gradients, which would lead to a violation of the operational reliability of Sokolniki station (Kobidze, Konukhov, 2022), it was closed to train traffic during the construction of the overpass tunnels with the organisation of scientific and technical support of construction, including the following works (Koval et al., 2022; Konukhov, Polyankin, 2019):

1. Development of technological regulations for tunnelling of the tunnels (Mazein et al., 2019), which described the controlled parameters of tunnelling, gave a diagram of bottom face loading pressure along the entire route of the tunnels, including under the existing Sokolniki station; the recommended loading pressure in the vault neck is 1.6 bar, in the flume is 2.3 bar.

Table 1. Results of calculation.

Tunnel structure	Calculated displacements, mm		
	Horizontal	Vertical	Sediment difference*
As a result of tunnelling of the left crossing tunnel			
Sokolniki station of Sokolnicheskaya line	1/2	12/11	1
Sokolniki station lobby (with drilling piles)	2	2	1
As a result of tunnelling of the left and right crossing tunnels			
Sokolniki station of Sokolnicheskaya line	2/4	17/16	1

* Difference between vertical deformations in zone I and II of station tracks (for the platform part of the station).

2. Automated monitoring of the planned height position of Sokolniki station structures with a frequency of 1 every 4 hours (Merkin et al., 2021).
3. Control of rail head height position and rail string difference with a frequency of 2 times a day.
4. Control of the planned height position of the internal structures of Sokolniki station lobby with the frequency of 2 times a day.
5. Visual inspection of technical condition of metro structures.
6. Geodetic observations of day surface deformations along the tunnelling axis.
7. Monitoring and interactive control of driving process parameters (loading pressure, volume of developed soil, injection pressure and volume of plugging solution) based on the results of geotechnical monitoring (Konyukhov, 2022).

The planned speed of tunnelling of the crossing tunnels was 7 rings per day.

Before the TBM entered the zone of influence at Sokolniki station, a technological stop was performed for maintenance and performance testing of the TBM systems to prevent it from stopping under the operating station.

The final deformations of Sokolniki station based on the results of excavation of two tunnels and their comparison with the results of calculations are given in Table 2.

According to the results of the tunnelling, it can be concluded that the tunnelling of the Big Circle Line tunnels did not affect the structures of the existing Sokolniki station.

As a result of the implementation of measures on scientific and technical support of construction and control of tunnelling parameters:

– maximum stabilised precipitation of Sokolniki station structures was 3.6 mm;
– safe, practically sediment-free tunnelling of the Big Circle Line tunnels was ensured at a depth of about 6 m under the existing Sokolniki station – a cultural heritage site of the station of the Sokolnicheskaya line of the Moscow Metro;

Table 2. Station deformations after driving the left and right crossing tunnels and stabilisation of deformations.

	Calculated		Based on the results of monitoring	
Tunnel structure	layout	depth	layout	depth
Sokolniki station of Sokolnicheskaya line	2/4	17/16	1	3,6
Sokolniki station lobby	2	2	-2,3	-4,3

– there was no need to install safety bags and their subsequent dismantling, waterproofing of the expansion joint, which could have entailed changes in the appearance of the historical monument and an increase in the cost of construction of the facility.

3 CONSTRUCTION OF PECHATNIKI STATION

The existing Pechatniki station of the Lyublinsko-Dmitrovskaya line of the Moscow Metro was built in 1995 using cut and cover method with cast reinforced concrete and prefabricated reinforced concrete structures. The maximum depth from the surface to the station cover is 1.5 m.

The tunnel inspection revealed sections where track subsidence occurred during operation. The recorded amount of subsidence ranged from 15 to 31 mm (Konyukhov et al., 2021).

Intervening ground mass – technogenic sediments, loams and sands mainly of medium coarseness with crumbs and fragments of bricks, concrete, in some places – with wood chips, glass fragments and pieces of metal; consolidated, low and medium degree of water saturation and water-saturated.

The Nishenka River collector, consisting of three prefabricated reinforced concrete pipes with a diameter of 3.5 mm and 6 chambers, runs under the station (Figure 2).

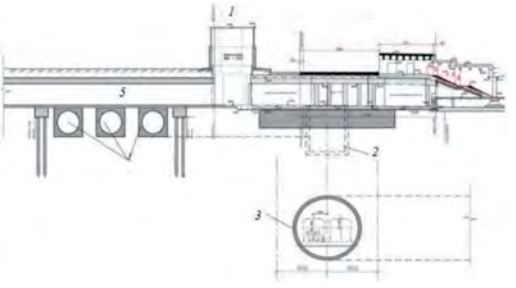

Figure 2. Mutual location of existing development and construction objects (cross-section: 1 –section along the axis of pechatniki station of the lyublinsko-dmitrovskaya line; 2 – the well of the nishenka river; 3 – tunnel of pechatniki station of the big circle line; 4 – the nishenka river collector; 5 – tunnel of pechatniki station of the lyublinsko-dmitrovskaya line.

The foundations of the chambers are monolithic reinforced concrete slabs 380 mm high, depth of embedment from the ground surface 7.0 m. The foundations under the collector pipes are precast reinforced concrete blocks with a depth of 6.5--10.5 m from the surface.

The construction of the tunnel from Pechatniki station to Nagatinsky Zaton station was carried out by a Herrenknecht 10.69 m diameter TBM with active soil loading of the face. Tunnelling of the Big Circle Line tunnels under Pechatniki station was carried out

at a depth of 13.6 m in the following engineering and geological conditions:

– vault part – in Jurassic clays of hard, with semi-hard interlayers;
– middle and lower parts – in Izmailovo limestones of medium strength, with marl and clay interlayers, fractured, interlayers broken to rubble and flour, water-bearing.

Hydrogeological conditions of the territory are characterised by the presence of groundwater of the Nadjursky and Izmailovsky aquifers.

The assessment of the impact of the construction of the double-track tunnel on the structures of the Pechatniki station of the Lyublinsko-Dmitrovskaya line and on the Nishchenka River collector was carried out, taking into account the technical condition of the station, its structural features and deformations obtained both during operation and as a result of the dewatering operation during the construction of the excavation of the Pechatniki station of the Big Circle Line (Znamenskaya, Zertsalov, 2022).

The calculation was carried out in the software package "Z_Soil" by the finite element method, in the volumetric formulation (Figure 3).

The calculation results are given in Table 3.

The minimum design safety factor for the Pechatniki station structures after the two-track tunnel is 1.15.

Based on the analysis of available materials, the following measures for scientific and technical support and interactive control of driving parameters were proposed (Konyukhov, 2022):

Verification of numerical modelling results (Konyukhov, 2023; Kulikova et al., 2022).

1. Prediction of geotechnical risks (Kulikova et al., 2023; Kulikova, Konyukhov, 2022).
2. Fixing of penetration parameters (loading pressure, volume of developed soil, injection pressure and volume of plugging solution).

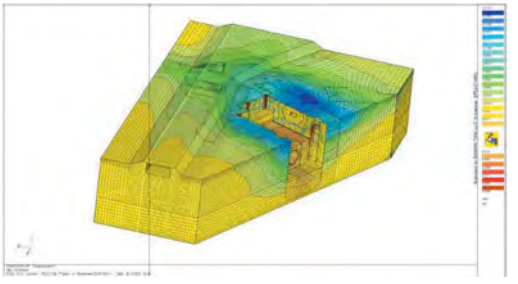

Figure 3. Isofields of vertical displacements during the excavation of a double-track tunnel.

3. Organisation of automated monitoring of the planned height position of the Pechatniki station structures with a frequency of once every 3 hours.
4. Geodetic observations of day surface deformations.

Table 3. Results of calculation by mathematical modelling method.

Object	Maximum displacements of station structures, mm		
	vertical	Along station	Across the station
Estimated displacements from tunnelling of the crossing tunnel			
Pechatniki station of the Lublinsko-Dmitrovskaya line	17.0	0	0
Concrete collectors of the Nishenka River that are 3500 mm in diameter	39.0	-	-

5. Georadiolocation survey of the ground massif in order to detect leaks from the Nishchenka River collector during shield sinking (Churkin et al., 2021).
6. Measurements using radio-wave geo-introspection of interwell space technology (Figure 4) in the intersection zone of active and under-construction tunnelling structures (Istratov et al., 2019; Kuznetsov, 2012).
7. Analysis of monitoring results and interactive control of tunnelling parameters.

In the course of tunnelling, the technological parameters of TBM operation were monitored and compared with the monitoring data. If necessary, real-time adjustments were made to the TBM loading pressure, which made it possible to ensure the maximum actual settlement of the Pechatniki station of 7.4 mm and of the Nishenka River collector of 4.2 mm (Table 4).

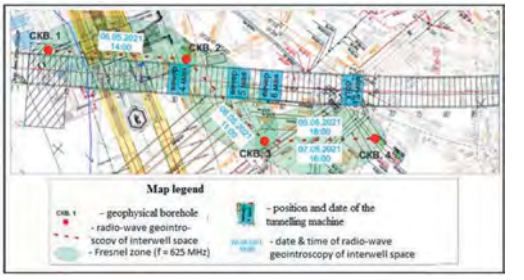

Figure 4. Schematic of measurements using radio-wave geointroscopy of interwell space (f = 625 kHz).

Table 4. Comparison of calculated and actual settlements of the pechatniki station and the nishenka river collector.

Tunnel structure	Settlements, mm	
	Calculated	Actual based on monitoring results
Pechatniki station of the Lublinsko-Dmitrovskaya line	17.0	7.4
Nishenka River collector	39.0	4.2

Measures on scientific and technical support of construction and interactive control of tunnelling parameters allowed:

– monitor changes in the physical condition of the soil mass, technical condition and deformations of the protected structures and make timely decisions to adjust the technological parameters of the TBM operation in real time;
– ensure structural reliability and further safe operation of the existing structures of the Pechatniki station and the Nishenka River collector without additional special construction methods.

4 CONSTRUCTION OF MARYINA ROSHCHA STATION

On 19 June 2010, Maryina Roshcha station was opened on the Lublinsko-Dmitrovskaya line. The station structure is a pylon, three-vaulted, deep-buried station (depth of embedment – about 57.0 m). The station was built by the trenchless method according to the standard design (Figure 5).

Figure 5. General view of maryina roshcha station of lublinsko-dmitrovskaya line.

The station lining is prefabricated cast iron, circular. The outer diameter of the side station tunnels is 8.50 m, the middle station tunnel is 9.50 m. The distance between the tunnel axis is 9.75 m. Pylons are arranged in two rows, distance between pylon axes 10.50 m, pylon width 6.759 m, opening width 3.759 m. The platform width is 19.10 m.

The northern lobby with an escalator tunnel was opened on 24 December 2012. Tunnel construction – reinforced concrete waterproof lining of high-precision blocks with a diameter of 10.6 m.

The construction of the Maryina Roshcha station of the Big Circle Line is of the pylon type with 3.755 m wide openings and 6.759 m wide pylons (Figure 6).

The middle tunnel is constructed with cast iron lining with a diameter of 9.5 metres. The side tunnels are built with cast iron lining with a diameter of 8.5 m. There are 22 openings between the side tunnel and the middle tunnel. The construction was carried out by a trenchless method through working-cable shafts.

In profile, the station is located at a depth of approximately 73 m from the ground surface; approximately 5 m below the crossing tunnels behind the Maryina Roshcha station of the Lublinsko-Dmitrovskaya line.

Figure 6. General view of the maryina roshcha station of the big circle Line.

The tunnel structures of Maryina Roshcha station of the Big Circle Line are located in stable sediments of Upper Stone Age of the Mescherinsky, Perkhurovsky, Neverovsky, Ratmirovsky and Voskresensky stages, represented by interspersed layers of calcareous, hard clays with marl interlayers; fractured marls of medium strength; fractured limestones of medium strength with interlayers of strong and low-strength marls and clays.

For the construction of the Maryina Roshcha station of the Big Circle Line perpendicular to the existing Maryina Roshcha station, pilot tunnels were constructed using Herrenknecht shield TBM equipped with active soil loading. Tunnel lining at the crossing section is prefabricated from cast iron tubing with a diameter of 6.00 m (Figures 7).

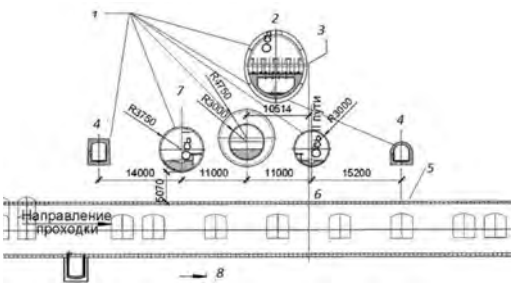

Figure 7. Mutual location of maryina roshcha stations of the big circle line and lublinsko-dmitrovskaya line (longitudinal section): 1 – existing lines; 2 – escalator tunnel centreline; 3 – sheremetyevskaya station centreline; 4 – cable collector centreline; 5 – line under construction; 6 – track II axis; 7 – track I axis; 8 – tunnelling direction.

In parallel with the construction of the pilot tunnels, construction of the middle station tunnel was started by counter faces. Installation chambers for tunnel lining pavers were built from the approach workings and the station paver was installed.

The project envisaged rock excavation of the station tunnel by drilling and blasting method outside the operating metro zone, under the operating station complex – Brokk type machine. When boring the station tunnels under the operating structures behind the Maryina Roshcha station of the Lublin-Dmitrovskaya line, the project provided for advance grouting of the rock to prevent settlement of its structures in the tunnel vault. After the cement mortar had maturing, the rock was excavated and a sprayed-concrete support was installed.

Construction of the middle station tunnel was stopped while the tunnels under the existing station complex were being driven. The blockage was secured with anchors and sprayed concrete.

After the completion of the middle station tunnel and pilot tunnels, the builders started bulkheading the side pilot tunnels from a diameter of 6.00 m to the design diameter of 8.50 m. The tunnelling was carried out in fractured limestone with hard clay interlayers and uniaxial compressive strength up to 70 MPa. Taking into account the high strength of the rock and the experience of excavation of the middle station tunnel, it was concluded that mining using a Brokk type machine increases the construction time. In order to speed up the works, we switched to the drilling and blasting method in the area of the existing metro structures. At the same time, special measures were developed to ensure safety and comfort of passenger transportations.

The basis for ensuring seismic-safe conditions of works is the limitation of the permissible vibration velocity at the base of the protected object (Verkholantsev et al., 2019; Vokhmin et al., 2022). For all underground facilities located in the area of blasting operations, including engineering systems of the Maryina Roshcha station, the permissible vibration velocity was assumed to be 30 mm/s.

The seismic permissible masses of instantaneously detonated charges depending on the distance to the structures of the Maryina Roshcha station were analytically calculated. The maximum mass of charges Qd = 4.3 kg is limited based on the impact on surface objects (construction was carried out at a depth of 61 m) located in the blasting area (Table 5).

The minimum distance from the places of planned drilling and blasting operations during pilot tunnel bulkheading in the technical zone of Maryina Roshcha station to the station structures was 9.0 m, to cable collectors – 6.74 m. The minimum distance from the places of planned drilling and blasting operations in the zone of influence of the station to the station structures was 5.57 m, to cable collectors – 7.5 m.

Then a geotechnical forecast of the impact of the construction of the Maryina Roshcha station of the Big Circle Line on the existing metro structures was made, taking into account the stage of tunnelling. Estimated displacements of the existing structures were obtained, on the basis of which a conclusion on the possibility of construction of the facility was given (Figures 8).

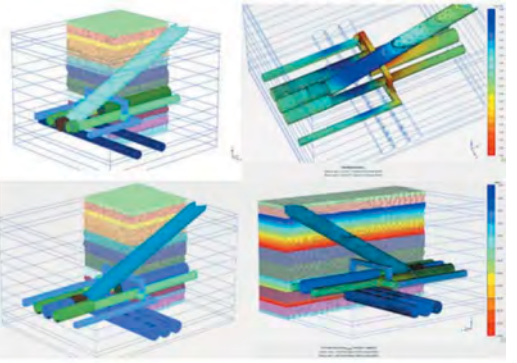

Figure 8. Three-dimensional mathematical model of maryina roshcha station construction.

For the entire period of construction of the Maryina Roshcha station of the Big Circle Line, a system of automated monitoring of the operating structures of the Lublin-Dmitrovskaya line was organised (Simutin et al., 2021).

Measurements of the planned and height position of the station structure were carried out at a frequency of once every 4 hours (Table 6).

Results:

1. Thanks to the use of the drilling and blasting method of rock excavation and the counter headway method, the construction time of the side

Table 5. Seismic safe masses of instantaneously detonated charges for bulkheading of station pilot tunnels of the sheremetevskaya station under construction.

Distance from the explosion site to the structure of Maryina Roshcha station *r*, m	5.5-7	7-8	8-9	9-10	10-12	12-15	15-17	17-20	20-22	22-25	25 and more
Permissible mass of instantaneously detonated charges Q_d, kg	0.067	0.1	0.15	0.2	0.3	0.5	0.9	1.4	2.2	3.0	4.3

Table 6. Values of predicted and actual vertical displacements of structures of maryina Roshcha station of the lublinsko-dmitrovskaya line.

Tunnel structure	Main line tunnel construction		Construction of Maryina Roshcha station of the Big Circle Line	
	Design displacements	Actual displacements	Design displacements	Actual displacements
Left side tunnel behind Maryina Roshcha station, track 1	6	-4.5	11.0	-11.1
Right side tunnel behind Maryina Roshcha station, track 2	6	-1.3	11.0	-12.0
Tension chamber of Maryina Roshcha station (north lobby)	3	-2.6	2.0	-7.0
Escalator tunnel (north lobby)	4	-2.6	6.0	-7.0

station and middle tunnels of the Maryina Roshcha station of the Big Circle Line was reduced by 25 %.
2. The developed measures (automated monitoring, calculation of charge mass and minimum safe distance) made it possible to ensure the safety of passenger transportations on the operating metro line without station closure and without other restrictions.

5 CONCLUSIONS

Scientific and technical support during the construction of the Big Circle Line allowed to:

1. develop and validate the analytical method of verification of mathematical modelling results when performing geotechnical calculations;
2. develop a methodology for calculating the coefficient of technological over-excavation of soil when using mechanised tunnelling;
3. monitor changes in the physical state of the soil mass, technical condition and deformations of the protected structures and to make timely decisions on the adjustment of technological parameters of TBM operation in real time mode;
4. develop and introduce into the practice of underground construction modern methods of automated monitoring and interactive control of tunnelling operations parameters;
5. ensure structural reliability and safe operation of the existing structures of the Moscow Metro during the construction of the Big Circle Line without the use of special construction methods;
6. reduce the time and cost of tunnelling works.

The experience gained during the construction of the Big Circle Line of the Moscow Metro will be relevant for further development of the underground space of Moscow and other megacities of the world.

REFERENCES

Churkin, A.A., Kapustin, V.V., Konyuhov, D.S., et al., 2021. Poslednie izmeneniya v rossijskoj praktike normativnogo regulirovaniya «tekhnicheskoj geofiziki». Geotekhnika. XIII, 56–70. (In Russ.).

Istratov, V.A., Kolbenkov, A.V., Kuznecov, N.M., et al., 2019. Sposob ob'emnoj radiovolnovoj geointroskopii gornyh porod v mezhskvazhinnom prostranstve. Patent RU № 2710874 ot 27.03.2019. (In Russ.).

Kobidze, T.E., Konyuhov, D.S., 2022. Osobennosti proektirovaniya i ustrojstva nadezhnoj i remontoprigodnoj gidroizolyacii dlya podzemnyh sooruzhenij transportnogo naznacheniya. Metro i tonneli. 3, 24–27. (In Russ.).

Konukhov D.S., Polyankin A.G., 2019. Ensuring the safety of the existing buildings during the construction of the underground in Moscow. Tunnels and Underground Cities: Engineering and Innovation meet Archaeology, Architecture and Art – Peila, Viggiani & Celestino (Eds). Taylor & Francis Group. London, pp. 5756–5766.

Konyuhov, D.S., Petunina, D.S., Kulikova, E. Yu., 2021. Nauchno-tekhnicheskoe soprovozhdenie prohodki dvuhputnogo peregonnogo tonnelya bol'shoj kol'cevoj linii Moskovskogo metropolitena pod dejstvuyushchej stanciej "Pechatniki". Proektirovanie, stroitel'stvo i ekspluataciya podzemnyh sooruzhenij transportnogo naznacheniya: sbornik statej "Lenmetrogiprotrans" JSC. Ed. M.O. Lebedev. M.: Izdatel'stvo "Pero". Pp. 144–152. (In Russ.).

Konyukhov, D.S., 2022. Interactive control of process variables in double-track tunnel driving between subway stations. Mining Informational and Analytical Bulletinthis link is disabled, 2022, (5). pp. 84–94.

Konyukhov, D.S., 2022. Safety of existing buildings during underground mining. Mining Informational and Analytical Bulletin. 8, 158–167.

Konyukhov, D.S., 2023. Forecast of technological deformations of the earth's surface during the construction of surface complexes of mines. Ugol, 2023, (4), p. 61–64.

Koval', S.V., Piskunov, A.A., Pestryakova, E.A., et al., 2022. Nauchno-tekhnicheskoe soprovozhdenie stroitel'stva mnogofunkcional'nogo kompleksa nad stanciej metro "Chkalovskaya". Metro i tonneli. 3, 16–19. (In Russ.).

Kulikova, E.Yu., Balovtsev, S.V., Skopintseva, O.V., 2023. Complex estimation of geotechnical risks in mine and underground construction. Sustainable Development of Mountain Territories, 2023, 15(1), p. 7–16.

Kulikova, E.Yu., Konyukhov, D.S., 2022. Accident risk monitoring in underground space development. Mining Informational and Analytical Bulletin, 2022, (1), p. 97–103.

Kulikova, E.Yu., Konyukhov, D.S., Potokina, A.M., et al., 2022. Analytical method for calculating the coefficient of technological soil sampling in the organization of mining and construction works with the use of mechanized tunneling. Mining Informational and Analytical Bulletin, 2022, (6), p. 305–315.

Kuznecov, N.M., 2012. Sposob 3D obrabotki dannyh radiovolnovogo prosvechivaniya mezhskvazhinnogo prostranstva. Vestnik KRAUNC. Nauki o Zemle. 1(19), 240–246. (In Russ.).

Mazein, S.V., Pankratenko, A.N., Polyankin, A.G., et al. 2019. Soil improvement in tunnel face using foam reagents in EPB TBM. Tunnels and Underground Cities: Engineering and Innovation meet Archaeology, Architecture and Art – Peila, Viggiani & Celestino (Eds). Taylor & Francis Group. London, 2019. pp.2663–2670.

Merkin, V.E., Pichugin, A.A., Medvedev, G.M., et al., E. A., 2021. Comprehensive Automated Geotechnical Monitoring System and Experience in its Application in the Construction of Underground Facilities. Soil Mechanics and Foundation Engineering, 2021, 58(3), p.230–236.

Simutin, A.N., Deineko, A.V., Zertsalov, M.G., 2021. Experience of Using the Home-Made Monitron Automated Hydrostatic-Leveling System for Monitoring of Hydraulic Structures. Power Technology and Engineering, 2021, 55(4), pp. 482–486.

Verholancev. A.V., Shulakov, D.YU., Dyagilev, R.A., 2019. Osobennosti ocenki sejsmicheskogo vozdejstviya burovzryvnyh rabot. Gornyj zhurnal. 5, 29–36. (In Russ.).

Vohmin, S.A., Kurchin, G.S., Kirsanov, A.K., et al., 2022. Raschet parametrov burovzryvnyh rabot pri stroitel'stve podzemnyh gornyh vyrabotok. Krasnoyarsk: Sib. feder. un-t, 180 p. (In Russ.).

Znamenskaya, E.A., Zercalov, M.G., 2022. Issledovanie vliyaniya shchitovoj prohodki tonnelya metropolitena na okruzhayushchuyu gorodskuyu zastrojku. Innovacii i investicii. 6, 167–170. (In Russ.).

Tunnelling for a Better Life – Yan, Celestino, Thewes & Eberhardt (Eds)
© 2024 The Author(s), ISBN 978-1-032-80042-4
Open Access: www.taylorfrancis.com, CC BY-NC-ND 4.0 license

Evaluation of impacts on existing structures induced by deep excavations in Bangkok MWA project

Phongkai Vonghirunyika & Wunchock Kroehong
Department of Civil Engineering, Faculty of Engineering and Architectural, Uthenthawai Campus, Rajamangala University of Technology Tawan-ok, Bangkok, Thailand

Tananat Yonjoho, Kangwan Kandavorawong, Arthit Chayaroon & Ochok Duangsano*
Geotechnical and Foundation Engineering Co., Ltd., Bangkok, Thailand

Pornkasem Jongpradist
Department of Civil Engineering, Faculty of Engineering, King Mongkut's University of Technology Thonburi, Bangkok, Thailand

ABSTRACT: The Metropolitan Waterworks Authority involves the construction of several shafts and a tunnel for the Water Transmission Tunnel Project in Bangkok, Thailand. In this project, numerous existing structures are located in close proximity to the underground construction areas. Consequently, these structures are susceptible to potential impacts due to the construction activities, particularly deep excavation of the shafts associated with excessive ground movements. This paper presents the evaluation of effects on the adjacent existing infrastructure resulting from the construction of two shafts with opening sizes of 12 m x 8 m and 10 m x 6 m, and the depth of excavation is around 30 m. A three-dimensional numerical analysis using PLAXIS 3D is carried out to investigate the responses, movements and imposed loads on the structures and piled foundations induced by the excavation in soft ground conditions. Extensive instrumentation and monitoring programs are implemented to observe such movements and to evaluate the serviceability of the existing structures. The monitoring results are in agreement with the analysis results and the construction has been successfully completed.

Keywords: Deep excavation, Impact assessment, Existing structures, Instrumentation

1 INTRODUCTION

The continuous expansion in the Bangkok metropolitan area has resulted in a rapid increase in demand for facilities. The 9th Master Plan Improvement Project of the Metropolitan Waterworks Authority (MWA) has been proposed to improve the efficiency of water supply distribution. The alignment of the project starts from the Mahasawat water treatment plant to the Samrong water pumping station, which is divided into four contracts.

According to the G-TN-9D project, the alignment of the tunnel commences from the Bangmod pumping station to the Samrong pumping station, covering a distance of about 13.4 km as shown in Figure 1. Seven shafts are proposed for construction, consisting of two rectangular diaphragm wall shafts, two octagonal diaphragm wall shafts and three circular sink caisson shafts. These shafts are utilized as the driving and receiving points for the Tunnel Boring Machine (TBM) at an approximate depth of 27.0 m below the ground surface.

Due to space constraints, shafts have to be excavated in close proximity to existing major structures. Typically, the construction of underground structures can result in soil displacements, leading to potential damage to nearby structures as depicted in Figure 2. Therefore, it is crucial to evaluate the possible impacts prior to the commencement of the construction. Figure 3 presents the relative positions between shafts (9D-1 and 9D-2) and the existing expressway viaducts. Preventive measures and risk mitigation strategies to reduce the effects are considered prior to the construction. A jet grout partition wall is proposed as a protection measure.

This paper focuses on the mitigation measure and the assessment of impacts on the existing viaduct adjacent to shaft construction by using 3D finite element analysis. The adjacent foundations are comprehensively evaluated in terms of foundation movements, pile structural capacity and pile geotechnical capacity due to the construction of both shafts. The comparison between computed foundation movements and the monitoring results is also discussed.

*Corresponding author: ochok_d@gfe.co.th

DOI: 10.1201/9781003495505-215

Figure 1. Layout Plan G-TN-9D.

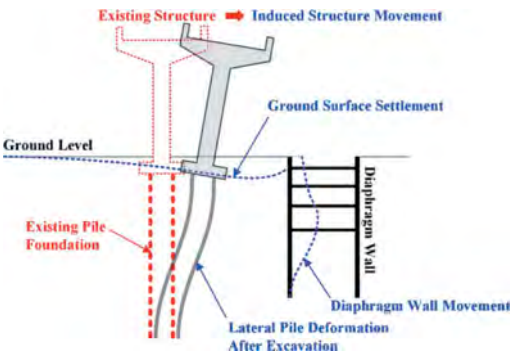

Figure 2. Structural movement due to deep excavation.

2 PROJECT DESCRIPTION

2.1 *Shaft 9D1 & 9D2*

Construction shaft 9D-1 exhibits a rectangular design, with internal dimensions measuring 8.0 m x 12.0 m. Similarly, shaft 9D-2 also follows a rectangular layout with internal dimensions of 6.0 m x 10.0 m. These shafts are constructed using a top-down method with a 1.2 m thick diaphragm wall. The toe of the diaphragm wall extends to approximately 57 m from the ground surface.

The internal structure of shaft 9D-1 comprises reinforced concrete walers. These walers have a cross-sectional size of 1.0 m x 1.2 m for the upper two levels (waler–1 and waler–2), and a cross-sectional size of 1.0 m x 2.0 m for the lower two levels (waler–3 and waler–4). The base slab has a thickness of 2 m.

The internal structure of shaft 9D-2 also features reinforced concrete ring beams, with a cross-sectional size of 1.2 m x 1.2 m for the upper two levels (waler–1 and waler–2), and a cross-sectional size of 1.2 m x 1.8 m for the lower two levels (waler–3 and waler–4). The Base Slab in this case also has a thickness of 2.0 m.

These components structurally act as a support system within the shaft during construction. The Base Slab of both shafts is situated at a depth of approximately 32 meters below the ground surface as shown in Figure 4.

2.2 *Existing viaduct structures*

Three adjacent foundations supporting the Kanchanaphisek outer ring road are considered in a detailed evaluation. The distance between viaduct No. MLP-46-1R and MLP-46-2R and Shaft 9D-1 are 11.8 m and 10.9 m, respectively. Similarly, viaduct No. MLP-46-2R and MLP-46-3R have clearances of 12.7 m and 13.9 m from shaft 9D-2. They are supported by several bored piles with a diameter of 1.20 m, and the pile tip level at 50 m below ground surface. The ultimate load of 1150 tons is considered for each pile.

Figure 3. Site Location of Shaft 9D-1 and 9D-2 and adjacent structures.

2.3 *Geological condition*

The geological condition of Bangkok is relatively uniform throughout the area. It is typically composed of fill material being approximately 0.5 to 2.0 m thick, soft clay layer generally ranges from the ground surface to a depth of 10.0 to 15.0 m. A medium stiff clay layer with a thickness of 1.0 to 3.0 is situated under the soft clay layer. Underlying the medium clay, a stiff clay layer can be found with a thickness varying from 5.0 to 15.0 m. Below the stiff clay layer, a thick layer medium dense to very dense first sand layer is located. The piezometric pressure head during construction is located around 13.0 m below the ground surface.

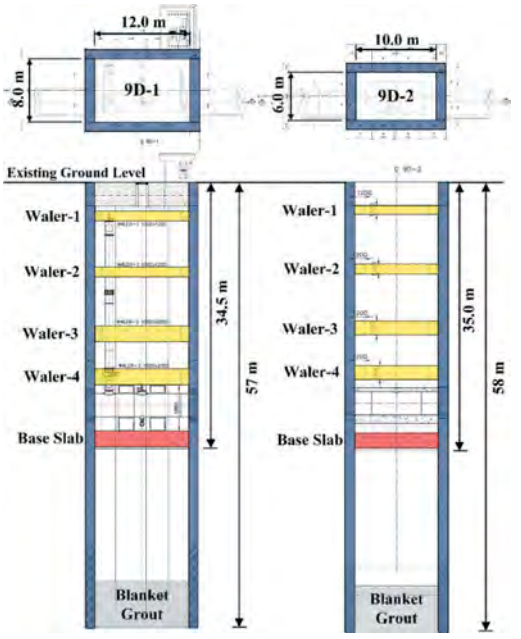

Figure 4. Cross-sections of shafts 9D-1 and 9D-2.

3 CONSTRUCTION OVERVIEW

According to the top-down construction sequences, the typical stages for excavation and construction of shafts 9D-1 and 9D-2 are represented in Figure 5, which are briefly outlined in the following sequence:

- The construction of shafts commences by excavation and casting of a 50 m-long diaphragm wall around the shaft boundary. Since the piezometric pressure in sand layer is high (approximately 230 kPa) at base slab level and may be susceptible to hydraulic uplift failure (upheaval) during excavation, therefore, TAM blanket grout is designed to create a watertight barrier at bottom of the earth retaining structure system to gain more counterweight with groundwater pressure. Moreover, joint grout within the sand layer is applied to ensure the ground water control during the excavation.
- Jet grout partition wall is constructed around the pile foundation of the existing viaduct to minimize the impacts due to the construction of shaft 9D-1 and shaft 9D-2.
- Jet grout blocks for TBM launching and receiving from both shafts are concurrently constructed. It is essential to complete jet grouting prior to commencing the top-down excavation.
- The top-down construction method is subsequentially utilized, involving a sequential excavation of soil inside the shaft area associated with the internal structure installation. It begins with the excavation of the 1st floor to a certain depth and the installation of a temporary support structure. The excavation continues to construct reinforced concrete permanent walers.
- Before reaching the final excavation level, the 2nd temporary bracing is installed due to the large span between waler-4 and the base slab.
- Final excavation is executed for base slab construction at approximately 34.0 m below the ground surface.
- The 2nd temporary bracing is removed after the completion of base slab casting to facilitate the subsequent tunnel excavation.

4 IMPACT ASSESSMENT

4.1 *Numerical model*

To address construction-related challenges and assess the impact of shaft 9D-1 and 9D-2 excavation on nearby structures, a numerical analysis has been performed by the commercial finite element software PLAXIS. Subsoil condition is referred from the borehole located in the construction site.

A three-dimensional finite element analysis (3D-FEA) is employed to simulate the rectangular shape of the shaft and the relative location of existing piles. The model size is 160 m in length and width. The bottom of the model is extended to 80 m below the ground surface corresponding to the approximated excavation depth of 34 m to ensure that the boundary effect is minimized. For the vertical boundaries, the horizontal movement is restrained. On the other hand, the movements for the bottom boundary are fixed in both horizontal and vertical directions. The mesh generation is intentionally refined in the zones around the considered structural members.

Soils are modelled as linear elastic-perfectly plastic material following the Mohr-Coulomb failure criterion. The correlation between E_u/S_u for Bangkok clay are based on the back-analysis by Phienwej (2008), Teparaksa et al. (1999), and Phienwej & Gan (2003). Likitlersuang et al. (2013) points out that the proposed correlation can be successfully used to simulate the ground movement due to the underground station excavation of the Bangkok MRT projects. Sand stiffness was estimated by using empirical correlations with the SPT-N value proposed by Stroud (1989). The FE model and parameters used in the analysis are presented in Figure 6 and Table 1, respectively.

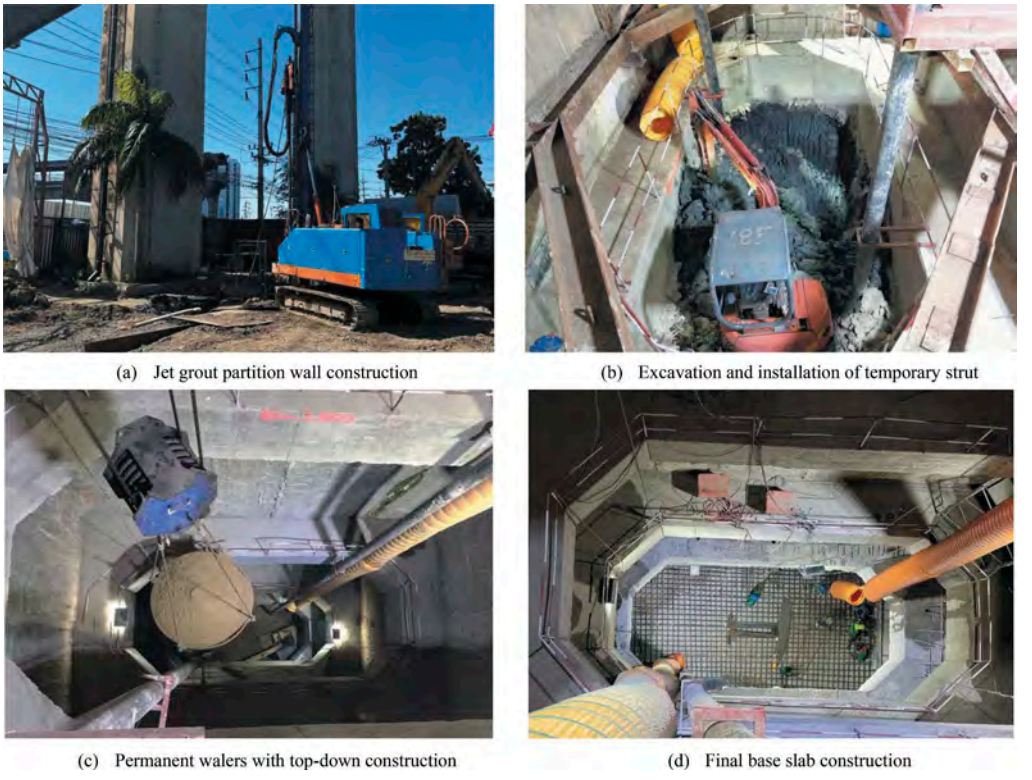

Figure 5. Shaft top-down construction.

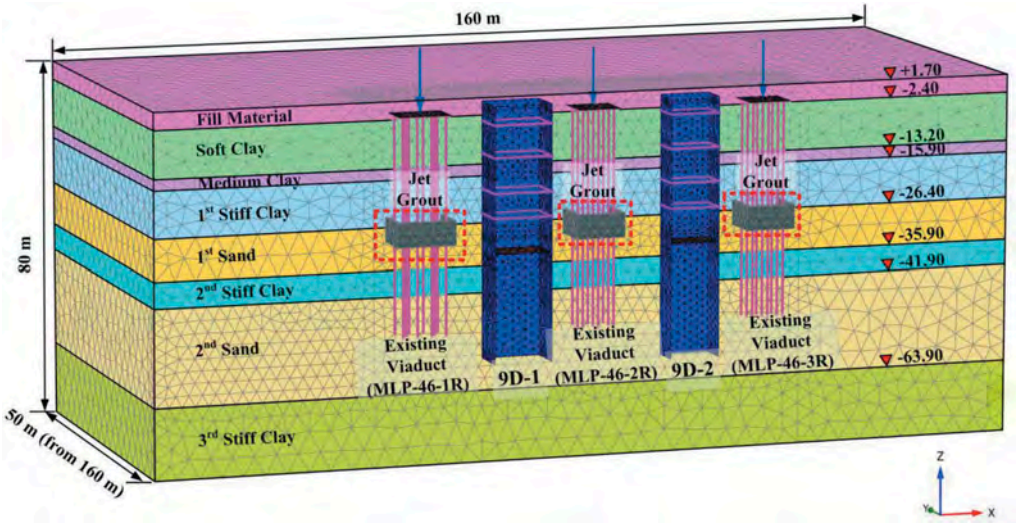

Figure 6. 3D-Finite element mesh for impact assessment analysis.

4.2 *Criteria for impact assessment*

Three important aspects are adopted to evaluate the possible impacts on the existing structures induced by ground movements during the deep excavation are as follows:

4.2.1 *Tolerable movements*

To maintain the serviceability of the existing viaduct, settlement shall be limited to under 15 mm, while the foundation tilting shall be lower than 1:500 according to the suggestion by the Building Construction Authority (BCA, 2021). The criterion for lateral

Table 1. Geotechnical parameters.

Soil Type	Elevation (MSL) Top	Bottom	γ (kN/m^3)	SPT-N (Blow/ft)	S_u (kPa)	ϕ (Deg.)	E' (kPa)	K_o
Fill	1.7	-2.4	16.0	-	25	0	10,400	0.60
Soft Clay	-2.4	-13.2	16.0	-	20	0	8,300	0.75
Medium Clay	-13.2	-15.9	17.0	-	40	0	25,000	0.71
1st Very Stiff Clay	-15.9	-21.9	20.0	26	170	0	141,600	0.68
2nd Very Stiff Clay	-21.9	-26.4	20.0	20	150	0	125,000	0.68
1st Dense Sand	-26.4	-30.9	21.0	55	-	38	110,000	0.43
2nd Dense Sand	-30.9	-35.9	21.0	10	-	43	200,000	0.43
3rd Very Stiff Clay	-35.9	-41.9	20.0	23	130	0	108,300	0.68
Very Dense Sand	-41.9	-63.9	21.0	100	-	38	200,000	0.41
Hard Clay	-63.9	-80.0	20.0	73	280	0	233,300	0.64

where γ is soil unit weight, S_u is undrained shear strength, ϕ is friction angle, E' is elastic modulus, *and* K_0 is coefficient of horizontal earth pressure.

foundation displacement and the angular distortion follows the recommendation of AASTHO Standard Specification for Highway Bridges (2002). The lateral movement is limited to under 25 mm, while the angular distortion shall be lower than 1:250.

4.2.2 *Pile structural capacity*
The additional structural forces induced along the adjacent piles shall be investigated so that the actual pile reinforcement can withstand the effect of nearby excavation. The moment-axial force interaction diagram in accordance with BS-8110 is used as a pile structural capacity.

4.2.3 *Pile geotechnical capacity*
The soil movement according to the deep excavation generally induced negative skin friction on the adjacent, which has a consequence on the axial force distribution along the pile. The mobilized negative skin friction will increase the compressive axial force in the pile (or tension in some cases). Therefore, the effect of this phenomenon will be verified if the available positive skin friction and the end bearing of the piles are sufficient to withstand the superstructure working load.

5 INSTRUMENTATION AND MONITORING

The geotechnical instrumentations are installed to observe the occurring ground movements as the construction control of excavation. The employed instrumentations as shown in Figure 7 including:

- The inclinometers installed in the diaphragm wall (INC) are used to measure the inclination of the diaphragm wall (D-wall) relative to a vertical plane.
- The inclinometers combined with extensometers (IEX) are used to monitor the movements of soil in response to changes in vertical and horizontal directions.
- Surface settlement points are used to measure and control soil movement in a vertical direction. The control values are determined based on the surface settlement near the excavation areas.
- Vibrating Wire Piezometers are used to monitor pore water pressure in soils. The control value of piezometers is set in accordance with the design piezometric profile.

Additional instrumentations are installed at the existing structures to ensure the safety and serviceability of the viaducts during the construction, as shown in Figure 7. The control values are typically set based on the allowable movements and distortion that have no adverse impacts on the existing structures. The Trigger – AAA values (Alert, Alarm and Action) of each instrumentation type are given in Table 2. Description of these devices are given below:

- Structural settlement points are used to measure the vertical movement of the existing viaduct near the excavation zone during construction.
- Tilt meters are used to measure the tilt of flyovers relative to one or two axial planes.
- Target prisms are used to measure the structural movements relative to 3 axes: vertical, horizontal, and in-plane axis, which can provide a more comprehensive understanding of the overall movements of the structure.

Table 2. AAA-Level for the Existing Structure.

Movement	AAA-Level Max 100%	Action 90%	Alert 80%	Alarm 70%
Vertical Movement	15 mm	13.5 mm	12 mm	10.5 mm
Horizontal Movement	25 mm	23 mm	20 mm	17 mm
Distortion	1:1,000	1:1,100	1:1,250	1:1,400
Foundation Tilting	1:500	1:550	1:625	1:700

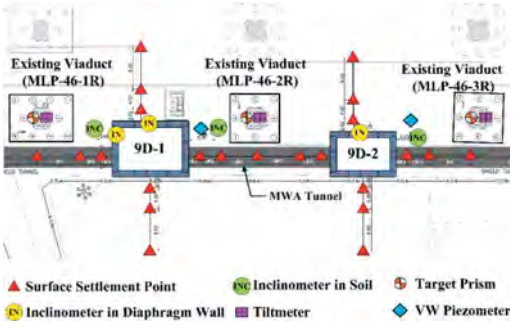

Figure 7. Instrumentation program for Shaft 9D-1 and 9D-2.

6 MONITORING RESULTS AND COMPARISONS

Figure 8 represents the corresponding lateral movements of INC monitoring in diaphragm walls and soil during construction compared to the computed results from the FE modelling. Note that, for the monitoring data, the results of only the final step (after removing the temporary steel bracing) are presented. In general, the shapes of lateral movement along the depth from the FE analysis agree well with the monitoring data, although the predicted values are smaller (particularly the INC in diaphragm wall 9D-2). This is probably due to the reason that a conservative evaluation concept has been considered.

The movements of the three adjacent piers (No. MLP-46-1R, MLP-46-2R, and MLP-46-3R) around the excavation area measured by the target prisms are depicted in Figure 9 together with the predicted results from FEA. As predicted by the computed results, insignificant settlement as well as the lateral movement of adjacent piers are presented by monitoring results. As illustrated in the figure, the maximum viaduct settlement of 2.0 mm is monitored during the shaft construction can be detected. Hence, the computed angular distortion and foundation tilting are 1:20,000 and 1:23,000, respectively. The maximum lateral foundation movement ranges between 1.0 to 3.5 mm. The observed pier movements are lower than the limiting value recommended by AASHTO (2002) and BCA (2021). Therefore, the monitoring results confirm the safety and structural stability of the excavation and existing structure, as evaluated in the impact assessment prior to the construction.

7 PILE IMPACT ASSESSMENT

Additional evaluations of the structural and geotechnical capacity of the pile were also performed. According to the comparison provided in Section 6, the 3D-FEA can be used to evaluate the effects of shaft 9D-1 and 9D-2 construction on the piles. The additional axial forces and bending moments along adjacent piles are computed and thus compared to available capacity according to the BS-8110 as illustrated in Figure 10. The values of all piles in each foundation are plotted by considering every construction stage. As the excavation process proceeds, the induced bending moments and axial forces change compared to the beginning stage. The predicted axial force-moment values in the piles represented the small change compared to the initial condition according to the relative location near the shaft corner. Moreover, the axial force-moment are enclosed within the interaction diagram, indicating that these piles have adequate structural capacity to withstand the nearby deep excavation activities.

8 CONCLUSION

This paper presents the responses of the existing viaducts in accordance with the ground movement during

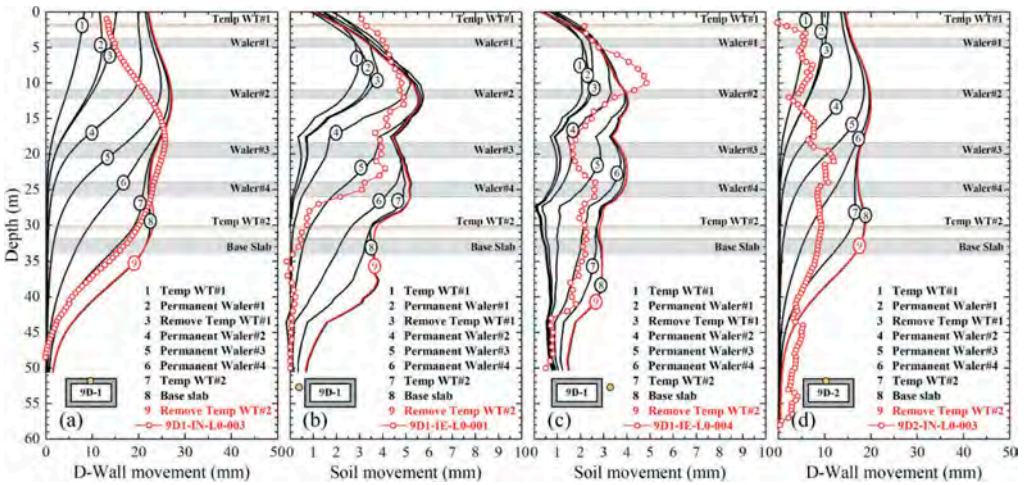

Figure 8. Comparison between monitoring and computed results of Diaphragm wall movement and lateral soil movement.

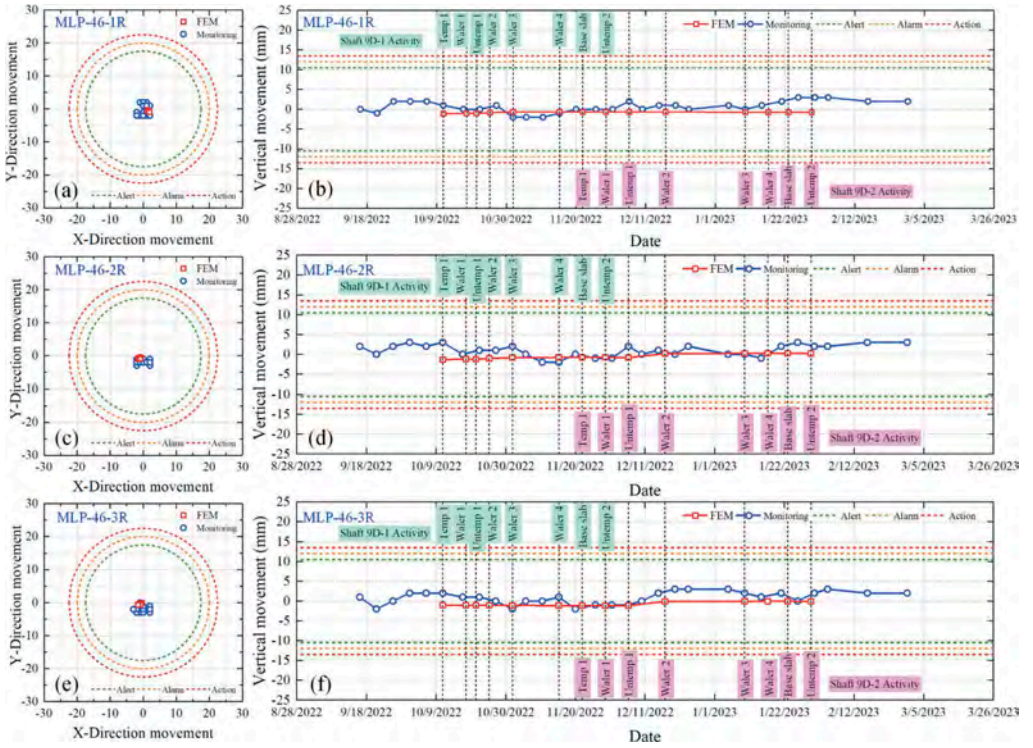

Figure 9. Comparison between monitoring and computed movements of adjacent viaducts.

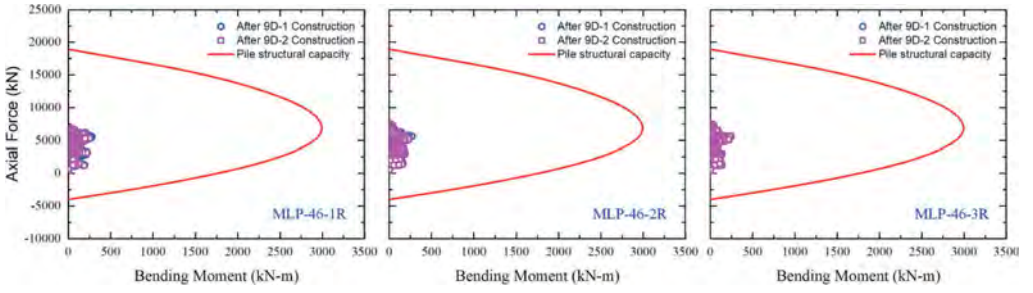

Figure 10. Development of axial force and bending moment in adjacent piles compared to available capacity.

the top-down construction of shafts in the 9th Master Plan Improvement Project of the Metropolitan Waterworks Authority (MWA). The impact assessment of the excavation of shafts 9D-1 and 9D-2 according to the G-TN-9D project on the Kanchanaphisek outer ring road viaduct is carried out. The results of the field measurement and three-dimensional finite element analysis are represented and discussed. According to this study, the following conclusions can be drawn:

1. The three-dimensional finite element analysis indicates that the impact of ground movement due to top-down excavation of shafts 9D-1 and shaft 9D-2 on the adjacent viaduct is acceptable in terms of viaduct movement, pile structural capacity and pile geotechnical capacity.
2. The predicted diaphragm wall movement and the lateral soil movement are consistently aligned with the measuring data. Moreover, the monitored vertical movement, horizontal movement and tilting of viaducts during the excavation are compatible with the finite element results. According to the criteria proposed by AASHTO (2002) and BCA (2021), their movements consistently remained within acceptable criteria, guaranteeing the safety and structural stability of the existing structure.
3. The computed results from three-dimensional numerical analysis reasonably agree well with the

field monitoring results. This reveals a suitability and practicality for adoption in future projects.

ACKNOWLEDGMENTS

The authors would like to appreciate to The Metropolitan Waterworks Authority (MWA) and CH. Karnchang Public Company Limited (CK) for their kind support.

REFERENCES

American Association of State Highway and Transportation Officials, 2002. Standard Specifications for Highway Bridges. Washington D.C., USA.

British Standards Institution, 1997. BS 8110:1997: Structural use of concrete. London, UK.

Building and Construction Authority, 2021. Framework on Performance Based Impact Assessment Associated with Earth Retaining or Stabilising Structures ("ERSS") And Tunnelling Works. Jurong East, Singapore.

Brinkgreve, R.B.J., Engin, E., Swolfs, W.M., 2013. Plaxis 3D 2013 Manual. Plaxis bv, The Netherlands.

Pheinwej, N., Gan, C.H., 2003. Characteristics of ground movement in deep excavations with concrete diaphragm walls in Bangkok soils and their prediction. Journal of the Southeast Asian Geotechnical Society. 34 (3), 167–175.

Pheinwej, N., 2008. Ground movements in station excavations of Bangkok first MRT. Proceeding of the 6th International Symposium on Tunnelling for Urban Development. Shanghai, China.

Stroud, M.A., 1989. The Standard Penetration Test – Its Application and Interpretation. Proceeding of the Geotechnology Conferences on Penetration Testing in the UK. London, UK.

Teparaksa, W., Thasnanipan, N., Tanseng P., 1999. Analysis of Lateral Wall Movement for Deep Braced Excavation in Bangkok Subsoils. Proceeding of the Civil and Environmental Engineering Conference, Bangkok, Thailand, pp. 67–76.

Taylor & Francis
Taylor & Francis Group
http://taylorandfrancis.com

Mechanized tunnelling (TBM, shield)

Taylor & Francis
Taylor & Francis Group
http://taylorandfrancis.com

Tunnelling for a Better Life – Yan, Celestino, Thewes & Eberhardt (Eds)
© 2024 The Author(s), ISBN 978-1-032-80042-4
Open Access: www.taylorfrancis.com, CC BY-NC-ND 4.0 license

Investigation of vibration patterns generated during rock cutting tests

Ugur Ates, Hanifi Copur* & Aydin Shaterpour-Mamaghani
Istanbul Technical University, Istanbul, Turkey

ABSTRACT: Tunnel boring machines (TBMs) are essential for infrastructure projects and they should be operated in accordance with the geological conditions. Thus, swiftly recognizing and adapting to geological changes plays a critical role for the excavation. In that aspect, vibrations generated during excavation by TBMs have been analysed for ground identification in various studies. However, those measurements are often complicated by numerous influencing factors and noise sources, which make it challenging to isolate the specific effects of rock cutting on vibrations. Due to this reason, there is a need for a better understanding of vibrations created during the rock cutting process under controlled environment. With this aim, laboratory rock cutting tests are realized by a full-scale linear rock cutting machine equipped with a 17-inch disc cutter and accelerometers on three different rock samples with uniaxial compressive strength values ranging from 21 to 82 MPa. Peak, root mean square (RMS), and interval RMS accelerations are calculated from the recorded vibration data and the relations between vibrations, cutting performance parameters, cutting geometry, and mechanical properties of rocks are analysed. The results reveal that there is a relationship between cutting forces (especially average and peak normal force), rock mechanical and mineralogical properties, cutting configuration and vibrations. In general, it is possible to say that the vibrations increase as penetration and rock strength increase.

Keywords: Vibration, Disc cutter, Rock mechanical properties, Full-scale linear rock cutting machine

1 INTRODUCTION

Understanding geological conditions during TBM excavation is crucial for project's success. However, most of the contractors rely on the geological data provided to them during the tendering stage or start the projects by performing additional geological surveys which can be considered as inadequate in general. During the excavation of tunnels, the best way to understand geological conditions is to check excavation face. However, continuous TBM excavation makes face inspections challenging and most of contractors are reluctant to stop excavation for face inspections unless it's deemed necessary, or forced by the contract. Another tool for understanding geological conditions ahead is probe drilling, which is generally not applied for the previously mentioned reasons. Therefore, monitoring muck and TBM operational data becomes essential, even though these methods may be interpreted inaccurately.

Vibrations generated during excavation operations, can provide valuable insights into geological conditions without the need for frequent face inspections. Several authors equipped TBMs with accelerometers and investigated vibration changes during excavation. Those accelerometers were either installed on the cutterhead (Shanahan, 2010; Huang et al., 2018; Wu et al., 2021) or behind the cutterhead (Walter et al., 2012; Walter, 2013; Mooney et al., 2014; Buckley, 2015; Hunt and Frank, 2021; Liu et al., 2021, 2022). Despite significant attention to TBM vibrations, the complexity of these machines and the multitude of factors influencing vibrations highlight the need for further comprehensive research conducted in a controlled laboratory environment.

To understand forces and vibrations generated during rock cutting several authors studied this topic. One of these researches was realized by Samuel & Seow (1984). Strain gauges were placed on the shafts of the disc cutters of a 4.1 m diameter TBM and force components acting on a disc cutter were investigated. Later, Gertsch (1993) conducted a detailed study on this area using a 17" constant cross section (CCS) disc cutter. This investigation involved frequency analyses of the forces, and it was carried out using a full-scale linear cutting machine (FLCM). Notably, these research used strain gauges rather than accelerometers to explore vibrations, which differentiates it from subsequent studies in the field. Huo et al. (2015) took a different approach by

*Corresponding author: copurh@itu.edu.tr

DOI: 10.1201/9781003495505-216

developing a dynamic multi-degree-of-freedom model for disc cutters. This model aimed to provide a deeper insight into the vibration characteristics and the transmission of loads within the cutters. Yang et al. (2020) performed laboratory tests using a Multi-Mode Boring Test System and investigated vibration characteristics of the cutterhead in soft-hard mixed strata.

In contrast to previous studies, Ates et al. (2019, 2022, 2023) and Ates and Copur (2023) conducted comprehensive and continuous measurements and analyses of TBM vibrations across multiple earth pressure balance (EPB) TBMs in three projects totalling 6 km. It was found that there was a relationship between geological conditions, TBM operational and performance parameters, and vibrations.

Three different rock block samples from a metro project site and a quarry are obtained in this study; then, full-scale linear cutting tests are performed by using a 17-inch diameter CCS disc cutter with varying line spacings and penetrations. The experimental setup includes load cells for tool force measurements and accelerometers for vibration measurements. Following the rock cutting tests, the acquired vibration data, comprising peak acceleration, root mean square (RMS) acceleration and interval RMS acceleration are correlated with cutting geometry (line spacing and penetration), cutting performance parameters (peak and mean normal, rolling and side forces, specific energy, and coarseness index), and mechanical properties of the rocks.

2 TESTING EQUIPMENT AND METHODOLOGY

A full-scale linear cutting machine (FLCM) utilized during this study, which is located at the Mining Engineering Department laboratory of Istanbul Technical University. Full-scale linear rock cutting test is widely acknowledged as one of the most reliable, cost-effective, and established methods for the selection, design, and prediction/optimization of mechanical miners' excavation performance. This approach minimizes uncertainties inherent in empirical methods and index tests (Bilgin et al., 2013). These tests involve measuring the forces acting on a cutter while it cuts a large block of rock sample encased in a sample box. The detailed information regarding FLCM is readily available in the literature (Bilgin et al., 2013; Copur et al., 2017). The machine incorporates a strain-gauge based load cell to measure the cutting tool forces. Additionally, five accelerometers, comprising both piezoelectric and MEMS types, are fixed to the various positions on the machine. They simultaneously measure and record vibrations occurring in conjunction with the cutting tool forces during the cutting tests.

A range of triaxial analog accelerometers and analog-to-digital converters are employed throughout the study for measuring/recording the vibrations. The specifications of the accelerometers are listed on the Table 1. USB-6009 and NI 9230 BNC analog-digital convertors from National Instruments are used for digitizing.

Table 1. Specifications of the accelerometers.

Manufacturer	Analog Devices	Analog Devices	PCB Electronics
Model	ADXL354BZ	ADXL356CZ	356A17
Type	MEMS	MEMS	Piezoelectric
Sensitivity (mV/g)	200	20	500
Measurement Range (±g)	4	40	10
Frequency Range (Hz)	0-1500	0-1500	0.5-3000
Internal Analog LP Filter (Hz)	1500	1500	N/A

The accelerometer placement, their identification numbers used throughout the study, and the directions of the axes are shown in Figure 1.

A specialized data recording software, tailored to the project's needs, is developed and employed for the recording of vibration data. The FLCM force data is obtained by using another dedicated software. The recorded vibration data is analysed in time and frequency domains using custom Matlab scripts and Excel macros are used for processing of vibration data.

After each cut, the length of the cut is measured, the muck is collected, weighed, and sieved. Subsequently, the rock box is laterally shifted by the specified spacing to simulate the actions of multiple cutters on the cutterhead of a mechanical excavator, and the experiment is repeated (Copur et al., 2017).

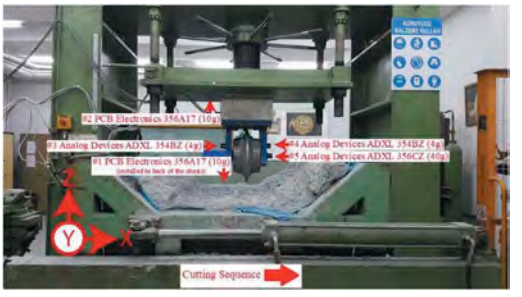

Figure 1. Locations of the accelerometers.

Single spiral pattern is used during cutting tests, and a constant-cross-section (CCS) disc cutter with a 17" diameter and an 18 mm tip width is used. The cutting speed is set at 12.7 cm/s, and the tests follow surface conditioning procedures as outlined by Copur et al. (2017). The line spacing and penetration configurations used in the tests are given in Table 2.

Table 2. Configuration of cutting tests (experimental matrix).

Formation	Siltstone	Mudstone	Marble (EC)	Marble (DC)
Line Spacing (s) (mm)	Penetration (d) (mm)			
70	5	5	-	-
	7	7	-	-
85	4	4	4	4
	6	6	6	6
	8	8	8	-
	-	10	-	-

The analysis of the collected vibration data involves various time-domain data analysis techniques, which include quantitative statistical methods. The initial phase of the analysis involves evaluating the data through time history graphs that show acceleration data alongside cutting parameters such as normal, rolling, and side forces. During this stage, the video recordings are used to identify the causes of specific vibration and cutting force peaks. Following this initial analysis, root mean square (RMS) and interval RMS accelerations are calculated. It's important to note that, since there are typically at least three cuts performed for each line spacing and penetration setting, the results are averaged to create a representative value for each configuration across all rock samples.

Vibration data is collected in the time domain; however, to gain a more comprehensive understanding of the frequency components of the signals, it can be beneficial to transform the data into the frequency domain. This transformation is achieved through a Fast Fourier Transform (FFT). It's important to note that the analyses show rock cutting generates broadband signals that are challenging to interpret directly in the frequency domain. Despite this, spectrograms and waterfall FFT plots are employed to examine the frequency content of the signals. Spectrograms are graphical representations that depict how acceleration signals vary concerning both time and frequency. They are particularly helpful in identifying the timing of specific activities within the recorded data (Rogers et al., 1997; Hanly, 2016).

3 ROCK SAMPLES

This study utilizes two rock blocks, mudstone from the Pendik Formation and siltstone from the Kurtkoy Formation, both obtained from the Goztepe-Umraniye -Atasehir Metro Line project site. Additionally, a beige marble sample from a quarry is included in the full-scale linear rock cutting tests. These rock samples exhibit various properties and characteristics. It's worth noting that the mudstone and siltstone samples had bedding planes, whereas the beige marble sample did not. The cutting direction is parallel to the bedding planes for mudstone and 45° angled for siltstone, as illustrated in Figure 2. The photos of the samples are shown on Figure 3.

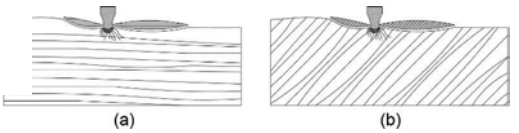

Figure 2. Bedding planes (a for siltstone and b for mudstone).

Pendik Formation (Mudstone): The rock sample is from the Pendik Formation's Kartal Member. The formation shows intercalation of micaceous shales, mudstones, and siltstones with rare micaceous sandstone of 5-10 cm thickness and bioclastic limestone (thickness of 5 - 10 cm to 40 - 50 cm) at various ratios. Frequently, the shales are severely altered/weathered along discontinuities and outcrops (Geodata Engineering S.p.A., 2016). The sample used during the rock-cutting tests belongs to mudstone units.

Kurtkoy Formation (Siltstone): Bakacak Member (Opkb) of the Kurtkoy Formation is dominant in the area where the rock block is obtained, and the lithology is composed of thin to medium bedded, parallel, and cross-laminated siltstone and sandstone. The lower parts show purple to brown colour banding; upwards in the sequence the purple colour becomes dominant and the grain size increases. Arcosic sandstones, conglomerates, and siltstones dominate within the Sureyyapasa Member (Geodata Engineering S.p.A., 2016).

Beige Marble (Sparitic Limestone): The Beige Marble sample was not homogenous in terms of strength and cuttability features. It was observed that one side of the sample was more difficult to cut during the FLCM tests than the other side. Thus, the data is evaluated in two different sections, which are difficult cuttability (DC) and easy cuttability (EC).

To better understand the distinction between the easy and difficult cuttability sections, petrographic analyses are performed on the thin sections. The ratio of intraclasts to pellets is observed to be the most significant difference between the two samples, as the intraclast ratio rises, the rock gets more difficult to cut and requires a greater tool force. It is also observed that the smaller pellet size requires a greater tool force.

Difficult cuttability section (DC): This section is described as "Fossilized Intra Pel Sparite or Fossilized Pel Intra Sparite". It includes sparitic cemented limestone, which consists of intraclasts, pellets (35-40%), and a slight number of fossils. Intraclastic parts are composed of micritic limestone fragments. It is mostly fractured with calcite fillings. Pellet size is between 0.1 and 0.4 mm.

Easy cuttability section (EC): This section is described as "Fossilized Intra Pel Sparite". Sparitic

cemented limestone includes more calcite fillings than the other section (DC). Pellets are larger in size (0.3-0.6 mm) and occupy more space (50%). Intraclast ratio is lower, while pellet size is bigger compared to difficult cuttability section. It includes a slight number of microfossils. It is mostly fractured with calcite fillings.

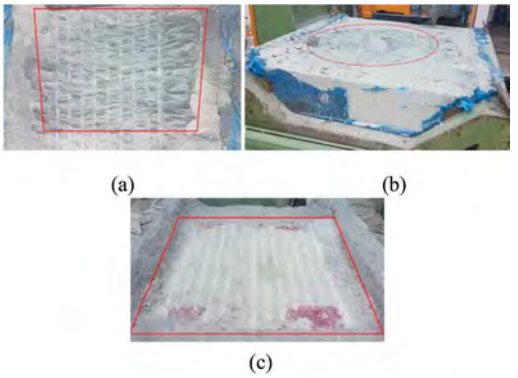

Figure 3. Photos of the rock samples (a for mudstone and b for siltstone and c for beige marble).

4 RESULTS OF ROCK CUTTING TESTS

The physical and mechanical properties of the rock samples are summarized in Table 3 and a total of 55 cutting tests were into consideration. As the difficult cuttability section of the beige marble sample had very high cutting forces, only 4 mm and 6 mm penetration values are applied to this section. Due to the limited rock sample size, the tests with 70 mm line spacing are not performed for the beige marble sample.

The rock cutting tests revealed that the difficult cuttability section of the beige marble required higher cutting forces; however, uniaxial compressive strength values for both the easy and difficult cuttability sections were not significantly different from each other. This observation suggests that the petrographic characteristics of the rocks have a substantial influence on their cutting behaviour.

Figure 4 shows that both average normal (a) and average rolling forces (b) increase with increasing penetration, as expected based on rock cutting science. Beige marble's difficult cuttability (DC) section requires a greater average normal force across all penetrations compared to the other rocks, while its easy cuttability (EC) section requires the lowest normal force. However, in contrast to the normal force, it's worth noting that the siltstone sample exhibits the highest average rolling force when the line spacing is 85 mm.

The correlation between specific energy and line spacing to penetration ratio is shown in Figure 4(c). The mudstone and beige marble (EC) exhibit an optimal S_L/p ratio of approximately 11, whilst the siltstone and beige marble (DC) demonstrate an optimal ratio of 14. However, to obtain a more accurate assessment of the optimal S_L/p ratio for the difficult cuttability section of beige marble, it is preferable to include at least one additional data point.

It is imperative to note that the normal force is typically correlated with the uniaxial compressive strength of the rock; however, the findings do not exhibit a similar pattern. Furthermore, the beige marble's difficult cuttability section requires higher tool forces than the easy cuttability section, although it is worth mentioning that the uniaxial compressive strength values of both sections do not display a substantial disparity. These results demonstrate

Table 3. Geomechanical properties of the tested rocks.

	Siltstone (Kurtkoy Formation)	Mudstone (Pendik Formation)	Beige Marble (EC)	Beige Marble (DC)
Density (gr/cm3)	2.73	2.52	2.68	2.69
Uniaxial Compressive Strength (MPa)	46.50	21.55	81.58	77.57
Indirect Tensile Strength (MPa)	6.94	4.95	5.83	6.51
Static Poisson's Ratio	0.31	0.11	0.19	0.11
Dynamic Poisson's Ratio	0.32	0.08	0.16	N/A
Static Elastic Modulus (GPa)	14.52	4.93	26.34	19.97
Dynamic Elastic Modulus (GPa)	29.38	19.33	17.29	17.03
P-Wave Velocity (m/s)	3903	2744	2695	2517
S-Wave Velocity (m/s)	2022	1850	1672	1784
Schmidt Hammer Hardness (L Type)	32.95	23.11	39.42	41.03
Shore Sclerescope Hardness	53.2	31.2	48.6	52
Brittleness (B1)[1] (by Hucka and Das, 1974)	6.62	4.35	13.99	11.91
Brittleness (B2)[2] (by Andreev, 1995)	0.73	0.62	0.86	0.84

[1] $B1 = \sigma_c/\sigma_t$ by Hucka and Das (1974)
[2] $B2 = (\sigma_c - \sigma_t)/(\sigma_c + \sigma_t)$ by Andreev (1995)

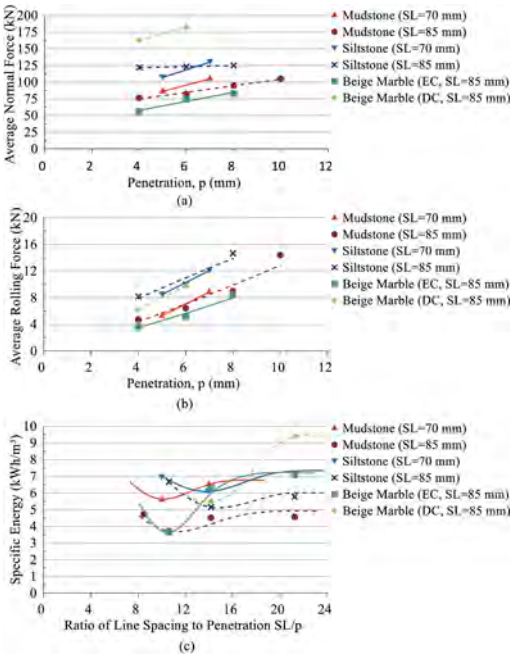

Figure 4. Variations of average normal force (a) and average rolling force (b) with penetration, and specific energy with S_L/p ratio (c).

that the petrographic characteristics of rocks have a significant impact on their cutting properties.

It is imperative to note that the normal force is typically correlated with the uniaxial compressive strength of the rock; however, the findings do not exhibit a similar pattern. The beige marble's difficult cuttability section requires higher tool forces than the easy cuttability section, although the uniaxial compressive strength values of both sections do not display a substantial disparity. These results demonstrate that the petrographic characteristics of rocks have a significant impact on their cutting properties.

5 RELATIONSHIPS BETWEEN CUTTING CONFIGURATION, CUTTING PERFORMANCE AND ACCELERATIONS

Following the investigation of the relationships between penetration, average rolling force, average normal force and interval RMS accelerations it was found that a general trend exists; vibrations tend to increase as these variables increase for all rock types (Figure 5). However, a notable exception is seen with siltstone at a line spacing of 85 mm, where vibrations decrease as the average normal force increases, which could be related with siltstone sample's bedding angle. Even the relationships can be categorized as moderately strong for normal force and weak for rolling force, by taking all data into consideration best fit lines are calculated and, equations (Equations 1 and 2) are presented for predicting the forces by utilizing the accelerations.

$$FN = 121.78RMS_{int} + 77.24 \quad (R^2 = \cdot 0.53) \qquad (1)$$

$$FR = 7.35RMS_{int} + 6.59 \quad (R^2 = \cdot 0.20) \qquad (2)$$

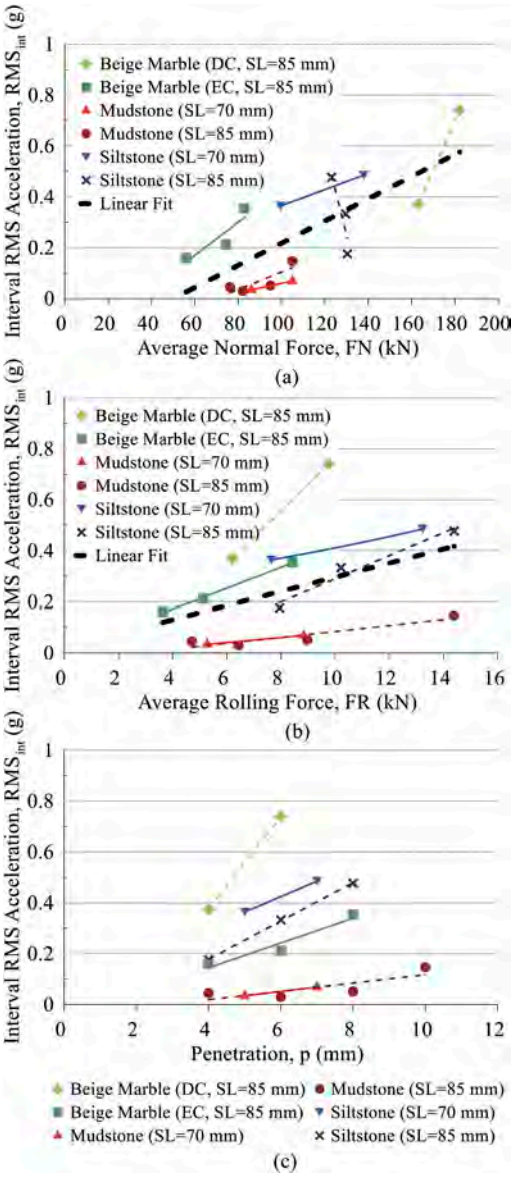

Figure 5. Variation of interval RMS acceleration with average normal force (a), average rolling force (b) and penetration (c).

As the forces also increase with penetration, it is possible assume that penetration is the major variable effecting the vibrations in terms of cutting parameters.

Figure 6 illustrates the relationships between interval RMS accelerations and peak forces, indicating another clear trend of increased vibrations with higher force values. These relationships can be categorized as strong for peak normal force and moderately strong for peak rolling force. The equations (Equations 3 and 4) are presented to formulize the relationship between interval RMS acceleration and peak normal force, providing a quantitative representation of this correlation.

$$F'N = 171.43RMS_{int} + 133.12\ (\mathrm{R}^2 = \cdot 0.74) \quad (3)$$

$$F'R = 22.58RMS_{int} + 13.04\ (\mathrm{R}^2 = \cdot 0.57) \quad (4)$$

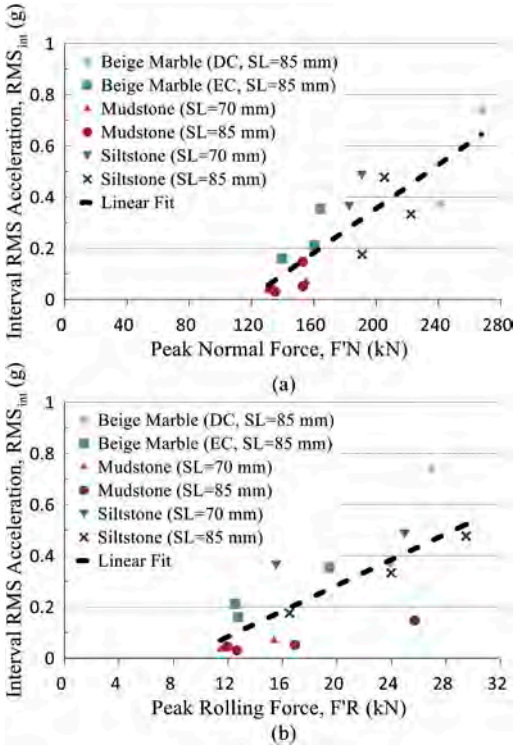

Figure 6. Variation of interval RMS acceleration with peak normal force (a) and peak rolling force (b).

Since the tunnelling machinery needs to withstand constant vibrations, this information is also particularly important and together with the tool force data, can be used during the design stage. If the vibration measurements become an integral part of the FLCM, together with force data, vibration data could also be provided to the related parties during the design stage.

Figure 7 presents the relationship between interval RMS acceleration values and chip size over 25 mm as a percentage of the total, as well as the coarseness index normalized by penetration. The relationships between interval RMS acceleration and coarseness index are not strong thus they are not presented; however, correlations are clearer for chip size >25 mm (Figure 7a) and coarseness index/penetration ratio. In simpler terms, when larger chips break off from the rock during cutting, it leads to higher tool forces and subsequently, greater vibrations. This observation aligns with video recordings that indicate vibrations occur when significant chips detach from the rock. Additionally, correlations with the coarseness index normalized by penetration are clearer, emphasizing the importance of chip size in understanding vibration dynamics during rock cutting. The relationship between interval RMS and chip size percentage over 25 mm are presented in Equation 5.

$$Chip\ Size\ (\%) > 25mm = 34.52\ RMS_{int} + 8.57\ (\mathrm{R}^2 = \cdot 0.32) \quad (5)$$

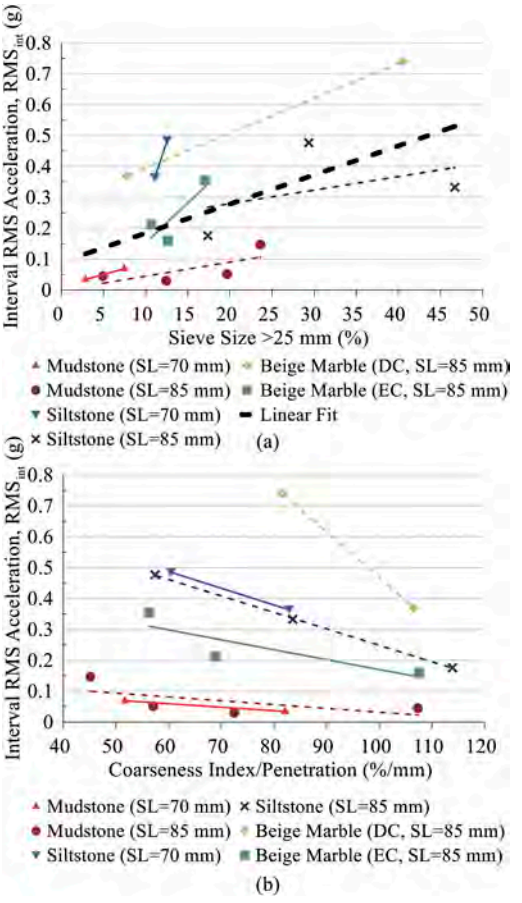

Figure 7. Variation of interval RMS acceleration with sieve size (>25 mm) (a) and coarseness index/penetration (b).

The study reveals that maximum accelerations during rock cutting increase as peak forces rise, and there is a moderately strong correlation between

these values exists. Typically, peak forces occur just before a significant chip breaks off from the rock, resulting in the generation of high-amplitude vibrations during this break-off process. This phenomenon explains the observed moderately strong relationships between peak forces and maximum accelerations, highlighting the influence of cutting forces on vibration amplitudes during rock excavation. Through the conducted analyses, Equations 6 and 7 are derived, which can be used for real-time prediction of peak normal and peak rolling forces by using the real-time measurements of maximum acceleration.

$$F'N = 5.85\text{Max.Acc} + 130.06 \ (R2 = 0.69) \quad (6)$$

$$F'R = 0.79\text{Max.Acc} + 12.46 \ (R2 = 0.56) \quad (7)$$

It is also found that maximum acceleration varies with penetration, and a general trend that suggests an increase in maximum acceleration as penetration levels rise. Penetration is considered a crucial parameter in TBM design, along with line spacing. Having knowledge of the maximum vibrations at specific penetration levels can provide valuable insights during the design phase, helping engineers and designers optimize TBM performance and component durability to withstand varying levels of vibration.

6 RELATIONSHIPS BETWEEN ACCELERATIONS AND ROCK STRENGTH

The primary aim of this study is to investigate the influence of rocks' mechanical properties on the vibrations generated during rock cutting. To achieve this, the interval RMS acceleration and maximum acceleration values are compared with the mechanical properties of the rocks. The samples tested at the same line spacing and penetration values are represented together in graph forms to investigate the effect of the rock's geomechanical properties on vibrations. It's important to note that the difficult cuttability section of the beige marble sample was only tested at 85 mm line spacing with varying penetration values of 4 mm and 6 mm (results for 8 mm penetration values are not available for this sample).

The impact of selected mechanical properties on vibration levels is visually presented in Figure 8 for interval RMS accelerations. Due to space constraints the figures showing maximum acceleration values are not presented, however, they follow similar trends. Although the coefficients of determination exhibit a wide range, indicating varying degrees of correlation from low to very strong, a general trend can be observed: as the rock's strength increases, vibrations tend to increase as well.

This trend is noticeable in mechanical properties such as uniaxial compressive strength, Schmidt hammer hardness, Shore scleroscope hardness, indirect tensile strength, dynamic elasticity modulus, dynamic Poisson's ratio, and brittleness (both B1 and B2, as listed in Table 3). However, static Poisson's ratio and P and S wave velocities do not show clear trends. It's important to emphasize that the strength of these correlations varies across different mechanical properties. For instance, Schmidt hammer hardness demonstrates moderately strong correlations with interval RMS accelerations, while uniaxial compressive strength (UCS) has a lower R^2 value of 0.52 (for SL = 85 mm, p = 4 mm).

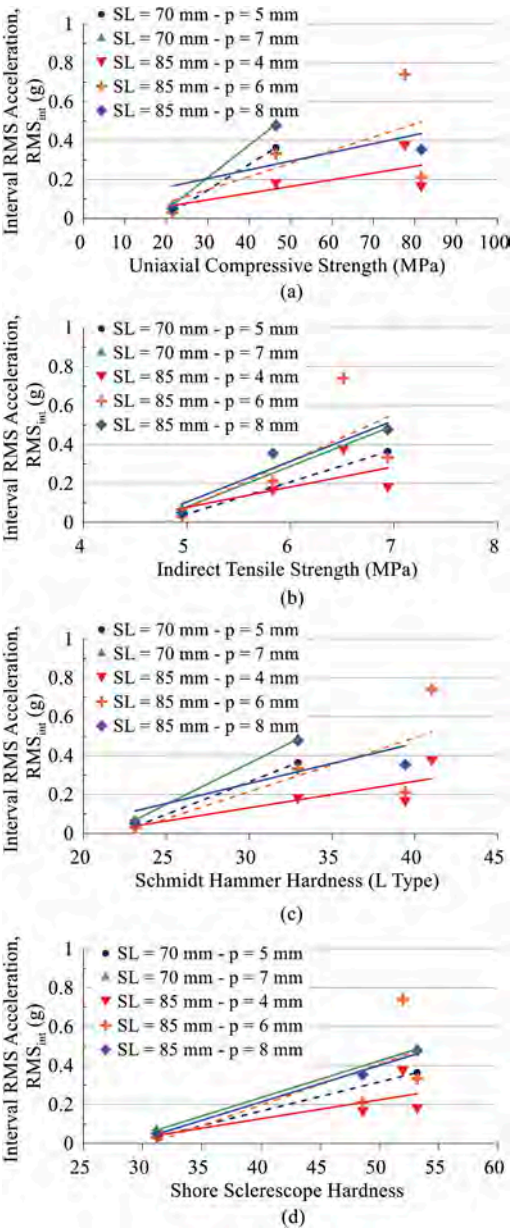

Figure 8. Variations of interval RMS acceleration with uniaxial compressive strength (a), tensile strength (b), Schmidt hammer hardness (c), Shore Sclerescope hardness (d).

Moreover, variations are observed between different penetration levels. Tensile strength and interval RMS accelerations, for example, have R^2 values of 0.49, 0.45, and 0.90 for 4 mm, 6 mm, and 8 mm penetration values, respectively. These findings align with previous studies and site observations, particularly with Ates and Copur (2023). Furthermore, it's worth noting that vibration levels tend to increase with higher penetration values for the same line spacing.

7 CONCLUSIONS

The study highlights the significant influence of cutting configuration, cutting performance parameters, rock mechanical properties, and mineral composition on vibration levels recorded during full-scale linear rock cutting tests. In general, it is observed that vibrations and forces tend to rise with increasing rock strength. Strong correlations are identified between peak normal force, interval RMS and maximum accelerations. As penetration increases, both tool forces and vibration levels increase.

Preliminary equations are provided for real-time prediction of tool forces (average and peak) based on acceleration measurements (both interval RMS and maximum acceleration). As these forces are related with the rock mechanical properties, rock strength can also be predicted during TBM operations, in especially locations where rock samples are difficult to obtain, by using the accelerations if a large database is created.

The analysis reveals that vibration shocks, with accelerations reaching up to 20g, occur after a significant rock chip breaks off, and the magnitude of these shocks is influenced by rock strength and cuttability.

The frequency content of the vibration signal is broadband, and vibrations can decrease as the tool force decreases, indicating stress relief in the rock during chipping.

Understanding expected vibration levels is crucial for TBM and component design, making vibration measurements an important aspect of full-scale linear cutting tests that can provide valuable insights for machine manufacturers.

For future studies, expanding the number of full-scale linear cutting tests would enhance the understanding of the relationships between rock properties, cutting configuration, cutting performance, and vibrations. It is recommended to use accelerometers with a measurement range of at least 20g due to the high amplitude vibrations observed in rock cutting.

ACKNOWLEDGMENTS

This paper presents a part of Ugur Ates' PhD studies. The authors are grateful to Gulermak-Nurol-Makyol Metro Construction J.V for providing rock samples, and Istanbul Technical University for providing fund within the scope of a Project numbered MDK-2017-40698.

REFERENCES

Andreev, G.E, 1995. Brittle failure of rock materials: Test results and constitutive models. A.A. Balkema, Rotterdam.

Ates, U., Copur, H., Mamaghani, A.S., Avunduk, E., Binen, I.S., 2019. Investigation of vibration patterns occurred during TBM excavation and rock cutting tests. In: Aydan, Ö., Ito, T., Seiki, T., Kamemura, K., Iwata, N. (Eds.), Proceedings of 2019 Rock Dynamics Summit, 7–11 May, Okinawa, Japan, pp. 704–709.

Ates, U., Copur, H., Kara, F. Cinar, M., 2022. Investigation of the vibration patterns generated during TBM excavation. World Tunnel Congress 2022, Denmark-Copenhagen.

Ates, U., Copur, H., Mamaghani, A. S., Aymir, M. E., 2023. Investigation of vibration patterns generated during rock cutting tests and TBM excavation. World Tunnel Congress 2023, Athens-Greece.

Ates, U., Copur, H., 2023. Investigation of parameters affecting vibration patterns generated during excavation by EPB TBMs. Tunnelling and Underground Space Technology, 138, 105185. https://doi.org/10.1016/j.tust.2023.105185

Bilgin, N., Copur, H., Balci, C., 2013. Mechanical excavation in mining and civil industries. CRC press.

Buckley, J., 2015. Monitoring the vibration response of a tunnel boring machine: Application to real time boulder detection. M.Sc. Thesis. Colorado School of Mines, USA.

Copur, H., Bilgin, N., Balci, C., Tumac, D., Avunduk, E., 2017. Effects of different cutting patterns and experimental conditions on the performance of a conical drag tool. Rock Mechanics and Rock Engineering, 50 (6), 1585–1609.

Geodata Engineering S.p.A., 2016. Final project services work of Ümraniye-Ataşehir-Göztepe Railway System Line, Preparatory Studies and Ground Site Investigation Final Design Phase - Report 2B2, Site, Laboratory and Geological & Geotechnical Studies Interpretative Report.

Gertsch, R. E., 1993. Tunnel boring machine disk cutter vibrations, M.Sc. Thesis. Colorado School of Mines, USA.

Hanly, S., 2016. Shock & Vibration Testing Overview eBook

Huang, X., Liu, Q., Liu, H., Zhang, P., Pan, S., Zhang, X., Fang, J., 2018. Development and in-situ application of a real-time monitoring system for the interaction between TBM and surrounding rock. Tunnelling and Underground Space Technology. 81, 187–208.

Hucka, V., Das, B., 1974. Brittleness determination of rocks by different methods. Int. J. Rock Mech. Min. Sci., 11, 389–392. https://doi.org/10.1016/0148-9062(74)91109-7

Hunt, S.W., Frank G.R., 2021. Abrasivity and cutter life assessment for TBM tunneling in cobbles and boulders. Rapid Excavation and Tunneling Conference 2021 Proceedings, SME.

Huo, Jz., Sun, Xl., Li, Gq., Li, T., Sun, W., 2015. Multi-Degree-Of-Freedom coupling dynamic characteristic of TBM disc cutter under shock excitation. Journal of Central South University. 22 (9), 3326–3337. https://doi.org/10.1007/s11771-015-2873-3

Liu, M., Liao, S., Yang, Y., Men, Y., He, J., Huang, Y., 2021. Tunnel boring machine vibration-based deep learning for the ground identification of working faces. Journal of Rock Mechanics and Geotechnical Engineering. 13(6), 1340–1357. https://doi.org/10.1016/j.jrmge.2021.09.004

Liu, M. B., Liao, S. M., Men, Y. Q., Xing, H. T., Liu, H., Sun, L. Y. 2022. Field monitoring of TBM vibration during excavating changing stratum: patterns and ground identification. Rock Mechanics and Rock Engineering. 55(3), 1481–1498.

Mooney, M., Walter, B., Steele, J., Cano, D., 2014. Influence of geological conditions on measured TBM vibration frequency. In: Davidson, G., Howard, A., Jacobs, L., Pintabona, R., Zernich, B. (Eds.), North American Tunneling 2014 Proceedings, Society for Mining, Metallurgy & Exploration, Englewood, USA (2014), pp. 32–41.

Rogers, M. J. B., Hrovat, K., McPherson, K., Moskowitz, M. E., Reckart, T., 1997. Accelerometer data analysis and presentation techniques. NASA Technical Memorandum, 113173.

Samuel, A. E., Seow, L. P., 1984. Disc force measurements on a full-face tunnelling machine. International Journal of Rock Mechanics and Mining Sciences & Geomechanics Abstracts. 21 (2), 83–96. https://doi.org/10.1016/0148-9062(84)91176-8

Shanahan, A., 2010. Cutter instrumentation system for tunnel boring machines. North American Tunneling 2010 Proceedings, 110–115.

Yang, Z., Pan, D., Zhou, J., Chen, J., Sun, Z., Liu, H., 2020. Vibration characteristics of cutter-head in soft-hard mixed stratum: an experimental case study on Su'ai Tunnel. KSCE Journal of Civil Engineering. 24 (4), 1338–1347.

Walter, B., Alavi-Gharahbagh, E., Frank, G., DiPonio, M., Mooney, M., 2012. Extending TBM reliability by detecting boulders. In North American Tunneling Conference, Indianapolis, IN.

Walter, B.W., 2013. Detecting changing geologic conditions with tunnel boring machines by using passive vibration measurements. PhD Thesis. Colorado School of Mines, USA.

Wu, F., Gong, Q., Li, Z., Qiu, H., Jin, C., Huang, L., Yin, L., 2021. Development and Application of Cutterhead Vibration Monitoring System for TBM Tunnelling. International Journal of Rock Mechanics and Mining Sciences. 146, 104887.

Tunnelling for a Better Life – Yan, Celestino, Thewes & Eberhardt (Eds)
© 2024 The Author(s), ISBN 978-1-032-80042-4
Open Access: www.taylorfrancis.com, CC BY-NC-ND 4.0 license

Bio-polymer sodium alginate application as an eco-friendly additive in slurry TBM excavation

Abraham Bae*
Civil and Environmental Engineering, Korea University, Seoul, South Korea

Young Jin Shin
Hyundai Engineering and Construction, Seoul, South Korea

Yongjoon Choe
Civil and Environmental Engineering, Georgia Tech. University, Atlanta, USA

Sangwoo Kim & Hangseok Choi
Civil and Environmental Engineering, Korea University, Seoul, South Korea

ABSTRACT: The objective of this study is to assess the applicability of sodium alginate, a bio-polymer, as an eco-friendly additive for maintaining face stability during the excavation of slurry Tunnel Boring Machine (TBM). The performance of sodium alginate was compared to that of Carboxymethyl Cellulose (CMC), a conventional polymer additive. Performance evaluation included measuring water loss infiltration quantity, filter cake thickness, and viscosity. Both additives were prepared by mixing with bentonite slurry liquid. To investigate the impact of seawater infiltration during excavation, both additives were evaluated under various concentrations of sodium chloride (NaCl) in the slurry liquid. Sodium alginate exhibited water loss quantities and filter cake thickness equivalent to CMC at practical NaCl concentrations. The concentration of NaCl was found to have no significant effect on the performance of either sodium alginate or CMC. The results indicate that sodium alginate has the potential to maintain face stability against seawater infiltration at practical NaCl concentrations. Increasing the quantity of sodium alginate reduces water loss and increases filter cake thickness. Based on the initial assessments conducted in this study, it can be concluded that sodium alginate is a viable and eco-friendly material for preserving face stability.

Keywords: bio-polymer, sodium alginate, eco-friendly, TBM, CMC

1 INTRODUCTION

In recent years, there has been a consistent increase in excavation work within urban areas in South Korea, Singapore, Hong Kong, and other Asian countries as part of infrastructure construction projects, encompassing civil, architectural, and plant development. Particularly, the use of Tunnel Boring Machines (TBMs) has been remarkable growth in urban aeras in South Korea. Among the various tasks involved in TBM excavation, ensuring face stability is of utmost importance. In slurry-type TBM tunnelling, stability is typically achieved by utilizing bentonite slurry (Min et al., 2015), often requiring the use of polymer additives to maintain viscosity (Chen et al., 2023).

To address the imperative of reducing carbon emissions, the global construction industry is increasingly focusing on substituting conventional construction materials with eco-friendly alternatives. In slurry TBM excavation, most additives employed to maintain face stability are chemically synthesized polymers (Amorim et al., 2007; Taheri and El-Zein, 2023). However, the use of these materials for natural ground and rock can potentially lead to adverse environmental consequences.

Sodium alginate, derived from brown seaweeds, is an eco-friendly bio-polymer. It possesses notable characteristics, including a high degree of hydrophilicity, the ability to form gels, and biodegradability. This eco-friendly material has been already applied in various industries (Wang et al., 2014; Kaneko et al.,

*Corresponding author: abebae@korea.ac.kr

DOI: 10.1201/9781003495505-217

1998). Specially, sodium alginate has been used in combination with bentonite for the decolorization of basic dyes (Mcyotto et al., 2020). Recently, in the infrastructure sector, sodium alginate's applicability has been explored in soil improvement and purification (Soltani et al., 2021; Liu et al., 2023).

This study investigates the potential of sodium alginate as a replacement for conventional polymer additives in bentonite slurry liquid used for maintaining the face stability during slurry TBM excavation.

2 SODIUM ALGINATE AS BIO-POLYMER

Sodium alginate is a bio-polymer extracted from seaweeds such as kelp and wakame. Notably, its production process results in a significant reduction in carbon emissions, making it an environmentally friendly material. This highly hydrophilic polymer electrolyte easily dissolves in water (Wang et al., 2014). In the food industry, it serves as a stabilizer in dairy products and is employed to enhance adhesiveness and viscosity. The characteristics of sodium alginate are summarized in Table 1.

Table 1. Characteristics of Sodium Alginate.

Variables	Contents
Basic Characteristics	- White to pale yellow in color - Granular in form - Odorless and tasteless - Possessing high absorbent properties
Chemical Form	$(C_6H_7O_6Na)_n$
pH	6 ~ 8
Viscosity	Barely changes in viscosity in solutions below 80°C
Applications in Industries	- Ice cream stabilizer - Thickener for ketchup and mayonnaise - Microcapsule and drug tables - A film and gel-forming agent

3 METHOD

To evaluate the performance of sodium alginate, three tests were conducted: water loss, filter cake thickness, and viscosity. Figure 1(a) is a filter press tester capable of measuring water loss infiltration volume and filter cake thickness. Figure 1(b) is a viscometer used to determine the viscosity of bentonite slurry liquid with a polymer additive.

These tests were typically conducted on bentonite slurry liquid before activating TBM excavation. Carboxymethyl Cellulose (CMC) was used as a comparative additive, as CMC is commonly employed in slurry TBM operations. Both Sodium Alginate and CMC were mixed with a 30 g/L concentration of bentonite slurry solution, which is typical for TBM operations. In excavations affected by seawater, it becomes crucial to assess the impact of sodium chloride (NaCl). Therefore, test solutions were prepared by varying the ionized concentration (IC) from 0 to 0.5 M. Furthermore, the effect of the quantity of sodium alginate was examined by varying it from 0 to 20 g/L. Table 2 summarizes the experimental variables.

(a) Filter Press Tester (b) Viscometer

Figure 1. Test Devices.

Table 2. Experimental Variables.

Variables	Contents	Cases
Additive Types	Sodium Alginate, Carboxymethyl Cellulose	2
Concentration of Bentonite Slurry	30 g/L	1
NaCl Concentration	0, 0.001, 0.005, 0.01, 0.1, 0.5 g/L	6
Quantity of Sodium Alginate	0, 1, 2, 5, 10, 20 g/L	6
Performance Test	Water Loss Infiltration Filter Cake Thickness Yield Stress (Viscosity Test)	3

4 RESULTS

4.1 *NaCl concentration effects*

Figure 2 presents the results of water loss and filter cake thickness tests concerning NaCl concentration. Sodium alginate was found to yield water loss volume and filter cake thickness equivalent to those obtained using the conventional additive, CMC. This trend remained consistent within the range of zero to 0.1 M of NaCl concentration. This result suggests that sodium alginate has a potential to maintain face stability against practical seawater infiltration during TBM excavation. Note that 0.5 M NaCl concentration is similar to that of seawater.

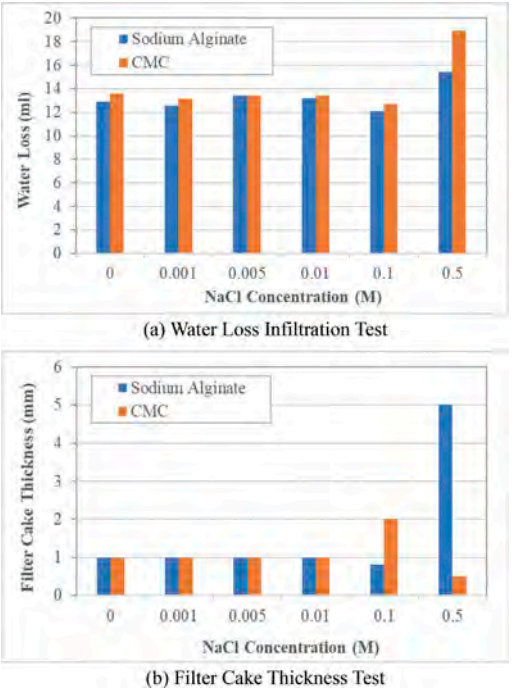

(a) Water Loss Infiltration Test

(b) Filter Cake Thickness Test

Figure 2. Filter Press Test as to NaCl Concentrations.

Figure 3 shows yield stress values obtained from the viscosity tests for both sodium alginate and CMC. In the NaCl concentration range of zero to 0.01 M, both sodium alginate and CMC demonstrated consistent yield stress values, although CMC exhibited slightly higher yield stress values than sodium alginate. However, at a NaCl concentration of 0.01 M or higher, both sodium alginate and CMC showed a sharp decrease in yield stress. Notably, at the highest NaCl concentration, sodium alginate exhibited a higher yield stress than CMC.

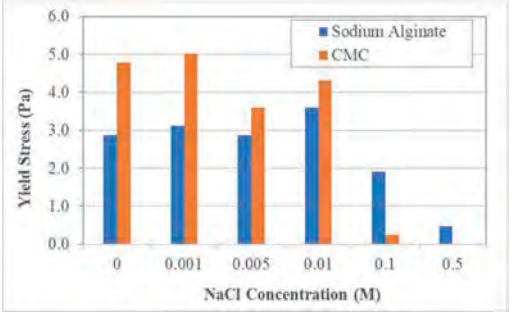

Figure 3. Yield Stress Corresponding to NaCl Concentrations.

4.2 *Sodium alginate quantity effects*

Figure 4 presents the results of water loss and filter cake thickness tests in relation to the quantity of sodium alginate. As the dosage of sodium alginate increased, the water loss volume gradually degreased, and filter cake thickness increased. Note that the application of only 1 g/L of sodium alginate significantly reduced water loss volume. This demonstrates the effectiveness of sodium alginate, a bio-polymer, in maintaining the face stability of slurry TBM.

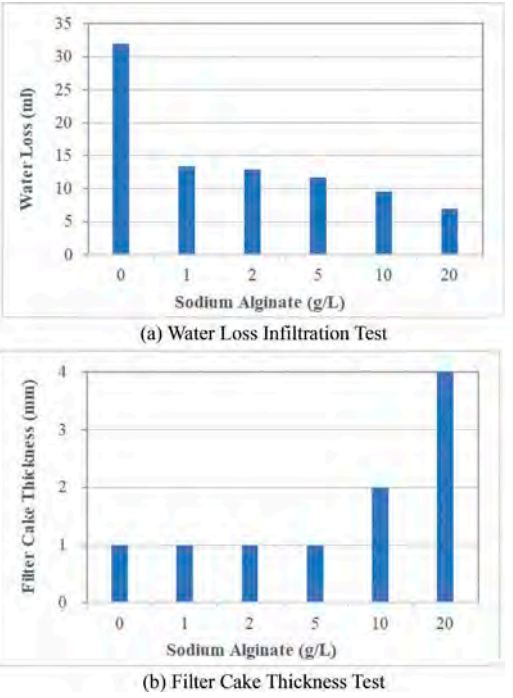

(a) Water Loss Infiltration Test

(b) Filter Cake Thickness Test

Figure 4. Filter Press Test with Sodium Alginate Quantity.

5 FINDINGS AND CONCLUSIONS

This study assessed the applicability of sodium alginate, as an eco-friendly bio-polymer, for maintaining face stability during slurry TBM excavation. Performance criteria for face stability were evaluated through filter press and viscosity tests. The findings and conclusion are summarized as follows,

- Sodium alginate demonstrated water loss volume and filter cake thickness equivalent to the conventional additive, CMC.
- In the NaCl concentration range of zero to 0.01 M, both sodium alginate and CMC demonstrated consistent yield stress values. However, at NaCl concentrations of 0.01 M or higher, both sodium alginate and CMC exhibited a sharp decrease in yield stress. Remarkably, at the highest concentration of 0.5 M NaCl, sodium alginate displayed higher yield stress than CMC.
- The test results suggest that sodium alginate has the potential to maintain face stability against seawater infiltration at practical NaCl concentrations.

- With an increase in the dosage of sodium alginate, water loss volume decreased gradually, while filter cake thickness increased. Note that the application of only 1 g/L of sodium alginate significantly reduced water loss volume.
- Based on the initial assessments conducted in this study, it can be concluded that sodium alginate is a viable and eco-friendly material for maintaining face stability.

ACKNOWLEDGMENTS

This work was supported by the National Research Foundation of Korea (NRF) grants funded by the Korea government (MSIT) (No. 2019R1A2C2086647, 2020R1A6A1A03045059, and RS-2023-00245022)

REFERENCES

Min, F., Zhu, W., Lin, C., Guo, X., 2015. Opening the excavation chamber of the large-diameter size slurry shield: A case study in Nanjing Yangtze River Tunnel in China. Tunnel Underground. Special Technol. 46, pp. 18–27.

Chen, F., Xiong, H., Yin, Z.Y., Chen, X., 2023. Impermeable and mechanical stability of filter cake under different infiltration conditions via CFD-DEM. Acta Geotech., 8.

Amorim, L.V., Barbosa, M.I.R., Lira, H. de L., Ferreira, H. C., 2007. Influence of ionic strength on the viscosities and water loss of bentonite suspensions containing polymers. Mater. Res., 10, pp. 53–56.

Taheri, S., El-Zein, A., 2023. Desiccation cracking of polymer-bentonite mixtures: an experimental investigation. Appl. Clay Sci., 238, 106945.

Wang, Y., Li, X., Wu, C., 2014. The role of sodium alginate in improving floc size and strength and the subsequent effects on ultrafiltration mem-brane fouling. Environ. Technol, United Kingdom, 35, pp. 10–17.

Kaneko, K., Kanada, K., Miyagi, M., 1998. Formation of water-insoluble gel in dry-coated tab lets for the controlled release of theophylline. Chem. Pharm. Bull., 46, pp. 728–729

Mcyotto, F.O., Wei, Q., Chow, C.W.K., Nadeem, Z., Li, Z., 2020. Eco-friendly decolorization of cationic dyes by coagulation using natural coagulant Bentonite and biodegradable flocculant sodium alginate. J. of Earth Sci. & Envir. Studies, 5(2).

Soltani, A., Raeesi, R., Taheri, A., Deng, A., Mirzababaei, M. 2021. Improved shear strength performance of compacted rubberized clays treated with sodium alginate biopolymer. Polymers (Basel). 13, pp. 1–21.

Liu, Q., Chen, H., Su, Y., Sun, S., Zhao, C., Zhang, X., Gu, Y., Li, L., 2023. Enhanced crude oil degradation by remodeling of crude oil-contaminated soil microbial community structure using sodium alginate/graphene oxide/Bacillus C5 immobilized pellets. Environ. Res., 223, 115465.

Tunnelling for a Better Life – Yan, Celestino, Thewes & Eberhardt (Eds)
© 2024 The Author(s), ISBN 978-1-032-80042-4
Open Access: www.taylorfrancis.com, CC BY-NC-ND 4.0 license

More efficient, cost-effective and reliable Slurry Treatment Plants (STPs) for mechanized tunnelling operations in the Asia-Pacific region

Kun Bai*
Herrenknecht (Chengdu) Tunnelling Equipment Co.Ltd., Chengdu, China

Gino Vogt*
Herrenknecht AG, Schwanau, Germany

ABSTRACT: In mechanized tunnelling operations performance, consumption and safety are main factors for jobsites. One of the most important components affecting these factors, especially in slurry TBM operations, are Slurry Treatment Plants (STPs). Inadequately/suboptimally dimensioned and designed STPs create bottlenecks for tunnelling operations and jeopardize time schedules and performance. Inefficiently planned STPs could drastically increase consumption figures such as electrical power, bentonite, water, polymers, etc. Inaccurately selected and treated suspension properties can cause a high-risk potential for the whole project. This paper debates the relevant key parameters for STPs from start to finish of a project and their results in influencing factors from the manufacturer's point of view.

In mechanized tunnelling performance, consumption and safety are main factors for operating jobsites. One of the most important, key components affecting these factors, especially in slurry Tunnel Boring Machine (TBM) operations, are Slurry Treatment Plants (STPs). Inadequately/suboptimally dimensioned and designed STPs which do not follow, for example, a detailed study of the geological baseline report with analysis of the influencing parameters could create bottlenecks for tunnelling operations and jeopardize time schedules and performance targets. Inefficiently planned STPs not adapted to environmental regulations (for example inner city operations) could negatively impact the jobsite surroundings and drastically increase disposal cost and consumption figures such as electrical power, bentonite, water, polymers, etc. Inaccurately selected and treated suspension properties can cause a high-risk potential for the whole project in terms of safety. A reliable process design based on experience is therefore a must for every jobsite to meet overall targets. Based on many years of Asia-Pacific experience, this paper debates the relevant interfaces and key parameters for designing and selecting STPs to operate in a more efficient and cost-effective way by the only global player manufacturing both TBMs and STPs (Herrenknecht). A further focus will be on the development steps of these machines in the history of the APAC region, including latest developments and innovations like data management and automatization.

Keywords: Mechanized Tunnelling, Slurry TBM, STP, Slurry, Treatment Plant, Performance, Efficient Operation, Circular Economy, Greener Tunnels

1 INTRODUCTION

Whenever tunnelling projects are realized with Slurry TBMs or multimode TBMs and therefore include a slurry circuit, Slurry Treatment Plants (STP) are required to remove particles of soil from the slurry suspension and rejuvenate the slurry before it is pumped back to the cutting face of the TBM. It is important the slurry remains in adequate quality ranges to maintain efficient excavation. Slurry treatment has direct influence on the reliability and performance of a slurry tunnelling job. Get the configuration of the slurry treatment plant wrong, and the TBM may be standing still. Apart from the primary use of STPs, protection of resources, recycling, classification and water treatment are steadily rising in importance all around the globe and therefore increasing the demands in separation units.

The STP in this context describes and stands for the complete setup and scope installed. Consisting mainly of equipment assembly groups such as Separation Plant, Centrifuge, Filter Press, Mixing Plant, Storage Tanks, Belt Conveyor, Slurry Management System, etc.

*Corresponding author: Bai.Kun@herrenknecht.com; Vogt.Gino@herrenknecht.com

DOI: 10.1201/9781003495505-218

The separation process itself could be divided into two main sections, as shown in Figure 1 below, separating the slurry suspension continuously from the by the boring process loaded solid particles in the slurry circuit. The active circuit (or primary separation, numbering 1 to 5 in the left box), consisting of the Separation Plant coarse screen, desanding- and desilting cut stages (dewatering screen combined with hydro cyclones), which are in continuous connection and communication with the Tunnel Boring Machine (TBM) from and to the Slurry Transport System (STS). The passive circuit (or secondary separation, numbering 6 in the right box) operates in a by-pass to the active circuit and consists of ultra-fine particle separation equipment such as a Centrifuge or Filter Press.

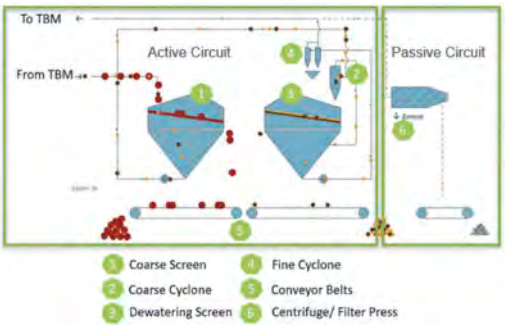

Figure 1. Working principle of a separation plant with active and passive circuit.

Following the separation process in detail inside the active circuit, the first stage of separation (coarse screen – numbering 1) can consist alternatively out of a of drum screen (for sticky geologies) or a horizontal shaker screen which take out large particles such as gravel and coarse sand with grain sizes bigger than 3 mm. For taking out even finer particles like fine sand and silt (up to 0.01 mm), two to three sets of hydro cyclones are commonly used in combination with a dewatering screen (numbering 2,3 and 4). Both the coarse screen and dewatering screen material can be classified by the help of a conveyor belt system (5). The secondary stage of separation, also known as fines treatment or passive circuit (6), is able to separate even finer solids as silt and clay particles from the suspension. This is possible with the help of centrifuges or filter presses that can reduce the remaining particles in the suspension to a bare minimum. Deciding for one of these technologies or a combination, several factors must be considered. In general, filter presses are more expensive and require more space on the jobsite due to their lower capacities. On the other side their solid outputs contain less water, which can be desirable in some disposal situations. The centrifuge on the other hand is cheaper, uses up less space, but has a higher level of residual moisture in the output. To achieve even better results in both secondary treatment technologies, polymers can be added to remove solids in the range of 0 – 0.05 mm.

To be optimally prepared for design and selecting the matching equipment for the specific geological sections of an STP, detailed geotechnical information is required. The results, gathered and evaluated by geological experts, give information about tunnel alignment, soil share distribution, grain size distribution and other soil characteristics.

1.1 *Safety factor*

Talking about STPs in relation to Safety Factors in tunnelling operations it is all about slurry quality aspects and monitoring and maintaining the rheological conditions in the given target range.

A properly maintained slurry quality/drilling fluid has a direct influence on a stable working face condition in the working chamber of the TBM to achieve a balanced supporting pressure against water and soil pressure as per following Figure 2 which shows the sealing function of the tunnel face by bentonite clay chemistry.

In most cases the suspension used in slurry operated TBMs is a bentonite suspension generated at the jobsite surface by mixing bentonite powder with water.

Bentonite is a natural clay mineral from the smectite clay group which has a so-called thixotropic structure to achieve a unique swelling behavior which is used in tunnelling to build up a filter cake and stabilize the working face. In some cases, polymers could also be added to the slurry to achieve particular results (for example against clogging potential, etc.). Besides the stabilization effect, the bentonite slurry is also used as a lubricant and transport medium for the solid loaded suspension via the STS out of the tunnel to the STP for recycling before it is taken back to the TBM.

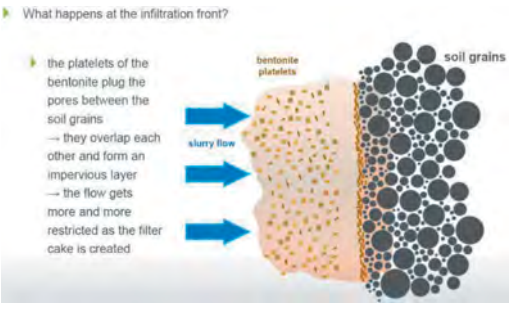

Figure 2. Stabilization of the working face of the tunnel operation by bentonite.

Key Performance Indicators (KPIs) for the drilling fluid are defined for each project individually based on the geological conditions encountered. The quality of raw bentonite varies a lot worldwide as there is a wide range of products and brands (also prices) on

the market showing different behaviors when mixed. It´s therefore essential to undertake consulting and tests upfront with reliable expert companies and suppliers to select matching products. Also, the water quality (pH, temperature, hardness, etc.) used for mixing can have a big influence on the quality of the drilling fluid. Often, soda ash could be of great benefit to waters not in the proper range for bentonite or polymer hydration (such as high hardness values which will retard the process). By adding soda ash the calcium hardness will be treated out and the pH value will increase slightly for better results. For the mixer itself it is important to select equipment with high shear strength. To mix bentonite with water a lot of "power" is required to enable the bentonite particles to react and to ensure optimum swelling behavior. Additionally, the drilling fluid quality will be affected by the constant solid load during the TBM advance. Therefore, KPIs must be monitored and logged during tunnel operations (often several times during one ring) to ensure they stay in the desired safe operation range. Typical main parameters are density (specific weight) to give an indication about solid load/ concentration resulting in wear and tear in pipelines and components together as well as the measurement of sand content. Another important parameter is related to viscosity and yield point to check the fluids carrying capacity and resistance to flow. An automated testing system as well as data management systems to monitor the parameters and warn the operator in case risks for the process should appear (settlements, etc.). Here, the selection of the right cut components inside the separation plant is essential to treat the incoming solid loaded slurry as well as possible and transfer it back with a quality as close as possible to that of fresh bentonite slurry. The quality delta between incoming and outgoing slurry shows the efficiency of the process and thus also has influence on the slurry lifetime.

1.2 *Performance factor*

What starts with the detailed TBM type selection should also be transferred to the STS and STP. Only when considered as one system with clear interface and communication definitions will the system display its full capability. Therefore, it is recommended for each project to specifically tender the STP and its components in all details to match the TBM and tunnelling operation maximum performance and most demanding geological parameters. If not, a lack of performance in operation is predictable.

The following checklist/rules of thumb provide contractors, clients and planners a brief overview of topics to consider with regard to STP selection so that plants are properly sized for performance:

- Size the STP for the fastest anticipated TBM advance rate.
- Size the STP based on maximum volumetric and solid flow rates that can be produced by the TBM and then add 10-20 percent redundancy to allow for the wear and inefficiency of mechanical equipment.
- Size all components to maximum flow rates that can be anticipated by pumps being used in the slurry circuit. Then build in 10-20 percent redundancy to allow for slurry inconsistency and wear and tear on cyclones and pump parts. Keep in mind that pump and hydrocyclone cut points are rated on water and "brand new" efficiency curves. Rates begin to drop quickly when wear occurs.
- Adjust components of the STP to meet the needs of anticipated geotechnical data. If you are anticipating mostly sands and gravels, you should concentrate your efforts on the primary screens, dewatering screens in combination with the hydrocyclones (desanding).
- If the geotechnical data indicates a large amount of clay with high plasticity (Thewes-Hollmann analysis), then your efforts should be geared to clay removal equipment.
- In geological sections where data indicates high amounts of fines (below 0.025 microns), your focus should be on a density regulation system (DRS/ third cyclone stage) and also on the Centrifuges/ Filter Press systems. The more times a solids particle is circulated through the system, the smaller the particle will become and the more expensive it is to remove.

For contractors, consulting STP experts via experienced suppliers or independent consultants is highly recommended due to their training, experience and expertise to alleviate many of the challenges before they have a chance to occur. In many cases these should be utilized prior to the bidding process.

1.3 *Cost factor*

Planning billion-dollar projects in a desired range of costs is a huge challenge itself but making some profits an even bigger one. Therefore, it is essential to know the influencing parameters on costs for an STP.

The biggest factor is not, as perhaps expected, the selected equipment but operation costs, therefore having to be as transparent as possible to identify savings.

Starting the cycle with the equipment cost, the factors for safety and performance stated in the previous chapters should be taken into account the most. As delays or slowdowns of the project due to poor performance and safety cost tens of thousands of dollars for every day the project schedule must be extended. Often contractors even have a contract which pays them supplements when the project is finished earlier than planned. An investment in properly adapted and highly efficient components with great availability is often beneficial in the long run. Also, decisions like not selecting in the first investment components matching the maximum values could cause problems and higher costs later if short notice add-ons must be purchased. Changes on the jobsite instead of already considering them in the planning/design stage can easily cost 10 times more.

Table 1. Exemplary project cost shares in relation with STPs on an EU jobsite.

Cost Factor	Equipment	Additional Comment
Equipment	25 – 45 %	Ultra-fines content dependent (Centrifuges/Filter Presses are biggest cost factors on site)
Civil Works	< 5 %	Site conditions, design dependent
Transportation	< 5 %	Incoterms, project location, design depending
Assembly	< 5 %	Scope of supply, experience, design dependent
Operation	45 – 55 %	Project location, experience, consumption figures, disposal cost, abrasivity, project duration dependent
Demobilization	< 5 %	Scope of supply, experience, design dependent

In cases where several TBMs start boring from the same launch shaft, STPs can also be combined to avoid redundancies as much as possible and to find savings especially in peripheral equipment like storage tanks, mixing plants, etc.

A common practice also for STPs is having a buy-back option available as contractors try to continuously avoid having their own machine parks. Accordingly, rentals can also be an option. In this case suppliers offer rental services most likely for modular, easily reusable systems. As for TBMs, to avoid cost-intensive surprises on jobsites it is recommended to carry out factory assembly and testing (FAT) in the suppliers' workshop for the main STP components.

The cost factors civil works, transportation, assembly and demobilization are the smallest portion in relation to equipment and operation costs. Still, these factors have high potentials for savings. A big difference in costs can be achieved with the use of modular, container type plants.

Table 2. Exemplary comparison between platform and containerized "mobile" water treatment plant.

	Mobile/Container	Platform
Equipment	120 %	100 %
	Add. Cost in relation to Equipment	
Assembly Personnel	7.5 %	15 %
Civil Works	5 %	10 %
Building/heating/lightning	Included	15 %
Cranes	1 %	2 %
Disassembly	3 %	6 %
TOTAL	136.5 %	148 %

Smaller footprints required on jobsites, improved handling and shipping due to pre-assembled and CSC-certified containers and faster assembly & demobilization thanks to the modularity, fewer parts and no requirement for civil works are the main advantages of using containerized STPs.

The biggest cost block for STPs by far are the operation costs. The following figure shows their approx. share which could vary for each project and circumstances (e.g. power cost, water cost, etc.)

Table 3. Exemplary operation cost for STPs (EU jobsite).

Operation Costs	Equipment	Depending on:
Personnel	5 – 15 %	Project location, setup, experience
Power	10 – 15 %	Project location, setup, design, operation
Bentonite	15 – 25 %	Type, quality, design, geology
Water	< 5 %	Project location, setup, geology dependent
Polymers and other consumers	5 – 10 %	Type, quality, design, geology
Spare parts	5 – 15 %	Scope of supply, geology, maintenance, design
Muck disposal	30 – 55 %	Project location, regulation, reuse options

To operate the STP it is required to have approx. three to four people available per shift including one for operating the active circuit components and communication with the TBM operator, a second one with mechanical skills to maintain the equipment and do routine inspections and a third one to operate the passive and secondary equipment. Additionally, it is recommended to have an electrician with PLC skills on call in case an electrical issue should occur.

On the electrical power side, installed kW (approx. 900-1200 kW for a standard metro TBM size STP), operation time and the final demand factor multiplied by local kWh cost define this block. Here the focus should be on efficient high-level components based on the latest electrical standards and a coordinated interface operation in advance, by-pass and ring building time between TBM, STS and STP.

Bentonite costs are usually the second highest in operation. As bentonite is indispensable for the safety aspect of most tunnelling operations it can generally not be avoided in tunnel construction, ultimately depending on the geo conditions and ground stability. The goal for contractors should be efficient utilization of this good in best relation to the set KPIs. High quality bentonites, for example, often show better thixotropic behaviors and therefore require much less kg per m³. Lower cut points maintain and extend the slurry lifetime and therefore less bentonite must be replaced. Also, reusing already excess "waste" bentonite slurry in some projects can

be an option to lower costs e.g., to prepare high-density (HD) bentonite slurries. Finally, bentonite costs are also highly linked to the geological section the TBM is mining in. In a more stable clay section, for example, less bentonite would be required than in a relatively unstable full sand layer section.

Depending on the jobsite location it might be advantageous to integrate a water treatment system to save costs for fresh water, wastewater and for the possibility of reusing recycled water.

Polymers and all related possible add-on products like lime, iron3, flocculants, etc. for the passive circuit equipment's efficient operation are a minor but not-to–be-forgotten cost indicator. As for bentonite, higher qualities often pay off in the long run. Training operators and regular maintenance are another hint how costs could be controlled.

For smooth operation, spare and wear parts play a key role especially in highly abrasive ground conditions which will influence slurry contacted parts. In close relation to regular maintenance shifts, properly installed spare parts could protect contractors from unplanned financial impacts. The relatively small share shown in Table 3 could increase dramatically if not controlled from the beginning. In case required job-stopper parts are not available on site or need a long delivery period, a loss of availability and overall project schedule impact is possible. It is therefore recommended to plan spare parts early enough to have the most important ones on site with the project ready to bore.

Finally, the biggest share of costs in operation in most projects is the muck disposal handling (restrictions, regulations vary worldwide). It is therefore a key element in early planning stages to have it settled even before the equipment is selected. The focus should be on how to control volumes coming out of the tunnel and what to do with it. Regarding volume, controlling water content is the key to success. Reducing the water content and with it the volume of muck coming from the STP can save hundreds of thousands or even millions of dollars within the total project duration, as disposal companies charge per tonne or m³. Nowadays in this context it is also predictable that what was declared as waste for a long period is now becoming a scarce resource which should be recycled as much as possible. Sustainability is a global trend. Classification and processing of different grain sizes should therefore be a target for modern and state-of-the-art STPs. Gravel and sand are scarce and expensive products in the construction sector so contractors may have good chances of selling their products to third parties to change a declared cost block to an income sector. The ultimate goal is to reuse those resources directly on the jobsites for example in shaft installation, segments or land filling.

2 FOCUS REGION ASIA-PACIFIC (APAC)

For the development and increase in importance of STPs the Asia-Pacific region has always played a key role. Simply because of its enormous size and due to the fact that ground and project conditions as well requirements in this area require slurry TBM operations more often than in others, the number of STPs used in this region is higher than anywhere else. As a result, contractors have acquired vast experience and transferred this knowledge to tender specifications also addressing new requirements and innovations.

Singapore, as one example, has been one of the hot spots in tunnelling globally in the past two to three decades. The DTSS2 project in particular, which had breakthrough of the last TBMs a couple of months ago, set new milestones in technology especially in data management (e.g. Excavation Management System "EMS") and innovations (e.g. Density Regulation System "DRS").

3 TRENDS AND INNOVATION

With the growing demands and requirements in separation technology, in recent years innovations have also been driven focusing on data management and automation. Another focus topic is how two reduce impacts such as noise and vibration on the jobsite surroundings and people living close by in particular in inner city operations.

Herrenknecht is moving these innovations forward as required by customers. Three example technologies deserve mention here:

3.1 *Density Regulation System (DRS)*

The Density Regulation System (DRS) was a development arising from Singapore DTSS2 requirements to increase the efficiency and cut point of the basic Separation Plant (as per Figure 1 numbering 1-4) in fine geological sections. Its function starts where standard components like screen machines and first plus second cyclone stage cannot cut off any more particles.

In principle it works with a third, ultra-fine cyclone to cut off particles in a range below 25 to 10 microns. By doing that the lifetime extends/ quality of the suspension increases and the discharge process will be delayed as long as possible. This reduction of volume to be exchanged per ring/day ultimately helps reduce the quantity of secondary fines treatment equipment such as Centrifuge or Filter Press. The second benefit and advantage created by the DRS is tackling the fact that Centrifuge or Filter press are not working perfectly efficiently (capacity and dryness of disposal) if the density/ solid content in the inflow is not constant and high. Target >1.2 kg/l. The DRS increases and controls this high, constant density level by means of the mechanical principle of the cyclone (dynamic thickener) and therefore further reduces the number of units required.

Advantages at a glance:

- Increase of fines treatment capacity due to thickened slurry

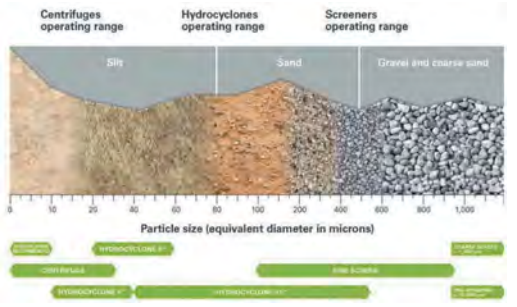

Figure 3. DRS (4" Hydrocyclone) working range in geological section.

- Lower operation costs due to longer slurry lifetime (bentonite savings, water, polymer savings)
- Less fines treatment equipment needed thanks to additional cut point (third cyclone stage)
- Less water content of muck due to increase of solids content
- Modular design & easily expandable

3.2 *Noise and Vibration Canceling System (NVCS)*

The next development arose from projects in Australia (Perth/Melbourne), mainly inner-city operations. Noise and vibrations caused by jobsite operations are becoming more and more problematic as the jobsite surroundings and people living close by suffer as a result of long duration noise impacts. It is therefore imperative to find optimizations and develop solutions to reduce this negative impact. The Noise and Vibration Canceling System (NVCS) tackles this problem. By means of phase-shifting (PSS) technology, which is also used in the latest headphones to cancel surrounding noise, the low frequencies caused mainly by the screen machine/shaker technology of Separation Plants is optimized as even at a distance they can cause rattling and noise e.g., to windows. The software and hardware used even controls for changes in ground conditions and adapts automatically. A positive side effect of the NVCS is that the overall sound power level L_{wa} of the STP is reduced by approximately 10 dB.

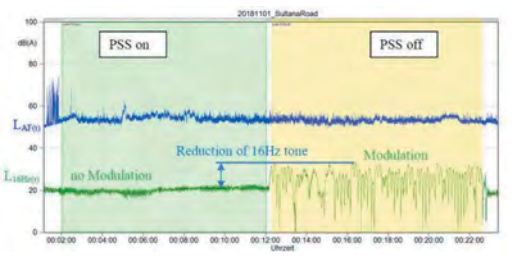

Figure 4. Working principle of NVCS using PSS method.

3.3 *HK.connected data management system*

The last innovation to be mentioned addresses the need to make data from more and more sensors installed in the machinery visible and used for further processes. With the new Herrenknecht.Connected customer portal, Herrenknecht tunnelling technology users can get digital performance reports and worldwide insight into the operators' cockpit monitors at any time and from any location.

These are, for example, consumption figures to be planned far ahead or efficiency and performance of the components to be supervised from the engineers' main offices to find optimization potentials.

The data management system allows digitalization of the overall jobsite processes in a user friendly and modern way.

All sensors and equipment provided by Herrenknecht can be integrated into the system by .ON modules like STP.ON which are stored in a web cloud and finally displayed by accessing using an internet browser. Customers can access a project license for their fleets and e.g. generate customized reports, check the live visualization of the TBM and STP or supervise functions using pre-set performance dashboards.

Figure 5. HK.Connected Overview And Interplay.

4 SUMMARY/CONCLUSION

Many clients, planners and even contractors underestimate the role of a Slurry Treatment Plant in the overall slurry operated tunnelling process in regard to safety, performance and costs. Increasingly stringent environmental regulations mean that the output of STPs is becoming more important than ever for sustainability. Challenging ground conditions, increasing regulations, tighter schedules and performance growth will increase and influence demands on STPs. So, there is a high chance that in future they won't be last minute thoughts anymore for some projects as their output is becoming more and more relevant in terms of the circular economy and greener projects. Latest developments for efficiency increases, surroundings impact and also data management underline the focus on this crucial part of a tunnelling project.

In conclusion, the functions of a properly designed and versatile STP are an absolute necessity to complete tunnelling projects successfully, on time and within budget. A properly selected STP while knowing the driving facts in terms of safety, performance and cost will save time and money and allow the contractor to concentrate on the front tunnelling process, instead of dealing with adverse slurry parameters and cost-intensive interfaces. Knowing that state-of-the-art developments and innovations such as autonomous functions, data visualization and management also help customers modernize jobsite management with Slurry Treatment Plants (STPs).

REFERENCES

Herrenknecht AG. Homepage. (2023), URL:https://www.herrenknecht.com/en/products/productdetail/separation-technology

Herrenknecht Separations. Homepage. (2023), URL:https://www.herrenknecht-separations.com

Sortenberg, B.L. (2012) Separation Plant Selection for Tunneling Projects. Tunnel Business Magazine.URL:
https://tunnelingonline.com/separation-plant-selection-for-tunneling-projects/

TJ. (09/2020) Overlooked and undervalued. Tunnelling Journal.
URL: https://tunnellingjournal.com/archive/tunnelling-journal-september-2020/

Tunnelling for a Better Life – Yan, Celestino, Thewes & Eberhardt (Eds)
© 2024 The Author(s), ISBN 978-1-032-80042-4
Open Access: www.taylorfrancis.com, CC BY-NC-ND 4.0 license

An evaluation of using different excavation methods related to specific geologic conditions in the Istanbul area

Cemal Balci* & Nuh Bilgin
Faculty of Mines Mining Engineering Department, Istanbul Technical University, Istanbul, Turkey

ABSTRACT: Mechanical excavation with tunnel boring machines is the most widely used excavation method in Metro tunnels in Istanbul. However, drilling and blasting, impact hammers, and roadheaders are also used in some cases, especially in metro station tunnels (platform tunnels). It is strongly emphasized that the prediction of the performance of the tunnelling machine plays an important role in the time scheduling for job termination and in the economy of tunnelling projects. In the past, the accumulated data in Istanbul Metro Tunnel drives served as a sound basis to model the performance prediction models of the excavation machines. This study gives a unique opportunity to compare; TBM's, impact hammers, and roadheaders performances with conventional drilling and blasting methods in a selected Metro Project. Although blasting in urban areas is restricted due to vibrations and difficulties in the transport of blasting agents, in extreme conditions its use becomes a necessity. Roadheader is proven to be more efficient than impact hammer in terms of machine utilization time and production rate. However, high pick consumption makes it a necessity to use impact hammers in similar conditions. An attempt is made to modify the equation used in the past to predict the net breaking rate of impact hammers and it is proved that a reduction factor in the breaking rate taking into account the thickness of the dykes improved the validity of the proposed model. One important point emerging from this paper is that the dip and strike of the joints of 45° in the direction of cutting of the roadheaders are found to be in favor of the cutting rate of roadheaders given higher values than predicted performance values. The dip and strike of the joints having an angle of 45° in favor of the cutting direction improves the net cutting rate of roadheaders.

Keywords: TBM, Roadheader, Impact hammer, Drill and blast

1 INTRODUCTION

In a metro project which is planned to be executed in complex geology like in Istanbul, it is inevitable to use different excavation methods in the same project. The main tunnels are usually excavated with EPB-TBMs. As seen in Table 1, in the last 5 metro projects of 194,121 m in length, 156,127 m of tunnels were excavated with EPB-TBM's, Station tunnels or crosscuts of 37,994 m were excavated with conventional methods such as drill and blast methods, impact hammers or roadheaders as in Kozyatagi-Kadıköy Metro project.

Table 1 clearly shows that conventional tunnelling methods are inevitable parts of mechanized tunnelling, since there is always room for conventional tunnelling in a metro project planned to be realized with TBMs, due to the short length of crosscuts and station (platform) tunnels. Before the introduction of TBMs in Istanbul in Moda and Baltalimani tunnels, the main excavation methods were with impact hammers and roadheaders leading to the accumulation of data and development of performance prediction models of these machines. Over time, the uniaxial compressive strength of andesite dykes surpassed 200 MPa necessitating the use of explosives. Therefore, tunnel project planners or practicing engineers who are responsible for the proper and economic excavation of the project

Table 1. The length of tunnels excavated with conventional tunnelling and with TBMs in 5 recently terminated metro projects in Istanbul.

Metro Project Tunnels	Tunnels with conventional methods (m)	TBM tunnels (m)	Total (m)
Gayrettepe New Airport	8,368	68,282	76,650
Halkalı Airport	6,961	55,617	62,578
Bakırköy Kirazlı	4,820	12,100	16,920
Ataköy İkitelli	10,200	16,200	26,400
Başaksehir Kayasehir	7,645	3,928	11,573
Total, m	37,994	156,127	194,121

*Corresponding author: cemalb@itu.edu.tr

DOI: 10.1201/9781003495505-219

should be aware of the difficulties which may be encountered when driving tunnels in complex geology and the use of performance prediction models for the proper time scheduling of the projects.

This paper is written with to introduce the readers understanding the performance of TBMs, roadheaders, impact hammers, and drill and blast tunnelling methods within the same geology of Goztepe Station of Kozyatagi-Kadıköy Metro Project and compare their performances. This paper includes the results of a reevaluated and enlarged paper already published, Ocak and Bilgin, 2010.

2 KOZYATAĞI-KADIKÖY METRO PROJECT, THE GEOLOGY AND GEOMECHANICAL PROPERTIES OF THE FORMATIONS

The geological cross-section of the studied area is given in Figure 1.

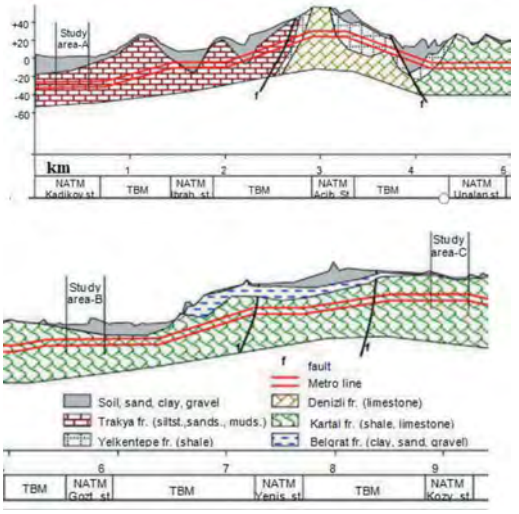

Figure 1. Geological cross-section of the metro line between Kadıköy and Kozyatağı stations, Ocak and Bilgin (2010).

The project is a part of Kadıköy-Kartal Metro line having a length of 8800 m, starting from Kozyatağı to Kadıköy. Sedimentary rocks are mainly found in the area. Tunnels between Kozyatagi–Kadiköy are excavated generally in the Trakya and Kartal formations. Trakya formation of carboniferous age consists of interbedded sandstone, siltstone, claystone, and mudstone. Diabase and andesite dykes having some 10 m in thickness are frequently encountered. In the east of the tunnel alignment, Kartal formation of Devonian age is found. Kartal formation consists of fine-grained, laminated, fractured, and interbedded siltstone, limestone, sandstone and shale. Water ingress is common in both Kartal and Trakya formations. Many faults dykes and geological discontinuities exist in the area. The rock material in the contact zone between dykes and the main rock is highly weathered. The overburden varies between 20 and 45 m, and the distance between twin tunnels is around 32 m. The geotechnical properties of the two rock formations show a wide range of variance which are summarized in Table 2.

The number of joint sets per meter occurring along the length of the tunnel can be classified as class 3 (one joint set plus random) and the number of discontinuities per meter changes between 15 and 20. In Figure 1, Kadıköy, Ayrılık Çeşme, Acıbadem, Unalan, Göztepe, Yenisahra, and Kozyatağı stations and associated tunnels are excavated with conventional tunnelling methods. Kadıköy, Göztepe and Kozyatağı stations (Zones A, B, and C) are the studied areas of the conventional tunnelling, drill and blast, impact hammers and roadheaders, Ocak and Bilgin (2009). As seen in this Figure 1 conventional tunnelling methods are used in Trakya Formation having interrelated, siltstone, mudstone, and sandst

one bands, and Kartal formation having shale and limestone layers.

Table 2. The geotechnical data of the formations.

Formation	γ kN/m^3	C kPa	σ_c MPa (+/- sd)	RQD +/-sd
Kartal	26.4	142	34.3 (+/-21.5)	48.5 (+/-11)
Trakya (W1-W2)	26.5	139	50.2 (+/-38.1)	20.3 (+/20)
Tuzla	26.4	210	58.0 (+/-12.3)	N/A
Baltalimanı	26.5	238	62.8 (+/-13.1	N/A

γ is density, C is cohesion, σ_c is the compressive strength

3 TBM, ROADHEADER, AND IMPACT HAMMER USED IN THE PROJECT

3.1 *TBM used in the metro the project*

Two identical Herrenknecht TBM's were chosen for Line 1 and Line 2, these machines can work in open and closed modes. The general view of the TBM's is seen in Figure 2, and technical data is given in Table 3.

Table 3. Main characteristics of the TBM.

Machine diameter	6.75 m
Rotational speed	1.65- 5.5 rpm
Number of cutters	28
Cutterhead power	4X315 kW
Cutterhead torque 1	5,200 kNm at 1.6 rpm
Cutterhead torque 2	1,515 kNn at 5.5 rpm
Maximum Thrust	42,575 kN at 350 bar
Opening ratio	%35

In the beginning, TBMs worked without a screw conveyor. Big blocks were coming from the face causing a lot of problems such as clogging the

cutterhead. The mean advance rate was 3 m/day at the beginning of the operation and this value increased up to 7 m/day after the modification of the cutterhead. However, it is interesting to note that the daily advance rate increased to 10.5 m (day) after installing a screw conveyor within the TBM chamber and passing to Earth Pressure Balance (EPB) mode. In the meantime in different tunnels in Istanbul, same remedial works were carried out for Beykoz and Marmaray Tunnels increasing the daily advance rates for those tunnels? to a great extent.

Figure 2. A view of the cutterhead of TBM used.

3.2 *Roadheader used in the project*

Transverse type roadheader of model WAV 178 Westfalia, was used in the station tunnels of upper and lower bench headings. The view of the machine is given in Figure 3. and the characteristics of the machine are in Table 4.

Figure 3. Transverse type roadheader used in the project.

Table 4. Characteristics of Westfalia WAW 178 model.

Weight, t	75
Cutting power HP/kW	402/300
Max.. excavation area m^2	61
Cutting head diameter, cm	88.8
Cutter type	Conical
Cutting number	82x2=164
Cutting head type	Transverse

3.3 *Impact hammer used in the project*

Hydraulic Hammers are widely used in tunnelling and several km of tunnels were excavated in Istanbul by hydraulic hammers mounted in excavators. The hammers used in Kozyatağı-Kadıköy metro station tunnels were Atlas Copco MB 170- type hydraulic hammers. All the hammers are the same and have the following characteristics: weight 1.7 t, oil flow rate 130–160 lt/min, working pressure 160–180 bars, impact frequency 320–600 impact/min, impact energy 4170 J. The selection of excavator is important for the success of the operations since the stability of the carrier plays an important role in the efficiency of the system. Volvo EC210B of 7 t, Sumitomo SH200LC OF 9.5 t, and Caterpillar 3066T of 7.5 t in weights were used with attached hammers. A general view of a hydraulic hammer is given in Figure 4.

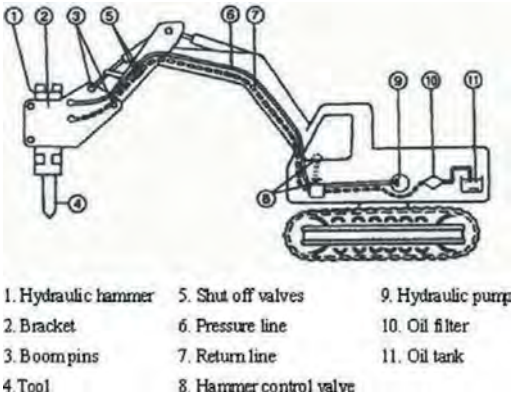

Figure 4. Schematic view of a hydraulic hammer mounted. on an excavator, After Tunçdemir (2007).

4 MAIN FACTORS AFFECTING THE PERFORMANCE OF TUNNELLING MACHINES

TBMs are mainly affected, by the geotechnical characteristics of the ground. Hard rock, soft ground or ground water level will affect the type of the TBMs used: gripper type TBMs, single shield TBMs, double shield TBMs, slurry or EPB TBMs. Weathering degree

of the rock formations, faults, transition zone, and plasticity of the ground affecting clogging of the cutters are among the most important parameters affecting the performance of TBMs. Swelling clays are the main reason of squeezing ground and it is the nightmare of the tunnelers. The main advantages of TBMs are being a continuous excavation system. However, excavation with roadheaders, impact hammers, and drill and blast method are not continuous systems. Due to this fact generally advance rates of tunnelling using these methods are used less frequently than TBMs. If the ground is not favorable, using roof bolts, forepoling, wire mesh, shotcrete and steel arches as seen in Figure 5 will be among the factors decreasing the advance rates.

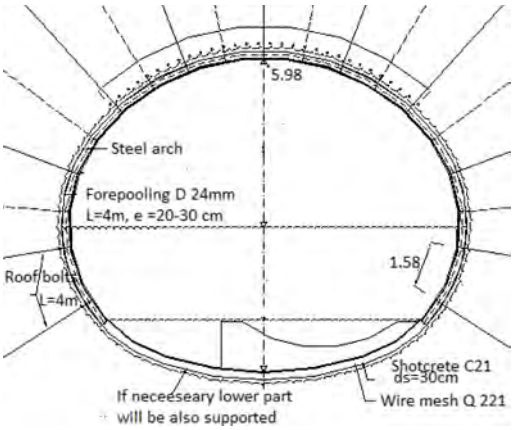

Figure 5. Cross section of the platform tunnel T1 excavated with roadheader, impact hammer and drill, and blast method, tunnel face has an area of 74 m^2.

5 THE PERFORMANCE OF TBM

A detailed analysis was carried out to investigate the effect of geotechnical properties on the performance of a TBM. Table 5 is a summary of the results of multiple regression analysis for dependent variables corresponding to 1 bar face pressure. The conclusion emerging from this statistical analysis was that geotechnical factors affecting the instantaneous cutting rate and penetration were the geological strength index as defined by Morinos et al. (2005), Cerchar abrasivity index, and destruction energy as defined by Thuro and Spaun (1996) and Thuro and Plinninger (2003). Thrust index and torque index were predicted best from the product of compressive strength times the Cerchar abrasivity index. Nizamoglu (1978) was the first who noticed this in 1978 during his field studies on Robbins and Wirth TBMs for his Ph.D thesis and he called this product an index of nocivité or index of harmfulness. Plinninger (2010) also noticed that the product of compressive strength times the abrasivity of the rock was a good indicator of drilling performance.

Table 5. The performance prediction equations of the TBM.

$ICR = 0,896GSI - 37,416CAI + 189,804\left(\frac{\sigma_c^2}{2E}\right), R2 = 0.84$
$p = 0,141\ GSI - 5,842\ CAI + 29,373\left(\frac{\sigma_c^2}{2E}\right), R2 = 0.83$
$\frac{TF}{p} = 0,1615(\sigma_c.CAI)^2 - 17,668(\sigma_c.CAI) + 737,37, R2 = 0.8$
$\frac{TF}{p} = 0,0366(\sigma_c.CAI)^2 - 3,4861(\sigma_c.CAI) + 203,15, R2 = 0.79$
$SE = \left(35,6 \cdot 10^{-3}\right)E - 0,0381(\sigma_c \cdot CAI), R2 = 0.69$

In the above equations, TF/p is thrust index in kN/(mm/rev), T/p is torque index in kNm/(mm/rev), SE is specific energy in kWh/m3, ICR is the instantaneous cutting rate in m^3/h, p is penetration in mm/rev, σ_c is compressive strength in MPa, CAI is Cerchar abrasivity index, E elasticity modulus in MPa, GSI is geological strength index, RQD is rock quality designation, $\sigma_c^2/2E$ is destruction work as defined by Thuro and Spaun (1996) Thuro and Plenninger (2003). A detailed analysis has been carried out using the data of the other projects to justify the validity of the predictor equation given in Table 4. It is hoped to publish the results soon.

Instantaneous cutting rate and penetration rates with machine utilization time are the parameters used to estimate daily advance rates. Machine utilization time is strictly related to job organization, the skill of the TBM operators, and the design of the tunnel operation parameters. A machine utilization time of 45% is a good number justifying the efficiency of the operational parameters used in the mechanized tunnelling

The major criticism of mechanized tunneling with TBMs in Kozyatağı Kadıköy Metro tunnels is that 27% is spent for excavation as seen in Figure, which is too low compared with the other projects. The main reason for this is that the muck is transported with rail system, and the muck is transported from the shaft to the surface with Floxewell vertical band. Sticky muck needed to be cleaned within the flyers plaques, with a ratio of 10% in the overall performance of tunnelling with EPB-TBMs

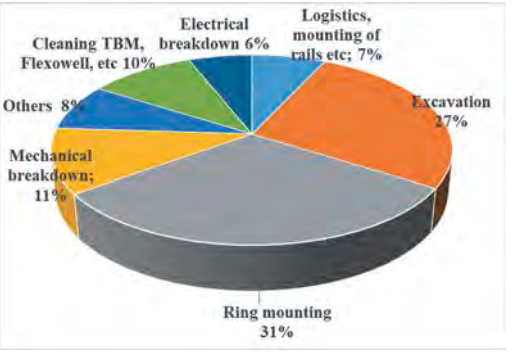

Figure 6. Overall performance of tunnelling with TBM.

6 THE PERFORMANCE OF TUNNELLING WITH DRILL AND BLAST, ROADHEADERS AND IMPACT HAMMER

Platform tunnels excavated with drill and blast tunnelling method have a crosse section area of 74 m^2 as illustrated in Figure 3. Drill holes were drilled using double boom Atlas Copco Rocket Boomer 282. Fracture characteristics of the rock mass were dictated by the blasting agent as Powergel Magnum 365 and Trimex (with density of 1,20 g/cm3, ideal blasting velocity of 6.437 m/s, and ideal blasting agent of 121.400 atm). The wedge cut, parallel- burn cut methods were used with blasting holes of parallel cuts having diameter of 89 mm and other blast holes of 41 mm in diameter. Nonel Exel MS/LP blasting cabs of 47 different blasting intervals were also used. A pie chart showing the work done in drill and blast tunnelling is given in Figure 7.

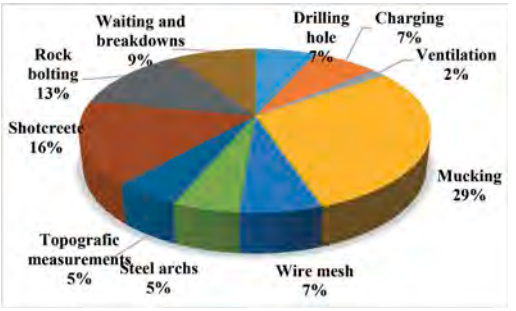

Figure 7. Pie chart showing the works done in drill and blast tunneling.

Roadheader and impact hammer used in the project are described in sections 3.2 and 3.3. Pie charts obtained for these machines are given in Figures 8 and 9.

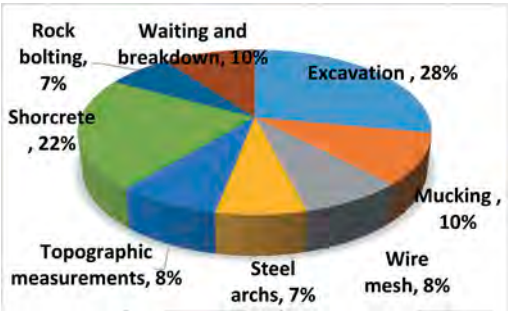

Figure 8. Pie chart obtained when using roadheader.

Machine utilization time is as important as the net cutting/breaking rate in determining the excavation efficiency and economy since daily advance rates are directly related to these factors for a given tunnel section. The performances of mechanical excavators and drilling and blasting methods are summarized in Figures 7, 8, and 9. These figures give a unique

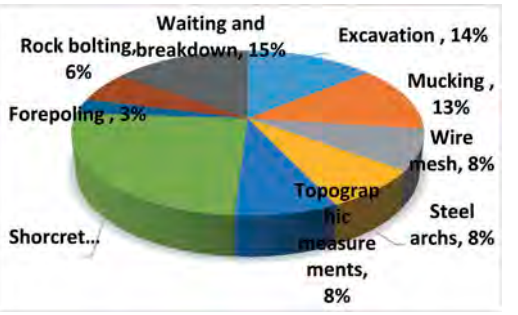

Figure 9. Pie chart obtained when using impact hammers.

opportunity to compare roadheaders, impact hammers, and drilling and blasting methods for a given job. As seen from these figures, machine utilization time for roadheaders is 28.2%, almost twice compared to impact hammers, and time spent for excavation in drilling and blasting is in the same order as the time spent in the excavation by impact hammers with a value of 15.4% (drilling, blast hole charging, blasting and ventilation). Mucking is another factor affecting job duration. In fractured rock formations like Kartal and Trakya formations, sometimes roadheaders excavate the rock in excess of their loading capacities with gathering arms and extra time is necessary to load the muck. The time spent for mucking was 9.8% for roadheader, 13.3% for impact hammers and as high as 29.4% for drilling and blasting methods. It is difficult to control muck size in fractured rock formations with conventional excavation methods, some big muck samples always create transportation problems and due to the disturbed zone, the number of bolts used for a unit length of tunnel is always higher compared to mechanical excavation methods. Time spent for rock bolting in drilling and blasting method is found to be twice as compared to the other excavation methods with a value of 13%.

The following equations 1,2, and 3 were already developed to predict the net production rates of roadheaders and impact hammers. The validity of these equations was tested also for Kozyatağı-Kadıköy Metro tunnels. However, the variety of the igneous dykes in thickness served to develop equation 4. K index which is a function of the thickness of the dykes is given in Table5. As a statistical test result the field values and predicted values are compared which are summarized in Table 6. The dip and strike of the joints of 45° in the direction of cutting are found to be in favor of the cutting rate of roadheaders given higher values than predicted performance values.

$$ICR = 0.28 \times P \times (0.974)^{RMCI} \quad (1)$$

$$RMCI = \sigma_C \times \left(\frac{RQD}{100}\right)^{\frac{2}{3}} \quad (2)$$

$$\mathrm{IBR} = 4,24\mathrm{xPx}(\mathrm{RMCI})^{-0.567} \quad (3)$$

$$IBR = Kx4,24xPx(RMCI)^{-0.567} \quad (4)$$

In the above equations, NBR is the net breaking rate (for impact hammers) in m3/h; Pi is the power output of the impact hammer in HP, it is found by multiplying the oil flow rate by working pressure; RMCI is the rock mass cutability index; UCS the uniaxial compressive strength in MPa; RQD the rock quality designation, %; NCR the net cutting rate(for roadheaders), m3/h; P the cutting power for roadheaders in HP., Bilgin et al. 2018.

Table 6. A guide to estimating reduction factor K used to predict net braking rates of impact hammers related to the related to the thickness of dykes.

The thickness of dykes (cm) (for UCS > 120 MPa)	Reduction factor K for net breaking rate
10-20	0.8-0-90
20-30	0-7-08
30-40	0.6-07
40-50	0.5-0.6
>50	D&B is recommended

Table 7. The relationship between net field production rate and the predicted production rate for impact hammers and roadheaders.

Impact hammer Equation 1	y=2.32x-10.02	R^2=0.82
Impact hammer Equation 2	y=1.98x-12.02	R^2=0.63
Roadheader	y=3.46x-40.97	R^2=0.80

In this table y is the field value in m^3/h; x is the predicted value in m^3/h

7 DISCUSSION OF USING TBMS, DRILL AND BLAST, ROADHEADER AND IMPACT HAMMERS

Conclusions will be drawn upon daily advance rates based on a tunnel diameter of 6.75 m as given in Table 8.

Table 8. Production rates obtained in Kozyatağı Kadıköy Metro tunnels with different tunnelling methods.

Method of excavation	Daily advance rate m/day
TBM	10.5
Drill and blast	5.5
Roadheader	6.4
İmpact hammer	1.3

Although drill and blast, roadheader and impact hammers were used in the platform tunnels of 74 m^2 area, production rates were converted for a tunnel of 6.7 m diameter which is the excavation diameter of the TBM. An advance rate of 10.5 m /day obtained for Kozyatağı Kadıköy is too low. Looking at Figure 4, 17% of overall time is spent for mounting of rails and 10% cleaning of Flexowell (vertical belt). A job organization with belts for muck transport would increase the time spent for excavation from 27% to 40-44% increasing consecutively the daily advance rate.

There is also a possibility of increasing the daily advance rates of impact hammers almost twice by using high-power impact hammers, since as seen from equation (3) net breaking rate of hammers is related to the power of impact hammers. The other alternative is to use impact hammers mounted on carriers having gathering arms eliminating the time spend for mucking.

8 CONCLUSIONS

TBMs are the most widely used in Metro tunnels in Istanbul. However, drilling and blasting, impact hammers, and roadheaders are also used in some cases, especially in metro station tunnels (platform tunnels). In Istanbul in the last 5 metro projects of 194121 m in length, 156127 m of tunnels were excavated with EPB-TBM's, Station tunnels or crosscuts of 37994 m were excavated with drill and blast method, impact hammers or roadheaders as in Kozyatağı-Kadıköy Metro project. In this project daily advance rates for TBM, drill and blast roadheaders and impact hammers were 10.5m, 5.5m, 6,4m, and 1.3m respectively. This paper made a concise criticism on the performance of these tunnelling methods and the modification of the some use of performance prediction models already developed using accumulated data in Istanbul.

REFERENCES

Alan, E. 2018. Determining "k" and "β" Coefficients of the Formation that Excavated by Blasting on Kadıköy-Kartal Metro Route, The Effect of Detonator Delay Time on Amplitude. Proceedings of the 4th International Symposium on Underground Excavations for Transportation, Organized by Turkish Tunnelling Society and Chamber of Mining Engineers of Turkey, Istanbul Branch.

Bilgin, N., Çopur, H., Balcı, C.,2014. Mechanical Excavation in Mining and Civil Industries, CRC Press, Taylor and Francis Group, London.

Bilgin, N., Çopur, H. and BalcI, C., 2016. TBM excavation in difficult ground conditions. Case studies from Turkey. Ernst & Sohn GmbH & Co.

Bilgin, N.,Yüksel, A, 2022. The effect of EPB face pressure on TBM performance parameters in different geological formations of Istanbul. Tunnelling and Underground Space Technology 138, 105184

Marinos, V., Marinos, P., Hoek, E., 2005. The geological strength index: applications and limitations. Bull Eng Geol Environ 64, 55–65.

Nizamoglu, Y.N., 1978. Contribution to the performance prediction of TBMs and analysis of the wear of disc cutters, Ph.D thesis (in French), Institute Nationale Polytechnique de Lorraine, Ecole Nationale Superieur de la Metallurgie et de L'industrie des Mines de Nancy, France, p.139.

Ocak, I., Bilgin, N., 2010. Comparative studies on the performance of a roadheader, impact hammer and drilling and blasting method in the excavation of metro station tunnels in Istanbul. Tunnelling and Underground Space Technology, 25, 181–187

Tuncdemir, H., 2007. Impact hammer applications in Istanbul metro tunnels.Tunnelling and Underground Space Technology 23, 262–264.

Thuro., K, Spaun., G, 1996. Introducing 'destruction work' as a new rock property of toughness referring to drillability in conventional drill- and blast tunnelling. In: Barla, G. (ed), Proceedings Eurock´96 conference, Vol.2, Rotterdam, Brookfield. Balkema, 707–713, 1996.

Thuro, K., Plinninger, R.J., 2003. Hard rock tunnel boring, cutting, drilling and blasting: Rock parameters for excavatability. Proceedings of ISRM 2003, 1227–1233.

Tunnelling for a Better Life – Yan, Celestino, Thewes & Eberhardt (Eds)
© 2024 The Author(s), ISBN 978-1-032-80042-4
Open Access: www.taylorfrancis.com, CC BY-NC-ND 4.0 license

Critical issues in selecting conventional and mechanized tunnelling methods, lessons learned from the past

Nuh Bilgin* & Cemal Balci
Faculty of Mines Mining Engineering Department, Istanbul Technical University, Istanbul, Turkey

ABSTRACT: The population is increasing rapidly in urban areas. Parallel to this, the need for a better life will necessitate tunnels for rapid mobility; tunnels to solve energy, water, and sanitation problems, etc. This is reflected in the current worldwide tunnelling market, which is growing fast. In light of these, this paper is prepared to summarize the basic requirements of conventional and mechanized tunnelling methods in a comparative way and to give several examples from the past to make it clear to understand the problems encountered while applying these two tunnelling methods. The incorrect choice between the two methods may lead to tunnel construction lasting several years more than expected and the cost may be 3 or 4 times higher than originally estimated, as happened in T26 high-speed tunnel in Turkey and Yacambu-Quibor Water Tunnel in Venezuela. First, geotechnical, geological, and environmental factors limiting the selection of the tunnelling methods will be discussed given examples of T26 high-speed tunnel, Uluabat, and Kargı power tunnels from Turkey. The paper will discuss the shortest tunnel ever driven 120 m in length with a 6.2m diameter EPB-TBM within the complex Marmaray Project in Istanbul, emphasizing the big cities' environmental restrictions.

Keywords: Drill and blast, TBM Tunnelling, T26 high speed-tunnel, Uluabat tunnel, Kargi power tunnel

1 INTRODUCTION

There are two tunnelling methods; conventional and mechanized tunnelling. Conventional tunnelling can be defined as the construction of underground openings of with a cyclic construction method consisted of excavation by using the drill and blast method or very basic mechanical excavators, mucking, placement of the primary support elements such as steel arch or wire mesh, soil nails or rock bolts, shotcrete or in situ cast concrete.

The second tunnelling method is generally called mechanized tunnelling with TBM or roadheaders. The basic comparison between both methods is summarized in Table 1.

2 HYBRID METHOD, CONTRIBUTION TO TUNNELLING ECONOMY AND EFFICIENCY

Choosing the most appropriate tunnelling method: drill and blast or TBM or the hybrid approach deliberately using both is discussed in detail by Barton (2012). However, in this section, it is intended to enlarge the topic by giving two examples from Turkey which contributed to the efficiency and the economy of tunnelling.

Table 1. The comparison of both tunnelling methods.

Parameter	Drill and blast	Roadheader	TBM
Geometry	Any shape	Any shape	Circular
Safety	Low	High	High
Handling of explosives	Risky	Avoided	Avoided
Advance rate	Low	Depends on geology	Depends on geology
Length	Any	Any	A limited length
Flexibility	High	High	Not
Operation	Cyclical	Cyclical	Continuous
Initial investment	Low	Low	High
Overbreak	High	Low	Low
Noise and vibrations	High	Low	Low

*Corresponding author: bilgin@itu.edu.tr

DOI: 10.1201/9781003495505-220

2.1 *Kaynarca Kadıköy Metro line*

The general layout of the Kaynarca Kadıköy Metro line of 26.5 km in two lines is given in Figure 1.

Figure 1. The general layout of the Kaynarca Kadıköy Metro line.

The first part of the project from Kozyatagi to Kadıköy of 8,800 m in length was finished first with 2 EPB-TBMs with a mean daily advance rate of 10.5 m/day. The platform tunnels of this project were opened with drill and blast, impact hammers, and roadheadres. The topic is discussed in detail in a paper titled "A Criticism of Using Different Excavation Methods Related to Specific Geologic Conditions in the Istanbul Area" which was submitted to WTC 2024, by Balci and Bilgin (2024). The second part of the project from of Kaynarca to Kozyatagi of 17,700 m in length was rewarded to another construction company than the first one. Due to the limited time to complete the project, the contractor decided to open the twin tunnels of 4.6 km in length from Kartal to Kaynarca by two EPB-TBM of 6.57 m diameter. TBM used is given in Figure 2 and the details of TBM are tabulated in Table 2.

Figure 2. TBM used in Kartal Kaynarca tunnel.

Table 2. Main characteristics of EPB-TBM used in the project.

Machine diameter	6.57 m
Rotational speed	0.0- 5.33 rpm
Number of cutters	32 single, 4 double
Number of rippers	72
Cutterhead power	8x160 kW
Cutterhead torque 1	3663 kNm nominal
Cutterhead torque 2	5018 kNm maximum
Maximum Thrust	42,575 kN at 350 bar
Opening ratio	%35

Eight station shafts existed between Kartal and Kozyatagi enabling 8 faces for drill and blast operations. It was decided to open a 13,100 m tunnel with conventional tunnelling methods, Ozcan (2011), Senol, (2014), Senol et al. (2014a). The tunnel area was highly populated and a special blasting methodology was used to minimize the blasting vibrations as given by Kahriman et al. (2008), Ozer (2008). TBM finished the tunnels of 4,600 m in length with a main daily advance rate of 11.6 m/day. From a tunnel face, a daily advance rate of 2.7 m/day was possible to obtain with the drill and blast method. A planned synchronized hybrid tunnelling method enabled the contractor to finish the project before the scheduled time. Pie charts for the works executed for drill and blast method and TBM operations are given in Figures 3 and 4.

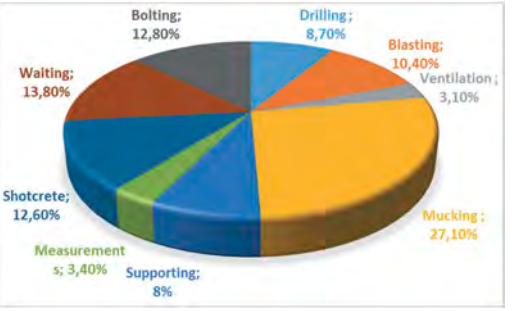

Figure 3. Work distribution in drill and blast, 2.7 m/day per round.

2.2 *Kargi project*

Another example of hybrid tunnelling project is Kargi hydropower project. As Barton mentions, "There are significant numbers of TBM projects that end up with difficult decisions to be made, namely to complete the projects by drill-and-blast from the other end of the tunnel. The deliberate selection of both TBM and drill-and-blast may often be a simple matter of common sense, giving schedule advantages and cost savings. This is the preliminary level of hybrid tunneling. Very often, time is lost while waiting for TBM

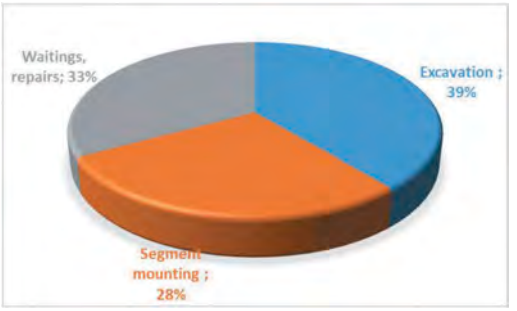

Figure 4. Work distribution in TBM excavation, mean 11.6 m/day.

delivery and assembly, and great advantages could be gained by selective use of drill-and blast for more than just the standard TBM assembly chamber and starter tunnel", Barton, 2002a, 2002b, 2016".

The 7.8 km of the total length of 11.8 km of Kargi tunnel was excavated with a double shield TBM of 9.84 m diameter, and 4 km of the tunnel from the inlet part was opened with NATM. TBM was launched in April 2012. After only a boring of 80 m, TBM became stuck in a section of the collapsed mixed ground face of hard rock and running ground. In the first 2 km of the tunnel, TBM jammed 7 times due to face collapses, and bypass tunnels were required to free the TBM. Continuous probe drilling was carried out for 5 km along the tunnel and an umbrella arch was applied in 9 different areas to stop face collapses excavation of the tunnel ended with success. Drilling and blasting at one end of the tunnel and TBM at the other end was a good alternative for decreasing the job termination time, Bilgin 2016. Figure 5 shows the comparison of advance rates of TBM against advance rates of drill and blast tunnelling through the Beynamaz Volcanites. It can be seen that the drill and blast operations took twenty-three months to complete 4,000 m of tunnel whereas it took less than 8 months for the TBM operations to complete the same length of the tunnel. Based on these production rates it would have taken approximately 32 months for the drill and blast operations to achieve the same production as the TBM achieved in 8 months.

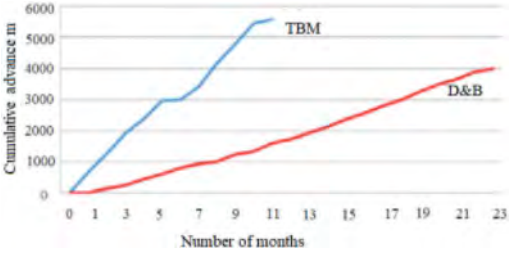

Figure 5. The comparison of TBM and drill and blast method based on cumulative advance and number of moths.

3 CHANGING THE TUNNELLING METHODOLOGY AFTER STARTING THE EXCAVATION

3.1 *T26 High-speed railway tunnel*

The complexity of the geology dictates the tunnelling methodology to be applied. Usually in such cases tunnel excavation starts with a conventional tunnelling method. Sometimes due to swelling of the rock or low Q values, the convergence experiences very high values which force the tunnelling method to be changed to mechanical excavation with TBMs. One example of this is T26 High Speed Railway Tunnel. The excavation started with the conventional tunnelling method in 2010. The tunnel is in the North-East of Turkey. Due to geological problems, shear zones, fault zones, and low RQD values, the daily advance rates were very slow. The tunnel excavation method was changed to mechanical excavation using a 13.7 m diameter single shield TBM at the end of 2011. Karakaya formation is the main formation in tunnelling area between the Pazarcik melange. It contains fault zones in several places. This formation has similarities with Karakaya Formation found in Uluabat Energy Tunnel, which will be discussed in the following paragraph. T26 tunnel is planned to pass through the predominated graphitic schist which includes frequently chlorite schist with a size of some tens of meters and rarely marble shear bodies with a dimension of a few tens of meters, Bilgin 2016. Graphitic schist is moderately weathered to fresh and very weak to weak and is extremely sheared along the foliation surface, which causes extreme loads to the precast segments. Finally, segments started failing on 16.11.2012 and the tunnel collapsed. TBM was buried. After tremendous efforts and remedial works tunnel excavation was decided to be carried out with drill and blast. Figure 6 shows the failure of the segment, and Figure 7 the thin section taken from the wall of the tunnel at Ring 484 (9 o'clock direction).

Figure 6. Failure of a segment in tunnel 26.

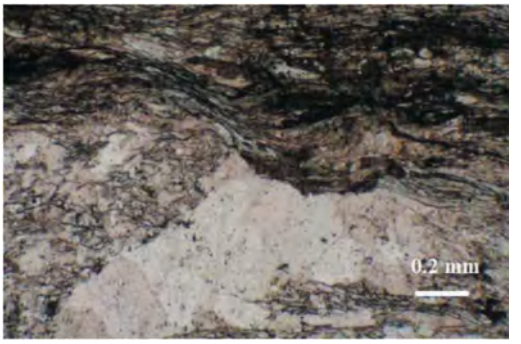

Figure 7. Thin secion of the graphitic schist from ring no 484, tunnel 26.

3.2 *Uluabat power tunnel*

Tunnel excavation commenced in 2002 from the portal next to Uluabat Lake, using conventional excavation methods with roof bolts, shotcrete, wire mesh, and steel arches as the primary tunnel support. Tunnelling operations were halted in November 2003 due to extreme roof deformations and floor heaves. Figure 8 shows the closure of the cross-section in the tunnel after a certain time for different stations. After the stoppage of tunnelling operations for about two and half years it was decided to continue the project with an EPB-TBM. During tunnel excavation, the TBM was stuck a total of 18 times. 192 days were spent on TBM rescue operations at different tunnel locations. A general view of the squeezing ground around the TBM shield, in Uluabat Tunnel is shown in Figure 9 The excavation terminated in March 2010, after a series of mitigation factors like injecting bentonite through the shield. It is reported that although the squeezing characteristics of the formations depend on several factors, it is closely related also to Q values, Barton and Bilgin, (2016).

This example shows how important it is to understand the squeezing characteristics of the formations and the mitigation factors to overcome the problems arising. The example is important since it dictates the time scheduling of a tunnelling project, to select the correct tunnelling methods and the mitigation factors to overcome.

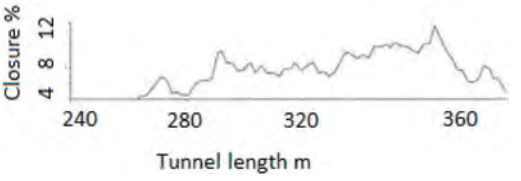

Figure 8. The closure of tunnel face area in % in conventional tunneling.

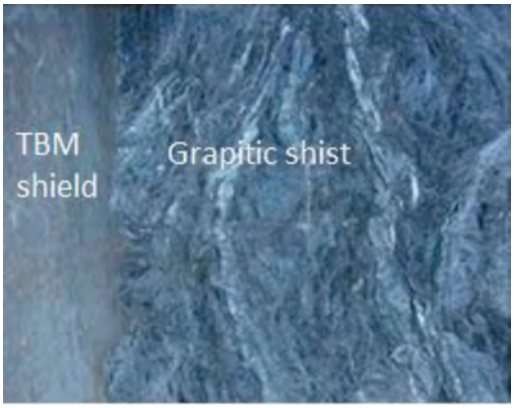

Figure 9. TBM shield and squeezing characteristic graphitic schist.

3.3 *Yacambu-Quibor water tunnel in Venezuela*

The project began in 1974, but it took 34 years to be completed, for technical, political, and financial reasons. Over those 34 years, the project was stopped and started up again eight times using TBMs, roadheaders, and conventional tunnelling methods. The tunnel, instead of costing $173 million as originally expected, ended up costing more than $800 million in current dollars, Ramonet, 2008. The geology consists of sandstone, phyllite, and limestone. The graphitic phyllite has a squeezing characteristic and has compressive strength changing between 15-50 MPa and the estimated GSI value is about 24, (tunnelbuilder.com., 12/08/2008) Graphitic phyllite is a very poor quality rock that causes serious squeezing problems which, without adequate support, results in the closure of the tunnel at an important level. Tectonically deformed graphitic phyllite on the tunnel face is seen in Figure 10 Hook and Guevara (209).

The readers are invited to to check the similarity of the rock material in Figure 9 and 10.

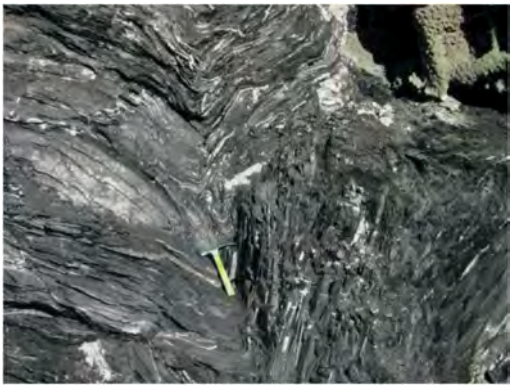

Figure 10. Graphitic schist at the Yacambú-Quíbor tunnel, Hoek and Guevara, 2009.

4 ENVIRONMENTAL CONDITIONS RESTRICTING THE USE OF TBM, ONE OF THE SHORTEST TBM TUNNELS OPENED

The north entrance tunnel of Sirkeci Station is a part of the Marmaray Project/Istanbul as outlined in Figure 11. It has a length of 120 m and it was originally designed to open with a conventional tunnelling method. Detailed geological investigation showed that the conventional tunnelling method was very risky due to bad ground conditions and a low overburden of 20 m. It was decided later to drive the tunnel with an EPB-TBM of 6.2 in diameter, which was the 6th TBM used in the first phase of the project, where 5 TBMs were slurry type. The launch EPB-TBM in the north entrance tunnel is shown in Figure 12. The excavation of the tunnel lasted one month without serious surface deformations. The final profile of the north entrance is shown in Figure 13. As far as the authors knowledge this tunnel is the shortest tunnel opened by mechanized tunnelling methods. To understand the construction concept of the Marmaray project, the readers are referred to consult Figure 13.

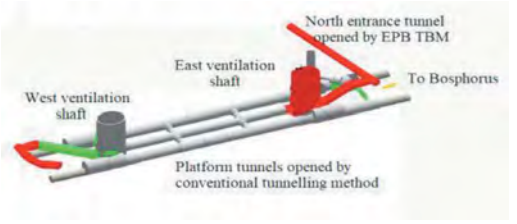

Figure 11. Marmaray project/Istanbul Sirkeci undrground station.The figure is kindly provided by Niyazi Sennazlı.

Figure 12. The portal of the tunnel.

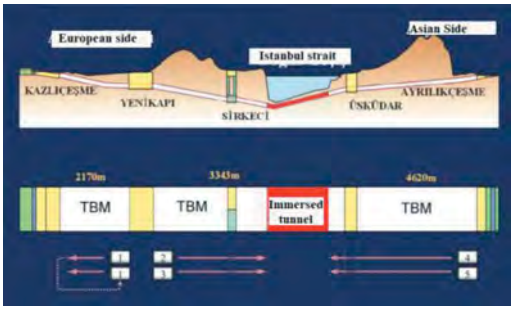

Figure 13. Construction concept of Marmaray tunnel.

5 CONCLUSIONS

The incorrect choice between conventional and mechanized tunnelling may lead to tunnel construction lasting several years more than expected and the cost maybe 3 or 4 times higher than originally estimated. First, the contribution of the hybrid method to tunnelling economy and efficiency is discussed given examples of Kargi power tunnel and, Kaynarca - Kadıkoy Metro tunnels in Istanbul. In this metro tunnel it was decided to open a 13,100 m tunnel with conventional tunnelling methods. The tunnel area was highly populated and a special blasting methodology was used to minimize the blasting vibrations. TBM finished the tunnels of 4,600 m in length with a main daily advance rate of 11.6 m/day. From a tunnel face, a daily advance rate of 2.7 m/day was possible to obtain with the drill and blast method. A planned synchronized hybrid tunnelling method enabled the contractor to finish the project before the scheduled time. Pie charts for the works executed for drill and blast method and TBM operations are given in Figures 3 and 4. Changing the tunnelling methodology after starting the excavation is another challenge as happened in T26 High-speed railway tunnel and Uluabat Tunnels in Turkey and Yacambu-Quibor Water Tunnel in Venezuela. One of the shortest tunnels of 120 m in length, driven with a EPB-TBM of 6.2 m in diameter EPB-TBM within the complex Marmaray Project in Istanbul, emphasis the big cities' environmental restrictions We hope that the summary of critical issues discussed in this paper in Selecting conventional and mechanized tunnelling methods will help in the future to decision makers of the tunnel designers.

ACKNOWLEDGMENTS

The information on section "Environmental Conditions Restricting the Use of TBM, one of the Shortest TBM Tunnel Opened" is provided by Nurettin Demir, Bülent Çakar and Niyazi Şennazlı. Şener Şenol provided his report on Kartal Kaynarca Tunnel. The authors are grateful to the people mentioned for their generous help in writing this paper.

REFERENCES

https://tunnelbuilder.com/News/Yacambu-Quibor-Water-Tunnel-Breaks-Through.aspx., 12/08/2008.

Alan, E. 2018. Determining “k” and “β” Coefficients of the Formation that Excavated by Blasting on Kadıköy-Kartal Metro Route, The Effect of Detonator Delay Time on Amplitude. Proceedings of the 4th International Symposium on Underground Excavations for Transportation, Organized by Turkish Tunnelling Society and Chamber of Mining Engineers of Turkey, Istanbul Branch.

Bilgin, N., 2016. An appraisal of TBM performances in Turkey in difficult ground conditions and some recommendations, Tunnelling and Underground Space Technology 57, 265–276.

Balci, C., Bilgin, N., 2024. A Criticism of Using Different Excavation Methods Related to Specific Geologic Conditions in the Istanbul Area, paper submitted to WTC 2024.

Barton, N., 2002a. Reducing risk in long deep tunnels by using TBM and drill-and-blast methods in the same project–the hybrid solution, Journal of Rock Mechanics and Geotechnical Engineering, 4 (2): 115–126.

Barton, N. 2012b Hybrid TBM and Drill-and-Blast from the start. Tunnelling Journal, p 22–32.

Barton., N, Bilgin, N, 2016. Fast or slow progress with TBM in ideal or faulted conditions, Rock Mechanics and Rock Engineering: From the Past to the Future – Ulusay et al. (Eds) © 2016 Taylor & Francis Group, London, ISBN 978-1-138-03265-1.

Hoek, E and Guevara, R. 2009. Overcoming squeezing in the Yacambú-Quibor tunnel, Venezuela. Rock Mechanics and Rock Engineering, Vol. 42, No. 2, 389–418.

Kahriman, A., Ozer, U., Adiguzel, D., Karadogan, A., Aksoy, M., Mustu, R., Dincel, E., Alan,E., Sefer, İ., 2007b. The analysis of ground vibrations induced by blasting on Istanbul Kadıköy–Kartal subway tunnel route. The 2nd Symposium on Underground Excavations for Transportation, 15–17 November 2007, pp. 571–582, symposium organized jointly by Turkish Chamber of Mines, Istanbul Branch, and ITU Faculty of mines, Proceedings, ISBN 978-9944-89-400-5.

Ozcan, A.K., 2011. M.Sc thesis, The performance of two TBMs in Kartal-Kaynarca section of Kartal-Kadıköy Metro Project, Okan University, Civil Engineering Department, Blasting Engineering Program, İstanbul, p.70.

Ozer, U., 2008. Environmental impacts of ground vibration induced by blasting at different rock units on the Kadikoy–Kartal metro tunnel, Engineering Geology 100 (2008) 82–90. doi:10.1016/j.enggeo.2008.03.006.

Ramonet.,D, 2008, Venezuela completes Yacambú-Quíbor water transfer tunnel, EIR, 35 (32) Number 32, p 32.

Senol, S., 2014. M.Sc Thesis. The comparison of TBM and drill and blast tunnelling performance in Doloyaba Formation, Okan University, Civil Engineering Department, Blasting Engineering Program, İstanbul, p.84.

Senol, S., Biberoglu, S., Posluk, E., Eitaz, I., 2014. The comparison of blasting excavation in the running tunnel being excavated through Doloyaba Formation. 67th Geological Congress of Turkey, 14-14 April 2.

Tunnelling for a Better Life – Yan, Celestino, Thewes & Eberhardt (Eds)
© 2024 The Author(s), ISBN 978-1-032-80042-4
Open Access: www.taylorfrancis.com, CC BY-NC-ND 4.0 license

Computational modeling of cutting disc-rock interaction in mixed ground conditions

Sahir N. Butt*
Institute for Structural Mechanics, Ruhr University Bochum, Germany

Jamal Rostami
Earth Mechanics Institute, Colorado School of Mines, USA

Günther Meschke
Institute for Structural Mechanics, Ruhr University Bochum, Germany

ABSTRACT: In this paper, we present a simulation tool based on the state-based peridynamic theory, developed to model the interaction between cutting discs of a TBM and the ground being excavated. As compared to existing TBM performance prediction models, this computational model allows to consider various heterogeneous and mixed ground conditions, different TBM and disc designs, as well as the direct coupling with wear models. Furthermore, the consequences of wear in terms of partially degraded or damaged discs on the excavation performance can be assessed numerically. The developed model is thoroughly validated using several benchmarks, including indentation tests on sandstone specimens and biaxial strength tests for concrete. The simulation model was further tested by simulating a full-scale LCM (Linear Cutting Machine) test conducted on Colorado Red granite, and the resulting cutting forces at various disc spacings are compared with experimental data. To investigate excavation in mixed ground conditions, which can lead to abnormal tool wear and even failure, an LCM experiment is performed where the cutting disc excavates through a series of rocks with a high contrast in UCS (Uniaxial Compressive Strength). These experiments successfully identify an overshoot in the cutting force as the disc enters the rock domain with a higher UCS which can cause localized damage to the cutting disc. The cutting forces obtained from scaled-down simulations using the developed model for mixed ground excavation scenarios exhibit qualitative agreement with the LCM experiment. Additionally, the simulation model is equipped with an abrasive wear model, which is verified using analytical solutions. This implemented wear model is able to identify the changes in wear rates as the cutting disc excavates through varying rock formations. Finally, the versatility of the simulation model is demonstrated by investigating various aspects of the cutting disc-ground interaction, including the efficiency of excavation with varying disc geometries.

Keywords: Hard rock excavation, Mixed ground, Performance prediction, Abrasive wear, LCM test, Peridynamic simulation

1 INTRODUCTION

Excavation processes involving a Tunnel Boring Machine (TBM) use cutting discs to fracture and excavate rock. These cutting discs are mounted on a rotating cutterhead of the TBM, which is pressed against the tunnel face. As the cutting disc penetrates the rock, the pressure in the contact area between the disc and the rock surface increases and a crushed zone develops (Rostami, 2013). The stresses in this zone continue to increase, leading to the initiation of radial cracks. These cracks grow and coalesce with adjacent cracks until the rock mass is disintegrated (Cho et al., 2010). The interaction between the rock and a cutting disc can be characterized by three-dimensional reaction forces at the disc. To accurately predict the performance of a TBM, including global thrust and torque requirements, and to design new cutter heads for specific ground geology, it is necessary to estimate the cutting forces for a single disc cutter. In addition, the loads on the disc cutters cause severe wear and damage to the tools. To plan maintenance stops and avoid unexpected TBM stoppages, it is necessary to estimate the working life of cutting tools in a given geology.

The cutting process in hard rock is modeled using the Peridynamics (Silling, 2000), (Butt and Meschke, 2021) continuum formulation. This class

*Corresponding author: sahir.butt@rub.de

DOI: 10.1201/9781003495505-221

of models allow, in contrast to standard continuum mechanics theories, for the modeling of complex fragmentation processes. The reason is, that the stresses are computed from a direct interaction of material point x, with a set of material points x´ within a volume defined by a cut-off radius δ known as the peridynamic horizon. This notion of direct connectivity between the material points is referred to as a bond. Fracture processes are modelled by irreversibly deleting the bonds between the material points once they reach a critical value. Once a bond fails, it does not further contribute to the internal force calculation. In this study, the critical energy required to break a bond is calibrated using the fracture energy of the rock.

2 ROCK INDENTATION

This section presents the indentation tests performed on a porous sandstone using a blunted tip indenter. The standard ordinary state-based peridynamic simulation model (Silling, 2000), (Silling et al., 2007), (Foster et al., 2011) is extended to consider the additional dissipation due to the pore-collapse phenomenon observed in porous rocks and applied to the indentation test of a sandstone. Qualitative features of indentation are analyzed through Acoustic Emission (AE) data obtained from the experiments performed on Bentheim sandstone (Yang et al., 2022). Quantitatively, the model is validated by comparison of force-penetration and indentation-penetration data obtained in the experiments by the simulation results.

2.1 *Consideration of the pore-collapse phenomenon*

Ordinary state-based peridynamic model has been thoroughly investigated for the tension-dominated fracture problems, including failure strengths and crack dynamics (Butt and Meschke, 2018), (Butt et al., 2022). However, for cases where the dominant loading is in compression (Butt and Meschke, 2021) and additional nonlinear dissipation phenomena, such as the pore-collapse, are present, the model underpredicts the failure strengths (Butt, 2023). To this end, the standard ordinary state-based peridynamic model (Silling et al., 2007), (Foster et al., 2011) is extended to consider the pore-collapse phenomenon in porous materials.

The mechanical properties and the deformation characteristics of Bentheim sandstone were studied under triaxial loads by Klein et al., 2001. The material parameters for Bentheim sandstone are presented in Table 1. It is a relatively homogeneous porous rock, and these pores collapse under compressive loads leading to stiffening of the material, this effect can be seen by comparing the volumetric strain predicted by a constant bulk modulus with the one obtained in the experiments under hydrostatic compression, as shown in Figure 1. This stiffening under compressive pressure, due to pore-collapse, contributes to a significant increase in the total dissipated energy.

Table 1. Material properties of bentheim sandstone.

Material parameter	Value
Young's modulus (GPa)	9.5
Poisson's ratio	0.18
Density (kg/m^3)	2011
Fracture energy (J/m^2)	10
Porosity (%)	24

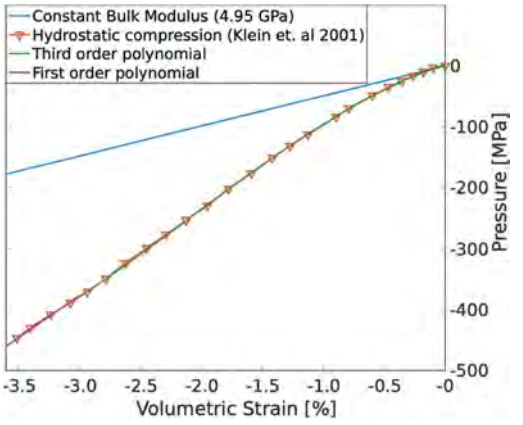

Figure 1. Relationship between hydrostatic pressure and volumetric strain from Klein et al., 2001, and a first- and a third-order polynomial fit to the experimental data.

The material stiffening due to pore-collapse is modeled by using the experimental relationship between the hydrostatic compression and volumetric strain (Figure 1) instead of just using a constant Bulk modulus. According to Klein et al., 2001, this relationship has one inflection point leading up to a compressive volumetric strain of 3.0% and after that, this relationship becomes linear again. So, the range of the volumetric strains from 0% to −3.0% is fitted with a third-order polynomial and for compressive volumetric strain greater than 3.0% a linear relationship is adapted. Additionally, these volumetric deformations are assumed to be irreversible, as pore-collapse is an irreversible process.

For the modification of the ordinary state-based linear elastic model, an additive split is defined for the dilatation under compressive deformation as:

$$\theta(\mathbf{x},t) = \begin{cases} \theta^e(\mathbf{x},t) & \text{if } \theta(\mathbf{x},t) > 0 \\ \theta^e(\mathbf{x},t) + \theta^{pc}(\mathbf{x},t) & \text{if } \theta(\mathbf{x},t) < 0 \end{cases} \quad (1)$$

Here $\theta^e(\mathbf{x}, t)$ is the reversible elastic part of the volumetric strain and $\theta^{pc}(\mathbf{x}, t)$ is the irreversible volumetric strain representing the pore-collapse under compression. Pressure $p(\mathbf{x}, t)$ is computed according to:

$$p(\mathbf{x},t) = \begin{cases} K\,\theta(\mathbf{x},t) \\ K_1 + K_2\,\theta(\mathbf{x},t) + K_3\,\theta(\mathbf{x},t)^2 + K_4\,\theta(\mathbf{x},t)^3 \\ K_5 + K_6\,\theta(\mathbf{x},t) \end{cases} \tag{2}$$

For the following different compression regimes, respectively.

$$\begin{aligned} &\text{if } \theta(\mathbf{x},t) > 0 \\ &\text{if } -0.03 < \theta(\mathbf{x},t) < 0 \\ &\text{if } \theta(\mathbf{x},t) < -0.03 \end{aligned} \tag{3}$$

In Equation 2, K is the Bulk modulus, K_1, K_2, K_3 & K_4 are calibrated for a third-order polynomial and K_5 & K_6 are calibrated for a first-order polynomial using the experimental data from Klein et al., 2001, as shown in Figure 1. The applicable range of volumetric strain for the third- and first-order polynomial are shown in Equation 3. For further details regarding the formulation of the state-based peridynamic pore-collapse model, the interested reader is referred to Butt and Meschke, 2023.

2.2 *Consideration of material heterogeneity*

Materials like rocks and concrete have inherent heterogeneity and random defects that must be accounted for in the model. To address rock heterogeneity in the simulations, strength parameters such as the fracture energy are sampled from a probability distribution. According to the literature (Hudson et al., 1969), Weibull's distribution has been found to well represent the distribution of micro-defects in the rocks. Therefore, the simulations will consider the strength parameters sampled from a Weibull distribution (Weibull, 1951), it is given by:

$$P(\sigma) = \frac{k}{\sigma_0}\left(\frac{\sigma}{\sigma_0}\right)^{k-1} \exp\left[-\left(\frac{\sigma}{\sigma_0}\right)^{k}\right] \tag{4}$$

Here, σ is the sampled parameter, σ0 is the mean value of the parameter to be sampled and k is known as the shape parameter. The shape parameter k represents the level of homogeneity of the material, where a larger k represents a more homogeneous material and vice versa (Figure 2). Simulations use a value of k = 3 for the shape parameter according to Liu et al., 2018.

The open-source software Peridigm (Parks et al., 2012) was extended to consider the pore-collapse model as well as the distributed strengths in the simulation domain. This extended version of Peridigm is used to carry out the simulations presented in the next section.

2.3 *Rock indentation simulations*

Numerical and experimental investigations (Yang et al., 2022), (Lindqvist et al., 1984) have shown that the rock fragmentation under indentation involves several progressive deformation mechanisms including the elastic deformations at an initial loading stage, then the volumetric compaction, plastic deformation, and finally the macro fracture. Thus, it is necessary for a simulation model to be able to reproduce these qualitative features observed in the indentation experiments.

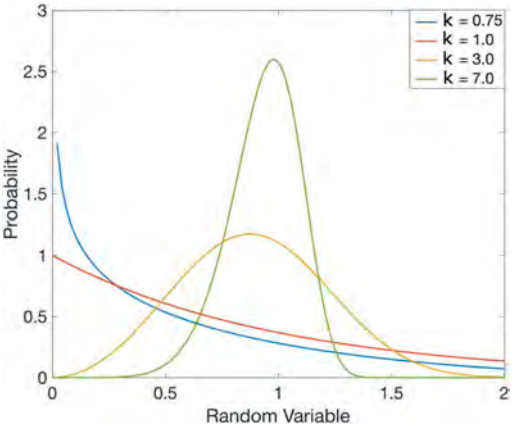

Figure 2. Weibull distribution for a scale factor 1.0 and various shape parameters *k* (top).

Simulations performed in this study for the indentation tests cover a total of six specimen sizes, with a combination of three diameters 30, 50 and 84 mm and two heights 50 and 100 mm. For validating the current model, we use the experimental data from indentation tests on Bentheim Sandstone reported in (Yang et al., 2022). The temporal evolution of fractures occurring due to the indentation load is presented in Figure 3 for a specimen with 30 mm diameter and 100 mm height. The simulation captures the experimental observation of the successive formation of the crushed zone and the initiation of a central macroscopic tensile fracture splitting the sample in half. Once the tensile stresses at the perimeter of this zone exceed a critical value, a tensile crack is formed which splits the specimen. As this tensile crack propagates, it exceeds a critical crack propagation velocity, at which the crack tip bifurcation takes place and the crack branches (Butt and Meschke, 2018), as shown in the middle column of Figure 3. Finally, the specimen splits into two main and several small fragments (right column of Figure 3).

The indentation pressure resulting from the indentation loads is calculated using:

$$p = \frac{F}{4\sqrt{2R_{\text{ind}}d - d^2\left(a_0 + \frac{d}{\tan\alpha}\right)}} \tag{5}$$

Here, F is the indentation load, d is the indentation depth, Rind is the radius of the indenter tip, a_0 denotes the half width of the indenter tip, and α is the angle between the indenter and the specimen surface (here 40°). For further details of the indenter

Figure 3. Temporal evolution (left to right columns) of the fracture process during the indentation test (top row), the associated damaged and cracked regions are filtered out for visualization (bottom row).

geometry, the interested reader is referred to Yang et al., 2022. The indentation force- penetration and the pressure-penetration relationship computed from the simulations are compared with the experimental data in Figure 4. The loading stiffness, the peak load as well as the peak indentation pressure predicted by the simulation are in a good agreement with the experiments.

3 LINEAR CUTTING MACHINE (LCM) TEST

LCM test (Rostami, 1997) was developed at the Colorado School of Mines (CSM) to predict the performance of a single cutting tool. In the LCM experiment, a cutting disc moves along a rock specimen at a known penetration level and tool spacing, and tool-rock interaction is characterized by the reaction forces on the cutting disc. Several cutting lines at a fixed spacing can be performed, which comprise a cutting pass, the cutting forces can then be averaged over these cutting lines. These forces are decomposed into normal, rolling, and side forces and they are used to predict the global thrust and torque requirements for a TBM.

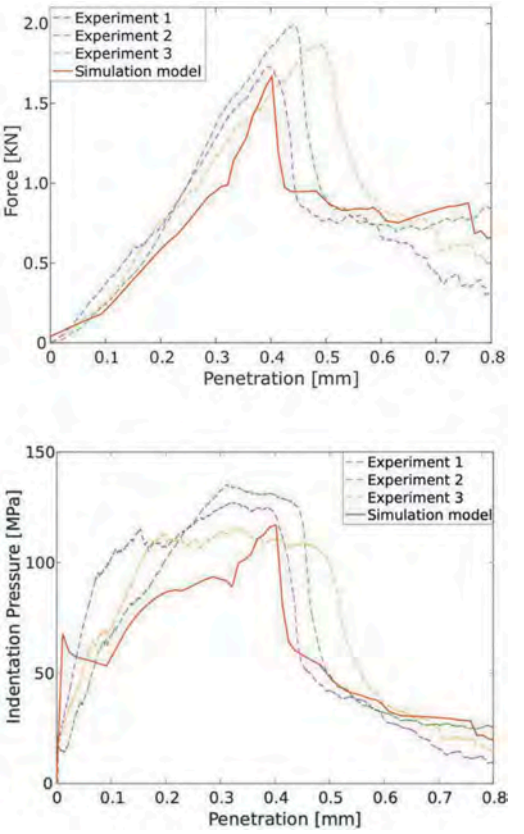

Figure 4. Comparison of the indentation force-penetration (top) and the indentation pressure-penetration (bottom) relationship measured in the experiments and computed from the simulations.

The LCM test is a widely used experimental procedure to predict the performance of a single cutting tool (Gertsch et al., 2007), and it uses cutting tools of the actual size instead of scaled-down versions (Entacher et al., 2014). This method facilitates direct measurement of the cutting forces under controlled process parameters, such as the tool penetration, spacing, and cutting speed. LCM testing is also suitable for validating rock cutting simulation models (Butt and Meschke, 2017, Cho et al., 2013, Labra et al., 2017). LCM-type simulations can be performed to predict the performance of a single cutting disc while varying different process parameters and tool geometries.

3.1 *Simulations of the LCM test*

This section presents peridynamic simulations of the LCM test carried out on Colorado red granite using an extended version of the open-source software

Peridigm (Parks et al., 2012). The simulations consider both relieved and unrelieved rock cutting cases. Relieved and unrelieved rock cutting modes refer to the stress state present in the rock during the excavation process. In relieved cutting mode, the fractures initiated from the adjacent cutting tools interact with each other and relieve the stress state in the rock, resulting in lower levels of cutting forces. In contrast, in unrelieved cutting mode, the surrounding rock mass is intact and stresses are not relieved, leading to higher forces on the excavation tools.

Table 2. Material properties of colorado red granite.

Material parameter	Value
Young's modulus (GPa)	41
Poisson's ratio	0.234
Density (kg/m^3)	2650
Tensile strength (MPa)	6.78
Compressive strength (MPa)	158

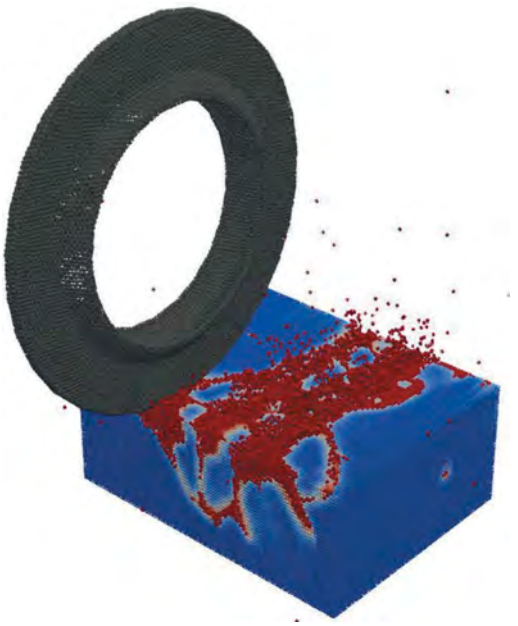

Figure 5. Simulation of the LCM test showing evolving damaged zones just before the third pass of the tool at a spacing of 76 mm and a penetration level of 7 mm.

The simulation model requires an initial calibration according to the pressure-dependent critical-energy model (Butt, 2023), in order to reproduce uniaxial tensile and compressive strengths (UTS and UCS), respectively. It should be noted that Brazilian tensile strength (BTS), commonly used in rock mechanics, can also be used to calibrate Gc, instead of the UTS used here. After calibrating UTS and UCS, simulations of the LCM test for both relieved and unrelieved cases are performed. The material parameters used for Colorado red granite, as reported in Gertsch et al., 2007, are presented in Table 2. The heterogeneous nature of the rock is considered using randomly distributed strength parameters, as explained in Section 2.2. For further details the interested reader is referred to Butt, 2023.

The simulation setup for LCM test presented here is similar to the one used by Butt, 2023. These simulations can be performed at various tool spacings and tool penetration depths. Simulations are conducted with three cutting disc passes at a fixed penetration and spacing, as shown in Figure 5. The first cutting line is used for rock conditioning to damage the rock and mimic the previous tool pass, as in the LCM test and rock cutting with a hard rock TBM cutterhead. The average cutting forces presented in this section are obtained by averaging the forces over the second and third cutting pass.

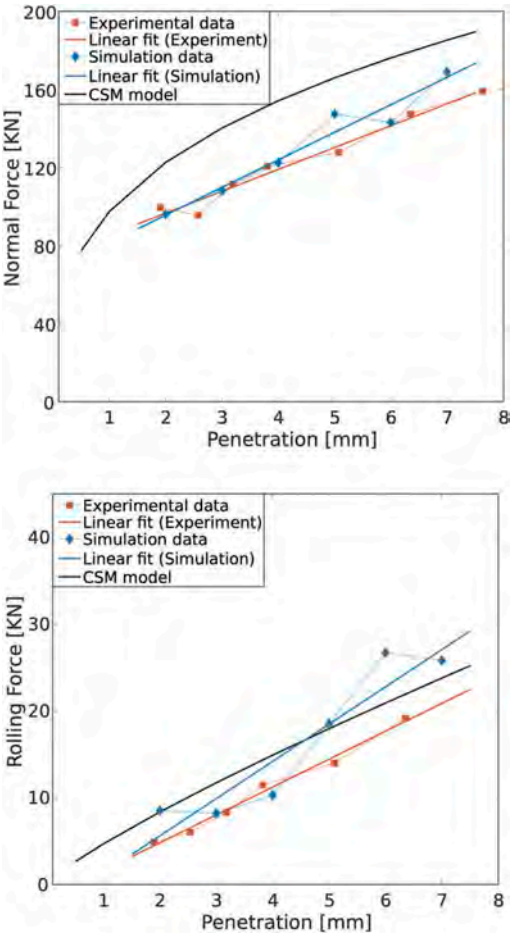

Figure 6. Average normal (top) and rolling (bottom) forces obtained from peridynamic simulations are compared with the CSM model and experimental data for various tool penetration levels and a tool spacing of 76 mm.

Simulation results show that the peridynamic approach can capture the chipping process and cutting forces in rock cutting simulations. For a tool penetration of 7 mm and spacing 76 mm, Figure 5 illustrates that the simulation captured the formation of rock chips between the tool passes. The average cutting forces obtained for a tool spacing of 76 mm at various penetration levels are compared with the CSM model (Rostami, 1997) and experimental data (Gertsch et al., 2007) in Figure 6. The normal cutting forces are in good agreement with the experiment, while the rolling forces are slightly overestimated. As the tool spacing is reduced, the chipping process becomes inefficient, leading to lower cutting forces but also lower excavated rock mass (Butt, 2023).

The average cutting forces obtained from the simulations in this section exhibit significant scatter due to the probabilistic nature of these simulations. As the strength parameters used to model the heterogeneous nature of the rock are randomly sampled from a Weibull distribution (Section 2.2), each simulation has a slightly different spatial distribution of material strength. These differences can result in the observed scatter. Ideally, a multi-simulation approach should be adapted for these cases to find an average solution. However, performing a large number of simulations with such high resolution would require a considerable computational effort and is outside the scope of the current work.

4 MIXED GROUND CONDITIONS

Mixed or heterogeneous ground conditions occur when a tunnel face has two or more layers of rock or soil with significantly different mechanical properties. Mechanized tunneling in such conditions results in highly variable loads on the cutting discs. As the cutting disc moves from soft to hard ground, an excessive load is exerted on the cutting disc at the point of contact with the hard ground layer, as shown in Figure 7. This excessive load contributes to the global torque fluctuation of the TBM and may substantially increase wear rates and cause localized damage to the cutting disc and bearings, leading to unexpected TBM stoppages and delays in the project timeline.

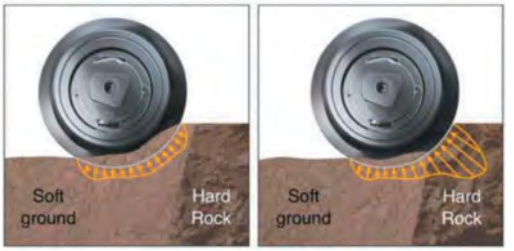

Figure 7. Schematic illustration of the forces acting on a cutting disc at a mixed face tunnel.

4.1 *Mixed-ground LCM experiment*

The contrast of material properties at the tunnel face is replicated in an LCM experiment with a rock sample constructed using limestone and granite casted in concrete (Butt, 2023). As the cutting disc moves through the various interfaces in the specimen (for e.g. concrete-granite interface) an abrupt change in the cutting forces is measured. Average normal forces obtained from four cutting passes are shown in Figure 8. It can be observed that as the cutting disc moves from concrete into granite (first dotted vertical line in Figure 8), the cutting disc experiences an overloading which can cause abnormal wear as well as localized damage to the cutting disc. In the next subsection, the potential of peridynamic modelling is explored to simulate the rock cutting process in in mixed-ground conditions.

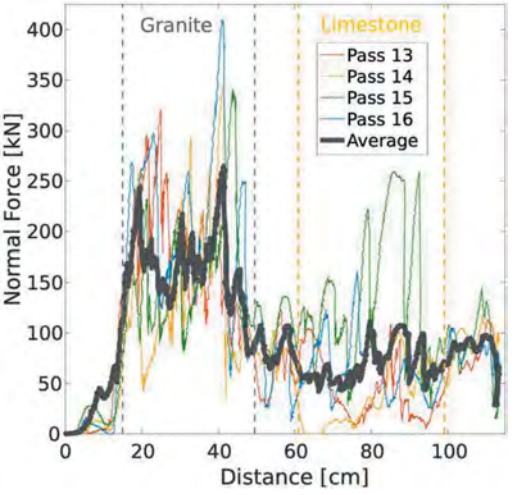

Figure 8. Average cutting forces obtained from four cutting passes in a mixed ground LCM experiment.

4.2 *Simulations of mixed-ground LCM test*

Mixed ground conditions are simulated in this section using LCM tests where a cutting disc moves from soft soil into a hard rock domain. The simulations used a scaled cutting disc of 56 mm diameter and a rock specimen of 0.2×0.15×0.075 m, as experimentalists have used such scaled cutting tests to facilitate the experimental setup and the availability of the apparatus in the laboratory (Entacher et al., 2014). Scaled tests were used here due to the large computational expense associated with a full-scale test.

The soil material is modeled using an elastic-plastic Drucker-Prager type plasticity model, and the rock material is modeled using an elastic-brittle constitutive relation. The objective of these analyses is to characterize the impulse load and resulting wear on the cutting disc as it moves through the interface between two materials with significantly different

mechanical properties. Such repeated impulse loads can cause excess vibration in the cutterhead and increased fluctuations in torque and thrust of the TBM, which may ultimately result in premature damage to the cutting disc.

Plastic deformations in the soil and the damage level in the rock obtained from the simulations of the cutting disc moving from soil to rock domain are presented in Figure 9. The reaction forces obtained fort two penetration levels (2 mm and 3 mm) are shown in Figure 10. These diagrams show that the normal cutting forces are negligible when the disc cutter is in the soil domain. However, as it reaches the soil-rock interface (cutting length = 0.05 m) and continues to move into the rock domain, the cutting forces show a peak of relatively high cutting forces. As anticipated, the comparison of cutting forces at the two penetration levels in this study shows that the peak cutting force increases proportionally with the tool penetration.

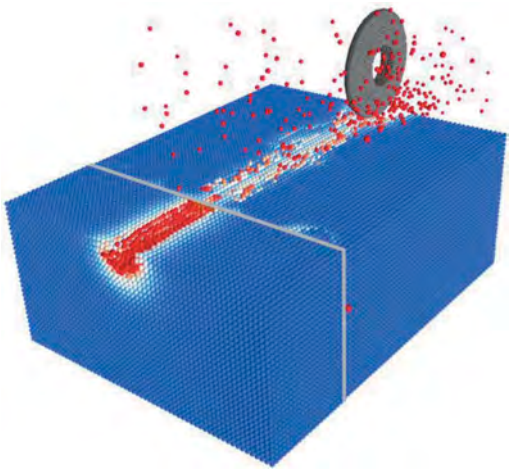

Figure 9. Plastic deformations and damage in hard rock obtained from a peridynamic simulation of a cutting disc working in mixed ground conditions (soft soil to hard rock domain) with a penetration of 3 mm.

An Archard type abrasive wear model (Archard, 1953) has been implemented in the open-source software Peridigm. The simulation model is verified based on a simple sliding test for the abrasive wear. For further details regarding the abrasive wear model, the interested reader is referred to Butt, 2023. The verified model for abrasive wear is utilized in conjunction with the simulations for mixed ground conditions to estimate the abraded volume on the cutting discs and localized wear occurring at the soil-rock interface. Figure 11 (top) displays the accumulated wear on the cutting disc, for a 180° rotation, for two penetration levels at three different stages: in the soil domain (left column), at the soil-rock interface (middle column), and in the rock domain (right column). The figure reveals a significant increase in accumulated wear on the cutting disc as it progresses into the rock domain. Figure 11 (bottom) presents the total volume loss due to abrasive wear on the cutting disc over the cutting length for both penetration levels. A notable change in wear rate is evident as the cutting disc moves from the soil to the rock domain.

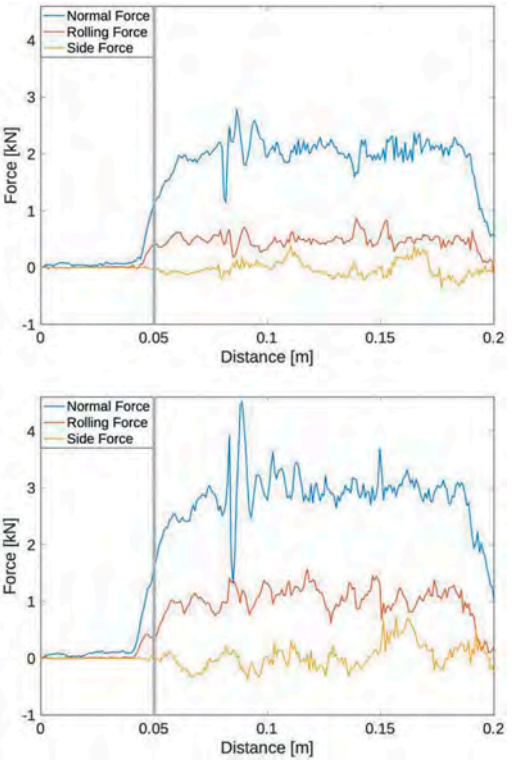

Figure 10. Cutting forces acting on a cutting disc working in mixed ground conditions (soft soil to hard rock domain) obtained from a peridynamic simulation for a penetration level of 2 mm (top) and 3 mm (bottom). The vertical grey line at 0.05 m cutting distance represents the soil-rock interface.

5 CONCLUSIONS

The rock indentation and excavation by means of cutting discs of a TBM has been investigated using an extended peridynamic simulation model. The simulation results for the indentation tests obtained using the extended model were validated through comparison with force-penetration and pressure-penetration data from experiments performed on Bentheim sandstone samples of various sizes. The simulation technique was further validated by simulating LCM tests on granite samples while considering the rock material heterogeneity through random sampling of strength parameters from a Weibull distribution. The cutting forces were found to be in good agreement with the experimental data and the

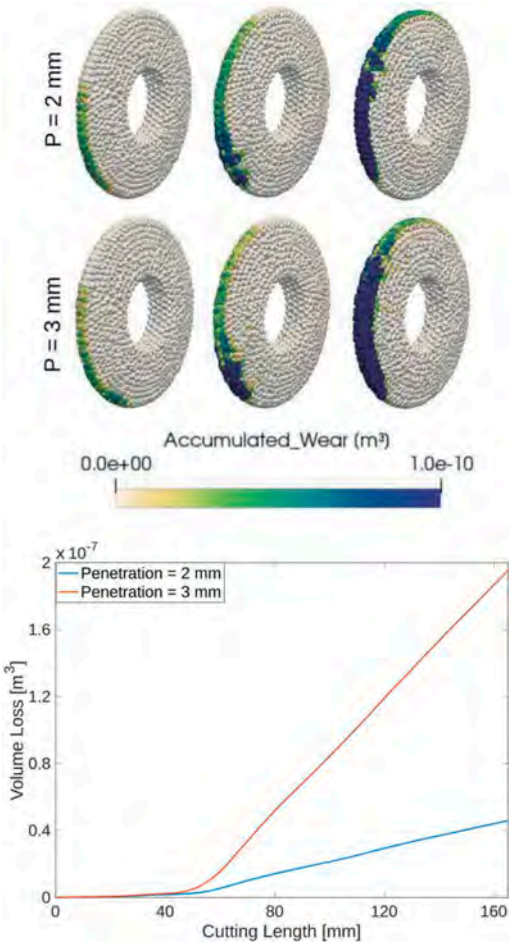

Figure 11. Comparison of the abrasive wear on the cutting disc working in mixed ground conditions (Figure 9 and 10) at two different penetration levels (top). Total volume lost on cutting disc due to abrasive wear over the cutting length (bottom).

CSM model predictions. In addition, the simulation model was used to perform LCM tests for mixed ground conditions where the cutting disc moves from a soil medium, modeled using a Drucker-Prager type plasticity model, to a hard rock medium. An Archard-type wear law was incorporated in the simulation model to simulate abrasive wear of the cutting discs. The mixed ground simulations revealed an abrupt increase in the cutting forces as the disc moves from soil to rock medium, resulting in uneven wear of the cutting disc. These results demonstrated the effectiveness of the proposed method in accurately identifying the cutting forces on the cutting discs working in changing ground conditions. The extended simulation model has a promising potential for modeling the rock excavation process in various scenarios.

ACKNOWLEDGMENTS

The authors gratefully acknowledge the financial support provided by the German Science Foundation (DFG) in the framework of project C4 of the Collaborative Research Center SFB 837 Interaction modeling in mechanized tunneling (Grant-No. 77309832).

REFERENCES

Archard, J. (1953). Contact and rubbing of flat surfaces. Journal of applied physics 24(8), 981–988.

Butt, S. and Meschke, G. (2017). A 3D peridynamic model of rock cutting with TBM disc cutters. Proceedings of the 7th GACM Colloquium on Computational Mechanics, Stuttgart, Germany, pp. 752–755.

Butt, S. and Meschke, G. (2018). A rate-dependent damage model for prediction of high-speed cracks. Proceedings in Applied Mathematics and Mechanics (PAMM).

Butt, S. and Meschke, G. (2021). Interaction of cutting disc with heterogeneous ground. Proceedings of Applied Mathematics and Mechanics 20, 20: e202000060.

Butt, S., A. Leon, and G. Meschke (2022). Numerical modeling of cutting tool-ground interaction. In M. Villeneuve, R. Galler, and N. Gegenhuber (Eds.), Proceedings of TBM DiGs 2022, Leoben, Austria.

Butt, S. N., & Meschke, G. (2023). Peridynamic simulations of rock indentation. Proceedings in Applied Mathematics and Mechanics, e202300051.

Butt, S. (2023). Computational fracture and fragmentation modeling using peridynamics: Application to mechanized excavation in hard rock. PhD thesis, Ruhr University Bochum.

Cho, J.-W., S. Jeon, H.-Y. Jeong, and Chang, S.-H. (2013). Evaluation of cutting efficiency during TBM disc cutter excavation within a Korean granitic rock using linear-cutting-machine testing and photogrammetric measurement. TUST 35, 37–54.

Entacher, M., S. Lorenz, and R. Galler (2014). Tunnel boring machine performance prediction with scaled rock cutting tests. International Journal of Rock Mechanics and Mining Sciences 70, 450–459.

Foster, J. T., S. A. Silling, and W. Chen (2011). An energy based failure criterion for use with peridynamic states. International Journal for Multiscale Computational Engineering 9(6).

Gertsch, R., L. Gertsch, and J. Rostami (2007). Disc cutting tests in Colorado Red Granite: Implications for TBM performance prediction. International Journal of rock mechanics and mining sciences 44(2),238–246.

Hudson, J. and C. Fairhurst (1969). Tensile strength, Weibull's theory and a general statistical approach to rock failure. In The proceedings of the civil engineering materials conference, pp. 901–904.

Klein, E., P. Baud, T. Reuschlé, and T. Wong (2001). Mechanical behaviour and failure mode of Bentheim sandstone under triaxial compression. Physics and Chemistry of the Earth, Part A: Solid Earth and Geodesy 26(1-2), 21–25.

Labra, C., J. Rojek, and E. Oñate (2017). Discrete/Finite Element Modelling of Rock Cutting with a TBM Disc Cutter. Rock Mechanics and Rock Engineering 50 (3),621–638.

Lindqvist, P. A., H. H. Lai, and O. Alm (1984). Indentation fracture development in rock continuously observed with a scanning electron microscope. International Journal of Rock Mechanics and Mining Sciences & Geomechanics Abstracts 21(4),165–182.

Parks, M. L., D. J. Littlewood, J. A. Mitchell, and S. A. Silling (2012). Peridigm Users'Guide v1. 0.0. Technical report, Sandia National Laboratories.

Rostami, J. (1997). Development of a force estimation model for rock fragmentation with disc cutters through theoretical modeling and physical measurement of crushed zone pressure. Ph. D. thesis.

Rostami, J. (2013). Study of pressure distribution within the crushed zone in the contact area between rock and disc cutters. International Journal of Rock Mechanics and Mining Sciences 57, 172–186.

Silling, S. A. (2000). Reformulation of elasticity theory for discontinuities and long-range forces. Journal of the Mechanics and Physics of Solids 48(1),175–209.

Silling, S. A., M. Epton, O. Weckner, J. Xu, and E. Askari (2007). Peridynamic states and constitutive modeling. Journal of Elasticity 88(2),151–184.

Weibull, W. (1951). A statistical distribution function of wide applicability. Journal of Applied Mechanics 18, 293–297.

Yang, H., J. Renner, L. Brackmann, and A. Röttger (2022). Normal indentation of rock specimens with a blunt tool: role of specimen size and indenter geometry. Rock Mechanics and Rock Engineering.

Tunnelling for a Better Life – Yan, Celestino, Thewes & Eberhardt (Eds)
© 2024 The Author(s), ISBN 978-1-032-80042-4
Open Access: www.taylorfrancis.com, CC BY-NC-ND 4.0 license

Pumice mineral using as a backfill grout injection in TBM excavations

Ufuk Cemali Çalışkan*, Seden Beyhan & Hasan Ergin
Istanbul Technical University, Istanbul, Turkey

ABSTRACT: Shielded full-face tunnel boring machines (TBM) have been used in the mining and construction industry for many years in underground tunnel excavations. There are two important elements of this manufacturing method, which is based on the principle of filling every voids in underground excavations that will meet certain strength values; the first is reinforced concrete structures consisting of precast segments, and the second is backfill injection injected between these segments and the ground cavity. In a tunnel opening in which the excavation-support cycle progresses rapidly, therefore it is desirable to improve the mechanical requirements of the backfill mortar, such as early setting, reaching high early strengths, maximum gap filling, easy pumpability, reducing water permeability into the precast segments, and at an affordable cost. In addition to being an expensive binder, the cement used in backfill mortar also causes CO_2 emissions during its production. All these factors motivate the tunnelling industry to reduce the use of cement in backfill mortar and to seek alternatives. In this direction, the use of different pozzolans as additives to improve the properties of the backfill mortar been examined. In this study, as a pozzolan named pumice was obtained by chemical synthesis from rocks containing high percentage of silica by weight. Cement backfill mortar samples mixed with different proportions of pozzolans at different ratios will be prepared and the optimum pozzolan ratio was be determined by strength tests. With the findings of this research provides to define the suitable pozzolan that's backfill mortar.

Keywords: Tunnelling, TBM, Backfill, Grout, Pozzolan, Pumice

1 INTRODUCTION

The TBM tunneling method is widely used in metro tunnels and infrastructure tunnels due to its high automation, fast construction speed and low impact on ground disturbance (Liu et al., 2018). To increase the stability of the layers and reduce ground settlement, grouting is often used to strengthen the layers for the shield tunnel. The backfill grouting consumption for the shield tunnel is enormous and the development of backfill grouting with high performance, environmentally friendly and low cost features is of great importance and has economic benefits (Ye et al., 2019).

In the TBM tunnel method, since the outer diameter of the machine's cutter head is larger than that of the segment, a ring-shaped gap is formed between the segment and layers after the machine's mattress and shield tail are separated from the segment (Liu et al., 2018). The task of synchronous injection is to fill the annular gap by injecting injections with appropriate early strength and final strength according to the prescribed injection pressure. With backfill injection, the segment can be supported against the surrounding ground pressure, which can effectively reduce ground deformation (Ding et al., 2019).

TBM backfill grouting is the filling of cement, mortar, bentonite or various organic-inorganic chemical substances under pressure into discontinuities in the rock mass and/or ground voids. By grouting under a certain pressure into the inaccessible gaps and cracks in the foundation;

- The bearing capacity of the foundation is increased,
- Leaks are either completely prevented or minimized,
- Ground settlements are minimized,
- Hydrostatic lifting pressures are prevented.

The backfill injection has to be;

Figure 1. Backfill grouting in TBM tunnelling (gulermak umraniye goztepe metro method of statement).

- Spreads easily around the precast segments,
- Setting times can be easily controlled,

*Corresponding author: caliskanuf@itu.edu.tr

DOI: 10.1201/9781003495505-222

- High durability,
- Low heat of hydration,
- No segregation after mixing,
- Short mixture preparation time,
- Low cost of injection mixture,
- It should not adversely affect health conditions.

A few scientific papers or tunnelling projects have so far reported the use of secondary cementitious materials in two-component grouts. A conference paper from 1950 presented characteristics of grouts formulated with slag cement bentonite and silicate (Florentin and Heriteau, 1950). Sculte- Schrepping and Breintenbucher (2019) demonstrated the interest of using ground granulated blast furnace slag, fly ash, or metakaolin to replace some of the ordinary Portland cement. According to these authors, the higher calcium content of the slag, compared to the other Al-Si materials, allows faster jellification and higher compressive strength. Other recent papers have associated fly ash for eco-friendly two-component grout design (Aboulayt et al., 2020; Song et al., 2020). However, grouts formulated in these studies used a lower water-to-binder ratio and a higher accelerator content than the mix-design presented in this work. One of the rare cases of a tunnelling project using SCMs in its two component grout design is the Warsaw metro. A blended CEM IV/B-P cement, containing between 36 and 55% of natural pozzolan (AFNOR, 2012) was used (Peila et al., 2015).

The aim of this paper is to assess the feasibility of using pumice as a alternative pozzolan for two-component grouting, by presenting the results of an experimental campaign that shows the effect of a partial replacement of Ordinary Portland Cement. It focuses on two main aspects of grout properties that must be managed: fresh state characteristics and compressive strength development.

2 EXPERIMENTAL

A two-part mortar typically consists of two components; Component A, which consists of cement, water, bentonite, and a retarder, and Component B, which usually consists of sodium silicate and water. The function of the retarder in Component A is to guarantee its workability from blending to transportation and injection into the annular space (Peila et al. 2011). When Component A is mixed with a sodium silicate-based accelerator, the mixture hardens rapidly due to the chemical action of the accelerator. The mixture begins to gel and begins to gain mechanical strength within a few seconds of mixing. The TBM backfill grout specifications listed in Table 1.

Table 1 . Specifications for grout properties, considered as acceptable quality parameters on jobsite.

Property	Criteria
Component A (only)	
Marsh cone flow time	30-45 sec
Bleeding	<3 % at 3h
Components A+B	
Gel time	5-15 seconds
Compressive strength	>0.6 MPa at 24 h
	>0.8 MPa at 7 days
	>1.20 MPa at 28 days

2.1 *Materials*

Pure cement mortars have various performance defects, so they are not used directly in TBM tunnel grouting. Quantitative industrial residues such as fly ash, slag, steel slag and silica fume, special pozzolans such as bentonite, gypsum, clay and metakaolin, chemical additives such as superplasticizers, dispersion resistance agents, setting accelerators, retarding agents, early strength agents, water reducer agents, microexpansion agents and viscosity modifying additives can improve the performance of mortars for shield tunnel (Wang et al. 2018).

Table 2. Typical composition of two-component backfill.

1 m^3 Content	Weight (kg)	Density (kg/m^3)	Volume (desi)
Cement	320	3150	101,59
Bentonite	30	2700	11,11
Plasticier	3,1	1100	2,91
Water	830	1000	830,00
Accelerator	75	1400	54,29
Total	1258		1000

First, bentonite is added to the water and mixed for 2 minutes. Afterwards, cement and pumice powder are added to the plasticizer mixture and mixed with a mixer for 3 minutes. Some of the material removed from here is taken into a measuring tape and kept waiting for slump testing.

Table 3. Grout design for laboratory (2 desi).

Content	2 desi Weight (g)	Volume (desi)
Cement	640	0,2
Bentonite	60	0,02
Plasticier	6	0,01
Water	1660	1,66
Accelerator	150	0,11
Total	2516	2,00

Pumice, a natural mineral source, has very few uses. However, the large amount of pumice stone reserves with high silica content in Turkey allows the use of pumice stone as an alternative to cement. Using pumice stone to improve binder hydration in

recipes by reducing the cement content in the backfill mortar can not only reduce the cost but also provide the opportunity to use more pozzolanic material (pumice). Development and/or promotion of low or inexpensive pumice use will be critical for the acceptance of nanomaterial application in backfill mortar injection technology in underground operations.

The cement industry is responsible for approximately 7% of CO_2 emissions, and it is predicted that this will increase further in the coming years. Since pumice particles have a high surface area, they fill the gaps between solid particles and serve as filler and pozzolan in cementitious materials**.**

Table 4. Composition of grout with pumice.

Components	Cement		Pumice		Water	
Unit	g	%	g	%	g	%
Cement (100%)	640	25,41	0	0,00	1660	65,90
Cement +Pumice (%90+%10)	576	22,87	64	2,54	1660	65,90
Cement +Pumice (%80+%20)	512	20,33	128	5,08	1660	65,90
Cement +Pumice (%70+%30)	448	17,79	192	7,62	1660	65,90

2.2 *Laboratory tests*

Marsh cone test

The Marsh cone test [UNI 11152:2005 (Italian Standards 2005) was conducted to evaluate the fluidity and viscosity of the grout before mixing with an accelerator, and this is expressed as the time required by 1,000 mL grout to flow through a standardized cone. The time required for a complete flow should range between 30 and 45 s.

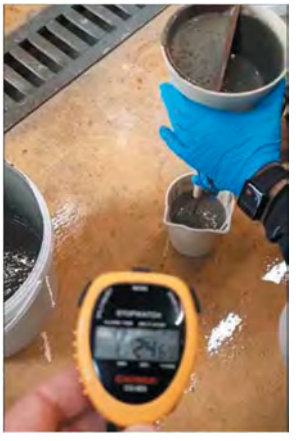

Figure 2. Flowing test with Marsh cone.

Bleeding test

The bleeding test was carried out by leaving an undisturbed grout sample (without accelerator) of 1,000 mL for 3h and measuring the water separation. In the technical literature (Peila et al. 2011), it is usually considered that a good mix should not exceed 3% water separation. The bleeding test
was carried out to test the water separation from the grout sample. In case of standstill during a TBM excavation, the water in the grout sample should not separate from the mix.

Figure 3. Bleeding test.

Hardening time evaluation

This hardening time evaluation test was carried out by mixing Component A with 6% of Component B (accelerator) until the grout was no longer workable. This is defined as the hardening time of the two-component mix. The usual hardening time for a two-component grout ranges from 5 to 15 s. Shorter values are avoided because they may lead to choking of the injection pipes, whereas larger values are unwanted because an immediate support is needed by the segmental lining as it exits from the TBM tai.

Figure 4. Gel time evaluation.

Uniaxial compressive strength test

Early strength is required to ensure that the segments can support the loads applied by the TBM back equipment and also to transfer the loads between the segments and the soil. However, testing relatively low 1-hour strengths has proven problematic as there are no directly applicable ASTM standards (Antunes, 2012). In this context, uniaxial compression tests were carried out based on the 1-7-28 day strengths accepted in Turkey.

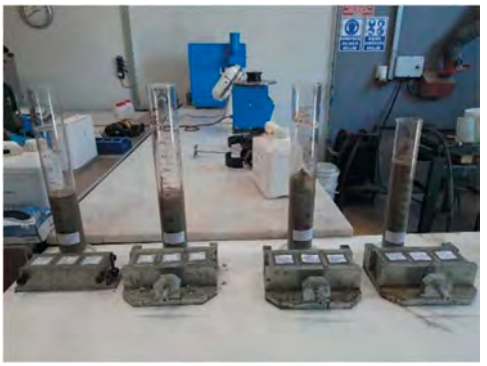

Figure 5. 5x5x5 cubes with different rates of pumice.

Characterization tests

Before mechanical tests are carried out, characterization experiments must be carried out to reveal the content of the CEM I 42.5 R cement and pumice to be used in the tests. In this context, CEM I 42.5 R type cement and pumice X-Ray Fluorescence (XRF) experiments were carried out in an accredited laboratory.

Figure 6. Pumice and cement samples.

3 RESULTS AND DISCUSSION

In order to determine most suitable bentonite the 4 different brand sample used in the tests. The fresh and hardened test carried out with 320 kg CEM I 42,5 R cement,

830 kg water, 30 kg bentonite, 3,1 kg EUCON NP205 plasticier additive, 75 kg CreteShot NS303 (%6) sodium silicate under the 2.60 w/c ratio. The bentonite which has a lesser bleed ratio chosen for further test process (Table 6).

Table 5. XRF test results.

Compound	CEM I (%)	Pumice (%)
SiO_2	19,28	72,95
Al_2O_3	4,83	13,12
CaO	62,23	1,07
MgO	3,30	0,74
SO_3	1,03	0,20
Loss of glow	3,23	0,00
Na_2O	4,36	3,34
K_2O	0,21	4,04
TiO_2	0,22	0,09
Mn_3O_4	0,07	0,05
P_2O_5	0,26	0,01
SrO	0,07	0,02
Total	99,94	100,09

Table 6. Grout mixtures with different bentonite brands.

	Mix #			
	1	2	3	4
Viscosity (sec)	35	35	35	35
Gel Time (sec)	6,9	7,8	7,2	7,1
3 hr Bleed (%)	1	3	3	2
UCS, average (MPa)				
1 day	0,63	0,57	0,69	0,58
7 days	0,95	1,27	0,82	0,89
28 days	1,35	1,45	1,02	1,20

*w/c=2,60, B/A ratio= %6
Accelerator: Euclid Chemical CreteShot NS303
Plasticier: Euclid Chemical EUCON NP205

In this study, the physical results of pumice stone, which has reserves in many regions in Turkey, when used in combination with cement in TBM backfill, were examined. Pumice stone powder; it was observed that when added into the Marsh cone, it flowed within 30-45 seconds and showed very similar properties to the cementitious mixture. In addition, when components A and B were mixed (with the addition of 6-10% sodium silicate setting accelerator), it was understood that they gelled in 7-8 seconds and showed almost the same properties as the cementitious mixture. In the slump funnel, which is another physical test, it is understood that the mixture prepared with pumice stone powder collapses at almost the same rate as the mixture prepared with cement, so it does not create a disadvantage.

When we look at the uniaxial compressive strengths, it is understood that when 10% pumice stone powder is used, the uniaxial compressive strengths are the same as cement, but after 20% it starts to decrease. The tests were carried out with 10-20-30% pumice stone powder additive, but these tests should be tried at dosages such as 5-15-25% to better investigate the diffraction point and determine the optimum point. In addition, water permeability

tests of the backfill prepared with pumice stone must be carried out and compared (Table 7-8).

Table 7. Fresh and hardened grout results with pumice and 6% accelerator additive.

	Mix #			
Pumice additive	%0	%10	%20	%30
Viscosity (sec)	32	33	34	33
Gel Time (sec)	7,3	8,1	9,4	9,4
3 hr Bleed (%)	1,5	2	2	2
UCS, average (MPa)				
1 day	0,65	0,61	0,46	0,38
7 days	0,92	0,83	0,71	0,58
28 days	1,34	1,30	1,22	1,10

*w/c=2,60, B/A ratio= %6
Accelerator: Euclid Chemical CreteShot NS303
Plasticier: Euclid Chemical EUCON NP205

Table 8. Fresh and hardened grout results with pumice and 10% accelerator additive.

	Mix #			
Pumice additive	%0	%10	%20	%30
Viscosity (sec)	32	33	34	33
Gel Time (sec)	7,3	8,1	9,4	9,4
3 hr Bleed (%)	1,5	2	2	2
UCS, average (MPa)				
1 day	0,89	0,78	0,73	0,52
7 days	1,00	0,90	0,80	0,70
28 days	1,62	1,50	1,33	1,29

*w/c=2,60, B/A ratio= %10
Accelerator: Euclid Chemical CreteShot NS303
Plasticier: Euclid Chemical EUCON NP205

4 CONCLUSIONS AND RECOMMENDATIONS

All tests in this article were performed with CEM I 42.5 R type cement. It will be beneficial to perform tests on cement types such as CEM I 52.5 R and examine the results. The tests performed under different B/A ratio, for TBM backfill grouting the most important requirements for TBM backfilling is that the grout begins to set as soon as possible in order to fill the gap open by the cutter head and reducing possible surface settlements to zero. This help to understand the importance of early strength, so uniaxial compressive strength tests should also carried out for 1-3-6 hour periods with all receipts. Also for the corrosive and high underwater projects its necessary to carry out permeability tests for TBM backfill.

One of the most important issues in creating alternatives in a region is the geographical proximity to the raw material as well as the availability of suitable raw materials. Pumice stone is a raw material with very high reserves in Turkey. It contains up to 75% SiO_2 in its entire state without any physical or chemical treatment.

According to the results obtained from all these results, the use of pumice stone as an alternative raw material to cement at a certain rate is promising in terms of mechanical tests and cost advantage. Pumice is a suitable pozzolanic material due to its lightness, porous structure, high SiO_2 content and amorphous structure and provides a more economical and environmentally friendly concrete production. Although 40% of the world's 18 billion tons of pumice reserves are in Turkey, they are still not used effectively (Gündüz et al., 2005).

ACKNOWLEDGMENTS

The authors are grateful Istanbul Technical University Scientific Research Projects Coordination Unit (BAP No: MGA-2023-44663) for their financial support to pursue this research program. Additionally, special thanks to Ege Kimya and Egecrete Yapi Kimyasallari A.S. for providing the use of the concrete laboratory and their additives.

REFERENCES

Aboulayt, A., Souayfan, F., Roziere, E., Jaafri, R., Cherki El Idrissi, A., Moussa, R., Justino, C., Loukili, A., 2020. Alkali activated grouts based on slag-fly ash mixtures: From early age characterization to long-term phase composition. Constr. Build. Mater. 260, 120510.

AFNOR, 2012. NF EN 197-1, Cement - Part 1: Composition, specifications and conformity criteria for common cements.

André, L., Bacquié C., Comin G., Ploton R., Achard D., Frouin L., Cyr1 M., (2022) "Improvement of two-component grouts by the use of ground granulated blast furnace slag", Tunnelling and Underground Space Technology, Volume 122, April 2022, 104369.

Antunes, P. (2012) "Testing procedures for two-component annulus grout", North American Tunneling, 14–22.

Ding, W.Q., Duan, C., Zhu, Y.H., Zhao, T.C., Huang, D.Z.,

Florentin, J., Heriteau, G., 1950. Le coulis de ciment thermocolloidal et ses possibilites d'application aux injections, aux travaux routiers. Presented at the Colloque international de mecanique rationnelle, Poitiers.

Gündüz, L., Şapçı, N., Davraz, M. 2005. "Pomza Madenciliği Endüstrisi ve Türkiye Açısından Önemi", Türkiye 19. Uluslararası Madencilik Kongresi ve Fuarı, IMCET2005, İzmir, pp. 397–407.

Liu J.L., Hamza, O., Davies-Vollum, K.S., Liu, J.Q. 2018. "Repairing a shield tunnel damaged by secondary grouting", Tunn. Undergr. Space Technol. 80, 313–321.

Rahman, F., Adil, W., Raheel, M., Saberian, M., Li, J., Maqsood, T. 2022. "Experimental investigation of high replacement of cement by pumice in cement mortar: A mechanical, durability and microstructural study", Journal of Building Engineering, 49, 104037.

Wang, S., Wang, J.F., Yuan, C.P., Chen, L.Y., Xu, S.T., Guo, K.B. 2018. "Development of the nano-composite cement: application in regulating grouting in complex ground conditions", J. Mountain Sci. 15 (7), 1572–1584.

Peila, D., Chieregato, A., Martinelli, D., Salazar, C.O., Shah, R., Boscaro, A., Negro, E.D., Picchio, A., 2015.

Long term behavior of two component back-fill grout mix used in full face mechanized tunneling. Geoing. Ambient. E Mineraria 144, 57–63.

Schulte-Schrepping, C., Breitenbucher, R., 2019. Two component grouts with alkali-activated binders, in: Peila, D., Viggiani, G., Celestino, T. (Eds.), Tunnels and Underground Cities: Engineering and Innovation Meet Archaeology, Architecture and Art. CRC Press, pp. 3078–3085.

Song, W., Zhu, Z., Pu, S., Wan, Y., Huo, W., Song, S., Zhang, J., Yao, K., Hu, L., 2020. Synthesis and characterization of eco-friendly alkali-activated industrial solid waste-based two-component backfilling grouts for shield tunnelling. J. Clean. Prod. 266, 121974.

Ye, F., Yang, T., Mao, J.H., Qin, X.Z., Zhao, R.L. 2019. "Half-spherical surface diffusion model of shield tunnel back-fill grouting based on infiltration effect", Tunn. Undergr. Space Technol. 83, 274–281.

Tunnelling for a Better Life – Yan, Celestino, Thewes & Eberhardt (Eds)
© 2024 The Author(s), ISBN 978-1-032-80042-4
Open Access: www.taylorfrancis.com, CC BY-NC-ND 4.0 license

Performance analysis of TBM excavation parameters related to small-diameter horizontal and inclined tunnels

Marilena Cardu*, Carmine Todaro, Oveis Farzay, Alfio Di Giovanni & Simone Saltarin
DIATI Politecnico di Torino, Turin, Italy

ABSTRACT: Horizontal, inclined, and vertical ways through the rock are needed for several mining and civil purposes (hydropower, transportation, sewer collector, underground transports), and quite often, in the same project, horizontal, inclined, and vertical ways are necessary. These cases offer a great opportunity for comparing the performance of the excavation systems in similar geological-geomechanical environments. The basic mechanism of rock breakage, either cyclical (Drill and Blast) or continuous (TBM or Raise Borer), is the same for horizontal or inclined ways. In the latter case, the fixed motor option (Raise Borer) tends to be preferred for short, small-diameter, easily accessible top-point cases. As to the Drill and Blast system, it tends to be employed only for horizontal ways or very short inclined ways. In the first part of the paper, a general discussion of the techniques for horizontal, inclined/vertical ways excavation is provided, comparing some real cases of tunnel driving by TBM under the aspect of the machine's average performance. The comparison of the cases makes it possible to draw some prediction criteria applicable to the TBM performance in horizontal and inclined tunnel driving.

Keywords: Tunnelling, TBM, Performance prediction, Inclined tunnel, Horizontal tunnel

1 INTRODUCTION

The use of the TBM for horizontal and inclined ways has become a widespread practice in Italy, both for the excavation of highway and railway tunnels and for the implementation of hydroelectric programs, for new plants and the adaptation of old plants, due to the general policy to transfer underground all the water conducts and powerhouses (Edvardsson & Broch, 2002). The cases examined here pertain to hydropower and water supply plants, and to the ventilation inclines of a large road tunnel, with diameters in the 2.5 to 4.2 m range (at places, subsequently enlarged). Although excavation with TBM potentially has the advantages of safety, respect for the environment, and speed, the cost and difficulty of realising the project, construction, and operation can be considerable (Zhu et al., 2019). It must be recalled that a hydropower tunnel project is far more complex than a road or railway tunnel (Nilsen, 2021). Today, tunnels are usually excavated through TBM, to ensure that construction is completed in a reasonable time; therefore, predicting TBM performance is a crucial issue and a primary requirement for implementing a tunnel project, both for planning purposes and for selecting the construction method (Graham, 1976; Farmer & Glossop, 1980; Hughes, 1986). Performance prediction for a hard rock TBM can be done in many different ways. The main approaches can be theoretical or empirical, the first being based on cutting force estimation and the other, on field performance. In general, over the past decades, various models and equations have been proposed to estimate the performance of TBM based on the properties of rock and machine, which employ various statistical analysis techniques (Yagiz, 2008; Yagiz et al., 2009; Gong & Zhao, 2009; Hassanpour et al., 2009, 2010, 2011, 2015, 2016; Khademi Hamidi et al., 2010; Farrokh et al., 2012; Delisio et al., 2013; Oraee & Salehi, 2013; Macias et al., 2014; Salimi et al. 2016; Zare Naghadehi & Ramezanzadeh, 2017). In the case under study, the aim is to assess and compare the data collected from tunnel boring machines used in both horizontal and inclined tunnels, identifying the correlations among

*Corresponding author: marilena.cardu@polito.it

DOI: 10.1201/9781003495505-223

the various parameters under consideration, taking into account the specific geological conditions of each project.

2 DATASET OF CASES EXAMINED

The main data of the examined cases are collected in Table 1. To be noticed, letters from A to F are used to recognise cases belonging to the same type of rock type crossed during the excavation: cases A pertain to granitic gneisses, B to limestones, C to calcschists and related, D to extremely hard gneiss-pegmatites, E to sandstone and marls, F to meta-ophiolites and meta-sediments.

Case A_1 refers to two inclined shafts for a pumped storage hydropower plant, subsequently enlarged to 6.4 m by D&B. A_2 is a pedestrian access tunnel, pertaining to the same plant as A_1, and is quoted to provide a comparison with a horizontal tunnel. Tunnel A_2 has been driven by TBM only for a short stretch (less than 2 km) and completed by D&B due to the excessive consumption of the tools and frequent machine failures; B_1 consists of two inclined tunnels for a hydropower plant, driven through comparatively soft limestones, subsequently enlarged to 5.8 m by mechanical excavation; B_2 is a horizontal tunnel driven through dolomitic limestone, harder than case B_1, as a part of an aqueduct; B_3 is an inclined tunnel for a hydropower plant, driven through a dolomitic limestone, whose strength is intermediate between B_1 and B_2; C_1 consists of a couple of inclined tunnels driven for ventilation purposes from a large road tunnel through calcschists, subsequently reamed to 5.8 m, again by TBM; $C_2 - C_3$ represent two stretches of a hydropower tunnel driven through calcschists (somewhat stronger than C_1); D is an inclined tunnel for a hydropower plant, driven through the most strong and abrasive rocks among the types considered in this report. Excavation by TBM has been discontinued because of a failure, unrelated to the machine. E refers to a horizontal tunnel that is part of a hydropower-water plant, while F serves as an inclined tunnel designed for the installation of a pipeline for a hydroelectric power plant.

Apart from cases A_1 and C_1 (the only cases where rolling tools with carbide buttons have been used), machines equipped with standard disc cutters have been used. Table 2 collects the main technical data of the machines used in the excavation works in terms of head diameter (D), maximum stroke (S), maximum thrust (T_{max}), number of tools (N), tool diameter (Φ), head revolution per minute (n), maximum power at the head (P_{max}). In case A_1, roller bits with buttons (RBB) were employed as the selected tools, whereas for cases A_2 and C_1, the TBMs utilized double-disc tools.

The properties of the rocks, as easily predictable, are not uniform along the alignments of the tunnels, and the variability is probably as important as the average strength value in determining the performance of the machines.

In Table 3, information pertaining to the rocks crossed are reported.

The uniaxial compressive strength (C_0) is reported in terms of range and, in brackets, the average reference value (C_{0av}). Furthermore, information concerning the indirect tensile strength (Brazilian test, T_0), the RMR (Rock Mass Rating), and the indicator of the rock abrasivity HK_{75} (upper quartile of the Knoop microhardness distribution) are also provided.

Table 1. General data of the inclined and horizontal tunnel cases examined. D: tunnel diameter; i: tunnel inclination; L_1: tunnel length; L_2: length excavated by TBM: TBM.

Case	i (°)	D (m)	L_1 (m)	L_2 (m)	TBM (%)	Lithotype
A_1	42	2.5	3150	2100	67	Gneiss
A_2	≈0	2.6	6215	1900	31	Granitic gneiss
B_1	43	3.0	472	472	100	Calcarenites
B_2	≈0	3.5	3052	2981	98	Dolomitic limestone
B_3	47	3.7	725	-	-	Dolomitic limestone
C_1	46	3.0-5.8	750	715	95	Calcschist
C_2 -C_3	≈0	3.5	14800	14800	100	Calcschist, conglomerate
D	44	3.9	752	450	60	Gneiss and amphibolite
E	≈0	3.5	6472	6204	96	Sandstone and marls
F	35	4.2	1750	1750	67	Meta-ophiolites, meta-sediments

Table 2. Machines data.

Case	S (m)	T_{max} (kN)	N (-)	Φ (mm)	N (rpm)	P_{max} (kW)	Total Power (kW)
A_1	-	1800	18	RBB	12	480	-
A_2	0.7	2800	17	300	12	380	-
B_1	1.0	4300	30	350	11.4	300	350
B_2	0.75	7155	27	397	9.6	552	680
B_3	1.1	2800	34	350	9.5	300	390
C_1	0.7	4400	17	300	12	360	460
C_2 -C_3	1.5	6200	26	412	10.6	600	900
D	1.6	8000	32	416	11	900	1050
E	1.1	4450	27	394	10	552	655
F	1.5	7920	36	432	5.5-11	600	-

Table 3. Geomechanical characteristics of the rocks encountered by tunnels.

Case	C_0 (C_{0av}) (MPa)	T_0 (MPa)	RMR (-)	HK_{75} (MPa)
A_1	100-150 (125)	-	-	-
A_2	70-170 (97)	7-12	70-85	5990
B_1	15-50 (25)	-	-	-
B_2	60-180 (70)	5	60-80	1500
B_3	(40)	2.9	60-85	3600
C_1	40-60 (50)	-	-	-
C_2 -C_3	60-130 (83)	5-7	30-70	6300
D	90-200 (112)	10-16	60-80	8200
E	49-80 (64)	4-7	-	900-4000
F	75-180 (126)	15	60-90	4300-8300

Unfortunately, the pattern of the information is not complete since, for the same case examined, some data are not available.

Besides numerical information reported in Table 3, further useful details and peculiarities recorded during the excavation by figures involved in the works are hereinafter concisely reported:

A_1: quite uniform rock, with scarce discontinuities;

A_2: rock strength progressively increases from the portal: as explained, the machine gave up after approximately 2 km excavated. A major fault has been crossed, with problems encountered;

B_1: calcarenites, softer, alternate with marls, harder; poor rock, faulted, is crossed in the last 50 m of the tunnels;

B_2: distinctly bedded dolomitic limestone, with marl-clay interlayers;

B_3: thick layers; homogeneous, apart from marl interlayers;

C_1: good rock quality, apart from a jointed rock stretch in the initial part of the layout;

C_2,C_3: problems due to some shear zones crossed; strength quite variable (calcschists, mica-schists and meta-conglomerates alternate along the tunnel);

D: hard gneiss with still harder lenses of pegmatites and amphibolites (machine thrust had to be improved after an initial unsuccessful attempt);

E: fairly regular alternation of homogenous strata of marl and sandstone;

F: schists and serpentinite show a foliated texture, while meta gabbro and metabasite are generally weakly foliated.

3 PERFORMANCE OBSERVED

A very important point in TBM operation, both horizontal and inclined, is thrust. It is seldom possible to exploit the full nominal thrust available from the machine (T_{max} of Table 2) and, consequently, being the thrust linked to the power consumed, to exploit the full power available (P_{max} of Table 2). The cases are examined under this aspect in Table 4: the values, where available, of T_{max}, of the average actual thrust (T_{av}), of P_{max}, and of the average power consumed considering only the head (P_{av}) are collected. Furthermore, values of thrust per disc (T_D) computed as the ratio between T_{av} and N are also reported.

Table 4. Thrust and power data for the cases examined.

Case	T_{av} (kN)	P_{av} (kW)	T_{av}/T_{max} (%)	P_{av}/P_{max} (%)	T_D (kN / disc)
A_1	-	340	-	70	-
A_2	1900	160	64-71	42	112
B_1	1200	186	28	62	40
B_2	4000	480	56	86	148
B_3	2000	174	71	58	59
C_1	-	140-180	-	39-50	-
C_2 -C_3	3960	504	64	84	152
D	5800	430	72	48	181
E	2390	389	54	70	89
F	5130	-	65	-	143

Table 5 provides information about the progression of the analysed tunnelling works. Specifically, data related to the net penetration rate (NPR), the basic penetration rate (p), the utilisation coefficient (UC), the average daily progression (ADP), the specific energy (Es), and the service life of the tool which is related to the efficiency of the tools (m^3 of excavated material per tool) (SL_v).

Referring to the last column of Table 5, it must be noticed that, in most cases, the tunnels are not long enough to provide reliable data regarding the service life of the tool, especially in soft rocks such as limestones: in B_1 - B_3 - C_1 the same discs set installed on the head at the beginning was still serviceable at the end of the work.

In scenario B_2, the parameter is computed based on the number of workdays to calculate the UC. Instead, for scenarios C_2-C_3, the rock reinforcement time is not factored into the calculation.

4 DISCUSSION

The cases examined refer to the use of different machines and, more importantly, in different rocks, which makes it difficult to answer the simple question: how much more difficult is it to drive by TBM an inclined tunnel with respect to a horizontal tunnel? To minimise the disturbance, at least, of the rock factor in comparison, in

Table 5. Parameters related to the progression of the analysed tunnelling works.

Case	NPR (m/h)	p (mm/rev)	UC (-)	ADP (m/d)	E_s (MJ/m^3)	SL_v (m^3/tool)
A_1	1.6	2.2	0.24	8.1	115.0	227
A_2	1.1	1.6	0.31	8.4	97.2	48
B_1	5.8-6.5	8.5-9.5	0.18	25-28	15.1	-
B_2	3.7	6.5	0.38	33.5	48.6	455
B_3	2.5	4.4	0.19	11.4	23.0	-
C_1	1.1-1.5	1.5	0.22-0.36	5.8-12.5	55.8-63.0	-
C_2-C_3	2.4	3.8	0.27	15.5	82.8	286
D	2.6	3.9	0.19	11.8	50.4	112
E	3.8	6.3	0.25	22.5	19.8	1000
F	1.4-2.5	3.8-4.2	0.18	5.0-9.1	86.9	244

Figures 1 to 4, some parameters have been selected and plotted against the rock strength indicator C_0. The choice of selecting the basic penetration rate, the specific energy, the thrust per disc, and the machine utilisation coefficient have been made to provide an easy understanding of the studied topic.

Considering Figure 1, in inclined tunnels, the basic penetration rates consistently fall near or below 4 mm/rev, suggesting that these machines operate at the limit of their boring capacity, apart from an outlier case (Case B_1). In contrast, horizontal tunnels exhibit a wide range of basic penetration rates, spanning from approximately 2 to 9 mm/rev, indicating their capacity to adapt to varying rock strength and geological conditions.

Considering Figure 2, the E_s - C_0 trend is similar for inclined and horizontal tunnels, i.e. an increase of C_0 leads to a growth of E_s. The same inferences can be made considering Figure 3; indeed, the correlation T- C_0 shows no differences in trends between inclined and horizontal tunnels.

Considering Figure 4, UC tends to be lower in inclined tunnels with values that never overcome 0.3. Cases examined, however, refer only to inclinations in a 35° – 47° range.

Figure 5 reveals a trade-off between SL_v and Es. Cases with higher Es values tend to have lower SL_v, indicating that when more energy is consumed per unit volume of rock, tools tend to have a shorter service life. Conversely, cases with lower Es values tend to have longer tool service lives. inclined tunnels generally result in lower SL_v values compared to horizontal tunnels. This suggests that tools used in inclined tunnels have a shorter service life, possibly due to increased wear and tear from the more complex excavation process.

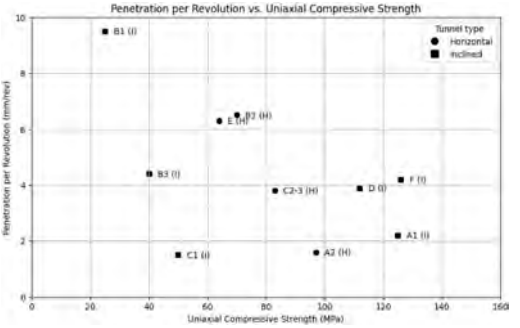

Figure 1. Penetration per revolution Vs. rock uniaxial compressive strength. Circles refer to horizontal tunnels, and squares to inclined tunnels.

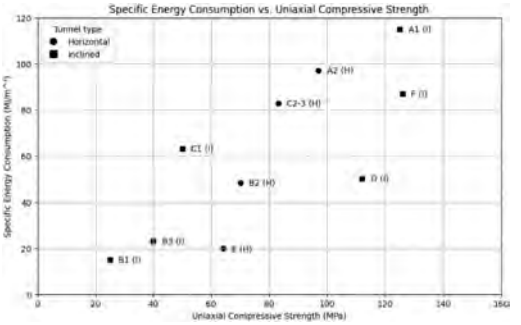

Figure 2. Specific energy consumption Vs. rock uniaxial compressive strength. Same symbols as in Figure 1.

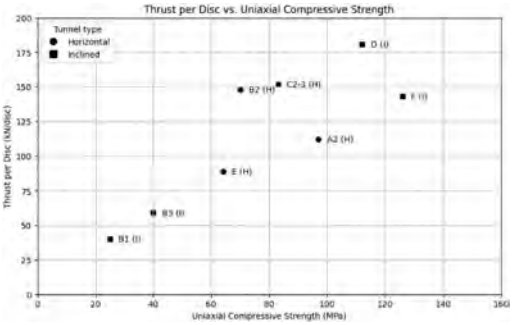

Figure 3. Thrust per disc Vs. rock uniaxial compressive strength. Same symbols as in Figure 1.

5 CONCLUSION

TBMs have been, and are, used in Italy in several projects. Historically, inclined tunnels are often driven by Drill & Blast, which is probably cheaper but tends to be abandoned. One reason is the scarcity of well-trained workers, but another important reason is the excavation speed, which undoubtedly favours the TBM. In fact, by analysing data presented in Table 1, inclined tunnels have been

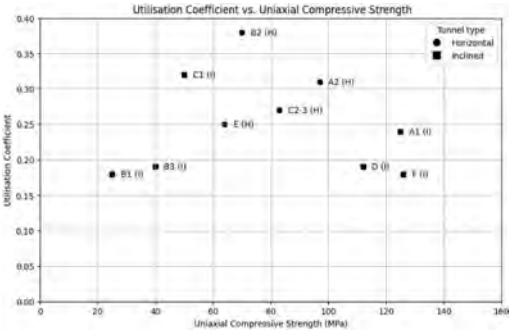

Figure 4. Utilisation Coefficient Vs. rock uniaxial compressive strength. Same symbols as in Figure 1.

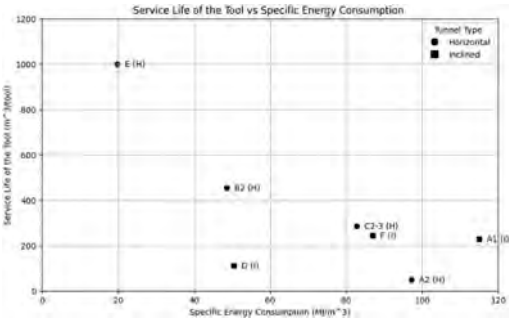

Figure 5. Service life of the tool Vs. Specific Energy Consumption. Same symbols as in Figure 1.

excavated for a percentage higher than 60 by using the TBM.

The paper mainly refers to the excavation of hydropower tunnels, presenting several cases. It should be clarified that analysing different case histories to summarise inferences generally validly is a hard issue since each machine, even if with similar diameter and similar power, has worked in different rock masses and in different conditions. The choice of select the basic penetration rate, the specific energy, the thrust per disc, and the machine utilisation coefficient have been done in the view to provide in an easy understanding of the studied topic.

Considering the ratio T_{av}/T_{max}, it can be concluded that the machines were quite reasonably exploited in horizontal and inclined excavations to within approximately 60 – 70 % of the capabilities. Exceptions are case B_1 (where the rock was particularly soft) and E (where clay beds were encountered). Considering instead the ratio P_{av}/P_{max}, values range between 40 – 85 %.

Considering Figures 1 to 4, Figures 2 and 3 do not provide useful information regarding the differences between inclined and horizontal tunnels. Indeed, the trends depicted are similar, and the different strengths of the rock dictate the differences. Instead, Figure 1 and 4 provide interesting detail: the basic penetration rate is lower for inclined tunnels, as well as the utilization coefficient. The rationale behind of this trend can be attributed to the fact that, despite the lower UCS, excavating an inclined tunnel poses greater challenges compared to a horizontal tunnel. Moreover, as highlighted in the study by Chu et al. (2022), it is imperative to assess the longitudinal and circumferential strain as well as stress characteristics specific to inclined TBM tunnels, under given geological and hydrogeological conditions.

Figure 5 reveals that higher energy consumption per unit rock volume results in reduced tool longevity, while inclined tunnels typically lead to shorter service lives for tools, likely due to the added wear and tear in their complex excavation process.

However, it is important to note that TBM performance relies heavily on geological conditions compared to the drill and blast technique. Numerous authors have emphasized the significance of in-situ rock parameters that can potentially influence TBM performance (Nelson et al., 1985; Bruland, 1998; Rostami et al., 2002; Zhang et al., 2003; Hassanpour et al., 2011). Nonetheless, it is worth mentioning that this paper does not take into account two important factors in TBM operations: drillability and the natural state of stress, as some research in this area might suggest (Bilgin et al., 2008; Yin et al., 2014; Ma et al., 2016).

Nonetheless, classification criteria could be implemented using the data collected from this research by combining them with in-situ rock structure parameters, drillability assessments, and abrasivity measurements. This approach would facilitate the implementation of knowledge and the identification of correlations among the various parameters involved in TBM excavation.

Another point is, however, important:

Coming to the cases here presented, the tunnel of case C_1 is served, in addition to the ventilation inclines driven by TBM, by other ventilation inclines, driven by Drill and Blast (Alimak method), practically of the same length. The excavation time by Drill and Blast has been 22 % longer, though considering the machine launching time for the TBM case. Both data are referred to as the pilot hole.

REFERENCES

Bilgin, N., Copur, H., Balci, C., Tumac, D., Akgul, M., Yuksel, A., 2008. The selection of a TBM using full scale laboratory tests and comparison of measured and predicted performance values in Istanbul Kozyatagi-Kadikoy metro tunnels. In: World Tunnel Congress, Akra, India, pp. 1509–1517.

Bruland, A., 1998. Hard rock tunnel boring Design and construction [Ph.D. thesis]. Trondheim: Norwegian Technical University.

Chu, Z., Wu, Z., Liu, B., Wu, K., Shi, X., Liu, Q., 2022. Mechanical response of inclined TBM tunnel due to drainage settlement of deep sandstone aquifer, Tunn. Undergr. Space Technol., 122, https://doi.org/10.1016/j.tust.2022.104393.

Delisio, A., Zhao, J., Einstein, H.H., 2013. Analysis and prediction of TBM performance in blocky rock conditions at the Lotschberg Base Tunnel. Tunn. Undergr. Space Technol., 33, 131–142.

Edvardsson, S., & Broch, E., 2002. Underground powerhouses and high pressure tunnels. Hydropower Development No. 14, Dept. Hydraulic and Environmental Engineering, NTNU, Trondheim, p. 105.

Farmer, I.W., Glossop, N.H., 1980. Mechanics of disc cutter penetration. Tunnels Tunn. Int. (12), 22–25.

Farrokh, E., Rostami, J., Laughton, C., 2012. Study of various models for estimation of penetration rate of hard rock TBMs. Tunn. Undergr. Space Technol. (30), 110–123.

Gong, Q.M., Zhao, J., 2009. Development of a rock mass characteristics model for TBM penetration rate prediction. Int. J. Rock Mech. Min. Sci. (46), 8–18.

Graham, P.C., 1976. Rock exploration for machine manufacturers. In: Bieniawski ZT (ed) Exploration for rock engineering. Balkema, Johannesburg, pp 173–180.

Hassanpour, J., Rostami, J., Khamehchiyan, M., Bruland, A., 2009. Developing new equations for TBM performance prediction in carbonate-argillaceous rocks: a case history of Nowsood water conveyance tunnel. Geomech. Geoeng. Int. J. 4(4), 287–297.

Hassanpour, J., Rostami, J., Khamehchiyan, M., Bruland, A., Tavakoli, H.R., 2010. TBM performance analysis in pyroclastic rocks: a case history of Karaj water conveyance tunnel. Rock Mech. Rock Eng. 43(4), 427–445.

Hassanpour, J., Rostami, J., Zhao, J., 2011. A new hard rock TBM performance prediction model for project planning. Tunn. Undergr. Space Technol., 26 (5), pp. 595–603, 10.1016/j.tust.2011.04.004

Hassanpour, J., Rostami, J., Zhao, J., Tarigh Azali, S., 2015. TBM performance and disc cutter wear prediction based on ten years' experience of TBM tunnelling in Iran. Geomec. Tunn. 8(3), 239–247.

Hassanpour, J., Ghaedi Vanani, A.A., Rostami, J., Cheshomi, A., 2016. Evaluation of common TBM performance prediction models based on field data from the second lot of Zagros water conveyance tunnel. Tunn. Undergr. Space Technol. (52), 147–156.

Hughes, H.M., 1986. The relative cuttability of coal measures rock. Min. Sci. Technol. 3, 95–109.

Khademi Hamidi, J., Shahriar, K., Rezai, B., Rostami, J., 2010. Performance prediction of hard rock TBM using Rock Mass Rating (RMR) system. Tunn. Undergr. Space Technol. |(25), 333–345.

Ma, H., Gong, Q., Wang, J., Yin, L., Zhao, X., 2016. Study on the influence of confining stress on TBM performance in granite rock by linear cutting test. Tunn. Undergr. Space Technol. (57), pp 145–150, https://doi.org/10.1016/j.tust.2016.02.020.

Macias, F.J., Jakobsen, P.D., Seo, Y., Bruland, A., 2014. Influence of rock mass fracturing on the net penetration rates of hard rock TBMs. Tunn. Undergr. Space Technol. (44), 108–120.

Nelson, P. Ingraffea, A.R., O'Rouke, T.D., 1985. TBM performance prediction using rock fracture parameters. Int. J. Rock Mech. Min. Sci. Geomech. Abstr., 22 (3), pp. 189–192, 10.1016/0148-9062(85)93234-6.

Nilsen, B., 2021. Norwegian oil and gas storage in rock caverns – Technology based on experience from hydropower development. J. Rock Mech. Geotech. Eng., Volume 13, Issue 2, Pages 479–486.

Oraee, K. and Salehi, B., 2013. Assessing prediction models of advance rate in tunnel boring machines-a case study in Iran. Arab. J. Geosci. 6(2): 481–489.

Rostami, J., Gertsch, R., and Gertsch, L., 2002. Rock fragmentation by disc cutter: a critical review and an update. Proc NARMS-TAC 2002, Eds. Hammah et al. Toronto, Canada.

Salimi, A., Rostami, J., Moormann, C., Delisio, A., 2016. Application of non-linear regression analysis and artificial intelligence algorithms for performance prediction of hard rock TBMs. Tunn. Undergr. Space Technol. 58, 236–246.

Yagiz, S. 2008. Utilizing rock mass properties for predicting TBM performance in hard rock condition. Tunn. Undergr. Space Technol. 23, 326–339.

Yagiz, S., Gokceoglu, C., Sezer, E., Iplikci, S., 2009. Application of two non-linear prediction tools to the estimation of tunnel boring machine performance. Eng. Appl. Artif. Intell. 22, 808–814.

Yin L.J., Gong Q.M., Zhao J., 2014. Study on rock mass boreability by TBM penetration test under different in situ stress conditions. Tunn. Undergr. Space Technol. 43, 413–425. https://doi.org/10.1016/j.tust.2014.06.002.

Zare Naghadehi, M. and Ramezanzadeh, A., 2017. Models for estimation of TBM performance in granitic and mica gneiss hard rocks in a hydropower tunnel. Bul. Engr. Geo. Env., 76, pp.1627–1641.

Zhang, Z.X., Kou, S.Q., and Lindqvist, P., 2003. In-situ Measurements of Cutter Forces on Boring Machine at Äspö Hard Rock Laboratory Part II. Characteristics of Cutter Forces and Examination of Cracks Generated. Rock Mech. Rock Engr. 36(1):63–83.

Zhu, H., Yan, J. and Liang, W., 2019. Challenges and development prospects of ultra-long and ultra-deep mountain tunnels. Engineering, 5(3), pp.384–392.

Tunnelling for a Better Life – Yan, Celestino, Thewes & Eberhardt (Eds)
© 2024 The Author(s), ISBN 978-1-032-80042-4
Open Access: www.taylorfrancis.com, CC BY-NC-ND 4.0 license

Wear prediction of disc cutter tools during shield tunnelling in composite stratum based on improved deep learning method

Jiaqi Chang*, Dongming Zhang & Hongwei Huang
Department of Geotechnical Engineering, College of Civil Engineering, Tongji University, Shanghai, China

ABSTRACT: As development of underground space, shield tunnels are developing towards large-diameter and long-distance. In upper-soft lower-hard stratum, the disc cutter tools are usually seriously worn, affecting the safety and efficiency of shield tunnel construction. The wear of tools is influenced by geological conditions, construction parameters and structure of cutter head, which is difficult to be predicted because the geological conditions are constantly changing along the longitudinal direction during tunnelling. Deep learning (DP) algorithm is an alternative method that can let the computer to learn from the driver's operation, geological conditions as well as record of tool detection, and try to model the relationship between construction parameters, geological condition and tools' wear. Thus, in this paper, an DP algorithm, Transformer, is improved by principal component analysis, K-means clustering and cutter location coding to predict the wear of cutter tool. Principle component analysis is used to reduce the dimension of input parameters, K-means clustering is used to identify the geological conditions in real time and cutter location coding is used to considering the influence of tool placement on cutter head. A set of parameters for shield tunnelling with geological conditions and tool detection records is extracted from the construction site of a Shenzhen tunnel. In total, 217 pairwise data points are collected and ten- fold cross validation is done. The final predicting errors of tools' wear is 3.3mm which is small compared with the critical wear of 40.0mm. The proposed method is helpful for the prediction of cutter wear in composite stratum.

Keywords: Tunnelling, Tool wear, Upper-soft lower-hard stratum, Transformer

1 INTRODUCTION

Tunnel boring machine, as the main method of tunnel construction, has been widely used because of its high safety, low disturbance to the surrounding environment, fast construction speed, and strong ground adaptability. With the development of tunnel construction in China, shield tunneling is developing in the direction of large diameter, large depth and long distance. Along with this, complex ground conditions such as composite strata, soft upper and hard lower strata bring great challenges to shield construction. As the main tool of shield machine for cutting and crushing strata, the tool is very easy to be severely worn under adverse geological conditions, and if the tool wear cannot be accurately predicted, it will often lead to problems such as damage to the cutter plate, difficulty in shield tunneling, and even affect the safety of shield tunneling. Therefore, it is necessary to predict the wear of shield tunneling tools under complex stratigraphic conditions.

Shield tools can be categorized into rock-breaking disc cutter and soil-cutting tooth, among which the disc cutter tend to wear more seriously and are the focus of scholars' research. In the study of the mechanism of wear, the CSM model of Colorado School of Mines (Rostami, 1997) and the NTNU model of Norwegian University of Science and Technology (Zare and Bruland, 2013) established the force model of the disc cutter and proposed the abrasive coefficient and abrasion value to predict the life of the disc cutter; Xue et al. (2021) established a discrete elemental model of disc cutter to analyze the rock-breaking process and the wear of the disc cutter; and Wang et al. (2015) analyzed the wear of disc cutter by the change of specific energy of the shield; Su et al. (2020) classified the wear of hob into abrasive wear, adhesive wear, and fatigue wear, in which abrasive wear and adhesive wear are the main causes of tool wear. Kilic et al. (2022) established Convolutional Neural Network models to predict the disc cutter wear based on shield construction parameters to predict the hob wear.

However, most of the above studies are aimed at homogeneous strata, and the rock breaking process of the disc cutter is relatively stable in homogeneous strata, whereas in composite strata, the strata on the face is not uniform, and the disc cutter force mechanism is more complicated, so the studies on the wear of the disc cutter in the upper-soft and lower-hard composite strata are fewer, and most of them

*Corresponding author: 1910278@tongji.edu.cn

DOI: 10.1201/9781003495505-224

are empirical summaries. Yang et al. (2021) moditied the tool wear model proposed by Japanese Tunnelling Society (JTS) for the heterogeneous grounds by assign different wear coefficients to cutters with different cutter diameters.

Traditional analytical and numerical simulation methods are difficult to analyze the complex interaction between construction parameters, ground conditions and cutter wear. And machine learning algorithms are able to establish complex models by mining the relationship between data, which have been widely used in the prediction of shield tunneling parameters (Huang et al., 2022). Some scholars have also tried to apply machine learning algorithms to tool wear prediction (Kilic et al.. 2022; Mahmoodzadeh et al., 2021), but it is still dominated by tool wear prediction in full-section hard rock, and tool wear prediction is very rare for tunnelling process in which soft and hard strata interact with each other.

Therefore, this paper relies on the construction process of a large-diameter slurry pressure balanced shield tunnel in Shenzhen, and establishes an improved deep learning model, taking construction parameters and ground conditions as the input parameters, and cutter wear as output parameters. And with the help of principal component analysis for input parameter dimensionality reduction, and with the help of clustering algorithm for the introduction of artificial experience.

2 ALGORITHMS

2.1 *Kmeans clustering method*

Kmeans is an unsupervised machine learning method, which cluster a sample set by calculating the Euclidean distance between samples (Wang and Bai, 2016). The basic principle of the algorithm is:

(a) Randomly select n points from the sample set as clustering centers;

(b) Calculate the distance l_i from each sample $\boldsymbol{s_i}$ $=\{s_{i1}, s_{i2}, ..., s_{in}\}$ to each cluster center $c_i=\{c_{i1}, c_{i2}, ..., c_{in}\}$:

$$l_i = \sqrt{(\boldsymbol{s}_i - \boldsymbol{c}_i)^2} \tag{1}$$

And classify the sample into the category that the closest cluster center belongs to;

(c) Calculate the geometric center $c_i^{'}$ of each category as the new clustering center:

$$c_i^{'} = \frac{\sum_{i=1}^{n} \boldsymbol{s}_n}{n} \tag{2}$$

(d) Repeat step (b), (c) until the change in the position of the clustering center is less than the specified value or the maximum number of iterations is reached.

2.2 *Spectral clustering method*

Spectral clustering is also an unsupervised machine learning method, based on the principle of graph connectivity optimization. The basic principle of the algorithm is:

(a) Initialize the weight matrix W and number of clusters n, where W is a $k*k$ matrix, k is the number of input parameters;

(b) Calculate Diagonal matric D where d_i is the sum of w_{ij} in W:

$$d_i = \sum_{j=1}^{n} w_{ij} \tag{3}$$

(c) Calculate the Laplacian matrix $L=D-W$ and the eigenvectors $e_i, ..., e_n$, set $E=[e1|e2|...|ek]$;

(d) For $i = 1, ..., n$, define ### the vector given by the i-th row of X;

(e) Calculate the eigenvalue, cluster the samples with the positive eigenvalue value in to the same category and repeat the steps until convergence.

Unsupervised clustering methods are able to automatically categorize construction parameters according to their correlations. Existing shield construction research shows that different construction parameter relationships reflect the tool wear: when the advance speed and thrust force are high, the cutter wears at a normal rate; the cutter wears faster when the chamber pressure is high and the total thrust is low; the cutter wears slowly when the total thrust is low, the cutter torque is low and the advance speed is normal. It can be seen that the cutter wear rate is different for different construction parameter relationships. Based on the clustering results of construction parameters in the above two methods, different cutter wear correction coefficients are assigned to different categories of construction categories, and this coefficient is used as an input parameter. The initial value of the correction coefficient is assigned according to the established research results, and the higher value represents the faster wear, the specific value is shown in Table 1.

2.3 *Transformer method*

Transformer algorithm was proposed by Vaswani et al. (2017), which is mainly used for natural language recognition problems. To apply it to the tool wear problem, its structure is slightly improved, and the structure of the improved Transformer model is shown in Figure 1: the input parameters are combined with the position encoding and fed into the encoder, and the number of encoders is N. Each encoder consists of a self-attention layer and a feed-forward layer and the residuals and regularization operations are immediately followed by each layer. After N encoders the data goes to decoders, the number of decoders is M. Each decoder consists of a self-attention layer, an

Table 1. Relationship between construction parameters and corresponding initial correction coefficients.

	Tool wear rate	Initial correction coefficient
Low thrust Low torque Normal advance speed Low chamber pressure	Normal	1.0
Low thrust Low torque Normal advance speed Low chamber pressure	Normal	1.1
Low thrust Low torque Normal advance speed Low chamber pressure	Fast	2.5
Low thrust Low torque Normal advance speed Low chamber pressure	Faster	3.0

encoding-decoding attention layer and a feed-forward layer, and each layer is also immediately followed by residual and regularization operations. After M decoders the data again goes through the feed forward layer with normalization and finally the predicted value is obtained.

Since different tools are installed on different cutter spokes and the cutting trajectories of neighbouring tools on the same spoke are usually not adjacent to each other, the interaction between tools is a complex spatial problem. The unique self-attention mechanism and position encoding method of Transformer is very suitable for this problem. To consider the position of the tools on the cutter head, the position code is adjusted. The original position code is:

$$PE_{(pos,2i)} = \sin(pos/10000^{2i/d_{mdoel}}) \quad (4)$$

$$PE_{(pos,2i+1)} = \cos(pos/10000^{2i/d_{mdoel}}) \quad (5)$$

where *pos* means the position of the feature, i.e., the installation radius of the tool. But on the cutterhead as shown in Figure 1, the tools with adjacent installation radius are not on the same spoke. Thus, the position code is adjusted as:

$$PE_{(pos,2i)} = \sin(pos/10000^{(2i+\theta/2\pi^*6)/d_{mdoel}}) \quad (6)$$

$$PE_{(pos,2i+1)} = \cos(pos/10000^{(2i+\theta/2\pi^*6)/d_{mdoel}}) \quad (7)$$

where θ is the angle between the spoke and the vertical direction. The coefficient of 6 means that there are 6 spokes on the cutterhead. By this adjustment, the position of the tools, including installation radius and angle of spoke, is taken into consideration. The position code after adjustment is shown in Figure 2.

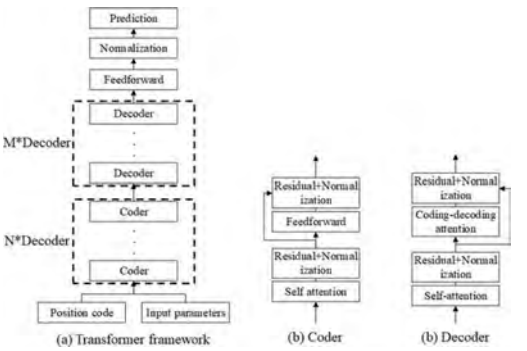

Figure 1. Improved Transformer model for predicting wear of disc tools.

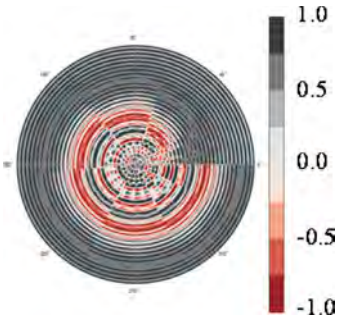

Figure 2. Adjusted position code.

Transformer's positional coding step can consider the positional relationship between the input parameters, and the installation radius of the tool itself, as one of the input parameters, responds to the spatial position of the tools, so it can be used for positional coding to input the positional information of the tools into the model. The self-attention mechanism takes into account the interaction between the input parameters, and assigns a higher attention value to other tools or construction parameters that have a greater influence on one tool, so the Transformer model is well suited for the prediction of tool wear on the cutterhead, which has spatial position information.

2.4 *Principle component analysis*

The principle component analysis is a popular method for dimension reduction. It projects high-dimensional data to low-dimensional space through linear projection and expect the maximum amount of information, i.e. maximum variance in the low-dimension space, of the data as shown in Figure 3. Since the prediction problem is a high dimension problem, PCA is applied to improving the stability and accuracy of models. The specific procedure for principle component analysis is described in (Huang et al., 2022).

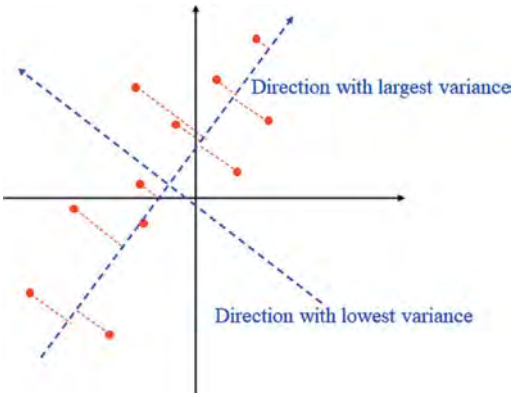

Figure 3. Schemes of principle component analysis.

2.5 *Predictive model based on clustering, PCA with Transformer algorithm*

The flow of the proposed prediction model based on clustering, PCA with Transformer algorithm is shown in Figure 4. The input parameters include four categories: construction parameters, tool parameters, stratigraphic parameters and wear correction coefficients. The construction parameters include total thrust, cutterhead torque, cutterhead rotation speed, chamber pressure and advance speed, which have obvious influence on the tool wear; the tool parameters include the installation radius of the tool and the cutting distance of the tool; the stratum parameters include the ratio of the area of soft and hard strata on the palisade surface; the wear modification coefficients are obtained by the kmeans clustering algorithm based on the construction parameters, and the initial value of the wear modification coefficients are assigned to the different clustering results. Different initial values of wear correction coefficients are assigned for different clustering results. The output parameter is the normal wear of the tools. The input parameters are fed into the Transformer model for training. The tool wear prediction model is obtained after the accuracy rate reaches the requirement or the maximum number of iterations.

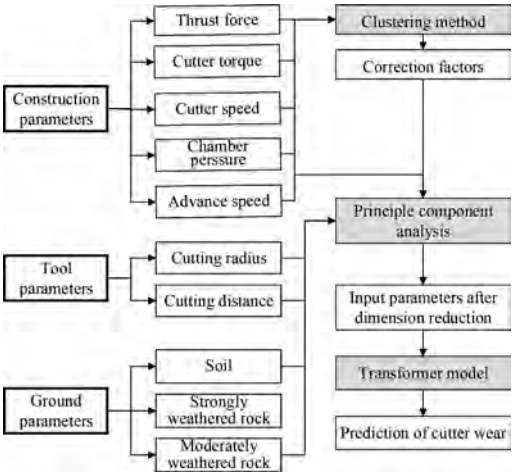

Figure 4. Prediction model based on kmeans clustering and Transformer regression.

3 DATA PREPROCESSING AND STRUCTURING

3.1 *Data collection*

Cutterhead of the shield machine as shown in Figure 5, the disc cutters are installed on the cutterhead. The installation radius of different disc cutter is different, and the distance crossed when the cutterhead rotates around is different. The larger the installation radius is, the longer the distance crossed when the cutterhead rotates around, and the corresponding wear is also larger. Therefore, the installation radius of the tool is used as an input parameter. In addition, the number of rotations of the cutterhead determines the cumulative cutting distance of the tools, so the number of rotations of the cutterhead is used as an input parameter.

Construction parameters are recorded by control system of shield machine, the construction parameters are recorded every 5 mins. As mentioned in Section 2.5, torque of cutterhead, cutterhead rotation speed, chamber pressure, total thrust, and advance speed are selected for the prediction of tool wear based on the existing research.

Based on the geological survey, the ground condition along the tunnel alignment can be obtained. For disc cutter, the wear is mainly caused by cutting hard rock. And the types of hard rock on the face of tunnel are strongly weathered rocks and moderately weathered rocks. For the same type of rocks, the physical properties are similar. Thus, the area proportion of different stratum on face is selected as the input parameters to reflect the ground condition.

3.2 *Data denoising*

The record of construction parameters usually contains noise. Thus, 3σ method is applied for the

Figure 5. Shield cutterhead and disc cutter.

denoising of construction parameters. The process of 3σ method is described in (Huang et al., 2022). Then, average of construction parameters during the construction of each ring is calculated for the represent of construction parameters of this ring. The reason for using the average is two-fold. One is that calculating the mean can eliminate some random errors. The other is that the wear of cutters are recorded after the construction of one ring and the data format based on the ring facilitates the data structure of the construction parameters and wear records.

3.3 *Data structuring*

The cutter wear, cutter radius, ground condition and construction parameters are multisource data. They should be structured to be used for the establishment of deep learning model. Analysing the problem, it can be seen that wear of cutter tools is the focus of this study. Thus, the data are structure based on the record of tool wear. Due to the complexity of tool wear detection, its detection frequency is uncertain. The ring number is selected for the description of the detection range of tool wear. Then, the averages of construction parameters are calculated as:

$$p_{ave} = \frac{1}{Ring_B - Ring_A} \sum_{i=Ring_A}^{Ring_B} p_i \qquad (8)$$

where p_{ave} is the average of construction parameters in this wear detection range, $Ring_A$ is the ring number of beginning of the wear detection, $Ring_B$ is the ring number of the end of the wear detection. For example, a cutter is detected in Ring 18, then detected in Ring 50, then for the record detected in Ring 50, $Ring_A$ is 18 and $Ring_B$ is 50. p_i is the average of construction parameters during the construction process of $Ring_i$.

For ground condition, the area proportion of different stratum is calculated at different ring number based on the geological survey. Then the averages of ground condition in each wear detection range is calculated as shown in formula (7).

For cutter installation radius, the radius of each cutter is shown in Figure 6. There are total 79 cutters on the cutterhead, each cutter has unique installation radius. In data structure, the corresponding installation radius is matched to the corresponding wear record.

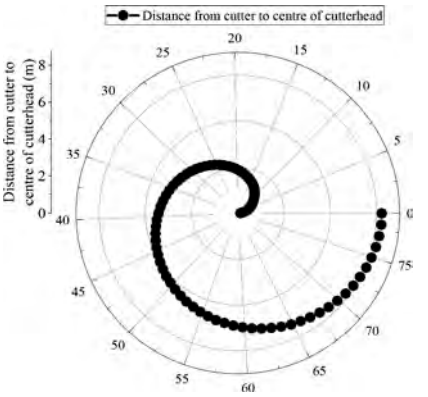

Figure 6. Installation radius of each disc cutte.

4 ENGINEERING APPLICATION

4.1 *Database for deep learning*

During construction, there are total 217 records of wear detection. Based on the method of data structuring, there are finally 217 samples in the database. For each sample, its dimension is 12, containing 5 construction parameters, namely torque of cutterhead, cutterhead rotation speed, chamber pressure, total thrust, and advance speed; 2 tool parameters, namely installation radius and cutting distance; 3 ground conditions, namely proportion of soil, strongly weathered rock and moderately weathered rock; 1 correction coefficient based on the results of clustering and 1 tool wear record. Among them, the construction parameters, tool parameters, ground conditions and correction coefficient are input parameters, tool wear is output parameters.

4.2 *Results of clustering*

In this research, two clustering methods are applied to cluster the construction parameters. For different categories, the values of construction parameters are different as shown in Figure 7. The black points, representing category 1, have low pushing force, low cutterhead torque and low advance speed, meaning that the wear speed of tools is low. The red points,

representing category 1, have normal pushing force, normal cutterhead torque and normal advance speed, meaning that the wear speed of tools is normal. The green points, representing category 2, have large pushing force, large cutterhead torque but normal advance speed, meaning that the wear speed of tools is fast. The brown points, representing category 4, have normal pushing force but low cutterhead torque and low advance speed, meaning that the wear speed of tools is large. Figure 7 shows the results of spectral clustering. For Kmeans method, the 4 categories have the similar relationship.

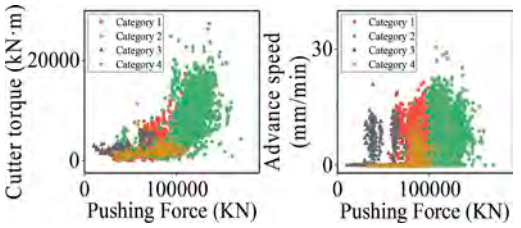

Figure 7. Relationship between construction parameters in the Kmeans results.

The stratum on the face include soil, strongly weathered rock and moderately weathered rock. Based on the geological survey report, the area proportion of these three strata along tunnel axis is shown in Figure 8 with the Kmeans results. The black line represents the area of soil on the face. The red represents the area of strongly weathered rock on the face. The blue line represents the area of moderately weathered rock on the face. The black semi-transparent box marks out the region of category 3 of Kmeans result. Similarly, the red box marks category 1, the green box marks category 2 and the brown box marks category 3. In category 3, it is the beginning of the construction and the driver set the construction parameters carefully, so the thrust force, cutterhead torque and advance speed are all low and the wear speed of tools is low. While in category 2 and category 3, the area of hard rock on face increases but the driver does not adjust the construction parameters properly. Thus, the wear speed of tools increases quickly. By assigning different values to different categories of clustering, the artificial experience is introduced into the model, i.e., higher correction coefficients represent higher tool wear rates.

In order to eliminate the influence of unit of the input parameters, a mix-min normalization is applied to the input parameters. The final size of dataset is 217*12. There are total 217 samples in the dataset with 12 features.

4.3 *Result of the model*

Training of each epoch requires about 0.1s and ultimately 1000 epochs were trained. Since the prediction of tool wear is regression problem the

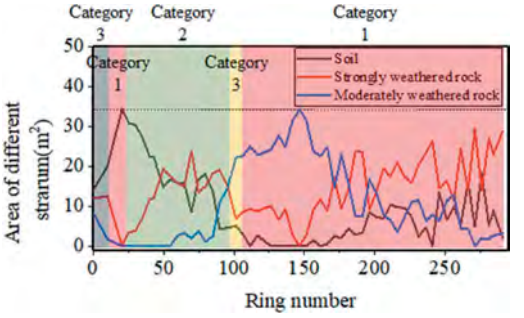

Figure 8. Area of different strata on tunnel face in longitudinal direction with the results of Kmeans.

evaluation factors are chosen as mean absolute error (MAE), mean squared error (MSE) and goodness of fit (R^2). They are calculated as:

$$MAE = \frac{\sum_{i=1}^{n_{test}} |y_i - y_{pi}|}{n_{test}} \tag{9}$$

$$MSE = \frac{\sqrt{\sum_{i=1}^{n_{test}} (y_i - y_{pi})^2}}{n_{test}} \tag{10}$$

$$R^2 = 1 - \frac{\sum_{i=1}^{n_{test}} (y_i - y_{pi})^2}{\sum_{i=1}^{n_{test}} (y_i - y_{ave})^2} \tag{11}$$

where y_i is the i^{th} true value, y_{pi} is i^{th} prediction value, y_{ave} is the average of true value. The lower values of MAE and MSE mean lower prediction error of model. R^2 ranges from 0 to 1, reflecting the proportion of real information reflected by the model. The closer R^2 to 1, the better the model is.

The tool wear detection results during the construction of this large-diameter slurry pressure balanced shield tunnel are used to validate the model, and the final model prediction results are shown in Figure 9, the the MAE is 3.3 mm, the MSE is 4.3mm and the R^2 is 0.73. In this project, the allowable tool wear of the disc cutter is 40 mm, and therefore the error of 3.3 mm or 4.3mm is acceptable for the complex problem of predicting the tool wear in composite stratum. And the prediction result of the model can provide a reference for the current tool wear, so as to arrange the replacement of tools in time to ensure the construction efficiency and safety.

5 RESULTS

An advanced Transformer method is proposed for the prediction of the tool wear of disc cutter during shield tunnelling in composite stratum. Clustering methods are applied to cluster the construction parameters for the introduction of artificial experience, position code is adjusted to consider the position of the disc cutter on the cutterhead, and

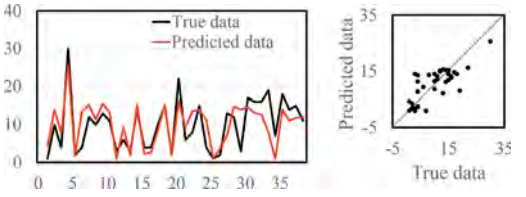

Figure 9. Results of predicting model.

principle analysis is applied for the dimension reduction of the input parameters. The following conclusions are obtained:

1) The clustering method can classify the construction parameters based on the relationship between the construction parameters, and the clustering results reflect the construction state of the shield. The wear rate of the tool varies in different construction states, and different correction coefficients are assigned to different construction states by the introduction of wear correction coefficients, so that the influence of the construction state is introduced into the prediction model to help the model accurately predict the wear of the tools.
2) Advanced position code is proposed to distinguish different location and relative positional relationship of disc cutters. The closer the cutters are, the more obvious the mutual influence of wear between them.
3) Considering the construction parameters, tool parameters, ground parameters and the correction coefficients, as well as optimizing the position code, the proposed Transformer model can predict the wear of disc cutter with the error of only 3.3 mm. The corresponding tool change program can be formulated according to the prediction results during construction.

REFERENCES

Chang J.Q., Zhang D.M., Huang H.W., Jia J.W. A hybrid sensing of rotation-induced stress of segmental lining during shield tunneling via WSN and surrogate numerical modelling[J]. Tunnelling and Underground Space Technology, 2023, 140, 105315.

Gong Y.W., Huang J., Zhang L.F. Study on Tunneling Parameter Setting of Shield Machine of Subway Tunnel Adjacent to River in Complex Strata[J]. Journal of Municipal Technology, 2022, 40(02): 91–96.

Huang H W, Chang J Q, Zhang D M, Zhang J, Wu H M, Li G. Machine learning-based automatic control of tunneling posture of shield machine[J]. Journal of Rock Mechanics and Geotechnical Engineering. 2022; 14: 1153–1164.

Huang J. H., Tang Z. C., Zhang X. H. Stratigraphic Correlation of EFPI and Evolution Regularity of Shield Tunneling Parameter in Complex Stratum[J]. Tunnel Construction, 2021,41(S2): 215–221. (in Chinese)

Kilic, K., Toriya, H., Kosugi, Y., Adachi, T., Kawamura, Y., 2022. One-Dimensional Convolutional Neural Network for Pipe Jacking EPB TBM Cutter Wear Prediction. Appl. Sci.-Basel 12

Mahmoodzadeh, A., Mohammadi, M., Ibrahim, H.H., Abdulhamid, S.N., Ali, H.F.H., Hasan, A.M., Khishe, M., Mahmud, H., 2021. Machine learning forecasting models of disc cutters life of tunnel boring machine. Autom. Constr. 128.

Rostami J. Development of a Force Estimation Model for Rock Fragmentation with Disc Cutters Through Theoretical Modeling and Physical Measurement of Crushed Zone Pressure[M]Golden: Colorado School of Mines, 1997.

Su, W.L., Li, X.G., Jin, D.L., Yang, Y., Qin, R.C., Wang, X.Y., 2020. Analysis and prediction of TBM disc cutter wear when tunneling in hard rock strata: A case study of a metro tunnel excavation in Shenzhen, China. Wear 446.

Vaswani A., Shazeer N., Parmar N., Uszkoreit J., Jones L., Gomez A.N., Kaiser L., Polosukhin I., 2017. Attention Is All You Need[C], 31st Annual Conference on Neural Information Processing Systems (NIPS), Long Beach, CA.

Wang, L.H., Kang, Y.L., Zhao, X.J., Zhang, Q., 2015. Disc cutter wear prediction for a hard rock TBM cutterhead based on energy analysis. Tunn. Undergr. Space Technol. 50, 324–333.

Xu W. H., Ni W. Y., Zhao H. T. Research on Driving Parameters of Large Diameter Slurry Shield Tunnel Under Complex Interbedded Strata[J]. Tunnel Construction, 2018, 38(S2): 373–378.

Wang, X.Y., Bai, Y.P., 2016. The global Minmax k-means algorithm. Springerplus 5.

Xue, Y.D., Zhou J., Liu C., Shadabfar M., Zhang J. Rock fragmentation induced by a TBM disc-cutter considering the effects of joints: A numerical simulation by DEM [J]. Computers and Geotechnics, 2021, 136: 1–14.

Yang, Z.Y., Sun, Z.Y., Fang, K.D., Jiang, Y.S., Gao, H.J., Bai, Z.Q., 2021. Cutting tool wear model for tunnel boring machine tunneling in heterogeneous grounds. Bulletin of Engineering Geology and the Environment 80, 5709–5723.

Zare S, Bruland A. Application of NTNU/SIN-TEF Drillability Indices in Hard Rock Tunneling [J]. Rock Mechanics and Rick Engineering, 2013, 46(1): 179–187.

Tunnelling for a Better Life – Yan, Celestino, Thewes & Eberhardt (Eds)
© 2024 The Author(s), ISBN 978-1-032-80042-4
Open Access: www.taylorfrancis.com, CC BY-NC-ND 4.0 license

A modified foam half-life time test method for EPB shield tunnelling

Zhongtian Chen*
Ghent University, Ghent, Belgium

Adam Bezuijen
Ghent University, Ghent, Belgium
Deltares, Delft, The Netherlands

Yong Fang
Southwest Jiaotong University, Chengdu, China

ABSTRACT: Soil conditioning is used in most earth pressure balanced (EPB) shied tunnelling projects and foam is one of the most used chemical additives. Foam with sufficient stability should have a suitable half-life time to ensure the effectiveness of soil conditioning during segment construction and through the whole process of excavated soil discharge. This study explained the limitations of current half-life time measurement method by introducing the influence of foam expansion ratio (FER) and foam column height. A modified foam half-life time test method is brought up by measuring the drainage of foam column with a certain height. The modified measurement method is specific enough to ensure that comparable results are obtained by scholars and engineers worldwide. It is found that both Cf (foam concentration) and FER play important roles in half-life time and they would influence each other, which can be explained by the surface tension of the foaming agent solution.

Keywords: EPB shield, soil conditioning, foam stability, half-life time, surface tension

1 INTRODUCTION

During EPB shield tunnelling, soil conditioning with foam can be used to reduce the permeability of sand, decrease the clogging potential in clay and increase the workability and compressibility of conditioned soil (Mori et al., 2018; Wang et al., 2020; Thewes and Budach, 2010; Thewes et al., 2012).

The stability of foam is crucial during the soil conditioning in sand, a sufficient foam stability is needed to ensure stable mechanical properties of conditioned soils during the mixing of excavated soil and the discharge of soil at the end of screw conveyor (Peila et al., 2007). The stability of foam can be evaluated by a parameter called half-life time. In shield tunnelling area, the half-life time is defined as the time needed for 80 g foam to lose 40 g weight (EFNARC, 2005). Bezuijen et al. (1999) found that foam can reduce the permeability of conditioned sand by replacing pore water in the sand, and foam could stay stable for over 24 h when mixed with sand. Wu et al. (2018) indicated that the half-life time of foam is much longer if evaluated by the foam volume loss than the foam weight loss. Wu et al. (2020) analysed the sand grain-foam pictures and performed compression and vane shear tests in 60 minutes after the foam-sand mixture is prepared; they found that foam is stable in the mixture during this period. Zhao et al. (2021) indicated that anti-clay agents could reduce the stability of foam bubbles. El Souwaissi et al. (2023) found that the half-life time measured by foam volume and foam weight loss share the same trend despite the differences in measured values.

It is found in chemistry area that foam stability changes with surface tension which is caused by the concentration change in foaming agent solution. In shield tunnelling area, Sebastiani et al. (2019) preformed extensive half-life time tests with various foaming agent products and concentrations, a foaming agent classification system was proposed based on the test results. Wan et al. (2021) and Li et al. (2022) measured the half-life time of foam at various concentrations and found

*Corresponding author: zhongtian.chen@ugent.be

DOI: 10.1201/9781003495505-225

that the half-life time trend to be stable after Cf is higher than 2%. Carigi et al. (2022) found that the stability of foam can be influenced by the concentration of foaming agent solution and the flow rate in the foam generator.

The extensive work about foam stability gives valuable instruction to soil conditioning, yet limited studies take the surface tension of foaming agent solution in consideration. This paper performs half-life time tests and explains the limitations of current measurement methods based on the test results. A modified measurement is brought up to avoid current limitations. The surface tension of foaming agent solution is also measured to further explain the stability of foam.

2 METHODOLOGY AND MATERIAL

A widely used commercial foaming agent is tested in this study and the foaming agent is diluted to desired concentration by tap water. The tested foaming agent is regular type for common use without any other polymer and anti-clogging chemicals.

The foaming agent is first mixed with tap water at rotation speed around 6 rpm to prepare the foaming agent solution. Foam is generated by a small-scale laboratory foam generation device which is introduced in detail in Chen et al. (2022). The flow rate of air and liquid is controlled carefully to provide foam with a precise and stable FER. A foam tester which meets the requirements of EFNARC 2005 is used to test the half-life time of foam, as shown in Figure 1. The test device consists of two acrylic parts, a cylinder and a funnel. Three cylinders are used in this study, the dimensions of these cylinders are shown in Table 1 and the funnel has inner height of 6 cm.

Table 1. Dimensions of test cylinders.

Test cylinder	Inner diameter (cm)	Height (cm)
A	13	10
B	5	20
C	13	30

A hydrophilic membrane with pore size 2 μm is placed between the cylinder and the funnel to separate foam bubbles and drainage. The diameter of foam bubbles with various concentrations at FER 10 is shown in Figure 2, it shows that the pore size 2 μm can separate all foam bubbles. The foam is filled in the test device after the hydrophilic membrane is saturated and installed. The actual FER of the generated foam is checked at the beginning and the end of filling process by measuring the weight of foam in a 70 ml container. It is found that the actual FER can be controlled at ±1 around the target FER. The weight of the drainage is recorded at a frequency of 1 Hz after the foam is filled in the container for the half-life test.

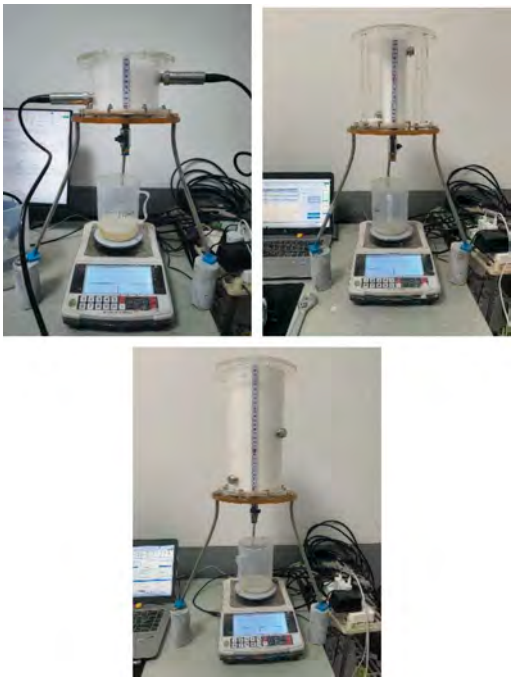

Figure 1. The half-life time test device.

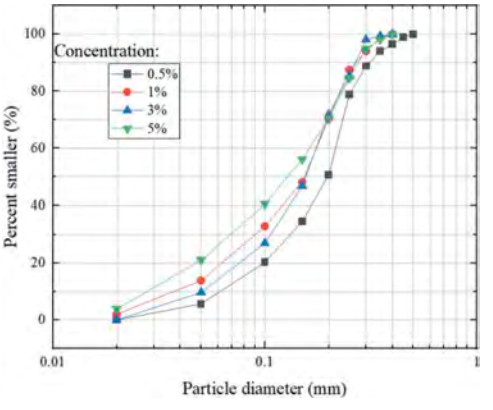

Figure 2. The foam bubble diameter at various concentrations.

The surface tension of the foaming agent solution used in this study is tested by the platinum plate method, which has an accuracy of 0.1 mN/m. The platinum plate is cleaned carefully before each test to ensure the accuracy of test results.

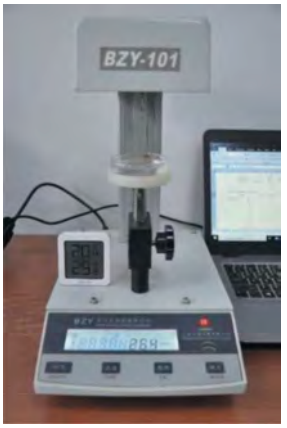

Figure 3. The platinum plate method device.

3 TEST RESULTS

3.1 *Results following current standard*

Half-life time tests are first performed following exactly the requirement of EFNARC (2005). The size of foam half-life time test device used in this section is shown in Table 1. The weight of tested foam is 80 g for all tests in this section, the weight of tested foam and the size of test device both meet the requirement of EFNARC (2005), where the size is regulated as 1 to 2 liters and the foam weight is regulated as 80 g. The concentration of foaming agent in this section is 3%, which is the suggested value by the foaming agent productor.

The test results following current standard are shown in Table 2, it shows that tests performed in the device with 5 cm diameter have longer half-life time (around 900 s) due to the higher foam column height. For tests performed in cylinder with diameter 13 cm, the half-life time measured is much shorter, which is around 385 s. Results show that although tests in Table 1 all follow the EFNARC (2005) standard, the half-life time measured by test cylinders with various diameters are completely different and even not comparable.

Table 2. Test results with different foam height.

Size (cm)	Target FER	Actual FER	Foam height (cm)	Half-life time (s)
D 5, H 20	5	4.7, 5.2, 5.1	20	905, 898, 909
D 13, H 10	5	5.0, 4.9, 5.2	3	380, 386, 389

Half-life time tests of foam with various FERs are performed in the foam test cylinder with diameter of 13 cm, the results are shown in Table 3. It shows that foam with FER 15 has much longer half-life time (around 1150 s). This is partly due to the higher foam column. The results show that the current standard for foam half-life time measurement is not suitable for the measurement of foam with different FERs, as foam with fixed weight will have different foam height with changing FER. The longer half-life time for foam with higher FER agrees well with the findings of Wu et al. (2018), where it is found that the longer foam column, the longer the half-life time.

Table 3. Test results with different FER.

Size (cm)	Target FER	Actual FER	Foam height (cm)	Half-life time (s)
D 13, H 10	5	5.0, 4.9, 5.2	3	380, 386, 389
D 13, H 10	15	14.7, 15.5, 15.4	9	1152, 1139, 1158

3.2 *Drainage curves at various FERs*

To further study the influence of FER, half-life time tests are performed in Cylinder C shown in Table 1. The tests with various FERs in this section are performed with a fixed foam column height of 30 cm to avoid the influence of foam column height difference. The drainage history curves are recorded in Figure 4. It shows that the drainage of foam with FER 5.6 starts directly at the beginning of the test, thus reaches the half-life time earlier than foam with higher FER. An obvious zero drainage stage shows for foam with FER 13.5, leading to a longer half-life time. For both FERs the drainage speed decreases after reaching the half-life time. The drainage history curves of Figure 4 show that the half-life time difference in Table 3 is not only influenced by the foam column difference, but also influenced by the permeability of foam

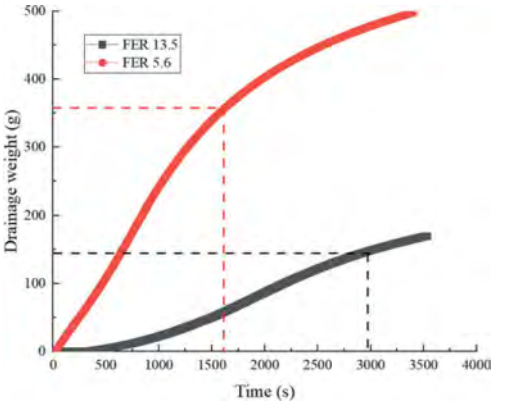

Figure 4. Typical drainage history curves, dash lines represents the half-life time and corresponding drainage weight.

column itself. It is difficult to analyse the permeability difference with current standard, as the influence of foam column height cannot be excluded.

3.3 *Half-life time at various concentrations*

Half-life time tests of foam with various concentrations are performed by the two test cylinders shown in Figure 1. The FER of tested foam for all tests in this section is 5. The test results in Figure 5 show that the half-life time increases with concentration until reaching a stable value at concentration of 3%. Further concentration increase does not lead to further half-life time increase. Foam with column height 20 cm has longer half-life time, yet the concentration 3% which corresponds to a stabilized high half-life time is not changed.

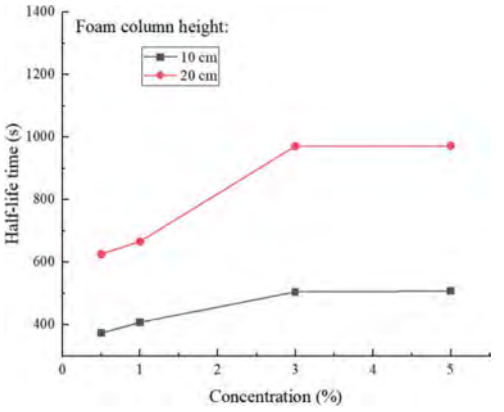

Figure 5. Half-life time with various concentrations.

3.4 *Surface tension with various concentrations*

The surface tension of foaming agent solutions with various concentrations is measured to further study the influence of concentration on foam stability. The results in Figure 6 show that the surface tension starts to decrease sharply at concentration 0.001% and reaches a relatively stable value at concentration 0.1%. The surface tension reaches the lowest value at concentration 3%, which corresponds well to the concentration with highest half-life time.

3.5 *Proposed new half-life time measurement method*

The half-life time test results reported above show that the major flaw of current half-life measurement method is, it that the size of the test device is not described sufficiently specific. Besides, the fixed initial weight regulation of current standard makes it difficult to evaluate the half-life time of foam with various FERs, as foam with various FERs will have different foam column height, it is difficult to tell

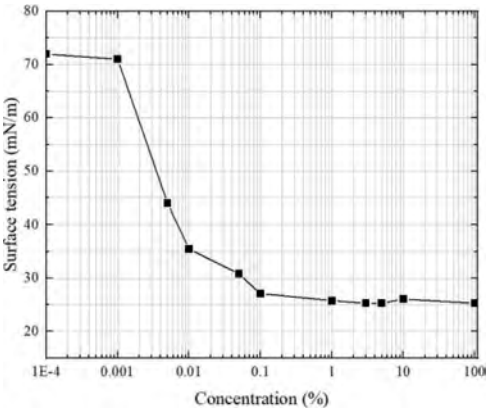

Figure 6. Surface tensions at various concentrations.

whether the stability difference is caused by foam column height or the permeability of foam itself. Both limitations are caused by the fact that the foam half-life time will be greatly influenced by the foam column height.

Thus, a modified foam half-life time test method can be proposed. In the new test method, the foam column height at the beginning of the test should be regulated instead of foam weight, while the half-life time is still the time needed for the drainage weight to reach half the initial foam weight.

4 CONCLUSIONS

This paper studies the stability of foam by performing extensive half-life time tests. Test results show that foam half-life time increases with foam column height and FER. Limitation exists in the current foam half-life time measurement method, as the current method did not regulate the size of the test device specific enough and the fixed foam initial weight could lead to various foam column height with changing FER. A modified half-life time measurement method is proposed with a fixed initial foam column height instead of a fixed initial foam weight. It is also found that for foam with FER 5, foam stability decreases with decreasing foaming agent solution concentration when the concentration is lower than 3%. The possible reason for the decreasing foam stability at low concentrations could be that foam has larger surface area than the foaming agent solution, the larger surface area leads to a lower surfactant density, thus decreasing the foam stability.

REFERENCES

Bezuijen, A., Schaminee, P. E. L., & Kleinjan, J. A. (1999). Additive testing for earth pressure balance shields. In Twelfth European Conference on Soil Mechanics and

Geotechnical Engineering (Proceedings) The Netherlands Society of Soil Mechanics and Geotechnical Engineering; Ministry of Transport, Public Works and Water Management; AP van den Berg Machinefabriek; Fugro NV; GeoDelft; Holland Railconsult (No. Volume 3).

Carigi, A., Todaro, C., Martinelli, D., & Peila, D. (2022). A More Comprehensive Way to Analyze Foam Stability for EPB Tunnelling—Introduction of a Mathematical Characterization. Geosciences, 12(5), 191.

Chen, Z., Bezuijen, A., Fang, Y., Wang, K., & Deng, R. (2022). Experimental study and field validation on soil clogging of EPB shields in completely decomposed granite. Tunnelling and Underground Space Technology, 120, 104300.

EFNARC, 2005. Specification and guidelines for the use of specialist products for soft ground tunnelling. European Federation for Specialist Construction Chemicals and Concrete Systems, Surry, UK.http://www.efnarc.org/pdf/TBMGuidelinesApril05.pdf

El Souwaissi, N., Djeran-Maigre, I., Boulange, L., & Trottin, J. L. (2023). Effects of the physical characteristics of foams on conditioned soil's flow behavior: A case study. Tunnelling and Underground Space Technology, 137, 105111.

Li, S., Wan, Z., Zhao, S., Ma, P., Wang, M., & Xiong, B. (2022). Soil conditioning tests on sandy soil for earth pressure balance shield tunneling and field applications. Tunnelling and Underground Space Technology, 120, 104271.

Mori, L., Mooney, M., & Cha, M. (2018). Characterizing the influence of stress on foam conditioned sand for EPB tunneling. Tunnelling and Underground Space Technology, 71, 454–465.

Peila, D., Oggeri, C., & Vinai, R. (2007). Screw conveyor device for laboratory tests on conditioned soil for EPB tunneling operations. Journal of Geotechnical and Geoenvironmental Engineering, 133(12), 1622–1625.

Sebastiani, D., Vilardi, G., Bavasso, I., Di Palma, L., & Miliziano, S. (2019). Classification of foam and foaming products for EPB mechanized tunnelling based on half-life time. Tunnelling and Underground Space Technology, 92, 103044.

Thewes, M., & Budach, C. (2010). Soil conditioning with foam during EPB tunnelling. Geomechanics and Tunnelling, 3(3), 256–267.

Thewes, M., Budach, C., & Bezuijen, A. (2012). Foam conditioning in EPB tunnelling. In Geotechnical Aspects of Underground Construction in Soft Ground (pp. 145–154). CRC Press.

Wang, S., Liu, P., Hu, Q., & Zhong, J. (2020). Effect of dispersant on the tangential adhesion strength between clay and metal for EPB shield tunnelling. Tunnelling and Underground Space Technology, 95, 103144.

Wan, Z., Li, S., Yuan, C., Zhao, S., Wang, M., Lu, Q., & Hou, W. (2021). Soil conditioning for EPB shield tunneling in silty clay and weathered mudstone. International Journal of Geomechanics, 21(9), 06021020.

Wu, Y., Mooney, M. A., & Cha, M. (2018). An experimental examination of foam stability under pressure for EPB TBM tunneling. Tunnelling and Underground Space Technology, 77, 80–93.

Wu, Y., Nazem, A., Meng, F., & Mooney, M. A. (2020). Experimental study on the stability of foam-conditioned sand under pressure in the EPBM chamber. Tunnelling and Underground Space Technology, 106, 103590.

Zhao, S., Li, S., Wan, Z., Wang, X., Wang, M., & Yuan, C. (2021). Effects of anti-clay agents on bubble size distribution and stability of aqueous foam under pressure for earth pressure balance shield tunneling. Colloid and Interface Science Communications, 42, 100424.

Tunnelling for a Better Life – Yan, Celestino, Thewes & Eberhardt (Eds)
© 2024 The Author(s), ISBN 978-1-032-80042-4
Open Access: www.taylorfrancis.com, CC BY-NC-ND 4.0 license

Automatic excavation system for directional control in shield tunneling using machine learning techniques

Jian Chen*, Hiroki Kamada, Naohiko Takamoto, Hirokazu Sugiyama, Shinya Yamamoto & Tetsuya Aoyama
Shimizu Corporation, Tokyo, Japan

ABSTRACT: In shield tunneling, it is essential to appropriately control shield jacks according to the attitude of a shield machine and geological conditions to follow a planned alignment. However, the quality of the directional control of a shield machine is dependent on the skill of its operator. Here, we develop an automatic excavation system that proposes the optimal method for controlling shield jacks equivalent to the techniques utilized by a skilled operator. The developed automatic excavation system has an algorithm consisting of two steps. In the first step, the necessity of operations of shield jacks is determined to avoid excessive operations. In the second step, the optimal point where the resultant force of shield jacks should be acted upon to control the propulsive direction of a shield machine is predicted. Both steps use the models trained by gradient tree boosting with the operational data related to the actions of skilled operators. Feature variables of these models are the monitoring data referred to operators such as the shield machine's yawing, pitching, rolling, deviation from the planned alignment, and so on. The moving average is also added to feature variables to consider temporal variations. To investigate the feasibility of the algorithm, the models were trained using the data obtained at a shield tunnel site. It was confirmed that the outputs of the models were comparable to experts' operations, comparing the actual operational data with the prediction results of the models. In addition, the shield machine was driven according to the automatic excavation system to validate its performance at the site. The deviation from the planned alignment and the attitude of the shield machine were within the tolerances. The result shows the applicability of the automatic excavation system in real environments. This indicates the future's possibility of self-driving shield machines.

Keywords: Gradient tree boosting, Digging instruction support AI, Jacking operation support AI

1 INTRODUCTION

Japan's rapidly declining birth rate and aging population will lead to a decline in the labor force, and many industries are predicted to have labor shortages in the future. In particular, the shortage of workers in the construction industry is a serious problem. This also means fewer highly skilled shield operators in the construction industry. Therefore, technological innovations in shield tunneling are expected to reduce labor time and assist inexperienced shield operators.

The quality of shield tunneling depends on the skill of the operator who controls the shield machine. Thus, the shortage of skilled operators leads to the deterioration of the shield tunnel's quality. Self-driving shield machines are effective in ensuring the accuracy and productivity of tunneling, but there have been several challenges in their development. For example, the operations of a screw conveyor for discharging excavated soil and shield jacks for advancing a shield machine were automated using fuzzy models (Kuwahara et al., 1988). There has also been a study in which the shield jacks to be activated were selected automatically by using monitoring data to estimate the physical properties of the ground and calculate the moment required for excavation (Tateyama et al., 1994). However, these methods did not lead to the full automation of shield machines: differences from ground and construction conditions in various locations meant that it was difficult to predict the proper operations of shield machines.

Recently, techniques of machine learning have attracted attention. It has become possible to build high-performance models easily. The realization of self-driving shield machines is feasible if machine learning techniques are applied to the monitoring data of shield tunneling. It has already been shown that models capable of making judgments equivalent to that of an operator can be constructed using machine learning (Sugiyama et al., 2017, Kubota et al. 2023). These models predict how the rotational speed of a screw conveyor should be set and the optimal point

*Corresponding author: jianchen77@gmail.com

DOI: 10.1201/9781003495505-226

at which the resultant force of shield jacks should be acted upon. To achieve self-driving shield machines, an automatic excavation system for directional control in shield tunneling using machine learning techniques was developed recently.

The automatic excavation system consists of two types of AI systems as core parts: a Digging instruction support AI system (hereinafter referred to as Instruction AI) for planning the excavation instructions and a Jacking operation support AI system (hereinafter referred to as Operation AI) for automatic jacking operation of shield machines.

This study presents the configuration and the applicability of the automatic excavation system. Firstly, the AI models were trained using the data obtained at a shield tunnel site and evaluated for accuracy. It was confirmed that the outputs of the models were comparable to experts' operations, comparing the actual operational data with the prediction results of the models. In addition, the shield machine was driven according to the automatic excavation system to validate its performance at the same site. The deviation from the planned alignment and the attitude of the shield machine were within the tolerances. The result shows the applicability of the excavation system in real environments. This indicates the future possibility of self-driving shield machines for more actual shield tunneling sites.

2 SHIELD TUNNELING METHOD

The upper half of Figure 1 shows an image of the conventional construction cycle in the shield tunneling method. In this method, a tunnel is constructed in day and night shifts. During the short shifts, the position and attitude of the shield machine and the finished shape of the tunnel rings are surveyed, and then the next construction plan is made based on the surveying results. In the construction plan, digging instructions are created for each ring that is scheduled to be excavated for half a day. The digging instructions include the instruction items for controlling a shield machine and assembling segment rings. A skilled shied operator then manipulates the shield machine with three types of actions: controlling the propulsive direction of the shield machine, making the pressure in the chamber equal to that of the ground, and injecting an additive agent to the chamber and a bulking agent to the tail voids.

Controlling the propulsive direction of a shield machine is the most important task in ensuring the accurate construction of a shield tunnel. The operator must manipulate the shield machine while comparing the instruction values with the values shown on the shield machine's sensors. The instruction values are the shield machine's azimuth direction, its pitch, the extension lengths of the shield jacks' strokes, and so on. It is not easy to manipulate a shield machine to match all the instruction values. When the operator activates only some shield jacks, the force acting on the shield machine is decentered, and the shield machine can veer to follow the planned alignment, so operators need to be skilled at their work.

3 DIGGING INSTRUCTION SUPPORT AI

3.1 *Overview*

In shield tunneling, tunnels are constructed by combing standard segments and taper-shaped segments for tunnel alignments that include curved sections. In addition, tunnel excavation in curved sections is performed by adjusting the shield jack stroke and using a combination of articulation mechanism and an over-cutting device.

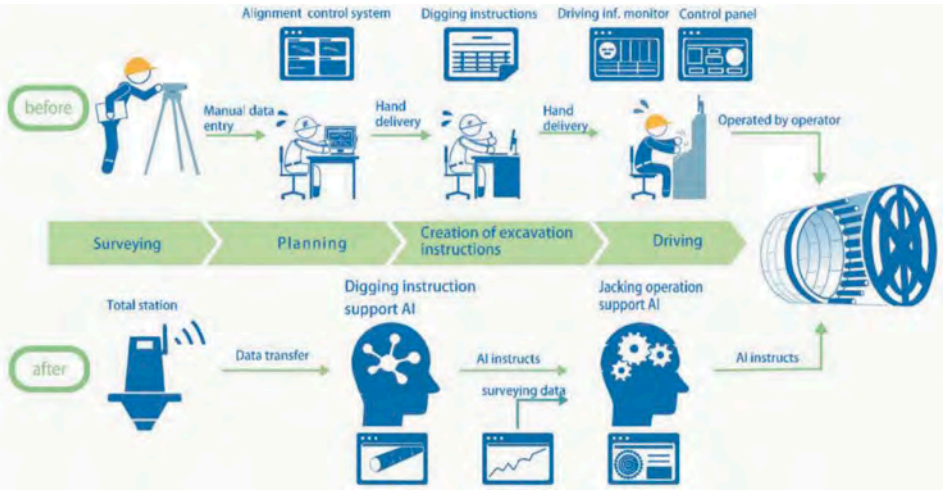

Figure 1. Shield tunnelling by the conventional method and AI-based methods.

The above considerations will be carried out before construction, but as errors will occur between the planned tunnel alignment and the actual measurements during construction, it will be necessary to conduct routine surveying and re-plan the digging instructions. Conventionally, these digging instructions disseminated to operators were calculated through theoretical calculations based on the geometry of the shield machine and the planned alignment.

To perform the above instructions, the Instruction AI searches for the optimal solution using machine learning and genetic algorithms through repeated three-dimensional simulations of segment allocation methods and shield machine tunneling methods, and then proposes the contents of digging instructions.

3.2 *Exploration of instruction AI*

In proposing the contents of the digging instructions, the Instruction AI will conduct a trial run on the following items.

3.2.1 *Segment assignment*

In the planning process, multiple types of segments such as straight and taper-shaped segments are provided and assigned along the planning tunnel alignment consisting of straight lines and curves so that the gaps between each segment and the planning alignment fall within a tolerance.

There are two demands in the segment assignment problem. (1) To make the gaps between each segment and the planning alignment fall within the tolerance. (2) To reduce the amount of soil excavated by the shield machine. The former demand is treated as an inequality constraint, and the latter demand is treated as an objective function. Segment assignment was defined as the constrained combinatorial optimization problem.

3.2.2 *Searching methods for optimal solutions*

The Instruction AI was built as an AI simulation program that combines shield construction experiences and a patented co-evolutionary combinatorial optimization algorithm inspired by evolutionary computation (Kato, et al. 2019).

The instruction AI performs simulated tunneling on a given planned alignment, based on trial conditions set by the AI, such as the digging plan of the shield machine and the allocation plan of segments. The AI scores the results using errors in the tunneling trajectory relative to the tunnel alignment and the degree of interference between the shield machine, segments, and excavated ground as evaluation indices. If the error exceeds the allowable value during the trial, or if there is a possibility of interference between the shield machine and the segment, the trial is terminated at that point and a new simulation is run with the trial conditions re-set. The AI evolves and learns what conditions can be selected to obtain the highest score over a large number of trials, and finally selects the plan that shows the highest score, which cannot be further improved, as the solution and develops it into a digging instruction plan.

3.2.3 *Reduction of impact on surrounding ground*

During curved tunneling, a copy cutter is used to expand the excavated cross-section (extra digging) while the shield machine passes through. The larger the excavated cross section, the greater the influence on the surrounding ground, such as loosening of the ground due to stress release.

This AI system can also propose a plan with no excess or deficiency in diameter expansion, thereby reducing the impact on the surrounding ground caused by the shield machine's passage and contributing to the reduction of construction waste volume by minimizing the amount of excavated soil.

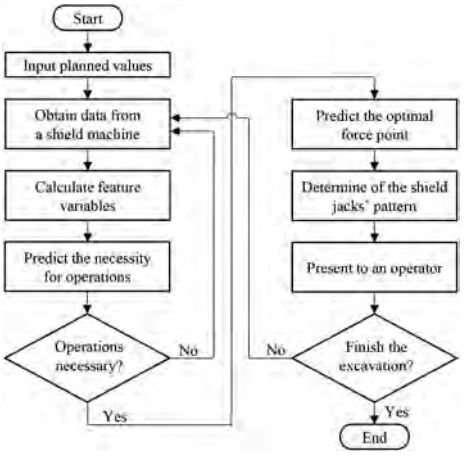

Figure 2. Processing flow executed by the operation AI.

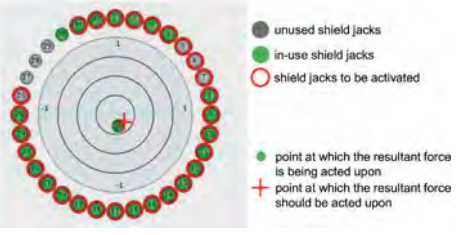

Figure 3. Example of the presented jacking pattern.

4 JACKING OPERATION SUPPORT AI

4.1 *Outline*

The Operation AI proposes the optimal way to control the shield jacks and to make a shield machine follow a planned alignment. Figure 2 shows the processing flow executed by the Operation AI. In the first step, digging instructions are prepared by the Instruction AI or a supervisor based on the surveying results for the daily excavation. When the shield

machine starts to excavate, the Operation AI obtains data from the shield machine and calculates the feature variables. The necessity for shield jacks' operations is predicted from the feature variables using a machine learning model. When necessary, other machine learning models are used to predict the optimal point at which the resultant force of the shield jacks should be acted upon to control the propulsive direction of the shield. The shield jacks to be activated are selected from the predicted point and presented to an operator, as shown in Figure 3.

4.2 *Gradient boosting decision tree*

A gradient boosting method (Jerome 2001) is one of the ensemble learning methods. A strong learner is built by combining multiple weak learners. When decision trees are used as weak learners, this method is called a gradient boosting decision tree (GBDT). The GBDT builds a strong learner through the following process. An initial strong learner $F_0(x)$ is given as

$$F_0(x) = f_0(x) \tag{1}$$

where x is a vector of feature variables and $f_0(x)$ is a weak learner of a decision tree. The root-mean-square error E_0 of $F_0(x)$ is calculated as

$$E_0 = \sqrt{(y - F_o(x))^2} \tag{2}$$

where y is a vector of the target values. A weak learner is $f_1(x)$ built with E_0 as the target value and connected to the strong learner:

$$F_1(x) = f_0(x) + f_1(x) \tag{3}$$

When this process is repeated M times, the following strong learner is obtained:

$$F_M(x) = f_0(x) + f_1(x) + \cdots + f_M(x) \tag{4}$$

The GBDT can build a high-performance learner by connecting weak learners to reduce the error. In this study, XGBoost, an open-source GBDT library, was used to build the machine learning models.

4.3 *Data for machine learning models*

Table 1 shows the data for three machine learning models used by the Operation AI. One model predicts the necessity for shield jacks' operations, using *F*c as the target variable (*F*c-Model). *F*c is given as 1 when in-use shield jacks were changed by an operator and as 0 when they were not. The other two models predict the horizontal and vertical coordinates of the point at which the resultant force of shield jacks should be acted upon, using *F*x and *F*y as the target variables (*F*x-Model and *F*y-Model). *F*x and *F*y are calculated from each thrust of the shield jacks. The variables other than *F*c, *F*x, and *F*y are the monitoring data that an operator refers to during the manipulations of a shield machine. These include the information on the shield machine's states and the deviation from the planned values. In addition, the moving averages between 1 and 10 s, 11 and 20 s, 21 and 30 s, and 31 and 60 s are added to feature variables because an operator would consider temporal variations.

4.4 *Predicting the necessity for shield jacks' operations*

The *F*c-Model predicts the necessity for shield jacks' operations to avoid excessive operations. These operations are deemed necessary when a few minutes have passed since the previous instruction of the operation system and when the output of the *F*c-Model is more than the threshold.

Table 1. Data for machine learning models.

Variable	Unit	Target	Machine's state	Difference from plan
Binary data of the operator's manipulations (*Fc*)	-	✓		
Horizontal coordinate of the resultant force point (*Fx*)	-	✓		
Vertical coordinate of the resultant force point (*Fy*)	-	✓		
Torque (*To*)	%		✓	
Velocity (*Ve*)	mm/min		✓	
Thrust (*Tr*)	kN		✓	
Face pressure (*Fp*)	MPa		✓	
Pitch (*Pt*)	deg		✓	
Roll (*Ro*)	deg		✓	
Deviation from the planned left-right difference of the extensions of shield jacks' strokes (*Dj*)	mm			✓
Deviation from the planned azimuth direction (*Dd*)	deg			✓
Deviation from the planned pitch (*Dp*)	deg			✓
Horizontal deviation from the planned path (*Dh*)	mm			✓
Vertical deviation from the planned path (*Dv*)	mm			✓

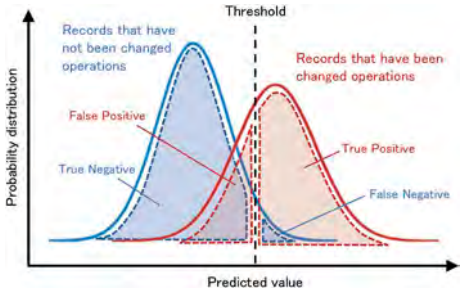

Figure 4. Probability distribution by the Fc-model.

Most of the *F*c are 0 because an operator controls shield jacks once in several tens of seconds to several hundreds of seconds. If the *F*c-Model is built using raw *F*c as the target variable, almost all values outputted by the *F*c-Model are 0. For this reason, the *F*c-Model is trained with weighted data.

The threshold must be set to predict whether the operations of shield jacks are necessary. Figure 4 shows the concept of the probability distribution of the predicted values outputted by the *F*c-Model. The numbers of true negatives (*TN*), false negatives (*FN*), true positives (*TP*), and false positives (*FP*) can be calculated if the threshold is fixed. Here, the threshold is set to minimize the balanced error rate (BER).

$$BER = 0.5 \times \left(\frac{FP}{TN + FP} + \frac{FN}{FN + TP} \right) \quad (5)$$

When the output value of the *F*c-Model is larger than the threshold, the operations of shield jacks are necessary.

4.5 *Predicting the optimal force point*

The optimal point at which the resultant force of shield jacks should be acted upon is predicted by the *F*x-Model and *F*y-Model. When the operations were predicted to be necessary, these models outputted the horizontal and vertical coordinates of the force point. The *F*x-Model and *F*y-Model are trained with the data classified as *TP* and *FN* in Figure 4. It is considered that more accurate models can be built because only characteristic data that were predicted to require the operations are used.

Furthermore, Operation AI calculates the pattern of shield jacks based on the resultant force point predicted by the machine learning models.

4.6 *Ensuring the safety of operation AI*

The Operation AI is equipped with a safety function for proper training and good-quality prediction of the aforementioned AI models. This function is divided into two parts, and if all of these are in order, the data is passed to the AI to make predictions.

4.6.1 *Input-data check*

The Operation AI reads the data to be passed to itself and checks for missing data or data that would be outside the measurement range of the instruments. Depending on how long such a condition persists, the AI determines if it is abnormal or urgent, displays an error, and asks the operator to make a decision.

4.6.2 *Unlearned check*

The Operation AI verifies if the data is within the training range of the AI model and if it can provide results according to the training results. If the data is not within the learning range, it is determined to be anomalous.

5 ON-SITE IMPLEMENTATION OF THE AUTOMATIC EXCAVATION SYSTEM

5.1 *Site description*

The shield machine was driven according to the automatic excavation system to validate its performance in a shield tunnel site. The shield tunnel site has a total length of 1,526 m, including two curve sections, which consist of 1 curve with a radius of 30 m, and 1 curve with a radius of 60 m respectively. It was constructed by a shield machine with a diameter of 4.08 m.

5.2 *Verification of instruction AI*

As a validation of the Instruction AI, a straight alignment composed with 40 rings (R1390 to R1429) was planned. Constraint conditions during planning were set as follows: alignment error within ±35 mm, tail clearance of 5 mm or more. Under these conditions, AI was able to complete the planning in approximately 5 minutes.

Figure 5 shows the calculated deviation by the Instruction AI from the planned alignment, and Figure 6 shows the calculated tail clearance. It can be said that the planning was successfully completed, as the set constraint conditions were satisfied.

In addition, the digging instruction values by the Instruction AI did not deviate significantly from the instruction values created by the staff, indicating that the Instruction AI was able to plan reasonable instruction values.

5.3 *Verification of operation AI*

As a validation of Operation AI, an automatic excavation process for the entire 16 rings was conducted for the directional operation of the shield machine. Figure 7 shows the management screen when automatic operation is being performed in the No. 751 ring.

Figure 8 shows the azimuth angle and their instruction values at the end of digging for each ring in the section where automatic excavation was

implemented, and Figure 9 shows the vertical coordinates of the shield machine and their instruction values. These figures indicate that the digging error by the automatic excavation was about ±0.02 degrees in azimuth and ±2 mm in vertical coordinates. This indicates that the developed automatic excavation system was able to dig the tunnel without any quality control problems in this verification experiment.

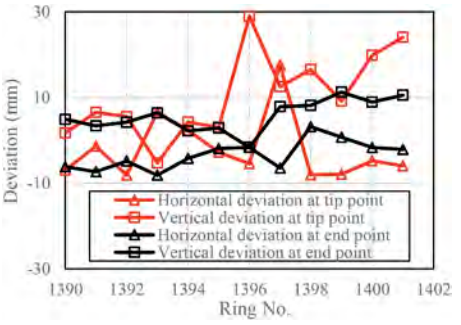

Figure 5. Deviation from the planned alignment.

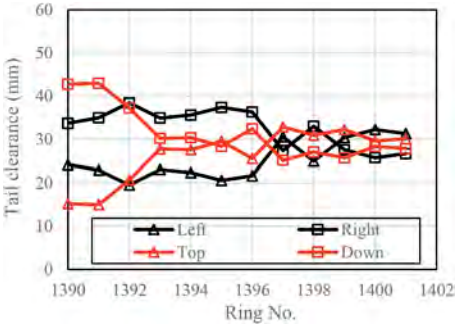

Figure 6. Tail clearance between the shield and segments.

Figure 7. Management screen of automatic operation.

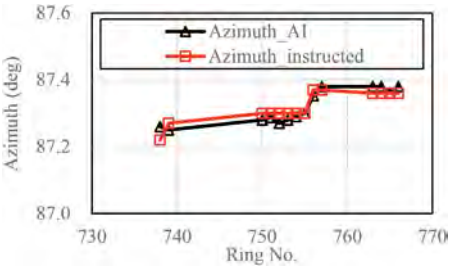

Figure 8. Azimuth results by automatic operation.

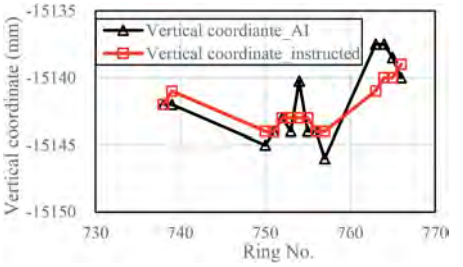

Figure 9. Vertical coordinate results by automatic operation.

6 CONCLUSIONS

This study developed an automatic excavation system for directional control in shield tunneling using machine learning techniques. By presenting how shield jacks operate, the automatic excavation system makes it possible to ensure the quality of shield tunnels in a way that does not depend on the skill of an operator. The following conclusions were derived by evaluating the performance of the machine learning models and the automatic excavation system.

The deviation from the planned alignment and the attitude of the shield machine were within the tolerance levels when the shield machine was driven by the automatic excavation system. No instruction that adversely affected the quality of the tunnel was outputted by the system. The result shows the applicability of the automatic excavation system in real environments.

The automatic excavation was limited to a straight alignment at this time, but shortly, automatic excavation in curved sections, where more frequent jacking operations are required, is planned.

ACKNOWLEDGMENTS

We would like to express our sincere gratitude to all the people involved, including the client, who kindly agreed to allow us to conduct on-site verification in the development of the system.

REFERENCES

Jerome, F., 2002. Greedy Function Approximation: A Gradient Boosting Machine. The Annals of Statistics, vol. 29, no. 5, pp.1189–1232.

Kubota, Y., Yabuki, N., Fukuda, T., 2023. Autopilot model for shield tunneling machines using support vector regression and its application to previously constructed tunnels. International Journal of Computer-Aided Civil and Infrastructure Engineering, pp. 1–17.

Kuwahara, H., Harada, M., Seno, Y., Takeuchi, M., 1988. Application of fuzzy reasoning to the control of shield tunneling (in Japanese). Journal of JSCE, vol 391, pp. 169–178.

Sugiyama, H., Wada, K., Nakaya, T., Ogi, T., 2017. Preliminary study on shield machine's operations by using artificial intelligence (in Japanese). In: 2017 JSCE Annual Meeting, Japan Society of Civil Engineers, Japan, vol. 6, pp.675–676.

Tateyama, K., Nishitake, S., Kazama, K., 1994. Automatic advancing control of shield machine (in Japanese). Journal of the Robotics Society of Japan, vol. 12, pp. 928–932.

Tunnelling for a Better Life – Yan, Celestino, Thewes & Eberhardt (Eds)
© 2024 The Author(s), ISBN 978-1-032-80042-4
Open Access: www.taylorfrancis.com, CC BY-NC-ND 4.0 license

Influence analysis and control measures of super-large diameter shield tunnel undercrossing the existing tunnel in upper-soft and lower-hard composite stratum

Jixiang Chen*
Shanghai Municipal Engineering Design Institute (Group) Co., Ltd., Shanghai, China

Zhijia Lv
CCCC Tunnel Engineering Co., Ltd., Nanjing, China

Hongjun Lou
Shenzhen University, Shenzhen, China

ABSTRACT: Setting a super-large diameter shield tunnel undercrossing an existing tunnel in upper-soft and lower-hard composite stratum in Southern China as an example, this paper studies the surface settlement and the deformation of the existing tunnel due to the undercrossing construction applying the FEA method. The results of the numerical simulation and the monitoring data indicate the surface settlement and the deformation of the existing tunnel are both within the control standard and the risk level of the undercrossing construction is under control. By setting up test sections, strengthening synchronous grouting, controlling driving posture and construction parameters, strengthening construction monitoring, and so on, the successful undercrossing construction by a super-large diameter shield tunnel through an existing tunnel can be ensured.

Keywords: Super-large diameter shield tunnel, Undercrossing construction, Upper-soft and lower-hard composite stratum, Numerical simulation, Control measures

1 OVERVIEW OF THE PROJECT

In Guangdong Province, southern part of China, there is currently undergoing a north-south-direction underground urban expressway project. The total length of the main road of the project is about 4.77km and the construction of the project consists of surface streets, a cross-line bridge, drilling & blasting (D&B) tunnels, shield tunnels and cut-and-cover tunnels, among which the main line shield tunnel under construction adopts the cross-section design of a single-tube, double-deck, 4-lane dual-carriageway tunnel with urgency parking strips.

The length of the main line shield tunnel is 1.71km and the shield tunnel is connected to the D&B tunnels and one cut-and-cover tunnel at each end. The outer diameter, inner diameter, thickness and width of the segment of the shield tunnel is 15.2m, 13.9m, 0.65m, and 2.0m respectively. To meet the demand of the small radius curve (R=599.5m) and to reduce the number of molds needed for segments prefabrication, the universal wedge-shaped segments with the wedge amount of 80mm is designed for the project. Segments are connected by oblique bolts and erected in the way of stagger jointed erection. And shear pins are installed between segment rings to promote the shear performance of the shield tunnel.

There are many sources of risk alongside the route to the shield tunnel construction, including shield crossing one operational cut-and-cover tunnel, one cut-and-cover tunnel under construction, more than 60 houses and buildings and some drainage and water supply pipelines, etc.

1.1 *Overview of the undercrossing construction*

The construction of the shield tunnel takes advantage of one super-large diameter slurry-balanced TBM. The excavation diameter is 15.76m. The undercrossing construction during which the shield travelled rightly under the cut-and-cover tunnel that was open to traffic in 2022 took place in March 2023. The floor plan of the undercrossing construction can be seen in Figure 1.

*Corresponding author: 897229441@qq.com

DOI: 10.1201/9781003495505-227

Figure 1. Floor plan of the undercrossing construction.

The construction of the existing tunnel is also part of the project. From what we can see in Figure 2, the existing tunnel is built in the form of a double-hole box culvert with width of 20500mm, floor thickness of 1000mm, roof thickness of 900mm, and tunnel clearance of 5500mm. Cast-in-place piles are applied for the excavation of the deep foundation pit and the waterproof curtain is formed by high-pressure spiral piles. Vertical distance from the shield tunnel to the cast-in-place piles is about 2.6m while to the tunnel floor is about 7.7m, as shown in Figure 3.

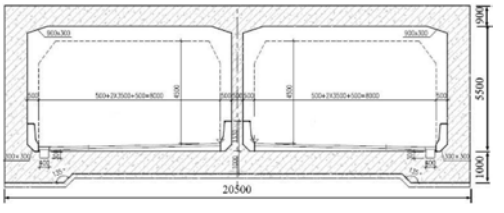

Figure 2. Cross section of the existing tunnel.

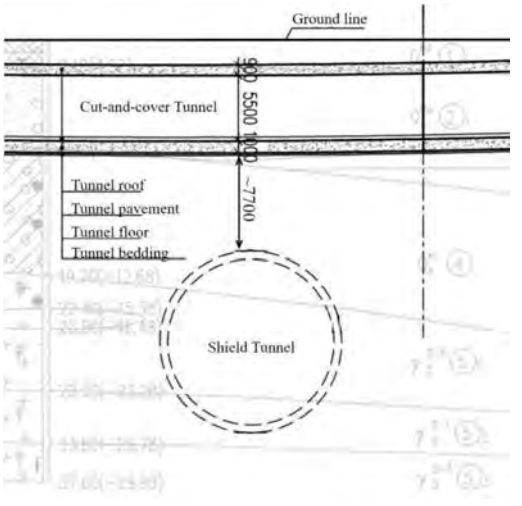

Figure 3. Cross section of the undercrossing situation.

1.2 *Geological condition*

From what we can see in Figure 3 and according to the geotechnical investigation report, during the undercrossing construction, the TBM crosses through the upper-soft and lower-hard composite stratum which consists of gravelly clayed soil (④), fully weathered granite ($⑤_1$) and strongly weathered granite ($⑤_2$). It is the typical ground in southern China. The description of soil strata can be seen in Table 1.

Table 1. Description of soil strata.

Layer No.	Soil Type	Description
①	plain fill	Cores are slightly compacted.
④	gravelly clayed soil	The liquid index of cores is mainly in the range of 0~0.25 and partly in the range of 0.25~0.75
$⑤_1$	fully weathered granite	Cores are hard soil.
$⑤_2$	strongly weathered granite	Cores are half blocky and half in soil state.
$⑤_3$	moderately weathered granite	Cores are in massive and short strut shape.

2 NUMERICAL SIMULATION

2.1 *3D numerical model*

To simulate the construction condition of the super-large diameter shield tunnel undercrossing the existing cut-and-cover tunnel in the upper-soft and lower-hard composite stratum, a 3D model for the numerical simulation is built using the software Plaxis 3D, as shown in Figure 4.

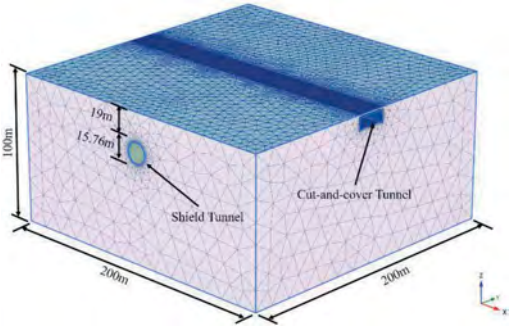

Figure 4. 3D numerical model.

The boundary conditions are set as free top surface, normal fixed side surfaces as well as fixed bottom surface. And the number of units and nodes of the model is 149870 and 234728 respectively.

Only gravity is considered in the 3D numerical model.

2.2 *Constitutive model and assumptions*

To simplify the numerical simulation, the constitutive model and assumptions are considered as follows.

1) The soil is isotropic, and the HSS model is chosen for the simulation. Parameters are determined according to the geotechnical investigation report and by applying the calculation method shown by Zhang (2022).
2) Since the excavation diameter is larger than the outer diameter of the shield tunnel, there is a gap between tunnel segments and the soil. Considering previous construction experience of the project and similar cases together, the ground loss ratio is taken as 5‰ to simulate the gap.
3) Assuming the surrounding rock and soil are relatively stationary during the tunnel excavation process.
4) The length of each advance of the TBM is 2m, which is the width of one segment ring.
5) The stiffness of the stagger-jointed segment is stable.

2.3 *Numerical analysis results*

The deformation curve of the cut-and-cover tunnel is shown in Figure 5. The settlement of the tunnel structure is 4.36mm due to the undercrossing construction, which meets the control requirement of no more than 20mm. The settlement of the tunnel floor shows the trend of firstly increasing and then decreasing. Due to the excavation face of the shield approached the existing cut-and-cover tunnel gradually, the disturbance caused to the soils also increased, resulting in the rising of settlement of the tunnel structure. After synchronous grouting as well as compensation grouting came into effect, the tunnel structure was lifted slightly, inducing the settlement value to decrease.

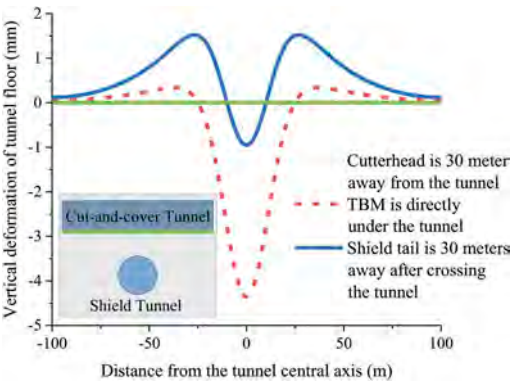

Figure 5. Deformation curve of the cut-and-cover tunnel.

3 ENGINEERING MEASURES

Referring to the case studies (Sun et al, 2022; Wu, 2022; Zhou, 2016; Zhou et al, 2020), following engineering measures are carried out.

3.1 *Design measures*

1) Add the number of grouting holes of the segments for the need of emergency grouting.
2) Install shear pins between segment rings to enhance the ability of the tunnel to resist uneven deformation, minimizing disturbance to the soil.

3.2 *Construction measures*

1) Set up trial section before TBM crossing the existing tunnel for better summarizing the construction parameters.
2) Check the condition of the cutterhead and the cutting tools in advance to make sure that TBM won't be forced to be in maintenance rightly under the existing tunnel.
3) During excavation, strictly control the attitude of TBM and apply reasonable construction parameters to minimize disturbance to the soil and to achieve continuous, balanced, and smooth shield advancing.
4) Select appropriate synchronous grouting materials to better control ground settlement and tunnel deformation.
5) Improve the quality of segment erection and waterproof work during shield tunnelling.
6) Choose grouting materials with short solidification time and grouting to form waterproof rings outside the segment ring at each end of the undercrossing area, thus preventing groundwater from running through to avoid soil erosion, which will otherwise lead to the subsidence of the existing cut-and-cover tunnel.
7) Strengthen monitoring of the existing tunnel, ground surface and etc. during undercrossing construction and grouting to control deformation when the monitoring result tells to do so.
8) Carry out geological radar survey to detect potential sources of risk, such as strong ground voids, collapses, looseness etc. and grouting to eliminate the risk promptly.

4 CONSTRUCTION MONITORING

4.1 *Layout of monitoring points*

To ensure the safe and sound passage of TBM, ground deformation and settlement of the cut-and-cover tunnel structure was monitored according to local standard. The layout of the monitoring points for the existing tunnel structure is shown in Figure 6.

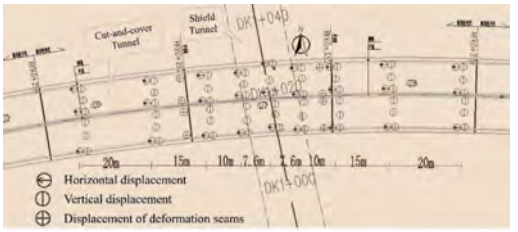

Figure 6. Layout of the monitoring points for the existing tunnel.

4.2 *Monitoring data*

The shield tunnel travelled under the existing tunnel from the mileage of DK1+004.459 to DK1 +045.235. Since the cutterhead of TBM entered the projection area of the existing tunnel on March 2nd, and until the shield tail left on March 8th, it turned out that the undercrossing construction was completed successfully. Monitoring data showed that the maximum surface settlement caused was 1.85mm, and the maximum uplift and settlement of the cut-and-cover tunnel pavement was 3.32mm and 2.87mm respectively. Other monitoring data was also within the range of control requirements.

Besides the construction monitoring, geological radar survey was also carried out with the aim of detecting any underground hazards. According to the report, no hazard was detected after the undercrossing construction.

5 CONCLUSIONS

1) According to numerical analysis and monitoring data, ground deformation and settlement of the cut-and-cover tunnel are within the range of control requirements, indicating the undercrossing construction is a total success.
2) By setting up trial sections, strengthening synchronous grouting, controlling driving posture, adopting reasonable construction parameters, strengthening monitoring and so on, the risk level of the undercrossing construction can be significantly downgraded.
3) Monitoring data is important for shield tunnelling. The number of monitoring points and the monitoring frequency should be improved appropriately for the undercrossing construction. Construction parameters should be adjusted timely in the guidance of the monitoring data.
4) With the rapid progress of urbanization in China, situations for super-large diameter shield crossing under existing tunnels will be more and more common. Reasonable design and construction plan as well as complete monitoring system is essential to ensure the safety of the undercrossing construction.

ACKNOWLEDGMENTS

The authors are grateful to Shanghai Municipal Engineering Design Institute (Group) Co., Ltd. and CCCC Tunnel Engineering Co., Ltd. for their supply of the information and data needed in this paper, and wish to acknowledge the technical and financial support of Dawn Project (No. K2022K127) of Shanghai Municipal Engineering Design Institute (Group) Co., Ltd.

REFERENCES

DBJ/T 15-213, 2021. Technical code for protection structures of urban bridge and tunnel. Department of Housing and Urban-Rural Construction of Guangdong Province, Guangzhou, Guangdong Province, China.

Sun, S., Shen, Y., Zhou Z., et al, 2022. Analysis of deformation and its control measures for large-diameter shield tunnels passing under building complexes. Mode. Tunn. Tech. 59(2), 103–110.

Wu Y., 2022. Study on deformation control of large diameter shield under metro line in use. Buil. Tech. Deve. 49 (09), 113–116.

Zhang H., 2022. Construction deformation control technology of large diameter shield undercrossing subway tunnel in operation. Mode. Tunn. Tech. 59(S1), 934–940.

Zhou Q., Li J., Wang R., 2020. Investigation of construction impact of super-large-diameter shield tunnel underneath existing subway tunnel. Mode. Tunn. Tech. 57(S1), 835–842.

Zhou J., 2016. Deformation control technology for an extra-large EPB shield machine crossing an operational subway tunnel in soft ground. Shan. Land & Reso. 37 (02), 57–60.

Tunnelling for a Better Life – Yan, Celestino, Thewes & Eberhardt (Eds)
© 2024 The Author(s), ISBN 978-1-032-80042-4
Open Access: www.taylorfrancis.com, CC BY-NC-ND 4.0 license

Influence of TBM cutter configurations on gravel excavation characteristics revealed by discrete element method

Yi-Fan Chen*, Tai-Tien Wang & Fu-Shu Jeng
National Taiwan University, Chinese Taipei

ABSTRACT: Over the past few decades, as urbanization has progressed, the demand for infrastructure has increased. The shield tunnelling method has been widely applied for underground space development, particularly in urban areas. The tunnel boring machine (TBM) contacts with the geological strata through a process of propelling and rotating. The complex excavation process often leads to severe wear on the cutting tools of the TBM cutterhead, especially in gravel layer, increasing construction costs and project durations significantly. This study establishes a methodology to investigate the influence of cutter configurations on gravel excavation characteristics and to evaluate the cutter wear during tunnel excavation. Numerical simulation using the discrete element method, PFC^{3D} is conducted to mimic the irregular shape and particle size distribution of gravel and their impact on gravel excavation. The effects of different opening ratios, type of cutting tools, and height of cutting tool of the cutterhead on gravel excavation, as well as the mechanism of cutting tool breaking through gravel layer are also examined. The simulation results indicate that cutter bits exhibit a peeling cutting mode, while disc cutters adopt cutting and fragmentation. Simultaneously employing both types of cutting tools on the cutterhead can enhance tunnel excavation efficiency. The method for simulating cutter wear on gravel developed in this paper can provide insights for the analysis and design of shield cutterheads in gravel layer.

Keywords: Shield tunnelling method, TBM, Gravel layer, Cutter wear, Discrete element method, Tunnel excavation

1 INTRODUCTION

In the field of tunnel engineering, the technology and application of the tunnelling method using a tunnel boring machine have matured significantly over the past few decades. Previous researchers have devoted efforts to analysing excavation effects on different common materials such as sand layers, clay layers, and rock layers. In soil tunnelling, the majority of excavation processes involve the use of Earth Pressure Balance (EPB) TBMs, where the cutterhead rotates and advances to excavate. Various cutter tools with tooth-like appearances, including ripper tools and scraper tools, are mounted on the cutterhead. Key factors in sand excavation involve the compression and friction of sand particles. In clay, the crucial factor is the soil's inherent cohesion, which makes cohesive soils challenging to be teared apart and significantly impacts the excavation performance of a TBM. In rock tunnels, the cutterhead configuration differs from that used in soil tunnels, with lower cutterhead opening ratios and primarily circular disc cutters (Fu et al., 2021; Tang et al., 2022; Jakobsen and Lohne, 2013; Berdal et al., 2018; Zhou and Zhai, 2018; Farrokh, 2021). Previous studies have focused on TBM performance related geological conditions involving small-grained soils and rock layers and their influences fruitfully. Nevertheless, limited study focuses on the mechanical properties of gravel layers and possible impact on TBM tunnelling.

When tunnelling using a TBM, the cutterhead's cutting tools experience significant wear inevitably due to the substantial friction generated during the forward rotation and advancement against the excavation face. Therefore, evaluating cutter tool wear is an important issue. Wen and Huang (2018) mentioned four different wear mechanisms: abrasion wear, adhesion wear, fatigue wear, and corrosive wear. Typically, hard rocks contain quartz minerals, resulting in quartz particles being pressed onto the cutter's surface, causing local plastic deformation of the surface material. Furthermore, the cutting action of the cutter may suffer from material losses in the ground surrounding a TBM. Under high-stress conditions, brittle fractures may occur, leading to wear of cutters of a TBM.

*Corresponding author: a109590065@gmail.com

DOI: 10.1201/9781003495505-228

Currently, there are considerable researches on simulating the mechanical behaviour or failure mechanisms of soil and rock materials using the discrete element method (DEM) such as PFC. For instance, Tian et al. (2018) used PFC^{2D} to simulate direct shear tests on coarse-grained soils. The results showed that the shape of particles significantly affected the mechanical properties of granular materials. Irregular particle shapes increased the peak shear stress ratio, the ultimate shear stress ratio, and the ultimate shear dilation ratio due to interlocking forces between particles. Su and Akcin (2011) employed PFC^{3D} to simulate conical pick cutting of rock to investigate the failure mechanism. In the initial cutting stage, micro-cracks initiated and propagated at the tool tip. As the cutting process continues, the rock occurs normal and shear failure. However, there is currently limited literature on DEM simulation of excavation in gravel layers. Therefore, this paper will utilize numerical analysis tools to explore the influence of cutter configurations on the characteristics of gravel excavation and establish a methodology for cutter wear assessment.

2 NUMERICAL ANALYSIS

PFC^{3D} is used to model the cutter wear during the TBM excavation in gravel. Major considerations regrading numerical model design and related modelling methods are introduced following.

2.1 *Numerical model design*

Figure 1 shows the numerical model developed in this study. The model consists of a rigid cylindrical container with a diameter of 310 mm and a length of 600 mm. It has an opening at the front, while the sides and rear parts are sealed. Two-thirds of the interior space of cylinder is filled with gravel soil. The base of the cutter tool model consists of a cross-shaped structure with a length of 240 mm. It has four cutter teeth at the front end in the basic case of this study, serving as the primary cutting and peeling tools. These cutters are oriented and have a size of 14 mm.

This study considers the irregular shape of gravel particles in the numerical model. Figure 2 shows a model of gravelly soil with 75% gravel content. In the numerical model, spherical particles are used to simulate the matrix part in a gravel layer with consideration on its grain size composition, while spherical clumps simulate the shape of large grain particles. The grain sizes are divided into two categories based on a 4.75 mm boundary, with smaller sizes representing sand and larger sizes representing gravel for simplification. Figure 3 illustrates the irregularly shaped gravel clumps in the model. Particles with irregular shapes are used to replace circular particles, introducing interlocking forces when particles undergo relative movement due to surface irregularities (Ting et al., 1995; Lu et al., 2017). This approach captures the characteristics of gravel in numerical simulations, resulting in generated gravel geometries that closely resemble nature.

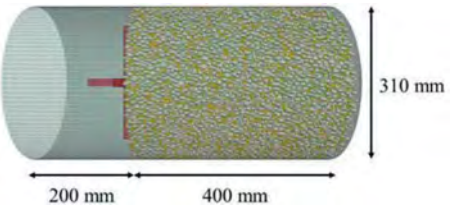

Figure 1. Geometry of the simulated container.

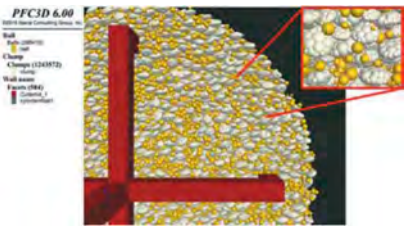

Figure 2. Gravel layer with 75% gravel content.

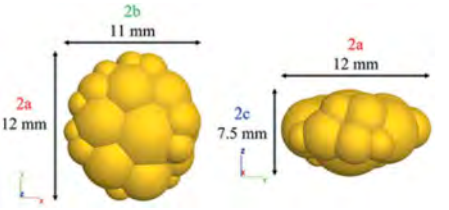

Figure 3. Clumps of gravel in the numerical model.

2.2 *Numerical model generation*

Figure 4 shows the schematic diagram of the wear test. The simulation on excavation process begins by generating two different sizes of balls within a rigid container. Subsequently, a three-dimensional model of gravel is imported. In PFC^{3D}, clumps are used to simulate gravel. Different contact models are then established between various particles, following the approach referenced by Hsieh et al. (2008). Three types of contact are defined, including contact between sand particles, contact between sand particles and gravel, and contact between gravel particles, ensuring their equilibrium.

The cutting tools in the numerical model are subjected to both rotational and translational motion conditions, with an angular velocity of 30 rpm and a translational speed of 5 mm/s. Additionally, this study has developed a FISH Function to record the

generation of cracks between clumps and balls within the model. This information, related to fracture patterns and crack propagation, is incorporated into the discrete network to visualize the excavation process in gravel and understanding of related failure mechanisms.

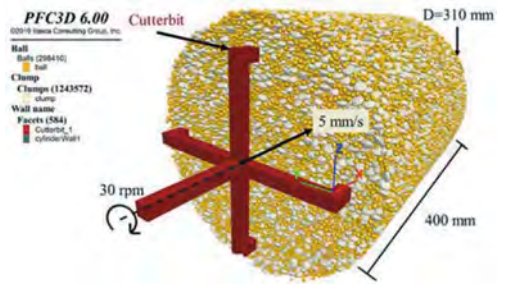

Figure 4. Numerical simulation model of gravel layer.

2.3 *Modeling of TBM cutterhead*

The design considerations for a shield machine cutterhead involve various factors such as geological conditions, subsurface data, excavation efficiency, and excavation face stability. Figure 5 shows four different cutterhead designs, categorized into four cases. The figure displays the numbering of cutter on the cutterheads for each case. The numbering is carried out counter clockwise from the outer ring to the inner ring, ranging from cutter number 1 to 7.

Afterward, we'll discuss the wear of each numbered cutter.

Case 1 features a cutterhead with four cutter bits, each having a height of 14 mm. In contrast, Case 2 consists of a cutterhead with seven cutter bits, each having a height of 14 mm and arranged in three concentric circles. The purpose of Case 2 is to compare the opening ratio with Case 1.

Case 3 involves a cutterhead with seven cutters, each having a height of 14 mm. Figure 6 shows the geometry of disc cutters used in this study. Unlike Case 2, Case 3 includes the configuration of four disc-cutters on the cutterhead. This case aims to investigate whether adjusting the proportion between disc cutters and cutter bits can increase the soil fragmentation capability and further reduce the wear on cutter bits.

In Case 4, the cutting tools are configured at different heights. The outer circle features two disc-cutters with a greater height of 26 mm, protruding a distance equivalent to one gravel particle. The middle circle of disc cutters has a height of 20 mm, while the heights of the remaining cutters remain unchanged. This configuration is employed to explore whether the use of high-low cutter height arrangements can enhance soil fragmentation and excavation efficiency or increase the load on higher cutters and lead to more severe wear.

3 RESULTS OF NUMERICAL ANALYSIS

Simulated cutting forces on various cutter bits are used to investigate the wear of cutters, associated with the damage and crack patterns in particles to interpret the excavation characteristics caused by cutters' motion.

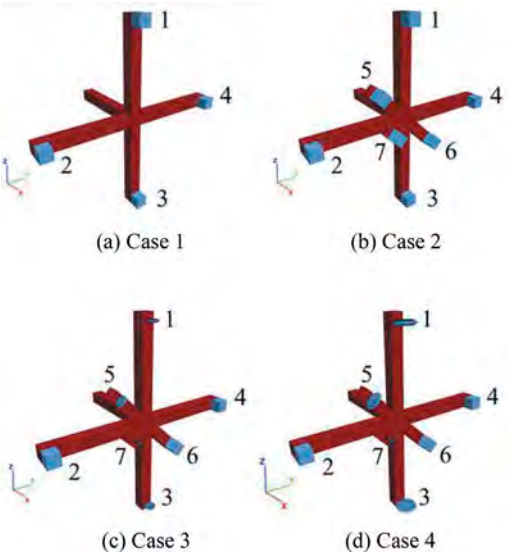

Figure 5. The layout of cutters on the cutterhead.

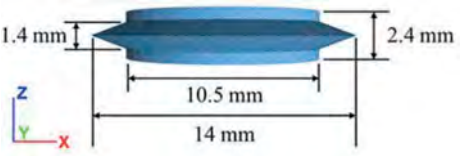

Figure 6. Disc cutters model.

3.1 *Analysis of cutter force*

In the numerical simulation, the cutting tools excavate the gravel layer by rotating concentrically. During this process, the irregularly shaped and varying-sized gravelly soils are worn down, reflecting frictional characteristics and interlocking effects. As a result, complex interactions of normal force, rolling force, and side force on cutting tools occur. Figure 7 illustrates the schematic representation of the direction of forces applying on the cutting tools. In the figure, θ represents the clockwise rotation angle of the tool. Since the internal coordinate system in PFC remains constant, by recording the forces exerted on the cutting tools in the X, Y, and Z directions during excavation and converting them through angle and quadrant transformation, the Fx, Fy, and Fz forces during the cutting process can be transformed into Fn (normal force), Fr (rolling force), and Fs (side force), as represented by Eq. (1), (2), and (3).

$$Fn = Fx \tag{1}$$

$$Fr = -Fy \cdot \cos\theta - Fz \cdot \sin\theta \tag{2}$$

$$Fs = -Fy \cdot \sin\theta + Fz \cdot \cos\theta \tag{3}$$

Figure 8 shows the forces acting on the cutting tool. The cutting tool penetrates and rotates within the ground, bringing it into contact with the gravel. The cutting tool is affected by frictional properties and the interlocking effects produced by the gravel particles. This necessitates the breaking of bonding between the particles to detach them. Additionally, the non-uniformity in size, shape, hardness of coarse particles, and the presence of potential voids and cavities lead to uneven loading on the tool. Over an extended excavation period, the wear due to friction becomes more pronounced.

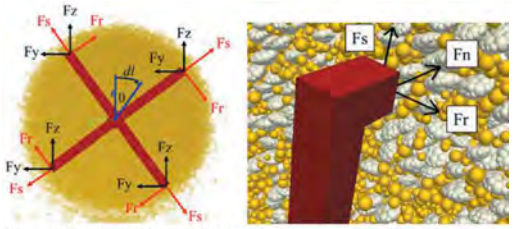

(a) y and z coordinates into tangential and radial directions
(b) Fn, Fr, and Fs for cutter

Figure 7. Transformation of forces for cutter bits.

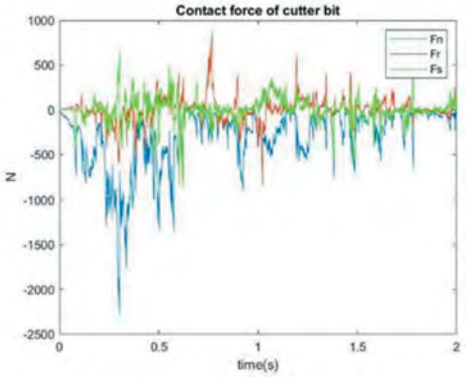

Figure 8. Record of cutter bit forces.

3.2 *Process of wear test*

Figure 9 shows the excavating process of cutter in gravel layer and the resulting failure pattern. When the cutter makes contact with the surface of the gravel, it exerts cutting and twisting forces to dislodge soil particles. In this study, the penetration of a single cutter into a gravel particle is used as a reference. When the cutting action exceeds the bonding strength of gravel particles, the particles are broken and then removed after subsequent cutter rotating. This also leads to the formation of depressions and protrusions on the cutting surface, creating an irregular surface.

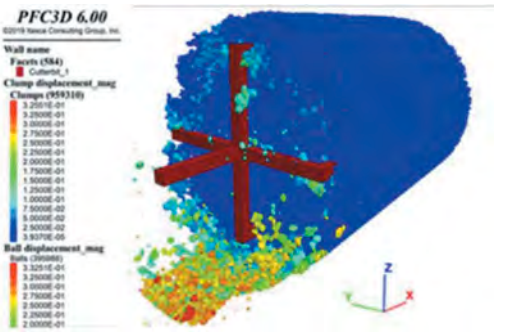

Figure 9. Displacement diagram of gravelly soil.

3.3 *Wear index*

Wear index is a quantification of the degree of wear. Common indexes include specific energy, work done by friction, cutting forces, weight loss, dimensional changes, and so on. In this study, the concepts of specific energy and frictional energy loss are adopted as indexes of cutter wear during excavation to represent the energy conversion and dissipation of the cutter during the cutting process.

3.3.1 *Specific energy*

The concept of specific energy was first introduced by Teale (1965). It is commonly used to compare the wear degrees of different materials or tools and evaluate the excavation efficiency. It represents the energy consumed per unit volume. In this study, we simultaneously recorded the relationship between cutting forces, torque, and the volume of cut material during the cutting process in numerical simulation. Eq. (4) represents the calculation formula. The numerator term represents the work done by the cutter, which is the sum of the total cutter moment work (Wm) and the excavation thrust work (Wn). The denominator term calculates the volume of particles removed by the cutter.

$$SE = \frac{\sum W}{V} = \frac{\sum (Wm + Wn)}{V} = \frac{\sum_{i=1}^{n} \left(\int M_i \cdot d\theta + \int Fn_i \cdot dx \right)}{V} \tag{4}$$

3.3.2 *Frictional energy loss*

Frictional forces are considered one of the main factors causing tool wear. Thus, the frictional energy loss is a key factor for wear, that is related with the frictional forces between the tool surface and the contact area. The phenomenon of energy dissipation and material loss leads to the conversion of energy into thermal

energy losses and mechanical energy losses. The calculation of frictional energy loss is shown in Eq. (5).

$$Wr = \sum_{i=1}^{n} \int Fr_i \cdot d1 \tag{5}$$

4 DISCUSSIONS

In this section, we will compare and explain the results of the four cases. To evaluate the influence of cutter configurations, including opening ratio, cutter type, and cutter height, based on the perspective of wear indexes.

4.1 *Cutterhead opening ratio*

Figure 10 shows the distribution of excavation-induced fractures for Case 1 and Case 2. In Case 1, fractures primarily occur along the cutting path of the cutter bits. These fractures are not interconnected, indicating that the excavation face has not undergone overall fragmentation. Therefore, increasing the number of cutter bits in the middle region of the cutterhead achieves overall fragmentation of the excavation face. In Case 2, with the cutter configuration, the number of fractures gradually increases and extends to both sides of the cutting path, forming a sheet-like fracture pattern. Eventually, these fractures connect to each other, resulting in fragmentation of the excavation face.

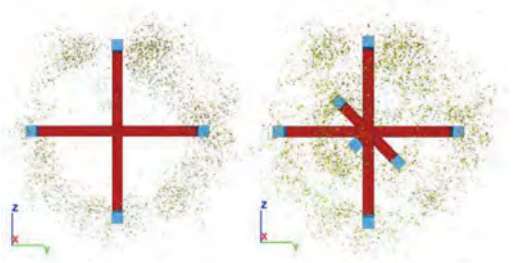

Figure 10. Fractures at different opening ratios.

4.2 *Type of cutters*

This paper analyses two types of cutters: cutter bits and disc cutters. Case 2 and Case 3 are designed to analyse the works doing on each cutter. Figure 11 shows the distribution of fractures after tunnel excavation in these two cases. The differences in crack positions and quantities between the two cases are not significant. Table 1 summarizes the simulated results of the work done for cutters 1 to 7. For cutter bits 1, 3, 5, and 7, the results indicate that when cutter bits are replaced with disc cutters, thrust, moment work, and frictional energy loss all decrease. The replacement of some cutter bits with disc cutters reduces the contact area, which increases the pressure on cutter bits. As a result, bits 2, 4, and 6 show slightly higher wear after changing the configuration. However, overall, adjusting the ratio of cutter bits and disc cutters effectively improves excavation efficiency.

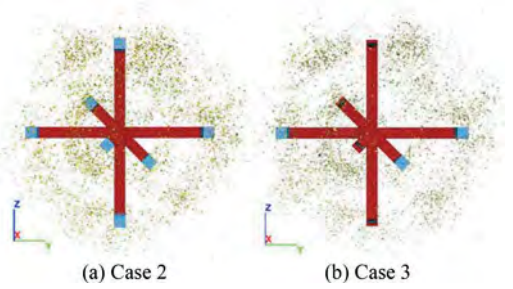

Figure 11. Fractures at different type of cutters.

Table 1. Work analysis for Cases 2 and 3.

	Wn (J)		Wm (J)		Wr (J)	
Cutter No.	Case 2	Case 3	Case 2	Case 3	Case 2	Case 3
1	0.35	0.04	5.48	0.85	12.85	1.94
2	0.27	0.42	3.92	8.72	8.14	13.36
3	0.30	0.10	6.32	2.18	16.37	4.70
4	0.59	0.53	8.43	9.70	15.03	18.46
5	0.96	0.33	4.10	2.13	12.04	7.97
6	0.71	0.74	5.14	5.80	18.76	20.72
7	0.74	0.31	2.04	1.20	6.16	4.59

4.3 *Height of cutter*

The purpose of designing the higher cutter bit is to cut and break the outer circle of the excavation face first, making it the leading cutter. This is expected to reduce the excavation load on the other cutter bits.

Figure 12 shows the crack distribution after excavation for Case 3 and Case 4. It can be observed that Case 4 has a wider and more numerous crack expansion, especially in the outer circle. Table 2 summarizes the results of the work analysis for each cutter. It is found that in Case 4, number 1, 3, and 5 cutters have significantly increased work done and frictional losses. For number 2, 4, 6, and 7 cutters, regardless of being cutter bits or disc cutters, there is a trend of reduced work done and lower frictional energy losses. This phenomenon indicates that the leading cutter bits perform as expected, consuming most of the energy required for excavation and reducing the wear of other cutters.

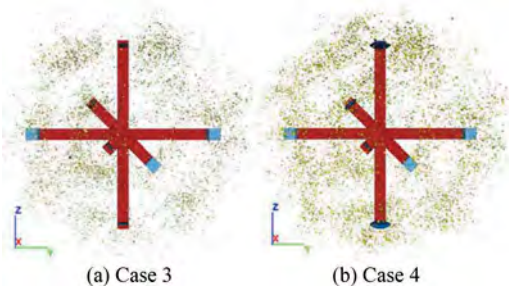

(a) Case 3 (b) Case 4

Figure 12. Fractures at different height of cutters.

Table 2. Work analysis for Cases 3 and 4.

	Wn (J)		Wm (J)		Wr (J)	
Cutter No.	Case 3	Case 4	Case 3	Case 4	Case 3	Case 4
1	0.04	6.16	0.85	57.86	1.94	113.60
2	0.42	0.17	8.72	2.43	13.36	4.89
3	0.10	0.57	2.18	14.97	4.70	45.20
4	0.53	0.35	9.70	4.31	18.46	9.68
5	0.33	0.91	2.13	10.02	7.97	31.83
6	0.74	0.32	5.80	1.60	20.72	4.77
7	0.31	0.24	1.20	0.97	4.59	3.88

4.4 *Excavation efficiency*

Figure 13 shows the differences mechanism of cutting tool breaking through gravel layer. Tooth-type cutters employ a mechanism of peeling off gravel particles, resulting in a larger crushed area due to the interlocking effects between particles. In contrast, disc-type cutters employ a cutting mechanism, breaking the excavation face by destroying the bonding between particles, with cracks predominantly growing along the cutting path. Figure 14 compares the total number of cracks generated by the four cases. Case 4, utilizing the pre-cutting tool configuration, leads to the highest number of cracks, with the largest expansion area and deepest depth.

Finally, data analysis of the four cutter configurations is presented in Table 3, summarizing the specific energy and frictional energy loss results. As Case 1's cutter configuration was insufficient to complete the cross-section excavation, and the cracks did not interconnect, it was excluded from the analysis concerning the overall fragmentation of the excavation face.

Using specific energy as an index for excavation efficiency evaluation, Case 3 with a mixed configuration of tooth-type and disc-type cutter demonstrates the highest excavation efficiency. This indicates that configuring both tooth-type and disc-type cutter teeth contributes to improved excavation performance. A similar trend is observed when using frictional energy loss as the tool index. Case 3 has the lowest frictional energy loss. Therefore, it is considered the most efficient cutter configuration for

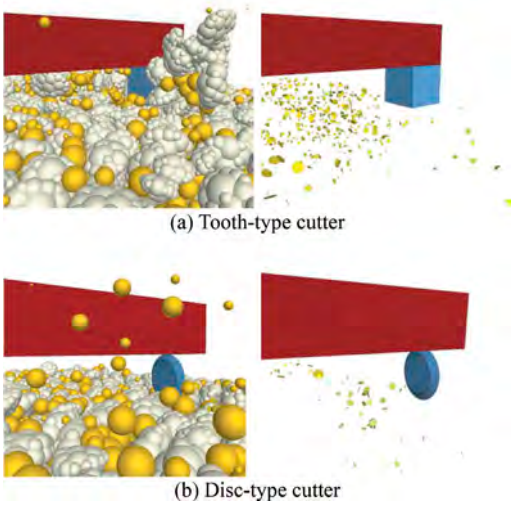

(a) Tooth-type cutter

(b) Disc-type cutter

Figure 13. Differences mechanism of cutting tool breaking through gravel layer.

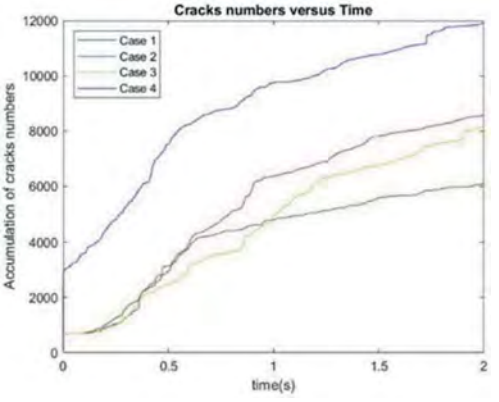

Figure 14. Accumulated crack count diagram during excavation for four cases.

Table 3. Wear index analysis results.

Case	ΣW(J)	V_{break} (m^3)	SE(kJ/m^3)	Efficiency by SE
1	25.25	0.000248	101.81	
2	39.35	0.000292	134.77	Medium
3	33.07	0.000268	123.26	High
4	100.86	0.000363	277.73	Low
Case	Wr(J)	Wear by Wr		
1	64.07			
2	89.35	Medium		
3	71.74	Low		
4	213.85	High		

excavation in the gravel layer. In contrast, Case 4, while reducing the wear of other cutter to some extent, experiences excessively high frictional energy loss overall, making it the cutter configuration with the highest wear among the four cases.

5 CONCLUSIONS

Based on the challenges encountered in tunnel engineering, this study investigated the severe wear issue of cutter in shield tunnelling through gravel layer, as well as the excavation efficiency of different cutter configurations on the cutterhead. A numerical model for cutter wear in gravel layer was developed. Various cutterhead designs were created to simulate tunnel excavation in gravelly soils, investigating the characteristics of different cutter opening ratios, cutter types, and cutter heights. The study yielded the following conclusions:

1. Four different cutterhead configurations were designed to investigate the influence of cutter configuration on excavation efficiency. From a microscopic mechanical perspective, cracks initially form along the cutting path. Subsequently, these cracks extended and increased in number, ultimately connecting with each other and breaking the entire excavation face.
2. The cutter bit breaks the soil by penetrating and cutting, subsequently removing the gravel particles during excavation. In contrast, the disc cutter operates by breaking and crushing. Cutter bits typically generate a significantly larger number of cracks and result in higher frictional energy losses compared to disc cutters.
3. Simultaneously incorporating cutter bits and disc cutters on the cutterhead effectively reduces the overall cutterhead forces, enabling the cutterhead to more efficiently break and remove gravel during excavation. This achieves optimal excavation efficiency while reducing cutter wear.

REFERENCES

Fu, J., Xia, Y., Lan, H., Wu, D., and Lin, L. (2021). A case study on TBM cutterhead temperature monitoring and mud cake formation discrimination method. Scientific reports, 11(1), 19983.

Tang, S. H., Zhang, X. P., Liu, Q. S., Xie, W. Q., Wang, H. J., Li, X. F., and Zhang, X. Y. (2022). New soil abrasion testing method for evaluating the influence of geological parameters of abrasive sandy ground on scraper wear in TBM tunnelling. Tunnelling and Underground Space Technology, 128, 104604.

Jakobsen, P. D., and Lohne, J. (2013). Challenges of methods and approaches for estimating soil abrasivity in soft ground TBM tunnelling. Wear, 308(1-2), 166–173.

Berdal, T., Jakobsen, P. D., and Jacobsen, S. (2018). Utilising excavated rock material from tunnel boring machines (TBMs) for concrete. In Proceedings of the SynerCrete'18 International Conference on Interdisciplinary Approaches for Cement-based Materials and Structural Concrete, 24–26.

Zhou, X. P., and Zhai, S. F. (2018). Estimation of the cutterhead torque for earth pressure balance TBM under mixed-face conditions. Tunnelling and Underground Space Technology, 74, 217–229.

Farrokh, E. (2021). Cutter change time and cutter consumption for rock TBMs. Tunnelling and Underground Space Technology, 114, 104000.

Wen, S., and Huang, P. (2018). Principles of tribology, fifth printing. Tsinghua University Press, Beijing, China.

Tian, J., Liu, E., Jiang, L., Jiang, X., Sun, Y., and Xu, R. (2018). Influence of particle shape on the microstructure evolution and the mechanical properties of granular materials. Comptes Rendus Mécanique, 346(6), 460-476.

Su, O., and Akcin, N. A. (2011). Numerical simulation of rock cutting using the discrete element method. International journal of rock mechanics and mining sciences, 48(3), 434–442.

Ting, J. M., Meachum, L., and Rowell, J. D. (1995). Effect of particle shape on the strength and deformation mechanisms of ellipse-shaped granular assemblages. Engineering computations, 12(2), 99–108.

Lu, Y., Tan, Y., Li, X., and Liu, C. (2017). Methodology for simulation of irregularly shaped gravel grains and its application to DEM modeling. Journal of Computing in Civil Engineering, 31(5), 04017023.

Hsieh, Y. M., Li, H. H., Huang, T. H., and Jeng, F. S. (2008). Interpretations on how the macroscopic mechanical behavior of sandstone affected by microscopic properties—Revealed by bonded-particle model. Engineering Geology, 99(1-2), 1–10.

Teale, R. (1965, March). The concept of specific energy in rock drilling. In International journal of rock mechanics and mining sciences and geomechanics abstracts, 2(1), 57–73.

Tunnelling for a Better Life – Yan, Celestino, Thewes & Eberhardt (Eds)
© 2024 The Author(s), ISBN 978-1-032-80042-4
Open Access: www.taylorfrancis.com, CC BY-NC-ND 4.0 license

Research on the application of high-strength burn-free building blocks made from shield muck

Hongshun Chen* & Yongqiang Xiao
Qingdao Qingtie Environmental Protection Technology, Co.,Ltd . Qingdao, China

Bo Chen, An Lin & Xiaowei Liu
Xinde (Shenzhen) Urban Building Environmental Protection Technology, Co.,Ltd, Shenzhen, China

ABSTRACT: A common way to utilize shield muck as a resource is to transform it into building materials products, such as building blocks. However, there is a significant difference in characteristics (such as clay content, composition and so on) between the shield muck and building materials such as sand and stone. The strength grade of building materials products which use shield muck as the main raw materials is usually low, and the dispersion of strength is significant, resulting in a small application scope and insufficient market competitiveness of building materials products made from shield muck, which ultimately affects the consumption of shield muck. In order to solve the problem of low strength grade of building materials products with shield muck as the main raw materials, on the basis of reasonably controlling the particle size and moisture of the raw materials of shield muck and using traditional cement as the cementitious materials, a geopolymer cementitious materials is used in a way of compounding in this study. Alkali and sulfate are used as activators for cementitious materials, besides, a small amount of functional additives are added. While improving the solidification effect of cement, the unique three-dimensional network structure of geopolymer cementitious materials is utilized to further compensate for the shortcomings of cement in solidification of fine clay particles. Thereby the strength of the building blocks is improved. Through the process of ingredient design, raw materials screening, homogeneous mixing, uniform distribution, static pressure forming, and maintenance, the shield muck is transformed into high-strength burn-free building blocks. Its compressive strength can be adjusted within the range of 20-40MPa after 28 days of curing suitable for different market demands, and the production cost can be controlled within a reasonable range, which provide an engineering reference for the resource utilization of different shield muck.

Keywords: shield muck, resource utilization, burn-free building blocks, compressive strength, geopolymer

1 INTRODUCTION

With the rapid development of urban underground space development, the shield tunneling method has been widely used in the construction of rail transit, municipal highways and other projects owing to the advantages of high efficiency,high safety and high degree of mechanization (Xie et al,2022). At the same time, a large amount of engineering muck will also be generated during shield tunneling construction. Taking subway construction as an example, 55 cities in mainland China have opened rail transit by the end of 2022 with a total operating mileage of 10,287.45 km, of which the subway mileage reaches 8,008.17 km. The subway mileage increased by 798.47 km compared with 2021 and most of them are constructed using shield tunneling technology. Based on the calculation that the average diameter of shield tunnel is 6.0m and the loose coefficient of the muck is 1.5 (Wei et al,2023), 33.8643 million m3 of shield muck will be generated in subway construction just in 2022.

Shield muck is generally a flow-plastic soil with high moisture content and low permeability containing clay minerals, foaming agents and polymer modified materials, and its particle size gradation, mineral composition, mechanical properties etc are closely related to the geological conditions and construction methods (Xie et al, 2022). Therefore, the properties of shield muck in different cities and regions vary greatly. At present, most cities in China are faced with the problem of "excavating" more than "filling" and need to "abandon". However, the land around the city is precious and it is difficult to

*Corresponding author: 1581100245@qq.com

DOI: 10.1201/9781003495505-229

find land for stacking or filling the muck. Therefore, in the era when the whole society is pursuing green and low carbon, resource utilization of the muck is the most expected way out (Wei et al, 2023).

In terms of resource utilization of shield muck, it is a common method to transform shield muck into building materials especially into burn-free building blocks. Guo Aifeng et al prepared a kind of burn-free building blocks using shield muck by pressing (Guo et al, 2023). The compressive strength, water absorption, softening coefficient and frost-resistance of the blocks all meet the MU15 requirements of JC/T 422-2007. However, this product is generally only used for wall materials and is difficult to be used as pavement materials due to the low strength level. Xi Zhiqin et al also prepared a kind of shield muck burn-free building blocks with a compressive strength of 50MPa by pressing,which can be used as pavement materials (Xi et al, 2021). However, the proportion of cementitious materials added especially expensive activators is too high in this method, resulting in low consumption of the muck and high cost of production.

The main purpose of this article is to improve the compressive strength of burn-free building blocks made from shield muck within a reasonable cost and expand the application scope of burn-free building blocks made from shield muck to adapt to different market demands, thereby accelerating the industrialization process of the resource utilization of the shield muck.

2 EXPERIMENTATION

2.1 *Materials*

2.1.1 *Shield muck*

The shield muck used for the experimentation was obtained from the naturally air-dried muck generated during shield tunnel construction at a subway station in Qingdao. The basic performance of the shield muck was tested according to JTG 3430-2020. The results of the particle size analysis are shown in Table 1 and Figure 1, and other performance indicators are shown in Table 2. The chemical composition of the shield muck is shown in Table 3.

Table 1. Particle size analysis of the shield muck.

Mesh size / mm	Cumulative percentage retained/ %	The mass fraction of particles smaller than a certain particle size/%
0.075	89.6	10.4
0.25	76.8	23.2
0.5	59.9	40.1
1	38.6	61.4
2	22.9	77.1
5	6,4	93.6

Figure 1. Curve diagram of particle size analysis of the shield muck.

Table 2. Physical properties of the shield muck.

Moisture content/%	Liquid limit	Plastic limit	Plasticity Index	Bulk density (kg/m3)	pH
5.3	40.4	24.9	15.5	1470	7.1

Table 3. Chemical composition of the shield muck.

Chemical composition	Content/%
SiO_2	72.84
Al_2O_3	13.81
Fe_2O_3	6.93
CaO	1.55
MgO	1.41
Na_2O	0.92
K_2O	2.54
Total	100

2.1.2 *Sand*

Common river sand from somewhere in Shandong was selected. The basic properties of the sand are shown in Table 4.

Table 4. Basic properties of the sand.

Fineness modulus	Clay content/%	Bulk density(kg/m3)
2.8	1.9	1490

2.1.3 *Cement*

Commercially available PO425 cement was selected. The basic properties of the cement are shown in Table 5.

Table 5. Basic properties of the cement.

Fineness (45μm)/%	10
Initial setting time/min	150
Final setting time/min	210
Specific surface area(m^2/kg)	360
Compression strength of 28 days/MPa	50.2
Requirement of normal consistency/%	26

2.1.4 *Fly ash*

Secondary fly ash from a power plant in Shandong was selected. The basic properties of the fly ash are shown in Table 6 and the chemical composition of the fly ash is shown in Table 7.

Table 6. Basic properties of the fly ash.

Water demand ratio/%	Specific surface area (m^2/kg)	Specific gravity
96	465	2.3

Table 7. Chemical composition of the fly ash.

Chemical composition	Mass fraction/%
SiO_2	48.43
Al_2O_3	32.58
Fe_2O_3	4.6
CaO	4.93
MgO	0.62
Loss on ignition	4.36
others	4.48
Total	100

2.1.5 *Water glass*

Commercially available liquid water glass was selected. The basic properties of the water glass are shown in Table 8.

Table 8. Basic properties of the water glass.

SiO_2 Mass fraction//%	Na_2O Mass fraction//%	modulus	Baume Degree (20°C)	Density (kg/m3)
28.21	8.74	3.33	39.6	1340

2.1.6 *Sodium hydroxide*

Commercially available granular industrial grade solid sodium hydroxide with a purity of 98.5% was selected.

2.1.7 *Calcium sulfate hemihydrate*

Commercially available industrial grade powdered calcium sulfate hemihydrate was selected, of which the effective content is no less than 60%.

2.1.8 *Superplasticizer*

Use self-made liquid high-performance polycarboxylate superplasticizer. The basic properties of the superplasticizer are shown in Table 9.

Table 9. Basic properties of the superplasticizer.

Solid content/%	Water reducing rate/%	Density (kg/m3)	pH
10.56	28	1023	5.1

2.2 *Methods*

2.2.1 *Preparation*

Weigh each material separately according to the designed proportion. The design proportions of different burn-free building blocks are shown in the Tables 10 and 11. The liquid materials are sequentially added to 1/3 of the designed total amount of water to dissolve. After dissolution, the solid materials and liquid materials are sequentially added to the star mixer and stirred for 4 minutes. Then the materials are transferred to the wheel mixer and stirred for 1 minute. After that, the materials are transferred to the distributor, distributing the material to the static pressure curing molding machine evenly. The molding pressure is set to 8MPa, and 25 burn-free building blocks are pressed at one time with a dimension of 200mm×100mm×60mm. When the pressing completed, the burn-free building blocks are coverd with plastic film. After 24 hours, the burn-free building blocks with intact appearance are picked out and transferred to the standard curing box. The burn-free building blocks are tested and analyzed after curing 28 days at 20°C and relative humidity above 95%.

2.2.2 *Test and analysis*

Compressive strength test. Take the burn-free building blocks that have been cured for 28 days in the standard curing box out, and wipe the surface of them with a wrung-out wet towel. Use the DYE3000 concrete pressure testing machine to test the compressive strength and control the pressurization rate at 0.4-0.6MPa/s. Test 10 burn-free building blocks for each designed proportion,then take the average value as the 28-day compressive strength under this proportion and list it in the table.

SEM analysis. Take the crushed samples after the compressive strength test of the burn-free building blocks, further break them into small pieces, use absolute ethanol to terminate the hydration reaction,

dry them in a vacuum drying oven at 50°C for 24 hours, and spray gold coating. A Regulus8100 cold field emission scanning electron microscope was used for microscopic morphology analysis.

3 RESULTS AND DISCUSSIONS

3.1 *Compressive strength of burn-free building blocks when cement is used alone as the cementitious material*

Table 10 show the relationship between the compressive strength of the burn-free building blocks and the proportion of cement when the proportion of shield muck is constant and the cementitious material is cement alone. It can be seen that as the amount of cement increase, the 28-day compressive strength of the burn-free building blocks also continues to increase. When cement accounts for 25% of the total solid mass, the 28-day compressive strength of the burn-free building blocks is 34.6MPa. Continuing to increase the proportion of cement, the 28-day compressive strength of the burn-free building blocks does not increase significantly. When cement accounts for 30% of the total solid mass, the 28-day compressive strength of the burn-free building blocks reaches 37.0MPa. However, the high proportion of cement in the burn-free building blocks results in high cost of material,making actual production difficult to achieve.

Table 10. The proportion and the 28-day compressive strength of burn-free building blocks when cement is used alone as cementitious material.

Number	A1	A2	A3	A4	A5
Shield muck/kg	50	50	50	50	50
Sand/kg	38	35	30	25	20
Cement/kg	12	15	20	25	30
Water/kg	10	10	10	10	10
28-day compressive strength/MPa	10.5	16.8	25.9	34.6	37.0

3.2 *Compressive strength of burn-free building blocks when cement is compounded with geopolymer cementitious materials*

Table 11 show the proportion and the 28-day compressive strength of burn-free building blocks when cement is compounded with geopolymer cementitious materials.

Comparing F1 and A3, the 28-day compressive strength of F1 is slightly higher than that of A3, indicating that the addition of fly ash has a certain promoting effect on the strength improvement of burn-free building blocks. This promotion mainly includes three aspects. On the one hand, it is the morphological effect of fly ash (Cai et al, 2018). The glass bead structure of fly ash can reduce the frictional resistance between cement particles and other particles such as muck and sand, making the cement more uniformly dispersed in the materials and increasing the cement hydration reaction area and reaction degree. on the other hand, it is the micro-aggregate effect of fly ash (Cai et al, 2018). The particles of fly ash are small and can fill the gaps between the mixed materials, increasing the density of the burn-free building blocks. Besides, it is the active effect of fly ash (Cai et al, 2018). Fly ash contains partially active SiO_2 and Al_2O_3 which can further react with $Ca(OH)_2$ generated by cement hydration and form a certain amount of C-S-H gel, which increase the total amount of the cementitious materials in the burn-free building blocks.

Comparing F2 with F1, the addition of sodium hydroxide increased the 28-day compressive strength of the burn-free building blocks from 27.6MPa to 32.5MPa. Analysis believes that the vitreous structure of fly ash is destroyed in the strong alkali environment provided by sodium hydroxide, releasing more active $[SiO_4]$ and $[AlO_4]$ monomers. These active monomers are further condensed to form amorphous geopolymer gels such as sodium aluminosilicate hydrate (N-A-S-H) and calcium aluminosilicate hydrate (C-A-S-H) that further solidify particles such as muck, thus improving the compressive strength of burn-free building blocks (Zhao et al, 2020) (Zhao et al, 2021) (Tong et al,2022) (Chen et al, 2022).

Comparing F3 and F2, the addition of water glass increased the 28-day compressive strength of the burn-free building blocks from 32.5MPa to 36.3MPa. Analysts believe that water glass can not only serve as a binding component, but also provide soluble silicates. Since the dissolution rate of aluminum in fly ash is much faster than that of silicon, the soluble silicates provided in advance can react with the previously released $[AlO_4]$ monomers to form a higher concentration of prepolymers in a shorter period of time (Chen et al, 2017) (Jafari et al, 2016) (Li and Fan, 2012), which is beneficial to improving the degree of polymerization of the geopolymer gel, thereby improving the strength of the burn-free building blocks.

Comparing F4 and F3, the addition of calcium sulfate hemihydrate increased the 28-day compressive strength of the burn-free building blocks from 36.3MPa to 38.7MPa. On the one hand, calcium sulfate hemihydrate can be further hydrated to form calcium sulfate dihydrate, which can consume part of the free water in the process and reduce the adverse effects of evaporation on the strength of burn-free building blocks in the later period. The formation process of calcium sulfate dihydrate crystals can further solidify the particles of the muck and reduce the voids in the burn-free building blocks. On the other hand, calcium sulfate hemihydrate introduces sulfate ions, which

can further react with cement hydration products to form hydration products such as ettringite, which improves the strength of the burn-free building blocks.

Comparing F5 and F4, the addition of superplasticizer increased the 28-day compressive strength of the burn-free building blocks from 38.7MPa to 40.1MPa. Analysis believe that the anionic groups (such as carboxyl groups, sulfonic acid groups, etc.) of the superplasticizer with a comb-shaped structure can be directionally adsorbed on the surface of the cement particles, forming an ion distribution of a diffusion double electric layer, causing the surface of the cement particles to carry charges with the same electrical properties, generating electrostatic repulsion, preventing cement particles from agglomerating, and promoting the dispersion of cement particles. Moreover,long-chain groups such as polyoxyethylene groups on the side chains can cause steric hindrance in the adsorption layer of cement particles, which is also beneficial to the dispersion of the cement particles (Li et al, 2012). The more uniformly the cement particles are dispersed, the higher the cement hydration reaction area and degree of reaction, and the higher the compressive strength of the burn-free building blocks.

Table 11. The proportion and the 28-day compressive strength of burn-free building blocks when cement is compounded with geopolymer cementitious materials.

Number	F1	F2	F3	F4	F5
Shield muck/kg	50	50	50	50	50
Sand/kg	25	25	25	25	25
Cement/kg	20	20	20	20	20
Fly ash/kg	5	5	5	5	5
Sodium hydroxide/kg	-	0.05	0.05	0.05	0.05
Water glass/kg	-	-	0.05	0.05	0.05
Calcium sulfate hemihydrate/kg	-	-	-	0.25	0.25
Superplasticizer/kg	-	-	-	-	0.5
Water/kg	10	10	10	10	10
28-day compressive strength/MPa	27.6	32.5	36.3	38.7	40.1

3.3 *Microstructure of burn-free building blocks*

Figures 2 and 3 show the micromorphology of A3 and F5.

The density and the amount of gel of F5 are significantly higher than those of A3, therefor the compressive strength of F5 is significantly higher than that of A3.

Not only fibrous and needle-like hydration products can be seen in the microstructure of F5, but also a large amount of amorphous gels. These amorphous gels are most likely geopolymer gels formed after fly ash is activated. These geopolymer gels with a unique three-dimensional network structure are filled between particles such as muck and sand, bonding them into a dense whole and greatly improving the compressive strength of the burn-free building blocks.

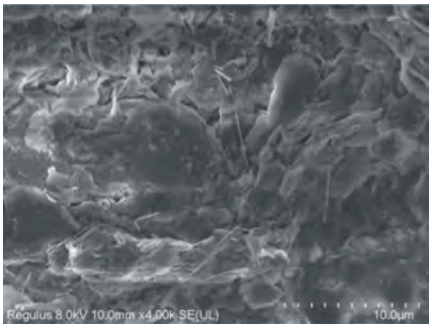

Figure 2. SEM of the burn-free building blocks of A3 after curing for 28 days.

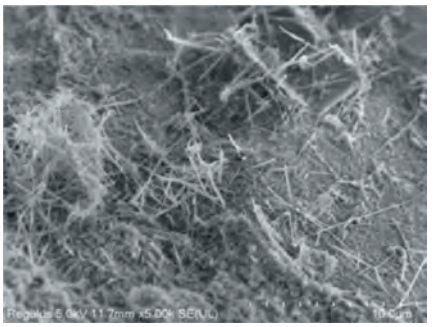

Figure 3. SEM of the burn-free building blocks of F5 after curing for 28 days.

4 CONCLUSIONS

Using cement and geopolymer cementitious materials, through the process of ingredient design, raw materials screening, homogeneous mixing, uniform distribution, static pressure forming, and maintenance,the shield muck can be transformed into high-strength burn-free building blocks. Its compressive strength can be adjusted within the range of 20-40MPa after 28 days of curing, suitable for different market demands, and providing an engineering reference for the resource utilization of different shield muck.

The formation of amorphous geopolymer gel is the key to product high-strength burn-free building blocks using shield muck. The addition of additives such as calcium sulfate hemihydrate and superplasticizer can improve the compressive strength of the burn-free building blocks made from shield muck.

REFERENCES

[1] Cai Yi, Wu Jian, Yang Gang, et al, 2018. Study on test analysis of fly ash properties and its application in baking-free brick. Coal and Chemical Industry. 41(9), 105–108.

[2] Chen Jiangang, Pan Zebin, Ma Yunlong, et al, 2022. Study on Mechanical and Microscopic Properties of Glass Powder and Fly Ash Based Geopolymer Concrete. China Concrete and Cement Products. 8, 91–95.

[3] Chen Xiao, Wang Jie, Zhu Guorui, et al, 2017. A Review of the Main Control Factors on Mechanical Properties of Geopolymers. BULLETIN OF THE CHINESE CERAMIC SOCIETY. 36(9), 2994–3002.

[4] Guo Aifeng, Wei Xiaofan, Wang Yao, et al, 2021. Study on Preparation and Properties of Unburned Brick by Building Waste. Non-Metallic Mines. 44(3), 99–102.

[5] Jafari Nadoushan, Mohsen; Ramezanianpour, Ali Akbar, 2016. The effect of type and concentration of activators on flowability and compressive strength of natural pozzolan and slag-based geopolymers. Construction and Building Materials. 111(0), 337–347.

[6] Li Lin, Fan Zhifang, 2012. Research Advance on Fly Ash Based Geopolymer. Liaoning Chemical Industry. 41(6), 598–600.

[7] Li Baijian, Tan Ruixin, Lin Yong, 2012. The performance difference between polycarboxylic acid-based and naphthalene-based water reducing agents based on their molecular structure. Guide of Sci-tech Magazine. 2012(19), 127,162.

[8] Tong Guoqing, Zhang Wuyu, Gao Yiting, et al, 2022. Mechanical Properties and Micromechanism of Alkali-activated Fly Ash Geopolymer. Materials Reports. 36(4), 125–130.

[9] WEI Bin, Zhu Wei, Qian Yongjin, et al, 2023. Physical and Mechanical Properties and Resource Utilization of Shield Tunnel Muck. HENAN SCIENCE. 41(4), 560–567.

[10] XIE Yipeng, Zhang Cong, Yang Junsheng, et al, 2022. Research and prospect on technology for resource recycling of shield tunnel spoil. Tunnel Construction. 42(2), 188–207.

[11] Xi Zhiqin, Li Shuisheng, Yang Dong, et al, 2021. Double-layer unfired paving brick with shield muck: designprinciples and engineering index testing. Proceedings of the 2021 Academic Annual Conference of China Civil Engineering Society. 2021, 2–13.

[12] Zhao Suning, Qu Lie, Zhang Quan, 2010. The mechanical properties and the chemical analysis of fly ash geopolymer. SHANXI ARCHITECTURE. 36(25), 1–3.

[13] Zhao Xianhui, Wang Haoyu, Zhou Boyu, et al, 2021. Research Development on Influencing Factors of Performances and Gel Products in Fly Ash-Based Geopolymer Material. BULLETIN OF THE CHINESE CERAMIC SOCIETY. 40(3), 867–876.

Tunnelling for a Better Life – Yan, Celestino, Thewes & Eberhardt (Eds)
© 2024 The Author(s), ISBN 978-1-032-80042-4
Open Access: www.taylorfrancis.com, CC BY-NC-ND 4.0 license

The key technology of large section pipe jacking for main structure of station in complex water-rich sand bed

Bin Cheng*, Weiran Huang, Xiaobing Shuai & Yangyu Tan
Guangzhou Rail Transit Construction Engineering Consulting Co., Ltd, Guangzhou, China

ABSTRACT: East extension of Guangzhou Rail Transit Line 3 and main structure of West End of Waterfront Station, due to the impact of the relocation of three large pipelines (from west to east are the National Pipeline Network finished oil pipeline, Dapeng natural gas pipeline, Guangzhou Gas Pipeline), it is not possible to adopt the open-cut construction method according to the original design plan, in order to promote the construction of the waterfront station, after safety assessment, the construction of the main structure of the west end adopts the pipe jacking method, which passes under three large pipes, the construction safety risk is bigger. This paper analyzes the technical difficulties and key techniques of pipe jacking in the main structure of metro station in the complex water-rich sand layer, taking the project of Haibang Station large section pipe jacking in the east extension of Guangzhou Metro Line 3 as an example.

Keywords: Complex stratum, type selection, large section, construction risk

1 INTRODUCTION

In the construction of the main structure of the subway station in our country, open excavation, cover excavation and mining method are mainly adopted, with the rapid development of urban rail transit construction in our country, some subway stations do not have the condition of large-scale open excavation because of the influence of underground pipelines, buildings and so on, therefore, it is urgent to find a suitable construction scheme to solve this kind of difficult problem. At present, in our country's Beijing, Shanghai, Shenzhen and other cities, construction schemes such as large section pipe jacking machine, multi-round shield machine and combined tunneling machine are being studied and gradually become the development direction of the industry.

2 PROJECT PROFILE

2.1 *Project profile*

The Waterfront Station is located at the southwest corner of the Asian Games City in Panyu District, on the east side of the Guangzhou-macao Expressway. The total length of the station is 559m, the width of the standard section is 23.9 m, the width of the enlarged end is 27.8 m, and the total height of the station is 14.53 m. The depth of the cover soil is about 3.0 m, the standard depth of the station is 17.73 m, and the depth of the extended end is 18.66 m. Under the influence of the surrounding environment, the construction of the waterfront station is divided into five stages, in which the fourth stage structure is the launching well of pipe jacking, the third stage structure is the receiving well of pipe jacking, and the fifth stage is the pipe jacking section. The section of pipe jacking is 11.1 * 8.1 m, and a rectangular pipe jacking machine with super large section is used to carry out the construction of left and right line successively. The length of pipe jacking passage is 48.5 m in left line, 52.5 m in right line, and the distance between pipe jacking passages is 1.5 m, it is designed as a plane straight-line, vertical two thousandth of the longitudinal slope, covering soil thickness of about 9.7 m.

Figure 1. Floor plan of Haibang Station construction site.

*Corresponding author: chb178@163.com

DOI: 10.1201/9781003495505-230

2.2 *Geological conditions*

From top to bottom, the geological range of pipe jacking is filled layer, mucky layer, mucky soil layer, silty clay layer, residual soil layer, fully weathered layer, strongly weathered layer, etc. . The depth of stable water level is 0.50-4.0 m, and the mud and muddy soil are thick. The excavation area of pipe jacking tunnel is located on silty clay. The geological condition of pipe jacking section is shown in Figure 2.

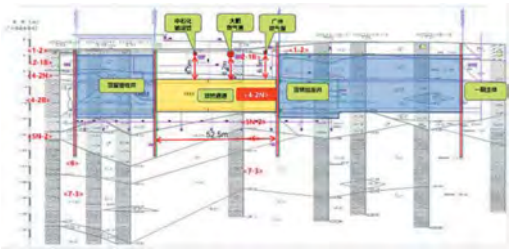

Figure 2. Geological map of pipe jacking section.

2.3 *Condition of underground pipelines*

The left and right channels of the jacking section pass through the D711 Guangzhou high-pressure gas pipeline, the D762 Shenzhen Dapeng ultra-high-pressure gas pipeline, and the D300 National Oil Pipeline Network (hereinafter referred to as the three large pipelines), pipeline operations in Guangdong, Guangxi, Guizhou, Yunnan, Sichuan, Shaanxi and other provinces. The shortest distance between the launching well and the receiving well is 6.3m and 7.1m, which meets the requirement of safety construction distance more than 5 m stipulated by the law of petroleum pipeline protection. The location relationship of the three main pipelines is shown in Figure 3. The basic situation of the pipelines is as follows:

The finished oil pipeline of National Pipeline Network: diameter is D323.9 mm, pipe material is X52 seamless steel pipe, wall thickness is 6.4 mm, buried depth is 3.68 m, distance from upstream valve chamber is 10 km, distance from downstream valve chamber is 5 km, design pressure is 9.5 mpa, Operation Pressure is 4.0 mpa, transportation medium: Diesel and gasoline alternate transportation.

Dapeng natural gas pipeline: pipe diameter D762MM, pipe material used X65M longitudinal submerged arc welding steel pipe, wall thickness 20.6 mm, buried depth 2.4 m, crossing point about 1.1 km from upstream valve chamber, 6 km from downstream valve chamber, Design Pressure 9.2 MPA, the operating pressure is 6.8 ~ 8.9 mpa, and the conveying medium is natural gas.

Guangzhou Gas Pipeline: pipe diameter is D711MM, pipe material is straight seam double-side submerged arc welding steel pipe, wall thickness is 17.5 mm, buried depth is 3.6 m, distance upstream pressure regulating station 2.4 km, distance downstream valve chamber 6.2 km, design pressure is 5.0 mpa, operating pressure is 3 mpa.

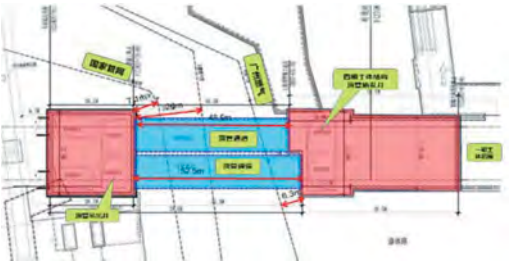

Figure 3. The plane relation diagram of oil and gas pipeline and pipe jacking construction.

3 CONSTRUCTION SAFETY RISK

There are the following construction safety risks in the construction of large section pipe jacking in the seaside station:

(1) It is difficult to control the formation subsidence, and the high-pressure pipeline protection is required. From top to bottom, the stratum is & LT; 1-2 & GT;, & LT; 2-1a & GT;, & LT; 2-1b & GT;, & LT; 4n-1 & GT;, & LT; 4-2b & GT;, & LT; 4n-2 & GT; from top to bottom. Pipe jacking is mainly located in the layer of & LT; 4n-2 & GT;, but there is a large range of deep silt and mucky soil in the upper part of pipe jacking, the maximum thickness is 5m, and the formation is easy to deform during pipe jacking.
The distance between the top of the jacking pipe and the upper pipe is about 6.5 m when the jacking pipe runs through three large pipes The grouting under the pipeline may cause the local uplift of the pipeline, and then cause the deformation of the pipeline, pipeline deformation may cause oil and gas leakage accidents, so high-pressure pipelines need to be protected during construction.

(2) the safety risk of starting and arriving is high, the pipe jacking is super-large section pipe jacking, the size of section is 11.1 x8.1 m, the location is not accurate and the direction is not well controlled during the starting and arriving of construction, or the quality problem of the end reinforcement, which results in the collapse, mud bursting and water gushing at the beginning and arrival of the pile, serious impact on construction safety.

(3) the construction risk of main pipe jacking is high, the main pipe jacking engineering consists of two parallel pipe jacking channels, the net distance between the channels is 1.5 m, the following problems are easy to occur during the construction: 1 the lateral pressure during jacking will affect the adjacent pipe-jacking passage, causing deformation and displacement of the adjacent pipe joints, and even causing damage; 2 the soil around the formed channel is disturbed again by the adjacent pipe jacking construction, which is easy to cause the ground and pipe settlement superposition,

causing the destruction of the surrounding environment; 3 at the same time, the attitude control of the pipe jacking machine is difficult during the pipe jacking construction.

4 KEY CONSTRUCTION TECHNOLOGY

4.1 *Selection of pipe jacking machine*

According to the particularity and difficulties of pipe jacking construction of rectangular tunnel in this project, in order to minimize the jacking construction risk, increase the controllability of the risk and ensure the safe and smooth construction, the project adopts 11.1 m × 8.1 m rectangular mud-water balanced pipe jacking machine construction. The cutter head of the pipe jacking machine is"The center big cutter head + the two sides rectangular cutter head type", the excavation rate reaches 95% . The cutter head and driving structure of pipe jacking machine are shown in Figure 4.

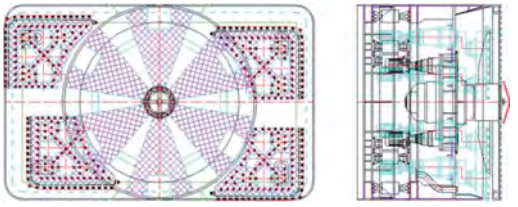

Figure 4. Drawing of cutter head and driving structure of pipe jacking machine.

The central cutter head structure and the cutter configuration are: The Banner Cutter Head, the opening rate is 35%, and the disk surface is evenly distributed, uses the 6 torsion leg 6 main beam 6 auxiliary beam structure, the main beam and the torsion leg uses the square structure, the auxiliary beam is a box-shaped structure, and the maximum equivalent stress of the cutter head structure is 160MPA, which can meet the force requirements of the cutter head in this standard section. When the cutter head rotates, the soil mass in the silo is forced to be stirred together with the two passive agitators on the front shield partition, the cut-off soil is fully stirred to improve the uniformity of the water-soil mixture in the mud silo.

The cutter head is driven by motor, equipped with 18 groups of 30kw motors, the total driving power is 540kw, the rated torque is 9600KNm, and the bailing torque is 11520KNm, which can meet the requirements of tunneling torque in this formation.

There are 3 kinds of center cutter: scraper, shell copying knife and center knife. The scraper is symmetrically arranged on both sides of the main beam of the cutter head. The shell profiling cutter is arranged on the surface of the auxiliary cutter box and the central part of the main beam, and the central cutter is placed on the central position of the Big Cutter Head. The principle of knife layout: the diameter of the cutter head is divided into three equal parts, the outer diameter part of each track line is arranged 3 knives, the inner diameter part of each track line is arranged 2 knives. Both scraper and shell profiling knife are 80mm apart; shell profiling knife is located between adjacent scraper. Scraper: 224; shell knife: 112; Outer Ring Knife: 12; Center Tip Knife 1, Pipe Machine Cutter as shown in Figure 5.

Figure 5. Actual picture of the cutter head of pipe jacking machine.

Corner cutter head structure and tool configuration: a total of 4 corner cutter head, using the panel-type cutter head, each corner cutter head configuration of 96 conical tooth cutter. The crankshaft bearing seat is connected with the flange and rotates eccentrically. The corner cutter head is shown in Figure 6.

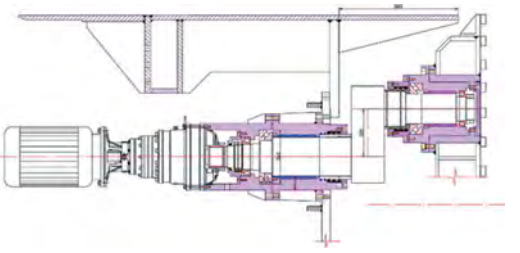

Figure 6. Eccentric drive diagram of corner cutter head.

4.2 *Pipe section lifting*

The pipe jacking section is divided into standard pipe section and 3 special pipe sections at head and tail. The biggest weight is the standard segment, the length of each segment is 1.5 m, the weight of each segment is about 106 tons, the hoisting safety risk is bigger, according to the site construction arrangement, the segment hoisting adopts 150 t gantry crane, the gantry crane is shown in Figure 13.

After many years of development, at present, the pipe section hoisting usually uses the special-purpose clamp type pole beam, the utility model has the advantages of firm structure, simple operation,

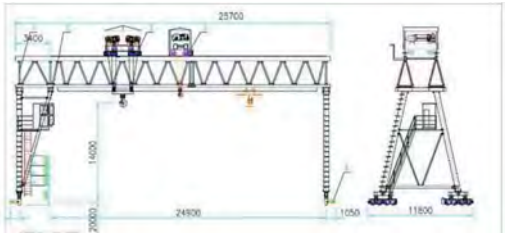

Figure 7. Schematic diagram of Gantry crane style.

good safety, minimum number of turning holes of the pipe joint (minimum influence on the structural strength), and no damage to the appearance quality of the pipe joint in the lifting process.

Figure 8. A picture of a clamped pole.

Figure 9. Pipe section lifting down well.

In this project, because the width of the wellhead is only 11.6 m and the width of the pipe joint is 11.1 m, the pipe joint can not go down the well because of using the original hoop-type pole, therefore, the vertical lifting hole of the pipe section is increased from the original 3 to 5. On the basis of the original special pole, the two sides of the hoop suspension devices were removed and replaced with wire ropes, so that the width of the suspension device was reduced to the maximum, only slightly wider than the latch, therefore, the lifting requirement in the narrow width working well can be met.

When the pipe section is erected, the eccentric roll-over hole is removed and the two upper lifting holes are used to lift the pipe down the well instead of the clamp structure. When the horizontal space of the working well is restricted by the factors such as the supporting beam and the side wall, pipe joints can also be lifted into the well.

Figure 10. Side hoisting hole of pipe section.

Figure 11. The pitch is erected by the eccentric vertical roll hole before it is lowered into the well.

Figure 12. Down-hole after changing lifting point.

4.3 *End reinforcement*

Head reinforcement close to important pipelines, high safety risk, small site. The ground reinforcement at the end of the pipe jacking well is carried out strictly outside the protected area of 5 m each of the pipeline center, and is carried out between the pipeline protection edge and the end wall. The ground reinforcement of the launching shaft is carried out by the single-axis mixing pile with a diameter of 1 m, and a row of SMW piles (inserted profiled steel) near the end wall of the launching shaft are used. The first row of Q235h profiled steel with a length of 21 m is fully inserted, and the size is 700 x 300, the second row is inserted one at a time. The width of initial well reinforcement is 1.3-5.4 m. The reinforcement range extends 3m

along the side of pipe jacking channel, during the construction of the mixing pile, the pile position, the verticality, the amount of cement, the down rod of the drill pipe and the speed of raising the rod should be mainly controlled. The design requires that the strength of the reinforcement should not be less than 0.8 mpa, the cement slurry water-cement ratio is 0.8 ~ 0.85, the speed of lower pole is ≤50cm/min, the speed of raising pole is ≤30cm/min, the amount of cement used per meter is about 305kg. The actual strength is 3.8 ~ 4.8 mpa by core-pulling test, and the effect of end reinforcement is shown in Figure 13.

Figure 13. Plan of reinforcement of starting well end.

Figure 14. Effect diagram of end reinforcement.

The receiving well end is reinforced by ground reinforcement combined with horizontal grouting in the tunnel, the ground end is reinforced by two rows of something 1000mm@750mm × 750mm large diameter mixing piles, and the horizontal grouting in the tunnel is reinforced by something 42 sleeve valve pipe grouting, the grouting range extends the direction of pipe jacking to 8m, and the position of transverse passage is 10m. The grouting hole is arranged in plum-shaped shape, the spacing is 1.5 MX 1.5 m, the grouting pressure is 0.4 ~ 0.6 mpa, the water cement ratio is 0.6 ~ 1:1. The grouting hole is made of cement. The plan of reinforcing the end of the receiving well is shown in Figure 15

4.4 *Breach*

4.4.1 *Initial breach*

Large section, big safety risk, before the hole is broken, first of all, the diaphragm wall to check the

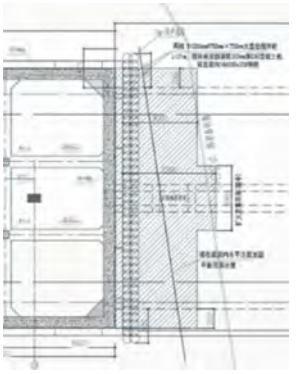

Figure 15. Receiving well head reinforcement plan.

end of the reinforcement, according to the hole depth of 2m control, the number of holes taken from a single hole 9.

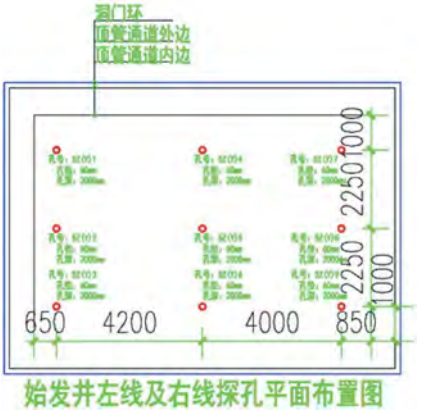

Figure 16. Layout of horizontal probe hole.

In order to reduce the amount of work and speed up the efficiency of the door breaking, the reinforcement cage is partially adjusted during the construction of the connecting wall at the part of the door, and part of the reinforcement is replaced by the box-shaped steel box, which is welded with 1 cm thick steel plate, the length is 8.5 m, the width is 1.05 m, the middle is provided with 4 baffles, and the tube silo is provided for the convenience of concrete pouring at the lower part of the steel box, the width is not less than 0.45 m, in order to prevent the steel box from floating during the concrete pouring process, two water injection pipes are embedded on the top of the steel box, and when the reinforcing cage is lowered, water is injected into the steel box through the water injection pipe embedded on the top.

When the hole door is broken, the time and sequence of the hole door should be mainly controlled. First, the steel plate on the surface of the steel box should be cut off and the connecting wall of 600mm thickness should be broken. Then, the

Figure 17. Connecting wall steel box processing.

Figure 18. Actual picture of the steel box with wall at the end.

pipe jacking machine should be assembled, after the pipe-pushing machine is assembled, the steel plate on the earth-facing surface of the steel box is cut off and the connecting wall with 200mm thickness of the earth-facing surface is broken.

In the course of hole breaking, we should pay close attention to the changes of the hole and set up monitoring points to monitor the structure of pipe jacking well.

24/2000

4.4.2 *Receive hole door broken*

The hole of the receiving well is destroyed by the gun and the manual air-axe. The first stage:

1. When the tip of the pipe ejector reaches the diaphragm wall, continue to push, let the tip of the knife into the diaphragm wall as much as possible, reduce the gap between the big disc and the diaphragm wall;
2. Stop digging, the grout is made of cement, bentonite and alumina, which can stop the water and keep the lubrication effect at the same time, easy to continue jacking machine.
3. empty the silo, observe whether there is groundwater infiltration and infiltration of water in the silo, when the infiltration is large, take other measures to deal with or receive the program;
4. then chisel the whole hole door diaphragm wall skin 10-20cm, chisel out the first layer of steel bar and cut.

Figure 19. Schematic diagram of the first stage.

The second stage: to determine the large cutter head, from the bottom to the upper chisel out of concrete and cut off the second layer of reinforcement, the whole break the whole center of the large cutter head;

Figure 20. Schematic diagram of the second stage.

The third stage: push the pipe machine forward to the upper and lower edge of the knife to reach the wall, pushing the process of injecting high-pressure water cooling;

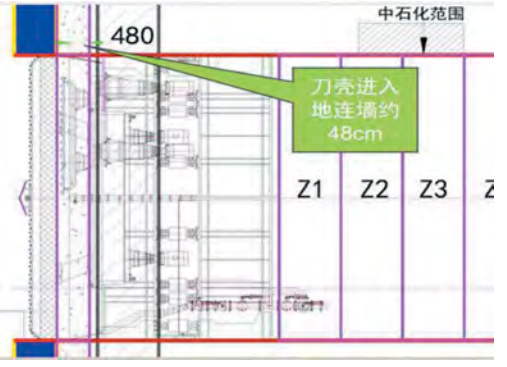

Figure 21. Schematic diagram of the third stage.

Figure 22. The third stage.

The fourth stage: First Chisel off the upper two edge knife disc parts of the connecting wall and reinforcement, after chisel off the lower part;

Figure 23. Schematic diagram of the fourth stage.

Figure 24. Fourth stage.

The fifth stage: pushing the pipe machine into and out of the hole.

In the same way as in the initial stage of tunnel excavation, the instability of the soil on the face of the tunnel may lead to the risk of collapse, mud bursting, water and sand gushing during the process of tunnel excavation and pipe jacking, due to the large size of the tunnel door, it will lead to a long time for manual chiseling. In order to ensure the safety of the pipe jacking machine, a number of measures have been taken:

Figure 25. The fifth stage.

(1) before the hole is broken, the pipe ejector is pushed into the connecting wall at the receiving end, and then the hole is broken, to ensure that the earth remaining behind the hole is the minimum. Once the hole is broken, the pipe ejector is pushed out of the face of the hole with the fastest speed, minimize water seepage channels;
(2) before breaking, divide into zones and layers according to the plan strictly, clean up the discarded materials in time, ensure the stress of the face is released evenly, and avoid the water gushing and sand gushing caused by single point breakdown;
(3) when conditions permit, excavator, Crusher and other large-scale equipment should be used to speed up the breaking speed and complete the breaking of the tunnel door during the period when the deformation of the soil on the face can be controlled;
(4) the above-mentioned reinforcement measures can also further ensure the stability of the soil on the face of the face and enhance the safety of the tunnel door.

4.5 *Double-line close-fitting pipe jacking deviation control*

When the large-section pipe-jacking method is used in this project, two tunnels on the left and right lines shall be constructed respectively. As the distance between the two tunnels is only 1.5 m, the latter tunnel on the right line will be more affected by the first tunnel on the left line. During the construction of tunnel by pipe-jacking method, it is necessary to inject drag-reducing mud to lubricate the pipe joints behind the tunnel wall, so the slurry shall be replaced after the construction of pipe-jacking method, the fluid resistance-reducing mud is replaced by a permanently solidified cement slurry to stabilize the tunnel. In the process of thixotropic slurry replacement in the left-hand tunnel, the slurry will diffuse to the surrounding stratum, and play a certain role in stratum reinforcement, due to the influence of unilateral hard formation, the horizontal attitude is difficult

to control. At this time, the ground rotary jet grouting pile (driving empty pile) method is used to soften the ground agitation and increase the horizontal deviation correction space of pipe jacking machine.

By using the external force to change the stratum state of the face of pipe jacking machine, the geological hardness of both sides of the face of pipe jacking machine tends to be uniform, later construction of the right-hand tunnel will suffer less reaction from the shaping of the left-hand tunnel. The pipe-pushing machine's edge cutter can also cut the soft soil layer better, and with the help of the pipe-pushing machine's own hinged oil cylinder, it is easier to achieve posture control, it is favorable for adjusting the attitude of pipe jacking machine. Finally, the attitude of pipe jacking machine is effectively controlled, and the schematic diagram of jet grouting pile is shown in Figure 26.

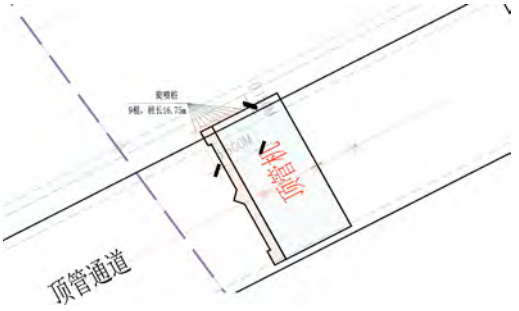

Figure 26. Schematic diagram of jet grouting pile.

13/2000

5 CONCLUSION

Through the application of key technologies such as pipe jacking machine selection, end reinforcement, pipe segment hoisting and tunnel door breaking, the left line pipe jacking of the large section pipe jacking project of the seaside station began to 2023 on January 28. On March 15, the 2023 pipe jacking was completed. It took 47 days for the pipe jacking to be completed, and the excavation time was 48.5 m, with an average of 1.03 m per day The right line pipe was 2023 on May 18 and 2023 on June 30. It took 44 days and 52.5 m, with an average of 1.19 m per day. During the pipe jacking construction, the monitoring of the ground and underground pipelines was normal and no early warning occurred.

The successful implementation of large section pipe jacking in Waterfront Station has become the first project of Guangzhou Metro to use pipe jacking method in the main structure of metro station, it solves the problem that the open-cut method and mine method can not be used in the construction of high-pressure pipeline in the main body of the station.

Figure 27. Actual picture of pipe jacking tunnel.

REFERENCES

[1] Yuen ha-wai, LÜ Dongbin, Wong siu-chuen. Construction method of mud-water balanced pipe jacking technology and points for attention [m]. First edition. Zhejiang: Journal of Shaoxing University, 2005

[2] Han Choon-kong. Construction principle and application of large underground pipe jacking [m]. Beijing: China Construction Industry Press. 2008.

[3] yu bin-chuen, Chan Chuen-chan. Pipe jacking technology [m]. Beijing: People's Transportation Publishing House. 1998.

[4] Wei Gang, Wei Xinjiang, Xu Riqing, etc.. Pipe jacking engineering [m]. First edition. Beijing: Chemical Industry Press. 2011.

Tunnelling for a Better Life – Yan, Celestino, Thewes & Eberhardt (Eds)
© 2024 The Author(s), ISBN 978-1-032-80042-4
Open Access: www.taylorfrancis.com, CC BY-NC-ND 4.0 license

Box jacking construction technology for large cross-section box culverts passing under existing high-speed railways

Chen Cheng, Jiahui Wang & Yuandong Li*
China State Construction Engineering (Hong Kong) Limited, Hong Kong, China

ABSTRACT: The APM & BHS tunnel construction underneath the MTR Airport Express Lane (AEL) railway is one of the critical projects for the Hong Kong International Airport's Third Runway System (3RS) as the railway is constructed on a reclaimed land and spans across the APM & BHS tunnels. This article demonstrates the example of APM & BHS TUNNELS ON EXISTING AIRPORT ISLAND project to describe the detail applications of i) TAM pipe full-section fan-shaped grouting technology, ii) MTBM tunneling machine advanced pipe shed support technology, and iii) combined push-pull technology for the precast box jacking. Firstly, the grouting curtain walls are well established in AEL areas to reinforce the soil in the early beginning of the construction, which seals up a closed box. Then, the grout materials are filled into the sealed area to enhance the integrity and quality of the reinforcements. Secondly, before excavating the tunnel, a row of large horizontal pipe shed supports are installed to strengthen the soil, which guarantees the ground settlement for the subsequent construction works to be within the allowable Alert-Alarm-Action (AAA) levels. Finally, by applying the Anti-jacking system on the tunnel roof level, along with the computerized control of the hydraulic jack system on the tunnel base level, the Pull and Push actions are generated on the precast box structure. With the above techniques, the stability of the box jacking operation is ensured.

Keywords: box jacking tunnel, Micro TBM, Alert-Alarm-Action, Grouting

1 INTRODUCTION

With the development of modern cities, it usually occurs that the to-be-constructed underground facilities pass under the existing important constructions, such as the high-speed railways. Thus, it is important to develop and deploy reliable techniques to efficiently carry out the new project while ensuring the structural safety and daily operation of the existing constructions.1

During the past decades, several construction techniques emerges [1-5], which provide many available choices for the engineers to build the new constructions under the existing facilities. The current techniques play a role in different stages of the construction. Specifically, in the early beginning of the construction, the soils around the to-be -constructed area need to be reinforced to ensure the construction safety of the sequential operations. Available techniques in this step include the TAM fan-shaped grouting technology. In advance of the tunnel excavation, the soil should be further reinforced in order to restrict the ground settlement. The technique used in this step includes the MTBM tunneling machine's advanced pipe shed support technology. Finally, during the box jacking operation, the stability of the structure must be secured to ensure the safety of both the existing construction and the current project. The available techniques include the Anti-jacking system on the tunnel roof level and the computerized control of the hydraulic jack system on the tunnel base level, which generates the Pull and Push action on the precast box.

The above techniques developed in the recent decades provide a reliable framework for the construction under an existing structure. Thus, we apply such techniques in the current project of the APM & BHS tunnel construction underneath the MTR Airport Express Lane (AEL) railway, which is one of the critical projects for the Hong Kong International Airport's Third Runway System (3RS). The railway is constructed on a reclaimed land and span across the APM & BHS tunnels, which is a typical example that

*Corresponding author: liyuandong@cohl.com

DOI: 10.1201/9781003495505-231

applies the advanced techniques mentioned in the last paragraph.

In the following parts of the article, we will firstly introduce the background of the APM & BHS TUNNELS ON EXISTING AIRPORT ISLAND project in section 2. Then, the critical techniques, including the TAM pipe full-section fan-shaped grouting technology, the MTBM tunneling machine advanced pipe shed support technology, and the combined push-pull technology for the precast box jacking will be introduced in section 3. The strategies to combine the techniques in this project is introduced in section 4. Concluding remarks are provided in section 5.

2 BACKGROUND

The Hong Kong Airport Authority's unmanned vehicle and baggage conveying tunnel project on the airport island is an ultra-large cross-section and ultra-shallow tunnel. It is located in the area which is both the old reclamation area of the Hong Kong Airport and the MTR Protection area. The conditions of the construction site are shown in Figure 1. The main structure of the 30m-long tunnel passes under the existing Airport Express railway. The geological conditions are poor, which increase complexity of the construction environment is complex, where the geological section of the box jacking location is shown in Figure 2. Thus, in order to reduce the ground settlement during the tunnel pushing process, the project team adopted the side-by-side jacking construction method of two box culvert tunnels based on the actual conditions of the construction site. The tunnel crossing was realized by pushing the precast box culvert. The construction starts from January 2022. By June 2022, the ground settlement during the entire construction process will not exceed 11mm, ensuring the smooth operation of the Airport Express Railway. Owing to the advanced construction techniques adopted in the project, the construction speed is ideal and the construction quality is extremely high, ensuring the smooth completion of the project.

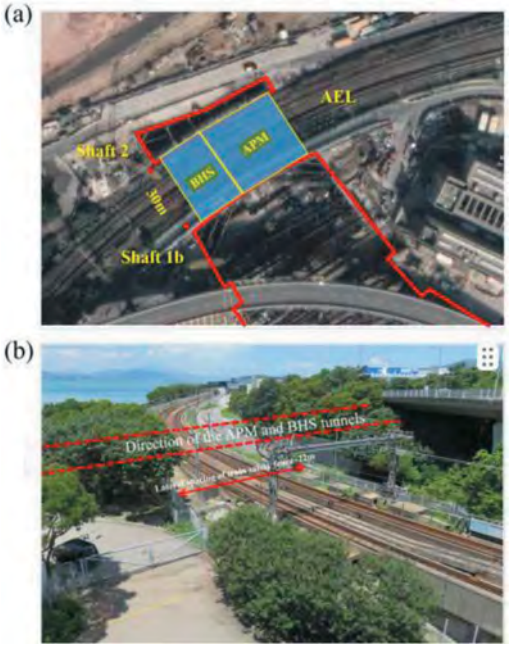

Figure 1. Sketch of the construction site.

During the construction process, there are several restrictions. Firstly, the nearby Hong Kong International Airport should be strictly ensured to be unaffected by the construction. Secondly, the construction machinery must comply with the height restrictions of the airport, operating time restrictions, construction under the AEL, to be carried out in the limited time (1:00 to 4:30 am). Thirdly, during the construction period, the operation of the three main traffic arteries around the airport shall not be affected. Moreover, the existing underground public facilities and pipelines of the airport are complicated, so they must be protected during construction and excavation, which increases the difficulty of construction.

3 CRITICAL TECHNIQUES

In this section, three critical techniques used in the project, including the TAM pipe full-section fan-shaped grouting technology, the MTBM tunneling machine advanced pipe shed support technology, and the combined push-pull technology for the precast box jacking, will be introduced. The applications of these three techniques in the real project will also be illustrated in detail.

3.1 *The TAM pipe full-section fan-shaped grouting technology*

The Tube-à-Manchettes (TAM) technique uses the sleeved perforated pipes to inject the grout into the soils, with partial or complete displacement of infilling ground water [6], as can be seen in Figure 3. According to the features of the grout injected into the soil, the TAM can be categorized into two stages, which is named as the cement bentonite grouting phase and the chemical grouting phase.

In the cement bentonite grouting phase, the grout fills up the relict joints of the soil mass and the large voids between the soil particles. In the chemical grouting phase, the chemical grout, which is a chemical solution penetrates and fills up the voids between the soils particles. All the infilling ground water is expelled. When the grout has set, the soil mass becomes a matrix of soil and grout and possess properties quite different from its original soil mass.

The cement bentonite grout with the same mix proportion as that used for the Rock Fissure grouting mentioned in the previous section is injected at 1m stages for each grout pipe from bottom upwards first.

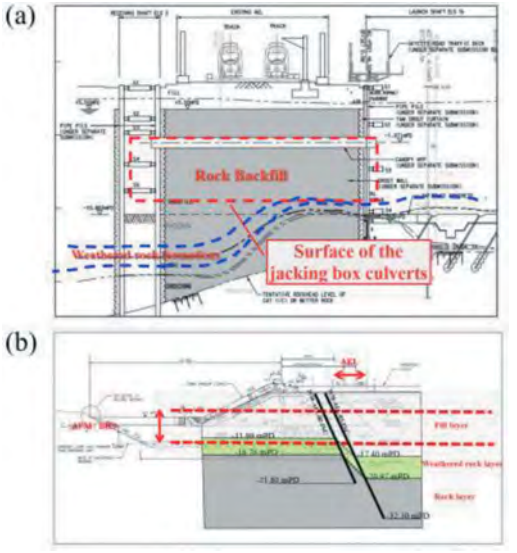

Figure 2. Geological section of the construction project.

Figure 3. Schematic sketch of the TAM technique.

After setting of the cement bentonite grout, chemical grout is injected at 0.33m stages from bottom upward as well for each grout pipe. Grouting records are kept as that for the rock fissure grouting.

A typical application of the TAM technique is to seal soil mass above and underneath a tunnel excavated in soil under compressed air condition, as used in our current APM & BHS TUNNELS ON EXISTING AIRPORT ISLAND project. From Figure 4, it is noticed that the cements is well injected into the rock layer, which seals up a reinforced closed box for the following construction procedures.

3.2 *The MTBM tunneling machine advanced pipe shed support technology*

After the reinforcement of the soils around the to-be constructed location, the soils are needed to be further strengthened in order to ensure that the ground settlement of the sequential constructions to be allowable within the AAA levels. Such targets can

Figure 4. Excavation surface of the grouting area.

be achieved by applying the Micro-Tunneling Boring Machine (MTBM) techniques [7-9].

The technology of MTBM is used for the advanced support of the pipe shed in the upper part of the box culvert tunnel. The pipe shed is used to bear the load of the covering soil above and provide space for excavation and box culvert pushing below. Especially, for a 30m long pipe shed, the construction error is only within 10mm, which is currently the most accurate pipe shed construction technology in the world. Since the MTBM uses full hydraulic power, the construction disturbance of MTBM is very small. This feature is very helpful for controlling the settlement of the airport railway line above and retaining the clearance height below the tunnel.

Next, we will illustrate the mechanism and procedure of the MTBM in detail.

3.2.1 *Preliminary preparation*

Since the construction site of the pipe shed is located under the existing Airport Express Railway (AEL), the elevation is -2.47mPD, which is lower than the groundwater level elevation (+3.50mPD). Therefore, relevant preparations should be properly handled before starting the pipe shed construction. The required preparations include (1) full-section grouting at construction location; (2) shaft excavation; and (3) the construction of the base slab and reaction walls. Note that the back-fill should be conducted seven days after the pouring of the reaction walls.

3.2.2 *Drilling and installation of the equipment*

The MTBM system consists of three parts, i.e., (1) the drilling system; (2) the slurry circulation system; and (3) the central control system, as shown in

Figure 5. Firstly, the drilling system consists of a slurry-water balance shield machine and a hydraulic jack, where each push can drill up to 3m. Then, the slurry system is used to supply clean water and process the slurry carried from the drilling system. The MTBM system is operated via the central control system, which controls the direction and speed of the drilling.

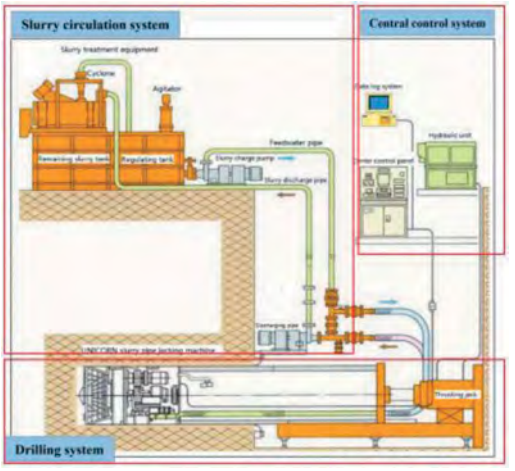

Figure 5. Schematic sketch of the MTBM system.

Besides the installation of the auxiliary equipment, that of the jacking equipment is also important. The pushing equipment mainly consists of four parts. The first part is the installation of the hydraulic jack, whose maximum push is 3000kN, with 1.5m/section. The second part is the installation of the steel backrest, which transmits the push applied to the reaction wall. The third part is the jacking iron, which is placed between the rear end of the steel pipe and the jacks, where the push is applied to the steel pipe sheds. The fourth part is the guide rails, which support the steel pipes and play a guiding role of the MTBM system.

After the installation of the auxiliary and jacking equipment, the drilling can be started. There are two steps for the drilling operation. Firstly, before starting drilling, an entrance ring needs to be installed, which has two functions: (1) serving as a guide for the drilling; (2) sealing the entrance of the pipe shed to prevent groundwater from flowing into the shaft during the drilling. Then, after the entrance ring is installed, the micro shield machine needs to be installed and checked.

During the drilling, the slurry-water balance should be guaranteed. This construction method uses a slurry-water balance shield machine to transport pressurized slurry into a sealed slurry-water tank to form a mud wall to maintain the stability of the excavation surface. The main component of the slurry is bentonite solution. In order to maintain the stability of the excavation surface, grouting will continue until the construction of the branch shed is completed regardless of whether the MTBM is operating or not. Finally, the laser system is utilized to monitor the drilling procedure and provide real-time corrections.

3.2.3 *Grouting*

The grouting operations are needed in the drilling process. According to the difference in targets, the grouting operations are categorized into four kinds, i.e., the gap grouting, the steel-pipe-filling grouting, water-stop grouting, and compensation grouting. The first kind is the gap grouting. It is known that the diameter of the micro-shield machine is slightly larger than the diameter of the steel pipe of the pipe shed. Therefore, there is a tiny gap left between the steel pipe and the drilled hole wall after the installation of the pipe shed. In order to minimize the risk of

Figure 6. The procedure of the MTBM tunneling machine advanced pipe shed support technology.

ground settlement, the gap needs to be filled immediately with grouting to. reduce. The grouting material is bentonite cement slurry with a design strength of 10MPa.

Then, the steel-pipe-filling grouting is conducted to enhance the rigidity of the pipe shed, which is operated after the gap grouting. The grouting material should be anti-shrink cement to ensure the validity of the grouting.

Besides the gap and steel-pipe-filling grouting, the water-stop grouting and compensation grouting are also needed to further improve the construction quality. In order to ensure that the water head remains below the design water level before drilling, or if an unexpected situation occurs when the groundwater level rises during drilling, water-stop grouting should be performed. The grouting fluid is obtained by mixing sodium silicate solution and cement slurry in equal volumes. On the other hand, during the drilling process of the micro-shield machine, it will cause ground settlement. In order to avoid irreparable losses, corresponding compensation grouting pipes must be installed before the construction of each pipe shed. The slurry is bentonite cement slurry.

3.2.4 *Applications in the construction projects*

In our current APM & BHS TUNNELS ON EXISTING AIRPORT ISLAND project, the MTBM technique is successfully deployed, where the construction procedure is shown in figure 6. Firstly, the entrance ring is installed to enable sequential operations. Then, both the guiding collar and the jacking equipment are installed with a high standard. After completing the preparations, the initial drilling is conducted. During the jacking process, the error is strictly controlled by the laser. At the outlet of the tunnel, the foundation ditch support is utilized. In the end, the TBM is connected at the exit of the tunnel.

The entire process was carried out during the night shutdown of the Airport Railway Line (1:00 to 4:30 am). During the construction process, no complaints were received from the MTR Corporation. Related parameters are listed in the following. Outer diameters of the pipe sheds are set as 1430mm, with the number of the pipe sheds equal to 26. The lengths of the pipe sheds are set as 30m for both APM and BHS. The drilling depths (from sea level height) are set as -0.6m for the BHS and -1.0m for the APM. The drilling area is the grouting backfill stone layer. Note that a pretty high standard is required for the drilling process.

3.3 *Combined push-pull technology for the precast box jacking*

3.3.1 *Patterns of the combined push-pull technology*

Commonly used tunnel crossing technologies include open excavation, underground excavation, shield tunneling, immersed tube method, etc., which have distinctive applicable scenarios. However, in ultra-shallow burial and ultra-large cross-section scenarios, traditional methods may not be applicable, or may cause significant interference to the surrounding soil and ground, making it difficult to meet engineering requirements.

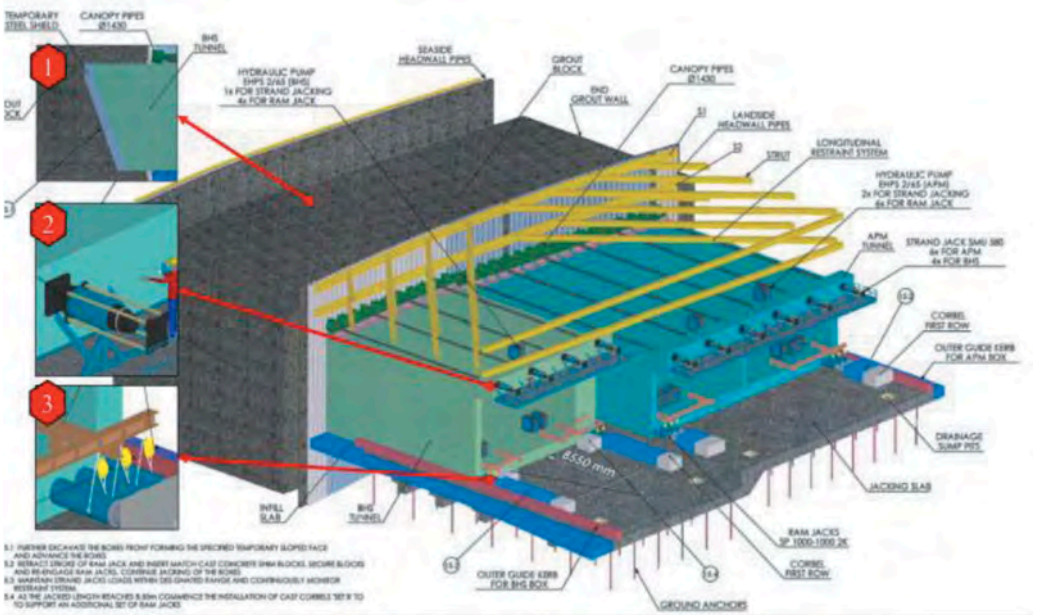

Figure 7. Schematic diagram of main tunnel box culvert jacking construction.

In comparison with the traditional approaches, the push-pull technology [10-12] introduced in this construction method has the admired characteristics of (1) combination of bottom push and top pull, which reduces the subsidence of the ground; (2) small jacking resistance, which relaxes the requirements of the force of the jacking system; (3) high smoothness in the construction process, which efficiently reduces the time consumption; (4) more auxiliary facilities; (5) small ground settlement; and (6) high degree of mechanization and low labour intensity for workers. Schematic sketch of the combine box jacking technique is depicted in figure 7.

3.3.2 *Applicable range*

This construction method is suitable for tunnel construction in complex urban environments and under existing railways, highways, buildings and other areas that have strict requirements for ground settlement. It is especially suitable for situations where the thickness of the covering soil is very shallow. It does not have high requirements on geological conditions and can still be applied even under loose surrounding rock conditions.

3.3.3 *Mechanism of the technique*

Schematic diagram of main tunnel box culvert jacking construction in figure 7. First, a push floor is constructed in the launch shaft and the floor is anchored to the formation. Construct two independent side-by-side box culvert structures (BHS, APM) on the push floor. The tunnel axis is not parallel to the direction of advancement. The outer contours on both sides of the two tunnel box culverts are appropriately thickened and designed to be parallel to the direction of advancement to ensure that the box culverts will travel straight along the horizontal plane in the direction of advancement during advancement.

The power of push-pull combined jacking is provided by a push system acting on the base plate at the bottom of the box culvert and a pulling force system acting on the upright plate at the top of the box culvert. The push force accounts for about 80% of the total power and the pulling force accounts for about 20%. In the push system, one end of the hydraulic jack contacts the base plate at the bottom of the box culvert, and the other end contacts the reaction block anchored on the push base plate to provide push. The pull system uses steel strand jacks to provide power. During the advancement process, friction will occur between the box culvert roof and the horizontal pipe shed support above. The main function of the pull system is to prevent the horizontal pipe shed support and the upper covering soil from moving forward under the action of friction.

The two box culverts are advanced alternately to minimize the resistance to advancement, and the tunnel surface is excavated while advancing. BHS will push forward first, and APM will follow closely, pushing about 1.5m each time until a pushing distance of about 30m is completed. The entire tunnel box culvert structure enters the receiving well position in the lower area of the Airport Express Railway to ensure that the tunnel crossing can be completed while not affecting the normal operation of existing facilities.

3.3.4 *Construction process and key points for operation*

To prepare for the construction, several steps are needed, which are listed in the following.

Firstly, the jacking floor is designed and constructed, as sketched in Figure 8. The jacking floor locates in the starter well. It serves as a platform for building the main structure of the culvert, which is used to fully support the reaction force generated by the culvert propulsion. The above approaches ensure that no force is transmitted to the surrounding lateral support system.

Secondly, the retaining wall is designed and constructed. A retaining wall is constructed around the jacking floor to bear the lateral load from the soil for the removal of the overhead and the subsequent construction of the box culvert structure. The construction of the retaining wall shall be carried out after the completion of the pouring of the nearby jacking floor, so that the installation of the ground anchor above the jacking floor can be carried out at the same time as the construction of the filling plate and retaining wall.

Thirdly, the tunnel main structure is designed and constructed. The main structure of the tunnel is the part of the BHS and APM tunnels located under the airport express line. The tunnel box culvert structure needs to be precast in the ejector shaft and pushed to the airport express line. Among them, BHS is 19.888m wide×10.995m high×32m long, and APM is 30.85m wide×9.019m high×32m long, with a cross-section area of more than 400m^2. The front section of the box culvert is not vertical. However, the top protrudes from the ground at an angle of 70° and is parallel to the front excavation face. A vertical plate is designed at the top of the rear end for the installation of the pulling system and temporary working table.

Figure 8. Construction of the jacking floor.

Figure 9. The procedure of the box jacking construction.

Finally, the ADMS system is utilized to monitor the ground settlement. The ground settlement requirements of the tunnel pushing are very strict, so we use the ADMS system to monitor the whole area 24 hours a day during the construction period. The system uses a total station, located in a fixed location, in accordance with the set procedure, every hour will be within the scope of all monitoring mirrors monitoring, and the relevant data transmission back to the office base station. When the settlement value of a certain location exceeds the preset warning requirements, the system will automatically contact the worker to deal with it according to the relevant regulations. The above processes are summarized in figure 9.

Basic information of the tunnel is listed as follows. The weight of the BHS tunnel is 7,700 ton, while that of the APM is 9,500 ton. The maximum design jack force for the BHS tunnel is 141,000kN, while that for the APM tunnel is 210,000kN. The footage per construction cycle is set as 1.5m. The angle of the excavation surface is set as 70°.

3.3.5 *Automated jacking system*

The automated jacking system includes three parts, i.e., the push system, pull system, and electronic monitoring system. We will introduce these two systems in the following.

The push system uses hydraulic jacks and is supported by a steel bracket fixed to the rear of the base plate of the box culvert, as shown in Figure 10. One end of the jack contacts a steel gasket welded to the rear of the foundation plate of the box culvert, and the other end contacts a row of concrete spacers. The end of the spacer block is supported by a reaction block anchored to the ejector bottom plate, which is restrained by shear keys and four horizontal bars. When the push has been carried out for a certain distance, the reaction block used earlier should be abandoned to avoid the arrangement of the spacer block is too long, resulting in a large eccentric force. There are two kinds of jacks used in the push system, namely SP460 and SEPS2200, respectively. The BHS propulsion will primarily use long-stroke SP460 jacks, However, the force of the SP460 jack needs to be supplemented by additional SEPS2200 jacks after the propulsion in halfway. APM uses a combination of two jacks from the start of propulsion. Both jacks are powered by an electric hydraulic pump with an additional fuel tank.

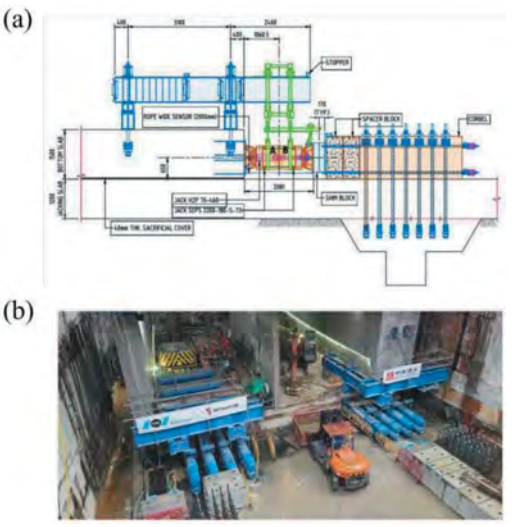

Figure 10. Layout (a) and construction (b) of the push system.

The pull system, also known as the anti-drag system (ADS), acts on the concrete vertical slab at the top of the box culvert. The harness of the steel strand jack used is placed in the respective conduit, located in the center of the horizontal pipe shed support and extends to the end of the horizontal pipe shed support in the receiving well. The main function of the pull system is to avoid the displacement of the horizontal pipe shed support under the action of friction with the top of the box and culvert tunnel, and to

reduce the settlement of the overlying soil. During propulsion, there are four stranding jacks for BHS and six for APM, the jack model is SLU580, which is also powered by an electric hydraulic pump with additional fuel tanks.

The hydraulic jacks and strand jacks mentioned above are connected to a central control station and are operated by staff in the central control room to push the box culvert. The electronic monitoring system is set up so that the staff can simultaneously control one or more sets of jacks, which need to be calibrated before they can be activated. The entire system is operated through an interface called the Bravo system, as shown in figure 11. The pushing load, jack stroke, and pushing distance during propulsion are closely monitored.

Figure 11. The central control station.

3.3.6 *Combined push-pull box jacking into the tunnel*

Before the jacking, the preparation work must first be completed: (1) the first row of reaction block is cast on the push bottom plate and pulled with the push bottom plate; (2) The temporary suspension system is installed at the end of the box culvert to support the push jack, and the temporary workbench of the wire jack is installed on the vertical wall at the end of the box culvert; (3) Complete the installation of the push jack, one end against the base plate at the end of the box culvert, one end against the reaction block on the bottom plate; (4) Jack hydraulic system and central monitoring system to complete the installation and testing, and complete the functional testing of the entire system.

After the preparations, the box jacking can be operated with two steps, i.e., (1) jacking towards the wall at the launch shaft, (2) jacking crossing underneath the railway line towards the reception shaft, which are illustrated in figure 12. The BHS tunnel weighs 7,700 tons and the APM tunnel weighs 9,500 tons. The footage of each construction cycle is 1.5m, and the tunnel excavation face is at a 70° angle to the ground.

Besides the above steps, a complete circle of the box jacking operation includes preparations of materials and facilities, controlling of the qualities, safety measures, environmental protections and benefit analysis.

3.3.7 *Applications*

The project of the Airport Island unmanned vehicle and baggage transport tunnel is an ultra-large

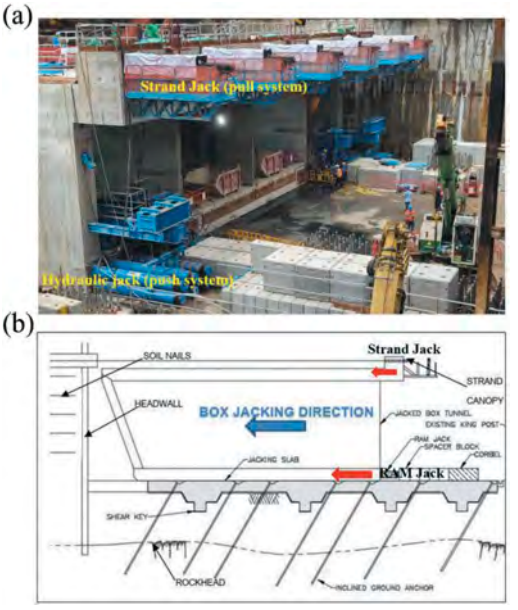

Figure 12. Layout of the box jacking.

section and ultra-shallow buried tunnel, located in the old reclamation area of the Hong Kong Airport and the MTR Protection area, with poor geological conditions and complex construction environment, in which the main structure of the tunnel about 30m long passes under the existing Airport Express railway. In order to reduce the ground settlement during the tunnel pushing process, the project team adopts the construction method of two box culvert tunnels side by side according to the actual situation on the site. The tunnel crossing is achieved by the precast box culvert jacking. The construction period is from January 2022 to June 2022, and the ground settlement during the whole construction process does not exceed 11mm. The combined pull-push box jacking technique ensures the smooth operation of the airport express railway and ideal construction progress. The resultant construction quality is very high, which ensures the smooth completion of the project.

4 CONCLUSIONS

In this article, we introduced the advanced technologies of the (1) TAM pipe full-section fan-shaped grouting technology, (2) MTBM tunneling machine advanced pipe shed support technology, and (3) combined push-pull technology for the precast box jacking and their applications in the APM & BHS TUNNELS ON EXISTING AIRPORT ISLAND project. These techniques show satisfying performances in the real applications. Such construction frameworks show large potential in further applications in future construction projects.

ACKNOWLEDGMENTS

We would like to express our sincerely gratitude to the supportive leadership colleagues on the construction site who made significant contributions to the completion of this article. We would also like to thank China State Construction Engineering (Hong Kong) Limited for providing financial support towards the submission of this paper.

REFERENCES

Song, Z., Shi, G., Wang, J., Wei, H., Wang, T., & Zhou, G. (2019). Research on management and application of tunnel engineering based on BIM technology. Journal of Civil Engineering and Management, 25(8), 785–797.

He, B., Armaghani, D. J., & Lai, S. H. (2022). A short overview of soft computing techniques in tunnel construction. The Open Construction & Building Technology Journal, 16(1).

Ye, X. W., Ni, Y. Q., & Yin, J. H. (2013). Safety monitoring of railway tunnel construction using FBG sensing technology. Advances in Structural Engineering, 16(8), 1401–1409.

Zhou, S., Ye, G. L., Han, L., & Jian-Hua, W. (2021). Key construction technologies for large river-crossing slurry shield tunnel: case study. Journal of Aerospace Engineering, 34(2), 04020118.

Zhang, C., Liu, N., & Chu, W. (2016). Key technologies and risk management of deep tunnel construction at Jinping II hydropower station. Journal of Rock Mechanics and Geotechnical Engineering, 8(4), 499–512.

Chan, Man Piu (2005). Analysis and modeling of grouting and its application in civil engineering.: 1–98.

Jebelli, J., Meguid, M. A., & Sedghinejad, M. K. (2010). Excavation failure during micro-tunneling in fine sands: A case study. Tunnelling and underground space technology, 25(6), 811–818.

Iseley, T., & Najafi, M. (1991). Micro-Tunneling. A Look at the Fastest-Growing Method of Trenchless Technology. Constructor, 73(8).

Alonso, M. P., Carney, P. A., Fernandez-Cuervo, V., Li, L., & Vega, E. A. (2013). Micro-Tunneling Under Urban Corridors-A Miami Beach Perspective. In Pipelines 2013: Pipelines and Trenchless Construction and Renewals—A Global Perspective (pp. 1101–1112).

Chaurasia, B., Tavakoli, H., Najafi, M., Williammee, Jr, R., Khankarli, G., & Daniel, A. (2013). Productivity study of box jacking for culvert installations. In Pipelines 2013: Pipelines and Trenchless Construction and Renewals—A Global Perspective (pp. 1126–1137).

Alkadour, F., Chelliah, A., Tzaveas, T., & Kara, A. (2023). Box Jacking Method Implementation in Rock for Mesaimeer Pedestrian Underpass Structure in Qatar.

Yang, Y. F., Liao, S. M., Liu, M. B., Wu, D. P., Pan, W. Q., & Li, H. (2022). A new construction method for metro stations in dense urban areas in Shanghai soft ground: Open-cut shafts combined with quasi-rectangular jacking boxes. Tunnelling and Underground Space Technology, 125, 104530.

Tunnelling for a Better Life – Yan, Celestino, Thewes & Eberhardt (Eds)
© 2024 The Author(s), ISBN 978-1-032-80042-4
Open Access: www.taylorfrancis.com, CC BY-NC-ND 4.0 license

City Rail Link – bored tunnel challenges in Auckland city centre, New Zealand

Thomas Cheung*, Shu Fan Chau & Tom Ireland
Aurecon NZ Ltd., Auckland, New Zealand

Sumi Eratne
City Rail Link Ltd., Auckland, New Zealand

ABSTRACT: The City Rail Link (CRL) Project is a major railway construction project underway in Auckland, New Zealand. It involves the construction of a 3.45 km underground rail link, which will connect the existing Waitemata (Britomart) and Maungawhau (Mount Eden) Stations.. For Contract 3, the project includes the construction of two new underground stations, Te Waihorotiu (Aotea) Station near Aotea Square and Karanga-a-Hape (KHP) Station near Karangahape Road along with the redevelopment of Maungawhau (Mount Eden) Station. The underground works include Twin Tunnel Boring Machine (TBM) tunnels, mined station platform tunnels, mined tunnels, caverns and cross passages, cut and cover tunnels and a cut and cover station. The City Rail Link is expected to significantly improve Auckland's public transport network, providing faster and more reliable train services across the city. The project is scheduled for completion in 2025. This paper describes the overall performance and challenges of Earth Pressure Balance (EPB) TBM tunnelling underneath Auckland's city center. The TBM started from the Mount Eden launching cavern, excavated under Eden Terrace, Central Motorway Junction (CMJ) and broke into KHP Station. The TBM was dragged through the station and re-launched in the mined stub tunnel. It continued her journey, passing through temporary anchors at the Aotea Centre and broke through at AOT station. The first TBM was launched on 17 May 2021, during the Covid-19 period and the last TBM tunnel was completed on 14 September 2022.

Keywords: Tunnelling, TBM, Performance, Bored Tunnel, EPB

1 INTRODUCTION

The construction of City Rail Link (CRL) includes a new 3.45 km double-track rail tunnel underneath Auckland's city center, extending the city's passenger rail system through the Waitemata (Britomart) Station in the Central Business District (CBD) and connecting to the existing regional rail network at Maungawhau (Mount Eden) in the city's inner South (Figure 1 and Figure 2). It is the largest transport infrastructure project ever in New Zealand (NZ) and will help Auckland cater for the demands of population growth over the next 30 years.

Contract 3 (C3) has included the main tunnel, stations, Western Line connection and rail systems and has been delivered by Link Alliance (LKA), comprising City Rail Link Ltd (CRLL), Vinci Construction Grands Projets S.A.S., Downer NZ Ltd, Soletanche Bachy International NZ Limited, WSP (NZ) Limited, AECOM NZ Limited and Tonkin + Taylor Limited. The reference design was undertaken by a Principal Technical Advisor (PTA) consortium led by Aurecon and including Jasmax, Grimshaw, Mott MacDonald, and Arup.

The Earth Pressure Balance (EPB) Tunnel Boring Machine (TBM), named Dame Whina Cooper, has excavated the two 1.6 km long tunnels from Mount Eden to central Auckland.

TBM, segmental lining production, TBM performance and overall tunnel construction quality control are of great importance for the success of a TBM tunnel project. The post construction review

*Corresponding author: thomas.cheung@aurecongroup.com

DOI: 10.1201/9781003495505-232

data from CRL C3 are valuable references for planning, design, and construction of future tunnelling projects in NZ. This paper aims to provide a summary of the post construction review of the CRL C3 TBM Tunnels.

Figure 1. Plan of CRL's alignment.

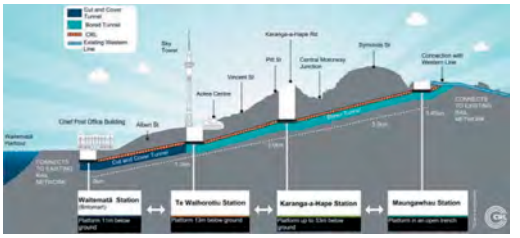

Figure 2. Section of CRL's alignment.

2 TBM TUNNEL WORKS

Tunnels comprise a cut-and-cover section connecting the completed C2 works in Albert Street to the Aotea Station with twin 7m diameter TBM bored section extending from Aotea Station to Newton Junction. There are two mined caverns at the southern end of the Newton Junction providing turnouts that are connected to cut and cover tunnels. The tunnels include emergency cross passages no greater than 325m centers.

The two bored tunnels are parallel and run underneath some of the city's most iconic areas, such as Grafton, the central motorway junction, KHP Road and the city centre.

The maximum longitudinal tunnel gradient is 3.25 per cent and the minimum horizontal tunnel radius is 141 m. Minimum cover at the Central Motorway Junction (CMJ) is about 7 m (a TBM tunnel diameter) and maximum cover is about 36 m above tunnel crown at Symonds Street.

The TBM worked 24/7, operated by a crew of 12 underground and a team of 12 above ground.

The machine's diameter is 7.15 m, weighs 910 tonnes, and the total length is 130 metres. The TBM was custom built for central Auckland soil conditions by the German tunnel machine company, Herrenknecht, for the Link Alliance. The driven lengths for Drive 1 MC30 and Drive 2 MC20 are 1631 m and 1619 m respectively and transition at KHP station.

The anticipated excavated material along the proposed alignment is East Coast Bays Formation (ECBF) which has both rock and soil (clay like) characteristics. Under the influence of severe mechanical working, the clay aggregations may be disaggregated and release clay mineral particles. Therefore, a closed mode EPB type TBM is suitable to the ground characteristics at City Centre.

Figure 3. CRL's EPB TBM, Dame Whina Cooper.

3 GEOLOGICAL AND HYDROGEOLOGICAL CONDITIONS

The tunnelling route traverses a wide range of geology and ground conditions. Most of the tunnelling are within the weak rocks of the Waitemata Group rocks (ECBF, a turbidite sequence of alternating Sandstones and Siltstones) that underlie much of the wider Auckland region, while shallower structures at the North and South of the project also encounter younger sediments (Tauranga Group); volcanic materials (Auckland Volcanic Field, AVF); made ground (including reclamation).

The TBM bored tunnel alignment is mainly within the slightly to unweathered very weak ECBF (EU2), the UCS is about 1 to 5 MPa, except near or within the KHP Station. Tunnel excavation at that section is predominately within massive EUs3 and EUg3 (slightly to unweathered weak to moderately strong ECBF, the unit is also referred as "channelized sandstone") materials. The Unconfined Compressive Strength (UCS) is about 10 to 25 MPa. The mined tunnel construction sequence requires at KHP Station that TBM is able to transit through the platform tunnels (MC30 and later MC20) from the South to North.

The section of bored tunnel approaching Aotea Station is expected to encounter weathered rock (EW), with residual weathered material (ER) at the crown level.

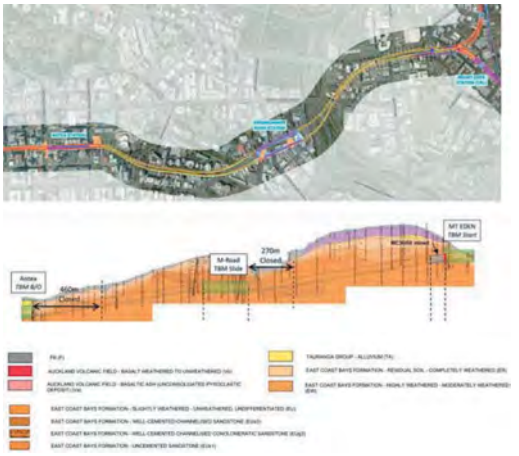

Figure 4. Geological longitudinal section of TBM.

The groundwater hydrogeology along the CRL alignment can be broadly summarised with typical two groundwater systems:

- Perched groundwater system: localized and non-continuous within the upper soils, fluctuates in response to rainfall events and flowing to local topographic sinks or shallow drainage infrastructure. This system is expected to be interrupted by structures including basements, service, roads etc.
- Regional groundwater system: a fully saturated groundwater generally observed below the surface of unweathered ECBF rock. The regional ECBF groundwater table is identified at a level slightly above or generally below the tunnel alignment within the ECBF rock.

Close shield TBM was running along the alignment with pressure so as to limit the ground movement and water ingress.

4 TBM SEGMENTAL LINING

The ring type designed for CRL bored tunnel is the universal type. This type of ring can be applied in both straight and curved sections of the tunnel alignment, without the need to include any special type elements to correct alignment deviation by the TBM during advancement.

The tunnel internal diameter is 6240 mm with six plus one keg segment parallelogram ring configuration with trapezoidal key and counter. The concrete lining is 300 mm thick and designed to provide a 100-year design life. It is equipped with a continuous two barrier EPDM-hydrophilic gasket system installed around the radial and circumferential faces of the segments.

The minimum horizontal tunnel alignment radius is 141 m. To accommodate this tight curve two different ring lengths are selected, and their respective tapers were designed to negotiate the full tunnel alignment curvature range. Rings of 1600 mm in length have been designed with a 60 mm taper to accommodate a minimum radius of 182 m, whilst 1100 mm long rings are designed with an 80 mm taper. The shorter rings will be used along sections with tighter curves and can accommodate down to curves with a -94 m horizontal radius.

The temporary spear bolts at circumferential joint (i.e. Ring to Ring) are distributed equally around the face of the ring. The pitch of lining rotation is 27.962 degrees. Only a spear bolt is provided on each radial joint (i.e. Segment to Segment) for the key segment. Shear cones are also provided next to the bolt for around circumferential joints at cross passage locations and at break-in or break-out locations. The shear cones are included to increase the shear capacity between rings. They also assist with reducing stepping between rings.

One guiding rod is provided at each radial joint to facilitate the segment installation and reduce the stepping between segments.

Two cone recesses have been detailed on the intrados face of each segment to facilitate the use of a TBM vacuum pad segment erector. Primary grouting of the annulus is undertaken from within the TBM tail skin and secondary grouting is carried out through grout sockets cast-in segments.

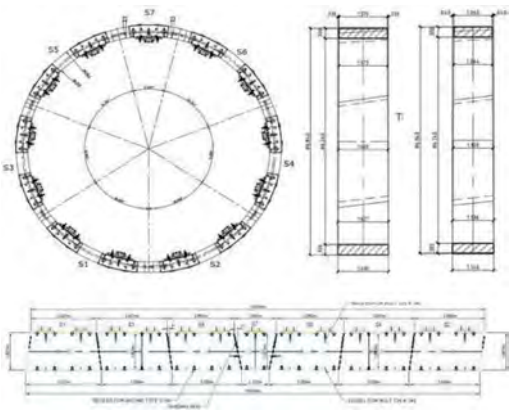

Figure 5. Segmental lining configuration.

The concrete compressive strength of the lining is 50 MPa (cylinder strength). Three types of segment reinforcement (see Table) were provided to take account of varying ground conditions and alignment depth. All segment types also included polypropylene fibres to reduce spalling in the event of a fire within the main line TBM tunnels.

5 TBM PERFORMANCE

The project used a 7.15 m bored diameter EPB shield TBM, which was capable excavating in mixed faced conditions and operating in either semi-EPB, chamber full mode and EPB modes. The working

Table 1. Segment type and details.

Type	Details
A1	Steel Fibre Reinforced Concrete (SFRC) with 1.6 m ring, "standard rings"
A3	SFRC and reinforcement bars with 1.6 m ring (Steel ratio around 150 kg/m^3)
B	SFRC and reinforcement bars with 1.1 m ring (Steel ratio around 110 kg/m^3)

EPB pressure at tunnel axis was specified as 4 bars. The TBM was designed for a theoretical advance rate of 80 mm/min.

5.1 *Cutterhead design*

The cutterhead was designed to consider the TBM operation under the city centre and its ground geology. A cutting wheel equipped with "rippers" and cutters for hard layers and with an opening percentage of 44% to overcome possible clogging due to the weak and plastic nature of ECBF. It did result in some clogging of the cutter discs and the foam ports. The cutter discs located within the centre and long the arms were removed and replaced with rippers to help mitigate clogging and subsequent flattening of the discs. Cutting knives were equipped to cut the cable strands in the temporary anchors at Aotea Centre.

5.2 *Penetration, thrust force and torque*

The TBM had 13 thrust cylinder pairs and capable of a maximum thrust force of 41,167 kN at 350 bar with maximum torque 7,187 kNm. Operation parameters on thrust force and contact force are summarised in Table 2 and the parameters along the tunnel alignment are presented in Figure 6 and Figure 7. The machine was operating well within its maximum capacity. The operation of thrust cylinders was divided into 5 Groups from A to F. It was noted that the difference in total thrust from each group especially the top and bottom was limited in order to control over-excavation and to manage TBM drive tilting or sliding. This value is not a constant and depends on the geology, alignment and operation diameters.

The designed nominal thrust force of the TBM was 3.16 MN per pad, no ladder reinforcement was required for SFRC segments where normal lower thrust forces were applied. The operational thrust load on the segments was below the design limit. No segment damage could be observed related to over-stress of the concrete capacity on site.

Table 2. TBM operational parameters.

	MC30 Tunnel		MC20 Tunnel	
Performance Items	Average	Max.	Average	Max.
Thrust Force (kN)	13,233	23,106	11,392	24,449
Contact Force (kN)	11,918	21,911	9,940	23,679

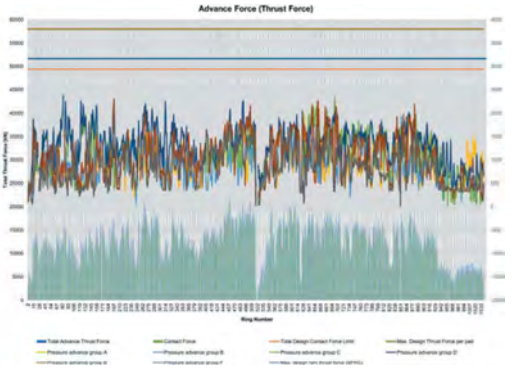

Figure 6. MC30 Drive thrust force data.

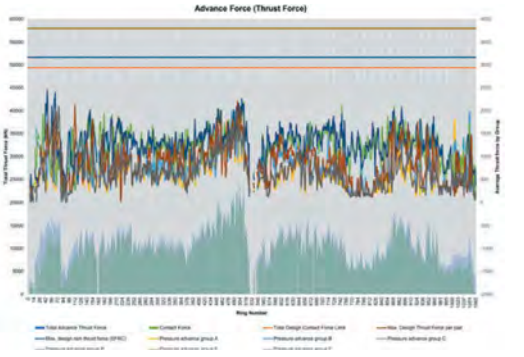

Figure 7. MC20 Drive thrust force data.

5.3 *Face pressure*

Daily Review Meetings (DRM) including the construction team, Construction Phase Services (CPS) team, instrumentation and monitoring team, geotechnical team and the owner verifier were held, and special meetings held during breakthroughs, traversing the temporary ground anchors at Aotea Centre, and during the Central Motorway Junction (CMJ) crossing. Face pressures, grouting with other TBM operational parameters and segment type were reviewed and discussed. A Permit to Tunnel (PTT) and associated parameter sheet were confirmed and issued to the construction team. The target and measured TBM face pressure at tunnel crown for both MC30 and MC20 tunnels are shown in Figure 8 and Figure 9. In general, the actual application face pressure was controlled well within the upper and lower bounds face pressures as confirmed from the DRM. It was noted that the face pressure was outside the bound at some locations, because the TBM operation parameters were adjusted according to the actual ground conditions and based on the monitoring results.

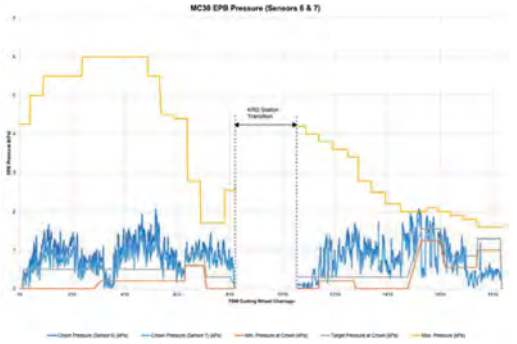

Figure 8. MC30 Drive TBM Face pressure data.

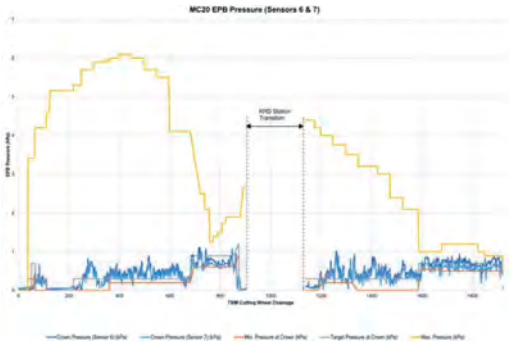

Figure 9. MC20 Drive TBM Face pressure data.

5.4 *Ground conditioning and clogging*

A foam agent was used for spoil conditioning of the EPB TBM spoil. During TBM operation, the foam agent was mixed with water and compressed air. The mixed material passed through the foam guns and injected into the front of the cutterhead via injection ports. Additional free water was injected into the chamber through independent lines to support and keep the foam in the chamber. Foam injection was controlled by 3 parameters: Foam Expansion Rate (FER); Foam Injection Ratio (FIR); and Foam concentration (C). These parameters were changed from time to time by the TBM operator, depended on the TBM advance. The average setpoint FIR mode of MC30 and MC20 Drives are 57% and 58% respectively. The average foam injection volume is 0.125 m^3/ring vary from 0.01 to 0.5 m^3/ring.

5.5 *Reliability and breakdowns*

During the TBM operation on both drives, the time for TBM operation and stoppage were recorded and grouped in 6 major categories: Excavation, Ring Building, Planned Stoppages/ Breaks and travel, Delay-Survey/ error -damage, Delay-System/ Cooling water/ Electrical and Delay-Conveyor/ Electrical. In general, the breakdowns include erector breakdown, TBM jacking rams breakdown, segment feeder damage, belt conveyor breakdown and cutterhead intervention with maintenance (Figure 10). For MC30 drive, the major stoppages were corona virus disease (COVID-19) lockdown, conveyor belt installation, and TBM thrust ram replacement; for MC20 drive, the major stoppages were MC20/50 mined cavern headwall construction, tower crane breakdown/ windy days and conveyor belt breakdown. Free air interventions were carried out in the project and the locations of stoppages were chosen prior to the critical zones such as cross passage locations, Central Motorway Junction (CMJ) and existing temporary ground anchors zone at Aotea Centre. Also, the major maintenance was scheduled at the station/ cavern transition. The disturbance to the tunnel programme was minimised. Low wear was observed on the TBM cutterhead and cutting tools – mix of discs and rippers during interventions.

Figure 10. Tunnel face inspection during maintenance.

6 TUNNEL CONSTRUCTION

6.1 *TBM launch, transition and retrieval*

The CRL TBM was shipped from Herrenknecht's factory in China to New Zealand. The machine arrived in kitset pieces in late 2020 and installed at Mount Eden Portal.

After the TBM assembly, the TBM was launched at Maungawhau (Mount Eden) portal in MC30 mined tunnel and advanced north towards the CBD. Temporary steel launching frame (Figure 11) was set up in the MC30 mined tunnel for transferring the launching thrust to the shotcrete lining and ground. For the launching operation, the TBM was operated at a limited thrust output until the completion of a length of tunnelling where the entire TBM and backup gantries were within the excavated tunnel.

Both MC30 and MC20 drives, were excavated under the Symonds Street, CMJ and broke through into KHP mined Station. For MC3 platform tunnel in KHP Station, the TBM transit occurred with only primary lining installed whereas for MC20 the transit occurred after installation of secondary (permanent) lining. Within 21 m at each end of the platform tunnels, the cavern profiles were widened. The widening was required to allow sufficient length for the TBM transit alignment to shift towards the middle of the station and clear the walls of the typical section as shown in

Figure 11. Temporary launching frame in MC30 drive.

Figure 12. Then the TBM was re-launched in the stub tunnel at the end of platform tunnel by using temporary thrust frame set up at the widening platform tunnel.

Figure 12. TBM Transition in KHP MC20 mined tunnel.

After the re-launching, the TBM excavated along the Pitt Street, turned to Vincent Street and finally broke into the Te Waihorotiu (Aotea) Station at Mayoral Drive after passing the temporary ground anchors outside the Aotea Centre.

Figure 13. TBM MC20 drive breakthrough at Aotea station.

The TBM was dismantled after the MC30 drive excavation and re-assemble at MC20 drive for the second drive. After the second tunnel was built, the TBM was dismantled and moved in pieces to the Ports of Auckland and transported back to the TBM manufacturer. The company deconstructed the machine and re-used suitable parts on multiple TBMs in the future.

6.2 *Production statistics and progress*

The tunnel production statistics and the time-chainage progress curves are summarised in Table 3 and presented in Figure 14 and Figure 15 accordingly. The production rate at MC30 for the first two months learning period was low, thereafter it was increased. The production was nearly stopped due to COVID-19

Table 3. Tunnel production statistics.

Items	MC30 Tunnel	MC20 Tunnel
Launch Date at Mount Eden Portal	17 May 2021	26 April 2022
Breakthrough Date at Aotea Station	22 Dec 2021	14 Sep 2022
Total Duration	7.3 Months	4.7 Months
Average Day (m)	7.4 m	9.4 m
Best Day (m)	33.6 m	34.0 m
Average Week (m)	51.9 m	69.5 m
Best Week (m)	162.1 m	187.2 m

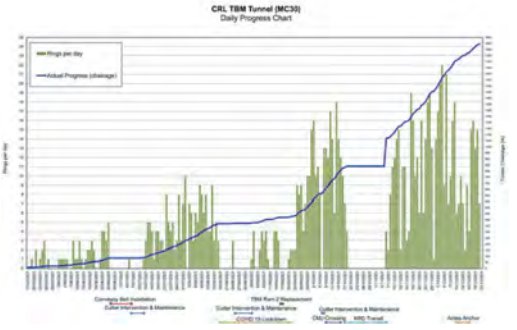

Figure 14. TBM MC30 drive progress chat.

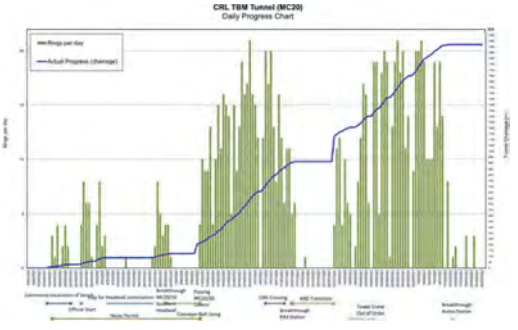

Figure 15. TBM MC20 drive progress chat.

Level 4 lockdown (i.e. approved to maintain minimum TBM operation with limited number of workers without segment production in the precast yard) for more than a month. Based on experiences gained from the first drive, the production rate in the second drive MC20 tunnel was higher.

6.3 *On-site segment damage*

The segment or ring damages during erection, excavation, advancing, and post construction activities were inspected and recorded. The damages were classified into three main groups: cracking, concrete spalling, and leakage. The damaged segments were inspected and repaired in accordance with the agreed repair. There were total 398 defects recorded for MC30 drive and 208 for MC20 drive. It indicated the damage rate occurred at every 2.6 rings in MC30 drive and improved to a frequency of 5.1 rings in MC20 drive. The majority of damage were cracks and it was improved by the experience in first drive and modification of the length of concrete pad on the segment.

6.4 *Grouting*

After the TBM excavation in the excavation cycle, the TBM left a gap between the excavation profile and the segmental lining. The theoretical cut diameter was 7.15 m, and the external diameter of the segmental lining was 6.84 m, leaving a theoretical void of 155 mm and 3.4 m^3/m. This void was filled with cementitious grout, which was pumped through the tail shield pipes during the excavation cycle. Grouting was performed to the theoretical volume within ± 10%. The injection pressure was monitored to ensure the surrounding ground and water pressures were balanced. Monitoring of the injection pressure indicated if any voids were present, or if there was a blockage in the grouting line. The lining was designed to withstand maximum grout pressure of 1 bar above prevailing groundwater pressure. Figure 16 and Figure 17 presented the grout volume against the ring number. The injection volume was generally within the tolerance. It was noted that the gap was filled up with primary grouting at the cross passage location (Figure 18).

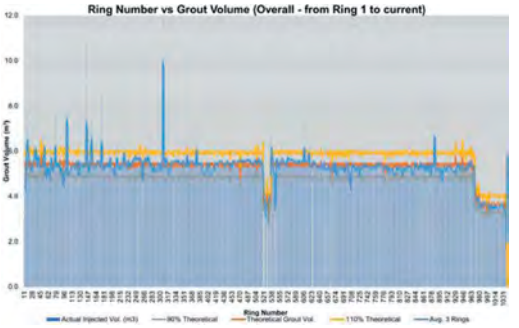

Figure 16. TBM MC30 drive grout volume.

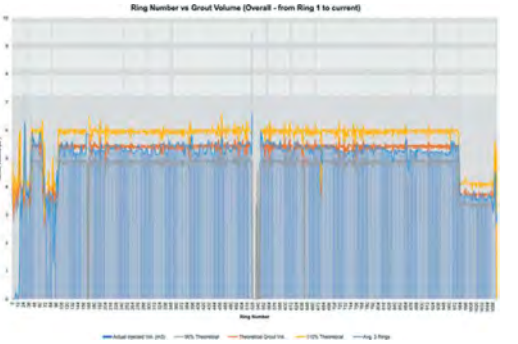

Figure 17. TBM MC20 drive grout volume.

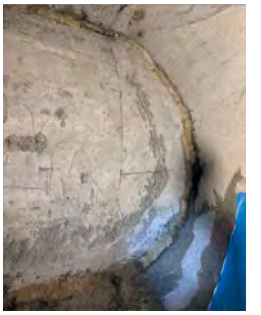

Figure 18. Primary grouting materials filled up TBM TAIL VOID.

Secondary grouting was also undertaken if there was evidence that primary grouting through the tail skin did not fully fill up the annulus between the lining and the ground.

6.5 *Tunnel spoil*

Up to 1,500 tonnes of spoil was excavated each day. Spoil from Mt Eden was a mix of clean fill, managed and contaminated. The spoil was either wet spoil extracted by the TBM from conveyor belt, or a clean, dry type of spoil removed during initial tunnelling operations. Clean fill was disposed of at the Three Kings Quarry in Mt Eden. All other spoil – managed or contaminated – was trucked to various disposal sites at Mercer in Waikato. The measured weight and excavated materials were important parameters to determine the ground geology and actual excavation volume. Depended on different ground conditions, the quantities of soil conditioner and additional free water were adjusted to obtain an optimum moisture content (MC) in spoil to ensure the effectiveness of TBM excavation, face support and mucking out.

6.6 *Central Motorway Junction (CMJ)*

The CMJ forms the intersection between three major motorways: Northern Motorway (SH1), Southern Motorway (SH1) and Northwestern

Motorway (SH16), which is one of the busiest roads in New Zealand. The MC30 and MC20 alignment lie in close proximity to three existing structures which are considered to be potentially adversely affected by the tunnelling works (Figure 19 and Figure 20). The structures are:

1) Upper Queen Street Retaining WallProposed MC30 alignment is approximately 1.5 m west of the nearest belled pile.
2) Newton Bridge No. 1The respective horizontal clearances to Abutment O and Pier N from MC20 are approximately 2.0 m and 6.5 m respectively.
3) Soil nail retaining wall adjacent to the SH16 off ramp Clearance between the CRL tunnel crown and the CMJ retaining wall is approximately 7.52 m for MC20 and 9.5 m for MC30.

The ground cover to the tunnel crown for MC30 ranges between 9.0 m and 25.4 m and for MC20 ranges between 7.2 m and 23.1 m. Considering the change in ground cover, 3D Finite Element Model for tunnelling under the CMJ (Figure 21) were set up by LKA to assess the induced effects and determine the required face pressure.

TBM intervention was carried out for maintenance before entering CMJ to minimise the risk of stopping at CMJ so as to avoid unacceptable ground movement. The last tunnelling crossing the CMJ was completed in July 2022 with negligible monitoring readings.

Figure 19. CRL Tunnels at CMJ (facing South).

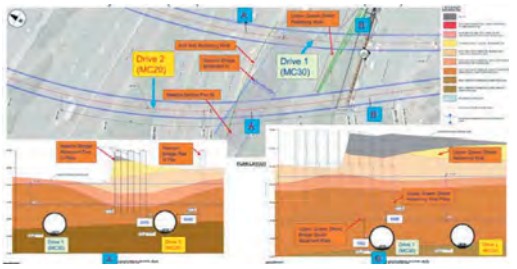

Figure 20. Geological Section at CMJ.

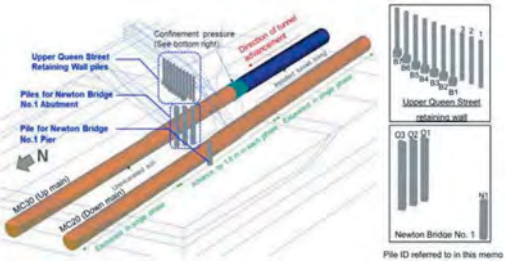

Figure 21. 3D finite element model for tunnelling under the CMJ.

6.7 *Existing temporary ground anchors at Aotea Centre*

Based on the desk study, there were ground anchors connected to Aotea Centre structures which were in the way of the CRL TBM drives (Figure 22). The retaining walls that were built during the construction are located along Mayoral Drive. Ground anchors investigations including investigation boreholes and CCTV were carried out at construction stage. It was found that the anchors are for temporary use and the head plates been cut which indicated that the anchors were inactive.

Knife tools were included on the Free air intervention was carried out within the anchor zone to remove the anchors from the tunnel face (Figure 23) which could reduce the risk of damaging the TBM. The last tunnelling crossing the ground anchors was completed successfully in September 2022.

Figure 22. Ground anchors at Aotea Centre.

6.8 *Ground volume loss due to TBM tunnelling*

The tunnels passed beneath residential and commercial areas, extensive and comprehensive instrumentations and monitoring were designed and implemented during construction. The instrumentations included individual and arrays of surface settlement markers and extensometers, piezometers, inclinometers, and convergence monitoring points inside the tunnels. The ground settlements recorded from the settlement marker arrays in different locations along the tunnel alignment have been back analysed by using the Gaussian ground movement model to determine the tunnelling volume loss. The

Figure 23. Ground anchors from excavation spoil.

trough width parameter of 0.7 was fitting the Gaussian curves. The range of volume loss was determined to be between 0.1% and 0.4%.

7 CONCLUSION

The CRL Tunnels was the first TBM tunnel passing through the CBD area. The last TBM breakthrough was completed on 14 September 2022. The use of the EPB machine made a significant contribution to the success of the Project. The post construction review on TBM operation and performance, segmental lining manufacturing and building, tunnel construction, and quality control, has been reviewed and a summary has been provided in this paper. It provides valuable reference for planning, design, and construction of future tunnelling projects in New Zealand.

ACKNOWLEDGMENTS

The paper is published with the permission of the City Rail Link Limited for which the authors would like to gratefully acknowledge. The design and construction of the project is currently undertaken by the Link Alliance.

REFERENCES

City Rail Link (CRL) Official Site (N.D.) from https://www.cityraillink.co.nz/.

R Mahajan, N Bsaibes and R Shi, 2021. Bored Tunnel Design for CRL Auckland – Design Challenges. Proceedings of Australasian Tunnelling Conference, ATS 2020+1, pp. 116–127.

T Ireland, P Kirk and S Eratne, 2021. Competitive Alliance procurement process for a major underground railway – City Rail Link, Auckland. Proceedings of Australasian Tunnelling Conference, ATS 2020+1, pp. 380–392.

T Ireland, R Bishop and M Sheffield, 2011. Project Hobson – new technology in Auckland. Proceedings of Australasian Tunnelling Conference 2011, pp. 99–110.

Tunnelling for a Better Life – Yan, Celestino, Thewes & Eberhardt (Eds)
© 2024 The Author(s), ISBN 978-1-032-80042-4
Open Access: www.taylorfrancis.com, CC BY-NC-ND 4.0 license

Research and application of multi-curve small turn continuous belt conveyor*

Liwei Cui, Huigan Xu, Jianyong Shen, Jinming Cheng, Pengyang Song, Qinghua Qin & Wang Yang
China Railway Engineering Equipment Group Co., Ltd., Zhengzhou, China

ABSTRACT: Through the analysis of the turning conditions, the definition of small turning belt machine is proposed, and the concepts of natural turning and forced turning are proposed for different turning radii. Through the force analysis of natural turning and forced turning, the corresponding turning adjustment measures are proposed. Through the analysis of turning radius and bandwidth under forced turning conditions, the concept of linear meter arc length difference is proposed, and it is used as an index to judge the difficulty of turning. Through the pumped storage power station project, the feasibility of forced turning measures under small turning radius is verified, and the theoretical and practical experience is provided for the slag discharge of the belt machine under the subsequent small turning condition.

Keywords: Small turn, Belt conveyor, Natural turns, Forced turns

1 PREFACE

Continuous belt conveyor as TBM supporting slag system, foreign countries as early as 1991 belt machine continuous slag system applied to tunnel construction, so far continuous belt machine slag technology has been very mature. Domestic tunnel continuous belt conveyor started late, as early as 2005 Liaoning Dahuofang water diversion tunnel project for the first time introduced continuous belt machine and TBM supporting slag system, which also marked the tunnel continuous belt machine officially applied in domestic tunnel construction. After the first stage of 21st century technology introduction, the second stage of 2010-2014 digestion and absorption, the third stage of 2015-so far independent research and development, continuous belt slag technology has been very mature, as a tunnel boring machine supporting slag extraction system is widely used in railway, highway, water diversion, urban subway, municipal water supply and other fields. The continuous belt conveyor has incomparable advantages over the slagging of mine carts. With the increasingly complex working conditions, new requirements are put forward for the belt conveyor to continuously transport slag under a small turning radius.

2 THEORETICAL ANALYSIS OF SMALL TURNING BELT CONVEYOR

According to its tape characteristics, the belt machine determines that the ideal movement route of the belt machine should be a straight line, that is, the belt machine head and tail connection and the trajectory of the tape material should be projected as a straight line in the horizontal plane; However, with the diversification of application scenarios, the belt machine curve should be the normal demand. When the belt conveyor is running in a curved (turning) section, the shape of the tape (mainly the upper branch tape) becomes the key point for reliable transportation. Therefore, the basic requirements for the turning section tape are not disengaged, not damaged, and not deviated.

2.1 *Definition of small turning belt conveyor*

According to the "Technical Code for Shield Construction of Metro Tunnel Engineering", "the radius of the curve of the subway tunnel plane is less than 300m as a small curve tunnel"; In rail transit design, less than 40D (D is the tunnel diameter) is defined as a small curve tunnel. The turning radius of traditional highways, railways and water conservancy tunnels is generally more than 1000m, and in recent years, TBM method has been gradually adopted for the excavation of roadways in the fields of pumped storage and metal mines, which has posed new challenges to the slagging of belt conveyors; According to the analysis of engineering characteristics, the slagging system needs to have a small turning radius slag discharge capacity, according to the different turning radius, the turning conditions of the belt conveyor can be divided into the following four categories.

2.1.1 *Super large curve turning (turning radius R> 1000m)*

Such working conditions have basically no effect on the long-distance belt conveyor system and do not require special consideration.

*Corresponding author: 1247992810@qq.com

DOI: 10.1201/9781003495505-233

2.1.2 *Large curve turning (turning radius 500<R<1000m)*

The running trajectory of the tape can be regarded as a curve, the turning radius has a significant impact on the running quality of the tape, and it is necessary to carry out special design for certain parameters of the parts (idlers) that support the tape in the turning section, which has made the tape naturally pass through the turning section.

2.1.3 *Small curve turning (turning radius 100<R<500m)*

Natural turning measures can no longer meet the turning needs of the tape, and mandatory measures need to be taken to force the tape to operate within a certain range.

2.1.4 *Ultra-small curve turning (turning radius R<100m)*

Super large curve turns and large curve turns belong to the natural turning range, and through reasonable design of relevant parameters, the tape can pass the turning section smoothly. Small curve turns and ultra-small curve turns belong to the forced turning range, and special structural design needs to be added to force the tape to operate within the specified range. The turning radius of the small radius turning belt conveyor is less than 500B (B is the belt width).

2.2 *Force analysis of natural turns*

In order to ensure that the plane turning belt conveyor can achieve autonomous guidance when bending operation, the conveyor belt needs to meet three conditions at the turn: first: the force balance condition of the turning section; Second: stress and strain constraints; Third: the conveyor belt on the outer roller cannot leave the roller and float up.

The resultant force balance condition of the turning section, when the tape is running steadily at the turn, its resultant force FTC direction is pointing to its inside along the radius of the turning line, and the resultant force acts on the tape to make it deviate inward. The gravity of the material and tape at the turning point is due to the existence of the curve elevation angle in the idler group, and its component produces the thrust force FG pointing to the outside of the curve; The centrifugal inertial force FQ when turning is directed to the outside of the curve; The inner curve elevation angle of the idler, the centrifugal friction between the conveyor belt and the idler FR points to the outside of the curve, and the combined force of the above forces is used to offset it. to ensure that the tape runs automatically in the corner. The tape is also affected by the reaction force of the roller and the action of the resistance during operation, where the direction of resistance points to the opposite direction of operation. Therefore, the stable operation of the tape at the plane bend should meet the following conditions (the positive direction of the specified force is to point to the outside of the bending line), as shown in the figure.

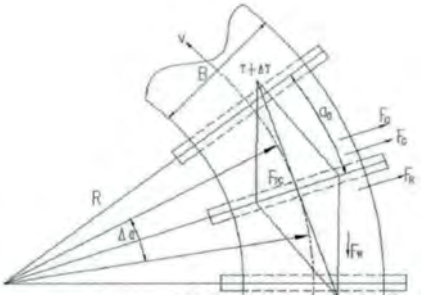

Figure 1. Mechanical model of plane turn.

When the material passes through the material in the plane bend of the force analysis trough idler group in operation, the cross-section of the material can be approximated as a combination of trapezoidal interface and chord arc section, and the idler corresponding to the cross-section is divided into three parts, and its force relationship is shown in the figure.

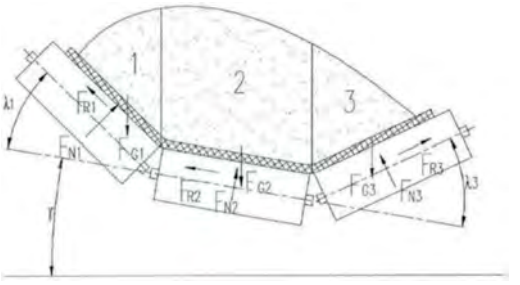

Figure 2. Friction between the material and the conveyor belt gravity and idler.

The tape turns naturally only through the following three measures:

(1) Increase the tilt angle of the idler frame γ;
(2) Increase the angle γ1 of the idler groove on the inner side of the turn;
(3) Reduce the angle γ3 of the idler groove on the outside of the turn;

When the tape turns, the resultant force of the tape tension is balanced with the gravity component of the material and the tape, the centrifugal force of the material and the tape, and the friction between the tape and the idler, the tape can achieve a natural turn.

2.3 *Force analysis of forced turns*

Within the forced turning range, the difficulty of the specific project can be evaluated according to the size of the linear meter arc length difference; Combined with similar TBM small turning engineering cases in the past, we derive the difference between the inner

and outer arc lengths within the unit length according to the arc length formula, that is, the arc length difference in linear meters as the difficulty factor for judging the turning difficulty of the belt machine.

$$N = B/R \quad (1)$$

In the formula:

N: Under the condition of a specific turning radius, the difference between the outer and inner motion trajectories of the inner tape per unit arc length, in mm/m;

B: Tape width, unit mm;

R: turning radius, unit m;

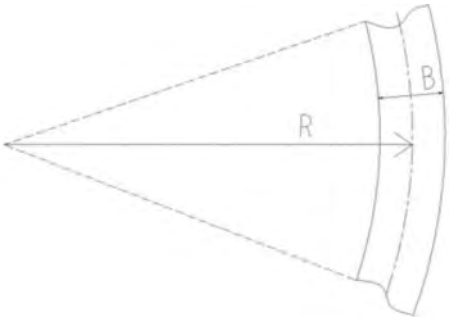

Figure 3. Turning diagram.
Note: N≤5 Less difficult; 5<N≤10 difficulty is moderate; 10<N≤15 Difficult; 15<N≤20 Extremely difficult.

When the tape is transported under small radius conditions, the inner tape of the turn is relaxed, and the tension of the tape on the outside of the turn is too large, so the stroke difference and tension difference between the inner and outer sides are too large, resulting in the combined force of the tape, that is, the misalignment force is relatively large, and the adjustment measures of natural turning are simply taken: increase the tilt angle of the idler frame γ; Increase the angle γ1 of the inner idler of the turn; Reduce the angle γ3 of the idler groove on the outside of the turn; The force equilibrium condition has not been reached; At this time, it is necessary to increase the pressure roller on the inside of the turn, the lower edge of the pressure roller is lower than the upper edge of the roller, so the inner side of the tape runs along the wavy line, the tension between the inner and outer sides of the tape is reduced, and the tension component of the inner tape is converted into the positive pressure of the roller and the upper roller, thereby increasing the friction between the tape and the roller, so as to achieve the balance of force.

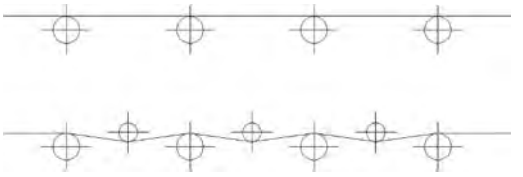

Figure 4. Running trajectory of the inner and outer ends of the tape in the turning section.

3 PROJECT OVERVIEW AND KEY DIFFICULTIES

3.1 *Project overview*

The power station consists of upper reservoir, lower reservoir, water transmission system and underground plant system, with a total installed capacity of 1.2 million kilowatts, the power station undertakes peak shaving, frequency regulation, project regulation, energy storage and other projects.

The ventilation tunnel passes through the roof arch of the factory building and is connected to the traffic hole, with a diameter of 9.53m and a total of 7 turning sections. The turning radius of the traffic hole plane is all R=100m, the longitudinal slope of the turning section is 3%, the maximum longitudinal slope of the local section is 4%, and the maximum longitudinal slope of the remaining cave sections is 5.9%; The plane turning radius before the ventilation tunnel enters the plant adopts R=90m, the turning radius of the remaining holes adopts R=100m, and the longitudinal slope is all 2.5%.

Figure 5. TBM tunneling route.

3.2 *Engineering difficulties*

(1) Small curves, many curves, annular slag out
The tunnel route is circular with a total turning angle of 430°, including 7 turns, 1 small turning radius of 90m + turning angle of 180°, and 6 turning radius of 100m. The overall route is complex, there are many turning sections, the turning angle is large, the turning radius is small, and the turning direction is inconsistent; At present, there is no similar tunnel line using belt machine system slag engineering case for reference.

(2) 180° continuous small turn to remove slag
The whole tunnel includes a continuous small turning route with a turning radius of 90m, a turning angle of 180°, and a turning section length of 300m; Small turning radius and large turning angle lead to large tension of the tape, the running resistance of the whole machine increases, the tension difference between the inside and outside of the tape increases, resulting in deviation, wear, inner folds and outer flipping tape phenomenon, due to the inner elevation of the turn, it is easy to scatter when turning.

(3) Large section, multiple crushing belt
The tunnel section excavation diameter is 9.53m, and there are many crushing zones in the construction route, the maximum particle size is 800mm, and the particle size of 400-500mm is more common. Due to the large diameter of the excavation hole and the large capacity of the belt machine system, there is a large amount of large particle size slag material at the crushing belt to put forward higher requirements for the belt machine slag discharge system, and at the same time bring the risk of material blocking, scratching the tape, damaging the roller, breaking down the funnel and so on.

4 BELT MACHINE SLAGGING SCHEME

4.1 *Technical solution of the whole machine*

This technical scheme adopts 3 sets of fixed small turning belt conveyor and 1 set of small turning continuous belt machine front and rear lap with slag discharge method, of which: the length of No. 1 belt machine is 330m, covering from the ventilation hole to the second turning section; The No. 2 belt conveyor has a length of 550m and covers the third turning section; The No. 3 belt conveyor has a length of 340m, covering the fourth turning section with a turning radius of 90m + a turning angle of 180°; Machine 4 is a continuous belt conveyor with a total length of 970 m, which dynamically passes through the 5th, 6th and 7th turns as TBM continues to advance. The technical scheme of the belt machine slagging system is shown in Figure 6, and the main technical parameters are shown in Table 1.

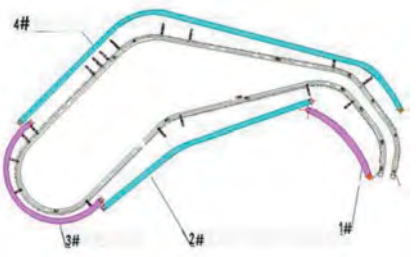

Figure 6. Layout diagram of the technical scheme of the belt machine slagging system of one project.

Table 1. Main technical parameters of belt machine slagging system.

Iems	With (mm)	Turning radius (m)	Turning angle (°)	Turn length (m)	Conveying length (m)
1#	1000	100	114°	200	330
2#	1000	100	33°	55	540
3#	1000	90	180°	330	340
4#	1000	100	100°	170	970

4.2 *Targeted design*

The cross-sectional layout of the turning section of the small turning belt conveyor is shown in Figure 5. Therefore, in order to ensure the smooth operation of the slagging machine in the turning section, the following targeted technical measures are taken:

(1) Multi-stage lap connection of the belt conveyor reduces the belt tension of the turning section and reduces the driving power;
(2) Adopt high-quality tape and lock edge design to prolong the life of the tape;
(3) The 180° turning section adopts a special structure, the upper idler group adopts a deep U-shaped design, and the lower idler group adopts a deep V-shaped or oblique arrangement, which reduces the tension difference on both sides of the tape, reduces the risk of mistracking, and prolongs the life of the tape;
(4) Adjustable idler sets, special stop rollers and pressure roller structures are arranged along the belt machine;
(5) Design protective functions such as tape anti-rollover, tape tear monitoring, etc;
(6) The reinforced belt conveyor bracket is adopted, which has a solid structure and can resist the large tensile load of the turning section;
(7) By converting the contact friction form between the tape and the roller line into surface contact friction, the pressure between the tape and the roller is reduced, thereby reducing the edge wear of the tape and improving the service life of the tape.

5 ENGINEERING APPLICATIONS

TBM equipment of pumped storage power station project began to boring in October 2021, the early use of dump truck slag, with the extension of the boring distance, the material transportation efficiency decreased, so TBM monthly advance is generally about 200m, when the boring mileage exceeds 1km, using car slag, TBM advance is generally about 150m.

From July to August 2022, the installation and commissioning of the belt conveyor will be carried

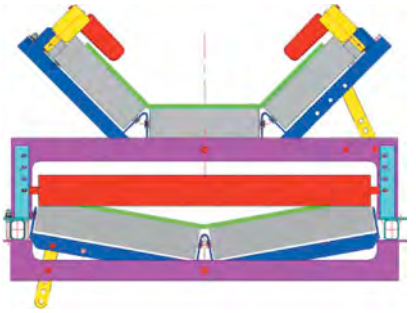

Figure 7. Structural layout of turning section.

out. After using the continuous belt conveyor in September, the monthly advance of more than 300 meters was created, the maximum daily advance was 21.6 meters, and the slag discharge of 180° turning radius + 90 turning radius and 6 100m small turns was completed.

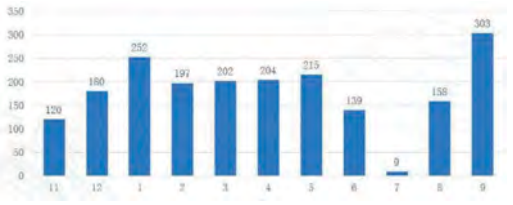

Table 2. TBM advance statistics.

6 CONCLUSIONS

Through multi-machine integrated control, multi-point drive, deep grooved section and flexible tape and other technical measures, the slag discharge system of small turning belt has completed the research and development and application of the first long-distance, high-speed, sharp-turn belt slagging system in China, greatly improving the excavation efficiency, solving the problem of slagging of a complete set of mechanized equipment for large-diameter and sharp-turn TBM, ensuring the synchronous progress of excavation and support, and the excavation efficiency is about 3 times that of manual drilling and excavation, while improving the image of safe and civilized construction of the tunnel.

With the continuous development of pumped storage power station and similar projects, the application of small turning belt machine technology in this field will continue to progress, it is recommended to combine the successful application experience of this project, fully consider the feasibility of belt machine system application, optimize the tunnel construction line, further promote and apply small turning belt machine technology, and promote the improvement of the construction level of TBM complete set of machinery.

REFERENCES

[1] Wang H Y, Liu J X, Jing X Y, et al. Selection of excavation equipment and TBM technology for underground cavern of Pumped Storage Power Stations [J]. China Rural Water and Hydropower, 2021(6): 148–152, 158.

[2] Liu Bing. Design and application of long-distance plane turning belt conveyor [D]. Dalian: Dalian University of Technology, 2013.

[3] Gao Hanli. Determination of radius of curvature of bending section of belt conveyor [J]. Coal Mine Electromechanics, 2010(1):67–68.

[4] Chang Xiaolin. Calculation and improvement measures of large angle plane turning belt conveyor [J]. Coal Mining Machinery, 2020, 41(2):26–28.

[6] Grimmer K J, Kessler F.The design of belt conveyors with horizontal curves [J], Bulk Solids Handing, 1992, 12(4):557–563.

[7] Kessler F, Grabner K, Grimmer K J.”bico-Tec” A new type of belt conveyor with horizontal curves [J], Bulk Solids Handing, 1993, 13 (4):741–747.

[8] Grabner K, Operation of the curve-going belt conveyor “biro-TEC”at Titan Cement [J], Bulk Solids Handing, 1997, 17(2):266–269.

Tunnelling for a Better Life – Yan, Celestino, Thewes & Eberhardt (Eds)
© 2024 The Author(s), ISBN 978-1-032-80042-4
Open Access: www.taylorfrancis.com, CC BY-NC-ND 4.0 license

Slurry treatment technology based on calcium oxide and seawater of extra-large diameter slurry balance shield machine in Zhuhai area muddy silty clay stratum

Ruiwen Dong*, Zhou Zhou & Wenjiang Liao
Guangzhou Rail Transit Construction Supervision Co., Ltd, Guangzhou, China

ABSTRACT: Aiming at the problem of insufficient slurry treatment efficiency caused by geological conditions during the excavation process of the extra-large diameter slurry balance shield machine in the Zhuhai tunnel project, this paper introduces the geological conditions of the shield machine excavation in detail, analyzes various factors and shortcomings that affect slurry treatment efficiency, and proposes methods to improve slurry treatment efficiency. A better additive ratio was obtained through slurry treatment experiments. The results show that additive combination of 6% calcium oxide and 50% seawater is beneficial to improve the slurry treatment efficiency under the good maintenance premise of slurry treatment equipment parts.

Keywords: Slurry separation equipment, Mix additions, Field experiments

1 INTRODUCTION

In recent years, with the continuous development and construction of China's infrastructure, medium and large urban subways, large-diameter tunnels and underwater tunnel projects, and based on the increasing requirements of settlement control, the demand and quantity of extra-large diameter slurry balance shield machine have increased. The slurry treatment function is becoming the key factor in choosing the construction method of super large diameter slurry balance shield machine.

In order to improve the efficiency of extra-large slurry treatment brought by the extra-large diameter slurry balance shield method, many technicians have carried out research. Chen et al. introduced the method of adding lime to improve silty soil, Zhang Lihua et al. introduced the method of adding lime and fly ash to improve dredging sludge with high water content. Zhao S et al. used sodium bentonite and dispersant to prepare slurry. Wan Z et al. studied the properties and interactions of soil improvement additives. Zumsteg R et al. found that some polymer solutions help mud to have high shear resistance and low clogging properties at the same time. Min et al. Zumsteg et al. found that the ratio of chemical additives in the slurry mixture was very important to the efficiency of the mixture. Yang W et al. studied the properties of the curing agent modified soil through experiments.

It can be seen that slurry treatment will affect the formation of mud film, slag carrying capacity, slurry making ability, etc., which will further affect the tunneling efficiency, and play a vital role in the extra-large diameter slurry balance shield.

2 BACKGROUND

The Zhuhai tunnel project passes through a 2276m full-section weak stratum, the length sea bedrock intrusion of the left and right lines is 387m and 464m. The composite strata of the shield tunneling bedrock protrusion are muddy silty clay, silty clay, medium coarse sand, sandy cohesive soil, fine medium sand, moderately weathered granite, and locally existing tough stone and quartz veins from top to bottom, as shown in Figure 1. In the interval of LK0+872~LK2+918 tunneling mileage, the tunnel vault is silt and muddy silty clay, the side wall is muddy silty clay, sand and silty clay, and the tunnel bottom is muddy silty clay, sand and silty clay, of which (2)-2-1 muddy silty clay accounts for about 65% of the main muck components after the tunnel face excavation, light and dark gray, containing organic matter and a small amount of shell debris, locally containing medium sand, with rancid smell, saturated, flow plastic-soft plastic state, soft soil, with high water content, micro permeability, high compressibility, large porosity ratio, low shear strength, high sensitivity, particle size of 0.005mm-0.05mm. (2)-2-1 physical properties of muddy silty clay are shown in Table 1. Due to the existence and high proportion of muddy silty clay, the slurry shield machine is prone to a large amount of slurry in the formation during the excavating formation process and the slurry is difficult to be treated in time, which leads to the adverse consequences of mud performance decline.

*Corresponding author: 516538316@qq.com

DOI: 10.1201/9781003495505-234

Table 1. (2)-2-1 Physical properties of muddy silty clay.

Physical property	Value
Natural water content W/%	48.4
Natural density ρ_0/g·cm^{-3}	1.7
Specific gravity Gs	2.68
Porosity ratio e	1.3
Saturation Sr/%	98.0
Liquid limit W_L/%	43.6
Plastic limit W_P/%	26.8
Plasticity index I_P/%	16.8
Liquidity index I_L	1.28

3 PROCESS

In order to realize slurry treatment function, the slurry treatment system is mainly composed of slurry inlet and outlet pipelines, slurry making and adjusting system, slurry separation equipment system, pressure filtration equipment system etc. The slurry outlet pipeline in the inlet and outlet slurry pipeline is the connecting pipeline between the shield machine slurry tank and the slurry separation equipment system, and the slurry inlet pipeline is the connecting pipeline between the adjusting poll and the shield machine slurry tank. The slurry making and adjusting system comprises 8 stage sedimentation pools, a making pool, a storage pool, an adjusting tank, and a water tank, which main function is to ensure that the slurry performance is in a good state by sedimentation, making and adjusting. To achieve the purpose of recycling, the slurry flows into the 8 stage sedimentation pool through the chute and then flows into the slurry inlet through the adjusting tank. Figure 2 is slurry treatment process and the dotted line part in the figure is for emergency use.

The main functions of slurry treatment include the following three points: (1) providing mud film for the tunnel face during shield tunneling to ensure the stability of the tunnel face; (2) The slurry is fed into the slurry bin to ensure pressure on the face, side, vault and bottom surface of the tunnel, so that the pressure on the outside of the slurry balance shield machine reaches a relatively stable equilibrium state; (3) After the slurry is discharged to the adjusting tank through multi-stage sieving treatment by slurry separation equipment, sedimentation pools and pressure filtration equipment. The slurry is re-fed to the adjusting pool to ensure the muck removal while improving the utilization rate of the slurry.

3.1 *Slurry separation*

The slurry separation equipment system comprises three sets of separation equipment and two centrifuge equipment system, as shown in Figure 3. Each set of separation equipment comprises a slurry distributor, a clay block-slurry separator, a coarse sieving equipment, A slot, B slot, a No.1 slurry pump,

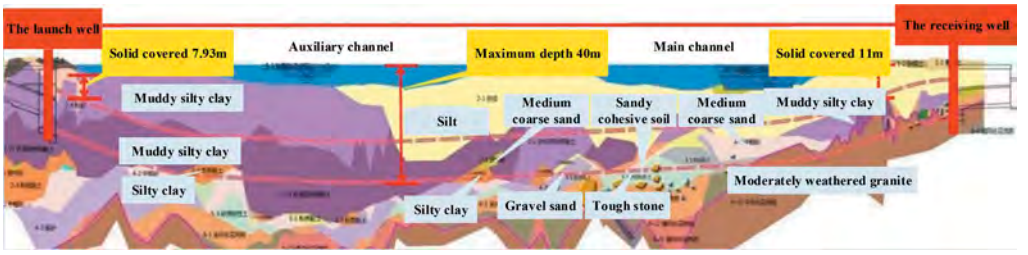

Figure 1. Vertical section.

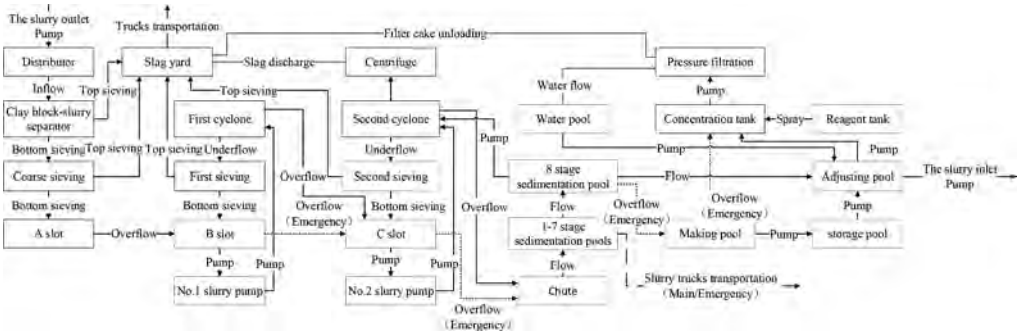

Figure 2. Slurry treatment process.

a first cyclone equipment, a first sieving equipment, a C slot, a No.2 slurry pump, a second cyclone equipment, a second sieving equipment. The first stage of the coarse sieve equipment filters with particles size greater than 0.2mm, the second stage of the first cyclone equipment filters with particles size of 0.074-0.2mm, and the third cyclone filters with particles size of 0.02-0.074mm.

Figure 3. The slurry separation equipment.

3.2 *Pressure filtration*

The plate pressure filtration equipment system includes a concentration tank, a reagent tank and five plate pressure filtration equipment (as shown in Figure 4.). The operation specific process of the plate pressure filtration equipment system needs to pump the slurry of the adjusting tank to the concentration tank and add the slurry flocculation and precipitation agent to the reagent tank. The reagent is sprayed into the chute through the pipeline and fully reacts with the slurry and then overflows into the concentrator tank. The slurry flocculation sediment at the bottom of the concentration tank is pumped to the plate pressure filtration equipment through the slurry pump. The plate pressure filtration equipment adopts the method of pressing the filter plate, filtering, one blowing, extrusion, diaphragm pressing, and two blowing to squeeze the water out of the slurry to the water tanks on both sides and recycle it. At the same time the slurry flocculation sediment form the filter cake with low water content and then the residual slurry overflows back into the concentration tank. The pressed filter plate is opened to start unloading and transporting to the slag yard.

4 PRESENT

The slurry treatment system mainly carries out the work of slurry preparation, filtration and slag removal, and adapts to the slurry preparation formula with the change of formation properties in the shield tunneling process and filters the slurry through the muck truck and transports the waste residue of the filter press out of slurry treatment plant. Due to the formation properties, sedimentation tank capacity,

Figure 4. The plate pressure filtration equipment.

separation equipment efficiency and filter press equipment efficiency of various factors, including the time spent repairing the filter press trolley, the time spent by the construction personnel cleaning the filter cloth, the time spent repairing the slurry pump, and the time taken to reduce the liquid level of the sedimentation tank, resulting in mud viscosity cause high specific gravity and sedimentation pools level, which affect slurry treatment efficiency and limit the efficiency of shield tunneling. The stratum geology is a natural attribute that cannot be changed. The capacity of the sedimentation pools need to expand the construction land to build a sedimentation pool with a larger capacity. The efficiency of the separation equipment need to be improved by increasing the separation equipment, but the separation equipment occupies a larger area. The construction land needs to be expanded to build a larger separation equipment foundation, and the expansion of the capacity of the sedimentation pools and the improvement of the efficiency of the separation equipment are difficult to achieve.

The capacity of the sedimentation pools on the left line of slurry treatment plant is 1,500 cubic meters, and the capacity of the adjusting pool is 2,000 cubic meters. The shield machine adds 550-750 cubic meters slurry and 350-360 cubic meters muck per ring, with a total of 900-1110 cubic meters per ring. There are 3 sets of the separation equipment, each set sieves 50-150 cubic meters slurry per ring. There are 8 filter press equipment, each of which processes about 16 cubic meters slurry per hour, totaling about 3,000 cubic meters. According to the analysis and calculation of the slurry and muck treatment in the excavation, it can be obtained that 3.3 rings can be excavated normally per day and 6 rings can be excavated on site. The slurry treatment efficiency at the construction site is low, which is far from meeting the excavation needs. Considering the lack of pressure filtration efficiency on the left line, three new plate pressure filtration equipment were added to the right line, each of which processed 40 cubic meters muck per hour, with a total of 2,880 square meters muck. At the same time, two new centrifuge equipment were added, each of which processed 40-50 cubic meters per hour,

totaling 1920-2400 cubic meters, and processed an average of 2160 cubic meters of muck per day. According to the analysis and calculation of the treatment of mud and muck and waste slurry in the excavation, it can be obtained that 5.6 rings can be excavated normally per day, and 6 rings can be excavated on site, which can basically meet the needs of excavation. In summary, based on the analysis of the left and right lines, it can be concluded that a total of about 9 rings of normal excavation can be carried out daily. If the number exceeds 9 rings, the muck can only be disposed of by slurry trucks. According to the on-site construction situation, it is difficult to improve the efficiency of slurry treatment on the left line by increasing personnel, equipment and physical methods. At the same time, the efficiency of slurry treatment on the right line still needs to be improved. Chemical methods can be used to improve the efficiency of pressure filtration equipment and slurry treatment.

In response to this situation, the construction site mainly improves the efficiency of slurry treatment by improving the efficiency of pressure filtration equipment and adopts the following methods. (1) adding a slurry pump in the 3 stage sedimentation pool to extract muck to the slurry trucks for slurry treatment, but it does not solve the root cause and has low economic benefits. (2) Adding 2‰ solid calcium oxide (as shown in Figure 5) to the making pool react with the slurry pumped from the 8 stage sedimentation pool to the making pool through an emergency slurry pump to improve the efficiency of the pressure filtration equipment. The calcium oxide undergoes a chemical reaction to release heat, generate calcium hydroxide, and consume the water in the slurry, achieving the goal of reducing viscosity and improving fluidity. At the same time, the calcium oxide increase the concentration of calcium ions and improve the slurry performance at the micro level. However, in order to ensure solid calcium oxide can undergo sufficient chemical reactions to achieve good results, this method can only add a smaller amount of calcium oxide, which will cause a little of slurry treated. (3) An external liquid preparation tank is set up next to the sedimentation pools to prepare about 2‰ calcium hydroxide solution, as shown in Figure 6. It is pumped to the making pool to fully blend with the solid calcium oxide and slurry mixture in the making pool. It should be noted that due to the presence of a large amount of carbon dioxide in the air, the calcium carbonate precipitation often occurs in the external liquid preparation tank. After adopting the methods mentioned in (2) and (3) above, the efficiency of the pressure filtration equipment will be improved to a certain extent. The construction site mainly adopts the method of (1) for slurry treatment, which can basically ensure the slurry circulation during conventional diameter shield tunneling, but it is obviously insufficient for extra-large diameter slurry shield tunneling.

Figure 5. 2‰ solid calcium oxide.

Figure 6. 2‰ calcium hydroxide solution.

5 EXPERIMENT

5.1 *Preparation*

According to slurry treatment construction site and the research status of scholars at home and abroad, a simple slurry treatment experiment was carried out for slurry treatment with high slurry gravity in Zhuhai tunnel project and the effect of different additives on slurry treatment was preliminarily analyzed. Yixin Chen et al. found that the version of plain soil was mud-like, which changed when pinched by hand and could not be compacted. After the silty soil was mixed with calcium oxide, the soil changed from lumpy to scattered. With the increase of calcium oxide content, the soil was more and more easy to crush, which also indicated that the improved soil was more and more easy to be compacted under the external force. From the macroscopic viscosity change, it can be seen that the mixed calcium oxide is conducive to the agglomeration and discretization of natural soil and the viscosity is greatly reduced. Min et al. found that through the study of slurry analysis of ζ potential, pore characteristics of filter cake and microstructure of filter cake indicates that the slurry prepared from water has a high ζ potential, less cations attracted to slurry particles, more water molecules, and thicker bound water film. At the same time, the electric repulsion between particles in the slurry is greater, making the particle dispersion more uniform. The thicker the bound water film and

the more dispersed the particles increase the distance between particles and aggregates in the filter cake. Based on comprehensive data analysis, it can be concluded that the total pore volume of water filter cake is relatively large, mainly composed of pores inside the filter cake. Low pore connectivity leads to less effective pores in the filter cake formed by seawater slurry than pores. The pores in the aggregated body, including bound water and free water, are blocked by a thick water film, which reduces the effective porosity and leads to high water content, high porosity and low permeability of the filter cake. For slurry prepared with different proportions of seawater, adding a large amount of cations to the slurry will reduce ζ potential. The repulsive force between particles weakens, and particles aggregate into a large number of aggregates. Due to a large number of cations adsorbed on the slurry particles surface, the number of adsorbed free water molecules decreased, which results in a relatively thin bound water membrane. Under the influence of pressure, particles in the aggregate become tightly packed. The pore size of the filter cake is small, mainly composed of pores between aggregates, with good connectivity. The thinner the water film, the fewer times the waterway is blocked. The effective porosity of the filter cake produced by seawater containing slurry is greater than that formed by the slurry prepared from water. As the seawater content increases, the permeability coefficient of the obtained filter cake also increases. The research results indicate that when the seawater content in the mud is less than 50%, filter cakes with permeable zones are formed. When the seawater content in the mud exceeds 50%, only filter cake is formed. As the seawater content in the mud increases, the thickness and permeability of the filter cake increase, while the water content and porosity decrease.

The strata in the LK0+872~LK2+918 section of the Zhuhai tunnel project are mainly composed of silty clay, which has strong slurry making ability and high mud slurry density and viscosity. Due to the poor economic efficiency of using slurry trucks to dispose, this experimental study mainly improves the efficiency of slurry treatment from two aspects including directing treatment through sedimentation and improving the efficiency of pressure filtration equipment. This experiment is based on on-site additive materials, using additives including seawater and calcium oxide. Seawater is mainly used for direct treatment through sedimentation, while calcium oxide is mainly used to improve the efficiency of pressure filtration equipment, with a focus on the study of calcium oxide additives.

5.2 *Working conditions*

According to the research of Yixin Chen et al. and Min et al., considering the slurry treatment situation of the pressure filtration equipment in the Zhuhai tunnel project, the optimal concentration of 6% calcium oxide is proposed. During the experiment, it is necessary to ensure that the temperature of each working condition is consistent. Based on the actual situation of the construction site, the slurry treatment work should be completed in a short period of time, mainly studying the mud situation of each working condition at 2 and 24 hours. Working conditions 1-8 are the slurry treated by the separation equipment at the outlet, as shown in Figure 7(a)-(h), with the slurry density of 1.41g/cm^3 during the experiment. The experimental conditions can be divided into four groups. The first group consists of conditions 1 and 2 to study the slurry treatment capacity of solid calcium oxide. The second group consists of conditions 3 and 4 to study the slurry treatment capacity of calcium hydroxide solution with different solvents. The third group consists of conditions 5 and 6 to study the sludge water treatment capacity under the sole action of excess solvents. The fourth group consists of conditions 7 and 8 to study the slurry treatment capacity under the action of excess calcium hydroxide solution. Working conditions 9-16 are the inlet mud of the adjustment pool, with the slurry density of 1.34g/cm^3. The experiment was operated in the same way and with the same purpose to study the effect of slurry density on slurry treatment. A total of 16 different working conditions were set up for the slurry treatment experiment, as shown in Table 2.

Table 2. Different working conditions experiment.

Working conditions	Slurry	Additions
1	Slurry at the outlet (100g, slurry density 1.41g/cm^3)	None
2		6%calcium oxide(6g)
3		6%calcium oxide(6g) and 6%water(6g)
4		6%calcium oxide(6g) and 6%seawater(6g)
5		50%water(50g)
6		50%seawater(50g)
7		6%calcium oxide(6g) and 50%water(50g)
8		6%calcium oxide(6g) and 50%seawater(50g)
9	Slurry at the inlet (100g, slurry density 1.34g/cm^3)	None
10		6%calcium oxide(6g)
11		6%calcium oxide(6g) and 6%water(6g)
12		6%calcium oxide(6g) and 6%seawater(6g)
13		50%water(50g)
14		50%seawater(50g)
15		6%calcium oxide(6g) and 50%water(50g)
16		6%calcium oxide(6g) and 50%seawater(50g)

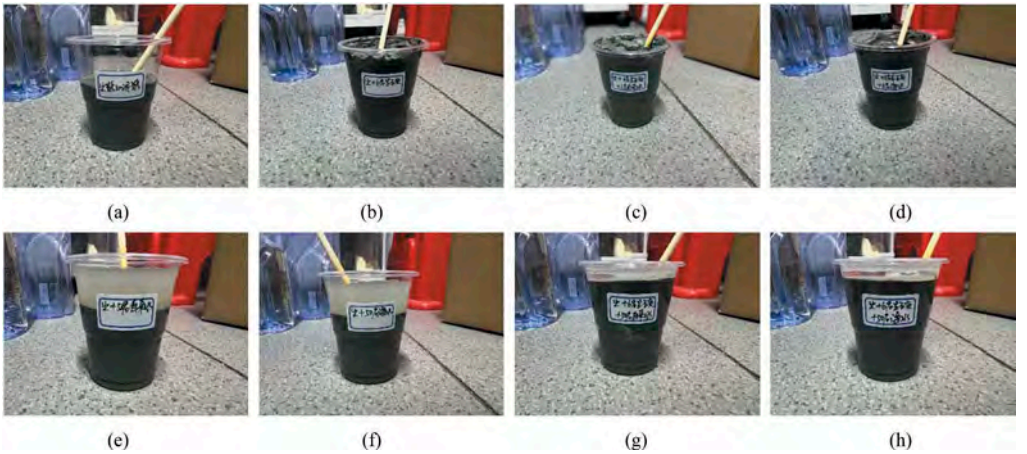

Figure 7. Field experiment diagram of working conditions 1-8.

5.3 *Results*

Under the same indoor temperature, different observations and mixing results were obtained for operating conditions 1-8 and 9-16 for 2 hours and 24 hours. Compared to working condition 1, working condition 2 has lower mud density and viscosity. Working condition 1 is the basic operating condition of operating condition 1-8 and operating condition 9-16 is the basic operating condition of operating condition 2, as shown in Table 3 and Table 4. From the comparison of the 2 hours and 24 hours stirring conditions recorded in Tables 3 and 4 above, it was found that there was little change by stirring observed in working conditions 1-8. The main difference was that the grainy increased in working conditions 7 and 8. The reason for this situation may be due to the reaction between calcium hydroxide solution and carbon dioxide in the air, which generated calcium carbonate precipitation. There is not much change in the mixing situation observed during the 2 hours and 24 hours of working conditions 9-16. The main difference is that there is a slight layering of the slurry in working condition 1, indicating that layering may occur under the static condition of low mud density slurry in the Zhuhai tunnel project and this situation is likely related to the geological properties of muddy silty clay. The grainy increased in working conditions 15 and 16, which may be due to the reaction between calcium hydroxide solution and carbon dioxide in the air, resulting in the precipitation of calcium carbonate. Observing the stirring situation at 2 hours and 24 hours under operating conditions 1-16 indicates that the reaction between additives and slurry is basically completed within 2 hours and the sedimentation and layering state is relatively stable. The states of low slurry density and high slurry density under the same additive conditions are basically similar, mainly analyzing working conditions 1-8. In the first set of working conditions, condition 2 has the strongest resistance and the highest viscosity at this time, which can cause pump jamming and pipe blockage. At the same time, the construction personnel cleaning the filter cloth for a longer time is not conducive to improving the efficiency of the pressure filtration equipment. In the second set of working conditions, condition 3 is similar to condition 4, with stronger resistance and higher viscosity at this time. This may be due to the proximity of the muddy silty clay in this project to the sea, resulting in its pore water already containing seawater components for experimenting. In the third set of experimental conditions, condition 5 is similar to condition 6. The effect of excessive solvent will greatly reduce the specific gravity and viscosity of the mud. Due to the fact that the pressure filtration equipment mainly relies on the slurry pump to pressurize the mud, excessive solvent will cause the slurry pump to have to be transported multiple times, resulting in a heavier load and reduced service life of the parts. This can easily form a “sandwich” situation of the filter cake, which is not conducive to improving the efficiency of the pressure filtration equipment. In the fourth set of experimental conditions, condition 7 is similar to condition 8. At this time, due to the presence of more solvents and solutes, more additional slurry needs to be treated after reacting with the slurry, increasing the load of the slurry pump. However, the slurry at this time meets the requirements for storage in the concentration tank, with good fluidity, high bottom density and viscosity and certain grainy, indicating a decrease in the density and viscosity of the bottom slurry during the mixing process. Based on the actual situation on construction site, it is ideal to add 6% calcium oxide and 50% seawater to the slurry outlet in the concentration tank under condition 8.

Based on the above experimental results, working condition 8 with 6% calcium oxide and 50% seawater added to the slurry outlet and working condition 16 with 6% calcium oxide and 50% seawater added to the slurry inlet are more ideal. This improves the

flowability while slightly increasing the specific gravity and viscosity of the bottom mud, in order to improve the efficiency of pressure filtration.

5.4 *Polymer mud treatment experiment*

Many scholars have found that polymers have a good effect on slurry treatment. In response to the current situation of this project, it has been decided to use 2‰ white powder agent PAM to flocculate the slurry in the concentration tank. After using PAM for slurry treatment, it was found that the effect was not ideal and the efficiency of the pressure filtration equipment was not significantly improved. Therefore, it was decided to add a mixed agent of 2‰ white powder agent PAM and 2‰ yellow powder agent PAC for flocculation. The efficiency of the pressure filtration equipment has been improved to a certain extent, but PAM and PAC flocculation are prone to pump jamming and pipe blockage, resulting in reduced service life of the slurry pump partsc and connection pipeline between the slurry pump and the pressure filtration equipment taking a long time to clear. In order to find suitable reagents to improve the efficiency of the pressure filtration equipment, solidification agent experiments and coating agent (polymer formed by copolymerization of propylene derivatives with different functional groups) treatment experiments were carried out. The experiments found that the solidification agent did not have an ideal effect on mud water treatment, and the coating agentsolution has an ideal effect on mud water treatment, as shown in Figure 8. However, the dosage of the coating agent solution needed to reach concentration of 20%. Considering the actual situation, the concentration tank capacity is not enough to use 20% concentration of coating agent, And the high price of the coating agent leads to lower economic benefits.

Figure 8. Coating agent treatment.

6 CONCLUSIONS

In this project, the slurry making slurry ability is strong and the slurry at the slurry outlet has high density and viscosity. However, the slurry treatment ability is weak. If the main reliance is on slurry trucks to dispose, it will lead to extremely low economic benefits. In response to this situation, construction site experiments were conducted to study ways to improve the efficiency of slurry treatment by using different additives to improve the efficiency of pressure filtration equipment. The main conclusions of the experimental research are as follows: (1) Firstly, the strata of the extra-large diameter slurry

Table 3. Observation of mixing conditions under working conditions 1-8 after standing for 2 hours and 24 hours.

	2h		24h	
Working conditions	Observe conditions	Mixing conditions	Observe conditions	Mixing conditions
1	No change	Resistance	No change	Resistance
2	Increased, wall adhesion	Strongest resistance	Increased, Highest Viscosity	Strongest resistance
3	Increased, wall adhesion	Stronger resistance	Increased, Highest Viscosity	Stronger resistance
4	Increased, wall adhesion	Stronger resistance	Increased, Higher Viscosity	Stronger resistance
5	No change, stratification, turbidity suspension	Resistance to weaker resistance	No change, stratification, turbidity suspension	Resistance to weak resistance
6	No change, stratification, turbidity suspension	Resistance to weaker resistance	No change, stratification, turbidity suspension	Resistance to weak resistance
7	Significant increased, slight stratification, clear suspension	Weak resistance, uneven resistance, bottom strong resistance, grainy	Significant increased, slight stratification, clear suspension	Weak resistance, uneven resistance, bottom stronger resistance, strong grainy
8	Significant increased, slight stratification, clear suspension	Weak resistance, uneven resistance, bottom stronger resistance, strong grainy	Significant increased, slight stratification, clear suspension	Weak resistance, uneven resistance, bottom strong resistance, stronger grainy

Table 4. Observation of mixing conditions under working conditions 9-16 after standing for 2 hours and 24 hours.

	2h		24h	
Working conditions	Observe conditions	Mixing conditions	Observe conditions	Mixing conditions
9	No change	Weak resistance	slight stratification	Weak resistance
10	Increased, wall adhesion	Stronger resistance	Increased, Higher Viscosity	Stronger resistance
11	Increased, wall adhesion	Strong resistance	Increased, Higher Viscosity	Strong resistance
12	Increased, wall adhesion	Strong resistance	Increased, High Viscosity	Strong resistance
13	No change, stratification, turbidity suspension	Weak resistance to Weakest	No change, stratification, turbidity suspension	Weak resistance to weakest resistance
14	Significant increased, slight stratification, clear suspension	Weak resistance to Weakest	No change, stratification, turbidity suspension	Weak resistance to weakest resistance
15	Significant increased, slight stratification, clear suspension	Weak resistance, uneven resistance, bottom stronger resistance, grainy	Significant increased, slight stratification, clear suspension	Weaker resistance, uneven resistance, bottom strong resistance, strong grainy
16	Significant increased, slight stratification, clear suspension	Weak resistance, uneven resistance, bottom strong resistance, strong grainy	Significant increased, slight stratification, clear suspension	Weaker resistance, uneven resistance, bottom resistance, stronger grainy

balance shield machine in this site is mainly composed of muddy silty clay, which contains high levels of powdery particles, causing significant losses to the slurry treatment equipment. Therefore, attention should be paid to the maintenance of equipment parts during slurry treatment, reducing their failure rate and extending their service life, which helps to improve the efficiency of slurry treatment. (2) Based on the actual needs and on-site treating conditions, a large amount of slurry is formed by extra-large diameter slurry shield tunnelling. Experimental research was conducted on the different concentrations combination of water, seawater and calcium oxide additives for muddy silty clay stratum. The results showed that the use of seawater has a good promoting effect on mud water treatment. On the other hand, in response to the current situation where the addition of low amounts of calcium oxide is insufficient to digest the slurry treatment requirements by increasing the amount of calcium oxide added and conducting group experiments. In order to improve the efficiency of the pressure filtration equipment and achieve the goal of treating a large amount of slurry, 6% calcium oxide and 50% seawater were determined to improve the slurry fluidity while slightly increasing the density and viscosity of the bottom slurry. (3)The theory of how the polymer formed by the additives combination in this project can promote the slurry treatment still needs further research. The this project experimental results can provide reference for the slurry treatment of extra-large diameter slurry balance shield tunneling method in muddy silty clay stratum and soft soil strata.

REFERENCES

Weibin Zhu, Shijian Ju, Hui Wang, 2020. Shield tunneling construction technology in composite strata (new version). Construction Industry Press, Beijing, China, pp. 171–181.

Yixin Chen, Baotian Wang, Yongqi Zhang, et al, 2014. Experimental study on lime improved muddy soil. Science and Technology and Engineering, 14 (34), 273–277

Lihua Zhang, Zhaoping Fan, 2013. Experimental study on lime fly ash improvement of high water content dredged sludge. Journal of Nanjing University of Technology (Natural Science Edition), 35 (01), 91–95

Zhao S, Li S, Wan Z, et al, 2021. Dispersant for reducing mud cakes of slurry shield tunnel tunneling machine in sticky ground. Advances in Materials Science and Engineering, 2021, 1–10.

Wan Z, Li S, Yuan C, et al, 2021. Soil conditioning for EPB shield tunneling in silty clay and weathered mudstone. International Journal of Geomechanics, 21 (9), 06021020.

Zumsteg R, Puzrin AM, Anagnostou G, 2016. Effects of slurry on stickiness of excavated clays and clogging of equipment in fluid supported excavations. Tunnelling and Underground Space Technology, 58, 197–208.

Min F, Du J, Zhang N, et al, 2019. Experimental study on property change of slurry and filter cake of slurry shield under seawater intrusion. Tunnelling and Underground Space Technology, 88, 290–299.

Zumsteg R, Puzrin A M, 2012. Stickiness and adhesion of conditioned clay pastes. Tunnelling and Underground Space Technology, 31, 86–96.

Yang W, Zhou F, Zhu R, et al, 2022. Strength performance of mucky silty clay modified using early-age fly ash-based curing agent[J]. Case Studies in Construction Materials, 17, e01595.

Tunnelling for a Better Life – Yan, Celestino, Thewes & Eberhardt (Eds)
© 2024 The Author(s), ISBN 978-1-032-80042-4
Open Access: www.taylorfrancis.com, CC BY-NC-ND 4.0 license

Field monitoring and numerical modelling of ground heaves due to shield tunnelling in soft ground conditions

Ochok Duangsano* & Arthit Chayaroon
Geotechnical & Foundation Engineering Co., Ltd, Bangkok, Thailand

Phatharaphong Yensri
University of Birmingham, Birmingham, UK

Auttakit Asanprakit
Geotechnical & Foundation Engineering Co., Ltd, Bangkok, Thailand

Noppadol Phienwej
Asian Institute Technology, Bangkok, Thailand

ABSTRACT: The main challenge of implementing and constructing a new tunnel in urban areas is to control and mitigate excessive ground surface disturbances. In general, ground surface settlements due to tunnel construction in soft ground conditions can be expected. According to detailed geotechnical monitoring results of the MRT Orange Line Project in Bangkok, significant ground heaves were observed during and after the passing of shield machines at shallow depth. This paper aims to reports unusual ground movements which developed when earth pressure balance shield machines were employed to excavate twin tunnels in the soft clay layers. A numerical simulation using a three-dimensional finite element method was also established to simulate the tunnelling process based on the operating parameters and in order to investigate the ground responses in this regard. Based on this finding, it can be seen that the computed results are presented in the same trend compared to the field measured data

Keywords: Tunnelling, Shield machines, Soft clay, Ground heaves

1 INTRODUCTION

Shield tunnelling method has been widely utilised in the construction of subway tunnels in urban areas. Excessive ground movements that may encounter during the construction should be strictly controlled to minimise the impacts on adjacent structures e.g. buildings, structures and utilities (Duangsano et al, 2023). These generally depend on several factors e.g. geological and geotechnical conditions, tunnel geometry, tunnel depth, and quality of workmanship and management (ITA/AITES, 2007).

Tunnelling in soft ground conditions with a shallow overburden may face the risk of instability due to ground heave and blowout (Bezuijen and Brassinga, 2015; Vu and Broere, 2023). In practice, the face pressure is a support pressure to balance the soil and water pressures. If it is not sufficient to resist against the surrounding pressures, active failure (collapse) is likely to occur. On the other hand, blow-out, also referred to as passive failure, and appears if the applied pressure is high enough to push the soil towards the ground surface (Vu et al., 2015). In addition, tail void grouting pressure is commonly high enough to guarantee the flow of grout material and to resist the ground moving into the gap between a shield and tunnel lining.

According to the construction of MRT Orange Line (East Section) Project in Bangkok, Thailand, twin bored tunnels were excavated and constructed in soft clay layers with shallow overburden. The soil cover from ground surface level to the tunnel crown is 6.6 m approximately which is equivalent to one time tunnel diameter (1D). During the excavation, foam and pressurized air travelled to the surface. In addition, significant ground heaves and blow-out were observed as presented in Figure 1.

This paper aims to present the responses of ground heaves and blow-out for due to tunnel excavation in soft clay layers in associated with operating pressures

*Corresponding author: ochok_d@gfe.co.th

DOI: 10.1201/9781003495505-235

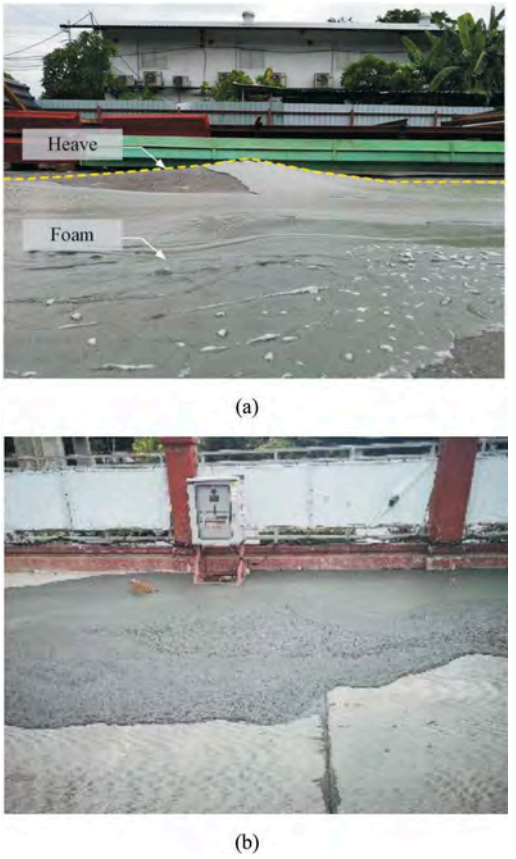

Figure 1. Ground heave and blow-out cases in MRT Orange Line Project; (a) first tunnel, (b) second tunnel.

of shield machines. In addition, a numerical computation is performed in order to investigate and compare the results with the field data.

2 PROJECT DESCRIPTION

Mass Rapid Transit Authority of Thailand (MRTA) has officially implemented the MRT Orange Line (East Section) Project to complete the mass railway system network. The project consists of both an underground and elevated structures within an approximate distance of 22.57 km. The underground section is divided into three contracts. The contents reported in this article focus for the design and construction of contract E1.

Twin tunnels of Westbound (WB) tunnel and Eastbound (EB) tunnel were utilized along the tunnel alignment. Since tunnels had to be initially commenced from the MRTA station (launching station), the observation test section was established to preliminary investigate the performance of Tunnel Boring Machine (TBM) and ground responses during the tunnelling process as shown in Figure 2. In this part of the initial drive, it was also used for trial and error in applying an optimum balance mode that resulted the acceptable ground settlement.

2.1 *Geological conditions*

Bangkok subsoil is relatively uniform throughout the entire area. The uppermost 2.0 m thick layer is the fill material, which is underlain by 6.0-15.0 m thick of soft clay layer. A medium clay layer is found at the depth of approximately 8.0 m from the surface. Below the medium clay is stiff clay; the thickness is about 4.0--15.0 m. The first sand layer is generally found at a depth of 25 to 30 m. The piezometric pressure head construction was observed at about 13 m below the ground surface during the construction.

The WB tunnel was excavated at the depth below the ground surface between 6.55 m and 8.12 m, while the elevation of the EB tunnel was 6.55 m throughout the soft soil conditions of the soft clay and medium

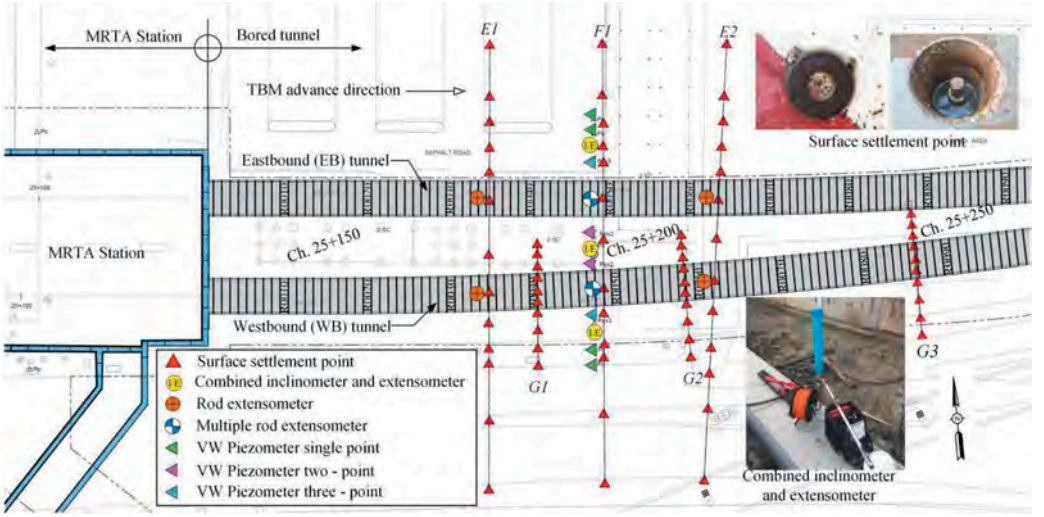

Figure 2. Plan view on the construction site at the observation test section.

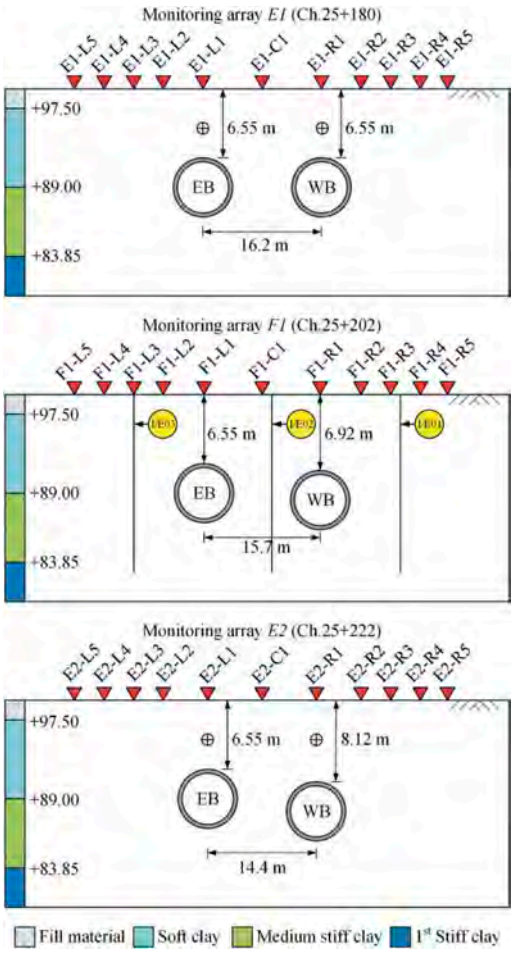

Figure 3. Layout of geotechnical instruments.

stiff clay layers. A center-to-center distance between twin tunnels varied from 16.2 m to 14.4 m at this area.

2.2 *Instrumentation and monitoring*

Instrumentation and monitoring system plays an important role in underground construction activities (Kong, 2003). Several geotechnical instruments were intensively installed to observe the potential ground responses along this area. Instrumentation layouts associated with tunnel positions and geological condition are illustrated in Figure 3.

Three main arrays of typical monitoring sections (E1, F1 and E2) were set to entirely cover the side-by-side twin tunnels. Each array consisted of 11 settlement markers located on the ground surface level to directly measure ground movements in the vertical direction. To capture the development of ground movements in the horizontal direction to the shield advances, there were three sets of combined inclinometer and extensometer were installed at section array F1. Three additional arrays of G1, G2 and G3 positioned in a part of WB tunnel alignment, were also proposed to observe ground surface settlement.

It is noted that particular attention in this article is paid to the surface settlements and lateral ground deformations induced by the tunnelling during the construction.

3 CONSTRUCTION OVERVIEW

3.1 *Tunnel construction*

Three Earth Pressure Balance (EPB) shield machines were employed to excavate and construct tunnel lining in this project. The main principle of the EPB shield machines is to control the stability of tunnel face by monitoring and adjusting the pressure inside the chamber to achieve a balance pressure (Suwansawat, 2002). Tail void grouting is injected simultaneously to fill the void between the TBM and tunnel lining. The shield machine has 6.58 m diameter and 9.615 m length. The main component of the EPB shield machine is illustrated in Figure 4.

A precast reinforced concrete of segmental tunnel lining was employed for twin bored tunnels. The internal diameter of the tunnel is 5.7 m. The thickness is designed to be 0.3 m and the segment length of 1.4 m is adopted. Each ring of tunnel lining consisted of five segments plus one key segment (5+1 configuration).

According to the construction plan, TBM no.1 was firstly used to excavate the WB tunnel from the MRTA station. Subsequently, TBM no.2 was operated for the construction of EB tunnel from the same station to the next station. The lagging distance between two shield machines along the tunnel alignment was more than 500 m.

Prior to the commencement of construction, target face pressures, tail void grouting pressures and other relevant parameters were entirely estimated along the tunnel route. During the early stage of tunnelling or also known as the initial drive, a number of data were recorded to observe the performance and control the quality for further excavation process (referred to the learning curve). The face pressure can be monitored using six pressure cells installed inside the earth chamber, whereas the injection of primary grouting pressure was measured by a pressure cell installed inside the shield machine.

3.2 *Shield operating parameters*

Face pressures and tail void grouting pressures monitored from the excavation of TBM no.1 are illustrated in Figure 5. The face pressure at tunnel axis of which 180 kPa was maintained throughout the monitoring area. Meanwhile, a fluctuation of the primary grouting pressure was recorded, ranging between 175 kPa and 220 kPa with an average pressure of around 195 kPa.

Furthermore, the actual face pressures at tunnel axis for excavation of the EB tunnel by TBM no.2

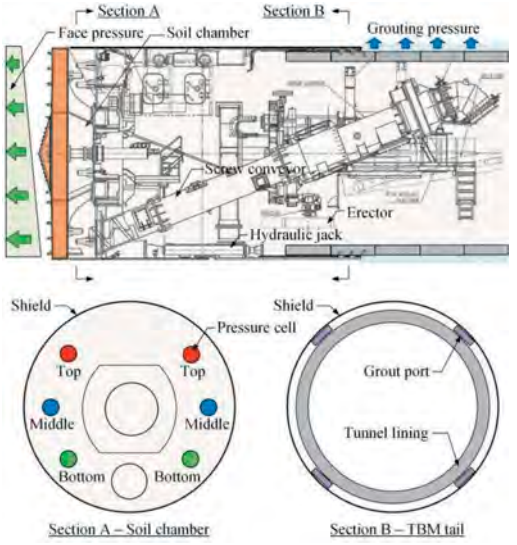

Figure 4. Shield machine component.

was typically operated with an average value of 160 kPa, being lower than that of TBM no.1. The tail void grouting pressure was measured at approximately 180 kPa. The shield parameters obtained from TBM no.2 are revealed in Figure 6.

Apparently, along the observational section, the face pressures and tail void grouting pressures applied for the construction of twin tunnels were significantly higher than the overburden soil pressure.

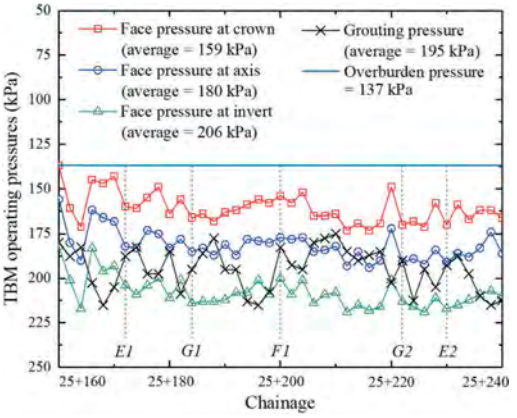

Figure 5. Recorded parameters of TBM no.1.

4 GROUND HEAVES

Due to large support pressures, an instability caused by a blow-out occurred during tunnel excavation at this location. To investigate the relationships between the ground responses and the advancement of the shield machines, maximum ground movements along each tunnel alignment are plotted

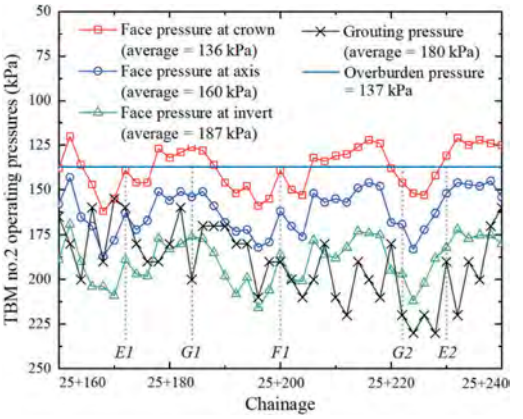

Figure 6. Recorded parameters of TBM no.2.

against the various positions of shield face. It should be noted that ground behaviour is considered affected by the process of tunnel excavation by shield machines only (i.e. before, during and immediately after shield passing) not by consolidation settlements (i.e. long term settlement).

4.1 *WB tunnel – 1st tunnel excavation*

Figure 7 presents longitudinal ground surface movements for six recording points measured in different distances from tunnel face induced by TBM no.1. It can be noticed that when the shield approached array E1 and G1, the ground surface experienced a small heave. However, it largely increased to almost 25 mm after the shield passing and reaching array F1. Obviously, ground heave continued to gradually rise, particularly monitoring point F1-R1 when the face of the shield was positioned at array G2. Array G3 was the last array at this section, ground deformation was still observed to move upward before and after shield passing. Based on the recorded data, the occurrence of ground heave appeared when the face of the TBM approaching, and it could be inferred that a higher ground heave was indicated during the primary grouting process.

4.2 *EB tunnel – 2nd tunnel excavation*

Surface heave was also recorded along the excavation route of the TBM no. 2 as shown in Figure 8. The development of upward ground displacement was observed, although the shield was operated and controlled at lower support pressures compared to the TBM no.1. Similarly, ground heave occurred more than 5 mm when the face of shield machine was approaching the monitoring point F1-L1. Moreover, there was a noticeable increase by almost 10 mm after the shield passing. In comparison, the recorded ground heave induced by the advancement of TBM no.2 was relatively smaller than that of the first tunnel excavation.

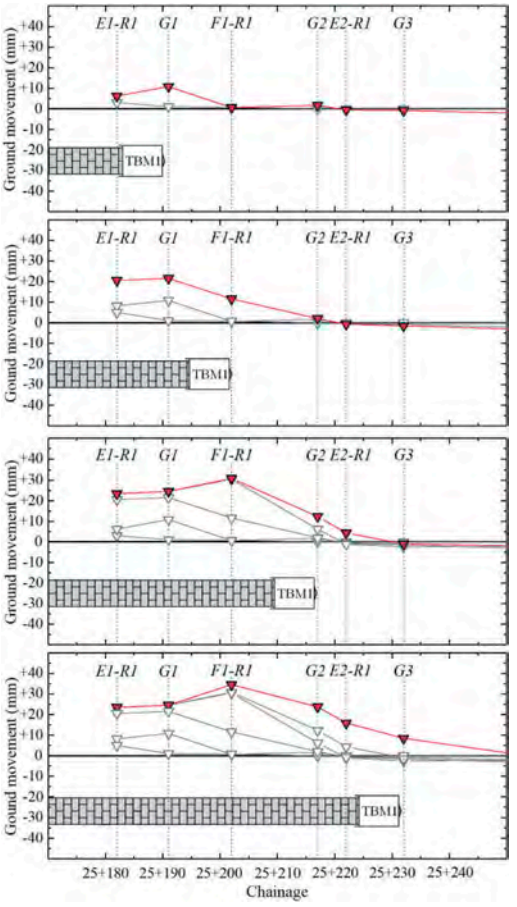

Figure 7. Longitudinal heave induced by TBM no.1.

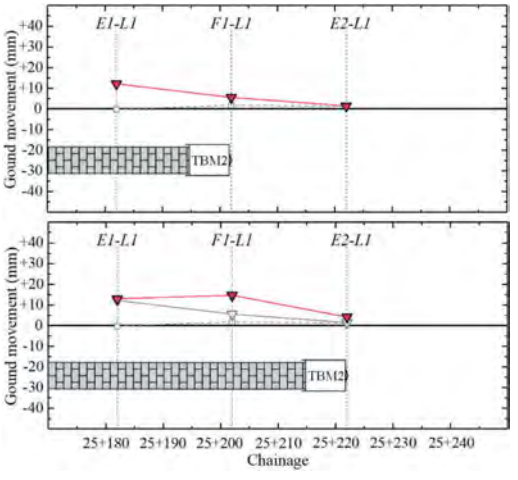

Figure 8. Longitudinal heave induced by TBM no.2.

5 NUMERICAL SIMULATIONS

5.1 *Numerical models*

A three-dimensional finite element analysis is employed to investigate the effects of TBMs excavation in a shallow section associated with face pressures and grouting pressures on ground surface settlements and ground lateral movements. To simulate the staged construction process and ground responses, finite element (FE) code PLAXIS3D is utilized. The 3D FE-model is set up with dimensions of 120 m long in x-direction, 100 m wide in y-direction and 50 m deep in z-direction. The discretization with a total number of 174,786 elements and the geometrical configuration of numerical simulation are illustrated in Figure 7.

It is should be pointed that this study is principally focused on the influence of soil movements due to tunnelling by EPB techniques, therefore, an advancement of the twin tunnels is simulated according to the step-by-step approach (Do et al., 2014; Do and Dias, 2017), with an advance rate of 1.4 m in each step (equal to the tunnel lining width). The simulation of TBM advancement is illustrated in Figure 8.

In the numerical simulation, the face pressures acting on the face from the shield machine at axes of the first tunnel and the second tunnel are applied as 180 kPa and 160 kPa, respectively. These pressures are modelled by considering a pressure distribution with a linear increase along with the depth by assuming as a trapezoidal profile to account for the increment of the pressure in the chamber based on the recorded data.

The tail void grouting pressure is simulated by applying a radial pressure perpendicular to the soil around the tunnel following the measured data. In the FE simulation, the values of grouting pressure are chosen as 194 kPa and 184 kPa applied for the first and second tunnels, respectively. These values are defined according to the average grouting pressures during the excavation in the observation test section. The tunnel lining is subsequently applied after TBM excavation. Both structures of TBM and tunnel lining are simulated by plate element. Material properties considered in the modelling are given in Table 1.

The excavation sequences for the twin tunnels are modelled as follows: the WB tunnel is excavated first, and then the EB tunnel is advanced following with a certain lagging distance behind the face of the WB tunnel. Thus, in the analysis model the first tunnel is driven and constructed through the boundary before the initial driving of the second tunnel is simulated.

Table 1. Material properties of TBM and tunnel lining.

Properties	TBM	Tunnel Lining
Elastic modulus, E (kN/m^2)	200E+6	26.4E+6
Poisson's ratio, ν (-)	0.30	0.20
Unit weight,γ (kN/m^3)	75	24.5

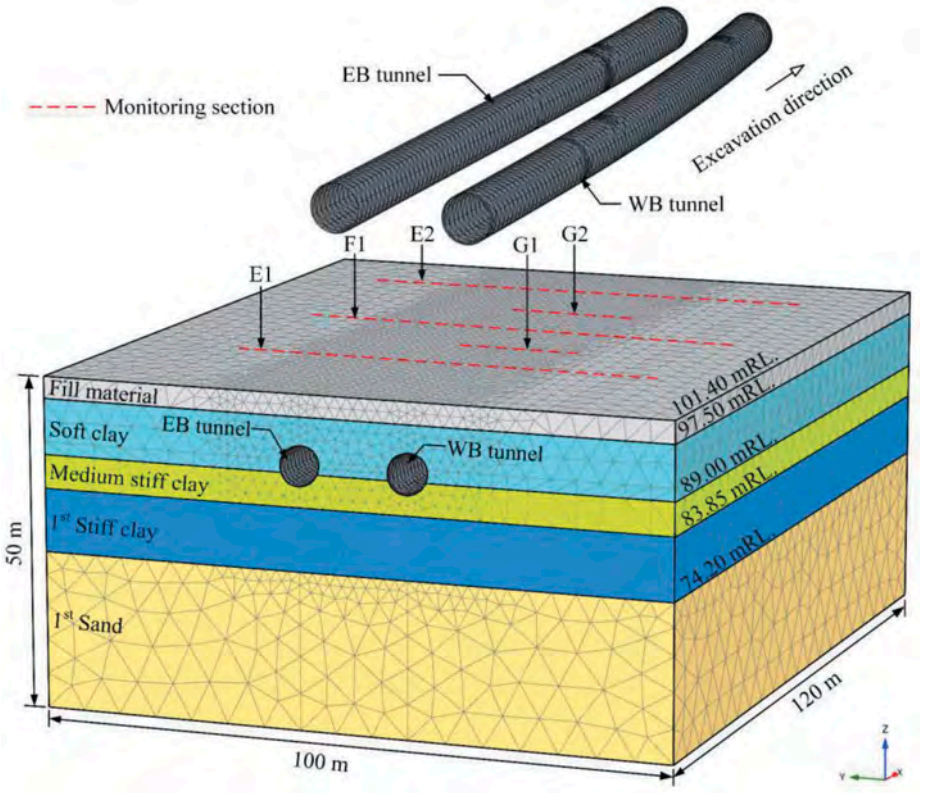

Figure 9. Geometry and finite element mesh of 3D model.

The soil is modelled using solid elements. A linear elastic, perfectly plastic Mohr-Coulomb constitutive model with non-associated flow rule is employed. Geotechnical design parameters are taken based on Geotechnical Interpretative Report (GIR) of the project as summarised in Table 2.

5.2 *Numerical results and comparisons*

This section presents the behaviours of ground movements in vertical and lateral directions during the excavation of the twin tunnels. In addition, a comprehensive comparison is made between ground movement induced by the EPB shield machines from the measured field data and the simulation results from the FE analysis. One typical monitoring array F1 is selected as a representative to present and analyse the developments of ground deformations induced by tunnel construction.

5.2.1 *Ground surface movements*

Figure 11 illustrates the development of the ground surface displacements in the transvers direction of the monitoring array F1, caused by the excavation of the WB tunnel and EB tunnel.

According to the measured field data as presented in Figure 11 (a), the response of ground surface

Table 2. Geotechnical parameters.

Soil type	SPT N-Value	γ_t (kN/m^3)	S_u (kN/m^2)	ϕ' (°)	E'_{ref} (kN/m^2)	E'_{inc} (kN/m^2)	ν (-)	k_0 (-)
Fill material	5 ± 3	18.5	25	-	8,500	-	0.3	0.60
Soft clay	-	15.5	15 – 25	-	3,750	500	0.3	0.75
Medium stiff clay	-	17.0	30 – 35	-	10,000	750	0.3	0.75
1st Stiff clay	35 ± 31	19.0	55 – 120	-	25,000	1,250	0.3	0.70
1st Sand	45 ± 38	21.0	-	35	100,000		0.3	0.43

where γ_t is unit weight, S_u is undrained shear strength, ϕ' is effective friction angle, E'_{ref} is Young's modulus at reference point, E'_{inc} is incremental Young's modulus, ν is Poisson's ratio, and k_0 is coefficient of horizontal pressure

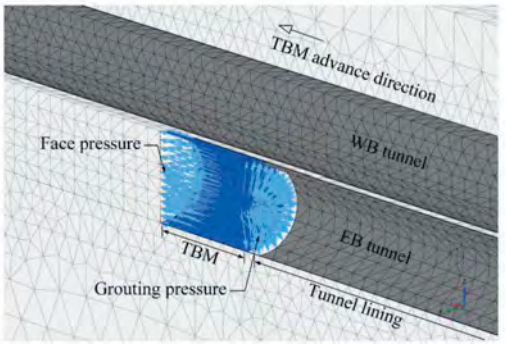

Figure 10. Simulation of TBM advancement.

tended to immediately move upward during the face approaching the observed section, an approximated value of 12.5 mm was recorded. Then, the ground deformation dramatically increased to around 30 mm above the tunnel centerline when the tail of the shield was positioned at the monitoring section. After the shield passing, the maximum value experienced a gradual rise to almost 35 mm.

Similarly, the measured ground heave resulting from the second tunnel (EB) was experienced as demonstrated in Figure 11 (b). As clearly shown in the plot, an initial small displacement as the shield approached was measured at the EB tunnel centerline, while a large heave up to 15 mm was observed after the shield passing. This also caused the peak value that gradually increased to 40 mm.

The surface vertical displacements computed by numerical analyses were compared to the field measured data at the monitoring section F1. As can be seen, the development of ground deformation obtained from numerical calculation showed a similar pattern and provided good agreement, although smaller displacements were demonstrated. The largest portion of ground movements occurred after shield passing and was mainly caused by tail void grouting process. A maximum predicted heave induced by twin tunnels based on numerical calculation was approximately 30 mm.

Moreover, the results showed that the maximum heave did not occur at the tunnel face immediately, it occurred well behind from the shield after the grouting pressure was performed.

The contour plots of the surface vertical movement obtained from the FE calculation of WB and EB tunnel excavation is presented in Figure 12. According to the simulation of WB tunnelling depicted in Figure 12 (a), ground surface movement occurred while the TBM face was approaching, and it significantly increased the at the tail section of the shield machine. The ground heave was characterized by a single peak curve behind the section F1 during the WB shield face was at the observed section.

After the WB tunnel passed through the model boundary, excavation of the EB tunnel was then simulated. In accordance with the EB tunnel excavation as

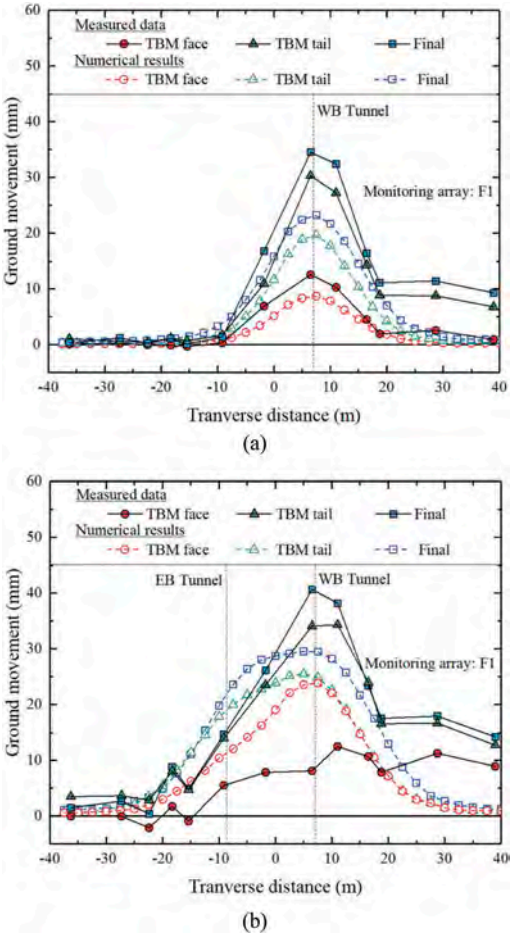

Figure 11. Ground surface displacement in transverse direction tunnelling; (a) WB tunnel, (b) WB & EB tunnels.

illustrated in Figure 12 (b), the ground heave began to exhibit the twin peak curves in front of the TBM face due to face pressure of EB tunnel. Then, the twin peaks moved toward each other gradually due to the grouting progressed and merged into one large single peak. The contour shades were densely distributed near the previous peak induced by WB tunnel, indicating the significant increments of vertical movement in those positions.

5.2.2 *Soil lateral movements*

In this project, a series of combined inclinometers and extensometers were mostly installed along the side of the tunnel alignment to measure ground deformations in horizontal direction. Figures 12 shows lateral deflections of three inclinometers (IEX1, IEX2 and IEX3) in the perpendicular direction to the tunnel axis during the excavation of the WB tunnel and the EB tunnel.

Based on the observation of the ground deformations after the excavation of the WB tunnel,

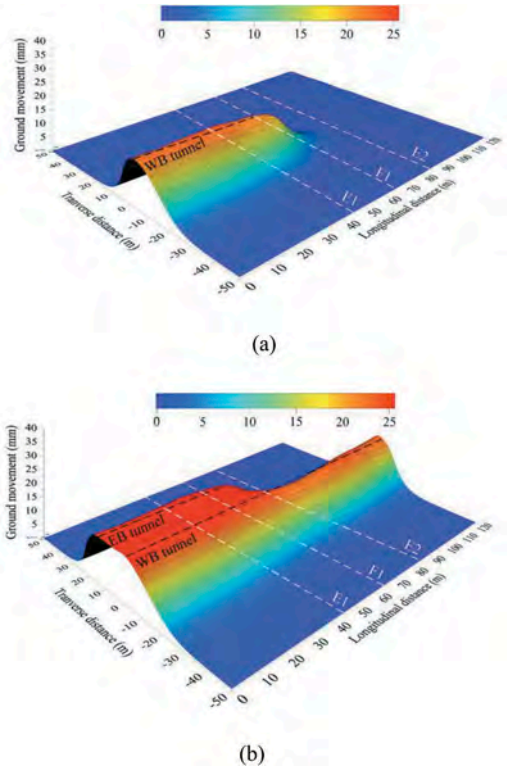

Figure 12. Contour of ground movement due to tunnelling; (a) after WB tunnel, (b) after WB & EB tunnels.

outward movement at the level of the tunnel springline as the shield passing was demonstrated. It was found that the maximum lateral magnitude measured by the IEX1 and IEX2 were 22.2 mm and 15.0 mm, respectively. On the contrary, the effect on the IEX3 due to excavation by TBM no.1 was minimal. This is because a distance between the position of the first tunnel and the instrument was very large.

Likewise, the outward movement measured by IEX2 and IEX3 were observed. The largest movement recorded in IEX3 was 12.6 mm which was nearly located at the level of tunnel axis. It is interested to note that the measured data of lateral movement by IEX2 substantially decreased to around 8.0 mm because of TBM no.2 advancement.

In addition, the general trend of the lateral movements resulting from the numerical simulations was similar to those measured data, with outward movements from the position of tunnels.

Overall, all inclinometers indicated a similar pattern of lateral ground movements. Large outward movements commonly appeared at the tunnel springline associated with high face pressures and grouting pressures. This outward deflection recorded by inclinometers reduced rapidly below the level of tunnel position.

6 CONCLUSIONS

The observation and comprehensive instrumentation data performed during the construction of twin

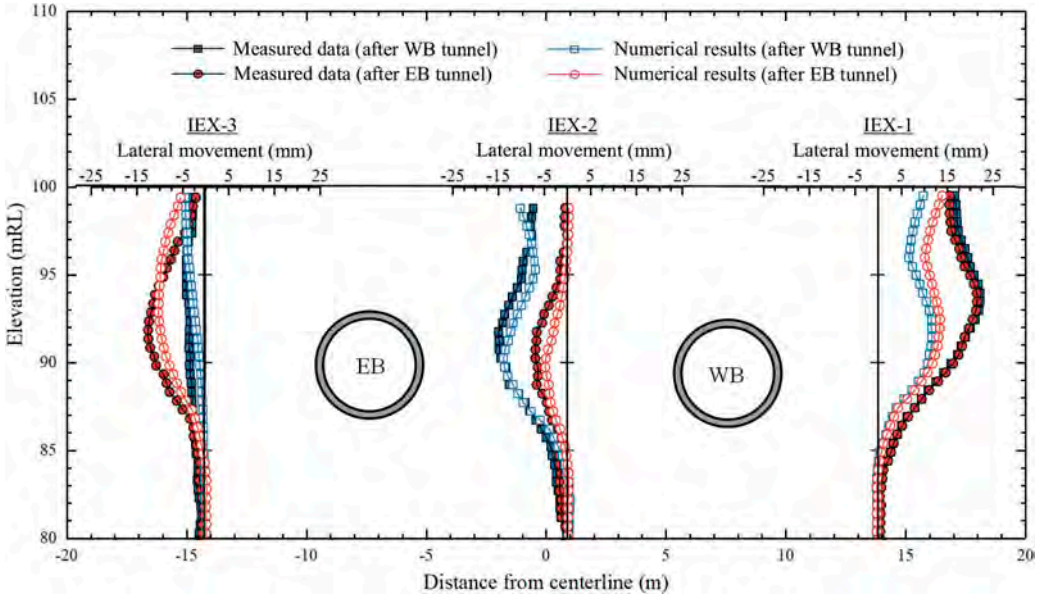

Figure 13. Lateral ground movements after excavation of twin tunnels in shallow overburden.

tunnels in the MRT Orange Line (East Section) project gave a better understanding of the interaction between the soil and the TBM during the tunnel process in a shallow overburden section. The numerical calculation was also carried out to compare the results obtained from the measured field data. Therefore, the main conclusions derived from this study can be summarised as follows:

- Based upon the observational test section, TBM driving parameters including face pressure and grouting pressure have significant effects on ground movements in both vertical and horizontal directions, particularly in shallow overburden.
- Two main parameters of the TBM driving parameters utilised along the monitoring section were recorded, and it can be clearly seen that ground heave and blow-out were obviously induced by applying relatively high face support pressures and tail void grouting pressures compared to the in-situ soil stress.
- The maximum ground heave of 35 mm was measured after the excavation of first tunnel (WB), while the highest upward movement at the tunnel centerline induced by the construction of the second tunnel (EB) was approximately 15 mm. This difference can be attributed to that the second tunnel mostly excavated by using lower support pressures.
- Ground heaves immediately occurred as the shield approaching the monitoring section, and it was found that a noticeable increase in upward ground movements were observed during the process of primary grouting injection.
- The numerical simulation of the EPB shield machine advancement by 3D FE analysis was conducted based on the operational parameters obtained from the recorded data. The simulation results provided the identification and confirmation of the behaviours of observed ground movements in both vertical and horizontal directions.

ACKNOWLEDGMENTS

The authors would like to appreciate Mass Rapid Transit Authority of Thailand (MRTA) and CKST joint Venture for their valuable project data.

REFERENCES

Bezuijen, A., and Brassinga, H., 2006. Blow-out pressures measured in a centrifuge model and in the field. Tunnelling: A Decade of progress, GeoDelf: 1995-2005. Taylor & Francis Group, pp. 143–148.

ITA/AITES (2007), 1995. Report 2006 on settlements induced by tunneling in soft ground. Tunnelling and Underground Space Technology 22, pp. 119–149.

Do, N. A., and Dias, D., 2017. A comparison of 2D and 3D numerical simulations of tunnelling in soft soils. Environ Earth Sci. 76(3).

Do, N. A., Dias, D., Oreste, P. 2014. Three-dimensional numerical simulation of a mechanized twin tunnels in soft ground. Tunnelling and Underground Space Technology. 42, pp. 40–51.

Duangsano, O., Yensri, P., Chayaroon. A., Timpong, S., and Jongpradist, P., 2023. Tunnelling impacts and mitigation on existing structures for Bangkok MRT Orange Line. Geomechanics and Tunnelling 16. No. 3, pp. 272–280.

Kong, S. K., 2003. Application of geotechnical instrumentations for safety control in basement construction works. BCA Seminar – Avoiding Failures in Excavation Works. Singapore.

Vu, M. N., and Broere, W., 2023. A compact blowout model for shallow tunnelling in soft soils. Tunnelling and Underground Space Technology. 138, 105167.

Vu, M. N., Broere, W., and Bosch, J., 2015. The impact of shallow cover on stability when tunnelling in soft soils. Tunnelling and Underground Space Technology. 50, pp. 507–515.

Suwansawat, S., 2002. Earth pressure balance shield tunneling in Bangkok: ground response and prediction of surface settlements using artificial neural networks. Doctoral Dissertation. MIT, USA.

Tunnelling for a Better Life – Yan, Celestino, Thewes & Eberhardt (Eds)
© 2024 The Author(s), ISBN 978-1-032-80042-4
Open Access: www.taylorfrancis.com, CC BY-NC-ND 4.0 license

Research and application of key technologies for the TBM tunnel construction under extremely complex geological conditions

Huan huan Feng* & Kai rong Hong
China Railway Tunnel Group Co., Ltd., GuangZhou China
State Key Laboratory of Shield Machine and Boring Technology, ZhengZhou China

ABSTRACT: With the Gaoligong Mountain Tunnel of Dali-Ruili Railway, Qinling Tunnel of Hanjiang to Weihe River Project, Xianglu Mountain Tunnel commenced successively in China, the TBM entrapment in water-rich fragmentation in extreme soft stratum and rockburst in extremely hard rock under high ground stress have been increasingly prominent problems in TBM construction. On the basis of the summary analysis on the cases of partial tunnel collapse and TBM entrapment and their contributory factors in the projects, we conduct systematic investigation of the key technologies for TBM tunneling: (1) For now there is no way to make accurate quantitative forecast of the geological conditions in medium or long distances ahead; for the soft and broken stratums with joint development, carbonaceous slate and fault fracture zone, special measures against machine entrapment must be taken and proper rescue solutions can be devised based on the length of the segment with unfavorable geological conditions; (2) The anomalies in the tunneling parameters are important indicators that reveal the geological conditions ahead of heading face. Before TBM tunneling, proper tunneling parameters should be chosen based on the preliminarily anticipated surrounding rock conditions such as full-section hard rock and weak and broken rock. In the boring process of TBM, it is necessary to correct the pre-estimation of geological conditions and take corresponding regulatory measures based on the abnormal changes of boring parameters; (3) Aiming at the situation that the existing TBMs are difficult to adapt to the existing geological conditions, the transformation technology of TBMs is analyzed and discussed with the engineering cases of Tao River Water Diversion Tunnel, Hongyan River to Shitou River Water Diversion Tunnel, and Hanjiang to Weihe River Water Diversion Tunnel. Finally, the new problems of TBM tunnel construction under extremely complex geological conditions and their countermeasures are prospected and discussed.

Keywords: TBM construction, fault, weak and broken, rock burst, jamming, TBM transformation, Standard registration

1 INTRODUCTION

Since the full-face hard rock tunnel boring machine (TBM for short) was applied to the water diversion tunnel of the Xi'erhe Cascade I Hydropower Station in Yunnan[1], the water diversion tunnel of the Tianshengqiao-II Hydropower Station[2], the water diversion tunnel of the Datong River-to-Qinwangchuan Basin Water Diversion Project, etc.[3] in the last century, the TBM equipment and construction technologies of China have been significantly improved[4], such as Shanxi Wanjiazhai Yellow River Diversion Project[5], Liaoning Dahuofang Water Tunnel[6], and Qinling Tunnel of the Xi'an-Ankang Railway[7] which were successfully completed later. However, as the Strategy for Large-Scale Development of Western China and the traffic network planning are making progress step by step, the geological conditions encountered during the construction of a TBM tunnel are more complex[8], and engineering problems or accidents, including rock burst[9], large deformation[10], sudden water inflow[11], tunnel collapse[12], etc., occur occasionally, having an extremely negative impact on the safety and high-efficiency construction of tunnels. Compared with China, the geological conditions of tunnels in other countries are less diversified, but many TBM tunnel projects have been also hampered by extremely geological conditions, for example, TBMs were struck in the construction of the Gotthard Base Tunnel in Switzerland[13]. To solve the rock burst problems of TBM tunnels, Huang Feng[14], Feng Xiating[15], Su Guoshao[16], Øyvind[17] et al. analyzed and researched the process of rock burst development, the sound signal characteristics of rock burst process, etc., and Qiao Zhibin[18], Zhao Xiangwei[19], Zhang Tianyu[20], Guo Yanhua[21] et al. put forward the identification method of rock burst levels of TBM tunnels; Du Lijie[22], Wu Haiyuan[23], Ma Tianhui[24] et al.

*Corresponding author: skl_fhh@163.com

DOI: 10.1201/9781003495505-236

conducted research into the rock burst prediction technology based on micro-seismic monitoring in TBM tunnels and its applicability; Xu Xiangdong[25] employed the discrete element method to carry out numerical simulation verification for common rock burst control methods, Zhang Peng[26], Wang Zuorong[27], Li Yuanlai[28] et al. used the rock burst problems in water diversion tunnel projects of the Jinping-II Hydropower Station and the HWWD Project as the research objects to summarize and analyze the countermeasures actually taken during their construction, and Du Li jie[29], Yang Chunbao[30] et al. summarized and refined the prevention and control technology for rock bursts in deep-buried tunnels and proposed preventive measures for different levels of rock bursts, involving slight, moderate and strong rock bursts. To solve the problems of TBM tunnel deformation, Kim[31], Huang Xing[32], Chen Weizhong[3] et al. separately conducted research into the surrounding rock deformation and reinforcement mechanism of TBM tunneling and impact of large deformation on the TBM tunneling process; Cai Dawei[34], Huang Xing[35], Shang Yanjun[36] et al. analyzed the deformation characteristics of surrounding rocks, TBM jamming process and countermeasures by taking the diversion tunnel of the Hongyan River-to-Shitou River Water Diversion Project, the diversion tunnel of the Water Diversion Project from Datong River to Huangshui River, the Shanggongshan Tunnel in Kunming, etc. as an example; Wang Yujie et al.[37] researched and put forward the classification standard for TBM construction adaptability under the large deformation conditions of surrounding rocks. Li Shucai[38], Kang, Daehun[39], Liu Bin[40] et al. conducted research into the application of advanced geological prediction technology to the prediction of mud gushing and water inflow of tunnels; Gao Kun[41], Li Zhaopeng[42] et al. carried out research and analysis of measures taken to solve mud gushing and water inflow in TBM tunnels by taking the water delivery tunnel of the Tao River Water Diversion and Supply Project and the Qinling Tunnel of the HWWD Project as an example. To solve the problems of rock bursts and large deformation of TBM tunnels, the predecessors have carried out long-term research into the formation mechanism, generation process, early prevention and control, treatment measures taken at a late stage, etc. and have obtained relevant results.

From the perspective of construction technology, this paper focuses on systematically summarizing and analyzing engineering difficulties and innovative technical measures based on the TBM tunnel project in typical complex geological conditions in China, with the aim to better solve technical difficulties of TBM construction under extremely complex geological conditions, and also proposed relevant recommendations in terms of equipment reconstruction, tunneling parameter regulation and control, and so on.

2 COMMON UNFAVORABLE GEOLOGICAL CONDITIONS IN TBM TUNNELS AND INFLUENCE

2.1 *Weak and broken surrounding rocks*

Within the range of influence of faults, the self-stability of surrounding rocks is poor, and stone falling and collapse easily occur, having a serious impact on the TBM tunneling speed. For example, for Lot 4 of the main line construction of the Water Supply Project of Transferring Water from the Songhua River, the TBM section includes 7km-long limestone and 39 fault fracture zones, with the width of zone of influence ranging from 50m to 250m. In the weak and broken strata where joints were developed, the excavation surface is irregular and peeling and stone falling occur very easily, causing TBM jamming (see Figure 1).

Figure 1. TBM Jamming.

2.2 *Extremely hard rock strata with high abrasiveness*

According to the current TBM equipment and construction technology level, the intensity of rocks which are relatively easy to tunnel ranges from 30MPa to 120MPa, and if the intensity varies between 180MPa and 250MPa, the construction schedule and cost risks incurred will be unaffordable; if it is higher than 250MPa, it will be difficult to tunnel, and in addition to the compressive strength of rocks, the quartz content, rock integrity, abrasiveness and other indexes will also have a direct impact on the TBM tunneling efficiency (e.g. the Qinling Tunnel of the HWWD Project passed through the complete granite section (see Figure 2), where the quartz content was up to 40%, the rock abrasiveness value was up to 5.24, and the single-cycle tunneling time reached 4~5h).

Figure 2. High-strength full-face granite.

The main engineering difficulties encountered by TBM in tunneling through extremely hard rocks with high abrasiveness include TBM tunneling failure, low rock-breaking efficiency of the cutter head, difficulty in ensuring the service life of the main shaft, serious damage to tools, etc., and will greatly reduce the TBM tunneling speed and the utilization rate of tunneling and significantly increase the construction schedule and costs.

2.3 *Rock burst in the hard rocks with high ground stress*

Under the conditions of high ground stress, rock bursts frequently occur in the process of TBM construction, having a serious impact on the construction of tunnel project, such as 43 rock bursts, with an accumulative length of about 1,894m[43], happened in the Qinling Tunnel of the Xi'an-Ankang Railway. As the burial depth of tunnels increases, the frequency of occurrence of rock bursts in mountain tunnel projects in China is increasing; for example, the in-progress Qinling Tunnel of the HWWD Project, the Xianglushan Tunnel of the Central Yunnan Water Diversion Project, etc. will face serious rock burst problems. Failure to treat rock bursts timely will endanger personal safety, safety of machinery and equipment and structural stability of tunnels (see Figure 3).

Figure 3. Damage of bracing system caused by rock burst.

2.4 *Comparison of construction efficiency under different conditions*

TBM utilization rate, tunneling speed, tool wear, etc. are the direct manifestations of the TBM construction efficiency and are also directly influenced by geological conditions. The preliminary geological survey is often hard to faithfully reflect the geological conditions encountered in the construction of tunnels at a later stage due to the large high burial depth of tunnels, etc. Even for the same class of surrounding rocks, the actual TBM tunneling progress is also not exactly the same as the expected progress. Taking the TBM tunneling of the Middle Tianshan Tunnel as an example, geological conditions are relatively poor, and the utilization rate of TBM equipment primarily ranges from 20% to 35%. The TBM tunneling efficiency varies under different surrounding rock conditions (see Table 1):

3 TBM CONSTRUCTION TECHNOLOGY IN UNFAVORABLE GEOLOGICAL SECTION

3.1 *Advanced geological prediction technology*

3.1.1 *Advanced geological prediction HSP technology*

This technique is mainly used to analyze and determine the scale, nature and extension of unfavorable geological bodies which may exist ahead of a tunnel, such as lithologic boundary, fault, and fracture zone of rock mass, and each monitoring cycle is 50m, and the number of times of prediction can be increased according to the actual surrounding rock conditions on site, and its main disadvantage is the low ability to predict groundwater.

3.1.2 *Induced polarization (IP)-based advanced water exploration technology*

For water-rich strata, the IP-based advanced water exploration technology shall be adopted, which provides a feasible approach to the advanced detection and positioning of water-bearing structures and the water quantity estimation of water-bearing bodies[44]. In a water inflow section, it is recommended to bore some deeper advanced water exploration holes to the greatest extent possible for the purpose of understanding as much as possible the development of groundwater over a longer distance ahead of the tunnel face.

Table 1. Comparison of boring efficiency of middle tianshan tunnel in different surrounding rocks.

		Actual average progress/ m/month				
Class of surrounding rock	Design progress m/ month	Metamorphosed sandstone	Keratophyre	Metamorphosed sandstone (fault)	Granite	Metamorphosed sandstone developed in the quartz vein
Class II	450	/	/	/	216	/
Class III	400	401	346	426	184	190
Class IV	260	180	147	150	141	154
Class V	150	/	/	/	52	/

3.1.3 *Integrated geological prediction technology*

In high-risk tunnel intervals, an advanced geological prediction technique combining multiple prediction methods is typically adopted to improve the accuracy and precision of geological prediction. For example, in the construction of the Middle Tianshan Tunnel, the integrated assurance technology of TBM construction safety in unfavorable geological sections is established, mainly including an integrated advanced geological prediction technology combining short-distance forecast and long-distance forecast, geophysical prospecting and drilling, and geological sketch and tunneling parameters.

Most of the existing techniques for geological prediction ahead of the tunnel are used for qualitative prediction of geological conditions and cannot accurately and quantitatively predict the geological conditions over a medium and long distance ahead of the tunnel, and it is also difficult to accurately identify the conditions of surrounding rocks ahead.

3.2 *Treatment measures for the rock burst section*

3.2.1 *Countermeasures against minor rock bursts*

1) Water spraying to soften surrounding rocks: Use the TBM water spraying system to directly spray high-pressure water onto the surface of rocks excavated to soften the surface and further promote the release of original stress of rock strata;
2) Densification of anchor bolts and short holes for stress relief: Set high-density anchor bolts within the range of 90° on the tunnel arch, and bore the short holes for partial stress relief within the range of 120° on the arch;
3) Emergency concrete spraying: After the surrounding rocks stand above the shield, the emergency concrete spraying system shall be used for the sealing treatment of rock surfaces as early as possible;
4) Reinforcement of the McNally support system: A combination of "arched truss + rows of rebars + connecting rebars" is one of the common measures against rock bursts.

3.2.2 *Countermeasures against moderate rock bursts*

To dispose of moderate rock bursts, the support methods are optimized and a combination of temporary support + permanent support is adopted: (1) The ordinary gasket-type anchor bolts are changed to the expansion shell-type prestressed hollow grouting anchor bolts with a large base plate to apply the prestressing force in advance; (2) ordinary concrete is changed to nanomaterials or steel fiber and imitation fiber concrete to quickly close and reinforce surrounding rocks; (3) it is recommended to use steel arches made of H150 profile steel, and meanwhile, the diameter of rebars in the rebar row is properly increased.

3.2.3 *Countermeasures against strong rock bursts*

In the section where strong rock bursts may occur, conventional support measures will be unable to cope with such rock bursts, and generally, advanced stress relief should be conducted. The following measures are taken to effectively reduce the intensity of rock bursts: bore holes with an advanced water hammer drilling rig, inject water within a certain range, change the physical and mechanical properties of rocks, and lower the brittleness of rocks and the ability of energy storage. After the rock mass stands above the shield, steel segments can be installed for initial support reinforcement for support reinforcement.

3.3 *Treatment measures in weak and broken strata*

3.3.1 *Grouting reinforcement for the strata where joints were developeds*

1) Advanced grouting reinforcement inside the cutter head. The technology for advanced grouting reinforcement inside the cutter head is widely used, i.e. chemical grouting is used in shallow holes in the cutter head to form the wall for grouting, while high-strength and fast-setting curing agents and cement-water glass slurry are injected in medium-length holes for reinforcement.
2) Advanced grouting reinforcement of TBM tailskin. The technology for advanced grouting with a drilling rig is employed in the position of TBM tailskin, and no construction experience is available for reference in China now. CRTG performed tests in the construction process of the Gaoli Gongshan Tunnel of the Dali-Ruili Railway, replaced multiple types of drill pipes and bits, tested fast drill pipes, self-feeding pipe roofs and geological drill pipes, and realized the integration of drilling and grouting.

3.3.2 *Support processing for carbonaceous slate stratum*

In the limestone section of the tunnel of the Water Supply Project of Transferring Water from the Songhua River, TBMs passed through a total of 2 carbonaceous slates surrounding rocks, leaving the cutter head and the cutter holes prone to be covered and plugged, and collapse and serious falling occurred on the top. The following countermeasures shall be taken:

1) Initial support reinforcement. After the surrounding rocks stand above the shield, supports shall be installed in time, and measures of reinforcement of fully-laid rebar rows, longitudinal connection of profile steel, densification of arches and concrete spraying for whole sealing, are formed to eradicate the hidden dangers of supports behind the shield. Different support methods shall be separately used for the crown, gripper shoe and tunnel bottom.

2) Cutter head cleaning. When the torque is close to the rated value, the cutter head shall be stopped immediately and cleaned manually according to the on-site tunneling situation to prevent the cutter head from being overloaded and protect the cutter head and tools from being damaged, and meanwhile, the aperture ratio of the cutter head is increased and the water spraying system for the cutter head is stopped to make the output of slate rock mass easy.

3.3.3 *Measures for passing through fault fracture zone*

1) Crown: A combination of supports, including steel arch, rebar row, connecting rebar, and shotcrete, can effectively deal with ordinary fracture zones; however, in addition to the above measures, the emergency shotcreting and supporting system can also be used to timely seal the serious fracture section if necessary;
2) If falling or collapse occurs in the position of gripper shoe, the measures are generally taken: square timber forms are put under the gripper shoe, concrete is poured, and emergency shotcreting is conducted in advance.

Different measures are taken for different types of weak and broken strata, such as joint development zone, carbonaceous slate zone and fault fracture zone. The classified support technology system shall be built for TRMs passing through the weak and broken strata, with the aim of better solving the problems in a targeted way, such as tunnel deformation and collapse and TBM jamming.

4 TBM TUNNELING PARAMETER REGULATION OF DIFFERENT STRATA

4.1 *Full-face hard rock*

The key to realizing the high-efficiency tunneling of TBMs is to properly master the matching relationship between the parameters and the compressive strength of surrounding rocks, without considering rock bursts. Taking the TBM tunneling data of the tunnel in the HWWD Project as an example, the main TBM tunneling parameters under different surrounding rocks are proposed (see Table 2):

4.2 *Soft surrounding rock*

The parameters of tunneling through weak surrounding rocks shall be controlled in a targeted way. Taking the TBM tunneling parameter control of the Water Supply Project of Transferring Water from the Songhua River as an example (see Table 3):

1) Speed of cutter head: From the cutter head thrust and the rock-breaking effect in the previous cycle, it is judged that the rock debris will be uniform with few large blocks and the speed of cutter head can be improved if the cutter head thrust is relatively large; the rock debris will not be uniform, with more large blocks, and the speed of cutter head should be lowered if the cutter head thrust is relatively small.
2) Torque of cutter head: Under the weak surrounding rock conditions, the torque of cutter head is typically controlled at about 75% of the rated torque;
3) Gripper shoe pressure: If the TBM tunneling conditions are met, the minimum gripper shoe pressure shall be selected.

If a tunnel collapses, corresponding control measures shall be taken for different positions of collapse:

1. If collapse occurs in the cutter head and the tunnel face, TBM tunneling shall be stopped immediately and the cutter and the belt conveyor shall continue to operate, and determine whether the cutter head needs to be retracted according to the quantity of rock debris;
2. If collapse occurs behind the shield, the TBM shall be stopped without delay and supports shall be set in case of serious collapse, and after the completion of support setting, tunneling can be resumed.

Table 2. Optimal range of tbm boring parameters in different surrounding rock conditions.

Compressive strength of surrounding rocks/ MPa	Average thrust cylinder pressure/ bar	Speed of cutter head/r/min	Torque/ kN·m	Penetration/ mm/r
≥260	300~310	6	850~950	0.9
240~260	300~310	6	850~950	1.0~1.2
220~240	300~310	6	850~1050	1.0~1.5
200~220	300~310	6	1050~1200	1.2~2.2
180~200	300~310	6	1200~1350	2.5~3.2
160~180	300~310	5~6	1350~1600	2.8~3.5
100~160	180~300	4~5	1500~2200	4~8
80~100	100~180	2~3	1800~2200	9~12

Table 3. TBM boring parameter comparison table under the full cross-section carbonaceous slate.

Different stratum conditions	Tunneling speed/ mm/min	Torque of cutter head/ kN·m	Speed of cutter head/r/min	Penetration/ mm/r	Thrust pressure/ bar	Gripper shoe pressure/ bar
Carbonaceous slate	10~26	400~3800	1.8~4.5	3~10	60~120	194~254
Fault fracture zone	52~70	1630~3360	4.8~5.9	9~13	255~294	255~294
Normal tunneling section	62~80	2200~3310	6~6.7	9~13	273~323	273~323

4.3 *Impact of different water contents*

In a dry and soft rock tunnel dominated by sandy mudstone and argillaceous sandstone, TBMs have strong adaptability, the fluctuation of various tunneling parameters is small, and the tunneling efficiency is relatively high; in a water-bearing loose sand layer, TBMs have a certain adaptability, and auxiliary measures are taken to ensure normal TBM tunneling. Taking the TBM construction of the tunnel in the Tao River Water Diversion Project as an example (see Figure 4), in the loose sand layer section with the water content of 6% ~11.8%, the TBM tunneling thrust increased with the water content. The maximum fluctuations of thrust and torque are 298% and 148%, respectively.

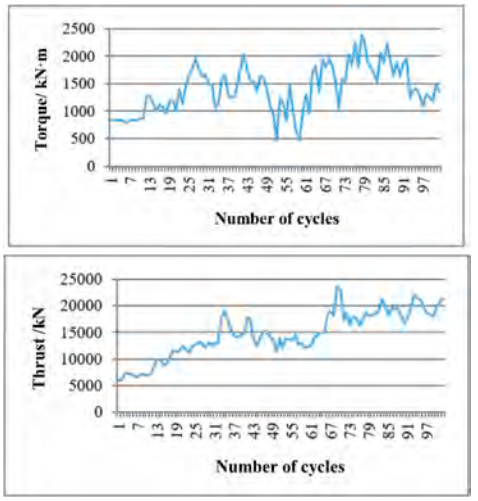

Figure 4. Changing curve of TBM boring parameters of aquiclude of tao river water diversion tunnel.

The changed rock conditions are reflected in the changes in various parameters related to TBM equipment and tunneling progress. Before TBM tunneling, appropriate tunneling parameters shall be selected according to the expected surrounding rock conditions; During the TBM tunneling process, the prediction of geological conditions shall be corrected and corresponding regulation measures shall be taken according to the abnormal changes in tunneling parameters, so as to ensure TBMs in the optimal tunneling state.

5 TARGETED TBM DESIGN AND RECONSTRUCTION TECHNOLOGY

To adapt to the demand for tunnel construction under various geological conditions, a variety of TBMs emerge, including open-type, single-shield and double-shield TBMs, and various types of TBMs have different abilities to adapt to the same geological condition, so the local system of a TBM shall be subject to targeted reconstruction for better meeting the construction demands when complex geological conditions are encountered or the existing TBM is difficult to adapt to the tunnel to be built.

5.1 *TBM tunnel reconstruction of the Hongyan River-to-Shitou River Water Diversion Project*

The TBM equipment used in the Hongyan River-to-Shitou River Water Diversion Project was second-hand, with poor adaptability. It was stuck a total of nearly 50 times. For this reason, targeted reconstruction of the equipment was conducted many times.

1) Main drive improvement: Add a set of variable frequency speed control devices, which can regulate the speed of cutter head to control the amount of muck according to the conditions of surrounding rocks of the tunnel face, so as to cope with poor geological conditions or pass through the fault fracture zone; improve the existing ABB two-speed motor into the 200 kW motor, which is a variable frequency motor having an IP67 rating for ingress protection; install 2 new variable-frequency drives to realize the "1+1" mode, use the bus control mode to realize synchronous running of 5 motors, and realize the vector control to make the cutter head drive have the function of low-speed rotation and large-torque output ;
2) An increase in excavation diameter: Move the side disc cutter housing outwards to increase the excavation diameter of the cutter head, so that the excavation diameter of a TBM increases from 3.655m to 3.755m and the amount of deformation is reserved for the TBM passing through the area of surrounding rock deformation quickly, and the TBM's ability to adapt to convergence and deformation of surrounding rocks can be improved;

3) An increase in the conveying capacity of belt conveyor: Replace a 10mm-dia. directional control valve with a 16mm-dia. one, so that all flows provided by a drive hydraulic pump can be used to drive 1# belt conveyor, the running speed can reach 2.3m/s, and the running ability can be increased by 15%; replace the hydraulic pump with a displacement of 100cc of 1# belt conveyor with one with a displacement of 140cc;
4) Optimization of the shield structure: lengthen the front shield: extend the front shield forward and lengthen it to protect the cutter head and reduce the amount of muck, so that the tunnel face has certain self-stability or a small amount of collapse will not make the cutter head stuck; bottom sealing of the internal telescopic shield: seal the telescopic shield to prevent muck from entering the shield, omit the muck removal process in the telescopic shield during the TBM tunneling period, and facilitate the rapid passage of a TBM; shortening and semi-sealing of the tailskin: the aperture opening ratio of the tailskin is 70° after reconstruction so that the inflow of slag caused by side arch collapse can be reduced.

After reconstruction, the geological adaptability of TBMs can be significantly improved, and especially after the completion of main drive reconstruction, the average daily footage is 11m, the maximum footage per shift is 26.7m and the daily maximum footage is 35.2m, and the TBM tunneling efficiency is increased by over 50% compared with that before reconstruction.

5.2 *TBM reconstruction of the tunnel of the HWWD project*

5.2.1 *Cutter head reconstruction*

1) Cutter head panel: Use the steel sheet of appropriate specifications for welding and repair according to the wear of the cutter head panel, so as to make it flush with the datum plane. a new wear-resistant composite plate with a welding thickness of 20mm is formed on the cutter head panel after repair, so as to improve the abrasive resistance;
2) Wear ring and slag-retaining block on the side: Increase the thickness of the first and second wear rings as well as the slag-retaining block on the side from 50mm to 70mm, and meanwhile, replace its material with Q690;
3) V-shaped guard block: On the premise that the same forming size can be ensured, use a 63.5mm-thick ASTM A572 steel plate as the bottom plate, set a 9~13mm wearing layer on the surface, and bevel the bottom welding position to ensure the welding quality;
4) Cutter housing: For a cutter housing which has been repaired multiple times and undergone large wear and deformation, the wear-prone contact surface can be designed as a replaceable block to avoid the whole cutter housing from being replaced after wear, provided that the original cutter housing size is not changed.

5.2.2 *Support system optimization*

To better deal with the complex geological conditions, such as weak and broken surrounding rocks, an emergency concrete-spraying manipulator shall be installed behind the TBM shield. The TBM equipped with a transfer pump behind a concrete conveying shield for shotcrete areas is used, the emergency concrete-spraying manipulator behind the shield is utilized for initial concrete spraying so that initial shotcrete can seal surrounding rocks, and after this section enters the mechanical shotcrete area, the mechanical injection method is employed to respray concrete until the design thickness is reached.

5.2.3 *Reconstruction of the bottom slag removal system*

Rock bursts frequently occurred in the process of TBM tunneling, so that more rock slag falls off from the main beam bottom of a TBM, seriously restricting the construction efficiency. The bottom slag removal system provided with the original TBM equipment fails to meet the requirements for quick slag removal from the main beam bottom on site due to the limited range of slag removal, complicated slag removal procedures and large quantities of transport. The adoption of an innovative belt conveyor will directly transport rock slag from the main beam bottom to the outside of a tunnel so as to accelerate slag removal and omit the processes of loading to dumper trucks, transport and reshipment.

5.2.4 *Reconstruction of the advanced drilling rig system*

To ensure the integrity of rocks after tunneling, there is an intact ring area of rock mass within 1m in the radial direction of the wall surface of an excavation hole; meanwhile, the regional stress within the vertical distance of 1m~5m in the radial direction of the wall surface of an excavation hole on the tunnel wall is released. A water hammer drilling rig is used to bore holes within the range of circumferential 100° on the upper part of a tunnel at an angle of elevation of 5°-9°. The borehole diameter should be the diameter of the supporting drill bit, the spacing between boreholes should be 60-100cm, and the appropriate and reasonable spacing should be kept to maintain the self-stability of surrounding rocks; tunneling shall be conducted at intervals of about 15-25m, and drilling shall be carried out once. Taking the water diversion tunnel of the HWWD Project as an example, it is especially necessary to introduce an advanced water hammer drilling rig and use it as a technical reserve for the construction of extremely strong rock burst sections.

6 CONCLUSIONS AND PROSPECTS

The characteristics of extremely complex geological conditions, such as weak and broken strata, full-face granite and high ground stress rock bursts, and their impact on the TBM construction are systematically compared and analyzed. The adoption of advanced geological prediction technology, targeted construction technology, tunneling parameter regulation technology, targeted TBM reconstruction technology, etc. can better guarantee the high efficiency and safety of TBM construction under complex geological conditions. However, more systematic and in-depth research shall be conducted to solve the engineering difficulties, such as rock bursts and large deformation, and relevant research recommendations are proposed according to the construction experience and research results of similar projects in the early stage:

1) Quantification of the advanced geological prediction technology. The advanced geological prediction technology is a powerful tool for helping TBMs deal with unfavorable geological conditions, but now, it is still in the qualitative or semi-quantitative stage in most cases, so it plays a limited role in guiding the safe and high-efficiency tunnel construction using TBMs, and the accuracy and degree of intelligence of geological prediction need to be improved;
2) Strengthening of the R&D of a new tunneling equipment technology. There is a lot of room for improvement of the existing open-type or shield-type TBMs in terms of dealing with extremely unfavorable geological conditions, including rock bursts or large deformation, and the R&D and application of new equipment, such as dual-structure and double-support[45] equipment, are urgently needed now; at the same time, a multi-purpose hybrid tunnel boring machine combining the advantages of shields and TBMs is developed, which is also one of the approaches to dealing with extremely unfavorable geological conditions.
3) In-depth analysis of the impact of tunneling parameters. The disturbance of surrounding rocks varies with different TBM tunneling parameters, including tunneling speed, penetration, speed, etc., so that its impact on the process of releasing the energy stored in surrounding rocks differs, and tunneling parameters are reasonably regulated to remove the necessary conditions for the occurrence of rock burst and large deformation, which may be an effective means to prevent rock bursts and large deformation.

ACKNOWLEDGMENTS

The authors would like to acknowledge the financial supports of a National Key Research and Development Program of China (No. 2020YFB1712100).

REFERENCES

[1] Chen Xiaodong, Chen Juqian, 2019. Development and Engineering Application of TBM in the 20th Century in China [J]. Water Resources Planning and Design, (01): 68–73.
[2] Wu Shiyong, Wang Ge, Xu Jinsong, etc, 2008. Research on TBM Type-Selection and Key Construction Technology for Jinping II Hydropower Station[J]. Chinese Journal of Rock Mechanics and Engineering, 27(10):2000–2009.
[3] Chen Xiaodong, Chen Juqian, 2018. Design and Technical Innovation of Long Tunnel and Large River-crossing Structure of Datong River to Qinwangchuan Diversion Project [J]. Gansu Water Resources And Hydropower Technology,54(10): 3–54.
[4] Hong Kairong, Wang Dujuan, Guo Rujun, 2018. Innovation and Practice of Hard Rock TBM in China[J]. Tunnel Construction, 38(04): 519–532.
[5] Xiao Xiaochun, Chen Guangcun, 2004. Application of full-face TBM on the international tender sections II and III of the southern artery in the Yellow River diversion project[J]. Modern Tunnelling Technology, 41(1): 46–50.
[6] Wei Yongqing, Du Shibin, 2006. Construction features of a super long water conveyance tunnel project with large cross section in construction[J]. Water Resources and Hydropower Engineering, (03): 8–11.
[7] Li Dianhuang, Yan Qihan, 1999. TBM Construction in Qinling Tunnel on Xikang Railway Line[J]. World Tunnelling,(01): 31–35.
[8] Hong Kairong, Feng Huanhuan, 2018. Construction Difficulties and Key Techniques for the Gaoligong Mountain TBM Tunnel[J]. Modern Tunnelling Technology, 55(04):c1–8.
[9] Fang Dunmin, Liu Ning, Zhang Chuanqing, etc, 2013. Rockburst Risk Control for Large Diameter TBM Boring in High Geostress Region[J]. Chinese Journal of Rock Mechanics and Engineering, 32(10): 2100–2107.
[10] Wang Yafeng, 2021. Key Technology of Resuming a Trapped TBM for Gaoligongshan Tunnel under Adverse Geological Conditions [J]. Tunnel Construction, 41(03): 441–448.
[11] Yuan Liang, Shi Zhao, 2012. Countermeasures against Water Inrush for TBM construction of Jinping II Hydropower Station[J]. Design of Hydroelectric Power Station, 28(S1): 9–12.
[12] Chen Z, Zhang Y, Li J, et al,202 1. Diagnosing tunnel collapse sections based on TBM tunneling big data and deep learning: A case study on the Yinsong Project, China[J]. Tunnelling and Underground Space Technology, 108.
[13] Dipl. I D T M, Sc. N E F M, Werner D, 2016. Gotthard Base Tunnel - Comparison of forecast and findings regarding engineering geology and tunnelling/ Gotthard-Basistunnel – Vergleich Prognose und Befund aus baugeologischer und tunnelbautechnischer Sicht[J]. Geomechanics and Tunnelling, 9(3).
[14] Huang Feng, Xu Zemin. 2009. On blasting perturbation mechanism of rock burst in tunnel by dynamic photo-elasticity[J]. Explosion and Shock Waves, 29 (06): 632–636.
[15] Feng Xiating, Xiao Yaxun, Feng Guangliang, etc, 2019. Study on the development process of rockbursts[J]. Chinese Journal of Rock Mechanics and Engineering, 38(04): 649–673.

[16] Su Guoshao, Shi Yanjiong, Feng Xiating, etc, 2016. Acoustic signal characteristics in rockburst process[J]. Chinese Journal of Rock Mechanics and Engineering, 35(06):1190–1201.
[17] Øyvind D, 2016. Prediction of Brittle Failure for TBM Tunnels in Anisotropic Rock: A Case Study from Northern Norway[J]. Rock Mechanics and Rock Engineering, 49 (6).
[18] Qiao Zhibin, 2021. Study on Rockburst Intensity Prediction Based on the Characteristics of In-situ Stress Field in Deep Tunnel on Sichuan-Tibet Railway[J]. Railway Standard Design, 65(02): 89–94.
[19] Zhao Xiangwei, 2020. Prediction of Tunnel Rockburst Intensity Based on Fuzzy Synthetic Evaluation Method[J]. Sichuan Architecture, Sichuan Architecture, 40(01):134–136.
[20] Zhang Tianyu, Li Jianpeng, Liao Wanhui, 2018. Application of Catastrophe Progression Method in Prediction of Rockburst Intensity in Tunnelling[J]. Highway, 63(09): 316–320.
[21] Guo Yanhua, Li Leyu, 2019. Evaluation of Rock Burst Level Based on the Improved Entropy Weight-Catastrophe Progression Method[J]. Journal of Hebei University of Engineering(Natural Science Edition), 36(03): 67–71.
[22] Du Lijie, Wang Jiaxing, Hong Kairong, etc, 2020. Research on Accuracy and Applicability of Rockburst Microseismic Monitoring in TBM Construction [J]. China Civil Engineering Journal, 53(S1): 278–285.
[23] Wu Haiyuan, Yu Qun, Du Zhiyuan, etc, 2020. Rockburst Early Warning Method Based on Microseismic Monitoring Technology[J]. Journal of Water Resources and Architectural Engineering, 18(03): 25–30.
[24] Ma Tianhui, Tang Chun'an, Tang Liexian, etc, 2016. Mechanism of rock burst forcasting based on micro-seismic monitoring technology[J]. Chinese Journal of Rock Mechanics and Engineering, 35(03): 470–483.
[25] Xu Xiang-dong, 2008. Preliminarily Exploration on the Function Mechanism of Prevention and Treatment of Rockbrust for Tunnel[J]. Journal of Railway Engineering Society, (10): 36–39.
[26] Zhang Peng, Zeng Xinhua, Li Xianchen, etc, 2011. Study on comprehensive measures for control of heavy rockburst during construction of diversion tunnel for Jinping Hydropower Station II[J]. Water Resources and Hydropower Engineering, 42(03):61–65.
[27] Wang Zuorong, 2014. Discussion on Rockburst Prevention Measures in Lingnan TBM Section of Qinling Tunnel of Hanjiang River to Weihe River Water Diversion Project[J]. Shaanxi Water Resources, (03): 91–92.
[28] Li Yuanlai, Wang Jun, 2017. Prediction and prevention measures of rock burst in No.4 construction adit of Qinling Water Conveyance Tunnel for Hanjiang-to- Weihe River Valley Water Diversion Project[J]. Water Resources and Hydropower Engineering, 48(08): 96–100.
[29] Du Lijie, Hong Kairong, Wang Jiaxing, etc, 2021. Rockburst Characteristics and Prevention and Control Technologies for Tunnel Boring Machine Construction of Deep-buried Tunnels[J]. Tunnel Construction, 41(01): 1–15.
[30] Yang Chunbao, Hu Guozhi, Li Lingzhi, etc, 2021. Study on prevention and control technology of hard rock rockburst in deep buried conveyance tunnel [J]. Water Resources Planning and Design, (04): 52–56.
[31] Kim D, 2021. Large deformation finite element analyses in TBM tunnel excavation: CEL and auto-remeshing approach[J]. Tunnelling and Underground Space Technology incorporating Trenchless Technology Research, 116.
[32] Huang Xing, Liu Quansheng, Liu Kaide, etc, 2015. Laboratory Study of Deformation and Failure of Soft Rock for Deep Ground Tunnelling with TBM[J]. Chinese Journal of Rock Mechanics and Engineering, 34(01): 76–92.
[33] Chen Weizhong, Chen Feifei, Zhao Wusheng, etc, 2017. TBM tunnel segment dislocation due to large deformation and reinforcement mechanism on surrounding rockmass[J]. Journal of Shandong University(Engineering Science), 47(02): 1–6.
[34] Cai Dawei, 2017. Soft Rock Deformation Characteristics and TBM Construction Control of Diversion Tunnel of Yinhongjishi[J]. Shaanxi Water Resources, (01): 39–41.
[35] Huang Xing, Liu Quansheng, Peng Xingxin, etc, 2017. Analysis and comprehensive prevention-control for TBM jamming induced by squeezing deformation of surrounding rock around water diversion tunnel from Datong river into Huangshui river[J]. Rock and Soil Mechanics, 38(10):2962–2972.
[36] Shang Yanjun, Shi Yongyue, Zeng Qingli, etc, 2005. TBM Jamming and Deformation in Complicated Geological Conditions And Engineering Measures[J]. Chinese Journal of Rock Mechanics and Engineering, 24(21): 60–65.
[37] Wang Yujie, Shen Qiang, Cao Ruilang, etc, 2020. Study on classification standard of TBM construction adaptability for large deformation surrounding rock[J]. Hazard Control in Tunnelling and Underground Engineering, 2(04): 37–43.
[38] Li Shucai, Liu Bin, Nie Lichao, 2018. The Practice of Forward Prospecting of Adverse Geology Applied to Hard Rock TBM Tunnel Construction:The Case of the Songhua River Water Conveyance Project in the Middle of Jilin Province[J]. Engineering, 4(01): 281–294.
[39] Kang D, Lee I M, Jung J H, et al,2019. Forward probing utilizing electrical resistivity and induced polarization for predicting soil and core-stoned ground ahead of TBM tunnel face[J]. Journal of Korean Tunnelling and Underground Space Association, 21(3).
[40] Liu Bin, Li Shucai, Li Jianbin, etc, 2016. Integrated acquisition method of adverse geology and rock properties ahead of tunnel face in TBM construction tunnel[J]. Journal of Shandong University (Engineering Science), 46(06): 105–112.
[41] Gao Kun, 2012. Tunneling in Mud/Sand Bursting Geology by Single-shield TBM[J]. Tunnel Construction, 32(01): 94–98.
[42] Li Zhaopeng, Li Peng, 2015. Discussion on Hanjiang River Diversion to Weihe River Qinling Tunnel TBM Construction Segment Sudden Surge Water Gushing Mud Construction Technology[J]. Water Resources Development & Management, 35(03): 12–14.
[43] Feng Xiating, Chen Bingrui, Zhang Chuanqing, etc, 2013. Mechanism, early warning and dynamic control of rock burst incubation process[M]. Science Press.
[44] Li Shucai, Liu Bin, Li Shuchen, etc, 2011. Study of Advanced Detection for Tunnel Water-Bearing Geological Structures with Induced Polarization Method[J]. Chinese Journal of Rock Mechanics and Engineering, 30(07): 1297–1309.
[45] Chen Kui, Feng Huanhuan, He Fei, 2021. Challenges in Tunnel Construction and Preliminary Study on Innovative TBM Design for Sichuan-Tibet Railway[J]. Tunnel Construction, 41(02): 165–174.

Tunnelling for a Better Life – Yan, Celestino, Thewes & Eberhardt (Eds)
© 2024 The Author(s), ISBN 978-1-032-80042-4
Open Access: www.taylorfrancis.com, CC BY-NC-ND 4.0 license

Evaluations and considerations on the squeezing rock tunnelling in twin TBM tunnel of Rishikesh to Karanprayag railway project in Himalaya

Mohammad Forooghi*, Vishal Bansal & Majid Tajik
Turkish Engineering Consulting & Contracting-TUMAS India Private Limited, India

Sumit Jain
Rail Vikas Nigam Limited, India

Soner Batuman & Pranshu Aggarwal
Turkish Engineering Consulting & Contracting-TUMAS India Private Limited, India

ABSTRACT: The new Railway line between Rishikesh and Karanprayag is under construction in the State of Uttarakhand, India with a total length of 125 km. Package 4 of the project includes 10.490 km (Twin bore TBM Tunnel, Upline & Downline) being constructed using two 9.11 m diameter Single Shield Hard Rock TBMs. Rock masses such as shale, slate, phyllite and schist, and the rock mass of weakness/fault zones are incapable of sustaining high stresses in such high overburdened tunnels leads to squeezing ground condition during tunnel construction in the tectonically active Himalayan region. Package 4 route is not an exception and mostly consists of high schistose Phyllite and Quartzite Phyllite rock mass being considered in TBM specifications which enables to investigate the ground ahead of TBM and monitor the constructed tunnel, aimed towards reducing the risk, using state of the art technologies in TBMs. Squeezing potential of rock strata along the Mechanized tunnel part being assessed with empirical, semi-empirical, analytical, and numerical methods based on the geotechnical and geomechanical parameters of the rocks, identified/interpreted in the tunnel route and presented through GBR, GDR and GIR Reports before tunnel construction and expected squeezing behaviour under average to high overburden conditions, which is also being evaluated during tunnel construction with the actual tunnel convergence measured around the shield. Void measurements around the shield is being done by adapting three special instruments along the shield near the tunnel crown capable to measure the void above after each advance and during stoppages of the TBMs. Comparison of the analytical and numerical analysis with the actual data collected in the first 2.7 km of upline tunnel path shows good corelations mostly with the previous studies done in the Himalayan region.

Keywords: TBM, Shield, Tunnel, Squeezing, Hard rock, Convergence

1 INTRODUCTION

The 125 km length Railway line between Rishikesh and Karanprayag in the State of Uttarakhand, India comprises of 17 tunnels 12 stations and 35 bridges. Tunnel 8 (Package 4) of the project from chainage 47+360 to 63+117, includes 15.1 km double line tunnel located between Devprayag and Janasu (Figure 1), out of which 10.490 km (Twin-bore TBM Tunnel) being constructed using two 9.11 m diameter Single Shield Hard Rock TBMs (Figure 2). Tunnel and TBM general specifications are mentioned in Table 1.

2 TBM INVESTIGATION AND MONITORING DEVICES

The utilization of Shielded TBMs for the Rishikesh to Karanprayag railway project Package 4 is a viable option, given the favourable conditions of the rock strata specified in the GBR, the expected topographical advantages along the tunnels, and the positive social, environmental, and financial considerations. To enhance the operation of these TBMs, state-of-the-art technologies have been incorporated, which offer the capability to precisely control the machines' advance rate and simultaneously assess the rock strata ahead of

*Corresponding author: mohammad.forooghi@tumas.com.tr; m.f.19800622@gmail.com

DOI: 10.1201/9781003495505-237

Figure 1. Rishikesh karanprayag package 4 project plan.

Table 1. Tunnel and TBMs general specifications.

TBM Boring Diameter	9,110 mm
TBM Front Shield Outer Diameter	9,050 mm
TBM Middle Shield Outer Diameter	9,030 mm
TBM Tail Shield Outer Diameter	9,010 mm
Total Shield length	10,675 mm
Nominal Radial Gap (Void) Behind TBM Front Shield	30 mm
Nominal Radial Gap (Void) Behind TBM Middle Shield	40 mm
Nominal Radial Gap (Void) Behind TBM Tail Shield	50 mm
Segment Outer Dia.	8,700 mm
Segment Inner Dia.	7,800 mm
Average Ring Length	1,700 mm
Number of Segments in Universal Ring	7 + 1 key
Total Installed Power	4,200 kW
Number of Thrust Cylinders	42
Nominal Thrust @ 420 bar	108,619 kN
Standby Thrust @ 500 bar	129,308 kN

Figure 2. TBM SHAKTI (S-1309A) factory acceptance test.

the TBM face and the excavated tunnel. These technologies include:

- Exploratory probe drilling equipment: Used to investigate the ground ahead of the TBM cutterhead through 20 inclined drill holes within the TBM shield perimeter and 6 horizontal drill channels through the cutterhead.
- Seismic investigation equipment: Enables extended investigation of the rock mass body in front of the TBM and verifies direct investigations conducted through boreholes and probe holes.
- Disc cutter load monitoring system (DCLM): Monitors the load on four disc-cutters positioned at different locations (radii) on the cutting wheel while the cutterhead rotates, providing insights into the rock strength in various positions on the face.
- Ring convergence monitoring system (RCMS): Monitors deformation and convergence of the segmental ring through effective measurements using a wireless system starting immediately after the ring installation.
- Muck weighing equipment: Measures the weight of the excavated material via the TBM conveyor belt.
- Variably sized TBM shields: Employed to create additional space in the tail shield to accommodate ground convergence during shield advance.
- Facilities to overcut up to 9310 mm diameter by shifting the 19" gauge cutters and changing with 20" disc cutters.
- Void measurement system (VMS): Measures the void between the shield and the rock using three cylinders in the front and middle shield's roof section. This system operates during TBM stoppages, such as ring building time. Continuous measurements during each advance, considering the distance between these cylinders (1700 mm as illustrated in Figure 3), allow for the recording of ground convergence in the same position during subsequent measurements.

3 GEOLOGICAL AND GEOTECHNICAL PROPERTIES OF THE ROCK ALONG THE TUNNEL ROUTE

The single shield TBMs shall excavate the twin tunnels of approx. length of 10.5 km each through the Chandpur formations of Jaunsar group comprising mainly of Phyllite and quartzitic phyllite with varying content of quartzite in them. Several drill hole investigations along with laboratory and geophysical investigations were performed to evaluate the rock mass conditions along the tunnel. The drill holes up to depth of 600 m were conducted to verify the expected site conditions based on site topography and geological traversing and mapping.

The in-situ state of stress was inferred from the hydrofracture field tests performed at the site. Vertical stress is one of the principal stresses and is due to gravity loading. The best estimates for the in-situ stress ratio for different overburdens and zones are calculated using Sheorey's equation validating from the site test results. The state of stress in the

horizontal plane is considered isotropic. Figure 4 Shows geological longitudinal section of package 4 and Table 2 represents the best and cautious estimates of various geomechanical properties along the various critical sections along the TBM tunnel lengths zone.

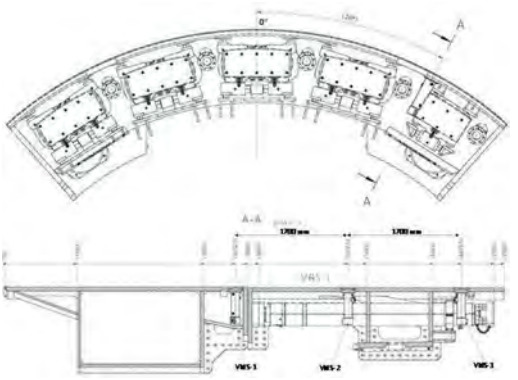

Figure 3. Void measurement cylinders position on the shield.

4 SQUEEZING ANALYSIS APPROACH AND METHODOLOGY

Squeezing of the host ground is the large time-dependent deformations that occur around the tunnel geometry. The time-dependent deformations are produced by the disturbance of the primitive stress field due to the excavation of the tunnel. The rock mass around the tunnel boundaries is strained under the influence of induced stresses. The deformations may terminate during construction or continue over a long period of time (Barla, 1995). In the landmark paper on tunnelling by Karl Terzaghi (1946), the prerequisite of the squeezing ground conditions is defined as the high percentage of microscopic or sub-microscopic particles of micaceous minerals or of clay minerals with low swelling capacity. Following the definitions of Terzaghi, several approaches are identified by various authors to assess the potential of squeezing problems in tunnelling.

4.1 *Singh et al. (1992) an empirical approach*

Using 39 individual case histories primarily from Himalayan formations, Singh et al. (1992) conducted a study in which they collected data on rock mass quality (Q) and overburden, led to the establishment of a discernible boundary line, clearly distinguishing between squeezing and those of non-squeezing rock, as presented in Equation 1, in which data points positioned above this demarcation line signify instances of squeezing conditions.

$$H = 350Q^{1/3} \tag{1}$$

Where, H is overburden (m); Q is rock mass quality (Barton et al. 1974).

Figure 4. Geological longitudinal section, package 4, rishikesh to karanprayag railway project.

Table 2. Geomechanical parameters of tunnel route.

Chainage	Overburden (m)	Density (kN/m^3)	E_{rm} (Mpa)	m_b	s	a	GSI	Q	UCS (Mpa)	m_r	K_0	Vertical Stress (Mpa)	Horizontal stress (Mpa)	Average stress (Mpa)
49+310	198	27	11411	1.261	0.0048	0.505	52	0.86	55	600	0.73	5.346	3.920	4.395
49+440	205	27	376	0.535	0.0003	0.526	28	0.01	15	350	0.27	5.535	1.469	2.825
51+020	108	27	376	0.535	0.0003	0.526	28	0.01	15	350	0.28	2.916	0.808	1.510
51+100	72	27	2564	0.851	0.0014	0.511	41	0.10	30	500	0.52	1.944	1.005	1.318
53+250	855	27	11411	1.261	0.0048	0.505	52	0.86	55	600	0.42	23.085	9.772	14.210
53+650	642	27	11411	1.261	0.0048	0.505	52	0.86	55	600	0.45	17.334	7.875	11.028
54+725	538	27	2564	0.851	0.0014	0.511	41	0.10	30	500	0.30	14.526	4.377	7.760
55+340	315	27	2564	0.851	0.0014	0.511	41	0.10	30	500	0.32	8.505	2.763	4.677
56+105	563	27	5367	0.982	0.0022	0.508	45	0.29	40	600	0.35	15.201	5.386	8.657
56+300	619	27	5367	0.982	0.0022	0.508	45	0.29	40	600	0.35	16.713	5.821	9.451
56+680	706	27	11411	1.261	0.0048	0.505	52	0.10	55	600	0.44	19.062	8.445	11.984
57+740	563	27	2564	0.851	0.0014	0.511	41	0.10	30	500	0.30	15.201	4.558	8.105

4.2 *Goel et al. (1995) an empirical approach*

Goel et al. (1995) proposed a straightforward empirical method that utilizes the rock mass number N. This number is defined as the stress-free Q, aiming to mitigate the uncertainties associated with determining the accurate rating of the SRF parameter in Barton et al.'s (1974) Q. The definition is as follows:

$$N = (Q)_{SRF=1} \tag{2}$$

Goel et al. (1995) conducted a comprehensive analysis of tunnel sections, taking into account overburden depth (H), tunnel span or diameter (B), and the rock mass number (N) and generated a log-log diagram (Figure 5) in which the plotted data points revealed a clear distinction between squeezing and non-squeezing cases, represented by Equation 3.

$$H = (275N^{0.33})B^{-1} \tag{3}$$

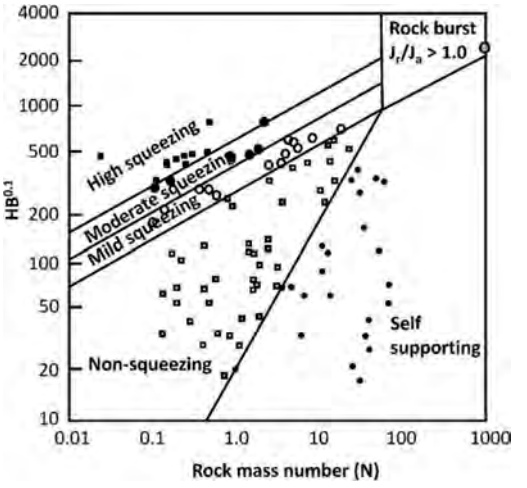

Figure 5. Goel et al. (1995), approach for predicting squeezing conditions.

4.3 *Verman (1993) an empirical approach*

In a field study involving nine Himalayan tunnels, Verman (1993) employed the ground reaction curves (GRC). Through the use of empirical correlations and the GRC, Verman developed a design chart for classifying ground conditions into three categories: self-supporting, non-squeezing, and squeezing. In this approach the maximum tunnel span (B_s) that the ground can sustain without experiencing squeezing is defined as Equation 4.

$$B_s = 3.2Q^{0.4} \tag{4}$$

Based on the actual span and the span defined in Equation 4, the ground is categorized as follows:

1) Self-supporting if $B - B_s < 0$,
2) Non-squeezing if $H\,(B - B_s)^{0.1} < 483Q^{1/3}$,
3) Squeezing or rock burst if $H\,(B - B_s)^{0.1} > 483Q^{1/3}$.

Where, H is overburden (m); B_s is tunnel span; Q is rock mass quality (Barton et al. in 1974).

4.4 *Jethwa et al. (1984) a semi-empirical approach*

Jethwa et al. (1984) delineate the degree of squeezing using the coefficient N_c which represents the ratio of the rock mass uniaxial compressive strength (UCS) to the in-situ stress and establish their approach for classification of degree of squeezing based on the Equation 5 and the criteria outlined in Table 3.

$$N_c = \frac{\sigma_{cm}}{P_0} = \frac{\sigma_{cm}}{\gamma H} \tag{5}$$

Where, σ_{cm} is rock mass uniaxial compressive strength; P_0 is in situ stress; γ is unit weight of rock mass; and H is tunnel overburden.

Table 3. Classification of squeezing behaviour Jethwa et al. (1984).

N_c	Type of behaviour
< 0.4	Highly squeezing
0.4 – 0.8	Moderately squeezing
0.8 – 2.0	Mildly squeezing
> 0.2	Non squeezing

4.5 *Aydan et al. (1993) a semi-empirical approach*

Drawing from their experience with Japanese tunnels, Aydan et al. (1993) introduced a relationship between the strength of intact rock (σ_{ci}) and the overburden rock pressure (γH), using the same equation as (5). This relationship assumes that the uniaxial compressive strength of the intact rock (σ_{ci}) and that of the rock mass (σ_{cm}) are equivalent. Based on the data from surveyed tunnels in squeezing rock conditions in Japan, Aydan et al. (1993) reveals that squeezing conditions are likely to arise when the ratio $\sigma_c/\gamma H$ is less than 2.0.

4.6 *Hoek and Marinos (2000) semi-empirical approach*

Hoek (1998) employed the ratio of the rock mass uniaxial compressive strength (σ_{cm}) to the in-situ stress (p_0) to gauge the likelihood of tunnel squeezing

issues. Hoek and Marinos (2000) further demonstrated that plotting tunnel strain ε_t against the ratio σ_{cm}/p_0 offers an effective method for assessing tunnelling problems in the presence of squeezing conditions.

Hoek (2000), through axi-symmetric finite element analyses involving derived an approximate relationship for tunnel strain ε_t using Equation 6 and Equation 7 considering $p_i = 0$.

$$\sigma_{cm} = \left(0.0034 m_i^{0.8}\right)\sigma_{ci}\left\{1.029 + 0.025 e^{(-0.1 m_i)}\right\}^{GSI} \quad (6)$$

$$\varepsilon = 100 \times \left(0.002 - 0.0025\frac{p_i}{p_0}\right)\left(\frac{\sigma_{cm}}{p_0}\right)^{\left(2.4\frac{p_i}{p_0}-2\right)} \quad (7)$$

Where, σ_{cm} is rock mass uniaxial compressive strength; σ_{ci} is uniaxial compressive strength of the intact rock; m_i is Hoek–Brown parameter for intact rock; *GSI* is Geological Strength Index; ε is tunnel strain (defined as the percentage ratio of radial tunnel wall displacement to tunnel radius); P_0 is in situ stress; P_i is internal support pressures.

Drawing from the above analysis and examining case histories, Hoek (2000) presented the curve depicted in Figure 6 as an initial estimate for evaluating tunnel squeezing problems.

The result of the empirical and semi-empirical approaches considering geomechanical properties of tunnel route is illustrated in Table 4. As it is clear from the following results, the approaches developed mostly from the Himalayan region shows almost same predictions for squeezing condition in this project. The Hoek and Marinos (2000) approach implemented to evaluate maximum deformation based on Equation 7 which the results are given in Table 4.

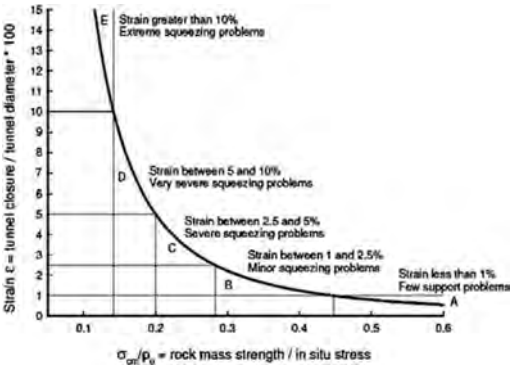

Figure 6. Classification of squeezing behaviour (Hoek and Marinos, 2000).

4.7 *Deformation analysis of tunnel at tail shield*

4.7.1 *Analytical analysis of deformations at tail shield*

Carranza-Torres and Fairhurst (2000) determined that the Convergence Confinement Method (CCM) consists of three fundamental components: the Longitudinal Displacement Profile (LDP), the Ground Reaction Curve (GRC), and the Support Characteristics Curve (SCC).

As an initial approximation, ground reaction curves were generated based on the estimated geomechanical properties using Rocsupport software, employing Carranza-Torres' approach (2004). These curves were used to assess the maximum ground deformations that may occur up to the point of first support contact, which corresponds to the end of the tail shield at 9.85 meters.

Tunnel boring machine (TBM) jamming in squeezing conditions arises when the available thrust is insufficient to maintain TBM progress or to facilitate a TBM restart, as indicated by Ramoni and

Table 4. Analysis of squeezing behaviour in critical section of the tunnel based on the empirical and semi-empirical approaches.

Chainage	Overburden (m) 0 – 855	Singh et al. (1992)	Verman (1993)	Goel et al. (1995)	Jethwa et al. (1984)	Aydan et al. (1993)	Hoek and Marinos (2000)	Max. Deformation Predicted (mm) H&M approach
49+310		Non Sq.	Non Sq.	Non Sq.	Mild Sq.	Non Sq.	Non Sq.	64.336
49+440		Sq.	Sq.	Mod. Sq.	High Sq.	Non Sq.	Severe Sq.	451.220
51+020		Sq.	Sq.	Mild Sq.	High Sq.	Non Sq.	Severe Sq.	451.220
51+100		Non Sq.	Non Sq.	Non Sq.	Mild Sq.	Non Sq.	Minor Sq.	157.099
53+250		Sq.	Sq.	High Sq.	High Sq.	Non Sq.	Non Sq.	64.336
53+650		Sq.	Sq.	Mod. Sq.	Mod. Sq.	Non Sq.	Non Sq.	64.336
54+725		Sq.	Sq.	High Sq.	High Sq.	Non Sq.	Minor Sq.	157.099
55+340		Sq.	Sq.	Mod. Sq.	High Sq.	Non Sq.	Minor Sq.	157.099
56+105		Sq.	Sq.	High Sq.	High Sq.	Non Sq.	Minor Sq.	113.549
56+300		Sq.	Sq.	High Sq.	High Sq.	Non Sq.	Minor Sq.	113.549
56+680		Sq.	Sq.	High Sq.	High Sq.	Non Sq.	Non Sq.	64.336
57+740		Sq.	Sq.	High Sq.	High Sq.	Non Sq.	Minor Sq.	157.099

Anagnostou (2011) and Zhao et al. (2012). To address this issue, one possible approach involves determining the closure of the TBM shield gap.

In the preliminary analysis utilizing Rocsupport, the maximum feasible deformation compared with the gaps between the TBM shield and the excavation diameter across various combinations of overcuts to assess the potential for TBM jamming in squeezing conditions. However, if these deformations surpass the prescribed limits, the point at which this gap closes concerning the tunnel face is determined using a Longitudinal Displacement Profile (LDP) plotting radial displacement against the distance from the tunnel face. Should the computed distance be less than or equal to the length of the TBM shield (9.85 meters), it signifies the development of a load buildup on the machine, which may lead to TBM jamming. In such cases, a more detailed analysis employing the Finite Element Method (FEM) undertook to assess and address the situation.

The LDP computed using the semi-analytical approach outlined by Vlachopoulos and Diedrichs (2009), which offers a preliminary estimation of expected deformations, guiding the identification of sections where FEM approaches may be required. The analysis will yield results in the form of a plastic radius (R_{pl}) and the maximum displacement at the tunnel perimeter ($u_{r,max}$).

The comprehensive analysis results for all critical sections, as determined through the analytical method employing Rocsupport, are provided in Table 5. These results are presented as the maximum expected displacement at the end of the tail shield, the anticipated maximum tunnel convergence, and the plastic radius of the excavated tunnel at each critical section.

Based on the analysis above, there is no anticipation of the ground making contact with the shield in any of the sections. Consequently, no pressure buildup is expected, provided that suitable overcuts are implemented at the appropriate locations. It's worth noting that second section (chainage 49+440) represents the scenario with the most significant deformation and convergence.

Table 5. Tunnel deformation at critical sections as per analytical approach (Rocsupport).

Chainage	Max displacement at tail shield (mm)	Tunnel Convergence at tail shield (%)	Plastic Radius (m)
49+310	1.59 mm	0.03%	4.93 m
49+440	123.37 mm	2.71%	10.94 m
51+020	36.63 mm	0.80 %	7.73 m
51+100	1.9 mm	0.04 %	4.8 m
53+250	8.39 mm	0.18 %	6.95 m
53+650	5.42 mm	0.12 %	6.29 m
54+725	32.94 mm	0.72 %	8.9 m
55+340	13.21 mm	0.29 %	6.94 m
56+105	12.75 mm	0.28 %	7.37 m
56+300	14.78 mm	0.32 %	7.68 m
56+680	6.24 mm	0.14 %	6.49 m
57+740	36.79 mm	0.81 %	9.13 m

4.7.2 *Numerical analysis of deformations at tail shield*

As stated above, based on the analytical analysis, most critical section will be at the chainage 49+440 which is further analysed using FEM (Plaxis) to further evaluate any squeezing risks.

The Axisymmetric finite element model provides more detailed results by incorporating the elasto-plastic behavior of the ground and accounting for the presence of the TBM shield and segmental lining. In FEM analysis, the initial stress is defined as the mean stress. Notably, the stepping of the shields has not been considered in this analysis, adopting a conservative approach. For all other sections not exhibiting squeezing issues according to analytical methods, control can be achieved through various overcuts, obviating the need for further refined analysis. It is also expected that in these sections, the ground will not come into contact with the TBM shields. Consequently, to drive the TBMs or initiate a restart, a nominal thrust force sufficient to overcome friction due to the machine's self-weight should suffice. The results of the FEM modelling are presented in Figure 7 to Figure 9.

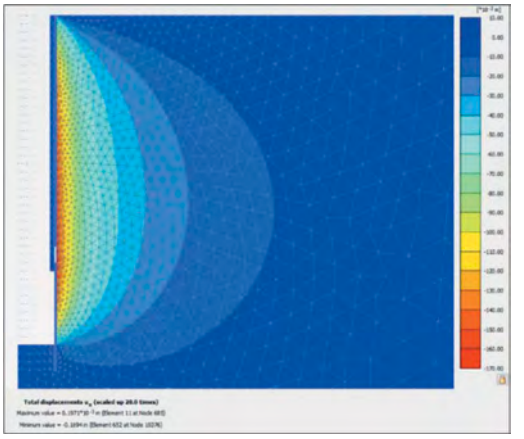

Figure 7. FEM analysis on chainage 49+440, Maximum ground displacement behind the TBM (170 mm).

The thrust required to overcome the friction force between the shield and the rock mass can be determined using Equation 8.

$$F_r = p_s S \mu \tag{8}$$

Where p_s is the pressure acting on the shield, μ is the friction coefficient, and S is the contact surface area between the shield and the rock mass.

The contact surface area of the shield and rock can be calculated as per Equation 9.

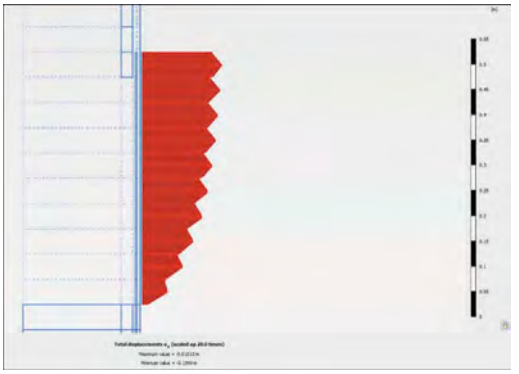

Figure 8. FEM analysis on chainage 49+440, maximum ground displacement at TBM tail shield (160 mm).

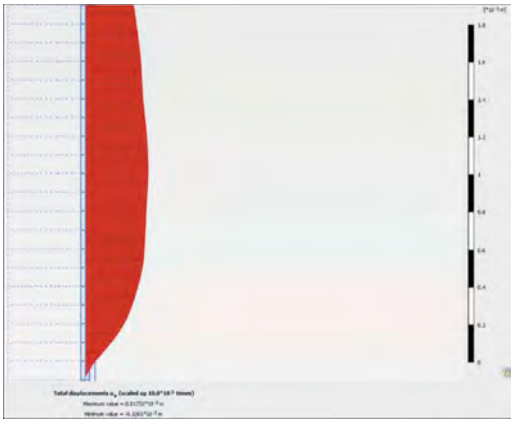

Figure 9. FEM analysis on chainage 49+440, maximum displacement on the segmental lining (0.33 mm).

$$S = 2\pi r_s L_c \tag{9}$$

Where r_s signifies the shield radius, and L_c is the length at which contact takes place.

The friction coefficient is variable, typically falling within the range of 0.15 to 0.35 for sliding friction during TBM advancement and 0.25 to 0.45 for static friction during TBM restart.

Likewise, the analysis to ascertain the maximum thrust necessary for both sliding and restarting the TBMs, utilizing the equations described in Equation 8, was carried out, yielding the following results:

- Maximum thrust required for sliding: 47,500 kN
- Maximum thrust required for TBM restart: 61,071 kN

Since the calculated thrust forces are lower than the maximum nominal thrust force of the TBM, they are deemed acceptable.

5 CONVERGENCE MEASUREMENT IN TBM TUNNELLING

As mentioned in Part 2, the machines are equipped with three void measurement cylinders along the shield, spaced at a distance equal to the advance length (1700 mm). These void measurements are conducted during TBM stoppages, both short stoppages (e.g., during ring building) and long stoppages (e.g., routine maintenance, probe drilling, tunnel conveyor extensions, etc.). The TBM operator measures the void behind the shield, recording this information along with the precise time and the shield's chainage in the data logger. These recorded data are used to assess the actual convergence around the TBM. Figure 10 displays the data obtained through the void measurement system at various chainages in the first 2.7 km of the upline tunnel.

To account for tolerances in the advance length and to exclude incorrect records (resulting from not measuring the same location with the void measurement cylinders), records in which two readings have a tolerance greater than ±50 mm in chainage are not considered in the Ground Convergence calculations. Ground Convergence is derived from the readings of the void measurement system during TBM advancement and is presented in Figure 11, where GC1-2 represents the convergence measured by the first and second void measurement cylinders, and the same format applies to GC2-3 and GC1-3.

Furthermore, the Ground Convergence Rate is calculated considering the time between two measurements. Figure 12 illustrates the Ground Convergence Rates, in which GCR1-2 representing the rates obtained from the first and second void measurement cylinder data, and the same nomenclature applies to GCR2-3 and GCR1-3.

Additionally, as previously mentioned, planned stoppages occur during tunnel execution, with durations ranging from several hours to one or more days. During these stoppages, void measurements are conducted, and the data analysis is carried out, utilizing precise convergence measurements taken at a single point while eliminating abnormal data. This process ensures a pure and accurate assessment of the Ground Convergence Rate, as depicted in Figure 13.

The most critical section within the 2.7 km length of the tunnel was situated between chainage 49+000 to 49+500, where the highest Ground Convergence Rate (GCR) was recorded. The ground closure around the shield in this specific section closely matched with the measurements derived from both the analytical and FEM analyses. Considering some convergences was attributed to wedge falls occurring

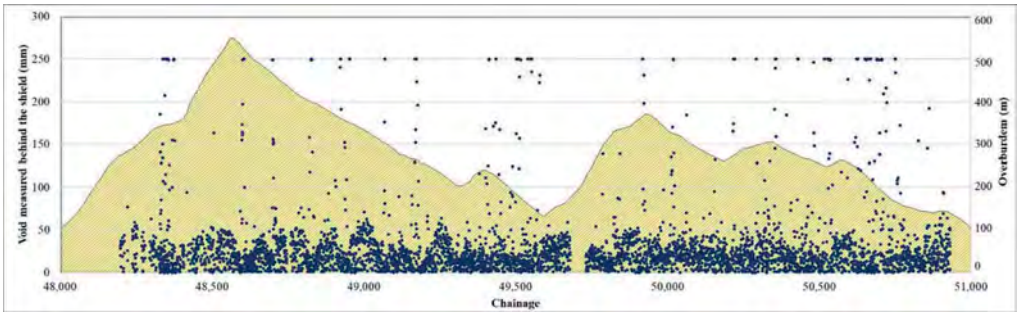

Figure 10. Gap/Void measured behind the shield along the shield using data obtained from three void measurement cylinders.

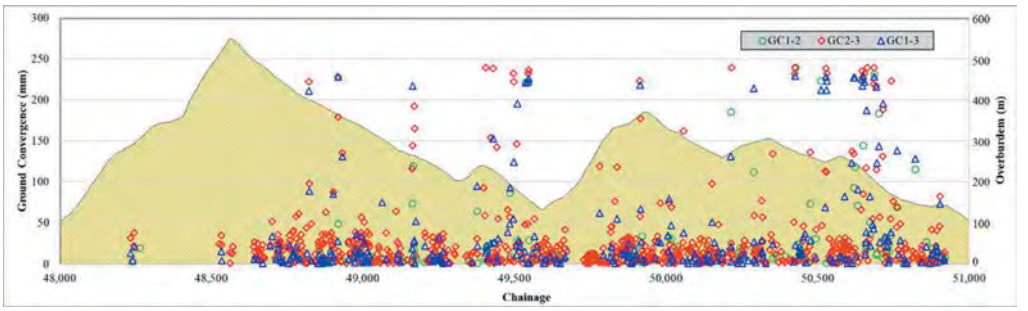

Figure 11. Actual ground convergence measured around the shield using data obtained from three void measurement cylinders.

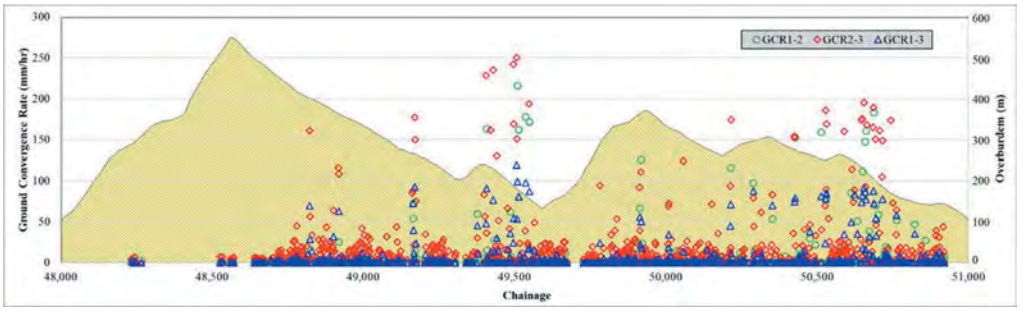

Figure 12. Ground convergence rates using data obtained from three void measurement cylinders.

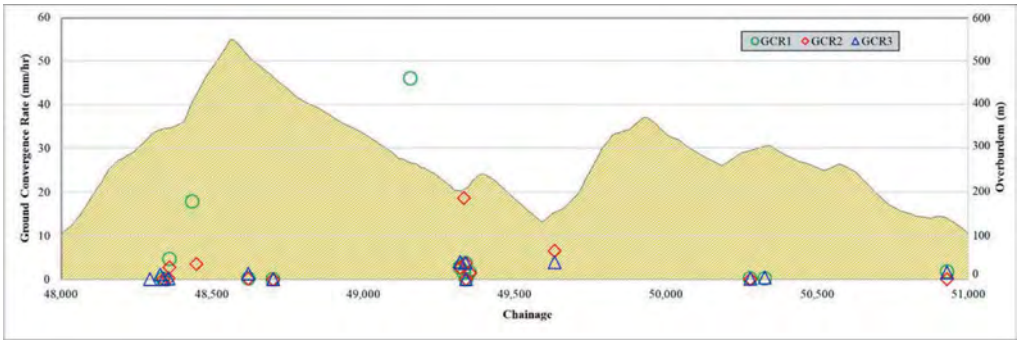

Figure 13. Ground convergence rates using data obtained from void measurement cylinders during TBM stoppages.

on the tunnel crown, resulting in the recording of 250 mm void behind the shield.

6 CONCLUSIONS

In this paper, a comprehensive exploration of various approaches for assessing squeezing ground conditions, spanning empirical, semi-empirical, analytical, and numerical methods, has been discussed and their applications have been demonstrated within the context of the Rishikesh to Karanprayag railway project, Package 4 (Tunnel 8). Notably, among the empirical and semi-empirical approaches, the Aydan et al. (1993) approach, based on a diverse dataset from different rock types and not confined to the same Himalayan region database, yielded distinctive results in the evaluation of squeezing conditions for this case study. Throughout these evaluations, it became evident that certain critical squeezing zones shared consistent outcomes across different methods, corroborated by FEM analysis. The most critical zone was identified around chainage 49+440, where site data were collected and meticulously assessed, employing state-of-the-art TBM technologies for monitoring tunnel convergence. In the initial 2.7 km of the upline tunnel (spanning from chainage 48+180 to 50+880), the highest Ground Convergence Rate was observed in close proximity to the same chainage, as evaluated through empirical, semi-empirical, and analytical approaches. Furthermore, continuous data collection and evaluation within the project are essential for adapting actual Ground Convergence (GC) and Ground Convergence Rates (GCR) to the evolving rock conditions and TBM excavation parameters.

ACKNOWLEDGMENTS

The authors express their heartfelt gratitude to Rail Vikas Nigam Limited as the project client, Larsen & Toubro as the project contractor, Herrenknecht as TBM supplier, and TUMAS-ALTINOK Joint venture as detailed design and project management consultant of the project for their invaluable support and collaborative efforts in providing a wealth of worthwhile and useful database. This data has been instrumental in commencing the journey of developing an approach to address squeezing conditions in TBM tunnelling in Himalaya.

REFERENCES

Aydan, O., Akagi, T. and Kawamoto, T. 1993. The squeezing potential of rocks around tunnels; theory and prediction. Rock Mechanics Rock Engineering, 26(2), pp 137–163.

Barla, G. 1995. Squeezing rocks in tunnels. ISRM News Journal, 3/4, pp 44–49.

Barla, G., Barla, M., Bonini, M., Debernardi, D., 2014. Guidelines for TBM tunnelling in squeezing conditions – a case study, Geotechnique Letters 4, 83–87,

Barton, N., Lien, R. and Lunde, J. 1974. Engineering classification of rock masses for the design of rock support. Rock Mechanics, Vol. 6, pp 189–236.

Carranza-Torres, C. and Fairhurst, C. 2000. Application of the convergence confinement method of tunnel design to rock masses that satisfy the Hoek-Brown failure criteria. Tunnelling and underground space Technology,15(2), pp 187–213.

Carranza-Torres, C. 2003. Dimensionless graphical representation of the exact elastoplastic solution of a circular tunnel in a Mohr-Coulomb material subject to uniform far-field stresses. Rock Mechanics Rock Engineering, 36(3), pp 237–253.

Goel, R. K., Jethwa U. L. and Paithakan, A.G. 1995. Tunnelling through young Himalayas - a case history of the Maneri - Uttarkashi power tunnel. Engng. Geol., 39, pp 31–44.

Hoek, E. 1998. Tunnel support in weak rock, Keynote address, Symp. On sedimentary rock engineering, Taipei, Taiwan, 20–22.

Hoek, E. and Marinos, P. 2000. Predicting tunnel squeezing problems in weak heterogeneous rock masses. Tunnels and Tunnelling International, part one-November 2000, pp 45–51; part two -December 2000, p 33-36.

Jethwa, J.L., Singh, B. & Singh, B. 1984. Estimation of ultimate rock pressure for tunnel linings under squeezing rock conditions—a new approach. In Design and Performance of Underground Excavations: ISRM Symposium—Cambridge, UK, Thomas Telford Publishing, 231238.

Ramoni, M. and Anagnostou, G. 2001. The interaction between shield, ground and tunnel support in TBM tunnelling through squeezing ground. Rock Mechanics and Rock Engineering. 44 (1), 2011, 37–61.

Singh, B., Jethwa, J. L., Dube, A. K. and Singh, B. 1992. Correlation between observed support pressure and rock mass quality. Tunnelling and Underground Space Technology, 7, pp 59–74.

Verman, M.K., 1993. Rock mass-tunnel support interaction analysis, Ph.D. Thesis, Indian Institute of Technology Roorkee, India.

Vlachopoulos, N., Diederichs, M., 2009. Improved Longitudinal Displacement Profiles for Convergence Confinement Analysis of Deep Tunnels. Rock Mech Rock Eng 42, 131–146.

Tunnelling for a Better Life – Yan, Celestino, Thewes & Eberhardt (Eds)
© 2024 The Author(s), ISBN 978-1-032-80042-4
Open Access: www.taylorfrancis.com, CC BY-NC-ND 4.0 license

Structural behaviour machenism of vertical jacking method on large sections and influencing factors analysis

Yi-min Gao*
College of Civil Engineering, Tongji University, Shanghai, China
School of Civil Engineering, Universitat Politècnica de Catalunya BarcelonaTech, Barcelona, Spain

Xian Liu & Zhen Liu
College of Civil Engineering, Tongji University, Shanghai, China

Gonzalo Ramos & Jose Turmo
School of Civil Engineering, Universitat Politècnica de Catalunya BarcelonaTech, Barcelona, Spain

ABSTRACT: The vertical jacking method has been widely used in water intake and drainage segmental tunnels. The construction method of standpipes by lifting could mainly be divided into upward shield method, vertical jacking method and vertical pipe jacking method. Comparing with the other two methods, the vertical jacking method has the advantage that its equipment is simpler. However, the vertical jacking force intensity is uncertain because it depends on many factors. The higher the pipe diameter, the higher the normal stresses, being the critical moment the starting of the jacking process. Based on numerical simulations, this paper intends to research on the structural behaviour of this method on large section standpipes and analyze the factors that controls the jacking process. The research results show: 1. The deformation of the main tunnel is a combination of two effects: the longitudinal sinking and the vertical ovalization. 2. The circumferential compressive stresses in the bottom segments of the main tunnel are greatly reduced due to the vertical force of the jack. 3. The shear of the transverse joint between two rings mainly appear in the joint between the opening ring and the contiguous one. 4. The thickness of the segment has little effect on the mechanical response of the structure for typical segment depth. 5. With the decrease of the opening area, the internal force of the open ring structure decreases, while the internal force of the contiguous rings decreases or remains basically unchanged.

Keywords: segmental tunnel, large section standpipe, vertical jacking method, mechanism, control factors

1 INTRODUCTION

When constructing large drainage outlets for extending into rivers, lakes, or seas in soft soil areas, water-based construction methods such as island construction pits or floating sinking pits are often used. Sometimes the method costs a lot, and it is also susceptible to the influence of wind and waves, resulting in longer construction periods. In recent years, mechanical methods for building vertical pipelines or tunnels have become increasingly common. Currently, three common mechanical methods have been adopted: upward shield method, vertical jacking method and vertical pipe jacking method.

The upward shield method is primarily carried out in Japan [Kondo et al., 2004, Ito K et al., 2004] (Midosuji Comprehensive Conduit Project in Osaka, Japan). The construction method is similar to shield machine boring and segment installation, with the only difference being that the boring is done in an upward direction.

The vertical pipe jacking method was applied in Argentina's "Riachuelo Lot 3" outfall project. The lifting equipment pushed the pipe sections upward into the soil layer The destruction mechanism and morphology of the overlying soil layer are analyzed in some tests [Wei et al., 2021, Wei et al., 2022, Wei et al., 2023].

*Corresponding author: yimin.gao@upc.edu

DOI: 10.1201/9781003495505-238

The vertical jacking method is mainly applied in China, which is similar to the vertical pipe jacking method construction process, but the difference lies in soil removal equipment. The vertical jacking method only need the lifting equipment to raise the pipe sections to the water surface.

Comparing with the other two methods, the vertical jacking method has the advantage that its equipment is simpler. However, the vertical jacking force is uncertain between different projects because it depends on many factors. The higher the pipe diameter, the higher the normal stresses, being the critical moment the starting of the jacking process. Different lifting forces will significantly affect the internal force response and mechanical properties of the tunnel structure, which are the points of the structure design.

In order to investigate the mechanical behavior of tunnel with vertical jacking method, many on-site experimental researches have been carried out. However, the most common monitoring is the structural convergence. [Dong et al., 2012, You et al., 2012, Wang et al., 2021].

Considering the limitations and cost-effectiveness of on-site experiments, numerical simulations were widely used to verify other structural responses. The results demonstrate: as the jacking force increases, the maximum misalignment deformation between the open ring and adjacent rings also increases. [Wang et al., 2011]. The crown of open ring and the adjacent three standard rings' deformation response is greater than that of bottom [Xu et al., 2021]. The applicability of numerical models in the vertical jacking method has been confirmed. Considering the research results mainly also concentrating on the deformation structural response and not considering more detailed load cases. This paper intends to research on more structural response throughout the entire vertical jacking construction process with shell-contact numerical model [Liu et al., 2021] Through parameter analysis, this study aims to provide support for the design of this construction method.

2 STUDY CASE

A certain power plant project is constructed near the coast in Shanghai. Its intake tunnel is constructed by the shield method, built at a depth of 8.45 meters below the seabed. The intake tunnel consists of 30 segments with an outer diameter of 3700mm and a segment thickness of 350mm. The segment ring width is 985mm, as shown in Figure 1.

The intake tunnel consists of 30 segment rings, with the 3rd, 4th, 9th, 10th, 15th, 16th, 21st, 22nd, 27th, and 28th rings being open rings (every six rings), while the rest are standard rings. The crown of the open rings is made of steel structure segments, used for vertical jacking. The opening range is two rings (1970mm×1970mm). Comparing other projects, the ratio of the open area to the inner diameter is relatively high, belonging to the large section [Wang et al., 2021].

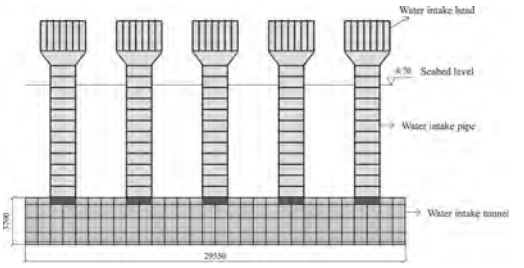

Figure 1. Illustration of study case.

As shown in Figure 2, the segmental lining ring consists of 3 stell-concrete segments and 4 reinforcement concrete segments, of a circular arc of 30.5°, 82.24°, 30.5°, 58°, 58°, 58° and 42.76°, respectively. Adjacent segments (including the radial and circumferential direction) are connected by 8.8-grade bolts (yielding strength 640 MPa). Concrete grade C50 is adopted for each component of the specimen, the main reinforcement bars are HRB400 steel bars (yielding strength 400 MPa) with a diameter of 28mm@150mm (inside face) and 22mm@150mm (outside face). The steel-concrete segments' steel parts are Q235 (yielding strength 235 MPa) and the concrete strength of grade was C50.

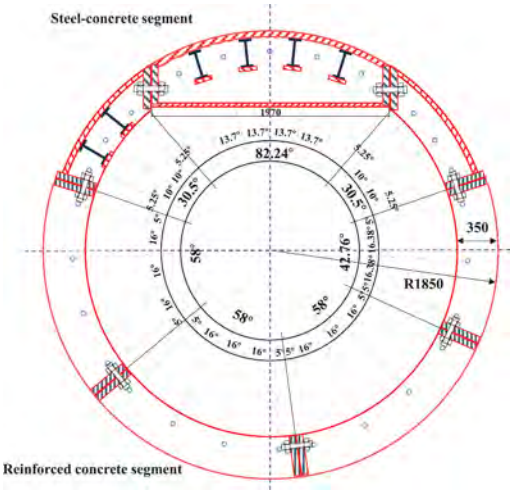

Figure 2. Layout of s tunnel linings (dimensions in mm).

According to the actual construction process, the process can be simplified the following steps (shown in Figure 3):

(1) Initial Stage
The intake shield tunnel has been constructed, loaded by external soil and water pressure, tunnel self-weight, etc. (including top vertical soil pressure of 61.57kPa, top water pressure of 235.1kPa, and a ground overload of 30kPa.)

(2) Vertical jack stage
The first pipe section is securely connected to the top cover of the tunnel. The circumferential bolts

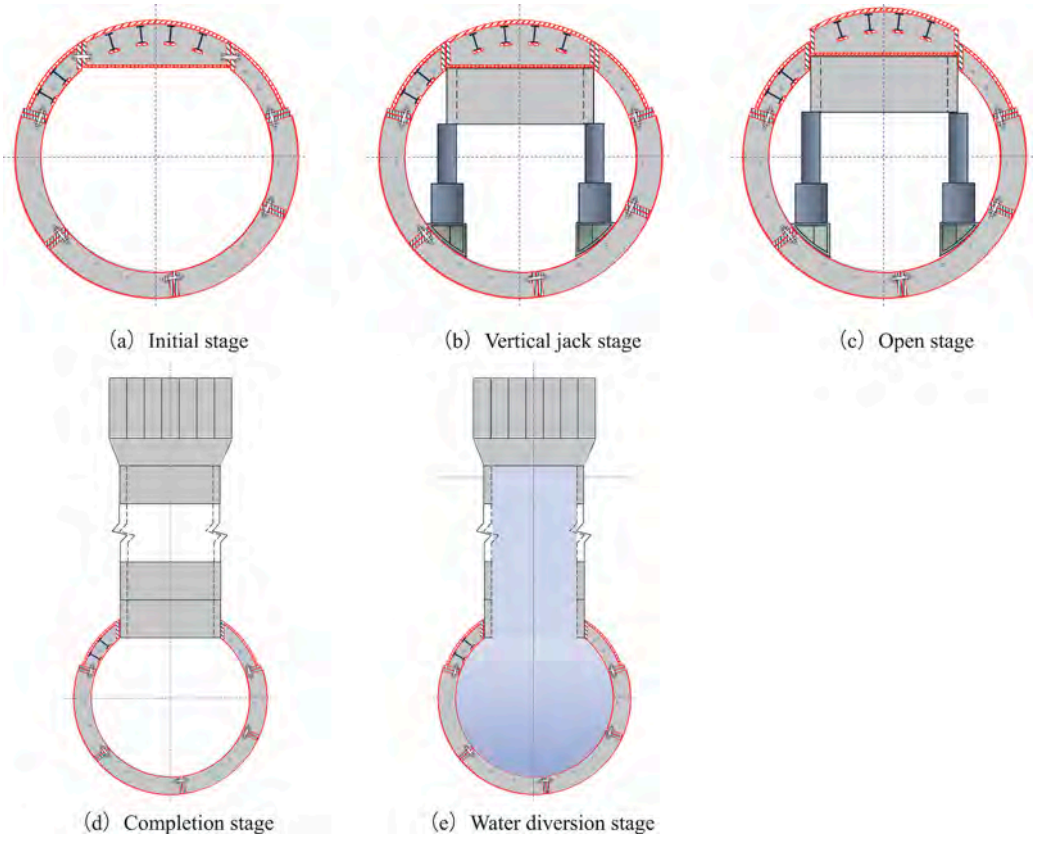

Figure 3. Schematic diagram of working condition.

connecting the special riser pipe section with the surrounding tunnel segments at the lifting port are removed.Vertical jack force is loaded at the bottom of open rings to lift the pipe upward. The force intensity is always variational according to the nonlinear variation of the frictional force of the structural lifting and the gravity of external soil, etc.

(3) Open stage
The first pipe section is vertical pushed out during construction, forming the open.After completing the lifting operation, two weighing beams are installed with tightening the tie rod bolts to secure the first pipe segment onto the beams. Once safety is confirmed, the hydraulic jack is used for the next pipe lift. Subsequently, the second section of the pipe is connected, the weighing beams are removed. The open is present throughout the entire process.

(4) Completion stage
The third stage is repeated multiple times until the vertical pipe is constructed, including the final vertical pipe structure, final joints, and longitudinal connecting beams. The vertical pushing force on the pipe is reduced to zero.

(5) Water diversion stage
Water is diversed into the tunnel. The self-weight of water, internal water pressure and water flow effects are included. The water pressure load consists of two parts. The first part is the self-weight of water, and the second part is the internal water pressure value, calculated at 254.10kPa based on the highest water level.

3 NUMERICAL MODEL

3.1 *Simulation assumptions*

The calculation principles are as follows:

(1) The calculation model is based on a load-structure pattern.
(2) Coulomb friction is used to simulate the "pressure-shear coupling" at the joints.
(3) Ideal elastic-plastic models are applied for the circumferential and longitudinal bolts.

3.2 *Model dimensions and materials*

Shell element is intended for simulation of segmental linings. A total of 30 ring segments are simulated, and the arrangement of the segments is the same as the chapter 2. (As shown in Figure 4).

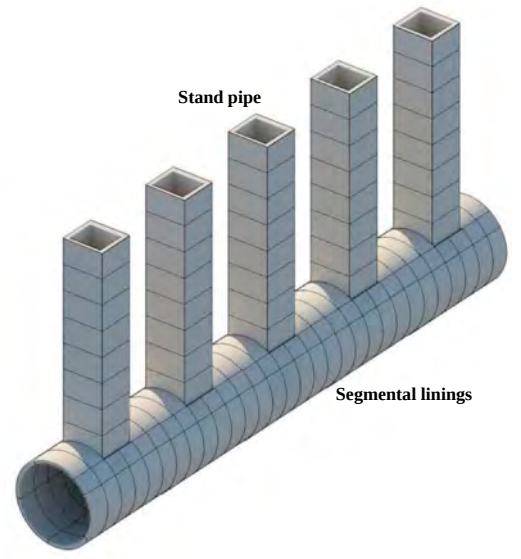

Figure 4. Medel of segments and standpipe sections.

The concrete structural portion is simulated by layered shell element. Both the concrete layer and the reinforcement layer are simulated. The steel structural portion is simulated by equivalent stiffness method. The flexural and compressive stiffness of the simulation structure is equivalent to that of the actual lining segments. The calculation formula is as follows.

$$E_{1x}A_{1x} = E_{2x}A_{2x} \quad (1)$$

$$E_{1y}A_{1y} = E_{2y}A_{2y} \quad (2)$$

$$A_{2x} = b_{2x}h_{2x} \quad (3)$$

$$A_{2y} = b_{2y}h_{2y} \quad (4)$$

Where, $E_{1x}A_{1x}$, $E_{1y}A_{1y}$ are the axial stiffness of the actual segments in x direction and y direction; $E_{2x}A_{2x}$, $E_{2y}A_{2y}$ are the axial stiffness of the segments in the equivalent model in x direction and y direction; $b_{2x}b_{2y}$, $h_{2x}h_{2y}$ are the width and height of the segments in the equivalent model in x direction and y direction. The material parameters used in the numerical model are listed in Table 1.

Table 1. Material models and parameters.

Type	Material	Young's modulus (N/m^2)	Poisson's ratio
Segment (Concrete part)	Concrete	3.45×10^7	0.167
Segment (rebar)	Steel	2.1×10^{11}	0.3
Segment (Steel part)	Equivalent model	2.08×10^7 (0.58m width)	0.3
Standpipe	Concrete	3.45×10^7	0.167

3.3 *Joints and bolts simulation*

Considering the actual joint of the project (the edge of the concrete is surrounded by the steel), a series of rigid beams are used to simulate the thickness of the segments and the steel joints. The contact parts are modeled with contact elements to simulate the joints' compressive behaviours. The circumferential and longitudinal bolt positions are set according to their actual locations. (As shown in Figure 5)

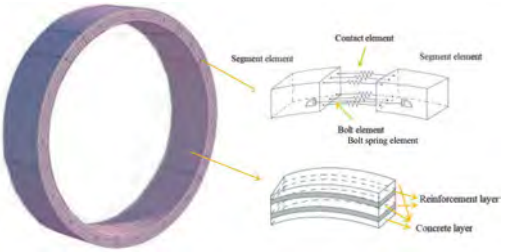

Figure 5. Model of segments and joints.

The parameters of the joints are shown in Table 2 below:

Table 2. Parameters of joints.

Type	Stiffness (N/m²)
Longitudinal joint compression	1.2×10^{10}
Longitudinal bolt tensile	1.7×10^{10}
Circumferential joint compression	2.5×10^{11}
Circumferential bolt tensile	2.9×10^{11}

3.4 *Boundary conditions*

The ground reactions corresponding to the tunnel deformation are simulated by ground springs located along the entire periphery of the tunnel. The geological parameters are shown in Table 3.

Table 3. Parameters of stratum.

Type	Stiffness (N/m²)
Horizontal direction	1.8×10^7
Vertical direction	1.3×10^7
Longitudinal direction	3×10^6

3.5 *Simulation loading process*

Based on the construction process in chapter 2, the simulation process is also divided into five loading cases.

(1) Initial stage
Following the previously mentioned method, the model and boundary conditions are established. Then the external soil and water loads are loaded.

(2) Vertical jack stage
The water-stop device is activated. In order to simulate the most extreme condition, the bottom of all open rings are loaded vertical downward (the vertical jack force is the maximum of the whole process).
(3) Open stage
All crown segments are pushed out in most dangerous condition. Since the pushed-out segments cannot transfer bending moments, the longitudinal axial force is primarily transmitted through the water-stop frame and the remaining segments. All crown segments are moved out.
(4) Completion stage
The final standpipe structure, the final joints are activated. Then the standpipe is loaded with soil and water loads.
(5) Water diversion stage
The self-weight of water and internal water pressure are loaded inside the main tunnel. The impact of water flow on the riser is also considered.

4 STRUCTURAL RESPONSE OF PROCESS

4.1 *Deformation characteristics*

Among all the loading cases, the two most significant deformation characteristics are as the longitudinal sinking and the vertical ovalization.

In the vertical jack stage, the tunnel is influenced by the invert force by the jack at the opening position, causing the entire tunnel to move downward. The maximum downward deformation is at the central position, reaching 28mm.

In the open stage, the open rings deform vertically, resulting in an 8mm convergence between the crown and invert. Influenced by the deformation of the open ring, the regular rings, under the internal force transmission from the open ring, also deform vertically. The closer to the open ring, the deformation phenomenon is more obviously. These two phenomena both occur under the open stage, as shown in the Figure 6.

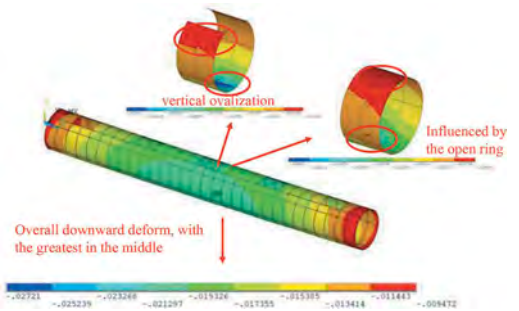

Figure 6. Deformation in y direction under open stage (dimensions in mm).

4.2 *Internal force characteristics*

In the initial stage, the bending moments and axial forces in each ring are the same. The maximum positive bending moment occurs at the crown of the lining ring(56 kN·m), and the maximum negative bending moment appears near the spring position (-60 kN·m). The axial force in the entire ring is maintained between -400 and -600 kN.

As shown in Figure 7, the greatest internal force changes happen in two stages. In the vertical jack stage, the positive bending moment at the crown and invert of the open ring decreases by 45 kN·m and the negative bending moment at the spring decreases by 40 kN·m. The axial force at the spring decreases by 50 kN, the axial force at the bottom decreases by 400 kN, which means it is virtually no axial force.

In the open stage, the negative bending moment at the spring changes from negative to positive (variation is around 25 kN·m), and the positive bending moment at the invert changes to negative. The axial force at the spring decreases by 100 kN, and the axial force at the bottom changes from compression to tension.

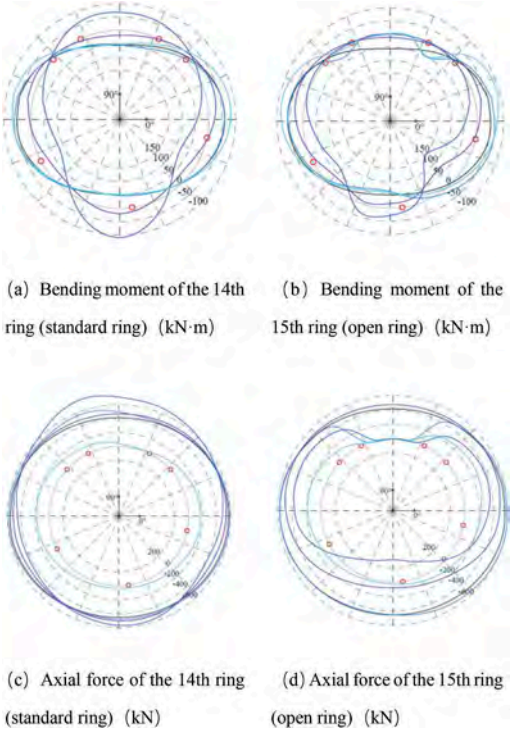

(a) Bending moment of the 14th ring (standard ring) (kN·m)

(b) Bending moment of the 15th ring (open ring) (kN·m)

(c) Axial force of the 14th ring (standard ring) (kN)

(d) Axial force of the 15th ring (open ring) (kN)

Figure 7. Internal force under different stages.

As shown in the Figure 8, the shear force between rings is primarily radial shear in the open stage, and the maximum radial shear occurs between the open ring and the contiguous one. The invert radial shear force between rings reaches 60 kN/m. The reason for this is that the open ring's vertical deformation trend

is stronger than that of the standard ring, resulting in inconsistent deformation, where the occurrence of inter-ring force transmission happens.

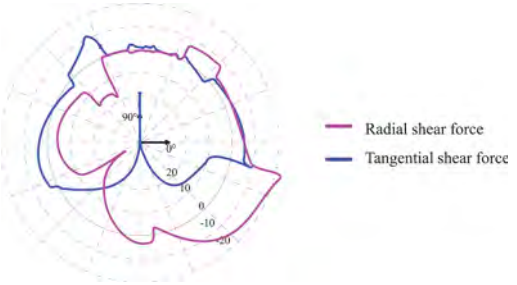

Figure 8. Shear force between 16th/17th ring in the open stage.

5 IMPACT ASSESSMENT OF DIFFERENT FACTORS FOR DESIGN

5.1 *Thickness influence*

In the case study project, calculations are carried out with thickness of 300mm and 350mm. In the initial stage, both schemes exhibited similar deformations under external loads, resulting in an 1mm convergence between the crown and invert. The deformation differences during the transition from the initial stage to the water diversion stage are within 1mm.

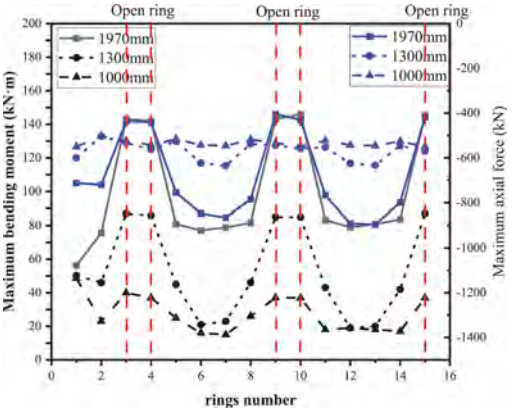

Figure 9. Maximum bending moment and axial force of different thickness in open stage.

The greatest differences in internal forces occur in the open stage. As shown in Figure 9,the bending moment of the 350mm thick scheme is larger than that of the 300mm thick scheme (less than 10 kN·m, with a difference of 5%), and the axial force is also larger (maximum less than 50 kN, with a difference of 5%). Therefore, the thickness of the lining segments has a relatively small impact on the structural internal forces.

5.2 *Open size influence*

In the case study project, calculations are also carried out with different open size (Original scheme: 1970mm×1970mm open, covering two rings in its entirety. Scheme 2: 1300mm×1300mm open. Scheme 3: 1000mm×1000mm open).

The different deformation trends of the two new schemes compared to the original scheme occur in the remaining structural portion at the crown of the open ring. The reason for this is that in the original scheme, two complete ring segments are moved out, whereas the two new schemes retain a portion of the segments.

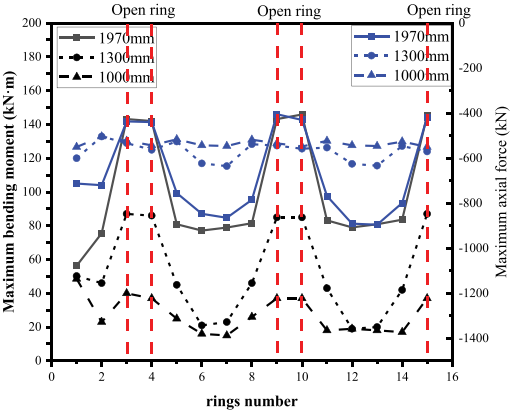

Figure 10. Maximum bending moment and axial force of different open size in open stage.

As shown in Figure 10, in open stage, as the open size decreases, the maximum bending moment of the open ring decreases, meanwhile the maximum axial force increases. With the open size decreases, the maximum bending moment and maximum axial force of the regular ring decrease. The smaller open area, the smaller jack force in use, enabling its internal force change.

In the completion stage, with the reduction in the open area, there is a partial stress concentration phenomenon at the crown of the remaining segments of the open ring. Although not illustrated in this paper, it should also be given attention.

6 CONCLUSIONS

In the summarized study case, shell-contact models have been used to simulate the structural behaviour of tunnels constructed by vertical jacking method on large section. The focus of the presented work was to explain the mechanism of this method and introduce the impact assessment of different factors for design.

The numerical results show that there are two most significant deformation characteristics during construction. The longitudinal sinking and the vertical ovalization deformation are caused by vertical jack force and the open area forming. At the same

time, the structural response of reduction in the axial force at the bottom of the open ring is obvious. The maximum radial shear occurs at the bottom between the open ring and the contiguous one.

Furthermore, the study also indicates that the thickness of the lining segments has a minimal impact on the structural mechanical response. The bending moment and axial force for 300mm thickness lining segments are smaller than those for 350mm thickness lining segments, but the variation is less than 5%. Different thicknesses of lining segments have almost no effect on the structural response. The design of lining segment thickness should primarily consider whether the cross-sectional reinforcement is reasonable. And as the open area decreases, the overall bending moment of the open ring structure decreases due to the reduced uplift load applied. At the same time, because of the reduced area, there are residual lining segments at the crown of the open ring, leading to an increase in structural axial force. The design of the lining segment open size should fully consider the different internal forces resulting from various open sizes, as well as the potential influence of residual lining segments on the structure and the possibility of stress concentration phenomena.

Future work related to this study includes the situ experiment check, in which promote the applicability of this numerical method.

ACKNOWLEDGMENTS

None

REFERENCES

Kondo F, Sakamoto H, Takaishi T, et al. “Construction of three vertical shafts using upward shield machine - the Bandai-Hannan sewer tunnel construction work”. Proceedings of the 30th ITA-AITES World Tunnel Congress, 2004, 19:491.

Ito K, Sakae T, Hara S, et al. “Development of Upward Shield Method”. Tunnelling and Underground Space Technology, 2004,19(4-5):488–489.

Wei Lixin, Yang Chunshan, Mo Haihong, et al. “Model tests and discrete element analysis on jacking force of shield shaft vertical pipe jacking”. Journal of Central South University (Science and Technology), 2021, 52 (10): 3595–3604.

Wei, Xinjiang, et al. “Study of the Indoor Model Test and CEL Simulation of Jacking Force in the Vertical Tunnelling Method.” Advances in Civil Engineering 2022 (2022).

Wei, Xinjiang, et al. “Numerical Simulation Analysis of the Jacking Force and Its Influencing Factors during the Vertical Tunneling Process.” Mathematical Problems in Engineering 2023 (2023).

Dong Shengxian, Luo Shuqing. “Application of Vertical Lifting Method to Water Supply and Drainage Tunnel Engineering in Power Plant”. Electric Power Survey & Design, 2012 (06):47-51+69.

You Xueti. “Application of Lager Diameter Vertical Lifting Water-intake Hats to Nuclear Power Station in Sanmen”. Electric Power Survey & Design, 2012 (05):48–52.

Wang Xiao, et al. “Vertical tunneling in China-A case study of a hydraulic tunnel in Beihai.” Tunnelling and Underground Space Technology. 2021(107): 103650.

Wang Lizhong, Wang Zhan, Li Lingling, et al. “Construction behavior simulation of a hydraulic tunnel during standpipe lifting”. Tunnelling and Underground Space Technology, 2011, 26(6):674–685.

Xu Shiyang, Liu Shuzhuo, Chen Junsheng, Yang Chunshan. “Tunnel Deformation in Vertical Jacking Construction Stage of Shield Shaft”. Henan Science, 2021, 39(01):76–83.

Liu Xian, Guo Zhenkun, Wu Pengli. “Shell-Contact Model with Nonlinear Joints for Shield Lining Design”. Tunnel Construction, 2021,41(S1):54–62.

Tunnelling for a Better Life – Yan, Celestino, Thewes & Eberhardt (Eds)
© 2024 The Author(s), ISBN 978-1-032-80042-4
Open Access: www.taylorfrancis.com, CC BY-NC-ND 4.0 license

Research on the automatic and synchronous construction technology of fully prefabricated internal structures inside large-diameter shield tunnels

Zhaoguo Ge
China Railway 14th Bureau Group Shield Engineering Co. Limited, Shanghai, China

Zeren Tang
College of Civil Engineering, Tongji University, Shanghai, China

Chen Chen
China Railway 14th Bureau Group Shield Engineering Co. Limited, Shanghai, China

Xian Liu*
College of Civil Engineering, Tongji University, Shanghai, China

ABSTRACT: The Shanghai Airport Connection Line is the first project to utilize fully prefabricated internal structures in a large-diameter shield tunnel in China. This paper elaborates on the automatic and synchronous construction of the fully precast internal structures in this project, including the design of internal structures, the automatic construction equipment, the process of synchronous assembly, and the control index of construction quality. To begin with, design information, involving precast arc parts and formed partition walls is introduced. Secondly, the composition and working principle of the adjustment device for prefabricated arc parts and assembling equipment for precast partition walls are carried out. In addition, automatic construction schemes and the process of synchronous shield excavation using those above devices are described respectively. Eventually, the construction quality control index of precast arc parts and prefabricated partition walls is elaborated. By utilizing the above-mentioned equipment and a series of construction techniques, automatic and synchronous construction of fully prefabricated internal structures in a large-diameter shield tunnel, which is in the form of a single hole with double tracks, has been realized. Moreover, the above approaches have significantly and effectively improved construction accuracy, quality, and efficiency.

Keywords: Fully Prefabricated Internal Structure, Automatic Construction, Synchronous Assembly, Prefabricated Arc Parts, Prefabricated Partition Walls

1 INTRODUCTION

With the continuous development of urban transit technology, the construction of large-diameter shield tunnels has increased gradually, and the method has also been improved continuously. Large-diameter shield tunnels are more suitable for single-hole with two tracks than single-hole with one track or double-hole with two tracks tunnels because they are capable of effectively shortening the construction duration and reducing risks and costs (Pan *et al.*, 2020).

Foreign projects, such as Line 9 in Barcelona, Spain (Ormazabal, Viñolas and Aguado, 2008); Apennine Tunnel in Italy (Finzi-Contini, Gori and Semproli, 1995); Seikan Tunnel in Japan(Matsuo, 1986), and so on, are explorations on the single-hole with double tracks tunnels form. Meanwhile, in recent years, domestic projects also carry out explorations on such forms of tunnels, such as Line 11(Zhou, 2015) and Line 16 (Cao *et al.*, 2015) of the Shanghai Metro; the Weisan Road river-crossing tunnel in Nanjing (Wang *et al.*,

*Corresponding author: xian.liu@tongji.edu.cn

DOI: 10.1201/9781003495505-239

2016); Laoshan Tunnel interval in Line 11 of Qingdao Metro (Wang *et al.*, 2017) and so on.

Internal structure in the tunnels from above projects adopts the form of cast-in-place or partially cast-in-place and partially prefabricated, which is characterized by high construction danger, construction difficulty, and low efficiency. However, utilizing fully prefabricated internal structures can effectively solve the above problems.

Additionally, for single-hole with two tracks tunnels, researchers have mainly focused on the aerodynamic effects on the internal structure caused by trains (Chen *et al.*, 2023; Peng *et al.*, 2023), or changes in mechanical properties of the structure under seismic effects lead by the constructional formation (Zhang *et al.*, 2013; Dai *et al.*, 2021; Yao *et al.*, 2022). Even fewer studies on fully prefabricated internal structures are presented, and construction technology and fabricated processes of tunnels are seldom described systematically.

Based on the JCXSG-2 section of the Shanghai Airport Line, this paper researches the automatic and synchronous construction technology of fully prefabricated internal structures inside large-diameter shield tunnels. This paper will elaborate on the automatic and synchronous construction of the internal structures in this project from the design information, automatic equipment, process of synchronous assembly, and control index of construction quality. By the above approaches, automatic and synchronous construction of fully prefabricated internal structures inside large-diameter shield tunnels has been realized, which may serve as experience and reference for similar projects in the future.

2 DESIGN INFORMATION

The Shanghai Airport Line (Chen *et al.*, 2022), which adopts the form of single-hole with double tracks, first utilized fully prefabricated internal structures in large-diameter shield tunnels in China. The total length of the JCXSG-2 Section is 4.97km, and the internal precast structures are divided into prefabricated arc parts, precast partition walls, top connecting parts, and evacuation platforms. The plan of the JCXSC-2 Section and the internal structures are shown below.

This section will introduce detailed design information on the internal structures including arc parts and partition walls.

Figure 1. Plan of the JCXSC-2 Section.

Figure 2. The internal structures.

2.1 *Design of arc parts*

The size of a single arc part, which uses the C40 concrete, is 9.5m×2.834m×2m, with a weight of 33.5 tons. The universal wedge block, which has a double-sided wedge, has the amount of 50mm. Four M36 leveling bolts are set under the arc parts for temporary support. In addition, C40 self-compacting fine gravel concrete is used to fill the gap between the arc parts and the tunnel segments after assembly to eliminate the influence of segment misalignment deformation. Six M36 bolts are used to connect adjacent arc parts. Detail of the prefabricate arc parts is illustrated in the following figure.

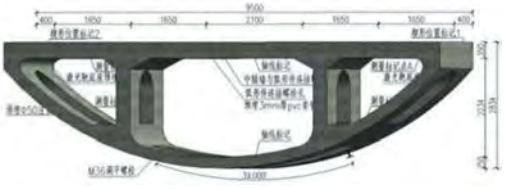

Figure 3. Detail of the prefabricate arc parts.

2.2 *Design of partition walls*

The size of prefabricated partition walls, which use C40 concrete, is 9.136m in height, 0.4m in thickness, and 1.99m in width, with each weighing 21.65t. Standard blocks, which can be divided into four types (I, II, III, and IV), are made for each single precast partition wall. Five M30 bolts are utilized to connect adjacent partition walls, and the bolt holes are sealed by polymer cement mortar after construction. Furthermore, the sealant is used to block the gaps between partition walls to prevent air leakage. The 30mm gap between bottom of the partition wall and top of the arc parts is firstly connected by double rows of M36 bolts (total 10 M36 bolts), then filled with self-compacting high-strength cement-based grout after assembling is completed. Details of the partition standard block and its bottom are revealed below.

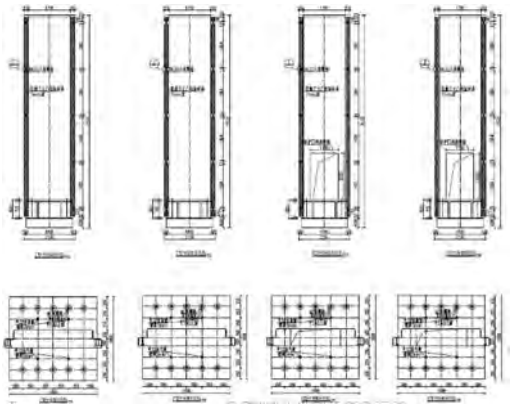

Figure 4. Detail of the partition standard block and its bottom.

The top connectors of the partition walls, consisting of top arc steel plate, steel ribbed plate, and steel baffle plate, are made of Q235B. Each upper part of a single set of top connectors is connected to the shield segments with eight M20 bolts, which are bonded with rigid epoxy adhesive. The gap in the top connectors is filled with C30 fine aggregate concrete. The top connectors of the partition walls are shown below.

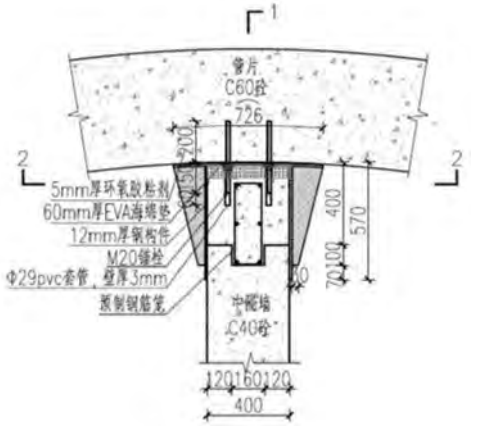

Figure 5. Top connectors of the partition walls.

3 AUTOMATIC CONSTRUCTION EQUIPMENT

This section will propose the fine-tuning equipment of arc parts and assembly equipment of partition walls.

3.1 *Fine-tuning equipment of arc parts*

The fine-tuning equipment consists of outrigger support shoes, walking slide shoes, fine-tuning mechanism assembly, stepping cylinders, stepping support shoes, and so on. The machine is set inside the arc parts to realize the functions of stepping, jacking, traversing, and yawing in three degrees of freedom. The fine-tuning equipment is shown in Figure 6.

Figure 6. Fine-tuning equipment of arc parts.

3.2 *Assembly equipment of partition walls*

Assembly equipment of partition walls mainly contains tracks, a traveling mechanism, a partition wall assembly mechanism, a frame, auxiliary mechanical arms, a top mounting platform, cranes, electrical cabinets, hydraulic pump stations, and so on. This instrument enables the adjustment of partition walls at six degrees of freedom and facilitates their high-precision assembly. The equipment is shown in Figure 7.

Figure 7. Fine-tuning equipment of arc parts.

4 PROCESS OF SYNCHRONOUS ASSEMBLY

This section will illustrate the synchronous assembly of arc parts and partition walls by utilizing the above devices.

4.1 *Synchronous assembly of arc parts*

Figure 8 illustrates the flowchart for the construction process of arc parts, which encompasses the following steps:

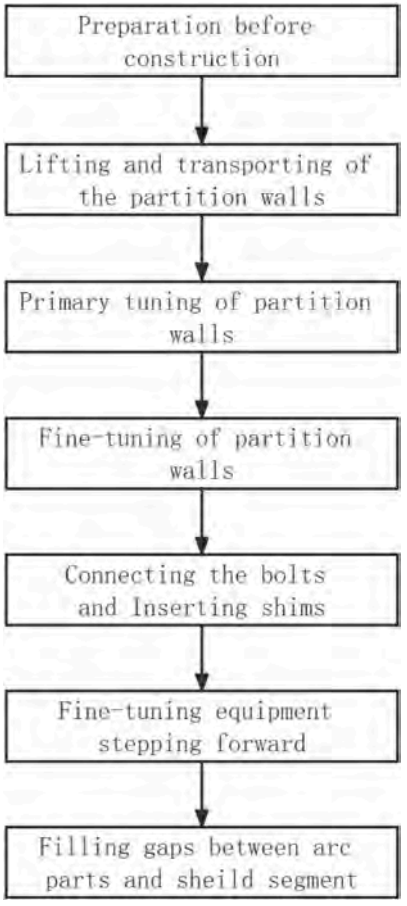

Figure 8. Flow chart for synchronized construction of arc parts.

1) Lifting and transportation of prefabricated arc parts. The fine-tuning equipment is set inside the assembled arc parts, which are shown in Figure 9.
2) Preliminary seating of prefabricated arc parts, including utilizing an arc part crane to assemble the arc parts and visually align the centrelines of the arc parts.

Figure 9. Location of the fine-tuning equipment.

3) Fine-tuning of prefabricated arc parts, involving the use of fine-tuning equipment to adjust the arc parts into their final positions. This step includes the utilization of internal support in arc parts and fine-tuning equipment to support the leg boots for the positioning of arc parts and attitude fine-tuning. Measurement systems are used on the arc parts to determine the degrees of freedom of the fine-tuning. After completing the above operation, the fine-tuning equipment steps forward and repeats the assembly cycle proceeds. Further details of this step are provided in Figure 10 and Figure 11.

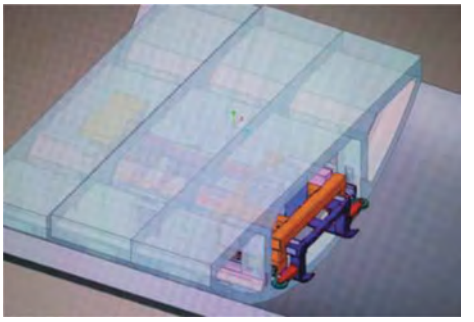

Figure 10. Adjustment and location of the arc parts.

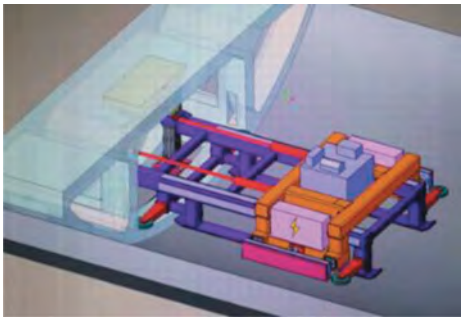

Figure 11. Fine-tuning of the arc parts.

4) Installation and pre-tightening of top connecting bolts and ground bolts, as well as the placement of shims in the bottom gap.
5) The fine-tuning machine steps forward into the preparation position for the installation of the subsequent arc parts, which is shown in the picture below.
6) Filling the gap between arc parts and shield segment through the reserved grouting holes.

4.2 *Synchronous assembly of partition walls*

Figure 13 depicts the flowchart for the construction process of partition walls, which involves the following steps:

1) Transportation of the prefabricated partition wall by a transport vehicle into the frame of

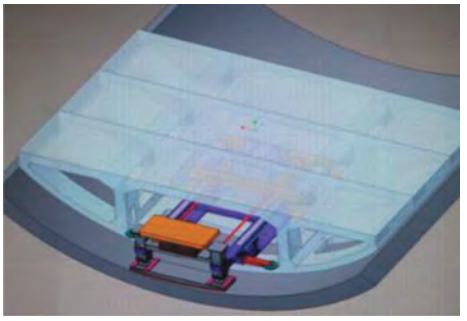

Figure 12. Fine-tuning equipment Stepping forward.

Figure 14. Fine-tuning equipment Stepping forward.

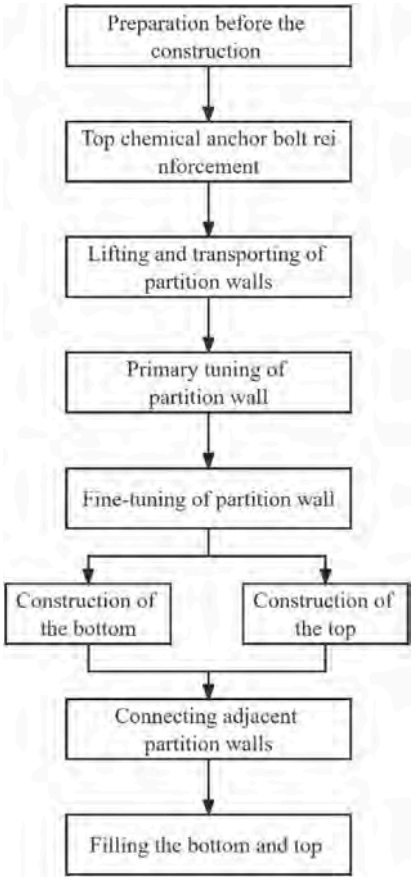

Figure 13. Flow chart for synchronized construction of partition walls.

the assembly cart, as shown in Figure 14. During this process, it is essential to ensure the marked points on the partition wall have entered the measurement range of the camera.

2) Utilizing the camera to detect the position information of the marked points on the partition wall. Position information is then used to calculate the stroke of the 6-degree-of-freedom control cylinder on the main mechanical arm, and guide the main mechanical arm to quickly align with the pin holes reserved on the partition wall.
3) Using the pin cylinder to push the pin into the interior of the partition wall. Once the pin is in place, the side of the partition wall is locked.
4) Extending 2 end face pressing cylinders and rotary pressing cylinders for partition walls in the thickness and width directions, respectively, which will complete the limitation of partition walls in the thickness and width direction.

Figure 15. Compression of the end face and rotary face.

5) Retracting the main mechanical arm lifting cylinder, and elevating partition walls from the transport vehicle. After all, the partition wall transporter exits the dolly frame area.
6) The laser distance measuring sensor is utilized to detect whether the turning gap of the partition wall meets the turning requirements. If the gap reaches the requirements, the lifting cylinder system will lift the partition wall to a certain height and turn it over. However, if the gap does

not meet the requirements, the system will issue an alarm signal, which indicates it is impossible to carry out the turning operation. When the partition wall is turned over, the overturning cylinder on the bow beam is utilized to pull the entire bow beam and partition wall to turn over together by 90 degrees.

Figure 16. Rotation and forward of partition walls.

7) The equipment of partition walls backs up and stops when it reaches the assembled partition walls. Simultaneously, adjusting the attitude of partition walls, which is based on the measured deviation between the 3 measuring points in the partition walls by total station and theoretical axis of the tunnel.
8) Fine-tuning of partition walls in three translational directions and three rotational directions is performed to align the partition walls with the middlebox culvert of the upper arc parts.
9) Inserting shims into the bottom of partition walls, tightening the bottom and side connected bolts. Furthermore, utilizing the installation platform to instruct the bolts between partition walls.

Figure 17. Tightening bolts in the bottom of partition walls.

Figure 18 Demonstrates the flowchart for the construction process of the top connector, which involves the following steps:

1) Drilling holes in the shield segment and placing anchors based on the central axis of the segment at the top arch of the tunnel.
2) Jacking up the top connector along with the prefabricated partition walls to the underside of the vault.
3) Coating epoxy adhesive on the outside of the curved plate of the top connector. Subsequently, installing the top connector promptly and fixing them with bolts.
4) Fill the top and bottom of the connector with sponge pads.
5) Installing the longitudinal prefabricated reinforcement cage. It is important to ensure that the joints of the cage and top connectors are in the form of staggered joints.
6) Fulfilling concrete after the deformation of the shield tunnel is stabilized.

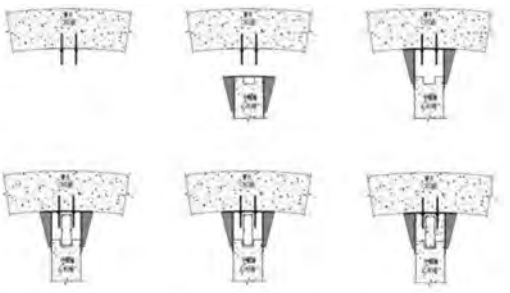

Figure 18. Detail of the partition standard block and its bottom.

5 CONTROL INDEX OF CONSTRUCTION QUALITY

This section innovates the control index of construction quality for prefabricated arc parts and partition walls.

5.1 *Control index of arc parts' construction quality*

The name and direction of each degree of freedom for precast arc parts and equipment are demonstrated in Figure 19. Based on the indicated directionality, the table below presents the construction standard of the precast arc parts.

The indexes proposed above define the translational directions X, Y, and Z and the rotational directions α (pitch), β (roll), γ (yaw), respectively. In addition, the maximum gap between each arc part is also a significant parameter to ensure the constructional quality. By adhering to these indexes, the quality of construction including assembled accuracy and safety can be effectively controlled.

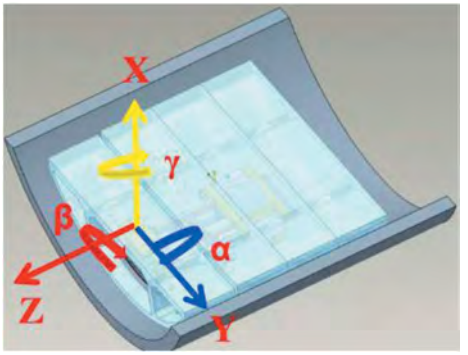

Figure 19. Directionality of the arc parts.

Table 1. Construction standard of the precast arc parts.

No.	Controlling parts	Tolerance	Note
1	Faulting in the vertical direction	8mm	dx
2	Faulting in the horizontal direction	8mm	dy
3	Maximum gap between each arc part	≤10mm	dz
4	Pitch angle α	±0.15°	
5	Roll angle β	±0.05°	
6	Yaw angle γ	±0.05°	
7	Gaps in the filler layer	50-100mm	

Figure 20. Directionality of the partition walls.

5.2 *Control index of partition walls' construction quality*

The name and direction of each degree of freedom for precast partition walls and equipment are demonstrated in Figure 20. Based on the indicated directionality, the table below presents the precision control indexes of the partition walls.

The indexes proposed above mainly define the rotational directions α (pitch), β (roll), γ (yaw), respectively, as well as deviation from the centrelines of partition walls and arc parts, the gap between each wall, and gaps in the filler layer. By adhering to these indexes, the quality of construction, including assembled accuracy and safety can be effectively controlled. Since the translational directions of the arc parts, which are the same as the partition walls, have been defined and controlled, only the deviation from the centrelines of partition walls and arc parts is required to command.

Table 2. Construction indexes of the prefabricated partition walls.

No.	Controlling parts	Tolerance
1	Pitch angle α	±0.15°
2	Roll angle β	±0.06°
3	Yaw angle γ	±0.05°
4	Deviation from the centrelines of partition walls and arc parts	±5mm
5	The gap between each wall	≤7mm
6	Gaps in the filler layer	20~30mm

6 CONCLUSIONS

Based on the Shanghai Airport Line, this paper carries out elaboration and study on the automatic and synchronous construction technology of internal structures inside large-diameter shield tunnels, conclusions are obtained as follows:

1. Utilizing fully prefabricated internal structures can effectively shorten the construction period, and improve the construction precision and quality simultaneously.
2. By using automated construction equipment, difficulties caused by large volumes and heavy quality of prefabricated parts can be effectively solved. Moreover, construction automation has been realized, and construction safety is effectively guaranteed.
3. Through a variety of reasonable construction techniques, automatic and synchronous construction of internal structures and shield tunnels are accomplished, which may serve as experience and reference for similar projects in the future.

ACKNOWLEDGMENTS

The authors would like to acknowledge the financial support from the National Natural Science Foundation of China (Grant No. 52078376).

REFERENCES

Chen, M., Mao, J. and Xi, Y. (2023) 'Aerodynamic effect analysis of high-speed train entering and leaving single and double track tunnels under crosswind', International

Journal of Rail Transportation, pp. 1–23. Available at: https://doi.org/10.1080/23248378.2023.2165182.

Dai, C. et al. (2021) 'Analysis of Three-Dimensional Vibration Characteristics of Single-Circle Double-Track Subway Tunnel under Moving Load', Mathematical Problems in Engineering. Edited by J. Gallardo Alvarado, 2021, pp. 1–13. Available at: https://doi.org/10.1155/2021/6620301.

Finzi-Contini, G., Gori, S. and Semproli, R. (1995) 'Road-Railway Tunnels Interested by Environmental Geophysical Evidences along the Adriatic Slope of the Apennine Ridge (Italian Peninsula)', in. 1st EEGS Meeting, European Association of Geoscientists & Engineers, p. cp. Available at: https://doi.org/10.3997/2214-4609.201407524.

Matsuo, S. (1986) 'An overview of the Seikan tunnel project', Tunnelling and Underground Space Technology, 1(3–4), pp. 323–331. Available at: https://doi.org/10.1016/0886-7798(86)90015-5.

Ormazabal, G., Viñolas, B. and Aguado, A. (2008) 'Enhancing Value in Crucial Decisions: Line 9 of the Barcelona Subway', Journal of Management in Engineering, 24(4), pp. 265–272. Available at: https://doi.org/10.1061/(ASCE)0742-597X(2008)24:4(265).

Pan, B. et al. (2020) 'Dynamic Responses of Soils around a One-Hole Double-Track Tunnel with the Metro Train Meeting', Shock and Vibration, 2020, pp. 1–16. Available at: https://doi.org/10.1155/2020/1782803.

Peng, H. et al. (2023) 'Deformation Control of the Existing Medium-Low-Speed Maglev Metro Viaduct over a Double-Line Bored Tunnel', Applied Sciences, 13(11), p. 6659. Available at: https://doi.org/10.3390/app13116659.

Yao, S., He, J. and Xu, P. (2022) 'The Change in Dynamic Response Distribution of Double-Track Tunnel Structure Caused by Adding Middle Partition Wall', Buildings, 12(10), p. 1711. Available at: https://doi.org/10.3390/buildings12101711.

Zhang, J. et al. (2013) 'Scheme Comparison of Single-Track and Double-Track Shield Railway Tunnel Based on Seismic Behavior', in ICPTT 2013. International Conference on Pipelines and Trenchless Technology, Xi'an, China: American Society of Civil Engineers, pp. 622–630. Available at: https://doi.org/10.1061/9780784413142.064.

Zhou J, 2015. Technologies for Assembly of Separation Wall of a Metro Tunnel on South Section of No.11 Line of Shanghai Rail Transit Works. Tunnel Construction. 35(04), 373–376.

Cao, J., Yang L., Chen K., 2015. Control on middle partition wall construction quality in single–hole double–track subway tunnel. Architecture Technology. 46(02), 177–179.

Wang K., et al., 2017. Key technology of construction of partition wall in Laoshan tunnel based on large diameter. Architecture Technology. 48(11), 1145–1148.

Wang S., et al., 2016. Precasting technologies for internal structure of single-tube double-deck extra-long shield tunnel: a case study on Yangtze River-crossing shield tunnel on Weisan Road in Nanjing. Tunnel Construction. 36(4), 451–457.

Chen Y., et al., 2022. Analysis of mechanical performance of precast middle partition wall in large diameter shield tunnel. Modern Tunnelling Technology. 59(S1), 406–411.

Tunnelling for a Better Life – Yan, Celestino, Thewes & Eberhardt (Eds)
© 2024 The Author(s), ISBN 978-1-032-80042-4
Open Access: www.taylorfrancis.com, CC BY-NC-ND 4.0 license

The Sicilian job, 21 TBMs simultaneously at work to modernize the railway infrastructure of the largest island in the Mediterranean Sea

Remo Grandori*
Director Plant & Equipment at Webuild, Milan, Italy
Senior TBM Expert at Webuild, Milan, Italy

Roberto Bono*
Senior TBM Expert at Webuild, Milan, Italy

ABSTRACT: The railway infrastructures in Sicily have recently undergone an important upgrade that involves new lines connecting the cities of Palermo, Catania and Messina. These railway lines develop largely underground and 21 TBMs will be simultaneously at work to excavate 184 km of tunnels. This extraordinary amount of tunnelling work is concentrated in a limited geographical area and shall be completed in very short time, 3 to 5 years depending on the lots. An enormous effort has been deployed to mobilize and set up the technical and logistic organization to satisfy the need for human resources, for TBMs and other machineries, for primary services such as water and power, for construction materials and transport services. The complex geological formations to be excavated, which mostly involve squeezing ground of sedimentary formations in presence of methane gas, required the development of important innovations for the TBMs, both in terms of structural design, safety devices and data management. In addition, all the TBMs have been designed and manufactured according to the Green TBM concept, a whole new design development by Webuild. Finally, to satisfy the massive requirements of precast segments, several automated, robotic and green precast segment factories have been developed and set up at different locations in Sicily. These factories allow to double the production capability for each working line and at same time to reduce the manpower and increase the quality of the product. These factories auto produce part of the power needed for their functioning and are almost completely autonomous in terms of water consumption thanks to recycling and the use of rainwater.

The article describes in detail the above summarized.

Keywords: Tunnelling, Green TBM, Gas, Squeezing, Precast, Robotic, Continuous Mining, Eko Cruise

1 INTRODUCTION

In Sicily, the railway infrastructures and network will undergo a dramatic implementation in the next 5 years. The works to be carried out, which is worth over 6 billions of euros, includes 184 km of new tunnels to be excavated by 21 TBMs contemporary in operation. The effort required to design the tunnels, procure the TBM, the plants, the equipment, the materials, the human resources and set up the logistics organization has been enormous.

The magnitude of the Project, the difficult logistic and the complex geologies required the implementation of several innovations and special measures.

2 THE PROJECT

The Project is quite complex given its geographical extension and the variability of the geological formations. For this reason, has been divided in two different lines, and each line in several construction lots (Figure 1):

- Messina-Catania Line:
  Lot 1 (Fiumefreddo – Taormina)
  Lot 2 (Taormina – Giampilieri)
- Catania-Palermo Line:
  Lots 1+ 2 (Fiumetorto–Montemaggiore-Lecarcara),

*Corresponding author: r.grandori@webuildgroup.com; r.bono@webuildgroup.com

DOI: 10.1201/9781003495505-240

Lot 3 (Lecarcara – Caltanissetta Xirbi),
Lot 4a (Caltanissetta Xirbi – Enna),
Lotto 4b (Enna – Dittaino)

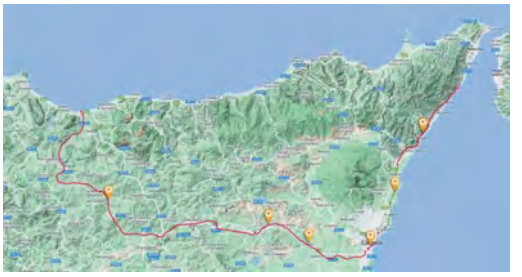

Figure 1. Sicily new rail lines Messina-Catania-Palermo.

2.1 *21 TBMs contemporary at works*

The 21 TBMs that will be used in Sicily are of different types based on the hydro-geological conditions to be faced:

- Messina Catania Line
  Lot 1: n°1 Dual Mode + n°1 EPB
  Lot 2: m°2 Dual Mode + n°1 EPB
- Catania-Palermo Line
  Lots1+2: n° 4 EPB
  Lotto3: n°5 EPB
  Lotto 4a: n° 6 EPB
  Lotto 4b: n°2 EPB

The excavation diameters vary between 9.16m and 9.48m, depending on segments thicknesses and shields conicities.

2.1.1 *Alignment and TBM site locations*

The project alignment from Messina to Catania runs almost parallel to the coast while from Catania to Palermo it crosses the Island from South-East to North-West

The chorography of the island, rich in mountains and hills, forces the railway to a continuous alternation of viaducts and tunnels, with only rare sections in embankment.

2.1.2 *Investments*

Over 1,2 billions € have been invested in the order for the 21 TBMs and related auxiliary plant, segment factories and Drill & Blast equipment used for the excavation of the shorter tunnels and connecting tunnels.

2.1.3 *Materials*

The amount of concrete and steel reinforcement to build the Project is huge and concentrated in a relative short lapse of time.

Beside the aggregates, that can be found in the island, all other construction materials shall come from Italy mainland by vessels, and this poses severe problems to the logistic organization for the construction of the project.

2.1.4 *Schedule*

All the TBMs have been ordered and the first Dual Mode TBM that will excavate the 9* 2=18 km long Sciglio Tunnel arrived on site in October 2023.

The other TBMs will be delivered to site progressively in the last quarter of 2023 and in the first half of 2024.

The Messina Catania Line shall be completed in 2028, while most of the Palermo Catania Lots are foreseen to be completed in 2026 and this places a strong pressure on the progress that the TBMs to be used on this line must achieve.

2.2 *Geology and main criticalities*

The geology of Sicily is complex and the tunnels alignments cross different formation, from hard rock (dolomite) to weak rock (fillades, marl, chalks, sandstone) to lose ground (mostly clays and locally sandy- gravel alluviums).

While crossing these different geologies it is expected to encounter several critical issues, the major of which are described below.

2.2.1 *Presence of gases*

126 km of tunnels out of the total 184 to be excavated in the Project will have to be bored in presence of methan and H2S gases.

Due to this, 17 out of the 21 TBMs have been designed and manufactured according to ATEX provisions as per the applicable norms in Italy (NIR 44).

The Multi Service Vehicles that transport the segments and the other tunnelling equipment will also be designed and manufactured to operate in presence of Gas.

2.2.2 *Squeezing*

The presence of week clay formations under cover will cause severe convergence of tunnel walls against the TBM shields and the segmental lining.

2.2.3 *Freatic water tables*

Ground water level is locally quite high above the tunnels routes and this required the TBMs and the lining to be able, where needed, to drain the water and reduce the pressure in the excavation chamber and on the precast lining.

3 TBM'S & INNOVATIONS

3.1 *TBM types*

As indicated in paragraph 2.1, out of the 21 TBMs, 3 will be Dual Mode TBMs (Open/EPB) and 18 EPB TBMs.

All these TBMs have been specifically designed for the application, with several innovations developed by Webuild in cooperation with the two suppliers (CREG and CRCHI).

Figure 2. The first green TBM dual mode by CREG.

Figure 3. The first CRCHI EPB TBM for the project.

3.2 *Operation in gassy formations*

All 17 TBMs for the Palermo-Catania line have been designed and manufactured to be able to advance in presence of methane gas. This according to the design guidelines and technologies developed in Italy and named NIR 44.

The basic concept of this design is (Figure 4) the physical separation volumes in the TBM system and along the tunnel as well the ventilation flows management.

Basically, the methane contaminated air is confined in the TBM excavation chamber (kept full of conditioned muck) and any eventual seepage of gassy air through the screw conveyor gate is kept separate and conveyed into a sealed back-up conveyor belt from where the contaminated air is sucked and conveyed through a pipeline behind the back-up where the gas is diluted by the main tunnel ventilation.

Naturally, in all volumes in which the TBM system and the tunnel are kept separated, gas sensors are installed which automatically intervene in the

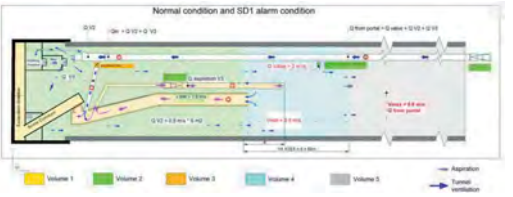

Figure 4. ATEX TBM system volumes schematic.

event of gas percentages exceeding established limit values.

3.3 *Dual mode TBMs*

N° 3 out the 5 TBMs that excavate the Messina-Catania railway line are Dual Mode TBMs, capable to operate in full EPB mode with screw conveyor as well in open mode with a belt conveyor.

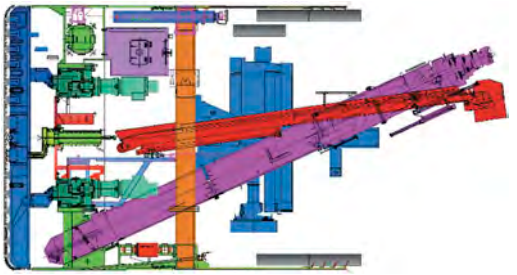

Figure 5. Dual mode TBM layout.

CREG developed a special design to allow to change the configuration from EPB to Open and viceversa in less than 5 working days.

This required a new special design of the cutterhead with mobile buckets that can be retracted and extended out of the cutterhead structure.

At the same time both the screw and belt conveyor have been permanently lodged inside the TBM shields despite their "full capacity" dimensioning.

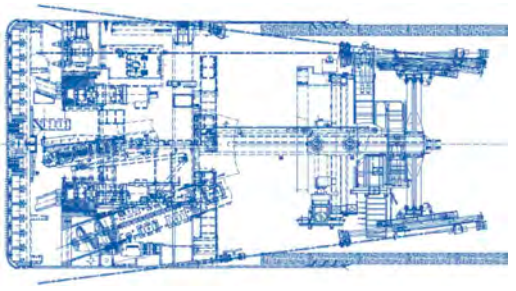

Figure 6. Dual mode TBM probe drill system.

3.4 *Continuous Mining two modes*

The Continuous Mining system (CMS) allows the installation of the segmental lining contemporary with the boring stroke (the last meter of the stroke).

In the TBMs for the Sicilian Projects this system has been improved and extended allowing two different operational modes automatically selected by the PLC of the TBM

- **Mode 1** is the standard mode in use when the boring thrust and its distribution in the different cylinders follow within the normal operating range. In this mode all segments could be assembled contemporary with the excavation provided that the TBM penetration allows sufficient time for the operation.
- **Mode 2** is automatically selected by the PLC when the distribution and level of thrust in the different cylinders follow outside certain parameters.

When in Mode 2 the first 2 segments in the ring are installed with the TBM in stand by and only the remaining 5 segments in the ring are installed while the TBM is completing the boring stroke.

When in Continuous Mining Mode:

- the PLC avoids the pressures in the different thrust cylinders to raise above of fall below the set triggers levels.
- The center of the boring thrust is maintained stable unless a steering action modifies its position.

The continuous mining system is expected to increase the average TBM production by 15-20% depending on the ground conditions.

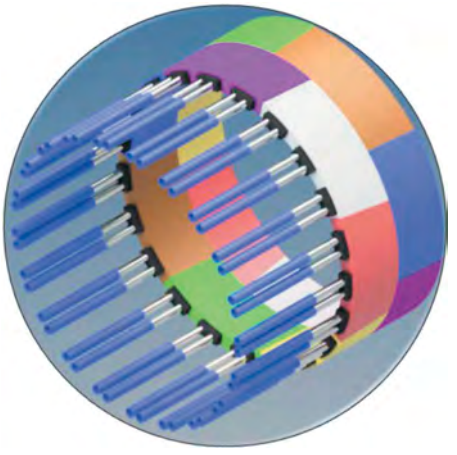

Figure 7. Thrust cylinders arrangement.

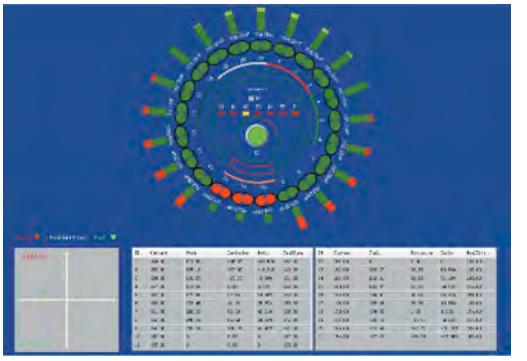

Figure 8. CMS control by center of thrust.

3.5 *EKO Cruise system*

The EKO Cruise is an automatic cruise system that has the target to optimize the TBM and auxiliary operating parameters reducing the power consumption of the TBM at equal Advance Rate.

Similarly to the cars cruise systems, the operator set the desired advance rate and then the PLC of the TBM adjust the operation parameters precisely for the purpose of optimizing energy consumption, reducing wear and maintaining (in EPB mode) the design pressure in the excavation chamber.

To achieve the goal, the system automatically:

- keep the muck pressure in the excavation chamber within the design range when in EPB mode
- optimizes the thrust and the revolution speed of the cutting head to maximize excavation efficiency
- optimizes the speed of the back-up conveyor belt adapting it to the actual penetration of the TBM

3.6 *Green TBM*

TBMs have been historically developed and selected considering mostly geology and productivity.

The Green TBM concept was introduced with the aim to reduce power consumption of TBMs without compromising on productivity, but on the contrary, focusing on an increase in productivity as one of the measures to reduce consumption.

The intended aim is to reduce power consumption by 20 -25% at same diameter and type of TBM.

This target is achieved with a package of interventions in the design, operation and management of the TBM, including:

3.6.1 *Cutterhead design improved efficiency*

Cutting head structures design reduces friction during rotation and favors the flow of material in the excavation chamber.

At same time the ground conditioning system is potentiated and high-pressure water jets have been introduced to help penetration & prevent clogging phenomena.

Figure 9. Ovoidal thrust rams to reduce friction.

3.6.2 *Use of high efficiency components*
High efficiency electric motors (IE4), Permanent Magnetic motors have been adopted as well VFD for the control of motors and Eko type Transformers.

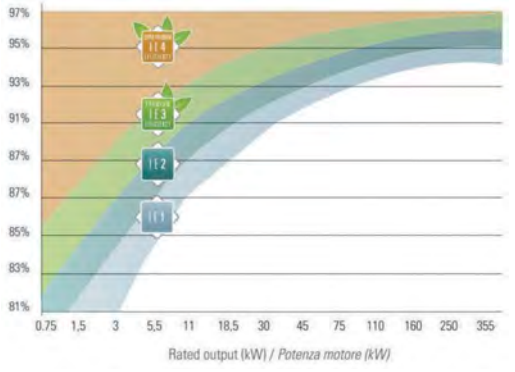

Figure 10. Increase of power efficiency by IE 4 motors.

3.6.3 *EKO Cruise*
See chapter 3.5 above.

3.6.4 *Continuous Mining – See chapter 3.4 above.*

3.6.5 *Automatic Utilities management system*
The TBM is equipped with an automatic control system targeted to save power consumption which acts in the following areas:

- it starts and stops the motors that drive the pumps of the hydraulic system according to the operational needs of use and power.
- turns on and off the other TBM and back-up service utilities according to the needs during the different phases of the advance.

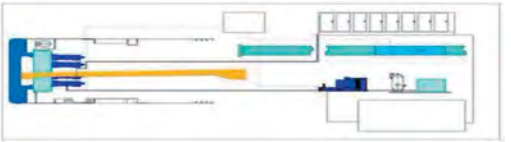

Figure 11. PLC switch on/off the system utilities.

3.6.6 *Optimal hydraulic system design*
The main thrust system pumps are activated automatically in sequence according to real needs.

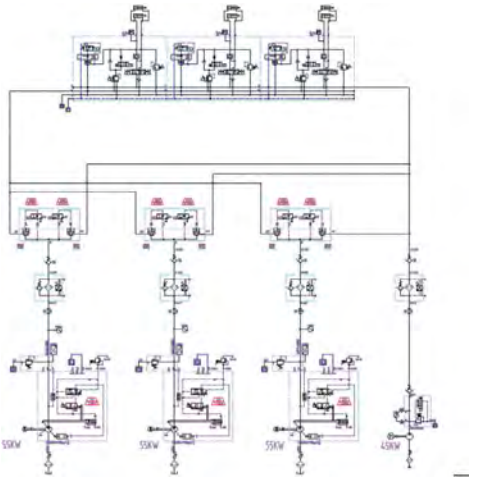

Figure 12. Hydraulic pumps activated in sequence.

3.6.7 *Optimize energy efficiency of the board systems*
Normal TBMs have a power factor correction system that allows them to maintain average values between 0.88-0.92. Through the installation of a more extensive power factor correction system the load factor is optimized to values of 0.95-0,97, thus reducing the absorbed power by about 5% and reducing the heating produced by the system.

The Power Quality required by the TBM system is then further improved by special devices that reduces the harmonics.

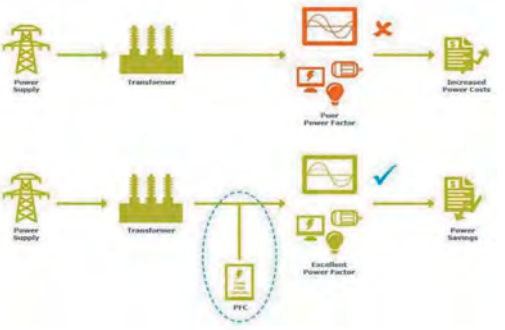

Figure 13. Improved power quality by reducing harmonics.

3.7 *Continuous in situ invert lining*

Tunnel design foresees a secondary invert lined in situ that form the base of the rails track.

A continuous casting system (Figures 7) was developed along the back-up of the TBM for the construction of this slab with the aim of:

- speed up the casting and avoid limiting the advancement of the TBM
- avoid secondary construction sites along the tunnel
- form a base for the transit and exchange of MSVs
- improve the safety of work

The railway

Figure 14. Continuous invert lining system.

3.8 *Predictive AI maintenance software system*

The TBMs are equipped with additional sensors and with a predictive maintenance software capable of scheduling maintenance interventions and prevent the occurrence of catastrophic failures to major components.

4 PRECAST SEGMENTS

4.1 *Segments design*

Starting from the segmental lining design initially developed by different design companies for each lot of the project, a standardization of the geometric design of the segments and of the related steel reinforcements was carried out, this to facilitate the centralized production of the segments in highly automated factories as well as the logistics of storage and transport to the different TBM portals.

This standardization was extended to segment accessories and seals.

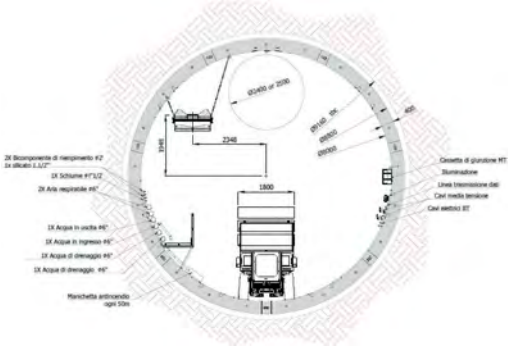

Figure 15. Typical tunnel section with service lines.

4.2 *Production strategy*

The amount of segments to be produced is extraordinary: 102.000 rings, 714.000 segments and 2,2 millions cubic meters of concrete.

The production of such a large amount of segments has been mostly concentrated in 2 main factories from where the segments where transported to the secondary storages located at the TBM portals.

Figure 16. The first robotic & green precast factory.

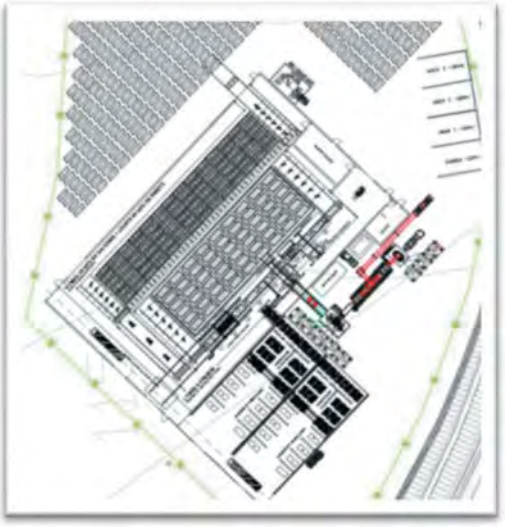

Figure 17. Precast factory layout.

4.3 *Robotic & Green factories*

The huge demand of segment to be produced required to develop new fully automated segment factory designs, able to produce from 170 to 270 segments per day per each production line with minimal manpower requirement.

These factories are equipped with solar panels to produce up to 40% of the total consumed power as well with water recycling systems integrated by the collection of the rain water which makes these factories substantially autonomous as regards the plant's water consumption.

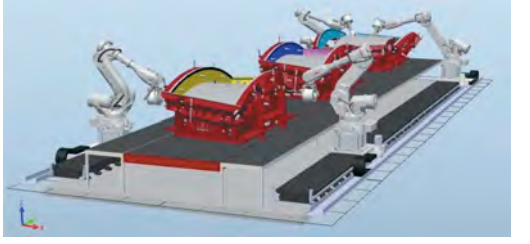

Figure 18. N° 4 robots ensure the short cycle and efficiency.

Further to the above recycled plastic spacers are used to store the segments in the store yard.

Figure 19. Demould and rotating clamp.

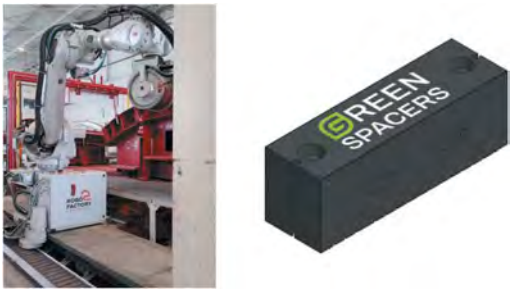

Figure 20. Robot detail and green spacer.

4.4 *Productivities*

The extensive use of robots and of innovative design arrangement of the production, curing and post curing lines allows to produce 1 segment every 4 or 6 minutes per production line depending on the specific factory design.

These productivities are obtained with reduced manpower been the entire process automated.

4.5 *Quality & Safety*

The extensive use of automation and robotic reduces the manual operations down to a minimum, thus reducing the probability of injuries to the personnel involved. Furthermore, a laser sensors system verifies the presence of personnel in dangerous areas and automatically stop production.

The curing process is monitored by sensors placed in each mould and recorded by the segment tracking system.

5 LOGISTIC CHALLENGES

Sicily is an island and all TBMs, plants and construction materials must be transported by ship from mainland Italy, except concrete aggregates available mainly in the Etna volcano area.

The huge amount of infrastructures works concentrated in a relatively short period of time risked putting the port and road infrastructures into crisis, especially during the summer season when the island is invaded by a flow of tourists from all over the world.

To overcome this criticality, alternative road solutions were studied, which involved the construction of new dedicated accesses to the island's motorway system.

At the same time, storage areas have been identified to accumulate materials during the wintertime and limit transport peaks in the summer months.

5.1 *TBM transport*

The transport of the TBMs from the port of arrival on the island to the different portals required careful verification of the road system, including viaducts, tunnels and urban crossings. The dimensions and weights of the major components of the TBMs have been limited so as not to exceed the limits permitted by the road system.

5.2 *Power supply & Generation*

Sicily, especially in its central area, does not have an electrical grid sufficiently widespread and capable to supply the power to all the TBM portals.

This problem has been overcome by providing for the use of liquid gas generating stations where the electrical grid was not available.

5.3 *Water supply*

An even bigger problem is the unavailability of sufficient water flows to support the contemporary mechanized excavation of all the tunnels. To overcome this problem, various aqueducts are being studied and will be constructed before the start of boring.

5.4 *Muck treatment & Disposal*

The TBMs used in the project are either EPB or Dual mode EPB/Open TBM.

Consequently, important settling and biodegradation pools systems have been provided in each TBM portal.

Part of this muck will be then added with lime for subsequent use in the project.

5.5 *Logistic camps*

To accommodate the several thousand of technicians and workers employed in the works, low environmental impact camps were created with extensive use of photovoltaic panels for the self-production of energy.

6 OTHER INNOVATIONS

6.1 *Segment tracking system*

Despite having maximized the standardization of the segment design, the variable geological conditions

required to adopt two different segments thicknesses and different types of steel reinforcement.

The planning of the production, storage and transportation of the different segments to each portals required to integrate the segment tracking software to allow the management of the logistics and produce the different types of segments according to the actual needs, so as to never stop the TBMs.

6.2 *WeView IT platform*

Figure 21. Operation data control.

A team of engineers from Webuild in cooperation with the specialized software house Tunnelsoft developed an IT platform, WeView, to monitor in real time from a central control room (Figure 21) the operation of the 21 TBMs and of all the related plants & systems utilized on the construction sites.

WeView monitors also the main environmental parameters, helping the management in keeping under control the environmental aspects and in the monitoring of the environmental targets (e.g. GHG reduction) and their achieving.

The platform allows also allows:

- the monitoring of the electric power consumption of each user.
- the control of the water consumption according to efficiency targets

The data are organized and elaborated automatically and notified by email and through app. Generate production reports, rock/support classification reports, geological mapping, QC/QA reports, water and energy consumptions and related efficiency.

Reports and alarms are automatically generated informing in real time the responsible staff through SMS and Email. The elaborated data are made available in real time to PC, smartphones and tablets and, as stated before, to the project control room.

Figure 22. Sicily new rail lines Messina-Catania-Palermo.

7 CONCLUSIONS

The complex of railway tunnels to be excavated in Sicily it is unprecedented due to the combination of the simultaneous excavation of so many TBMs, the geological complexity, the presence of gas, the many innovations introduced and the difficult logistic and lack of basic infrastructures on the island.

The technical details of the individual innovations implemented and their behavior during the execution of the works will be the subject of separate presentations as the works will progress.

The same will be for the productions and the geological difficulties that the 184 km of tunnel will reserve and the special measures that will be eventually necessary to overcome them.

The project, once completed, will allow Sicily the infrastructural development that was missing since ever and, once connected to the Messina bridge which construction is expected to start soon, will finally connect Sicily to Italy and to the rest of Europe.

ACKNOWLEDGMENTS

The authors would like to thank Webuild partners in the project construction, Ghella and Pizzarotti, the designers Rocksoil, Proger, SWS, PINI, the Client RFI and the TBM suppliers CREG and CRCHI.

REFERENCES

Remo Grandori, Roberto Bono, Luca Castelli, 2022. WeView – An Integrated data & elaboration system of global underground projects. World Tunnel Congress WTC 2022 Copenhagen.

Heikkilä, R., Kaaranka, A., & Makkonen, T. 2014. Information Modelling based Tunnel Design and Construction Process. The 31st International Symposium on Automation and Robotics in Construction and Mining (ISARC Proceedings2014). Sydney, Australia, July 2014.

Tunnelling for a Better Life – Yan, Celestino, Thewes & Eberhardt (Eds)
© 2024 The Author(s), ISBN 978-1-032-80042-4
Open Access: www.taylorfrancis.com, CC BY-NC-ND 4.0 license

Evaluating TBM design and performance, 30 years apart: The Lesotho Highlands Water Tunnel, phase 1 and phase 2

Brad Grothen*
Robbins, Solon, Ohio, USA

ABSTRACT: Two massive tunnel projects 30 years apart: The Lesotho Highlands Water Project (LHWP) is a multi-phased project that has taken place over decades to provide water to the Gauteng region of South Africa and to generate hydroelectricity for Lesotho. Phase I tunneling began in 1992 and utilized multiple Main Beam TBMs to bore long tunnels in basalt and dolerite ground conditions.

Phase II, now under construction, consists of 38 km of transfer tunnel to be excavated by both TBM and drill & blast. Water from the Polihali reservoir will flow by gravity through the Polihali Transfer Tunnel on its way to Katse Dam. Two 5.4 m diameter Double Shield TBMs will bore 17 km long sections of the Polihali Transfer Tunnel, one designated Polihali-West and the other Katse Outlet-East. The tunnels will travel through basalt and dolerite with some sections of breccia, pillow lava, tuff and agglomerate at depths ranging from 91 to 994 m below the surface.

In order to bore in the challenging conditions, the machines are fitted with 19-inch disc cutters and two-speed gearboxes that efficiently use power to generate high torque at low RPM when in sections of squeezing geology or fracture zones.

This paper will detail the design for the TBMs to be used on the Phase II tunnel, while comparing the modern-day machines to the history-making Main Beams used in the 1990s. It will derive some conclusions and lessons learned about boring in volcanic rock at depth utilizing Main Beam vs. Double Shield TBMs.

Keywords: Tunnelling, Hard rock, Main Beam, Africa

1 INTRODUCTION – PROJECT BACKGROUND

The Lesotho Highlands Water Project (LHWP) is decades in the making. A cooperative effort between Lesotho and South Africa, Phase 1 of the project sought to rejuvenate South Africa's heavily populated and arid Gaucheng Province. Its first phase began in 1992 and involved construction of the 180 m high Katse Dam, part of the Orange (Sequ) River system in Lesotho. The dam, finished in 1998, supplies water to South Africa's Vaal river system via a water transfer tunnel and two delivery tunnels. A total of 82 km of tunnels were constructed between 1992 and 1996. The project went online in 2003.

Today, the contribution of Phase 1 of the LHWP to the economic activity of Lesotho has been remarkable. Royalties, the sale of electricity, construction activities and other project-related revenue have provided an important economic boost to Lesotho. In 2002, it was calculated that the project's contribution to the economic activity of Lesotho was 5.4% of the GDP (lhda.org.ls, 2023).

The water from the LHWP is used in six provinces of South Africa. It cools the Eskom power stations in Mpumalanga, keeps Sasol and Free State gold mines operational, supplies the vast industries and sprawling urban areas of Gauteng, provides water to some of the southern towns of Limpopo and the platinum mines of the northwest, as well as the diamond mines and people of Kimberley and surrounding areas. Under drought conditions, emergency water can, and has, been transferred to the Caledon River and to the Eastern Cape and southern Free State through the BloemWater network.

Phase 2 of the Lesotho Highlands Water Project, now underway by the Lesotho Highlands Development Authority (LHDA), builds on the successful completion of Phase 1 in 2003. It delivers water to the Gauteng region of South Africa and utilises the water delivery system to generate electricity for Lesotho. Phase II will increase the current supply rate of 780 million cubic metres per annum incrementally to more than 1.27 billion cubic metres per annum. At the same time, it will increase the quantity of electricity generated at the Muela hydropower

*Corresponding author: grothenb@robbinstbm.com

DOI: 10.1201/9781003495505-241

station and is a further step in the process of securing an independent electricity source to meet Lesotho's domestic requirements (LHDA, 2020).

The water transfer component of Phase 2 comprises a Concrete-Faced Rockfill Dam (CFRD) and saddle dam at Polihali, downstream of the confluence of the Khubelu and Senqu (Orange) Rivers, and a gravity tunnel that will connect the reservoir at Polihali to the Katse reservoir. In addition, two 1 km long, drill and blasted river diversion tunnels were built prior to the construction of the Polihali Dam.

The 38 km long Polihali Transfer tunnel will be constructed by both TBM and drill and blast, and allows water from the Polihali Reservoir to flow by gravity to the reservoir at Katse.

2 PHASE 1

The first phase of the massive project included approximately 80 km of tunneling and construction of two dams and an underground power station. The project's co-owners, the Kingdom of Lesotho and the Republic of South Africa, awarded the contract for the 13 km-long south delivery tunnel and the 45.6 km-long transfer tunnel, both located in Lesotho, to the Lesotho Highlands Project Contractors (LHPC). LHPC was a joint venture of Spie Batignolles (France), LTA Ltd. (South Africa), Ed Zublin AG (Germany), Balfour Beatty Ltd. (U.K.) and Campenon Bernard (France).

LHPC leased a refurbished Main Beam TBM to excavate the shorter delivery tunnel. The contractor also ordered three new open-type TBMs, manufactured by Robbins, to bore the longer transfer tunnel. Yet another Main Beam TBM, manufactured by Wirth, was ordered for the North Delivery Tunnel.

The 5.18 m diameter south delivery tunnel connects the Muela adit with ventilation shaft #5 to the north. At this point the excavation junctures with the 5.1 m diameter north delivery tunnel, which continues 22 km to the Axle River outfall in South Africa.

The transfer tunnel, proceeding from the Katse Dam to the Muela Power Station, is one of the world's longest water supply pressure tunnels. It is made up of three 4.99 m diameter drives with lengths of 10.9 km, 17.3 km and 17.4 km. The transfer tunnel diverts water from the dam to the power station (see Figure 1).

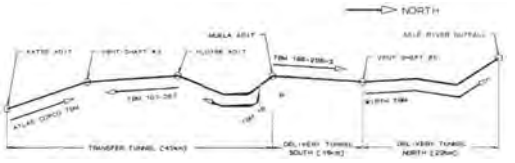

Figure 1. Schematic Overview of the Lesotho Highlands Tunnels (Finnsson, 1994).

2.1 *Geology*

The transfer tunnel route passes through basaltic flows of the Lesotho/Drakensberg formation, volcanic rock with variable amygdaloidal content. The area includes blocky conditions in faulted areas and within some of the doleritic dykes also found along the route. The unconfined compressive strength (UCS) of these rock formations ranges from 80 MPa to 176 MPa.

The south delivery tunnel site lies in sedimentary rock of the Stormberg Group, upper formation of the Karoo sequence, a deposit formation in the extensive Karoo Basin. Most of the tunnel route passes through the Clarens formation, located beneath the Lesotho/Drakensberg formation. The Clarens section consists mainly of horizontally layered sedimentary rocks composed of fine- to medium-grained siltstone and sandstone with occasional doleritic dykes and layers of claystone. The UCS of the softer rocks in this area varies from 10 MPa to 40 MPa.

3 TBM DESIGN AND EXCAVATION

3.1 *The south delivery tunnel*

The 5.18 m dia machine, the first TBM to begin work at Lesotho, featured 37 cutters, each 432 mm in diameter. Six 185 kW motors provided 1,110 kW to the cutterhead, which operated at 7.28 rpm. The 270 metric ton machine had a 1.5 m boring stroke and a thrust of 7,400 kN. Manufactured in 1979, the refurbished Main Beam was already a tunneling veteran before its journey to Lesotho, having bored more than 24 km on projects in the U.S. and Canada.

The refurbished Robbins Model 186-206 began boring the 13 km-long south delivery tunnel in February 1992 and achieved breakthrough in August 1993, an astounding 20 months ahead of schedule. The tunnel excavation consisted of three drives: 2.1 km from Hololo south to Muela, 5.2 km from Ngoajone south to Hololo and 5.7 km from Ngoajone north to ventilation shaft #5.

The refurbished Main Beam achieved outstanding results on the south delivery tunnel despite two breakthroughs and start-ups of the TBM and back-up system along the way. The machine's average rate of penetration (ROP) was 3.86 m per hour (8.8 mm per revolution). The TBM advanced at an average 39.9 m per day in three eight-hour shifts and 878 m per 22-day month. The best day advance of the drive was 82.9 m, with a best week of 384.0 m and a best month of 1,324.4 m. Rock support measures in the south delivery tunnel included spot bolting as well as some systematic rock bolting with mesh and shotcrete (see Figure 2).

3.2 *The transfer tunnel*

3.2.1 *Design of the TBMs*

The new Robbins MK 15, an open hard rock machine, offered a bore diameter of 5.018 m. The

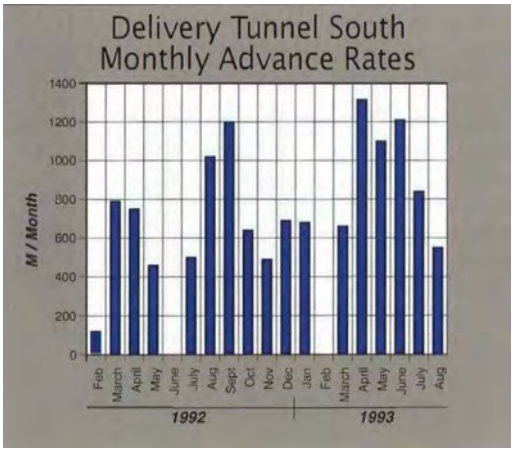

Figure 2. Advance rates in the South delivery tunnel.

TBM's cutterhead was dressed with four center cutters, 22 face cutters and eight gauge cutters, all 432 mm in diameter. Three 560 kW motors supplied 1,680 kW to the cutterhead, producing a torque of 1,588 kNm. The 320 metric ton machine had a 1 1.525 m boring stroke and a thrust of 8,300 kN. Cutterhead speed was 10.1 rpm (see Figure 3).

Figure 3. The MK15 open-type TBM at the tunnel portal.

The two Robbins Main Beam TBMs were supplied with boring diameters of 5.03 m. At Lesotho these machines were equipped with 35 disc cutters, each 432 mm in diameter and load rated to 222 kN, producing a total cutterhead thrust of 9,723 kN. The machines were both equipped with backloading cutterheads. The flexible design of these high-performance TBMs also allowed later installation of 483 mm dia cutters to achieve a cutter load of up to 312 kN for situations in which increased power was needed for superior performance on the job. The machines also featured five 315 kW water-cooled motors supplying a total of 1,575 kW to the cutterhead. The TBMs have a boring stroke of 1 .866 m and a cutterhead speed of 10.0 rpm.

Each of the four Robbins TBMs on the Lesotho Project had its own trailing back-up system, including a rock drill. The drill was part of an assembly mounted on a 7 m-long sliding deck about 20 m behind the cutterhead on the top level of each TBM's backup. This arrangement allowed probe drilling concurrently with TBM advance (see Figures 4 and 5).

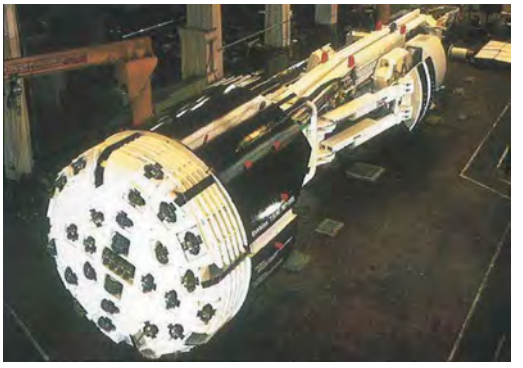

Figure 4. One of the 5.03 m diameter main beam TBMs supplied for the transfer tunnel.

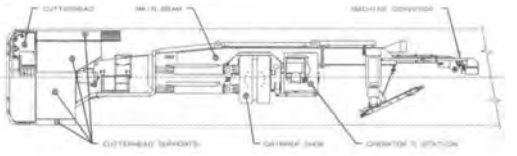

Figure 5. Schematic of the main beam TBMs provided for Phase 1 transfer tunnel.

Locomotives and rotadump cars operated behind each of the TBMs to remove muck produced during tunneling operations. Each service train was made up of seven 12 m^3-capacity muck skips. Depending on the difficulty of the excavation gradient, either 25 metric ton, 180 hp or 35 metric ton, 200 hp diesel locomotives were used to haul the filled muck trains.

LHPC installed a precast concrete invert segment in each tunnel to support tracks for the muck-handling trains. These segments remained in the operating water delivery system to facilitate tunnel maintenance and repair.

3.2.2 *TBM excavation*

The Robbins MK 15 began boring the Katse tunnel section from the Katse Dam site to ventilation shaft #3, a distance of 10.9 km, in May 1992, and reached breakthrough in September 1994. With an average ROP of 3.89 m per hour (6.4 mm per revolution), the TBM achieved an average monthly advance of 364 m, with a best day, week and month of 62.9 m, 289.0 m and 987.0 m, respectively.

Difficult rock conditions prevailed in the non-amygdaloidal basalt areas of this section of the transfer tunnel. Blocky ground at the tunnel face and rock

falls from the crown area resulted in substantial downtime to clean the invert and cutterhead and install appropriate rock support. In addition, some challenging conditions forced reductions in TBM thrust and ROP, decreasing the machine's advance rate in these areas to about 30 percent of the progress achieved in stable rock. Although the tunnel route also included two doleritic dykes, one 95 m long and the other 82 m long, the TBM advanced surprisingly well through these difficult sections. About 15 percent of total job time was devoted to rock support, which included bolting, rock straps, mesh and shotcrete. Overall, TBM utilization reached 31 percent (see Figure 6).

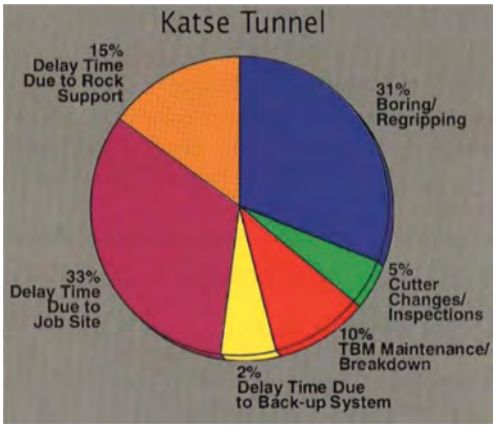

Figure 6. Katse tunnel utilization.

The first Main Beam TBM (Muela tunnel section) began boring the 17.4 km-long transfer tunnel section from Muela south to the Hlotse adit in June 1992. Maintaining an average ROP of 4.59 m per hour (7.7 mm per revolution), the machine broke through in September 1994. The TBM's average advance rate was 33.4 m per day and 656 m per month. The Main Beam set world tunneling records for its diameter class with a best day advance of 86.3 m, a best week of 399.8 m and a best month of 1,344.3 m.

The TBM set these records despite some challenging geology along the tunnel route. Rock jointing necessitated rock support measures, especially at the beginning of the drive. Overall, rock support required 24 percent of total job time, with machine utilization reaching 29 percent (see Figure 7).

In July 1992, shortly after boring began on the transfer tunnel's Muela-Hlotse section, the Robbins Model 167-267 TBM started its 17.3 km long drive from Hlotse to ventilation shaft #3. The machine achieved an average ROP of 4.10 m per hour (6.8 mm per revolution), while maintaining average advance rates of 27 .6 m per day- and 620 m per month. The TBM turned in a superior performance with a best day advance of 66.8 m, a best week of 325.0 m and a best month of 1221.0 m.

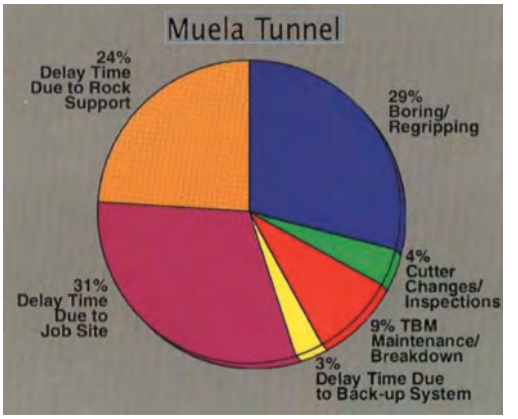

Figure 7. Muela tunnel utilization.

Challenging rock conditions in this section of the transfer tunnel required rock support measures accounting for 11 percent of total job time, with another substantial delay (29 percent) due to job site problems. Nevertheless, machine utilization reached 38 percent (see Figure 8). Final breakthrough occurred on October 14, 1994.

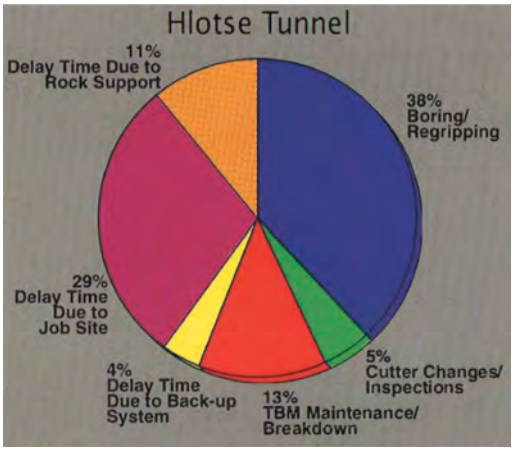

Figure 8. Hlotse tunnel utilization.

4 PHASE 2 TUNNELING

In 2022, the 38 km long Polihali Tunnel was announced as part of the LHWP Phase 2. The approximately M9.2 billion Polihali Transfer Tunnel contract was awarded to the Kopana Ke Matla joint venture, which includes Yellow River Company (China); Sinohydro Bureau 3 (China); Unik Civil Engineering (South Africa) as the main joint venture partners. Subcontractors include Nthane Brothers of Lesotho, Esor Construction and Mecsa Construction of South Africa.

The Polihali Transfer Tunnel will transfer water by gravity from the Polihali reservoir to the Katse reservoir. From Katse, water is transferred via the

delivery tunnel to the 'Muela Hydropower Station constructed in Phase I, and then on to the Ash River outfall outside Clarence in the Free State on its way to Gauteng (see Figure 9).

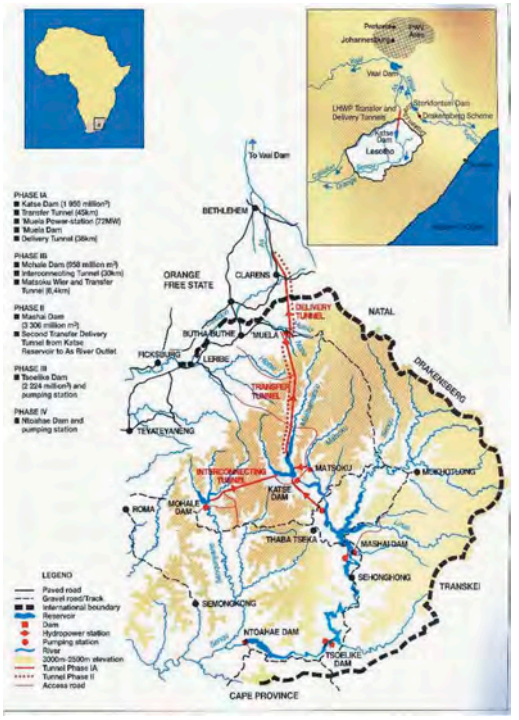

Figure 9. Map of LHWP works, Phases I and II (Lhda. org).

4.1 *Tunnel specifications & geology*

The Polihali tunnel includes two approximately 17 km long TBM-driven tunnels, designated as TBM Drive from Polihali-West and TBM Drive from Katse Outlet-East, and two approximately 1.5 km long D&B-driven connecting tunnels (one at each end), designated as Polihali Connecting Tunnel and Katse Outlet Connecting Tunnel. The Polihali Tunnel will have a finished diameter (ID) of 4.5 m and a relatively flat slope of 0.032%. The tunnel will be constructed in hard rock at depths to invert ranging from 91 to 994 m below ground surface. The TBM-driven portion of the tunnel will be lined with a drained, initially-bolted, gasketed, precast concrete segmental tunnel lining (PCTL) installed concurrently with TBM tunnel excavation (see Figure 10).

Geology along the tunnel alignment consists of highly amygdaloidal basalt (28%), moderately amygdaloidal basalt (28%), non-amygdaloidal basalt (28%), doleritic basalt (10%), and dolerite (5%). About 1% of the geology is estimated to consist of other rock types including breccia, tuffites, pillow lavas, olivine basalts, and agglomerate. These rock types are often associated with problems in terms of tunnel stability and excavation.

Figure 10. Schematic of Polihali tunnel path.

4.2 *TBM design for challenging conditions*

In order to excavate in the challenging conditions, the two 5.4 m diameter Double Shield TBMs have been designed with advanced features.

4.2.1 *Multi-speed gearboxes*

Customized cutterhead drives can be instrumental in getting through difficult ground. Designing a machine with high-torque, continuous boring capabilities allows that machine's cutterhead to restart with break-out torque in difficult ground. The net effect is that the machine can keep boring in the event of a face collapse and can effectively bore through fault zones and running ground where the potential for cutterhead jamming exists. Multi-speed gearboxes give the machine the ideal EPB torque if larger sections of soft ground are anticipated (Figure 11).

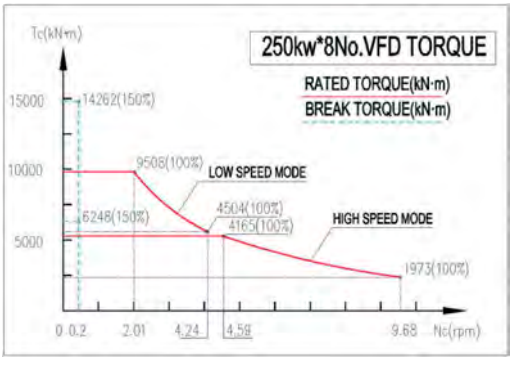

Figure 11. Torque-speed curve for the LHWP Phase II TBMs.

When compared to the Phase I TBMs, the Phase II machines also have much higher thrust – in some cases nearly four times higher (see Table 1). The combination of higher thrust capabilities and multi-speed gearboxes is ideal for variable rock conditions.

Table 1. Comparison of 5 m diameter TBMs, Then and Now.

	Cutterhead Power (kW)	Thrust (kN)
LHWP Phase I MB TBMs	1,110 to 1,680	7,400 to 9,473
Modern MB TBM	2,310	10,898
LHWP Phase II DS TBMs	1,920	29,500

4.2.2 *Stepped shields and shield lubrication*

When blocky rock or squeezing ground is expected, using a shielded TBM can be tricky. The risk of a machine's shield becoming stuck is real and can be the source of major delays. Designing for these conditions involves creating the shortest possible shield length, with stepped shields if necessary (particularly if a Double Shield TBM is used). Stepped or tapered shields involve each successive shield having a slightly smaller diameter than the last to accommodate for any squeezing or ground convergence as the TBM excavates. Radial ports in the shields can be used for application of Bentonite to provide lubrication between the shield and tunnel walls, again to avoid a stuck machine. Should the machine become stuck, there are additional solutions: hydraulic shield breakout can be used in trapped conditions. The radial ports can be made to inject pressurized hydraulic lubricants to free a shield that has already become stuck (see Figure 12). Lastly, additional thrust jacks between the normal thrust cylinders can supply added thrust in a short stroke to break loose a stuck shield.

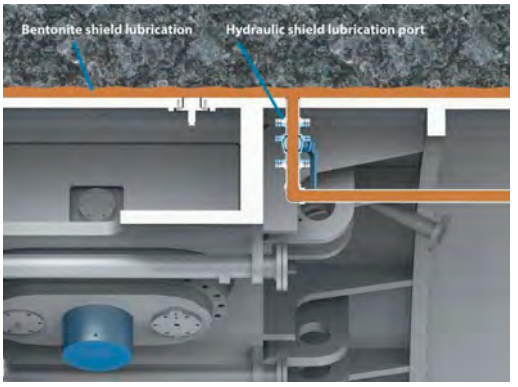

Figure 12. Shield lubrication system.

4.2.3 *Enhanced probe drilling and grouting*

One of the key lessons learned from projects in difficult ground is that more drill ports, and more types of drills, are necessary components of shielded tunneling in difficult ground. Multiple probe drills can be installed on the TBM, with ports to provide probing patterns in a 360-degree radius. High-pressure grout injection can be done through these same ports to stabilize ground up to 40 m ahead of the face (or more if using specialized drills). The type of grout injected can also be specialized—for example chemical or polymer grout can be used to seal off groundwater.

In order to minimize water inflows and increase water tightness of the segments, grouting can be done through the TBM tail shield as well.

4.3 *TBM supply*

The two Double Shield TBMs are currently being built at Robbins partner facilities, CCCC Tianhe Mechanical Equipment Manufacturing Co., Ltd. (CCCCTH) in Jiangsu Province, China. A representative example of a Double Shield TBM is shown in Figure 13 below.

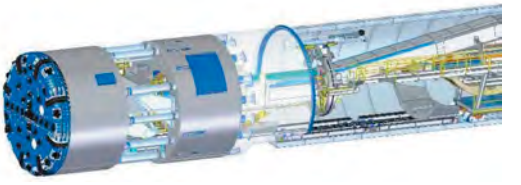

Figure 13. Example high-performance double shield tbm design.

5 CONCLUSIONS

While the original Main Beam TBMs provided for Phase I were able to excavate in the challenging conditions, there were many delays and stoppages. Modern TBM design, from 360-degree probe drilling to multi-speed gearboxes, offers advantages in these types of challenging ground. They have been proven to get through fractured, and variable ground by detecting such conditions ahead of the TBM grouting to seal off water inflows and utilizing multi-speed gearboxes. While the Double Shield TBMs have not yet been launched at the Polihali Tunnel, these two epic projects, 30 years apart, clearly elucidate the advances of the TBM industry. Advance rates and utilization will be monitored throughout these tunnels in order to compare and contrast to the Phase 1 TBMs.

REFERENCES

Lesotho Highlands Development Authority. 2020. Press Release: LHWP Phase II Diversion Tunnel Excavation Starts. https://www.lhda.org.ls/lhdaweb/Uploads/documents/Press_Office/Press_releases/DiversionTunnel.pdf

Lhda.org.ls. 2023. Lesotho Highlands Development Authority. https://www.lhda.org.ls/lhdaweb/about/ourStory.

Finnsson, S., 1994. Two tunnel-boring machines for Lesotho: A Design and Case History. Tunnelling '94. © Springer Science+Business Media Dordrecht 1994

Tunnelling for a Better Life – Yan, Celestino, Thewes & Eberhardt (Eds)
© 2024 The Author(s), ISBN 978-1-032-80042-4
Open Access: www.taylorfrancis.com, CC BY-NC-ND 4.0 license

Load condition effect based on functional model for the ultimate bearing capacity of segmental lining

Chengchao Guo, Renxiang Dong & Xinping Dong*
Zhengzhou University, Henan, China

Chuan He
Southwest Jiaotong University, Sichuan, China

Yingchun Cai
Zhengzhou University, Henan, China

ABSTRACT: Based on the principles of influence and the path of factors on the ultimate bearing capacity of a segmental lining, this study investigates the relationships between the load-bearing capacity of the lining members, the structure function of tunnel failure, the ultimate bearing capacity of the segmental lining, and load conditions. This research provides fundamental knowledge for assessing the safety of segmental lining and designing the loading procedure. The ultimate bearing capacity of a tunnel structure depends to a large extent on its failure behavior. The load or action leading to tunnel failure is diverse, including but not limited to sudden local loading or unloading, accidents, crashes, vehicle fires, and terrorist bombings. A functional model for the ultimate bearing capacity of a segmental lining has been developed. Then, the principles of influence and action path of loading on lining capacity, as well as the effects of loading path, loading mode on the structure function of failure, are analyzed. Finally, the principle of equivalent loading for the model test is discussed. The results indicate the ultimate bearing capacity of a segmental lining is influenced by the forms and paths of loads acting on the tunnel lining, in addition to the strength of materials, structural dimensions and interaction between components. The capacity of the tunnel lining is a variable that is significantly affected by load conditions. Therefore, when considering the results from specific full-scale tests or model tests, it is important to take into account their application scope and limitations. The failure mode of a segmental lining is an important factor that affects the tunnel capacity. The approximation of load conditions in model tests cannot alter the value of structure function of system failure. Additionally, the similarity criterion for the structure function of system failure must be met.

Keywords: segmental lining, load conditions, ultimate bearing capacity, analytical solution, functional model

1 INTRODUCTION

Compared to the traditional sequential tunneling method, the shield tunneling method offers advantages of safety and fast construction, especially for tunnels located in soft and water-rich ground, such as those under-crossing rivers or requiring strict ground settlement control. However, due to the application of shield tunnels in different strata and the presence of numerous joints in the lining system, they are susceptible to various disasters. These include man-made disasters such as water gushing (Feng et al., 2023), local loading (Zhang Y. M., et al., 2023), or unloading (Zhang J. Z., et al., 2023), as well as natural disasters, like earthquakes (Zhang S. H., et al., 2020). The consequences of these disasters can be catastrophic. Moreover, the design and construction of shield tunnels are facing a trend of larger cross-sections and complex structural forms (Zhu, et al., 2022; Liu et al., 2018). All of the phenomena prompt research concerning the tunnel safety, including the ultimate bearing capacity (Lu et al., 2012; Blom et al., 1999; Afshan et al., 2017), failure mechanisms (Zhang et al., 2019), and long-term performance (Zhu et al., 2022) of segmental linings, among others.

Owing to the complexity of determining the ultimate bearing capacity of a segmental lining

*Corresponding author: dxp3000@163.com

DOI: 10.1201/9781003495505-242

system (referred to as the lining system), the model testing is one of the primary research approaches. According to the simulation methods for the surrounding ground, the model test is classified into two categories: the ground-lining model (Feng et al., 2023; Zhang Y. M., et al., 2023; Zhang J. Z., et al., 2023; Zhang S. H., et al., 2020; Wang et al., 2020) and the load-lining model (Liu et al., 2018; Lu et al., 2012; Blom et al., 1999; Afshan et al., 2017; Zhang L., et al., 2019). The ground-lining model mostly adopts a small-scale, such as 1:10, 1:15, and uses materials like gypsum, micro-concrete or organic plastic to simulate the tunnel lining, as well as the rock mass. On the contrary, in a load-lining model, either a full-scale 1:1 or a small-scale 1:10 is typically used. The tunnel lining is modeled alone, and jacks are positioned along the normal direction of the lining to simulate the surrounding rock. It is well known that the ultimate bearing capacity of a lining system is significantly influenced by the segment joints (Lu et al., 2012; Blom et al., 1999; Afshan et al., 2017; Zhang L., et al., 2019; Ye et al., 2011; Wang et al., 2021). Thus, in addition to satisfying geometric similarity and material similarity, what principles or similarities should be followed in designing the model test to assess the strength of the lining? To address this problem, firstly, a functional model for the ultimate bearing capacity of a lining system is described. Then, a comparative study is conducted to examine the effects of loading conditions on the ultimate bearing capacity of lining components. The structure failure function is also analyzed, along with the principles and pathways of how loading conditions impact the ultimate bearing capacity of a lining system. Finally, a case study is conducted on the failure history of a single-ring lining system. The study investigates the equivalence principle, method and effect of the loading scheme in small-scale model tests.

2 LOADING SCHEMES FOR LOAD-LINING MODEL TESTS

In a load-lining model, the loading is directly applied to the model lining through jacks, making it easier to accurately control the direction and magnitude of the load. The load-lining model is discussed in this paper.

In the load-lining model, the loading scheme is subdivided into three types based on the loading path and the degree of load concentration:

(1) Constant eccentricity and distributed loading method. According to this method, the jacks are grouped, and the loading ratio between the groups is maintained in loading history (Lu, 2019; Liu, 2017). For example, in the study of the subway section tunnel with an outer diameter of 6.2m, Lu et al. (2012) used 24 jacks to simulate the ground resistance, soil and water pressure, surcharge, etc. Afshan et al. (2017) used 18 jacks. For this incremental loading mode, a constant ratio, M/N, between bending moment M, and the axial force N at any cross-section of the lining structure is maintained, as shown by curve A in Figure 1.

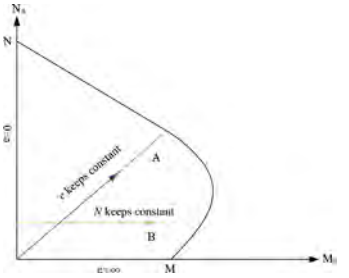

Figure 1. Loading path.

(2) Constant eccentricity and point loading methods. For example, the water pressure is applied first, and then, the 4 jacks are utilized to simulate the earth pressure. The incremental load is applied until the lining structure fails (Zhang L., et al., 2019). In loading history, the ratio between the vertical and horizontal loads, as well as eccentricity, is kept constant. Nakamura et al. (2003) used a 6-point loading method for double-circular rectangular-shaped shields.
(3) Constant axial force N and radial distribution loading method. This loading method is employed in all the full-scale tests for the BRT tunnel (Blom et al., 1999; Blom, 2002; Vervuurt et al., 2007), using 28 jacks to simulate the ground pressure.

The loading procedure is as follows: firstly, a radial uniform pressure is applied to generate an axial force N in the lining structure. Then a radial load distributed in the form of cosine function (Figure 2) is applied until the lining structure fails. Throughout this process, the axial force N is maintained at a constant level, as shown by curve B in Figure 1.

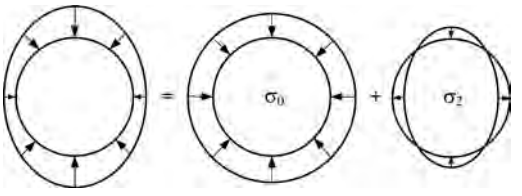

Figure 2. Loading subdivided into uniform load and an ovalization load.

It should be noted that in the aforementioned loading scenarios, multiple jacks can be arranged for the full-scale test. Nevertheless, in the small-scale

model test, a large number of jacks cannot be used due to insufficient space. To address this dilemma, the impact of loading conditions will be analyzed first, using the functional model for the ultimate bearing capacity of a lining system.

3 FUNCTIONAL MODEL FOR THE ULTIMATE BEARING CAPACITY OF A SEGMENTAL LINING SYSTEM

Ultimate bearing capacity is an important research topic in the field of lining system failure behavior (Blom et al., 1999; Ye et al., 2011; Wang et al., 2011). A functional model for the ultimate bearing capacity of the segmental lining with inclined bolts was proposed by Chen and Dong, et al. (2023).

The system capacity can be expressed in terms of the failure mode function, joint capacity, and segment capacity, as follows:

$$\begin{aligned} F &= \Phi\left(M_{\lim}^{joint}, M_{\lim}^{seg}\right) \cdot \mathrm{F}_{mode} \\ &= \Phi\left(M_{\lim}^{joint}, M_{\lim}^{seg}\right) \cdot \chi(\mathbf{I}(t)) \end{aligned} \tag{1}$$

Where, $\Phi\left(M_{\lim}^{joint}, M_{\lim}^{seg}\right)$ is a dimensional quantity that represents the strength contribution of the joint and segment, and $\mathrm{F}_{\mathrm{mode}}$ is a dimensionless quantity that represents the contribution of the system failure mode function. Function F represents the ultimate bearing capacity of the lining system

Two critical parameters are calculated as follows:

$$M_{lim}^{seg'} = -\frac{N^2}{2f_c b} + \frac{h}{2} \cdot N + f_y A_S (h_0 - a'_s) \tag{2}$$

$$M_{\lim}^{\mathrm{joint}} = \frac{-3N^2 + 3Nh_{joint} f_c b}{6 f_c b} \tag{3}$$

Where, M_{lim}^{seg} , M_{lim}^{joint} is segment and joint strength, respectively; f_c is the concrete compressive strength; f_y is the yielding strength of the reinforcement rebar; A_s is the cross-sectional area of the reinforcement; h_0 is the effective height of the segment cross section; h is the segment height; b is the segment width; N is the axial force; and a'_s is the concrete cover; h_{joint} is the joint height.

Note that the ring joint is considered an irrelevant component in terms of its load-bearing functionality within a segmental lining system, as indicated by the "relevant/irrelevant" notation. In tunnel engineering, the ring joint typically cannot be designed in practice to serve as a load-carrying part, even though the ring joint is of significant importance to a lining system.

The failure mode can be expressed in terms of the state variable vector at time t, as follows:

$$\begin{aligned} F_{\mathrm{mode}} &= \chi(Y_i(t)) = \chi(x_i(t)) = \chi(I_i(t)) \\ &= \chi\left(I_1^{joint}, I_2^{joint}, \ldots, I_{NJ}^{joint}, I_{NJ+1}^{seg}, I_{NJ+2}^{seg} \ldots, I_{NJ+NS=n}^{seg}\right) \\ &= \chi(\mathbf{I}(t)) \end{aligned} \tag{4}$$

Where, $\mathrm{F}_{\mathrm{mode}}$ is the failure mode function of the lining system in terms of the failure index vector at time t.

$\mathbf{I}(t) = (I_1(t), I_2(t), \cdots I_n(t))$ is the failure index vector at time t.

$$I^{\mathrm{Joint}} = \frac{M^{\mathrm{joint}}}{M_{\lim}^{\mathrm{joint}}} \tag{5}$$

$$I^{\mathrm{Seg}} = \frac{M^{\mathrm{Seg}}}{M_{\lim}^{\mathrm{Seg}}} \tag{6}$$

Where, $\mathrm{I}^{\mathrm{Joint}}$, $\mathrm{I}^{\mathrm{Seg}}$ is the failure index of the segment joint and segment, respectively; M is the moment induced by the external load and can be computed using a theoretical or numerical model.

The advantage of expressing the failure mode function expressed in terms of the failure index vector instead of the bending moment is discussed below.

The joint failure index and segment failure index are dimensionless quantities that range from 0 to 1. The failure index has a clear physical interpretation. Thus, the load-bearing states of segments or joints can be evaluated and compared using a universally normalized measuring scale.

The functional model for the ultimate bearing capacity of a segmental lining establishes a direct mapping relationship between various causal factors and the ultimate load-bearing capacity of the lining system, which clarifies the constituent elements of the ultimate load-bearing capacity of the segmental lining, as well as the principle of each influencing factor on the ultimate bearing capacity. From Equations. (2)- (6), it can be seen that all three components of lining strength are sensitive to the loading conditions, such as type, direction, distribution, and path of loading.

4 INFLUENCE PRINCIPLE AND PATH OF LOADING EFFECT ON LINING STRENGTH

4.1 *Analysis method and verification*

Based on a series of full-scale tests, Blom (2002) derived an analytical method for the mechanical response of segmental lining, which can consider the nonlinear rotation characteristics of segment joint, and analyzed a single-ring failure history using this analytical method. For verification purpose, the analytical case is chosen as study case. The study case is based on Botlek Railway Tunnel, with physical and material parameter is shown in Table 1.

Segment joints are illustrated as shown in Figure 3.

Table 1. Physical dimensions and material properties.

Parameter and symbol	Values	Unit
Tunnel radius, r	4.525	m
Ring width, b	1.5	m
Segment thickness, h	0.4	m
Joint height, h_{joint}	0.17	m
Young's elastic module of concrete, E_c	36	GPa
Poisson's ratio of concrete, v	0.2	
Compressive strength of concrete, f_c	64	MPa
Joint compressive stiffness, k_c	230	GPa/m

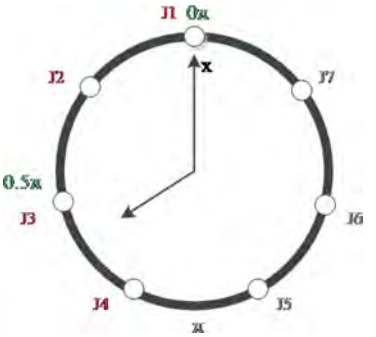

Figure 3. Geometry of lining: i is location index of segment joint.

The loading mode is as shown in Figure 2. In Blom's model, non-linear behavior of a single ring is analyzed without considering the interaction between the soil and the lining. The loading procedure is as follows:

(1) Firstly, the uniform load is applied (σ_0 =0.5MPa).
(2) Then, the ovalization load (σ_2).is applied step by step.

In this study, the moment-search-method (MSM), developed by Dong (2015), is used to calculate the failure history of the lining system. The MSM adopts the segment joint model proposed by Dong (2013). According to Dong, the rotation curve of the segment joint is shown in Figure 4.

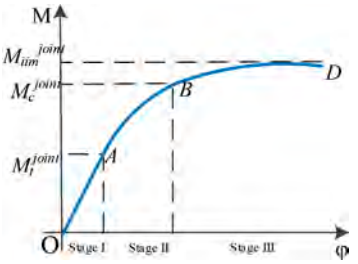

Figure 4. M-φ curve of segment joint.

The M-φ curve in Figure 4, can be described by the following formula (Dong, 2013):

$$\theta_{\text{joint}} = \begin{cases} \dfrac{M}{k_c I_{\text{joint}}} & M \le M_{\text{t}}^{\text{joint}} \\ \dfrac{2N}{9k_c b\left(\frac{h_{\text{joint}}}{2}-\frac{M}{N}\right)^2} & M_{\text{t}}^{\text{joint}} < M \le M_c^{joint} \\ \dfrac{1}{2}\dfrac{f_c{}^2 b}{k_c\left(3Nbf_c h-6Mbf_c-3N^2\right)^{1/2}} & M_{\text{c}}^{\text{joint}} < M \le M_{\text{lim}}^{\text{joint}} \end{cases} \tag{7}$$

Where, M_t^{joint} is the critical moment for joint opening; M_c^{joint} is the critical moment for joint yielding; M_{lim}^{joint} is the joint capacity; I_{joint} is the joint inertia moment; and k_c is the joint compressive stiffness.

In addition, the critical moment is derived as follows (Dong, 2013).

$$M_{\text{t}}^{\text{joint}} = \frac{N \cdot h_{joint}}{6} \tag{8}$$

$$M_{\text{c}}^{\text{joint}} = N\left(\frac{h_{joint}}{2} - \frac{2N}{3bf_{\text{c}}}\right) \tag{9}$$

The vertical displacement at ring bottom obtained using MSM is compared with that of Blom in Figure 5.

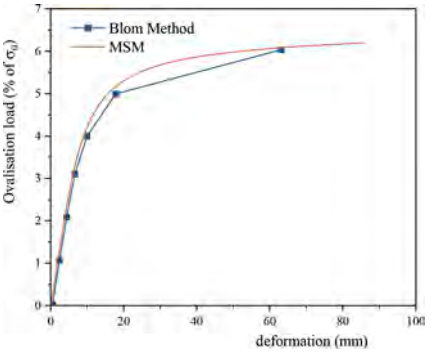

Figure 5. Comparison of displacement at ring bottom between MSM and Blom's algorithm.

It can be seen that the displacement history at bottom obtained by MSM agrees well with the calculation results of Blom, and the load effect will be analyzed by MSM in this study.

4.2 *Effect of loading conditions on lining strength*

To simplify the calculation of equivalent resultant loads under different loading conditions, two cases are constructed based on blom's analysis. The cases are used to compare loading mode 1 and 2, which are the distribution loading and centralized loading, respectively, under constant eccentricity:

Case 1: vertical uniformly distributed load p + horizontal uniformly distributed load q (p>q);

Case 2: vertical concentrated load P_V + horizontal uniformly distributed load q;

The load magnitude is as follows: based on Blom's analysis case, σ_0=0.5MPa, and the maximum ovalization load σ_2 is σ_0×8%. Thus, uniform distribution load p, q is 810kN/m, 690kN/m, respectively. In accordance with the loading procedure, firstly apply uniform loading q=690k/m, and then apply ovalization loading (p-q)=120kN/m. Ovalization loading (p-q) is divided into 80 load steps, the incremental load in each loading step is 1.5kN/m in Case 1 and the corresponding point load is 6.7875kN in Case 2.

Since the magnitude of individual load step at the ovalization loading stage (Stage 2) for Cases 1 to 2 is equivalent, the number of load steps is then used as the representation of the loading history.

The comparison of the ultimate bearing capacity of the lining system for Case 1 to 2 is shown in Figure 6.

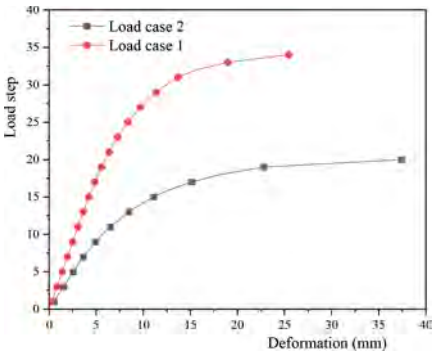

Figure 6. Comparison of the lining strength.

For Case 1 and 2, loading stage 1 is identical and loading stage 2 is equivalent. However, the lining strength of Case 1 is 1.7 times that of Case 2. From Figure 6, it can be observed that in the ultimate bearing capacity test of a lining system, it is not appropriate to design the loading procedure solely based on the "load equivalent" principle. What causes the formation of this phenomenon? It will be investigated in the following manner.

4.3 *Influence principle and path of load effect*

Based on the functional model for lining strength, the influence of load effect on the composition elements of lining capacity can be analyzed separately. Firstly, the influence of the load effect on segment and joint strength is investigated. The variation of axial force in Case 1 is shown in Figure 7.

In Figure 7, it can be observed that the axial force increases with the increase in ovalization loading. The axial force reaches its peak at the load step LS=34. Among them, the axial force at segment joints increases, while the axial force at the ring bottom decreases. The axial force at the bottom decreases at a rate of 0.4%, and the rates of increase for J1 to J4 are: 0.4%, 4.9%, 7.14%, and 1.08%, respectively. Thus, the axial force remains approximately constant (less than 10%) throughout the ovalization loading (p-q) history. Consequently, the

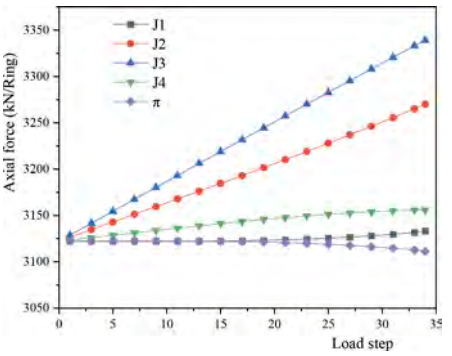

Figure 7. Axial force history in load case 1.

ultimate bearing capacity of the joints and segments remains essentially constant in the failure history. The variation of the ultimate bearing capacity of the joints is shown in Figure 8.

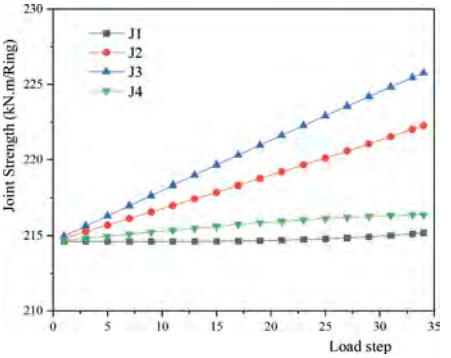

Figure 8. Variation of the joint strength in case 1.

The variation rates of the strength of the joints J1 to J4 in ovalization loading stages are 0.3%, 3.7%, 5.3%, and 0.8%, respectively. Thus, the strength of the joints is approximated to remain constant during ovalization loading.

The variation of joint strength for Case 2 is shown in Figure 9. From the Figure 9, it can be seen that the change in the strength of the segment joint is within 10kN.m/Ring. Compared with 215kN/Ring before the ovalisation loading, the change rate of the ultimate bearing capacity of the joints from J1 to J4 is 0.6%, 2.8%, 2.9%, and 0.8%. The ultimate bearing capacity of the segment joints is approximately constant.

According to the function model for segmental lining strength, it is evident that the influence of Case1 and Case 2 on the component's strength function Φ is not the primary factor contributing to the significant difference in the ultimate bearing capacity of the lining system.

Another factor that affects the ultimate bearing capacity of the lining system is the failure mode. In fact, the failure modes of Case 1 and Case 2 are significantly different, even though they have equivalent load magnitude. The evolution of the failure indices for Case 1 and Case 2 is shown in Figure 10.

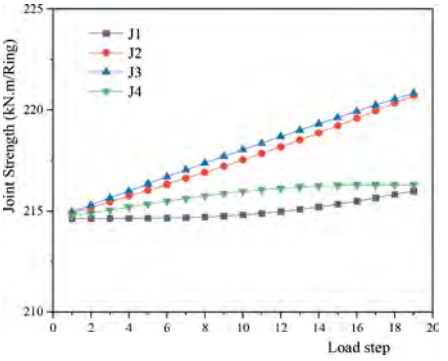

Figure 9. Variation of the joint strength in case 2.

As can be seen in the Figure 10, there is a significant difference between the failure mode functions for Case 1 and Case 2. In Case 1, the structure functions at failure are as follows:

$$\begin{cases} I_1 = 0.99 \\ I_2 = 0.40 \\ I_3 = 0.99 \\ I_4 = 0.96 \\ \quad \vdots \end{cases} \tag{10}$$

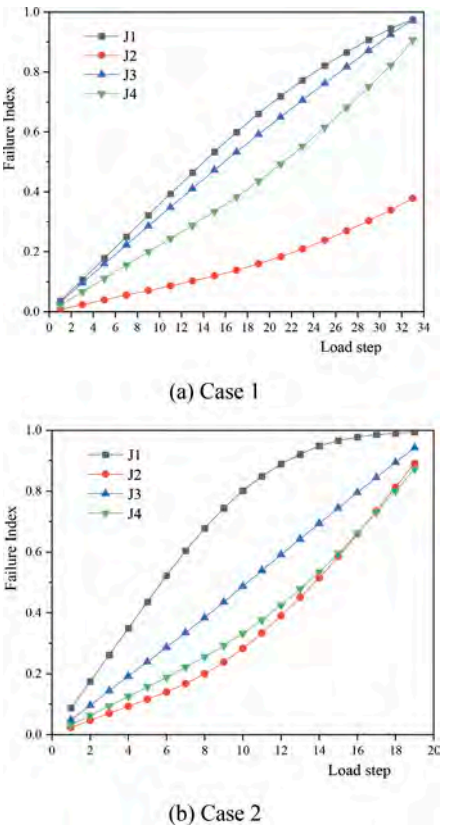

Figure 10. Failure mode of case 1 and case 2.

For Case 2, the structure functions at failure are as follows:

$$\begin{cases} I_1 = 1.00 \\ I_2 = 0.97 \\ I_3 = 0.99 \\ I_4 = 0.95 \\ \quad \vdots \end{cases} \tag{11}$$

The difference in the structure of the failure mode function is the main reason for the significant disparity in the ultimate bearing capacity between Case 1 and Case 2,

As can be seen from the examples of Case 1 to 2, the loading have an influence on influence the ultimate bearing capacity of the lining system by affecting the failure mode function.

5 DESIGN PRINCIPLE OF LOADING PROCEDURE BASED ON THE FUNCTIONAL MODEL FOR LINING STRENGTH

As mentioned previously, the loading conditions have a significant impact on the ultimate bearing capacity of the segmental lining system. Meanwhile, in the small-scale model test, it is not possible to arrange as many jacks as in the full-scale test due to the limitations of model dimensions. So, how can we balance this contradiction in the model test?

The Blom's constant axial force N loading is selected as the study case. As shown in Figure 2, according to Blom, a uniform loading σ_0 (0.5 MPa) is applied initially, followed by a cosine-distribution ovalization loading with a maximum value of 1/80th of 8% of σ_0 per step. In other words, the maximum load p_0 at each loading step is 0.75 kN/m. When this case was implemented in the Netherlands laboratory, 28 radial jacks were used to simulate the uniform and ovalization cosine loading. Obviously, if a small-scale model test with a similarity ratio of n=10 is used, the maximum diameter is within 1m. In this case, it is impossible to implement the arrangement of 28 jacks, and the centralized loading method is generally used for small-scale test. So, how should the jacks be arranged to achieve the approximation of the cosine loading?

Two points loading methods are examined, as shown in Figure 11.

For centralized loading in Figure 11a, the vertical and horizontal directions are loaded with the incremental equivalents of the cosine loading, i.e:

$$P_V = \frac{1}{3} p_0 r = 2262.5\text{kN/ring} \tag{12}$$

$$P_H = P_V = 2262.5\text{kN/ring} \tag{13}$$

For centralized loading in Figure 11b, the load is applied only in the vertical direction. The value of the load is 2 times the P_V.

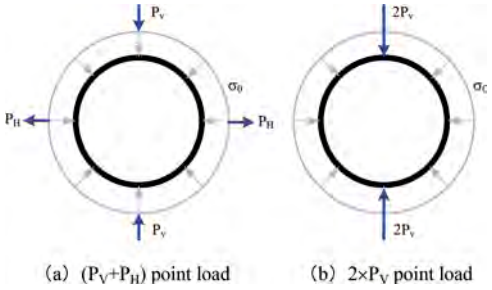

Figure 11. Centralized loading.

The comparison of ultimate bearing capacity is shown in Figure 12. The ultimate bearing capacity of (P_V+P_H) and 2×Pv point loading increases 18.88% and 22.64% compared to the cosine loading method, respectively. The rate of change in ultimate bearing capacity of segment joints is less than 1.5% for cosine mode loading until the failure of the segmental lining system. The rate of change in the ultimate bearing capacity of the joints in the (P_V+P_H) and 2×P_V loading methods is less than 1.5% and 3%, respectively. Therefore, the change in the ultimate bearing capacity of the segmental lining system is not caused by a change in joint strength.

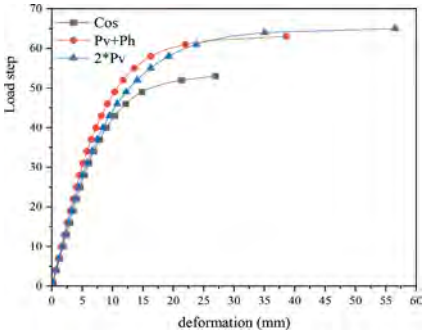

Figure 12. Effect of loading pattern on lining strength.

In fact, the primary reason for the change in lining strength is the alteration of the lining failure mode due to the loading mode. For example, the failure index of J2 under different loading patterns is shown in Figure 13.

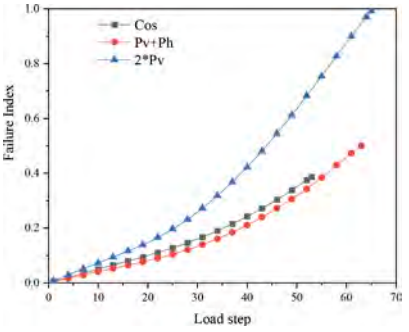

Figure 13. Effect of loading mode on failure index of J2.

Therefore, it is not appropriate to replace the ovalization cosine loading with the vertical centralized loading. Meanwhile, from Figure 13, it can be seen that the (P_V+P_H) loading method does not fundamentally alter the failure mode structure. Thus, an attempt is made to add a correction factor ϖ=1.1 to the point loading, i.e., applying the load ϖ× (P_V+P_H). The ultimate bearing capacity and the structure of the failure function are shown in Figures 14 and 15.

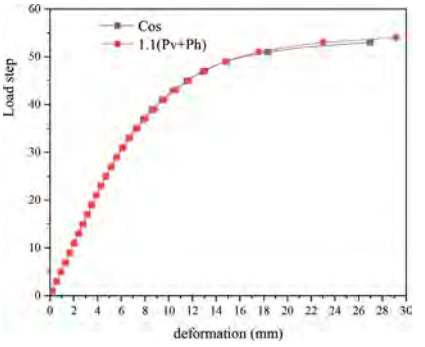

Figure 14. Lining strength for (P_V+P_H) multiplied by correction factor ϖ.

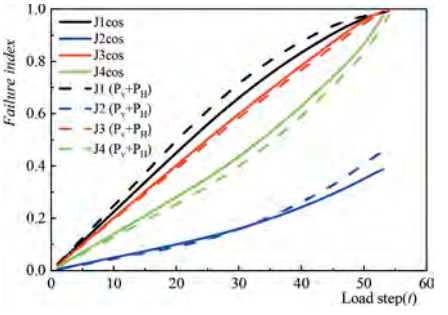

Figure 15. Failure mode for (P_V+P_H) multiplied by correction factor ϖ.

It can be seen that multiplying (P_V+P_H) by the correction factor ϖ to replace cosine loading is feasible. As long as the ultimate bearing capacity of components and the failure modes are similar, the ultimate bearing capacity of the lining system must also be similar, according to the functional model for lining system strength. This paper provides a theoretical basis for the design of loading in small-scale model tests.

6 CONCLUSION

(1) Currently, the ultimate bearing capacity of segmental lining is primary determined through the full-scale and small-scale tests. It should be noted that the ultimate bearing capacity of a segmental lining system is not an inherent property of the tunnel structural system itself, and the lining

capacity is influenced by various factors, including the load conditions imposed on the structural system, the lining materials, lining structure and dimensions of component, and the interaction between these components. The ultimate bearing capacity of a lining system is a variable greatly influenced by the loading conditions. Therefore, the results of a specific capacity test should explicitly indicate its scope and limits.

(2) In the design and data analysis of model tests, the loading conditions should be carefully and thoroughly considered. It is evident that selecting an appropriate load condition for model testing, whether it is full-scale test or small-test, is not a simple task. This includes considering factors, such as the type and forms of loading, the magnitude of loads and the path (whether to keep the ratio of M/N constant or the axial force N constant).

(3) The ultimate bearing capacity of a segmental lining is a function in terms of the ultimate bearing capacity of the segment joints and segments, failure mode of the lining system.

(4) In the segmental lining test for ultimate bearing capacity, it is necessary to ensure similarity in geometric dimensions, material properties (such as the elastic modulus, compressive strength of segment concrete), component strength, and structural failure mode. This means that the strength of the lining system must exhibit similarity. The approximation of loading conditions in the model test should not alter the failure mode structure function of the lining system.

(5) The function model for the ultimate bearing capacity of segmental lining provides a theoretical basis for loading design in small-scale model tests. For different loading procedure, as long as the component capacity and failure mode similarities are satisfied, the ultimate bearing capacity of the lining system must be similar.

REFERENCES

Afshan, S., Yu, J. B. Y., Standing, J. R., et al, 2017. Ultimate capacity of a segmental grey cast iron tunnel lining ring subjected to large deformations. Tunnelling and Underground Space Technology. 64, 74–84.

C. B. M. Blom., 2002. Design philosophy of concrete linings for tunnels in soft soils. PhD Thesis. Technische Universiteit Delft, NL.

C. B. M. Blom., E. J. van der Horst and P. S. Jovanovic, 1999. Three-dimensional structural analyses of the shield-driven “Green Heart” tunnel of the high-speed line south. Tunnelling and Underground Space Technology. 14(2), 217–224.

Dong, X. P., 2013. Analytical solution of segment joint model for segmented tunnel lining. Chinese Journal of Geotechnical Engineering. 35(10), 1870–1875.

Dong, X. P., 2014. Failure mechanism of the full-ring for segmented tunnel lining. Chinese Journal of Geotechnical Engineering. 36(3), 417–426.

Dong, X. P., 2015.Incremental analytical solution for failure history of a single ring of segmented tunnel lining. Chinese Journal of Geotechnical Engineering. 37(1), 119–125.

Chen, X. Y, Dong, X. P. et al., 2023. Functional model based on FMEA methodology for ultimate bearing capacity of segmental lining, to be published.

Feng, Y., Chen, Y. M., 2023. Experimental study on water gushing-sand bursting in shield tunnels based on transparent soli. J. Tunnel Construction. 43(1), 75–81.

Liu, X., Ye, Y. H., Liu, Z., et al, 2018. Mechanical behavior of Quasi-rectangular segmental tunnel linings: First results from full-scale ring tests. Tunnelling and Underground Space Technology. 71, 440–453.

Liu, X. Z., Lai, H. R., Sang, Y. L., et al, 2020. Model tests on effect of bonded steel plate reinforcement of shield tunnels under different deformation conditions. Chinese Journal of Geotechnical Engineering. 42(11), 2115–2123.

Liu, Z., 2017. Shield segment deformation performance test and simulation analysis under complicated working condition. Master thesis. China academy od railway sciences corporation limited, CHN.

Lu, L., Sun, Y. F., Liu, X., et al, 2012. Full-ring experimental study on the ultimate bearing capacity of the lining structure of the metro shield tunnel. Structural Engineers. 28(6), 134–139.

Lu, Y.,2019. Full-scale model test of shield tunnel segment and simulation analysis of circumferential joint. Master thesis. China academy od railway sciences corporation limited, CHN.

Nakamura, H., Kubota, T., Furukawa, M., et al, 2003. Unified construction of running track tunnel and crossover tunnel for subway by rectangular shape double track cross-section shield machine. Tunnelling and Underground Space Technology. 18, 253–262.

Vervuurt, A., & den Uijl, J. A.,2007. Bezwijkveiligheid boortunnels. meetrapport en evaluatie proevenserie C.

Wang, J. C., Xie, J. C., Huang, W. M., 2021. Review on nonlinear mechanical response analysis of shield tunnel lining. Tunnel Construction. 41(2), 22–35.

Wang, S. M., Wang, X. M., Chen, B., et al, 2020. Critical state analysis of instability of shield tunnel segment lining. Tunnelling and Underground Space Technology. 96, 1–13.

Zhang, J. Z., Huang, H. W., Zhang, D. M., et al, 2023. Experimental study of the coupling effect on segmental shield tunnel lining under surcharge loading and excavation unloading. Tunnelling and Underground Space Technology. 140, 1–14.

Zhang, L., Feng, K., Guo, C., et al, 2019. Failure tests and bearing performance of prototype segmental linings of shield tunnel under high water pressure. Tunnelling and Underground Space Technology. 92, 1–15.

Zhang, S. H., Yuan, Y., Li, C., Herbert, M.A., et al, 2020. Effects of interior structure as double deck lanes on seismic performance of segmental linings. Tunnelling and Underground Space Technology. 103, 1–11.

Zhang, Y. M., Liu, T. J., Zhu, C., et al, 2023. Model test on deformation and failure characteristics of shield tunnel in soil-rock composite stratum under surface surcharge. J. Journal of Railway Science and Engineering.

Zhu, M., Chen, X.S., Wang, X.T., 2022. Analysis and thinking on structural performance evolution of shield tunnel lining. Engineering Mechanics. 39(3), 33–50.

Tunnelling for a Better Life – Yan, Celestino, Thewes & Eberhardt (Eds)
© 2024 The Author(s), ISBN 978-1-032-80042-4
Open Access: www.taylorfrancis.com, CC BY-NC-ND 4.0 license

Negligible ground surface movement with EPB TBMs in Singapore marine clay and fluvial sand

Grace Christine Hangadi*
Arup Singapore Pte Ltd, Singapore

Leslie Jonathan Pakianathan
Tunnelling and Underground Construction Society (Singapore), Singapore

Chee Keong Poh & Johnny Lim
Land Transport Authority (Singapore), Singapore

Raymond Koh
Shanghai Tunnel Engineering Co (Singapore) Pte Ltd, Singapore

ABSTRACT: Past experiences of EPB TBM projects in soft sedimentary deposits such as Singapore Marine Clay and Fluvial Sand demonstrated the relatively high ground movement during tunnel boring operations. A volume loss of up to 3% is therefore adopted during the preliminary impact assessment and execution of tunnelling in these soils. In end 2022, five tunnels of excavation diameters ranging from 6.7m to 12.2m under-crossed an almost-flat, highly settlement sensitive pavement with ground cover between 11m to 20m. A comprehensive set of control measures were established to limit the surface ground movement. These measures included real-time remote settlement monitoring with readings published hourly in the vicinity of the TBM, application of higher-than-normal face pressure (more than 90% of the full ground overburden), robust muck reconciliation regime counter-checked amongst three independent measurement methods, regular testing of excavated spoil samples for each advance, selection of appropriate ground conditions and timely adjustment of the conditioning quantities injected to suit the changing geology during TBM advancement. With these measures, the surface movement was controlled during the parallel boring of the five tunnels to within the bounds of monitoring accuracy. This paper shares the lessons learnt in particular the success of the observational method and the implementation of relatively higher face pressures during TBM driving.

Keywords: Tunnelling, Settlement, Observational, Volume loss, PVD, Face Pressure

1 INTRODUCTION

Past experiences of TBM tunnelling in Singapore Marine Clay and Fluvial Sand suggest high surface settlement with volume loss of up to 3% [1, 2, 3] and occasionally reaching as high as 5% or beyond [4]. Even with the advancement in TBM technology and increased tunnelling experience in such geology, volume loss of up to 1.89% is still recorded in Thomson-East Coast Line, the most recent Mass Rapid Transit (MRT) tunnelling project in Singapore [5]. The Singapore Land Transport Authority (LTA) Civil Design Criteria recommends volume loss of 3% for impact assessment arising from EPB (Earth Pressure Balance) TBM (Tunnel Boring Machine) tunnelling of up to 6.6m excavated diameter in Kallang Formation [6].

In 2022, 5 nos. of tunnels with almost parallel alignment were launched almost simultaneously at the Eastern Region of Singapore and the ground settlement after the TBMs have passed was almost negligible or within the bounds of monitoring accuracy (less than 5mm). Towards the last 300m of the tunnel drive, the TBMs encountered Marine Clay and Fluvial Sand while undercrossing an operational pavement with stringent settlement criteria. The project site is situated on reclaimed land which generally comprises of Reclamation Fill and Kallang Formation (Marine Clay and Fluvial Sand) overlaying Old Alluvium. Prior to development of the area, Prefabricated Vertical Drains (PVD) with surcharge were installed in 1970s to accelerate the consolidation process. In addition to undercrossing an operational pavement in Marine Clay and Fluvial Sand, the TBMs had to

*Corresponding author: Grace.Hangadi@arup.com

DOI: 10.1201/9781003495505-243

tunnel through a cluster of PVDs which were installed some 40 years ago and left-in-place.

In order to mitigate the risks that could adversely affect the sensitive pavement, several measures were put in place including carrying out trials for each TBM to fine tune operating parameters, developing special tools to cut the PVDs and verifying through trial the ability of the TBM to cut cleanly without dragging, allowing only one TBM to under cross at a time, selecting closely-spaced surface settlement points and carrying out real-time (hourly) monitoring, etc. This paper will elaborate on some of these measures put in place to achieve safe tunnelling in Marine Clay and Fluvial Sand with negligible surface movement.

2 TUNNEL ALIGNMENT AND GEOLOGY

The 5 constructed tunnels are of the following excavated diameter: 1 no. of 12.3m, 2 nos. of 7.5m and 2 nos. of 6.7m.

The 12.3m diameter tunnel axis ranges from 13m to 35m deep below ground level whereas the 7.5m diameter tunnel axis ranges from 16m to 35m deep below ground level. The 6.7m diameter tunnels' depth at axis ranges from 17m to 26m.

The TBMs traversed through Old Alluvium, mainly of Class B and C for 1.3km followed by mixed face of Old Alluvium (OA) and Kallang Formation for 300m under an operational pavement. The simplified geological condition along the tunnel alignment is illustrated in Figure 1.

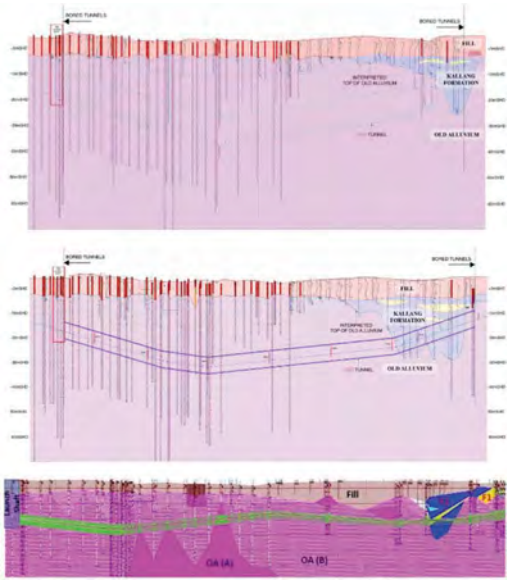

Figure 1. Geological profile along tunnel alignment (12.3m diameter – top, 7.5m diameter – middle, 6.7m diameter – bottom).

Due to limited surface access to carry out extensive and intrusive site investigation in the vicinity of the pavement, the interface between the Reclamation Fill/ Kallang Formation and Old Alluvium were inferred based on non-intrusive geophysical survey data and the available site investigation boreholes and Cone Penetration Tests (CPT) data in the vicinity. Figure 2 illustrates the geophysical survey data gathered along the tunnel alignments in the vicinity of the pavement.

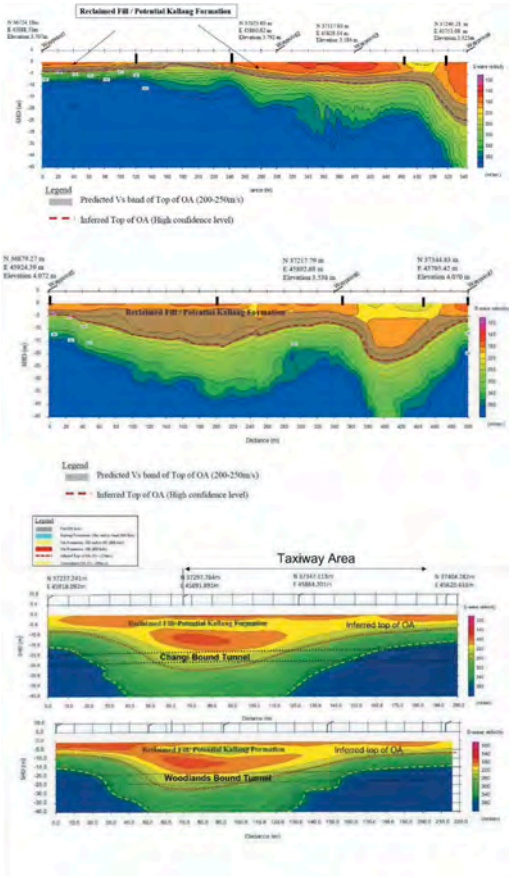

Figure 2. Geophysical survey data along tunnel alignments in the vicinity of the pavement.

The geotechnical design parameters for indication of ground properties can be referred from Table 1.

3 INSTRUMENTATION AND MONITORING

Conventional instruments such as surface settlement markers and borehole instruments which protrude above the ground surface and require access for reading collection could not be installed in the project site environment. Automatic Deformation Monitoring System (ADMS) comprising of optical prism and automated total station was adopted to monitor settlement of turf and non-pavement structures in real-time. Reflectorless ADMS which utilised an

Table 1. Geotechnical design parameters.

			FILL	KALLANG FORMATION		OLD ALLUVIUM				
STRATIFICATION			FILL	FLUVIAL SAND	MARINE CLAY	RESIDUAL	DESTRUC-TURED	DIS-TINCTLY WEA-THERED	PARTIALLY WEATHERED	UNWE-ATHER-ED
GEOLOGICAL CLASSIFICATION		UNIT	FILL	F1	MC	O(E)	O(D)	O(C)	O(B)	O(A)
Bulk Unit Weight	γ	kN/m^3	18 (min. 15, max. 20)	20	16-17	20	20	20.5	20.5	20.5
Effective Angle of Friction	ϕ'	°	32	30	22	30	32	35	35	35
Effective Cohesion	c'	kPa	0	0	0	0	1	15	15	15
Undrained Shear Strength	c_u	kPa	-	-	1.3(10.6-z) where -2.5mSHD > z > -17.5mSHD; 30 where z ≤ -17.5 mSHD	40	100	200	300	400
At Rest Earth Pressure Coeffi-cient	K_0	-	0.65*	0.5	1.0	0.8				
Elastic Modulus	E_u	kPa	-	-	$300c_u$	1.2E'				
Effective Elastic Modulus	E'	kPa	12000	1500N	Eu/1.2	4000N (For ERSS) 2500N (For Tunnelling)				
Permeabil-ity	k	m/s	1×10^{-5}	1×10^{-6}	1×10^{-9}	1×10^{-7}				

1. z = elevation in mSHD
2. N = SPT blow count
3. *To be considered on case by case basis to reflect lateral stress increases from manmade processes such as but not limited to compaction of fill materials post deposition
4. Stated K_0 values are meant for ERSS design only
5. The above parameters are not appropriate for use to assess excavability nor are they intended for selection of construction equipment and method. The Contractor may use factual site investigation data for selection of construction equipment and method.

automated total station to measure and track the alteration of a point on the surface with preset coordinates was adopted for monitoring of pavement in real-time.

The accuracy of reflectorless ADMS is influenced by monitoring radius, rain and sunlight glare. With 3m high total station, the monitoring accuracy is within 2mm for up to 100m of monitoring radius. During light rain, the monitoring radius is reduced to 80m for similar accuracy range, however, during heavy rain, reading may not be able to be taken. During early afternoon between 12noon to 4pm, high fluctuation of readings was observed due to sunlight glare.

3.1 *Monitoring of pavement*

The pavement was monitored in grid of 15m by 7.5m as per required Standards set by the relevant Authority of Singapore. In order to remain operational, the Standard requires the pavement to maintain longitudinal slope not exceeding 1.5%. However, considering the criticality of the pavement, strict settlement control was imposed and the settlement limit for the cumulative bored tunnelling works is set at 45mm with maximum rotation of 1/400.

4 TRIAL DRIVES

In order to verify the TBM operating parameters in similar ground condition as that under the pavement as well as to demonstrate that the cumulative settlement achieved during tunnelling is less than the settlement limit, trial drives were conducted for each TBM prior to undercrossing of the pavement. During the trial

drive process, the instrumentation readings were reviewed closely and frequently and TBM operating parameters were adjusted and fine-tuned according to the actual tunnelling performance. The trial also considered the materials and mix proportions of the ground conditioning.

4.1 *Muck testing and soil conditioning*

During the trial drives of approximately 35m long, the TBMs transitioned from the stronger Old Alluvium into weak and more permeable Kallang Formation. As the TBM approached the geological transition, muck testing was carried out at every ring (approximately 1.6m to 2m interval) to monitor the change in density, slump as well as water content. The frequent muck testing provided an indication on the actual ground type being tunnelled through and enabled timely adjustment of soil conditioning. In Old Alluvium, combination of 40% foam and 10% dispersant was adopted to minimise cutter wear and at the same time, adequately workable for muck disposal by conveyor belt. In mixed-face Old Alluvium and Marine Clay, combination of 15% foam and 20% encapsulator was adopted and adjusted to 10% foam and 30% encapsulator if Fluvial Sand was also observed. In Kallang Formation, only encapsulator was adopted and the injection ratio ranged from 15% to 30% depending on the percentage of Fluvial Sand observed. To mitigate risk of uncontrolled water inflow in the event of TBM encountering Fluvial Sand, water absorbing and binding polymer was made available on standby and to be injected into screw conveyor with injection ratio of 2% to 5%.

4.2 *Face pressure and muck reconciliation*

In Old Alluvium, the applied face pressure ranged between 40% to 50% of overburden pressure. As geological transition was largely interpreted and there was limited geological information due to access constraints, face pressure was stepped up gradually from 40% to 80% of overburden pressure as the TBM approached the theoretical transition zone.

During the trial drives, muck reconciliation was carried out for every ring and the applied face pressure was adjusted according to the muck reconciliation percentage and surface settlement monitoring. For 7.5m and 6.7m diameter diameter tunnels, the muck reconciliation was carried out by muck skip count and belt weigher in the tunnel or weighing bridge/gantry crane at the shaft. For the 12.3m diameter tunnel, conveyor belt sensors and muck pit volume were utilised for reconciliation. Rather than solely basing the over-excavation ratio on the permissible limit of 10% (for tunnel diameter more than 10m) and 15% as stipulated by the Building Control Authority, the trend of the muck reconciliation percentage was also considered in the face pressure and backfill grout pressure adjustment.

During the undercrossing of the pavement, the TBM was climbing up at a gradient of 3.5% to 5% and the ground cover to the tunnel crown was approximately 12m for the 12.3m diameter tunnel and 15m for the 7.5m diameter tunnels. Low ground cover and low undrained shear strength of Marine Clay in the area were a concern for adopting a high face pressure and backfill grout pressure in view of potential blow-out or excessive heave. The Recommendations for Face Support Pressure in Soft Ground [7] suggests that the applied pressure at tunnel face should be kept below 90% of the vertical overburden pressure at tunnel crown. Past experiences in Singapore [4] demonstrate that higher face pressures in the range of 90% to 120% of vertical overburden pressure have been used. However, these tend to cause higher settlement sometime after the passage of the TBM. Therefore, it was decided not to exceed 100% overburden pressure, however, when necessary, depending on actual real-time surface settlement monitoring readings and over-excavation trend, the face pressure could be increased to beyond 90%. The maximum face pressure applied during tunnelling under the operational pavement was 92% of vertical overburden pressure for the 7.5m diameter tunnel and 89% for the 12.3m diameter tunnel. The face pressures were reviewed for each ring and adjusted as required. Considering the limited ground cover, the soft Marine Clay with OCR close to 1 and the stringent settlement limit, the close review of muck properties, muck reconciliation trend and real-time instrumentation readings were crucial factors in dynamically adjusting the TBM operating parameters. With this approach, despite the significant challenges the measured settlement was maintained below 5mm at the operational pavement. As of today, one year after completion of bored tunnelling works, there is no significant post-tunnelling settlement observed.

5 TUNNELLING THROUGH PVDS

Tunnelling through PVDs poses risk of excessive settlement arising from downdrag during cutting and entanglement of the PVDs with the cutting tools of the TBM [8]. To mitigate the risk, a trial was conducted during the design stage of the TBM to verify suitability of the cutting method and devices. The setup of the trial is illustrated in Figure 3. During the trial, comparison between tensile strength of the PVD and friction between PVD and ground which holds the PVD from being dragged during cutting, observations on cuts made on PVD, pulling force and surface settlement during cutting were made. The proposed PVD cutting tools with Castolin coating shown in Figure 4 were also tested. These special cutting tools were installed at some of the ripper, scrapper and bucket locations of the cutting wheel immediately prior to entering the zone influencing the operational pavement.

PVDs were encountered as anticipated during the TBM drive in Kallang Formation, however, no significant ground movement or variation in TBM parameters was observed when tunnelling through the PVDs. Some of the PVDs were observed in the

muck being discharged and some were found in the TBM cutterhead chamber during cutterhead intervention (CHI) as shown in Figure 5.

Figure 3. PVD cutting trial setup.

Figure 4. PVD cutting tools – fresh cutters (left), worn cutters (right).

Figure 5. PVD encountered during tunnelling.

6 DISCUSSIONS AND LESSONS LEARNT

The control of ground movement when tunnelling through Kallang Formation and the interface of Old Alluvium mixed with Kallang Formation has been a challenge in Singapore. This is partly as a result of the nature of the soils forming the Kallang Formation namely very weak Marine or Estuarine clay as well as the saturated and permeable fluvial sand that is often present in the form of discrete lenses making detection through site investigations difficult. Sections of Singapore MRT projects such as North-East Line, Circle Line, Downtown Line and Thomson East Coast Line have been bored through this medium, with greater understanding being gained and tunnelling performance improving progressively.

The key improvements can be attributed to: a) better identification of the Kallang Formation boundaries during site investigations, b) selection, trial and injection of ground conditioning materials and frequent testing of the excavated spoil and changing the type, quantity and mix ratio of the conditioning accordingly to suit, c) application of appropriate face pressure with minimum fluctuations, d) uninterrupted injection of backfill grouting during TBM advance using redundant ports in case of chokage, and e) more accurate methods of muck reconciliation. The frequent, accurate and timely monitoring of surface settlements is another contributory factor which promptly informs in the event any revision is needed to the applied face pressure. It is worthy to note that all cutter tool changes were carried out either in competent Old Alluvium or in a pre-installed grout block prior to entering the zone of the operational pavement. In the case of the five tunnels described in this paper, all the above-mentioned mitigation measures were put in place.

With the development in instrumentation and monitoring technology, real-time settlement readings using automated instruments with minimal physical installation and access could be taken in the vicinity of the TBM to enable timely adjustment of TBM face pressure. Applied face pressure plays a critical role in controlling ground movement directly above and ahead of the tunnel face. Whereas over the length of the shield, the settlement is controlled by the injection of bentonite slurry into the annulus and behind the shield by the backfill cementitious grout. The injection pressures of bentonite slurry along the shield and backfill grout depend on the magnitude of the applied face pressure and therefore, indirectly influenced by the applied face pressure. For all the five TBMs, the face pressure applied in Kallang Formation did not exceed the overburden pressure though it was close. As the pressures applied was closed to overburden pressure, timely adjustment of the pressure, especially at the geological transition, was crucial in controlling the ground settlement.

The experience from North-East Line showed that at certain times face pressure was increased to 120% of overburden pressure and the corresponding volume losses were higher compared to when the face pressure was kept within the range of 80% to 100% of overburden pressure. Similar experiences were noted in a project in South Korea [9] and the optimal face pressure was numerically demonstrated to be below full overburden pressure. That study also reported an increase in long-term consolidation settlement with the adoption of high face pressures.

Singapore LTA Civil Design Criteria recommends a volume loss of 3% for impact assessment arising

from EPB TBM tunnelling in Kallang Formation. In the light of recent experiences, should this be considered as over-conservative? There is no clear answer to this question since the bigger challenge is knowing exactly where the boundary of Kallang Formation and its constituent members especially Fluvial Sand are located. Furthermore, it also depends on the capability of the tunnelling equipment as well as the experience and competency of the tunnelling crew. For this project, a volume loss of 1% (for the 12.3m diameter tunnel) and 1.5% (for the 7.5m and 6.7m diameter tunnels) in Kallang Formation was assumed during the design stage and for the setting the settlement limit or work suspension levels which proved to be satisfactory.

The lessons learnt from this project to control ground settlement in both Kallang Formation and at the mixed interface between Old Alluvium and Kallang Formation to negligible magnitude are summarised as follows:

- Comprehensive site investigation to locate the boundary of Kallang Formation as well as Fluvial Sand.
- Incorporating additional features on the TBM for smooth injection of different types of ground conditioning to suit Old Alluvium, Marine Clay, Fluvial Sand and a mixture thereof.
- Allocating sufficient ports with redundancy for injection of: ground conditioning to tunnel face, excavation chamber and screw conveyor; bentonite slurry around the shield; and backfill grout behind the shield.
- Taking frequent soil samples at screw conveyor discharge and testing (preferably at each ring when approaching geological transition) to identify the changes in ground type.
- Measuring real-time ground movements in the zone of influence of the TBM.
- Changing the face pressure as necessary based on ground settlement and over-excavation trends.
- Accurate muck reconciliation.
- Setting up a clear protocol and following up with good communication among tunnel crew and supervision team.

7 CONCLUSIONS

In conclusion it can be stated that with appropriate control measures, it is possible to achieve negligible surface movement while tunnelling in Singapore Kallang Formation consisting of Marine Clay and Fluvial Sand. The special tools installed on the TBM cutterheads were designed and trialled to cut PVDs cleanly without dragging down and the tools performed as expected. The key lessons learnt from the project are summarised in the paper.

ACKNOWLEDGMENTS

The Authors express their appreciation to the developers, consultants, contractors and suppliers who contributed to the successful outcome of the project.

REFERENCES

[1] Shirlaw, J. N. and Copsey, J.P.: Settlements over tunnels in Singapore marine clay, 5th International Geotechnical Seminar, Singapore, December 1987.
[2] Broms, B.B. and Shirlaw, J.N.: Settlements caused by earth pressure balance shields in Singapore, Tunnelling and microtunnelling in soft ground, Paris, 1989.
[3] https://core.ac.uk/reader/48812510 Su, Thiri: Study on Ground Behaviour associated with tunnelling in mixed-face soil condition, National University of Singapore, PhD thesis, 2015.
[4] Shirlaw, J. N.: Controlling the risk of excessive settlement during EPB tunnelling, IES- NTU Conference, 2002.
[5] Ma et al.: Volume Loss induced by Tunnelling of Downtown Line and Thomson-East Coast Line Projects, Underground Singapore, 2021.
[6] Singapore Land Transport Authority Civil Design Criteria
[7] German Tunnelling Committee (DAUB): Recommendations for Face Support Pressure Calculations for Shield Tunnelling in Soft Ground, Version 10/2016.
[8] Zhang, F., Huang, L., Liang Y.: Calculation of Soil Deformation caused by Shield Tunnelling through the Sludge Layer with Plastic Drainage Plates.
[9] Kiseok, K., Juyoung O., Lee, H., Choi, H.: Critical face pressure and backfill pressure in shield TBM tunnelling on soft ground, ASEM17 World Congress, 2017.

Tunnelling for a Better Life – Yan, Celestino, Thewes & Eberhardt (Eds)
© 2024 The Author(s), ISBN 978-1-032-80042-4
Open Access: www.taylorfrancis.com, CC BY-NC-ND 4.0 license

Development and application of supersized tunnelling technology for China's large-scale construction of underground infrastructure

Shengli Hu*
Herrenknecht (Guangzhou) Tunnelling Equipment Co., Ltd. Beijing Branch, Beijing, China

Jürgen Hoss
Herrenknecht AG, Schwanau-Lahr, Germany

Wen Sun
Herrenknecht (Guangzhou) Tunnelling Equipment Co., Ltd. Beijing Branch, Beijing, China

ABSTRACT: To cope with the high population density and intense commercial activities in China's metropolitan cities, multifunctional large-diameter tunnelling projects have sprung up in recent years as examples of safe and efficient underground transportation infrastructure. Since 2006, when two of the world's largest Mix-shield machines (Φ15.43m) were used in the Shanghai Yangtze River Tunnel Project, dozens of mega tunnel projects with diameters exceeding 14m have been completed in China up to now. On the basis of accumulated experience in real projects, mega-diameter tunnel boring machines have realized long-term improvements in design and manufacturing, and the technology in this field has also developed significantly in terms of safety and performance. This paper focuses on one of the key technologies in this field – long-term technology development of the accessible cutting wheel, in terms of its upgrading with regard to reliability, pressure resistance and sealability. This paper analyses the technical challenges presented by different geological conditions to the design of the cutting wheel through project examples in Shanghai, Nanjing, Wuhan, Shantou, Jiangyin, Jinan and other places, as well as the solutions and technological innovations.

Keywords: Tunnel project, Ultra-large Diameter Shield, Accessible Cutting Wheel

1 PREFACE

Since the 1990s, because of the rapid development of China's transportation infrastructure construction, the shield method has been used widely for construction on large-scale urban subway projects. Since 2000, railway and highway tunnel construction also began to use the large shield method, therefore the shield tunnel diameter continues to increase, the tunnel one-time excavation distance continues to extend. Many tunnels go through rivers, lakes and oceans, the depths are ever-increasing, which poses a challenge to construction safety. In 1994, Herrenknecht designed a 14.2m accessible cutting wheel for the Elbe Tunnel with complex hydrogeology in Hamburg. And in 2006, Herrenknecht applied the accessible cutting wheel technology to two 14.43m Mix-shield machines in the Shanghai Yangtze River Tunnel project. Since then, the accessible cutting wheel has been adopted in the Nanjing Yangtze River Tunnel, Wuhan Sanyang Road Tunnel, Shantou Suai Tunnel, Jinan Yellow River Tunnel, Jiangyin Jingjiang Yangtze River Tunnel and so on, with the rapid development of the technology.

Accessible cutting wheel means that the internal atmospheric pressure space in the cutting wheel for the operation personnel to carry out the cutter tools changing operation is created by increasing the thickness of the cutting wheel on the basis of the conventional cutting wheel. All the cutter tools that need to be replaced in this space are installed in the cutter house, and the gate set in the cutter barrel seals the atmospheric pressure space in the cutting wheel from the external environment. Thus, the cutter tools inside the cutting wheel can be replaced under normal pressure.

*Corresponding author: hu.shengli@herrenknecht.com

DOI: 10.1201/9781003495505-244

Table 1. The comparison between accessible cutting wheel and conventional cutting wheel.

	Accessible cutting wheel	Conventional cutting wheel
Structure	The cutting wheel is a closed box structure with complex structure and certain air tightness	The cutting wheel is simple in structure and easy to maintain
Cutter tool	Higher manufacturing precision of the cutter house and barrel, and the cutter tools can be replaced under normal pressure	Cutter tool installation structure is simple, easy to install
Scope of application	Suitable for geological environments with high water pressure or unstable formations	The ground adaptability is good
Cutting tool changing	Cutter tool change can be achieved under normal pressure, short tool change time, high efficiency, low tool change cost	Cutter tool replacement requires pressure operation, low tool change efficiency, high risk, and high tool change cost

Table 2. Cutting wheel layout.

Layer	Tool Type	Height
1st layer	Replaceable ripper and center tool	210mm
2nd layer	Advance ripper	190mm
3rd layer	Replaceable scraper	180mm
4th layer	Standard scrapers and bucket	160mm

2 ACCESSIBLE CUTTING WHEEL IN SOFT GROUND

2.1 The accessible cutting wheel technology of Herrenknecht's large-diameter Mix-shield was introduced to China for the first time on the Shanghai Chongming Yangtze River Tunnel Project (Figure 1). The total length of the tunnel is about 7,470m, and the main strata are primarily silt and sandy silt. The cutting wheel structure adopts the structural form of 6 star-shaped main arms and 6 triangular auxiliary arms, with an excavation diameter of 15.47m and an opening ratio of about 28%.

Since the Shanghai Chongming Yangtze River Tunnel project, other projects represented by this cutting wheel type include the Nanjing Yangtze River Tunnel (Figure 2), Shanghai Changjiang West Road Tunnel, Hangzhou Qianjiang Road Crossing Tunnel, Shanghai A30 Tunnel and Shanghai Beiheng Road Crossing Tunnel (Figure 3), among others.

2.2 The total length of the Nanjing Metro Line 10 Yangtze River-Crossing Tunnel is 3,600m, with a segment inner diameter of 10.2m and outer diameter of 11.2m, single-hole two-line surface. Minimum curve radius 1,500m, with the maximum longitudinal slope of 28‰. Tunnel maximum overburden is 37m, while the minimum overburden is 9.4m (receiving shaft), the overburden is generally between 14-18m in the middle river section. The stratum encountered by the tunnel is mainly clay, silt, fine sand, coarse gravel and conglomerate and gravelly mixed soil.

Figure 1. Shanghai Chongming Yangtze River Tunnel project.

Figure 2. Nanjing Yangtze River Tunnel project.

Figure 3. Shanghai Beiheng Road Crossing Tunnel project.

After experiencing the construction process of the Shanghai Chongming Yangtze River Tunnel and Nanjing Yangtze River Tunnel, the design was further developed in terms of safety and efficiency of tool change method. The Herrenknecht design team successfully designed an accessible cutting wheel for this project, which is suitable for the range of 11m-12m segment outer diameter.

Compared with the Shanghai Chongming Yangtze River Tunnel and Nanjing Yangtze River Tunnel, the design of the cutting wheel is limited by the space

Figure 4. Nanjing metro line 10 crossing the river section.

layout, and its structural type is in the form of 5 main arms and 5 small auxiliary arms, with an excavation diameter of 11.64m and an opening ratio of 35% (Figure 4).

For the kind of cutting wheel type as accessible cutting wheel suitable for the segment outer diameter of the 11m-12m range there are representative projects such as the Beijing-Zhangzhou High-Speed Railway Qinghuayuan Tunnel (Figure 5), Hangzhou Wangjiang Road River Crossing Tunnel and the Sutong GIL Tunnel (Figure 6).

Figure 5. Beijing-Zhangzhou High Speed Railway Qinghuayuan.

Figure 6. Sutong GIL integrated pipe corridor.

2.3 The main geology encountered in the Jinan Yellow River Tunnel is silty clay, fine sand, calcareous nodules and fully weathered diorite.

In view of the geological characteristics of the project, summarizing the experience with accessible cutting wheels in past tunnel construction, combined with the 6 main arms of the accessible cutting wheel in the Shanghai Chongming Yangtze River Tunnel and other similar projects, as well as the large opening ratio of the accessible cutting wheel in Nanjing Metro Line 10 and other similar projects, the cutting wheel structure of this project is designed with 6 main arms and 6 auxiliary arms, with an opening ratio of about 50% (Figure 7).

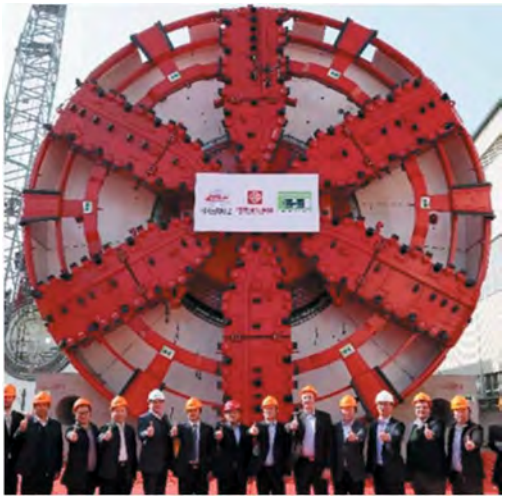

Figure 7. Yellow River Tunnel in Jinan.

At present, the accessible cutting wheel type is mainly applied in the range of segment outer diameter 13m-17m, the representative projects for this cutting wheel type also include the Nanjing Five Bridges River Tunnel (Figure 8), Hangzhou Gengshan East Road Tunnel (Figure 9), Hangzhou Xiasha Road Tunnel, GuangZhan Railway Zhanjiang Bay Tunnel (Figure 10), and Jiangyin Jingjiang Yangtze River Tunnel (Figure 11).

Figure 8. Five Bridges Clip River Nanjing Tunnel.

Figure 9. Hangzhou Genshan East Road.

Figure 10. Zhanjiang Bay Tunnel of Guangzhou-Zhan High Speed Rail.

Figure 11. Jiangyin Jingjiang Yangtze River Tunnel.

3 ACCESSIBLE CUTTING WHEEL UNDER COMPLEX GEOLOGY

3.1 The total length of the Qingdao Jiaozhou Bay 2nd Sea Crossing Tunnel is about 14.36km, with a shield section of 3.25km. Three tunnels, namely two main tunnels and one service tunnel respectively. The main tunnel segment has an outer diameter of 15m and a width of 2.1m. 88% of the tunnels are in rocky terrain for the whole face, and the remaining part is in complex geology. The rock strata include tuff, andesite, breccia, orthogneiss and long quartzite. Soft soils are clayey soft soils and silty clays. Several fracture zones or transition zones are widely distributed.

For this project profile and its geological conditions, the optimized design structure based on the summary of the past composite cutting wheel, this accessbile cutting wheel is 6 main arms and 6 small auxiliary arms, the opening ratio 30% (Figure 12).

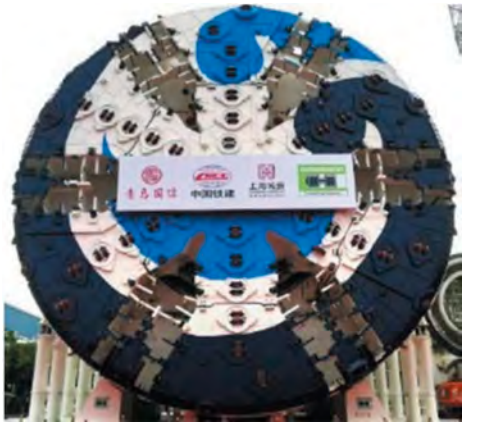

Figure 12. Qingdao Jiaozhou Bay 2nd Sea Crossing Tunnel.

Other projects represented by this cutting wheel type are the Wuhan Sanyang Road Tunnel (Figure 13), Foguan Intercity Shiziyang Tunnel (Figure 14), Nanjing Jianning West Road Tunnel (Figure 18), Shantou Bay Tunnel of Shantou Railway (Figure 19) and Wuhu Yangtze River Tunnel (Figure 20).

Figure 13. Wuhan Sanyang Road Tunnel.

Figure 14. Foguan Intercity Shiziyang Tunnel.

Figure 15. Shantou Su'ai Tunnel.

Figure 16. Nanjing Heyan Road Tunnel.

Figure 17. Shenzhen Mawan Sea Crossing Tunnel.

3.2 Wuhan Metro Line 8 Yangtze River Crossing Tunnel is the fourth river crossing subway line in Wuhan. The tunnel length is 3,186m, the distance of crossing the Yangtze River 1,500m, tunnel excavation diameter 12.5m.

Figure 18. Nanjing Jianning West Road.

Figure 19. Shantou Bay Tunnel.

Figure 20. Wuhu Yangtze River Crossing Tunnel.

The tunnel crosses both sides of the Yangtze River for a total of about 2100m through the upper part of the stratum of soft soil (4-2 to 4-2b), the lower part of the layer of fine sand, less abrasive to the tools; in the middle section of the river crossing for the upper part of the layer of fine sand, the lower part of the composite strata such as weathered rock, including: about 495m of Q4 rounded conglomerate; about 1370m of (15b-1) strong weathering conglomerate; about 705m of (15b-2) weakly cemented conglomerate; about 430m of (15b-3) moderately cemented conglomerate; and three kinds of rock layers overlap the top and the bottom (Figure 21).

As the main stratum of the river central section is soft at the top and hard at the bottom, and the range of weathered rock in the lower part is relatively small, a mixed configuration of disc cutter and rippers is adopted, which means that it can handle the long-distance excavation in the soft ground layer,

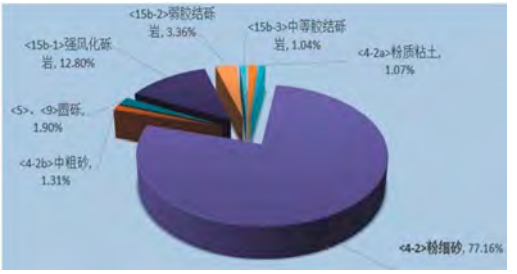

Figure 21. Distribution of geological conditions of Wuhan Metro Line 8.

Figure 22. Wuhan Metro Line 8 River-Crossing Section.

and also effectively solve the problem of the weathered rock layer in the smaller range.

4 TARGETED INNOVATION

4.1 *Layered design of the cutter tool*

Based on the analysis of geological conditions of coarse gravel sand and cobble-gravel mixed soil in the Nanjing Metro Line 10 Yangtze River Crossing Tunnel, and the research on the wear condition of the cutting wheel in similar geological conditions of the past projects, the height of the cutting tools is specially designed, and the layout of four layers of cutting tools is adopted.

4.2 *Further development of accessible cutting tool change*

An anti-disorder device for detecting the cutting tool is provided on the replaceable cutting tools. Additional signs and devices are installed to prevent the cutting tool from being assembled at the wrong angle.

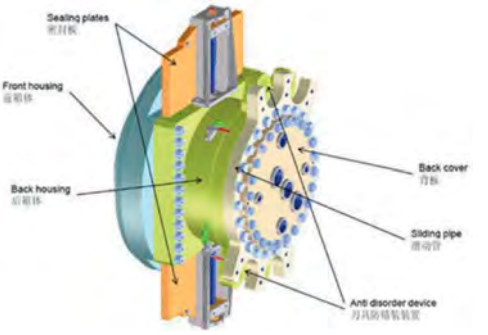

Figure 23. Improved schematic of the atmospheric tool change.

4.3 *Video monitoring system for excavation chamber and air cushion chamber*

It was the first time for the Nanjing Metro Line 10 Yangtze River Crossing Tunnel that a camera device was applied to the monitoring of the tunnel surface and cutter tool to facilitate the checking and observation of the condition of the tool and surface. The detection technology can accurately and safely monitor the angle, depth and distance of the target object. Accurate images can be recorded, stored and retrieved (Figure 24).

Figure 24. Camera peering into tool conditions.

The video monitoring system for excavation and air cushion chamber has been widely used on large diameter shield machines in subsequent projects since the Nanjing Metro Line 10 Yangtze River Crossing Tunnel, such as the Wuhu Yangtze River Crossing tunnel, Nanjing Jianning West Road, Jiangyin Jingjiang Yangtze River Tunnel and Qingdao Jiaozhou Bay 2nd Sea Crossing Tunnel.

During the advancing process of the shield tunnelling machine, most of the cutting tools on the cutting wheel can be easily inspected using the relevant functions of the accessible cutting wheel, but the wear of bolt mounted scrapers and bucket lips cannot be detected. In addition, sometimes when the shield machine is stopped, it is necessary to check the excavation surface in front of the cutting wheel to observe whether there are foreign objects inside the excavation face and whether the excavation face is stable. When carrying out maintenance work for shield tunnelling machines in the excavation and air cushion chambers, it is also necessary to monitor the operation of personnel in the excavation and air cushion chambers to

ensure safety. Therefore, the shield tunnelling machine for this project is equipped with a set of pressure-resistant, waterproof and self-illuminated telescopic cameras above the excavation chamber, and a set of pressure-resistant, waterproof and self-illuminated fixed cameras are installed above the air cushion chamber. The telescopic camera can extend to the back of the cutting wheel to observe the steel structure of the cutting wheel, the side tools of the main arm of the cutting wheel, the bucket lips, and the tunnel face. The fixed camera observes the air cushion chamber.

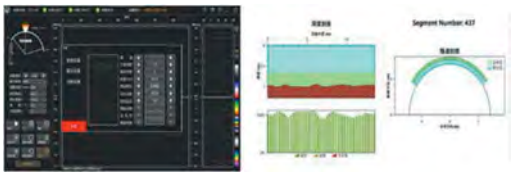

Figure 25. Schematic of the working process of the telescopic camera in the excavation bin.

During the construction process of the Nanjing project, the telescopic camera was used to observe the structure of the cutting wheel, the tunnel face and the clogging situation on the cutting wheel. The camera imaging was clear and the effect was good (Figure 26).

Figure 26. Picture taken by telescopic camera.

4.4 *High-flow flushing system of cutting wheel center*

To reduce the probability of mud cake formation in the cutting wheel center for the accessible cutting wheel, a high flow center flushing system is used (Figure 27).

- ➢ 6 center flushing nozzles are set to flush the center of the cutting wheel
- ➢ 6 center flushing nozzles between the main arms of the cutting wheel, flushing outward toward the center of the cutting wheel
- ➢ The independent center flushing pump has a maximum flow of 920m3/h and a maximum pressure of 16.2bar.

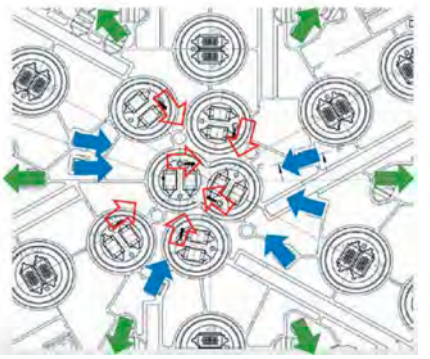

Figure 27. Center flushing nozzles arrangement.

The center flushing system in the accessible cutting wheel with disc has been upgraded on the basis of the center flushing system used for the Nanjing Yangtze River Crossing Tunnel and other projects, as well as of the center flushing system used for the Jinan Yellow River CrossingTunnel and other projects, which has been optimized based on the anti-clogging measures of the center cutter and to realize the flushing targeted at the center disc.

The center area of the cutting wheel is designed with a high flow mud and water flushing cycle:

- ➢ Flushing port to realize sub-area control, to ensure the flushing flow rate
- ➢ 6 center flushing ports
- ➢ Flushing between 6 main arms
- ➢ 6 cutter house flushing ports
- ➢ Center flushing pump flow: 1000m³/h

4.5 *Disc rotation monitoring system*

The disc cutter rotation monitoring system (DCRM) is an independent monitoring system. The disc rotation monitoring device is installed on the fixture of each disc, which can continuously monitor the rotation and temperature status of the disc and display the status of the disc in the main control cabinet.

The goal is to monitor non rotating cutters and improve efficiency in cutter maintenance.

Downtime required for manual inspection of disc cutters can be reduced.

The overall downtime by maintance could be minimized. This allows for a better tool management plan, facilitates full utilization of the disc cutters service life and makes the entire tunnel boring process more efficient. In addition, damages or secondary wear on adjacent disc cutter housings or cutting wheel steel structure could be reduced.

4.6 *Disc cutter spacing*

Herrenknecht carefully researched and analyzed the arrangement characteristics of the disc cutters and realized a disc spacing of 80mm, which plays

a certain role to break through hard rock and improve the excavation efficiency. The disc cutter spacing for the same size disc from 100mm to 80mm has gone through three stages:

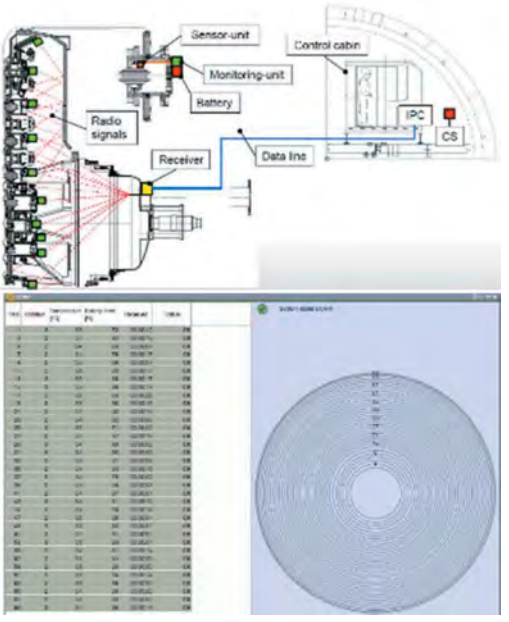

Figure 28. Schematic of cutter rotation monitoring.

Phase I: represented by Shantou Su'ai Tunnel Project and Nanjing Heyan Road Tunnel, the disc is designed with two axes and two blades, and the disc spacing is 100mm.

Phase II: represented by Shantou Bay Tunnel of Shantou-Shantou Railway and Nanjing Jianning West Road Tunnel, the cutter is designed as a double-axis with a disc spacing of 90mm.

Phase III: represented by Qingdao Jiaozhou Bay 2nd Sea Crossing Tunnel, with disc spacing of 80mm.

4 SUMMARY

The innovative features of Herrenknecht's accessible cutting wheel in the course of engineering practice in large-diameter shield tunnel projects are as follows:

- ➢ Installation of 19-inch single-edged disc (full-section rock formation)
- ➢ Mixed arrangement of accessible disc cutters and accessible ripper on the cutting wheel.
- ➢ Accessible disc and accessible ripper can be interchangeably mounted in the same housing.
- ➢ Real-time monitoring of disc rotation, temperature
- ➢ Wear monitoring of steel structure
- ➢ A safer aid for access, replacement and trouble-shooting of accessible cutting tools in the cutting wheel
- ➢ Procedures for tool management, tool replacement planning and forecasting
- ➢ Improvement and enhancement of high flow flushing capacity and efficiency of cutting wheel centers
- ➢ Excavation chamber telescopic camera monitoring system

Accessible cutting wheel technology still needs to be further improved. For example, in the formation dominated by clay soil, by increasing the flushing system capacity or other measures to improve the flow of slag to increase the efficiency of excavation. In the hard rock stratum with relatively high rock strength, how to improve the rock breaking ability of the accessible cutting wheel and boring efficiency and how to improve the stability of the installation structure of the cutter house still need further study.

REFERENCES

Battistioni, F., Burger, W., Bappler, K., 2023, Evolution of accessible cutterhead TBMs.

Burger, W., 2018, Accessible cutterheads-Herenknecht's long term development towards safety in large diameter TBM operation.

Tunnelling for a Better Life – Yan, Celestino, Thewes & Eberhardt (Eds)
© 2024 The Author(s), ISBN 978-1-032-80042-4
Open Access: www.taylorfrancis.com, CC BY-NC-ND 4.0 license

Failure analysis and coping suggestions for TBM tools under complicated geological conditions

Huan Huan Feng*
China Railway Tunnel Group Co., Ltd., GuangZhou, China
School of Civil Engineering, Central South University, ChangSha, China

Shu Ying Wang
School of Civil Engineering, Central South University, ChangSha, China

Lu Wei Yang
China Railway Tunnel Group Co., Ltd., GuangZhou, China

Yan Dong Yang
State Key Laboratory of Shield Machine and Boring Technology, ZhengZhou, China

ABSTRACT: The complicated geological conditions and unreasonable tunneling parameters will cause the abnormalities or damage of the TBM tools and increase the tool consumption, which are adverse to the tunneling efficiency of TBM and the construction cost control. Based on the systematic description of the common failure modes of the TBM tool, we have studied and analyzed such tunneling parameters as total thrust, cutterhead speed and tool penetration, such geological parameters of different surrounding rocks as uniaxial compressive strength and quartz content, as well as the influence rule for the wear, abnormalities or damage of the tool. Taking Zhongtianshan Tunnel as an example, we have made statistics for and analyzed the tool consumption and failure modes, and proposed the specific optimization methods in terms of tool selection, inspection and maintenance. Finally, we have proposed that the configuration technology for the tools with adjustable clearance shall be further developed, to ensure the rock-breaking efficiency of tools under different geological conditions. In the meantime, we will intensify the R&D and application of the new tool condition monitoring system strongly adaptive to the work environment of TBM.

Keywords: tunnel, TBM, hob, complicated geology, tunneling parameters, tool failure, tool wear

1 INTRODUCTION

Tools are the core part of a rock tunnel boring machine (TBM), so their performance and type selection are directly related to the construction efficiency of TBM and also influence the economic cost of engineering projects[1,2]. According to the statistics, the TBM downtime caused by inspection and tool replacement and tool consumption cost under complex geological conditions separately account for about 15% and 30% of the total construction time and cost of TBM[3]. The failure modes and causes of tools are analyzed, and it is particularly important to conduct research into the optimization measures in terms of type selection of tools, tunneling parameter control, etc.

Jonak, et a[4] held that the prediction for TBM cutter load and life is crucial for TBM cutter design and maintenance, and they studied the feasibility of using a multilayer perceptron neural network as tool for predicting. Moosazadeh, S, et al[5] did the research that the impact to EPB-TBM cutter life, reliability and maintainability from the mixed geological condition and underground water, based on on-site data of Tabriz urban railway projects. Farrokh, E.[6] summarized different methods for TBM cutter life and wear in soft soil formations, and found the predictability of TBM cutter life by comparing the data of 23 TBM cutter projects in soft soiled formation around the world. It made great values for establishing the TBM cutter wear model that Mousapour, H, et al[7] designed and constructed a tunnel boring machine laboratory simulator for measuring the TBM cutter wear rate, penetration rate, and torque. Karami, M, et al.[8] believe that the volume of the plastic zone as well as the actual

*Corresponding author: skl_fhh@163.com

DOI: 10.1201/9781003495505-245

penetration depth in the highly fracturing rocks are also about 40% and 42% higher than in the slightly fractured rocks under applying the same TBM parameters.

Duan Zhiwei[9] carried out field tests on domestic tools under different surrounding rock conditions based on the Xinjiang EN Tunnel Project and concluded that the wear rate of a disc cutter in the marlite stratum is 1/8 of that in diorite and granite strata; Wu Zhipeng et al.[10] analyzed the failure modes and damage causes of tools by taking the TBM construction in a hydropower plant in Vietnam as an example and proposed that tool wear was primarily affected by tool quality, surrounding rock conditions, construction environment, etc.; Yan Changbin et al.[11] established a prediction technique of tool consumption based on different surrounding rock conditions and different disc cutter diameters through the fit analysis of tool consumption data, and verified this technique through field tests in a water delivery tunnel project of Lanzhou water source region; Ebrahim et al.[12] researched and analyzed the quantitative relation between different abrasion indexes and the amount of tool wear through the laboratory abrasion tests for disc cutters abrasion based on multiple cases of TBM tunnel projects; Yang Yandong et al.[13] established a tool consumption evaluation method and a prediction model through theoretical formula model inference and regression analysis of field data and concluded that there was an exponential function relationship between the tool wear rate and the product of rock mass integrity coefficient and rock abrasion index. Xia Ming[14] established a selection method of TBM tools and a method for repairing cutter heads and tools through field tests in the tunnel for the Hanjiang-to-Weihe River Water Diversion (HWWD) Project; Zhang Ling[15] made a solution to the improvement of tool mounting structure through the cause analysis of TBM tool failure; Li Jinlin[16] analyzed the consumption of TBM tools in the highly-abrasive hard rock section by taking the Qinling Tunnel Project of the HWWD Project as an example. Li Xiaoling[17] analyzed the failure modes of tools for shield construction engineering and proposed measures for tool management and maintenance. The above-mentioned research was conducted into the evaluation and prediction of TBM tool wear, selection and repair of tools, etc. and was of guiding significance to the type selection, optimization and consumption evaluation of tools to some degree; however, there is a lack of systematic research on different failure modes of tools and influencing factors, so it is difficult to provide a solid basis for the optimization of tools and the establishment of management measures, and more engineering practice data will be combined for a more in-depth summation and analysis.

This paper analyzed the influencing factors of tool consumption by relying on the Qinling Tunnel Project of the HWWD Project, the Middle Tianshan Tunnel Project, etc. and producing the statistics on the consumption of tools under different geological conditions so as to analyze the deficiencies in the application and management of tools and made recommendations on optimization to better solve the problems of type selection and management of tools and further to improve the construction efficiency of TBM and save construction costs.

2 COMMON FAILURE MODES OF TOOLS

2.1 *Normal wear*

When tools are used for rock breaking, the rock breaking efficiency is related to the edge width of cutter ring, and as the amount of cutter ring wear increases, the crushing area also increases and if such an increase reaches a certain range, the tunneling speed will be influenced; the wear that occurs in this case is called normal wear.

2.2 *Chord wear*

Chord wear is the phenomenon that the disc cutter ring wears into one or more chords, which is the most common mode of abnormal tool wear. The main causes of chord wear of cutter rings are as follows:

1) The cutter ring itself has a quality problem;
2) The tool bearing is damaged and fails to rotate;
3) Starting torque is not set properly during the tool assembly;
4) Seal assembly damage results in oil leakage of tools; meanwhile, rock slag enters the seal chamber, causing damage to the tool bearing;
5) Stones enter the gap between the disc cutter and the cutter housing, causing tools to be stuck;
6) Parameters are not properly controlled during the tunneling of equipment, resulting in overloading of bearings;
7) The tool bearing locks due to overheating.

2.3 *Cutter ring breaking*

During the process of tunneling, the cutter ring breaks from time to time. The main causes are as follows:

1) Geological conditions suddenly change or a foreign object is stuck between the cutter edge and the surrounding rock, resulting in local overloading of the cutter ring;
2) The interference fit between the cutter ring and the cutter body is too large;
3) The cutter ring has a quality problem;
4) When the cutter head starts rotating, the thrust force is too large or the advance rate is too fast, resulting in a sudden collision between the tool and rocks;
5) When the direction of TBM is adjusted, the magnitude of adjustment is too large.

2.4 *Oil leakage of tools*

There are plenty of causes for oil leakage of tools, mainly including:

1) Failure of tool bearing or seal assembly;
2) Inappropriate assembly or inclusion of foreign objects during the repair of tools;

3) Insufficient performance of the water spraying system for the cutter head, causing overtemperature of shafts and lubricating oil;
4) Overloading of tools caused by a sudden change in geological conditions or improper manual operation, so that bearing rollers peel off, while the peeled-off metal fragments and particles further cause the failure of seal assembly;
5) A quality problem of the seal assembly itself.

3 INFLUENCING FACTORS OF ABNORMAL DAMAGE TO TOOLS

3.1 *Analysis of the impact of tunneling parameters on the abnormal damage to tools*

3.1.1 *Total thrust force*

If tunneling is conducted through soft surrounding rocks or low-intensity surrounding rocks, only a small amount of total thrust force will be imposed on the cutter head to break rocks from the tunnel face. The load force on the tool is relatively small, the cutter ring wears slowly, and the service life of disc cutter bearings is relatively long in a low-load state; meanwhile, the temperature at which the tool can operate normally is relatively low, and the sealing elements are not prone to abnormal damage. If tunneling is conducted through high-intensity surrounding rocks, a relatively large amount of total thrust force should be imposed on the cutter head to break rocks from the tunnel face. The load force on the tool is relatively large, the cutter ring wears quickly, and in particular, the side disc cutter area undergoes more wear and tear; the disc cutter bearing rotates in a high-load state, causing its service life to be significantly shortened; the temperature at which the tool operates is relatively high, lubricating oil and grease are failure-prone at a high temperature, and sealing elements fail due to fracture after aging. As the intensity of rocks increases during the tunneling of a TBM, the higher the total thrust force required by the cutter head to break rocks from the tunnel face is, the larger the tool consumption is.

3.1.2 *Tool penetration*

If a TBM is used for tunneling under similar geological conditions and at the same speed of rotation, the thrust force applied to the cutter head must be increased to get larger tool penetration and enhance the tunneling speed. As the tool penetration increases with the thrust force, i.e. the force applied to the tool increases to cause the cutter ring to undergo plastic deformation to different degrees and leave its edges twisted or broken, the wear of cutting ring increases; the bearing load is too large and even overloading occurs, resulting in abnormal damage, such as large-spot pitting, peeling and spalling.

3.1.3 *Speed of cutter head*

During the tunneling of a TBM, the tool penetration and the speed of cutter head are typically increased to improve the tunneling speed. The penetration of cutter head curvilinearly varies with the thrust force of cutter head, and when this thrust force reaches the rated thrust force, the tunneling speed can further increase only by improving the speed of cutter head. After the speed of cutter head increases, the linear distance of the tool rotation per unit time increases accordingly. Firstly, the rotation of tools speeds up, the edge is prone to breaking after overloading of the cutter ring, and the abnormal consumption of tools increases; secondly, the tool temperature significantly rises, leaving seal assembly, lubricating oil and grease prone to failure.

Taking the Qinling Tunnel Project of the HWWD Project as an example, (1) the hydraulic cylinder thrust of a TBM is controlled at 280~320bar: when the tool penetration is 2mm/r, the rate of abnormal damage to tools is 8.83%; when the tool penetration is 4mm/r, the rate of abnormal damage to tools is 12.22%; (2) the TBM penetration is controlled at 3~4mm/r: when the hydraulic cylinder thrust of a TBM ranges from 260bar to 280bar, the rate of abnormal damage to tools is 11.54%, and when the hydraulic cylinder thrust of a TBM varies between 280bar and 320bar, the rate of abnormal damage to tools is 12.22%. It can be seen that the rate of abnormal damage to tools is directly proportional to the tool penetration and the TBM thrust force, but it is very difficult to accurately analyze the degree of influence of a factor because there are many factors that cause abnormal damage to tools. In the construction of a TBM, full consideration shall be given to the impact of different tunneling parameters, geological conditions and type selection of tools on the abnormal damage to tools as well as the impact on the TBM tunneling efficiency.

3.2 *Analysis of the impact of geological conditions on the tool wear*

Based on the statistics on the actual replacement of tools in a TBM interval of the Qinling Tunnel Project of the HWWD Project, the impact of the uniaxial compressive strength (UCS) of different surrounding rocks and the quartz content on the tool wear is analyzed through the comparison of tool consumption under different conditions.

3.2.1 *UCS of surrounding rocks*

When the quartz content is fixed, an interval in which the quartz content is 70% is taken as an example (Figure 1), and it can be seen from Figure 1 that the higher the uniaxial compressive strength is, the larger the tool consumption is, the higher the degree of influence on the tool wear is.

3.2.2 *Quartz content of surrounding rocks*

When the uniaxial compressive strength is fixed, an interval in which the uniaxial compressive strength is 150MPa is taken as an example (Figure 2), and it can be seen from Figure 2 that the tool consumption is positively correlated to the quartz content and the rate of change gradually increases.

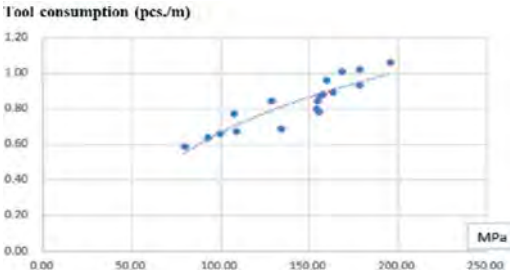

Figure 1. Curve of uniaxial compressive strength - tool consumption relation.

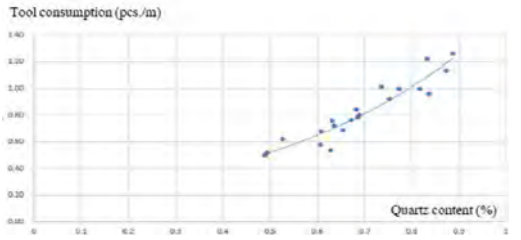

Figure 2. Curve of quartz content - tool consumption(the vertical axis - tool consumption (pcs./m), the horizontal axis - quartz content (%)).

Combined with the engineering statistics of Qinling Tunnel Project and the above-mentioned analysis results, the relation curve of uniaxial compressive strength, quartz content and tool consumption is drawn (Figure 3).

From the above Figure 3, it can be judged, on the whole, that there is an approximately linear relationship among the uniaxial compressive strength, the quartz content and the tool consumption to deduce the tool consumption under different conditions (as shown in Table 1), which can be used for tool replacement and management in the process of similar TBM project in the future. In addition, however, tool consumption is also affected by multiple factors, and in special cases, such as collapse of tunnel face and rock burst, tool consumption will also be greatly influenced. For example, the first peak between K28-29: this is a transition section between quartzite and granite, where the rocks on the tunnel face are broken, joints are developed, and a lot of abnormal damage to tools occurs, resulting in a deviation from the uniaxial compressive strength and the quartz content and trend; peak after K34: after K33+860, the burial depth of the tunnel exceeds 1,300m, the frequency of rock bursts is relatively high, and the rock bursts are dominated by moderate rock bursts or above, and strong rock bursts occasionally happen, leading to an irregular law of tool consumption.

4 ENGINEERING CASE ANALYSIS

4.1 *Middle tianshan tunnel*

Middle Tianshan Tunnel is located in the east segment ridge area of the mid-range of the Tianshan Mountains between Toksun County and Hoxud County and is the controlled project of the new Turpan-Korla section of the Southern Xinjiang Railway. The tunnel, with a total length of 22,467m, passes through different strata, mainly including metamorphosed sandstone, granite, and schist with marble. The inlet section was constructed with 8.8m-dia. open-type TBMs, and the surrounding rocks of Classes II and III approximately accounted for 78.8% of the total tunnel length (Table 2).

4.1.1 *Tool consumption*

1) Analysis of total tool consumption

The TBM cutter head is configured with a total of 6 single disc center cutters, 62 frontal disc cutters, 3 side disc cutters and 2 double-edged reaming cutters, all of which are made of 17″ disc cutters; in addition, 8 edge buckets and 4 front buckets are provided (see Figure 9). In the process of TBM construction, a total of 4,407 frontal disc cutters, 445 side disc cutters, 154 center cutters and 32 reaming cutters were replaced. For the statistics on the replacement reasons of tools, see Table 3.

Through study and comparison, the TBM tunneling parameter control of the Middle Tianshan Tunnel is basically reasonable, and two major

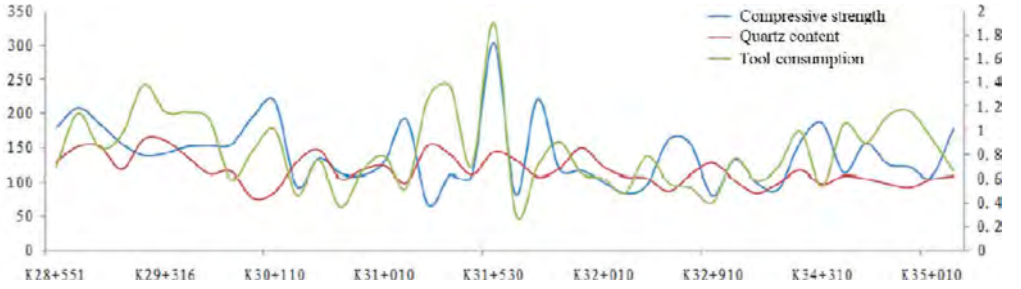

Figure 3. Construction chainage - uniaxial compressive strength, quartz content and tool consumption (the left vertical axis - USC (mpa), the right vertical axis - quartz content (%)/tool consumption (pcs./m), the horizontal axis - construction chainage).

Table 1. Tool consumption for different intensities of surrounding rocks and different quartz contents (pcs./m).

Uniaxial compressive strength (MPa)						
Quartz content (%)	75~100	100~125	125~150	150~175	175~200	200~230
45~55	0.34	0.42	0.48	0.54	0.62	0.68
55~65	0.42	0.49	0.55	0.62	0.7	0.75
65~75	0.55	0.59	0.64	0.70	0.77	0.86
75~85	0.67	0.71	0.76	0.80	0.88	1.02
>85	0.74	0.84	0.92	1.04	1.08	1.19

Table 2. Surrounding rocks in TBM section.

Surrounding rock grade					
Item	II	III	IV	V	Total
Length/m	3309	7343	2722	140	13514
Proportion/%	24.5	54.3	20.2	1.0	100

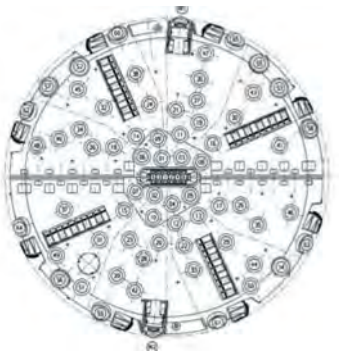

Figure 4. Schematic diagram of tool configuration.

reasons for the large abnormal consumption of tools are as follows: 1) TBMs passed through 4 dense zones of granite joints (with a total length of over 600m) and 1 fracture zone of dense sandstone joints with schist developed in the quartz vein in total. The hardness of surrounding rocks was uneven, joints were well developed, the direction of principal stress was basically consistent with that of tunnel axis, and large rocks frequently collapsed, causing tools to be smashed and edges to be broken; meanwhile, tools were stuck between large stones and failed to rotate, causing chord wear as well as the failure of tool bolts, oil leakage of tools, and other forms of damage; 2. The TBM passed through the 2,755m-long complex tunnel section of the Variscan granites. In this section, geological conditions were extremely complex, the tunnel face and the tunnel walls on both sides underwent rock bursts and collapse from time to time, and steps and boulders were formed on the tunnel face, causing the cutter head to impact on boulders in the process of rotation and further causing the abnormal damage to tools, and the tool consumption increased by geometric progression.

2) Consumption of frontal and side disc cutters
A total of 2,367 frontal and side disc cutters were normally replaced, accounting for 48.8% of the total consumption and a total of 2,485 frontal and side disc cutters were replaced due to abnormal causes, such as chord wear, oil leakage, and cutter ring fracture, accounting for 51.2%, and the abnormal replacement of tools greatly affected the tunneling progress of TBMs.
3) Center cutter consumption
A total of 119 center cutters were normally replaced, accounting for 77.4% of the total consumption, and 35 center cutters were replaced due to abnormal causes, accounting for 22.6%.

Table 3. Statistics for replacement reasons of tools.

	Frontal and side disc cutters		Center cutter		Reaming cutter	
Replacement reason	Qty. (pcs.)	Percentage (%)	Qty. (pcs.)	Percentage (%)	Qty. (pcs.)	Percentage (%)
Normal wear	2367	48.8	119	77.4	18	56.3
Chord wear	1218	25.1	31	20.1	8	25.0
Oil leakage	485	10.0	1	0.6	/	/
Cutter ring breaking	298	6.1	3	1.9	6	18.8
Peeling of a retainer ring	90	1.9	/	/	/	/
Others	394	8.1	/	/	/	/
Total	4852	100	154	100	32	100

4.1.2 *Analysis of tool failure modes*

1) Tool wear
   Tool wear accounted for nearly 3/4 of the tool failure, among which normal wear of tools accounted for 48.8%, and this type of tool replacement should be arranged as a whole and tools should be replaced in bulk, with the aim to minimize the impact on tunneling; chord wear of tools accounted for about 25.1% of the tool failure, and it would be very difficult if chord wear occurred in a tool but was not timely found, and in this case, its failure cause could be accurately identified only after the tool subjected to chord wear was dismantled and was fully tested.
2) Oil leakage of tools
   The oil leakage of tools was also common, accounting for 10% of the tool failure.
3) Fracture or peeling of a retainer ring
   A retainer ring peeled off from time to time during construction, accounting for 1.9% of the total tool failure. The main cause of this situation was improper installation, poor welding, being broken by stones, or peeling of the retainer ring.
4) Loosening, falling, breaking, and stripping of tool bolts
   Tool bolts were also subjected to loosening, falling, breaking and stripping frequently, accounting for 8.1% of the tool failure. The causes of these tool bolt problems mainly included degradation of tool bolt performance, improper installation of tools, quality problems of bolts, failure of the pretension torque of tool bolts to reach the given value, etc.

4.2 *Tunnels in the HWWD project*

The length of the Qinling Tunnel in the HWWD Project is 81.779km, and by taking a lot located in the high and middle-altitude mountainous zone of the ridge area of the Qinling Mountains and the low and middle-altitude mountainous area south of the Qinling Mountains as an example, the total length of this lot was 18.717km and its elevation ranged from 1,050m to 2,420m, the maximum burial depth of the tunnel was about 2,000m, and the quartzite, granite and diorite through which the tunnel passed accounted for more than 75% of the total surrounding rocks, among which the quartz contents in the quartzite, granite and diorite could be up to 97%, 30% and 18%, respectively; in the lot, the maximum rock intensity was up to 320MPa, so 8.02m-dia. open-type TBMs were used for construction. 17″ center disc cutters, 20″ frontal disc cutters and side disc cutters were mainly used for rock breaking; the tool layout is shown in Figure 5:

Figure 5. Schematic diagram of tool layout.

4.2.1 *Analysis of tool consumption*

In the HWWD Project, tools were badly worn during the tunneling due to high uniaxial compressive strength, high wear value and high quartz content, resulting in high tool consumption and frequent replacement of tools. Tool consumption is primarily caused by normal wear; in addition, abnormal wear will occur occasionally, mainly including edge breaking or fracture of cutter ring, eccentric wear of tools, etc.

1) Consumption of single disc cutters
   In a TBM construction section, a total of 5,961 single disc cutters were replaced, including 5,094 cutters replaced due to normal wear, accounting for 85.46%, and 867 cutters replaced due to abnormal wear (see Figure 6), accounting for 14.54%. The specific proportion is shown in Figure 7 below.

Figure 6. Abnormal wear of tool.

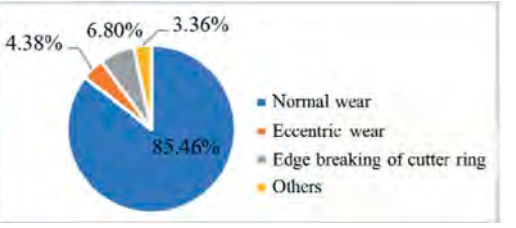

Figure 7. Failure statistics of single disc cutter.

2) Center cutter consumption
   In the first TBM tunneling section, a total of 161 double center cutters were replaced (see Figure 8), including 90 cutters subjected to normal damage and 71 cutters subjected to abnormal damage (see Figure 9).
3) Cutter gear consumption
   In the first TBM tunnel section, a total of 2,687 cutter gears were replaced, reaching 0.32 pieces

Figure 8. Failure statistics of center cutter.

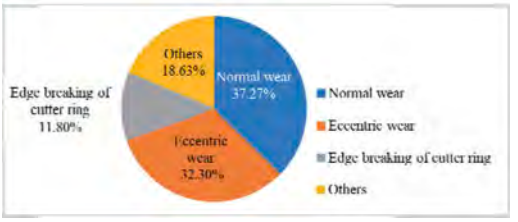

Figure 9. Statistics for center cutter failure.

per linear meter; the replacement of cutter gears was mainly caused by normal wear, accounting for 91%, while the abnormal replacement was primarily due to bolt fracture and peeling of cutter gears caused by the impact of high-intensity rock mass, accounting for 9%; the consumption of cutter gears mainly occurred in the transition area of the cutter head where tools were worn quickly, resulting in the replacement of cutter gears in this area accounted for over 80%.

4.2.2 *Analysis of tool failure modes*

In the first tunneling section of the HWWD Project, a total of 938 disc cutters were subjected to abnormal wear, of which the edge breaking of cutter ring was 44%, eccentric wear was 32% and other causes accounted for 24%, and the specific analysis was as follows:

1) With the frequent rock bursts in the HWWD Project, rock collapse was caused by rock bursts and hit disc cutters violently, resulting in edge breaking and fracture of curter rings, which was the main factor causing the edge breaking and damage of cutter rings.
2) There were many reasons for the eccentric wear of disc cutters; for example, ① tool bearings, cutter body and cutter rings were damaged by the impact of overloading and failed to be timely replaced; ② stones squeezed into the gap between the cutter housing and the disc cutter, causing tools to be stuck; ③ seal assembly damage resulted in oil leakage of tools; meanwhile, rock slag entered the seal chamber, causing damage to the bearing; ④ during the assembly of tools, an improper adjustment to the starting torque caused tools to fail to rotate normally.
3) In addition to the two major failure modes (viz. edge breaking and eccentric wear) hereinbefore, the proportion of other causes, such as bolt loosening or fracture, end cover displacement, and broken threads of end cover, also reached 24%, and the "loosening, peeling and breaking" of bolts fixing tools were among the technical difficulties encountered in the use and management of TBM tools in extremely hard strata.

5 COUNTERMEASURE ANALYSIS

5.1 *Type selection of tools*

In the strata where disc cutters are prone to wear, wear is the main form of tool consumption. According to different geological conditions, the corresponding cutter head and tool configuration shall be selected, the clearance between tools shall be properly adjusted to protect tools from the secondary wear caused by excessive crushing of rock surface, the frequency of cutter head inspections shall be increased during construction so as to find any problem in advanced and solve it timely, and the normal operation of all tools shall be protected from being affected by a problem of any individual tool, such as quick wear and edge breaking. After the external reasons for the quick wear of a disc cutter, such as equipment, are eliminated, the configuration of the disc cutter itself is particularly critical:

1) Select a reasonable torque configuration, adjust the tool torque accordingly in case of a change in geological conditions, and improve the service life of tools to prevent eccentric wear and chord wear of tools due to insufficient force of friction;
2) Select high-quality floating seals and bearings to ensure that disc cutters will not be subjected to abnormal wear due to the failure of floating seals and bearing when tools operate;
3) Select cutter rings suitable for the current geological conditions; for example, where surrounding rocks seriously collapse and peel from the tunnel face, the thickened cutting edges and cutter rings shall be used, the medium and high gradient hardness treatment shall be adopted to improve toughness, and other measures shall be taken; where the intensity of rock is relatively high, a cutter ring with a wider cutting edge should not be used; otherwise, the rock-breaking efficiency will be reduced and the rate of wear of cutter rings accelerated.

In the strata where disc cutters are prone to wear, the new process treatment of cutter rings can also produce good results; for example, if a cutter ring is inlaid with a superhard alloy, the service life of the cutter ring can be extended in case of low intensity of rock strata (≤40MPa), and the high wear resistance of the alloy can be utilized to improve the tool wear resistance.

5.2 *Tool inspection method*

5.2.1 *Requirements for tool inspection frequency*

1) Routine inspection standard for tools: The routine inspection frequency of tools is determined according to the TBM tunneling velocity (v), and in case of v<2.6m/h, tools shall be inspected once every 3 tunneling cycles; in case of 2.6m/h<v<3m/h, tools shall be inspected once every 4 tunneling cycles; in case of v>3m/h, tools shall be inspected once every 5 tunneling cycles;
2) If the main engine violates greatly, abnormal noise is produced from the cutter head, and an abnormal increase in the cutter head torque or the tunneling thrust force occurs, the TBM shall be stopped immediately and the cutter head shall be inspected;
3) If a tool inspector finds that long strips of slag are produced continuously for over 5min when observing the mucking conveyor belt, the TBM shall be stopped and tools shall be inspected;
4) If any objects, such as tool bolts and scrapers, appeared on the conveyor belt, the TBM shall be stopped and the cutter head shall be inspected.

5.2.2 *Main contents of tool inspection*

1) Remove slag from the cutter head and clean it;
2) Measure the tool wear at intervals of 20m~30m. The limit value of wear of a center cutter is 38mm, the limit value of wear of a frontal disc cutter is 38mm, the limit value of wear of a side disc cutter is 18mm, and a daily inspection will be considered, as appropriate, in special cases;
3) Inspect whether tools are subjected to chord wear, oil leakage, breaking and displacement of cutter rings, and peeling of retainer rings and whether tool bolts are loosened, broken, and peel off, and use a tool to hit bolts to judge the fastening of bolts;
4) Inspect the conditions of the scraper and its bolts;
5) Inspect whether the water spraying system for the cutter head is intact.

5.3 *Judgment criteria for tool replacement*

Different types of tools shall be replaced according to different criteria:

1) Normal replacement of tools: The wear of a cutter ring reaches its limiting value, the wear of a frontal disc cutter and a center cutter reaches 38mm, and the wear of a side disc cutter reaches 18mm;
2) Abnormal replacement of tools: Tools are subjected to chord wear, oil leakage, cutter ring breaking and a displacement cutter ring (more than 5mm);
3) Tool replacement due to an adjustment to height difference: the height difference between two adjacent frontal disc cutters is less than 15mm and the height difference between side disc cutters is less than 5mm;
4) Replacement of a group of tools: the 1# frontal disc cutter must be replaced when a group of center cutters is replaced; No. 55~No. 62 frontal disc cutters shall be replaced at the same time when side disc cutters are replaced.

5.4 *Relevant requirements for tool replacement*

1) In case of tool replacement, all contact surfaces of a tool must be polished with an angle grinder to ensure the contact surfaces are smooth and free of foreign objects; the contact surface between the bracket and the tool must be washed thoroughly with clean water and dried with clean cotton cloth before assembly, and finally, a torque wrench shall be used to tighten it to the required torque;
2) The brackets disassembled from an old tool must be matched in an exact way (i.e. the brackets on the cutter body side with a retainer ring and the brackets on the cutter body side with a retainer ring shall be separately arranged), and a cutter that is removed from a cutter housing shall be replaced by a new cutter and this new cutter shall be installed on the corresponding cutter housing. If brackets and cutter housings need to be replaced, they must be replaced in sets, i.e. 4 cutter housings and 2 brackets need to be replaced;
3) Before a cutter is installed in a cutter opening, inspect whether the cutter housing is secured, and then install the cutter after no problem is found. If a sign of wear is found or a cutter housing bolt is broken, reinstallation shall be conducted, and glue shall be applied to a bolt before the bolt is connected with the cutter housing; before bolts are installed, bolt holes shall be thoroughly washed to ensure that no impurities exist in bolt holes and then bolts can be installed. A bolt must be manually screwed into 4-5 threads and then tightened with an impact wrench, and it is strictly forbidden to use an impact wrench to install bolts; finally, a torque multiplier shall be used to tighten bolts in place as required, and the bolt tightening sequence is diagonal fastening;
4) The personnel responsible for tool replacement shall record in the tool replacement record form the cutter housing No., mileage of tool replacement, operating time of cutter head, new cutter body No., old cutter body No., new tool condition, and person responsible for tool installation, and notify the records to the chief operator for recording.

6 CONCLUSIONS AND RECOMMENDATIONS

Different types of surrounding rocks, such as full-face hard rocks and fault fracture zones, produce different failure modes of TBM tools; a variety of geological parameters, such as UCS and quartz content of surrounding rocks, have varying degrees of impact on tools; inappropriate TBM tunneling parameters will also cause abnormal damage to tools, such as total thrust force, speed of cutter head, and tool penetration. For the consumption of different types of tools, the causes shall be accurately analyzed and targeted measures shall be taken to effectively control the consumption of tools and finally realize a reduction in construction costs and an increase in the construction efficiency. On the basis that the causes of damage to tools are accurately analyzed and countermeasures are

properly taken, research into tool configuration technology, tool status monitoring technology, etc. shall also be strengthened to reduce the abnormal damage to tools. The specific conclusions and recommendations are as follows:

1) There is an approximately linear relationship among the uniaxial compressive strength, the quartz content and the tool consumption on the premise that the impact of special circumstances (e.g. tunnel face collapse and rock burst) on the abnormal damage to tools is not considered.
2) The tool configuration technology with an adjustable cutter clearance is further researched and developed. At present, the design of TBM tool configuration is mostly based on the configuration experience and construction effect of similar projects in the early stage for analogical design, and once the tool configuration mode is determined, it will not be changed in the later construction; thus, it is difficult to meet the rock breaking requirements under different geological conditions of the same tunnel. Given that the optimal rock-breaking clearance of disc cutters varies with different surrounding rock conditions, the adjustable cutter clearance is only realized on the laboratory test platform now but has not been applied to projects, so the cutter head design and manufacturing technology with an adjustable cutter clearance shall be further researched to ensure the TBM tunneling efficiency under different geological conditions.
3) The R&D and application of a new tool status monitoring system shall be strengthened. The tool status monitoring system has now been widely applied to super-pressure disc cutters on a large-diameter shield, but as there is violent vibration, external interference and other adverse impact during the tunneling of TBM equipment, causing the existing disc cutter status monitoring system shows poor adaptability and low data acquisition accuracy in the TBM tunneling process; on the other hand, there are relatively convenient conditions for checking the TBM tool status on site, so the tool status monitoring system is rarely used in TBM devices. Meanwhile, driven by the trends of unmanned, information-based and intelligent development of equipment, manual inspection of the tool status from time to from is difficult to meet the demands, so it is necessary to master the tool status in real time and predict its running status, and it is most urgent that a new monitoring system that can highly adapt to various TBM working environments should be further researched and developed on the basis of the existing tool status monitoring systems, such as ultrasonic detection method and electrical method.

ACKNOWLEDGMENTS

The authors would like to acknowledge the financial supports of a National Key Research and Development Program of China (No. 2020YFB1712100).

REFERENCES

[1] Jonak, J; Kuric, I; Drozdziel, P, et al. Prediction of load on the cutting tools in tunnel boring machines[J]. Acta Montanistica Slovaca, 2020, 25(4): 444–452.
[2] Moosazadeh, S; Hoseinie, SH; Ghodrati, B. Effects of mixed-ground condition on tool life and cutterhead maintenance of tunnel boring machines[J]. International Journal Of System Assurance Engineering And Management, 2023, 14(6): 2586–2594.
[3] Farrokh, E. Primary and secondary tools' life evaluation for soft ground TBMs[J]. Bulletin Of Engineering Geology And The Environment, 2021, 18(6): 4909–4927.
[4] Mousapour, H; Chakeri, H; Darbor, M, et al. Evaluating the wear of cutting tools using a tunnel boring machine laboratory simulator[J]. Mining Of Mineral Deposits, 2023, 17(02): 28–34.
[5] Karami, M; Zare, S; Rostami, J. Real-Rcale Numerical Analyzing Dynamic Process of TBM Boring in Jointed Rock; a Case Study: Kerman Water Conveyance Tunnel in Iran[J]. Journal Of Mining And Environment, 2022, 13(3): 643–666.
[6] Hong Kairong, Wang Dujuan, Guo Rujun, 2018. Innovation and Practice of Hard Rock TBM in China[J]. Tunnel Construction, 38(04):519.
[7] Hong Kairong, 2019. Study on rock breaking and wear of TBM hob in high-strength high-abrasion stratum. Hazard Control in Tunnelling and Underground Engineering, 1(1): 76.
[8] Jiang Qiao, 2018. Brief Discussion on TBM Tool Failure Modes and Influencing Factors[J]. Engineering Machinery and Maintenance, (03):82.
[9] Duan Zhiwei, Wang Jiahai, Liu Leitao, etc, 2020. Field Tests and Comparative Analyses of the Performance of Domestic TBM Cutters[J]. Modern Tunnelling Technology, 57(S1): 1214.
[10] Wu Zhipeng, Liu Suyan, 2020. Analysis the Wear and Tear of Cutters in Small Section TBM Construction[J]. Mechanical & Electrical Engineering Technology, 49 (07):222.
[11] Yan Changbin, Jiang Xiaodi, Yang Jihua, etc, 2018. Prediction of TBM Cutter Consumption Considering Geological Suitability and Disc Cutter Diameter[J]. Tunnel Construction, 38(7): 1243.
[12] Ebrahim F, Dae Y K, 2018. A discussion on hard rock TBM cutter wear and cutterhead intervention interval length evaluation[J]. Tunnelling and Underground Space Technology incorporating Trenchless Technology Research, 81.
[13] Yang Y, Hong K, Sun Z, et al, 2018. The Derivation and Validation of TBM Disc Cutter Wear Prediction Model[J]. Geotechnical and Geological Engineering, 36 (6): 3391.
[14] Xia Ming, 2018. Research on high abrasion formation TBM hob field test[J]. Construction Mechanization, 39 (04):37.
[15] Zhang Ling, Zhang Aiwu, Yu Yongsheng, etc, 2019. Fracture Failure Analysis of Cutter Shaft of Disc Cutter for Full-Face Tunnel Boring Machine (TBM)[J]. Rock Drilling Machinery & Pneumatic Tools, (02): 31.
[16] Li Jinlin, 2018. Tool consumption analysis of TBM construction in high-erosion hard rock section of tunnel High Abrasive Hard Rock Tunneling and TBM Tools Consumption research[J]. Shaanxi Water Resources, (05):127.
[17] Li Xiaoling, 2019. Discussion on Tool Damage and Repair Measures in Shield Tunneling [J]. Journal of Ezhou University, 26(06):104.

Tunnelling for a Better Life – Yan, Celestino, Thewes & Eberhardt (Eds)
© 2024 The Author(s), ISBN 978-1-032-80042-4
Open Access: www.taylorfrancis.com, CC BY-NC-ND 4.0 license

Construction method for rapid construction of station by use of large-diameter shield tunneling machines expanding small-diameter shield tunnels and its application

Liping Huang
Shenzhen Metro Group Co., Ltd, Shenzhen, China

Ke Jia, Jian Zhang* & Deyong Yu
Shenzhen Metro Construction Group Co., Ltd., Shenzhen, China

Tiantian Song
Shenzhen Metro Group Co., Ltd, Shenzhen, China

ABSTRACT: Aiming at the construction method of "tunnel first and station later" in subway project, this paper proposes an innovative construction method of rapid station construction of tunnel with large shield tunneling and small shield construction. In this construction method, the small shield tunnel passes through the station section first, and then the large shield tunnel is used to dig and expand the small shield tunnel to form the side platform station. This construction method was first applied to Zhangbei station of Shenzhen Metro Line 14. Compared with the traditional construction method, the construction method has good economic and social benefits as well as technical innovation and advanced nature, which enrich the construction technology of subway engineering and provides a reference for subsequent similar projects.

Keywords: Metro stations, Stations posterior to tunnels, Shield tunneling method, Construction method, Engineering application

1 INTRODUCTION

The development of urban rail transit has brought more and more convenience to people. At the same time, with the continuous expansion of urban rail lines, various situations that may occur in the process of line selection, planning and construction need to be considered. For example, due to the influence of external reasons such as land expropriation and demolition, the construction period of subway stations lags behind, or the decision to add stations in the construction process of subway lines leads to major changes in the overall construction period planning, which restricts the key goals of subway line tunnel "tunnel" and station "roof". As a result, the trial operation node of the whole subway line is delayed, resulting in the delayed opening of the subway. The construction method of "tunnel before station" is a better way to solve the above problems. For this reason, the domestic and foreign engineering circles have actively explored the construction technology of "tunnel before station" [1,2], and formed a variety of construction methods. The main difference lies in the differences in the excavation methods of the station after the shield tunnel passes through the station section, such as mine method, pipe shed method, joist method, half-shield method, open excavation method, cover excavation and reverse work [3].

The pipe shed method means that a curved pipe shed is built above two intersectional tunnels at the same time as the two tunnels, and soil is excavated below the pipe shed and part of the pipe segments are removed to form an island platform. This method has been widely used in the construction of subway stations in Iran [4].

In China, the construction method in which the shield tunnel is formed first and then the station is excavated by mining method was used earlier, that is, after the shield tunneling machine passes through the station section, the mining method is used to expand the excavation, dismantle the shield tunnel segments in the station section, and build the underground station [5]. This technology is applied to the East [6] Shankou station of Guangzhou Metro Line 6 and the intersection section of the tunnel of the left

*Corresponding author: 11021234@qq.com

DOI: 10.1201/9781003495505-246

line of Zhengzhou Metro Line 2 and the tunnel of the liaison line of Line 1 and Line 2 [7].

The construction method of shield tunneling first and open excavation means that after shield tunneling passes through the station section, the station is excavated according to the traditional open excavation construction method of underground station. During the construction process, the tunnel structure of the station section was protected to avoid collapse, and finally the tube segments in the station were removed to form an underground station [8]. The application cases of this construction method in China include Wuyangcun Station of Guangzhou Metro Line 5 [9], Beihe East Station of Beijing Metro Line 6 Phase 2 [10], Jingshun Road Station of Beijing Metro Line 14 [11], and Gaolin Station of Xiamen Railway Line 2 [12]. Typical examples abroad include Line 5 in Riyadh, Saudi Arabia [13], and the western section of the Tel Aviv Metro Red Line in Israel [14]. In addition, the shield tunneling method was applied in the construction of Shenzhen Metro Renmin South Station [15].

This paper puts forward a fully mechanized "tunnel first and station later" construction method, that is, small shield tunneling first enlarging and digging forming station construction method. This paper elaborate the technical key points of this construction method and introduce the first application project case of this construction method in the country, so as to provide reference for subsequent similar projects.

2 CONSTRUCTION METHOD FOR METRO STATIONS BY USE OF LARGE-DIAMETER SHIELD TUNNELING MACHINES EXPANDING SMALL-DIAMETER SHIELD TUNNELS

2.1 *Construction technology flow*

The principle of this construction method is that the small shield adopts glass fiber reinforcement segments, the small shield passes through the station section first, and then the large shield is used to expand and dig, and the large shield tunnel is used as the platform of the station, and the station is quickly constructed. The construction process is shown in Figure 1, and the specific construction steps include:

(1) Make four end walls of the two shafts at both ends of the station (Figure 2 (a)).
(2) The shield machine has passed through the end wall and the section of the station (Figure 2 (b)). After arriving at the next station to complete acceptance, the shield machine falls out of the shaft.
(3) The shafts at both ends of the station are dug from the ground, and some internal structures such as the bottom plate and side wall are applied (Figure 2 (c)).
(4) Remove the connection bolts of the shield lining segments, and backfill the shield holes in sections and layers (Figure 2 (d)).
(5) The large shield machine is hoisted into one of the shafts and started (Figure 2 (e)).
(6) The large shield traverses the section where the station is located, receives and lifts out of another shaft, and finally completes the expansion of the station (Figure 2 (f)).

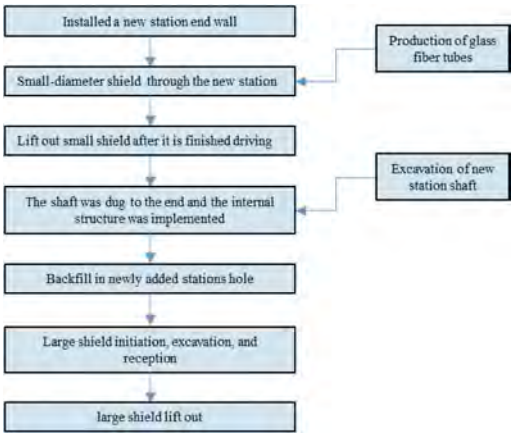

Figure 1. Construction technology flow for metro stations by use of large-diameter shield tunneling machines expanding small-diameter shield tunnels.

2.2 *Construction characteristics*

(1) Safe and reliable.The shield tunneling machine is used to complete the station construction, which has higher safety performance than the underground excavation and open excavation.
(2) High construction efficiency. Shield tunneling method is a fully mechanized tunnel construction method, which is used in both section tunnels and stations, and the construction efficiency is guaranteed.
(3) Avoid long shutdown of shield, save the overall construction period. The small shield first adds the station, continues the subsequent excavation task, and synchronously carries out shaft excavation, which not only reduces the downtime of the shield, shortens the impact of the shaft on the total construction period, can greatly save the construction period and reduce the cost of large equipment idle.

2.3 *Scope of application*

This construction method is applicable to the situation that the new station scheme is stable and lagging behind, the ground environment and geological conditions of the station are poor, the overall construction period is tight, the existing station is not suitable for the transformation of the construction period is long, and the station cannot provide the starting conditions as scheduled.

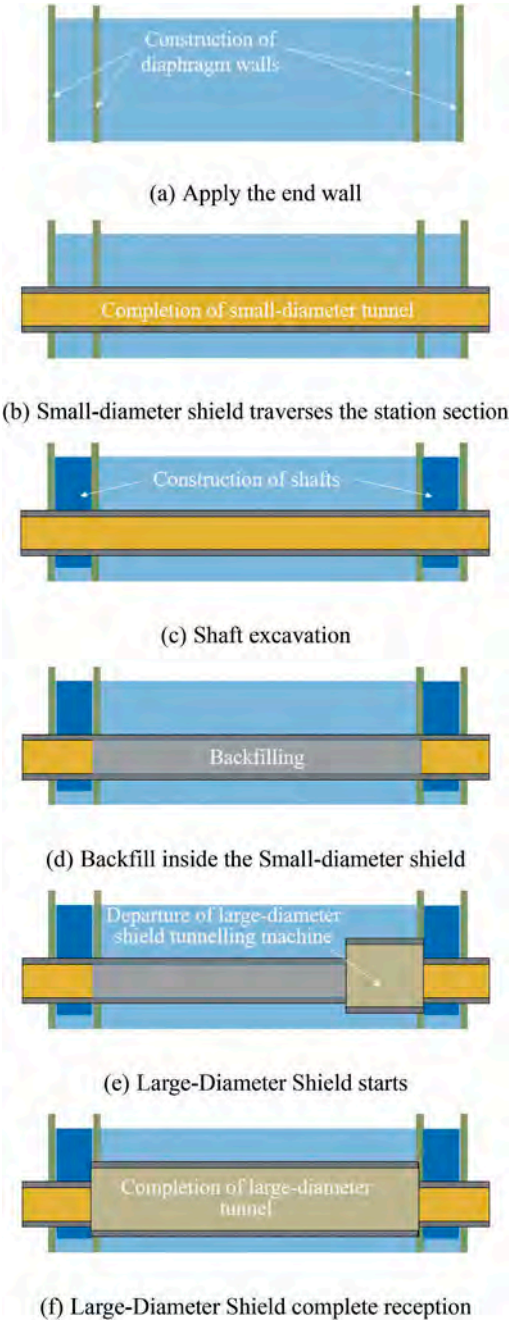

Figure 2. Schematic diagram of construction steps for metro stations by use of large-diameter shield tunneling machines expanding small-diameter shield tunnel.

3 APPLICATION CASE

3.1 *Project overview*

Shenzhen Metro Line 14 Dayun Station, Baohe station and its intermediate air shaft have been completed, according to the project plan to carry out the shield tunneling construction between the two stations. At this time, due to urban planning reasons, it was necessary to add Zhangbei station between Dayun Station and Baohe Station (Figure 3). Zhangbei Station is a side-platform station with a length of about 264m, and the newly added works include station platform, station hall, shaft, evacuation exit, etc. The project mainly passes through massive heavily weathered sandstone and partially through heavily weathered carbonaceous shale, soil-like strongly weathered sandstone and breezy limestone. The geological profile is shown in Figure 4. The massive heavily weathered sandstone is heavily weathered, the joint cracks are very developed, there are more moderately weathered rock blocks in the local area, and there are unevenly weathered interlayers in the layer, and the rock mass is broken into fragments. The standard penetration test measured 52 ~ 97 blows, with an average of 62.1 blows. Strong weathering carbon shale and earth-like strong weathering sandstone are easy to soften when exposed to water, and their strength decreases. The hammer number measured by standard penetration test is 71 ~ 113, with an average of 80.4 blows. The joints and fissures of breezy limestone are more developed, and the weathered fissures are more developed. The measured saturation uniaxial compressive strength is 63 MPa.

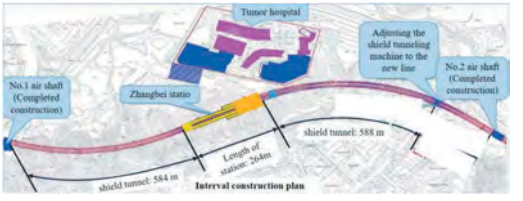

Figure 3. Plan of Zhangbei station of Shenzhen Line 14.

In order to ensure that the opening target of Metro Line 14 remains unchanged, the construction method and project planning adjustment of the new project are carried out, that is, the construction method of adding station sections through small shield tunneling is adopted first, and then the construction method of expanding and digging small shield tunnel segments to build stations is adopted. The feasibility of the construction scheme is established through model test research.

3.2 *Key points of construction technology*

(1) The small shield adopts glass fiber reinforcement segments in the station section (Figure 5). The normal design segment strength of this section is C50. In order to reduce the strength difference between the segment and the surrounding strongly weathered sandstone, and considering that the glass fiber segment is only a temporary structure, the

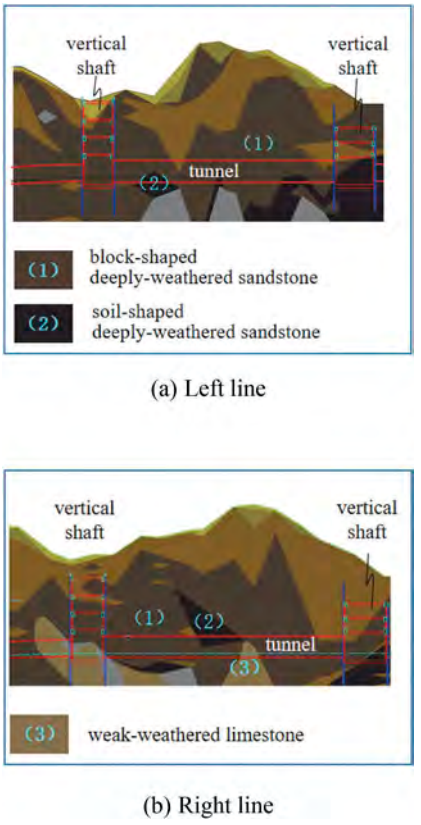

Figure 4. Section view of engineering geology of Zhangbei Station on Shenzhen Line 14.

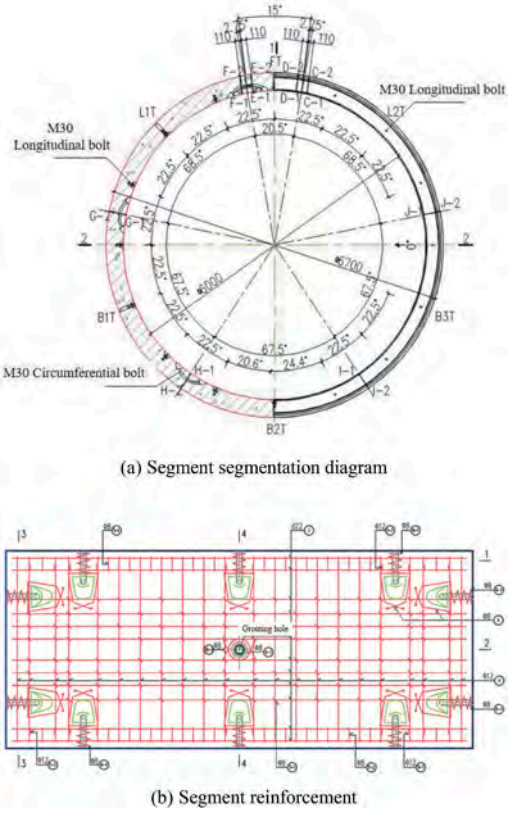

Figure 5. Reinforcement diagram of small-diameter shield segment.

empirical calculation uses C40 concrete with concrete impervious grade P12. The main rib of the annular tension is replaced by glass fiber rib of equal diameter. At the same time, considering the unified diameter type of glass fiber bars, the longitudinal tensile steel bars are replaced by glass fiber bars with a diameter of 22 mm, and the inner and outer main bars are connected by double rows of 14 mm U-type steel bars. The distribution bars are replaced by glass fiber bars with a diameter of 12 mm, and the inner and outer distribution bars are connected by 12 mm U-type steel bars. The joint between the glass fiber bar and the steel bar, and the glass fiber bar and the glass fiber bar should be fixed by binding both ends of the U-type steel bar. To facilitate subsequent removal and segment stability, the bolts are of a smaller specification class (normally M30), including sixteen M24 ring bolts and twelve M24 longitudinal bent bolts.

(2) Linear adjustment. The outer diameter of the small shield segment is 6.7 m, and the outer diameter of the large shield segment is 8.83 m. The line centers of the small and large shield segments are not completely coincident (Figure 6). If part of the small shield segment is not within the cutting range of the large shield cutterhead, the formation disturbance may be intensified during the excavation process, and the residual segments after cutting will accumulate and form a monolithic effect. Therefore, it is necessary to adjust the small shield route within the cutting range of the large shield cutter head. Theoretically, the small shield segment can be cut as a whole during expansion construction. In the scope of the small shield tunnel near the shaft, the plane adjustment of 46 cm (0.88cm/ ring) to ensure that the large shield cutter can cut the small shield segment as a whole.

(3) Backfill the hole. The amount of backfill is large, and a single line needs to be backfilled 5567 m³. A platform pump is arranged on the ground, and the mortar is pumped into the tunnel through the discharging pipe of A400 of the wellhead to the tunnel for backfilling. The backfill in the hole is divided into three layers (Figure 7). The first layer is 1.5 m, the second layer is 2.5 m, the third layer is 2 m, the first layer is not segmented as a whole, the second and third layers are divided into three sections of backfill, each section is 66 m, and forty-nine sealing walls are built in the middle, and the pump pipe is set up a pouring point every 20 m, and has an overall slope. Remove the bolt before backfilling,

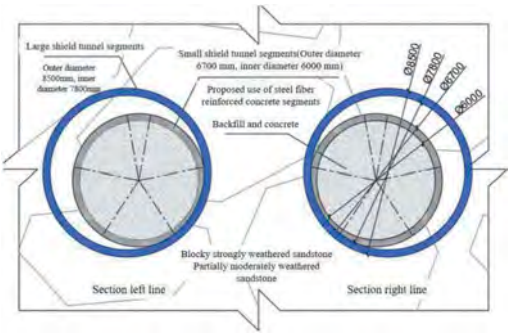

Figure 6. Section diagram of large shield tunnelling.

remove the section by section, and set the convergence monitoring in the hole.

(4) Large shield type selection and cutter head preparation. The large shield equipment DZ512 and DZ513 of the expansion and excavation station were selected initially. The maximum propulsion speed of the shield machine was 4.8 m/h, the maximum thrust was 81905 kN and the rated torque was 17960 kN·m. Cutter head diameter of 8840 mm, using six spokes and surface plate design, equipped center disc cutter with six 17-inch double disc cutters, thirty-five 19-inch front disc cutters, thirteen 19-inch edge disc cutters, a total of eleven tracks, including the outermost two tracks have two each, seventy-six cutting knives, twenty-two pairs of scrapers. The center disc cutter spacing is 101.5 mm, the front disc cutter spacing is 78 mm, and the cutter -cutter spacing is 200 mm. The height of the disc cutter is 160 mm and the height of the cutter is 115 mm. There are six wear detection points (two disc cutters continuous wear detection, four disc cutters continuous wear detection) the maximum rock breaking capacity of 200 MPa. Cutter head opening rate is 34%, the center opening is about 40%. Screw conveyor adopts shaft screw, barrel body diameter is 1020 mm, the maximum passing particle size is 380 mm×570 mm, the maximum slag capacity is 550 m^3/h, the maximum torque is 249 kN·m.

(5) Shield tunneling control. After the initial injection into the hole, it was found that there was basically no water on the palm surface, and 100~110 L of foam liquid should be injected into each ring in normal excavation. When the workability of residue soil was poor, the cutter head should be sprayed. After opening the warehouse, it was observed that the palm surface was stable, there was no clear water, and the top of the backfill in the hole was not dense. Under the premise of stable palm surface, the glass fiber bar cut by the cutter head will not accumulate at the bottom, and the small steel bar is not easy to wind the tool or the tool holder. The driving speed is 20 mm/min and the cutter speed is 1.5 r/min. The excavation site of large shield is shown in Figure 8.

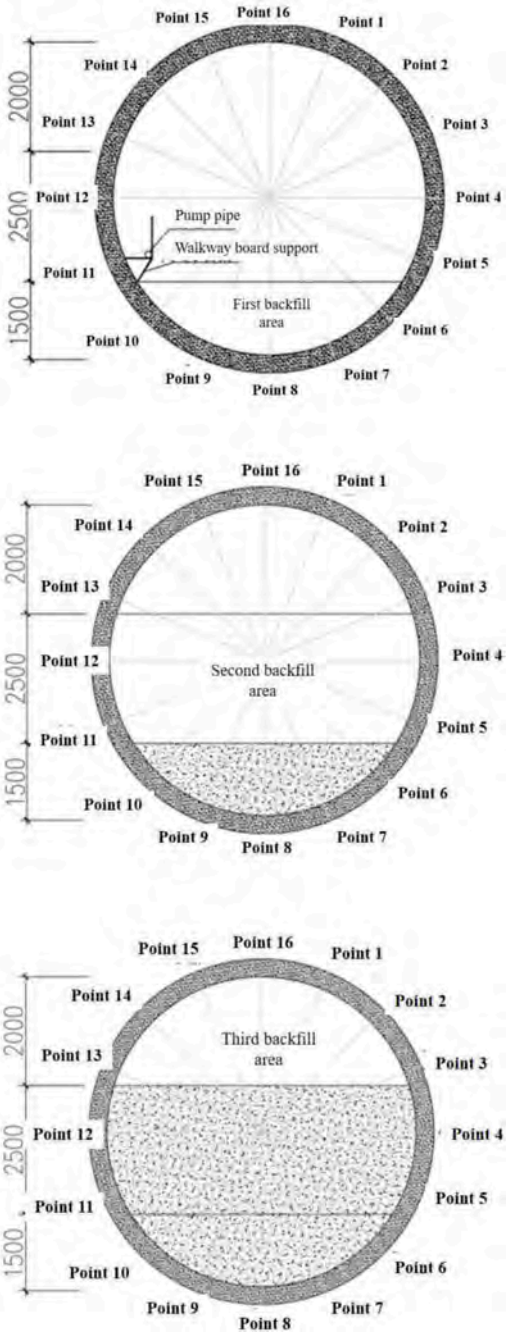

Figure 7. Schematic diagram of layered backfilling in the cave.

3.2 *Benefit analysis*

The direct economic benefits of large shield tunneling and small shield tunneling are mainly derived from the adjustment of the overall construction plan, greatly shortening the construction period, and reducing the idle cost of personnel and equipment for

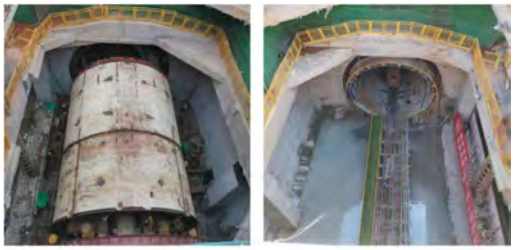

(a) Before the large shield (b) After the large shield

Figure 8. Construction site.

a long time. The indirect economic benefits are derived from the implementation of the excavation task in advance, reducing the increase in construction costs caused by rush work in the later period, and ensuring that the overall opening operation target of Metro 14 is not delayed. Compared with the completion of the new station shaft, the small shield is hoisted out of the station, and then the large shield construction is carried out, which shortens the construction period of the whole project by ten months and ensures the construction period node of Shenzhen Metro Line 14, which is highly recognized by the supervisor and the owner.

The social benefits of this construction method mainly include two aspects. On the one hand, this process enriches the construction method of "tunnel before station", and adopts large shield tunneling to improve the mechanization level of existing tunnel expansion and avoid the construction risk of underground excavation station. On the other hand, the small shield adopts a new type of glass fiber reinforcement segment, which provides a successful case for the engineering project that needs to use glass fiber reinforcement as the main reinforcement of the segment.

4 CONCLUSIONS

Generally speaking, subway construction adopts the construction sequence of "station first, tunnel later", and the station shaft constructed first provides the receiving and starting conditions for the small shield tunneling in the section tunnel. However, due to special reasons such as line changes, new stations, and limited station construction sites, the following situations may occur: the small shield machine arrives at the station first, but the station construction progress is slow, and the shield lifting conditions cannot be provided. The construction method of large shield tunneling and small shield tunneling has become an effective solution.

(1) The main construction procedures of the construction method include: the end wall of the shaft, the small shield through the station, the excavation of the shaft, the backfill in the hole, and the expansion of the large shield.
(2) The construction method has the characteristics of safety and reliability, efficient construction and saving the overall construction period.
(3) This construction method was first applied to the newly added Zhangbei station between Dayun Station and Baohe Station of Shenzhen Metro Line 14, which shortened the construction period of the whole project by 10 months, ensured that the overall opening and operation target of Metro Line 14 was not delayed, and achieved good economic and social benefits.

REFERENCES

[1] Xiong Qian, 2009. Subway tunnel before station method [J]. Railway Standard Design, 2009(12), 106–111.
[2] Wu Fei, Wang Bin, 2020. Construction technology of subway project "tunnel before station" [J]. Building Technology, 51(07), 800–802.
[3] Ren Ke, Li Jian, Hu Lin, 2019. Analysis on key points of construction technology of tunnel and station in subway station [J]. Building Materials and Decoration, 2019(33), 258–259.
[4] Sadaghiani M. H., Dadizadeh. S., 2010. Study on the effect of a new construction method for a large span metro underground station in Tabriz-Iran [J]. Tunneling and Underground Space Technology, 25, 63–69.
[5] Wang Zhanbing, 2019. Operation of key technologies for construction of tunnel and station in subway station [J]. Metallurgical Management, 2019(23), 64+81.
[6] Liao Hongyan. Construction technology of metro station by expanding shield tunnel with mine method [J]. Urban Express Rail.
[7] Chen Ruizheng, Hu Weidong, Li Xinping, 2016. Construction technology of large-section tunnel by expanding shield tunnel in mine [J]. Tunnel Construction, 36(11), 1372–1378.
[8] Zou An, 2019. Research on the construction plan of the red line light rail tunnel and then station [J]. Railway Construction Technology, 2019(10), 44–48+54.
[9] Zhong Changping, Zhou Cuiying, Wei Kanglin, 2013. Research on construction technology of subway station by open-cut shield tunnel expansion [J]. Guangdong Civil and Architecture, 20(7), 46–50.
[10] He Yonghong, 2015. Key technologies for construction of tunnel and Station of Beijing Metro North Canal East Station [J]. Science and Technology Outlook, 25(14), 9–10.
[11] Ding Guisong, 2017. Construction technology of tunnel before station in subway station [J]. Building Technology, 48(06), 613–616.
[12] Lin Yin, 2018. Discussion on the subway station construction of Xiamen Railway Line 2 Gaolin Station by "tunnel first and station later" method [J]. Fujian Construction Science and Technology, 2018(1), 14–16+23.
[13] Schneider G r, Molina A g-f, Mendiola V t, Lavin J a, 2018. Innovative solutions for intersection of TBM tunnel and station in Riyadh Line 5 metro [J]. Tunnelling and Underground Space Technology, 80, 26–37.
[14] Du Chuangdong, Zhang Jie, Wu Lebin, 2020. Application of construction technology of red line tunnel and station in Tel Aviv, Israel [J]. Tunnel Construction (Chinese and English), 40(04), 562–568.
[15] Ding Xianli, 2016. Design and construction of Shenzhen Metro Renmin South Station under complex environment [J]. Tunnel Construction, 36(08), 960–967.
[16] Zhang Jian Long, Gao Yimin, Zhang Jian, Zhou Hao, Pan Ye, Ke Lei, Liu Xian, 2021. A model test design principle and method for simulating rock breaking process of shield cutter [J]. Tunnel and Underground Engineering Disaster Control.

Tunnelling for a Better Life – Yan, Celestino, Thewes & Eberhardt (Eds)
© 2024 The Author(s), ISBN 978-1-032-80042-4
Open Access: www.taylorfrancis.com, CC BY-NC-ND 4.0 license

Breaking the tunnel vision: Generalizing TBM performance prediction across projects

Shengfeng Huang*
Department of Civil Environmental, and Ocean Engineering, Stevens Institute of Technology, Hoboken, USA

Rita Sousa
Department of Civil Environmental, and Ocean Engineering, Stevens Institute of Technology, Hoboken, USA
Civil and Urban Engineering, New York University Abu Dhabi, Abu Dhabi, UAE

George Korfiatis
Department of Civil Environmental, and Ocean Engineering, Stevens Institute of Technology, Hoboken, USA

ABSTRACT: Accurately predicting the Penetration Rate (PR) in tunneling is crucial for evaluating the performance of Tunnel Boring Machines. However, a significant shortcoming of many existing studies is that the predictive models are developed using data from a single project, which limits their applicability to future tunneling projects. This research addresses this issue by examining whether the model can generalize to other tunneling projects and investigates the impact of an incremental learning strategy on its performance. In this study, the Extreme Gradient Boosting (XGBoost) model was initially trained and tested using data from one tunnel project and then generalized to a different tunneling project with similar geological conditions. To improve the model's generalization performance, an incremental learning strategy was used, which involved iteratively incorporating new data from the second tunneling project into the existing data from the first tunneling project to update the model. Additionally, the study analyzed how the generalization ability of XGBoost varies with the incremental size of new data. The findings indicate that there is a promising potential for enhancing the model's generalization ability using incremental learning techniques. However, additional research is needed to address the challenges related with skewed data and mitigating the effects of catastrophic forgetting.

Keywords: EPBM performance, Penetration Rate, XGBoost, Generalization, Incremental Learning

1 INTRODUCTION

The rapid urbanization and the need to reduce traffic congestion has led to an increase in underground construction projects. Tunnel boring machines (TBMs) have become a popular choice for tunnel excavation due to their efficiency, safety, and minimal impact on the environment (Huang et al., 2023).

To accurately predict TBM performance, many researchers have employed machine learning techniques using real-world data (Huang et al., 2023b; Shreyas and Dey, 2019). Several machine learning models have been employed (Mokhtari and Mooney, 2020), extreme gradient boosting (XGBoost) model (Zhou et al., 2021), artificial neural networks (Armaghani et al., 2019), deep learning (Pan et al., 2022). However, these models are constructed and tested using data from a single project. To establish confidence in these approaches and extend their applicability, it is essential to validate these models across various projects (Sheil et al., 2020). Moreover, the environment in tunneling projects is subject to dynamic changes, necessitating the development of more intelligent models capable of continuous learning and adaptation. Traditional machine learning models are typically trained on static, identically distributed, and well-labeled data (He et al., 2016). Hyperparameter optimization and model selection are typically performed using the provided data before training begins. This process assumes that the data and its inherent structure remain static. However, these models often struggle to capture the dynamic characteristics of data collected in tunneling projects.

In sharp contrast to machine learning models, engineers have the capacity to progressively acquire new skills and expertise through the diverse range of projects they encounter throughout their professional careers. Incremental Learning refers to a learning

*Corresponding author: shuang54@stevens.edu

DOI: 10.1201/9781003495505-247

system's ability to continuously assimilate new knowledge from fresh data while retaining the bulk of previously acquired knowledge. It aims to bridge the gap in incremental learning capabilities between natural and artificial intelligence (van de Ven et al., 2022). This approach empowers models to continually adapt and enhance their performance as new data becomes accessible. In the context of distinct tunneling projects, it is important to note that the underlying data distribution may undergo changes as construction progresses. Incremental learning serves as a valuable tool, enabling models to adapt to these shifts by seamlessly incorporating new data. This adaptive process plays a pivotal role in maintaining the models' ability to generalize effectively across various projects.

The primary objective of this paper is to delve into the possibilities offered by incremental learning to enhance the model's generalization performance in predicting penetration rate (PR) as tunnel construction progresses. Additionally, we seek to examine how the model's generalization capacity will change with varying data incremental sizes which represent the amount of incoming new data. Our primary objective is to create a model that not only demonstrates excellent generalization abilities but also has the adaptability to respond to changing situations. This will pave the way for a more effective and intelligent tunneling system in the future.

2 DATA DESCRIPTION

2.1 *Porto metro case*

We obtained tunneling data from two segments of the Porto Light Metro Project in Porto, Portugal (Sousa and Einstein, 2012), to conduct and validate our study on TBM performance prediction. These two segments, Line C and Line S, traverse the city center of Porto in Portugal and are illustrated in Figure 1. Line C extends for a distance of 2.3 kilometers, stretching from Campanhã to Trindade. In contrast, Line S spans 3.7 kilometers, connecting Salgueiros to São Bento. Both tunnels were constructed using earth pressure balance shield tunnel boring machines (EPBMs) equipped with 300 mm thick segments. The outer diameter of Line C measures 8.7 meters, while Line S boasts an outer diameter of 8.9 meters (Centis and Giacomin, 2004). These EPBMs are engineered to excavate in mixed conditions, making them well-suited for the diverse soil compositions encountered in Porto. The soil conditions in the region exhibit significant heterogeneity, ranging from fresh granite to residual soil.

Before initiating the construction of the Porto Metro light metro project, an extensive geological survey was undertaken. This survey encompassed the drilling of over 500 boreholes to thoroughly assess the geological conditions in the area. The geological findings were categorized into seven distinct

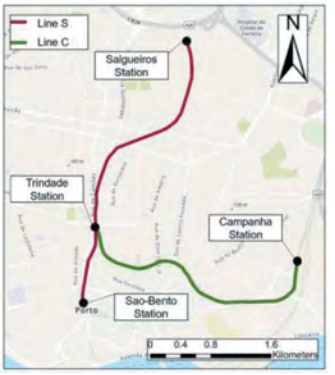

Figure 1. Top-down layout visualization of tunnelling projects.

geomechanical groups, denoted as g1 to g7. Groups g1 to g4 were indicative of rock-like materials, while g5 to g6 encompassed soil-like materials, including saprolite and residual soil. The seventh group, g7, included man-made materials and alluvial soils. Detailed longitudinal geological profiles and data pertaining to PR for both lines are presented in Figures 2 and 3.

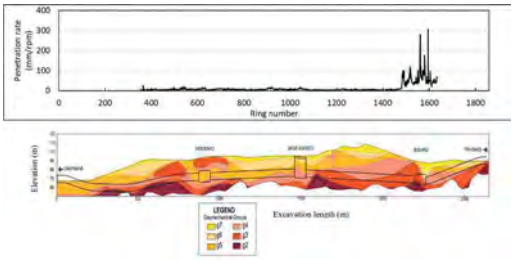

Figure 2. Geological profile and penetration rate of Line C tunnel (Sousa and Einstein, 2012).

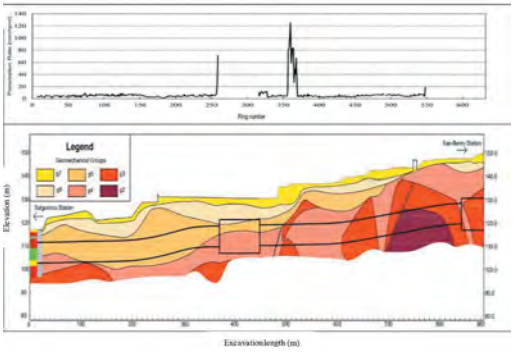

Figure 3. Part of geological profile and penetration rate of Line S tunnel (private communications with Transmetro).

2.2 *Feature selection and processing*

The EPBM deployed for the Porto Metro tunnel project was outfitted with an extensive array of sensors.

These sensors captured 195 variables at 10-second intervals during both excavation and stationary phases of construction. Only the data recorded during the excavation phase was utilized in the model to predict tunnelling performance. Additionally, parameters that held no relevance within this specific context, such as tank temperature and CH4-monitoring, were disregarded for the analysis.

A systematic feature selection procedure was executed to accurately forecast the PR. This process was guided by insights drawn from previous research studies (Koopialipoor et al., 2019; Pan et al., 2022; Yu et al., 2022) as well as practical knowledge garnered from industry expertise. Consequently, a set of nine parameters was chosen as features for the PR prediction task. These encompass attributes such as: torque cutting wheel, pressure force cutting wheel, thrust force, torque screw, cutting wheel speed of rotation, thrust pressure, excavated material flow, earth pressure, and foam lance pressure. PR, expressed as millimeters per rotation (mm/rpm), is adopted as the label, serving as the target variable that the models endeavor to predict. The PR distribution of tunnel Line C and Line S is depicted in Figure 4. It is worth noting that both projects produced skewed PR distributions. Commonly, the skewed points would be treated as outliers as they deviate dramatically from the main distribution and thus are removed. However, it is the authors' opinion that doing so would remove from consideration some important situations, such as drastic geology changes, encountering voids, or fault zones. Thus, in this paper, we consider both PR < 125 mm/rpm and PR < 25 mm/rpm.

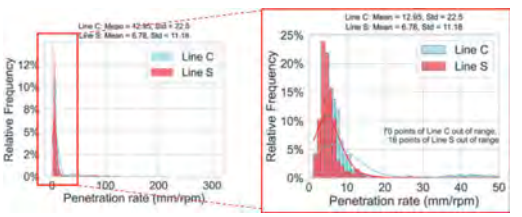

Figure 4. PR distribution of tunnel Line C and Line S.

During the excavation of each 1.4-meter tunnel ring, an averaged representative value was computed for all features and the corresponding label. This approach was adopted to smoothen the data and enhance the robustness of the subsequent analysis. The purpose of this smoothing process is to counteract the inherent fluctuations present in the 10-second interval time series data. By mitigating extreme variations, this technique highlights the overall trends, which is particularly advantageous for the development of models. Furthermore, specific variables like earth pressure and foam lance pressure are measured through multiple sensors situated at various positions on the cutterhead. In this particular EPBM, seven sensors are allocated for earth pressure and four for foam lance pressure. For the purpose of model development, the average of these sensors' values was used. Consolidating measurements from different sensors contributes to a more comprehensive and representative dataset for further analysis and modelling.

3 METHODOLOGY

The primary objective of this paper is to offer valuable insights into the generalization capabilities of models concerning tunneling performance prediction. To achieve this goal, the study places particular emphasis on exploring how the model's performance and its generalization ability varies with different incremental data sizes. By systematically updating the model using varying sizes of incremental data, this research aims to shed light on the intricate relationship between incremental learning and model performance, as well as its impact on generalization. Through this investigation, the paper seeks to contribute a deeper understanding of how incremental learning influences the overall performance and ability of models to generalize in the context of tunneling projects.

Figure 5 provides a detailed depiction of the incremental learning process employed in this study. Extreme Gradient Boosting (XGBoost), proved to be robust in generalization performance base on our previous research, was selected as the base model. The continuously acquired new data are segmented into sequential datasets through chronological order based on a predefined incremental size, which can be denoted as $\{T_1, T_2, \ldots, T_n\}$. Here, T_i represents the i-th new dataset. The initial phase of the study involves training and validating the model using Line C data, with a training-validation stratified split of 70% for training and 30% for testing. Subsequently, the model is generalized to the entire Line S dataset. In each subsequent iteration, a new dataset T_i, corresponding to a newly excavated part of line S, is integrated with the previously existing data. For instance, during the first iteration, T_1 (first increment of data from Line S) is added to Line C data; in the second iteration, T_2 (second increment of data from Line S) is added to the combined dataset of Line C data and T_1. It's worth noting that each T_i dataset is also divided into a 70% portion for training and a 30% portion for testing. This expanded and updated dataset is then utilized to retrain the mode, fine-tuning its hyperparameters to enable it to accommodate the newly incorporated data. Ultimately, the model's predictions are generalized to encompass the remaining data from Line S, resulting in an iterative and progressively refined learning process. The model performance will be evaluated by coefficient of determination (R^2) and root mean square error (RMSE).

To assess the incremental learning performance on different incremental size, a range of different incremental data sizes was employed in this study. These sizes include 200, 150, 100, 60, 30, 10, and 5.

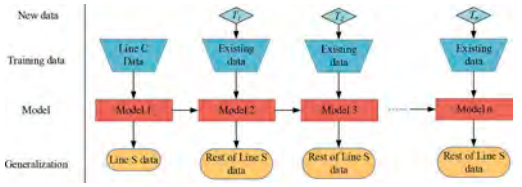

Figure 5. Flowchart of incremental learning process.

4 RESULTS

4.1 *Model performance*

Figure 6 illustrates the incremental learning performance of the XGBoost model, specifically developed for PR values less than 125 mm/rpm, with an incremental data size of 5. In this analysis, considering that the Line S dataset consists of 602 data points, the study investigates the impact of incorporating new data on both model performance and generalization. To do so, new data sizes ranging from 60 to 545 were examined. It's important to note that a few results are missing from the Figure 6 due to a technical constraint of stratified split. When dealing with imbalanced data, the common practice is to use the stratified split method to maintain a proportional representation of each range in both the training and testing datasets. However, this method may encounter difficulties when trying to create sections with zero instances, which can lead to the omission of these results in this analysis.

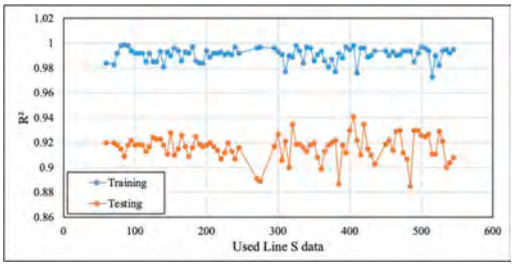

Figure 6. Incremental learning performance of XGBoost model on PR < 125 mm/rpm.

From Figure 6, it's evident that the XGBoost model demonstrates strong performance on both the training and testing datasets. This is substantiated by the R^2 values, with the R^2 for training exceeding 0.97 and the R^2 for testing surpassing 0.88. These high R^2 values indicate that the model is capable of explaining a significant portion of the variance in the data, reflecting its effectiveness in making accurate predictions for both the training and testing datasets. A noteworthy observation is made when incorporating more than 300 Line S data points into the model development process. At this point, the model's performance on the testing dataset exhibited instability. This phenomenon can be attributed to the increasing skewness of the data as more samples are added for model development. As the model is exposed to an increasingly imbalanced dataset, it may start to overfit to the training data, attempting to fit it very closely. Consequently, this can lead to a degradation in testing performance as the model struggles to perform well effectively beyond the training set, ultimately resulting in the observed instability in performance. Another reason of downgraded performance could be "catastrophic forgetting", where the model forgets or degrade its ability to perform well on tasks it previously mastered when exposed to new data (French, 1999). That is, when XGBoost learns new knowledge on new sequential data, it adjusts its hyperparameters to minimize the loss on this new data. However, it may significantly modify its parameters, which can lead to a drop in performance on the knowledge it had previously learned.

Figure 7 illustrates the incremental learning performance of the XGBoost model, focusing on PR values less than 25 mm/rpm. In this analysis, PR values ranging from 25 to 125 mm/rpm were excluded, resulting in a dataset of 587 remaining data points. Despite of this adjustment, the study continued to investigate the impact new data sizes varying from 60 to 545. It's important to note that there is one missing result for the scenario where 65 Line S data points were integrated into Line C data. This omission is also due to technical constraints. In general, the XGBoost model exhibits strong performance for both training and testing, with the R^2 values for training consistently exceeding 0.85, and the R^2 values for testing mostly surpassing 0.7. However, it's observed that the model's performance becomes less stable in both training and testing when more than 200 Line S data points are incorporated for model development. This instability could also be attributed to catastrophic forgetting. In comparison to the previous scenario, the impact of the catastrophic forgetting is more pronounced when considering the model trained on PR values less than 25 mm/rpm.

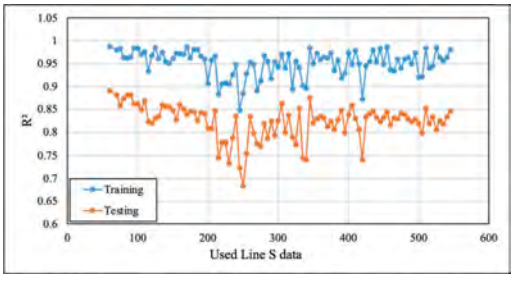

Figure 7. Incremental learning performance of XGBoost model on PR < 25 mm/rpm.

The underlying reason behind this phenomenon is highlighted in Figure 8. Balanced data, referring to PR values below 25 mm/rpm, tends to exhibit a simpler structure compared to imbalanced data with PR values below 125 mm/rpm. When dealing

with balanced data, the model may not need to learn as highly complex patterns in the data. This simplicity makes it more vulnerable to forgetting when new data is introduced, as indicated by the significant structure change in upper right part of Figure 8. Conversely, imbalanced data is often more intricate, which in turn compels the model to learn a more intricate and robust representation of the data. This greater complexity in imbalanced data can contribute to a model that is less prone to catastrophic forgetting, as indicated by smaller structure change in lower right part of Figure 8.

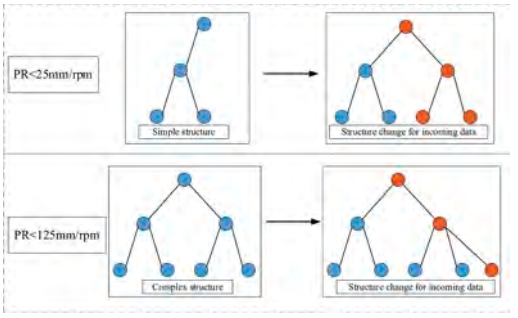

Figure 8. Catastrophic forgetting example of XGBoost model.

4.2 *Model generalization*

Figure 9 presents the model's generalization performance for PR < 125 mm/rpm with incremental data sizes of 60, 100, 150, and 200.

In Figure 9a, these plots reveal a noticeable trend: as new data is introduced, the model's generalization ability tends to deteriorate. This decline is evident through the decrease in R^2 and the increase in RMSE values. It's worth highlighting an interesting observation: there is a decrease in RMSE when the model begins incorporating 200 new data points, and this trend continues until 400 data points. This phenomenon can be attributed to the fact that the skewed data, which significant deviate from main distribution, start to become part of the model development process. Figure 10 illustrates how skewed data are incorporated and how R^2 and RMSE vary during this process. Additionally, upon closer examination of the Line S data distribution, it becomes apparent that the second quarter of the data includes 10 skewed data points, as presented in Figure 11.

When we closely examine the model performance for incremental data sizes of 5, 10, and 30, several intriguing observations in Figure 9b and Figure 9c come to light. Firstly, it becomes evident that the model's generalization performance is inherently unstable as new data is introduced. Remarkably, even the inclusion of just 5 new data points can result in a significant drop of 0.15 in the R^2 value, indicating a notable impact on the model's predictive accuracy. Secondly, a noteworthy pattern emerges during the incorporation of new data, particularly

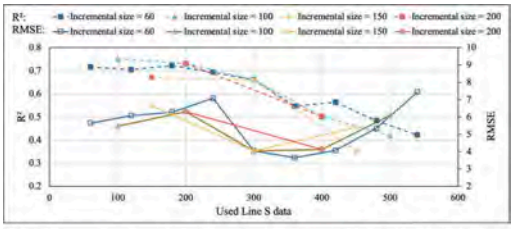

a. Model generalization performance on incremental sizes 60, 100, 150, 200

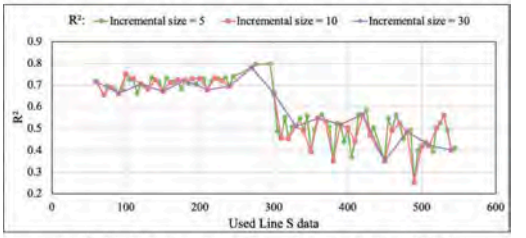

b. R^2 of model generalization on incremental size 5, 10, 30

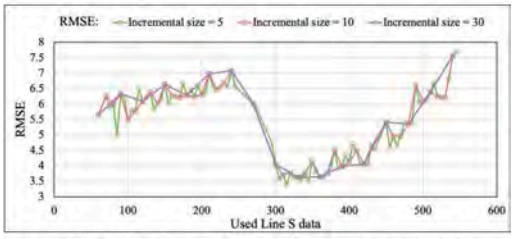

c. RMSE of model generalization on incremental size 5, 10, 30

Figure 9. Incremental generalization performance of XGBoost model on PR < 125 mm/rpm.

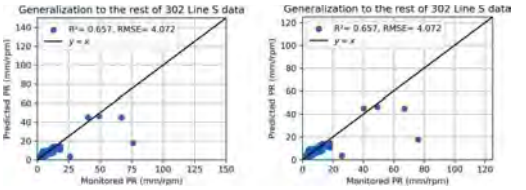

Figure 10. Model generalization showing skewed data involved.

when the number of data points falls within the range of 240 to 300, instead of 400 which is concluded before from rough incremental size. During this phase, the model's generalization performance undergoes dramatic changes. Initially, R^2 values decrease, suggesting a decline in predictive power. However, RMSE exhibits a different behavior—it decreases initially due to the inclusion of skewed data but then increases in subsequent iterations. This fluctuation in RMSE is a result of the incorporation of data that initially deviates significantly from the existing dataset and subsequently affects the model's overall predictive accuracy.

Figure 12 presents the model's generalization performance for PR < 25 mm/rpm with incremental data sizes of 60, 100, 150, and 200. R^2 in most cases

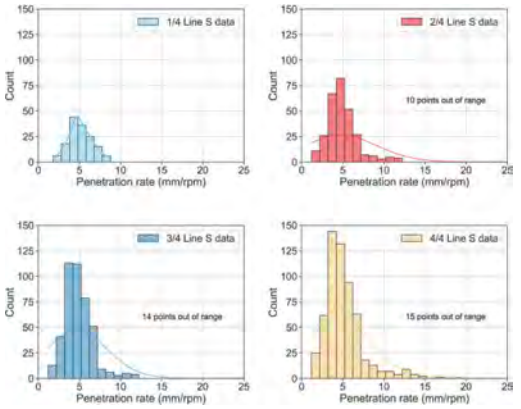

Figure 11. Incremental PR distribution of Line S data.

are larger than 0.5 and RMSE, compared to previous case, decreases significantly whose values mostly are between 1.5 to 2. The RMSE is much smaller than the one of the models built on PR < 125 mm/rpm, showing the robust performance of incremental learning on balanced data.

In Figure 12a, a noticeable trend emerges as new data is incorporated: the model's generalization ability shows slight improvement, as evidenced by the increase in R^2 from around 0.4 to approximately 0.8, while the RMSE remains relatively stable. An interesting observation worth noting is that beyond the inclusion of 500 Line S data points, the model's performance experiences a significant decline. This phenomenon could be attributed to the limited number of testing data points available for generalization. With only 47 data points remaining for generalization testing when 540 data points are incorporated, even a small deviation in one data point can exert a notable influence on the model's generalization performance, potentially leading to the observed degradation in performance.

Upon closer examination of the model performance with incremental data sizes of 5, 10, and 30, a general trend emerges: these plots consistently show improved generalization performance as new data is incorporated. However, it's important to highlight a remarkable observation when the model incorporates more than 500 Line S data points. During this phase, there are significant fluctuations in generalization performance, as indicated by the substantial variations in both R^2 and RMSE values. R^2 can reach values of approximately 0.88, with RMSE at 1.8, but it can also drop to as low as 0.13, with RMSE increasing to 3.5. These fluctuations can likely be attributed to the random nature of the limited number of remaining data points available for generalization testing. A poor prediction could result in much worse generalization performance than before.

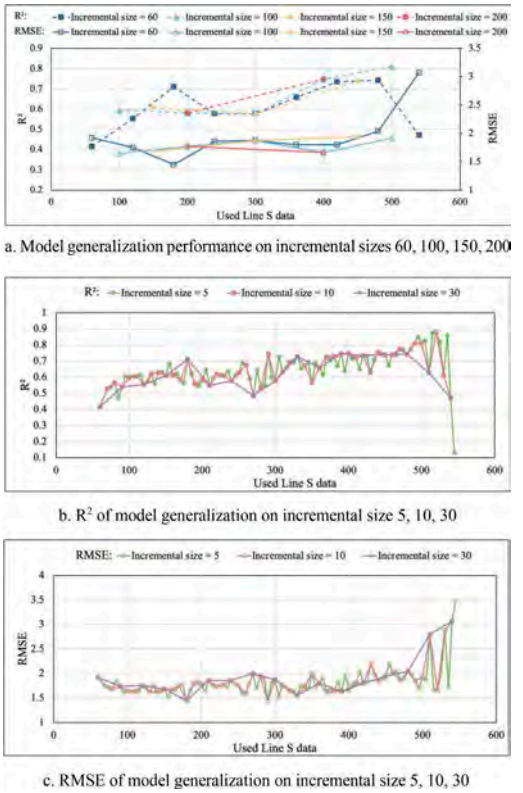

a. Model generalization performance on incremental sizes 60, 100, 150, 200

b. R^2 of model generalization on incremental size 5, 10, 30

c. RMSE of model generalization on incremental size 5, 10, 30

Figure 12. Incremental generalization performance of XGBoost model on PR < 25 mm/rpm.

5 CONCLUSIONS

This paper examines the generalization capability of the XGBoost model and explores the feasibility of enhancing it through the application of incremental learning. The research delves into the variance of model's generalization ability on various incremental data sizes. Recognizing that skewed data may hold valuable insights, the study considers two scenarios: one that includes skewed data where PR values are below 125 mm/rpm and another where skewed data is excluded and PR values are restricted to below 25 mm/rpm. Our conclusions are as follows:

1. In both scenarios, the XGBoost model generally demonstrates strong performance for both training and testing datasets. However, the model's performance can experience degradation as a result of incorporating skewed data and encountering the phenomenon of catastrophic forgetting.
2. Incremental learning has the potential to improve model generalization, as indicated by the increasing R^2 and decreasing RMSE. However, skewed data can significantly impact the model's generalization performance.

3. Incremental learning shows more promising results when applied after the removal of skewed data. However, further research is needed to explore the value of the information contained in skewed data and develop strategies that mitigate the impact of skewed data on model performance and generalization.

ACKNOWLEDGMENTS

This research was conducted with the support of the "Interactive decision support system for planning and construction of large-scale tunneling projects" funded by UTC region 2 Center CAIT under USDOT.

REFERENCES

Armaghani, D.J., Koopialipoor, M., Marto, A., Yagiz, S., 2019. Application of several optimization techniques for estimating TBM advance rate in granitic rocks. Journal of Rock Mechanics and Geotechnical Engineering 11, 779–789. https://doi.org/10.1016/j.jrmge.2019.01.002

Centis, S., Giacomin, G., 2004. EPB tunnelling in highly variable ground – the experience of Oporto Light Metro. Tunnelling and Underground Space Technology 19, 358. https://doi.org/10.1016/j.tust.2004.01.058

French, R.M., 1999. Catastrophic forgetting in connectionist networks. Trends in Cognitive Sciences 3, 128–135. https://doi.org/10.1016/S1364-6613(99)01294-2

He, K., Zhang, X., Ren, S., Sun, J., 2016. Deep Residual Learning for Image Recognition, in: 2016 IEEE Conference on Computer Vision and Pattern Recognition (CVPR). Presented at the 2016 IEEE Conference on Computer Vision and Pattern Recognition (CVPR), IEEE, Las Vegas, NV, USA, pp. 770–778. https://doi.org/10.1109/CVPR.2016.90

Huang, S., Dastpak, P., Esmaeilpour, M., Kaijian, L., Sousa, R., 2023a. Comparison between machine learning algorithms for TBM advance rate prediction, in: Expanding Underground - Knowledge and Passion to Make a Positive Impact on the World. CRC Press.

Huang, S., Esmaeilpour, M., Dastpak, P., Sousa, R., 2023b. EPBM Advance Rate Prediction Using Hybrid Feature Selection and Support Vector Regression Modeling. Presented at the TMIC 2022 Slope Stability Conference (TMIC 2022), Atlantis Press, pp. 253–264. https://doi.org/10.2991/978-94-6463-104-3_22

Koopialipoor, M., Nikouei, S.S., Marto, A., Fahimifar, A., Jahed Armaghani, D., Mohamad, E.T., 2019. Predicting tunnel boring machine performance through a new model based on the group method of data handling. Bull Eng Geol Environ 78, 3799–3813. https://doi.org/10.1007/s10064-018-1349-8

Mokhtari, S., Mooney, M.A., 2020. Predicting EPBM advance rate performance using support vector regression modeling. Tunnelling and Underground Space Technology 104, 103520. https://doi.org/10.1016/j.tust.2020.103520

Pan, Y., Fu, X., Zhang, L., 2022. Data-driven multi-output prediction for TBM performance during tunnel excavation: An attention-based graph convolutional network approach. Automation in Construction 141, 104386. https://doi.org/10.1016/j.autcon.2022.104386

Sheil, B.B., Suryasentana, S.K., Mooney, M.A., Zhu, H., 2020. Machine learning to inform tunnelling operations: recent advances and future trends. Proceedings of the Institution of Civil Engineers - Smart Infrastructure and Construction 173, 74–95. https://doi.org/10.1680/jsmic.20.00011

Shreyas, S.K., Dey, A., 2019. Application of soft computing techniques in tunnelling and underground excavations: state of the art and future prospects. Innov. Infrastruct. Solut. 4, 46. https://doi.org/10.1007/s41062-019-0234-z

Sousa, R.L., Einstein, H.H., 2012. Risk analysis during tunnel construction using Bayesian Networks: Porto Metro case study. Tunnelling Underground Space Technol. 27, 86–100. https://doi.org/10.1016/j.tust.2011.07.003

van de Ven, G.M., Tuytelaars, T., Tolias, A.S., 2022. Three types of incremental learning. Nat Mach Intell 4, 1185–1197. https://doi.org/10.1038/s42256-022-00568-3

Yu, H., Zhou, X., Zhang, X., Mooney, M., 2022. Enhancing earth pressure balance tunnel boring machine performance with support vector regression and particle swarm optimization. Automation in Construction 142, 104457. https://doi.org/10.1016/j.autcon.2022.104457

Zhou, J., Qiu, Y., Armaghani, D.J., Zhang, W., Li, C., Zhu, S., Tarinejad, R., 2021. Predicting TBM penetration rate in hard rock condition: A comparative study among six XGB-based metaheuristic techniques. Geoscience Frontiers 12, 101091. https://doi.org/10.1016/j.gsf.2020.09.020

Tunnelling for a Better Life – Yan, Celestino, Thewes & Eberhardt (Eds)
© 2024 The Author(s), ISBN 978-1-032-80042-4
Open Access: www.taylorfrancis.com, CC BY-NC-ND 4.0 license

Study on soil discharge efficiency of earth pressure balance shield tunneling in deep buried depth sandy strtum

Siyuan Huang & Xiaochun Zhong
College of Civil and Transportation Engineering, Hohai University, Nanjing, China
China Railway Construction South China Construction Co., Ltd., Guangzhou, China

Zhi Zhou
China Railway Construction South China Construction Co., Ltd., Guangzhou, China

Tugeng Feng
College of Civil and Transportation Engineering, Hohai University, Nanjing, China

ABSTRACT: Controlling the rate of soil discharge is a key technology for earth pressure balance shield tunneling to maintain dynamic stability of the excavation surface. In order to ensure the safe excavation of earth pressure balance shield tunneling in rich water sandy stratum with large burial depth, the soil is classified into fluid state, hard plastic state, and transitional state between the two based on slump tests. Based on the Π theorem, Darnell-Mol theory, and the discrete element numerical model of soil discharge, empirical formulas for soil discharge in three states are established. Finally, the three empirical formulas is coupled to obtain the empirical formula for soil discharge in the full state of the soil by using slump as an index, And verified through the monitoring data in practice. The results show that the theory of soil discharge in full state is reliable; The soil discharge rate increases with the increase of slump, pressure in pressure chamber, and speed of screw conveyor. For the construction of EPB shield tunneling with a buried depth of 30m, the reasonable range of slump for conditioned soil should be 102-192mm. This research can provide a theoretical basis for the application of earth pressure balance shield tunneling in deep buried stratum.

Keywords: earth pressure balance shield, slumps, soil discharge, soil condition, discrete element theory

1 INTRODUCTION

EPB shield tunneling is widely used in urban subway construction. In recent years, the overall construction trend of EPB shield tunneling has developed towards complex stratum such as deep burial depth and high water pressure stratum (Ma and Najafi, 2008; Qiao and Peng, 2016; Qiao et al., 2017; Zhao et al., 2016). The advantage of EPB shield tunneling is weak perturbation. In engineering, according comparison between the setting pressure of the pressure chamber and the monitoring pressure, the soil discharge can be controled by adjusting the speed of the screw conveyor to achieve dynamic stability of the excavation surface support pressure, ensuring weak perturbation to the surrounding environment (Zhong, 2022). However, When the shield machine excavates in the deep buried depth, high water pressure, and cohesionless stratum, such as sand stratum and sand pebble stratum, it is difficult to control the soil discharge based on existing experience, and the support pressure of excavation surface fluctuates greatly, which may cause the excavation surface to collapse. Therefore, it is urgent to establish the soil discharge theory, which can consider the engineering scale and guide shield tunneling (Borio and Peil, 2010; Liu et al., 2018).

During the shield tunneling, the soil is cut down by the cutter and enters the pressure chamber. Soil is transported to the screw conveyor by the blades, and finally transported to the conveyor belt. In the pressure chamber and screw conveyor, the soil is transported under pressure, and considering the properties of the conditioned soil, the soil discharge process is relatively complex. Therefore, it is difficult to establish a complete and scientific soil discharge theory. Maild (1995) proposed a diagram of the transport process and pressure distribution of soil in pressure chamber and screw conveyor, and analyzed the relationship between soil discharge and pressure difference, screw conveyor inclination angle, soil fluidity, and other factors; Merrit

*Corresponding author: 1013984090qq.com

DOI: 10.1201/9781003495505-248

and Mair (2006, 2008) assumed the soil as a solid and explored the effects of spiral blades and shaft size on the pressure gradient inside a screw conveyor. Based on above study, a soil discharge theory was proposed; Pena et al. (2007) established a 1:11 soil discharge model test, and studied the soil discharge law with different content of foam, bentonite slurry and other modifiers; Huang (2009) simplified the soil discharge, and established an soil discharge model using Fluent, and analyzed the influence of cutterhead opening rate on soil discharge and soil pressure distribution; Zhu et al. (2020) analyzed the velocity, motion trajectory, and mass flow rate of particles in sandy gravel stratum using the discrete element method, and obtained the flow characteristics of particles in the pressure chamber.

In summary, most soil discharge theories have a relatively small scope of application, which only assumed the soil as fluid or solid, these theories lack understanding of the conditioned soil state. Most of the soil is a semi liquid and semi solid body, and the description of the soil discharge in existing theories is far from sufficient. Therefore, it is significant to establish a comprehensive theory of soil discharge in all soil states considering deep burial depth engineering. Therefore, this paper conducts the following research work to address the above issues: 1) Based on self-designed soil discharge model test, we explored the influences of screw conveyor speed, pressure in pressure chamber, and conditioned soil state on soil discharge rate; 2) According to the slump test, the soil is divided into fluid state, hard plastic state, and transitional state between the two. empirical formulas were established for soil in three conditioned states, and verified with model tests; 3) Taking the slump of soil as an index, the empirical formulas of soil in three states were coupled, and the full state soil discharge considering engineering scale was proposed; 4) Based on the shield tunneling construction between Hengli Station and Panyu Square Station on Guangzhou Line 18, and combined with the empirical formula of full state soil discharge, a reasonable slump range in deep buried engineering is proposed to guide the soil condition plan and construction in practice.

2 MODEL TEST OF SOIL DISCHARGE

The soil discharge is the key factor affecting the excavation of shield tunnel. Therefore, in order to study the influence of screw conveyor speed, pressure, and soil state on the soil discharge, the model test of soil discharge was established, as shown in Figure 1.

The main part of the model test is the construction simulation system, which mainly consists of two parts: pressure chamber and screw conveyor. The inner diameter of the screw conveyor sleeve is 50mm, the length is 785mm, the screw diameter is 14m, and the screw pitch is 35mm.The soil in the test is mainly fine sand, with a density of 1.585 g/cm^3.

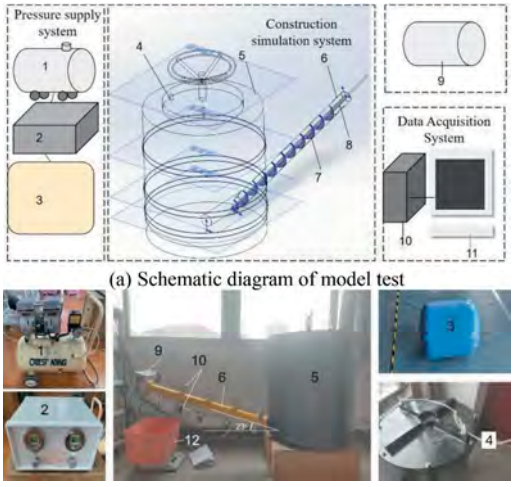

(a) Schematic diagram of model test

Figure 1. Model test of soil discharge. (a) Schematic diagram of model test (b) Model testing device. 1-Air compressor, 2-Pressure regulator, 3-Pressure airbag, 4- Pressure inlet, 5- Pressure chamber, 6- Sleeve, 7- Spiral blade, 8- Spiral rod shaft, 9- Rotating motor, 10- Data acquisition instrument (mainly including 4 soil pressure sensors and 4 water pressure sensors), 11- Computer, 12- Soil collection box.

The particle size distribution is shown in Figure 2. To investigate the influence of screw conveyor speed, pressure in pressure chamber, and conditioned soil state on the soil discharge rate, the following experimental conditions were designed: screw conveyor speed (2rpm, 4rpm, 6rpm, 8rpm), pressure in pressure chamber(20kPa, 40kPa, 60kPa), and soil state (dry sand, conditioned soil). The conditioned soil is modified by adding 15% foam by volume, 12% bentonite slurry by mass and 10% water by mass. Bentonite slurry is prepared in a ratio of 1:5 to water, which is fermented for 8 hours after stirred thoroughly. The concentration of the foaming agent mixture is 3%, and the foaming rate is 20 times. The slump of conditioned soil was measured to be 125mm, as shown in Figure 3. According to the above experimental conditions, the soil discharge rate is shown in Figure 4.

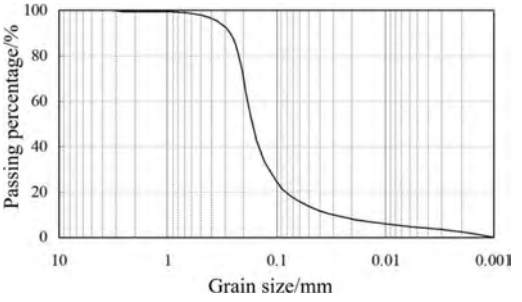

Figure 2. Particle size distribution of sand in the test.

From Figure 4, it can be seen that as speed and pressure in pressure chamber increase, the soil

Figure 3. Conditioned soil with a slump of 125mm.

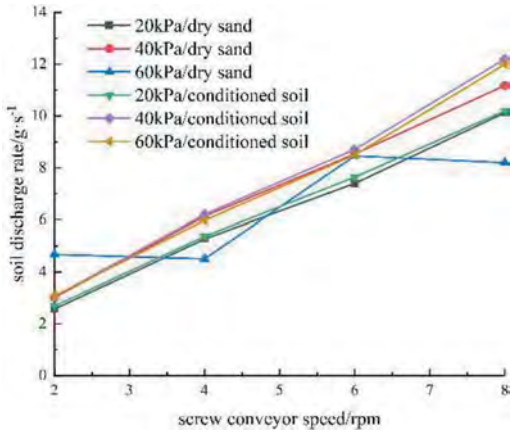

Figure 4. Result of soil discharge.

discharge basically shows a linear increasing trend. However, for dry sand in high pressure condition (60kPa), the soil discharge rate is out of control, which basically does not meet the above rules. This is because sandy soil has poor workability and a large internal friction angle. Under high pressure, a tight soil plug is formed inside the screw conveyor, which greatly affect the soil discharge. The friction between the soil plug and the inner wall of the screw conveyor is extremely high. Before it reaches the outlet, it hinders the efficiency of soil discharge. However, once the soil plug moves to the outlet, the stress is instantly released, which causes a large amount of soil to spray, ultimately leads to a sudden increase in soil discharge rate. Therefore, the 60kPa/dry sand condition has no obvious pattern with the increase of screw conveyor speed. Under the same pressure and screw conveyor speed conditions, the soil discharge rate of the conditioned soil is basically higher than that of dry sand. This is because foam is added as conditioner, and foam is filled into the pores between sand particles, playing a "ball bearing" which can reduce friction between soil particles, and greatly improving the fluidity of soil.

3 STUDY ON SOIL DISCHARGE OF EPB SHIELD TUNNELING

According to the slump test, the fluidity of soil with different slumps is different, so the corresponding soil discharge rate will not be consistent. For example, when slump of fully fluidized soil is 300mm, compared to dry hard soil with a slump of 0mm, its soil discharge rate must be much higher than that of dry hard soil. Therefore, this paper divides the soil into hard plastic state (slump 0mm), fluid state (slump 300mm), and transitional state between the two states (slump 0-300mm).

3.1 *Empirical formula for soil discharge in fluid state*

In order to derive the empirical formula of soil discharge when soil state is fluid, this section uses the Π theorem and CFD to establish a numerical test for soil discharge, and fits the empirical formula for soil discharge when soil state is fluid. The specific details are as follows: the flow of fluidized soil inside the screw conveyor is essentially pipeline flow phenomenon. The inclination angle, pitch, and other physical structures of the screw conveyor all effect the soil discharge. However, in essence, these structural physical parameters effect the soil discharge by changing the pressure gradient dp/dx inside the screw conveyor, so the pressure gradient dp/dx is the first parameter involved in the soil discharge phenomenon. Similarly, the other involved parameter are: the diameter of the screw conveyor (D), the average velocity of the soil discharge (U), and the density of the soil (ρ), The viscosity of soil (μ) (To simplify calculations, Newtonian fluid is used to simulate the fluidized soil), and the speed of screw conveyor (ω). There are six parameters involved in the soil discharge. The dimensional matrix of the above parameters in the CGS unit system is as follows:

$$\begin{array}{c|c} & \begin{matrix} \mathrm{D} & \rho & \mathrm{U} & \mu & \mathrm{dp/dx} & \omega \end{matrix} \\ \begin{matrix} L \\ M \\ T \end{matrix} & \begin{bmatrix} 1 & -3 & 1 & -1 & -2 & 0 \\ 0 & 1 & 0 & 1 & 1 & 0 \\ 0 & 0 & -1 & -1 & -2 & -1 \end{bmatrix} \end{array}$$

In the above matrix, L, M and T are the basic variables of the CGS unit system, including length, mass, and time. The values in the matrix represent the dimensional indices of each involved variable. I. e, $\dim(\rho)=L^{-3}\cdot M$, dim is a dimensional representation. The above dimensional matrix are converted into a row simplest form matrix, as shown below. From this, it can be seen that the diameter D, the average flow velocity U, and the density ρ are dimensionally independent. Pressure gradient dp/dx, fluid viscosity μ, speed of screw conveyor ω can be represented by these three dimensionally independent quantities, as shown in equation (1). Therefore,

based on the Π theorem, three independent similarity criteria can be established, as shown in equation (2).

$$\begin{array}{c} \quad \mathrm{D} \quad \rho \quad \mathrm{U} \quad \mu \quad \mathrm{dp/dx} \quad \omega \\ \left|\begin{array}{c} L \\ M \\ T \end{array}\right| \left[\begin{array}{cccccc} 1 & 0 & 0 & 1 & -1 & -1 \\ 0 & 1 & 0 & 1 & 1 & 0 \\ 0 & 0 & 1 & 1 & 2 & 1 \end{array}\right] \end{array}$$

$$\begin{aligned} &\dim\mu = (\dim \mathrm{D})(\dim\rho)(\dim U) \\ &\dim\frac{dp}{\mathrm{dx}} = (\dim D)^{-1}(\dim\rho)(\dim U)^2 \\ &\dim\omega = (\dim D)^{-1}(\dim U) \end{aligned} \tag{1}$$

$$\Pi_1 := \frac{\rho U D}{\mu} \quad \Pi_2 : \frac{dp}{dx}\frac{D}{\rho U^2} \quad \Pi_3 := \frac{\omega D}{U} \tag{2}$$

where Π_1, Π_2, and Π_3 are the three independent similarity criteria for soil discharge. Π_1, Π_2, and Π_3 satisfy the Π theorem, then the three similarity criteria satisfy the relationship as shown in equation (3).

$$\Pi_2 = f(\Pi_1, \Pi_3) \Rightarrow \frac{dp}{dx}\frac{D}{\rho U^2} = f(\frac{\rho U D}{\mu}, \frac{\omega D}{U}) \tag{3}$$

From equation (3), it can be seen that as long as the form of the function f is determined, the relationships of Π_1, Π_2, and Π_3 can be obtained, and an empirical formula of the average flow velocity U can be derived. Now, baseed on fluent, a numerical model of soil discharge are established: 1) Model establishment. The screw conveyor model is shown in Figure 5. The length of the screw conveyor is 450mm, the diameter of the screw conveyor is 104mm, the diameter of the central shaft is 68mm, and the screw pitch is 90mm. The model is divided into 68768 grids by using unstructured grids. The inlet and outlet boundary conditions are set as constant pressure boundary conditions, while the rest, such as sleeves, blades, and screw conveyor shaft, are set as non inflow and non slip wall boundaries. 2) Parameter settings. In the model, Newtonian fluid is used to simulate the fluid state of the soil. The entire calculation is set to steady calculation.

In numerical calculations, it was found that the speed of the screw conveyor has little influence on the velocity. Therefore, it can be considered that the ω is not involved parameter of soil discharge. Therefore, equation (3) is modified to obtain a new Π theorem relationship equation:

$$\Pi_2 = \varphi(\Pi_1) \Rightarrow \frac{dp}{dx}\frac{D}{\rho U^2} = \varphi(\frac{\rho U D}{\mu}) \tag{4}$$

Equation (4) is a unary function related to Π_2, with an independent variable of Π_1. Therefore, as long as the $\varphi(\Pi_1)$ curve is obtained, Π_2 values of similar phenomena can be obtained, and the fitted function relationship can be used to obtain an empirical formula.

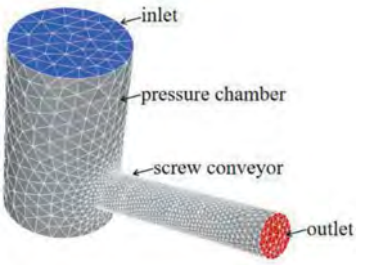

Figure 5. Numerical model of soil discharge.

Figure 6. Numerical models of slag discharge at different scales.

In order to study the same soil discharge phenomenon (i.e. similar phenomenon) at different scales, Figure 4 is taken as Condition 1, and it is magnified 10 times as Condition 2. The screw conveyor is lengthened to twice as Condition 3, as shown in Figure 6. The φ relationship of the different conditions under similar conditions is explored, that is, each working condition controls the Π_1 value to be equal, Ensuring that all working conditions are similar, and Π_2 is calculated at this time. The results are shown in Figure 7.

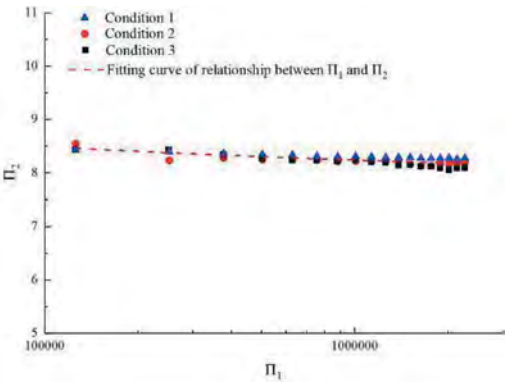

Figure 7. Numerical experimental relationship of Π_1 and Π_2.

From Figure 7, it can be seen that the dimensionless values Π_2 of the three working conditions are basically equal, and decrease with the increase of Π_1. So, according to Figure 8, the empirical formula

for soil discharge can be summarized when the soil state are fluid state. Firstly, the functional relationships φ of Π_1 and Π_2 are fitted. In order to facilitate subsequent solutions, the empirical formula adopts a linear fitting, as shown in equation (5). Further substituting equation (5) into equation (4), a cubic equation about the average flow velocity U of soil are obtained. For the concise of formula expression, the U^2 term is placed on the right side of the equation and represented by Π_1. Finally, the empirical formula for flow rate Q is obtained based on the average flow velocity U, as shown in equation (6).

$$\pi_2 = \varphi(\pi_1) \Rightarrow \pi_2 = -1.026e^{-7}\pi_1 + 8.36 \quad (5)$$

$$\begin{aligned} U &= \frac{dp}{dx}\frac{D}{\rho U\phi(\pi_1)} \\ &\Downarrow \\ Q &= \frac{\pi(D_f^2 - D_s^2)D_f}{4\rho U\phi(\pi_1)}\frac{dp}{dx} \\ &= \frac{\pi(D_f{}^2 - D_s{}^2)D_f^2}{4\mu\frac{\rho U D_f}{\mu}\varphi(\pi_1)}\frac{dp}{dx} = \frac{\pi(D_f{}^2 - D_s{}^2)D_f^2}{4\mu\pi_1\varphi(\pi_1)}\frac{dp}{dx} \end{aligned} \quad (6)$$

Where D_f is diameter of the screw conveyor, and D_s is the diameter of the screw conveyor shaft.

3.2 *Formula for soil discharge in hard plastic state*

When the soil is not conditioned or the condition effect is poor, the soil basically presents a hard plastic state. At this time, the slump of soil would be very small, the soil would hardly collapse. At this point, the soil can be regarded as a hard plastic solid in the screw conveyor. So, based on Darnell Mol solid transportation theory, the formula for soil discharge can be obtained as follows:

$$Q = \frac{(D_f^2 - D_s^2)}{4}\frac{\pi^2 D_f N\tan\varphi_f\tan\theta}{\tan\theta + \tan\varphi} \quad (7)$$

$$\theta = \arcsin\left(\frac{\sqrt{1 + K^2 - M^2 - KM}}{1 + K^2}\right) \quad (8)$$

$$\begin{aligned} M &= 2\frac{H\mu_1\sin\varphi_f}{l\mu_2}(K + \frac{\overline{D}}{D_f}\cot\varphi_f) \\ &+ \frac{\mu_2\sin\theta}{\mu_2}(K + \frac{D_s}{D_f}\cot\varphi_f) \\ &+ \frac{H\sin\theta}{z_b\mu_2}(K + \frac{\overline{D}}{D_f}\cot\varphi)In\frac{P}{P_0} \end{aligned} \quad (9)$$

$$K = \frac{\overline{D}}{(\mu_1\sin\phi_f - \cos\phi_f)D_f} \quad (10)$$

Where Q is the soil discharge per unit time; D_f is the diameter of the screw conveyor; D_s is the diameter of the screw conveyor shaft; N is the speed of the screw conveyor; $\overline{D}$ is the sum of the D_f and the D_s; φ_f is the blade inclination angle of the screw conveyor; θ is the angle between the velocity of the soil and the x-axis is referred to as the conveying angle in this article; μ_1 is the friction coefficient between the screw and the soil; μ_2 is the friction coefficient between the inner wall of the screw conveyor and the soil; l is the height of the soil section inside the screw conveyor; P_0 is the pressure of the pressure chamber; P is the pressure at any position inside the screw conveyor.

3.3 *Study for soil discharge in transitional state*

Based on the above study, the soil discharge laws under the fluid state and hard plastic state of soil has been obtained. However, the soil generally is the transitional state between the two, so it is difficult to calculate the soil discharge through one of these theories. Therefore, based on the discrete element software EDEM, the soil discharge law of the soil in the transitional state were explored.

As the main conditioner affecting the fluidity of soil, foam content for a large proportion in the soil and has a significant influence on the soil discharge. foam, as an unstable system composed of bubbles, would produce defoaming phenomena such as drainage, consolidation, coarsening, etc. in the process of screw conveyor transportation of slag, which would further affect the fluidity of soil, so the soil discharge process of soil in transition state is very complex. In the whole soil discharge process, stability of foam will increase due to the existence of solid particles and the increase of internal pressure, so it can be considered that the foam of soil under pressure is more stable than the foam of soil in air. Therefore, according to the characteristics of foam in soil, a simplified foam-soil contact model and calculation scheme are proposed to simulate the soil discharge, which could consider defoaming phenomenon. The assumptions are made: (1) foam are regarded as particles, foam particles are incompressible in the whole soil discharge process; (2) Foam defoaming occurs instantaneously, without considering the process of drainage, consolidation and coarsening; (3) Material intrinsic parameters and conventional contact parameters of the foam particles are consistent with the soil particles, and the defoaming amount is only considered in post processing; (4) The foam defoaming in the pressure chamber is not considered. The radius of soil particles is 4mm, and that of foam particles is 2mm. The contact between all particles and the wall is Hertz-Mindlin contact model.

The soil is conditioned with bentonite slurry and foam. Therefore, the specific contact model is as follows: (1) Soil-soil contact model. Considering the bonding effect of bentonite slurry between soil and soil, the JKR contact model is adopted. (2) Foam-foam contact model. The Hertz-Mindlin contact model is adopted for foam and foam because of the smoothness of the contact liquid film. (3) Foam-soil

contact model. It can be seen from the defoaming process of foam during soil discharge that, with change of time and position migration, foam will defoaming due to liquid discharge and the increase of pressure difference between inside and outside the liquid film. At this time, there is a gap at the position originally filled by foam, and the surrounding soil particles will be immediately filled under the pressure. At this time, the lubricated effect of foam is weakened, and the internal friction of soil particles becomes larger due to contact, and the cohesiveness between particles is enhanced. In order to simulate this process, before foam particle defoaming, the JKR contact model is used for the contact between soil particles and foam particles. When the normal force is less than a predefined value, as shown in equation (11), foam are considered to be broken. At this time, in post-processing, foam particles are regarded as soil particles with the same volume, the foam particles that does not defoaming is considered as a particle with a mass of 0. At this point, the normal force is calculated according to equation (12). The intrinsic parameters of the material are defined (Zhu, H.H, 2020), and the contact parameters are calibrated by establishing a virtual slump test, as shown in Figure 8. Due to limited space, the virtual slump will not be introduced. The intrinsic parameters and contact parameters of the material are ultimately shown in Tables 1 and 2.

Figure 8. Virtual slump test.

$$F_n < F_{npre} \tag{11}$$

Where F_n is the normal force of foam and soil particles, F_{npre} is the threshold of normal force when defoaming.

$$\begin{aligned} F_n^* &= -4\sqrt{\pi\gamma E^* \alpha^{\frac{3}{2}}} + \frac{4E^*}{3R^*}\alpha^3 - KA \\ \delta &= \frac{\alpha^2}{R^*} - \sqrt{\frac{4\pi\gamma\alpha}{E^*}} \\ A &= \pi R^{*2} \end{aligned} \tag{12}$$

Where F_n^* is the normal force between foam particles and soil particles after foam defoaming, γ is the particle surface energy, A is the area of the contact surface between foam particles and soil particles, R^* is the radius of the contact surface between foam particles and soil particles, K is the adhesion energy density, and E^* and R^* are both Hertz Mindlin basic parameters, which are calculated from the modulus and radius of the contact particles.The damping force and tangential force are consistent with the JKR contact model. Considering that the tangential rolling friction increases after the foam particles defoaming, the torque of the contact surface is used for explanation, as shown in equation (13).

$$T = -k\mu_r F_n R\omega \tag{13}$$

Where k is the friction amplification coefficient, set to 1.5 in this working condition, μ_r is the rolling friction coefficient, R is the distance from the particle center of mass to the contact point, and ω is the unit angular velocity vector of the particles at the contact point.

Table 1. Material intrinsic parameters.

Material	Soil particles	Foam particles
Poisson's ratio	0.25	
density/kg·m^{-3}	2500	
Young's modulus/Pa	2.5×10^8	
Radius/mm	8	4

Table 2. Material contact parameters.

contact type	Soil-soil (JKR contact)	Foam-foam (Hertz-Mindlin contac)	Soil-foam (custom contact)
Coefficient of restitution	0.01		
Coefficient of static friction:	0.1		
Coefficient of rolling friction:	0.1		
Surface energy/J/m^2	0.36	—	0.36
Foam burst threshold/N	—	—	5e-5

The established numerical model for soil discharge is shown in Figure 9, and the geometric dimensions of the screw conveyor are consistent with the model test in first section. A total of 140026 particles were generated.

From Figure 10, it can be seen that as the speed of the screw conveyor and the pressure of pressure chamber increase, the soil discharge rate shows an increasing trend, which is consistent with the law obtained from the experiment. In order to verify the rationality of the numerical model, the experimental results in the second section were compared with the numerical results, as shown in Figure 10.

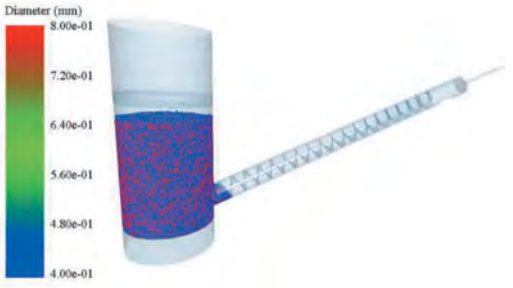

Figure 9. Numerical model of soil discharge.

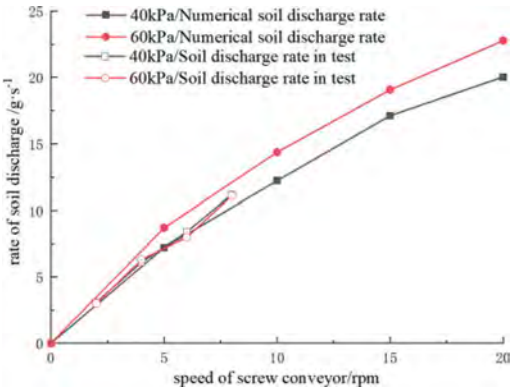

Figure 10. Comparison between numerical results and model test results.

It can be found that the numerical model has a good agreement under the working condition of 40kPa, and the numerical results under the working condition of 60kPa are greater than the experimental values. This is because during the test process, the soil consolidates under pressure, the effective stress increases, the internal friction of the soil increases, and the fluidity decreases. Therefore, compared to the slag discharge rate under the working condition of 40kPa, there is no obvious trend of increasing, and even a slight decrease. Therefore, it can be considered that the numerical model has certain rationality.

3.4 *Empirical formula for soil in full state*

The soil discharge largely depends on the fluidity of the soil. Slump is commonly used in engineering to evaluate the fluidity of soil. Therefore, slump can be used as an evaluation index to explore the relationship between the fluidity of soil and the soil discharge rate when it is in the transitional state. The contact parameters of soil with different slumps were calibrated according to the virtual slump test in Figure 8 (Due to the fact that the soil particles established in EDEM are spherical, There is friction between particles, so the complete collapse fo soil is impossible. Therefore, the maximum slump is taken as 225mm, and the slump is normalized), and then based on numerical model in section 3.3, The soil discharge under different slump conditions can be obtained.

Figures 12, 13, and 14 show the variation of soil discharge with different slump . It can be seen that the soil in the transitional state has a fluidity greater than that in the hard plastic state and less than that in the flowing state. Therefore, the soil discharge of soil in transitional state is basically between the the hard plastic state and the flowing state, and increases with the increase of slump, which is basically in line with the actuality.

From section 3.3, it can be seen that soil discharge of soil in transitional state is based on laboratory scale, which is difficult to meet the engineering scale. Therefore, in order to overcome this problem, this paper combines the soil discharge theories in sections 3.1, 3.2 and 3.3, then couples the three soil discharge theories to obtain the full state soil discharge. From Figures 11, 12, and 13, it can be seen that the soil discharge rate of the transition state slag is between the other two types of soil discharge rates, and increases with the increase of slump. Therefore, the formulas in sections 3.1 and 3.2 can be modified using the slump as a variable, and the correction equation is:

$$\begin{aligned} Q^*(h) = & f_1(h)\frac{\pi(D_f^2-D_s^2)D_f^2}{4\mu\pi\phi(\pi_1)}\frac{dp}{dx} \Rightarrow Q_1 \\ & + f_2(h)\frac{(D_f^2-D_s^2)\pi^2 D_f N}{4}\frac{\tan\phi_f\tan\theta}{\tan\phi_f+\tan\theta} \Rightarrow Q_2 \end{aligned} \tag{14}$$

Where $Q^*$is the soil discharge rate of soil in transitional state, Q_1 is the soil discharge rate of soil in

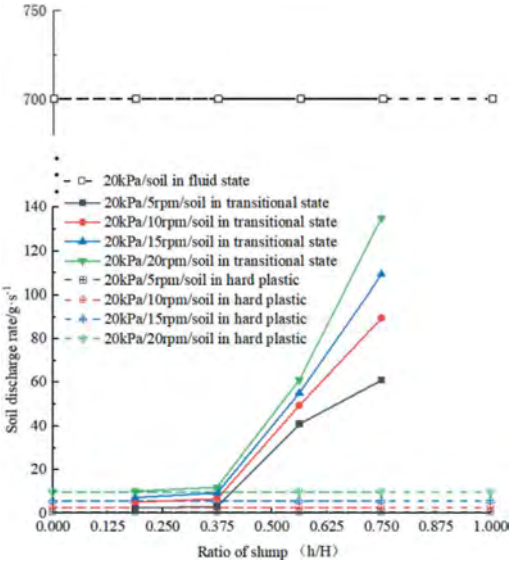

Figure 11. Full state soil discharge rate under 20kPa pressure.

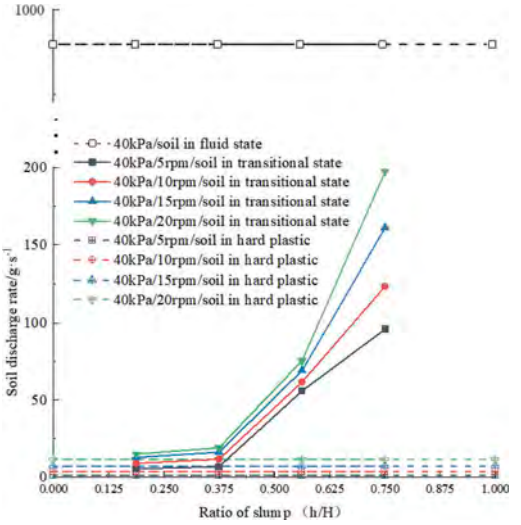

Figure 12. Full state soil discharge rate under 40kPa pressure.

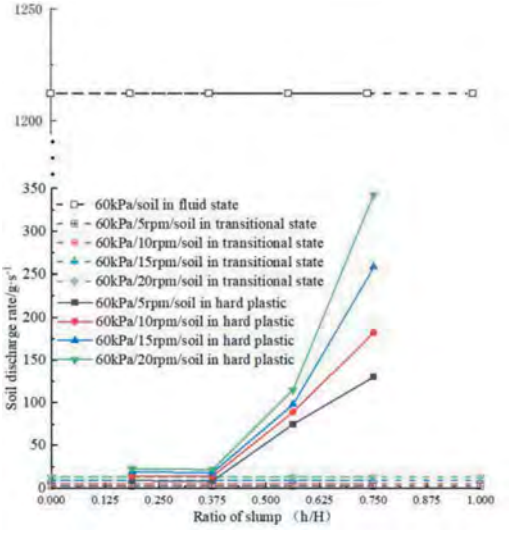

Figure 13. Full state soil discharge rate under 60kPa pressure (In Figures 11, 12, and 13, h represents the slump of the soil, and H represents the height of the slump cone).

fluid state, Q_2 is the soil discharge rate of soil in hard plastic state, $f_1(h)$ and $f_2(h)$ are respectively the correction functions of Q_1 and Q_2. h is the slump.

To determine the expression of $f_1(h)$ and $f_2(h)$, the slump ratio is used as the independent variable. So when h/H is 0 and 1, the state of the soil is in a hard plastic state and a fluid state, respectively, that is, when h=0, $f_1(h/H)$=0, $f_2(h/H)$=1. when h=H, $f_1(h/H)$ =1, $f_2(h/H)$=0. Substitute the data from Figures 11, 12, and 13 to fit f_1 and f_2 functions..

From Figure 14, it can be seen that as the slump ratio increases, $f_1(h/H)$ decreases, $f_2(h/H)$ increases,

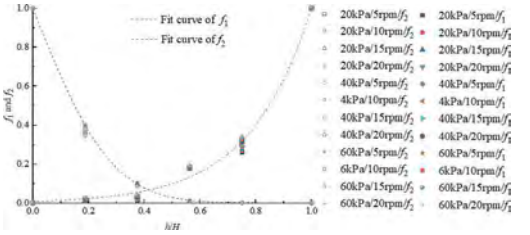

Figure 14. Correction function for soil discharge f_1 and f_2.

which represents the change in the properties of the soil from a hard plastic state to a fluid state. So the function form of fitting curve is as follows:

$$\begin{aligned} f_1 &= e^{-4.67214+54.81351\frac{h}{H}-0.14258(\frac{h}{H})^2} \\ f_2 &= e^{-3.563\frac{h}{H}-7.0223(\frac{h}{H})^2} \end{aligned} \tag{15}$$

The above equation is brought into equation (14) to obtain the empirical formula of soil discharge for the full state soil discharge considering engineering scale:

$$\begin{aligned} Q^*(\frac{h}{H}) &= (e^{-4.67214+4.81351\frac{h}{H}-014258(\frac{h}{H})^2})\frac{\pi(D_f^2-D_s^2)D_f^2}{4\mu\pi_1\phi(\pi_1)}\frac{dp}{dx} \\ &+ (e^{-3.563\frac{h}{H}-7.0223(\frac{h}{H})}\frac{(D_f^2-D_s^2)\,\pi^2 D_f N}{4}\frac{\tan\phi_f\tan\theta}{\tan\phi_f\tan\theta} \end{aligned} \tag{16}$$

4 APPLICATION

To verify the reliability of equation (16), The shield tunneling between Hengli Station and Panyu Square Station on Guangzhou Line 18 has been used as the engineering background. The main crossing stratum of the right line are: medium coarse sand, muddy soil, fine sand, slightly weathered conglomerate, and strongly weathered granite. Geological longitudinal sections are shown in Figure 15. The burial depth of the shield tunnel vault is about 33.2 m, and the monitoring pressure of the pressure chamber is about 300 kPa. The engineering used 8.8 meter earth pressure balance shield to excavate, and the diameter of the screw conveyor is 1.02m, the length of screw conveyor is 13.321m, and the diameter of screw shaft is 0.285m, the speed of screw conveyor are 0~20rpm. Based on the dimensions of the screw conveyor and the monitoring data, the theoretical soil discharge is calculated using equation (16) and compared with the monitoring data, as shown in Figure 16.

From Figure 16, it can be seen that the monitoring data is within the maximum soil discharge rate based on equation (16) and the minimum soil discharge rate based on equation (16), which indicates that the equation (16) is reliable and can be extended to engineering applications.

The control of soil discharge is one of the key guarantees for the operation of EPB shield tunneling.

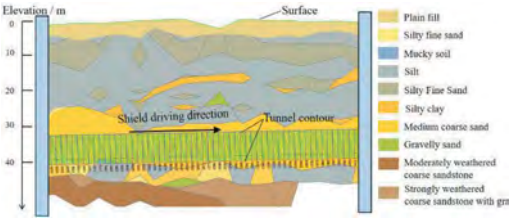

Figure 15. Geological section of shield tunnel crossing.

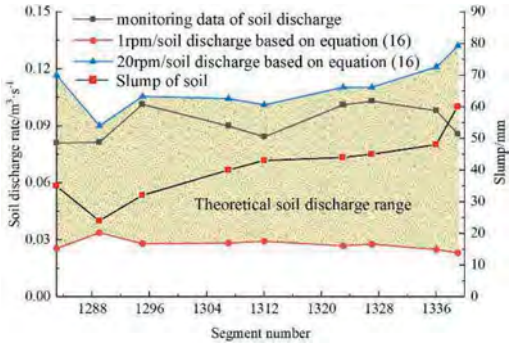

Figure 16. Comparison between soil discharge rate based on equation (16) and monitoring data.

In engineering, it is required that the theoretical soil discharge Q_s and the theoretical soil volume Q_0 determined by the excavation speed are basically equal. When $K = Q_s/Q_0$ is greater than 1, it indicates that the slump of soil is large, the properties of soil are soft and fluid, and the soil discharge is too large. Therefore, it is necessary to reduce the speed of screw conveyor. When K is less than 1, it indicates that the slump of the soil is small and its properties are dry and hard, and it is necessary to increase the speed of screw conveyor. It can be seen that for soil with different slumps, different speeds of screw conveyor are required to meet the excavation requirements. However, due to the different conditioning status of the soil, the actual soil discharge would differ from Q_s. This is because there is relative movement between the soil and the inner wall of the screw conveyor, which involves the soil discharge efficiency of the screw conveyor, which is related to factors such as the conditioning status of the soil and construction conditions. Based on the shield tunneling construction of the section from Hengli Station to Panyu Square Station on Guangzhou Line 18 as the engineering background, and the slumps of soil are used as evaluation index, the efficiency of soil discharge in different slumps is analyzed. The soil discharge efficiency is calculated according to equation (17).

$$Q_x = V_x N \quad Q_0 = AVn_0 E_s = Q^*/Q_s \qquad (17)$$

Where V_s is the theoretical soil discharge per revolution of the screw conveyor, N is the speed of the screw conveyor, A is the cutting area of the cutter head, n_0 is the factor of loose, E_s is the soil discharge efficiency of the soil discharge, Q^* is the soil discharge based on equation (16).

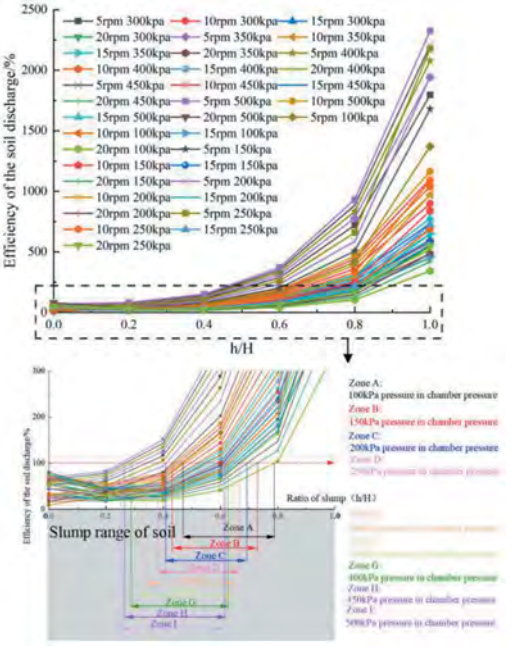

Figure 17. Efficiency of the soil discharge.

From Figure 17, it can be seen that as the slump increases, the efficiency of the soil discharge shows a non-linear growth trend, and the growth gradient becomes larger and larger. When the ratio of slump reaches 1, that is, the soil is in fluid state. Under the conditions of 500kPa pressure and 5rpm speed of the screw conveyor, the efficiency of soil discharge reaches 2326%. It is obvious that the soil discharge at this time is basically uncontrollable, which are greater than soil discharge calculated Q_s by equation (17). The efficiency of soil discharge further increases under high pressure, which requires the use of small slump soil in deep burial depth engineering, that is, the slump of the soil has a adaptability to the burial depth of tunnel. In engineering, it is necessary to ensure that the soil discharge is basically consistent with the actual soil discharge. the soil discharge efficiency of the screw conveyor is required to reach 100%, which is related to the burial depth of shield tunneling, the speed of the screw conveyor, and the slump of soil. Therefore, in order to provide a reference basis for similar projects, according to Figure 17, the suggested conditioned range for the slump of the soil under different burial depths can be obtained. Assuming that soil excavation and soil discharge is balance, earth pressure at rest can be used as the support pressure, and the pressure in pressure chamber basically follows a linear variation

relationship with burial depth. The monitoring pressure in pressure chamber is basically around 300kPa under the condition of burial depth of 30m, so it is not difficult to determine the earth pressure under other burial conditions. Finally, the suggested range for the slump of soil is shown in Table 3.

Table 3. Suggested conditioned range of soil.

Pressure in pressure chamber/kPa	Speed of screw conveyor/rpm	Slump range/mm	Burial depth of tunnel vault/m
100	5~20	141~237	10
150		126~216	15
200		121~208	20
250		117~204	25
300		102~192	30
350		93~186	35
400		87~183	40
450		81~181	45
500		75~180	50

5 CONCLUSION

This paper divides the soil state into fluid state, hard plastic state, and transitional state between the two. Empirical formulas and numerical models for soil discharge in three different states are proposed, and finally, the soil discharge theory of the three states is coupled by the slump to obtain the empirical formula for soil discharge in the full state of the soil, and the following conclusions are obtained:

(1) The pressure in pressure chamber, speed of screw conveyor, and soil slump are the key factors that affect the soil discharge. The slag discharge is positively correlated with the pressure in pressure chamber, speed of screw conveyor, and soil slump.

(2) Based on the Π theorem and CFD, an independent similarity criterion for the soil discharge phenomenon and the relationship between the similarity criteria were obtained when soil state is fluid. Based on the Darnell-Mol theory, the theoretical formula of soil discharge were obtained when soil state is hard plastic state. The discrete element numerical model of soil discharge considering foam defoaming was established when soil state is transitional state, and the soil discharge under different working conditions was calculated based on this numerical model, which was verified with the model test, and the reliability of the numerical model was verified.

(3) This paper uses slump as an evaluation index of soil fluidity to couple the soil discharge theory of fluid state, hard plastic state, and transitional state, and then proposes an empirical formula for the soil discharge of full state soil, which can consider engineering scale. The shield tunneling construction between Hengli Station and Panyu Square Station on Guangzhou Line 18 was taken as the engineering background, based on the monitoring data of soil discharge, the reliability of the theory of soil discharge in full state soil was verified..

(4) There is a adaptability between the slump of conditioned soil and the tunnel burial depth. As the tunnel burial depth increases, the reasonable slump of the soil should be appropriately reduced. When the burial depth of the tunnel vault of 30m, the range of soil slump should be 75-180mm, which is more suitable.

REFERENCES

Borio, L., Peila, D, 2010. “Study of the Permeability of Foam Conditioned Soils with Laboratory Tests”. American Journal of Environmental Sciences, 6 (4): 365–370.

Huang, B.Q., 2009. The Adaptive Research on Cutterhead Design Parameters for Shield Machine. Master Thesis. Tianjin University.

Liu, P., Wang, S., Ge, L., et al, 2018. “Changes of Atterberg limits and electrochemical behaviors of clays with dispersants as conditioned agents for EPB shield tunnelling”. Tunnelling and. Underground Space Technology, 73(3): 244–251.

Ma, B.S., Najafi, M, 2008. “Development and applications of trenchless technology in China”. Tunnelling and Underground Space Technology, 23(4), 476–480.

Maild, U, 1995. Erweiterung der Einsatzbereiche der Erddruckschilde durch Bodenkonditio nierung mit Schaum. PhD Thesis. Ruhr-University, Bochum, Germany.

Merritt, A.S., Mair, R.J, 2006. “Mechanics of tunnelling machine screw conveyors: model tests”. Geotechnique, 56(9): 605–615.

Merritt, A.S., Mair, R.J, 2008. “Mechanics of tunnelling machine screw conveyors: a theoretical model”. Géotechnique, 58(2):79–94.

Pena. Duarte, M.A, 2007. Foam as a soil conditioner in tunnelling: physical and mechanical properties of conditioned sands. PhD Thesis. University of Oxford, Oxford, Britain.

Qiao, Y.K., Peng, F.L, 2016. “Lessons learnt from Urban underground space use in Shanghai-from Lujiazui business district to Hongqiao central business district”. Tunnelling and Underground Space Technology, 55(5), 308–319.

Qiao, Y.K., Peng, F.L., Wang, Y, 2017. “Monetary valuation of urban underground space: a critical issue for the decision-making of urban underground space development”. Land Use Policy, 69(12), 12–24.

Zhao, J.W., Peng, F.L., Wang, T.Q., et al, 2016. “Advances in master planning of urban underground space (UUS) in China”. Tunnelling and Underground Space Technology, 55(5), 290–307.

Zhong, J.Z., Wang, S.Y., Liu, P.F., et al, 2022. “Investigation of the Dynamic Characteristics of Muck during EPB Shield Tunnelling in a Full Chamber Model Using a CFD Method”. Journal of Civil Engineering, 26(9): 4103–4116.

Zhu, H.H., Cheng, P., Zhuang, X. et al, 2020. “Assessment and structural improvement on the performance of soil chamber system of EPB shield assisted with DEM modeling”. Tunnelling and Underground Space Technology, 96(2): 92–103.

Tunnelling for a Better Life – Yan, Celestino, Thewes & Eberhardt (Eds)
© 2024 The Author(s), ISBN 978-1-032-80042-4
Open Access: www.taylorfrancis.com, CC BY-NC-ND 4.0 license

Muck discharge efficiency depending on soil conditioning by laboratory-scale model test

Byeonghyun Hwang* & Abraham Bae
Korea University, Anam-ro, Seongbuk-gu, Seoul, Republic of Korea

Dongjoon Lee
Daewoo E&C, Eulji-ro, Jung-gu, Seoul, Republic of Korea

Kyuhyeong Lim & Hangseok Choi
Korea University, Anam-ro, Seongbuk-gu, Seoul, Republic of Korea

ABSTRACT: The Earth Pressure Balance (EPB) shield Tunnel Boring Machine (TBM) ensures face stability of the face by introducing additives like foam and polymer to make excavated soils viscoplastic. The screw conveyor, serving as the muck discharge device in the EPB shield TBM, controls face pressure, impacting TBM excavation performance. This study aimed to construct a laboratory-scale model of the screw conveyor to determine the optimal muck discharge conditions for EPB shield TBM excavation. To create the model, the specifications of an 8m EPB shield TBM commonly used in road tunnels were analysed and scaled down by a ratio of 1:20. The torque measured for the conditioned artificial sandy soil in the lab-scale model were compared with the rheological properties assessed through the laboratory pressurized vane shear tests. The findings revealed that the screw blade torque decreases under moderate additive conditions and increases when over-applied. Furthermore, a relationship between the yield stress and screw blade torque was established, which is also linked to the slump value that measures the workability of the conditioned soil. These insights contribute to enhancing EPB shield TBM operations by predetermining more accurate injection of additives at the design stage.

Keywords: Earth Pressure Balance (EPB) shield Tunnel Boring Machine (TBM), additives, Screw conveyor, Torque, Rheological properties

1 INTRODUCTION

The Earth Pressure Balance (EPB) shield Tunnel Boring Machine (TBM) is a device designed for excavating the ground and filling its chamber, located at the rear of the cutterhead, with excavated soil. This process serves to support and stabilize the tunnel face. Typically, the excavated soil is discharged through a screw conveyor, and chamber pressure is regulated by adjusting parameters such as the rotational speed of the screw blades and the opening and closing of the discharge gate. The screw conveyor plays a crucial role in the excavation process, and it features a mechanism to reduce the pressure to atmospheric levels as the excavated soil travels along the screw toward the discharge gate.

The efficiency of excavation for an EPB shield TBM is highly dependent on the ground conditions at the tunnel face and the properties of the excavated soil. Ideally, EPB shield TBMs perform optimally in ground conditions characterized by relatively fine-grained clayey silt, mud, and sand. These soils should have low permeability and high plasticity during excavation. These characteristics enable consistent transmission of support pressure to the tunnel face and allow for control over the transportation of excavated soil through the TBM. In addition to mechanical controls, soil conditioning is carried out by introducing additives into the tunnel face, chamber, and screw conveyor to maintain chamber pressure and to reduce pressure and torque on the screw conveyor. The application of additives is determined based on ground survey data collected before excavation, and the slump test results for muck during excavation. However, the slump test is conducted at atmospheric pressure and can yield different results depending on the operator. To address this limitation, it should be complemented by vane shear tests, which provide rheological properties that aid in designing

*Corresponding author: bh2917@korea.ac.kr

DOI: 10.1201/9781003495505-249

the injection of additives. Nevertheless, vane shear tests alone cannot fully assess the impact on the screw conveyor and the overall efficiency of the EPB TBM excavation process. Therefore, there is a need for research into the efficiency of excavation through reduced-scale model experiments. In this study, a typical EPB shield TBM was scaled down to a 1:20 ratio to create a laboratory-scale model. This model was used to evaluate discharge efficiency while using foam and polymer as additives.

2 ADDITIVES AND RHEOLOGICAL PROPERTIES

2.1 *Additives*

Soil conditioning involves the injection of additives, such as foam and polymer, to transform the excavated soil into a viscoplastic state (Lee et al., 2022). This method has broadened the spectrum of ground conditions that are suitable for EPB shield TBMs because the effective utilization of additives improves the properties of the excavated soil (Merritt et al., 2003). Additionally, it plays a vital role in maintaining face stability by decreasing the load on TBM equipment and minimizing the risk of face collapse.

2.1.1 *Foam*

As an additive, foam can effectively reduce surface tension and induce electrostatic repulsive forces, allowing soil particles to separate from each other and to fluidize the soil (Langmaack, 2000). Additionally, it can significantly alter the mechanical and rheological properties of the excavated soil, such as reducing internal friction angle, ensuring plasticity and workability, decreasing permeability, and minimizing wear on TBM cutters (Quebaud et al., 1998). Foam is typically composed of water, air, and a foaming agent. To produce foam, water and the foaming agent are injected into a foam generator at the desired concentration, where they combine with air. The injection process involves three key parameters: Foam Injection Ratio (FIR), Foam Expansion Ratio (FER), and Concentration of Foam (C_f), which are represented in Eqs. (1) – (3).

$$FIR = \frac{V_f}{V_{es}} \times 100(\%) = \frac{V_{lf} + V_a}{V_{es}} \times 100(\%) \quad (1)$$

$$FER = \frac{V_f}{V_{lf}} = \frac{V_{lf} + V_a}{V_{lf}} \quad (2)$$

$$C_f = \frac{V_t}{V_t + V_w} \times 100(\%) = \frac{V_t}{V_{lf}} \times 100(\%) \quad (3)$$

Where V_f is the volume of expanded foam (m^3), V_{es} is the soil volume (m^3), V_{lf} is the volume of aqueous foam solution (m^3), V_a is the air volume (m^3), V_t is the volume of foaming agent (m^3), and V_w means the water volume (m^3).

2.1.2 *Polymer*

Polymers serve the crucial function of maintaining uniform chamber pressure and preventing the collapse of the tunnel face. They also contribute to the enhancement of foam stability and a reduction in the permeability of excavated soil (Kwak et al., 2022). One crucial characteristic of polymers is their substantial water-binding capacity, enabling them to absorb moisture from the excavated soil upon injection and retain it even when subjected to external forces. These are particularly useful in highly permeable soils where foam alone is insufficient for effective soil conditioning. The polymers typically consist of water and a polymer solution and are applied in liquid form without air bubbles. There are two injection parameters for polymer injection: Polymer Injection Ratio (PIR) and Concentration of Polymer (C_p), which are expressed by Eqs. (4) – (5).

$$PIR = \frac{V_{lp}}{V_{es}} \times 100(\%) \quad (4)$$

$$C_p = \frac{V_p}{V_p + V_w} \times 100(\%) = \frac{V_p}{V_{lp}} \times 100(\%) \quad (5)$$

Where V_{lp} is the volume of aqueous polymer solution (m^3), V_p is the volume of polymer solution (m^3).

2.2 *Rheological properties*

To determine the optimal conditions for injecting additives into the target ground, it is essential to assess the rheological properties of the excavated soil after treatment with these additives. This assessment provides insights into the mechanical and rheological behavior of the treated soil, focusing on key rheological properties such as workability, peak strength, and yield stress.

Workability is closely associated with the transformation of the excavated soil, achieved through soil conditioning, into a state of plastic fluidization, which exists between the solid and liquid states. Enhancing the workability of the excavated soil, resulting in plastic fluidization, ensures uniform pressure at the tunnel face and facilitates the continuous discharge of soil through the screw conveyor. Typically, slump tests are conducted to evaluate the workability of conditioned soil.

Shear properties are assessed by deriving rheograms using raw torque data obtained from vane shear tests to determine peak strength and yield stress. The flow curve represents the relationship between shear rate and shear stress, both of which are rheological variables. These variables are calculated as described in Eqs. (6) – (7). The shear stress is calculated assuming that the surface is cylindrical in shape and that a uniform shear stress is applied to the surface (Karmakar et al., 2007). The shear rate assumes that the vane rotates in a cylindrical shape without upper and lower boundaries during the vane shear test (Meng et al., 2011).

$$\tau = \frac{2T_m}{\pi D_v{}^3 \left(\frac{H_v}{D_v} + \frac{1}{3}\right)} \quad (6)$$

$$\dot{\gamma} = \frac{4\pi D_c{}^2}{60\left(D_c{}^2 - D_v{}^2\right)} \omega_{vane} \quad (7)$$

Where τ is the shear stress (Pa), T_m is the measured torque value ($N \cdot m$), D_v is the vane diameter (m), H_v is the vane height (m), and $\dot{\gamma}$ is the shear rate (1/s), D_c is the chamber inner diameter (m), and ω_{vane} is the vane rotation speed (rpm).

3 LABORATORY TEST

3.1 *Soil specimens*

An artificial sandy soil was prepared by combining 30% illite and 70% silica sand for laboratory testing. Artificial sandy soil is classified as SM (Silty Sand) according to the Unified Soil Classification System (USCS). The particle size distribution curve of the samples is shown in Figure 1. This artificial sandy soil belongs to the ground conditions suitable for EPB shield TBMs, as proposed by Maidl (1995). The target unit weight of the soil specimens was set to be 1.8 t/m^3.

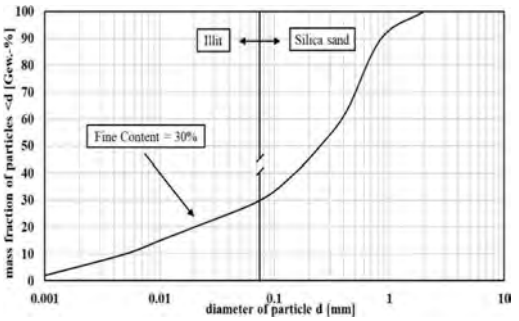

Figure 1. Particle size distribution of artificial sandy soil.

3.2 *Test setup and apparatus*

The recommended foam injection parameters for optimal performance have been proposed as follows: FIR of 30-60%, FER of 5-30, and C_f of 0.5-5% (Oh, 2021; Shin, 2020). Foam injection parameters were determined by considering a range of slump values for optimal workability (i.e., 100-200 mm). Consequently, the selected parameters were 40% of FIR, 15 of FER, and 3% of C_f. Regarding appropriate polymer injection, it has been advised to utilize PIR values within 20% (Merritt et al., 2003). As indicated by the manufacturer, C_P was tested at 0.2 and 0.4% (Table 1).

After obtaining the target foam injection parameters (FIR, FER, and C_f) using the foam generator, the foam was injected into the sand soil specimens.

Table 1. Laboratory test cases and slump results.

No	FIR (%)	Cp (%)	PIR (%)	Slump (mm)
1	40	0	0	150
2	40	0.2	5	120
3	40	0.2	10	72
4	40	0.4	10	7

On the other hand, the polymer was mixed with water corresponding to the specified PIR and C_p targets. Afterward, it was stirred for 10 minutes in a small mixer before injection. The foam and polymer-infused artificial sandy soil were stirred for 2 minutes at a constant speed using a hand mixer.

3.2.1 *Laboratory pressurized vane shear test*

The rheological properties of conditioned soils were evaluated using a laboratory pressurized vane shear test apparatus developed by Lee (2021). This apparatus is designed to pressurize the soil specimen within a chamber, where a rheometer with a rotating vane applies shear to the soil specimen. In addition, the apparatus is equipped with a torque sensor that records the torque generated as the vane rotates. Two pressure gauges are installed to measure the pressure inside the chamber. The torque value can be monitored in real-time during the test. The apparatus adopted in the laboratory pressurized vane shear test is shown in Figure 2. In this test, a confining pressure of 200 kPa was applied to simulate TBM operation at a depth of 20 m.

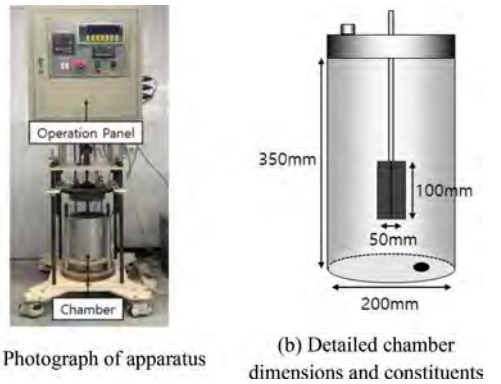

(a) Photograph of apparatus (b) Detailed chamber dimensions and constituents

Figure 2. Laboratory pressurized vane shear test apparatus.

3.2.2 *Laboratory-scale model test of EPB shield TBM*

The 8-meter EPB shield TBM was downsized to a 1:20 scale, and the screw blade featured an optimal shaft shape for sandy soil. The equipment was made of transparent acrylic to enable visual monitoring of the placement process. The scale model chamber had an inner diameter of 300 mm, a height of 500 mm, while the inner diameter of the screw conveyor casing measured 50 mm, with a total length of 460 mm. The

chamber was equipped with two pressure gauges, one at the top and one at the bottom. Similarly, the screw conveyor casing was equipped with three pressure gauges evenly spaced to facilitate real-time pressure measurement. Additionally, a torque sensor was installed to enable continuous torque measurement. The assembly of the manufactured equipment is shown in Figure 3, the adopted screw blade in Figure 4, and find detailed specifications in Table 2.

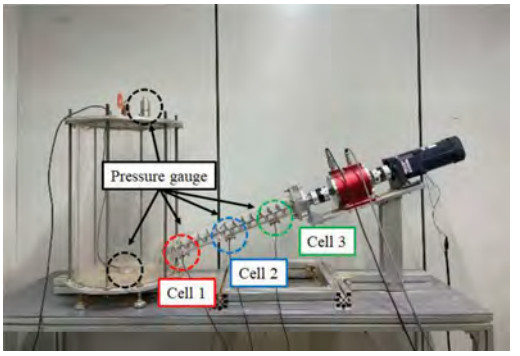

Figure 3. Laboratory-scale model of EPB shield TBM.

Figure 4. Laboratory-scale screw blade.

Table 2. Component and value of screw blade.

Component	Value
Total screw length (mm)	550
Screw shaft diameter (mm)	12
Screw flight diameter, D_f (mm)	46
Screw flight thickness (mm)	3
Number of pitches	16
Screw pitch, t (mm)	27.5
Pitch to diameter ratio, t/D_f	0.6

The conditioned soil specimen was placed in the chamber at a height of 400 mm, factoring in the 1:20 scale. Following this, the chamber was pressurized until 100 kPa, and it remained in a pressurized state for the discharge process. The screw blade rotated at a speed of 10 rpm, and real-time discharge measurements were recorded. In this study, the beginning of screw blade rotation marked the initiation of the experiment. The entire experiment lasted for 800 seconds, a duration standardized for each experimental case to ensure equitable comparisons.

4 TEST RESULTS

4.1 *Rheological properties*

The laboratory pressurized vane shear test was conducted for Cases 1 to 4 to examine the effect of polymer on the rheological properties of conditioned soils. Figure 5 presents a comparison of torque data over time, while Figure 6 illustrates the peak strength and yield stress for each case.

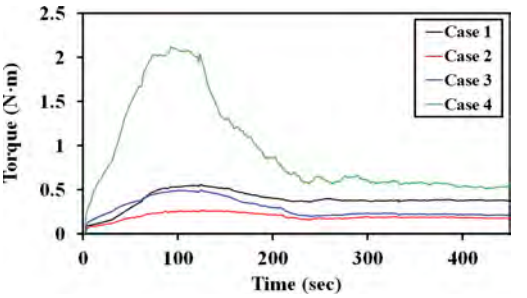

Figure 5. Torque results according to polymer injection.

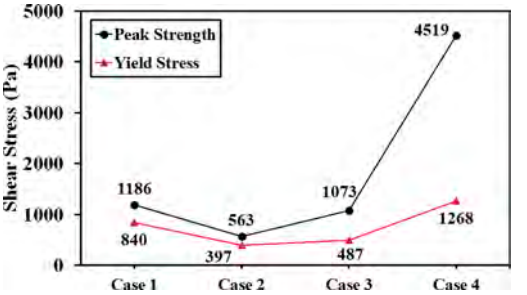

Figure 6. Peak strength and yield stress.

In Cases 1, 2, and 3, injecting the appropriate amount of polymer resulted in a reduction of both peak strength and yield stress. Furthermore, due to the water-binding capacity of the polymer, the slump value also decreased. However, Case 4 demonstrates that excessive polymer injection led to increased torque and peak strength.

4.2 *Screw torque and muck discharge rate*

The laboratory-scale model test was conducted for Cases 1 to 4 to investigate the effect of polymer on the efficiency of muck discharge. The torque and pressure data over time are compared in Figures 7 and 8, respectively. In addition, the mass flow rate of muck discharge is illustrated in Figure 9.

Compared to Case 1, where no polymer was injected, Cases 2 and 3 exhibited lower torque measurements. The pressure results, analysed cell-by-cell, indicated a decrease in pressure as the muck moved from the chamber to the muck discharge gate. However, Case 4 showed very low workability and took a long time to stabilize. Notably, the injection of

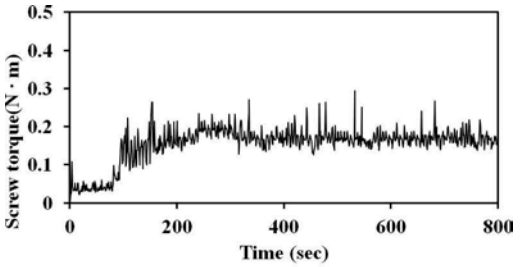

(a) Torque data of Case 1

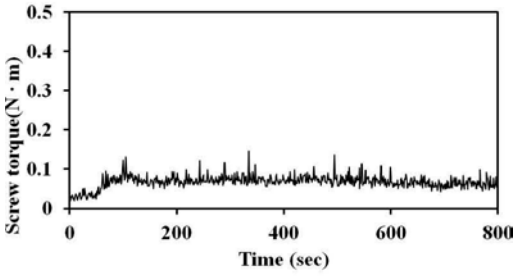

(b) Torque data of Case 2

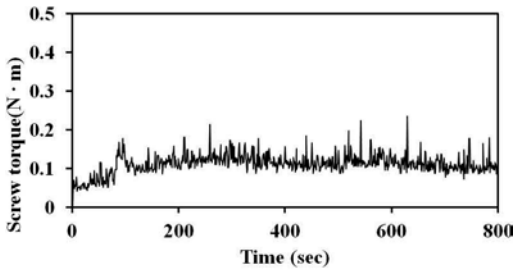

(c) Torque data of Case 3

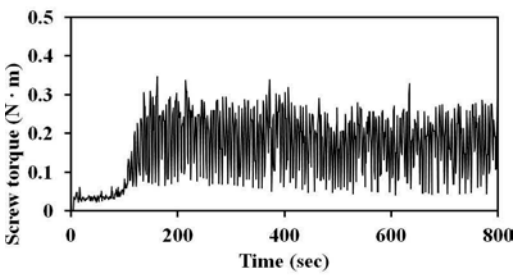

(d) Torque data of Case 4

Figure 7. Torque data of screw blade.

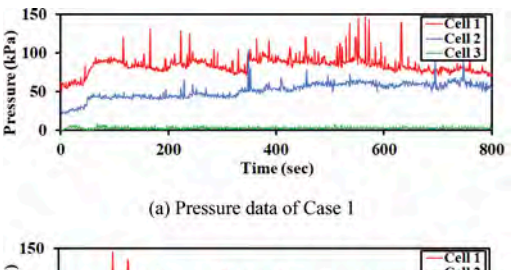

(a) Pressure data of Case 1

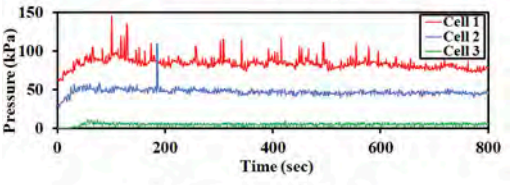

(b) Pressure data of Case 2

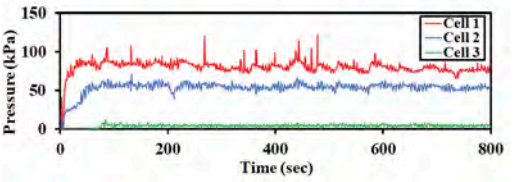

(c) Pressure data of Case 3

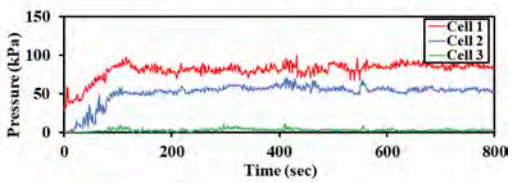

(d) Pressure data of Case 4

Figure 8. Pressure data of screw barrel.

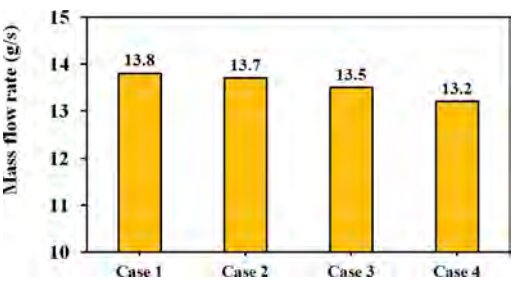

Figure 9. Mass flow rate of muck discharge.

polymer resulted in a reduction in the amount of muck discharged per hour, similar to the observed slump results.

4.3 *Discussion of test results*

The average screw blade torque after stabilization is depicted in Figure 10. Similar to Cases 2 and 3, injecting the suitable polymer reduced the machine's load. When comparing the torque results for each condition with the yield stress determined through the laboratory vane shear test, a correlation was identified, as shown in Figure 11. Conditions with optimal workability are marked with solid circles, while those with workability outside the optimal range are marked with solid triangles. The results of the laboratory-scale model test validate that proper conditioning can reduce the equipment load, even when it does not fall within the optimal workability range.

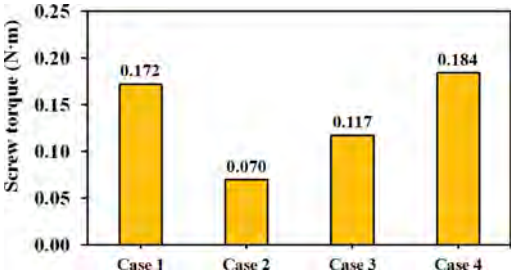

Figure 10. Compare torque results of each case.

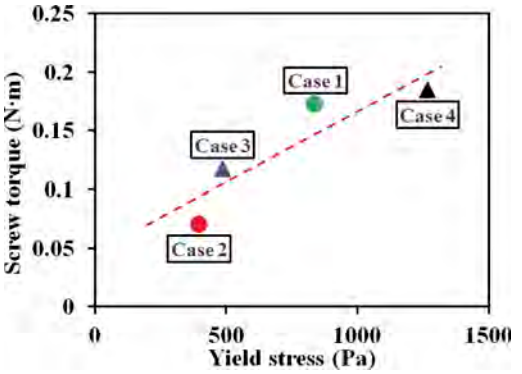

Figure 11. Torque and yield stress of conditioned soil.

5 CONCLUSIONS

The Earth Pressure Balance (EPB) shield Tunnel Boring Machine (TBM) is a device that maintains face pressure by filling the chamber with excavated soil, and controlling the screw conveyor is crucial for the machine's efficiency. Discharging muck through the screw conveyor significantly impacts the overall load of the equipment and the construction period.

This paper evaluated the efficiency of muck discharge from conditioned soil using a laboratory-scale model test and compared it with the rheological properties measured through a laboratory pressurized vane shear test. The correlation between the yield stress from the laboratory pressurized vane shear test and the torque of the screw blade was confirmed. The following conclusions can be drawn:

1) When the polymer was added to the conditioned artificial soil with foam, the slump value was lower than in the condition without polymer (Case 1), and both peak strength and yield stress were reduced. However, when the polymer content became excessive, as in Case 4, workability became very low, and peak strength increased.
2) Similar to the rheological properties, the proper application of polymer reduced the torque of the screw blade, while excessive application significantly increased the torque. Muck discharge decreased with increasing polymer injection, also similar to the slump results.
3) There is a correlation between screw blade torque and yield stress, and even in Case 3, which had low yield stress but was not an optimal workability condition, it was identified that applying suitable additives can reduce equipment loads. Incorporating the results of the laboratory-scale model test into the construction process will improve constructability.

ACKNOWLEDGMENTS

This research was conducted with the support of the "National R&D Project for Consecutive Excavation Technological Development Project of Tunnel Boring Machine (RS-2022-00144188)" funded by the Korea Agency for Infrastructure Technology Advancement under the Ministry of Land, Infrastructure and Transport, and managed by the Korea University.

REFERENCES

Karmakar, S., Kushwaha, R. L., 2007. Development and Laboratory Evaluation of a Rheometer for Soil Visco-plastic Parameters. Journal of Terramechanics, 44, pp. 197–204.

Kwak, J., Lee, H., Hwang, B., Choi, J., Choi, H., 2022. A Laboratory Pressurized Vane Test for Evaluating Rheological Properties of Excavated Soil for EPB Shield TBM: Test Apparatus and Applicability. Korean Tunnelling and Underground Space Association, 24(5), pp. 355–374.

Langmaack, L., 2000. Advanced Technology of Soil Conditioning in EPB Shield Tunnelling. Proc. North American Tunnelling '00, Balkema, Rotterdam, pp. 525–542.

Lee, H., 2021. Evaluation on Performance of EPB Shield Tunnelling with Foam Conditioning. PhD Thesis. Korea University, Republic of Korea.

Lee, H., Kwak, J., Choi, J., Hwang, B., Choi, H., 2022. A Lab-scale Experimental Approach to Evaluate Rheological Properties of Foam-conditioned Soil for EPB Shield Tunnelling. Tunnelling and Underground Space Technology incorporating Trenchless Technology Research, 128, 104667.

Maidl, U., 1995. Erweiterung der Einsatzbereiche der Erddruckschilde durch bodenkonditionierung mit Schaum. PhD Thesis. Institut für Konstruktiven Ingenieurbau, Ruhr-Universität Bochum.

Meng, Q., Qu, F., Li, S., 2011. Experimental Investigation on Viscoplastic Parameters of Conditioned Sands in Earth Pressure Balance Shield Tunneling. J Mech Sci Technol, 25, pp. 2259–2266.

Merritt, A.S., Borghi, F.X., Mair, R.J., 2003. Conditioning of Clay Soils for Earth Pressure Balance Tunnelling Machines. In: Underground Construction 2003, London, pp. 455–466.

Oh, J., 2021. Laboratory Study on Optimum Foam Injection Condition for EPB Shield TBM in Weathered Granite Soil. Master Thesis. Korea University, Republic of Korea.

Shin, D., 2020. Evaluation of EPB TBM Excavation Performance on Artificial Sandy Soils with Foam Injection Conditions. Master Thesis. Korea University, Republic of Korea.

Quebaud, S., Sibai, M., & Henry, J. P., 1998. Use of chemical foam for improvements in drilling by earth-pressure balanced shields in granular soils. Tunnelling and underground space technology, 13(2), pp. 173–180.

Tunnelling for a Better Life – Yan, Celestino, Thewes & Eberhardt (Eds)
© 2024 The Author(s), ISBN 978-1-032-80042-4
Open Access: www.taylorfrancis.com, CC BY-NC-ND 4.0 license

Use of biomass as soil conditioner to improve clay rheology in EPB tunneling

Muhammad Ishaq*, Benjamin Appleby, Jamal Rostami & Joseph Samaniuk
Colorado School of Mines, Golden, USA

ABSTRACT: Mechanized tunneling in soft ground presents inherent challenges, with clay clogging emerging as a particularly troublesome issue that leads to increases in downtime and project delays. The rheology of clay is influenced by several variables, such as its composition, mineralogy, groundwater chemistry, soil pH, and moisture content. This study focuses on clay conditioning with a biomass product made of glucose and oil, generated from industrial biomass production by algae. The objective of this study is to evaluate the impact of adding a solution containing varying concentrations of biomass on the rheology of clay at a laboratory scale. The observations made during and after tests on clay samples, each with different quantities of biomass agent, along with quantitative data obtained from a large-scale rheometer under constant moisture and rpm conditions, will be presented. The findings of this study confirm that the rheological properties of clay can be effectively modified, similar to drilling mud in the petroleum industry, to control and alter the rheological properties of clay, including its viscosity and clogging. Further testing and modeling efforts are currently underway to assess the optimal clay rheology achieved through the utilization of biomass in soft-ground tunneling.

Keywords: Clay Rheology, Biomass, Clay Conditioning, Clogging

1 INTRODUCTION

Mechanized soft ground tunneling projects often encounter material clogging predominantly due to clay content overloading the muck transportation-related components of tunnel boring machines, mainly in the excavation chamber and screw conveyor. Maintaining proper earth pressure balance at the tunnel face and operating the screw conveyor becomes challenging when the muck is prone to clogging (Feinendegen et al., 2011; Garroux et al., 2018; Hu., 2020; Sebastiani et al., 2022; Todaro et al., 2022; Yang et al., 2023).

"Clogging," in the context of soft ground tunneling, refers accumulation and packing of clay particles in pore spaces of native soils making them difficult to transport (Mair, 2008; Zumsteg et al., 2013).

To facilitate consistent material flow and easy transportation, the muck should possess certain properties including workable viscosity, compressibility, and low permeability (Jeong et al., 2010; Dudhat et al., 2016; Sonebi and Perrot, 2019; Hu and Rostami, 2020; Xie et al., 2021; Zhang et al., 2021). Achieving all the necessary properties in natural soil is nearly impossible. Therefore, the use of different soil conditioners is common in soft ground tunneling to adjust and improve its rheological properties and prevent clogging. Chemical additives and foaming agents are often used as soil conditioners to modify the rheological and mechanical properties of soils (Nelson and Miller, 1992, Puppala et al., 2006, Bhadriraju et al., 2008, Pedarla et al., 2011, Yi et al., 2016). In clay-rich soils, oil-based additives perform better at reducing the clogging phenomenon due to their inherent stability and easy integration with the soil than chemical and foam alternatives (Maidl et al., 1996; Mair, 2008; Vinai et al., 2008; Zumsteg et al., 2012; Hu and Jamal, 2020; Hu., 2020). Addressing environmental concerns related to chemical additives in muck disposal and the added advantages of oil-based additives, current research emphasizes testing eco-friendly additives and biodegradable materials. The goal is to alter the rheology of clay, a primary contributor to clogging in natural soils to avoid overloading or disruption in tunneling operation.

*Corresponding author: mishaq@mines.edu

DOI: 10.1201/9781003495505-250

Clay is a term used to identify fine soil particles less than 2 microns in diameter (Adam and Hooper, 2001; Bleam, 2017; Brindley, 2006; Huggett, 2015; Matsui et al., 2022). Clayey soils are more prone to clogging due to the stickiness of clay particles caused by adhesion, inherent cohesion, composition, mineralogy, chemical setting, soil pH, and moisture content (Kooistra et al.1998; Bleam, 2017; Kang et al., 2019). Bentonite is a term used for commercially available clay often used as stabilizing fluid for drilling and laboratory tests (Cumaraswamy and Mohammed, 2020; Hua et al., 2012; Fernandez et al., 2021; Mat, 2023; Zhang et al., 2022a, b). In North America, commercially available bentonite clay is mined in Wyoming and South Dakota, where the biggest deposits of volcanic ash are found in the Black Hills of Wyoming and South Dakota and the Big Horn Mountains of Wyoming (U.S. Geological Survey, n.d.; Hannon et al., 2019, 2020a). In most of the laboratory tests related to clay rheology, bentonite clay is used as the base material (Chaudhuri, 2020, Jefferis and Merritt, 2013). This study uses Wyoming Bentonite to conduct small and full-scale laboratory tests.

Avoiding deeper discussion of clay chemistry, clogging links to various factors outlined in Figure 1. Two states, aggregation, and flocculation, decrease viscosity in clay-rich materials, while dispersion and deflocculation increase viscosity. The close packing of clay particles significantly decreases medium permeability, posing challenges in excavating soft ground mechanically. Figure 1 illustrates the clogging effect with a 25% moisture content bentonite mix for visual reference. Water serves as a widely-used technique employed by field crews to minimize clogging and enhance the workability of materials in soft ground conditions during mechanical excavation. Clogging intensity depends on clay plasticity, flow velocity, groundwater chemistry, and relative movement of working surfaces.

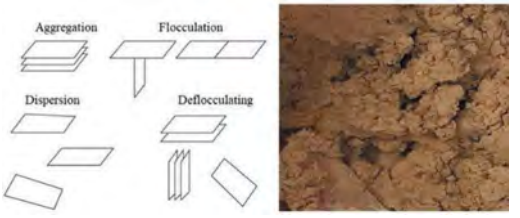

Figure 1. Clay particle state, Left: Four states of clay particles[1], Right: Clay mix with 25% moisture content.

Due to the many heterogeneities in clay soils including granular particles and large viscosities, traditional shear rheometers could not accurately characterize the fluid properties of real soils. Thus, there was a need to develop a fully capable rheometer specifically designed to evaluate the mechanical properties of soil mediums, considering their varying particle size distribution. Consequently, modifications were made to an existing Soil Abrasion Index Unit at Earth Mechanics Institute (EMI), Colorado School of Mines, integrating the necessary attachments to measure the rheological properties of materials while preserving their original composition, particle size distribution, and moisture content (Hu and Rostami, 2020; Hu., 2020). In this paper, the device is referred to as a "Full-Scale Rheometer." To compare against standard rheometers, a commercially available benchtop TA Instruments DHR-3 rheometer will be used.

This study investigates the use of a biomass product (commercially known as Encapso™) made from algae to modify the rheology of clay and reduce clogging during tunneling operations. The test matrix was designed to comprehensively assess the impact of the additive on the clay rheology and compare the results with measured values by the DHR-3 and Full-Scale Rheometer. Tests were conducted on clay samples with different moisture levels and biomass concentrations. Observations during and after these tests along with quantitative analysis of the data for each clay sample provided insights into how the biomass additive affects the flowability of bentonite clay.

2 EQUIPMENT AND MATERIALS

2.1 *DHR-3 rheometer*

The TA Instruments Discovery Hybrid Rheometer Series-3 (DHR-3) represents the latest advancement in a series of rheometers (shown in Figure 2). It is considered one of the world's most advanced combined motor and transducer (CMT) rheometers. The DHR-3 rotational rheometers have a maximum torque capacity of 200 mN·m and can exert a maximum normal force of 50 N (TA Instruments, 2014).

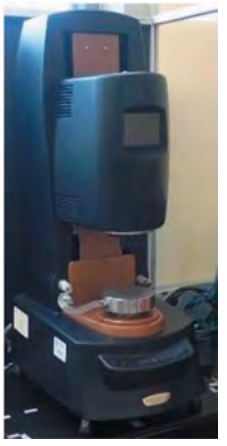

Figure 2. DHR-3 rheometer.

1 Figure retrieved from clay chemistry book (Bleam, 2017)

2.2 *Full-scale rheometer*

The full-scale rheometer is an industrial drill press modified with a Variable Frequency Drive (VFD) to control rpm, loadcells holding the sample chamber to measure torque, and a mixer attachment to become a rheometer, as seen in Figure 3. Due to its capability to characterize soil materials with large particle sizes and viscosities, covering many heterogeneities found in real-world geology and soil properties at various sites, it is referred to as the "Full-Scale Rheometer" in this manuscript.

Figure 3. Full-scale rheometer.

A full-scale rheometer consists of a cylindrical chamber with a 330 mm internal diameter and 450 mm height. A chamber lid is attached at the drive shaft under the adjustable head and impeller mount at the lower end of the spindle nose. The backup motor capacity powering the drive shaft consists of 3.7kW. The torque is measured using two sensors attached on opposite sides of the chamber and the chamber sits on a turn table mount so that it can freely rotate. A variable frequency drive is installed to the unit to control motor rpm. The unit is capable of driving shafts between 0 rpm to 1000rpm speeds. Detailed descriptions of the components can be found in the literature (Rostami et al., 2019; Gharahbagh et al., 2013b; Gharahbagh et al., 2014b, Hu and Rostami, 2020; Hu., 2020).

2.3 *Impeller*

There are two impellers used in the Full-Scale Rheometer given in Figure 4 and one impeller in the DHR-3 rheometer.

The auger impeller has a 148mm radius. The auger attachment was used to simulate the condition within the screw conveyor of TBM. The Pin Rotor has a 296mm radius

The impeller used with the DHR-3 rheometer is a 4-vane aluminum rotor 42 mm in length and 15 mm in diameter.

Figure 4. Impeller, Left: Pin Rotor, Right: Auger.

2.4 *Schematics of the mechanisms*

Two different rheometers are used for testing the rheological parameters of mixtures, each featuring slightly different torque measurement mechanisms. The commercial rheometer directly measures torque by utilizing impeller force input, while the full-scale rheometer uses an indirect torque measurement method, utilizing load cells positioned on the sides of the material chamber. Refer to Figure 5 for schematics depicting the mechanisms in both rheometers.

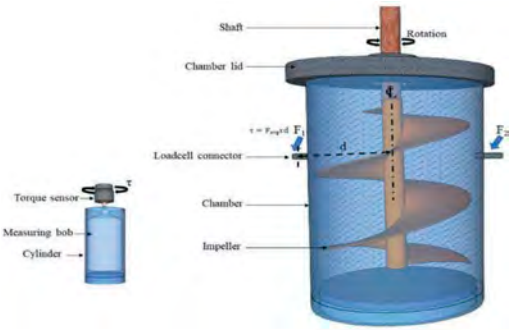

Figure 5. Schematics of the mechanism, Left: Commercial rheometer, Right: Full-scale rheometer.

2.5 *Base materials*

This study uses two base materials: a) Wyoming Bentonite and b) Denver clay. Wyoming Bentonite (details in the introduction) was purchased from a local distributor, whereas, Denver clay was obtained from a construction site in Arvada, Colorado, shown in Figure 6.

Bentonite is used to compare full-scale and DHR-3 rheometer results. This determines the quality of data from a full-scale rheometer. Denver clay was used to investigate Encapso's ability to change the rheological

Figure 6. Base material, Left: Denver clay, Right: Wyoming Bentonite.

Table 1. Mineralogy and material characteristics of base materials.

Properties	Description	Denver Clay	Wyoming Bentonite
Mineralogical composition (wt%)	Quartz	58	4
	Smectite	15	88
	Illite	10	3
	Kaolinite	9	19
	Calcite	3	0.38
	Potash Feldspar	3	0.1
	Sodium Feldspar	2	2.34
Material characteristics	Specific Gravity	2.72	2.55±0.1
	Bulk density (kg/m^3)	1280	833±48

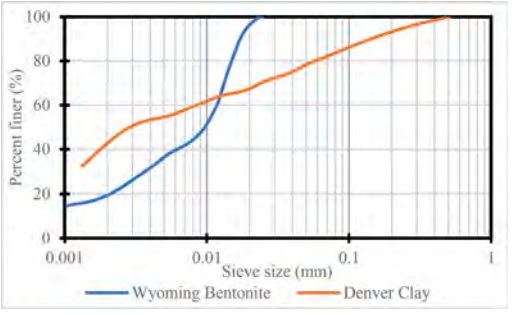

Figure 7. Particle size distribution of base materials.

properties of clay materials. Each test sample consists of around 60 kgs of wet batch of mixture. Table 1 shows the mineral characteristics and Figure 7 shows the particle size distribution curves of both materials (Anderson and Low. 1957; Hauser and Colombo. 1953; Hu., 2020).

2.6 *Biomass*

The conditioner, Encapso™, is a form of biomass derived from algae oil, characterized by particles sized between 5-10 microns and coated with glucose. This particular coating renders Encapso™ highly effective in various extreme conditions, including elevated temperatures, high pH levels, increased calcium concentration, and the presence or absence of water. Its primary application lies in optimizing drilling processes by mitigating friction without inducing excessive greasiness or foaming. Furthermore, Encapso™ exhibits biodegradable properties, as confirmed by OECD 301B testing methods, thus it is an environmentally friendly soil conditioner. Customized packaging options are available for Encapso™. To ensure its integrity, protection from moisture is essential, and it has a shelf life of approximately 2 years. Storage requirements dictate a dry environment (humidity level below 70%) at a cool temperature (below 25°C). Detailed material characteristics are outlined in Table 2.

Table 2. Material characteristics of Biomass.

Description	Numerical Value
Total algae oil by weight	50-70%
Moisture	<4%
Bulk Density	240-360kg/m^3
Specific Gravity (Gs)	1.0- 1.1
Recommended Concentration	34-53 Kg/m^3
Cell wall stability	390°F
Lubricant stability	650°F

Figure 8 shows a dry biomass with comprehensive view of material texture, along with a detailed micron-level view.

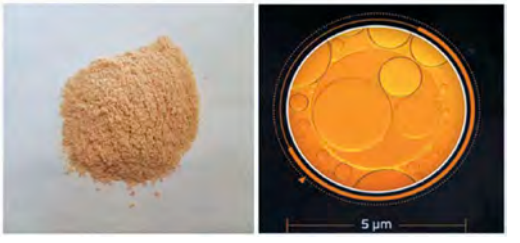

Figure 8. Biomass, Left: Dry material, Right: Micron-level[2].

2.7 *Test matrix and sample preparations*

The test matrix aimed to quantitatively analyse how the biomass agent affects bentonite, first employing the DHR-3 rheometer. Subsequent tests were carried out using a material mix with the same composition in a Full-Scale Rheometer. In the next phase, two distinct impellers were tested to comprehend their geometric influence on clay rheology. The final testing phase incorporated Denver clay into the matrix with

2 Image sourced from Corbion's Encapso product pamphlet.

a reasonable moisture content to further explore the impact of biomass concentration at lower effective shear rates.

Utilizing high moisture with bentonite was necessary due to the torque capacity limitation of the DHR-3 rheometer. In the case of Denver clay, the moisture content was initially selected to facilitate the hand-mixing process, which was challenging with lower moisture content. Later, a lower water content was considered to simulate in-situ ground conditions.

The mixing process involved hand-mixing all samples, varying in water content, for a minimum of 3 hours, followed by mechanical agitation using an electric drill with a mixing flat beater. All samples were allowed to hydrate for 24 hours before testing in a full-scale rheometer to ensure homogeneity. For the DHR-3 rheometer, approximately 80g of samples were extracted from large samples, with proper moisture content records. A detailed text matrix is given in Table 3.

Table 3. Test matrix.

Rheometer	Base Material	Water Content (%)	Biomass Concentration kg/m^3
DHR-3	Wyoming Bentonite	200	0
		200	39
Full-scale	Wyoming Bentonite	200	0
		200	38
		500	0
	Denver Clay	25	20
		25	30

3 RESULTS

This section is subdivided into two subsections to separately present results from the DHR-3 and full-scale rheometer.

3.1 *DHR-3 Rheometer results*

Two sets of tests were conducted (shown in Figures 9 and 10), each consisting of two tests, involving varied shear rates (both increasing and decreasing) using bentonite as the base material, mixed with a moisture content of 200 wt%. These tests were conducted using the DHR-3 rheometer.

The first set of tests aimed to establish a torque and viscosity baseline without incorporating biomass. The results indicated a torque of 4427 μN-m at a shear rate of 1 s^{-1}. However, as the shear rate increased to 400 s^{-1}, the torque rose to 5538 μN-m. Concurrently, in this test, viscosity decreased from 1221 Pa . s to 8.25 Pas as the shear rate increased from 1 to 400 s^{-1}.

In the same set of tests, where the shear rate decreased from 400 to 1 s^{-1}, the torque measurements

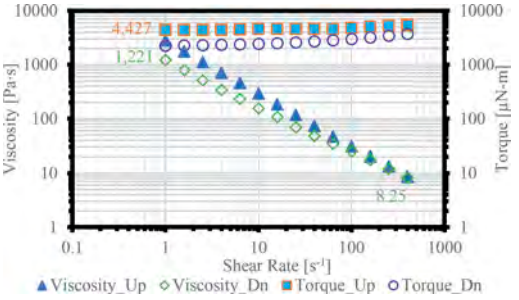

Figure 9. Test set -1 (Wyoming Bentonite with 200% Moisture).

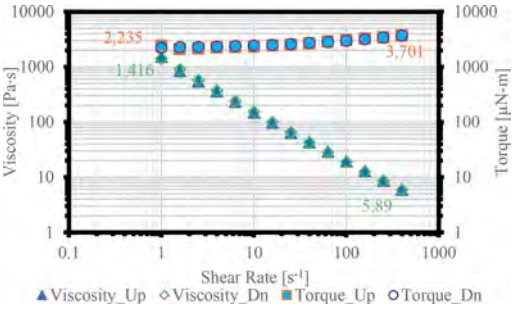

Figure 10. Test set -2 (Wyoming Bentonite with 200 Moisture and 20 kg/m^3 concentration biomass).

shifted from 5184 to 1905 μN-m, and viscosity values changed from 8.25 to 1212 Pa . s. Refer to Figure 9 for a visual representation of the results of the first test set.

The second test set aimed to assess the influence of biomass on the matrix. The data shows less divergence between increasing and decreasing shear rate conditions. When increasing the shear rate from 1 to 400 s-1, the recorded torque ranged from 2406 to 3726 μN-m, while viscosity ranged from 1532 to 5.9 Pa . s. Conversely, in the scenario of reducing the shear rate from 400 to 1 s-1, torque ranged from 3701 to 2225 μN-m, and viscosity ranged from 5.9 to 1417 Pa . s, as illustrated in Figure 10.

3.2 *Full-scale rheometer results*

The first two tests were conducted on the same material sample which was tested in the DHR-3 rheometer, to validate the result and ensure the sensitivity of the Full-Scale Rheometer. In the first two tests, the Pin Rotor was used and only the increasing effective shear-rate scenario was recorded.

The results of torque shown in Figure 11 are in N-m. The first test using bentonite with 200 wt% water content without biomass shows 55 N-m torque at 0.08 s-1 shear rate, whereas 50 Pa . s was the viscosity. At 0.16 s-1 effective shear-rate torque increased to 59 N-m and viscosity decreased to 3.46 Pa . s.

In the subsequent test, biomass was introduced into the 200 wt% water content bentonite sample. This alteration resulted in torque fluctuation ranging from 25 to 38 N-m and a viscosity shift from 22 to 2.59 Pa . s, corresponding to an ascending effective shear rate of 0.08 to 0.16 s-1. The outcomes are shown in the accompanying Figure 12.

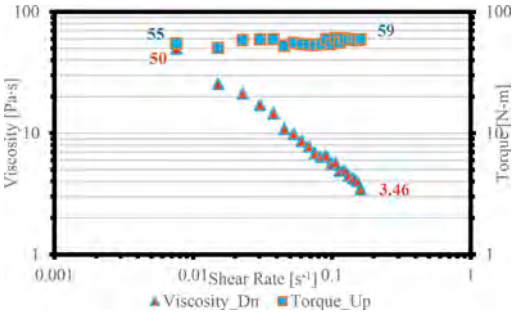

Figure 11. Full-Scale Rheometer test -1 (Wyoming Bentonite with 200 wt% Moisture).

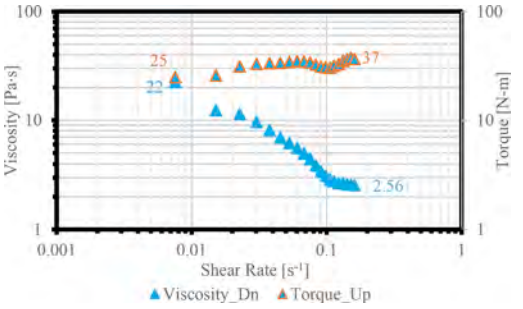

Figure 12. Full-Scale Rheometer test-2 (Wyoming Bentonite with 200 wt% Moisture and 20kg/m^3 biomass).

The third test using a Full-Scale Rheometer was to investigate how different impeller geometries affect the rheology of bentonite. The test involved using a Pin Rotor and an auger. Since the auger mimics the screw conveyor in an Earth Pressure Balance Tunnel Boring Machine (EBP TBM), incorporating geometric parameters into the test matrix was deemed essential for interpreting the results.

The bentonite mixture in this test had a water content of 500 wt% and contained no biomass. The primary goal of this test was to comprehend the relationship between impeller geometry and rheological properties. Therefore, efforts were made to maintain test conditions and preparation as consistent as possible. The results indicated a significant torque applied by the auger compared to the Pin Rotor, shown in Figure 13.

The recent series of tests aimed to replicate real-world conditions and assess how varying biomass concentration affects torque and viscosity in a material. Denver clay served as the base material, with water content reduced to 25%. Two specific biomass concentrations were examined, utilizing an auger as an impeller to understand their impact on material behavior. Graphed in Figure 14 are the peak torque and viscosity results. At a biomass concentration of 20 kg/m^3, the torque measured approximately 1200 N-m, and viscosity was around 10937 Pa . s. In contrast, a 30 kg/m^3 biomass concentration yielded a torque of 956 N-m and a viscosity of 8552 Pa . s.

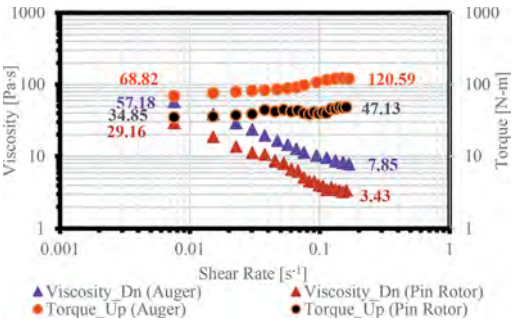

Figure 13. Rheology vs impeller geometry.

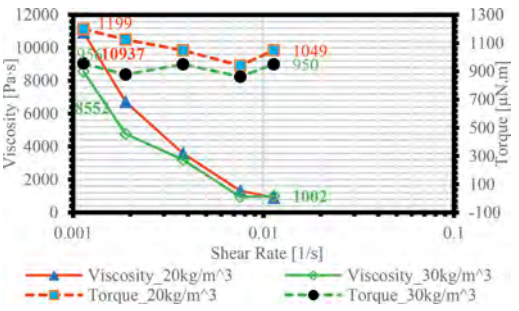

Figure 14. Variation in Biomass Concentration - Viscosity and Torque Vs. Effective Shear Rate - Full-Scale Rheometer.

4 DISCUSSION

The use of biomass in tunneling operations offers a chance to offset environmental concerns linked to using alternative chemical soil conditioners. Integrating biomass with water as a soil conditioner provides an eco-friendly alternative, improving workability and addressing environmental concerns during muck disposal.

The test matrix was designed to analyze how Biomass affects clay rheology, and how beneficial in tunneling operations with EPB TBM. A precise method employing the advanced rheometer DHR-3 was initially utilized, followed by utilizing a Full-Scale Rheometer. The significant benefit of employing a Full-Scale Rheometer was to mitigate the challenges of characterizing the rheological properties of soil materials with large particle sizes and high

viscosities, that traditional steady-shear rheometers are not capable of measuring.

The initial testing phase aimed to establish baseline measurements using a mix of Wyoming Bentonite clay with 200 wt% moisture content. This same composition was then utilized with a biomass concentration of 20 kg/m^3.

With the inclusion of biomass, the torque decreased by approximately 50 %, while viscosity increased by about 14 % in the DHR-3 rheometer. This notable reduction in torque highlights the biomass's efficacy in clay-rich soils.

Using the Pin Rotor on a Full-Scale Rheometer to examine the material's composition, the data revealed a significant reduction of 55 % and 56 % in torque and viscosity, respectively, for Wyoming Bentonite at a low effective shear rate. The discussion focuses on a low shear rate, which is feasible in the EPB TBM operation.

The Full-Scale Rheometer was used with geometry similar to a screw conveyor in EPB TBM. A comparative analysis of the Pin Rotor and Auger was conducted to understand the shear surface's influence on rheology. The findings revealed a 17 % difference in torque and a 15 % difference in viscosity at lower effective shear rates, underscoring the influence of impeller geometry. This signifies that soil muck with a significant clay content might affect the screw conveyor's efficiency if the geometry is altered for any reason during operation.

The last set of tests aimed to assess how varying biomass concentration affects the rheological properties of clay materials. Denver clay was chosen as the base material, and an auger was employed as an attachment in a Full-Scale Rheometer to closely mimic real-world conditions of tunneling in clay. The impact of biomass concentration was particularly noticeable at lower effective shear rates, with a substantial difference observed. Conversely, the viscosity of the mixture exhibited almost no variation at higher effective shear rates. The findings highlighted a 20 % reduction in torque at a biomass concentration of 30 kg/m^3 compared to 20 kg/m^3. Furthermore, a significant 22 % difference in viscosity was noted at an effective shear rate of 0.0011 s-1. These results emphasize that a standardized biomass concentration is not universally applicable across all material types. Rather, tailored laboratory tests are necessary to determine the optimal biomass concentration for soil material at each tunneling site.

5 CONCLUSIONS

Incorporating biomass into tunneling operations presents the opportunity for an environmentally friendly solution to reduce mechanical workload in the cutting chamber and screw conveyor. Experiments investigated the impact of biomass on the rheological properties of clay, including viscosity and torque at varying shear rates, using advanced rheometry (DHR-3) and a Full-scale rheometer. Tests with Bentonite clay having 200 wt% moisture showed ~50% torque reduction with biomass addition, confirmed in both small-scale and full-scale rheometers. After having the full-scale test results validated with advanced rheometry, a real-world simulation was designed using the Denver Clay at low moisture content which was deemed to be prone to clogging. Varying biomass concentrations in the Denver Clay mix further confirmed the impact of biomass on viscosity and torque requirement at a certain range of effective shear rates in a mix with 25 wt% moisture content. Site-specific full-scale testing is critical to determine optimal biomass levels, moving beyond a one-size-fits-all approach. This research highlights biomass's potential for decreasing clay viscosity and required torque, easing muck transportation and disposal.

ACKNOWLEDGMENTS

We gratefully acknowledge the generous support of Corbion company for providing the biomass Encapso™, to conduct this research endeavor. Additionally, we extend our appreciation to the Earth Mechanics Institute at the Colorado School of Mines and its staff for providing us with the requisite help in the successful execution of this research.

REFERENCES

Adams, J., and Hooper, J. 2001. Clays. In Elsevier eBooks (pp. 1236–1242). https://doi.org/10.1016/b0-08-043152-6/00234-5

Anderson, D. M., and Low, P. F. (1957). Density of Water adsorbed on Wyoming Bentonite. Nature, 180(4596), 1194. https://doi.org/10.1038/1801194a0

Bentonite deposits of the northern Black Hills district, Wyoming, Montana, and South Dakota | U.S. Geological Survey. (n.d.). https://www.usgs.gov/publications/bentonite-deposits-northern-black-hills-district-wyoming-montana-and-south-dakota

Bhadriraju, V., Puppala, A. J., Madhyannapu, R. S., and Williammee, R. 2008. Laboratory procedure to obtain Well-Mixed soil binder samples of medium stiff to stiff expansive clayey soil for deep soil mixing simulation. Geotechnical Testing Journal, 31(3), 100936. https://doi.org/10.1520/gtj100936

Bleam, W. F. 2017. Clay Mineralogy and Chemistry. In Elsevier eBooks (pp. 87–146). https://doi.org/10.1016/b978-0-12-804178-9.00003-3

Brindley, G. W. 2006. Clays, clay minerals. In Kluwer Academic Publishers eBooks (pp. 69–80). https://doi.org/10.1007/0-387-30720-6_23

Chaudhuri, S. D., Mandal, A., Dey, A., and Chakrabarty, D. 2020. Tuning the swelling and rheological attributes of bentonite clay modified starch grafted polyacrylic acid based hydrogel. Applied Clay Science, 185, 105405. https://doi.org/10.1016/j.clay.2019.105405

Cumaraswamy, V., and Mohammed, A. 2020. Effect of drilling mud bentonite contents on the fluid loss and

filter cake formation on a field clay soil formation compared to the API fluid loss method and characterized using Vipulanandan models. Journal of Petroleum Science and Engineering, 189, 107029. https://doi.org/10.1016/j.petrol.2020.107029

Dudhat, S. M., Kettler, C. N., and Dave, R. H. 2016. To study capping or lamination tendency of tablets through evaluation of powder rheological properties and tablet mechanical properties of directly compressible blends. AAPS PharmSciTech, 18(4), 1177–1189. https://doi.org/10.1208/s12249-016-0576-1

Feinendegen, M., and Ziegler, M., and Weh, M. and Spagnoli, G. 2011. Clogging during EPB-tunneling: Occurrence, classification and new manipulation methods. 12.

Garroux G. de Oliveira, D. and Thewes, M., and Langmaack, L., and Diederichs, M. 2018. Proposed Methodology for Clogging Evaluation in EPB Machines.

Gharahbagh, E. A., Qiu, T., and Jamal, R., 2013b. Evaluation of granular soil abrasivity for wear on cutting tools in excavation and tunneling equipment. Journal of Geotechnical and Geoenvironmental Engineering, 139(10), 1718–1726. https://doi.org/10.1061/(asce)gt.1943-5606.0000897

Gharahbagh, E. A., Jamal, R., and Talebi, K. H. S. 2014b. Experimental study of the effect of conditioning on abrasive wear and torque requirement of full face tunneling machines. Tunneling and Underground Space Technology, 41, 127–136. https://doi.org/10.1016/j.tust.2013.12.003

Hannon, J. S., Huff, W. D., and Sturmer, D. M. 2019. Geochemical relationships in Cretaceous bentonites as inferred from linear discriminant analysis. Sedimentary Geology, 390, 1–14. https://doi.org/10.1016/j.sedgeo.2019.07.001

Hannon, J. S., Dietsch, C., and Huff, W. D. 2020. Trace-element and Sr and Nd isotopic geochemistry of Cretaceous bentonites in Wyoming and South Dakota tracks magmatic processes during eastward migration of Farallon arc plutons. Geological Society of America Bulletin, 133(7–8), 1542–1559. https://doi.org/10.1130/b35796.1

Hauser, E.A., and Colombo, U. 1953. Colloid science of montmorillonites and bentonites. Clays and Clay Minerals, Second National Conference, V0l. 2. 439–461.

Hu, W. 2020. Developing a System to Measure Rheology of Conditioned Soil for Soft-Ground TBM Tunneling (Order No. 27834424). Available from Dissertations and Theses @ Colorado School of Mines; ProQuest Dissertations and Theses Global; Publicly Available Content Database. (2415421697). http://mines.idm.oclc.org/login?url=https://www.proquest.com/dissertations-theses/developing-system-measure-rheology-conditioned/docview/2415421697/se-2

Hu, W., and Jamal, R. 2020. A new method to quantify rheology of conditioned soil for application in EPB TBM tunneling. Tunneling and Underground Space Technology, 96, 103192. https://doi.org/10.1016/j.tust.2019.103192

Hua, M., Zhang, S., Pan, B., Zhang, W., Lv, L., and Zhang, Q. 2012. Heavy metal removal from water/wastewater by nanosized metal oxides: A review. Journal of Hazardous Materials, 211–212, 317–331. https://doi.org/10.1016/j.jhazmat.2011.10.016

Huggett, J. 2015. Clay Minerals□. In Elsevier eBooks. https://doi.org/10.1016/b978-0-12-409548-9.09519-1

Jefferis, S., and Merritt, A. 2013. Exploiting physico-chemical modification of soils in closed face tunneling. 10.1201/b15004-73.

Jeong, S. W., Locat, J., Leroueil, S., and Malet, J. 2010. Rheological properties of fine-grained sediment: the roles of texture and mineralogy. Canadian Geotechnical Journal, 47(10), 1085–1100. https://doi.org/10.1139/t10-012

Nelson, J. D., and Miller, D. J. 1992. "Expansive Soils: Problems and Practice in Foundation and Pavement Engineering," John Wiley and Sons Inc., New York.

Kang, C., Wu, Y., Yi, Y., and Bayat, A. 2019. Assessment of the clogging potential of two clays. Applied Clay Science, 178, 105134. https://doi.org/10.1016/j.clay.2019.105134

Kooistra, A., Verhoef, P., Broere, W., and Van Tol, F. 1998. Appraisal of the stickiness of natural clays from laboratory tests. ResearchGate.

López-Fernández, M., Matschiavelli, N., and Merroun, M. L. 2021. Bentonite geomicrobiology. In Elsevier eBooks (pp. 137–155). https://doi.org/10.1016/b978-0-12-818695-4.00007-1

Mair, R.J. 2008. Tunneling and geotechnics: new horizons. Geotechnique, 58(9), 695–736. https://doi.org/10.1680/geot.2008.58.9.695

Maidl, B., Herrenknecht, M., Mitzel, M., and Anheuser, L. 1996. Mechanised shield tunneling. Ernst and Sohn.

Mat, M. 2023. Bentonite. Geology Science. https://geologyscience.com/minerals/silicates-minerals/bentonite/?amp

Matsui, M. S., Carle, T., and Costa, M. 2022. The interaction of metals and the skin: The good, bad, and the ugly. In Elsevier eBooks (pp. 407–420). https://doi.org/10.1016/b978-0-12-823292-7.00011-5

Mosleh, M., Hu, W., and Jamal R. 2019. Introduction to Rock and Soil Abrasivity Index (RSAI). Wear, 432–433, 202953. https://doi.org/10.1016/j.wear.2019.202953

Pedarla, A., Chittoori, S., and Puppala, A. J. 2011. Influence of mineralogy and plasticity index on the stabilization effectiveness of expansive clays. Transportation Research Record, 2212(1), 91–99. https://doi.org/10.3141/2212-10

Puppala, A., Punthutaecha, K., and Vanapalli, S. K. 2006. Soil-Water characteristic curves of stabilized expansive soils. ResearchGate. https://doi.org/10.1061/(ASCE)1090-0241(2006)132:6(736)

Sebastiani, D., Spagnoli, G., De Amici, M., and Mangifesta, S. 2022. Geotechnical characterization of natural clays for the prediction of clogging risk for TBM. Research Square (Research Square). https://doi.org/10.21203/rs.3.rs-1645803/v1

Shrivastava, A. K., Jain, D., and Vishwakarma, S. 2016. Frictional resistance of drilling fluids as a borehole stabilizers. International Journal of Geo-engineering, 7 (1). https://doi.org/10.1186/s40703-016-0026-7

Sonebi, M., and Perrot, A. 2019. Effect of mix proportions on rheology and permeability of cement grouts containing viscosity modifying admixture. Construction and Building Materials, 212, 687–697. https://doi.org/10.1016/j.conbuildmat.2019.04.022

TA Instruments. 2014. Discovery Hybrid Rheometer (DHR Series). TA Instruments -Waters LLC

Todaro, C., Carigi, A., Peila, L., Martinelli, D., and Peila, D. 2022. Soil conditioning tests of clay for EPB tunneling. Underground Space, 7(4), 483–497. https://doi.org/10.1016/j.undsp.2021.11.002

Vinai, R., Oggeri, C., and Peila, D. 2008. Soil conditioning of sand for EPB applications: A laboratory research. Tunneling and Underground Space Technology, 23(3), 308–317.

Wang, Y., He, T., Yin, D., Han, Y., Zhou, X., Zhang, G., and Tian, X. 2020. Modified clay mineral: A method for the remediation of the mercury-polluted paddy soil. Ecotoxicology and Environmental Safety, 204, 111121. https://doi.org/10.1016/j.ecoenv.2020.111121

Xie, J.; Cui, X.; Guo, N.; Liu, G., 2021: Influence of Mix Proportions on Rheological Properties, Air Content of Wet Shotcrete—A Case Study. Applied Sciences., 11, 3550.

Yang, Z.; Liu, P.; Chen, P.; Li, S.; Ji, F., 2023: Clogging Prevention of Slurry–Earth Pressure Balance Dual-Mode Shield in Composed Strata with Medium–Coarse Sand and Argillaceous Siltstone. Applied Sciences., 13, 2023.

Zhang, Y., Xu, P., Xu, M., Pu, L., and Wang, X. 2022. Properties of bentonite slurry drilling fluid in shallow formations of deepwater wells and the optimization of its wellbore strengthening ability while drilling. ACS Omega, 7(44), 39860–39874. https://doi.org/10.1021/acsomega.2c03986

Zhang, Y., Xu, P., Xu, M., Pu, L., and Wang, X. 2022b. Properties of bentonite slurry drilling fluid in shallow formations of deepwater wells and the optimization of its wellbore strengthening ability while drilling. ACS Omega, 7(44), 39860–39874. https://doi.org/10.1021/acsomega.2c03986

Zumsteg, R., and Puzrin, A.M. 2012. Strain hardening and softening of saturated clay: Plasticity and damage modeling. Géotechnique, 62(6), 569–579.

Tunnelling for a Better Life – Yan, Celestino, Thewes & Eberhardt (Eds)
© 2024 The Author(s), ISBN 978-1-032-80042-4
Open Access: www.taylorfrancis.com, CC BY-NC-ND 4.0 license

TBM jamming and statistical estimators: Case of a long and deep tunnel

Daniel Kasal, Alberto Flor*, Federico Amadini & Andrea Oss
Systra-SWS, Trento, Italy

ABSTRACT: TBM jamming events caused by caving can be difficult to predict and can cause significant delays and cost overruns. This study proposes a new method for predicting jamming events using aggregated quantities calculated on the TBM raw excavation data. These statistical estimators tend to reach extreme values when in proximity of recorded TBM blockages. By classifying each excavation section with a score based on the statistical estimator's deviation from normality, the TBM advancement can be monitored, helping operators and construction crew to anticipate difficult situations. The method is applied to three long and deep tunnels excavated through the Alps, where an extensive dataset is available.

Keywords: TBM, Excavation, Caving, Prediction, Statistical estimators

1 INTRODUCTION

In mechanized tunnel excavation, the unexpected stop (jamming) of the Tunnel Boring Machine (TBM) is one of the worst occurrences, in terms of cost, time and workers' safety. The ability to predict the likelihood of a TBM jamming event is therefore of paramount importance during the excavation. Early warnings of impending TBM failure (even just one ring ahead) are essential for implementing effective countermeasures.

There are many articles focusing on real time prediction during excavation, especially with Machine Learning techniques. For example: in Wu et al. (2021) a method is proposed to predict the encountered rockmass class, classified by their boreability, while Gao et al. (2019) describe the use of Recurrent Neural Networks able to predict the future values of important TBM operating parameters, by using in-situ monitoring.

Hasanpour et al. (2020), on the other hand, propose a method to predict the jamming risk at design phase by using artificial neural network (ANN) and Bayesian network (BN) trained on synthetic data that model ground convergence and the possibility of machine entrapment.

In this paper the case of deep and long tunnel is discussed, using the dataset of three TBMs, that encountered critical sections and underwent prolonged stops due to difficult geological conditions and severe overburden. The jamming events were nine in total, eight of which caused by caving and one by squeezing.

The goal is to test whether these critical occurrences could be predicted by analysing the TBM data, such as Advance Rate or Torque, called Key Performance Indicator (KPI). These quantities, sampled at regular time intervals (every 3 seconds), tend to assume anomalous behaviours in the rings preceding critical sections.

This work aims to quantify the perceived spread and erratic trend of the TBM KPIs, proposing and discussing the usage of statistical estimators that can signal the upcoming critical phenomenon, showing that their extreme behavior is correlated to recorded jamming events.

2 PROJECT OVERVIEW

The Brenner Base Tunnel (BBT) will connect Fortezza (Italy) to Innsbruck (Austria). With total length of 56 km it will join the existing Innsbruck railway tunnel, reaching a total length of 64 km and becoming the longest railway tunnel in the world. This paper focus on the mechanized excavation with double shielded TBMs of the Mules 2-3 lot (Citarei et al. 2020), consisting of three parallel tunnels: an exploratory tunnel and two mainline tunnels. The distance between the main tunnels is 70 m, while the exploratory tunnel is located 12 m below them, as shown in Figure 1.

*Corresponding author: aflor@systra.com

DOI: 10.1201/9781003495505-251

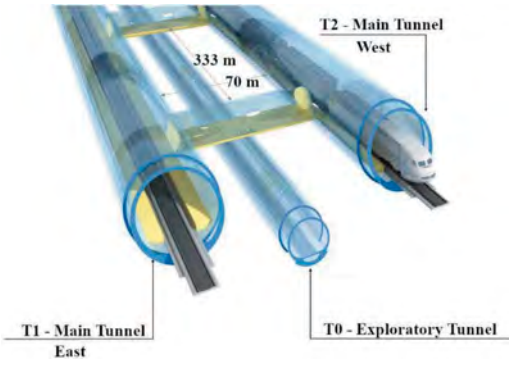

Figure 1. Cross section of the BBT tunnels, modified from (BBT, 1999).

The overburden ranges from 595 to 1715 m. The alignment crosses a complex geology, passing through the Subpenninic core of the Tauern Window, which is wrapped by a stratified layer of Penninic and Austroalpine. The geological context is characterized by a great heterogeneity of the rock masses and by the presence of numerous faults. The main lithologies are phyllites, schists, granite, granodiorites and gneiss, as shown in the design and as-built geological profile in Figure 2. A complete geological description is presented in Schiavo et al. (2015).

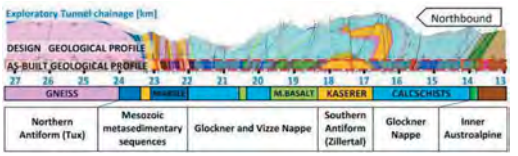

Figure 2. BBT Lot Mules 2-3 as-built geological profile according to the Joint Venture (Pescara et al. 2020).

3 DATA

The datasets employed contain the measurement of TBM parameters for the three parallel tunnels. We will codename them T0 (the exploratory tunnel), T1 and T2 (the two main tunnels). At the time of writing, T0 and T1 are completed, while T2 is still under construction. Specifics of the three tunnels, and respective data, are reported in Table 1. The raw data samplings are the number of rows in the datasheet. The dataset is substantially larger than those reported in many other publications.

The dataset contains the measurement (sampled with a 3 second interval) of the TBM parameters, called Key Performance Indicators (KPI) (Maggio et al., 2022).

The KPI considered in the discussion are:

- Torque (T).
- Thrust force (TF).

Table 1. Tunnels details.

	T0	T1	T2
Total length [km]	14	14	11
Rings number [-]	9456	8130	6165
Excavation diameter [m]	6.8	10.7	10.7
Number of blocks occurred [-]	3	1	5
Raw data samplings	$9 \cdot 10^6$	$9 \cdot 10^6$	$6 \cdot 10^6$

- Rotational speed (RPM).
- Advance rate (AR).
- Penetration rate (PR).

A total of nine jamming events occurred to the TBMs in the three tunnels. Most of these were caused by caving, or face instability. One event was caused by squeezing, i.e., severe convergence of rock mass in plastic conditions (Working Group n°17, 2017). Some of these jamming events are described in detail in Amadini et al. (2021).

The events analysed and their causes are:

- T0.0 – caving;
- T0.1 – squeezing;
- T0.2 – caving;
- T1.1 – caving;
- T2.0 – caving;
- T2.1 – caving;
- T2.2 – caving;
- T2.3 – caving;
- T2.4 – caving and squeezing.

A caving event is induced by poor rock mass quality, high stress and, possibly, by water inflows. The excess of excavated material leads to a decrease in advance rate and rotational speed, with an increase in torque. When caving occurs, the TBM jamming is caused either by the machine reaching the maximum torque available or by problems to the material extraction's system, such as the backfilling of the cutterhead or the falling of excavated material from the conveyor bell.

A squeezing event is caused by the inability of the TBM's jacks to exert the necessary thrust force to contrast the friction between rock mass and shields.

3.1 *Aggregated data vs raw data*

To analyze the TBM functioning, it is common practice to consider aggregate values for each KPI (aggregated data), usually averaged on some length (every centimetre, every ring length, etc.). By looking at the mean per ring, one may anticipate whether some anomalies in the excavation are occurring. The main reason to use the ring-averaged values, instead of the more detailed time sampling (raw data), is twofold. On one hand the parameters behaviour inside a ring is wild and sometimes very difficult to analyse, therefore engineers or scientists may prefer to work with just the mean of the TBM quantity for

each ring (aggregate the information); these quantities are, most of the time, sufficient to summarize the situation. On the other hand, there is a computational and storage necessity: for a long tunnel, the datasheet with the recorded key indicators averaged per ring is of the order of thousands of rows times hundreds of columns. If one were to store the timestamped samplings (for example every 3 seconds) the rows can easily explode to the millions (the raw data are in the order of 10^3 per ring).

However, using only the KPI's average values per ring could lead to a significant loss of information. A comparison between two rings with a similar torque average is shown in Figure 3. In the second graph, it can be clearly seen that the average value is not representative of the whole situation. The goal is to quantify the extreme behaviour in the second graph, by aggregating the information with an estimator that could complement mean per ring.

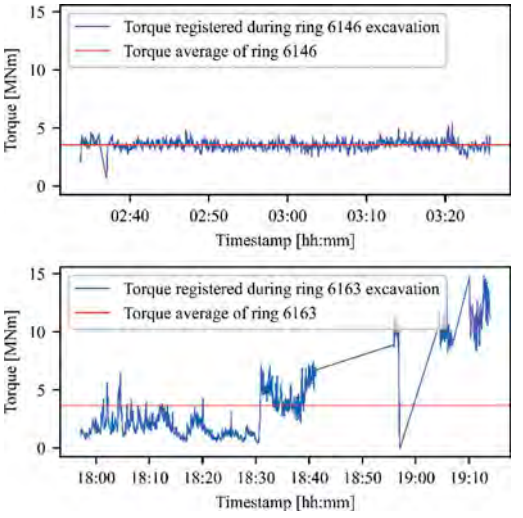

Figure 3. Torque values during excavation of two different ring. Both images have the same mean value (red line), but they present two distinctively different situations.

4 PROPOSED ESTIMATORS

We present a collection of statistical quantities that may give a further understanding on the TBM's advancement, helping to describe KPI's anomalous readings.

Given a sample $x_1, x_2, \ldots, x_n$ of a measured quantity during the excavation of a single ring, the following statistical quantities can be calculated:

- **Mean**:

$$\mu = \frac{1}{n}\sum_{i=1}^{n} x_i$$

- **Standard deviation (SD)**:

$$\sigma = \sqrt{\frac{1}{\mathrm{n}}\sum_{i=1}^{n}(x_i - \mu)^2}$$

- **Max variation (MaxVar)**: difference between 95$^{\text{th}}$ percentile and 5$^{\text{th}}$ percentile range

$$max_{\text{var}} = P_{95} - P_5$$

- **Interquartile range (IQR)**: the range between the 75$^{\text{th}}$ percentile (Q3) and the 25$^{\text{th}}$ percentile (Q1)

$$\mathrm{IQR} = Q_3 - Q_1 = P_{75} - P_{25}$$

- **Coefficient of variation (CV)**:

$$CV = \frac{\sigma}{\mu}$$

The previous statistical quantities will be called **statistical estimators** for the rest of the paper. These are aggregated quantities calculated for each ring using the raw data (3 seconds sampling) recorded during ring excavation.

A graphical representation of the statistical parameters chosen is shown in Figure 4 (applied to torque distribution), while a procedure chart of aggregating raw data to obtain the statistical estimator for three rings is depicted in Figure 5.

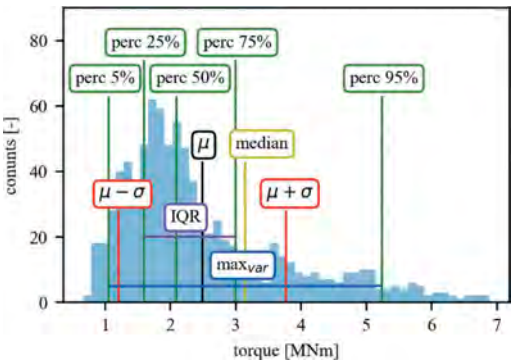

Figure 4. Graphical representation of the statistical quantities, applied to the torque distribution for the excavation of one ring.

In the following paragraphs, we will use the estimators as aggregate quantities per ring. Specifically, for each TBM parameter, we will calculate the estimators for each ring.

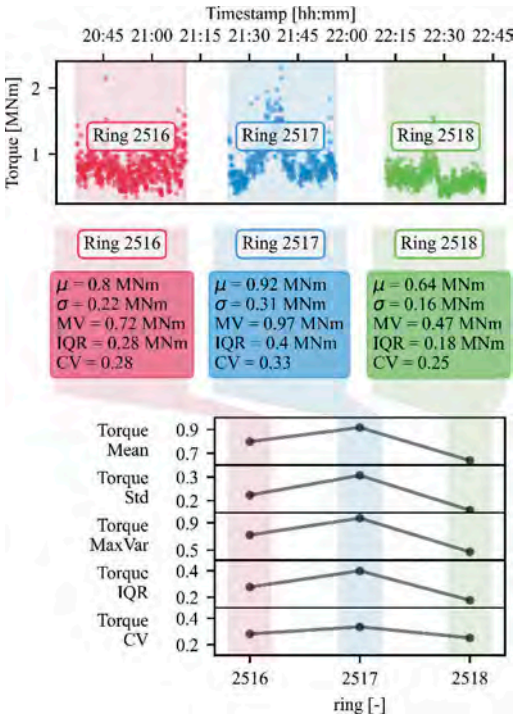

Figure 5. Example of the aggregating procedure, from raw data to statistical estimators, for three rings.

5 RESULTS

In addition to mean and standard deviation, we aggregate the TBM data during a ring excavation cycle by calculating the estimators described in the previous paragraph (max variation, interquartile range, coefficient of variation), for the TBM KPI's described in Paragraph 3 (torque, thrust force, rotational speed, advance rate, penetration rate).

As a preliminary step, the estimators' values are studied, looking for anomalous behaviours in the rings preceding a jamming episode. First empirical evidence is inferred by plotting the estimators' trends. Afterwards a scoring system to quantify the deviation of the estimators from their usual baseline is proposed, correlating this deviation with the occurrence of critical phenomena.

5.1 *Estimators behaviour*

The trends of the estimators in rings close to the recorded TBM's jamming events show that they tend to reach extreme values near the stops.

Among the aggregated quantities, the proposed estimators can alert of a critical section earlier than the mean, at least one ring earlier. IQR and MaxVar in particular, as shown in Figure 6 and Figure 7, signal the critical zone with one ring in advance. In both Figures the last 100 rings before the jamming events are plotted.

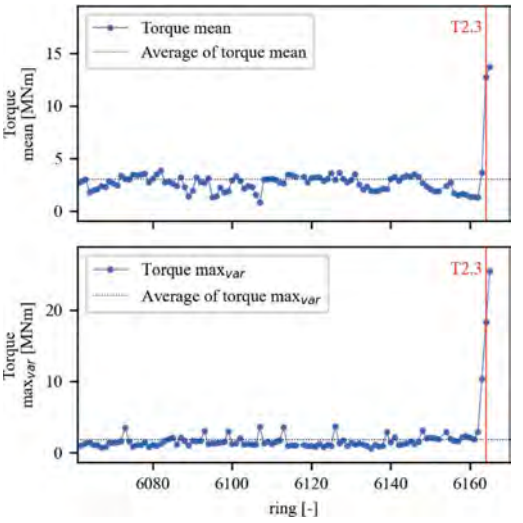

Figure 6. Torque mean value for each ring (above) and Torque maximum variation for each ring (below). Vertical line: the ring where T2.3 TBM stop happened.

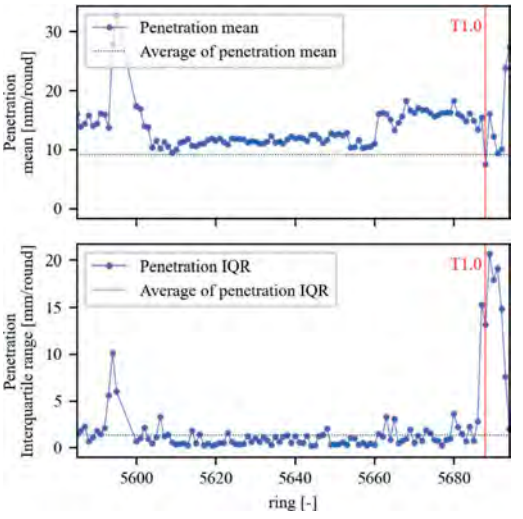

Figure 7. Penetration mean value for each ring (above) and penetration interquartile range for each ring (below). Vertical line: the ring where T1.0 TBM stop happened.

The comparison of the same estimator close to all jamming events can be plotted, by stacking the lines together for each critical event of the three tunnels. The curves show a positive trend in the 10 rings before the stops, for all nine cases recorded.

Torque – maximum variation (Figure 8): in the two rings before the jamming event, there is a relevant increase in torque maximum variation for the events T0.0, T0.2, T1.0, T2.3 and T2.4. In the jamming ring, for all the events analysed the quantity is at its peak, except for T0.1. The increase in torque maximum

variation seems to be correlated with the occurrence of caving, and T0.1 is the only event caused exclusively by squeezing.

Penetration – interquartile range (Figure 9): In this case, there is also a perceivable increase of the value while approaching the jamming event. The TBM stops showing the steepest trend in penetration IQR are the same of torque max variation, except for T2.4, where the variation is not that perceivable.

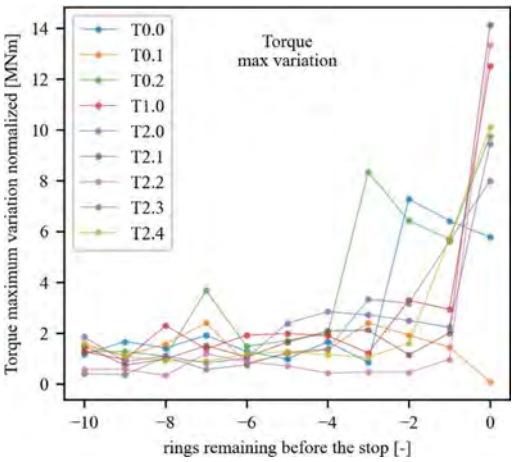

Figure 8. Trend of torque maximum variation in the last ten rings before the critical events. The estimators have been normalized for visibility, making results from the three tunnels comparable.

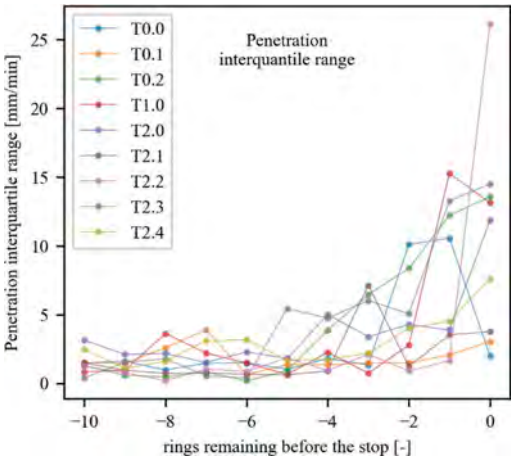

Figure 9. Trend of penetration interquartile range in the last ten rings before the critical events.

5.2 *Scoring the estimators*

Up to this point it has been shown that by employing statistical quantities of Paragraph 4, we can correlate their evolution during excavation with the presence of critical sections. Graphically we showed that the estimators tend to spike when close to the ring of a recorded TBM stop.

This qualitative understanding must be formalized. The next step is to construct a scoring system, based on the statistical aggregations per ring, able to classify all excavation sections according to the likelihood of a jamming episode.

This next paragraph may appear complex at first glance, since we are going to construct a statistical distribution of statistical estimators. The core idea is that, once calculated for each ring, the estimators form a statistical population and, for each KPI, we have the collection of the estimator outcomes. Every new value of the estimator can be compared to said distribution and ranked accordingly.

By doing so, one can quantify the sentence "the estimators assume quite an extreme value", by defining the extremity of the value compared to its other occurrences.

We assign the following score, called **variability score**, to each ring, based on the value of the statistical estimators:

- "H": high variation compared to the estimator history, when the value is above the 99th.
- "M": medium variation if the value is above the 90th percentile.
- "L": low variation, all other cases.

With this scoring system we can classify the tunnel sections according to the severity of each KPI deviation from a "normal" behaviour.

As shown in Figure 10, the whole tunnel can be divided into three sections, according to the estimator variability score. The rings that have estimators with a score "H" are those that in the previous sections were described as anomalous and with extreme values.

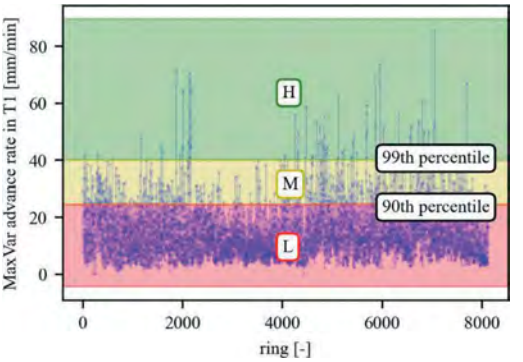

Figure 10. Visual aid for the variability scores: variability score for the Max Var value of advance rate, calculated at each tunnel ring for all the recorded values. The rings for which the advance rate Max Var is above the 99th percentile of its distribution are ranked as "H" (High) score.

The intuitive idea in Paragraph 5.1 (see Figure 8) can now be formalized, by looking at the estimators score in the rings preceding a jamming event. Table 2 shows the highest variability score between the two rings before these events. For each recorded TBM stop (rows), we report the variability score of the statistical estimators (standard deviation, maximum variation, coefficient of variation, inter-quartile range) for the KPI (torque, thrusts, rounds per minute, advance rate, penetration).

An "H" value of the variability score means that either one or both rings before the critical section have a very unusual value of the statistical estimator. In many cases, the critical section is anticipated by an abnormal value, i.e. "H" score.

Table 2. Variability scores for estimators of KPI close to critical zone.

	Standard deviation					**Maximum variation**				
	T	*TF*	*RPM*	*AR*	*P*	*T*	*TF*	*RPM*	*AR*	*P*
T0.0	**H**	**H**	M	M	**H**	**H**	**H**	M	M	**H**
T0.1	L	**H**	L	M	M	M	**H**	L	**H**	M
T0.2	**H**	L	L	M	**H**	**H**	L	M	M	**H**
T1.0	**H**	L	M	**H**	**H**	**H**	M	M	**H**	**H**
T2.0	M	L	L	L	M	M	L	L	L	M
T2.1	L	L	L	L	M	M	L	L	M	M
T2.2	L	L	L	L	L	L	L	L	L	L
T2.3	**H**	M	L	L	**H**	**H**	M	L	L	**H**
T2.4	**H**	**H**	**H**	**H**	M	**H**	**H**	**H**	**H**	M

	Interquartile range					**Coefficient of variation**				
	T	*TF*	*RPM*	*AR*	*P*	*T*	*TF*	*RPM*	*AR*	*P*
T0.0	**H**	**H**	M	**H**	**H**	M	**H**	**H**	**H**	**H**
T0.1	L	**H**	M	M	M	M	L	L	M	M
T0.2	**H**	L	M	**H**	**H**	M	L	M	**H**	**H**
T1.0	**H**	M	M	**H**	**H**	**H**	M	**H**	**H**	M
T2.0	M	L	L	M	M	M	L	L	M	L
T2.1	M	L	M	M	M	M	L	M	M	L
T2.2	L	L	L	L	L	L	L	L	L	L
T2.3	**H**	M	L	L	**H**	L	M	M	**H**	**H**
T2.4	**H**	M	M	**H**	M	**H**	**H**	**H**	**H**	**H**

The statistical estimators that have a variability score between "H" and "M" in all the TBM stop events but one (T2.2) are:

- Maximum variation of the torque.
- Standard deviation, maximum variation, and interquartile range of penetration.
- Coefficient of variation of advance rate.

It is then important to point out that there are some critical events that did not show great variability of any statistical estimator before the ring of the jamming. This is the case of T2.0, T2.1 and especially the stop T2.2, which did not show any "H" or "M" behaviour in any parameter analysed.

5.3 *Combining the scores*

From previous section, the statistical estimators with variability score "H" on most of the jamming events are:

- Torque standard deviation (T SD);
- Torque maximum variation (T MaxVar);
- Torque interquartile range (T IQR);
- Advance rate coefficient of variation (AR CV).

This leads to the idea of highlighting only the rings where all these four statistical estimators have score "H". As it turns out, many of this high-estimators rings are in proximity of jamming events.

The most important are those preceding the critical section (to be an information of practical use).

In Table 3 are reported the fraction of events that have 4 High-score estimators in the ring(s) preceding the stop. All the events for T0 and T1 tunnel were signalled by extreme estimators' behaviour, while 2 out of 5 of the T2 events had this alert.

Table 3. Critical events in lot Mules 2-3.

	T0	T1	T2
Total caving events	2	1	5
Events with at least 4 estimators scored 'H'	2	1	2

The 3D scatter plots in Figure 12, Figure 13 and Figure 15 show the estimators listed above (Torque SD, Torque MaxVar, Torque IQR and Advance Rate CV) for the three tunnels. The vertical red planes indicate the critical events. The markers colors are chosen as follows:

- Red: the rings where the jamming took place.
- Green: rings with all 4 estimators scored "H" and preceding the jamming event (these are the most important).
- Yellow: rings with all 4 estimators scored "H", that are either following the jamming event or far from any event (false positives).
- Blue: all other rings.

Tunnel **T2**:

For the tunnel T2 the predictive capacity is limited. By highlighting the rings that have the 4 estimators scored High, one can see that only 2 out of 5 caving events have a warning. The highlighted dots can be seen in the 3D scatter plot (Figure 11), together with the 4 estimators' behavior along the whole excavated tunnel (Torque SD, Torque MaxVar, Torque IQR and Advance Rate CV). In Figure 12 only one of the 4 plots has been chosen for clarity, but the colored marks still indicate rings with all 4 estimators scored 'H'. One can see that only the two rightmost critical events have a green-colored ring preceding them.

For the T2 tunnel there are 15 rings exhibiting abnormal behaviour. These rings are as follows (from left to right):

- The ring where event T2.0 occurred;
- The ring where event T2.1 occurred and the ring after this;
- The ring where event T2.2 occurred and the ring after this;
- A ring approximately 30m after T2.2;
- The ring where event T2.3 occurred, the ring before and the ring after;
- 3 consecutive rings approximately 90 m after T2.3;
- The ring where T2.4 occurred, the ring before and the ring after.

These results show that, in two cases, it is possible to detect abnormal behaviour (green rings) before the critical ring (red). The other three events exhibited an unpredictable behaviour.

Moreover, there are two "false positives". One of these (the one with three consecutive rings) was in fact a short jamming event, that was not included among the studied jamming occurrences since it did not require excessive effort to restart the TBM in that occasion.

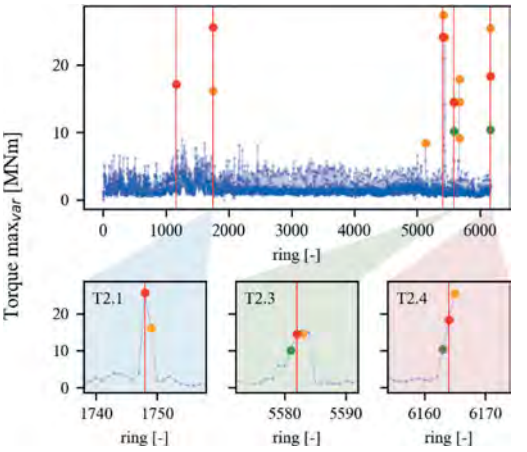

Figure 12. Torque maximum variation per ring in T2, highlighting rings with large variation in the 4 statistical estimators. Rings antecedent to the events are green, the ring of the event is red, while all others are yellow.

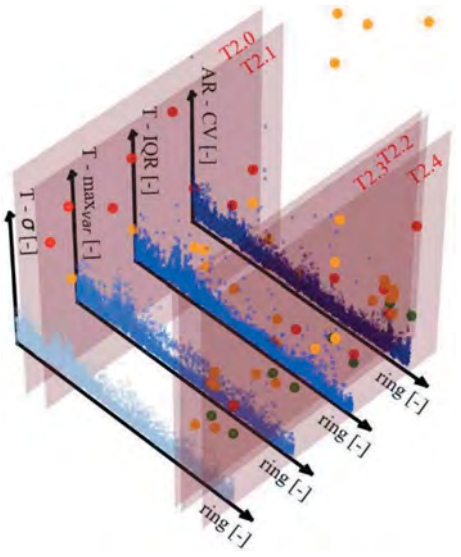

Figure 11. The four estimators for the tunnel T2: Torque SD, Torque MaxVar, Torque IQR and Advance Rate CV. Vertical planes coincide with rings where critical events took place.

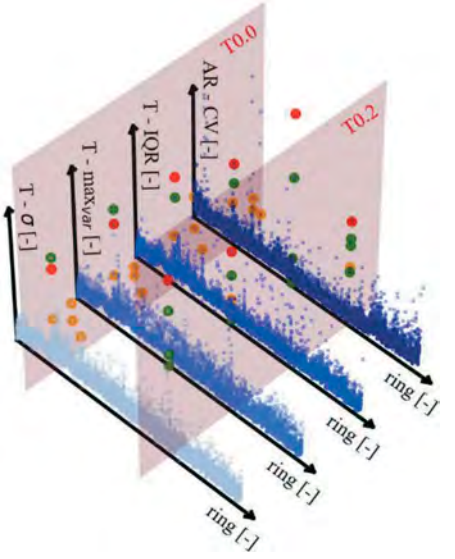

Figure 13. The four estimators for the tunnel T0: Torque SD, Torque MaxVar, Torque IQR and Advance Rate CV. Vertical planes coincide with rings where critical events took place.

Tunnel **T0** and **T1**:

For the tunnels T0 and T1, the estimators analysis works better. As for T2, the 3D scatter plots (Figure 13 and Figure 15), show the 4 estimators evolution along the excavated tunnel, with the red planes denoting the critical regions and the red-yellow-green points been the rings variability score "H" for all 4 estimators. In Figure 14 and Figure 16, a 2D slice of the previous graphs, with only one estimator (torque Max Var).

We see anomalies one ring before for T0.0 and T1.0, and for T0.2 up to three rings before.

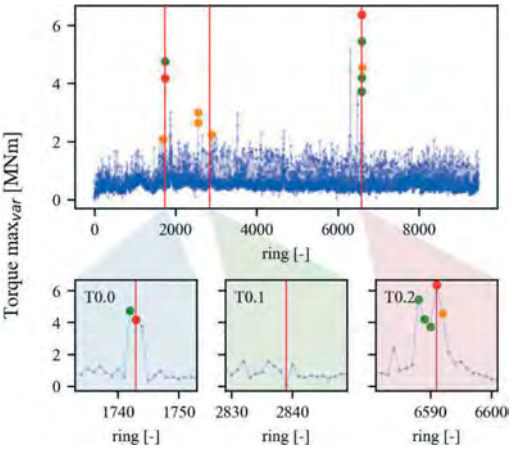

Figure 14. Torque maximum variation per ring in T0, highlighting rings with large variation in the 4 statistical estimators. Rings antecedent to the events are green, the ring of the event is red, while all others are yellow.

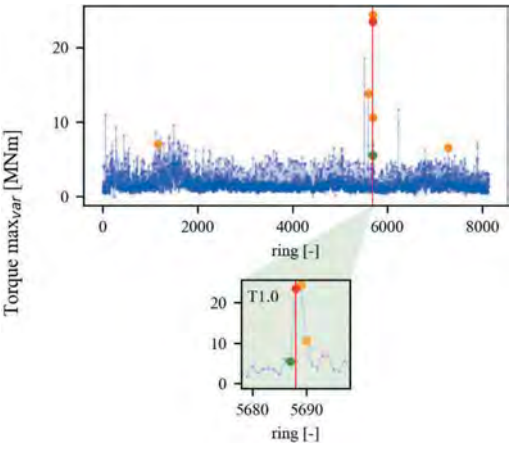

Figure 16. Torque maximum variation per ring in T1, highlighting rings with large variation in the 4 statistical estimators. Rings antecedent to the events are green, the ring of the event is red, while all others are yellow.

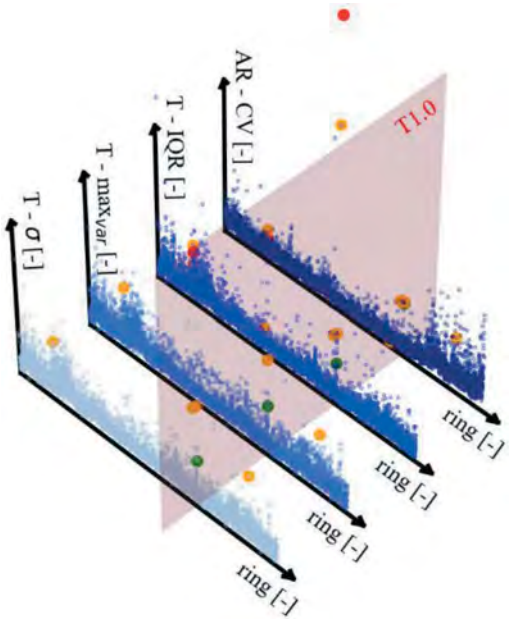

Figure 15. The four estimators for the tunnel T1: Torque SD, Torque MaxVar, Torque IQR and Advance Rate CV. Vertical planes coincide with rings where critical events took place.

The T0.1 event needs to be studied separately, because it was caused by squeezing and the parameters behaviour in a squeezing event differ from those of a caving event.

In T0 there was a false positive, in a complex zone 100m before the squeezing jamming T0.1 occurred.

There were three false positives in T1: one 100 m before T1.0 event, where a minor stop of four days occurred, and the other two in different areas. It should be noted that the excavation of these two rings was difficult, having taken about a day for each ring.

5.4 *Results interpretation*

While the proposed methodology demonstrated overall reliability, it underperformed in T2 predicting two out of five critical sections, as delineated in Table 3.

The challenges encountered in T2 can be attributed to its status as the last tunnel excavated. In brittle rock masses, T2 experienced detensioning induced by the prior excavation of tunnels T0 and T1. This, coupled with the presence of sub-vertical fault systems in the BBT project and the inherent unpredictability of TBM operation influenced by human factors, resulted in more abrupt TBM stops in T2.

It is crucial to recognize that, as expected with a predictive tool, the proposed methodology encounters difficulties in predicting such sudden events.

6 CONCLUSIONS

In this paper the use of KPIs statistical estimators is proposed. Their use can help monitoring the TBM advance to anticipate TBM jamming events, caused by caving. An extensive dataset has been analysed from the combined samplings of three long and deep rock tunnels (BBT railway project between Italy and Austria).

The statistical estimators avoid the loss of information that comes with using only the ring average of KPIs and are relatively simple quantities compared to the huge amount of the raw data samplings.

It has been proved that for some KPI, the statistical estimators tend to spike when approaching

a jamming event. By combining these quantities, a method is proposed that leads to the identification of excavation anomalies one ring (or even two rings) before, for 5 caving events out of 8, although some false positives were highlighted in other zones of the excavation.

It should nonetheless be noted that even in the false positive rings the TBM stopped for a short period of time and risked being jammed.

The scoring of rings based on the estimators can help monitoring TBM advancement, by being displayed on a dashboard in real time during excavation and serving as a supportive tool for decision-making, complementing human judgment.

Another application is to employ the estimators for automated data labelling for machine learning classification tasks. Most Machine Learning applications for TBM excavation are regressions and (time)series forecasting, see Flor et al (2023) and references therein. Classification would require the labelling of data and the proposed scoring system seems a good candidate to differentiate rings according to the value of IQR or Maximum Variation, as shown in Table 2.

The authors want to stress that this method requires some adjustments when applied to a real excavation case, when the full information of the whole tunnel is not available, since we still need to score the estimators based on their percentiles. The solution could be to use the z-score of the quantities calculated on the recent rings, i.e., on the moving statistics, as discussed in Amadini et al. (2023).

REFERENCES

Amadini, F., Flor, A., Secondulfo, M., Baliani, D., Cernera, F., La Morgia, M., Mei, A., Sassi, F., 2023. BBT, Lot Mules 2–3. Application of Machine Learning on TBM parameters for Risk Prediction tools. WTC 2023, May 12–18, 2023, Athens, Greece.

Amadini, F., Buttafoco, D., Cucino, P., Giacomin, G., Oss, A., & Schiavinato, L., 2021. Case studies related to jammed TBM in rock. Gallerie e Grandi Opere Sotterranee n.140, p. 15–25.

BBT, 1999. Project overview. URL: https://www.bbt-se.com/en/tunnel/project-overview/.

Citarei, S., Secondulfo, M., Buttafoco, D., Debenedetti, J. & Amadini, F., 2020. BBT, construction lot Mules 2–3. Production management and site logistics organization. WTC 2019, May 3–9, 2019, Naples, Italy.

Flor A., Sassi F., La Morgia M., Cernera F., Amadini F., Mei A., Danzi A., 2023. Artificial intelligence for tunnel boring machine penetration rate prediction. Tunnelling and Underground Space Technology, Volume 140, 105249.

Gao X., Shi M., Song X., Zhang C., Zhang H., 2019. Recurrent neural networks for real-time prediction of TBM operating parameters, Automation in Construction, Volume 98.

Hasanpour R., Rostami J., Schmitt J., Ozcelik Y., Sohrabian B, 2020. Prediction of TBM jamming risk in squeezing grounds using Bayesian and artificial neural networks, Journal of Rock Mechanics and Geotechnical Engineering, Volume 12, Issue 1.

Maggio, G., Voza, A., Egger, H., 2022. Key machine parameters for classification of rock mass in TBM excavation in BBT. WTC2022, Copenhagen 2–8 September 2022.

Pescara, M., Spanò, M & Della Valle, N., 2020. BBT, Lot Mules 2–3. Management of data gained by the pilot tunnel drive for the twin main tubes. *WTC 2019, May 3–9, 2019 , Naples, Italy.*

Schiavo, A., Dal Piaz, G. V., Monopoli, B., Bistacchi, A., Dal Piaz, G., Massironi, M., Toffolon, G., 2015. Geology of the Brenner Pass-Fortezza transect, Italian Eastern Alps. Journal of Maps, 11:1, 201–215.

Working Group n°17, 2017. ITA/AITES Report n°19 – TBM Excavation of Long and Deep Tunnels Under Difficult Rock Conditions. Longrine, Avignon, France.

Wu Z., Wei R., Chu Z., Liu Q., 2021. Real-time rock mass condition prediction with TBM tunneling big data using a novel rock–machine mutual feedback perception method, Journal of Rock Mechanics and Geotechnical Engineering, Volume13, Issue 6.

Tunnelling for a Better Life – Yan, Celestino, Thewes & Eberhardt (Eds)
© 2024 The Author(s), ISBN 978-1-032-80042-4
Open Access: www.taylorfrancis.com, CC BY-NC-ND 4.0 license

Construction of a Horseshoe-shaped trenchless tunnel using the rectangular element propulsion method

Daiya Koizumi*
Japan Railway Construction, Transport and Technology Agency, Yokohama, Japan

Tatsuya Shimotsu
Japan Railway Construction, Transport and Technology Agency Tokyo Regional Bureau, Tokyo, Japan

Takashi Tanaka
TODA CORPORATION, Tokyo, Japan

ABSTRACT: The Sotetsu-Tokyu-Link Line is a connecting line whose length is approximately 10 km in the city of Yokohama from Hazawa Yokohama-kokudai Station on the Sotetsu Line to Hiyoshi Station on the Tokyu Line. Shin-Tsunashima Station is a new intermediate station and locates on the fourth underground floor, approximately 35m deep (at the deepest) and 14 to 25m in width and 240m in length. Because there are several buildings on the surface at the 35m south of the station and eviction of tenants from those buildings was impossible, we decided to construct the tunnel by the square steel propulsion method, one of the trenchless method. Firstly, a series of square steel pipe boxes were constructed around the outer circumference of the tunnel to form the outer shell, and then the internal section was excavated. The cross section of the tunnel is a horseshoe shape (224m^2 internal area), and 42 square steel pipes were combined with each other. The method involved three critical challenges. (1) Accurate positioning in propulsion. (2) Closure of the steel pipes with minimum displacement. (3) Prevention of the inflow of groundwater into the launching shaft. To overcome these challenges, we adopted the following measures. (1) A new jack controller for on the propulsion machine (2) Newly developed steel shell joint structure which can tolerate construction errors (3) A double entrance packing waterproof device to be installed at the launching shaft. In this way, we are confident that these measures successfully coped with this difficult situation.

Keywords: Outer Shell Precedent, Digging accuracy, Cross-section closure, Water prevention measures

1 INTRODUCTION

The Sotetsu-Tokyu-Link Line from Hazawa Yokohama-kokudai Station on the Sotetsu-JR link line to Hiyoshi Station on the Tokyu Lines via Shin-Yokohama Station opened on 18 March 2023 (Figure 1). The length of the line is 10 km. Shin-Tsunashima Station is a new intermediate station and 240m in length, 35m of the north of the station (Tokyo side) is a trenchless tunnel. We report on the construction plan and results of this trenchless tunnel.

Figure 1. Route map of the Sotetsu-Tokyu-Link Line.

*Corresponding author: koizumi.dai-b8wm@jrtt.go.jp

DOI: 10.1201/9781003495505-252

2 OVERVIEW OF THE CONSTRUCTION PLAN

2.1 *Overview of Shin-Tsunashima Station*

Shin-Tsunashima Station locates 7.8km apart from Hazawa Yokohama-kokudai Station, at the fourth underground floor, approximately 35 m deep (at the deepest part) and 14 to 25 m in width. Both ends of the station shaft were used as launching shafts for shield type TBMs. In addition, the first 34.5m portion of the tunnel requires a large cross-section with an inner space of 224 m^2 (Height:14m, Width:19m) to envelop a platform. Given the restrictions due to surface the (Figure 2) and geological conditions around the tunnel with thin solid strata above the tunnel and abundant groundwater, we constructed an outer shell with a small section of 1,000 mm × 1,000 mm in advance to minimize the impact on the surrounding ground during the excavation. The NATM and the shield widening method were denied due to concerns about the impacts on the surrounding area, such as ground surface subsidence and groundwater level lowering caused by loosening of the surrounding ground.

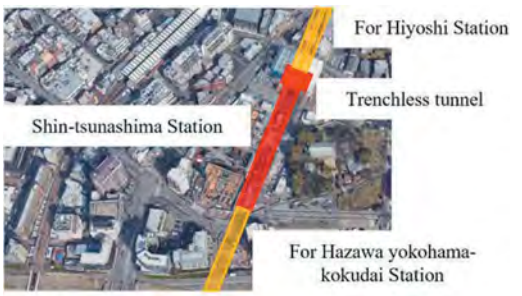

Figure 2. Aerial photograph of Shin-Tsunashima station.

2.2 *Summary of geological features*

The strata at this site are a solid upper stratum group with an N value of 50 or more and there are alternating layers of sand and mudstone. The distribution of the sand layer is unclear and abundant groundwater is observed (Figure 3).

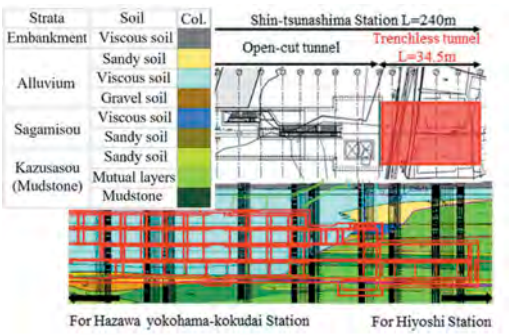

Figure 3. Ground plan and geologic cross section.

3 IMPROVEMENT OF PROPULSION METHOD

In this construction, we adopted a structurally improved version of the rectangular cross section used in previous construction of trenchless section. Figure 4 shows a cross-sectional view of the trenchless section of the Tsukuba Express Rokucho Station constructed in 2005, and the construction length of the section was about 15 m, and the N value of the ground to be excavated was about 1 through 10.

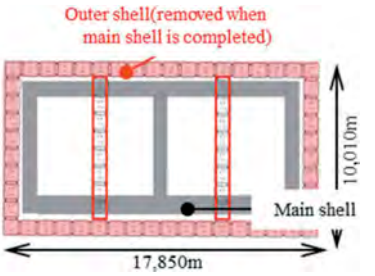

Figure 4. The cross section of Rokucho Station.

Improvement of this rectangular element propulsion method was studied for this paper's case because this section was constructed in relatively solid ground compared to previous construction results, the sandstone layer has abundant groundwater, the construction extension is long with large cross-section, and these elements can be used as permanent body.

Improvements of the construction method are as follows: (1) the propulsion machine is retrieved from the launching side because no reaching shaft was available, (2) a new joint structure to close the square steel pipe, (3) high propulsion accuracy including rolling measures was required for long-distance (35m) propulsion, and (4) prevention of joint work during construction under pressurized groundwater.

4 IMPROVEMENT OF ELEMENT JACKING METHOD

4.1 *Retrieval from the launching side of the machine*

Water cutoff on the arrival side was ensured by injecting chemical grout, and only the propulsion drive unit was retrieved while the outer shell of the propulsion machine was left in the ground. The machine could be reasonably and economically retrieved thanks to newly developed extraction device of the retrieval cart shown in Figure 5 and using the drive unit repeatedly. In order to ensure that water is blocked when retrieving the propulsion equipment, we decided to backfill propulsion equipment reaching area with cement bentonite after retrieving the propulsion drive unit, with the aim of stabilizing the ground in front of the face and preventing the inflow of groundwater.

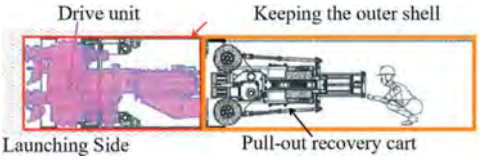

Figure 5. The drive unit of the rectangular element.

4.2 *Adoption of a new joint structure*

We have developed a new joint that secures an appropriate amount of clearance so that it can be closed in any shape, and that can reliably stop flowing water during construction with shut-off valves and sealing materials (Figure 6).

In addition, the clearance inside the joint, which was traditionally 4 mm horizontally and 4 mm vertically, has been expanded to 28 mm and 9 mm respectively, which improves ability to cover construction errors during the propulsion, and makes it easier to clean and fill the inside of the joint with mortar. Furthermore, we decided to enlarge the joints because of ease of construction. To reduce the resistance during propulsion, the soil at the sites was replaced in advance with high-quality low-strength cement bentonite.

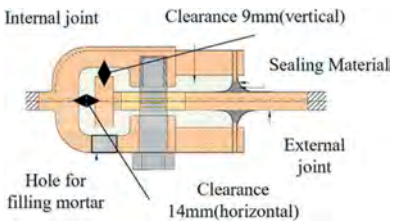

Figure 6. The joint between rectangular elements.

4.3 *A new control mechanism for accuracy*

Since the rectangular element was used for the main body and the position of the main body structure had to be fixed, strict propulsion accuracy was required. Rolling control was also important because the position of the joint installed at the edge of the rectangular element could be easily changed due to rolling. For this reason, a folding jack was installed on the propulsion machine, and new control jacks were installed on the top and bottom of the propulsion unit for adjusting the sled to correct the rolling (Figure 7).

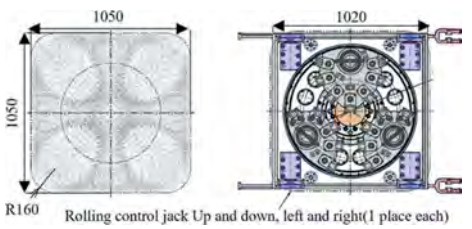

Figure 7. The cross section of the propulsion machine.

4.4 *Water influx during construction*

As a measure against water leakage from the launching shaft, we developed new equipment to block water at the well-head with double entrance packing made of two types of rubber bonded together. A high-viscosity sealing material was also used to stop water between the double entrance packings (Figure 8). Since this was the first time of this construction method, a pre-construction test was conducted using a large-scale experimental device to confirm water blocking performance. In this test, it was found that the waterproof effect of the entrance packing was deteriorated and water leakage occurred due to vibration.

Furthermore, we decided to make improvements such as changing the shape of the rubber entrance packing according to the construction stage and confirm the improvement effect in additional tests before applying it. This is because it was necessary to improve the ability to follow the sway that occurs during propulsion.

Additionally, we improved the propulsion pipe joint with flange structure that can control the load during propulsion and extraction which is required in the control.

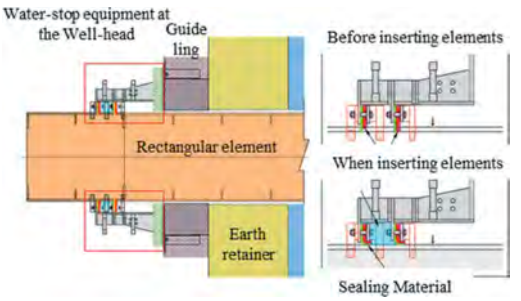

Figure 8. Water blocking equipment (Rectangular element).

In addition, since it is necessary for the water-blocking equipment to ensure waterproof in both directions of pushing and pulling in the propulsion of pipe and passing of flange, two lip-seal type rubber packings that are strong against turnover and have excellent water blocking performance when pulling in were used. By making the gap between the entrance rubber packings larger than the dented section (300 mm) of the joint, even when the joint passes through an entrance rubber packing, the other packing could stop water (Figure 9).

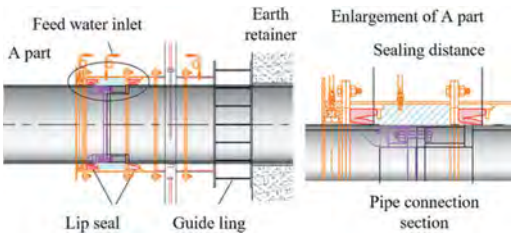

Figure 9. Water-blocking equipment (Joint replacement).

A feed water inlet was equipped between the two tiered lip seals to control fluctuations in water pressure and to fill the sealing material in an emergency.

5 CONSTRUCTION PLAN FOR TRENCHLESS TUNNEL

5.1 *Construction procedure for trenchless tunnel*

Figure 10 shows the construction procedure for the trenchless section. After completion of joint replacement, a standard element that serves as a guide was installed by the jacking method, and the external joints of the other elements to be installed subsequently were fitted to the internal joints of the installed elements, then sequentially pushed and connected. After above installation, concrete was filled inside the standard element and space between adjacent elements, and the inside of the fitted joint is cleaned.

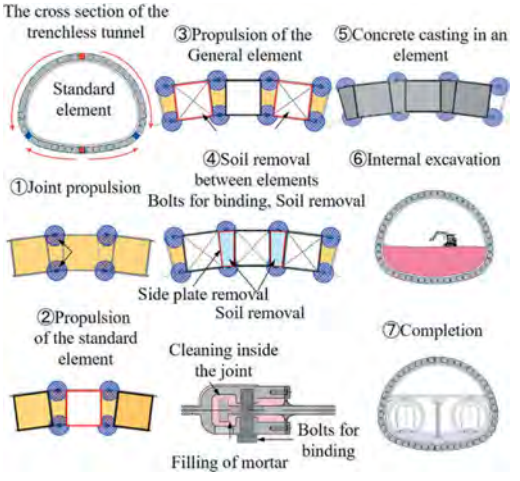

Figure 10. Construction procedure for trenchless tunnel.

While repetitive cleaning and filling with mortar and filling concrete between and inside the elements, all square elements were assembled and closed and then excavated inside the large horseshoe shape section. The station platform was finally to be constructed.

5.2 *Preceding replacement for joints*

Prior to the construction of the rectangular element, the ground through which the joint passes was replaced with cement bentonite (low-strength) by a small-diameter jacking method (φ600 mm). Figure 11 shows the joints between the elements protruding from the excavation range of the rectangular propulsion machine to decrease resistance and secure accuracy. Several tests were conducted to confirm the solidification strength, fluidity, material non-separability, incompressibility, etc. of cement bentonite.

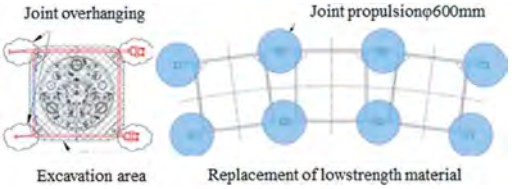

Figure 11. Preliminary joint replacement.

Table 1. Composition of cement bentonite.

A Liquid (Clay sand solution)			B Liquid Particular water glass
Tackment (hardening agent) 120.2kg	TAC-α (aid) 60.1kg	Water 929.9L	TAC-3G (plastic material) 3L

5.3 *Rectangular element propulsion*

The main pushing-device in the launching shaft was extended to penetrate the ground (Figures 12 and 13), and the subsequent elements were connected in sequence.

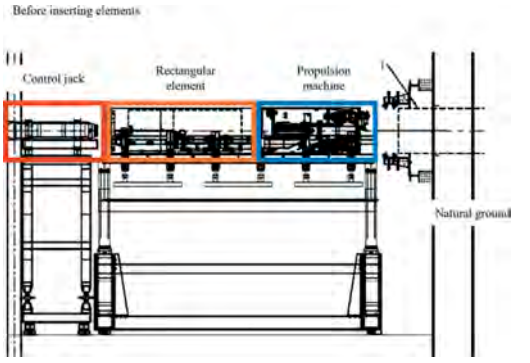

Figure 12. Preliminary joint replacement (before propulsion).

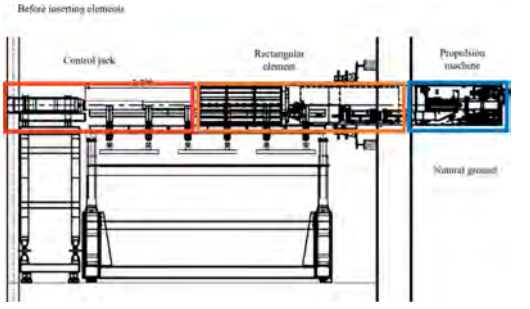

Figure 13. Preliminary joint replacement (after propulsion).

High propulsion accuracy was required for rectangular element propulsion because the propulsion position determines the final body structure. Therefore, for the propulsion unit, a new rolling control jack was added to the front body of the propulsion unit so that not only

vertical and horizontal displacement but also rolling could be controlled and managed with a high degree of precision. A pressure-type water level gauge for vertical displacement and a target for horizontal displacement were installed on the propulsion unit and a gyro for rolling was installed on the subsequent elements (Figure 14). Table 2 shows allowance for location accuracy of the standard element and other ones. The propulsion machine used in the square element jacking work was retrieved and reused together with the propulsion drive unit. The structure of the water-blocking equipment was set based on a preliminary waterproof test, and maximum water pressure was assumed as 0.45MPa, 1.2 times of 0.35MPa considering safety factor for vibration of elements during propulsion.

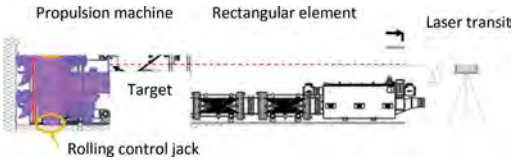

Figure 14. Precision management of rectangular elements.

Table 2. Target value of elements.

Direction	Standard	Other
Horizontal	±10 mm	±25 mm
Vertical	±10 mm	±25 mm

5.4 *Internal excavation*

Ground might be loosened by installation of gable wall and rapid excavation of large section. Therefore, the process was divided into three parts(Figure 15). After removing the earth retaining wall at the end of the excavation section of the station, excavation was started from the top of the trenchless cross-section using a backhoe. Therefore, we set up measuring points for subsidence on the city road surface above the trenchless area, and proceeded with the excavation while checking the impact of the excavation on the surrounding ground.

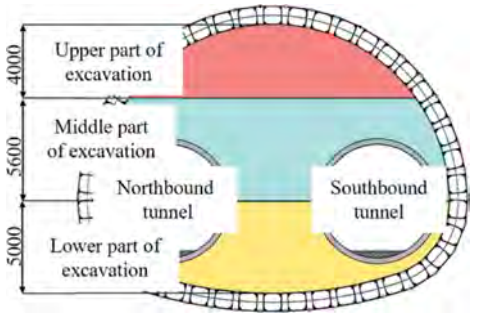

Figure 15. Internal excavation of the trenchless tunnel.

5.5 *Estimation by preliminary deformation analysis*

In the trenchless section, after preceding replacement of the joint, the joint was connected from the top of the tunnel in sequence, and the square element was pushed forward to close it. Because this trenchless section was built with several methods, impacts from each work might accumulate into larger ground settlement. A step analysis was performed using the two-dimensional finite element method (FEM) to predict the ground deformation accompanying construction in advance which impacts on gas pipes on the city road above the trenchless section.

The deformation of the outer shell of the tunnel and the amount of settlement of the gas pipe were predicted by reproducing step analysis for the construction of a single-track tunnel, which was constructed simultaneously with the promotion of 42 rectangular elements in the outer shell of the tunnel and the excavation inside the tunnel. Figure 16 shows the analysis model, and Table 3 shows the analysis results. After internal excavation, the vertical displacement at the top of the non-excavated tunnel was 10.8 mm (displacement due to internal excavation: 5.8 mm). The analysis results were within the control values determined in negotiation with the surrounding facility owners.

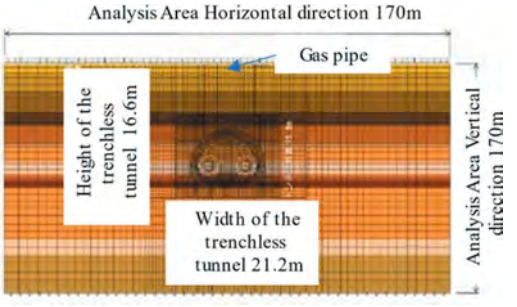

Figure 16. Two dimension FEM analysis of internal excavation.

Table 3. Result of FEM analysis.

	Vertical settlement displacement (mm)	
Status	Gas pipe	General pipe
Completion (the upper half)	0.98	1.54
Outbound shield tunnel passage	1.70	2.67
Completion (the lower half)	3.23	4.86
Inbound shield tunnel passage	3.48	5.00
Completion (Internal excavation)	6.03	10.80

6 CONSTRUCTION RESULTS

Works for the rectangular element jack had to share the limited space of the vertical shaft with TBM works. In order to obtain space, as shown in Figure 17, a total of 42 rectangular elements were divided into two stages: 17 of upper half and 25 of lower half.

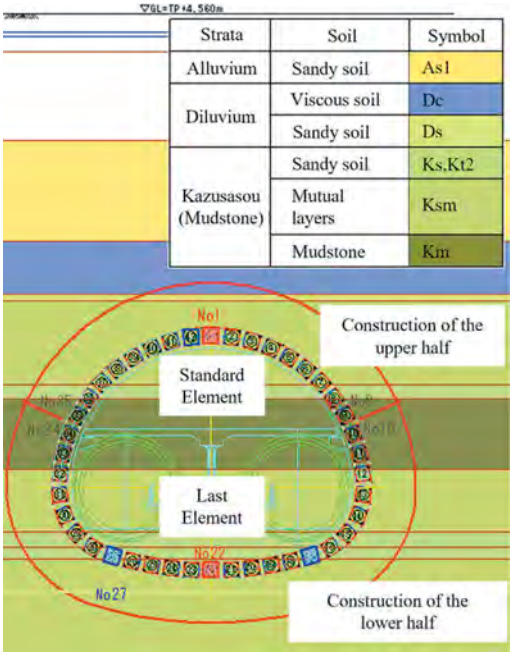

Figure 17. Two-phased approach of the propulsion.

6.1 *Preceding replacement of joints*

In the first half of the construction, the propeller tended to deviate downward at the sloping boundary between the sand layer and the mudstone alternate layer, so the propulsion speed had to be slowed down (Figure 18).

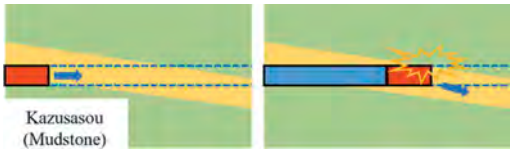

Figure 18. Descriptive sketch of the propulsion deviation.

Even if the above measures had been taken, it was still not possible to propel within the control target value (horizontal and vertical ± 50 mm). So it would be necessary to push and pull repeatly and re-promote them.

At the same time, the overcut amount of the propulsion was reduced before the next replacement work from 11mm to 7mm, etc. so that the propulsion accuracy could be all within the control target in the end (Figure 19).

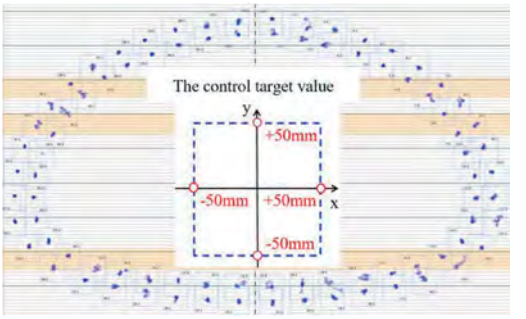

Figure 19. Result of preceding replacement.

In the preceding replacement work at the lower half, improved tunnel peripheral area was warped upward due to the grout lump involved under the propelling machine which exceeded the control target. It is thought that pieces of the shattered modified material, in lump form, went underneath the propulsion machine. By reducing the speed near the modified material to grind the modified material into small pieces, as a countermeasure, we were able to finally keep the propulsion accuracy within the control target value.

6.2 *Rectangular element Propulsion*

6.2.1 *Result of the upper half*

Figures 20 and 21 show the displacement generated in the propulsion machine and the rectangular element.

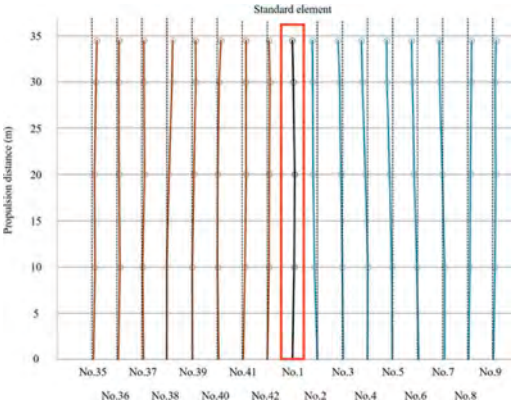

Figure 20. Result of horizontal displacement (upper half).

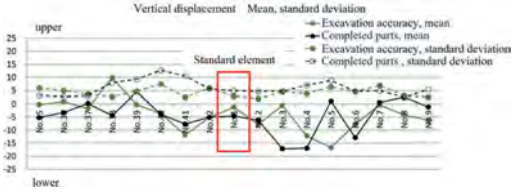

Figure 21. Result of vertical displacement (upper half).

The vertical displacement in Figure 21 is averaged number of measurements taken every 1m of the propulsion proceeding.

All horizontal displacements of the rectangular elements were within the control target of ±25 mm. As for the tendency of the displacement, it was displaced to the side of the previously installed element.

It is presumed that ground was loosened due to early installation.

The average vertical displacement was about ±15mm, and the standard deviation was about 10mm. Basically, the propulsion accuracy and the finished shape accuracy of the elements showed the same tendency.

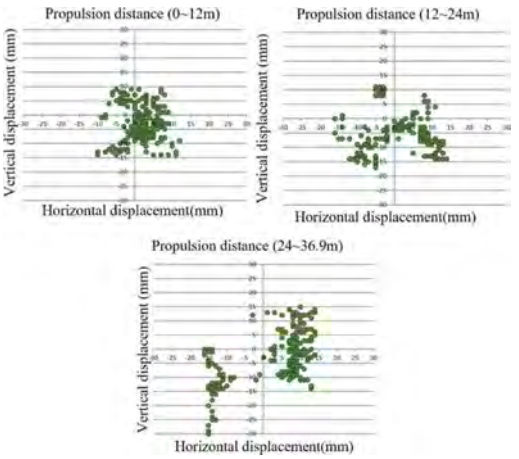

Figure 22. Displacements (every 1m of propulsion distance).

Figure 22 shows the result of classifying the displacement of the propulsion machine that occurred in every 1m of propulsion proceeding into three ranges.

This figure shows that the propulsion accuracy varies as the propulsion distance increases. In order to block the confined groundwater that acts on the pit mouth during propulsion, we tried to block the water by using two-staged entrance rubber packing and a high-viscosity sealing material filled between them. Nevertheless, water leakage occurred and the leakage was thought to be the cause of ground surface subsidence. In the lower half, it is lower than in the upper half construction due to higher water pressure, so prevention measures against water influx was required.

6.2.2 *Result of the lower half*

Figure 23 shows the horizontal displacement generated in the rectangular element, and Figure 24 shows the average vertical displacement of the excavator and the element.

It was within ±25mm of the control target value except for two closing locations. At the closing location, it was necessary to cover the displacement of each element on the left and right to fit the joint. To

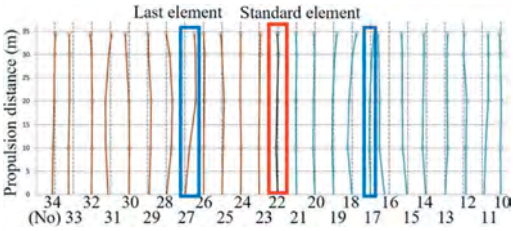

Figure 23. Result of horizontal displacement (lower half).

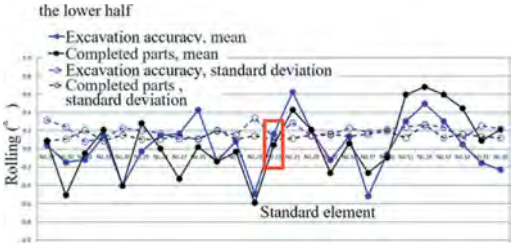

Figure 24. Result of vertical displacement (lower half).

do so, we decided to increase the inner space of the internal joint and change the shape and length of the tip of the external joint so that the joint could be securely fitted (Figures 25 and 26).

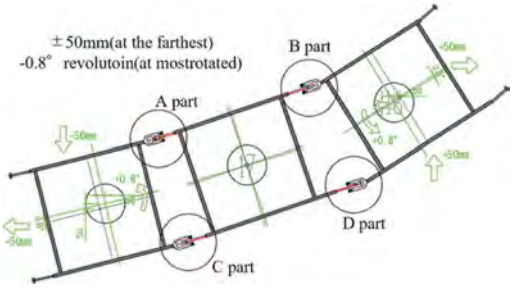

Figure 25. One of the closing locations.

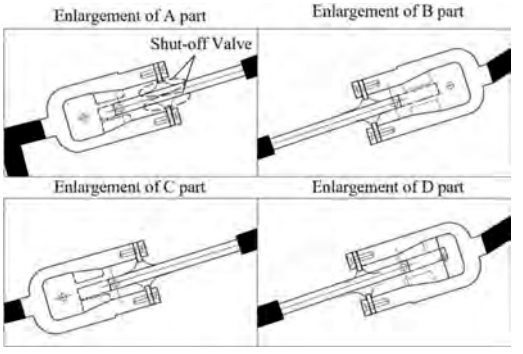

Figure 26. Adjustment of the closing locations.

As a result, the propulsion of the closed section was smooth, but the displacement at the time of closing increased and slightly exceeded the control target value because restraint by the joint during propulsion was released and the flexibility increased. For No. 16 through No. 28, where the orientation of the element is almost horizontal, it was observed that there was a tendency to displace in the direction of the reference element that was installed earlier. For No.29 through No.34, no clear tendency was observed in the direction of displacement.

The average vertical displacement and standard deviation were generally within the control target values. As in the first half, the propulsion accuracy and the finished form accuracy of the element show the same tendency, and it is crucial to control the propulsion machine accurately.

As a result of classifying the displacement of the propulsion machine that occurred in every 1m of propulsion distance into three ranges according to the propulsion distance (Figure 27), there was a tendency for the displacement to increase as the propulsion progressed. The geology of the lower half is alternating layers of mudstone and sand layers, and it is presumable that the stratum boundary affected attitude control during propulsion, and displacement occurred regardless of the propulsion distance.

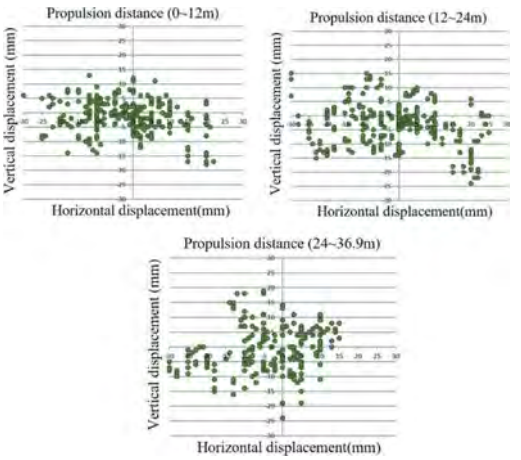

Figure 27. Displacements (every 1 m of propulsion distance).

Water leakage of about 20L/min occurred due to the change of the waterproof device at the wellhead and the outflow of the sealing material and the deformation of the steel guide ring installed at the wellhead. Most of these water leakages could be stopped.

6.2.3 *Considerations on rotation of elements*

Figure 28 shows the results of the rotation angle in rectangular element propulsion.

The average rotation angle of the rectangular element in the upper half was about -0.4° to +0.6°, and the average rotation angle in the lower half was

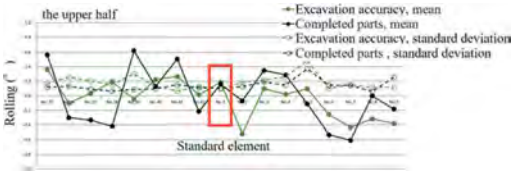

Figure 28. Results of rotation of rectangular elements.

about -0.6° to +0.7° (positive direction: clockwise, Negative direction: counterclockwise), within the propulsion accuracy control value (±0.8°). The addition of a hydraulic roll correction jack to the front body of the propulsion machine made it possible to immediately correct rolling during propulsion. Thanks to these measures, the rolling angle could be controlled and managed within the control target value.

Figure 29 shows the completion of the upper and lower halves of the rectangular elements' propulsion.

Figure 29. Completion of upper and lower halves propulsion.

6.3 *Excavation inside elements*

After the rectangular elements were propelled and the joints were filled with mortar and the elements were filled with concrete, excavation inside elements was started from the crown. During the construction of the upper level, the displacement of the element was measured using a laser transit. The vertical displacement of the top of the tunnel (No.1 element) was 4mm from the start of measurement to the completion of the upper excavation, 7mm at the completion of the middle excavation, and 8mm before the completion of the lower excavation. This result approximates the prediction of 5.8mm in the FEM analysis for element excavation conducted in advance.

Furthermore, the ground surface subsidence was up to 13mm at its maximum after the commencement of the excavation inside elements and it has ceased and converged after the completion of the excavation. The reason why this value was larger than the displacement at the top of the tunnel is considered that it was influenced by fluctuations in underground movements.

Additional achievement is successful grouting during excavation in this work which waterproof was required at the horizontal joint surface of the end wall concrete and the boundary with the outer

shell. As a result, water leakage due to the elastic deformation of the rectangular elements during excavation was successfully prevented.

The fact that the ground surface subsidence was suppressed to about 10mm in the construction of a large-section tunnel with an inner space width of 19m and a height of 14m indicates that it is possible to minimize the impact on the surrounding ground when constructing a large-section tunnel by square element jacking was appropriate.

7 CONCLUSION

We could construct a large horse-shape tunnel with 42 elements by the rectangular element propulsion method with fine accuracy under the challenging condition of a large amount of pressurized groundwater. The deformation of the surrounding ground due to internal excavation was also well-controlled (Figure 30).

The results show that the propulsion method could be efficient and that the degree of flexibility of the cross-sectional shape of the tunnel and the required accuracy can be attained. It is expected that this method will be adopted when constructing underpasses and underground spaces in urban areas.

Figure 30. Completion of the internal excavation.

Tunnelling for a Better Life – Yan, Celestino, Thewes & Eberhardt (Eds)
© 2024 The Author(s), ISBN 978-1-032-80042-4
Open Access: www.taylorfrancis.com, CC BY-NC-ND 4.0 license

Decision-making approach for parallel earth pressure balance machine advancements for tunnel construction

Niranjan Kumbhar* & Sanket Tirpude
MIT-WPU, Pune, India

ABSTRACT: Tunnel excavation with Tunnel Boring Machine is more systematic and safer due to in house deformation control by operator but when excavation done for parallel tunnels then tunnel construction became more slower because any one tunnel excavate entirely then go for 2nd tunnel to avoid this delay in tunnel excavation in this study highlights the influence of two parallel (||) TBM construction processes when this two TBMs Tunnel Boring Machine) which is used to excavate tunnel in numerical model . 7 construction sequences (decisions) where adopted for checking its feasibility in parallel tunnel construction simultaneously. In this study Excavation Cycle Sequence (ECS) introduced for representing excavation of tunnel and they are ECS-D1, ECS-D2, ECS-OEO, ECS-EOO, ECS-OM. All this ECSs complete tunnel excavation in different excavation cycles which are nothing but excavation for ring or rings as per ECS also installation and applicable for that particular ECS. This study shows that if adopt time dependent excavation (time=more or less installation of rings in numbers) make influence on deformation pattern between (ux=lateral deformation) parallel tunnels as well as in vertical deformation (uz). In tunnel advancement direction (uy= longitudinal deformation) as per excavation and installation of rings in Plaxis 3D model are constant (0.59mm) deformations because of application of constant thrust force which is required for the TBM movement in construction advancement direction (along +Y=axis) in Plaxis 3D model, we will suggest to implement variable thrust force models for further studies. This study shows that to minimize deformation use minimum excavation cycle such as ECS-OEO (Odd Even Order) and ECS-EOO (Even Odd Order), and if excavation cycle increases for more safer construction approach such in adverse geological sections in underground simultaneous excavation of parallel tunnels then increase drift (distance between excavation faces) to minimize deformation such as in ECS -OM (4.6m).

Keywords: Construction sequence, Deformation, Plaxis 3D , || Tunnels, TBM Advancement

1 INTRODUCTION

Tunnelling works increase day by day and its need to provide a safe, rapid, and sustainable transport system to society. During the construction of metro tunnels, special awareness should be taken to minimize surface settlement and the safer foundation of high-rise buildings from the arching effect of the tunnels. To counteract this situation, more reliable machines deployed to construct a tunnel in urban areas call it as Earth Pressure Balance (EPB), the obvious reason for that is, it has the capability to maintain face pressure in terms of to avoid excess excavation in the face. Mechanized TBM (Tunnel Boring Machine) tunnelling method has been majorly used for constructing metros in many urban areas in the world is because this method has several advantages over the other methods, the advantages are, for example, reduced environmental impacts in relation to noise, dust, ground settlement, vibrations and interruption to neighbouring infrastructure; reduced labour cost and danger to the existence of workers; improved tunnelling rate, majorly in soft soils

Fu et al. discussed that when new tunnel construction is done with existing tunnel max stress lining increases by 80 % to protect the existing tunnel stress monitoring done [1], relate to this study, in the present study ECS adopted to minimize the stress path during || simultaneous tunnel construction. Jiang et.al. discussed in two working conditions (excavation methods-1st up then down, 1st down then up) are 2 respective tunnel construction, which can affect the radial stress on the tunnel lining [2], on the basis of it in this study || tunnel construction sequentially modified in the form of ECS. Backer et al. discussed distance between horizontal twin tunnels plays a key role in settlement, previous study related to this shows that intermediate distance between two parallel lying horizontal tunnels

*Corresponding author: tunnelengineer123@gmail.com

DOI: 10.1201/9781003495505-253

increases then settlement decreases [3]. Raja Kanagaraju and Premalatha Krishnamurthy presented a tunnel depth-related settlement study in FEM to isolate its influence zone [4], in this study the influence zone isolated between two || parallel tunnels along the springline of parallel tunnels. As discussed by Ma et al. for TBM tunnelling effects on adjacent environment, several research has been carried out, numerical simulation, an examination of field data of settlement in soft ground tunnelling by indicating that a major proportion of total soil deformation occurs immediately after construction as well as Ma et. al. remarks deformation of the existing tunnel is relevant to the relative position of the TBM-EPB shield, the settlement development can be divided into three stages according to shield position change, shield approaching subsidence, shield crossing heave, and shield leaving subsidence [5], and this deformation characteristics are important in the present research study because with drift and ECS all above parameters can interact in || tunnel construction advancement. The ground movements associated with tunnelling and found that the main hazards related to tunnel construction in urban areas include poor ground conditions, the presence of a water table above the tunnel, shallow overburden, and tunnelling-induced ground settlement with potential damage to the existing structures and utilities on the top of the tunnelling area.

Taylor et. al discussed in his study about how stratification will affect the settlement [6]. Palassi et.al shows that face supporting pressure has more effect on settlements that grout injections [7]. Muhammed et.al. discussed construction advances during the construction stage for 1.5m of each stage were considered for analysis to check settlement using FEM software Plaxis [8], in this study the tunnel advancement is considered as 1.5 and for ECS it is different for the respective pattern of advancement. Bin-Chen Benson Hsiang describes that ground movement during excavation is mainly caused by the absence of sink in tunnel construction operations such as material discharge [9], and this study suggested that further data is desired to support their finding, so that a drift is introduced between simultaneous || tunnel construction Excavation Cycle Sequence [ECS] also some construction cycle patterns are suggested in this study. Shahriar et al discussed interaction of twin tunnels and adjacent structures are a complex problem because 3D software has significant power on the intensity of interaction and it can conclude that among TBM operation parameters face pressure influence [10].

Md Shariful Islam and Magued Iskandar [11] studied the important parameters of tunnel which is the construction sequence of twin tunnel, the settlement profile is directly influenced by the construction sequence and the position of maximum settlement shift towards the new tunnel [11], so that in this study included different construction sequence Excavation Cycle Sequence [ECS]. Daud et.al discussed that numerical analysis done in finite element for tunnels closely spaced settlement, and moments of tunnels are considered important [12], in this study || tunnels are closed spaced to identify the deformation behaviour during ECS, the centre to distance of || tunnels is taken as 1.84D where D is external diameter of both tunnels. Liu et al. describes, the face support pressure doesn't have significantly influence on the 1st tunnel convergence [13], that is why in this study all || tunnel stimulations ECS are performed with the same face support pressure to check its impact on ECS. Previous study conducted by Adugna et al. tunnel-induced ground deformation in Plaxis 3D for EPB TBM and its control using grout pressure and pressure in their research [14], in the present study the face pressure is constant to check the drift effect during a || tunnel advancement, so it will help to better TBM excavation in the present study the face pressure is constant in ECS to normalize effect during || tunnel advancements and it will help to see drift effect in || tunnel construction. Suwansawat et. al. throw light in face pressure, shield element, grouting process, and lining element are most important parameters of mechanized tunnelling well described in previous studies along with the phases in Plaxis 3D FEM software for EPB-TBM tunnel [15], in this study throw light on the 5th factor which can control TBM excavation with is drift (face distance between two || simultaneous excavation along Y direction in global coordinate system in Plaxis 3D). Liu et al. describes excavation of the 1st tunnel shows greater surface settlement than that of the 2nd tunnel, especially for twin-tunnelling operations in which the excavation of the 2nd tunnel imposes a remarkable effect on the adjacent first tunnel [16].

2 MATERIALS AND METHODS

2.1 *Materials*

Instead of creating virtual new stratification, in this study included geotechnical data (Table 1) and TBM machine data (Tables 2 & 3) from a previous study. Geotechnical Materials (Data Set*)* and EPB (Earth Pressure Balance) TBM Properties taken from previous studies conducted in IIT, Chennai [14], to implement mix geological condition which is suited for Earth Pressure Balance machine TBMs for excavating tunnel. For Geotechnical properties Mohr-coulomb model assigned for this study because as per Plaxis 3D manual this model is suitable for preliminary studies so that 3 soil layers (Figure 1) along with a water head that is located -3m from the surface in the XZ plane and this will fulfil EPB TBMs working environment in Plaxis 3D model. In mix geological conditions EPB machine balance earth pressure Infront of cutter head to minimize excavation face collapse as well as minimizing surface settlement.

2.2 *Methodology*

2.2.1 *Working environment in Plaxis 3D*

In this study, we take half the portion of 2 TBMs because of its isotropic geometry (both tunnels have

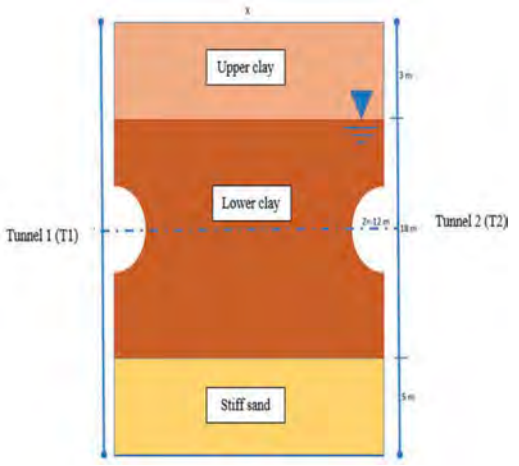

Figure 1. Front view parallel tunnels in the Plaxis 3D model.

Table 1. Borehole data for Plaxis 3D.

Parameter	Name	Upper Clay	Lower Clay	Stiff sand
Material Model	Model	Mohr-Coulomb	Mohr-Coulomb	Mohr-Coulomb
Type of Material Behavior	Type	Undrained	Undrained	Drained
Dry unit weight (kN/m2)	γunsat	16	16	17
Saturated Unit weight (kN/m3)	γsat	18	18	20
Young's modulus (kN/m2)	E	8.4e3	1e4	2.5e4
Poisson's ratio	ν	0.35	0.35	0.3
Undrained shear strength (kN/m2)	C	48	70	3
Friction angle (°)	φ	10	20	30
Permeability (m/day)	Kv, Kx	0.001	0.05	1
Dilatancy angel	ψ	0	0	0

Table 2. TBM shield (plate) data for Plaxis 3D.

Parameter	Name	Segmental Lining
Behaviours Types	Material type	Elastic
Normal stiffness [kN/m]	EA	2.20e6
Flexural rigidity [kN/m2 /m]	EI	8.38e4
Equivalent thickness [m]	D	0.35
Unit weight [kN/m3]	w	0.3
Poisson's ratio	v	0.3

the same dimensions) and this condition benefits towards the isolation of the investigation zone between 2 || tunnels ux(s) according to advancement (ECS).

Table 3. TBM concrete lining data for Plaxis 3D.

Parameter	Name	Segmental Lining
Identification	-	concrete
Type of material behaviour	Model	Linear-elastic
Material type	type	Non-porous
Volumetric weight (kN/m3)	Ƴunsat	24
Young's modulus (kN/m2)	Eref	3.1e7
Poisson's ratio	υ	0.2
Interface strength reduction	Rinter	1.0 (Rigid)

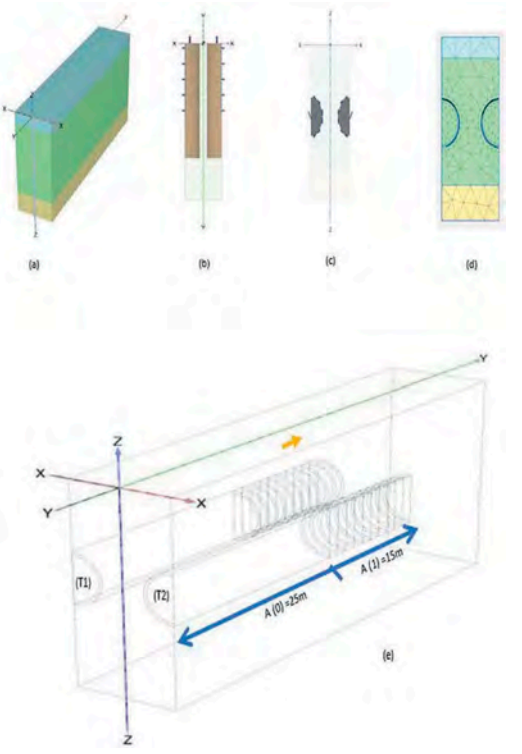

Figure 2. Representation of the Plaxis 3D model (a) Borehole of stratification, (b) Top view, Structure of || tunnels, (c) front view of || tunnels, (d) Meshing front view and (e) wireframe view || tunnel structural geometry.

2.2.2 *Tunnel dimensions*

In metro tunnels has approximate 6 m diameter to achieve standardization that's why in this study we take external diameter = 6.2 m [2]. Segmental lining thickness = 0.35 m [2] taken to avoid max deformation in parallel tunnel construction. Thrust force = 1166 kN/m^2 (assumed) which is applied in Plaxis 3D software without increment and decrement for all ECS for isolation of deformation check. As per International Tunnelling Association guidelines width Segmental lining width taken as 1.5 m each [10] and in this study total number of 10 rings constructed for each ECS. Distance between two tunnels = Overt of T1 to Overt of T2 = 5 m for checking lateral deformation between parallel tunnels [2].

Table 4. TBM concrete lining data for Plaxis 3D.

Sr. NO.	Global Coordinates	Length (m)
1	Xmin	-5.6
2	Xmax	5.6
3	Ymin	0
4	Ymax	54.6
5	Zmin	-26
6	Zmax	0

2.2.3 *Tunnel orientation*

Both Tunnels (T1 and T2) located the XZ plane in Plaxis 3D where Zmin = 12 m along the Springline (s) and the advance direction is Ymax parallel to the XY plane (Figure 2-e).

2.2.4 *Tunnel advancement*

FEM model constructed in structure mode (Figure 2) in the tunnel designer window with external diameter of the tunnel is 6.2m and the segmental lining thickness is 0.35m. It is assumed that both tunnels have constructed 25m, which is the initial advancement A (0) not monitored, next to it 10 segments of 1.5 m in width (A1=15m) are constructed with different Excavation Cycle Sequences (ECS) in the Ymax direction from the XZ plane. Tunnel advancement modelled in phase tab in Plaxis 3D. Initial phase software automatically calculates the insitu stress for the model and in phase 1 A (0) is assigned. From phase 2 construction, advancement of the tunnel for the next 10 rings begins manually (Figure 3).

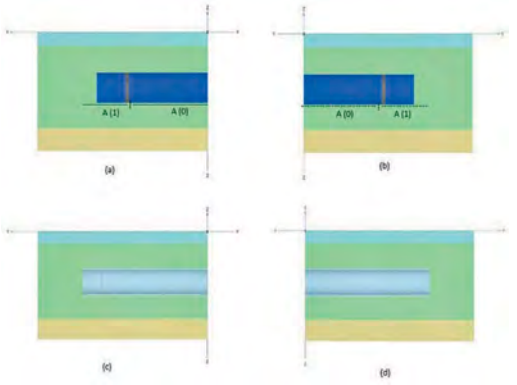

Figure 3. Ring building methodology (a & b); after ring build (c & d).

2.2.5 *Excavation Cycle Sequence (ECS)*

A] Conventional approach

a. D1 represents the decision of advancement with no drift, simultaneously constructing 1segment from each TBM, that is, from TBM 1 and TBM 2.

b. D2 represents the decision of advancement without drift, simultaneously constructing 2 segments from each TBM, that is, from TBM 1 and TBM 2.

B] Serpent approach (S)

a. Version 1 (v1) In this approach, the first segment constructed simultaneously from both TBMs and then one tunnel (T2) became a pilot tunnel with 1.5m drift.

b. Version 2 (v2) In this approach, the 1st segment constructed simultaneously and then both tunnels advance alternatively (sometimes T1 advance, and sometimes T2 advance with 1.5 m drift for respective phase).

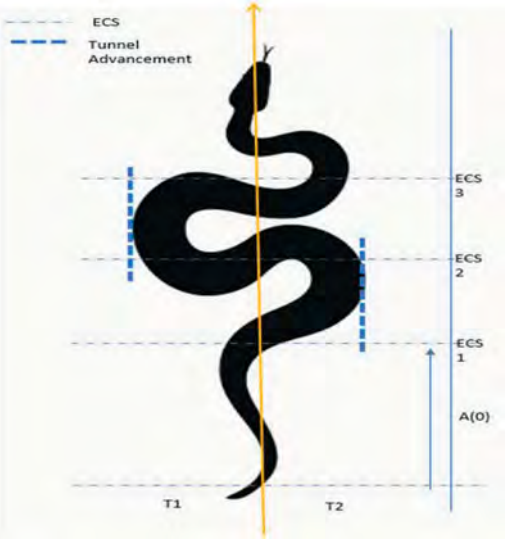

Figure 4. Serpent Method of Tunnelling (SMT).

In SMT (Figure 4), Serpent (Snake) represents the directional advancement (snake head) T1 and T2 are Tunnel 1 and Tunnel 2 respectively. A (0) is initial advancement which represents area of tunnel before 10 segments constructions (snake tail). ECS is excavation cycle Sequence which decide number of segments installation and vertical distance (bold dash lines) between two ECS is referred as Tunnel advancement. Two different tunnel advancements which is nothing but tunnel construction methods (S-v1 and S-v2) are adopted to excavate tunnel. Serpent version 1 (S-v1) is site specific because if in site conditions found that T1 shows more ahead of face deformation (which found in early stage of modelling) after constructing 1 segment from each (T1 and T2) TBMs then don't overstress the situation let T2 advance 1st as a pilot tunnel with 1segment (1.5m drift) ahead of T1 in simultaneous excavation. Whereas in S-v2 when both tunnels construct 1 segment simultaneously then T2 achieve its 2st ECS by installing 2nd segment then T1 will achieve its 2nd ECS at this situation T2 is stopped then T1 will construct its 2nd segment and achieve its 2nd ECS dame scenario follows and all 10 rings build done by using two vice versa TBM coordination.

C] Modified approach

a. OEO tunnels constructed in Odd Even Order like odd number of sets of linings (3 – 1.5 m each) from || TBM selected for installation (tunnel advancement), then go for even sets of linings (2-- 1.5 m each) from || TBMs likewise tunnel advancement(construction) go ahead.

b. EOO tunnels constructed in Even Odd Order like an even number of sets of linings (2– 1.5 m each) from || TBMs selected for installation (tunnel advancement), then go for sets of odd linings (3-1.5 m each) from || TBMs likewise tunnel advancement(construction) go ahead.

D] OM

It is Observational Methods which includes the experience of the tunnel engineer during construction related to what that person experiences during advancement, this approach is adopted in Plaxis 3D by observing the output window, so for this consider 0, 4.5 and 6 m drift at various phases (ECS).

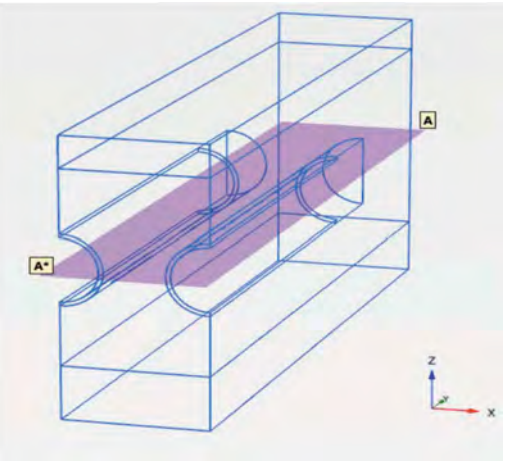

Figure 5. Horizontal c/s along || tunnel springline A-A* in Plaxis 3D output window.

3 RESULTS AND DISCUSSION

3.1 *Results*

Total deformation |u|, lateral deformation (ux), longitudinal deformation (uy), vertical deformation (uz) represents the tunnel advancement effect during ring installation in global coordinate system, whereas lateral deformation ux (s), longitudinal deformation uy(s), and vertical deformation uz(s) represent the tunnel advancement effect during ring installation along the springe line of || tunnels. Active = Segment installed or TBM advanced; pause = Segment already installed or TBM Paused. As per table 5 deformation values changes as construction sequence (ECS) change

Table 5. Last phase results of all ECS.

TBM Sequence	Phase No. (LAST)	Deformation [mm]							
-	-	|u|	|u|(s)	ux	ux(s)	uy	uy(s)	uz	uz(s)
D1	11	65.53	63.47	13.14	13.33	1.30	0.17	25.25	6.80
D2	6	64.49	62.23	11.84	12.01	1.80	0.16	23.31	6.56
S-v1	12	65.34	63.26	13.67	13.90	1.26	0.14	25.39	6.65
S-v2	20	65.68	63.64	13.55	13.72	1.21	0.18	25.21	6.93
OEO	5	63.83	61.30	11.10	11.32	2.19	0.15	26.11	7.12
EOO	5	63.73	61.26	12.35	12.58	2.47	0.14	23.80	7.306
OM	6	61.20	59.10	19.46	19.39	1.00	0.12	23.49	5.84

3.2 *Discussion*

In Figure 5 represents the cross section along springline which cut in horizontal plane of parallel tunnels to see lateral deformation ux(s). In Figure 5 shows the deformation of 10th ring build for each ECS.min and max deformation trends between parallel tunnels are varies ECS to ECS. In Figure 6 represents last phase lateral deformation (deformation between parallel tunnels along springe line) of 7 approaches of a parallel TBM advancement reveal different results from each other In parallel tunnel, overt to overt has a special connection in terms of stability especially during parallel (||) tunnel advancement. In D1, D2 approach, Figure 5 (a & b) represents the deformation for each advancement along springline of a || tunnels in D1 and D2 approach, respectively. In D1 the approach, the trend for the min lateral deformation for T1 is continuous, whereas in D2 it has a discontinuous min lateral deformation trend for T2. Figure 5 (c & d) represents all phases of ux(s) for Serpent v1 and Serpent v2, respectively, during the advancement of tunnel. Min and max deformation trends are quite similar for both approaches which are continuous for min deformation and discontinuous for max deformation, and an important difference is that the min deformation trend changes from T1 to T2 when almost half the excavation done for Serpent v2 and max deformation effect reduced at early phases for a || tunnel advancement Figure 5 (e&f) shows OEO and EOO with the same criteria ux(s), OEO shows less Max deformation coverage between a || tunnels than EOO. Figure 5 (g) represents the ECS-OM which shows the min and max lateral deformation along TBM drive for T1 and T2 || tunnel along TBM drive in springline which shows the min deformation trend is discontinuous for T2 tunnel and the max deformation trend starts with T2 tunnel advancement and shift towards T1 at end of the excavation cycle.

Figure 7 represents the deformations (whole model + along the springline of a parallel tunnels), which shows that the model deformation for the respective deformation is more than its relevant springline deformation. Serpent version (S-v1) shows

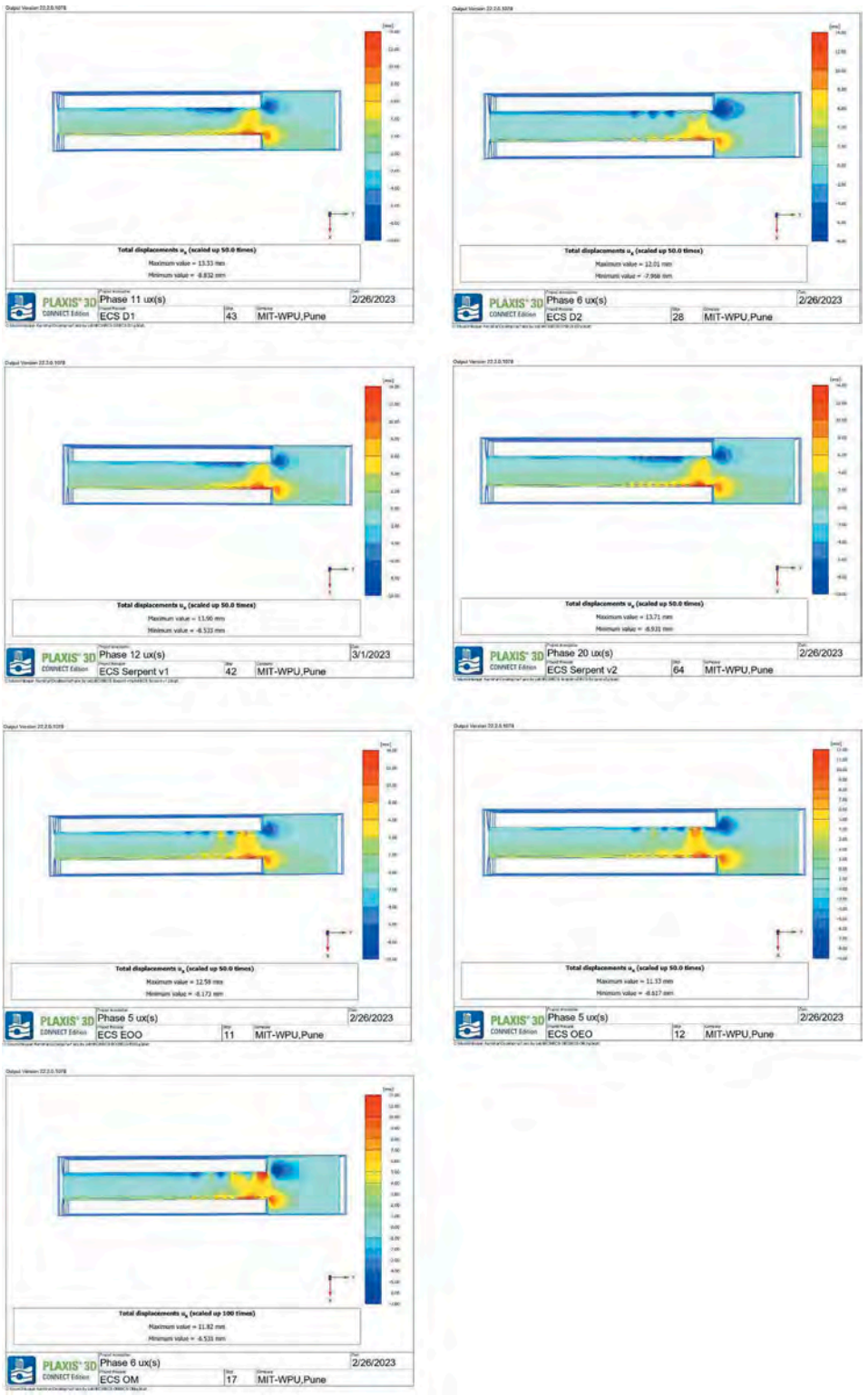

Figure 6. Top view of the final phase where the upper tunnel is T1 and the lower tunnel is T2, and (a) D1, (b) D2, (c) Serpent v1 (d) Serpent v2 (e) EOO (f) OEO and (g) OM that represents ECS.

the maximum total deformation |u|, whereas Odd Even Order OEO shows Min, Max deformation |u|.

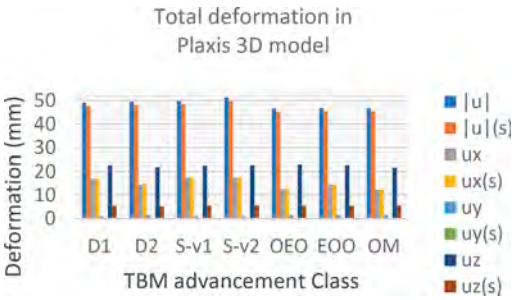

Figure 7. The general deformation for the model is |u|, ux, uy, uz, and the deformation along the springline for a || tunnels are |u|(s), ux(s), uy(s), uz(s).

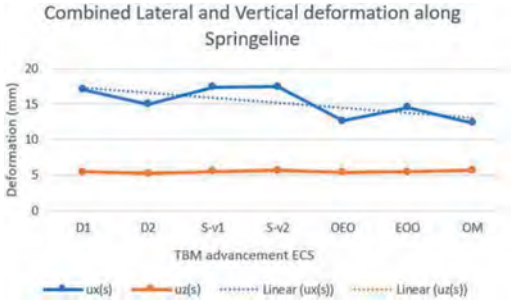

Figure 8. The general deformation for the model is |u|, ux, uy, uz, and the deformation along the springline for a || tunnels are |u|(s), ux(s), uy(s), uz(s).

During the construction of the | | tunnel with TBM lateral deformation, the ux (s) is the key factor for a safe and efficient construction process. So that ux(s) behaviours need to be checked with vertical and longitudinal deformation. Figure 8 shows graphical representation of ux(s) and uz(s) along springe line for all construction approaching Excavation Cycle Sequences (ECS) show almost close linear deformation for vertical displacement in the horizontal direction whereas lateral deformation goes linearly decreasing toward the observational method (ECS-OM).

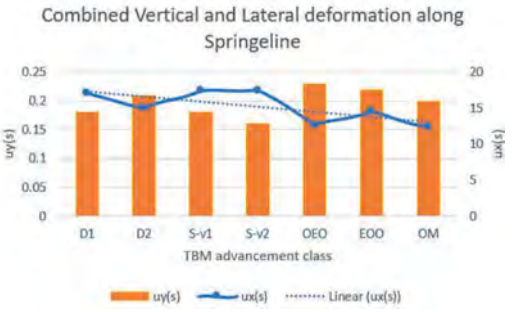

Figure 9. Deformation along the springline for a || tunnels which are uy(s), ux(s).

In Figure 9, compared to vertical deformation, OEO is more sensitive about vertical deformation, and it has more uy(s) than other ECS. uy(s) for D1, S-v1, S-v2 less than ux(s).

4 CONCLUSION

Plaxis 3D is a very useful tool to predict the effect of parallel tunnel construction simultaneously implemented in this study, showing a satisfactory and prominent result in | | tunnel construction. This study will help to understand the behaviour of deformation during simultaneous excavation. By following the trend of ECS, one can choose the appropriate sequence for a particular geology as well as for critical sections such as D2, S-v2, OEO has the capabilities to divert the deformation effect from one tunnel to another by selecting an appropriate ECS which is relevant to ECS on site conditions, the adverse effect on a particular tunnel will be minimized in || simultaneous construction. From this study, with EPB TBMs in urban areas for surface and subsurface safety in undrained clay, the class (B)-subclass (III) has more capabilities. The response of || tunnel construction to different geotechnical properties, different tunnel diameter, and TBM properties is the scope of future studies.

*Conclusion is divided into 3 important outcomes obtained in this study;

I. Plaxis 3D and parallel tunnels

Table 6. Excavation sequence classes and its deformation for phase 1 (mm).

ECS	|u|	|u|s	ux	ux-s	uy	uy-s	uz	uz-s
D1	22.32	22.23	12.47	12.42	0.72	0.59	18.62	3.53
D2	22.32	22.23	12.47	12.42	0.72	0.59	18.62	3.52
S-v1	22.32	22.24	12.47	12.43	0.72	0.59	18.62	3.51
S-v2	22.32	22.24	12.47	12.43	0.72	0.59	18.62	3.51
OEO	22.32	22.23	12.47	12.42	0.72	0.59	18.62	3.52
EOO	22.32	22.23	12.47	12.42	0.72	0.59	18.62	3.53
OM	22.32	22.23	12.47	12.42	0.72	0.59	18.62	3.52

For Phase 1, as per Table 6, model deformation less than springline deformation (s) for all ECS and also model deformation shows consistency in deformation for all ECS, whereas for springline deformation, longitudinal deformation shows constancy for all ECS as well as longitudinal and vertical deformation shows fluctuation that is a sign of Plaxis 3D has potential to generate accurate results along springline of || tunnels. Reason behind Longitudinal deformation (uy) consistency is that constant thrust force is applied for TBM advancement and it totally depend on actual insitu geological conditions which diversify in nature whereas in this model layering is done while excavating tunnel cutterhead will cut constant layers ahead of face in longitudinal direction that means it does not cut another layer in another direction while advancing. Jointing, fracture, intrusion water ingress such geological features are cooperated in cutting layer in scope of future studies to study more longitudinal deformation and it is very precise and construction site specific.

II. Tunnel Industry Utilization (TIU)

Table 7. ESC for ECS to achieve min deformation in the respective direction, min deformation between sub-classes is taken as the final value for that particular class and for Class-D Min deformation check with Class-C because both have close results.

ESC	Scale	ECS	|u|	|u|s	ux	uxs	uy	uys	uz	uz s
A	I	D1	✓	✓			✓	✓		
	II	D2			✓	✓			✓	✓
B	III	S-v1	✓	✓	✓	✓			✓	✓
	IV	S-v2					✓	✓		
C	V	OEO	✓	✓	✓	✓	✓			✓
	VI	EOO						✓	✓	
D	VII	OM			✓	✓		✓	✓	

As per Table 7 Min deformation between sub-classes is taken as the final value for that particular class and for Class-D Min deformation check with Class-C because both have close results. **()** represents the decision of parallel TBMs advancement construction methodology to achieve minimum deformation specially in soil between two parallel tunnels (ux-s= lateral deformation along springe line) to avoid deformation during simultaneous excavation it will lead towards time saving sustainability tunnel construction approach along with improving safety.

III. With drift and without drift aspects in parallel tunnel construction

Table 8 and Figure 10 shows its graphical representation of drift its total phases in numbers of that particulate ECS numbers and it conclude that (Excavation cycle of S-v1 and OM have equal construction cycles with drift of 1.5m and 4.5,6 in certain phases, which shows that the continuation of drift will increase the deformation, so it needs to vary after a certain pattern

Table 8. Drift suitability in simultaneous parallel tunnel excavation

ECS	Phases	Drift[m]	|u|[mm]
D1	11	0	49
D2	6	0	49.48
S-v1	12	1.5	49.83
S-v2	20	0,1.5	51.29
OEO	5	0	46.63
EOO	5	0	46.83
OM	12	4.5,6	46.85

of excavation. In drift situation, the deformation will be higher when the increase of excavation cycle. From this study, it suggested that using 1.5 m drift for clay is not suitable instead of this suggested that use OEO or EOO approach during a || tunnel construction. Moreover, it notices that by comparing ECS-S-v1 from Phase 4 onwards in ECS-OM continuous drift with more than 1.5m such as 4.5m,6m gives satisfactory results for the same excavation cycle because Phase 4 onwards in ECS-OM values of |u| constantly reduce. For rapid and safe construction, the approach from this study suggested that in | | simultaneous construction in case of drift 4.5 to 6 m and for non-drift excavation use modified patterns like ECS-OEO and ECS EOO. This graph concludes that if you need to increase excavation cycles for more safer construction approach then increase drift to minimize deformation (S-v1 < OM).

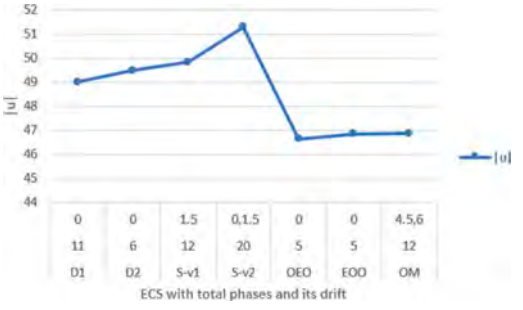

Figure 10. Drift aspects in ECS decisions.

ACKNOWLEDGMENTS

Expressing gratitude towards my parents (Gajanan Kumbhar and Sushama Kumbhar); my university MIT-WPU, Pune; my software training institute RamCaddsys Chennai (Mr. Siva Subramaniam Sir & Mr. Jitendra Pradhan Sir) and all invisible hands who make this research happen.

REFERENCES

[1] Zhen Huang, Chenlong Zhang, Helin Fu et al. 2020, "Numerical Study on the Disturbance Effect of

Short-Distance Parallel Shield Tunnelling Undercrossing Existing Tunnels," Advances in Civil Engineering, vol. 2020, Article ID 8810658, 14 pages.

[2] Zhiyong Yang, Yaowen Ding, Yusheng Jiang et al. 2020, "Study of the Construction Sequence of Overlapping Tunnels by the Shield Tunnelling Method: A Case Study of the Longest Overlapping Tunnel in China," Advances in Civil Engineering, vol. 2020, Article ID 4909750, 9 pages.

[3] Ahsan Naseem, Ken Schotte, Bart De Pauw and Hans De Backer. 2019, "Ground Settlements due to Construction of Triplet Tunnels with Different Construction Arrangements," Advances in Civil Engineering, vol. 2019, Article ID 8637837, 18 pages.

[4] Raja Kanagaraju and Premalatha Krishnamurthy. 2020, "Influence of Tunnelling in Cohesionless Soil for Different Tunnel Geometry and Volume Loss under Greenfield Condition," Advances in Civil Engineering, vol. 2020, Article ID 1946761, 11 pages.

[5] Xinjiang Wei, Mobao Zhang, Shaojun Ma et al. 2021, "Deformation Characteristics of Existing Twin Tunnels Induced by Double Shield Undercrossing with Prereinforcement: A Case Study in Hangzhou," Advances in Civil Engineering, vol. 2021, Article ID 7869899, 15 pages.

[6] Toshiyuki Hagiwara, R.J., Grant M. Calvello and R. N. Taylor et al. 1999, "The Effect on Overlying Strata on the Distribution of Ground Movements induced by Tunnelling in Clay," Soils and Foundation, vol. 39, no.3, 10 pages.

[7] Masoud Forsat, Mohammad Taghipoor, Masoud Palassi. 2021, "3D FEM Model on the Parameters' Influence of EPB-TBM on Settlements of Single and Twin Metro Tunnels During Construction," International Journal of Pavement Research and Technology, 15:525–538, 14 pages.

[8] Waad A. Zakaria, Qasim A. Mahdi, Halah Hashim Muhammed. 2019, "Prediction of Stresses and Settlement for TBM Tunnel Surrounding Soil," DJES, vol.12, no.4, 10 pages.

[9] Bin-Chen Benson Hsiung. 2011, "A Case Record of Bored Tunnels in Sand based on the Kaohsiung Mass Rapid Transit System Project," Journal of Geoengineering, vol. 6, no.3, 10 pages.

[10] Mohammad Afifipour, Mostafa Sharifzadeh, Kourosh Shahriar et al. 2011, **"**Interaction of twin tunnels and shallow foundation at Zand underpass, Shiraz metro, Iran,**"** ELSEVIER Tunnelling and Underground Space Technology, Article ID 26(2011) 356-363, 8 Pages.

[11] Md Shariful Islam and Magued Iskander. 2022, "Effect of Geometric Parameters and Construction Sequence on Ground Settlement of Offset Arrangement Twin Tunnels," Article ID 12010041, 30 Pages.

[12] Adel A. Al-Azzawi, Khalida A. Daud and Halah A. Daud.2018, "Finite Element Investigation on the Interaction between Shallow and Deep Excavated Twin Tunnels," Article ID ISSN 1819-6608, 9 Pages.

[13] Chao Liu, Zhuohua Peng, Liufeng Pan, Hai Liu et al. 2020, "Influence of Tunnel Boring Machine (TBM) Advance on Adjacent Tunnel during Ultra-Rapid Underground Pass (URUP) Tunnelling: A Case Study and Numerical Investigation, MDPI- Applied science article, 25 Pages.

[14] V.B. Maji, A. Adugna. 2016, "Numerical Modelling of tunnelling induced ground deformation and its control," *Physical Review Letters*, vol. 50, no. 2, Article ID 183-188, 6 pages.

[15] Prateep Lueprasert, Pornkasem Jonpradist and Suchatvee Suwansawat. 2017, "Tunnelling simulation in soft ground using Shell elements and Grouting layer," *International Journal of Geomate*, vol. 12, Article ID ISSN 2186-2990, 6 pages.

[16] Shaohua Li, Pengfei Li, Mingju Zhang and Yi Liu. 2019, "Influence of Approaching Excavation on Adjacent Segments for Twin Tunnels," Applied Science Article, 19 pages.

Tunnelling for a Better Life – Yan, Celestino, Thewes & Eberhardt (Eds)
© 2024 The Author(s), ISBN 978-1-032-80042-4
Open Access: www.taylorfrancis.com, CC BY-NC-ND 4.0 license

Short launch of TBM to overcome economic and logistic difficulties in Sri Lanka

David Lees*
Chief Resident Engineer, MWSIP, PMDSC, Dambulla, Sri Lanka

Juan Sánchez
Resident Engineer UECP-2A, PMDSC, Habarana, Sri Lanka

Yi Chengzhi
Chief Engineer UECP 2A, China State Construction Engineering Corporation Ltd, Habarana, Sri Lanka

Seneviratne Banda
Project Director PIU, MWSIP, Madatugama, Sri Lanka

David Denman
Tunnel Consultant, Geo Consult, Bankok, Thailand

Perumal Muniyandy
Rock Mechanics & Tunnel Construction Engineer, PMDSC, Dambulla, Sri Lanka

ABSTRACT: The Mahaweli Water Security Investment Program (MWSIP) is a major project in Sri Lanka to provide water resources to the dry North-East of the country and enable two crops of rice per year. The current phase includes the construction of 76 km of waterway via canal, aqueduct and tunnel.

Contract UEC-ICB-2A is the biggest component of this current phase and includes the excavation of 27 km of underground waterway which will be the longest in South-East Asia when complete. The tunnels are being constructed by two, purpose built, Double Shielded Chinese TBMs of 7.6 m diameter. The construction is being carried out by China State Construction Engineering Corporation (CSCEC) for the Ministry of Mahaweli. The Engineer is a JV called the Project Management Design and Supervision Consultants (PMDSC) and the Client is represented by a Project Management Unit (PMU) and a Project implementation Unit (PIU).

During the economic crisis in 2022 the Country suffered many shortages including diesel and explosives. The original plan was to excavate a full launch chamber for the TBM from the bottom of the 23 m deep, 26 m diameter Northern Start Shaft. However, due to shortages of explosives and limitations on imports it was instead decided to launch the TBM in a short mode of only 65 m length and then to stop and complete the installation and commissioning of the TBM once the tunnelling had reached 200 m.

This paper will describe the actions taken to promote the tunnel progress and to achieve the best result for the TBM in very challenging circumstances.

Keywords: Tunnelling, TBM, short launch

1 INTRODUCTION

The Mahaweli Water Security Investment Program, financed by the Asian Development Bank and the Government of Sri Lanka, aims to complete the Mahaweli Development Program, started in the 1970s to improve farmer incomes, food security, equity between different parts of the country, public health, and domestic, municipal and industrial water supplies. Up to 900 million m^3 of water will be transferred annually through canals, reservoirs and tunnels from the Mahaweli River to the water-scarce north and north-west, where smallholder farmers have traditionally practiced single-season rice cultivation. The transfer will facilitate cultivation of a second, diversified, crop and must be shared with competing consumptive demands, as well as meeting daily peak energy demands through releases for hydropower (Chegwin and Kumara, 2018).

Phase 1 of the North Central Province Canal Project under the Mahaweli Water Security Investment

*Corresponding author: David.Lees@external.tractebel.energie.com

DOI: 10.1201/9781003495505-254

Program comprises three components – namely the Minipe Left Bank Canal Rehabilitation Project (MLBCRP), the Kalu Ganga – Moragahakanda Transfer Canal (KMTC) and Upper Elahera Canal Project (UECP), and the North Western Province Canal Project (NWPCP).

The objective of the 65.5 km long Upper Elahera Canal (UEC) is to transfer 100 MCM of Mahawelli water from the Morakahander Reservoir to the Yan Oya basin (Figure 1).

The UES is implemented in three program tranches:

1. Tranche 1 comprises the construction of the UEC from 0+100 km to 6+226 km (UECP-ICB1).
2. Tranche 2 includes the construction of the UEC from 6+226 km to 17+700 km (UECP-ICB3), UEC Tunnel 3 and Tunnel 4 from 27+509 to 55 +600 km (UECP-ICB2A), and the Kalunganga-Morahakanda Transfer Canal (KMTC) from 0 +000 to 8+830 km (UECP-ICB2B).
3. Tranche 3 comprises the construction of the UEC from 17+700 to 27+509 km (UECP+ICB4), from 55+600 to 65+500 km (UECP-ICB5, and the transfer canal from the end of the UEC to the Mahakanadarawa Reservoir (UECP-ICB6).

Funding is provided by the Asian Development Bank (ADB) under all three Tranches.

The tunnels for UECP-2A consist of a short length of drill and blast excavation to be excavated under NATM principles (Tunnel 4) and two TBM drives one from the north and one from the southern portal (Tunnel 3). Access at the northern site is via a 26 m diameter vertical shaft and the intention was to excavate start tunnels for full assembly of the TBM from the bottom of the shaft.

However due to the economic situation that developed in Sri Lanka in 2022 where the provision of many resources became very difficult, due to a lack of availability of explosives for the drill and blast development it was necessary to consider an alternative methodology for commencing the TBM excavation namely a "Short Launch" option.

2 SHORT LAUNCH

The original concept was to excavate a launching pilot tunnel 370 (200+170) m long. However, due to limits on explosive availability it was decided to excavate 65 m in T4 and 15 m in T3.

Although the short launching method increased the working time of secondary assembly of the TBM, due to the low excavation rates achieved in the NATM excavation it was expected that the short launching method could expect to be completed up to 44 days ahead of the programme.

The original method proposed to excavate 170 m in Tunnel 4 of 1100 m and 200 m in Tunnel 3. Then to fully assemble the TBM in Tunnel 4 (except No 9 gantry) and push it forward 130 m into Tunnel 3, which would enable normal excavation to start after an initial excavation of 70 m. This is presented in Figure 2.

Firstly, The No 5, No. 4, No. 2 and No.1 gantry were assembled and pushed back into the T4 Tunnel. Then the cutter head was lowered into the shaft and assembled at the head of the TBM. A special Crawler Crane had to be imported to lift the 150 tons cutter head, and due to import restrictions at the time in Sri Lanka, this had been arranged on a specific import/export permit. The total length of the first stage is 83 m as shown in Figure 4.

The next step was to push the TBM into the 15 m of excavated Tunnel 3 and install the first ring segments as shown in Figure 5.

Step 3 was initial tunnelling of 76 m. This is shown in Figure 6. The first 55 m using a temporary belt conveyor and gantry crane to lift muck from the shaft, and from 55 m to 76 m using bucket for mucking.

3 TBM 2ND ASSEMBLY

After completing 76 m of excavation the remaining gantries of the TBM (except No. 9 gantry which is the pipeline extension gantry) were assembled underground this gave a total length of the TBM of 153 m. The total available excavated length was 90 m in Tunnel 3 and 65 m in Tunnel 4 with 26 m for the shaft diameter giving a total of 181 m.

To perform this the gantries were moved back to Tunnel 4 removing them one at a time with the gantry crane, inserting the shotcrete bridge and reconnecting the gantries and moving the completed TBM back into Tunnel 3 as shown in Figure 7.

The next step was to excavate a further 98 m until the total length of Tunnel 3 reached 188 m. Then the No 9 gantry and belt conveyor system could be installed. When this was completed, normal tunnelling operation with full TBM launching could commence. This is shown in Figure 8.

4 TBM MODIFICATIONS

To facilitate the short launch a number of modifications were required to the TBM firstly the belt conveyor for the removal of the muck. The TBM belt drive was originally located in the No 8 gantry this was relocated to the end of the No 5 gantry and a temporary muck chute was installed.

The mucking conveyor was temporarily installed in Tunnel 4. The muck was first transferred to the shaft, and then lifted vertically to the ground by the gantry crane.

The mucking conveyor was temporarily installed in Tunnel 4. The muck was first transferred to the shaft, and then lifted vertically to the ground by the gantry crane as shown in Figure 11.

5 ELECTRICAL MODIFICATIONS

The cutter head transformer, ordinary transformer, capacitor compensation cabinet, power distribution

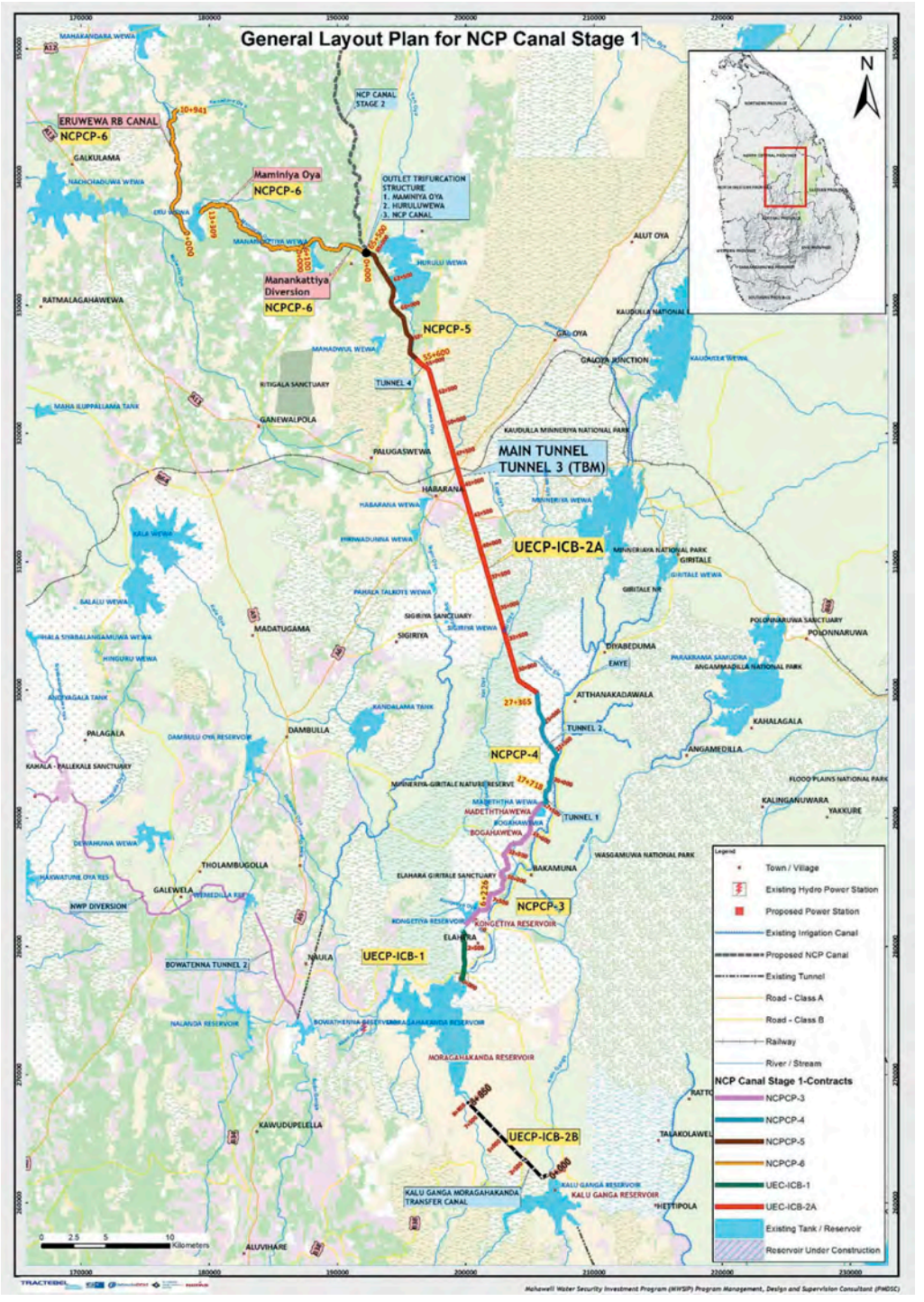

Figure 1. General layout plan for northern central province canal stage 1.

cabinet, frequency conversion cabinet, control room, etc. are all in place, and the main functions of TBM are ready for operation. Equipment not in place was powered separately.

The emergency generator on the right side of the No 5 gantry was removed and the transformer and capacitor compensation cabinet on the left side of gantry No.6 crane was modified.

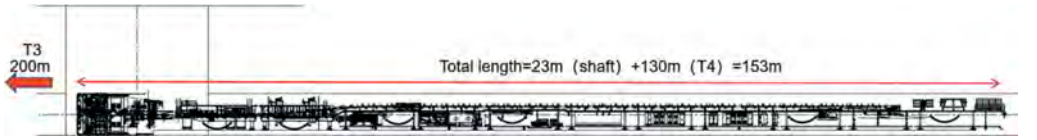

Figure 2. Original concept long launch.

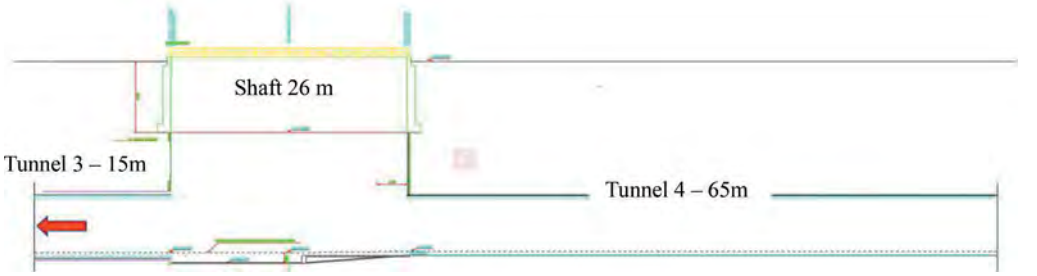

Figure 3. Northern access shaft and start tunnels.

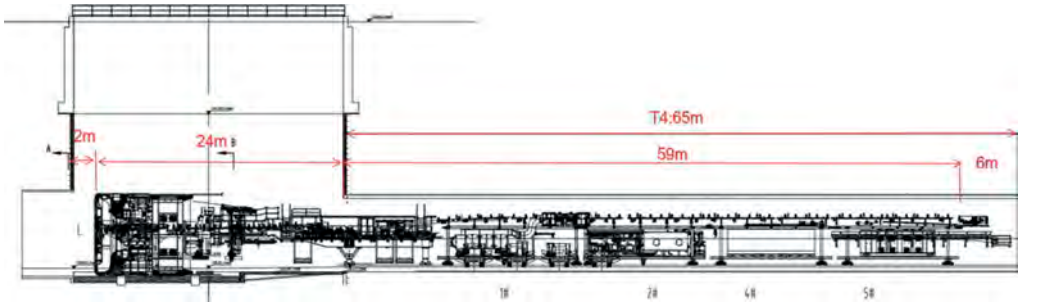

Figure 4. First assembly - short launch.

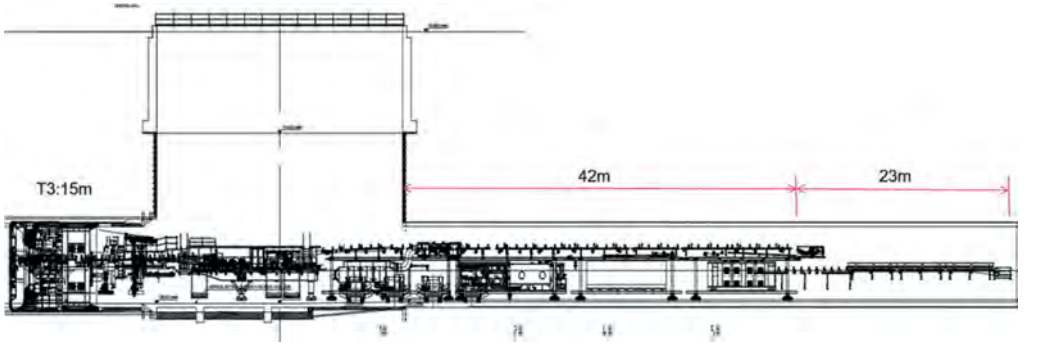

Figure 5. CommenceTBM excavation – short launch.

The TBM belt drive cabinet (MDO) needs was transferred from the left side of the No. 7 gantry to the top of the No. 5 gantry.

Due to the missing of shotcrete bridge and No. 3 gantry, there was a surplus of cables in the order of about 30 m, including the main drive motor cable, pump station motor cable and most of the control cables. These were protected from dust and damp and temporarily stored in the headroom space.

The pea gravel pump was removed and relocated at the shaft bottom. This was an independent system, so power was supplied from surface.

6 OTHER SYSTEMS

The TBM supply pipe route from the ground extends through the hose to the water tank located at the rear

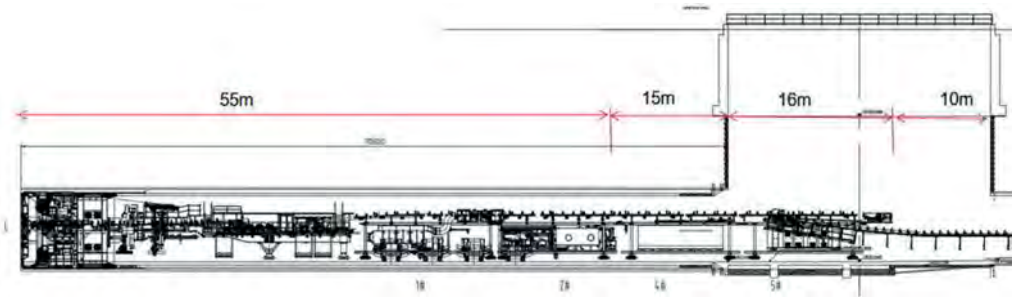

Figure 6. Initial TBM tunnelling – short launch.

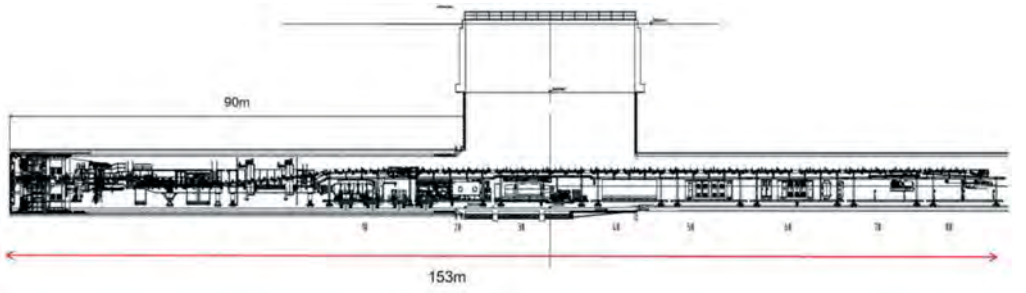

Figure 7. 2nd Assembly – short launch.

Figure 8. Completion of short launch tunnelling.

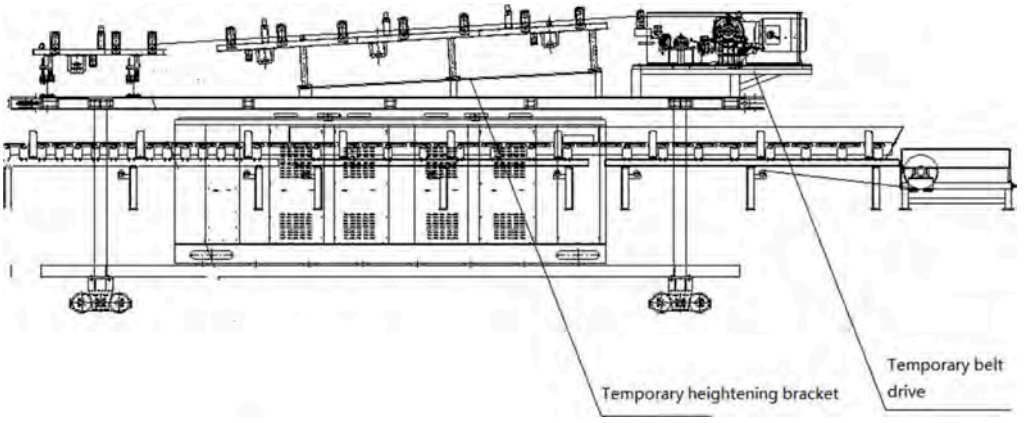

Figure 9. Modification of No 5 gantry.

of the No. 5 gantry. During the initial stage, temporary water pumps were used instead of the TBM dewater system for drainage.

The Pneumatic oil pump is suspended during the initial launching period, and oil filling was carried out manually.

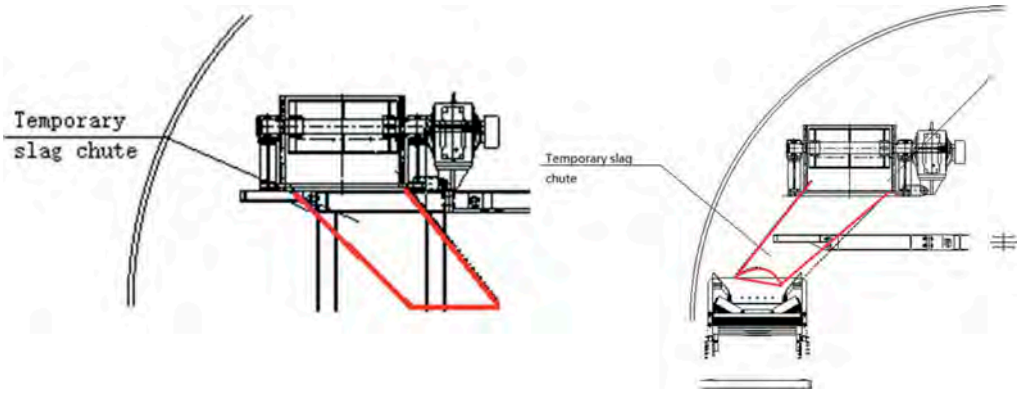

Figure 10. Temporary muck chute.

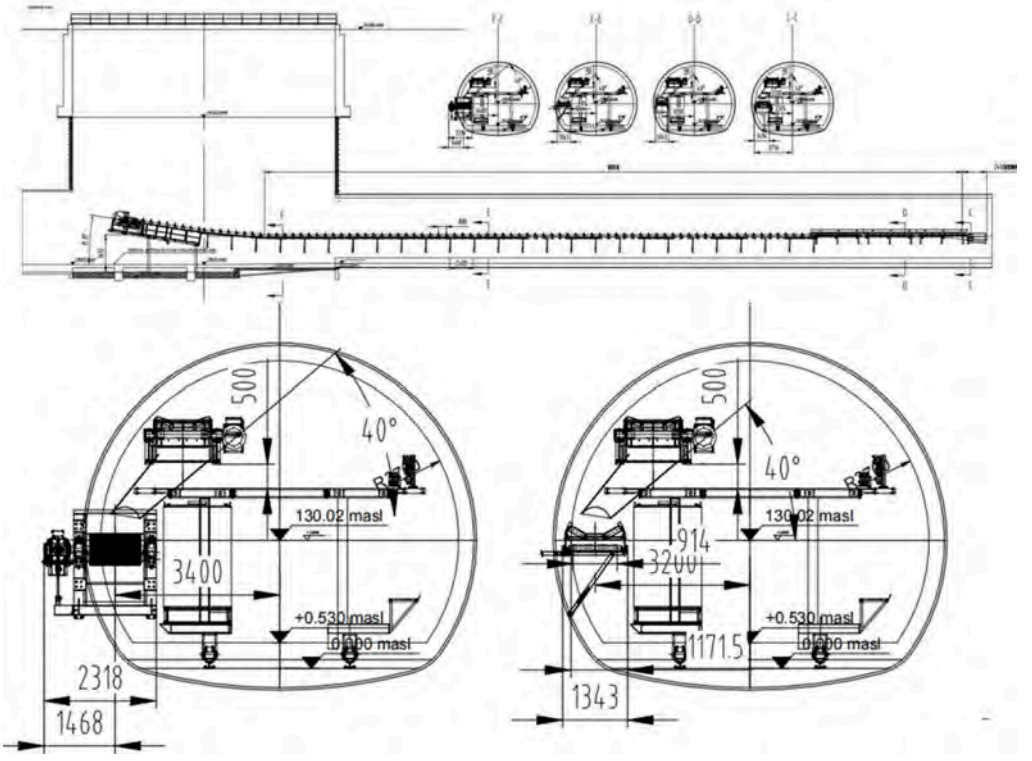

Figure 11. Temporary belt conveyor in tunnel 4.

The air compressor and gas tank are located on the surface at the shaft, from which a pipeline supplied compressed air to gantry No 5.

7 PROGRESS

The NATM excavation and support was completed on November 15, 2022.

First assembly of the 83 m of the TBM for the first launch commenced on November 16, 2022, and was completed on December 6, 2022.

The initial 90 m of TBM excavation commenced on December 27, 2022, and was completed on January 29, 2023. Excavation rate was slow due to the temporary mucking arrangement from the bottom of the shaft and due to commissioning work of some parts of the TBM during this period.

The second step in the excavation commenced on January 29, 2023, and finalized on 20 March 2023.

After that, was planned to prepare full commissioning of TBM, it was completed on April 10, 2023.

The TBM then excavated the initial 500 m of tunnelling to complete its full commissioning. This 500 m excavation was completed on May 9, 2023.

ACKNOWLEDGMENTS

The Authors would like to acknowledge the support of the Mahaweli Ministry and the Project Management Unit for the MWSIP, the other members of the Engineers Team from PMDSC and the Contractor CSEC for their assistance in preparing this paper.

REFERENCES

Chegwin, M.R., Kumara S, 2018. Energy, land and water nexus in Sri Lanka's Mahaweli basis. Energy: Volume 171 Issue EN3, ICE, 5th June 2018

Tunnelling for a Better Life – Yan, Celestino, Thewes & Eberhardt (Eds)
© 2024 The Author(s), ISBN 978-1-032-80042-4
Open Access: www.taylorfrancis.com, CC BY-NC-ND 4.0 license

Adaptability design and application of TBM cutterhead in Beishan extremely hard rock geological conditions

JianFang Li*
China Railway Construction Heavy Industry Corporation Limited, Changsha Hunan, China

ABSTRACT: As a key part of rock TBM, the cutterhead bears great load during excavation and rock breaking. Under extremely hard rock geological conditions, higher requirements will be meant for cutterhead rock breaking efficiency and structural bearing performance. This paper analyzes the geological characteristics and project engineering difficulties of TBM long-distance spiral downhill construction in Benshan Laboratory, carries out adaptive design from the aspects of cutter selection and layout, disk structure, etc., analyzes and checks the balance performance and mechanical properties of the cutterhead, and designs and manufactures a TBM cutterhead suitable for Beishan extremely hard rock working conditions. The project engineering application results show that the tunneling efficiency and cutter usage of TBM meet the design requirements, which is of reference significance to the cutterhead design under similar extremely hard rock conditions.

Keywords: extremely hard rock, TBM, cutterhead, adaptability

1 INTRODUCTION

With the increasing acceleration of infrastructure construction in China, there are more and more large-scale projects in these fields as underground resource excavation, underground space development, nuclear industry laboratory and highway construction. As a major key technical equipment for human beings to carry out underground space construction in the 21st century, TBM is also widely used and its demand is constantly rising. Therefore, the R&D of TBM for applications under various complex geological conditions has become a technical key point that all manufacturing powers in the world focus on and compete to seize [1-4]. As the core component of TBM, cutterhead is in direct contact with rock surface and bears all rock breaking loads. Its adaptive design such as static analysis, cutter matching and balance calculation are necessary links and steps for cutterhead design[5-6].

Many scholars both at home and abroad have done a lot of design analysis on TBM cutterhead. Zhang Zhaohuang put forward the concept of curved cutterhead, which can reduce the vibration of cutterhead during tunneling by increasing the strength and rigidity, thus improving the service life of cutters and the rock breaking efficiency of TBM[7]. Zhao Zhenwei analyzed the plane, conical and spherical cutterhead structures under different tunneling conditions to obtain the maximum deformation and equivalent stress of three types of cutterheads[8]. Sun Jianping analyzed the adaptability of related geological conditions, tunneling parameters, engineering construction, durability and safety[9].

The above studies mainly focus on the conventional TBM cutterhead, but there are few related structural research designs for spiral downhill tunneling cutterhead for extremely hard rock. Relying on the Beishan Underground Laboratory Project, this paper carries out adaptability research on the key technologies of cutterhead in view of the key and difficult problems in the process, and selects extremely hard rock cutterhead with strong geological adaptability, good comprehensive performance and comprehensive functions.

2 PROJECT INTRODUCTION

2.1 *Project overview*

The spiral ramp of the main project of Beishan Underground Laboratory is constructed by open TBM, with a total length of 7 km, an overall slope of -10% and R250 m horizontal turn. The rock mass is granodiorite, mainly Class I and II surrounding rocks. The uniaxial compressive strength of the rock is 110-260 MPa, with an average of 170 MPa. It is the tunnel project with the most complete rock and the highest strength in the

*Corresponding author: lijianfang@crchi.com

DOI: 10.1201/9781003495505-255

projects of the world under construction. The main difficulties in TBM design are spatial spiral downhill excavation and long-distance extremely hard rock construction.

2.2 *Analysis of important and difficult points*

The Project mainly faces the following technical difficulties:

1. Rock fissures are not developed. The core with RQD>90 accounts for 86.2% of the total core length, and the core with RQD>75 accounts for 93.4% of the total core length. The rocks generally have good integrity;
2. The uniaxial compressive strength of rock ranges from 110 MPa to 235 MPa, and the average uniaxial compressive strength is 170 MPa. The tensile strength of rock ranges from 6 MPa to 15 MPa, with an average tensile strength of 11 MPa. The rock friction index (CAI) is between 4.31 and 5.29, with high strength and abrasiveness;
3. The tunneling mode is spatial spiral downhill tunneling, which affects the service life of cutters.

Figure 1. Schematic diagram of rock core.

3 TARGETED DESIGN OF CUTTERHEAD

3.1 *Structural design of cutterhead*

3.1.1 *Conical cutterhead design*

There are plane, conical and spherical TBM cutterheads, as shown in the figure.

Figure 2. Schematic diagram of cutterhead structure.

The plane cutterhead is widely used due to its easy manufacturing, shorter cantilever length and good adaptability to various soft and hard surrounding rock conditions. In horizontal tunneling projects, the cutterhead is basically a plane cutterhead. Conical and spherical cutterheads are difficult to manufacture because the disk body composed of face plate and back plate is conical or spherical. The tapered surface or spherical surface of the disc body has a larger coverage area relative to the plane, so that the cutter spacing can be made smaller than that of the plane cutterhead. However, there is a free face between the conical and spherical cutterheads relative to the plane cutterhead hob during tunneling, so the rock breaking efficiency will be higher than that of the plane cutterhead. However, the crushed and peeling rocks at the upper part of the tunnel face are not easy to fall to the bottom during the process of horizontal tunneling. The smaller the cone angle and spherical diameter, the lower the ballast chute efficiency, resulting in secondary or more wear of the hob and cutter head, accelerating the wear of the hob and cutterhead and shortening the service life of the cutterhead. Therefore, the cone and spherical cutterheads are mainly used in inclined shaft and vertical shaft tunneling, but less used in horizontal tunneling.

The advantages and disadvantages of the three structural forms of cutterheads are shown in the table below.

Table 1. Advantages and disadvantages of cutterhead type.

S/N	Structural Type	Advantages	Disadvantages
1	Plane type	It is relatively easy to manufacture and is widely used, suitable for various soft and hard surrounding rocks	Rock breaking efficiency is lower than that of conical and spherical surfaces
2	Conical type	It is mainly used in inclined shaft and vertical shaft TBMs, with high rock breaking efficiency	Difficult to manufacture and low ballast chute efficiency
3	Spherical type	Less case of application, difficult to manufacture	Relatively difficult to manufacture and low ballast chute efficiency

According to the advantages and disadvantages of the three types of cutterhead structures, combined with the downhill extremely hard rock tunneling of Beishan Ramp Project, in order to improve the rock breaking efficiency of the cutterhead under extremely hard rock working conditions and take into account the smoothness of ballast chute, and considering the cutterhead height, cutter installation method and manufacturing difficulty, the cutterhead is designed as a conical cutterhead.

3.1.2 *Design of high-load cutter head*

The tunneling efficiency of TBM is related to the structural characteristics of the device itself, cutterhead, type of cutterhead used, cutter arrangement, geological conditions of construction and other factors. Among them, the bearing capacity and service life of cutter head structure are one of the key factors that could affect tunneling efficiency.

There are two types of cutter installation: back-mounted and front-mounted. The former is convenient for cutter operators to replace and inspect the cutters inside the cutterhead. At the same time, the hob holder is embedded in the cutterhead body, with better structural strength and higher stability. However, due to the embedded cutterhead body and limited by its large structural size, the cutter spacing of the cutterhead cannot be made smaller, and the strength of the cutterhead will be affected. Front-mounted cutter installation type, or the latter: The hob is disassembled from the tunnel face, so the size of the cutter head can be shortened from 630 mm to 520 mm. The strength and rigidity of the cutter head itself are better than those of the back-mounted type, or the former and the cutter arrangement is more symmetrical. Due to the reduction in structural size, the strength and rigidity of the cutterhead are better than those of the back-mounted type. However, there are some safety risks due to tool replacement in the tunnel face.

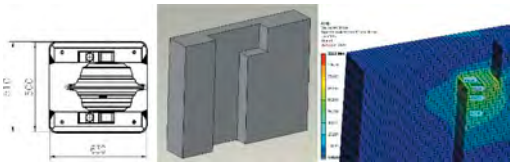

Figure 3. Back-mounted cutter head.

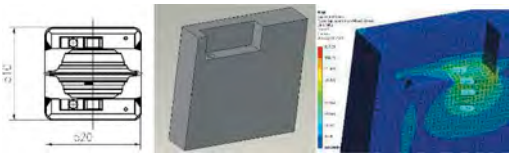

Figure 4. Front-mounted cutter head.

According to the characteristics of good integrity, high rock strength and extremely hard rock conditions, cutter installation form and cutter position in the Project, as well as the small space in the edge area and a certain inclination angle between the edge hob and the tunneling direction, the center and front side are front-mounted, and the edge hob is back-mounted.

3.1.3 *Structural strength analysis*

Taking the TBM cutterhead of Beishan Project as the research object, the cutterhead's structural strength is analyzed. The cutterhead is an integrated cutterhead, which mainly consists of the front panel, rear panel, flange, rib plate, back plate and cutter. To ensure the feasibility of analysis and calculation, some chamfers and slight gaps are omitted in the solid modeling process, and grid division is carried out, as shown in the figure.

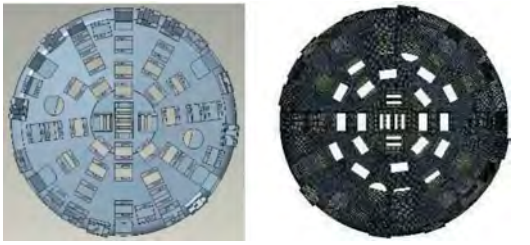

Figure 5. 3D model and grid model.

The static analysis method should be used to analyze the stress of TBM cutterhead. According to the installation method and movement requirements of TBM cutterhead, full displacement constraint should be applied on the bottom surface of flange plate of the cutterhead. In rock breaking, the blade penetrates into the rock and soil, causing cracks in the rock and thus spalling. Therefore, the hob cutter edge is stressed at some nodes. To better simulate the hob load, a rigid element is established to connect some nodes of the cutting edge so that the nodes on the cutting edge will be stressed at the same time. Considering the simultaneous action of vertical force, rolling force and lateral force on the hob, a local coordinate system will be established for non-horizontal and vertical hobs to facilitate loading.

After calculation, the structural stress and displacement nephogram of cutterhead can be obtained. It can be seen from the displacement diagram that the deformation at the center of the cutterhead is the largest, at 1.06 mm, and the degree of deformation gradually decreases from inside to outside. Due to gravity, the deformation at the bottom of the cutterhead will be greater than that in the surrounding area. The strain of deformation relative to the overall thickness of cutterhead is about 0.627‰. The deformation of the flange and support plate is relatively small.

It can be seen from the stress nephogram that the maximum stress is 215.4 MPa and the statistical average of the maximum stress is 131.6 MPa. The stress of the cutterhead is mainly distributed in the support rib area, including six main support ribs and the connection position between each support rib and the flange.

3.2 *Cutter and layout design*

TBM tunnels in extremely hard rock strata and mainly breaks rock with hobs. Therefore, the

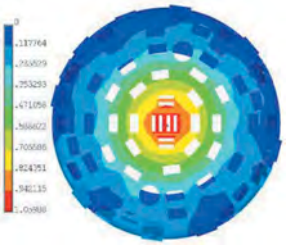

Figure 6. Cutterhead displacement Nephogram.

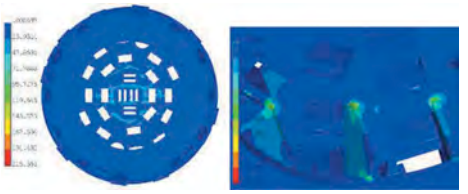

Figure 7. Stress Nephogram.

arrangement of hobs is a key factor in cutterhead design. According to different geological conditions and different cutter layout modes, the rock breaking efficiency of the cutterhead will be affected, which will impact the service life of the cutterhead and cutters.

The disc hob is the first part to contact rock on TBM and also a key part for breaking rock. Its main structure includes cutter ring, cutter shaft, cutter body, bearing, floating seal, etc.

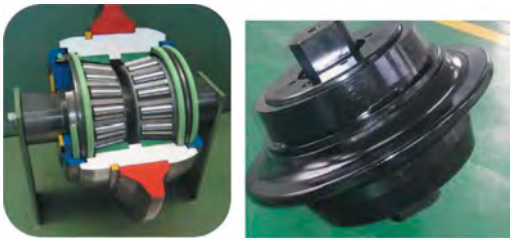

Figure 8. Structure of disc hob.

The average uniaxial compressive strength of Beishan Ramp Project is 170 MPa, and the overall rock strength is extremely high. According to the most widely used disc hob stress CSM model proposed by Rostami[10], the greater the compressive strength of rock is, the greater the force applied by the disc hob to crush rock will be.

Therefore, to improve the rock breaking efficiency of the cutterhead of Beishan Ramp Project, the cutterhead hob is designed as a large-load 20-inch hob. Compared with conventional 19-inch hobs, the inner diameter, outer diameter, inner width and outer width of the large-load 20-inch hob bearing are increased, and the corresponding shaft diameter, end cover and installation size of the hob are increased accordingly, thus finally increasing the bearing capacity of the hob by 19% to 375 kN, as shown in the table.

Table 2. Parameters of hob bearing.

S/N	Parameter	20-inch hob	19-inch hob	Improvement rate
1	Bearing model	HH932132/ HH32110	HH926749/ HH926710	
2	Bearing bore diameter/mm	127	120.65	5.3%
3	Outer diameter of bearing/mm	304.8	273.05	11.6%
4	Inner width of bearing/mm	82.55	82.55	/
5	Outer width of bearing/mm	88.9	82.55	7.7%
6	Rated bearing capacity/kN	375	315	19%
7	Shaft diameter/mm	127	120.65	5.3%
8	Wear limit/mm	35	35	/

According to the geological conditions and actual layout of cutterhead, the final configuration of cutterhead is determined as shown in Table 3.

Table 3. Configuration of cutterhead and tools.

Name	Diameter of hob/mm	Quantity	Cutter spacing/mm	Cutter height
Central hob	457	4 (duplex)	100	145
Front hob	508	35	60	145
Edge hob	508	12	60 degressive	/
Number of buckets	/	6	/	105

3.3 *Cutter spacing design*

Disc hob spacing is defined as the shortest radial distance between two adjacent disc hobs, which is different from that the cutter layout must cover the whole section. The main requirement of disc hob layout is that the crushing area between adjacent disc hobs must be connected, and the related disc hob spacing becomes one of the most critical factors for disc hob layout. The spacing between the most important rolling hobs on the TBM cutterhead and the front disc hob is generally equal and a constant

value, which is 40-120 mm. The size is related to rock properties and tunneling parameters. Reasonable disc hob spacing can improve the tunneling efficiency of the cutterhead and reduce cutter wear.

The specific energy consumption for rock breaking by disc hobs is an extremely important indicator in the process of rock breaking by disc hobs, which is defined as the work done by disc hobs when crushing unit volume of rock. If the specific energy consumption is small, it indicates that less energy is required to crush unit volume of rock and the rock breaking efficiency is high. Therefore, the optimal cutter spacing between disc hobs can be determined based on the specific energy consumption[11].

Simplified calculation formula for specific energy consumption improvement:

$$SE = \frac{W}{V} = \frac{F_R l}{V} = \frac{F_R l}{m/\rho} \tag{1}$$

Where: FR is the average rolling force; l the cutting distance of hob; S the cutter spacing; p the penetration; A is the rock breaking area below; V the volume of rock debris V=A·l.

The physical and mechanical parameters of rock specimens made with the standard method by using rock samples collected on site measured in the mechanical test center are shown in the table.

Table 4. Parameters of rock materials.

Rock Type	Density/ (g/mm³)	Compressive Strength/ MPa	Tensile Strength/ MPa	Crushing Angle/(°)
Granite	2.97×10-3	156.2	26.5	120

First, the disc hob indentation test should be carried out to record the penetration of the disc hob and the length of the lateral crack when the rock lateral crack penetrates the free surface. The rock sample is loaded by a hob until the lateral crack penetrates the free surface and then unloaded, as shown in Figure 3. The maximum penetration of the disc hob and the width of broken rock (i.e. lateral crack length) are collected and analyzed.

Figure 9. Hob indentation experiment.

Considering the randomness of lateral crack length in the test, it is necessary to carry out multiple indentation tests and eliminate singularity data to obtain a trend curve between crack length and penetration, as shown in Figure 4.

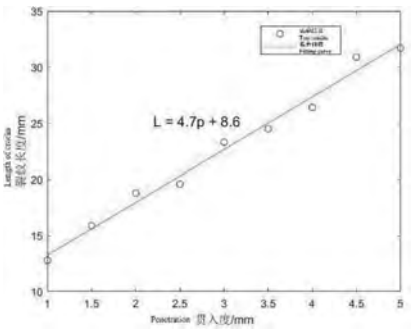

Figure 10. Crack length at different penetrations.

In general, the lateral crack length increases generally linearly with increasing penetration. According to the fitting of measuring points, the first-order function of lateral crack length with respect to penetration is

$$L = 4.7p + 8.6$$

The specific energy consumption model of hob cutting the above rocks can be obtained as follows:

$$SE = \begin{cases} \frac{TR\phi P^0 \sin(\frac{\varphi}{2})}{\lambda pS} & 0 < S \le 9.4p + 39.2 \\ \frac{TR\phi P^0 \sin(\frac{\varphi}{2})}{p^2 \tan\beta + Tp} & S > 9.4p + 39.2 \end{cases}$$

To compare the relationship between different penetrations, cutter spacing and specific energy consumption, the penetration is taken as 1, 2, 3 and 4 mm respectively. By substituting the above parameters into Eq., the calculation results of rolling force

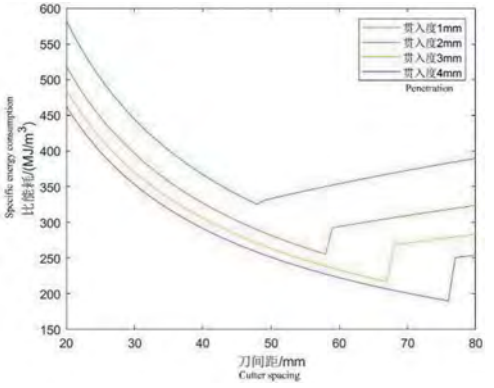

Figure 11. Energy consumption change of different tool spacing ratio.

and vertical force under common tool spacing can be obtained.

It can be seen from the figure that with the increase of cutter spacing, the specific energy consumption gradually decreases and then increases gradually when it is reduced to a certain extent. With the increase of penetration, the excavation volume increases and the specific energy consumption decreases gradually. According to the geological conditions in Beishan, the specific energy consumption of hob rock breaking process can be calculated by using force prediction model. The analysis shows that under the geological conditions of Beishan, the cutter spacing is set to 60 mm.

3.4 *Cutter balance calculation*

The existence of overturning moment may cause the cutterhead to deflect through the center and perpendicular to the cutting direction, which will lead to uneven stress on the cutterhead and spindle, accelerate the wear of edges and some hobs, and adversely affect the rock breaking performance and service life of the cutterhead. When the cutterhead rotates for one circle, the overturning moment along X and Y directions is shown in the figure.

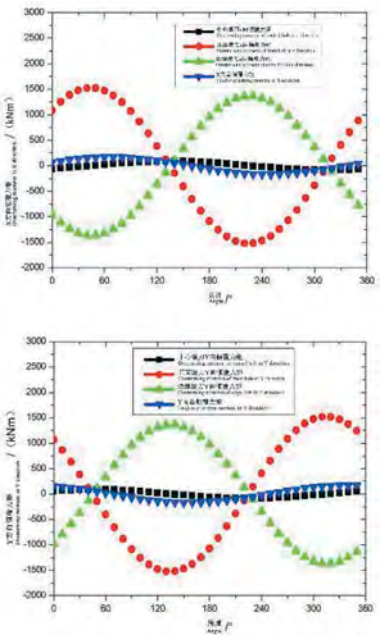

Figure 12. Overturning moments of cutterhead in X and Y directions.

It can be seen from the figure that the overturning moment generated by the front hob and the edge hob is obvious, which is related to the layout of cutters. The central hob has a small number and is located in the center of the cutterhead, so the overturning moment is small; the overturning moment generated by the cutterhead in X and Y directions is 170 km, less than 3.3% of the overall torque, meeting the use requirements.

Figure 13. Physical cutterhead and tunnel formation.

4 PROJECT APPLICATION EFFECT

The Beishan underground laboratory project is under excavation now, with a maximum daily footage of 20.4 m and a maximum monthly footage of 340 m.

At present, the tool wear is normal and conforms to the wear law, with a low abnormal failure rate of tools.

In general, Beishan TBM runs steadily during tunneling and mucking is smooth. The cutterhead has good adaptability to project engineering geology and meets the construction requirements.

5 CONCLUSIONS AND SUGGESTIONS

1) For spiral downhill extremely hard rock tunneling, the conical cutterhead can realize free face and high rock breaking efficiency;
2) The knife spacing can better match the extremely hard rock tunneling conditions, with low specific energy consumption and high rock breaking efficiency;
3) By analyzing the geological characteristics of extremely hard rock in Beishan, TBM cutterhead is designed with targeted innovation, which can better meet the tunneling needs of the project and show good application effect.

In short, the selection and design of cutterhead are not determined by any single factor. On the basis of engineering geology, following the principles of technical reliability and economic rationality, it is necessary to comprehensively consider factors such as cutterhead structural type, cutter layout, cutter load characteristics, balance calculation, etc., so as to match more adaptable cutterheads and meet project requirements.

This paper relies on the actual project conditions to carry out targeted design and solve practical engineering problems. In the next step, more in-depth theoretical analysis and research need to be carried out on multi-objective optimization modeling and analysis.

REFERENCES

[1] Acaroglu, and, et al. A fuzzy logic model to predict specific energy requirement for TBM performance prediction[J]. Tunnelling and Underground Space Technology, 2008, 23(5):600–608.

[2] Qi Mengxue, Yang Guoqing, Ceng Shaoyi. *Overview and Thinking of Advanced Disposal Technology for Full-face Rock TBM Construction* [J]. Tunnel Construction (Chinese and English), 2021, 41 (09): 1555–1564.

[3] Gong Jiangfeng, Wang Wei, Zhou Junchao. *Statistics and Analysis of Railway Shields and TBM Tunnels in China by the End of 2021* [J]. Railway Standard Design, 2022,66(03):1–5. DOI:10.13238/j.issn.1004-2954.202202230004.

[4] Qi Mengxue. *Development, Status quo and Prospect of TBM Tunneling Technology in China* [J]. Tunnel Construction (Chinese and English), 2021,41 (11):1964–1979.

[5] Nie Rui, Zhao Haifeng, Wang Xueke et al. *Research on Cutterhead and Cutter Arrangement Method of Miniature Earth Pressure Balance TBM Machine in Sandy Pebble Stratum* [J]. Manufacturing Automation, 2015, 37(21): 52.

[6] Liu Jianqin, Liu Mengmeng, Guo Wei et al. *Analysis of Key Problems in Research on Structural Performance Evaluation of TBM Cutterhead* [J]. Modern Tunneling Technology, 2014, 51(2): 5.

[7] Zhang Zhaohuang, Ji Wei, Weng Zicai. *Determination Theory and Simulation Analysis of Main Parameters of Conical Cutterhead Shield* [J]. Journal of Mechanical Engineering, 2021,57 (11):243–256.

[8] Zhao Zhenwei, Zheng Kangtai, Li Nan, Ma Changcheng. *Comparative Analysis of Static Performance of TBM Cutterheads with Different Geometries* [J]. Tunnel Construction, 2016,36(01):102–107.

[9] Sun Jianping, Tang Zhaoping. *Research and Evaluation on Design Adaptability of Shield Cutterhead System* [J]. Modern Tunneling Technology, 2020,57 (4):27–36.

[10] Rostami J. Study of pressure distribution within the crushed zone in the contact area between rock and disc cutters[J]. International Journal of Rock Mechanics and Mining Sciences, 2013, 57: 172–186.

[11] Tan Qing, Yi Nian'en, Xia Yimin et al. *Study on Calculation Formula of Optimal Disc Hob Spacing for Full-face Rock TBM* [J]. Geomechanics, 2016, 37 (3): 883–892.

Tunnelling for a Better Life – Yan, Celestino, Thewes & Eberhardt (Eds)
© 2024 The Author(s), ISBN 978-1-032-80042-4
Open Access: www.taylorfrancis.com, CC BY-NC-ND 4.0 license

Real time estimation and early warning of rock mass strength and integrity in TBM tunneling

Qingwei Li*
School of mechanical engineering, Shijiazhuang Tiedao University, Shijiazhuang, China

Lijie Du
Collaborative innovation center for performance and safety of Large-scale infrastructure, Shijiazhuang Tiedao University, Shijiazhuang, China

Yalei Yang
School of mechanical engineering, Shijiazhuang Tiedao University, Shijiazhuang, China

Xiangbo Zhao
Xinjiang Irtysh River Investment and Development (Group) Co., Ltd., Wulumuqi, China

Yong Zhao
China State Railway Group Co.,Ltd., Beijing, China

Yongwei Quan & Shan Su
Xinjiang Irtysh River Investment and Development (Group) Co., Ltd., Wulumuqi, China

ABSTRACT: Real time estimation and early warning of rock mass strength and integrity are very important for TBM safe and efficient tunneling. However, the previous research on the correlation model between rock core strength and FPI established without distinguishing the rock mass integrity has a large deviation in estimating the strength of jointed rock mass, and can't show the integrity of rock mass. In this study, firstly, based on the statistical analysis and fitting of field data collected at several tunnels with different geological conditions and different TBM diameters, a general correlation model between intact rock mass strength and FPI was established, and the concept of rock mass equivalent strength was put forward for the jointed rock mass. Then, a real-time method of estimating rock mass equivalent strength and integrity coefficient using FPI was proposed, the accuracy and applicability of which were verified in several project cases. Finally, based on the real-time estimated rock mass equivalent strength and integrity coefficient, the classification method and early-warning threshold of TBM digging rock mass was given, which can predict and warn the rock mass real-timely. The research provides a more practical and feasible idea and method for real-time estimation and early warning of rock mass strength and integrity in TBM tunneling.

Keywords: Tunnel, TBM, Rock mass strength, Rock mass integrity coefficient, Rock mass classification, Early warning

1 INTRODUCTION

In recent years, full face hard rock tunnel boring machine (TBM) has been rapidly developed in tunnel construction due to its advantages of fast construction speed, safety and environmental protection, gradually becoming the first choice. Rock strength and rock mass integrity, as the key parameters characterizing rock mass quality, are the main judgment indexes for engineering rock mass quality classification and TBM driving performance. It is crucial to evaluate the rock strength and rock mass integrity of tunnel face timely and accurately during TBM excavating. However, limited by the TBM mechanical structure such as cutterhead and shield, the surrounding rock condition of tunnel face can't be observed directly, and the quality characteristics of surrounding rock can't be tested and evaluated in TBM

*Corresponding author: 1737459678@qq.com

DOI: 10.1201/9781003495505-256

tunnelling. At present, the traditional test method of rock strength and rock mass integrity can only be used after TBM stopped, lacking of real-time, which is difficult to provide TBM with online identification and early warning of surrounding rock. Therefore, according to the change of TBM tunneling parameters, establishing a real-time method of estimating rock strength and rock mass integrity to determine whether the rock mass is easy to boring or is broken, and to implement the real-time identification and warning of rock mass, is of great significance for ensuring TBM safe and efficient tunneling and improving the intelligent level of TBM construction.

Previous studies and engineering practices have shown that the TBM tunneling parameters are correlated with rock strength and rock mass integrity. In 1979, Hamilton and Dollinger (1979) proposed the concept of field penetration index (FPI). Subsequently, many scholars found that the relationship between rock strength and FPI was proportional through the laboratory analysis or the field measured data analysis respectively, and used this parameter to evaluate the rock mass (Nelson et al, 1983; O'Rourke et al., 1994; Hamidi et al., 2010; Farrokh et al., 2012; Saimi et al., 2017). Hassanpour et al. (2010, 2011, 2016) proposed and verified the relational model of rock strength, rock quality designation (RQD) and FPI based on several diversion tunnels in Iran. Du et al. (2015) analysed the correlation of FPI and main geological parameters through field data, and established a multiple regression model of FPI, rock uniaxial compressive strength (UCS) and rock mass integrity coefficient (K_v). Wu et al. (2020), taking the UCS, K_v and tunnel diameter as the main influencing factors and the FPI as the evaluation index, established an empirical prediction method of rock mass boreability and carried out the boreability classification by the analysis of measured data from five TBM tunnels.

According to laboratory test results, a rock strength estimation model based on TBM technical parameters (number and diameter of disc cutter) and tunneling parameters (thrust, torque and penetration) was put forward, the accuracy of which was verified by engineering examples, and an idea to solve the K_v was given (Fukui et al. 1999, 2003, 2006). Ma et al. (2017) and Zhang et al. (2022) proposed a rock strength estimate method according to the statistical analysis of measured data from TBM tunnel engineering, which has the same idea as the Fukui's method except for adding a parameter of tunnel diameter. Chen et al. (2017) analysed the correlation of tunnelling parameters and UCS based on the site data of N-J hydropower project in Pakistan, and found that the FPI had the best correlation with UCS, so as to put forward a fast evaluation model of rock strength based on FPI.

From all the research above, it can be found that a higher rock strength and integrity coefficient correspond to a smaller penetration and a greater thrust, which means that estimating the rock strength by TBM tunneling parameters is feasible. However, there are some shortcomings in the current research: (1) some of the results are a semi-quantitative description on the basis of the laboratory test, without giving a general quantization formula for engineering; (2) some empirical models, based on the site data of a certain project, are only applicable to this project or similar projects, and are not universal; (3) the rock strength estimate models based on tunnelling parameters actually establish the relationship of the FPI with rock core strength, rather than with the excavated rock mass strength, which ignores the influence of rock mass integrity. The models have limitations in real application. In practical engineering, the rock strength is usually represented by rock core test strength (UCS). For the intact rock mass, the rock mass strength is close to the UCS, so the model estimated results have a good accuracy. But for the jointed rock mass, the rock mass strength is generally lower than the UCS. The tunneling parameters actually reflect the rock mass strength, so the model results estimated by the tunneling parameters are different from the UCS.

During TBM construction, the practical need is to estimate the rock mass boreability real-timely, that is, to know the rock mass strength as well as integrity. If the relation model of UCS and FPI is established without distinguishing the rock mass integrity, the model computing results will lack accuracy in jointed rock mass, which can't truly reflect the strength and integrity of rock mass. Therefore, this paper proposes a real-time estimate method of rock mass strength and integrity based on the TBM tunneling parameters. Firstly, different from previous studies, an empirical model between the intact rock mass strength (R_c) and FPI is established by the statistical analysis of field data from the intact rock mass sections with different lithologies in multiple projects. At the same time, considering that the rock masses with same FPI have same boreability, the concept of rock mass equivalent strength (R_{ec}) is introduced to reflect the model estimated results of jointed rock mass. Secondly, a real-time method to estimate the R_{ec} and K_v is established, the accuracy and applicability of which is verified by several project cases. Finally, based on the real-time estimated R_{ec} and K_v, the classification and early-warning method of rock mass in TBM tunneling is proposed, which can provide technical support for TBM safe and efficient tunneling.

2 CORRELATION MODEL BETWEEN INTACT ROCK MASS STRENGTH R_C AND FPI

2.1 *Project overview*

The research data in this paper is from 9 TBM construction projects (10 TBM in total). The main

Table 1. TBM specifications.

Project Name	TBM type	Cutterhead diameter/m	Number of disc cutter	Face cutter spacing /mm	Maximum thrust /kN	rotational speed /rpm
Zhuxi Reservoir diversion Project	open type	4.03	26	75	14 200	0~12
Nabang water diversion tunnel	open type	4.53	30	70~90	12 200	0~12
A northeast water diversion project	open type	8.53	53	—	20 491	0~7.98
A water diversion project in Xinjiang	open type	7.0	49/48	75/78	23 562/27 489	0~10.9
A water diversion project in Jilin	open type	7.93	56	75~80	23 260	0~3.97~7.6
Gaoligongshan tunnel	open type	9.03	62	80	25 133	0~3.4~6.5
Chongqing Rail Transit Line 6	Single shield	6.28	38	80	17 040	0~5.44~11.97
A water diversion project in Shanxi	double shield	5.06	33	—	8 811	0~5.4~11.4
HJ tunnel project	open type	8.53	53	90	25 991	0~6.7

Table 2. Geological conditions.

Project Name	Tunnel Length/km	Main Lithology	UCS / MPa	Maximum Depth/m
Zhuxi Reservoir diversion Project	15.94	Breccia fused tuff, fused tuff	60~240	800
Nabang water diversion tunnel	9.748	biotite hornblende plagioclase gneiss, granite	100~200	600
A northeast water diversion project	35.441	Giant porphyritic granite, alaskite-granite, granite porphyry	80~175	500
A water diversion project in Xinjiang	20.823 /17.67	Tuffaceous sandstone, granite, tuff, andesite, quartz diorite	50~170	774
A water diversion project in Jilin	20.198	Limestone, tuffaceous sandstone, granite	50~130	260
Gaoligongshan tunnel	29.307	Granite, dolomite, slate, schist	40~90	1 155
Chongqing Rail Transit Line 6	5.631	Sandstone, sandy mudstone	5~39.9	371
A water diversion project in Shanxi	23.28	Limestone, mudstone, shale	30~90	610
HJ tunnel project	37.69	Chorismite, breccia lava, granite porphyry	35~120	1000

technical parameters and geological conditions of each TBM project are shown in Table 1 and Table 2, respectively.

2.2 *Data source of geology and tunneling parameter*

To establish a more accurate and widely applicable model, the in-situ data of different projects and geological conditions are collected and sorted out. As shown in Table 1 and Table 2, the data used in this research, from different tunnel diameters, TBM types and rock types (including sedimentary rock, magmatic rock and metamorphic rock, etc.), include tunneling parameter data and geological data. The tunneling parameter data, recorded in the field or copied in the TBM data acquisition system, mainly include the cutterhead thrust and penetration, which are used to calculate the field penetration index (FPI). The FPI is the ratio of single-cutter thrust to penetration, and the calculation formula is as Eq. (1). The geological data include uniaxial compressive strength (UCS) and rock mass integrity coefficient (K_v). Among them, the UCS is obtained from the uniaxial compressive strength test or point load test, and the K_v is

obtained from geologic sketch and analysis of volumetric joint count of rock mass, or from the calculation of geophysical exploration test.

$$FPI = F/(n.P) \quad (1)$$

Where, F is cutterhead thrust (*kN*); P is penetration (mm/r); n is the number of disc cutters.

2.3 *Establishment of model between R_c and FPI*

In TBM construction, the tunneling parameters actually reflect the rock mass strength. When the rock mass of tunnel face is intact with undeveloped joint or structural surface, the rock mass quality is mainly affected by the rock strength. At this time, the rock mass strength is approximately equal to the rock core strength, namely the test results of UCS. When the rock mass of tunnel face is broken with developed joints, the rock mass strength, affected by the rock strength and rock mass integrity, is generally lower than the UCS. At this time, the FPI actually corresponds to the jointed rock mass strength rather than the rock core strength (UCS). Therefore, the corresponding FPI and UCS under the intact rock mass in each project mentioned above are selected to fit the empirical formula of intact rock mass strength R_c (i.e. UCS) and FPI, so as to obtain a more accurate and widely applicable prediction model. According to the actual engineering surrounding rock classes and rock mass conditions, all the data of above projects are filtered. And a total of 165 valid data were selected for fitting. The UCS ranged from 10.2MPa ~224MPa, as shown in Table 3.

After fitting, the correlation model between the intact rock mass strength R_c and FPI is as follows (Figure 1):

$$R_c = 64.98\ln(FPI) - 140.32 \left(R^2 = 0.9146\right) \quad (2)$$

In this empirical model, the R_c increases with the FPI, and there is a good logarithmic relationship between them. The correlation coefficient of this model is 0.914 6. The error between the actual R_c (namely the UCS) and the predicted R_c (calculated by FPI) is small, indicating that this empirical model can be used to predict the strength of intact rock mass.

3 REAL TIME ESTIMATION METHOD OF ROCK MASS STRENGTH AND INTEGRITY COEFFICIENT

3.1 *Real time estimation of rock mass equivalent strength R_{ec}*

In TBM construction, it is necessary to know the rock mass boreability, and to know the strength and broken degree of the rock mass.

Table 3. The practical data.

R_c(UCS)/ MPa	Thrust /kN	Penetration/(mm/r)	FPI
224	4720	0.25	464.74
218.57	7250	0.5	483.36
182.59	7062	1.5	156.92
175	7055	1.25	146.56
168.0	6480	1.5	106.34
…			…
137.73	5657	3	62.85
126.23	6113	4	50.94
114.4	16287	5.4	42.66
107.0	16940	6.7	39.51
91.0	16830	7.6	34.6
89.0	14810	7.3	31.70
…			…
70.0	14120	7.8	28.29
60.21	18388	8.59	24.86
56.91	19021	9.87	22.38
43.2	13084	10.23	17.13
32.8	5214	7.1	14.79
…			…

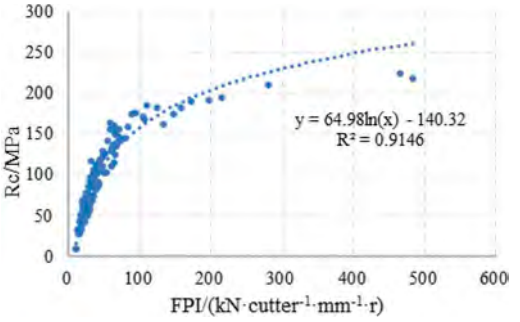

Figure 1. The relationship model between FPI and R_c.

For the intact rock mass, the rock mass strength can be regarded as the UCS. In actual engineering, based on the proposed model (Eq. (2)), the strength of intact rock mass can be directly estimated using the real-time FPI calculated by the tunneling parameters from TBM data acquisition system, instead of rock core testing.

For the jointed rock mass, to describe the proposed model estimated result, the concept of rock mass equivalent strength (R_{ec}) is introduced, that is, the excavated rock mass strength

with the same penetration difficulty as an intact rock mass strength is called the equivalent strength of TBM excavated rock mass. In other words, some jointed rock mass with the same FPI has the same rock mass boreability as the other intact rock mass, that is, the boreability of a rock mass with higher rock strength and developed joints is similar to that of another intact rock mass with lower rock strength. In this way, regardless of the rock mass integrity, based on the proposed model (Eq. (2)) and the proposed concept of R_{ec}, the equivalent strength of rock mass (including jointed rock mass and intact rock mass) can be directly estimated using the real-time FPI.

To illustrate the accuracy of the real-time R_{ec} estimation method mentioned above, the estimated R_{ec} are compared with the quasi-rock mass strength. Quasi-rock mass strength (i.e. rock mass integrity coefficient correction method) is an empirical method to determine rock mass strength, which is to modify rock strength with certain simple test index as the estimated value of rock mass strength. The calculation formula is shown in Eq. (3).

$$\sigma_{cm} = \left(V_{pm}/V_{pr}\right)^2 \sigma_{ci} \tag{3}$$

Where, σ_{cm}: uniaxial compressive strength of rock mass; σ_{ci} : uniaxial compressive strength of rock; v_{pm}: elastic longitudinal wave velocity of rock mass; V_{pr}: elastic longitudinal wave velocity of rock; $(v_{pm}/v_{pr})^2$: rock mass integrity coefficient, k_v. Joints, cracks and structural planes are the main factors affecting rock mass. Taking the product of UCS and k_v as the estimation value of rock mass strength avoids many subjective factors and is simple, which is one of the commonly used rock mass strength estimation methods in practical engineering.

Taking the field data of Northeast project and HJ project in China as examples (Table 4), the R_{ec} estimated by the FPI is compared with the results calculated by the Eq. (2) to verify the accuracy of the proposed method. The comparison results and error analysis are shown in Figure 2. The error analysis formula is as follows:

Table 4. The field data of projects.

Project Name	Lithology	UCS/ MPa	K_v
Northeast diversion project	granite	78~175	0.56-0.89
HJ project	migmatite	74~107	0.24~0.72

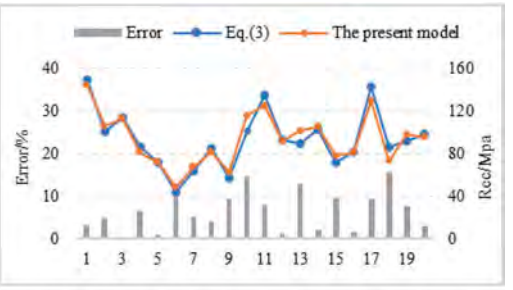

(a) Northeast diversion project (20 sets of data)

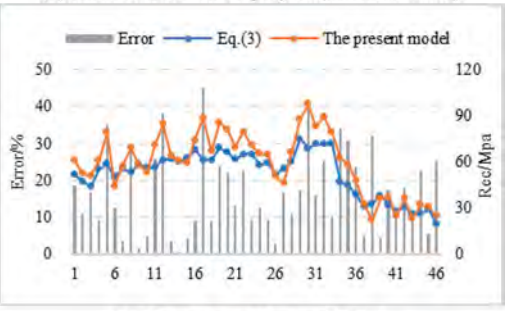

(b) HJ project (46 sets of data)

Figure 2. Comparison of results and error analysis.

$$E = \left|\frac{R_{ec} - \sigma_{cm}}{\sigma_{cm}}\right| \times 100\% \tag{4}$$

From the comparison results of above two projects, the R_{ec} estimated by the proposed model is close to the calculation results of the empirical formula (3), with the mean error of 6.53% and 16.76%. The errors of some results are relatively high, but the whole variant trend of the results estimated by two methods is identical with minor error. In addition, in the actual engineering the rock strength obtained through tests also have a certain discreteness, and the estimates of empirical method have a certain error.

3.2 *Real time estimation of rock mass integrity coefficient K_v*

The rock mass equivalent strength (R_{ec}) is a comprehensive reflection of rock block strength and rock mass integrity. The R_{ec} estimated by FPI in real time can reflect the rock mass boreability ahead of the tunnel face, but it can't reflect separately the rock strength and the broken degree of rock mass. Under the same R_{ec}, the condition of rock mass may be diverse. For example, the value of R_{ec} with lower strength and better integrity may be the same as that with higher strength and poorer integrity. Therefore, during TBM tunneling, it requires to know not only the boreability and equivalent strength of rock mass, but also the broken degree of rock mass, which is

crucial for identifying and warning the risk of TBM stuck in rock collapse and preparing appropriate support measures in advance. It's necessary to find a real-time estimation method for the rock mass integrity.

Applying the model to a practical project, the rock mass integrity coefficient (K_v) can be estimated real-timely based on the R_c under the intact rock mass with same lithologic measured in advance and the R_{ec} estimated by the model (Eq.2). The formula for the rock mass integrity coefficient estimation is as follows:

$$K_v = R_{ec} / R_c \tag{5}$$

The intact rock mass strength R_c can be measured by the rock core test in the stage of pre-geological investigation, or in the early stage of TBM tunneling under the intact rock mass.

However, affected by the sampling and testing error of the rock, the rock strength under the same lithology still has certain discreteness, so the mean compressive strength of the rock samples is taken as R_c. At this time, if the K_v estimated by the Eq. (5) is within a certain range, for example, the range of rock mass integrity classification as Table 5, it is enough to identify the risk caused by broken rock, and can be considered that the estimated results are accurate and effective.

Table 5. The correspondence between K_v and rock mass integrity.

K_v	>0.75	0.75~ 0.55	0.55~ 0.35	0.35~ 0.15	<0.15
Rock mass integrity degree (BQ)	Intact	Relatively intact	Relatively broken	Broken	Extremely broken

4 PROJECT APPLICATION AND VERIFICATION

In the following, the accuracy of the real-time estimation method above is verified through three application examples: Zhuxi reservoir diversion project, a diversion project in Guangzhou, and Gaoligongshan tunnel project. The predicted equivalent strength and integrity of rock mass will be compared with the exposed actual rock strength, surrounding rock classification and support, and analyzed in combination with the TBM driving thrust and penetration.

(1) Example 1: A tunnel section of Zhuxi reservoir diversion project: 15+916~15+716(200m).

In this tunnel section, the lithology is breccia fused tuff with the mean UCS of 145MPa (under the intact rock mass), and the class of surrounding rock is class II. The surrounding rock is intact with undeveloped joints and smooth surface, no water seepage and no rock support, except that the surrounding rock are partially broken in the mileages of 15+870~15+860 and 15+732~15+726, which is supported with mesh and shotcrete. The change of the model estimated results (R_{ec} and K_v) and the tunneling parameters (thrust (F) and penetration (P)) is shown in Figure 3.

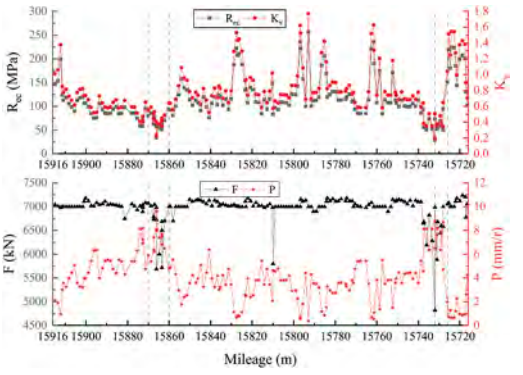

Figure 3. Changes trend of R_{ec}, k_v, F and P of example 1 (176 sets of data).

From Figure 3, the thrust is basically maintained at 7 000kN, and the penetration ranges from 0.5 mm/r to 8mm/r, with great changes. The R_{ec} estimated by Eq. (2) is in the range of 50~250MPa, with an average of 114MPa. Among them, affected by the rock mass integrity, the R_{ec} of the sections (15+875~15+860 and 15+737~15+728) is lower than that of the intact rock mass sections, which is reflected in the relative increase of penetration and the decrease of thrust in TBM tunneling parameters. It can be seen that the R_{ec} is close to the UCS for the intact rock mass, and lower than the UCS for the jointed rock mass. In addition, at 15+784, 15+737 and 15+724, the UCS are 175MPa, 83.1 MPa and 162MPa respectively, corresponding to the penetration of 1.3mm/r, 6.3mm/r and 1.0mm/r, and the R_{ec} are 172MPa, 94MPa and 184MPa. The rock core samples are from the intact rock mass section, and the model estimated results (R_{ec}) are close to the rock core test results (UCS), so the model prediction is relatively accurate.

Under the same lithology, the ratio of R_{ec} to R_c (the mean UCS of this lithology is taken here) is the K_v. Therefore, the R_{ec} and the K_v estimated by the

model have the same variation. Under the sections of 15+875~15+860 and 15+737~15+728, the surrounding rock is partially broken, and the corresponding values of K_v are small, ranging from 0.25 to 0.55. Under the rest of sections, the K_v is relatively high, keeping above 0.55. The breccia fused tuff belongs to hard rock, which is complete or relatively complete in the surrounding rock II, and the K_v is above 0.55. Therefore, the K_v calculated in this paper is in line with the real situation, and the variation trend of K_v is basically consistent with the actual rock mass condition.

(2) Example 2: A tunnel section of Gaoligongshan tunnel project: 225+504~225+410(94m).

In this tunnel section, the lithology is granite with the mean UCS of 53MPa (under the intact rock mass). In the mileages of 225+504~225+419, the class of surrounding rock is class IIIa, and the surrounding rock is broken on the part of right side and weathered at 11 o 'clock, with relatively developed fractures and developed groundwater in the section (225+504~225+477), and the surrounding rock is relatively intact with undeveloped crack and groundwater in the section (225+477~225+419). The bolting with wire mesh is carried out for the surrounding rock. In the mileages of 225+419~225+410, the class of surrounding rock is class IVa, and the surrounding rock has poor integrity, local strong weathering and quartz zone intrusion, which is supported with steel arch, systematic rock bolt and shotcrete. The change of the model estimated results (R_{ec} and K_v) and the tunneling parameters (F and P) is shown in Figure 4.

It can be seen from Figure 4 that the R_{ec} and K_v vary regularly with the actual rock mass conditions. The rock mass under the section of 225+504~225 +421 is class IIIa. The section (225+477~225+421) has good integrity, so the values of R_{ec} and K_v are relatively high, with means of 47.25MPa and 0.89, respectively. The corresponding mean of thrust, penetration and FPI is 16 897kN, 10.74mm/r and 18.68, respectively, and the rock mass condition is good and easy to penetration. However, in tunnel section (225+504~225+477), the right side of surrounding rock is locally broken with developed cracks, so the R_{ec} and K_v are relatively low, with the means of 30.8MPa and 0.6. In terms of TBM tunneling parameters, the thrust decreases to 14 711kN, the penetration increases to 12.5mm/r, and the mean FPI is 14.5. The rock mass under the section of 225+421~225+410 is class IVa with poor integrity, so the R_{ec} and K_v are low, with means of 19.88MPa and 0.38. Correspondingly, the mean thrust is 11 202kN, penetration is 10.98mm/r, and FPI is 12.11. Compared with surrounding rock class IIIa, the penetration of class IVa remains basically unchanged and the thrust decreases, indicating that the rock mass is weak and broken with strong support. Therefore, the overall change trend of estimated R_{ec} and K_v is basically coincident with the construction practice.

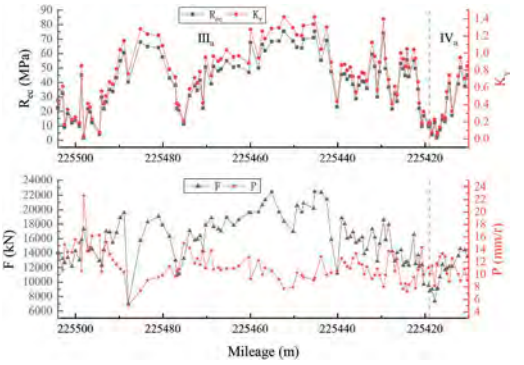

Figure 4. Changes trend of R_{ec}、K_v、F and P of example 3 (109 sets of data).

The above two typical application examples show that the rock mass equivalent strength and integrity coefficient estimated by the method are in agreement with the actual rock mass conditions from the overall trend. There is a little error in some tunnel sections because the surrounding rock classification is to divide infinite rock mass sequence into several classes by the indexes of rock strength and rock mass integrity, which is no clear demarcation between the surrounding rock classes, so there may be some judgment errors in the classification of surrounding rock on site. From this, it indicates that the real-time estimation method of rock mass equivalent strength and integrity coefficient presented in this paper is feasible.

5 REAL TIME CLASSIFICATION AND WARNING OF ROCK MASS IN TBM TUNNELING

At present, the commonly used classification methods of tunnel surrounding rock stability are mainly proposed for the traditional drilling and blasting method, not TBM adaptability classification, and not online real-time intelligent classification. The intelligent identification and early warning of TBM tunneling rock mass is of great significance for judging the surrounding rock boreability timely and preventing the risk of tunnel collapse and TBM trapped. For this purpose, using the rock mass equivalent strength and integrity coefficient estimated by the real-time method in this paper, a classification and early-warning method of rock mass in TBM tunneling is established.

The rock strength is the key factor to measure the difficulty of TBM tunneling. For TBM, too high (i.e. extremely hard rock) or too low (i.e. extremely soft rock) rock strength is unfavorable for TBM tunneling. Too high rock strength means the rock mass boreability is poor, leading to the TBM tunneling difficult and the cutter replaced frequently due to serious wear,

which seriously affects the construction speed and increases the construction cost. Too low rock strength means the rock mass is weak and broken with poor stability, leading to an increase in corresponding support amount and time and a reduction in construction efficiency, which are often located in the bad geological zone and more prone to collapse, so that the TBM tunneling is blocked, or even stuck and trapped. At present, in the engineering circle, there is the underlying idea that the rock strength range of 30~150MPa is perfect for TBM tunneling. For the rock strength greater than 150MPa or less than 30MPa, the TBM construction efficiency is low, which is not conducive to TBM tunneling speedily. In addition, the existing studies (He et al., 2002; Li and Peng, 2006; Wang et al., 2020) and TBM construction practice analysis show that, for the rock strength greater than 200MPa or less than 15MPa, it is extremely difficult for TBM to boring. Based on the above analysis, in this paper, the 150MPa and 200MPa are used as the two levels warning threshold of extremely hard surrounding rock. And the 30MPa and 15MPa are taken as the two levels warning threshold of soft surrounding rock.

Rock mass integrity, measured by the K_v, is also a main factor affecting the efficiency of TBM construction. In general, the smaller the K_v is, the more developed the rock mass structural plane, and the higher the TBM tunneling speed is. However, when the K_v is too small, the surrounding rock integrity is very poor with especially well-developed rock mass structural plane and no self-stabilization ability. In this case, the TBM tunneling efficiency will be reduced due to the increase of surrounding rock support. From the TBM construction projects, when K_v is less than 0.35, the tunnel surrounding rock is very broken, mostly located in the fault fracture zone, and is prone to collapse and instability, which not only seriously affects the TBM construction speed, but also has the construction risk of TBM being stuck.

Based on the above analysis and the classification of rock mass basic quality in *Standard for Engineering Rock Classification of Rock Mass (GB/T 50218-2014)*, the rock mass boreability and safety risk during TBM excavating are classified by the real-time estimation of R_{ec} and K_v, thereby establishing a real-time classification and early-warning method of tunnel surrounding rock for TBM tunneling, as shown in Table 6.

For Table 6, the following explanations are given.

1. For the rock mass with equivalent strength of 30~150MPa, or 15~30MPa and integrity coefficient greater than 0.35, it is suitable for TBM tunneling, relatively easy to penetrate and safe, and the TBM construction will not have big risk even if there is occasionally local collapse. So, there is no need for warning.
2. For the rock mass with equivalent strength of 150~200MPa or greater than 200MPa, TBM tunneling penetration is very difficult. But even if there is local collapse, TBM construction will not pose a big risk. However, early warning can remind the operator that the rock is extremely hard, and attention should be paid to the inspection of cutter damage and appropriate adjustment of tunneling parameters. Therefore, two level rock extremely hard early warning are given.
3. For the rock mass with equivalent strength of 15~30MPa and integrity coefficient lower than 0.35, or rock mass lower than 15MPa, TBM tunneling penetration is very easy, but the rock mass may be broken or extremely broken or very weak at this time. Early warning can remind the operator of the risk of TBM being stuck due to collapse or deformation of surrounding rock, and attention should be paid to geological check and support adjustment. Thus, two level rock extremely soft early warning are given.

Table 6. Real-time classification and early warning of rock mass for TBM tunnelling.

Class	R_{ec}	K_v	Rock mass conditions	Boreability and collapse risk	Early warning
B-I	30~150	~	Suitable rock hardness and integrity	Easy or relatively easy penetration Low or relatively low collapse risk	No need for warning
	15~30	>0.35			
B-II	150~200	~	Very hard rock and intact rock mass or occasionally local collapse	Difficult penetration Cutter wear fast and low risk	Second-level warning
	15~30	<0.35	Soft weak or broken rock mass	Easy penetration Relatively high risk	
B-III	>200	~	Extremely hard and intact rock mass	Extremely difficult penetration Cutter wear extremely fast and low risk	first-level warning
	<15	~	Extremely weak or broken rock mass	Easy penetration High risk of collapse or deformation	

It should also be noted here that this paper focuses on the impact of rock mass strength and integrity, while the impact of rock burst and groundwater will be studied separately.

Compared with the previous surrounding rock classification methods for TBM construction, the proposed approach adopts the simple classification index parameters which is easy to get online. Using the R_{ec} and K_v estimated by the model in this paper can classify and warn the rock mass in TBM tunneling real-timely. According to the rock mass boreability and risk degree, the tunneling parameters and construction strategy could be adjusted timely, and the countermeasures could be made in advance to guide TBM safe and efficient tunneling.

6 CONCLUSIONS

(1) Through the statistical analysis and fitting of field data under intact rock mass sections in a variety of lithologies from multiple TBM projects, a correlation model with general applicability of the intact rock mass strength (R_c) and the filed penetration index (FPI) is established, and the correlation coefficient reaches 0.914 6. The model prediction is close to the actual value, which can be used to predict the intact rock mass strength (i.e. rock strength).

(2) For the jointed rock mass in actual TBM tunneling, the concept of rock mass equivalent strength (R_{ec}) is introduced. Then the real-time estimation method of R_{ec} based on FPI is proposed, that is, the FPI of excavated rock mass, calculated by the TBM cutterhead thrust (F) and penetration (P), is plugged into the proposed model to obtain the R_{ec}. Furthermore, the rock mass integrity coefficient (K_v) can be calculated via $K_v = R_{ec}/R_c$. In this way, the equivalent strength and integrity coefficient of rock mass in TBM tunneling can be estimated online instead of offline sampling and testing, thereby monitoring the boreability and broken degree of rock mass in real time.

(3) Based on the model estimate results of R_{ec} and K_v, the real-time rock mass classification and bad geology warning threshold values are given. The research can predict the rock mass conditions real-timely and warn the bad geology timely in TBM tunneling, which provides the technical support for the TBM safe and effective tunneling.

In this paper, the real-time estimation method of rock mass strength and integrity coefficient for TBM tunneling is based on the relationship between rock mass strength and FPI, which is different from the previous models between rock block strength and FPI established without distinguishing rock mass integrity during sampling. In addition, the goal of this method is not to calculate accurately the strength and integrity coefficient of rock mass, but to estimate its range real-timely using TBM tunneling parameters, intuitively know the boreability and broken degree of rock mass, and give the early-warning for TBM safe and efficient tunneling. Therefore, from the perspective of the TBM actual tunneling requirements, the method has good applicability.

ACKNOWLEDGMENTS

This research was supported by the Research Plan of Xinjiang EH Project of China (Grant No. EQ075/FY056) and National Key R&D Program of China (Grant No. SQ2022YFB2300029). The authors are very grateful for the huge support of all members of this research project.

REFERENCES

Chen, E.Y., Deng, S.W., Chen, F.M., et al, 2017. Development of a novel rock strength estimation model based on TBM boring performance. Journal of Shandong University (Engineering Science) 47(02), 7–13 (in Chinese).

Du, L.J., Qi, Z.C., Han, X.L., et al, 2015. Prediction method for the boreability and performance of hard rock TBM based on boring data on site. Journal of China Coal Society 40(06), 1284–1289 (in Chinese).

Farrokh, E., Rostami, J., Laughton., C., 2012. Study of various models for estimation of penetration rate of hard rock TBMs. Tunn. Undergr. Space Technol. 30, 110–123.

Fukui. K., Okubo, S., 1999. Rock-properties estimation by TBM cutting force.: In Proceedings, The 9th International Congress on Rock Mechanics. Paris, France, pp. 1217–1220.

Fukui. K., Okubo, S., 2003. TBM cutting forces with particular reference to cutter and tunnel diameters. In: Proceedings, The 10th International Congress on Rock Mechanics. Sandton, South Africa, pp. 1343–1346.

Fukui. K., Okubo, S., 2006. Some Attempts for Estimating Rock Strength and Rock Mass Classification from Cutting Force and Investigation of Optimum Operation of Tunnel Boring Machines. Rock Mech. Rock Eng. 39(1), 25–44.

Hamidi, J.K., Shahriar, K., Rezai, B., et al, 2010. Performance prediction of hard rock TBM using Rock Mass Rating (RMR) system. Tunn. Undergr. Space Technol. 25(4), 333–345.

Hamilton, W.H., Dollinger, G.L., 1979. Optimizing tunnel boring machine and cutter design for greater boreability. In: RETC Proceedings, vol. 1, Atlanta, pp. 280–296.

Hassanpour, J., Rostami, J., Khamehchiyan, M., et al, 2010. TBM Performance Analysis in Pyroclastic Rocks: A Case History of Karaj Water Conveyance Tunnel. Rock Mech. Rock Eng. 43, 427–445.

Hassanpour, J., Rostami, J., Zhao, J., 2011. A new hard rock TBM performance prediction model for project planning. Tunn. Undergr. Space Technol. 26(5), 595–603.

Hassanpour, J., Vanani, A.A.G., Rostami, J., et al, 2016. Evaluation of common TBM performance prediction

models based on field data from the second lot of Zagros water conveyance tunnel (ZWCT2). Tunn. Undergr. Space Technol. 52, 147–156.

He, F.L., Gu, M.C., Wang, S.C., 2002. Study on Surrounding Rockmass Classification of Tunnel Cut by TBM. Chinese J. Rock Mech. and Eng. 9, 1350–1354 (in Chinese).

Li, C.M., Peng, Y.R., 2006. Discussion about surrounding rock classification of tunnel excavate by TBMs. Journal of China and Foreign Highway 3, 235–237 (in Chinese).

Ma, C.S., Chen, W.Z., Tian, H.M., et al, 2017. Discussion on rock strength estimating method based on TBM parameters. Rock Soil Mech. 38(S2), 295–303 (in Chinese).

Nelson, P., O'rourke, T.D., Kulhawy, F. H., 1983. Factors affecting TBM penetration rates in sedimentary rocks. In: Proceedings, 24th U.S. Symposium on Rock Mechanics, Texas A&M, College Station, TX, pp. 227–237.

O`Rourke, J.E., Springer, J.E., Coudray, S.V., 1994. Geotechnical Parameters and Tunnel Boring Machine Performance at Goodwin Tunnel, California. In: Proceedings of the 1st North American Rock Mechanics Symposium, Rotterdam: A. A. Balkema, pp. 467–473.

Salimi, A., Rostami, J., Moormann, C., et al, 2017. Examining Feasibility of Developing a Rock Mass Classification for Hard Rock TBM Application Using Non-linear Regression, Regression Tree and Generic Programming. Geotechnical & Geological Engineering, (1):1–15, DOI:10.1007/s10706-017-0380-z.

Wang Y.J., Cao, R.L., Wang, S.L., et al, 2020. Study on Classification Index and Determination Method of Extra-hard Rock for TBM Tunnel. Tunnel Construction 40(S2), 38–44 (in Chinese).

Wu, X.L., Zhang, X.P., Liu, Q.S., et al, 2020. Prediction and classification of rock mass boreability in TBM tunnel. Rock Soil Mech. 41(05), 1721–1729 (in Chinese).

Zhang, H.L., Tang, Y., Ren, T., et al, 2022. Real-time estimation of surrounding rock strength in composite strata tunnels. Rock Soil Mech. 43(07), 1877–1883 (in Chinese).

Tunnelling for a Better Life – Yan, Celestino, Thewes & Eberhardt (Eds)
© 2024 The Author(s), ISBN 978-1-032-80042-4
Open Access: www.taylorfrancis.com, CC BY-NC-ND 4.0 license

Three-dimensional centrifuge modelling of the effects of TBM on adjacent piles

Xing Liang* & Stuart Haigh
Department of Engineering, University of Cambridge, UK

ABSTRACT: The demands of urban tunnel applications will continue to provide a major impetus to achieving improved understanding of the behaviour of piles due to TBM excavation. This research investigated the effects of new built tunnel by TBM method to the adjacent bored piled structures by applying a mini-TBM model. The novel miniature TBM designed in Cambridge geotechnical centrifuge has been proven successful in excavating soft clay. Results show that the undrained shear strength exhibits good agreements both in measurements by T-bar and estimations by Modified Cam-clay and SHANSEP method. Compared to tunnelling in softer clay, it shows a bigger settlement trough as expected and well agrees with the general understanding of longitudinal settlement trough, although limited by the size of strong box. TBM induced pore pressure variation can be perfectly explained as a result of thrust force and peripheral volume loss. Comparison with reported centrifuge tests presents the repeatability of the test and a larger settlement was obtained for smaller transverse distance from the tunnel axis. Recorded bending moments explains the influence of continuous tunnelling rather than simple change of volume loss. They were in a good agreement with previous reports but provided more details involving thrust and tapered shape of TBM. Finally, the capabilities of current mini TBM are discussed together with potential modifications.

Keywords: Mechanised tunnelling, reduced scale physical modelling, centrifuge, soil-pile interaction

1 INTRODUCTION

The growing population and extensive urbanisation of communities has led to a need for increased urban infrastructure inclusive of undergrounds. The overused infrastructures above ground left limited surface space in such dense urban area. Consequently, the construction of underground transportation (i.e., also known as tubes, metros, subways) has been undertaken in highly populated areas.

As the construction of urban tunnel develops rapidly, various tunnelling techniques were employed to maintain the ground safety. Among them, tunnel boring machines or TBMs were widely used due to its evident advantages of limiting the disturbance to the surrounding ground and producing a smooth tunnel wall. This significantly reduces the cost of lining the tunnel and makes them suitable to use in heavily urbanized areas. Like any other construction methods, however, tunnelling causes stress relief to the surrounding soil leading to ground movements around the tunnel which propagate through the soil to the ground surface. These movements might have an impact (e.g., axial load, bending moment, and pile capacity) on the piled structures. Researchers have been carried out investigating the damage caused by tunnelling to near buildings (Burland et al., 1977; Potts and Addenbrooke, 1997; Mair, 2011) but a relatively small amount of scholars worked on the effects of these ground movements on piled foundations and the resulting interaction with the overlying structures. As a result of the lack of knowledge and case studies, the behaviour of piled structured due to the tunnel excavations is not completely understood.

One of the most common techniques to study the tunnel-soil-pile interaction problem is by small-scale physical modelling, both at 1g (e.g., Lee and Yoo, 2006; Hu et al., 2022; Meguid and Mattar, 2009) and high g-level in centrifuge tests (e.g., Loganathan et al., 2000; Jacobsz, 2003; Marshall, 2009; Williamson, 2014; Franza and Marshall, 2018). However, the common limitations of above literature are that they considered the tunnelling process in a 'two dimensional' scenario rather than three-dimensional one, which is completely accurate in practical application. In such models, a latex membrane is wrapped around a metal cylinder, where the gap between them is filled with a fluid to achieve a pressure similar to the overburden pressure around the tunnel. A controlled volume loss can thus be obtained by adjusting extraction rata of the pressurised fluid. Ng et al., (2015) made an attempt to address the problem by splitting the tunnelling stages by applying multiple pressurised late membranes. However, such method still failed to capture the actual mechanism due to neglecting the continuity of TBM tunnelling. More recently,

*Corresponding author: xl539@cam.ac.uk

DOI: 10.1201/9781003495505-257

Cambridge Geotechnical Group has made great efforts and designed a new mini-TBM system to simulate the TBM excavations. Based on the work of Viggiani et al., (2022) and Alagha (2023), the mini-TBM system has been assembled, successfully tested and some convincing data was obtained. This offers us to investigate the issue from a three-dimensional perspective. This research is aiming to provide a better understanding of the effects of TBM excavation on adjacent bored piles. This paper presents obtained data from recent centrifuge tests and discusses the effects of tunnelling on adjacent piles in soft clay.

2 EXPERIMENTAL ARRANGEMENTS BY CAMBRIDGE MINI TBM

The latest mini-TBM model was designed by Viggiani et al., (2022) and has been employed to conduct a series of tests. The machine is able to reproduce the mechanisms of shield tunnelling and to account for most sources of volume loss outlined above and has been proved to successfully investigate the effects of TBM tunnelling both in greenfield conditions and in scenarios where piled foundations exist (see Figures 1 and 2).

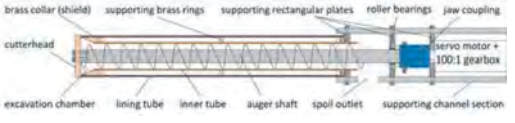

Figure 1. Conceptual drawing of Cambridge mini TBM (after Viggiani et al., 2022).

Figure 2. Model TBM system attached to tunnelling box.

The cutterhead has a diameter of 78 mm, while the diameter of the shield at the face is 77.2 mm. As the current mini TBM system aims to be operated in soft clay, a cutterhead with an opening ratio of 45% was employed. To imitate a tapering shield, a conical brass collar is placed at the front of the lining tube, with a diameter decreasing from 77.2mm at the cutterhead junction to 76.2mm at the tail. The inner diameter of the chamber decreases from 70 mm to 50.8 mm, corresponding to the outer diameter of the inner tube. The soil is removed from behind the cutterhead by a horizontal auger with a diameter of 40 mm. The outer lining tube was carefully chosen to represent extremely stiff lining segments at prototype scale thus eliminating the contribution of lining deflection to the overall volume loss. The auger is driven by a servo motor and a 100:1 reduction drive gearbox that can provide a maximum torque of 27 Nm. The TBM is advanced into a strongbox filled with soil using a linear actuator that can provide a thrust of up to 20 kN. All tests were conducted in 50-g acceleration equivalent to a prototype of about 4 m. Specific details of the mini TBM system can be found in Viggiani et al., (2022) and Alagha (2023).

2.1 *Experimental layout*

2.1.1 *Design of model pile*

Model pile foundations were designed and fabricate to conduct a comprehensive study with respect to tunnelling effects on pile and further pile groups. The following sections provide a complete description of the design process in this study.

Based on works of Williamson (2014), two primary behaviours of a structural element, i.e., axial behaviour and flexural behaviour, are governed by their axial stiffness (EA) and bending stiffness (EI). In this regard, an equivalent model pile has to possess similar axial and bending stiffness to those of prototype so that the centrifuge model can represent the real structures. Under 50g level intended to adopt in this study, a 11 mm outer diameter and 1 mm thickness round aluminium tubes supplied by RS PRO were found to offer the best match in terms of piles within pile group. Here listed the detailed comparison between the properties of the model pile presented in Table 1.

The two significant behaviours of model piles used in this study are similar to the prototype. With respect to axial behaviour, the axial stiffness of model pile is slightly smaller than that of the prototype (around 16% less); In terms of bending behaviour, the bending stiffness of the model pile is larger than that of the prototype (around 37% more). The discrepancies could not be avoided due to the limitations of materials but would not exert great influences on a geotechnical problem.

2.1.2 *Length and size for pile*

All piles employed in this study are the same (235 mm in model dimension). The length corresponds to that the pile tip located at the tunnel centreline. In addition, the piles were distributed at a different distance horizontally to the tunnel axis.

As aluminium tubes have a quite smaller roughness than that of reinforced concrete, a thin layer of epoxy fine mixture was coated in the model piles to ensure that a rough pile shaft is modelled. Araldite rapid adhesive epoxy was used for its excellent adhesive strength

Table 1. Comparison between the properties of the model pile and prototype.

Property	Desired prototype pile	Prototype pile scaled down with 50 g	Selected model pile
Material	Reinforced concrete	Reinforced concrete	Aluminium
Cross section	Solid circular	Solid circular	Hollow tube
Outer diameter (mm)	550	11	11
Thickness	-	-	1
Young's modulus (GPa)	30	30	70
Axial stiffness EA (N)	7.13×109	2.86×106	2.40×106
Bending stiffness EI (Nm)	13.48×107	21.55	29.69

and waterproofing characteristics. Photographs of coating process are shown in Figure 3.

Figure 3. Details of coating process: (a) putting araldite cohesive to a clean plate; (b)pouring sands to another clean plate; (c) stick the model pile with sand by araldite cohesive; (d) leave the new coated pile for half a day.

2.1.3 *Pile instrumentation*

Single piles (piles A, B and C) were all instrumented with LVDTs to monitor their vertical movements during tunnelling. Strain gauges were installed in single piles to measure their bending moments (see Figure 3(d)). Pile A and pile B were employed with 7 strain gauges while the pile C was instrumented with 8 strain gauges (see Figure 4). Details and description of strain gauges system can be found in Williamson (2014) and Alagha (2023).

2.1.4 *Clay property*

Speswhite Kaolin powder, supplied by Imerys Performance Minerals, was chosen to model the clay samples in this study. This clay type has been widely used in previous studies (e.g., Elmes, 1985; Williamson, 2014; Lau 2015; Gue 2017; Garala, 2020) for its mineral homogeneity. In addition, the small permeability makes it suitable for modelling undrained geotechnical processes as tunnelling. The parameters reported by researchers have been listed in the Table 2.

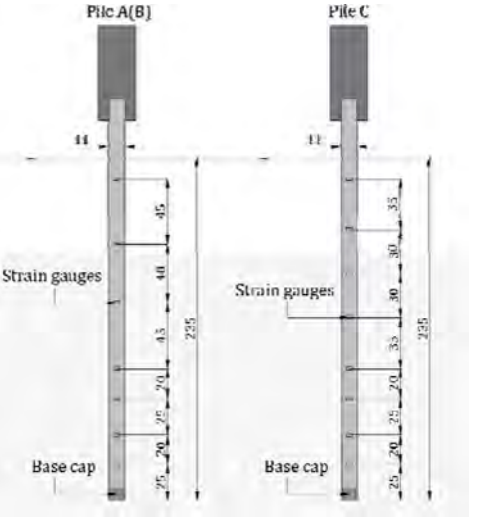

Figure 4. Details of strain gauges in single piles (dimensions in mm).

2.1.5 *Test layout*

Figure 5 shows the experimental setup used in the centrifuge test. The inner dimension of the strong box is 780 mm × 460 mm × 620 mm. The buried depth of the tunnel centreline is z_0= 235 mm (i.e., around three times of diameter with the cover-to-diameter ratio of 2.5). It is worth noting that the model TBM was inserted in the clay by a length of 110 mm, which is also the length of the shield body plus cutterhead. This is to ensure a tight fit between the porthole and the tunnel lining tube, resulting in the tunnelling length of 300 mm.

Thirteen LVDTs (L1 to L13) were used to measure surface displacement in the transverse (TS) and longitudinal section (LS) and pile head settlements. LVDTs L2, L6-L9 were employed in section TS and LVDTs L1-L5 were used in section LS. It is noted here that LVDTs were only placed on one side due to the symmetrical condition. LVDT L10 was used in the far field to measure surface settlement. LVDTs L11, L12 and L13 were used to measure the pile head settlements, namely Pile A, Pile B, Pile C, respectively. Six PPTs (P1 to P6) were performed in the test. PPTs P1 to P4 were placed around the mini-TBM to measure the pore water pressure variation due to tunnelling. Specifically, P1 and P4 were placed at both sides of the TBM while P2 and P3 were placed at the top and bottom of the TBM. P5 was placed at the tunnel. centreline and in front of the cutterhead at the end of excavation. P6 was used to measure the pore water pressure in the far field. Single piles A, B and C were placed at the same side as that of LVDTs measuring transverse troughs. Piles B and C were at the same transverse section and Piles A and B were around 2D away from tunnel axis at the same longitudinal section. Pile group was placed on the other side with the edge around 1D away from tunnel axis.

Table 2. Properties of speswhite kaolin clay.

Material property	Elms (1985)	Williamson (2014)	Lau (2015)	Gaudio et al. (2022)	Value
Liquid limit, w_l (%)	-	-	63	58	63
Plastic limit, w_p (%)	-	-	30	34	34
Plasticity Index, PI (%)	-	-	33	24	24
Specific gravity, G_s	2.61	2.61	2.6	2.61	2.61
Slope of critical state line in q-p' plane, M	0.82 (comp)	0.89 (comp) 0.69 (ext)	0.9 (comp)	0.8 (avg)	0.9 (avg)
Critical state friction angle, ϕ_{crit}	21°	23°	-	20.7°	21°
Intercept of normal consolidation line at p' = 1 kPa in v - $ln\ p'$ plane, N_λ	2.98	2.26	3.49	2.98	3.22*
Intercept of critical state line at p' = 1 kPa in v - $ln\ p'$ plane, Γ	2.87	3.13	3.31	2.87	3.08*
Slope of normal consolidation line, λ	0.14	0.18	0.22	0.14	0.17*
Slope of unloading-reloading line, κ	0.03	0.047	0.039	0.03	0.027*

*measured during clay preparation in this study.

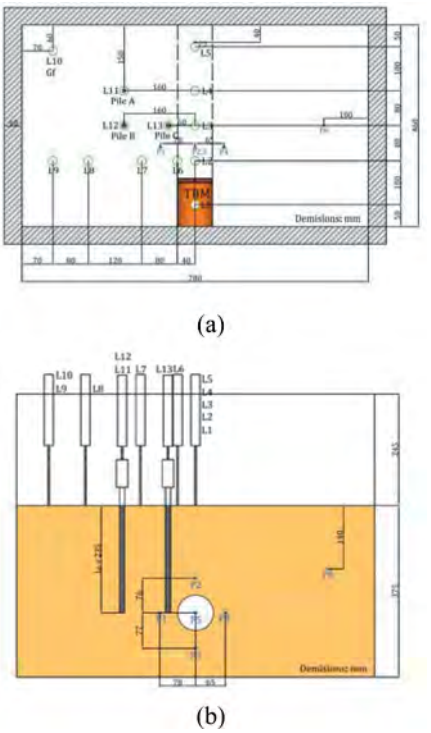

Figure 5. Layout performed in this centrifuge test: (a) plan view; (b) section view.

A T-bar test was performed during the flight after reconsolidating the clay to measure the undrained shear strength profile.

2.2 *Experimental procedure*

The centrifuge test was carried out following the procedures described as follows:

1. Prepare a normal consolidated clay;
2. Attach the mini-TBM to the tunnelling box;
3. Install pile/pile groups in the model clay;
4. Install monitoring instruments and assemble the centrifuge model;
5. Load the centrifuge package to the beam centrifuge;
6. Swing up to a centrifugal acceleration to 50 g;
7. Verify that the mini-TBM's drive system is operating well; if not, swing down and solve the issue;
8. Leave the clay reconsolidated for an hour under 50 g;
9. Activate T-bar at a rate of around 2.3 mm/s up to a maximum distance of 200 mm;
10. Operate the TBM to simulate mechanised tunnelling in the centrifuge;
11. Allow clay to post-tunnelling consolidate for approximately an hour;
12. Swing down and unloading.

3 EXPERIMENTAL RESULTS

All test results presented in this paper are in model scale, unless stated otherwise.

3.1 *Undrained shear strength of clay*

Determining the undrained shear strength profiles of clay is vital for analysing the force acting on the mini-TBM and understanding the physical behaviour of piled foundations during tunnelling. In-flight T-bar best was conducted to assess the undrained shear strength in this study. It should be noted that the T-bar performing rate should be such that the undrained penetration is achieved without causing any resistance increase due to partial consolidation. The T-bar undrained shear strength was calculated based on the T-bar penetration resistance, q_{T-bar}, which was computed by dividing the measured load by the projected area of the T-bar.

$$s_u = \frac{q_{T-bar}}{N_{T-bar}} \quad (1)$$

where N_{T-bar} is the T-bar bearing factor. Randolph and Houlsby (1984) concluded that the dimensionless load factor varied from 9.14 for a perfectly smooth pile (i.e., adhesion factor $\alpha = 0$) to 11.94 for a rough pile (i.e., adhesion factor $\alpha = 1$) and recommended an average value of 10.5 (i.e., adhesive factor α is around 0.4). Therefore, the value of 10.5 has been widely accepted to predict the T-bar undrained shear strength. Alagha (2023) carried out T-bar penetration test and miniature vane tests to verify the non-dimensional load factor. A total of six tests were performed and the results showed that all values have an average of approximately 11.6, which falls within the range reported by Randolph and Houlsby (1984) but is closer to the upper limit. This is also evidenced by the work of Gaudio et al. (2022). $N_{T-bar} = 11.6$ was used to compute the undrained shear strength as the test conducted in this investigation employed the same T-bar as that in the work of Alagha (2023).

The normalised soil parameter (NSP) concept, called "stress history and normalised soil engineering properties" (SHANSEP) can also be utilised to estimate the undrained shear strength profile of the soil (Ladd and Foott, 1974). The undrained shear strength, s_u of overconsolidated clay can be determined as follows:

$$\left(\frac{s_u}{\sigma'_v}\right)_{OC} = \left(\frac{s_u}{\sigma'_v}\right)_{NC} OCR^m \quad (2)$$

where m is a soil parameter indicating the relationship between over consolidation ratio (OCR) levels and s_u.

Based on the critical state soil mechanics by Schofield and Wroth (1968), Wood (1990) reported the calculation of soil parameter m as follows:

$$m = \frac{\lambda - \kappa}{\lambda} \quad (3)$$

Subtitling the data from Table 2 to the Equation (3), the computed value of m is 0.84. This value compares well with the m values that result from the λ and κ values of Elmes (1985), Lau (2015) and Alagha (2023). Utilising these values, the estimated S_u profiles determined by SHANSEP and Modified Cam-clay were illustrated in Figure 6.

Overall, the undrained shear strength profiles measured using the T-bar results show a steady increase in s_u with depth, which can be expected due to the increasing OCR values. The T-bar test was capable of measuring up to a depth of 300 mm, which fully covered the thickness of the mini-TBM. Two approaches determining the s_u are quite accurate while s_u obtained from SHANSEP was larger than that attained from Modified Cam-clay. At a depth from 150 mm to 300 mm, the computed

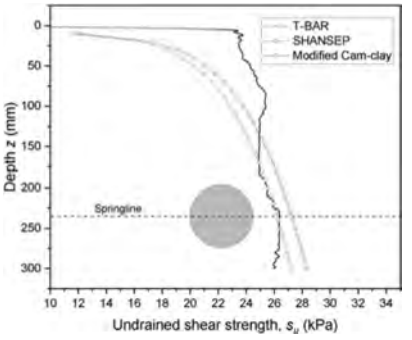

Figure 6. Comparison for pre-consolidated clay.

undrained shear strength from MCC can be believed to represent the soil behaviour around the TBM. Meanwhile, it was verified that the T-bar was suitable for the measurement of the strength of soft clay.

3.2 *Ground surface settlement*

3.2.1 *Vertical settlement trough*

Figure 7 shows the extents of ground surface vertical settlement (S_v) measured by LVDTs 2,6-9 in this test. In addition, the result from a former test by the same machine but a softer clay (s_u = 15 kPa) was given (Viggiani et al., 2022). The transverse distance from the centreline of the TBM were normalized by the diameter of tunnel (D).

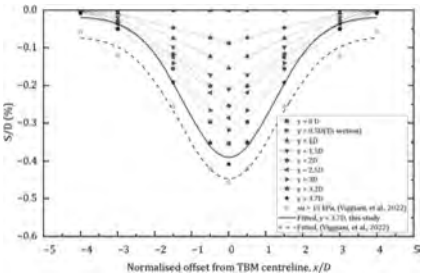

Figure 7. Surface settlement induced by tunnel excavation.

In this test, only half of the ground surface settlement trough was measured. At the end of the TBM excavation, the measured maximum settlement was 0.32 mm (0.41% D) above the centreline of the tunnel. At a distance of 1.5 D from the centreline of the tunnel, a surface settlement of 0.19% D was also measured. When it comes to tunnelling in softer clay, the maximum settlement was measured as about 0.46% D above the tunnel.

Equation (4) was used to fit the measured displacements induced by TBM excavation. As expected, the measured maximum settlement $S_{v,\max}$ was located above the centreline of tunnel. The best-fitted curve using an i of 1.23D (4.80 m in prototype) is shown in Figure 8.

$$V_s = \int_{-\infty}^{\infty} S_v dy = \sqrt{2\pi} i S_{v,\max} \quad (4)$$

where V_s is the settlement trough volume, S_v is the vertical settlement at a certain distance from the tunnel centreline, $S_{v,\max}$ is the maximum vertical settlement of the trough (i.e., usually to be above the centreline) and i is the horizontal distance to the point of inflection.

As proposed by O'Reilly and New (1982), i can be represented by Kz, where z is the vertical distance between from the centre of tunnel and ground surface.The deduced K value for the best-fitted curve is 0.41, which is within the envelop bounded by 0.4 and 0.6 suggested by Mair and Taylor (1997) for tunnelling in clay.

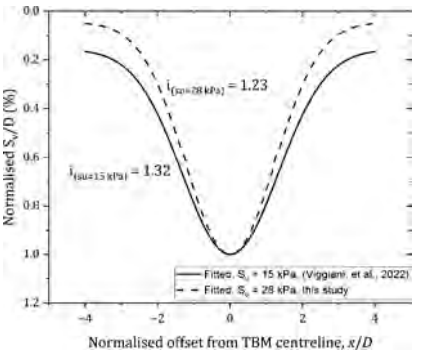

Figure 8. Settlement troughs induced by single tunnelling regressed by normal probability curves at various s_u.

3.2.2 *Longitudinal settlement trough*

Measurements from LVDTs L1 to L9 versus TBM advancement were shown in Figure 9. As TBM advanced, all LVDTs measured settlements increased. As discussed in Section 2.1.5, LVDTs L1 to L5 were used to measure the longitudinal settlement trough as illustrated in solid line. As L1 and L2 has been settled to some extents due to attaching TBM into the box, the slopes of these two curves decrease. In other words, the settlements in these two surface positions tend to be stable. On the contrary, the other three surface positions in front of the TBM measured by LVDTs L3 to L5 present rising trend due to tunnelling. The results well agree with the general understanding of longitudinal settlement trough (Attewell and Woodman, 1982 and Mair and Taylor, 1997).

It should be noted that the due to the limited strong box size, the settlements failed to reach an equilibrium, resulting in that we cannot get the final maximum settlement $S_{v,\max}$. Another reason might be the continuous reconsolidation as a result of water level decrease. Nevertheless, we could build the three-dimensional settlements through all LVDTs data shown in Figure 10.

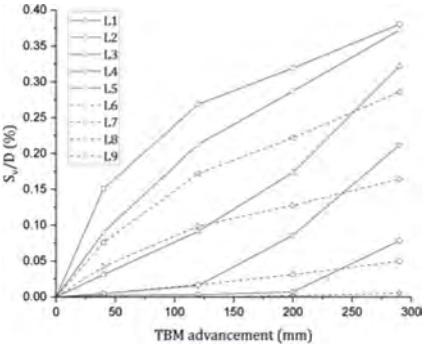

Figure 9. Settlements of L1 to L9 vs TBM advancement.

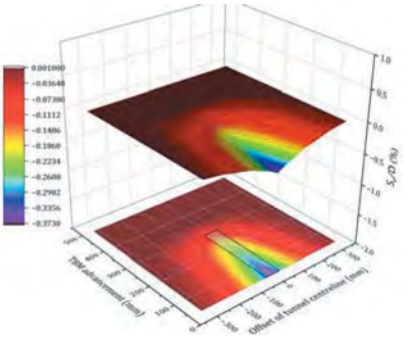

Figure 10. Three-dimensional settlement due to tunnelling.

3.3 *Excess pore water pressures*

Figure 11 shows the normalised excess pore water pressures during and after tunnelling as a function of time. Two indications of TBM positions are given at relevant times. The excess pore water pressures were normalised by the initial maximum pore water pressures measured by PPTs. Looking closely to Figure 11, just after TBM started excavation, all PPTs around the machine (i.e., P1 to P4) recorded positive pore water pressures due to the thrust force of the cutterhead. It should be noted here that P1 to P3 showed a decrease after the initial thrust effect, but the value measured by P4 remained increasing until face past the it. Once face past the PPTs, P1 remained almost constant until tail past PPTs; P2 suffered from flat variation before measured high positive excess pore pressure and persisted until the very end of tunnelling; P3, in contrast, recorded the pore water pressure remaining negative and gradually reducing until tail past PPTs; the pore pressure measured by P4 reduced to zero by the end of tunnelling; P5 remained low positive pore pressure but presented a rising trend. After the tail past PPTs, P1 remained positive pore pressure during the tunnelling and post consolidation; P2 kept increasing due to the tail gap; P3 reduced to zero by the end of tunnelling; P4 remained positive but gradually reduced to zero; P5, located at ahead of the final TBM face position,

began measuring significant positive excess pore pressure as TBM approached. This phenomenon was also reported in Viggiani et al., (2022) and Alagha (2023). Once the TBM stopped, the positive excess pore pressure turned into negative pore pressure very shortly due to the suctions of clay. As one would expect, PPT 6 positioned in the far field, did not exhibit any changes during tunnelling.

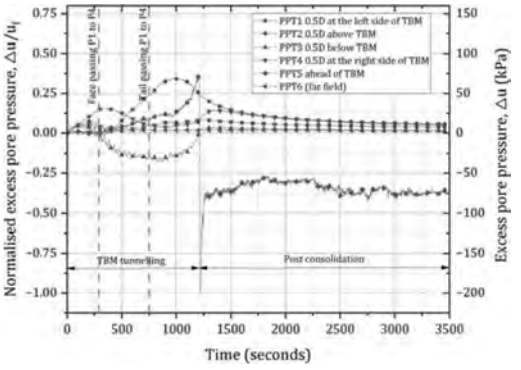

Figure 11. Normalised excess pore water pressure vs time.

3.4 *Tunnelling effects on piled structures*

3.4.1 *Influence of transverse distance on piled structures*

As mentioned above, the undrained shear strength of clay used in this study is 28 kPa. Figure 12 shows the settlement due to tunnelling. By comparing the normalised pile settlement with P2 and P12 in Alagha (2023), for piles at the monitoring section, a larger settlement was obtained for smaller transverse distance from the tunnel axis; for piles at the same transverse distance from the tunnel axis, the parallel curves exhibit the repeatability of the test. This is consistent with both previous centrifuge tests (Loganathan et al., 2000) and numerical studies (Jongpradist et al., 2013). It should be mentioned that the settlements of piles A and B are not presented here as the LVDTs employed for them did not work well during the flight.

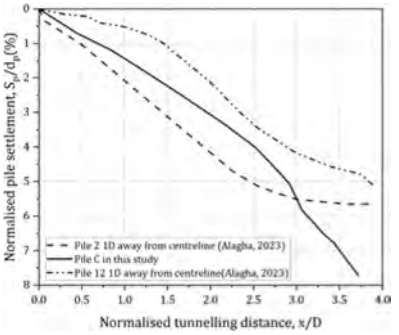

Figure 12. Normalised pile settlement versus normalised tunnelling distance.

3.4.2 *Tunnelling induced bending moments along piles*

Bending moments were taken to be positive if tensile stress was induced at the side facing the tunnel. As introduced in Section 2.1.3, seven strain gauges were used in piles A and B while eight strain gauges were installed in the pile C to measure the bending moments. Herein the strain gauges are labelled as the pile name plus number from the bottom to the top. For instance, the strain gauge at the bottom of pile A was labelled as A1. Figure 13 (a) (b) and (c)

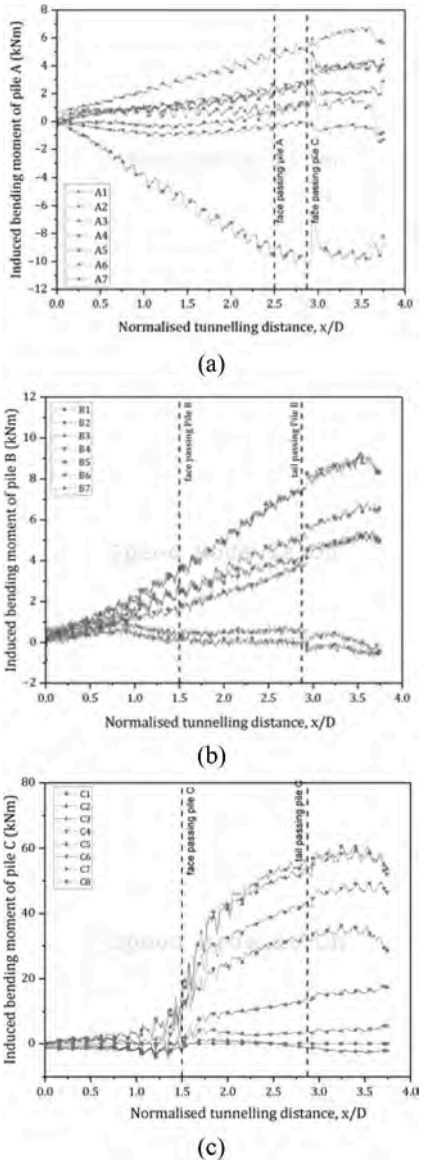

Figure 13. Tunnelling induced bending moments: (a) bending moments on pile A; (b) bending moments on pile B; (c) bending moments on pile C.

illustrated the bending moments induced by mechanised tunnelling on single piles versus tunnelling distance.

As TBM approaches, the bending moments of all three piles increased. In terms of pile C, which is the closest to the tunnel axis, once face past the pile C, the bottom strain gauges recorded a rapid rise; while once tail past the pile C, a sudden increase was observed. The reason might be the volume loss of the tunnel increased due to the end of conical shield body. Similar observations also be captured in piles A and B as shown in Figure 13(a) and (b). Although the bending moment curves exhibit similar trend regarding piles A and B, the extent on pile A is apparently larger than that on pile B. This is because the existence of pile C blocked the horizontal soil movements due to tunnelling. Similar conclusions have been reported in Ng et al. (2015) and Alagha (2023). Figure 14 shows the summarised bending moments versus normalised depth.

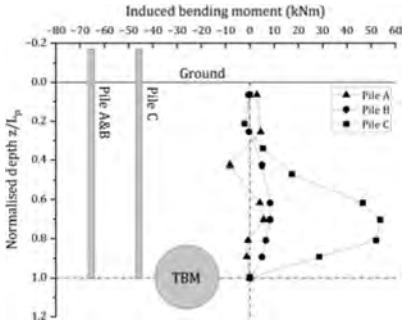

Figure 14. Bending moments versus normalised depth.

4 CONCLUSIONS AND PERSPECTIVES

The novel miniature TBM designed in Cambridge geotechnical centrifuge has been proven successful in excavating soft clay with an undrained shear strength of about 28 kPa. This work sets the foundation for further developments and improvements. In this paper, the undrained shear strength shows good agreements both in measurements by T-bar and estimations by Modified Cam-clay and SHANSEP method. Compared to tunnelling in softer clay (s_u = 15 kPa), this test results show bigger settlement trough as expected and well agree with the general understanding of longitudinal settlement trough, although limited by the size of strong box. The change of excess pore pressure due to continuous tunnelling was captured and analysed. TBM induced pore pressure variation can be perfectly explained as a result of thrust force and peripheral volume loss. A larger settlement was obtained for smaller transverse distance from the tunnel axis; for piles at the same transverse distance from the tunnel axis, the parallel curves exhibit the repeatability of the test. Recorded bending moments show the influence of continuous tunnelling rather than simple change of volume loss. They were in a good agreement with previous reports but provided more details involving thrust and tapered shape of TBM.

Although the current design includes important features of an earth pressure balance machine, some features are still hard to simulate, like tail void gap. In addition, the size of the strong box limited by the centrifuge restricted the tunnelling length. But the size of TBM can be reduced to obtain a wider greenfield whereas that of box is fixed. A smaller and sophisticated mini-TBM under higher g-level is on the way.

REFERENCES

Alagha, A.S.N. (2023). *Centrifuge modelling of the impact of mechanised tunnelling on piled foundations using a miniature TBM*. Ph.D. Thesis, University of Cambridge.

Attewell, P.B. and Woodman J.P. (1982) Predicting the dynamics of ground settlement and its derivatives caused by tunnelling in soil. *Ground Engineering*, 15 (8):13–36.

Burland, J.B., Broms, B.B. and De Mello, V.F.B. (1977) Behaviour of foundations and structures. In *Proceedings of the 9th International Conference on Soil Mechanics and Foundations Engineering*, volume 2, pp. 495–546, Tokyo.

Elmes, D. (1985). *Creep and viscosity in two kaolin clays*. PhD thesis, University of Cambridge.

Franza, A. and Marshall, A. M. (2018). Centrifuge modeling study of the response of piled structures to tunneling. *Journal of Geotechnical and Geoenvironmental Engineering*, 144(2):04017109.

Garala, T. K. (2020). *Seismic response of pile foundations in soft clays and layered soils*. PhD thesis, University of Cambridge.

Gaudio, D., Madabhushi, S. G., Rampello, S., and Viggiani, G. M. (2022). Experimental investigation of the seismic performance of caisson foundations supporting bridge piers. *Géotechnique*, pp. 1–16.

Gue, C. Y. (2017). *Effects of tunnelling under an existing tunnel in clay*. PhD thesis, University of Cambridge.

Hu, X., Fang, Y., Walton, G., He, C. (2022) Laboratory model test of slurry shield tunnelling in saturated sandy soil, *Géotechnique*, pp. 1–22.

Jacobsz, S. W. (2003). *The effects of tunnelling on piled foundations*. PhD thesis, University of Cambridge.

Jongpradist, P., Kaewsri, T., Sawatparnich, A., Suwansawat, S., Youwai, S., Kongkitkul, W., and Sunitsakul, J. (2013). Development of tunneling influence zones for adjacent pile foundations by numerical analyses. *Tunnelling and Underground Space Technology*, 34:96–109.

Ladd, C.C. and Foott, R. (1974) New design procedure for stability of soft clays, *Journal of the Geotechnical Engineering Division*, 100(7), pp. 763–786.

Lau, B. H. (2015). *Cyclic behaviour of monopile foundations for offshore wind turbines in clay*. PhD thesis, University of Cambridge.

Lee, Y. and Yoo, C. (2006). Behaviour of a bored tunnel adjacent to a line of loaded piles. *Tunnelling and Underground Space Technology*, 21(3-4).

Loganathan, N., Poulos, H., and Stewart, D. (2000). Centrifuge model testing of tunnellinginduced ground and pile deformations. *Géotechnique*, 50(3):283–294.

Mair, R.J (2011). Tunnelling and deep excavations: Ground movements and their effects. In A. Anagnostopoulos, M. Pachakis, and C. Tsatsanifos, editors, Geotechnics of Hard Soils Weak Rocks: *Proceedings of the 15th European Conference on Soil Mechanics and Geotechnical Engineering*, volume 4, pp. 39–70, Athens, Greece. IOS Press.

Mair, R.J., and Taylor, R.N. (1997) 'Theme Lecture: Bored tunnelling in the urban Environment', *In 14th International conference on soil mechanics and foundation engineering*, pp. 2353–2385.

Marshall, A. (2009). *Tunnelling in sand and its effect on pipelines and piles*. PhD thesis, University of Cambridge.

Meguid, M. A. and Mattar, J. (2009). Investigation of tunnel-soil-pile interaction in cohesive soils. *Journal of Geotechnical and Geoenvironmental Engineering*, 135 (7):973–979.

Ng, C. W. W., Hong, Y., and Soomro, M. A. (2015). Effects of piggyback twin tunnelling on a pile group: 3d centrifuge tests and numerical modelling. *Géotechnique*, 65 (1):38–51.

O'Reilly, M.P. and New, B.M. (1982) Settlements above tunnels in the United Kingdom - their magnitude and prediction. In M.J. Jones, editor, Tunnelling '82: *Proceedings of the 3rd International Symposium*, pp. 173–181, London. Institution of Mining and Metallurgy.

Potts, D.M. and Addenbrooke, T.I. (1997) A structure's influence on tunnelling-induced ground movements. *Proceedings of the Institution of Civil Engineers: Geotechnical Engineering*, 125(2):109–125.

Randolph, M. F. and Houlsby, G. (1984). The limiting pressure on a circular pile loaded laterally in cohesive soil. *Géotechnique*, 34(4):613–623.

Schofield, A. N. & Wroth, C. P. (1968). Critical State Soil Mechanics. London: McGraw-Hill.

Viggiani, G., Alagha, A. S. N., & Haigh, S. K. (2022). Reduced scale modelling of mechanised tunnelling-challenges and perspectives. *Physical Modelling in Geotechnics*.

Williamson, M. G. (2014). *Tunnelling effects on bored piles in clay*. PhD thesis, University of Cambridge.

Wood, D.M. (1990) *Soil Behaviour and Critical State Soil Mechanics*. Cambridge: Cambridge University Press.

Tunnelling for a Better Life – Yan, Celestino, Thewes & Eberhardt (Eds)
© 2024 The Author(s), ISBN 978-1-032-80042-4
Open Access: www.taylorfrancis.com, CC BY-NC-ND 4.0 license

Geotechnical dimensioning of TBMs and new technological challenges

Giuseppe Lunardi, Giovanna Cassani, Martino C. Gatti* & Andrea Zimbaldi
Rocksoil S.p.A., Milan, Italy

ABSTRACT: The ever-growing need of transportation networks has led to considerable development in tunnelling works. Mechanized excavation is increasingly being applied, especially in the presence of high overburdens and squeezing rock-mass conditions. The advantages of the method are mainly to be found in an industrialization of the construction process, which enables greater excavation rates, as well as safer working conditions. The application of mechanized tunnelling in geotechnically complex contexts, however, forces to deepen the geotechnical dimensioning, considering the behaviour of the core-face, the face chamber-pressure and the interaction between the rock mass and the tunnel system, mainly the shield during excavation, to avoid jamming. These geotechnical analyses allow the design of the technical requirements for the TBM construction, in terms of chamber-pressure, shield conicity, over-excavation, and total thrust. The Authors will present a methodology approach to define in detail the correct technical specification for the TBM. A risk assessment must address the most critical aspects, towards which to choose the most appropriate risk mitigation interventions. The focus will refer to squeezing and geological complex conditions, where recent experiences have allowed projects to define very high-performance TBMs, according to the state-of-the-art. Numerical modelling is presented to analyse the problem and as a tool to help designers in defining with key technical specifications for the TBM advance. Based on monitoring data, specific "guidelines" will allow projects to calibrate operative parameters during excavation and to manage residual risks.

Keywords: geotechnical dimensioning, TBM, mechanized excavation, critical contexts

1 INTRODUCTION

The ever-growing need of transportation networks has led to considerable development in tunnelling works, with increasing excavation diameter requirements and facing adverse geological and geotechnical conditions. Mechanized tunnelling is increasingly being applied, not only in urban areas where it has always been preferred over conventional excavation, but also, nowadays, in the presence of high overburdens and, sometimes, in severe squeezing rock-mass conditions. The advantages of the mechanised system are mainly to be found in its industrialization of the construction process, which determines greater excavation rates, as well as safer working and better environmental conditions. However, the application of this excavation methodology in geotechnically critical contexts, by means of EPB-TBMs or hydro-shield TBMs, forces projects to carefully deepen the geotechnical dimensioning, considering in detail the behaviour of the core-face, according to the ADECO-RS Approach (Lunardi, 2008), and the interaction between the rock mass and the tunnel system, mainly the shields. The definition of the correct pressure value, to be adopted in the excavation chamber to assure face-stability, as well as the TBM thrust, are crucial elements for the success of the advancement excavations. Jamming conditions must be especially avoided, which can lead to excavation stops or the shield's ovalization.

In this paper, a methodological approach to examine the problem and to define the correct technical requirement for the TBM to be used is described. In the design stage, once the geological and geotechnical model has been defined (survey phase), a risk analysis must be developed in order to identify the critical issues regarding TBM excavation (diagnosis phase). Regarding each risk, the TBM design strategies must be identified, according to the potential offered by the TBM manufacturing market, and numerical analyses must be performed to size in detail the technical specifications to be envisaged (therapy phase). Finally, in the construction stage, specific "guidelines" should be adopted, to monitor the key parameters of the TBM advance with respect to each risk, and to calibrate the excavation system according to design variabilities.

*Corresponding author: martino.gatti@rocksoil.com

DOI: 10.1201/9781003495505-258

2 GEOLOGICAL INVESTIGATIONS AND GDM MODEL

An accurate geological, geotechnical and hydrogeological model along the tunnel axis has to be constructed. This requires an investigation campaign with boreholes deepened 10 m down the future tunnel invert, in addition to desk studies of the area and relevant bibliographic research. All of the collected stratigraphic and piezometric data must be inserted in the GDM and used to produce an accurate predictive geomechanical profile considering geological sequences, contacts between formations, presence of faults or sliding structures and landslides. Lithological and geotechnical properties (strength and deformability parameters) of the rock-mass should be defined; it's also important to detect the presence of boulders or mixed face conditions. Finally, hydrogeological context should be assessed, that is to define distribution of aquifers, rock permeability values and groundwater levels.

3 RISK ASSESSMENT

Based on the GDM model, a risk analysis for TBM advance must be developed. The main typical risks, linked to geotechnical and hydraulic conditions, are described in the following and must be investigated with respect to TBM behaviour during excavation.

3.1 *Squeezing or swelling phenomena*

In poor rock-mass conditions, mainly in clays or argillitic shales, especially in the presence of high overburden (>80-100 m, with geostatic stresses greater than 2.0-2.5 MPa), it's very frequent to encounter the risk of squeezing conditions. These generate large convergence of the excavation profile, extensive plastic yielding around the cavity, and swelling phenomena due to the volume and stress variation in the rock-mass during excavation. The risk is the activation of high ground pressures on the TBM shields, which could exceed their static resistance, with ovalization and/or deformations. These high pressures on the shield, combined with the need to operate adequate balancing pressures at the face and to impart the cutters' energy to advance the excavation, can generate high thrust values for the TBM, exceeding the capabilities of the machine. The consequential risk is the TBM becomes trapped.

3.2 *Core-face instability*

When the state of stress in the ground is considerably greater than the strength properties of the material, even in the zone around the face, an unstable core-face condition occurs (category C, referring to ADECO-RS Approach), coupled by the risk of face collapses. Moreover, deformation of the core-face, in terms of extrusion and pre-convergence, could cause decay of the strength parameters of the ground, if it's affected by "strain-softening" behaviour, further deepening the band of plastic yielding. So, it's necessary to enact pre-confinement operations at the core-face, by proper pressure in the TBM excavation chamber, minimising ground deformation and strength decay. This is clearly stated by extrusion tests, specifically applied to the sizing of the pressures to be maintained at the TBM face (Gatti, 2011 and Lunardi, 2013).

3.3 *Presence of boulders or mix-face condition*

Homogeneous face conditions, characterized by uniform stiffness and strength of the material to be excavated, allow regular and efficient advancement of the TBM. Otherwise, the presence of stone boulders, especially inside a weak rock-mass, or mixed face conditions characterized by different rock components can be critical for the TBM excavation. Some examples are reported in Figure 1.

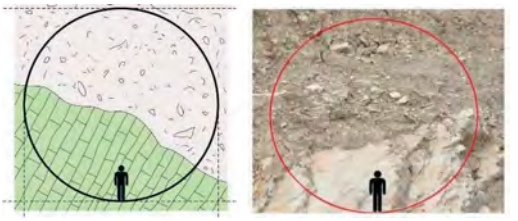

Figure 1. Example of mix-face conditions.

Thus, the excavation tools of the TBM must guarantee adequate flexibility in relation to the variety of stiffness and strength of the excavated materials, providing suitable devices for their easy replacement in relation to the lithological variability of the rock-mass to be excavated.

3.4 *Landslides or existing superficial interferences*

The presence along the tunnel alignment of landslides or pre-existing interferences, such as buildings, roads or utilities, requires to limit the "lost volumes" during the excavation, in order to avoid subsidence at ground level and consequently damage to the pre-existing structures or accelerations to the movements of landslide. Generally, this risk occurs with low overburdens (with limited geostatic stresses), so that it is possible to maintain pressures in the TBM excavation chamber close to geostatic pressures, and drastically reduce deformations during the excavation phase. Similarly, care must be taken to backfill the segmental lining, in order to avoid settling at the tail of the TBM (Gatti, 2007).

3.5 *Water leaks and high hydraulic heads*

With reference to the hydrogeological context, the main risks are linked to the interception, during

excavation, of high-water inflows and to the presence of high groundwater pressure. The first risk can be mitigated through consolidation and/or drainage systems to be carried out at the face of the TBM and through the shield (dewatering system). For the second one, if the hydrostatic pressures exceed the static resistance of the concrete linings, drainage systems must be used, generally installed along the base of the sidewalls, so as to facilitate easy collection and disposal of the drained water (Figure 2).

Figure 2. Drainages systems.

The effectiveness of the drainage action can be verified, in the long term, by pressure monitoring systems mounted behind the segmental lining.

3.6 *Presence of in-situ gas*

The presence of in-situ gas can be identified through detailed analysis of the geostructural context (i.e., lithological and fault successions) and according to the results of boreholes that identify gas emissions. The gas risk is very high in mechanized excavations, considering that not all TBM equipment can be ATEX, such as the cutterhead. The Italian "Interregional Note 44" (NIR, 2009) provides useful advice to mitigate the risk of operating excavations with TBMs in a gas context. The TBM must be compartmentalized by sectors, to avoid the diffusion of gas in the different working environments. In the presence of gas, the excavation must be carried out with a full chamber (closed mode) to prevent possible formation of a "combustion chamber", and a special gas-proof duct to enclose the top of the screw conveyor and the conveyor belt, for approximately the first 80 m, up to the protected tunnel sectors should be provided. Systems for monitoring and controlling the concentration of gas in the atmosphere must also be activated, coupled with ventilation systems (Lunardi, 2012).

3.7 *Clogging phenomena*

Clogging phenomena are linked to the presence of clayey soils, which are difficult to condition and subject to "cooking" and packing. The resulting risk is not allowing the correct pressures to be maintained at the face and the correct extraction of material from the screw. It may be necessary to use anti-clogging additives in addition to ordinary foaming agents.

3.8 *Other risks*

Other risks may be linked to structural geological conditions, such as the crossing of fault zones or highly fractured rock, as well as anomalous thrust conditions (for example of a tectonic nature or due to schistosity). These risks present similar problems to those already discussed in Section 3.1. Sometimes, in very sound rocks, problems may arise related to difficulties in penetrating and breaking the rock, with high wear of the cutting edges due to abrasiveness.

To identify the magnitude of the described risks, it is necessary to determine the frequency (F_E) of occurrence of the events identified above, evaluating the length of the tunnel sections in which they will have to be addressed. Furthermore, the impact (I_E) of each event must be assessed considering the possible consequences, in terms of health/safety, effects on the development of works to be carried out, economic and environmental impacts during construction. The risk will be identified as the impact for the probability of occurrence ($R = F_E \times I_E$).

4 DESIGN APPROACH AND TBM REQUIREMENT

The TBM design strategy is to consider mitigation measures, which will have the aim of mitigating the risks within residual acceptable values. With reference to risks of geotechnical nature, mainly linked to squeezing or complex geological conditions, it is necessary to adopt measures capable of governing the stress-strain distribution into the rock-mass all around the TBM, keeping the pressures on the shields below fixed values. This can be achieved by avoiding the relaxation of the rock-mass by applying counterbalancing pressures at the TBM's face and along the contour of the shield, as well as by preparing a gap around the TBM by overcutting in order to accommodate the inevitable convergence of the rock-mass. It is therefore necessary to define the pressure value to adopt in the chamber pressure and choose the correct excavation diameter, coupled with TBM's shield conicity. Modern TBMs can operate pressures at the excavation face of up to 5-6 bar, thanks to the maintenance of conditioned soil in the excavation chamber in the case of EPB or by means of bentonite slurry in the case of hydroshield. At the same time, they can inject bentonite along the gap between the shield and the excavation profile, using pressure injectors of up to 5 bar. Modern TBMs have also the possibility of modulating the excavation diameter during advance, to face different geotechnical contexts, and increasing the excavation diameter in the presence of squeezing conditions. This can be achieved both through the adoption of fixed "overcutting", which is managed along the perimeter of the cutterhead, and through temporary "copy-cutters", with hydraulic opening. Radial fixed overcutting values of up to 100-150 mm can be achieved, for single steps of 20-40 mm; additional copy-cutters can further increase the excavation radius by a further

50-60 mm. Typical shield conicities are between 50 mm and 130 mm. Considering that the shields, with a total length of 10-12 m, are generally divided into three sections (front, intermediate and tail shields), the conicity is guaranteed by providing a first step between the excavation diameter and the front shield (20-30 mm) and two reductions in diameter between the intermediate and the tail sectors (30-50 mm each), as represented in Figure 3.

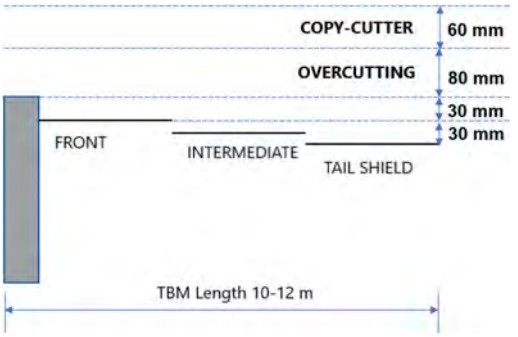

Figure 3. Typical TBM shield conicity.

It follows that the maximum radial over-excavation can reach up to 250-300 mm. It is therefore necessary to equip the TBM with measures to facilitate driving if the expected convergences do not occur and the driving position may be lost. For example, 4 to 6 fin stabilizers are placed around the lower part of the shield and 2 to 4 round stabilizers in the upper part. It could also be useful to provide an "active articulation system" of the head, located in the front-shield, so as to manage the vertical guidance of the TBM. If a significant gap, between the excavation profile and the extrados segments is present, it's necessary to make sure it is perfectly filled with bicomponent backfilling; the filling systems, carried out by 8-10 injection lines, must be able to guarantee an injection volume of 50-60 m^3/hour.

The ground pressures, which will be active around the shield, will generate frictional forces that must be overcome by the thrust of the jacks. It is therefore necessary to size the overall thrust of the TBM to take into account all the necessary components: mainly the pressure to be maintained at the face, the force of the cutters for excavation, the friction forces along the shields, the weight of the machine and the back-up (Maidl, 1996 and Gatti, 2011). In the squeezing context, a total thrust in the range of 200-300 MN is recommended, depending on the TBM's diameter. Numerical modelling must be performed to define in detail the proper chamber pressure, the excavation diameter (using overcutting and/or copy-cutter) and the total TBM thrust. A proposal is described in Section 5.

Another important strategy in managing mechanised excavations in squeezing conditions is to guarantee regular and continuous advances, avoiding prolonged stops, which can generate the release of ground pressure on the shields and considerably increase the friction forces. This is the situation in which trapped TBMs most frequently occur. Some modern TBMs are equipped with the "continuous mining" system (CMS), which allows the installation of the segmental lining at the same time as the advancement. During the installation of a segment, the corresponding thrust cylinders must be temporarily retracted while the remaining pistons remain actively pushing on the rest of the ring; the TBM's PLC manages the necessary redistribution of pressure in the active cylinders, to keep the centre of the thrust unchanged during the advancement of the TBM, as showed in Figure 4.

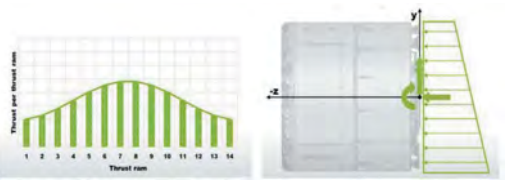

Figure 4. Redistribution of pressure in the active cylinders.

Another important tool is the "sliding continuous conveyor" system (SCC) and service extension. This solution consists of the installation of a single sliding belt of 1000 m in length with a bridge function between the machine belt and the ordinary tunnel belt, capable of advancing autonomously while following the TBM. Finally, it's necessary to reduce as much as possible the maintenance interventions. This can be achieved by increasing the cutter positions of the cutterhead, adopting anti-wear protections on the cutterhead, on the edge of the shield and on the screw. It may be useful to install two high-pressure water injections of 300 bar (10 l/s) at the face to break up the rock-mass and foam injection points to lubricate the screw conveyor. With reference to the equipment for backfilling injection at the back of the segments, it could be useful to adopt a greater number of injection lines in the tail shield (10-12), with additional lines installed as spares. These can provide an automatic high-pressure washing system that will be activated on each line at the end of each excavation stroke of the TBM, to avoid blockage of the lines. The main TBM mechanical parts must be designed with a view to facilitating replacements and maintenance interventions.

5 NUMERICAL AXIAL-SYMMETRIC MODELLING

The interaction analysis between the rock-mass and the TBM shield during the excavation can be conveniently carried out with an axisymmetric model created with the software FLAC 2D ver. 8.0 by

Itasca. The result in terms of pressure on the shield can be considered as an upper limit because the axi-symmetric model is not gravity oriented and the convergence along the tunnel boundary is the same on the whole circumference. In the analyses presented in the following, the mesh has a width of 50m and a height of 125m, to avoid boundary effects during the calculations of the stresses in the rock-mass; the mesh is composed of 25000 square elements, sized 0.5m. Excluding the boundary of the axisymmetric model, the geostatic load is applied on the other three boundaries from the initial phase of the model (the geostatic step), and, in the first excavation step, the lower boundary is fixed to avoid movements in the longitudinal direction of the excavation, due to the increase of stresses in that direction.

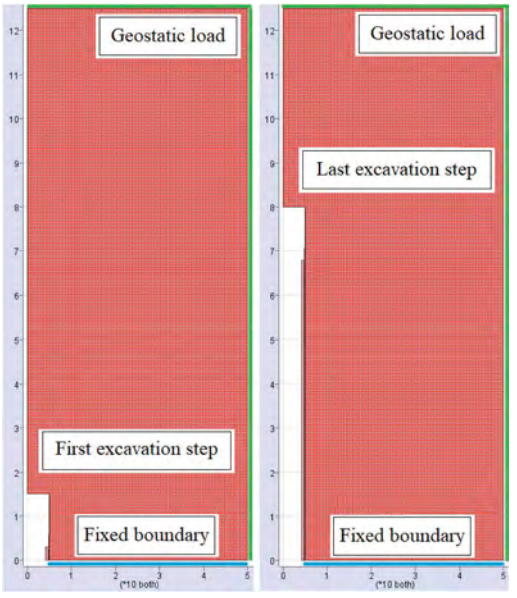

Figure 5. Axisymmetric model.

The model includes excavation steps of 1m each to simulate the advance of the excavation face from 15m to 80m, in the middle of the mesh. In each step, the geometry of the mesh is updated as a function of the calculated displacements, using the "set large" command in the software, to correctly evaluate the progressive contact between the rock-mass and the shield and the tunnel lining.

In each step, following the advance of the excavation face, one additional meter of the TBM shield, of the tunnel lining and of the backfilling is activated. The TBM pressure, which is constant at the face and decreases linearly to null pressure in the first 4 meters of the tunnel, is moved forward 1 meter too.

Mesh elements representing the steel TBM shield and the concrete tunnel lining, concrete class C35/45, are modelled with an Elastic behaviour. For the backfilling, the Mohr-Coulomb criterion is applied.

In Table 1, properties of the structural parts are reported. Mesh elements of the rock-mass and of the backfilling are fully connected ("attached"), while the interaction between the rock-mass and the shield is managed by an "interface" which is activated only in the case of contact between the two elements.

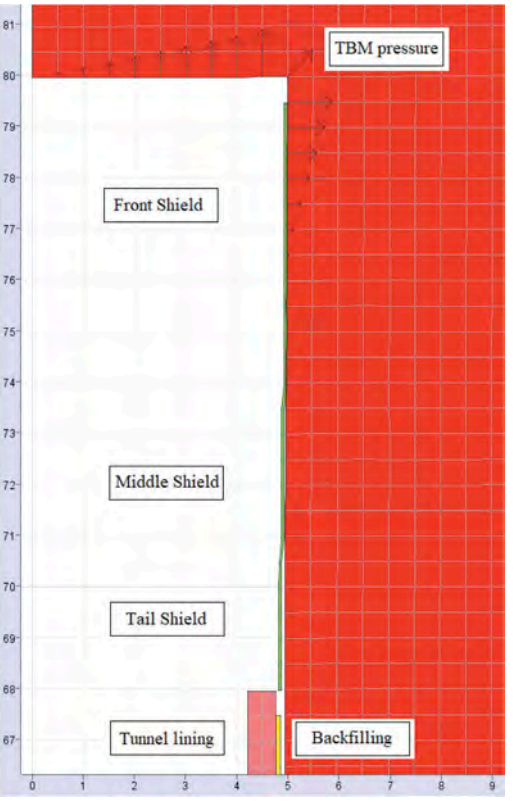

Figure 6. Detail of the FDM model for the high conicity TBM.

Table 1. Properties of the structural components.

Structural part	Thickness [m]	γ [kN/m^3]	E [GPa]	c' [kPa]	Φ [°]
TBM shield	0.05	78.5	200		
Tunnel lining	0.55	25	34		
Backfilling	≥ 0.1	20	0.5	0	25

The considered TBM shield has a typical length of 12 m and the nominal excavation diameter is equal to 10 m. Two types of TBM shapes are evaluated: one with "low conicity" (40 mm), for the excavation in good rock, and one with "high conicity" (130 mm), where relevant convergence is expected during excavation at the tunnel boundary (see Table 2). The evaluation of how far from the front face is the contact zone between the rock-mass and the shield and its extension is surely more reliable with respect to what can be

found with a simplified closed-form solution, such as the one used by Panet (1982). A geostatic isotropic pressure of 5.125 MPa is initialised in this application, for each of the cases studied below, considering a tunnel overburden of 200 m and a rock-mass unit weight γ equal to 25kN/m^3. Three geomechanics contexts are analysed, with a different response of the core-face, as classified by the ADECO-RS approach (Figure 7):

A – good rock, with "stable" behaviour
B – fault zone with "short term stable" behaviour
C – weak rock with "unstable" behaviour.

In the geomechanics context A, a TBM with a low conicity (Model 1) is compared with a high conicity TBM (Model 2), varying the TBM pressure from 1 bar (a) to 3 bars (b) and up to 5 bars (c).

Table 2. Geometry of the TBM.

TBM type	Low conicity	High conicity
Cutterhead		
R_{nom} [m]	5	5
ϕ_{nom} [m]	10	10
TBM Front shield		
R [m]	4.98	4.97
ϕ [m]	9.96	9.94
L [m]	6	6
gap from Cutterhead	0.02	0.03
TBM Middle shield		
R [m]	4.96	4.92
ϕ [m]	9.92	9.84
L [m]	3	3
gap from Front shield (m)	0.02	0.05
TBM Tail shield		
R [m]	4.96	4.87
ϕ [m]	9.92	9.74
L [m]	3	3
gap from Middle shield	0	0.05
gap from Cutterhead (m)	**0.04**	**0.13**
Tunnel lining		
R_{int} [m]	4.2	4.2
ϕ_{int} [m]	8.4	8.4
Thickness [m]	0.55	0.55
R_{ext} [m]	4.75	4.75
ϕ_{ext} [m]	9.5	9.5
gap from Tail shield (m)	0.21	0.12
gap from Cutterhead (m)	0.25	0.25

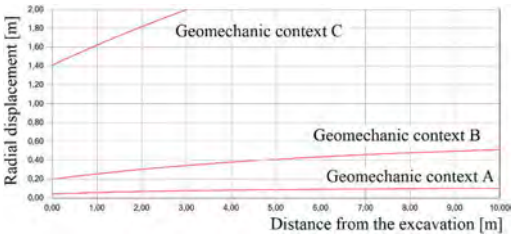

Figure 7. Radial tunnel displacement along the shield.

The analyses' results are reported in Figures 8 to 11, representing:

– Radial displacement along the tunnel,
– Deconfinement rate, equal to the ratio between radial stresses at the tunnel boundary and geostatic pressure,
– Pressure along the interface between medium and shield, and
– Axial – circumferential stress in the TBM shield.

It can be noticed that different levels of pressure, always less than 10% of the geostatic load, have a slight impact on the tunnel convergence at the core-face and at the tunnel boundary. With the high conicity TBM, bigger radial displacements are allowed and a lower pressure acts on the shield, even avoiding the contact with the middle and tail shield (Figure 10), thus reducing both the friction force on the shield and the thrust force required by the TBM to advance.

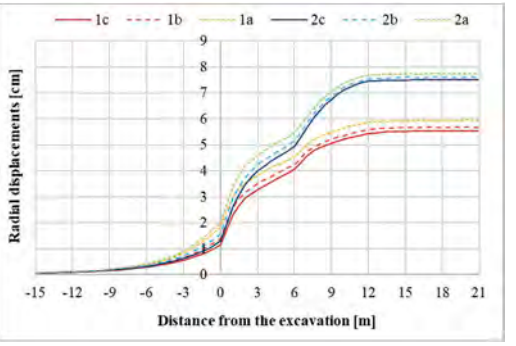

Figure 8. Geo-context A – Models 1 and 2 - Radial displacement.

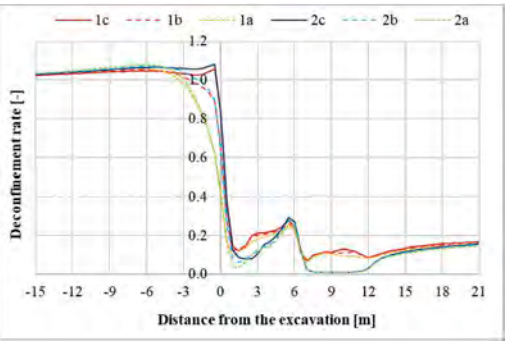

Figure 9. Geo-context A – Models 1 and 2 – Deconfinement rate.

In Model 1, preconvergence at the tunnel face is around 1.5 cm and along the shield the entire gap of 4 cm, between the cutter-head and tail shield, is used. In Model 2, preconvergence at the tunnel face is around 1.5-2.0 cm and along the shield only 6 cm of the available 13 cm is used (Figure 8).

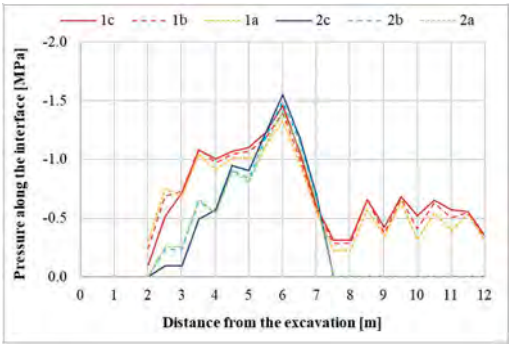

Figure 10. Geo-context A – Models 1 and 2 – Pressure along interface.

In the geomechanics context B, the high conicity TBM (Model 3) is compared with the same geometry but with the activation of a copy-cutter (Model 4), which increases by 5 cm the excavation diameter. The copy-cutter, allowing higher tunnel convergence, significantly reduces the contact zone between the soil and the shield, maintaining the average pressure along the interface around 1.5MPa (Figure 14), which means a maximum axial stress of about 150MPa at the end of the front shield and lower stress in the tail shield. Considering that the tail is the weakest part of the shield, it is difficult to put structural reinforcement in the inner part, where segments are to be placed (Figure 15). Even in this case, different front-face pressures have a small impact on the tunnel convergence and on the TBM shield, especially in Model 3.

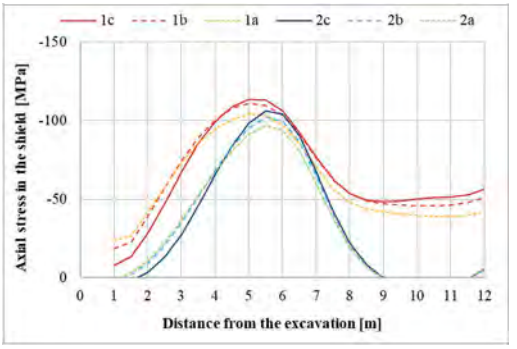

Figure 11. Geo-context A – Models 1 and 2 – Axial stress in the shield.

Finally, in the geomechanics context C, the comparison is between the high conicity TBM (Model 5) and the same geometry but with an excavation diameter increase of 15 cm (Model 6), due to overcutting. With low pressure at the tunnel face (case a, Figure 16), the support given by the soil ahead the excavation face tends to be null causing a significant increase in the preconvergence at the tunnel face and subsequent tunnel convergence, with a higher risk of instability of the excavation.

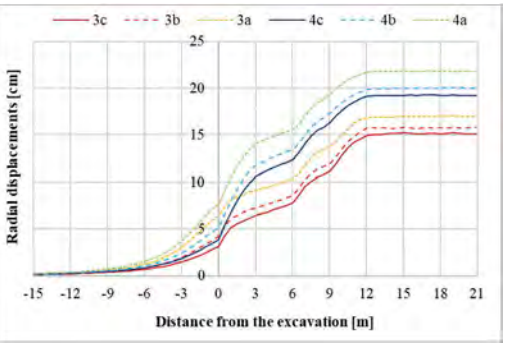

Figure 12. Geo-context B – Models 3 and 4 - Radial displacement.

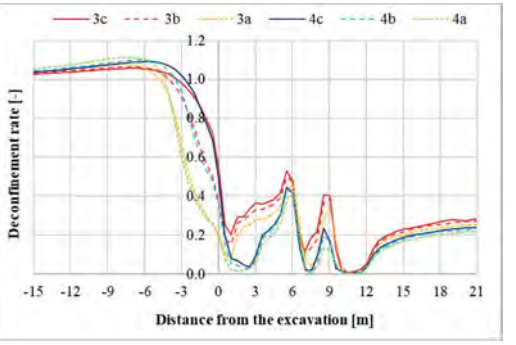

Figure 13. Geo-context B – Models 3 and 4 – Deconfinement rate.

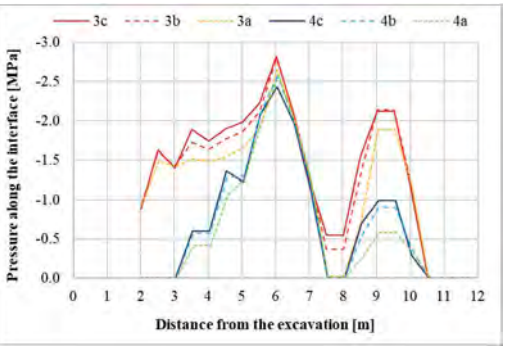

Figure 14. Geo-context B – Models 3 and 4 – Pressure along interface.

The increase of the excavation diameter has a positive impact, reducing the contact zone between the soil and the shield (Figures 18 and 19). The contact zone has to be adequately evaluated to assure the feasibility of the excavation, even in terms of stresses in the shield and TBM thrust needed to advance.

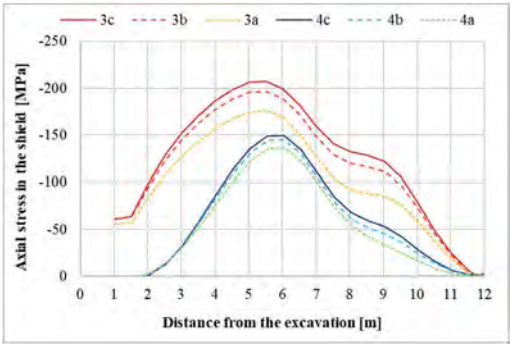

Figure 15. Geo-context B – Models 3 and 4 – Axial stress in the shield.

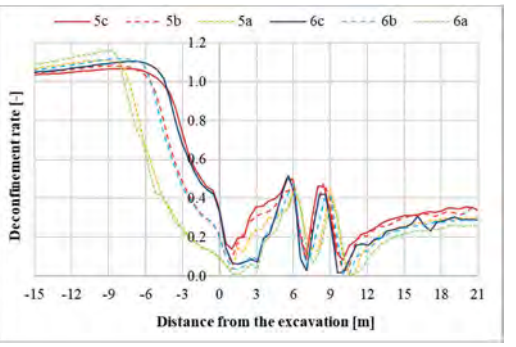

Figure 17. Geo-context C – Models 5 and 6 – Deconfinement rate.

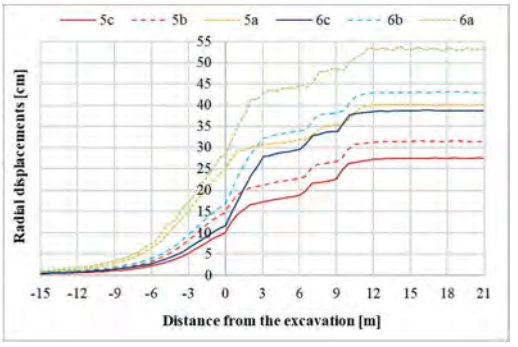

Figure 16. Geo-context C – Models 5 and 6 - Radial displacement.

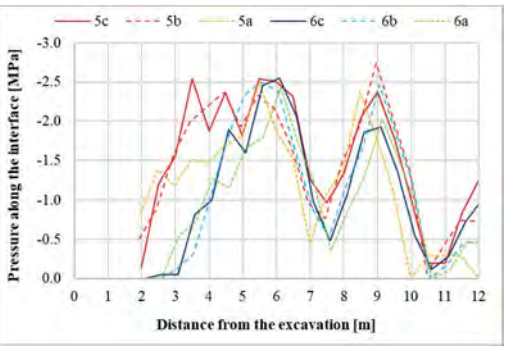

Figure 18. Geo-context C – Models 5 and 6 – Pressure along interface.

6 GUIDELINES FOR THE CONSTRUCTION STAGE

Once the risks have been defined and the mitigation measures have been identified for the TBM project, it is also important to define "guidelines" for the management of the TBM advance and to calibrate the interventions during construction. The main design inputs, such as the chamber pressure at the face and the actual excavation diameter, can be varied during advancement and adjusted according to the evidence collected. Other parameters to be collected during advancement in order to verify the processes are being carried out efficiently, are the pressures on the shields, the annular gaps around the shield, the thrust values and the volumes of backfilling injected.

It should be noted that to record the annular gap around the shields and, in the event of contact, the acting ground pressures, it is necessary to equip the shields with fonti-meters and pressure cells. Generally, three control sections are arranged, one in the central position of each shield sector; 3 instruments are provided for each section, corresponding to the crown and the lateral sidewalls. The TBM control system allows the systematic recording of the pressures at different levels in the excavation chamber, the total TBM thrust, and the volumes of back-filling

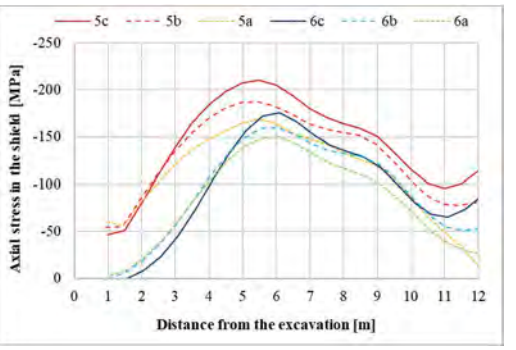

Figure 19. Geo-context C – Models 5 and 6 – Axial stress in the shield.

injected for each advance stroke of the TBM. Furthermore, to ensure that the annular gap has been perfectly filled, the backfilling will be verified continuously by means of Pulse-Echo ultrasonic tomography based on the reflection of short pulses of elastic waves at the extrados of the tunnel lining segments, and by adopting the Ground Penetrating Radar (GPR) technique.

For each control parameter, a reference value (design value) and a range of possible excursions

must be set. The limits of this range represent threshold, attention and alarm values. For some parameters which refer to the most critical risks, such as for example the gap at the intermediate shield or the pressure on the tail shields to control the jamming risk, it is advisable to set a maximum limit, so as to implement urgent corrective actions in its proximity; warning and alarm values can be suggested at 70% and 90% respectively of the set value. The following scenarios can be identified:

1. If the values of the measured control parameters are consistent with the design value, within a minimum expected variability (+/- 10%), it's possible to proceed with the project operating parameters.
2. If the values of the control parameters are lower than expected, for example fewer thrusts, less convergence of the excavation profile and, therefore, less pressure on the shields, it will be possible to reduce the operating parameters (reduction of overcutting, pressure values at the front, etc.).
3. Vice-versa, if the values of the control parameters are greater than expected, or if there is a tendency towards greater difficulty in TBM advance, with thrust values higher than expected, higher ground pressure on the shields, it will be necessary to increase the operating parameters (increase in the excavation diameter with insertion of overcutting and/or copy-cutters, increase the pressure at the face, etc.).

Any change in the operating parameters must arise from an analysis of the monitoring data considering the trend over time on a significant number of readings and data collections. The analysis must therefore be conducted considering at least the values deriving from 2-3 strokes, before leading to variations during construction. If the planned actions are not able to resolve the problems, it's necessary to implement further measures to mitigate the residual risk, especially with reference to the risk of high pressures acting on the shields and therefore trapping the TBM. Some useful solutions to keep in mind relate to the use of the "clay-shock" mixture or hydro-demolition. To apply both solutions it is necessary to leave provisions in the shields for additional injectors. In the first case, a mud containing bentonite, fillers and additives is injected which has the property, when activated with a component B, of rapidly thickening so as to reduce, even partially, the convergences of the soil, and drastically reduce the friction of the shields facilitating the start/restart of excavation. In the second case, the hydro-demolition of the ground around the shields is carried out through the nozzles, to unlock the shields and allow the TBM to restart.

7 CONCLUSION

In this paper, a methodological approach to examine TBM excavation, especially in squeezing and complex geological contexts, is presented, to define the correct technical requirement for the TBM to be used. Once the geological and hydrogeological model has been defined, a risk assessment is necessary to address the critical issues to be carefully investigated in the design stage. The main parameters to be considered are the pressure to maintain in the excavation chamber and the modulation of the TBM diameter during excavation. Indeed, the nominal TBM diameter can be increased by overcutting and using copy-cutter systems, so as to calibrate the gap between the shields and the surrounding rockmass and to control the ground pressure on the tail shield. These pressures and the correlated friction forces are responsible for the most important risk related to ovalization and/or deformations of the shield, and trapping the TBM. A proposal of using a numerical axial-symmetric model is presented, through which an understanding of the behaviour of the TBM excavation is gained and used to define the design aspects in detail. The examples presented allow focus to be placed on how different excavation radii can affect the static of the shields.

REFERENCES

Gatti, M., Cassani, G., 2007. Ground loss control in EPB TBM tunnel excavation, Proceedings of the 33rd World Tunnel Congress "Underground Space - The 4th Dimension of Metropolises", Prague.

Gatti, M., Lunardi, P., Cassani, G., 2011. The largest TBM-EPB machine in the world, designed to the Appennines. The experience of the Sparvo Tunnel. Proceeding of the 1st Int. SEE Con. «Using underground space», Dubrovnik

Lunardi, G., Selleri, A., 2012. Design of « Martina », the World's Largest EBM TBM. Geological and geotechnical issues. Swiss Tunnel Congress Colloquium, Luzern

Lunardi, P., 2008, "Design and Construction of Tunnels – Analysis of Controlled Deformation in Rock and Soils (ADECO-RS)", Springer, Berlin

Lunardi, P., Cassani, G., Gatti, M., 2013. Evidenze raccolte durante lo scavo della prima canna della Galleria Sparvo, mediante « Martin », la TBM più grande al mondo. Gallerie e Grandi Opere nel Sotterraneo, n. 105

Maidl, B,. Herrenknecht, M., Anheuser, L., 1996. "Mechanised Shield Tunneling", Ernst&Sohn, Berlin

Nir, Nota Interregionale n. 44, 2009, "Scavo meccanizzato di grande sezione con TBM – EPB in terreni grisutosi. Grisù – TBM"

Panet M., Guenot A. 1982. Analysis of convergence behind the face of a tunnel - Proc. Int. Symp. "Tunneling 82", Brighton.

Tunnelling for a Better Life – Yan, Celestino, Thewes & Eberhardt (Eds)
© 2024 The Author(s), ISBN 978-1-032-80042-4
Open Access: www.taylorfrancis.com, CC BY-NC-ND 4.0 license

Line 2 y Ramal - Red Básica Metro Lima y Callao – Conditioning of different types of soils encountered during the tunnel excavations with 2 TBMs (EPB and Variable Density)

Juan Luis Magro*
Equipment Division - Dragados, Madrid, Spain

Marcos Calleja*
Equipment Division – FCC Construcción, Madrid, Spain

Roberto Bono*
Design Services – WeBuild, Rozzano, Italy

Salvatore Iacullo*
Consorcio Constructor Metro 2 Lima, Lima, Perú

ABSTRACT: The Project for the Lima and Callao Metro Line 2 and a branch of Line 4 (Av. Faucett – Av. Gambetta) consists in the construction of an automatic underground metro line, on the East-West route of the city of Lima, with a length of 27 km (Line 2 of Red Base of Lima) and an 8 km section (Line 4) in correspondence with Elmer Faucett Avenue, from Óscar Benavides Avenue (Colonial) to Néstor Gambetta Avenue. The area of the city served by this new metro line will include approximately 2,4 millions of people.

The mechanized tunnel section will be 17,5 km long and located between 15 and 25 m with a maximum working pressure of 3 bar. The Project also contemplates the construction of 35 stations (no. 27 on Line 2 and no. 8 on Line 4) built with the Cut & Cover methodology and the construction and commissioning of two railway depots underway serving Line 2 and Line 4 of the metro. Due to the highly variable geological conditions, the tunnel will be executed by using two Tunnel Boring Machines (TBMs), one Earth Pressure Balance (EPB) and the other Variable Density (VD) TBM type. These two TBMs are manufactured by Herrenknecht (HK) and have the excavation diameter 10,27 m and 9,26 m the final inner diameter.

The geology along the tunnel alignment is particularly complicated, based on large alluvial deposits with low presence of fines and excavating sections under water table with high permeability ground.

The conditioning of the different types of soils encountered along the excavation of the tunnels plays a crucial role in the appropriate operations of the machines, for the correct maintenance of the pressure at the excavation face, the performance optimization, and the mitigation of the cutterhead wear.

Keywords: TBM, EPB, Variable Density, Underground, Conditioning, Metro

1 INTRODUCTION

This paperwork focuses on the various soil conditioning strategies implemented for the excavation of the Metro Lima tunnels, set after an extensive testing program performed prior to start tunneling but that have been continuously adjusted based on the results in the field and to accommodate the different geological conditions encountered while tunnel boring.

One of the major challenges for carrying out the excavation of these tunnels in EPB mode, besides the adverse ground conditions, was dealing with the sudden ground changes that occur within small distances. Once the soil conditioning strategies were in

*Corresponding author: jlmagroe@dragados.com; mcallejam@fcc.es; r.bono@webuildgroup.com; siacullo@ccmetrolima.com

DOI: 10.1201/9781003495505-259

place, it was crucial to pay close attention to any change of the excavation parameters and to assess the properties of the muck extracted from the excavation chamber.

Any delay to properly respond to these changes of geology by applying the correct conditioning strategy could be very detrimental for the excavation process and might lead to additional corrective measures, increasing costs and causing delay to the critical path of the overall project schedule.

2 PROJECT DESCRIPTION

The TBM bored tunnels of the Metro Lima project were divided in two stretches, according to the selected excavation method: 12.6 Km of pure EPB tunneling (including stations pass through) in Line 2, from the launching station E19 (San Juan de Dios) until the Switch Box in Parque Murillo, next to the station E11 and from there to the station E04 (Insurgentes). And 11.4 Km of VD tunneling, from station E04 to the Ventilation Shaft PV01Bis, by Callao Port in Line 2 and the 7.4 Km of Line 4.

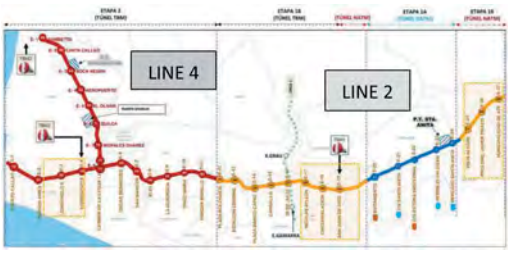

Figure 1. Lima Metro Lines 2 and 4 under construction.

The alignment develops through the city of Lima, mainly below main roads, but also underneath various critical private buildings, some of them in poor structural condition, as well as below several live infrastructures, such as roads and railway, bridges and sensitive underground services, like two sewers of 1,4 and 2,1 m diameter, just 2,3 and 3,1 m above TBM path, one of them very old, installed through the excavation of an open trench, poorly backfilled. Ad hoc local ground improvements have had to be implemented as risk mitigation measures in some locations.

These challenging conditions have driven the TBM type selection and design. In particular, the tunnels to be excavated with the EPB TBM (from E19 to E04 of Line 2) are located above the water table with poorly graded and very dense sandy gravel, with high presence of boulders and minimum fine content.

On the other hand, the tunnels to be executed with the Variable Density Multimode TBM (from E04 to the end of Line 2 and Line 4) are quite like the other ones but under the water table.

The complex geological conditions of this tunnels are prone to cause overexcavation, especially in areas of bigger grain size gravel, embedded in a non-cohesive matrix, as well as clogging of cutterhead openings, blockage of screw conveyor and even difficulties to maintain face pressure within the planned range, because of high permeability.

On the other end, the presence of sand and boulders has caused high wear and damages by impact to the cutting tools, mitigated using a tailored soil conditioning for each case and customized cutting tools to accommodate the different conditions along the alignment.

The classic EPB excavation mode has been used so far, despite soil conditioning and TBM parameters having to be quickly adapted during excavation to adjust to rapidly changing conditions.

Other factors that may have enhanced the effect of conditioning the soil are mounting longer cutting tools, sticking out more from the cutterhead face, which allows an early remixing of the excavated soil with the foam injected in the front whilst keeping the high water pressure on within the excavation chamber from the bulkhead, to avoid damaging the sandy matrix of the face.

Moreover, the Variable Density Multimode TBM has mined in our preferred pure EPB mode too for the time being, assisted by a second in-line horizontal screw conveyor, to ensure the pressure drop from the excavation chamber up to the TBM conveyor when needed, such as when sudden pressure increase episodes.

3 GEOLOGICAL CONDITIONS

Both Line 2 and Line 4 tunnels run across the alluvial deposits of the Rimac River, below groundwater table for most of the alignment, up to 25 m above the tunnel crown, especially in the Callao Section. Some of the challenges of such ground conditions are the lack of fines in an always mixed face, featuring large boulders of up to 1 m in diameter and of high strength, and the great amount of gravel of 100 mm diameter and above. High permeability is also a factor, especially in Line 4 alignment, with up to 10^{-3} m/s in gravel.

The ground encountered so far while mining Line 2 is mostly large-size pebbles, from 150 to 400 mm size, and sand, with some stretches of clayey sand tongues or just clay.

The pebbles ratio in the soil matrix is also relevant, averaging 50% greater than 50 mm but, at a certain depth, it rises to 75%. The abrasion rate is also high, usually over 3.5 Abrasivity Cerchar Index (ACI) but with peak values up to 5.25 ACl. Permeabilities are between $5x10^{-6}$ m/s and $1,5x10^{-4}$ m/s. The maximum water table height is 20 m above the tunnel invert.

On the other hand, the uniaxial compression strength tests on the extracted rocks gave values of 130 to 150 MPa, which could be considered as strong-medium resistance.

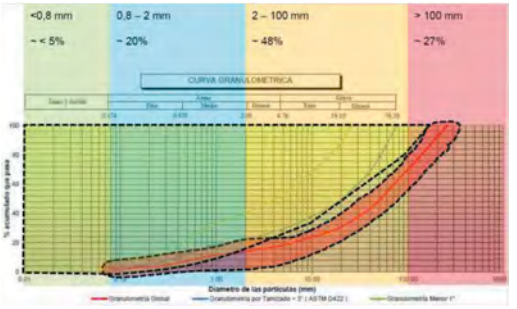

Figure 2. Grain size distribution considered at bidding phase.

Figure 3. Soil samples and excavated ground.

The main geological formations present in the project are summarized in the table below, where the following descriptions are provided: R: Backfilling/Top Soil contaminated and with a low level of compaction; CL/ML: Inorganic Clay with low/medium plasticity and silt with low plasticity; SM: Silty Sand; GP-Ss: Poorly Graded Gravel with sand, clay and silt with clayish/silty sand with low level of compaction; GP-Sm Poorly Graded Gravel with sand, clay and silt with clayish/silty sand with medium level of compaction; Gp-Sf: Poorly Graded Gravel with sand, clay and silt with clayish/silty sand with high level of compaction.

Table 1. Geotechnical parameters of the ground formations.

FORMACIÓN	γ_{ap} kN/m³	% Finos	C kPa	ϕ (°)	E carga MPa	G MPa	Vs (m/s)	Vs, adop. (m/s)	Gd MPa	Ed MPa
R	16,7	25	0	28	17	7	200	100	15	50
CL/ML	17,4	80	8	26	23	9	260	150	40	115
SM	16,9	34	5	30	35	14	280	225	85	250
GP-Ss	20	0	15	34	42	16	< 450	350	250	715
GP-Sm	21	0	25	36,5	82,5	31	450-600	500	535	1530
GP-Sf	22	0	32	39	183	70	> 600	650	950	2700

Their distribution in the excavation face varies along the alignment but in general, the stretch from the station E19 to E06 (EPB) is manly GP-Sm, with lenses of SM that are generally very small, whilst in the portion from the E06 to PV01Bis (VD) is GP-Ss with layers of SM ad CL/ML at the top of the tunnel face in most of the stretch. The average granulometric distribution of this area is in Figure 4.

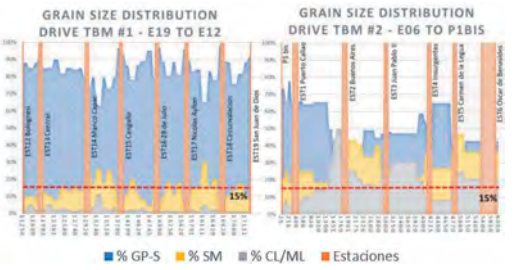

Figure 4. Grain size distribution (E19-E12 and E06-PV01Bis).

In Figure 5 there is a typical graph with the permeability and grain size distribution encountered so far during most of the excavation of the two TBMs. In particular, the first curve was taken from a sample where the geological formation is described as poorly graded gravel with high level of compaction (Average Vs > 600 m/s) with sand, clay and silt and clayish/silty sand. The second one was taken from samples where the geological formation is the same but with a low level of compaction (Average Vs < 450 m/s) and lenses of silty sand. Apart from the presence of fines, which is very low in the first one (fines 0,075 mm are about 2%) and higher in the second one (fines 0,075 mm are about 10%), the distribution of particles, which can be classified as pebbles and cobbles, is also different. For instance, cutting from the particles having size equal or greater than 100 mm, the percentage of the sample reaches in the first case 30% whilst in the second one is less than 20%.

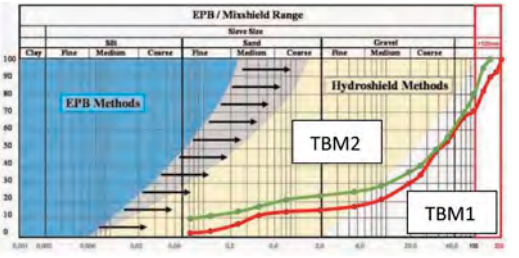

Figure 5. Typical EPB and slurry mode application range with project grain size distribution.

It must be noted that where granulometry was discontinuous, with large amount of big grain sizes, mostly all TBM excavation parameters increased respect to those planned according to the previous lab tests, in which maximum grain size was restricted by the own limitations of the testing workbench.

Also, in the tunnel section to be excavated with the TBM 1 (EPB) from station E19 to station E11, random presence of larger boulders has been observed so far

from E19 to E16 stations, whose dimensions exceeded those represented in the graph (up to 400-500mm).

And again, the field experience during the tunnel excavation, particularly for the TBM S-973 stretch, has shown rapid changes of the ground permeability. This variability, especially during sharp transitions, has made the excavation more challenging. The permeability values measured before the excavation within the tunnel footprint have been found near the limit of what is considered suitable for the EPB application, as shown in Figure 6.

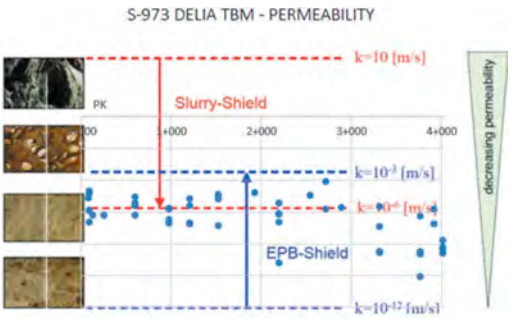

Figure 6. Ground permeability from E04 to PV01bis.

4 TBMS SELECTION

Both TBMs were selected based on the geological and geotechnical conditions defined in the Geotechnical Baseline Report (GBR), but also based on the risks of excessive ground settlement, efficiency and cost optimization and a general criterion of safety and environmental protection. As a result, one EPB and one VD TBMs were selected.

4.1 *Analysis parameters before TBM design*

TBMs type was selected considering all the information from geotechnical investigations and permeability analysis, grain size distribution, soil composition, abrasiveness, front face stability and presence of many boulders. A comprehensive review was performed, resulting in a risk assessment, including clogging potential, muck hauling and handling, performance, and TBM operation, as well as previous experiences.

From the granulometric analysis point of view, the operational area appeared to be more suitable for a Hydroshield or Mixshield, but the presence of large boulders and big-size cobbles could have compromised the effective performance of the necessary stone-crusher, prior to muck extraction.

Also, higher equipment investment and operational costs of the slurry type TBMs were considered a factor for this decision.

Conversely, going with an EPB would be limited by the maximum boulder size the screw conveyor could handle. Also, the high permeability of the ground in some sections of the alignment, together with the lack of fines, would compromise the ability to maintain and control face stability due to the difficulties to gradually drop the pressure from inside the excavation chamber, passing thru the screw conveyor, up to the extraction belt conveyor.

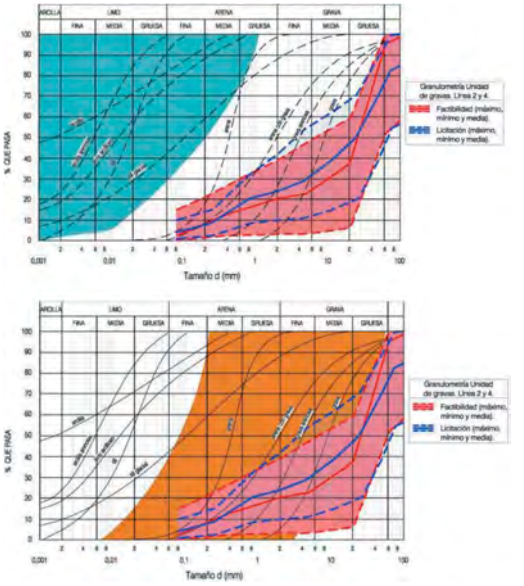

Figure 7. EPB (top) and Mixshield (bottom) application range according to granulometric distribution.

An assessment of the pros and cons of both technologies, EPB and Mixshield was performed, based on the commonly accepted application range for them, as follows:

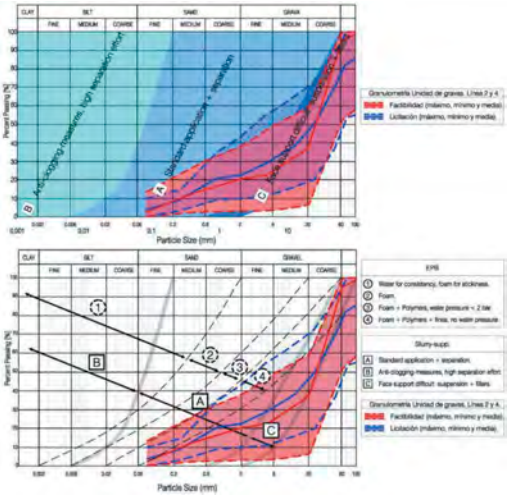

Figure 8. EPB (top) and Mixshield (bottom) application range according to granulometric distribution and conditioning.

4.2 *Summary of TBM design concepts*

The TBM design was done considering the most reasonable assumptions that could be made with the data available at the time, with emphasis on the machine flexibility to leave options open to mitigate risks during the construction phase.

fter a detailed assessment of all the risks, the following features were implemented to our TBMs:

Double screw conveyor to drop the pressure from the front to the discharge conveyor on the TBM, to deal with permeable ground.

EPB mode machines designed with slurry prechamber to be able to add fines quickly to the excavation chamber to compensate any sudden pressure drop caused by gravel, cobbles, boulders and porous ground in the face.

Strong anti-wear protection in cutter head and screw conveyors to protect them from highly abrasive granular soils.

Quick change of operations modes EPB/Slurry, to be able to deal with mixed face conditions.

Limit the boulder size passing through cutter head to 400 mm and maximize the dimensions of screw conveyors and crusher to deal with the many of them expected and prevent them from damaging the machine.

In turn, Cutterhead openings were narrower than those of a regular EPB TBM (less than 30%) and therefore, easier to clog than what would have been desired.

Those boulders were also considered a limiting factor for the excavation process (a lot of crushing involved) and for muck conveyance through slurry lines, due to their high resistance and abrasiveness, which was also an advantage for the EPB technology. Thus, we did select a first TBM to work over water level, to operate in EPB mode, with enhanced ground conditioning systems; and a second other TBM to work under water pressure, dual-mode (variable Density or VD) convertible to pure EPB or to Slurry mode, featuring two muck conveyance systems (conveyor belt, and slurry circuit and separation plant).

Figure 9. TBM VD at the factory and at site before launching.

5 TBM TYPE & CHARACTERISTICS

5.1 *TBM 1 ("Delia")*

It is an Earth Pressure Balance machine manufactured by Herrenknecht in Germany, serial number S-972, of 10,19 m excavation diameter, designed to hold 3 bar at spring line while mining. It weighs 1.750 T and its total length is 111 m with 5 backup cars. "Delia" was designed to mine up to 80 mm/min, with a maximum thrust of 107 MN at 350 bar hydraulic pressure and to rotate cutterhead up to 3 rpm, with 27,8 MNm maximum torque and 7.800 kW of installed power.

It does mount a 18,3 m long screw conveyor of 1,25 m diameter, shaft type; a vacuum erector to mount a 6+1 concrete segments ring and features all Hyperbaric Interventions means needed, including a man lock and a tool lock.

As previously said, it does have a slurry prechamber, to be able to quickly react to sudden pressure losses and mixed face conditions.

Figure 10. TBM EPB Herrenknecht S-972.

5.2 *TBM 2 ("Micaela")*

It is a Variable Density (VD) machine manufactured by Herrenknecht too in Germany, serial number S-973, also 10,19 m excavation diameter and designed to hold 3 bar at spring line while mining.

"Micaela" was designed to mine up to same speed than its sister machine, 80 mm/min. It is heavier (1.980 T) and longer (148 m) than "Delia" because of a more stuffed shield and longer back up (7 backup cars) to hold systems for conveyor belt and slurry lines muck conveyance, but key parameters such as maximum thrust and torque are alike Delia's.

Figure 11. TBM VD Herrenknecht S-973.

Unlike "Micaela", it features a two in-line screw conveyor system, 18+14 m long, same 1,25 m nominal diameter and a jaw crusher within a slurryfier box, designed to crash rocks up to 1.200 mm size and features state-of-the-art Hyperbaric Interventions means too, including a man lock and a tool lock.

This TBM allows for mining either as an EPB, mucking out by means of one or the two in-line

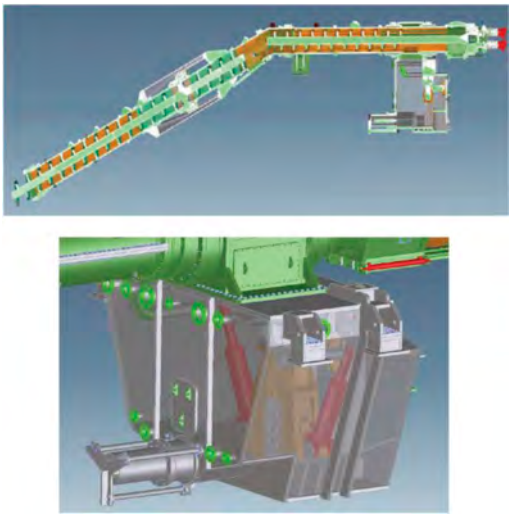

Figure 12. Screw conveyor with slurryfier box and crusher.

screw conveyors onto a continuous conveyor belt; or as Misxhield, conveying muck out of the excavation chamber by means of a two in-line screw conveyors and a slurryfier box with a crusher inside and from them, pumping it out through the slurry circuit to the Slurry Treatment Plant (STP) overland, back in the staging area; and combination of modes (open, semi-closed and closed), according to the following chart.

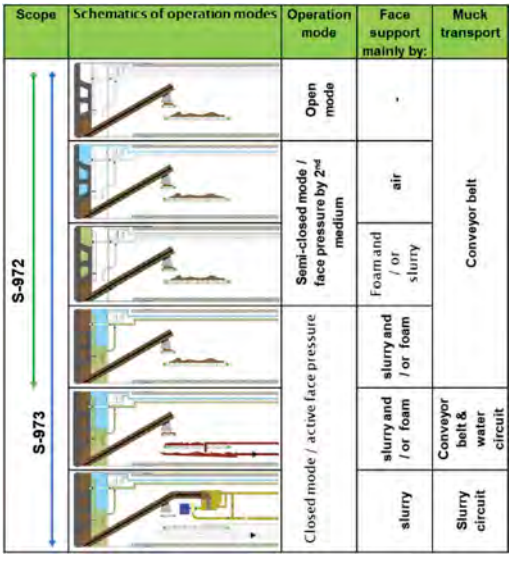

Figure 13. Operational modes of TBMs S-972 and S-973.

Both TBMs have cutting wheels designed for mixed-face conditions, including opening ratio of slightly less than 30%; 19" disc cutters, interchangeable with rippers; anti-wear plates 40mm + 20mm bimetallic; extensive wear detection for cutting tools and cutting wheel structure; High Pressure Water (HPW) injection and 12 ground conditioning injection ports.

6 SOIL CONDITIONING

6.1 *Preliminary tests during TBM design process*

Initial tests were performed to determine and design an adequate conditioning system to operate the TBMs in EPB mode in a challenging geology as much as possible during the project.

Additional tests were performed later on, focused on ground water content for potential water ingress, to determine the impact of conditioning with foam on the cutterhead torque measured with a laboratory mixer and the capacity of the additives to reduce the ground permeability.

6.2 *Tests while tunneling*

More testing was performed prior to start tunnel boring and during tunneling. Samples were taken, representing typical particle distribution, making sure to also include the bigger size elements to truly replicate the actual ground conditions, even they had to be cut to a maximum particle size of 40 mm for slump tests.

The results showed that a FIR ranging from 30% to 50% gave good plasticity, depending on the water content added to the sample, which could be suitable for forming an EPB paste.

Additional tests were performed at the site using the TBM foam generators, calibrating the parameters and verifying the expansion rates by measuring before each test, in this case without removing the bigger particles from the sample. The materials for the soil conditioning used in these tests included, beside the foam, bentonite and polymer diluted in water.

Different recipes have been tested, finding the optimum results with the values indicated below, which anyhow are to be assessed considering real conditions, where the scale factor, temperature or pressure in the chamber can influence the actual results in the TBM.

It was observed that without removing the bigger particles (cobbles to boulders), Foam expansion rate (FER) and Foam injection rate (FIR) needed to be increased to achieve a proper EPB paste.

Figure 14. Sample of gravel with sand, clay, and silt before (left) and after conditioning (right).

Accordingly, the following parameters were set as a baseline to work in EPB mode: FER between 12 y 15, foam agent concentration up to 3% and FIR up to 90%. Moreover, it was anticipated that adding polymer to control ground water may be needed at some point in time.

6.3 *Soil conditioning for TBM EPB S-972*

Our soil conditioning program for the EPB TBM was focused on two main aspects: prevent cutterhead clogging when passing from very dense sandy gravel only to the same formation with large lenses of silt/clay and mitigate cobbles segregation in the excavation chamber, impeding muck extraction, which would cause performance issues, as well as accelerate screw conveyor and cutterhead secondary wear.

Figure 15. Water and gravel extracted by the screw conveyor.

Clogging prevention was managed mainly by adding high water pressure injection ports from the bulkhead and eventually, to the cutterhead.

And ground segregation by increasing FIR from 110% to 180% average with even higher peaks, with a 2,2 to 3% foam concentration and FER between 15 and 20.

In turn, stable face pressure, good consistency of the extracted muck, an excavation speed between 35 and 45 mm/min were achieved. Temperature measured in the bulkhead ranged from 32 to 45ºC, cutterhead torque from 3,5 MNm to 4,5 MNm, contact force nominally from 4.000 kN to 6.500 kN (up to 12.000 kN in case of cutterhead clogging) and thrust force of circa 22.000 kN to 25.000 kN.

It must be noted that initially, bentonite was added from the bulkhead lines and through some of the foam lines in the cutterhead, to add cohesive particles into to the mixed material in the excavation chamber and to thicker the EPB paste, but no beneficial results were observed and as such, this practice was discarded from the soil conditioning plan.

On the other hand, having the right amount of fines in the ground improves the muck consistency but creates a fast-clogging effect of the cutterhead openings, which affects quickly to the main excavation parameters, like contact force or bulkhead temperature, reducing advance speed and jeopardized excavation face stability, specially above the shield, causing higher consumption of backfill grout and

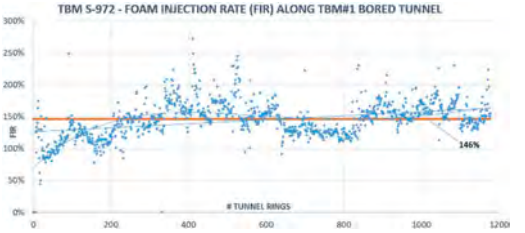

Figure 16. FIR vs mined rings E19-E16 (TBM 1).

potential ground deformation. When this happens, conditioning parameters had to be quickly adjusted and increasing the volume of high-pressure water (an average of 4 m³ with peaks up to 10 m³ per excavation) in the cutterhead and reducing the FER were found highly effective. However, more liquified muck would alter the pressure balance, causing unsteady pressure drops along the screw conveyor and making muck more difficult conveying and disposal.

6.4 *Soil conditioning for VD TBM S-973*

The Soil conditioning with the Variable Density Multimode TBM can be divided in four different geological scenarios.

The first one being exactly like the one described for the EPB TBM tunnel sections and in particular, for the same geology but without groundwater; in this case, the recommended soil conditioning would be equivalent to the one previously mentioned.

Another case was where higher fines content appear (30%). When gravel size is smaller and compaction levels are less dense, being these either above or below the groundwater level, then FER and FIR had to be slightly adjusted. From the experience gained during excavation, in non-saturated ground like described above, FIR can go up to an average of 300%, foam concentration from 2% to 3%, FER from 18 to 20 and high pressure water injection volume over the 7 m^3 per excavation.

However, if groundwater was present in most of the excavation face, FIR could be decreased to circa 170%, surfactant concentration from 2% to 2,5%, FER from 6 to 18 and high-pressure water volume would be maintained still within the same range.

Finally, the last scenario, which is probably the most critical for EPB mode, involved the presence of groundwater with water table roughly 10 m above the crown, high permeability (in the range of $2x10^{-3}$ to $8x10^{-4}$ m/s), low fines content (less than 30%) and high variability of particle size in a loose sandy gravel formation, with potential presence of cobbles and boulders. The challenges in this case are characterized by the increased risk of segregation of heavier elements on the bottom of the excavation chamber and high-water inflow if a proper

conditioning is not achieved. Excavation muck bleeding inside the excavation chamber may result in screw conveyor blockages, while excessive water ingress may lead to difficulties to maintain the pressure drop along the screw conveyor. Both these issues are addressed by adding a synthetic liquid polymer to the foam and high-pressure water we were using, injected directly into the excavation chamber in a percentage up to 0,04% of the excavated muck volume.

During the excavation in these geological conditions, it has been observed a drastic reduction of Foam Injection Ratio to values ranging from 40% to 80%, with a concentration of foam agent of 2,5% and FER of around 6.

It must also be noted that in these specific conditions, the foaming agent was enriched with a natural lubricating polymer that has thicker treated material.

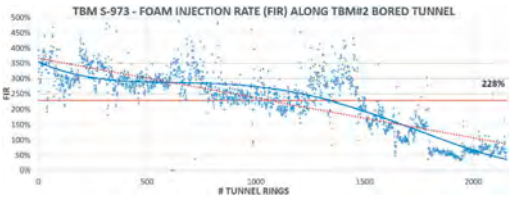

Figure 17. FIR vs mined rings E04-PV01Bis (TBM 2).

In conclusion, these additives and proportions have allowed to maintain stable face pressures, good consistency of the extracted muck, an proper excavation parameters in very challenging conditions, while reaching 30 and 40 mm/min speed of mining, bulkhead temperature ranging from 32 to 42ºC, cutterhead torque from 4,5 MNm to 7 MNm, Cutterhead contact force from 5.500 kN to 6.500kN and total thrust force ranging from 22.000 kN to 25.000 kN.

7 PRODUCTION RATES OF BOTH TBMS

Up to the date of this article (September 2023) the TBM1 (EPB) has excavated more than 2.4 Km from stations E19 to E16 and the TBM2 (VD) has excavated 4 Km, which is all its planned section of Line 2 and is about to be dismantled and reassembled at the Ventilation Shaft Gambetta to excavate Line 4.

TBM1 (EPB) has been able to mine 303 rings the best month, 69 rings the best week and 24 rings the best day while TBM2 (VD) did mine 378 rings the best month, 108 rings the best week and 23 rings the best day, considering a 6+1 precast concrete ring configuration, 1,7 m long and 32 cm thick.

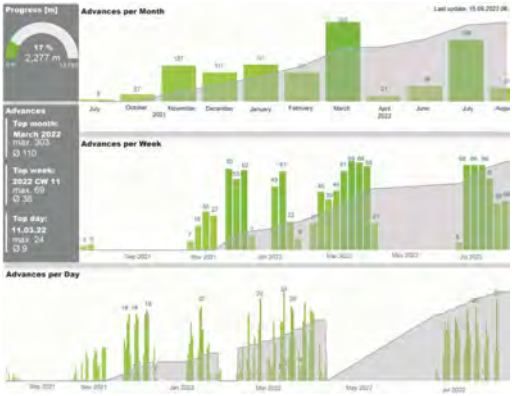

Figure 18. TBM 1 production summary (Oct-23).

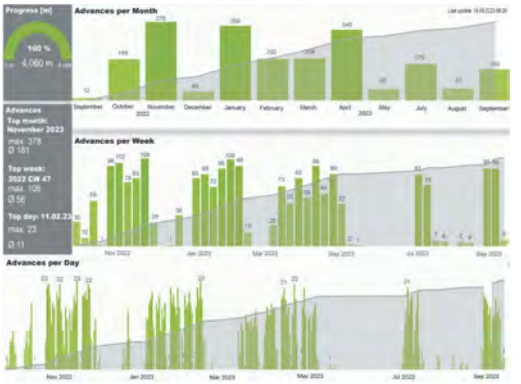

Figure 19. TBM 2 production summary (Oct-23).

8 CONCLUSIONS & LESSONS LEARNED

Our TBM S-972 “Delia” is cutting the edge, proving that an EPB machine can successfully mine through granular soils, mostly gravels and above all, lacking what was considered the minimum amount of fines needed (30%) to mine in pure EPB mode, mostly thanks to the great development of conditioners in recent years, but also to a correct cutterhead and cutting tools selection and configuration and to a quick reaction to every change of conditions in the field.

As for the conditioning, it should be noted that it all started with extensive preliminary studies performed by conditioners manufacturers and Universities, but that they had to be flexible to accommodate site conditions and must be customized on site later on, in real time, according to the actual ground conditions the TBM is encountering at any given moment and the experience gained while mining though them.

To be able to work with an EPB in gravel and without fines and to do it safely, not only the Foam Injection rate (FIR) but the overall rate of ground treatment, including water, bentonite, or polymer,

shall be remarkably high, almost always above 100. And that accounts for both, the conditioning of the excavated ground and the saturation of the granular and unstable soils in the face and around the shield.

Ground conditioning must continue not only while mining but also during ring building and long stoppages, to prevent pressure losses that could compromise face stability, initiating overexcavation for the next ring. Conditioners shall be injected to the excavation chamber as needed to maintain it pressurized.

In addition, TBM must be sufficiently prescribed and dimensioned, especially thrust and torque, to be able to deal with an excavation chamber completely full of pressurized muck, which is the best way to prevent over excavating in unstable and crumbling ground conditions.

When pore water pressure adds up to the ground conditions depicted above, second screw conveyor helped to control and reduce the face pressure to atmospheric and to control the flow of muck and therefore, to ensure face stability. This was also successfully proven in similar circumstances in the excavation of the SR99 Bored Tunnel in Seattle, WA (USA).

Finally, full slurry mode is planned to be implemented when water pressure will be even higher, coming up next in the excavation of Line 4 and natural ground even more unstable than it has been so far, besides mining under and close to extremely sensitive utilities and structures, to ensure the finest face pressure control possible.

ACKNOWLEDGMENTS

The authors would like to thank Consorcio Constructor M2 Metro Lima (CCM2L), Consorcio EPC, Metro de Lima Linea 2 S.A., Herrenknecht AG, Lombardi and specially, our three companies, Dragados, FCC and WeBuild, for making this amazing project happen.

REFERENCES

Consorcio Nuevo Metro de Lima. Proinversión. Documento A, Diseño de Ingeniería número A.4. Geología y geotecnia del proyecto.

Consorcio Nuevo Metro de Lima. Proinversión. Documento A, Diseño de Ingeniería número A.6.5. Selección de TBM.

Freimann, S., M. SC of Institute for tunneling and construction management. Laboratory investigations on soil conditioning Metro Lima line 2/4. Ruhr-Universität Bochum, Germany.

Escoda, R., Magro, J.L., Vázquez J., 2017. SR99 AWV Replacement Performance and Challenges of “Bertha”, the largest TBM Ever. Proceedings of the Rapid Excavation Tunneling Conference in San Diego, CA, USA, pp. 472–487.

Herrenknecht AG, 2016. S972 Escudo de presión de tierra Lima Metro Line 2/4 Ø10210 mm. 77963 Schwanau, Germany.

Herrenknecht AG, 2016. S973 Escudo de presión de tierra Lima Metro Line 2/4 Ø10210 mm. 77963 Schwanau, Germany.

Tunnelling for a Better Life – Yan, Celestino, Thewes & Eberhardt (Eds)
© 2024 The Author(s), ISBN 978-1-032-80042-4
Open Access: www.taylorfrancis.com, CC BY-NC-ND 4.0 license

Large diameter slurry TBM tunnels with very low cover: A comparison of approaches

Michael Mains*
AECOM, Burnaby, Canada

S. Sánchez, L. Içik & C. Mora
AECOM ECC Europe, Madrid, Spain

ABSTRACT: A critical aspect of the design of large diameter pressurized TBM tunnels in low-cover areas is whether the minimum required face pressure can be maintained below the maximum heave/frac-out pressure while accounting for TBM operational tolerances. In shallow tunnels, usually defined as having less than 1.5 times the excavation diameter of overburden, the minimum calculated pressure is typically very close to or exceeds the maximum permissible pressures as defined by frac-out or heave limit. Further, the available closed form solutions produce a wide variety of results making it very difficult to properly evaluate the risks and stability of a given low-cover alignment. The following paper provides a brief overview of some of the most common methods for determining the minimum confining pressures and frac-out limits for pressurized TBM tunnels including both closed form and 3D Finite Difference Modelling. The results of each method from a recent project in Latin America involving a Ø13.5m slurry TBM with less than 1.5 diameters of cover in a dense urban environment are presented for comparison. The paper concludes by emphasizing that 3D numerical modelling is essential for evaluating risk in these critical areas and that in all cases strong engineering judgement is required.

Keywords: Low Cover Tunnelling, Large diameter TBM, Slurry Pressure, Face Stability, Frac-out

1 INTRODUCTION

There is an industry trend in many parts of the world towards single bored tunnels rather than twin tube tunnels in the transportation sector. There are many advantages to the single bore option including a generally lower cost, faster construction schedule, and the deletion of several types of complicated structures like cross passages and crossover boxes. One of the primary disadvantages, however, is that single tube projects require a deeper tunnel alignment and consequently deeper stations and shafts. Unlike tunnel excavation, the complexity and cost of station and shaft construction is quite sensitive to depth. Deeper stations not only require higher excavation volume, but all structural elements for both support-of-excavation and permanent internal structures become heavier and more costly. Construction of these deep station boxes also carries higher risk of impacting neighbouring buildings and infrastructure. These implications are especially true in soft ground projects where slurry TBMs are commonplace. Consequently, an option to minimize these impacts is to place the tunnel alignment as shallow as possible near stations and shafts.

Placing large diameter tunnels in low cover areas (generally defined as having less than 1.5 diameters of cover) often triggers a whole host of additional risk analyses and often incurs additional costs associated with the tunnel rather than the station. However, the most critical aspect of the design is whether the minimum face pressure to maintain stability can be achieved without causing the ground to heave or frac-out. Only by first assessing this minimum feasibility requirement can other evaluations regarding safety, settlements, and the potential need for installation of pre-support and/or ground improvements be carried out.

The following sections provide a brief overview of some of the most common methods for determining the minimum confining pressures and frac-out limits for pressurized TBM tunnels including both closed form and 3D Finite Difference Modelling.

*Corresponding author: Mike.Mains@aecom.com

DOI: 10.1201/9781003495505-260

The results of each method are shown for a recent project in Latin America involving a Ø13.5m slurry TBM with less than 1.5 diameters of cover are presented for comparison.

2 MINIMUM CONFINING PRESSURE FOR FACE STABILITY

The calculation methods available to determine face stability and the minimum face pressures have not been covered in detail in any North American or European design codes or standards (For example AASHTO, FHWA, and EuroCode 7 do not cover the topic), nor has it been the subject of any ITA/AITES recommendation. Although specific to the German Context, DAUB's (the German Tunnelling Committee) "Recommendations for Face Support Pressure Calculations for Shield Tunnelling in Soft Ground" (2016) provides the closest thing to comprehensive summary of face stability calculations and seems to be the most referenced document on the topic in many projects in Europe and the Americas. France's Centre for Tunnel Studies (CETU) also issued a useful and informative document in 2022 on face stability, although not specific to pressurized TBM tunnelling and has yet to be adopted widely outside of France.

In practice, most face stability calculations are either executed using closed form approaches, the numerical modelling approach, or in critical areas a combination of both.

2.1 *Closed form approaches*

2.1.1 *Drained condition without seepage*

Pressurized TBM excavation can typically be categorized into either undrained or drained conditions. The choice between drained and undrained conditions can have a considerable impact on support pressure estimation. In the authors' experience, most soft ground tunnels fall into the "cohesive-frictional" soil category where the drained state is uncertain. In low permeability soils ($k<10^{-6}$m/s), the ground is probably in an undrained state if the TBM is advancing. In higher permeability soils or during TBM stoppages, drained or at least a partial drained is more likely.

For a drained condition in a cohesive-frictional soil, the calculation is done in effective stress according to a limit-equilibrium philosophy. First introduced by Horn (1961), the limit-equilibrium essentially models a failure wedge develops ahead of the excavation face and is surcharged by the overburden soils. The sliding of this wedge into the tunnel is resisted by friction and when this friction is insufficient a support pressure from the TBM is required to keep the wedge in place. The simple balance of forces approach is illustrated in the figure below.

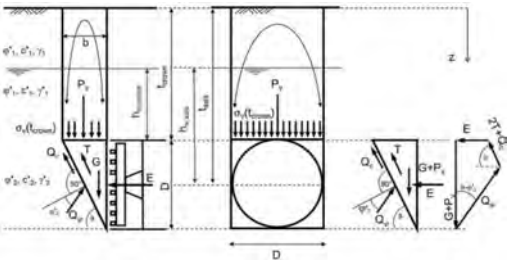

Figure 1. Driving and resisting forces on an active wedge (DAUB, 2016).

To prevent seepage into the tunnel, the TBM support pressure also has to maintain hydrostatic equilibrium. Thus, the required pressure is equal to the minimum to support the sliding wedge plus the hydrostatic pressure. Typically, the support pressures for ground and water are factored by 1.5 and 1.05 respectively. The step-by-step procedure and all relevant equations are summarized well in the DAUB (2016) recommendation.

2.1.2 *Undrained condition*

Although it is much less common that the full face and overburden meets the criteria for an undrained analysis, it is nevertheless an important case to evaluate in cohesive dominant soils since it could be the prevailing failure mechanism. The undrained calculation is carried out in total stress using the undrained shear strength, Cu (φ=0) and the stability ratio philosophy. The stability ratio is essentially expressed as the vertical stress at tunnel axis minus the support pressure, all divided by the undrained shear strength, as shown in the following equation.

$$N = \frac{\sigma_s + \gamma \cdot H - \sigma_r}{C_u} \qquad (1)$$

Where N is the stability ratio, σ_s is the surcharge on surface, $\gamma \cdot H$ is the vertical stress at tunnel axis, and σ_T is the confining pressure exerted by the TBM.

If the critical stability ratio, N_{crit}, below which the face collapses is known, the minimum face pressure can then be back calculated from Equation 1. CETU (2022) provides an excellent comparative summary for N_{crit} as a function of the cover/diameter (C/D) ratio as calculated by the various approaches, project observations, and scale mode lab testing found in the literature.

This chart not only provides a quick and easy way to estimate face pressure, but also helps illustrate an important risk relating to low cover tunnelling. A large variability in N_{crit} exists for any given C/D depending on the method used. In deeper tunnels, a conservative approach is to simply use the lower bound line shown in Figure 2. However, in the low cover case even

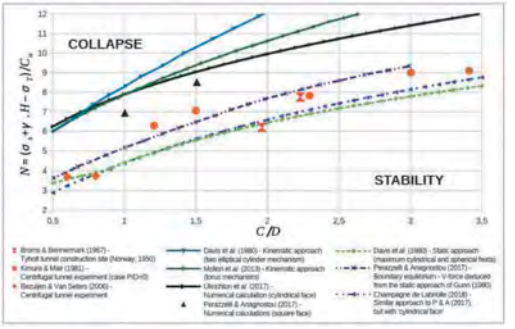

Figure 2. Comparison of N_{crit} lines based on existing models (CETU, 2022).

the higher bound lines may produce pressures which approach or exceed the blow-up/frac-out limit of the ground thereby requiring a more sophisticated way of managing risk and defining operational pressures of the TBM.

3 MAXIMUM PERMISSIBLE CONFINING PRESSURE

The other principal failure mechanism that is critical in low cover is when excessive pressure heaves or ruptures the overburden soils, more commonly known as blow-up or frac-out. In low-cover, a small amount of heave can be expected and as long as it remains minimal, say below 5mm, it is not considered an issue in most cases. However, larger amounts of heave can cause damaging deformations for nearby structures. Even worse, frac-outs cause a "spill" incident with possible environmental issues and could erode/compromise nearby foundations. The TBM could also become stuck and require a rescue shaft. All of these risks are more prevalent in low cover areas and are much more consequential at larger diameters.

DAUB (2016) proposes the simplest method to estimate the limit pressure by recommending that the maximum permissible TBM pressure at the crown remain below 90% of the overburden stress. However, in shallow tunnels, it is relatively common that the minimum stability pressure exceeds the overburden stress. In this case, Hong Kong's Geo Report No. 249 (2009) acknowledges that the factored shear strength of the ground can be mobilized to resist failure of the ground upwards in an ULS calculation. An example of this approach is Mollon (2013):

$$\sigma_b = \gamma\, D \cdot N\gamma - C_u \cdot Nc \qquad (2)$$

Where σ_b is the blow-up pressure, γ is the soil unit weight, D is the tunnel diameter, and C_u is undrained shear strength and N_γ and N_c are estimated from the below design chart.

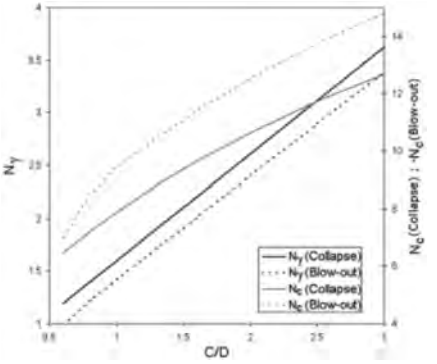

Figure 3. Design chart for N_γ and N_c Mollon (2013) for cohesive soils.

However, in purely cohesive soils, maximum permissible pressure can be governed by the fracturing mechanism caused by high localized pressure which exceeds clay shear or tensile capacity.

A simple approach for purely cohesive soils is that provided by Soga et al. (2005) where the blow-up pressure P_f is calculated using Equation (3).

$$P_f = s_0 + n \cdot C_u \qquad (3)$$

Where n=1.25 can be assumed (Atkinson et al. 1994).

There are however two major issues with relying on shear strength to set maximum operating pressures. The first is that although the factor of safety against rupture may be satisfactory, the maximum pressure limit may induce significant heave deformations. The second is that cohesive soils at low cover are often weathered and contain weaker seams which may have much lower shear strength that the representative value of the soil. Other preferential slurry paths may also exist such as existing boreholes, pipe bedding, or any other granular or weak zones that can be extremely difficult to detect prior to excavation.

4 NUMERICAL CALCULATIONS

As discussed in the previous sections, the available closed form approaches to calculate minimum face pressures produce a large margin of values. Further, the maximum limit pressure may generate large heaving displacements not captured in the closed-form calculation. Thus, it is clear that the available closed form solutions do not provide adequate information to properly assess risk in critical areas such as low cover zones, especially at large diameters.

3D finite element or finite difference modelling is an important method to add to the toolbox because it can account for all pressures in the excavation (face, around the shield, and grouting pressures), as well as account for mixed face conditions and complicated geometries.

By iterating the 3D model with varying excavation pressures, the deformation at face and surface can be traced as a function of pressure, creating a sensitivity curve which can be compared to an "admissible" zone relating to deformations. This allows an SLS approach for the definition of both the maximum and minimum TBM operating pressures. It is also the only method which allows for the extent of ground yielding to be investigated.

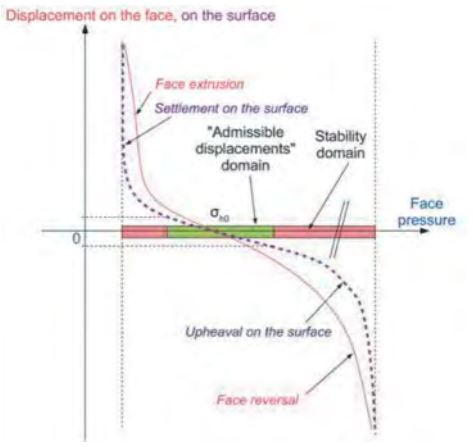

Figure 4. Example sensitivity curve (CETU, 2022).

Numerical modelling is however not without its limitations. For example, the risk of hydraulic fracture along weak zones or slurry loss through pre-existing or unknow paths are very difficult to model meaningfully in practice. It is still nevertheless a powerful tool which compliments the existing analysis types and may even be necessary in critical locations of the tunnel alignment.

4.1 *The settlement problem*

The use of 3D numerical modelling often reveals a common issue seen in low cover scenarios. For example, we sometimes see large settlements generated at surface even though the TBM pressure is within the acceptable operational range. Peculiarly, this settlement can get worse if we increase the confining pressure which is the opposite of what we would normally expect for a deeper tunnel in more competent ground.

Consider a scenario where the TBM pressure is exactly equal to the vertical in-situ stress at the crown. The forces at node located in the crown of the excavation perimeter would be perfectly balanced. Now consider the nodes at spring line elevation for a soil with k_0=0.5 where the horizontal stress is about half of the vertical stress. the slurry fluid pressure will have increased as a function of its unit weight and the ground load will have decreased due to the k_0 condition. Thus, there is a nodal force imbalance which pushes the sides of the tunnel outward to re-establish equilibrium. In soft ground, this effect causes the crown to "sag" which translates to settlements on surface and increasing the TBM pressure only makes deformations increase.

The effect is demonstrated in a FLAC Model shown in Figure 5.

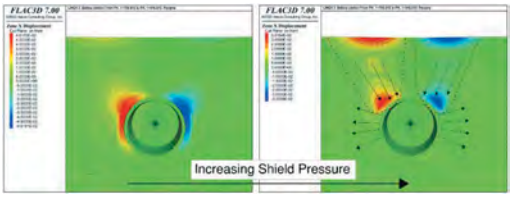

Figure 5. Deformation trend in low cover for increasing TBM pressure.

5 COMPARISON BY EXAMPLE

As described in the previous sections, to adequately design large diameter alignments at low cover in soft ground, it is necessary to carry out both ULS and SLS analyses for face stability and frac-out/heave to define the TBM pressure operating window. An example analysis from a project in Latin America involving a Ø13.5m slurry TBM in soft ground is presented herein. The example shown is in mixed face conditions of predominantly soft cohesive soils with some weathered rock in the invert.

In mixed face conditions, the closed form approaches become even less reliable as they are only suitable for homogenous ground. In practice, mixed face conditions are usually handled by either averaging the soil parameters or taking the lower bound strength directly. If part of the face is in rock, the results can be skewed since rock strength is often an order of magnitude higher and could incorrectly imply that the face is stable when it isn't. Although these closed form approaches are important to understand what failure mechanisms may be governing, they must be supplemented by a numerical model to provide an adequate understanding of the problem.

5.1 *Finite difference analysis*

To address the aforementioned limitations of closed form calculation, finite difference modelling was used to further evaluate feasibility and risk of the Ø13.5m tunnel directly adjacent to one of the station boxes. TBM excavation would be excavated in mixed face conditions of soft fractured rock in the invert with the remainder of the face and overburden consisting of very soft fine grained and residual soils. The excavation cover is less than 1.5 diameters.

The analysis was carried out using FLAC 3D V7.0 and iterated by applying a steadily decreasing (collapse) and increasing (heave) face pressure,

starting from the operational minimum and maximum values initially estimated using the DAUB (2016) methodology.

Figure 6 shows an example of the displacement magnitude and vectors at one calculation stage with a high pressure value applied to the face.

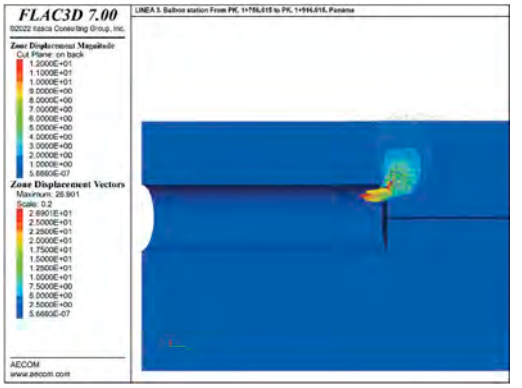

Figure 6. FLAC 3D output showing displacement vectors during maximum pressure analysis.

The operational window can then be defined by plotting the displacements compared with the applied face pressure as shown Figure 7. Here the heave limit pressure is identified in the model by noting the pressure that triggers large displacements. A similar approach can be done for the minimum face pressure to maintain stability. The model also highlights importance of coupled analyses where the stress state is updated at every stage according with the compatible pore pressure.

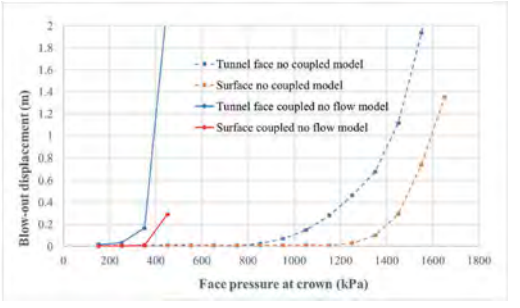

Figure 7. Displacements at face and surface obtained in FLAC analysis.

5.2 *Comparison of results*

The comparison of results using various closed form methods as well as the 3D FLAC results can be found below in Figure 8.

We note that the numerical model correlates reasonably well with the lower bound stability limit pressures. However, the comparison of heave limits is much less clear. Numerical analyses suggest

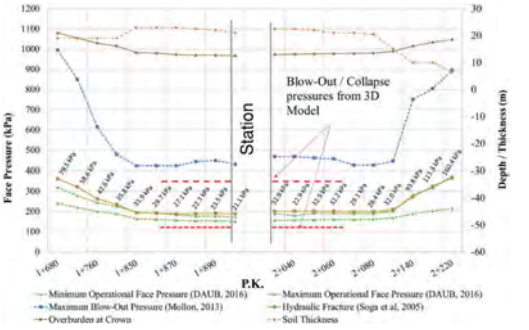

Figure 8. Comparative analysis of face pressure.

a heave limit as much as 100kPa below the limit calculated using Mollon (2013) and about 100kPa higher the hydraulic fracture limit (Soga et al. 2005).

Additionally, iterations of the FLAC model all produced very large settlements on surface due to the phenomenon discussed in section 4.1 which ultimately led to additional risk mitigation measures being required. Thus, even though the FLAC analysis is the only method capable of capturing these large deformations, it was in this case is not capable of capturing the potentially more critical hydraulic fracture failure mode. This further underscores that no single calculation method is capable of analysing all probable failure mechanisms and that a combination of approaches should always be considered at critical locations of the alignment.

6 CONCLUSIONS

With shallow tunnels becoming an increasingly common means to lower the cost of stations and ancillary shafts, the particular problem of excavation stability in low cover requires special attention. The risks associated with a failure of the face, either from collapse or frac-out/heave, are significantly higher with larger diameter tunnels. The design of large diameter slurry TBM tunnels in low cover is not codified and recommendations are notably absent from the ITA/AITES working groups. The available closed form solutions provided in commonly referenced guidelines from Germany, Hong Kong, and France give varied results and are not sufficient to fully evaluate the risks associated with shallow excavation. Supplementing these calculations with finite element or finite difference modelling is essential but still doesn't capture all of the potential failure mechanisms. Thus, a healthy dose of engineering judgement and experience is always required regardless of how much computation has been carried out.

REFERENCES

DAUB, 2016. Recommendations for Face Support Pressure Calculations for Shield Tunnelling in Soft Ground. German Tunnelling Committee (ITA-AITES), Germany.

CETU, 2022. Tunnel Face Stability; collapse mechanisms, design and construction principles. Ministère Chargé des Transports: Centre d'Études des Tunnels, France.

Golder Associates, 2009. Geo Report No. 249: Ground Control for Slurry TBM Tunnelling. Government of Hong Kong Special Administrative Region, Hong Kong.

Horn, M., 1961, Alagutak homlokbiztositstasra hato vizszintes földnyomasgalat néhany eredménye, Azorszdgos mélyépitoipari konferencia éloadasai, Közlekédési Dokumentacios Vallalat, Budapest (in Hungarian)

Mollon G., Dias D., Soubra A.H., 2013, Continuous velocity fields for collapse and blowout of a pressurized tunnel face in purely cohesive soil, International Journal for Numerical and Analytical Methods in Geomechanics, vol 37, n°13, pp. 2061–2083

Soga, K., Ng, M. Y. A., and Gafar, K., 2005. Soil fractures in grouting. Proc., 11th Int. Congress on Computer Methods and Advances in Geomechanics, Turin, Italy, 397–406.

Atkinson, J. H., Charles, J. A., and Mhach, H. K. 1994. Undrained hydraulic fracture in cavity expansion tests. Proc., 13th Int. Conf. on Soil Mechanics and Foundation Engineering, Vol. 3, Oxford & IBH, New Delhi, India, 1009–1012.

Tunnelling for a Better Life – Yan, Celestino, Thewes & Eberhardt (Eds)
© 2024 The Author(s), ISBN 978-1-032-80042-4
Open Access: www.taylorfrancis.com, CC BY-NC-ND 4.0 license

The mechanised excavation of the exploratory tunnel of the Brenner Base Tunnel: The major challenges

David Marini*
BBT SE, Bolzano, Italy

Andrea Lussu
BBT SE, Innsbruck, Austria

Giuseppe Venditti
BBT SE, Bolzano, Italy

ABSTRACT: The exploratory tunnel of the Brenner Base Tunnel was excavated for over 40 km in mechanised mode, using both double shield TBMs and an open TBM. The peculiar characteristic of this tunnel is precisely that its excavation occurs immediately before that of the main tunnels, with the primary purpose of providing greater certainty in terms of geological-geotechnical data for their excavation. During the excavation of the exploratory tunnel, some specific situations occurred which blocked the TBMs and required special measures to unblock them. This article describes the most striking construction challenges encountered, presenting the main interventions that were applied in the field to allow excavations to resume.

Keywords: Brenner Base Tunnel, exploratory tunnel, double shield TBM, open TBM, construction challenges

1 THE BRENNER BASE TUNNEL

1.1 *Introduction*

The Brenner Base Tunnel is a flat railway tunnel that connects two States and is the central part of the new Munich-Verona railway corridor, along the extended Scandinavian-Mediterranean corridor within the European TEN-T transport network. It stretches between Innsbruck (Austria) and Fortezza (Italy) for a total length of 64 km (including the Innsbruck bypass) and will be the longest underground railway link in the world.

The BBT is a complex system of tunnels with a total length of almost 230 km, of which 160 have been completed to date, the main ones being the two railway tunnels and the exploratory tunnel. It will offer a viable alternative for freight transport and will create a new travel opportunity for passenger traffic.

The main benefits of the project include the shift of freight and passenger traffic to rail, eliminating traffic congestion, to the benefit of people and the environment, greater safety from natural hazards and a significant reduction in journey times. Today, travelling by train from Fortezza to Innsbruck takes 80 minutes for passenger traffic and 105 for freight traffic, while in the future, when the tunnel is completed, it will take 25 and 35 minutes respectively.

1.2 *The purpose of the exploratory tunnel*

The excavation of the exploratory tunnel extends from the Sillschlucht (at Innsbruck) to Aica (near Fortezza) and runs along the axis of the main tunnels for about 85 per cent of the route. By anticipating the excavation of the line tunnels, it considerably reduces geological-geotechnical and hydrogeological uncertainties and thus limits the risks in the excavation of the main tunnels.

Depending on the complexity of the rock mass to be excavated and on logistics, the excavation is performed either using traditional methods or with tunnel boring machines.

The most critical fault zones to cross were the Periadriatic Lineament in Italy and the Hochstegen fault zone in Austria, both excavated using traditional methods.

*Corresponding author: david.marini@bbt-se.com

DOI: 10.1201/9781003495505-261

Important stretches of respectively 24.5 km in Italy and 16.5 km in Austria were excavated by machine, and still provided useful and effective information of the rock mass in advance of the main tunnel excavation.

2 GEOLOGICAL FRAMEWORK

The Brenner Base Tunnel route is geographically located in the central part of the Eastern Alps and it crosses the Alpine arc from Innsbruck (Austria) to Fortezza (Italy), east of the Brenner pass.

From a geological point of view, the Brenner Base Tunnel crosses the major tectonic units that make up the Alpine chain. These units, which take the form of several overlapping strata, represent the remnants of the collision zone between the Eurasian (European) and Adriatic (African) plates, forming a dome at the centre of which the Pennidic and Subpennidic units of the Tauern window appear, the deepest tectonic units forming the core of the Alpine chain. The deepest structural sectors of the Tauern Window are represented by the central gneiss cores (Tux core to the north and Zillertal core to the south), which constitute the sub-Pennidic paraautochthonous basement, continental tectonic units of European origin, cloaked by the oceanic Pennidic units of the Vizze and Glockner Plateau complex, on which lie the Austroalpine units of African origin (Adria). To the south, the important fault zone forming the Periadriatic Seam separates the Austroalpine from the Southalpine.

The current structure of the Alpine mountain range is the result of the polyphasic deformation process that occurred during Alpine orogenesis (see Figure 1).

3 THE EXPLORATORY TUNNEL IN ITALY AND AUSTRIA

3.1 *The excavation of the exploratory tunnel inconstruction lots in Italy*

3.1.1 *Exploratory tunnel construction lots*

In the construction lots B0021 'Aica-Mules Tunnel' and B0131 'Mules Lot 2-3′, most of the exploratory tunnel was excavated with TBMs. Mechanised excavation began in the Aica-Mules lot on 10/06/2008 starting from Aica northwards, and after 10,269 m of excavation the section was completed in November 2010. In the Mules 2-3 lot, the 'Serena' TBM began its journey on 25/05/2018 in the vicinity of the Trens emergency stop and after advancing 14,209 m northwards, it reached the end of the lot in November 2021 by the Brenner.

3.1.2 *The TBM used in the mechanised sections of the exploratory tunnel*

Two double shield TBMs with an excavation cross-section of 6.6 m and 6.8 m respectively were used for the excavation of the exploratory tunnel in Italy. The thickness of the tubbing rings varies from 20 cm to 30 cm, as does the geometric arrangement of the segments and their performance characteristics (see Figure 2).

Advance surveys and geoseismic investigations, excavation front surveys during maintenance activities and interpretation of tunnelling data were systematically carried out.

3.1.3 *Excavation difficulties encountered*

In various situations, these advance investigations and the interpretation of real-time data made it possible to solve excavation difficulties with special interventions (over-cutting, advance consolidation by means of GRP anchors, foam injections, hydro-demolition and micro-loading behind the shield, etc.).

In the mechanised excavation of the total 24.5 km of exploratory tunnel in Italy, some unusual circumstances occurred, which forced the TBMs to stop and required special interventions to restart them.

The two most significant standstills are described below.

3.1.4 *Exploratory tunnel section from km 49 to km 59 (Aica-Mules construction lot)*

On 7 August 2009, after excavating approximately 6 km of the tunnel (at km 53+149, corresponding to km 6+190 from the Aica portal), during the TBM advancement phase, some cracks were observed in the left face at approximately 20 m from the face; 24 hours later, these had extended in the direction of the face, until they reached the TBM shield.

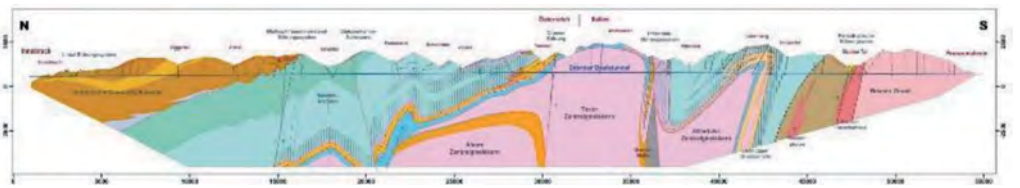

Figure 1. Geological profile along the axis of the Brenner Base Tunnel; legend with the structural units: brown-orange…Innsbruck quartz phyllite; blue-greenish…limestone schist; orange-blue…Hochstegen fault zone; pink…central gneiss, brown…paragneiss; red…tonalite with Periadriatic Lineament; pink…granite.

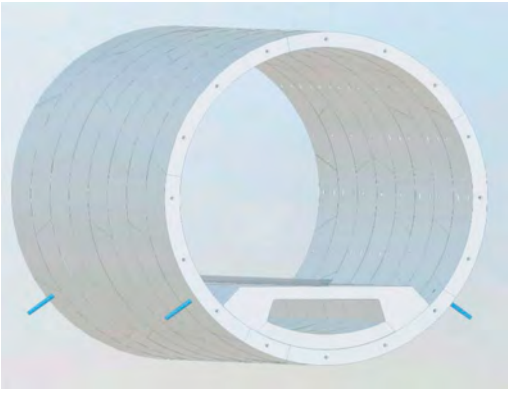

Figure 2. Model of the tubbing ring lining of the Exploratory Tunnel - Lot Mules 2-3.

The cracks and fractures moved in an exclusively horizontal direction and directly affected the body of the reinforced concrete cones even when they occurred near the joints. A resumption of the phenomenon limited to the approximately 10m portion of the tunnels occurred on 18/08/09 following the execution of a geognostic borehole on the left wall, which intercepted a pressurised water flow at a depth of approximately 20m from the wall itself. On this occasion, the cracks already present in the tubbing rings widened to the point of generating a real fracture, forcing four rings to protrude into the tunnel itself. (see Figure 3).

Figure 3. Damaged and shifted precast concrete segments.

Basically, in the last 150 m the rock mass surrounding the tunnel was generally good quality granitic rock (although it did cross two more fractured bands approximately 20 m thick located sub-vertical and sub-orthogonal to the route), though it was however almost tangential on the left wall to a sub-vertical fault sub-parallel to the route, 5-10 m thick, consisting of bands of very fractured rock and bands of completely transformed dark green tectonic breccias.

The position of the fault with respect to the direction of advancement made it impossible to predict through the tunnel face mapping, which had highlighted the sub-orthogonal fractured bands. On the other hand, seismic surveys systematically carried out during excavation are unable to detect reflectors parallel to the tunnel axis.

The additional investigations carried out allowed subsequent reconstruction of the geological situation.

Before the re-start, safety measures had to be taken consisting of radial bolts, retraction of the back-up wagons and installation of HEB100 profile ribs.

Restoration work then took place, consisting of:

- disassembly of those parts of TBM that had not been blocked by the shifted precast concrete segments,
- injections of expanding organic-mineral resin to solidify the areas subject to the most intense loosening, directly behind the precast concrete segmental rings on the left wall,
- injections of organic-mineral resins in a 3m thick strip on the left wall
- installation of RN32 self-drilling radial anchors, 3 m to 6 m long.
- cutting, demolition and replacement of the reinforced concrete segments with excessive displacement and/or breakage, for successive portions of reduced size with steel panels (see Figure 4).

Figure 4. Repaired stretch with steel panels.

These interventions made it possible to secure the precast concrete segmental rings, carry out the

necessary work on the TBM including back-up, and re-start excavation.

No special work was required at the TBM shield before restarting. After less than four months of downtime, it was possible to re-start excavation of the TBM.

For the following section, metal segments specially dimensioned to support high loads were laid over an extension of approximately 60 m (see Figure 5).

Figure 5. Stretch with steel ribs.

3.1.6 *Exploratory Tunnel section from km 32 to km 46 (Construction Lot Mules 2-3)*

On 27 March 2019, after approximately 4.2 km of mechanised excavation of the exploratory tunnel with the 'Serena' TBM (at km 42+007, corresponding to km 17+332 from the Aica portal), main piston thrusts of 21,000 kN were recorded, which required excavation to continue with re-gripping equipment and in single-shaft mode. On 30 March, the thrusts, still proceeding in single-shield mode, reached values of 70,000 kN, no longer allowing advancement. The pressure cells on the front shield went all the way to the end of their scale, registering a pressure of 6 MPa.

A geological reconstruction shows a meta-archite rock mass with interlayers of quartz and mica schist in bands with horizontal schistosity. Due to the high overburden (1500m) and the horizontal schistosity, large blocks detached from the dome and on the left side of the TBM, favoured by the millimetric layers of mica with smooth, cohesionless joints, also causing an asymmetrical pressure on the shield.

In the first few days of the standstill, attempts were made to remove and lighten the material on the left side of the front shield by means of micro-charges.

The geological and seismic investigations carried out, and the reconstruction of the rock mass behaviour determined that the most effective approach to unblocking the TBM would be the construction of an approximately 13m lateral tunnel immediately behind the shield in order to decrease the pressures acting on around the shield.

The works that allowed the re-start of the tunnel boring machine were designed by the construction contractor, based on the specific solutions aimed at solving TBM standstill situations which had been presented in the technical section of their bid during the tender procedure.

This lateral tunnel was built on the left wall (west side of the TBM) and secured mainly with ribs and steel sheets placed on steel arches which are driven upwards and outwards into the rock at a flat angle until a new steel arch can be placed underneath (see Figure 6). More specifically, the following interventions were carried out:

- preparation of the 1.5mx2m side opening on the left face of the precast concrete segmental ring behind the shield: injection with epoxy resins, installation of 2m radial anchor bolts, installation of UPN 140 beams around the opening (see Figure 7);
- cutting and removal of precast concrete segment;
- drilling and micro-loading;

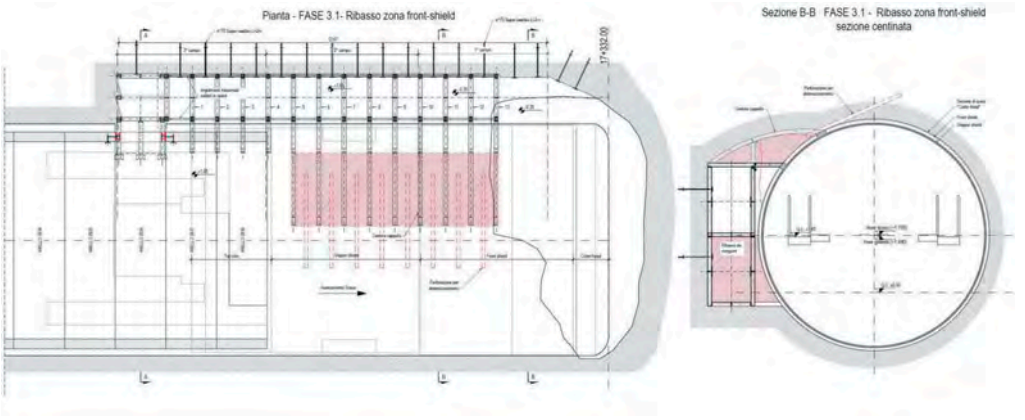

Figure 6. Diagram of the repair works.

Figure 7. Junction to the lateral tunnel.

- Securing with HEB 120 ribs and the above mentioned steel sheets on steel arches, with 0.75m spacing along the entire length of the shield (see Figure 8).

Figure 8. Lateral tunnel parallel to the TBM shield.

In addition to freeing the shield along the left wall and in the dome, it was necessary to lower the lateral tunnel, to further decrease the contact between rock and shield.

A special metal push frame was constructed to perform re-start attempts. It was then necessary to backfill the exploratory tunnel with pea-gravel and cement mortar, after properly protecting the shield.

After 44 days of stoppage, excavations could be resumed.

3.2 *The excavation of the exploratory tunnel in construction lots in Austria*

3.2.1 *Exploratory tunnel construction sections*

In Austria, the exploratory tunnel was excavated in 3 sections. A first section in the northernmost area, i.e. in the Innsbruck quartz phyllite, had already been excavated conventionally by blasting in 2009. A 16.5 km long section in the central area between the Innsbruck emergency stop and St. Jodok was excavated between 2015 and 2019 using an open gripper TBM.

3.2.2 *Mechanical excavation of the exploratory tunnel section from km 8 to 23*

The decision to drive the section between km 8 and 23 with an open gripper TBM was based on the acknowledgments from the first conventionally driven exploratory tunnel section in the quartz phyllite and the geological explorations from the surface. The decision to use an open TBM was made in order to guarantee best possible documentation and sampling of the open area behind the shield in order to obtain accurate geological - geotechnical information for the main tunnel tenders. Furthermore, an open TBM was put out to tender in order to be able to react more flexibly during excavation through predicted fault zones, the location of which was not known. Appropriate supporting measures such as injections and drilling shields for difficult sections were also included in the tender.

During excavation between September 2015 and July 2021, a total of 9 relevant fault zones were encountered, which led to collapses and delays.

The first relevant fault was encountered about 1 km after the start of driving at project kilometre 9. In this section, a rock structure with shallow dipping, poorly interlocked schistosity was encountered in conjunction with clustered shear traces and a fault zone with a thickness of approx. 10 m. This unfavourable combination and the shallowly dipping course of the fault zone led to a large-volume collapse above the TBM shield with a cavity volume of approximately 750 m³ (see Figure 9), and lead to

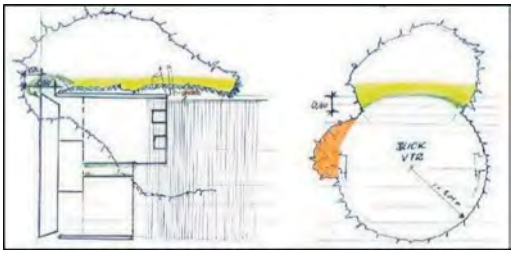

Figure 9. Fault zone progression at km 9.000; legend: green…foam; yellow…concrete; orange…cement injections.

notable deformations of the primary structure in the area behind the shield (see Figure 10).

Figure 10. Deformation of the steel profiles in the top heading.

At the beginning, collapses and advance fractures were recorded around the drill head; the belt scale recorded the production of significantly higher tonnage of excavation material compared to the theoretical excavation volume. First smaller collapses, so-called "Zipfelmützen (jelly bag caps)", were overcome by "controlled spoil removal" without significant driving disturbances. In the area of the damage zone, despite intensified constructive measures behind the shield to prevent outbreaks, further collapses and an enlargement of the cavity occurred due to the spoil removal. When it became foreseeable that a cavity would expand backwards over the shield, the excavation process was stopped for safety reasons and the following immediate measures were initiated:

- a barrier was created with radially bored and injected IBO anchors in the area behind the finger shield to prevent the cavity from spreading to the rear;
- intensification of deformation measurements to keep the effects of the cavity on the tunnel lining under control.

Before further crossing of the cavity, the project team identified, planned and evaluated various solutions and options (pipe shield, bypass) for crossing the areas of fault zone interference. The greatest challenge here was to ensure worker safety behind the finger shield. As excavation continues, the collapse in the area of the crown moves backwards beyond the finger shield. Finally, it was decided to apply the "continuous steel profile" solution. In the "continuous steel profile" solution, UNP 180 special profile ribs were installed shoulder-to-shoulder between the existing shotcrete shell and the finger shield in the "open area" with the required shotcrete backing (double metal grid mats and fleece insert or expanded metal) (see Figure 11).

Figure 11. "Continuous steel profile" solution UNP 180 profiles set shoulder-to-shoulder.

These special profiles have the same steel cross-section and therefore the same axial resistance as the tendered TH ribs; like the TH ribs, the UNP 180 profiles were equipped with adjustable clamps to allow deformation at very high support pressure. Compared to the TH profiles, the UNP 180 profiles have a lower modulus of resistance, at the other hand they have the advantage that they can be additionally secured with IBO anchors. The holes for the IBO anchors were designed as slotted holes to ensure that the ribs can deform inside each other.

The excavation was continued slowly and the UNP 180 profiles were positioned shoulder-to-shoulder under the protection of the finger shield. After placing 6-7 UNP-180 profiles, metal grid mats were placed and the whole section was covered with a sprayed concrete layer to reinforce the steel structure. This strengthened the tunnel lining and ensured safe working in the A1 area.

After 3-4 work fields (i.e. 4-5m) had been excavated using this method and there was still no stable rock in the drill head area, the tunnel lining behind the finger shield was additionally reinforced for safety reasons by injecting and poring a concrete slab over the UNP 180 profiles to provide additional protection against collapse for the workers. Concrete was pumped into the cavity above the TBM via backfill pipes that had already been installed during tunnelling. To prevent the concrete from penetrating into the drill head, it was sealed and stabilized with silicate foam before starting the concrete casting process (see Figure 9).

The casting took place under constant monitoring of the deformations. After the concrete had hardened, driving was continued using UNP-180 profiles positioned shoulder-to-shoulder until the drill head had reached stable rock again and there was therefore no danger of jamming or caving. Before re-starting regular driving, the remaining cavity above the lining was filled with concrete and injected in a controlled manner via the backfill pipes. A total of 26 days was required to excavate through and secure

the fault zone. Jamming of the TBM was avoided thanks to the quick action of all parties involved.

At project kilometer 16.6, another collapse occurred in the Bündner Schiefer section. Shortly before the drill head entered the major fault zone, the excavation encountered folded alternating sequences of limestone phyllites and limestone schists. The main fault dipped steeply at about 70° obliquely against the excavation direction and entered the cavity from the right-hand side (about 25° to the axis). When the formation of a collapse was detected, the measures that had been tried and tested up to that point and successfully used in several collapses (analogous to the collapse described above) were immediately initiated. However, this time the fault zone progression was very steep. The thickness of the core zone was similar in size to the previous collapses, at about 4-5m, but this time the cavity spread further and further upwards as driving continued (see Figure 12).

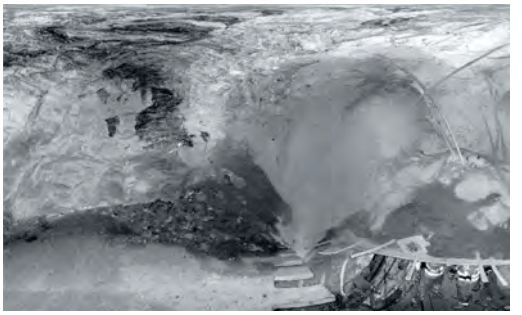

Figure 12. Laser scan of the cavity above the finger shield at the beginning of the collapse.

At a certain point the laser measurements showed heights up to 17 m and more. Subsequently fractured material fell on the shield and, in combination with lateral pressures due to the lack of vault action, led to jamming of the TBM. Despite several attempts, the TBM could not be started. Therefore, it was decided to drive two lateral side tunnels (see Figure 13) by means of micro-blasting and the use of a small excavators in order to free the drill head.

To the excavation of the lateral side tunnels lead to a decrease of the lateral pressure on the cutter head and allowed to continue the excavation process. Estimates of the mucked excavated material have revealed a cavity volume of over 5,000 m³. Due to the large amount of loose material above the lining and the shield, it was also not possible to refill or inject the cavity from the TBM as in previous collapses. The excavation through the fault zone at km 16.6 required 45 working days. Since the safety was ensured and the static load capacity of the exploratory tunnel was guaranteed by the lining and the concrete cover above it, the TBM excavation continued even without the complete refilling of the cavity.

Figure 13. Excavation of one lateral side tunnel to free the cutter head.

Even though the load-bearing capacity for driving the exploratory tunnel was ensured, an impact of the cavity on the main tunnel tubes still to be excavated above the exploratory tunnel could not be excluded, due to the great height of the collapse and the still present cavity. For this reason, after TBM driving had been completed it was decided to access the cavity by means of a ramp dug from the exploratory tunnel using the conventional drill&-blast excavation method, to backfill and ensure the cavity professionally. Furthermore, it was decided to use the ramp required for backfilling to excavate the sections of the main tunnel tubes through the fault zone conventionally at main tunnel level in order to prevent future jamming of the TBMs and thus delays in the further construction lots (see Figure 14).

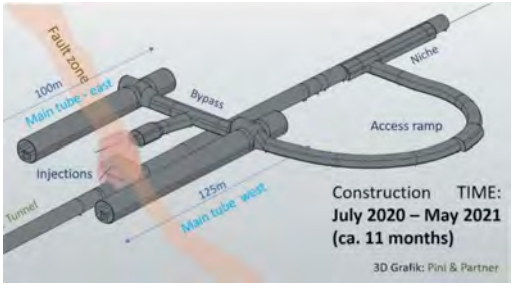

Figure 14. Ramp to the main tunnel level and excavation through the fault zone.

This measure led to significant risk reduction in the main construction lots, as it was possible to avoid the TBM stucks and excavation delays in these areas. The measures were carried out parallel to other ongoing construction activities, thus minimising the impact on the overall time schedule.

4 CONCLUSIONS

Despite various difficulties in excavating the exploratory tunnel, average advance rates of 10-12m/day could be achieved. The usefulness and necessity of an exploratory tunnel in deep-lying tunnel systems was confirmed, as it was possible to explore the geologically relevant areas in advance, with a smaller diameter excavation.

Not only did this provide valuable knowledge for the excavation and the further tender procedures of the main tunnels, but the advance excavation of the exploratory tunnel also allowed construction measures to be taken to secure fault-zones in the main tunnel tubes, from the exploratory tunnel, which led to a significant reduction in risk as well as cost and time.

On the basis of the knowledge gained during excavation of the exploratory tunnel, it was possible to redesign and move positions of assembly caverns, other necessary caverns and cross-passages before excavation of the main tunnels. In some cases, as shown, it was advantageous to anticipate the construction of singular tunnel sections, to reduce jamming risk of the main tunnel TBMs.

Last but not least, the continuous exploratory tunnel can also be used during the operational phase of the BBT to maximize the availability of the tunnel system by allowing time-relevant maintenance and servicing work on the rail tunnels to be carried out from the exploratory tunnel via shafts without impact on the rail operation.

ACKNOWLEDGMENTS

We would like to express our sincere thanks to BBT SE CEOs Martin Gradnitzer and Gilberto Cardola, both for their willingness to share the technical experience of the Project and their support of our active participation in international events in our sector.

REFERENCES

[1] Zhao K., Janutolo M., Barla G., Chen G., 2014. 3D simulation of TBM excavation in brittle rock associated with fault zones: The Brenner Exploratory Tunnel Case; Engineering Geology 181.

[2] Bergmeister, K.; Reinhold, C., 2017. Lernen und Optimieren vom Erkundungsstollen – Brenner Basistunnel - Learning and optimization from the exploratory tunnel – Brenner Base Tunnel; Geomechanics & Tunneling 10, no. 5.

[3] Lussu A, Grüllich S., Kaiser Ch., Fontana A., 2019. 15 km TBM exploratory tunnel excavation in the construction lot H33 of the Brenner Base Tunnel – Geomechanik and Tunneling geot. 201900039.R1

[4] Skuk S., Egger H., Barnabei E., Conti U. M., Foderà M. G., Liuzzi G., Maggio G., Renghi D., Spaziani A., Toro M., Voza A., 2023. Brenner Base Tunnel: three DS-TBMs excavation in parallel under the Alps in Italy – Findings, difficulties and achievements form a geological-geotechnical point of view; 15Th ISRM congress 2023 – Challenges in Rock mechanics & rock engineering.

Tunnelling for a Better Life – Yan, Celestino, Thewes & Eberhardt (Eds)
© 2024 The Author(s), ISBN 978-1-032-80042-4
Open Access: www.taylorfrancis.com, CC BY-NC-ND 4.0 license

Excavation management system for mechanized tunnelling in urban areas

Massimo Marotta*, Jeyatharan Kumarasamy, Alvin Sim, Chee Keong Poh & Kin Boon Chang
Land Transport Authority, Singapore

ABSTRACT: The Land Transport Authority (LTA) of Singapore has been planning and constructing the expansion of the rail networks since 1995. Bored Tunnelling by Earth Pressure Balance (EPB) and Slurry Pressure Balance (SPB) TBM have been extensively used to build up the network. Apart from monitoring the tunnelling operation parameters and ground related movements using monitoring instrumentation, Singapore has developed and implemented a comprehensive Excavation Management System (EMS) to ensure improve the accounting and reconciliation of the excavated soil and rock. Excavation management is a major risk mitigation measures as it allows for early identification of over-excavations which, if undetected, will potentially impact the surrounding area with risks of large settlements or sinkholes. However, the muck reconciliation is complex is nature as affected by several factors such as the variable nature of the geological conditions, the effect of advance speed, the effects of accuracy of the instrumentation used to measures flow and density, and more. For this reason, a more holistic approach is necessary where different methods based on volume or mass are employed to provide sufficient data to the tunnel engineers. This paper will the describe different muck reconciliation methods, and will discuss practical application of the Excavation Management system using Slurry and Earth Pressure Balance Boring Machines in Singapore.

Keywords: Mechanized Tunnelling, Excavation Management, Muck Reconciliation

1 INTRODUCTION

In conjunction with Singapore's vision to have sustainable, efficient and extensive Mass Rapid Transit (MRT) system across Singapore Island, more and more underground rail tunnels are being planned and constructed.

A total of 148 TBMs, both Slurry type and Earth Pressure balance, have been extensively used for tunnelling for the variuos MRT lines, from the North East Line (NEL), to the Circle Line (CCL), the Downtown Line (DTL) and the Thomson East Coast Line (TEL).

Table 1. TBM used in Singapore MRT from 1995 to 2017.

MRT Line	EPB	Slurry	Open Face
Phase 1-2	1	0	1
NEL	14	0	2
CCL	19	8	0
DTL1/CCLe	3	0	0
DTL2	8	11	0
DTL3	29	0	0
TEL/TELe	28	24	0
Total	**102**	**43**	**3**

Tunnelling under densely populated and developed cities and towns has been gathering momentum over the last two decades in Asia and other parts of the world.

With growing scarcity of land space, tunnels for transportation, conveyance of clean and wastewater and utility services are being located under public roads, buildings, and other infrastructure.

As such, any ground movement associated with tunnelling activities has to be carefully estimated and controlled in order to prevent damage or disruption.

In Singapore, mechanised tunnelling started with open shields during the nineteen eighties, supplemented by compressed air as face support mainly to deal with ground water, moved on to earth pressure balance TBMs in the nineties and to slurry machines in the new millennium which have contributed to the improved control of ground movements and groundwater control.

In Singapore, the continued use of slurry TBMs, starting from Circle Line MRT, then Downtown Line MRT followed by the East-West-North-South Power Cable Tunnels, the Thomson East-Coast MRT and the Deep Tunnel Sewage System (DTSS) phase 2, has contributed to progressive improvements to slurry TBM technology, slurry transportation systems as well as separation systems.

*Corresponding author: marotta_massimo@lta.gov.sg

DOI: 10.1201/9781003495505-262

In addition to these, another major advance is the way excavated spoil is quantified and compared to the theoretical excavation quantity at the tunnel face.

This allows early and accurate reconciliation to detect and deal with any over excavation during tunnelling, although the methods deployed for measurement of the excavated soil/rock are different under EPB and Slurry machine respectively.

The objective of Excavation Management System (EMS) is therefore to early identify potential over-excavation and take appropriate actions promptly when necessary.

This is achieved by reconciling the measured quantity of excavated volume and mass with theoretical values estimated based on geometry of excavation and expected ground condition.

An allowable deviation from the theoretical values is set and follow-up actions should be taken once limit is exceeded.

However, it is important to understand that the reliability of the Excavation Management System is highly dependent on variation of geological conditions at the tunnel face, the accuracy of the measuring instruments and other operational factors, and therefore it is essential to understand that an holistic assessment is required, often comprising the assessment of other relevant TBM parameters, i.e. variation in face pressure, torque, etc.

2 SOIL PHASES

In soil or rock skeleton, it consists of solid particles, water and air. Figure 3 below represents the schematic phases diagram of the soil and rock composition by both mass and volume.

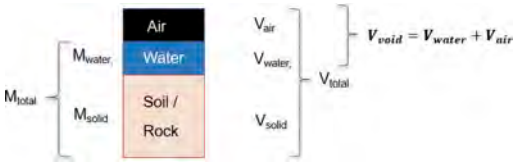

Figure 1. Soil phases diagram.

In Excavation Management, the Dry Volume V_{dry} refers to the volume of the solids (V_{solid}), while the Dry Mass M_{dry} refers to the mass of the solids (M_{solid}), and following equation express the relationship between the two:

$$M_{dry} = V_{dry} \rho_{solid} \quad (1)$$

With reference to the equations included in the paper, the following abbreviations are used:

ρ_{bulk} = bulk density of the soil
ρ_{solid} = solid (particle) density
n = porosity
S = degree of saturation

3 EXCAVATION MANAGEMENT FOR SLURRY TBMS

3.1 *Slurry transportation system and solids separation*

Mode of transportation of excavated materials from TBM is through bentonite flow via Slurry Transport System (STS) to Separation Treatment Plant (STP) During excavation, bentonite-based slurry is delivered from the STP to the TBM excavation chamber via slurry feed line. At the same time, excavated materials are transported from the chamber, via slurry discharge line to the STP for the separation of solid particles. Not every particle size is separated at the STP. As the STP is designed to retain bentonite, fines from the excavation (i.e. silt/clay) are also be retained in the system, causing an increase in the slurry density and a decrease in the slurry rheological properties.

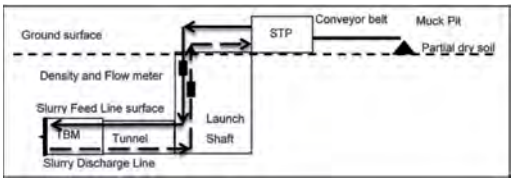

Figure 2. Schematic of slurry transportation and separation.

As the Excavation Management System is affected by the interpretation of geological information and by instrumentations accuracy, LTA has, in the recent years, required for provision of secondary reconciliation systems to be done at the Slurry Treatment Plant. Additionally, LTA has introduced rigours check on slurry physical and rheological properties using Key Performance Indicators and stringent testing regime since Circle Line projects (Marotta, 2010).

3.2 *Assumptions and limitations*

Excavation management is based on a comparison between theoretical and actual values of excavated volume or mass.

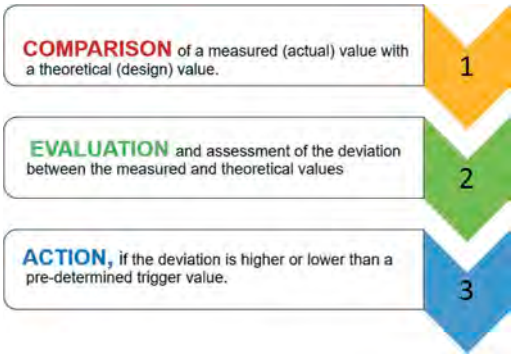

Figure 3. Excavation management process.

For the excavation management to be as accurate as possible, an important assumption is operating in a closed system where the difference in volume or mass between the slurry discharge and slurry feed can be used to determine the actual volume or mass of the excavated material. For slurry TBMs, the above is achieved when tunnelling with a membrane model at the tunnel face, where the formation of an impermeable filter cake can prevent major slurry losses into the ground. In reality, a overlap of both models can be assumed to govern the interactions at the tunnel face. Especially in highly permeable ground conditions such as coarse gravel, the penetrating filter cake model becomes more dominant.

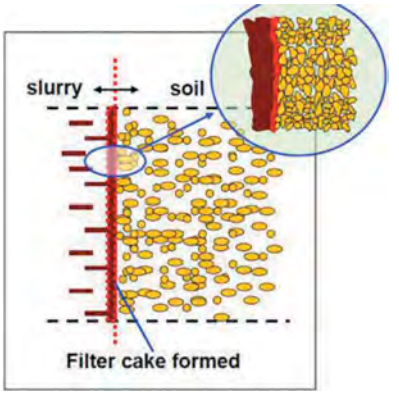

Figure 4. Schematic membrane model.

A closed system implies no major water seepage into the excavation chamber during tunnelling. Seepage cannot be measured and if present would drastically affect the results of the Excavation Management System.

For tunnelling in Singapore, the membrane model is generally achievable based on the characteristics of the local geological formations. However, minor losses or ingress in the system could still be one of the many factors contributing to the accuracy of the Excavation Management System.

3.3 *General approach on excavation management*

Muck reconciliation is done by volume and by weight. As described in Yee et al (2018), the traditional reconciliation method is by Volume, as its theoretical value is very simple to be calculated based on TBM cutting area and the advance length, with the actual Volume measured by the instruments (flowmeters) installed in the slurry feed and discharge line.

However, the experience with over 40 Slurry TBMs confirm that a reconciliation by volume only is often not sufficient, due to several reasons. Firstly, there are risks that an Over Excavation by Volume may not be captured by the system if the void if filled with slurry from the feed line.

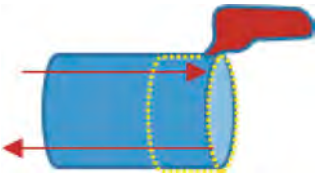

Figure 5. Schematic over-excavation.

To be accounted for, any void created by over-excavation shall remain empty. If filled by slurry, the volume of slurry filling the cavity will offset the over-excavated volume measured through the discharge line. That`s why it is important to assess all the other available data such as variation in the Slurry Tank Level, variation in Face Pressures, Deviation Flow, which would help assessing if an over-excavation has occurred.

Figure 6. Slurry treatment plant active tank.

Additionally, as explained in the previous paragraph, any alteration to the system volume may occur in case of seepage in the chamber, filtration outside the chamber or even seal water introduced to the slurry pumps.

Therefore, to rely only on muck reconciliation by volume has its own limitations and having muck reconciliation by Mass can allow for a better assessment. Mass measurements are done using Density Meters installed in the slurry the feed and discharge lines. Additionally, further measurement by mass can be taken for verification purpose at the Slurry Treatment Plant, if equipped with compartmentalized muck pit and measuring weighing system on the conveyor belts.

3.4 *Excavation management by total volume*

The Theoretical Excavation Volume depends on the TBM cutting diameter and the excavation length of the advance, and can be calculated as:

$$V_{theor} = \frac{\pi d_T^2}{4} L_{advance} \quad (2)$$

where d_{tbm} is the cutting diameter of TBM and $L_{advance}$ is the length of advancement, which is typically 1.4 meters to 2m for TBM size used in Singapore MRT construction projects.

The actual excavated volume can be measured using flowmeters installed at the feed and discharge slurry line.

The comparison between theoretical and actual excavation volume can be tracked in real time:

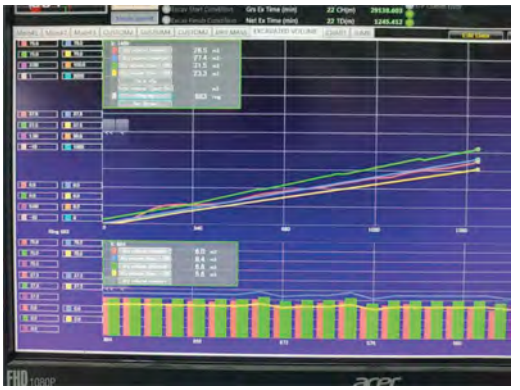

Figure 7. Real time visualization of EMS by total volume.

3.5 *Excavation management by dry mass/dry volume*

As described in Yee et al (2018), different TBM suppliers used different equations for the calculation of the theoretical dry mass/dry volume, and it may not be so evident that some of the equations were written for tunnelling in Saturated soil (S=1). To avoid errors in muck reconciliation, it is advisable to use equations which are applicable to soil of any degree of saturation, such as:

$$M_{dry} = V_{tot_th} \frac{(\rho_{bulk} - \rho_{water} \times S)}{(\rho_{solid} - \rho_{water} \times S)} \rho_{solid} \quad (3)$$

$$M_{dry} = V_{tot} \rho_{dry} \quad (4)$$

$$V_{dry} = V_{tot_th} \ (1 - n) \quad (5)$$

The theoretical dry mass/ dry volume is highly dependent on the density of the soi/rock at the tunnel face.

Therefore, when tunnelling in rock soil mix face conditions, the calculation of the theoretical mass can be challenging.

As shown in the figure below, for a Metro tunnel size the variation in Dry mass for a 1.4 m excavation length can range from 63 to 130 Tons.

While having sufficient Soil Investigation can help, there are always possible deviations between the expected and the encountered ground conditions. Common practice is therefore to analyse the ground conditions encountered in the previous ring to estimate rock and soil distribution for the following ring. During excavation, the gradient of dry mass/ dry volume graph will be monitored and compared with excavated materials collected. This is possible

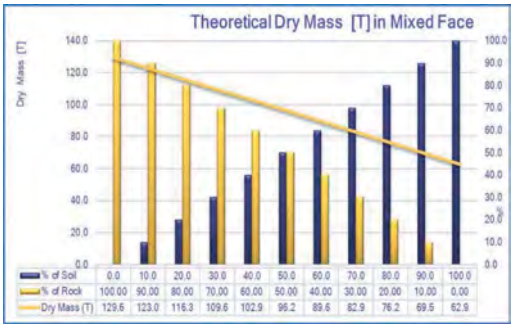

Figure 8. Variation of Dry Mass in mix rock/soil conditions.

Figure 9. Abrupt soil/rock interface observed at the tunnel face.

as the Slurry Treatment Plant is equipped with compartmentalized pits, belt weigher and density meters to measure the quantity of rock chips, sand, and fines remaining in the system.

Measurements of Dry Mass and Dry Volume is done using both flowmeters and density meters installed along the slurry feed and discharge lines.

As described by Yee et al (2018b), most of the flow meters available in the market is of electromagnetic type. Location of flow meters would affect their accuracy. It is generally recommended to position the magnetic electrodes perpendicular the direction of steady flow and reasonably distance away from density meter so to avoid interference.

To measure the corresponding density, density meter is also recommended to install at vertical pipe position where the soil particles are better evenly distributed across the pipe as compared with horizontal pipes position. Wear in the slurry pipe would affect its accuracy over time. Density meter of radioactive type has higher accuracy as compared with electromagnet density meter. (Yee et al, 2018a)

To have better accuracy of the density meters, it is advisable to perform multiple points calibration prior

to commencement of tunnelling. The calibration should be done with water and with sample of drilling fluid of a density equal or higher to the maximum expected density on discharge line during tunnelling.

A quick check on the accuracy of the density meter can be done during by-pass operation when slurry circulation is done outside the excavation chamber with no solid ingress. Under this by-pass mode, the density in feed and discharge should be equal. However, it takes some time to reach a stable reading once the slurry in the system is homogeneous. Should a major deviation be observed, it is advisable to engage the density meter supplier or agent for a re-calibration (Yee et al, 2018b)

3.6 *Secondary muck reconciliation*

The secondary reconciliation measurements are carried out with weigher installed at conveyor belt transporting soil from STP to muck pit.

Figure 10. Muck Pit for gravel.

Figure 11. Muck Pit for sand.

However, belt and muck pit would collect only the relatively large solid particles that are successfully separated in the Slurry Treatment Plant (STP), and not the fines (including bentonite) which are below the STP separation capacity (usually defined as d50 of the cyclones). Therefore, for accounting purpose, the fines in the system need to be estimated by comparing the difference in the total slurry volume and density at the start and at the end of each excavation cycle (Yee et al, 2018)

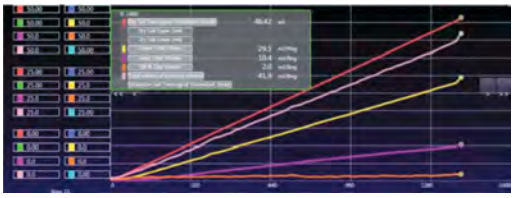

Figure 12. Automatic measuring of fines in the system.

3.7 *Evaluation and assessment*

With many data available, it is important to understand that assessment on the occurrence of a potential over-excavation shall be done holistically with the understanding that muck reconciliation method has his own limitations.

In general, the allowable limits of under or over excavation (i.e. +/- 15%) do not represent an acceptable variation in the excavated quantity, but are set to reflect the reliability of the excavation management as a comparison between a measured and a theoretical value, where both are affected by a large number of external factors as described in this paper.

For instance, when tunnelling in rock/soil mix face, great variation on dry mass/dry volume is expected. In this case, accounting by total volume may be more reliable than accounting by mass.

When tunnelling in ground with very high content of clay, the soil separated at the STP and collected in the muck pit (gravel/sand) may only be a small percentage of the excavated one. In this case the estimation of fines in the system is very important for the secondary muck reconciliation at the STP.

Where multiple methods are used, analysing trends and outliners can be a better methodology then simply reply on individual measurement as number. Having this approach, and executing holistic assessment, has proven to be effective in identifying potential over excavations.

4 EXCAVATION MANAGEMENT FOR EPB TBMS

4.1 *Muck reconciliation by volume (EPB)*

Traditionally and for a long time the quantity of spoil excavated by an EPB TBM has been measured by volume based on the number of muck skips.

The reliance only on the volume can lead to inaccuracies related to computation of the bulking factor of the spoil, injection volume of soil conditiioning, sticking of spoil to the interior of the muck skip and the like.

Unlike for Slurry TBMs, it is more complex to reconcile the excavated spoil for EPB TBMs. For a start the injection of ground conditioning foam to the cutterhead and excavation chamber leads to

Figure 13. Muck skip for soil disposal (EPB TBM).

accumulation of air in the chamber. Often this accumulated air is not purged. As a result, the excavation could proceed with a partially full chamber thus leading to significant fluctuations in the volume and weight of the spoil removed from the chamber for individual rings. This can be avoided by releasing any air that has accumulated in the excavation chamber at periodic intervals during tunnel boring or once every advance towards the end of the boring cycle, for example 300mm before completing the advance.

Other than using the muck skips, muck reconciliation by volume can also be done using scanner, measuring the soil on the conveyor belt and providing real time visualization (Veenuganan et al (2023)

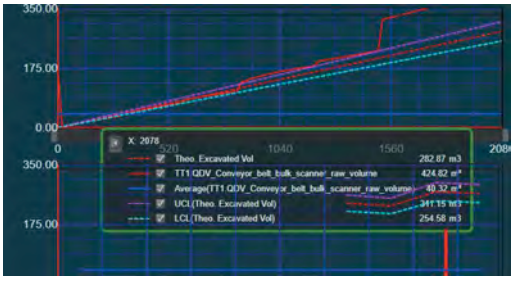

Figure 14. Volume scanner real time visualization.

The belt scanners principally scan the profile of the spoil which is carried on the belt using special laser devices installed on top of the conveyor belt at a specified height.

As shown in Veenuganan et al (2023), recent Singapore experience in large diameter TBM in alluvial soil has shown the measurement by the scanner largely be within the allowable limit.

It is important to understand that any muck reconciliation by volume is affected by the quantity of water/foam injected, by the air content as a result of soil conditioning. The quantity of water or conditioning injected shall be therefore accounted for in order to determine the net excavation volume

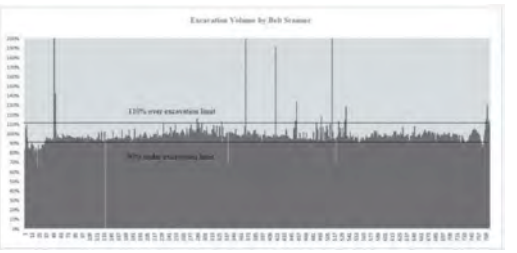

Figure 15. Belt scanner results (% of theoretical).

4.2 *Muck reconciliation by Mass (EPB)*

Muck reconciliation by Mass can be executed by different means depending which muck transportation method is used. Generally, weighers are installed at the conveyor belts transporting the soil out of the TBM (TBM belt). For long drives where conveyor belt is used for soil transportation to surface, additional weighers can be installed along the tunnel belt.

If muck skips are used and gantry crane employed to lifting the skips for soil disposal into muck pit, the excavated total mass can be calculated by measuring each skip before and after it is loaded by the excavated soil.

The advantage of muck reconciliation by Mass, is that it is not affected by the tunnelling bulking factor, including by the presence of air as a result of soil conditioning. The measurement by mass can be relatively accurate as long as any fluid added during excavation (water, conditioning) is accounted for and is subtracted from the measured total mass in order to derive the net excavated mass.

4.3 *On Board Muck Weighing System (OBMWS)*

The OBMWS is an enhanced version of weight measurement, introduced and developed by the Land Transport Authority and currently adopted in some of the Cross Island Line tunnelling project.

It follows the same principles of the Gantry Crane method, where muck reconciliation by Total Mass is done by measuring the weight of skips. However, instead of measuring the weight of the skips when they reach the gantry crane, load measurements of the skips are done directly using load cells embedded on the flat bed of the rolling stock, as seen in Figure 15.

The load cells can transmit data in real time and can be integrated directly into the PLC system, allowing for real time visualization (Veenuganan et al, 2023) for each skip as it the soil come from the EPB Screw conveyor.

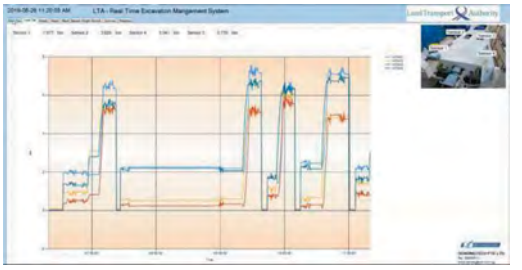

Figure 16. OBMWS Real Time Visualization.

Figure 17. Flat car equipped with load cells for OBMWS.

5 CONCLUSIONS

The paper has outlined the principles, limitations, and applicability of various muck reconciliation methods, for tunnelling using Slurry and EPB Boring Machines.

The aim of Excavation management System is to detect potential over-excavations so that actions can be taken before escalating into large ground movement or sinkholes.

Nevertheless, it is important to understand that the system is influenced by various factors as outlines in the paper, and therefore the Excavation Management System should consist of a holistic interpretation of the various measurements by volume and mass measurements and their comparison with their theoretical "expected" values based on tunnel dimension, advance rate and ground conditions.

This systematic approach to excavation management is especially beneficial when tunnelling in urban environment where the allowable tunnel induced ground movement are often limited and governed by serviceability limits. Tunnelling in Singapore has developed a state-of-the-art approach on Excavation Management thanks to the contribution of all industry partners, from Contractors to TBM Manufacturer to consultants. The continues development of more advanced software solution in this field would, is and will continue to be highly beneficial.

REFERENCES

Connors, R. (2017) The Challenges Of Tunnelling With Slurry Shield Machines In Mixed Ground, The David Sugden Young Engineers Writing Award 2017.

Deutscher Ausschuss für unterirdisches Bauen e. V. German Tunnelling Committee (ITA-AITES), (2016) Recommendations for Face Support Pressure Calculations for Shield Tunnelling in Soft Ground.

Dhume, R., Rasanavaneethan, R., Pakianathan. L. & Herud, A., 2015. Therotical basis of slurry shield excavation management system. In: International Conference on Tunnel Boring Machines in Difficult Grounds (TBM DiGs) Singapore, 18-20 Nov.2015.

Duhme, R. & Kleine, E. (2018). Excavation Management of Slurry TBMs – Long Term Operational Accuracy Evaluation. Proceeding of Underground Singapore 2018.

Marotta, M. (2010). Singapore Bukit Timah granite: Slurry quality control for TBM. Proceedings of the World Urban Transit Conference 2010 (pp. 237–245). Singapore: Research Publishing.

Nakano, A., Sahabdeen, M., Kulaindran, A. & Seah, T. (2007) Excavation Management for Slurry TBMs Tunnelling under Residential Houses at C853 (CCL3) Project. Proceeding of Underground Singapore 2007.

Peng, S., Kulaindran, A. & Ow, C. N. (2007). Construction of Rail Tunnels Using Slurry Machines on Circle Line Stage 3. Proceeding of 11th ACUUS Conference: Underground Space: Expanding the Frontiers. Athens.

Veenuganan, S., Pakianatha, L., Marotta, M., Velu, D. (2023) Theoretical Basis and Practical Application of Excavation Management System for Tunnelling with EPB TBM, Proceeding of Underground Singapore 2023.

Yee, T.C. Marotta, M, & Ow, C.N. (2018) Excavation Management System for Slurry TBM in Singapore. Proceeding of the World Tunnelling Congress 2018, Dubai.

Yee, T.C. Marotta, M, & Ow, C.N. (2018) Theory and Application of Excavation Management System for Slurry TBM in Singapore. Proceeding of Underground Singapore 2018.

Tunnelling for a Better Life – Yan, Celestino, Thewes & Eberhardt (Eds)
© 2024 The Author(s), ISBN 978-1-032-80042-4
Open Access: www.taylorfrancis.com, CC BY-NC-ND 4.0 license

Advancing mechanized tunneling through integrated digital design, simulation, and data-driven techniques

Günther Meschke*, Yaman Zendaki, Abdullah Alsahly & Ba Trung Cao
Ruhr University Bochum, Bochum, Germany

ABSTRACT: Towards the digitalization in tunneling industry, interactive digital planning as well as model and data driven steering support during construction is at the forefront of modern tunnel projects. Project stakeholders are then possible to collaboratively explore and visualize various design alternatives in a virtual environment in real-time, which leads to optimized tunnel design and reduced construction risks. For this purpose, a digital interactive platform has been developed for collaborative planning and construction in tunneling projects, in which digital data, numerical simulation, and the damage assessment of existing infrastructure, is integrated and visualized in real-time. In this work, firstly, an interactive tunnel alignment design example utilizing the digital platform is presented. Secondly, a simulation-and-monitoring-based example, which adopts risk-oriented models for the steering of Tunnel Boring Machines considering interactions with the built environment, in association with monitoring and process data to enable an informed real-time adjustment of the construction process, is also illustrated. This contribution provides an insight into the latest advancements in the field, focusing on digital design, integration of Building Information Model and numerical simulation, interactive planning, and real-time steering support during tunnel construction.

Keywords: Real-time prediction, Numerical simulations, Interactive design, Tunnel alignment, TBM steering

1 INTRODUCTION

With the move toward digitalization in the tunneling industry, data from different sources in a tunnel project are required to be digitally transformed, efficiently stored, processed and displayed. Digitalized data is then used to collaboratively explore, to process and to visualize in a virtual environment, which leads to not only optimized tunnel design but also reduced construction risks.

With respect to the design task, the development of a real-time interactive digital platform for planning and design of tunneling projects, particularly in urban areas, provides a valuable tool to support the decision-making process in the design phase, such as the tunnel alignment design problem. In this paper, a simulation-based interactive platform, which allows to quickly investigate different possibility of planning the tunnel alignment in real-time, is introduced to better enrich the alignment design process. The platform is established based on a combination of several approaches, such as the Building Information Model (BIM) (Borrmann et al., 2015), Finite Cell Method (FCM) (Düster et al., 2008) and surrogate models. Similar to the Tunnel Information Model in (Koch et al., 2017), a BIM-based data management model, which contains four essential components in mechanized tunneling including a ground model, a TBM model, a tunnel model and a built environment model, has been generated in Revit software. In (Alsahly et al., 2020), a BIM-to-FEM concept has been introduced and developed to properly transform necessary data from the digital model to numerical simulations based on the Finite Element Method (FEM). This concept has been extended in this paper namely BIM-to-FCM approach in order to connect the BIM-based model to a 3D FCM model for the simulation of tunneling processes in soft soils, which can efficiently simulate different tunnel alignments. The simulation results are then utilized to create a surrogate model using a combination of the Proper Orthogonal Decomposition (POD) and the Radial Basis Functions (RBF) to substitute the time-consuming FC model (Zendaki et al., 2023). The POD-RBF model has the capability to quickly

*Corresponding author: guenther.meschke@rub.de

DOI: 10.1201/9781003495505-263

provide the system responses (e.g. surface settlement, risks of building damages) with respect to an arbitrary tunnel alignment created by the design engineer in an interactive environment.

Simulations and data-driven techniques are employed not only to assist the design tasks but also to enhance the tunnel construction process. The process-oriented 3D FC model is also used together with the POD-RBF model in a concept of combining simulation and monitoring data to support the TBM steering. In this approach, the operation of TBMs is suggested for future construction steps based on the possible system responses (e.g. surface settlement and risks of damages on existing buildings). Similar to the alignment design problem, a bunch of simulations is carried out using the FC model to generate a dataset, which can be learned using the POD-RBF model. During the construction process, corresponding to each configuration of operational parameters, the POD-RBF model can quickly provide the surface settlement as well as the associated risks of damages on building.

The paper is structured as follows. Section 2 presents the methodology of the FCM, the BIM-to-FCM approach, and the POD-RBF method. Section 3 describes the concept of interactive tunnel alignment design and simulation and monitoring supported TBM steering. Section 4 is devoted to the illustration of digital design, simulation and data-driven techniques in mechanized tunneling through two respective application examples. Finally, the work is summarized and some conclusions are drawn in Section 5.

2 METHODOLOGY

2.1 *FCM for the simulation of tunneling processes*

To accommodate for the flexibility in varying the tunnel alignment in analysis and design, a tunnel analysis model based on the FCM is proposed (Bui et al., 2022).

FCM allows for the use of one structured background mesh for all simulations, which removes the need to create a custom mesh for each track alignment in every simulation. This is particularly important for the generation of synthetic data where thousands of simulations are needed. The soil domain is discretized using the structured background mesh, whereas the other tunnel components like grouting and lining are discretized with a boundary-fitted mesh and tied to the background mesh. Different soil layers are modeled using a boundary representation that completely cuts through the background mesh. The material properties are then assigned to integration points depending on their position with respect to each of the soil layers' boundary representations. Figure 1 shows a tunnel section simulated with the FCM model for the Wehrhahn Linie Düsseldorf reference project. More details about the simulation model can be found in (Bui et al., 2022, Zendaki and Meschke, 2022).

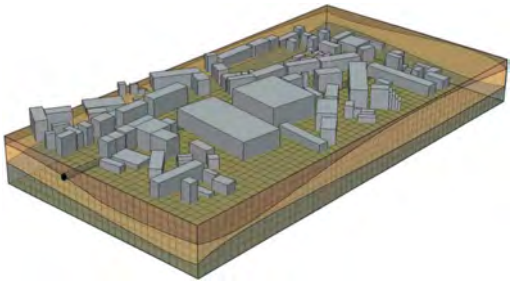

Figure 1. FCM model for tunneling processes in soft soils.

2.2 *BIM-to-FCM approach*

For the assessment of the impact of various tunnel alignments or steering scenarios of the TBM (e.g., settlements, damage criteria), the process-oriented FCM model is coupled with a BIM model to automatically exchange data between the two models. This coupling allows automatic extraction of all relevant information needed for the numerical model and subsequently performing a numerical analysis for the tunnel drive.

A BIM model including information of geology, alignment, lining, existing infrastructure, material, and process parameters in a tunnel project is developed in Revit. The varying parameters (e.g. the tunnel alignment or the operational parameters) are parameterized using Dynamo. After defining expected parameters of an arbitrary scenario of the tunneling process, the corresponding simulation model can be quickly obtained using the developed automatic framework. Figure 2 presents the BIM model in Revit of a reference tunnel project with the information of geology, alignment, lining, TBM, existing buildings, material properties, and process parameters. For a better description of the BIM to numerical analysis concept, readers are refered to the work of Alsahly et al. (2020) and Ninic et al. (2021).

Figure 2. BIM model of a reference tunnel project with all relevant information.

2.3 *POD-RBF model*

Instead of the time consuming FCM simulations, the POD-RBF is employed to efficiently substitute the

numerical model in order to enable the real-time predictions for different purposes in tunneling.

The data obtained from M simulations (e.g. settlements and building damages) is arranged into a matrix $\boldsymbol{Q}$ (N rows x M columns). N output values in each column represent the number of settlement points and maximum principal strains in all buildings corresponding to a specific scenario (a tunnel alignment or an operational scenario). The POD basis vectors $\boldsymbol{\Phi}$ (Smith et al., 2005), which characterizes the matrix $\boldsymbol{Q}$, can be obtained by solving the eigenvalue problem of the sample covariance matrix $\boldsymbol{C}$ of $\boldsymbol{Q}$. A reduced basic functions of K ($K \ll M$) dimensions are kept to approximate $\boldsymbol{Q}$. The reduced or truncated POD basic matrix $\widehat{\boldsymbol{\Phi}}$ then consists of the first K POD modes. The original snapshots matrix $\boldsymbol{Q}$ is approximated by

$$\boldsymbol{Q} \approx \widehat{\boldsymbol{\Phi}} \cdot \widehat{\boldsymbol{A}} \tag{1}$$

Where, the truncated matrix $\widehat{\boldsymbol{A}}$ contains constant values associated with the given matrix $\boldsymbol{Q}$. Here, only snapshots, which were included in the given $\boldsymbol{Q}$, can be approximated. To obtain responses with an arbitrary snapshot, a nonlinear interpolation function of input parameters needs to be integrated into the matrix $\widehat{\boldsymbol{A}}$. Therefore, an expression of $\widehat{\boldsymbol{A}}$ using interpolation functions $\boldsymbol{F}$ of input parameters and an unknown matrix of constant coefficient $\boldsymbol{B}$ is as follows

$$\widehat{\boldsymbol{A}} = \boldsymbol{B} \cdot \boldsymbol{F} \tag{2}$$

In this work, a type of Radial Basis Functions (RBF), the inverse multi-quadric radial function (Hardy, 1990) has been adopted as the interpolation function. Finally, an approximation of responses corresponding to an arbitrary input is obtained by

$$\boldsymbol{Q}^a = \widehat{\boldsymbol{\Phi}} \cdot \boldsymbol{B} \cdot \boldsymbol{F}^a \tag{3}$$

More details about the POD-RBF algorithm are given in (Cao et al., 2016, Zendaki et al., 2023).

3 SIMULATION-SUPPORTED-TUNNELING CONCEPTS

3.1 *Interactive tunnel alignment design*

A schematic illustration of the interactive tunnel alignment concept is presented in Figure 3. In the first step of the procedure, a number of possible tunnel alignments are generated. The process-oriented FCM model is then used to simulate the mechanized tunneling processes with various tunnel alignments. The inputs in each simulation are the coordinates of alignment points, which represent the tunnel alignment. Afterwards, a POD-RBF model is established using these coordinates of points as inputs and strains in buildings in all alignment scenarios as outputs.

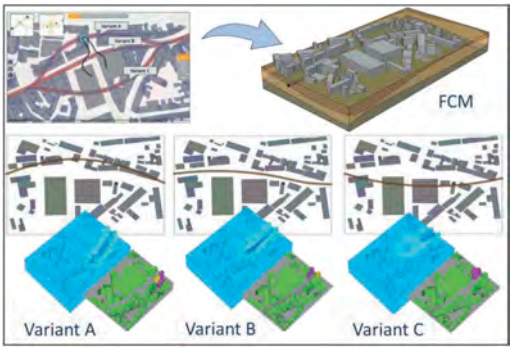

Figure 3. Scheme of interactive tunnel alignment design.

Considering predefined design criteria and constraints with respect to tunnel serviceability, e.g. fixed position of stations and curvature tolerance according to the design speed of the train, a tunnel alignment can have different shapes. In this work, a set of twenty-one control points following a cubic function are chosen to represent the alignment. For a general case, where an arbitrary number of points is used to represent the alignment, the proposed strategy is still valid. Figure 4 illustrates a collection of possible tunnel alignments in 3D space within an investigated area. The coordinates of all alignments scenarios, which are regarded as inputs of the POD-RBF surrogate model, are then sent to the FCM model to execute the simulations.

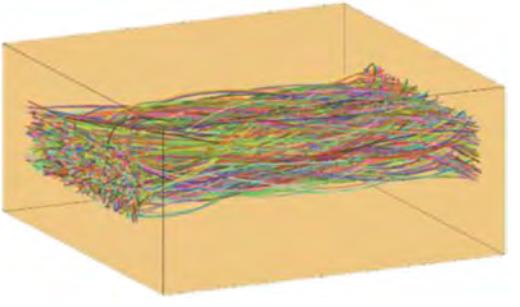

Figure 4. Possible three-dimensional tunnel alignments.

3.2 *Simulation-monitoring supported TBM steering*

This concept employs the advantages of simulations and monitoring data to support a possible extreme scenario occurring during the tunnel construction in

an urban area, which encounters a soil layer change between two soft soil layers (see Figure 5). In this case, designed steering parameters for the second half of the tunnel section are required to be adapted to the new geological condition.

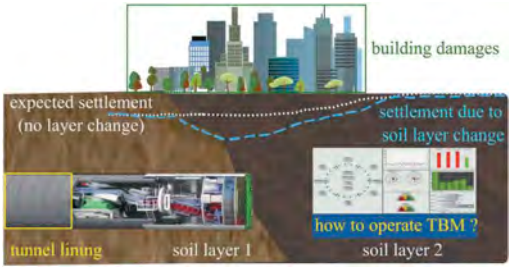

Figure 5. TBM operation support in a scenario of soil layer change between 2 soft soils layer.

In general, numerical simulations considering the new geological condition can be executed to roughly estimate soil-structure interactions; however this approach is not realistic for a practical application during the tunnel construction due to the expensive computation time from simulations. Therefore, the POD-RBF surrogate model is utilized to substitute the numerical model. Figure 6 presents the operation concept exploiting simulation data as the basis of surrogate models for real-time predictions.

To construct the surrogate model, a number of operation scenarios, which can be applied to the new situation, are firstly simulated using the FCM model to generate the necessary data. During the real-time application, i.e. the construction stage, engineers can investigate different steering possibilities before making a decision by adjusting process parameters with arbitrary scenarios. Quick evaluations of multi-output quantities from the POD-RBF provide engineers suggestions on the decision-making process. To better support the steering decision, real-time predictive simulation models will be continuously updated with monitoring data during the construction.

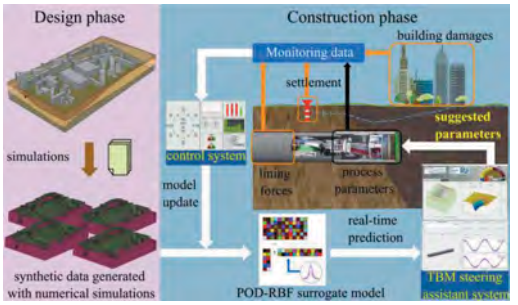

Figure 6. Concept of simulation-supported TBM steering.

4 APPLICATION EXAMPLES

4.1 *Interactive tunnel alignment design*

This section presents the application of the digital design approach in a scenario of tunnel alignment design in an urban area. A section of 400 x 300 meters inspired by the tunnel project Wehrhahn Line Metro in Düsseldorf, Germany is generated. A tunnel with an excavation diameter of D = 9.5 meters, see Figure 7, is assumed to be constructed using the shield tunneling method. The length of the computational model is 400 meters. The bottom surface of the model is fixed in both horizontal and vertical directions since it is assumed that deformations in deeper soil layers can be neglected. Buildings located at the ground surface are modeled depending on the Level of Details (LOD) (Ninic et al., 2019). The LOD varies from a simple substitute model using shell elements with equivalent thickness and stiffness; 3D block volume elements; or a detailed structure with connected walls, columns, and slabs. To efficiently simulate the problem, an adaptive searching algorithm, which assigns higher LOD to critical buildings based on their position with respect to the tunnel alignment, is employed to reduce unnecessary degree of freedoms of less important buildings, see Figure 7.

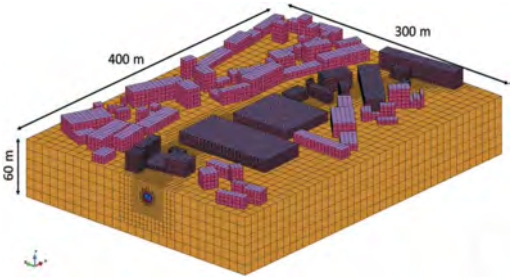

Figure 7. Simulation model of a section with buildings.

A total of 85 buildings at the top surface used in this application example are illustrated in Figure 7. The design task is to interactively create an arbitrary tunnel alignment and visualize immediately the possible associated damages on all buildings. In a way similar to (Cao et al., 2022), the building damage assessment is performed by estimating the principal tensile strains in each building individually. A POD-RBF model, which considers the coordinates of the alignment control points as the inputs, is used to predict the tensile strains in 85 buildings.

Quality of the POD-RBF model is evaluated using the 5-fold cross validation with the data from a total number of 2000 simulations of three-dimensional tunnel alignments. In this example, the 2000 samples are generated with a constraint such that in each alignment the Y coordinates of any alignment points are within the range from 50 to

250 meters. On the other hand, to maintain the design of a shallow tunnel with a cover depth in the range of 1.2D to 3.3D (D as the excavation diameter), the variation of Z coordinates of alignment points is kept between 16 meters and 36 meters. Table 1 summarizes the mean L_2 norm errors of all validation cases in each fold of the 5-fold cross validation for the prediction of maximum tensile strains in buildings as compared to the reference solutions from FCM simulations. It is shown that with an average error of only 2.7% and similar prediction accuracy in all 5 folds, the POD-RBF surrogate model can efficiently substitute the FCM simulation model to predict the maximum tensile strain in the buildings.

Table 1. Prediction performance of the POD-RBF model: L_2 norm error (in [%]).

5-fold cross validation	Building strain error [%]
1	3.8
2	2.0
3	3.4
4	2.2
5	2.0
Average	2.7

Based on the proposed computational strategy, an interactive real-time simulation software namely "TunAID" (Tunnel Alignment Interactive Design) is developed to support the decision-making of tunnel alignment selection during the design phase of a tunnel project. With the help of TunAID, a real-time prediction of TBM-soil interactions, i.e. the surface settlements and the associated risks of damage on buildings, are enabled for an arbitrary tunnel alignment design. A screenshot of the developed software is depicted in Figure 8. In an interactive design manner, corresponding to each movement of the pointer an alignment following a predefined criterion is created and visualized immediately. Consequently, the associated risks of damages on all existing buildings are quickly estimated and shown in the developed software package.

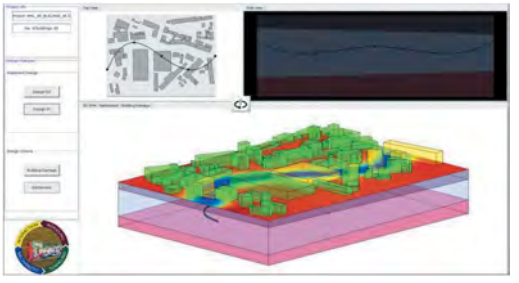

Figure 8. A screenshot of the TunAID application.

4.2 *Simulation-monitoring supported TBM steering*

This section is devoted to the application of the simulation-support TBM operation concept. The simulation model generated in this example represents a tunnel section of a reference project, where the tunnel is excavated underneath an urban area with a large number of buildings. The target to operate the TBM in this example is to minimize the possible damages on existing buildings in the area. The computational domain, the tunnel alignment, the associated buildings, and the geological conditions of the section are depicted in Figure 9. The shield tunneling method is used to construct a tunnel with a diameter of 11.34 m. The cover depth in this section varies from 17 m to 20 m. The simulated tunnel alignment consists of 57 concrete lining rings, each with a length of 2 m and a thickness of 0.4 m. There are in total 108 masonry residential buildings, which are typically two to three-story buildings, taken into consideration in the simulation. However depending on their locations to the tunnel alignment, different LODs are used to model the buildings, see Figure 9(a).

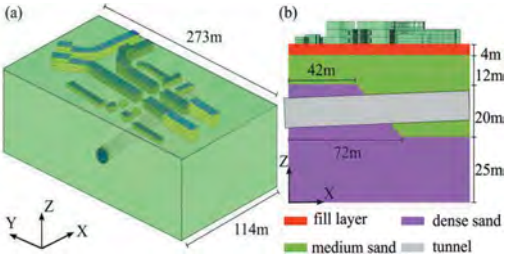

Figure 9. Simulation model of the section with buildings: (a) Computational domain with 108 buildings; (b) Geological conditions of the simulated section.

Along the simulated tunnel section, three soil layers including a filling layer, a medium sand layer, and a dense sand layer exist as depicted in Figure 9(b). In the Y direction, the soil layers are assumed to be horizontal. In the first half of the section, the TBM advances in the dense sand layer (with a modulus of elasticity E_3 = 66 MPa), while in the rest of the alignment, the tunnel is constructed in the medium sand layer (E_2 = 37 MPa). A soil layer change situation with the transition zone of 30 m appears in the area from ring 21 to ring 36, i.e., in the range of 42 m to 72 m from the left boundary of the computational domain.

A total number of 324 operation scenarios considering different face support pressures in two tunnel sections and the steering time (i.e. where starting to adjust the pressure) are created and used as inputs to execute corresponding FCM simulations. The respective POD-RBF models take these operational parameters as inputs and the simulated settlements at 931 surface points and the simulated

damages on 108 buildings as outputs. To estimate the risks of damages on buildings in practice, categories of damages converted from associated strain values (Boscadin and Cording, 1989) are usually used, therefore the POD-RBF models in this example will predict the tensile strains on multiple positions of buildings. The building strains are then converted to categories and visualized as shown in Figure 9 to indicate the building damage levels. Table 2 shows the prediction accuracy of POD-RBF models for both surface settlements and strains.

The settlement can be excellently predicted using the POD-RBF model with a L_2 norm error of only 2.4% as compared to FCM results. The prediction of non-linear strains on buildings also shows a great agreement between the two models (FCM and POD-RBF). The overall L_2 norm error of 5-fold cross-validation for the strain prediction is 7.52%, while the computation time is significantly reduced from 10 hours to only 1 second.

Table 2. Prediction performance of POD-RBF models in TBM control example with buildings: L_2 norm error (in [%]).

5-fold cross validation	Settlement	Tensile strain
1	2.4	7.40
2	2.39	7.10
3	2.51	7.59
4	2.32	8.10
25	2.39	7.27
Average	2.4	7.52

The presented simulation-based strategy has been integrated into a real-time simulation software called SMART (Simulation and Monitoring based Assistant for Real-time steering in mechanized Tunneling) to support the TBM operation during the tunnel construction (Cao et al., 2016; Zendaki et al., 2023). In this paper, the SMART application focuses on the possibility to quickly estimate the surface settlement and the risk of building damages.

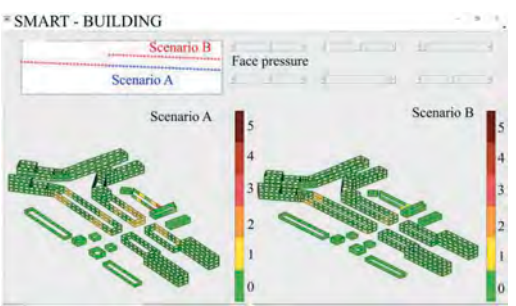

Figure 10. A screenshot of the SMART application illustrating the simulation-supported TBM steering.

Figure 10 shows an application of the SMART app for an investigation of TBM process control in an urban area. Two investigated scenarios: scenario A with the blue line and scenario B with the red line, are shown in the top left of the panel. In scenario A, the relative change of face pressure is kept constant, while a moderate increase of 40 kPa for the face pressure is applied in scenario B. The resulting damage categories are plotted respectively at the bottom of the application panel. The results show that the pressure adjustment in scenario B will lead to a safer situation with lower damage categories in critical buildings in this area. Generally, by changing the sliders of model inputs on the top right panel (i.e., the relative change in support pressure), the associated damage categories of buildings can be quickly estimated and visualized, which provides a real-time assistant tool for site engineers to make a decision on how to select the face pressure in next excavation steps.

5 CONCLUSIONS

In this paper, a framework for advancing TBMs in mechanized tunneling through the support of digital design, numerical simulations and data-driven techniques has been presented. The digital BIM-to-FCM concept has enhanced the data exchange between a BIM-based data management system and a FCM simulation model. The FCM simulation model serves as the main investigation tool for the numerical analyses in tunneling process, both in design stage and tunnel construction. To activate the interactive alignment design and the real-time TBM steering support in construction stage, surrogate models based on POD-RBF method have been utilized.

In both application examples, the POD-RBF models have proven to be able to substitute efficiently the FCM simulation model. The associated computation time is substantially reduced from 7 to 10 hours (using FCM simulations) to only several seconds (using POD-RBF model), while the prediction capability remains. Two user-friendly applications namely TunAID and SMART have been developed to support the tunneling work. The TunAID software allows to interactively determine (in real-time) optimized tunnel alignments resulting in minimal settlement-induced damage within a predefined section of a tunnel project. On the other hand, the developed simulation-based SMART application can be used as an assistant system for real-time TBM operation support in practical tunneling.

ACKNOWLEDGMENTS

This research is funded by the Deutsche Forschungsgemeinschaft (DFG, German Research Foundation) – Project number: 77309832 within subproject C1 of the Collaborative Research Center SFB 837 “Interaction Modeling in Mechanised Tunnelling”.

REFERENCES

Alsahly, A., Hegemann, F., König, M., Meschke, G., 2020. Integrated bim-to-fem approach in mechanised tunneling. Geomechanics and Tunnelling, 13 (2), 212–220.

Borrmann, A., Kolbe, T.H., Donaubauer, A., Steuer, H., Jubierre, J.R., Flurl, M., 2015. Multi-Scale Geometric-Semantic Modeling of Shield Tunnels for GIS and BIM Applications. Comput-Aided Civ Inf 30(4): 263–281.

Boscardin, M., Cording, E., 1989. Building response to excavation-induced settlement. ASCE Journal on Geotechnical Engineering (115), 1–21.

Bui, H.-G., Schillinger, D., Zendaki, Y., Meschke, G., 2022. A cutfem based framework for numerical simulations of machine driven tunnels with arbitrary alignments. Computers and Geotechnics 144, 104637.

Cao, B.-T., Freitag, S., Meschke, G., 2016. A hybrid rnn-gpod surrogate model for realtime settlement predictions in mechanised tunneling. Advanced Modeling and Simulation in Engineering Sciences 3(1),1–22.

Cao, B.T., Obel, M., Freitag, S., Heußner, L., Meschke, G., Mark. P., 2022. Real-time risk assessment of tunneling-induced building damage considering polymorphic uncertainty. ASCE-ASME Journal of Risk and Uncertainty in Engineering Systems, Part A: Civil Engineering 8(1): 04021069.

Düster, A. Parvizian, J., Yang, Z., Rank, E., 2008. The finite cell method for three-dimensional problems of solid mechanics. CMAME 197, 3768–3782.

Hardy, R. L., 1990. Theory and applications of the multiquadric-biharmonic method: 20 years of discovery 1968-1988. Computers & Mathematics With Applications 19, 163–208.

Koch, C., Vonthron, A., König, M., 2017. A tunnel information modelling framework to support management, simulations and visualisations in mechanised tunnelling projects. Automation in Construction 83, 78–90.

Ninic, J., Alsahly, A., Vonthron, A., Bui, H.G., Koch, C., König, M., Meschke, G., 2021. From digital models to numerical analysis for mechanised tunnelling: A fully automated design-through-analysis workflow, Tunnelling and Underground Space Technology 107, 103622.

Ninić, J., Bui, H.G., Koch, C., Meschke, G., 2019. Computationally efficient simulation in urban mechanized tunneling based on multilevel bim models. Journal of Computing in Civil Engineering, 33(3): 04019007.

Smith, T., Moehlis, J., Holmes, P., 2005. Low-dimensional modelling of turbulence using proper orthogonal decomposition: A tutorial. Nonlinear Dynamics 41, 275–307.

Zendaki, Y., Meschke, G., 2022. Adaptive mesh refinement using octree for finite cell simulation and its application for tunneling in saturated soils. PAMM22, 1–4.

Zendaki, Y., Cao, B.T., Alsahly, A., Freitag, S., Meschke, G., 2023. A simulation-based software to support the real-time operational parameters selection of tunnel boring machines. Underground Space, in print.

Tunnelling for a Better Life – Yan, Celestino, Thewes & Eberhardt (Eds)
© 2024 The Author(s), ISBN 978-1-032-80042-4
Open Access: www.taylorfrancis.com, CC BY-NC-ND 4.0 license

TBM design and special features for boring through highly squeezing ground

Maurizio Monina*
Webuild, Milan, Italy

Marco D'Ambrosio & Fabio Del Rossi
Seli Overseas, Rome, Italy

ABSTRACT: The Italian railway network systems is under rapid expansion and several new railway lines are under construction in the Country. Most of these new lines in Italy include numerous long tunnels and more than 40 TBMs will be in operation simultaneously to complete the works in the tight schedule imposed by the European Community that, through the Next Generation EU funds, contributes to finance these infrastructures. However, many of these tunnels cross clayey formations in extremely poor local conditions, with strongly converging and squeezing behaviour in presence of gas. The difficulties posed by such geological conditions could not be faced by the "standard" TBM designs available on the market. Indeed, without the introduction of substantial innovations, the mechanical excavation of these tunnels would have been impossible. At the same time the execution of these tunnel by conventional excavation would have required extremely long times, not compatible with the challenging schedule foreseen. To deal with these criticalities and ensure at same time high productions of the TBMs, specific and innovative technical and design solutions have been developed, such as: excavation with variable diameter, accentuated shields conicity, redundant cutting tools arrangement on the cutterhead, dynamic hydrodemolition "on the go", static hydrodemolition, continuous mining system, reinforced shields, extended sensors for preventive maintenance and gap monitoring, exceptional thrust, active articulation, high viscosity lubricant injection capability. The muck transport and the services along the tunnels have also been improved to reduce the TBM stand by times for the extension operations. Some of the mentioned design features have been tested in previous and on-going projects while some others have been developed for these applications. The article will describe the adopted solutions and innovations, the rational for their introduction and the first outcomes from the project sites where the TBMs have already started the excavation.

Keywords: convergence, gas, clay, thrust, hydrodemolition, innovation

1 INTRODUCTION

The rapid expansion of the Italian railway network has ushered in a wave of construction projects that demand the creation of an extensive network of tunnels. To meet the ambitious schedule imposed by the Client Rete Ferroviaria Italiana (RFI) and to be fulfilled by Webuild as main contractor, more than 40 Tunnel Boring Machines (TBMs) are planned to be in operation at the same time.

These projects span the entire Italian peninsula, with a notable concentration in southern Italy. Notably, they involve the Naples-Bari and Salerno-Reggio Calabria connections, and the new Messina-Catania-Palermo railway line in Sicily.

A substantial portion of these tunnels, especially those in Sicily, cross clayey formations marked by exceptionally challenging geological conditions. These include pronounced convergence and squeezing behaviours, particularly in presence of gas. Conventional TBM designs proved to be insufficient to address these formidable challenges, necessitating the introduction of substantial innovations to enable mechanical excavation within the strict project timelines. To overcome these geological hurdles while ensuring optimal TBM productivity, a collaborative effort between Webuild Group engineers and the TBM's manufacturers has resulted in the development of pioneering technical and design solutions. This article provides an in-depth exploration of the innovative solutions and design features adopted to overcome the geological challenges posed by clayey formations. It elucidates the rationale behind their integration and presents initial outcomes from

*Corresponding author: m.monina@webuildgroup.com

DOI: 10.1201/9781003495505-264

project sites where TBMs have commenced excavation. Some of the described design features have been tested in prior and ongoing projects, while others have been developed specifically for these demanding applications. These innovations not only enable the successful completion of tunnels in adverse geological conditions but also contribute to the efficiency and reliability of TBMs in the ever-expanding Italian railway network.

2 METHODOLOGIES AND SOLUTIONS

In this chapter are described only the main innovations introduced on the TBMs, that supplement the general improvement of other well-known systems, such as extensive probe drilling facilities, grouting and increased dewatering capabilities, not part of the current focus.

2.1 *Excavation with variable diameter*

Acting on the excavation diameter can be one of the most effective actions to prevent the TBM from being blocked when it must face highly squeezing ground. At this purpose during the TBM's design phase a package of "special features" has been defined to make it possible the adaptation of the excavation profile, when necessary. A combination of main drive vertical displacement and enlarged cutting profile with additional and extended tools in the most peripherical positions, are effectively a good practice to let the TBM passing fast through the highly squeezing ground tunnel zones.

The sequence to increase the final boring diameter includes first the use of a copy cutter which creates empty space in the crown so that the cutting wheel can bore into a larger diameter. Once enough room is created, the gauge cutters can be shimmed out and installed at the most peripherical positions into the empty spare housings. The cutting tools are commonly shimmed out in subsequent steps up to a final total exposure of 130 mm (case of ripper tools) with respect to the nominal boring diameter. In addition, there is the possibility of the main drive displacement, commonly executed in two increasing steps, up to 65 mm each, for a total amount of 130 mm extra bore on radius. These features are activated in the most critical situation, where an extra bore exceeding the 80 mm on radius is required, to guarantee the steerability of the TBM even with high overcut. Moreover, the main drive can be designed with an initial offset between cutting wheel and center of shield, in the range of 10÷20mm, which gives an additional possibility to extra-bore.

Here below a schematic representation of the steps to increase the bore diameter:

In such case the total overcutting TBM capacity at crown is 260 mm, resulting from the combination of 130 mm of the main drive displacement and 130 mm of the gauge cutters shimming out.

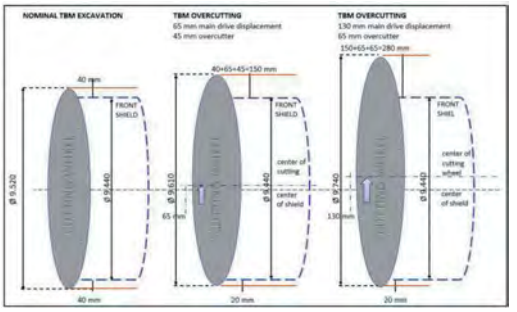

Figure 1. PA-CT maximum overcutting.

2.2 *Accentuated shields conicity*

In addition to the possibility of varying the excavation diameter as described in the previous paragraph, the TBM must have an adequate conicity or stepped geometry and the shortest possible length (compatible with the dimensions of the internal elements of the machine) to reduce friction with the ground.

In these regards, all the TBMs that will be used in the mentioned new projects, are designed with a much more accentuated conicity and a more stepped geometry compared to common practice. This allows for a greater gap between the ground and the shield and reduces the influence of the rock squeezing against the shield in terms of friction and load.

The proposed mitigation measures, aimed at addressing all the risks, therefore have a particular focus on those related to deformations and poor rock mass conditions in presence of high coverage, both in the excavation phase (problems related to the TBM and excavation management) and in the long-term phase (lining design).

In the figure below is included a schematic representation of the typical shield's conicity that has been applied in the recent TBM design development.

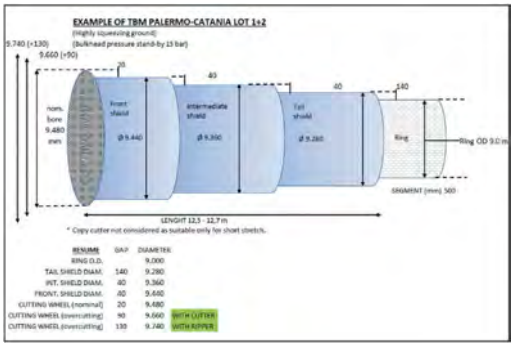

Figure 2. Shield conicity in Palermo-Catania Project Lot 1+2.

Particular attention was paid to maintain an appropriate gap between the tail shield and the extrados of the tunnel lining ring. This gap was estimated at 140 mm as shown in the figure below (case of TBM of Circonvallazione di Trento Project).

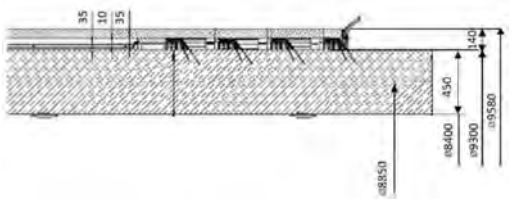

Figure 3. Tail shield gap in Trento Project TBM.

2.3 *Increased wear resistance*

On the cutterhead, the installation of an additional cutting line, for a total of 3 lines (long rippers/cutters, short rippers, scrapers), guarantees an extended protection against wear of the face and especially of the gauge part of the cutting structure.

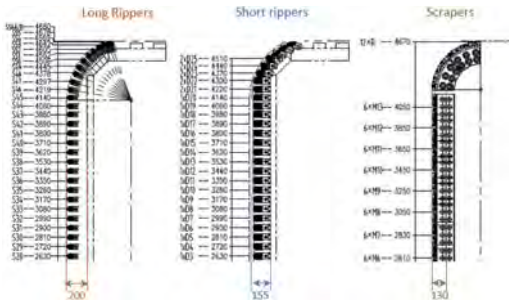

Figure 4. Cutting lines protrusion in mm on ME-CT lot 2 - forza d'agrò TBM.

The excavating tools, provided with a massive amount of tungsten carbide inserts employed to increase hardness and wear resistance, reduce the frequency of replacement in hyperbaric conditions and often in presence of gas.

Special passive protection, like Vautid or similar on the gauge, are foreseen as well.

To avoid clogging phenomena, water nozzles in the center can inject water up to 300bar, while a minimum opening of 38% of the center optimizes the muck flow.

On the tail shield, the adoption of special wear resistant brushes with Teflon inserts and the employ of an additional grease chamber, has proved to be an effective measure to extend the sealing life.

2.4 *Static and dynamic hydrodemolition*

In case of shields blockage, there have been already successful experiences of application of the hydrodemolition system with high pressure water (up to 1600 bar) through holes arranged along the shield, to achieve the disintegration of the pile resting on the TBM. Nevertheless, in case of extended and extremely quick squeezing conditions, the single application of the system might not be decisive. Therefore, an enhanced version of the system while advancing, called "hydrodemolition on the go" or "dynamic hydrodemolition", has been developed. Such system, first employed by the Webuild group's company Seli Overseas on Cociv Radimero Project, allowed to halve the thrust required to advance the TBM. The spacing of the nozzles, together with a 12° slope of the jet with respect to the surface of the shield, is essential to provide a connection between the fractures created by two adjacent nozzles, creating a continuous and more effective fracture surface along the tunnel kidneys and reducing the compression of clay material on the TBM shield.

The coming TBMs, are all factory provided with pre-drilled holes for hydrodemolition to cope with these exceptional conditions, designed for cases where thrust values around the shields are excessive.

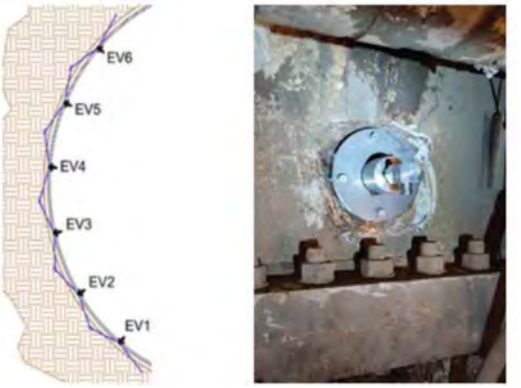

Figure 5. Nozzle detail and distribution on the shield in cociv radimero TBM.

2.5 *Continuous mining system*

One of the main limitations in the performances of the single shield TBMs is that its cycle of advance foresees to alternate the excavation with the segments erection. The Continuous Mining System instead allows the segments erection of the ring during the boring stroke, with a consequent decreasing of the cycle time. This requires the TBM to be equipped with adequate thrust cylinder stroke (about 3.1-3.2m for 1.8m long segment) and an intelligent steering control system that keeps unchanged the position of the center of thrust of the TBM. This is possible thanks to the PLC adjusting the pressure of the cylinders when some are retracted for ring building. The number of segments installed while the TBM is boring may vary from 3 segments to the full ring depending on the penetration rate of the machine. The Continuous Mining system, as prepared, allows the ring assembly to begin when the TBM has excavated about half of its advance stroke, installing part of the segments simultaneously with the excavation of the second half of the stroke. The decision to begin ring installation only in the second half of the excavation stroke made it possible to

contain the elongation of the thrust cylinders and thus the length of the machine shields.

The number of segments the TBM is able to mount "in shade" at the excavation stage varies according to the TBM's speed; the slower this is, the more segments can be installed. The hourly output of the TBM increases in terms of meters/hour of advance by a percentage ranging typically from 20% to 30%.

In addition, the shorter TBM standby time between excavations allows for more continuous shield advance, a very important factor in crossing critical areas to avoid shield entrapment and to reduce face instabilities.

In conclusion, the combination of higher productivity and shorter stand-by times significantly reduce the operating hours of the TBM and consequently the working hours of its electromechanical parts, reducing the need of maintenance of the parts themselves.

2.6 *Reinforced shields*

Another critical factor for the TBMs operating in clay as the ones of Palermo-Catania project, is to accommodate the special condition of anisotropic loads on the shields, with anticipated pressures reaching up to 15 bar under static conditions.

Three distinct scenarios, as illustrated in Figure 6, have been meticulously examined and designed for the shields, with particular focus on the tail shield.

In Scenario 1, we have considered the potential presence of horizontal thrusts surpassing vertical thrusts. The value under consideration is K0 = 1.5, representing the maximum value observed in hydraulic fracturing tests.

Similarly, in Scenario 2, we have considered the possible existence of voids in the crown area and/or along the excavation profile. In this scenario, thrust does not engage certain sections of the shield. Due to the presence of these voids, the shield will remain unconfined, allowing for free outward deformation.

Lastly, in Scenario 3, we have accounted for the potential presence of voids in the crown area and/or along the excavation profile. Here, the thrust does not affect specific portions of the shield. As with the previous scenario, the shield is not constrained due to the presence of voids, permitting unrestrained outward deformation.

The three load conditions described above led to the joint choice with the TBM manufacturers for a Q690D type steel (yield strength ≥ 690 MPa, ultimate tensile strength 730-940 MPa) with a tail shield thickness of 70/80 mm, reinforced with 30 mm thick ribs, arranged both longitudinally and in cross-section as depicted in Figure 7.

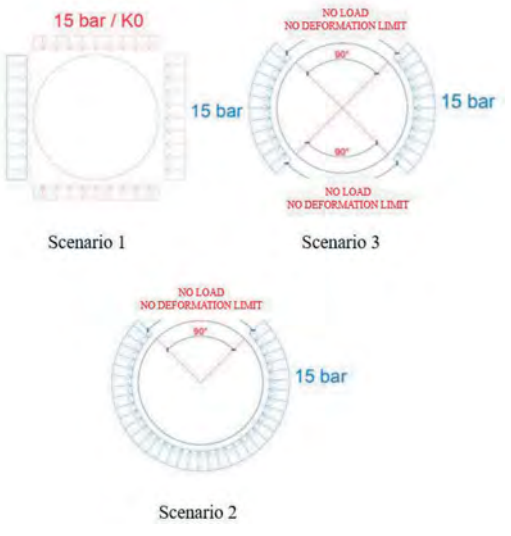

Figure 6. Three different load scenarios for shield dimensioning .

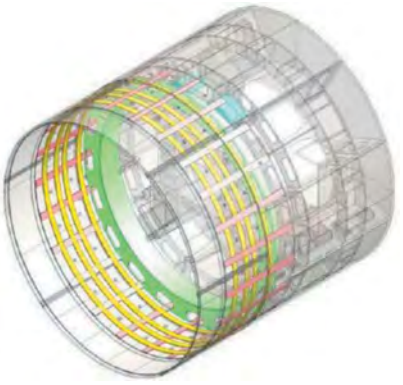

Figure 7. Tail shield: in yellow highlighted the internal reinforced ring 30mm thick.

2.7 *Extended sensors for preventive maintenance*

The TBMs will be provided with an extensive amount of sensors, controlling critical components such as main bearing seals, lubrication oil, main drives reducers and electric motors, VFDs, hydraulic pumps, cutting tools, critical parts of the belt conveyor system. The information provided by these sensors, will be elaborated by a specific software (named "S.M.I.L.E."), that is being introduced by Webuild with the target of facilitating the maintenance of the TBM and conveyor systems and automatically elaborates a complete planning of the maintenance interventions based on the actual operating cycles and sensors data of the machine.

Making use of the most recent technologies of the digital world (Internet Of Things, Digital Twin, Big Data, Artificial Intelligence and Machine Learning) is able to provide a practical and simple tool that allows to schedule daily, medium-long term and extraordinary maintenance, reducing drastically the failures that stop the production process. The software is used for the maintenance of the TBM and Backup System, the Tunnel Conveyor and the Cutterhead. A full integration with the already existing Weview web platform (also developed by Webuild) is guaranteed, from

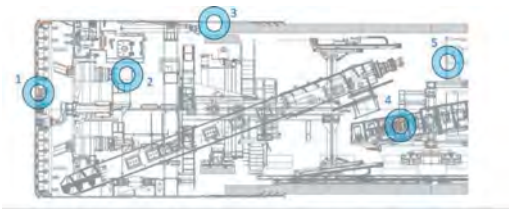

Figure 8. Main families of sensors on the TBM and belts: 1-cutting tools; 2 gear and lube sensors; 3 void detection; 4 belt system; 5 gas sensors.

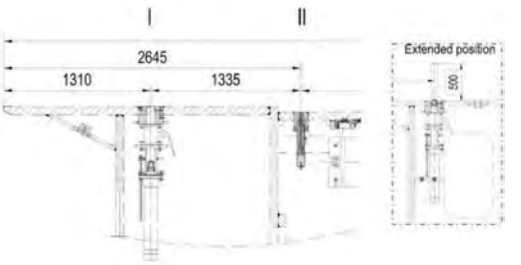

Figure 9. Fontimeters along the shields and detail.

which to collect the operating & sensors data of the TBM and to which send the maintenance reports for the creation of the database and the relative inspection and maintenance sheets.

The three types of maintenance can therefore be properly planned and by doing so anticipate/prevent the failures that could stop the entire excavation process:

- Preventive Maintenance: programming of Interventions performed at regular time intervals or when a certain usage threshold is exceeded;
- Predictive Maintenance: correct/fine tune the preventive maintenance program considering the operational and sensors data of the TBM;
- Corrective or extraordinary maintenance: by analysing the operational and sensors data will also detect when a component is near to fail and automatically instruct an extraordinary maintenance intervention before of a catastrophic failure occur.

2.8 *Gap monitoring*

During mechanized excavation operations in the geological formations being traversed, an important feature planned in the shields are extensometers (fontimeters) and additional pressure cells in the three shields that make up the entire TBM.

Three pressure sensors and three extensometers are equipped on each shield - front, middle, and rear - to provide crucial data to the machine operator or the supervising engineer during excavation phases, such as monitoring over-excavation (through the extensometers) and increasing pressure on the shields (via the pressure cells).

In each shield, three extensometers are positioned just behind the excavation chamber: one in the center at 12 o'clock, the second on the right at 2 o'clock, and the third on the left at 10 o'clock. The extension of each individual piston is 500mm in the front shield. The extension of the extensometers in the middle and tail shield is 150mm because at this distance from the excavation face, a less extensive void presence is expected as increasing the distance from the excavation face results in reduced over-excavations.

The additional pressure cells, three for each shield (front, middle, and tail shields), are placed near the extensometers, in the positions previously mentioned.

2.9 *Exceptional thrust and active articulation*

To facilitate efficient and uninterrupted excavation operations with TBMs in the planned squeezing clay soils, particularly those in Sicily, as well as all other machines used in Webuild projects throughout Italy, we have specified two levels of primary thrust from the TBM suppliers. The first level is intended for standard operation, while the second level is meant for unlocking the TBM in case it becomes stuck due to squeezing on the shields.

Additionally, each TBM is equipped with an active articulation system for the front shield. This system serves to enhance the machine manoeuvrability and, when required for inspection or replacement of excavation tools like cutters, rippers, or scrapers, allows for the retraction of the front shield and the cutting head.

In the Palermo-Catania project (excavation diameter 9.32/9.48m), for instance, the primary thrust is distributed among no.42 thrust pistons (no.21 pairs) with diameters of 300/240mm (casing/rod) and a stroke length of 3200mm. These pistons act upon the 7 segments comprising the precast ring, with 3 pairs assigned to each segment. As for the active articulation, it comprises 16 cylinders with diameters of 420/300mm (casing/rod) and a 350mm stroke.

The total thrust values are summarized below:

- Total Thrust at maximum operating pressure: 118792 kN @ 400bar
- Total exceptional thrust for shield unlocking (Emergency): 163201 kN @ 550bar
- Maximum Articulation Thrust Cylinder Force: 77584 kN @ 350 bar.

2.10 *High viscosity lubricant injection capability*

In order to minimize the risk of the shield entrapment due to downtime, a further enhancement has been considered through the possibility of lubrication of the shield mantle with bentonitic mixtures, improved in terms of effectiveness and redundancy through three sections of nozzles uniformly distributed along the circumference, able to limit soil convergence in place, especially at soils that have a particular predisposition to this phenomenon.

Studies and tests have been carried out together with La Sapienza University of Rome to use a high

viscosity lubricating mixture and with the TBM manufacturers to set up the necessary injection systems. This solution ensures better lubrication of the shield by further decreasing the friction and counteracts subsidence, as far as possible, before the injection of the backfilling mortar.

Figure 10. Tests on high density lubricating mixture.

2.11 *Services extension time reduction*

Together with the "special features" designed to let the TBM passing through the tunnel sections, where a high squeeze ground behaviour is expected, there is a series of improvements on the extension of the services lines which contribute to reducing downtime.

Those are related to:

- Increase of the capacity of the conveyor belt cassette up to 1500 m belt storage
- Increase of the capacity of the ventilation duct cassette at the TBM's back up, up to 200 meters duct storage
- Optimization of the HV cable extension in the way to install the fixed cable that feeds the TBM together with the temporary cable of the back up cable reel
- Increase of the capacity of the hose reel at the TBM's back up, up to the double of the standard storage capacity
- Introduction in the back up of a dedicated platform that allows the extension of the tunnel pipes easier, faster and safer by means of lifting hoist.

The above measures have the target to avoid impacting heavily the TBM production cycle and reduce the downtime specially in the most critical zone, where the ground have highly squeezing behaviour and the TBM needs to pass through quickly.

2.12 *Dealing with gas*

In consideration of the geologic formations and the risk associated with the presence of gas, it has been necessary to design the TBM and other tunnel equipment in an ATEX configuration and in accordance to local italian regulations (NIR 44), which defines the specifications for the advancement of mechanized excavation in presence of gas in the rock mass. Based on Cociv Radimero experience, a dual aeration and air intake system is foreseen. The aeration system enables uncontaminated pressurized air to converge inside the excavation chamber and into the frontal area of the TBM, allowing dilution of the methane concentration.

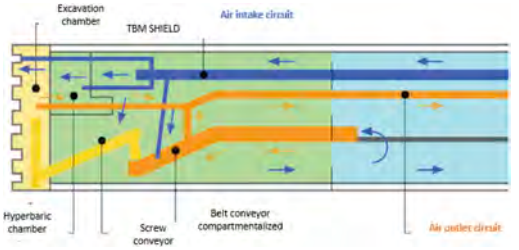

Figure 11. Air circulation in atex TBM.

The suction system is designed to extract contaminated air no longer into the tunnel belt duct (which often causes the TBM to stall) but directly outside the tunnel via an isolated and dedicated pipe. This solution ensures room compartmentalization by creating a flow path in the tunnel that is hydraulically isolated from the surrounding environment.

3 CONCLUSIONS

The paper highlights several significant innovations that have been introduced, often based on recent experiences within the Company Group. These innovations are designed to mitigate the risk of machine blockages in challenging conditions, such as those arising from soil squeezing, high overburden, and gassy soil. However, the success of the upcoming projects, which must be compliant to the tight schedule mandated by the European Community, will also heavily rely on effective project management.

Engineers, geologists and specialists on site, armed with machine data and geological information, will be tasked with meticulously planning the advance of the Tunnel Boring Machine. This includes identifying the most suitable areas for planned stoppages and harnessing the additional features integrated into these new-generation TBMs.

REFERENCES

Amadini, F., et al., 2021. Case studies related to jammed TBM in rock. Gallerie e grandi opera sotterranee, Italy, pp. 15–25.

Ashton, P.J., et al., 2021. Analysis of two-component clay sand backfill injection in Japan. WTC 2019 Proceedings.

Grandori, R., et al., 2022. WeView - An Integrated Data & Elaboration System of Global Underground Projects. WTC2022 Proceedings.

Tunnelling for a Better Life – Yan, Celestino, Thewes & Eberhardt (Eds)
© 2024 The Author(s), ISBN 978-1-032-80042-4
Open Access: www.taylorfrancis.com, CC BY-NC-ND 4.0 license

The application of tunnel boring machines in the execution of incline and decline tunnels in mining projects

M. Nasiri*
Sound Mining Solution (Pty) Ltd, Johannesburg, South Africa

H. Moammeri
Project Managers and Design Engineers Limited (PMDE), Mahe, Seychelles

G. Stripp
Sound Mining Solution (Pty) Ltd, Johannesburg, South Africa

ABSTRACT: Tunnel boring machines (TBMs) have gained considerable attention in recent years due to an increased demand from investors and mine owners to deliver mining operations at the earliest possible timeline, along with increasingly demanding environmental restrictions and global health and safety trends. The TBM has been used to address different objectives in mining projects, such as access to ore bodies or mining areas, water supply and exploration. Several technical and financial parameters should be considered in the selection of the right TBM type and method statement. One of the most important design parameters is the gradient of the tunnel, especially in access tunnel planning and development. In circumstances where ore bodies occupy either a high depth from the surface or in mountainous areas, the vertical alignment of planned mine access tunnels may have a relatively high gradient. Addressing the issues around these high gradient requirements creates unique TBM design and planning challenges. This paper briefly reviews several recently executed and studied tunnelling projects using current TBM technology. The findings will assist mining industry clients, consultants and contractors when evaluating TBM applications in future projects.

Keywords: Tunnelling, TBM, Mining, High gradient

1 INTRODUCTION

There is currently an increasing focus amongst investors and mine owners to consider the utilisation of Tunnel Boring Machines (TBMs) in mining projects. This can be explained by the capacity of this tunnelling system to deliver rapid and safe ore body access, which in turn can secure early project revenue generation.

Table 1 presents a list of projects where TBMs have been used to construct tunnels for access, conveyance, drainage, exploration and water diversion purposes for new and existing mines (Brox, 2013).

The application of TBM tunnelling systems requires that the following technical areas be investigated to achieve the benefits of rapid TBM excavation. These areas include:

- Geological and hydrogeological conditions
- Site access roads
- TBM assembly and disassembly
- Tunnel alignment and gradient
- Contractor experience
- Project schedule and procurement
- TBM size
- Tunnel support and lining
- Muck disposal and transport system
- Logistics

Tunnel alignment and gradient remain one of the most important technical areas in mining project evaluation. In circumstances where ore bodies occupy either a high depth from the surface or in mountainous areas, the vertical alignment of planned mine access tunnels may have a relatively high gradient.

This paper briefly reviews several executed and recently studied tunnelling projects using current TBM technology. The findings may assist mining industry clients, consultants and contractors when evaluating TBM applications in future projects.

*Corresponding author: mnasiri@soundmining.co.za

DOI: 10.1201/9781003495505-265

2 SOME EXAMPLES OF EXECUTED PROJECTS

The history of TBM tunnelling for mine exploration and access tunnels started more than fifty years ago with the Step Rock Iron Mine in northwestern Ontario, Canada. After the earliest applications and attempts of TBMs in mining operations (often using machines not originally or specifically designed for mining projects), the mining industry has witnessed more successful TBM applications. A significant amount of experience has been gained over the last three decades, with an increasing willingness of the manufacturers to design TBM machines specifically suited for mining operations. Some more recent TBM applications are considered below;

Table I. TBM Use in the mining projects (Brox, 2013).

Project	Location	Project Start	Length (km)	Diameter (m)
Step Rock Iron	Canada	1957	0.3	2.74
Nchanga	Zambia	1970	3.2	3.65
Oak Grove	USA	1977	0.2	7.40
Blyvoor	South Africa	1977	0.3	1.84
Fosdalen	Norway	1977	0.67	3.15
Blumenthal	Germany	1979	10.6	6.50
Weatfalen	Germany	1979	12.7	6.10
Donkin Morien	Canada	1984	3.6	7.60
Autlan	Mexico	1985	1.8	3.60
Kiena	Canada	1986	1.4	2.30
Stillwater EB	USA	1988-1991	6.4	4.00
Fraser (CUB)	Canada	1989	1.5	2.10
Rio Blanco	Chile	1992	11	5.70
San Manuel	USA	1993	10.5	4.60
Cigar Lake	Canada	1997	>20	4.50
Port Hedland	Australia	1998	1.2	5.00
Stillwater EB	USA	1998-2001	11.2	4.60
Mineral Creek	USA	2001	4.0	6.00
Amplats	South Africa	2001	0.35	2.40
Monte Giglio	Italy	2003	8.5	4.90
Tashan Coal	China	2007		4.90
Ok Tedi	PNG	2008	4.8	5.60
Los Bronces	Chile	2009	8.0	4.20
Stillwater Blitz	USA	2012-2013	6.8*	5.50
Grosvenor Coal	Australia	2013	1.0*	8.00
Oz Minerals	Australia	2013	11*	5.80
Norhparkes	Australia	2013	2.0*	5.00
EI Teniente	Chile	2014	6.0*	10.00

* Planned TBM excavation.

2.1 *The grosvenor decline tunnel, Australia*

The Grosvenor Decline Tunnel is a metallurgical coal project owned by Anglo American in Moranbah, Central Queensland, approximately 180km southwest of the coastal port city of Mackay and about 1,000km north of Brisbane (Scialpi, Ofiara, 2013).

The Grosvenor Coal Mine considered two decline tunnels, creating mine access to the shallowest coal seam depth at 130m. Longwall panels are 300m in width with lengths up to 6,200m. The first decline tunnel is used for the transportation of coal from the longwall to the deposit area on the surface, while the second decline tunnel is designed to transport staff and machinery (Figure 1).

Both decline tunnels are approximately 1,000m in length with a gradient of 1:6 or 16.7%, see Figure 2 (Tunnel Talk website), approximately 9.5º for the conveyor drift and 1:8 or 12.8%, approximately 7º for the transport drift. Except for the vertical curve (400m radius) between the assembly area on the surface and the launch tunnel, there are no curves along both drifts' alignments.

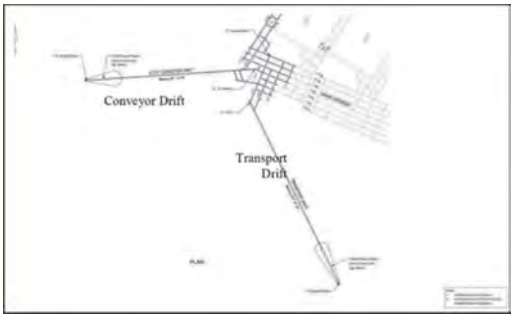

Figure 1. Plan view of conveyor and transport drifts.

Figure 2. Long access tunnel is at 16.7% incline.

Each drift has an internal diameter of 7.0m and consists of a steel-fibre-reinforced concrete segmental lining (universal ring in 5+1 segments).

The TBM decline tunnels at the Grosvenor Coal Mine are designed to be "blind headings", i.e., excavation ceases when the TBM reaches the coal seam. The TBM developed one tunnel at a time and must be retracted back up the slope through the pre-cast concrete-lined tunnel it has just completed. The TBM must be retracted quickly so that continuous mining machines can access the coal seam to begin the follow-on mine development work. The TBM is also needed to begin excavation of the second drift as soon as possible. Both drifts need to be completed and cleared to allow effective mine development work to proceed.

The Grosvenor Earth Pressure Balance (EPB) TBM design incorporated special features to allow quick demobilisation in a "blind heading" without the need for a large disassembly chamber. Underground disassembly on the steep gradient would have been difficult, costly and time-consuming due to the mine's strict roof support requirements for such a large chamber.

The Grosvenor Project was successfully completed and proved that TBMs are well-suited in mining operations for main access and conveyor haulage tunnels as well as ventilation tunnels, offering numerous advantages compared to drill and blast or road header excavation tunnelling methods, such as

- improved personnel safety;
- higher advance rates;
- better precision and control;
- improved ventilation;
- smoother tunnel profile; and,
- reduced ground disturbance and ground support.

2.2 *The Monte Giglio incline tunnel, Italy*

This tunnelling project involved the construction of a 9,500m tunnel for the installation of a conveyor belt linking the "Colle Pedrino" quarry to the new cement production factory of Calusco D'Adda in Bergamo (Busillo et al., 2006). The tunnel portal was located in the area of the Monte Giglio quarry near the cement factory. The tunnel route has a gradient of 6.2° for approximately 850m, a shallow rise of 0.5° to 1.25° for approximately 5,800m and a final sharp rise with an ascending slope of up to 11.86° for approximately 2,900m. The tunnel was bored using a double-shielded Robbins TBM with a diameter of 4.88m and was lined with 200mm hexagonal-type pre-cast reinforced concrete segments.

2.3 *Parbati H.E. incline tunnel, India*

The project consisted of boring two inclined pressure tunnels of the Parbati-II Hydroelectric project by one double shield TBM. The project consists of 1,546m twin tunnels with a finished diameter of 3.5m, each with an incline of 30º (Khali et al., 2013). The TBM could excavate through rock at steep inclinations but also install the tunnel lining with hexagonal-shaped pre-cast concrete segments mechanically. Figure 3 shows the breakthrough (ITA newsletter, 2008).

Figure 3. Breakthrough in inclined pressure shaft with TBM.

2.4 *"Linth-Limmern" (KLL), Switzerland*

The AXPO power station Linth-Limmern built between 1957 and 1968, is located in the Swiss Alps, at Glarus" south of Zürich (Burger, 2012). The existing plant, approximately 300 MW, was modified and extended to a pump storage plant with an additional capacity of approximately 1,000 MW at peak power. The new underground powerhouse was positioned close to the existing dam reservoir at 1,850m above sea level and connected to the natural but now extended lake Muttsee, at approximately 2,450m above sea level. Part of the connection was the two new, 1km long inclined pressure shafts of 5.2m excavated diameter at a gradient 40°. The Gripper TBM was assembled in the horizontal position and moved to the launch position onto a ramp with a 14° incline. The final shaft inclination, 40°, was then achieved by a TBM-bored vertical curve with a radius of 150m (Figure 3).

2.5 *Snowy 2.0 project, Australia*

Snowy 2.0, a major pump-hydro expansion of Australia's renowned Snowy Mountains Scheme, is underway, with tunnelling to commence. The majority of the tunnels on Snowy 2.0 will be constructed by TBMs, including a pre-cast segmental lining support system (Snowyhydro website). Figure 5 shows a schematic profile of the plan (Energymatters website).

The remainder of the underground works, including the access tunnels, shafts, and power station complex, will be constructed by a drill and blast method. Future Generation, the client, has procured

Figure 4. A view of gripper TBM.

three single-shielded TBMs for the construction of the Snowy 2.0 underground works, including two open-mode and one dual-mode machine. The TBMs will have a nominal excavation diameter of 11m and will be compatible with a common concrete segment geometry.

Whilst relatively similar in this regard, the challenges faced by each TBM differ substantially due to the respective tunnel arrangements, construction strategies and anticipated ground conditions. The second TBM to commence excavation is supplied by Herrenknecht, and will excavate a 2.7km long emergency, cable and ventilation tunnel, which will access the power station complex parallel to the main access tunnel. Beyond this point, the TBM will continue its drive up a 25º inclined pressure shaft to the upstream surge shaft before continuing into the western portion of the headrace tunnel.

Figure 5. Snowy 2.0 scheme.

3 SIMILAR TBM PROJECTS BY SOUND MINING GROUP

Sound Mining Solution (Proprietary) Limited (Sound Mining), in collaboration with Project Managers and Design Engineers Limited (PMDE), assisted two different clients by providing professional consulting services for Preliminary Feasibility Studies (PFS) which considered orebody access by TBMs. The two case studies are considered further.

3.1 *TBM for twin decline access tunnels*

Inspired by the Grosvenor decline tunnel in Australia, mechanised tunnelling by means of a TBM has been considered for developing twin decline access tunnels in an underground Iron Mine Project.

In consideration of the design approach, the geometry and dimensions of the orebody, including shape, size, dip, strike, depth and extent of the orebody, are critical parameters for mine design purposes. An oblique view of the orebody under consideration is presented in Figure 7. It shows views looking northeast (almost perpendicular to the strike) and a side view with approximate dimensions. Sublevel caving (SLC) was selected as the preferred underground mining method.

All required TBM studies have been completed at a Preliminary Feasibility Study (PFS) level. The TBM tender has been awarded, along with the selection of the EPC Contractor to execute the project.

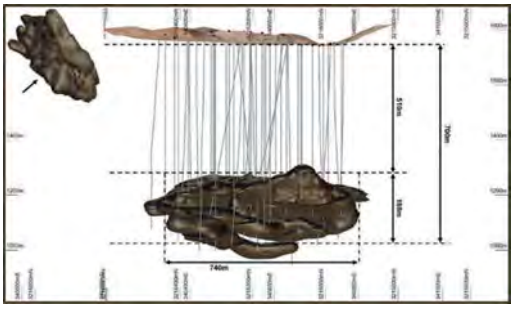

Figure 6. Generalised views of the underground orebody.

3.1.1 *Tunnels geometry and alignment*

Different alternatives were considered to access the underground orebody. One of the alternatives considered was implementing a twin decline tunnel system. An alignment (route) of the decline system was designed and is presented in Figure 8.

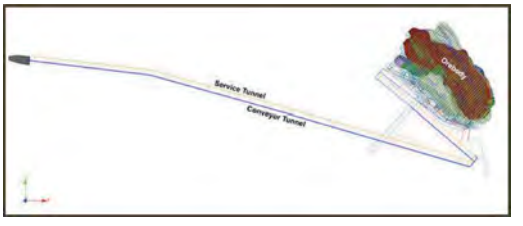

Figure 7. Plan view schematic of twin decline.

In order to design the decline route, the following parameters were carefully considered:

- geometry and location of the orebody;
- stope and development designs;
- crusher(s) position;

- position of the existing portal; and,
- Maximum gradient of 16% for the decline tunnels.

It should be noted that the start coordinates of the declines were considered fixed points due to the previously excavated tunnel portal.

Different options for designing the twin decline tunnels were investigated and considered in the following steps:

- development of the mine design criteria;
- design of the stoping (production) area in the orebody;
- design of the underground infrastructure to link all the underground tunnels and excavations;
- design of the access underground from the surface.

The twin decline's cross sections are illustrated in Figure 9.

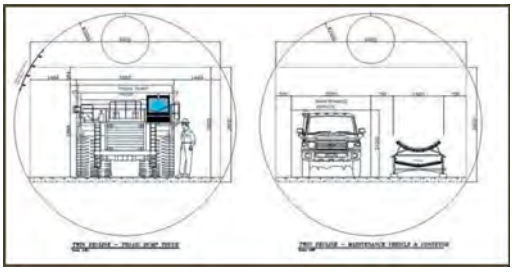

Figure 8. Cross section of twin decline tunnels.

This consists of a conveyor decline equipped with a conveyor belt and a maintenance roadway adjacent to the conveyor belt. The maintenance roadway is wide enough to accommodate a utility vehicle which will transport conveyor belt spares, tools, equipment and maintenance personnel. The conveyor decline will transport the rock from the mining area to the stockpile area on the surface. The second decline tunnel (service decline) will be designed at a 7m diameter to transport personnel, equipment, machinery logistics and support ventilation requirements.

Figure 10 Provides a profile view of the declines.

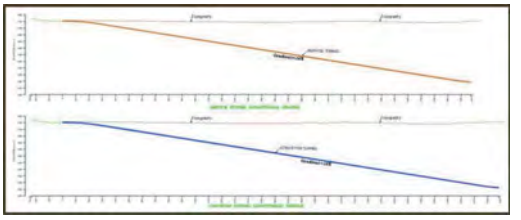

Figure 9. Profiles of the decline tunnels, mechanized section.

3.2 *TBM for an incline ore conveyor tunnel*

Inspired by several incline tunnels worldwide, TBM tunnelling has been selected for an Ore Transfer Tunnel excavation. This was a separate project in a very different international locality, and the project scope focused on providing the shortest possible access route to transport the mined ore from the deposits down from higher elevation mountainous areas to lower elevation areas where the ore would be discharged onto the designated stockpile areas. In order to navigate the environmentally sensitive areas on the surface, it was decided to investigate the use of an underground tunnel between the deposits at the top of the mountain and the low-lying areas.

The selected access design is a 7.5 m internal diameter underground tunnel equipped with a conveyor belt to transport 34 Mtpa (Million tonnes per annum) of mined ore from the deposits at the top of the mountain to the low-lying area. It has been assumed that all heavy-duty and large equipment would be transported on the surface via the construction roads.

Various technical areas were identified during the scoping of the PFS and formed the basis of the scope of work. These included:

- Tunnel geometry and cross-section
- Geology and geotechnical studies
- General method statement
- Portal designs
- Tunnel Boring Machine (TBM)
  - o TBM selection
  - o TBM backup system requirements
  - o TBM launching structure design
  - o TBM ventilation system
  - o TBM assembly and disassembly plans
  - o Muck handling
- Tunnel lining and inlay segments design, including waterproofing
- Tunnel Services
  - o Tunnel power supply
  - o Compressed air supply
  - o Industrial water supply
  - o Tunnel drainage system
  - o Tunnel ventilation
- Site mobilisation plan
- Risk assessment

3.2.1 *Tunnels geometry and alignment*

Several alternatives for the tunnel alignment were studied, and the finally selected characteristics at the PFS design stage are as follows:

- The tunnel will be a single tube with no transfer point or cross passages along the route.
- The tunnel length is about 5km.
- Vertical alignment will be according to the variable gradients from the Lowland's Portal 0.5°, 6° and 15°, see Figure 10.

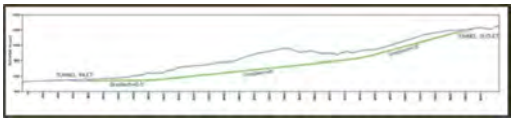

Figure 10. Longitudinal profile of the tunnel.

- Horizontal alignment will be rectilinear with no curves at the ends.
  The final cross-section of the tunnel is presented in Figure 11. According to execution and operational requirements, the final diameter and excavation diameter will be 7.5 m and 8.3 m, respectively.

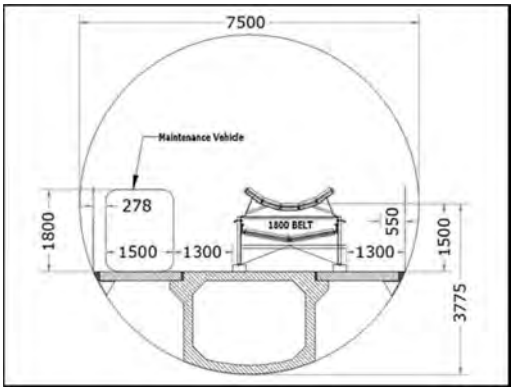

Figure 11. Cross section of the tunnel.

3.2.2 *General method statement*
Three principal alternatives for the method statement were identified as described below:

- Alternative I: Tunnel construction by one shielded TBM (Length = 5,030m). In this alternative, a dual-mode TBM, which can work in closed soil, will be the optimal choice.
- Alternative II: Tunnel construction from two working faces by one shielded TBM (Length = 3,645m) from the tunnel inlet and conventional method (Length = 1,385m) from the tunnel outlet.
- Alternative III: Tunnel construction by one Gripper TBM (Length = 5,030m). Depending on waterproof requirements, two sub-alternatives with or without cast in place for concrete lining is considered

A study was compiled on these alternatives for the method statement describing and discussing key comparisons. For this exercise, no constraints around the project were assumed. This approach assisted the project team to consider all possible method statements at the PFS level. The TBM was assumed to be the main excavation equipment for the tunnel. A Multi-Criteria Analysis (MCA) was used to compare the alternatives and select the optimal option. The following principal goals have been targeted to select the optimal alternative:

- Minimise the construction time
- Minimise the total project costs
- Minimise the impact of the construction on the environment
- Maximise the technical adequacy (directly related to the reduction of the construction time)

As a preliminary result, Alternative I was selected as the basis for further studies at the PFS level.

4 CONCLUSIONS

The main advantages of TBM tunnelling compared to drill and blast or road header excavation (conventional/traditional methods) are:

- Higher advance rates by TBMs;
- Successful excavation through heterogeneous and loose rocks by using the correct TBM type;
- Successful excavation of hard to very hard rocks like Quartzite;
- Their optionality to manage groundwater control at the tunnelling face through closed-face TBMs and heavy-duty drainage pumps in the tail shield area;
- Improvement in health conditions for workers by providing a safe place in the shield, along with the support benefits of concrete segmental lining erection;
- Better ventilation control; and
- Smoother tunnel profile and clean working environment.

The main disadvantages of the use of TBMs for mining projects are as follows:

- High initial investment for the TBM purchase or for the modification requirements for the second-hand TBMs, along with their supporting logistical systems, including concrete moulds and transport systems, etc;
- TBM tunnelling should be considered as a separate project itself within the mining project programme, which needs to be carefully managed by specialists with TBM insight;
- Long lead times are required for TBM projects; this includes site establishment at the job site (12 to 14 months), TBM installation (2 to 3 months) and finally, TBM commissioning (1 to 2 months);
- The circular shape of TBM excavations creates their own design constraints when compared to conventionally excavated tunnel shapes.
- In circumstances where one TBM is being used to excavate two tunnels, it is necessary to consider two separate assembly and disassembly operations;
- Similarly, when using one TBM to excavate two declines, it is necessary to order a spare set of TBM shield skin due to burying the first set into the

ground if using one TBM only to excavate the twin declines.

TBM tunnelling systems can be viable techno-economic alternatives to conventional tunnelling approaches in mining projects. The TBM must be designed for the tunnel route's ground conditions.

ACKNOWLEDGEMENTS

The authors thank Sound Mining Solution (Pty) Ltd (Sound Mining) for their support of this project.

REFERENCES

Brox, D., 2013. Technical considerations for TBM tunnelling for mining projects. Proceedings of Transactions of the Society for Mining, Metallurgy and Exploration, Vol. 334, pp. 498–505.

SCIALPI. M., D. OFIARA, 2013. Unique Hybrid EPB Design for use in Coal Mine Drifts. Proceedings of ITA WTC 2015 Congress, Dubrovnik, Croatia, www.tunnel talk.com, TBM success signals coal access opportunity.

Busillo, A., D. Vizzino, R. Grandori, 2006, "The Monte Giglio Tunnel- Bergamo (Italy): Italcementi: Provisioning of Quarry Material for The New Cement Factory at Calusco D'adda". Felsbau 2006.

Khali, R.K., 2013. Boring of inclined pressure shafts by double shield TBM and problems of casting concrete in the Parbati H E Project Stage-II (Lot PB-3), Kullu, HP, India – a case study. Proceedings of ITA WTC 2013 Congress May 22-28, Geneva, Switzerland. ITA newsletter No. 32 Focus on India – June 2008 – ISSN 1267-8422, p. 8.

Burger W., 2012. Mechanised Excavation for Hydropower Projects. Proceedings of Montréal TAC 2012 (Tunnels and Underground Spaces: Sustainability and Innovations. www.snowyhydro.com.au www.energymatters.com.au

Tunnelling for a Better Life – Yan, Celestino, Thewes & Eberhardt (Eds)
© 2024 The Author(s), ISBN 978-1-032-80042-4
Open Access: www.taylorfrancis.com, CC BY-NC-ND 4.0 license

Soil conditioning for TBM performance advancement in mixed geology

Enrico Dal Negro, Alessandro Boscaro & Enrico Barbero
Mapei S.p.A, Milan, Italy

Alessio Menghini
Ferrovial, UK

Christopher Butterworth*
Mapei UK, Birmingham, UK

ABSTRACT: Soil conditioning is critical for optimising the performance of Tunnel Boring Machines (TBMs), especially in complex ground conditions such as those experienced at the Silvertown Tunnel Project, a 1.4 km long twin-bored tunnel under the Thames in London, excavated with a 12-meter diameter Earth Pressure Balance (EPB) machine by Herrenknecht. Mixed geology, which consists of various soil types with different properties, poses significant challenges to TBMs due to variations in soil composition, strength, and water content along the tunnel alignment. Soil conditioning techniques are employed to enhance the properties of the soil and improve its excavation properties. Foaming agents, or "Foams" are branded by type, some are dedicated for excavation through cohesive soils, while some foam types are relatively more efficient for heterogeneous ground. Other polymers can be considered emergency measures for the optimal management of mixed geology mining. Foams are injected into the soil to reduce its density and permeability, making excavation operations more efficient by reducing the resistance encountered by the TBM's cutting tools. Selecting the appropriate foam for soil conditioning is crucial to optimise TBM performance, meaning that the best results are obtained with efficient cooperation between the chemical supplier and the contractor. This study highlights the critical role of foam additives for soil conditioning in optimising the TBM performance for the Silvertown Tunnel Project, by comparing the adaptation of two different foams in specific geological conditions. Valuable insights have been gained regarding their effectiveness in reducing soil resistance and improving the overall performance of the TBM. The findings emphasise the importance of selecting the most suitable foam and adaptable strategy for each geological section of the tunnel alignment. The success experienced in the Silvertown Tunnel project is thanks to foam conditioning strategies, enhanced by support from supplier's collaboration since the preliminary stages of the project.

Keywords: Soil Conditioning, Tunnel Boring Machines, Tunnelling, Silvertown, EPB-TBM

1 INTRODUCTION

TBMs play a pivotal role in underground infrastructure construction, permitting efficient excavation through various geological conditions. One of the central factors influencing EPB operation performance is soil conditioning, a process aimed at developing the properties of the excavated soil, enabling improved extraction, transportation, and disposal. This paper discusses and explores the role of soil conditioning regarding performance, particularly the use of foaming agents in assisting TBM performance, with a specific focus on data from the Silvertown Tunnel Project. The complex geology with diverse properties encountered during the drives posed unique challenges for soil conditioning, requiring a dynamic approach and constant input from contractors and support from the chemical supplier.

The Silvertown Tunnel Project, a new twin-bore road tunnel under the Thames, will be the first in London in over 30 years. Serves to improve cross-river public transport, improving the reliability and resilience of the wider road network. Data from this project functions as an ideal case study for investigating the effectiveness of different soil conditioning agents and related strategies to enhancing TBM performance in diverse geological conditions.

The research presented in this paper aims to contribute to the knowledge base of TBM performance optimisation and soil conditioning techniques. It provides an in-depth analysis of the performance of four different foams from two suppliers in the application at Silvertown Tunnel Project's specific geological conditions. Valuable insights are gathered from this comparative study, shedding light on the effectiveness of these foams in reducing soil resistance and enhancing overall performance.

*Corresponding author: c.butterworth@utt.mapei.com

DOI: 10.1201/9781003495505-266

Figure 1. Silvertown break through southbound.

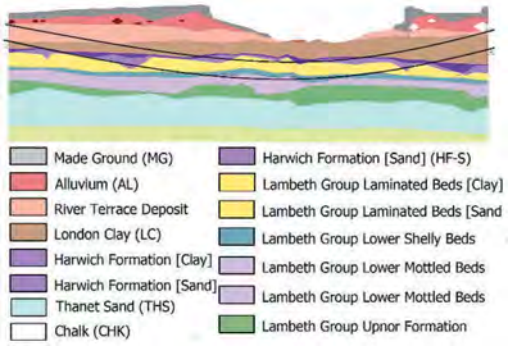

Figure 2. Geological cross section.

Soil conditioning is an essential element in the successful execution of tunnelling projects employing TBMs. Its significance arises from the intricate practice of modifying soil properties using various agents, such as foaming agents, polymers, or water, to facilitate excavation. The capacity to significantly diminish soil resistance is at the core of its importance, by modifying the soil's characteristics, particularly its density and permeability, flowability and also compressibility (Herrenkecht et al, 2011) should be taken into consideration, inevitability conditioned soil becomes more susceptible and responsive to excavation.

This reduction in resistance minimises the wear and tear on the TBM's cutting tools. Substantially enhancing the tunnel construction efficiency and allowing progress to run more smoothly and faster is advantageous on multiple fronts, reducing project timelines and curtailing energy consumption, resulting in reduced operational costs. Additionally, soil conditioning plays a pivotal role in extending the operational lifespan of TBMs and, in turn, reducing maintenance requirements. Given these machine's intricate nature and costliness, this aspect is of utmost importance and can translate into considerable financial savings over a project lifespan.

2 SILVERTOWN TUNNEL GEOLOGICAL CONTEXT

The geological profile along the alignment of the Silvertown Tunnel exhibits significant variation in ground conditions. It is composed of River Terrance deposit, a medium dense to dense slight clay, sandy to very sandy, angular to rounded, fine to coarse flint gravel with occasional cobbles; London Clay, a 100% clay mineral, plastic, stiff and sticky; Harwich formation, silty sand with gravel and cemented beds, fine-grained sand with varying proportions and pebble beds. Finally, the Lambeth Group includes Woolwich Formation laminated beds, lower shelly clay, and Reading Formation with lower mottled clay (Figure 2).

In summary, the varying geological scenarios along the tunnel alignment demonstrate a complex interplay of soil types and properties for the different formations. These diverse ground conditions necessitate careful consideration and selection of soil conditioning techniques, including the use of foaming agents, to assist the TBM operations.

2.1 *Geological scenarios*

The varying proportions have been categorised into distinct scenarios along the tunnel alignment. The scenarios have been strategically considered to align with the changes in soil composition, consistency, and the presence of specific geological profiles along the chainage. This deliberate approach serves a twofold purpose; facilitating a more precise interpretation of the data for the study and enhancing our understanding of the performance within the specific geological context. The data was analysed across six studies to capture the difference in foaming agents across the twin tunnels, by further tailoring the scenarios to match the geological conditions, we can draw more meaningful insights and conclusions about how the TBM behaves in response to the variations in the geological profile.

2.1.1 *Scenario 1*

Chainage 1240 – 1340, there is a predominance of River Terrace Deposits, with a lower amount of London Clay, this scenario features sandy gravel with low cohesive fraction and high permeability conversely, the presence of cohesive soil with excellent permeability values add complexity to the ground condition.

2.1.2 *Scenario 2*

Chainage 1340 – 1420, As we move into Scenario 2 the ground conditions become more mixed with a progressively decreasing presence of River Terrace Deposits, increasing presence of London Clay, and lower presence of Harwich Formation and Woolwich Formation.

2.1.3 *Scenario 3*

Chainage 1420 – 1530, London Clay becomes the dominant geology feature, accompanied by Woolwich

Formation Laminated Beds, the Harwich Formation is less prominent in this scenario, further emphasising the transition towards London Clay-dominated ground conditions. This section exhibits stiff and sticky silty sand with clay and is characterised by angles of shearing resistance and cohesion intercepts within specific ranges.

2.1.4 *Scenario 4*

Chainage 1530-2250, is marked by the predominance of Woolwich Formation Laminated Beds. This geological formation is composed of silty sand with clay, with relatively high angles of shearing resistance and minimal cohesion intercepts. However, the presence of the Harwich Formation and Woolwich Formation lower shelly clay introduces variability in ground conditions within this section.

3 IMPACT OF MIXED GEOLOGY ON TBM PERFORMANCE

Mixed geology in tunnelling projects introduces various challenges, through ranges in soil composition, strength, water content etc (Oliveira et al., 2017; Shirlaw, 2016). The soil composition can undergo significant shifts along the tunnel alignment, encompassing clay, sand, gravel, or combinations of geological ratios. Each soil type unique properties impact the TBM performance differently, requiring the careful selection of soil conditioning techniques, products and approaches to address the encountered soil types effectively. Additionally, merged variations in soil strength present shifting circumstances, with some sections featuring cohesive soils possessing high shear strength and others holding weaker or less stable soil layers. Managing these fluctuations in soil strength requires dedicated real-time monitoring and operational adjustments to maintain face stability (Anagnostou et al, 1996) and excessive wear issues.

Mixed geology can naturally affect the content of water and bring about dramatic changes, varying between well-drained, drier soils to submerged or saturated sections. Excessive water content presents difficulties, such as over-excavation, settlement and instability, requiring careful control and management of pressure differentials to uphold excavation efficiency and assist soil transportation and storage (Pixoto et al,2017). TBMs deployed in such conditions must be capable of managing these challenges to maintain operations, for the geology encountered by adapting the parameters and soil conditioning strategies. Certainly, successful navigation of mixed geology hinges on multiple factors, such as real-time monitoring and effective planning, however, the importance of soil conditioning adaptation cannot be emphasised enough for successful TBM operations, inevitably ensuring the integrity of the project.

4 SOIL CONDITIONING WITH FOAMS

Soil conditioning on TBMs encompasses several critical aspects. Firstly, it involves modifying the soil's inherent properties, including cohesion, density, and permeability, to render it more suitable for extraction, thus, effectively transmitting the pressure in the excavation chamber and along the screw conveyor (Herrenknecht,1994; Anagnostou and Kovari, 1996; Nomoto et al., 1999). For example, loose or granular soils may be compacted to support stability, while sticky cohesive soils are treated to alleviate adhesion and enhance ease of disintegration (Zumsteg et al, 2012),. A principal component of soil conditioning is the reduction of soil cohesion, this has the potential to restrict TBM progress substantially. As cohesive soils are characterised by their tendency to adhere together, appropriate soil conditioning strategies must be adapted this includes the use of chemical agents, such as foaming agents or polymers, to diminish cohesion to transform the soil properties into a more easily extractable state. This transformation prevents the TBM from becoming clogged and immobilised and additionally minimises excessive wear on its cutting tools.

Benefits can also be observed from enhancing soil permeability, particularly relevant in instances where developed drainage and prevention of water ingress into tunnels is crucial. Soil conditioning agents are utilised to promote the permeability of the soil, assisting challenges during tunnelling associated with water ingress. Adapting to geological profiles is fundamental to this process, as different conditions demand tailored approaches to mitigate risk and manage the desired soil properties for efficient excavation. Therefore, soil conditioning agents and techniques are distinct to the unique geological characteristics encountered in each tunnelling project.

4.1 *Silvertown foaming agents*

During this project, two specific foaming agent types were employed, Foam 1 and Foam 2, utilised for the primary purpose of soil conditioning. These foams have been carefully selected and tailored to address the unique geological conditions encountered along the tunnel alignment. Foam type 1 enhances excavation efficiency in granular and heterogeneous ground conditions, where soils may mix sand, gravel, and other granular materials. Designed to reduce soil cohesion, allowing for smoother TBM advancement by mitigating resistance and wear on cutting tools.

Foam type 2 is for cohesive ground conditions, typically characterised by sticky and adhesive soils, such as clay-rich substrates. This foam is engineered to break down soil cohesion effectively, making the soil more workable and less adhesive. Facilitating efficient TBM progress in such challenging geological environments by reducing stickiness and enhancing soil properties. Choosing the appropriate

foam type for soil conditioning is a critical decision that impacts TBM performance significantly. This paper explains the beneficial partnership between the chemical supplier and the contractor in selecting the most suitable foam for each geological section of the tunnel.

Many other foam types are available such as high-expansion and low-density foams, environmentally friendly, biodegradable foams (Dal Negro et al, 2022), and polymer-based foams, each one addresses specific soil conditions as needed and offers adaptability and flexibility in soil conditioning strategies. This paper focuses on the use of Foam 1 and Foam 2 types along with the personalised strategies selected to assist the tunnel excavation and related performance in the distinct geological scenarios encountered along the tunnel alignment with respect to the project.

5 IMPACT OF FOAM SELECTION

The importance of selecting the appropriate foam type for soil conditioning in tunnelling projects cannot be overstated, as it significantly influences the efficiency and overall success of excavation endeavours. Several critical factors related to foam selection highlight its significance, Principal the foam concentration should be considered a central figure in determining how effectively the foam and related consumption alters the soil properties. Next, the expansion characteristics or foam expansion ratio (FER) is important for achieving the optimum soil conditioning effects without causing over-expansion that could lead to ground instability. Additionally, the appropriate foam injection ratio (FIR) or total foam volume proportional to the treated soil, supports efficient conditioning while curtailing waste and cost. However, it is also important to recognise the foam types are not standardised across suppliers thus, each supplier entails a unique formulation that impacts overall performance in different geological conditions. Therefore, specific factors are related to suppliers and foam type, such as foam stability, which is essential to maintain the conditioned soil properties over time, inhibiting soil reaggregation. The ability to control water content is also crucial, finding a balance with soil conditioning parameters ensures the stability of the ground and minimises the associated risks.

Furthermore, the flexibility to change foam selection to support the different geological conditions along the tunnel alignment can be beneficial for efficient extraction. This holistic approach to adapting foam selection contributes to cost-effective and safe tunnelling and can also align with environmental requirements to minimise the ecological footprint for soil conditioning activities. In summary, the educated selection of foaming agents and appropriate strategy for geological encounters is a multifaceted decision that directly impacts the outcomes of TBM tunnelling works.

6 COLLABORATION WITH CHEMICAL SUPPLIER

The relationship between the chemical supplier and the contractor in implementing soil conditioning strategies for tunnelling works is a beneficial and communicative process that develops across multiple phases. It begins during the tender phase, where the contractor seeks to collaborate with the chemical supplier. During this initial stage, the chemical supplier engages closely with contractors to understand the project's specific requirements, geological complexities, and performance objectives. This early involvement ensures that soil conditioning strategies are considered from the project's initiation, setting the requirements for bespoke solutions.

A key stage of developing this collaboration is a comprehensive laboratory testing phase. Here, the chemical supplier and the Contractor work together to propose and conduct rigorous tests, as discussed by EFNARC (2005), Peila (2016) & ASTM (2017) simulating the project's geological conditions. These tests evaluate the performance of various soil conditioning agents, such as foaming agents, in modifying soil properties. Collaborative data analysis and interpretation help the Contractor make informed decisions regarding selecting the most effective conditioning agents in the field.

Once the project is in construction, the chemical supplier provides valuable on-site support and training. This entails close cooperation with the Contractor's on-site team, including TBM engineers and operators, to ensure that selected foaming agents are applied correctly and at the appropriate parameters. Recommendations and training include equipment setup, safety protocols, and contingency measures to address unforeseen challenges during tunnelling. This continuous support and guidance foster a collaborative environment that ensures the effective implementation of soil conditioning strategies throughout the project's duration, ultimately contributing to its success.

Finally, effective soil conditioning often requires collaboration between the project's engineers and chemical suppliers. Chemical suppliers bring their expertise to bear in selecting the most appropriate agents and techniques tailored to the specific soil types. This collaborative effort ensures that the conditioning process aligns seamlessly with the project's objectives, schedules, and successful execution.

7 SOIL CONDITIONING EVALUATING PERFORMANCE

Advancement operations for TBMs are performed and guided by numerous parameters: speed, thrust, main-drive torque, screw torque, contact force and EPB pressures, as these values are indicative of the TBM advancement, they provide insight into the overall performance. Comparing this average data

for these parameters across geological scenarios may correlate results, highlight trends, and identify variations.

Relationships can also be identified between the TBM parameters and the soil conditioning parameters to indicate TBM performance, specifically with respect to the proportion of foam to soil, indicated by FIR percentage. Understanding this impact of FIR on the excavation advancement illustrates if higher volumes of foam are associated with enhanced progress for the geological conditions. Establishing the optimal foam-to-soil ratio should generate performance increases whilst supporting efficient excavation effects. Acquiring this balance is the objective, as this assists in minimising resistance and the efficient use of foam resources, noting that in the situation finding the balance is key it should be recognised for foam conditioning "more" does not always translate to an improved situation establishing an equilibrium is essential for excavation efficiency and foam consumption for well-conditioned soil (Figure 3).

Figure 3. Conditioned soil southbound drive.

To further illustrate the performance differences within the range of TBM and Soil conditioning parameters, calculations can be made to demonstrate normalised performance indications (NPIs) in the context of TBM advancement, resistance reduction and excavation efficiency. The use of these NPIs, in conjunction with direct observations, to assist with each performance assessment, emphasises how foam conditioning strategies can be tailored to different geological scenarios. TBM advancement NPI can be defined as the difference between thrust and main drive torque, used as an indication of resistance. Moreover, the ratio can indicate how effectively the TBM is advancing through soils with reduced resistance, higher thrust and lower torque would be observed, and conversely, lower thrust and high torque may suggest increased resistance in the geological profile. An NPI for resistance reduction incorporates thrust, main drive torque and contact force, likewise providing value associated with resistance relative to the applied force providing a measurement of resistance reduction relative to applied force, a Lower ratio indicates reduced resistance reduction and contrariwise. An NPI for excavation efficiency includes values from multiple parameters to illustrate excavation efficiency, considering the cutterhead diameter, TBM speed, thrust and torque from the main drive, A Higher NPI may suggest that the TBM is achieving greater excavation progress for the energy and cutterhead size used.

8 COMPARATIVE STUDY OF FOAM TYPES

The paper uses data from both drives of the TBM, northbound nine hundred metres and southbound nine hundred metres, capturing the average TBM and related soil condition values across the opposing tunnel chainage for each advancement, divided into six studies enabling a systematic comparison of the foam types and suppliers in different instances. The data set captures 1.8 kilometres of tunnelling across the six studies, studies 2 and 4 are further divided into scenarios to give additional comparison with reference to the change in geology, we can also consider the difference in foam type and supplier (Table 1).

Table 1. Key study data.

Study	South Bound Advance	North Bound Advance	Scenario	Chainage
1	Supplier 1 - Type 2 (S1T2)	Supplier 2 - Type 1 (S2T1)	1	1252.6-1316.8
2	Supplier 1 - Type 1 (S1T1)	Supplier 2 - Type 1 (S2T1)	1 & 2	1316.8-1368.8
3	Supplier 1 - Type 1 (S1T1)	Supplier 1 - Type 2 (S1T2)	2	1368.8-1398.8
4	Supplier 1 - Type 1 (S1T1)	Supplier 2 - Type 1 (S2T1)	2, 3 & 4	1398.8-1756.5
5	Supplier 2 - Type 1 (S2T1)	Supplier 2 - Type 1 (S2T1)	4	1756.5-1872.5
6	Supplier 1 - Type 1 (S1T1)	Supplier 2 - Type 1 (S2T1)	4	1872.5-2154.3

All the results within the data sets have been analysed against one another, to obtain a clear

understanding and representative comparison, we can consider the data to have two areas of interest to directly associate to arrive at a performance-related conclusion in the comparison. Data values from the soil conditioning system; Consumptions of water and foaming agent, foam expansion ratio (FER) and foam injection ratios (FIR) and the data values from the TBM systems; thrust, main drive and screw torque, advance speed, penetration, cutterhead rotation contact force, EPB crown pressure.

9 CASE STUDY FINDING & DISCUSSION

Analysis of the data from the advancement average, NPIs and larger analysis values all show the same general trends associated with the FIR regarding the TBM parameters, namely thrust, main drive torque, speed, and pressures. Increasing FIR values show reductions in the discussed parameters, and, conversely, decreased values of FIR show increased values in the TBM parameters. This can also be demonstrated when comparing FIR, thrust and main drive torque values against the geological profile, in scenario 1, the average thrust and torque were the lowest, increasing when advancing into scenarios 2, then 3 and finally highest at scenario 4, the associated FIR values decreasing against this trend as the Thrust and Torque increase see Figure 4.

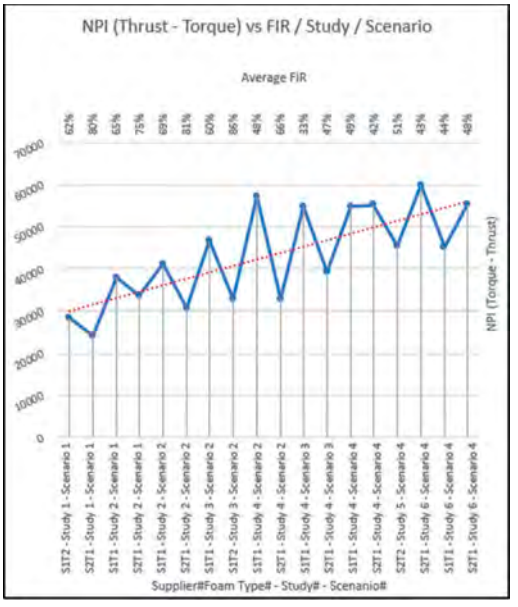

Figure 4. Average NPI 1 vs FIR, Study & Scenario.

As discussed, geological scenario 1 demanded a larger volume of water to support the extraction the EPB pressures were lower in this case, lower FER values were adopted, and given the lowest values for thrust, torque, and contact force, the related FIR values were observed to be higher. As the geology changes to scenario 2, FIR values peaked along with the foam and water consumption, but this translated to the highest values in the screw conveyor torque. thrust torque, and contact force values, on average, increased. Moving into scenario 3, these values peaked, and FIR values dropped along with water and foam consumption. In scenario 4, contact force peaked, thrust and torque remained level, but the water consumption was at the lowest along with the screw torque. It is essential to keep in mind that this summary is a generalisation of the values across the different geological scenarios. Therefore, variability is an inherent aspect of these results due to a multitude of variables and factors that can influence these results in such complex conditions. It is important to recognise that data organisation can be a valuable tool to reduce variability, additional in the evaluation of the scenarios, the data was deliberately arranged by advancing speed, such as, 40mm/min by refining that narrowed data set, it was possible to carefully scrutinise the effect of the TBM parameter within the specific scenarios, allowing for a more precise evaluation.

Comparing the average data sets from each study and related scenarios given northbound and southbound advances, we see the variation in all parameters, a difference of the FIR ranging 8-35% is observed, and commonly the higher this difference, the higher the difference in TBM parameters (Table 2). Across the average data sets for the study and scenario, mostly, TBM parameters show differences however we do see some isolated cases where individual parameters are similar, but not all parameters within the set are the same. For example, in study two scenario one, north and southbound advances are the same for an average torque of 8.46MNm corresponding soil conditioning values show a 16% difference for FIR and a 56% difference for concentration, giving an extra 195 litres of foaming agent. In this case, the entire TBM parameters only vary by 10%, considering this, it would be expected that northbound with increased concentrations to show favourable results in performance, but this is not the case. We see an average thrust increase of 24% and an average increase of contact-force of 9%, albeit the advance speed is 4mm higher, this case illustrates, given that the foam type is the same, better performance can be seen from adjustments in the soil conditioning parameters and foam supplier, leading to an optimum balance translating to benefits in the TBM performance.

The trends clearly reflect how geological conditions cause variations in the TBM parameters and related performance. The soil conditioning strategy is intern adapted to support these variations; thus, the performance of the said strategies should be the difference between the northbound to southbound trends in TBM parameters, not the effect of the change in geology. The distinction in the difference can be directly attributed to the performance of these strategies, as the geological conditions are the same. If we deliberate the specific challenges posed by

Table 2. Average data from study 1-6.

Study	1		2		3		4		5		6	
Supplier & Type	S1 - T2	S2 - T1	S1 - T1	S2 - T1	S1 - T1	S1 - T2	S1 - T1	S2 - T1	S2 - T2	S2 - T1	S1 - T1	S2 - T1
Average Thrust [kN]	36232	30491	47841	39954	55750	39698	65072	57651	55288	69802	54619	65040
Average MD Torque [MNm]	7.80	6.37	8.23	8.02	9.07	6.87	10.10	8.83	9.86	9.96	9.59	9.75
Average Speed [mm/min]	40.2	28.4	40.8	35.5	42.4	29.5	42.4	41.4	39.8	44.7	42.0	39.9
Average Penetration [mm/rpm]	20.0	14.0	20.3	18.1	20.8	15.0	20.9	20.5	19.7	21.9	21.0	19.8
Average Min Drive D Speed [rpm]	2.0	2.0	2.0	2.0	2.0	2.0	2.0	2.0	2.0	2.0	2.0	2.0
Contact Force [kN]	9784	8362	15470	13587	16696	14041	15883	14189	18031	18269	15721	15858
Average Screw Conveyor Torque [kNm]	55.0	46.4	52.5	62.9	56.9	40.4	33.1	27.6	34.9	29.2	32.7	27.8
Average Earth Pressure Crown [bar]	1.0	1.0	1.3	1.2	1.5	1.3	2.6	2.4	2.4	2.5	2.4	2.3
Average Foam Water Pump [l]	30924	43149	31363	40228	25367	49981	18646	17689	21359	15828	18884	14837
Average Foam agent pump [l]	401	528	587	482	507	735	300	245	350	275	336	294
Average CF %	1.3	1.2	1.9	1.2	2	1.5	1.6	1.4	1.6	1.7	1.8	2
Average FER %	4.1	3.8	4.3	4.0	4.8	3.5	4.8	5.2	4.8	5.5	4.7	6.5
FIR	0.6	0.8	0.7	0.8	0.6	0.9	0.4	0.5	0.5	0.4	0.4	0.5

mixed geology at Silvertown Tunnel, it is clear from the data that as the geology changes from study to study and, more importantly, across the scenarios, adapting the conditioning parameters is essential.

While different soil conditioning strategies were implemented from Northbound to Southbound drives, a consistent trend in TBM parameters emerges across the geological scenarios. Focusing on studies 2, 4 and 6, we see the same foam type 1 used opposingly, but from different suppliers in relation to the drives, supplier 1 for north-bound and supplier 2 for south-bound. Consider that these three studies are also representative of all the geological scenarios from 1 to 4, from the average data for these cases, the soil conditioning strategies vary from north to southbound. For the Northbound drive, the water used for the foam system was approximately 24-45% lower until geological scenario 4 was reached at this point, it remained 28% higher compared to the South. The foaming agent concentration followed a similar trend to the water consumption, given a 0.6% difference across the geology leading to a foam consumption average ranging from 336 to 714 litres per advance. The average FER values remained similar across all the scenarios at a 4.2 to 4.9 ratio, Hence, FIR followed the same trend as the water utilised, ranging on average from 69 to 44%. For the Southbound drive, we see a larger variation in the parameter values, with an average range in the water consumption of 14,837 to 42,877 litres, the trend showing a reduction in water consumption moving from scenarios 1 to 4. The concentration varied by 0.8%, with an average total foam consumption varying from 232 to 519 litres. Across the geology, the average FER and FIR varied by 52% and 68%, respectively. The approach to increase FER for granular profiles not only aids the increased FIR but is crucial for maintaining EPB pressure, face stability, water control, etc.

All the average TBM parameters apart from the screw torque are all lower for the southbound drive until study 4, scenario. 4, given that the speed was also lower until this instance, it is difficult to make an assessment for the respective drives and associate the variations in soil conditioning parameters and associate these changes to the difference in the TBM parameters across the two drives.

However, a unique situation presents to draw firm conclusions over a period of 114 advances, in study 4, scenario 4 and can give us an interesting insight into the soil conditioning strategies and related foam parameters as the average data for the TBM is almost the same in this occurrence, the TBM parameters align given very similar values apart from the screw torque. Given this situation, we isolate the supplier for foam type 1 and soil conditioning parameters to indicate contributions to performance. Table 3 indicates the average values across this instance, 28% difference in water consumption, 34% difference in foaming agent, 12% difference in FER, and 16% difference in FIR.

Considering these differences and the general trends discussed earlier for the association of FIR and TBM data, it would be presumed that an increased FIR and average additional foaming agent

Table 3. Average data from study 4 – Scenario 4.

Case & Study	Study 4/Scenario 4	
Drive/ Supplier/Foam Type	Northbound Supplier 1 Type 1	Southbound Supplier 2 Type 1
Average Thrust [kN]	64451	64869
Average MD Torque [MNm]	9.62	9.64
Average Speed [mm/min]	40	41
Average Penetration [mm/rpm]	19.5	20.3
Average Main Drive Speed [rpm]	2.0	2.0
Contact Force [kN]	16603	15645
Average Screw Conveyor Torque [kNm]	32	24
Average Earth Pressure Crown [bar]	2.8	2.7
Average Foam Water Pump [l]	20829	15770
Average Foam Consumption [l]	329	234
Average FER	4.8	5.4
Average Concentration	1.6%	1.5%
Average FIR	49%	42%

consumption of 95 litres would yield better performance for the Northbound drive, however this is not the case with reduced foaming agent consumption and FIR percentage but higher FER ratio for the geology in scenario 4 supplier 1 - foam type 1 resulted in equivalent performance apart from screw conveyor torque which showed a 30% improvement in performance. This ultimately illustrates that a better balance was achieved in the southbound drive as the data for the foam-to-soil ratio and consumption has provided the same performance from significantly reduced consumption and a more adaptive strategy form to the geological condition given the supplier and foam type.

10 CONCLUSIONS

The data analysis consistently shows a relationship between soil conditioning parameters and TBM advancement parameters, more specifically, the association of FIR can be related to thrust, main drive torque and face pressures. The increased FIR relates to reductions in TBM parameters, for some scenarios, this influence can be attributed to the predominance of cohesive soil. However, the question of improved performance for a given advancement is struck with a balance of the FIR to reach an optimum for each geological situation and the importance of the ability to adapt a tailored strategy. The FIR value is a figure based upon all the conditioning parameters and this optimum value is dynamic in its approach within changing geological conditions.

As the performance of the TBM relies on the soil conditioning systems, generally, it is difficult to substantiate the related performance increase to a given foam, as there's more than one way to arrive at increased FIR and other soil conditioning parameters are important and must be deliberated. Therefore, the contributing factors should account for the required change in soil properties to enable efficient extraction. This approach is evident in the different strategies adopted for Northbound and Southbound drives. Considering the same TBM performance in the same geological profile but significant reduction in the soil conditioning consumption with on average 34% less foaming agent for 114 advances on the Southbound drive with foam type 1 from supplier 2. The challenges posed by mixed geology as Silvertown Tunnel highlights the significance of adapting the soil conditioning parameters to the condition of the geological profile. Moreover, the key understanding should be focused on the point of balance between TBM and conditioning parameters and proactively adjusting and fine-tuning the foam concentration, water consumption, and FER to reach the optimum FIR for a given geology to support extraction and enhance TBM performance.

Strategies for foam soil conditioning and related parameters should first consider geological conditions so that the appropriate foam type can be selected, it may be where multiple foam types should be considered in the case of mixed geology. Secondly, the selection of soil conditioning parameters should be constantly reviewed and optimised based on the geological situation and the required TBM performance. This process can be significantly improved if the suppliers and contractor take a collaborative approach, as each party has specialised knowledge that can contribute to beneficial outcomes. From laboratory testing, knowledge of technology and site support, the supplier's input can substantially bolster the contractor's operations.

Various factors guide the effectiveness of a foam's influence on this balance, and this complexity that develops is even more evident when we consider the mixed geology experienced in projects like the Silvertown Tunnel. To negotiate these challenges effectively, it is imperative to accept a customisable strategy, one that prioritises a holistic understanding of geological conditions and proactively regulates soil conditioning systems to reach the ideal soil properties for each instance along the tunnel alignment.

ACKNOWLEDGEMENTS

We extend our gratitude to the Riverlinx CJV tunnelling department for facilitating analysis and cooperation in the development of this paper.

REFERENCES

Anagnostou, G., Kovari, K, 1996. Face stability conditions with Earthpressure-balanced Shields. Tunnelling and Underground Space Technology 11 (2), 165–173.

ASTM D4318-17, 2017. Standard test methods for liquid limit, plastic limit, and plasticity index of soils. ASTM International, https://doi.org/10.1520/D4318-17

Anagnostou, G. and Kovari,K, 1996. "Face stability conditions with earth-pressure balanced shields". Tunneling and Space Technology. Vol 11, No 2, pp 163–173

Dal Negro, E, Boscaro, A, Barbero E, Picchio, A, and Martini, M, 2022, EPB Tunnelling for the "Riachuelo – Lote 3" project in Buenos Aires, 22–28, ITA-AITES WTC 2022

EFNARC, 2005, Specification and Guidelines for the use of specialist products for mechanised tunnelling (TBM) in soft ground and hard rock. EFNARC

Herrenknecht, M., Thewes, M., Budach, C, 2011, The development of earth pressure shields: from the beginning to the present. Geomechanics and Tunnelling 4, No. 1, pp. 11–35. https://doi.org/10.1002/geot.201100003

Herrenknecht, M, 1994. EPB or slurry machine: the choice. Tunnels and Tunnelling International (June), 35–36.

Nomoto, T., Imaura, S., Hagiwara, T., Kusakabe, O., Fujii, N, 1999, Shield tunnel construction in centrifuge. Journal of Geotechnical and Geoenvironmental Engineering (April), 289–300. ASCE.

Oliveira, D.G.G, Diederichs, M.S., Thewes, M., Freimann, S., Aguiar, G, 2017, EPB conditioning of mixed transitional ground: investigating preliminary aspects. WTC 2017 Bergen

Peila, D., Picchio, A., Martinelli, D., Dal Negro, E, 2016, Laboratory tests on soil conditioning of clayey soil. Acta Geotechnica 11, S. 1061–1074. https://doi.org/10.1007/s11440-015-0406-8

Peixoto da Silva, M.A.A., Katayama, L.T., Leyser, F.G., Aguiar, G., Ferreira, A.A, 2017, Twin tunnels excavated in mixed face conditions. WTC 2017 Bergen

Shirlaw, N, 2016, Pressurized TBM tunnelling in mixed-face conditions resulting from tropical weathering of igneous rock.Tunnelling and Underground Space Technology 57, pp. 225–240.

Zumsteg, R., Puzrin, A.M, 2012, Stickiness and adhesion of conditioned clay pastes. Tunnelling and Underground Space Technology 31, S. 86–96. https://doi.org/10.1016/j.tust.2012.04.010

Tunnelling for a Better Life – Yan, Celestino, Thewes & Eberhardt (Eds)
© 2024 The Author(s), ISBN 978-1-032-80042-4
Open Access: www.taylorfrancis.com, CC BY-NC-ND 4.0 license

Tunnel excavation with EPB: Development of new conditioning agents to reduce the amount of water required for soil conditioning

Enrico Dal Negro, Alessandro Boscaro* & Enrico Barbero
Mapei S.p.A., Milan, Italy

Carmine Todaro & Daniele Peila
DIATI - Polytechnic University of Turin, Turin, Italy

ABSTRACT: Tunnel excavation with TBM requires large amounts of water that are necessary for several different applications. When EPB machines are used, an important contribution to the water consumption is due to the soil conditioning, in particular when the excavation is in cohesive formations. The proper amount of liquids necessary for the soil conditioning depends on several aspects (such as geology, type of conditioning agents used, configuration of the TBM, earth pressure applied at the tunnel face, etc.), however values of WIR (Water Injection Ratio = Volume of pure added water/Volume of soil excavated) in the range of 10%-30% are common.

The development of new conditioning agents allows to significantly reduce these amounts of water. The laboratory of the University "Politecnico di Torino" carried out a thorough campaign of tests using a reference clay, whose results show that new conditioning agents allow to save water in a range between 20 and 33% compared to the traditional products. This reduction of the WIR means thousands of tons of water saved for tunnel excavation, with consequent advantages under several points of view: technical, economical, and environmental. The reduction of water means lower volume of tunnel muck, less trucks necessary to transport the muck to its destination, which means lower CO_2 emissions due to downscaled logistics, etc. All these advantages are more and more relevant nowadays, especially in those countries where water has become a precious and scarce resource.

The paper describes the tests carried out and obtained results.The advantages of these new conditioning agents are presented in detail and contextualized in the view of a sustainability approach in tunnel construction.

Keywords: Tunnelling, TBM, EPB, Soil conditioning, New products, Water, Environment

1 INTRODUCTION

Mapei S.p.A., is at the forefront of innovation in sustainable TBM operations by developing new products capable of reducing the environmental impact of mechanized tunnelling. This has resulted in a wide range of products dedicated to reducing the amount of CO_2, emissions and the overall environmental impact of a TBM project.

As is well known, water is a very valuable resource and an increasingly rare commodity, which in the later years is demanding an increase in sensibility regarding the way it is utilised, especially in territories where its scarcity makes it even more of a precious asset to be carefully managed.

TBM tunnelling, similarly to many other industrial processes, requires a massive amount of water to be performed. The non-contaminated portion of water employed in mechanized tunnelling jobsites is continuously re-used during the activity, such as the water used for the cooling systems of the TBM. Part of the water is instead lost into the muck, such as the groundwater extracted during the excavation or the large water quantities which are necessary for soil conditioning during the excavation itself, especially when cohesive grounds are excavated.

The main issue stands in the fact that some soils, in order to be excavated with EPBs, require large amounts of liquid to be added, either as pure water (defined by the parameter of WIR = Water Injection

*Corresponding author: boscaro@utt.mapei.com

DOI: 10.1201/9781003495505-267

Ratio) or in foam generation. Moreover, greater values of WIR are generally required in order to condition cohesive soils with particularly high stickiness, such as clays, mudstone, shale, etc.

Since soil conditioning constitutes the greater part of the water needs of these jobsites, reducing the environmental impact of soil conditioning can also be linked to reducing the amount of water used in TBM tunnelling projects.

1.1 *Creating a new type of soil conditioning agent*

As part of Mapei's Water Saving Program (WSP), a new range of products have been specifically introduced to allow for a reduction of the WIR parameter.

In this paper we will describe the experimental phase of Polyfoamer ECO WSP and Mapedisp ECO WSP when applied in comparison with a reference soil conditioning product.

In detail, the following chapters have been produced to describe the operational methods for carrying out laboratory tests aimed at the characterisation of a clay extracted from a quarry near Reggio Emilia, in accordance with the technical partenership between DIATI of the Politecnico di Torino and Mapei S.p.A.

The new generation products were designed and manufactured with a view to achieving good conditioning of the clays by reducing the amount of water required by the soil to be conditioned.

The laboratory tests performed are:

- Mini flow test.
- Mini slump and flow table test.
- Slump test.
- Dynamic adhesion test.

1.2 *Reference nomenclature*

The following nomenclature for technical parameters has been adopted throughout the entire experimental phase.

w_n (%) – natural water content, computed on the dry weight of the soil;

w_{add} (%) – additional water content, calculated on the dry weight of the soil;

w_{tot} (%) – total water content, calculated on the dry weight of the soil;

c w/w (%) – concentration of the solution calculated as weight of conditioning agent per 100 g of soil;

c v/v (%) – volume concentration of foaming agent on volume of generating liquid;

φ_{BJ} (mm) – base diameter of the sample in the mini slump test, before application of the jolts;

φ_{AJ} (mm) – base diameter of the sample in the mini slump test, after application of the jolts;

h_{BJ} (mm) – height of the sample in the mini slump test, before application of the jolts;

h_{AJ} (mm) – height of the sample in the mini slump test, after application of the jolts;

w_{saved} (%) – amount of water saved. Percentage value computed on the w_{add} value of the considered conditioning and the w_{add} value of the reference soil conditioning;

T (Nm) – average torque value, calculated in the dynamic adhesion test.

For the calculation of water contents, percentage values are rounded. Values with a decimal part greater than or equal to 0.5 are rounded up, values with a decimal part less than 0.5 are rounded down.

2 UTILIZED MATERIALS

The purpose of the experimentation described in this report is to study, by means of laboratory tests, the conditioning of "Reggio" clay using specific conditioning agents for clays. Specifically, 3 different soil conditioning agents supplied by Mapei S.p.A. have been tested, defined as follows:

- reference conditioning agent - "REF";
- next-generation conditioning agent - "Polyfoamer ECO WSP";
- next-generation additive - "Mapedisp ECO WSP".

Both the soil conditioning products as well as the clay used in the experimental phase will be described thoroughly in the following paragraphs.

2.1 *"Reggio" clay*

The clay soil used for the experiments was supplied to the Tunnels & Underground Space Research Center of the Turin Polytechnic University directly by Mapei S.p.A., in hermetically sealed containers carrying a total of approximately 400 kg of material. The mineralogical analysis, certified by the supplier (Movimento Terra e Trasporti Ruggi) of the clay and carried out semi-quantitatively by XRD spectrometry showed the following composition:

- Clay Material: 43%
- Feldspar: 19%
- Quartz: 35%
- Other: 3%

The Atterberg limits are instead:

- Liquid limit: 54%
- Plastic limit: 30%

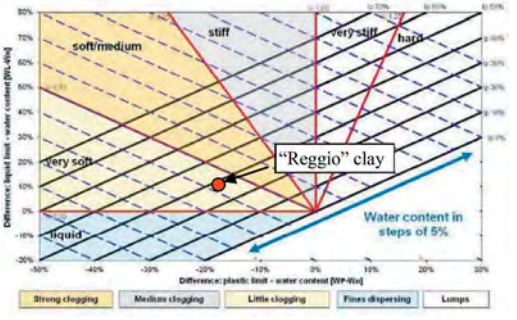

Figure 1. Thewes graph for "Reggio" clay.

Further analysis based on the Atterberg limits and the natural water content equal to 13%, shows that "Reggio" clays could be classified as prone to clogging risk, as shown in Figure 1.

The material was then processed in order to make it suitable for the planned tests.

Specifically, two different types of clays were produced:

- dry crushed clay (w_n = 0 %), hereinafter referred to by the acronym "DCC"
- chip clay (w_n = 12.6 %), hereinafter referred to by the acronym "NCC".

Figure 2. Clay samples used in the laboratory for the test campaign. DCC (left) e NCC (right). The difference in color is due to the different water content in the samples.

The two variants of clay material employed in the tests can be seen in Figure 2, while their particle size distributions are shown in Figure 3.

2.2 *Conditioning agents*

Conditioning agents play a key role for the correct conditioning of soils, expressly in clayey ones (Peila et al., 2016). For this testing campaign, three different specific conditioning agents for clays were used in addition to water taken from the water network of the metropolitan city of Turin. Specifically:

a) "REF" (reference) conditioning agent. "Traditional" foaming agent, formulated with anionic surfactants of the SLES (Sodium-Lauryl -Ether-Sulphate) type, characterised by the following chemical composition reported on the safety data sheet in section 3: alcohols, C12-14, ethoxylates, sulphatates, sodium salts; CAS number: 68891-38-3, 500-234-8; Concentration: ≥ 10% - < 20%;
b) "Polyfoamer ECO WSP" conditioning agent. Next generation foaming agent, formulated with the aim of reducing the amount of water required in comparison to 'traditional' foaming agents;
c) "Mapedisp ECO WSP" additive. A next-generation dispersing additive, to be used in combination with foam to further reduce the amount of water required for conditioning.

3 LABORATORY TEST CAMPAIGN

The two types of tests carried out on the conditioned samples, namely Mini Flow tests and Mini Slump/ Flow Table tests, will be described in detail in the following paragraphs.

3.1 *Mini flow tests*

The mini flow test campaign was performed according to the procedure described in the article published in an international scientific journal: C. Todaro, A. Carigi, L. Peila, D. Martinelli, D. Peila, Soil conditioning tests of clay for EPB tunnelling, Underground Space, Volume 7, Issue 4, 2022, Pages 483-497, ISSN 2467-9674.

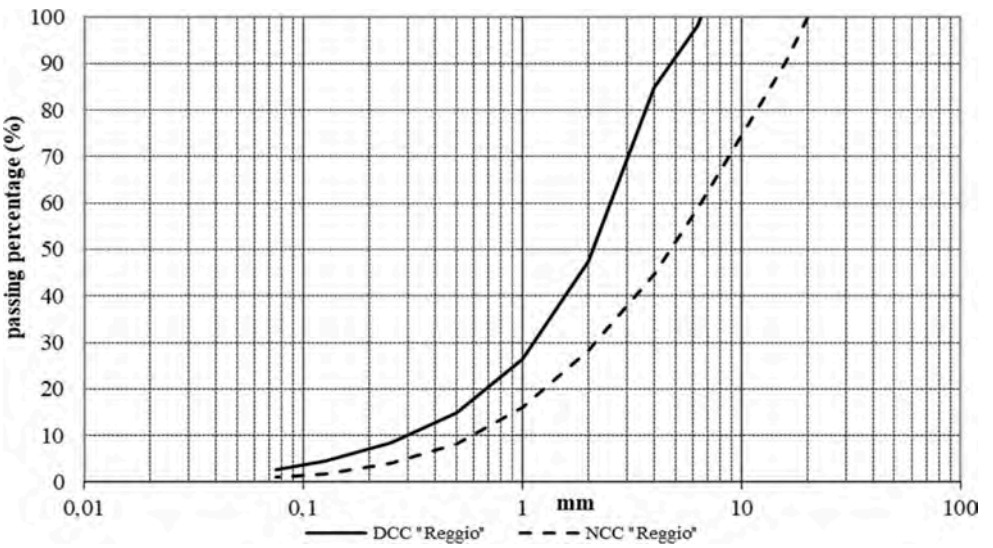

Figure 3. Grain size distributions of the clay samples used for the test campaign.

Mini flow" tests have been recently introduced into the scientific literature and laboratory experimental practises for the characterisation of conditioned clays. These tests involve the use of a mini-cone (Figure 4), a scale reduction of the one used for slump tests (CEN 2009).

The cone base diameter is 44 mm, while its height is 66 mm.

Table 1. Mini flow tests results for "Reggio" clay.

ID	Conditioning agent	w_{add} (%)	flow (%)	slump (%)	w_{saved} (%)
6	REF	90	16	24	/
7	Mapedisp ECO WSP	90	126	84	0
8	Polyfoamer ECO WSP	90	126	83	0
9	Mapedisp ECO WSP	70	43	56	22
10	Polyfoamer ECO WSP	75	61	69	17

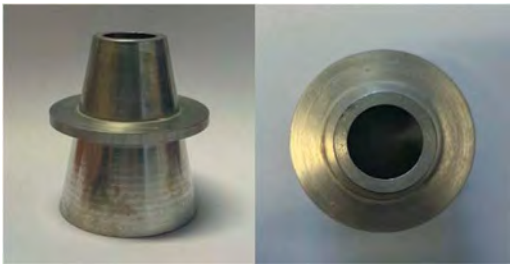

Figure 4. Mini flow cone front and from-above views.

3.1.1 *Mini flow test results*

The obtained results are shown in Table 1, while pictures of performed tests can be seen in Figure 5. Flow and slump values refer to height and diameter of the conditioned material downstream of the cone lift (computed on the dimensions of the mini-flow cone) and are shown in percentage value. The amount of conditioning agent, which remained constant for all tests (ID 6-10), is 0.5 g, equivalent to a dosage on the treated soil in concentration w/w equal to 0.5%.

Regarding results on "Reggio" clay specimens, given the same dosages used in terms of the amount of water added and the amount of conditioning agent (ID 6, 7 and 8), adopting the new generation products results in flow values increased by around 8 times and slump values were more than three times as much. Polyfoamer ECO WSP in the ID 10 test shows flow and slump values approximately 4 and 3 times higher than in the ID 6 comparison test, despite the fact that the amount of water added is approximately 17% less than in the reference test.

The specimen treated with Mapedisp ECO WSP (ID 9), although made with a w_{saved} of 22%, shows values for flow and slump respectively about 3 and 2 times higher in relation to those obtained in the reference (ID 6).

Figure 5. Mini Flow tests for "Reggio" clay. IDs are labelled.

3.2 *Mini slump tests*

The tests performed by using the mini slump (geometries shown in Figure 6) involve the use of NCC "Reggio" clay, which is characterised by its natural water content. The mixing of the soil with the correct amount of water and foam is carried out until a homogenous material is achieved. The conditioned material thus obtained is then placed inside a mini slump cone, using the surface of the flow table as a base support. A first slump test is thus performed, and the values of the base diameter (φ_{BJ}) and height (h_{BJ}) are measured. Fifteen jolts are then applied at a height of 25 mm after which base diameter (φ_{AJ}) and height (h_{AJ}) are measured.

Table 2. Mini slump and flow tests results.

Test ID	Conditioning agent	w_{add} (%)	w_{tot} (%)	φ_{BJ} (mm)	h_{BJ} (mm)	φ_{AJ} (mm)	h_{AJ} (mm)	flow (%)	slump (%)	w_{saved} (%)
1	REF	45	58	114	57	171	104	71	31	/
2	Polyfoamer ECO WSP	45	58	160	75	211	104	111	31	0
3	Polyfoamer ECO WSP	35	48	116	49	174	96	74	36	22
4	REF + Mapedisp ECO WSP	45	58	145	70	202	104	102	31	0
5	REF + Mapedisp ECO WSP	38	50	141	63	195	104	95	31	17

The cone base diameter is 100 mm, while its height is equal to150 mm.

The density value of the "Reggio" clay γ = 1.786 kg/L was used as a constant for all mini slump test campaign.

The conditioning parameters, which have been kept constant for all tests, are:

- c(%): 2.0
- FER(-): 8
- FIR(%): 60

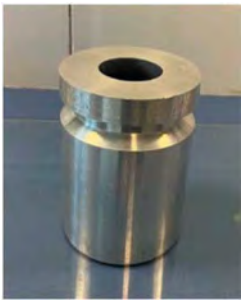

Figure 6. Mini-slump tool.

3.2.1 *Mini slump test results*

The results are summarized in Table 2, while images of the test for ID5 are shown in Figure 7 as example. The values for flow and slump are referring to height and diameter values measured after the jolts, calculated in comparison to the original mini slump dimensions. ID 4 and ID 5 tests have been carried out with a conditioning procedure which made use of Mapedisp ECO WSP with a fixed dosage of di 0.8 g over 1500 g of clay, corresponding to a dosage of 1 kg of polymer over 1 m^3 of soil in situ. The additive dosage, in the range of one tenth of a gram, is negligible for the calculation of water content. For the calculation of w_{saved}, ID 2-5 refer to ID 1.

Considering the use of Polyfoamer ECO WSP, while keeping the water content and conditioning parameters constant (comparison between test ID 1 and 2), the flow percentage increases by about 1.5 times, from a value of 71% to a value of 111%. Considering instead tests ID 1 and 3, equivalent results in terms of flow are obtained by conditioning the soil with a w_{saved} of 22%.

If, on the other hand, we consider the conditioning obtained by adding Mapedisp ECO WSP to the REF, keeping the water content and conditioning parameters constant (comparison between test ID 1 and 4), the flow percentage increases by about 1.5 times, from a value of 71% to a value of 102%. Considering instead tests ID 1 and 5, similar results in terms of flow are obtained by conditioning the soil with w_{saved} equal to 17 %.

The "slump" parameter is irrelevant, with values in the range of 30-36% regardless of the conditioning they were subjected to.

Figure 7. ID5 mini slump test pictures before jolting (left) and after (right).

3.3 *Slump tests*

he slump test is probably the first that was used for characterise the conditioned soil even if it was originally applied to cohesionless soils (Peila et al., 2009; Borio abd Peila, 2011; Peila et al., 2013). The slump test campaign has been performed in compliance with the procedure described in the article published in the international scientific journal: C. Todaro et al. (2022).

The slump tests foresaw the use of NCC "Reggio" clay, which is characterised by its natural water content.

3.3.1 *Slump tests results*

The results obtained are summarised in Table 3 while images of the tests performed can be found in Figure 8, Figure 9,Figure 10, 11 and 12.

Test ID 5 was carried out with a conditioning which employed Mapedisp ECO WSP with

Table 3. Slump test results.

Test ID	Conditioning agent	w_{add} (%)	w_{tot} (%)	Slump A (cm)	φ_A (cm)	Slump B (cm)	φ_B (cm)	Slump C (cm)	φ_C (cm)	w_{saved} (%)
1	REF	32	45	19	28	11	25	25	49	/
2	Polyfoamer ECO WSP	22	34	13	27	0	20	17	34	33
3	Polyfoamer ECO WSP	26	38	17	34	5	22	22	41	20
4	REF	26	38	12	23	1	20	18	38	/
5	REF + Mapedisp ECO WSP	26	38	16	30	7	21	24	46	20

a fixed dosage of 2.02 g on 12000 g of clay, equivalent to 0.3 kg of polymer on 1 m^3 of soil in situ. The amount of additive, in the order of one gram, is negligible when calculating water content. For the calculation of w_{saved}, ID 2-3 refers to ID 1, while ID 5 refers to ID 4.

The analysis of a slump test is not only based on the numerical value of the slump at the cone. In all materials, but especially in clay materials, other parameters must be considered such as the overall homogeneity of the sample, its pulpy consistency and stickiness. Only from the careful evaluation of all these parameters can an overall judgement of the slump test be considered reliable. The writers, in order to facilitate reading, introduced a simple scale of pulpy consistency (1 - not very pulpy; 5 - very pulpy) and stickiness (1 - not very sticky; 5 - very sticky). The evaluations in terms of pastiness and stickiness were made after the execution of slump B and C.

Further comments for direct comparisons of "REF" tests and the other conditioning combinations are listed below:

ID 1 vs ID 2: Slumps A are comparable in terms of pulpy consistency and stickiness. Slumps B are also comparable, although ID 2 is characterised by a w_{saved} of 33%. It should also be considered that ID 1 - slump C is an unacceptable slump as it is excessively fluid. In fact, the conditioned soil leaked abundantly from the plate downstream of the execution of the shots, whereas ID 2 - slump C shows a slump at the cone in the ranges, without any material leaking from the plate.

ID 1 vs ID 3: Slumps A are comparable in terms of pulpy consistency and stickiness. Slumps B are also comparable, although ID 3 is characterised by a w_{saved} of 20%.

ID 3 - slump C shows a slump value at the cone in the range, with no material escaping from the plate.

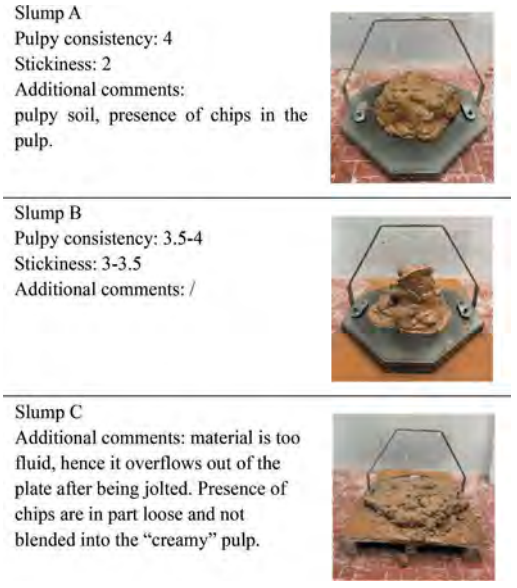

Figure 8. ID 1 slump tests.

Figure 9. ID2 slump tests.

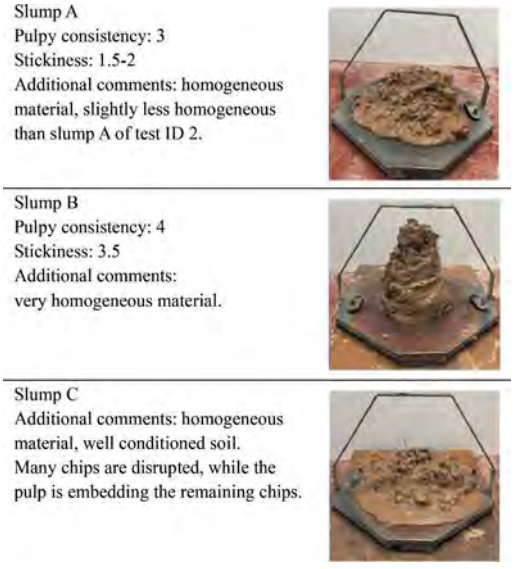

Figure 10. ID3 slump tests.

ID 4 vs ID 5: Conditioned soils with equal water content. Comparing Slump As, the better result obtained in ID 5 in terms of pulpy consistency is evident. ID 5 - slump B was less stiff than the corresponding ID 4 - slump B (with slump values at the cone of 7 and 1 cm respectively), as well as showing a more limited stickiness. ID 5 - slump C slightly off the plate but with fewer chips and more paste than ID 4 - slump C.

ID 3 vs ID 4: Conditioned soils with equal water content. ID 4 - slump A is slightly stickier than ID 3 - slump A. ID 3 - slump C was much pulpier than ID 4 - slump C. It should be noted, however, that ID 4 - slump C exhibited a high degree of stickiness during lifting of the cone, which was not the case in ID 3 - slump C.

Slump A
Pulpy consistency: 2
Stickiness: 3.5
Additional comments:less homogeneous material, the creamy outside hides the chips, which are still hard to the touch.

Slump B
Pulpy consistency: 2.5
Stickiness:4
Additional comments: less pulpy yet very sticky material, the cone would not detach easily from the conditioned material.

Slump C
Additional comments:
homogeneous material, scarce presence of non-disrupted chips.

Figure 11. ID4 slump tests.

Slump A
Pulpy consistency: 3.5-4
Stickiness: 2.5
Additional comments:
homogeneous material, creamy paste.

Slump B
Pulpy consistency: 3.5
Stickiness: 2.5
Additional comments:
homogeneous material, creamy paste.

Slump C
Additional comments:
Homogeneous material, well conditioned, chips present but with small. Slight excess of fluidity, with limited material falling out of the plate downstream of the jolts.

Figure 12. ID5 slump tests.

3.4 *Dynamic adhesion tests*

The dynamic adhesion test campaign was carried out on the basis of the procedure described in Todaro et al. (2022) and Carigi et al. (2023).

The dynamic adhesion test is based on the rotation of an aluminium disc, 120 mm in diameter and 10 mm thick, placed in contact with the clay material under specific conditions in order to assess the developed adhesion. The test, specifically designed for the study of clays, involves placing the disc in rotation within the material to be tested, with a constant rotation of 90 rpm (Figure 13). The clay material then adheres to the surface of the disc and the contact is ensured by applying a pressure of 1 bar to the conditioned material. The pressure is applied by means of a plate which, pushed by 2 hydraulic pistons, moves downwards in contact with the soil, thus making sure that the intended pressure is applied to the conditioned soil. The test provides important information about the resistance exerted by the clay soil to the rotation of the disc, due to the adhesion/clogging forces typical of clay soils. During the test, the torque required to ensure a constant disc rotation speed is constantly measured and recorded.

Dynamic adhesion tests foresaw the use of NCC "Reggio" clay, conditioned by its natural water content.

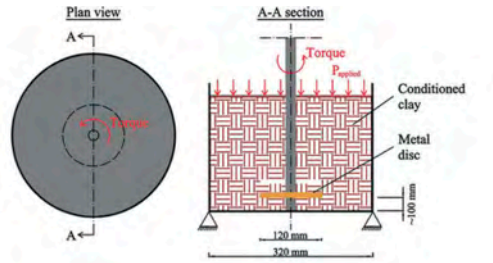

Figure 13. Schematic diagram and picture of the dynamic adhesion test apparatus. 1. steel container; 2. torque transducer; 3. hydraulic pistons; 4. steel cover; 5. hydraulic unit.

Table 4. Dynamic adhesion tests results.

Test ID	Conditioning agent	w_{add} (%)	w_{tot} (%)	c (%)	FER (-)	FIR (%)	T (Nm)	w_{saved} (%)
1	REF	27	40	2	8	45	4	/
2	Polyfoamer ECO WSP	23	35	2	8	45	3	17
3	REF + Mapedisp ECO WSP	23	35	2	8	42	4	17

3.4.1 *Dynamic adhesion test results*

The conditioning parameters of the tests and the results obtained in terms of average torque T (Nm) and w_{saved} are shown in Table 4 while Figure 16 shows the trends in torque as a function of time. The average torque was calculated over the 300 s of the actual test, after the pressure stabilisation transient phase which lasted an average of 120 s for all 3 tests. This reduction in FIR was evaluated in agreement with the commissioning company's technicians in order to maximize adhesion phenomena during the test, consistent with obtaining good conditioning results.

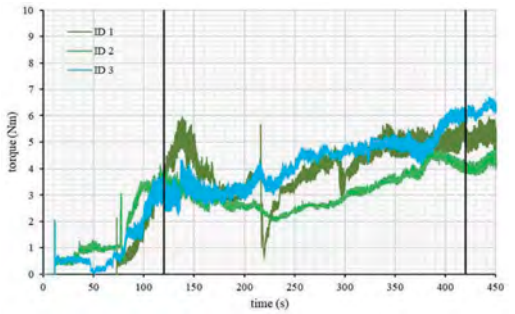

Figure 14. Torque over time graph for dynamic adhesion tests.

The reference test, i.e. ID 1 is highlighted in grey color. ID 3 was carried out by conditioning using Mapedisp ECO WSP with a fixed dosage of 2.55 g per 15000 g of clay, equivalent to 0.3 kg of polymer per 1 m^3 of soil in place. The amount of additive, in the order of a gram, is negligible for the purpose of calculating the water content. For the calculation of w_{saved}, ID 2-3 refer to ID 1.

Figure 15 shows some shots of the significant phases of the dynamic adhesion test. For illustrative purposes only, the images shown refer to ID 1.

Figure 15. Dynamic adhesion test ID 1. Material completely poured into the steel container (left), material at the end of the test (right), extraction and visual analysis of the disc (right).

An analysis of Figure 14 shows that the 3 torque trends as a function of time are very similar, despite the fact that IDs 2 and 3 were carried out with a w_{saved} of 17%. Regardless of the test considered, the torque values never exceeded the value of 7 Nm, an indication that the conditioning used ensures that adhesion/clogging phenomena are controlled. The T values, between 3 and 4 Nm, also show a high degree of similarity in the behaviour of the materials tested with dynamic adhesion testing.

4 FINAL CONCLUSIONS

The study of the conditioning of clays is a complex analysis which is difficult to carry out using a single type of laboratory test. In the present study, the conditioning of the "Reggio" clay was evaluated by means of tests considering both homogenised clay (obtained from the DCC sample) and clay in chips (NCC sample), conditioned with products specifically designed and manufactured for the conditioning of cohesive materials.

The different conditioners adopted, adjusted each time depending on the type of test carried out, highlighted the effectiveness of Polyfoamer ECO WSP and Mapedisp ECO WSP (the latter used as an additive alongside a reference conditioning agent) in guaranteeing good conditioning, comparable to that obtained with REF, while using reduced quantities of added water.

Specifically speaking, mini-flow and mini-slump tests denoted a potential water saving ranging from 17 to 22 % when comparing samples conditioned with Polyfoamer ECO WSP to the ones conditioned with the REF conditioning agent. Similar results (w_{saved} = 17-22%) for the same tests were observed by comparing the samples treated using REF with an addition of Mapedisp ECO WSP with the ones conditioned using REF only.

With Slump tests, the best results highlighted a potential water saving between 20 and 33% using Polyfoamer ECO WSP.

Dynamic adhesion tests evidenced samples treated with next generation products, which are the ones conditioned with either Polyfoamer ECO WSP or with a combination of REF and Mapedisp ECO WSP result in a potential water saving of 17%.

In conclusion, with regard to technical performance parameters, a potential water saving of a minimum of 17 % has been consistently observed, denoting a great potential for the reduction in water

demand for TBM jobsites which would result in a significantly lower environmental impact as well as an economical advantage.

REFERENCES

Borio L., Peila D. (2011), Laboratory test for EPB tunnelling assessment: results of test campaign on two different granular soils. Gospodarka Surowcami Mineralnymi, 27(1), 85–100.

Carigi, A., Di Giovanni, A., Saltarin, S., Peila, D., Todaro, C. 2023. "Influence of chip-size on development of adhesion for conditioned clayey soils" Proceedings of the ITA-AITES World Tunnel Congress 2023 (WTC 2023), 12-18 May 2023, Athens, Greece

Peila D., Oggeri C., Borio L. (2009), Using the slump test to assess the behavior of conditioned soil for EPB tunneling, Environmental & Engineering Geoscience, XV (3), 167–174.

Peila D., Picchio A., Chieregato A. (2013) Earth pressure balance tunnelling in rock masses: Laboratory feasibility study of the conditioning process. Tunnelling and Underground Space Tech., 35, 55–66.

Peila D., Picchio A., Martinelli D., Dal Negro E. (2016) Laboratory tests on soil conditioning of clayey soil. Acta Geotechnica. DOI: 10.1007/s11440-015-0406-8.

Todaro C., Carigi A., Peila L., Martinelli D., Peila D. (2022) Soil conditioning tests of clay for EPB tunnelling, Underground Space, Volume 7, 4, 2022, 483–497, http://dx.doi.org/10.1016/j.undsp.2021.11.002

Dal Negro E., Boscaro A. and Plescia, E. (2014). Two-component backfill grout system in TBM: The experience of the tunnel "Sparvo" in Italy, Proceedings of TAC Congress 2014: "Tunnelling in a Resource Driven World", Vancouver, 26–28 October 2014.

Dal Negro E., Schulkins R., Boscaro A., Pediconi, P. (2014). Two-component backfill grout system in double shield hard rock TBM. The "Legacy Way" tunnel in Brisbane, Australia, Proceedings of ITA-AITES World Tunnel Congress 2014: "Tunnels for a better life", Foz do Iguacu, Brazil, May 2014.

Dal Negro E., Boscaro A., Barbero E., (2023) Mechanized tunnelling: improving the environmental impact of chemical products without impacting technical performance, Proceedings of the ITA-AITES World Tunnel Congress 2023 (WTC 2023), 12-18 May 2023, Athens, Greece.

Thewes M., and Budach C. (2009). *Grouting of the annular gap in shield tunnelling – An important factor for minimization of settlements and production performance*, Proceedings of the ITA-AITES World Tunnel Congress 2009 "Safe Tunnelling for the City and Environment", Budapest, 23-28 May 2009.

Tunnelling for a Better Life – Yan, Celestino, Thewes & Eberhardt (Eds)
© 2024 The Author(s), ISBN 978-1-032-80042-4
Open Access: www.taylorfrancis.com, CC BY-NC-ND 4.0 license

Managing tunnelling risks in urban environment using first earth pressure balance/variable density slurry Tunnel Boring Machine (TBM) in Hong Kong for the MTR East Rail Line Cross Harbour Extension of the Shatin Central Link project

Neil Ng*
Project Manager, MTR Corporation Limited, Hong Kong SAR, China

Derek Kwok
Chief Engineering Manager – Geotechnical, MTR Corporation Limited, Hong Kong SAR, China

Ken Kwok
Technical Director – Bouygues Construction, London, UK

Didier Jacques
Construction Director, Bouygues Construction, London, UK

ABSTRACT: The opening of the East Rail Line (EAL) Cross-Harbour Extension has re-shaped the public travel pattern and metro network in Hong Kong. The history of the century old EAL has also been rewritten as a direct rail link, connecting the city boundary and the Northeast New Territories with the Central Business District area on Hong Kong Island. It brings people from the Northeast New Territories closer to the city's financial hub with one railway line. Variable density TBM was first used in Hong Kong for this project to minimize the inherent risk for one of the TBM drives with very shallow ground cover and within heterogenous soil in reclaimed land. Advanced obstruction removal and protection of existing structures was carried out to mitigate the tunnelling risks. Rigorous numerical analysis has been carried out to predict the ground behaviour and design the confinement pressures. Performance of the TBM drives and the Variable density TBM has been reviewed based on the monitoring data from a suite of comprehensive geotechnical instrumentation.

Keywords: Tunnel boring machine (TBM), Variable density (VaD), Shallow ground cover, Tunnelling risk, Performance prediction

1 INTRODUCTION

The opening of the East Rail Line (EAL) Cross-Harbour Extension in 2022 has re-shaped the public travel pattern and metro network in Hong Kong. The history of the century old EAL has also been rewritten as a direct rail link and the city's fourth railway cross-harbour tunnel, connecting the city boundary and the Northeast New Territories with the Central Business District area on Hong Kong Island. It brings people from the Northeast New Territories closer to the city's financial hub with one railway line. The new connection also helps alleviate the congested sections of the railway corridor as well as road traffic via the vehicular Cross-Harbour Tunnel.

Hong Kong is densely populated with 1,110 km^2 of land mass. Its mass transit system operated by Mass Transit Railway Corporation Limited (MTRCL) is one of the main modes of transportation for the public. The 6km long EAL Cross-Harbour Extension, situated between the Kowloon Peninsula and the central business district on Hong Kong Island, includes an Immersed Tube Tunnel (IMT) below Victoria Harbour, an overrun tunnel below the hills in Admiralty, modification, and extension of the existing Hung Hom Station and Admiralty Station and four TBM tunnels connecting the IMT to Admiralty Station via the brand-new Exhibition Centre Station (EXC). Figure 1 shows alignment and connectivity of the EAL Cross-Harbour Extension.

*Corresponding author: ngneil@mtr.com.hk

DOI: 10.1201/9781003495505-268

The EAL Cross-Harbour Extension alignment features various engineering solutions to overcome complex geology, varying topography and many other site constraints. There exist various and distinct inherent risks for one of the TBM drives with excavation below only 6m of ground cover in reclaimed land. The possibilities of uncontrolled ground collapse due to compressed air leak during TBM cutterhead maintenance, compressed air blowout due to excessive confinement pressure, loss of confinement pressure if encountering underground obstruction which can result in over-excavation as the TBM attempts to drive through the ground at shallow depth necessitated detailed review of the risks and implementation of advanced mitigation measures.

One of the key successes to the shallow cover TBM drive was the use of a hybrid variable density slurry TBM combining Earth Pressure Balance (EPB) and Slurry (Mixshield) processes. The slurry density inside the excavation chamber was adjusted based on the geology and TBM operation mode. This mitigated the chance of pressurised slurry leaking onto the ground surface while minimizing ground settlement. This was particularly important in the developed Wan Chai area and below the busy road network. This paper will discuss the underground risks and technical aspects of the mitigation measures that were undertaken prior to commencing the TBM excavation under shallow ground cover in an urban environment at the north Wan Chai area of Hong Kong Island.

Figure 1. EAL Cross-Harbour Extension alignment.

2 ALIGNMENT AND GEOLOGY OF TBM TUNNEL DRIVES

The EAL Cross-Harbour Extension involves construction of two sets of twin 7.45m Ø TBM tunnels to the east and west respectively of the Exhibition Centre Station. The Eastern Bored Tunnels are approximately 680m and Western Bored Tunnels are approximately 470m in length. Figure 2 shows the horizontal alignment of the four TBM tunnels.

The ground topography for the entire TBM tunnel alignment is on flat low-lying ground along the

Figure 2. Horizontal alignment of TBM tunnels.

northern coastline of Hong Kong Island, all in reclaimed land. The reclaimed Fill materials below the ground level consist of Marine Deposits, Alluvial Deposits and generally underlain by Completely Decomposed Granite (CDG) soil and Slightly Decomposed Granite bedrock. For the upper Eastern Bored Tunnel, the risks involve excavation under shallow ground cover in soft Marine Deposits, Alluvial Deposits with the tunnel crown just below the bottom of the reclaimed Fill and old seawall revetments. Figure 3 shows the typical geological profile for the tunnel section between Canal Road and Wan Shing Street in the north Wan Chai area.

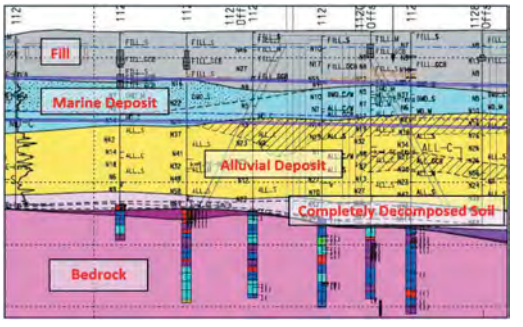

Figure 3. Typical geological profile of Eastern Downtrack Tunnel.

Based on project specific site investigation results, the Eastern upper downtrack alignment was found to have a complex geological profile. The solid geology consists of Granite bedrock at 20 to 30m below surface level. Above the bedrock stratum, Completely Decomposed Granite (CDG) is overlain by a stratum of sandy to clayey alluviums and sedimentary marine deposits of varying thicknesses below the top reclaimed fill layer. The reclaimed fill is identified to contain construction debris e.g. reinforced concrete, bricks, plastics, woods and steel bars as well as rubble mound that had previously formed as parts of temporary or permanent sea walls. At the shallowest location, the tunnel excavation took place with cover of less than one TBM diameter and at some

locations, the TBM passed closed to existing live structures with less than 1m of very soft soil in between. Figure 3 highlights one of the significantly more challenging areas in terms of ground cover and potential obstructions. To minimize the risk of excessive ground settlement and impact to existing underground facilities and to reduce the risk associated with cutterhead and cutting tools (disc, picks and scrappers) maintenance under compressed air intervention (CAI), the vertical alignment of the upper and lower tunnels was revised with small but significant changes.

- Deeper Uptrack Tunnel: raised to a higher level to minimize excavation in the transition zone between the CDG and granite bedrock;
- Upper Downtrack Tunnel: lowered generally by 0.5m, deeper at localized areas, to avoid old seawall and revetments below the TBM, thereby increased the margin of confinement pressure design which is under the influence of daily hydraulic gradient fluctuation near Victoria Harbour.

The revised and lowered alignment of the Upper Downtrack Tunnel minimized the risk of slurry leaks into old seawall rubbles along stretch of the alignment. However, the revised vertical alignment also increased the risk of TBM excavation closer to existing facilities including a trunk sewer which required extensive geotechnical instrumentation and a stringent monitoring programme. Alternative alignment of the upper and lower Eastern Bored Tunnels and the surrounding geology are shown in Figures 4(a, b).

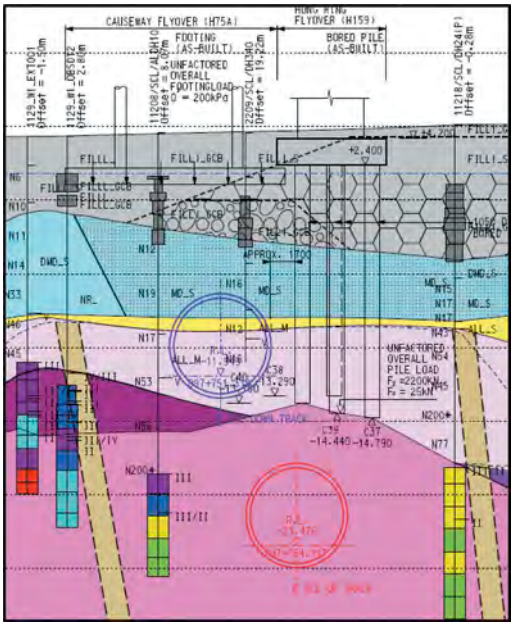

Figure 4a. Tunnel level and typical geological sections.

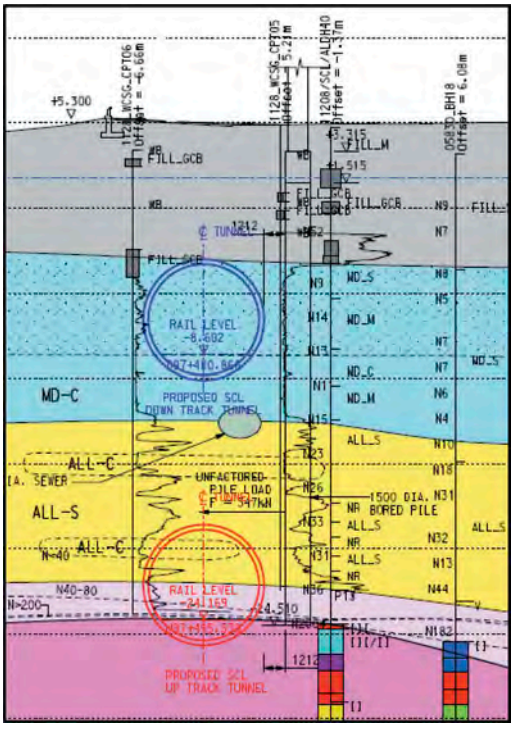

Figure 4b. Tunnel level and typical geological sections.

3 SITE CONSTRAINTS

The Causeway Bay and Wan Chai districts are highly developed with its coastline extended under various phases of reclamation. The Easter Bored Tunnels traverse below reclamation constructed in the 1960s and 1970s which are now built with multi-lane carriageways, vehicular flyovers and viaducts, commercial buildings and other major underground utilities. In additional, there are pile foundation

Figure 5. Historic reclamation up to 2000s.

supporting box culverts, trunk sewers, footbridges, abandoned ferry piers and left-in temporary works for the development in this area. Figure 5 shows the tunnel alignment in the historic reclamation.

The contract Geotechnical Baseline Report compiled at the design stage of the project involved extensive record search and desktop study followed by advanced ground investigation programme to identify known structures, pile foundations and underground obstructions. At the construction stage with new project interface and further desktop studies, additional major obstructions were identified in the form temporary left-in sheetpiles and old pile foundation coinciding with both the Uptrack and Downtrack tunnel alignment. The risk assessment also included the possibility of encountering old World War II ordnance.

With the existing obstructions identified at various locations along the alignment at the design stage, an advanced works contract was awarded to remove and clear the underground obstructions from the ground surface. The buildings and structures protection works and removing some of the existing obstructions including those identified after contract award were executed by the tunnelling contractor. Figure 6 shows the location of major pile obstructions below the Canal Road Flyover and Wan Shing Street Footbridge.

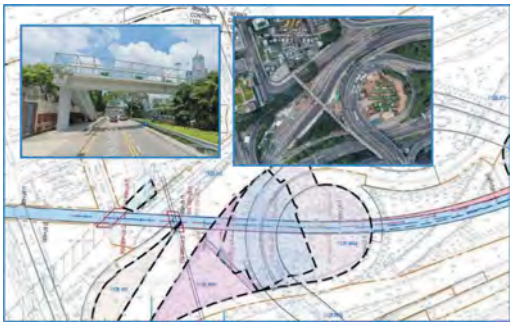

Figure 6. Major pile obstructions below Canal Road Flyover and Wan Shing Street Footbridge.

4 ADVANCED WORKS

4.1 *Pile obstruction removal*

Removal of pile obstructions behind the TBM cutterhead in the excavation chamber has been done in previous MTR projects. However, such operation, particularly under compressed air intervention (CAI) at depth or under shallow ground cover, is complex and carries inherent risks to the tunnel workers, tunnelling operation, and other stakeholders.

With several structures supported by piles that conflicted with the TBM alignment, advance works to remove these obstructions were carried out to mitigate tunnel excavation risks. They include piles supporting the Percival Footbridge (9 nos. bored piles), Canal Road Box Culvert (21 nos. pre-stressed concrete piles) servicing the Wanchai district, Canal Road Flyover (6 nos. pre-stressed concrete piles) which is a main artery connecting the south of Hong Kong Island and the Cross Harbour Tunnel, and the Marsh Road drainage sewer (2 nos. precast concrete pile). As-built records of the latter pile obstructions on Marsh Road were not available. Their presence and locations were instead confirmed by site trial pits and geophysical survey.

The sheetpile obstructions at Wan Shing Street was critically identified prior to the shallow Downtrack tunnel drive. A study of this project interface and old site photos revealed the risk of left-in temporary works from the cable trench which could result in slurry leak, excessive ground settlement and programme impact. Subsequent geophysical survey confirmed this risk and help identified up to 100 nos. sheetpiles that clashed with the tunnel alignment. With the assistance of the utility company and government departments, temporary traffic management scheme was quickly implemented to allow safe removal of the sheet piles without impact to the 11kV and 132kV electrical cables prior to the TBM excavation.

Figure 7. Traffic management and temporary trenching for sheetpile removal at Wan Shing Street.

4.2 *Protection of existing facilities and structures*

The advanced works associated with pile obstruction removal involved well planned engineering schemes. To remove the piles supporting the Canal Road Box Culvert, full diversion of the culvert and complete reinstatement was done. Adjacent to the box culvert, underpinning of the Canal Road Flyover was undertaken before removing the piles under low headroom condition with specially designed plant.

One of the most critical protection measures was designed and implemented for the Hung Hing Flyover and Causeway Flyover trunk artery. These two individual bridge structures, spanning over the tunnel alignment, are both supported by pile foundation at one end and shallow foundation at the other ends and pile

removal was not necessary. However, the two structures separated by a longitudinal movement joint and its combination of foundation types posed a unique challenge to excavating the shallow Downtrack tunnel in reclaimed fill just underneath the structures.

Furthermore, the Canal Road Flyover, Hung Hing Flyover and Causeway Flyover are "red routes" meaning traffic stoppage at any stage during construction was not allowed. Despite these challenges, ground treatment below one of the shallow foundations was carried out to improve ground stiffness and hydraulic jacks were installed below Hung Hing Flyover to control excessive movement. The protection measures combined with use of the Variable Density TBM resulted in just 5mm movement and well below structural capacity and serviceability of the bridge structures.

Figure 8. Underpinning of Canal Road Flyover to facilitate pile obstruction removal.

Figure 9. Hung Hin Flyover and Causeway Flyover.

5 TBM TUNNELLING STRATEGY

5.1 *Choice of TBM*

During the project's tender stage, the three deepest tunnels under the same contract were specified to be excavated by using Mixshield TBMs. However, the shallow cover east Upper Downtrack tunnel was initially specified to be completed by an EPB TBM, avoiding the potential risk of slurry blowouts that could occur using a Mixshield TBM.

One of the tenderers highlighted the key concerns in using an EPB TBM with greater risk of collapse, higher ground settlement due to inefficiencies in managing the confinement support because of the complex geology, limited cover and possibility of encountering unforeseen obstruction in reclaimed ground. Further risks using the EPB TBM included foam blowouts, a more complex process for completing compressed air interventions and given the geology, a concern of the moisture content for spoil disposal (to be below 25%) not easily achieved.

The project team was aware of the experience from the Klang Valley MRT project in Kuala Lumpur, where a Variable Density (VaD) TBM was used for the first time, to overcome the complex Karstic limestone geology where problems (slurry blow-outs) had previously occurred using Mixshield TBM's (Schaub, 2014; Bäppler, 2016). The machine was developed to give the advantage of both a Mixshield TBM and an EBP TBM in providing an adequate face support medium (Bappler, 2016). The Variable Density TBM can make use of a thicker, denser slurry inside the excavation chamber instead of a thin slurry or earth paste. By using a higher density at the excavated face than a normal Mixshield TBM, the VaD TBM was more suited to the shallow eastern Downtrack tunnel. The proposal to use a VaD TBM for the first time in Hong Kong was then adopted.

5.2 *Special features of Variable Density (VaD) TBM*

To mitigate the risk of blow out to the ground surface while controlling stability of the excavation face, a range of slurry density was considered. The project's VaD TBM operated in two different modes of excavation, a Low-Density mode where slurry is supplied similarly to a slurry TBM (roughly 1.05-1.20T/m^3) through the slurry circuit, and a High-Density mode that took the TBM to the lower boundary of an EPB TBM where density in the excavation chamber was limited to 1.50T/m^3. This value is the maximum density that can be applied with the variable density process against the geology to avoid a blow out. Above this density, a full switch to EPB mode would have been required including foam conditioning to prevent plugging inside the cutter head and installation of a conveyor belt for spoil mucking out. The concept of the Low and High-Density modes and basic formula to determine the recommended density between the TBM axis and the ground level is shown in Equation (1) and Figure 10.

$$\text{Slurry Density} = \frac{\text{Design confinement pressure at axis (kPa)}}{\text{Depth from surface to TBM axis(m) x9.81}} \quad (1)$$

Excavated material is removed from the pressurised excavation chamber through a screw conveyor. For

operation, the screw was not required to reduce the support pressure from the front like a regular EPB TBM as a slurryfier box remained pressurised with the slurry circuit. The primary function of the slurryfier box is to dilute material removed from screw to a suitable density thereby allowing hydraulic transportation to the Slurry Treatment Plant (STP) for separation.

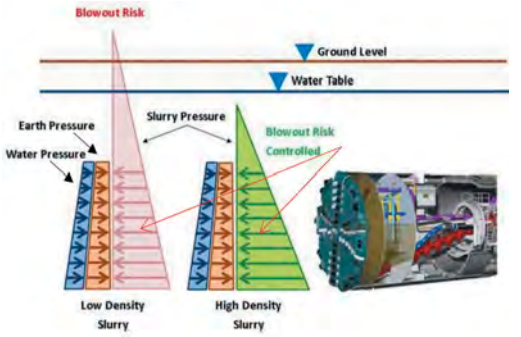

Figure 10. Blow out control using Low or High Density with same confinement pressure (Straesser, 2016).

To enable the higher density slurry mode in the excavation chamber, regulation of slurry injected to the excavated face is necessary. The Bentonite Injection Ratio (BIR) controlled this injection. The BIR is the flow of slurry sent to the excavation chamber divided by the flow of material physically excavated, with the basic formula shown in Equation (2).

$$\text{BIR}\ (\%) = \frac{\text{Flow of slurry}\ (\text{m}^3/\text{hr})}{\text{Flow of excavated materials}\ (\text{m}^3/\text{hr})} \quad (2)$$

The ratio is adjusted by the operator depending on the density of slurry measured in the excavation chamber. When the density is too low in the excavation chamber, the flow of slurry must be reduced and vice versa, if the density it too high, the flow of slurry must be increased.

Part of slurry injected to the front is sent to the working chamber where it is pushed to the excavation chamber through the communication pipe. The remaining slurry is directed through the face injection lines located on the cutter head which work the same as the foam injection lines found on an EPB TBM. A $2m^3$ tank supplies slurry to the 6 individually controlled pumps with the facility to add a polymer to aid dispersion in the excavation chamber if necessary. In semi-automatic mode, the PLC system regulates the flow through the face injection lines to make up the total slurry reaching the set BIR. In manual mode, the operator has control of the pumps which can be adjusted independently.

6 TBM PERFORMANCE

6.1 *Confinement pressure*

The complexity of the geology in conjunction with the shallow ground cover for the Downtrack tunnel, circa 6.5m made up of fill material in reclamation as far back as 50 years ago required specialist design and technology. As such the TBM was operated as a standard slurry mix shield or in a high density mode to avoid slurry blow out using specific verifications to limit the slurry and face support pressure.

Face support pressures, annulus grout pressures and compressed air intervention pressures were designed for ultimate limit state and serviceability limit state. Reference was made to GEO Report No. 249, GEO (2009) and GEO Report No. 298, GEO (2014) for the confinement pressures design. This ULS confinement pressure defines the minimum face support pressure. For the Service Limit State (SLS), the ground and building settlements at surface are verified with the 2D finite element models, to define the recommended pressure. Finite element analysis for soil-structure interaction were also carried out for validation and rigorous analysis for sensitive areas. To define the confinement pressures to be applied, a set of 2D (plain strain) Finite Element models were developed along the tunnel alignment. Slurry pressure to support the excavation and grout pressure injected by TBM behind the segmental lining are considered in the models to account for their interaction and the associate effect on the surface settlement. PLAXIS 2D revision 2015 is used to model the excavation.

6.2 *VaD TBM excavation performance*

Despite the eastern tunnels were relatively short (~680 m each) and learning curves considered, the Eastern Downtrack tunnel excavated with the VaD TBM completed the drive in 81 days with an average excavation of 8.3 m/day including stoppages for assembly, break in and false tunnel dismantling. In comparison, the Eastern Uptrack tunnel excavated with a Mixshield TBM completed the drive in 86 days, excavating an average of 7.9 m/day. The difference is largely a result of more rock and transition sections for the Mixshield drive, due to the deeper alignment, requiring more CAI interventions. Table 1 provides a comparison of average excavation rates for the various types of geology encountered by the Mixshield TBM and the VaD TBM.

The VaD TBM was driven through an initial long transition of rock/CDG and mixed face soil with boulders and several CAIs were required to maintain and replace the excavation tools. For the remainder of the drive, due to the shallow ground cover and potential unstable ground conditions, most of the CAIs were pre-planned and carried out as much as possible in defined and ground treated locations. This minimized

risks to the public on the surface, as well as the workers working in compressed air.

In addition, the TBM design included the contractor's in-house system which monitors the instrumented disc cutters during excavation, reduced the risk of failure and improper maintenance of the cutter head. Due to the complexity and challenges within the complex geology of the Eastern Downtrack excavation within transitions and reclaimed areas, the cutting tools system provided the TBM operator with accurate data including the ground repartition at the excavation face, unforeseen obstructions, and presence of corestones.

The progress of the VaD TBM was impacted by the processing time to treat the excess slurry in the Marine Deposit area with up to 60% fines content. As a result, the processing time of the filter presses at the STP was restrictive to TBM progress but this was anticipated due to limited works area available has restricted the capacity of the STP.

Upon completion of the TBM drives, the measured volume loss of the two upper Downtrack and the lower Uptrack tunnels are found to be in between 0.1 – 1.0% which is well within the predicted volume loss of 0.5 – 1.5% from the confinement pressure analysis. Reasons for this better than expected performance could be due to conservative soil parameters, effective advanced ground treatment implemented on site and diligent operation of the VaD TBM. The VaD TBM performed within the expected settlement values based on the designed confinement definition.

There was continual monitoring along the alignment with a suite of geotechnical instrumentation including numerous Automatic Deformation Monitoring System (ADMS) and monitoring points on the ground surface, roads, existing structures and services as the TBM progressed (Auvergne, 2017). No TBM stops or impacts to the surface (roads, footbridge) occurred as a result of either effects on the surface settlement or risk to the safety of the public.

7 RISK MANAGEMENT

Generally, TBM projects, particularly in an urban environment, comprise of an initial stage with advanced works to clear the tunnel alignment of obstructions and prepare for construction. This is then followed by execution of the construction contract and tunnelling operation. The tunnelling works for the project adopted the requirements set out in A Code of Practice for Risk Management of Tunnel Works (The International Tunnelling Insurance Group, 2006) to manage the tunnelling risks from feasibility to the design stage and throughout the construction period including the early contractor involvement process in the procurement stage. The risk assessments for various aspects related to the project and 3rd party stakeholders were systematically identified with mitigation measures and action implemented in advance of procuring the works contract. The resulting live "design for safety and constructability" risk register were taken forward to the procurement and construction stage. The MTR project team was well involved in the risk assessment at each stage of the project with designers, tenderers and the winning contractor.

In addition to the hazards and risks identified at the design and procurement stage, lead information received post contract award was act upon promptly to minimize the risk to the TBM excavation. Conducting comprehensive ground investigations and geophysical survey at Marsh Road and Wan Shing Street and the subsequent pile removal works are just two examples of the risk management process. The project also had the benefit of an International Expert Panel consisting of world-renowned tunnelling expert Dr. Alastair Biggart and experts in geotechnical and structural engineering, Professor John Burland of Imperial College London and Mike Glover of ARUP respectively, to provide expert advice on the design and construction. The input from the panel members included technical review of particular design matters and site constraints

Table 1. Comparison of excavation rates for the Mixshield TBM and VaD TBM.

	Up Trak Tunnel (Mixshield TBM)			Down Track Tunnel (VaD TBM)		
		Av Progress Rate			Av Progress Rate	
Stoppage times removed are those not link to The TBM production	Length	With stoppages	Without stoppages	Length	With stoppages	Without stoppages
Rock (learning curve)	172m	3.5m/day	5.4m/day	35m	3.5m/day	5.0m/day
Mixed Rock/CDG	82m	8.2m/day	9.1m/day	122m	4.4m/day	6.8m/day
CDG or CDG/All	419m	14.0m/day	15.0m/day	-	-	-
Soft (All, MD)	-	-	-	160m	10.0m/day	12.3m/day
MD (Marine Deposits)	-	-	-	210m	11.7m/day	14.0m/day
Seawall (Rubble Mound)	-	-	-	150m	16.7m/day	16.7m/day
Duration of drive		86 days	67 days		81 days	62 days
Total Length/Av rate	673m	7.9m/day	10.0m/day	677m	8.3m/day	11.1m/day

against construction methodologies via workshops and site visits with project team members. The input and support from the panel members is one of the key steps in mitigating the project risks.

8 CONCLUSIONS

Undertaking the shallow Eastern Downtrack tunnel alignment has significantly raised the risk profile of the project. The decision to adopt he hybrid EPB/ VaD TMB for the ground condition was deemed a success. The ground settlement associated with the tunnel excavation was well below the predicted level, there was no impact to the existing buildings, structures and utilities along the alignment and road traffic in the busy districts was not affected. Although the EPB mode was not necessary for the entire 670m long tunnel drive, the TBM and its multi-density slurry mode operated efficiently with good maintenance and production.

The success of the tunnel drive can also be summarized with a risk management process which include relentless approach to record search on construction history and having a good geological model along the tunnel alignment and comprehensive advanced works to remove obstructions.

ACKNOWLEDGEMENT

The authors would like to thank the Railway Development Office of Highways Department of the Government of the Hong Kong Special Administrative Region for its permission to publish this paper and their support particularly during the construction stage of the project. Although this paper bears the names of the authors, the staff from design consultant Ove Arup & Partners, contractor Dragages Bouygues Joint Venture and their suppliers, and the MTR project team all played a vital role on the success of the project.

REFERENCES

A Code of Practice For Risk Management of Tunnel Works, The International Tunnelling Insurance Group 2006.

Auvergne, S., Gauffre,J., Prost, A., (2017) Extensive use of I&M to Enable Safe TBM Drive in Urban Dense Area, a Focus on SCL1128 Eastern Downtrack Drive, Proceeding of the HKIE Geotechnical Division Annual Seminar 2017,Hong Kong.

Bäppler, K., New Developments in TBM tunnelling for changing grounds, Tunnelling and Underground Space Technology, 57, 2016, 18–26.

Kwok, K.; Bracq, G.; Barrett, T.; (2017) Hong Kong MTR Shatin to Central Link Contract1128 (Eastern Approach) – Tunnelling in Sensitive and Congested Urban Environment, Proceedings of the HKIE Geotechnical Division Annual Seminar 2017, Hong Kong.

Ng, N; Jacques, D, Reilly, B; Cheung Michael; (2108) Shatin Central Link – First Variable Density Tunnel Boring Machine in Hong Kong for a Shallow Tunnel Drive, Proceedings of the World Tunnel Congress 2018, Dubai.

MTR Geotechnical Base Line Report – Deliverable No 3.6H, Works Contract 1128, Consultancy Agreement No. C1108 (2014), SCL Hong Kong Section – Construction Scoping and Sequencing.

Schaub, W., Duhme, R., (2014) Multi-Mode and Variable Density TBMs – Latest Trends in Development, Underground Singapore 2014, Singapore.

Straesser, M. (2012), Klang Valley Mass Rail Transit Kuala Lumpur, Malaysia, Final Report of the Predesign for the Variable Density TBM, Herrenknecht AG, Schwanau.

Straesser, M., Klados, G., Thewes, M.; Schoesser, B.. Developments of LDSM and HDSM Concept for Variable Density TBM's. Tunnel, No. 7, 2016, 18–37.

Tunnelling for a Better Life – Yan, Celestino, Thewes & Eberhardt (Eds)
© 2024 The Author(s), ISBN 978-1-032-80042-4
Open Access: www.taylorfrancis.com, CC BY-NC-ND 4.0 license

Is a large TBM diameter unfavourable under squeezing conditions?

Alexandros N. Nordas*, Thomas Leone & Georgios Anagnostou
ETH Zurich, Zurich, Switzerland

ABSTRACT: A notable hazard in shield tunnelling through squeezing ground is the entrapment of the tunnel boring machine (TBM) due to insufficient thrust force. One often associates larger tunnel diameters with higher risks compared to smaller ones, mainly due to the higher propensity for problems related to an increased tunnel face size. However, depending on the tunnel diameter, different technical limitations exist that are associated with particular TBM parameters and the construction process, the effects of which are complex to assess and often mutually competing with respect to the TBM entrapment risk; all such limitations considered, the question arises: is a larger tunnel diameter always more critical? The present paper addresses this question by numerically investigating the effect of the tunnel diameter on the risk of TBM entrapment during mechanised excavation and after construction standstills, considering relevant technical limitations, a broad range of geotechnical conditions, as well as the effect of time-dependency of squeezing. The investigations yield an interesting finding – larger diameter tunnels are more favourable in poor quality ground, while the opposite holds in higher quality ground, as well as in the case of pronouncedly time-dependent ground behaviour. Besides their theoretical value, the results of the presented investigations also provide practice guidance concerning the use of experiences acquired from existing tunnels about the required thrust force as a reference for different diameter tunnels constructed under the same geotechnical conditions.

Keywords: tunnel boring machine, shield jamming, scale effect, creep, consolidation

1 INTRODUCTION

A situation sometimes encountered in tunnelling practice is that of different diameter tunnels constructed under practically the same geotechnical conditions, *e.g.* a smaller diameter pilot tunnel constructed prior to the main tunnel for exploration, advance drainage or ground improvement; or a road tunnel upgraded by later construction of a safety tunnel of smaller diameter. In such cases, the larger diameter tunnel usually poses a higher risk during construction, as a large cross-section is unconditionally less favourable for certain hazards (*e.g.,* collapse of the tunnel face), and more likely to encounter adverse conditions (*e.g.,* weak zones, water inflow *etc.*; Kovári 1979; Schneider 2002). In the cases of mechanised construction with a shielded tunnel boring machine (TBM), one of the most critical hazards is TBM entrapment due to insufficient thrust force ("shield jamming"; Ramoni and Anagnostou 2010). Although one may tend to think that a larger diameter tunnel is also more critical in relation to this hazard, this is not always straightforward when it comes to assessment for two reasons.

First, depending on the tunnel diameter, there are different technical limitations for certain TBM parameters, including the annular overcut around the shield, shield length, shield and lining stiffnesses and installable thrust force (Ramoni and Anagnostou 2010). These limitations often have mutually competing influences on the risk of shield jamming, which render their combined effect complex to assess.

Second, the tunnel diameter also poses limitations on certain parameters of the construction process, including the TBM advance rate during excavation and the duration of construction standstills. These are only relevant in the cases of time-dependent ground behaviour, and thus in squeezing ground. The latter may undergo rapid convergences following excavation, but its behaviour is often characterised by continuous deformations over a period of days, weeks, or even months due to creep or consolidation (Kovári and Staus 1996; Barla 2001; Anagnostou and Kovári 2005; Anagnostou 2007).

Considering all aforementioned factors, the question of whether a larger diameter tunnel is more critical than a smaller one in relation to the risk of shield jamming becomes complex and far from straightforward to answer qualitatively. Although the problem of shield jamming in mechanised tunnelling through squeezing ground – additionally considering creep and consolidation effects –has overall attracted significant attention in the literature (for a recent review see Leone *et al*. 2023), the effect of the tunnel diameter on the risk of shield jamming

*Corresponding author: anordas@ethz.ch

DOI: 10.1201/9781003495505-269

(henceforth referred to as "scale effect") has not been addressed thus far in the literature.

This question will be numerically investigated here, considering all factors mentioned above, a broad range of geotechnical conditions including pronounced creep of the ground, and the main two operational conditions – ongoing excavation and restart after a construction standstill. For details concerning the case of consolidation, the reader is referred to Nordas *et al.* (2023), which focuses principally on time-dependent ground behaviour and examines the differences between creep and consolidation.

The paper starts with the problem definition and the computational assumptions adopted in the numerical investigations (Section 2). Subsequently, it presents some theoretical considerations that improve the understanding of the problem (Section 3), as well as the practical considerations and limitations concerning the TBM and construction process parameters which must be considered in the simulations (Sections 4 and 5). Finally, it presents the results of the numerical investigations into the scale effect; first, for the case of time-independent ground behaviour, where the scale effect is associated solely with the TBM parameters (Section 6), and then for the case of time-dependent behaviour, where the construction process parameters are also relevant and a distinction must be made between the conditions prevailing during excavation (Section 7) and those during restart after a longer standstill (Section 8).

2 COMPUTATIONAL ASSUMPTIONS

Consideration is given to the rotationally symmetric problem of a deep, cylindrical tunnel of radius R, crossing homogeneous and isotropic rock subjected to a hydrostatic *in-situ* stress field (σ_0). A numerical model of the advancing tunnel heading has been developed in Abaqus® (Dassault Systèmes, 2018) to simulate the mechanised excavation and lining installation, as well as the conditions during a subsequent TBM standstill of arbitrary duration (Figure 1). A detailed description of the computational assumptions can be found in Nordas *et al.* (2023), while some key aspects of the model are discussed hereafter.

On account of rotational symmetry, the model assumes uniform overcut ΔR and backfilling around the segmental lining. The excavation process, which in reality consists of intervals of continuous TBM propulsion (with the net advance rate v_N) regularly alternating with standstills for lining erection (zero advance rate), is simulated as continuous with an average advance rate v; this simplification has been shown to be sufficiently accurate in most cases (Leone *et al.*, 2023). At each numerical excavation step, part of the ground equal to the 0.5 m round length (Figure 1) is removed ahead of the face and an equal part of lining is installed immediately behind the shield tail (step-by-step simulation method; see, *e.g.*, Franzius and Potts, 2005). The tunnel face is considered unsupported, taking into account the fact that open shield TBMs are employed in most practical cases of mechanised tunnelling through squeezing rocks. The tunnel support is modelled by radial springs that account for the shield and lining stiffnesses (K_s and K_l) as well as for the radial overcut ΔR (for details see Ramoni and Anagnostou, 2010).

In transient analyses considering creep, a linear elastic-viscous perfectly plastic constitutive model is adopted for the rock, with a Mohr-Coulomb yield condition and a non-associated visco-plastic flow rule based on Perzyna's theory (Perzyna, 1966); this is suitable for modelling rheological processes in squeezing ground, where the dominant portion of time-dependent deformations is plastic. The model has six parameters – Young's Modulus E, Poisson's ratio ν, uniaxial compressive strength f_c, angle of internal friction ϕ, angle of dilation ψ, and the viscosity η, which determines the rate of visco-plastic deformations. Details on its formulation and numerical implementation in Abaqus® can be found in Leone *et al.* (2023). In the absence of creep ($\eta = 0$), the constitutive model degenerates into the classic elastoplastic model.

The model provides the longitudinal distribution of the rock pressure $\sigma_R(x)$ on the shield at any time instance. The simulated excavation length is set equal to 60 excavation steps which is sufficiently long for achieving steady state with respect to the advancing heading; the standstill phase of duration t is initiated thereafter.

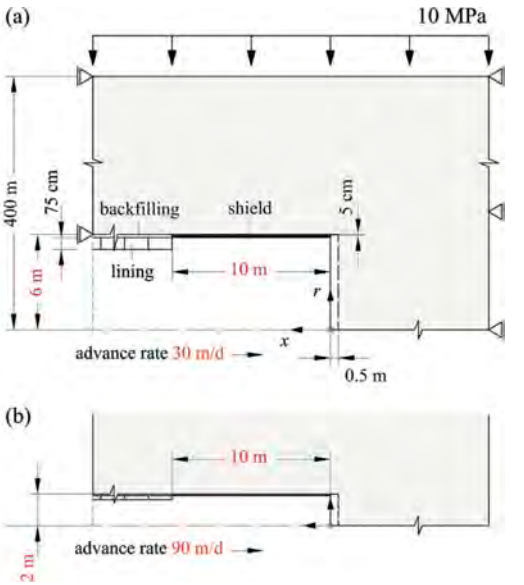

Figure 1. Axisymmetric computational model of the advancing tunnel heading for tunnels with diameter of 12 m (a) and 4 m (b) (Parameters: Table 1).

3 THEORETICAL CONSIDERATIONS

The risk of shield jamming is assessed based on the required thrust force to overcome shield skin friction, which depends on the rock pressure exerted on the shield (Ramoni and Anagnostou, 2010). In the following, the average pressure $\overline{\sigma}_R$ will be considered. It is obtained via integration over the shield length L and depends in general on all problem parameters, including the *in-situ* stress σ_0, tunnel radius R, ground parameters E, ν, f_c, ϕ, ψ, η, TBM parameters K_s, K_l, L, ΔR, and process parameters, *i.e.* advance rate v, and standstill duration t (Nordas *et al.*, 2023):

$$\frac{\bar{\sigma}_R}{\sigma_0} = f\left(\frac{E}{\sigma_0}, \frac{\Delta R}{R}, \nu, \frac{f_c}{\sigma_0}, \phi, \psi, \frac{L}{R}, \frac{K_s R}{E}, \frac{K_l R}{E}, \frac{\mathrm{v}\,\eta}{R E}, t\frac{E}{\eta}\right) \quad (1)$$

In practice, different technical constraints exist for the TBM parameters and the advance rate depending on the size of the tunnel cross-section (here the tunnel radius R), while the rock parameters may also differ at the representative material volume which, however, is not as relevant in weak, squeezing ground (Section 4). Therefore, the dimensionless parameters in Eq. (1) cannot in general take the same values for tunnels of different size, which gives rise to the scale effect.

Evidently, there is not much use in trying to quantify the combined influence of all parameters qualitatively; even by neglecting time-dependency to simplify matters (the last two terms in Eq. 1 become irrelevant), the combined influence of the TBM parameters is cumbersome to assess, due to their mutually competing effects (*e.g.*, L/R and $\Delta R/R$ both decrease with increasing R, but the former is favourable for the rock pressure, while the latter is unfavourable). Therefore, one must resort to numerical simulations. However, before undertaking this it is useful to understand the influence of each parameter, as it offers a better comprehension of the problem. The influence of the TBM parameters is generally known (Ramoni and Anagnostou, 2010), and so in this instance we focus on the last two parameters related to the advance rate v and the standstill duration t, which are only relevant in the cases of time-dependent ground behaviour due to creep. To examine their influence, we consider an idealised situation where all other dimensionless parameters in Eq. (1) related to the ground and TBM are fixed regardless of R.

First, let us examine the isolated influence of the last term related to the standstill duration t. We can do this by considering a case where the excavation occurs rapidly in relation to the rate at which the ground to responds to it ($\mathrm{v}\,\eta \to \infty$), which renders the penultimate parameter infinite regardless of R and the rock pressure only dependent on the last parameter. Since R does not appear in the last parameter of Eq. (1), one can conclude that the rock pressure develops at the same rate regardless of the cross-section size.

Next, let us examine the influence of the penultimate term related to the advance rate v, by considering a case where the excavation is not followed by a standstill and the last term becomes irrelevant. First of all, in order to compare the rock pressure in tunnels with different R, v alone is not the most suitable measure of the rate of advance. When the shield reaches any given tunnel cross-section, it remains exposed to pressure at that section for as long as it is required for its entire length L to pass through it; therefore, the shield pressure that ultimately develops depends on the time required for the TBM to advance by one shield length, *i.e.* L/v (= $(L/R)/(\mathrm{v}/R)$), which is only a function of v/R since L/R is considered fixed here regardless of R. A more suitable measure of the rate of advance would thus be v/R – considering the same v/R means that the TBM takes the same time to advance by one shield length irrespective of R. For a given v/R, the normalised advance rate $(\mathrm{v}/R)\cdot(\eta/E)$ is constant, which means that the pressure develops at the same rate irrespective of R – exactly as in the case of the standstill examined previously.

Combining the above, for both conditions – during advance and for restart after a standstill of the TBM – there would be no scale effect in the case of time-independent ground behaviour, but also in the case of creep, if the same dimensionless parameters related to the ground and the TBM could be specified for different diameter tunnels and these could be excavated with the same rate v/R. In all other cases, there will be a scale effect, which can only be quantified numerically.

4 PRACTICAL CONSIDERATIONS

Notwithstanding the value of the theoretical considerations discussed in Section 3, the scale effect resulting from the combined influence of all parameters is far more complex due to the aforementioned constraints and limitations concerning the advance rate, the TBM parameters and, possibly, also the ground parameters. These are discussed in the following subsections.

4.1 *Advance rate*

The assumption adopted in Section 3 – that v/R can be the same for the two tunnels, *i.e.* v is proportional to R – is particularly erroneous, as it means that a larger diameter tunnel could be excavated at a higher rate. In practice, it is well-known that the larger the boring diameter, the slower the TBM advances, *i.e.* v decreases with increasing R. In fact, v can be assumed inversely proportional to R, which then makes v/R inversely proportional to R^2, as discussed hereafter.

Mechanised excavation can be idealised as a "stop-and-go" process, where intervals ΔT_1 of continuous TBM propulsion over the length of one prefabricated segmental lining ring L_T regularly

alternate with standstill intervals ΔT_2 for the corresponding ring installation. The net advance rate of the TBM during continuous excavation can thus be expressed as $v_N = L_T/\Delta T_1$, while the average advance rate during the "stop-and-go" process considered in this work (Section 2) can be expressed as $v = L_T/(\Delta T_1 + \Delta T_2)$ (Leone *et al*., 2023).

The net advance rate is defined as v_N = ROP*RPM, where ROP is the rate of penetration and RPM the number of rotations of the TBM cutterhead per minute. For tunnels under identical ground conditions ROP can be assumed to be the same, provided that the installed thrust force is higher in the larger TBM, as is common in practice. RPM can be assumed inversely proportional to R, considering that the linear velocity of the gauge cutters is limited to 150-200 m/min to avoid overheating, irrespective of the TBM diameter (Rispoli *et al*., 2020; Hamburger and Weber, 1992). Under these assumptions, v_N becomes inversely proportional to R. Assuming that the lining ring length L_T is the same regardless of R, ΔT_1 becomes proportional to R. It is reasonable to assume that ΔT_2 is also proportional to R (see, *e.g.*, Tahernia and Rostami, 2021; Farokh, 2013, 2020), which then makes v inversely proportional to R.

It is indicatively noted here that, by incorporating the above realistic assumption in the theoretical analysis of Section 3, the conclusions concerning the scale effect during advance already change completely – the normalised advance rate $(v/R)\cdot(\eta/E)$ becomes inversely proportional to R^2, which means that the pressure develops faster in a larger tunnel. In practice, this means that if the tunnel diameter was, *e.g.*, four times larger, the pressure would develop 16 times faster (as if the ground viscosity η was lower by a factor of 16). On the other hand, the scale effect during a standstill preceded by a rapid advance ($v\ \eta \rightarrow \infty$) is not influenced; however, as the tunnel size influences the advance and standstill phases differently, the overall scale effect already becomes very complex to assess – this is even more so the case when the technical constraints for the TBM parameters are additionally considered, as discussed next. This underscores the importance of incorporating these limitations in our numerical investigations.

4.2 *TBM parameters*

The TBM parameters (overcut ΔR, shield length L and shield and lining stiffnesses K_s and K_l) that can be materialised in practice are limited to a specific range, regardless of the tunnel diameter. Therefore, the nondimensional parameters $E\Delta R/(\sigma_0 R)$, L/R, K_sR/E and K_lR/E cannot in general take the same values for a large and small tunnel. Furthermore, when evaluating potential scale-effects with respect to the risk of shield jamming, it is not sufficient to only consider the shield loading or the required thrust force (which depend on the parameters in Eq. 1), but also the installed or installable thrust force. The latter increases with the tunnel diameter, which introduces an additional scale effect to be considered. Typical values for these parameters based on technical data gathered from various TBMs can be found in Ramoni and Anagnostou (2010).

4.3 *Ground parameters*

The strength and stiffness of the ground tentatively decrease with increasing representative volume and, in turn, tunnel diameter, hence scale-effects may exist also in relation to the ground parameters. However, as squeezing ground is often weak at the scale of specimen, the differences between a small and a large diameter tunnel with respect to the ground parameters are not significant and can be neglected.

5 ASSUMPTIONS OF QUANTITATIVE ANALYSIS

Two tunnels with diameters D = 4 m and 12 m excavated under identical ground conditions will be analysed numerically using the computational model introduced in Section 2 (Figure 1) and considering practically relevant TBM and process parameters based on the limitations discussed in Section 4, as given in Table 1.

The average advance rates during the stop-and-go operation are selected to be inversely proportional to the diameter (Section 4.1). The common overcut ΔR = 50 mm and shield length L = 10 m adopted for both tunnels are realistic, considering that the corresponding normalised values $\Delta R/R$ = 2.5% and 0.8%, and L/R = 5 and 1.7, are typical for D = 4 m and 12 m, respectively (*cf.* Fig. 6 in Ramoni and Anagnostou, 2010). The thicknesses d_s of the shield and d_l of the lining are assumed proportional to the radius R; this assumption is reasonable and makes the normalised radial stiffnesses $K_sR/E = (E_s/E)\ d_s/R$ and $K_lR/E = (E_l/E)\ d_l/R$ identical for the two tunnels, and dependent only on the Young's moduli E_s, E_c and E of steel, concrete and the ground, respectively.

To assess the risk of shield jamming, the required thrust force F_r must be considered in combination with the installed thrust force F_i. Therefore, the comparison between the two tunnels is based on the ratio F_r/F_i, which expresses the percentage of F_i utilised by F_r and will be hereafter referred to as "thrust utilisation factor" (TUF). The required thrust force F_r is computed as $\mu\ 2\pi R\ L\ \mu\ \bar{\sigma}_R$, where μ denotes the static friction coefficient. Strictly speaking, this expression holds for the conditions during TBM restart after a standstill and not during advance; however, the former is the most critical operational stage in most cases (see Ramoni and Anagnostou, 2010), hence the expression in general provides a conservative estimate. The installed TBM thrust force is assumed to increase proportionally with the cross-section area, and thus with R^2, according to the

expression $F_i = 5\ R^2$ MN/m^2 which provides values in the high end of the range of technical data collected from various TBMs (*cf.* Fig. 7 in Ramoni and Anagnostou 2010).

The scale effect is first analysed by disregarding creep (rapid squeezing development), where it is solely influenced by the TBM parameters (Section 6). Subsequently, the case of time-dependent ground behaviour due to creep is examined, considering the conditions during TBM advance (Section 7) and at restart after a 200-day long TBM standstill (Section 8).

Table 1. Parameters considered in the numerical simulations.

Ground	
Young's Modulus, E [GPa]	1
Poisson's ratio, ν [-]	0.25
Uniaxial compressive strength, f_c [MPa]	var.
Angle of internal friction, ϕ [°]	25
Dilatancy angle, ψ [°]	5
Depth of cover, H [m]	400
In-situ stress at tunnel axis, σ_0 [MPa]	10
Viscosity, η [MPa·d]	var.
TBM	
Boring diameter, D [m]	4 or 12
Radial overcut, ΔR [mm]	50
Shield length, L [m]	10
Radial shield stiffness, K_s [MPa/m]	875 (D = 12m) 2625 (D = 4m)
Shield thickness, d_s [m]	0.15 (D = 12 m) 0.05 (D = 4 m)
Young's modulus of steel, E_s [GPa]	210
Average Advance rate, v [m/d]	30 (D = 12 m) 90 (D = 4 m)
Shield skin friction coefficient, μ [-]	0.15
Installed thrust force, F_i [MN]	180 (D = 12 m) 20 (D = 4 m)
Lining	
Young's modulus of concrete, E_c [GPa]	30
Lining thickness, d_l [m]	0.75 (D = 12 m) 0.25 (D = 4 m)
Radial lining stiffness, K_l [MPa/m]	625 (D = 12 m) 1875 (D = 4 m)

6 RESULTS DISREGARDING CREEP

Figure 2 shows the thrust utilisation factors of the two tunnels with D = 4 m (solid lines) and D = 12 m (dashed lines) as functions of the rock quality, expressed by its uniaxial compressive strength f_c.

The results of Figure 2 contradict the common perception that a smaller diameter tunnel is less vulnerable than a larger one. This may be unconditionally true for other potential hazards (*e.g.*, instability of the tunnel face), but not for shield jamming, where it is only true in higher quality ground (f_c > 3.2 MPa), while the opposite holds in weaker ground. The TUF

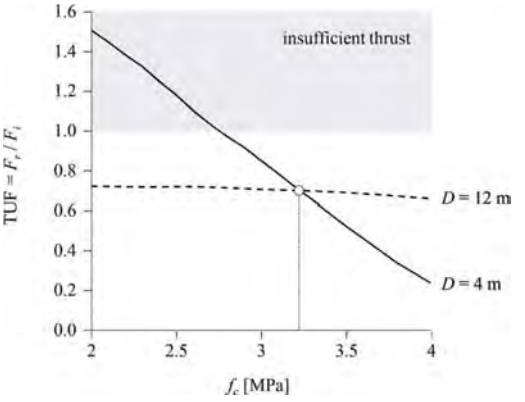

Figure 2. Thrust force required to overcome shield skin friction normalised by the installed thrust force ("thrust utilisation factor", TUF), as a function of the uniaxial compressive strength of the ground f_c (no creep; parameters: Table 1).

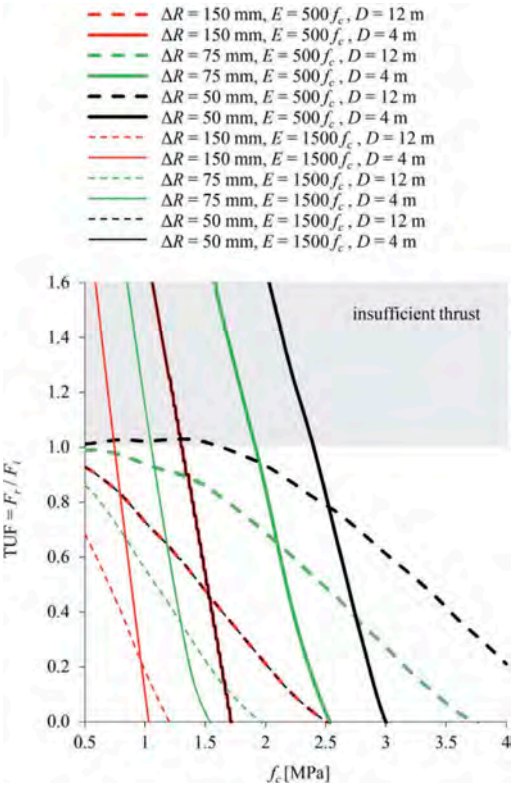

Figure 3. Results of a parametric study about the effects of rock strength f_c, rock stiffness E and overcut ΔR on the thrust utilisation factor (TUF) (F_r after the design nomograms of Ramoni and Anagnostou, 2010, for a 400 m deep tunnel with σ_0 = 10 MPa, ν = 0.25, f_c = 0.5 – 4 MPa, ϕ = 25°, ψ = 5°, L = 10 m, K_sR/E = 10, K_lR/E = 0.5, μ = 0.15,F_i = 20 and 180 MN for D = 4 and 12 m, respectively).

of the TBM in the larger diameter tunnel is generally less sensitive to variations of rock quality than in the smaller diameter tunnel and is consistently lower than 1, which means that the tunnel excavation is feasible for the considered strength range, whereas the small tunnel excavation is only feasible in higher quality ground (f_c > *ca.* 2.7 MPa).

Considering this interesting finding, a more extensive parametric study was conducted to assess its general validity. The computations concern a 400 m deep tunnel (σ_0 = 10 MPa) and have been performed using the design nomograms of Ramoni and Anagnostou (2010). Concerning ground parameters, consideration is given to variable uniaxial compressive strength f_c = 0.5 – 4 MPa, Young's moduli $E = 500\, f_c$ and $1500\, f_c$, which respectively correspond to the lower and upper limits of possible stiffnesses for a geomaterial with given f_c, and otherwise identical parameters to those given in Table 1, which were also considered by Ramoni and Anagnostou (2010).

Concerning TBM parameters, consideration is given to overcuts ΔR = 50, 75 and 150 mm, which respectively correspond to the relatively small value adopted in the computational example (Table 1), an intermediate value and an unusually large value. The shield length and installed thrust force are as given in Table 1, but different normalised radial stiffnesses of the shield $K_s R/E = 10$ and the lining $K_l R/E = 0.5$ are considered, which correspond to those assumed by Ramoni and Anagnostou (2010) for producing the design nomograms; although the latter assumption leads to more conservative predictions for the required thrust force, it does not affect the conclusions of the study otherwise.

The results of the parametric study (Figure 3) confirm that a larger diameter tunnel is always less vulnerable than a smaller one in weak ground (dashed lines for D = 12 m consistently below solid lines for D = 4 m in the range of low f_c). Moreover, it is less sensitive to variations of the ground quality and its excavation is practically feasible in all cases considered, in contrast to the smaller diameter tunnel, which exhibits a much higher sensitivity to the ground quality and its excavation is only feasible in higher quality ground.

7 RESULTS FOR CREEP AND TBM ADVANCE

In the example of Figure 2, the TUFs of the two TBMs are equal for f_c = *ca.* 3.2 MPa, which means that the competing effects of the TBM parameters (Section 3) outweigh one another and the scale effect associated with these is eliminated. Therefore, the transient computations have been performed for this strength (and the parameters of Table 1). This enables examining the isolated influence of the advance rate v or, equivalently, the viscosity η in the case of creep (note the dimensionless expressions in Eq. 1).

Figure 4 shows the thrust utilisation factor as a function of η for the two tunnels with D = 4 m (solid lines) and D = 12 m (dashed lines).

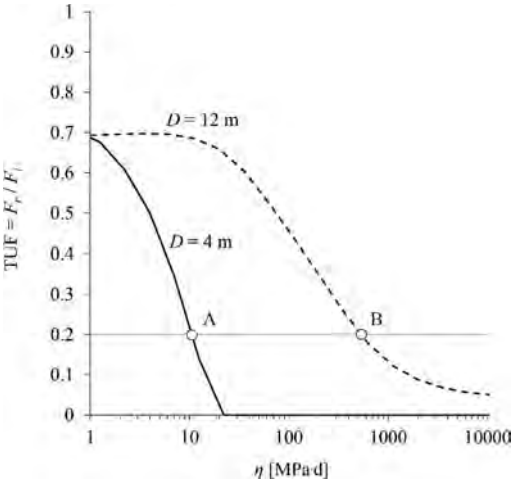

Figure 4. Thrust utilisation factor (TUF) as a function of the viscosity η (f_c = 3.2 MPa; other parameters: Table 1).

With the exception of the range of high viscosities, a scale effect clearly exists with respect to the risk of shield jamming: an increase in diameter results in a higher utilisation of the thrust force, as reflected by the vertical distance between the dashed line and the solid line that is consistently below it. This means that in the case of time-dependent ground behaviour, the situation is more favourable for the smaller diameter, which is also consistent with the results discussed in Section 6 and shown in Figure 2: time-dependency delays squeezing, hence the rock responds to tunnel excavation as if it were of a higher quality, and an increase in rock quality renders a smaller diameter more favourable. It is noted here that this result is qualitatively consistent with the theoretical considerations discussed in Section 4.1, according to which the rock pressure on the shield develops faster on the larger TBM for a given advance rate (or, equivalently, viscosity η herein).

The scale effect is negligible in the range of high viscosities because the rock behaviour is practically elastic, hence the convergences around the advancing shield area are small anyway, regardless of the tunnel diameter.

The scale effect can also be demonstrated in an alternative way. Let us consider a case where the 4 m diameter tunnel was constructed first, and the actual applied force was equal to 20% of the installed one (TUF = 0.2). Assuming that the strength and stiffness parameters of the rock are known and correspond to the ones in Figure 4, the rather low required thrust force could be explained on the basis of the convergence delay due to time-dependency (point A in Figure 4). What could one expect for the main, larger diameter tunnel? In order to limit the effect of squeezing and maintain the same, low TUF = 0.2, the viscosity η would have to be higher by a factor of about 50 (point B vs. A); equivalently, for the same η (as in point A), the

advance rate v in the main tunnel would have to be about 50 times higher (note dimensionless expressions in Eq. 1). This is, of course, impossible, but provides another interpretation of the scale effect.

For the parameters adopted in this example, the TUFs of both TBMs are consistently lower than the value of ca. 0.7 which corresponds to time-independent behaviour (very low viscosity; *cf.* Figure 2), indicating that the excavation of both tunnels is thoroughly feasible. However, the assumed values for the installed thrust force $F_i = 5\ R^2$ MN/m^2 (20 MN for $D = 4$ m, 180 MN for $D = 12$ m; Table 1) are very high for rock TBMs; with a moderate assumption, *e.g.* $F_i = 3\ R^2$ MN/m^2 (12 MN for $D = 4$ m, 108 MN for $D = 12$ m), jamming of the larger TBM might occur in the range of η = *ca.* 10–100 MPa·d, while the smaller TBM would remain entirely in the safe region.

8 RESULTS FOR CREEP AND RESTART AFTER STANDSTILL

Transient computations have been performed considering the same parameters as before (Table 1 and $f_c = 3.2$ MPa), as well as a high viscosity $\eta = 10{,}000$ MPa d to ensure that the behaviour during advance is elastic and, therefore, relevant shield loading develops only during the standstill (see TUF < 0.1 for $\eta = 10{,}000$ MPa d in Figure 4). This enables an examination of the isolated influence of the standstill duration t.

Figure 5 shows the thrust utilisation factor as a function of t for the two tunnels with $D = 4$ m (solid lines) and $D = 12$ m (dashed lines).

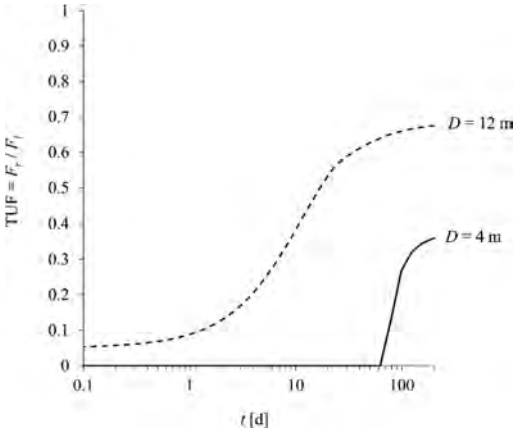

Figure 5. Thrust utilisation factor (TUF) as a function of the standstill duration t ($f_c = 3.2$ MPa; $\eta = 10^4$ MPa·d, other parameters: Table 1).

The same conclusions as for the advance stage examined in Section 7 can basically be drawn also here. There is a clear effect of the tunnel diameter on the thrust force required for restart after a standstill and the associated shield jamming risk, as expressed by TUF. This scale effect is reflected by the width of the band defined by the dashed and solid lines.

9 CONCLUSIONS

The present paper numerically investigated the effect of the tunnel diameter on the risk of shield jamming during mechanised tunnel construction in squeezing ground, considering the various technical limitations concerning the TBM and construction process parameters depending on the tunnel diameter and the markedly time-dependent response that squeezing ground often exhibits. Exemplary numerical simulations with practically relevant parameters demonstrated that a larger diameter is always more favourable than a smaller one in poor quality ground, while the opposite is true in the case of higher quality ground or ground exhibiting time-dependent behaviour, where the delay in ground deformations is equivalent to an improvement of the ground quality.

The paper only considered time-dependency due to creep, but the conclusions drawn hold also for the case of consolidation – the other common mechanism of time-dependency in squeezing ground. Scale effect in this case is slightly less pronounced. For more details, the reader is referred to Nordas *et al.* (2023).

Provided that data are available concerning the required thrust force in an existing tunnel, the findings of the present paper provide useful indications and guidance concerning the risk of shield jamming during the later construction of an adjacent, different diameter tunnel.

REFERENCES

Anagnostou, G., 2007. Practical consequences of the time-dependency of ground behavior for tunneling. Proceedings - Rapid Excavation and Tunneling Conference, 255–265.

Anagnostou, G., Kovári, K., 2005. Tunnelling through geological fault zones. In: International symposium on design, construction and operation of long tunnels, Taipei, vol 1. Chinese Taipei Tunnelling Association, Taipei, pp 509–520.

Barla, G., 2001. Tunnelling under squeezing rock conditions. In: Eurosummer-school in tunnel mechanics, Innsbruck. Logos Verlag, Berlin, pp 169–268.

Dassault Systèmes, 2018. ABAQUS 2018 Theory manual. Dassault Systèmes Simulia Corp., Providence, Rhode Island.

Farrokh, E., 2013. Study of utilization factor and advance rate of hard rock TBMs. Ph.D. thesis, Pennsylvania State University, USA.

Farrokh, E., 2020. A study of various models used in the estimation of advance rates for hard rock TBMs. Tunnelling and Underground Space Technology, 97, 103219.

Franzius, J. N., Potts, D. M., 2005. Influence of mesh geometry on three-dimensional finite-element analysis of tunnel excavation. International Journal of Geomechanics, 5(3), 256–266. doi: 10.1061/(ASCE)1532-3641(2005)5:3(256).

Hamburger, H., Weber, W., 1992. Tunnelbau im Untertagebau – Tunnelvortrieb mit Vollschnitt- und Erweiterungsmaschinen für grosse Durchmesser im Festgestein. Taschenbuch für den Tunnelbau 1993, 139–197, Verlag Glückauf GmbH Essen.

Kovári, K., 1979. Basic considerations on the design of underground openings. IABSE Surveys = Revues AIPC = IVBH Berichte, 3, 23.

Kovári, K., Staus, J., 1996. Basic considerations on tunnelling in squeezing ground. Rock Mechanics and Rock Engineering 29(4), 203–210.

Leone, T., Nordas, A., Anagnostou, G., 2023. Effects of creep on shield tunnelling through squeezing ground. Rock Mechanics and Rock Engineering. (Accepted for publication).

Nordas, A., Leone, T., Anagnostou, G., 2023. Comparison of creep and consolidation in tunnelling. Part B: Transferability of Experience. Rock Mechanics and Rock Engineering (under review).

Perzyna, P., 1966. Fundamental problems in viscoplasticity. In G. G. Chernyi, H. L. Dryden, P. Germain, L. Howarth, W. Olszak, W. Prager, R. F. Probstein, H. Ziegler (Eds.), Advances in Applied Mechanics, Elsevier, Vol. 9, 243–377.

Ramoni, M., Anagnostou, G., 2010. Thrust force requirements for TBMs in squeezing ground. Tunnelling and Underground Space Technology, 25(4), 433–455.

Rispoli, A., Ferrero, A. M., Cardu, M., 2020. From Exploratory Tunnel to Base Tunnel: Hard Rock TBM Performance Prediction by Means of a Stochastic Approach. Rock Mechanics and Rock Engineering, 53(12), 5473–5487.

Schneider, A., 2002. Sicherheit gegen Niederbruch im Untertagbau. Ph.D. Thesis. ETH Zurich. (in German).

Tahernia, T., Rostami, J., 2021. The effect of TBM Diameter on Ring installation time. In: Carlson, J.E., Davidson, G.W. (Eds.) Rapid Excavation and Tunnelling Proceedings 2021. Society for Mining, Metallurgy & Exploration.

Tunnelling for a Better Life – Yan, Celestino, Thewes & Eberhardt (Eds)
© 2024 The Author(s), ISBN 978-1-032-80042-4
Open Access: www.taylorfrancis.com, CC BY-NC-ND 4.0 license

Developments in large diameter subaqueous tunnels

Ozturk Ozgur*
Executive Director, Hong Kong SAR, China

Terry Ma
Technical Director, Hong Kong SAR, China

Jackie Cheung
Senior Engineer, Hong Kong SAR, China

ABSTRACT: Over the last two decades, large diameter Tunnel Boring Machine (TBM) tunnels have been increasingly utilized for underground road and rail transportation projects. Among those, longer and deeper subaqueous tunnels also became feasible and competitive with increased technological developments and applying innovative solutions. Notably in recent years, several subaqueous large diameter tunnels have been designed and safely constructed under high water pressures and in challenging environmental conditions, e.g. seismic regions, with the aid of smart technologies and digital tools.

This paper discusses developments of large diameter subaqueous tunnels; focusing on special considerations in design and construction, risk management and sustainable low carbon solutions using key examples from recent projects.

Keywords: TBM, Large diameter, Subaqueous, Sustainable solutions

1 INTRODUCTION

In recent years, several subaqueous TBM tunnels have been successfully designed and constructed in depths greater than 100m, lengths extending over 4km, and in highly seismically active regions (≥7.0Mw). In order to overcome environmental challenges, innovative and robust design and construction techniques together with sustainable solutions have had to been considered and effectively applied. Constructing subaqueous tunnels using TBM, by their very nature, face higher risks against blowouts and/or sinkholes. Therefore a more rigorous risk management approach is required to help identify and mitigate, or eliminate if feasible, the associated risks.

2 SUBAQUEOUS TUNNELLING METHODS

For large scale subaqueous tunnelling projects, mainly four types of tunnelling methods are utilized, including:

- TBM Tunnels
- Immersed Tube Tunnels
- Mined Tunnels (Drill & Blast, Sequential Excavation Method)
- Offshore Cut-and-Cover Tunnels

2.1 *Subaqueous TBM tunnels*

In recent years, longer and deeper, large diameter subaqueous TBM tunnels are being constructed. For example the Eurasia subsea tunnel, located in Turkey, is a 106m deep, double-deck road tunnel. This was constructed with a TBM designed to withstand up to 12 bar hydrostatic pressure. In Hong Kong SAR, a number of subaqueous tunnels have been constructed with TBM diameter ≥13m. Table 1 below shows details of some of the larger diameter subaqueous TBM tunnels together with lengths, depths and tunnel lining outer diameters. The projects shown in Table 1 are all road tunnels, including three lane per tube and double-deck tunnels. There are some large diameter TBM tunnels accommodating double-track railways such as Riyadh Metro (completed), three contracts in Singapore (CRL Phase 2) which are under construction and few others. Those tunnels are smaller in diameter compared to the road tunnels listed in Table 1, in the range of 10m ~ 13m OD.

*Corresponding author: ozturk.ozgur@aecom.com

DOI: 10.1201/9781003495505-270

Table 1. Some of the Large Diameter Subaqueous Tunnels.

Project	Length below Sea/ River (m)	Depth below Sea/ River (m)	Outer Diameter (m)
Eurasia Tunnel (Turkey)	3340	106	13.2
Shantou Su Ai Tunnel (China)	3046	65	14.5
Tokyo Bay Aqua Line (Japan)	9400	60	13.9
Tuen Mun – Chek Lap Kok Link (Hong Kong, SAR of China)	5000	55	13.5 & 16.9
Karnaphuli River Crossing (Bangladesh)	2450	50	11.8
Chong Ming South Tunnel (China)	7470	60	15.0
Shenzhen Mawan Subsea Tunnel (China)	2063	40	15.0
Port of Miami Tunnel (USA)	1300	37	12.5

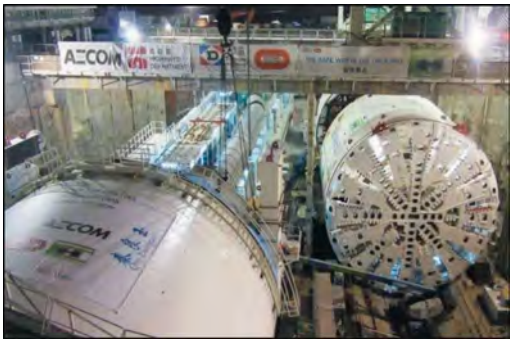

Figure 1. Tuen mun – Chek lap kok link TBM tunnel, Hong Kong, SAR of China.

2.2 *Immersed tube tunnels*

There are over 180 immersed tube tunnels in the world, including those under construction. In recent years, with the help of advancing technology, deeper and longer immersed tube tunnels could be designed and built. Figure 2 and Figure 3 show the deepest and longest immersed tunnels constructed to-date.

2.3 *Subaqueous mined tunnels*

Large scale subaqueous mined railway or road tunnels are generally deep, passing through rock strata. The longest mined tunnel to-date is the Seikan railway tunnel located in Japan. This railway tunnel passes beneath the Tsugaru Strait and connects the Aomori Prefecture on Honshu Island and the Hokkaido Island.

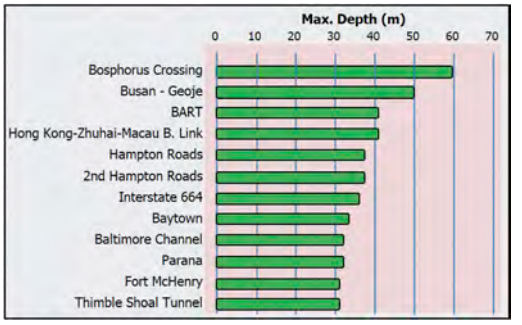

Figure 2. Deepest immersed tube tunnels.

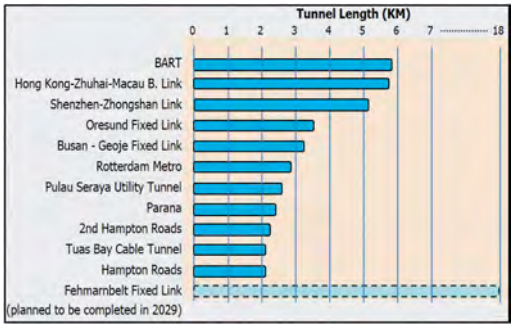

Figure 3. Longest immersed tube tunnels.

Figure 4. Tunnel element prefabrication and floating at casting yard (HZMB Link).

Its 23.3km long subsea section, extends approximately 240m below the sea level (approximately 100m below seabed). The deepest mined tunnel for transportation is the Ryfylke tunnel, located in Norway, extending 292m below the sea level at its deepest point.

2.4 *Subaqueous cut-and-cover tunnels*

Subaqueous Cut-and-Cover tunnels are also called off-shore Cut-and-Cover tunnels. The construction method utilized for these types of tunnels usually involves marine cofferdams or sheet/pipe piling, constructing the cut-and-cover tunnel in dry condition, and

backfilling after completion of the tunnel. Subaqueous cut-and-cover tunnels are usually shorter and shallower compared to subaqueous TBM and mined tunnels. A road tunnel example is show below in Figure 5.

Figure 5. Central - Wan Chai Bypass, Hong Kong, SAR of China.

3 SUBAQUEOUS TBM TUNNELS IN SEISMIC REGIONS

Tunnels generally perform better during earthquakes than above-ground structures such as bridges, buildings, towers and similar. Tunnels are constrained by the surrounding ground and, in general, cannot be either excited independent of the ground or be subjected to strong vibratory amplification during earthquakes except when the tunnel passing through or near the active fault zone. In addition, as it gets deeper below the ground, the amplitude of seismic ground motion attenuates, and therefore the magnitude of damage to the tunnel structure is smaller compared to above-ground structures.

A Probabilistic Seismic Hazard Assessment (PSHA) returns the probability of a given ground motion to be exceeded within a year, which is usually called "return period". Most commonly referred return periods for seismic design of tunnels are as follows:

- 100 years return period (40% probability of exceedance in 50 years)
- 475 years return period (10% probability of exceedance in 50 years)
- 975 years return period (5% probability of exceedance in 50 years)
- 2475 years return period (2% probability of exceedance in 50 years)

As an example, the AREMA (2020) design code in the US gives three levels of seismic design motion i.e., at PGA_{100}, PGA_{475} and PGA_{2475} which are corresponding to return period of 100 (Serviceability), 475 (Ultimate) and 2475 (Survivability).

Circular tunnels undergo three primary modes of deformation during seismic shaking:

- Ovaling
- Axial
- Curvature deformations

Axial and curvature deformations are induced by components of seismic waves that propagate along the longitudinal axis (see Figure 6) (Wang, 1993; Owen and Scholl, 1981).

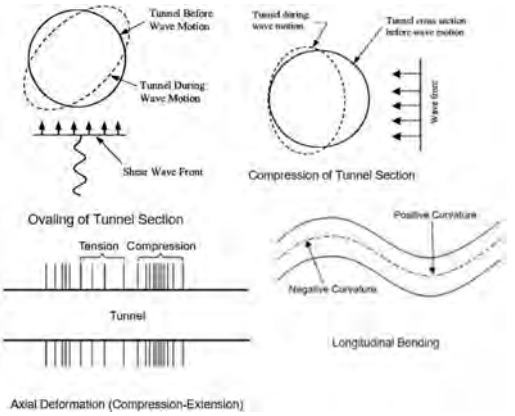

Figure 6. Deformation modes of circular tunnels due to seismic waves.

As mentioned above, the effect due to earthquake on the tunnels is generally less significant than above-ground structures. However, careful assessment is required especially there is risk of liquefaction, or significant change in ground types at high seismic regions (Figure 7). In such cases, special mitigation measures may be required.

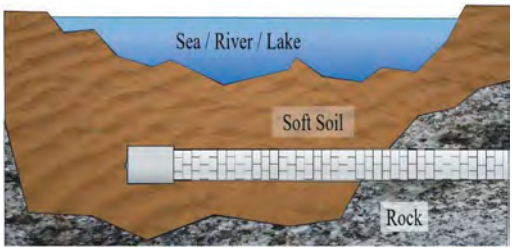

Figure 7. TBM tunnel excavating through rock and soft soil.

Seismic waves travel faster through hard rock strata compared to soft soil layers. The deformation or shaking is stronger at soft soil layers which may cause excessive deformation in longitudinal and/or transverse direction of the tunnel at the vicinity of boundary between soft soil layer and the rock. For some projects, seismic joints are installed at the vicinity of soft soil/rock

boundary to minimize the effect of seismic activity at high seismic regions. These seismic joints are full ring like a flexible joint allowing a certain amount of movement in longitudinal and transverse directions. A sample application on a TBM tunnel constructed in a high seismic region is shown in Figure 8.

Figure 8. Seismic joint application on a TBM tunnel.

4 CROSS PASSAGES LINKING SUBAQUEOUS TBM TUNNELS

Cross passages are provided between two TBM tunnels at regular spacing for evacuating passengers to non-incident tunnel in case of emergency (Figure 9).

Figure 9. Cross passage between two TBM tunnels.

In some cases, the cross passages may also used to house the MEP equipment of other services. Depending on the country and local regulations, whether it is rail or road, the spacing between two cross passages varies. For railway tunnels, one of the most common design codes referred to is NFPA 130 which limits the spacing between two cross passages to maximum 244m (800ft).

Cross passage construction for subaqueous tunnels is higher risk than one constructed on land due to high water pressures, and difficulties in employing ground improvement under marine condition. Ground improvement from above the sea or river surface may not be feasible or quite costly, which may require other methods such as ground freezing (Figure 10) or ground improvement from inside the cross passage.

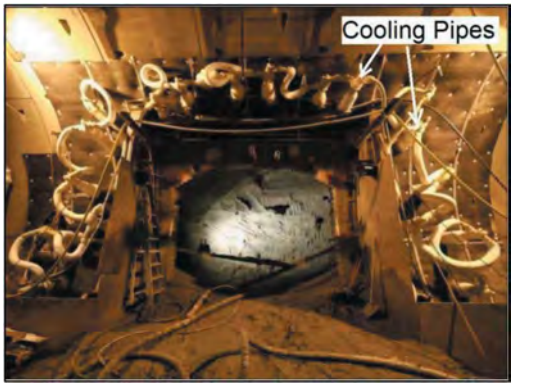

Figure 10. Ground Freezing at Cross Passage location.

Another innovative construction method, applied for the first time and proved successful at Tuen Mun - Chek Lap Kok Link project (Hong Kong, SAR of China), uses a mini-TBM for most of the cross passages sub-sea section. Local regulations required two large-diameter sub-sea TBM tunnels to be linked at every 100m which resulted a total of 57 cross passages.

A 3.665m diameter slurry mini-TBM was used to construct the sub-sea cross passages. On the launching side of the cross passage, a jacking-pipe system was setup for the mini-TBM break-in. On the retrieval side, a steel pressurized chamber was installed to receive the mini-TBM for break-out. A pipe-jacking system was adopted to excavate the cross passages using a mini-TBM (Figure 11, 12, 13). This innovative method helped safely construct 39 cross passages in about 13.5 months.

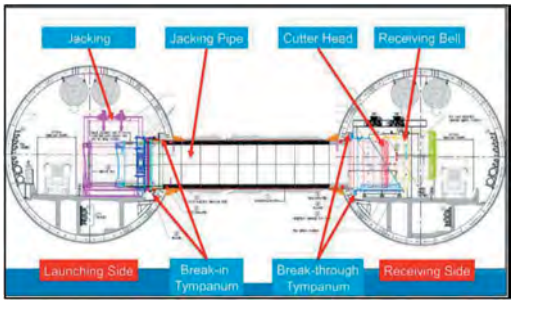

Figure 11. Cross Passage construction with mini-TBM.

Figure 12. Mini-TBM (OD 3.665m) for cross passage construction.

Figure 13. Steel pressurized chamber for receiving mini-TBM.

5 SATURATION DIVING FOR CUTTERHEAD INTERVENTION (CHI)

Disc replacement or cutterhead maintenance for subaqueous large diameter TBM tunnels is an extremely high-risk activity. Apart from the planned cutterhead interventions, there may be the need of unplanned interventions as well for TBM reparation as emergency. In order to minimize unplanned interventions, grouted blocks are created as safe havens, which, enable the intervention at atmospheric conditions.

However, in some cases where the ground condition is unstable under atmospheric condition, hyperbaric interventions may become necessary, especially when the pressures exceed 3.5bar for cutterhead maintenance. A compressed air intervention cannot be carried out at high (>5~8 bar) pressures. In such hyperbaric environments, saturation diving techniques could be employed. This comprises a team of divers living in a man lock under hyperbaric habitat and being transported to the TBM in a pressurized shuttle that docks with an airlock on the pressure bulkhead.

The divers breathe mixed gases throughout their stay in the habitat before decompression. Decompression can take a few days as the pressure is reduced step by step until atmospheric pressure is achieved.

Figure 14. Hyperbaric Shuttle, TM-CLKL, Hong Kong, SAR of China.

For TM-CLKL project, a team composed of 4 workers, specialized in hyperbaric works have been deployed. The duration of the work cycles was 28 days. For that purpose, a living habitat was built on the ground (Figure 15).

Figure 15. Living habitat for saturation diving on the ground.

6 CONFINEMENT PRESSURE

A slurry TBM can be used in almost all ground conditions under high water pressures. The principle of the slurry TBM is to apply an adequate pressure on the slurry contained in the excavation chamber. This pressure is thus transferred to the excavation face to obtain a pressure value as close as possible to that calculated in relation to the in-situ stress.

In subaqueous tunnels, high pore pressures can occur at very shallow depths of ground cover, resulting in particularly adverse effects on face stability and deformation. In the event that a tunnel connection opens to the seabed, potential hazards may include high water inflows or even complete flooding of the tunnel. It is imperative to control TBM confinement pressure to prevent face collapse, blowout, excessive ground settlement, and excessive ground heaving.

7 CASE STUDIES – LARGE-DIAMETER SUBAQUEOUS TBM TUNNELS

7.1 *Tuen Mun – Chek Lap Kok Link (TM-CLKL), Hong Kong, SAR of China*

TM-CLKL is a strategic subsea traffic route serving as a direct connection between the Northwest New Territories and Hong Kong – Zhuhai – Macao Bridge (HZMB), the Airport and North Lantau and also an alternative route to the Airport (Figure 16). This project comprises a dual two lane, trunk road about 10km long, of which about 5km consist of TBM and cut & cover tunnels, connecting a 16.5 hectares of reclaimed land in Tuen Mun (Northwest New Territories) and the reclaimed site of HKBCF. TM-CLKL also comprises a toll plaza together with associated tunnel operation facilities at north. Cross passages are provided at every 100m spacing between the two tunnel tubes for emergency escape purposes.

TM-CLKL is a pioneering subsea TBM project in Hong Kong with the following key features:

- The World's largest TBM tunnel in 17.6m excavation diameter constructed in mixed ground conditions;
- The Longest and deepest TBM subsea tunnel in Hong Kong at 5km long 17.6m/14m excavation diameter bored tunnels; max. water head of above 5 bars respectively;
- Two mini TBMs deployed to construct large amount of cross passages connecting twin cubes of main tunnels (57 cross passages including 48 subsea cross passages);
- New technologies adopted for better and safer tunnel operation, such as changing TBM cutterhead of different diameters; saturation diving approach to smooth and shorten the TBM maintenance procedures; articulated robot arm to access the excavation chamber at hyperbaric conditions

Figure 16. TM-CLKL Project Location.

Figure 17. TM-CLKL – Twin TBMs (14m dia) break-out.

7.2 *Chongming south tunnel, Shanghai, P.R.china*

The 7.5 km Chongming South Channel Tunnel was the largest diameter TBM tunnel when it was completed in 2009. This tunnel is part of the 25.5 km long Shanghai – Chongming expressway, linking the Changxing and Chongming islands to the city. The expressway consists of the tunnel and a cable bridge from Chang Xing Island to Chongming Island (Figure 18).

The tunnel section comprises two 15.0m OD tunnels and the TBM diameter is 15.43m, connected by eight cross passages. The length of each tunnel is approximately 7.5 km and there is a further 1.5 km approach road. The upper part of the tunnel is a three lane road and the lower part is for the utilities and accommodating a light railway.

Due to high hydrostatic pressures and hyperbaric environment, similar to TM-CLKL, saturation diving technique was adopted for cutterhead interventions. The tunnels were excavated in soft ground. Ground freezing technique was also used for cross passage construction. Cast iron lining segments were replaced the 650mm thick reinforced concrete segmental linings at the junction between the bored tunnel and cross passage. The gallery at the lower part of the tunnel was constructed as precast boxes (Figure 19).

7.3 *Shanghai bund tunnel, Shanghai, P.R.China*

This project is located at one of the busiest commercial areas of Shanghai city. The 1km long, 13.95m OD TBM road tunnel has double-deck with three

Figure 18. Chong Ming south project location.

Figure 19. Chong Ming south tunnel during construction.

lanes in each direction, accommodating total six lanes in a single TBM tunnel (Figures 20, 21).

Figure 20. Shanghai bund project location.

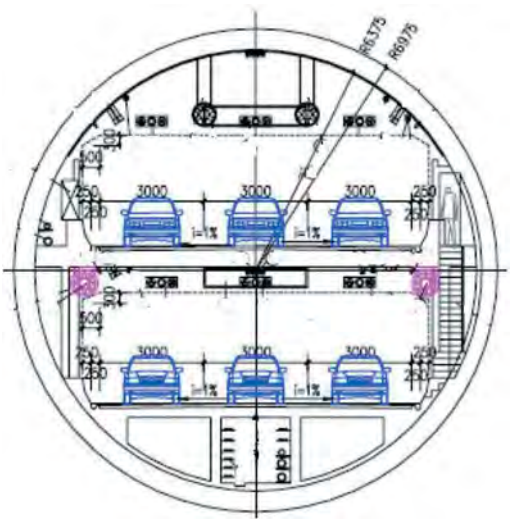

Figure 21. Shanghai bund TBM tunnel cross section.

The tunnel had very shallow cover and passed through several sensitive structures including existing metro tunnels (with small separations), existing bridges, subways and is very near to many historical buildings such as the old Hong Kong Shanghai Bank Building located along the river bank

8 CONCLUSIONS

This paper discusses the design and construction development of large scale subaqueous tunnels, focusing on large diameter TBM tunnels. It explains some of the challenges specific to subaqueous TBM tunnels, giving innovative and, practical application examples. With recent technological developments and innovative solutions, larger diameter and longer subaqueous TBM tunnels are expected to be constructed in the future.

REFERENCES

Frew, B., 2020. Advancements in Large Diameter TBM Tunneling, Tunnel Business Magazine.

Schwob, A., Guedon, F., Combe, B., Lockhart, T., 2019. Tuen Mun – Chek Lap Kok Link in Hong Kong – Innovative solutions for construction of an outstanding Subsea Tunnel Tunnels and Underground Cities: Engineering and Innovation meet Archaeology, Architecture and Art – Peila, Viggiani & Celestino (Eds).

Tunnelling for a Better Life – Yan, Celestino, Thewes & Eberhardt (Eds)
© 2024 The Author(s), ISBN 978-1-032-80042-4
Open Access: www.taylorfrancis.com, CC BY-NC-ND 4.0 license

Design and construction excellence at Tuen Mun-Chek Lap Kok Link tunnels: An engineering marvel beyond boundaries

Patrick W.H. Ng
Highways Department, Hong Kong SAR, China

Etienne Baranger & Kelvin Choi
Dragages-Bouygues Joint Venture, Hong Kong SAR, China

Peter Thompson & Andy Raine
ARUP, Hong Kong SAR, China

ABSTRACT: The Tuen Mun-Chek Lap Kok Link (TM-CLKL) project is one of the most impressive infrastructure developments in Hong Kong. The project comprises a 9km two-lane carriageway connecting Tuen Mun and North Lantau via 5km long sub-sea tunnels, which presented complex hydrogeological conditions and numerous technical and geotechnical difficulties. The project was completed successfully through the application of innovative techniques, including the world's largest Tunnel Boring Machine (TBM), the first use of saturation diving in Hong Kong, TBM tunnelling in newly reclaimed land, and the first deployment of innovative pipe jacking of cross passages.

The construction team deployed a 17.6m diameter slurry-type Mix shield TBM for the northern approach tunnels, followed by two 14.2m diameter slurry-type Mix shield TBM's for sub-sea tunnel construction. The large diameter of the TBMs facilitated efficient and speedy construction while eliminating risk of high-pressure sea water ingress up to 5.8 bars. Additionally, the use of saturation diving technique was applied for TBM cutterhead interventions, with robot cutter-changing to manage complicated ground conditions, providing a safe and stable work environment.

The project also utilized ground-breaking designs such as the peanut shafts in the northern landfall and the world's first 15-cell caterpillar-shaped cofferdam in the southern landfall, reducing costs and improving safety while minimizing environmental impact. The tunnels and buildings' construction involved large volumes of precast concrete elements manufactured off-site, improving quality, efficiency, and working conditions inside the tunnel while reducing the number of workers required onsite.

The TM-CLKL project's commitment to innovation and the application of novel construction techniques overcame numerous challenges, raising the project to global acclaim. Understanding the project's success may contribute to the development of sustainable infrastructure worldwide, where future developments continue pushing the boundaries of construction excellence.

Keywords: Tunnelling, TBM, Performance, Cross passages, Peanut shaft, Saturation diving

1 INTRODUCTION

The TM-CLKL comprises a 9km dual two-lane carriageway between Tuen Mun and North Lantau. It commences at the Lung Mun Road and Lung Fu Road Roundabout in Tuen Mun Area 46, before heading southeast on elevated structure to a landing point on the newly formed reclamation, referred as the northern landfall. The landing of the northern landfall marked the beginning of the sub-sea tunnel as the road alignment turns south. The sub-sea tunnel stretched for 4.2km, passing beneath the Urmston Road, the busiest navigation channel in Hong Kong cited between Lantau Island and Tuen Mun. The alignment daylights at the eastern edge of the newly reclaimed land of Hong Kong-Zhuhai-Macao Bridge Hong Kong Port, referred as the southern landfall, as illustrated in Figure 1.

The tunnel alignment passes through a number of complex geotechnical interfaces as is shown on figure 2.

DOI: 10.1201/9781003495505-271

Figure 1. Site location plan (Chan et al., 2019a,b).

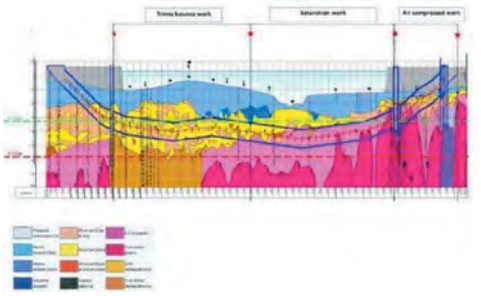

Figure 2. Geological profile of the TM-CLKL sub-sea tunnels (Chan et al., 2019a,b).

The sub-sea tunnels, with the internal diameter of 12.4m, each contained a two-lane carriageway, made up to an external diameter of 14.2m (S882) for tunnel excavation as shown in Figure 3. However, in the tender design, it was proposed to replace an approximately 500m length of cut and cover structure within the northern landfall reclamation area in Tuen Mun with a bored tunnel through an extension of the sub-sea bored tunnels.

The proposed scheme required the northbound exit tunnel to contain a third climbing lane, which was a challenge as it required the internal diameter to be increased to 15.6m with a corresponding increase to the external diameter of 17.6m for excavation, making it the largest diameter TBM in the world, as illustrated in Figure 4. Due to the large dimension of the bored tunnels and shallow cover within freshly reclaimed areas, a similarly innovative solution needed to be developed for the associated launching shaft at the northern landfall to house such a large machine.

This Technical Paper will focus on the world first and pioneering aspects of the TM-CLKL project.

Figure 3. 14.2m diameter TBM (S882) in the Nansha factory.

Figure 4. 17.6m diameter TBM (S880).

2 DESIGN INNOVATION

2.1 *Peanut shafts*

With a typical large diameter tunnel boring machine of up to 10m it is possible for a conventional cut and cover structure system to span vertically to provide sufficient working space for the tunnel boring machine launching operations but requires a number of horizontal struts and waling beams to provide lateral support. However, in the northern landfall, due to high lateral loads from the still consolidating newly reclaimed land and the adjacent sea such a design would be expected to be bulky which would limit the use of excavators and vehicles inside making excavation slow. Furthermore, for a machine with an external diameter of 17.6m, a typical TBM launching system becomes practically infeasible due to the need for a minimum clear height of 19m inside the excavation and therefore an alternative approach was required.

In order to cater for the large dimensions of the two tunnel boring machines used for the TM-CLKL project, an innovative strut free multi-cell system, namely the multi-cell "peanut" shaft was adopted as shown in Figure 5. The peanut shaft comprised three interconnected circular diaphragm walls with a varying thickness of 1.2m in Cell 1 and 1.0m in Cells 2 and 3, approximate dimension is 100m by 50m. The cells are designed to work in hoop stress by transferring the radial earth pressure forces acting on the outside of the excavation in compression around the perimeter walls. Only two cross walls and two cross beams between Cells 1 & 2 and Cells 2 & 3 are required as lateral support for the excavation, the cross-wall thickness was 1.2m.

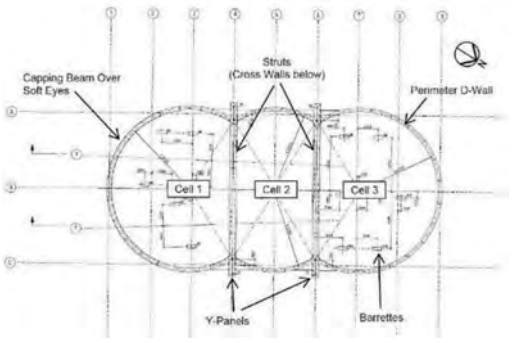

Figure 5. Interconnected cellular cofferdam solution.

This method allows more flexibility in geometry, having the width of the excavation determined by the cell diameter and the length by the number of cells used.

2.2 *Caterpillar shafts*

To the south of the TM-CLKL, where it approaches the man-made island of the Hong Kong-Zhuhai-Macao Bridge Hong Kong Port, an innovative 15-cell Caterpillar Cofferdam was used to cope with the adverse site geology at the newly reclaimed area as illustrated in Figure 6, with very thick (over 30m) and very deep (up to 50m below ground level) layers of marine deposits and alluvium clays. The cofferdam has a length of 500m and a depth of 43m, circular cells are formed by a perimeter diaphragm wall in an arch shape, ranging from approximately 25 to 37m long and 44 to 57m wide each, hoop forces induced on the walls are transferred at the junction of the cells to the "Y-panels", which are transversally supported by reinforced concrete struts and cross-wall. Fewer rebars were used, allowing unobstructed construction space and maximising working space for the TBMs and cut and cover tunnel.

Figure 6. Caterpillar-shaped cofferdam for southern cut and cover tunnel (Schwob. a, et. al, 2020).

2.3 *Tunnel lining design for largest diameter tbm*

The TM-CLKL used the world's largest slurry-type Mixshield TBM (S880), creating an internal diameter of 15.6 m with an excavated diameter of 17.6m as shown in Figure 7, composing the northern approach tunnel. The TBM tunnel was lined with pre-cast universal concrete segmental lining, and the lining was designed as an undrained lining with a design life of up to 120 years (Chan, et. al, 2019). To enable an adequate tunnel lining, its structural stability and deformation of the lining were checked. Structural stability was checked in compliance with the Code of Practice and the crack width of the lining was controlled to be not more than 0.2mm for durability assessment.

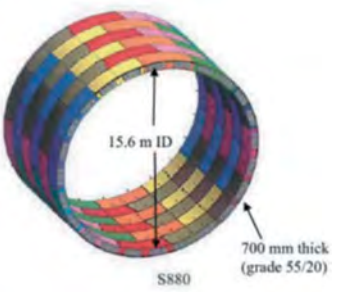

Figure 7. Typical cross section of the 17.6m tbm.

The lining segments are grade 55/20 concrete, with 700mm thick for the tunnel internal. The tunnel itself is made up of twelve precast concrete segments which sequentially assembled to form a ring as illustrated in Figure 8.

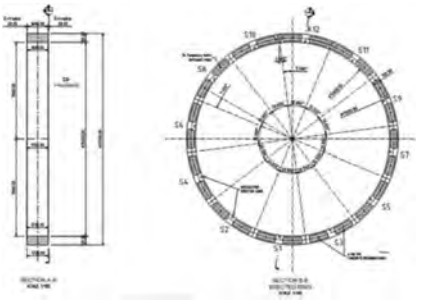

Figure 8. Typical cross section of segmental lining (Chan, et. al, 2019).

2.4 *Tunnel settlement control design principles for largest diameter tbm*

A large portion of the initial 17.6m TBM drive was in freshly reclaimed land, which was a major challenge as it required some enhancements to the northern reclaimed land. The original land was composed of

layers of marine deposits and clayey alluvium, the layers were disturbed by the backfilling work and consolidated under the new loads from the tunnelling works.

In order to achieve the strength parameter of the compressible soil, it was taken as the surcharge imposed on compressible soils, in which bands of drains of high permeability were installed, after that the reclamation was backfilled, with the surcharge of up to 12.5m and during the process, water was squeezed out of the soil matrix and particles were squeezed more tightly together, leading to an increase in the shear strength of the material. The consolidation period was scheduled to be up to 4 to 6 months, according to Schwob et. al (2020), a final efficiency of 90% consolidation under the weight of the surcharge was reached at the end of the consolidation period.

If the ground condition did not meet the success conditions, local ground improvement by jet grouting would be performed. Reaching the end of the consolidation and surcharge period, the twin tunnels were excavated.

2.5 *Tunnel internal structures and integration of design for manufacture and assembly (DfMA) principles*

Efficient space proofing of the tunnel was carried out to enhance the functionality of the large diameter of tunnel, the majority of the E&M equipment were placed underneath the carriageway, a dedicated service gallery underneath the road deck was provided for operational and maintenance access without disrupting tunnel traffic, also the provision of undercarriage ventilation duct, for the supply of fresh air to the main tunnel carriageway through openings in the parapet and an E&M ventilation duct, for the supply of fresh air and extract smoke from the service corridor through the damper openings in the event of fire, as required in the tender design.

Large portions of the sub-sea tunnel internal structures were precast elements, which were fabricated at an off-site precast yard. The service gallery, the overhead ventilation deduct (OHVD) and the road barrier were all precast elements, utilising DfMA extensively. The construction programme for the tunnel internal structure was extremely tight, access to TBM needed to be maintained during the internal structure construction, therefore a dedicated service gallery installation gantry were designed and placed behind the TBM, allowing installation of the precast service gallery units whilst maintaining uninterrupted access for the TBM tunnelling logistics.

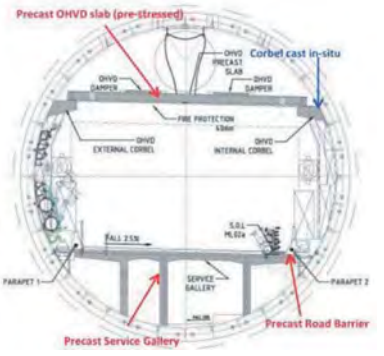

Figure 9. Typical sub-sea tunnel internal structure (Chan, et. al, 2019).

2.6 *Cross passage head wall and reaction block design*

Cross passages between the two main tunnels were constructed at every 100m interval, three methods were adopted to excavate a total of 57 cross passages, and a total of 46 cross passages were within the sub-sea tunnel section. Two types of cross passage, namely the Type A and Type B cross passage were introduced in the original scheme, for which Type B was very large. By introducing the underroad gallery, the cross passages were unified to just one single type (Type A), as the E&M installations were removed from Type B.

Due to the high hydrostatic pressure at the subsea condition, it has made the cross-passage construction a potentially high-risk activity for a conventional ground freezing or grouted solution. To mitigate these risks, a pipe jacking method using a mini tunnel boring machine (MTBM) was devised for the construction of cross passages in the sub-sea tunnel section.

2.7 *Cross passage lining design to suit construction methodology*

One of the most critical challenge was within the interface between cross passages and the main tunnels. Construction of the cross passages were carried out after the erection of the main tunnel lining. In order to stabilise the main tunnel segmental lining at cross passage locations, area of special segment with increased quantity of reinforcement was provided. The redistribution of stress induced by cross passage opening was taken up by six special heavily reinforced segments and by cast-in-situ Tympanum structure, which were constructed at both ends of the cross passage. These were used to resist the temporary and permanent loads around the cross passage opening, allowing the MTBM of cross passage to excavate through the reinforced concrete of the main tunnel lining.

During the break-in and excavation stage of the cross passages, temporary and permanent sealing system installed between the circumferential faces of segmental lining was induced to prevent water ingress and leakage under high water pressure. Each segment of the cross passage was fitted with two layers of 65mm thick of ethylene

propylene diene monomer compressible gasket which provided sufficient redundancy in the event that one seal failed.

3 CONSTRUCTION INNOVATIONS

3.1 *Saturation diving*

The TM-CLKL project faced challenges due to the adverse geology along the alignment, including transition from granite to decomposed granite and alluvium. These conditions required specialized maintenance and interventions for the cutter heads. The soft marine deposits on the seabed further complicated face stability. Two specially designed TBMs were driven in parallel. A slurry pressure system maintained the face, ensuring confinement pressure of up to 5.8 bars at the deepest sections. Efficient maintenance of the cutter tools was crucial to meet demanding production rates. The abrasive granite in the initial part of the alignment caused rapid wear on the disc cutters, necessitating daily hyperbaric interventions.

The saturation technique, implemented for the first time on such a large scale in an underground project, involved lengthening the cycles to 28 days. This technique avoids subjecting workers to daily compression/decompression cycles and allows for longer periods of intervention. A specialized team of four workers trained in hyperbaric works was housed in a pressurized living habitat on the surface. The habitat included hyperbaric chambers, compression/decompression chambers, and medical caissons equipped with necessary equipment for providing care in the event of injury. To maintain the proper functioning of the installation, various parameters such as chamber pressure, temperature, humidity, and gas mixture had to be constantly monitored. Surface teams, operating from a fully equipped control room, were responsible for monitoring and ensuring the installation's proper functioning. Additionally, a doctor certified for hyperbaric works was available full-time to intervene if necessary. In total, the team comprised of six doctors, three nurses (day/night), forty-five professional hyperbaric workers, twelve live support technicians and three hyperbaric operation supervisors.

The worker's team was transported daily through a pressurized shuttle from the living habitat to the TBMs. The shuttle connected directly to the hyperbaric chambers of the TBMs, allowing for the replacement of the disc cutters to commence. This allowed for efficient cutter tool replacement while minimizing risks.

The implementation of the saturation technique improved safety and efficiency. With support from the Client, necessary approvals were obtained for this innovative technique in Hong Kong. The pressurized living habitat and continuous monitoring of parameters ensured worker well-being and safety. The shuttle system facilitated easy access to the hyperbaric chambers for cutter tool replacement, contributing to steady tunnel excavation progress. Total Saturation Dives since Dec 2015: > 300, Total discs changed in Saturation: 1000, The best dive: 13 discs changed, Maximum Intervention Pressures: 5.8 bars, and no decompression illness or other health problems since the commencement in December 2015.

Figure 10. Living habitat in surface.

Figure 11. Pressurized shuttle transferred daily to tbm.

3.2 *Development of robotic cutter change*

"Telemach" robotic cutter change system, developed by Bouygues Travaux Publics, has revolutionized the replacement of worn TBM disc cutters. This teleoperated robotic system allows for safer and more efficient cutter replacement without the need for manned interventions. The project made a step further in the automation of maintenance systems with the "Telemach" robot. The "Telemach" is in a dedicated air locked chamber in the TBM shield. It can access the excavation chamber under hyperbaric conditions of up to 7 bars and replace worn or damaged disc cutters with new one. This robot, similar to those used in the car industry but with greater difficulty, is equipped with advanced features such as stereoscopic laser vision, force control with touch sensors, water cleaning jet of 400 bars, and torque control tensioning device. The robot has an industrial robotic arm of 500 kg payload and is stored inside its own pressurisation locker where it can be maintained between intervention. The system can locate the disc cutter and adapt the movements of the robot accordingly in a compressed air environment in the presence of spoil. Telemach successfully performed a fully automated disc cutter replacement cycle in January 2016, proving its effectiveness on the TM-CLKL project, and it has been used on several projects by Bouygues Construction. This innovation was recognised with the ITA Tunnelling Award 2017 for safety initiatives of the year.

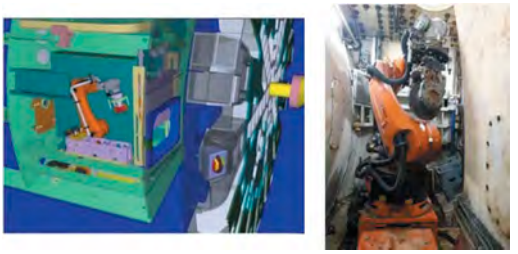

Figure 12. Robotic arm in the TBM shield.

Figure 13. New cutter disc fixation (Bouygues's patent).

3.3 *Development of TBM monitoring systems*

The TBM Monitoring System was implemented in TM-CLKL project to improve intervention efficiency by providing advanced knowledge of the cutter head's condition. Bouygues Travaux Publics developed innovative technologies equipped on the TBMs, such as the Mobydic system. This system offers real-time mapping of the cutterhead (temperature, rotation, wear state, load), identifying each disc cutter and detecting any abnormal behaviour caused by excessive wear. It also assesses the ground type based on disc cutter pressure, providing an accurate view of the TBM's operating environment. The data is collated, analysed, and displayed both numerically and pictographically. The Mobydic system optimizes excavation processes, reduces hyperbaric interventions, and improves accuracy in assessing excavated volumes. Moreover, it produces automated reports and develops geotechnical models of the excavation. This system is especially powerful in heterogeneous condition, by avoiding disc cutter overload and brake away. It identifies geological conditions, obstructions encountered, spoil clogging of the cutter chamber and areas of cutter tool wear/damage which in turn reduces the duration of hyperbaric interventions.

The Snake system is another crucial component of the TBM Monitoring System. This remote-controlled, poly-articulated arm is equipped with a high-quality zoom camera and a high-pressure water jet of 400 bars for cleaning and inspecting the cutterhead. The snake-arm robot has a diameter of 125mm and a 3m horizontal reach, with a pressurization system to operate in hyperbaric conditions. It cleans the TBM heads and eliminate clogging before the Snake's inspection. The Snake system allows inspections in areas where it is not possible to send workers, enhancing maintenance organization and optimizing TBM usage.

These systems have proven to be essential in TM-CLKL project in ensuring the optimal operation of TBMs while reducing human interventions. As a result, they are now widely implemented in most of the company's TBMs.

3.4 *Mini-TBM for cross passage construction*

To ensure the safety of road users during emergencies, a total of 57 cross passages were built every 100m of varying length from 8m to 13m to provide a means of egress between the two tunnel tubes. The construction of these cross passages presented a significant challenge, as they had to be built under 6 bars (max.) high pressure conditions due to being located under the sea. Instead of using traditional ground freezing techniques, the project team developed an innovative solution by utilizing MTBM with a diameter of 3.6m. This world's first groundbreaking mechanized approach allowed for better control over the construction schedule and minimized the exposure to geological risks, resulting in a significant reduction in construction time.

Initially, ground freezing was proposed as the stabilization method for the construction of these cross passages. However, detailed technical reviews found that the design parameters were weaker and it required additional drilling and freezing time, leading to delays. As an alternative, the Contractor proposed using a pipe jacking method with a MTBM. This method offered several advantages, including enhanced safety, suitability for high water pressure conditions, the elimination of the need for ground treatment, and reduced impact on the main tunnel's internal structure. Additionally, it provided greater certainty in terms of construction time.

The operation of the MTBM involved tunnelling through hard rock and soft ground. The cross passages were excavated after the main tunnel lining had been erected. The stress redistribution around the cross-passage opening was managed through segment ring and a tympanum - a reinforced concrete structural frame. Each main tunnel intersected the cross passage, with one ring being completely cut while the adjacent rings were partially cut. The MTBM was equipped with a soft eye using fiberglass reinforcement to prevent damage to the cutterhead. The loads from the centre cut ring were effectively transferred to the adjacent rings through shear keys or shear cones. The jacking frame, equipped with hydraulic jacks, was pulled on the tympanum on the launching side of the cross passage. With cutterhead power of 400kW and torque of 800kNm, the MTBMs' excavation was carried out in short advances, with a typical length of each jacking pipe being 1.33m.

The jacking pipe was composed of permanent pre-cast reinforced concrete, with the internal

diameter of 3,000mm. Six types of precast concrete jacking pipes were designed for the cross passages, known as first pipe, last pipe, standard pipe A, standard pipe B, lubrication pipe A and lubrication pipe B, with lubrication pipe A had the longest length of 1,330mm. At each of the pipe connection, a double wear barrier was adopted to ensure long-term water tightness with a design life of 120 years against corrosion.

A jacking pipe was installed at each advance, and on the receiving side, the MTBM would break out to a pressurized steel bell to maintain the pressurized regime and prevent water or soil ingress into the main tunnel. Emergency seals provide additional inundation prevention in case of water ingress.

This project marked the first time that cross passages had been constructed using TBM pipe jacking methodology between two main tunnel tubes. The innovation could achieve construction of 39 cross passages within less than 13.5 months, in average 3 numbers per month. The excavation cycle is approx. 18 days, with the average advance rate of the MTBM was 2.3m/day, and a best record of 13.2m/day. The MTBM and associated equipment were designed and developed by the Contractor and the TBM supplier. Overall, the use of the MTBM and pipe jacking technology proved to be a successful and efficient method for constructing the cross passages.

Figure 14. Cross passages with MTBM.

3.5 *World's largest tbm – guinness world record*

At early stages of the project, the North Approach Tunnels were initially planned as a cut and cover structure. However, the land above the North Approach tunnels had to be made available for partial handover to third parties and for a timely start of the sub-sea TBM drives. To address the time constraints and minimize earth movements, the Contractor proposed using two TBMs instead. The world's largest TBM, the Mixshield S-880 "Qin Liangyu," (in Chinese "秦良玉") was employed to excavate one of the 630m long tunnel. With its impressive power output of 5,600kW and a torque of 27,722kNm, the TBM has a shield diameter of 17.6m, an overall length of 120m and weighs 4,850 tonnes.

The 17.6m tunnel section was excavated up to a point the TBM's shield was converted into one of 14.2m diameter to complete the rest of the tunnel alongside another TBM. Core components and the back-up plants were taken from the largest machine to continue the excavation. The two 14.2m TBMs broke through at the same time to complete the tunnels on 27 February 2019. This achievement marked the first double breakthrough in Hong Kong and set the Guinness World Record for the World's Largest TBM.

Figure 15. World's largest TBM tunnel.

Figure 16. First double TBM breakthrough in hong kong.

3.6 *Development of tailor-made launching gantry – overhead ventilation duct slab installation*

To optimize the utilization of DfMA principles, the Contractor and her sister company, VSL, collaborated on the design and manufacturing of an internal slab structure gantry (ISSG). This self-launching gantry was tailored to install over 5,000 precast slabs for the OHVD in the two tunnels.

The OHVD slabs, which are precast and pretensioned, span across previously cast corbels and come in different lengths and weights, ranging from 11.5 to 23t. Additionally, there are shorter slabs that combine to form longer slabs, with openings in between and spanning across two long slabs at regular intervals.

The ISSG gantry consists of longitudinal main beams of 800mm in depth supported by front and rear lower crossbeams spanning 20m, with an additional movable crossbeam for launching operations. The rear and movable crossbeams are equipped with mechanical and hydraulic jacks, while the front crossbeam rolls on nylon wheels along the corbels. The outrigger extensions of the three crossbeams are designed to accommodate different corbel spacings, ranging from 9.0 to 12.5m. The main beams support a winch trolley lifting unit with a chain drive system, allowing movement of the slabs along the main beams.

The lifting process involves picking up a slab, clearing the traffic window, moving the main beams to the center for rotation by about 45 degrees and adjustment in crossfall and gradient, and then lifting the slab above the corbels. The slab is then moved backwards to its final position and lowered onto the corbels. Remote control via a touch panel manages slab installation and gantry launching. Various sensors have been installed to enable automation and coordination of different movements, reducing reliance on the gantry operator and minimizing the risk of slab collisions with corbels or tunnel lining. Typically, 16 to 20 slabs can be installed per shift. Overcoming the technical challenge of designing the specialist equipment to fit the available headroom, the ISSG gantry was easily dismantled and reassembled inside the tunnel to accommodate multiple relocations between tunnels during the construction sequence.

Figure 17. Launching gantry – overhead ventilation duct slab installation.

4 CONCLUSION

The TM-CLKL project has developed a large number of world first achievements, such as the world's largest TBM, first large-scale deployment of Peanut and Caterpillar shaft deign and first large scale deployment of microtunnelling techniques for inter tube cross passages. This deep undersea and geotechnically complex project has seamlessly integrated world class design innovation with state of the art construction methodology and the Project is globally recognized as a true benchmark.

The deep collaboration between the Contractor and the Contractor's designer has been an exemplar model, together with the huge support from the Client in facilitating the solutions to a large number of design and construction challenges has been major contributing factors in the success of this Project.

ACKNOWLEDGMENTS

The Authors would like to record appreciation to Highways Department, Hong Kong SAR (the Client), and Ms Natelie Mak who coordinated the inputs into this paper. The Authors would also like to thanks the literally hundreds of people involved in the design and construction of the TM-CLKL project, we salute you all, a truly global team effort.

REFERENCES

Chan, A.W.Y., Yeung, C.H.C., et al,2019a. Use of saturation diving technique for tunnel boring machine cutterhead intervention in the Tuen Mun-Chek Lap Kok Link sub-sea tunnel project, Hong Kong. Proceedings of the Hong Kong Institution of Engineers. 28(1), pp. 31–38.

Chan, A.W.Y., Yeung, C.H.C., et al,2019b. Construction of the Tuen Mun-Chek Lap Kok Link sub-sea tunnels in Hong Kong. Proceedings of the Hong Kong Institution of Engineers. 28(3): 139–153.

Kwong, A.K.L., Ng, C.C.W. and Schwob, A., 2019. Control of settlement and volume loss induced by tunnelling under a recently reclaimed land. International Journal of Underground Space. 4(4): 289–301.

Munfah, N., 2019. Challenges of large diameter TBM tunnels. [PowerPoint presentation]. 12th Annual Breakthroughs in Tunnelling short course.

Schwob, A., 2019. Tuen Mun-Chek Lap Kok Link Northern connection sub-sea tunnel section, Hong Kong. [PowerPoint presentation]. ITA Tunnelling Awards

Schwob, A., Cagnat, E., et al.2020. Tuen Mun-Chek Lap Kok Link: an outstanding sub-sea tunnel project in Hong Kong. Proceedings of the Institution of Civil Engineers – Civil Engineering 173(5): 33–40.

Tunnelling for a Better Life – Yan, Celestino, Thewes & Eberhardt (Eds)
© 2024 The Author(s), ISBN 978-1-032-80042-4
Open Access: www.taylorfrancis.com, CC BY-NC-ND 4.0 license

TBM sub-sea tunnelling in the Arabian Gulf

G. Peach
Project Manager, Mott MacDonald, Doha, Qatar

H. Vigil*
Tunnel Manager, HBK-PORR JV, Doha, Qatar

Khalid Saif Al-Khayareen
Manager of Drainage Networks Projects Department, Public Works Authority

ABSTRACT: Musaimeer outfall tunnel is one of the longest storm water tunnels in the world with a total length of 10.2 km. The tunnel will accommodate surface and storm water received from the drainage networks from 270 km² of urban areas in southern Doha. The tunnel was excavated by Tunnel Boring Machine (TBM) and encountered three distinct rock masses Rus formation, Midra-Shale and Simsima Limestone along with water inflows at high pressure, complex mixed ground, and weaker ground strata prone to cavities with the presence of vertical and lateral fractures connected to the sea bed. The geotechnical parameters in sub-sea tunnelling were assessed through all main project stages; a) Evaluation b) Verification and c) Application. The TBM required periodic atmospheric or hyperbaric interventions at the cutter head for cutter tool maintenance. During this process, the face was mapped and compared to off-shore borehole logs. Geophysical seismic reflection/refraction and resistivity surveys were also carried out. A non-intrusive radar system facility, installed on the TBM cutter-head, able to probe ahead in real time the ground conditions was used continuously. By monitoring TBM excavation parameters such as, thrust force, torque, penetration, cutter head rotation speed correlation with encountered ground conditions were made.

Keywords: TBM, Sub-sea tunnel, hydrostatic pressure, offshore geophysics, non-intrusive radar system, face mapping, TBM parameters

1 INTRODUCTION

The outfall tunnel extends from the pump station, 10.15 km off-shore discharging drainage flows in to the Gulf. The discharging will be performed through a vertical riser shaft and a marine outfall diffuser field. Figure 1 shows the project location.

2 TENDER GEOTECHNICAL INVESTIGATION

The Client Public Works Authority (Ashghal) undertook a significant geotechnical investigation program for this particular project which consisted of 22 off-shore boreholes at 500 m centers, which provided the following geotechnical data.

1. Cores for inspection
2. In-situ packer tests.
3. Pressure meter tests at each location.
4. Geophysical surveys including Sonar Bathymetry, Magnetometer, Seismic Reflection and Seismic Refraction.

Figure 1. Project Location.

5. laboratory mechanical and chemical tests on soil, rock and water samples.

This investigation data was combined on a long geotechnical profile and become the basis for

*Corresponding author: hernan.vigil@porr.qa

DOI: 10.1201/9781003495505-272

selection of the selection of TBM and tunnel segmental lining type. Figure 2 shows the long geological profile, with the tunnel alignment superimposed.

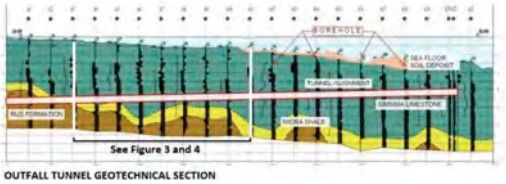

Figure 2. Outfall tunnel geotechnical section.

The detailed evaluation of this geotechnical data was a challenge, although there was significant experience of TBM tunnelling in the Doha area, there was no previous experience on subsea tunnelling in the area. The above data indicated the rock quality to be fairly competent along the tunnel alignment, however, there were two major tunnelling risks which required mitigation by the Designer and Contractor.

2.1 *Karstic features*

The first risk was the possibility of the TBM encountering karstic features along the tunnel alignment. Although the tender geotechnical investigation has shown no evidence of karstification within the calcareous formations of Rus, Midra and Simsima limestone. However, the risk was still valid. The size of a potential kasrtic feature was also very important resulting in limited mitigation measures, considering that the accessing and intervention from offshore would be very expensive and time prohibited. To mitigate this risk the TBM was installed with grouting ports and associated drilling and grouting equipment.

2.2 *Hydraulic connection to seabed*

The second risk was associated with the hydraulic connection between the seabed and the TBM tunnel. In this case the full hydraulic water pressure, would be directed to the advancing TBM cutterhead, requiring an increase in the face pressure and thrust accordingly to balance and advance the tunnel. However, there were significant factual evidence that along approximately 55% of tunnel alignment, competent and low permeability rock would be encountered by the TBM, providing protection against water infiltration from above. This assessment was based on Rock Quality Designation records and the Lugeon field tests performed in the offshore boreholes. Evaluation indicated that 25 % of the tunnel alignment, was rock of poorer quality with increased permeability based on lugeon tests. To mitigate this risk, the TBM was designed to withstand the full hydraulic pressure of 4.5 bar.

3 TENDER GEOTECHNICAL INVESTIGATION

The TBM selected to excavate the outfall tunnel was an EPB (Earth Pressure Balance) designed to support a maximum face working pressure of 4.5 bar. EPB configuration has a cutterhead, excavation chamber, main bearing or drive, screw conveyor, front, middle and tail shields, man locks, thrust system, articulation, erector and brushes as part of the tail shield seal system. In addition, there are 18 gantries, 180 m long accommodating all electromechanical parts, additive tanks and rescue chambers.

To minimize or eliminate the risk uncontrolled water inflow into the tunnel during construction, the TBM had double "guillotine gates" located at the end of the screw conveyor. These are used during normal operation and closed automatically in case of power failure. To accommodate 4,5 bar of water pressure the TBM screw was a total length 13.5 m. A fourth row of wire brush seals was also installed in the tailskin.

4 POST TENDER INVESTIGATIONS

The Contract requirements specified the possible implementation of an additional 24 offshore boreholes if required. It was considered that in terms karst identification and possible hydraulic connection to the sea, the drilling of further boreholes would provide minimal benefit to the TBM operation, and would provide additional isolated data on the alignment, and limited understanding to the overall hydrogeological and structural conditions along tunnel alignment.

The Contractor decided to implement a detail geophysical investigation survey as a more beneficial approach to mitigate the major geotechnical risks and provided more complete geotechnical information regarding variations in geology, areas of seawater saturation, areas of cavities, weak disturbed zones or other discontinuities under the seabed between the existing 22 boreholes. This alternative was accepted by the Client.

Two different types of offshore geophysical surveys were conducted along the outfall tunnel alignment. The Electrical Resistivity Tomography (ERT) and the Seismic Reflection Geophysical Tomography.

4.1 *Electrical resistivity tomography survey*

The objective of Electrical Resistivity Tomography (ERT) is to determine the subsurface distribution in two or three dimensions (2D and 3D) of resistivity, using geological parameters such as soil/rock type and mineral content, as well as the porosity and degree of water saturation in the rock. The ERT survey was performed satisfactorily in good weather conditions and the data was processed, analysed and interpreted. The survey covered 10 km of triple, parallel ERT marine profiles, aligned along the tunnelling corridor (West to East), at 3 m spacing, then integrated into sixteen transversal ERT marine profiles distributed in a North to South direction along the tunnel alignment.

After conducting the offshore survey, the most accurate electro stratigraphic model was developed and refined. Correlation between resistivity value variations and the main three different geologic units was then identified. A number of "conductive anomalies" and "resistive anomalies" were detected along ERT profiles and documented accordingly. Figure 3 is an extracted section from the ERT survey. The chainages start from zero at the TBM launch chamber and increase with tunnel alignment.

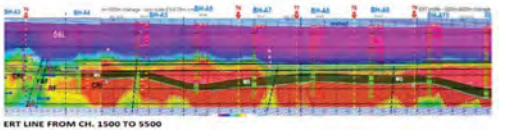

Figure 3. ERT for alignment Ch.1+500 to 5+500.

4.2 *Seismic reflection geophysical survey*

The Seismic Reflection Geophysical (SRG) process consists of recording the acoustic waves generated at the surface which have been reflected back by sub-surface structures or interfaces. A reflection will occur when the density and/or the velocity changes occur at the boundary between two different materials. The acoustic waves are recorded from numerous hydrophones, installed at fixed distance along a seismic cable (streamer).

The SRG survey was used to correlate the existing borehole defined stratigraphy, confirm the extend of topsoil formations and identified possible vertical weak zones, that may result in excessive water ingress along the TBM tunnel alignment. Figure 4 shows a typical section of this survey.

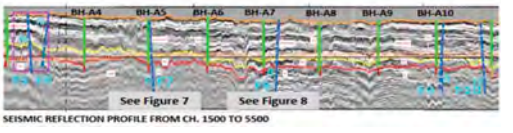

Figure 4. SRG for alignment Ch.1+500 to 5+500.

Based on the interpretative of Seismic Reflection Long and Cross sections certain structural vertical zones/faults were identified indicating possibilities of increased water ingress, these are features are marked F5 to F10 in Figure 4, and are points on the survey were abrupt changes in the seismic wave received profiles. This assessment identified 20 locations coded these F1 to F20.

5 PREDICTED GEOTECHNICAL CONDITIONS ALONG THE TUNNEL ALIGNMENT

With the use of the pre and post tender geotechnical and geophysical data, it was possible to build up an overall picture, of the underground conditions, indicating critical tunnelling areas, schedule possible and preferred locations for the TBM interventions and reduce the tunnelling risk level. In order to ensure the TBM advances smoothly the cutterhead requires regular inspection, maintenance and repair. The most efficient way to carry this out is in ground conditions which are safe under atmospheric conditions. This operation becomes more complex and time consuming in poorer ground conditions which require hyperbaric support. To mitigate the impact of various ground conditions an assessment is made by linear meter of the likely hood of favourable sections where only atmospheric interventions is anticipated, on moderate sections where atmospheric interventions is anticipated but hyperbaric may also be required and on unfavourable sections where TBM interventions should be avoided, unless absolutely required. Figure 5 illustrates a typical section of the predicted geotechnical profile, the favourable (green), moderate (blue) and unfavourable (red) zones are colour coded accordingly.

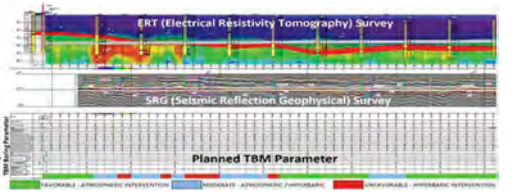

Figure 5. Predicted geotechnical conditions profile.

6 REAL TIME NONDESTRUCTIVE RADAR SYSTEM

The TBM is provided with a non-intrusive electrical induced polarization prediction system able to provide predictions of the ground conditions and interpretations up to three tunnel diameters ahead and two thirds of the tunnel diameter in real time. The Bore-tunnelling Electrical Ahead Monitoring (BEAM) System is based on a geotechnical principle that rock mass has different resistivities at varying frequencies, expressed with the Percentage Frequency Effect (PFE). The information is displayed in a matrix which combines both resistivity and PFE.The interpretation of the matrix, which is shown in Figure 6, is based on the columns and rows; factors on the columns refer to the karst interpretation (P1:P4) while factor on the rows (R3: R1) refer to the possibility of water inflow. There was a computer located in the TBM operators cabin where the information and interpretation are showed on real time as the TBM advances, the TBM operator can monitor and correlate with other parameters, if required.

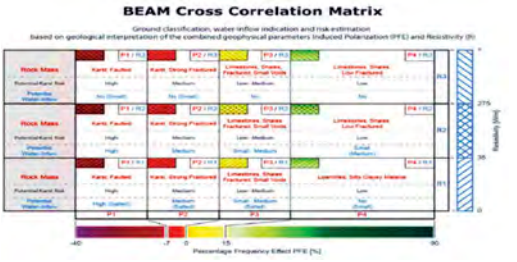

Figure 6. Beam correlation matrix.

Figure 7 Shows the real time Beam display the TBM passing through an limestone strata with low fracture and small voids, potential karst risk is low-medium and potential aquifer risk is small-medium.

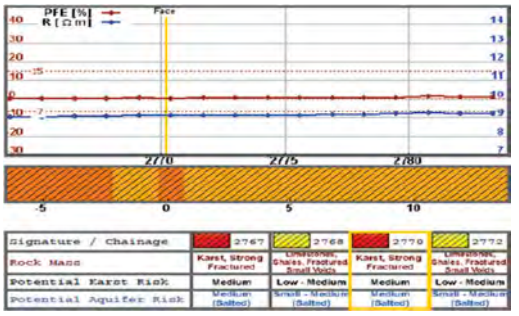

Figure 7. Beam display.

However, in Figure 8 the TBM is shown tunnelling in a rock mass with higher potential risk of karsts and aquifers, this particular location refers to a previously identified fault F8. The interpretation from the matrix is compared with specific parameters on the TBM, like torque, thrust force, penetration rates, advance speed and cutterhead rotation speed.

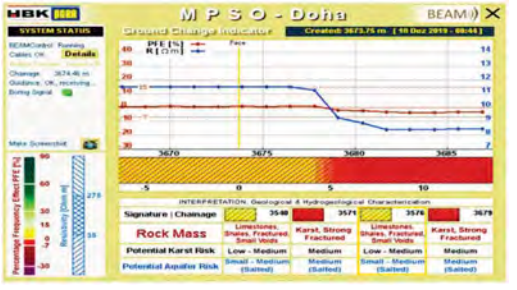

Figure 8. Beam display for F8.

Refer to the predicted geotechnical conditions profile the TBM expected to encounter F1 to F20. The BEAM system gave indication 10-15 m before entering those zones. Table 1 contains all the predicted data from the predicted geotechnical conditions profile shown in Figure 5 along with an estimation relative to the tunnel chainage, The next column then records the actual chainage any anomaly was encountered. The next column records if the BEAM detected the feature and the final column indicates the face pressure required to successfully advance through the particular section. It can be observed that 11 of the 20 F zones were correctly identified and a good correlation with predicted condition. It can is also noted that the correlation greatly increased over the tunnel alignment Chainage from 2,600 to 10,200 m when 10 out of 14 F features were identified and allowing appropriate TBM operations to be executed to maximize advance rates.

However, there are limitation in that the actual ground water pressure can not be predicted. The system can provide an estimation of the possibility that water inflow or aquifers might be encountered. The system is not able to identify whether the TBM is advancing though Rus formation, Midra Shale or Simsima limestone, it can only identify intrinsic properties of rock mass.

7 TBM ENCOUNTERED ROCK MASS

TBM tunnelling operations commenced on 03 February 2019 and tunnel completion had encountered 741 m of Rus formation (full face), 205 m of Rus formation affiliated with Midra Shale formation, then 660 m of Midra shale formation (full face), then 298 m of Midra Shale affiliated with Simsima Limestone formation, then 406 m of Simsima Limestone formation (full face), then 328 m of Simsima Limestone affiliated with Midra Shale formation, then finally from chainage 2,638 m geological formation was Simsima Limestone (full face) which continued until the tunnel completion at the riser shaft, at chainage 10,156 m on 03 February 2021.

Those geotechnical factors found along of Midra shale constrained the performance of the TBM in terms of advance rates. The torque of the TBM increased up to 75 % of its nominal capacity, the penetration rates were very low. The injection of water and other conditioning agents in the excavation chamber reached 25m³ per ring which in effect doubled the excavated volume per ring. However, this increase in conditioning made it possible to reduce scenarios of clogging of the cutterhead and severe damages to the cutting tools which still required a high number of cutterhead interventions in atmospheric conditions. Logistics in the tunnel were significantly affected and required a re-configuration of the trains regarding to the number of skips required to dispose the excavated material due the doubling of the volume per ring.

In the Simsima Limestone formation divided into 2 conditions, i.e. Simsima Limestone with high pressure of groundwater (3.8- 4.0 bar) and Simsima Limestone with low pressure of groundwater (below 2.0 bar). The Simsima Limestone with highest pressure of

Table 1. Predicted geotechnical condition actual and BEAM.

No	Fracture Zone	Predicted Location Chainage	Actual Condition From	To	BEAM Indication Yes	No	Remarks
1	F1	500	528	608	☐		2.6 bar
2	F2	900	-	-		☐	No impact on TBM operation
3	F3	1150	-	-		☐	
4	F4	1300	-	-		☐	
5	F5	1750	-	-		☐	
6	F6	1900	-	-		☐	
7	F7	2600	2638	2756	☐		3.5-4.0 bar
8	F8	3700	3678	-	☐		3.5-4.0 bar
9	F9	5200	-	5247	☐		
10	F10	5500	5437	5600	☐		2.4-3.4 bar
11	F11	5800	5808	5884	☐		2.4-3.2 bar
12	F12	6100	6079	6170	☐		2.4-2.8 bar
13	F13	6350	-	-		☐	
14	F14	7000	6620	6820	☐		2.2-2.7 bar
15	F15	7100	-	-		☐	
16	F16	7300	-	-		☐	
17	F17	8250	7820	8260	☐		2.2-2.7 bar
18	F18	8450	-	-		☐	
19	F19	9550	9550	9650	☐		1.5 bar
20	F20	9750	9650	9760	☐		1.6 bar

groundwater at chainage 2638 m – 2756 m (118 m), and chainage 3678 m – 5247 m (1569 m).

In both cases geotechnical engineers and TBM team were monitoring and correlating the geotechnical profile and BEAM system profiles to adjust and optimized the performance of the TBM.

7.1 *TBM production in different geological formation*

Referring to boreholes information, additional geophysical investigation and actual geological conditions recorded the TBM advance through six different formations with associated high or low ground water pressure, with some formation occurring more than once. The six formations are:

- Rus Formation (RF) – full face
- Rus Formation with Midra Shale (RF+MS)
- Midra Shale (MS) – full face
- Midra Shale with Simsima Limestone (MS+SL)
- Simsima Limestone (SL) – full face
- Simsima Limestone with Midra Shale (SL+MS)
- High water pressure (HP) and Low water pressure (LP)

Figure 9 shows the graph of averages TBM production in different geological formation, from start to completion of the tunnel. The average advance rates are shown as Tunnel rings per day. Each tunnel ring is 1.30 m long. The baseline programme (BLP) was based on 14 rings per day and the overall average for the project was 13.2 rings per day.

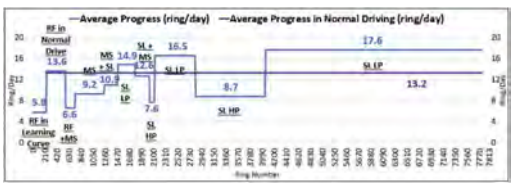

Figure 9. Averages progress in geological formations

7.2 *TBM progress and BLP*

The BLP for the tunnel construction is divided into an initial learning curve of 300 m in length, followed by 27 No. drives of varying length and duration and was based on 24 hours per day and 6 days per week. Actual TBM production rate compared to the BLP is shown in Figure 10.

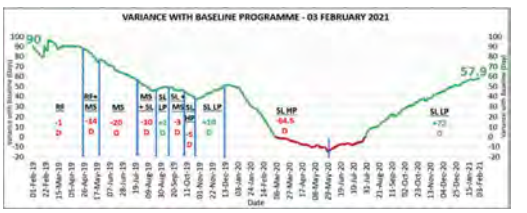

Figure 10. Variance with BLP from 03 February 2019 to 03 February 2021.

The actual variance with the BLP is shown in Figure 10 as green (ahead of BLP) and red (behind BLP) and the various geological formations as explained in section 7.1 are also shown. TBM excavation commenced 90 days ahead of BLP and over the course of the construction period deteriorated to 14 days behind programme before recovering and eventually completing the tunnel 57.9 days ahead of BLP.

7.3 *TBM production in different geological formation*

The TBM progress can be split down into five sections:

Firstly, when the TBM excavated through the Midra shale starting from ring no. 571 to ring no. 1465 (Ch. 743m – 1905m), from 21 April 2019 to 20 August 2019, the TBM lost 43.36 days from the BLP, variance started at +89.5 and become +46.14. In this geological formation, TBM advance speed was slow due to the need to inject water and soil conditioner, averaging more than 25m^3 per ring, this bulked up the excavated material to more than 8 skips (4 Skips normal) this resulted in boring times of 90 minutes per ring. In this period there were eight cutterhead intervention changing 20 cutters.

The second section was when the TBM excavated through mixed Simsima limestone/ Midra shale from ring no. 1,778 to ring no. 2029 (Ch. 2312m – 2638m), from 15 September 2019 to 7 October 2019, TBM losing 3.02 days from the BLP, variance started at +48.67 and become +45.66. Midra shale excavation reduced TBM progress slower due to need to inject soil conditioner.

The third section was when TBM excavated through the Simsima limestone with high groundwater pressure up to 3.5 bar, resulting in slower TBM progress due to a significant increase in all the boring parameters. From ring no. 2,020 to ring no. 2,120 (Ch. 2,626m – 2,756m), from 8 October 2019 to 21 October, TBM losing 5.28 days from the BLP, variance started at +45.66 become +40.37.

The fourth period was when the TBM excavated Simsima limestone with high groundwater pressure for a second time. This was expected from geological information in boreholes BH-A7 to BH-A10. Starting from ring no. 2830 (Ch. 3679m) on 11 December 2019 to 29 May 2020, with EPB pressure more than 3.4 bar, reducing the TBM advance rate. Additionally in this section two series of cutterhead intervention had to be carried out in compressive air conditions that are significantly more difficult for smaller TBM. Special divers working in hyperbaric condition with pressure 3.5 bar to 4.0 bar really consumed the time because one intervention period was only 120 minutes. In this period the TBM lost 64.54 days from the BLP, variance deteriorated from +50.36 to -14.18.

The fifth period was from 30 May 2020 until tunnel completion on 03 February 2021. Simsima Limestone formation with UCS max. 23-24 MPa is favorable for the TBM operation, only problem is when it is encountered with high groundwater pressure. In Figures 9 and 10 can see that progress in Simsima limestone with low pressure was always higher than other formations. From 30 May 2020 to 03 February 2021, TBM gained 72 days from the BLP, variance started at –14.18 and ended at +57.90. In this geology formation, all TBM boring parameters are low and muck material only 4 to 5 skips per ring, allowing the TBM to advance at higher speeds.

8 CONCLUSIONS

Tunnelling works is considered a highly challenging part of this project, due to the fact that is constructed on subsea conditions, has a small inner diameter (3700 mm), long length with no intermediate access points. The need for comprehensive, accurate and in-depth geotechnical information was critical to a successful tunnel completion. There is no single advance ground investigation method that can completely predict the ground conditions in front of a TBM. There are however a number of systems that can give an insight into a particular aspect of the geological conditions that lie in front of the TBM. When the results of these methods are integrated, the prediction can be comprehensive.

On this project, the key issue was the cross correlation with other methods and observed geology in a standard format which allows the identification of patterns and trends. This may well be unique to this project.

The BEAM had good correlation with the identified F features in the tunnel alignment 2,600 to 10,200 m.

Simsima limestone is favourable for TBM mining, except when associated with high groundwater pressure.

REFERENCES

Karagkounis, N., Sayers, K., Latapie, B., and Mulinti, S.R. Geology and geotechnical evaluation of Doha rock formations. ICE Geotechnical Research UK, 3. 3. pp120–121.

Poulos, H.G., A review of geological and geotechnical features of some Middle Eastern countries – Innovative Infrastructure solutions 2018, Springer, pp 6–8.

Public Works Authority. (2017). Contract Documents for Design, Build, Operate and Maintain of Musaimeer Pimping Station and Outfall, Project ID: IA 14/15 C 015 G, Contract Number: C2017/109.www.ashghal.gov.qa.

Sadiq, A.M., Nasir, S.J., "Middle Pleistocene Karst Evolution in the state of Qatar, Arabian Gulf. Journal of cave and Karst studies, pp 137–139.

Specification for tunnelling, Third edition, The British Tunnelling Society, and Institution of Civil Engineers, 2010.

Tunnelling for a Better Life – Yan, Celestino, Thewes & Eberhardt (Eds)
© 2024 The Author(s), ISBN 978-1-032-80042-4
Open Access: www.taylorfrancis.com, CC BY-NC-ND 4.0 license

Green TBM: Design targets, features and power efficiency

Andrea Petriccioli*, Laura Tafuri & Remo Grandori
Webuild S.p.A., Milano, Italy

ABSTRACT: The awareness of the importance and the need to reduce the energy consumption in any human activity, including in the execution of large infrastructures, has led the major construction companies to set very ambitious targets for reducing their energy consumption. The type, design and specifications of the TBMs to date have been developed with the main targets of increasing their productivity and their capability to deal with the most different geological formations and ground behaviors without much consideration of the energy aspects as the installed power and consumptions. Moreover, for several decades until today, technicians, consultants and manufacturers, specified more and more power to be installed on the TBMs, increasing the energy absorption during the tunneling process. The TBMs and the auxiliary systems are highly energy-intensive and are responsible for a large part of the power consumptions of an infrastructure project. Considering that more than 40 TBMs will be used simultaneously in the coming years in Italy for an important expansion of the Italian railway network, Webuild has developed the concept design of the Green TBM. The Green TBM encompasses various equipment, systems and control logics in an overall vision with the target of reducing the energy impact of tunnel excavation by about 20%, with comparable or lower boring times. The article describes how, from the initial concept, the first Green TBMs have been designed and manufactured in cooperation with the manufacturers. The different systems are analyzed, describing their contribution for the reduction on energy consumption and improved power quality.

Keywords: TBM, green, efficiency, energy, Webuild

1 INTRODUCTION

The Tunnel Boring Machine (TBM) is a complex system which requires the integration of capital aspect of civil, mechanical, electrical and control engineering. The evolution of the TBM to increase the productivity in a wide range of geological formations has led to an increase of the installed power on the machine, and the TBM represents the highest energy user for a construction site.

The EU Recovery Fund is increasing the investments in infrastructure projects. The Italian high-speed/high-capacity rail network will be expanded, especially in inland region of southern Italy, where the geographical aspects require to excavate hundreds of kilometers of tunnels in various lots. More than 40 TBMs will be used in the years 2024-2027.

Webuild is the biggest Italian infrastructure construction company, and is leader in many joint-ventures selected to build the new railway lines. Targets to increase the efficiency of the projects, reducing energy costs and CO_2 emissions led to development of a new concept design for a more efficient TBM, called the "Green TBM".

The target of the Green TBM is to reduce the energy incidence during the tunnel construction, defined as (1), by a factor of 20%.

$$I = \frac{E}{V} \tag{1}$$

Where I is the intensity (kWh/m^3), E is the total energy absorbed by the TBM to bore the tunnel (kWh) and V is the total excavated material (m^3).

The first project where the Green TBM is applied is the Messina – Catania Lot. 1&2 in Sicily, with four TBMs, 2 EPB and 2 dual-mode EPB-open, 9.3 meter diameter. The first one (in Figure 1) will start to bore by the end of 2023.

The paper will begin to introduce the main components of the electric systems onboard the machine.

Then it will describe how the concept of the Green TBM has been applied to the various parts of the machine, furthermore deepening all the different points of the concept design in two sections,

*Corresponding author: a.petriccioli@webuildgroup.com

DOI: 10.1201/9781003495505-273

Figure 1. FAT of the first green TBM for ME-CT lot. 2.

dedicated to the systems and to the equipment. In the end, the paper will present the testing activities that will be carried out to validate the expected target, and the conclusion with a recap of the main aspects.

2 ELECTRIC SYSTEM OF A TBM

The following section will describe the electric system applied to shielded TBM in the 8÷12 m diameter range, which is of interest for the railway projects in Italy, but could be generalized for different type of machines.

The power required to a TBM construction site is in the range of 7÷9 MW. The highest part is dedicated to the machine, that generally has more than 6 MW of installed power. The TBM is fed by a high voltage line, in Italy at 15 or 20 kV 50 Hz, via a cable reel.

These data give the idea of how important is to increase the electric efficiency of the TBM to reduce the energy used by the project.

2.1 *Main drive*

The main drive motors accounts for around 60÷70% of the installed power. The motor speed is regulated by variable frequency drive (VFD). Given the high power demand, the VFDs are fed by dedicated transformers at 690 V. For ME-CT project, the main drive has a 11×350 kW or 10×400 kW configuration.

2.2 *Backup*

One or two transformers power the backup low voltage network at 400V. The loads are mainly motors and, in residual portion – less than 50 kW – lights, sockets and controllers. The motors that require speed regulation are fed by VFD (e.g., foam, bentonite and dewatering pumps), otherwise directly by the grid (e.g., hydraulic power pack, compressors).

3 CONCEPT DESIGN OF THE GREEN TBM

The Green TBM concept was conceived in 2020. Preliminary specifications were issued the following year, and in 2022 the detailed design was developed for Italian railway projects. In 2023 the first Green TBMs have been manufactured, and excavation work will soon begin.

The target of a 20% reduction in the energy incidence is ambitious, and can be reach only gathering different solutions. Some of the solutions that will be exhibited have already been engineered and are in use. The special feature of the Green TBM was to bring together elements that were originally separate, or not applied to the tunnelling industry, adding to this automation logic aimed at minimizing energy consumption.

The following discussion will be divided into "systems" and "equipment". "Systems" refers to those control logics that act simultaneously on multiple TBM items. By "equipment", on the other hand, we mean the individual items with specific functions that make up the various systems of the machine. This subdivision is not only conceptual but also practical.

3.1 *Systems*

Indeed, the development of "systems" logic is tied to finding a solution through a problem-solving process. These solutions must first be conceived, and then integrated within the complex automation system of the TBM so that they do not create interference with other control logics nor between each other. The effectiveness of the solution must then be evaluated in the field in order to proceed, if necessary, with calibration or modification of the logic.

The systems that have been implemented are:

- Automatic utilities management
- Eco cruise mode
- Continuous mining

3.2 *Equipment*

Instead, the work on "equipment" has been of a different kind. First, the main components that could be worked on in terms of energy efficiency were identified. Then, for each item, the technical solutions currently in use, those available on the market and those already applied to the tunnelling sector were studied. In choosing the systems to be adopted, consideration was given to higher technical standards, the EU Ecodesign directive and the EU Commission Regulation 2019/1781.

The improvements on the equipment that have been implemented regard:

- Cutterhead design
- Transformers
- Electric motors
- Power quality
- Diesel generator

The two following chapters will describe the solutions implemented in the Green TBM, entering in detail in systems and equipment.

4 TBM SYSTEMS

The following TBM system have been integrated in the TBM main PLC.

4.1 *Automatic utilities management*

The "Automatic utilities management" is a control system that act on electric motors of the machine, with two separate logics.

4.1.1 *Automatic stop-start of motors*

The hydraulic power pack absorb much of the energy of the TBM backup. Thrust and screw conveyor hydraulic circuits are generally managed by more than one electric pump: trust pumps can be two to four (or more) and screw conveyors pumps are generally two.

The "automatic stop-start" function detects when the load demand is low and switch off the pumps in excess, in order to keep running the minimum requested electric motors. When the load demand increases, the motors are automatically reactivated.

The TBM operator does not need to select which motor need to be started, because the TBM PLC manages all the operations automatically. To avoid overuse of one motor and underuse of the others, the system cycles the "default" motors among the available ones.

4.1.2 *Automatic belt speed*

TBM conveyor belt is usually kept at a fixed speed when in operation, even if the TBM advance speed is low and the excavated material is less than the nominal one. The "automatic belt speed function" regulates the VFD of the belt according to the actual advance speed, estimating the amount of muck discharged by the screw conveyor.

The scale system along the TBM belt provide the feedback to the control loop, so that the system can better adapt to the actual discharged muck.

4.2 *Eco cruise mode*

The "Eco cruise mode" (ECM) refers to an automatic management of thrust and cutterhead rotation speed during the advance. The link between advance speed, penetration and cutterhead rotation speed is described in (2).

$$A = P \cdot \Omega_c \tag{2}$$

Where A is the advance speed [mm/min]; P is the penetration [mm/rev] and Ω_C is the cutterhead rotation speed [rev/min].

The starting point that led to the conception of the ECM is that the energy incidence described in (1) is higher when the Ω_C provided by the main drive motor is minimized and the thrust – thus, the penetration – is maximized. Due to mechanical and geotechnical constraints, P and Ω_C cannot exceed predefined values. Moreover, these two limits are different when it comes to EPB and open excavation mode, and this is taken into account in the logic.

Figure 2 describes the functional logic of ECM in EPB mode, while Figure 3 is related to the Open mode. It has to be noted that the first two TBMs for ME-CT Lot. 2 are dual mode Open-EPB, so the ECM is present in both variants.

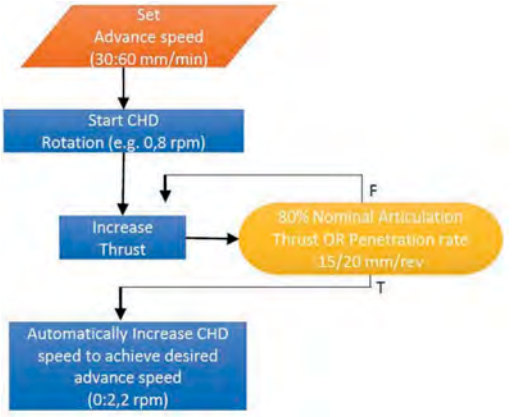

Figure 2. Eco cruise logic in EPB mode.

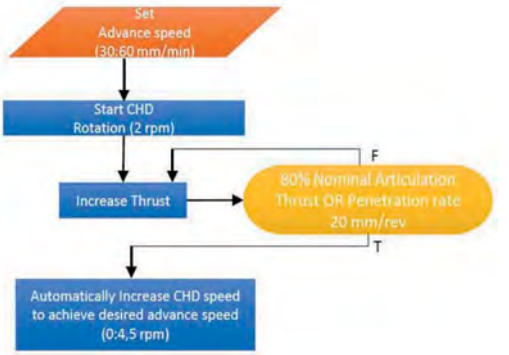

Figure 3. Eco cruise logic in open mode.

Once advance speed is set by the operator in the HMI, the ECM automatically adjusts rotation speed and thrust to reach the target speed with the minimum energy incidence.

4.3 *Continuous mining*

Continuous mining is a well know excavation method that allows shield TBM to excavate while mounting the ring. This is possible because the pressure of the thrust cylinder groups that need to be retracted to install the segment is redistributed on the adjacent groups, to keep the same center of thrust. Figure 4 shows in blue the redistribution of the pressures (y-axis, in bar) when the cylinder group 4, 5, 6 (x-axis) are retracted to install the segment, compared to the normal advance pressures in green. The new pressures are computed automatically by the TBM PLC, also considering the constraint of the pressure limit of the cylinders.

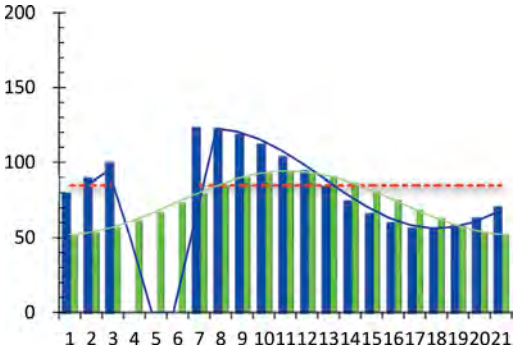

Figure 4. Pressure distribution during Continuous Mining.

The first target of the continuous mining is to increase the productivity of the TBM, decreasing the excavation time of the tunnel. There are also two side effect that are very important when it comes to energy efficiency, and this is the reason why it is included in the Green TBM framework.

4.3.1 *Baseload energy*

The first one is that the continuous mining energy absorbed is less than the sum of the energy requested by the excavation sequence and the ring mounting sequence. The reason of this is that the baseload power of the machine – usually 100 to 300 kW – would be requested for the time of both sequences, while during the continuous mining the sequences take place at the same time, the advancing time per ring is reduced and so it is for the baseload energy.

4.3.2 *Auxiliary tunnel systems*

Tunnel excavation requests a various amount of auxiliary system, which are necessary for the TBM operation. Some of these system (e.g., the conveyor belt), run only when the machine is advancing, while some others are requested to run uninterruptedly for safety reason. Among these, the most energy demanding ones are lighting and ventilation. The power requested by these systems can be more than 500 kW for long tunnel: reducing the time they have to be active will lead to a relevant energy saving.

5 TBM EQUIPMENT

The improvements related to TBM equipment are in mechanical, electromechanical and electric fields. The equipment may vary according to the different TBM manufacturers, but generally speaking the framework concepts are the same.

5.1 *Cutterhead design*

The design of the cutterhead is optimized to improve the outflow of excavated material, reducing the advance resistance. This target is achieved using three solutions:

- Connection to main bearing via rounded connection arms (Figure 5)
- Increased central opening
- Increased number of loading buckets

Figure 5. Rounded connection arms.

5.2 *Transformers*

Commission Regulation (EU) 2019/1783 defines new efficiency requirements for power transformers, implementing the new technical standard EN 50078 as additional requirement to the IEC EN 60076 standard. From July 2021 the highest standard for transformer efficiency have shifted from Tier 1 to Tier 2, with new requirements in terms of maximum full-load and no-load losses and to the peak efficiency index (PEI), defined in (3) for ONAN transformers.

$$PEI = 1 - \frac{2P_0}{S_r\sqrt{P_0/P_k}} \tag{3}$$

Where P_0 is the no-load losses [W], S_r is the rated power [VA] and P_k is the full-load losses [W]. These new requirements are different according to insulation and power, Table 1 compares Tier 1 and Tier 2 class for a 2500 kVA ONAN transformer, commonly used on TBM.

Table 1. Comparison between Tier 1 and Tier 2 transformer.

2500 kVA ONAN	Tier 1	Tier 2
Max. load losses [W]	22000	18500
Max. no-load losses [W]	1750	1575
Min. PEI [%]	99.737	99.797

Although Tier 2 standard is not mandatory in underground mining applications, Webuild's choice is to adopt it to reduce energy losses of the transformers.

5.3 *Electric motors*

The vast majority of the power absorbed in the TBM is used by electric motors: the increase in efficiency in these components is essential to the Green TBM concept. The standard IEC EN 60034-30-1:2014 state minimum requirements to meet different levels of efficiency, varying according to power and number of

poles, from IE1 (worst) to IE4 (best). Figures 6 shows the IE classes for 4-pole 50 Hz motors.

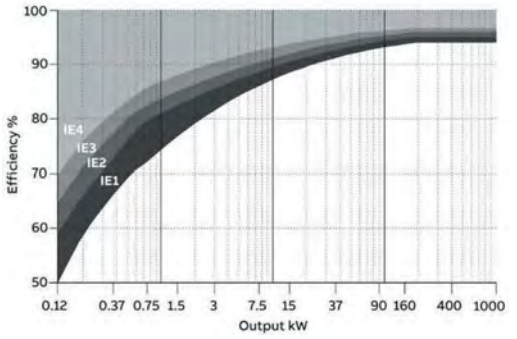

Figure 6. IE classes for 4-pole 50 Hz motors. [From ABB, 2018].

Since July 2023, the EU Regulation on electric motors and variable speed drives 2019/1781 requires three-phase motors to be IE3, between 75 kW and 200 kW to be IE4.

5.3.1 *Backup motors*

In order to achieve a better result than the minimum EU regulation, Webuild requires to install IE4 motors in the backup regardless of the power, except for those applications where suitable motors are not yet available. The shift from IE3 to IE4 for motor under 75 kW and over 200 kW impacts around 70 motors per TBM, accounting for 70% of the installed power in the backup. The expected energy saving is 2÷3%, and include energy intensive users as hydraulic, bentonite and grout pumps.

5.3.2 *Main drive motors*

Main Drive is the most energy intensive user of the TBM: improving its efficiency is a key point to reduce energy consumption. Some peculiar aspects must be considered: Main Drive motors are the most powerful in the machine (350÷400 kW each), they operate in a wide range of different speeds and load levels, they need to provide high torque at low rotation speed.

Generally, the type of motor used in the Main Drive is the cage asynchronous motor (AM). In this motor, the rotating magnetic field is produced by the stator windings through a magnetization current. On some TBMs, Webuild chose and will evaluate a more innovative technology: the permanent magnet synchronous motor (PMSM). In the PMSM the magnetic field is produced by permanent magnets on the rotor, increasing efficiency especially at partial load. This is clearly visible comparing the 3D plots of Figure 7 and Figure 8 (courtesy of CRCHI).

The rotation speed of the motor is indicated in RPM, power in kW, the efficiency is on the vertical axis.

These plots highlight the higher efficiency of the PMSM with respects to the AM in the whole operative range, and the great improvement at partial speed and load, where the difference broads. Analysis and comparison of data during mining, considering the type of excavated material, will allow to evaluate the motors in real operating conditions.

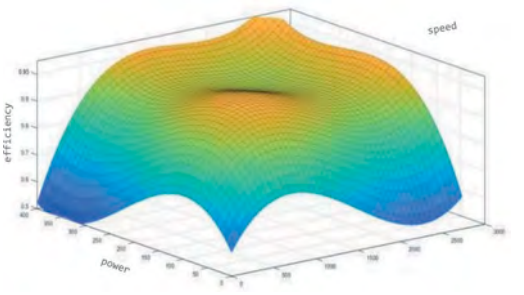

Figure 7. Efficiency of asynchronous motor.

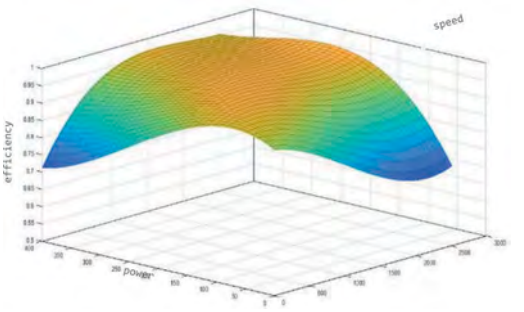

Figure 8. Efficiency of permanent magnet synchronous motor.

5.4 *Power quality*

Power quality is a topic of close concern for TBMs, as electrical disturbances produced by large motors and VFDs can greatly affect the electric grid. In particular, asynchronous motors fed directly from the grid absorb a large amount of reactive energy to produce the rotating magnetic field, increasing the phase shift between voltage and current sinewave, while VFDs produce harmonic sinewaves, which induce losses and disturbances on the grid.

5.4.1 *Displacement power factor*

Displacement power factor (DPF) is defined as per (4).

$$DPF = \frac{P_1}{A_1} = \frac{A_1 \cos\varphi}{A_1} = \cos\varphi \qquad (4)$$

P_1 is the real power of the fundamental sinewave (at 50 Hz), A_1 is the total apparent power of the fundamental sinewave, cosφ is the phase shifting between voltage and fundamental current. Lower DPF means that for the same amount of real power, the apparent power required is higher, thus the

circulating current and the Joule losses on the distribution network are higher. Induction motors have low power factor (0.75 to 0.88), requiring correction capacitors. Italian distribution system operators require an average minimum of 0.95. Webuild enhance this requirement, adopting automatic displacement power factor corrector to reach 0.97.

5.4.2 *Harmonic currents*

Harmonic currents are waveform multiple of the fundamental current (50 Hz in Europe) produced by the rectifying bridges of the VFDs. The distortion power factor is defined in (5), assuming cosφ=1.

$$PF_{THDi} = \frac{P_1}{A} = \frac{\sqrt{3}VI_1}{\sqrt{3}VI_{rms}} = \frac{I_1}{I_{rms}} = \frac{1}{\sqrt{1+THDi^2}} \quad (5)$$

THD_i is the total harmonic distortion, defined in (6).

$$THD_i = \frac{\sqrt{\sum_{h=2}^{\infty} I_h^2}}{I_1} \quad (6)$$

I_1 is the fundamental current, I_h are the harmonics multiple of the fundamental.

Harmonics cause energy losses, overheating, vibrations, disturbances on electronic devices. Webuild decided to adopt the IEEE 519:2022 standard "Harmonic Control in Electric Power Systems", requiring the TBM manufacturers to comply to the limits of section 5.2, and containing the THD_i under 10%.

5.4.3 *Improvement in total power factor*

The total power factor (PF) is defined in (7) from (4) and (5).

$$PF = DPF \cdot PF_{THDi} = \cos\varphi \frac{1}{\sqrt{1+THDi^2}} \quad (7)$$

The apparent power A absorbed the grid is shown in (8).

$$A = \frac{P}{PF} = P\frac{\sqrt{1+THDi^2}}{\cos\varphi} \quad (8)$$

The current is determined by A. To reduce the circulating current (and thus the losses) using the same power the electric equipment must have high cosφ and low harmonics. The impact of cosφ and THD_i on the total power factor PF is shown in Table 2, the value obtained by Webuild is in bottom right.

Table 2. Resulting power factor.

	THD_i 50%	THD_i 25%	THD_i 10%
cosφ 0.75	0.67	0.73	0.74
cosφ 0.90	0.80	0.87	0.89
cosφ 0.97	0.87	0.94	0.96

The result achieved can be considered the best in class regarding power quality, ensuring the minimum energy losses and the minimum disturbance on the electric grid of the construction site and the distribution network.

5.5 *Diesel generator*

During high-voltage cable extension or in case of power outage, the essential supply loads are powered by an emergency diesel generator. The generator has no requirement in terms of efficiency or emission control. However, the choice of Webuild is to adopt a Stage V engine, defined in EU Regulation 2016/1628, which is the most advanced in the world. Stage V generators are designed to optimize diesel consumption and to reduce the pollutant emission (PM, CO, NO_x), implementing the selective catalytic reduction (SCR).

Table 3 offers a comparison between a non-regulated and a Stage V engine, all values are in g/kWh.

Table 3. Engine stage comparison.

	non-regulated	Stage V
Fuel cons.	213	191
CO	>5.0	3.5
NO_x	>9.2	0.4

This equipment has not a direct effect on reducing the energy incidence defined in (1), but it has been included in the Green TBM framework due to its effect on reducing CO_2 and pollutant emissions.

6 TESTING ACTIVITIES

The effectiveness of the innovations implemented for the Green TBM will be evaluated with extended testing activities along the duration of the projects. TBMs for Messina – Catania project will start to bore at the beginning of 2023. The data analysis during the first months will allow to collect a preliminary dataset and to tune the systems.

Three categories of tests will be adopted:

- ON/OFF test: a section of the tunnel will be excavated with the system off, then the system will be turned on and a section of equal length will be excavated;
- Comparison: electricity consumption will be compared between a TBM equipped and one not equipped with the innovation;
- Calculations: if the previous two methods are not applicable, calculations based on the equipment utilization parameters will be used.

Table 4 present which type of test will be used according to the different improvements introduced by the Green TBM.

Table 4. Testing activities.

Improvement	Test	Note
Automatic utilities management	ON/OFF	
Eco cruise mode	ON/OFF	According to geology
Continuous mining	ON/OFF	According to geology
Cutterhead design	Calculation	
Transformers	Calculation	
Electric motors	Calculation/ comparison*	*Comparison only regarding PMSM and AM of Main Drive
Power quality	Calculation	
Diesel generator	Comparison	With diesel generators of other TBMs

The results will be presented in a future paper, following the data analysis of the first tunnels.

7 CONCLUSIONS

Green TBM represents a new approach to reduce CO_2 emission and energy cost in infrastructure projects with a mix of new and existing state-of-the-art technologies. TBM systems and equipment have been integrated to increase energy efficiency an operational performance. The high number of TBMs for Italian projects will allow to significantly reduce the energy consumption of the construction sites. An extensive evaluation of the effectiveness of the innovations implemented will be performed in 2024.

ACKNOWLEDGMENTS

The authors would like to thank the engineers of TBM manufacturers CREG, CRCHI, Herrenknecht, and Webuild Plant and Equipment department for their efforts in the development of the Green TBM concept design.

REFERENCES

Ragonnaud G., 2023. Ecodesign for sustainable products. European Parliamentary Research Service EPRS, Brussels, Belgium.

ABB Motion, 2018. IEC 60034-30-1 standard on efficiency classes for low voltage AC motors, Technical note, Zurich, Switzerland.

Elbaz K., Tao Y., Zhou A., Shen S.L., 2022. Deep learning analysis for energy consumption of shield tunneling machine drive system. Tunnelling and Underground Space Technology, vol. 123.

Perera S., Elphick S., 2023. Impact and management of power system harmonics. In: Applied Power Quality Analysis, Modelling, Design and Implementation of Power Quality Monitoring Systems. Elsevier, Amsterdam, Netherlands, pp. 71–130.

Zhang, Q.; Qu, C.; Cai, Z.; Huang, T.; Kang, Y.; Hu, M.; Dai, B.; and Leng, J., 2012. Modelling specific energy for shield machine by non-linear multiple regression method and mechanical analysis. 2011 2nd International Congress on Computer Applications and Computational Science, Bali, Indonesia, vol. 1, pp. 75–80.

Acaroglu, O.; Ozdemir, L.; and Asbury, B., 2008. A fuzzy logic model to predict specific energy requirement for TBM performance prediction. Tunnelling and Underground Space Technology, vol. 23, pp. 600–608.

Tunnelling for a Better Life – Yan, Celestino, Thewes & Eberhardt (Eds)
© 2024 The Author(s), ISBN 978-1-032-80042-4
Open Access: www.taylorfrancis.com, CC BY-NC-ND 4.0 license

On the interplay between face extrusion and shield loading in squeezing conditions

Th. Pferdekämper* & G. Anagnostou
ETH, Zürich, Switzerland

ABSTRACT: This paper investigates the risk of shield jamming in mechanized tunnelling through heavily squeezing rocks that already experience large deformations at the tunnel face (extrusion), close the gap around the shield at a small distance behind the face and practically start exerting pressure upon the shield immediately after excavation. This may lead to the entrapment of the tunnel boring machine (TBM), if the installed thrust force is not sufficient to overcome shield skin friction. In addition, the excavation of the extruding ground, which happens continuously as part of the advance process, leads to additional extrusion and deformations ahead of the tunnel face and, due to longitudinal arching, to a potentially considerable additional shield loading. This paper investigates this aspect, comparing the results of a novel computational method that accounts for the continuous excavation of the extruding face with those of conventional tunnel advance simulations, which do not account for the cutterhead-ground interaction. According to our simulation results, the conventional simulations are adequate for moderate squeezing, but underestimate the pressure developing under heavily squeezing conditions.

Keywords: TBM, Shield jamming, Face extrusion, Thrust force requirements

1 INTRODUCTION

Squeezing occurs when tunnelling through weak and highly deformable rocks at high depth of cover. Large convergences of the cavity wall and extrusions of the tunnel face have been observed in several conventionally excavated tunnel stretches through weak rocks. In mechanized tunnelling, however, cavity deformations can be assessed only indirectly during advance, by measuring the weight of the spoil material at tunnel face and recording the necessary torque and thrust force.

The risk of TBM entrapment in squeezing ground conditions can be counteracted by installing a sufficiently high thrust force and, to a certain extent, excavating a larger tunnel diameter ("overcut") to accommodate the ground convergences (thus preventing the ground from establishing contact with the shield). However, the radial overcut is limited to 15-25 cm at the tunnel face, as a larger overcut would make the steering of the TBM difficult. If the squeezing intensity is high, the radial gap around the shield may close already during the tunnel advance, leading to the development of a ground pressure upon the shield extrados (σ_R in Figure 1).

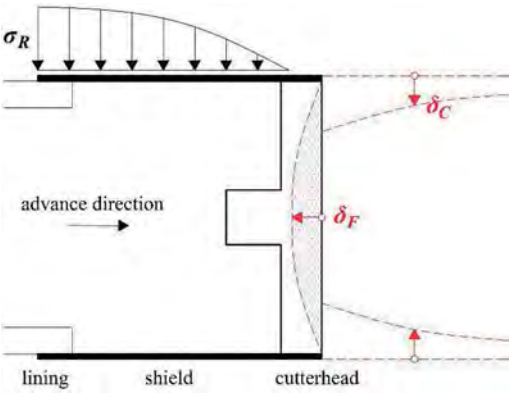

Figure 1. Radial pressure σ_R acting upon the shield during TBM advance, tunnel face extrusion δ_F and core deformation δ_C.

In addition, the TBM dimensions limit the number and diameter of the installable thrust cylinders too. In this case, if the installed thrust force is not sufficient to overcome the friction caused by the ground pressure, the TBM gets trapped. This results in

*Corresponding author: thomas.pferdekaemper@igt.baug.ethz.ch

DOI: 10.1201/9781003495505-274

expensive, time-consuming repair works, and, if it occurs frequently, may endanger the economic viability of a TBM drive.

For this reason, assessing the risk of shield jamming and estimating the required thrust force is probably the most important preliminary design step in the case of potentially squeezing ground.

To assess the interaction between ground, shield and lining, various methods have been proposed in the literature over the last decades (see Leone *et al*., 2023, for a recent review). Anagnostou *et al*. (2018) and Pferdekämper *et al*. (2023) showed that, due to the extrusion of the face, the excavation volume during TBM advance under severe squeezing conditions can significantly exceed the theoretical tunnel volume. This is because the TBM continuously excavates material that was originally outside the theoretical tunnel cross-section but enters it during the tunnel advance (δ_C in Figure 1). This raises the question of whether the extrusion induced over-excavation might lead to an increase in the ground pressure acting upon the shield extrados (via arching in longitudinal direction). The potentially unfavourable interaction between the shield and the behaviour of the tunnel face has not yet been investigated.

This paper quantifies the aforementioned interaction taking explicitly into account the extrusion-induced over-excavation in the numerical analyses, which provide the rock pressure developing on the shield σ_R during advance in heavily squeezing rock.

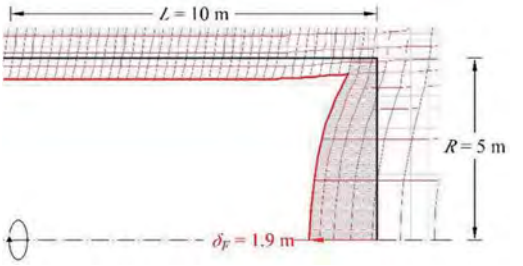

Figure 2. Deformed tunnel boundaries with large tunnel face extrusion δ_F (steady-state method after Anagnostou 2007).

Table 1. Parameter set.

Tunnel radius R	5 m
Shield length L	10 m
TBM overcut ΔR	0.15 m
Shield stiffness K_S	2000 MPa/m
Lining stiffness K_l	100 MPa/m
In-situ stress σ_0	10 MPa
Uniaxial compressive strength fc	0.5 MPa
Friction angle φ	15°
Dilation angle ψ	1°
Young's modulus E	1000 MPa
Poisson's ratio ν	0.25

2 NUMERICAL TBM ADVANCE ANALYSES

To quantitatively investigate the influence of face extrusion on shield loading, we compare results of TBM advance analyses that do not consider this interaction with results of finite element (FEM) computations with a novel computational model that accounts for the excavation of the extruding face.

2.1 *Without considering continuous face excavation*

Figure 2 shows, exemplarily, the result of a TBM advance analysis performed with the numerical FEM code HYDMEC (see Anagnostou 2007). The tunnel radius R is equal to 5 m and the shield length L to 10 m (typical values for a traffic tunnel). Table 1 summarises the parameters used for this computation.

The black and the red bold lines in Figure 2 represent the theoretical and actual (deformed) tunnel boundaries, respectively.

The limitation of conventional TBM advance computations becomes evident in severe squeezing ground conditions, as the volume of ground that entered the tunnel face during advance might be considerable (red dotted area in Figure 2). Numerically, the extruded volume supports the surrounding tunnel core limiting its deformation and, presumably, the ground pressure acting upon the shield σ_R. In reality, however, such a convex face cannot occur during TBM advance, because the rotating cutterhead continuously removes the ground extruding at the tunnel face. This process results in a vertical tunnel face but a larger-than-expected excavation volume ("over-excavation").

2.2 *Considering excavation of extruding ground*

A novel computational model was developed within the framework of the feasibility study for a demanding tunnel project (Anagnostou *et al*. 2018). The model, that includes a re-profiling and stress re-mapping algorithm, was implemented in a Python script and executed with the commercial FE software Abaqus® (see Pferdekämper *et al*. 2023).The first results, considering a rigid shield and zero overcut for the purposes of simplicity, have been published by Pferdekämper *et al*. (2023).

As schematically indicated by Figure 3, the novelty of the developed algorithm lies in the repeated excavation of the extruding ground at the face ("re-profiling"). The continuous TBM advance is approximated by discrete excavation steps of finite length Δx. The simulation of every excavation step begins with the deactivation of the core region of length Δx (volume V_0) in front of the tunnel face (Figure 3a). This causes additional radial

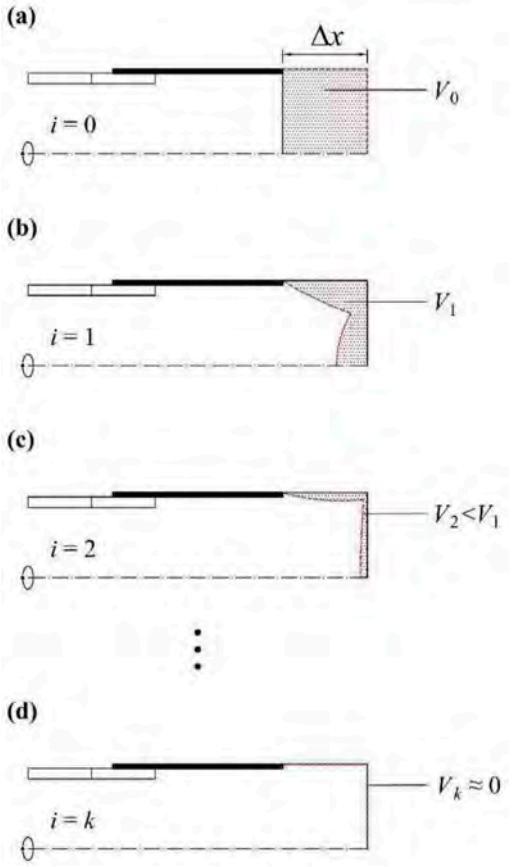

Figure 3. Schematic representation of the numerical re-profiling algorithm within a step-by-step advance computation.

displacements of the ground around the shield, which eventually lead to the gap closure and to an increase in shield loading. Additionally, in highly deformable grounds, the deactivation of volume V_0 may also lead to considerable extrusion of the tunnel face and radial displacement of the excavation boundary (V_1 in Figure 3b). In contrast to any previous investigation, the numerical algorithm makes sure that before simulating the next excavation step, the TBM excavates the volume V_1 too, which leads to an additional increase of the ground pressure acting upon the shield and to further displacements of the core boundaries (Figure 3c). The latter becomes increasingly smaller with each re-profiling round, hence core boundary displacements converge towards zero after a sufficient number of iterations (Figure 3d). As soon as the displacement at the face reaches a sufficiently small length (less than 1% of the step length Δx), the numerical re-profiling is considered complete and the algorithm continues with the next excavation step.

The algorithm tracks the shield-ground interaction storing the actual radial gap and contact pressure between shield and ground in an array after each computation and writing the values into the input file of the subsequent re-profiling round or excavation step.

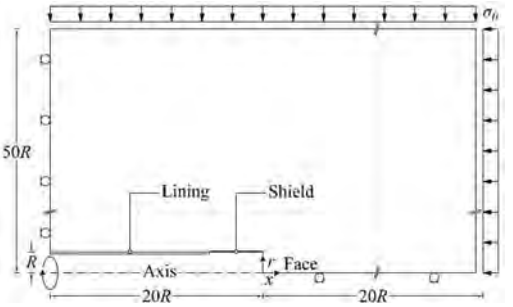

Figure 4. Numerical model setup.

Figure 4 schematically shows the numerical model setup used to investigate the TBM advance problem. For a deep tunnel in a hydrostatic *in-situ* stress field (σ_0), an axisymmetric model can be considered, which in the present case extends radially for 50R, where R is the tunnel radius. The TBM advance is simulated from the left boundary up to the middle of the model for a length of 20R, to avoid boundary effects. Three different step lengths with increasing degrees of precision (and computational effort) are considered for the step-by-step procedure (Δx = R/5, R/10 and R/20). The ground is taken to be linearly elastic (with Young's modulus E and Poisson's ratio ν), perfectly plastic obeying the Mohr-Coulomb yield criterion (with friction angle φ and cohesion c). The flow rule is non-associated (dilation angle ψ). Shield and lining are modelled by radial springs that account for their stiffnesses (K_s and K_l) as well as for the radial overcut ΔR (Ramoni and Anagnostou, 2010).

3 RESULTS

To quantify the difference in the required thrust force F_f between conventional and novel TBM advance computations, we consider the results presented by Ramoni and Anagnostou (2010) for a single-shield TBM with typical dimensions (see Figure 5). In general, the required thrust force to overcome skin friction F_f is a function of all the parameters given in Table 1, but, for dimensional reasons, the significant parameters of the problem are only the following (Ramoni and Anagnostou, 2010):

$$\frac{F_f}{\mu 2\pi RL\sigma_0} = f\left(\frac{L}{R}, \frac{\Delta RE}{R\sigma_0}, \frac{f_c}{\sigma_0}, \frac{K_s R}{E}, \frac{K_l R}{E}, \nu, \varphi, \psi\right) \quad (1)$$

Considering the favourable effect of the friction angle on face extrusion, we compare the worst case investigated by Ramoni and Anagnostou (2010), that is $\varphi = 15°$ (with $\psi = 1°$ and $\nu = 0.25$) and moderate to heavy squeezing ground conditions ($fc/\sigma_0 = 0.05 \div 0.2$, where fc is the uniaxial compressive strength). Moreover, for comparison purposes, we assume the same shield and lining stiffnesses. The complete set of dimensionless parameters is given in Table 2.

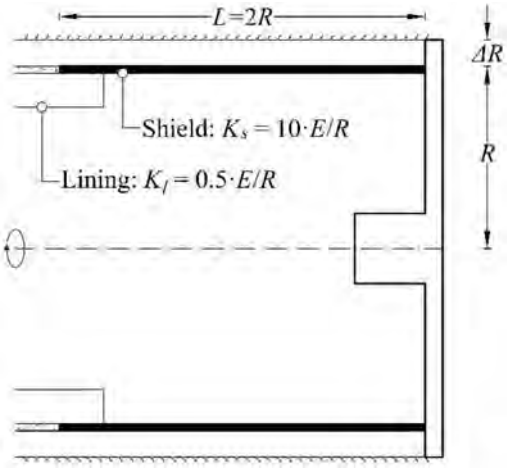

Figure 5. TBM dimensions and shield and lining stiffnesses considered in the comparative axisymmetric analyses (single shield TBM).

Figure 6 graphically represents Equation 1; it shows (in dimensionless form) the determined required thrust force F_f as a function of the overcut ΔR and of the normalized strength fc/σ_0. The lines represent the results after Ramoni and Anagnostou (2010) and the diamonds are the numerical results obtained with the novel numerical algorithm and hold for an excavation step length $\Delta x = 0$ (obtained by linear extrapolation).

The required thrust force F_f can be obtained by multiplying the results of Figure 6 with the shield surface ($2\pi RL$), the primary in *situ-stress* σ_0 and the skin friction coefficient μ.

Table 2. Dimensionless parameters of this study.

Shield length L/R	2
TBM overcut $\Delta RE/R/\sigma_0$	1; 3; 5
Shield stiffness $K_S R/E$	10
Lining stiffness $K_l R/E$	0.5
Uniaxial compressive strength fc/σ_0	0.5; 1; 1.5; 2
Friction angle φ	15°
Dilation angle ψ	1°
Poisson's ratio ν	0.25

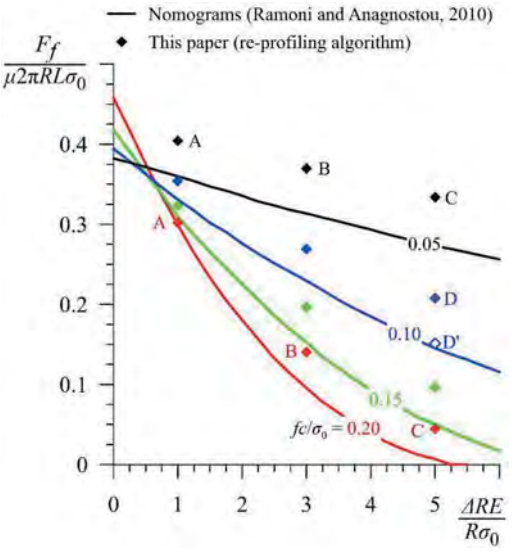

Figure 6. Dimensionless required thrust force as a function of the TBM overcut and the ground strength ($\nu = 0.25$, $\varphi = 15°$, $\psi = 1°$).

According to Figure 6, conventional TBM advance computations generally underestimate the required thrust force. In terms of absolute values, the underestimation is rather slight. The relative error, too, is small in the potentially critical case of very weak and soft ground (low f_c, low E).

3.1 *Influence of TBM overcut*

The influence of TBM overcut on required thrust force and maximum ground pressure is discussed based on the results for cases A, B and C in Figure 6. The parameters of the black point B are the same as the ones given in Table 1.

Figures 7 and 8 show the distribution of the radial stress acting upon a 10 m-long shield, considering a short excavation step length ($\Delta x = 0.25$ m) and a uniaxial compressive strength f_c of 0.5 MPa or 2.0 MPa, characterising severe and rather moderate squeezing conditions, respectively.

In the case of severe squeezing and small overcut (A in Figure 7), the radial gap around the shield practically closes at the tunnel face ($x = -0.25$ m). The maximum pressure in the region of shield-tail ($x = -9.75$ m) is about 85% of the primary *in-situ* stress, and is caused by the stiffness change between shield K_s and segmental lining K_l. This maximum pressure might be relevant for the structural design of the steel shield.

Integrating the radial pressure over the shield length and considering a lubrication of the shield with friction coefficient $\mu = 0.2$ (a conservative assumption for a lubricated shield, see *e.g.*, Gehring 1996), we obtain a required thrust force of 258 MN, which is high. From a design perspective, it is possible to reduce the shield-ground friction by increasing the

overcut ΔR. However, in severe squeezing conditions, the increase of the overcut from 5 cm to 25 cm leads to a reduction in the required thrust force of only 19% (see A and C in Figure 7).

On the contrary, in the case of moderate squeezing, the increase of the overcut from 5 cm to 25 cm leads to a considerable 85% reduction of required thrust force and, in addition, to a significantly lower maximum ground pressure (4 MPa instead of 8.5 MPa in Figure 8). Therefore, the overcut is very beneficial for the design of the TBM in moderate squeezing conditions, but not in severe squeezing conditions.

3.2 *Influence of re-profiling*

The influence of the re-profiling algorithm on the load acting upon the TBM is discussed considering the results for cases D (with re-profiling) and D' (without re-profiling) of Figure 6.

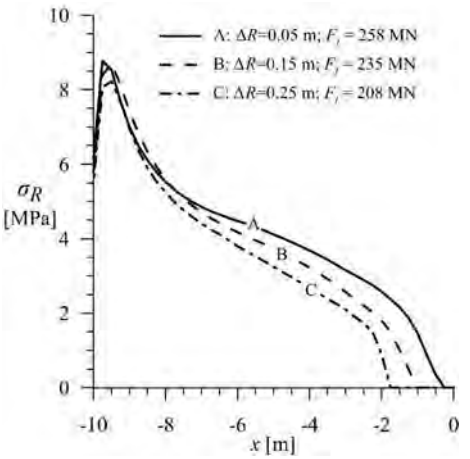

Figure 7. Radial stress distribution along a 10 m-long shield for severe squeezing (f_c = 0.5 MPa, σ_0 = 10 MPa).

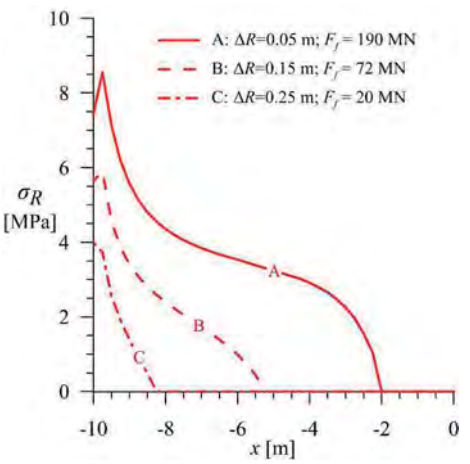

Figure 8. Radial stress distribution along a 10 m-long shield for moderate squeezing (f_c = 2 MPa, σ_0 = 10 MPa).

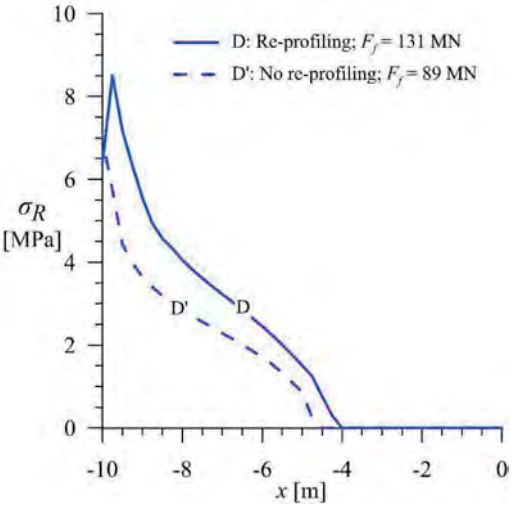

Figure 9. Radial stress distribution along a 10 m-long shield, with and without the re-profiling algorithm (f_c = 1 MPa, σ_0 = 10 MPa, ΔR = 0.25 m).

According to the stress distributions (Figure 9), a consideration of the continuous excavation of the extruding material at the face results in an earlier closure of the gap between shield and ground (4.00 m vs. 4.75 m behind the face) and in a higher maximum radial pressure in the shield tail area (8.5 MPa vs. 7.0 MPa) and in a higher thrust force (131 MN vs. 89 MN).

4 CONCLUSIONS

This paper focused on severe squeezing conditions, characterised by a large extrusion of the ground at the face, and investigated whether the continuous excavation of the extruding ground might affect shield loading to a considerable degree. This was done by comparing the shield loading obtained from conventional TBM advance simulations with the loading obtained by means of a novel numerical algorithm that takes into account the interaction between cutterhead and ground at the face by means of successive re-profiling rounds. The excavation of the extruding ground results in an increase in the excavated tunnel volume. The latter considerably exceeds the theoretical tunnel volume in the case of severe squeezing (see Pferdekämper *et al*. 2023). Besides the practical implications for the spoil removal, mucking-out logistics and disposal site size, the aforementioned over-excavation results – via longitudinal arching – in a higher shield loading and a higher risk of shield jamming. This was confirmed by the performed comparative analyses. Conventional numerical simulations of the TBM advance, which do not take into account the excavation of the extruding ground during the boring

process, underestimate the ground pressure that develops upon the shield, but the effect is rather small (less than 20%) in the potentially critical situation of highly deformable ground.

REFERENCES

Anagnostou, G., 2007. Continuous tunnel excavation in a poro-elastoplastic medium. In: Pande & Pietruszczak (Eds.) „Numerical Models in Geomechanics - NUMOG X“, 183–188. Taylor & Francis Group, London.

Anagnostou, G., Mezger, F., Pferdekämper, Th., Syomik, A., Vrakas, A., 2018. *The Gibraltar Strait Tunnel - On the feasibility of mechanized tunnelling through the breccias*. ETH Zurich. Unpublished report prepared on behalf of SECEG SA, Madrid, Spain, and SNED, Rabat, Morocco.

Gehring, K.H., 1996. Design Criteria for TBM's with Respect to Real Rock Pressure. In: Schulter & Wagner (Eds.): *Tunnel Boring Machines: Trends in Design and Construction of Mechanical Tunnelling: Proc. of the Int. Lec. Series, Hagenberg Castle*, pp. 43–53.

Leone, T., Nordas, A., Anagnostou, G., 2023. Effects of creep on shield tunnelling through squeezing ground. Rock Mechanics and Rock Engineering. (Accepted for publication)

Pferdekämper, Th., Vrakas, A., Anagnostou, G., 2023. Numerical modelling of face extrusion in shield tunnelling through squeezing ground. In: M. Barla *et al*. (Eds.): *Challenges and Innovations in Geomechanics: Proc. of the 16th Int. Conf. of IACMAG*, vol. 3, pp. 422–429.

Ramoni, M., Anagnostou, G., 2010. Thrust force requirements for TBMs in squeezing ground. *Tunnelling and Underground Space Technology*, vol. 25, no. 4, 433–455.

Tunnelling for a Better Life – Yan, Celestino, Thewes & Eberhardt (Eds)
© 2024 The Author(s), ISBN 978-1-032-80042-4
Open Access: www.taylorfrancis.com, CC BY-NC-ND 4.0 license

Research on curved tunneling and bending angle calculation of articulated shield tunneling machine*

Wei Qiao, Xiangyu Zhou & Xingsheng Liang
China Railway Construction Heavy Industry Corporation Limited, Changsha Hunan, China

ABSTRACT: In order to accurately control the curve of articulated shield tunnelling machine and provide a theoretical basis for the size design of shield tunnelling machine and the selection of hinged form, the working principle of active hinged shield tunnelling machine, passive hinged shield tunnelling machine and double hinged shield tunnelling machine was firstly analyzed in detail, and its performance characteristics and application scenarios were compared. Then, according to the tunnelling attitude of the shield body in the tunnel curve section, the calculation method of bending angle between shield bodies was analyzed by analytic geometry, and the corresponding range of active and passive hinged bending angles of the double articulation system was calculated under the set turning radius of the tunnel trajectory curve. Finally, the telescopic stroke of the articulated cylinder was calculated to control the hinged bending angle, and the double-articulated shield tunnelling machine was used for example analysis, and the angle was checked in the range of no interference between the cylinder and the tunnel. This method accurately simulates the curve driving attitude of the shield tunnelling machine, thus providing a theoretical reference for the design of shield body size and cutter head overcutting tool when considering the minimum turning radius.

Keywords: shield tunnelling machine, articulation system, analytic geometry, the curve of driving

1 INTRODUCTION

TBM is a large-scale underground equipment used for tunnel excavation. At present, shield tunneling is the most promising and competitive tunnel construction method. Compared with other excavation methods, it has the advantages of safety and reliability, highly automated,fast excavation speed, etc. Therefore, the TBM is widely used in underground tunnel, pumped storage project and metro project [1]. The full-face TBM is mainly composed of three core systems: cutterhead drive system, hydraulic propulsion system and articulated system (attitude positioning system) [2], which play different important roles, as shown in Figure 1. The cutterhead drive system makes the TBM cutterhead rotate at a certain speed to cut and excavate the soil body; the hydraulic propulsion system makes the TBM cutterhead advance along the tunnel axis at a certain speed; the articulated system makes the TBM cutterhead follow the excavation direction of the tunnel.

The deviation between the actual axis of tunnel and the design axis is directly related to the construction quality of shield tunnel. During tunnel excavation, it is necessary to adjust the attitude of TBM in real time to change its movement direction, so as to control its movement trajectory. The moment and thrust of attitude adjustment are provided by articulation cylinder. Therefore, to reasonably control the thrust and stroke of articulation cylinder is the key to reduce tunnel excavation error and improve tunnel construction quality. The articulated system is an important part of TBM, which consists of dozens of hydraulic cylinders used to adjust the tunneling attitude of TBM and control the bending angle of TBM during curved tunneling. However, the existing articulated turning technology has not yet formed a systematic technical theory.

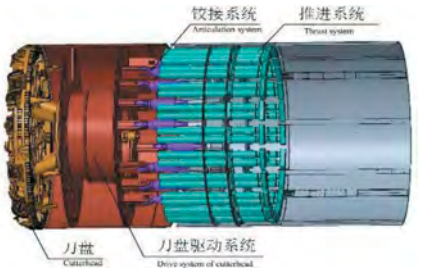

Figure 1. Schematic diagram of TBM structure.

*Corresponding author: 1434493225@qq.com

DOI: 10.1201/9781003495505-275

At present, the articulated TBM is mainly divided into three forms: passive articulation, active articulation and double articulation. Many scholars at home and abroad have analyzed and studied it. It mainly includes innovative design and research on the structure and composition of articulated system, articulated sealing system, etc., comparative analysis of the advantages, disadvantages and application scenarios of active articulation and passive articulation, and analysis and research in combination with the layout method of propulsion system considering the influence of articulated system [3-5]. Han Xue, et al. studied the characteristics and working principle of the articulated system of TBM, established a simulation model of the articulated hydraulic system, and analyzed the working characteristics of the hydraulic valve group [6]. Dong Weidong, et al. used the prism method of ENZAN to precisely calculate the attitude of active articulation TBM during tunneling [7].

2 WORKING PRINCIPLE OF ARTICULATED SYSTEM

Working principle of active articulation: As shown in Figure 2, the articulation cylinder is connected between the front shield and the middle shield, the middle shield and the shield tail are connected into a whole by bolting or welding, and the thrust cylinder is fixed on the supporting ring plate of the middle shield of TBM, that is, the articulation cylinder is at the front end of the fixed point of thrust cylinder; the whole middle shield and shield tail are pushed by the reaction force of the thrust cylinder supported on the segment, while the articulation cylinder connects the middle shield with the front shield. The acting force of the articulation cylinder is transmitted to the front shield and cutterhead, and then the telescopic stroke of the articulation cylinder is adjusted in zones to control the turning angle, thus realizing curved tunneling of the TBM. Since the middle shield and shield tail are coaxial with the segment, the reverse thrust F formed by the thrust cylinder and the segment is consistent with the radial direction of the segment, so that no lateral force will be generated.

Working principle of passive articulation: As shown in Figure 3, the articulation cylinder is connected between the middle shield and the shield tail, the front shield and the middle shield are connected into a whole by bolting or welding, and the thrust cylinder is fixed on the supporting ring plate of the middle shield of TBM, that is, the articulation cylinder is at the rear end of the fixed point of thrust cylinder; the front and middle shields are moved forward by the reaction force of the thrust cylinder supported on the segment, and the articulation cylinder drags the shield tail to move forward, that is, the shield tail moves forward in a serpentine shape with the front and middle shields. The articulation cylinder adjusts the telescopic length of the cylinder in zones and then generates a bending angle between the shields to realize turning. It can be observed in Figure 3 that since the middle shield is not coaxial with the shield tail and the segment, the reverse thrust F formed by the thrust cylinder and the segment has a certain angle with the radial direction of the segment, which will generate lateral force.

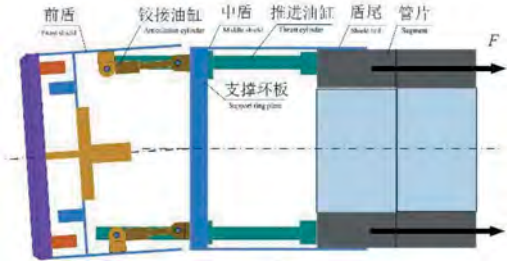

Figure 2. Active articulation.

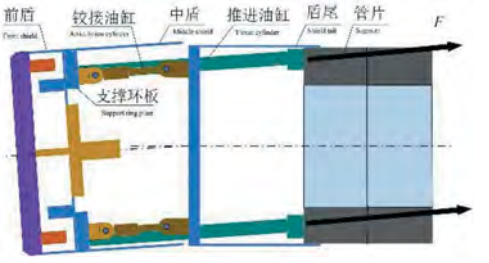

Figure 3. Passive articulation.

There is an active articulation system between the front shield and the middle shield, and a passive articulation system between the middle shield and the shield tail, so that the TBM forms two sets of articulation systems, which are called double-articulated TBMs. Working Principle of Double Articulation: As shown in Figure 4, the front shield and middle shield are connected by an active articulation cylinder, the middle shield and shield tail are connected by a passive articulation cylinder, and the thrust cylinder is fixed on the supporting ring plate of the middle shield of TBM; the middle shield is moved forward by the reaction force of the thrust cylinder supported on the segment, and the passive articulation cylinder drags the shield tail forward, while the front shield and cutterhead are pushed by the action force of the active articulation cylinder, so as to adjust the telescopic stroke of the active articulation cylinder in zones to control the bending angle of the front shield and the middle shield, and adjust the telescopic stroke of the passive articulation cylinder to control the bending angle of the middle shield and the shield tail, thus realizing curved tunneling of the TBM. Similar to the passive articulation system, since the middle shield is not coaxial with the shield tail and the segment, the reverse thrust F formed by the thrust cylinder and the segment has a certain

angle with the radial direction of the segment, which will generate lateral force.

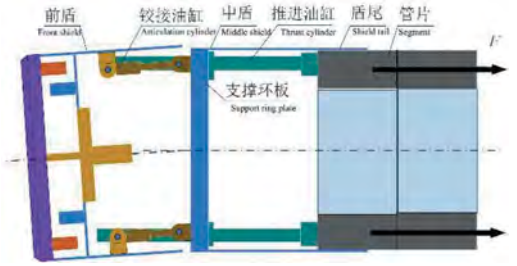

Figure 4. Double articulation.

Table 1. Comparison of characteristics and applicable working conditions of various articulation forms.

Articulation type	Performance characteristics	Applicable working conditions
Active articulation	Good deviation correction operability, large thrust of articulation cylinder, no lateral force for propulsion, uniform stress on segment, small requirements for internal space of shield,	accurate stroke control, adaptable to tunnels with small turning radius
Passive articulation	Large minimum turning radius, small drag force of articulation cylinder, large lateral force of thrust cylinder on segment, easy to cause fragmentation of segments,	adaptable to tunnels with certain turning radius
Double articulation	Two articulation systems, more adaptable to curved tunneling of the tunnel, small lateral force of thrust cylinder, small requirements for internal space of shield,	adaptable to tunnels with larger long diameter and smaller turning radius in shield design.

3 CALCULATION OF BENDING ANGLE BETWEEN SHIELDS

3.1 *Calculation of front shield rotation range and cutterhead over-excavation length*

During tunneling along a curved trajectory, the central perpendicular line passing through the cutterhead plane needs to be tangent to the axis of excavation trajectory, as shown in Figure 5(a). The cross section of turning plane of the curved tunnel is taken for analysis, and the contour line of the front end face of cutterhead needs to point to the center of the tunnel curve [8-9]. Through analysis on the shield body of TBM, its front shield and cutterhead are fixed as a whole, while the outer diameter of cylinder of front shield is designed to be slightly smaller than that of cutterhead. During curved tunneling, the over-excavation cutter shall be extended as required to meet the distance requirement between shield body and curved tunnel, without mutual interference affecting shield attitude [10]. Therefore, the over-excavation radius is calculated to ensure that the rear end face of the front shield does not interfere with the contour trajectory of the tunneling section, and the curve radius is also changed when the front shield and cutterhead carry out curved tunneling. Then, when the over-excavation is t, the rotation angle range of the front shield and cutterhead is calculated to meet the movement of the front shield in the tunnel.

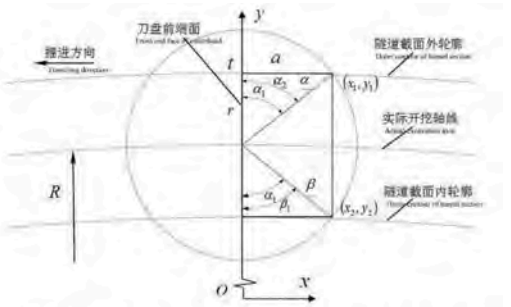

(a) Schematic Diagram of Front Shield and Cutterhead Positions on Cross Section of the Curved Tunnel

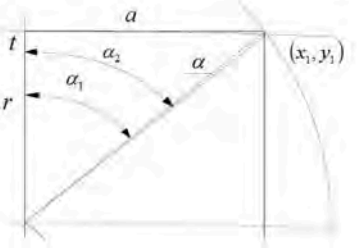

(b) Schematic Diagram of Bending Angle of Front Shield

(c) Intersection point between the upper turning point on the rear end face of front shield and the outer contour of tunnel

Figure 5. Attitude of front shield during curved tunnelling.

When the TBM is tunnelling with a certain radius of circular curve, the cross section passing through the center of the curve is analyzed. The plane coordinate axis is established with the center of the tunnel contour curve as the origin and the front end face of the cutterhead is used as the y axis, so that the trajectory function of the outer contour of tunneling section can be derived:

$$x^2 + y^2 = (R + r + t)^2 \tag{1}$$

As shown in Figure 5(a), R is the radius of tunnel circular curve, r is the radius of outer cylinder of front shield, and t is the over-excavation length of cutterhead. Inner contour trajectory function of tunneling section:

$$x^2 + y^2 = (R - r - t)^2 \tag{2}$$

When the curve radius is changed for tunneling, the front shield and cutterhead rotate with the center of the front end face of cutterhead as the circle center. The trajectory function of upper turning point on the rear end face of the front shield of TBM is:

$$x^2 + (y - R)^2 = \left(\frac{a}{2}\right)^2 + (r)^2 \tag{3}$$

其中: a为刀盘加前盾长度。

Where: a is the length of cutterhead plus front shield.

As shown in Figures 5(b) and (c), the calculation equations of intersection point can be derived from the coordinates (x_1, y_1) of the intersection point between the trajectory of upper turning point on the rear end face of front shield and the outer contour trajectory of tunneling section:

$$\begin{cases} x^2 + (y - R)^2 = \left(\frac{a}{2}\right)^2 + (r)^2 \\ x^2 + y^2 = (R + r + t)^2 \end{cases} \tag{4}$$

The calculation equations of intersection point can be derived from the coordinates (x_2, y_2) of the intersection point between the trajectory of lower turning point on the rear end face of front shield and the inner contour trajectory of tunneling section:

$$\begin{cases} x^2 + (y - R)^2 = \left(\frac{a}{2}\right)^2 + (r)^2 \\ x^2 + y^2 = (R - r - t)^2 \end{cases} \tag{5}$$

When the TBM rotates through the circle center position of the front end face of the cutterhead until the trajectory of upper turning point on the rear end face of front shield intersects with the outer contour trajectory of tunneling section, the rotation angle is as follows:

$$\alpha = \alpha_2 - \alpha_1 \tag{6}$$

Where

$$\alpha_1 = \arctan\left(\frac{a}{2r}\right) \tag{7}$$

$$\alpha_2 = \arctan\left(\frac{x_1}{y_1 - R}\right) \tag{8}$$

When the TBM rotates through the circle center position of the front end face of the cutterhead until the trajectory of lower turning point on the rear end face of front shield intersects with the inner contour trajectory of tunneling section, the rotation angle is as follows:

$$\beta = \alpha_1 - \beta_1 \tag{9}$$

Where

$$\beta_1 = \arctan\left(\frac{x_2}{-y_2 + R}\right) \tag{10}$$

Through calculation, when the front shield and cutterhead conduct curved tunneling and the curve radius is changed, the rotation angle range of the front shield and cutterhead is (α, β).

The range of over-excavation t is calculated to meet the requirement that the upper and lower turning points on the rear end face of the front shield of TBM are within the contour of tunneling section, and it can be derived that:

$$t > \sqrt{a^2 + (R + r)^2} - R - r \tag{11}$$

3.2 *Calculation of bending angle of middle shield*

During tunneling with curved trajectory, a certain angle will be formed between the middle shield and the front shield to ensure that the outer cylinder of the middle shield does not interfere with the tunnel, while thrust and steering are conducted between the front shield and the middle shield through active articulation. As shown in Figure 6, for the convenience of calculation and understanding, it can be simplified as that the middle shield rotates around O_1. Therefore, the outer diameter of cylinder of the middle shield can be calculated to meet the distance requirement between the shield body and the curved tunnel so that they do not interfere with each other. It is easy to see from this that the middle shield can rotate at a certain angle without interfering with the

inner wall of the tunnel. Therefore, the rotation angle range of the middle shield can be calculated to meet the movement of the middle shield in the tunnel.

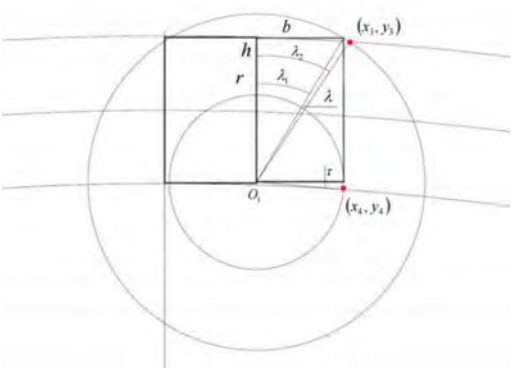

Figure 6. Attitude of middle shield during curved tunneling.

Where, h is the radius difference between the middle shield and the front shield, and b is the length of the middle shield. The calculation equations of intersection point can be derived from the coordinates (x_3,y_3) of the intersection point between the trajectory of upper turning point on the rear end face of front shield and the outer contour trajectory of tunneling section:

$$\begin{cases} (x-a)^2 + (y-R-r+h)^2 = b^2 + (2r-2h)^2 \\ x^2 + y^2 = (R+r+t)^2 \end{cases} \tag{12}$$

When the middle shield of TBM rotates through the circle center O_1until the upper turning point on the rear end face of middle shield intersects with the inner contour trajectory of tunneling section, the rotation angle is as follows:

$$\lambda = \lambda_2 - \lambda_1 \tag{13}$$

Where

$$\lambda_1 = \arctan\left(\frac{b}{2r-2h}\right) \tag{14}$$

$$\lambda_2 = \arctan\left(\frac{x_3 - a}{y_3 - R + r - h}\right) \tag{15}$$

The calculation equations of intersection point can be derived from the coordinates of the intersection point between the trajectory of lower turning point on the rear end face of front shield and the inner contour trajectory of tunneling section:(x_4,y_4)

$$\begin{cases} (y-R+r-h)^2 + (x-a)^2 = b^2 \\ x^2 + y^2 = (R-r-t)^2 \end{cases} \tag{16}$$

When the middle shield of TBM rotates through the circle center O_1until the lower turning point on the rear end face of middle shield intersects with the inner contour trajectory of tunneling section, the rotation angle is as follows:

$$\tau = \arctan\left(\frac{R-r+h-y_4}{x_4-a}\right) \tag{17}$$

The bending angle range of the middle shield is calculated when the curve radius of the tunnel is R to ensure that the outer cylinder of the middle shield does not interfere with the tunnel, and the rotation angle range of the middle shield is (λ, τ). Similarly, the bending angle range corresponding to the shield tail of the passive articulation system in a tunnel with a certain turning radius can be derived.

3.3 *Calculation of bending angle of double articulation system*

Since the middle shield and the shield tail form an articulation angle with the front shield and middle shield respectively under the action of the active articulation cylinder and passive articulation cylinder, the value of articulation angle is taken within a range, and its range depends on the condition that the cylinders of middle shield and shield tail do not interfere with each other in the tunnel. Here, an angle suitable for tunneling can be taken. As shown in Figure 7, the center of the tunnel curve where the rear end face of the middle shield passes through and the center of the curve where the rear end face of the shield tail passes through can be taken to make the thrust cylinder parallel to the segment, reduce the generation of lateral force, calculate its articulation angle, and check whether the angle is within the range where the cylinder doesn't interfere with the tunnel.

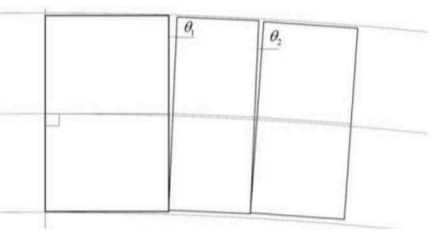

Figure 7. Attitude of shield body during curved tunneling.

In order to simplify the calculation, the cylinder length can be regarded as the chord length and the articulation angle can be calculated. The articulation angle is:

$$\theta = \theta_1 + \theta_2, \quad \theta_1 = \frac{a+b}{R} \cdot \frac{180}{\pi} \quad \theta_2 = \frac{c}{R} \cdot \frac{180}{\pi} \qquad (18)$$

4 CYLINDER STROKE DERIVATION AND CALCULATION EXAMPLE ANALYSIS

4.1 *Cylinder stroke derivation*

Active articulation or passive articulation makes an angle between the front shield and the middle shield of the TBM, or between the middle shield and the shield tail, which is controlled by the telescopic stroke of the articulation cylinder. The telescopic stroke of the articulation cylinder at each location when the angle δ is generated is calculated here. In Figure 8(a), the normal direction of TBM turning direction is X axis, and the shaft center of TBM is Z axis to obtain the distribution diagram of its articulation cylinders. From the projection of ZOX plane, Figure 8(b) is obtained, where δ is the articulation bending angle; from the projection of XOY axis plane, Figure 8(c) is obtained. By taking the position (x_i, y_i) of any articulation cylinder, its stroke is calculated.

Assuming that the radius of the trajectory circle at the articulation point of the oil cylinder is r_1, and the uniform extension distance of the oil cylinder is l, then the extension distance $L_i$of the oil cylinder at the location (x_i, y_i) vis:

$$L_i = l + (r_1 - x_i) \cdot \tan\delta \qquad (19)$$

4.2 *Calculation example analysis*

The bending angle and over-excavation size of each shield body under the minimum design curve radius of 150,000 mm are calculated by taking a certain type of soil pressure balance TBM with double articulation system as the analysis object. Its main dimensional parameters are shown in Table 2.

During normal tunneling, the over-excavating cutter is not extended. That is to say, during over-excavation $t = 0$, it is only necessary to calculate the rotation angle range of the front shield and cutterhead when the front shield and cutterhead carry out curved tunneling and change the curve radius, so as to meet the movement of the front shield in the tunnel. The rotation range of front shield is calculated, which is derived from Section 2.1 and solved by Equations (4), (5), (7), (8) and (10):

$$(x_1, y_1) = (1665, 153991), (x_2, y_2) = (1621, 145991),$$
$$\alpha_1 = 23.077^\circ, \alpha_2 = 22.645^\circ, \beta_1 = 22.015^\circ$$

$$(x_1, y_1) = (1665, 153991), (x_2, y_2) = (1621, 145991),$$
$$\alpha_1 = 23.077^\circ, \alpha_2 = 22.645^\circ, \beta_1 = 22.015^\circ$$

When the TBM rotates through the circle center position of the front end face of the cutterhead until

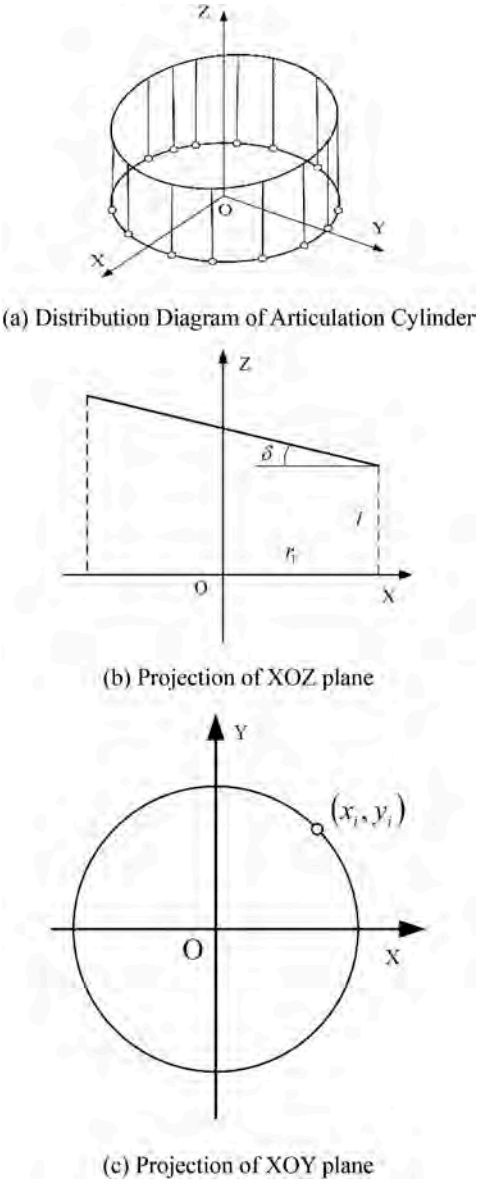

Figure 8. Geometric simplification diagram of articulation cylinder.

Table 2. Main dimension parameters of TBM.

Item	Size/mm
Length of front shield plus cutterhead	3400
Length of middle shield	3170
Length of shield tail	3245
Stroke of active articulation cylinder	310
Stroke of passive articulation cylinder	200
Diameter of outer cylinder of front shield	3990
Cutterhead diameter	4000

the upper and lower turning points on the rear end face of front shield are within the contour of tunneling section, the rotation angle range is as follows:

$$(\alpha, \beta) = (0.432^\circ, 1.062^\circ)$$

The range of over-excavation t is calculated to meet the requirement that the upper and lower turning points on the rear end face of the front shield of TBM are within the tunnel, where

$$x_1 = a, y_1 = R + r, x^2 + y^2 = (R + r + t)^2$$

So:

$t > 37.5$mm

The rotation angle range of middle shield is calculated under the over-excavation distance of 37.5 mm. When the middle shield of TBM rotates through the circle center O_1 until the upper and lower turning points on the rear end face of middle shield intersect with the inner and outer contour trajectories of tunneling section, the rotation angle range is as follows: The following can be obtained through the Equations (12), (14), (15) and (16):

$$(x_3, y_3) = (6833, 153875), \lambda_1 = 21.390^\circ,$$
$$\lambda_2 = 23.594^\circ, \lambda = 2.204^\circ$$

$$(x_4, y_4) = (6564, 145827), \tau = 3.400^\circ$$

Rotation angle range:

$$(\lambda, \tau) = (2.204, 3.400)$$

Here, an angle suitable for tunneling can be taken. The center of the tunnel curve where the rear end face of the middle shield passes through and the center of the curve where the rear end face of the shield tail passes through can be taken to calculate the bending angle and check whether the angle is within the range where the cylinder doesn't interfere with the tunnel. The solution obtained is as follows:

$$\theta_1 = 2.510^\circ, \theta_2 = 1.239^\circ, \theta = 3.749^\circ$$

The bending angle of middle shield is $2.510 \in (2.204,\ 3.400)$, meeting its non-interference condition. The bending angle of shield tail is $\theta_2 = 1.239^\circ$. As the shield tail is less than the length of front shield plus cutterhead, the shield tail also meets the condition of no interference with the tunnel contour under the over-excavation distance of 37.5 mm when there is no bending angle. The soil pressure balance TBM with double articulation system has a bending angle of 3.749° under the minimum design curve radius of 150,000 mm.

The telescopic stroke of articulation cylinder is calculated when it rotates at a certain angle. As shown in Figure 9, if the radius of trajectory circle at the articulation point of oil cylinder is 3,700 mm, the uniform extension length l is 50 mm for the oil cylinder at the location (2110,3039). If it turns left and the articulation bending angle is 1.24°, the 270° direction is the forward direction of the X axis, and the calculated extension distance of cylinder 1 is 175.8 mm.

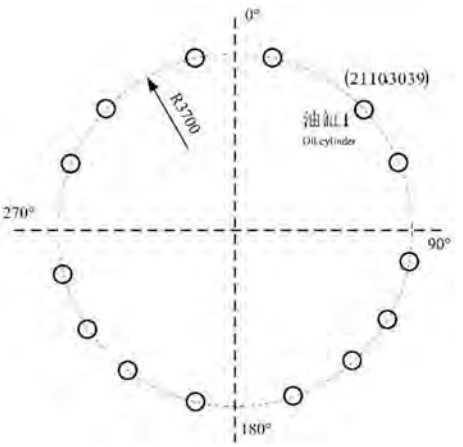

Figure 9. Layout diagram of oil cylinders.

5 CONCLUSIONS

In order to accurately control the curved tunneling of articulated TBM and provide theoretical reference for the design of shield size, cutterhead over-excavation cutter size and selection of articulation form, three articulation forms (active articulation, passive articulation and double articulation) are studied for TBM.

(1) Analyze the working principles and characteristics of three articulation forms of TBM, show the shield attitude during curved tunneling and the stress of thrust cylinder on segment, and compare the tunneling conditions applicable to the three articulation forms.

(2) By analyzing the articulated TBM, study the bending attitude of shield body during curved tunneling, and put forward an analytical geometry method to calculate the boundary conditions for the movement of shield body in the tunnel, so as to calculate the rotation angle range of each shield. Here, calculate the rotation angle rage of front shield and cutterhead when the front shield and cutterhead carry out curved tunneling and change the curve radius; calculate the over-excavation range of cutterhead over-excavation cutter to meet the requirement that the upper and lower turning points on the rear end face of front shield are within the contour of tunneling section; and calculate the range of bending angle of middle shield under a certain

radius of tunnel curve to ensure that the outer cylinder of middle shield doesn't interfere with the tunnel.

(3) Analyze the rotation angle corresponding to the stroke of each cylinder to obtain the corresponding relation between the telescopic stroke and the bending angle of the cylinder. Calculate the rotation angle of each shield during curved tunneling of double articulation system through an example, and check whether its angle is within the range where the cylinder of shield body doesn't interfere with the tunnel.

REFERENCES

[1] He Chuan, Feng Kun, Fang Yong. Technical Status and Prospect of Metro Tunnel Construction by Shield Method [J]. Journal of Southwest Jiaotong University, 2015, 50(1): 97–109.

[2] Guan Huisheng. Design and Calculation of TBM [M]. Chengdu: Southwest Jiaotong University Press, 2018.

[3] Deng K, Huang J, Wang H.Layout optimization of non-equidistant arrangement for thrust systems in shield machines[J]. Automation in Construction,2015, 49(pt.a): 135–141.

[4] Zhang Xu, Zhu Limin. Optimization and Selection Method of TBM Attitude Control Points [J]. China Mechanical Engineering, 2009 (8): 902–906.

[5] Zhao Y, Pan H, Wang H, et al.Dynamics research on grouping characteristics of a shield machine's thrust system[J]. Automation in Construction, 2017, 76 (APR.): 97–107.

[6] Han Xue, Li Pei. Application of Articulation System in TBM [J]. Hydraulics Pneumatics & Seals, 2011, 31 (10): 29–32.

[7] Dong Weidong, Guo Hao, Luo Haibo, et al.Measurement and Attitude Precision Solution Method for Automatic Guidance System of Active Articulated TBM [J]. Bulletin of Surveying and Mapping, 2022 (1):149–154+158.

[8] Pan Hong, Su Wenyuan, Zhai Guolin, et al.Measurement and Analysis of Shield Construction Disturbance in Turning Tunnels with Small Curvature Radius [J]. Chinese Journal of Rock Mechanics and Engineering, 2017, 36(4):1024–1031.

[9] Deng Huangshi, Fu Helin, Shi Yue. Calculation of Ground Subsidence Caused by Shield Tunnel Excavation with Small Turning Radius Curve [J]. Chinese Journal of Geotechnical Engineering, 2021, 43(01):165–173.

[10] Chen Jian, Li Zhiming. Theoretical Algorithm of Shield Over-excavation and Articulation Angle in Sharp Curved Tunnels [J]. China Journal of Highway and Transport, 2017, 30(8): 66–73.

Tunnelling for a Better Life – Yan, Celestino, Thewes & Eberhardt (Eds)
© 2024 The Author(s), ISBN 978-1-032-80042-4
Open Access: www.taylorfrancis.com, CC BY-NC-ND 4.0 license

Analysis of motion characteristics of large-sized irregular particles in long pipelines

Zhen Ren*
China Railway Engineering Equipment Group Co.Ltd., Zhengzhou, China
School of Automation Science and Electrical Engineering, Beihang University, Beijing, China

Shaoping Wang
School of Automation Science and Electrical Engineering, Beihang University, Beijing, China

Youzeng Wang & Xiaolei Zhou
China Railway Engineering Equipment Group Co.Ltd., Zhengzhou, China

ABSTRACT: To study the motion law and characteristics of large-sized particles in the slurry discharge pipeline of slurry TBM, the two-way coupling method based on FVM-DEM is used to simulate the solid-liquid two-phase flow in long pipelines. In order to verify the feasibility of the numerical method, the solid-liquid two-phase flow in vertical pipelines is simulated. The calculated results are in good agreement with the experiments with the error of pressure drop being less than 5.0%. Then this method is used to simulate the motion characteristics of large-sized particles with irregular shapes in long-distance continuous pipelines. It is found that the increase of mud viscosity has little effect on particle velocity compared with the results of clear water. Local convergence phenomenon of large-sized irregular particles appears, which is easy to cause pipeline blockage. Therefore, the second blockage of large particle size slag is needed in advance in circulation system to prevent blockage of the pipeline.

Keywords: Slurry TBM, CFD-DEM, Two-way coupling, Long pipelines, Slurry circulation system

1 INTRODUCTION

In the planning and construction of urban subway tunnel, The slurry balance shield has become a priority construction machinery for the construction of cross-river tunnels, because there are some advantages such as less construction impact, strong adaptability to geological conditions, safety and speed. The slurry circulation system is an important part of the slurry TBM. However, there are few studies on the circulation system of slurry TBM and its slag carrying capacity, especially on the transportation characteristics of large-size slag.

At present, researchers have carried out a lot of research on the transportation of solid particles in pipelines. Zhou et al, (2011) analyzed the relationship between particle composition characteristics and conveying speed and obtained the particle volume fraction. F. Ravelet et al, (2013) studied the influence of particle size and density on the formation of fixed bed or dispersed flow of particles through experiments and revised the empirical formula. Wang et al. (2015), adopted the experiments to study the influence of different hydraulic parameters on the pressure loss of the pipeline and determined the functional relationship between different hydraulic parameters and pressure loss. Edelin et al, (2015) analyzed the optimal concentration of particles transported in clear water from the perspective of energy. In the experiments of Cao et al, (2016), the hydraulic characteristics of coarse particles under different hydraulic parameters was analyzed by high-speed camera. Wu (2019) designed a slurry circulation system. With water as the carrier fluid, the critical velocity law of large-sized pebbles in different pipeline positions in the circulation system, as well as the typical movement pattern and velocity of different pipeline forms under different flow velocities are obtained.

With the rapid development of computer technology, the numerical simulation method is increasing widely applied to the study of pipeline transportation. Compared with the experimental method, the numerical

*Corresponding author: renzhen90@163.com

DOI: 10.1201/9781003495505-276

method has the advantages such as short research cycle and low investment cost. Jiang et al. (2012) used eulerian multiphase flow model to study the influence of flow velocity and average solid volume fraction on the flow characteristics of nitrogen slurry. Gopaliya et al. (2016) constructed a solid flow model by using two-phase flow theory, and analyzed the flow state of iron ore filling slurry and sand slurry in horizontal pipe. Xia et al, (2017, 2018) studied the influence of shape coefficient, constant volume particle size and quantity of rock slag on the starting speed of rock slag and the influence of shield machine operation parameters on the pressure loss of circulation system and the conveying speed of rock slag. Yang et al. (2018) studied the transport characteristics of slag in the horizontal straight pipe of the slurry TBM circulation system. Yang et al. (2018) used CFD and DEM to establish the corresponding model, and pointed out that the stones were mainly distributed at the bottom of the horizontal straight pipe. Dai et al (2021) simulated the pipeline internal flow by coupling software Fluent and EDEM. From the perspective of computational fluid mechanics, the movement performances of particles such as concentration distribution and velocity distribution in the vertical pipeline are obtained. In addition, the wall shear stress under different working conditions is also analyzed. Song et al. (2021) simulated the characteristics of solid-liquid two-phase flow under different working conditions in vertical pipelines and analyzed the influence of large particle solid-liquid two-phase flow with different properties on deep-sea mining transportation system. Chen, et al (2022) studied the internal mechanism of pipeline wear through the results of motion trajectory, flow state and solid volume distribution during the transportation of particles with three different length-to-diameter ratios by coupling CFD and DEM.

Scholars have done a lot of research on the transportation of slag in the pipeline, but there are relatively few studies on the movement of large and medium-sized slag in long distance. This paper makes a preliminary study on the transportation of large irregular slag in horizontal long pipelines. This paper includes the following parts, the first part is introduction, the second part is the numerical method, and the third part is the numerical method verification and simulation results analysis. Finally is the conclusion.

2 NUMERICAL METHOD

2.1 *CFD-DEM model*

CFD method is one of the important means to solve complex flow problems and plays an important role in the numerical simulation of solid-liquid two-phase flow. The discrete element model (DEM) in the commercial CFD software STARCCM+ has three advantages in the numerical simulation of the solid-liquid two-phase flow of large-size particles in the pipeline. Firstly, the particles are solved in the Lagrangian coordinate system, so that the position of each particle can be tracked. The second is to consider the interphase force between particles and liquid at the same time to realize the two-way coupling of flow field and particles. At last, the interaction force between particles is considered to explain the interaction between particles.

The motion of the particles is solved in the Lagrangian coordinate system and the position of each particle in the flow field is located. The flow of liquid is solved in the framework of Euler coordinate system. The interaction between liquid and solid particles is considered by introducing the volume fraction of the solid-liquid two-phase.

The continuity equation of liquid phase is:

$$\frac{\partial(\varepsilon_1\rho_1)}{\partial t} + \nabla\cdot(\varepsilon_1\rho_1 u) = 0 \tag{1}$$

The momentum equation of the liquid phase is:

$$\frac{\partial(\varepsilon_1\rho_1 u)}{\partial_t} + \nabla\cdot(\varepsilon_1\rho_1 uu) = -\varepsilon_1\nabla p + \nabla\cdot(\varepsilon_1\mu\nabla u) + \varepsilon_1\rho_1 g + F_{pl} \tag{2}$$

where

$$F_{pl} = -\frac{\sum F_{pl,i}}{\Delta V_{cell}}$$

where ρ_1 is the density of the liquid; t is time; ε_1 is the volume fraction of the liquid phase; u is the velocity of liquid; p is the static pressure of liquid; μ is liquid dynamic viscosity; F_{pl} is the sum of the forces of the discrete phase (solid phase) to continuous phase (liquid phase) in the grid cell; ΔV_{cell} is the grid element volume.

The particle motion including the varaition of particle velocity and position with time is calculated by DEM model based on Newton's law of motion. The equations of translational motion and rotational motion of a single particle are respectively shown as:

$$m_i\frac{dv_i}{dt} = \sum_j F_{c,ij} + \sum_k F_{nc,ik} + F_{lp,i} + F_{g,i} \tag{3}$$

$$I_i\frac{d\omega_i}{dt} = \sum_j (M_{t,ij} + M_{r,ij}) \tag{4}$$

where m_i is the mass of a single solid particle i; vi is the moving speed of particle i; $F_{c,ij}$ is the contact force between particle i and particle j; $F_{nc,ik}$ is the non-contact force between particle i and particle j; $F_{lp,i}$ is the acting force of fluid on the particle i; $F_{g,i}$ is the

body force on particle i; I_i is the moment of inertia of particle i; ω_i is the rotation speed of particle i; $M_{t,ij}$ is the tangential friction torque between particle i and particle j; $M_{r,ij}$ is the normal friction torque between particle i and particle j.

2.2 *Geometry model and boundary condition*

The pipe material is carbon steel, length L=10m, pipe diameter D=100mm, roughness 100μm. The mixing transport speed V_{mix} is 3.0m/s and solid particle volume transport concentration C_V is 5%. The RNG k-ε turbulence model was used for liquid phase simulation. The velocity inlet and pressure outlet are used to set the boundary conditions. The fluid calculation domain is shown in Figure 1. The thickness of the first layer boundary layer is set to 10.0 mm and the boundary layer is set to 4 layers with an elongation of 1.4. The model is divided by trimmer mesh with a total of 536,512 mesh elements and 557,865 mesh nodes.

The Lagrangian phase model selects composite particles, two-way coupling, turbulent dissipation, pressure gradient force, drag force and DEM particle model.

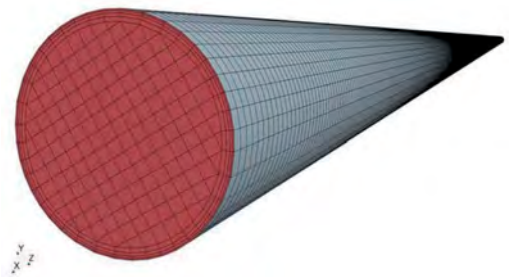

Figure 1. Pipeline and grid distribution.

2.3 *Two-way coupling procedure*

In STAR-CCM+, the interactions between the dispersed phase and the continuous phase are simulated as one-way coupling or two-way coupling (CD-adapco (2022)).

With one-way coupling, only the continuous phase influences the dispersed phase, but not in the reverse direction. With two-way coupling, the effects of the dispersed phase on the continuous phase such as displacement, interphase momentum, mass, and heat transfer are taken into account.

The displacement of the continuous phase by the dispersed phase is accounted for through the volume fraction. The volume fraction of a Lagrangian phase is the fraction of the local cell volume which that phase occupies. It is calculated for both discrete material particles and DEM particles.

Figure 2 depicts the two-way coupling procedure. The volume fraction, force distribution and flow field information of the fluid phase and the solid phase are calculated in CFD. At the end of a time step calculation, the force acting on the particles is transferred to the DEM model. The position and velocity of particles are updated in DEM. After the DEM calculation is completed, the position and velocity of the particles are transferred to the flow field of the FVM.

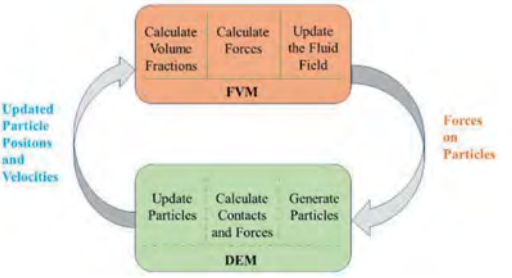

Figure 2. Two-way coupling procedure.

2.4 *Source smoothing method*

To make the CFD-DEM method can be used for the calculation of large particles and ensure its calculation accuracy, the source smoothing method is introduced in StarCCM+ (CD-adapco (2022), Liu (2019)). The main idea is that when the grid resolution is less than the particle, the multiple grids containing the particles are combined to form a large virtual grid cluster which is used to calculate the volume fraction of the particles, the movement of the particles, the force and other parameters. At the same time, the effect of particles on the fluid will also be assigned to each grid in the virtual grid cluster. Figure 3 describes the treatment of large-sized particles.

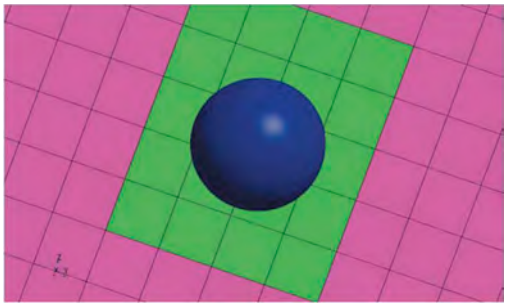

Figure 3. Source smoothing method.

3 ANALYSIS OF SIMULATIONS

3.1 *Experiment verification*

In order to verify the reliability of the numerical simulation method, simulation results and experimental data of solid-liquid two-phase flow in vertical pipe are compared as shown in Figure 4. The experimental results are obtained from the tests of Xia (2004). The

solid phase transport concentration is 5.0%, the diameter of solid particle is 15.0mm. As shown in Figure 4, the numerical simulation results are in good agreement with the experiments. The maximum error between the two is less than 5%. This shows that the current numerical simulation method is credible.

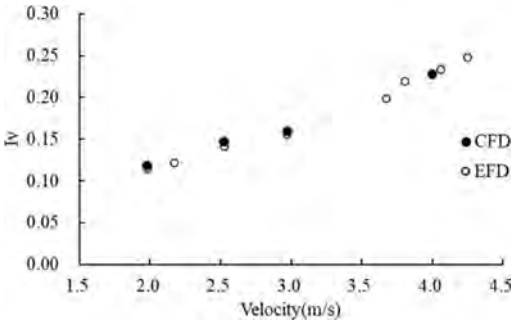

Figure 4. Comparison between CFD and EFD.

3.2 *Effect of viscosity on slag transportation*

In order to simulate irregular particles, the composite particle model is selected. The composite particles model uses multiple shapes (spheres) to represent non-spherical particles. The shapes are fixed together and do not separate during the simulation.

The slag stone transported by the circulation system is mostly pebbles. In order to simulate the shape of pebbles, 15 spherical particles were used to form irregular pebble particles, as shown in Figure 5.

Figure 5. Irregular particle.

In the numerical simulations, the influence of viscosity on particle transport is studied. Water and slurry with viscosity being from 0.02 to 0.05 mpa-s were selected for comparative analysis. In the simulations, taking the slurry TBM with diameter being 15.0m as an example, the amount of slag stone can be calculated according to the tunnelling speed of 15.0mm/min. When the particles are generated, the maximum particle size is set to 50.0mm and the average particle size is 30.0mm.

In order to monitor the distribution and motion state of particles in the local area, two cylindrical sections with a length of 1.0m in the middle and outlet of the pipeline are selected, as shown in Figure 6.

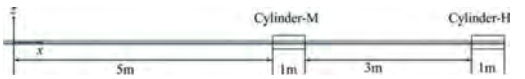

Figure 6. Local monitoring area layout.

Figure 7 describes the variation of solid particle concentration under different working conditions. It is shown that the solid particle concentration under clean water condition is higher than that under other conditions. However, the concentration of solid particles does not change much under different viscosity conditions. It indicates that the slurry with slightly larger viscosity is beneficial to the transportation of slag, but the change of viscosity has little effect on the transportation of slag.

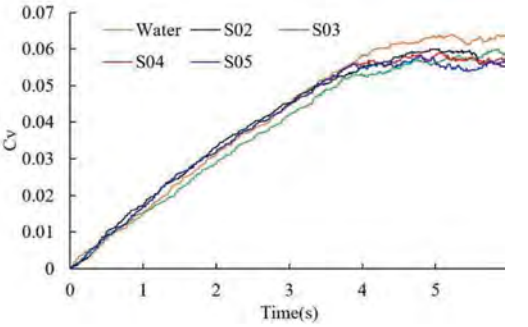

Figure 7. Time history of concentration at different viscosities.

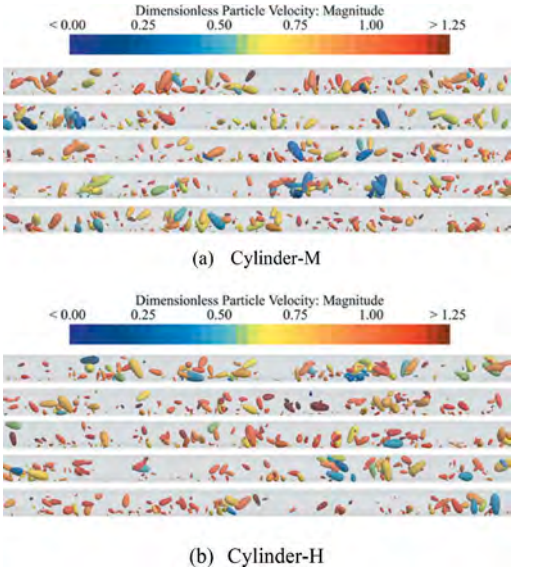

Figure 8. Dimensionless particles velocity in local pipe.

Figure 8 shows the dimensionless particle velocity in the local regions. The variation of dimensionless particle velocity is little under different viscosity conditions. However, under different working conditions, there is a same phenomenon, that the large size particles will gather in different positions. The main reason for this phenomenon is that the large

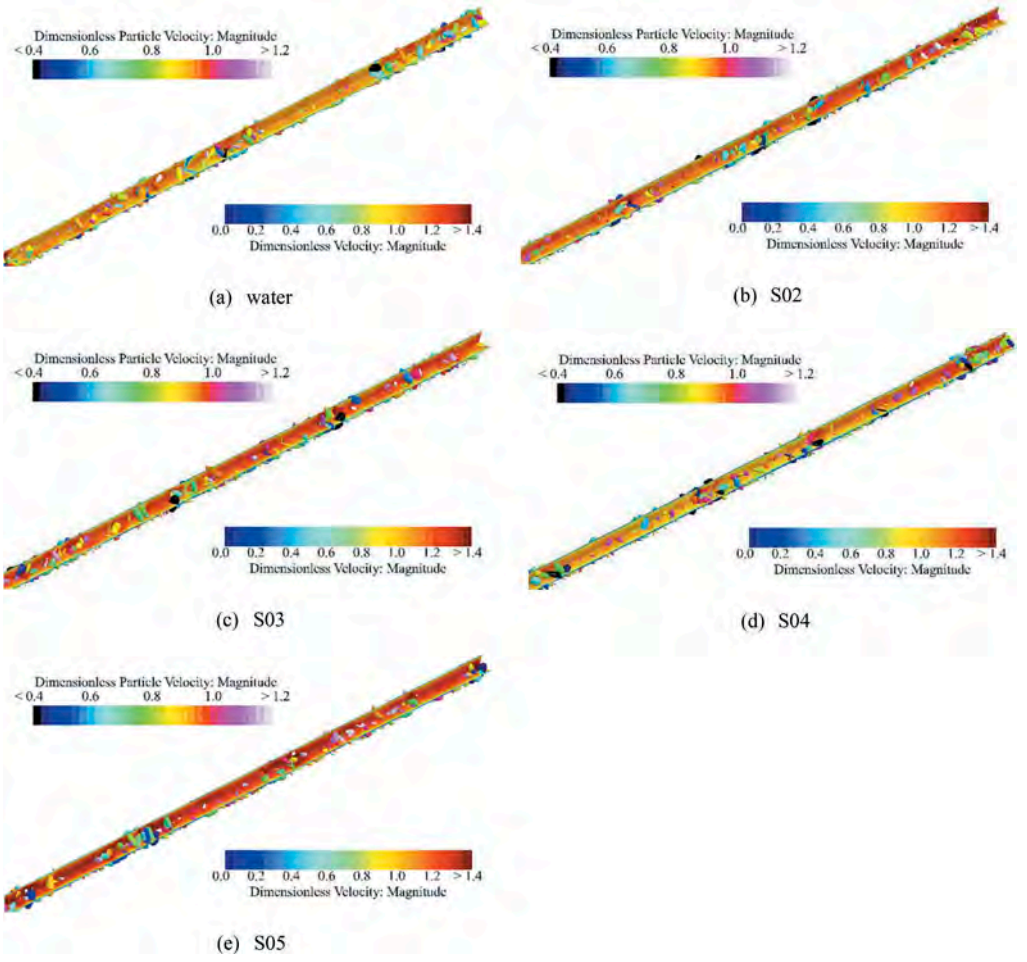

Figure 9. Dimensionless particle velocity and dimensionless fluid velocity.

mass of the particles leads to a relatively low speed so that they are not easy to transport.

Figure 9 describes the dimensionless velocity of particles and the dimensionless velocity of flow field under different viscosity conditions. It can be more obvious that large particle size particles will occasionally aggregate. This leads to the pipeline is easy to block in the process of conveying slag. Moreover, the velocity of the flow field will increase at the location of large particle size slag aggregation. This is because the accumulation of large-size slag blocks the pipeline, resulting in a decrease in the flow area and an increase in the flow rate.

4 CONCLUSIONS

In this paper, STARCCM+ software is used to simulate the transport characteristics of large-size irregular particles in long-distance pipelines. The combination of FVM and DEM are used to simulate the two-way coupling of particle motion. In order to simulate the large particle size irregular slag stone, the source term smoothing method is adopted in the current numerical simulation. The current numerical results are good agreement with experiments with the error of pressure drop being less than 5%.

By comparing the motion characteristics of particles under different viscosities, it can be found that the viscosity has little effect on the transport characteristics of slag. However, due to the large mass, large-size slag stones are prone to local convergence, resulting in pipeline blockage. Therefore, for the slurry TBM circulation system, it is not recommended to transport slag stones with a particle size exceeding more than half of the pipe diameter.

REFERENCES

Cao B, Xu X Y, Xia J X, 2016. Movement Status Change of Coarse Particlesand it's Discriminant Parameter in Hydraulic Transporting Pipeline. Journal of Basic Science and Engineering, 24(4), pp. 672–679.

CD-adapco, 2022. User Guide, STAR-CCM+[M]. CD–adapco.

Chen W, Zhang P, Sun Y C, 2022. Numerical simulation of hydraulic transport of non-spherical particles based on CFD-DEM. China Powder Science and Technology. 28 (5), pp. 82–91.

Edelin D, Czujko P C,Castelain C,et al, 2015. Experimental Determination of the Energy Optimum for the Transport of Floating Particles in Pipes[J]. Experimental Thermal & Fluid Science, 68, pp.634–643.

Gopaliya M, Kaushal D, 2016. Modeling of Sand-Water Slurry Flow Through Horizontal Pipe Using CFD [J]. Journal of Hydrology and Hydromechanics, 64(2), pp.261–272.

Jiang Y Y, Zhang P, 2012. Numerical Investigation of Slush Nitrogen Flow in a Horizontal Pipe[J]. Chemical Engineering Science, 73, pp. 169–180.

Liu L, 2019. Research on Dynamic Performance of Solid-Liquid Two-Phase Flow in Hydraulic Transport in Deep Sea Mining. PhD Thesis. ShanghaiJiaoTong University, Shanghai, China.

Ravelet F, Bakir F, Khelladi S,et al, 2013. Experimental Study of Hydraulic Transport of Large Particles in Horizontal Pipes[J]. Experimental Thermal and Fluid Science, 45(2), pp.187–197.

Song L B, Teng S, Cao Q, et al, 2021. Solid-liquid two-phase flow characteristics in pipe during large solid particles lifting [J]. Journal of Drainage and Irrigation Machinery Engineering, 39(11), pp. 1111–1117.

Wang S P, Wu A X, Yin S H, et al, 2015. Influence factors of pressure loss in pipeline transportation of paste slurry, Chinese Journal of Engineering, 37(1), pp. 7–12.

Xai Y M, Yao J, Wu D, et al, 2018. Study of Pickup Velocity of Pebbles in Horizontal Straight Pipe of Slurry Shield, Tunnel construction, 38(3), pp. 392–398.

Xai Y M, Wang Y, Wu D, et al, 2017. Transport characteristics of shield slurry system, Journal of Central South University (Science and Technology), 48(11), pp.2889.

Xia J X, Ni J R, Mendoza C, 2004. Hydraulic lifting of manganese nodules through a riser. Journal of offshore mechanics & arctic engineering, 2004, 126 (1) pp. 72–77.

Yang G D, Xia Y, Wu D,et al, 2018. Numerical Investigation of Pipeline Transport Characteristics of Slurry Shield Under Gravel Stratum[J]. Tunnelling and Underground Space Technology, 71 pp.223–230.

Dai Y, Zhang Y Y, Li X Y, 2021. Numerical and experimental investigations on pipeline internal solid-liquid mixed fluid for deep ocean mining, Ocean Engineering, 220, 108411,

Zhou Z J, Liu A J, Xia Y M, et al, 2011. Influence of particles component properties on transporting speed in lifting pipeline, Journal of Central South University (Science and Technology), 40(9), pp. 2692–2697.

Tunnelling for a Better Life – Yan, Celestino, Thewes & Eberhardt (Eds)
© 2024 The Author(s), ISBN 978-1-032-80042-4
Open Access: www.taylorfrancis.com, CC BY-NC-ND 4.0 license

Experimental study and simulation verification of slurry penetration process

Zhen Ren*, Lei Ye, Xiaolei Zhou & Yue Wang
China Railway Engineering Equipment Group Co., Ltd., Zhengzhou, China

Shaoping Wang
School of Automation Science and Electrical Engineering, Beijing University of Aeronautics and Astronautics, Beijing, China

ABSTRACT: The matching degree of slurry characteristics and formation parameters has great significance for maintaining the stability of the working face and safe and efficient construction in slurry TBM. Based on CFD-DEM fluid discrete element numerical coupling method, the slurry penetration process was modelled and simulated for summarizing the microscopic mechanism of slurry film formation and the effect of slurry characteristic parameters on slurry film. The self-designed slurry penetration test apparatus was used to compare and verify the simulation conclusions. The neural network genetic algorithm was used to fit the test data, and the slurry penetration prediction function for specific formation was obtained. The results show that the formation-slurry particle size ratio has an important effect on the morphology of filter cake, with the increase of slurry density as well as viscosity, slurry invasion depth decreases, and filter cake thickens. The fitting function is verified by the slurry penetration test of the drilled core formation in engineering field, and good feedback is obtained.

Keywords: Slurry TBM, Slurry characteristics, Slurry penetration process, Neural network

1 INTRODUCTION

With the advancement of urbanization in China, slurry shield tunnelling method has been widely applied. Especially for the underground space construction in high-density areas, landmark buildings, cross-river and cross-sea tunnels, the excellent control effect of slurry shield tunnelling on the stability of excavation surface and its ability against ground settlement are particularly outstanding. The key of slurry shield tunnelling technology lies in the slurry film formed by the slurry at the excavation surface, which converts the slurry pressure into effective stress that can balance the earth pressure to maintain the stability of the excavation surface. As the "blood" of slurry shield tunnelling, the characteristics of slurry play a vital role in the quality of the slurry film. In this regard, domestic and overseas scholars have conducted some research on the formation of the slurry film, and have reached some conclusions from both theoretical and application perspectives, with slurry penetration test being the main research method.

Fritz (2007) conducted slurry penetration film-forming experiments to address the issue that slurry could not provide support to the excavation surface in formations with permeability coefficients much greater than 10^{-3}m/s. It was found that adding appropriate coarse particles and high polymer additives to the slurry helps to form a slurry membrane in high permeability formations. Han et al. (2008) conducted penetration experiments with different slurry viscosities under the same slurry ratio and density, and concluded that the higher the slurry viscosity, the thinner, denser and more physically stable the formed slurry film. Min et al. (2013) carried out penetration tests in 5 types of formations with different permeability coefficients by using different slurry ratios, and divided slurry penetration film formation into 3 types: "filter cake", "filter cake + infiltration zone" and "infiltration zone" type. Lin et al. (2020) carried out penetration experiments in sandy soil layers with different permeability coefficients. They concluded that using the D15/d85 value can roughly divide the slurry film types, and the relationship between formation permeability coefficient and filter cake thickness can obtain the k-line theory of filter cake. Xia W. (2023) carried out research on the reasonable slurry ratio based on the Zirui Tunnel project of Chengpu Railway. The study found that: the slurry ratio has a significant impact on the efficiency of slurry TBM excavation. Slurries with low density and

*Corresponding author: renzhen90@163.com

DOI: 10.1201/9781003495505-277

viscosity can lead to excessive slurry loss and inability to timely build slurry pressure; while slurries with high density and viscosity can lead to filter cake buildup on the cutterhead, reducing excavation efficiency. Min et al. (2014) verified the relationship between formation permeability coefficient and film formation type through penetration experiments, and pointed out that the amount of filtrate mass can be used as a criterion for judging the formation of filter cake, and can also be used as an evaluation criterion for slurry film quality. Lian (2017) analyzed the effects of slurry properties and formation permeability coefficient on slurry film formation through slurry penetration experiments, and proposed the relationship between slurry effective stress conversion rate and film formation type. Jiang et al. (2016) analyzed the effects of slurry density, ratio, pressure and other factors on the gas tightness of the slurry membrane through self-made slurry penetration experiments. Min et al. (2015) carried out closed air experiments on slurry membranes formed under different slurry penetration modes in the sandy cobble formation crossed by the Nanjing Weisan Road Cross-River Tunnel using a self-developed slurry membrane air tightness apparatus. The test concluded that: first use low-density and low-viscosity dilute slurry to penetrate the formation to form a stable penetration zone, then replace the dilute slurry with high-density and high-viscosity slurry to form a slurry cake type membrane on the excavation surface, thus forming a composite membrane with better air tightness. Ni et al. (2013) used discrete element numerical simulation to simulate the slurry penetration process and summarized the influence of different formation-slurry particle size ratios on film formation. Liu (2019) realized the simulation of the slurry penetration process by using Fluent and EDEM coupling, analyzed the factors affecting film formation and the relationship between particle size ratio and film formation type. It was proposed that under the same conditions, the slurry density has a greater influence on the invasion depth, while the slurry pressure has less influence.

To address the issue of difficult slurry film formation in high permeability formations, fluid discrete element simulation technology has been used to simulate the slurry film formation process and summarize the effects of formation-slurry particle size ratio, slurry density, viscosity on slurry film formation. This paper focuses on verifying the simulation conclusions through self-made slurry penetration test equipment; and fitting a Slurry permeability prediction function based on test data using neural network. This function can predict the slurry film type according to the slurry properties and formation attributes, and provide reference for adjusting parameters to ensure safe excavation.

2 SIMULATION CONCLUSIONS OF SLURRY PENETRATION PROCESS

The Fluid-discrete element numerical coupling technology was used to simulate the slurry infiltration process, and the influence of the particle size ratio D/d, slurry density, and viscosity on the slurry film was analyzed. The following conclusions were drawn: When D/d<3, slurry infiltration forms a “filter cake”; when 3<D/d<7.5, it forms a “filter cake + infiltration zone”; when D/d>7.5, it forms an “infiltration zone”, as shown in Figure 1.

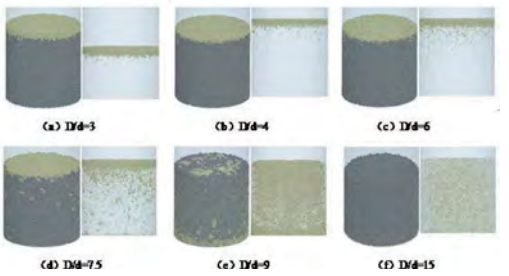

Figure 1. Influence of particle size ratio on film.

As the slurry density increases, the number of particles that can block the formation pores per unit volume increases, and the blocking ability becomes stronger. The depth of particle infiltration decreases, and the filter cake formed becomes thicker, as shown in Figure 2.

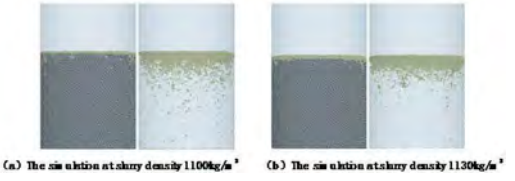

Figure 2. Influence of density on film.

The greater the slurry viscosity, the better the cohesion between particles, and the stronger the “bridging effect”. The depth of slurry infiltration decreases, and the filter cake formed becomes thicker, as shown in Figure 3.

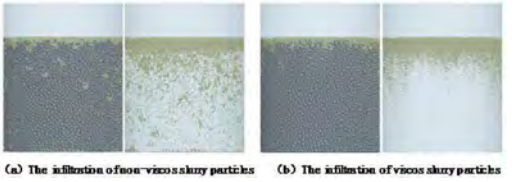

Figure 3. Influence of viscosity on film.

3 SLURRY PENETRATION TEST

A self-made slurry penetration test apparatus (Figure 4) was used to verify the simulation

conclusions. The test apparatus mainly consists of three parts: a pressure loading device, a penetration column body, and a data acquisition device.

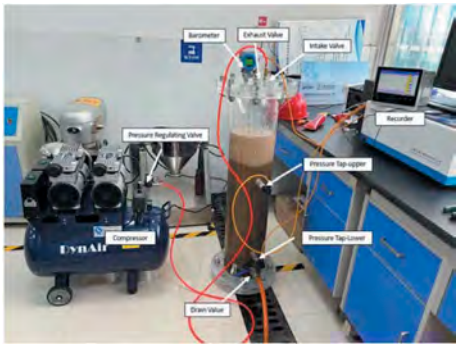

Figure 4. Experimental apparatus.

3.1 *Formation-slurry particle size ratio*

A fixed slurry formulation was used. The slurry properties were determined using a slurry balance, soviet funnel and medium pressure water loss tester. The particle size d85 at 85% on the slurry particle distribution curve was taken as the representative particle size. Different experimental formations were prepared. The particle size D15 at 15% on the formation particle distribution curve was taken as the representative particle size, to study the effects of different formation-slurry particle size ratios (D15/d85) on slurry permeability. Tables 1 and 2 show the slurry formulations and properties, respectively.

Table 1. Slurry composition.

Material	water	Bentonite	CMC
Quantity	1000 mL	70 g	1.5 g

Table 2. Slurry performance parameters.

Performance	proportion	Viscosity	API filter loss	d85
Parameter	1.06	25.03 s	18 mL/ 30 min	0.074 mm

Natural river sand was sieved into different size fractions using a standard sieve shaker. Experimental formations with different particle size distributions were prepared by mixing the fractions in certain proportions (Figure 65). A total of 4 different formations were prepared in this test (Table 3).

In this test, the same slurry formulation was used to perform pressurized penetration tests in the differently prepared formations. Pore pressure in the formations

Table 3. Strata information.

Num.	ST1	ST2	ST3	ST4
D15	0.225 mm	0.4 mm	0.5 mm	0.7 mm
F-S particle ratio	3.04	5.40	6.80	9.46

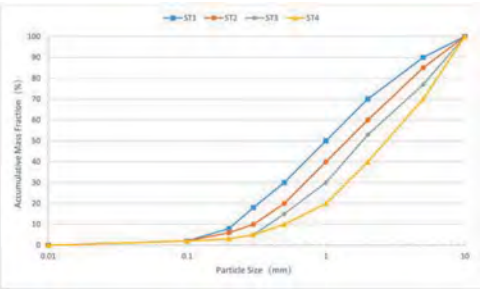

Figure 5. Grading curve.

and filtrate volume were recorded to observe and analyze the effects of different formation-slurry particle size ratios on slurry permeability. The test involved 5 pressure steps, each being 50 kPa, up to a maximum pressure of 250 kPa. At each pressure step, the pressure was held constant for 3 minutes. Figure 6 shows the test results for the four formations.

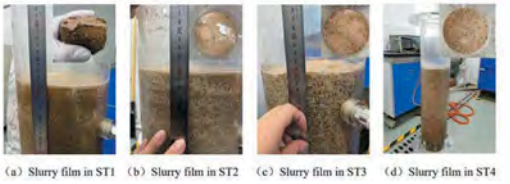

Figure 6. The particle ratio test results.

As shown in Figure 6a, due to the high content of fine particles in the formation, as pressure increased, it was difficult for the slurry particles to penetrate into the formation. There was almost no slurry invasion, and the filtrate was clear. Eventually, a filter cake of about 5 mm formed on the surface, showing a "filter cake" type membrane. As shown in Figure 6b, the slurry invaded the formation incompletely with relatively clear filtrate, forming a "filter cake + infiltration zone "type membrane. A filter cake of about 4 mm formed on the surface. In the ST3 formation, the slurry was not completely lost, but the filtrate was slightly turbid. A filter cake of about 2 mm formed on the surface, but with lots of pores on the surface, resulting in poor sealing capacity. The final membrane was a "filter cake + infiltration zone" type (Figure 6c). In the ST4 formation, the slurry was completely lost, without filter cake building up on the surface. The turbid filtrate indicated an "infiltration zone" only (Figure 6d).

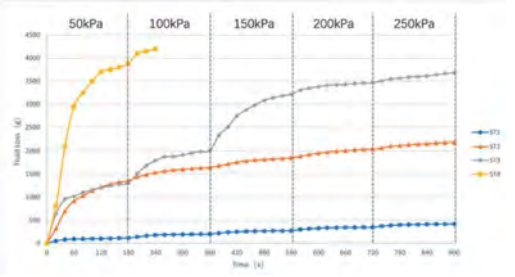

Figure 7. The fluid loss curves.

As shown in Figure 7, as the formation-slurry particle size ratio increased, the filtrate mass also increased. In the ST1 and ST2 formations, the filtrate mass versus pressure curves showed a "step-ladder" shape, and the filtrate mass changed stably at each pressure step. This indicates that the slurry film reached a steady state, and the pressure change had little influence on the slurry film structure. In the ST3 formation, there was a sudden increase in filtrate mass at the third pressure step, indicating slurry film instability. The slurry film structure gradually stabilized after holding the pressure constant for 3 minutes. In the ST4 formation, the slurry started slowly invading the formation even without applied pressure. With the first pressure step, the slurry quickly penetrated into the formation, and was completely lost when pressure reached 100 kPa. However, the filtrate curve showed a stabilizing trend, indicating the slurry particles still played a role in plugging the formation pores.

3.2 *Slurry proportion*

Using the fixed ST2 formation, two groups of slurries with the same viscosity (±2s error) but different proportions were prepared by adjusting the slurry formulations. Penetration tests were conducted to study the effect of slurry proportions on permeability. The slurry formulations and properties are shown in Table 4.

Table 4. Slurry performance parameters of different density.

		Material			Performance		
Num.	Mark	water	S/B	CMC	Prop.	water	S/B
1	S1	1000 mL	80 g	0.5 g	1.07	26.2 s	15.5 mL/ 30min
	S2	1000 mL	120 g	0	1.10	25.0 s	17.5 mL/ 30min
2	S3	1000 mL	80 g	1.1 g	1.07	38.3 s	12.5 mL/ 30min
	S4	1000 mL	150 g	0	1.13	39.4 s	14.5 mL/ 30min

Figure 8. The proportions test results.

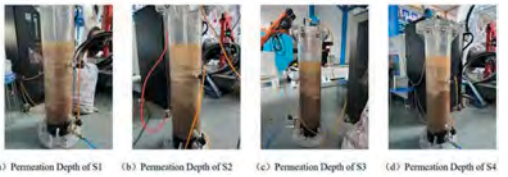

Figure 9. The invasion depth results.

At the end of the test, as shown in Figure 8, the S1, S2, S3 and S4 slurrys formed "filter cake + infiltration zone" type membranes in the formation, with filter cake thicknesses of 2mm, 5mm, 4mm and 8mm, respectively. The comparison between S1 and S2, and between S3 and S4 shows that under the same viscosity, higher slurry proportion leads to thicker and denser filter cake.

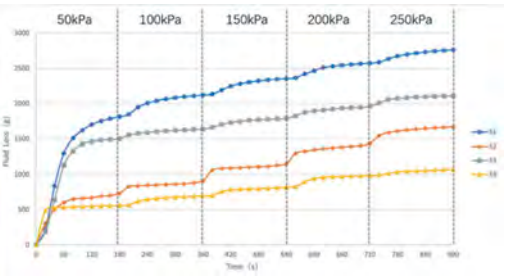

Figure 10. The Fluid Loss Curves.

3.3 *Slurry viscosity*

Using the fixed ST2 formation again, four slurry samples with the same density but different viscosities were prepared by adjusting the CMC content while keeping the degree of hydration constant. Penetration tests were conducted to study the effect of slurry viscosity on slurry film. The slurry formulations and properties are shown in Table 5.

As shown in Figure 11, the S5 was completely lost in the formation without forming a filter cake on the surface. The S6, S7 and S8 slurries formed "filter cake + infiltration zone" type membranes, with filter cake thicknesses of 2mm, 4mm and 7mm, respectively. It shows that under the same density, higher viscosity leads to thicker filter cake and shorter maximum invasion depth (Figure 12).

Table 5. Slurry performance parameters of different viscosity.

		Material			Performance		
Num.	Mark	water	S/B	CMC	Prop.	Vis.	API
1	S5	1000 mL	80 g	0	1.07	18.4 s	22.5 mL/ 30min
2	S6	1000 mL	80 g	0.5 g	1.07	26.2 s	15.5 mL/ 30min
3	S7	100 0mL	80 g	1.1 g	1.07	38.3s s	12.5 mL/ 30min
4	S8	1000 mL	80 g	1.5 g	1.07	48.6 s	10.5 mL/ 30min

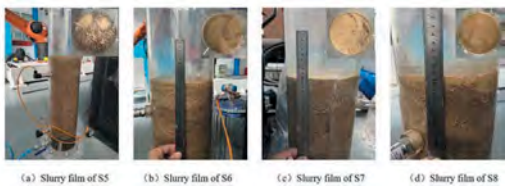

Figure 11. The viscosity test results.

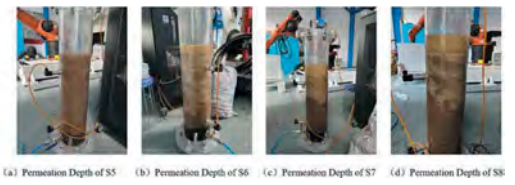

Figure 12. The invasion depth results.

The comparison shows that different viscosities can lead to different membrane morphologies in the same formation (size ratio 5.4). This indicates that the formation-slurry particle size ratio is not the only factor in determining the membrane type. Minimum requirements for slurry density and viscosity must also be met in order to form corresponding membranes within the respective size ratio range.

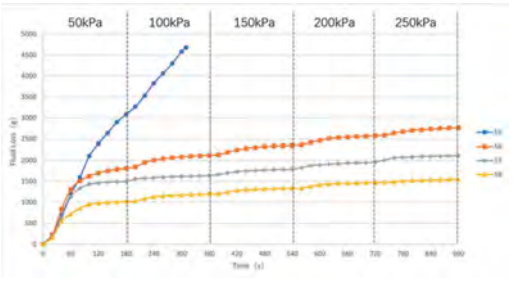

Figure 13. The fluid loss curves.

Figure 13 shows that when slurry density is the same, higher slurry viscosity leads to lower filtrate mass, and the membrane transitions from an unstable state to a stable state. When CMC dissolves in water, it forms a viscous gel-like substance. This gel has swelling capacity to fill and plug pores and fractures in the formation. The gel barrier prevents loss of slurry solids and water into the formation. Meanwhile, CMC can adsorb onto the formation surface, increasing adhesion between the slurry and formation. This effectively prevents slurry invasion into the formation.

3.4 *Comparison of simulation and experimental results*

Slurry penetration tests were conducted to verify the effects of formation-slurry particle size ratio, slurry proportion, and viscosity on the slurry film. The results show that when the size ratio falls around the three ranges for slurry film classification, the test results matched well with the simulation predictions. Higher slurry density and viscosity led to shorter invasion depth and thicker filter cake, consistent with the simulations. The test results agree well with the simulation conclusions.

4 SLURRY PERMEABILITY PREDICTION FUNCTION

During shield tunnelling, as the formation is not fixed and parameters like permeability and representative particle size change constantly, the required slurry properties need to be adjusted accordingly to maintain a stable working face. Therefore, a slurry permeability prediction function is developed, which can predict the slurry film type formed by the current slurry properties based on real-time formation conditions, providing references for selecting tunneling parameters and ensuring safe, intelligent tunneling.

The input of the prediction function considers four factors: formation permeability (A), formation represent particle size D15 (B), slurry density (C), and slurry viscosity (D). The output is the permeability prediction coefficient (O), also called slurry loss coefficient. When $O \leq 0.15$, it is belong to "filter cake" type; when $0.15 < O < 0.85$, it is belong to "filter cake + infiltration zone"; when $O \geq 0.85$, it is belong to "infiltration zone". Higher O means more slurry loss and deeper invasion.

The BP neural network can approximate arbitrary nonlinear functions with strong fitting capabilities. It can adapt to complex data patterns and relationships by learning and adjusting the network weights and biases. Using the experimental results as the dataset for function fitting and testing, the weights of various factors are adjusted through forward and back propagation until the error between predicted and actual values reaches a given criterion, ending the network training.

Table 6 and Figure 14 show examples of the training dataset and BP neural network structure, respectively.

Table 6. Train data set examples.

S/N	Factor A (cm/s)	Factor B(mm)	Factor C	Factor D(s)	Factor E
1	0.052	0.4	1.07	26.3	0.51
2	0.012	0.35	1.06	23.2	0.12
3	0.125	0.8	1.07	38.5	0.92
4	0.072	0.6	1.10	33.2	0.83
5	0.063	0.5	1.06	25.2	0.37
…					

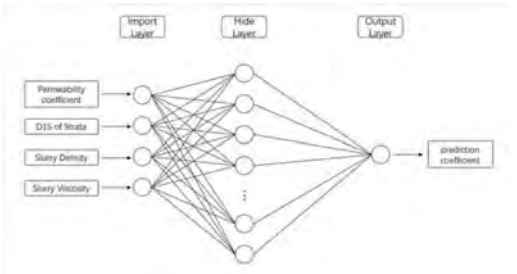

Figure 14. BP neural network structure.

Slurry penetration tests were conducted using core samples from 5 different periods at a construction site, using a fixed slurry formulation. The prediction function was used to calculate predicted values and compare with test results, to verify the applicability of the prediction function.

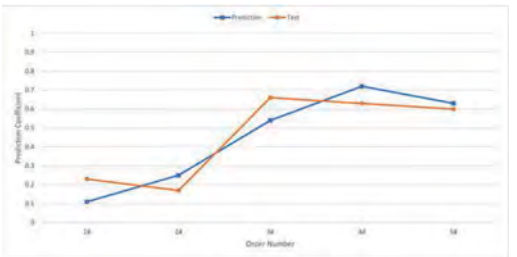

Figure 15. BP neural network structure.

5 CONCLUSIONS

Regarding the problem of slurry film formation in high permeability formations, simulation analysis and experimental verification were used to study the slurry penetration process and types, as well as the effects of different slurry properties on the slurry film. The conclusions are:

(1) The formation-slurry particle size ratio has a significant impact on the film structure. The "filter cake + infiltration zone" type is optimal, providing effective wellbore strengthening while the impermeable filter cake helps maintain stable formation pressure.

(2) Under the same viscosity, higher slurry density means more particles per unit volume to plug the formation, resulting in shorter invasion and thicker filter cake.

(3) Under the same density, higher viscosity means more viscous particles per unit volume, increasing friction between particles and formation pores, resulting in shorter invasion and thicker filter cake.

(4) The size ratio alone does not determine film type. Minimum requirements for density and viscosity must also be met to achieve the expected film type.

(5) Based on experimental data, a neural network prediction function was developed and verified to effectively predict slurry permeability using formation and slurry parameters.

The simulation conclusions are verified by the slurry penetration tests, with excellent agreement. Simulations can provide quick solutions for complex conditions and greatly shorten research cycles. Machine learning algorithms can also be integrated to predict slurry film conditions based on available data, providing reliable support for intelligent tunnelling.

REFERENCES

Fritz, P., 2007. Additives for Slurry Shields in Highly Permeable Ground. Rock Mechanics and Rock Engineering 40(1):81–95.

Min, F. L., Zhu W., Han X. R., 2013. Filter Cake Formation for Slurry Shied Tunneling in Highly Permeable Sand. Tunnelling and Underground Space Technology 38 (3):423–430.

Han X. R., Zhu W., Liu Q. W., et al, 2008. Influence of Slurry Property on Filter-cake Quality on Working Face of Slurry Shield. Rock and Soil Mechanics 29 (s1):288–292.

Lin Y. F., Zhang S. D., Fang Y., et al, 2020. Experimental Study on Filter Cake for Slurry Infiltration in Different Permeability Strata. China Journal of Highway and Transport 33(12):190–199.

Xia W. Y., 2023. Experimental Study on the Composition of Slurry in the Pebble Soil and Slurrystone Intrusive Strata. Science Technology and Engineering 23(5):2100–2109.

Min F. L., Wei D. W., Jiang T., et al, 2014. Experimental Study of Law of Slurry Infiltration in Strata. Rock and Soil Mechanics 35(10): 2801–2806.

Lian F. L., 2020. Experimental Study on Penetration Mechanism of Large Diameter Slurry Shield Excavation Face. Master thesis. Zhengzhou University, Zheng zhou, Henan, China.

Jiang T., Xiap J., Min F. L., 2016. Experimental Study on the Influence of Slurry Properties on the Airtightness of the Filter Cakes of Slurry Shields.Modern Tunneling Technology 53(02): 134–140.

Min F. L., Zhao X. P., Zhu W., et al, 2015. Airtightness of Filter Cakes Formed under Different Slurry Infiltration Modes. Modern Tunnelling Technology 2015,52(4):68–73.

Ni H. J., Xu Y., Li Y., 2013. Numerical Simulation of Filter-Cake Formation Law in Slurry Shield Tunnelling. YELLOW RIVER 35(3):135–137.

Liu F., 2019. Study on the Slurry Performance and Face Stability of SPB Shield Tunnel in Cobble-rich Soil. PhD thesis. Chongqing Jiaotong University, Chongqing, China.

Tunnelling for a Better Life – Yan, Celestino, Thewes & Eberhardt (Eds)
© 2024 The Author(s), ISBN 978-1-032-80042-4
Open Access: www.taylorfrancis.com, CC BY-NC-ND 4.0 license

Passage of TBM EPB under buildings with deep foundations, with physical interference

Hugo Rocha*, Fernando Hirata, Guilherme Robbe, Waldir Giannotti & Thiago Pires
São Paulo Metro Company, São Paulo, Brazil

ABSTRACT: The excavation of tunnels in urban areas often encounters existing building foundations within the excavation sections. Passage through, and potential cutting of, these foundations generally require sophisticated engineering techniques. However, the difficulties are much greater when it comes to mechanized excavation compared to conventional excavations.

For the excavation of 10,764 meters of track tunnels on Line 5 of the São Paulo Metro, three tunnel boring machines were used. Two machines with a diameter of Ø 6.9m excavated 5,021 meters, while one machine with a diameter of Ø 10.5m excavated 5,743 meters, crossing deep foundations of buildings. One with a Ø 6.9m diameter traversed an area where precast piles were expected, near the outlet shaft. The second, with a Ø 10.5m diameter, cut through the foundation piles of two housing condominiums in the region of Chacara Klabin station, also near the outlet region. For all passages, several geotechnical studies, risk analyses, and monitoring using accelerometers in the properties were conducted, which were vacated for this purpose.

The article provides a descriptive summary of the passages beneath the buildings, the conducted geotechnical studies, monitoring, measures adopted, and the obtained results. In all cases, the measures proved to be effective and led to success.

Keywords: Tunnelling, TBM, Subway, EPB, Foundation, Structure Behavior

1 INTRODUCTION

The São Paulo Metro in Brazil commenced its implementation in the 1970s, making it more than 50 years old. Compared to other major Western cities like New York, London, and Paris, whose main lines were established in the early 20th century, São Paulo's metro system is relatively recent. Due to this delayed implementation, there were challenges in acquiring free surface areas and limited urbanized spaces for installation, as well as fewer existing obstacles that interfered less with urban life. São Paulo, during the initial implementation phase, was not fully developed, yet it faced high traffic levels and significant surface occupation.

However, during the implementation of the first Line 1, a substantial part of the line was executed through a long Cut and Cover (C&C) method, covering approximately 10.5 km from the city center to the south (Figure 1). This occurred during a historical period with limited interference from civil society and fewer environmental constraints compared to today, resulting in extensive expropriation requirements. Presently, such an approach is unfeasible due to increased civil society influence, stricter legislation, environmental limitations, and the soaring cost of expropriations. In fact, Cut and Cover construction is now more expensive than their tunnel counterparts. As a result, in the ongoing construction of new lines, the use of C&C is limited to shallow stations, ventilation shafts, and a few work access points.

Tunnel layouts offer more flexibility in development as they are not bound by street layouts and can be constructed deeper. However, they often encounter various surface obstacles and subsurface structures, posing challenges to their construction and development.

The most recent completed and operational line of the São Paulo Metro is Line 5, situated in the southern part of the city. The backbone of this line comprises track tunnels excavated using EPB TBMs, including one section with a TBM of Ø 10.6 m and another section with two TBMs of Ø 6.9 m. Throughout the line's trajectory, several notable interferences with surface and subsurface structures were encountered, necessitating detailed studies to navigate these obstacles effectively without causing significant damage to the structures. Notable interferences include:

*Corresponding author: hcrocha@metrosp.com.br

DOI: 10.1201/9781003495505-278

Figure 1. Cut & Cover in the south of the city - Line 1 - 1970s.(Metrô-SP).

Figure 2. Location of Line 5 - São Paulo Metro.

a) House at Rita Joana de Souza 297 - encountered interference with the TBM of Ø 6.9 m.
b) Residencial Klabin/Residencial Souza Ramos - encountered interference with the TBM of Ø 10.6 m.
c) Platinum Tower Building - encountered interference with the TBM of Ø 10.6 m.

2 CASE STUDIES

2.1 *Residence at Rita Joana de Souza 297*

The house located at Rua Rita Joana de Souza 297 falls directly on the alignment of the tunnel, set to be constructed by a TBM EPB Ø 6.9 m. The tunnel's shallow coverage was necessary due to the proximity of the breakthrough (refer to Figure 3). This three-floor house, approximately 25 years old, includes a lowered garage and is in an average state of conservation, requiring repairs that, however, do not entail any structural risks (see Figure 4). The house is built on a soft surface layer of soil (peat), necessitating deep foundations supported by a series of piles driven to depths of 13-15 meters. These piles consist of alternating layers of sand and clay without encountering a more resistant layer (see Figure 5). The depth of these piles resulted in interference by 2 to 3 meters with the excavation section of the tunnel boring machine tasked with excavating route 1.

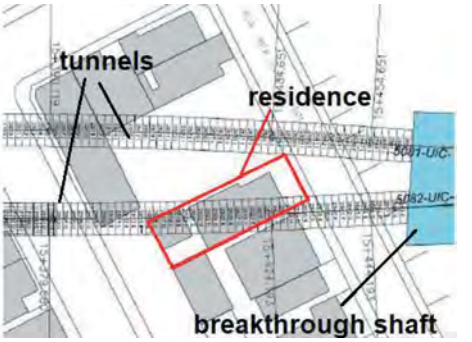

Figure 3. Location plan of the building in relation to the tunnels.

The most viable solution to avoid property demolition involved the partial demolition of the piles to the extent of interference using the discs on the head of the tunnel boring machine. This approach aimed to preserve the property while addressing the interference. Given the existing chronic foundation problems and numerous structural cracks, special care was essential during the TBM installation.

Figure 4. Photo of the house façade.

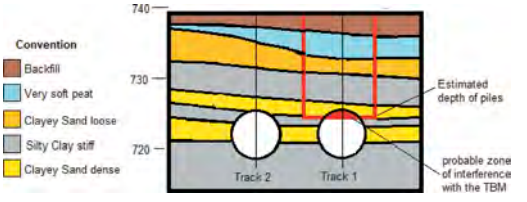

Figure 5. Geological/geotechnical section of the site.

After conducting down-hole seismic geophysical tests and evaluating the potential loads on the foundations, it was determined that the foundations were oversized. It was concluded that localized cutting of part of the pile tips would be viable without causing significant damage. During the passage of the TBM, the structure would be monitored using precision leveling and accelerometers.

Extreme executive care was recommended during the process regarding:

Installation of cutting tools on the perimeter and the 4 arms of the cutting head. Ensuring that the foundation of House 297 would be cut regardless of its position in relation to the excavation section.

Reduction of TBM speed to 15 mm/min at each encounter with House 297's piles. This speed allowed the process to be controlled so that if any problem occurred, it would be detected in time to act on and resolve it.

Implementation of outlined mitigation measures to ensure that the work was prepared for the eventual implementation of contingency measures. This allowed for greater ease and safety in tunnel excavation beneath House 297.

Through this, the speed was obtained by integrating the acceleration graphs and, as mentioned above, the established limit was 40 mm/s. According to DIN 4150-3 standard 'Structural Vibration – Effects of Vibration on Structures,' vibrations exceeding this value would pose risks of damage to the property's structure. During the monitoring conducted, the highest speed value recorded was 0.1 mm/s (Figure 6).

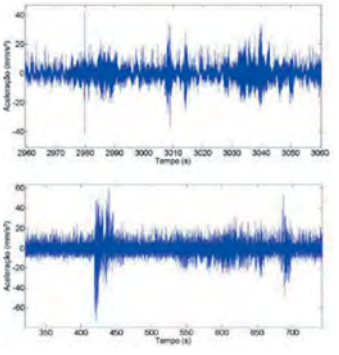

Figure 6. Acceleration (mm/s^2) versus Time (s).

No significant vibrations were observed during the passage of the TBM, nor were there any changes in the TBM control parameters indicating pile cutting. The passage under the building was successfully completed without incident.

2.2 *Residential Klabin/Residential Souza Ramos*

The excavation of the section between Santa Cruz and Chácara Klabin stations, in its final portion, was carried out beneath two single-family house complexes: Residential Souza Ramos and Residential Klabin. Both were built on soft soil areas, and their foundations were supported by precast piles that would be intersected by the TBM.

Figure 7. Overall view of the section with influence curves and risks.

Each set of houses did not have a sufficient amount of available information; however, to make the project feasible, the following activities had to be developed:

• Residential Condominium Souza Ramos.

a) Determination of loads on each pile

• Residential Condominium Klabin.

a) Determination of pile depth: Down-hole tests (Figure 8)

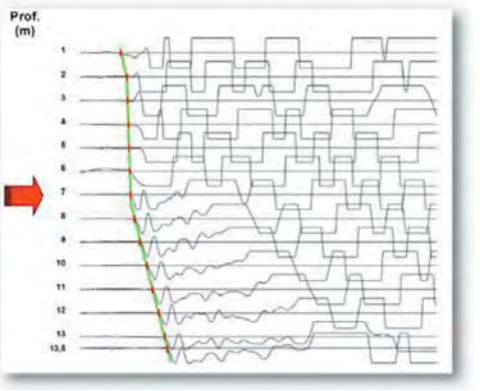

Figure 8. Downhole geophysical profile indicating pile depth at 7 meters.

b) Determination of the load-bearing capacity of each pile: based on local soil (Figure 9)
c) Determination of the quantity of piles.
d) Determination of loads on each pile.

The following potential damage types were identified in the buildings:

- Surface damages (ground floor, connections, boundary walls) due to settlements originating from the tunnel.

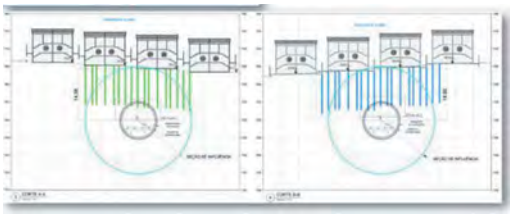

Figure 9. Indication of pile positions.

- Structural damages to the houses, due to settlements originating from the tunnel and due to the loss of pile capacity.

To evaluate the settlements originating from the tunnels, two scenarios were considered with different levels of soil loss, depending on the local massif and coverage (Figure 10).

Based on the zoning of potential effects from the TBM's passage under the properties, a risk map was developed, and a preventive evacuation of selected properties was carried out due to vibration effects and structural risks (Figures 11 and 12).

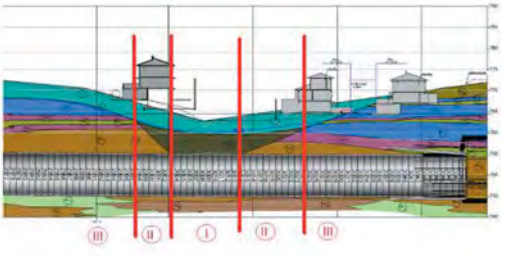

Figure 10. Profile indicating the separation into regions with different levels of risks.

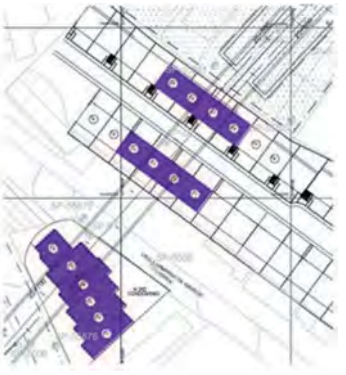

Figure 11. Profile indicating the separation into regions with different levels of risks.

2.3 *Platinum tower case*

Near to the breakthrough of the TBM at Moema station, there was an expectation of proximity to a diaphragm wall and tie rods installed for the

Figure 12. Resulting from structural damages (Scenario 1).

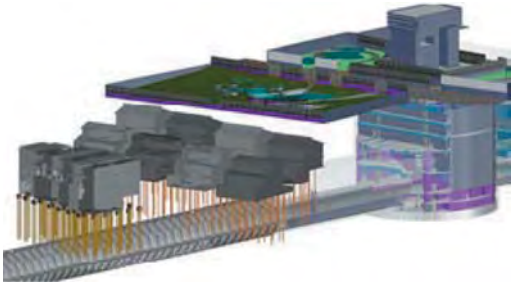

Figure 13. 3D model of the TBM passing beneath the houses and intersecting their foundations.

basements of the 13-story Platinum Tower building, adjacent to the route (Figure 14). This building was constructed after the design of Line 5 but before the passage of the TBM. At that time, an agreement was made with the building's construction company to install the tie rods in a way that ensured no physical interference with the future tunnel. However, the construction company did not guarantee the exact location of the tie rods, which could physically interfere with the TBM, potentially causing serious operational

Figure 14. General view of the location with the building and TBM.

problems, especially at the cutting head and screw conveyor (Figure 15).

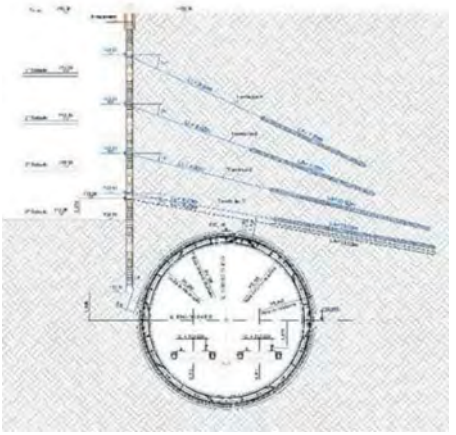

Figure 15. Schematic section of the location.

The passage of the TBM alongside the building would pose a high risk under these conditions. To mitigate this risk, in addition to all the instrumentation of the building and diaphragm walls, the tie rods were extracted by over-drilling and removal of the tie rods' strands (Figure 16) from the building's garage, thus minimizing the risk. The passage of the tunnel boring machine occurred with very low impact on the building and no interception of tie rods by the TBM (Figure 17).

Figure 16. Removal of tie rods' strands.

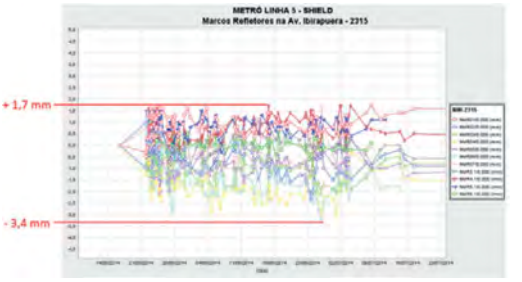

Figure 17. Deformations observed in the building structure.

3 CONCLUSIONS

The passage of tunnel boring machines in densely urbanized areas, although theoretically causing fewer surface deformations than conventional methods, requires careful consideration of existing interferences. The possibility of intervention in the excavation face is much more restricted, and the contact of the equipment with these buried structures can cause serious damage to both the structures and the machine. The prior determination of these interferences and their treatment with adequate risk management greatly minimizes their effects on both the surroundings and the equipment.

ACKNOWLEDGMENTS

The authors would like to thank the São Paulo Metro Company for the opportunity to conduct this study and for granting permission for its publication.

REFERENCES

CJC – Engenharia - TBM interference with the foundations of houses in the Souza Ramos residential condominium and Klabin residential condominium - Metro Internal Report – 2015.

Della Vale, N., Tunnelconsult - Study on the issue related to the interference of deep foundation piles of property 297 on track 1 in the vicinity of the Bandeirantes shaft - Metro-SP Internal Report – 2015.

Giannotti, W. - Mechanized Tunnels: Construction Aspects - Tunnel Course, Metro - UNiMETRO – 2016.

IEME Brasil - Vibration monitoring in a building during the passage of the TBM - Metro-SP Internal Report – 2015.

Tunnelling for a Better Life – Yan, Celestino, Thewes & Eberhardt (Eds)
© 2024 The Author(s), ISBN 978-1-032-80042-4
Open Access: www.taylorfrancis.com, CC BY-NC-ND 4.0 license

TBM performance in rock conditions of water diversion tunnel constructions (Mae Ngad-Mae Kuang tunnel) in Chiang Mai Province, Thailand

Kaisorn Sarapagdee*, Anchalee Laddakul & Thanaphon Saelao
Geotech Pillar Co., Ltd., Bangkok, Thailand
Panya Consultants Co., Ltd., Bangkok, Thailand

ABSTRACT: The knowledge of rock type and technology using for tunnel opening is essential for any mechanical excavation. The double shield TBM (DS TBM) was selected to excavate the complex geological structures for the water diversion tunnel construction projects (Mae Ngad-Mae Kuang Tunnel) in Chiangmai Province, Northern Thailand. The TBM tunneling contains several factors to control in the TBM excavation and the tunnel construction, the overall machine performance and factors controlling the TBM performance are important to summarize in detail. Furthermore, the impact of unfavourable ground conditions affected the tunnel construction times such as the bad rock conditions, the fault zones, the high pressure of groundwater ingress, and unplanned downtimes. Machine utilization and boring cycle are the most important factor illustrating the overall TBM performance related to construction times. The major incidents during TBM excavation need to be comprehended as the key parameter indicating the machine performance in the problematic zones. In addition, this study summarized the tunneling time consumption and evaluated the machine utilization and boring cycle time of the DS TBM. The consistency of TBM boring was an important key to increasing productivity, while the standstills must be reduced as much as possible. The DS TBM have proved that the field penetration index (FPI) can be indicated the problematic zone and the difficult ground conditions. In conclusion, the FPI could be used to warn the problem zones in adverse ground conditions and the complex ground conditions zones. Additionally, the overall machine performance of the TBM, the machine utilization, and the TBM boring cycle are the essential factors considering an impact on the construction times.

Keywords: TBM Performance, Difficult Ground, Rock Conditions, FPI

1 INTRODUCTION

The Mae Ngad-Mae Kuang (MNMK) tunnel project was designed by jointly attended members of Royal Irrigation Department (RID), Panya Consultants Co., Ltd. (PY), and 3G Gruppe Geotechnik Graz ZT GmbH, according to the solely selected option for the construction of each tunnel project, there is the double shield TBM (DS TBM) accounted for the geological, geotechnical, and hydrological uncertainties and associated costs as well as a risk analysis. Hence, the identification of the actual rock mass type (actual RMT) and the actual behaviour (actual BT) can be determined or reviewed during the construction to detect these variable ground conditions as much as possible. Consequently, the information in the detail design stage can be clarified and reappraised the adverse geological situations during the implementation, as well as the relevance between the ground conditions and the TBM performance can also be explained.

Overall, TBM performance needs to be predicted during the design stages to appropriately determine the right machine operation and a plan for tunnel construction. Obviously, the actual TBM performance is significantly different from the predicted TBM performance because some unknown factors cannot be evaluated in the predictive models, which some TBM performance parameters are exaggerated because of a wrong prediction of geological conditions. Hence, major factors affecting the TBM performance need to be summarized and concluded. Likewise, a deep understanding of the background in the TBM tunneling must be clear to recap the TBM performance, including the ground conditions, the TBM selection, the TBM tunnel designs, the cutter

*Corresponding author: Kaisorn_s@panyaconsult.co.th

DOI: 10.1201/9781003495505-279

head designs, the TBM performance parameters, construction operations of the DS TBM, major incidences in the projects, and so on. Following a summary of overall TBM performance, the TBM database need also be improved, and solid comprehension of the factors affecting the overall TBM operation must be clarified.

Due to the lack of subsurface information of the geological and geotechnical investigations in the detail design stage, the hard rock DS TBM boring processes during the operation can be predicated the actual ground condition. As uncertainties of the complex geology affected mainly the time of tunnel construction, the key issues during TBM excavation should be realized factors affecting the productivity of TBM tunneling.

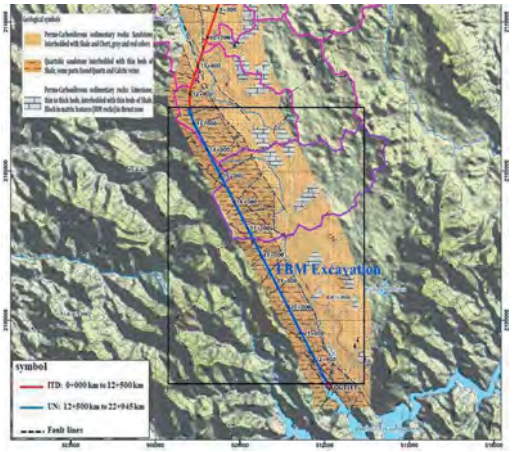

Figure 1. The geological mapping along the MNMK tunnel alignment in scale 1:10,000.

2 BACKGROUND

2.1 *Geological and geotechnical models*

2.1.1 *Geological history*

The geological models of the MNMK tunnel were delineated in the design stage. The geological uncertainties are inevitable to eliminate as the costs of geological investigation are limited to provide clearly descriptive information of the rock formations. However, the geological interpretation of geologists is helpful to indicate the ground conditions in the study area to provide general information for the engineering design. The complexity of the geology along the tunnel alignments is a tough task to accurately interpret the geological models because the rocks/soils are not uniform. Which, the tunneling projects are located on the complex rock formations in the Inthanon zone where the Palaeozoic and Mesozoic rocks were detached overlying the crystalline complex rocks. Moreover, the orogenic of the Triassic – Jurassic Granitoids is also observed in the study area.

2.1.2 *Geological models*

The geological conditions were proposed by Schubert et al. (2005a) in the design phases of the MNMK tunnel project based on the publication in the Geology of Thailand (Ridd et al., 2011). The Thung Song Group is the oldest rock group in late Ordovician – Silurian in the study area, which the formation consists mainly of Limestone and Shale. The upper parts of rock formations are covered by the Lower – Upper Paleozoic, Tertiary, and Quaternary sedimentary rocks. The Permo – Triassic Volcanic rocks and Triassic Granitoid intrusion are related to the main granite belts.

The geological mapping of the MNMK tunnel project can be shown in Figure 1 as the previous studies for the review of geological models of the MNMK by Sutiwanich et al. (2006) can also be shown in Figure 2.

2.1.3 *Rock mass type (ground type)*

The guideline for the determination of ground type was proposed by the Austrian Guideline for Geomechanical Design of Underground Structures (Austrian Society for Geomechanics, 2010) used in the tunnel projects. The outline information was gained by the geological investigation (e.g., the field investigation, core drilling, and laboratory testing) which the key parameters will be used to define the rock mass type based on similar geotechnical properties. Therefore, the geotechnically relevant parameters (Table 1) are used to determine the ground types. The geotechnical parameters are basically included lithology, the thickness of rock formations, joint/fracture conditions, rock mass/intact rock strength, degree of weathering, and so forth.

The selection of parameters depends on the project phase and a certain extent on the possible construction methods. For this project, 18 rock mass types (Table 2) have been determined using the criteria listed as the classes used in each criterion are shown in brackets.

− Rock types such as Marble, Limestone, Quartzite, Sandstone, Siltstone, Plutonic rock, Volcanic rocks, and fault rocks distinguished according to the source material, and alluvial deposits

− Bedding thickness (>60 cm, 60 – 20 cm, and 2 – 20 cm)

− Joint persistence (low and high)

− Fracturing (low and high)

− Joint roughness (rough and smooth)

− Karstification (none, small cavities, and large cavities)

− Intact rock strength (< 10 MPa, 10 – 50 MPa, 50 – 150 MPa, and 150 –250 MPa)

2.1.4 *Rock mass behavior (ground behavior)*

The ground behaviors are predicted by the influencing factors for each section of the tunnel. The

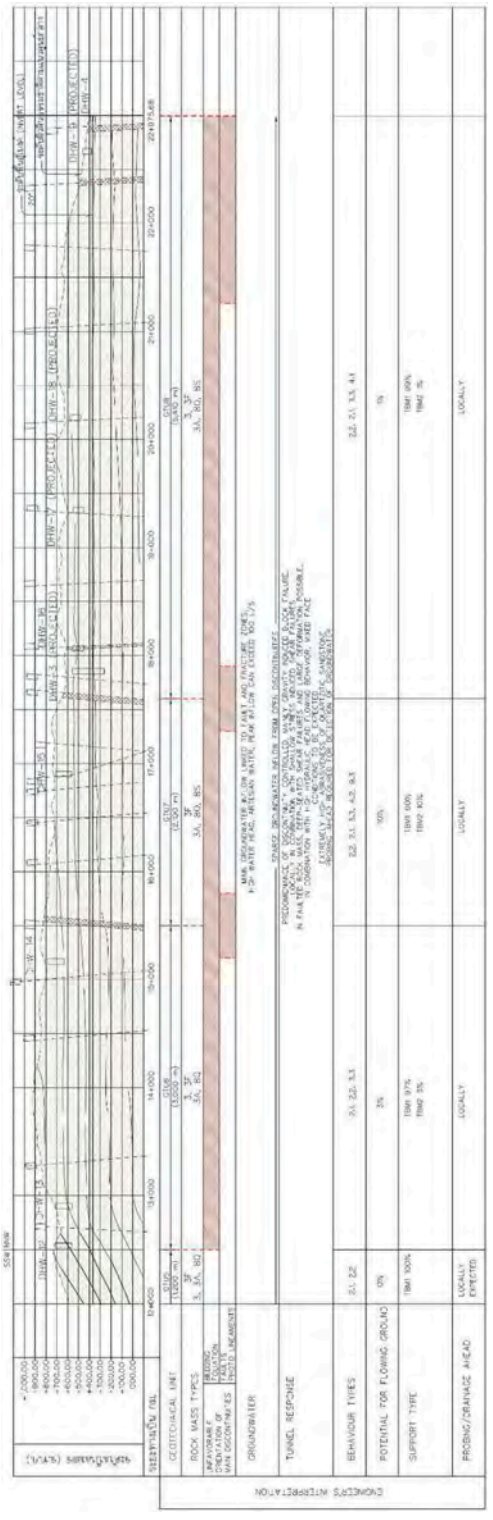

Figure 2. The geological model of the MNMK tunnel (Sutiwanich et al., 2006).

Table 1. Example of selected key parameters for different general rock types (Austrian society for geomechanics, 2010).

BASIC ROCK TYPES		KEY PARAMETERS: INTACT ROCK PROPERTIES — Mineral Composition	Clay Mineral Composition (qualitative)	Clay Mineral Composition (quantitative)	Cementation	Grain Size	Texture	Ratio Matrix/Fragments	Porosity	Alteration/Weathering	Solubility Phenomena	Swelling Properties	Strength Properties	Anisotropy	KEY PARAMETERS: DISCONTINUITIES — Block Shape	Block Size	Persistence	Aperture	Shear Strength/Roughness	Infilling
ROCKS	Plutonic Rocks	■				■	■			□			■		■	■		■	■	
	Volcanic Rocks (massive)	□					□		■	■			■		■	■				■
	Volcano-Clastic Rocks	□	□			□		■	■	■			□							
	Coarse-grained Clastic Rocks (massive)	□		□		■	□	■		□			■		□	□	□	■		
	Fine-grained Clastic Rocks (massive)		■	■		■					□		□		□					
	Coarse-grained Clastic Rocks (bedded)	□		□	■	■		■	□	□		■	□	■					■	
	Fine-grained Clastic Rocks (bedded)		■	■		■				□		□		■						
	Carbonatic Rocks (massive)	■											■		□	■	□	■	□	□
	Carbonatic Rocks (bedded)	■										■	■		■					
	Sulfatic Rocks	■									■	■	□							
	Metamorphic Rocks (massive)	■			■	■				□			■		■	■	□	■		
	Metamorphic Rocks (bedded)	■			■	■				□			■	■	■	■	□	■		
	Fault Rocks	□	■	■	■			■				■	■						■	■
SOILS	Coarse-grained Soils (gravel)					■		■	□	□			■							
	Coarse-grained Soils (sand)					■		□	□				■							
	Coarse-grained Soil Mixtures	□		■		■		■	□			□	■							
	Fine-grained Soils (silt)					■			□				■							
	Fine-grained Soils (clay)	□		■		■			□			■	■							

Legend ■ Significant Parameter □ Less important Parameter

Table 2. Rock mass type and classification parameters in the detail design stages of the tunnel projects (Schubert et al., 2005a).

RMT	rock type	bedding thickness >60cm	60-20 cm	20-2cm	fracturing low	fracturing high	joint persistence high	joint persistence low	joint roughness v. rough	joint roughness rough	joint roughness smooth	karstification none	karstification small cav.	karstification large cav.	intact rock strength <10MPa	intact rock strength 10-50MPa	intact rock strength 50-250MPa	intact rock strength 150-250MPa
RMT 1	limestone (marble)	X			X		X			X			X				X	
RMT 1f	limestone (marble) fractured	X				X	X			X				X			X	
RMT 2	limestone		X		X		X			X				X			X	
RMT 2f	limestone fractured	X				X	X			X				X			X	
RMT 3	quartzitic sandstone		X		X		X				X	X						X
RMT 3a	qu.sandst. / siltstone - shale intercallations		X			X	X			X	X	X				X		
RMT 3f	qu. sandstone fractured			X		X	X				X	X				X		
RMT 4	sandstone / siltstone - shale intercallations		X	X	X			X			X	X			X	X		
RMT 4f	sandstone / siltstone -shale intercal. fractured			X		X		X			X	X			X			
RMT 5	siltstone - shale			X	X			X			X	X			X			
RMT 5f	siltstone - shale fractured			X		X		X			X	X			X			
RMT 6	plutonic rocks	X			X		X			X		X					X	
RMT 6f	plutonic rocks fractured	X				X	X			X		X					X	
RMT 7	volcanic rocks	X			X		X			X		X					X	
RMT 7f	volcanic rocks fractured	X				X	X			X		X					X	
RMT 8q	fault rocks / sandstone origin	n.a.	n.a.	n.a.	n.a.	n.a.	n.a.	n.a.	n.a.	n.a.	n.a.	n.a.	n.a.	n.a.		X		
RMT 8s	fault rocks / siltstone - shale origin	n.a.	n.a.	n.a.	n.a.	n.a.	n.a.	n.a.	n.a.	n.a.	n.a.	n.a.	n.a.	n.a.		X		
RMT 9	alluvial deposits	n.a.	n.a.	n.a.	n.a.	n.a.	n.a.	n.a.	n.a.	n.a.	n.a.	n.a.	n.a.	n.a.	n.a.	n.a.	n.a.	n.a.

factors influencing the rock mass behaviors are essentially tunnel size, primary stresses around the opening, water conditions, and the relative orientation of discontinuities in the rock mass to the tunnel axis. The ground behaviors are estimated as the ground reaction to the excavation under unsupported conditions (i.e., without consideration of supports) or other construction measures.

After estimation of the rock mass behaviors for each tunnel section, the behavior type (BT) can be grouped the single rock mass behavior into the basic categories as shown in Table 3. Methods for determining rock mass behaviors can be empirical or analytical, using closed-form solutions block analyses or numerical simulations as appropriate. The excavation method and the support systems are then designed based on the behavior types as a ground response in a way to meet the requirements, like constructability, stability, serviceability, and economic aspects.

Table 3. General categories of behavior types (Schubert et al., 2005a).

	Behavior Type (BT)	Description of potential failure modes/mechanisms during excavation of the unsupported rock mass
1	Stable	Stable rock mass with the potential of small local gravity induced falling or sliding of blocks
2	Stable with the potential of discontinuity controlled block fall	Deep reaching, discontinuity controlled, gravity induced falling and sliding of blocks, occasional local shear failure
3	Shallow shear failure	Shallow stress induced shear failures in combination with discontinuity and gravity controlled failure of the rock mass.
4	Deep seated shear failure	Deep seated stress induced shear failures and large deformation
5	Rock burst	Sudden and violent failure of the rock mass, caused by highly stressed brittle rocks and the rapid release of accumulated strain energy
6	Buckling failure	Buckling of rocks with a narrowly spaced discontinuity set, frequently associated with shear failure
7	Shear failure under low confining pressure	Potential for excessive overbreak and progressive shear failure with the development chimney type failure, caused mainly by a deficiency of side pressure
8	Ravelling ground	Flow of cohesion-less dry or moist, intensely fractured rocks or soil
9	Flowing ground	Flow of intensely fractured rocks or soil with high water content
10	Swelling	Time dependent volume increase of the rock mass caused by physical-chemical reaction of rock and water in combination with stress relief, leading to inward movement of the tunnel perimeter
11	Heterogeneous rock mass with frequently changing deformation characteristics	Rapid variations of stresses and deformations, caused by block-in-matrix rock situation of a tectonic melange (brittle fault zone)

2.2 *Double shield TBM (DS TBM)*

The MNMK tunnel project was initially studied by 3G Gruppe Geotechnik Graz ZT GmbH in the detail design stage in 2005 in which the first hard rock TBM excavation was recommended for excavation around 10+476 km from the outlet at the Mae Kuang reservoir to 12+500 km along the tunnel alignment (Figure 1). The DS TBM were chosen as the best choice to excavate through some parts of the long water diversion tunnel projects in the complexity of a geological setting in Northern Thailand. According to the geological, geotechnical, hydrological uncertainties, and associated costs, a risk analysis was performed to evaluate the options for the tunnel constructions in the tender design stage (Schubert et al., 2005b). However, the DS TBM must properly be designed the special measures when the TBMs are going to encounter such as the squeezing ground phenomena, the rock bursting, the swelling or slacking ground, the blocky ground or jointed rock, the clay clogging, the effects of high strength rocks and high abrasion, and significant water inflows, etc.

2.3 *TBM Performance prediction models*

The MNMK tunnel project is used the NTNU model, which has been developed by the Norwegian University of Science and Technology since 1976 using the statistics based on field studies of 35 tunnel jobs with more than 250 km in the database of tunnels documented in detail (Bruland, 2000c). The philosophy of the NTNU model is to predict the reliable TBM performance combining relevant rock properties and machine parameters (Mascias, 2016). Furthermore, the factors influencing the TBM performance as shown in Table 4 can also be evaluated by the RMi parameters to characterize rock masses for TBMs in which the rock material, the jointing, and TBMs are considered as the main factors affecting the TBM performance, as shown in Figure 3 (Palmström, 1995).

Table 4. Hard rock mass and machine factors influencing TBM performance (Palmström, 1995).

Rock mass factors	Machine factors
- Rock mass jointing (k_j) ° type and continuity ° frequency ° orientation - Rock porosity - Rock drillability (DRI) - Rock hardness/abrasiveness - Stress in rock	- Thrust per cutter (M) - Cutter edge bluntness (b_j) - Cutter spacing (A) - Cutter diameter (d) - Torque capacity and RPM - The machine's capacity for handling large chips or blocks - General solidity against blows and vibrations - Cutterhead curvature and diameter (D) - Backup equipment

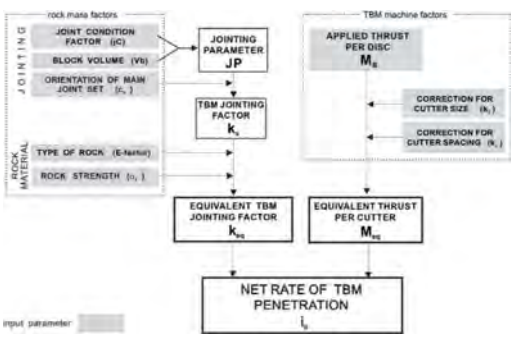

Figure 3. Layout of a method to predict TBM penetration using RMi parameters based on the NTH mode (Palmström, 1995).

2.4 *TBM performance analysis*

The TBM performance and an impact on the time of the tunnel construction, there are various details of actual TBM operating in the tunnel projects. The time of construction is controlled by the overall machine performance, which this term can be illustrated through machine hours spent to excavate the length of the tunnel, basic machine operation parameters (e.g., applied thrust, torque, and cutterhead RPM, etc.). The overall performance is also expressed as the gross advance rate of the machine and illustrated in terms of tunneling time consumption (Figure 4).

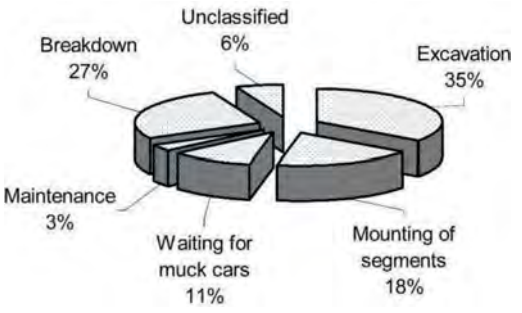

Figure 4. Summary of machine performance (Bilgin et al., 2005).

However, machine utilization is very difficult to predict in actual TBM tunneling. There are some of the most important concepts needed to review for the evaluation with the TBM utilization including the rock mass boreability, the boring cycle time of the TBM tunneling, and cutter consumption. Basically, the machine utilization can be calculated as the (1) (Moosazadeh et al., 2018).

$$U(\%) = \frac{Boring\ Time}{Total\ Time} = \frac{T_b}{T_i} \qquad (1)$$

Where the boring time (T_b) is the net boring time, and the total time ($\sum T_i$) is the summation of the duration of the main activities and TBM downtimes.

The utilization factors (i.e., classification of the main activities and the downtimes) can be varied depending on the prediction models to estimate the machine utilization in percentages of total tunneling time. The utilization factors in the real construction of TBM tunneling are collected in performance records based on the objectivity of the shift log data.

3 DATA COLLECTION

3.1 *Rock mass parameters*

In the geotechnical design, the ground conditions were interpreted in the design stages to distribute the expected rock mass types (RMT), rock mass behaviors type (BT), and groundwater ingress to consider the support types and the additional measures along the tunnels. Hence, the TBM excavation relies on the interaction between the machines and the rock mass behaviors elaborated in the geotechnical sections along the tunnels. Due to closed face tunneling machines for handling wide ranges of ground conditions, the DS TBM are quite difficult to collect the data for rock mass characteristics in front of the cutterhead or behind the shields. Generally, the TBM tunneling in the MNMK tunnel used muck logging to assess the RMT and the BT during the TBM excavation. The parameters in muck logging forms include as follows.

− Rock mass types (RMT) depend on the geological information in the tender documents of tunnel.

− Weathering conditions are used to describe the weathering degree of rock chips.

− Roughness conditions are used to illustrate the characteristics of surfaces of fractures/joints.

− Rock Strength is one of the most useful parameters used to clarify the stability of the tunnel and indicate weakness zones. The strength tests in the field can be observed by using empirical methods such as geological hammers smashing, point load testing, and Schmidt hammer testing.

− Chip sizes are probably ambiguous to interpret the rock mass characteristics. The percentages of each size for muck logging are implied to the frequency/spacing of joint sets. The appropriate chip sizes should be in medium size, whereas the large size and the small size are related to the blocky ground and the faulted rocks, respectively.

− The shape of muck chips is generally used to empirically distinguish whether existing fractures or mechanical fractures.

− Joint spacing is difficult to interpret in the field because the DS TBM. Normally, the geologist can roughly estimate the spacing by their experiences in which the open slots behind the tail shield for invert segments may be used to calibrate or clarify the joint spacing in the back-mapping.

− Water Inflows are also one of the most important factors affecting the TBM performance in every tunnel project.

− The coarseness index (CI) was defined as the sum of the cumulative weight percentages retained on each sieve used, which compares a measure of the size and distribution of the produced debris, as shown in Figure 5.

3.2 *Machine performance and records*

TBM operational parameters are recorded by the onboard acquisition system gathering signals in the machine control panel. The machine operational parameters are varied by the TBM operation in the TBM excavation encountering different ground conditions. To compute the TBM performance parameters, the operational parameters, and some

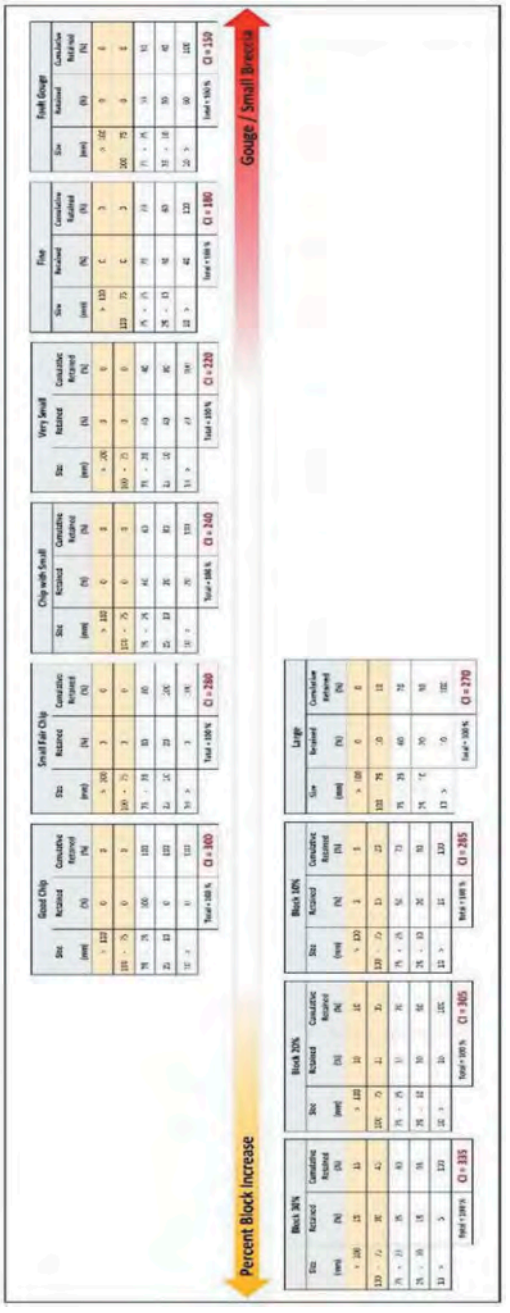

Figure 5. The coarseness index (CI) classification chart.

parameters of the TBM configurations were used to calculate in the analysis. These data sets can be used to estimate other important factors considered while describing basic TBM performance parameters.

The main activities and sub-activities of the tunneling performance were collected and recorded in the shift logs. The records can be used for back-analyses of machine performance.

3.3 *Time Consumption and majors issues*

In TBM tunneling, the additional time consumption is difficult to estimate as used to speculate the machine utilization in tunnel projects. The overall machine performance was reduced the efficiency since the major issues during the DS TBM operation resulted from several factors as follows.

− Downtime TBM: The downtime for TBM systems and system elements can be categorized as (1) Machine Breakdown (2) Lining systems (3) Muck Removal Systems (4) Utilities (5) Surveys (6) Personnel and (7) Miscellaneous.

− Unexpected Rock Mass Conditions: Due to the complexity of rock masses, unpredictable geological conditions may affect TBM performance, which are an impact on the time of the construction.

− TBM Stopped for Stabilizing Zones of Difficult Ground Conditions: About difficult ground conditions, the DS TBM need to be stopped to treat the problematic zones of adverse ground conditions such as squeezing ground, extremely high groundwater ingress, karst filling with sand/water, and so on.

3.4 *TBM performance parameters*

Basic machine performance parameters were used to summarize the field performance study approaches compared with the engineering back-mapping as follows.

− Penetration rate (PR) is defined as the advance or the excavated distance divided by the operating time during a continuous excavation phase (i.e., the penetration rate is not considered the time required for installing rock supports, maintenance, etc.).

− Machine Utilization (U) is defined as the ratio/percentage between net boring time and total shift time (i.e., the TBM utilization expresses the amount of time in which the machine has been effectively used for boring). The utilization factors (UF) can be assessed and evaluated by using the main activities of the TBM operation based on data from the shift logs/performance records. The UF can be subdivided into more specific activities and evaluated for given time periods (e.g., shift, day, week, or month) or for given tunnel sections (e.g., tunnel length or geological conditions).

− Advance rate (AR) is defined as the TBM advance speed for a period computed by considering the TBM delays due to rock support, maintenance, and so on.

− Field penetration index (FPI) is calculated as the ratio between average cutter load and attained penetration per cutterhead revolution. The FPI can also be defined as FPI_{blocky} as the TBM field performance to the rock mass conditions in the blocky ground. To compare possibly, the FPI is calculated in (2).

$$FPI - \frac{D}{c}\ \frac{F_n}{p} \tag{2}$$

Where D is the diameter of the cutterhead and the total number of cutter discs on the cutterhead.

4 RESULTS

4.1 *Summary of the MNMK TBM*

The first hard rock TBM tunneling in Thailand was successfully constructed in early 2021 with the total length 10.45 km. The DS TBM was selected to operate in the Carboniferous sedimentary rocks where there are several interruptions to deal with the difficult ground conditions such as high-water ingress, blocky ground, severe inrush materials, and squeezing ground during TBM excavation.

The TBM is also located in the thrust fault zone, where the minor systematic faults crossing the alignment were interpreted 20 lines in the geological models. During the TBM excavation, the major issues from high groundwater ingress, geological hazards, and mechanical breakdowns that reduce the productivity of the TBM excavation.

The overall machine performance of the TBM was mainly influenced by excessive groundwater ingress and the major incidences caused by geological conditions.

The total number of days for 10.45 km was 1,350 days, where the total production was 54%, and the total no production was 46%. The maximum average machine utilization was 66.7% in the period of the best performance, whereas the mean was just 21.2% compared to the whole period of TBM excavation. The top gross advance rate was 203.4 m/week, while the mean was 48.6 m/week of the total tunnel length. The Figure 6 shows the tunneling time consumption that the most time-consuming is standstill TBM around 24.9%, which the DS TBM had waited for excavation. The time needed to overcome the major incidences of the TBM was 17.1%, of which the times of segments fallen were spent more time to recover the machine performance and a large amount of groundwater ingress. On the other hand, the TBM downtimes are defined as the time during the machine is unavailable for use, which the major

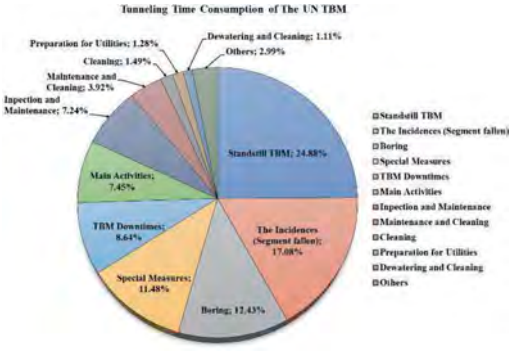

Figure 6. The tunneling time consumption of the MNMK TBM.

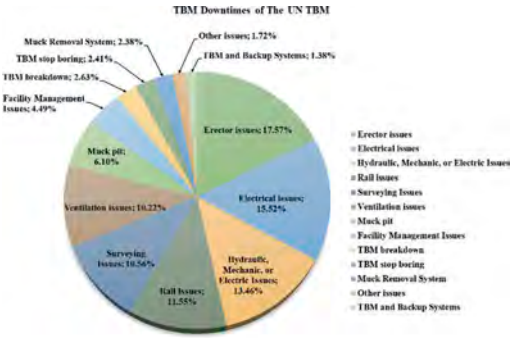

Figure 7. The TBM downtimes of the MNMK TBM.

influences of TBM downtimes consisted of segment erector issues 17.6%, electrical issues 15.5%, hydraulic/mechanic/electric system issues 13.5%, rail issues 11.6%, and so on, as shown in Figure 7.

During TBM excavation in the fault materials such as RMT 8Q and RMT 8S, the discharged fractured rocks or completely weathered rocks were flowed into the TBM with the high-water ingress.

4.2 *Overall machine performance*

The TBM was launched from the outlet of the Mae Kuang reservoir to the upper section. In the first period, the TBM learning curve had taken for almost 29 weeks, where the tunnel chainages were 22 +947 km to 21+593 km or around 1.35 km, as the average advance rate was 46.97 m/week. The top performance during this period was reached 134.38 m/week, in which the achieved machine utilization was gone to the maximum of 79.17% for the available shift time, and the mean was 34.67% for the learning curve. The Figure 8 and Figure 9 are shown the distribution of the gross advance rate and the net advance rate of the machine utilization was explicitly illustrated the variation of TBM productivities.

4.3 *Summary of the geological conditions*

The actual rock mass types were different from the expected rock mass types, as summarized in Figure 10. The Quartzitic-Sandstone fractured (RMT 3F) was mainly found in the Carboniferous sedimentary rock formation as 43.57% along the tunnel. The Sandstone/Siltstone – Shale intercalation fractured (RMT 4F) was 32.29%, while the Siltstone – Shale fractured (RMT 5F) was 0.44% of the total actual rock mass types. However, the faulted rock masses including RMT 8Q and RMT 8S were found almost 24%, which was completely different from the expected ground types.

The groundwater conditions were slightly increased to more than 50 L/sec. The cumulative amount of water in the TBM exceeded the limit to

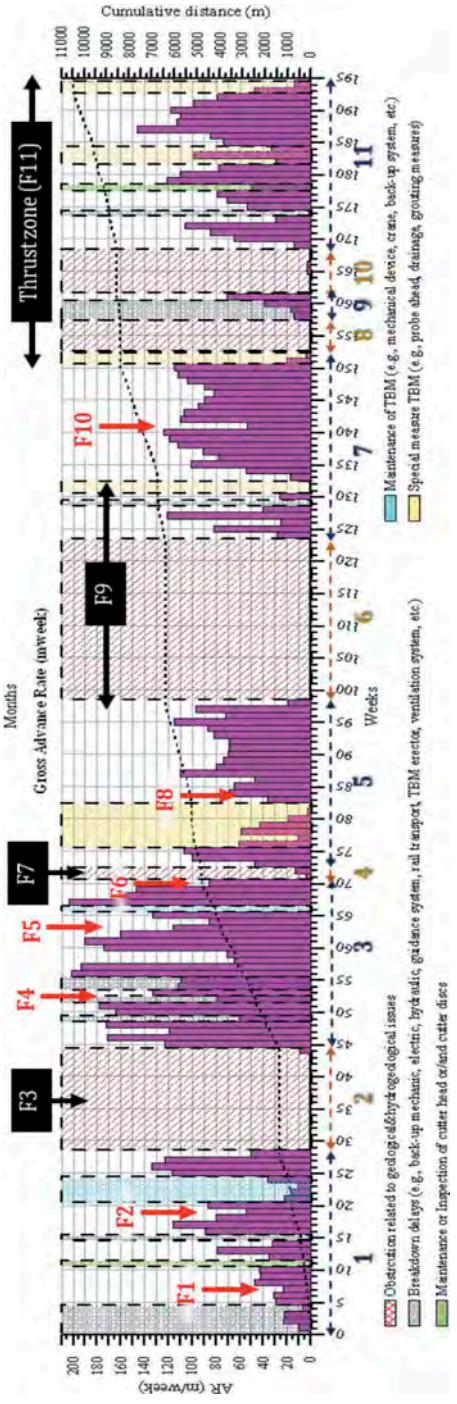

Figure 8. The summary of the overall machine performance of the MNMK TBM (F or black background is the fault zones and the double line arrows with the labelled numbers are the periods of machine performance used in the analysis.).

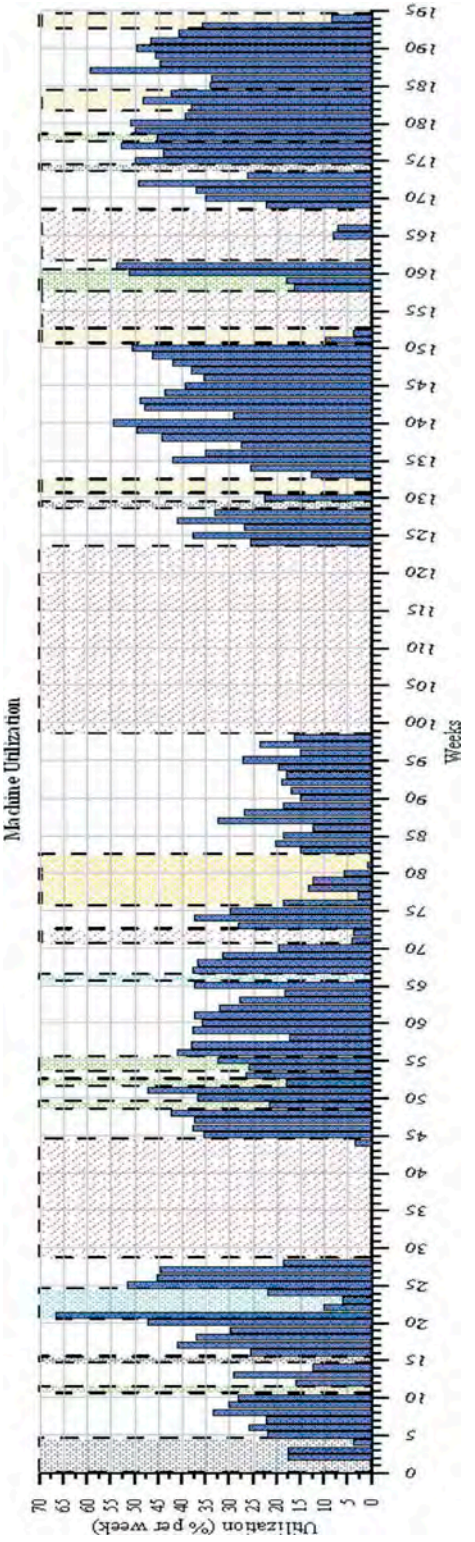

Figure 9. The summary of the gross advance rate compared to the machine utilization and the TBM downtimes.

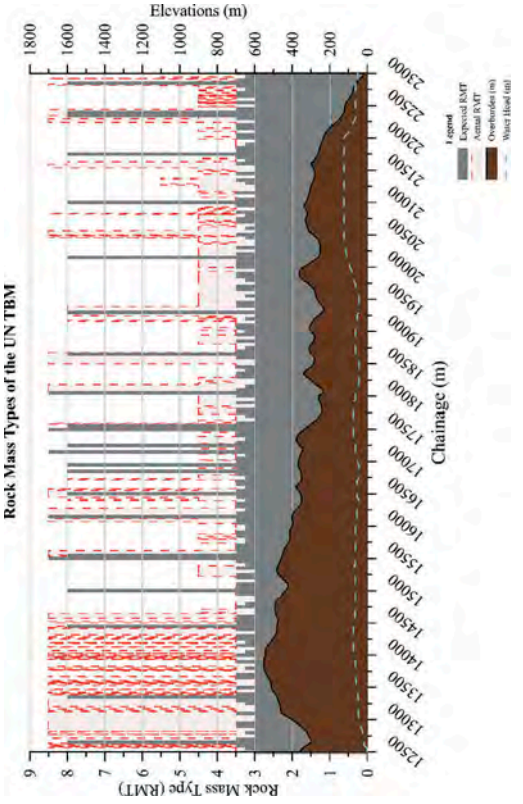

Figure 10. The actual rock mass types encountered along the TBM section.

Figure 11. The summary of water ingress in the TBM tunnel.

more than 320 L/sec, as shown in Figure 11. According to the design, the extremely high-water ingress was excessive 100 L/sec, where the TBM should be stopped boring to treat the ground or block the water ingress.

4.4 *Collapsed segments*

4.4.1 *At chainage 16+563 km*

One of the major incidences is that the precast lining concretes, including No. 4559 to 4561 were collapsed in chainage 16+563 to 16+561 in the 6th period (Figure 12). At chainage 16 +582 km the rock chips were found as the faulted rock mass (RMT 8S) and the 5 L/sec of the groundwater ingress. The faulted meta-sandstone formation was grey color, moderately weathered, highly fractured, and iron oxides covering a fracture surface. The chip sizes were average cutting size around 1 to 3 cm and a large cutting size around 3 to 9 cm with blocky angular and poorly sorted chip sizes. Then, the groundwater ingress had increased to approximately 10 L/sec at the cutterhead while the cumulative water in the tunnel had been almost 230 L/sec. In the night shift, the segment C of ring No. 4556 at chainage 16+563 km to 16 +561 km was fallen over the conveyor in the Deck-1 and bridge areas (Figure 13), where there was an abundant inflow of rock material and water through the opening at the collapsed segment in the top section. The inrush material resulted in the major obstruction in correspondence of the backup bridge, and the access to the TBM area has been inhibited.

Figure 12. The major stoppage (i.e., the 1st incidence of the collapsed segment) (a) collapse occurred (b) water inflows into the tunnel (c) inrush materials with water inflows (d) the collapsed segments (e) cleaning the inrush materials (f) support tunnel with H-beam steel arch.

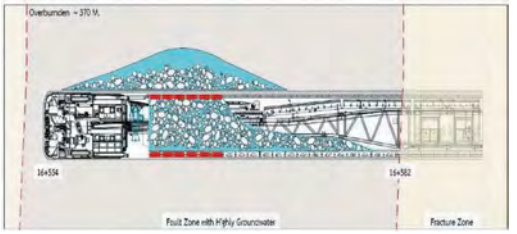

Figure 13. The constructed model after the TBM tunnel inspection for the collapsed segments in chainage 16+582 to 16+554.

The summarized in the field performance studies, the cutterhead coefficient (i.e., a ratio between the cutter torque and the thrust force) was a primary indicator to review the machine behaviors, as shown in Figure 14. During the TBM had excavated via the RMT 8S in chainage 16+583 km to 16+553 km in which the cutterhead coefficient had slightly dropped into 0.10 to 0.05 indicating the squeezing ground. The FPI will be higher values when the blocks of rocks are ruptured from the tunnel face, and face collapse occurs. The cutterhead coefficient was decreasing while the FPI was increasing from approximately 20 kN/mm/rev to almost 80 kN/mm/rev. The loosen segment was also induced to fall by the water ingress because the stability of the rock mass was degraded by groundwater. The cutter torque and the cutter rotation increased in the highly fractured rock mass when the cutting wheel friction decreased. Furthermore, the auxiliary thrust during re-gripping had increased before the TBM stuck as the TBM struggled to push forward, leading to excessive pressures on the segmental lining.

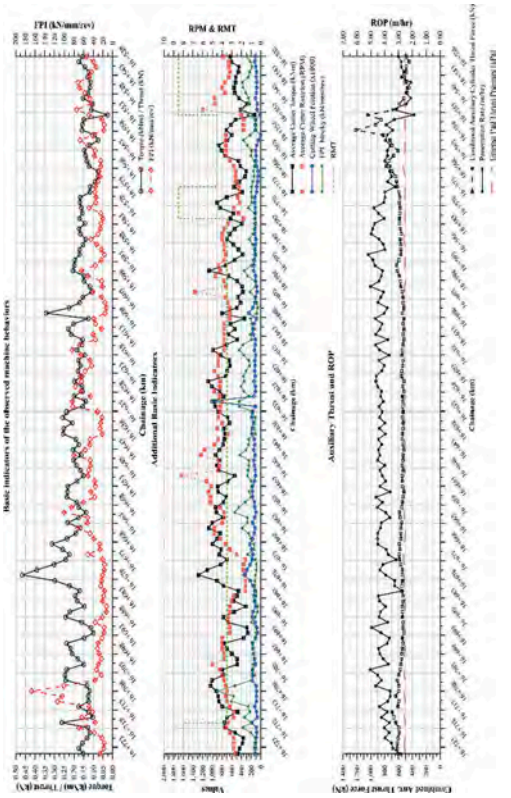

Figure 14. The key indicators reviewing the machine behaviors in the major stoppage.

4.4.2 *At chainage 14+475 km*

The major incidence of the TBM was the segments collapsed in the thrust zone (Figure 15). The field performance data (Figure 16) could be well indicated the problematic zones in this incidence. The cutterhead coefficient slightly dropped from 0.18 to 0.10 in around chainage 14+574 to 14+576 km, while the FPI was starting to increase from approximately 20 kN/mm/rev to 60 kN/mm/rev at chainage 14 +575 km. These factors are a good indicator used to caution against the adverse behavior of the ground interacting with the machine. The cutter torque and the RPM had raised in accordance with the cutterhead coefficient and the FPI.

4.5 *Extremely high-water ingress*

After the first incidence through the number nine fault zone, the advance rate slightly increased around 69.07 m/week. The maximum advance rate was 123.40 m/week in the extremely high-water ingress conditions. The achieved machine utilization was an average of 36.7%, where the TBM still dealt with the high groundwater inflow. The water inflows had

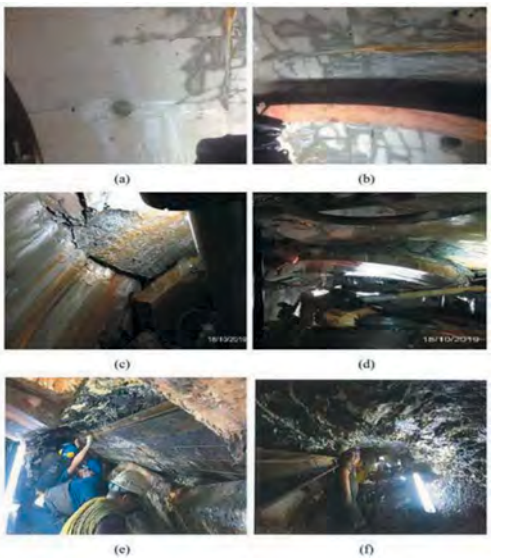

Figure 15. The major stoppage (a) segmental lining cracking (b) cluster cracks of the collapsed segments (c) damage of the segmental lining (d) the collapsed segments (e) H-beam steel rib used for supporting the problematic zone (f) inspection and working for support the ground.

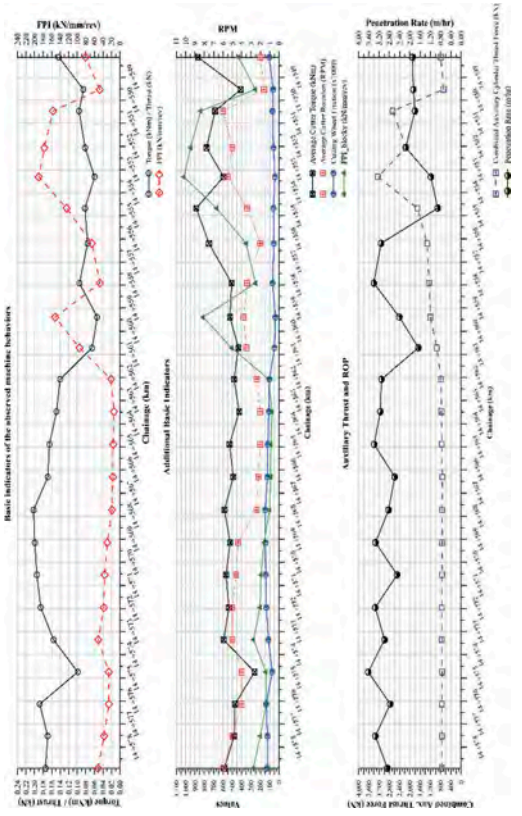

Figure 16. The key indicators reviewing the machine behaviors in the major stoppage.

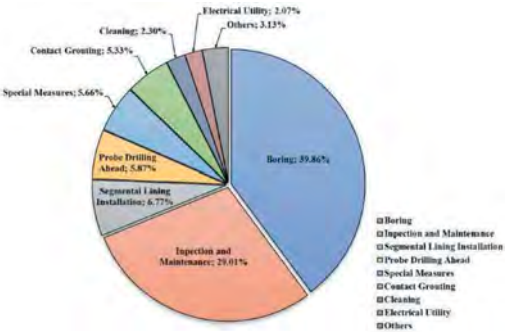

Figure 17. The boring cycle time during the TBM excavation in the thrust zone.

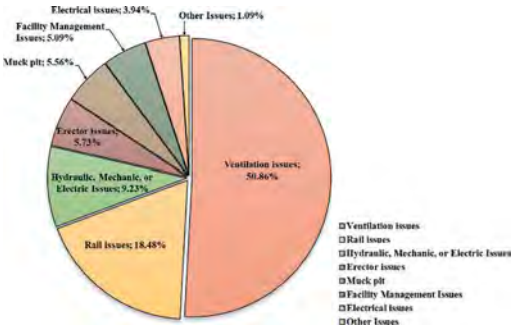

Figure 18. The major TBM downtimes during the TBM excavation in thrust zone.

increased up to 170 L/sec, where the TBM needed to stop to implement the special measures. The boring cycle time had increased by 11.9%.

4.6 *TBM excavation in the thrust zones.*

The TBM had been operated in the difficult ground conditions as the utilization was reduced by the inrush materials and high-water inflows around 120 L/sec to 140 L/sec. The advance rate during the TBM excavation through the thrust zone was an average of 73.24 m/week. The maximum of advance rates was 146.24 m/week. The achieved machine utilization was on average 42%, and the maximum of achieved machine utilization was 82%. The boring was 40% of the total available shift time, and inspection and maintenance of the cutterhead and backup systems were 29%. Figure 17 is showed the boring cycle time almost 12% of the total shift time for the special measures in the thrust zone. Figure 18 is showed the major TBM downtimes, which were ventilation issues 50.86%, rail issues 18.48%, hydraulic/mechanic/electric issues 9.23%, erector issues 5.73%, and so on.

5 CONCLUSIONS

The MNMK water diversion tunnel construction projects in Northern Thailand was selected the double shield TBM to excavate the ground based on the geological conditions related to risks and uncertainties. The TBM-data analysis was performed using the collected data from the TBM to summary of the overall TBM performance and the recommendation for future TBM tunnel projects in hard rocks can be established as follows.

1) The TBM had finished the TBM excavation in the Carboniferous clastic sedimentary rock formation with a tunnel length of 10.45 km, The operation days was 1,350 days, the total production was 54% and the total no production was 46%. The best gross advance rate was 203.42 m/week, as well as the best net advance rate was 40.59 m/day. The average rate of advance could be summarized as 48.6 m/week.
2) The maximum average machine utilization was 66.7%, and the mean was 21.2% of the whole period of the TBM operation. On the other hand, the tunneling time consumption shows the standstill TBM was 24.9%, the incidences of the collapsed segments were 17.1%, the net boring was

12.4%, special measures were 11.5%, TBM downtimes were 8.6%, other main activities were 7.5%, and the TBM maintenance/inspection/cleaning/utilities were around 18.0%.

3) The explicit difference between the actual RMTs and the expected RMTs was almost 24% in the faulted rock mass types where the RMT 8Q and the RMT 8S were mostly found in the thrust zone as more than the prediction.

ACKNOWLEDGMENTS

I would first like to give special thanks to Dr. Thanu Harnpattanapanich who provided the best suggestion and the comprehension in the TBM tunneling, and their profound knowledge in the TBM tunnel design. I appreciatively acknowledge the Consults Team of Construction Supervisions for support big data. My thanks are also provided by the GEO team of GTP and PYG, who always helpful to support data.

REFERENCES

Austrian Society for Geomechanics. (2010). The Guideline for the Geotechnical Design of Underground Structures with Conventional Excavation. Austrian Society for Geomechanics, 2.1.

Bilgin, N, Feridunoglu, C., & Tumac, D. (2005). The performance of a full-face tunnel boring machine (TBM) in the performance of a full-face tunnel boring machine (TBM) in Tarabya (Istanbul). April. https://doi.org/10.1201/NOE0415374521.ch122

Bruland, A. (2000c). Hard Rock Tunnel Boring Vol. 1 Background and Discussion (Vol. 1, Issue February) [Norwegian University of Science and Technology]. https://doi.org/10.13140/2.1.4930.4322

Bruland, A. (2000d). Performance Data and Back-mapping Amund Bruland Hard Rock Tunnel Boring (Vol. 6, Issue February) [Norwegian University of Science and Technology]. http://doi.org/10.13140/RG.2.1.4674.1924

Kaewkongkaew, K., Phien-wej, N., Harnpattanapanich, T., & Sutiwanich, C. (2013). Geological Model of Mae Tang-Mae Ngad Diversion. 2013(September), 340–351.

Mascias, F. J. (2016). Doctoral thesis Francisco Javier Macias Hard Rock Tunnel Boring Performance Predictions and Cutter Life Assessments Francisco Javier Macias Hard Rock Tunnel Boring Performance Predictions and Cutter Life Assessments Thesis for the degree of Philosophiae D (Vol. 5). Norwegian University of Science and Technology.

Moosazadeh, S., Aghababaie, H., Hoseinie, S. H., & Ghodrati, B. (2018). Simulation of tunnel boring machine utilization: A case study. Journal of Mining and Environment, 9(1), 53–60. http://doi.org/10.22044/jme.2017.5707.1384

Morya, P. (2019). Evaluation of Multi-Standpipe Grouting Technique and RTGC Method for Mae Ngad - Mae Kuang Water Diversion Tunnel Project (Issue May 2019). Asian Institute of Technology.

Palmström, A. (1995). RMi parameters Applied in Prediction of Tunnel Boring Penetration. RMi – a Rock Mass Characterization System for Rock Engineering Purposes, 0, 1–14.

Paltrinieri, E. (2015). Analysis of TBM tunnelling performance in faulted and highly fractured rocks. 6724(November), 18–20. https://doi.org/10.5075/epfl-thesis-6724

Ridd, M. F., Barber, A. J., & Crow, M. J. (2011). The Geology of Thailand (pp. 23–40).Rostami et al. (1996). C Omparison B Etween Csm and Nth. Geology, 1–11.

Schubert, Fasching, & Vigl. (2005a). Mae Ngad – Mae Kuang Tunnel Project (Detail design) (Issue November).

Schubert, Fasching, & Vigl. (2005b). Mae Ngad – Mae Kuang Tunnel Project (Tender design) (Issue November).

Sutiwanich, C., Phienwej, N., Harnpattanapanich, T., & Fasching, A. (2006). Investigation and Preliminary Design of Mae Ngat-Mae Kuang. February, 513–520.

Viglconsult. (2016). Mae Tang - Mae Ngad Diversion Tunnel: Segmental lining and Geotechnical Design (Issue August).

Tunnelling for a Better Life – Yan, Celestino, Thewes & Eberhardt (Eds)
© 2024 The Author(s), ISBN 978-1-032-80042-4
Open Access: www.taylorfrancis.com, CC BY-NC-ND 4.0 license

A new AFTES guideline: Suitability and selection process of pressurized TBMs in urban contexts

Magali Schivre*
Incas Partners, Paris, France

François Renault
Vinci Construction Grands Projets, Nanterre, France

ABSTRACT: The aim of this new AFTES (French Tunneling & Underground Space Association) recommendation is to provide a guide for assessing the suitability of pressurized TBMs for use in urban contexts, together with an approach for documenting the choices made. While soil-related constraints are a prime factor in this choice, there are sometimes several types of machines that may be suitable, and it is other constraints, such as environmental or economic ones, that will guide the final choice. The purpose is not to guide towards a single choice of machine, but to make each of the parties involved aware of the importance of the constraints that can influence this choice, and therefore the program and economics of a project.

The recommendation defined by the AFTES working group is structured around achieving three major objectives for the successful implementation of a project using a pressurized tunnel boring machine in an urban context: safety, transparency, and performance.

Furthermore, as the range of applications for these machines continues to expand, with multi-purpose machines with additional equipment, the guideline recommends determining the most suitable types of confinement (e.g. paste, liquid, or gaseous) before selecting the machine's typology and its equipment.

Similarly, taking into account specific configurations and risks are reviewed (e.g. presence of boulders) to define the design of the tunnel boring machine and its complementary equipment (e.g. crusher), and countermeasures are proposed if available and necessary.

Additionally, the working group suggests that the adopted approach for selecting the confinement type and tunnel boring machine, be outlined and synthesized in an "environment and excavation conditions" model.

Keywords: TBM, urban, pressurized, suitability, model approach, confinement mode

1 DIFFERENT OBJECTIVES OF AN URBAN PROJECT INFLUENCING TBM'S SELECTION

The comparison between urban tunnels and other underground structures reveals two major sets of challenges. First, insertion constraints include restricted alignment, limited construction space, engagement with multiple stakeholders, presence of neighbouring structures, and the potential discovery of forgotten anthropic objects in the subsoil. Second, technical complexity arises from poor ground quality, the water table's presence, difficulties in obtaining permits for preliminary investigations, and the relatively shallow ground cover. These constraints represent substantial risks to nearby residents and third parties, necessitating careful project design to ensure success.

The aim of the new AFTES (French Tunneling & Underground Space Association) recommendation "*Suitability and selection process of pressurized TBMs in urban contexts*", is to provide a guide for assessing the suitability of pressurized TBMs for use in urban contexts, together with an approach for documenting the choices made.

The selection of tunnel boring machines (TBM) and their equipment is a critical step in any project, and it must ensure the fulfilment of three major project objectives:

Safety: Safety is the fundamental requirement for any excavation project, emphasizing the protection of both third parties and personnel involved. This involves maintaining the stability of the excavation face, minimizing the impact of TBM operations on the surrounding environment, and ensuring the safety of all personnel throughout the project.

Transparency: Beyond safety, gaining acceptance from local residents in urban projects requires a design that optimally utilizes available space and

*Corresponding author: mschivre@incas-partners.com

DOI: 10.1201/9781003495505-280

minimizes the project's impact on the broader environment. This includes considerations like road congestion, noise and dust emissions, vibrations, and respects of working hours. Proper disposal of excavated materials and the overall logistics of the construction site significantly affect nearby residents. As a result, the entire project should aim to be as "transparent" as possible to address these concerns.

Performance: The project needs to be optimized in terms of costs and scheduling, making it essential to consider efficiency and timely completion.

The new AFTES Guideline suggests that it is essential to consider these major objectives related to urban projects, rather than just geological and geotechnical aspects, when selecting the TBM. The process of selecting the TBM begins with the exclusion of confinement methods that do not meet the fundamental safety requirements mentioned earlier. Subsequently, an analysis of various criteria is conducted to compare the remaining confinement methods, ultimately choosing the one that best aligns with the project's overall objectives.

2 STUDYING THE FEASIBLE FACE CONFINEMENT TYPES, RATHER THAN MACHINE TYPES

Applying pressure to the excavation boundaries serves to ensure the stability of the cutting face, limit water ingress, and minimize ground displacement. Tunnel boring machines (TBMs) with face confinement mechanisms achieve these objectives.

There are three main types of face confinement, determined by the consistency of the material used to fill the excavation chamber:

- Paste Confinement: Involves filling the chamber with excavated materials, possibly with additives, to create a viscous mixture.
- Liquid Confinement: Uses a viscous fluid to fill the chamber.
- Gaseous Confinement: Fills the chamber with compressed air.

The choice of face confinement depends on the geotechnical context in which it will be deployed. Some pressurized TBMs can operate with different types of face confinement, and certain TBMs are "multimodal," meaning they can switch between different confinement modes.

The capacity of various pressurized TBMs to implement the different confinement modes mentioned above is summarized in Figure 1 below. Obviously, even without considering multimodal tunnel boring machines, some machines can operate with multiple types of face confinement.

Therefore, the approach suggested by the new AFTES recommendation is to first focus on identifying the possible face confinement options before selecting a machine technology.

The evolution of the last 15 years demonstrates that there is more overlap between pressurized shielded TBM thanks in particular to continuous improvements and technological developments that make it possible to extend the application scope of the various types of TBM, with also addition of specific equipment to compensate for deficiencies:

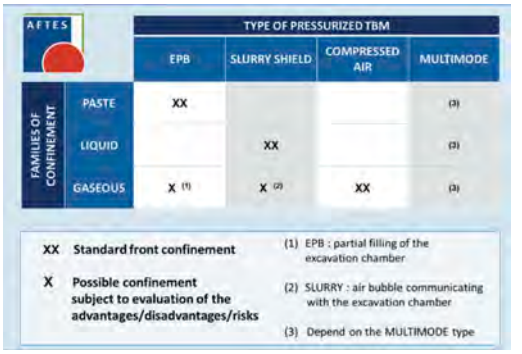

Figure 1. Type of pressurized shield versus confinement.

- Increasing confinement pressures, particularly for slurry TBMs.
- Enhancing the precision with which face support is managed by injecting pressurized bentonite to limit variations in chamber pressure, for the various types of TBM.
- Adaptability, enabling use in ground with different particle size distributions and permeability, with for slurry TBM: anti-clogging measures and improved behaviour in cohesive soils; managing cutting face stability by generating cake. And for EPB TBM: modifying the mechanical properties of excavated earth by injecting additives directly into the cutting chamber.

3 ANSWERING TO "SAFETY" OBJECTIVE

Ensuring Front Stability and Minimizing the TBM's Impact on the Surrounding Area.

3.1 *Identification of current conditions and suitable confinement*

As the range of applications for these pressurized machines continues to expand, with multi-purpose machines with additional equipment, The AFTES guidelines discuss in a very precise way the optimal conditions for implementing various face confinement types (e.g. paste, liquid, or gaseous) and the potential corrective measures to expand standard application fields.

The optimal conditions are primarily characterized by:

- The grain size and/or permeability of the soils being traversed.
- Their Atterberg limits and moisture content.
- Hydrogeological conditions.

- Mechanical strength parameters affecting the minimum and maximum confinement pressure to be maintained.
- The deformability of the overlying soils.

Ground investigation campaigns should, therefore, focus on providing these pieces of information. In a very concise manner, the optimal conditions for applying paste, liquid, and gas face confinement modes are illustrated in Figure 2.

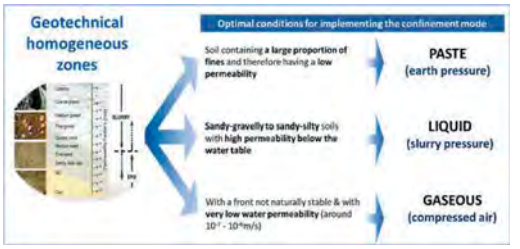

Figure 2. Optimal condition for the different type of confinement.

The grain size and Atterberg limits help evaluate the feasibility of implementing the face confinement type. The strength and deformability parameters of the overlying soils determine the required confinement pressure values to maintain front stability and keep settlements within acceptable limits. It is important to compare the maximum confinement pressure with the acceptable range for each confinement mode.

3.2 *Addressing specific configurations and risks to determine the TBM design and supplementary equipment*

The specific configurations and risks which have influence on the pressurized TBMs are reviewed. For each of them, the guideline introduces a common technical language, gives an indication on the predictability (spatial and temporal) of the following phenomenon:

- Sticky/clogging soils
- Erratic blocks & boulders or anthropic obstacle (cf. Figure 3)
- Voids of natural or anthropic origin
- Mixed fronts
- Polluted soils

For each specific configuration, the AFTES guidelines provides recommendations in identifying the consequences on the TBM type based on the type of confinement and evaluating the level of impact (cf. Figure 4).

The AFTES guidelines also provides recommendations in anticipating appropriate mitigation measures that can be implemented regarding the type of TBM.

- assessing the difficulty of implementing these countermeasures.

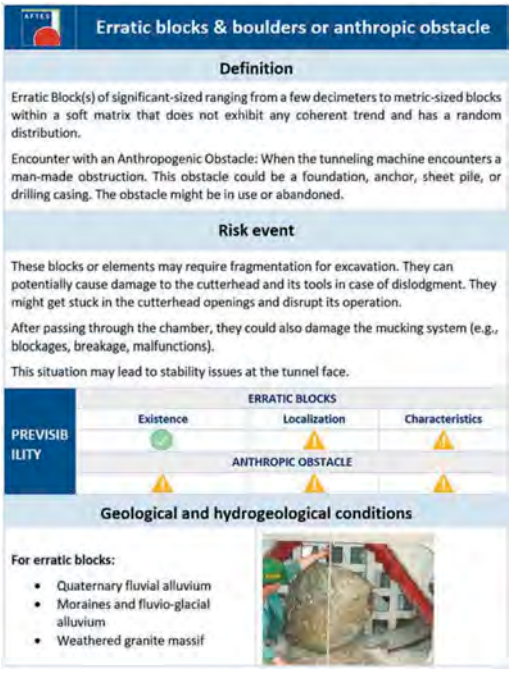

Figure 3. AFTES definition of "Erratic blocks & boulders or anthropic obstacle".

- anticipating the impacts on the TBM design and its equipment (e.g., crushers).

Mitigation measures are classified as "easy to implement on-site" provided that their implementation has been considered during the TBM's design, including the TBM equipment, as illustrated on Figure 5.

4 ANSWERING TO "TRANSPARENCY" OBJECTIVE

The succeed of a project will pass through limiting the impact on the environment and aligning with available worksite areas.

4.1 *Environmental impact of construction works*

4.1.1 *Excavated materials*

Regarding **excavated material management**, more than the type of confinement, it's primarily the **mucking system** that should be considered. For instance, it's possible to install a dilution system at the rear of an Earth Pressure Balance (EPB) TBM and evacuate the muck through a hydraulic system (as seen in the example of the Botlek tunnel in the Netherlands). Similarly, a multimodal TBM capable of EPB and slurry confinement can be associated with a hydraulic mucking disposal system with a surface separation plant.

The Figure 6 illustrate a separation plant, placed on a temporary deck over the bench and the Seine River to minimize impact on the city life.

TBM CONSEQUENCES - Erratic blocks / anthropic obstacle

CONSEQUENCES	Initial IMPACT level			Localization				Comments / Examples
	PASTE	LIQUID	GASEOUS	Extraction Chamber	Cutterhead	Shield	Back-up / Logistic Train	
Block/element larger than the wheel sizing or causing obstruction to the aspiration, requiring a TBM stop to remove it.	3	3	3	X	X			The machine should be stopped as soon as possible to minimize the consequences
Breaking or damaging cutting tools or bits upon impact, necessitating a near-term TBM stop for replacement	1	1	1		X			Depending on the geology or nature of the obstacle, the breakage of cutting tools/bits may require a specific TBM stop
Damage to the screw conveyor	2	2	2	X				In extreme and rare cases, this could result in the breakage of the screw conveyor or casing tear
Disruption of the hydraulic mucking operation when encountering anthropogenic elements (bars, piles, etc.).	NC	1	NC				X	Be cautious of the risk of water hammer (a sudden surge of pressure).
Damage in the mucking conveyor system.	2	NC	2				X	If there is no crusher or grizzly behind the screw, there is a risk of blocks falling from the conveyor (human risk) Belt tear, which can be more serious when encountering metallic elements.
Challenges in TBM guidance and maintaining confinement.	2	2	3	X	X	X		The risk is heightened in unstable terrains.

Note: In cases of repeated encounters with pebbles/blocks, this can lead to wear and damage to the marinage pipes.

It may also be necessary to consider protections for the cutting wheel face against wear, including potential reinforcements.

CONSEQUENCES and INITIAL IMPACT LEVEL

The possible consequences of the main geotechnical risks or specific configurations are evaluated for the different types of confinement concerning their impact on the operation of the tunnel boring machine and worker's safety

0	**Negligible Without impact or Not concerned (NC)**	No further consideration of the hazard is needed
1	**Significant,** but presumably acceptable	Construction can begin, but risk factors must be closely monitored through appropriate procedures, and the project must be supplemented with a series of predefined measures that can be adapted during the execution phase
2	**Important**	Construction cannot commence until the risk is reduced or eliminated. Risk mitigation measures should be identified and implemented as long as their cost is not disproportionate to the risk reduction achieved.
3	**Unacceptable**	Risk-taking is unacceptable regardless of the potential benefit. It should be avoided at any cost or impact on the schedule. The impact should be rédduque to at least "important."

Figure 4. Impact and consequences on TBMs regarding confinement "Erratic blocks & boulders or anthropic obstacle".

MITIGATION MEASURES - Erratic blocks / anthropic obstacle

MITIGATION MEASURES	Preventive (P) Corrective (C)	Level of difficulty to implement it			Comments / Examples
		PASTE	LIQUID	GASEOUS	
Equip the TBM with a **crusher** to reduce the size of blocks	P	⚠	✓	⚠	Determine type of crusher regarding the expected block nature (e.g., jaw or roller crusher). For paste confinement, the crusher (or a "grizzly") is located behind the screw conveyor, while in the case of liquid confinement, it is located at the bottom of the excavation chamber.
Determine **the sizing of the cutterhead openings** based on the desired calibration	P	⚠	✓	✓	The cutterhead must gradually gnaw away at the block(s). The cutterheads with liquid confinement may have larger openings, limited by the block size.
Appropriately size the screw conveyor (pitch, strength, diameter) and casing	P	⚠	⚠	⚠	Limited by the block size and the cutterhead openings.
Outfit the cutterhead with **specialized tools** for encountering metallic obstacles	P	✓	✓	✓	
Include **inspection hatches** for clearing metallic elements or facilitating repairs	P	✓	✓	✓	Stone traps ahead the pumps or inspection hatches on a screw conveyor.
Use **pipes with sizes compatible** with the block size coming out of the crusher, with suitable mesh screens	P	NC	✓	NC	
Instrumentation of the cutterdiscks	P/C	✓	✓	✓	Instrumentation allows for the detection of block/obstacle encounters and the reduction of penetration pitch, reducing the risk of cutter breakage
Install a **metal detector and/or electromagnet** to detect potential tool breakage or the presence of metallic obstacles	P/C	✓	⚠	✓	In the case of liquid confinement, detection can only be carried out from the surface.
Equip the TBM with **non-destructive surveying equipment** (seismic, radar, etc., currently in development)	P/C	✓	✓	✓	Various advanced inspection techniques exist, but their effectiveness varies depending on the context, with few conclusively successful experiences. These are promising technologies whose use should be encouraged, as they contribute to overall risk management
Perform **preventive maintenance** on the cutterdiscks and tools	C	⚠	✓	⚠	Increase the frequency of cutterdisks and tool inspection and maintenance. These zones should be pre-identified in the PAT
Advance at **reduced speed** when the occurrence is predicted	C	✓	✓	✓	Advancing at very slow speeds (e.g., microspeed, penetration speed, rotation speed) should be considered in the design to make it feasible. These zones should be pre-identified in the PAT
Remove the obstacle or block with **hyperbaric intervention.**	C	⚠	✓	⚠	

DIFFICULTY LEVEL TO IMPLEMENT MITIGATION MEASURE ON SITE

NC	**Not concerned**
✓	**Easy to implement on site, to be previously considered in the design**
⚠	**medium difficulty of implementation**
◆	**very difficult to implement, (*could have an impact on the requirements*)**

Figure 5. Countermeasures regarding confinement on TBMs regarding confinement "Erratic blocks & boulders or anthropic obstacle".

The choice of mucking disposal system will impact both the nature and quantities to be evacuated and their potential reuse in case of revaluation. It's important to remember that the in-situ soil is different from the excavated muck, which accumulates in the muck pile. This difference can be attributed to the confinement method (e.g., addition of additives or bentonite) and the mucking disposal method.

The AFTES guideline discusses and compares the mucking disposal methods using conveyors belt (suited for paste and/or gaseous confinement) and the hydraulic mucking disposal method (suitable for all types of confinement):

- Nature of excavated material depending on their conditioning in the case of conveyor belt mucking
- Nature of excavated material in the case of hydraulic transport
- Difference in quantities of excavated material based on the mucking method
- Possibility of reuse or future valorization

4.1.2 *Vibrations, noise and pollution*

As of today, there is no evidence to suggest that one type of confinement TBM generates more vibrations than another type. This is a non-discriminatory factor for choosing the confinement method. However, it remains true that this issue should be addressed during the early phases of a project. The building survey should identify structures sensitive

Figure 6. EOLE separation plant, Slurry TBM D11,4m – 6km.

to vibrations (laboratories, recording studios, hospitals, etc.) and prioritize alignment options that keep a distance from these buildings.

Most of the surface equipment generating noise is the same regardless of the type of machine. Typically, the loudest sources are the mortar preparation plant, ventilation, and transport vehicles. However, there are differences related to the slurry disposal method: the separation plant in the case of liquid confinement and material chutes in the case of conveyor belt mucking.

The ground that the TBM will encounter can contain various types of pollutants. Depending on the type of machine chosen, these pollutants can have an impact on the safety of workers and the deposition of excavated materials. Without specific processes, paste and gas confinement methods expose workers more to existing pollutants such as hydrocarbons, H2S, and asbestos fibers compared to liquid confinement.

4.2 *Urban site constraints for construction*

The worksite is the visible part of the construction site. It serves as the Owner's showcase and acts as the primary point of contact with local residents. It must prioritize discretion to ensure effective acceptance. Proper dimensioning of the worksite is crucial for achieving and controlling the project's planning objectives.

4.2.1 *Areas for worksite installations and access*

Substantial differences exist in terms of required surface of worksite installation regarding the different confinement mode.

For each type of tunnel boring machine technology, there is a minimum size of worksite installation below which it is no longer feasible and an optimal size from which no loss of productivity is expected.

The AFTES guideline suggests that the optimal area depends on several key parameters:

- The TBM excavation diameter.
- Work organization (which can be carried out 5 days a week, 6 days a week, or 7 days a week, for example), authorized hours for slurry disposal or material supply, which will dictate the number of buffer stock days required.
- The maximum excavation speed. Note that to guarantee the project's average excavation speed, a common approach is to consider a ratio of 2 between the maximum speed and the average speed.
- The TBM confinement technology (paste, liquid, gas, or multimodal).
- The management mode and characterization of excavated materials (bins for chemical identification or space required for revaluation).
- Activities that are conducted concurrently or sequentially with the excavation on the same site (e.g., starting shaft or metro station for a metro project).

The chart provided by the AFTES Guideline in Figure 7, illustrates based on past projects that the space needed increases with the diameter, and that separation plants need large spaces potentially restricting the space available for other site facilities, especially in urban locations.

4.2.2 *Starting shaft size*

The challenge of acquiring a substantial land area in urban areas leads to a desire to reduce the dimensions of the starting shaft. The choice of the starting shaft size can determine the type of tunnel boring machine that can be used and also have significant implications for the project schedule.

There is a minimum starting shaft size below which it is no longer possible to assemble and launch a TBM. This size corresponds to the length of the TBM pushed against the face, plus sufficient space for supplying the first segments. Furthermore, TBMs equipped with a screw conveyor (compressed air pressure, earth pressure, or variable density) require a sufficient assembly area length to insert the screw conveyor into its casing.

Using a slurry TBM can, therefore, be advantageous when the starting shaft size is severely constrained.

The assembly and startup phases are often accident-prone due to the use of excavation equipment in degraded mode. From a safety perspective, it is essential to prefer a starting shaft size that limits the number of temporary phases.

5 ANSWERING TO "PERFORMANCE" OBJECTIVES

After considering aspects related to face stability and the project's impact on the environment, economic and scheduling factors should also be considered when choosing the type of tunnel boring machine.

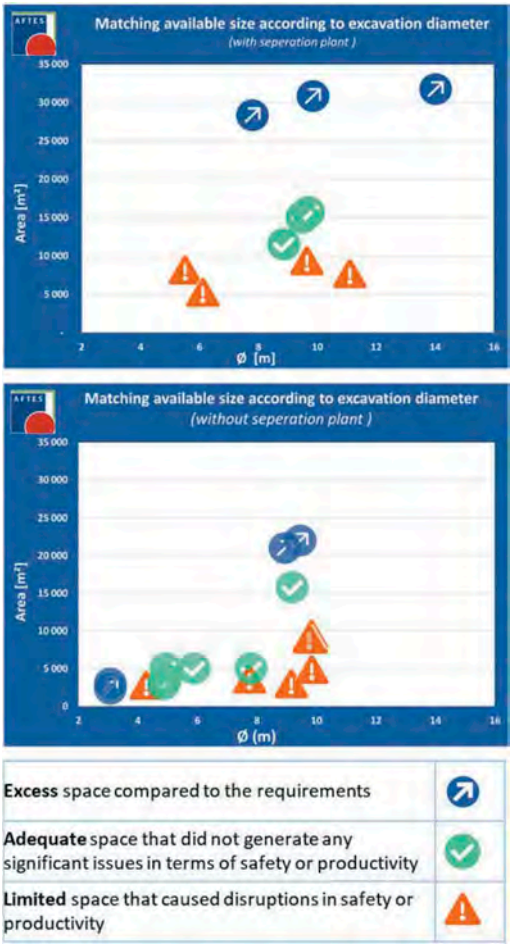

Figure 7. Illustration of lessons learned: Matching available size according to excavation diameter and mucking type – GT4 database.

Some elements of the cost of tunnel construction depend on the type of TBM used, primarily including equipment investment costs, operating costs, and excavation material disposal costs.

The "bare" machine costs refer to the machine itself without the specific equipment indicated below. The chart provided by the AFTES Guideline in Figure 8 shows that within the same diameter range, EPB and SLURRY TBMs are in a similar price range, while Multimode TBMs have slightly higher investment costs.

In the assessment of the investment gap between machines, specific equipment associated with each TBM technology should be taken into account. The main elements include:

- Cost of a hydraulic slurry circuit per kilometer for liquid confinement.
- Cost of a conveyor per kilometer for paste or gas confinement.
- Cost of a separation plant per excavated diameter.

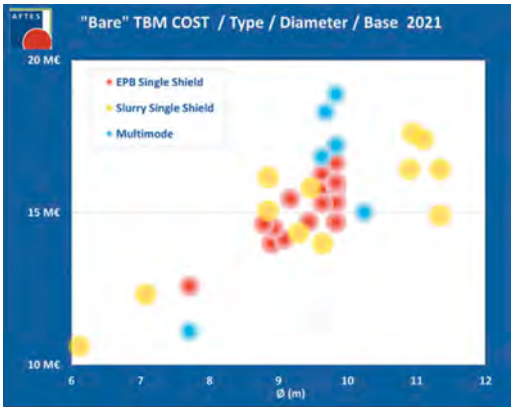

Figure 8. Cost of a "bare" new TBM based on its type and diameter – GT4 database.

Similarly, since tunnel excavation activities are often on the critical path for projects, it's important to assess the time differences in project completion based on the chosen TBM technology. For example, the project duration depends on:

- Assembly/startup
- Excavation rates vs. geology: they are highly dependent on the presence of clay, influenced by the strength and abrasiveness of the ground. They also depends on the size of the worksite and the size of the separation plant
- Stop-time and maintenance time

However, there can be significant differences in the duration of stop-time. The Figure 9 highlights different types of downtime based on the technology used, leading to significantly different expected durations.

TBM stop-time can be categorized into four main families:

- Planned stops, primarily due to inevitable tasks such as extending easements.
- Waiting times, which encompass machine downtime due to external breakdowns unrelated to the TBM.
- Scheduled maintenance.
- Miscellaneous breakdowns.

	PRESSURIZED TBM DOWNTIME			
MUCKING or CONFINEMENT	Unavoiding Tasks => Planned Stops	Waiting Times	Maintenance	Breakdowns
LIQUID confinement + Hydraulic mucking	Extension of Slurry Lines Relay Pump Installations	Waiting at the Slurry Treatment Station (e.g., drumming blockage)		Slurry pumps
LIQUID confinement + Conveyors mucking	Extension of Conveyor Belts Installation of boosters	Conveyor Belt Blockages		Belt tear
All types	Extension of Utilities (air/water) Extension of Electrical Power Cable Extension of Ventilation Cleaning of Mortar Injection Lines	Downtime Waiting for the TSV or other Segment Supply; Waiting for the Mortar Plant (excavation interruption if no mortar to inject)	Daily maintenance Hyperbaric interventions	TBM TSV Mortar Plant

Figure 9. Stop-time tasks regarding confinement/mucking.

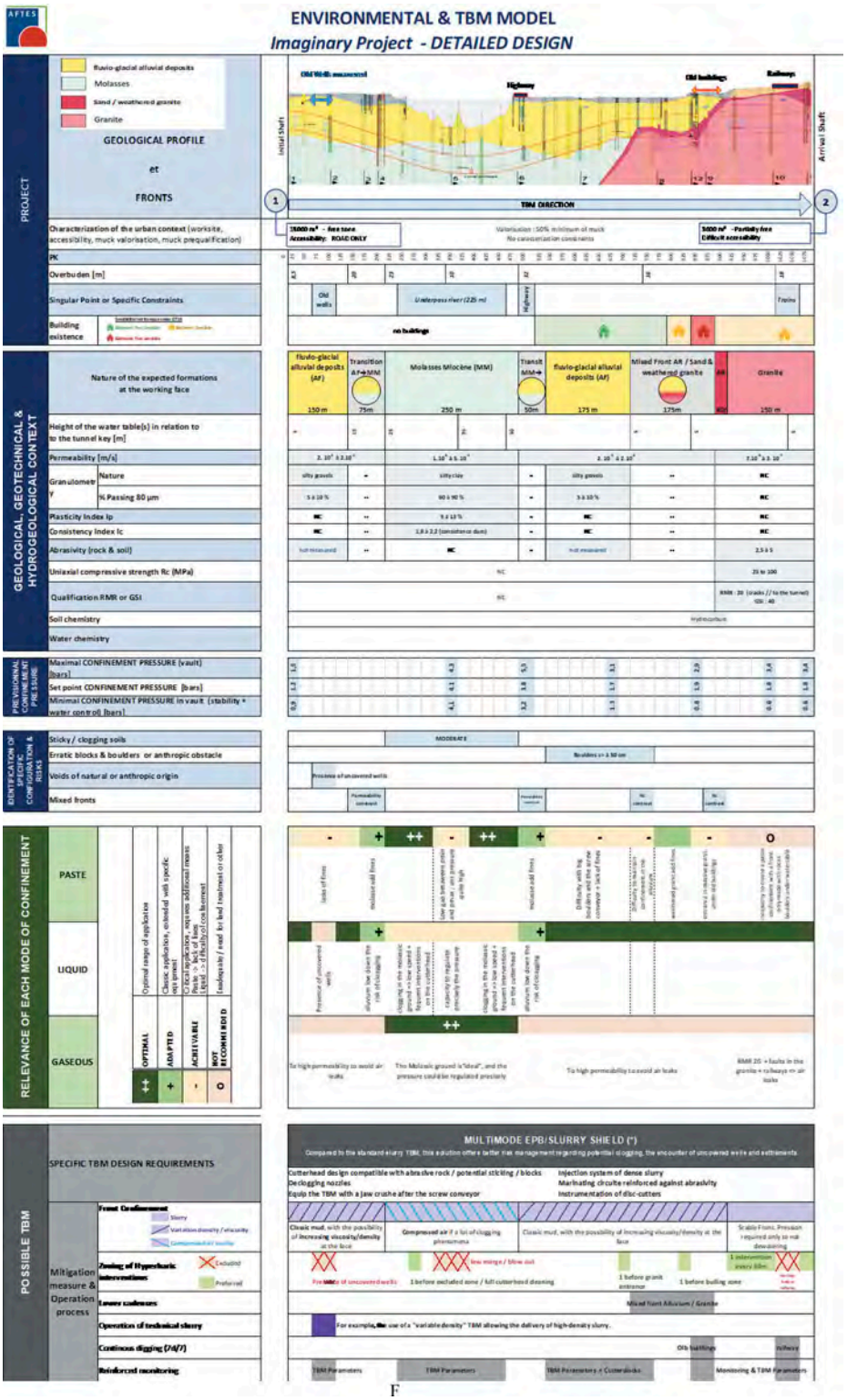

Figure 10. AFTES environnemental & Excavation conditions model.

6 SUGGESTING A STEP-BY-STEP APPROACH FOR CHOOSING FACE CONFINEMENT AND TBM

The aim of the AFTES approach is not to propose a logic for defining the "ideal" TBM for a given project because, as mentioned earlier, there are numerous parameters, some of which are difficult to quantify, that can influence this assessment.

Among these parameters, one should not overlook the unique experience of each company, which enables them to master the technology they intend to implement. Instead, the objective is to present an approach that addresses all the criteria discussed earlier, ensures traceability, and provides a concise overview.

During the design phase, it is necessary to gradually reduce uncertainties until a project is developed that meets the required program while maintaining acceptable costs and residual risks. This is an iterative process, and assessing the suitability of a TBM type is a part of it.

This methodology can be applied during the design phases and when selecting the TBM by the company. Its secondary goal is to guide the necessary geological studies and assessments for managing construction risks effectively. Furthermore, it allows for maintaining a concise record of the considerations made during the project's development.

The AFTES guidelines suggests that the adopted approach for selecting the confinement type and TBM machine, should be outlined and synthesized in an "Environmental and Excavation Conditions Model", in a concise document.

Its primary objectives are to:

- Ensure traceability.
- Locate the elements of the project context, including obstacles and structures traversed by the project, all along the layout.
- Include geotechnical and hydrogeological characteristics of the ground that impact the choice of excavation methods.
- Present confinement pressure values, all along the layout.
- Identify specific configuration & risks.
- Asses the relevance of each mode of confinement (paste/liquid/gaseous), with a classification from "not recommended" to "optimal" as illustrated in Figure 11.

++	OPTIMAL	Optimal range of application
+	ADAPTED	Classic application, extended with specific equipment
-	ACHIEVABLE	Critical application, requires additional means Paste -> lack of fines Liquid -> difficulty of confinement
o	NOT RECOMMENDED	Inadequate / need for land treatment or other

Figure 11. Relevance of confinement mode.

- Select the design & the equipment of the machine:

The identification of preliminary measures for the TBM's design, including the implementation of specific equipment based on the TBM's type. This involves referring to the countermeasures detailed previously (as in Figure 5) and considering technological advancements that enable the use of a tunnel boring machine outside its typical domain.

- Anticipate the operation phase of the TBM, with the location of the mitigation measures with:

The listed measures include the zoning of confinement mode based on the recommended TBM type. For example, for slurry TBM, it involves identifying areas where the machine can operate under air pressure mode in regions affected by clogging soils in the presence of an impermeable environment. For EPB, it entails locating areas that require working in full-face mode with slurry confinement and proper conditioning.

The topics also cover hyperbaric interventions zoning, including the identification of areas where interventions should be excluded or prioritized, work with specific technical mud, slow-rate excavation, continuous 7/7 excavation, enhanced monitoring of TBM parameters, and implementing suitable control thresholds, vigilance zones for mud loss, and preventive maintenance integrated into the TBM's advance plan, which may necessitate interventions at the face.

Using this model, which provides an overall and cross-sectional view of the project's challenges, the designer and after the contractor can determine which types of confinement are compatible with the project and whether additional ground treatments or other accompanying measures are necessary.

An example of a concise Environmental and Excavation Conditions Model, suggested by the guideline, is illustrated on Figure 10. It is entirely based on a theoretical imaginary project.

7 CONCLUSIONS

The aim of the new AFTES guidelines "Suitability and selection process of pressurized TBMs in urban contexts" is to provide a guide for assessing the suitability of pressurized TBMs for use in urban contexts, together with an approach for documenting the choices made.

While soil-related constraints are a prime factor in this choice, there are sometimes several types of machines that may be suitable, and it is other constraints, such as environmental or economic ones, that will guide the final choice. It is essential to address Specific Configurations and Risks to Determine the TBM Design and Supplementary Equipment (e.g., crushers).

The purpose is not to guide towards a single choice of machine, but to make each of the parties involved aware of the importance of the constraints that can influence this choice, and therefore the program and economics of a project.

The AFTES guidelines also suggest to study the Feasible Face Confinement Types, rather than Machine Types, and after suggest a Step-by-Step Approach for Choosing Face Confinement and TBM, summarized in an Environmental and Excavation Conditions Model.

ACKNOWLEDGMENTS

We would like to express our deep gratitude to the dedicated team of the AFTES Working Group "Mechanization". Their unwavering commitment and voluntary contributions of their valuable time were instrumental in the development and sharing of this methodology. Without their efforts, this work would not have been possible.

REFERENCES

Suitability and selection process of pressurized TBMs in urban contexts", AFTES Recommendation GT4R8F2 – 2024.

Review of developments in TBMs and their capabilities over the period 2000-2019", AFTES Recommendation GT4R6A1 – 2021.

"Slurry for use in slurry shield TBM" AFTES Recommendation GT4R4A1 – 2005.

Tunnelling for a Better Life – Yan, Celestino, Thewes & Eberhardt (Eds)
© 2024 The Author(s), ISBN 978-1-032-80042-4
Open Access: www.taylorfrancis.com, CC BY-NC-ND 4.0 license

JWPCP effluent outfall tunnel in Los Angeles, California – Anticipated challenges and slurry TBM performance in the soft ground section of the alignment

Martino Scialpi*
Pini Group USA Inc., Washington, DC, USA

Miriam Piemontese & Roberto Schürch
Pini Group Ltd., Zurich, Switzerland

Matt Kendall & Nicholas Karlin
Dragados USA, Costa Mesa, CA, USA

ABSTRACT: The Los Angeles, California JWPCP effluent outfall tunnel will transport secondary-treated effluent from the Joint Water Pollution Control Plant in Carson to the White Point Manifold. Upon completion, through ground conditions ranging from soils to hard rock, the tunnel will be approx. 11km long with a finished internal diameter of 5.5m. This paper will present the Tunneling Conditions Assessment Report (TCAR) and Tunnel Operation Plan (TOP) developed prior to construction, as well as the actual TBM performances achieved along the northern portion of the alignment in soft ground, shallow cover, and beneath a densely urbanized area.

Keywords: Tunnelling, Slurry TBM, Performance prediction, Soft Ground

1 INTRODUCTION

The aim of the new Los Angeles, California JWPCP effluent outfall tunnel is to provide relief and redundancy to the existing tunnels (shown in red in Figure 1) as well as providing additional overall conveyance capacity. Upon completion, the tunnel – approximately 11 km long with a finished internal diameter of 5.5 m – will transport secondary treated effluent from the Joint Water Pollution Control Plant (JWPCP) in Carson to the White Point Manifold on the coast.

The tunnel is currently under construction using a Mixshield TBM with precast segmental concrete lining designed to cope with the baseline maximum water pressure of 9.1 bar (according to the Geotechnical Baseline Report – GBR 2018). This paper focuses on the northern portion of the alignment (i.e., approximately 5.5 km), completed in November 2023 (shown in blue in Figure 1).

Figure 1. Project area, with existing and new tunnel alignments.

2 EXPECTED TUNNELLING CONDITIONS

The geological conditions and the tunnelling conditions expected along the northern portion of the alignment determined in the pre-excavation phase (Schuerch et al., RETC 2023) are summarized in the following section. For the southern portion of the alignment, refer to Schuerch et al., WTC 2023).

*Corresponding author: martino.scialpi@pini.group

DOI: 10.1201/9781003495505-281

2.1 *Geology and hydrogeology*

Along the northern portion of the alignment, the TBM was expected to encounter heterogeneous soils of the Lakewood Formation and San Pedro Sand. Locally, the Timms Point Silts and the Alluvium were expected to reach the tunnel elevations. Table 1 shows the expected geology along the different tunnel reaches of the northern portions:

- Lakewood Formation, San Pedro Sand: Predominantly sand, sand with varying amount of silt and clay, lenses of gravels and shells.
- Alluvium: Clays, silts and sands with organic debris, gravels, cobbles and boulders.
- Timms Point Silt: Predominantly silt, siltstone, claystone and mudstone with seams of sand, organic fragments, shells and gravel.

The overburden, consisting of the abovementioned heterogeneous deposits, varies approximately from 14m to 35m. The hydraulic head varies along this portion between 3 and 18 m. The hydraulic conductivity of the soils is highly variable ranging from very low to very high (10-9 to 1 cm/s).

Table 1. Tunnel reaches and expected geology.

Reach	Length [m]	Geology
1	3900	Lakewood, San Pedro Sand
2	180	San Pedro Sand, Timms Point Silt, Alluvium
3	1700	San Pedro Sand, Alluvium, Timms Point Silt

2.2 *TBM technical specifications*

The 6585 mm dia. Mixshield TBM shown in Figure 2 was designed and manufactured for the specific project conditions. The key technical specifications are summarized in Table 2.

Table 2. TBM specifications.

Type	Mixshield TBM
Bore Ø	6585 mm
TBM Length	13 m
Operating Pressure	Max: 10 bar
Cutterhead Speed	0-3.8 rpm
Torque	Nominal: 4.5 MNm; Breakout: 5.6 MNm
Cutter Type	17" – 18"
No. Cutters	40
Thrust per Cutter	267 kN
Thrust Force	Nominal: 79 MN; Max: 158 MN
Total Length	242 m
Min Curve Radius	240 m

Figure 2. Mixshield TBM "Rachel" being assembled at the Carson launch shaft.

2.3 *Main geotechnical hazards*

Based on the anticipated tunnelling conditions, the potential geotechnical hazards identified in the pre-excavation phase in this portion of the alignment are summarized in Figure 3:

- Face instability, blow-up, and large settlements: Main hazard scenarios to be expected when tunneling through low cohesion soil with low overburden in urban environment. To mitigate these risks, the TBM is to be operated in pressurized mode within the operational ranges of support pressure determined in the design phase, based on the quantitative assessment of these risks.
- Clogging: The excavated material, at its natural moisture content, may stick to the steel of the cutterhead and cutting tools obstruct muck flow and machine advance. This phenomenon, commonly referred to as "clogging", leads to the wear of the cutterhead and muck handling system, causing downtimes and economic loss. The clogging potential of a material increases with increasing clay content. The risk of clogging can be mitigated by frequent cutterhead cleaning and by introducing ground conditioners.
- Mixed face: During excavation in mixed face conditions, low advance rates can be experienced. Excessive or uneven wear of the cutting tools and, in the worst case, damages to the cutterhead may be caused by strength contrast between softer and harder layers, with impact loading of tools and eccentric/asymmetrical loading of the head.
- Boulders and cobbles: Boulders may jam against the cutterhead openings first and against the rock crusher second, making the muck handling process, out of the excavation chamber more difficult. Boulders and cobbles may lead to severe wear of the cutterhead, tools and tool mountings, as well as generate local instability in case of over-excavation, frequent stops for maintenance works, downtimes and economic loss.

- Inflow of hydrocarbons, gasses or abandoned oil wells: The tunnel alignment develops across known active and dormant oil fields (Torrance Field and Wilmington Oil Field). Oil well removal as well as gassy conditions management may be very time consuming and expensive. Based on this, the tunnel was classified as "gassy", with direct impact on TBM and ancillary equipment specifications.

These risks are discussed in more detail in Schuerch et al., RETC 2023 along with possible impacts on TBM performances and mitigation measures. As a result, the Tunneling Operational Plan (TOP) was developed to provide recommendations on the TBM operation alongside with a flowchart to assist the Contractor in the decision-making process (i.e., Decision Making Tree). This tool allows a timely reaction to any deviation of the encountered conditions from the ones assumed in the design, through the early assessment of the geological conditions during advance (Tamburri et al., RETC 2019, Schuerch at al., RETC 2023).

3 CONSTRUCTION OF THE EFFLUENT OUTFALL TUNNEL

3.1 *Overview of the construction progress*

The construction progress through the northern portion of the alignment is shown in Figure 4. The TBM excavation started with umbilical's (Karlin, RETC 2023) on September 27, 2021 and reached Sta 195+50 on November 8, 2023. On November 10, 2021, after installation of 75 rings, the advance was paused to add back-up gantries no.2 to no.9, perform all electric and hydraulic connections, and test/commission the whole system. On January 10, 2022 the advance was intermittently resumed to allow progressive installation of back-up gantries no.10 to no.18 and perform final field testing and commissioning. TBM launching and commissioning was officially completed in correspondence of ring no. 161 (Sta 8+25), on February 17, 2022.

Total tunnel excavation duration was 110 weeks (773 days). Figure 4 shows monthly, weekly and daily production. The overall average advance rate was 7.5 m/day.

24 x 1.5m advances were completed on the best day, 101 in the best week, and 302 in the best month.

A total of 12 interventions (9 hyperbaric and 3 under atmospheric conditions in improved ground areas – "safe havens") were performed along this portion of the alignment.

3.2 *Encountered geological conditions*

The encountered geological conditions were mainly assessed based upon the observations of the muck (Figure 5) at the Slurry Separation and Treatment Plant (STP) and excavation face inspections. In general, sand with clay and silt in variable amount were observed all along the alignment. Locally, presence of crushed rock (sandstone, mudstone) and Alluvium was encountered.

3.3 *TBM operations*

With respect to the potential geotechnical hazards identified in the design phase, Figure 3 shows the main challenges encountered during advance:

- Clogging between Sta. 10+50 and 27+00: The clayey component of the ground progressively clogged the cutterhead causing the blockage of numerous disc cutter bearings and obstruction of the cutterhead openings. This generated rapid and excessive wear of all components exposed to the ground and frequent stoppages for maintenance. The adopted countermeasures included: addition of anti-clogging polymers; frequent stoppages to clean the cutterhead form the accumulated muck; reduction of the thrust force and advance speed to lower the flow rate of excavated material.
- Jamming of the articulated tail shield: High thrust force levels were observed between Sta. 40+50 and 69+70. Within this area, recurrent issues with the tail shield advancement were experienced, with frictional forces exceeding the capacity of the passive articulation cylinders. The adopted countermeasures included: bentonite injection through radial ports; tail shield vibration; increase of face pressure; installation and utilization of 4 auxiliary hydraulic cylinders to advance the tail shield.
- High wear: no significant/excessive cutter wear was observed, generally being higher in Reach 3 than in Reach 1.
- Inflow of hydrocarbons and/or toxic/explosive gas: low level readings of hydrocarbon in slurry and benzene in muck pile at STA 124+45. In general, either no gas was encountered, or the slurry system managed to keep it within the pipelines (with no dispersion in the tunnel environment).
- Boulders and cobbles, other obstructions: no unknown objects were encountered during the drive, and generally no significant cobbles or boulders.

The more relevant TBM performance parameters are discussed in the following paragraphs based on the analysis of the TBM data and geotechnical monitoring data presented in Figure 6.

3.3.1 *Advance rate*

Figure 6a shows the net advance rate (in mm/min) along the northern portion of the alignment. For most of the drive (approximately 54% between Sta. 25+00 and 130+00), it was in the high range of 40-80 mm/min. The maximum advance rate was governed by the maximum

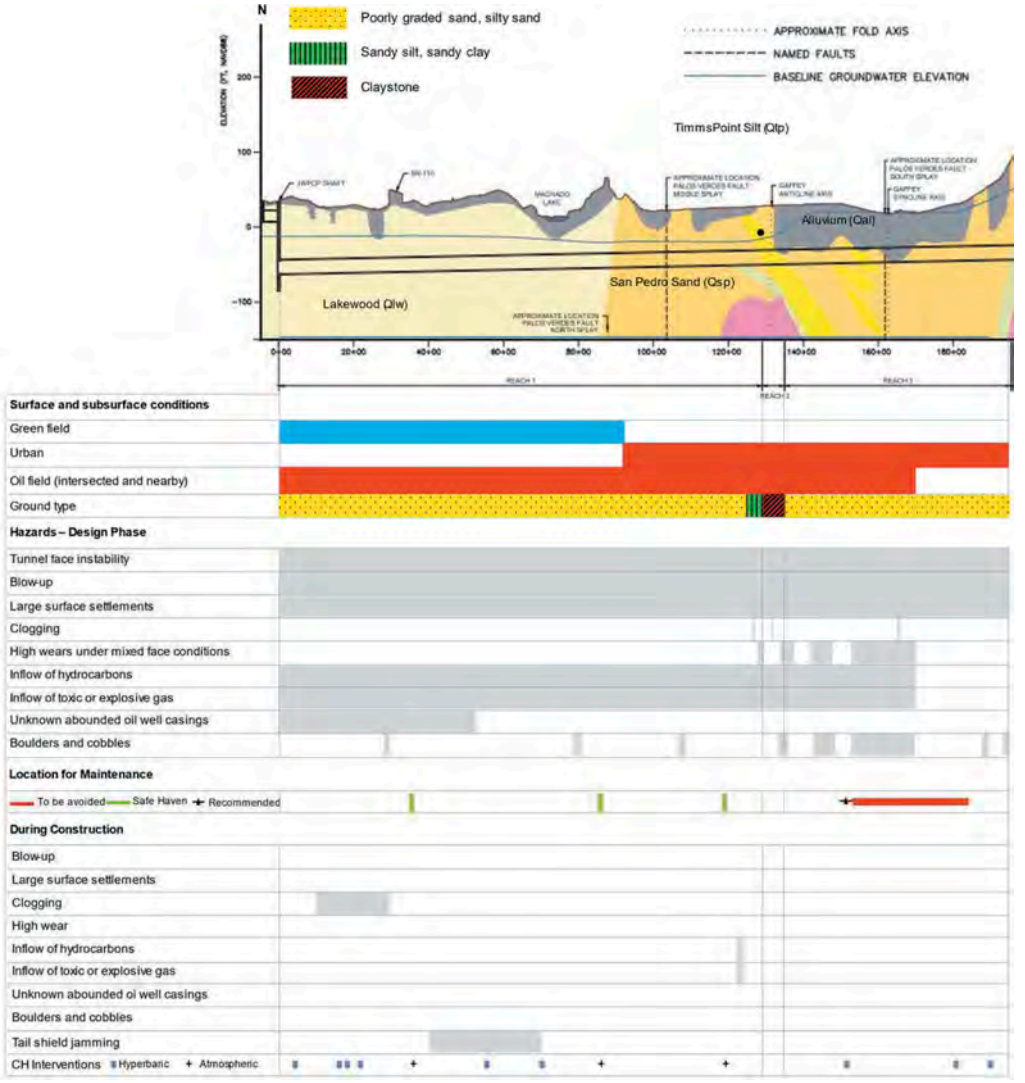

Figure 3. Expected hazards without considering support pressure for the northern section identified in the design (Schuerch et al., RETC 2023) Vs. Actual challenges encountered during excavation (Sta. 0+00 to 195+50).

muck-out capacity of the slurry circuit and the STP. The advance rate was in general lower, in the 20-60 mm/min range, over approximately 41% of the alignment, at the beginning of the excavation up to Sta. 25+00 and again along the last 1675 metres between Sta. 140+00 and 195 +00. The lowest advance rate values, down to 8 mm/min, were recorded between Sta. 130+00 and 140+00 where mixed face conditions (soils and crushed rock) were encountered.

3.3.2 *Face pressure*

Figure 6b shows the face pressure applied during advance along the northern portion of the alignment. The operational range defined in the design phase is also indicated in the chart. The recommended pressures (green line) were defined as target values to compensate groundwater pressure and to avoid face instability and large surface settlements. During operation, the applied face pressure was consistently kept in line or above target but always below the defined maximum limit (red dashed line) determined in the design phase to avoid blow-up. In particular, between Sta. 160+00 and 180+00 where the allowed operational range was extremely narrow (i.e., min 0.1 bar), the TBM operators carefully managed to always keep the face pressure within the recommended upper/lower limits. As shown in Figure 6.e, the ability to accurately control the face pressure kept surface settlements even below the predicted values (i.e., settlements of 4 to 10 mm).

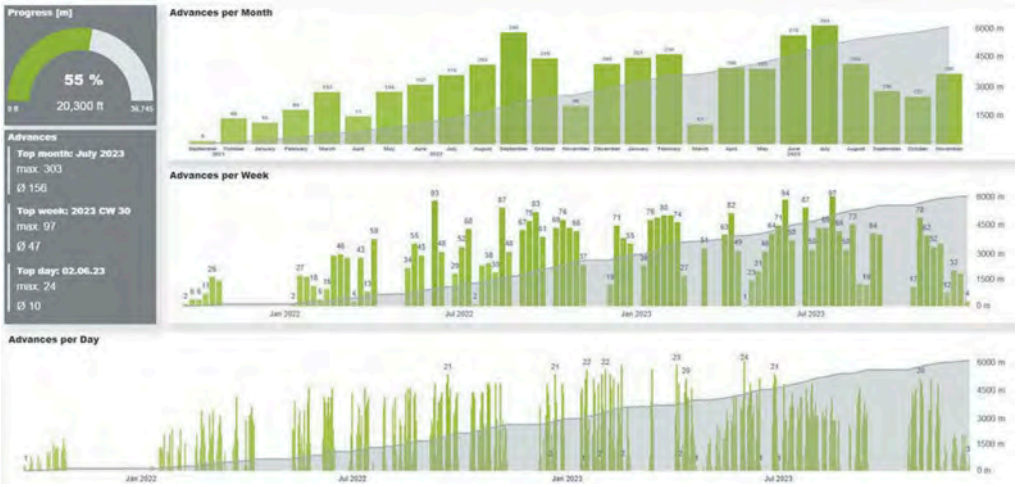

Figure 4. JWPCP Effluent Outfall Tunnel Northern Drive – Daily, Weekly, and Monthly Production charts.

Figure 5. Pictures of the muck (sand; shell fragments).

3.3.3 *Thrust force*

Figure 6c shows the total thrust measured during advance along the northern portion of the alignment along with the required thrust estimated in the design phase (15-18 MN). In line with design estimations, the total thrust was measured below 20 MN along most of the alignment except:

- between Sta. 2+00 and 18+00, in part due to cutterhead clogging issues;
- between Sta 40+00 and 70+00, mostly due to higher frictional resistance along the shields, up to jamming of the tail shield;
- between Sta. 180+00 and 185+00 possibly due to mixed face with Alluvium.

Nevertheless, the total thrust was always well below the TBM installed nominal capacity of 79 MN.

3.3.4 *Cutterhead torque*

Figure 6d shows the cutterhead torque measured during advance along the northern portion of the alignment. With the rotation speed being set at 3 rpm almost over the entire stretch, the measured torque was mainly below the maximum nominal torque of 3.5 MNm. The highest torque was measured between Sta. 170+00 and 190+00, where Alluvium was encountered at the tunnel elevation, and between Sta. 10+50 and 27+00 where challenges related to cutterhead clogging were experienced.

When filled with sticky ground the head tends to become heavier to turn for the main drive. Moreover, an uneven distribution of this additional weight (by buckets, pockets, or entire quadrants more clogged than others) would shift the cutterhead centre of gravity and generate eccentric loading. In this scenario, the head requires more effort for rotation and generates unsteady load patterns on main drive motors and frequency converters.

3.3.5 *Surface settlements*

Figure 6e shows the surface settlements estimated in the design phase for the northern portion of the alignment and the actual vertical displacements measured with the multipoint borehole extensometers installed along the alignment. A1, A2 and A3 indicate the three rods of the instrument installed at different depths.

In the design phase, the assessment of the expected settlements was performed by means of analytical calculations taking into account two different values of volume loss: 0.3% as expected conditions (black line) and 0.5% as conservative assumption (red line). The abovementioned values of volume loss were set according to literature and verified by means of numerical analysis for the most critical sections identified along this portion of the alignment.

The actual ground movements were mainly below the expected values and always below the conservative assumption. The back-analysis of the measured settlements indicates a maximum volume loss of 0.35% and a minimum volume loss of 0.01% with an average of 0.1% that is significantly lower than the one assumed for the design.

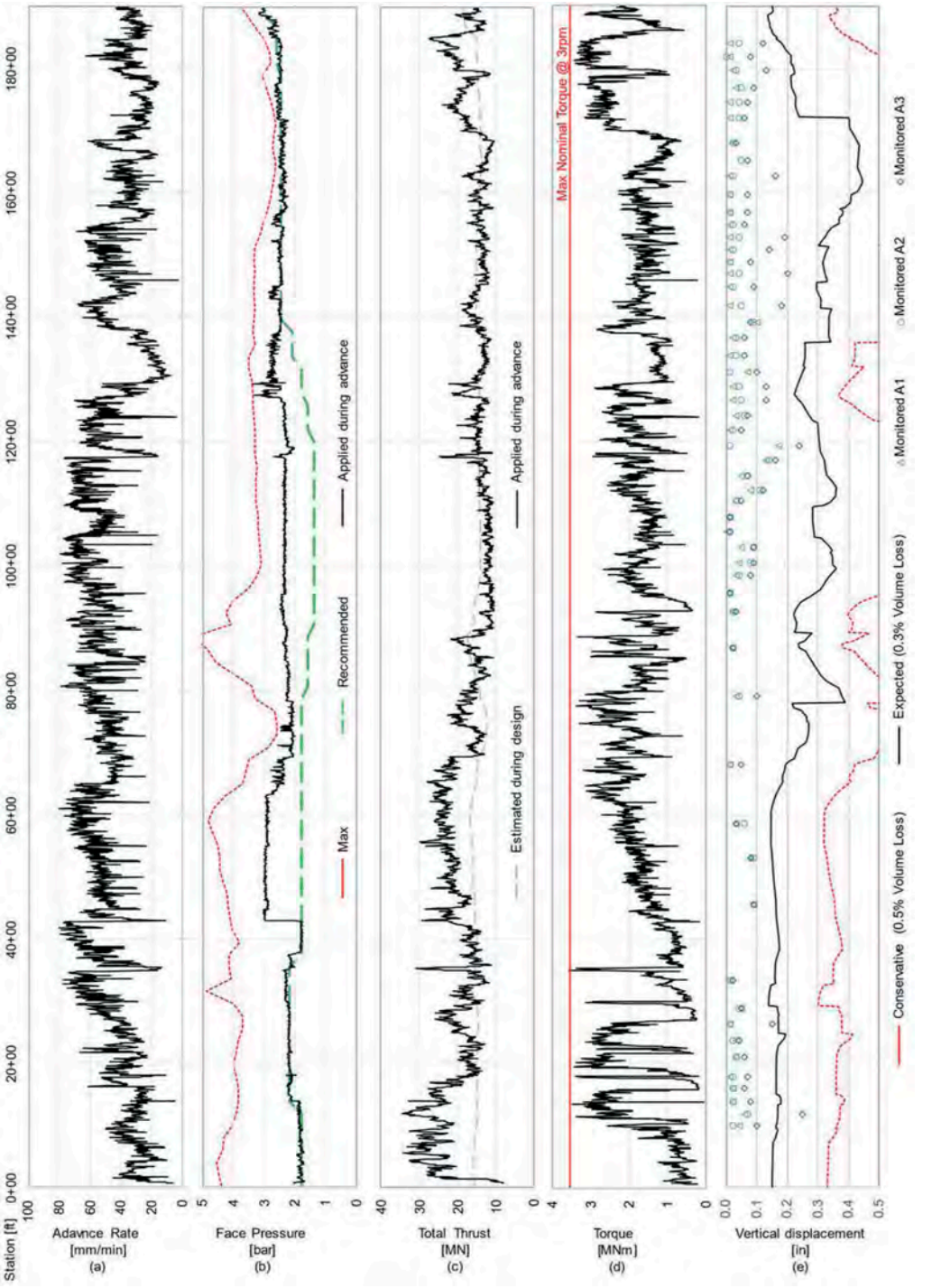

Figure 6. Main TBM operation parameters and geotechnical monitoring data (Sta. 0+00 to 195+50).

The data monitored during advance show in general small ground deformations over the entire tunnel stretch:

- ≤ 3.3 mm for A1,
- ≤ 4.3 mm for A2,
- ≤ 6.35 mm for A3.

These values are mainly below the "Warning Level I" for extensometers and always below the "Maximum Level", defined as follows:

- Warning Level I: Relative vertical movement of 2mm for anchors A1; Relative vertical movement of 6mm for anchors A2; relative vertical movement of 23 mm for anchors A3.
- Warning Level II: Relative vertical movement of 3 mm for anchors A1; Relative vertical movement of 9 mm for anchors A2; relative vertical movement of 25 mm for anchors A3.
- Maximum Level: Relative vertical movement of 4mm for anchors A1; Relative vertical movement of 12mm for anchors A2; relative vertical movement of 36mm for anchors A3.

3.3.6 *Annular grout*

Mainly three (two upper ports and one below springline) out of five ports were consistently used to uniformly inject bicomponent (A+B) grout in the annular gap. Figure 7 shows the total grout volume injected at every ring from all the active ports along with target values. The green line indicates the target volume of 7.3 m^3 or 7,300 liters, as defined in the pre-excavation phase according to the expected conditions. From Sta. 46+90 to 125+00 a revised target volume was defined, reduced to account for a narrower annular gap around the segmental lining and to mitigate the risk of cementation of the tail shield. The red line shows the lower bound that corresponds to the volume in case of full closure of the tail shield gap. The injected grout volumes were consistently on or close to the theoretical target, and well above the minimum recommended value. Proper control of the injected grout volume concurred to the low settlements observed on surface and subsurface.

3.3.7 *Quality of the slurry*

The functions of the slurry in TBM tunneling are to support the tunnel face and wall, to control groundwater, to lubricate the cutterhead and the muck-out system, to carry the muck in suspension, to facilitate the separation of the muck. The bentonite is used to ensure the micro-stability of the soil grains and to seal the tunnel face in order to transfer the support pressure onto the soil skeleton. To seal the tunnel face, the bentonite slurry has to infiltrate the soil and form a filter-cake.

The quality of the slurry is constantly verified by monitoring specific properties (e.g., density, yield

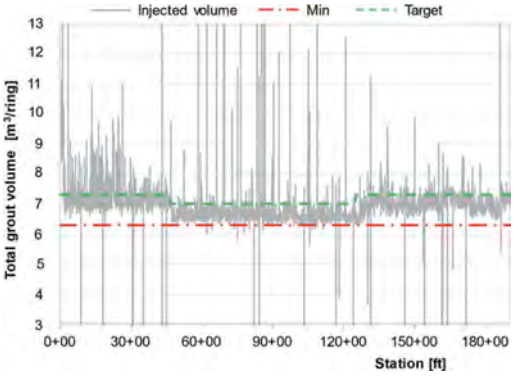

Figure 7. Total grout volume during TBM advance.

point, sand content) and performances. The used bentonite is adjusted by discharging part of it and by adding fresh bentonite or water in order to fulfil the target values of the bentonite slurry parameters.

Figure 8 shows the density of the slurry (feed and return lines) along the northern portion of the alignment and compares it with the target values defined in the design phase (min-max thresholds in red, target range within the green lines). It can be observed that the density in the return line was consistently above the maximum target value of 1.15 t/m³. The local drops below the red-line were usually measured immediately after cutterhead interventions. After treatment at the STP, the density in the feed line was more often lower than 1.15 t/m³. Nonetheless, the density of the slurry resulted being clearly higher than target range defined in the design phase, possibly due to the higher-than-expected amount of fines in the soil matrix.

Figure 8. Density of the slurry during TBM advance.

4 CONCLUSIONS

The northern portion of the new JWPCP Effluent Outfall Tunnel, for a length of 5,960 m, was excavated through soft ground in a highly urbanized area

at low overburden (14 to 35m). Despite the challenges identified in the design phase, the Mix-shield TBM tunneling was successful, also due to the Contractor's ability to operate the TBM within the face pressure ranges and backfill grout volume ranges recommended during the design stage. This resulted in no impacts on existing surface and subsurface structures and utilities, also at very shallow covers (as low as two tunnel diameters at some location). Ground movements were below 5mm for most of the drive and well within the tolerances allowed by contract. However, the heterogeneous nature of the ground, at times, enhanced some of the predicted hazards (i.e., clogging and jamming) to a magnitude or severity that required proactive TBM data analysis, parameters adjustments and specific countermeasures promptly implemented in the field to mitigate impacts on estimated advance rates and project schedule.

REFERENCES

JWPCP Effluent Outfall Tunnel Project, Geotechnical Base Line report (GBR), May 2018. County Sanitation, District No. 2 Los Angeles County, CA, USA.

Schürch, R., Perazzelli, P., Piemontese, M., Scialpi, M., 2023. TBM Excavation under High Water Pressure. Proceedings of the World Tunnel Congress 2023. Athens, Greece.

Schürch, R., Perazzelli, P., Piemontese, M., Halton, P., Cimiotti, C., Karlin, N., 2023. Los Angeles, California JWPCP Effluent Outfall Tunnel Project – Tunneling Under Extremely Challenging Conditions. Proceedings of the the Rapid Excavation & Tunneling Conference 2023. Boston, MA, USA.

Karlin, N., 2023. Unique Umbilical Launch of a Slurry TBM in Los Angeles. Proceedings of the Rapid Excavation & Tunneling Conference 2023. Boston, MA, USA.

Tamburri, E., Pizzarotti, L., Perazzelli, P., Schürch, R., Moranda, G., 2019. The Three Rivers Protection and Overflow Reduction Tunnel (3RPORT) – Decision-making during construction. Proceedings of the Rapid Excavation & Tunneling Conference, Chicago, IL, USA.

Tunnelling for a Better Life – Yan, Celestino, Thewes & Eberhardt (Eds)
© 2024 The Author(s), ISBN 978-1-032-80042-4
Open Access: www.taylorfrancis.com, CC BY-NC-ND 4.0 license

A review of deterministic approaches in the performance evaluation of Raise Boring Machines (RBMs)

Aydin Shaterpour-Mamaghani*
Geological Engineering Department, Istanbul Technical University, Istanbul, Turkey

Hanifi Copur, Cemal Balci & Deniz Tumac
Mining Engineering Department, Istanbul Technical University, Istanbul, Turkey

ABSTRACT: The raise boring technology was initially developed to meet the requirements of the underground mining sector. However, it was also found extensive application in infrastructure projects, including tunnelling for ventilation and the excavation of deep shafts. The selection and precise performance prediction of Raise Boring Machines (RBMs) during the feasibility (planning) stage of a shaft excavation project are crucial for project budgeting and scheduling. The ability to accurately predict and optimize RBM performance leads to more realistic planning that reduces overall shaft excavation costs. Deterministic approaches are one of the most widely used methods to predict the performance of mechanical miners such as RBMs. Deterministic models offer a more detailed and precise approach to performance prediction by considering various parameters. However, they rely heavily on accurate and adequate input data and initial conditions to produce reliable outputs. This paper aims to review the deterministic models used for predicting the operational and performance parameters of RBMs. The applicability of the available models is discussed and examples are presented for field validation.

Keywords: Shafts, Raise boring machines, Performance prediction, Deterministic model

1 INTRODUCTION

The excavation of tunnel and shaft with mechanical miners has been increasing around the world. These equipments provide two significant advantages over the conventional methods as cutting down the time of tunnel/shaft construction and creating safe working conditions. Raise Boring Machine (RBM) is one of the mechanical miners that is commonly used in mining and construction projects for excavation of shafts. These machines offer an economic, safe, and rapid excavation operation compared to other excavation methods. However, capital cost of these machines is high; assembly and disassembly time could be long in some cases (Shaterpour-Mamaghani et al., 2023).

Ability of the operator and prediction of RBM performance are two crucial aspects significantly affecting shaft construction uncertainty. Performance and success of an RBM is influenced by various variables. One of these variables is the geological and geotechnical characteristics of drilled or excavated rocks. Other variables include RBM related mechanical features and operational parameters (available thrust and torque, reamerhead rotational speed, etc.) and technical-environmental parameters (Shaterpour-Mamaghani and Copur, 2017).

Early studies on RBM performance attempted to predict performance based on physical-mechanical properties of the drilled or excavated core samples, as well as the results of indentation tests conducted on the samples (Morris, 1969; Bilgin, 1989; Breeds and Conway, 1992; Dollinger et al., 1998; Shaterpour-Mamaghani et al., 2016, 2018, 2023; Shaterpour-Mamaghani and Copur, 2021). However, the research on performance prediction of RBMs based on rock cutting tests, which provide essential data for deterministic prediction of excavation performance, is limited. Deterministic performance prediction based on full-scale linear rock cutting tests is the most commonly used and more reliable method among the many other prediction methods such as empirical, theoretical, computer simulation, testing a prototype machine in laboratory, and in situ testing of a real machine (Copur et al., 2014; Bilgin et al., 2014). Takaoka et al. (1973) investigated cutting performance of spherical and gear type cutters (with a constant load type rotary cutting test device) on a granite and two andesite rocks at different vertical forces and

*Corresponding author: mamaghani@itu.edu.tr

DOI: 10.1201/9781003495505-282

indicated that for both cutters, the depth and width of the grooves increased as the vertical force increased. Lindqvist (1982) investigated the cutting characteristics of two different single disc cutters (9 mm of blunting radius for regular edge single disc cutter and 9 mm of concave blunting radius of disc cutter) and a three-row button cutter (having hemispherical inserts with 18 mm of diameter and 60 mm of kerf spacing) during cutting tests (in single-spiral pattern on conditioned rock surface) on the fine to medium grained granite with 188 MPa of uniaxial compressive strength. He mentioned that optimum depth of cut in combination with smooth side chipping would increase the utilization of available thrust and torque, but also would decrease vibrations and pulse on inserts, cutters, cutterhead, and boring unit. Savidis (1982) performed cutting tests at static and dynamic rates of loading, using spheres and model cutters equipped with buttons on the sandstone, marble, and granite samples. He stated that in the marble and granite samples, optimum spacing to penetration ratio was almost constant for all levels of pitch; therefore, wider button spacing required deeper penetration to achieve a similar level of efficiency. Shaterpour-Mamaghani et al. (2022) discussed the full-scale linear cutting characteristics of the single slice (row) of a real-life multi-row button cutter used with RBMs in double-spiral cutting pattern on five different rock samples and suggested two deterministic approaches (direct and indirect) to predict operational and performance parameters of RBMs; they also proved that a real-life multi-row (multi-kerf) button cutter could be simulated by using only one row of a multi-row button cutter so that the force limitation of the cutting test equipment was overcome.

The main purpose of the current study is to summarize the basic concepts of deterministic models used for estimating performance of RBMs. Some performance estimation examples are also presented by using these methods.

2 BASIC CONCEPTS OF DETERMINISTIC MODELING

Deterministic modeling is a mathematical approach used to describe and analyse systems or processes where outcomes are entirely predictable and certain, given specific inputs and conditions. In deterministic modeling, there is no randomness or uncertainty involved, and the results are based on precise mathematical or physical relationships.

One of the earlier deterministic models was introduced for hard rock Tunnel Boring Machines (TBMs), (Rostami and Ozdemir, 1993). Copur et al. (2014) used a stochastic model implemented into a deterministic model to predict performance of earth pressure balance TBMs using full-scale linear cutting test to predict instantaneous penetration and cutting rates of the constant cross section and/or V-type disc cutters. In addition, Shaterpour-Mamaghani et al. (2022) used the deterministic methodology given in Rostami and Ozdemir (1993) and Copur et al. (2014) to predict performance of RBMs. This direct deterministic concept is based on directly the full-scale linear cutting tests (limiting or restrictive normal and rolling forces). The details of this deterministic concept are summarized below.

Total thrust ($FT_{cutting}$) (in kN) required for penetrating a cutter into a rock body can be estimated by Equation (1):

$$FT_{cutting} = FN \times N_{cutter} \times f \tag{1}$$

where, FN is average normal force obtained from the full-scale linear cutting tests at optimum cutting conditions (kN), N_{cutter} is the total number of cutters on the reamerhead (it can be taken as total number of rows in this case) and f is a constant related to friction between cutting tool-reamerhead and the excavated rock, and it can be taken as 1.0 for RBMs, since all the cuttings (debris, excavated material) fall down by gravity without causing any important friction on the reamerhead.

The reamerhead net torque requirement ($Tq_{cutting\text{-}net}$) (in kNm) can be estimated by Equation (2):

$$Tq_{cutting-net} = FR \times N_{cutter} \times f \times \left(\frac{D_{RBM}}{4}\right) \tag{2}$$

where, FR is average rolling force obtained from the full-scale linear cutting tests at optimum cutting conditions (kN), D_{RBM} is reamerhead diameter (m), and the other parameters are as defined above.

The total net power requirement ($P_{total\text{-}net}$) of the RBM reamerhead at optimum cutting conditions (in kW) can be estimated by Equation (3):

$$P_{total-net} = 2\pi \times Tq_{cutting-net} \times \left(\frac{RPM}{60}\right) \tag{3}$$

where, RPM is reamerhead rotational speed (in rpm) and the other parameters are as defined above. RPM can be estimated by Equation (4):

$$RPM = \frac{V_{max}}{\pi \times D_{RBM}} \tag{4}$$

where, V_{max} is maximum allowable cutter speed (for gauge/corner cutter) (m/min).

Different RBM manufacturers may suggest different rotational speeds for reamerheads. Sandvik company recommends maximum RPM based on reamerhead diameter and rock characteristics. For example, it was recommended to use 10 rpm (which gives 75 m/min linear rotational speed) for reamerhead with 2.44 m diameter (Sandvik catalogue). Atlas Copco recommends that the maximum rotational speed should be peripheral speed of the head under 107 m/min (350 ft/min) (Brooke, 2008). Liu

and Meng (2015) stated that speed of side (corner) cutters in reamerhead had to be controlled at 0.7-1.0 m/s. In this study, 10 rpm of the rotational speed is assumed and used for the example calculations given in the next section.

Total consumed (gross) power requirement of the reamerhead ($P_{consumed}$) (in kW) is estimated by Equation (5):

$$P_{consumed} = \frac{P_{total-net}}{\eta} \quad (5)$$

where, η is system efficiency factor of reamerhead rotation motor and is assumed and used 0.85 in this study.

The instantaneous penetration rate (IPR) of RBMs (in m/h) can be estimated by Equation (6):

$$IPR = d_R \times RPM \times \frac{60}{1000} \quad (6)$$

where, d_R is depth of cut per revolution (mm/rev) giving the optimum specific energy for a certain (constant) line spacing, and RPM is rotational speed of reamerhead (rpm).

Indirect deterministic concept is another method that can be used to predict performance of RBMs. It is not always possible to perform full-scale linear cutting tests due to some difficulties such as obtaining large blocks of rock samples from the site, extensive time consumption for experiments and costly experiments, as well as requirement of skilled-trained personnel to run the tests. To overcome these problems, the relationships between rock properties and cutting parameters obtained from the full-scale linear cutting tests can be indirectly used as input in the direct deterministic model, which is called indirect deterministic approach in this study. Shaterpour-Mamaghani et al. (2022) suggested some empirical models (Equations 7-11) based on the relationships between physical-mechanical properties of the rocks and normal force (FN), rolling force (FR), FR/FN, specific energy (SE), and ratio of line spacing to depth of cut per revolution (s_L/d_R) found at optimum cutting conditions. In these equations the FN and FR values are normalized by d_R values obtained at the optimum cutting conditions.

$$\left(\frac{FN}{d_R}\right)_{opt} = 0.00003 \times UCS^{2.858} \; R^2 = \; 99\% \quad (7)$$

$$\left(\frac{FR}{d_R}\right)_{opt} = 0.014 \times (UCS \times BTS)^{0.759} \; R^2 = 98\% \quad (8)$$

$$\left(\frac{FR}{FN}\right)_{opt} = (-0.001 \times UCS) + 0.284 \; R^2 = 91\% \quad (9)$$

$$SE_{opt} = 0.35 \times (UCS \times BTS)^{0.83} \; R^2 = \; 98\% \quad (10)$$

$$\left(\frac{s_L}{d_R}\right)_{opt} = 0.00001 \times UCS^{2.711} \; R^2 = \; 98\% \quad (11)$$

3 CASE STUDIES

The results of physical-mechanical property tests, full-scale linear rock cutting tests, and field measurements from some shaft excavations by RBMs given by Shaterpour-Mamaghani et al. (2022) are used to evaluate the deterministic performance prediction models. In Shaterpour-Mamaghani et al. (2022), five rock samples with different geological origins were used in the investigation. The uniaxial compressive strength of the tested samples varied between 77.90 and 130.67 MPa. Moreover, the Brazilian (indirect) tensile strength of the tested samples ranged from 4.90 to 11.09 MPa.

Shaterpour-Mamaghani et al. (2022) mentioned that Sandvik Rhino 1088DC RBM was used in the investigated raise boring projects. Rhino 1088DC RBM is a hydraulically driven rig with maximum 4,000 kN operating thrust. The machine is capable of operating at a torque of 300 kNm in pilot hole drilling and 160 kNm in reaming operation. The reamerhead diameter of this RBM was 2.44 m and equipped with 14 multi-row button cutters. Seven cutters consist of five rows of tungsten carbide inserts and another seven cutters consist of four rows of tungsten carbide inserts (Figure 1). Multi-row button (carbide-insert) cutters (with steel kerfs) with row spacing of around 30-60 mm (with arithmetic average of 45 mm) was used in the RBM. CMR41 (four-row) and CMR52 (five-row) cutters were used as a pair with 180° circumferential (angular) spacing on the reamerhead. The row spacing value sets the cut spacing, while its half is the line spacing. Thus, cutting pattern of the cutters on Rhino 1088DC was double spiral, as its details are described in Copur et al. (2017). Spacings (pitch) between the inserts on a row vary from the inner rows to the outer rows to prevent tracking. Total number of the inserts having a diameter of 22.2 mm in a cutter are 104/four-row-cutter + 128/five-row-cutter (as a pair).

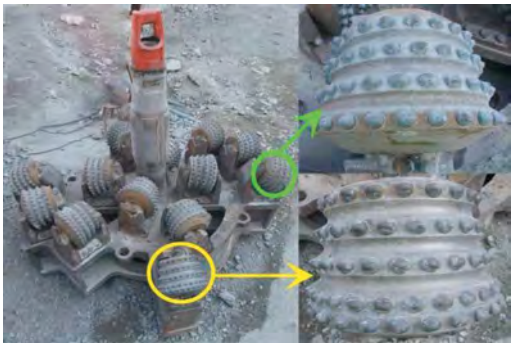

Figure 1. Reamerhead, four and five rows cutters of Sandvik Rhino 1088DC RBM.

The thrust capacity/limit of the cutters used with the RBM (which is a durability limit for the cutters as being important for cutter life) and torque capacity/limit of the RBM reamerhead are considered in the performance prediction. The achievable maximum

depth of cut per revolution is calculated for a certain rock by using these limit values and the force-depth of cut relationships obtained from the full-scale linear cutting tests stated in Shaterpour-Mamaghani et al. (2022). Sandvik company recommended 265 kN/cutter (27 tonnes/cutter) as maximum operating cutter load (Sandvik catalogue). By considering this recommendation, the limiting FN value for average thrust per row is obtained to be 53.0 kN/row (265 kN/cutter/5 rows/cutter). By using torque capacity of the machine (160 kNm) and Equation (2), the limiting FR value is obtained to be 18.74 kN/cutter, and 3.75 kN/row (considering 5 rows). The 5 rows in a cutter is taken into consideration instead of 4 rows, since the maximum force is critical for durability of the 5-row cutters.

By using the limiting FN and FR values as well as force-depth of cut equations (FN-d_R and FR-d_R) mentioned in Shaterpour-Mamaghani et al. (2022) and given in Table 1, it is possible to calculate the achievable maximum depth of cut for each rock. The results of these calculations are summarized in Table 2. It should be noted that the d_R values estimated in Table 2 are not the values obtained at optimum cutting conditions; they are lower than that of the ones obtained at optimum cutting conditions. Then, the smaller depth of cut value limiting either normal force capacity or rolling force capacity is selected for calculation of the instantaneous penetration rate by using Equation (6) for all of the rocks and assuming a rotational speed of 10 rpm as recommended by Sandvik company.

Table 1. Force-depth of cut equations of the investigated rocks (Shaterpour-Mamaghani et al., 2022).

Rocks	FN (kN/row)	FR (kN/row)
Granodiorite	$FN = 48.10 \times {d_R}^{0.53}$	$FR = 2.05 \times {d_R}^{1.25}$
Diabase	$FN = 58.55 \times {d_R}^{0.47}$	$FR = 2.74 \times {d_R}^{1.13}$
Skarn	$FN = 27.83 \times {d_R}^{0.51}$	$FR = 2.14 \times {d_R}^{0.88}$
Limestone-1	$FN = 26.22 \times {d_R}^{0.55}$	$FR = 2.07 \times {d_R}^{0.87}$
Limestone-2	$FN = 16.43 \times {d_R}^{0.67}$	$FR = 0.67 \times {d_R}^{1.28}$

FN normal force per row, FR rolling force per row.

Table 2. Calculated achievable maximum depth of cut values and deterministically predicted instantaneous penetration rates based on the limiting force values.

	d_R (mm/rev) *		
Rocks	Based on FN	Based on FR	IPR (m/h)
Granodiorite	**1.20**	1.62	0.72
Diabase	**0.81**	1.32	0.49
Skarn	3.54	**1.89**	1.13
Limestone-1	3.60	**1.98**	1.19
Limestone-2	5.74	**3.84**	2.30

* Bold values of d_R are used for calculation of IPR.
d_R depth of cut per revolution, IPR instantaneous penetration rate.

By considering the limiting depth of cut values obtained based on the force-depth of cut equations (bold values in Table 2) and using Equations 1, 2, 3 and 5, the total thrust, torque, net and consumed power requirements of the reamerhead can be calculated. For example, as seen in Table 2, the maximum achievable depth of cut is obtained as 0.81 mm/rev in the diabase sample by use of FN-d_R equation, which is smaller than the depth of cut value of 1.32 mm/rev obtained based on FR-d_R equation. In this case, for obtaining total thrust ($FT_{cutting}$), FN (kN/row) is first calculated by using FN-d_R equation given in Table 1 for 0.81 mm/rev depth of cut value; then, $FT_{cutting}$ is estimated by using Equation (1) as shown below for diabase sample:

$$FT_{cutting} = FN \times N_{cutter} \times f = 53 \times ((5 \times 7) + (4 \times 7)) \times 1 = 3,339kN$$

where, 5×7 part of the equation indicates 7 cutters with 5 rows and 4×7 indicates 7 cutters with 4 rows, giving totally 63 rows for 14 multi-row cutters in the reamerhead. In addition, for estimating reamerhead torque ($Tq_{cutting\text{-}net}$), FR (kN/row) is calculated as being 2.16 kN/row for 0.81 mm/rev based on FR-d_R equation for the diabase sample given in Table 1. Then, $Tq_{cutting\text{-}net}$ is estimated by using Equation (2) as shown below for diabase sample:

$$Tq_{cutting-net} = FR \times N_{cutter} \times f \times \left(\frac{D_{RBM}}{4}\right) = 2.16 \times (5 \times 7 + 4 \times 7) \times 1 \times \frac{2.44}{4} = 83.0\ kNm$$

Equation (3) is used to estimate the total net power ($P_{total\text{-}net}$). When estimating the gross (consumed) power requirement of the reamerhead ($P_{consumed}$) as in Equation (5), $P_{total\text{-}net}$ value is divided by the efficiency factor η that is assumed to be 0.85 in this study. The results of these estimations are summarized in Table 3 for all of the rocks. As seen, the thrust (4,000 kN) and torque (160 kNm) capacities of the RBM are not exceeded.

Table 3. Estimated operational parameters of RBM by using direct deterministic method.

Rocks	FT_{cuting} (kN)	$Tq_{cutting\text{-}net}$ (kNm)	$P_{total\text{-}net}$ (kW)	$P_{consumed}$ (kW)
Granodiorite	3,339	99	104	122
Diabase	3,339	83	87	102
Skarn	2,426	144	151	177
Limestone-1	2,404	144	151	177
Limestone-2	2,549	144	151	177

$FT_{cutting}$ reamerhead total thrust,
$Tq_{cutting\text{-}net}$ reamerhead net torque requirement,
$P_{total\text{-}net}$ reamerhead total net power requirement, $P_{consumed}$ reamerhead consumed (gross) power requirement

Another example here is given based on the indirect deterministic performance estimation concept. If diabase sample having a uniaxial compressive strength of 130.67 MPa and a tensile strength of 7.81 MPa is considered, the normal and rolling forces normalized by the depth of cut per revolution are obtained as 33.51 kN/row/mm/rev and 2.69 kN/row/mm/rev by using Equations (7-8), respectively. Then, by using limiting cutter normal and rolling forces (FN = 53.0 kN/row and FR = 3.75 kN/row, respectively), the maximum depth of cut values are calculated as shown below:

$$d_R = (53\text{kN/row})/(33.51\text{kN/row/mm/rev}) = 1.58\text{mm/rev}$$

$$d_R = (3.75\text{kN/row})/(2.69\text{kN/row/mm/rev}) = 1.39\text{mm/rev}$$

As seen, the achievable maximum depth of cut per revolution for diabase is obtained as 1.39 mm/rev, which is the limiting value for the torque and smaller than the d_R value (1.58 mm/rev) limiting the cutter thrust. Then, the instantaneous penetration rate is obtained by using Equation (6) as 0.84 m/h for 10 rpm rotational speed. In addition, by considering 1.39 mm/rev of depth of cut per revolution and using Equations (7-8), the normal and rolling forces are obtained as 46.58 kN/row and 3.74 kN/row, respectively, as shown below:

$$\left(\frac{FN}{1.39}\right) = 33.51\,\text{kN/row/mm/rev} \rightarrow FN = 46.58\,\text{kN/row}$$

$$\left(\frac{FR}{1.39}\right) = 2.69\,kN/row/mm/rev \rightarrow FR = 3.74kN/row$$

Finally, by using Equations (1, 2, 3, 5), operational parameters of the RBM are calculated. The results of indirect deterministic estimations by implementing the relationships between the rock properties and linear cutting performance parameters are summarized in Table 4.

Table 4. Estimated operational-performance parameters of RBM by using indirect deterministic method.

Rocks	IPR (m/h)	FT_{cuting} (kN)	$Tq_{cutting\text{-}net}$ (kNm)	$P_{total\text{-}net}$ (kW)	$P_{consumed}$ (kW)
Granodiorite	0.76	1,415	144	151	178
Diabase	0.84	2,934	144	150	177
Skarn	1.39	1,596	144	151	177
Limestone-1	1.63	1,505	144	151	178
Limestone-2	1.76	1,410	144	151	178

IPR instantaneous penetration rate, $FT_{cutting}$ reamerhead total thrust,
$Tq_{cutting\text{-}net}$ reamerhead net torque requirement,
$P_{total\text{-}net}$ reamerhead total net power requirement, $P_{consumed}$ reamerhead consumed (gross) power requirement

When the results of the direct and indirect deterministic performance estimation concepts are compared with the field results mentioned in Shaterpour-Mamaghani et al. (2022), a certain difference is seen between the field performance (unit penetration, instantaneous penetration rate) and operational parameters (thrust, torque, power). As stated by Shaterpour-Mamaghani et al. (2022), these differences are due to the different physical-mechanical (intact) properties of the rocks and the rock mass characteristics (especially existence of joints and fractures) between the samples tested by the full-scale linear cutting and the rock mass excavated in the field at the shaft locations. Massive (joint-free, competent with RQD of 100%) rock blocks were used in the full-scale linear cutting tests, while the rock masses excavated in the shafts have usually some joints and fractures that would also generate a difference and a discrepancy on the predictions.

Another reason for deviations between the predicted and realized (field) performance is the applied levels of the operator dependent parameters in the field, especially reamerhead rotational speed. The operators applied around 3.5-4.0 rpm in the field, while it is assumed in this study that the reamerhead rotational speed is 10 rpm as suggested by the RBM manufacturer. Therefore, these issues generating deviations on the predictions should be properly managed to obtain more precise and reliable predictions. The effects of strength values on the predictions are taken into consideration if the deterministic method by implementing the relationships between rock properties and cutting parameters obtained from full-scale linear cutting tests are used. However, the effect of rock mass characteristics and rotational speed of reamerhead should also be taken into consideration.

Among the tested samples in Shaterpour-Mamaghani et al. (2022), the limestone-2 sample looks like massive or without too much fractures (with high RQD value). The only difference between the core samples and block samples are the uniaxial compressive strength and Brazilian tensile strength (Table 5).

Table 5. Geotechnical properties of the limestone-2 core and block samples.

Samples	RQD (%)	Uniaxial Compressive Strength (MPa)	Brazilian Tensile Strength (MPa)
Core Sample	89 (field)	115.8	5.41
Block Sample	100 (block)	77.90	4.90

It is seen that the unit penetration is well predicted for the limestone-2 sample by the indirect deterministic model. In Equation (6), if an RPM value of 3.8 rpm as in the field application is used instead of 10 rpm along with a predicted d_R value of 2.93 mm/rev, an IPR value of 0.67 m/h is obtained. This indicates that the model suggested in this study works very well for predicting unit penetration and instantaneous penetration rate of

massive rock masses. However, the predicted values of the operational parameters ($FT_{cutting}$, $Tq_{cutting\text{-}net}$, and $P_{consumed}$) deviate from the realized field parameters, which requires further investigations in future. The influence of joints within the rock mass on predictions should also be further investigated.

4 CONCLUSIONS

There are quite limited studies on performance prediction of RBMs based on the deterministic model. In this study, some of the recent literature on deterministic performance estimation are summarized. In addition, the direct and indirect deterministic concepts of Shaterpour-Mamaghani et al. (2022) are discussed with examples.

The direct deterministic method (based on limiting normal (thrust) and rolling (torque) forces) uses directly results of the full-scale linear cutting tests if a large block rock sample (~50x60x80 cm) is obtained at the same location of the excavated shaft. The indirect deterministic method uses the statistical relationships between the physical-mechanical properties of rocks and the tool forces obtained from the full-scale linear cutting tests if any large block of rock sample is not obtained (only core samples are available).

It is seen that the direct and indirect methods of deterministic performance estimations for RBMs are reliable methods for especially unit penetration and instantaneous penetration rates within the limits of the available data. However, an improvement is needed for predicting thrust force and torque as well as consumed power parameters of RBMs.

ACKNOWLEDGMENTS

This study summarizes some of the results of PhD study carried out by Aydin Shaterpour-Mamaghani. The authors are grateful to the Scientific and Technological Research Council of Turkey (TUBITAK) for their financial support in Project MAG-217M729. The contributions of Esan Eczacibasi (Balya lead-zinc mine), DSI (State Hydraulic Works), Joint-venture Limak-Cengiz-Kolin and Sargin Construction and Machinery Industry Trade Inc are acknowledged, without whom this study could not be accomplished.

REFERENCES

Bilgin, N., 1989. Applied Rock Cutting Mechanics for Civil and Mining Engineers. 1st ed. Istanbul: Birsen (In Turkish).

Bilgin, N., Copur, H., Balci, C., 2014. Mechanical excavation in mining and civil industries. 1st ed. CRC Press, New York.

Breeds, C.D., Conway, J.J., 1992. Rapid Excavation. SME Mining Engineering Handbook, Second edition, senior editor: Howard L. Hartman, Littleton, Colorado. pp. 1871–1917.

Brooke, S. 2008. Rock drillability. In: Atlas Copco Rock Drills AB (ed) Raise boring in mining and construction, first edition, Örebro, Sweden, pp. 3–6.

Copur, H., Aydin, H., Bilgin, N., Balci, C., Tumac, D., Dayanc, C., 2014. Predicting performance of EPB TBMs by using a stochastic model implemented into a deterministic model. Tunnelling and Underground Space Technology. 42, 1–14.

Copur, H., Bilgin, N., Balci, C., Tumac, D., Avunduk, E., 2017. Effects of different cutting patterns and experimental conditions on the performance of a conical drag tool. Rock Mechanics and Rock Engineering. 50, 1585–1609.

Dollinger, G.L., Handewith, H.J., and Breeds, C.D., 1998. Use of the Punch Test for Estimating TBM Performance. Tunnelling and Underground Space Technology. 13 (4), 403–408.

Lindqvist, P.A., 1982. Energy consumption in disc cutting of hard rock. In: Tunnelling 82: papers presented at the third international symposium, organized by the Institution of Mining and Metallurgy, (ed) M.J. Jones, London: The Institution of Mining and Metallurgy, pp. 189–196.

Liu, Z., Meng, Y. 2015. Key technologies of drilling process with raise boring method. Journal of Rock Mechanics and Geotechnical Engineering. 7, 385–394.

Morris, R.I., 1969. Rock drillability related to a roller cone bit. In: Proceedings of society of petroleum Engineers of AIME. Paper No. SPE 2389. pp. 79–86.

Rostami, J., Ozdemir, L. 1993. A new model for performance prediction of hard rock TBMs. Proceedings of Rapid Excavation and Tunnelling Conference, USA, pp. 794–809.

Sandvik Catalogue. Rock drilling tools, Raise boring heads, user manual. Sandvik Mining and Construction Tools AB, pp. 1–44.

Savidis, G.M., 1982. Fundamental studies on the excavation of rock by button cutter. Doctoral Dissertations, University of New South Wales, Australia.

Shaterpour-Mamaghani, A., Bilgin, N., Balci, C., Avunduk, E., Polat, C., 2016. Predicting Performance of Raise Boring Machines Using Empirical Models. Rock Mechanics and Rock Engineering. 49 (8), 3377–3385.

Shaterpour-Mamaghani, A., Copur, H., 2017. Factors affecting the selection and performance of raise boring machines (RBMs) and case studies from Turkey. In: 26th International Symposium on Mine Planning & Equipment Selection Conference, Luleå, Sweden, pp. 153–161 (ISBN: 978-91-7583-935-6).

Shaterpour-Mamaghani, A., Copur, H., 2021. Empirical Performance Prediction for Raise Boring Machines Based on Rock Properties, Pilot Hole Drilling Data and Raise Inclination. Rock Mechanics and Rock Engineering, 54, 1707–1730.

Shaterpour-Mamaghani, A., Copur, H., Balci, C., Tumac, D., Kocbay, A., Dogan, E., Altintas, E., Erdogan, T., Sirin, O., Gumus, A., 2023. Suggestion of new models for predicting performance of raise boring machines based on indentation tests. Tunneling and Underground Space Technology, 138, 105181.

Shaterpour-Mamaghani, A., Copur, H., Dogan, E., Erdogan, T., 2018. Development of new empirical models for performance estimation of a raise boring machine. Tunnelling and Underground Space Technology. 82, 428–441.

Shaterpour-Mamaghani, A., Copur, H., Gumus, A., Tumac, D., Balci, C., Erdogan, T., Dogan, E., Kocbay, A., 2022. Full-scale linear cutting tests using a button cutter and deterministic performance prediction modeling for raise boring machines. Tunnelling and Underground Space Technology 127, 104609.

Takaoka, S., Hayamizu, H., Misawa, S., Kuriyagawa, M., 1973. Studies on the cutting of rock by rotary cutters. Part II: Cutting using a spherical chip and a milled tooth cutter. Tunnels and Tunneling. 5 (3), 276–283.

Tunnelling for a Better Life – Yan, Celestino, Thewes & Eberhardt (Eds)
© 2024 The Author(s), ISBN 978-1-032-80042-4
Open Access: www.taylorfrancis.com, CC BY-NC-ND 4.0 license

Distinctive considerations in the design and construction of large diameter TBM-built tunnels in urban environment – a UK perspective (ID: 379)

Si Shen*
TYPSA UK & Ireland, London, UK

ABSTRACT: Large diameter TBM-built tunnels, particularly in soft ground conditions, is of significant technical challenges in an urban environment. The challenges can be divided into technical and construction related categories. From a design perspective, the volume loss from a large diameter tunnel will result in a significant amount of surface settlement. The utilisation of tunnel space, spatial requirement at launch, lining deformation control and ground settlement control are all technical challenges that the designer should bear in mind. From a construction perspective, substantial power requirement, logistics for transporting the heavy tunnel segments and spoil removal required for the large diameter tunnel is of particular importance in the project delivery. TBM selection for large diameter tunnels in the context of the local ground condition is also different from that for the normal sized tunnel. This paper will provide a general overview of the design and construction of large diameter TBM-built tunnels, with particular reference to case studies from the United Kingdom.

Keywords: Tunnelling, Large diameter tunnel, TBM technology, variable density

1 INTRODUCTION

In recent years, the United Kingdom (UK) has witnessed remarkable transformations in tunnel construction, primarily driven by the advancements in tunnel boring machine (TBM) technology. One of the most noteworthy trends in this evolving landscape is the continuous increase in the diameter of tunnels being constructed. The most recent project examples include hs2 and Silvertown tunnel which are under live construction; projects of large diameter such as A303 Stonehenge tunnel and Lower Thames Crossing are also planned down the pipeline.

Figure 1 illustrates the evolution of tunnel sizes of major projects in London, where the vast majority of tunnelling works take place, using data from a number of well-known projects both in the past and planned down the pipeline. A strong trend of increase in tunnel diameters can be observed, from the vintage London Tube to modern infrastructural projects such as Crossrail, HS2, Silvertown, and the Lower Thames Crossing down the pipeline.

The significance of tunnel dimensions is evident as tunnel design and construction inherently entail specific size-related implications. Based on personal experience, the author would like to acknowledge that with increased tunnel diameter, comes a host of unique and multifaceted challenges, encompassing both construction-related and design-related aspects.

This trend in tunnel diameter is not merely a numerical progression; it represents a profound shift in the capabilities and possibilities of underground infrastructure development in the UK. As we delve deeper into the intricacies of this phenomenon, it becomes evident that this evolution is reshaping the way we perceive and harness subterranean spaces, with far-reaching implications for transportation, utilities, and urban development. In this exploration, we will delve into the factors driving this trend, its impact on various sectors, and the exciting prospects it presents for the future of infrastructure in the United Kingdom.

In the context of this paper, we define a 'large diameter tunnel' as one that has an excavation diameter of close to or greater than 10m. This paper aims to provide an overview of the following challenges that are unique to large diameter TBM mined tunnels, using plain English, without the reference to any equations, making it accessible to a wider audience. The larger the tunnel diameter is, the more pronounced the following challenges tend to be.

- Construction and logistics:
  - High power requirement, especially for EPB
  - Large and heavy tunnel segments

*Corresponding author: sshen@typsa.es

DOI: 10.1201/9781003495505-283

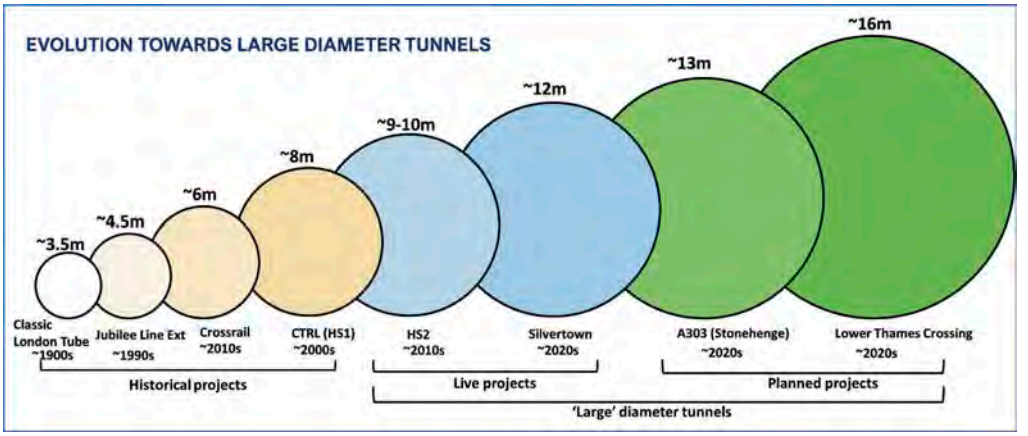

Figure 1. The trend of evolution towards large diameter tunnels in London (diameter from each project indicative only).

Figure 2. TBMs from Silvertown (left) and hs2 C1 contract (right) respectively. Image credit: Herrenknecht.

  - Long ring assembling time
  - Large spoil and grout volume
- Face stability and intervention
  - Mixed face condition
  - Pressure control
  - High groundwater pressure
  - Face intervention
- TBM selection
- Design:
  - Spatial utilisation
  - Low overburden at launch
  - Deformation control
  - Surface settlement
  - Buoyancy uplift

2 CHALLENGES IN CONSTRUCTION AND LOGISTICS

Firstly, a substantial amount of torque is required to operate large diameter cutterheads. Bambridge et al. (2013) find that the TBM torque is cubically proportionate to the tunnel diameter, which means a 10m diameter TBM requires a torque output of approximately 8 times that from a 5m diameter one under the same ground conditions, as an example. The required torque is even higher in the case of Earth Pressure Balance (EPB) tunnel boring machines, which inherently involve more abrasive cutting processes, handling the muck in a solid or semi-solid state. This necessitates a considerable amount of power, making the engineering of power systems a paramount concern. Availability of electric supply in large diameter TBM may be a show-stopper for certain rural locations or cities that are unable to facilitate a significant increase in local power demand, especially if two TBMs are driven simultaneously. The biggest diameter TBM in the UK on a live project is from the Silvertown project, at an excavated diameter of 11.87m, with a cutterhead power of 5,600 kW and a torque of 31,093 kNm (source: Herrenknecht).

Furthermore, the thickness of tunnel segments presents another noteworthy aspect. Segments of 500mm to 600mm or even beyond in thickness are not uncommon around the world for large diameter tunnels, as the segment thickness largely follows a linear relationship with tunnel diameter (Salas and Della Valle, 2012). This places significant demands

on the volume capabilities of the tunnel logistics. Width, height and weight restrictions of highways and bridges apply if the segments are transported via roads. Due to the limits logistics capacity, it is common practice to divide a full tunnel ring into more segments, making each segment smaller in size and lighter in weight, albeit at the expense of prolonging the ring assembly cycle. For a normal sized tunnel, typical ring assembly cycle time is approximately 20-30 minutes; whereas for a large diameter tunnel, the assembly cycle time can be 40 minutes or more. Therefore the decision-making process on the segment geometry usually involves a trade-off between ease of construction logistics and speed of assembly.

The problem of prolonged ring-building cycle makes measures that can achieve continuous mining more cost-effective. Whilst in hard-rock conditions, this can be achieved by a 'double-shield' TBM, where the TBM advancement thrusts off a pair of grippers as the ring building is taking place, it is relatively more challenging to achieve in soft ground conditions that prevails in the UK. As an UK example, Hs2 Chiltern tunnel adopted a 'semi-continuous mining' methodology for the TBM ring building, allowing the TBM to re-start advancement thrusting off a partially completed ring (Reilly and O'Keefe, 2022). This makes the excavation and ring building to become a more continuously cyclic activity.

Moreover, the considerable quantity of excavated materials conveyed out from and into tunnel face simultaneously presents a monumental challenge, necessitating meticulous logistics planning and execution of spoil handling. Spoils are usually required to be disposed of at a defined location due to environmental considerations, and this may require logistics via the road, or usually better, the railway or barge. Hs2 S1/S2 contractor SCS adopted a 'NEMO' concept (Hooton et al., 2020) to maximise re-use of spoil locally on site for landscaping, based on a multi-disciplinary collaboration. They have also adopted a spoil conveyor belt to reduce disruption to road traffic (Moore, 2022). At the Chiltern tunnel site, the C1 contractor ALIGN adopted an innovative method of treating chalk spoil, turning it into 'chalk cakes' to be re-used for slope landscaping (hs2, 2021).

Simultaneous parallel operation is another particular challenge as well as opportunity for large diameter tunnels, due to its inherent large available space on cross-section. When planned right, simultaneous operation can be permitted to all or a number of activities in the TBM including but not limited to: out-logistics (mainly excavated spoil removal), in-logistics (mainly segments, tunnel internal structures and consumables such as grout), ground treatment, installation of tunnel internal structure, cross passage construction, TBM maintenance such as change of cutter tools. The 'scale factor' of large diameter tunnels increases the volume of these elements in a non-linear manner. For example, the volume of excavated spoil and the annulus grout are both in a squared relationship to the tunnel diameter. Nevertheless, on the flip side of the coin, the large available cross-sectional area may permit parallel installation of multiple TBM configurations, which will be discussed in later sections of this paper.

3 CHALLENGES IN FACE STABILITY AND INTERVENTION

Tunnelling in the UK, and especially in and around London, where the majority of tunnelling work takes place, is primarily situated within the 'soft ground' remit, i.e. soil, as opposed to rock (Jones, 2022). In the context of this paper, chalk is also classified as 'soft ground'.

In 'soft ground' tunnelling, the stability of the tunnel face assumes critical importance, particularly in the case of large diameter tunnels. In the case of large diameter TBMs, considerable mixed face conditions, encompassing diverse rock types, soil compositions, fault zones, dissolution features and water table variations, may be inevitable. Even if a homogenous route is planned, the excavation may uncover unexpected ground conditions. Different layers could bear different face pressure, which calls for a higher level of accuracy in the face pressure control of the TBM.

The pressure control of EPB TBM is relatively less accurate compared to slurry, since it mostly relies on the muck itself to balance the pressure, which tends to be variable. The balancing pressure of a slurry TBM better follows a hydraulic gradient thanks to the presence of bentonite fluid, as well as an air bubble mechanism serves to regulate face pressure. When facing particular challenges such as high ground permeability, low ground cover or karst features, adopting a thicker and heavier bentonite suspension (slurry) can be a suitable solution – this will be further discussed later in this paper.

Furthermore, large diameter tunnels typically require deeper ground cover, resulting in high groundwater pressure at the face. Consequently, the management of hydrostatic pressure gradients at the face presents a multifaceted challenge. The implementation of robust dewatering systems, including wellpoints, pumping mechanisms, and grouting techniques, can be complementary measures for the control and prevention of water infiltration into the tunnel.

Bambridge et al. (2013) find that the TBM ram thrust increases almost quadratically with the tunnel diameter in order to resist the face pressure and overcome the shield friction. This places high importance on the TBM specifications and the structural capacity of the tunnel segments to resist such ram thrusts.

In addition, mixed face conditions, as well as the presence of boulders are likely to result in more

wear of the cutter tools. This leads to higher frequency of face interventions for maintenance, and stoppage of construction progress. Consequently, it is obviously imperative to minimize the frequency and duration of such face interventions, such as the replacement of cutters. Notably, Slurry Tunnel Boring Machines (TBM) exhibit a relatively reduced need for face maintenance compared to other alternatives.

Certain face interventions entail substantial costs and pose significant health and safety hazards, particularly when conducted under hyperbaric conditions, which underscores the paramount importance of meticulous planning for face intervention, in conjunction with the judicious utilization of so-called 'safe havens' wherever possible, to mitigate negative impact to human health when conducting hyperbaric face intervention. 'Safe havens' are discrete locations along the tunnel drive where face intervention can be undertaken under the atmospheric pressure, either under natural ground conditions or with human interventions such as ground treatment. These have been used on Lee Tunnels in chalk even under almost 8 bars of water pressure (Newman et al., 2016). Tunnels with large diameters pose greater challenges in identifying suitable 'safe havens' for conducting free air face interventions, primarily owing to their large span and heightened internal pressure. To ensure the ground is self-standing, prior ground treatment may be required, and this can possibly be achieved from within the TBM through the cutterhead.

Given the increased complexity associated with facilitating human access for face intervention within such tunnels, it becomes increasingly appealing to establish means for performing essential face maintenance tasks, including the replacement of cutting tools, without necessitating human presence. Various advanced technologies are currently accessible for ensuring accessibility to the cutterhead under free air conditions or for employing robotic arms to execute cutter tool replacements.

'Saturation diving' may be required in certain circumstances for situations where high water pressure is present and hyperbaric intervention is unavoidable. Regulatory authorities in the United Kingdom places tight restrictions over the exposure of compressed air and the use of saturation diving to achieve hyperbaric intervention. In the UK, the health of individuals is regulated by "The Work in Compressed Air Regulations 1996", and accompanied by guidance document L96 (The Stationary Office, 1996; HSE, 1996).

4 CHALLENGES IN TBM SELECTION

4.1 *TBM selection in soft ground conditions*

There is a wide variety of TBMs available in the market, with each specifically designed to tackle a given type of ground conditions at maximum efficiency (high speed, low cost and risk). In 'soft' ground conditions, particularly in an urban area, a tunnelling shield is usually compulsory, in order to control ground movement.

In the context of 'soft ground' tunnelling predominant in the UK, face pressure support can be achieved by one or more of the following measures:

- **Excavated material** – this type is typically called "Earth Pressure Balance (EPB)" machine. It uses the excavated material itself, mixed with conditioner to make it more fluid, to balance the pressure. As an example from the UK, the hs2 Northolt tunnel TBM "Sushila" is EPB type.
- **Hydraulic pressure** – this type is typically called "slurry" machine, because the fluid typically takes the form of slurry (bentonite), which is water with suspension of fine clay particles. As an example from the UK, the Thames Tideway East TBM "Selina" is slurry type.
- **Compressed air or mechanical support** – typically during a face intervention activity when the shield is backed away from the tunnelling face. These are not systematically used in the UK for large diameter tunnelling.

For major tunnelling projects in soft ground, particularly in an urban environment, the choice of the TBM usually comes down to a decision between EPB and slurry. The decision-making comprises a number of factors including the expected ground particle size, presence of ground water, production rates, upfront cost, and so on.

Nevertheless, EPB and Slurry machines do not necessarily have to be mutually exclusive. A TBM can be configured to include function for both modes. Multi-mode TBMs offer the flexibility of adapting to changing ground conditions, to cope with all foreseeable ground condition changes during the drive. However, the conversion typically can take between days and weeks to complete, during which is the TBM's downtime (no production). This is particularly true if an additional stone crusher is required in front of the slurry circuit intake screen (Billota et al., 2022), which is commonly used to de-risk bands of flint which often occur in chalk in the ground conditions of the UK. Therefore the conversion has to be limited to as few times as possible, and typically only 1 to 2 times during the drive. Also, the upfront cost for procuring such a mechanically complex TBM is naturally higher compared to its peers.

4.2 *'Variable density' TBM*

The 'variable density' TBM, which has been used on the hs2 project as the first in the history of the United Kingdom (smith, 2020), is a type of multi-modal TBM that permits switching modes almost freely without any significant internal system alteration. Especially in the case of large diameter

tunnels, the available space is sufficient to accommodate parallel installation of screw conveyor and slurry circuit in the invert section of the TBM. The 'variable density' TBM is by far the most versatile and mechanically sophisticated type of soft ground TBM in use. The variable density TBM used on hs2 project has four modes, EPB, slurry, mixed EPB and slurry, and high density slurry (source: Herrenknecht). It is capable of adapting to a large variety of benign and hostile ground conditions with short response time, reducing the need for pre-engineering and mitigation. Therefore it shines when dealing with long drive, variable face conditions and large diameter, for which a large number of swift switch-overs in mode is beneficial.

Needless to say, the capital cost of type of TBM can be prohibitive for the majority of tunnelling projects. However, in large scale and large diameter tunnelling, the capital cost of TBM procurement usually becomes less significant compared to their conventional peers, and more importantly a high-spec TBM can prove to be more cost-effective in providing risk mitigations for long drives and complex ground conditions, maintaining high efficiency and low risk throughout the drive alignment.

4.3 *High density slurry*

'High density slurry' is one of the four available modes in the variable density TBM used on hs2, as stated above. As the name suggests, this mode utilises 'high density' slurry, for which the following features are more pronounced, as illustrated in Figure 3:

- Firstly, it has higher viscosity. Due to its insignificant shear capacity, slurry suspension fluid to a large extent behave as a liquid, seeping into the pore space of the ground. It has certain penetration distance into the ground ahead of the tunnelling face (DAUB, 2016). The larger grain size the soil has, the greater the penetration distance is. Higher viscosity increases its shear capacity, making it behave less like a liquid and more towards a solid. This way the frictional resistance between the slurry and the soil particles is increased, reducing the distance of penetration before equilibrium is reached. Therefore high density slurry can be used in ground with higher permeability, such as coarse sands and gravels.
- For the same principle, high density slurry also has significant advantages of bridging across fault zones or karstic features, to help prevent or reduce loss of slurry at these significant but frequently encountered ground hazards in tunnelling. It can allow the TBM pass some of these features without disruption from the necessity of other mitigation measures such as grouting.
- Due to higher solid suspension rate, high density slurry has higher density. This results in steeper hydraulic pressure gradient. For any given tunnelling face pressure to be balanced, the pressure at the crown of the tunnel is lower (low hydraulic head, as shown in Figure 3), and this reduces the

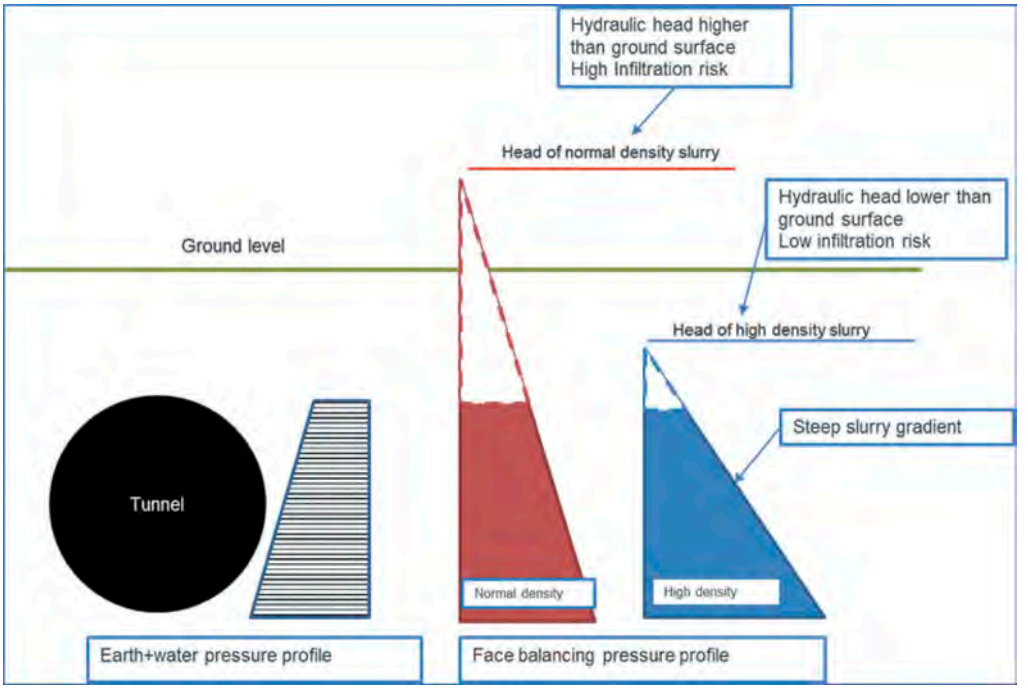

Figure 3. How high density slurry help mitigate blow-out risk.

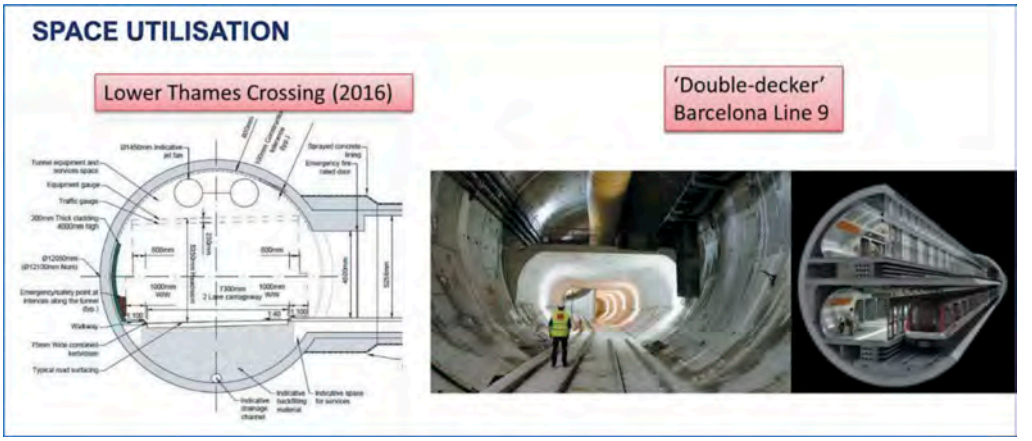

Figure 4. Space utilisation examples from Lower Thames Crossing (image credit: Tunneltalk) and Barcelona Line 9 (image credit: TYPSA).

risk of ground heave or blow-out at the ground surface level

- Following on from above, since the hydraulic head of the balancing pressure is lower, and this can mitigate the risk of slurry infiltration to the ground surface (through an unfilled borehole or other natural cavities), especially for large tunnel with low cover.

5 CHALLENGES IN LARGE DIAMETER TUNNEL DESIGN

5.1 *Space utilisation*

This chapter shifts our attention to the realm of design considerations, beginning with the challenge of space utilization. In the context of metro or highway tunnels, one prominent issue frequently encountered by tunnel engineers revolves around the endeavor to reconcile the circular cross-section of the tunnel bore with the rectangular traffic envelope from vehicles. As illustrated in Figure 4, the cross-sectional profile of the Lower Thames Crossing (LTC) project in its early stages, it is evident that there exists a substantial amount of unutilized space beneath the deck, although this mass concrete is useful for anti-buoyancy purpose, which will be discussed later on in this paper. In subsequent design development of LTC, the under-deck space has been utilised for maintenance and emergency access. In contrast, when we look to international examples such as Barcelona's Line 9, a double-decker approach has been employed, showcasing a significantly more efficient utilization of space. This arrangement also eliminates the need for cross passages in the case of twin bore tunnels. It is worth noting that these are two distinctively different projects, one designed for highway usage and the other tailored for railway operations, thus no direct comparisons can be made between them due to different project requirement.

5.2 *Waterproofing*

The deep alignment of large diameter tunnels leads to challenges in the waterproofing design of the tunnels. In segmental lined tunnels, the waterproofing of the tunnel is usually provided by the gaskets around the perimeter of each segment. For a given compressive stress, the gasket can only resist water pressure up to a given limit. In the case of hs2 Chiltern tunnel, due to the high section depth, double gaskets, one on the intrados and another on the extrados, were used to provide sufficient resistance against the high groundwater pressure encountered on the Chiltern tunnel (Reilly and O'Keefe, 2022).

5.3 *Shallow launch*

As a fundamental guideline in tunnelling, it is advisable to have at least 1 time the tunnel diameter as ground cover. This first-principle criterion ensures that the surrounding ground provides sufficient confinement, increasing bending moment capacity, and more uniform ground support to the tunnel ring. Furthermore, this can help distribute movement in the ground, leading to a more even settlement trough, and also prevents possible 'blow-out' of TBM face pressure. However, in the case of large-diameter tunnels, particularly within urban environments, achieving this required depth for launch can be notably challenging, since for a given alignment gradient, a significantly long section of tunnel would be required to lower the tunnel alignment sufficiently deep to achieve the 1 diameter ground cover. Launching the TBM with less than 1 tunnel diameter of ground cover can be defined as "shallow launch" in the context of this paper, and it introduces several critical hazards including reduced confinement and bending moment capacity of the tunnel segments, higher risk of tunnel face blow-out, more liable to encountering soft ground conditions, and less resistance to buoyancy and floatation. As a design oriented solution, Hs2 adopted a design of

piled slab confinement in combination with ground treatment and embankment (Torello et al., 2020).

5.4 *Large spatial requirement at launch*

The construction of large tunnels often necessitates sizable shafts for the launch and reception of TBMs. If a TBM is launched within a deep shaft, typically a front/back shunt mined tunnel (typically in the form of sprayed concrete lined tunnel) would be required for a full TBM assembly including all backup gantries. The construction of the front/back shunt tunnel in the case of large diameter tunnels can be particularly challenging since they are 'hand'-mined. Occasionally when it is driven by programme, the 'umbilical' launch, or partial launch is chosen, such as Thames Tideway (Tideway, 2019). In the case of large diameter TBMs, the front/back shunt tunnel option may not be feasible given the large tunnel diameter required, whereas the umbilical launch may cause logistics bottleneck up and down the shaft due to the heavy weight of the elements and large volume of spoil. A third possible solution is to provide a long trench, which would result in excessive propping required due to the depth and width.

In response to this challenge, a novel solution known as the 'caterpillar' shaft has gained more use in recent years. Notably, caterpillar shafts have found application in large diameter tunnelling projects in the UK in the most recent years including HS2 (High Speed Rail Group, 2021) and the Silvertown tunnels (Smith, 2021), emerging as a cost-effective method for deploying these large TBMs. The circular structural arrangement of caterpillar shaft maximises the arching effect of both the concrete structure and the ground itself, achieving optimal structural arrangement, reducing element thickness and propping.

5.5 *Deformation control and structural capacity*

It is stated earlier in this paper that large diameter tunnels tend to have higher number of segments per ring due to logistic constraints. More longitudinal joints will result in higher ring deformation and joint rotation. This is particularly challenging in a soft ground condition such as the UK, especially where the tunnel face condition traverses multiple hard-and-soft layers or is subject to perched water table, leading to local peaks in bending moments or joint rotations, which may result in excessive cracks and loss of water tightness. Experiment results have also shown that fibre reinforced segments perform less well than conventional bar reinforced segments. Therefore, in certain challenging soft ground conditions, or where fire design is governing, fibre reinforcement alone may not provide sufficient robustness and conventional bar reinforcement, or a mixture of the two, may be necessary.

The TBM gantries run as trailers behind the shield supported by wheels, which exert concentrated loadings on the tunnel segments, creating localised bending, especially when the annulus grout is relatively fresh. Large diameter TBM gantries usually carry a lot more service units, adding significant weight to them, exerting higher concentrated loads on the segments. Particular attention should be paid to the design of the TBM and the grout mix, for the grout to cure long and fast enough before bearing the wheel loads.

5.6 *Ground movement and settlement control*

A feature pronounced for large diameter tunnels is the large annulus gap. The dimension of the annulus gap for conventional tunnels is in the order of 100mm, subject to project requirements. With regard to large diameter TBM, however, the annulus gap can usually reach 150mm or 200mm, or even beyond. This is one of the key reasons leading to large settlement for constructing large diameter tunnels. Bambridge et al. (2013) coined the phrase of "scale factors", describing the phenomenon of non-linear numerical relationship between the tunnel diameter and some key metrics in tunnel design, including the annulus gap, grout volume and surface settlement.

In terms of prediction of surface settlement due to tunnelling works, the conventional assumption of 1% volume loss assumed by default in tunnel design would need to be challenged and mitigated, otherwise this may lead to overly conservative assumptions. For example, a 1% volume loss on a large diameter tunnel could result in a theoretical maximum surface settlement in the order of 100mm to 200mm. Bambridge et al. (2013) find that a single bore large diameter TBM at an excavated diameter of 17.48m needs to be able to control face loss to a figure of approx 0.04% if it is to yield a surface settlement value which is equivalent to that of a 4m diameter tunnel with the same depth to the tunnel crown.

Actual ground settlement data as reported by Cording (2018) and Yang, Z. et al. (2010), from Seattle SR-99 tunnel and Yangtze River tunnel respectively, both suggest actual volume loss to be lower than 0.5%.

Since large diameter tunnels are usually buried deeper to achieve sufficient cover, the settlement trough extends well beyond the normal range, causing settlement effects on a much wider range of surface and underground assets.

5.7 *Buoyancy stability control*

Buoyancy stability is a failure mode of underground structures where the minimum guaranteed self weight of the structure and any ground directly above it, must be sufficiently high compared to the buoyancy uplift force of the groundwater, after load factors are applied. However, it is not usual to for buoyancy stability to govern for a normal sized tunnel, as in the vast majority of cases, simply by inspection, the factor of safety is sufficiently high. However, large diameter tunnels in particular, face the buoyancy uplift issue in a much more pronounced way – the tunnel alignment is usually shallow relative to its ground cover, and the tunnel is usually without sufficient backfill to increase its

weight. From the author's experience, as a 'rule of thumb' a minimum ground cover of 0.5 times tunnel diameter should be maintained throughout the route, subject to more explicit buoyancy stability checks.

6 CONCLUSIONS

Based in the particular context of tunnelling in the United Kingdom, this paper has presented a number of technical challenges in large diameter tunnelling. It has categorised these challenges into four categories.

- In terms of construction and logistics, a vast amount of spoil and material to will be handled, and the weight of the tunnel segments will be quite significant.
- From a face stability and intervention requirement perspective, large diameter tunnelling is more susceptible to mixed face conditions, high groundwater pressure, more geological hazards such as karst or faults. Wear of the cutter tools can also be expected to be heavier than usual, with more frequent need for face intervention. Hyperbaric intervention must be best avoided through sound planning and the use of 'safe havens' where possible.
- In terms of TBM selection, this paper provided a high level comparison between EPB TBM and slurry TBM in the use of soft ground tunnelling. It went on to explain the use of multi-modal TBM and then the latest technology of the 'Variable Density' TBM, and the advantages of high-density slurry. In large scale tunnelling projects, these prominent technologies are more likely to be adopted, since the capital cost of the TBM itself plays a smaller part proportion compared to the gigantic overall project cost, and are therefore more cost effective in risk management.
- With regard to the design aspects, this paper explained the challenges in space utilisation by reconciling the rectangular profile and the circular tunnel bore, higher water pressure necessitating more robust waterproof design, the high demand of 'shallow launch', large spatial requirements at launch leading to the more frequent use of the 'caterpillar' type of shafts, large ground movement, difficult settlement control and also noted the importance of checking buoyancy stability of the tunnels.

ACKNOWLEDGMENTS

The author would like to thank TYPSA Group and particularly colleagues within the Tunnelling and Geotechnics department for their technical and mental support in the production of this paper. A particular thanks is owed to Helena Castellvi who provided extremely valuable comments on the draft of this paper.

REFERENCES

Bambridge, C., Wongkaew, M., Kennedy, E., 2013. Factors of Scale Planning Design and TBM Considerations for Large Diameter Bored Tunnels. RETC (Rapid Excavation Tunneling Conference) - June 26, 2013.

Billota, Casale, di Prisco, Miliziano, Peila, Pigorini and Pizzarotti, 2022. Handbook on tunnels and underground works, volume 2 Construction – Methods, Equipment, Tools and Materials.

Cording, E. J. 2018. Monitoring and Controlling Ground Behavior at the Source - Recent Applications to Pressurized Tunneling, Muir Wood Lecture 2018, AITES/ITA.

DAUB, 2016. Recommendations for Face Support Pressure Calculations for Shield Tunnelling in Soft Ground. German Tunnelling Committee (ITA-AITES)

GREAT BRITAIN. The Work in Compressed Air Regulations 1996. London: The Stationery Office.

High Speed Rail Group, 2021. HS2 construction of the Victoria Road Crossover Box. https://www.rail-leaders.com/industry-news/hs2-construction-of-the-victoria-road-crossover-box/

Hooton, M., Doughty, L., Newton, L., Huthison, S. 2020. Minimisation of spoil to landfill from a collaborative approach to re-use on site. Hs2 learning legacy.

Hs2, 2021. HS2 reveals the innovative slurry treatment technology supporting the Colne Valley 'rewilding' project. https://mediacentre.hs2.org.uk/news/hs2-reveals-the-innovative-slurry-treatment-technology-supporting-the-colne-valley-rewilding-project

HSE. 1996. A guide to the Work in Compressed Air Regulations 1996 [L96]. Bootle:HSE, 1996.

Jones, B. 2022. Soft Ground Tunnel Design. Oxon, United Kingdom. CRC Press.

Moore, 2022. HS2 spoil conveyor network begins operation at Old Oak Common. New Civil Engineer. https://www.newcivilengineer.com/latest/hs2-spoil-conveyor-network-begins-operation-at-old-oak-common-22-11-2022/

Newman, T., Bellhouse, M., Corcoran, J., Sutherden, R., Karaouzene, R., Shirlaw, J. 2016. TBM performance through the engineering geology of the Lee Tunnel. Proceedings of the Institution of Civil Engineers. Geotechnical Engineering 170 December 2017 Issue GE6.

Reilly, J. and O'Keefe, S. 2022. HS2 C1 Tunnel Construction – 1 year on. British Tunnelling Society.

Salas and Della Valle, 2012. Segmental lining thickness vs. Internal diameter ratio: a perspective approach for lining dimensioning. Tunnelconsult.

Smith, C., 2020. HS2 will use UK's first multi-mode TBMs. Ground Engineering. https://www.geplus.co.uk/news/hs2-will-use-uks-first-multi-mode-tbms-19-05-2020/

Smith, 2021. Parts for the UK's largest tunnel boring machine start to arrive on Silvertown Tunnel site. New Civil Engineer. https://www.newcivilengineer.com/latest/parts-for-the-uks-largest-tunnel-boring-machine-start-to-arrive-on-silvertown-tunnel-site-15-12-2021/

Tideway, 2019. First tunnelling machine reaches 100 metre mark in battersea. https://www.tideway.london/news/site-news/2019/january/first-tunnelling-machine-reaches-100-metre-mark-in-battersea/

Torelló, X., Castellvi, H., Doulkas, G., Rogala, T., 2020. Shallow TBM launch of the Northolt Tunnel West TBMs at West Ruislip. Hs2 Learning Legacy.

Yang, Z., Huang, H., Zhang, D., 2010. Analysis of Ground Deformation Caused by Tunneling of Large-Diameter Tunnel Boring Machine. In: Proceedings GeoShanghai 2010, ASCE.

Tunnelling for a Better Life – Yan, Celestino, Thewes & Eberhardt (Eds)
© 2024 The Author(s), ISBN 978-1-032-80042-4
Open Access: www.taylorfrancis.com, CC BY-NC-ND 4.0 license

Smarter, larger, leaner, greener – trends of the tunnelling industry towards a sustainable future in the United Kingdom

Si Shen* & Arabel Vilas Serin
TYPSA Limited, London, UK

ABSTRACT: The latest trend of the tunnelling industry in the United Kingdom can be summarised as 'Smarter, Larger, Leaner, Greener'. This paper provides an overview of a number of leading-edge technologies and methodologies in practical application in the tunnelling industry, attributed to the aforementioned 4 categories, using case studies of projects in the UK. On the 'Smarter' front, this paper will discuss the importance of good practice in ground investigation data management and automatisation for its interpretation, as well as the application of BIM and design processing technologies. In terms of 'Larger', there is an observable trend of tunnels getting bigger over time, right from the classic London Tube to Crossrail, HS2 and Silvertown and Lower Thames crossing. Advancement of TBM technology has enabled bigger and bigger tunnels, which in turn makes certain types of projects feasible. As tunnels get bigger comes a raft of challenges, some construction related, some design related, and this paper will select several aspects of challenges specific to large diameter tunnels to discuss. With regard to being 'Leaner', it means to reduce material wastage by combining temporary works and permanent works, which often requires a collaboration between the permanent works designer and the contractor, and sometimes the temporary works designer. Certain advanced design and testing methods can also be used to improve the efficiency. In terms of becoming greener, the UK tunnelling industry has been world-leading in terms of reducing road congestion, noise, carbon and air pollution, for which numerous examples from the hs2 project provide good practice.

Keywords: TBM, design, sustainability, United Kingdom, large diameter, lean construction

1 INTRODUCTION

Through the experience and observation of the authors, the trend of technological advancement in the United Kingdom (UK) can be summarised as "Smarter, Larger, Leaner, Greener". This means: the integration of digital technology in design; the trend of increase in tunnel diameter; less materials and temporary works and a more sustainable way of working. The authors believe that the UK has been standing at the forefront of all these aspects and will continue to do so in the foreseeable future, taking the lead in the tunnelling industry across the world. For each of these four aspects, this paper will provide a brief overview of selected case studies for leading-edge but tried-and-tested technologies and techniques used in the United Kingdom. It will not delve into great depth about any of the case studies but aims to provide a conceptual framework for the latest technological advancement and demonstrate the trend of future developments. The case studies are of course non-exhaustive, but selected based on the authors' personal experience. This paper aims to use plain English, without reference to any equations, making it accessible by a wider audience.

2 SMARTER TUNNEL DESIGNS

2.1 *The importance of data*

In the recent years, the amount of information designers receive from ground investigation campaigns has increased immensely. Data analysis has become an indispensable skill for geotechnical and tunnel engineers and plays a crucial role in order to optimize processes, improve efficiency and support the decision-making process during tunnel design.

Understanding the geotechnical behaviour of the ground is the only path to make informed decisions during the design, considering site-specific factors, assess risks, and optimize design solutions.

For this, data analysis is a powerful tool to optimize the process for geotechnical interpretation, visualisation and extraction of meaning insights from data. However, any engineer in charge of efficiently and effectively manage data for the design face some challenges during the analysis for parameter derivation and generation of ground models from ground investigation data. In addition, the extracted data need to be understandable and

*Corresponding author: sshen@typsa.es; avilas@typsa.es

DOI: 10.1201/9781003495505-284

readable for other departments working on the project. Figure 1 shows a glimpse of an in-house data management and visualisation tool that TYPSA has developed, used on projects worldwide.

Figure 1. Data management and visualisation (image credit: TYPSA Group).

2.2 *AGS data & data-related challenges*

In the UK, AGS is a standardised format to transfer geotechnical and environmental data between parties from ground investigation, laboratory testing and monitoring. Although there is a common dictionary to transfer

geotechnical data, every company needs to figure out how to deal with this vast amount of data and how to face the issues related to data quality, data variability, uncertainties in the data base for data validation, interpretation and visualisation. In the end, how efficiently and effectively engineers manage ground investigation data will have a direct impact on productivity, risk mitigation for safe and cost-effective construction projects, and therefore in the success of the project.

As an example, an automated workflow was developed to convert AGS format data into 3D geological surfaces in a BIM environment, requiring minimal manual input. The output is a CAD file stored in Common Data Environment that allows digital traceability and internal baselining (Bottomley and Fernandez, 2020).

2.3 *Turning data into information*

Challenges during ground investigation data collection, management and analysis arise at the early stages of a tunnel project. Data pre-processing techniques along with a good understanding of the dictionary of the data base is key to make sure that data is turned into design information. Therefore, it is of utmost importance to ensure an appropriate workflow/framework is in place for data quality (inaccurate, inconsistent or contain error), data integration and data analysis for data visualisation before the results are distributed. These steps must be followed while engineers do not lose sight of the fundamental, which is dealing with a non-linear issue: geology. It is a 3D problem with 3D site conditions, so it is important to critically address any piece of data to work towards more value-engineering designs, while understanding the geohazards, raise them to other disciplines and controlling the risk during the design. For example, with LiDAR scanning results, the risk of faulting was automatically mapped and visualised on hs2 contract C1 (Sercombe et al., 2023).

2.4 *Geotechnical data integration*

The field of data analysis is constantly evolving. Emerging trends and technologies that are shaping the future of data analysis – integrating BIM and GI data.

Analysing large volumes of data to ensure reliable insights and decision-making processes is one of the main challenges to be addressed. The integration of the data into other software, e.g. GIS that correlates ground parameters with topographical data, can lead to the visualisation of wrong or missing data in the wrong place. For this, it is important to understand geo-statistics and how interpolations are done by the software in order to understand lateral variability of non-linear properties to improve accuracy and risk management.

2.5 *Present and future trends*

By employing effective analysis techniques and considering site-specific factors, engineers can extract valuable insights, assess risks, and optimize design solutions. As advancements in data analysis continue to unfold, ground investigation data analysis will remain a cornerstone of tunnel engineering.

Automatising these processes is key to reduce human error in validating the data during the error detection/data correction process. Programming language such as MySQL, R, Python, etc. allow us to improve the timing in the process.

The field of ground investigation data analysis is continuously evolving. There are some emerging trends and advancements in geotechnical data analysis, such as the integration of artificial intelligence, machine learning algorithms, and geospatial data analysis techniques that will be soon incorporated if they are not yet.

3 'LARGER' TUNNEL DIAMETERS

Figure 2 illustrates the evolution of tunnel sizes in London, using data from a number of well-known projects both in the past and planned down the pipeline. A discernible trend is evident in the expansion of tunnel diameter over time, extending from the venerable London Tube to modern infrastructural projects such as Crossrail, HS2, Silvertown, and the Lower Thames Crossing. This progression has been facilitated by advancements in Tunnel Boring Machine (TBM) technology, enabling the constructability of increasingly larger tunnels. Consequently,

the feasibility of specific types of projects has been significantly enhanced. Notably, the latest and largest diameter tunnel projects Silvertown and Lower Thames Crossing exemplify this trend as they represent highway tunnel infrastructure developments, whereas other projects are from the rail infrastructure sector.

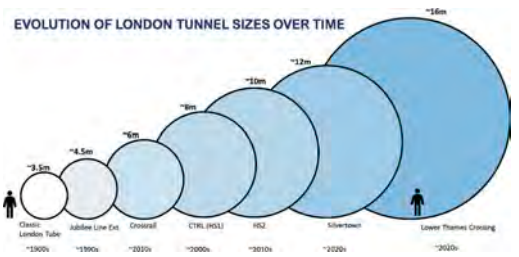

Figure 2. Evolution of tunnel sizes in London over time.

The significance of tunnel diameter is evident as tunnel design and construction inherently entail specific size-related implications. Based on our personal experience, the authors would like to acknowledge that with increased tunnel diameter, comes a host of unique and multifaceted challenges, encompassing both construction-related and design-related aspects.

Due to the page limit of the paper, the authors will provide only a cursory overview of these considerations. These will be further detailed in another paper the authors have submitted – "Distinctive considerations in the design and construction of large diameter TBM-built tunnels in urban environment – a UK perspective".

3.1 *Challenges in construction and logistics*

The first challenge pertains to the substantial torque requirements necessary for the operation of large cutterheads, particularly in the case of Earth Pressure Balance (EPB) tunnel boring machines, which inherently involve more abrasive cutting processes. This necessitates a considerable amount of power, highlighting the importance of sufficient power supply.

Furthermore, the thickness of tunnel segments presents another noteworthy aspect. Segments of 500mm to 600mm in thickness or even beyond are not uncommon around the world (Salas and Della Valle, 2012). Coupled with significant width and ring perimeter, the large concrete volume which leads to significant weight places significant demands on the weight-bearing capabilities of the tunnel infrastructure. To mitigate this, it is common practice to divide tunnel rings into smaller, lighter segments, albeit at the expense of prolonging the ring assembly cycle.

Furthermore, the management of materials transported into and out of the tunnel bore represents a significant logistical challenge. For example, how excavated materials (spoil) are transported and disposed of; how materials transportation is shared with other simultaneous works in the tunnel.

In addition to spoil handling, ensuring face stability remains a critical concern, particularly due to the larger tunnel diameter. Variability in ground conditions across the tunnel face is more likely in such cases, necessitating rigorous evaluation. Moreover, the deeper burial often required for larger tunnels results in increased groundwater pressures, making the management of hydrostatic pressure gradients at the tunnel face a complex endeavor. These challenges underscore the importance of meticulous planning for face intervention and the judicious use of safe havens for free air intervention, where feasible. Adherence to safe pressure limits for hyperbaric intervention is essential, given the high groundwater pressures involved.

3.2 *Shallow launch*

One notable challenge associated with large tunnels is the concept of shallow launch. As a guideline, it is advisable to have at least 1 time the tunnel diameter as ground cover above the tunnel crown. This first-principle criterion ensures that the surrounding ground can effectively mobilize its shear capacity to achieve arching effect, ensuring minimum required confinement of the tunnel, and leading to a more uniformly loaded tunnel ring. Furthermore, this can help distribute movement in the ground, leading to a more even settlement trough, and also prevents possible 'blow-out' of TBM face pressure. However, when dealing with large-diameter tunnels, particularly within urban environments, achieving this required depth for launch can be notably challenging, since a significantly long section of tunnel would be required to lower the tunnel alignment sufficiently deep to achieve the 1 diameter ground cover. Launching the TBM with less than 1 tunnel diameter of ground cover can be defined as "shallow launch" in the context of this paper, as it introduces several critical hazards:

1. Reduced Confinement: The lack of ground cover reduces confinement of the tunnel, thereby reducing the bending moment capacity of the tunnel segments. From a serviceability perspective, the lack of confinement also leads to higher joint rotation under the same bending moment, resulting in higher risk of water leakage through the gaskets.
2. Face Stability and Slurry Infiltration: The shallow depth aggravates the vulnerability of the tunnel face against blow-out or ground heave. Where there are unfilled boreholes or cracks in the surrounding ground, it could potentially lead to slurry infiltration at the surface causing loss of slurry and contamination.
3. Soft Ground: At shallow levels, encountering ground with low deformation modulus such as

alluvium or peat is highly likely. This introduces challenges related to controlling ground settlement and segment joint rotation.

4. Buoyancy and Floatation: Large tunnels, in particular, face a somewhat uncommon issue—buoyancy floatation. This problem is more pronounced for large tunnels due to the sheer size of void in the ground the tunnel creates.

To address these challenges, a holistic solution was implemented in the case of HS2. This solution involved the adoption of a permanent slab with piles, and a permanent embankment immediately following the slab. As shown in Figure 3, for Part A (immediately adjoining the portal), a concrete slab is cast at the surface level, supported by piles situated below. The piles are designed to resist both compression and tension, with the compression capacity for the scenario of heavy crane operating on the platform, and the tension capacity for resisting uplift force from either the face pressure from the TBM, or long term buoyancy floatation. Within the enclosure created by this setup, ground treatment measures are implemented. For Part B that is immediately downstream from Part A, a permanent embankment is placed, preventing buoyancy and floatation issues, thus ensuring the long-term stability and safety of the tunnel. This innovative approach effectively addresses the unique challenges posed by shallow launch in the context of large-diameter tunnels, particularly within urban environments like HS2.

3.3 *'Soft' ground*

'Soft' ground – ground with low deformation modulus, exemplified by Peat, is a typical ground hazard for tunnelling in the UK. Peat has certain presence in the Greater London region and has been encountered during the construction of HS1 (Gallagher et al., 2003). The presence of Peat can pose notable challenges, particularly in the context of large-diameter tunnelling, owing to its inherently low stiffness and high creep, low bulk density, low shear strength and potential flammable gas content. Measures commonly employed to mitigate the presence of Peat include pre-loading with surcharge, installing vertical drainage system and ground improvement, including dig-and-replace, jet grouting, deep soil mixing and soil reinforcement.

3.4 *The 'caterpillar' shaft*

The construction of large diameter tunnels often necessitates the use of large diameter and long Tunnel Boring Machines (TBMs), which, in turn, require sizable shafts for their installation. In response to this demand, a novel solution known as 'caterpillar' shafts has gained prominence in recent years. Notably, caterpillar shafts have found application in prestigious projects such as HS2 S1/S2 (High Speed Rail Group, 2021) and the Silvertown tunnel (Smith, 2021), emerging as a cost-effective method for deploying these large TBMs. Figure 4 illustrates their outline configurations from the two projects. The shaft consists of multiple circular shaped

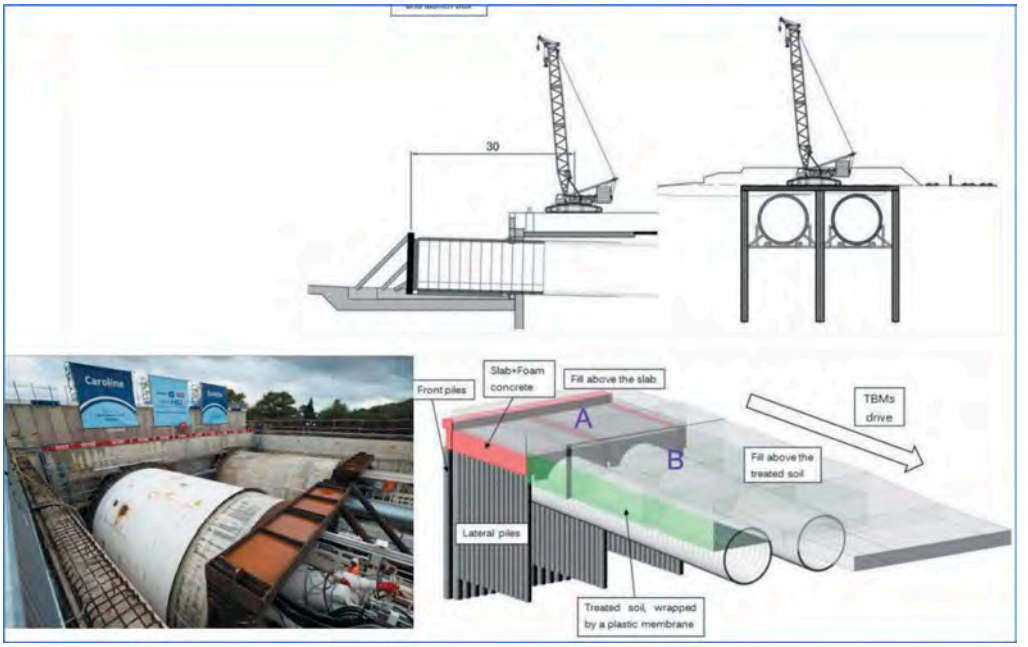

Figure 3. HS2's solution to 'shallow launch' (image source: Torello et al., 2020; hs2).

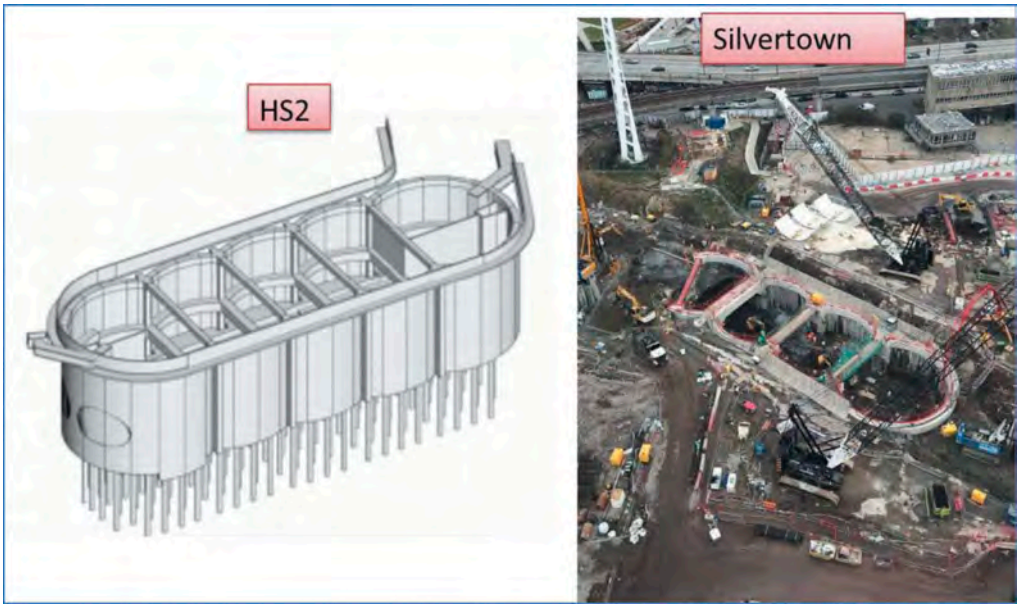

Figure 4. Examples of 'caterpillar' shafts (source of images: Rail-leaders.com and NCE, respectively).

vertical bores in a continuous manner with intersections, forming a long, wide and deep trench.

Characteristics of caterpillar shafts include:

1. **Space Optimization**: Caterpillar shafts provide a generous allocation of space, accommodating the size and requirements of large and long TBMs.
2. **Structural Efficiency:** These shafts are designed with a focus on structural integrity and efficiency, ensuring the safe launching of the TBMs.
3. **Reduced Propping:** Caterpillar shafts are engineered to minimize the need for additional structural support, streamlining the construction process and reducing associated costs.
4. **Minimal Ground Displacement:** The caterpillar shafts contributes to minimisation of ground movement, reducing the potential impact on the surrounding environment and infrastructure.

However, it's important to emphasise that the design and construction of intersection panels (so called 'Y' panels) remain a technical challenge within this innovative approach. Careful consideration and engineering expertise are required to address this aspect effectively, ensuring the temporary stability of these intersection panels. In difficult ground conditions, ground treatment or other temporary works may be required.

4 'LEANER' TEMPORARY WORKS

4.1 *Umbilical launch*

The concept of "lean" in this context pertains to minimizing spatial demands due to launch for a given situation. Typically, a TBM's full length falls within the range of 100 to 200 meters. However, in urban environments, spatial constraints often prevail, placing doubts over the feasibility of a full sized launch.

For launching a TBM at significant depths, a method known as "umbilical launch" has been employed in the UK tunnelling industry as a lean design for spatial demand, as illustrated in Figure 5. The term 'Umbilical Launch' refers to the methodology where the TBM is launched with a minimal operational setup, ensuring that its operations are sustained through the utilisation of 'umbilical' cables and pipelines. As the TBM progresses, auxiliary gantries are incrementally deployed, resulting in an extended launch duration but a reduced spatial requirement. This method derives its name from the analogy of a baby's umbilical cord, as the TBM initially relies on pipelines and cables extending to the surface worksite for its operations.

Umbilical launch was used on Thames Tideway in London (Tideway, 2019). In this scenario, the TBM was launched with the bare essentials, primarily consisting of the shield and the minimum required backup gantries, while relying heavily on the umbilical cord infrastructure. As the TBM excavated the earth, it generated space for itself, and the supplementary gantries were progressively dropped down as additional space became available. It should be noted that this approach necessitates a protracted launch duration, but it becomes particularly advantageous in situations where spatial constraints are a predominant concern. Moreover, programme saving is possible as it can achieve a launch milestone sooner since less work is required to create space.

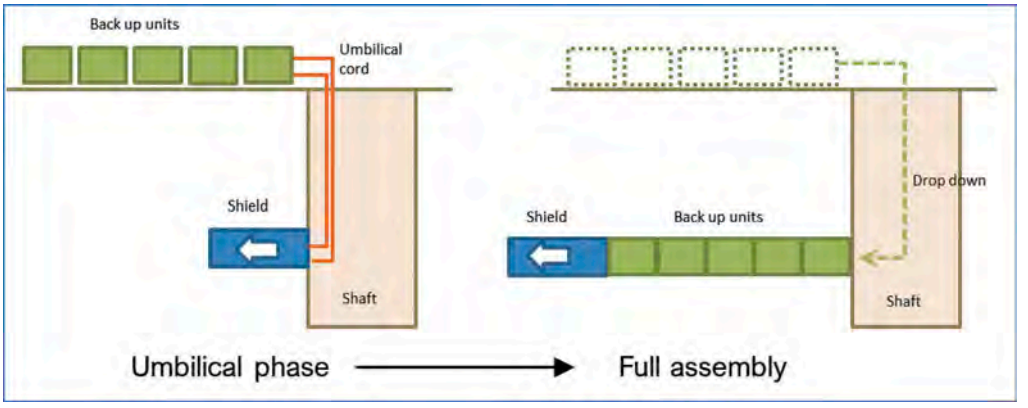

Figure 5. Schematic illustration of 'umbilical launch'.

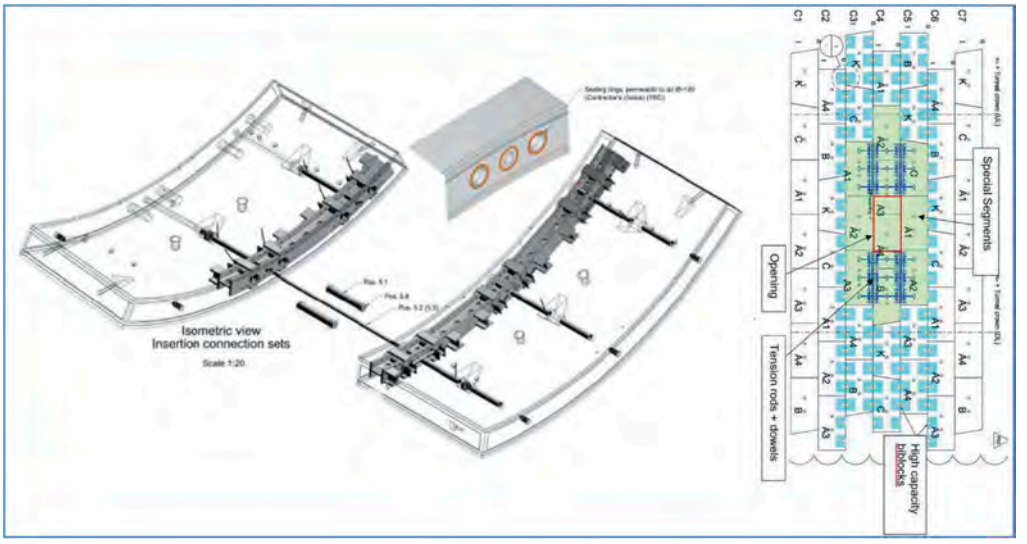

Figure 6. Layout of the 'special segments' (Source: Torello et al., 2021).

4.2 *Saving of temporary propping*

Lean construction principles encompass not only cost and time efficiency but also a reduction in temporary works. Conventionally, when creating openings within segmental tunnels for cross passages, the industry has relied on steel half-moon propping, or cast iron tunnel segments, as means to control deformation within the tunnel structure. However, on the HS2 project (Castellvi et al., 2023; Torelló et al., 2021; Gutierrez and Serna, 2020), an innovative and forward-thinking approach has been adopted in the form of "special segments."

The overarching concept behind these special segments involves a departure from propping reliance, instead focusing on imbuing the segments with a high structural capacity around the opening area. This structural fortification allows for effective shear transfer into the adjoining rings and serves as a pivotal element in deformation control. The special segments encompass four key structural components:

1. **Heavily Reinforced Segments**: These segments are engineered with robust reinforcement to bolster their bending moment capacity.
2. **Embedded Steel Beam**: Integration of a steel beam within the segments forms a composite section, enhancing their load-bearing capacity.
3. **High-Capacity Shear Dowels**: Utilization of high-capacity shear dowels facilitates effective deformation control of the segments once the opening is created, to limit stepping and lipping.
4. **Tension Rods**: Tension rods play a critical role in managing deformation and enhancing the stability of the tunnel structure above and below the opening.

Furthermore, a noteworthy aspect of this approach is the meticulous design of the segments to precisely match the width of the cross passage opening, thereby minimizing the amount of cutting required. This not only contributes to improved health and safety conditions but also enhances the overall quality of the construction process. By integrating these innovative techniques, the HS2 project exemplifies a commitment to lean construction practices that optimize efficiency, safety, and structural integrity in tunnel construction.

4.3 *Composite sprayed tunnel lining*

This paper now switches focus to the realm of lean construction towards the realm of Sprayed Concrete Lined Tunnels (SCL), which are also recognized as New Austrian Tunnelling Method (NATM) or sequential excavation method (SEM) in other parts of the world. The conventional construction employs a double-shell configuration, comprising a primary outer lining and a secondary inner lining, with a sheet of waterproof membrane sandwiched in between. Historically, the primary lining was viewed as temporary infrastructure and, consequently, was not factored into the assessment of permanent works. However, it is now becoming widely recognised practice in the United Kingdom to consider load sharing between the primary and secondary linings, specifically concerning effective earth pressure.

A more novel development has seen increase in use, wherein the waterproof layer is also sprayed onto the structure, subsequently hardening to attain a stiffness akin to concrete. This innovative approach fosters composite action between the primary and secondary linings (Su, 2022). In practical terms, this implies that no materials are considered redundant in load sharing. Moreover, this advancement holds the potential to significantly diminish the requisite thickness for the secondary lining, thus optimising efficiency and sustainability in tunnel construction.

5 'GREENER' TUNNEL CONSTRUCTION

5.1 *Conveyor belt instead of lorries*

Figure 7. HS2 spoil conveyor belt (source: NCE).

Undoubtedly projects at the scale of hs2 will produce a gigantic amount of spoil. At the Logistics Hub alone, over 430,000 tonnes of spoil will be produced and transported to its end destination (Moore, 2022). In order to eliminate the presence of muck-away lorries on the roadways, HS2 contractors SCS JV and BBVS JV have adopted a solution in the form of a conveyor belt system (Moore, 2022) that to the author's minds is reminiscent of baggage handling systems at airports – refer to Figure 7. The conveyor network is considered to have achieved a reduction of a million lorry journeys on the road. This innovative concept represents a remarkable advancement, characterized by its continuous operation, resistance to adverse weather conditions, minimal noise emissions, and a reduced requirement for human oversight and management.

5.2 *Low carbon solutions*

HS2 is at the forefront of implementing strategies to achieve low carbon emissions, with several notable examples showcasing their commitment to sustainability:

1. **Fibre Reinforced Tunnel Segments**: In the realm of tunnel construction, fibre reinforced tunnel segments have emerged as the predominant choice. They have essentially become the industry default solution in the UK, and widely adopted on Crossrail (King, Thomas and Stenning, 2017), Thames Tideway (Jewell et al., 2014; Rossi, 2020) numerous sections of hs2 (Rossi and Monks, 2022) due to their sustainability, efficiency and durability. Rebar reinforced tunnel segments remain to be important for scenarios where additional structural capacity is essential, such as soft ground sections, low ground cover zones and adjacent to cross passage openings.
2. **Low Carbon Concrete**: HS2 places a significant emphasis on the use of low carbon concrete, adopting it in general in its constructions (hs2, 2020) to reduce carbon emissions. This involves the incorporation of a high dosage of cement replacement binders such as slag or fly ash, which are commonly employed in the construction of tunnel segments. Low carbon concrete has also been used in the largest ever concrete pour to date in the UK at the Euston site (hs2, 2022a). These materials not only enhance the sustainability of the project but also contribute to the reduction of carbon emissions associated with concrete production.
3. **Hydrogen Power Generators**: On-site, HS2 (hs2, 2022b) has adopted the use of hydrogen power generators, marking a substantial step toward minimizing their carbon footprint. improving air quality for workers and the local community.. Hydrogen is renowned for its clean-burning properties and its potential to serve as

a green energy source, thereby aligning with HS2's dedication to eco-friendly practices.

By implementing these measures and continuously evaluating their environmental impact, HS2 underscores its commitment to achieving low carbon emissions and promoting sustainability in the field of infrastructure development. These initiatives represent a progressive approach to construction that seeks to balance infrastructure demands with ecological responsibility.

6 CONCLUSIONS

This paper has presented a number of case studies representing the 'tried and tested' technological advancements in the UK tunnelling industry. This demonstrates that the UK tunnelling industry is heading towards a future of 'Smarter, Larger, Leaner and Greener' future. 'Smarter' is exemplified by the vital role data analysis play in understanding the ground and make informed decision; 'larger' diameter tunnels lead to associated challenges such as logistics, 'shallow launch', 'soft' ground issues and the necessity of large launching shafts such as a 'caterpillar' shaft; 'leaner' mainly themes a reduction in temporary works such as propping around tunnel opening with 'special segments', an improvement in the utilisation of what traditionally was considered to be 'temporary' works only by using composite lining behaviour, substantial reduction in the spatial requirement for tunnel launch by using the 'umbilical launch' approach; as for the 'greener' front, hs2 has pushed the frontier significantly further ahead by adopting numerous green designs including conveyor belt system for removing spoil replacing road transport, fibre reinforced tunnel segments, low carbon concrete and hydrogen power generators.

ACKNOWLEDGMENTS

The authors would like to thank TYPSA Group and particularly colleagues within the Tunnelling and Geotechnics department over the world for their technical and mental support in the production of this paper. A particular thanks is owed to Helena Castellvi and Alberto Gomez-Elvira (both TYPSA) who provided extremely valuable comments on the draft of this paper.

REFERENCES

Bottomley, J. and Fernandez, E., 2020. Incorporation of digital ground investigation data and geological model into the 3D BIM environment. HS2 learning legacy.

Castellvi, H., Torelló Ciriano, X., Denia, A., Baró López, L., Hoerrle D. 2023. An approach for geotechnical numerical modelling of tunnels lining longitudinal behaviour. Proceedings 10th NUMGE 2023.

Gutierrez, J., Serna, L., 2020. Design of shafts and tunnels to decouple the construction programme. Hs2 Learning Legacy.

High Speed Rail Group, 2021. HS2 construction of the Victoria Road Crossover Box. https://www.rail-leaders.com/industry-news/hs2-construction-of-the-victoria-road-crossover-box/.

Hs2, 2020. HS2 uses new pioneering low carbon concrete to reduce carbon emissions in construction. Hs2 media centre. https://mediacentre.hs2.org.uk/news/hs2-uses-new-pioneering-low-carbon-concrete-to-reduce-carbon-emissions-in-construction.

Hs2, 2022a. HS2 completes largest ever UK pour of carbon-reducing concrete on Euston station site. Hs2 media centre. https://mediacentre.hs2.org.uk/news/hs2-completes-largest-ever-uk-pour-of-carbon-reducing-concrete-on-euston-station-site.

Hs2, 2022b. HS2 reveals successful results of hydrogen generator trial. Hs2 media centre. https://mediacentre.hs2.org.uk/news/hs2-reveals-successful-results-of-hydrogen-generator-trial.

Jewell, P., Barker, A., Bellhouse, M., Matta, C. and Sefton, A., 2014. Innovative shaft and tunnel lining for the Thames Water Lee Tunnel. Proceedings of North American Tunnelling Conference.

King, M., Thomas, I., Stenning, A., 2017. Crossrail project: machine-driven tunnels on the Elizabeth line, London. ICE Proceedings, Civil Engineering, Volume 170 Issue CE5.

Moore, 2022. HS2 spoil conveyor network begins operation at Old Oak Common. New Civil Engineer. https://www.newcivilengineer.com/latest/hs2-spoil-conveyor-network-begins-operation-at-old-oak-common-22-11-2022/.

Rossi, B. 2020. United Kingdom Leads the SFRC Usage for The Tunnel Lining Segments - A success story: Thames Tideway Tunnel - Central Section. ITA-AITES World Tunnel Congress, WTC2020 and 46th General Assembly Kuala Lumpur, Malaysia 11-17 September 2020.

Rossi, B. and Monks, D. 2022. HS2 is going to use steel fibres for the rail tunnel lining segments. World Tunnel Congress, Copenhagen, Denmark.

Salas and Della Valle, 2012. Segmental lining thickness vs. Internal diameter ratio: a perspective approach for lining dimensioning. Tunnelconsult.

Sercombe, G. Paraskevopoulou, C., Bedi A., Vazaios, I., 2023. Automating fault identification along the hs2 Chilterns tunnel alignment from aerial LiDAR scanning. Taylor and Francis.

Smith, C., 2020. HS2 will use UK's first multi-mode TBMs. Ground Engineering. https://www.geplus.co.uk/news/hs2-will-use-uks-first-multi-mode-tbms-19-05-2020/.

Smith, 2021. Parts for the UK's largest tunnel boring machine start to arrive on Silvertown Tunnel site. New Civil Engineer. https://www.newcivilengineer.com/latest/parts-for-the-uks-largest-tunnel-boring-machine-start-to-arrive-on-silvertown-tunnel-site-15-12-2021/.

Su, J. 2022. Adopting "less is more" principle for efficient design of Composite SCL Tunnels. World Tunnel Congress 2022. Copenhagen, Denmark.

Tideway, 2019. First tunnelling machine reaches 100 metre mark in battersea. https://www.tideway.london/news/site-news/2019/january/first-tunnelling-machine-reaches-100-metre-mark-in-battersea/.

Torelló, X., Castellvi, H., Doulkas, G., Rogala, T., 2020. Shallow TBM launch of the Northolt Tunnel West TBMs at West Ruislip. Hs2 Learning Legacy.

Torelló, X.; Hoerrle, D.; Castellvi, H.; Doulkas, G.; Rogala, T. 2021. Special segments design for cross passages and shaft passages. High Speed Two (HS2): Infrastructure Design and Construction - Volume 1. 181–191. ICE Publishing, London.

Tunneltalk, 2016. TBM preferred for Lower Thames Highway Crossing. https://www.tunneltalk.com/UK-28Jan2016-TBM-preferred-for-Lower-Thames-highway-crossing.php.

TYPSA, 2018. BARCELONA METRO LINE 9. https://www.typsa.com/en/proyectos/barcelona-metro-line-9/

Gallagher, Tauschinger, Heron, Watson, Warren, 2003. Construction of the CTRL Thames Tunnel. Conference: Underground Construction 2003.

Tunnelling for a Better Life – Yan, Celestino, Thewes & Eberhardt (Eds)
© 2024 The Author(s), ISBN 978-1-032-80042-4
Open Access: www.taylorfrancis.com, CC BY-NC-ND 4.0 license

Tunneling successes in West Los Angeles - Purple Line Project Section 3

Eleanor Sillerico*
Mott McDonald, Los Angeles, USA

Martin Ellwood & Codie Davis
WSP, Los Angeles, USA

Angel del Amo
Aldea Services, Orange, USA

Edouard Whitman
Frontier Kemper Constructors, Los Angeles, USA

ABSTRACT: Construction of bored tunnels for the Los Angeles Metro's Purple Line Extension Section 3 started in October 2020 and was completed in April 2023. Twin earth pressure balance (EPB) tunnel boring machines (TBM), each 23.5 feet in diameter, mined 27,077 feet (5.12 miles both tunnels) with crown elevations ranging between 50 to 120 feet below ground. The tunnels contract included a launch shaft 90 feet in diameter and 89 feet deep, twin bore tunnels, 14 cross passages mined with SEM (sequential excavation method), stations end-walls and ground treatment under critical utilities. The underground work was constructed in the soils of the Los Angeles Basin, a gassy environment. This paper presents the performance of the TBMs while tunneling in a challenging environment that included major sensitive structures such as the I-405 freeway, a 96-inch cast iron water main, and deep shoring piles at a commercial property.

Keywords: Tunneling, TBM, sensitive structures, gassy ground, gassy tunnel, permeation grouting

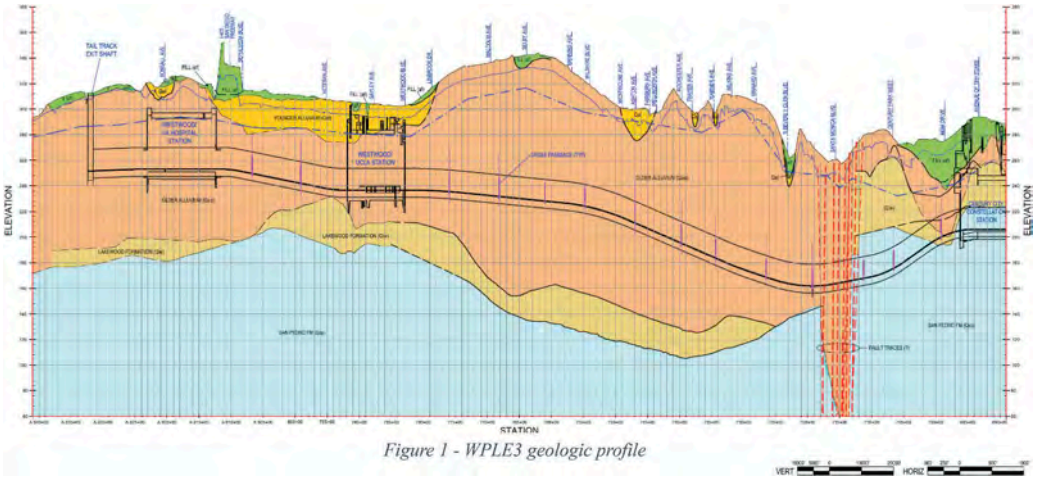

Figure 1. WPLE3 geologic profile.

1 INTRODUCTION

The Westside Purple Line Subway Extension (WPLE) project is heavy rail transit subway that will operate as an extension of the Metro Purple Line in Los Angeles. This mega-project brings seven underground stations and nine miles of twin-bore tunnels westward to the UCLA and VA Campuses in West LA, and through the Beverly Hills, Century City and Mid-Wilshire areas.

*Corresponding author: Eleanor.sillericomayta@mottmac.com

DOI: 10.1201/9781003495505-285

The project is separated into three Sections; this paper focuses specifically on the tunneling in the final (most westward) Section 3 (WPLE3), a 2.56-mile section of the project comprising twin 23.5-foot diameter tunnels excavated EPB TBMs and varying in crown depth from 50 feet to 120 feet below ground. Refer to Figure 1.

The tunnel design was developed to mitigate risks through several challenges along the alignment:

- Tunneling beneath the I-405 Freeway,
- Minimizing settlements for major utilities at Sepulveda Boulevard,
- Tunneling within five feet of building support of excavation piles,
- Tunneling in gassy ground,
- General TBM performance requirements.

The design/build project definition documents (bridging documents/contract documents) specified a series of measures to mitigate potential issues. The Final Designer generally incorporated these measures, and in some areas was able to amend them through design, analysis and TBM performance. This paper describes how each process unfolded and the means by which the mitigation measures were implemented or amended. The bored tunnels were successfully constructed between 2021 and 2023.

2 TUNNELING BENEATH THE I-405 FREEWAY

The Westside Purple Line Extension alignment terminates at the Veterans Affairs campus in West Los Angeles. To reach this terminus, the tunnels had to cross beneath the Interstate 405 (I-405) Freeway. This is a major north-south transportation corridor constructed in 1957, widened in 2007-2010, and reconfigured (on/off ramps) in 2013-2014. The tunnels pass under the Wilshire overpass bridge abutment structure, between two bridge bent structures and mechanically stabilized earth (MSE) walls constructed in 2013-2014 (see Figures 2 and 3).

Figure 2. I-405/Wilshire Boulevard intersection looking south.

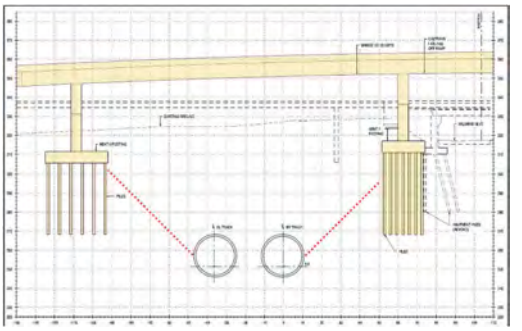

Figure 3. Tunnel influence zone with respect to bridge bents.

Metro, WSP, Mott MacDonald (Metro's Construction Management Consultant), Frontier Kemper-Tutor Perini JV (FKTP), and Aldea worked closely with Caltrans District 7 representatives throughout the design and construction process to ensure all criteria were achieved.

2.1 *Preliminary engineering*

The project requirements included a Project Study Report – Project Report (PSR/PR) which was undertaken by WSP, Metro's design consultant, and approved by Caltrans in 2012. A further revision was approved in 2016 for work impacting the I-405 freeway and its ramps. WSP also prepared a Joint Permitted Use and Maintenance Agreement (JPUMA) in 2018, with amendments in 2020 and 2021. This was needed to grant approval for rights to build, operate and maintain Metro's facilities within the Caltrans right-of-way.

These documents were provided to the final designer for compliance, as well as additional performance requirements identified in the contract documents, such as a robust instrumentation program. This program included horizontal inclinometers positioned about three feet above each tunnel crown, arrays of Multipoint Borehole Extensometers (MPBXs) in the public roadway and VA property either side of the I-405 and surface settlement markers on the I-405 Freeway embankment. A Building Protection report was produced which assessed the impact of the tunneling from a preliminary design perspective. This was reviewed by Caltrans. The initial results showed that the maximum movements of the existing I-405 bents would be less than 0.02 inches for a tunneling volume loss of 0.35%. This is far less than the allowable settlement of 0.5 inches of total differential settlement across the bent structures or 1/600 (i.e., 0.002 radians) of slope across a structure/bay in accordance with Metro Rail Design Criteria (MRDC) Chapter 5. AASHTO LRFD Strength Limit States allow for 0.7 inches of settlement, but the MRDC governs as the more stringent project requirement.

Discussions with Caltrans and others resulted in several additional measures added to the contract documents:

- Hold Points – The contractor may not proceed with work until each Hold Point has been released by Metro, contingent upon the approval of a report demonstrating performance requirements have been met.
- Tunnel Construction Review Points (TCRP) – The contractor may not proceed beyond the TCRPs until it demonstrates that preconstruction surveys are complete, that instrumentation is installed and functioning, that Caltrans approval is received, and that previous instrumentation data is received and compliant.
- Continuous tunneling beneath the I-405 – Tunnel construction is to be continuous, without stopping work and with no planned interventions to reduce ground relaxation/settlement.
- Tunneling with greater control – The allowable settlement three feet above each tunnel, measured by Multi Point Borehole Extensometer (MPBX) and Horizontal Inclinometer (SAAX Array), is 0.35 inches for Action Level and 0.5 inches for Alert Level (reduced from 1 inch for Action Level and 1.5 inches for Alert Level in areas with general control).

2.2 *Final design*

The final designer (Aldea Services) performed the detailed analyses and presented them to Caltrans. Metro's tunneling contractor FKTP (Frontier-Kemper Tutor Perini JV) prepared a pre-construction survey of Caltrans structures with an analysis of the current Caltrans bridge load rating assessment and inspection reports, including a LiDAR survey. FKTP developed a geotechnical investigation program to define geotechnical parameters for the design and construction of the tunnels. Aldea then used the geotechnical parameters to develop a Midas model and perform a numerical analysis to assess the effects of vertical, horizontal and transverse ground movements/deformations and induced strain on each Caltrans structure, the results and analysis of which were presented in a Structure Impact Assessment Report (refer to Figure 4).

Aldea concluded that the increase in loads in the bent piles, the increase in the stresses in the abutments, and movements of the abutments and bent piles due to TBM tunnel excavation were negligible for a predicted volume loss of 0.35%, and that no special mitigation measures were required.

FKTP simultaneously prepared and submitted the Plans, Specifications and Estimate (PS&E) Documents for the project elements within Caltrans right-of-way in order to obtain encroachment permits. Metro engaged a third party (STE LLC) to perform an independent check of the final design documents in compliance with Caltrans requirements.

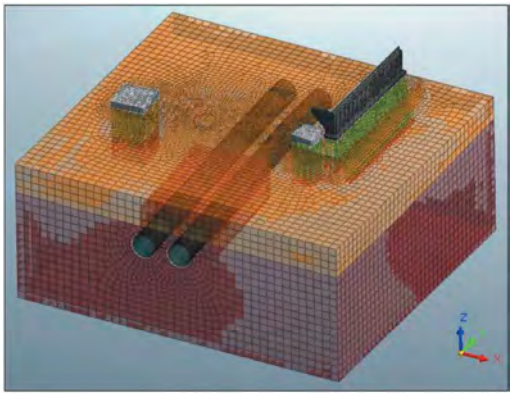

Figure 4. Portion of I-405 Midas FLAC model with tunnels.

2.3 *Performance during construction*

Both TBMs completed mining beneath the I-405 and Sepulveda Boulevard in nine days each, including the installation of 100 precast concrete rings while working in continuous mining mode 24/7 (2 x 12-hour shifts). The horizontal inclinometers comprised 147 anchors and measured 0.4 inches of maximum settlement above both the westbound (BR) and eastbound (BL) tunnel crowns, and no movement was observed at surface level, demonstrating the success of the permeation grouting operation. Measured settlement fell within allowable limits and Aldea's prediction to the satisfaction of Caltrans.

3 MINIMIZING SETTLEMENTS AT SEPULVEDA BLVD

3.1 *Reason for enhanced ground control*

Sepulveda Boulevard (at Wilshire Boulevard) is located towards the west end of the PLE3 tunnel alignment, adjacent to the I-405 Freeway. Sepulveda is a dense utility corridor and contained two critical utilities of significant interest to the tunneling: a 96-inch diameter water mainline, and a reinforced concrete box (RCB) storm drain measuring 12 feet x 12.5 feet.

The water line, with an inside-diameter of 96 inches, is a mainline feeder constructed in 1969 as a prestressed concrete pipe inside a steel jacket, at an invert depth of EL 280 feet, only 12 feet above the tunnel crowns. This pipe carries a significant amount of fresh water to the Los Angeles region under high pressure. Since the 96-inch water main would govern the design, this was the focus of the team in relation to minimizing settlements at Sepulveda Boulevard.

The preliminary design utilized an initial two-dimensional FLAC analysis of the tunnels and the

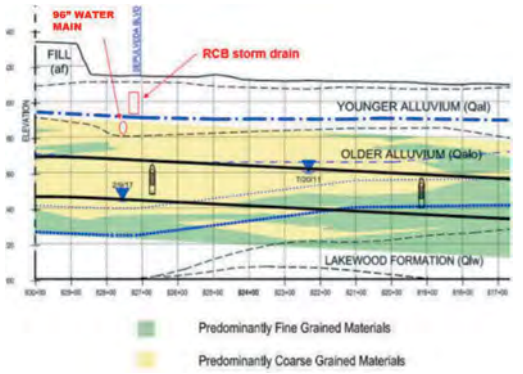

Figure 5. Geologic profile at Sepulveda Boulevard.

96-inch water main. The ground conditions consist of Young/Old Alluvium and San Pedro formations (see Figure 5), predominantly silty sandy material with lenses of gravel/cobbles, and reasonable stiffness. The water table is approximately EL 250 feet, which is 65 feet below grade, at the location of the top of rail in the tunnels.

The analysis was run initially for one tunnel passing under Sepulveda Boulevard, followed by the second tunnel, adopting various parameters including both non-grouted and grouted ground. The results were compared to the standard curves calculated from a basic Gaussian Distribution Approach representing a ground loss of 0.35%, to ensure ground stiffnesses were being reasonably represented in the non-grouted model. The analysis concluded that without grouting the soil matrix, the maximum settlement of the pipe invert would be 0.6 inches and with grouting it could be reduced to less than 0.2 inches.

3.2 *Criteria and coordination with water utility owner*

The project engaged with the water utility owner prior to, during, and after tunneling to ensure that communication was clear and criteria were being met. The owner mandated a maximum settlement criterion of 1/5 inch maximum for its waterline pipe. This requirement was added to the contract documents, along with a mandate to provide ground improvement above and around the entire tunnel cross section for a length of about 125 feet and a width of approximately 80 feet. This was anticipated to require permeation grouting techniques, a technique in which the space between soil grains is filled with grout injected at a steady pressure and which does not disturb the soil structure. Since this is performed at low pressures, it is ideal for use in close proximity to existing sensitive utilities.

An instrumentation and testing program was specified. This consisted of utility monitoring points (UMPs) along the length of the 96-inch water main within the zone of influence of the tunnels, arrays of MBPXs, a horizontal inclinometer placed above each tunnel crown, and core testing of the grouted area to ensure the soil shear strength was achieved throughout.

Metro also required continuous TBM mining under a zone that started west of the I-405 and continued east under Sepulveda Boulevard until the zone of influence of the 96-inch water main was passed. This required the contractor to continuously operate the TBM machine within this zone, regardless of time of day or week.

Metro also included strategic Hold Points along the alignment. This included demonstration that key performance indicators were met at the machine measuring tail skin grout, face pressure, spoil removal and bentonite slurry injection behind the cutter head. Having documentation of indicators all performing correctly was considered a key element to controlling settlement under the 96-inch water main.

3.3 *Final design*

During final design, Aldea Services designed a permeation grouting plan which did not require the full cross section of the tunnel to be grouted. Instead, FKTP proposed a block of grout from the tunnel spring line to approximately eight feet above the tunnel crown. Finite Element Analysis using 2D and 3D models was produced in the MIDAS program to validate the approach and demonstrate that the design would meet the strict settlement criteria. An emergency response plan was prepared in the event that an incident occurred, identifying appropriate mitigation measures.

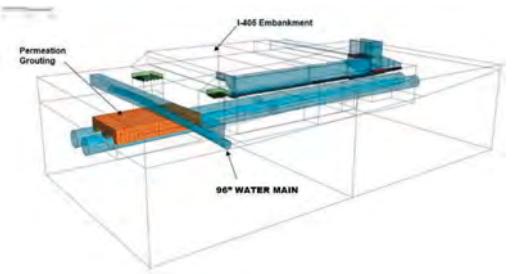

Figure 6. Proposal for compensation grouting beneath 96-inch water main.

3.4 *Performance during construction*

The ground improvement was undertaken by Keller and consisted of 53 grout holes approximately seven feet apart to create the grouted envelope. The Shape Accel Arrays (SAA), aka horizontal inclinometers, and the permeation grout holes were constructed by horizontal directional drilling (HDD) from the surface, from a starter pit approximately 200 feet from Sepulveda Boulevard. The top row of grout pipes was approximately five feet below the 96-inch water main

invert. Sleeve ports every 48 inches along the grout pipes allowed the sodium silicate chemical grout to be pumped in with momentary high-pressure injection of water through the packer rod. Post-grouting, Keller performed three vertical cores with logging and sampling to ensure the target grout strength of 100psi at 28 days was achieved (refer to Figure 6).

During installation of the permeation grout pipes, a magnetic survey system installed in the roadway continuously collected survey information for each HDD borehole. The as-built survey information was provided to WSP which was then modeled in 3D and viewed in Navisworks to verify the design grout coverage was achieved. It was discovered that the HDD boreholes were installed higher than anticipated, and an additional row of boreholes was added by Keller. This coordination among the project team proved to be extremely valuable in meeting the performance requirements set by the owner and the design grout coverage area set by Aldea (refer to Figure 7).

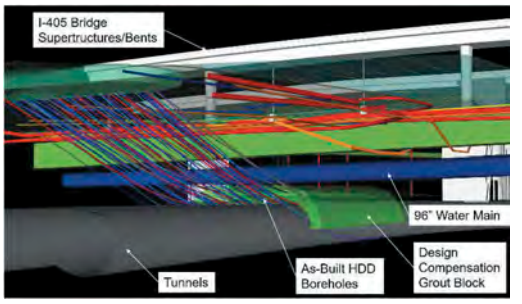

Figure 7. Navisworks as-built model of compensation grouting beneath 96-inch water main.

Tunneling was undertaken on a continuous basis as required by the contract, including over weekends. The owner was engaged in daily briefing meetings with FKTP and Metro to ensure communication was clear. These meetings included a summary of the instrumentation readings such as the UMPs, horizontal inclinometers and MPBX readings, which were available from the prior shift.

Construction was successfully completed for both tunnels with minimal settlement, less than 0.1-inches above the BR tunnel and even less for the BL tunnel, which was well within the 0.2-inch limit set by the owner. No surface settlement was measured for either tunnel. Communication was well coordinated through all stages of the tunneling, particularly with the owner.

4 TUNNELING WITHIN FIVE FEET OF SOE PILES

The low point of the tunnel alignment between Constellation Station and Westwood/UCLA Station is near a commercial building located within a mixed commercial and residential corridor with mid-rise buildings. The brick-clad building was constructed in 1984 and comprises a four-story commercial building on top of four parking basements, with a particularly deep row of support of excavation (SOE) friction piles along the north property line, approximately 80 feet deep at the toe. It is likely the deep piles were required because the adjacent road is a narrow alley and insufficient space was available for traditional tiebacks, which were used in other parts of the basement excavation. These piles are no longer in use structurally, as the building adopted a shallow foundation solution for the permanent structure consisting of pad foundations on competent ground. However, the steel H-piles are embedded into the permanent concrete basement walls. The Metro tunnel alignment was designed to provide five feet of clearance from the bottom of the steel SOE piles to the top of the tunnels. However, with limited record drawings available from the building owner, Metro elected to perform field investigations to verify the clearance in advance of tunneling and mitigate any risk of the TBM striking the steel piles. No load was expected to be present in the toe of the piles (refer to Figure 8).

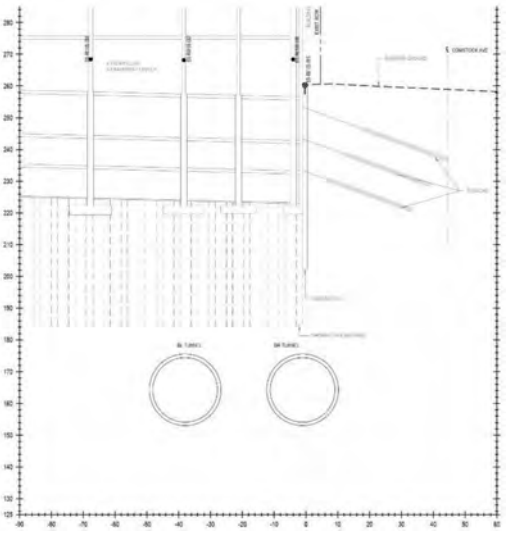

Figure 8. Section showing Metro tunnels beneath deep SOE piles (design).

4.1 *Pile investigation*

Metro's design consultant, WSP USA, engaged specialty geotechnical consultants (Wood PLC and Olson Engineering, Inc.) to undertake a non-destructive investigation utilizing parallel seismic testing. The parallel seismic test consisted of dropping a hydrophone down ten water-filled PVC-cased borings and taking measurements along 20 steel soldier piles encased in concrete and located 65 feet to 85 feet below ground surface.

Each borehole was used to test the two adjacent soldier piles. The testing was performed by impacting the exposed piles to generate seismic compressional/primary wave (P-wave) energy down the pile to the hydrophone receiver at one-foot vertical test depth intervals. An inflection point in P-wave velocities experienced between saturated soils and steel W-beams indicates the pile tip. The results indicated that several piles were within five feet of the Metro tunnels.

Metro then elected to perform a second investigation using a magnetometer testing to obtain better accuracy on the closest piles. New borings were installed within two feet of the targeted soldier piles to improve the accuracy of the results.

The magnetometer test was performed by lowering a borehole magnetometer (gradiometer) into the PVC-cased boreholes to detect magnetic field strength between two sensors on the instrument which detects the greatest differential magnetic field at the tip of the steel pile when it transitions to concrete encasement at the toe.

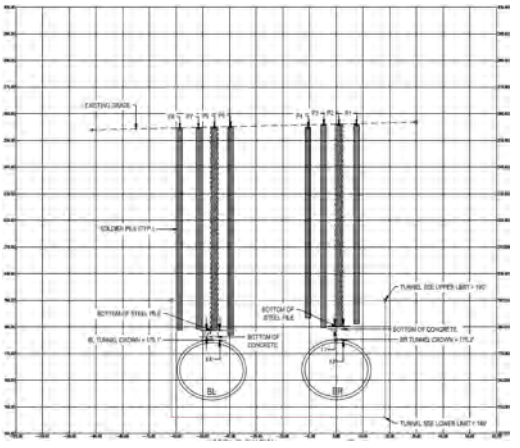

Figure 9. Section at north SOE deep pile line based on investigation results.

The results of the magnetometer test provided the depth of the steel piles with an accuracy of +/- one foot. The combination of the two tests showed that the tunnels had 3.6 feet (BL tunnel) to 5 feet (BR tunnel) of clearance to the steel piles and 1.2 feet (BL tunnel) to 3.9 feet (BR tunnel) of clearance to the concrete encasement around the tip of the piles (refer to Figure 9).

4.2 *Performance during construction*

The successful non-destructive testing gave Metro and FKTP the confidence to proceed with tunneling beneath the deep SOE piles, which was successfully completed without incident. Metro and the building owner worked hand in hand to conduct the field investigation, prepare an emergency response plan and utilize continuous mining to minimize potential building settlement.

5 TUNNELING IN GASSY GROUND

During the initial geological investigation that Metro and WSP undertook between 2011 and 2017, methane (CH_4) and hydrogen sulfide (H_2S) were encountered along the alignment. Methane is less dense than air and is highly explosive; hydrogen sulfide is denser than air and is highly toxic. These results confirmed the findings of Los Angeles Department of Building and Safety, City Ordinance 175790, which includes a map of Methane and Methane Buffer Zones for the City of Los Angeles. The map indicated that the Purple Line Project, including WPLE3, would be inside the gassy zones.

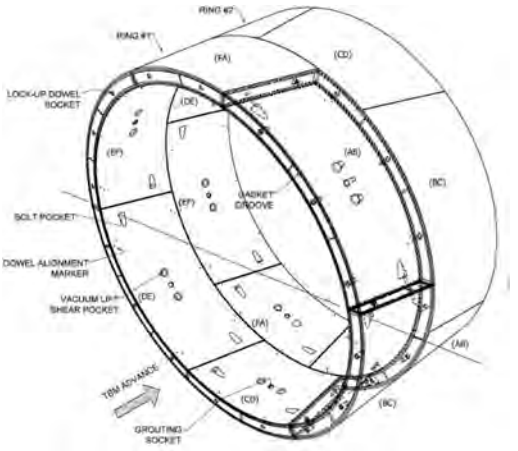

Figure 10. Tunnel precast ring assembly showing double gasket.

Extensive studies were undertaken to determine suitable measures to deal with the elevated levels of gases on the project. The highest density of gas was found on Section 1 near the La Brea Tar Pits. However, the entire nine-mile alignment falls into the category of "gassy ground".

For the tunnels, it was determined that double gaskets should be incorporated as a mitigation measure between the concrete segments along the circumferential and radial joints. This was included in all three sections of the project, including WPLE3 (refer to Figure 10).

Furthermore, the provision for a possible future "Secondary Liner" was incorporated in the tunnel internal diameter, which was increased by 12 inches to allow for a 6-inch liner all round should gases be found to be entering the tunnel during operation. This would not be installed in the current project but would be available for Metro in the future in the event of a gas/water leak which could not be remedied by grouting or other primary means of mitigation.

During construction, it was also required that CH_4 and H_2S gas sensors be placed along the TBMs as well as backup, self-rescuing equipment at strategic

locations and a certified gas tester present at all times when employees were in the tunnels. Employees entering the tunnel were required to undertake special training and carry self-rescue equipment including gas testing devices.

5.1 *Probe Drilling from the TBM – CalOSHA variance*

Due to the gassy ground, the contractor was required to probe ahead of the TBM in accordance with CalOSHA. Title 8, Subchapter 20, Tunnel Safety Order (TSO), Article 9. This requires "Tunnel-based horizontal probe hole drilling" where the likelihood of a dangerous accumulation exists.

EPB TBMs were used for excavation and support for both tunnels. With this method, the gas is controlled and measured to ensure that there is no dangerous accumulation of hazardous gases and that automated shut-down safety measures are incorporated into the TBMs.

During tunneling, the TBMs were always operated in the closed face EPB modes. This meant that the plenum and screw conveyor were full of conditioned material. A guillotine-type valve is at the end of the screw where the conditioned ground depressurizes. This would constitute the "true" face of the excavation in the context of the exposure to any hazardous gasses or contaminated soil.

In addition, a negative-pressure TBM and tunnel ventilation system was designed to dilute and capture any potentially harmful gases. The ventilation system was specified to supply an airflow rate of 100,000 cfm, which was sufficient to dilute the maximum off-gassing volumes to an allowable exposure limit. Large fans were installed in TBM gantry 12. The fans were capable of handling 100,000 cubic feet per minute (cfm) airflow but operated at reduced speeds using variable frequency drives (VFDs). These fans removed gases coming out of the auger directly into a ventilation hood, located approximately 12 feet behind the screw discharge, and into a steel duct which contained the exhaust air, discharging it directly to the surface.

In the event that CH_4 and H_2S gas levels were detected in excess of that anticipated by the TBM safety plan, the TBM would automatically shut down and cut operational power. This would be followed by closure of the screw discharge gate in under 60 seconds which would seal the entire tunnel immediately against any gas inflows. CalOSHA granted a variance for probe drilling, in lieu of the numerous measures described above, in 2022. At the end of mining of both tunnels, there were no incidents where gas levels were measured in excess of the allowable limits.

6 GENERAL TBM PERFORMANCE ALONG THE TUNNEL REACHES

The PLE3 tunneling commenced from the western-most end of the alignment (Tail Track Exit Shaft) and proceeded east 2.56 miles towards the PLE Section 2 Century City Constellation Station, which would receive the TBMs. Reach 6 refers to the tunnels between Century City Constellation Station and Westwood/UCLA Station. Reach 7 refers to the tunnels between Westwood/UCLA Station to the Tail Track Exit Shaft at the alignment terminus (refer to Figure 11).

Figure 11. BL TBM "Aura" cutterhead being lowered into the launch shaft.

The BR TBM began mining in October 2020 and the BL TBM in April 2021. Due to spatial constraints in the 90-foot diameter launch shaft, mining started with umbilicals (temporary cables and connections to the support equipment) until the four TBM starter gantries were constructed, at ring 100, approximately 500 feet into the tunnel.

An assembly period then commenced for commissioning the full mining mode, with a TBM support structure composed of 13 gantries that enable the installation ring 101 to 2703 (505 feet to 13,530 feet). Tunneling in full mining mode started in August 2021 for the BR TBM, and in November 2021 for the BL TBM. TBM and segmental lining specifications are listed in Table 1.

Table 1. TBM and segmental lining specifications.

Machine type	EPB
Bore diameter	7160 mm
Installed power	4000 kW
Nominal thrust force	56068 kN
Length TBM + back-up approx.	140 m
Theoretical thrust speed	30 mm/min
Working pressure (at axis)	6 bar
Tunnel curve radius (min.)	274 m
Segmental liner type	Universal 4+2
Outer ring diameter	6858 mm
Segment thickness	330 mm
Length	1524 mm
Backfill grout type	A (grout) + B (accelerator)

6.1 *TBM performance*

Regular tunneling operation by FKTP occurred in two 10-hour shifts for five days per week (Monday to Friday). The overall daily production average was 37 feet/day for the BR TBM and 42.7 feet/day for the BL TBM, with a maximum for both TBMs of 87 feet/day. This daily production was calculated for full mining mode and accounts for a learning curve, holidays, interventions, and maintenance stoppages excluding the breakthrough into the adjacent PLE2 structure. Figures 12 and 13 show the monthly production for both TBMs in Reach 6. Special operating modes occurred at strategic locations near or under sensitive structures. In these locations, additional tunneling shifts were implemented until the TBM's were clear of the sensitive facility. Higher rates of production were achieved in these locations, up to 55.6 feet/day. However, this required a highly focused effort from Metro, the contractor, stakeholders, and consultants.

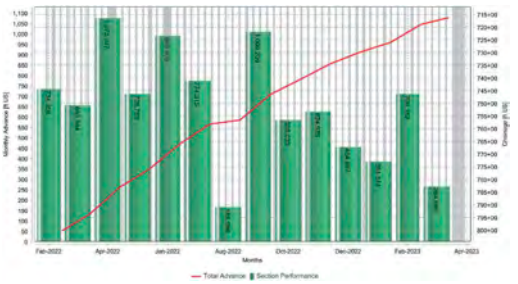

Figure 12. BR TBM Reach 6 (Rings 797 to 2703) monthly production and total advance.

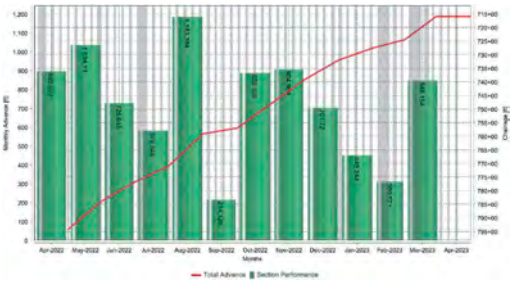

Figure 13. BL TBM Reach 6 (Rings 811 to 2703) monthly production and total advance.

6.2 *Earth pressure balance pressures*

In general, the face pressure was maintained within the range established during the design phase for Reach 7 for BR TBM (rings 1 to 796) and for BL TBM (rings 1 to 810). However, as the TBMs were gaining depth in Reach 6, the face pressures were adjusted based on actual geology and existing water table, maintaining the face pressure at a minimum of 1.20 bar above the ambient combined hydrostatic and ground pressures at the TBM crown. The piezometers installed in the

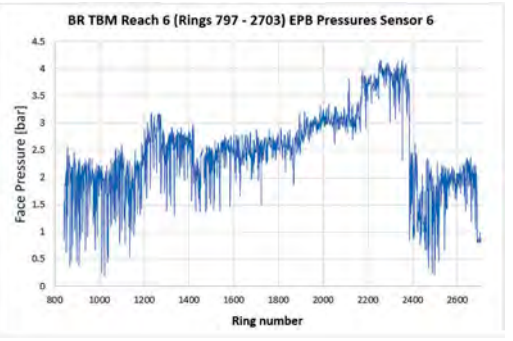

Figure 14. BR TBM Reach 6 face pressures.

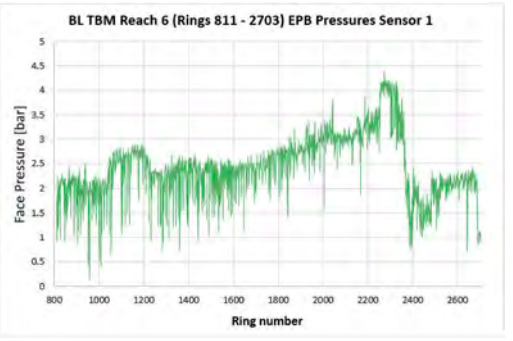

Figure 15. BL TBM Reach 6 face pressures.

MPBXs every 200 to 300 feet along the alignment provided actual water table levels. Figures 14 and 15 show the measured EPB pressures for both TBMs in Reach 6.

6.3 *Mucking system and annular grouting*

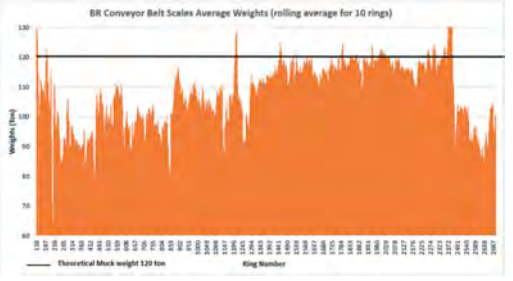

Figure 16. BR conveyor belt scales average weights.

The mucking system was composed of horizontal conveyor belts being fed in the tunnels from vertical supply structures (cassettes). Along the 2.56 miles of tunnel length, no booster stations were installed. Once the muck was delivered from the excavation face to a muck pit (max capacity of 4.5 advances) in the launch shaft, the muck was extracted using a crawler crane and two circular buckets 18 cy capacity each.

The muck weight was monitored with two scales installed at TBM gantry 12. While the theoretical weight per advance was calculated to be 120 tons, this figure was derived from the interpretation of limited exploratory boring samples gathered during the design phase. Figure 16 shows the average weights of the two BR TBM scales, and reflects actual geological conditions encountered by both TBMs. Note that while the actual weight of material extracted by advance was at times substantially less than what the theoretical average had anticipated; the geotechnical instrumentation installed along the alignment did not indicate under-excavation or uplift. If over-excavation was suspected at any time, the contractor proceeded to perform secondary (check) grouting through the tunnel liner.

Grout was injected in the annular gap behind the tunnel lining simultaneously with each TBM advance. The injection pressures were maintained between 0.5 and 1.2 bar above the EPB face pressure. The theoretical volume was 5.07 m3 for a five-foot ring. The grout was a two-component A+B where A is a mix of bentonite, cement and stabilizer and B is an accelerator: a sodium silicate base activating the A component at the rear of the tail skin. The grout gel time was between five and ten seconds. The tail skin was equipped with four grout ports facilitating the homogeneous distribution of grout behind the tunnel lining. Figure 17 shows the grout volume injected along the BL and BR tunnels (average volume across the four grout ports). The data collected offered no indication of a corelation between the grout takes per advance displayed in Figure 17 and the geologies encountered as reported by the belt scales in Figure 16.

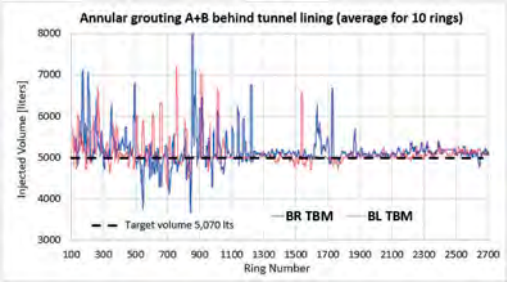

Figure 17. BR and BL annular grouting volumes.

7 CONCLUSIONS

The Purple Line Extension Section 3 tunneling project included some significant challenges in both design and construction. These were overcome by the following strategies:

- Mitigations were included in the contract documents to safeguard the construction at sensitive structures such as the Sepulveda Boulevard 96-inch diameter water main, I-405 Freeway, and for encountering known gassy ground conditions.
- The contractor followed the mitigations in the contract and was able to add value by modifying some of the mitigations during final design.
- The contractor was able to control settlement below allowable limits during the project, which provided confidence to Metro to allow some of the design mitigations to be adjusted based on calculations using the standard TBM ground loss.

ACKNOWLEDGMENTS

The authors acknowledge Los Angeles Metro for supporting and advancing the development and construction of public transportation for the County of Los Angeles.

REFERENCES

Building Response to Excavation-Induced Settlement – Boscardin and Cording, 1989.

Assessment of Excavation-Induced Building Damage – Cording et al, 2010, Proceedings of the ASCE 2010 Earth Retention Conference.

Los Angeles Department of Building and Safety Ordinance 175790 – City of Los Angeles Methane and Methane Buffer Zones.

Comis, E, Ebrahimi, Y., Peterson, J., 2022. The North East Boundary Tunnel – A TBM Performance Review. North American Tunneling 2022 Proceedings. NAT 2022. UCA., USA, pp. 660–670.

Tunnelling for a Better Life – Yan, Celestino, Thewes & Eberhardt (Eds)
© 2024 The Author(s), ISBN 978-1-032-80042-4
Open Access: www.taylorfrancis.com, CC BY-NC-ND 4.0 license

Application of EPB-TBM dual-mode shield tunneling technology in Shenzhen Metro

Tiantian Song*, Junwu Yang, Liping Huang, Jiangsong Lei, Ke Jia & Jizheng Huang
Shenzhen Metro Group Co., Ltd, Shenzhen, China

Jianwei Lu
Shenzhen Metro Group Co., Ltd, Shenzhen, China
Key Laboratory of Urban Security and Disaster Engineering of Ministry of Education, Beijing University of Technology, Beijing, China

ABSTRACT: Based on the geological conditions of Shenzhen region, the experience of traditional single mode shield tunneling was summarized. Studied the adaptability and technical characteristics of shield tunneling, proposed the concept of EPB-TBM dual mode shield tunneling machine, and fully applied it to the fourth phase of Shenzhen Metro project. This paper analyzes and studies the practical applications of multiple engineering projects, summarizes and analyzes the efficiency, consumption of cutter tool, mode switching, economy, and existing problems of dual mode shield tunneling, and puts forward relevant suggestions to provide reference for similar projects in the future.

Keywords: Shenzhen Metro, EPB, TBM, dual-mode shield

1 APPLICATION BACKGROUND OF EPB-TBM DUAL-MODE SHIELD

After 25 years of construction, nearly 98% of underground excavation in the Shenzhen Metro utilizes the shield tunneling method. Taking the fourth phase of the Shenzhen Metro construction project as a case study, a total of 150 shield tunneling machines were deployed, with a peak of nearly 120 machines simultaneously in operation in 2020. In that year, the total tunneling length reached 140 km, marking the highest in its history, a rarity compared to other cities in China and abroad.

With the ongoing expansion of the Shenzhen Metro construction, the geological conditions and surrounding environments along metro lines have become increasingly complex and variable. Traditional single-mode Tunnel Boring Machines (TBM) are no longer adequate for meeting the demands of construction projects, leading to the gradual development and implementation of multi-mode TBMs. Since 2019, Shenzhen Metro has invested in 16 EPB-TBM double-mode shields across eight sections of Metro Line 12, Line 13, and Line 14 in the fourth phase of metro construction, as well as Metro Line 8 Phase II in the third phase of metro construction project. In subsequent projects, such as Line 8 Phase III, Line 13 Phase II, Line 16 Phase II, and the construction of the pipe gallery, a total of 13 EPB-TBM dual-mode shields have consistently been deployed to ensure the smooth progress of these projects. As of now, approximately 45 km of tunneling has been completed across multiple sections, with 14 successful in-tunnel mode transitions, as seen in Figure 1.

2 APPLICATION OVERVIEW OF EPB-TBM DUAL-MODE SHIELDS

2.1 *The key characteristics of the equipment*

The EPB-TBM dual-mode shield machine combines the design principles and functionalities of both Earth Pressure Balance (EPB) shield machines and Single Shield Tunnel Boring Machine (TBM), as seen in Figure 2. It can function in two different modes for spoil removal. In soil and broken rock conditions, the EPB mode is utilized to ensure construction safety. In hard rock conditions, it switches to the open-mode Single Shield TBM to prevent secondary abrasion of the cutterhead and cutters, thereby prolonging their lifespan and reducing the frequency of tool replacement. Additionally, the cutterhead is engineered to operate at higher rotational speeds (up to 6.6 RPM), leading to increased tunnelling efficiency compared to traditional single-mode EPB shields.

The EPB-TBM dual-mode shield is classified into two types depending on the spoil removal system:

*Corresponding author: stt5@163.com

DOI: 10.1201/9781003495505-286

Figure 1. Distribution diagram of Shenzhen Metro EPB-TBM dual-mode shield section line.

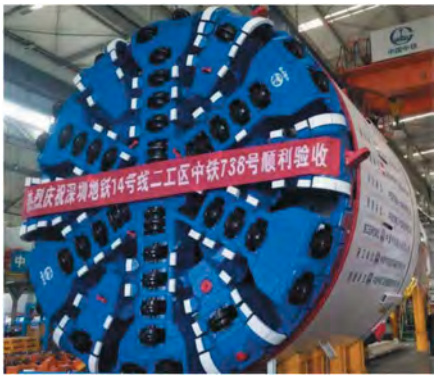

Figure 2. The first EPB-TBM dual-mode shield CREC738 applied in Shenzhen Metro.

central screw conveyor type and central belt conveyor type, as seen in Figure 3. Out of the 29 dual-mode shields used in the Shenzhen Metro, 22 belong to the central screw conveyor type, while 7 are of the central belt conveyor type, as seen in Table 1.

2.2 *Key parameters of the equipment*

The initial set of dual-mode shields (TBM) is equipped with a cutterhead excavation diameter ranging from 6470 to 7000 mm, an overall opening ratio of 28 ~ 32%, and a maximum rotation speed of 6.6 RPM. The cutterhead is exclusively electrically driven, boasting a total drive power of 1400 ~ 2100 kW, a rated torque of 5920 ~ 7200 kNm, and an extricating torque of 7100 ~ 11000 kNm. The

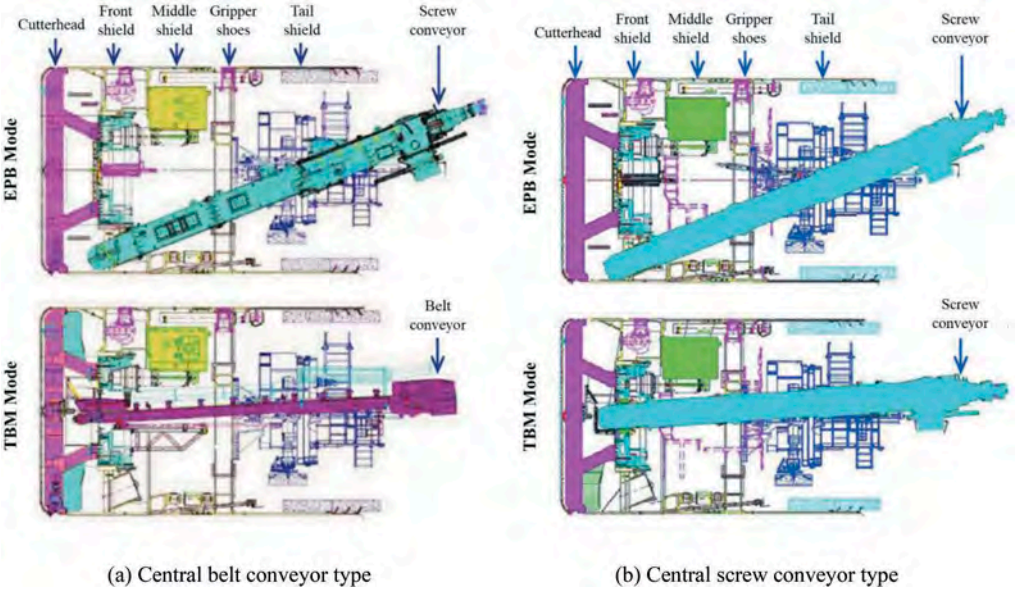

Figure 3. Schematic diagram of main arrangement for EPB-TBM dual-mode shield.

Table 1. Information table for the first batch of deployed EPB-TBM dual-mode shields in Shenzhen Metro.

No.	Line	Construction company	Section	Section length (km)	Equipment number	Tunnelling pattern and length (m)	Spoil removal system
1	Line 12	China Hydropower First Bureau	Huaide Station – Fuyong Station (left)	1.7	CREC755	EPB(320)→TBM (1132)→EPB (264)	Central belt conveyor type
2			Huaide Station – Fuyong Station (right)	1.7	CREC756	EPB(320)→TBM (1132)→EPB (264)	Central belt conveyor type
3	Line 13	China Construction Fifth Engineering Bureau	Liuxiandong Station – Liubaifeng Well (right)	2.2	CREC779	TBM(279)→EPB (458)→TBM (1483)	Central belt conveyor type
4			Liuxiandong Station – Liubaifeng Well (left)	2.2	CREC780	TBM(258)→EPB (729)→TBM (1234)	Central belt conveyor type
5			Baimang Station – Liubaifeng Well (right)	2.4	CREC781	EPB(525)→TBM (1822)	Central belt conveyor type
6			Baimang Station – Liubaifeng Well (left)	2.4	CREC782	EPB(483)→TBM (1871)	Central belt conveyor type
7		No.3 Engineering of China Construction Eighth Engineering Bureau	Baimang Station – Yingrenshi Station (left)	2.2	DL589	EPB (1088)→TBM (614)→EPB(551)	Central screw conveyor type
8			Baimang Station – Yingrenshi Station (right)	2.2	DL590	EPB (1112)→TBM (592)→EPB(527)	Central screw conveyor type
9	Line 14	China Railway Tunnel Group Co., LTD	Qingshuihe Station – Buji Station (left)	2.1	CREC740	EPB(644)→TBM (1362)→EPB (123)	Central screw conveyor type
10			Qingshuihe Station – Buji Station (right)	2.1	CREC741	EPB(638)→TBM (1321)→EPB (149)	Central screw conveyor type
11		No.2 Engineering of China Railway Tunnel Group Co., LTD	Buji Station – Bushifeng Well (left)	2.1	CREC738	TBM(421)→EPB (910)→TBM (375) →EPB(376)	Central screw conveyor type
12			Buji Station – Bushifeng Well (right)	2.1	CREC739	TBM(421)→EPB (910)→TBM (375) →EPB(376)	Central screw conveyor type
13			Bushifeng Well – Shiyaling Station (left)	0.95	CREC512	EPB(453)→TBM (546)	Central screw conveyor type
14			Bushifeng Well – Shiyaling Station (right)	0.95	CREC517	EPB(453)→TBM (546)	Central screw conveyor type
15	Line 8 Phase II	Affiliated to CCCC First Highway Engineering Group	Dameisha Station – Xiaomeisha Station (left)	1.8	THDG-20310	EPB(50)→TBM (1140) →EPB(630)	Central screw conveyor type
16			Dameisha Station – Xiaomeisha Station (right)	1.8	DL815	EPB(50)→TBM (1140)→EPB (630)	Central screw conveyor type

cutterhead's main bearings come in two sizes, with diameters of 3400 and 3600 mm. The maximum thrust of the cutterhead reaches 40860 ~ 50600 kN. For a comprehensive overview of the parameters, please refer to the table below.

2.3 *Analysis of performance of dual-mode shields*

2.3.1 *Tunnelling performance of dual-mode shields*

This paper conducted a statistical analysis based on the tunneling progress in three specific segments of

Table 2. Key parameters of the first batch of EPB-TBM dual-mode shields in Shenzhen Metro.

			Cutterhead				Main drive			
No.	Equipment number	Diameter (mm)	Opening ratio (%)	RPM	Weight (kN)	Total drive power (kW)	Rated torque (kNm)	Extricating torque (kNm)	Main bearing diameter (mm)	Maximum thrust (kN)
1	CREC755	6470	30	0-2.5-5.0	700	1750	6686	8023	3400	40860
2	CREC756	6470	30	0-2.5-5.0	700	1750	6686	8023	3400	40860
3	CREC781	6980	30	0-2.47-5.59	750	1575	6080	7296	3400	50600
4	CREC782	6980	30	0-2.47-5.59	750	1575	6080	7296	3400	50600
5	CREC779	6980	30	0-2.47-5.59	750	1575	6080	7296	3400	50600
6	CREC780	6980	30	0-2.47-5.59	750	1575	6080	7296	3400	50600
7	DL589	7000	32	0-4.5	730	2000	8780	9760	3600	46510
8	DL590	7000	32	0-4.5	730	2000	8780	9760	3600	39910
9	CREC740	6480	30	0-2.26-5.4	720	1400	5920	7100	3400	40860
10	CREC741	6480	30	0-2.26-5.4	720	1400	5920	7100	3400	40860
11	CREC738	6990	30	0-2.65-5.39	750	1400	5924	7108	3400	50600
12	CREC739	6990	30	0-2.65-5.39	750	1400	5924	7108	3400	50600
13	CREC512	6990	30	0-1.43-3.43	700	1400	9030	11000	3400	50600
14	CREC517	6990	30	0-1.43-3.43	700	1400	9030	11000	3400	50600
15	THDG-20310	6600	27	0-2.95-6.6	720	2100	6800	8160	3400	45000
16	DL815	6580	28	0-5.34	750	2000	7200	7920	3600	44600

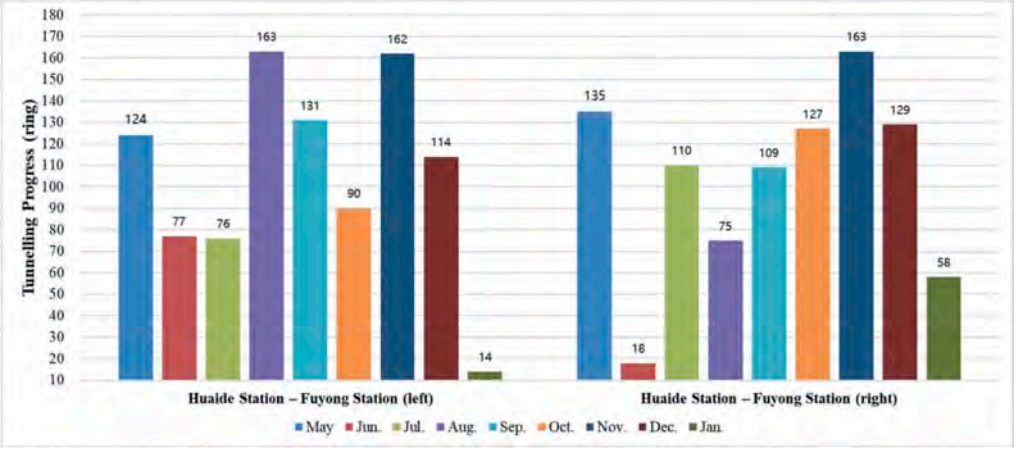

Figure 4. Monthly advance rate bar chart of dual-mode shield in selected segments of Shenzhen Metro Line 12, from Huaide Station to Fuyong Station section.

the Shenzhen Metro Phase IV Project, focusing on Line 12 and Line 14, as seen in Figures 4 ~ 6. The details of the statistical analysis are outlined below.

In the Huaide Station to Fuyong Station section of Shenzhen Metro Line 12, the left line's dual-mode shield began operations in April 2020. The dual-

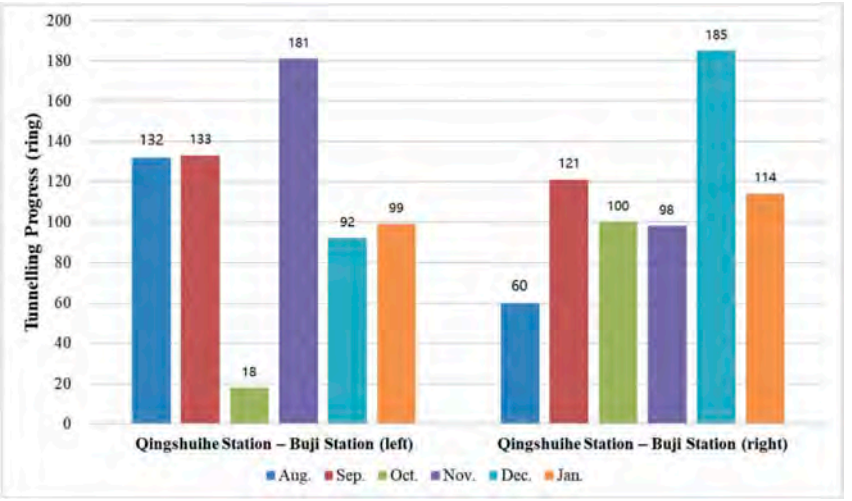

Figure 5. Monthly advance rate bar chart of dual-mode shield in selected segments of Shenzhen Metro Line 14, from Qingshuihe Station to Buji Station section.

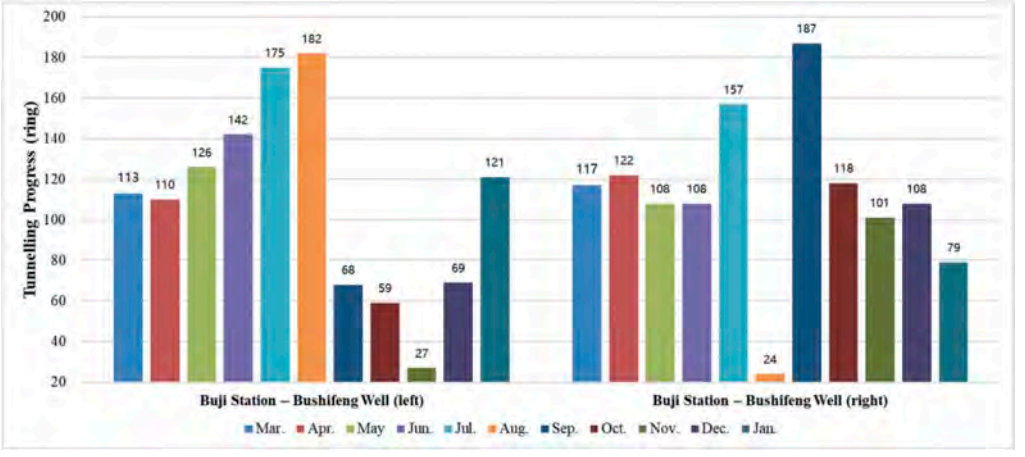

Figure 6. Monthly advance rate bar chart of dual-mode shield in selected segments of Shenzhen Metro Line 14, from Buji Station to Bushifeng Well section.

Table 3. Comparison of the cutter consumption between the dual-mode shield in the Huai-Fu section and the EPB shield in the adjacent Cui-Huai section.

Section	Shield type	Ring No.	Tunnelling length (m)	Normal abrasion	Abnormal abrasion	Replaced cutters number	Cutter consumption index (cutter/m)
Huai-Fu section (left)	EPB-TBM	223-328	157.5	19	3	22	0.14
Huai-Fu section (right)	Dual-Mode shield	208-310	153.0	11	4	15	0.10
Cui-Huai section (left)	EPB	195-290	142.5	67	38	105	0.74
Cui-Huai section (left)		204-360	234.0	163	19	182	0.78

mode shield utilized EPB mode with an average advance rate of 2.8 rings/day and TBM mode with an average advance rate of 4.4 rings/day. Similarly, the right line's dual-mode shield started operations in March 2020, employing EPB mode with an average daily advance rate of 2.7 rings/day and TBM mode

Table 4. Comparison of cutter consumption between TBM mode and EPB mode of dual-mode shield in the left Bu-Shi section of Line 14.

Tunnelling Mode	Stratigraphic Type	Ring No.	Tunnelling length (m)	Cutter abrasion type		Replaced cutters number	Cutter consumption index(cutter/m)
				Normal abrasion	Abnormal abrasion		
TBM	Slightly weathered hornstone	0-347	520.5	98	39	137	0.26
EPB	Slightly weathered hornstone	491-600	165.0	35	26	61	0.37
		951-1165	322.5	75	73	148	0.46

with an average advance rate of 3.8 rings/day. During this period, the TBM mode encountered light weathered granite ground with a compressive strength of 130-150MPa, achieving a maximum daily advance of 16.5m and a maximum monthly advance of 271.5m.

In the Shenzhen Metro Line 14 section from Qingshuihe Station to Buji Station, the left-line dual-mode shield commenced excavation in July 2020 using the EPB mode, achieving an average advance rate of 3.7 rings/day. Simultaneously, the right-line dual-mode shield initiated excavation in August 2020 also using the EPB mode, achieving an average advance rate of 4.2 rings/day. During this period, the EPB mode encountered geological formations of light weathered schist with a compressive strength exceeding 120MPa, achieving a maximum daily advance of 13.5m.

In the section from Buji Station to Bushifeng Well of Shenzhen Metro Line 14, the left-line dual-mode shield began excavation in January 2020. In this case, EPB mode achieved an average advance rate of 3.6 rings/day, while the TBM mode achieved an average advance rate of 3.3 rings/day. Similarly, the right-line dual-mode shield started excavation in February 2020, achieving an average advance rate of 3.7 rings/day using the EPB mode and 4.7 rings/day using the TBM mode. During this period, the TBM mode encountered geological formations of light weathered schist with a compressive strength exceeding 100MPa, achieving a maximum daily advance of 18m and a maximum monthly advance of 294m.

2.3.2 *Statistical analysis of cutter abrasion and replacement quantity*

In the context of the sections on Shenzhen Metro Lines 12 and 14, this study performed a comparative analysis of cutter abrasion and replacement quantities in full cross-section hard rock strata. The analysis centered on two distinct tunneling methods: the EPB-TBM dual-mode shield and the traditional EPB shield. Furthermore, within the dual-mode shield tunnel boring, the study delved into the variations in cutter abrasion and replacement quantities between two different excavation modes.

As depicted in Table 3, in the Huai-Fu section of Line 12, the dual-mode shield averaged 6.9 rings per cutter replacement under normal abrasion conditions, one cutter replacement for every 29.6 rings under abnormal abrasion conditions, and an average of 5.6 rings per cutter replacement. In the Cui-Huai section, the EPB shield experienced an average of 1.1 rings per cutter replacement under normal abrasion conditions, one cutter replacement for every 4.4 rings under abnormal abrasion conditions, and an average of 0.9 rings per cutter replacement.

The tool consumption for the EPB shield is 6.2 times that of the EPB-TBM dual-mode shield. Cutter abrasion is significantly higher for the EPB shield tunnel boring machine, particularly under abnormal wear conditions.

Based on the data presented in the Table 4, it can be deduced that, in this specific section, the Dual-Mode shield demonstrates an average cutter consumption rate of 3.79 cutters per meter in TBM mode and 2.33 cutters per meter in EPB mode. The cutter lifespan in TBM mode is 1.6 times that observed in EPB mode.

According to the aforementioned statistical analysis, it is evident that in high-strength hard rock strata, both the EPB shield and the EPB-TBM Dual-Mode shield with EPB mode lead to the accumulation of rock debris at the soil bin and cutterhead bottom. This results in significant secondary abrasion on the cutters, reducing their lifespan, increasing the cutter consumption, and leading to a higher number of cutters exhibiting abnormal wear. The TBM mode of the EPB-TBM dual-mode shield proves effective in mitigating this issue.

2.3.3 *Comparative analysis of main economic indexes of EPB-TBM dual-mode shield*

In the context of the same hard rock strata, a comparative analysis was conducted between the Dual-Mode shield operating in TBM mode in the Huai-Fu section of Line 12 and the adjacent section employing a traditional EPB shield. The analysis focused on major economic indicators, including the construction period, labor costs, and electricity expenses.

Regarding the construction period, the length of this section is 2340m, and the Dual-Mode shield achieves a daily average excavation rate of 6.5m/d, resulting in a total construction period of 360 days.

$$2340\text{m} \div 6.5\text{m/d} = 360\,\text{days} \tag{1}$$

In contrast, the single EPB shield achieves a daily average excavation rate of 1.75m/d, resulting in a total construction period of 1337 days.

$$2340\text{m} \div 1.75\text{m/d} = 1337\,\text{days} \tag{2}$$

The former saves approximately 977 days compared to the latter.

Regarding labor costs, under normal construction organization with two shifts per day and a labor cost standard of 350 RMB/d, the Dual-Mode shield requires 65 personnel per day per machine, resulting in labor costs of 8.19 million RMB.

$$360\,\text{days} \times 65\,\text{people/d} \times 350\,\text{RMB/d} = 8.19\,\text{million RMB} \tag{3}$$

On the other hand, the EPB shield requires 50 personnel per day per machine, resulting in labor costs of 23.40 million RMB.

$$1337\,\text{days} \times 50\,\text{people/d} \times 350\,\text{RMB/d} = 23.40\,\text{million RMB} \tag{4}$$

The former saves approximately 1520.75 million yuan compared to the latter.

Based on the actual construction conditions in this section, the economic advantages of the EPB-TBM dual-mode shield TBM primarily stem from the higher excavation efficiency of the TBM mode in full cross-section hard rock strata. The longer the distance of TBM mode excavation, the more pronounced the economic advantages become.

3 TECHNOLOGY FOR MODE TRANSITION IN EPB-TBM DUAL-MODE SHIELD

3.1 *Principles of mode transition in tunnel*

According to the design and construction principles of the EPB-TBM dual-mode shield, and considering construction safety, the machine is brought to a stop for mode transition under specific conditions. When transitioning from TBM mode to EPB mode, the cutterhead should be halted for conversion when it is 10 ~ 15m away from the soil-rock interface, as seen in Figure 7. Similarly, when transitioning from EPB mode to TBM mode, the cutterhead should be stopped for conversion after entering full cross-section hard rock formations at 20 ~ 25m, as seen in Figure 8.

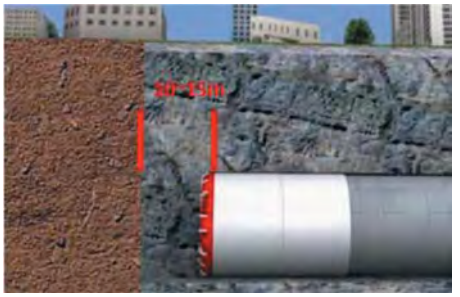

Figure 7. Schematic diagram of transition point from TBM to EPB mode.

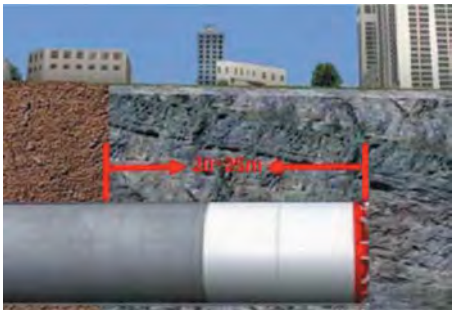

Figure 8. Schematic diagram of transition point from EPB to TBM mode.

3.2 *Procedure for mode transition within dual-mode shield in tunnels*

This section provides an overview of the mode transition process within tunnels, using the Central Belt Conveyor Dual-Mode Shield with the central belt conveyor as a case study.

3.2.1 *Transition from EPB to TBM mode*

The transition from EPB mode to TBM mode in the dual-mode shield with central belt conveyor involves the replacement of the muck removal equipment, namely the belt conveyor and screw conveyor. The main process includes preparatory work, removal of the screw conveyor, modification of the muck chute, installation of the belt conveyor, and modification of the chamber interior, as illustrated in Figure 9.

3.2.2 *Transition from TBM to EPB mode*

The primary process of transitioning from TBM mode to EPB mode includes preparatory work, modification of the soil bin, removal of the belt conveyor, installation of the screw conveyor, finalization, and debugging, as illustrated in Figure 10.

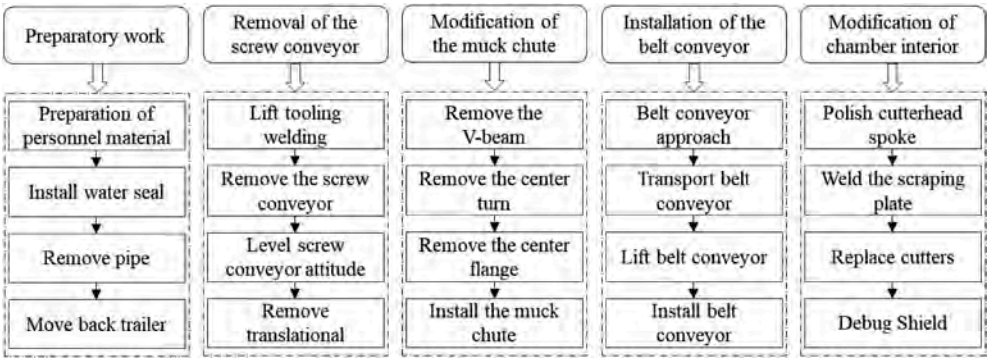

Figure 9. Flowchart of transition from EPB to TBM mode.

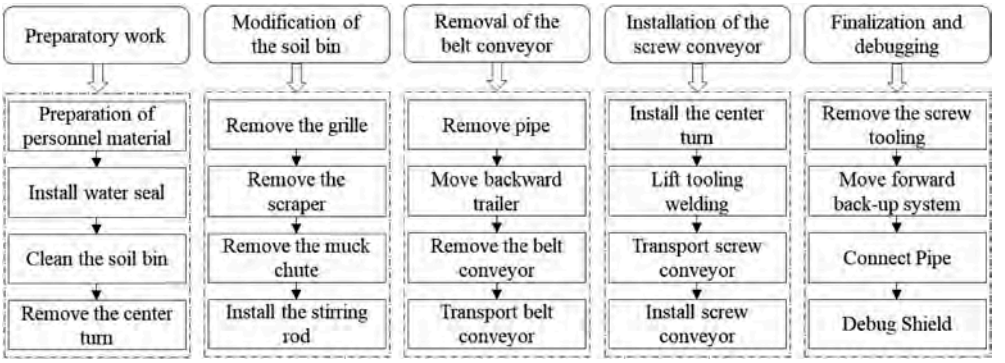

Figure 10. Flowchart of transition from TBM to EPB mode.

3.3 *Duration of mode transition within tunnels*

Based on the practical experience gained from 14 instances of in-tunnel mode transition in the EPB-TBM dual-mode shield utilized in the Shenzhen Metro, the typical duration for a single transition from EPB to TBM mode is 12-15 days, and from TBM to EPB mode is 11-15 days, with an average duration of approximately 13.5 days. Notably, the dual-mode shield tunnel boring machine CREC779 in the Liuyue to Baihe section of Line 13 achieved the shortest transition period, completing the TBM to EPB mode transition in just 11 days.

Taking the example of the EPB to TBM mode transition in the left-line of the Huai-Fu section of Line 12, the total duration was 12 days, with individual process times illustrated in Figure 11. Due to the confined operational space within the soil bin and the high welding process requirements, the welding operation during the mode transition process took a considerable amount of time, emerging as a critical step in controlling the overall transition period. Through technical enhancements and optimizations in the disassembly tools for the original screw conveyor, the operation safety was improved, and the transition efficiency was increased. As a result, the overall transition period was reduced by approximately 3 days compared to the pre-improvement duration.

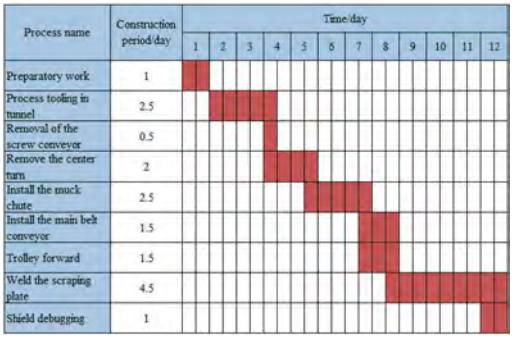

Figure 11. Gantt chart for the duration of EPB to TBM mode transition in the left-line of Huai-Fu section of Line 12.

4 MAJOR PROBLEM ENCOUNTERED FOR EPB-TBM DUAL-MODE SHIELD

In the excavation of high-strength and highly abrasive hard rock strata, encountering shield jamming against the surrounding rock mass becomes a significant operational risk for dual-mode shields. Similarly, such challenges have been recurrently encountered in the application of EPB-TBM dual-mode shields in the

Shenzhen Metro. For instance, during the excavation of an extremely hard rock stratum in a specific section, as seen in Figure 12, there was a notable deviation in tunneling parameters, with the cutterhead thrust increasing to 15000 kN, cutterhead torque decreasing to 800 kNm, and the penetration rate dropping to 4 mm/min. Upon conducting a cutterhead inspection, it was discovered that three disc cutters had experienced uneven wear, with the outermost edge cutters exhibiting varying degrees of deviation. This resulted in insufficient excavation diameter, causing the shield to become jammed against the surrounding rock mass.

Figure 12. The tunnel face of high-strength and highly abrasive hard rock formations.

Blasting excavation emerges as a highly effective method to address the challenge of shield jamming in tunnel boring machines, as seen in Figure 13. This technique involves strategically placing explosive charges at the cutterhead's muck discharge port and the location where the cutter tools are removed. After manually drilling boreholes and loading them with explosives, blasting is initiated. The sequence typically follows the order of "trial blast - groove excavation - section enlargement - reverse excavation", resulting in high efficiency in surrounding rock mass excavation. However, due to the limited space within the soil bin and the need to protect the cutterhead and shell of the shield machine, careful precautions are necessary. Depending on the specific conditions at the site, the duration for resolving shield jamming using this method typically ranges from 15 to 45 days.

5 CONCLUSIONS

In the construction process of the Shenzhen Metro Phase IV project, the EPB-TBM dual-mode shield was successfully applied on a large scale for the first time. Tunneling under complex and variable geological conditions and sensitive surrounding environmental conditions, the dual-mode shield has obvious advantages over the traditional single-mode shield. The application of dual-mode shield technology realized the concept of "one machine, two uses" in long-distance tunnels. This approach reduced the number of shield machine launch and retrieval shafts, as well as the quantity of different types of shield equipment, contributing to energy conservation, environmental friendliness, and low-carbon subway construction. Additionally, it significantly improved the efficiency of tunnel construction in long-distance, high-strength hard rock strata, generating substantial economic and social benefits.

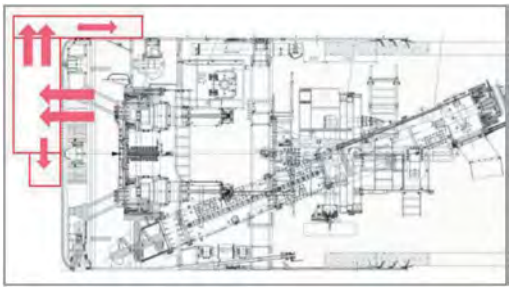

Figure 13. Schematic diagram of explosive excavation method for dealing with shield jamming.

Drawing on the practical application of nearly 30 instances of EPB-TBM dual-mode shields, improvement measures were proposed to address issues such as frequent problems with the cutterhead and cutters, as well as excessive shield vibration and torsion. The insights gained from this endeavor provide valuable guidance and reference for optimizing equipment and on-site construction in similar projects. The successful application has been extended to highway, water management, and intercity projects, serving as a model case for rail transit engineering construction both domestically and internationally. This achievement is of great significance in promoting the rapid development of the industry.

REFERENCES

Song Tiantian, Lou Yonglu, Wu Weibo, et al, 2020. Mode conversion technology of EPB-TBMdouble mode shield machine. Modern Urban Transit. 12, 59–64. (in Chinese)

JIA Ke, SONG Tiantian, SUN Qianwei et al, 2022. Analysis of Tunneling Performance of Earth Pressure Balance/Tunnel Boring Machine Double-Mode Shield in Complex Strata. Tunnel Construction. 42(S2):479–486. (in Chinese)

Tunnelling for a Better Life – Yan, Celestino, Thewes & Eberhardt (Eds)
© 2024 The Author(s), ISBN 978-1-032-80042-4
Open Access: www.taylorfrancis.com, CC BY-NC-ND 4.0 license

A newly developed reduced CO_2 backfill grout system for TBM operations

Mike A. Sposetti*
Master Builders Solutions Construction Chemicals LLC, Dubai, United Arab Emirates (owned by Sika AG)

ABSTRACT: The TBM Tunnelling industry has used two component grouts (A+B) as major backfill application for the last twenty years. Two component grouts have become so widely used that this conventional technology has become simple to handle in matter of specifications, performance expectations and application. However, being primarily focus on pricing, the TBM industry has lost the technical focus of backfill grouts, which is to primarily to avoid surface settlements and tunnel lining floating. Low quality cheap constituents significantly contribute to low quality grouts, in addition to the high carbon footprint. Conventional grout formulations contain a range of cement varying between 260 to 330Kg/m³ and they are responsible for an average of 300-340Kg of CO_2 eq./m^3 emissions of injected grout. The newly developed Component A ensures net CO_2 emissions in the atmosphere in the range between 180 to 220Kg/m^3, thus contributing to a decisive and substantial reduction of carbon footprint in the range of 45-55%. A good and performing annulus grouting is crucial for sustainability in mechanized tunnelling; more specifically, it should provide more durability to ensure a longer service life of the structures and reduce the cement content as the main source of CO_2 emissions.

Keywords: Tunnelling, TBM, Two components backfill grouts, reduced carbon footprint emissions, new technologies

1 HOW THE TBM INDUSTRY PERCEIVES THE BACKFILL GROUT TODAY

The TBM Tunnelling industry has lost the technical reasons why backfill grouts are pumped behind the tunnel lining during TBM advance.

Primary objective is the avoidance of ground settlements that can be automatically generated by the creation of the annulus void due to the passage of the TBM in the ground.

Secondary objectives, not less important, are:

- The avoidance of segment floating
- The prevention of water ingress into the tunnel, and
- The mild transfer of longitudinal and radial stresses from ground to lining

All backfill grouts objectives are strictly linked to raw material quality, TBM operations and the quality of the final tunnel as a product per se.

Unfortunately, in most of the cases, conventional two-components grouting methods do not fulfil the above basic requirements, thus jeopardizing the quality of the final tunnel and putting at risk the life of people using the final tunnel on daily basis.

In this context, the backfill grout durability concept is still, anachronistically speaking, highly dominated by the concrete industry mentality where the Unconfined Compressed Strength (UCS) is measured at 28 days.

However, accountability on curing of laboratory samples and detailed procedures of testing, quality control is not yet properly addressed by the industry due to the lack of a proper tailored-made standard to regulate TBM backfill grouts.

The Global Warming Potential (GWP), defined as the impact of carbon footprint emissions (CO_2 eq. Kg) per cubic meter of grout, considering how long it remains active in the atmosphere, is however still rarely calculated.

In an average 300-340 GWP/m^3, cement as binder of component A and sodium silicate as activator of component B are the major contributors of approx. 90% of the total CO_2 eq./m^3.

This paper illustrates a new Component A backfill grouts solution with reduced carbon footprint emissions, that hopefully will be accepted by the industry.

*Corresponding author: mike.sposetti@mbcc-group.com

DOI: 10.1201/9781003495505-287

2 THE CHALLENGES FACING CONVENTIONAL ANNULUS GROUTING METHODS

The major undisputable limitation in annulus grout injection methods is that after placement, they are located behind the concrete segments and are therefore not visible for quality inspection.

Under these circumstances, with the inability by stakeholders to review the final product, material quality has not been the focus of operations over the last decade.

For more sustainable results, annulus grouts should focus on quality, be more durable for longer lasting structures and reduce cement consumption to reduce CO_2 carbon footprint emissions.

Also, conventional logistics, mixing and placement pose several other operational challenges.

There are many influencing factors which contribute to supply chain complexity and overall quality fluctuations over project time.

A conventional formulation includes cement as binder, water, bentonite, other admixtures as component A, and sodium silicate as accelerator of component B. Each raw material requires its own storage tank with the materials procured and delivered separately by multiple suppliers.

These raw materials are stored and mixed at the site batching plant located outside the tunnel. There are many influencing factors which contribute (negatively) to supply chain complexity and overall quality fluctuations over project time. Cement, bentonite and accelerator are the raw materials that suffer the fluctuation of quality more than others.

3 THE REASONS FOR A NEW SUSTAINABLE, ECO-FRIENDLY FORMULATION

In a standard annulus grout, regardless the TBM excavation diameter the average percentage CO_2 emissions is around 20-22 range%.

Figure 1. CO_2 equivalent for segmental concrete and annulus grout per linear tunnel meter (Tunnelling Journal – April-May 2021).

Goal for a new environmentally sustainable formulation is to reach a total impact of 12-13% of CO_2 emissions in a TBM tunnelling project, reducing the overall impact to one third of the current one with conventional grouting methods.

4 THE ENVIRONMENTAL OPPORTUNITY

Conventional grout formulations contain between 260 to 330Kg of cement in every m^3, being responsible for an average of 320Kg of CO_2 eq. emissions for every m^3 of injected grout in the ground.

In order to reduce CO_2 emission to around 200Kg/m^3, the challenges rest in retain all the key performance properties (density, viscosity, bleeding, gel time, compressive strength) and operational parameters (pumpability, flowability, stability leading to no segregation) and keeping the costs within the present range.

A significant reduction in cement content and overall CO_2 carbon footprint emissions represents an opportunity as long as negligible leeching by limiting free water and increased durability are ensured.

The solution the new grout has focused on is using unique admixture technologies, thanks to the mining backfill experience and the adoption of less reactive, inert materials.

5 THE NEW GROUT (COMPONENT A) AND HOW IT WORKS

With the new solution cement and water generate a stronger interbond between the binder and inert materials to reduce free water, reduce leaching, increase strength, control hardening behavior and reducing permeability.

Component A is a combination of binder, inert materials and admixtures delivered as a single dry powder which must be mixed at site with water, pumped into the TBM and then mixed at the injection point with sodium silicate as activator of component B.

Mixing benefits

- Component A mixing procedure follows the same protocol (and time) for standard grouts
- Only water is needed in the shear mix colloidal tank at the batching plant

Infrastructure & logistic benefits at batching plant & TBM

- Smaller batching plant with fewer tanks/silos for less complexity
- No retro fitting required
- No changes of pipes, pumps, tanks outside the tunnel and inside the TBM
- No changes in the injection points in TBM

Logistics and procurement benefits

- Single powdery material
- One supplier
- One point of contact for site technical support
- One supply contract

6 THE ROLE OF FREE WATER

Free water in backfill grout methods is very much linked to water volume losses in the surrounding grounds.

Critical argument for water volume losses is how much water is bonded in each component of the mix and, reversibly, how much water has a critical volume loss potential.

Free water in conventional backfill grouts goes over 60%, a huge factor that impacts on durability, affecting shrinkage and permeability of the final product.

In the new grout method there is significant less free water in net volume (overall 5-10% range, regardless the higher water/binder ratio).

Thanks to the high volume of inert aggregates, binder is bonded in the solids and aggregates are bonded in the water, reducing the net volume of free water by much.

In these conditions the net unbonded free water is better stabilized leading to a much better and more durable final product; anti washout properties are improved after gelling; leaching and shrinking are almost erased; early strength does contribute to lining stabilization.

How much water can potentially leach will heavily depend on the surrounding ground's porosity and water content.

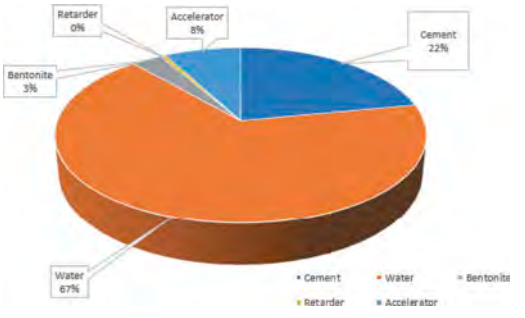

Figure 2. Average Conventional raw materials distribution in conventional backfill two components grouts.

Why water?

- Water is needed to trigger the hydration process of cements
- Water is needed to ensure pumpability and flowability of Component A
- Accelerators need water to create the gelling matrix

What is the solution

The technical solution is the increase of solids in the mix to reduce the free water and, at the same time, to let the remaining water to continue doing its job at the same time

Less free water means:

- Shrinkage is insignificant with limited net water leaves the grout after placement
- Fewer cracks
- Improved waterproofing properties
- Increased durability
- Leaching is almost erased
- Anti Wash-Out properties are improved immediately after gelling
- No segregation, making the grout compatible with any ground

7 PROPERTIES COMPLIANCE WITH TECHNICAL PARAMETERS

In addition to the consistently reduced CO_2 carbon footprint emissions per m^3, with the new backfill grout solution the pre and post injection technical performance of main parameters can still be ensured.

- Ensured pumpability, flowability and stability of Component A
- Very limited bleeding of Component A @T24hrs
- Sodium silicate with low solid content dosage as Component B
- Limited shrinkage @T24hrs for reduction of free water and leeching capacity
- Fewer cracks, improved waterproofing and increased durability
- No segregation, allowing the new solution to be compatible with any ground
- Improved anti washout properties

7.1 *Quality control*

In order to ensure a positive reception in the market, we have kept unchanged all the laboratory tests in use for the qualitative assessment of the grouts. The Table 1 below summarizes these tests.

8 CO2 CARBON FOOTPRINT EMISSIONS SOURCES OF INFORMATION

When calculating GWP, it's important to list the source of information to give credibility to the work.

GWP needs also to be formally stated in EPD (Environmental Product Declaration (EPD) drafted in accordance with EN15804+A2 & ISO14025/ ISO21930 standards.

Generic (global) dataset from Ecoinvent 3.6, Generic (European) dataset from CEPE database v3.0 (2016) and EFCA Model EPD: EPD-EFC-20150091-IAG1-EN (Europe) are just some of these sources.

Table 1. Summary of lab tests.

Property	QC Test	Average Conventional Grouts	The New Grout
Flowability	Marsh Cone @T0 hour	30 – 45 seconds	35 – 55 seconds
Stability	Marsh Cone @T24 hrs	45 – 55 seconds	35 – 70 seconds
Bleeding	Bleeding Test @T24 hrs	3 – 8%	1 - 3%
Gel Time	Beaker by Beaker Test Method @T0 hr	It depends on Accelerator dosage	It depends on Accelerator dosage
Early Strength	Penetration Test @T1 hr	0.05 – 0.10 MPa	0.10 – 0.15 MPa
Was-Out	Anti Wash-Out test @T0 hr	Seldom required	3 - 5% max weight loss
Shrinkage	Volumetric Test @T24 hrs	Never required	1 - 2%
Late Strength	UCS Test @T24 hrs	0.20 – 0.50 MPa	0.40 – 0.80 MPa
Late Strength	UCS Test @T28 days	2.0 – 3.0 MPa	1.50 – 2.0 MPa
Elastic Deformation	E-Modulus @T28 days	Seldom required	0.70 – 1.20 GPa
GWP (Global Warming Potential)	Calculation based on Sources	Never measured or required	Net 170 – 230 CO_2 eq. Kg/m3 (30 – 45% reduction on raw materials)

Figure 3. Conventional grout @T24hrs after 15 strokes on Hagermann flow table at room temperature.

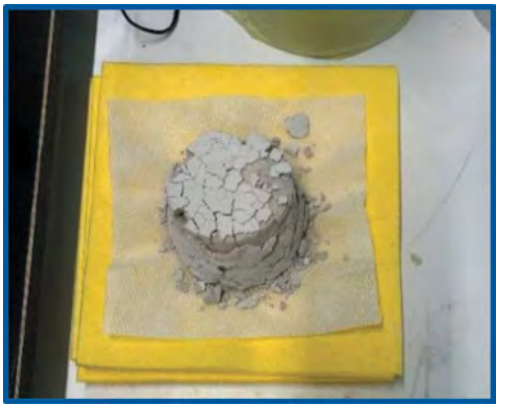

Figure 4. Conventional grout @T28days at room temperature.

Figure 5. The new grout solution @T24hrs after 15 strokes on Hagermann flow table with improved rheology & no cracks.

Figure 6. The new grout solution @T28days at room temperature with improved durability, no segregation.

9 THE BENEFITS OF THE NEW, INNOVATIVE ANNULUS GROUT

9.1 *Environmental benefits*

- Reduced CO_2 emissions on raw materials by 35-45%
- Reduced CO_2 emissions from transport – one only source to supply Component A
- Insignificant leeching levels into the surrounding ground/water table

9.2 *Benefits for operators and contractors*

- More predictable outcome
- Less risk of secondary grouting
- One supply contract
- Use of present plant infrastructure
- Less logistic complexity
- Mixing and injection unchanged
- Costs comparable to conventional solutions

9.3 *Benefits for employers and end users*

- Increased durability
- Less chance of water ingress in tunnels
- Fewer water leak repairs
- Less downtimes
- Longer, uninterrupted service operation

10 CONCLUSIONS

The new sustainable technologies introduced in this paper are brand-new solutions designed to work in the industry for very long time, compatible with the new Green TBM concept but also with any type of TBM currently serving the market.

The benefits are particularly advantageous for the environment, in terms energy and water reduction, and carbon footprint emissions.

The advantages of the new technology of foaming agents and backfill grouts match with the constant increase of the diameter of final tunnels (tunnel ID) that leads to a corresponding increase of the volume of soil to be excavated and, ultimately, the volumes of chemicals to be used during TBM operation.

Contractors have now a new way to approach the protection of the environment; with these new technologies they are now able to contribute to a substantial reduction of environmental pollution in grounds and into the atmosphere.

REFERENCES

Wolfgang Aldrian, Tunnelling Journal, April-May (2021).

EFNARC, "Specification and Guidelines for the use of specialist products for Mechanized Tunnelling (TBM) in Soft Ground and hard Rock" (April 2005).

CSN EN 15804+A2, "Sustainability of construction works - Environmental product declarations - Core rules for the product category of construction products' (2019).

ISO 21930:2017, "Sustainability in buildings and civil engineering works — Core rules for environmental product declarations of construction products and services" (2023).

ECOINVENT, "Generic (global) dataset from Ecoinvent 3.6" (2023).

CEPE, "Generic (European) dataset database v3.0" (2016).

EFCA, "Model EPD: EPD-EFC-20150091-IAG1-EN (Europe)' (2022).

Tunnelling for a Better Life – Yan, Celestino, Thewes & Eberhardt (Eds)
© 2024 The Author(s), ISBN 978-1-032-80042-4
Open Access: www.taylorfrancis.com, CC BY-NC-ND 4.0 license

Successful tunnelling in the desert, Wakrah and Wukair Drainage Tunnel, Doha, Qatar

J.B. Stypulkowski* & Khalid Saif F S Al-Khayareen
Public Works Authority (ASHGHAL), Doha, Qatar

ABSTRACT: The Wakrah and Wukair Drainage Tunnel is a 13km-long and 4.5m-ID sewer tunnel which includes several adits with provisions for future connections as well as four work shafts, four intermediate access shafts and ancillary hydraulic structures. Two TBM drives with a length of 5877m and 7198m were both mined using two CREG TBMs with an excavated diameter of 5.9m. The tunnel is supported with a 300mm-thick precast segmental lining made from Fiber Reinforced Concrete (FRC). The tunnel is also lined with a secondary cast-in-place Corrosion Protection Lining (CPL) consisting of sacrificial concrete and a HDPE membrane to cope with an aggressive sewer environment for the next 100 years. The ground surface levels along the alignment range from approx. +5 to +25 m above the Qatar National Height Datum 95 (QNHD95) with shaft depths ranging from 50 to 60m thus making this the deepest and most challenging TBM tunnelling project in Qatar to date. Connecting branches and a new sewage treatment plant will be delivered under different contracts. The authors will link the design considerations and results of the geotechnical data collection system for weak/soft rock mass commonly found in Doha, Qatar presented in the previous papers with the results of performed geological mapping and show how they correlate with the actual TBM performance. The recent advancements in research related to TBM performance and how they relate to the mechanized tunnelling in the Rus Calcareous (RUS) and Rus Gypsum (RUSGYP) formations will be assessed as well.

Keywords: Tunnelling, EPB TBM, Performance prediction, weak/soft rocks, deep shafts, durability

1 INTRODUCTION

The Wakrah and Wukair Drainage Tunnel (WWDT) is 13 km long with 4.5 m ID sewer water tunnel about 50 to 60 m below ground surface which is part of a bigger sewer scheme serving Doha's growing population in the years to come. The Owner (or Employer), PWA-ASHGHAL, is the designated Engineer, who is represented by the Engineer's Representative Parsons International (PIL). PIL design team provided engineering design review, verification and approval services for all the design produced by the Contractor's team PORR-HBK-MIDMAC (PHM). PIL was also the Construction Manager on this project. Authors of this article expect the readers to refer to introductory publication by Stypulkowski et al. (2023) on the same subject for omitted details. The basic statistical terminology used is explained in www.cuematch.com The author's preference is to use "mode" to find the most common value, average is used only if mode can't be calculated.

2 PROJECT OVERVIEW

Integral to the project are several adits with provisions for future connections as well as four work shafts, four intermediate access shafts, ancillary hydraulic structures and an Odour Control Facility. The shaft depths range from 50 to 60m, which will make this the deepest and most challenging TBM tunnelling project in Qatar to date, with water pressures potentially reaching 6 bars. Connecting branches and a new sewage treatment works will be delivered under different contracts.

Two TBM drives with a length of 5,877m and 7,198m respectively were mined using two identical CREG TBMs with excavation diameter of 5.9m. The tunnel is supported with a 300mm-thick precast segmental lining made from Fiber Reinforced Concrete (FRC). The tunnel is currently lined with a secondary cast-in-place Corrosion Protection Lining (CPL) consisting of sacrificial concrete and a HDPE membrane.

Logistics and launch tunnels were excavated using NATM/SEM technology (bench & heading) with a cross section area between 31.2 m^2 and 43.8 m^2.

*Corresponding author: jstypulkowski@ashghal.gov.qa

DOI: 10.1201/9781003495505-288

The project site is mostly undeveloped with sparse desert vegetation and is surrounded by Qatar Energy (QE) lines, overhead high-voltage transmission lines, and other utility services, as well as expressways. The ground surface levels along the alignment range from approx. +5 to +25 m above the Qatar National Height Datum 95 (QNHD95).

Figure 1. WWDT project layout/progress.

Access Shafts WS10 and AS09 were used to launch two Tunnel Boring Machines (TBMs) mining upstream provided access for tunnel construction. Access Shaft AS09 is centralized along the alignment and is a launching shaft as well as receiving shaft. List of all the shafts is in Table 1. After completion of construction a smaller diameter permanent shafts will be constructed within the temporary shaft and the excess space around is backfilled. Two shafts are intended as TBM reception shafts: WS07 and AS09. The shafts intermittently served as tunnelling shafts and after TBM passed it facilitated CIP liner installation in already completed sections (Figure 1).

Table 1. Shaft summary.

Shaft	Temporary shaft ID		Permanent shaft OD		Permanent shaft ID
			(m)		
	Conical		Conical		
	Base	Top	Base	Top	
WS08	10.2	14.5	10.2	11.1	7.8
AS10	10.2	14.0	10.2	11.1	7.8
WS09	15.2	19.5	15.2	16.1	12
AS11	15.2	19.5	10.2	11.1	7.8
WS10	17.1	20.7	17.1	18.2	14.1
	Vertical		Vertical		
WS07	15		15		12
AS09	15		15		12

3 ALIGNMENT CONSIDERATIONS

The tunnel horizontal alignment has been confined to the assigned utility corridors. For additional consideration please refer to Stypulkowski et al. (2023).

4 GEOLOGY

An extensive ground investigation works has been performed along the alignment. For detailed description please refer to Stypulkowski et al. (2023).

The project area is geologically a part of the Arabian Gulf Basin as described in detail by Cavelier et al. (1970) and Sadiq and Nasir (2002). Only two underlying lower geological units: the Rus Calcareous (R) and Rus Gypsum (RG), (Karagkounis, 2016) were encountered during tunnelling.

The encountered R can be described as fine-grained calcarenite characterized by chalky and bioclastic limestone with occasional nodules of gypsum and beds of laminated shale, siltstone, claystone, and clayey silt. Very closely to medium-spaced fractures were reported, as well. RUS was encountered in different colours, including greyish brown, grey, brownish grey, and white.

The encountered RG can be described as fine-grained gypsum and calcareous siltstone with beds of fine- to medium-grained bioclastic limestone, calcareous siltstone, soft to stiff silty clay and claystone, with very closely to widely spaced fractures. RG was encountered in different colours, including grey, brown, brownish grey, bluish grey and brownish grey.

5 INTACT ROCK PROPERTIES

Laboratory tests were conducted on rock samples obtained from borings before construction. For the Rus unit Uniaxial Compressive Strength (UCS) test results (Figure 2) range between 1 – 51 MPa (mode 4.1MPa). For the Rus Gypsum unit Uniaxial Compressive Strength (UCS) test results range between 2.2 – 31 MPa (mode 16MPa). While the maximum values are lower the USC in mode terms for RG is almost 4 time larger. Tensile strength from Brazilian tests (Figure 3) range between 0.1 – 11MPa (mode 3MPa) for R and for RG range between 0.1 – 12MPa (mode 2MPa). While the maximum values are similar the Brazilian in mode terms for R is 38% higher. $Is_{(50)}$ from point load testing (Figure 8) ranges between 0 – 4MPa (mode 0.2MPa) and 0 – 3MPa (mode 0.5MPa) for R and RG respectively. While the maximum values are higher the $Is_{(50)}$ in mode terms for RG is almost 3 time larger. Young's modulus from UCS testing (Figure 7) range between 0.4 and 39GPa (mode 12GPa) for R and between 0.8 and 47.5GPa (mode 23.5GPa) for RG. The maximum values are 21% higher for RG and the

Young's modulus in mode terms for RG is 2 times larger. Poisson's ration in mode terms is 0.36 for both units. Slake Durability Index (SDI) (Figure 4) ranges between 10 and 99 (mode 75) and 32 and 99 (mode 97) for R and RG respectively. The SDI in mode terms for RG is 30% higher. Schmidt Rebound Hardness (SRH) (Figure 5) is similar for both rock units, however in mode terms it is 35% higher for RG. Maximum Swelling Strain Index (Figure 6) values are 4 times larger for RG.

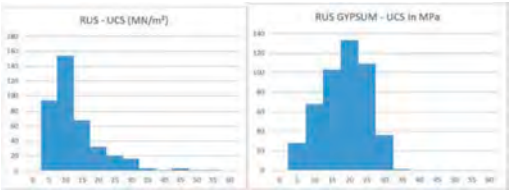

Figure 2. Rus & Rus Gypsum all tests UCS in MPa and MN/m².

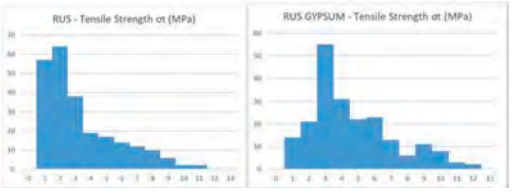

Figure 3. Rus & Rus Gypsum all tests, Tensile Strength σ_t (MPa).

Series of Triaxial Tests were carried out on 241 Rus samples and 209 Rus Gypsum samples. Resulting Angles of Friction φ (°) were similar yielding 38 to 40 deg mode terms and average cohesion was from 2 to 2.4 MPa.

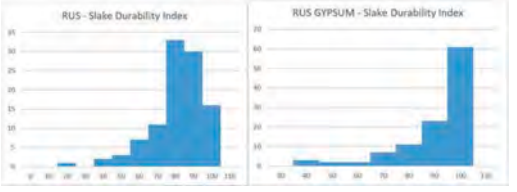

Figure 4. Rus & Rus Gypsum all tests, slake durability index.

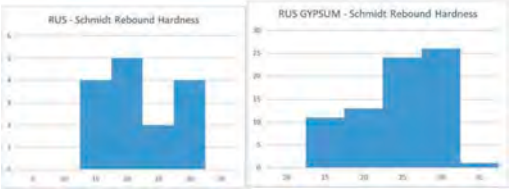

Figure 5. Rus & Rus Gypsum all tests, schmidt rebound hardness.

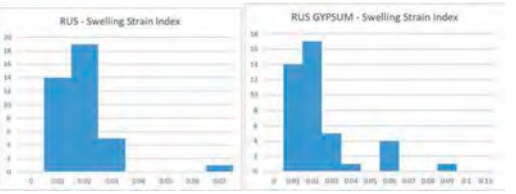

Figure 6. Rus & Rus Gypsum all tests, swelling strain index.

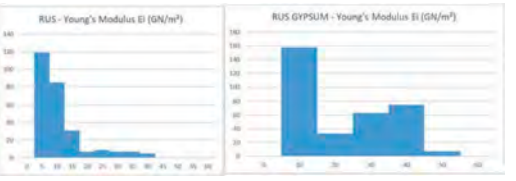

Figure 7. Rus & Rus Gypsum all tests young's modulus E_i (GN/m²).

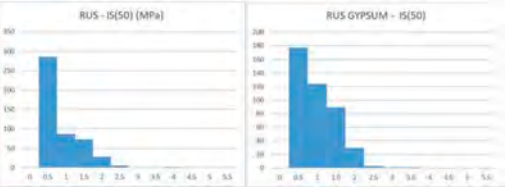

Figure 8. Rus & Rus Gypsum all tests, $Is_{(50)}$ (MPa).

The RMR system (Bieniawski, 1989) while it was developed for hard rock tunnels it is commonly used by designers since it is related to GSI which in turn is often used as an input for the Hoek-Brown failure criterion. Its inapplicability to soft/weak rocks has been discussed in detail by Stypulkowski et al, 2014, 2016, 2018, Pathak et al 2015, Vucemilovic, H. 2021. Since extensive triaxial testing has been conducted yielding Mohr-Coulomb (M-C) criteria parameters the authors decided to omit it.

6 EXAMINATION OF THE TBM DATA

6.1 *General*

The excavation is still carried out by one of two CREG TBMs with rotating cutter-head which was fitted with cutting tools (disc cutters, scrapers, rippers). TBM drives AS09 to WS07 with a length of 5,877 m started 2/28/22 with a breakthrough 5/4/23 and WS10 to AS09 with a length of 7,198 m started 1/27/22 with expected breakthrough in October 2023. Both TBMs have an excavation diameter Ø5,9m. The permanent lining of the tunnel consists of dowelled, pre-cast concrete segments reinforced with steel fibres. For additional details please refer to Stypulkowski et al. (2023).

6.2 *TBM performance and utilization*

Five earth pressure sensors in the bulkhead were used for controlling the stability of the tunnel face. Continuous measurements of the earth pressure in the excavation chamber allowed control of the face support pressure. The contractor estimated in its Plan for Advance of Tunnels (PAT) maximum supporting pressure of 5.22 and assumed 1.2 bar as a minimum.

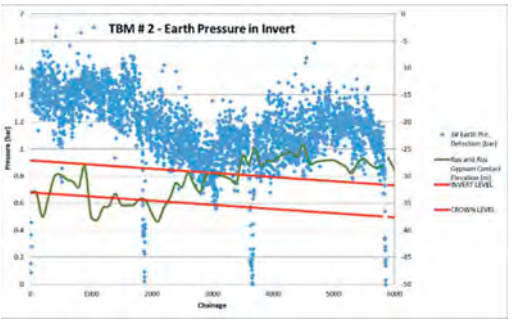

Figure 9. TBM Earth Pressures – Invert (bar).

Face pressures calculated using methodology described in Anagnostou et al.(1994) is commonly used for estimation. Since most of the measured results in mode terms are about 1.14 bar there is no corelation between soil type of materials and weak rocks of Doha (Figure 10).

The excavated material was measured via the belt scales installed on the conveyor belt and compared to the theoretical volume.

Since the rate of advance mainly depends on geological conditions, ground stand-up time, stability, mode of advance, condition of cutters, etc. the authors looked at the collected data (Figure 11). These boundary conditions have a direct influence on the cutter head torque and the contact force, which limit the advance rate.

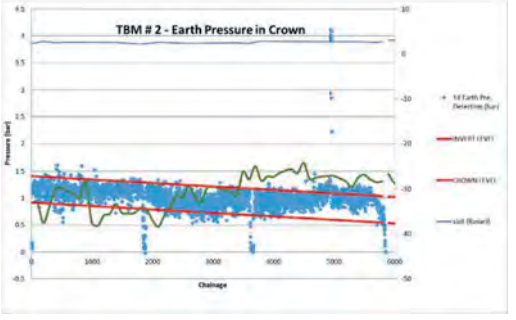

Figure 10. TBM Earth Pressures – Crown and σ_{tot} (bar).

The maximum speed designed for this TBM was 80 mm/mi (Figure 11). The advance speed associated with cutter head rotation speed, was well below expected maximum 5.5 rpm (Figure 12).

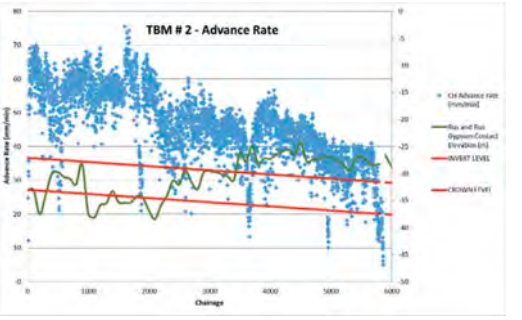

Figure 11. TBM Advance Rate (mm/min).

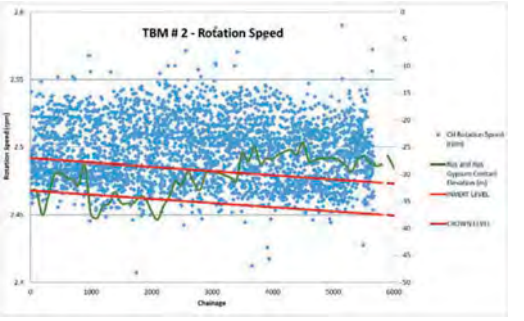

Figure 12. TBM Rotational Speed (rpm).

The cutter head rotation speed and thrust force were adjusted during the TBM excavation for optimized advance rate (Figure 14). The contractor estimated in PAT expected maximum thrust forces from: ground face resistance, water pressure, shield friction, cutter tools, drag forces from back up systems and tail skin seal to be 27,715kN and minimum 12,478kN. What was recorded during tunnelling is shown on Figure 12. Maximum thrust recorded was 17,389kN with a mode of 8,453kN which is about 30% of what was anticipated.

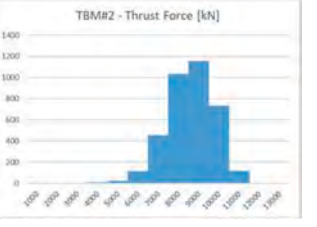

Figure 13. TBM Thrust (kN) with 12 high values eliminated out of 3649.

There were 12 interventions at the face, 3 involved double disc replacement (Table 2).

6.3 *Ring building*

The tunnel was lined with segments immediately after the TBM advance under the protection of the

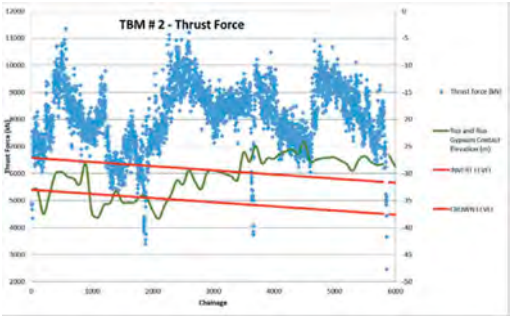

Figure 14. TBM Thrust Force (kN).

Table 2. TBM#2 Cutter head intervention summary.

TBM#2 Cutter Head Intervention Summary			
Date	Chainage (m)	Distance between interventions (m)	Tools changed
3/22/2022	5765		No Tools replaced
5/17/22	5391	375	No Tools replaced Disc no: (19 & 20)
5/26/22	5313	77	Double disc, replaced Disc no: (33 & 35)
6/6/22	5115	199	Double disc, replaced
7/3/22	4662	453	No Tools replaced
7/27/22	4287	375	No Tools replaced Disc no: (9 & 10)
8/22/22	3911	376	Double disc, replaced
10/16/22	3144	767	No Tools replaced
10/24/22	2447	697	No Tools replaced
12/25/22	1902	545	No Tools replaced
3/15/23	827	1075	No Tools replaced
5/3/23	19	809	No Tools replaced

shield. The segments were moved into position by an erector, a remote-controlled crane arm, which picked them up mechanically and then put in place. In TBM tunnelling it is the most important operation which when it is done efficiently contributes greatly to overall success of tunnelling operations.

The ring build time has been filtered and after elimination of stoppages longer than 8 hrs it has been established that installation time in mode terms was 75 minutes (Figure 16 and Figure 15).

Detailed description of typical installation process has been presented in Stypulkowski et al (2018).

6.4 *EPB face pressure effect on TBM performance*

The authors looked at how different face pressure may affect tunnelling parameters after Bilgin (2023). The results were split into four pressure intervals of 0.5bar each. As shown in Table 3 and of figures Figure 16 and Figure 17. Contrary to the findings made by Bilgin (2023) thrust and torque were not linearly related to the face pressure.

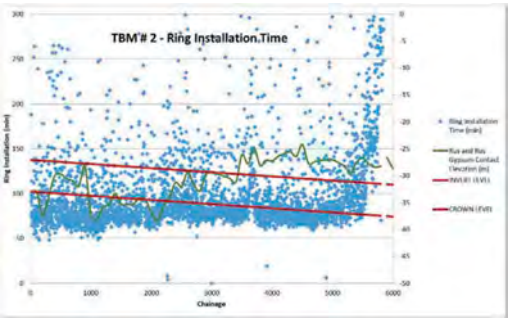

Figure 15. TBM Ring Build Time (min).

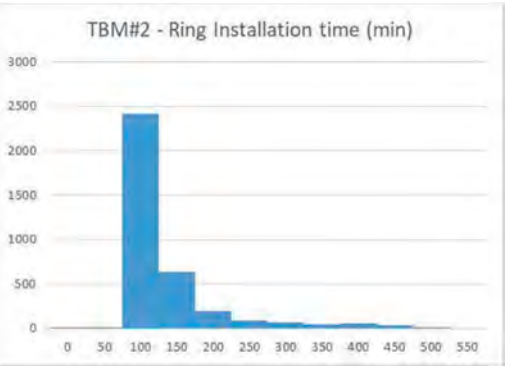

Figure 16. Ring installation time shorter than 480 min (99 instances out of 3649 eliminated).

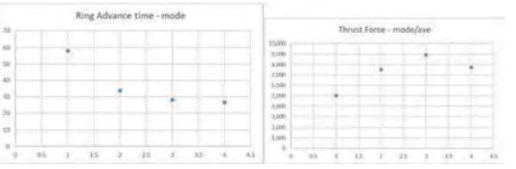

Figure 17. Ring Advance time (min) & Thrust Force (kN) vs EPB face pressure.

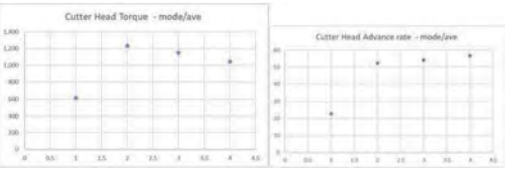

Figure 18. Cutter Head Torque (kNm) & Advance Rate (mm/min) vs EPB face pressure.

Table 3. EPB face pressure effect on TBM performance.

TBM#2 Face Presure	Ring Advance time - mode	Thrust Force - mode/ ave	Grout Pressure - mode/ ave	Cutter Head Advance rate - mode/ave	Cutter Head Advance Rate/ Penetration - mode/ave	Total Grout Volume Ratio (Actual/Theor-etical) - mode/ave	Total Grout Volume	Cutter Head Torque - mode/ave
bar	[min/ Ring]	[kN]	[bar]	[mm/min]	[mm/rev]	[%]	[m³]	[kNm]
0 to 0.5	58	5,018	0.98	23	10	106	4.98	615
0.5 to 1	34	7,502	2.01	52	18	127	5.01	1,234
1 to 1.5	28	8,931	2.06	54	17	115	4.94	1,153
1.5 to 2	27	7,745	3.44	57	23	142	5.02	1,044

notes: correlations don't follow published patterns, EPB face pressure increase doesn't automatically result in proportional increase in tunneling parameters for both TBMs

6.5 *TBM penetration considerations*

Since UCS test results concluded that Rus Gypsum is 4 times stronger than Rus and $Is_{(50)}$ is 3 times higher, the authors decided to look if the difference in strength affected TBM performance in those units. Most of the tunnelling was done along the boundary between those units with significant portion in the mixed face condition. In addition, tensile strength for Rus Gypsum is 38% higher and young's modulus values are 2 times larger supporting trends in other data. However, triaxial test results show very similar results for both units.

6.6 *Torque and thrust*

When comparing thrust forces recorded in both units in mode terms, we have 8,249 and 9,565 (kN) in R and RG respectively (Figure 12) which is 16% higher for RG. When comparing advance rates, we have units in mode terms 47.3 vs. 37.7 (mm/min) which is which is 29% lower for RG (Figure 20).

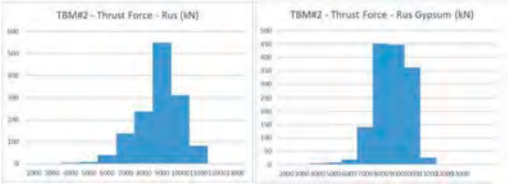

Figure 19. Thrust force in Rus vs Rus Gypsum.

When looking at torque recorded in both units in mode terms, we have 1,211 and 1,196 (kNm) in R and RG respectively which are similar indicating constant driving parameters for the TBM.

In general no in-crease of penetration can be associated with thrust and torque increase.

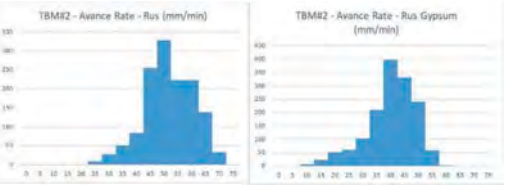

Figure 20. Advance rates in Rus vs Rus Gypsum.

6.7 *Boreability*

The boreability have been used in rock tunnelling to express ease or difficulty of TBM tunnelling. Most frequent input parameters in hard rock models are: UCS, data on discontinuities, thrust per cutter and cutter diameter. Applicability of this approach for weak/soft rocks of Doha was addressed by Stypulkowski et al (2016).

The authors used Boreability Index (BI) to analyse the variations of rock mass conditions along the alignment. BI also known as FPI is the thrust force per cutter (kN) divided by penetration rate (mm/rev). The

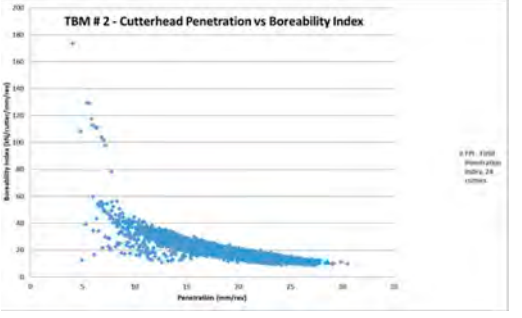

Figure 21. Correlations made with Boreability Index (BI) were not observed with thrust and torque.

authors looked at this relationship before in Stypulkowski et al (2018). The index again shows similar characteristics for weak/soft rocks of Doha.

6.8 *UCS and penetration in weak/soft rocks*

The relationships between UCS and penetration, torque and thrust are shown on Figure 22 to Figure 27 for R and RG separately. Unlike previously UCS test results from tunneling horizon do not correlate well.

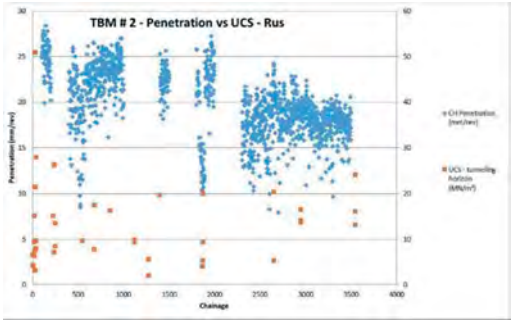

Figure 22. TBM Penetration (mm/rev) vs UCS in tunnelling horizon (MPA) in R.

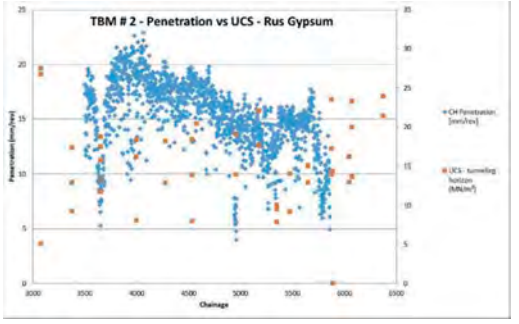

Figure 23. TBM Penetration (mm/rev) vs UCS in tunnelling horizon (MPA) in RG.

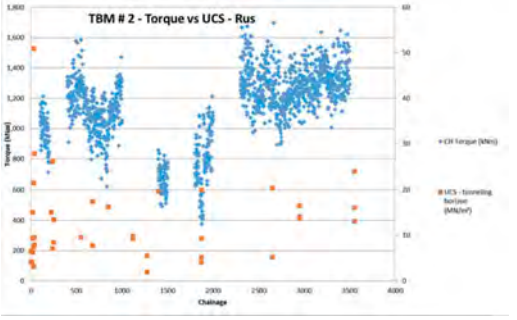

Figure 24. TBM Torque (kNm) vs UCS in tunnelling horizon (MPA) in R.

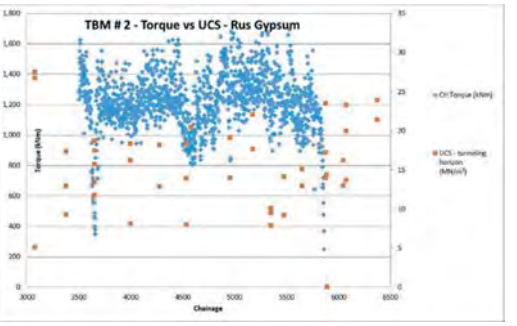

Figure 25. TBM Torque (kNm) vs UCS in tunnelling horizon (MPA) in RG.

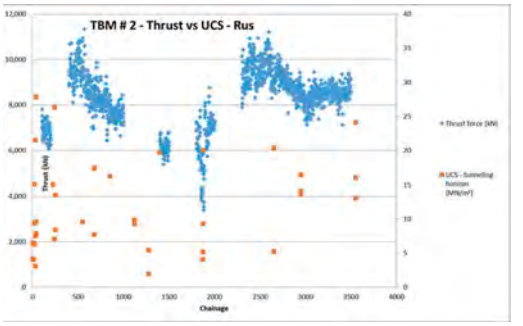

Figure 26. TBM Thrust (kN) vs UCS in tunnelling horizon (MPA) in R.

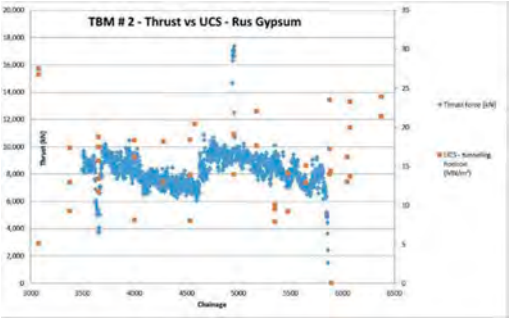

Figure 27. TBM Thrust (kN) vs UCS in tunnelling horizon (MPA) in RG.

7 CORRELATIONS OF TBM DATA WITH ROCKMASS

Forecasting of excavation behaviour in tunnelling using classification systems rely on previous case histories.

7.1 *QTBM*

Penetration rates were used to calculate Q_{TBM} using well known empirical approximation after Barton,

2006 (Q_{TBM} = (5/PR)^5). Figure 28 shows distribution of QTBM with median 19 yielding good to very good tunnelling for most of the drive in Q_{TBM} terms.

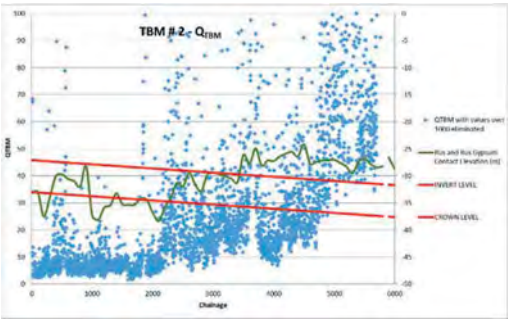

Figure 28. QTBM less than 100 with 87 high values eliminated.

8 CONCLUSION

Since the project is still ongoing with the second TBM mining in the same geology the authors intended this paper to provide a second "progress report".

ACKNOWLEDGMENTS

The writers acknowledge PHM for all the construction and design effort and Volkan Salepciler from PIL for actively managing the project. A special acknowledgement is owed to Murat Canpolat of PHM for providing and reviewing all geotechnical information included herein.

REFERENCES

Anagnostou, G., Kovari, K., The face stability of slurry-shield-driven tunnels. Tunnelling and Underground Space Technology 9, 165–174, 1994

Barton, N. (2006) TBM tunnelling in sheared and fractured rock masses, Cartagena, Colombia.

Bieniawski, Z.T. 1989. Engineering rock mass classifications. New York: Wiley.

Bilgin, N., Yuksel, A., The effect of EPB face pressure on TBM performance parameters in different geological formations of Istanbul, Tunnelling and Underground Space Technology 138 (2023) 105184

Brown, J., Salepciler, V., Stypulkowski, J., and Sheikh Abdulrahman Al-Thani, Launching a 148m-long Tunnel Boring Machine from a 15m-inner diameter shaft, CIC 2023, Doha, Qatar

Karagkounis, N., Latapie, B., Sayers, K. & Mulinti, S.R. 2016. Geology and geotechnical evaluation of Doha rock formations. ICE, Geotechnical Research 3(3): 119–136.

Sadiq, A. & Nasir, S. 2002. Middle-miocene karst evolution in the state of Qatar, Arabian Gulf. Journal of Cave and Karst Studies 64(2): 132–139.

Stypulkowski, J.B., Najder Olliver, A.M., Khalid Saif F S Al-Khayareen, Tunnelling in the Desert, Wakrah and Wukair Tunnel, Doha, Qatar, in "Expanding Underground. Knowledge and Passion to Make a Positive Impact on the World" Anagnostou, Benardos & Marinos (Eds) © 2023 The Editor(s), ISBN 978-1-003-34803-0, Open Access: www.taylorfrancis.com, CC BY-NC-ND 4.0 license, ITA-AITES WTC2023, Athens, Greece

Stypulkowski, J.B., Pathak, A.K. & Bernardeau, F.G. 2014. Abu Hamour, TBM Launch Shaft – A Rock Mass Classification Attempt for a Deep Shaft in Doha, Qatar. EUROCK14, ISRM International Symposium, May 27 – 29, 2014. Vigo, Spain. CRC Press, Taylor & Francis Group: pp 117.

Stypulkowski, J.B., Pathak, A.K. & Bernardeau, F.G. 2016. Engineering geology for weak rocks of Abu Hamour surface and ground water drainage tunnel Phase-1 Doha, Qatar. International Conference on Recent Advances in Rock Engineering, Specialized Conference of ISRM in Bengaluru, India, 16 – 18 November 2016. RARE2016. Bengaluru: 85–90.

Stypulkowski, J.B., Bernardeau, F.G. & Sandell T.D. 2018. Mechanized tunneling technologies for weak rocks of Middle East, revisited. UIAU2017 - Underground Infrastructure of Urban Areas 4 – Madryas et al. (Eds) © 2018. Taylor & Francis Group, London: 211–222.

Stypulkowski J.B., Bernardeau F.G. (2018) Abu Hamour Tunnel Phase I the First TBM Tunnel in Qatar: The Art of Tunneling in a New World. In: Agaiby S., Grasso P. (eds) Engineering challenges for sustainable underground use. GeoMEast 2017. sustainable civil infrastructures. Springer, Cham

Vest, S. 2018. The Midra Shale/Rus Formation unconformity and the potential for groundwater inflow in-to deep excavations, Doha, Qatar. Proceedings of the World Tunnelling Congress 2018. Dubai: 10 p.

PHM-JV., 2022, C8532-PHM-GEN-DES-SPK-26 Detail Design – TBM Support Pressures & Thrust Forces and Plan for Advance of Tunnel, 2022, PORR-HBK-MIDMAC C853/2 JV, Doha, Qatar

Tunnelling for a Better Life – Yan, Celestino, Thewes & Eberhardt (Eds)
© 2024 The Author(s), ISBN 978-1-032-80042-4
Open Access: www.taylorfrancis.com, CC BY-NC-ND 4.0 license

TBM design for operation in gassy formation

Laura Tafuri* & Omar Bonfanti
Webuild, Milan, Italy

Andrea Lisardi
Collins srl, Fiumicino, Italy

ABSTRACT: The Italian railway new network system at present under construction in south of Italy foresees the excavation of several long tunnels to be bored by TBMs in clayey sedimentary formations in presence of gas. The inflows of gas along most of these tunnels are foreseen to be frequent if not continuous in some area. The standard TBM design features and predispositions adopted to deal with the presence of gas are instead suitable for formations in which the presence of gas is only possible or occasional. Consequently, the systems installed on these "standard" TBMs are oriented, according EN16191, towards measuring the gas concentration and, in the event of critical thresholds being exceeded, to automatically shutdown the power supply, evacuate the tunnel and leave the TBM in standby until the dilution of the gas concentration by the ventilation system. The expectation of frequent gas inflows for long stretches of tunnel in projects to be carried out in Southern Italy required a different approach, and more advanced systems to increase the workers safety and at the same time allow, within certain limits, the advancement of the TBM even in the presence of gas inflows, using a safety system that adopt ATEX equipment, procedures, compartmentation, ventilation, drainage and monitoring system. Starting from the guidelines (NIR 44), developed in Italy for large diameter TBMs excavating in gassy formations and adopting EN1127-2 and EN80079-38 for guidance, Webuild has developed, in collaboration with specialist consultants, university institutes and TBM manufacturers, the design, the technical characteristics and the specifications of the TBMs to be used in these projects. The article describes the philosophy behind the design of these TBMs, how this design was developed, the associated procedures and the specifications of the auxiliary equipment and systems supporting the TBM for muck transport and services along the tunnel.

Keywords: Tunnelling, TBM design, gassy formations, ATEX, underground, safety

1 INTRODUCTION

The new Italian railway network currently under construction in the southern part of Italy, utilizing mechanized excavation, is part of a complex and heterogeneous geological context, specifically involving clayey sedimentary formations. In addition to these geological challenges, there is a significant presence of gas, which is not occasional or discontinuous, as observed in other contexts, but continuous and characterized by high quantities and pressures.

Furthermore, the new foreseen railway network, include several projects, located in Campania and Sicily regions, as following indicated:

- *Napoli-Bari HV,* with the lots of Hirpinia-Orsara, Orsara-Bovino and Apice-Hirpinia, for a total tunnel length of 71km
- *Palermo-Catania HV*, that include the lots:
  - Lot 4B Enna-Dittaino
  - Lot 4A – Caltanissetta-Xirbi-Nuova Enna
  - Lot 3 – Lercara-Caltanissetta-Xirbi
  - Lots 1&2 – Fiumetorto-Lercara

for a total tunnel lenghts of 124 km

The various tunnels to be realize, which involve the use of more than 20 TBMs, challenging construction timelines, in addition to the difficult geological context, the strong and continuous gas presence mentioned earlier, and the primary need to ensure the highest safety standards for all individuals

*Corresponding author: l.tafuri@webuildgroup.com

DOI: 10.1201/9781003495505-289

involved, while allowing for the continuity of excavation, have led to the necessity to revolutionize the traditional ATEX concept. The article will describe, starting from the classic ATEX concept, the approaches and improvement interventions undertaken to define the new explosion-proof design of the TBM.

2 ATEX CONCEPT: EVOLUTION AND IMPLEMENTATIONS

Essentially, the reference for the design of ATEX TBMs is based on the Best Practices recommended by the NIR 44 regulation, typically defined and applied to large-diameter TBMs. In these TBMs, the design is primarily focused on measuring gas concentration, and in the event of critical thresholds being exceeded, automatically interrupting the power supply, evacuating the tunnel, and placing the TBM on standby until the gas concentration is diluted by the ventilation system. In the specific context of projects in Southern Italy, this standard design and working approach are not sufficient and need to be implemented. Specifically, the design of the TBMs for transformation into ATEX includes the following macro-intervention areas:

- Compartmentation of volumes/work areas;
- Use of suitable equipment certified for use in gas environment.
- Implementation and optimization of operational activities on board the machine.

The objective was to improve the continuity of excavation while prioritizing safety; the evolution of this specific aspect has been a focal point in conceptual development over the years. To achieve these goals, a suitable machine configuration has been established, starting from NIR44 and drawing upon previous Italian experiences (Sparvo tunnel, Santa Lucia, COCIV). Additionally, by studying and subsequently implementing new technologies, specific procedures have been devised for workers to follow during the operational phase. This ensures the proper utilization of these innovations and, consequently, maximizes excavation efficiency.

There has been an increased emphasis on machine design, aiming to establish a design methodology that, regardless of variations across projects, can provide a universal approach to ATEX design. In the following sections, starting from the overarching concept of ATEX, all the implementations developed to achieve the new concept of explosion-proof TBM design will be outlined.

2.1 *TBM main concept and previous implementations*

The design of TBM-EPB in gassy formations is based on the concept of managing emission sources and confining the air-methane atmosphere within an ATEX volume.

General TBM concepts comply to EN 16191 that, for use TBM in potentially explosive atmospheres, require EN 80079-38 *(Equipment and components in explosive atmospheres in underground mines*) for guide, and comply the Italian guideline NIR44.

Consequently, the risk assessment is performed according EN 1127-2 and equipment are Ex Group I. Analyses of previous experience in gassy formations like Sparvo tunnel (Bandini et al, 2017), Santa Lucia e Pavoncelli tunnels (Bandini et al, 2020) have provided know-how, implemented and tested in Radimero tunnel in a gassy formation, where emissions are quite ordinary.

The new TBM design is an evolution of all previous experience; solutions are provided to avoid both presence of explosive atmosphere and ignition sources, by technical innovations, monitoring, procedures, ventilation system, avoiding potential emission source by increasing sealing of shield elements, and using a drainage system from the excavation chamber.

A confined ATEX volume, designed with specific ventilation, are built around screw conveyor discharge, considered an effective and almost continuous emission source.

2.1.1 *TBM volumes -NIR44*

TBM volumes concept is realized according NIR44 criteria, using a new solution for compartmentation and ventilation of Volume 3. The main conceptual layout is depicted in Figure 1. General NIR44 criteria (Bandini et al, 2017) establish four distinct volumes characterized by different risk assessments and varied solutions aimed at risk mitigation:

- **Volume 1** – always full of muck or material during the advance,
- **Volume 2** – Non ATEX Volume, around Volume 3 housing, where are implemented ATEX solution to monitoring and increase sealing of shield elements and emergency system.
- **Volume 3** – ATEX volume confined by an air proof housing and aspiration ventilation system, from screw conveyor discharge (Figure 2) to last gantry.
- **Volume 4** – ATEX Volume from the end of Volume 3, extended for 500 m
- **Volume 5** – Non ATEX Volume. It is a new implementation respect to NIR44, managed by monitoring and alarms procedures.

2.1.2 *Emission source*

The first step of analysis is to characterize the emission source on the TBM. These can be categorized into two groups:

- Potentially continuous, that can't be avoided during advance;
- Discontinuous, emissions resulting from a temporary malfunction or inefficient of sealing systems adopted to compartmentalize the machine's volumes and to segregate them from ground.

Figure 1. Main Concept Layout and Ventilation concept in normal and SD1 alarm conditions.

Full ATEX volumes are associated to the first type of emission. For the second type of emissions have been implemented solutions, to avoid emission, by developing new sealing system, managed by ATEX control systems, improving their efficiency and managing emergencies. In the volumes where there are second type of emission source, all emergency and control system are ATEX, while other equipment are standard, with temperature control procedures and automatic shut-down managed by methane monitoring system.

2.1.3 *Maintenance in hyperbaric conditions*

In hyperbaric condition is not possible to use ATEX equipment to eliminate ignition source: ATEX

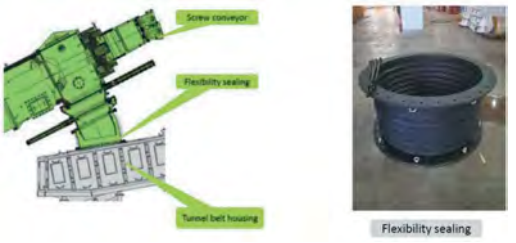

Figure 2. Compartmentation between volume 1 and 3 (Photo and scheme courtesy of CREG).

standard are applicable only in normo-baric conditions. The working procedure adopt a system to realize a cake, by slurry or cement grout, or clay-shock method (Shao-Hui Tang et al, 2021). Pressure and air flow rate are monitored, managing alarm conditions. Methane sensors are in normo-baric atmosphere connected by a probe to a suction point inside excavation chamber. If methane is detected inside excavation chamber alarm condition are activated. In alarm condition, due to pressure drop or air flow rate variation or methane concentration detected, all equipment are turned off, people leave excavation chamber, closing the door, reaching man-lock. Special lights are used to communicate alarm condition in excavation chamber. These equipment are tested by a specialized laboratory in 5 bar methan-air atmosphere, to ensure that they haven't ignition source in working conditions (5 bar). Lights protections dedicated solutions are developed improving ATEX protection method Ex M (encapsulation - EN 60079-18).

2.1.4 *Alarm shut down concept*

All emergency and monitoring equipment in TBM and tunnel are ATEX, allowing emergency managing during alarm condition. According En 1127-2, in an explosive atmosphere (concentration greater than LEL), Ex I M2 (Mb) equipment needs to be capable of being disconnected or made safe. During evacuation and for a short time, it might be necessary to operate M2 equipment in an explosive atmosphere.

According to the risk assessment, in tunnel and on TBM, equipment and plants are both ATEX or standard. Methane monitoring system manage two shutdowns: SD1 for non ATEX equipment in alarm condition and SD2 for ATEX Ex I M2 (Mb) equipment, if explosive atmosphere is present on for a longer time than evacuation time from TBM. In the Figure 3 is showed the electrical line concept, in which one ATEX line (armored high voltage cable and ATEX junction box) from portal reaches the ATEX cable reel on TBM. This cable reel is then connected to the high voltage junction box from where start two lines: the first to the ATEX transformer cabinet and the second to the switchgear cabinet for standard line. In SD1 condition is activated the braker on TBM to shut down from safe volume

standard line. In SD2 condition is activated the switch gear present on the portal and all the tunnel equipment are automatically turned off.

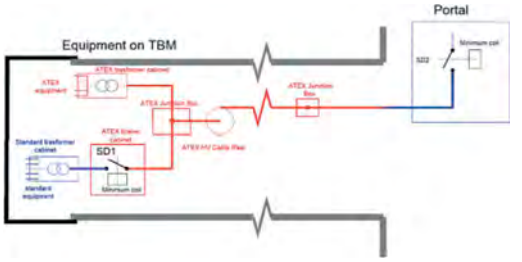

Figure 3. Electrical line concept.

According to the emergency plan and risk analysis, monitoring system, telephones, SOS system and rescue chamber on TBM are not turned off both in SD1 and SD2 condition: all these equipment is energized by backup-UPS.

In SD1 condition still work ventilation system and emergency equipment, like lights, dewatering pumps, tail and articulation sealing systems, and second crane mechanical protection system.

In SD2 condition, ATEX line is shutter down from portal, after short time. Ventilation fan on TBM, both blower and aspiration one, are switched off. In these conditions remain blower ventilation system by portal fan, blower ventilation flow up fresh air to the shield while the secondary fan is off, by closing valve before secondary fan. Proportional valve for blower ventilation in volume 3 is fully opened to maximize flow rate. The ventilation concept changes to the layout showed in the Figure 4. The ventilation inside Volume 3 (belt conveyor housing and duct) changes direction, blowing from screw conveyor discharge. Different threshold limits are defined for each volume, according to the risk assessment and the NIR44 guideline. Table 1 shows the percentage methane volumes that trigger the various situations.

Figure 4. SD2 Alarm condition – ventilation procedure.

The same conditions are activated for different threshold limits. In alarm condition all standard (not ATEX) equipment are shutter down (SD1) from a safe volume and it is activated evacuation procedure using the ATEX evacuation vehicle, always available on the TBM. On the TBM there are several

Table 1. Threshold limits.

	C % methane in air			
Alarm condition	Volume 3	Volume 4	Volumes 2 and 5	
Normal	< 0,3	< 0,3	< 0,15	
Attention	0,3	0,3		Reduce advance Pump grease articulation and brushes
Pre alarm	3	0,7	0,15	Stop advance Increase ventilation Close guillotine
Alarm	3,5	1	0,35	Shut down standard equipment evacuation

alarm lights and trumpet managed by gas monitoring system. These alarm stations are even along tunnel every 500 m, connected by optical fiber to TBM monitoring system. At the portal there is a control room with PC with real time display, data logger, alarm log and managing system to operate, by password, to the gas monitoring system.

2.2 *New implementations/optimizations for ATEX*

Based on the previous operational experiences, it has been studied new aspects and/or implement and improved previous adopted solutions for increasing the safety and the continuity of the excavation. These aspects are all oriented to extend the operativity on TBM board, and are listed below:

- Ventilation Concept
- Gas Drainage Concept
- Upgrading of gas monitoring system
- Solution for parking and use of ATEX emergency vehicle
- Other improvement and applications
  - Shield articulation and tail brushes
  - Extension of Volume 4

In the following paragraphs are described in details.

2.2.1 *Ventilation concept*

Ventilation plant is a "safety device" according to ATEX; it is compliance to a risk-based approach considering Safety Integrity Level, SIL1 level according to EN 61508.

The main features are:

- UPS station,
- Flow rate and pressure monitoring system with associated safety procedures,
- portal fan station redundancy

For this last aspect typically are provided two fans coupled, considering a degraded mode due to failure. All control and monitoring system are compliance to a SIL1 level.

On the TBM the ventilation system is made by two different plants, that working together and in a balanced way: blower ventilation from portal with a secondary ATEX fan on TBM, and aspiration system dedicated to Volume 3.

In the Figure 5 is showed the schematic detail.

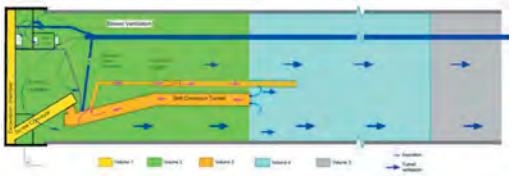

Figure 5. Ventilation concept.

Blower ventilation is provided to the shield area and to working chamber, to excavation chamber during maintenance in normobaric conditions, and to Volume 3, by blowing line close to screw conveyor gate to move and dilute emission from screw conveyor. All lines are managed by a proportional valve.

Volume 3 flow rate is defined by balancing all flows in TBM and considering minimum air speed in the belt conveyor housing of 1,5 m/s.

Main ventilation design parameters are:

- Air speed inside the belt conveyor housing,
- distance between suction line end section and Volume 3 end section,
- avoid air recirculation,
- emergency gate on the front of housing to be opened if ventilation inside Volume 3 is off,
- minimum air speed in TBM is 0,5 m/s.

2.2.2 *Gas drainage concept*

To increase the continuity of the excavation, one of the main aspects considered is the removal of gas presence to avoiding any ignition source. For this reason has been developed various operative procedures and technical implementation that combine ventilation and new systems. These implementations consist in:

– Procedures that allow the gas reduction during TBM advancing;
– Procedures that allow the intervention in the excavation chamber;
– Systems that permit the gas removal from the excavation chamber and the evacuation through the tunnel

The first aspect is illustrated in the Figure 6

Figure 6. Void detection system (photo on CREG courtesy)

This system is installed on the top of bulkhead and permit to monitor the voids presence. Normally the advance of the TBMs is possible only in "Closed" mode, with excavation chamber always full. The absence of absence of void volumes into the excavation chamber shall prevent the release of gas from the excavated material and consequently the formation of potentially explosive gas bubbles.

The second aspect is depicted in Figure 7a and 7b, illustrating the two phases, one before and the other after the intervention in the excavation chamber. As shown in the pictures, the presence of additional air lines allows interventions in hyperbaric conditions with a higher level of safety. This is because they enable the introduction of clean air into the excavation chamber, thereby reducing the methane concentration to safe levels.

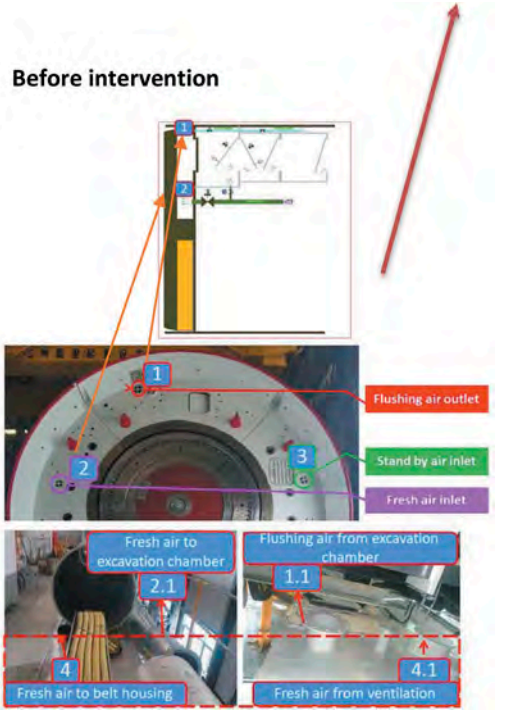

Figure 7a. Procedures for interventions in excavation chamber in atmospheric conditions – Before the maintenance (on CREG courtesy).

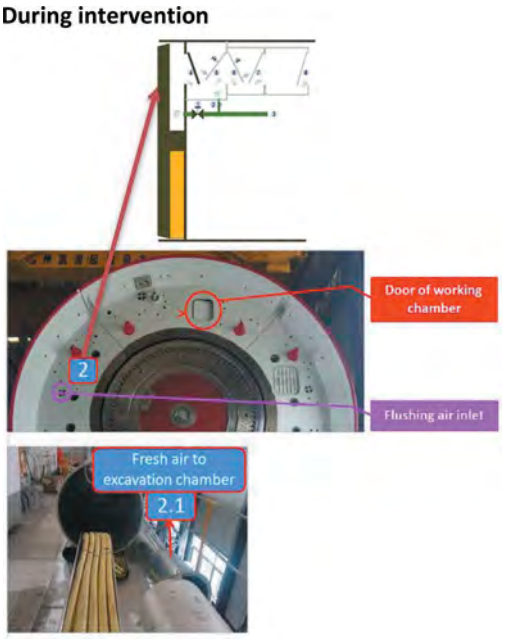

Figure 7b. Procedures for interventions in excavation chamber in atmospheric conditions – During the maintenance (photo on CREG courtesy).

Furthermore, considered the third aspect mentioned before, a drainage system has been designed to allow the discharge of the gaseous volumes from the excavation chamber to the surface through a dedicated conduit (Figure 8 for schematic and Figure 9 for details).

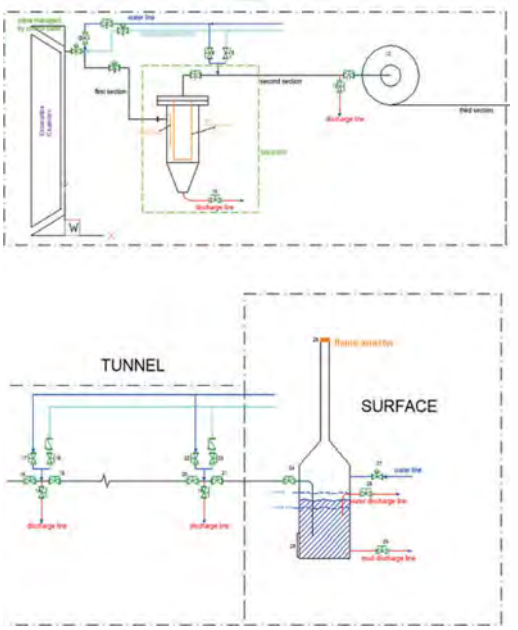

Figure 8. Drainage system Schematic.

The primary objectives are as follows: to reduce the pressure within the excavation chamber, expel exhaust air from the excavation chamber during the flushing procedure, eliminate air bubbles from the excavation chamber during excavation, and facilitate the drainage of methane to the surface. The design has been developed with due consideration of past experiences in the Pavoncelli tunnel (Bandini et al, 2020) and requirements described in EN 14983:2007, (*Explosion prevention and protection in underground mines - Equipment and protective systems for firedamp drainage*).

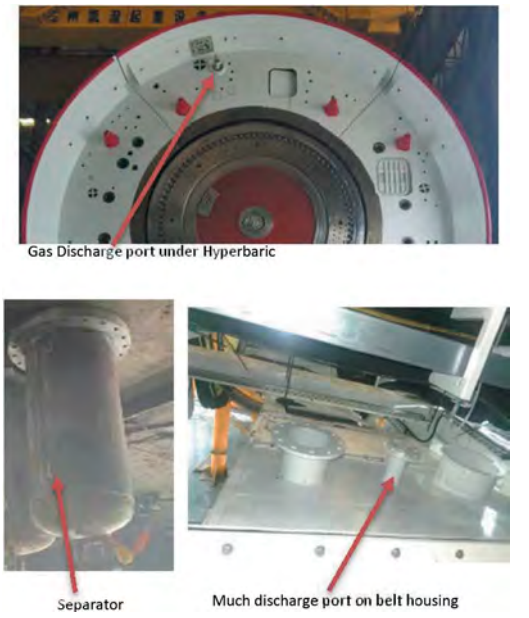

Figure 9. Drainage system Details (photos on CREG courtesy).

This system is designed to reduce the occurrence of an explosive atmosphere within the tunnel and the TBM back-up during operations. It achieves this by maintaining operational pressure limits for all sealing systems and minimizing impulsive emissions from the screw conveyor. The entire system and its components operate under hyperbaric pressure in an air-methane atmosphere, in compliance with the Pressure Equipment Directive (PED) and the ATEX directive.

A separator, designed in accordance with the ATEX directive, is installed near the excavation chamber. To prevent frictional ignition, the internal surfaces and filters are constructed using non-sparking materials. The objective is to segregate solids and mud (clasts, foam, muck) from gas and water, facilitating their passage into the second section of the drainage system. Procedures have been established for flushing the entire line and separator using inlet water and compressed air, managed by

valves. A hose reel on the TBM ensures continuous line integrity during advancement, with dedicated procedures developed for maintenance.

It is possible to flush the entire line by filling it with water propelled by compressed air to the portal. The water will travel from the reel to the surface through the separator, the second section of the line, and the hose. A water seal drum with a flame arrester on the discharge line is installed at the surface. Emissions from the line are intermittent, and the flow can consist of air or a methane-air mixture at various concentrations, with no flame being utilized.

2.2.3 *Methane monitoring system*

The monitoring system functions as a pivotal safety device, designed in adherence to the ATEX standard, achieving a Safety Integrity Level (SIL) 1 in accordance with EN 61508. Monitoring sensors align with the specifications outlined in EN 60079-29-1:2016 (Explosive atmospheres - Part 29-1: Gas detectors - Flammable gas detector performance requirements). The strategic positioning of sensors, illustrated in Figure 10, is carefully defined to oversee emission sources and the gas path on the TBM.

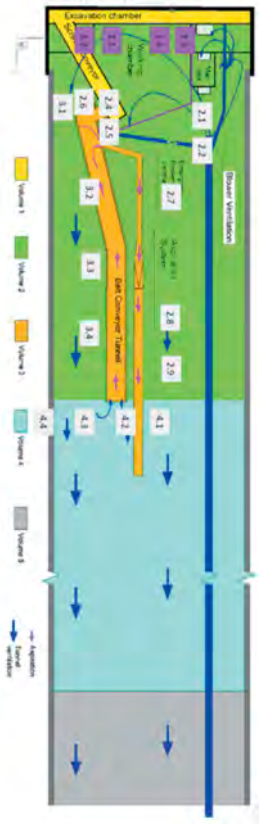

Figure 10. Sensor Positioning concept (on CRCHI courtesy).

In this specific application, a deliberate augmentation of the sensor count has been implemented, further fortifying the monitoring capabilities and safety levels.

The sensors for the excavation chamber and the work chamber are located in Volume 2 within a safe area and are connected to a sampling point in the excavation chamber during maintenance. This is due to the fact that the sensors do not function properly under hyperbaric conditions, and direct installation is not feasible. The schematic representation is provided in Figure 11.

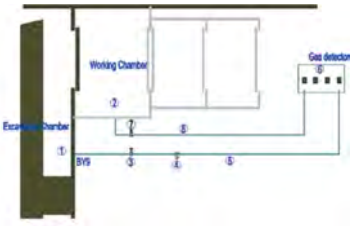

Figure 11. Sensors for working and excavation chamber (on CREG courtesy).

2.2.4 *Emergency vehicle and solution for evacuation*

An emergency vehicle is consistently present on the TBM to facilitate the evacuation of the entire crew from the tunnel at any given moment. To accommodate this requirement, a dedicated gantry has been implemented.

In an ATEX configuration, the system is designed to enable evacuation at any time, and, for this purpose, a specific system has been developed to facilitate this in emergency situations. In Figure 12, the hoisting system used to transfer the vehicle from the platform to the ground is depicted. The entire system, comprising hoisting and hydraulic components utilized for moving the emergency vehicle, adheres to a Safety Integrity Level (SIL) of 1 according to IEC 61508.

The evacuation procedure is initiated in alarm conditions at SD1. Upon activation at SD2, personnel commence the evacuation of the tunnel. If gas concentration rapidly rises to the Lower Explosive Limit (LEL) level, the emergency vehicle system remains operational even after power shutdown from the portal, allowing the relocation of the vehicle from the parking area by personnel.

A semi-manual system employing compressed air, sourced either from a bottle or supplied by the tunnel line, is utilized to relocate the vehicle from the platform even under SD2 conditions.

2.2.5 *Other improvements and applications*

2.2.5.1 Shield articulation and tail brushes

To enhance the tightness of shield articulation, seals and cameras have been incorporated, along with an

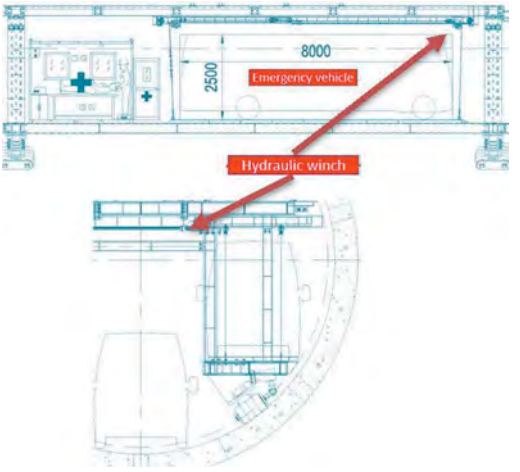

Figure 12. Emergency Vehicle Platform in ATEX configuration (on CREG courtesy)

ATEX control system and ATEX grease pumps. A redundant injection procedure is in place to seal the articulation. In the event that local sensors of the methane monitoring system or grease flow monitoring indicate a malfunction in the shield articulation sealing, an emergency gasket can be deployed (refer to Figure 13).

The sealing system for tail brushes is equipped with three cameras and an ATEX tail grease system. Additionally, it features ATEX pressure monitoring, an ATEX grease distribution system, valves, and ATEX pumps.

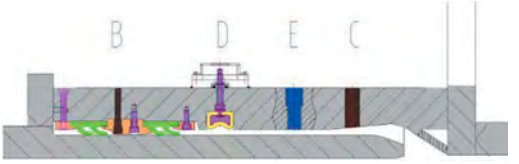

Figure 13. Articulation sealing system (on CRCHI courtesy).

The entire grease pumping system automatically activates for a predetermined duration in alarm conditions to ensure the sealing of the tail brushes system.

2.2.5.2 Volume 4 extension

The ATEX volume 4 extension is defined to ensure that a potentially explosive atmosphere introduced into volume 4 reaches volume 5 only when hot surfaces are cooler than 300°C (Bandini et al, 2013). Similar monitoring on dumpers or excavators has indicated that the maximum cooling time is approximately 11 minutes. Including these times, along with alarm activation and the shutdown procedure performed by the operator, results in a total cooling time of about 14 minutes. Considering a tunnel flow rate of 0.6 m/s, the safety cooling system can be calculated over 500m. The cooling time for electrical equipment may be shorter than that for engine hot surfaces; however, after shutdown, they require several minutes to cool. This procedure can operate efficiently only if an effective monitoring system is installed, and cooling tests are conducted on all equipment operating in Volume 5.

2.2.5.3 Specialized people and procedures

All the implemented solutions cannot overlook the presence of trained personnel and expertise, and the meticulous adherence to detailed and specific procedures for all excavation and maintenance phases. A constant presence of a technician responsible for on-board monitoring and verification of the adopted solutions for compartmentalization and ventilation is anticipated.

The team is led by a manager who examines and analyzes issues, identifying technical and procedural solutions. Personnel working in the tunnel receive training from the responsible technician at the beginning of excavation and during continuous site inspections. Each operator, according to their role, undergoes dedicated training covering general risks, the management of alarm conditions, and specific working methods for their tasks.

Risk minimization is achieved through the adoption of technical and technological solutions, but it cannot disregard the method of advancement. Experiments conducted have confirmed the ability to contain impulsive emissions that trigger alarm conditions through careful management of advancement methods and material conditioning.

3 CONCLUSIONS

The innovative approach to the TBM design and the further implementation of the ATEX setup concept, as described in preceding chapters, were necessitated by the need to establish a comprehensive and systematic approach to the challenge. This need arose due to the considerable number of machines involved and the length of the tunnel to be constructed. The overarching objective was to enable the construction of the involved tunnels in a reasonable and systematic manner, specifically addressing the following aspects:

- Ensuring continuity of excavation, which would otherwise not be feasible.
- Enhancing TBM efficiency.
- Elevating the safety standards for the workforce.

Operational implications and all implementations were executed drawing on experiences from past construction projects, and more critically, through the engagement of sector experts and the close, robust collaboration with TBM suppliers.

The achieved results have facilitated and continue to support a systematic approach to design, offering the potential for replication across a broad spectrum of cases that encompass different machine groups.

ACKNOWLEDGMENTS

The authors extend their sincere appreciation to Collins consultants and TBM manufacturers CREG and CRCHI for their unwavering support throughout the development of solutions and for facilitating the practical realization of the studied concepts.

REFERENCES

AA.VV., 2012. Nota Interregionale n° 44 “Grisù TBM” Scavo meccanizzato di grande sezione con TBMEPB in terreni grisutosi. Prot. n° PG/2012/132178 del 28/05/2012. Ed. Regioni Emilia Romagna e Toscana.

Bandini, Berry, Colaiori, Lisardi, 2013. Il franco di sicurezza nello scavo di gallerie grisutose, In: Atti Congresso Internazionale Expotunnel, Bologna 17-19 Ottobre 2013. Gallerie e Spazio Sotterraneo nello Sviluppo dell’Europa, Patron Editore (BO), p. 1091–1102. ISBN: 978-88-555-3253-2

Bandini, Berry Cormio, Colaiori, Lisardi. 2017. Safe excavation of large section tunnels with Earth Pressure Balance Tunnel Boring Machine in gassy rock masses: The Sparvo tunnel case study. IN: Tunnelling and Underground Space Technology 67: 85–97. DOI: 10.1016/j.tust.2017.05.001

Bandini, Cormio, Berry, Battisti, Lisardi, Bernardini Urso,, 2020. Innovative solutions for safety against firedamp explosions in small section EPB-TBM tunnelling. In: Tunnels and Underground Cities: Engineering and Innovation meet Archaeology, Architecture and Art. DOI: 10.4324/9781003031666-7

Gui Fu1, Ziqi Zhao1, Ping Chen and Ying Ge1. 2018. Analysis of key unsafe acts in major and particular major gas explosion accidents. In: IOP Conference Series: Materials Science and Engineering. volume 452, number2, pages 022032, doi: 10.1088/1757-899X/452/2/022032.

Shao-Hui Tang, Xiao-Ping Zhang, Quan-Sheng Liu, Wei-Qiang Xie, Xin-Lin Wu, Peng Chen, Yu-Hua Qian, 2021. Control and prevention of gas explosion in soft ground tunneling using slurry shield TBM. In: Tunnelling and Underground Space Technology, Volume 113, , https://doi.org/10.1016/j.tust.2021.103963.

EN16191:2014, Tunnelling machinery - Safety requirements. CEN, the European Committee for Standardization

EN ISO/IEC 80079-38:2016 Explosive atmospheres - Part 38: Equipment and components in explosive atmospheres in underground mines. CEN, the European Committee for Standardization

En 1127-2:2014, Explosive atmospheres - Explosion prevention and protection - Part 2: Basic concepts and methodology for mining. CEN, the European Committee for Standardization Directive 2014/34/EU of the European Parliament and of the Council of 26 February 2014 on the harmonisation of the laws of the Member States relating to equipment and protective systems intended for use in potentially explosive atmospheres. IN: Official Journal of the European Union, L 96/309

EN 14983:2007, Explosion prevention and protection in underground mines - Equipment and protective systems for firedamp drainage. CEN, the European Committee for Standardization

EN 60079-29-1:2016 Explosive atmospheres - Part 29-1: Gas detectors - Performance requirements of detectors for flammable gases

Tunnelling for a Better Life – Yan, Celestino, Thewes & Eberhardt (Eds)
© 2024 The Author(s), ISBN 978-1-032-80042-4
Open Access: www.taylorfrancis.com, CC BY-NC-ND 4.0 license

Successful steering control with partial soil excavation for station crossing of a 13.08 m diameter EPB TBM in Lodz, Poland

Marcin Tomaszewski* & Soren Nortoft
PBDiM, Mińsk Mazowiecki, Poland

Fabrizio Bove & Marco D'Ambrosio
Seli Overseas, Rome, Italy

ABSTRACT: The Lodz Railway Node project in Poland, includes the excavation of an approximately 2.7 km tunnel in a densely urbanised area with an earth pressure balance (EPB) tunnel boring machine (TBM) of 13.08 m in diameter. To optimize the project schedule, the TBM crossing through Polesie station has been carried out with only a partially excavated face. Considering the geometrical station constraints, such as the slabs already in place, and the lack of face pressure, controlling the steering of the machine within the small tolerances allowed by the alignment required the application of special measures. The task has been particularly challenging due to the features of the large diameter TBM employed, not provided of any active articulation, the alternance of layers of very different soil and the low area accessibility. The paper highlights the difficulties encountered and the solutions adopted, providing a valuable numerical reference of the actual TBM parameters through the back-analysis of the data recorded during the advance. Additionally, the correctness of the theory and assumptions, that had been previously developed before the execution of this challenging task, is demonstrated.

Keywords: station crossing, partial soil excavation, TBM guidance, alignment

1 INTRODUCTION

The tunnel boring machine (TBM) tunnel from Odolanowska chamber to Fabryczna Lodz railway station is a section of the Lodz Railway Node (TEN-T) Stage II – Section Lodz Fabryczna – Lodz Kaliska/ Lodz Zabieniec which, when completed, will constitute a new modern junction between the terminal station of Fabryczna and the existing railway line between Kaliska and Zabieniec (see Figure 1).

Figure 1. General layout of Lodz Railway Node.

The tunnel,excavated with a 13.08 m diameter earth pressure balance (EPB) TBM, is 2660 m long with an overburden ranging between 14 and 18 m.

To date, approximately 40% of the complete length of the TBM tunnel has been bored, including the 885 m stretch of the tunnel from Odolanowska up to Polesie station, the 165 m of Polesie station crossing with partial soil excavation, and further 100 m underneath the ancient historical buildings of the city of Lodz.

For the excavation, a refurbished EPB TBM manufactured by Herrenknecht was employed, with the features relevant for the station crossing summarized below:

- Boring diameter 13.08 m
- No active or passive articulation
- No applicable tilting for steering of the cutterhead

The tunnel lining is designed with 500 mm thick precast segments wide and 1.6 m long, with an 8+0 configuration (i.e., without a small key segment) and a 11.7 m internal diameter.

Moreover, a summary of the main events of the whole drive to date are shortly presented hereby:

*Corresponding author: m.tomaszewski@pbdim-obt.pl

DOI: 10.1201/9781003495505-290

- The first 100 m of the TBM has been carried out with an umbilical configuration, with the backup gantries preassembled at the top of the launching shaft and extracting the muck by a temporary de-mucking system.
- The TBM experienced severe steering difficulties in the first meters of the alignment, following a narrow horizontal curve radius of 600 m. Thus, they have been solved by the rearrangement of thrust cylinder groups and a full ripper configuration instead of disk cutters, to adapt tool configuration to actual soil conditions, where at the beginning it has been faced a majority of clay face that later became mostly sand.
- Due to the shallow overburden (slightly more than one diameter), the variable soil characteristics, and the urbanized area above, tighter control on the settlements has been carried out.
- A massive activity of consolidation (as well as evacuation, demolishment, and reconstruction of already damaged buildings where possible and needed) is currently still ongoing in the old city in the proximities of the tunnel.

Further details related to the above have been already shown by Bove et al. (2022).

2 BEFORE THE STATION CROSSING

At the beginning of 2022 the partial execution of the first station Polesie (see Figures 2 and 3) required consideration of an alternative crossing with a partially excavated section, as TBM excavation was on the critical path of the overall project. Hence, a new study for the station crossing has been conducted to advance through the station safely and avoid jeopardizing the project's construction schedule.

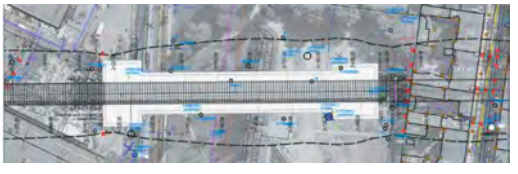

Figure 2. Plain view of Polesie station and TBM alignment.

This led to the conclusion that a theoretical "static condition" for TBM excavation should be applied, with a minimum theoretical thrust force of roughly 15 MN, to be carried out according to the following actions:

- Excavating along an 8 m high partial face (5 m missing on the top), similarly to a single shield TBM advancing in open mode through soft material with a small cavity on top of the section.

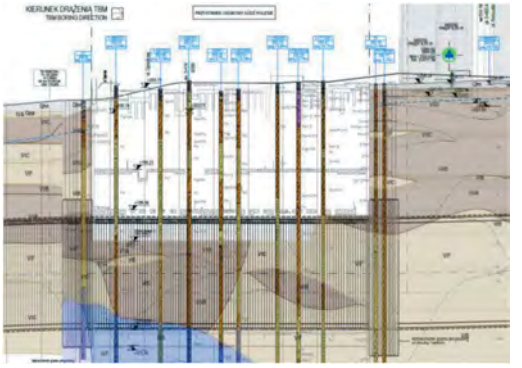

Figure 3. Polesie station longitudinal profile: silty clay and clayed sand.

- Reducing the cutter-head revolution speed (to about 1 rpm) as well as penetration rate during the advance, to achieve a continuous advance in a quasi-static process and equilibrium.
- Limiting the pressures on thrust cylinders during ring assembly.
- Installing the full ring to allow the steering of the TBM in all directions.
- Reducing the TBM cutterhead boring diameter, by removal of gauge rippers and disc cutters, to limit the undercutting below the shield and the tendency of the machine to dive.
- Tight control of the TBM alignment and adherence to the threshold limits for stopping the advance, according to the previously set limitations on excavation, due to the small gap between the TBM and the already existing slab (see Figures 4 and 5).

Eventually, previous successful station crossings already recorded (Concilia et al., 2021, Goodboy et al., 2021, Maccan et al., 2011) speeded up the process of decision-making toward this challenge.

Figure 4. Polesie station crossing: the TBM advances with limited gap on the top.

Figure 5. Polesie station crossing: general overview of the TBM, in situ soil and concrete walls.

3 THE "CROSSING CONCEPT"

According to what has been practically carried out, a model for station crossing is presented in Figure 6.

Conversely to typical EPB mode, where there is a clear cylindrical symmetry among tunnel, TBM and ring alignment, during the excavation in the station this obvious concept has been twisted, thus creating a misalignment between the tunnel axis and TBM axis, that is now positioned approximately 15 mm lower. In such a case it is almost clear that the advance is more similar to a hard rock TBM, asymmetric with respect to the tunnel alignment and with the shields lowered toward the bottom of the excavation, whose reaction is totally borne and balanced by the natural soil underneath.

4 DATA ANALYSIS

The station crossing, for a total length of 165 m, has been carried out in 52 days between October 13th (break-in into the station) and December 6th, 2022 (completion of Polesie station crossing), i.e. 3,2 m/day of advance on average, including all the following stops:

- Removal of unsafe concrete blocks and mud (mixture of soil, reactivated crushed cement, foams and water) after the break-in.
- Adjustment of the checks in situ, i.e. identification of the actual TBM position and relative maneuvering spaces between level -2 and level -3 with forecast of any possible interference with structural elements, like steel anchors already present inside the Polesie Station: just 27 cm of gap has been detected as minimum tolerance value!
- Ad hoc reconfiguration of the cutting tools configuration for the station crossing.
- One high voltage cable extension.
- Maintenance and reconfiguration of the cutterhead for the break-out.
- Mechanical overhaul, including the replacement of any damaged tail brush.

The peak of advance during the station crossing was reached on November 29th with 11 meters excavated within 24 hours.

Starting with an analysis of the main relevant parameters during the station crossing, it can be observed as follows:

- The average height of ground not removed by TBM is approximately 4,3 m with a muck

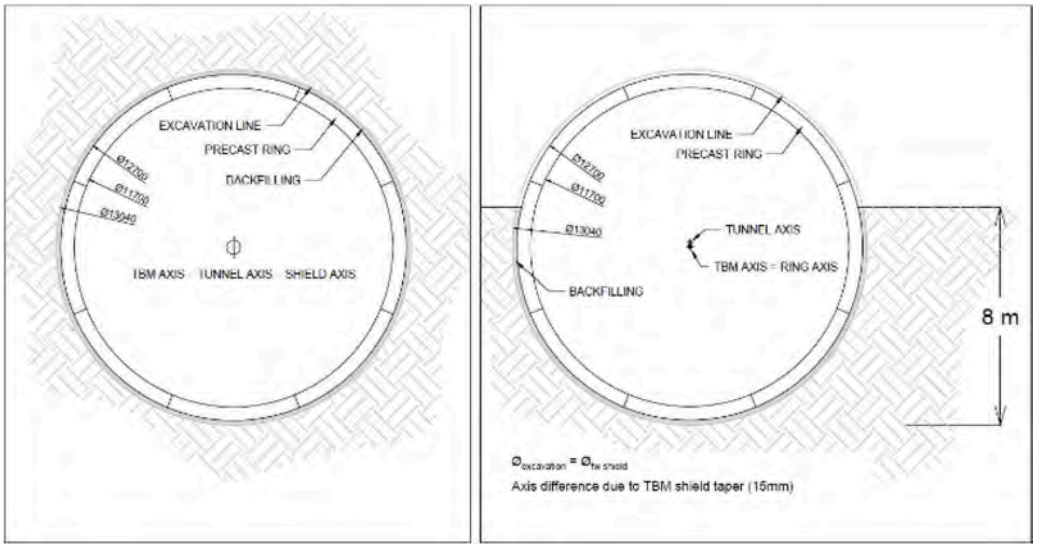

Figure 6. EPB mode (left) vs. station crossing mode (right).

Figure 7. Horizontal deviation along the Polesie station.

extracted of 219 tons per ring, approximately the 61% of the full excavation

- The deviations can be summarized hereby:
  - Horizontal deviation: 0.41 mm on average with peak value of 12 mm (see also Figure 7)
  - Vertical deviation: 0,5 mm on average with peak value of 20 mm

Thus, the maximum value of deviation with respect to the diameter of excavation is no more than 0,11%, that is totally neglectable, confirming the successful expectations.

Further to the above, the following average parameters are significant:

- penetration rate: 20 mm/min
- RPM: 0,8
- Cutterhead Torque: 10 MN
- Thrust force: 26.000 kN

Focusing on the thrust, the distribution of the forces among the thrust cylinders' groups (see Figure 8) is significant, with approximately 51% of the total thrust applied on the bottom (Group D), since the TBM has the natural tendency to dig, moreover considering that the soil changed to "softer" during the ongoing advance. Going into deeper details, the thrust applied in the lower part (Groups C, D and E) sums up to 79% of the total thrust (see Table 1), with an asymmetric variation between Group C and F, most likely due to the direction of the TBM rotation.

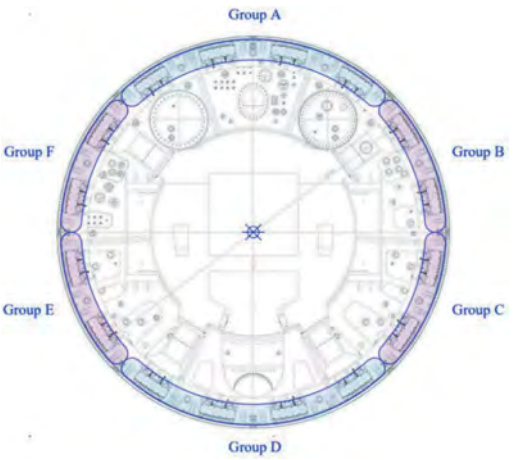

Figure 8. Arrangement of the thrust cylinders' groups.

Table 1. Average distribution of the thrust force.

Position	Thrust cylinders' groups	Total thrust (kN)		Total thrust (%)	
Top	Group A	5.633	1.968,26	21,10	7,37
	Group B		1.268,57		4,75
	Group F		2.396,14		8,98
Bottom	Group C	21.066	2.819,26	78,90	10,56
	Group D		13.620,76		51,02
	Group E		4.625,82		17,32

Additionally, a proper partial backfilling has been carried out with grout injection of bicomponent of around 7,6 m^3 per ring, roughly 60% of the value injected during standard EPB operation.

Eventually, the total thrust force used has been higher than the one expected by theory, thus meaning that most likely the friction between shields and natural soil, as well as the reaction of the back-up, had been underestimated.

5 ADJUSTMENTS DURING THE STATION CROSSING

In this paragraph, it is also important to mention some practical adjustments that have been carried out during the advance like:

- Segments that have been connected each other through temporary steel supports instead of designed connectors, pins and bolts: this in order to simplify the future dismantling of the rings into the station (see Figure 9).
- A window created on the top of the segments to smooth the access.
- Instead of using sealing rings at break-in and break-out into the station, it was preferred to lower the piezometric level by the use of drainage shafts all around the station, thus pumping out the water.

Figure 9. Temporary supports for rings to simplify their future removal.

6 MONITORING

A sound net for monitoring (see Figure 10) with tachymeter prisms and inclinometers has been used in order to assess and promptly act in case of any problem. In any case the maximum settlement value recorded was less than 5 mm, i.e. neglectable.

Moreover, particular care has been carried out regarding the risk due to the narrow gap between the slab already in place and the TBM, by a continuous control during the advance. To ensure that no damage will occur to the permanent structures of the

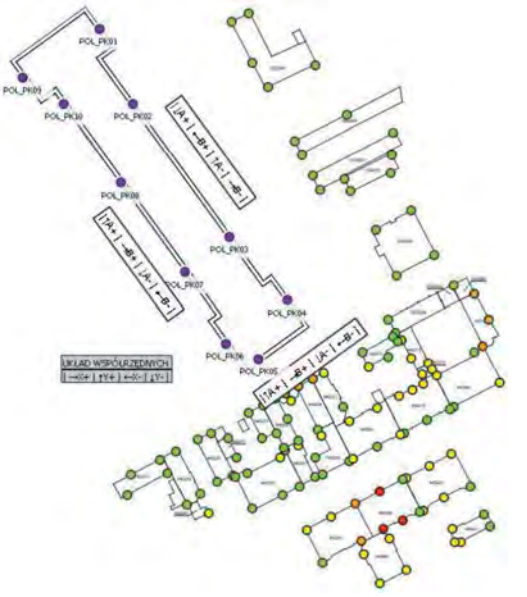

Figure 10. Monitoring points positions of Polesie station (level 0).

stations, the following trigger values have been established (Bove et al., 2022):

- Bottom: right and left: max misalignment allowed 200 mm.
- Top: max misalignment allowed 100 mm (reduced due to the proximity of the slab).

It is worth pointing out that during the full run into the station, the maximum deviation values were no more than 10% of the aforementioned threshold values, as shown in Figure 11, where the higher values have been automatically read by tachymeters.

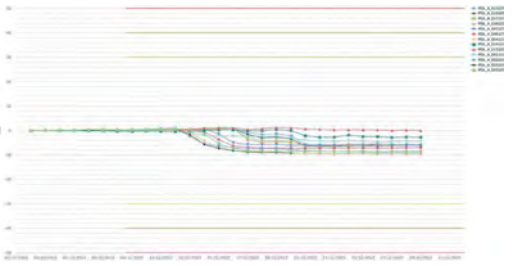

Figure 11. Polesie station (level -2): tachymeter prisms values.

7 CONCLUSIONS

The safe passage through Polesie station presented unique challenges, that was possible to overcome by adjusting thrust force, excavation method, and cutterhead configuration while adhering to strict alignment controls and settlement limitations. Data

analysis reveals that the TBM, maintained impressive performances during the station crossing, including neglectable deviations, high penetration rates, and effective force distribution. In summary, the way of execution of the TBM tunnel, especially the complex station crossing, through the diligent monitoring and strategic adjustments to the excavation process, have collectively contributed to the overall success of the project. As the Lodz Railway Node Stage II progresses, the experiences and insights gained from this experience can guide future projects of similar magnitude and complexity.

ACKNOWLEDGMENTS

Special thanks to PKP Polish Railway Lines for their cooperation in the implementation of this demanding project, which is a pilot project in TBM technology in railway Poland market. This project paves the way for series of future challenging projects planned by PKP PLK, for implementation in the upcoming close future.

Furthermore, an additional acknowledgement to Mr. Mariusz Serzysko, PBDiM Director, for the overall experience and support provided.

REFERENCES

Bove, F., D'Ambrosio, M., Grandori, R., Konstantinou, A., 2022. Challenging station crossing by a 13,08 m diameter EPB TBM in Lodz, Poland, with partial soil excavation. Sancot Symposium 2022 – Tunnel boring in civil engineering and mining, 7-8 November, Stias, Stellenbosch, Western Cape, South Africa.

Concilia, M., Armentano, F., Tamburri, M. 2021. The machine selection for the construction of lot T2C of the new Paris Metro Line 15 and the crossing of an interconnection shaft by the combination of conventional and mechanised excavation methods. *Gallerie e grandi opere sotterranee*, no. 138/2021, pp. 47–55.

Goodboy, A. 2021. Robbins XRE TBMs make final breakthroughs for Mumbai Metro Line 3 (accessed 04 August 2022).

Maccan, S., Stefanizzi, S., Bontempi, F. and Palomba, M. 2011. Sochi tunnels for the 2014 winter Olympic games: an example of a coupled mechanised and conventional excavation approach. *Underground Spaces for tomorrow*, AFTES International Congress, Lyon.

Tunnelling for a Better Life – Yan, Celestino, Thewes & Eberhardt (Eds)
© 2024 The Author(s), ISBN 978-1-032-80042-4
Open Access: www.taylorfrancis.com, CC BY-NC-ND 4.0 license

Planning, design and construction for mechanised cross passage excavation

Chor Kin Tsang* & Tong Joo Sia
SMEC Australia Pty Ltd, Australia

Zhi Guo Zhang, Lei Sun & Kunpeng Chen
China Railway Engineering Equipment Group Co. Ltd, China

ABSTRACT: Cross passages between twine bored tunnels are typically provided at regular interval to allow people to evacuate from one tunnel to the other in the event of an emergency. Constructing these cross passages is considered as a high-risk construction activity particularly in soil and water bearing ground. Traditionally, ground treatments (such as jet grouting and ground freezing) are conducted before opening of the main tunnel lining for cross passage construction. Mechanised method by mini-TBM and pipe jacking machine is developed and have been used in several projects around the world. CREG's Cross Passage (CP) Machine is specifically designed and manufactured for cross passage construction between two mainline TBM tunnels. The CP Machines have been successfully adopted in several projects in China and valuable knowledge are consolidated. This paper will discuss the key considerations during the planning stage, design of special tunnel segments and cross passage opening, temporary works design to facilitate launching and retrieval of CP Machine, permanent CP lining and impact assessment to the main tunnel segmental lining. In addition, detailed construction methodology and experienced gained in several projects will be summarised.

Keywords: Tunnel Boring Machine (TBM), Cross Passage (CP), Cross Passage Machine

1 INTRODUCTION

Cross passages between twine bored tunnels are typically provided at regular interval to allow people to evacuate from one tunnel to the other in the event of an emergency. Constructing these cross passages is considered as a high-risk construction activity particularly in soil and water bearing ground. Traditionally, ground treatments (such as jet grouting and ground freezing) are conducted before opening of the main tunnel lining for cross passage construction. The quality of ground treatment highly depends on the ground conditions and skill of specialist ground treatment contractor. Even though ground treatment is provided however in some cases, ground collapses are reported during the CP construction. In addition, the construction of CP by traditional method need several months to complete and it will significantly affect the programme of the project. Mechanised method by mini-TBM and pipe jacking machine is developed and have been used in several projects around the world. CREG's Cross Passage (CP) Machine is specifically designed and manufactured for cross passage construction between two mainline TBM tunnels. The construction of CP by mechanised method takes a few weeks to complete both excavation and permanent lining installation. It also eliminates safety and health concerns associated with manual excavation for workers under exposed ground. The CP Machines have been successfully adopted in several projects in China and overseas.

This paper will discuss the key considerations during the planning stage, design considerations of special tunnel segments and cross passage opening, temporary works design to facilitate launching and retrieval of CP Machine, permanent CP lining and impact assessment to the main tunnel segmental lining. In addition, detailed construction methodology and experienced gained in several projects will be summarised.

2 TRADITIONAL CP CONSTRUCTION

The construction of CP, especially in soft ground, between the twin bored TBM tunnel is one of the most high-risk construction activities for

*Corresponding author: ck.tsang@smec.com

DOI: 10.1201/9781003495505-291

tunnelling projects. The CP is generally constructed using traditional mining techniques to create a link between two tunnels as shown in Figure 1. Depending on the ground conditions and site constraints, different ground treatment methods such as TAM grout, jet grout or ground freezing can be implemented. The overall sequence of works is described below:

- Carry our ground treatment works for the ground surrounding the CP
- Opening of main tunnel segmental lining
- Excavation of CP by mined method, generally not more than 2m advance.
- Shotcrete the excavated roof and walls and provide temporary support as necessary
- Continue excavation, shotcrete and temporary support, stage by stage, until reaching the receiving end
- Apply smoothing shotcrete before the installation of waterproofing membrane
- Spray permanent shotcrete or cast in-situ concrete to form the CP permanent structure
- Construction of collar structure between the CP and main tunnel

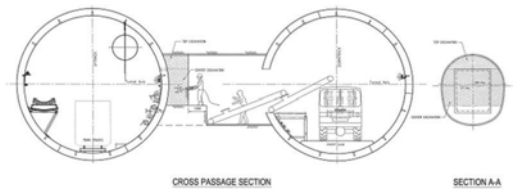

Figure 1. Typical construction of cross passage.

There are mainly two types of risk for traditional CP construction which need to be considered during the design. The first one is the stability of tunnel segment opening and CP excavation. The second one is the CP induced settlement and its impact on surrounding assets. Some of key risks are summarised below:

- Geotechnical design parameters not reflecting the condition observed on site, or unforeseen ground conditions encountered.
- Instability of segmental lining during opening (before CP excavation)
- Damage to existing tunnel structure near the opening
- Instability of segmental lining at the receiving tunnel (near completion of the CP excavation)
- Unforeseen ground conditions causing unsuccessful ground treatment
- Higher than expected water ingress leading to excessive ground loss.
- Excessive ground movement affecting nearby existing building, structures and utilities.

In addition to the high risk associated with CP excavation, the construction programme usually takes several months to complete. The health and safety issue are also a concern for CP construction. Therefore, mechanised method by mini-TBM and pipe jacking machine are developed to minimise the risks and to improve the production rate compare to the traditional method.

3 PLANNING FOR MECHANISED CP EXCAVATION

The key concerns for using mechanised CP excavation is the available working space inside the mainline TBM tunnels. The launching and receiving devices, TBM and backup equipment, precast segments/pipes, TBM launching frame, grouting pipelines, slurry pipelines, water supply and power supply need to be fit within limited space. The diameter of CP machine needs to satisfy the functional requirements for the CP. Detailed space proofing of the CP need to be carried out for approval by the Authorities. Since the construction of the CP by mechanised method will fully occupied the mainline tunnel and will obstruct any construction activity inside the tunnel. Careful construction planning needs to be carried out to minimise the impact of the overall construction programme of the project.

4 DESIGN CONSIDERATIONS

The use of the mechanised method for CP construction highly depends on the equipment developed by the machine manufacturer. The designer of the mainline TBM tunnel segmental lining and cross passage lining need to have very good understanding on the construction methodology and sequence of works developed by the machine and equipment manufacturer. Based on the experience of using CREG's CP machines for metro projects in China, the typical arrangement of the machine and the special tunnel segments are shown in Figure 2 and Figure 3 respectively.

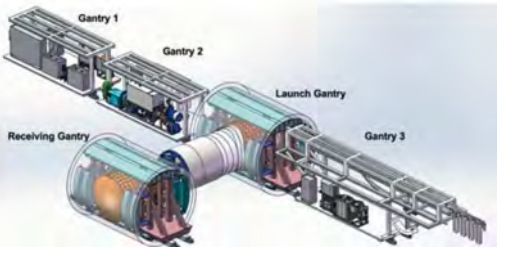

Figure 2. Typical arrangement of CREG CP machine.

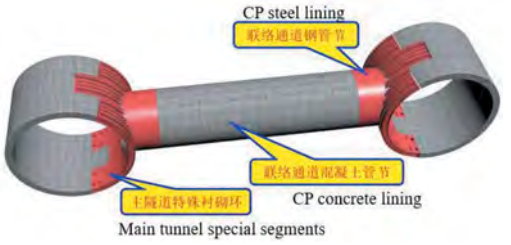

Figure 3. Typical arrangement tunnel and CP segments.

The following special design and assessment need to be carried out:

- Permanent Steel Segmental Lining for CP opening
- Temporary glass fibre reinforced concrete segments at CP opening
- CP permanent linings
- Temporary structures
- Launching frame and receiving frame
- Launching sleeve and receiving sleeve
- Waterproofing details
- Carrier & work platform
- Impact assessment of the permanent lining structural capability and deformation
- Ground movement induced by cross passage construction

5 MECHANISED METHODS FOR CP CONSTRUCTION

The mechanised method for CP construction can be classified into TBM method and pipe jacking method. These methods will be descried in the following sections.

5.1 *TBM method*

TBM method is a fully mechanized construction method to cooperate excavation, mucking out and segment erection in sequential process.

5.1.1 *Case study*

The first TBM method for CP excavation was adopted in Ningbo Rail Transmit Line 3 in 2017. The project locates between the Southern Business District Station and Yinzhou Government Station with a total section length of about 733.7m. There are a lot of sensitive buildings and structures along the tunnel alignment. The CP is under the greenery of a park at the intersection of Yinzhou avenue and Tiantong south road, with an overburden of 17.8m. The distance between the centers of the two main metro tunnels is 17.4m and the geology is mainly muddy clay and silty clay. The two main metro tunnels are lined with 5500mm I.D. segmental lining, and the cross passage is also lined with circular segmental lining. The segmental lining of CP is designed with 3150mm OD, 2650mm I.D with segment thickness and width of 250mm and 550mm respectively. The general arrangement of the CP is shown in Figure 4.

Figure 4. CP general arrangement.

5.1.2 *Machine configuration and key features*

The TBM method for CP construction consists of main machine (including cutter head, shield structure, main drive, screw conveyor, segment erector, thrust system, etc.), back-up system, launch and receiving devices, and other auxiliary construction systems. The arrangement of the machine is shown in Figure 5. The TBM key parameters are shown in Table 1.

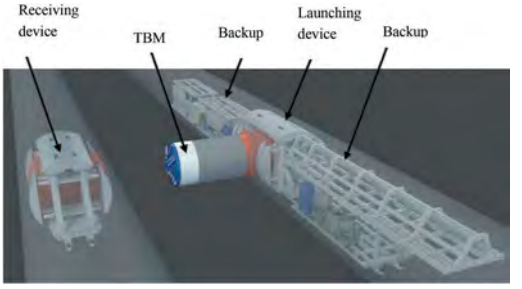

Figure 5. Cross passage TBM configuration.

Table 1. Cross passage TBM key parameters.

Item	Description	Parameters	unit
1	Excavation diameter	Φ3290	mm
2	Cutter head rotation speed	0-3.8	r/min
3	Maximum thrust	10500	kN
4	Drive power	200	kW
5	Maximum torque	862	kNm

Different from the conventional TBM design, the cross passage TBM will be launched and received in the concave and convex shape of main tunnel segments respectively. Therefore, the cutter head of cross passage TBM is designed with big and small arc structures (see Figure 6). This is to allow the diameter of the big convex arc structure of cutter head to fit to the inner diameter of main tunnel segment so that the force on the cutter head is evenly distributed across the opening. This can also enhance

a better tilt control of the machine during the launching operation. The diameter of the small concave arc structure of center cutter is similar to the outer diameter of main tunnel segment so as to allow a better tilt control of machine during receiving.

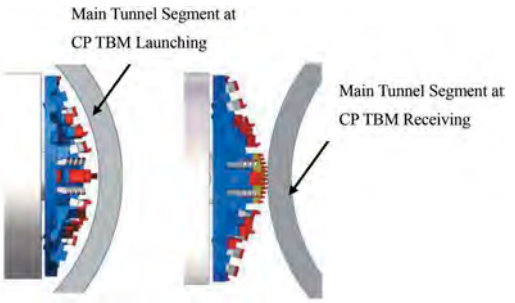

Figure 6. Design of tapered cutter head and center cutter.

To deal with the main tunnel segment deformation caused by the thrust of cross passage TBM during launching, advancing and receiving. Stabilizing support devices are designed in the main tunnels as shown in Figure 7. The stabilizing support device consists of the outer gripper system, inner trolley system, hydraulic system and electrical control system. During construction, the jacking force on the main tunnel segments can be adjusted to prevent over stressing the main tunnel segment.

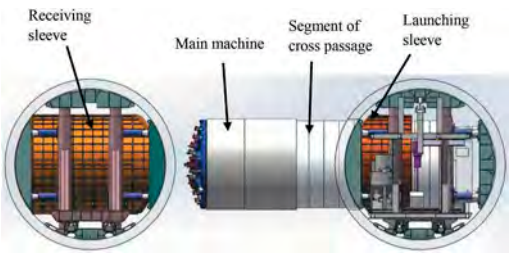

Figure 7. Stabilizing support and seal devices at launch and receiving.

To deal with possible water inflow at the CP opening during launching and receiving of TBM, the use of steel sleeve for launching and receiving is developed. Traditionally ground treatment is required to prevent groundwater inflow however under this construction method, minimal ground treatment and even without ground treatment is needed. This can significantly reduce the construction risks, cost and programme.

5.1.3 *Construction sequence and key technical issues*

Construction sequence

The construction sequence includes preparation, launching, excavation, receiving and T-joint treatment.

During preparation, the main tunnel is clear for installation of rails for cross passage TBM and rolling stocks. The assemble the cross passage TBM will be carried out in the surface and it is transported to the CP location. The TBM can then be connected to the launch sleeve and the launching portal set up in the main tunnel. The launching sleeve will be filled up with slurry and pressurised for TBM to start boring. After cutting the segmental lining, the TBM will continue boring, mucking out, installation of CP segmental lining and back grouting will be carried out progressively. At the same time, the receiving device is set up in the opposite side of CP. The receiving sleeve is filled up with slurry and pressurised to receive the TBM. After the whole main machine of cross passage TBM enters the receiving sleeve, the TBM will be disconnected for water and electricity connection. Removal of the receiving device together with the main machine out of the main tunnel. Finally, T-joint treatment will be carried out between the finished cross passage and the main tunnel.

Key technical issues

(1) Special tunnel segments for the CP opening

The CP opening at the main tunnel is lined with special segments. As shown in Figure 8, the special segments include steel segments surround the CP opening, fibre reinforced concrete segments at the CP opening and steel ring at the junction to enable even distribution of load after the CP opening is cut. This can also facilitate the connection of launch and receiving sleeves.

Figure 8. Cross passage portal.

(2) Segment erection

The segments of cross passage adopt stagger-jointed erection with circumferential joints and longitudinal joints connected with M24 curved bolts. A segment ring consists of 5 segments as shown in Figure 9 and a photo showing the completed CP is shown in Figure 10. The details of CP segment are shown in Table 2.

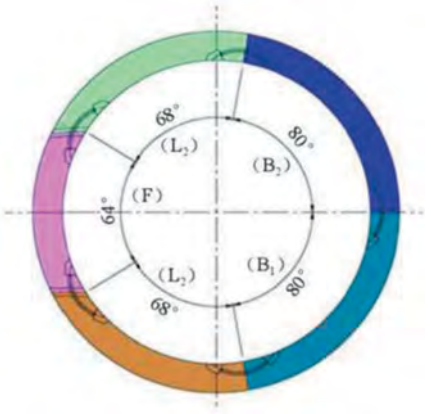

Figure 9. Cross passage segments.

Table 2. Details of cross passage segments.

Details	Dimensions	Description	Remarks
I.D.	2650mm	Erection method	Staggered
O.D.	3150mm	Joint connection	M24 curved bolt
Thickness	250mm	Segment type	Five segments (one 64°key segment + two 68°adjacent segments + two 80° standard segments)
Width	550mm	Erection method	Staggered

In order to facilitate the installation of CP segments in the congested space, the segment erector adopts the main beam with rotary erector installed in the center of machine to allow longer axial movement stroke to pick up segments. A simple trolley runs on the steel rail at the bottom of cross passage to transfer segments of cross passage from the back-up gantry to the area below segment erector.

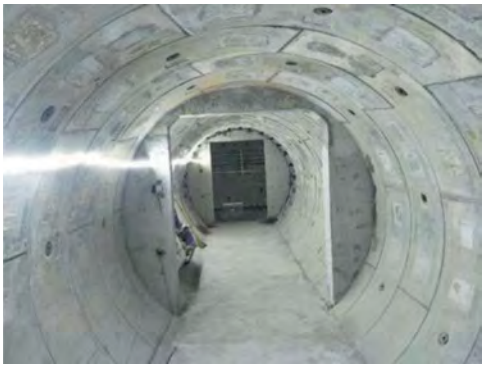

Figure 10. CP after segment erecting.

(3) Treatment at the CP opening

Steel segment rings are used at the CP opening in both the launching and receiving ends. This is used to facilitate the construction of CP opening structure that normally constructed by cast in-situ reinforced concrete. The completed CP opening structure and is connected to the steel segment is shown in Figure 11.

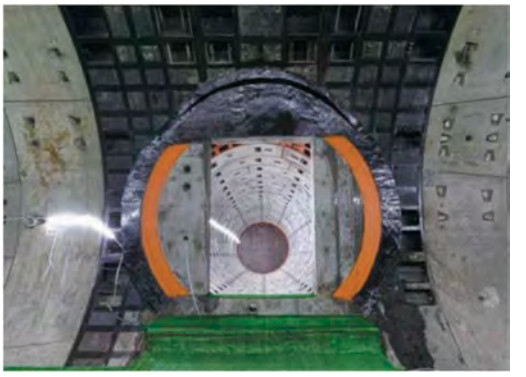

Figure 11. CP opening structure.

5.2 *Pipe jacking machine*

Th pipe jacking machine for CP construction is very similar to the TBM method. For the two methods, the machines can usually adopt similar designs in the excavation and drive systems, and thus their systems are convertible. The major difference is the installation method of lining. For the TBM method, segments will not move forward along with the TBM, which are erected by segment erector and then follow with back grouting. For pipe jacking method, pipes are pushed forward along with the main machine until the completion of cross passage. Back grouting will be carried out

Table 3. Summary of projects using pipe jacking machines for cross passage construction.

Project	Characteristic	Machine type
Cross passage of Mexico's Emisor Oriente Tunnel	Geology: sand and clay; Pipe I.D.: 1800mm.	Slurry pipe jacking machine
Cross passage of Hong Kong Tuen Mun - Chek Lap Kok Link	Geology: granite and alluvium; Pipe I.D.: 3000mm; CP length: about 13m.	Slurry pipe jacking machine
Cross passage of East Gaolang Road Station - Zhoujingxiang Station section of Wuxi Metro Line 3 Phrase 1	Geology: clay	EPB pipe jacking machine

after completion of excavation and installation of pipes. Table 3 shows a summary of the projects with cross passages excavated by pipe jacking machines in China and overseas.

5.2.1 *Case study*

The project is located at East Gaolang Road Station - Zhoujingxiang Station section of Wuxi Metro Line 3 Phrase 1 Project. The overburden of tunnel is about 17.5m and the TBM tunnel has O.D. and I.D. of 6200mm and 5500mm respectively. The tunnel lining thickness of 500mm and segment length of 1500mm. The distance between the center of two main tunnels is 14m with overburden of 19.2m. The geology at the CP location is mainly in clay The O.D. and I.D. of CP is 3260mm and inner diameter of 2760mm respectively. The length and thickness of pipe is 900mm and 250mm respectively. The are totally 10 numbers of pipes installed to complete the CP.

5.2.2 *Machine configuration and design features*

The earth pressure balance (EPB) pipe jacking machine for the CP of Wuxi Metro Line 3 is composed of main machine (including cutter head, shield structure, main drive, screw conveyor and steering system, as shown in Figure 12), jacking system, back-up system, launch and receiving devices and support system. The technical details of the CP pipe jacking machine are shown in Table 4.

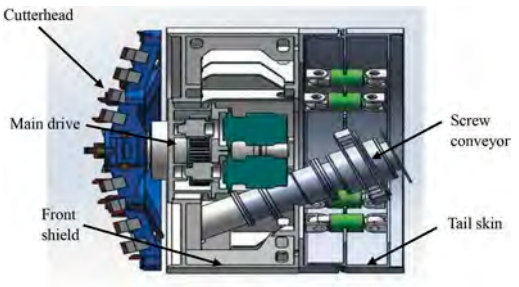

Figure 12. Main features of EPB pipe jacking machine.

Table 4. Technical details of the CP pipe jacking machine.

Item	Parameter	Unit
Excavation diameter	3290	mm
Cutter head rotation speed	0-1.8	r/min
Maximum thrust	12000	kN
Drive power	180	kW
Maximum torque	1100	kNm

Compared with the TBM method, the pipe jacking method has the advantages of simple construction process, low costs and high applicability in a narrow space. But it also has the disadvantages that it is only adapted to short and straight CP alignment.

5.2.3 *Construction sequence and key technical issues*

Construction sequence

The pipe jacking method shares the similar construction process with the TBM method, which also includes preparation, launch, excavation, receiving and T-joint treatment. The major difference is the excavation and pipe installation process. Figure 13 shows the launching of CP pipe jacking machine for Wuxi Metro Line 3 project.

Figure 13. Launching of the pipe jacking machine in the cross passage of Wuxi Metro Line 3.

Key technical issues

The CP is constructed by an EPB pipe jacking machine. Similar to the TBM method described in Section 2, special segments in the main tunnel are required at the CP openings.

Due to the limited working space within the main tunnel, the pipe is divided into upper pipe and lower pipe with angular degree of 150° for the smaller pipe. The general arrangement of the pipe is shown in Figure 14. This arrangement is different from conventional construction by pipe jacking machine.

Figure 14. The upper and lower rings arrangement of pipe.

The pipe is erected in a staggered arrangement and its technical details are shown in Table 5. Generally, when using a pipe jacking machine to bore a cross passage with single pipe, the power cable of main machine will be disconnected during pipe installation process. For the upper and lower rings arrangement, the power cable is keep connected during the pipe installation process.

The pipe jacking machine equipped with a single beam structure with double hoists that allow the two

Table 5. Technical Details.

Item	Parameter	Description
Pipe diameter	O.D. 3260mm and I.D. 2760mm	Precast reinforced concrete
Pipe thickness	250mm	Joint connection with 10 M24 longitudinal bolts
Pipe length	900mm	Joint connection with 4 M24 circumferential bolts

hoists move independently or simultaneously. This allow easy adjustment of the lifting point and orientation of the pipe. The whole erection procedures are as follows:

- lift the lower pipe by changing the height of lifting hooks and position of lifting points.
- move the power cables to the inside of the pipe.
- lift the upper pipe and connect to the lower pipe by controlling the gap between the pipes

Figure 15 And Figure 16 show the installation of the lower and upper pipes respectively.

Figure 15. Installation of lower pipe.

Figure 16. Installation of upper pipe.

6 CONCLUSIONS

6.1 *Pros and cons of mechanical excavation method*

In general, the mechanised CP construction has a high degree of automation such that excavation and lining installation can be carried out concurrently. In addition, the machine can be reused for all CP construction if the dimension of CP is the same. It will significantly reduce the costs and shorten construction period. It also provides a better health and safety control over traditional mined excavation and cast in-situ lining construction. The risks associated with ground settlement and water inflow are significant reduced by the mechanised CP construction with special segment installed in the main tunnel.

On the other hand, the mechanical equipment also has some disadvantages over traditional mined method. This is less flexible for different dimensions of CP. More sets of CP machines need to be manufactured for different dimensions of CP and consequence the cost will be increased. Due to limited working space within the main tunnel, the logistic for installation of the CP machine is quite challenge that need a proper planning. Since special segments in the main tunnel need to be designed and installed at the CP locations, the design of steel segments, fibre reinforced segment and steel ring need special design and assessment based on the equipment features and construction sequence. The T-joint treatment between the main tunnel steel segment and cross passage lining need special connections against water leakage.

6.2 *Future development*

The mechanical equipment for cross passage construction has been adopted for several projects in the world. Different projects have different requirements and the developed CP machines have different unique features. New equipment leading to new construction methods has become a new approach for the innovative development of underground space. This paper provides some insights potential new developments of the mechanical equipment for cross passage construction.

(1) Intelligent TBM construction

Intelligent TBM technology is a development that deeply integrates the new generation of information technology and intelligent data analyses. Based on current TBM technology development, the modern TBM has the functions of self-prediction, self-judgment, self-learning, self-decision-making and self-control system. These form an important part of future industrialized development for TBM tunnel construction. It will provide a safer and energy saving construction with less man-power input.

Since cross passages are generally short in length, the excavation machine after launching and will be ready for retrieval. The control of CP machine alignment is therefore challenging. Moreover, the main machine needs to break through the special segment and the pre-installed steel ring at the receiving end, which requires high construction accuracy. The application of intelligent TBM technology in cross passage construction can overcome these difficulties. In addition, the main tunnels construction are completed with better understanding of the geological conditions at the CP locations. This provides important geological information for CP machine to develop automatic operation

parameters for precise construction control and to reduce construction risks.

(2) Application under extreme conditions
Subsea tunnel is developing rapidly in China and oversea. The construction of proposed sub-sea tunnels such as Qiongzhou Strait Tunnel and Bohai Strait Tunnel will face significant technical challenges such as safety of tunnel drives for super long distance and super high water pressure. Under such circumstances, the application of slurry TBM/pipe jacking machine for cross passage construction can reduce the risks water inflow by use of sealing of shield structure, main drive, launch sleeve and receiving sleeve.

(3) Application in more construction fields
In addition to common cross passages of metro tunnels, the mechanical equipment can also be widely used for the construction of underground fire exits and escape routes, cross passages between underground shopping malls, cross passages between utility tunnels and sewage tunnels., short underground passages with small cross-sections mainly for personnel passing, and underground structures with limited launch and receiving sites.

REFERENCES

GB 50157-2013 Code for design of metro [S]. China Architecture & Building Press, 2018(7): 13.

Yang Zhuangzhi. Suggestions on Design and Construction of Pump Stations of Shield-bored Running Tunnels in Beijing [J]. Tunnel Construction, 2015, 35(10): 1071–1076.

Jin Zhou. Research and Application on Horizontal Freezing Method in Connected Aisle of Nanning Rail Transit Line 1 [D]. Nanning: Guangxi University, 2018.

Zhu Yaohong, Dong Zibo, Yin Tiefeng, et al. Exploration of T Connected Tunnel Construction Technique Using Mechanical Method with Local Reinforcement for Underground Connecting Passage [C]. Proceedings of 2017 Annual Academic Conference of China Civil Engineering Society. China City Press, 2017: 138–147.

Zhu Yaohong. Innovative Application of the Built-in Pump House in Urban Rail Transit Engineering [J]. Urban Mass Transit, 2018, 21(8): 12–16.

Shi Jiyao. Application of Freezing Method: Case Study on Metro Connected Aisle [J]. Tunnel Construction, 2011, 31(S2): 152–156.

Xu Liming, Chen Xiaojian, Peng Zhengyong, et al. Study of Health Monitoring Technology for Cross-passage in Subsea Tunnel Constructed by Freezing Method [J]. Tunnel Construction, 2018, 38(2): 295–299.

Liu Xunhua. Risk Analysis of Freezing Construction Method Applied to Connection Passage for Cross River Tunnel over Difficult Stratum [J]. Modern Urban Transit, 2011(5): 43-46+6.

Jiang Hong. Risk Assessment & Recognition of Freezing Method for Cross-Passage Construction [J]. Journal of Shanghai Jiao Tong University, 2011, 45(S1): 38–41.

Huang Dawei, Zhou Shunhua, Gong Quanmei, et al. Characteristic Analysis of Non-uniform Settlement for Different Structures of Metro in Soft Soil Districts [J]. Journal of Tongji University (Natural Science) 2013, 41(1):95-100+158.

Wang Kun, Ye Lei, Cheng Yonglong, et al. Sealing Device for Launching and Receiving of Tunneling Machine for Connection Gallery with Mechanical Excavation Method [J]. Tunnel Construction, 2020, 40(1): 134–142.

Zhu Yaohong, Wang Jingyu, Dong Zibo, et al. Design of Sealing Gasket of Connection Gallery Bored by Shield and Its Waterproofing Test [J]. Tunnel Construction, 2019, 39(1): 110–118.

Cheng Yonglong, Jia Xingmin, Ye Lei, et al. Study and application of semi-automatic segment assembling technology for micro shield machine [J]. Construction Mechanization, 2018, 39(8): 54–57.

Shen Zhangyong. Study on structural design of mechanical method liaison tunnel [J]. Modern Urban Transit, 2019 (11): 58–63.

Estelle Cagnat, Morgan Oleron, Thibaut Lockhart. Mechanized cross-passage construction in soft soil under high pressure: the Tuen Mun-Chek Lap Kok link-northern connection sub-sea tunnel section project, Hong-Kong. Proceedings of ITA-AITES World Tunnel Congress, April 2018: 706–718.

Yan Jianbiao, Ge Jiajia, Zhang Xiangchen. Pipe Installation Technology in Mechanical Methods for Cross Passage Construction [J]. City & House, 2021, 28(12):235-236 +239.

P. Schmaeh. Mechanized solutions for cross passage construction. Bergen ITA-AITES World Tunnel Congress, June 2017.

Jiang Guoping. Key Technologies for and Application of Open Shield [J]. Tunnel Construction, 2015, 35(6): 601–609.

Qian Qihu, Li Chaofu, Fu Deming. Application Situation and Outlook of TBM in Underground Project in China [J]. Construction Machinery, 2002(5): 28-35+4.

Li Jianbin, Jing Liujie, Yang Chen, et al. Discussion on Technical Characteristics and Realization-Path of Intelligent TBMs [J]. Tunnel Construction, 2023, 43(3): 355–368.

Liu Yingbin, Liao Shaoming, Du Hua, et al. Research on Intelligent Predicting and Controlling Method of Shield Tunneling Parameters Based on Machine Learning [J]. Railway Standard Design, 2023, 67(7):137-145+154.

Song Chaoye, He Weiguo, Wu Yijun. Feasibility Analysis on Key Technologies to Cope with High Water Pressure and Long Distance of Subsea Shield Tunnel [J]. Tunnel Construction, 2020, 40(5): 717–726.

Zhao Yiting, Wu Kejie, Shi Xiaodong. Underground Space Planning Control Methods under Territorial Space Planning System: a Case Study of Beijing Sub-City Center Project [J]. Tunnel Construction, 2020, 40(5): 717–726.

Ng, W H, Tsang, C K, Shut, S C and Hu, Y M. Pre-Treatment for TBM Break-outs and Break-ins, in Proceedings of International Conference and Exhibition of Tunnelling and Underground Space. Kuala Lumpur 2015.

Tsang, C K, Yu, H Z, Kong, C S and Hu, A. Artificial Ground Freezing Application for Tunnelling Works in Hong Kong, in Proceeding of the 13th Australia New Zealand Conference on Geomechanics 2019.

Wang, K, Ye, L and Cheng, Y. Sealing device for launching and receiving of tunneling machine for connection gallery with mechanical excavation method, Tunnel Construction 2020, 40(1), pp 134.

Hu, X and Wang, G. Construction methods for cross passage in soft ground tunnels in China, in 2011 International Conference on Electric Technology and Civil Engineering (ICETCE) 2011. IEEE, pp. 193–196.

L Lu, C K Tsang, L Jia, L Sun and N Xu, 2021 Key Challenges on Cross Passage Design and construction, ATS2020+1 Australian Tunnelling Conference, Melbourne, Australia 2011.

Tunnelling for a Better Life – Yan, Celestino, Thewes & Eberhardt (Eds)
© 2024 The Author(s), ISBN 978-1-032-80042-4
Open Access: www.taylorfrancis.com, CC BY-NC-ND 4.0 license

A study on intelligent assembly technology for Mid-partitions in shield tunnels and application

Hua Wang
China Railway Tunnel Group Co., Ltd., Guangzhou, Guangdong, China
China Railway Tunnel Consultants Co., Ltd., Guangzhou, Guangdong, China
Guangdong Provincial Key Laboratory of Intelligent Monitoring and Maintenance of Tunnel Structure, Guangzhou, Guangdong, China

ABSTRACT: In order to solve great construction interference, complex construction procedures, backward construction techniques and difficulty to guarantee construction quality in the integral or partial cast-in-situ construction of mid-partitions inside the shield tunnels, key intelligent assembly technologies such as multi-sensor information fusion vision camera recognition and positioning, dual 6-axis mechanical arm and active visual posture control, heavy-duty servo displacement feedback control, etc. were developed by adopting the construction concept of intelligent equipment design and prefabricated assembly and manufacturing one-button intelligent assembly robots based on Lot JCXSG-11 of the Shanghai Airport Connecting Line, ensuring the assembly posture and control accuracy of mid-partitions, and realizing the intelligent assembly of prefabricated mid-partitions. The results show that: 1) The control and synchronization accuracy of the mid-partition assembly robot system reaches 0.5mm, and the assembly accuracy of mid-partitions reaches ±2mm, resulting in high-precision assembly; 2) With the aid of intelligent control technology, one-button operation is realized for mid-partition assembly. Each cycle takes 38min and the efficiency is more than 10 times higher than that of the traditional cast-in-situ construction, bringing about intelligent, efficient and green assembly of mid-partitions.

Keywords: shield tunnel, mid-partition, intelligent prefabricated assembly, high precision, synchronous construction, gantry-type, assembly robot

1 INTRODUCTION

With the rapid development of traffic construction in China in recent years, shield tunneling has become an important method for tunnel and underground engineering construction due to its advantages such as high efficiency, fast speed, safety and reliability. The internal structure of a shield tunnel is usually constructed by the cast-in-situ and prefabrication methods. According to the construction organization mode, the internal structure can be constructed synchronously with shield tunneling or after shield cut-through. In general, mid-partitions of the internal structures of the tunnels are of a semi-prefabricated and semi-cast-in-situ structure, with cast-in-situ bases and partial walls prefabricated, and will be constructed after shield advancement. The mouth-shaped prefabricated components are installed synchronously with shield advancement, and the arched bottom plates and rail bearing plates are cast-in-situ structures and will be constructed synchronously after shield advancement for a certain distance.

At present, some progress has been made in the research of prefabrication and assembly technology for mid-partitions in the internal structures of the shield tunnels. Scholars Zhou Junli[1], Jiang wenxing[2], Yang Chenglong[3], Wang Zhihua[4], Shen Yongping [5], Wu Kui[6]studied the installation machine for precast middle partition wall in the practical shield tunnel construction projects in China and explored systematically the key technology of assembling and synchronous construction, etc., and a series of research results has been achieved.

It can be seen from the above studies that the following problems are involved in the prefabrication and assembly of mid-partitions of internal structures of tunnels in China: 1) Prefabrication has not been completely realized, and many components are still cast in situ; 2) Synchronous progressing of mid-partition construction and shield tunneling has not been fully realized, resulting in great construction interference; 3) The degree of automation is low, and intelligent assembly has not yet been realized. The assembly equipment is modified with special mechanical arms or designed with special "sucker-type" cranes, and operated manually. The performance, structure and intelligence of the equipment need to be further improved. Therefore, for the construction technology for prefabricated mid-partitions of underground structures in China, a corresponding system or specification has not yet been established, the application scope is relatively single, the assembly

DOI: 10.1201/9781003495505-292

technology is fragmented, and the construction process and technology are not mature enough. In terms of assembly equipment, the special assembly machine for internal components of shield tunnels features low construction efficiency, low intelligence, low assembly accuracy and great construction interference.

In order to solve the problems in the prefabrication and assembly of mid-partitions in shield tunnels, such as great construction interference, complex construction procedures, backward construction techniques and being difficult to guarantee construction quality, it is of great significance to carry out systematic and in-depth research on the assembly technology and equipment of mid-partitions in the internal structures of the tunnels, so as to enhance the intelligent level of construction technology and equipment, thus ensuring that the assembly quality of finished products of prefabricated components is controllable, improving the construction environment and realizing intelligent, efficient and green construction.

2 TECHNICAL BACKGROUND

2.1 *Project overview*

This paper is based on the tunnel works of Lot JCXSG-11 of Airport Connecting Line of Shanghai Rail Transit Regional Line Project, which is located in Pudong New Area, Shanghai, including 1 transfer shaft and 1 section. The transfer shaft is a shield launching shaft, 209m long, 15.6~30.5m wide and 26.4~28.5m deep, with two underground box frame structures. The total length of the transfer shaft section is 4,721.099m, and the sectional tunnel is of single-tube double-track layout. A slurry shield with a diameter of Φ14.04m is used for construction. The internal structure mainly includes arc members, mid-partitions, top connectors, evacuation platforms and cable trenches. See Figure 1 for the schematic diagram of cross-section design of the internal structure of the tunnel.

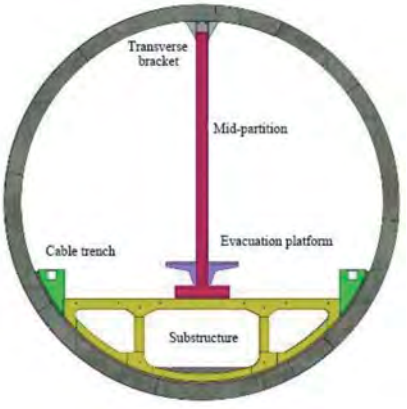

Figure 1. Cross-section design of internal structure of tunnel.

2.2 *Design scheme of mid-partition*

The mid-partition is designed to be 9.116m high, 0.4m thick and 2m wide. It is made of C40 concrete, and the structural outline of the mid-partition with each section weighing 22.65t is shown in Figure 2.

Figure 2. Structural outline of Mid-partition.

As shown in Figure 3, a 30mm thick cushion is provided between the mid-partition and the substructure, with a flatness of not less than 3mm. The gap is filled tightly with fine aggregate mortar and 20 Grade 8.8 M36 bolts are adopted for connection. As shown in Figure 4, Grade 8.8 M30 bolts are used for longitudinal connection of the mid-partition; 33*100mm cross bolt holes are set up for connection of adjacent walls, and the joint surface is assembled in an "L" shape, with required assembly caulking of 20 mm.

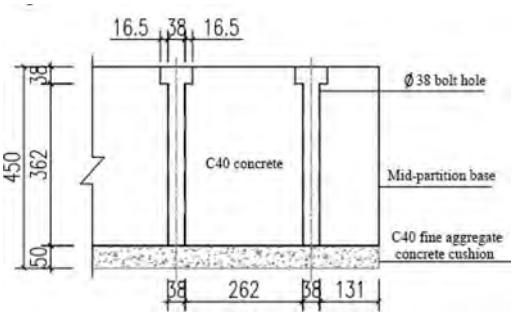

Figure 3. Connection between substructure and Mid-partition (Unit: mm).

As shown in Figure 5, the top of the mid-partition and the segment are fixed with brackets, and the steel plate bracket and the segment are fixed with bolts by using bolt holes embedded on the segment. Sealing strips are designed between the mid-partitions to block gaps and prevent air leakage. The top connectors of the mid-partitions are metal brackets, which have the characteristics of lateral restraint of the mid-partitions and vertical relative movement.

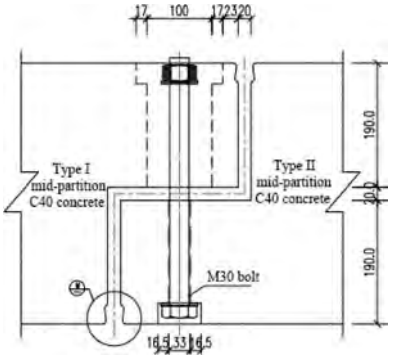

Figure 4. Connection between Mid-partitions (Unit: mm).

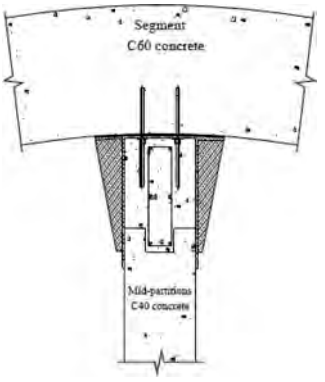

Figure 5. Connection between Mid-partition and segment.

2.3 *Assembly accuracy requirements for mid-partition*

For the assembly accuracy of the mid-partitions, the bolt connection and the control of the gap between the mid-partitions shall be taken as the control objectives and the smoothness and aesthetics of the tunnel shall be taken into account. See Table 1 for the installation quality control indicators.

Table 1. Quality control indicators for Mid-partition installation.

S/N	Control item	Control deviation	Control density
1	Elevation angle α	±0.15°	Per piece
2	Maximum gap difference at the bottom	≦ 5mm	Per piece
3	Inclination β	≦ 0.06°	Per piece
4	Side verticality	≦ 10mm	Per piece
5	Corner γ	±0.15°	Per piece
6	Centerline deviation between mid-partition and arc member	≦ 5mm	Per piece
7	Gap between walls	≦ 7mm	Per piece
8	Filling the gap	20-30mm	Per piece

3 GENERAL DESIGN OF INTELLIGENT ASSEMBLY ROBOTS FOR MID-PARTITIONS

3.1 *General design concept*

The general design of intelligent assembly robots for mid-partitions aims to achieve the basic functions for stable operations of procedures such as grabbing, rotating, walking, fine adjustment and assembling of mid-partitions, and ensure high precision and intelligent control of assembly. In order to ensure the normal passage of construction transport vehicles, the gantry of the erector is provided with a walk-through design with large clearance to meet the requirements for the passage space of construction vehicles; it has the function of fine adjustment for 6 degrees of freedom in various postures to ensure installation accuracy, efficiency and safety. The gantry-type intelligent erector for mid-partitions features posture adjustment with 6 degrees of freedom, with the installation trolley having fine adjustment functions such as longitudinal back and forth movement, transverse back and forth movement, upward and downward expansion, rotation and swing, and it also features automatic walking and positioning; it has intelligent construction functions such as automatic detection and perception, automatic calculation and analysis processing, automatic decision-making and action execution, human-machine interaction and information storage.

The main design concept of the intelligent control systems for mid-partition assembly robots is as follows: project the structured light onto a reference mid-partition and that to be installed in a visual guidance mode with the aid of two 6-DOF mechanical arms of the erector, an integrated laser rangefinder, a limit switch and other detection elements, as well as the active binocular vision camera module to calculate position and posture parameters; complete the closed-loop control of the visual servo through multi-sensor information fusion to provide basis for subsequent fine adjustment of mid-partitions; finally control the hydraulic cylinder and drive motor through software calculation and analysis to complete such 4 procedures as parallel posture adjustment of partitions, mid-partition grabbing and turning, fine posture adjustment and assembly of mid-partitions, and erector return posture adjustment.

3.2 *Main structural composition and parameters*

3.2.1 *Main structure of assembly machine*

According to the construction space characteristics and robust structural requirements in the tunnel, the intelligent erector for mid-partitions is designed with a double-span gantry structure, with supporting structures at both ends and an assembly working mechanism in the middle. The intelligent erector for mid-partitions is mainly composed of a gantry system, a rotating system, a traversing system, a walking system, an electronic control system, a hydraulic system and an intelligent control system. See Figure 6 for the conceptual design of the gantry-type intelligent erector for mid-partitions.

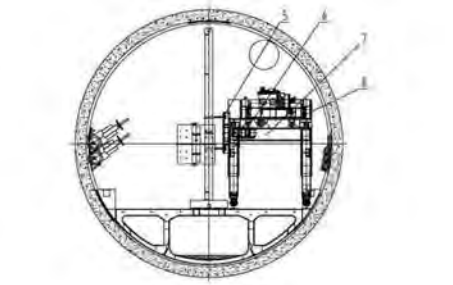

(a) Front View

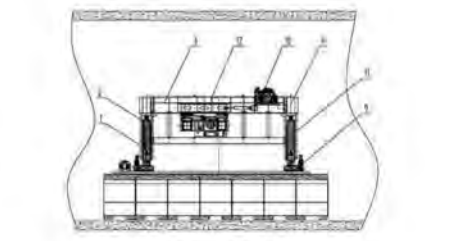

(b) Side View

1-Inner sleeve of gantry column;2-Outer sleeve of gantry column;3-Longitudinal beam of gantry;4-Lateral beam of gantry;5-Rotating disc assembly;6-Rotary drive assembly;7-Outer sleeve assembly for vertical swing;8-Longitudinal moving slider assembly;9-Walking system;10-Hydraulic system;11-Intelligent control system;12-Working platform

Figure 6. Conceptual design of gantry-type intelligent erector for Mid-partitions.

3.2.2 *Technical parameters of erector*

According to the assembly requirements, the main technical parameters of the gantry-type intelligent erector for mid-partitions are shown in Table 2.

Table 2. Main technical parameters of Gantry-type intelligent erector for Mid-partitions.

Technical parameter	Value
Overall dimensions of the erector (mm)	11576×6350×6185
Total weight of the erector(t)	80
Degree of freedom in installation	6-axis control
Operating pressure of the hydraulic system (MPa)	18
Lifting height of the gantry column (mm)	1600
Lateral traversing distance (mm)	1400
Longitudinal displacement distance (mm)	600
Lateral angle adjustment distance(mm)	±50
Longitudinal angle adjustment distance (mm)	±50
Turning distance of the mid-partition (mm)	800
Laser ranging sensor (mm)	Measurement accuracy: 0.02, 0.5
Photoelectric sensor (mm)	Measuring range: 0-800
Active vision camera (mm)	Measurement accuracy: 0.5
6-DOF mechanical arm (mm)	Repeated positioning accuracy: ±0.02
Walking method	Frequency converter + electric drive
Walking speed(m/min)	6.7
Assembly time of a single mid-partition (min)	38
Operation mode	Gantry-type
Control mode	One-button intelligent control + remote control

4 PROCESS OF INTELLIGENT ASSEMBLY OF MID-PARTITIONS

4.1 *Process of intelligent assembly of mid-partitions*

In accordance with the multi-sensor information fusion positioning system, an erector coordinate system is established. The coordinate transformation is carried out with the mechanical arm vision positioning system as the core. With the aid of the closed-loop control of the visual servo and the laser ranging redundancy information, real-time positioning of the mid-partitions during installation is realized through strong robust visual feature selection for accurate position and posture adjustment.

The assembly process with intelligent assembly robots for mid-partitions mainly includes 4 procedures: parallel posture adjustment of mid-partitions, grabbing and turning of mid-partitions, fine posture adjustment and assembly of mid-partitions, and erector return posture adjustment. It takes 2,280s (38min) in total, including 1,800s for the erector and 480s for manual installation of bolts. See Figure 7 for the assembly process flow of mid-partitions.

4.2 *Workflow of intelligent assembly robots for mid-partitions*

4.2.1 *Step 1: Parallel posture adjustment of mid-partitions*

As shown in Figure 8, the erector moves to the zero working position and communicates wirelessly with the mid-partition. The 4 laser ranging sensors installed with the aid of the grabbing pin shaft of the erector is used to adjust the vehicle carrying platform device to make the mid-partition relatively parallel and transverse to the grabbing mechanism. The grabbing mechanism and pin shaft are aligned with the five center holes of the mid-partition through visual recognition cameras and laser ranging sensors. See

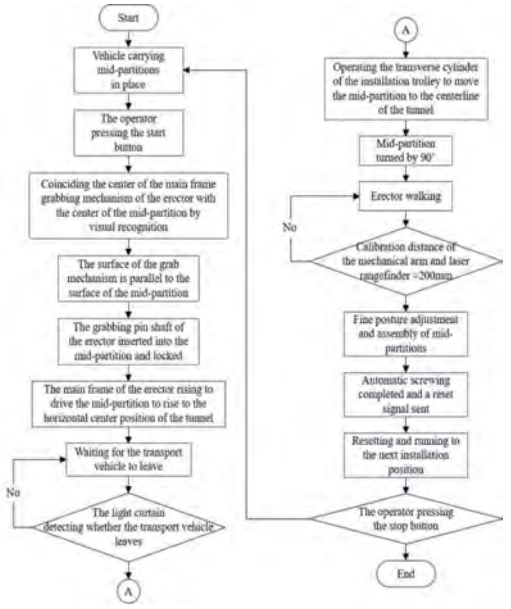

Figure 7. Flow chart of intelligent assembly of Mid-partitions.

Figure 9 for the alignment of the grabbing mechanism and pin shaft with five center holes of the mid-partition.

Figure 8. Erector moving to the zero working position.

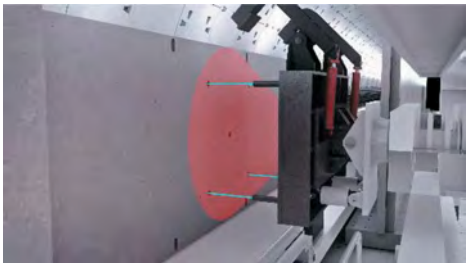

Figure 9. Alignment of the grabbing mechanism and pin shaft with five center holes of the Mid-partition.

4.2.2 *Step 2: Grabbing and turning of mid-partitions*

As shown in Figure 10, the laser ranging sensor for positioning is used to insert the grabbing pin shaft into the mid-partition and lock it; according to the set procedure, the transport vehicle leaves after the mid-partition is lifted; the transverse cylinder retracts, and the mid-partition moves transversely to the centerline of the tunnel; the main frame lifting cylinder rises, and the mid-partition rises to the horizontal center position of turning. The mid-partition is rotated 90° to reach the vertical state, as shown in Figure 11.

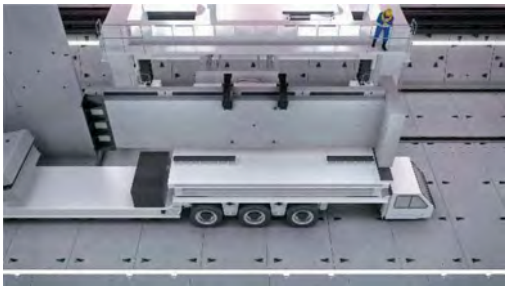

Figure 10. Grabbing pin shaft Inserted into the Mid-partition and locked.

Figure 11. Mid-partition rotating 90° to reach vertical state.

4.2.3 *Step 3: Fine posture adjustment and assembly of mid-partitions*

As shown in Figure 12, two 6-DOF mechanical arms of the erector and laser ranging sensors are used to detect the distance from the installed mid-partition; when the distance is 200mm, the erector stops and the fine adjustment position is reached; as shown in Figure 13, with the aid of active vision cameras of the two mechanical arm systems, the structured light is projected onto the reference mid-partition and that to be installed and then identified, and the relative position and posture parameters between the mid-partitions are calculated, all posture positions of the mid-partitions are adjusted through the closed-loop control, and then, fine adjustment and assembly are completed.

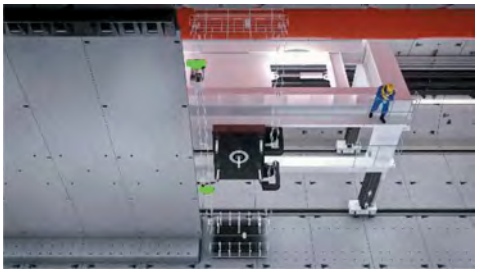

Figure 12. Schematic diagram of two 6-DOF mechanical arms and laser ranging sensors.

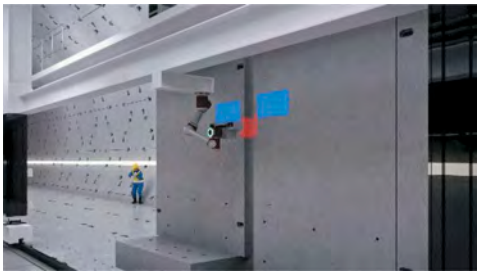

Figure 13. Projecting structured light onto reference Mid-partition and that to be Installed and identifying status.

4.2.4 *Step 4: Erector return posture adjustment*

As shown in Figure 14, after the assembly of the mid-partition is completed, the bottom is temporarily fixed with appropriate metal gaskets and the bolts at the bottom and between walls are tightened. The operator presses the reset button; and then, the grabbing pin shaft is separated from the mid-partition, and the erector automatically moves to the zero working position for the next procedure. The erector automatically moves to the zero working position, as shown in Figure 15.

Figure 14. Grabbing pin shaft separated from the Mid-partition.

Figure 15. Erector automatically moving to the zero working position.

5 KEY TECHNOLOGIES FOR INTELLIGENT ASSEMBLY OF MID-PARTITIONS

5.1 *Multi-sensor information fusion positioning technology*

The intelligent installation of mid-partitions is based on multi-sensor information fusion data, and the mechanical arm vision positioning system of the erector as well as the strong robust visual feature, high-precision displacement sensors, laser range-finders, optical sensors and other detection elements are used to measure and detect actual relevant data. The hydraulic cylinder is finally controlled through software calculation and analysis.

As shown in Figure 16, key information data are extracted with the aid of multi-sensor information such as laser ranging information, vision information, cylinder stroke information and structured information of the equipment; the structured light is generated by a point cloud camera generator, the vision camera extracts point cloud data information to form an image characteristic value of the target mid-partition, which is compared with the expected characteristic value of the fixed mid-partition image, and the visual servo loop control is used to calculate their relative positions and postures.

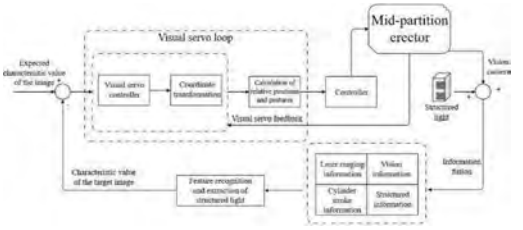

Figure 16. Block diagram of intelligent control system for Mid-partitions.

An erector coordinate system is established. The coordinate transformation is carried out with the mechanical arm vision positioning system as the core. With the aid of the closed-loop control of the visual servo and the laser ranging redundancy information, real-time positioning of the mid-partitions during installation is realized through strong robust visual feature selection for accurate position and posture adjustment.

5.2 *Center hole positioning by vision camera recognition*

In the center hole alignment stage, a visual recognition camera is used to identify the round hole for center positioning reserved at the center of the prefabricated slab of the mid-partition, and it is necessary to feed back the coordinate position of the circle center for adjusting the center of the grabbing mechanism of the erector to align with the center of the prefabricated slab.

As shown in Figure 17, the grabbing pin shaft is aligned with the hole of the mid-partition. The industrial vision camera positioning technology and the built-in deflection angle of the vision camera are adopted to compare the coordinate information of the hole image taken with the standard image and feed back the coordinate position of the circle center for adjusting the center of the grabbing mechanism of the erector to align with the center of the mid-partition. The identification and positioning process of the round hole for center positioning includes image loading, image pre-processing, edge detection of the center hole, hough-circle transform, and output of coordinates of the fitted circle and circle center, aiming to obtain the rotation angle, height difference and horizontal difference, control the relative movement of the rotating cylinder, lifting cylinder and longitudinal horizontal cylinder of the erector, and insert the grabbing pin shaft into the mid-partition. See Figure 18 for the application effect of recognition of the center hole of the mid-partition by the vision camera.

Figure 17. Recognition results and adjustment of current grabbing hole and standard positions and postures.

Figure 18. Effect of recognition of the center hole of the Mid-partition by the vision camera.

5.3 *Dual Six-axis mechanical arm and active visual posture control technology*

After the mid-partition reaches the fine adjustment position, with the aid of two mechanical arm systems with active vision cameras (see Figure 19 and Figure 20), the structured light is projected onto the reference mid-partition and that to be installed respectively and then identified, so as to calculate the relative position and posture parameters between the mid-partitions and adjust the postures and positions of the mid-partitions through the closed-loop control.

The dual six-axis mechanical arm guides the camera to accurately obtain the position and posture coordinates of the mid-partitions, converts the image coordinates into the erector coordinates that can be recognized by the erector, and issues instructions according to the coordinate system calculation and PLC calculation of the erector. The hydraulic control system adopts a load-sensitive electrical proportional control scheme to complete the automatic centering and grabbing of the intelligent assembly robots for the mid-partitions, the automatic rotation of the mid-partitions by 90°, the automatic walking of the erector to the installation position, the fine adjustment of the mid-partitions, the installation of the mid-partitions and other procedures, and then guides the hydraulic cylinder of the erector to complete the positioning, grabbing and posture adjustment of the mid-partitions.

Figure 19. Upper active vision camera and structured light generator in working.

Figure 20. Lower active vision camera and structured light generator in working.

5.4 *Heavy-duty servo displacement feedback control*

The hydraulic system adopts the combination mode of the load sensitive pump and the proportional multi-way valve to realize the flow control technology with constant output of system flows and independent of load changes; the proportional valve adjusts the speed curve of the cylinder according to requirements to ensure stable actions; when integrated with displacement sensors, the cylinder realizes multi-cylinder compound action control with accuracy of millimeter level to meet the action accuracy requirements of the erector.

The intelligent assembly robot for mid-partitions obtains external information through the multi-sensor information fusion positioning system based on the measured data and analysis of the current and target positions of components. The high-performance industrial personal computer makes calculations and judges whether the perception meets the working conditions in real time, and imports the collected position and posture errors into PLC to calculate the current control amount in accordance with the coordinate system analysis information of the erector, so that hydraulic cylinders and other actuators can execute the current drive amount, calculate the displacement of each actuator and send it to the hydraulic control system, so as to achieve the required working condition.

6 FIELD APPLICATION EFFECT

6.1 *Assembly efficiency of erector*

From June 2022 to July 2023, after factory test and field application, a total of 2,361 mid-partitions were assembled on site, with a cumulative assembly length of 4,722 m. The intelligent assembly robot for mid-partitions completed four procedures, with a total duration of 38min (including 5 min for fastening bolts and removing lock pins). The field application of the intelligent assembly robot for mid-partitions is shown in Figure 21.

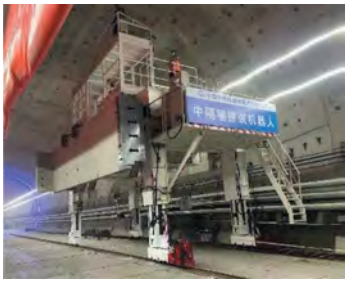

Figure 21. Field application of intelligent assembly robot for Mid-partitions.

6.2 *Quality control effect of assembly*

The assembly quality of the intelligent assembly robot for mid-partitions is mainly reflected in the control of assembly accuracy, which refers to the relative deviation from the previous mid-partition. If the assembly accuracy of the mid-partitions reaches ±2mm, high-precision assembly is realized. and the installation quality control indicators of the mid-partitions are shown in Table 3.

Table 3. Statistics of quality control eviations for Mid-partition assembly.

Control item	Design deviation	Measured deviation	Control density
Elevation angleα	±0.05°	±0.05°	Per piece
Maximum gap difference at the bottom	≦ 5 mm	≦ 0.5 mm	Per piece
Inclinationβ	≦ 0.06°	≦ 0 .01°	Per piece
Side verticality	≦ 10 mm	≦ 2 mm	Per piece
Cornerγ	±0.15°	±0.05°	Per piece
Centerline deviation	≦ 5mm	≦ 1mm	Per piece
Gap between walls	≦ 7mm	≦ 0.5 mm	Per piece
Filling the gap	20-30mm	20-30mm	Per piece

7 CONCLUSIONS AND DISCUSSION

Based on the problems that need to be solved urgently for intelligent assembly of prefabricated mid-partitions for shield tunnels, and in combination with the assembly process, equipment intelligence degree and status of the resource organization mode, this paper studies the design scheme of the gantry-type intelligent erector for mid-partitions and key technologies for one-button intelligent high-precision assembly, and draws the main conclusions as follows:

1) The conceptual design of the intelligent control system for the intelligent assembly robot for mid-partitions: An erector coordinate system is established. The coordinate transformation is carried out with the mechanical arm vision positioning system

as the core. With the aid of the closed-loop control of the servo of the double-sided vision camera module and the laser ranging redundancy information, real-time positioning of the mid-partitions during installation is realized through strong robust visual feature selection for accurate position and posture adjustment, resulting in the assembly accuracy ≦±2mm.

2) The posture measurement technology of mid-partitions based on the dual six-axis mechanical arm and active vision servo technology: The structured light image is recognized by a vision camera, and the position difference between two mid-partitions is identified and calculated by an algorithm, thus realizing accurate position and posture adjustment of parallelism of mid-partitions. The efficiency is more than 10 times higher than that of the traditional cast-in-situ process.
3) The application of full prefabrication and assembly technology and intelligent equipment for the internal structures of shield tunnels has great technical and practical significance and provides a reference for construction technologies and new equipment in the field of full prefabrication and assembly. In the next step, it is recommended to carry out systematic and in-depth research on the connection between mid-partitions and bottoms, design forms of mid-partitions, connection between mid-partitions and top brackets, intelligent assembly application function integration and intelligent fastening of circumferential and longitudinal bolts, etc. to standardize construction and improve construction efficiency.

REFERENCES

Yang Jifan,2011. Mechanical Design of Assembling Construction of Tunnel Precast Mid-Partition Wall. China Municipal Engineering (4):52–55+92.

Zhou Junli, 2015. Technologies for Assembly of Separation Wall of a Metro Tunnel on South Section of No.11 Line of Shanghai Rail Transit Works. Tunnel Construction 35(4): 373–376.

Jiang Wenxing, Hu Xinpeng, Yu Jing, et al, 2022. Study on design and construction technology of prefabricated components for internal structure of large-diameter shield tunnel. Modern Urban Transit (9): 57–62.

Yang Chenglong, 2022. Research on assembly technology of middle partition wall in large diameter rail transit tunnel of city line. Shanxi Architecture 48(12):109–112.

Wwang Zhihua, 2020. Key Technologies for Synchronous Construction of Internal Structure of Super-large Diameter Tunnel. Construction Technology 49(13):28–31.

Shen Yongping, 2014. Mid-Partition-Wall Construction Technology within Large Diameter Rail Transit Running Tunnel. Underground Engineering and Tunnels (1):20–24.

Wu Kui, 2017. Synchronous construction technology of large diameter shield tunnel. Shan Dong Jiao Tong Ke Ji (1):94–96.

Tunnelling for a Better Life – Yan, Celestino, Thewes & Eberhardt (Eds)
© 2024 The Author(s), ISBN 978-1-032-80042-4
Open Access: www.taylorfrancis.com, CC BY-NC-ND 4.0 license

Creative design for Herrenknecht TBM used in Jiangyin Jingjiang Yangtze River crossing tunnel construction

Hai Wang*
Herrenknecht (Guangzhou) Tunnelling Equipment Co., Ltd. Beijing Branch, Beijing, China

Renjun Jin & Guanghong Lin
Guangzhou Herrenknecht Tunnelling Machinery Co., Ltd. Guangzhou, China

Wen Sun
Herrenknecht (Guangzhou) Tunnelling Equipment Co., Ltd. Beijing Branch, Beijing, China

ABSTRACT: The Jiangyin Jingjiang Yangtze River Tunnel Project has a total length of approximately 11.825 kilometers, of which 6,445 meters cross the Yangtze River using the TBM tunnelling method (with a TBM tunnelling length of 4,952 meters), and the outer diameter of the tunnel segment is 15.2 meters. The TBM used in this project has a long one-time excavation distance, and the strata it crosses are mainly composed of cohesive and sandy silt, with the sand layer containing a high quartz content and contains high-strength calcareous nodules. The tunnel has deep overburden, high water pressure, and noxious gases in the formation, making it very challenging project.

This article elaborates on the innovative design of the Herrenknecht TBM used in right line of this project, which was aimed at addressing the challenges of the project including the long excavation distance, high water pressure, strong wear from soil, the presence of noxious gases in the formation and high construction quality requirements.

The TBM used on this project has an excavation diameter of 16.09 meters, a working pressure of 1 MPa and is equipped with a large opening ratio accessible soft ground cutting wheel, a displaceable main drive and an automatic pressure-regulating main drive sealing system. It is also equipped with a SSP-E geological forecasting system, a tailskin two-components synchronous grouting system, an adaptive tailskin sealing grease injection system, a tailskin grouting quality scanning system, a telescopic camera in the excavation chamber, and a high-flow flushing system among other customized features.

Thanks to all these TBM design innovations, the right line tunnel excavation was successfully completed on May 17, 2023.

Keywords: TBM, Tunnel project, Design

1 INTRODUCTION

In recent years, with the development of economy and society and the progress of engineering technology, the shield tunnelling method has been widely used in the construction of highway tunnels due to its advantages such as fast construction speed, good safety, and low environmental impact. Due to the functional requirements of highway tunnels, the diameter of shield tunnelling machines used in highway tunnel construction is usually over 10m, with the diameter greater than 14m being the majority. According to statistics, there are currently 50 ultra- large diameter shield tunnelling projects with a diameter of >14m in China, most of which are underwater tunnels.

The shield tunnelling machine applied to ultra-large diameter underwater tunnels needs to be designed, manufactured, and used in accordance with the characteristics of ultra-large diameter underwater tunnels, such as long excavation distance, high underground water pressure, large excavation section, complex geological changes, and high requirements for tunnel forming quality. A targeted design should be carried out to ensure the safety and efficiency of the tunnel construction. This article takes the design of the Herrenknecht shield machine for

*Corresponding author: wang.hai@herrenknecht.com

DOI: 10.1201/9781003495505-293

the right line tunnel of the Jingjiang Yangtze River Tunnel in Jiangyin as an example to explain the application of shield machine design tailored to the characteristics of the project.

2 PROJECT OVERVIEW

The Jiangyin Jingjiang Yangtze River Tunnel Project is located in Jiangsu Province, starting from the intersection of Jingjiang Gongxin Highway and Chengxi Avenue, crossing the Yangtze River south and ending at the intersection of Jiangyin West Outer Ring Road and Furong Avenue. The total length of the route is appoximately 11.825 kilometres, and the entire line adopts the construction standard of a two-way, six-lane expressway with a design speed of 80 km/h and a roadbed width of 33 meters; three interchanges are set up along the entire line, including Jingxi, Jiangyin West, and Qingshan.

The main tunnel of the Jiangyin Jingjiang Yangtze River Tunnel Project starts from about 300m north of S356 in Jingjiang City, passes south through S356 and Binjiang 1st Road before entering the Yangtze River. After reaching Jiangyin City, it passes down through Jiangfeng Road, Binjiang Road, and Tongfu Road, and is grounded at about 270m south of Tongfu Road. The total length of the tunnel is about 6445 meters (the main tunnel is calculated based on the left and right lines, with chainage YK2+720-YK9+170 on the right line, and 6450 meters long; the chainage ZK2+720-ZK9+159.238 on the left line, and 6439.2 meters long).

The tunnel crossing the river section is constructed using the shield tunnelling method. The inner diameter of the tunnel segment lining is 14.2 meters, and the outer diameter is 15.5 meters. The shield tunnelling section on the right line is 4952 meters long (chainage YK3+433-YK8+385), and the shield tunnelling section on the left line is 4937.19 meters long (chainage ZK3+432.396-ZK8+369.590).

Figure 1. Overview of jiangyin jingjiang yangtze river tunnel project.

The strata crossed by the tunnel mainly consist of soft plastic to hard plastic silty clay, muddy silty clay, loose to dense silt, silt, fine sand, dense gravel medium coarse sand, etc. The quartz content of the silt layer is about 55-75%, the quartz content of the fine sand is about 55-85% and the quartz content of the medium coarse sand is about 80-90%. There are high strength calcareous nodules sandwiched in the sand layer. Noxious gases are present in the muddy silty clay.

The main characteristics of the project are:

- "Large cross section", with an outer diameter of 15.5m for the segment, and the excavation diameter of the shield machine will exceed 16m;
- "Long distance", with a one-time tunnelling distance of approximately 4.95km for the shield tunnelling machine;
- "High pressure", refers to the tunnel crossing the Yangtze River with a large burial depth and high water pressure. The maximum soil and water pressure at the tunnel axis exceeds 0.9Mpa;
- "Difficult geology", the tunnels pass through various strata, and hard plastic silty clay can easily lead to clogging and blockage on the cutting edge; dense powder fine sand and medium coarse sand have a high quartz content, are highly abrasive, and in some areas are also mixed with calcareous nodules, which can easily cause wear of the cutting tool; there are also noxious gases present in the formation.

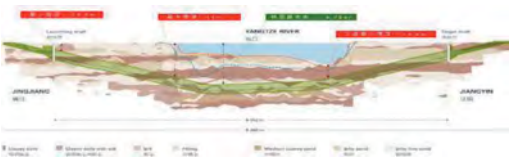

Figure 2. Geological longitudinal section of jiangyin jingjiang yangtze river tunnel engineering.

3 TARGETED DESIGN AND INNOVATION OF SHIELD TUNNELLING MACHINES

3.1 *Overview of overall design of shield tunnelling machine*

Based on the engineering geological and hydrogeological conditions and difficulties of the Jingjiang Yangtze River Tunnel in Jiangyin, the overall design concept of the shield tunnelling machine was determined through theoretical analysis and calculation, as well as summarizing the design experience of similar projects in the past. The shield machine adopts a MIX shield with the following main technical parameters:

- Working pressure of the shield tunnelling machine: 1Mpa
- Cutter head excavation diameter: 16,130mm
- Front shield diameter: 16,100mm
- Middle shield diameter: 16,070mm
- Tailskin diameter: 16,040mm/16,020mm
- Main drive power: 4,900KW
- Cutting wheel speed: 0-2r/min
- Nominal torque: 37,593KNm
- Maximum torque: 46,991KNm
- Breakout torque: 50,751KNm
- Total thrust: 28,7064KN
- Theoretical maximum advance speed: 45mm/min

3.2 *Cutting wheel*

The geology of this project is complex and the fine sand, coarse sand and calcareous nodules can cause wear on the cutting tools. Under the working conditions of deep overburden and high water pressure, if the cutting tools are worn out to the point where they cannot be used and need to be replaced, using the conventional way to enter the chamber with compressed air to replace the cutting tools will result in high construction risks and low tool replacement efficiency. Therefore, in the design of the cutting wheel, a targeted design of an accessible cutting wheel was adopted, and the safety of the cutting wheel and cutting tools during long distance excavation is ensured by tool configuration, wear resistance design, and tool wear monitoring.

The cutting wheel structure adopts an accessible type, consisting of 6 accessible main arms and 6 small spokes. The cutting wheel is equipped with accessible ripper tooth holders and sealing gates, accessible scraper holders and sealing gates, and conventional scraper holders, which can facilitate the replacement of the cutting tool.

Figure 3. Cutting wheel for the right line tunnel of Jiangyin Jingjiang Yangtze River Tunnel.

The cutting wheel opening ratio is approximately 45%. 12 DN100 flushing ports are set in the center area of the cutting wheel, and a separate P0.1 flushing pump is used for flushing. The flushing of each nozzle has been optimized and designed to concentrate the flushing at two of the flushing points. The flow rate is concentrated for a short period of time, the flushing pressure is increased, and the central area of the cutting wheel is washed in time to prevent clogging formation at the cutting wheel center.

The layout of the shield tunnelling tools is shown in Figure 5. The height of the accessible center tool is 245mm, the height of the front welded rippers and the accessible rippers is 225mm, the height of the accessible scraper on both sides of the main arms is 185mm, and the height of the bolt fixed scraper and bucket lips on both sides of the main arm is 165mm. The reasonable height difference configuration of the cutting tools can effectively meet the requirements of cutting strata and fully utilize the service life of the tools.

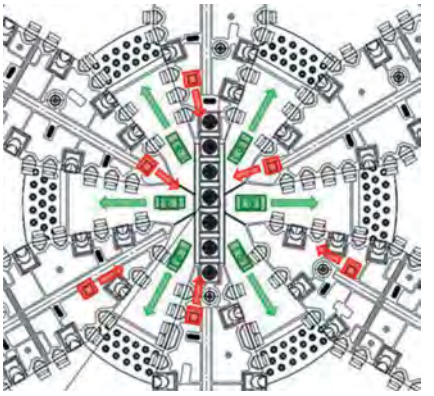

Figure 4. Center flushing of cutting wheel.

Figure 5. Cutting tool configuration.

When excavating in dense powder fine sand, medium coarse sand, and formations containing calcareous nodules, the cutting tools are prone to wear. Once excessive wear occurs, it will greatly reduce the service life of the cutting tools and even endanger the structure of the cutting wheel, causing irreparable losses. In response to this phenomenon, the cutting wheel is equipped with an accessible scraper/ripper wear monitoring device at key positions, which can display the tool wear status in the shield machine control cabin, as shown in Figure 6.

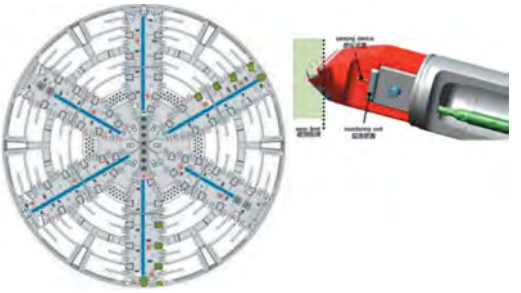

Figure 6. Wear monitoring of cutting wheel and cutting tools.

3.3 *Main drive and sealing system*

Considering the geological conditions of the shield tunnelling in this project and the uncertainties encountered in the geological conditions (such as boulders, dead wood, and sunken ships), the main drive adopts a variable frequency motor drive, equipped with 14 gearboxes, with a total power of 4900kW, a nominal torque of 37,593KNM, a maximum torque of 46,991KNM, and a breakout torque of 50,751kNm.

Considering the main excavation in clay and sand layers, the maximum speed is 2.0rpm. The torque curve of the driving part is shown in Figure 7.

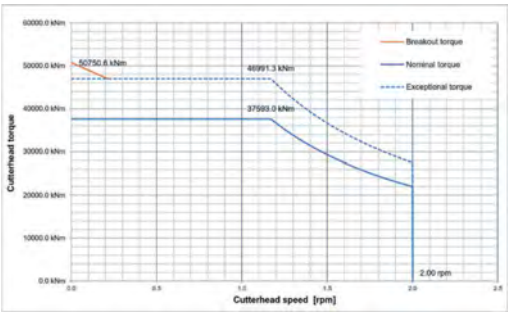

Figure 7. Main drive torque curve.

The main drive of the cutting wheel is shown in Figure 8. The main drive adopts a 7.6m diameter three row roller heavy-duty main bearing produced by Rothe Erde in Germany, equipped with 18 pieces of Φ 400/280-400mm telescopic cylinders.

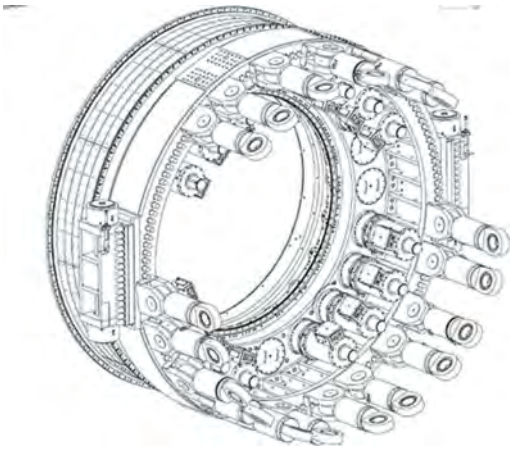

Figure 8. Main drive structure.

The inner and outer seals of the main drive sealing system are composed of four lip-shaped rubber seals. The outer seal is equipped with an automatic pressure regulating device, which can adjust the sealing back pressure according to the changes of the slurry pressure in the excavation chamber, and the pressure resistance can reach 1.2MPa. The structure and installation method of the main seal can ensure that the external seal can be replaced inside the tunnel in emergency situations.

3.4 *Synchronous grouting system*

In order to reduce the phenomenon of segment stepping and joint leakage, and to ensure the quality of the formed tunnel, it is necessary to use shield tail

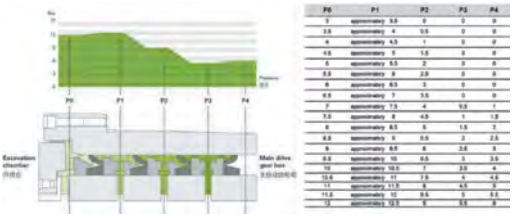

Figure 9. Automatic pressurizing system for main bearing sealing.

grouting in a timely manner to stabilize the segment ring after it comes out of the shield tailskin, thereby reducing the floating of the segment ring. In response to the characteristics of this project, the shield tailskin grouting adopts a synchronous bi-components grouting system, which greatly shortens the setting time of the grout, timely and effectively controls the floating of the ring segments, avoids the occurrence of segment stepping, joint leakage etc., and the quality of the formed tunnel is high.

The structure of the shield tailskin synchronous bi-components grouting system is shown in the Figure 10. Equipped with component A pipe, component B pipe, cleaning piston, and cleaning water circuit, the structure is exquisite, the piston action is reliable, cleaning is convenient, and the two-component mixing position is close to the end of the shield tailskin, making it difficult to block the pipe.

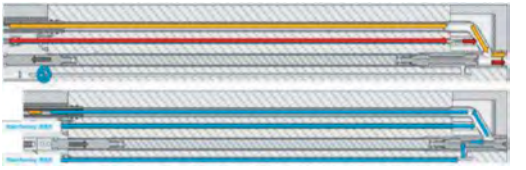

Figure 10. Layout of Bi-component grouting system in tailskin.

The capacity of the component A and B screw pumps equipped in the system can meet the grouting volume requirements at the maximum advance speed of the shield machine, accurately control the mixing ratio of component A and B, and effectively control the grout setting time. In the grouting mode, component A and component B enter the mixing zone at the end of tailskin of the shield through their respective pipelines and mix before injecting into the annular gap between the outer wall of the segment and the inner wall of the excavation tunnel. At this point, the cleaning piston is in the retracted position, blocking the cleaning circuit.

In the cleaning mode, the cleaning piston extends, and the slurry injected into the annular gap is blocked by the piston and will not flow back into the shield tailskin. The cleaning water enters the component A and B pipelines through the space around the cleaning piston to clean the

pipelines. The cleaning water flows back to the waste water tank to ensure the cleanliness of the environment inside the tunnel.

3.5 *Grouting quality inspection system*

After the segment is moving out from the tailksin and grouted, whether the grout timely and completely fills the annular gap outside the segment directly affects the stability of the structure and the buoyancy of the segment. It also has an important effect on controlling soil deformation and prevention of ground settlement. In order to confirm the quality and effectiveness of grouting behind the segment wall, and to ensure the stability and quality of the formed tunnel, it is necessary to test the quality of grouting behind the segment wall in order to take timely measures to compensate for the adverse effects of insufficient synchronous grouting at the shield tail during the shield tunnelling process.

The shield tunnelling machine of this project is innovatively equipped with an independent segment grouting quality detection system behind the erector. The system mainly consists of an arc arch structure, a geological radar that can move on the arc arch, and the associated data processing laptop and software.

After the segments have been assembled, as the shield tunnelling machine advances, the segments gradually detach from the shield tailskin and reach the area where the grouting quality detection system is located. At this time, the system is activated to scan the wall of the segments using geological radar. The data obtained is automatically processed by the corresponding data processing software and presented in the form of a graphical report. The operator can visually see the thickness and uniformity of the grouting behind the segment wall, determine whether the synchronous grouting at the shield tailskin is sufficient, and whether secondary grouting behind the segment wall is necessary.

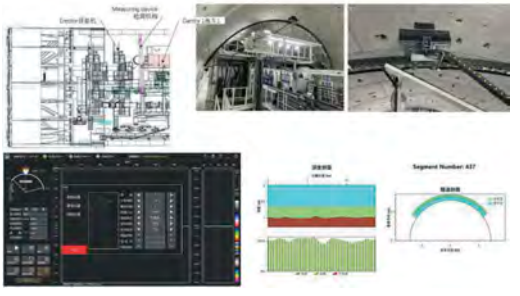

Figure 11. Grouting quality inspection system.

3.6 *Shield tailskin grease injection system*

The shield tailskin sealing system consists of 4 rows of shield tailskin brushes, 1 row of steel plates, and 1 row of grout extruders. During the advancing process of the shield tunnelling machine, the shield tailskin sealing system plays a role in isolating the water and soil pressure and grouting outside the shield tailskin, to ensure tunnel safety. It is necessary to continuously inject shield tailskin sealing grease during the advancing process to ensure the sealing ability of the shield tailskin sealing brush and extend its service life.

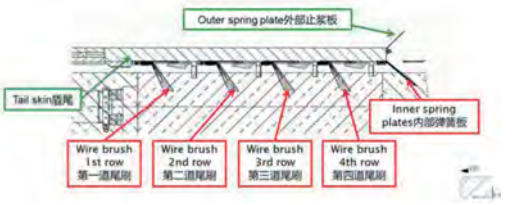

Figure 12. Layout of shield tailskin sealing.

In the past, traditional shield tailskin grease injection systems, although equipped with automatic and manual modes, often experienced excessive grease injection in actual use, affecting the effectiveness of shield tailskin sealing and wasting shield tailskin grease. The shield tunnelling machine of this project innovatively adopts a new adaptive shield tailskin grease injection system. The system can automatically adjust the injection amount of shield tailskin grease into each sealing chamber based on the physical characteristics of the shield tailskin sealing grease, the required amount of shield tailskin grease per square meter of segment surface area and the pressure of different shield tailskin sealing brush chambers, ensuring that the grease is evenly injected into each shield tailskin brush sealing chamber and applied to the shield tailskin sealing brush. After practical use, it has been proven that the system has a good control effect on the injection of shield tailskin grease, ensuring the sealing effect of the shield tail sealing system and effectively saving the amount of shield tail grease injection, demonstrating good effectiveness.

3.7 *Video monitoring system for excavation chamber and air cushion chamber*

During the advancing process of the shield tunnelling machine, most of the cutting tools on the cutting wheel can be easily inspected using the relevant functions of the accessible cutting wheel, but the wear of the bolt mounted scrapers and bucket lips cannot be perceived. In addition, sometimes when the shield machine is stopped, it is necessary to check the excavation surface in front of the cutting wheel to observe whether there are any foreign objects inside the excavation surface and whether the excavation surface is stable. When carrying out maintenance work on the shield tunnelling machines in the excavation and air cushion chambers, it is also necessary to monitor the operation of personnel in the excavation and air cushion chambers to ensure safety. Therefore, the shield tunnelling machine of this project is equipped with

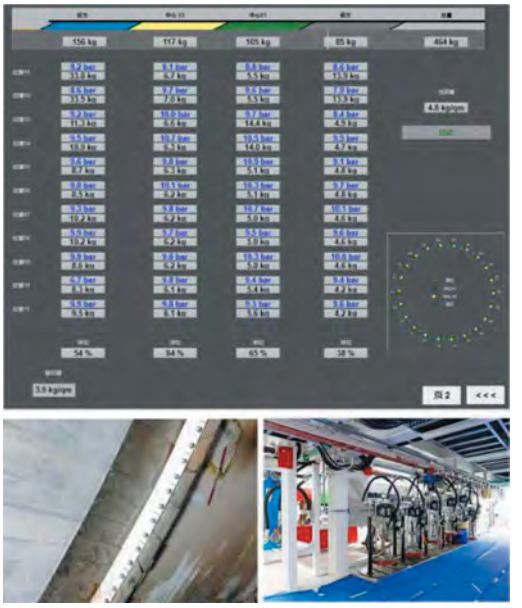

Figure 13. Adaptive tailskin grease injection system.

a set of pressure-resistant, waterproof and self-illuminating telescopic cameras above the excavation chamber and a set of pressure-resistant, waterproof, and self-illuminating fixed cameras are installed above the air cushion chamber. The telescopic camera can extend to the back of the cutting wheel to observe the steel structure of the cutting wheel, the side tools of the main arm of the cutting wheel, the bucket lips, and the tunnel face. The fixed camera observes the air cushion chamber.

During the construction process of this project, the telescopic camera was used to observe the structure of the cutting wheel, the tunnel face, and the clogging situation on the cutting wheel. The camera image was clear and the effect was good. As shown in Figure 14.

Figure 14. Snapshot from telescopic camera.

3.8 *Geological advance prediction system*

Due to the long distance of the tunnel crossing the Yangtze River in this project, there are certain uncertainties in the geological conditions and the geological conditions encountered (such as boulders, dead wood, and sunken ships). In addition to the reserving advance drilling channels, the shield tunnelling machine is also equipped with a soft soil sonic geological advance prediction system (SSP-E), which can detect the soil in front of the shield tunnelling machine through geophysical exploration.

The system includes a transmitter located below the side of the shield, receivers located on the front of the shield, and corresponding data transmission and processing software. When the shield tunnelling machine stops to assemble segments, the system is activated and the transmitter extends to touch the tunnel wall, emitting sound signals. The receivers extend to touch the excavation surface through the cutting wheel opening to receive signals. The system collects the reflected waves of the sound waves and processes and analyses the data, recording the magnitude of the reflected wave reflectivity. Subsequently, the same steps will be carried out again when the shield tunnelling machine stops and assembles the segments. Through the accumulation of a certain amount of measurement data, abnormal reflectance sections can be discovered, which can help determine if there are foreign objects or voids in the soil ahead and provide support for making construction plans.

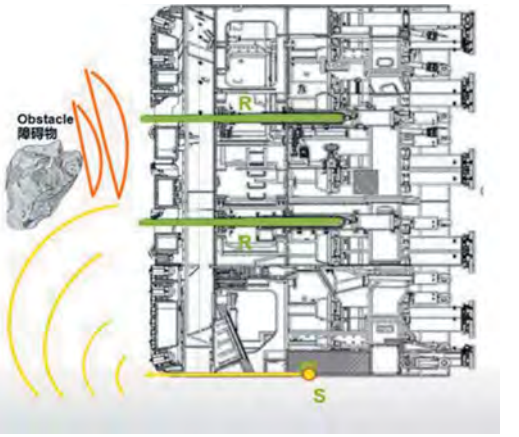

Figure 15. Geology forecasting system.

In the actual operation process, due to a leakage of a gate valve in front of one receiver and the need for compressed air intervention to repair completely, the contractor ultimately gave up on repairing the system considering the cost and time needed. The system was not actually used.

3.9 *Slurry circuit and flushing system*

This project adopts a MIX shield machine which relies on the slurry circuit to provide bentonite slurry

to maintain stable support pressure and ensure the stability of the excavation surface, and to ensure that the relevant parts of the cutting wheel, excavation chamber and air cushion chamber are flushed and the excavated materials from the cutting wheel is transported to the ground slurry treatment system.

The slurry circuit includes P1.1, P1.2 feed pumps, P2.1, P2.2, and P2.3 discharge pumps, P0.1 center flushing pump, P0.2 air cushion chamber bottom flushing pump, P0.3 excavation chamber bottom flushing pump, feed and discharge pipelines, valves, flow meters, density meters, etc. The diameter of the slurry feed and discharge line is DN500, with a slurry inlet flow rate of 2600m^3/h and a slurry discharge flow rate of 2800m^3/h. Considering the long tunnelling distance of the shield tunnelling machine and the high ground abrasiveness, the slurry circuit pipelines of the entire machine adopt more wear-resistant tri-base composite material wear-resistant pipes, and the tri-base wear-resistant layers in the straight jet area inside all the flushing pipelines and slurry discharge pipeline bends have been thickened.

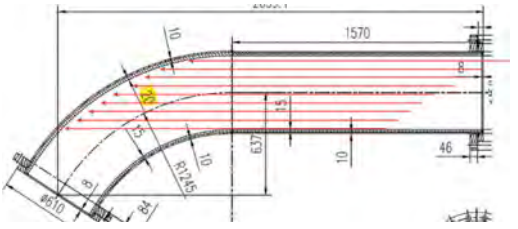

Figure 16. Thickened three base composite material wear-resistant pipe.

The slurry circuit has various operating modes, such as excavation, stoppage, pipe extension, weekend and equipment maintenance, to ensure smooth excavation of shield tunnelling in complex geological conditions.

4 TARGETED DESIGN APPLICATION EFFECT

The shield machine started excavation on December 31, 2021 and successfully breakthrough on May 15, 2023. Throughout the entire tunnelling process, the performance of the shield machine was stable, with a maximum daily advance of 11 meters and a maximum monthly advance of 234 meters. The targeted designs have basically played a full role, among which the accessible cutting wheel works normally, the tool has no abnormal wear, the main drive torque reservation and the main drive sealing pressure resistance are sufficient, the shield tailskin bi-components synchronous grouting and adaptive shield tailskin grease effect are well used, the grouting quality detection system, excavation chamber & air cushion chamber video monitoring system, and slurry circuit work normally, providing technical support for the final tunnel connection.

Figure 17. Performance of shield machine of right line tunnel of jiangyin jingjiang yangtze river tunnel.

5 CONCLUSION

Based on the geological and hydrogeological conditions of the right line of the Jiangyin Jingjiang Yangtze River Tunnel Project, especially when crossing the Yangtze River, the tunnel has a large overburden depth, a large excavation diameter, high water pressure, complex geological conditions, and the presence of adverse geological conditions such as calcareous nodules and harmful gases. There are many uncontrollable factors and Herrenknecht has innovatively designed the shield tunnelling machine. The main technologies include accessible cutting wheel, telescopic main drive, and automatic pressure regulating main drive sealing system, shield tailskin bi-components synchronous grouting, adaptive shield tailksin grease injection system, grouting quality detection system, excavation chamber and air cushion chamber video monitoring system, geological advance prediction system, and slurry circuit have achieved good application results in construction, ensuring the safe and smooth tunnel construction according to plan, and playing a good demonstration role for the design and application of shield tunnelling machines in similar projects.

REFERENCES

Wang G.A., Wang K., et. al, 2021. Proceedings of the National Engineering Construction Industry Construction Technology Exchange Conference (Volume II), Current Situation and Prospects of Large Diameter Shield Tunnel Construction Technology, China

China Railway Bridge Survey and Design Institute Group Co., Ltd., 2020, Engineering Geological Survey Report for Construction Drawing Design Phase of Jiangyin Jingjiang Yangtze River Tunnel (Shield Tunnel Section)

Tunnelling for a Better Life – Yan, Celestino, Thewes & Eberhardt (Eds)
© 2024 The Author(s), ISBN 978-1-032-80042-4
Open Access: www.taylorfrancis.com, CC BY-NC-ND 4.0 license

Research on settlement control of large diameter shallow buried shield tunnel crossing railway and reservoir embankments

Jianhong Wang & Shaohang Yan*
Shandong University, Jinan, China

Chao Wang, Qinglin Yang, Jing Sun & Shunqiang Xue
China Railway 14th Bureau Group Mega Shield Construction Engineering Co., Ltd., Nanjing, China

ABSTRACT: Ground subsidence is a common geological hazard generated during shield tunneling construction, and if not controlled, it can have a catastrophic impact on the safety of existing buildings. Due to the large shield face and shallow burial depth from the ground, large-diameter shallow buried shield tunnels are more prone to ground deformation. Therefore, the study of the impact mechanism and deformation control of large-diameter shallow buried tunnels on ground deformation is of great engineering significance. This study is based on model experiments and on-site measurement methods to conduct targeted research on deformation caused by large-diameter mud water balance shield tunneling through railways, reservoir embankments, and surface uplift and settlement, including indoor scaled model tests that can simulate the shield tunneling process and grouting behind the wall. The study is based on the actual engineering of the Jinan Yellow River North Extension Tunnel. The model test results show that the surface deformation first experiences uplift, followed by settlement, with a maximum settlement of 10mm, and the settlement trend conforms to the Peck formula prediction results; And compared with the on-site measurement results, a control technology for railway and reservoir embankments using large-diameter shallow buried shield tunnels is proposed, which is to reinforce railway tracks through D-beams or control surface deformation through controlling grouting pressure combined with real-time monitoring, in order to provide guidance and reference for engineering practice and reduce the impact of ground settlement and uplift on existing buildings.

Keywords: Shield tunneling method, Reservoir embankment, Railway subgrade, Settlement control, Model test

1 INTRODUCTION

With the development of society and urban expansion, more and more tunnel projects are being planned for construction. Among them, large-diameter shield tunnels are widely used due to their high construction efficiency and automation level. However, at the same time, as the diameter of shield tunnels increases, construction risks also increase synchronously. It is crucial to explore the impact mechanism of large-diameter shield tunneling on the surface.

Scholars at home and abroad have conducted some research on this section. Regarding the aspect of shield tunneling through existing railways, Lv Peilin[1] et al. found based on observation data that during the process of shield tunneling under railways causing line settlement, subsequent settlement accounts for a relatively large proportion of the total settlement, and it takes a long time for settlement to reach stability; Du Hu[2] used a combination of finite element analysis and on-site practice to study and found that sleeve valve pipe grouting can be used to treat railway roadbed, set up pile isolation protection, and closely implement secondary grouting during shield tunneling through existing railways, which can effectively reduce the impact of shield tunneling; Huang Long[3] et al. conducted a study on the shield tunneling under the newly built railway of Ningbo Metro Line 1 and found that the shield tunneling construction had a relatively small impact on the deformation of the pile plate structure roadbed. The settlement of the pile plate structure after shield tunneling construction can meet the requirements of the specifications; Gao Zhigang[4] et al. conducted numerical simulation analysis based on the S8 line of the Nanjing Metro, and adopted foundation grouting reinforcement measures for the railway roadbed and dynamically adjusted construction parameters during shield tunneling, achieving the role of ensuring construction safety; Li Qi[5] et al. introduced the

*Corresponding author: sduyan_sh@163.com

DOI: 10.1201/9781003495505-294

use of D-beam reinforcement schemes and excavation parameter control techniques to control the settlement of shield tunneling through existing railways. Throughout the monitoring process, the settlement was less than the control value, proving the feasibility of the control technology; Sun Bo[6] et al. used the example of Qingdao Metro Line 2 crossing the Jiaoji Railway, and used ABAQUS to dynamically simulate the process of crossing the existing railway. They analyzed the settlement of ballasted and ballastless railways, and proposed that setting up a reinforcement area for grouting can reduce settlement by about 50% and reduce ground disturbance.

In terms of shield tunneling through reservoir embankments, Yuan Dajun[7] et al. relied on the Nanjing Yangtze River super large diameter mud water shield tunnel to study the disturbance mechanism and laws of mud water balance shield tunneling on soil at various stages; Cheng Xuewu[8] conducted research on the mud water balance shield tunneling through the Haihe River, summarizing the lateral and longitudinal settlement laws of the overlying soil layer of the tunnel, as well as settlement control methods; Zhu Muyuan[9] et al. analyzed the settlement law and characteristics of the large embankment section during the shield tunneling process, and proposed settlement control methods based on the Jinan Jiluo Road Yellow River Crossing Tunnel Project; Huang, J[1o] et al. used ABAQUS to numerically simulate the settlement caused by construction and study and control construction measures based on the Luoyang Metro Line 2 Undercrossing Luohe River Project; Zhang Xiaoyong[11] et al. analyzed the displacement law of the Yellow River embankment surface when the mud water balance shield tunneling passes through it, and studied the influence of different mud support pressure ratios on the stability of the excavation surface; Zhang Longbo[12] combined three-dimensional finite element analysis and Peck formula calculation, comprehensively considering factors such as tunnel burial depth and grouting, and introduced a correction coefficient α and β, The modified Peck formula obtained can more accurately predict the surface lateral settlement of large-diameter shield tunneling tunnels; Wang Xin[13] et al. used a finite difference program to conduct a three-dimensional model analysis of a super large diameter shield tunnel crossing a large embankment, and found that the shield tunneling had the greatest impact on the soil settlement of the embankment before reaching it. The main impact area of the embankment was from 1D outside the dam foot on the back surface (D represents the outer diameter of the tunnel) to 1.71D outside the dam foot on the upstream surface. However, there is still a lot of research space for the construction of double track tunnels with burial depths less than the diameter of shield tunneling studied in this article, as well as the impact of shield tunneling on existing railways and embankments.

This article first uses indoor model tests to explore the surface deformation situation, and compares and analyzes the experimental data with on-site measurements. The two are combined to study the control methods of surface deformation during large-diameter shallow buried shield tunneling construction, providing control methods and technical references for surface deformation caused by future large-diameter shallow buried shield tunneling projects.

2 PROJECT OVERVIEW

This study is based on the Jinan Jiluo Road North Extension Tunnel Project, which is a double track large-diameter slurry shield tunnel designed as a public rail joint construction. The double track tunnel starts 50 meters from the north bank of the Yellow River and crosses the Handan Jinan Railway. Then, less than 100 meters of excavation begins to penetrate the south bank embankment of the Queshan Reservoir, entering a continuous water section of 1550 meters. The total length of the shield tunnel section is 2040m. The project uses a shield tunneling machine with a diameter of 15.76m and an outer diameter of 15.2m for the shield tunnel segments. When crossing railway and reservoir embankments, the burial depth is 11.7m, and the distance between double track tunnels is about 12m. The geological conditions at the construction site are complex, mainly composed of silty clay and silt, accompanied by sand layers, calcareous nodules, etc. The reservoir area was once a village, and there are unexplored abandoned wells along the route, which poses a threat to shield tunneling construction. The reservoir embankment is 6-8 meters above the ground, with the highest water level about 6 meters above the ground. The bottom of the reservoir area is a thick layer of cohesive soil, and the surface of the reservoir embankment is covered with composite geomembrane. The dam foundation has a vertical plastic layer to cut off seepage. However, after 20 years of operation, the anti-seepage material of the dam body is partially damaged, resulting in varying degrees of leakage. Queshan Reservoir is an above ground regulation and storage reservoir, covering an area of 7.4 square kilometers with a net water supply of 400000 cubic meters per day. It is a centralized drinking water source for the Yellow River regulation and storage reservoir as well as Jinan City. The water source is a first-class protected area, so shield tunneling through railways and reservoir embankments requires extremely high settlement requirements.

Figure 1. Engineering plan diagram.

Figure 2. Schematic diagram of engineering profile.

3 TEST SIMULATION

This study used a 100:1 similarity ratio to scale down the engineering situation. The model experiment designed similar soil layers and tunnels, and used laser displacement meters to monitor and simulate surface deformation during shield tunneling. The size of the model test box was 1550 × nine hundred × 1000mm, the soil layer is taken by on-site small diameter earth pressure balance shield tunneling machine, the shield tunneling machine is made of 157mm outer diameter steel pipe, and the pipe segments are made of 152mm outer diameter PE material pipe. Based on the similarity ratio of size similarity ratio: C_L = 100:1 and bulk density similarity ratio: C_γ = 1:1, achieve full similarity in controlling various physical and mechanical parameters within the elastic range: similarity ratio of elastic modulus: C_E = 100:1, similarity ratio of bending stiffness: C_{EI} = $(100{:}1)^5$, similarity ratio of tensile stiffness: C_{EA} = $(100{:}1)^2$, Poisson's ratio, similarity ratio of internal friction angle: $C_\mu = C_\varphi = 1$. Permeability coefficient similarity ratio: C_K = 10:1. Given actual segment weight γ_p = $25kN/m^3$, elastic modulus $E_p = 31GPa$, elastic modulus PE (polyethylene) pipe $E_p = 0.55GPa$, acrylic elastic modulus $E_p = 2.7GPa$, then: (1) Simulate the similarity ratio of actual elastic modulus of shield tunnel: C_E = 31:0.55 = 56, outer diameter similarity ratio: 1570:15.7 = 100, inner diameter similarity ratio: 1390:13.9 = 100, pipe thickness similarity ratio: 650:6.5 = 100; (2) Model soil bulk density similarity ratio: C_γ = 1:1.

The shield tunneling adopts a casing pipe jacking method, using a large diameter pipe to simulate the cutter head of the shield tunneling machine. The pipe is pushed forward by hydraulic pressure, and a small diameter pipe is placed behind the large diameter pipe to simulate the tunnel lining. During the process of small diameter circular pipe jacking, rubber pipes are tied between the soil layer and the pipe segments, and water is injected into them. The grouting pressure can be controlled through water pressure simulation to simulate the deformation of the soil during the grouting process.

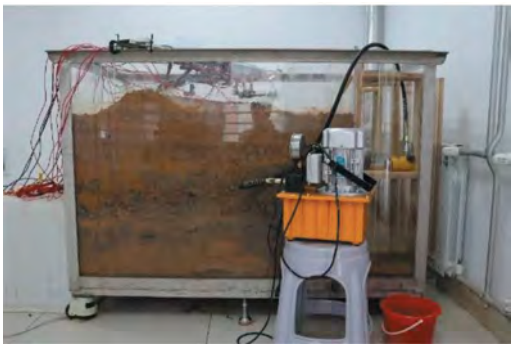

Figure 3. Model testing device.

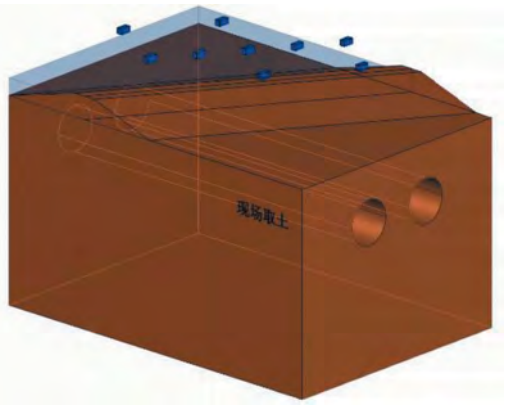

Figure 4. Schematic diagram of the layout position of the model test soil box and laser displacement meter.

The experimental process mainly includes: filling the soil box with on-site soil and compacting it, measuring the density of the soil layer to meet the requirements of similarity ratio; After the soil layer reaches its height, make an earth dam on the surface of the soil layer, and conduct a water storage test after compaction; Install laser displacement meters at the top and bottom of the dam; The reservoir area is filled with water, and after waiting for the water in the reservoir area to slowly seep into the formation, shield tunneling is started and real-time monitoring is carried out. Firstly, the drill bit is used to extract soil 50mm forward, then the shield cutter is used to insert 50mm into the top of the head, and finally the PE pipe tunnel model is pushed forward 50mm until the tunnel is fully penetrated.

4 TEST RESULTS AND ON-SITE MEASURED VALUES

4.1 *Model test results*

The monitoring results of the laser displacement meter at the dam crest during the model test are shown in Figure 5.

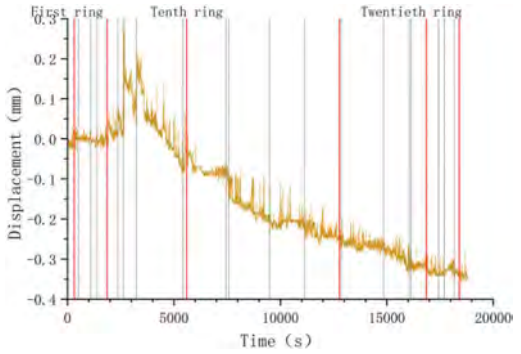

Figure 5. Model test results.

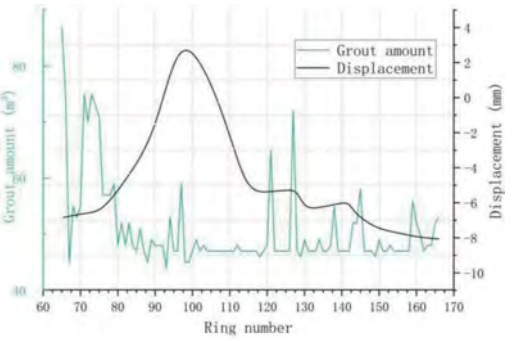

Figure 6. Dam monitoring results.

The model test results show that as the shield tunneling progresses, a partial uplift occurs at the top of the dam, and after the shield tunneling machine passes through, a settlement of about 0.1mm is generated, corresponding to a settlement of about 10mm on site. During the shield construction process, it is necessary to strictly control the shield tunneling speed and grouting amount, which will be discussed in detail in the following text.

4.2 *Dam monitoring results*

An electronic level is used for settlement monitoring on site, and a new method is adopted for on-site monitoring and testing, which is based on the micro pressure ground deformation area surface monitoring system and method. Multiple measuring lines including micro pressure sensors are laid on the surface to collect real-time water pressure values at each measuring point. After processing the pressure change data monitored by the micro pressure sensors, differential settlement values are obtained The settlement rate and settlement trend curve, based on the absolute coordinate elevation information of the initial point, calculate the relative settlement uplift deformation displacement of each measuring point based on the initial point, and then obtain the absolute deformation displacement value. The on-site monitoring points are arranged horizontally along the dam foot and crest, the on-site monitoring results of the embankment are shown in Figure 6.

The on-site monitoring results are similar to the model test results, with a protrusion of about 10mm first, followed by a settlement of 10mm. Finally, through settlement control measures, the overall settlement is about 1mm. The monitoring data of the electronic level deployed along the axis of the dam crest is shown in Figure 7, and the settlement trough caused by the single line shield tunnel conforms to the theoretical solution of the Peck formula.

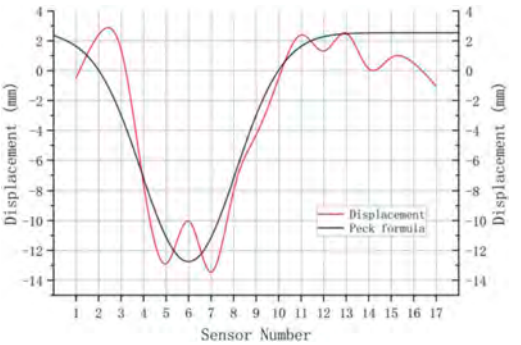

Figure 7. Comparison between the monitoring results at the top of the embankment and the Peck formula.

4.3 *Railway monitoring results*

Due to the extremely high requirements of railways for surface subsidence, detailed monitoring and control areas have been set up in the vicinity of the railway on site. The location relationship between the railway and the originating well, embankment, and Queshan Reservoir is shown in Figure 8.

Figure 8. Schematic diagram of railway protection area.

On site monitoring of the railway protection line using an electronic level, the deformation monitoring results of the railway track are shown in Figure 9.

The trend of railway monitoring results is similar to that of embankment settlement, with about 5mm uplift occurring first, followed by about 4mm settlement. The surface gradually rises over time, with a total uplift of about 1mm within 20 days. The overall settlement is smaller than that of embankments,

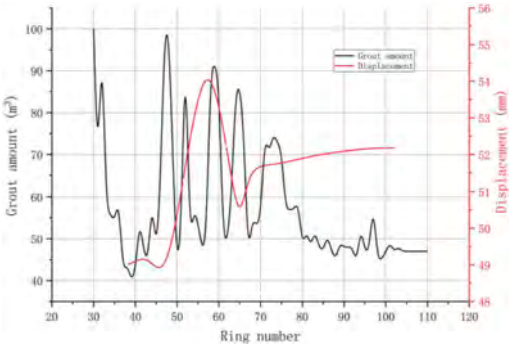

Figure 9. Monitoring results of railway settlement.

due to the use of more stable rail reinforcement methods by the railway to control surface uplift and settlement caused by shield tunneling.

5 SHIELD TUNNELING CONTROL METHOD

5.1 *Control of shield tunneling machine construction parameters*

The construction site adopts a 15.76m outer diameter mud water balance shield machine, which monitors real-time excavation parameters such as thrust, speed, torque, rotational speed, steering, rolling angle, as well as grouting parameters such as grouting amount and grouting position during the excavation process. At the same time, it monitors axis deviation and soil cover thickness. At the same time, real-time monitoring of the dam traversed by the shield tunneling is carried out on the construction site to adjust the construction strategy based on this.

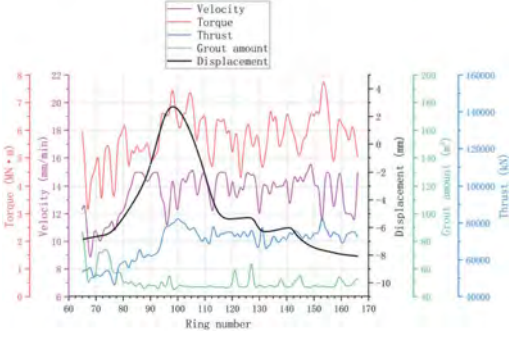

Figure 10. Settlement and excavation parameters at the top of the embankment.

According to on-site construction records, the crossing of the south bank of the reservoir embankment starts around 25 rings, which is about 50 meters from the start of the shield tunneling, and is completed around 150 rings, which is about 300 meters from the start of the shield tunneling. As the shield tunneling machine advances, due to the increase in tunnel burial depth and changes in soil layer, the thrust and torque of the shield tunneling machine gradually increase. Subsequently, due to the gradual fixation of burial depth, the shield tunneling machine moves forward parallel to the ground, and the thrust and torque of the shield tunneling machine gradually stabilize. During the process of crossing the embankment, the speed of the excavation machine is an average of 15mm/min, which is adjusted appropriately according to the soil layer situation.

During the shield tunneling process, two steps are mainly used for surface deformation control, namely synchronous grouting and secondary grouting. According to the trend of the change in grouting amount, it can be seen that during the process of shield tunneling machine passing through the dam, from ring 25 to ring 150, the grouting amount is significantly larger. By controlling the deformation of the dam top through grouting, excessive settlement can be prevented from causing the dam to collapse, leak, and other situations.

5.2 *Railway foundation reinforcement methods*

Due to its sensitivity to deformation, railways require special reinforcement. On site, the reinforcement of the cross section between the railway and shield tunnel was completed before the shield tunneling under the Handan Jinan Railway. The reinforcement of the strata was carried out using sleeve valve pipes and rotary jet grouting piles. The boundary of the reinforcement area is perpendicular to the railway line, with a minimum distance of 5m from the outer side of the shield tunnel, and the reinforcement depth is up to the arch of the shield tunnel. The specific reinforcement method is shown in Figure 11.

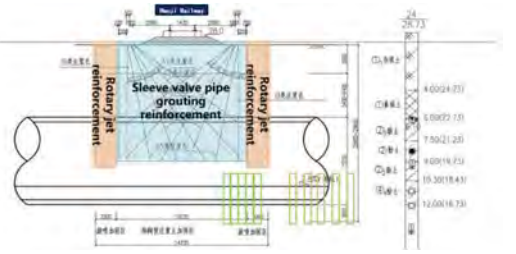

Figure 11. Schematic diagram of railway track reinforcement.

At the same time, in the reinforcement area, D-shaped temporary beams are used to erect railway tracks to prevent excessive settlement during shield tunneling through the railway, affecting railway traffic and even threatening the safe passage of trains. D-shaped temporary beams can ensure that shield tunneling does not interrupt the operation of the railway business line when passing under it. The relationship between D-shaped beam and fulcrum pile is shown in Figure 12. After actual testing, the deformation of the railway during the shield tunneling process has not

affected the opening of vehicles. At the same time, in order to prevent safety accidents, trains need to slow down during construction. The design speed of the Hanji Railway is 120km/h, starting from 800m away from the construction site. When it reaches the deceleration landmark, it slows down to 45km/h. After the tail of the train departs from the deceleration landmark on the other side, it starts to accelerate to the design speed.

Through the reinforcement of rotary jet grouting columns, the joint reinforcement of temporary beams and support piles, and the control of train speed during the passing process, various measures

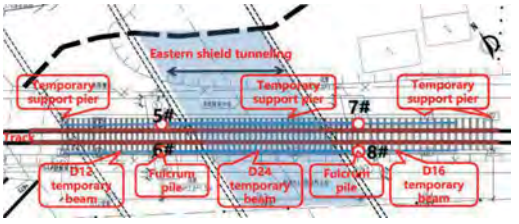

Figure 12. Layout plan of temporary beam and support Pile.

can be implemented together, which not only does not affect the normal operation of the railway, but also achieves the purpose of settlement control.

6 CONCLUSIONS

Based on model testing and on-site monitoring, combined with construction technology methods, the following conclusions have been drawn from this study:

(1) For surface settlement caused by large-diameter mud water balance shield tunneling, the deformation of the ground conforms to the concave settlement groove calculated by the Peck formula. The maximum settlement is located at the tunnel axis, and the settlement gradually decreases towards both sides. This proves that the indoor simulation method is more accurate and can accurately reflect the working conditions;

(2) Large diameter mud water balance shield tunneling, due to its significant disturbance to the soil and the tunnel depth being smaller than the diameter of the shield tunnel, has a significant impact on the surface without control, which can easily cause deformation and collapse of surface buildings. Therefore, it is necessary to reinforce the foundation of existing buildings. For example, in this study, the railway track is reinforced with rotary jet grouting in advance, and D-shaped beams are used to reinforce the railway track, which can control surface deformation, Simultaneously ensuring the normal passage of railways;

(3) For existing reservoir embankments, especially those discussed in this article that were constructed earlier and lacked soil information, settlement control can be achieved through monitoring and dynamic adjustment of grouting. By controlling the grouting pressure, monitoring the deformation of the dam, reducing the grouting pressure when the surface rises, and increasing the grouting pressure when the surface settles, surface deformation can be controlled and the risk of shield tunneling through the dam construction can be reduced.

REFERENCES

Lv Peilin, Zhou Shunhua, 2007. Analysis of the settlement law of the railway line caused by shield tunneling under the main railway line in soft soil areas. China Railway Science, 2007 (02): 12–16.

Du Hu, 2020. Research on the Technology of Shield Tunnel Crossing Existing Railways in Poor Strata Journal of Railway Engineering, 2020, 37 (4): 63–68.

Huang Long, Zhou Shunhua, Gong Quanmei, 2013. Research on the Foundation Treatment Plan for Shield Tunnels Undercrossing New Railways in Soft Soil Areas. Research on Urban Rail Transit, 2013, 16 (2): 56–61.

Gao Zhigang, Feng Chao, 2015. Analysis of foundation reinforcement during the construction of subway tunnels crossing existing railways. Research on Urban Rail Transit, 2015, 18 (06): 105–108.

Li Qi, Yan Fuhua, 2023. Safety technical measures and parameter control for shield tunneling through existing railways. Shanxi Architecture, 2023, 49 (19): 130–134, 188.

Sun Bo, Li Wenqiang, Li Suozai, etc, 2023. Deformation analysis of shield tunneling through existing railway subgrade tracks. Heilongjiang Transportation Technology, 2023, 46 (7): 129–132.

Yuan Dajun, Yin Fan, Wang Huawei, et al, 2009. Research on the Disturbance of Soil Mass Caused by Large Diameter Slurry Shield Tunneling. Journal of Rock Mechanics and Engineering, 2009, 28 (10): 2074–2080.

Cheng Xuewu, 2018. Numerical analysis of bottom settlement caused by mud water balance shield tunneling under the Haihe River. Railway Construction, 2018, 58 (10): 51–54.

Zhu Muyuan, Wei Lifeng, Fang Yong, et al, 2022. Analysis and control of settlement of a super large diameter shield tunnel crossing the Yellow River embankment. Modern Tunnel Technology, 2022, 59 (3): 211–219.

Huang J, Xu P, Huang Z., 2023. Settlement Analysis of Mud-Water Shield Passing Full Face Water Rich Sand and Cobble Stratum Under Luo River. Geotech Geol Eng (Dordr), 2023.

Zhang Xiaoyong, Liu Yongqiang, Ma Anzhen, et al, 2023. Stability analysis of mud water balance shield tunneling through the Yellow River embankment. Construction Technology (Chinese and English), 2023, 52 (3): 140–145.

Zhang Longbo, 2023. Analysis and Discussion on Surface Settlement Prediction Method for Large Diameter Shield Tunnel Construction. Tunnel and Rail Transit, 2023 (01): 45–48.

Wang Xin, Wang Xiaobo, Wang Yinchang, 2012. Numerical analysis of the influence of super large diameter shield tunnel crossing the embankment. Wuhan, Hubei, China: 2012.

Tunnelling for a Better Life – Yan, Celestino, Thewes & Eberhardt (Eds)
© 2024 The Author(s), ISBN 978-1-032-80042-4
Open Access: www.taylorfrancis.com, CC BY-NC-ND 4.0 license

Slaking characteristics of clay blocks and the influence of dispersant

Shuying Wang
School of Civil Engineering, Central South University, Changsha, Hunan, PR China
Tunnel and Underground Engineering Research Center of Central South University, Central South University, Changsha, Hunan, PR China
MOE Key Laboratory of Engineering Structure of Heavy Haul Railway, Central South University, Changsha, Hunan, PR China

Hanbiao Zhu*
School of Civil Engineering, Central South University, Changsha, Hunan, PR China
Tunnel and Underground Engineering Research Center of Central South University, Central South University, Changsha, Hunan, PR China

Pengfei Liu
CCCC Second Harbour Engineering Company Ltd., Wuhan, Hubei, PR China

ABSTRACT: Shield clogging is a common issue when tunneling through cohesive soil layers. Dispersants are frequently employed to disintegrate and disperse the clay adhered to the cutter head and cutters. This paper uses slaking tests to investigate the slaking characteristics of a mixed soil composed of kaolin and montmorillonite with different void ratios under the influence of dispersants and pure water. The results indicate the following: (1) Surface slaking is the primary process in mixed soil slaking, resulting in a slightly turbid solution and continuous peeling of clay debris from the clay block surface; (2) Influenced by the extent of the water-soil interaction area, the slaking percentage over time displays an "S" shaped curve; (3) The equivalent slaking thickness of clay blocks can better evaluate clay slaking characteristics in terms of size change. The equivalent slaking thickness gradually increases over time, followed by a steady acceleration, and it can be divided into the initial stable and rapid development periods. (4) With an increased void ratio, the initial stable period of mixed soil gradually shortens, and the slaking rate in the rapid development period first increases and then decreases. Dispersants can significantly shorten the initial stable period of mixed soil.

Keywords: Clay, Slaking characteristics, Void ratio, Dispersant

1 INTRODUCTION

When shield tunneling in cohesive soil, clay easily adheres to the cutterhead and cutters' surfaces. If not dealt with in time, under the influence of high temperature and consolidation, the clay will quickly solidify into tough mud cakes, blocking the cutterhead openings and seriously affecting the tunneling efficiency of the shield machine. To mitigate this issue, dispersants or dispersible foam agents are commonly injected into the shield machine's cutterhead and soil bin. These agents help disintegrate and disperse the mud cakes, detaching them from the cutterhead and cutters' surfaces (Du et al., 2022; Fang et al., 2022). An in-depth analysis of the slaking characteristic of clay is helpful for better carrying out the prevention and control of shield clogging.

In recent years, many scholars have researched the slaking characteristics of clay. Moriwaki and Mitchell (1977) conducted the slaking experiments on kaolin, illite, and montmorillonite, pointing out that soil slaking can be divided into four modes: swelling slaking, dispersion slaking, surface slaking, and body slaking. Swelling slaking is manifested as excessive expansion leading to loose clay structure and slaking; dispersion slaking is displayed as the dispersion of clay particles without macroscopic cracking; surface slaking is manifested as the continuous falling of debris and fragments on the surface of clay blocks; body slaking is displayed as the overall fracture of clay blocks. The mass variation curve of clay during the slaking process can be derived by monitoring the changes in the mass of clay blocks. Typically, this curve exhibits an 'S' shape. Li et al.(2019) and Wang et al. (2019) divided the slaking

*Corresponding author: zhuhanbiao@csu.edu.cn

DOI: 10.1201/9781003495505-295

process of loess into three stages: immersion, softening, and slaking, based on the variation curve of slaking. The softening stage is the main stage of clay slaking. According to the variation law of the slaking curve, multiple evaluation indicators of clay slaking can be obtained, such as the slaking rate in the middle section of the slaking rate curve(Wang et al., 2019), the slaking rate at 8 hours(Große et al., 2015), the time required for 30% of the soil mass to disintegrate(Große et al., 2015), the initial slope of the slaking rate curve(Lim, 2006), the average slaking rate(Yin et al., 2020; Ze et al., 2019), the relative surface area of the aggregate at 10 minutes of slaking(Jones et al., 2021), and the ratio of the final slaking rate to the slaking time(Wei et al., 2022), etc. However, there are currently no widely recognized evaluation indicators and methods for clay slaking, so it is necessary to analyze the slaking characteristics of clay in depth to better evaluate its slaking properties.

The types of forces that affect the slaking of clay are diverse, including electrostatic repulsive forces, expansion or hydration repulsion, pore pressure, and mechanical breakdown(Große et al., 2015; Hu et al., 2018). These forces can disrupt the connections between particles and cause clay slaking. At the same time, moisture content is also an essential factor affecting the characteristics of clay slaking. Ze et al.(2019) pointed out that the slaking rate of Moscow covering loam decreases with increasing moisture content. There is a "critical moisture content" above which the soil does not entirely slake. Robinson and Dasari(2004) studied the slaking characteristics of kaolin clay and found that soil blocks with moisture content close to the liquid limit are the most difficult to slake. In shield tunneling projects, the tunnel is often located below the groundwater level, and the saturated soil is the main geological layer that shield tunneling passes through. Saturated soil usually does not have matric suction, and the void ratio is one of the main factors affecting the structure of saturated soil. Therefore, the variation of void ratio may be one of the main reasons for the differences in saturated clay slaking characteristics, and there is currently little research on the influence of void ratio on clay slaking characteristics. In addition, factors that affect clay slaking also include clay matrix properties and solution properties(Wang et al., 2017), but the role of solution properties in existing studies is often overlooked. In the shield tunneling process, the dispersant is commonly used to treat the shield clogging by soaking it in the chamber, causing the mud cake in the dispersant to slake and disperse, and detach from the surface of the metal cutterhead (Du et al., 2022; Wei et al., 2022). Investigating the influence of dispersants on clay slaking helps prevent and treat shield clogging and deepens the understanding of clay slaking.

To deeply investigate the characteristics of clay slaking and the influence of dispersants, this paper first studied the slaking characteristics of the mixed soil blocks of kaolin and montmorillonite over time through slaking experiments. Then, based on the proposed equivalent slaking thickness, the slaking law of the mixed soil under the action of dispersants and pure water is explored under different porosity ratios.

2 EXPERIMENTAL RESEARCH

2.1 *Testing materials*

The mixed soil of kaolin and montmorillonite was used as a typical clay material. It comprises 10% montmorillonite and 90% kaolin, with a liquid limit of 54.43%, a plastic limit of 27.47%, and a plasticity index of 26.96. It belongs to high liquid limit clay, and its mineral composition is shown in Table 1. The commercial dispersant was used to study the effect of changes in solution properties on clay slaking, and their role in promoting clay slaking has been confirmed (Du et al., 2022; Liu et al., 2019). Chemical composition analysis showed that the main components of the dispersant are anionic surfactant sodium alkane sulfonate, combined with cationic surfactant Dodecyl trimethyl ammonium chloride, nonionic surfactant Polyethylene glycol (PEG500), and Lauryl Alkaline-8.

Table 1. Results of mineral composition analyzation.

Mineral name	Chemical formula	Mass percentage/%
Kaolinite	$Al_2(Si_2O_5)(OH)_4$	75.33
Muscovite	$KAl_{2.2}(Si_3Al)_{0.975}O_{10}((OH)_{1.72}O_{0.28})$	12.6
Na-montmorillonite	$Na_{0.3}(Al,Mg)_2Si_4O_{10}(OH)_2$	4.88
Soda feldspar	$NaAlSi_3O_8$	2.83
Quartz	SiO_2	2.32
Ca-montmorillonite	$Ca_{0.2}(Al,Mg)_2Si_4O_{10}(OH)_2$	1.41
Microcline	$(K_{0.95}Na_{0.05})(AlSi_3O_8)$	0.55
Calcite	$CaCO_3$	0.08

Table 2. Component analysis results of dispersants.

Component name	Characteristics	Mass percentage/%
Dodecyl trimethyl ammonium chloride	Cationic surfactant	1.5
Polyethylene glycol	Nonionic surfactant	1.5
Lauryl Alkaline-8	Nonionic surfactant	0.75
Sodium alkane sulfonate	Anionic surfactant	4.5
Water	Solvent	92.5

2.2 *Testing approach*

The slaking test is commonly used to evaluate the slaking characteristics of clay (Moriwaki et al., 1977; Qi et al., 2020), as it can intuitively observe the slaking features of clay blocks and obtain time-varying parameters for clay slaking. A new slaking apparatus (Figure 1) is used to study the law of clay block slaking. The slaking apparatus consists of an organic glass cylinder, a high-precision buoyancy scale (with an accuracy of 0.001g and a range of 500g), a mesh plate, etc. In the test, the clay block was placed on the mesh plate under the buoyancy scale, and the mesh plate and the clay block were immersed in the solution in the organic glass cylinder. The curve of clay slaking mass over time was obtained by collecting the readings of the buoyancy scale. The change in the reading of the buoyancy scale is mainly due to the slaked clay falling off the mesh plate and the decrease in buoyancy caused by the escape of pore bubbles in the clay block. When considering the correction of the buoyancy scale reading by the pore gas, it is usually assumed that the block mass and the pore gas are uniformly distributed (Zhang and Tang, 2013). Therefore, when the clay and pore gas of a certain buoyancy and volume detach from the block during slaking, their buoyancy accounts for a certain proportion of the total buoyancy of the clay and pore gas. In other words, the change in volume of the slaked clay block is proportional to the change in buoyancy (reading of the buoyancy scale). The slaking percentage of the sample can be obtained by applying Equation 1, and the slaking percentage represents the ratio of the slaked block's volume to the original block's(Tinebra et al., 2019).

$$A_t = \frac{R_0 - R_t}{R_0 - R_z} \times 100\% \qquad (1)$$

where: A_t is the slaking percentage (%) of the clay block at moment t; R_0 is the buoyancy scale reading at the beginning of the clay block slaking; R_t is the buoyancy scale reading at moment t of the soil block slaking; R_z is the buoyancy scale reading when the soil block is completely slaking.

Figure 1. The new slaking apparatus.

When the soil block is a polygon with corners, the corners disintegrate first, eventually leading the soil block to a more rounded shape (Moriwaki et al., 1977). To reduce the influence of shape changes during clay slaking, a cylindrical soil block with a radius (R) of 25mm and height (H) of 35mm was used for the slaking test. The mesh plate aperture is a key parameter determining whether the slaked unit falls off. The preliminary tests showed that surface slaking is the dominant mechanism for clay slaking, and the slaked unit was usually smaller than 5mm. In order to prevent the slaking unit from blocking the mesh plate aperture, the mesh plate aperture was set to 10mm according to relevant specifications(Yang and Wang, 1999). Furthermore, consistent with the Atterberg limit test(GB/T50123, 2019), the clay was fully compacted to remove air from the soil, and a fully saturated and uniform state was ensured for the soil blocks under different working conditions in the test. The specific test steps are as follows:

(a) A predetermined mass of dry clay was mixed with water to achieve a specified water content, w. After thorough mixing, the mixture was sealed and left undisturbed in a cool environment for 24 hours, allowing for uniform water distribution within the soil sample and the complete hydration of clay minerals.
(b) The compactor was placed on a rigid foundation. And the surface of the compaction meter hammer and base was covered with a layer of cling film to prevent clay adhesion.
(c) The soil sample was divided into four equal portions, added to a compaction mold, and then leveled. After each addition, a compaction hammer with a mass of 482.5g was dropped from a height of 26.5cm to compact the clay. The clay was compacted ten times on both the front and back sides, with enough compaction cycles to fully release the gas in the soil sample and ensure its saturation. The adjacent interfaces between each layer were roughed, and finally, a fully saturated and uniform test specimen was obtained.
(d) The soil block was pushed out of the compaction mold using a compaction hammer, and the volume and mass of the soil block were recorded. The soil sample's void ratio (e) and saturation (S) were measured using appropriate instruments or calculations.
(e) The glass cylinder was filled with the specified solution level for slaking. The buoyancy scale was zeroed, and then the soil block was placed in the center of the mesh plate and hung from the buoyancy scale. The mesh plate was quickly immersed in the solution, ensuring the clay block was positioned approximately 3cm below the water level. Photographs of the soil block's slaking state were taken at intervals of one minute or smaller, and the readings from the buoyancy scale were recorded. Enough readings were obtained to plot a continuous and smooth curve.

(f) The experiment concludes when the soil block has completely passed through the mesh plate.

The slaking test conditions are shown in Table 3, with three tests conducted for each condition. The obtained saturation of the soil samples in all conditions is greater than 95%. Therefore, it can be assumed that all the soil samples were fully saturated. And the experiment aimed to investigate the influence of different void ratios on clay slaking.

Table 3. The slaking test conditions.

Soil Types	Water content (w)/%	Void ratio (e)	Saturation (S)
mixed soil composed of kaolin and montmorillonite	27.47	0.754	0.969
	30.84	0.829	0.989
	34.21	0.909	1.000
	37.58	0.999	1.000
	40.95	1.089	1.000
	44.32	1.178	1.000
	47.69	1.268	1.000

3 ANALYSIS OF THE TESTING RESULTS

3.1 *Time-varying characteristics of clay slaking percentage*

Figure 2 shows a schematic diagram of clay slaking. It is evident that among the four slaking modes described by Moriwaki and Mitchell, namely, swelling slaking, dispersion slaking, surface slaking, and body slaking(1977), the clay blocks in the experiment mainly undergo surface slaking, with a slight dispersion slaking observed (the solution is slightly turbid). During the slaking process, the clay debris on the clay block surface continuously peeled off, gradually reducing volume. Figure 3 presents the variation curve of the slaking percentage of the clay blocks under different void ratios. Due to the abundance of recorded data, a continuous smooth curve is used to represent the clay slaking process. The slaking curve of the clay blocks generally follows an "S" shape. In the initial stage of slaking, there is no significant peeling of the clay debris. However, in some instances, such as when the void ratio of the clay block is 0.754 and the water content is relatively low, incomplete saturation of the block leads to a negative slaking percentage due to the release of air. As the soaking time of the clay block increases, the repulsive force between clay particles continues to develop, gradually offsetting the interparticle cohesive force, thus increasing the clay's slaking rate. When the slaking rate reached its maximum, the volume of the clay block decreased continuously, and the slaking rate decreased due to the reduction in the interaction surface area between the solution and the clay block. It can be observed that the surface area of the clay block constrains the development of the slaking curve. When the surface area is large, the water-soil interaction area is also large, resulting in a higher slaking rate. During the slaking process of the specimen, the surface area continuously decreases, making it difficult to reflect the essential characteristics of clay slaking through the variation of slaking percentage or slaking mass over time.

3.2 *Time-varying characteristics of the equivalent slaking thickness of clay*

Considering the influence of the contact area between soil blocks and solution on the slaking percentage, Equation (2) defines the d_t value as the ratio of the soil block slaking volume to the soil block's surface area at time t. Clearly, d_t represents the equivalent slaking thickness of the soil block during that period,

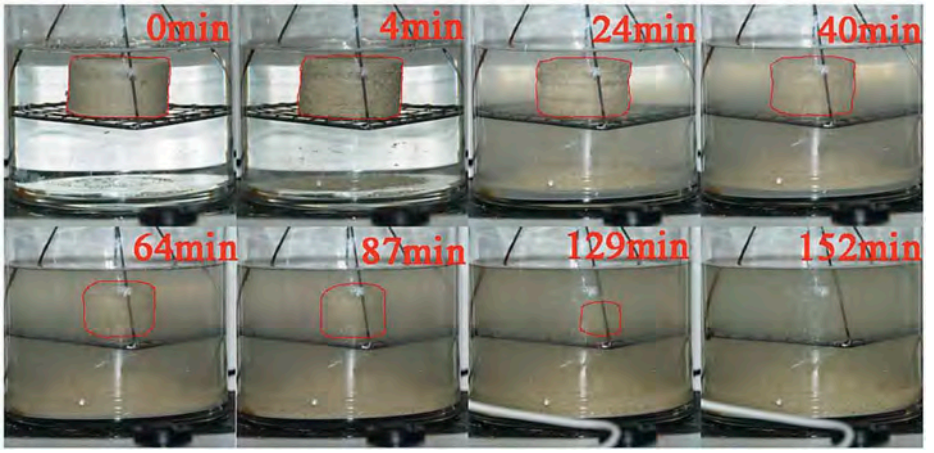

Figure 2. Schematic diagram of clay slaking.

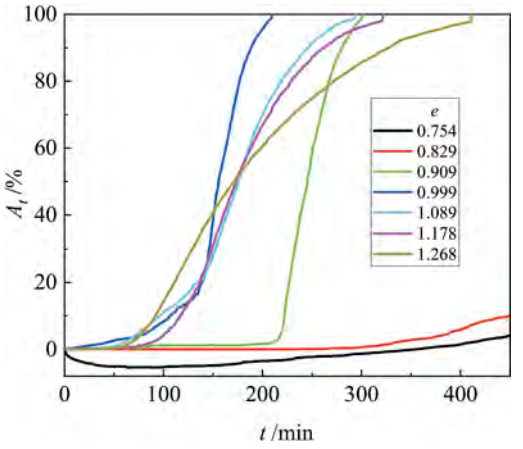

Figure 3. The change in the slaking percentage of the clay blocks over time with different void ratios under the action of pure water.

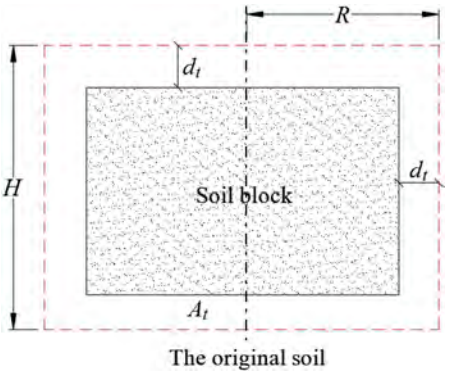

Figure 4. Schematic diagram of the axial section.

indicating the soil block's size change. It eliminates the influence of surface area changes on the characteristics of the slaking curve and better reflects the slaking law of the soil block. As discussed in section 3.1, the clay block follows a surface slaking mode, where the shape of the block remains changed little during the slaking process. Therefore, as shown in Figure 4, starting with the change in the equivalent slaking thickness of the clay, we assume that the slaking rate is the same at any position of the soil block surface. By equal slaking rate, Equation (3) was established to convert the slaking percentage At into the equivalent slaking thickness d_t of the soil block, representing the cumulative reduction in the size of the soil block during slaking.

$$d_t = \frac{V_t}{S_t} \tag{2}$$

where: d_t is the equivalent slaking thickness of the soil block at time t; V_t is the block volume slaked at time t; S_t is the surface area of the soil block at time t.

$$\frac{(H - 2 \times d_t) \times (R - d_t)^2 \times \pi}{H \times R^2 \times \pi} = 1 - A_t \tag{3}$$

where: A_t is the slaking percentage at time t; H is the original thickness of the soil block, with a value of 35mm in this study; R is the original radius of the soil block, with a value of 25mm in this study.

Figure 5 shows the changes in the equivalent slaking thickness of the mixed soil over time under the influence of pure water and dispersant. The change in the equivalent slaking thickness of the clay can generally be divided into two stages: the initial stable and the rapid development period. During the initial stable period, the solution infiltrates the clay pores, and the inter-particle connection force is gradually weakened under the action of the solution, causing the rate of change in the equivalent slaking thickness to increase gradually. After reaching the maximum change rate of the equivalent disintegration thickness, it enters the rapid development period, after which the rate of change in the equivalent slaking thickness of the clay remains unchanged. Meanwhile, since the height of the soil block is 35mm, the soil block is completely slaking when the equivalent slaking thickness d equals 17.5mm. When the size of the soil block is smaller than that of the mesh plate aperture, the direct fall of the soil block from the mesh plate causes a sudden change at the final moment on the slaking curve. In Figure 5a, the mixed soil with a small void rate was more difficult to slake under pure water than with a large void rate. When the void rate is less than 0.829, the initial stable period exceeds 7 hours, and as the void rate increases, the total slaking time of the clay first decreases and then increases. In Figure 5b, the action of the dispersant significantly accelerates the soil slaking. When the void rate is 0.829, the slaking of the mixed soil is the fastest.

3.3 *Analysis of slaking characteristics parameters*

The previous section revealed that the equivalent slaking thickness of the soil exhibits two stages: the initial stable and rapid development periods. Clearly, the pore ratio and dispersant have different effects and mechanisms on the soil slaking in these two stages. Therefore, to analyze the characteristics of these two time-varying stages, the initial stable period duration (t_0) is selected to characterize the initial stability of the soil, and the slaking rate (v_t) during the rapid development period is selected to represent the speed of slaking in this stage. As shown in Figure 6, the initial stable period duration refers to the time the soil undergoes before entering the rapid development period, and the slaking rate during the rapid development period represents the change rate in the equivalent slaking thickness in this stage, as shown in Equation (4). Specifically, when the soil sample exhibits block-like "splitting", the slaking curve before the occurrence of "splitting" is used as the basis for obtaining t_0 and v_t.

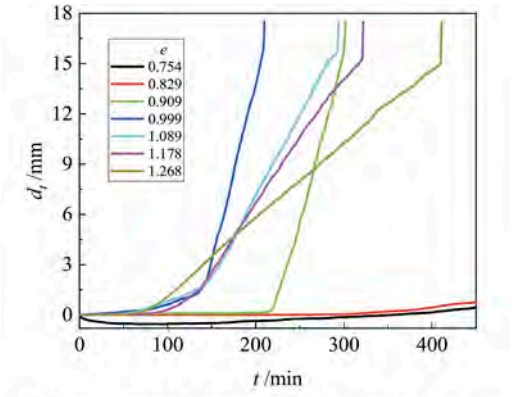

(a) Time-varying curve of the equivalent slaking thickness of the mixed soil under the action of pure water

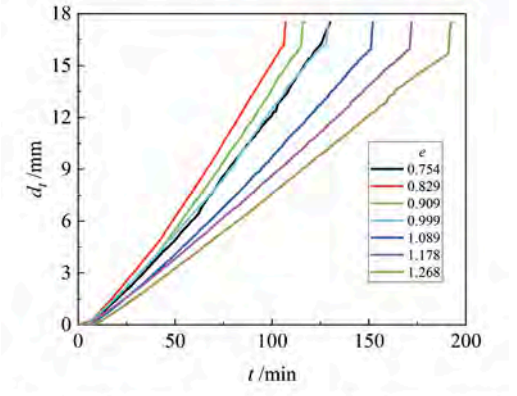

(b) Time-varying curve of the equivalent slaking thickness of the mixed soil under the action of dispersant

Figure 5. The change in the equivalent slaking thickness of mixed soil blocks slaking overtime under the different void ratios.

$$v_t = \frac{d_t - d_{t+\Delta t}}{\Delta t} \tag{4}$$

where: v_t is the change rate of equivalent slaking thickness at any given time t, d_t is the equivalent slaking thickness at time t (in mm), and $d_{t+\Delta t}$ is the equivalent slaking thickness at time t+Δt (in mm).

Figure 7 shows the variation of the initial stable period duration and the rapid development period slaking rate of the mixed soil under the action of pure water and dispersant. Since the void ratio is less than 0.829, the clay does not slake within 7 hours under the action of pure water, so there are no corresponding data points in the figure. Under pure water, as the void ratio increases, the interparticle bonding strength between clay particles decreases, resulting in a shorter initial stable period of the mixed soil. However, due to the synchronous reduction of clay slaking mechanisms such as expansion repulsion, the slaking rate during the rapid development period first increases and then decreases. In addition, compared to pure water, the surfactant in the dispersant reduces the solution's surface tension, accelerates the liquid infiltration into the clay block, and promotes the dispersion and

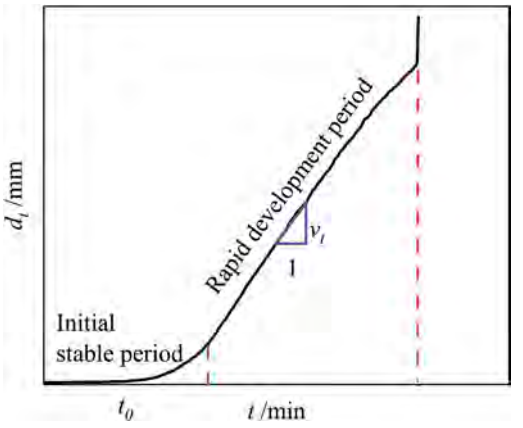

Figure 6. Schematic diagram for determining characteristic parameters of slaking.

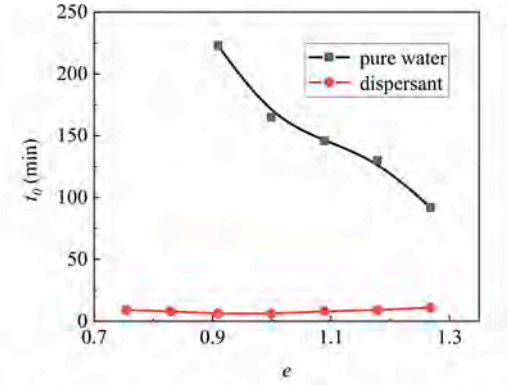

(a) Changes in the initial stabilization period duration of the mixed soil

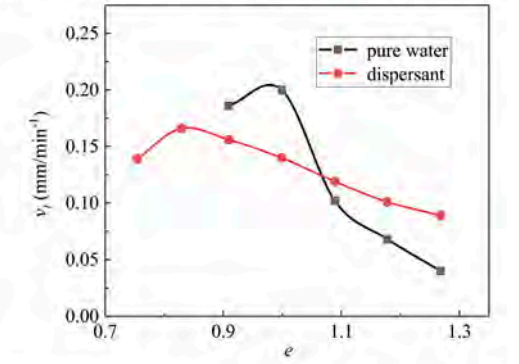

(b) Changes in the slaking rate during the rapid development period of the mixed soil

Figure 7. The change of the initial stable period and the slaking rate of the rapid development period of mixed soil over void ratio under different solutions.

slaking of the clay. Therefore, under the action of the dispersant, the initial stable period duration of the soil is significantly shortened, and it is less affected by the void ratio. The slaking rate during the rapid development period also shows a characteristic of increasing first and then decreasing with the increase of the void ratio.

4 CONCLUSIONS

This paper investigates the time-varying slaking characteristics of kaolin and montmorillonite mixed soil through slaking tests. Based on the proposed equivalent slaking thickness, the slaking patterns of the mixed soil with different void ratios under the influence of dispersants and pure water were explored. The main conclusions are as follows:

(1) Among the four types of slaking modes, the primary mode of mixed soil slaking is surface slaking, with the solution becoming slightly turbid and clay debris continuously peeling off the clay block surface during the process;
(2) Influenced by the extent of the water-soil interaction area, the slaking rate displays an "S" shaped curve over time. The equivalent slaking thickness of clay blocks can better evaluate clay slaking characteristics from the perspective of size change.
(3) The equivalent slaking thickness increases gradually over time and then steadily increases at a certain speed, and it can be divided into the initial stable and rapid development periods. Under pure water, the slaking of the mixed soil becomes more difficult when the porosity is small. With the increase of porosity, the slaking duration first decreases and then increases, while the dispersant can significantly accelerate the soil slaking.
(4) With the increased void ratio, the initial stable period of mixed soil gradually shortens, and the slaking rate in the rapid development period first increases and then decreases. Dispersants can significantly shorten the initial stable period of the mixed soil.

REFERENCES

Du C Y, Zhu H B, Wang S Y, et al, 2022. Test and application study on dispersion and disintegration of mud cake on slurry shield. Tunnel Construction, 42(05): 847–853. (in Chinese)

Fang Y, Yao Y, Song T, et al, 2022. Study on disintegrating characteristics and mechanism of cutterhead mud-caking in cohesive strata. Bulletin of Engineering Geology and the Environment, 81(12): 510.

Moriwaki Y, Mitchell J K, Sherard J L, et al, 1977. The role of dispersion in the slaking of intact clay. Dispersive Clays, Related Piping and Erosion in Geotechnical Projects, ASTM STP, 623: 287–302.

Li X A, Wang L, Yan Y, et al, 2019. Experimental study on the disintegration of loess in the Loess Plateau of China. Bulletin of Engineering Geology and the Environment, 78(7): 4907–4918.

Wang J, Gu T, Zhang M, et al, 2019. Experimental study of loess disintegration characteristics. Earth Surface Processes and Landforms, 44(6): 1317–1329.

Große A K, Cantré S, Saathoff F, 2015. The applicability of disintegration tests for cohesive organic soils. Journal of Environmental Engineering and Landscape Management, 23(1): 1–14.

Lim S S, 2006. Experimental investigation of erosion in variably saturated clay soils. UNSW Sydney.

Yin L J, Zhao F D, Liu Z Q, et al, 2020. Impact factors and mechanism of red sandstone disintegration. Rock and Soil Mechanics (S2): 1–12 (in Chinese)

Ze Z, Vadim P, Svetlana N, et al, 2019. Disintegration characteristics of a cryolithogenic clay loam with different water content: Moscow covering loam (prQIII), case study. Engineering Geology, 258: 105159.

Jones E J, Filippi P, Wittig R, et al, 2021. Mapping soil slaking index and assessing the impact of management in a mixed agricultural landscape. Soil, 7(1): 33–46.

Wei L F, Ye L B, Huang J Z, et al, 2022. Disintegration Characteristics of Mud Cake on Shield Cutterhead in Cohesive Strata. Tunnel Construction,42 (02): 275–282. (in Chinese)

Hu F, Liu J, Xu C, et al, 2018. Soil internal forces initiate aggregate breakdown and splash erosion. Geoderma, 320: 43–51.

Robinson R G, Dasari G R, Tan T S, 2004. Three-dimensional swelling of clay lumps. Geotechnique, 54 (1): 29–39.

Wang L Q, Shao S J, Lu Z G, 2017. Influence of physical properties on the initial structure of loess. Rock and Soil Mechanics, 38 (12): 3484–3490. (in Chinese)

Liu P, Wang S, Shi Y, et al, 2019. Tangential adhesion strength between clay and steel for various soil softnesses. Journal of Materials in Civil Engineering, 31 (5): 04019048.

Qi Y Z, Jiang P M, Liu X Y, et al, 2020. Influences of soil disintegration in water on slope stability. Chinese Journal of Geotechnical Engineering, 42 (S2): 214–218. (in Chinese)

Zhang S, Tang H M, 2013. Experimental study of disintegration mechanism for unsaturated granite residual soil. Rock and Soil Mechanics,34 (06): 1668–1674. (in Chinese)

Tinebra I, Alagna V, Iovino M, et al, 2019. Comparing different application procedures of the water drop penetration time test to assess soil water repellency in a fire affected Sicilian area. Catena, 177: 41–48.

Yang W H, Wang X J, 1999. Study on testing method of slaking property of expensive soil (rock). China Railway Science(1): 31–42. (in Chinese)

GB/T50123-2019, 2019, Standard for geotechnical testing method. Beijing: China Planning Press. (in Chinese).

Tunnelling for a Better Life – Yan, Celestino, Thewes & Eberhardt (Eds)
© 2024 The Author(s), ISBN 978-1-032-80042-4
Open Access: www.taylorfrancis.com, CC BY-NC-ND 4.0 license

Revealing inherent mechanism affecting loess-metal interface adhesion properties: Insights from macro- and atomic-scale tests

Bin Wu, Wen-Chieh Cheng* & Xue-Dong Bai
School of Civil Engineering, Xi'an University of Architecture and Technology, Xi'an, China
Shaanxi Key Laboratory of Geotechnical and Underground Space Engineering (XAUAT), Xi'an, China

ABSTRACT: Although previous studies have greatly enhanced our understanding regarding adhesion, the interplay of the loess with cutting tools is still not clear raising the potential of unplanned downtimes. In this study, three laboratory tests were applied to explore the inherent mechanism affecting the loess-metal interface (termed interface hereafter) adhesion properties, in which the sand-loess, kaolinite-loess, and montmorillonite-loess mixtures were considered. The pull-out and sliding plate tests were introduced to measure the normal and tangential adhesion forces at the interface, while the mixing test was used to determine the adhesion ratio of the soil mixtures. In addition, the atomic force microscopy (AFM) test was applied to investigate the surface morphology and adhesion characteristics. Results showed that the normal adhesion force at the interface is governed by the intermolecular force and the capillary tension. The flatter the contact interface, the easier the water ring development. The sand addition of 75% significantly reduced both the normal and tangential adhesion forces. Further, the adhesion ratio applied to the sand-loess mixtures remained below 0.4, indicating that the sand acted as an addition against interface adhesion. Apart from that, both the normal and tangential adhesion forces generally increased with increasing kaolinite and montmorillonite fractions. The adhesion ratio applied to the loess-kaolinite mixtures remained above 0.4, whereas it applied to the montmorillonite-loess mixtures remained way higher than 0.4. These results indicated that the kaolinite and montmorillonite are featured with a high adhesion potential and a high clogging anomaly possibility (soil consistency prior to its peak). Practitioners, while shield tunnelling, should be aware of groundwater intrusion preventing the montmorillonite-loess mixtures from turning into critical sticky materials.

Keywords: Soil adhesion ratio, Soil consistency, Tangential adhesion force, Normal adhesion force

1 INTRODUCTION

While tunnelling in the loess strata, the shield cutterhead is often adhered with the soil, and then the "mud cake" will be formed on the cutterhead after extrusion, which causes the clogging of the soil inlet hole on cutterhead. The formation of mud cake will cause the problems such as increased torque of cutterhead, slower tunnelling speed and tool wear, delaying the construction schedule. Therefore, accurate evaluation of the loess adhesion properties is essential in the development and utilization of underground space so that appropriate preventive and disposal measures can be taken.

A series of researches targeting soil adhesion characteristic have been carried out till now. Thewes et al. (1999, 2004, 2012, 2013, 2016) proposed several basic mechanisms which cause clogging of soil in shields, including adhesion, bridging, cohesion and insolubility, and concluded that adhesion is the main cause of clogging. The researches also related the adhesion risk to the consistency index of soil as well as plasticity index, and presented the empirical prediction plot for predicting the clogging risk, which provides a reference for subsequent researches. Fountaine et al. (1954), based on the study of the adhesion behaviour at soil-metal interface, concluded that interface adhesion occurs due to the cohesive force between soil particles being smaller than the soil-metal interface adhesion, and proposed two models of interface adhesion: the soil with low moisture content and large particles contacts the metal with the water rings, and the other is for soil with high moisture content and fine particles, in which the water rings between the soil particles and the metal

*Corresponding author: w-c.cheng@xauat.edu.cn

DOI: 10.1201/9781003495505-296

have linked to form a water film. As for laboratory tests, Zumsteg et al. (2013) put forward the mixing and plate shear test to quantify the adhesion and clogging behaviour of clay, and used these methods to further establish the relationship between adhesion and the soil physical properties, in particular the relationship between adhesion and soil strength. Then Oliveira et al. (2019a, 2019b) continued the research by proposing a simple laboratory test to characterize adhesion properties of cohesive soil, considering different soil components. Kang et al. (2019) evaluated the clogging potential with laboratory drilling test and semi-empirical plot, and found that bentonite samples have higher clogging potential than the pure kaolinite samples. In addition, Wang et al. (2020) carried out the plate shear test and investigated the variation rule of tangential adhesion strength of bentonite-kaolinite mixture with consistency index under different normal stresses. The test results showed that as the water content increased, the tangential adhesion strength first decreased significantly and then remained almost constant.

The normal adhesion force and the tangential adhesion force are usually not measured in a separate manner by the existing works, causing difficulty in exploring the role of intermolecular force and capillary tension in the change in normal adhesion force and tangential adhesion force. The above reveals several research gaps and shortcomings that remain to be addressed. The main objectives of this study are to (1) measure the normal adhesion force and the tangential adhesion force at the soil mixture-metal interface separately using the proposed pull-out and plate sliding tests respectively, and the adhesion ratio using the mixing tests; (2) explore the role of intermolecular force and capillary tension in affecting the interface adhesion properties; and (3) reveal further the adhesion reduction mechanism.

Table 1. Physical properties of the loess.

Natural moisture content (%)		17.3
Specific gravity G_s		2.6
Plastic limit (%)		21.2
Liquid limit (%)		33.9
Particle size distribution (%)	> 4.75 mm	0
	0.075~4.75 mm	5
	< 0.075 mm	95
USCS classification symbol		CL

2 TESTING MATERIALS AND METHODS

2.1 *Testing materials*

Loess that contains mainly silt particles and is widespread in Northwest China at a depth range of 4-5 m was taken from Lantian County, Shaanxi Province. The physical property parameters of the loess were summarized in Table 1. Since the loess is featured with 5% sand, 85% silt, and 10% clay and possesses a plasticity index of 12.75%, it was classed as low plasticity clay (CL) according to the Unified Soil Classification System (USCS). In this study, three additions, namely sand, kaolinite, and montmorillonite, were added to the loess forming the soil mixtures. The soil mixtures were applied to the pull-out, sliding plate, and mixing tests. The Atterberg limits of the soil mixtures are tabulated in Table 2.

2.2 *Methods*

The laboratory tests were designed as the pull-out, plate sliding and mixing test to measure the tangential and normal soil-metal interface adhesion forces and the adhesion ratio. The equipment of plate sliding test is shown in Figure 1(a), specifically a metal plate controlled by the hand winch to uniformly stabilized tilt 0-90°. And the tangential adhesion forces are measured with following steps.

Table 2. Atterberg limits of the soil mixtures.

Soil mixture	Sand or kaolinite or montmorillonite fraction (%)	Plastic limit (%)	Liquid limit (%)	Plasticity index (%)	Classification symbol
Sand-loess	25	19.9	32.4	12.5	CL
	50	17.5	27.4	9.9	SC
	75	16.6	24.7	8.1	SC
Kaolinite-loess	30	20.9	33.1	12.2	CL
	50	20.2	32.2	12.0	CL
	70	19.3	30.6	11.3	CL
	100	18.6	28.9	10.3	CL
Montmorillonite-loess	30	24.7	46.9	22.2	CL
	50	30.4	56.1	25.7	CH
	70	32.5	66.9	34.4	CH
	100	34.2	83.7	49.5	CH

(1) Firstly, configure the soil mixture at the preset moisture content and mineral fraction, then fill it into ring-shaped container with a jackhammer at the certain level of compaction;
(2) Subsequently, put the soil mixture on the metal plate and applied positive pressure for 60 s to ensure a certain degree of contact between the soil mixture and the metal plate;
(3) Remove the positive pressure, and slowly lift one side of the metal plate to make it tilt with a uniform speed until it stops when the soil mixture begins to slide. Then, record the tilt angle θ of the metal plate, and calculate by Equation 1 to obtain the tangential adhesion strength at the soil-metal interface.

$$\alpha_\tau = 4mg \cdot \sin\theta/\pi D^2 = 4F_\tau/\pi D^2 \quad (1)$$

where, α_τ is the tangential adhesion strength at the soil-metal interface (Pa); m is the mass of the soil mixture and the container (kg); g is the acceleration of gravity (9.8 N/kg); θ is the inclination angle of the metal plate when the soil mixture starts sliding (°); D is the contact diameter of the soil mixture (m); F_τ is the tangential adhesion force at the soil-metal interface (N).

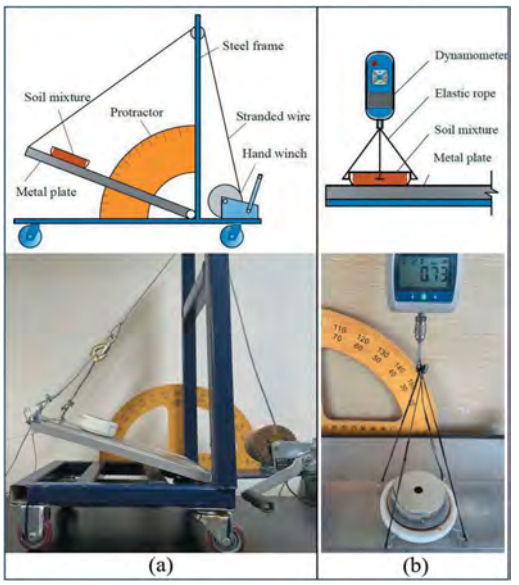

Figure 1. Proposed apparatus applied to the loess-metal interface adhesion tests: (a) plate sliding test and (b) pull-out test.

The operation of the pull-out test used to measure the normal adhesion force at the soil-metal interface is shown in Figure 1(b). The soil mixture was prepared in the same way as described above and positive pressure was applied for 60 s. Subsequently, the elastic rope was driven by a dynamometer to lift the soil mixture at a constant slow speed until the sample was detached from the metal plate. Recording the maximum value measured by the tensiometer and the gravitational force of the soil mixture, the normal adhesion force at the soil-metal interface can be obtained by Equation 2. In addition, the friction coefficient tanδ between the soil mixture and the metal can be calculated from the measured tangential and normal adhesion forces, as shown in Equation 3.

$$\alpha_n = 4(F_{\max} - mg)/\pi D^2 = 4F_n/\pi D^2 \quad (2)$$

$$\tan\delta = F_\tau/(mg \cdot \cos\theta + F_n) \quad (3)$$

Where, α_n is the normal adhesion strength at the soil-metal interface (Pa); $F_{\max}$ is the maximum tensile force indicated by the dynamometer (N); F_n is the normal adhesion force at the soil-metal interface (N); tanδ is the interfacial friction coefficient between the soil mixture and the metal plate.

An apparatus applied to the mixing tests is depicted in Figure 2. The mixing tests measured the masses of soil mixtures adhered to the agitator, which reflected the soil adhesion characteristics from a more macro perspective. The soil mixtures were stirred with the agitator at a constant rate and time. Then the agitator was dropped from the same height for seven times, weighing the adhered soil after each falling. The soil adhesion ratio can be calculated with Equation 4 and 5.

$$\lambda_x = G_{MTx}/G_{TOT} \quad (4)$$

$$\overline{\lambda} = (\lambda_0 + \lambda_1 + \lambda_2 + \lambda_3 + \lambda_7)/5 \quad (5)$$

Where, G_{MTx} is the adhesion mass of soil after dropping x times (g); G_{TOT} is the total mass of soil (g); $\overline{\lambda}$ is the average adhesion ratio.

The microscopic atomic force microscopy (AFM) test was also carried out to characterize the three-dimensional morphology of the loess, kaolinite, and montmorillonite sample surfaces, and to measure the adhesion force between the metal probe and the soil particles, which was used to reveal the adhesion mechanism between the soil mixture and the metal.

The testing scheme is shown in Table 3. The adhesion tests applied to the soil mixtures of 200 cm^3 take the effect of addition fraction and soil consistency into account at the normal pressure of 2 kPa. Each test is repeated three times, ensuring repeatability.

Figure 2. Apparatus applied to the mixing tests.

Table 3. Testing scheme applied to the adhesion tests.

Soil mixture	Sand or kaolinite or montmorillonite fraction (%)	Consistency index	Normal pressure (kPa)
Sand-loess	0\25\50\75	1.2\1.0\0.8\	2
Kaolinite-loess	10\30\50\ 70\100	0.6\0.4\0.2\0	
Montmorillonite-loess	10\30\50\ 70\100		

3 RESULTS AND DISCUSSION

3.1 *Results of sand-loess mixture*

When subjected to a sand fraction being 0%, the normal adhesion force first increases with increasing moisture content (I_c = 0 equal to the liquid limit and I_c =1 equal to the plastic limit) and then decreases after reaching a peak (see Figure 3a). The maximum normal adhesion force is generally attained at I_c = 0.4. In case the moisture content of the loess cannot provide conditions favourable for developing water rings, the loess-metal interface contact falls into intergranular, meaning that intermolecular forces play major parts in developing the normal adhesion force. By contrast, when the moisture content is high enough, water rings are present with the interface frictional coefficient (e.g., 0.2-0.6) developing closed spaces between soil particles. Capillary tension accompanies the closed spaces' formation. When subjected to the pull-out effect, the capillary tension builds up, causing a substantial increase in the normal adhesion force. As the moisture content surpasses a threshold that corresponds to I_c = 0.4, the water rings transform to a water film. The higher the moisture content, the lower the capillary tension, and the lower the normal adhesion force. Despite that, the soil shear strength lower than the interface adhesion strength is deemed as the root cause leading to a decline in the normal adhesion force when subjected to I_c < 0.4. The maximum normal adhesion force is shifted to the left to a place where I_c is about zero when subjected to a sand fraction equal to 50%. When subjected to a sand fraction of 75%, the normal adhesion force remains at approximately zero, irrespective of I_c, in which the interface frictional coefficient falls within a 0.6-0.7 range (see Figure 3c). On the whole, the normal adhesion force generally increases with increasing sand fraction, with the exception of a sand fraction equal to 75%. When subjected to a sand fraction of 75%, intermolecular forces play major parts in developing the normal adhesion force. The water rings accompany the interface frictional coefficient varying in a 0.2-0.6 range and help develop the capillary tension toward promoting the normal adhesion force development. By contrast, the water film prevents the capillary tension from developing impeding the normal adhesion force development.

Similarly, the tangential adhesion force first increases with increasing moisture content (I_c = 0 equal to the liquid limit and I_c =1 equal to the plastic limit) and then decreases after reaching a peak (see Figure 3b). The maximum tangential adhesion force is generally attained at I_c = 0.6. The maximum normal adhesion force due to the interface frictional coefficient differs from the maximum tangential adhesion force. Despite that, the soil shear strength lower than the interface adhesion strength is considered to be the root cause that explains the formation of a reduction in the tangential adhesion force when subjected to I_c < 0.6. Apart from that, the adhesion ratio decreases with increasing sand fraction, and the lowest adhesion ratio is attained at a sand fraction of 75%. meaning that the higher the sand fraction applied, the lower the adhesion ratio, and the lower the potential of interface adhesion (see Figure 3d).

3.2 *Results of kaolinite-loess mixture*

The normal adhesion force first increases with increasing moisture content and then decreases after a peak is attained at I_c = 0.4. Water rings are not present at the interface when the moisture content of the loess remains at lower levels (corresponding to I_c = 1 to 1.2) (see Figure 4a). Under such a circumstance, intermolecular forces dominate the normal adhesion force development. The water rings accompany the moisture content high enough and help develop the capillary tension toward contributing to the normal adhesion force formation. It can also be seen from Figure 4c that a reduction in the interface frictional coefficient to 0.2 helps develop the capillary tension. As the moisture content of the loess is in excess of a threshold that corresponds to I_c = 0.4, the water film forms, thereby impeding the capillary tension and normal adhesion force developments. This also tallies with the formation of a decline in the normal adhesion force when subjected to I_c < 0.4. Apart from that, the normal adhesion force increases notably when the kaolinite fraction > 10%. To summarize, the normal adhesion force in general increases with increasing kaolinite

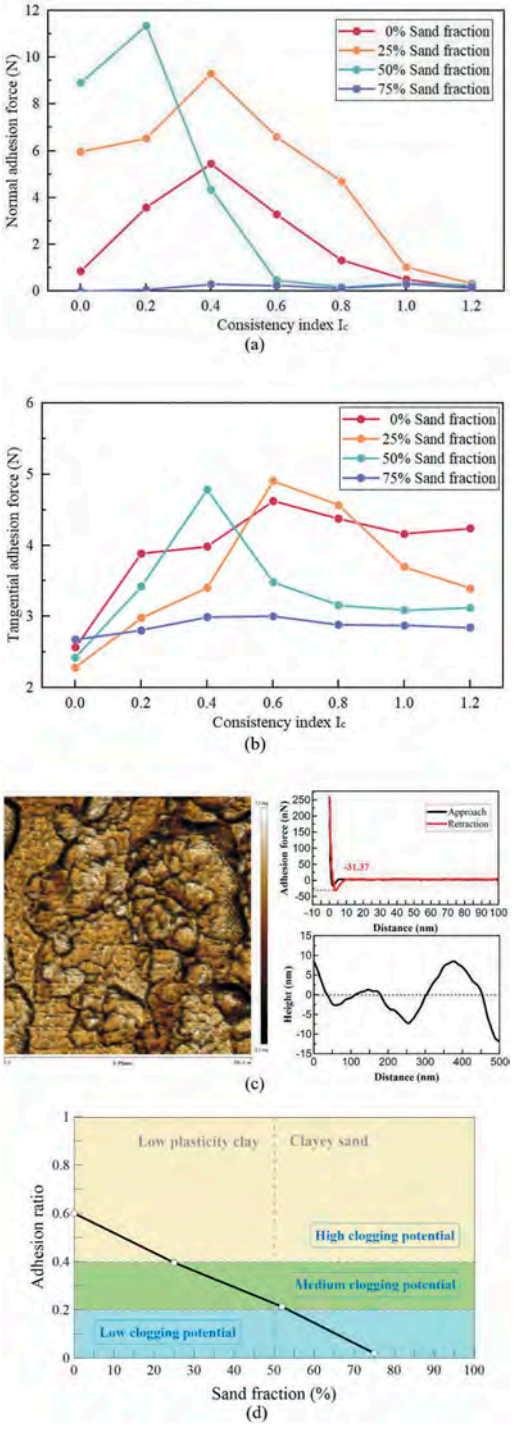

Figure 3. Results applied to the sand-loess mixture: (a) normal adhesion force, (b) tangential adhesion force, (c) AFM test, and (d) adhesion ratio.

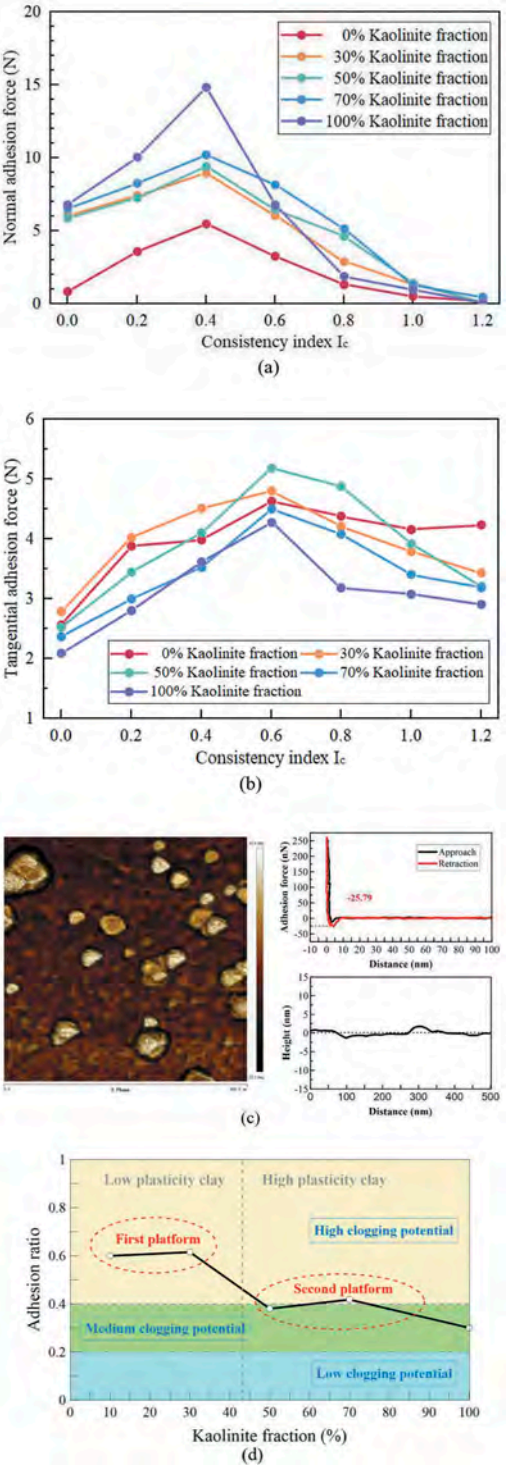

Figure 4. Results applied to the kaolinite-loess mixture: (a) normal adhesion force, (b) tangential adhesion force, (c) AFM test, and (d) adhesion ratio.

fraction. The water rings accompany the interface frictional coefficient of approximately 0.2 promoting the normal adhesion force formation, whereas the water film prevents the capillary tension from developing impeding the normal adhesion force formation.

The tangential adhesion force increases in the first place with increasing moisture content and then decreases after a peak that corresponds to $I_c = 0.6$ is attained (see Figure 4b). The maximum normal adhesion force links to the maximum tangential adhesion force using the interface frictional coefficient. Notwithstanding that, the soil shear strength lower than the interface adhesion strength is considered the main contributor to a sharp decline in the tangential adhesion force when $I_c < 0.6$. Furthermore, a reduction in the tangential adhesion force is noted as well when the kaolinite fraction surpasses 50%. Moreover, the adhesion ratio of above 0.4 is measured, although the tangential adhesion force reduces when subjected to the kaolinite fraction > 50% (see Figure 4d). These results lead us to conclude that the adhesion ratio remains above 0.4 when the kaolinite addition intervenes in shield tunnel excavations. When subjected to $I_c < 0.6$, a sharp decline in the tangential adhesion force occurs. Although the water film prevents the capillary tension from developing, the soil shear strength lower than the interface adhesion strength is the main contributor to a substantial drop in the tangential adhesion force. As a result, the kaolinite addition raises not only the interface adhesion potential but also the clogging anomaly possibility. I_c prior to its peak aggravates further the clogging anomaly possibility.

3.3 *Results of montmorillonite-loess mixture*

Similarly, the normal adhesion force goes up initially with increasing moisture content and subsequently goes down after a peak that corresponds to $I_c = 0.2$ is attained (see Figure 5a). Water rings do not develop at the interface as the moisture content remains at lower levels (e.g., $I_c = 1$ to 1.2). In this case, intermolecular forces, in turn, play major parts in the normal adhesion force development. The water rings form along with the moisture content at high levels and help develop the capillary tension, contributing to the normal adhesion force formation. A reduction in the interface frictional coefficient to 0.2 provides testimony supporting the above claim (see Figure 5c). As the moisture content of the loess goes beyond a threshold (i.e., $I_c = 0.2$), the water film forms, preventing the capillary tension and normal adhesion force from developing. A slight decline in the normal adhesion force, when subjected to $I_c < 0.2$, shows good correspondence with the said phenomenon. On the other hand, the normal adhesion force increases dramatically when the montmorillonite fraction > 50%. In short, the normal adhesion force increases with increasing montmorillonite fraction. The water rings form along with the interface frictional coefficient of approximately 0.2 encouraging the normal

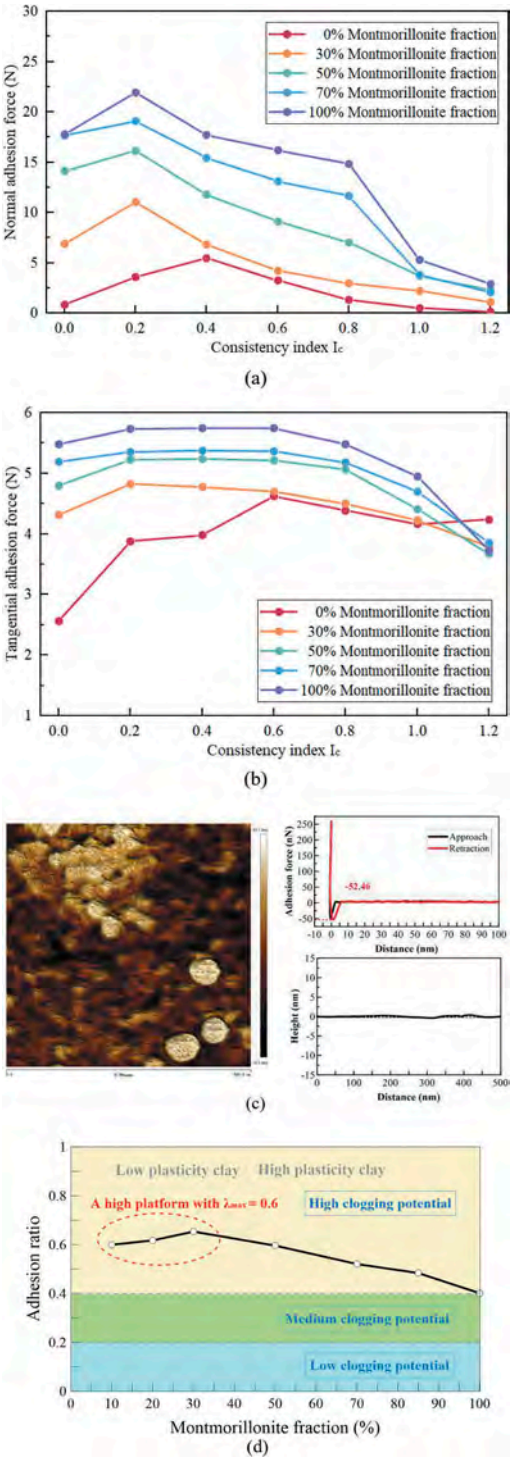

Figure 5. Results applied to the montmorillonite-loess mixture: (a) normal adhesion force, (b) tangential adhesion force, (c) AFM test, and (d) adhesion ratio.

adhesion force formation. While the water film prevents the capillary tension from developing causing difficulty in forming the normal adhesion force.

The tangential adhesion force increases in the first place with increasing moisture content and then decreases after a peak that corresponds to $I_c = 0.2$ is attained (see Figure 5b). The interface frictional coefficient explains the fact that the maximum normal adhesion force differs from the maximum tangential adhesion force. However, the soil shear strength lower than the interface adhesion strength is the main contributor of forming a decline in the tangential adhesion force when subjected to $I_c < 0.2$. Unlike the said two mixtures, the tangential adhesion force increases all the way with increasing montmorillonite fraction. Further, the adhesion ratio way above 0.4 is measured when the montmorillonite addition intervenes in tunnelling activities. Therefore, the montmorillonite addition more significantly lifts up the interface adhesion potential in comparison with the kaolinite addition and the clogging anomaly possibility. I_c prior to its peak further intensifies the clogging anomaly possibility.

4 CONCLUSIONS

According to the results of the pull-out, sliding plate, and mixing tests applied to the soil mixtures, some main conclusions can be drawn as follows:

(1) The loess-metal interface normal adhesion force is affected by the intermolecular force and the capillary tension. While the tangential adhesion force at the loess-metal interface links to a combination of the normal adhesion force and the interface frictional coefficient. The moisture content of the soil mixtures high enough helps develop the water rings and capillary tension promoting the normal adhesion force formation. The interface frictional coefficient varying in a 0.2-0.6 range supports the above claim. The water film develops as the moisture content of the soil mixtures surpasses the threshold. It prevents the capillary tension from developing toward impeding the normal adhesion force formation.

(2) The sand addition of 75% dramatically reduces both the normal and tangential adhesion forces. Furthermore, the adhesion ratio applied to the sand-loess mixtures remains below 0.4. These results show that the sand can act as an addition against interface adhesion. Apart from that, the normal adhesion force goes up with increasing kaolinite fraction, although the tangential adhesion force goes down with increasing kaolinite fraction in some circumstances. The adhesion ratio applied to the kaolinite-loess mixtures remains above 0.4, indicating that the kaolinite cannot act as an addition against interface adhesion. I_c prior to its peak intensifies the clogging anomaly possibility as well.

(3) Both the normal and tangential adhesion forces increase generally with increasing montmorillonite fraction. This is especially pronounced when the montmorillonite fraction is in excess of 50%. Further, the adhesion ratio remains way higher than 0.4, indicating that the montmorillonite cannot act as an addition against interface adhesion. Moreover, the montmorillonite-loess mixtures are featured with not only the highest adhesion potential but also the highest clogging anomaly possibility (when I_c prior to its peak). Therefore, practitioners should be aware of groundwater intrusion while tunnelling, preventing the montmorillonite-loess mixtures from turning into critical sticky materials.

REFERENCES

ASTM D2487-17, 2017. Standard Practice for Classification of Soils for Engineering Purposes. ASTM International, West Conshohocken, PA, USA.

Fountaine E. R., 1954. Investigations into the mechanism of soil adhesion. Journal of soil science, 5(2), 251–263.

Hollmann F. S., Thewes M., 2013. Assessment method for clay clogging and disintegration of fines in mechanised tunnelling. Tunnelling and Underground Space Technology, 37, 96–106.

Kang C., Wu Y., Yi Y., Bayat A., 2019. Assessment of the clogging potential of two clays. Applied Clay Science, 178, 105134.

Oliveira D. G. G., Thewes M., Diederichs M. S., 2019. Clogging and flow assessment of cohesive soils for EPB tunnelling: Proposed laboratory tests for soil characterisation. Tunnelling and Underground Space Technology, 94, 103110.

Oliveira D. G. G., Thewes M., Diederichs M. S., 2019. EPB machine excavation of mixed soils–Laboratory characterisation. Geomechanics and Tunnelling, 12 (4),373–385.

Thewes M., 1999. Adhesion of clays during tunnelling with slurry shields. PhD Thesis. University of Wuppertal, wuppertal, German.

Thewes M., Burger W., 2004. Clogging risks for TBM drives in clay. Tunnels & Tunnelling International, 36(6).

Thewes M., Hollmann F., 2016. Assessment of clay soils and clay-rich rock for clogging of TBMs. Tunnelling and Underground Space Technology, 57, 122–128.

Thewes M., Budach C., Bezuijen A., 2012. Foam conditioning in EPB tunnelling. Geotechnical Aspects of Underground Construction in Soft Ground, 127.

Wang S., Liu P., Hu Q., Zhong J., 2020. Effect of dispersant on the tangential adhesion strength between clay and metal for EPB shield tunnelling. Tunnelling and Underground Space Technology, 95, 103144.

Zumsteg R., Plötze M., Puzrin A, 2014. Reduction of the clogging potential of clays: new chemical applications and novel quantification approaches. Bio-and Chemo-Mechanical Processes in Geotechnical Engineering: Géotechnique Symposium in Print 2013. ICE Publishing, pp. 44–54.

Tunnelling for a Better Life – Yan, Celestino, Thewes & Eberhardt (Eds)
© 2024 The Author(s), ISBN 978-1-032-80042-4
Open Access: www.taylorfrancis.com, CC BY-NC-ND 4.0 license

Challenges and solution of super large diameter TBM tunnel construction in urban center

Xiaochun Xiao*, Lei Jiao & Yong Li
Shanghai Tunnel Engineering Co. Ltd, China

ABSTRACT: With the super large diameter TBM tunnel construction expanded from river-crossing passage to urban central expressway, new challenges would be inevitably encountered. Taking Shanghai Beiheng Expressway Package II which being opened now as an example, lots of technical difficulties and challenges including slurry TBM with diameter of 15.56m negotiating tight S curves, mining through all kinds of buildings and under-crossing live metro lines during the 6.4km tunnelling journey were introduced. To overcome the mentioned challenges, technical solutions such as TBM tailored design, lining special consideration, construction risk control measures etc. were adopted. The super large diameter TBM had negotiated 4 tight S curve sections with minimum plane radius of 500m merely, tunnelled through 89 buildings, and under-crossed 3 live metro lines successfully. The project results revealed that the quality of the tunnel was excellent, the max. ring ovality was 5cm and ring steps were less than 6mm, and disturbances to the environment, namely the ground subsidence, buildings tilt and live metro tunnels displacement were precisely controlled within the criteria, the max. rail displacement was 12.58mm which was less than specified criteria. The experience and data gained in this project could provide valuable references for similar projects in future.

Keywords: Slurry TBM, Super large diameter, Sensitive environment, Tight S curve, Tunnel through buildings, Under-cross metro tunnel

1 INTRODUCTION

In recent decades, more than 30 super large TBM tunnels whose diameter were bigger than 14m were constructed successfully in China, and the achievements gained in this field attracted worldwide attention. With the rapid development of TBM tunnel construction technologies and the growing needs of city development, extra-large TBM tunnel was gradually being expanded from river/sea crossing passage to urban centre expressway. TBM construction in urban centre indicated a more sensitive and limited construction environment, rules of 'precise control, stable balance and slight disturbance' must be followed, and new challenges would be inevitably encountered. Shanghai Beiheng Expressway Project (hereafter referred as BEP) was one of the above mentioned typical examples.

To make Shanghai move, a '3 Horizontal plus 3 Vertical lines' expressway skeleton net was being planned and developed. As north horizontal line of it, BEP started from Beihong interchange of Middle ring in west and ended at the Neijiang road in east, refer to Figure 1. It run through 5 urban central districts with total span of 19.1km, and 8 pairs of ramps were arranged along the route. The traffic flow of Middle ring and North-south elevated road was further reduced by interconnecting with BEP.

BEP was designed with combination of tunnels, elevated roads, flyovers and underpasses etc., and tunnel with length of 14.7km including 12km bored tunnels and 2.7km C&C was the main portion of the project. The single tube bored tunnel with outer and inner diameter of 15.0m and 13.7m respectively accommodated double decks, dual-way 6 lanes with design speed of 60km/h to serve motorcars, refer to Figure 2. The TBM tunnels were divided into 6 sections by 8 shafts and excavated with 3 slurry TBMs with 15.56m excavation diameter each.

BEP package II (hereafter referred as BEP II) was about 8km fully underground section constructed by Shanghai tunnel engineering Co.ltd, consisting of 2 tunnel drives in middle portion and 2 C&C sections at both ends, refer to Figure 1. The BEP II was completed successfully and opened to public on 18 June 2021.

Grand item of BEP II, the two tunnel drives namely section 1&2 in Figure 1 were constructed with one slurry TBM supplied by Herrenknecht. The TBM was

*Corresponding author: xxchstec@163.com

DOI: 10.1201/9781003495505-297

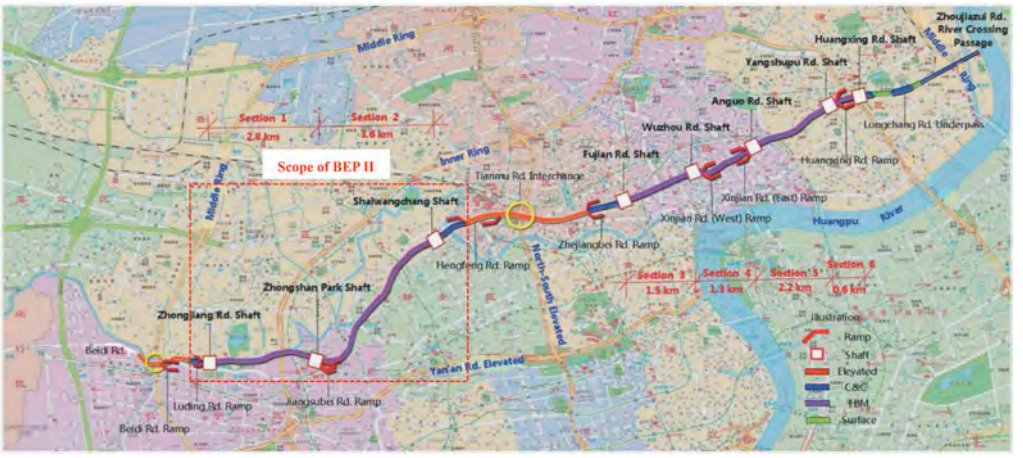

Figure 1. General layout of BEP in Shanghai part print map.

launched from Zhongjiang Rd. shaft on 26 December 2016, and received in Zhongshan park intermediate shaft on 23 December 2017, and completed the 1st drive after 2761m eastward excavation in one year. Then moved by 72m and launched again on 10 June 2018 in middle shaft. After 3665m eastward drive, the TBM finally entered into Shaiwangchang shaft on 28 October 2019 and completed the 2nd drive.

Figure 2. Bored tunnel cross section.

2 FEATURES AND CHALLENGES OF BEP II

Compared with other large diameter tunnel, one of notable features was that the BEP II tunnels run along densely residential and commercial corridor. The tunnel route passed through a large number of structures including buildings, flood retaining walls, subway system and utilities. During the crossing process, adverse factors such as tight S curves, low overburden, and unfavorable soil strata were also encountered. Such large-scale and high-risk crossings with mega TBM were unprecedented events worldwide. All these made the project known as "A cyclopedia of TBM underground boring through". The main features and challenges of BEP II were described as follows:

2.1 *Tight S curves*

Referring to the definition in Chinese code, the tunnel alignment could be defined as tight S curve if its radius was smaller than 300m for metro tunnel, while 40 times of tunnel diameter for large section tunnel. As for BEP, its excavation diameter was 15.56m, so the threshold for tight S curve alignment in this project was R= 602.24m. Accordingly, the tight curve section accounted for 44.8% in the 1st drive and 57.9% in the 2nd drive. The distribution of the curve sections in the 2nd drive was shown in Figure 3.

Tight curve excavation would lead to severe problems such as big steps of segmental lining rings, tail skin wear by segments, failure of the tail seal due to uneven tail skin gap, and the scraping of the inner lining by the TBM backup gantries etc.

2.2 *Tunnelling through buildings*

As per defined effect zone along the tunnel route, 89 buildings fallen within it, including residential blocks, commercial offices and historical monuments etc., and 30 ones were above the tunnel crown and 59 ones were the case of tunnel passed within close proximity. To ensure buildings safety, the disturbance of the saturated soil strata caused by the tunnel construction must be strictly controlled within specified criteria. This was the most challenge issues faced by the construction teams.

2.3 *Under-crossing live metro lines*

The BEP II intersected with rail transit at 5 locations, namely line 15 (in planning), line 3(4), line 11, line 14 (in planning) and line 7 from west to east. For

Figure 3. Curve sections distribution in 2nd drive.

case of line 3 (4) which was an elevated viaduct, TBM passed by the pile foundation with horizontal clearance of 18m, the risk was therefore relatively low. On the other hand, while BEP under-crossed line 11 and 7, the vertical clearance was only 7m. It was the first time that a 15m diameter TBM crossed beneath a metro tunnel with such small clearance, and no references could be provided.

3 TIGHT S CURVES EXCAVATION

Aiming at the technical difficulties and challenges of such tight S curves excavation with super large TBM, researches focused on the TBM selection, segment special design and risk control measures were carried out.

3.1 *TBM selection and design*

To reserve certain safety margin, the TBM adaptability was designed based on alignment curve with minimum radius of 350m. Generally, for the curvature tunnel construction, the articulated shield TBM was preferred. Thus, 3 options of shield design including passive articulation, active articulation and fixed tail skin were proposed. The shield design was governed by the load case of 36m overburden plus additional 6-story building overload. Under this condition, the radial shield deformation at the articulation would be more than 10cm, and no strengthening measures could be taken because of the articulation. Leakage of the articulation seal would therefore be inevitable. Based on comprehensive analysis and in-depth review, STEC and Herrenknecht concluded that a shield with a fixed tail skin was the only solution for BEP II.

In order to increase the TBM ‘s flexibility and decrease the friction between TBM skin and the ground soil, the large diameter TBM was designed to be conical. For the BEP II TBM, diameters of the front shield, middle shield and tail shield gradually decreased by 3cm respectively, and the overall conical volume was 90mm.

In addition, 4 nos. of copy cutters were equipped on the cutter edge. The extension was calculated based on curvature of the alignment. The maximum extension of the copy cutter was 50mm, corresponding to the curve with radius of R=300m.

After adopting the above measures, the selected TBM flexibility was significantly increased and met the requirements to negotiate specified tight curves. However, this caused severe disturbance on the soil strata. In this project, the TBM would tunnel through a large number of sensitive structures. In order to ensure low disturbance and safety of structures, the grouting system including synchronous grouting with 10 points, shield injection system and secondary grouting was also designed specially.

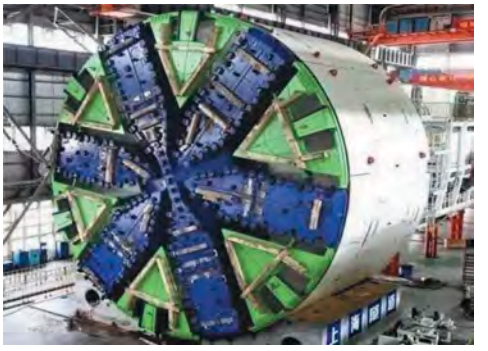

Figure 4. The TBM used in BEP II.

3.2 *Segment lining design*

For the extra-large diameter shield tunnel, universal segment lining and staggered assembly were always used. In case of tight curve simulation, segment taper and width were two important parameters to be considered. Generally, the segment taper was determined empirically based on factors of alignment curve radius, ring width, tail skin clearance and manufacturing etc. At the beginning of design stage, two types of universal segmental lining with segment width of 1.5m and 2.0m were comparatively studied, as shown in Table 1.

Referring to Table 1, comparison analysis showed that unique ring width had obvious advantages. Using 2m ring width would be beneficial to construction efficiency, tunnel quality and cost control. Instead, to fit the tight curve sections, the segment taper needed to be optimized based on 2m width. According to the statics data of previous large-diameter shield tunnels in Shanghai, most taper size

Table 1. Optimal analysis for different segment width.

No.	Items	Segment width (m)		
		1.5	1.5+2.0	2.0
1	Rings	4285	2339 (for 2.0m) 1460 (for 1.5m) 3799 in total	3214
2	Ring build efficiency	Low	Moderate	High
3	Joints	Maximum	Moderate	Minimum
4	Segment molds	①One type of mold. ②8 sets molds	①Two types of molds for various width. ②4 sets for 1.5m + 3 sets for 2m	①One or two type for various tapers. ②6 sets for 2m
5	TBM design	①Shortest shield tail, small tail skin clearance ②Erector: 1set	①Longer shield tail, more tail skin clearance required ②Erector:2 sets	①Longer shield tail, more tail skin clearance required ②Erector: 1 set

was 40mm, and the maximum was 80mm. Considering TBM tailskin clearance was 50mm, a variety of taper size (ranged from 40mm to 100mm) were used for DTA fitting analysis using 3-D numerical simulation model. When the fitting deviation was relatively small, two taper sizes of 40mm and 80mm (double-side tapered) were proposed. The 80mm taper size corresponded to the ring wedge slope of 1:375 (theoretical turning radius of 375m), which met the R=500m tight curve construction requirements. Based on above analysis and calculation, rules of segmental ring layout were determined as per Table 2.

Table 2. Rules of segmental ring layout.

Axis curve (m)	Ring width (m)	Arch radius R (m)	Taper (mm)
R<1000	2.0	375	80
R>1000	2.0	750	40

In addition, the gasket water resistance experiments had been carried out for tight curve cases. Important parameters were obtained to ensure the segment joints waterproof.

3.3 *Tight curved section construction*

In total, the length of the tight curved sections of BEP II was 2842m, which included the launching, receiving and normal drive sections. The construction records showed that, except for the launching and receiving sections, the average production rate reached 5.2r/d, and the peak value was 9r/d. All tight curved sections had been completed with high quality, ring joint openings was less than 5mm and maximum axis horizontal deviation was controlled within 9mm.Taking the first tight S curve as example, it started at ring No.555 and ended at ring No.631 in 1st drive. There were 77 rings in total. The construction duration was 13 days, and construction rate was 5.9r/d, and the maximum construction rate reached 8 r/d.

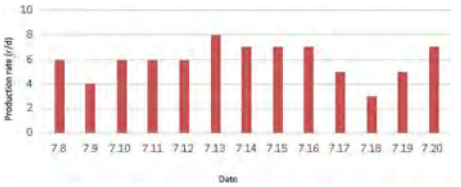

Figure 5. Production rate of 1st tight curved section.

With the aid of efficient planning and rigorous construction management, the time of excavation and segment assembly accounted for 70%. Considering the factors such as interruption and transportation, the construction efficiency reached 80%.

(a) Turn left (b) Turn right

Figure 6. Tight curved tunnel photos.

4 TUNNELLING THROUGH BUILDINGS

4.1 *Influence zone definition*

Firstly the influence zone along the tunnel route need to be determined to confirm the affected structures and buildings because of tunnel excavation. In

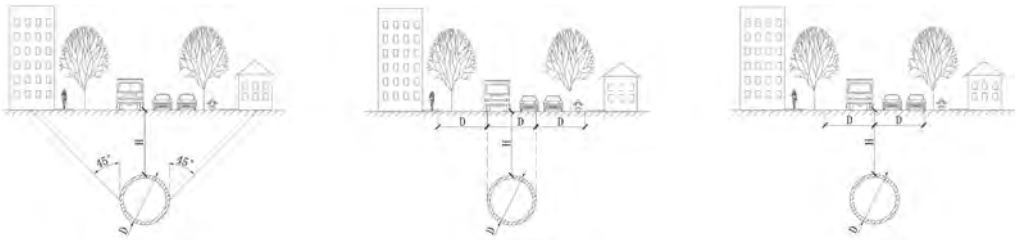

Figure 7. Influence zone definition for different cases.

terms of extra-large TBM construction influence zone, no regulations were specified in China. To formulate the construction method statement, 3 different cases listed as follows were studied and reviewed,

(1) case a, the 45°lines from both sides of the tunnel waist
(2) case b, 1D offset from each side of the tunnel edges
(3) case c, 1D offset from tunnel centre line at both sides

refer to Figure 7 for details.

According to above 3 cases, the numbers of buildings within influence zone were 173, 137 and 89 nos. respectively. Considering safety, society stability and construction cost issues, referring to previous experiences, case c was preferred as the influence zone. For BEP II, the TBM diameter was 15.56m, which meant that it had an influence zone with width of 31.12m along the tunnel route. Based on this criteria, BEP II affected 89 buildings, which the TBM under-crossed 30 buildings and side passed 59 buildings within the tunnelling influence zone in the 2nd drive.

4.2 *Risk assessment*

Extra-large TBM tunnelling through buildings was a typical multi-factor issue. With reference to previous engineering experience, the main parameters affecting the buildings' safety included TBM equipment, geology condition, building structure conditions, tunnel alignment, and level of the construction team etc.

For the same project, the equipment and construction team were fixed, so the risk of tunnelling through buildings was basically determined by the conditions of the soil stratum, building structures, and the tunnel alignment. Reference was made to similar projects, especially the experiences gained from the 1st drive, 6 factors were selected in the risk assessment model. Sorting by importance, they were overburden, foundation type, structure type, crossing pattern (under-crossing or passing by), structural status, tunnel alignment respectively. The risk of tunnelling through buildings could be calculated as function of the above 6 factors. The importance of each factor was expressed by weight coefficient. Thus, the risk value for TBM tunnelling through one building could be expressed as:

$$F = \sum_{i=1}^{7} \alpha_i \bullet F_i \qquad (1)$$

Where, F was the gross risk value; F_i was the risk value of a certain factor; α_i was the weight coefficient of a certain factor, and the sum of all the 6 factors' weight coefficient should be 1.0.

Each factor was specifically categorized into three levels, i.e., high, moderate and low risk. In order to distinguish the risk level in number, risk estimates of each level were assigned as score of 10, 5 and 1 respectively, which denoted high risk, moderate risk and low risk respectively, as listed in Table 3.

As per formula (1), the risk of TBM tunnelling through 89 buildings within influence zone could be evaluated case by case. Based on the risk assessment results, risk management strategies and control measures for all cases were classified into 3 groups ranked grade I to III representing high risk, moderate risk and low risk respectively. Different prevention and risk control strategies were adopted for corresponding risk cases, refer to Table 4 for details.

4.3 *Risk management for high risk cases*

According to Table 4, 26 buildings involved with high risk (grade I) were the main focuses and challenges in BEP II. For these cases, to ensure the effectiveness of risk prevention measures, the risk resources for every high risk case were identified firstly, then composite measures targeting the major risk resources were tailored designed for the case. Some of the risk sources and corresponding methods for high risk cases were listed in Table 5. Taking case of TBM tunnelled through Zhaofeng villa F (3-6) as example, major risk resources were listed as shallow foundation, tight curve alignment, thin overburden, and risk control measures including automatic building monitor, early strength grouting, highest contingency response level were recommended.

Table 3. Risk scores for different factors.

Factor	Rate	Description	Score
Overburden (H)	Shallow	H <1 5m	10
	Normal	15m < H < 25m	5
	Deep	H > 25m	1
Foundation	No foundation	Including independent column foundation	10
	Shallow foundation	Strips or raft foundation	5
	Deep foundation	Pile foundation	1
Structure type	Brick-concrete, masonry	Multi-layer buildings	10
	Concrete frame	Most high-rise buildings	5
	Core tube (shear wall) structure	High-rise and sky scrapes	1
TBM crossing pattern	Under-crossing	Distance < i	10
	By-pass	i< distance < 2i	5
	Beyond influence	Distance > 2i	1
Building conditions	High risk	Age > 30ys, inclination more than 10‰, cracked	10
	Moderate risk	30ys>age> 10ys, inclination 5~10‰, moderate cracked	5
	Low risk	Age < 10ys, small inclination less than 5‰	1
Tunnel Alignment	Tight curve	R < 600m	10
	Normal curve	600m < R < 1000m	5
	Transition or straight line	R > 1000m	1

Table 4. Risk classification and risk management strategy.

Range	Risk grade	Buildings	Risk management strategy
6.5~10.0	I (High)	26 nos. (29.21%)	General measures for tunnelling through structures + special measures.
4.0~6.5	II (Moderate)	42 nos. (47.19%)	General measures for tunnelling through structures.
1.0~4.0	III (Low)	21 nos. (23.60%)	Treat as normal situation.

4.4 *Construction results*

In the 2nd drive, the TBM tunnelled through 89 buildings totally, and the section between ring 45 to ring 155 right after the initial drive was the worst case. In this 220m section, the tunnel alignment was a R500 tight curve with 3.8% downward slope. The overburden was 10.2-23.5m which belongs to thin overburden. The TBM tunnelled through 10 buildings including Zhaofeng villa (7 buildings), Xunfa Apartment (2 buildings) and No.330 Huayang Rd. (1 building) etc, refer to Figure 8. All these buildings were shallow foundation, and Zhaofeng villa group was the historic preserved buildings with age of over 80 years. According to the risk assessment, they were cases of grade I, and measures of automatic monitoring, arly strength grouting, highest contingency level were adopted. The buildings displacement time history curves from TBM mined into the influence zone to 1 month after TBM left the building were depicted in Figure 9.

Table 5. Risk source identification and control measures for high risk buildings.

No.	Building	Risk sources	Recommended measures
1	Zhaofeng villa F(3-6)	Shallow foundation + Tight curve + Shallow overburden + Under crossing	Automatic monitor + Early strength grouting + Highest contingency response level
2	Shanghai public administration center (7)	Shallow foundation + Tight curve + Under-crossing	Automatic monitor + Shield grouting + Highest contingency response level
3	Rixu Business Center (18)	Shallow foundation + Tight curve + Under-crossing	Automatic monitor + TBM Shield grouting + Highest contingency response level
4	Galaxy Securities(22-1)	Shallow foundation + Under-crossing	Automatic monitor + Shield grouting + Highest contingency response level
5	No.234 Changning Rd (25)	Shallow foundation + Tight curve + Under-cross	Shield injection + Highest contingency response level
6	No.487 Yuyao Rd(50-1)	Shallow foundation + Tight curve + Under-crossing	Automatic monitoring + Shield grouting + Highest contingency response level
7	Yaoxi Community(50-3)	Shallow foundation + Tight curve + Under-crossing	Automatic monitoring +Shield grouting + Highest contingency response level

Learning from Figure 9, it could be known that due to the relatively shallow overburden, the house appears to heave between TBM cutter head entered the influential zoon and the shield tail left. In this stage, the maximum displacement was 12mm. After the tail left, the building started to sink down. The maximum absolute

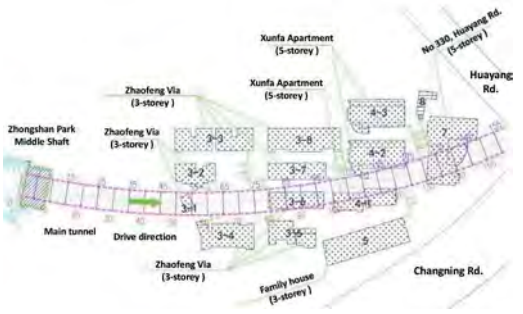

Figure 8. Plan of 2nd initial drive.

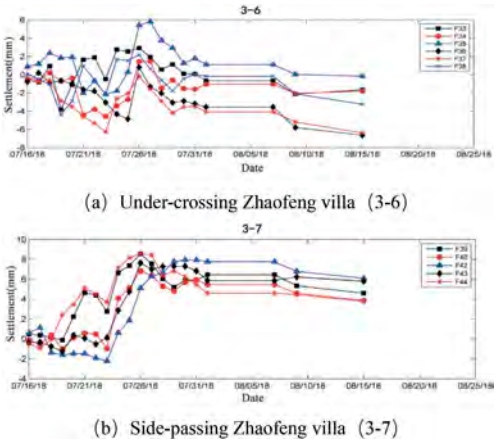

Figure 9. Settlement curve of Zhaofeng villa.

subsidence was -7mm (1 month after tail shield left). During the whole under-crossing process, the buildings were relatively stable. For both cases of under-crossing and by-passing, the max. differential settlement of the buildings was less than 10mm. Even if the old structures such as Zhaofeng villa were so fragile, there no unfavorable conditions such as structure cracks occurred.

To date, the TBM tunnelled through 89 buildings in 2nd drive successfully without any incidents reported. Instrumentation results revealed that all structures were well controlled within the allowable deformation and settlement criteria (-20mm~ +10mm). During tunnelling through, the buildings were heaved slightly first, and then followed by gradually falling back after the shield had left, and the subsidence would converged 6 months later.

5 UNDER-CROSSING LIVE METRO LINES

5.1 *General*

Among the three cases of tunnelling through live metro lines, the TBM first crossed the viaduct of line 3 (4), and then under-crossed metro lines 11 and 7 both with about 7m clearance. The cases of passing through metro line 11 and 7 were much more challenge and quite similar, so case of line 11 was introduced as an example in this paper.

Referring to design tunnel route, the TBM would under-cross metro line 11 between chainage K5+915 and K5+943 (ring 386 to 400 of 2nd drive) which was in the vicinity of Changning road and Jiangsu north road intersection. The intersection angle between two tunnels was 68 degree. The overburden of metro Line 11 and BEP II were 20.8m and 34.6m respectively with a clearance of 7.06m, the alignment of the BEP II was a R=500m tight curve in plane. Metro Line 11 located within ⑤$_1$(Grey silty clay) layer and covered with ① (Filled), ②$_1$(Brown yellow grayish yellow clay), ③(Grey muddy silty clay), ④(Grey mucky clay) soil layers above the tunnel crown and BEP II tunnel located within ⑦$_2$ (Straw grey silty fine sand) layer, ⑦$_1$ (Straw-grey silt) layer at the tunnel crown and ⑧$_{1\text{-}1}$ (Grey clay) layer at the invert. There was a 4m layer of ⑥(Dark green silty clay stiff clay) in between two layer tunnels. Details were illustrated in Figure 10, 11.

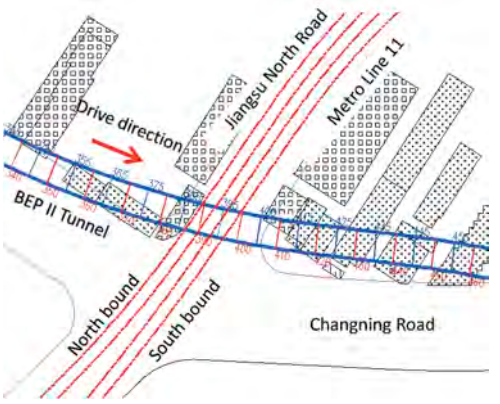

Figure 10. Plane of BEP tunnel and metro line 11 intersection.

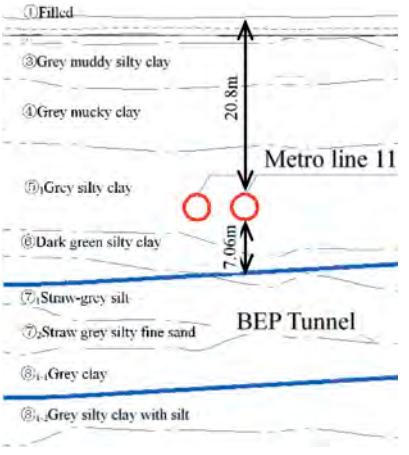

Figure 11. Cross section of the intersection.

Construction of under-crossing live metro lines faced lots of technical difficulties and challenges including: (1) no similar experiences could be provided; (2) the protection standards for the metro tunnel were not specified; (3) BEP II tunnel's alignment was R=500 tight curve; (4) it also under-crossed lots of buildings and utilities at this intersection.

5.2 *Metro tunnel displacement control criteria*

In view of the fact that displacement control criteria for the large-diameter TBM tunnelling through metro tunnel under such conditions were not defined. At the early stage of scheme design, previous cases were investigated and summarized in detail, including other under-crossing metro tunnel cases and the BEP II's TBM performance of tunnelling through buildings. Considering the geological and environment condition at the intersection, lots of special expert consultations were held. Criteria of the metro tunnel allowed displacement were agreed and defined as -20mm~ +20mm for both cases of line 11 and 7.

5.3 *Construction organization*

To avoid accidents especially big impact to the rail traffic caused by TBM mining construction, some experts and government officials suggested shutting down the metro system during under-crossing construction. After in-depth evaluation, it was considered that the train outage would lead a great impact on the society, especially in the later stage, the situation of large TBM mining through live rail transit will occur frequently in other projects. Thus, in the process of scheme demonstration, two options were put forward on the premise that the train did not stop operation, i.e. intermittent drive and continuous drive. A detailed comparison was carried between the two options, and the option 2 was selected eventually. Considering the vibration influence on the excavation face stability caused by the train movement, Shentong group the metro system owner determined to limit trains' speed from normal 60km/h to 15km/h in this section based on field tests during the TBM tunnelling construction.

5.4 *Under-crossing drive*

Referring to the BEP's earlier experience on tunnelling through buildings, the process of under-crossing the live metro tunnels was divided into three phases which considered different parameter setting and optimization, they were phase I: before the cutter head arrived metro projection range, phase II: the TBM under the live metro, phase III: the tail shield left the projection range. On 16 November 2019, the cutter head began to enter into projection range. On 19 November shield tail left the projection range, and the shield left the influence zone on 23rd November. During the under-crossing construction, the maximum heaving recorded was 9.05mm for the north bound tunnel and12.42mm for the South bound tunnel. After the shield tail passed line 11, the North bound tunnel shown settlement trend and the final reading recorded a heaving of 7mm. For the South Bound Tunnel, the tunnel continues to heave up to 12.5mm before dipping.

5.5 *Metro tunnel displacement*

In order to monitor the metro tunnel displacement and deformation, automatically instrumentation device such as EL beam was used to real time monitor the displacement of the metro tunnel. The monitoring zone was 86m each side from the BEP tunnel center line and cover a total length of 172m. A monitoring point was set every 2 rings (2.4m), which was consistent for the south bound and the north bound line. Laser diameter convergence survey was also applied, which install every 5 rings (6m) in the range of 120m.There were 42 laser diameter convergences in total were installed. All the monitoring data were read and send to control center every 5 minutes. The tunnel displacement monitoring results at two layer tunnels intersection points were shown in Figure 12 below.

Since the shield cutter head entered the influence zone of Metro Line 11, the tunnel closer to the crossing area showed a downward trend with a max. subsidence of -0.38mm. As the shield continued to advance, the tunnel of Line 11 began to be uplifted. With the driving continued, the south bound reached

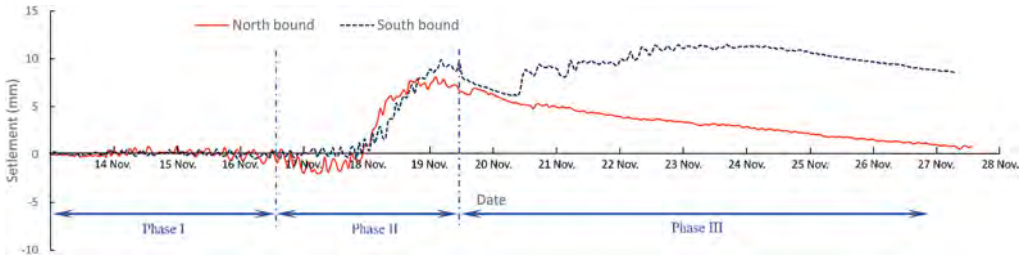

Figure 12. Displacement time history curves of metro tunnel.

a maximum elevation of +9.6mm. While the shield left influence zone, the metro tunnels began to sink, with a subsidence of 3.02mm. In the whole process, displacement of the south bound tunnel reached +12.58mm which was less than specified criteria (-20mm~+20mm). As the shield machine moved away, the tunnels gradually sank.

During the under-crossing, the metro tunnel horizontal diameter increased firstly and then decreased. The maximum convergence deformation of the north bound tunnel was +4.8mm ("+" denoted transverse diameter increased). And the convergence value decreased to +0.7mm afterwards. The maximum convergence deformation of the south bound tunnel was +6.4mm, and the convergence value decreased to +1.1mm afterwards. This shown that the deformation of the metro tunnels was mainly recoverable elastic deformation.

After tail shield left the projection range of metro tunnel (after Ring No.412) on 24 November 2019, the tunnel's uplift began to fall down. Before 9 July 2020, the maximum absolute settlement of the north bound tunnel reached -9.58mm, and the south bound tunnel was -7.29mm. In order to control the settlement, the post-perturbation grouting was applied inside the subway tunnel using the pre-set holes on 12 July 2020. From12 July to 2 August 2020, 7 rounds of grouting had been carried out. By the end of 2 August the perturbation grouting finished and final settlement of the tunnel was successfully controlled within 5mm.

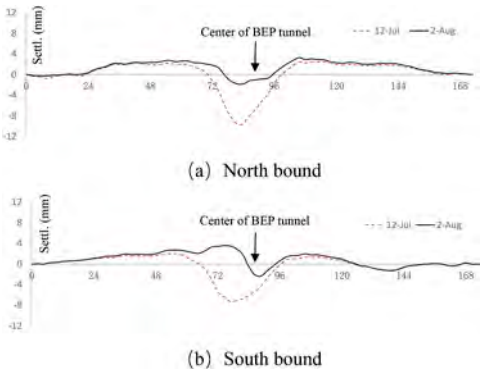

Figure 13. Metro tunnel settlement comparison before and after perturbation grouting.

6 CONCLUSIONS

In this paper the BEP II which was opened to public on 18 June 2021 was studied as an example. The extra-large slurry TBM with diameter of 15.56m had successfully tunnelled 6.42km, during which it faced many technical challenges such as continuous tight S curves excavation, tunnelling within close proximity to buildings and under-crossing live metro lines. Focusing on each difficulty, technical solutions such as TBM selection, segmental lining design, construction risk control, etc. were adopted, and the project team successfully achieved the goals of 'precise control, stable balance and slight disturbance'.

(1) In order to negotiate the tight S-curve sections using slurry TBM with extra-large diameter of 15.56m, a comparative study was conducted to determine whether the shield skin should be articulated or fixed. Then, the conical shield, the copy cutter configuration and the overall design of the TBM machine were studied. Comparative studies were also performed on segmental rings, optimizing their width (2.0m/1.5m) and tapers (40mm/80mm). The TBM has tunnelled through 4 sections of tight S-curve, and the construction quality was excellent. Results shown that the overall tunnel axis deviation was less than 10mm. The average working efficiency reached 5.2r/d in normal condition.

(2) Regarding TBM tunnelling through buildings, the influence zone along the tunnel route was defined firstly. A multi-factor and multi-level risk assessment model was formulated. Risks of TBM tunnelling through 89 buildings within influence zone in 2nd drive were estimated case by case. According to each building's risk grade, corresponding construction methodologies were recommended. In case of high-risk situation, the source of risk must be considered, and each case would have its own construction scheme. The entire under-crossing process was successful, and the building tilt and settlement were controlled within specified criteria. During the under-crossing process, the buildings heaved at first, and it gradually fell back after the shield tail left, and the subsidence became stable and converged after 6 months.

(3) There was no such precedent for a Φ15.56m TBM to under-cross live metro tunnel with clearance of 7m before. The displacement criteria of the metro tunnel were discussed and determined as -20mm~20mm. A variety of schemes were optimized, and the overall methodology of 'Reduce speed, Uniform speed and Continuous drive' was adopted. Metro tunnel's displacement and deformation were monitored automatically. The perturbation grouting was adopted in case of settlement, and the final displacement of the metro tunnel was successfully controlled within 5mm.

The success of BEP II had accumulated valuable experiences and data, formed a comprehensive technical system, and established a rich case library, which could provide references for similar constructions in the future, and further promote the development progress of entire TBM tunnel industry, and also find new solutions for urban center expressway construction.

ACKNOWLEDGMENTS

The authors appreciate all construction team members from Shanghai Chengtou Group Corporation, Shanghai Municipal Engineering Design Institute (Group) Co., Ltd., Herrenknecht AG, Shanghai Shengtong Group etc, and thanks also give to our STEC colleagues worked in BEP II.

REFERENCES

R. Huang, 2008, The Shanghai Yangtze River tunnel – Theory, Design and Construction (Eds.), Taylor & France Group, London, UK.

Shanghai Tunnel Engineering & Rail Transit Design and Research Institute et al, Shanghai road tunnel design code (DG-TJ08-2003-2008), July 2008, in Chinese.

Ministry of Housing and Urban Rural Development of the People's Republic of China, Code for construction and acceptance of shield tunnelling method (GB50446_2017), China.

Yuqian Zhou, Jinrong Yuan et al, 2020, Construction simulation of large diameter TBM tunnelling in a sharp curve alignment in soft clay using 3D numerical analysis, ITA-AITES World Tunnel Congress, WTC2020 and 46th General Assembly Kuala Lumpur Convention Centre, Malaysia 15–21 May 2020.

Xingbao Song, Construction Technology of extra-large diameter slurry shield under-crossing operation rail transit tunnels with small clearance, Tunnel and Rail Transit, 2020(4):35–40, in Chinese.

Tunnelling for a Better Life – Yan, Celestino, Thewes & Eberhardt (Eds)
© 2024 The Author(s), ISBN 978-1-032-80042-4
Open Access: www.taylorfrancis.com, CC BY-NC-ND 4.0 license

Research on vertical dry tailings conveying technology and equipment of shaft boring machine

Chuge Yang*
China Railway Construction Heavy Industry Corporation Limited-CRCHI, Changsha Hunan, China

ABSTRACT: The vertical rock slag conveying technology has always been an important research direction in the field of shaft construction, and how to collect and lift the rock slag at the bottom layer of the shaft to the corresponding transfer height through continuous mucking equipment is the core technical problem. In this paper, by comparing and studying the application scenarios and technical characteristics of existing mature vertical conveying equipment, carrying out targeted research on mucking equipment in consideration of shaft construction conditions, and trial-manufacturing the prototype of vertical slag removing machine for relevant lifting tests and verifications, the effective vertical lifting operation of rock slag has been successfully realized, providing a reference breakthrough for solving the "bottleneck" mucking technical problems in the field of shaft construction.

Keywords: shaft boring machine, vertical slag removing

1 INTRODUCTION

Non-blasting rock breaking technology represented by mechanical rock breaking is an important orientation for the development of shaft sinking technology at present, and a feasible technical approach to solving the problems such as large number of underground operators, complex working procedures, serious occupational injuries and consequences and environmental pollution in existing drilling blasting shaft sinking [1]. Liu Zhiqiang [2] introduced the shaft sinking technology of mechanical rock-breaking shaft TBM using guide hole for slag discharge, and discussed the matters concerning tunneling equipment; Zheng Kangtai [3] formed a set of schemes and equipment specific to the adaptability of shaft boring machine slag discharge technology according to the research and test on key technologies of full-face shaft boring machine.

At present, the shaft construction methods both at home and abroad include drilling and blasting method, raise boring machine/undercut type shaft boring machine, cutting type shaft boring machine, full-face boring method, etc. The drilling and blasting method is in the slagging mode of rock grab loading → bucket mucking, with flexible device and equipment configuration and low cost; however, the construction efficiency is low, a large number of personnel are required for underground operation, the labor intensity of workers is high, and the construction safety risk is also high.

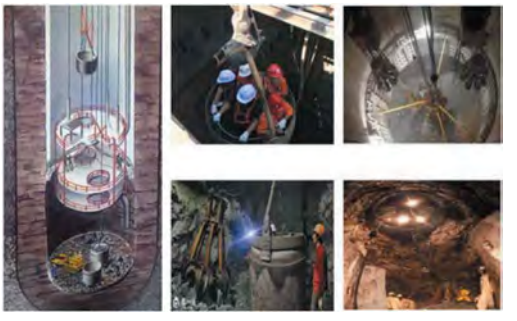

Figure 1. Main device and equipment configuration of drilling and blasting well construction system.

The deep shaft boring machine has equipment such as cutterhead scraper to scrape slag and bucket elevator to transfer slag from the cutterhead to the main engine. This mucking form distributes the slag

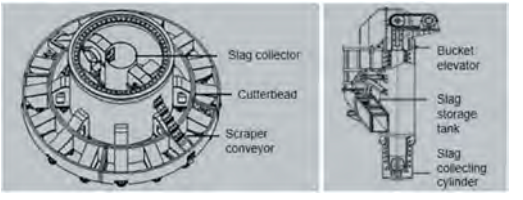

Figure 2. (a) Slag scraping by scraper conveyor (b) Slag conveying by bucket elevator.

*Corresponding author: yangchuge@crchi.com

DOI: 10.1201/9781003495505-298

scraping and transferring in two independent devices, and each needs to provide an independent power system, which has high requirements for equipment operation reliability, mucking speed and efficiency matching, and will be poorly adaptable to water-rich strata due to its low position of power unit.

The lower part of the main engine of the cutting type shaft boring machine is equipped with a telescopic cutting arm and a pick-type cutting head, which is flexible and can rotate up, down and around the vertical centerline of the main engine to cut and excavate the working face. The machine is suitable for construction in soft rock strata without water. During construction in hard rock, the pick could wear quickly, and the whole section cannot break rock at the same time, so the well completion speed would be slow. Typical products include Herrenknecht SBM and VSM models, with a maximum device excavation.

The mucking method of this type can also be divided into the two kinds of mucking: upper mucking or lower mucking, in which the upper mucking is mainly carried out by mud pump or vacuum suction, and the lower mucking also requires a bottom hole mucking channel.

Figure 3. Cutting type shaft boring machine.

The full-face shaft is excavated from top to bottom by the cutterhead, and the excavated rock slag is continuously lifted vertically and discharged to the ground. During construction, there is no need to excavate chute holes and underground mucking channels, which has high construction efficiency and low safety risks, and can implement working procedures synchronously such as shaft wall support and boring guidance. The slag discharge mode of the machine can be divided into mechanical slag discharge and fluid slag discharge, which can adapt to different geological conditions. For rocks and composite water-poor strata, the muck will be discharged by mechanical slag discharge; for water-rich strata, the muck can be discharged by fluid slag discharge.

According to the engineering characteristics of deep shaft construction by the boring machine, it is easy for the rock excavated in the shaft to sink after being crushed under dry tailings mucking mode, and it is very difficult to transfer and collect muck due to the large range of working face. If the slag is not

Figure 4. Full-face shaft boring machine.

scraped in time, it is easy to pile up slag and even cause cutterhead burial, resulting in excessive device torque load and affecting normal boring. When the muck is transferred to the slag receiving device, a certain height difference needs to be formed to meet the slag receiving requirements. However, it is difficult to form the height difference under the action of gravity when the muck rotates with the cutterhead, resulting in great difficulty in entering the slag receiving device. Therefore, how to realize automatic and fast muck transfer operation of tunnel face is one of the key factors that could affect mucking efficiency.

2 OVERALL DESIGN

According to the current technical characteristics of shaft mucking, the overall height and size of the main engine of the shaft shall be reduced as much as possible to reduce the excavation quantities of the launching shaft. It is considered to integrate the slag shoveling and slag-carrying lifting functions of the cutterhead tunnel face on the main engine mucking device, and in combination with the excavation characteristics of the cutterhead of the shaft boring machine, it is necessary to meet the slag carrying capacity under large particle size mucking and water-rich working conditions. The corresponding bucket opening shall be ≥ 2 times the limit size, and a screen plate shall be designed in the bucket body to realize the dual material lifting function of slag and water.

2.1 *Technical principle*

The vertical slag removing machine is driven by the upper double sprockets, and the traction chain and bucket rotate. During the action of the bucket, the slag is shoveled into the bucket from the bottom. After shoveling, it is vertically lifted with the traction chain, and runs to the arc top for unloading to complete the muck transfer under a single cycle. The

working principle and structure of the device and equipment are close to those of the existing removing machines. However, due to the differences in the types of conveyed materials and operating conditions, targeted design improvement is required for structures and materials, and the structural design of buckets needs to ensure smooth muck unloading.

2.2 *Slag conveying capacity of vertical slag removing machine*

The calculation formula is$Q = 3600 \frac{uc}{a} v$

Where: Q is the hourly slag transfer volume of vertical slag removing machine, m³/h; u is the bucket volume, m³; c is the bucket filling coefficient; a is the bucket spacing, m; v is the chain speed of vertical slag removing machine, m/s. Q shall meet ≥ unit excavation volume Q1 of cutterhead to avoid large-area slag accumulation on the cutting face of the cutterhead.

2.3 *Test schemes*

To verify the feasibility of vertical slag removing technology, it is planned to carry out prototype slagging test verification, complete the prototype design of vertical slag removing machine and reserve support frame interface, design chute muck box to simulate the size of cutterhead excavation chamber and muck flow state. The vertical slag removing machine and muck box form a shoveling state. A spiral chute is set at the upper drive end to guide the discharge of removing machine back into the muck box for circulation. To ensure the normal operation of the vertical slag removing machine, a gap of 30~50 mm shall be reserved between the bucket and the arc bottom of the muck box, so that when the cutterhead hob cuts into the rock surface, there is still a certain safety margin between the lowest point of the bucket and the excavation face.

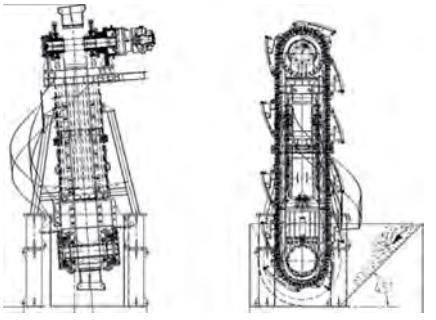

Figure 5. Test scheme of slag removing machine.

3 TEST VERIFICATION

After the trial production of test equipment and tooling is completed, assembly and commissioning shall be carried out as per the test scheme. The vertical slag removing machine shall be started and stopped in no-load state to ensure that its functions such as stable start and stop and chain tensioning are normal, and the noise of drive device, deviation of drive chain, speed of drive chain and oil pressure of drive motor meet the design expectations;

Fill the muck box with composite muck and gravel, observe the shoveling, vertical lifting and unloading of the vertical slag removing machine for composite muck and gravel, and record the inspection results; add water to the composite muck and gravel in the silo to reach a surplus state, and observe and record the water-carrying lifting capacity of the vertical slag removing machine for water-rich slag;

Figure 6. (a) Bucket surface of vertical slag removing machine (b) Slag chute surface.

Figure 7. (a) Conventional slag bucket (b) Water-carrying slag bucket.

Figure 8. (a) Chain tension state (b) Filling of slag silo.

Figure 9. (a) Muck and Gravel (b) Water-rich Muck and Gravel.

Table 1. Statistics of vertical slag removing machine operation.

S/N	Item	No-load standard value	No-load test value	Standard value with load	On-load test value
1	Chain speed	≮0.8m/s	0.8-1m/s	≮0.8m/s	0.8-1m/s
2	Drive motor oil pressure	≯2MPa	1~1.5M-Pa	≯5MPa	3~4MPa
3	Slag removing machine starts and stops smoothly	Normal	Normal	Normal	Normal
4	Slag shoveling, vertical slag lifting and unloading effect	/	/	Slag quantity of discharge hopper ≥0.5 efficiency coefficient	Slag shoveling, vertical slag lifting and unloading are normal, and the slag amount is close to 2/3
5	Water-carrying effect	/	/	Slag liquid volume in water-carrying chamber of slag bucket ≥0.5 efficiency coefficient	The water storage capacity of the water-carrying chamber is normal, and the amount of slag liquid is close to 1/2 of its volume

During the no-load operation of the vertical slag removing machine, the overall operation is relatively stable, the sprocket and chain are bonded smoothly, the driving oil pressure is within the range of 1~2 MPa (the lifting height of the prototype is smaller than that of the installed vertical slag removing machine, and the oil pressure is low), and the operating speed is 0.8~1 m/s. Due to the restriction of the working mode, there is certain noise interference. In the on-load operation test, the test muck is a mixture of shield soil and rock slag at the boring machine site. The driving oil pressure for on-load operation is within 3~4 MPa, and the test running speed is 0.8~1 m/s, which all meet the calculation requirements. The basic functions of bucket shoveling, vertical slag carrying and arc top slag unloading process have achieved their design effects, verifying that the principle of the vertical slag removing machine with integrated muck conveying function is feasible and can further promote its engineering application. The installed height and slag type of the device in this test deviate from the actual on-site loading conditions to some extent, so the engineering application will face a more severe actual test than this test.

4 CONCLUSION

(1) Aiming at the difficult problem of vertical transportation of dry tailings in shaft boring machine construction, this paper puts forward a technical method of vertical slag extraction and removing integrating slag shovel and slag extraction, and expounds the working principle of vertical slag extraction and its matching relationship with excavation chamber.

(2) By simulating the tunneling slag discharge test of vertical slag removing machine, it is proved that the performance of muck lifting system meets the design requirements, the particle size and slag discharge effect of rock slag meet the expected indicators, and the vertical muck extraction equipment runs well.

(3) The vertical slag extraction equipment has been verified by the slag extraction and removing test, but there is a certain difference between the engineering test conditions and the actual boring and tunneling and mucking state. The performance of the vertical slag extraction and removing system needs to be technically verified in specific engineering applications.

REFERENCES

[1] Liu Zhiqiang, Li Shucai, Wang Dujuan. *Exploration and Analysis of Key Technologies and Research Paths for Shaft Sinking by Full-face Boring Machine in Hard Rock with a Thousand-meter Vertical Shaft* [J]. Journal of China Coal Society. 2022, 47 (08).

[2] Liu Zhiqiang. *Shaft Boring Machine Shaft Sinking Technology* [M]. Beijing: China Coal Industry Publishing House, 2018.
[3] Zheng Kangtai, Jia Lianhui. *Development and Key System Test of Full-face Shaft Boring Machine* [J]. Tunnel Construction (Chinese and English). 2021, 41 (10).
[4] Xu Dapeng, Chen Wusheng, *Several Problems to be Noticed in Shaft Engineering Construction* [J]. Engineering and Technology 2014, (6).
[5] Jing Guoye, Han Bo. *Shaft Sinking Technology of Full-face Shaft Boring Machine* [J]. Coal Engineering 2020, 52 (10).
[6] Cai Jianfeng, *Design of 500 m Deep Shaft Hoisting System* [J]. Test and Research 2018, (5).
[7] Li Guangke, *Comparison and Selection of Excavation Methods for 500 m Ultra-deep Shaft Body* [J]. Construction Machinery. 2020 (08).
[8] Ding Zhangfei, *Key Technologies of Full-Face Shaft Boring Machine* [J]. Construction Mechanization. 2022,43(11).
[9] Lyu Dan, Jia Lianhui. *Shaft Sinking Technology and Application of Upper Muck Discharge Type Full-Face Shaft Boring Machine* [J]. Tunnel Construction (Chinese and English), 2023, 43(1): 151.

Tunnelling for a Better Life – Yan, Celestino, Thewes & Eberhardt (Eds)
© 2024 The Author(s), ISBN 978-1-032-80042-4
Open Access: www.taylorfrancis.com, CC BY-NC-ND 4.0 license

Study on classification prevention and control technology of hard rock rockburst in TBM construction

Yalei Yang
School of Mechanical Engineering, Shijiazhuang Tiedao University, Shijiazhuang, China

Lijie Du*
Collaborative innovation center for performance and safety of Large-scale infrastructure, Shijiazhuang Tiedao University, Shijiazhuang, China

Cheng Gong & Yin Song
PowerChina Chengdu Survey and Design Research Institute Co. Ltd., Chengdu, China

Qingwei Li
School of Mechanical Engineering, Shijiazhuang Tiedao University, Shijiazhuang, China

Minyuan Wang
School of Safety Engineering and Emergency Management, Shijiazhuang Tiedao University, Shijiazhuang, China

ABSTRACT: Rockburst is a difficult problem in construction of deep-buried tunnels by full-face rock tunnel boring machine (TBM) due to its great impact on the safety and speed of TBM tunneling. This paper relies on the Yinhanjiwei (YHJW) Project, Xinjiang AiBiHu (ABH) Project, Jinping II Hydropower Station Project and Xinjiang EHe (EH) Project, and obtains the influence degree and temporal and spatial characteristics of rock burst on TBM construction speed through a large number of data analysis and research. The prevention and control objectives of TBM construction with four grades of slight, moderate, strong and extremely strong rockburst and four prevention and control criteria of TBM construction with speed control, risk control, space-time control and grading control are put forward. According to four grades of rockburst, the corresponding effective prevention and control technical schemes are given respectively. Furthermore, the theoretical and technical system of 4-4-4-4 graded rockburst prevention and control is constructed, which is controlled by monitoring, equipment, excavation and support. These results have been verified and applied in practical projects, and can provide a reference for the subsequent construction of ultra-deep tunnels.

Keywords: Rockburst grading, TBM, Graded prevention and control, Guideline, Technical methods

1 INTRODUCTION

The full-face rock boring machine (TBM) is a large underground engineering equipment with the characteristics of parallel process of excavation, support and slag discharge, so it has been widely used in various infrastructure construction fields. With the development of underground engineering construction towards "long, large and deep", however, TBM construction is also facing new challenges. Especially for the super-deep tunnel, the ground stress is high and rockburst is easy to occur, which has a serious impact on the construction progress of TBM and the safety of construction personnel and equipment [Du, 2017]. From the practical experience of previous TBM projects, a large number of strong rockbursts or even extremely strong rockbursts occurred in the excavation process of Jinping II hydropower station project. As a result, the construction of two water diversion tunnels was stopped actively, and one drainage tunnel was destroyed and buried, causing casualties and huge economic losses [Yang et al.,2023, Yu et al., 2014]. Under construction, the Yinhanjiwei (YHJW) project also encountered a strong rockburst. The existing support was destroyed many times in early construction, and the TBM equipment was seriously damaged by rockburst impact. It has greatly affected the construction safety and progress [Xue, 2019].

*Corresponding author: dulj@stdu.edu.cn

DOI: 10.1201/9781003495505-299

Two TBM tunnels of Pakistan's N-J hydropower project suffered frequent rockbursts, causing casualties and serious equipment damage [Abdul, 2019]. Rock burst in TBM construction of Kobbelv HPS water conveyance tunnel in Norway also brought casualties [Øyvind, 2016].

At present, in order to better prevent and control rockburst, there are mainly three aspects of research work during construction. Namely, rock burst occurrence mechanism and theoretical method of rock burst prediction, microseismic monitoring and prediction of rock burst, and key technologies and methods of rock burst prevention and control. The theoretical research on rockburst prediction is earlier and there are many achievements. C.S.Ma et al. [2018] put forward a rockburst criterion based on the N-J hydropower project in Pakistan. The rockburst can be judged according to the ratio of the strength of rock mass to the horizontal stress perpendicular to the axis of the tunnel. In the aspect of rockburst microseismic monitoring, Zhao et al. [2017] relied on the monitoring data of rockburst microseisms and rockburst cases of Jinping II hydropower station project to analyze the temporal and spatial law of rockburst from the perspective of microseismic monitoring results. It shows that microseismic events have strong temporal and spatial correlation with rockburst. Yu et al. [2014] analyzed the changes of microseismic monitoring data before and after the rockburst of Jinpin II Hydropower Station project, and found that most rockbursts have microfracture precursors that can be monitored. It is preliminarily proved that the microseismic monitoring system is feasible for early warning of rockburst risk in TBM construction. Chen et al. [2011] analyzed the law of microseismic activity in the process of TBM excavation, and found that the faster the TBM excavation speed, the stronger the microseismic activity. The high incidence period of rockburst is 4 - 6h when the tunneling starts again after TBM maintenance. Wang [2019] made statistics on the monitoring results of rockburst microseisms and rockburst conditions in the upstream and downstream of No.3 and No.4 tunnels of Qinling Tunnel from the YHJW project, and found that the prediction accuracy rates were 95.89%, 90.00% and 88.46%. Ma et al. [2016] analyzed the rock bursts in the Jinping II hydropower station project and found that the accuracy of rock burst prediction in this project can reach 80.6 %. Du et al [2020] studied the accuracy and applicability of rockburst microseismic monitoring based on the big data analysis verified by comparison between rockburst microseismic monitoring and actual rockburst in the YHJW project and Xinjiang AiBiHu (ABH) project. It is concluded that the higher the rockburst grade, the higher the accuracy of microseismic monitoring, and the accuracy of strong rockburst risk grade prediction is close to 80%. In the key technology of rockburst prevention and control, slight rockburst and moderate rockburst have little influence on the safety and progress of TBM construction in terms of engineering practice. The main measures taken are steel mesh support, mechanical shell-expanding prestressed grouting anchor, water-rising anchor, nano-steel fiber-like concrete and other comprehensive prevention measures [Chen et al., 2015]. For strong rockburst, TBM construction progress has a great influence. TBM equipment and personnel still face great security risks. It is difficult to get complete prevention and control. The main reason is that when the rockburst happens, firstly, the support is not done in time, and the personnel and equipment are at risk of being smashed. Second, the support was destroyed and the amount of slag removal was large. For example, after the TBM construction of the drainage tunnel of Jinping II Hydropower Station entered the strong rockburst area, the construction speed of TBM decreased a lot due to the destruction of the support and the huge workload of slag cleaning and support restoration, and only 600 m was excavated from July to November 2009 [Zhang et al., 2011]. In this project, in order to prevent the risk of strong rockburst ahead, the construction scheme of advanced pilot tunnel is put forward. That is, the pilot tunnel is excavated at the upper part of the tunnel face by drilling and blasting, and then the remaining section is excavated by TBM [Xiao et al., 2011]. In particular, it should be pointed out that this drilling and blasting pilot scheme is beneficial as an experimental research and exploration. However, it is difficult to be accepted by all parties as the construction technical scheme of TBM crossing the strong rock burst tunnel section. Because if so, it is better to excavate by full-face drilling and blasting.

To sum up, we can find that the accuracy of rockburst prediction needs to be improved. Higher than the actual prediction result of rockburst will increase the cost of prevention and control and affect the construction progress; The prediction result lower than the actual rockburst will bring greater safety risk and schedule risk. Moreover, even if the occurrence of rock burst is accurately predicted, it is ultimately necessary to rely on rock burst prevention and control measures to ensure the safe crossing of TBM.

2 PROJECT OVERVIEW

2.1 *Project overview*

The total length of the main tunnel of Xinjiang ABH project is about 41 km, of which 9 km is excavated by drilling and blasting, and 32 km is excavated by two open TBM. The tunnel is located in the strong uplift area of the northern Tianshan Mountains, with developed folds and faults, strong seismic activity and high ground stress. Hard and brittle rocks such as siltstone, metamorphic mudstone and granodiorite are distributed along the line, and the compressive strength of the rocks is 55.6-148.7 MPa, which has the geological conditions for rockburst.

The YHJW project is located in the Qinling Mountains in south-central Shaanxi Province, China. The total length of the project is 98.3 km, which is excavated by drilling and blasting method and two

8.0m diameter open-type TBMs. The elevation of the tunnel ranges from 1050-2420 m, the maximum buried depth is about 2012 m, and the ground stress is high. Hard rocks such as quartzite, granite and diorite are mainly distributed along the line. The compressive strength of rock is 107-317 MPa, and the average value is about 160-170 MPa, which has the conditions for strong rockburst.

2.2 *Rockburst situation*

The excavation pile number of the III section of ABH project studied in this paper is K9+600-K23 +600. Up to August 2019, there were 151 rockbursts during the TBM excavation of this project, including 101 slight rockbursts, 18 slight to moderate rockbursts and 32 moderate rockbursts. There was no strong to extremely strong rockburst. The impact on the construction is not great.

The total length of the Lingnan section of the YHJW project studied in this paper is 18.28 km, and the pile numbers are K28+085-K46+360. Among them, the pile numbers K28+490-K37+011.5 are the first tunneling section of TBM, and the pile numbers K39+511-K46+360 are the second tunneling section of TBM. Up to November 2019, there were 795 rockbursts during TBM excavation, including 302 slight rockbursts, 84 slight to moderate rockbursts, 158 moderate rockbursts, 80 moderate to strong rockbursts and 171 strong rockbursts. It has a great impact on TBM construction.

3 IMPACT ANALYSIS OF ROCKBURST ON TBM CONSTRUCTION

3.1 *Impact of rockburst on TBM construction safety*

Once a rockburst occurs during TBM construction, it will not only slow down the construction speed, but also threaten the construction safety. Moreover, the impact of different grades of rockburst on TBM construction is generally different. The impact of rockburst on construction is shown in Figure 1.

a) Rockburst occurs in the exposed shield

b) Rockburst damage the support and equipment

Figure 1. Impact of rockburst on TBM construction.

3.2 *Impact of rockburst on TBM construction efficiency*

The construction speed of TBM, i.e. the feed rate, is mainly affected by both the pure digging speed and the pure digging time of TBM. It is mainly affected by TBM pure advance speed and pure tunneling time. After classifying and summarizing the construction parameters of rock burst section, we can get the influence law of rock burst on TBM construction speed by comparing with the construction parameters of non-rock burst section. After the statistical analysis of types of surrounding rock with rockburst risk in two supporting projects, it is found that the Class IV surrounding rock with rockburst risk is only about 150m, and only 20 rockbursts have occurred. Due to the lack of rockburst data in Class IV surrounding rock, this paper only discusses the influence of rockburst on TBM construction speed under the conditions of Class I, Class II and Class III surrounding rock.

3.2.1 *Influence of rockburst on TBM pure advance speed*

The advace speed of TBM in rockburst section and non-rockburst construction tunnel section in two supporting projects is counted. The influence of rockburst on TBM advance speed is analyzed. The results are shown in Figure 2.

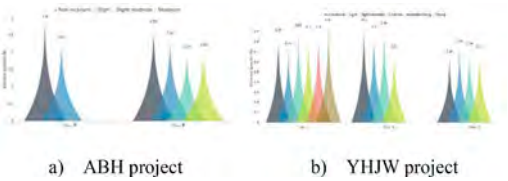

a) ABH project b) YHJW project

Figure 2. Comparison of advance speed under different surrounding rock classification and different rock burst grades.

It can be seen from Figure 2a that the advance speed of TBM is obviously reduced due to the existence of rockburst in ABH project. And in a certain range, the influence of rockburst on TBM advance speed is gradually strengthened with the improvement of rockburst grade. The main reason is that the compressive strength of rocks is low in ABH project, which is suitable for TBM excavation. If there is no rockburst, the pure advance speed of TBM is faster. Once rock burst happens, the advance speed will be obviously reduced. This is mainly due to the active control of TBM advance speed by rock burst tunnel section. However, it can be seen from Figure 2b that the influence of rock burst on TBM advance speed is not obvious in YHJW project. In some cases, the advance speed of rock burst section is even slightly higher than that of non-rock burst section. And only from the statistical results of this project, it can be found that the correlation between advance speed and rockburst grade is weak. The reason is that the rock compressive strength is extremely high in YHJW project. Even without rockburst, the pure advance speed of TBM is very low. After the rock burst happens in this extremely hard rock, the pure advance speed will not increase or decrease obviously, and it does not

need to be actively controlled. Therefore, the easier it is for surrounding rock to penetrate, the greater the proportion of rock burst will affect the construction speed of TBM. Moreover, the main factor affecting the construction speed of TBM is not the pure advance speed, but the pure advance time.

3.2.2 *Influence of rockburst on TBM pure advance time*

Rockburst will increase the workload of slag cleaning, support and equipment repair. It takes up pure advance time, which further affects the penetration speed of TBM construction. Generally speaking, under the same kind of surrounding rock, the higher the rockburst grade, the more the delay of pure advance time. The pure tunneling time of TBM in rock burst section and non-rock burst construction section of two supporting projects is counted. The influence of rockburst on TBM pure tunneling time is analyzed, as shown in Figure 3.

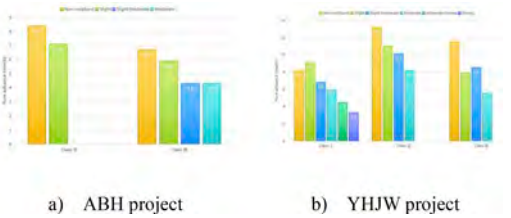

Figure 3. Comparison of pure advance time under different surrounding rock classification and different rock burst grades.

3.2.3 *Influence of rockburst on TBM construction speed*

The daily footage of TBM is counted in the rock burst section and the tunnel section without rock burst in two supporting projects. This paper analyzes the influence of rock burst at all levels on the construction speed of TBM under different surrounding rock classification. Taking the construction speed of the non-rockburst section as a reference, the construction speed is expressed as 100%. Then, under the influence of different grades of rockburst, the percentage of construction speed of rockburst section is non-rockburst section, as shown in Table 1.

The above construction speed takes into account the influence of rock burst prevention and control support measures. From the statistical analysis in Table 1, it is found that: (1) In the same project with the same rockburst grade, the influence of rockburst on the construction speed of Class II surrounding rock is more obvious than that of Class III. Under the condition of similar surrounding rock of different projects, the influence of rock burst of different grades on the construction speed of ABH project is more obvious than that of the YHJW project. The reason is that the rock strength of ABH project is low and it is easy to penetrate. If there is no rockburst, the supporting capacity of Class II surrounding rock is very small. A very high advance speed can be obtained. Once there is the possibility of rockburst, it is necessary to take support measures similar to broken surrounding rock. This will increase the impact on the proportion of pure advance time. Therefore, rockburst has a great influence on the construction speed. (2) The active control of daily footage in Class I surrounding rock is not considered in the YHJW project. When moderate rockburst occurs in two projects, the construction speed is only about 1/2-3/4 of that without rockburst. This shows that rockburst has great influence on construction speed. (3) Within the scope of the tunnel studied in this paper, the strong rockburst occurred only under the condition of Class I surrounding rock in the YHJW project. The construction speed of strong rockburst tunnel section is less than 1/2 of that of non-rockburst tunnel section. It shows that rockburst has a great influence. If the same strong rockburst occurs in ABH project, because its rock strength is lower than that of the YHJW project, it is easy to penetrate and the pure tunneling speed is high. Moreover, there is a big gap between the pure tunneling time with strong rockburst and that without strong rockburst. Therefore, if a strong rock burst occurs in ABH project, the influence degree on the penetration speed of TBM construction is far more than half. In fact, especially the prevention and control of strong rockburst, preventive measures are generally taken in advance.

4 TEMPORAL AND SPATIAL CHARACTERISTICS OF ROCKBURST

It is very important to know the characteristics of rockburst in TBM construction for rockburst prevention and control. This paper will focus on the study and analysis of the “space-time effect” of rockburst.

Table 1. Comparison of construction speed between rock burst section and non-rock burst section.

Project	Class	Non-rockburst	Slight	Slight -Moderate	Moderate	Moderate -Strong	Strong
ABH	II	100%	67.8%	—	—	—	—
	III	100%	77.2%	49.5%	48.4%	—	—
YHJW	I	100%	95.8%	87.3%	74.6%	54.9%	45.1%
	II	100%	76.7%	73.6%	45.0%	—	—
	III	100%	78.9%	82.9%	51.3%	—	—

That is to say, the characteristic law of rockburst is analyzed from three aspects: the occurrence time (tunneling lag time), the occurrence position (the distance to the heading face) and the influence range. Due to the low rockburst grade of ABH project, there is no rockburst with medium or above grade. There are few rockburst data, so the accuracy of the conclusion may be biased. This will make the research less meaningful. Therefore, the following only summarizes the temporal and spatial characteristics of rockburst in the YHJW project.

For the convenience of statistics, T is used to represent the lag time of rockburst (that is, the time from the excavation of a certain pile number to the occurrence of rockburst). According to the construction time of the project, T is grouped with 12 h, 24 h, 48 h and 72 h as nodes. S is used to represent the distance from the position of rockburst to the working face. According to the structural characteristics of TBM, 5 m, 15 m and 60 m are used as nodes for grouping. D is used to represent the influence range of rockburst (including the length of rockburst section and the circumferential position of rockburst). Among them, the length of the rockburst section is the distance from the starting pile number to the ending pile number of the rockburst location. The location of rockburst refers to the location of rockburst on the circumference of tunnel section. The upper 120 range is divided into top arch, the lower 120 range is bottom arch, and the left and right sides are side walls.

4.1 *Statistical analysis of rock burst characteristics*

Because some rockburst data are incomplete, 788 groups of relatively complete rockburst data are selected for analysis in YHJW project, including 301 minor rockbursts, 83 minor-moderate rockbursts, 157 moderate rockbursts, 80 moderate-strong rockbursts and 167 strong rockbursts. The temporal and spatial characteristics of rockburst are obtained by statistical analysis of T, D and S in these data. The relatively complete rockburst data recorded in the YHJW project are classified according to the rockburst grade. T, D and S of rockburst at all levels are statistically analyzed, and the statistical results are shown in Figure 4.

As can be seen from the statistical analysis results in Figure 4, the rockburst occurred has the following characteristics in the YHJW project. (1) More than 90% of rockbursts occur within 24 h, and the frequency of rockbursts is the highest within 10 - 24 h after excavation, and about 9% of strong rockbursts occur within 24 - 48 h.. Therefore, the key prevention and control time of rockburst should be within 24 h after excavation. (2) The distance from the rockburst position to the tunnel face is mostly 5-15m. With the increase of rockburst grade, the distance from rockburst to heading face decreases. The proportion of strong rockburst before the shield is 31.1%. According to the characteristics of open

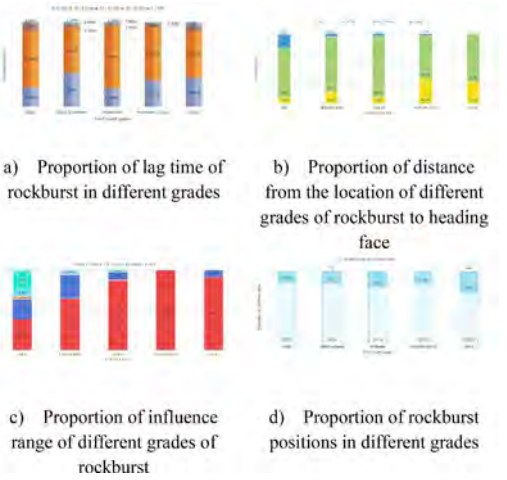

Figure 4. Temporal and spatial characteristics of rockburst.

TBM, the main girder is usually located within the range of 5 - 15 m from the tunnel face. The personnel and equipment here are relatively concentrated, so the prevention and control of rockburst must be done well. (3) The length of single rock burst section is mostly within 5 m. 100% moderate to strong rockburst and 98.2% strong rockburst are in the range of 5m. Rockburst mostly occurs within 120 of the top arch, and 98.1%, 97.5% and 100% of moderate rockburst, moderate-strong rockburst and strong rockburst occur in the top arch respectively. There are 15.9% - 38.9% rockbursts on both side walls. There are cases where the top arch and the side wall rock burst simultaneously. Rock burst at the bottom arch accounts for very little. Therefore, the key prevention and control positions can be determined according to the influence range of rockburst at all levels. At the same time, the support of rock burst section should be mainly within 120 of the top arch.

4.2 *Characteristic of strong rockburst controlling TBM daily footage*

The influence of strong rockburst is reduced by actively controlling the daily footage of TBM excavation in the YHJW project. In order to clarify its prevention and control effect, the moderate ~ strong and strong rockburst in this project is verified in groups with the daily footage of 3 m as the node. In the selected data of this project, there are 80 moderate to strong rockbursts, and 13 times with daily footage below 3 m. There were 167 strong rockbursts, and 46 times the daily footage was below 3 m. Data with daily footage above 3 m can be represented by medium-strong A and strong rockburst A, and data with daily footage below 3 m can be represented by medium-strong B and strong rockburst B. The statistical results are shown in Figure 5.

It can be seen from Figure 5 that after the daily footage is reduced, more than 90% of rockburst still

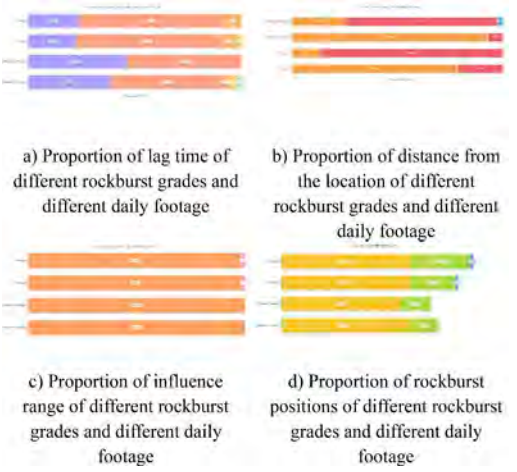

Figure 5. Characteristic of strong rockburst controlling TBM daily footage.

occurs within 24 hours, and there is no obvious change in T and D, but S is significantly reduced. The proportion of moderate-strong and strong rockburst occurring within 5m (i.e. from shield to tunnel face) increased obviously, reaching 92.3% and 78.3%. This is of great significance to the prevention and control of rock burst in TBM construction.

5 PREVENTION AND CONTROL OF ROCKBURST

The concept and technology of rock burst prevention and control in TBM construction are put forward based on the understanding of the above characteristics and laws of rock burst, combined with the structural characteristics and construction methods of TBM.

5.1 *Criteria of rock burst prevention and control in TBM construction*

Engineering practice shows that even if there is good rock burst prevention and control technology, it is difficult to achieve good prevention and control effect if the technical scheme cannot be selected and implemented according to certain theoretical criteria. For example, the support can not be completed at the right time, or the technical scheme can not be selected according to the rock burst grade. Therefore, the prevention and control of rockburst must first consider the characteristics of TBM construction and the law of rockburst occurrence, and follow the correct concept and theoretical criteria of rockburst prevention and control. Four theoretical principles of rock burst prevention and control are put forward based on the characteristics of TBM construction, the characteristics and laws of rock burst occurrence and the practical experience of rock burst prevention and control in engineering.

(1) Construction speed control criterion. The construction speed control here refers to controlling the footage every day or within a certain period of time.
(2) Risk control criteria. The concept of risk here refers to the risk brought by rock burst, that is, the safety risk of rock burst to TBM construction personnel and equipment, and the risk of the impact of TBM construction speed, construction period and trapped. The corresponding prevention and control technical measures shall be taken according to the magnitude of risk hazards and the probability of occurrence.
(3) Temporal and spatial control criterion. Engineering practice shows that rockburst may occur instantly or in a short time after excavation, which is called instant rockburst. This kind of rockburst mainly occurs in the tunnel face and TBM cutter head or shield area. Rockburst may also occur after a period of delay after excavation. As mentioned above, the probability of such rockburst occurring within 24 hours is very high. Individual occurrence in a longer period of time. The location is mainly concentrated in the TBM host area.
(4) Graded control criterion. Different surrounding rock conditions have different rock burst grades. Rockburst is generally divided into no rockburst, slight rockburst, moderate rockburst, strong rockburst or even extremely strong rockburst. Different rockburst grades have different hazards. Different prevention and control technical measures have different prevention and control effects. The influence on the construction footage speed and the construction cost are different. The technical measures for prevention and control of minor and moderate rockburst may not solve the fundamental problem for strong rockburst and extremely strong rockburst.

5.2 *Prevention and control technology of rock burst in TBM construction*

The technical system of classified prevention and control of rock burst in TBM construction based on coordinated control of equipment-excavation-support is put forward according to the influence law, space-time effect, equipment structure and construction method characteristics, as well as the prevention and control objectives and guidelines of rock burst. Compared with open TBM, the shield-type TBM is generally easier to prevent and control rockburst, and the control is relatively simple, because the main engine area is protected by shield and the back supporting part is supported by prefabricated segments. Therefore, the following mainly discusses the technical scheme of rock burst prevention and control with the open TBM.

5.2.1 *Rockburst prevention and control technology of different grades*

For slight rockburst, the conventional open TBM is equipped with anchor drilling machine at the tail of

shield, which is convenient for anchor operation. Moreover, the combined support of bolt and mesh can resist slight rockburst. The operation speed of bolt and mesh support is also relatively fast. Basically, it can keep up with the TBM excavation, even if it can't keep up with the excavation for a while, it will generally not bring the safety threat of equipment and personnel, and even can remedy the support. Therefore, it is not necessary to actively control the pure tunneling speed of TBM, but it is necessary to ensure that the support follows the tunneling. Rock burst prevention and control support may actually cause some delay to TBM construction speed, i.e. footage speed. And if the rockburst occurs in front of the shield tail and is a large-scale continuous rockburst. In this case, the use of anchor rod and steel mesh is invalid, because it will cause a lot of slag to be cleaned up. The technical scheme of the combination of arch frame and steel bar row with large spacing should be adopted. It not only ensures safety, reduces slag falling, but also greatly improves the construction speed. According to the above analysis, the prevention and control technical scheme of minor rockburst is a combination of conventional TBM design and bolt mesh or large-spacing arch reinforcement row support and support following excavation without actively controlling footage speed. For moderate rockburst, ordinary bolt and mesh support are difficult to resist the impact of rockburst. The support by spraying concrete at the main engine of TBM will pollute the main engine and the strength will increase slowly. It is not a good choice, unless the concrete with low price, no rebound and high speed can be developed. Therefore, it is proposed that the continuous closed support method combining steel arch frame and steel bar row is adopted for moderate rockburst. In this case, the TBM construction speed does not need to be actively controlled. Because the support may not keep up with the excavation, the construction speed will be passively controlled. In addition, in order to enable the TBM shield to store steel bars and achieve uninterrupted closed support, it needs to be designed as a shield with storage interlayer. Thus, the medium rockburst prevention and control technical scheme is constructed, which includes the design of storage bunker shield, the support of arch reinforcement row with regular spacing and the passive control of excavation. For strong rockburst, the past engineering practice shows that the conventional steel arch support is difficult to resist the impact of strong rockburst. Support is often damaged. And a lot of slag cleaning work will be brought. It will threaten the safety of equipment and personnel and seriously affect the construction progress. Nevertheless, according to the analysis results of the characteristics and laws of rockburst, the active control of the daily footage in the case of strong rockburst has a significant impact on the location of rockburst. So most strong rockburst can occur in the face and shield area by actively controlling the daily footage. In this way, not only the equipment and personnel behind the shield are protected. It is more important that the problem of rock burst protection with huge impact energy can be transformed into the problem of landslide and broken zone support. Namely, the rockburst and its falling rocks fall in the area from the tail of shield to the front face, and the cutter head and shield play a role in resisting the impact of rockburst. Small-spacing steel arches and steel bars can be combined at the tail of the shield to support rockburst and rockfall. On this basis, a strong rock burst prevention and control technical scheme is put forward, which combines the design of robust cutter head shield, active control of footage speed and steel bar row support of small spacing steel arch frame. Generally, the distance from the tunnel face to the shield tail is about 6m, and more than 90% of the strong rockburst occurs within 24h. According to this law, the daily footage of TBM excavation can be actively controlled below 3 ~ 5 m. With the excavation process, the combined support of steel arch frame and steel bar row at the tail of shield follows closely. After the footage control index is completed, the machine can stop and wait. The spacing between steel arch frames is reduced to enable TBM support shoes to cross. If the smaller spacing cannot be crossed, concrete pouring can be used to smooth it. For extremely strong rockburst, there are actually local extremely strong rockbursts in the strong rockburst tunnel section of the Han-Ji-Wei Water Diversion Project. The concept and technology of rock burst prevention and control can be controlled with reference to strong rock burst. The specific footage speed index, arch spacing and model can be adjusted appropriately. At the same time, the water hammer drilling rig equipped with TBM can be used to carry out advanced drilling to degrade the extremely strong rockburst energy. Then, the tunneling support method mentioned above is adopted for crossing. In addition, double-type support TBM can also be selected. On the basis of the traditional open TBM, it adds a steel sheet installer and an auxiliary propulsion system, which is closely behind the shield to support the steel sheet. This further improves the safety and construction speed of TBM crossing strong rockburst. But its disadvantage is high cost.

The technical schemes of rock burst prevention and control with different grades are shown in Figure 6.

5.2.2 *Engineering application effect of graded rockburst prevention and control technology*

The technical scheme of prevention and control of minor rockburst has been fully applied in Xinjiang ABH project and Xinjiang EHe (EH) project. The ABH project in Xinjiang had 101 slight rockbursts by August 2019. The rock burst can be completely controlled by the support, and no equipment damage and casualties have occurred. Because of the compressive strength and integrity of surrounding rock of ABH project, it is easy to tunnel. The construction speed under slight rockburst is about 70 - 90% of that without rockburst. In Xinjiang EH project, a large area of continuous minor rockburst to moderate rockburst occurred in

Figure 6. Different grades of rock burst prevention and control technical schemes.

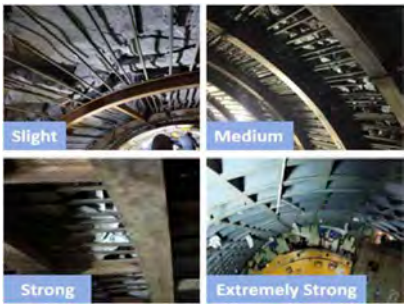

Figure 7. Engineering application effect.

front of the shield tail, and the slight rockburst adopted the technical scheme of combining long-distance arch frames and steel bars. The field application of tunneling for several kilometers, the effect is obvious, the safety is controlled, and the monthly footage can reach about 400m

In the ABH project and the YHJW project, the monitoring and prediction of rockburst microseisms include moderate rockburst, slight-moderate rockburst or moderate-strong rockburst, all of which adopt the above-mentioned rockburst prevention and control technical scheme. From the start of TBM excavation in ABH project to August 2019, there were 18 slight-moderate rockbursts and 32 moderate rockbursts. From the excavation to November 2019, there were 84 slight-moderate rockbursts, 158 moderate rockbursts and 80 moderate-strong rockbursts in the YHJW project. By adopting the above prevention and control technical scheme, the support resisted the impact of rockburst, no casualties occurred and the equipment was not greatly damaged. Moreover, it has reached a relatively fast TBM construction speed, which is about 50% - 70% of the construction speed without rockburst. The daily footage is about 10m when steel arch frame and steel bar row are used for support in ABH project.

The application of double-type support TBM in the construction of plateau railway provides another technical means for TBM to cross the extremely strong rock burst. There is no engineering case list of steel pipe segments in dealing with extremely strong rockburst, but the steel pipe segments in dealing with large deformation of soft rock in Xinjiang EH project have been verified by engineering, and the effect is very good.

The actual effect of engineering application of graded rockburst prevention and control technology is shown in Figure 7.

6 CONCLUSIONS

The paper takes the YHJW project and Xinjiang ABH project as the main cases to study the characteristics and prevention technology of rock burst in TBM construction of deep-buried tunnel. The results are compared with Jinping II hydropower station project. This study covers all three TBM construction projects in China with a buried depth of more than 2000m and strong rockburst. The technical scheme of TBM construction prevention and control of classified rockburst is put forward through engineering practice exploration, data statistics and theoretical analysis. It is verified in engineering and draws the following main conclusions.

(1) Different grades of rockburst have different effects on the construction speed, equipment and personnel safety of TBM. In particular, strong rockburst poses a great threat to the safety. However, the safety risk of rock burst in TBM construction can be basically controlled by adopting appropriate prevention and control concepts and technologies. By comparing and analyzing the construction speed with and without rockburst, the construction speed of TBM is reduced to about 70 - 90% of that without rockburst when the rockburst is slight. It decreases to about 50% - 70% in moderate rockburst and to about 25% - 50% in strong rockburst. Hence, the influence of rockburst should be fully considered in the surrounding rock classification, construction period and cost prediction of TBM construction.

(2) The occurrence time of rockburst shows that about 20% - 40% of rockburst occurs within 10h after excavation. The frequency of rockburst is the highest within 10 h - 24 h after excavation. More than 90% rockburst occurred within 24 h after excavation. About 9% of the strong rockburst has a lag time of 24 h - 48 h. From the location of rockburst, more than 30% moderate and strong rockburst occurred in the area from shield to tunnel face. Above 90% moderate and strong rockburst occurred within 15m behind the tunnel face. The scheme of actively controlling the penetration speed of TBM can make about 80% - 90% of strong rockburst occur in the area from TBM shield to heading face. This provides favorable conditions for TBM rockburst prevention and control. The penetration speed of TBM actively controlled by strong rockburst is generally about 3 m - 5 m per day, which can be determined according to different engineering conditions.

(3) On the basis of the influence of rockburst on TBM construction and its temporal and spatial characteristics. The structure, construction characteristics, safety and speed of TBM are comprehensively considered. For four levels of rockburst, namely, slight, moderate, strong and extremely strong, this paper puts forward the corresponding rockburst prevention and control objectives, rockburst prevention and control criteria (i.e., construction speed control, risk control, time and space control, hierarchical control) and rockburst prevention and control technical scheme. Thereby, a 4-4-4-4 theoretical and technical system of rock burst prevention and control based on monitoring, equipment, excavation and support is constructed.

To sum up, using the prevention and control technical scheme proposed in this paper, one of the TBM in Xinjiang ABH project has safely and efficiently passed through all the medium rock burst tunnels, and completed the 14km excavation of the bid section. TBM in Lingnan section of the YHJW project passes through the 18km rockburst tunnel section. During the construction of the second tunneling section of TBM, it has passed through the 5km continuous strong rockburst tunnel section, and the average monthly footage of the strong rock burst tunnel section has reached 110m. The proposed concept and technology of rock burst prevention and control have achieved good prevention and control effect in practical engineering application, which can provide important reference for subsequent ultra-deep tunnel construction.

ACKNOWLEDGMENTS

Financial support from the PowerChina Chengdu Survey and Design Research Institute Co. Ltd. (Grant No. NZL022) and Xinjiang Irtysh River Investment and Development (Group) Co. Ltd. (Grant No. EQ075/FY056) are gratefully acknowledged. Valuable comments and constructive suggestions from Editor and anonymous reviewers are also acknowledged.

REFERENCES

Du, L.J., 2017. Progresses, Challenges and Countermeasures for TBM Construction Technology in China. Tunnel Construction, 37(09), pp. 1063–1075.

Yang, Y., Du, L.J., Li, Q.W., et al, 2023. Predicting the Accuracy and Applicability of Micro-Seismic Monitoring of Rock Burst in TBM Tunneling Using the Data from Two Case Studies in China. Sustainability, 15(5), pp. 4232.

Yu, Q., Tang, C.A., Li, L.C., et al, 2014. Nucleation process of rockbursts based on microseismic monitoring of deep-buried tunnels for Jinping IIHydropower Station. Chinese Journal of Geotechnical Engineering, 36(12), pp. 2315–2322.

Xue, J.P., 2019. Construction Technology of Open TBM Safely and Rapidly Pass through Strong Rockburst Formation of Lingnan Section on Qinling Tunnel of Hanjiang River-Weihe River Water Conveyance Project. Tunnel Construction, 39(06), pp. 989–997.

Abdul, M.N., Hafeezur, R., Muhammad Z.E., et al, 2019. Static and Dynamic Influence of the Shear Zone on Rockburst Occurrence in the Headrace Tunnel of the Neelum Jhelum Hydropower Project, Pakistan. Energies, 12(11), pp. 2124.

Øyvind D., 2016. Prediction of Brittle Failure for TBM Tunnels in Anisotropic Rock: A Case Study from Northern Norway. Rock Mechanics and Rock Engineering, 49 (6), pp. 1–23.

Ma, C.S., Chen, W.Z., Tan, X.J., et al, 2018. Novel rockburst criterion based on the TBM tunnel construction of the Neelum-Jhelum (NJ) hydroelectric project in Pakistan. Tunnelling and underground space technology, 81(2018), pp. 391–402.

Zhao, Z.N., Feng, X.T., Chen, B.R., 2017. Activity laws of microseisms and rockbursts in deep tunnels by TBM tunneling. Chinese Journal of Geotechnical Engineering, 39(07), pp. 1206–1215.

Chen, B.R., Feng, X.T., Zeng, X.H., et al, 2011. Real-time microseismic monitoring and its characteristic analysis during tbm tunneling in deep-buried tunnel. Chinese Journal of Rock Mechanics and Engineering, 30(02), pp. 275–283.

Wang, J., 2019. Study on rock burst prediction of Hanjiang River-to-Weihe River Qinling Water Conveyance Tunnel based on microseismic monitoring. Water Conservancy Construction and Management, 39(11), pp. 7–12.

Ma, T.H., Tang, C.A., Tang, L.X., et al, 2016. Mechanism of rock burst forcasting based on micro-seismic monitoring technology. Chinese Journal of Rock Mechanics and Engineering, 35(03), pp. 470–483.

Du, L.j., Wang, J.X, Hong, K.R., et al, 2020. Research on Accuracy and Applicability of Microseismic Monitoring of Rock Burst in TBM Construction. China Civil Engineeering Journal, 53 (S1), pp. 278–285.

Chen, X.R., Liu, N., Pan, Y.B., et al, 2015. Researches on rock burst mechanism and engineering prevention measures of deep buried tunnel.Water Power, 41(11), pp.67–71.

Zhang, P., Zeng, X.H., Li, X.C., et al., 2011. Study on comprehensive measures for control of heavy rock burst during construction of diversion tunnel for Jinping Hydropower Station II. Water Resource and Hydropower Egineering, 42(3), pp. 61–65.

Xiao, Y.X., Feng, X.T., Chen, B.R., et al, 2011. Rockburst risk of tunnel boring machine part-pilot excavation in very strong rockburst section of deep hard tunnel. Rock and Soil Mechanics, 32(10), pp. 3111–31118.

Hou, J., Zhang, C.S., Shan, Z.G., 2011. Rockburst Characteristics and the Control Measures in the Deep Diversion Tunnel of Jinping II Hydropower Station. Chinese Journal of Underground Space and Engineering, 7 (6), pp. 1251–1257.

Wu, S.Y., Zhou, J.F., Chen, B.R., et al, 2015. Effect of excavation schemes of tbm on risk of rock burst of long tunnels at jinping ii hydropower station. Chinese Journal of Rock Mechanics and Engineering, 34(4), pp. 728–734.

Li, H.P., 2017. Rock burst prevention and control technology for diversion tunnel of Jin-ping two hydropower station. Construction Machinery, 04, pp. 79–82.

Tunnelling for a Better Life – Yan, Celestino, Thewes & Eberhardt (Eds)
© 2024 The Author(s), ISBN 978-1-032-80042-4
Open Access: www.taylorfrancis.com, CC BY-NC-ND 4.0 license

Prediction model of TBM tunneling speed based on geological parameters

Yalei Yang
School of Mechanical Engineering, Shijiazhuang Tiedao University, Shijiazhuang, China

Lijie Du*
Collaborative innovation center for performance and safety of Large-scale infrastructure, Shijiazhuang Tiedao University, Shijiazhuang, China

Rong Tang
School of Mechanical Engineering, Shijiazhuang Tiedao University, Shijiazhuang, China

Fei Wei & Huilan Zhang
Xinjiang Irtysh River Investment and Development (Group) Co., Ltd., Urumqi, China

ABSTRACT: The penetration rate (PR) of tunnel boring machine (TBM) is often used to evaluate the tunneling performance and predict the construction period cost. But most prediction models of penetration rate are based on a single specific project, which leads to poor universality of the models. Besides, the selection of cutter head speed in the prediction of construction period in the survey and planning stage depends on manual experience and lacks theoretical guidance. Therefore, based on several TBM engineering data of different surrounding rocks and different diameters, this paper statistically analyzes the distribution law of cutter head speed (N) and the relationship between field penetration index (FPI) and geological parameters (uniaxial compressive strength (UCS) and rock mass integrity coefficient (Kv)) and penetration (P). The results show that FPI is significantly related to geological parameters and P is significantly related to FPI. Geological parameters and tunneling parameters are the main factors affecting the penetration rate. Based on this, the FPI prediction model, P prediction model and the calculation model of cutter head speed are established, and then the prediction model of penetration rate is obtained. The accuracy and reliability of this model have been verified and analyzed by the ErHe (EH) project in Xinjiang, and the average prediction error is 15.15%, which has a good effect and can provide theoretical support for the cost prediction of the construction period in the survey and planning stage.

Keywords: TBM, penetration rate, Geological parameters, Different projects, Prediction model

1 INTRODUCTION

The tunnel boring machine (TBM) has been widely used in many tunnel construction projects such as railway, highway, water conveyance and hydropower development because of its many advantages in construction efficiency, tunneling safety and ecological protection. Recently, the analysis and prediction of tunneling performance has become a hot issue in TBM industry (Shang et al.,2007) The penetration rate (PR) is one of the main indexes to evaluate the tunneling performance of TBM. The research on the prediction of PR can provide theoretical support for TBM tunneling performance evaluation and construction period prediction. Nowadays, the research on TBM PR prediction mainly focuses on two aspects: on the one hand, it is based on theoretical analysis of indoor tests or numerical simulation; On the other hand, it is the analysis of engineering data based on tunneling parameters. In theoretical analysis, Boyd (1986) made full use of numerical simulation to make dimensional analysis of tunneling performance, and puts forward the concept of specific energy. By calculating the driving power required by the cutter head, the PR can be obtained. But the specific energy can't be calculated and analyzed at present, so the prediction model has little practical application. The CSM model (Luo, et al.,2018; Wu, et al., 2020) mainly calculated the hob penetration of TBM based on the force balance method through many linear cutting tests. Nevertheless, the data obtained from the indoor cutting test ignores the actual rock characteristics,

*Corresponding author: dulj@stdu.edu.cn

DOI: 10.1201/9781003495505-300

which leads to the relatively conservative prediction results of the model. The NTNU model (Jing, 2022) was based on a large number of geological parameters and many laboratory tests, and considers many factors that affect the tunneling parameters, and uses various mechanical variables to predict the PR. But the model relies heavily on the previous engineering data, so it is necessary to re-introduce the revised data for the new tunnel project. Thus, the model has great limitations. In the aspect of engineering data analysis, Alber (2000) put forward the concept of specific penetration based on field excavation data, and established the relationship model between specific penetration and UCS. But the model only considers the UCS and ignores the influence of other factors, so the prediction accuracy of the model is low. Du et al. (2015) studied the field data of a super-long tunnel in Northeast China, and selected factors such as UCS and integrity coefficient (Kv) to establish a field penetration index (FPI) prediction model by multivariate nonlinear fitting method. Zhou et al. (2021) used data mining clustering method to select geological and excavation parameters to build a prediction model of excavation speed. Gholaimi (2012) selects UCS, structural plane conditions and other influencing factors, and establishes a prediction model of PR by using neural network. Mahdevari et al. (2014) selects UCS, Brazilian tensile strength (BTS) and brittleness index (BI), etc., and establishes the prediction model of PR through support vector machine. Yagiz (2011) and Armaghani et al. (2017) used particle swarm optimization algorithm to predict the PR. Luo et al. (2018) analyzed the relationship between penetration and cutterhead thrust and torque, and established the prediction model of PR with UCS, Kv and cutterhead thrust as inputs. Wu et al. (2020) analyzed the engineering data of several tunnels, and established the prediction formula of FPI based on factors such as UCS, Kv and tunnel diameter (D). Xu et al. (2021) established penetration prediction formulas by curve fitting and multiple linear regression respectively according to the analysis of several engineering data. Feng et al. (2021) predicted the cutterhead thrust, rotating speed and FPI of TBM based on the data of Jilinyinsong project, and the results showed that the prediction effect was good. To sum up, it can be found that most of the PR prediction models are based on the actual tunneling data of TBM in a single specific project. The model has poor universality. Some real-time prediction models of PR are based on the data after excavation and cannot be used in the planning stage of construction period.

2 FACTORS AFFECTING TBM PR

Based on the previous related research literature and a large number of engineering practices, it is shown that UCS, Kv, F and N are the main factors affecting the PR of TBM. Kv can be obtained by testing rock mass and rock wave velocity during exploration or construction. It can also be calculated by the number of joints of surrounding rock exposed after excavation, so as to verify the measured Kv. Code for Geological Exploration of Water Resources and Hydropower Engineering (GB 50487-2008) states that the integrity of rock mass is closely related to the degree and stability of rock mass fragmentation, and the degree of correlation is shown in Table 1. With the increase of Kv, the surrounding rock is more complete and the stability of rock mass is better.

The size of P is determined by F and surrounding rock condition. The N is mainly regulated by TBM drivers according to geological conditions and combined with subjective experience. Under the condition of poor surrounding rock, TBM driver actively controls the thrust and speed of cutter head, and then limits the penetration. Therefore, this paper introduces the field penetration index FPI to establish the relationship between tunneling parameters and geological parameters. The FPI can comprehensively reflect the difficulty of TBM tunneling in rock mass. The calculation formula is shown in formula (1).

$$FPI = \frac{F}{nP} \tag{1}$$

Where n represents the number of disc cutters.

3 PREDICTION MODEL OF FPI BASED ON GEOLOGICAL PARAMETERS

3.1 *Correlation analysis between FPI and geological parameters*

With the data in the range of 82+606-77+548 in Dahuofang Project (DHF), the influence of UCS and Kv on the distribution of FPI is analyzed, and the three-dimensional scatter and color map of the data is drawn. The result is shown in Figure 1.

It can be seen from Figure 1 that the distribution law of FPI based on UCS and Kv is obvious. In the case that both UCS and Kv are small or UCS is small but Kv is large, FPI is at a low level, which indicates that TBM is easy to penetrate. However, in the range where UCS and Kv are both large, the distribution of FPI is also obvious. When UCS is in the range of 60-70 MPa and Kv is in the range of 0.6-0.7, FPI is in

Table 1. The relationship between Kv and rock integrity degree.

Kv	>0.75	0.75~0.55	0.55~0.35	0.35~0.15	<0.15
Integrity degree	complete	Relatively complete	Relatively broken	Broken	Extremely broken

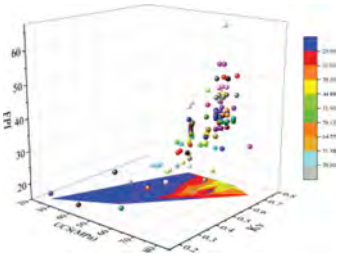

Figure 1. Three-dimensional scatter and map of FPI, UCS and Kv.

the range of 38-44 kN·r·mm^{-1}. The distribution of FPI is annular when UCS is 60-80 MPa and Kv is 0.5-0.7. Above all, FPI has a significant correlation with UCS and Kv, and its distribution law is obvious.

3.2 *Prediction model of FPI*

The engineering data of Zhuxishuiku (ZXSK) Project, DHF Project and ErHe (EH) Project (including TBM7 and TBM8) are selected, and the pile numbers are 21 +891-17+731, 82+620-77+546, 172+578-169+816 and 173+863-177+410, respectively. The correlation between FPI and UCS and Kv is analyzed. The scatter plot of FPI, UCS and Kv is drawn, and its fitting analysis is carried out. The result is shown in Figure 2.

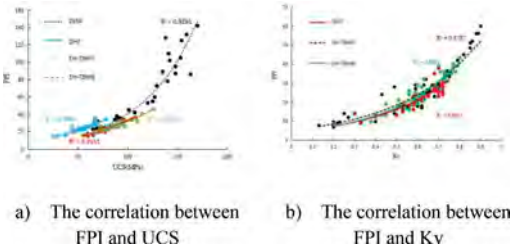

a) The correlation between FPI and UCS

b) The correlation between FPI and Kv

Figure 2. The correlation between FPI and UCS and Kv.

As can be seen from Figure 2, the FPI of the four TBM is highly correlated with UCS and Kv. The correlation coefficient R^2 is close to 0.9, showing an obvious exponential relationship and a significant positive correlation. With the increase of UCS and Kv, FPI also increases. As the rock becomes harder and more complete, it is more difficult for TBM to penetrate for tunneling, which is consistent with the actual working conditions.

Based on the analysis, it is found that FPI has obvious correlation with UCS and Kv. However, the correlation between other geological parameters and FPI is not significant, or there is collinear superposition effect with UCS and Kv, and its data is not easy to obtain in the exploration stage. Therefore, UCS and Kv are taken as independent variables, and FPI is taken as dependent variables for prediction and analysis. Furthermore, FPI has a nonlinear relationship with UCS and Kv. Both of them show exponential distribution. So the FPI, UCS and Kv were regressed by multiple nonlinear regression.

Select 400 groups of data from 4 TBMs of ZXSK Project, EH Project (including TBM7 and TBM8) and DHF Project for multivariate nonlinear regression fitting, and initially set the optimal mathematical expression as shown in Formula (2).

$$FPI = \mathrm{a} \times \exp(b \cdot UCS + c \cdot Kv + d) + e \qquad (2)$$

Where: a, b, c, d and E are all mathematical regression parameters; The initial set values are a=0.328, b=0.017, c=2, d=1 and e = 0.15; Set constraints a≥0, b≥0 and c≥0.

After 19 iterations, the sum of squares of residuals has remained unchanged and the value is too small. By fitting, the estimated values of the optimal regression parameters are a=0.497, b=0.014, c=0.683, d=2.190, and e=0.836. At this time, the correlation coefficient R2 of the fitting formula is 0.801. To sum up, the empirical formula of multivariate nonlinear regression of FPI is shown in Formula (3).

$$FPI = 0.497\exp(0.014UCS + 0.683Kv + 219) + 8.367 \qquad (3)$$

The formula has a high overall fitting degree, and the corresponding FPI value can be obtained according to the geological data in the preliminary investigation stage of the project.

4 PREDICTION MODEL OF P BASED ON FPI

The previous literature research [Du et al.] shows that P has a significant correlation with FPI. However, previous studies are based on a single engineering data fitting, and the prediction model lacks universality. Therefore, this paper brings TBM cluster data into the relationship model between P and FPI.

The pile number ranges of DHF project, EH project (including TBM1, TBM2 and TBM3), Shenzhen Metro Line 6 (SZM-6) project and Gaoligongshan (GLGS) project are 82+620-77+546, 14+133-17 +922, 57+797.40-54+415.19 62+973-67+570, 0 +242-2+757 and 226+126-225+784 respectively. Based on these tunneling data, the fitting relationship between P and FPI is established by fitting regression method, as shown in Figure 3.

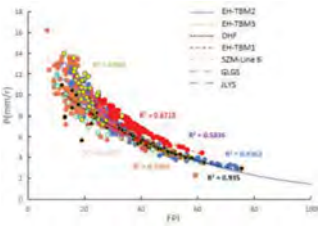

Figure 3. The correlation between P and FPI in different projects.

It can be seen from Figure 3 that there is a strong correlation between P and FPI, and the correlation coefficient R^2 is close to or greater than 0.9. The decrease of P with the increase of FPI indicates that the drivability of rocks is getting worse. When the FPI is small, the dispersion degree of P is large. With the increase of FPI, the fluctuation degree of P is smaller. This is mainly because when the FPI is small, the rock can be excavated better, and the main driver can cause a large fluctuation of P by adjusting F slightly. However, when the FPI is large, the rock mass is difficult to tunnel, and the change of P will be small if the main driver increases the thrust. Furthermore, it can be seen that the fitting curves of the seven projects are very close. It can effectively avoid the problem of poor universality of the prediction model caused by a single project to some extent if a unified fitting formula of P and FPI is established through the TBM data of multiple projects. Based on this, 800 groups of excavation data of the above seven projects are fitted and regressed as a whole, and a P prediction model suitable for multiple projects is established, as shown in Figure 4.

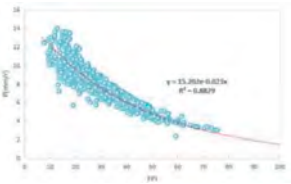

Figure 4. The fitting relationship between P and FPI based on multi-engineering.

By fitting and regressing the data of the above seven projects as a whole, it can be seen from Figure 4 that the relationship between P and FPI is exponential and has a strong correlation, and the correlation coefficient R^2 reaches 0.883. The data in Figure 4 shows the same trend as that in Figure 3. The prediction model of P is shown in Formula (4).

$$P = 15.202\exp(-0.023\mathrm{FPI}) \tag{4}$$

5 THE THEORETICAL CALCULATION METHOD OF CUTTER HEAD SPEED UNDER DIFFERENT SURROUNDING ROCKS AND DIFFERENT DIAMETERS

The cutter head speed is related to surrounding rock and cutter head diameter. But in the stage of survey and design or construction period planning, there is no theoretical calculation method for selecting cutter head speed under different surrounding rocks and different diameters, and the selection is always based on experience. Thus, based on the engineering data of TBM with different diameters, this paper puts forward the theoretical calculation formula of cutter head speed by using mathematical statistics method.

5.1 *The theoretical calculation formula of cutter head speed*

When designing a TBM, it is considered that if the cutterhead speed is too high, it will generate high temperatures, which will affect the performance and life of the bearings and some seals. At the same time, the side cutters will be quickly damaged. Therefore, the allowable peripheral linear speed (v) of the cutterhead is generally 2.5m/s. Based on this principle, the cutterhead speed can be determined by the formula (5).

$$\mathrm{N} = v/\pi D = 2.5 \times 60/\pi D = 47.7/D \tag{5}$$

Furthermore, the relationship between the speed of the cutterhead and its diameter can be written in the form of formula (6).

$$\mathrm{N} = x/D \tag{6}$$

Where x is the cutter head speed factor, generally taken as 45-50, and the corresponding circumferential linear speed of the cutterhead is 2.4-2.6m/s.

In addition, considering that the rotation of the cutter head during TBM tunneling will cause a certain amount of centrifugal force on the rock slag. The slag tapping effect of TBM will be affected if the centrifugal force is too large. Hence, in the design of the rotational speed, the centrifugal acceleration generated by the rock debris should be smaller than its own gravitational acceleration g. That is, the requirement of formula (7) should be met.

$$v^2/r \le g \tag{7}$$

Where r is the radius of the cutter head.

The formula (8) can be further derived from the formulas (5) and (7).

$$v = N\pi D/60 \le \sqrt{gD/2} \tag{8}$$

Then, the allowable cutterhead speed meeting the design requirements is obtained, as shown in formula (9).

$$N \le 42.6D^{-0.5} \tag{9}$$

It can be seen from formula (8) that the cutter head speed is often calculated according to the maximum cutter head speed in TBM design. However, in practical engineering, the TBM operator will adjust the cutter head speed according to his personal experience and the change of surrounding rock conditions, so it will be quite different from the maximum cutter head speed.

In order to obtain a reasonable formula for calculating cutter head speed, firstly, the cutter head diameter and rated speed of some representative TBM projects in China, such as ZXSK project, Nabang (NB) project, Chongqing Metro (CQM) project (including Line 5 and Line 6), Xinjiang EH project

(including VII and IV sections), Jilinyinsong (JLYS) project, DHF project, Shaanxi Yinhanjiwei (YHJW) project, Gaoligongshan (GLGS) project and Jinping (JP) II hydropower station project, are statistically analyzed. The distribution law of rotating speed of TBM cutter heads with different diameters is studied, and the results are shown in Table 2.

Table 2. Statistics of cutter head diameter and rotation speed of some representative TBM projects in China.

Proejct	TBM type	Diameter/(m)	Cutter head speed/(r/min)
ZXSK	open-type	4.03	0-12
NB	open-type	4.53	0-12
CQM-6	open-type	6.36	0-10.53
ABH	open-type	6.53	0-9.8
CQM-5	Single shield	6.83	0-0.54-11.9
EH-VII	open-type	7	0-10.9
EH-IV	open-type	7	0-10.9
JLYS	open-type	7.93	0-6.7
DHF	open-type	8.03	0-4.63-6.93
YHJW	open-type	8.05	0-6.87
GLGS	open-type	9.03	0-3.4-6.5
JP	open-type	12.4	0-4.5

From Table 2, it can be seen that with the increase of cutter head diameter, the rated speed of cutter head also decreases. It shows that the diameter has a certain influence on the speed of TBM cutter head. Moreover, the influence of surrounding rock conditions on the speed of TBM can be obtained through the speed distribution law of different surrounding rock types in different projects. The regular distribution statistics are shown in Figure 5.

Figure 5 shows that the cutter head speed decreases with the increase of cutter head diameter under the same surrounding rock conditions. The overall trend of cutter head speed in different surrounding rock types is that it also decreases with the deterioration of surrounding rock. The same diameter TBM, under the same surrounding rock grade, the cutter head rotation speed is similar, showing only a small change, such as EH-TBM1, EH-TBM2, EH-TBM10 and EH-TBM5. The average rotation speed of cutter head varies in the range of 0~1.4 r/min under the same surrounding rock grade. But the rotating speed distribution of TBM cutterheads with different diameters is quite different under the same surrounding rock grade. Take NB project and EH project for example, the average rotating speed of TBM cutter head changes by 41.15% under class II surrounding rock. It is further explained that diameter and surrounding rock are the main influencing factors of cutter head speed. The average and peak values of the rotating speed of eight TBM cutterheads under various surrounding rock grades are statistically analyzed, as shown in Table 3.

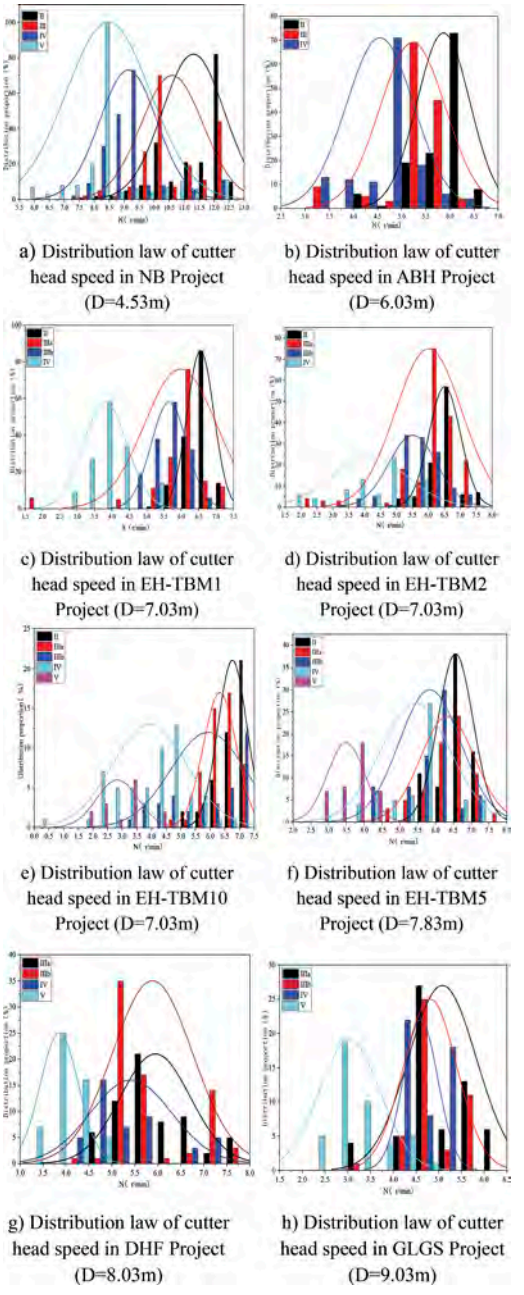

Figure 5. Speed distribution law of TBM cutter head with different diameters in different projects.

To sum up, it is further explained that the diameter and surrounding rock are the main influencing factors of cutter head speed. So the factors of surrounding rock and diameter are included in the calculation of cutter head speed, which are reflected in the form of correction coefficient respectively. The diameter factor is represented by k_1, and the surrounding rock factor is represented by k_2. In this

Table 3. Distribution statistics of rotating speed of eight TBM cutterheads under different surrounding rock types.

	II		IIIa		IIIb		IV		V	
Project Class	Mean	Max	Mean	Max	Mean	Max	Mean	Max	Mean	Max
NB	11.3	11.2	10.6	10.6	10.5	10.5	9.1	9.1	8.5	8.6
ABH	5.9	5.7	5.2	5.2	5.2	5.2	4.6	4.5	—	—
EH-TBM1	6.5	6.6	6.0	6.0	5.6	5.6	3.8	3.7	—	—
EH-TBM2	6.5	6.5	6.0	6.0	5.5	5.5	4.1	4.0	—	—
EH-TBM10	7.0	6.8	6.3	6.4	5.9	5.7	3.9	4	2.8	2.7
EH-TBM5	6.6	6.6	6.3	6.2	5.8	5.7	5.4	5.2	3.5	3.5
DHF	—	—	5.9	6.0	5.9	6.1	5.4	5.4	3.9	3.7
GLGS	—	—	5.1	5.2	4.8	4.7	4.6	4.5	3.0	3.0

paper, TBM with D=7.03 m is taken as reference diameter. So the calculation formula of cutter head speed is as shown in Formula (10).

$$N = k_1 k_2 N_0 \tag{10}$$

Where: N- cutter head speed, r/min. k_1- diameter coefficient. K_2- surrounding rock coefficient. N_0- cutter head speed under reference diameter, r/min.

5.2 *Determination of cutter head diameter correction coefficient*

According to the research of [Du Yanliang et al. [2]], the influence of TBM diameter on cutter head speed is mainly related to the linear speed of edge cutter. The relationship between cutter head speed and TBM diameter in TBM design is shown in Formula (11).

$$N = \frac{X}{D} \tag{11}$$

Where: X- velocity coefficient, generally 45 or 50; D- cutter head diameter.

While the calculation formula of reference speed N_0 is formula (12).

$$N_0 = \frac{X}{D_0} \tag{12}$$

The influence of diameter on TBM cutter head speed can be measured by calculating the ratio of cutter head speed N to reference cutter head speed N_0, that is, the diameter coefficient k_1. The formula for calculating the diameter coefficient k_1 is as shown in Formula (13) with reference to the ratio of the diameter D_0 to the design diameter D.

$$k_1 = \frac{N}{N_0} = \frac{D_0}{D} \tag{13}$$

5.3 *Selection of correction coefficient of surrounding rock*

To obtain the cutter head rotation speed of TBM reference diameter, the average rotation speed of six 7.03m diameter TBM cutter heads in Xinjiang EH Project was statistically compared and analyzed, and the results are shown in Figure 6.

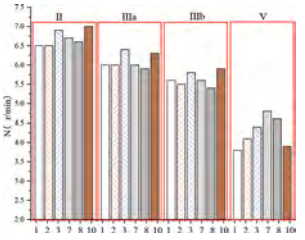

Figure 6. Statistical analysis of cutter head speed under TBM reference diameter (D=7.03m) in EH project.
Note: The horizontal axis number in the figure is the code name of TBM in EH project.

From the comparative analysis of the average cutter head speed in Figure 6, it can be seen that the distribution of TBM cutter head speed is in a small range under the same surrounding rock grade. The maximum and minimum values of cutter head speed are only 0.5 r/min under Class-II and Class-IIIb, 0.6 r/min under Class-IIIa, 1.6 r/min under Class-IV and 1r/min under Class-V, and the overall fluctuation range is small. It can be seen that different surrounding rocks have different effects on the cutter head speed. The reference rotational speed N_0 of the reference diameter D_0(7.03m) under different surrounding rock grades can be obtained by averaging the rotational speeds of six sets of 7.03 m diameter TBM under the same surrounding rock grade. The results are shown in Table 4.

Table 4. Reference cutterhead speed N_0 under different surrounding rock grades.

	N_0(r/min)				
D_0(m)	II	IIIa	IIIb	IV	V
7.03	6.6	6.0	5.5	4.5	3.0

It is necessary to study and analyze the law of cutter head speed under the same TBM diameter in different

projects considering the influence of surrounding rock factors. Therefore, the tunneling data of TBM in NB Project (D=4.53m) and Beijiangyinshui (BJYS) Project (D=4.53m) are selected respectively, and the cutter head speed is statistically compared and analyzed. The results are shown in Figure 7.

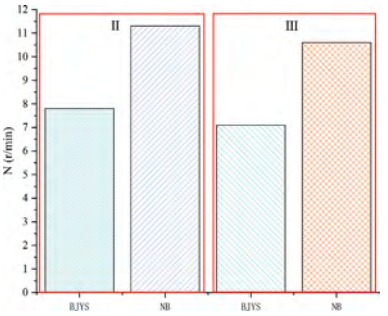

Figure 7. Statistical analysis of cutter head speed under the same TBM diameter in different projects.

As can be seen from Figure 7, the diameter of TBM in BJYS project and NB project is the same, but the cutter head speed is obviously different under the same surrounding rock grade. The main reason is the influence of surrounding rock factors. The physical and mechanical properties of the two projects are different from the surrounding rock lithology under the same surrounding rock grade. The UCS of BJYS project is 60.15-203 MPa, the content of quartz is 20%-45%, and the lithology is medium-coarse grained biotite granite. The UCS of Nabang project is 100-220 MPa, the content of quartz is 25%-35%, and the lithology is mixed gneiss. Without the influence of the diameter factor, the TBM cutter head rotation speed of BJYS project under Class-II surrounding rock is about 0.68 of that of NB project, and it is about 0.67 under Class-III surrounding rock. The k_2 can be obtained from Formula (10) without the influence of the diameter factor, as shown in Formula (14). The TBM cutter head rotation speed of BJYS project under class II surrounding rock is about 0.68 of NB project, and it is about 0.67 under class III surrounding rock. That is, the correction coefficient k_2 of surrounding rock is 0.67 and 0.68 respectively.

$$k_2 = \frac{N}{k_1 N_0} \tag{14}$$

In order to cover more specifications of TBM, the cutter head speeds of TBM in ABH project (D=6.53m), DHF project (D=8.03m) and GLGS project (D=9.03m) are statistically analyzed, which can be obtained from Table 2. First, k_1 is calculated according to Formula (7), and then the distribution range of surrounding rock correction coefficient k_2 is obtained according to actual cutter head speed n and cutter head speed N0 under reference diameter, as shown in Table 5.

In summary, according to Formula (10) and Formula (13), and referring to Table 4 and Table 5, the rotating speed of TBM cutter head with different diameters and different surrounding rock grades can be calculated.

Table 5. The range of the correction coefficient k_2 of surrounding rock.

Class	k_2
II	0.65~0.75
IIIa	0.75~0.85
IIIb	0.85~0.95
IV	0.95~1.05
V	1.05~1.15

6 PREDICTION MODEL OF PR

The PR represents the tunneling distance of TBM per unit time, which can be expressed by N and P and is the product of them, as shown in Formula (15).

$$PR = N \cdot P \tag{15}$$

Based on the above prediction model, the prediction model of PR can be obtained as shown in Formula (16).

$$PR = 15.202 k_1 k_2 N_0 \cdot e^{-0.023FPI} \tag{16}$$

The application flow of the PR prediction model is shown in Figure 8.

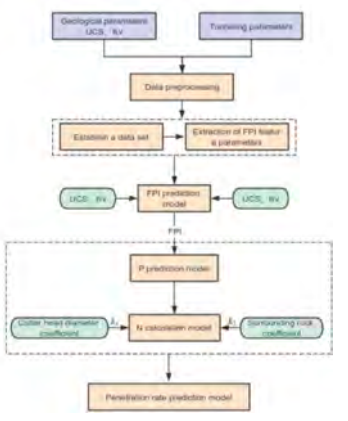

Figure 8. The application flow of the PR prediction model.

Based on the geological parameters (UCS and Kv, etc.) obtained in the geological exploration stage or construction stage, firstly, the data is cleaned to eliminate abnormal data, and then the FPI value is obtained by inputting the FPI model. Thirdly, the FPI is substituted into the P model to get the value of P. Fourthly, considering the influence of TBM diameter and surrounding rock, the diameter correction coefficient $k_1$and surrounding rock correction

coefficient $k_2$are selected and substituted into the theoretical calculation formula of N, and the value of n is obtained. Finally, based on the above model, the prediction model of tunneling speed is obtained.

7 VERIFICATION AND ANALYSIS OF THE MODEL

7.1 *Project verification of FPI prediction model*

Based on the geological data in the investigation stage, the FPI prediction model can get the corresponding FPI value. The prediction results of FPI were compared and tested by selecting 30 sets of data from DHF project, EH-TBM7 project and EH-TBM8 project. The comparison between FPI prediction and actual value is shown in Figure 9.

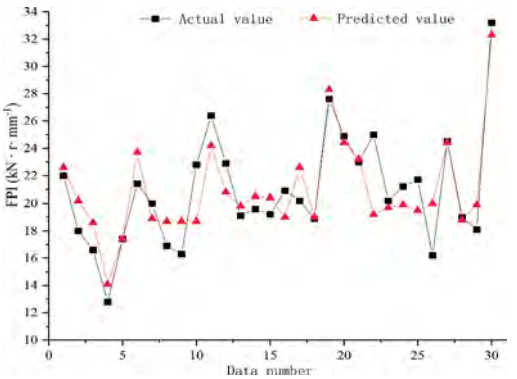

Figure 9. Comparison between predicted value and actual value of FPI.

It can be seen from Figure 9 that the predicted value of FPI is generally close to the actual value, with the maximum prediction error of 23.5% and the average prediction error of 7.84%. The verification of project site data shows that the prediction accuracy of this model is good.

7.2 *Project verification of penetration prediction model*

Select 30 groups of data from EH-TBM7 and EH-TBM8 projects to verify the prediction effect of P model. The comparison between the predicted value and the actual value of p is shown in Figure 10.

As can be seen from Figure 10, the actual value of p is close to the predicted value, with the maximum prediction error of 25.5% and the average prediction error of 11.91%. The prediction errors of some data points in Figure 10 are relatively large, one is that FPI itself has certain prediction errors, and the other is that it may be caused by the artificial regulation of TBM drivers. But on the whole, the prediction effect of P is good, which can better reflect the relationship between P and FPI, and can lay a foundation for the subsequent prediction of PR.

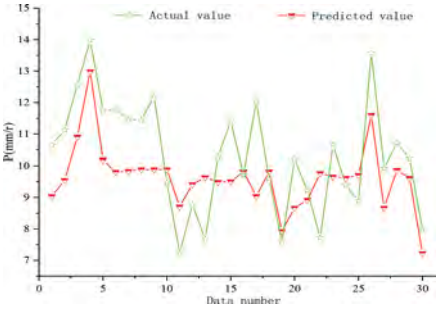

Figure 10. Comparison between predicted value and actual value of P.

7.3 *Project verification of PR prediction model*

The universality and accuracy of the PR prediction method are verified by selecting 40 groups of data from EH-TBM7 and EH-TBM8 projects in Xinjiang. Some prediction results are shown in Table 6.

Table 6. The statistics of PR prediction.

		Predicted				Actual	RE
UCS	Kv	FPI	P	N	PR	PR	(%)
66	0.6	25.22	8.5	5.8	49.4	50	1.28
76	0.69	28.98	7.8	6.8	53.1	49	8.32
80	0.63	29.30	7.7	7.1	55.0	44	25.1
69	0.63	26.31	8.3	6.6	54.8	47	16.6
…	…	…	…	…	…	…	…
81	0.7	30.63	7.5	6.9	51.9	50	3.71
65	0.56	24.54	8.6	5.2	45.0	48	6.34
82	0.73	31.41	7.4	6.8	50.2	47	6.79
76	0.59	27.62	8.1	6.5	52.3	48	9.06

The data in Table 6 are plotted as a point chart to clearly show the comparison effect between the predicted value and the actual value of PR, and the result is shown in Figure 11.

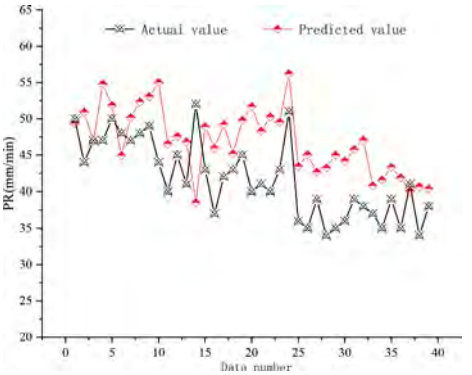

Figure 11. Comparison between predicted value and actual value of PR.

It can be seen from Figure 11 and Table 6 that the predicted value of PR is consistent with the actual value, but the predicted value is slightly larger than the actual value on the whole. The main reason is that in the actual tunneling process of TBM, the main driver will take the initiative to reduce the cutterhead speed or thrust due to the influence of geological conditions and tools. The predicted value is based on the previous high tunneling parameters, which leads to the predicted value slightly larger than the actual value. However, through validation analysis, the average prediction error is 15.15%, the maximum prediction error is 28.7%, and the minimum prediction error is only 0.14%. Overall, this indicates that the PR prediction effect is good. At the same time, since the validation analysis data is randomly selected and indicates that the prediction model is applicable, it can provide reference for the prediction of other engineering PR.

8 CONCLUSIONS

This paper, based on the data of several engineering sites, analyzes the main influencing factors of excavation speed from how to accurately estimate the construction period cost in the engineering investigation stage. The FPI prediction model and P prediction model are established. The theoretical calculation method of cutter head speed with different diameters and different surrounding rock grades is put forward. Furthermore, the relationship model between geological parameters and PR is established. The following research results are obtained: (1) The cutter head speed is mainly related to the diameter of TBM and surrounding rock. With the increase of TBM diameter or the deterioration of surrounding rock, the rotation speed also decreases. Therefore, the diameter correction coefficient and surrounding rock correction coefficient are put forward, and the value method of correction coefficient is determined. The theoretical calculation method of cutter head speed suitable for different diameters and different surrounding rock grades is established. (2) The fitting relationship between FPI, UCS and Kv is established, and both of them are exponentially distributed. Through multivariate nonlinear regression fitting, the empirical model of FPI is obtained and verified in project. The average prediction error is 7.84%. The P and FPI data of seven projects are analyzed by regression, and a more universal P prediction model is established. The average prediction error is 11.91% verified by field data. (3) The prediction method of PR is put forward, and the prediction model of PR is established based on geological parameters. Through engineering verification and analysis, the maximum prediction error is 28.7%, the minimum prediction error is only 0.14%, and the average prediction error of PR is 15.15%.

A more universal PR prediction model is established in this paper, based on the field data of several projects and considering the influence of geology and TBM diameter on PR. It can not only meet the cost prediction of the construction period in the early stage of TBM project, but also provide theoretical guidance for tool consumption prediction and tunneling performance evaluation.

ACKNOWLEDGMENTS

Financial support from the Xinjiang Irtysh River Investment and Development(Group) Co. Ltd. (Grant No. EQ075/FY056) is gratefully acknowledged. Valuable comments and constructive suggestions from Editor and anonymous reviewers are also acknowledged.

REFERENCES

Shang, Y.J., Yang, Z.F., Zeng, Q.L., et al, 2007. Retrospective analysis of TBM accidents from its poor flexibility to complicated geological conditions. Chinese Journal of Rock Mechanics and Engineering, 2007(12), pp. 2404–2411.

Alber, M., 2000. Advance rates of hard rock TBMs and their effects on project economics. Tunnelling and underground space technology, 15(1), pp. 55–64.

Boyd, R.J., 1986. Hard rock continuous mining machine: Mobile Miner MM-120. Rock Excavation Engineering Seminar; Howarth, DF, Ed. Department of Mining and Metallurgical Engineering, University of Queensland: Brisbane, Australia.

Du, L.J., Qi, Z.C., Han, X.L., et al, 2015. Prediction method for the boreability and performance of hard rock TBM based on boring data on site. Journal of China Coal Society, 40(06), pp.1284–1289.

Zhou, Z.l., Tan, Z.S., Li, Z.L., 2021. A data mining based prediction model for penetration rate. Journal of Basic Science and Engineering, 29(05), pp. 1201–1219.

Gholami, M., Shahriar, K., SharifzadYE, M., et al, 2012. A coMParison of artificial neural network and multiple regression analysis in TBM performance prediction. ISRM Regional Symposium 7th Asian Rock Mechanics Symposium: [s. n.].

Mahdevari, S., Shahriar, K., Yagiz, S., et al, 2014. A support vector regression model for predicting tunnel boring machine penetration rates. International Journal of Rock Mechanics and Mining Sciences, 72, pp. 214–229.

Yagiz, S., Karahan, H., 2011. Prediction of hard rock TBM penetration rate using particle swarm optimization. International Journal of Rock Mechanics and Mining Sciences, 48(3), pp. 427–433.

Armaghani, D.J., Mohamad, E.T., Narayanasamy, M.S., et al, 2017. Development of hybrid intelligent models for predicting TBM penetration rate in hard rock condition. Tunnelling and Underground Space Technology, pp. 63: 29-43.

Luo, H., Chen, Z.Y., Gong, G.F., et al, 2018. Advance rate of TBM based on field boring data. Journal of Zhejiang University(Engineering Science), 52(08), pp. 1 566–1 574.

Wu, X.L., Zhang, X.P., Liu, Q.S., et al, 2020. Prediction and classification of rock mass boreability in TBM tunnel. Rock and Soil Mechanics, 41(05), pp. 1 721-1 729+1 739.

Xu, H.Y., Gong, Q.M., Lu, J.W., et al, 2021. Setting up simple estimating equations of TBM penetration rate using rock mass classification parameters. Tunnelling and Underground Space Technology, 115(2021), pp. 104065.

Feng, S.X., Chen, Z.Y., Luo, H., et al, 2021. Tunnel boring machines (TBM) performance prediction: A case study using big data and deep learning. Tunnelling and Underground Space Technology, 110(2021), pp. 103636.

Jing, L.J., 2022. Research on TBM Tunneling Performace Predication and Intelligent Auxiliary Control. PhD Thesis. China University of Mining and Technology, China.

Tunnelling for a Better Life – Yan, Celestino, Thewes & Eberhardt (Eds)
© 2024 The Author(s), ISBN 978-1-032-80042-4
Open Access: www.taylorfrancis.com, CC BY-NC-ND 4.0 license

Research on prefabricated metro station structure and key assembly technologies

Xiuren Yang* & Fang Lin*
Beijing Urban Construction Design and Development Group co., Ltd, Beijing, China
National Engineering Research Center for Green & Safe Construction Technology in Urban Rail Transit, Beijing, China

ABSTRACT: The prefabrication and assembly construction technology for metro stations provides a new industrial construction mode for urban rail transit underground stations. It not only solves the winter construction problems in severe cold areas, but also demonstrates irreplaceable advantages in terms of quality, efficiency, safety, and environmental protection. This paper is based on the research and application of this technology by the research team in Changchun, Qingdao, and Shenzhen, China since 2012. It is a brief introduction to the prefabricated metro station structure system as well as the key technical achievements in the research and application of prefabricated assembly construction technology for metro station structures in the past 10 years, mainly including joint connection technology, key technology for the design of closed-cavity thin-walled components, structural mechanical behavior and calculation method of fabricated station, structure assembly design method and key technology, joint waterproof technology, etc. It has been proved by engineering practice that the prefabrication and assembly construction technology for metro stations significantly improves engineering quality and reduces operating and maintenance costs; Greatly improve construction efficiency, save labor, and shorten construction period; Green environmental protection, emission reduction and noise reduction, sustainable development; With wide applicability, it has significant technical, economic, and social benefits.

Keywords: metro station, prefabricated, grouted mortise-tenon joint, closed-cavity thin-walled components, prefabricated structure waterproof

1 INTRODUCTION

Promoting the industrialization of construction and the development of prefabricated building technology is an important measure to realize the optimization and upgrading of China's construction industry, practice the concept of green development and promote the realization of the dual carbon goals. In recent years, the country has constantly introduced policies to promote the development of prefabricated building technology and applications, and has made remarkable achievements. The proportion of prefabricated building in new construction projects around the country keeps rising, and the development of prefabricated building presents a prosperous situation.

Compared with the booming field of prefabricated buildings, the research and application of prefabricated technology in the field of underground engineering in China started late and the development was relatively lagging behind, especially in the application of prefabricated construction technology for large and complex underground structures. Ten years ago, in 2012, it was still in a blank state. The main application of prefabricated assembly technology for underground structures was basically limited to tunnel lining, municipal pipeline and utility tunnel structure constructed by shield tunneling method. Its application characteristics are relatively simple in structure type (circular or simple rectangular), small in structural section size, and simple in structure assembly method (such as using prefabricated assembly of whole ring pipe sections).

For the purposes of solving the problem of cast-in-place concrete construction in severe cold winter, the former Soviet Union carried out research and application of prefabricated assembly construction technology for the first time in metro stations and interval tunnel engineering in the 1980s (Frarov, 1994). The same problem existed in the construction of rail transit in the severe cold areas of Northeast China, where winter break lasted as long as 5 months a year, imposing huge pressure on the construction period.

In 2012, the author's research team carried out the research and application of the prefabricated structure construction technology for cut-and-cover metro stations based on the Changchun Metro Line 2

*Corresponding author: yangxr@bjucd.com; felyo@foxmail.com

DOI: 10.1201/9781003495505-301

Project. Up to now, a total of 21 prefabricated stations have been successfully built. It has been proved by practical engineering applications that prefabricated construction technology can not only solve winter construction challenges in severe cold areas, but also demonstrate irreplaceable advantages in terms of high quality, high efficiency, safety, environmental protection, etc. (Lawson, 2011; Baghchesaraei et al., 2016;Jiang et al., 2018; Yang et al., 2019, 2021 & 2022; Lin et al., 2023). This technology is also applicable to other non-severe cold areas. In the present age that the concept of engineering construction in China is gradually changing from the traditional economic applicability and aesthetics to the energy conservation, environmental protection and sustainable development, the successful construction of the first prefabricated station of Changchun Metro is a significant milestone, arousing the widespread concern of industry and society. This innovation is of great significance to promote the deep integration of rail transit engineering construction with industrialization and informatization, as well as the transformation of the construction industry from the traditional labor-intensive industry to the high-end industry.

Based on the prefabricated stations of Changchun Metro, this paper briefly discusses the research achievements and applications of the research team in the construction technology of fully prefabricated structures in the past 10 years (Yang 2020) for reference in the industry.

2 STRUCTURE SYSTEM OF PREFABRICATED STATION

Take the prefabricated stations of Changchun Metro as an example. All prefabricated stations of Changchun Metro are 2-storey underground standard stations with 11m island platforms, and the largest prefabricated station structure is 246m long. Except for the air ducts at both ends of the station and the shield working shafts in the section, which are of cast-in-place concrete structure, the standard sections in the middle are all of prefabricated structure. Figure 1 shows the schematic diagram of the prefabricated station structure system.

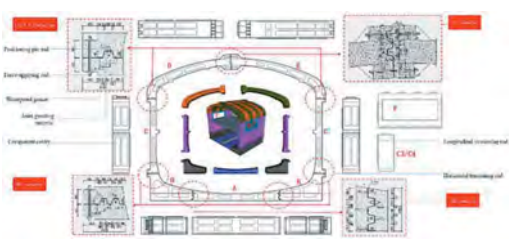

Figure 1. Schematic diagram of prefabricated station structure system.

2.1 *Prefabricated metro station structure*

The metro station is of large size. In addition to longitudinal splitting into several standard structural rings, the horizontal structural links shall also be split into several standard components. The standard rings used in the prefabricated station structure of Changchun Metro consist of 7 large prefabricated components with a ring width of 2m, as shown in Figure 2. In prefabricated structures, except for the longitudinal joint between the top arch components D and E, which is assembled in a staggered joint manner, the rest are assembled in a straight joint manner.

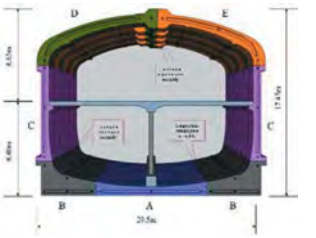

Figure 2. Schematic diagram of single-arch long-span structure type of prefabricated station.

After the lining structure is assembled as a whole, a stable tunnel-type bearing structure will be formed under the restraint of the hard backfill in the lateral extra trench for the foundation pit. The internal structures such as the mid-floor slabs, columns, and beams can be of prefabricated structure according to the engineering conditions and be assembled with the lining structure, or be cast in place or superposed as a whole after the assembly of lining structure.

2.2 *Prefabricated closed-cavity thin-walled components*

Each prefabricated component is a new-type lightweight "closed-cavity thin-walled component", which can effectively reduce the weight of the component and facilitate transportation and construction assembly under the condition of meeting the structural stress, and reduce the hydration heat of large prefabricated concrete components while reducing the amount of concrete used for the components.

See Figure 3 (a) for the schematic diagram of the section of closed-cavity thin-walled components, and Figure 3 (b) for the perspective view of single-ring fully prefabricated structure. The single-ring fully prefabricated structure has a weight of 292.5t and a total volume of 144m³. The volume of the cavity is 27m³, and the cavity rate is 18.75%.

2.3 *Grouted mortise-tenon joint*

The grouted mortise-tenon joint is composed of mortise, tenon, and later joint grouting. One of the two

(a)Sectional view (b) Perspective view of single-ring prefabricated structure

Figure 3. Closed-cavity thin-walled components.

opposite ends of the prefabricated components is a tenon, and the other end is a mortice, see Figure 4. After the assembly of the components is completed, grout is injected into the gap between the mortise and the tenon through the reserved grouting hole to effectively fill the gap between the mortise and tenon, so as to effectively transmit the internal force of the section and limit the interface dislocation between the mortise and tenon.

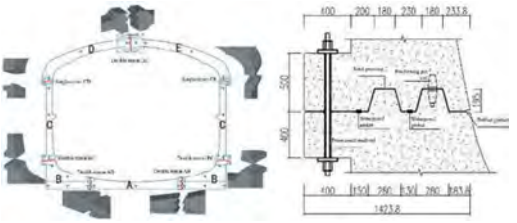

Figure 4. Closed-cavity thin-walled components.

2.4 *Joint waterproofness*

The waterproof mode of prefabricated station shall be structure waterproof + joint waterproof, without an outer waterproof layer required. For structure waterproof, the scheme of "two gaskets + one injection + one caulking" is adopted, as shown in Figure 5, that is, two composite expansive rubber gaskets are arranged at the joint, modified epoxy resin is injected into the joint, and waterproof caulking is carried out for the reserved grooves of the joint inside the tunnel.

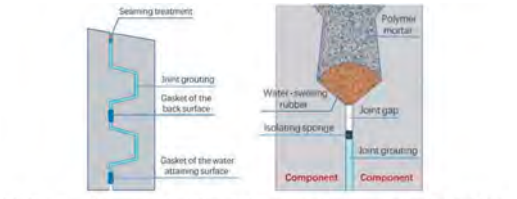

(a) Waterproof measures for joints (b) Waterproof measures of embedded joint

Figure 5. Waterproof measures for joints.

2.5 *Structure assembly*

In each lining ring, the floor component joints are tensioned and compressed by prestress, while the joints of the upper components are mainly compressed by their own weight, and are connected by auxiliary bolts. Relay-type prestressed reinforcement is used to tension and compress the ring-ring joints ring by ring, as shown in Figure 6 (a). To ensure the assembly accuracy of prefabricated components and prevent collisions between components during assembly, a guide positioning pin rod is specially provided at the joint, as shown in Figure 6 (b), to guide the assembly movement direction of the components and limit unexpected assembly dislocation of joints.

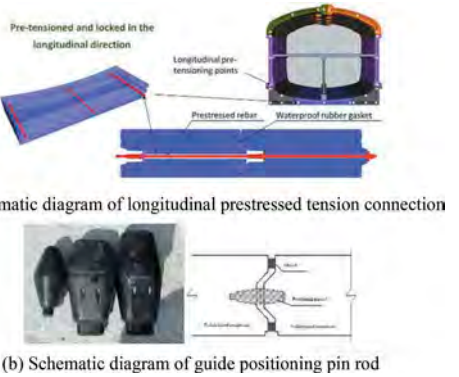

(a) Schematic diagram of longitudinal prestressed tension connection

(b) Schematic diagram of guide positioning pin rod

Figure 6. Auxiliary devices for structure assembly.

2.6 *Assembly steps*

The assembly of prefabricated station structures starts from the fixed end of the first ring in the longitudinal direction and advances in one direction. In the process of circumferential assembly of prefabricated station structures, the "bottom-up" sequence is adopted, that is, starting from the lower floor structure and continuing the assembly upward in a block by block and layer by layer manner, similar to the way of "building blocks". In the case that a horizontal structure such as floor, floor slab, or roof is assembled from multiple components, it is recommended to place the middle components in place first, and then assemble the components on both sides. Figure 7 (a) is a schematic diagram showing the assembly steps of fabricated station structures, while Figure 7 (b) is a schematic diagram showing the main assembly steps of the fabricated station structure of Changchun Metro Line 2 under the pile-anchor support system.

3 KEY TECHNOLOGY RESEARCH

3.1 *Joint connection technology*

"Grouted mortise-tenon joints" are a new type of connection joints specifically developed for prefabricated underground structures. The research team has conducted a comprehensive and in-depth discussion on the mechanical properties and design methods of grouted mortise-tenon joints from the perspectives of joint type, mechanical behavior, failure mode, bearing

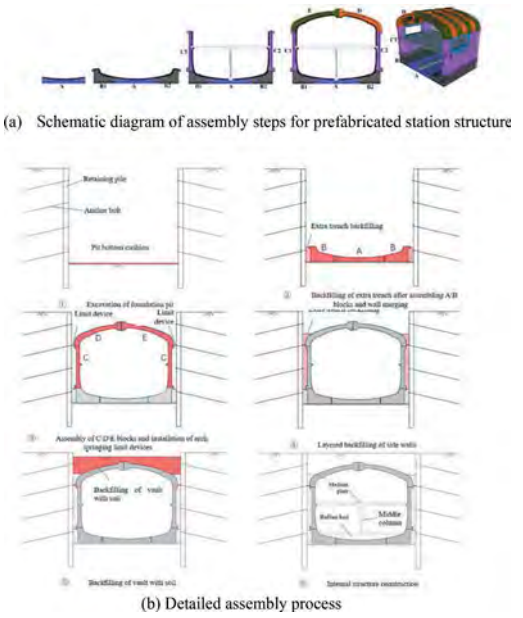

Figure 7. Schematic diagram of assembly steps for prefabricated station structure of Changchun Metro.

capacity, and key design technologies, etc. by means of 1:1 prototype test and theoretical analysis. It mainly involves experimental research on the basic mechanical properties of joints, research on bending resistance characteristics, research on bending stiffness characteristics, research on bending and shear bearing capacity and failure modes, research on the design and calculation methods of compression bending bearing capacity, research on the design and calculation methods of shear bearing capacity, and research on key technologies for constructional design of joints.

Regarding different joint types, grouting materials, grouting ranges, and bending combinations, a self-developed joint prototype bearing performance and destructive loading test system was used to conduct a series of 1:1 full-scale prototype mechanical property tests (Figure 8).

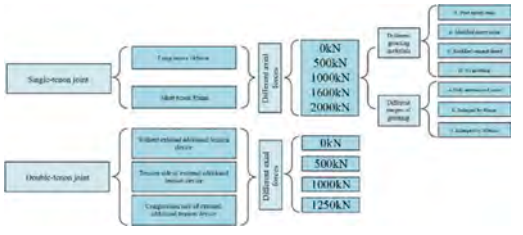

Figure 8. Schematic diagram of assembly steps for prefabricated station structure of Changchun Metro.

Main conclusions from the test:

a. The test revealed the bending resistance characteristics of grouted mortise-tenon joints under axial force, and proposed the concept of "resistance moment". As an important basic index of joint bearing capacity, "resistance moment" is a strong support for subsequent research on joint mechanical behavior.
b. It revealed the "variable stiffness" characteristic of the stiffness of grouted mortise-tenon joints changing with axial force and bending moment, formed an empirical formula for the bending stiffness of the joints by deriving the fitted M-θ curve, and proposed the main factors affecting the bending stiffness of the joints.
c. The bearing characteristic curve of various joints and the proportion of bearing capacity at different bearing stages were revealed.
d. Based on the impact of the above indexes on the bearing capability, fabrication, and construction convenience of joints, a set of joint constructional design steps (see Figure 9) and requirements are proposed.

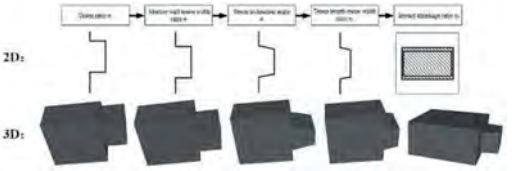

Figure 9. Steps for joint constructional design.

3.2 *Key technologies for the design of closed-cavity thin-walled prefabricated components*

The use of closed-cavity thin-walled components is an important means for the lightweight design of large prefabricated components in underground structures. Cities such as Changchun, Qingdao, and Shenzhen have taken the lead in adopting closed-cavity thin-walled components in the lining structure of prefabricated metro stations. Given the fact that the structure types, stress environments, and mechanical behaviors of closed-cavity thin-walled components in underground structures are relatively complex, and there are no applicable norms and standards available for reference, a discussion will be made in this section on the key points of lightweight design for large fabricated underground structural components and the key technologies for closed-cavity thin-walled component design in conjunction with theoretical research and practical engineering applications, mainly involving lightweight methods for commonly used structural components, research on mechanical properties of closed-cavity thin-walled components, and key points of structural design and calculation analysis of closed-cavity thin-walled components. Research has shown that closed-cavity thin-walled components have significant lightweight effects, excellent mechanical properties, and similar characteristics to ribbed components with T-shaped, I-shaped and box-shaped sections in terms of shear lag effect and shear stress distribution law. The internal cavity ratio,

flange plates, longitudinal rib plates, diaphragm plates, and end plates of the components have a certain impact on the mechanical properties of the components. In practical engineering applications, it is necessary to, based on the specific situation of the project, grasp the mechanical behavior characteristics of components through numerical analysis or experimental research, determine the section type and constructional measures of closed-cavity thin-walled components in a reasonable manner, effectively control the influence of shear lag effect on the section, and ensure that the whole process of prefabricated components from production, lifting, transportation, assembly to use meets the design requirements of bearing capacity limit state and normal use limit state.

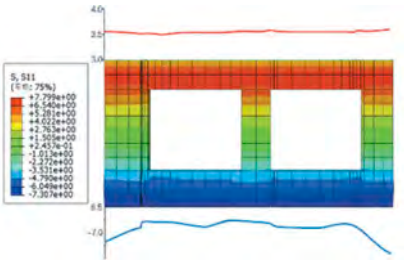

Figure 10. Schematic diagram of the normal stress distribution on the section of closed-cavity thin-walled components (Display effect scaled up).

3.3 *Structural mechanics behavior and calculation method of prefabricated stations*

Grouted mortise-tenon joints have typical variable stiffness characteristics. The existence of joints makes the mechanical behavior of fabricated station structures significantly different from that of traditional cast-in-place one-piece structures. In this section, numerical simulations of multiple models, multiple construction stages, multiple load conditions, and multiple structure types are conducted, and field tests are made for comparative analysis to study the mechanical behavior of fabricated station structures. The research focuses include the research on the calculation and analysis method of overall action effect of prefabricated structures based on variable stiffness joint connection, the research on the influence of joint stiffness on mechanical behavior of prefabricated structures, the research on the structural mechanical behavior characteristics in assembly construction process and the main influencing factors, and the comparative research on in-situ testing of fabricated station structures, etc.

Based on the structural characteristics of prefabricated metro stations, and by means of dynamic time-history analysis and response displacement methods, and numerical model analysis, the seismic performance of prefabricated station structures is studied by comparing the seismic response laws of prefabricated station structures and the same type of cast-in-place structures. The research focuses include the research on seismic response laws of prefabricated metro station structures, the influence of joints on the behavior characteristics of prefabricated structures under earthquake action, the research on the follow-up characteristics of prefabricated station structures and strata, and the influence of formation hardness on the seismic response of prefabricated station structures.

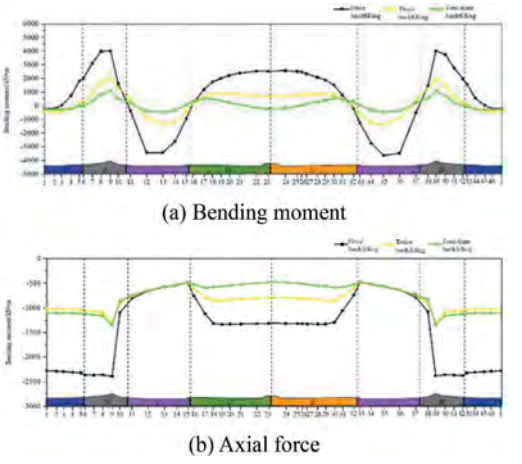

Figure 11. Structural internal forces in different backfill schemes when concrete materials are used for extra trench backfilling.

3.4 *Key technology of joint waterproof*

Regarding the characteristics of the structure construction, component manufacturing and construction technology of prefabricated stations, the main influencing factors and control indexes of two key parameters, “joint opening” and “gasket dislocation”, which are highly related to the waterproof performance of joints, are analyzed in this section. Based on the experimental research on gasket waterproof performance and the monitoring results of practical engineering applications, the key technology of “two gaskets + one injection + one caulking” multiple defense lines for joints has been proposed and fully demonstrated. In the double-gasket mode, the EPDM elastic gasket serves as the main waterproof, and the composite water-swellable rubber as the reinforced waterproof, forming a composite sponge and multi-groove gaskets. The gaskets are the main line of defense for joint waterproof, while grouting and caulking are auxiliary lines of defense. According to the existing and under-construction projects, both the measured maximum opening and surface dislocation of the station structure joints meet the requirements of the joint waterproof performance control standards. In places where no enclosed waterproof layer is set, there is no water leakage at the joints.

4 APPLICATION EFFECT

The above technologies have been promoted and applied in many cities such as Changchun, Qingdao and Shenzhen, and the first batch of prefabricated stations in China have been built. As of now, the number of existing and under-construction prefabricated stations has reached 44, becoming the largest cluster of prefabricated stations in China and even the world. No safety accidents occurred during the construction period, and the stations are safe and reliable after operation, without structural water leakage. The technical, economic, and social benefits are significant. Figure 12 (a) is a schematic diagram of different prefabricated station structures in different cities, Figure 12 (b) shows photos of the assembly sites for prefabricated stations, Figure 12 (c) shows photos of the fabrication and assembly sites for prefabricated components, and Figure 12 (d) shows photos of the first batch of prefabricated metro stations in China opened to traffic. Among them, Xinglongpu Station is rated as one of the top ten most beautiful stations in China.

Moreover, this technology has also achieved extended application in other engineering fields such as highway tunnels and deep and large vertical shafts. Figure 13 (a) shows the schematic diagram and on-site construction photo of the highway tunnel (under construction) structure on Xinsen Avenue in Jinfeng Park, Chongqing. Figure 13 (b) shows the cross section of the fabricated vertical shaft structure of Terminal 3 (T3) of Chongqing Rail Transit Line 15 Phase I Project (under construction).

5 MAIN TECHNICAL ECONOMIC AND SOCIAL BENEFIT ANALYSIS

With the prefabricated stations of Changchun Metro as the measurement basis, compared with the cast-in-place concrete structure, the main advantages of the prefabricated structure for standard cut-and-cover station of the same scale are as follows:

a. In the assembly link, more than 70% of the construction time can be saved, and the duration of each station can be shortened by 4-6 months, equivalent to the duration shortened by 25%-30%.
b. In the assembly link, the construction personnel on the construction site are reduced by 85-90%; the operators during peak hours are reduced from 150-180 per shift to about 20.
c. About 800t steel bars can be saved for each station.
d. About 800m3 of timber used temporarily for construction can be saved.
e. Construction wastes generated in construction are reduced by more than 50%.
f. The land for construction can be reduced by about 1,000m^2.
g. The comprehensive carbon emission can be reduced by about 19%.

Rail transit is the traffic artery of modern cities, which plays an important role in urban development and residents' life. The metro stations are usually built in the center of densely populated and busy commercial areas, located at the main traffic routes and are highly sensitive to construction.

Completely different from the cut-and-cover cast-in-place concrete structure, precast concrete components are used for prefabricated structure construction technology to enable quick mechanical assembly on site without wet concrete placing operation, so as to minimize the construction activities on site, give full play to the greatest advantage of prefabricated assembly. This construction technology with industrialization mode as the core has played an important role in social development, mainly in the following aspects:

a. Project quality and construction safety have been greatly improved.
   The industrialized and mechanical automation construction mode makes the prefabricated structure have higher production accuracy, better quality assurance and durability. The on-site high-risk operation links are reduced, and manpower is greatly reduced, which is convenient for project management and risk reduction in personal injury.
b. Comprehensive benefits improved
   The operation time on the assembly construction site is reduced by 70%, and the labor is saved by 85%. By reducing the duration and man-day, the comprehensive duration of a prefabricated station can be shortened by 4~6 months. Considering the above two advantages, the indirect economic benefits generated can reach RMB 10 million. Meanwhile, improving construction efficiency and speeding up construction are conducive to reducing the impacts of construction on urban land, transportation, commerce and the environment, alleviating labor shortages, and greatly improving the comprehensive benefits of urban rail transit construction.
c. Employee-oriented principle
   The industrialized construction mode will greatly change the low-end situations of the traditional construction industry, provide a clean work environment, reduce labor intensity, save labor, improve construction safety, and improve the happiness of employees as a whole.
d. Green and environmental protection
   No operations such as formwork erection on site, steel rebar binding and concrete placing & vibration on site during assembly can effectively reduce the pollution of construction noise and dust to the surrounding environment, and thus the satisfaction of residents is greatly improved. Wood consumption can be reduced by 800m3, construction waste can be reduced by more than 50%, and carbon emissions can be effectively controlled, which is conducive to reducing the impacts on the global environment.

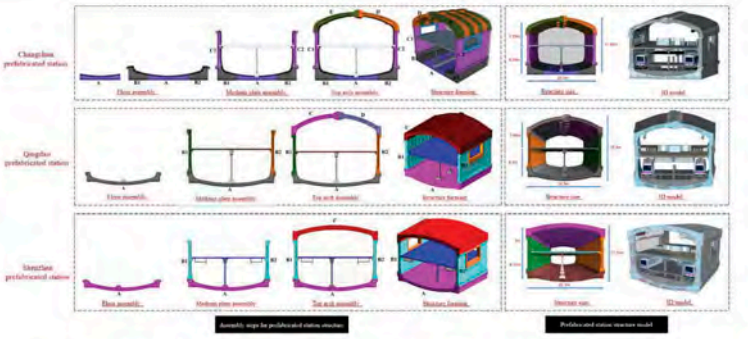

(a) Schematic diagram for structure assembly of different prefabricated stations

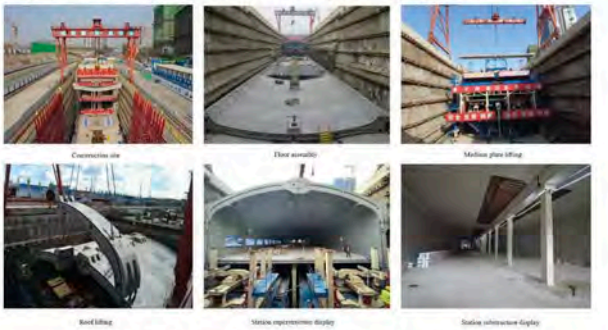

(b) On-site assembly of prefabricated station structure

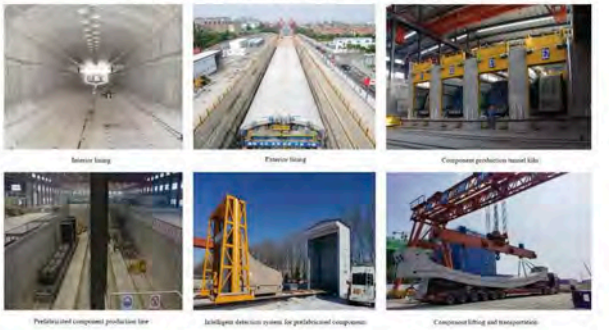

(c) Component production and assembly

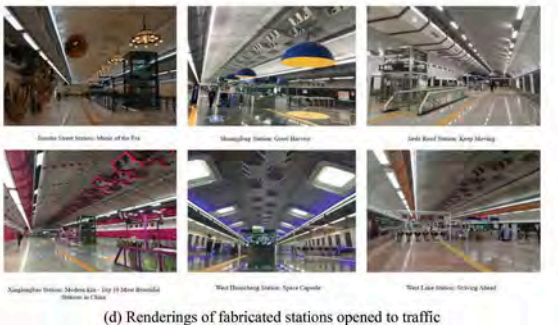

(d) Renderings of fabricated stations opened to traffic

Figure 12. Schematic diagram of entire construction process of fabricated station.

(a) Schematic diagram and on-site construction photo of the prefabricated highway tunnel structure on Xinsen Avenue in Jinfeng Park, Chongqing

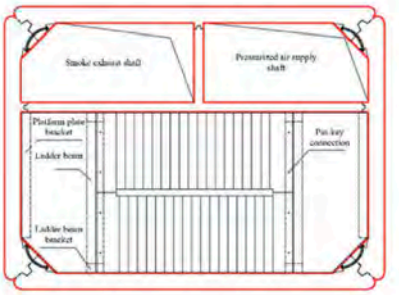

(b) Schematic diagram of the cross section of the prefabricated vertical shaft structure of Terminal 3 (T3) of Chongqing Rail Transit Line 15 Phase I Project

Figure 13. Technical expansion.

e. Promoting the development of construction industrialization and industry science and technology progress
The transformation from traditional labor-intensive mode to industrialization mode is of great significance to promote the optimization, upgrading and sustainable development of the construction industry. The R&D and successful application of fabricated station technology have led the development direction of green construction technology and strongly promoted the scientific and technological progress of the industry.

6 CONCLUSIONS AND RECOMMENDATIONS

For prefabricated structure construction technology of metro stations, a series of core achievements in industrialized construction covering engineering design, component production, construction technology and equipment, etc. have been achieved, forming a technical system supporting the whole process of construction, e.g. standardized design methods, high-accuracy fabrication methods for large precast components, intelligent testing devices, automatic mechanical assembly processes and technical standards, and providing a new construction mode for underground rail transit stations. This technology is an industrialized construction method developed for metro stations developed to solve the problem of construction impossibility in the severe cold winter in Changchun, China, and is also applicable to the metro construction in other cities under various environmental conditions. This technology has been currently applied in Changchun, Qingdao and Shenzhen Metros.

The prefabricated construction technology developed for metro station structures is also applicable to other cut-and-cover underground structures such as metro section structures, entrance and exit passageways, air duct structures, and underground pipe racks. The structure type can be a single-arch long-span tunnel structure or a rectangular frame structure. The cut-and-cover foundation pit support system can be applied for slope setting, soil nail wall, shotcrete and rockbolt support, pile (wall) + anchor cable, and pile (wall) + interior support, etc. This innovative technology has broad applicability.

Although the outstanding achievements have been made for this technology after more than 10 years of development, there are still many problems to be solved and the technology shall be further improved and upgraded, e.g. improving the prefabrication ratio of the structure, reducing engineering investment, improving the concept of assembly, and strengthening innovation, deepening the integration of industrialization, increase the further development of informatization and intellectualization, and strengthening the promotion and application. This requires the joint efforts of the industry and continuous exploration to make this advantageous technology play a greater role and create more value.

ACKNOWLEDGMENTS

We thank you China Association of Metros (Project: CAMET-KY-2022016) and State Grid Corp. of China (Project: 5108-202218280A-2-324-XG) for sponsoring this article.

REFERENCES

Baghchesaraei O.R., Lavasani H.H., Baghchesaraei A., 2016. “Behavior of prefabricated structures in developed and developing countries”, Bulletin de la Société des Sciences de Liège. 85:1229.

Frarov., 1994. “New conception of underground railways”, Moscow.

Lin F., Yang X.R., 2023. “Mechanical properties analysis of joints for prefabricated metro station structure based on whole-process in-situ monitoring”, Tunnelling and Underground Space Technology, 138:105202.

Lin F., Yang X. R., Wang C., 2023, “Influence of key structural parameters of grouted single-tenon joints. urban rapid rail transit”. 36(2): 34–44.

Lawson R., Mark, A. M, Ogden, R. G., Bergin R., 2011, “Application of Modular Construction in High-Rise Buildings”, Journal of Architectural Engineering. 18(2):148–154.

Jiang L, Li Z, Li L, et al. 2018, “Constraints on the promotion of prefabricated construction in China”, Sustainability. 10(7).

Yang X, Huang M, Lin F., 2019, “Research strategies on new prefabricated technology for underground metro stations”, Urban Rail Transit. 5(3):145–154.

Yang, X. R., 2020, “Theory and application of prefabricated open-cut metro station structure”, Beijing Jiaotong University.

Yang, X. R., Lin, F., 2021. “Prefabrication technology for underground metro station structure”, Tunnelling and Underground Space Technology. 108:103717.

Yang X, Lin F, Huang M., 2022, “Analysis of the law of joint deformation for grouted mortise-tenon joint”, Advances in Civil Engineering. 1–13.

Tunnelling for a Better Life – Yan, Celestino, Thewes & Eberhardt (Eds)
© 2024 The Author(s), ISBN 978-1-032-80042-4
Open Access: www.taylorfrancis.com, CC BY-NC-ND 4.0 license

Numerical investigation of the excess pore water pressure generated by TBM tunnelling in saturated and unsaturated aquifers: A comparable study

Chenghao Zhang*
Department of Civil Engineering, Ghent University, Ghent, Belgium

Adam Bezuijen
Department of Civil Engineering, Ghent University, Ghent, Belgium
Geo-Engineering, Deltares, Delft, The Netherlands

ABSTRACT: Understanding the distribution of excess pore water pressure induced by the TBM is of importance when assessing the stability of the tunnel face. The presence of high excess pore water pressure is not favourable in this regard. Previous studies have extensively investigated the excess pore water pressure generated by TBM tunnelling in saturated aquifers using field measurements and numerical simulations. However, there is a lack of investigation into the excess pore water pressure in the front of the TBM when excavating in unsaturated soils. To address this knowledge gap, a CFD (Computational Fluid Dynamics) model is introduced in this paper to simulate the water flow in front of the tunnel excavation face under both saturated and unsaturated soils. Results show that in the case of saturated soil, the distribution of excess pore water pressure obtained from the model calculation exhibited excellent agreement with the measurements taken during the excavation of the second Heinenoord Tunnel in the Netherlands. Excess pore water pressure in unsaturated soil exhibited a much shorter influence zone compared to saturated soil conditions. Moreover, the influence zone of excess pore water pressure in unsaturated soil expands as a function of infiltration time and saturation degree.

Keywords: Excess pore water pressure, TBM, CFD, Saturated, Unsaturated

1 INTRODUCTION

During the drilling process of a slurry TBM, the infiltration of bentonite triggers the generation of excess pore water pressure within the soil in front of the tunnel face. This phenomenon may pose challenges for tunnel face stability, as the excess pore pressure will reduce the effective tunnel face pressure (Bezuijen et al., 2001, Broere, 2002).

Extensive research has been conducted on the excess pore water pressure induced by slurry TBM in saturated soil conditions. Through analysis of the field measurements during the construction of the Second Heinenoord Tunnel, the Netherlands, Bezuijen et al. (2016) concluded that excess pore water pressures can be expected when drilling in saturated sand, and the formula developed can be used to calculate the pore water pressure distribution at a certain distance from the tunnel face, assuming unconfined flow in the aquifer where the tunnel is constructed. This formula was subsequently validated using 3D simulations (Zizka et al., 2017). Furthermore, Xu and Bezuijen (2018) compared this model with the transition model for estimating the excess pore pressure in a semi-confined aquifer, proposed by (Broere and van Tol, 2001). It was found that these two models gave comparable results, and both can be fitted to the field measurements. In the case of the Second Heinenoord Tunnel, the maximum influence distance of excess pore water pressure was found to be up to 30 m. Mori et al. (1995) reported a similar value of 30 m in sandy soil based on laboratory tests, numerical modelling, and field observations.

Compared to the well-studied saturated conditions, there is a notable lack of research examining excess pore pressure in the unsaturated soil influenced by the slurry TBM. Some investigations explored the stability of the tunnel face in unsaturated soil through centrifuge tests and numerical

*Corresponding author: Chenghao.Zhang@Ugent.be

DOI: 10.1201/9781003495505-302

analysis. Soranzo et al. (2015) found that suction played a favourable role in enhancing the effectiveness of tunnel face. Dziuban et al. (2018) observed that with the increase of the saturation degree of the soil, the failure zone decreases, while the settlement of the ground surface increases. To bridge the knowledge gap, this study deals with the excess pore water pressure distribution in the unsaturated sandy soil just in front of the tunnel. The results were compared with the saturated condition.

2 NUMERICAL MODELLING

COMSOL Multiphysics computer software was used to perform the finite element analysis, incorporating the porous media and subsurface flow models. The 2D finite element model built has a length of 150 m, a width of 100 m, and a 50 m × 10 m opening, while the dimension of 3D model is 150 m × 100 m × 100 m, with a cylindrical tunnel opening (diameter in 10 m and length in 50 m). It is important to highlight that achieving convergence in 3D models can be notably challenging when simulating unsaturated conditions. As a result, 3D modelling is only reserved for saturated conditions in this study. A free triangular mesh for 2D model or a free tetrahedral mesh for 3D model was generated across the entire domain, with a refined mesh strategically applied around the tunnel face to enhance the precision of calculation results.

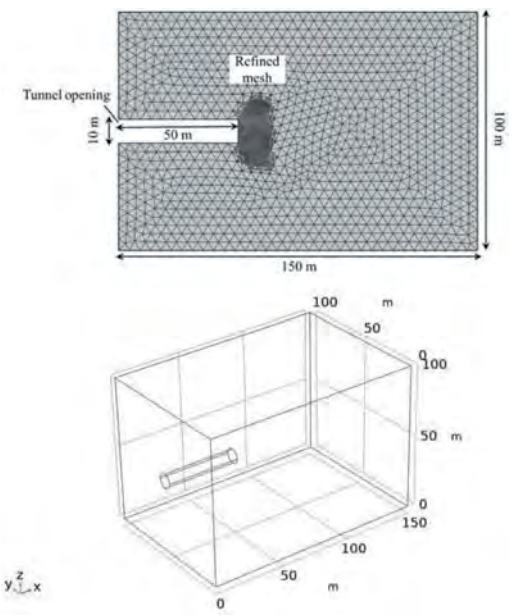

Figure 1. Geometry of the tunnel models, 2D model (top), and 3D model (bottom).

2.1 *Governing equations for the water flow*

In the case of saturated soil, the governing equation comprises a combination of Darcy's law and the continuous model:

$$\frac{\partial \varepsilon_p \rho}{\partial t} + \nabla \cdot \rho \boldsymbol{u} = 0 \tag{1}$$

$$\boldsymbol{u} = -\frac{K}{\mu}(\nabla p - \rho g) \tag{2}$$

With ε_p the porosity, ρ (kg/m^3) the fluid density, t (s) the time, $\boldsymbol{u}$ (m/s) the Darcy's velocity or specific discharge vector, K the intrinsic permeability of the porous medium (m^2), μ (Pa·s) the fluid dynamic viscosity, p (Pa) the pore water pressure, and g (m/s^2) the acceleration of gravity.

To describe water flow in unsaturated soil, Richards' equation, as depicted in Equation (3), was chosen as the governing equation.

$$\rho(C_p + Se \cdot S)\frac{\partial}{\partial t}p + \nabla \cdot \rho\left[-\frac{K \cdot k_{\mathrm{r}}}{\mu}(\nabla p + \rho g \nabla D)\right] = 0$$

With ρ (kg/m^3) the fluid density, C_p (m^{-1}) the specific moisture capacity, Se(-) the effective saturation, S (m^{-1}) the storage coefficient, p (Pa) the pore water pressure, K (m^2) the intrinsic permeability of the porous medium; k_r the relative permeability (a function of saturation for a given fluid), μ (Pa·s) the fluid dynamic viscosity, g (m/s^2) the acceleration of gravity, and D (m) the coordinate (for example, x, y, or z) of vertical elevation.

The specific moisture capacity C_p depends on changes in the effective saturation with respect to the capillary pressure as

$$C_p = (\theta_r - \theta_{\mathrm{s}})\frac{\partial \mathrm{Se}}{\partial p_{\mathrm{c}}} \tag{4}$$

where θ_s is the total porosity or saturated volume fraction; θ_r is the residual volume fraction; so the difference θ_s-θ_r is the available pore space for phases to move.

The capillary pressure p_c is commonly defined as the difference between the pressure of the nonwetting (p_{nw}) and wetting phases (p_w).

$$p_{\mathrm{c}} = p_{\mathrm{nw}} - p_{\mathrm{w}} \tag{5}$$

It is assumed in Richards' equation that the air in the soil is supposed to be at atmospheric pressure, suggesting p_{nw}= 0 and then p_c= - p_w.

The storage coefficient S represents the ratio of the change in the volume of groundwater that can be extracted from or released into an aquifer to the change in the hydraulic head (water level) within that aquifer.

$$S = \rho g(\chi_p + \theta\chi_f) \tag{6}$$

Here, ρ is the fluid density, (kg/m^3), g is the acceleration of gravity, (m/s^2), while χ_p and χ_f are the compressibility constants of the solid particles and fluid, respectively, (m·s^2/kg).

The solution to the governing equation, Equation (3), can be obtained if the simultaneous variations of θ, C, Se, k_r, and p_c are addressed. These relationships are defined by specific equations, such as the Van Genuchten-Mualem formulas (Van Genuchten, 1980), see Equation (7).

$$\begin{aligned}
\theta &= \begin{cases} \theta_r + \mathrm{Se}(\theta_s - \theta_r) & H_c > 0 \\ \theta_s & H_c \le 0 \end{cases} \\
Se &= \begin{cases} \frac{1}{[1+|\alpha H_c|^n]^m} & H_c > 0 \\ 1 & H_c \le 0 \end{cases} \\
C_m &= \begin{cases} \frac{am}{1-m}(\theta_s - \theta_r)\mathrm{Se}^{\frac{1}{m}}\left(1 - \mathrm{Se}^{\frac{1}{m}}\right)^m & H_c > 0 \\ 0 & H_c \le 0 \end{cases} \\
k_r &= \begin{cases} \mathrm{Se}^L\left[1 - \left(1 - \mathrm{Se}^{\frac{1}{m}}\right)^m\right]^2 & H_c > 0 \\ 1 & H_c \le 0 \end{cases}
\end{aligned} \tag{7}$$

where S_e is the effective saturation; θ_s is the total porosity or saturated volume fraction; θ_r is the residual volume fraction; H_c is the capillary pressure head, = $P_c/\rho g$; C_m is the specific capacity, =$C_p \cdot \rho g$; α, n, and m are the parameters in the Van Genuchten model; and L is a lumped parameter that incorporates both pore tortuosity and pore connectivity.

The excess pore water pressure reported in the subsequent sections originates from determining parameter p in Eq. (1) under saturated conditions or in Eq. (3) under unsaturated conditions.

2.2 *Boundary conditions and input parameters*

The boundary conditions for both saturated conditions and unsaturated conditions are demonstrated in Figure 2. In both scenarios, a pressure head of 5 m (consistent with the pressure head used in the Second Heinenoord Tunnel) was imposed at the tunnel face. The roof and bottom of the tunnel were modelled as impermeable, no flow. For the remaining domain and boundaries, an initial pressure head of 0 m was applied in the case of saturated condition, while in unsaturated conditions, an initial pressure head which is related to the initial degree of saturation was employed (for example, -0.05 m, for initial saturation of 0.8). Additionally, a pressure head of 0 m was specified at the bottom boundary of the unsaturated soil model, suggesting this is a saturated boundary.

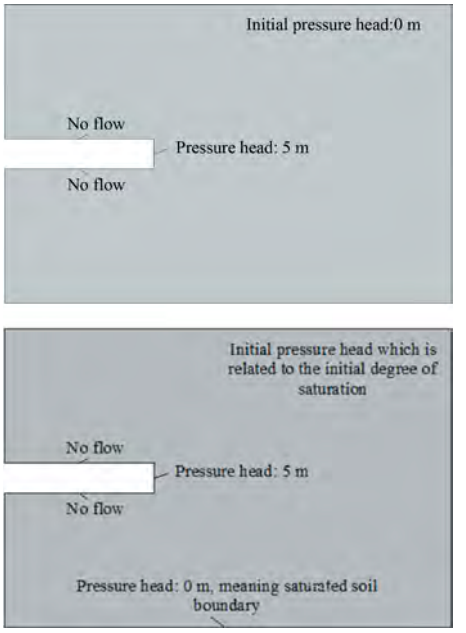

Figure 2. Boundary conditions for saturated soil model (top) and for unsaturated soil model (bottom).

The values for the input parameters are listed in Table 1.

Table 1. Summary of the input parameters.

Variable	Description	Unit	Value*
ρ	Fluid density	kg/m^3	1000
μ	Fluid dynamic viscosity	Pa·s	1*10^{-3}
K	Intrinsic permeability of the porous medium	m^2	4*10^{-11}
θ_s	Saturated volume fraction	-	0.4
θ_r	Residual volume fraction	-	0.021
α	α parameter	m^{-1}	14.5
n	n parameter	-	2.68
m	m parameter	-	1-1/n
L	Lumped parameter	-	0.5
χ_p	Compressibility of the solid particles	m·s^2/kg	0
χ_f	Compressibility of fluid	m·s^2/kg	4.4*10^{-10}

* The parameters in the Van Genuchten model (α, n and m) were set to typical values for sandy soils. (Brunner et al., 2010). The value for L is an optimal value for a data set of 45 samples (Mualem, 1976).

3 SIMULATION RESULTS

3.1 *Saturated conditions, 2- and 3-D modelling*

The express pore pressure in the saturated sandy soil just in front of the tunnel face was demonstrated in Figure 3.

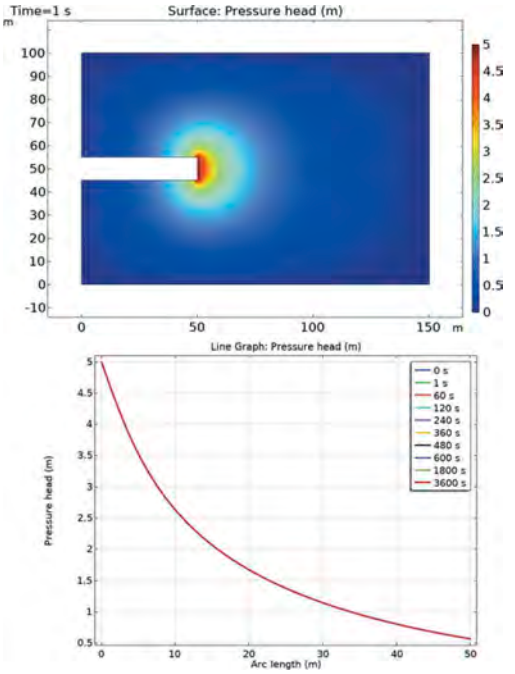

Figure 3. Excess pore water pressure distribution, surface (top), and central axis (bottom). Arc length means the distance from the tunnel face.

Based on the observations from Figure 3, it becomes evident that excess pore pressure is immediately present up to 50 m in front of the tunnel face. There is some difference with the field measurement data recorded during the construction of the Second Heinenoord Tunnel, suggesting that the 2D model may not accurately depict the actual geological layers. Additional 2- and 3-D numerical calculations were conducted using models of varying sizes to gain a more comprehensive understanding of how the excess pore pressure varies with distance from the tunnel face. The resulting data was then subjected to fitting using a model proposed by Bezuijen et al. (2001) for an unconfined aquifer, see Equation (8). The outcomes and the quality of the fit can be examined from Figure 4.

$$\phi=\phi_0(\sqrt{1+(x/R)^2}-x/R) \tag{8}$$

With ϕ_0 the pressure head at the tunnel face in front of the infiltrated zone, ϕ the pressure head at a distance x in front of the tunnel face, and R the radius of the tunnel, assuming a pressure head of zero far from the tunnel in the pore water.

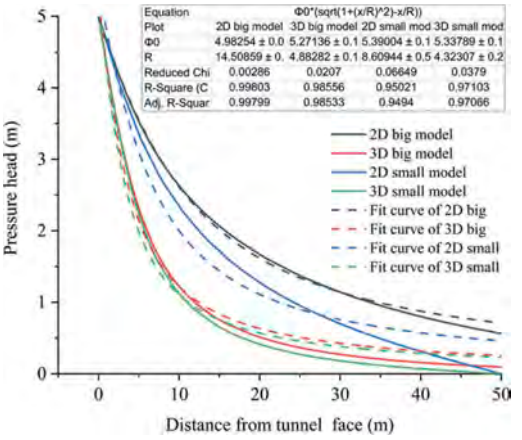

Figure 4. Excess pore water pressure distribution of 2D and 3D modelling (central axis). 2D big model (150m*100m), 3D big model (150m*100m*100m), 2D small model (70m*70m), and 3D small model (70m*70m*70m).

From Figure 4, it can be concluded that both the 2D and 3D models proposed exhibited a satisfactory fit with Equation (8). The 3D model proved to be more accurate, closely mirroring the excess pore water distribution observed in the actual field measurements, and values ϕ_0 and R used in the project and as input in the numerical model. It is worth noting that the model size substantially affects the outcomes of the 2D simulation, whereas its impact on the 3D simulation is relatively modest. Only the 3D model results in a value for R which is comparable to the radius of the tunnel (5 m).

3.2 *Unsaturated conditions*

The distribution of excess pore water pressure within the unsaturated soil at 80 % saturation is demonstrated in Figure 5. Additionally, Figure 6 displays the corresponding variations in the degree of saturation.

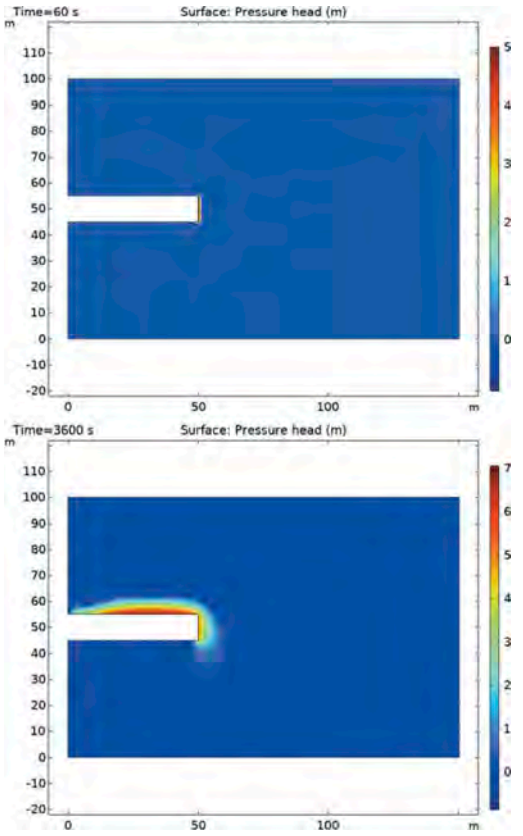

Figure 5. Pressure head changes with time (t=60 s, top and 3600 s, bottom), 80 % saturation.

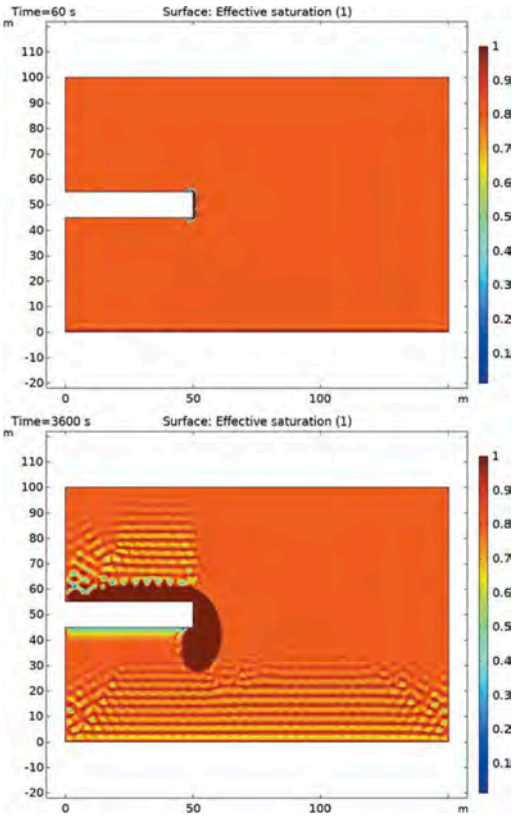

Figure 6. Degree of saturation changes with time (t=60 s, top and 3600 s, bottom), 80 % saturation.

Based on Figure 5, it can be observed that the pressure head increased as the fluid arrived. The remaining aspects remained unaltered, signifying the initial pressure. The initial pressure assumed a negative value due to the unsaturated nature of the soil.

In a manner similar to the pressure head variation, the degree of saturation increased upon the arrival of the fluid, as depicted in Figure 6. The remaining components were constant, representing the initial saturation. At 3600 s, alterations in saturation occurring at the upper boundary of the tunnel are primarily attributable to gravitational effects, whereas changes at the lower boundary of the entire model stem from capillary pressure.

Moreover, it is interesting to see an emergence of a saturated flume at 3600s, flowing from the upper section downward at the tunnel face, which will influence the excess pore water pressure in front of the tunnel face to some extent, as discussed in more detail in the following section.

From a practical perspective, it is important to highlight that the unsaturated condition with a constant degree of saturation in sand over 100 m does not align with reality. In real-world scenarios, saturation typically increases at the bottom and decreases at the top. Therefore, the overall calculated pressure distribution is not correct. However, this calculation can still be valuable when assessing the excess pore water pressure distribution in front of the TBM since the laminar flow conditions are applied.

Figure 7 illustrates the distribution of excess pore water pressure along the central axis of the tunnel, accompanied by the corresponding variations in effective saturation.

Figure 7 reveals that excess pore pressure is evident within a limited zone in front of the tunnel face, even with 80 % saturation, which is considerably less than that seen in saturated conditions. In real TBM projects, penetration times typically range from 20 to 60 seconds or even longer (Zizka et al., 2019), derived by calculating the timespan between subsequent cutting

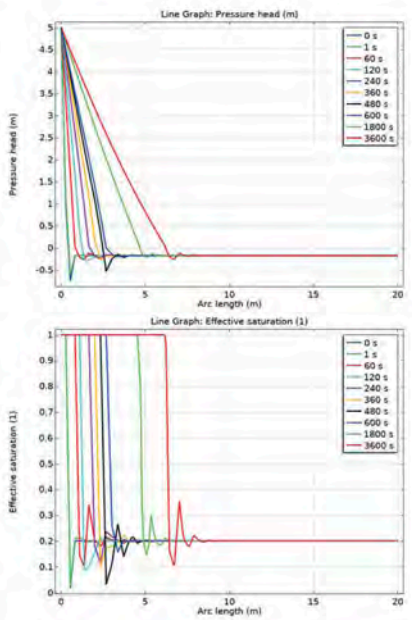

a) initial degree of saturation: 0.2, pressure head (top), effective saturation (bottom).

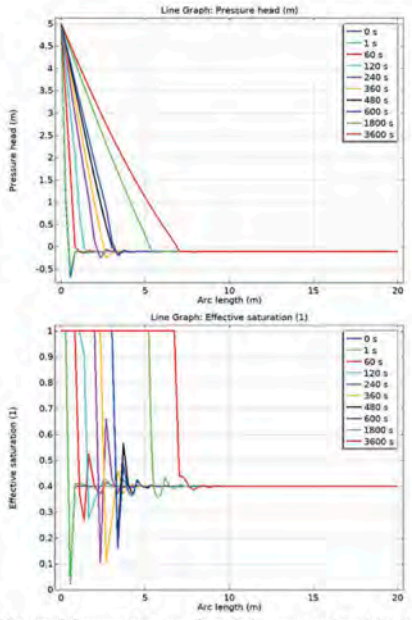

b) initial degree of saturation: 0.4, pressure head (top), effective saturation (bottom).

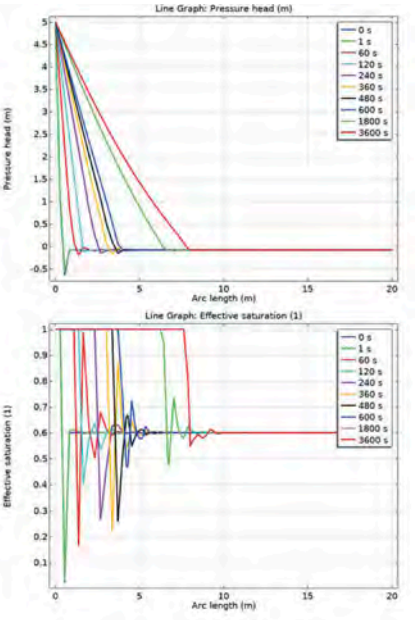

c) initial degree of saturation: 0.6, pressure head (top), effective saturation (bottom).

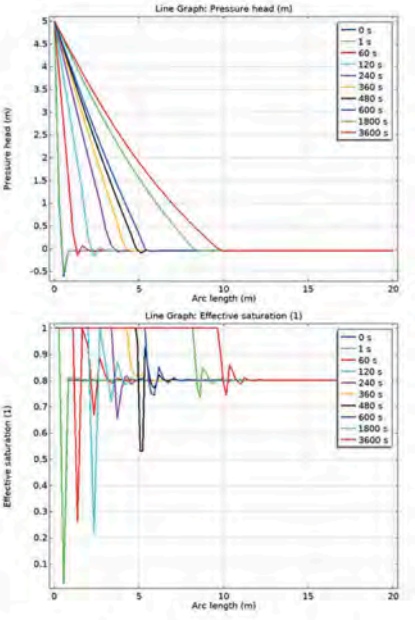

d) initial degree of saturation: 0.8, pressure head (top), effective saturation (bottom).

Figure 7. Pressure head and saturation variations along the central axis over time.

tool passing. Consequently, the influence zone typically spans less than 1 m. In saturated soil scenarios, however, the influence zone can be 50 m.

Given the presence of a saturated front entering the previously unsaturated soil, as evident in Figure 7, an analytical calculation can be made to determine the penetration distance x:

$$q = k\frac{\phi_0}{x} \tag{9}$$

With q (m/s) the Darcy's velocity, k (m/s) the permeability of the soil, and ϕ_0 (m) the difference in piezometric head.

Regarding pore velocity, Equation (9) transforms into:

$$n(1 - Se)\frac{dx}{dt} = k\frac{\phi_0}{x} \tag{10}$$

With n (-) the porosity, and Se (-) the degree of saturation.

Integration of Equation (10) with t=0, x=0, leads to:

$$x = \sqrt{2\frac{k}{n(1 - Se)}\phi_0 t} \tag{11}$$

By utilizing the same parameters employed in the numerical simulation, namely a water permeability of 4×10^{-4} m/s (k) and a porosity of 0.4 (n), the penetration distance of water in the unsaturated soil at 60% saturation was calculated using the analytical model Equation (11). The calculated results are depicted in Figure 8, alongside the results derived from the numerical analysis.

It follows from Figure 8 that the analytical model Equation (11) provided a comparable prediction of the excess pore pressure when compared to the numerical simulation (without considering the gravity influence). As previously stated, it is clearly seen from Figure 8 that gravity induced a downward saturated flow, which reduced the excess pore pressure in front of the tunnel face. This downward flow only happened after a prolonged penetration time, around 3600 s in this case study. However, this long penetration time is impossible in the real slurry TBM project due to the cutting of TBM tools and the potential formation of a filter cake.

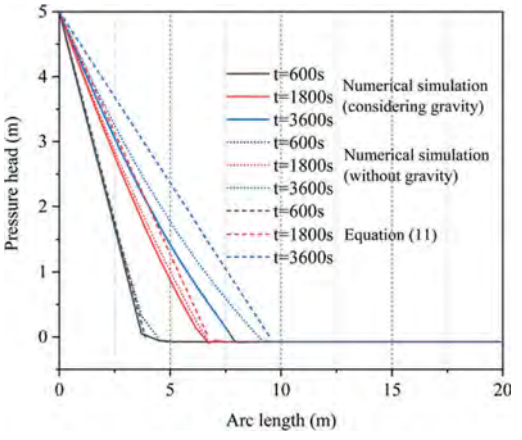

Figure 8. Distribution of excess pore water pressure in front of the tunnel face, both from numerical simulation and analytical calculation.

4 DISCUSSION

The simulations conducted in this study highlight a significant difference in the behaviour of excess pore water pressure in saturated versus unsaturated soils. When drilling in saturated sandy soil, the excess pore water pressure can extend as far as 50 m ahead of the tunnel face. In contrast, the impact of excess pore water pressure is confined to around 1 m, see next sections, when dealing with unsaturated sandy soil. Based on the experiences with slurry-filled trenches (Kilchert and Karstedt, 1984), it is advisable to consider that only the pressure drop within the wedge width, roughly equivalent to half of the tunnel diameter (Broere, 2002), may be reckoned in the effective support force. The excess pore water pressure beyond the wedge can lead to an upward force and a force on diagonal of triangle of the wedge, diminishing the effective support pressure. For a tunnel with a diameter of 10 m, the estimated critical failure wedge width may be around 5 m. This suggests that excess pore water pressure can exert a detrimental influence on tunnel face stability when excavating saturated soil. However, its impact is significantly less pronounced when the soil is unsaturated. These findings for unsaturated soils need field verification, especially when the saturated degree is high. This is because the simulation, which solved Richards' equation, does not account for the air pressure. In soils with lower degrees of saturation, air can be interconnected, implying that the pressure is close to the atmospheric pressure. However, in soils with higher degrees of saturation, air might become entrapped in the water, leading to a pressure that deviates from atmospheric conditions. In this latter scenario, it becomes imperative to carefully monitor and assess the air influence during the drilling of slurry TBM.

It is worth noting that this paper does not explore the influence of bentonite slurry infiltration. If considering the infiltration of bentonite into saturated soil, certain insights may emerge. Specifically, if the drilling velocity of the TBM is lower than the infiltration rate, there will be some slurry infiltration zone in front of the tunnel face and a certain percentage of the pressure drop will happen in this infiltrated zone, causing a reduction in excess pore water pressure

(Kaalberg et al., 2014). Consequently, the diminished pore water pressure aligns with a reduced risk of tunnel face instability. On the other hand, when the drilling velocity of TBM exceeds the infiltration rate, the distribution of excess pore water pressure remains comparable to the findings presented in this paper (Bezuijen et al., 2016).

In the case of unsaturated soil, the distribution of excess pore water pressure in a real slurry TBM drilling in the same soil, as studied in this paper, would be shorter than the simulated results. Assuming the permeability of sand for bentonite slurry is 4×10^{-5} m/s, ten times smaller than the water permeability, the excess pore pressure would extend up to 0.39 m at 60 s and 3 m at 3600s when the soil is at 60% saturation, as determined by Equation (11). These values are significantly smaller than the corresponding values (1.22 m at 60 s and 9.49 m at 3600 s) when considering only water penetration, as demonstrated in Figure 8. This indicates the excess pore water distribution is limited during the drilling of TBM in fine and medium-coarse sand. Only for coarse sand and gravel can the penetration depth be large enough to influence the stability of the front face.

Furthermore, our ongoing experimental tests reveal that the penetration of the bentonite slurry in unsaturated soil is notably faster than that in saturated soil, and there probably will be a filter cake formation before the subsequent TBM cutting tool passing. This suggests the main pressure drop will happen within the slurry infiltrated zone or almost entirely over the thin filter cake, which is favourable for enhancing the stability of the tunnel face.

In our future work, the influence of bentonite slurry penetration on the excess pore pressure is planned to be incorporated into the modelling. Field assessments should be conducted to monitor the influence of air, and the collected data will be valuable for back analysis. Additionally, for unsaturated soil, our current simulations for unsaturated soil has solely centred on 2D models. The future work will shift its focus towards the implementation of 3D models to investigate potential disparities when compared to the 2D models.

5 CONCLUSION

The numerical simulation presented, and the results discussed in this paper allow the following conclusions to be drawn.

1) In the case of saturated sandy soil, the excess pore pressure was observed at a significant distance from the tunnel face, which closely aligns with field measurements. Notably, the 3D model exhibits better fit compared to the 2D model.
2) When dealing with unsaturated sandy soil, the zone of excess pore water pressure expanded with increasing saturation levels; however, it remains significantly smaller than what is observed in saturated conditions, even at 80% saturation. This finding needs field verification because the simulation relies on the assumption of atmospheric air pressure, which may not be valid, particularly in unsaturated soils with high saturation degrees. Since there is a saturated front entering the unsaturated soil, an analytical calculation can be made to determine the penetration distance.
3) The limited extent of the excess pore water pressure zone in unsaturated soil implies that it has a minimal impact on tunnel face stability. In contrast, the longer excess pore pressure distribution zone in saturated sandy soil exerts a noticeable unfavourable influence on tunnel face stability.

ACKNOWLEDGEMENTS

The first author thanks the China Scholarship Council for their generous funding.

REFERENCES

Bezuijen, A., Pruiksma, J. P. & Van Meerten, H. H. (2001). Pore pressures in front of tunnel, measurements, calculations, and consequences for stability of the tunnel face In *Proceedings of Proc. of the Intl. Symp. on Modern Tunneling Science and Technology*.

Bezuijen, A., Steeneken, S. & Ruigrok, J. (2016) Monitoring and analysing pressures around a TBM. In *13th International conference underground construction*.), vol. 1, pp. 1–9.

Broere, W. (2002) Tunnel face stability and new CPT applications.

Broere, W. & Van Tol, A. (2001). Time dependant infiltration and groundwater flow in a face stability analysis. In *international symposium on modern tunneling science and technology*). CRC Press/Balkema-Taylor & Francis Group, pp. 629–633.

Brunner, P., Simmons, C. T., Cook, P. G. & Therrien, R. (2010). Modeling surface water-groundwater interaction with MODFLOW: Some considerations. *Groundwater.* **48(2)**:174–180.

Dziuban, B., Ling, H. I. & Li, L. (2018). Failure mechanisms of shallow tunnel in sandy ground. *Transportation Infrastructure Geotechnology.* **5**:318–331.

Kaalberg, F., Ruigrok, J. & De Nijs, R. (2014) TBM face stability & excess pore pressures in close proximity of piled bridge foundations controlled with 3D FEM. *Geotechnical Aspects of Underground Construction in Soft Ground*:555–560.

Kilchert, M. & Karstedt, J. (1984). Schlitzwände als Tragund Dichtungwände, Band 2, Standsicherheitberechnung von Schlitzwänden. Berlin, DIN.

Mori, A., Kurihara, K. & Mori, H. (1995). A study on face stability during slurry-type shield tunnelling. In *Underground construction in soft ground*, pp. 261–264.

Mualem, Y. (1976) A new model for predicting the hydraulic conductivity of unsaturated porous media. *Water resources research.* **12(3)**:513–522.

Soranzo, E., Tamagnini, R. & Wu, W. (2015).Face stability of shallow tunnels in partially saturated soil: centrifuge testing and numerical analysis. *Géotechnique.* **65(6)**:454–467.

Van Genuchten, M. T. (1980). A closed-form equation for predicting the hydraulic conductivity of unsaturated soils. *Soil science society of America journal.* **44 (5)**:892–898.

Xu, T. & Bezuijen, A. (2018) Analytical methods in predicting excess pore water pressure in front of slurry shield in saturated sandy ground. *Tunnelling and Underground Space Technology.* **73**:203–211.

Zizka, Z., Schoesser, B., Popovic, I. & Thewes, M. (2017) Excess pore pressures in front of the tunnel face during slurry shield excavations due to different time scales for excavation sequence of cutting tools and penetration time of support fluid. *EURO: TUN*.

Zizka, Z., Schoesser, B., Thewes, M. & Schanz, T. (2019) Slurry shield tunneling: new methodology for simplified prediction of increased pore pressures resulting from slurry infiltration at the tunnel face under cyclic excavation processes. *International Journal of Civil Engineering.* **17(1)**:113–130.

Tunnelling for a Better Life – Yan, Celestino, Thewes & Eberhardt (Eds)
© 2024 The Author(s), ISBN 978-1-032-80042-4
Open Access: www.taylorfrancis.com, CC BY-NC-ND 4.0 license

Launching technology with shallow overburden for super-large diameter slurry shield

Bo Zhang*
Guangzhou Rail Transit Construction Supervision Co., Ltd, Guangzhou, China

Hui Wang
Guangzhou Metro Construction Management Co., Ltd, Guangzhou, China

XiaoBing Xie, YangYi Lu & Zhao Chen
Guangzhou Rail Transit Construction Supervision Co., Ltd, Guangzhou, China

ABSTRACT: In order to solve the problems of shallow overburden, large slope of launching section, mixed face ground condition (upper sand layer, middle and lower whole, strong and medium-weathered pelitic siltstone), curve radius launching with umbilical system, etc., combined with the implementation conditions and the geological condition of the launching area of the project. Measures such as breaking the launching eye wall in stratified sections, two-time sealing the launching gate, enhancing the water dispersion resistance of synchronous grouting and in time secondly grouting, strictly controlling the excavation speed, slurry density, strengthening CW central flushing, washing exaction chamber invert while ring building, replacing alloy-inserted cutting tools, strengthening settlement monitoring interval and timely feedback of monitoring results, etc, ensuring the successfully launch of the shield machine in Guangzhou Haizhu Bay Tunnel. The paper summarized the key technology of shield machine launching with shallow overburden in Haizhu Bay Tunnel, to provide reference for similar projects.

Keywords: Super large diameter slurry shield, Shallow overburden launching, Mixed face ground condition, Risks of launching

1 INTRODUCTION

As a key link of shield construction, initial test driving is also an important and difficult point in shield construction [1,2], which has been studied by relevant scholars. Such as: You Yongfeng et al[3] developed a set of construction techniques for ultra-shallow soil cover of Chunfeng tunnel, aiming at the problems that the tunnel door seal is prone to soil erosion, and the driving attitude and section attitude are difficult to control. Zhang Boyang [4] summarized the key technologies of shield tunnel initiation based on a river crossing project in Nanjing. Du Chuangdong et al[5] gave a detailed introduction to each process of underground assembly and start-up construction of mud shield in the Shiziyang Tunnel of the new Guangzhou-Shenzhen-Hong Kong Passenger Special Line, and summarized the construction experience of shield assembly and start-up; Fang Xinsheng et al[6] summarized the experience of shield tunneling in Qinghuayan Tunnel, studied its driving parameters and the layout of engineering components such as reaction frame, and used finite element software to analyze and calculate the static strength of the reaction frame. In addition, some scholars have studied the initiation of steel sleeves[7], the sealing technology of tunnel doors[8], the emergence of segment floating[9] and the formation of mud with shield cutters [10,11] during the initial test driving.

Taking Haizhuwan Tunnel in Guangzhou as an example, this paper analyzed and studied the construction risks and problems in the preparation and test driving stage, and summarized the key technologies of Haizhuwan Tunnel.

2 PROJECT OVERVIEW

2.1 *Project introduction*

The length of the western line of Haizhuwan Tunnel is 2093.13m, and the length of the eastern line is 2102m. The length of the initial test driving section of the double-line shield tunneling is 100 rings (200m), and two slurry shield tunneling machines with excavation diameter of 15.07m are used for construction. Among them, the western shield is a normal pressure cutter head, and the eastern shield is a pressure cutter head. The minimum flat surface radius of the line is 1000m, and the maximum slope is 4%.

*Corresponding author: Bo Zhang 42730697@qq.com

DOI: 10.1201/9781003495505-303

2.2 *Hydrogeological conditions and surrounding environment*

2.2.1 *Hydrogeological condition*

The covering thickness at the beginning of the shield is 8.87~24.95m. The strata from top to bottom are mainly: mixed fill soil, silt, fine sand, medium coarse sand, whole, strong and medium-weathered argillaceous siltstone, and the excavated section is mainly located in the sand layer and whole, strong and medium-weathered argillaceous siltstone. The clay mineral content of the argillaceous siltstone is about 30%, and the maximum uniaxial compressive strength of the rock is about 50MPa.

The surface water and groundwater at the beginning of the shield are as follows:

(1) Surface water: The project runs through the Lijiao River and Sanzhixiang River, which are major rivers of the Pearl River System. At the same time, there are also four inland river surges along the route, which are important flood drainage channels for Haizhu District, Luoxi Island and Nanpu Island to communicate with the Pearl River.

(2) Ground water:

① Type: There are mainly water retention in the upper layer, pore diving in the quaternary sand layer and confined water in the pore fissure of bedrock.

② Groundwater level and dynamic changes: The groundwater level of the site is generally shallow. According to the observation 24 hours after the final hole of the drilling, the buried depth of the mixed stable water level of the site is generally 0.10 ~ 3.30m, and the elevation is generally 3.09 ~ 6.04m. Every year from May to July is the rainy season, the atmospheric rainfall is abundant, the water level will rise slightly, and in winter due to the decrease of precipitation, the groundwater level will drop slightly. The variation range of the water table is about 1.0m.

2.2.2 *Surrounding environment*

The surface environment is mainly self-owned roads and river surges. The surface environment is shown in Figure 1.

Figure 1. Surface environment plan of the starting section.

3 ACTUAL CONSTRUCTION SITUATION

The Haizhuwan Tunnel started smoothly with a super large diameter slurry shield tunnel, however, there were still problems such as crack removal at the entrance of the tunnel, leakage of slurry from the sealing of the initial warehouse entrance, surface monitoring and warning, pipe leakage, deterioration of excavation parameters (mud accumulation at the cutterhead opening), and severe tool wear. The specific problems were analyzed and summarized below, and suggestions were provided for the subsequent excavation construction under similar conditions.

3.1 *Cracks appear in the tunnel door and slurry leakage from the initial construction tunnel door seal*

3.1.1 *The tunnel door cracks*

(1) Briefing

On February 9, 2023, the shield machine of the western line began to break the concrete of the tunnel door. On February 12, 2023, transverse cracks were found in the tunnel door and stopped breaking.

(2) Causes analysis

1) The 1.2m range of the tunnel door is reinforced with fiberglass bars (without hooks on the inner and outer layers) and a washing tank joint, and there is no rigid connection between the ground and wall.

2) During the hoisting of large components such as the cutterhead and main drive of the shield tunneling machine on the western line, a single track of an 800 ton crawler crane was pressed above the ground connecting wall of the tunnel portal, while the other track was in the end reinforcement area. Although the monitoring data of the ground and the side walls of the main structure were normal, cracks have appeared inside the connecting walls.

(3) Targeted measures

1) Disposal measures: A 300mm I-beam support was set up at 1.5m below the crack position of the ground link wall (Figure 2), and the two ends were welded with the tunnel door steel ring. In the middle, three I-beams were arranged evenly to the cutters of the shield tunneling machine, and the bottom I-beam supports were arranged according to the monitoring situation of the tunnel door. The I-steel support was close to the palm surface of the ground connecting wall, and the gap position was filled with wood wedges to ensure that the I-steel fits the ground connecting wall; The reinforced area at the end of the west line shall be enclosed, and large equipment shall not be allowed to walk.

Table 1. Statistical table of internal monitoring control value of tunnel door at the end of Nanpu working well.

Number	measuring items	Methods and tools	Measurement frequency	
			Allowable value /mm	Average rate control value mm/d
1	Site inspection	Photography observation	/	/
2	Horizontal displacement	Total station	30	3
3	Vertical displacement	Total station	30	3

2) Monitoring measures: In order to ensure the safety state of the internal structure of the tunnel door ring, 6 small L-shaped prisms were evenly arranged at the ground connecting wall inside the tunnel door ring to monitor the internal structure, and the monitoring frequency is 3 times /d. By comparing and analyzing the monitoring data in real time, the changing trend of the horizontal displacement and vertical displacement of the palm surface can be grasped, and timely warning can be made to ensure the construction safety. Specific control values and change rates of monitoring items were listed in Table 1.

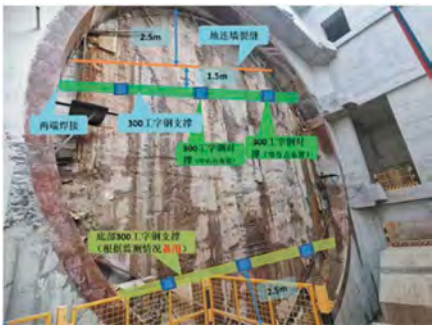

Figure 2. Layout diagram of I-beam support.

3.1.2 *Initial warehouse door seal leakage*

(1) Briefing
During the construction of the west line shield, leakage occurred at the bottom and middle of the tunnel door sealing device.

(2) Causes analysis
1) Under the influence of the anti-planting cushion in the outer door ring, the folding plate and curtain rubber plate interfered with the outer edge hob, which caused the bottom folding plate and curtain rubber plate to crack during the shield advancing process, resulting in large leakage at the bottom of the door ring.
2) The internal filling of the sealing device at the cave door was not timely, resulting in a small amount of mud leaking from the middle of the sealing device at the cave door.

(3) Targeted measures
At the bottom of the external tunnel door ring, a secondary sealing seal was applied in advance to seal the bottom leakage. At the same time, before the departure of the eastern line, the position of the anti planting head cushion layer, curtain rubber plate, and folding pressure plate inside the tunnel door ring should be confirmed to ensure that the curtain rubber plate and folding pressure plate were intact and undamaged. By taking the above measures, the sealing condition of the door of the shield tunnel starting from the east line was good and there was no leakage.

3.2 *Surface monitoring and early warning*

(1) Briefing
Surface monitoring and early warning of the western Shield: On April 9, 2023, the accumulated change of the settlement value of the surface monitoring points exceeded the red warning value.

(2) Cause analysis
① The settlement area was mainly in the area of Dongxiangcun River, and the buried depth of the tunnel vault was about 12m. When the shield tunneling was driven in the upper soft and lower hard stratum, the upper stratum was easily disturbed when the cutter cut the soil layer, resulting in the instability of the undisturbed soil and the ground settlement.
② The shield body of the shield machine was a conical structure, with a maximum gap of 110mm between the excavation diameter of the cutterhead and the diameter of the shield tail, and a gap of 570mm between the protruding pipe segment and the shield tail. Improper grouting filling in this area can easily lead to ground settlement;
③ There was F237 fault zone near the River, with a width of about 20m. The rock mass was broken to relatively broken, and the sidewall stability was poor. When the shield tunneling in this stratum, the instability of the palm surface may also affect the surface settlement.

(3) Targeted measures
① Considering the surrounding environment of the project and expert advice, the monitoring level of the 150m starting excavation section of the project was considered as three levels. The

cumulative monitoring control value of surface settlement was 45mm, and the change rate was used as a reference value.

②Through the radial grouting hole of the shield tunneling machine, the effect of mud removal was injected into the shield shell to effectively fill the gap between the shield shell and the excavation profile and prevent the natural settlement of the formation.

③ Timely secondary grouting and increase the incision pressure to achieve "head and tail protection".

3.3 *Analysis and countermeasures of quality problems in segment forming*

(1) Briefing

When the shield segment was assembled into a ring, the overall quality was good, but it is easy to produce misalignment, cracking and leakage after the shield tail is removed. The maximum misalignment was 15mm between the rings, with 13 damaged pipe segments and 37 water leaks.

(2) Cause analysis

1) When assembling the inner segments of the shield tail into a ring, they were constrained by the shield tail brush and had no buoyancy effect, resulting in better forming quality of the segments. However, due to the effect that the hole passes through the upper stratum of medium coarse sand and fine sand, it was difficult to solidified after simultaneous grouting slurry injection, which cannot restrain the segments in time and provide the first waterproof protection, and the segments were easy to float up and then misalignment between rings occurs.
2) The segment design of this project was a concave and convex tenon structure, the stiffness between pipe rings was large, but the segment is prone to stress concentration failure after the relative displacement, resulting in the cracking of the pipe segment concrete and the formation of leakage channel.

(3) Targeted measures

1) Strengthen segment prefabrication quality control: avoid large transverse cracks forming leakage channels.
2) Improved synchronous grouting slurry: shorten the initial setting time and enhance the anti-dilution ability of the slurry, so that the mortar solidifies early, constrains the segment and provides the first waterproof effect.
3) Strengthen secondary grouting: double liquid injection was carried out at the leaking position to restrain segment displacement in time and provide the rear waterproof effect of segment wall.
4) Tightening measures for strengthening segment bolts: strictly implement the triple tightening system of segment bolts, especially for the newly removed shield tail segment to strengthen segment bolts, and further enhance the overall stiffness between segments.

3.4 *Deterioration of excavation parameters and severe tool wear*

(1) Briefing

1) Deterioration of excavation parameters

According to the rock and mineral identification report, the clay mineral content of the shield through the formation at the initial stage was about 30%. Slurry shield tunneling in the stratum with high clay mineral content for a long time was very easy to lead to the deterioration of tunneling parameters, serious tool wear, limited tunneling efficiency, and even the phenomenon of the cutter head opening burning and the cutter head forming mud cake.

Due to the large excavation section of super-large diameter shield, there may be great differences in formation lithology and weathering degree, so the adaptability of tool configuration and selection was very important for shield tunneling efficiency. According to statistics, a total of 77 cutting tools were sampled during the excavation of the project, of which 48 were normal wear and 29 were abnormal wear (5 were ring damage and tooth breakage).

(2) Cause analysis

1) The stratum through the excavation was mainly muddy siltstone with high clay mineral content. In the process of excavation, under the condition of low specific gravity, most of the residue disintegrates into the mud, resulting in a rapid increase in the specific gravity of the mud, and at the same time, the burden of centrifugal equipment was increased, the centrifugal effect was poor, and the slurry abandonment pressure was large. After the specific gravity increases, the residue no longer disintegrates, and was easy to attach to the cutter head and gradually form accumulation. If not controlled, a large number of panel friction torque provides a large amount of heat, resulting in clay minerals mixed with other residue to burn into secondary rock blocks, and then form mud cake.
2) The driving parameters were adjusted during the driving process, and it was found that the cutter head torque changed periodically, with a fluctuation close to 8MN*m, and the driving speed was inversely proportional to the cutter head torque (Figure 3). It was concluded that the slagging delay has caused the blockage of the slagging mouth in part of the cutter head, which further aggravates the slagging delay in front of the cutter head.
3) The sludge in front of the cutter head caused the sludge to enter the inside of the cutter

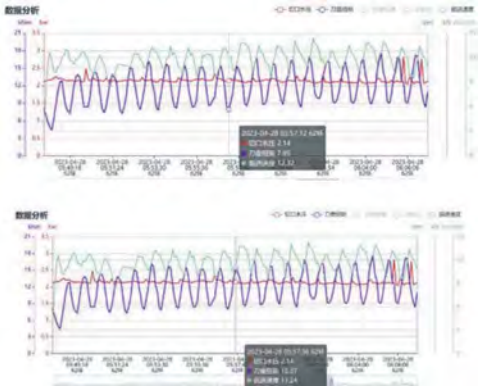

Figure 3. Line chart of shield tunneling parameters for the western route.

head and accumulate, which led to the increase of starting torque and serious secondary wear. At the same time, due to the mud formation in front of the tool barrel, the actual partial extrusion pressure was transmitted to the palm surface through the slag accumulation, and was not transmitted to the palm surface through the tool, resulting in the starting torque of the tool was not enough to rotate, and the formation of partial grinding.

Figure 4. Photo of tool partial grinding.

Figure 5. Tool secondary wear.

(3) Targeted measures

1) Strictly control the density of mud and increase the circulation flow
Increase the centrifuge and filter press, improve the mud processing capacity, control the specific gravity of mud in 1.1~1.15, and constantly wash the slurry circulation with large flow and low specific gravity to improve the environment in the warehouse.

2) Staged washing According to the torque as the criterion, when the overall torque was too large, the washing operation was carried out to reduce the accumulation of slag in front of the cutter head. In order to avoid overexcavation caused by warehouse washing, the standard for the end of warehouse washing was subject to the reduction of cutter head torque to idle torque.

3) Using inlaid gear hobs
Due to the low hardness and poor wear resistance of the smooth hob, the secondary wear was seriously affected by the accumulation of slag in front of the superimposed cutter head. Meanwhile, according to the detailed survey report, the uniaxial saturation compressive strength of the breezy argillaceous siltstone is 20-30 MPa. Therefore, the inserted tooth type hob was more suitable for the geology of this project.

(4) Auxiliary pressure driving mode or center scour aeration
According to the previous experience of similar formations in South China, after adopting measures such as auxiliary pressure driving mode or central scour gas filling, the driving parameters and driving efficiency will be greatly improved. However, there was sand layer in the excavation section at the initial stage, which was prone to breakdown and formation of channels due to strong gas flow, and there was a risk of pressure loss. In the subsequent excavation process, due to the gradual reduction of rock weathering degree, it was expected that the slag stagnation and drainage conditions and excavation parameters will develop well. If the deterioration continues, auxiliary pressure excavation mode or central scour aeration excavation can be adopted after judging the air tightness of the face of the face.

4 CONCLUSION

The double-line shield of Haizhuwan Tunnel has been successfully launched, and the key technologies were summarized below:

1) In order to offset the impact of “upward drift” that may occur due to shallow soil cover, it was necessary to strictly control the reinforcement quality of the control end. When the shield was driven,

the deviation between the shield center and the design elevation of the tunnel was controlled within -30mm, and the plane deviation was controlled within ±30mm.At the same time, the main excavation parameters were strictly controlled, and the low speed excavation were adopted to avoid large disturbance to the soil mass and prevent overexcavation.

2) When the tunnel door was broken, the I-steel support face can be set up according to the situation, and the end reinforcement area was enclosed during the breaking period, and large-scale equipment was prohibited to walk;
3) Before starting, confirm the position of the anti-planting head cushion, curtain rubber plate and folding plate in the tunnel door ring to prevent the tunnel door seal from being damaged. After the leak of the tunnel door seal, fill the internal void of the tunnel door seal device in time, and made a secondary seal of the tunnel door in advance at the position of the external tunnel door ring to block the leakage;
4) In the process of excavation, the cut pressure was properly increased, and the mud effect was injected into the shield shell through the radial grouting hole of the shield machine to prevent the natural settlement of the formation. Shorten the initial setting time of synchronous grouting slurry and enhance its resistance to water dispersion, timely secondary grouting to avoid misalignment, cracking, leakage, and effectively guarantee the quality of formed tunnel; If necessary, increase the monitoring frequency, feedback the monitoring data in time, and strictly implement the monitoring guiding construction principles;
5) Affected by the high content of clay minerals in the starting formation, there was a hysteresis in the driving process, and in serious cases, the cutter head opening forms a mud cake. During the process, the efficiency of shield tunneling has been greatly improved by strict control of tunneling speed, mud gravity, strengthening central scour, stage washing of silo and replacement of insert cutting tools.

REFERENCES

Zhu, W. B, Ju, SJ., Wang H. Shield tunneling technology in mixed face ground conditions[M]. New version. Beijing: China Architecture & Building Press, 2020.

Lian, W. B. The Initial Technology of Subway Shield and the Prevention and Treatment of Common Problems[J]. Chinese & Overseas Architecture, 2019 (06): 254–255.

You Y, F., Liang K, S., Du C, D. et al. Launching Technology with Shallow Overburden for Super-Large Diameter Shield in Chunfeng Tunnel[J]. Tunnel Construction, 2021, 41 (S1): 382–387.

Zhang B, Y. The Key Technology of Super Large Diameter Shield Tunnel[J]. Journal of Underground Space and Engineering, 2013,9 (03): 633–639.

Du C, D, Wang K, You y, F. Starting technology of large-diameter slurry shield tunneling for the Shiziyang Tunnel on the Guangzhou Shenzhen Hong Kong Passenger dedicated line [J]. Modern Tunnel Technology, 2008,45 (S1): 371–377.

Fang X, S., Ye L, B, Zhu M,Y., et al. Analysis on launching control tunneling of large diameter slurry shield in Qinghuayuan tunnel[J] Railway Survey, 2022, 48 (01): 81–86.

Wu W. L, Zhu H.H.,Zou Y,. et al. Study of Key Technologies of Steel Sleeve Launching and Receiving of Shield[J]. Tunnel Construction, 2017, 37 (07): 872–877.

Bai X, L. Bullflex cave door sealing technology and its application [J]. Railway Construction Technology, 2018 (02): 86-88+111.

Shu Y, Zhou S, H, Ji C, et, al. Analysis of shield tunnel segment uplift data and uplift value forecast during tunnel construction in variable composite formation [J] Journal of Rock Mechanics and Engineering, 2017, 36 (S1): 3464–3474.

Wang Z, F, H., Feng Clay Cake Prevention for a Slurry Shield Cutterhead in Argillaceous Siltstone Stratum[J] Modern Tunnel Technology, 2017, 54 (06): 217–222.

Fu X, H, Mo t, Z C, et al. Formation and Precautions of Mud Cakes in Mixed Strata[J] Chinese Journal of Underground Space and Engineering, 2020, 16 (S2): 864–869.

Tunnelling for a Better Life – Yan, Celestino, Thewes & Eberhardt (Eds)
© 2024 The Author(s), ISBN 978-1-032-80042-4
Open Access: www.taylorfrancis.com, CC BY-NC-ND 4.0 license

Experimental research on foam performance and intelligent injection control of foam additive system of tunnel boring machine

Chengjie Zhang*
Shanghai Urban Construction Tunnel Equipment Co., Ltd., Shanghai, China

Yixin Zhai
Shanghai Shield Research Centre Co., Ltd., Shanghai, China

ABSTRACT: As an important soil conditioner in TBM tunnel construction, foam additive system composition, foaming effect and injection control mode have a great impact on the actual construction, especially in complex formations. Aiming at the problems of poor foaming effect and low degree of automation control in the foam additive injection system of tunnel boring machine, this paper develops an experimental platform, by simulating and setting the TBM's actual construction parameters, six possible factors affecting the foaming and spraying effect (such as different foaming ratios, etc.) were explored and tested. The intelligent monitoring and automatic control logic of foam injection were matched, through the collection, analysis and comparison of test data, it was verified that the developed control system could meet the adaptive driving requirements of the tunnel boring machine.

Keywords: TBM, Foam additive, Foaming Performance, Intelligent Control, Experimental Research

1 BACKGROUND

Figure 1. Foam injection diagram.

With the continuous development of rail transit construction, tunnel boring machines[1,2] have become the main underground excavation process equipment for urban tunnel construction due to their advantages such as less impact on the surrounding environment, safe and efficient construction, and low labor intensity. However, in complex soil conditions such as sand, pebble, and clay layers, especially in round gravel and pebble layers, tunnel boring machine may encounter varying degrees of difficulties in the following aspects during excavation construction:

The problem of difficult to achieve dynamic balance of soil pressure on the excavation surface. In the formation of round gravel and pebbles, the plastic flow of the debris and soil cut by the cutterhead during tunnel construction is poor, the working pressure cannot be smoothly transmitted, making it difficult to achieve continuous dynamic balance. The working face is prone to instability, leading to over excavation.

The problem of excessive torque on the cutterhead and screw conveyor. After the soil layer is disturbed by the cutterhead, the sand and gravel layer will become soft, and larger particles of pebbles are prone to accumulate at the bottom of the cutterhead, causing excessive torque during TBM mining operation and "blockage" of the cutterhead. However, in clay layers, the phenomenon of "mud cake" on the cutterhead is prone to occur frequently.

The problem of abnormal wear and rapid wear of cutting tools. Due to the high friction of the pebbles, the impact between the cutting tools and the pebbles, and the locking effect of the excavated soil on the cutting tools, which is prone to cause rapid wear, impact wear, eccentric wear and abnormal wear of the cutting tools.

During the tunnel construction in strong permeable layers of sand and gravel layers, excessive water pressure on the excavation surface can lead to

*Corresponding author: zhangchengjie@stecmc.com

DOI: 10.1201/9781003495505-304

soil erosion, resulting in gushing[3]. In severe cases, can cause surface subsidence and affect the smooth construction of the project.

Since the foam improvement technology was developed in Japan in the early 1980s, the research on the effect of foam additive has been ongoing for more than 40 years. It has been confirmed from relevant research and engineering practice that foam additives[4] have obvious effects on improving the characteristics of slag soil, such as improving the fluidity of soil in excavation chamber, stabilizing the cutting surface, reducing the torque of cutterhead and screw conveyor, reducing structural wear, and reducing the permeability coefficient of soil and sand. The research on foam additives is mainly focused on the development and characteristics of foam agent materials[5], the improvement of foam additives on the construction soil layer and the impact of construction parameters[6,7,8], and the exploration and research on the factors affecting the foam performance is relatively lacking. At the same time, with the development trend of automated driverless tunneling machines, the foam injection control based on the operator's construction experience now is lack of accurate monitoring, fault diagnosis and adaptive adjustment of the injection process, with high blindness and low intelligence. The development of automatic injection control of foam additives is urgent.

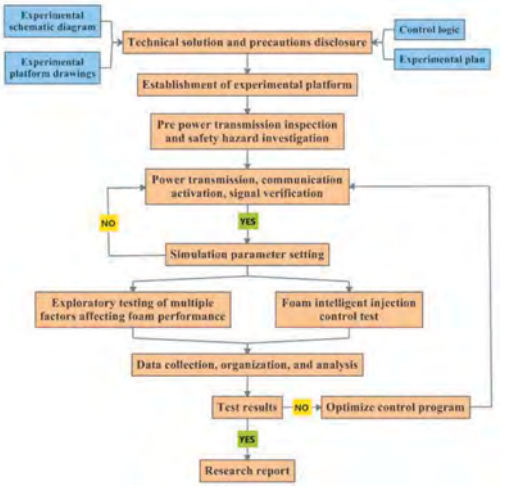

Figure 2. Foam experimental flow chart.

Figure 3. Composition and physical diagram of the test platform.

2 EXPERIMENTAL RESEARCH

2.1 *Test method and process*

This test is based on building an experimental platform for testing and research[9]. By simulating the setting of the TBM's actual construction parameters, a single factor contrast injection test is carried out on the foam generator, air control valve, pipeline "Ω" device, foam generator setting position, foaming ratio, foam solution concentration and other factors that may affect the foaming performance effect, while matching adaptive data acquisition and fault monitoring, intelligent control logic programs, the foam automatic injection control adjustment and accuracy of the TBM in the unmanned mode are optimized through experiments. The main line revolves around design (experimental system principles, control program development, experimental technical solutions, etc.), experimental platform construction, exploration and testing of factors affecting foam performance, intelligent injection control testing, scheme and program optimization, and acceptance report process execution. The experimental process is shown in Figure 2.

2.2 *Composition of testing platform*

The experimental platform shown in Figure 3 is designed in conjunction with the tunnel boring machine additive injection system, mainly consisting of a simulated cutterhead, injection pump, agitator, valve components, additive tank, monitoring sensors, control room, and pipeline components. This test platform can simulate and set up various functional controls of foam injection system under the tunnel construction condition through the man-machine operation interface, including foam solution proportioning supply, solution mixing, solution regulation, air conditioning, foam manual injection, semi-automatic injection, automatic injection, data monitoring and fault alarm. At the same time, it can also conduct comparative exploration, test and research on factors that may affect the foam performance.

2.3 *Principle of foam injection test*

As shown in Figure 4, the foam injection test system is mainly composed of foam solution proportioning, solution injection circuit and foaming circuit. The ratio of foam solution is transferred from the submersible pump of Part 9 located in the foam stock solution tank of Part 31 to the foam solution tank of Part 32 through the control of the pneumatic ball valve of Part 13, and mixed with the industrial water transferred to the solution tank through the pneumatic ball valve of Part 14 to form foam solution. The ratio concentration of foam solution can be

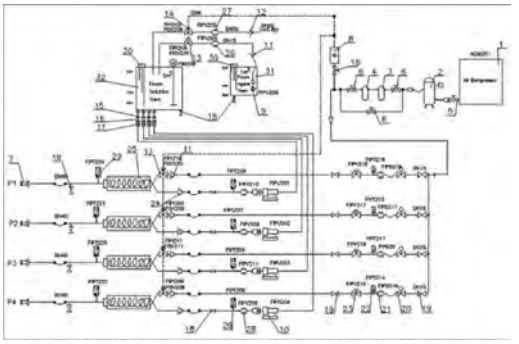

Figure 4. Schematic diagram of foam injection.

adjusted by changing the transfer amount of foam stock solution and industrial water. The transfer amount of stock solution and water is converted and accumulated through the flow meter of Part 26 and Part 27 respectively. At the same time, both the foam stock solution tank and the solution tank are equipped with a 30 liquid gauge to monitor the liquid level of the medium in the tank and participate in the liquid level alarm and control; The foam solution is pumped and filled through the solution pump of Part 10. The outlet of the solution pump is equipped with a flow meter of Part 28 and a pressure sensor of Part 29 to monitor the flow and pressure of the circuit. When the flow is too low or the pressure is too high, the operation status of the pump is interlocked; The foaming circuit injects foam solution into the foam generator of Part 25 at a certain rate of air to make the solution produce more bubbles foam to achieve foaming effect. The foam solution after mixing foam solution and air is sprayed to the front through the nozzle of Part 7. The air entering the generator is generated by the air compressor of part 1 and adjusted through the regulating valve of part 23. At the same time, the air circuit is equipped with a pressure differential flow meter of part 21 and a pressure sensor of part 22 to monitor the air flow and pressure. In automatic mode, it is matched with automatic interlocking control for injection.

2.4 *Experimental contents*

In foam injection system, factors such as foam generator structure, air control valve form, foam generator setting position, foaming ratio and foam solution ratio concentration may affect the foaming performance. In order to verify the influence of the above factors on the foaming performance, comparative injection tests are were conducted on each factor, measuring the visual state of the foaming effect, fading time, and pipeline pressure. At the same time, combined with the actual excavation parameters of a tunnel project, the adaptive control program of the foam injection system was compiled and revised to verify that the quantitative indicators of automatic interlocking function control and feedback adjustment in the automatic mode were within the deviation of the theoretical calculation value[1].

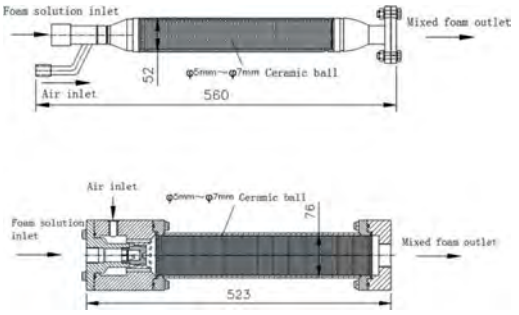

Figure 5. Two foam generators with different structure (1st: specification 1; 2nd: specification 2).

2.4.1 *Influence test of foam generator on foaming performance*

The contrast test of two foam generators with different structure as shown in Figure 5 was conducted under the same injection conditions (the injection flow of foam solution pump was consistent with the air input). The test results showed that the foam solution of specification 2 foam generator was sprayed fully and continuously, and the foam path was fluffy and spongy, while that specification 1 foam generator was sprayed intermittently, and the bubbles were scattered, as shown in Figure 6. This may because of the air channel internal structure of the foam generator in Specification 2 and the volume of the ceramic ball in the cavity are more reasonable, which enables better mixing of foam solution and air, so as to obtain better foaming effect. Monitoring the fading time of two types of foaming agents, it was found that the fading time of foaming solution for specification 1 and specification 2 was 210 minutes and 170 minutes respectively. The fading of foaming agents for specification 1 in discrete state was faster.

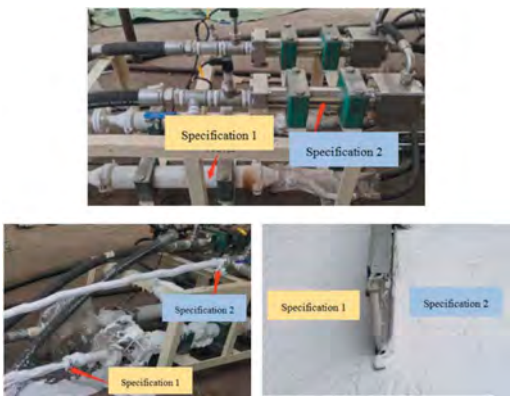

Figure 6. Comparison test diagram of foaming effect of different foam generators.

Figure 7. Different forms of air regulator used in foam injection system.

2.4.2 *Response and accuracy testing of regulating valves on air conditioning*

The amount of air injection will directly affect the mixing and foaming performance, and its adjustment mainly depends on the control valve 23 in Figure 4. At present, there are several commonly used forms of control valves on the market with different adjustment characteristics (control mode, adjustment response, and control accuracy). Three different forms of control valves, pneumatic, electric (with locator), and electric (without locator), are selected for injection simulation tests. The tests include the time required for valve opening from closed to fully open, and the response speed when adjusting to the same flow value. The test results in terms of control accuracy (flow stability) and ease of operation are shown in the table below.

Table 1. Comparison test with different types of air regulators.

Test item	Pneumatic regulator	Electric regulator (with locator)	Electric regulator (without locator)
Time taken from close to fully open	5s	38s	44s
Air regulator response and accuracy in automatic mode (flow rate increases from 0NL/min to 600 NL/min)	Flow rate stabilizes at 626 NL/min after 10s	Flow rate stabilizes at 630 NL/min after 32s	Flow rate fluctuates between 500-600NL/min in 40s, and stabilizes at 620 NL/min after 72s
Drive mode	Pneumatic +4-20mA	24V voltage +4-20mA current	24V voltage AC
Ease of operation	Interface percentage input	Interface percentage input	Interface percentage input
Cost	High	Low	Lower

2.4.3 *Influence test of pipeline "Ω" device on foaming performance*

In the actual foam injection system, the foam generator is often positioned at the rear gantry frame. The length of the pipeline from the foam generator outlet to the shield and then into the cutterhead injection port is at least 30m. At this time, the mixed foam from the generator may appear gas-liquid stratification in the long-distance pipeline. The air is dispersed on the top of pipeline, and the foam quality decreases, as shown in Figure 8. In order to explore the influence of giving appropriate back pressure and mixing in long-distance pipelines on the foam foaming effect, the "Ω" device was designed, and comparative tests were conducted under the same injection conditions (foam solution flow and air flow), as shown in Figure 9. From the test results, it can be seen that the circuit equipped with an "Ω" device has a more fluffy and spongy effect on the foaming liquid. Whether the "Ω" device is set horizontally or vertically, both method have a promoting effect on the foam performance.

Figure 8. Distribution diagram of foam additive in pipeline.

Figure 9. Foam injection test with "Ω" device.

2.4.4 *Influence test of foam generator different position on foaming performance*

When the foam generator is placed far away from the injection port, the pressure loss will increase due to the long pipeline, which will also have a certain impact on the foaming performance. Select the distance between the foam generator and the injection port as 10m and 30m respectively, and conduct the contrast test of foam injection under the same conditions.

It can be seen from the test results that when the foam generator is 10m away from the nozzle position (Figure 10-4 #), the distance of foam injection is longer. According to the mechanical pressure

Figure 10. Comparative test on foaming effect of different distance between foam generator and nozzle.

gauge installed at the injection port, the injection pressure is 2.3 bar, and the foaming effect is flocculent. When the foam generator is 30m away from the injection port (Figure 10-2 #), the injection pressure is 2 bar, there is a pressure loss of 0.3 bar compared, and the foam is dispersed and fluid.

2.4.5 *Influence test of foaming ratio on foam fading degree*

In the foam automatic injection system, the foaming ratio will affect the output of foam solution and air, making the foaming solution produce different performance. In order to explore the influence of different foaming ratios on the fading degree of foam, under the same foam concentration and injection conditions, respectively adjust the foaming ratios to 10 times, 15 times, 20 times, and 30 times to test the fading degree of foam. The test results are shown in the following figure.

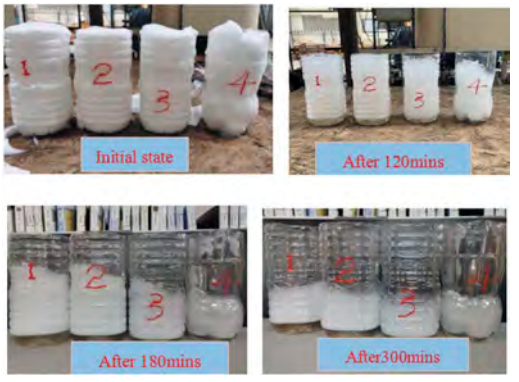

Figure 11. Comparative test on foam fading of different foaming ratios.

Table 2. Comparative test on foam fading time of different foaming ratios.

Foaming ratios	Fading time (in half cup)
10 times - 1# cup	230 min
15 times - 2# cup	210 min
20 times - 3# cup	160 min
30 times - 4# cup	140 min

It can be seen from the test results that when the foaming ratio is 10 times and 15 times, the fading time of foaming is more than 200 min, while when the foaming ratio is 20 times and 30 times, the fading time of foaming is around 150 min. This indicates that the foaming ratio is not as larger as better. When the foaming ratio exceeds a certain ratio, the hollow gas content of foam increases, the solution content decreases, and it cannot reach the high-quality foaming solution.

2.4.6 *Influence test of foam solution concentration on foam fading degree*

The foam concentration in the foam solution will affect the stability and performance of the foam solution. To explore the influence of foam concentration on the foam fading degree, under the same injection conditions, compare and test the foam fading time of three concentrations: 1%, 3% and 5%, and record the fading speed of the foam solution at different concentrations, as shown in the following figure.

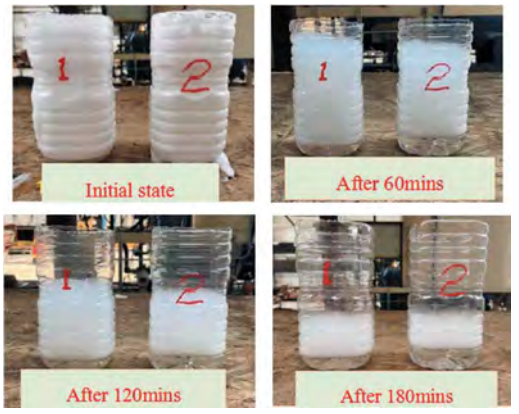

Figure 12. Comparative test on foam fading of different foam concentration.

It can be seen from the data in Table 3 that under the same test conditions, when the concentration of foam solution is 5%, the fading time of bubbles is 230 min, and the foaming effect is also good. When the concentration of foam solution is below 3%, the decay time of bubbles becomes shorter, and the foaming effect becomes worse with the decrease of concentration. This is because the proportion of

Table 3. Comparative test on foam fading time of different foam concentration.

Test item	1% foam concentration Figure 12 - 1# cup	3% foam concentration Figure 12 - 2# cup	5% foam concentration Figure 11 - 1# cup
Foaming effect	Large amount of bubbles	Foam dispersion	Foam fluffy
Fading time (in half cup)	120 min	140 min	230 min

foam agent in foam solution decreases, and the proportion of water increases.

2.4.7 *Test of foam automatic injection control*

The foam automatic injection control can adapt to the automatic driving of the TBM, and intelligently realize functional control in the unmanned operation mode. Its injection volume adjustment is based on the actual injection demand of the tunneling construction calculated according to the tunneling speed of the shield machine, the excavation area of the shield machine, and the injection rate of foam mixture, and then calculate the flow required for foam solution pump and gas supply according to the foaming ratio, by averaging the number of actual injection circuits, the required output flow of each solution in use is obtained[11], which is feedback to the PLC control program. After comparing with the PLC program, the frequency output value of the frequency converter of the solution pump in actual injection is adjusted (the speed of the solution pump is adjusted to adjust the output flow of the solution pump) and the opening of the gas supply regulating valve, so that the output flow of the solution pump and the gas supply is matched with the injection amount required for construction, this stage is a dynamic matching compensation process. Figure 13 shows the mechanism diagram of foam automatic injection control.

Advanced Mitsubishi Q series CPU is used for foam automatic injection control, and CC Link communication mode is used. The CPU is connected with the proface human-machine interface through Ethernet. PLC can collect digital input signals such as start/stop of motor and opening/closing of valve, as well as analog input signals of foam pressure, flow and liquid level. PLC can output digital output signals for valve switches, as well as analog signals for adjusting valve opening output from frequency converters[12]. Only to set the excavation area, foam mixture injection rate, thrust speed, foaming ratio of the TBM on the operation interface, so that the foam system can be activated adaptively. At the same time, the liquid level, flow, pressure and other states during the injection process can be observed in real-time, as shown in Figure 14.

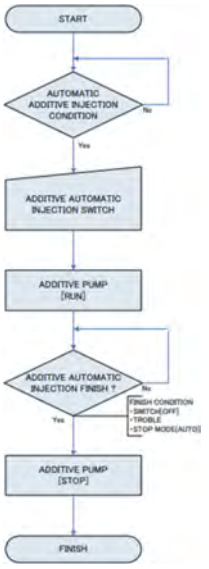

Figure 13. Control mechanism of foam automatic injection.

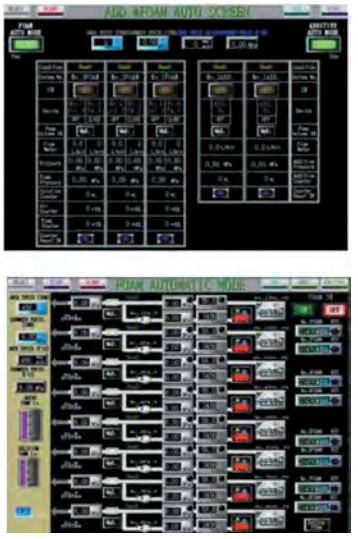

Figure 14. Foam automatic injection operation interface.

Calculation formula of foam automatic injection demand flow:

Mixed foam demand flow Qmix (L/min) = excavation area (m2) * excavation speed (mm/min) * injection rate (%);

Foam solution demand flow Qsol (L/min) =Qmix (L/min)/foaming ratio;

Air supply demand flow rate QAir (NL/min) =Qmix (L/min) * [Pearth (MPa)+0.1] * (foam rate -1)/Foam rate /0.1.

It can be seen from the test data in Table 4 that under the simulated setting of different thrust speed, injection rate and foaming ratio parameters, each

Table 4. Foam automatic injection test data record.

Test data record of foam volume when injection rate is 105% and foaming ratio is 10 times

Thrust speed mm/min	Theoretical demand of foam solution L/min	Actual measured value of foam solution L/min	Theoretical demand of foam air NL/min	Actual measured value of foam air NL/min
10	43.68	46	393.12	390.2
15	65.52	68.3	589.68	555
20	87.36	93.3	786.24	762

Test data record of foam volume when injection rate is 110% and foaming ratio is 15 times

Thrust speed mm/min	Theoretical demand of foam solution L/min	Actual measured value of foam solution L/min	Theoretical demand of foam air NL/min	Actual measured value of foam air NL/min
10	30.51	32.6	427.09	420
15	45.76	48	640.64	620
20	61.01	63	854.19	826

Test data record of foam volume when injection rate is 120% and foaming ratio is 10 times

Thrust speed mm/min	Theoretical demand of foam solution L/min	Actual measured value of foam solution L/min	Theoretical demand of foam air NL/min	Actual measured value of foam air NL/min
10	49.92	53.2	449.28	435
15	74.88	79	673.92	660
20	99.84	105	898.56	850

Test data record of foam volume when injection rate is 130% and foaming ratio is 10 times

Thrust speed mm/min	Theoretical demand of foam solution L/min	Actual measured value of foam solution L/min	Theoretical demand of foam air NL/min	Actual measured value of foam air NL/min
10	36.05	38	504.75	483
15	54.08	56	757.12	712
20	72.11	75	1009.5	960
20	72.11	75	1009.5	960

function of the foam injection system is controlled normally under the automatic mode, and the output of the actual solution and air filled is within the deviation of the theoretical calculated value (± 5%), which meets the design and construction requirements.

3 CONCLUSION AND PROSPECT

By setting up a test platform to simulate the TBM actual construction parameters, a comparative injection test was conducted on the foam generator, air control valve, pipeline

"Ω" device, foam generator setting position, foaming ratio, foam solution concentration and other factors that may affect the foaming performance in the foam injection system. The test results can be obtained as follows:

1) From the foaming effect and fading time, it can be concluded that the foaming quality of specification 2 foam generator is superior to specification 1 foam generator in terms of foaming quality;
2) Combined with the response speed and control accuracy test of the three types of air control valves on air conditioning, the pneumatic type response speed and accuracy control are optimal, which is suitable for the automatic control of the foam system under the automatic driving of TBM, while the electric control valve with positioner has more advantages in cost performance;
3) Adding "Ω" device (horizontal installation and vertical installation) to foam concentrate pipeline can improve the performance of foam concentrate;

4) When the foam generator is set close to the fill port, it will have better foaming performance than that set far from the fill port;
5) The foaming rate will affect the fading of the foaming solution. Under the same injection conditions, the fading time of the foaming solution at 10- and 15-times foaming rate is longer than that at 20- and 30-times foaming rate;
6) The foam concentration will affect the foaming performance. Under the same injection conditions, the foam test results with the concentration of 1%, 3% and 5% show that the foam with the concentration of 5% has the slowest fading speed and the highest stability.

At the same time, by optimizing the foam automatic injection control logic and integrating data monitoring and sensing, collection, deviation correction, control and fault alarm, it can actively adjust the transmission parameters of foam solution and air to meet or close to the theoretical demand of foam additives, and the test shows that the control of each function is normal under the automatic mode of foam injection system The output of the actual solution and air injected is within the deviation range of ±5% of the theoretical calculated value.

This test provides technical support for the design, development and intelligent control of the foam additive system of the tunnel boring machine, and also conforms to the development demand of the current tunnel boring machine towards intelligence and automation. However, there is also a lack of foam solution matching for different soil layers and the verification of the control effect of foam automatic injection during actual stratum excavation. In the future, the optimal foaming solution can be obtained by combining automatic ratio adjustment for different soil layers, and an automatic control system that is adaptive to the excavation parameters of the tunneling machine can be used.

REFERENCES

[1] Japanese Civil Engineering Society. Standard Specification for Tunnels [Shield Section] and Commentary [M]. Translated by Zhu Wei. Beijing: China Construction Industry Press, 2011.
[2] Berhard Maidl, Martin Herrenknecht. Mechanised Shield Tunnelling, Second Edition[M]. 2012.
[3] Wei Kanglin. Research on the Mechanism and Prevention Measures of Spilling Problems in Earth Pressure Balanced Shield Construction [D]. Hohai University, 2003.
[4] Zhang Fengxiang, Zhu Hehua, Fu Deming. Shield Tunnel [M]. Beijing: People's Communications Press, 2004.
[5] Qiao Guogang. Development of new foaming agent for EPB shield and research on foam soil improvement [N]. China University of Mining and Technology (Beijing), 2009.
[6] Chen Chunlin. The role of foam agent in EPB shield construction [J]. Shanxi Construction Engineering, 2007, 33 (7): 307–308.
[7] Song Kezhi, Wang Bo, Kong Heng, Yuan Dajun. Research on foam technology of earth pressure shield construction in water free sandy pebble stratum [N]. Journal of Rock Mechanics and Engineering, 2005,24 (13): 2327–2332.
[8] Wang Hui. Analysis on application efficiency of foam agent in shield construction of subway tunnel [J]. Heilongjiang Traffic Science and Technology, 2014,11:134–136
[9] Li Xiaofeng. Experimental Study on the Performance of foam for Shield [J]. China's New Technology and New Products, 2013.
[10] Guo Tao. Evaluation and Research on the Performance Method of Foam Agents for Shield Tunnelling [J]. Dalian: Hehai University, 2005.
[11] Liu Xiuzheng. Parameter Design and Application of Shield foam System [J]. Shanxi Construction Engineering, 2008,34 (3): 344–345.
[12] Chu Guangdong, Zhang Wang, Liang Long. PID control of foam system of EPB shield machine [J]. China Science and Technology Journal Database, 2015,39:94–95.

Tunnelling for a Better Life – Yan, Celestino, Thewes & Eberhardt (Eds)
© 2024 The Author(s), ISBN 978-1-032-80042-4
Open Access: www.taylorfrancis.com, CC BY-NC-ND 4.0 license

Visualization study on stability of shield tunnel face with transparent soil model

Honghua Zhao*, Zhi Jia & Yang Liu
The School of Mechanical and Aerospace Engineering, Dalian University of Technology, Dalian, China

ABSTRACT: Due to design optimization and geological conditions, shield tunnels often work with different longitudinal inclination angles. In this case, it is very important to understand and master the failure mode of the tunnel face. In this study, a transparent soil model was set up in the laboratory to visualize the full 3D deformation field of the tunnelling. The failure mechanism of tunnel face in soft clay stratum is studied under different longitudinal inclination angles δ and the ratio of buried depth to diameter C/D. The results show that the failure shape of the shield tunnel face shows a ' ring ' mode under different longitudinal inclination angles δ and C/D conditions. The deformation process of soft clay has different development stages, and the failure modes in different areas vary. The deformation zone is mainly divided into subsidence areas and uplift areas. With the increase of the longitudinal inclination angles, from δ = -20 °, 0 ° to 20 °, the instability area, the maximum displacement, and the vertical pressure all changes, and the 3D reconstruction also obtains the same failure mode. Compared with other cases, the tunnel has a higher collapse risk with shallow buried and upward inclination angles. Long-term upward inclined excavation in soft clay stratum should be avoided in engineering practices.

Keywords: Tunnelling, Transparent soil, 3D visualization, Failure, Soft clay

1 INTRODUCTION

Tunnel construction is commonly used in urban metro construction in China due to its distinct advantages and the country's rapid infrastructure growth. Mastering failure mechanisms ahead of the tunnel face is essential to ensure a stable construction process. Due to complex engineering geological conditions or design optimization, the shield machine's running route may not always remain horizontal in reality. And it has been demonstrated that the stability of the tunnel varies significantly under different longitudinal inclination angles. Thus, this study focuses on investigating the failure mechanism of the excavation face with various longitudinal inclination angles.

The damage mechanism in the vicinity of the shield face has been well investigated by previous researchers, using three main types of analysis: (1) Indoor tests, (2) Theoretical analysis, and (3) Numerical methods. Indoor tests are mainly carried out by centrifuge experiments and 1-g model tests etc.(Weng et al., 2020; Yin et al., 2021). Alternatively, simulation of tunnel face collapse by rigid plate retreat was adopted in several research works (Ads et al., 2021; Ahmed and Iskander, 2011a; Cheng et al., 2021; Kirsch, 2010; Ma et al., 2022; Yin et al., 2021). The impact of tunnel face opening and anisotropy of seepage conditions on tunnel face stability was investigated undergoing a series of centrifuge experiments and finite difference numerical simulation analysis(Yin et al., 2021). The findings demonstrate that tunnel face stability benefits from the seepage caused by water ingress. By applying water pressure to the shield face, Ahmed and Iskander (2011) estimate the minimum support pressure, the failure mode, and the expansion of the failure area. Weng et al. (2020) investigated the failure of the excavation face driven by the longitudinal slope angles and steady-state seepage using centrifuge experiments and numerical simulation analysis. Researchers (Ma et al., 2022; Sang et al., 2019; Zhao et al., 2022) carried out a systematic study on the destabilization patterns of excavation faces in transparent clay with different burial depths and clay-gravel composite strata. They undertook it by controlling the retreat of the excavation face to simulate the lack of support pressure.

*Corresponding author: zhaoh@dlut.edu.cn

DOI: 10.1201/9781003495505-305

Huang et al. (2019) conducted six indoor tests to investigate the specific failure pattern of excavation face in dense sand layers at various longitudinal inclination angles.

Limit analysis and limit equilibrium methods are the two primary categories of theoretical methods, with the majority of the remaining approaches being variations of these two types(Hou and Yang, 2022; Huang et al., 2022; Lee and Nam, 2004; Li et al., 2021; Man et al., 2022; Perazzelli et al., 2014; Zhang et al., 2011; Zou et al., 2019). Using the upper limit solution from the limit analysis, Lee and Nam (2004) estimated the seepage pressure on the tunnel face. The 3D kinematic tolerance mechanism for upper limit analysis has been enhanced by Tang et al. (2014) to predict potential damage within various stratums. Cheng et al. (2021) developed a three-dimensional failure mechanism in dense sand, segmenting the unstable area into a fracture slip zone and an upper loosening zone, based on the limit equilibrium theory and findings from previous model tests. Senent and Jimenez (2015) proposed that the recent rotating surface collapse mechanism could be expanded to estimate critical pressures for tunnels in stratified (or layered) strata in the context of the upper limit analysis. Zhang et al. (2011) adopted an improved wedge prism model based on the limit equilibrium approach as well as an improved three-dimensional rotation failure model based on the limit analysis method.

In numerical methods, the finite element method (Ahmed and Iskander, 2011b; Alagha and Chapman, 2019; Han et al., 2021; Huang et al., 2019; Ukritchon et al., 2017; Wang et al., 2020) and discrete element method (Chen et al., 2011; Zhang et al., 2011) are also widely used to discuss the stability of tunnel face under different conditions. Based on 140 numerical analyses, Alagha and Chapman (2019) determined the collapse pressure required for tunnel excavation in homogeneous or layered soil. According to the analysis of the water head, Huang et al. (2019) performed a three-dimensional coupled pore fluid flow and stress finite element simulation to estimate the seepage pressure in the limit equilibrium and took a novel wedge mechanism into consideration. The spatial variation of soil mechanical characteristics can be explained by the gradient between soil masses. Chen et al. (2013) investigated the failure mechanism and limit support pressure of the tunnel face in a dry sand layer using the discrete element method. This method has unique advantages in revealing the mechanical properties of granular materials. Zhang et al. (2011) develop a 2D particle flow approach to explicitly consider explicitly soil excavation from the face, effects of varying face support pressure, and the influence of buried depth.

The main focus of the aforementioned study and analysis is on the stability of the horizontal tunnel and the failure mechanism, including the impact of layered soil, seepage, weak and cracked zones, and layered soil. Shield tunnels frequently operate at varying longitudinal inclinations in practice as a result of design optimization and the influence of stratum qualities, but there is little research on this topic, particularly in the clay stratum. Knowing the failure characteristics and instability mode of tunnel at varied longitudinal inclinations can greatly simplify selecting support parameters in engineering. In addition, considering the development of transparent soil technology, it is now possible to detect soil deformation in three dimensions in a more intuitive and non-intrusive manner(Ahmed and Iskander, 2011a; Guzman et al., 2014; Iskander et al., 2015; Liu et al., 2022; Sang et al., 2019; Yuan et al., 2019; Zhang et al., 2019). Hence, utilizing the self-designed shield model test device along with image processing and 3D reconstruction algorithm, this study analyzed the failure mechanism of the tunnel face under various longitudinal inclination angles and burial depths in the clay stratum.

2 EXPERIMENTAL SETUP

In this study, the preparation methods of transparent clay are as follows: 1) Take an appropriate amount of Laponite RD powder and deionized water (the ratio of powder to total mass is 4.5%); 2) To avoid the influence of bubbles, the deionized water is evacuated and monitored until no bubbles escape from the liquid surface; 3) After evacuation, pour deionized water into the container and swirl vigorously for 30 minutes or more while slowly putting in Laponite RD powder; 4) After vacuuming the mixture, then settling and consolidate for 14 days. After vacuuming the mixture, it is allowed to consolidate for 14 days. Tracer particles (refraction index: 1.582, size: 50μm, density: 1.03g/cc) are added to the dispersion procedure to enable clear image capture(Ads et al., 2020b; Ma et al., 2022).The strength of samples undergoing self-weight consolidation for 14 days was 0.44 kPa, 0.50 kPa and 0.63kPa for 5cm,15cm and 20cm below the surface.

A model box and a shield tunnelling device was design for the test as shown in Figure 1.

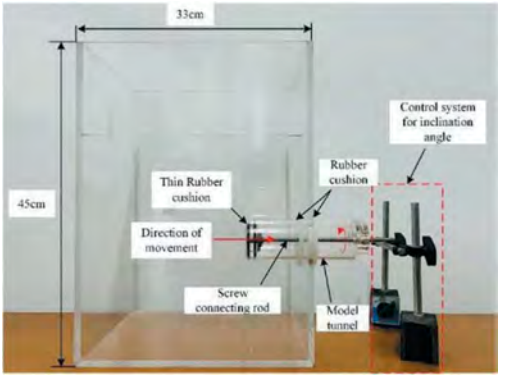

Figure 1. Schematics of the model box and tunnel.

The model box is mainly composed of the main body and plugging device. To reduce the effect of the model border, the diameter of the tunnel D was set to 80 mm and placed in the center of the side wall, 120 mm from the bottom of the model box and 250 mm from the top of the box.

The shield simulator, as shown in Figure 1. The shield shell consists of a round Plexiglas tube with an inner diameter of 70 mm, a thickness of 10mm, and a length of 200 mm. There are two rubber cushions around the outer wall where it contacts the shield shell. The back of the model is 20 mm thick, and two holes with a diameter of 15 mm are opened to balance the pressure when the center distance is 39 mm. A bearing is installed 10 mm behind the support panel, and a wire rod with a 1mm pitch and a length of 250 mm is secured with its rear end through the locking cap. The screw rod's back end is connected to the rotating motor via the processed sleeve, so that during motor rotation, the central connecting rod drives the support panel backward using the thread of the locking cap, replicating the tunnel excavation face's insufficient support force.

Meanwhile, to investigate the effect of overburden depth C on the damage pattern of the shield face, assume that the model conditions are δ=±10°,0° and C/D=1.5,3. The definitions of the ratio of overburden depth to model diameter (C/D) and inclination angle δ are shown in Figure 2. The surface of the model box and shield model is roughened to minimize laser reflections.

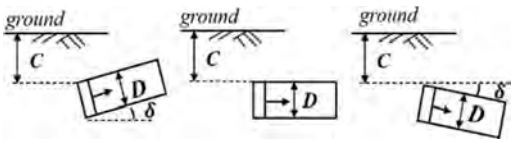

Figure 2. Layout of shield inclination.

A loading subsystem, two measuring systems, a transparent soil model, a laser, a CCD camera (charge-coupled device camera), and other components were designed for a scanning and image acquisition device as shown in Figure 3. Continuous laser speckle images are recorded by an industrial camera during the experiment. The camera is a model USB3 Vision TL from Daheng Galaxy Device Lt., with a 3840 × 2748 pixels resolution. Image processing is mainly used with MATLAB software programming.

The CCD camera and laser are controlled by two high-precision linear platforms to maintain synchronous motion, and the entire model is scanned to obtain cross-sectional photographs at various places as shown in Figure 4 (a). The displacement field at various positions is then obtained by using MATLAB software to analyze the slice photos captured at various deformation times at the same position. Finally, the whole three-dimensional displacement field is constructed by a reconstruction algorithm.

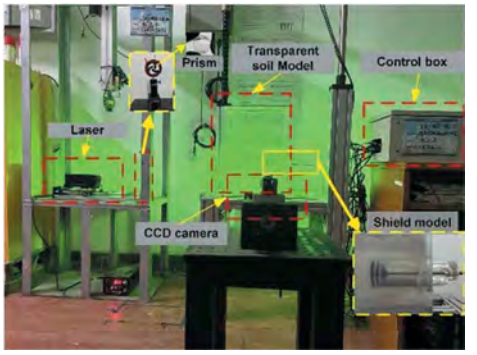

Figure 3. Experimental setup for the transparent soil tunnelling model.

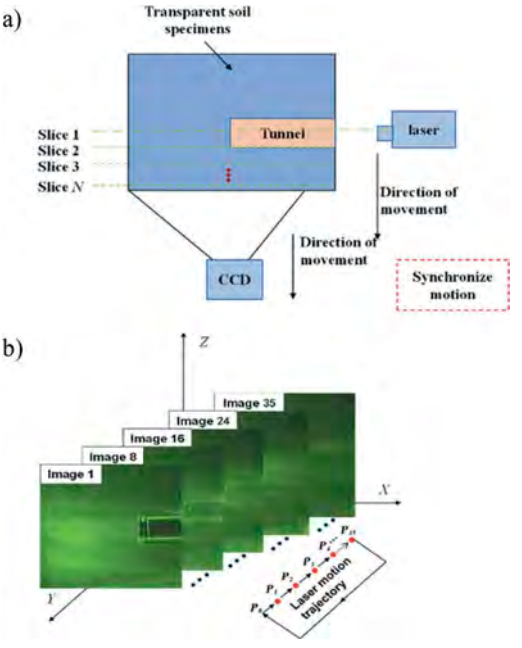

Figure 4. Test principle: a) Principle of tomographic scanning; b) Principle of laser speckle image scanning.

3 RESULTS AND ANALYSIS

3.1 *Horizontal deformation analysis*

Figure 5 depicts the evolution of the displacement field with δ= -10°, 0°, 10°, and C/D = 1.5 or 3. The ground begins to deform as the rigid plate begins to travel backward. The failure area that forms in front of the tunnel face varies depending on the three conditions. The failure area is different from the typical 'wedge + prism' shape in sandy soil stratum. The failure of the excavation face in the soft soil stratum presents an 'ellipsoidal' flow to the tunnel, with a wider influence area than the sandy soil stratum in

front of and above the excavation face. It's consistent with the failure mode of excavation face in clay stratum established by Mollon et al. (2013) based on continuous velocity field distribution.

The soil in front of the tunnel flows smoothly into the tunnel, and the failure pattern and influence zone are basically consistent with Schofield et al. (1980)'s experimental results and the numerical simulation of Huang et al. (2019).

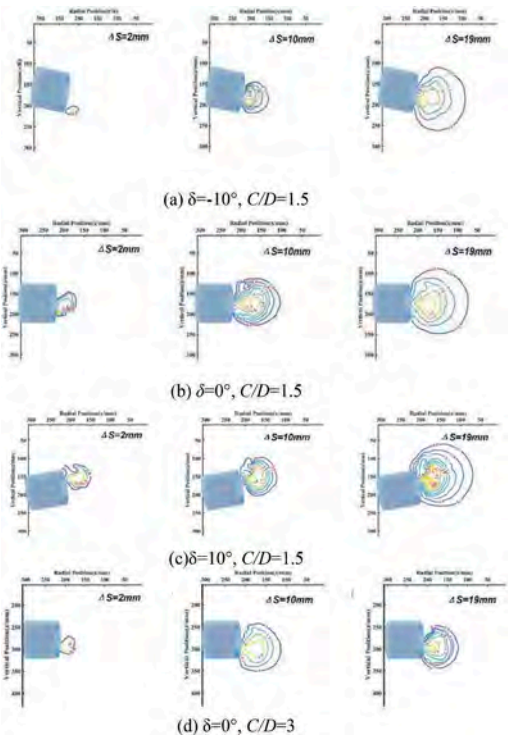

Figure 5. Two-dimensional horizontal displacement of central axis plane.

Figure 5 is a horizontal displacement contour map of different inclined angles and different buried depths at varying rigid plate retreat distances. Figure 5(a) - (d) show that when ΔS increase, the damaged area in front of the tunnel gradually forms, extending vertically from the tunnel invert and center to the top of the tunnel in a ' ellipsoidal ' expansion. As shown in Figure 5 (a) - (c), when ΔS = 19 mm, the influence area and deformation increase as the inclination angle δ increase, and the failure zone extends to the surface, from δ = −10 ° corresponding to 100mm to δ = 10 ° corresponding to 50 mm. Figure 5 (a) shows that when the inclination angle δ = -10 °, the horizontal deformation gradually increases with the increase of the retreat distance. However, compared with Figure 5 (b) and Figure 5 (c), its horizontal deformation is smaller, thus the soil around the tunnel with a downward inclination angle shows better stability. According to the displacement contour map in Figure 5 (b) and Figure 5(d) , when the C/D ratio is 1.5 and 3, the deformation area and value gradually decrease with increasing C/D due to the soil arching effect of clay (Lee et al., 2006).

3.2 *Vertical deformation analysis*

Figure 6 is a vertical displacement contour map of different inclined angles and different buried depths at various rigid plate retreat distances. According to Figure 6 (a) - (d), when the pressure is reduced to very small (ΔS = 2mm), the displacement is small except for the displacement of 0.3-0.5mm in front of the tunnel. The vertical displacement increased together with the retreat distance. When the retreat distance reaches 10 mm, the deformation in front of the tunnel increases sharply. As the inclination angle changes from downward to upward, the influence range further expands, and some areas begin to bulge (As shown in the blue lines below the model in Figure 6 (b) and (c). When ΔS = 19mm, the maximum value of the displacement is developed from 2mm corresponding to δ = -10 ° to 2.8 mm corresponding to δ = 10 °. In other words, with the inclination angle increases, the soil deformation is gradually increasing, and the failure zone develops toward and eventually reaches the ground. Figure 6 (b) and 9(d) show that for various overburden depths, the vertical influence area is bigger for smaller C/D, whereas the vertical influence area declines as C/D increases, and the maximum failure zone is approximately 2/3 of the shallow overburden.

3.3 *Deformation mode analysis*

The displacement vector field under various retreat distances is analyzed as follows in order to investigate the disturbance and deformation with the retreat of the rigid plate.

As shown in Figure 7, the size of the vector arrow represents the displacement, and the angle represents the direction of motion. According to Figure 7 (a) - (c), the excavation of a cohesive soil layer presents a stage-by-stage failure process. At the initial stage of deformation, the tunnel moves slowly backward, causing the loosening zone in front of and above the tunnel, and slipping along some of its micro-crack surfaces, resulting in soil moving into the tunnel. In the expansion stage, driven by the early sliding soil, the soil moves along the vertical and longitudinal direction, and the influence area are further expanded. The soil close to the surface eventually moves as a result of the retreat distance growing farther. The deformation of the soil mass in front of the shield can be approximately separated into three portions, as shown in Figure 7(b) and (c). The uplift area beneath the tunnel makes up one portion. The

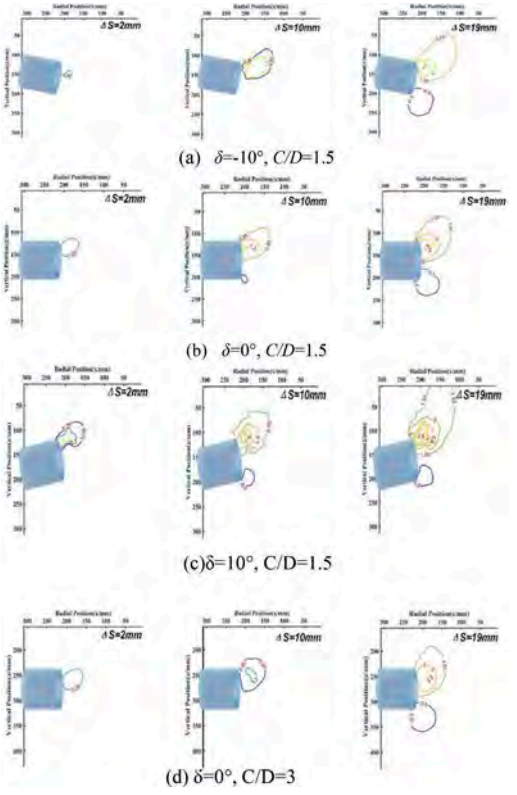

Figure 6. Two-dimensional vertical displacement of central axis plane.

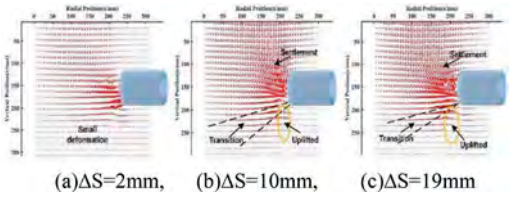

Figure 7. Deformation vector diagram of clay shield tunnel.

soil is driven toward the tunnel's interior as a result of the shield tunnel's retreat. The soil underneath is raised as a result of cohesiveness between the particles, and the uplift area rises with the retreat distance. The settling zone is the other part where soil masses pour into the tunnel as a result of shield retraction. Between these two parts, there is a transition area as well.

The displacements under different working conditions are shown in Figure 8 According to continuous velocity field and upper bound theory of limit analysis, the region enclosed by the black curve represents the region envelope of clay failure (Li et al., 2019; Mollon et al., 2013, 2011). The dotted line is the area with the maximum velocity.

$$\dot{W}_D \geq \dot{W}_e = \dot{W}_\gamma + \dot{W}_s \tag{1}$$

Where $\dot{W}_e$ represents the total rate of the external forces' work; $\dot{W}_D$ is the rate of the energy dissipation within the soil mass undergoing plastic deformation; $\dot{W}_\gamma$ and $\dot{W}_s$ refer to soil gravity and overload power respectively.

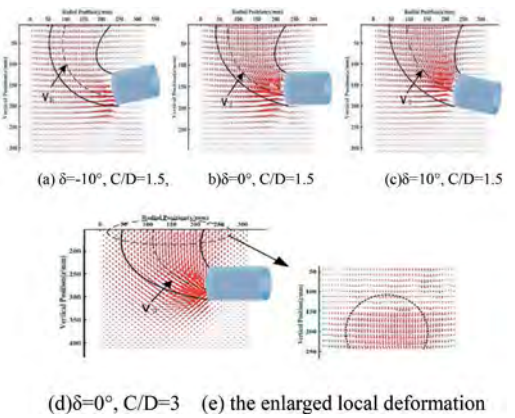

Figure 8. Displacement vector diagram of shield tunnel in clay stratum.

From Figure 8(a) - (d), the shape of the failure zone is essentially the same as Mollon 's theory (see Figure 8(c), Mollon et al., 2013). The instability area reaches the ground in an ellipsoidal shape (Klar et al., 2007).

In addition, it can be clearly seen from Figure 8-(a)-(c) that the failure area in front of the tunnel expands laterally as the inclined angle of the tunnel decreases. Vertical settlement starts to happen as the failure area's circular curvature steadily reduces above the tunnel. This is similar to the engineering example where there is a high risk of instability in upward sloping tunnels. Figure 8(d) is the deformation vector diagram with C/D = 3. Since the observation area is concentrated near the tunnel, the analysis should be combined with Figure 8(f) (soil deformation above the tunnel). The results show that when the buried depth is higher, the failure area does not reach the surface, but gradually tends to be stable within about 1.5D above the tunnel.

The relationships between different retreat distances and the maximum ground subsidence are shown in Figure 9. The ground subsidence starts to build up as the retreat distance grows, with the maximum ground settlement occurring in the 1D range in

front of the shield tunnel. The influence on soil deformation is minimal in the early stages of deformation because of the tiny change in the supporting force. As can be observed from Figure 9(c), when the supporting force is reduced quickly, the ground settles quickly and the upward inclination's influence is more noticeable, which causes the deformation to occur more quickly. Furthermore, when taking the overburden depth into account, it is evident that as it increases, the soil mass tends to remain completely stable, regardless of the growth rate of settlement or the maximum deformation. This might be caused by the transparent clay's high compressibility and initial high initial water content. Long-term compression will contribute to consolidation, which will increase the material's strength. This confirms the viability of using this substance to simulated clay and is similar to the characteristics of soft clay.

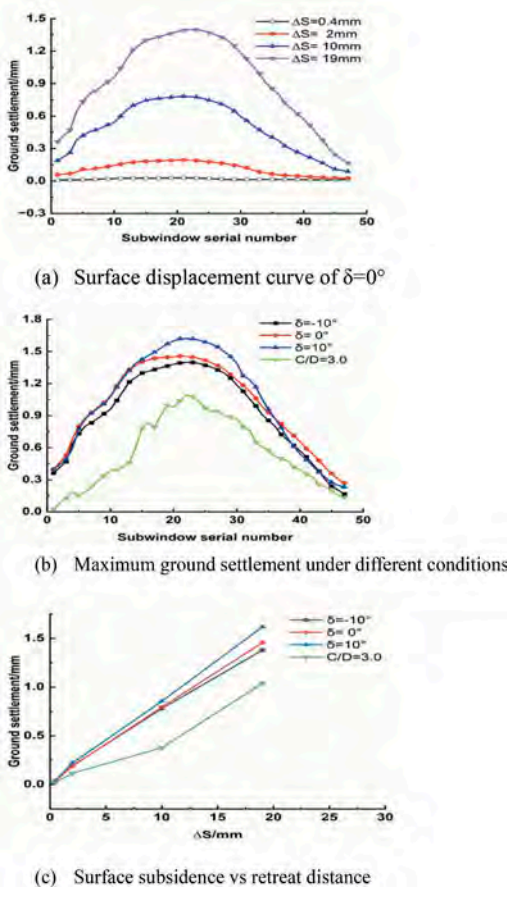

Figure 9. Ground subsidence of shield tunnel in a clay stratum.

3.4 *Analysis of 3D reconstruction results*

The 40 2D slice scanning images are first calculated using the improved adaptive image measurement method to determine the deformation matrix of the corresponding slice position, and then the 3D displacement field is created using the 3D reconstruction method, which can reflect the out-of-plane displacement to a certain amount.

Figure 10 shows the 3D reconstruction failure model of the tunnel face under various inclination angles δ and ratio of C/D. Compared with the two-dimensional analysis, the movement trajectory and failure mode of the soil can be observed more intuitively. In the Figure s, the positive value of vertical displacement represents compression and settlement, while the negative value represents uplift, and the unit is mm. According to Figure 10 (b), (d), (f), and (h), the soil deformation may be approximately separated into the settlement area in front of and above the shield, the uplift area below, and the transition area between them. This essentially corresponds to Zhang et al. (2011)'s description of the failure mode of clay. The shear strength of the soil will withstand this deformation as the rigid surface gradually moves backward, generating a force that will flow into the tunnel due to soil particle friction and cohesion. On the other hand, a tiny pore will be created for pressure release when the soil above and in front of it moves. The soil below will swell as a result of the unloading and the cohesiveness between particles, and it will gradually change as the damaged region grows. As demonstrated in Figure 10(a)-(f), the maximum horizontal displacement in front of the tunnel changes as the inclination angle changes. This

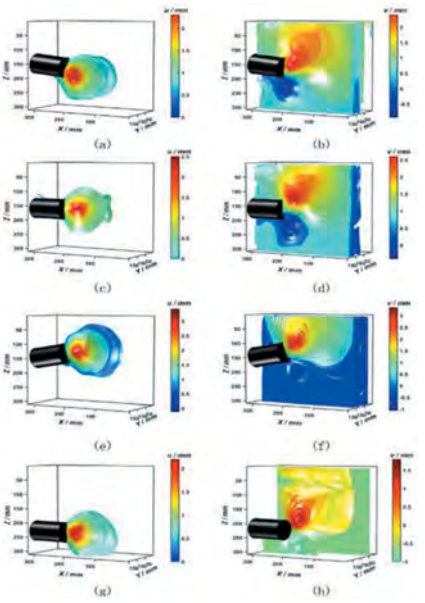

Figure 10. Three-dimensional reconstruction results of the failure zone (Horizontal displacement on the left, Vertical displacement on the right, (a) and (b) are for δ=-10°, C/D=1.5, (c) and (d) are for δ=0°, C/D=1.5 (e) and (f) are for δ=10°, C/D=1.5 (g) and (h) are for δ=0°, C/D=3.0).

displacement follows a similar trend and gradually decreases in the horizontal direction with this angle. The maximum displacement ranges from 2.3 mm at the downhill inclination to 3.2 mm at the upward inclination at a distance of 0.5D in front of the tunnel. The vertical displacement diagrams in Figure 10(b), (d), (f), and (h) show that the influence area gradually moves towards the ground as the inclination angle increases. It develops to the surface when the angle $\delta = 10$ °, and the influence zone is likewise larger than under other conditions.

As demonstrated in Figure 10(c), (d), (g), and (h), the maximum soil deformation decreases to 0.4mm as the C/D ratio increases, and the deformation zone similarly shrinks. The increase in C/D improves the soil's vertical stability from the perspective of vertical displacement. While the maximum displacement value has decreased by roughly 1mm, the deformation zone has shrunk and is located farther from the ground. This deformation progressively stabilizes once it reaches a particular height. The soil is more stable when the inclination angle is downhill as opposed to upward under the same C/D ratio. The soil with deeper buried depths is more stable at the same inclination angle.

4 CONCLUSIONS

This study conducted a series of shield model tests using transparent soft clay. The failure modes of the tunnel face under various longitudinal inclination angles δ and buried depths are simultaneously depicted and methodically investigated. The following are the primary conclusions:

1) Using transparent soil experimental technology, a set of model test systems for shield tunnel excavation under various longitudinal angles were established. By precisely managing the motor's tunnel face withdrawal, the shield tunnel's insufficient support force is reproduced.
2) The deformation process of soft clay has different development stages, and the failure modes in different areas vary. The soil in front of and above the excavation face drives the soil in the instability zone to move together towards the interior of the tunnel, gradually extending the disturbance and eventually causing overall subsidence of soil ground. The soil under the shield tunnel will have a small uplift zone due to drag force, which will be more obviously when the angles downward.
3) Under various inclination angles and buried depths, the damage shape of soil in front of tunnel shows an 'ellipsoidal' deformation pattern. The same failure mode was obtained by 3D reconstruction. When the failure occurs, soil settlement on the surface and above the tunnel rises along with the longitudinal inclination angles and the maximum velocity point also gradually moves downward. The increase of buried depth ratio not only reduces the critical support force required by the face, but also limits the soil settlement of the surface and tunnel roof, and improves the stability of the soil mass. Compared with other conditions, shallow buried, upward sloping tunnels have a higher risk of collapse.

The 3D reconstruction results are more effective and intuitive than the traditional 2D displacement field analysis. It shows that the deformation and instability of the shield tunnel is a three-dimensional problem.

REFERENCES

Ads, A., Iskander, M., Bless, S., 2020a. Shear Strength of a Synthetic Transparent Soft Clay Using a Miniature Ball Penetrometer Test. Geotech. Test. J. 43, 20190020. https://doi.org/10.1520/GTJ20190020

Ads, A., Iskander, M., Bless, S., Omidvar, M., 2020b. Visualizing the effect of Fin length on torpedo anchor penetration and pullout using a transparent soil. Ocean Engineering 216, 108021. https://doi.org/10.1016/j.oceaneng.2020.108021

Ads, A., Shariful Islam, M., Iskander, M., 2021. Effect of Face Losses and Cover-to-Diameter Ratio on Tunneling Induced Settlements in Soft Clay, Using Transparent Soil Models. Geotech Geol Eng 39, 5529–5547. https://doi.org/10.1007/s10706-021-01843-7

Ahmed, M., Iskander, M., 2011a. Tunnel Face Support Pressure and Associated Risk, in: GeoRisk 2011. Presented at the Georisk 2011, American Society of Civil Engineers, Atlanta, Georgia, United States, pp. 939–947. https://doi.org/10.1061/41183(418)101

Ahmed, M., Iskander, M., 2011b. Analysis of Tunneling-Induced Ground Movements Using Transparent Soil Models. J. Geotech. Geoenviron. Eng. 137, 525–535. https://doi.org/10.1061/(ASCE)GT.1943-5606.0000456

Alagha, A.S.N., Chapman, D.N., 2019. Numerical modelling of tunnel face stability in homogeneous and layered soft ground. Tunnelling and Underground Space Technology 94, 103096. https://doi.org/10.1016/j.tust.2019.103096

Chen, R., Li, J., Kong, L., Tang, L., 2013. Experimental study on face instability of shield tunnel in sand. Tunnelling and Underground Space Technology 33, 12–21. https://doi.org/10.1016/j.tust.2012.08.001

Chen, R.P., Tang, L.J., Ling, D.S., Chen, Y.M., 2011. Face stability analysis of shallow shield tunnels in dry sandy ground using the discrete element method. Computers and Geotechnics 38, 187–195. https://doi.org/10.1016/j.compgeo.2010.11.003

Cheng, C., Jia, P., Zhao, W., Ni, P., Bai, Q., Wang, Z., Lu, B., 2021. Experimental and analytical study of shield tunnel face in dense sand strata considering different longitudinal inclination. Tunnelling and Underground Space Technology 113, 103950. https://doi.org/10.1016/j.tust.2021.103950

Guzman, I.L., Iskander, M., Suescun-Florez, E., Omidvar, M., 2014. A transparent aqueous-saturated sand surrogate for use in physical modeling. Acta Geotech. 9, 187–206. https://doi.org/10.1007/s11440-013-0247-2

Han, K., Wang, L., Su, D., Hong, C., Chen, X., Lin, X.-T., 2021. An analytical model for face stability of tunnels traversing the fault fracture zone with high hydraulic pressure. Computers and Geotechnics 140, 104467. https://doi.org/10.1016/j.compgeo.2021.104467

Huang, M., Li, Y., Shi, Z., Lü, X., 2022. Face stability analysis of shallow shield tunneling in layered ground under seepage flow. Tunnelling and Underground Space Technology 119, 104201. https://doi.org/10.1016/j.tust.2021.104201

Huang, Q., Zou, J., Qian, Z., 2019. Face stability analysis for a longitudinally inclined tunnel in anisotropic cohesive soils. J. Cent. South Univ. 26, 1780–1793. https://doi.org/10.1007/s11771-019-4133-4

Iskander, M., Bathurst, R.J., Omidvar, M., 2015. Past, Present, and Future of Transparent Soils. Geotech. Test. J. 38, 20150079. https://doi.org/10.1520/GTJ20150079

Kirsch, A., 2010. Experimental investigation of the face stability of shallow tunnels in sand. Acta Geotech. 5, 43–62. https://doi.org/10.1007/s11440-010-0110-7

Klar, A., Osman, A.S., Bolton, M., 2007. 2D and 3D upper bound solutions for tunnel excavation using 'elastic' flow fields. Int. J. Numer. Anal. Meth. Geomech. 31, 1367–1374. https://doi.org/10.1002/nag.597

Lee, C.J., Wu, B.R., Chen, H.T., Chiang, K.H., 2006. Tunnel stability and arching effects during tunneling in soft clayey soil. Tunnelling and Underground Space Technology 21, 119–132. https://doi.org/10.1016/j.tust.2005.06.003

Lee, I.-M., Nam, S.-W., 2004. Effect of tunnel advance rate on seepage forces acting on the underwater tunnel face. Tunnelling and Underground Space Technology 19, 273–281. https://doi.org/10.1016/j.tust.2003.11.005

Li, W., Zhang, C., Tan, Z., Ma, M., 2021. Effect of the seepage flow on the face stability of a shield tunnel. Tunnelling and Underground Space Technology 112, 103900. https://doi.org/10.1016/j.tust.2021.103900

Liu, C., Tang, X., Wei, H., Zhao, H., 2022. Visualization Investigation of the Plugging Effect on Open-Ended Pipe Pile Jacked in Transparent Sand. Int. J. Geomech. 22, 04022176. https://doi.org/10.1061/(ASCE)GM.1943-5622.0002455

Ma, S., Duan, Z., Huang, Z., Liu, Y., Shao, Y., 2022. Study on the stability of shield tunnel face in clay and clay-gravel stratum through large-scale physical model tests with transparent soil. Tunnelling and Underground Space Technology 119, 104199. https://doi.org/10.1016/j.tust.2021.104199

Man, J., Huang, H., Ai, Z., Chen, J., 2022. Analytical model for tunnel face stability in longitudinally inclined layered rock masses with weak interlayer. Computers and Geotechnics 143, 104608. https://doi.org/10.1016/j.compgeo.2021.104608

Mollon, G., Dias, D., Soubra, A.-H., 2013. Continuous velocity fields for collapse and blowout of a pressurized tunnel face in purely cohesive soil: INSTABILITY VELOCITY FIELDS OF A PRESSURIZED TUNNEL FACE. Int. J. Numer. Anal. Meth. Geomech. 37, 2061–2083. https://doi.org/10.1002/nag.2121

Mollon, G., Dias, D., Soubra, A.-H., 2011. Rotational failure mechanisms for the face stability analysis of tunnels driven by a pressurized shield. Int. J. Numer. Anal. Meth. Geomech. 35, 1363–1388. https://doi.org/10.1002/nag.962

Perazzelli, P., Leone, T., Anagnostou, G., 2014. Tunnel face stability under seepage flow conditions. Tunnelling and Underground Space Technology 43, 459–469. https://doi.org/10.1016/j.tust.2014.03.001

Sang, Y., Zhao, J., Duan, F., Sun, W., Zhao, H., 2019. A novel automatic device to measure deformation inside transparent soil based on digital image correlation technology. Meas. Sci. Technol. 30, 035202. https://doi.org/10.1088/1361-6501/aafaa0

Schofield, A.N., 1980. Cambridge Geotechnical Centrifuge Operations. Géotechnique 30, 227–268. https://doi.org/10.1680/geot.1980.30.3.227

Senent, S., Jimenez, R., 2015. A tunnel face failure mechanism for layered ground, considering the possibility of partial collapse. Tunnelling and Underground Space Technology 47, 182–192. https://doi.org/10.1016/j.tust.2014.12.014

Tang, X.-W., Liu, W., Albers, B., Savidis, S., 2014. Upper bound analysis of tunnel face stability in layered soils. Acta Geotech. 9, 661–671. https://doi.org/10.1007/s11440-013-0256-1

Ukritchon, B., Yingchaloenkitkhajorn, K., Keawsawasvong, S., 2017. Three-dimensional undrained tunnel face stability in clay with a linearly increasing shear strength with depth. Computers and Geotechnics 88, 146–151. https://doi.org/10.1016/j.compgeo.2017.03.013

Wang, P., Sang, Y., Guo, X., Shao, L., Zhao, J., Ji, X., 2020. A novel optical method for measuring 3D full-field strain deformation in geotechnical tri-axial testing. Meas. Sci. Technol. 31, 015403. https://doi.org/10.1088/1361-6501/ab3c80

Weng, X., Sun, Y., Yan, B., Niu, H., Lin, R., Zhou, S., 2020. Centrifuge testing and numerical modeling of tunnel face stability considering longitudinal slope angle and steady state seepage in soft clay. Tunnelling and Underground Space Technology 101, 103406. https://doi.org/10.1016/j.tust.2020.103406

Yin, X., Chen, R., Meng, F., 2021. Influence of seepage and tunnel face opening on face support pressure of EPB shield. Computers and Geotechnics 135, 104198. https://doi.org/10.1016/j.compgeo.2021.104198

Yuan, B., Sun, M., Wang, Y., Zhai, L., Luo, Q., Zhang, X., 2019. Full 3D Displacement Measuring System for 3D Displacement Field of Soil around a Laterally Loaded Pile in Transparent Soil. Int. J. Geomech. 19, 04019028. https://doi.org/10.1061/(ASCE)GM.1943-5622.0001409

Zhang, M., Xu, P., Li, J., Wang, R., 2019. Mining-induced ground movements and displacements using transparent soil model test. Geotechnical Research 6, 252–264. https://doi.org/10.1680/jgere.18.00031

Zhang, Z.X., Hu, X.Y., Scott, K.D., 2011. A discrete numerical approach for modeling face stability in slurry shield tunnelling in soft soils. Computers and Geotechnics 38, 94–104. https://doi.org/10.1016/j.compgeo.2010.10.011

Zhao, H., Zhang, D., Liu, C., Deng, A., Ji, S., 2022. Experimental investigation of rapid penetration of cylindrical rods into granular materials. Granular Matter 24, 22. https://doi.org/10.1007/s10035-021-01181-8

Zou, J., Chen, G., Qian, Z., 2019. Tunnel face stability in cohesion-frictional soils considering the soil arching effect by improved failure models. Computers and Geotechnics 106, 1–17. https://doi.org/10.1016/j.compgeo.2018.10.014

Tunnelling for a Better Life – Yan, Celestino, Thewes & Eberhardt (Eds)
© 2024 The Author(s), ISBN 978-1-032-80042-4
Open Access: www.taylorfrancis.com, CC BY-NC-ND 4.0 license

Application study of combined machining in the cutterhead design for hard rock tunnel boring machine

Michael B. Zhou*
Independent Advisory Engineer, USA

ABSTRACT: The principle of Hard Rock Tunnel Boring Machine (TBM) is to use the roller cutters to grind, drill, and break hard rock and smash it locally as big piece by rotating cutterhead and roller cutter into a depth from rock surface by depth with the pushing forward jacks electrically or hydraulically thrust. Since the mechanics compressive and tensile strength of hard rock is similar to the metal materials with different basic crystal and joint size, and strength scale MPa (10^6Pa =10^6 x 1.02 kgf/cm^2), or 145 psi, it is exaggerated to say the principle of TBM were a machining process, too.

The efficiency of the TBM is dependent on the cutter head design and being machined rock material. In light of this, adopting the principles of the proper combined machining could raise the efficiency of the cutting, possibly.

It is a good idea to explore to transplant the proper process of combined machining to the hard-rock machining to get a good rate of penetration (ROP) and performance of tunneling of TBM. It also proposes its new design principle and outlines the design process and mechanics analysis with the pneumatic machining process. The paper tries to evaluate a new machining method combined with conventional hard rock TBM to seek its feasibility as potential alternative machining process for hard rock to advance a new generation of the TBM. It might save construction cost and shorten construction duration of tunneling capital contract for a better project performance.

Keywords: TBM, Hard Rock, Cutterhead, Thrust, Design, Combined Machining, Tunnel, Tunneling, Pneumatic Cylinder, Machining

1 INTRODUCTION

In the contemporary, TBM is undoubtedly the first chosen and critical equipment and tool of digging and excavating for the hard rock tunnel construction. Many study papers and summarized reports have concentrated in the analysis of the TBM function and work performance including some typical technical specifications, costs, geological conditions with TBM capabilities and adaptabilities, and case studies. A few experts are aimed in the general future development, such cutter technology, RPM, ROP, cutter replacement, instrumentation and monitoring, manufacturing and assembly. A few cutterhead designers dealt with the detailed cutterhead design sceneries and profile, and TBM performance with the cutter layout and structure design.

This paper is trying to use mechanical engineering principles to analyze the regular and special combined machining process as well as counter directional mechanical design measure to degrade rock strength parameter. In this way, it can promote TBM relative thrust force, raise rate of cutter penetration and abrasive ability, decrease downtime, extend whole TBM life, and save tunnel construction time and cost.

Hard rock tunnel is applied in many engineering and business field, such as water works, rail road, and transportation road, etc. The current machining process combined with the TBM cutterhead design improvement might cause some technical advance and breakthrough in the tunnel digging velocity and specific energy, utilization percentage, and cutter and TBM life cycle.

2 HARD ROCK TBM PERFORMANCE

Hard rock is generally classified by its unconfined compressive strength (UCS) and with three categories as below Table 1.

Sometimes, information used in the paper and magazine uses the uniaxial compressive strength as MPa, that is consolidated, drained, and lateral confining process test is not equal to zero. More papers

*Corresponding author: mbzengineerpc@yahoo.com

DOI: 10.1201/9781003495505-306

Table 1. Hardness and unconfined compressive strength of rock materials (1).

Hardness category	Typical range in unconfined compressive strength (MPa)	Strength value selected (MPa)	Field test on sample
Hard rock	50–100		Handheld specimen requires more than one hammer blow to break it. Can be faintly scratched with 20d common steel nail. Resistant to abrasion or cutting by a knife blade, but can be easily dented or broken by light blows of a hammer.
Very hard rock	100–250		Specimen breaks only by repeated, heavy blows with geologic hammer. Cannot be scratched with 20d common steel nail.
Extremely hard rock	> 250		Specimen can only be chipped, not broken by repeated, heavy blows of geologic hammer.

and specifications use unconfined compressive strength (UCS) stands for the maximum axial compressive stress that a cohesive soil or rock specimen can bear under zero confining stress. To secure the lasting proper work status, it is sometimes to select to layout the water work tunnel in the deep hard rock layer to protect it from structure damage or cracking and water leaking.

There are several water tunnels with the hard rock strength and TBM tunneling information and performance to be listed as following two cases.

- NYC Delaware Aqueduct Hard Rock Bypass Water Tunnel: 12,448 ft (2.357 mile = 3.792 km) over 582 days, 270 m (900 ft) maximum deep with penetration rates of 6m (20ft) per hour, 6.8 m (22.3 ft) diameter Robbins Single Shied TBM, tunneling completed in August 2019; TBM excavated 27.4 m (89.8 ft) m on its most productive day, 108.1 m (354.8 ft) during its best week, and 288 m (945 ft) during its most productive month, tunnel completed 2019 (2).
- Atlanta Water Tunnel, 3.8 m (12.5 ft) diameter Robbins Main Beam TBM, 8.5 km (5.282 mile) length, extremely hard rock condition as 117 and 310 MPa (17,000 and 45,000 psi USC, best day of 38.4 m (126 ft), completed on October 4, 2018 (3).

Therefore, the practical measurement of tunneling construction performance with TBM are based on the advanced distance m (ft) best hourly, daily, weekly, and monthly operation and total days for completion of tunneling because it will consider many encountered conditions, such as fault area, water flooding, TBM stuck and downtime including maintenance and replacement of roller cutter, etc. However, it could not be precisely evaluate the TBM cutterhead real efficiency as rate of penetrated (ROP) and as depth by per TBM revolution. In light of difficult evaluation, it has better improve the tunneling efficiency of TBM cutterhead system to get its performance with a good completed day for the performance.

3 IMPACT TO HARD ROCK TBM PERFORMANCE WITH CUTTERHEAD FUNCTION

The TBM cutterhead is consisting of opened space central disc rotor and outer circular shell, inner muck ring and chamber, muck guide segment, roller cutter with shaft and bearing, connection nuts and screws between central disc and outer circular shell, connection parts between central mechanical rotating and transmission and power system, and joint back base and frame between with articulation joint and thrust articulation cylinder as the Figure 1 and 2 (4) (6).

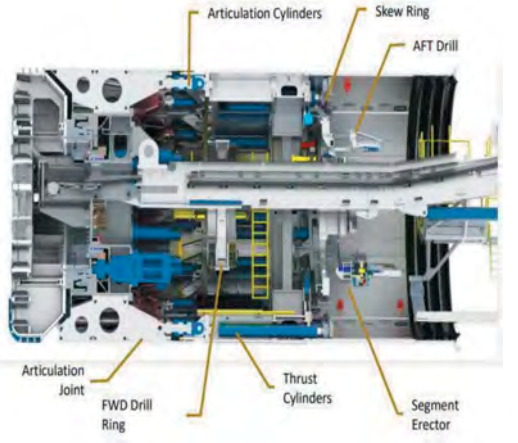

Figure 1. Hard rock TBM cutterhead and main beam structure section view (4).

The cutterhead cutting performance is based on its load force capacity KN and Torque. That is to determine the depth of penetration (ROP), width of cutter tip, cutting space, velocity limit for disc cutters, cutterhead shape and profile, etc. Its rotational speed on hard rock TBMs is a function of disk cutter size and velocity limit, and the diameter of TBM and cutting geometry, cutting force, spacing and location of cutters on the profile (5).

Figure 2. Hard rock TBM cutterhead central disc rotor and outer circular shell front view (6).

The first step of cutterhead design is to evaluate its given geology (7) and decide to select ideal cutterhead structure and materials to adapt to the geological condition for smooth and efficient digging. Some evaluation has progressed to establish the assessed index of geology adaptation to TBM in the linear algebra, such as assessment of uniaxial compressive strength > 200 MPa for TBM as less adaption (8). Otherwise, the cutters of cutterhead would be damaged, stuck, changed more often, down time-increased. But the real operation function is a little far to the theoretic design of hard rock TBM due to the depth of the tunnel structure and geologic deviation, and rock sampling restriction. Therefore, the macro improvement of the TBM cutterhead is a good way for its mechanical process and tunneling innovation.

4 POSSIBILITY OF SIGNIFICANT IMPROVEMENT FOR FUNCTION OF HARD ROCK TBM CUTTERHEAD

As mentioned above, TBM is a special machining except the materials being machined is difference between hard rock and metal. Generally, the upper limit of compressive (USC) and tensile stresses of hard rock Granit, limestone, quartzite is around 250/25, 300/25, 250/30 MPa, Concrete 42/5 MPa, and steel 250/750 (tool) MPa (9).

TBM is a merely machine to break the hard rock locally by tool roller cutter pressing, grinding, cutting, and twisting, then transporting and excavating muck. Compared with the general turning machine (lathe), its work piece is static and machining cutter is rotated with the cutterhead, vice versa to the turning machine. However, the uniaxial compressive strength of hard rock is sometimes close to the low carbon steel compressive one as 250 MPa. It might consider the material similarity then pay more attention from the mechanical process principles.

Due to the weak tensile strength of hard rock, it might adopt clockwise and enter counter clockwise rotating of the central disc rotor with the short hock alternately to generate some tensile force except the designed compressive force system.

More importantly, it needs to change its machining function from sole work machine system. Considered its large volumetric inner muck ring as chamber of cutterhead and huge forged steel mass and high mechanic strength, there are some avenues to insert another alternative machining system to raise TBM working function or use it to degrade the hard rock mechanical strength referencing other conventional and custom machining process and technology.

5 APPLICATION OF COMBINED MACHINING TO IMPROVE CURRENT SINGLE MACHINING OF CUTTERHEAD

Current popular TBMs use one machine to obtain mechanical pressing of roller cutter and cutting to hard rock of passive rotated cutter, twisting moment by roller and cutter circular-moving with cutterhead rotating. Due to the high hard rock compressive strength and surface hardness, and narrow cutter tip width, it cannot provide too large rotating energy due to cutter side areas as TBM revolution per minutes, sometimes only 8.3 revolutions per minute (10). Excessive rotating velocity and twist energy of TBM can cause the cutter break from its side resistant moment. This is because the energy as work done and power of rotating rigid body is proportion to the machine angular rotation speed ω and rotating angles Θ from the circular motion formula (11).

The work done and power for one roller cutter and whole cutterhead with rotating of TBM Central Disc Rotor (12) can be calculated roughly from following formulas.

Work done = Torque (RF) x angle in radians = $R\ ma \times \Theta = R\ mv^2 / R \times \Theta = R\ m\ (\omega R)^2 / R \times \Theta = m^2 \omega^2 R^2 \Theta$ (13)

Power = Torque x Angular Velocity = RF x ω = $Rmv^2/R \times \omega = R\ m\ (\omega^2 R^2)/R \times \omega = m\ \omega^3 R^2$ (14)

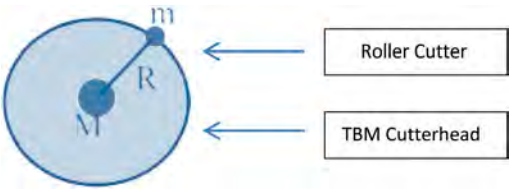

Figure 3. TBM roller cutters and cutterhead circular Motion.

From the above analysis of the energy and work done by the TBM roller cutter and high USC for hard rock, it is propose to improve the mechanical process efficiency referencing special mechanical process system.

The special machining has included the multiple work machines and processing systems, such as machining center with combination of drilling, turning, milling and grinding; four-cylinder combined die with press machine to form metal end and die cutting circle to cut four sides by the press stroke downward to automatic produce the ends of metal container.

It might imitate the combined machining concept and try to add another machine transmission and mechanical process system to the current popular TBM cutterhead to improve its penetration depth per TBM machine revolution then prompt the TBM performance.

Due to the limited space of interior cutterhead chamber as muck ring with being optimized mechanical process and transmission mechanism, it is difficult to insert the second mechanical machine into the chamber or outside chamber. The other better way is

to utilize the pneumatic and hydraulic with water or oil. The hydraulic oil processing system has the problem in the oil leakage and low work speed and cycle, and water press machine with its thrust force needs big system and less function than current motor thrust system and low work speed.

Finally, it is explored to adopt the transmit system of pneumatic work with the pneumatic control components. With the available pneumatic system on site or remote air compressor system, the operation process of pneumatic working system could be compacted and fit it to interior chamber space of cutterhead and TBM work process. The advantages of pneumatic are less impact to environment due to leakage and rapid action frequency, and easy maintenance, adapt to dust and explosive site (15).

There are many kinetic mechanism of pneumatic work system, for instance piercing hole, light forge, cutting material, and breaking rock. In term of the pneumatic work system, the impact cylinders that can generate the not light forge and break materials will be a good candidate to combine it with the current TBM cutterhead mechanical system to increase it work performance.

6 DESIGN PRINCIPLE OF COMBINED PNEUMATIC IMPACT CYLINDER WITH TBM CUTTERHEAD SYSTEM

The impact cylinder is a special cylinder with simple structure and less power to produce a big impact striking force. The impact cylinder is classified as two types: quick air discharge and non -quick air discharge. But, the quick air discharge possesses a higher work impact frequency and it is satisfactory to hard rock breaking.

The quick air discharge cylinder is consisting of 1. guide cover of quick discharge 2. rubber seal gasket of quick discharge, 3. piston of quick discharge, 4. cylinder of quick discharge, 5. middle cover of quick discharge, 6: push bar, 7. gas resistor, 8. gas storage. The function of quick mechanism can make cavity below piston has enough avenue of flow area to connect to outside atmosphere quickly. It can let the back pressure of low cavity to lower air pressure to a very small quickly. This system is operated and controlled by three electrical and pneumatic solenoid valves: two – two ways and three ports and one two ways and four ports (Figure 4) (16).

Application of impact cylinder is very broad, such as metal rivet, bending, piecing hole, press-assembly, forging, crushing ore, and big hammer-striking. It can add the impact cylinder into the interior muck ring as chamber of cutterhead to form the second mechanical system or said second work system to generate the impact force on the hard rock surface before the TBM initial mechanical process for each cycle. In this way, the pneumatic striking on the hard rock surface can result in cracking the fracture of hard rock near by the striking area then degrade hard rock USC and other mechanical strength.

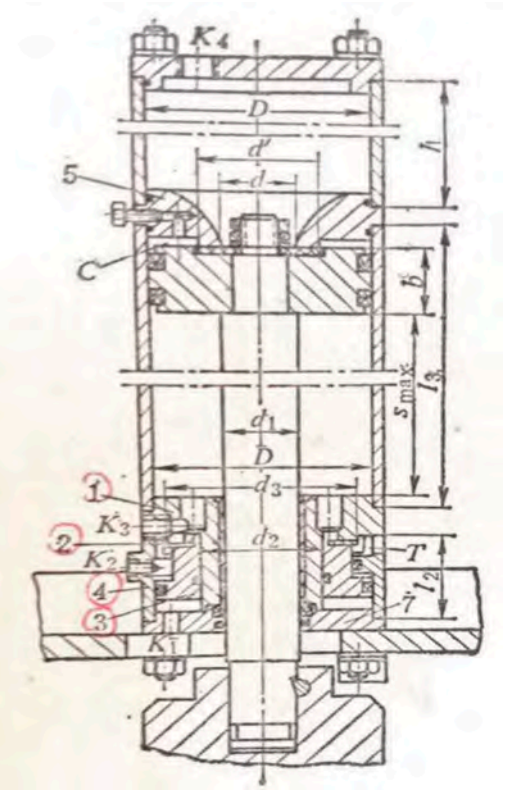

Figure 4 . Pneumatic quick discharge impact cylinder.

Hereafter is the Table 2 to list the referenced structure dimension and specification of the quick air discharge cylinder for the possible application in combination with the current popular TBM cutterheads.

Since the quick air discharge cylinder is especially for vertical gravity falling to the object, its maximum impacting work, when applied in the horizontal impact striking, will be changed roughly with the supplied air pressure and stroke distance neglecting its front pressure for the case to the back. Therefore, it will only count for the force acting on the piston times its stroke for the work done horizontally.

However, the method and process of quick air discharge cylinder can only be utilized to generate the striking work on the hard rock and result in the fractures inside rock to degrade the compressive strength of hard rock horizontally.

Roughly to calculate piston thrust force and impact work from forge steel acted horizontally for 200 mm diameter impact cylinder D, neglecting the masses (G) of piston and piston rod, and pressure P_a in the piston rod cavity (20) as

Table 2. Referenced structure size and specification of Quick air discharge impact cylinder (17) (18) (19).

Application,	Forge Steel, Compressive Stress MPa= 250 x 1.3 = 325 (17)	Crushing Cast Iron Compressive Stress MPa = 220 – 2,520 (18)
Diameter of Cylinder, D, mm	200	250
Piston Rod, d, mm	120	150
Width of Piston, b mm	70	75
Length of Air- storage, l mm	220	250
Stroke Distance, l_1 mm	460	525
Length of Quick Exhaust, Cylinder, l_2 mm	90	110
Max Impacting Frequency , times/min #/s	30	25
Gravity of Moving Part, G Newton	900	1500
Impacting Work, W Newton-m	2500	4650
Efficiency, η %	24	24.5
Application to Hard Rock Grade, MPa	Very Hard 100 - 250	Extreme Hard >250

$$F\,(\text{NewTon}) = 0.785 \times D^2(\text{m}) \times p\,(\text{bar})10^5\,\text{Newton/bar}$$
$$= 0.785 \times (0.2)^2 \times 5 \times 10^5$$
$$= 15,700\,\text{Newton} \times 70\%(\text{resistantforce}\,30\%)$$
$$= 10,900\ \text{Newton}$$
$$W\,(\text{N} - \text{m}) = 10,900\ \text{Newton} \times 0.23\text{m}\,(50\%\,\text{stroke dis.})$$
$$= 2,527\ \text{Newton} - \text{m}$$

It is close to 2,500 vertical gravity impact work W = 2,500 Newton-m) (21)

However, its exact mathematic solution of the impact work for the cylinder can be obtained by the differential and integration equations. (20)

7 POSSIBLE PASSIVE MACHINING TO DEGRADE OF HARD ROCK MECHANIC PROPERTY TO IMPROVE TBM WORK

So far it has predicted that the passive machining measure with the quick air discharge cylinder can change the material property being machined. It provides a feasible way for lowering difficulty extent of cutterhead to cut and excavate hard rock.

Study of hard rock property is a very important task before the TBM and special cutterhead is designed. Most rock properties include mass, type, hardness, strength, color, particle size and texture, permeability, consolidation, shearing resistance, rock structure, discontinuity, water content, compressive stress (USC), friction angle, etc. In addition to, there are some Lab test items, such as DRI (Drilling Rate Index), porosity, brittleness, and mass degree of fracturing %. But for cutterhead, unconfined compressive strength (UCS) is more directly to the TBM performance and to the popular performance grading as m (ft) advance per day, week and month, or total days of complete, and or mm/rev. (22).

Degrading USC of the hard rock by generating the fractures with impact work and energy of impact cylinder will lower its popular index MPa and offer a chance to increase the rate of penetration per machine cycle. If the hard rock MPa is really closed to the forge steel and cast iron MPa or similarity during the case, it will be a good opportunity like getting the striking and crunching cast iron and deforming the steel and dramatically improve the rate of penetration of TBM with the combination of machining process.

8 NEW LAYOUT OF ROLLING CUTTER AND IMPACT PNEUMATIC CYLINDER ON THE CUTTERHEAD

Generally, the friction angle of hard rock is round 30 degrees (23) and it is proposed the impact cylinders are layout with 60 degree interval to affect left and right 30 degrees that means 6 cylinders per circle with 2 circles beyond the central roller cutter set. It results 6 x 0.2 m = 1.2 m opening per circle on the profile of cutterhead. It should be fines compared to one 18" (0.4572m) and one 19 "(0.4826m) roller cutter linear length. Meanwhile, it is necessary to add the cast steel outside of cylinder to protect the abrasive damage of cylinder shell.

In addition, the depth of the inner muck ring chamber of cutterhead is possible to room the impact cylinder length around 0.9 m with the one stroke distance. But the opening structure of back based plate might be redesigned to fit the connection between the cylinder and cutterhead disc and with cushioning part to reducing vibration.

The front end structure of hole for stroke of piston rod in the impact cylinder needs to be fabricated as sunken head. When impact cylinder is not working it will not be protrusion outside the cutterhead. Moreover, end of piston rod should be machined as screw to be connected with the tip or flat end tool pit pal.

9 CONCLUSION

a) Combined machining can increase the efficiency of machining by reducing preparation and mutual connection of individual work step. It also adapts to TBM cutterhead machining to improve its performance.
b) Potential increasing TBM rate of penetration to obtain better TBM performance can degrade hard rock UCS. With the technical development of TBM, to make opposite effort for degrading material strength can get further success to break technical bottle neck.

This potential degrade of hardrock process strength is also application of strength of materials, advanced theory. That means there will be appeared some circular holes on the hardrock surface after it is impacted by tool pit pal striking with piston rod stroke of the pneumatic cylinder. If the random hardrock segment is modeled as similar to are rectangular plate being compressed, there will be 3 σ compressive stresses at the

contract point n intersected between circle and horizontal n-n axis perpendicular to vertical compressive stress, Figure 5 (24).

In the term of above theories, the stress concentration of material being compressed at the circular point n of hole, will be similar to the structure shape resulted in by the compressive force of roller and cutter with rotated twist moment and cutterhead trust compressive stress.

If the smashed area of hardrock after being striking by impact cylinder is 30% by 30° angle interval rotating, it could degrade 50% compressive strength with increasing compressive stress with the 1.5 σ effects. And overall degrade effect and rate of penetration and tunneling performance increasing would be 30% x 50% = 15%

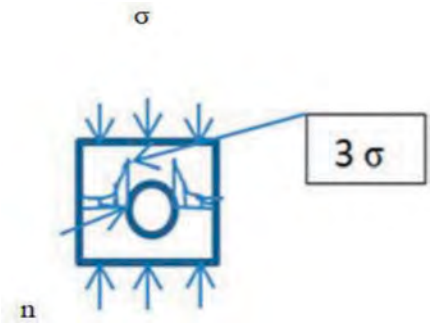

Figure 5. 3 σ compressive stresses at n on plate with circular hole being compressed.

c) It is feasible to add the pneumatic discharge impact cylinder to TBM cutterhead with its high strength steel-forged disc frame, around 3-ft big inner muck ring chamber space, 6 cylinders' circle length per circle equal to 3 (three) roller cutter linear length per circle. It is forecasted that pneumatic transmitted machining is going to be formed first machining system. The second popular pressing, cutting and grinding, twisting, and machining system for the hard rock is the current and breaking mechanical process by the sole work machine. Meanwhile, it could install LIDAR laser scanning to get the point clouds by software with the fracture distribution and depth, and percentage of cracked hard rock area, then start to run the second machining system main disc cutterhead imitated to CNC machining.
d) Pneumatic impact cylinder application can be applied to degrade hard rock mechanic property. If the degrade of hard rock UCS could be reaching to 30% fractured areas to lower grade level by the impact cylinder striking like forge and crush, the rate of penetration would be advancing a big advanced step. The benefit of the cost aroused could be significant if the rate of penetration per minute could be increased by 20% due to fractures of hard rock, its specific energy could save $20\%^2$ = 4% due pneumatic less energy consumption.
e) It is predicted that the rate of penetration for TBM could have big progress and increase penetration by 1.0 mm/ revolution compared to theoretical values between 3mm – 8 mm per revolution (25) to save cost and time of tunneling construction by 15%. It will definitely cause some interests from construction business and develop this breakthrough in theory and practical application for the combined machining with TBM cutterhead design and manufacture and tunneling.

REFERENCES

1. Department of Agriculture Natural Resources Conservation Service, Issued January 2012, USA, Part 631 Geology National Engineering Handbook Chapter 4 Engineering Classification of Rock Material, pp. 42.
2. The Robbins Company, October 2019, USA, Delaware Aqueduct Bypass, Tunnel Boring Now Complete, Tunnel Business Magazine, October 2019, USA, pp. 16–18.
3. The Robbins Company, Usa, October 2018, Robbins TBM Breaks Through on Atlanta Water Tunnel Project, Tunnel Business Magazine, USA, December 2018, pp. 10.
4. Brian B. Khalighi and Joseph J. Diehl, Atlas Copco Robbins Inc. and Grow Tunneling Corp, 1997, USA, High Performance Tunnel Boring Machine for Queens Water Tunnel No.3: A Design and Case History, 1997 RETC Proceedings, USA, pp. 1–3.
5. Brad Grothen, P.E., Technical Director, Robbins Company, Dec 18, 2018, Case Studies in Challenging Geology: Gerede Water Tunnel and Delaware Aqueduct Repair, Presentation, USA, https://robbins.com, Google
6. Jamal Rostami, Soo-Ho Chang, December 2017, A Close Look at the Design of Cutterheads for Hard Rock Tunnel – Boring Machines, USA and Korero, Science Direct, pp. 1–7.
7. Brad Grothen, P.E., Technical Director, Robbins Company, Dec 18, 2018, Case Studies in Challenging Geology: Gerede Water Tunnel and Delaware Aqueduct Repair, Presentation, USA, https://robbins.com, Google
8. Jamal Rostami, Soo-Ho Chang, December 2017, A Close Look at the Design of Cutterheads for Hard Rock Tunnel – Boring Machines, Science Direct, pp. 4.
9. Li Qin Bo, Yang Ji Hua, Qi San Hong, Yang Feng Wei, 2018, Huang River Surveying, Planning and Design Limited P.C., Zheng Zhou, China, Papers' Book, Water Works Tunnel Technical Application and Development, Association of Survey and Design of Hydraulic and Electricity, China, August 2018.
10. Carlos Liu, Some Useful Numbers on the Engineering Properties of Materials (Geologic and Otherwise), GEOL 615, https://www.academia.edu, pp. 57–64.
11. Brian B. Khalighi and Joseph J. Diehl, Atlas Copco Robbins Inc. and Grow Tunneling Corp, USA, High Performance Tunnel Boring Machine for Queens Water Tunnel No.3: A Design and Case History, 1997 RETC Proceedings, USA, pp. 5.

12. Slide Player, Circular Motion, images, https://slide player.com, Google
13. Slide Player, Circular Motion, images, https://slide player.com, Google
14. Slide Player, Circular Motion, images, https://slide player.com, Google
15. Hongshen Zhen, Pneumatic Transmission, 1981, China, Northeast University, Mechanical and Industrial Publisher, China, pp.1.
16. Hongshen Zhen, Pneumatic Transmission, 1981, China, Northeast University, Mechanical and Industrial Publisher, China, pp. 23.
17. Overview of Materials, Cast Iron, https://www.matweb.com, USA, Google
18. Overview of Materials, Steel, https://www.matweb.com, USA, Google
19. Hongshen Zhen, Pneumatic Transmission, 1981, China, Northeast University, Mechanical and Industrial Publisher, China, pp. 36.
20. Hongshen Zhen, Pneumatic Transmission, 1981, China, Northeast University, Mechanical and Industrial Publisher, China, pp. 39–41
21. Hongshen Zhen, Pneumatic Transmission, 1981, China, Northeast University, Mechanical and Industrial Publisher, China, pp. 36
22. The Robbins Company, October 2019, Delaware Aqueduct Bypass, Tunnel Boring Now Complete, Tunnel Business Magazine, USA, pp. 16 – 18
23. Carlos Liu, Some Useful Numbers on the Engineering Properties of Materials (Geologic and Otherwise), GEOL 615, https://www.academia.edu, pp. 57 – 64.
24. S Timoshenko, 1956, Strength of Materials, Part II, Advanced Theory and Problem, Stanford University, USA, D. Van Nostrand Company, Inc. Third Version, 1957, Chinese Version Translated by Wang Yi Lin, Shanghai Jiatong University, 1960, China, pp. 259–262.
25. Jean-Daniel Brahant and Ruben Duhma, 2017, Singapore, Herrenknecht Asia Headquarters, pp. 10.

Tunnelling for a Better Life – Yan, Celestino, Thewes & Eberhardt (Eds)
© 2024 The Author(s), ISBN 978-1-032-80042-4
Open Access: www.taylorfrancis.com, CC BY-NC-ND 4.0 license

Shield self-driving technology and its application

Wenbo Zhou*
Shanghai Tunnel Engineering Co., Ltd, Shanghai, China

Min Hu
SHU-SUCG Research Centre for Building Industrialization, Shanghai University, Shanghai, China
SILC Business School, Shanghai University, Shanghai, China

Huiming Wu
Shanghai Tunnel Engineering Co., Ltd, Shanghai, China

Bingjian Wu
SHU-SUCG Research Centre for Building Industrialization, Shanghai University, Shanghai, China
SILC Business School, Shanghai University, Shanghai, China

Jing Lu
SHU-SUCG Research Centre for Building Industrialization, Shanghai University, Shanghai, China
School of Mechatronic Engineering and Automation, Shanghai University, Shanghai, China

ABSTRACT: With the continuous growth of the demand for underground space construction, shield self-driving technology has become a research hotspot in recent years. In this paper, focusing on the characteristics and difficulties of shield tunnel construction, inspired by Rasmussen's human performance model, we design an intelligent decision-making and control system for shield tunnelling, called Zhiyu_IDCS. In addition, we propose a series of technologies, such as autonomous and fast recognition of the environment based on the conceptual drift, control model reconstruction mechanism based on explanatory machine learning, and multi-model collaborative control based on reinforcement learning, to cope with the challenges brought by complex, changing and uncertain construction scenarios. The shield tunnelling intelligent decision-making and control system includes shield attitude control, ground settlement control, soil improvement, soil-cutting, muck-discharging control, tunnel sealing control, etc., to accomplish long-distance tunnelling tasks without human intervention. The "Zhiyu" shield self-driving intelligent controller, developed by Zhiyu_IDCS, has been installed on shield machines of different manufacturers and models and has been applied in tunnelling in many cities such as Shanghai, Zhengzhou, Nanjing, Ningbo, and Shaoxing. The shield machines have crossed various soil layers, such as clay, sand, rock, and composite soils, and diverse engineering scenarios like rivers and bridges. Its cumulative advancing mileage has exceeded 10 km. The paper analyses the tunnelling performance and features of the "Zhiyu" intelligent controller from four aspects: tunnel quality, environmental safety, tunnelling efficiency, and control stability, and compares it with manual control. Finally, we give opinions and suggestions on the future development direction of shield self-driving technology.

Keywords: Shield, Tunnelling, Self-driving, Intelligent, Autonomous control

1 INTRODUCTION

With the rapid development of underground space, the size、length, and complexity of underground construction are increasing, and the demand for shield tunnelling has also risen significantly. However, the complex construction environment and tight construction schedule make the traditional manual tunnelling mode face significant challenges, and the potential risk of tunnelling projects is increasing. The tunnel construction industry faces a significant shortage of experienced construction personnel. In addition, even for experienced construction personnel, whose construction experience is limited to the tunnels they have driven through. They often get into trouble when an entry into a new

*Corresponding author: zhouwb@stec.net

DOI: 10.1201/9781003495505-307

geological environment or an unmet engineering phenomenon occurs. Tired workers and blind acceleration pose a great threat to the quality and safety of tunnelling projects. Therefore, it has become a consensus to use automation and intelligent means to change the existing construction methods and improve project safety, quality, and efficiency.

Since 2018, shield autopilot has been accelerating, and the research results have increased significantly. In 2018, Shimizu Corporation of Japan and Nagoya University cooperated to complete the shield attitude trajectory planning by using AI technology; in 2019, MMC AMUDA MRT of Malaysia developed the A-TBM automatic tunnelling module, which realizes the automatic control according to the attitude target given by the expert, which was applied in the Kuala Lumpur Metro Line 2 project. In the same year, Shanghai Tunnel Engineering Co., Ltd. and Shanghai University cooperated to develop the "ZhiYu" shield self-driving control system V1.0, which was installed in an articulated earth-pressure balance shield tunnelling machine, realizing the independent planning and control of the shield attitude, ground settlement, and tunnel sealing, and achieving success in the Hangzhou-Shaoxing Intercity Railway Project. In 2020, Shimizu Corporation of Japan developed an automatic shield attitude guidance system, which achieved good results in a small horizontal radius of curvature axis control of tunnels. In 2021, Tokyu Construction Co. of Japan realized automatic earth pressure and attitude control, and Ohayashi Group of Japan developed the "OGENTS® intelligent shield," which completed the automatic control of shield attitude. In 2022, China Railway Tunnel Bureau Group Co., Ltd. realized a one-button start for shield intelligent tunnelling in the 12th section of Shanghai Airport Line. In June 2023, the "Zhiyu" shield self-driving control system V2.0 developed by Shanghai Tunnelling Engineering Co. Ltd. in cooperation with Shanghai University completed the independent tunnelling of the whole line (5695 meters) of the 12th section of the Shanghai Airport Line (7# wind shaft ~ Lingkong Road), creating the records of 19 rings of tunnelling in a single day, 461 rings of tunnelling in a single month, and 829.8 meters of tunnelling of 9-meter-diameter shield. Moreover, shield self-driving decision-making and control systems (Zhiyu_IDCS) is applied in different geological environments, brands, and EPB shield machines in many cities, with a total tunnelling distance of more than 10 kilometres. Self-driving shield technology is gradually moving from research to practice. Shield intelligence and automation have become an inevitable trend in tunnel construction development, promoting underground space development into a new era.

2 SHIELD SELF-DRIVING DECISION AND CONTROL SYSTEM

Shield tunnelling engineering is a complex and massive system, which has the following difficulties:

1) The tunnel construction situation is complex, changeable, and incompletely knowable. With the shield tunnelling, the surrounding geology, force environment, and shield machine properties may change, and the whole tunnelling process is characterized by time lag and sudden change.
2) A shield machine is a complex, large-scale equipment, including cutting, propulsion, sealing, grouting, soil improvement, and other independent subsystems that affect each other.
3) The relationship between the control systems and control tasks is complex. The shield machine accomplishes attitude, settlement, and sealing control through more than ten independent control subsystems in cooperation. However, these tasks own complex relationships, coupled control parameters, and conflicting control objectives in different situations.

Aiming at these problems, we introduced human performance model (Rasmussen,1983) to design the "ZhiYu" shield self-driving decision-making and control system(Figure 1), which is divided into four levels: real-time perception, control and execution, system coordination and planning and decision-making. The perception layer is the "*eyes*" of the whole system, which utilizes various sensors and monitoring devices to obtain the ground deformation, shield machine work and movement characteristics, and the state of the completed part of the tunnel; the execution layer is the "*hands*" of the system, which consists of controllers of various subsystems. The execution layer is the "hands" of the system, which consists of the controllers of each subsystem and operates according to the control target given by the coordination layer; the coordination layer is the "*cerebellum*" of the system, which coordinates the relationship of each subsystem according to the requirements of the decision-making layer, determines the targets of the subsystems, and ensures the balance of the system; the decision-making layer is the "*brain*" of the system, which judges the engineering situation and predicts control effects and plans the control strategy of the whole system according to the engineering objectives dynamically.

Therefore, reinforcement learning (Sutton,1998) is adopted in the decision-making layer to continuously learn and optimize autonomously by receiving rewards (feedback) from the environment and simulated environment, with the exploration-exploitation phase balancing mechanism to ensure that the shield machine maintains good performance in complex or incompletely knowable scenarios. Since reinforcement learning requires a large amount of data for training, the environment simulator is trained using historical engineering data.

In Zhiyu_IDCS, environment identification, situation simulation, collaborative control, and objective evaluation are the most important key technologies, which will be described in detail in Section 3.

Figure 1. "ZhiYu" shield self-driving decision and control system.

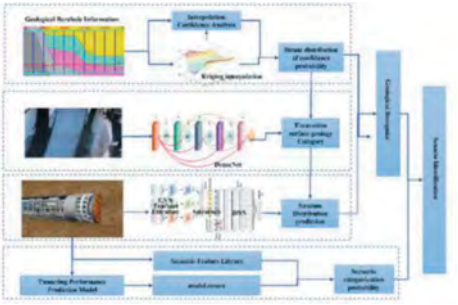

Figure 2. Tunnelling scenario identification.

3 KEY TECHNOLOGIES

3.1 *Scenario self-identification mechanism based on multi-source information*

During the shield tunnelling process, factors such as location movement, human activities, and equipment wear and tear lead to gradual changes or sudden changes in the tunnelling scenario, which triggers the drift of the control model. Therefore, correctly and quickly recognizing the context changes is the basis for improving shield structure control.

The mechanism of scenario identification is studied from two perspectives: mechanism tracing and difference analysis. Sudden geological change is the most crucial reason for contextual change in tunnelling. Although the geological exploration information and the state of excavated soil cannot accurately reflect the geological changes, they can be an essential basis for scenario identification. In addition, the deep learning model for geologic identification based on shield tunnelling data also provides a reference for scenario analysis. When the model drift analysis is performed, this information is used as the a priori condition, combined with controlling the model error and the data distribution changes in the adjacent time windows and finally completing the autonomous recognition of the tunnelling scenario based on the Bayesian classifier.

Figure 2 shows the process of scenario identification. First, the initial confidence probability of stratum distribution is determined based on exploration information. Then, deep learning is used to determine the geological type of the excavation surface using the slag monitoring video. Then, based on the geological distribution prediction model established from the shield excavation information and the drift of the excavation performance prediction model, the probability of a change in the context is calculated. Finally, based on multiple diagnostics and the Bayesian principle, synthesize the feature recognition results and the likelihood of occurrence of scenario change to realize the fast and accurate identification of engineering scenarios.

3.2 *Predictive model reconstruction based on XAI*

Since the shield tunnelling system has significant hysteresis characteristics, if the judgment is only based on the current system feedback, it will lead to the instability of the control system. Therefore, an environment simulator with predictive capability is essential in the control system, which can improve the control strategy and parameter accuracy, especially to overcome the problem of poor adaptability of the shield structure into a new situation. Considering the characteristics of small data sample size and complex situation, we utilize the interpretive machine learning idea, combined with transfer learning, to guide the model reconstruction and avoid the application risk brought by the black-box model.

First, we start from the engineering scenario, cluster the historical engineering construction according to the basic information of tunnels, shields, geology, and environment, and extract several typical scenario categories; then, classify and train according to the scenario, constituting the scenario base model library; then, adopt the LIME (Local Interpretable Model-Agnostic Explanations) interpretive method (Ribeiro,2016) is used to rank the importance of the core features of the model and the directional interpretation of the control relationship, to form intellectual control rules, and to form a scenario knowledge base where the model and the rules coexist. Finally, when a new engineering situation occurs, according to the engineering characteristics and the statistical characteristics of the data, the base model with a certain degree of situational similarity is selected as a sub-model for constructing the control model. The model transfer from the multi-source domain to the target domain is accomplished through model reconstruction to quickly adapt to the new situation. (Figure 3).

3.3 *Reinforcement learning-based cooperative control of multiple intelligences*

As a large-scale mechanical equipment, the shield machine accomplishes attitude control, settlement control, sealing control, and performance enhancement

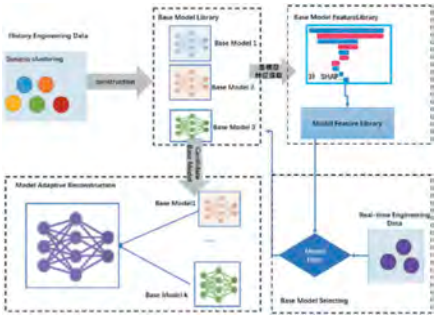

Figure 3. Shield excavation prediction model construction.

through more than ten independent control subsystems cooperating. However, these tasks have complex relationships in different scenarios, coupled control parameters, and conflicting control objectives.

Therefore, we design a collaborative optimization control method. First, from the perspective of the comprehensive performance of tunnelling, we construct a complete evaluation index system of tunnelling in the short, medium, and long term, focusing on the four dimensions of environmental safety, tunnel quality, tunnelling efficiency, and control performance.

Based on the shield tunnelling mechanism and engineering data, deep learning and other methods are used to design a relationship model for settlement, attitude, and performance prediction, construct a shield tunnelling simulator, analyse the possible changes of the shield tunnelling machine and the surrounding environment under different control strategies, and analyse the control effect. The strategy's reward value is calculated using the simulator and the control feedback. The strategy optimization is carried out with the goal of the maximum reward value. On this basis, each control parameter's importance ranking and search direction are determined according to the optimization strategy, and the control value of each subsystem is determined after passing the constraint check. (Figure 4).

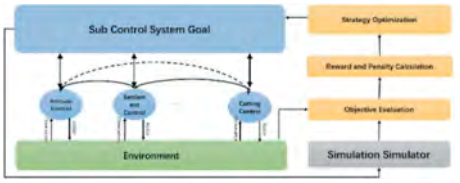

Figure 4. Multi-system collaborative control.

4 ENGINEERING APPLICATIONS

4.1 *Application overview*

Zhiyu_IDCS has been applied in many cities such as Shaoxing, Zhengzhou, Nanjing, Shanghai, and Ningbo, traversing a variety of geologies such as clay, pulverized soil, sandy soil, rocky and composite soil layers, etc., with the diameter of the shield machine ranging from 6-9 m, and the list of completed projects is shown in Table 1.

Table1. List of completed self-driving projects.

Project	Tunnel	Mileage(m)	Shield Maker	Geologic	Automation Rate	Evaluation of control effects		
						HD	VD	S
Hangzhou-Shaoxing Intercity Railway	Ke-Di Left	528	STEC	Silt\muddy clay\Clayey silt	0.871	6	6	13
	Ke~Ji Left	939.6	STEC	Silt-clay/gray silty clay	0.805	10	12	15
Shanghai Line 14	Xie-Long Up	596.4	CCCC	Silt\muddy clay\Clayey silt	0.875	4	7	3
Nanjing Metro Line 5	Ke-Zhu Left	739.2	STEC	muddy Silty clay\Silt	0.971	7	9	6
	Ke-Zhu Right	734.4	STEC	\Silty clay\clay\Silty sand	0.926	12	10	2
	Wen-Cha Left	1278	STEC	\intense or moderate weathered munstone	0.881	4	7	3
	Wen-Cha Right	1273.2	STEC		0.763	3	5	4
Zhengzhou Metro Line 8	Pu-Pu Right	2126.4	JISTRONG	Silty sand\Fine sand	0.832	5	5	3
	Pu-Pu Left	2097.6	JISTRONG	\Clayey silt	0.854	3	6	1
Ningbo Metro Line 3	Yong-Zhen Right	1836	KMQ	muddy Silty clay\Silty sand	0.951	6	13	4
Shanghai Airport Line	Ling-feng left	5695.2	STEC	Gray muddy clay\Gray	0.94	10	27	3
	Ling-feng Right	5715	STEC	clay\Gray Silty clay	0.893	10	13	4

Note: HD is horizontal deviation of shield Tail, VD is vertical deviation of shield tail, S is cumulative ground settlement; Evaluation of control effects is calculated by average of absolute values

4.2 *Performance analysis*

We take the Shanghai Airport Line Ling-Feng right line as an example to analyse the control performance of shield self-driving from attitude control, settlement control, propulsion speed, and cutting energy consumption. We compared a similar tunnelling section (200 rings) to the Ling-Feng right line, which is manual tunnelling. The working conditions are: the horizontal line shape is a gentle curve (left), the elevation line shape is a downward straight section, and the traversing geology is a mixed layer of gray silty clay and gray clay.

4.2.1 *Engineering background*

Shanghai Rail Transit City Line Airport Liaison Line, with a total length of 68.627km, is a fast channel connecting the east and west areas of Shanghai, which will not only be responsible for transporting most of the passengers between Pudong and Hongqiao airports but also be an essential channel for external railroad passenger transportation in Shanghai. Shanghai Airport Line Ling-Feng tunnel length is 5.7 kilometres. The right line adopts a 9.3m "Zhiyu" self-driving EPB shield machine (Figure 6) for construction. The shield machine of left line was equipped with the Zhiyu_IDCS. The Ling-Pudong tunnel is tunnelled manually (Figure 5).

Figure 5. Shanghai Airport Line.

4.2.2 *Performance analysis*

1) Attitude Control

The attitude control of "Zhiyu" adopts the dual control mode of shield head and tail positions. Figure 6 shows the distribution of the horizontal deviation of the shield head, the vertical deviation of the shield head, the horizontal deviation of the shield tail, and the vertical deviation of the shield tail under autonomous driving. It can be seen that the deviation variation of the whole shield machine is between -50mm and 50mm for both the head and tail, and the symmetry of the deviation distribution is better, with most of the deviations between -20mm and 20mm.

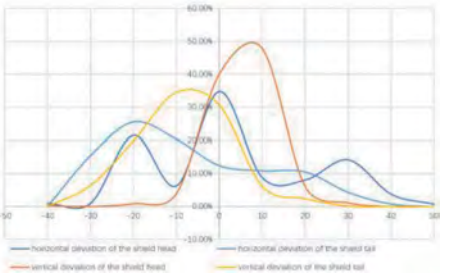

Figure 6. Distribution of shield attitude deviation.

Figure 7 illustrates the box plots of attitude deviations for automatic and manual control (box plot quantile are 5%, 15%, 85%, and 95%, respectively). The comparison shows that horizontal and vertical attitude autonomous control is superior to manual control, the distribution of deviation intervals is more reasonable, and the advantage is more evident in elevation deviation control.

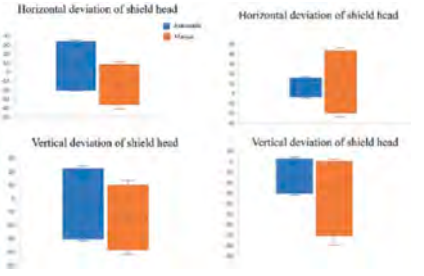

Figure 7. Attitude deviation comparison between automatic and manual controls.

2) Settlement Control

The autonomous tunnelling control system of the "Smart Driver" shield structure controls the whole process of ground settlement utilizing cutting-face pressure control and grouting control at the end of the shield. Figure 8 shows the distribution of the cumulative settlement in front of the shield, the cumulative settlement behind the shield, and the final ground settlement. It can be seen that the ground settlement is between -8mm and 10mm during the whole excavation process, and the settlement mainly varies from -5mm to 5mm, with little disturbance to the environment.

Figure 9 compares the ground settlement under automatic and manual control, with box plots at quartiles of 5%, 15%, 85%, and 95%, respectively. It can be seen that both have excellent settlement control with little difference.

3) Tunnelling speed

Zhiyu_IDCS allows on-site technicians to set the upper-speed limit. Figure 10 shows the trend of ring average speed change after the field technicians released the upper-speed limit (after 1800 rings). The

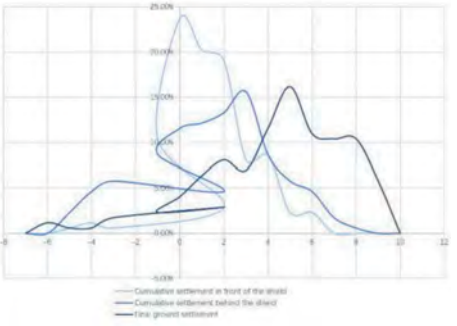

Figure 8. Distribution of ground settlement.

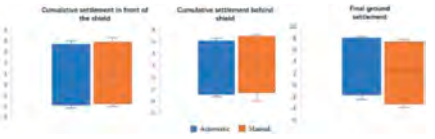

Figure 9. Ground settlement comparison between automatic and manual controls.

self-driving system can motivate the potential capacity of the shield machine as much as possible to realize high-speed and balanced construction when conditions allow.

After the statistics, the average speed of the automatically controlled section reached 85mm/min after the upper-speed limit was raised. In comparison, the ring average speed using the same type of shield machine was 70mm/min when manually controlled.

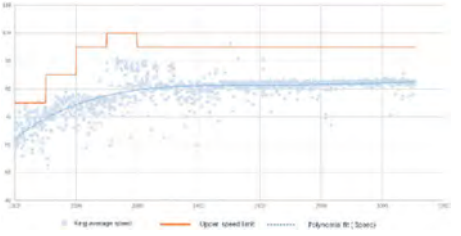

Figure 10. Tunnelling speed.

4) Cutting energy consumption

Shield machines are large power consumption equipment, so how to save energy and reduce emissions is also a problem to be considered. Therefore, the Zhiyu_IDCS continuously optimizes the energy consumption in the tunnelling process. Figure 11 shows that the upper limit of propulsion speed is gradually released, and the electric energy efficiency per unit distance of the shield machine changes (calculated by dividing the propulsion speed by the current). The utilization efficiency of electric energy is constantly optimized and improved during the tunnelling process.

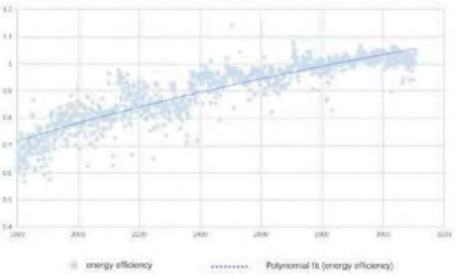

Figure 11. Tunnelling energy efficiency.

5 CONCLUSIONS

With the development of information technology, shield self-driving has shown a bright future, and its unique advantages have been reflected in engineering applications. Zhiyu_IDCS V2.0 adopted the ideas of reinforcement learning and transfer learning, and compared with V1.0, the control effect is more stable in complex geological situations. Of course, for the Zhiyu_IDCS, there are still problems, such as poor control flexibility and lack of timely response in some cases. Therefore, if the shield autonomous driving technology can be more widely accepted and applied, it should learn more historical engineering data, adapt to various engineering situations faster and better, and always maintain safe, stable, and efficient performance. However, although the informatization level of shield machine construction is improving now, the data between each company is independent, with inconsistent data meanings and low data quality, which makes it challenging to learn big data in the later stage. Therefore, constructing the standardization of data and improving data quality are very important.

This paper describes the autopilot architecture and key technologies from the perspective of intelligent control. However, the success of the autopilot technology is also related to the performance of the communication system of the shield machine, the shield machine equipment, and the supporting equipment. All of these factors can constrain the performance of the autopilot capability. Developing a more high-speed and efficient shield machine based on self-driving is also a future development direction that should be emphasized. In addition, there must be a digital and lean project management mode to improve the efficiency and quality of tunnelling projects.

ACKNOWLEDGMENTS

Grant to the Engineering Project Departments of Shanghai Tunnel Engineering Co., Ltd. for support and assistance in applying the “Zhiyu” self-driving system.

REFERENCES

Justin, C.J.H. 2020, In Pursuit of the Autonomous TBM. North American Tunneling Journal. (2-3): 18–22.

Hirokazu Sugiyama, Koichi Masuda. 2020. Rationalization of Shield Tunnel Construction Management by AI. Research Report of Shimizu Corporation. 98: 13–20.

Hu M, Wu B, Zhou W, et al. 2022. Self-driving shield: Intelligent systems, methodologies, and practice[J]. Automation in Construction. 139: 104326.

OBAYASHI CORPORATION, 2021. Developed "Shield AI automatic directional control system". Japan.

Rasmussen. 1983. Skills, rules, and knowledge; signals, signs, and symbols, and other distinctions in human performance models. IEEE Transactions on Systems, Man, and Cybernetics 13:257–266.

Ribeiro, Marco Tulio, Sameer Singh, and Carlos Guestrin. 2016. Explaining the predictions of any classifier. Proceedings of the 22nd ACM SIGKDD international conference on knowledge discovery and data mining. Association for Computing Machinery, New York, USA.

Sutton R, Barto A, 1998. Reinforcement Learning: An Introduction. MIT Press. USA.

Shanghai State owned Assets Supervision and Administration Commission, 2023.The first subway in Shanghai constructed by Tunnel Co., Ltd. using "unmanned driving" shield tunneling technology has successfully started construction. Shanghai, China.

Shimizu Corporation, 2018. AI based Support System Developed for Shield Excavation Planning. Japan.

TOKYU Construction Co. 2021.Demonstration of Shield Machine AI Excavation System, a support tool for shield tunnel construction. Japan.

Xinhua News Agency, 2022.The intelligent construction technology of shield tunnels in China has reached the world's leading level, Beijing, China.

Tunnelling for a Better Life – Yan, Celestino, Thewes & Eberhardt (Eds)
© 2024 The Author(s), ISBN 978-1-032-80042-4
Open Access: www.taylorfrancis.com, CC BY-NC-ND 4.0 license

Research on frontier technology of shield machine/hard rock machine selection and mode innovation

Weibin Zhu*
Chinese Society for Rock Mechanics & Engineering, Beijing, China
Guangzhou Metro Group Co., Ltd, Guangzhou, China

Junbin Wang & Wenda Xie
Guangzhou Rail Transit Construction Engineering Consulting Co., Ltd, Guangzhou, China

ABSTRACT: The classical theory of shield machine selection is based on single or homogeneous formation, and the essential risks while TBM tunnelling, such as "mud cake", "screw conveyor blow-out" and "hindered mucking", are mostly presented separately. These essential risks would occur together while TBM works at mixed face ground condition, result in extra difficulties and even surface collapse. In general, preventive measures of improving TBM design, to enhanced single mode shield machine adaptability and safety, such as adding cutterhead agitators and foaming pipes, optimizing the cutterhead opening ratio, using accessible cutterhead, etc., or taking auxiliary civil measures prior to machine crossing.: such as blasting boulders or rocks, filling karst formation caves, etc. However, in the past 10 years, big number of projects is increasing together with larger diameter, deeper overburden and longer distance tunnel, the probability of essential risks combination and the losses of project caused by mixed face ground condition and/or "mud cake", "screw conveyor blow-out" and "hindered mucking" have increased significantly, even leaded to major engineering accident. Author establishes the elements and principles of mixed face condition shield/hard rock machine selection system, based on experience and lessons learned from the application of 30 years of experience and systematic summary, as well as more than 1,000 shield machines under various geological and working conditions. By studying the upgrade and limitation on single mode shield machine/hard rock machine, provides original and ground-breaking key technology of TBM mode integration and explores the paths of overcoming the challenges. Expect to inspire you to similar projects.

Keywords: shield machine type selection, mixed face ground condition, essential risk, superposition of essential risks, mode integration and innovation, frontier key technology

1 INTRODUCTION

The "type" and "mode" of the shield machine, e.g. type of EPB, mode of Slurry, must be "tailor-made" according to specific geological conditions and other construction environments, machine's adaptability determines the success or failure of the project.

Since the development of the closed-face mechanical balanced shield machine in the 1960s, especially after the Guangzhou Metro took the lead in trying to use the balanced shield machine to build tunnels in rich water mixed face ground condition in the 1990s, the shield construction method has been rapidly promoted in China. During this period, many difficulties were encountered, which led to thorough reflections on the theory of the traditional shield machine selection and mode choice based on uniform stratum conditions by industry aspirants. At the same time, the engineering geological conditions are becoming more and more complicated: the same project section has both uniform strata and composite strata; some sections are greatly lack of water, and some sections are extremely abundant in water; there are both full face complete rock masses and broken rock masses formed by the development of fracture joints, uneven weathering, etc.; there are both super-hard (≥90MPa) monoliths and holes formed by karst development. The series of concrete difficulties further promote the innovation and optimization of the theory of the shield machine selection and mode choice.

With the rapid development of China's tunneling equipment industry and the application of nearly 5000 modern shield machines, especially the practice of super-large diameter (≥12m) shields in water-rich

*Corresponding author: Wang.Junbin@hotmail.com

DOI: 10.1201/9781003495505-308

mixed face ground condition in recent years, China's shield machine selection and mode innovation research has made significant progress and is at the forefront of the world. For example, in 2012, Guangzhou Herrenknecht factory produced 6 no. φ6.6m slurry/earth pressure tandem dual-mode shields for the karst composite strata in Malaysia; at the same time, Guangzhou Metro led China Tunnel Construction Co., Ltd. and Mitsubishi to develop a 6-meter parallel slurry/earth pressure dual-mode shield machine. In 2020, China Railway Engineering Equipment Co.,Ltd developed a 6-meter three-mode tunneling machine for the second phase of Guangzhou Metro Line 7; the φ12.84m slurry/earth pressure dual-mode shield machine produced by China Railway Engineering Equipment Group Co.,Ltd (CREG) successfully penetrated the pebble under mudstone composite strata in Chengdu Zirui Tunnel. In April 2022, CREG developed a φ15.09m super-large diameter accessible cutterhead dual-mode shield to across the Wuhan East Lake; in the same year, Tianhe Mechanical Equipment Manufacturing Co., Ltd. developed the world's largest diameter (φ16.07m) accessible cutterhead dual-mode shield machine (with spiral conveyor + accessible cutterhead slurry shield machine) to deal with the overlapping risk sources of composite strata coexisting with mudstone, limestone, quartz sandstone and developed fractures, reducing safety risks and improving efficiency.

At present, the multi-mode shield tunneling machines manufactured in China, which are independently innovated, developed, has become the best option or cutting-edge technology to tackle the challenge of shield construction in mixed face ground conditions.

2 SHIELD /TBM SELECTION PRINCIPLE

Geological body is the object of underground space development. Understanding the characteristics of geological body and scientific classification is the basis of shield /TBM selection and innovation.

For shield construction method, the construction object is generally divided into two categories: one is homogeneous stratum and the other is composite stratum. Among them, composite strata are further divided into soil/soil, soil/rock, rock/rock and other multiple combinations of composite strata.

2.1 *Conventional shield machine/hard rock machine selection theory*

The conventional theory of shield machine selection is established for a single or homogeneous soil layer (Quaternary/Q 2 million years before present/Q4 10,000 years before present). That is, the selection is based on the permeability coefficient and particle grading of the soil layer (Figure 1 and Figure 2).

According to the conventional shield selection theory, the slurry balanced shield machine is

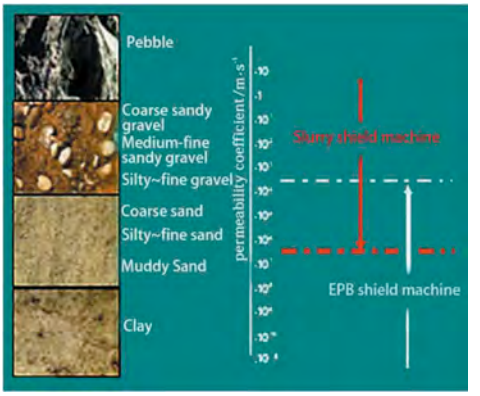

Figure 1. Relationship between permeability coefficient and shield machine selection.

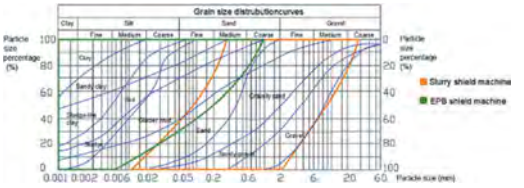

Figure 2. Relationship between particle gradation and shield machine selection.

generally chosen for water-rich sand, pebble, gravel strata with large permeability coefficient; and for sandy soil, silt, clay strata with permeability coefficient less than 10-4 m/s earth pressure balanced shield machine are often being used.

However, in the actual decision-making phase of the selection, cognition, experience, habits, as well as soil conditioning technology and economic considerations will also affect the selection of shield machine. With the development of soil conditioning improvement technology, soil discharging compatibility can improved EPB machine application in water-rich sand layer. Therefore, in China, the proportion of choosing EPB shield is much more than slurry shield, accounting for more than 80%.

2.2 *Elements and principles of shield machine/ hard rock machine selection system for mixed face ground condition*

Composite stratum and its geotechnical properties are far more complex than single or homogeneous stratum, the traditional selection theory is simply not applicable, the selection of the shield machine need to take into account the following system elements.

(1) Geological elements: including rock strength, rock integrity, geotechnical composition and structure, geotechnical stability (excavation surface flatness), water content (permeability) and so on. Adopt the technical route from macro (geomorphology + geohistory + stratigraphic

lithology combination) to micro (site geotechnical properties) to analyze;
(2) Tunnel burial depth and its deviation;
(3) Tunnel section diameter size;
(4) The nature of the soil (particle size, specific gravity), the amenability and its conditioning improvement system;
(5) Advance speed (decreasing speed results in mechanical energy converted to thermal energy leads to mud cake and other series of problems);
(6) Environmental requirements (ground settlement, groundwater level control requirement).

Therefore, the selection of composite formation shield machine /hard rock machine is more based on the comprehensive analysis and selection of geological elements, engineering section diameter, buried depth, environmental control requirements, the drainage of residual soil, the controllability of "dynamic balance", as well as the production capacity of shield manufacturers, the experience and economy of the construction party. Of course, after the selection process, the shield type is determined, there may still be local adaptability and engineering risks. Generally, the adaptability and safety of the shield structure when the shield machine in single mode are enhanced by improving the design of the shield machine, such as increasing the cutterhead mixing agitators and foam pipes, optimizing the opening ratio of the cutterhead, and adopting the accessible cutterhead or adopting auxiliary measures outside the shield, such as millisecond blasting of the rock beforehand and filling up the caves in karst strata.

3 THE PROBLEM OF SUPERPOSITION OF ESSENTIAL RISKS IN MIXED FACE GROUND CONDITION WHILE SHIELD CONSTRUCTION

From 1995 to 2005, Zhu Weibin and Ju Shijian put forward the concept of defining the basic risk sources of composite formation shield construction as "mud cake", "screw conveyor blow-out" and "hindered mucking" according to the subway construction practice of Guangzhou Metro Line 1, 2, 3 and 4 and Shenzhen Metro Line 1. In the past 20 years, thousands of shield construction cases have proved that the essential risks of shield construction, whether uniform formation or composite formation, are still "mud cake", "screw conveyor blow-out" and "hindered mucking", as shown in Figure 3. These three factors are the main factors that affect the progress of shield construction and induce engineering safety accidents. In the homogeneous formation, most of them are independent. For example, when the earth pressure shield is constructed in the formation of water-rich sand gravel and water-rich fracture zone, it is mostly manifested as "screw conveyor blow-out" and rarely occurs "hindered mucking" and "mud cake". Slurry shield tunneling in the stratum with high viscosity content, the common risk is "mud cake". However, in the construction of mixed face ground condition, a single mode shield machine will experience superposition of essential risks altogether, as shown in the following examples: (1) In Chengdu, China, the upper part of the tunnel is sand and pebble, and the lower part is mudstone. If a single mode slurry shield machine is selected, mud cake will be formed on the cutter head, and at the same time, pebble "hindered mucking" will occur in the excavation chamber and slurry circulation pipeline. (2) In the composite strata of Qingdao, Jinan, Xuzhou, Shenzhen and other places of China, there are water-rich sand layers overlying the tunnel, the upper part of the section is a clay layer, and the lower part is a limestone or granite layer. Earth pressure shield machine was used in early year construction, and the phenomenon of "screw conveyor blow-out" and "mud cake" superposition was frequent, and the subsidence or collapse events induced by it were frequent. After the summary and analysis, the root causes are as follows:

(1) The understanding of the adaptability of shield machine using under mixed face ground condition is limited or misled by the traditional classical selection theory, resulting in improper selection.
(2) The limitations of the development of shield equipment technology.
(3) There is insufficient risk awareness of single mode boring in composite formation, and no timely adoption of enhanced technical measures.

4 SINGLE-MODE SHIELD MACHINE /HARD ROCK MACHINE TECHNOLOGY UPGRADE AND ITS LIMITATIONS

The most direct result of the essential risks and superposition of those risks in composite formation shield construction is cutter or cutterhead wear/damaged and machine stuck, which need to be replaced and repaired frequently by accessing excavation chamber. It not only affects the tunnelling progress, but also has safety risks such as unbalanced over the face and collapse. At present, the "mud cake", "screw conveyor blow-out" and "hindered mucking" caused global engineering losses (direct + indirect) more than 10 billion.

4.1 *Single-mode shield machine/hard rock machine technology upgrade*

In response to the above problems, industry pioneers continue to innovate technology to upgrade shield equipment, including:

(1) Earth pressure shield: the cutter head equips with one foam pump to one nozzle design for improving soil condition efficiency, add the active agitators and strengthens the mixing capacity in support arms behind the cutterhead

(a) mud cake in the center of the cutter head (b) blow-out event (c) hindered mucking

Figure 3. Risk source of shield construction.

centre area to improve the "workability" of soil; Double screw or double discharge gate is adopted to strengthen the muck improvement design in the screw cylinder to prevent the superposition of "mud cake" and "screw conveyor blow-out".

(2) Slurry shield: Increase the cutter flushing system, install additional crushers, rock collecting boxes and cutterhead active agitators to prevent the superposition of "mud cake" and "hindered mucking".

(3) The conventional cutter head is equipped with a tool wear detection device to monitor tool wear in real time. Figure 4.

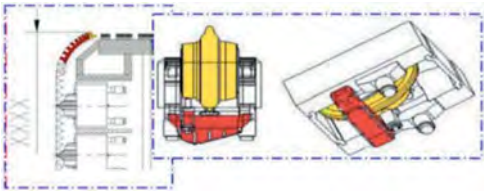

Figure 4. Schematic diagram of real-time detection device for conventional cutter hob mode.

(4) Auxiliary pressure balanced excavation, that is, the lower part of the excavation chamber is slag soil, the upper part is compressed gas, and the slag gas jointly balances the excavation surface. Figure 5.

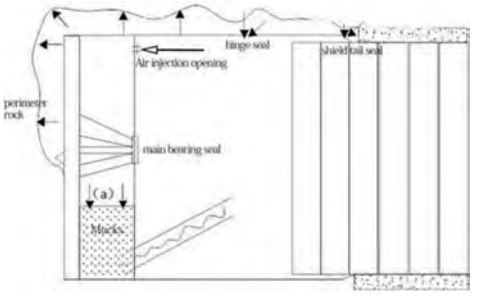

Figure 5. Mechanism of auxiliary pressure balancing.

(5) Equipped with freezable cutterhead (patent of CTC).

(6) Develop a variety of dispersants and polymers.

(7) Large diameter shield (>12m) adopts "scraper type atmospheric pressure cutter" (Figure 6) at full-section soil layer.

Figure 6. Jinghua: (16.07m) spatula type atmospheric pressure cutter head.

(8) Large diameter shield (>12m) adopts "disc cutter + scraper combined type atmospheric pressure cutter" (Figure 7) composite formation.

Figure 7. Tuodao: (13.42m) hob and scraper combined type atmospheric pressure cutter head.

(9) hard rock machine: open type → single shield → double shield.

The upgrade of shield machine/hard rock machine technology in single mode greatly improves the security and adaptability of shield. However, with the

dramatic increase of large diameter, large buried depth and long distance tunnel projects, the probability and the degree of loss caused by the superposition of the risks such as "mud cake", "screw conveyor blow-out" and "hindered mucking" and the encounter of the complex formation have significantly increased, and even induced major engineering events.

4.2 *Limitations of shield equipment technology development*

(1) Limitations of cuter tool wear detection and ex. change safety assurance for conventional cutterhead in mixed face ground condition.
It is difficult to allocate the "first damaged cutter tool" in time, there is the problem of not changing the cutter tool in time, and under the joint action of "mud cake", "screw conveyor blow-out" (earth pressure) and "hindered mucking", it is easy to cause the "domino effect" type of damage of cutter tools (Figure 8).

Figure 8. Damage of conventional cutter head of shield tunnelling machine.

(2) Limitations of medium and small diameter (<12m) shield machine/hard rock machine configuration with accessible cutter head in composite formation

If the disc cutter is applied, the area of the central closed area of the cutter head is increased, and the opening rate is reduced, the risk of mud cake and "hindered mucking" - stagnation superposition - will be increased. For example, the Nanjing Metro Line 10 crossing Yangtze river tunnel Φ11.6m slurry balance shield machine, Changde Yuanjiang crossing River tunnel Φ11.7m slurry balance shield machine (Figure 9), during the construction, the "hindered mucking" and "mud cake" superposition events occurred, lead to the need to have shield machine maintenance and extraction process which result in the extension of the construction period.

5 SHIELD MACHINE/HARD ROCK MACHINE MODE INNOVATION AND PRACTICE

Based on the limitations of shield machine/hard rock machine in dealing with complex geological and

(a) Nanjing Metro Line 10 crossing River tunnel

(b) Changde Yuanjiang Crossing River Tunnel shield machine cutter head

Figure 9. Superposition of "hindered mucking" and "mud cake".

construction risk sources and their superposition in a single mode, a breakthrough can be achieved only by combining the advantages of slurry, earth pressure and hard rock single shield mode.

In 2012, Guangzhou Metro and CTC developed the world's first "slurry and earth pressure parallel" dual-mode shield machine (Figure 10), and successfully applied to Guangzhou Metro Line 9. In a variety of composite strata such as clay and karst combination, sand and karst combination (Figure 11), the system design of integrating different driving modes and soil discharge modes on the same TBM is realized. According to actual needs, the driving function of specific modes can be set, and can be quickly switched in the tunnel.

Figure 10. Cutter head of shield machine in Hua-Guang section of Guangzhou Metro Line 9.

Based on the success application of dual-mode shield construction, as it is difficult for single-mode shield machine to adapt to the complex and changeable geological conditions in the granite distribution area (Figure 12) and meet the construction schedule requirements, in 2018, Guangzhou Metro again proposed the world's first three-mode TBM integrating

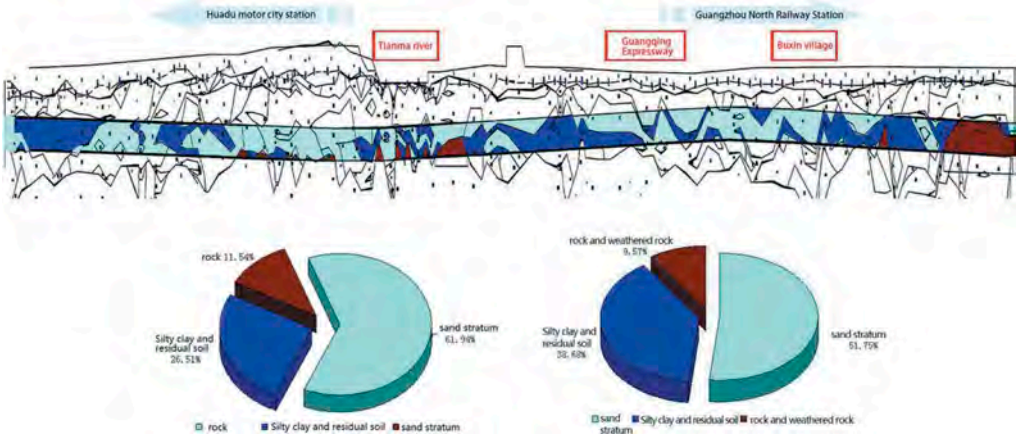

Figure 11. Geological profile of Hua-Guang section and stratigraphic distribution of left and right lines of Guangzhou Metro Line 9.

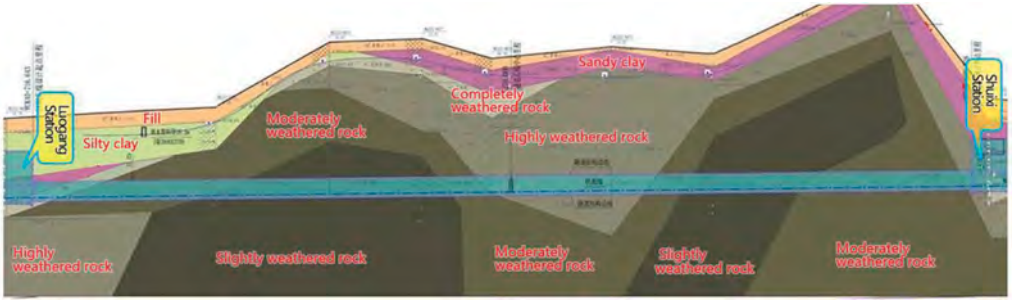

Figure 12. Geological section of the shield section between Luogang Station and Shuixi Station of Guangzhou Metro Line 7 Phase II.

Figure 13. A three-mode TBM completes the first tunnel boring.

"slurry, earth pressure and single shield" jointly developed by CREG and CRTG (Figure 13). In 2020, it was successfully rolled off the production line and applied to the section of Luogang to Shuixi Tunnel of Guangzhou Metro Line 7 Phase II.

6 CONCLUSION

The shield machine mode fusion innovation has gradually been widely used in shield design, the "type" of shield, from the past earth pressure balance, slurry balance and hard rock single shield. It has evolved into slurry/EPB dual-mode, EPB/single shield dual-mode, EPB/double shield dual modes, slurry/ single shield dual modes and EPB/slurry/ single shield three modes. There are three different methods of soil discharging at EPB/slurry dual mode machine: serial, parallel and double channel. EPB/ shield shield dual-mode machine capable of the center belt and center screw conveyor two kinds of discharge method while applicating single shield mode. According to the characteristics of the stratum, the dual-mode or multi-mode shield machine can choose the appropriate mode to balance the excavation face, and the soil discarge method is more reasonable, so as to avoid the risks of "mud cake", "screw conveyor blow-out" and "hindered mucking".

The integrated innovation of construction technology theory comes from large-scale engineering practice, and has been verified, improved and promoted in guiding problem solving. At present, the challenging problems in front of us still need to be overcome, such as: the selection of the shield and the configuration of cutter tool in the rich water and large buried depth of mixed face ground condition;

The utility of earth pressure shield foaming system; Timely and accurately discovery of the "first damaged cutter tool"; Shield, especially super large diameter shield main bearing seal lifespan extension or protection problems; Timely detection of excavation face and rock face flatness and effective contact thrust force and stress distribution problem; The performance monitoring and protection of tailskin seal brush still need to be studied and required breakthroughs in the industry.

"Methods are always more than difficulties", as long as perseverance, large-scale engineering practice as the basis, always problem-oriented, adhere to "geology is the foundation, shield is the key, management is fundamental", theory with practice, superposition of essential risks in mixed face ground condition and induce engineering difficulties will eventually be overcome, mixed face ground conditon shield construction theory will continue to walk in the forefront of the world.

REFERENCES

Zhu W. B., Ju S. J., 2006. Shield Construction Technology in composite strata. Science and Technology Press of China, China.

Zhu W. B., Liu L. H., Zheng X., et al, 2022. Study on the improvement formula of earth pressure balance shield dregs based on slump. Tunnel Construction, 42(02), 208–214.

Zhu W. B., Ju S. J., 2003. Causes and countermeasures of mud cake (secondary rock block) in shield construction. Underground Engineering and Tunneling, 02, 25–29+48.

Zhu W. B., Zhong C. P., Huang W. R., et al, 2014. Cause analysis and countermeasures of "delay discharge" in shield construction. Modern Tunnel Technology, 51(05), 23–32.

Gong Q. M., Wang Q. H., Wang D. J., et al, 2021. Development of real-time monitoring system for cutter head in shield tunnel construction. Modern Tunnel Technology, 58(02), 41–50.

Zhu W. B., Zhong C. P., Huang W. R., et al, 2017. Research on key technologies of auxiliary pressure balance in shield tunneling. Modern Tunnel Technology, 54(01), 1–8.

Tunnelling for a Better Life – Yan, Celestino, Thewes & Eberhardt (Eds)
© 2024 The Author(s), ISBN 978-1-032-80042-4
Open Access: www.taylorfrancis.com, CC BY-NC-ND 4.0 license

Development and application of a synchronous shield tunnelling technology combining advancement and segment fabrication

Yeting Zhu* & Yanfei Zhu
Shanghai Tunnel Engineering Co., Ltd., Shanghai, China

Xiangli Bi & Xiuzhi Wang
Shanghai Shentong Metro Co., Ltd., Shanghai, China

Zixin Zhang
Department of Geotechnical Engineering, Tongji University, Shanghai, China

Jian Chen
School of Civil and Hydraulic Engineering, Huazhong University of Science and Technology, Wuhan, China

Yuan Qin & Song Duan
Shanghai Tunnel Engineering Co., Ltd., Shanghai, China

ABSTRACT: To solve the problem of long construction period caused by the application of traditional shield construction method in long-distance shield projects, a synchronous shield tunnelling technology combining advancement and segment assembly was proposed. Then, a super-large mixed shield machine equipped with this technology was successfully applied in Shanghai Airport Railway Link Line project.

The on-site test results showed: the actual oil pressure fluctuated around the target values with the error rate of ± 5%, and the other two response conditions were also discovered; the phenomenon of the quick recoveries after the sudden changes of the total thrust force were observed, and the error rate of which was controlled at ± 3%; shield speed was directly affected by the total thrust vector, while the shield postures was not sensitive to it since the shield machine was wrapped in the surrounding soil, and the deviations of which in both of the horizontal and vertical directions were controlled in the range of ±10 mm of the initial values. The construction data of 351 segmental rings achieved in a single month was analysed to find that: approximately 2.4 blocks per ring could be assembled synchronously, and the construction efficiency had been improved by about 27% compared with traditional method; the starting stroke of the oil cylinder for the synchronous operation and the segment assembly proficiency had the greatest impact on the construction efficiency, and the time management was suggested to be improved. Finally, a continuous slurry pipe connection technology was provided as a supportive method to further promote the construction efficiency through adopting two pipe system alternately employed during the shield tunnelling.

Keywords: Shield tunnelling, Segmental assembly, Synchronous operation, Engineering application, Efficiency analysis

1 INTRODUCTION

The traditional shield construction method connecting the shield excavation and segment assembly in series has been solidified for over a hundred years, which requires the assembly operation to be conducted after the propulsion hydro-cylinders reach the maximum stroke, and the times for excavation and assembly are often similar in length. With the increasing demand for long-distance shield tunnels, construction period has become a decisive but uncontrollable issue that needs attention and breakthroughs, although the working performances of shield machines and related supporting technologies

*Correspondong author: zhuyeting@stecmc.com

DOI: 10.1201/9781003495505-309

have been well-optimized or developed to improve construction efficiency (DING et al., 2019; WEI et al., 2019; ZHANG et al., 2020).

From a construction perspective, low-speed continuous advancement is preferred for long-distance shield tunnel projects in urban core areas, as shortening shield downtime will significantly reduce the risk of shield machine failure and excessive ground surface settlement, while high-speed shield driving combined with synchronous assembly may improve construction efficiency and shorten the construction period in open terrain areas. Therefore, the synchronous shield tunnelling technology combining advancement and segment assembly is undoubtedly a feasible solution, and the total tunnelling duration can be reduced by increasing the overlapping time of these two procedures, i.e., by synchronising the fabrication of the segment with the advance of the shield.

Japan has conducted corresponding technical research and equipment development since 1970s as the first country in the world, and the main technical solutions can be divided into four categories as showed in Table 1: double hydro-cylinders in front and rear shield, front shield equipped independent steering function, total thrust vector control method, and special-shaped segments. The obvious limitations such as large structural size, high economical cost and control difficulty, complex design for segment and its erector could be discovered after a particular comparison. Several equipment manufacturers and construction enterprises in China also have inversed considerable time and efforts to develop related synchronous shield methods in recent years, but no publicly available data from engineering application could be found. Overall, regardless of the technical paths, the shield machine will have to be stopped and wait until the assembly is completed, if the assembling time for a single ring exceeds the advancement time. Therefore, the overlapping time that can be used for synchronous operation is a core factor for selecting the technical path.

Given that the stock of conventional shield machines in the domestic market is gradually becoming saturated, how to revitalize the "old" shield machines and how to upgrade the new are a hot topic for us. This article proposed a synchronous shield tunnelling technology based on the steady-state control of the total thrust vector (ACTT method) by adding control valves, improving sensor accuracy, and upgrading the hydraulic control system, which is suitable for both the old and new shield machines without changing the original structural design of the shield machines and segments as well as the operation experiences of the working staff. Then, this technology was applied in a super-large slurry balanced shield tunnelling project. After the analysis of construction data, the feasibility of this technology was verified, and some referable suggestion was provided to promote the construction efficiency furthermore.

Table 1. Comparisons of existing synchronous technologies.

Program	Institutions	Main technical features
Double-cylinder synchronous tunnelling method (HIROSHI, 2005)	KAJIMA	Double hydro-cylinders in front and rear shield, difficult turning, large size of the shield machine
Lattice hydro-cylinder shielding method (SUZUMI et al., 1999)	HONGCHI	
"F-Navi" shielding method (HAYASHI et al., 2008)	SHIMIZU	Front shield equipped independent steering function, high economical cost, difficult sealing method
"LoseZero" shielding method (FUKUAKYOSI, 2007)	TOBISHIMA	Inaccurate thrust vector control method, transform existing shield machine, partial synchronization
ASC-OM system	OBAYASHI	
Honeycomb-typed segment (OKUMURA, 2006)	OKUMURA	Special-shaped segment, complex structures of the segments and its erector

2 OVERVIEW OF DEMONSTRATION PROJECT

As figured in Figure 1, Shanghai Airport Railway Link Line project achieves the connection between the Pudong International Airport and the Hongqiao International Airport with the length of 68.66 km. Lot 3 of this project (JCXSG-Lot 3) consists of two section tunnels: one from Meifu Road working well to Huajing Station receiving well, and the other from Meifu Road working well to No. 2 air shaft receiving well, and the later with the length of 5658 m was constructed by "Jiyue" super-large (Φ14.07 m) mixed shield machine equipped with ACTT system.

The sketch maps of the shield machine and segmental lining structure were shown in Figure 2. "Jiyue" had a cutterhead with an excavation diameter of 14.07 m, the propulsion system of which comprised 34 sets of dual hydro-cylinders, and the inner diameter of the hydro-cylinder, the diameter of the piston-rod, and the largest cylinder stroke were 360, 280, and 3600 mm, respectively. The segmental ring was divided into 9 blocks with the outer diameter of 13.6m, the width of 2m, and the thickness of 0.65m. 4 groups of hydro-cylinders were located in each standard and adjacent block, and 2 in key block. The assembly sequence was B3, B4, B2, B5, B1, B6, L1, L2, and K, one more group on both two sides of the segment to be assembled retracted to provide enough space during the actual synchronous operation.

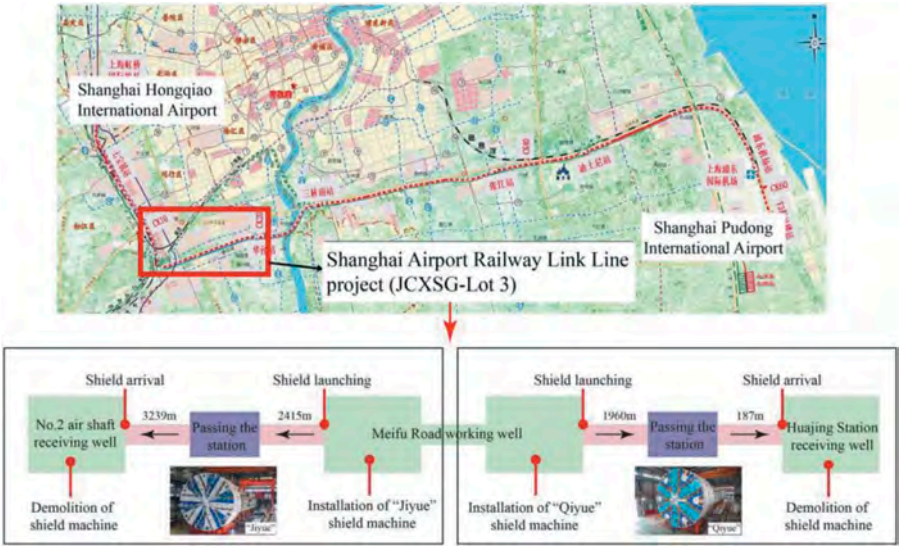

Figure 1. Project overview.

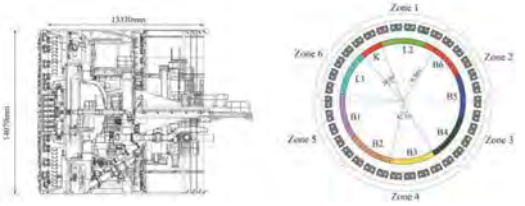

Figure 2. "Jiyue" shield machine and segmental blocks.

3 DATA ANALYSIS OF SYSTEM RESPONSE

3.1 *Control algorithm of total thrust vector*

As illustrated in Figure 3, the distribution method of the total thrust vector in the full cylinder mode and redistribution method of the missing thrust in the synchronous assembly mode have been explained in corresponding references (Zhu et al., 2023). The number of the dual hydro-cylinder groups in propulsion zone A was equal to zone B in the former mode, and which of the first pressurization zone was also equal to the second in the later mode. Effective range of target oil pressures (f_{min}, f_{max}) for all dual hydro-cylinders was set in advance to ensure that the calculated values were executable, where f_{min} is the lower limit as the minimum force to support the segment being assembled and prevent it from falling, f_{max} is the upper limit to avoid the calculated values that exceed the output capacity of the propulsion pump.

It should be noted that the numbers of the groups for the propulsion zone A and the decompression zone could be self-adaptively adjusted according to the preset rules. More specifically, when certain target oil pressures calculated by the preset grouping method were judged to be less than f_{min}, the numbers of the groups of propulsion zone A and decompression zone would be increased one after another to raise them, and the opposite operation would be conducted if the maximum calculated pressure exceeded f_{max}. The segment would be prohibited to be synchronously assembled if the calculation finally failed.

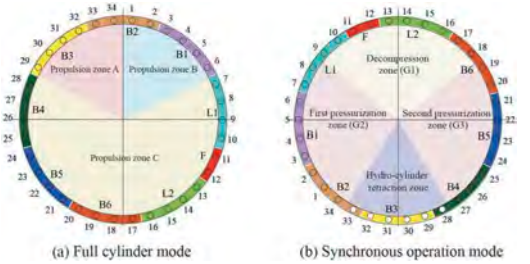

Figure 3. Calculation modes of total thrust vector.

3.2 *System response of shield machine*

The section tunnel from Meifu Road working well to No. 2 air shaft receiving well with total ring number of 2846 was completed on September 8th, 2023, and over 2000 rings were constructed by adopting ACTT synchronous technology. Among them, Ring 1022 with the overburden thickness of 15m which was marked in Figure 4 in the form of five-pointed star was selected as a characteristic rin to demonstrate the actual system response, and the total thrust force (F_T), its resultant horizontal (M_{Th}) and vertical (M_{Tv}) moments during the synchronous operation were 60869 kN, -20901kN · m, -93795kN · m, respectively. As shown in Figure 5, three blocks were synchronously assembled when the cylinder stroke extended from 2302 mm

to 2955 mm, which took about 16 minutes at the shield speed of approximately 40 mm/min.

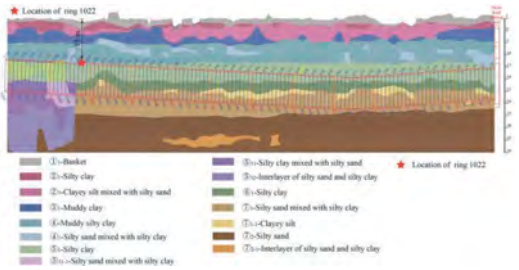

Figure 4. Geological map and arrangement of the segments.

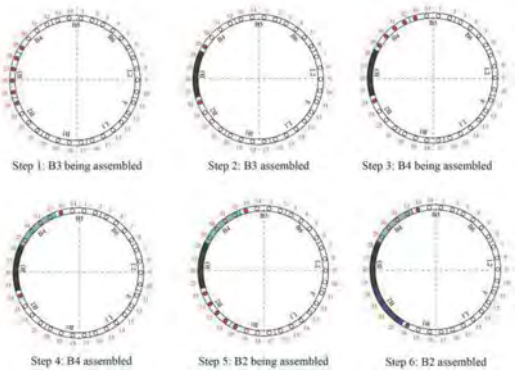

Figure 5. Assembly sequence of ring 1022 in synchronous period.

As shown in Figure 7, based on the assembly condition of ring 1022, one hydro-cylinder from the corresponding range of each segment (9 in total) was selected to present the execution of the target oil pressures. It can be seen that, consistent with the model test results (YUAN et al., 2023), the actual pressure fluctuated with a small amplitude near the target pressure values under PID closed-loop control (with the error rate of ± 5%), and a short-term response delay was observed once the target pressure changed. Owing to the fluctuations of the water-soil load on the excavation path, response performances of proportional reduction valves, shield deviation correction operations and et al., the execution of target pressure also shows the following two typical conditions: (1) obvious overshoots happened if the target pressures were slightly higher than that the hydraulic system could respond, and the error rate was controlled within 10%; (2) although the executed oil pressures could not reach the target values that exceeded the response capacity of hydraulic system, fixed deviations between the two could be remained. Overall, no significant irregular fluctuations were discovered during the whole applying process.

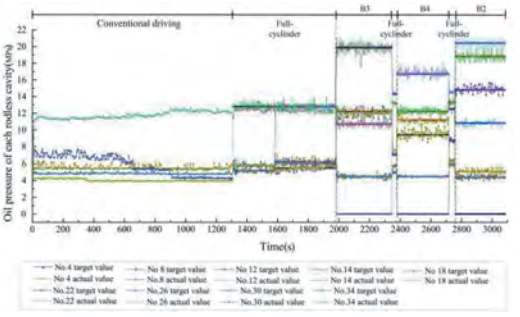

Figure 6. Oil pressure response of each cylinder in the whole process.

The total thrust force was generally stable during the synchronous period because of the effective responsiveness of the propulsion system to the target oil pressures (Figure 7), the error rate of which was controlled at ±3%. an interesting phenomenon was discovered that the total thrust showed a sudden drop and quick rebound when the hydro-cylinders in the range of the segment to be assembled retracted, and a quick fall after a rise when the abovementioned hydro-cylinders extended and touched the segment assembled. The fluctuation amplitude of the resultant vertical moment was more significant than its total thrust force, and a timely recovery after a sudden change also happed at the moment of mode switching.

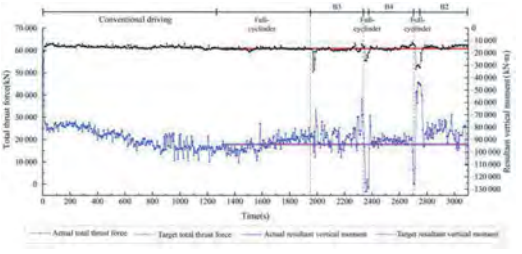

Figure 7. Total thrust vectors of shield propulsion system.

It could be observed from Figure 8 that the performance of the total thrust force when the hydro-cylinders retracted and extended reflected in the same pattern of changes in the shield speed, which was controlled at ± 5mm/min of the initial value, and small drops and rises were always allowable in the actual construction.

Different from the results of the model test, the fluctuation of the total thrust vector did not cause unstable changes in the shield postures due to the shield machine being wrapped in the surrounding soil. During the synchronous operation period, the shield postures in both horizontal and vertical directions were controlled at ± 10m of the target values. This result was within a completely acceptable range since the accuracy of the guidance system during conventional shield tunnelling is also 10mm.

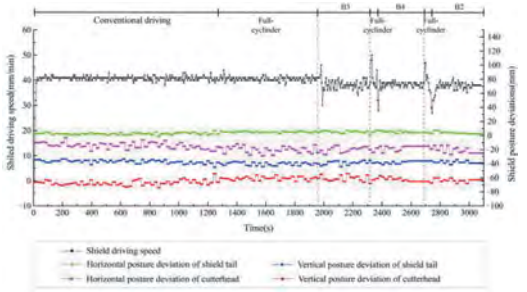

Figure 8. Shield tunnelling speeds and attitudes.

4 DATA ANALYSIS OF CONSTRUCTION EFFICIENCY

As shown in Figure 10, 351 rings were constructed in Lot 3 of Shanghai Airport Railway Link Line project in a month from December 4th, 2022 to January 4th, 2023 (a total of 31 days), which was also a tunnelling record (702m) of 14-meter slurry balanced shield machine in soft strata. An average of 11.3 rings per day and a maximum of 15 rings one day were achieved. Among them, 289 rings accounting for 82.3% were conducted by ACTT synchronous technology, and the rest 62 rings were done by the conventional method as the strategy of shield advancement firstly and waiting for the subsequent segments to be in place was adopted since the cleaning of shield tail grease took a long time, and the delay of the segment transportation inside and outside of the site was another main reason. Slurry pipe connection was a key factor affecting the construction efficiency, and a creative continuous connecting method as a supportive technology will be proposed in section 5.

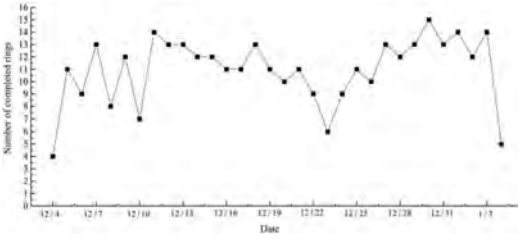

Figure 9. Number of rings completed for each day.

The cylinder stroke that could be used for synchronous segment assembly was a main factor affecting the construction efficiency of this technology, and the ideal cylinder strokes at the beginning and end of the synchronous operation were suggested to be 2200mm (200mm wider than the width of the pipe segment) and 3100mm for "Jiyue" shield machine, respectively. As shown in Figure 10, the end strokes were stably controlled at around 3000mm, while the starting stokes fluctuated slightly around 2250mm. Among them, 28 rings began to be assembled when the starting strokes exceeded 2500mm, which was mainly due to the failure to achieve the seamless shifting of duty between two working teams. The average values of the starting and end stroke were approximately 2280mm and 3006mm, respectively, which were both close to the ideal values, and average cylinder stroke of 706mm could be used for the synchronous operation.

Seen from the actual on-site construction, time management should be improved if other external factors were not considered, the hydro-cylinders in range of the first segment should wait to retract after the stroke of which exceeded about 1900mm since the hydro-cylinder retraction also took some time, and the grabbing of the first segment could be conducted in advance.

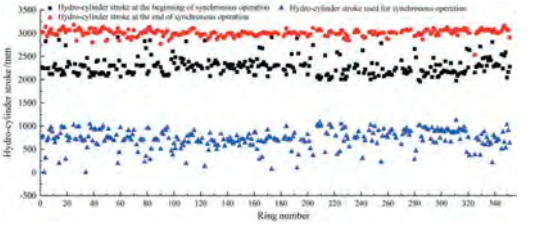

Figure 10. Usages of hydro-cylinder strokes in the synchronous operation mode.

Figure 11 provided the average shield driving speed for each ring. It can be seen that except four rings ranging from 321 to 324 with the speed approaching 60 mm/min, the speed for the remaining rings was generally controlled within the range of 40-50 mm/min, with an average of approximately 45.4 mm/min. The efficiency analysis of this synchronous technology (ZHU et al., 2023) indicated that although improving the shield driving speed would reduce the overlapping time, the total time spent on a single ring would still be shorten. After considering the performance and safety of the shield machine, as well as the disturbance to the ground, this project had decided to maintain the conventional driving speed and only explore the efficiency potential from the perspective of system management.

Given the stable shield speed, the variation of the overlapping time was similar to which of the hydro-cylinder strokes used for synchronous operation (see Figure 11), and approximately 18.11 minutes per ring was calculated to be an average value.

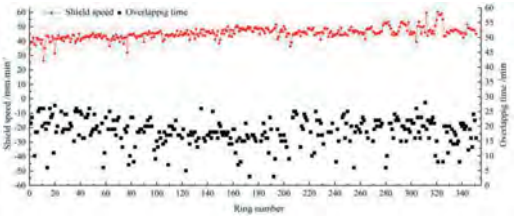

Figure 11. Shield speed and overlapping time for each ring.

Time consumptions of shield tunnelling and segment assembly for each ring were figured in Figure 12, and the average tunnelling time was about 45.0 minutes due to the stable driving speed.

The assembly time was obviously another main factor that affected the application efficiency of this synchronous technology, while the prerequisite of this technological development was to basically not change the operating habits of the construction teams, mainly by upgrading the control system and optimizing the operation process. Therefore, the workers of the three construction teams were not intentionally adjusted, the optimized operation method with high acceptance was verified to be simple and easy to understand. Finally, the assembly time for each ring was relatively discrete, with an average of about 57.0 minutes.

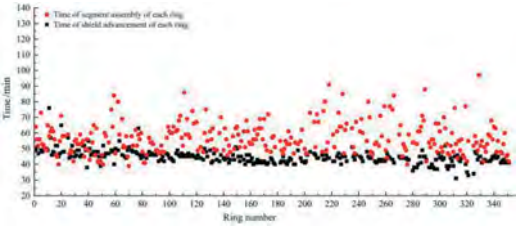

Figure 12. Time consumptions of shield tunnelling and segment assembly for each single ring.

The number of segmental blocks synchronously assembled for each ring was given in Figure 13. Apparently, it always took relatively longer time to install the first segment compared with the rest ones as no adjacent segments were available to assist in positioning. An average of approximately 2.4 blocks per ring (with a maximum of 5 blocks) was calculated to indicate that the proficiency level of the assembly workers significantly affected the number of the synchronously assembled blocks. Improving the proficiency in assembly operation or combining it with the upcoming automatic segment assembly technology would greatly improve the construction efficiency.

According to statistics, an average of 83.9 minutes was finally obtained adopting this synchronous technology for a whole ring, which was 27.0% shorter than the traditional operation time (average of about 115 minutes).

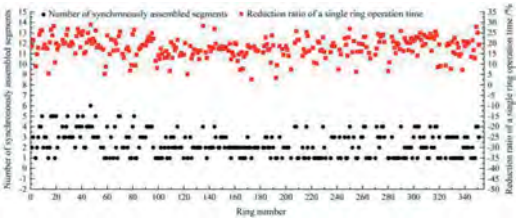

Figure 13. Numbers of segments assembled synchronously and efficiency promotion for each ring.

5 SUPPORTIVE TECHNOLOGY: CONTINUOUS CONNECTION METHOD OF SLURRY PIPES

During the advancement of the slurry balanced shield machine, the rigidity slurry pipes with no retractility has been fixed on the internal tunnel surface, and cannot move forward in the tunnelling direction. The pipeline has to be extended to ensure the circulation of the slurry feeding and discharging after shield driving a distance equal to the length of a pipe, which is always integral multiple of the corresponding segment width. The slurry circulation system has to be shut down, and the original pipeline path will be disconnected. Then, a new pipe will be welded between the front and rear ones. The entire connection operation may take approximately one to two hours, which is a repetitive and time-consuming process that plays an important role in the construction efficiency of slurry-balanced shield machines.

Therefore, it is extremely necessary to develop a continuous connection method of slurry pipes, i.e., integrating the connection time into the shield tunnelling. Then, an original continuous connecting technology of the slurry pipe was then proposed. As drown in Figure 14, a Y-typed branch pipe was designed through drilling a hole in the main pipe where a branch pipe was welded to. Then, two pipe systems including the main and auxiliary connecting devices with respective slurry hoses could be interchangeably employed.

As shown in Figure 15, the general operation process was as follows:

Step 1: the main slurry hose was connected to the main pipe by the main connecting device, and the auxiliary pipe system followed the same way, the main connecting device was at the forefront of the track at this point; the slurry circulation was switched in the main pipe system;

Step 2: shield tunnelling began, and the main and auxiliary connecting devices remained stationary relative to the tunnel; shield machine moved forward a distance exactly equal to the length of the slurry pipe;

Step 3: the shield machine continued moving, and the slurry circulation was switched in the auxiliary pipe system; after the main connecting device was pulled to the forefront of the track, the pipe connecting operation began;

Step 4: after the pipe connection was done, the slurry circulation was switched in the main pipe system; the auxiliary connecting device was pulled forward, and the auxiliary slurry hose was connected to the branch pipe as showed in step 1; one cycle of the work completed, repeat steps 1 to 4 until the tunnel construction was completed.

This continuous connection technology can greatly save time and cost, and is of great significance for improving the shield construction efficiency. The detailed operation procedures and control methods will be provided in the following research articles.

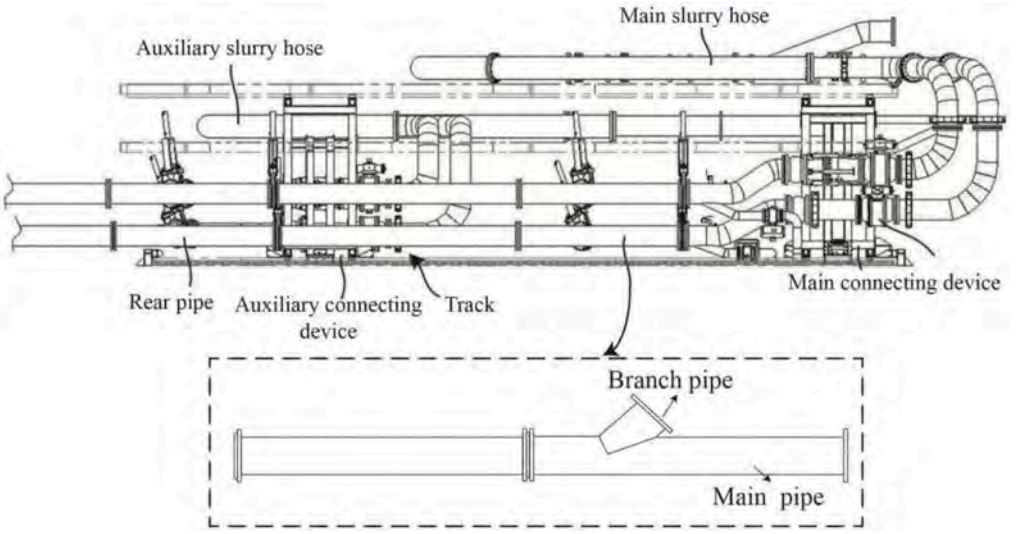

Figure 14. Y-typed slurry pipe.

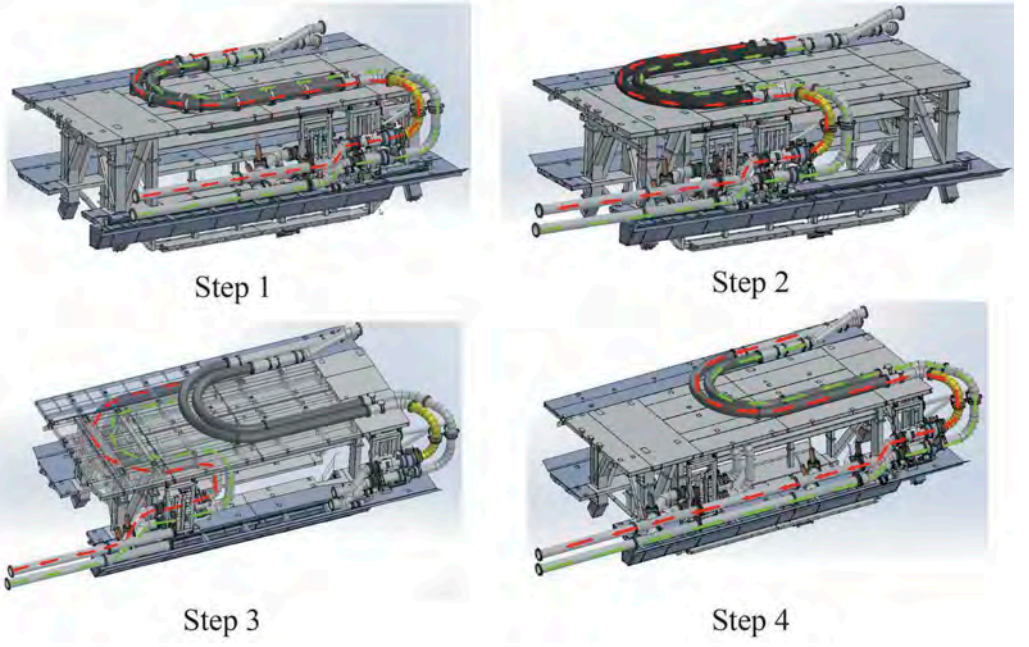

Figure 15. Continuous connection technology of slurry pipes.

6 CONCLUSIONS

A synchronous technology combining shield tunnelling and segment assembly was developed through the active closed-loop control on the oil pressure of the shield propulsion system. The effectiveness of the proposed technology was evaluated through onsite application in the Shanghai Airport Railway Link Line project. The major findings are given below:

(1) The response characteristics of the oil pressures of the propulsion system could be generally divided into three categories in the synchronous tunnelling mode. Benefiting from the accurate setting of the target thrust vector, the fluctuations of the propulsion oil pressures were overall stable, and no irregular jumping happened;
(2) During the synchronous operation process, the phenomena that the total thrust suddenly dropped and then quickly rebounded when the

oil cylinder retracted was observed, as well as a quick fall after a rise when the abovementioned hydro-cylinders extended and touched the segment assembled, the error rate of the total thrust was controlled at ±3%.

(3) Due to the sudden change in total thrust force, there was a synergistic change in the shield driving speed, but which was controlled within the set speed of ± 5mm/min. The shield machine was wrapped in the surrounding soil, and the shield posture was not sensitive to small changes of the total thrust vector, and was in a fully controllable range;

(4) On the premise of maintaining the conventional shield tunnelling speed, the starting stroke of the propulsion cylinder and the proficiency of the segment assembly workers were the main factors affecting the total operation time of a single ring. An average of 2.4 blocks were synchronously assembled in a ring, and the total operation time for a single ring taken by adopting this synchronous technology was reduced by approximately 27% compared with the traditional method.

(5) An original continuous slurry pipe connecting technology was proposed to integrate its operation time into the shield tunnelling, which as a supportive method could improve the construction efficiency furthermore.

ACKNOWLEDGMENTS

The research was supported by State-owned Assets Supervision and Administration Commission of Shanghai (Grant number 2022020), Shanghai Tunnel Engineering Co., Ltd. (Grant number 2023-SK-07) and Shanghai Shentong Metro Co., Ltd. (Grant number JS-KY23R009S).

REFERENCES

Ding W., Duan C., Zhu Y., et al., 2019. The behavior of synchronous grouting in a quasi-rectangular shield tunnel based on a large visualized model test. Tunnelling and Underground Space Technology, 83, 409–424.

Fukuakyosi, 2007. LoseZero method - partial synchronization shield construction method. Land Improvement, 45, 1–3.

Hiroshi S., 2005. Development of double hydro-cylinder type shield method (Part 3) -Application to gas conduit project connecting East and West (Futsu works). The 60th Annual Lecture of Civil Engineering Society,9, 193–194.

Hayashi Y., Ryunosuke K., Toshio S., 2008. Case introduction of F-NAVI high-speed shield construction method-construction examples of synchronous operation combining the shield tunnelling and segment assembling. Construction Machinery and Equipment, 44(8), 20–26.

Okumura K., 2006. "New technology flexible use system" won the best award, using the synchronous construction method of honeycomb segments. Construction Insights, 13, 1–4.

Suzumi S., Norihiko M., Kunio Y., 1999. Long distance shield tunnel construction by lattice tunneling method-project of Eizugawa River main line in Neyagawa River, Osaka Prefecture. Tunnels and Underground, 30, 717–724.

Wei G., Zhang X. H., Xu Y. F., et al., 2019. Prediction of Ground Settlement Due to Excavation of a Quasi-Rectangular Shield Tunnel Based on Stochastic Medium Theory. Geotechnical and Geological Engineering, 37(5), 3605–3618.

Yuan X. H., Zhu Y. F., Zhu Y. T., 2023. Test verification of synchronous technology combining shield tunneling with segment assembling based on the principle of maximum pressure redundancy. Modern Tunnelling Technology, 59(6), 106–113.

Zhang C., Li W., Zhu W., et al., 2020. Face stability analysis of a shallow horseshoe-shaped shield tunnel in clay with a linearly increasing shear strength with depth. Tunnelling and Underground Space Technology, 97, 103291.1–103291.19.

Zhu Y. T., Zhu Y. F., Chen E. J., et al., 2023 Synchronous shield tunnelling technology combining advancement and segment fabrication: Principle, verification and application. Underground Space, 13, 23–47.

Immersed tunnels

Taylor & Francis
Taylor & Francis Group
http://taylorandfrancis.com

Tunnelling for a Better Life – Yan, Celestino, Thewes & Eberhardt (Eds)
© 2024 The Author(s), ISBN 978-1-032-80042-4
Open Access: www.taylorfrancis.com, CC BY-NC-ND 4.0 license

Achieving sustainable immersed tunnel projects

Jonathan Baber*, BEng, CEng, FICE
Technical Director, Tunnels Practice Leader Australia, Mott MacDonald Ltd., Sydney, Australia

ABSTRACT: Guidance for applying sustainability targets and the Three-Rs principle of the circular economy to immersed tunnel projects has not been published to date. Principles have generally been developed project by project according to local practice. This paper consolidates work undertaken on immersed tunnel projects worldwide to give insight into the construction activities and project components that can be targeted to make a tangible benefit to carbon reduction. The two major material components for an immersed tunnel that have significant impact on the carbon usage during construction are the concrete works and the marine earthworks. Projects where extensive or wholesale re-use of dredged materials has been achieved during construction are described and the challenges explained. In particular, projects in Scandinavia have demonstrated success in this area with early planning by the projects Clients.

Immersed tunnels have particular requirements for watertightness and durability due to their marine environment. Historically this has driven the use of cement replacement material in concrete mixes to control heat of hydration during curing and to produce dense impermeable concrete. The reduction in cement gives a naturally improved carbon footprint but this outcome has been driven by other factors. This approach should now be used as a default for sustainable outcomes. Another area for consideration is the re-use of facilities for prefabrication of tunnel elements. The opportunity for this is outlined with case studies presented for successful examples. In addition some commonly applied initiatives such as the use of recycled aggregates are described and there applicability to immersed tunnels.

The paper gives Owners, designers and contractors some guidelines and case study examples showing how carbon reductions can be made to immersed tunnel projects. It highlights the items that need specific attention from Clients during the early planning of the project and the development contractual frameworks for delivery.

Keywords: Submerged tube, Sustainability, Reduce, Reuse, Recycle, embodied carbon

1 INTRODUCTION

The three Rs of the circular economy – Reduce, Reuse and Recycle - are a long established foundation of sustainability thinking. They are applicable across a multitude of industries, but the detail of how they can be realised within a specific industry is necessarily different. There are well developed strategies in place and continually emerging initiatives for the construction industry due to the ever-increasing focus on sustainability, managing greenhouse gas emissions and minimising the embodied carbon in construction projects.

Guidance for specific subsectors is not always available and for niche construction methodologies there can be a need for new thinking each time. In the case of immersed tunnel projects, this is a unique and distinct construction methodology of which there are fewer than 200 examples in the transport sector worldwide, so understandably, there is no specific guidance published to date. However there are some significant opportunities available to enable a highly sustainable approach, and there are some excellent examples of initiatives taken in the past that meet the three R's principles. This paper aims to draw together some guidance on these opportunities, illustrated by some past examples, so that clients, planners, designers, builders and operators can consider them and hopefully deliver their immersed tunnel projects in a sustainable manner.

It also reviews how immersed tunnels compare to other forms of tunnel, how ongoing industry initiatives can be applied, which forms of immersed tunnel offer the most carbon efficient solutions, how specific considerations can be made in design to reduce embodied carbon, and draws attention to previous immersed tunnel projects that have adopted good sustainable approaches. It looks at the opportunities for

*Corresponding author: jonathan.baber@mottmac.com

DOI: 10.1201/9781003495505-310

extending asset life that are specific to immersed tunnels, and makes some recommendations for clients to consider in future project development.

It is not the intention to discuss efficiency in operation, or the broader benefits of transport corridors. Nor is it the intention to look at the different frameworks that can be applied for managing sustainability, as these are much broader topics.

2 WHY CHOOSE AN IMMERSED TUNNEL

Immersed tunnels historically have often been chosen as a solution to overcome particular circumstances. For example there are a number of projects where an immersed tube tunnel was selected in preference to a bridge that might interfere with airport flight paths. They have also been selected where land is not available for the long approaches required for a deeper bored tunnel, where there is soft marine geology, or where multi-modal transport solutions are required with multiple tunnel tubes. More recently there have been a number of projects where immersed tunnels have been found to be the optimal solution on cost and environmental grounds, such as the Fehmarnbelt Tunnel in Denmark. But what about from a sustainability perspective? If this were to be the key driving criteria for selection would an immersed tunnel be favoured over other forms of construction?

To answer this question a comparison was made between the immersed tunnel and bored tunnel design solutions developed as options for the Silvertown tunnel in the UK during the early planning phase. This comparison considered the river crossing element of the project only and the main construction components of concrete, earthworks and interior fill/mass concrete. The conclusions drawn from the study were:

- Concrete volumes: The bored tunnel utilised 43% more reinforced concrete. It is noted that the use of SFRC in the bored tunnel lining concrete would improve the carbon footprint for the bored tunnel. However, there is greater opportunity for use of substitute cementitious materials (SCM) in the immersed tunnel. These two opportunities broadly balanced in the assessment of embodied carbon. Hence the volume increase remains a significant factor.
- Infill beneath the roadway: The bored tunnel utilised >300% more imported material vs the mass concrete required in an immersed tunnel. However granular fill in the bored tunnel will have significantly lower embodied carbon per m^3 compared to mass concrete.
- Earthworks spoil: The immersed tunnel generated >100% more spoil. The impact of this will be largely determined by whether a beneficial re-use of materials from either the immersed tunnel dredging or the bored tunnel excavated spoil can be realised.

The conclusion from the comparison was that the bored tunnel required a 40-50% increase in embodied carbon compared to the immersed tunnel. This difference is primarily driven by the fact that the bored tunnel overall length is approximately 50% greater due to the extra depth required for the bored tunnel. Therefore the benefit of utilising an immersed tunnel solution in keeping the overall tunnel length as short of possible is clearly an advantage to minimising material quantities and therefore embodied carbon.

2.1 *Concrete vs steel immersed tunnels*

Two main structural forms are available to immersed tunnel projects – concrete or steel. Although it should be noted that concrete tunnels contain a high proportion of steel and, vice versa, steel shell tunnels rely on a high volume of structural concrete. Many immersed tunnel projects have undertaken options studies in their early stages to confirm the optimal structural form from the point of view of cost. This is often done by contractors bidding Design and Construct contracts, where cost is the primary driver, as means to secure a contract. But what about the relative sustainability benefits? Using one such past study it is simple to compare the embodied carbon between two solutions.

The project utilised for this was the Marmaray Tunnel beneath the Bosphorus Strait in Istanbul, a twin bore rail tunnel. During the tendering of this project a comprehensive options study was prepared looking at alternative structural forms - reinforced concrete, single steel shell, and double steel shell. Multiple cross section shapes were also considered, but for this comparison the most economic rectangular section for the reinforced concrete tunnel was compared to the curved binocular cross section for the steel single and double shell solutions as these were the most cost effective options considered. These tunnel sections are shown in Figure 1.

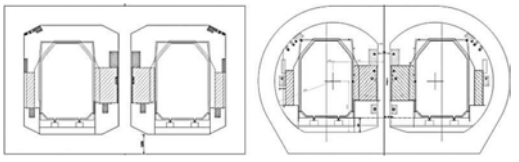

Figure 1. Marmaray tunnel options study cross sections.

The primary components of the construction were considered only, namely the structural and mass concrete, reinforcement, structural steel, and formwork. The marine earthworks and casting facilities were taken as common across all solutions. The conclusions drawn from the comparison were:

- The reinforced concrete tunnel was the most carbon efficient design.
- The segmental form of reinforced concrete construction is slightly favourable compared to

a monolithic form of construction due to the heavier reinforcement requirement in the monolithic tunnel elements.
- The double shell steel sandwich construction required 10% more carbon useage than the reinforced concrete solutions.
- The single steel shell tunnel required 17% more carbon useage than the reinforced concrete options.

So in this instance the reinforced concrete solution is seen to offer the best solution for minimum embodied carbon. It happens that this was also the conclusion of the cost evaluation between the solutions. Whilst this is informative, the project specific circumstances and local market conditions will always need to be taken into account for any particular project. What the study shows however is that the differences are relatively small and so it is worthwhile to make this type of detailed comparison to arrive at a clear conclusion for a specific project.

3 OPTIMISING IMMERSED TUNNEL DESIGN

There are some key topics to consider when optimising the design of an immersed tunnel to achieve a sustainable outcome. These are predominantly associated with minimising embodied carbon but some relate to re-use opportunities. They are:

- Reinforced concrete
- Mass concrete
- Steelwork
- Earthworks re
- Temporary works
- Tunnel element casting facilities

3.1 *Reinforced concrete*

The majority of recent immersed tunnels have been built as reinforced concrete structures. There are two forms of concrete tunnel that can be adopted: 1) using segmental tunnel elements with regular articulation joints through the structure at 20-25m spacing, and 2) using monolithic tunnel elements where articulation can occur at the immersion joints between the tunnel elements only.

A tunnel with monolithic tunnel elements will have a significantly higher reinforcement content to carry longitudinal bending moments in the tunnel structure. It will also feature an external membrane to achieve watertightness. There are circumstances where this type of structure is preferred for the site conditions but there is likely to be a modest cost penalty. In addition there will be an increased embodied carbon with this type of structure due to the increase in material quantities.

3.1.1 *Optimisation of concrete vs steel*

In the design process for an immersed tunnel structure, the normal optimisation of concrete sections takes place in the transverse design of the tunnel cross section. This is the same process irrespective of whether the tunnel elements are segmental or monolithic. However there is a design step before this section optimisation is performed that is to balance the cross section to achieve the desired buoyant behaviour. This ensures the tunnel elements are able to float in the temporary condition, be immersed with the application of a sensible amount of water ballast, and then be secured against permanent uplift using ballast concrete within the tunnel.

Often the sizing of the tunnel cross section results in thicker sections than would be needed for structural adequacy. The temptation to optimise the structural sections further and manage buoyancy using other means is strong and deemed to be beneficial to achieving low cost solutions. However is this the correct approach for an optimal sustainable design solution?

To test this a simple parametric study was undertaken for a typical load level on a structural slab. The section thickness was gradually reduced and reinforcing steel increased to maintain a constant section capacity. Total embodied carbon was then measured for the resulting quantities and the results can be seen in Figure 2. It can be seen that there is a sweet spot for minimum embodied carbon where the balance of section thickness vs reinforcement ratio is optimal. In the example investigated, it can be seen that this is typically when reinforcement ratios are in the order of 250kg/m^3 to 300kg/m^3. For the thick sections in an immersed tunnel structure this is actually quite a high reinforcement content. It shows that there is merit in slimming down the sections beyond what is needed just for structure buoyancy control. However as soon as the reinforcement design begins to feature multiple layers of large diameter reinforcement bars or bundles of bars it can be seen that the overall embodied carbon will begin to increase rapidly compared to a moderately reinforced thicker section.

To incentivise designers to reach the optimal embodied carbon, mechanisms could be introduced within the contract requirements to ensure designers demonstrate that the sustainability objectives are being achieved. A possible approach to this would

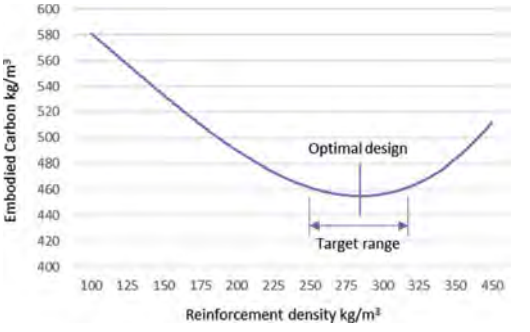

Figure 2. Idealised curve indicating optimal reinforcement density.

be to require that structural design aims to achieve the optimal point of the steel-concrete sustainability curve within a tolerance of, say, +/-10%. This could be easily demonstrated in the design output using simple automated algorithms to enable quick efficient testing of designs section by section, or for the structure as a whole, to show they are in the desired range. This approach would not be specific to immersed tunnel projects of course and could be adopted more widely.

3.1.2 *Cement replacement in concrete mixes*

High percentages of cement replacement materials have been used in concrete mixes for immersed tunnel structures for decades. This is because immersed tunnels are designed to be watertight structures, and to achieve this with the thick sections required (to carry the external loading on the structure) requires a sophisticated approach to concrete curing. In many countries a simplistic approach to controlling thermal gradients in the concrete during curing has been used in conjunction with the application of an external membrane or permanent prestressing of the structure. In Europe a more sophisticated approach of cooling the concrete by passing chilled water through a network of embedded cooling pipes has been adopted. For either approach it is highly beneficial to minimise the heat of hydration in the concrete and this is done by replacing Portland Cement with GGBFS or PFA. Cement mixes with up replacement levels in the order of 70% have therefore been relatively commonplace.

However, in recent years tunnel structures have become wider with larger internal spans to accommodate greater number of traffic lanes, meaning structures are working harder. Coupled to this, longer tunnels using factory style production techniques demand higher concrete strength and early strength gain to support rapid construction programmes. Also in general terms there is a continued drive for achieving structural efficiency and reducing cost that has often resulted in thinner structural sections and higher reinforcement ratios. These factors mean that high cement replacement ratios may not be preferred as they result in slower strength gain.

However, compared to optimising section thickness where typically a 10% improvement in embodied carbon may be achieved for a 20% thickness reduction, significant gains can be made by using cement replacement materials. Moving from zero SCM content to 70% SCM content will give in the order of 50-60% reduction in embodied carbon. To realise these benefits clients need to be firm in their requirements for achieving a target cement replacement content. If, say, a 70% target was mandated, the tunnel can still be designed, programmes can still be achieved, and the cost premium is likely to be small. This has already been demonstrated in many immersed tunnel projects and so can be considered an achievable approach.

3.1.3 *Recycled aggregates*

It is quite feasible for recycled aggregates to be used in immersed tunnel structures but this has not been widely adopted or investigated. The challenge is to obtain clean reliable materials with the necessary mechanical and durability characteristics in the locality of a project. One concern for an immersed tunnel structure however is the potentially increased porosity of recycled concrete aggregates, as noted by Panda et al. This could be detrimental to achieving the desired low permeability concrete and protection against chloride penetration through the outer cover zone of the structure.

There is however a large quantity of mass concrete used in immersed tunnels for ballasting the structure and this lends itself to the use of recycled materials. There are few durability concerns and only low strength requirements for this component of the tunnel. This could even become a mandatory requirement for projects.

3.2 *Mass concrete*

There is opportunity to use high cement replacement material content in mass concrete used for permanent ballasting of the tunnel. The concrete does not have a high strength or performance requirement. In addition, as mentioned above, recycled aggregates could easily be used. Typically a layer of concrete in the order of 1m thick is placed throughout the width and length of the tunnel, so this accumulates to an appreciable volume of concrete and so it is important to explore these opportunities for a good sustainable outcome. There could be a cost penalty for this and so Clients should consider mandating requirements or incentivising contractors to go down this path.

3.3 *Steelwork*

As mentioned above there is a fundamental choice in the structural form of an immersed tunnel that is taken at a very early stage of design. Contractors may have a preference according to their experience, or the solution may be driven by the market conditions. In recent years the majority of tunnels have been built as reinforced concrete structures being the most competitive market solution.

However, there are other steelwork components used in all forms of immersed tunnel, notably the immersions joints that typically feature a cast-in steel frame to aid the accurate seating of Gina and Omega sealing gaskets. These details have evolved in time and are important for the correct functioning of the joint. Although reducing the amount of steelwork is a good objective, optimisations will result in relatively limited gains and care should be taken in this area to ensure the desired performance is achieved. Initiatives to omit the steelwork need to be considered extremely carefully.

3.4 *Earthworks*

The construction method for an immersed tunnel requires the dredging of a trench beneath a waterway in which the tunnel elements are progressively placed and backfilled. The nature of dredged material can vary considerably according to the particular site conditions. In marine, estuarine and river environments there is typically a degree of soft alluvial material that must be removed. In harbour and industrial areas there can be a layer of material that is contaminated and may require special treatment. One of the main challenges for an immersed tunnel project is to aim to re-use the material either within the project or for a designated purpose. This is a significant issue for immersed tunnels that should be carefully and continually addressed through the project development and delivery stages.

3.4.1 *Re-use within the project*

The ability to reuse dredged material depends on a number of factors:

- Suitability for engineering fill material
- Suitability for use as general fill material
- Presence of contaminants or unsuitable content
- Availability of land for temporary storage
- Need for treatment e.g. settling, drying, screening
- Practicality of handling material from the dredger

Assessing the suitability for different uses is an important part of early the planning work. Ground investigation along the marine alignment will be required for this. Backfill for the tunnel comprises different components that will have a different level of opportunity to consider re-use, described in Table 1.

Table 1. Opportunities for dredge material re-use.

Marine earthwork	Opportunity for re-use
Sand foundation layer	This has a carefully selected grading curve to facilitate pumping and limit consolidation settlement. Opportunity if dredging uniform sands.
Gravel foundation layer	This has a carefully selected grading for placing and mechanical properties of the placed layer. Unlikely opportunity to use of dredged spoil.
Engineering fill adjacent to tunnel structure	Material will need to be granular and largely self-compacting on placement. Opportunity if dredging granular material.
General fill away from the tunnel structure	Material has few requirements other than reinstation the bed level. Opportunity for use of all dredged material.
Transition layers between backfill and rock protection layer	Will have carefully selected grading to meet filter requirements. Opportunity if dredging granular material.
Rock protection above the tunnel	Rock size will depend on protection requirements, usually large size stones meeting grading for layer stability and load dissipation. Not suitable for re-use of dredge materials.

Once a determination has been made of the possibility for re-use the next challenge is to address the practicalities. It is unlikely to be practical to dredge material and immediately place it in its final re-use position. Even if a very long tunnel is being constructed, and the material can be re-used directly without treatment, the plant for placing the material may need to be very different to the barges typically used to carry away spoil from the dredging operation. This infers that double or triple handing of the material may be needed, and land be available for temporary storage. This is generally the reason why dredged materials are not re-used in the works as backfill as the volumes of material are large and so the practicality of stockpiling (on land or at sea) for re-use may make this unachievable.

If a project client wants to achieve this outcome it may therefore come at a cost, and they will need to provide early support with the relevant land acquisition, environmental investigations and approvals if needed. They may also need to mandate the solution in the contract. Otherwise the building contractor will likely prefer to simply dispose of the dredged material and import new material.

Nevertheless, the opportunity for re-use and the need for treatment of the spoil, storage facilities, handling facilities etc. should be considered as part of any project's planning, so that the project client can make a conscious decision for the project. If left to builder to solve the issue, the best commercial outcome will likely drive the solution which may be sub-optimal for carbon usage.

3.4.2 *Use in reclamation works*

A more likely approach to managing the dredged spoil is to investigate the possibilities for re-use on another part of the project. On many immersed tunnel projects dredged spoil has been used for creation of reclamation in which the tunnel approaches are constructed. An example of a pro-active approach to this is the Jack Lynch Tunnel in Cork, Ireland where spoil was used to create a new area of landscaped public amenity alongside the River Lee, see Figure 3. The reclaimed land was also used for the temporary casting basin for tunnel element construction. This was a solution decided by the project client from the outset and the necessary work to understand the impacts to the river flow regime was undertaken early to assess environmental impacts and obtain planning approval.

A similar approach was taken for the Øresund Tunnel in Denmark where the Kastrup peninsula was extended for the construction of the tunnel approach. In addition, the dredged limestone was used for the creation of an artificial island that served as the transition between the immersed tunnel and the bridge,

Figure 3. Reclaimed southern approach at Jack Lynch Tunnel.

see Figure 4. This approach, again dictated by the project client, enabled full re-use of the dredged material. Major sea crossings of this type that feature artificial islands particularly lend themselves to this re-use philosophy.

Figure 4. Artificial Island on Øresund Tunnel project.

3.4.3 *Off-site beneficial re-use*

A further option is to look for opportunities for beneficial re-use outside of the project. Two examples illustrate this well. During construction of the Limerick Tunnel in Ireland material dredged from the river bed was removed and stored in a purpose built lagoon and settlement area adjacent to the tunnel site. The settlement area and lagoons have been subsequently converted into a permanent wetland area for wildlife.

On a larger scale the Fehmarnbelt Tunnel construction will generate some 19million m^3 of dredged sand and clay materials that will stored and re-used, partially to reinstate the construction facilities but also to create new beach areas, flood protection dykes, coastal lagoons and wetlands, for environmental, wildlife and recreational benefits.

3.5 *DfMA principles*

There are many elements of an immersed tunnel project that lend themselves to a Deign for Manufacture and Assembly (DfMA) approach. Arguably when factory casting methods are used the whole construction process becomes a DfMA production process that maximises material and carbon efficiency. On a conventional project where the tunnel works are effectively insitu works, there can still be opportunity that is not often realised:

- Mass concrete infill beneath roadways could be largely precast blocks, with a final topping layer applied to form the base to the running surface asphalt.
- Internal structural walls could be prefabricated as often they are lightly loaded, are thinner and more lightly reinforced than the tunnel perimeter walls and slabs.
- Immersion joint infill sections that are complex to cast insitu can be precast beneath the road construction and also for walls and roof.
- Suspended floors in service galleries should be precast.

Steel fibre reinforced concrete (SFRC) is not generally used in immersed tunnel structures as the structural capacity requirements for the main tunnel structure requires conventional reinforcing. However, for the elements of the structure that can be considered for DfMA this may be a reasonable approach.

3.6 *Temporary works*

A growing trend amongst the specialist marine contractors who construct immersed tunnels is to manufacture temporary works items that can be re-used from project to project. Items such as ballast tanks, bulkheads, temporary tunnel element supports, access towers survey equipment and specialist barges can be adapted for different projects and the impact of transporting them to a new location is considerably less that fabricating new items for each project. One of the best examples is the Multi-purpose pontoon designed and built for the Øresund Tunnel project for laying the gravel bed foundation and placing backfill. This has subsequently been used on multiple immersed tunnel projects around the world.

3.7 *Casting facilities*

A variety of facility types can be used for casting the tunnel elements of an immersed tunnel. Historically the industry has often taken the approach to leave it to the builder to determine the most economical solution. If the objective is to arrive at the most sustainable solution, then clients need to take the initiative in this respect and identify the opportunities for a project.

3.7.1 *Use of dry docks*

The use of a dry dock is highly advantageous for reducing cost and achieving a fast construction programme as it avoids the need to construct a new facility. Recent tunnels that have taken this approach include the Maasdeltatunnel in Rotterdam, Netherlands, and the 2nd Midtown tunnel in the USA, see Figure 5. This is a highly sustainable approach.

Figure 5. 2nd Midtown Tunnel dry dock, Virginia USA.

One concern often voiced is that ready-made facilities are not available in the locality of the construction site. However, the cost and risk of towing tunnel elements, even up to hundreds of kilometres, is small so the search for a suitable dock can be quite wide. Political and economic drivers for the work to be carried out in a specific country may also come into the decision making of course.

3.7.2 *Use of quarries*
This is slightly less common as quarries adjacent to waterways are not plentiful. However, the Shek O quarry in Hong Kong is an example where a disused quarry has been used for the construction of multiple immersed tunnel projects in the region. Again this is a highly sustainable approach.

3.7.3 *Use of casting basins*
Many immersed tunnel projects have utilised purpose-built casting basins. This is not a good sustainable approach as a large volume of work and material is required. Therefore, this should be the last resort approach. However, if a Re-Use approach is taken then this could become a sustainable approach. A successful example is the Barendrecht casting basin in the Netherlands that has been retained as a facility specifically for immersed tunnel projects and has been re-used multiple times. Another example of re-use is the casting basin at the Conwy Tunnel in the UK, see Figure 6. This was created for the project to build the tunnel element in but afterwards was converted to a marina which in turn stimulated the development of housing and community facilities at the location.

3.7.4 *Use of factories*
Casting factories are economic for large and long immersed tunnel projects but require high carbon useage to construct the factory. If a programme of tunnel works is envisaged, then such a facility could be beneficial for following projects, but this is a relatively unusual circumstance. Unfortunately, the factory built for the Øresund Tunnel (Figure 7) which was the first of its kind, has never been able to be re-used but there should be greater opportunity with the factory being built for the Fehmarnbelt

Figure 6. Conwy Marina (tunnel approach in foreground).

Tunnel. The factory built for the HZMB tunnel in Hong Kong has been re-used for the Shenzen-Zhongshan tunnel, albeit with modification, and is a good example of re-use through innovative thinking. The factory was built initially for a concrete segmental tunnel and it has been converted for carrying out the concreting operations for a steel double shell sandwich type monolithic tunnel.

Figure 7. Øresund Tunnel casting factory.

4 EXTENDING ASSET LIFE

Immersed tunnels are relatively simple structures. The most complex items are the immersion joints but the design and construction methods for these is well established, and provisions are readily made to ensure durability for the desired design life. However, experience in their application is necessary to carry through lessons from previous projects. It is not an area to be over-experimental with given the sensitive nature of the details for maintaining water-tightness of the tunnel.

Durability provisions for immersed tunnels typically include:

- Concrete mixes feature high cement replacement materials content (GGBFS or PFA) that provides improved heat of hydration performance of the concrete to limit early age cracking, and also

reduces permeability to increase the resistance to chloride penetration through the outer cover zone of the concrete section;
- Additional concrete additives such as silica fume to further introduce fines to the concrete matrix and enhance resistance to chloride penetration;
- Cathodic protection systems are applied to steelwork elements of immersion joints. These can be relatively simple passive systems e.g. connection of sacrificial anodes for cathodic protection;
- Choice of materials for non-replaceable components e.g. uses of high grade stainless steel for embedded items and inaccessible items in immersion joints;
- Structural health monitoring systems are often used. In particular embedded probes to detect chloride ingress and predict corrosion potential. These measure the progression of chloride to enable a choice of when to activate additional protective measures;
- Provision for future intervention is common. This is typically the welding of reinforcement cages and provision of connection points to enable a cathodic protection system to be installed in the future should chloride penetration reach a level that risks onset of corrosion.

Steps are usually taken to protect the asset in the event of extreme or accidental event, such as:

- Passive fire protection is generally applied to the interior of the tunnel. This is to protect against catastrophic collapse from progressive spalling of concrete in the tension zones to the underside of roof slabs.
- Structural adequacy is designed for extreme events such as flooding, fire, explosion, internal vehicle impact and external vessel collision/sinking such that the asset can remain in service or be readily returned to service with minimal disruption.
- In seismic regions there would usually be a performance requirement to maintain the integrity of the structure and joints such that the asset can remain in service or be quickly returned to service. This requires careful design of the immersion joint details to prevent opening and water inundation occurring.

Measures can be implemented to enable ease of inspection and maintenance. As described by Baber et al (2009), access can be provided to the voids formed at immersion joints for camera inspections and for water ingress detection, and measures implemented to manage potential water ingress at the joints. Standardisation of the approach to extending asset life across immersed tunnel projects globally would be beneficial. Not all clients and their advisors are aware of the possibilities that exist, and reference to publications such as the ITA Owners Guide to Immersed tunnels (Annex 25 Cathodic Protection & Annex 32 Durability) is encouraged.

5 CLIENT AND CONTRACT INITIATIVES

Based on the issues and opportunities identified, some recommendations for clients are:

- Consider sustainability outcomes in scheme selection giving it appropriate weighting in MCAs at the early stage of project development e.g. steel tunnels vs concrete tunnels and bored tunnel vs immersed tunnels.
- Set ambitious targets for cement replacement in concrete mixes.
- Request design submissions to demonstrate optimal (minimum) embodied carbon in primary elements of the construction – concrete, steel, earthworks.
- Do sufficient early preparation to identify pre-existing facilities that can be used.
- Do sufficient early preparation to facilitate re-use of earthworks in the construction or in environmental enhancement projects e.g. reclamation and habitat creation.
- Reward contractors through appropriate contract mechanisms for achieving, and going beyond, sustainability targets.

6 CONCLUSIONS

Some excellent examples of good practice with regard to sustainability exist on immersed tunnel projects around the world. By distilling these lessons frameworks can be developed to inform new projects about the possibilities and to help drive some consistent thinking for future immersed tunnel projects. Table 2 summarises the opportunities on immersed tunnel projects that can be considered to maximise the response to the principles of circular economy in construction.

Table 2. Summary of immersed tunnel sustainability opportunities.

3 Rs	Opportunity	Impact
Reduce	Cement replacement materials	High
	Steel/concrete balance	Medium
	Shortest possible tunnel length	High
	DFMA principles	Medium
	Factory casting	High
Reuse	Casting facilities	High
	Earthworks re-use	High
	Recycled aggregates	Medium
	Temporary plant and equipment	Medium
Recycle	Extending asset life	Medium

There are clear benefits that can be realised by early consideration. Project Clients can play the strongest role in realising these benefits, by giving full consideration in the early stages of a project development and encapsulating requirements and incentives into project scopes and specifications.

ACKNOWLEDGMENTS

Mott MacDonald's in-house PAS 2080 certified Moata Carbon Portal tool has been used for the measurement of embodied carbon for the comparisons made in this paper.

REFERENCES

Marine Works operations and Environmental Considerations when Building the Fehmarnbelt Tunnel/ J Anderson, C Iversen, E v Putten/Terra et Aqua | Number 127 | June 2012.

Proceedings of the Fifth Symposium on Strait Crossings, Trondheim, Norway, 2009/Maintenance Considerations for Immersed Tunnels, with particular reference to the Bjørvika Tunnel, J.Baber, L. Narvestad,.

ITA report no.7 An Owners Guide to Immersed tunnels - N° ISBN:978-2-9700858-7-4/April 2022.

ITA Immersed Tunnels in the Environment, Working Group 11 publication, www.ita-aites.org

Lunniss, R., & Baber, J. (2013). Immersed Tunnels (1st ed.). CRC Press. ISBN: 9780415459860.

The Use of Recycled Aggregates on Mechanical Properties of Concrete: A Review: S. Panda and T. Jena 2022 IOP Conf. Ser.: Earth Environ. Sci. 982 012027.

Tunnelling for a Better Life – Yan, Celestino, Thewes & Eberhardt (Eds)
© 2024 The Author(s), ISBN 978-1-032-80042-4
Open Access: www.taylorfrancis.com, CC BY-NC-ND 4.0 license

Research on fire resistance limit standard of steel-encased concrete immersed tunnel structure

Peng Cao*
College of Water Resource & Hydropower, Sichuan University, Chengdu, China
China Merchants Chongqing Communications Technology Research & Design Institute Co., Ltd., Chongqing, China

Shenyou Song
Shenzhen-Zhongshan Channel Management Center, Zhongshan Guangdong, China

Mengjun Wu
China Merchants Chongqing Communications Technology Research & Design Institute Co., Ltd., Chongqing, China

Shouchao Jiang
College of Civil Engineering, Tongji University, Shanghai, China

Enlong Liu
College of Water Resource & Hydropower, Sichuan University, Chengdu, China

ABSTRACT: The Shenzhen-Zhongshan Passage is a super-large cluster project integrating "bridge, island, tunnel and underwater interchange". The submarine immersed tunnel, main works of the Passage, follows the two-way eight-lane technical standard. It is a new steel-encased concrete composite structure, with both technical indicators and project scale at the world's leading level. For the steel-encased concrete immersed tunnel, the steel case has dual functions, i.e. waterproofing and load bearing. So, its stability under fire and high temperature is of great significance to the safety of the entire tunnel structure. At present, researches on fire resistance limit standards for tunnel structures are mostly focused on reinforced concrete structures. It is lack of relevant technical reserves for how to establish fire resistance limit standards for steel-encased concrete immersed tunnel structures. This paper proposes a fire resistance limit standard for steel-encased concrete immersed tunnels through standardized research and analysis and high-temperature mechanical testing: for steel-encased concrete composite structures, the fire resistance time in the RABT standard temperature-time curve test is not shorter than 2 hours. (1) For the main segment structure, the maximum temperature of the steel case surface should be lower than or equal to 300°C within 2 hours of fire resistance; (2) for the waterstop of the segment joint, the maximum temperature of OMEGA and GINA waterstops should be lower than or equal to 150°C, and the resistance time for temperatures above 100°C should not be longer than 1h and that for above 70°C should not be longer than 2h.

Keywords: Immersed tunnel, composite structure, fire resistance limit, segment structure, segment joint

1 INTRODUCTION

The steel-encased concrete immersed structure is an application direction of steel concrete composite structure in immersed tunnels. As it is seldom used in projects at present, its fire resistance has been studied scarcely. The existing studies and specifications on fire resistance of steel concrete composite structures focus on composite components in building structures. Therefore, the research on the fire resistance limit standards for steel-encased concrete immersed tunnel structures can further improve the fire protection regulations for immersed tunnels and provide references for subsequent research on the fire resistance of composite structures of immersed tunnels.

At present, there are few standards for the fire resistance limit of tunnel structures and most research results are based on the fire resistance performance and

*Corresponding author: caopeng1@cmhk.com

DOI: 10.1201/9781003495505-311

protective measures of tunnel structures under the existing fire resistance limit standards. For example, Chen Changqing [1] et al. verified the effectiveness of the designed fire prevention nodes through the fire resistance limit test with full-scale specimens. Li Pingli [2] et al. developed a fire protection decoration system for immersed tunnels of steel-encased structure, of which the fire resistance performance was tested with the 2h RABT temperature-time curve. Xi Yang [3] et al. conducted the fire mechanical response test on the scaled (1:3) components in the roof structure of the steel-encased concrete immersed tunnel, selected the RABT fire standard temperature-time curve and found in the test that the mechanical properties of the steel significantly deteriorated at 300 °C.

The studies on rubber waterstops for immersed tunnel segment joints were also limited to mechanical properties, durability and fire protection design. For example, Chen Zhonghai [4] et al. conducted the thermal oxygen accelerated aging tests and stress relaxation tests on OMEGA rubber and the results showed that both the rubber material and the waterstop product had a design service life of 120 years. Peng Liqun [5] et al. studied the effects of rubber hardness, compression deformation and specimen length on compression load and stiffness as well as the effect of compression displacement on stress relaxation changes. Tuo Yongfei [6] et al. carried out the numerical simulations for tunnel lining segments under three different fire conditions and found that the waterstop would be burnt and damaged when the maximum temperature near the inner waterstop was close to 300 °C under operating conditions if a fire lasted for 2h without fire prevention measures; the waterstop was safe when its maximum temperature should be kept below 100 °C if there is a 30mm-thick fireproof plate for protection and a fire lasted for 2h. However, the above studies have not addressed the fire resistance limit standards for the waterstop of immersed tunnels.

In allusion to main segment joint structure of steel-encased concrete immersed tunnel, this paper proposes a method of researching and analyzing the fire resistance limit standards and specifications at home and abroad so as to summarize and obtain the fire resistance limit standards of the main segment joint structure. The high-temperature mechanical test is adopted for OMEGA and GINA waterstops at the segment joints of steel-encased concrete immersed tunnels to consider the waterproof characteristics of the waterstop rubber and explore the tensile strength, elongation at break, modulus, compression set and stress relaxation of the waterstop rubber at different temperatures. Then, the experimental results are analyzed to obtain the fire resistance limit standard.

2 FIRE RESISTANCE LIMIT STANDARD FOR MAIN SEGMENT STRUCTURE

The existing fire resistance limit determination criteria are studied to obtain the fire resistance limit standards for the main segment structure of steel-encased immersed tunnels:

The Permanent International Association of Road Congress (PIARC) [9] and the International Tunnelling Association (ITA) [10] have recommended the fire resistance limits for main load-bearing structures and some ancillary structures of tunnels based on the type of tunnel structure, working environment, traffic type, etc. The Code for Fire Protection Design of Buildings (GB 50016-2014) [11] divides tunnels into four categories based on their lengths and traffic conditions and specifies the fire resistance limit requirements for each category. The requirements for immersed tunnel structures in these suggestions or regulations are shown in Table 1.

Table 1. Fire resistance limits for immersed tunnel structures.

Institution/ Specification	Condition	Fire resistance target of main structure	Fire resistance target of ventilation duct	Fire resistant target of escape exits
PIARC	Small car	1h (ISO)	1h (ISO)	0.5 h (ISO)
	Large car	2 h (RWS/ HCinc)	2 h (ISO)	0.5 h (ISO)
ITA	Small car	1h (ISO)	1h (ISO)	0.5 h (ISO)
	Large car 1-2	2 h (RWS/ HCinc)	2 h (ISO)	0.5 h (ISO)
	Large car >2	3 h (RWS/ HCinc)	2 h (ISO)	0.5 h (ISO)
GB 50016	Class I tunnel	2 h (RABT)	—	—
	Class II tunnel	1.5 h (RABT)	—	—
	Class III tunnel	2 h (HC)	—	—

There are few profound studies on the criteria for determining the fire resistance limit state of tunnel structures. Some domestic and foreign standards or regulations, e.g. Technical Code for Concrete Filled Steel Tubular Structures (GB 50936-2014) [10], specify the practical calculation method for the fire resistance limit of concrete-filled steel tubular components, of which the temperature fields of the components are calculated and the material data at different temperatures are introduced to calculate the ultimate bearing capacity of the components. The Code for Fire Protection Design of Buildings (GB 50016-2014) and Code for Fire Protection Design of Tall Buildings (GB 50045-1995) [11] also specify the fire resistance limits of concrete-filled steel tubular components, but there is no research on the determination criteria for fire resistance limit of steel-encased concrete immersed structures. Determination criteria for structural fire resistance limit in some national tunnel fire resistance codes are shown in Table 2.

Table 2. Determination criteria for fire resistance limits of some national highway tunnel structures.

Country	Specification/standard	Fire temperature-time curve	Determination criteria		
			Concrete surface	Steel reinforcement	Steel case
Netherlands	2008-Efectis-R0695	RWS	< 380°C	<250°C	—
USA	NFPA 502	RWS	< 380°C	<250°C	< 300°C
Austria	OVBB	RWS	< 350°C	<250°C	—
France	CETU	HCM	< 380°C	<250°C	—
Germany	ZTV-ING	RABT	—	<300°C	—
China	GB 50016	RABT、HC	< 380°C	<300°C(RABT) <250°C(HC)	—

According to the prescribed fire temperature-time curves, these temperature determination criteria can be divided into three categories: RWS fire temperature-time curve represented by the Netherlands, including USA, Austria and other countries; RABT fire temperature-time curve represented by Germany, and HC or HCM fire temperature-time curve represented by France. These fire temperature-time curves are shown in Figure 1.

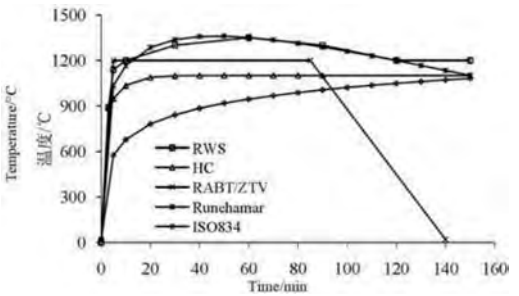

Figure 1. Common fire temperature-time curves for tunnels.

The criteria for determining the fire resistance limit of concrete are 380 °C in the Code for Fire Protection Design of Buildings (GB 50016-2014) and NFPA 502 [12]. For steel bars, the national standard - Code for Fire Protection Design of Buildings (GB 50016-2014) stipulates that: the temperature of the steel bars at a distance of 25mm from the bottom surface of the concrete is critical when the RABT temperature rises to 300 °C and the HC temperature rises to 250 °C. NFPA 502 specifies that the temperature of the steel bar at a distance of 25mm from the bottom surface of the concrete rises to 250 °C of the critical state.

By comparing the fire resistance limit determination criteria for tunnel structures between the national standard - Code for Fire Protection Design of Buildings (GB 50016-2014) and NFPA 502, it has been found that NFPA 502 stipulates that the temperature of the steel case cannot be higher than 300 °C, while no relevant regulation is provided in the Code for Fire Protection Design of Buildings (GB 50016-2014).

In summary, based on the analysis of the determination criteria for fire resistance limit of highway tunnel structures at home and abroad, the fire resistance time determined by the RABT standard temperature-time curve test should not be shorter than 2h for steel-encased concrete composite structures and the maximum temperature of the steel case surface should be lower than or equal to 300 °C within 2h of fire resistance for main segment structures.

3 FIRE RESISTANCE LIMIT STANDARD FOR SEGMENT JOINT WATERSTOPS

In order to obtain the fire resistance limits of OMEGA and GINA rubber waterstops at the segment joints of steel-encased immersed tunnels, the model test has been carried out for OMEGA and GINA rubber waterstops.

3.1 *Preparation of specimens*

Refer to relevant provisions of the Rubber, Vulcanized or Thermoplastic - Determination of Tensile Stress-Strain Properties (GB 528-2009) [13] and the Rubber, Vulcanized or Thermoplastic - Determination of Compression Set at Ambient, Elevated or Low Temperatures (GB 7759-1996) [14]. OMEGA and GINA rubber is used to make dumbbell-shaped tensile specimens to perform the high-temperature tensile testing and make cylindrical compression specimens to perform the high-temperature compression testing, as shown in Figures 2 and 3.

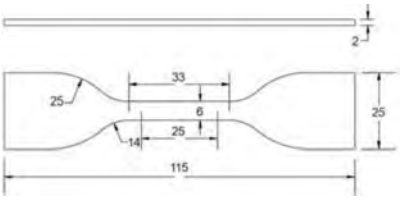

Figure 2. Dumbbell-shaped tensile specimen (unit: mm).

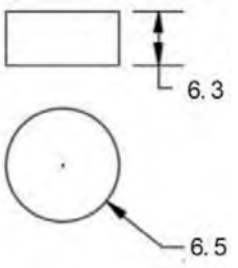

Figure 3. Cylindrical compression specimen (unit: mm).

3.2 *Test conditions*

The conditions for tensile performance test and compression test of OMEGA and GINA rubber waterstops are detailed in Tables 3 and 4.

Table 3. Tensile test conditions.

Test type	High-temperature duration	Test temperature/°C
Determination of high-temperature tensile strength, elongation at break and modulus of rubber	The movement speed of the tester gripper is 500 ± 50mm/min and the time is subject to the point that the specimen is pulled apart.	20 40 55 70 85 100 125 150 175 200 225 250
Determination of tensile strength, elongation at break and modulus of rubber after high-temperature cooling	2h	40 70 100 150 200
Determination of tensile strength, elongation at break and modulus of rubber after high-temperature stress cooling	2h	40 70 100 150 200

3.3 *Test method*

The test is conducted with an electronic universal tester. As shown in Figures 4 and 5, the specimen should be placed in a constant temperature box before testing, the dumbbell-shaped tensile specimen should be preheated for 6 minutes while the cylindrical compression specimen for 2 hours. The test is performed after the predetermined operating temperature is achieved. The tensile strength, elongation at break and modulus are obtained through tensile tests. Then, the high-temperature compression set and compression stress relaxation trends of OMEGA and GINA rubber waterstops are mainly obtained through compression tests.

Table 4. Compression test conditions.

Test item	High-temperature duration	Temperature/°C
OMEGA rubber - Determination of compression set at high temperature	24.0h	20 40 70 100 150 200
OMEGA rubber - Determination of compressive stress relaxation at high temperature	24.0h	20 40 70 100 150 200
GINA rubber - Determination of compression set at high temperature	24.0h	20 40 70 100 150 200
GINA rubber - Determination of compressive stress relaxation at high temperature	24.0h	20 40 70 100 150 200

Figure 4. Electronic universal tester for tensile test.

4 ANALYSIS OF RESULTS

4.1 *Analysis of tensile test results*

The changing trend of tensile strength as function of temperature is shown in Figure 6 and 7. The high-temperature tensile test shows that the tensile strength shows a decreasing trend as the temperature rises. When the thermal treatment temperature is lower than

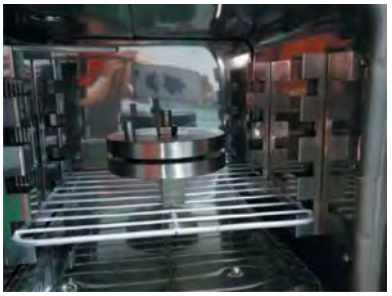

Figure 5. Electronic universal tester for compression test.

or equal to 150 °C, the tensile strength of OMEGA and GINA rubber waterstops after high-temperature cooling is basically the same as that of direct tensile fracture at room temperature, and the high-temperature cooling process has no effect on the tensile strength of OMEGA and GINA rubber waterstops. When the temperature is higher than 150 °C, the tensile strength at break decreases significantly after high-temperature cooling and the physical properties of the rubber waterstops undergo significant changes. The tensile strength characteristics of OMEGA and GINA rubber waterstops after high-temperature stress and cooling are basically the same as those after high-temperature cooling. Within the test temperature range and under the stress level, the stress during the high-temperature process has little effect on the tensile strength of OMEGA and GINA rubber waterstops after high-temperature cooling.

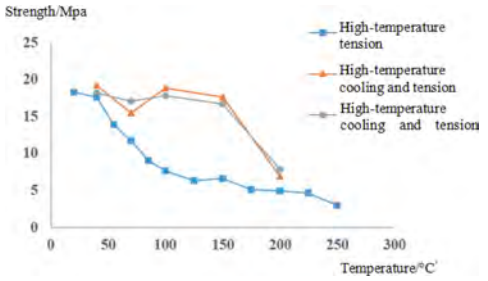

Figure 6. Tensile strength of OMEGA rubber waterstop.

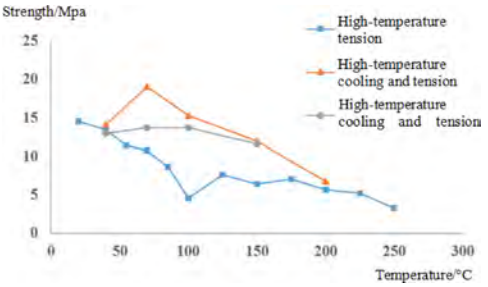

Figure 7. Tensile strength of GINA rubber waterstop.

The changing trend of elongation at break as function of temperature is shown in Figure 8 and 9. The high-temperature tensile test shows that the elongation at break presents a decreasing trend as the temperature rises. When the thermal treatment temperature is lower than or equal to 150 °C, the elongation at break of OMEGA and GINA rubber waterstops after high-temperature cooling is basically the same as that of direct tensile fracture at room temperature, and the high-temperature cooling process has substantially no effect on the elongation at break of OMEGA and GINA rubber waterstops. When the maximum temperature is higher than 150 °C, the elongation at break decreases significantly after high-temperature cooling and the physical properties of the rubber waterstops undergo significant changes. Within the test temperature range and under stress level, the stress during the high-temperature process has little effect on the elongation at break of OMEGA and GINA rubber waterstops after high-temperature cooling.

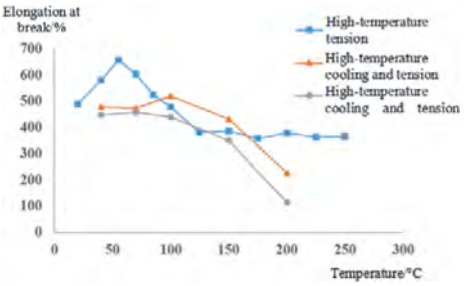

Figure 8. Elongation at break of OMEGA rubber.

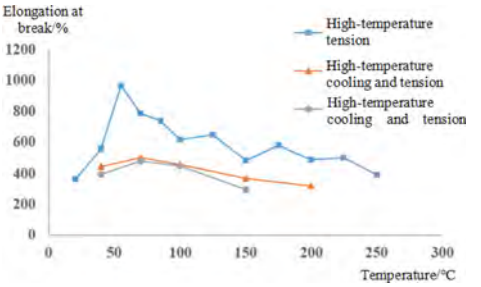

Figure 9. Elongation at break of GINA rubber.

The changing trend of modulus as function of temperature is shown in Figures 10-13. The high-temperature tensile test shows that 100% and 300% moduli present a decreasing trend along with the rise of temperature. The modulus of OMEGA and GINA rubber waterstops decreases along with the rise of temperature. When the thermal treatment temperature is lower than or

equal to 150 °C, 100% and 300% moduli after high-temperature cooling are basically the same as when direct break at room temperature. The high-temperature cooling treatment has no effect on the moduli of OMEGA and GINA rubber waterstops. When the temperature is higher than 150 °C, 100% and 300% moduli after high-temperature treatment and cooling present a significant increase and the physical properties of the rubber undergo a significant change. Within the test temperature range and under stress level, the stress during the high-temperature process has little effect on the modulus of OMEGA and GINA rubber waterstops after high-temperature cooling

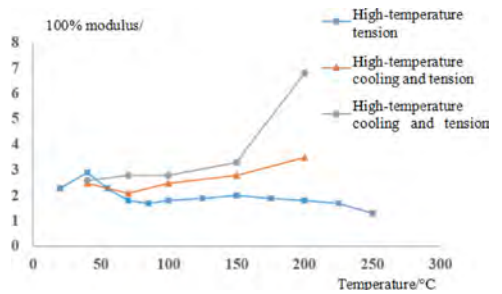

Figure 10. 100% modulus of OMEGA rubber.

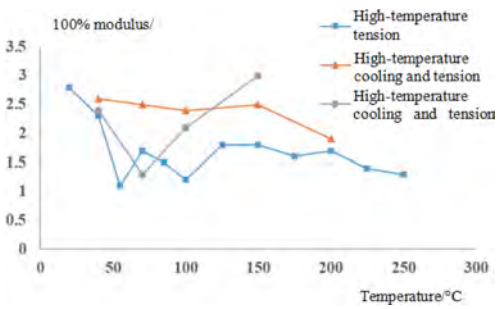

Figure 11. 100% modulus of GINA rubber.

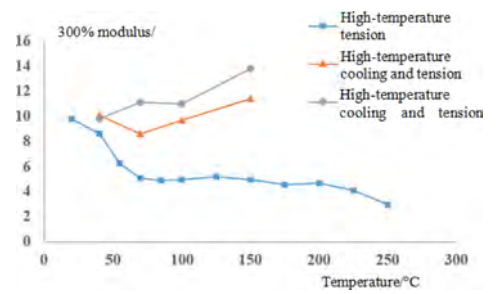

Figure 12. 300% modulus of OMEGA rubber.

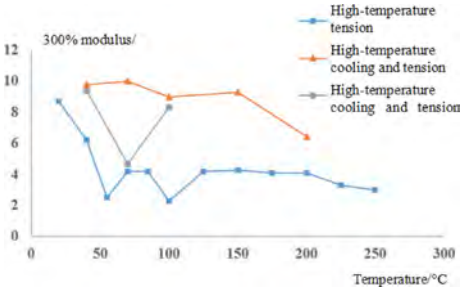

Figure 13. 300% modulus of GINA rubber.

4.2 *Analysis of compression test results*

The mechanical properties of OMEGA and GINA rubber waterstops are consistent in compression tests. As the temperature increases, the compression stress relaxation and compression set of the rubber present an upward trend. The compression set is about 25% at 100 °C and increases sharply to 65% at 150 °C, as shown in Figures 14 and 15.

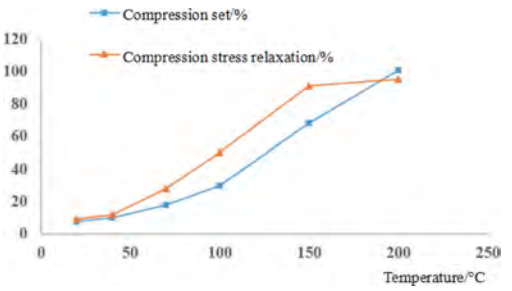

Figure 14. Compression test of OMEGA rubber.

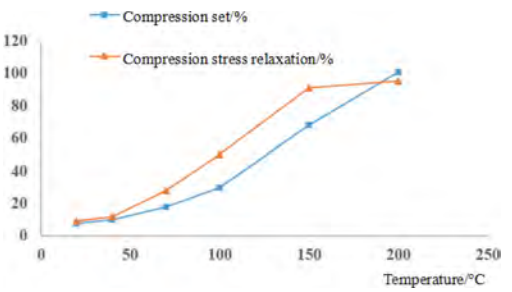

Figure 15. Compression test of GINA rubber.

5 CONCLUSIONS

This paper proposes a fire resistance limit standard for steel-encased concrete immersed tunnels through research and analysis of current fire resistance limit

standards and specifications for tunnel structures, as well as high-temperature mechanical tests of rubber waterstops at segment joints. For steel-encased concrete composite structures, the fire resistance time tested through the RABT standard temperature-time curve is not shorter than 2h. The conclusions are as follows:

For the main segment structure, the maximum temperature of the steel case surface must be lower than or equal to 300°C within 2 hours of fire resistance;

The high-temperature tensile test of rubber waterstops at segment joints shows that the tensile strength of OMEGA and GINA rubber waterstops decreases along with the rise of temperature. When the temperature is higher than 150 °C, the tensile strength at break decreases significantly after high-temperature cooling and the physical properties of the rubber waterstops undergo significant changes.

The high-temperature compression test of rubber waterstops at segment joints indicates that the mechanical properties of OMEGA and GINA rubber waterstops are consistent in compression tests. As the temperature increases, the compression stress relaxation and compression set of the rubber present an upward trend. The compression set is about 25% at 100 °C and increases sharply to 65% at 150 °C.

For the waterstop of the segment joint, the maximum temperature of OMEGA and GINA rubber waterstops should be lower than or equal to 150°C, and the resistance time for temperatures above 100° C should not be longer than 1h and that for above 70°C should not be longer than 2h.

ACKNOWLEDGMENTS

This research was financially supported by the National Key Research and Development Program of China (No.2018YFCO809600), the National Natural Science Foundation of China (No. 52127814), Natural Science Foundation of Chongqing (CSTB2022NSCQ-MSX1656).

REFERENCES

Chen Changqing, Tong Anqi, Wei Zhikai. The design and fire endurance text for fire protection system of immersion joint[C]. Chinese Society of Civil Engineering. Proceedings of the 2020 Academic Annual Meeting of the Chinese Society of Civil Engineering. China Construction Industry Press, August 2020.

LI Ping-li, MAO Chao-jun, ZHANG Ze-jiang,etc.Fire protection technology of caisson tunnel with steel shell structure[J]. Fire Science and Technology, 2018,37 (11): 1510–1512.

Xi Yang. Mechanical Behavior of A Composite Structure with Steel-shell and Concrete Under High Temperature of Fire[D]. Chongqing Jiaotong University, 2022.

Chen Zhonghai OMEGA, rubber waterstop for immersed tunnel. Zhuzhou Times New Materials Technology Co., Ltd., Hunan Province, 2012-05-12.

Peng Liqun, Luo Yonghuan, Wu Xinglei, etc.Mechanical Property Test of Gina Seal Blet in Immersed Tunnel[J]. Special rubber products, 2020,41 (04): 56–60.

Tuo Yongfei, Shu Heng, Guo Xiaohong, etc.Fireproof characteristics of lining and waterproof of shield tunnel with super-large diameter[J]. Journal of Geotechnical Engineering, 2013,35 (S1): 269–274.

Fire Protection Standard for Highway Tunnel Structures [R] International Road Association 2007:190–203.

Russell H A.Ita GUIDELINES FOR STRUCTURAL FIRE RESISTANCE OF ROAD TUNNELS[J].Routes/roads, 2004(324):p.72–81.

Code for Design of Buildings Fire Protection [S] Beijing: State Planning Commission of PR.China, 2014.

Technical Specification for Steel Pipe Concrete Structures [S]. Beijing: Construction Industry PR. China, 2014.

Code for fire protection design of tall buildings [S] Beijing: State Planning Commission of PR.China, 2014.

Standard for Road Tunnels, Bridges, and Other Limited Access Highways[J].NFPA 502,2017.

Determination of tensile properties of vulcanized rubber and thermoplastic rubber. [S] Beijing: China standard press, 2009.

Rubber, Vulcanized or thermoplastic - Determination of compression set at ambient elevated or low temperatures. [S] Beijing: China standard press, 1996.

K. H. Tan, C. Y. Tang. Interaction Model for Unprotected Concrete Filled Steel Columns under Standard Fire Conditions. Journal of Structural Engineering. 2004, 130(9): 1405~1413.

Timo Inha. A Simple Method for the Structural Fire Design of Composite Structures. Proc. of an Engineering Foundation Conference on Steel-Concrete Composite Structures. New York, the Structure Division of the ASCE, 1992: 210~223.

Kodur, V. K. R. Performance-Based Fire Resistance Design of Concrete-Filled Steel Columns. Journal of Constructional Steel Research,1999,51:21–26.

T. T. Lie. Fire and buildings. Applied Science Publishes LTD. 1972.

R. Hass. On Realistic Testing of the Fire Protection Technology of Steel and Cement Supports. Translations of BHPR/NL/T/1444. 1991:171.

W. Klingsch. New Developments in Fire Resistance of Hollow Section Structures, Symposium on Hollow Structural Sections in Building Construction. ASCE, Chicago Illinois, 1985: 1–34.

Haack A. Fire protection in traffic tunnels: General aspects and results of the EUREKA project[J]. Tunneling and Underground Space Technology, 1998,13 (4):377–381.

Tunnelling for a Better Life – Yan, Celestino, Thewes & Eberhardt (Eds)
© 2024 The Author(s), ISBN 978-1-032-80042-4
Open Access: www.taylorfrancis.com, CC BY-NC-ND 4.0 license

Stability and deformation analysis of dry dock slope in Haihe Tunnel, Tianjin, China

Chun Ning He*, Ying Qu, Er Chun Qing & Jie Qing Shen
Shanghai Tunnel Engineering & Rail Transit Design and Research Institute, Shang Hai, China

ABSTRACT: This paper mainly deals with the stability and deformation of dry dock slope in Haihe Tunnel, Tianjin, China. For a dry dock to be built in soft soil, the key issue is to set the correct calculation model and use the correct calculation method to develop a safe and economical slope gradient and the proper structure of the slope to meet the requirement of overall schedule and the cost control. The slope gradient of Haihe Tunnel was calculated by limit equilibrium method, then based on the data of vertical and horizontal displacements monitored on site in construction, the study on the whole deformation shape of the slope was carried out. And the monitored data was compared with the theoretical analysis results calculated by PLAXIS. From the analysis conducted in this study, the maximum settlement occurs on top of the slope, about 0.6% of the excavation depth; the maximum horizontal displacement also occurs on top of the slope, about 0.72% of the excavation depth; during construction, the whole slope behaviour changes with the excavation of the slope in different stages. Based on data monitored on site, corresponding empirical formula in expressions of time are set up to predict the deformation of the slope.

Keywords: dry dock, slope stability, settlement, horizontal displacement, slope behaviour

1 INTRODUCTION

The dry dock is named as a place in which the tunnel elements of Haihe Tunnel were prefabricated, see Figure 1. The stability of dry dock is essentially a problem of slope stability. While it is different from the general slope and also different from the general excavation, it is necessary to maintain the stability of the dry dock slope during excavation and also during the construction of the elements. Generally, the whole period as mentioned above will be about two years, much longer than the average exposure time of any other general excavations.

According to the requirements of element fabrication, floating and outfitting, the excavation depth of the dry dock is 11.8m; the bottom transverse width is 157.8 m, and the axis length is 115 m. The complex geological conditions and the poor mechanical properties of the soil on site make the project more complex.

Based on the background of the dry dock slope in Haihe Tunnel, methods such as the Sweden slice method and the Bishop method were used to calculate FS (factor of safety) of the slope in different conditions, to determine the appropriate slope gradient, to carry out the general design and detail design of the slope. The whole slope was completed in six months. In the construction process, deformation data of the slope with time were monitored and recorded in detail. Then the finite element method was used and the corresponding results obtained were compared with the data monitored on site. On this basis, the distribution of the deformations of the whole slope could be studied and the empirical formulas for the deformation of the slope could also be obtained, see Figure 2.

2 COMPLEX GEOLOGICAL CONDITIONS

The soil layers within the dry dock belong to quaternary new series. Different era and genetic types result the soil on site being different both in horizontal and vertical directions. According to the geological investigation report, from top to bottom, the soil layers mainly constitute of 1-1 backfill, 2-1 clay, 2-2 silty clay, 3-1 silty clay, 3-3 alluvial clay and 3-4 soft clay sublayers, see Figure 3.

The mechanical properties of the soil are generally poor, mostly soft or very soft soils with large natural water content, and are in the soft plastic ~ plastic flow state with high compression and low strength, see Table 1.

*Corresponding author: he.chunning@stedi.com.cn

DOI: 10.1201/9781003495505-312

Figure 1. View of a dry dock for an immersed tube tunnel.

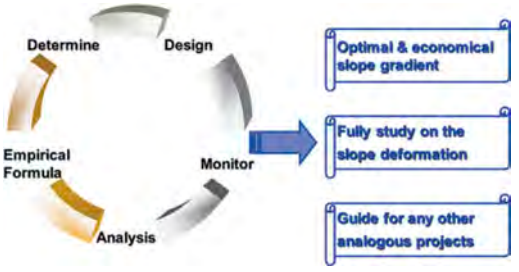

Figure 2. Research objective.

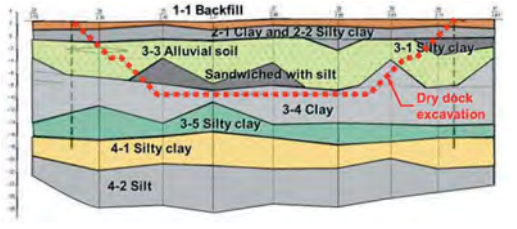

Figure 3. Transverse geological profile of dry dock.

Table 1. Main physical and mechanical parameters.

					CD test	
	Sublayer	ω (%)	γ sat (kN/m^3)	e	c' (kPa)	φ' (kPa)
2-1	Clay	33.1	18.8	0.94	20.33	18.67
2-2	Silty clay	32.0	18.8	0.91	17.00	14.60
3-1	Silty clay	34.4	18.5	0.97	19.10	20.01
3-2	Silt	26.7	19.2	0.79	13.13	25.60
3-3	Alluvial soil	43.2	17.7	1.22	12.40	14.82
3-4	Clay	40.5	17.9	1.15	14.44	14.08
3-5	Silty clay	26.4	19.6	0.74	15.25	24.03
4-1	Silty clay	27.5	19.8	0.77	19.76	19.91
4-2	Silt	22.6	20.1	0.65	18.50	23.24
4-3	sand	20.0	19.9	0.63	0	32.1

3 DETAIL CALCULATION AND DESIGN

3.1 *Calculation model*

Based on limit equilibrium, the Swedish slice method and the Simplified Bishop method were carried out separately. Totally nine slope gradients and three different methods were assumed for analysis and comparison, to determine the final appropriate slope gradient. Nine slope gradients were considered from 1:3.0 to 1:7.0. Three different methods were considered as total stress analysis (TSA), effective stress analysis (ESA) and effective stress analysis with seepage.

Groundwater was considered as 1.0 m below the ground level.

3.2 *Calculation results and comparisons*

The overall calculation results of different slope gradients in different methods are shown in Table 2; corresponding curves are shown in Figure 4.

Table 2. Calculation results.

	Swedish slice method			Simplified Bishop method		
Slope gradient	TSA	ESA	with seepage (ESA)	TSA	ESA	with seepage (ESA)
1:3.0	1.61	2.63	1.11	1.74	2.81	1.14
1:3.5	1.75	2.87	1.25	1.86	3.03	1.27
1:4.0	1.91	3.09	1.40	2.03	3.18	1.45
1:4.5	2.09	3.01	1.55	2.19	3.11	1.61
1:5.0	2.24	2.92	1.73	2.36	3.06	1.77
1:5.5	2.43	2.93	1.9	2.55	3.06	1.95
1:6.0	2.59	3.08	2.00	2.7	3.18	2.09
1:6.5	2.77	3.23	2.15	2.88	3.31	2.26
1:7.0	2.97	3.38	2.40	3.09	3.46	2.45

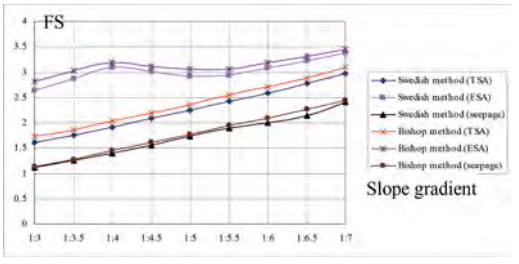

Figure 4. FS in different slope gradients and different methods.

Both the Swedish slice method and Simplified Bishop method regard the slip surface as a circular surface, owing to the brief concept and being able to analyse the slope stability under complex conditions, the methods above are widely used. Because of different assumptions, distinct differences can be found

comparing the two calculation results. The Swedish slice method neglects the interslice forces, results a lower value of FS than the Simplified Bishop method. Generally speaking, for TSA, ratio of the FS obtained by the Simplified Bishop method to the FS obtained by the Swedish slice method is between 1.04 ~ 1.08; for ESA, the ratio is between 1.02 ~ 1.07; and for ESA with seepage, the ratio is between 1.02 ~ 1.05. So for layered soils or in complex conditions, the Swedish slice method should be used combined with the Simplified Bishop method.

For the project, most part of the slope is in the range of soft clay. Because of the low permeability of the soils, during construction process, it's impossible or very difficult to exclude the porewater in the soils, resulting in decreasing the effective stress of the soils and generating seepage force along the slope from the top to the bottom, increasing the sliding force and decreasing the anti-sliding force. Also the above calculation results as ESA with seepage reveal this phenomenon. Therefore, ESA method should be used to determine the stability, considering the impact of porewater pressure, and also this is the most adverse condition.

3.3 *Comprehensive evaluation of slope stability*

In the process of slope design, not only the stability should be taken into account, but also the economy of the project. High factor of safety would lead to large cost in project. Considering the dry dock project as a temporary work, taking unit investment for slope gradient as 1:3.0, the investments of the other slope gradients could be obtained in proportion with the excavation volume, and the cost effective ration as FS/cost could also be obtained, see Figure 5.

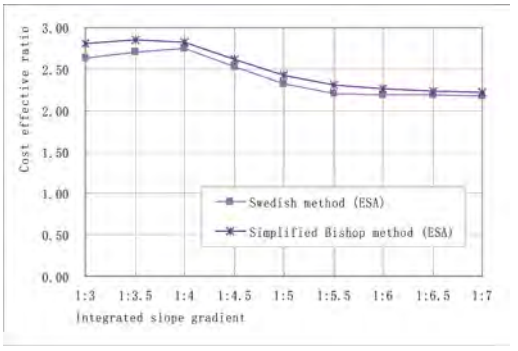

Figure 5. Cost effective analysis for slope gradients.

In ESA analysis, the cost effective ratio rose up with the slope gradient, and at 1:3.5 and 1:4.0 it reached the peak value. After that it decreased with the increasing of the slope gradient. Through the cost effective ratio analysis, it's obvious that 1: 3.5 and 1:4.0 were the appropriate slope gradients for the project. For more safety, slope gradient 1:4.0 was adopted.

3.4 *Slope design*

The whole slope was under three excavations, with 1.5 m wide terrace located between each level. φ700 mm diameter soil cement piles were built up around the dry dock, with a pile length of 20.5 m, reaching into the 4-1 impermeable layer of clay, to form a closed area, which could not only act effectively as waterproof curtain, but could also enhance the whole stability of the slope, see Figure 6.

Protection measures were taken into account as the slope of the dry dock standing for quite a long exposure time. Transverse arc-shaped concrete beams and vertical concrete beams were poured on the slope surface with 80mm thickness C20 reinforced concrete inside. Bamboos were inserted in the concrete beams at spacing 1500 mm, embedded 2 ~ 3 m depth into the soil as to enhance the surface stability, see Figure 7.

Dry dock can be considered as a large excavation, so the drainage system is an important part of design. Drainage system in dry dock can be classified as the surface drainage system and underground drainage system.

Surface drainage system as drainage holes were set on the surface of the slope to dissipate water pressure inside the soil. In the second and the third terrace, 300×200 mm transverse gutter were built up, connecting with the longitudinal gutters, to drain the water into the bottom gutters and finally into collection wells. Underground drainage system named as blind ditch, which was made of φ100 mm diameter PVC pipes with open holes on its surface and laid perpendicular to the gutters at the bottom of the dock, was mainly used to exclude the groundwater in the soil.

4 MONITORING AND ANALYSIS

Continuous monitoring was carried out from the beginning of the excavation to the completion of the slope. The monitoring data for typical sections were analysed and put into figures, including the vertical and horizontal displacements. The whole slope was with three excavations, each excavation including curing of the concrete lasted about 10 days.

In vertical displacement curves, positive displacement means upheaval, negative displacement means settlement; in horizontal displacement curves, positive displacement means displacement towards the excavation direction, negative displacement means displacement reverse to the excavation direction.

4.1 *Deformation relationship of the whole slope*

During the whole period, the vertical displacement of the points on top of the slope and the points in the middle of the first slope show settlements, while the other points on the slop show upheavals or both settlements and upheavals. The maximum settlement occurs

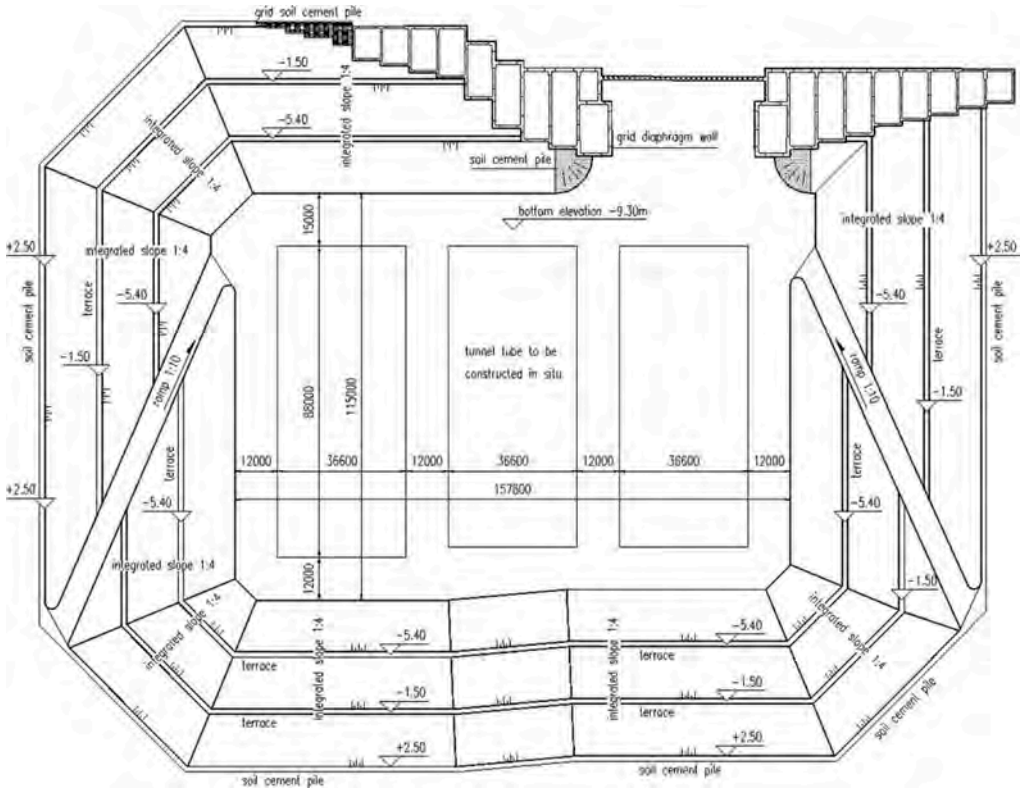

Figure 6. General layout of the dry dock.

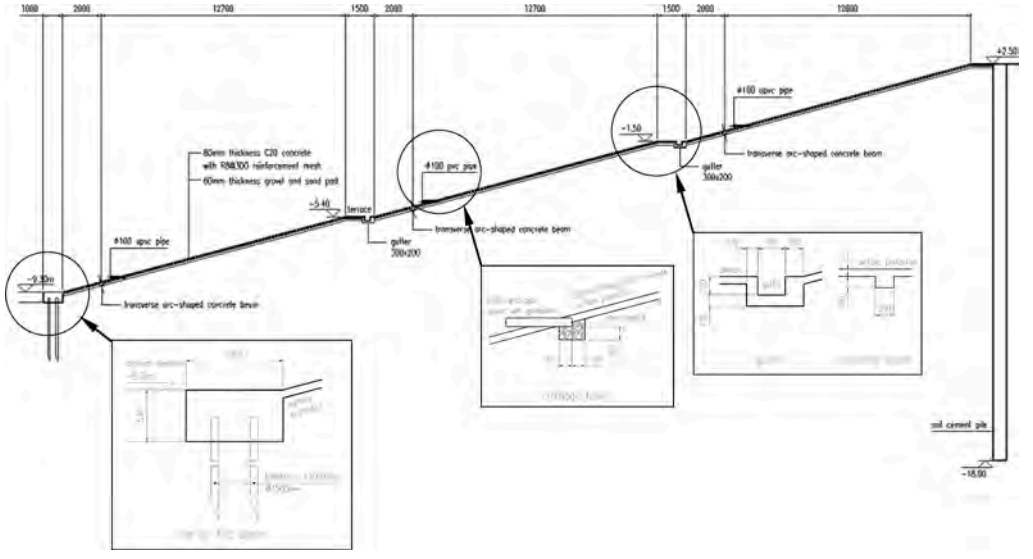

Figure 7. Profile and detail design.

on top of the slope, and the settlement of the middle of the first slope is nearly 50% of maximum settlement. With the excavation of the slope, the vertical displacement shape of the slope, from top to the bottom, turns from settlement to upheaval gradually. Generally, the vertical displacement of the corresponding points on the slope increase with the next excavation. See Figure 8.

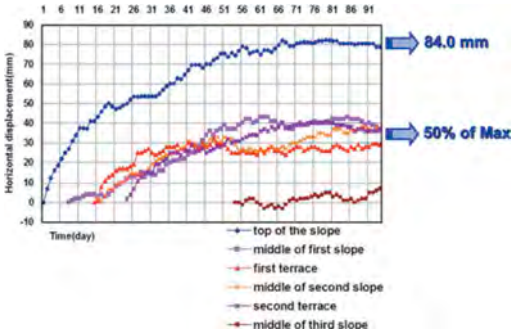

Figure 8. Typical vertical displacement of the slope.

During the whole period, all the points on the slope show horizontal displacements towards the excavation direction. The maximum displacement occurs on top of the slope, and the displacements of the other points are within 60% of maximum displacement. For the points on the first terrace, the displacement is generally less than the points in the two adjacent slopes. Generally, the horizontal displacements of the corresponding points on the slope increase with the next excavation. See Figure 9.

The whole displacement of the slope turns stable usually about 30 days after the completion of the final excavation.

Figure 9. Typical horizontal displacement of the slope.

4.2 *Deformation relationship on top of the slope*

At the beginning of excavation, the vertical displacement on top of the slope behaves with great settlement. After the completion of the first excavation and the construction of the concrete protection surface, the settlement keeps stable with performance of local upheaval. Then the settlement increases with second slope excavation, and tends to slow down again with the curing of the concrete protection surface, and so as the third excavation. After the whole slope is completed, the settlement slows down and keeps stable gradually. The maximum settlement is about 0.6% of the excavation depth. See Figure 10, symbols A ~ D represent different profile positions.

Daily vertical displacement increment shows settlement and upheaval alternately, and it can be

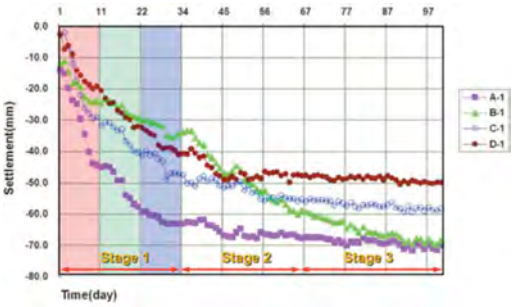

Figure 10. Vertical displacement – time curve.

classified into four stages, the maximum increment occurs in the first excavation. See Figure 11.

Stage1: during the first excavation (the first 10 days), daily settlement or upheaval increment varies between +1.0 mm ~ -5.8 mm.

Stage2: during the second and third excavation (the following 10 days), daily settlement or upheaval increment slows down, varies between +1.5 mm ~ -3.0 mm.

Stage3: middle period after the whole slope is completed (next 10 days), daily settlement or upheaval increment varies between +2.5 mm ~ -3.0 mm.

Stage4: at the end, increment varies between +2.0 mm ~ -2.0 mm and keeps stable.

At the beginning of excavation, the top of the slope behaves with great horizontal displacement. After the completion of the first excavation and the construction of the concrete protection surface, the displacement slows down. Then horizontal displacement increases with second slope excavation, and tends to slow down again with the curing of the concrete protection surface, and so as the third excavation. After the whole slope is completed, the displacement slows down and keeps stable gradually. The maximum horizontal displacement is about 0.72% of the excavation depth. See Figure 12.

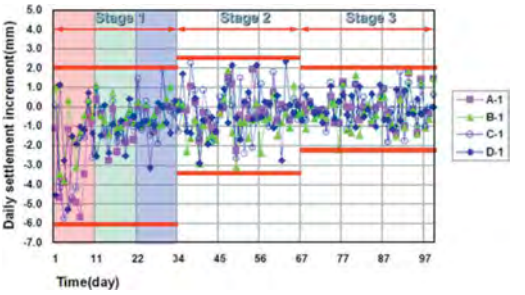

Figure 11. Daily vertical displacement increment.

Daily horizontal displacement increment can be also classified into four stages, the maximum increment occurs in the first excavation. See Figure 13.

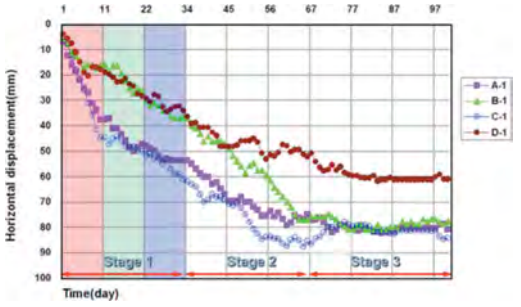

Figure 12. Horizontal displacement – time curve.

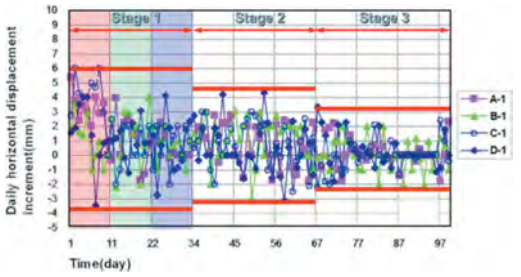

Figure 13. Daily horizontal displacement increment.

Stage1: during the first excavation (the first 10 days), daily displacement increment varies between +6.0 mm ~ -3.6 mm.

Stage2: during the second and third excavation (the following 10 days), daily displacement increment varies between +4.0 mm ~ -3.0 mm.

Stage3: middle period after the whole slope is completed (next 10 days), daily displacement increment varies between +4.5 mm ~ -3.0 mm.

Stage4: at the end, increment varies between +2.0 mm ~ -2.0 mm and keeps stable.

The ratio of the settlement to horizontal displacement on top of the slope for different sections is shown in Figure 14. The relationship can be found as:

At the beginning, the ratio is in disorder. After the slope is completely excavated, about 30 days after the whole slope is completed, the ratio turns stable gradually and at last reaches a certain value about 0.7 ~ 0.9.

4.3 *Empirical formula for slope deformation*

The deformation of the slope is mainly the results of release of the load during excavation and the consolidation of the soils. Both the release of the load and the consolidation of the soils tie up with the time, so in other words, the deformation of the slope ties up with the time, and the behaviour of the slope can be illustrate with time. The adverse points where the maximum displacement usually occurs on top of the slope. Once any empirical formula can be set up, the maximum displacement and settlement can be predicted.

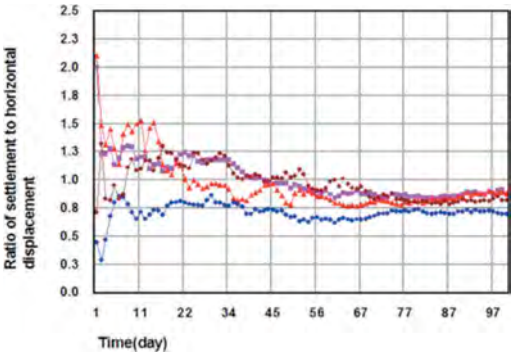

Figure 14. Daily ratio of settlement to horizontal displacement.

Based on the monitoring data, the behaviours of the points on top of the slope change with the excavation of the slope in different stages. In the first 30 days during excavation of the slope, the settlement and horizontal displacement develop greatly, 79 ~ 90% of the total settlement and 46 ~ 66% of the total horizontal displacement occur in this period. In the next following 30 days, the settlement and horizontal displacement slow down gradually but still go up, mainly about 4 ~ 17% of the total settlement and 31 ~ 44% of the total horizontal displacement. And then the whole settlement and horizontal displacement keep in stable, only about 5 ~ 7% of the total settlement and 2 ~ 10% of the total horizontal displacement occur, see Figure 15 and 16.

Based on the characteristic of the settlement on top of the slope, the corresponding formula can be set up in three stages. Stage 1, the first 30days, the settlement can be expressed in polynomial function of time; Stage 2, the next 30 days, the settlement can be expressed in Ln function of time; Stage 3, the following days, the settlement can be expressed in linear function of time.

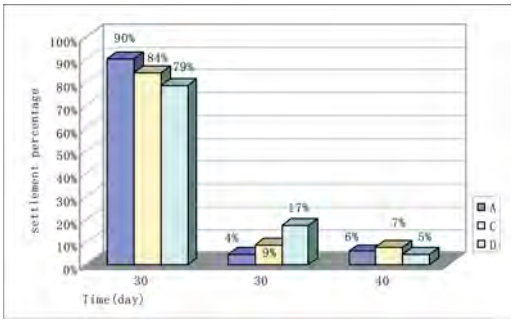

Figure 15. Settlement distribution in different period.

Empirical formula for the settlement on top of the slope can be expressed as:

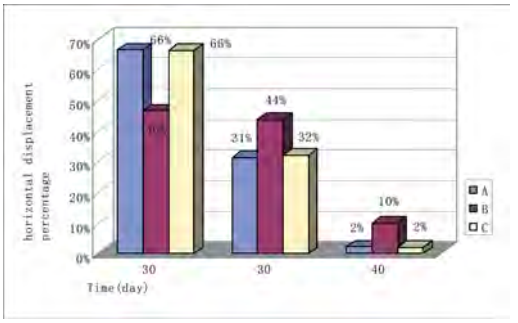

Figure 16. Horizontal displacement distribution in different period.

$$V_d = \begin{cases} \alpha_1 t^4 + \alpha_2 t^3 + \alpha_3 t^2 + \alpha_4 t + \alpha_5 & 0 \le t \le 30 \\ \beta_1 \mathrm{Ln}(t) + \beta_2 & 30 \le t \le 60 \\ \gamma_1 t + \gamma_2 & t \ge 60 \end{cases} \quad (1)$$

Where V_d is the settlement on top of the slope (mm), t is time (day); $\alpha_1 \sim \alpha_4$, β_1, β_2, γ_1 and γ_2 are the coefficients, which mainly depend on the process of excavation, the protection of the slope constructed in time or not and the characteristics of the soil on site.

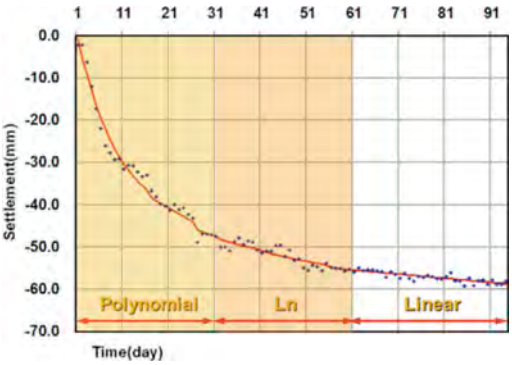

Figure 17. Comparison of settlement obtained by empirical formula and monitor data on site.

Based on the characteristic of the horizontal displacement, the corresponding formula can be set up in three stages. Stage 1, the first 30days, the deformation can be expressed in Ln function of time; Stage 2, the next 30 days, the deformation can be expressed in power function of time; Stage 3, the following days, the deformation can be expressed in linear function of time.

Empirical formula for the horizontal displacement on top of the slope can be expressed as:

$$H_d = \begin{cases} \omega_1 \mathrm{Ln}(t) + \omega_2 & 0 \le t \le 30 \\ \psi(t)^{\upsilon} & 30 \le t \le 60 \\ \xi_1 t + \xi_2 & t \ge 60 \end{cases} \quad (2)$$

Where H_d is the horizontal displacement on top of the slope (mm), t is time (day); $\omega_1 \sim \omega_2$, ψ, υ, ξ_1 and ξ_2 are the coefficients, which mainly depend on the process of excavation, the protection of the slope constructed in time or not and the characteristics of the soil on site.

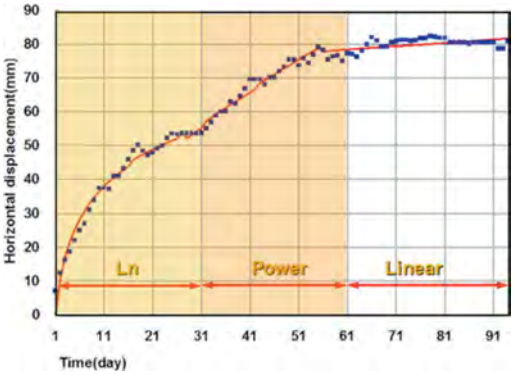

Figure 18. Comparison of horizontal displacement obtained by empirical formula and monitor data on site.

5 DEFORMATION ANALYSIS BY PLAXIS

5.1 *Deformation analysis by PLAXIS*

In calculation, Morh-coulomb material model, drained material type for the soil, plane strain and 15-Node elements model were used. Based on slope gradient as 4.0, four different types of slopes were considered as slope without any protections(type A), slope with surface protections(type B), slope with waterproof curtain(type C) and slope both with surface protections and the waterproof curtain(type D).

All the calculations were carried out following with the excavation steps of the slope. The results of type A and D are as shown in Figure 19 and 20.

5.2 *Comparison of calculation with the data measured*

All the points on the slope calculated in different conditions combined with the data monitored on site are shown in Table 3, Table 4 and depicted in Figure 21.

From the calculation results, points of view could be obtained as followed:

- The vertical deformation shape of the slope, from top to the bottom, turns from settlement to upheaval gradually and all the points on the slope show horizontal displacements towards excavation direction, which show accordance with the data monitored on site. Combined with the four deformed slope surface and the monitored slope surface, the turning point of the vertical deformation shape is the point about one third of the second slope.

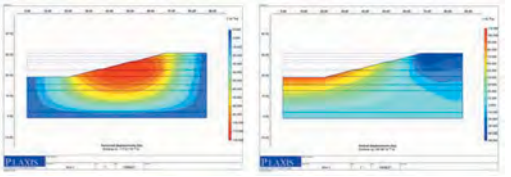

Figure 19. Horizontal and vertical displacement for the slope without any protections(type A).

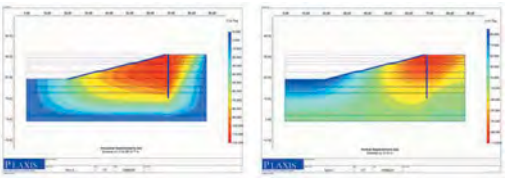

Figure 20. Horizontal and vertical displacement for the slope with waterproof curtain and surface protections(type D).

Table 3. Horizontal displacement comparison.

		Calculation results			
Slope gradient	Monitored data	Type A	Type B	Type C	Type D
toe	/	64.53	60.22	44.31	44.74
Third slope	34.75	92.73	91.67	64.36	64.87
Second terrace	37.25	105.73	101.95	74.22	75.63
Second slope	40.00	111.75	111.19	87.14	86.55
First terrace	31.75	108.96	108.14	94.48	93.60
First slope	31.75	94.96	108.63	107.58	104.09
Top of slope	76.00	69.70	95.14	109.35	113.50

Table 4. Vertical displacement comparison.

		Calculation results			
Slope gradient	Monitored data	Type A	Type B	Type C	Type D
toe	/	109.56	96.52	90.88	89.25
Third slope	40.3	88.56	86.36	74.26	71.36
Second terrace	26.7	78.48	77.05	47.17	45.03
Second slope	8.23	58.65	56.85	6.61	6.15
First terrace	-1.05	38.2	34.18	-28.53	-32.72
First slope	-44.15	8.83	4.4	-68.11	-68.34
Top of slope	-61.6	-34.74	-33.78	-107.1	-99.72

- Comparing with the deformed slope surface without any protections and with surface protections calculated above, the two curves show almost the same shape, though the latter one shows partial prevention to the toe of the slope from upheaval. That means the surface protections have little contributions to reduce the deformation of the slope during excavation, so its function is mainly to prevent the erosion of the slope surface.
- Comparing with the deformed slope surface without waterproof curtain and with waterproof curtain, distinct difference can be found as:
  For the slope without waterproof curtain, the maximum horizontal displacement occurs near the slope surface in the middle part of the second slope, while for the slope with waterproof curtain, the maximum horizontal displacement occurs inside the soil layers near the middle part of the waterproof curtain. The above two maximum horizontal displacement values are almost the same, but the whole deformed shape of the soil layers is different. The horizontal displacement on the slope surface for the slope with waterproof curtain is much lesser than the slope without waterproof curtain. That means the soil cement pile around the dry dock, can not only act effectively as waterproof curtain, but also can provide great contribution to minimize the surface horizontal displacement and enhance the stability of the slope.
  For the vertical displacement, the whole deformed shape is also different for these two conditions. Through the ground water monitor outside the dry dock, the ground water keeps stable during the whole period of excavation, so the soil cement pile waterproof curtains can be proved available. Because of the dewatering inside the dry dock, for the slope with waterproof curtain, the consolidation of the upper part of the soil causes more settlement.
- The calculations results of the two slopes with waterproof curtains and the monitored data show almost the same deform shape, while the value of the former is a little bigger than the data monitored on site. The following aspects may explain the above phenomenon. First of all, due to the complex stratified soils, the distribution of the soil used in calculation may not represent the actual stratified soil on site. Secondly, the calculation results mainly depends on the physical and mechanical properties of the soil, the shear strength indexes of the soils obtained in indoor experiments usually will be different via different experiment instruments and methods, especially for these soft clay. Thirdly, in construction, the surcharge acting on top of the slope is a mobile load while in calculation it can only be simulated on top of the slope all the time, so the load in calculation may be magnified. Then the last, the process and speed of construction such as the surface protection and drainage system to be

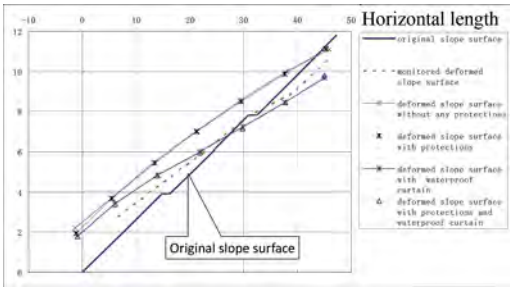

Figure 21. Total deformation of the slope surface in different conditions.

constructed in time or not will also have influences on the deformation of the slope.

6 CONCLUSIONS

In this paper, the study mainly deals with comprehensive analysis and evaluation on the stability and deformation of the slope, based on the background of dry dock slope in Haihe Tunnels, and some preliminary conclusions can be obtained as followed.

- Based on limit equilibrium, the Swedish slice method and Simplified Bishop method were used to determine the final appropriate slope gradient as 1:4.0. And on this basis, general design and detail design of the slope were carried out. In the practice of the project, the whole design was proved successful.
- With excavation of the slope, the vertical displacement shape of the slope, from top to the bottom, turns from settlement to upheaval gradually. The maximum settlement occurs on top of the slope, about 0.6% of the excavation depth. All the points on the slope show horizontal displacements towards excavation direction. The maximum displacement occurs on top of the slope, about 0.72% of the excavation depth. The ratio of the final settlement to the horizontal displacement on top of the slope is within 0.7 ~ 0.9.
- Based on the monitoring data, slope behavior changes with the excavation of the slope in different stages. Empirical formula as polynomial function, Ln function, linear function and power function with respect to time can be set to express the deformation of the slope.
- In practice, the detail structural design of the slope and all the protection measures used are proved available and effective. The soil cement pile around the dry dock can not only act effectively as waterproof curtain, but also can provide great contribution to control the surface deformation of the slope and enhance the whole stability of the slope.
- The successful implementation of the project provides a useful reference for any other analogous projects. All the preliminary conclusions mentioned above are just based on the study on stability and deformation of dry dock slope in Haihe Tunnel, whether these conclusions are reasonable and reliable should be tested and adapted in more practices, such as the parameters in the empirical formula and the analysis methods and the deformation relationships.

REFERENCES

Chun N. H., 2021. Summary on design of Haihe immersed tube tunnel, Tianjin. Tunnel and Rail Transit, 2, 14-19, 29,64.

Tunnelling for a Better Life – Yan, Celestino, Thewes & Eberhardt (Eds)
© 2024 The Author(s), ISBN 978-1-032-80042-4
Open Access: www.taylorfrancis.com, CC BY-NC-ND 4.0 license

Research on online intelligent prediction of service status of immersed tunnel based on artificial intelligence

Hao Ding & Peng Cao*
National Engineering Research Center of Road Tunnel, Ltd., China
China Merchants Chongqing Communications Technology Research & Design Institute Co., Ltd., China

ABSTRACT: Due to the complexity of the construction process of immersed tube tunnels and the dynamic nature of the operating environment, the key parameters of immersed tube tunnels after service are difficult to know and measure; However, using traditional forward numerical simulation methods can only analyze the service conditions for determining parameters. Aiming at the prominent technical bottleneck of online evaluation of service status of immersed tunnels, this paper constructs a 3D refined model for immersed tunnel element joints, and establishes a large database of service status under massive working condition analysis; The BP neural network method was introduced to establish an intelligent prediction model for predicting the displacement changes of the full section waterstop and shear key of the element joints; Driven by on-site monitoring data, the reliability of the intelligent prediction model was verified, and high-precision prediction of the displacement changes of the element joint water stop and shear key was achieved. The above methods have achieved full coverage of key characterization indicators for the service status of immersed tube tunnels, providing a solution for online evaluation and early warning of service safety of immersed tube tunnels. They have important engineering significance for optimizing the operation and maintenance management methods of immersed tube tunnels and improving operation and maintenance efficiency.

Keywords: immersed tunnel, Service status, Intelligent prediction, Artificial intelligence, neural network

1 INTRODUCTION

The evaluation of service status is an important prerequisite for safe operation and maintenance of an immersed tunnel. During online evaluation and early warning of tunnel structures, the key step is to construct appropriate models by scientifically and effectively processing monitored data [1]. However, due to the complexity in the operating environment and structure of immersed tunnels as well as the lagging development of sound monitoring systems in the tunnel field, existing monitoring data is insufficient to support the safety assessment of in-service structures [2-3].

Scholars at home and abroad have performed extensive research in the field of the service status of immersed tunnels. Xu Xiangchun, et al. combined different types of data from multiple sensors and obtained the comprehensive evaluation value of immersed tunnels by the fuzzy analytic hierarchy process [4]; Shao Junjiang compared and analyzed the settlement records and actual damage data of 10 immersed tunnels and provided the allowable settlement control standards for immersed tunnels [5]; Gong Hao and Huang Minghua separately used finite element software to conduct static and dynamic analysis for different immersed tunnels and carried out exploratory research for the sound monitoring system of immersed tunnels [6-7]. The existing data mostly provides parameter references for analysis of defect causes or construction of numerical simulation, but has not been fully utilized in structural safety assessment and early warning [8-12]. In recent years, the development of artificial neural networks in the field of geotechnical engineering opened up more research avenues for processing and analysis of monitored data, mainly focusing on predicting surrounding rock or settlement deformation of the tunnel to guide design and construction [13-18]. Some research results have also been obtained on deformation prediction during tunnel service. Meho Saša Kovačević, et al. [19] adopted the neural model with particle swarm optimization to predict the long-term deformation behavior of soft rock tunnels; Liu, et al. [20] established an intelligent decision-making neural network model for tunnel monitoring systems based on historical databases and association rules. Chen Jianzhong, et al. [21] constructed an ARIMA system to predict future

*Corresponding author: caopeng1@cmhk.com

DOI: 10.1201/9781003495505-313

time series of SHM data and proposed a three-level dynamic warning scheme.

Currently, researchers usually adopt numerical simulation or model testing to study the deformation characteristics and warning standards of immersed tunnels and their research results provide significant support for the design stage of immersed tunnels. However, the load, boundary conditions and geological parameters of simulation models or model tests only represent typical working conditions and cannot cover or restore the actual service status of immersed tunnels. Therefore, these research results cannot effectively support the structural safety evaluation of immersed tunnels during service. In summary, the research on deformation prediction and safety evaluation during the service period of immersed tunnels is still in its infancy.

Therefore, this paper proposes a new research solution: a three-dimensional refined model is established for element joints at key parts of the immersed tunnel to fully reflect the working characteristics of the waterstop and shear key at the element joints and obtain the mechanical response at different positions of the element joint through massive calculation of working conditions, so as to form a large database of the service status of immersed tunnels; since it is difficult obtain the monitored data for the waterstop and shear key of element joints, a BP neural network algorithm is introduced on the basis of a large numerical simulation database to establish an intelligent prediction model for deducing the displacement changes in the full-section waterstop and shear key of element joints; then, the data monitored on the site is substituted into the intelligent prediction model of the joint components of the immersed tunnel to verify the reliability of the intelligent prediction model through the analysis of the data deduction results and finally achieve high-precision prediction of the displacement changes in the waterstop and shear key of the element joint.

2 TECHNICAL BOTTLENECKS IN STRUCTURAL SAFETY EVALUATION OF IMMERSED TUNNEL DURING SERVICE PERIOD

Common defects of immersed tunnels during the service include deformation, water leakage, crack and joint dislocation. The quantitative description of these indicators by reasonable evaluation methods forms the basis for evaluating the service status of immersed tunnel. Moreover, accurate evaluation of the service status plays an important role in technically supporting the maintenance and management decisions for the immersed tunnel. At present, there are three main weight classification methods applied in safety evaluation of structural service status: subjective weighting method, objective weighting method and combined subjective-objective weighting method. For the subjective weighting method, the experts assign corresponding weights to different indicators based on experience and judgment and then perform the weighted average for the indicators based on the weights to obtain overall evaluation results. This method is susceptible to subjective factors of experts, but still has certain application value in the absence of data and models. The objective weighting method mainly relies on source data but underestimates the knowledge and experience of experts, such as common neural network method, principal component analysis method, etc. The combined subjective-objective weighting method simultaneously considers the impact of subjective and objective factors on the rationality of weights and integrates two methods through relevant theories.

The precondition for reliable structural safety evaluation during the service period of an immersed tunnel is that the source data must be accurate. Currently, researchers mainly obtain evaluation source data through the following two channels:

(1) Structural soundness monitoring data during the service period of the immersed tunnel: this data can directly reflect the service status of the immersed tunnel and the preferred solution is to use this data to evaluate the safety status of the structure. The safety evaluation object for the service status of immersed tunnels is the overall safety state of the structure. It requires multiple types, wide ranges and large quantities of monitoring data. However, the current monitoring data available during the service of the immersed tunnel far falls short of the requirements for safety evaluation.

(2) Numerical or physical model test data: Due to the limitations of on-site monitoring data, researchers usually adopt the means of numerical simulation or physical model test to obtain structural deformation and stress data of immersed tunnels under typical working conditions. However, the service life of the immersed tunnel involves massive calculation or simulation of working conditions. Traditional numerical or model test methods cannot simulate the structural service status of immersed tunnels at the very moment because it is unable to obtain critical data, such as accurate foundation parameters, stress state of immersed tunnel upon completion and prestressed state of the segment joints. It is impossible to obtain the same numerical simulation or test model as current service status of the immersed tunnel. In addition, the external environment of the immersed tunnel is constantly changing. Even if we barely obtain a simulation or experimental model similar to the service status of the immersed tunnel at this moment, different states will occur along with the changes of external environmental factors, e.g. loads and movements from settlements, temperature variations, etc. Accordingly, it is necessary to modify the parameters for

numerical simulation calculations or model tests again. Therefore, this method can only represent the service status of the immersed tunnel under typical working conditions, but it is unfeasible and unachievable to perform structural safety evaluation during the service period of the immersed tube tunnels.

3 INTELLIGENT EVALUATION MODEL FOR SERVICE STATUS OF IMMERSED TUNNEL

3.1 *Overall idea*

The overall idea of the research method proposed in this paper is as follows:

Try best to consider the boundary parameters and geological parameters, which can be obtained under actual service conditions, based on the service characteristics and evaluation requirements of the immersed tunnels, and then establish a three-dimensional refined numerical simulation model for element joints at key parts of the immersed tunnel.

Take deformation postures (compressive deformation, horizontal dislocation, vertical dislocation, vertical bending, horizontal bending and torsion) of the immersed tunnel, changes in foundation parameters, changes in overlying loads and other factors as variables, and propose a massive calculation condition under multi-factor coupling to ensure that the calculation condition is sufficient to cover the changes in the state of the immersed tunnel under external environmental effects and establish a numerical simulation database in advance.

Then, adopt a neural network model to establish a mapping relationship between actual monitoring data and simulation database, match and screen target working conditions of simulation data and actual monitoring data on the basis of actual service monitoring data of the immersed tunnel, complete the self-learning process of numerical simulation database, and input a small amount of monitoring data to output the deformation, stress and other data of key monitoring points required for structural evaluation during service in order to meet the needs of structural safety evaluation and early warning data, establish an intelligent evaluation model for immersed tunnel structure based on multi-source data and achieve online evaluation and early warning of immersed tunnel structures.

3.2 *Overall idea*

The specific implementation process is as follows:

(1) Building of a refined numerical model
Considering that the element joint is an important control part for the service status of the immersed tunnel, a three-dimensional refined numerical model is established for the element joint. The important structures at the joints mainly include waterstops and shear keys.

(2) Setting of calculation conditions
The sudden sedimentation caused by typhoons, mud brought by ocean currents and siltation during flood season may lead to uneven settlement along the longitudinal and transverse directions of the immersed tube. As deformation modes may exist in general element joints of the immersed tunnel, 6 typical deformation modes (compression deformation, horizontal dislocation, vertical dislocation, vertical bending, horizontal bending and torsional deformation) are selected as deformation factors and all possible deformation zones in the joints are taken into consideration to determine the deformation level.

(3) Data extraction and output
Based on the three-dimensional refined simulation calculation results of the immersed tunnel, the deformation data of joint structures and key parts of the immersed tunnel under massive working conditions are extracted and mainly divided into the output information of the element joint structure and that of the shear key and waterstop, including deformation of joint structure and that of shear key and waterstop.

(4) Establishment of a simulation database
The results of all working conditions are summarized and sorted to form a numerical simulation database. The distribution of monitoring points in the service status database of the immersed tunnel is shown in Figures 1-4. The database mainly consists of two parts. The first part is the monitoring data that can be obtained daily for the immersed tunnel, including tensional displacement monitoring and dislocation displacement data. The second part is the data difficult to monitor/detect, including longitudinal displacement data of waterstop at the roof, side wall and floor of joint components, as well as dislocation displacement data of the side wall, middle wall and floor.

(5) Building of an artificial neural network model
To establish an artificial network model based on the established simulation database is mainly to utilize the displacement at typical positions of immersed tunnel joints (specific selection can be determined based on the actual monitoring position) to predict the displacement and stress variation of shear keys and waterstops at different monitoring points of the element joints; and to find the optimal fitting for the nonlinear relationship between these data and ultimately build an artificial neural network algorithm model.

(6) Training and verification of intelligent inference model
80% data in the established simulation database of immersed tunnel element joint is randomly selected as the training set and the remaining 20% as the test set. The training set is used to train and

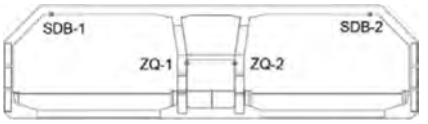

Figure 1. Monitoring point of tensional displacement.

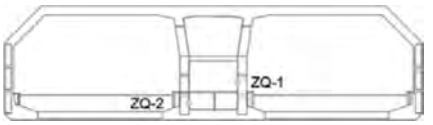

Figure 2. Monitoring point of dislocation displacement.

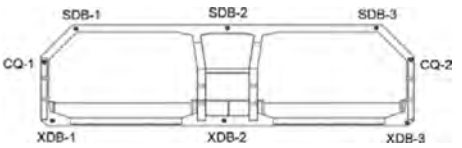

Figure 3. Monitoring point of waterstop displacement.

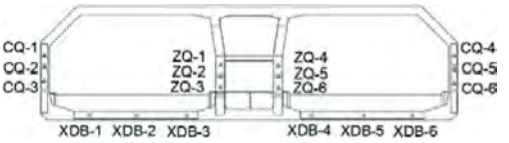

Figure 4. Monitoring point of shear key displacement.

select the optimal neural network model and then the data of the test set is entered into the neural network model to compare the difference between the deformation data output from the model and the data in the database. Meanwhile, the on-site monitoring data is entered into the neural network model to analyze the differences between the model data results and the monitored data and verify the reliability and accuracy of the established deduction model, to ensure the engineering practicality of the intelligent deduction model.

3.3 *Overall idea*

3.3.1 *Data standardization*

Due to the differences in the input training data, the deformation of each shear key and waterstop is different under each service condition and the displacement is different as well. So, in order to facilitate model training, these data should be normalized before training so as to normalize the input and output data between 0 and 1. The specific normalization method is shown in the following equation. As 0 may exist in the data, the normalization processing is adopted to output 0 as 1 at default. Finally, the predicted data is normalized back to its original form to verify the accuracy of the predicted results.

$$X = \{x_n\} = \frac{x_n - x_{\min}}{x_{\max} - x_{\min}} \tag{1}$$

3.3.2 *Adjustment of network model parameters*

Parameter adjustment is the most crucial step for whole model training. The network parameters in this study mainly include training frequency (maxepochs), learning rate (learnrate), error final (errorfinal), hidden unit number (hidden unit number), etc. Each of these parameters may affect the training effect of the model.

3.3.3 *Evaluation of network model*

The BP neural network can be used to achieve regression analysis of the research data. Finally, the mean square error (MSE), root mean square error (RMSE) and coefficient of determination (R2) are selected as evaluation indicators for the model training results.

MSE, known as mean square error, refers to the expected value of the square of the difference between the estimated value of a parameter and its true value. It reflects the degree of deviation between the true value and the predicted value. So, the smaller the MSE, the better the model quality and the more accurate the prediction. Its mathematical expression is as follows:

$$MSE = \frac{1}{n}\sum_{i=1}^{m} \omega_i (y_i - \hat{y}_i)^2 \tag{2}$$

Where, n is the number of samples, represents the true values on the test set and is the predicted value on the test.

R^2, called the coefficient of determination, refers to the goodness of fit of the model. It is the degree to which the regression line fits the observed values. Its value is between 0 and 1. The closer the R^2 value is to 1, the better the fitting degree of the straight line to the observation value is; otherwise, the smaller the R^2 value is. Its mathematical expression is as follows:

$$R^2 = \frac{\sum_i^{\mathrm{n}} (\hat{y}_i - \bar{y}_i)^2}{\sum_i^{\mathrm{n}} (y_i - \bar{y}_i)^2} \tag{3}$$

Where, n is the number of samples, y_i is the true value on the test set and y_i is the predicted value on the test set.

4 EXAMPLE ANALYSIS

4.1 *Refined modeling*

With the element joint of a reinforced concrete immersed tunnel as the research object, a three-

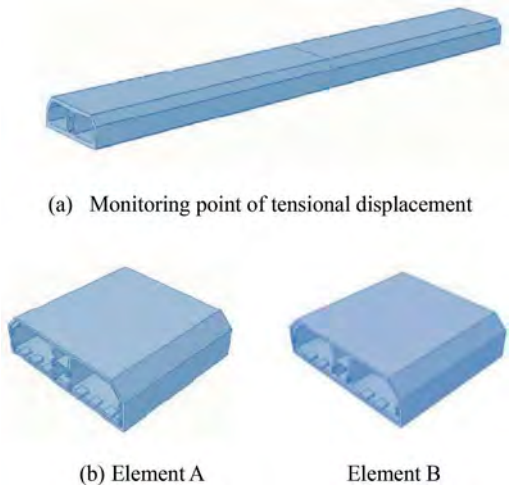

Figure 5. Schematic diagram of immersion Joint.

dimensional refined model is established for the element joint structure of the immersed tunnel. The ABAQUS software is adopted to establish a FEM analysis model for two element joints of the immersed tunnel. The solid elements are used to simulate the tunnel structure, including roof, floor, side wall and middle partition wall. All cross-sectional dimensions of the numerical model are based on the middle section of actual tunnel structure. The longitudinal length of the model is consistent with the actual tunnel section. Moreover, the elements at the element joints are refined. As shown in Figure 5, Type A represents the end face of the element joint with GINA installed and Type B represents the end face of the element joint without GINA.

4.2 *Calculation conditions*

For different deformation modes, the gradual process from conventional small deformation to large deformation under extreme load is considered when the calculation conditions are formulated. For example, the compression of GINA waterstop gradually increases from 100mm to 180mm and the dislocation deformation of horizontal shear keys gradually increases from 0mm to 15mm. For each element joint, in case the deformation mode, deformation range and operating environment mentioned above are taken into consideration, it is necessary to calculate about 300 simulated conditions, some of which are shown in Table 1.

4.3 *Data extraction and simulation database establishment*

Based on the 3D refined simulation model calculation results of the immersed tunnel, the deformation data of key positions and parts of the immersed tunnel structure is extracted under massive working conditions, including deformation of element structure and that of shear key and waterstop. a basic database is provided for the subsequent use of neural network methods for deformation prediction and cross fusion with site data.

4.4 *Intelligent deduction of service status data for immersed tunnel*

80% data in the intelligent simulation database of immersed tunnel joint components is randomly selected as the training set and the remaining 20% as the test set. The data of the training set is entered into the neural network model for parameter training. The fitting training results of the waterstop are shown Figure 6. It can be seen from the figure that the output prediction of the model for waterstop is relatively accurate through debugging. The average R2 is as high as 99.3% and meets the requirements for model accuracy and the error is less than 0.01mm. So, the model can effectively and accurately predict the waterstop. When the model is used to predict the output of the shear key, the average R2 is 97.02%. Compared with the Model III, the prediction accuracy of this model is further improved. For the shear key, the prediction accuracy of the displacement is greater

Table 1. Simulated calculation conditions for deformation of element joint.

Factor	Compression	Horizontal dislocation	Vertical dislocation	Vertical bending	Horizontal bending	Torsion
Unit	mm	mm	mm	rad	rad	rad
1	100	2	8	0.006	0.002	0.002
2	100	12	14	0.002	0.012	0.003
3	100	0	0	0	0	0
4	100	10	2	0.002	0.01	0.002
5	100	16	6	0	0.002	0.004
6	100	14	4	0.008	0	0
7	100	8	12	0.01	0.008	0.003
8	100	4	16	0.012	0.004	0.001
9	100	6	10	0.004	0.006	0.001
10	110	12	16	0.004	0	0.004
…	…	…	…	…	…	…

than 95% in the XY direction and the mean square error is less than 0.01mm. It can be seen from the prediction results that the intelligent deduction model for joint components of the immersed tunnel can accurately predict the output data and meet the accuracy requirements of the model.

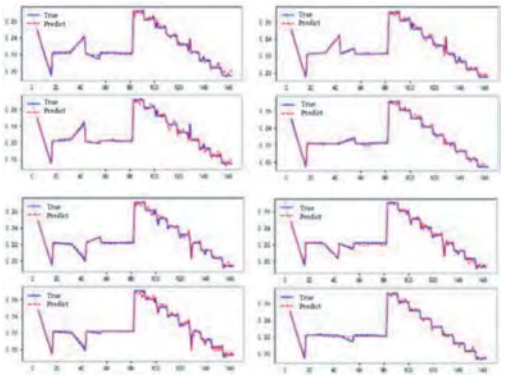

Figure 6. Diagram for monitoring points of output information (deformation of waterstop).

4.5 *Intelligent deduction of service status data for immersed tunnel*

(1) Verification of test data

The above neural network model is trained based on the training set in the intelligent simulation database of immersed tunnel joints and the constructed model is validated and analyzed with the test data. The test data is entered into the model to compare its deduction results with the displacement results in the intelligent simulation of immersed tunnel joint components, as shown in Figure 7.

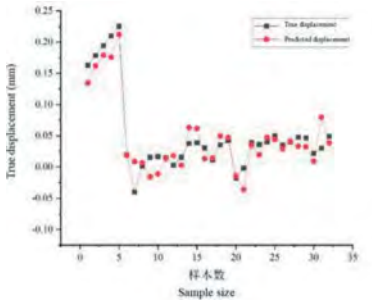

Figure 7. Comparison of simulated and inferred values.

It can be seen from the figure that the trend of simulation results and model deduction results is relatively consistent. The error difference between two results is small with an average error of 0.02mm. The model results are more accurate.

In order to effectively distinguish the stability and accuracy of the model, this study calculates the R2 and root mean square error of the feedforward neural network and support vector machine based on the same training set, and the results are shown in Table 2.

Table 2. Title of the table.

Algorithm model	R^2(%)	RMSE
BP neural network	95.3	0.03
Support vector machine	89.6	0.16
Feedforward neural network	90.5	0.11

It can be seen from the table that, compared to the other two algorithm models, the R2 of the BP neural network is greater than that of the support vector machine and feedforward neural network model, and its root mean square error (RMSE) is smaller than the other two algorithms. It means that the intelligent inference model established for immersed tunnel joint components with the BP neural network has high accuracy and its error is relatively smaller than similar inference algorithms.

(2) Verification of site monitoring data

The accuracy and stability of the model are clarified through self-inspection of the model and comparison with other relevant models. In order to further apply the model to practical works, the intelligent deduction model is experimentally verified by measuring the dislocation displacement at 6 monitoring points on the site.

It can be seen that the intelligent deduction model for the joint components of the immersed tunnel has a small gap between the actual application process and the monitored data. The error results are less than 0.01mm in different directions and the error is smaller than 0.1mm in Y direction. It means that the intelligent deduction model can be used to more accurately calculate the displacement changes at various parts of the immersed tunnel.

5 CONCLUSIONS

This paper has summarized technical bottlenecks in structural safety evaluation during the service of immersed tunnels. It can be believed that the key issue in achieving reliable structural safety evaluation during the service of the immersed tunnel is to accurately obtain the source data required for evaluation. The source data must have three key characteristics: trueness, extensiveness and real-time.

(1) In response to the technical bottleneck in structural safety evaluation during the service of immersed tunnels, this article proposes an intelligent evaluation method for the service status of immersed tunnels based on the neural network and systematically elaborates on the overall idea and specific implementation steps of this method.
(2) Based on a certain immersed tunnel, the example analysis is performed for the intelligent evaluation method for the service status of

immersed tunnel based on the neural network, including 3D fine modeling, data extraction and output, establishment of simulation database, establishment of artificial neural network model, and verification and analysis of online monitoring data.

(3) The displacement and stress data of the waterstop and shear key at the element joint of a certain immersed tunnel has been predicted based on the established artificial neural network model, and the accuracy of the model prediction is not less than 95%. Moreover, the reliability of the established neural network model has been verified to provide data support for safety evaluation of the immersed tunnel structure.

(4) The artificial neural network method has laid the technical foundation for efficient and high-precision prediction of changes in element structure. Later, the fusion of actual monitoring data and numerical simulation database can be established to form a service status database of immersed tunnel structures based on multi-source data so as to achieve online evaluation and early warning of immersed tunnel structures.

ACKNOWLEDGMENTS

This research was financially supported by the National Key Research and Development Program of China (No. 2019YFB1600700), Natural Science Foundation of Chongqing (CSTB2022NSCQ-MSX1656).

REFERENCES

Xiongyao Xie, Naiyuan Zhang, Biao Zhou, et al. Analysis on Evolution Laws and Causes of Structure Performances for Coastal Immersed in Soft Soil[J]. Industrial Constuction,2021,51(7):1–6.

Hongzhe Li, Guodong Jiang, Guozhu Zhang, et al. Consideration on Common Diseases of Immersed Tunnel and Its Inspection and Maintenance[J]. Tunnel Construction, 2019, 39(s1):465–470.

Hao Gong,Kesu Sheng. Research on Health Monitoring of Immersed Tunnel [J].Journal of Yangtze University,2006(02):91–94.

Xiangchun Xu, Liyuan Tong, Songyu Liu, et al. Evaluation model for immersed tunnel health state: A case study of Honggu Tunnel, Jiangxi Province, China[J]. Tunnelling and Underground Space Technology incorporating Trenchless Technology Research,2019,90.

Junjiang Shao. Research on Health Monitoring of Immersed Tube Tunnels Settlement Prediction and Control of Immersed Tube Tunnels [D]. Tongji University, 2003.

Hao Gong. Research on immersed tunnel health monitoring[D]. Jinan University,2006.

Huang Minghua. Running Performance Analysis and Health Monitoring System Design of YongJiang Underwater Tunnel[D]. Harbin Institute of Technology,2008.

Hongzhou Liu,Guoping Xu,Yi XU, et al. Analysis of progressive failure mode of immersed tunnel joints in complex environments [J].Road,2022,67(02):308–314.

Zhan Wang, Baohu Zhang, Yanmeng Zhang, et al. Damage and Deformation of Chebei Raod Immersed Tunnel Based on Multiple Lateral Differential Foundation Stiffness[J]. Tunnel Construction, 2021, 41 (S2):209–214.

Yanning Wang,Huanzhu Zhou,Jin Yu. Long-term settlement model for immersed tube tunnels under back silting loads during operation and maintenance periods [J]. Chinese Journal of Geotechnical Engineering, 2023,45 (2):292–300.

Gang Wei, Huijie Qiu, Xinjiang Wei. Analysis of Settlement Reasons and Mechanism in Immersed Tunnel[J]. Applied Mechanics and Materials, 2012, 2080(238-238): 803–807.

Glenda Abate, Maria Rossella Massimino. Parametric analysis of the seismic response of coupled tunnel–soil–aboveground building systems by numerical modelling-[J]. Bulletin of Earthquake Engineering, 2017, 15(1): 443–467.

Yangyang Zhang, Tianyu Sui, Jun Pei,et al. Artificial Neural Network Technology and Its Application in Geotechnical Engineering [J]. Applied Technology,2021 (03):62-64+69.

Fei Xu and Ke Wang. Study and Application of Slope Displacement Time Series Forecast Based on CO-WLSSVM[J]. Advanced Materials Research, 2012, 2091(594-597): 2932–2935.

Renpeng Chen, Pin Zhang, Xin Kang, et al. Prediction of maximum surface settlement caused by earth pressure balance (EPB) shield tunneling with ANN methods[J]. Soils and Foundations,2019,59(2).

Masahiro Nakata, Yoshinori Araki, Shoji Suzuki, et al. A Study on the maximum displacement estimation model of neural network for tunnel construction with NATM [J]. Doboku Gakkai Ronbunshu,1997,1997 (581).

Bofeng Liu. Analysis and Application of Displacement Monitoring Data of Large Deformation Tunnel Based on BP Neural Network Algorithm [J]. Railway Engineering,2022,62(07):106–109.

You Chen, Tao Ren, Peng Deng,et al. Prediction of Tunnel Settlements by Optimized Wavelet Neural Network Based on ABC [J].Modern Tunnelling Technology,2019,56(04):56–61.

Kovačević Meho Saša, Bačić Mario, Gavin Kenneth, et al. Assessment of long-term deformation of a tunnel in soft rock by utilizing particle swarm optimized neural network[J]. Tunnelling and Underground Space Technology incorporating Trenchless Technology Research,2021,110.

Liu Liu, Chengqian Ma. Research on Intelligent Monitoring System on Tunnel Based on Neural Network[J]. Advanced Materials Research,2014,3530(1044–1045).

Chen Jianzhong, Jiang Xinghong, Yan Yu, et al. Dynamic Warning Method for Structural Health Monitoring Data Based on ARIMA: Case Study of Hong Kong–Zhuhai–Macao Bridge Immersed Tunnel[J]. Sensors,2022, 22 (16):6185–6185.

Wenhao Xiao, Yong Yuan, Haitao Yu, Lu Jing, Yue Chen. Numerical Analysis Of Mechanical Behaviours Of Immersion Joint[C]. 11th World Congress On Computational Mechanics; 5th European Conference On Computational Mechanics; 6th European Conference On

Computational Fluid Dynamics, Vols Ii - Iv, 2014, Spain, 1388–1397.

Peng Liu,Wenqi Ding,Bo Yang. Model for stiffness of joints of immersed tube tunnel [J]. Chinese Journal of Geotechnical Engineering,2013,35(S2):133–139.

Chi Zhang,Yuan Guo, Ming Li. Review of Development and Application of Artificial Neural Network Models [J].Computer Engineering and Applications,2021,57(11):57–69.

Rong Liu. Overview of the Basic Principles of Artificial Neural Networks[J]. Computer Products and Circulation,2020(06):35+81.

Lei Wang. Principles, Classification, and Applications of Artificial Neural Networks[J].Science & Technology Information,2014(03):240–241.

Zhenhua Zhao,Xipeng Hu, Heming Sun,et al. Application of BP Neural Network in Prediction of Ground Settlement in Urban Shield Tunneling [J]. Subgrade Engineering,2020(04):170–175.

Linjun Tang,Xiaojun Ning, Yang Li, et al. Forecast of Tunnel Surrounding Rock Deformation Based on Grey Theory and BP Neural Network [J]. Industrial Safety and Environmental Protection,2021,47(10):88–93.

Song GUo, Jinping Lu,Yu Zhou. Application of Improved BP Neural Network Model in Tunnel Deformation Analysis [J]. Urban Geotechnical Investigation & Surveying,2017(01):137–141.

Jiayin Jia,Yuhao Liu,Xiaojun Li,Chengping Wang, Menghuan Li. Time Series Prediction of Surrounding Rock Deformation in Shallow Buried Tunnel Based on Improved PSO-BP Neural Network [J]. Journal of Water Resources and Construction Engineering,2021,19 (05):19-22+51.

Tunnelling for a Better Life – Yan, Celestino, Thewes & Eberhardt (Eds)
© 2024 The Author(s), ISBN 978-1-032-80042-4
Open Access: www.taylorfrancis.com, CC BY-NC-ND 4.0 license

Key developments of world's immersed tunnel design and construction solutions

Ard Doorduyn*, Ying Li, Hans de Wit & Marcel 't Hart
Tunnel Engineering Consultants, Amersfoort, The Netherlands

Weibin Chen
CCCC Fourth Harbor Engineering Co. Ltd

ABSTRACT: Immersed road/rail tunnels (IMT) have a long history, some 120 years. During the period various evolutions have taken place, and each region had their own particular designs and methodologies, e.g. tubular steel tunnels in the U.S.A., rectangular concrete in the Netherlands (Europe) and rectangular steel shell in Japan. These developments and its contributions to the world IMT technology will be addressed in the first part of this paper. The second part addresses the great impact from China on world IMT industry with its fast developments in the new century. The paper which will focus mainly on the new innovations of immersed tunnel with relate to the design theory, construction methodologies, new material, equipment, et al. In all these developments, how sustainable ideas are in-cooperated will be highlighted such as energy saving, carbon reduction and green construction.

Keywords: Immersed tunnels, innovations, world wide, coverage, key developments, design and construction

1 INTRODUCTION

This paper discusses the key developments of world's IMT design and construction solutions. And it is divided into two parts, 1st part addresses the world IMT developments except China; and the 2nd part addresses the impact from China on world IMT industry with its fast developments in the new century.

2 IMT HISTORY IN THE WORLD

The first immersed tunnel ever, was built across the Detroit River. The tunnel consisted of 2 steel tubes, each accommodating 1 railway. The tunnel was operated in 1910, and has been the base for the design and construction of most of the USA IMT's.

It has taken many years before the first immersed tunnel in Europe was realized. The first was the Maas tunnel in Rotterdam, Netherlands.

Later, in the 1970's in the Netherlands scheduled several immersed tunnels, amongst which an immersed metro tunnel under de maas which extended onshore (still as immersed elements).

2.1 *Detroit river tunnel (Wilson S.K. 1911)*

2.1.1 *Introduction*

In the late 1800's the initiative for a tunnel between the United States and Canada was considered. The link would replace the ferries that provided the services between Detroit and Windsor. The plans were delayed several times, and only once it was clear that electrification of the railway traffic had become possible, i.e. it would replace steam locomotives.

The selection for an immersed tunnel was made due to the significant difficulties for the generally used compressed air and shields.

A relevant feature of this new method of immersed tunnel construction is the small labor cost, as compared with the compressed air and shield method. On the other hand, the aggregate cost of the materials will generally be larger, but not enough to overbalance the labor cost; the result is a stronger and more durable construction, certainly a desirable quality in a subaqueous tunnel.

At Detroit this method effected a saving of about $2 000 000 over a shield-driven tunnel with compressed air, and this should be added the capitalized

*Corresponding author: a.doorduyn@TEC-tunnel.com

DOI: 10.1201/9781003495505-314

saving in annual cost of operation on account of the tunnel being placed some 15 ft. higher.

2.1.2 *Tunnel design*

The selection for a steel immersed tunnel was made, with 2 tubes, 1 tube for a rail line. The steel tubes were stiffened with diaphragms. The connection of the steel plates and the diaphragms were made using the techniques common at the shipping production.

The plates for the tubes were riveted together with lap-joints and attached to the steel diaphragm by an angle-iron, running entirely around the tube, riveted to the diaphragm and to the tube plate, the diaphragms being spaced so as to come at the center of the plate between the lap-joints.

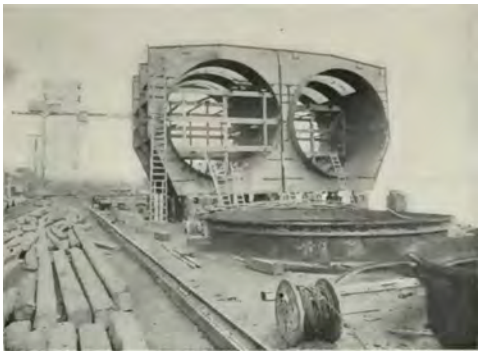

Figure 1. Tube during erection at shipyard.

When an entire section of tubes was erected and securely bolted, and before riveting was started, the tubes were checked for alignment and grade, and any necessary change was made by moving the diaphragms.

Figure 2. Completed tube at shipyard.

2.1.3 *Sinking of the tubes*

ln advance of the sinking of a section of tubes, and before placing the grillage for the temporary end support, it was necessary to determine the condition of the trench as to depth and width, this was done by divers. The actual excavation was done by the derrick scow.

At intervals, marking the joints between the different sections of tubes, a steel grillage of I -beams was placed at the required level, under which concrete was deposited until the beams were engaged. These grillages formed temporary supports until the

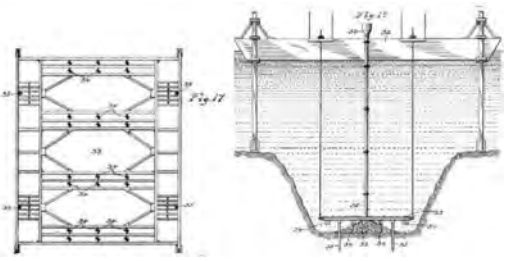

Figure 3. Grillage (left) & the tremie installing the concrete below the steel grillage (right).

foundation concrete could be deposited. A plan of the grillage is shown by Figure 3.

For sinking, the ends of the tubes were fitted with water-tight bulkheads. Each of these bulkheads was equipped with a 14-in. gate-valve, which could be opened from the outside. The sections were sunk by opening valves and permitting the tubes to fill with water. The time required for submerging a section of tubes was approximately 2 hours.

Four air cylinders, or buoys, were used for floating and ballasting the tubes to correct position, two being placed over each tube and connected to the diaphragms.

After a section of the tubes was in proper position in the bottom of the trench and sufficiently anchored by concrete, the air cylinders were detached by a diver, brought to the surface, and held in readiness for use on the next section. One set of cylinders was used for all the sections.

Figure 4. Tunnel element prepared for immersion.

Figure 5. Immersion in progress.

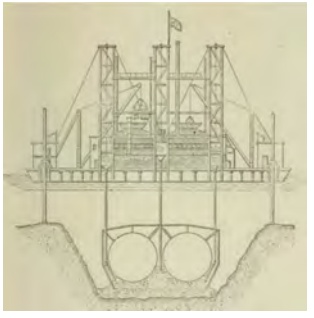

Figure 6. Method of placing concrete by Tremie to ballast the tunnel element in the permanent situation.

2.2 *Maas tunnel (H. Dekking, 1937-1941, Erwin Schnitter, 1941, H. van Tongeren, 1978)*

For the Maastunnel it was decided to make a monolithic reinforced concrete tunnel with an external waterproofing steel shell accommodating 2 x 2 road traffic lanes and specific bicycle traffic and pedestrian tubes, as shown below.

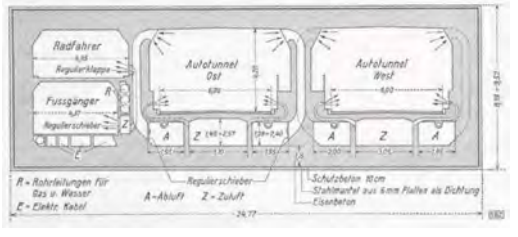

Figure 7. Cross section of maastunnel.

The Maas tunnel is the first rectangular tunnel. This was possible due to the development of a system that could fill the space between the trench bottom and the tunnel element with sand, e.g. by using a Sand-jetting system.

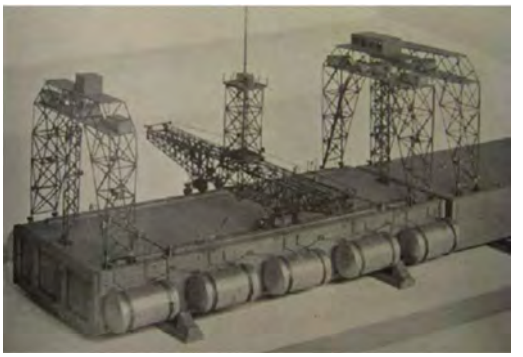

Figure 8. Model of the maas tunnel element with the towers at both ends, the sand jet system and buoyancy cylinders.

In short, by placing two extraction pipes next to the outflow opening of the injection pipe of the sand-water mixture, rapid consolidation and sufficiently tight packing of the sand under the tunnel is ensured.

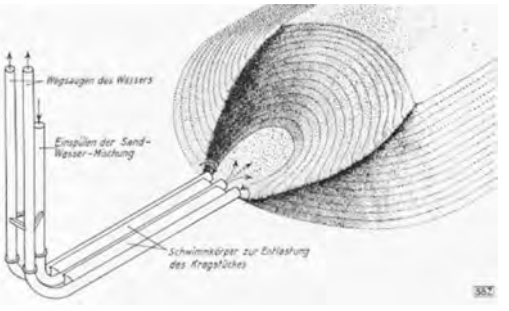

Figure 9. The sand-jet concept by Christiani & Nielsen.

The maas tunnel elements were placed on a pre-installed concrete support beam. The beams were provided with supports on both sides with horizontal jacks to fine tune the alignment of the tunnel element. In addition, also vertical jacks were installed in the tunnel element walls to fine tune the vertical position of the tunnel element.

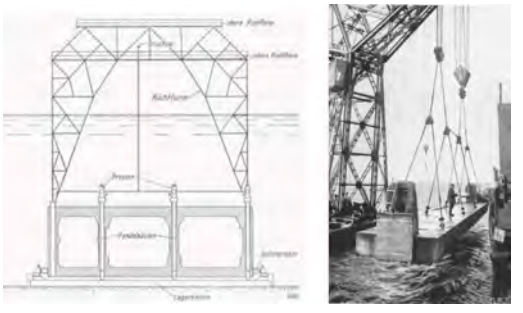

Figure 10. Element on beam (left) and support beam (right).

This picture shows the floating tunnel element with the end-frame (left) needed for the positioning of the element as well as for the completion of the immersion joint. In addition, the sand-jet frame is shown with the travel frame.

Figure 11. Tunnel element with tower & sand jet system.

For the connection of the immersion joints half Larssen XI planks were arranged at the ends of the tunnel sections and firmly anchored in the concrete of the side walls. Next the space of the roof slab is provided with a diving bell that covers the whole length. See below Figure.

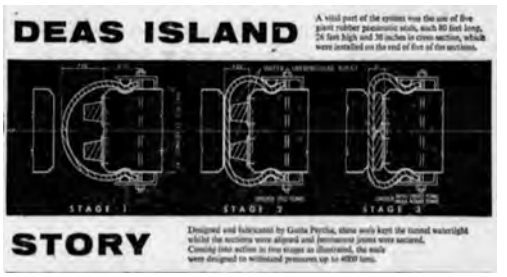

Figure 12. Immersion joint completion with diving bell.

2.3 *Deas island (Carson Kerr, 1959)*

In 1959, the first use of a rubber profile to realize watertightness at the immersion joint was done at the George Massey tunnel in Vancouver, Canada.

Figure 13. Combination of gasket with inflatable tube.

A special inflatable rubber seal was developed to speed up joining of the elements and finish from the inside.

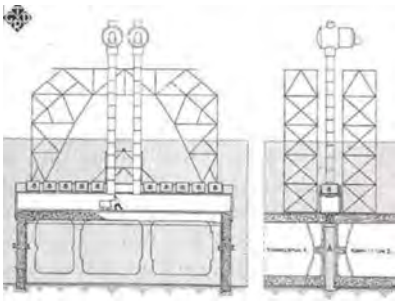

Figure 14. Immersion joint inflatable rubber seal.

2.4 *Rotterdam metro tunnel (G. Plantema, 1968, H. van Tongeren, 1978)*

The Rotterdam metro tunnel is partly located inshore (for a significant length) and a limited length across the river. For the inshore part, the tunnel elements are placed on specially designed adjustable piles and adjusting beams. The immersion joints between the tunnel elements adopted a new design, using so-called Gina and Omega gaskets for the watertightness. Gina appeared common since then.

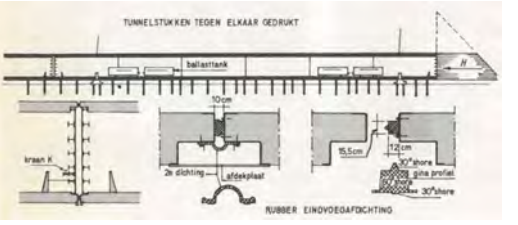

Figure 15. Details immersion joint with the gaskets.

2.5 *Later developments*

2.5.1 *Øresund tunnel (R. Spreng, et. al, 2000)*

Figure 16. The first industrial tunnel element production facility with 2 production lines.

2.5.2 *Sandwich structure elements (Akifumi Kojima, et al, 1995) (R. Ojima et al, 1996)*

The sandwich structures (mostly in Japan) can be open sandwich with steel plates at the out-side with stiffeners and studs for a proper connection to the concrete. Furthermore, at the inner-side conventional reinforcement is used.

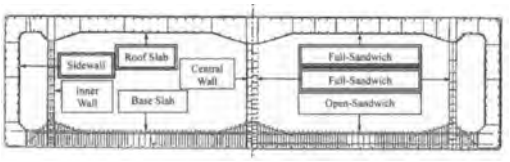

Figure 17. Example of sandwich immersed tunnel options.

Figure 18. Example of open sandwich (left) full sandwich (right).

The second option is the full sandwich where the in- and out-side of the walls are of steel plates. Between the plates, diaphragms are installed in longitudinal and in transverse direction, thus realising boxes of typical 10m^3, that are filled with highly fluid concrete.

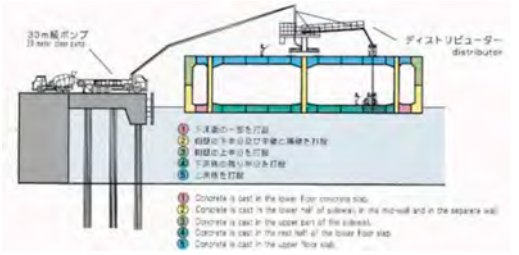

Figure 19. Casting of full sandwich immersed tunnel element in floating position.

2.5.3 *Japanese closure elements (Kazunari Umeyama & Haruo Shibuyama, 1995) (M. Shimoishi, et. Al, 2001)*

The V-block method was newly developed for the closure joint. The method was developed to achieve safe, rapid and economic construction.

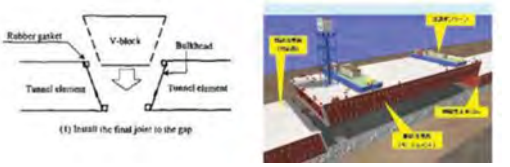

Figure 20. V-Block (left) and closure element (right).

2.5.4 *Japanese joint - bellow (Kazunari Umeyama & Haruo Shibuyama, 1995) (Hideo Kimure, et. Al., 2003)*

Immersed tunnels in Japan are subject to significant earthquakes. One of the solutions are the bellows joints that are made from steel and has a high allowable deformation. The reference paper shows the development of bellows joint adopted as the flexible joint for the immersed tunnel elements in lieu of conventional seismic joints.

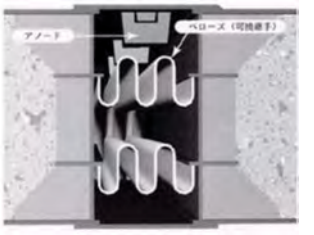

Figure 21. Bellow joint.

2.5.5 *Japanese joint – crown seal (Shuji Eguchi. Et. al, 2005)*

Another innovated joint with large deformation capacity to withstand earthquakes and uneven settlement of tunnel elements that may occur in the future between the land section and the seabed section or earthquakes, may causing displacement at the submerged box joint. As a result of various studies were conducted of a new type of joint that can follow such displacements, a new crown seal type joint was developed is the Crown Seal.

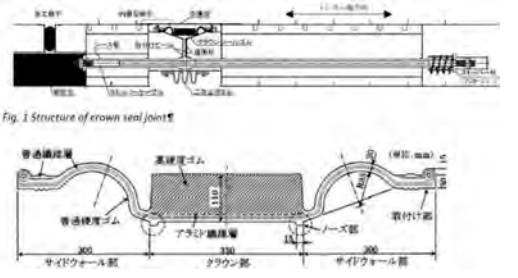

Figure 22. Crown seal & restraining bars.

3 NEW DEVELOPMENTS IN CHINA

The first immersed tunnel in China originates from 1972 in HK and 1993 in mainland. In this century, China has demonstrated strong development momentum which contribute to the world IMT industry. Till now, more than 22 IMTs have been realized and about 10 are under construction. Due to page limits, only typical examples are selected with key developments from the aspects of design, construction, material, equipment, et al. In all these new developments, how sustainable ideas are incooperated will be highlighted.

Undoubtedly, the immersed tunnel of the Hong Kong Zhuhai Macao Bridge (HZMB) is the most important milestone project in the history of China's IMT development. Its successful implementation has transformed China from a small IMT country to one of the world's leading countries and has also driven the great development of China's IMTs and the continuous emergence of innovative technologies in recent 5-10 years.

3.1 *Innovation in design and construction*

3.1.1 *"Semi-rigid" concept in longitudinal behavior*

HZMB project brought new "semi-rigid" theory with respect to the longitudinal behavior of reinforced concrete immersed tunnels, in which generally two basic structural forms are distinguished, e.g., the rigid tunnel (one element behaves as one rigid body) and the flexible tunnel (one element subdivided in various segments that allow flexible behaviour in segment joints.

HZMB immersed tunnel took segmented element. However, it changed the temporary use of the longitudinal post tensioning cables for transport and immersion phase into permanent for operational phase, still allowing opening of the segment joint in case the bending moment capacity provided by the pre-stressing is exceeded. special design of local debonding of the post tension cables at the segment joints was applied to provide the segment joint with a certain rotation capacity.

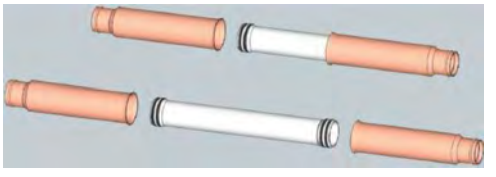

Figure 23. Principle of de-bonding of post tension cables (Hans de Wit, et al., 2018).

The semi rigid method combines the advantages of the flexible (segmental) and rigid (monolithic) tunnel concept. Especially in offshore tunnel projects that involve challenging transport and immersion conditions and resulting in a significant amount of post tensioning, the semi rigid concept is very interesting. But leaving the post tensioning in place will make the tunnel more cost effective (all cutting work can be omitted) and movements in tunnel segment joints will be reduced significantly, or avoided, which is beneficial to the water tightness performance of the tunnel.

The Piet Hein tunnel in the Netherlands was the first segmental tunnel in which the post tensioning was kept in place, using some basic ideas of the semi rigid concept. The Chinese engineers really brought this idea to the next level and turned it into a real innovation in which the segment joint detailed design allows some rotation when the bending moment capacity of the post tensioning is exceeded and that will cap the forces in the joint. At the same time the segment joint detailed design is using the normal force (of which post tensioning is a significant part) to increase the shear capacity of the segment joint (Hans de Wit, et al., 2018)

3.1.2 *Closure joint*

An exceptional innovation of HZMB project was the successful installation of the world's first steel "sandwich" closure joint, using the world's largest single arm floating crane with a lifting capacity of 12.000 ton. The length of the bottom structure was 9.5 m and that of the roof was 12 m with total weight of about 6000tons.

Figure 24. Closure joint installation of HZMB (Su Quanke, at el., 2022).

Following the HZMB project, two other large sea crossings in China, the Dalian Bay Crossing and the Shenzhen-Zhongshan Link, have adopted similar concept of convenient offshore installation with high accuracy, further optimizing the design and construction of its closure joint.

Dalian Bay subsea tunnel has 18 elements of 180m each. The closure joint with segment-jacking method mainly consists of an external sleeve, jacking segment, water stop structure, jacking device, locking structure, and post pouring strip structure. It connects the 18th element with C&C section.

The closure joint of Shen-Zhong Link immersed tunnel adopts the overall prefabrication and underwater pushing out construction method consisting of an expansion section,

a push-out section, and a post welding section. The push-out section is hidden within the expansion section, and by the hydraulic and jack push-out system, it is pushed out and connected with the previous immersed tunnel element. The post welding section is welded inside the tunnel; A deviation correction jack system is used to control the position of the push-out section.

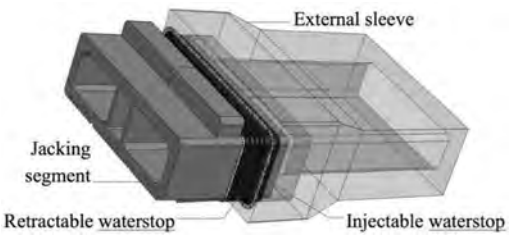

Figure 25. Closure joint by segment jacking of Dalian Bay crossing (Ren Dongsheng, 2022).

Figure 26. Closure joint of Shen-Zhong Link (DENG Bin, et al, 2023).

3.1.3 *Steel sandwich structure*

Shen-Zhong Link is another world-class project composed of "bridge, island, tunnel and underground interchange" after the HZMB Project in China. In order to deal with the structural stress and reduce the engineering risk regarding the complex construction condition, max 24.0m span of one traffic tube and extra thicker soil cover (partly larger than 10m) on top of the tunnel, the steel-concrete sandwich structure is applied. This is the world's first bi-directional 8-lane immersed tunnel built with steel-concrete sandwich structure. Mechanism of this structure, technologies for intelligent manufacturing of Steel Shell, mixture and intelligent pouring of high strength self-compacting concrete had been detailed studied and realized successfully.

3.1.4 *Full sectional casting for monolithic element*

Very sound concrete quality had been realized by fully sectional casting method in the three segmented immersed tunnel projects: HZMB, Oresund Link and

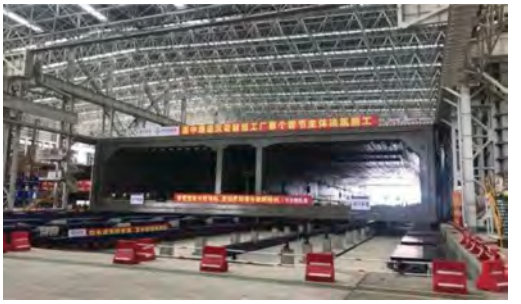

Figure 27. First steel sandwich element casting construction (Picture by Ying Li in 2019).

Busan-Gorge Link. It avoided cold joints by traditional staged casting method. In order to increase the overall performance of the structure, control the development of structural cracks, and enhance the waterproof performance of the structure, Chinese engineers further had developed this technology for monolithic immersed tunnels.

Xiangyang- Hanjiang Tunnel in Hubei province has 120.5 m and 86.5 m long elements which are divided into 5 and 4 segments along the longitudinal direction, respectively. All segments adopt a sequential full sectional casting process one by one without a post pouring belt between segments. The control of concrete cracks was studied through numerical and physical model tests.

Figure 28. Full-section casting and prefabrication with integral hydraulic formwork of Xiangyang- Hanjiang Tunnel (WANG Yong, et al.2022).

In Chebei-XinJiao East Road immersed tunnel Guangzhou, one element is divided into 6 segments with the length range from 14.5 to 16m, with 1.6m post-pouring band which is different from Xiangyang- Hanjiang Tunnel. But one segment uses full sectional casting as well. the formwork is designed with an external truss structure and a no-tie-rod system to ensure the precast quality of the segments. It is similar to HZMB project. This technology has been promoted and applied in subsequent projects such as the Ruyifang Tunnel.

Figure 29. Full-section casted elements with post-pouring band in between (source: CCCC4th Harbor Engineering Co. Ltd).

Figure 30. Full-section casting formwork of Chebei-Xinjiao West Road tunnel (source: CCCC4th Harbor Engineering Co. Ltd).

3.2 *New equipment*

A lot of new equipment had been developed in IMT industry in China, here only two examples are picked up.

3.2.1 *Intelligent trolley system*

Factory production of IMT elements is becoming attractive for long tunnels after Oresund Link and HZMB projects. Intelligent trolley system was developed in China to move the heavy elements more efficiently and safely with self-adapting jacking for fast transporting in the factory. For example below Figure shows a system made of 200 trolleys for Shen-zhong Link project. Each trolley can bear 800tons. It can intelligently control and manage of synchronous forward, lifting, and automatic deviation correction for 200 trolleys.

Figure 31. Intelligent trolley system for Shen-zhong Link project.

3.2.2 *Integrated equipment for transport and installation*

In response to adverse meteorological conditions such as busy and complex waterways, deep water, and complex wind, wave, and currents in the route of floating transportation of tunnel element, in order to improve the accuracy and efficiency of construction, Shenzhen-Zhongshan Link has developed the first specialized operation vessel that integrates the functions of floating transportation, positioning, sinking, and installation of immersed elements. The ship has a length of 190.4m, a width of 75.0m, and a molded depth of 14.7 meters. When carrying element, the speed can reach 5 knots. The hull is equipped with a side thrust engine, which has DP power positioning, tracking, and deviation correction functions.

Figure 32. Transport & installation integrated vessel for Shenzhen-Zhongshan Link (Chen Hong, at el. 2022).

3.3 *Improvements on materials*

3.3.1 *Machine-made sand*

Based on the Dalian Bay subsea tunnel project in cold area, concrete made from machine-made sand is firstly used in large immersed tunnel prefabrication. After numerous mixture tests, a concrete mixture suitable for cold areas had been found, which can meet the design requirements of immersed concrete in terms of working performance, strength, hydration heat, shrinkage, early crack resistance, and durability. This application provided a good reference for future projects where shortage of naturel sand is a problem.

3.3.2 *Self-compacting concrete*

The steel shell sandwich structure is a global challenge in achieving concrete filling density in closed compartments. The self-compacting concrete for the closure joint of the immersed tunnel of HZMB is a successful start. The Shen-zhong link project adopts a super large-scale steel shell sandwich structure and has undergone hundreds of separate compartments model pouring tests. Based on research on the mixture, long-term performance, quality control,

and construction quality inspection, a self-compacting concrete with high robustness, good flowability, filling performance, and anti- segregation performance has been developed. Reasonable processes and structures have been proposed for self-compacting concrete pouring.

3.4 *Sustainability considerations*

Sustainability has been paid more and more attention in the new century in China, the same in the world. For every new development or innovation, sustainability is always one of the important factors to check.

The development trend of IMTs in China since the new century: simplified construction, intelligence, industrialization, more durable and environment friendly, energy-saving and low-carbon. Taking the HZMB and the Shenzhen-Zhongshan Link as examples, the design has begun to pay attention to the full life cycle consideration, and increasingly focuses on the maintenance free, easy to maintain, or easy to replace issues of the structure during the operational stage. The factory prefabrication has improved the quality and durability of the structure, greatly reducing the cost of future maintenance.

The trench excavation is often considered the most environmentally affected process, and both projects use specialized equipment such as dredgers and siltation cleaning vessels to maximize accuracy and reduce environmental disturbance caused by underwater construction. All types of offshore construction strictly control environmental pollution and its impact on aquatic animals and plants. Especially for the protection of local white dolphins. Minimize offshore construction time and processes as much as possible, and reduce the pollution of the marine environment caused by repeated shuttling of ships. For example, both projects have adopted innovative and fast steel cylinder technology for artificial island formation.

Shared utilization of resources is another characteristic. The prefabrication yard for immersed tubes is a very high part of the cost. The re-use of dry docks or prefabrication yards has become a trend, such as the re-use of prefabrication factory of the HZMB for the tunnel of Shenzhen-Zhongshan Link, and the re-use of dry dock and formworks from the Chebei-XinJiao East Road Tunnel for the Huizhan West Tunnel in Guangzhou, etc.

4 CONCLUSIONS

It is fascinating how immersed tunnel construction has developed of the past century. it is our good fortune that the construction methods of the first immersion tunnels have been documented and still accessible to us. Archives are accessible and provide the design documents and patents of several IMT's.

Where patents provide technical information, they also provide restrictions and may restrict progress when new designs need to be developed. An example of an important design that was not restricted due to a patent was the GINA gasket as developed in Rotterdam, the Netherlands and has freely been used all over the world.

Ultimately, however, always new designs are developed. Next to longer, wider, and at deeper location, immersed tunnels are developed in new countries and at more remote locations that are outside the main (economic) parts of countries, and IMT technologies are constantly innovating towards a more efficient, high quality, and cost-effective direction.

REFERENCES

Akifumi Kojima, Takaaki Jojiro, Yuki Nakajima, Keiji Ozawa,1995, Minatojima tunnel steel sandwich structure two-structure immersed box [Japanese]; Construction of high fluidity concrete; Proceedings of the Japan Concrete Institute Volume 17, No. 2.

Carson Kerr, 1959, A Prefab Tunnel Conquers a Tough River (Deas Island), Popular Mechanics

Erwin Schnitter, 1941, The construction of the river section of the car tunnel under the Maas in Rotterdam, Schweizerische Bauzeitung (in German) part 1 to 3.

Chen Hong, He Chunning, Zeng Yi, 2022. Engineering Difficulties and Innovation of Immersed Tunnel of Shenzhen-Zhongshan Passage, TUNNEL AND RAIL TRANSIT, 2022 No.4.

Deng Bin, et al, 2023. Rationally Constructed of Immersed Push-out Final Joint in Water of Shen-Zhong Link[J], Tunnel Construction, First online paper, 2023- 06-27.

G. Plantema, 1968, Metro construction in Rotterdam -The Tunnel Construction part 1 & 2 (in Dutch), De Ingenieur.

Hans de Wit, René Kuiper, Ying Li, et al, 2018. An innovative design concept for the Immersed Tunnel of the Hong Kong Zhuhai Macao Bridge Project- Following an alternative review approach for the approval of an innovative concept, Proceedings of ITA Congress 2018, Dubai.

Kazunari Umeyama & Haruo Shibuyama, 1995, Construction work of Osaka Nanko submerged tunnel [in Japanese]; Third Port Construction Bureau, Ministry of Transport, Osaka Port and Airport Construction Office

M. Shimoishi, O. Kiyomiya, T. Katsuumi, 2001, New Technology for Immersed Tunnel Construction (V-Block Method), Proceedings ITA WTC Milan 2001, Vol 2, page 445–452

H. Dekking, 1937–1941. The Maastunnel, Monthly magazine dedicated to the interests of the city of Rotterdam in general and the construction of the Maastunnel in particular (in Dutch).

Hideo Kimure, Yoshisuke Katayama and Shingo Toyonaga, 2003, The Development of Bellows Joint for Immersed Tunnels. Tunnel engineering research paper/Report Volume 13 November 2003 [in Japanese]

H. van Tongeren, 1978, The Foundation of Immersed Tunnels, Delta Tunneling Symposium 1–Netherlands.

R. Ojima, T. Jodai, Y. Nakashima and K. Kozawa, 1996. Pouring Works of High Fluidity Concrete for Kobe Port Minatojima Tunnel [in Japanese]; Concrete Journal, Vol. 34, No. 8, pp. 21–28

R. Spreng, R. Bittner, B.C. Gerwick, P Gernigon, A Piquet, 5-7 April 2000, Prefabrication of Tunnel Elements

(Øresund Tunnel Project); The Development and Design of the Casting Yard; Immersed Tunnel Conference, Proceedings, Copenhagen, Denmark

Ren Dongsheng, 2022. Waterproofing Design of the Final Joints of Dalian Bay Immersed Tunnel, China Building Waterproofing, 2022, No. 6, PP47–50

Shuji Eguchi, Yoshikazu Shimazaki, Toshifumi Ikeda, Susumu Kitao, Akira Matsuyama, Yukio Hoshino, Masaru Shinkai, Shigekazu Kawakita, 2005, Regarding construction of new joints for immersed tunnels, The 60th Annual Academic Conference of the Japan Society of Civil Engineers (September 2005) - 539-

Su Quanke, Zhu Yongling, et al, 2022.Hong Kong Zhuhai Macao Bridge-Tunnel project immersed tunnel and artificial islands – From an Owners' perspective, Tunnelling and Underground Space Technology 121 (2022) 104308.

Wang Yong, XU Guoping, LI Yong, et al. (2022). Key Technologies in the Design of the Xiangyang Hanjiang Immersed Tube Tunnel[J].Modern Tunnelling Technology, 2022, 59 (2):192-199+219.

Wilson Sherman Kinxear, 1911. The Detroit River Tunnel. Transactions Paper No 1212, American Society of Civil Engineers

Xiao Jitao, et al, 2022. Comprehensive study on bottom sliding system of segment-jacking method for tunnel closure joint, China Harbour Engineering (J), Vol.42, No. 12, PP13–17.

Tunnelling for a Better Life – Yan, Celestino, Thewes & Eberhardt (Eds)
© 2024 The Author(s), ISBN 978-1-032-80042-4
Open Access: www.taylorfrancis.com, CC BY-NC-ND 4.0 license

Structural optimization design of seamless expansion joint based on finite element analysis

Wei Jiang, Shuangjiao Zhang, Yinghui Wang, Rui Bao & Jinhuan Shan
School of Highway, Chang'an University, Xi'an, China

ABSTRACT: The expansion joint structure is usually installed at discontinuous positions in bridge and immersed tube tunnel projects, serving as a transitional structure while also having the ability to accommodate deformation. To address issues such as stress-induced damage and bonding interface cracking that occurred during the use of expansion joints in immersed tube tunnel, this study conducted a detailed finite element numerical simulation analysis of seamless expansion joints. Firstly, the sources of stress in the seamless expansion joints of the immersed tube tunnel were analyzed clearly. The structural model of the seamless expansion joints was built. Secondly, combined with material variations at different structural locations, stress concentration in the seamless expansion joints under two extreme conditions was analyzed. Finally, the structure of the seamless expansion joint was changed. The impacts of design factors such as chamfer, angle steel component, and layered bonding interfaces on structural stress were analyzed, thus determining an optimized structural design scheme for seamless expansion joints. The results indicated that stress concentration occurred particularly at interfaces A and C of the seamless expansion joint structure. The increase of chamfer structure in the design effectively alleviated stress concentration, reducing maximum principal stress by 52%. Simulation results suggested that the optimal position for the angle steel component was 40 mm from the base point, with an optimal height of 40 mm. For the bonding interface, the layered design was proposed, with a recommended thickness of 50 mm for the lower layer. All three structural optimization designs effectively mitigated stress concentration, improving the crushing failure of the ballast concrete corners and the bonding failure between the expansion joint filling materials and road pavement materials. The relevant research results can provide a reference basis for the design of seamless expansion joint structures.

Keywords: Immersed tube tunnel, Expansion joint structure, Finite element analysis, Stress concentration, Structural optimization

1 INTRODUCTION

Bridges and the pipe joints of immersed tube tunnels experience multidirectional repetitive deformations (Chen et al., 2022). To accommodate these deformations, expansion joints are installed at discontinuous locations within bridges and immersed tube tunnels (Marques et al., 2006). As an integral component of bridge and tunnel engineering, the quality of expansion joints directly impacts the quality and safety of these projects (Lu et al., 2021a; Qian et al., 2000). If the selection of filling materials or the structural design is not reasonable, expansion joints will be prone to defects (Wang et al., 2020; Lee et al., 2019). Seamless expansion joints are a type of expansion joint that use viscoelastic materials as sealing materials, relying on the deformable properties of the filling materials to accommodate deformations in different directions of the expansion joint structure (Xiao, 2016a). Asphalt-based seamless expansion joint materials are typically special asphalt mixtures with excellent deformability. Seamless expansion joints offer advantages such as smoothness, comfort, and noise reduction (Xie et al., 2013). Consequently, they are widely used in small and medium-sized bridges with expansion requirements less than 60mm (Bramel et al., 2000).

However, it has been observed during usage that seamless expansion joints can experience defects like high-temperature rutting, low-temperature cracking, and bond interface delamination (Ren et al., 2021; Li et al., 2021). Asphalt-based sealing materials exhibit significant temperature dependence, becoming soft at high temperatures in summer, making them prone to rutting and extrusion under loads. In contrast, they become stiff and brittle in cold temperatures in winter, leading to reduced deformability and susceptibility to low-temperature cracking and debonding (Mo et al., 2013). Cracks in

DOI: 10.1201/9781003495505-315

seamless expansion joints can progress to material delamination, negatively impacting road smoothness and driving comfort(Marques et al., 2009). Among these, high-temperature rutting and bond interface delamination are relatively common occurrences (Mogawer et al., 2004). In addition to the performance of sealing materials (Liu et al., 2016), the structural design of seamless expansion joints also has a significant impact on the incidence of defects (Partl et al., 2011; Park et al., 2010). Structural optimization and research on sealing material properties are crucial steps in improving the quality and widespread application of seamless expansion joints.

In previous research, scholars mainly focused on filling materials for seamless expansion joints (Jiang. et al., 2023), especially the performance of the binders (Lu et al., 2021b). Min prepared rubber modified asphalt seamless expansion joint what binder using different proportions of recycled rubber powder. The study found that when used the content of recycled rubber powder was 30%, the prepared seamless expansion joint mixture exhibited excellent mechanical properties, with higher high-temperature performance compared to BJ200 mixtures, while their low-temperature performance was similar (Min et al., 2022). Teltayev's research found that using polymer-modified asphalt and measures like adding polyphosphoric acid could effectively improve the low-temperature crack resistance of seamless expansion joint materials (Teltayev et al., 2019). Polyurethane materials have gradually been introduced as an alternative to traditional asphalt-based sealing materials in seamless expansion joints (Meng et al., 2017). Polyurethane flexible expansion joints are considered an optimal solution for small displacement expansion joints in bridge engineering (Kovach et al., 2022), likely due to the robust strength and elasticity of polyurethane materials (Shen et al., 2022). Gallai and colleagues developed a novel polyurethane material. The filling materials that made from this material exhibited superior lifespan and deformability (Gallai, 2016, 2014; Gallai et al., 2018). Therefore, measures such as optimizing material properties (Cao et al., 2023), optimizing mixture composition (Lu et al., 2022), and developing new materials (Funabashi et al., 2021) can enhance the performance of seamless expansion joints, effectively addressing issues of high-temperature rutting and low-temperature cracking (Mo et al., 2012).

The structure of seamless expansion joints in immersed tube tunnels undergoes longitudinal deformation and nonuniform settlement due to some factors such as temperature and vehicle loads. Tensile forces generated by pavement material shrinkage, horizontal forces from vehicle acceleration and deceleration, and vertical pressures from vehicles can lead to stress concentration in certain parts of the seamless expansion joint (Lu et al., 2023). Therefore, research and optimization of seamless expansion joint structures are necessary (Park et al., 2011; Reid et al., 1998). Jiang et al. conducted finite element simulations of longitudinal displacement induced by temperature. The author found that increasing the width of seamless expansion joints could effectively reduce stress at the bonding interface (Jiang. et al., 2020). The bonding interface between the expansion joint filling material and the road pavement material is one of the weak points in the structure (Xiao, 2016b), Xiao studied the main factors influencing interface tensile stress, shear stress, and vertical displacement of the APJ interface. The author found that measures such as changing the properties of the expansion joint filling material, the roughness of the interface, and pavement layer thickness effectively mitigate interface damage behaviors (Xiao, 2016c). Lu et al. used finite element simulation to study the influence of cross over joint steel plates with rectangular and arc-shaped sections on the internal stress of seamless expansion joints, concluding that optimizing the cross-seam steel plate's section shape effectively improves the mechanical performance of seamless expansion joints (Lu et al., 2023). Moor found that adding steel support components to seamless expansion joints can extend their service life (Moor et al., 2016). It indicates that altering the structure of seamless expansion joints can address some of the issues encountered during their use (Ghafoori et al., 2015).

While the above research has investigated the structure and stress of seamless expansion joints, the focus has primarily been on those used in bridge engineering. Currently, there is a limited amount of research on seamless expansion joint structures in immersed tube tunnel engineering. Therefore, leveraging immersed tube tunnel engineering of the Shenzhen-Zhongshan Bridge and employing finite element simulation analysis, this paper, from the perspective of internal stress, combines the condition of seamless expansion joint defects to conduct structural optimization. First, utilizing the Abaqus finite element analysis program, a finite element structural model for the seamless expansion joint in the immersed tube tunnel is constructed. Subsequently, according to the finite element simulation calculations of the original structure, the stress responses within the seamless expansion joint structure are analyzed. Stress concentration phenomena are studied, and the most critical load positions are identified under different limit states. Finally, based on the observed stress concentration within the structure, some structural optimized designs for the seamless expansion joints are proposed, and the optimization rates are determined through finite element simulation calculations.

2 ESTABLISHMENT OF SEAMLESS EXPANSION JOINT STRUCTURAL MODEL

2.1 *Stress sources of seamless expansion joint*

During the operation of immersed tube tunnels, multiple sources of stress act on seamless expansion joints, primarily caused by traffic loads, segment

nonuniform settlement, and temperature variations. The combined stress from multiple sources leads to multidirectional deformation in seamless expansion joints, especially in stress concentration areas, where rapid deformation occurs. It will result in defects such as cracking or bonding interface delamination in seamless expansion joints.

Traffic loads result in compressive, tensile, and shear stresses at seamless expansion joint structures. When the vehicle wheel is positioned above the seamless expansion joint, the load is transmitted downward from the surface of the joint, causing compression deformation in the seamless expansion joint. At this point, the uppermost part of the seamless expansion joint material experiences maximum compressive stress, the lowest part experiences maximum tensile stress, and shear stress develops between the seamless expansion joint filling materials and the road pavement materials. When the vehicle wheel is positioned on the road surface either behind or in front of the seamless expansion joint, minor downward deformation occurs in the road surface, potentially leading to high shear stress between the seamless expansion joint and the road pavement material, as shown in Figure 1.

(a) The loads acting on the expansion joint filling materials

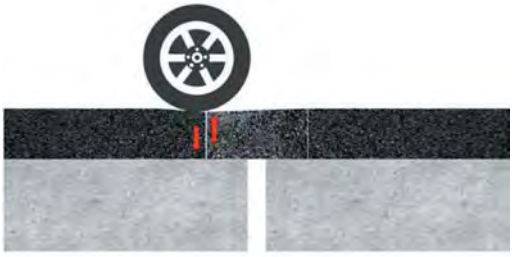

(b) The load acting on the road pavement materials

Figure 1. Schematic of stress changes caused by traffic loads.

Influenced by the uneven settling of the foundation cushion and the siltation above the immersed tunnel segments, nonuniform settlement may occur between segments in the immersed tube tunnel. It results in height differences on both sides of the seamless expansion joint. This leads to vertical shear stresses within the seamless expansion joint, as illustrated in Figure 2.

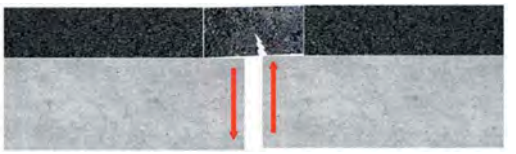

Figure 2. Schematic of stress changes caused by nonuniform settlement.

With temperature variations, the lower ballast concrete and upper road pavement materials undergo longitudinal shrinkage or expansion deformations, causing changes in the spacing between segments. Seamless expansion joints will be stretched or compressed, resulting in longitudinal tensile or compressive stresses within the structure, as shown in Figure 3. The greater the temperature gradient, the more significant the deformation, and consequently, the greater the longitudinal stress within the seamless expansion joint.

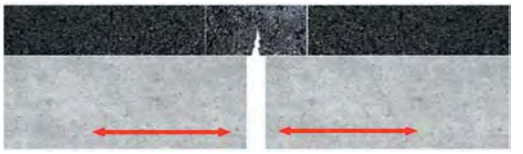

Figure 3. Schematic of stress changes caused by temperature variations.

2.2 *Original structure of seamless expansion joint*

The original structure of seamless expansion joints is depicted in Figure 4(a), primarily comprising ballast concrete, road pavement materials, seamless expansion joint materials, and cross-joint plates. Considering the influence of contact area and boundary conditions, the longitudinal length of the finite element model is set at

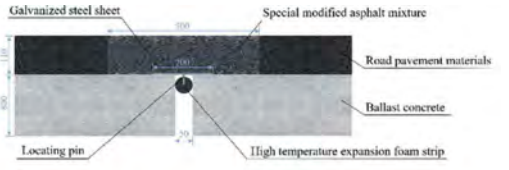

(a) Original structure of seamless expansion joint

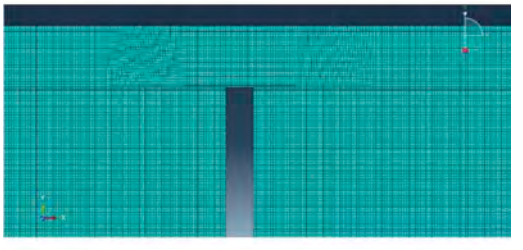

(b) Abaqus model of seamless expansion joint

Figure 4. The structure of seamless expansion joint.

2500mm, with a height of 910mm (Bao, 2021). The finite element model of seamless expansion joints was established by the software ABAQUS 2021, using a four-node bilinear plane stress quadrilateral element (CPS4R). Figure 4(b) shows the finite element model of seamless expansion joints.

Due to variations in material properties and construction times at different sections, the interface between the expansion joint filling material and other components is considered a structural weak point. Park et al. noted that cracks in seamless expansion joints typically occur first at the contact points with the cross over joint steel plates and bridge pavement layers. Based on the current usage of seamless expansion joints, detachment and cracking at the interface are common issues (Park et al., 2011). These detachment and cracking issues often result from excessive local stresses. Therefore, the surfaces, sides, and bottoms of the expansion joint filling material were selected for study. Figure 5 illustrates the schematic of the internal interfaces within the seamless expansion joint structure. Among these, interface A refers to the interface between the cross over a joint steel plate and ballast concrete, interface B refers to the interface between the bottom of the expansion joint filling material and the ballast concrete, interface C pertains to the interface between the expansion joint filling material and the tunnel road pavement material, and interface D represents the upper surface of the expansion joint filling material in contact with the load, with appropriate contact points selected as needed.

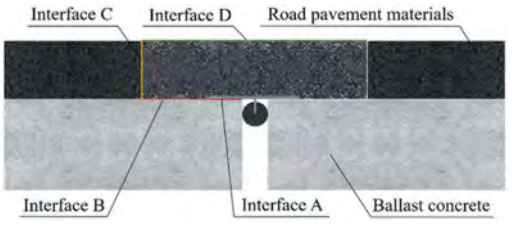

Figure 5. Interface schematic of seamless expansion joint.

2.3 *Parameters of structural model*

Based on the material composition of seamless expansion joints in the reference Shenzhen-Zhongshan Tunnel, this study utilized C30 cement concrete for the ballast concrete, SMA-13 asphalt mixture for the road pavement material, Q235A steel plate for the cross over joint plate, and elastic concrete for the seamless expansion joint filling material. Table 1 presents the parameters of the materials used in various parts of the seamless expansion joint.

The bonding state between seamless expansion joint filling materials and cross over joint steel plates and ballast concrete is not in a fully bonded state. The coefficient of interlayer friction was selected as 0.35. The model was loaded using the standard axle load BZZ-100, with a contact pressure of 0.7 MPa between the tire and the road surface. The applied load was simplified as a rectangular load with dimensions of 192 mm in length and 184mm in width.

Based on the study of the positions of the most unfavorable load for the seamless expansion joint structure, this paper set the load in four different locations. (Load-1)The load was located in the middle of the expansion joint structure; (Load-2) The load's centerline was directly above the left edge of the cross-joint plate; (Load-3) The load was positioned to the left of the expansion joint material, with the left edge of the load coinciding with the left edge of the expansion joint material; (Load-4) The load's centerline was positioned above the bonding interface between the expansion joint material and the road pavement material. Figure 6 shows the schematic diagram of load locations.

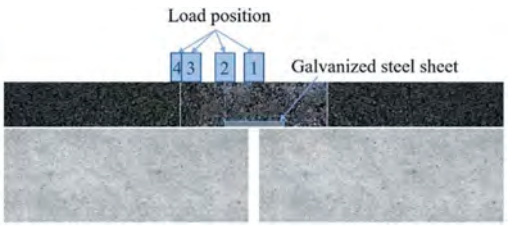

Figure 6. Schematic of load locations.

3 MECHANICAL ANALYSIS OF SEAMLESS EXPANSION JOINT STRUCTURES

3.1 *Stress in nonuniform settlement condition*

The siltation above the immersed tunnel and nonuniform settlement between pipe sections can result in vertical relative displacement in seamless expansion

Table 1. Material parameters of the seamless expansion joint structural model.

Components	Materials	Elastic Modulus/ (MPa)	Poisson's Ratio	Thickness/ (mm)	Density/ (kg/m^3)
Road Pavement Material	Asphalt Mixture	1400	0.30	110	2600
Ballast Concrete	Cement Concrete	30000	0.25	800	2100
Cross Over Joint Plate	Galvanized Steel Sheet	206000	0.28	4	7850
Expansion Joint Filling Material	Elastic Concrete	800	0.40	110	2200
Anchor Bolt	Angle Steel	206000	0.28	4	7850

joints. According to the design data of the Shenzhen-Zhongshan Tunnel, a maximum relative displacement of up to 10 mm vertically between pipe sections has occurred. One side of the seamless expansion joint structure was fixed, while the other side experiences a 10 mm settlement. The structural maximum principal stress, structural maximum shear stress, and maximum principal stress and shear stress at interface A of the seamless expansion joint structure have been calculated when subjected to different load positions.

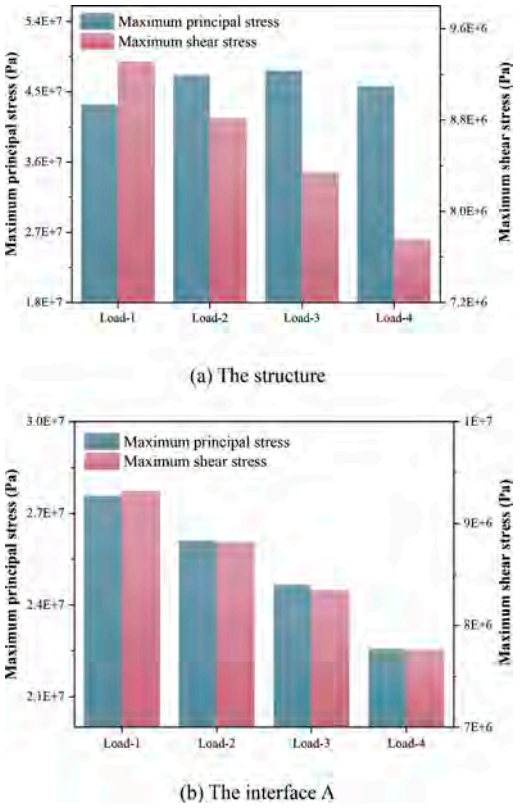

Figure 7. Stress changes in seamless expansion joint structure under different load application positions in nonuniform settlement condition.

Figure 7 presents the stress in seamless expansion joint structure under different load application positions in nonuniform settlement conditions. Under conditions of maximum nonuniform settlement, the maximum principal stress and maximum shear stress in the seamless expansion joint structure and interface A varied with different load positions. When the load was applied at Load-2 and Load-3 positions, the maximum principal stress in the seamless expansion joint structure was the highest, followed by the Load-4 position. When the load was applied at the Load-1 position, the maximum principal stress in the seamless expansion joint structure was the lowest, but the maximum shear stress was the highest. The maximum shear stress and maximum principal stress at interface A were ranked from highest to lowest as Load-1, Load-2, Load-3, and Load-4, indicating that Load-1 is the most unfavorable load position for interface A. The maximum principal stress at interface A was 64%, 55%, 52%, and 49% of the maximum principal stress in the structure, respectively, showing that stress concentration at interface A was more pronounced when Load-1 was applied. The reason may be Load-1 is closest to the corner of the ballast concrete.

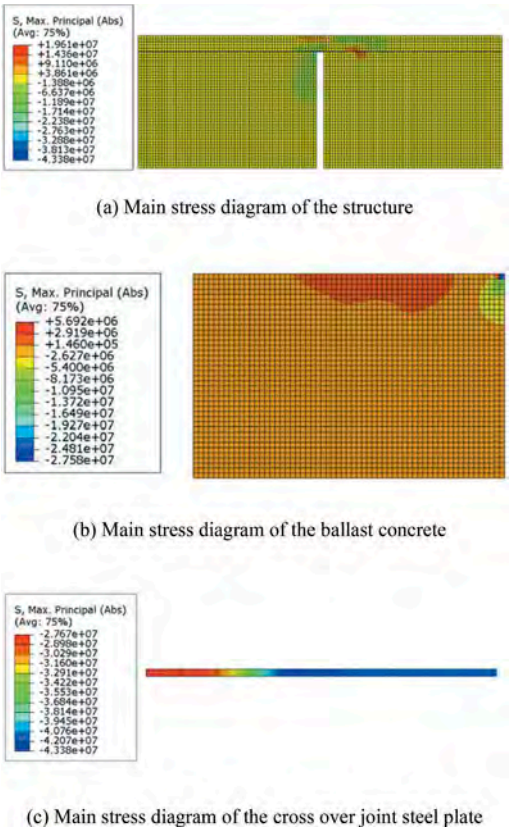

Figure 8. Main stress diagram of seamless expansion joint in nonuniform settlement condition.

Figure 8 shows the stress distribution in the seamless expansion joint structure when the load is at the Load-1 position. When there was a 10 mm vertical displacement between pipe sections, the maximum principal stress in the seamless expansion joint was 43 MPa, occurring at the cross-joint steel plate. Stress concentration was observed on the upper surface of the ballast concrete just below the cross-joint steel plate (interface A), with a maximum compressive stress of 28 MPa at the corner of the ballast concrete. Prolonged loading may lead to localized stress concentration, potentially causing crushing failure at the corner of the ballast concrete. This phenomenon may be attributed to the gap between the segments of the submerged tunnel

below the Load-1 position, where stress cannot propagate downward, resulting in significant stress concentration at interface A.

3.2 *Stress in longitudinal tension condition*

Changes in temperature and the longitudinal effects of traffic loads can lead to longitudinal stretching or compression of the seamless expansion joint structure. Temperature variations cause different degrees of deformation in various parts of the seamless expansion joint, resulting in changes in its length. During the driving process, horizontal forces are resulted between traffic loads and the road surface, which have a certain impact on the dimensions of the seamless expansion joint. According to the design data of the Shenzhen-Zhongshan Tunnel, the seamless expansion joint structure was designed to undergo a 25 mm longitudinal stretching. When subjected to loads at different positions, the maximum principal stress, maximum shear stress, and maximum principal stress and shear stress at interface C of the seamless expansion joint structure have been calculated.

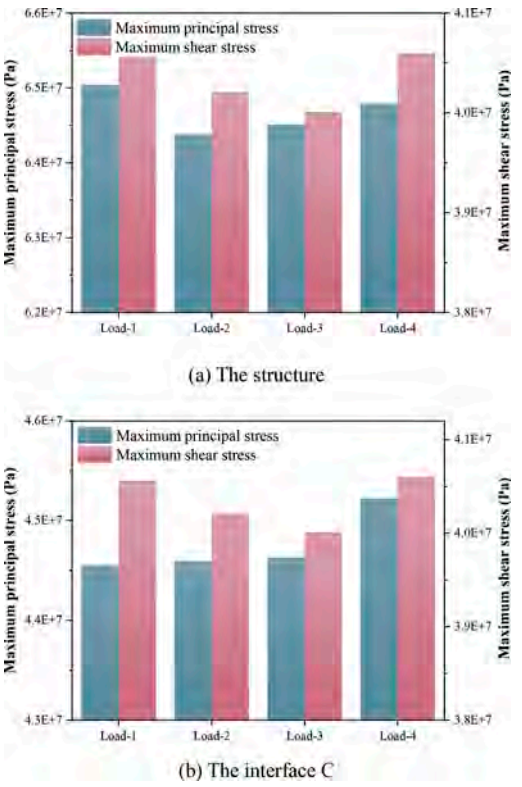

Figure 9. Stress changes in the seamless expansion joint structure under different load application positions in longitudinal tension condition.

Figure 9 shows that the stress in the seamless expansion joint structure under different load application positions in longitudinal tension conditions. Under conditions of longitudinal stretching, the maximum principal stress of the seamless expansion joint structure was in descending order, which is Load-1, Load-4, Load-3, and Load-2. The maximum principal stress at interface C was ranked as Load-4, Load-3, Load-2, and Load-1. The maximum principal stress at interface C was 68%, 69%, 69%, and 70% of the maximum principal stress in the structure, respectively. It indicates that the stress concentration at interface C is relatively more pronounced when the load is at Load-4. The maximum shear stress at interface C was ranked in descending order as Load-4, Load-1, Load-2, and Load-3, indicating that Load-4 is the least favorable load position for interface C. Although both Load-3 and Load-4 edges coincide with interface C, Load-4 is farther from the edge of the ballast concrete than Load-3. Consequently, the load at Load-3 causes greater vertical deformation of the ballast concrete, leading to a decrease in relative displacement between the road pavement material and the expansion joint material, resulting in higher shear stress at interface C for Load-4.

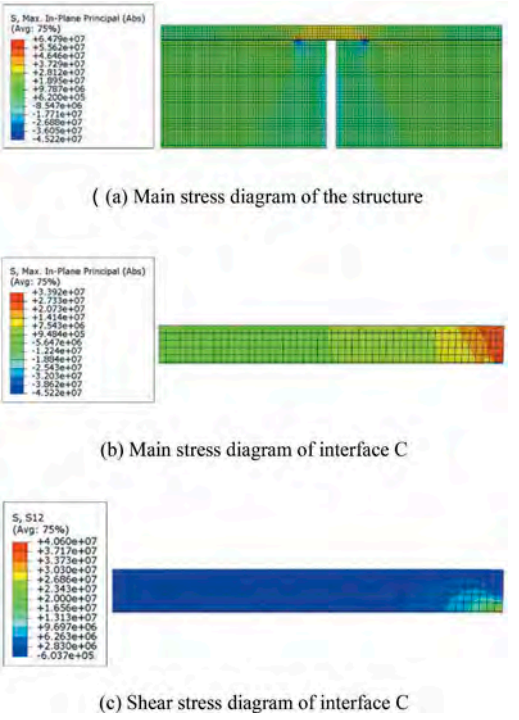

Figure 10. Stress diagram of seamless expansion joint in longitudinal tension condition.

Figure 10 depicts the strain condition of the seamless expansion joint structure when the load is applied at position Load-4. When there was maximum longitudinal stretching between pipe sections, the maximum shear stress in the seamless expansion joint was 41 MPa, occurring at the bonding interface between the seamless expansion joint material and the paving

material, namely, interface C exhibits stress concentration. This result may be due to the differences between the road pavement material and the expansion joint material. The road pavement material undergoes vertical deformation under load. Due to the bonding between the road pavement material and the expansion joint material, interface C experiences higher stress to accommodate the deformation of the road pavement material. It also explains why the seamless expansion joint is highly prone to delamination and cracking at the bonding interface.

4 OPTIMIZATION DESIGN OF SEAMLESS EXPANSION JOINT STRUCTURE

4.1 *Optimization design of the ballast concrete section*

To mitigate stress concentration at the corners of the ballast concrete, chamfer structures are introduced at the edges of the ballast concrete, simultaneously filled with elastic composite material. Figure 11 depicts the optimized design of the ballast concrete section and the contact points a_1 and a_2, which are the vertices of the ballast concrete. The finite element simulations were performed on the expanded joint structure with added chamfer structures (Optimized Structure 1) under maximum differential settlement conditions. The load was at the position of the most unfavorable load. The stress of the seamless expansion joint structure under extreme conditions has been calculated and analyzed.

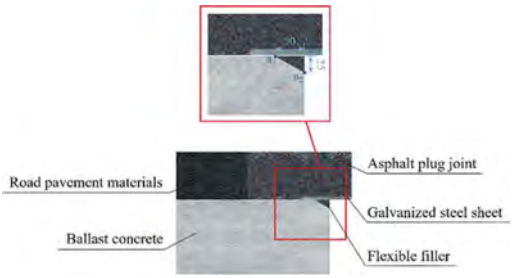

Figure 11. Schematic diagram of optimized design for the ballast concrete part.

Figure 12 presents stress results for the overall structure, interface A and the two contact points. The Optimized Structure 1 features chamfer structures added to the seamless expansion joint. It is evident that under maximum settlement conditions, the maximum principal stress in the Optimized Structure 1 shows little change compared to the original structure. However, the maximum principal stress at interface A decreased from 28 MPa to 13 MPa, a reduction of 52% compared to the original structure. The principal stresses at the corners of the ballast concrete were reduced by 72% and 57%, respectively. The addition of chamfer structures significantly reduced the maximum shear stress in the seamless expansion joint structure, decreasing it from 9 MPa to 4 MPa, a reduction of 56% compared to the original structure. Shear stresses at contact points a_1 and a_2 were reduced by 75% and 85%, respectively, compared to the original structure. This reduction is likely due to the stress-buffering effect of the filling material at the chamfer locations. Adding chamfer structures in seamless expansion joints can reduce the principal and shear stresses in

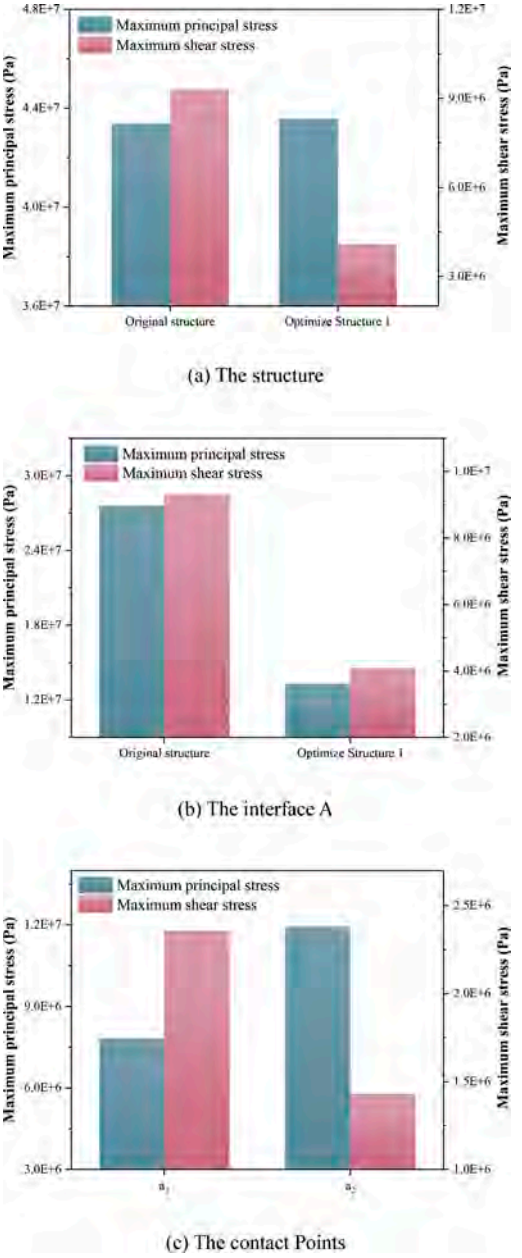

Figure 12. Stress changes in the seamless expansion joint after increasing chamfer in nonuniform settlement condition.

the ballast concrete, effectively improving stress concentration at the corners. Therefore, in conditions with significant vertical deformation of the seamless expansion joint structure, the recommended structural optimization approach is to add chamfers.

4.2 *Optimization design of the expansion joint filling material section*

To improve the stress concentration, at the bonding interface between the expansion joint filling material and the road pavement material, an attempt was made to introduce the angle steel components within the seamless expansion joint to reduce stress at the bonding interface. Figure 13 provides a schematic representation of the optimized design for a portion of the seamless expansion joint. The distance between the bonding interface and the cross over joint steel plate was 150 mm. The optimal position of the angle steel component was determined through finite element analysis. The thickness of the angle steel component matched that of the cross over joint steel plate. The height of the angle steel component was determined through finite element analysis. Finite element simulations were conducted on the seamless expansion joint structure with added angle steel components (Optimized Structure 2) under maximum longitudinal stretching conditions. The load was applied at the most critical position to analyze stress responses under extreme conditions. The lowest point on the bonding interface was selected as contact point c_1.

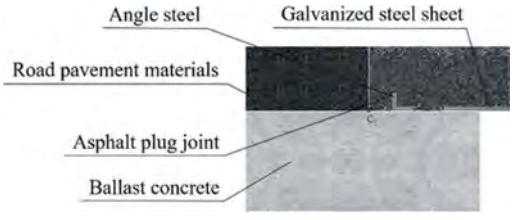

Figure 13. Schematic diagram of optimized design for the expansion joint filling material part.

4.2.1 *Position of the angle steel component*

When determining the horizontal position of the angle steel component, the height of the angle steel component was selected as 40 mm. The contact point c_1 was considered as the base point. The distance between the angle steel component and the base point was 10 mm, 20 mm, 30 mm, 40 mm, 50 mm, 60 mm, and 70 mm. Figure 14 and Figure 15 show the simulation results.

Figure 14 illustrates the schematic of the shear stress on interface C, comparing the shear stress in the original structure to those in the structures with adding the angle steel components. It is evident that without the angle steel components, the shear stress values on interface C were consistently higher than in the optimized structures. Contact point c_1 represented the location of maximum shear stress on interface C, making the stress value at contact point c_1 the crucial

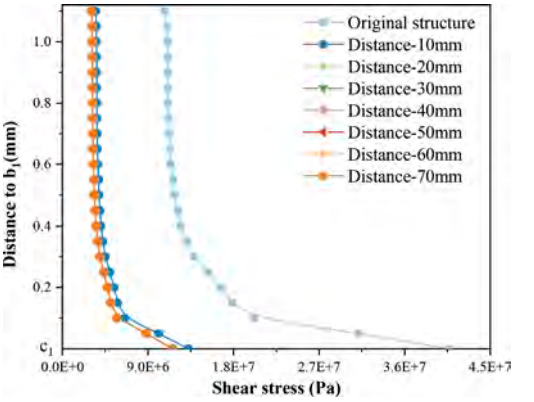

Figure 14. Shear stress diagram of interface C when the angle steel component is at different horizontal positions.

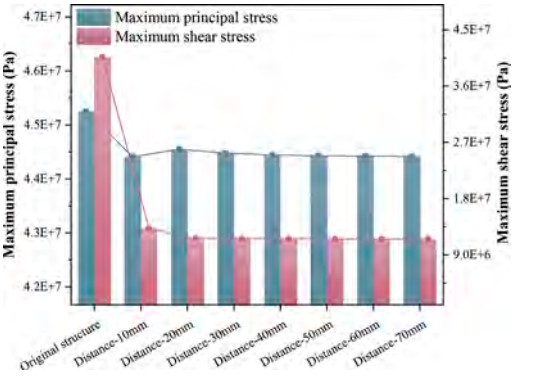

Figure 15. Stress changes of interface C when the angle steel component is at different horizontal positions.

parameter for determining the optimal placement of the angle steel component. Figure 15 shows the maximum principal stress and maximum shear stress on interface C. The maximum principal stress and maximum shear stress at interface C of the original structure reached 45 MPa and 41 MPa, respectively. As for the optimized structure, the position of the angle steel component varied, resulting in differences in the maximum principal stress and maximum shear stress on interface C. However, these values were overall lower than in the original structure. As the distance between the angle steel component and the base point increased, the maximum principal stress on interface C initially rose and then stabilized. The maximum principal stress reached a stable state when the distance was 40mm. The maximum shear stress on interface C decreased with increasing distance from the angle steel component to the reference point. And as the distance increased, the decreasing trend gradually stabilized. When the distance between the angle steel component and interface C was 40 mm, the decreasing trend reached a stable state, with a decrease rate of about 72%. Therefore, the recommended distance between the angle steel component and the reference point is 40 mm.

4.2.2 *Height of the angle steel component*

Based on the previous finite element analysis results, the distance between the angle steel component and the reference point was set to 40 mm. The height of the angle steel component was 10 mm, 20 mm, 30 mm, 40 mm, and 50 mm, respectively. Figure 16 and Figure 17 show the finite element simulation results.

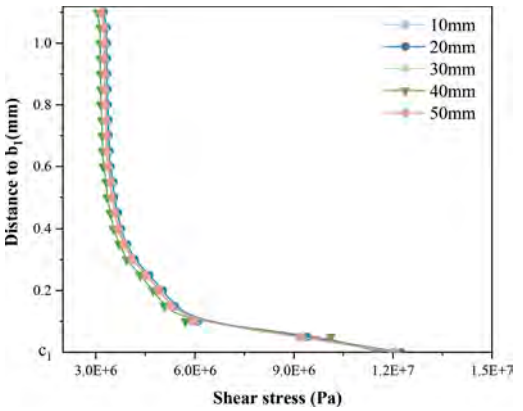

Figure 16. Shear stress diagram of interface C when the angle steel component is of different heights.

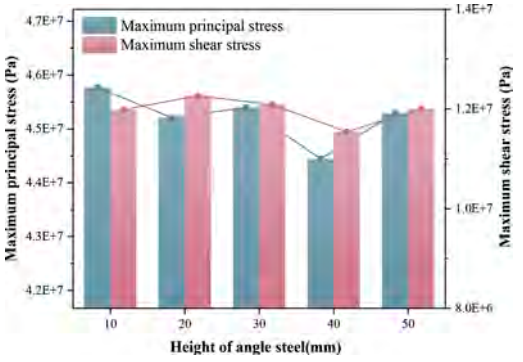

Figure 17. Stress changes of interface C when the angle steel component is of different heights.

Figure 16 provides the schematic of the shear stress on interface C for different heights of the angle steel components. From the figure, it can be observed that the height of the angle steel component has a relatively minor impact on the principal stress on interface C. However, when the height of the angle steel component was 40mm, the stress of interface C was slightly lower than the stress at other heights. Figure 17 illustrates the maximum principal stress and maximum shear stress on interface C for different heights of the angle steel components. The relationship between the maximum principal stress and maximum shear stress on interface C and the height of the angle steel component is not significant. Following the trend of increasing maximum principal stress on interface C, the order of the angle steel component heights was 40 mm, 20 mm, 50 mm, 30 mm, and 10 mm. Following the trend of increasing maximum shear stress on interface C, the order of the angle steel component heights was 40 mm, 10 mm, 50 mm, 30 mm, and 20 mm. It indicates that when the height of the angle steel component is 40 mm, the values of maximum principal stress and maximum shear stress on interface C are lowest, resulting in the most optimal design effect. Therefore, a height of 40 mm for the angle steel component can be recommended. The optimization design involving the addition of the angle steel components not only significantly reduces the shear stress in the seamless expansion joint structure but also, to some extent, diminishes the principal stress in the same structure. Therefore, it is suggested to adopt this optimization design under heavy traffic load conditions.

4.3 *Optimization design of the road pavement section*

To mitigate the stress concentration at the bonding interface between the seamless expansion joint filling material and road pavement material and to reduce the relative deformation between these materials, an approach involving stepped layering in the road pavement section is adopted. Considering the relatively small road thickness, a two-stage cutting method was employed. During construction, cutting can be carried out separately, followed by the pouring of the expansion joint material together. Figure 18 depicts the optimized design for the road pavement section. For the seamless expansion joint structure with adding a stepped layered design (Optimized Structure 3), the finite element simulation was performed in the maximum longitudinal stretching state. The load was applied at the position of the most unfavorable load to analyze stress responses under extreme conditions. Figure 19 presents the finite element simulation results.

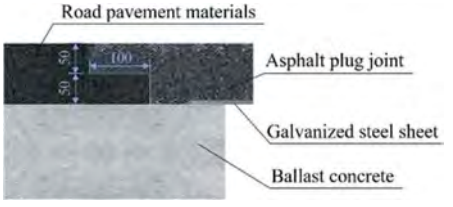

Figure 18. Schematic diagram of optimized design for the road pavement part.

Figure 19 displays the simulation results for the maximum principal stress and maximum shear stress of the overall structure and interface C. The Optimized Structure 3 represented the seamless expansion joint structure by adding a stepped layered design. When the longitudinal tensile deformation reaches its maximum state, the maximum principal stress in the Optimized Structure 3 increased from 41 MPa to 70 MPa, and the maximum principal stress on interface C increased from 45 MPa to 49 MPa. Compared to the original structure, these values increased by 8% and 9%,

respectively. This result could be attributed to the higher stress transfer efficiency within the expansion joint filling materials compared to the road pavement materials. After optimizing the road pavement section, the maximum shear stress in the seamless expansion joint structure significantly decreased. The maximum shear stress in the structure reduced from 41 MPa to 33 MPa, and the maximum shear stress on interface C decreased from 41 MPa to 12 MPa. Compared to the seamless expansion joint before optimization, these values decreased by 19% and 71%, respectively. The reason may be that the stepped layered design can reduce the relative deformation between the expansion joint material and road pavement material. Due to there being no joint in the upper part of the road pavement material section, the shear stress is shared by both the expansion joint filling material and part of the interface. It indicates that adding a stepped layered design to seamless expansion joints can reduce shear stress occurring at the bonding interface and effectively improve stress concentration at the bonding interface. Although the stepped layering design can effectively fall shear stress at the bonding interface, it may increase the principal stress of the structure to some extent. Therefore, incorporating the structural optimization method with the stepped layering design can be adopted under light traffic load conditions.

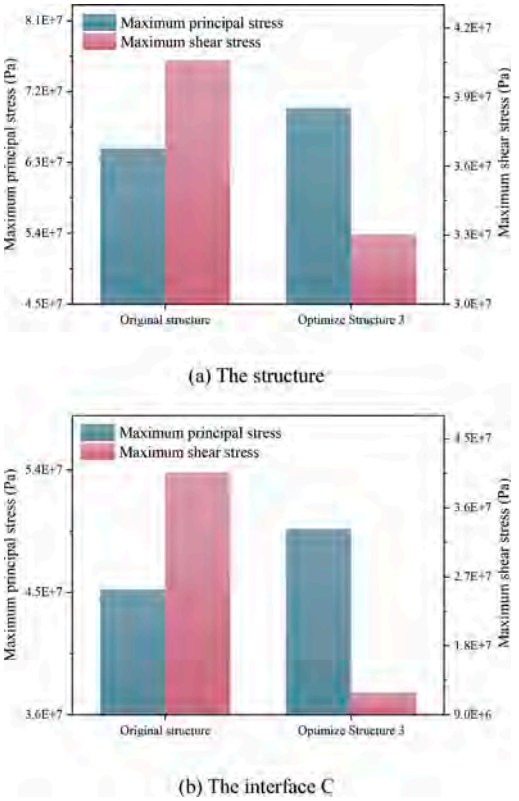

Figure 19. Stress changes in the seamless expansion joint after increasing layered design in longitudinal tension condition.

4.4 *Comparison of different optimization designs*

Figure 20 illustrates the optimization rates of different seamless expansion joint structural stress compared to the original structural stress. It can be seen that all three optimization structures significantly improve the shear stress in the structure and interfaces. The Optimized Structure 1 had a minor adverse impact on the principal stress of the structure, but the maximum principal stress in the Optimized Structure 1 occurred at the cross over joint steel plate, and the stress values were within the allowable stress range. Therefore, the Optimized Structure 1 exhibits good optimization results. The Optimized Structure 2 reduced the principal stress in the structure and interfaces to some extent but involved relatively complex construction processes. Hence, it can be recommended for use on road surfaces with heavy traffic loads. The Optimized Structure 3 harmed the principal stress in the seamless expansion joint structure and interfaces. However, this structure significantly improved the phenomenon of shear stress concentration at the bonding interface of the seamless expansion joint. Therefore, it can be suggested for use under conditions of light traffic loads.

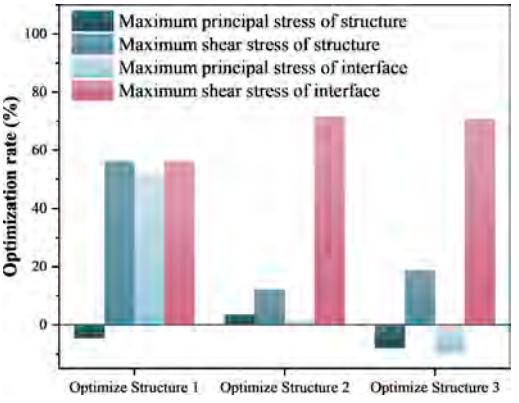

Figure 20. Optimization rate of different optimize structures.

5 CONCLUSIONS

(1) Finite element analysis indicated that under non-uniform settlement conditions, the seamless expansion joint structure was prone to stress concentration at interface A, between the cross over joint steel plate and the ballast concrete, with the middle position of the expansion joint structure representing the position of the most unfavourable load. In the longitudinal deformational state, the seamless expansion joint structure was susceptible to stress concentration at interface C, between the expansion joint filling material and the road pavement material, with the position where the load's centerline coincides with the bonding interface being the position of the most unfavourable load.

(2) The structural design of adding chamfer to the ballast concrete section resulted in a 52% reduction in maximum principal stress and a 56% reduction in maximum shear stress between the cross over joint steel plate and ballast concrete, effectively improving stress concentration. This design optimization can be recommended for use in conditions where vertical deformation of the seamless expansion joint structure is significant.

(3) Finite element simulation results indicated that the optimal position for adding the angle steel component was 40 mm from the base point, with an optimal height of 40 mm. After adding the angle steel components to the expansion joint material, the maximum principal stress and maximum shear stress between the expansion joint material and road pavement material decreased by 2% and 72%, respectively, effectively improving stress concentration at the bonding interface. This optimization can be recommended for conditions with significant longitudinal stretching deformation and heavy traffic loads.

(4) Adopting a stepped layering design in the road pavement section with a recommended lower layer thickness of 50 mm resulted in a 9% increase in maximum principal stress and a 71% decrease in maximum shear stress between the expansion joint filling material and road pavement material compared to original structure. This result significantly reduced shear stress at the bonding interface. However, the addition of a stepped layering design had an adverse effect on the principal stress of the seamless expansion joint structure. Therefore, it can be recommended for use under conditions with significant longitudinal stretching deformation and light traffic loads.

ACKNOWLEDGMENTS

This project was jointly supported by Key Technologies R&D Program of Guangdong Province (2019B111105002) and National Natural Science Foundation of China (Grant No. 52122809, Grant No. 52038001).

REFERENCES

Bao, R. 2021. *Research on Design and Performance of High Elastic Filling Material Used for Pavement Segment Joint of Immersed Tube Tunnel*. Master Thesis. Chang'an University, Shaan'xi, China.

Bramel, B. K., Dolan, C. W., Puckett, J. A., et al. 2000. Asphalt plug joints: Refined material tests and design guidelines. *Transportation Research Record*(1740), 126–134. doi:10.3141/1740-16.

Cao, L., Li, L., Yang, H., et al. 2023. Gradation design and performance evaluation of modified asphalt mixture for bridge asphalt plug joint design. *Constr Build Mater, 367*. doi:10.1016/j.conbuildmat.2022.130211

Chen, W. L., Zhang, S. J., Jin, W. L., et al. 2022. Review of Research Status and Development of Seamless Expansion Joints Materials. *Transport Research*, *8*(05), 64–74. doi:10.16503/j.cnki.2095-9931.2022.05.008

Funabashi, K., Sakano, M., Gallai, G. 2021. *Superior PU-based alternative to the asphaltic plug expansion joint - The "PA joint" in Japan*. Paper presented at the 10th International Conference on Bridge Maintenance, Safety and Management, IABMAS 2020, April 11, 2021 - April 15, 2021, Sapporo, Japan.

Gallai, G. 2014, 2014//. *The First European Approval for an Expansion Joint Flexible Plug Joint System with New Material*. Paper presented at the The Eight International Conference "Bridges in Danube Basin", Wiesbaden.

Gallai, G. 2016. *Flexible Plug Joint System with New Material*. Paper presented at the 9th International Conference Bridges in Danube Basin, BDB 2016, September 30, 2016 - October 1, 2016, Zilina, Slovakia.

Gallai, G., Mettner, K., Savioz, P. 2018. *Next-generation flexible plug expansion joints*. Paper presented at the IABSE Conference, Kuala Lumpur 2018: Engineering the Developing World, April 25, 2018 - April 27, 2018, Kuala Lumpur, Malaysia.

Ghafoori, N., Sharbaf, M. 2015. *Bridge deck asphalt plug joints: Problems and solutions*. Paper presented at the 6th International Conference on Bituminous Mixtures and Pavements, ICONFBMP 2015, June 10, 2015 - June 12, 2015, Thessaloniki, Greece.

Jiang, S. J., Hailesilassie, B. W., Hean, S., et al. 2020. Modelling structural response of flexible plug expansion joints under thermal movements. *Road Materials and Pavement Design*, *21*(4), 1027–1044. doi:10.1080/14680629.2018.1534695

Jiang, W., Yuan, D. D., Zhang, S. J., et al. 2023. Experimental analysis of deformation-adapted binders and their mixture performance. *Constr Build Mater, 389*. doi:10.1016/j.conbuildmat.2023.131733

Kovach, F., Moor, G., Ortmann, D. 2022. *A state-of-the-art, flexible, easy-to-replace plug-type expansion joint for the Delaware Memorial Bridge*. Paper presented at the IABSE Symposium Prague 2022: Challenges for Existing and Oncoming Structures, May 25, 2022 - May 27, 2022, Prague, Czech republic.

Lee, K. A., Atadero, R. A., Mahmoud, H. N. 2019. Life Cycle Cost Analysis of Deteriorated Bridge Expansion Joints. *Practice Periodical on Structural Design and Construction*, *24*(1). doi:10.1061/(ASCE)SC.1943-5576.0000407

Li, C., Pan, K., Wang, L. 2021. Low-temperature cracking performance of asphalt mixture based on stepwise loading bending creep test. *Zhongnan Daxue Xuebao (Ziran Kexue Ban)/Journal of Central South University (Science and Technology)*, *52*(7), 2450–2458. doi:10.11817/j.issn.1672-7207.2021.07.030

Liu, S., Mo, L., Wang, K., et al. 2016. Preparation, microstructure and rheological properties of asphalt sealants for bridge expansion joints. *Constr Build Mater*, *105*, 1–13. doi:10.1016/j.conbuildmat.2015.12.017

Lu, P. Z., Huang, S. M., Shen, Y., et al. 2022. Mix design of asphalt plug joint based on response surface method and grey relational analysis. doi:10.1080/10298436.2022.2032699

Lu, P. Z., Wang, J. H., Ye, K., et al. 2023. Asphalt plug joint geometric analysis and improvement. *Case*

Studies in Construction Materials, 18. doi:10.1016/j.cscm.2023.e02011

Lu, P. Z., Zhou, C. H., Huang, S. M., et al. 2021b. Study on rheological properties of asphalt binders for seamless expansion joints of bridges. *Australian Journal of Structural Engineering*, *22*(1), 10–18.

Lu, P. Z., Zhou, C. H., Huang, S. M., et al. 2021a. Experimental Study on Mix Ratio Design and Road Performance of Medium and Small Deformation Seamless Expansion Joints of Bridges. *Transportation Research Record*, *2675*(5), 48–59.

Marques, L. J., Brito, J. 2009. Inspection survey of 150 expansion joints in road bridges. *Engineering Structures*, *31*(5), 1077–1084. doi:10.1016/j.engstruct.2009.01.011

Marques, L. J., De Brito, J. 2006. *Road bridge expansion joints: Existing systems and most common defects*. Paper presented at the 3rd International Conference on Bridge Maintenance, Safety and Management - Bridge Maintenance, Safety, Management, Life-Cycle Performance and Cost, July 16, 2006 - July 19, 2006, Porto, Portugal.

Meng, N., Gallai, G., Bailles, B. 2017. *Polyurethane flexible plug expansion joints - Characteristics, benefits and case studies*. Paper presented at the 39th IABSE Symposium in Vancouver 2017: Engineering the Future, September 21, 2017 - September 23, 2017, Vancouver, BC, Canada.

Min, Z. H., Wang, Q. C., Zhang, K., et al. 2022. Investigation on the properties of epoxy asphalt mixture containing crumb rubber for bridge expansion joint. *Constr Build Mater, 331*. doi:10.1016/j.conbuildmat.2022.127344

Mo, L. T., Shu, D. L., Li, X., et al. 2012. Experimental investigation of bituminous plug expansion joint materials containing high content of crumb rubber powder and granules. *Materials and Design*, *37*, 137–143. doi:10.1016/j.matdes.2012.01.003

Mo, L. T., Xie, Y. J., Dai, Y., et al. 2013. Review on asphalt plug joints: Performance, materials, testing and installation. *Constr Build Mater*, *45*, 106–114. doi:10.1016/j.conbuildmat.2013.03.089

Mogawer, W. S., Austerman, A. J. 2004. Evaluation of asphaltic expansion joints. *Bituminous Binders*.

Moor, G., Gallai, G., Meng, N. 2016. *Flexible plug expansion joints - Benefits of polyurethane versus bituminous*. Paper presented at the 19th IABSE Congress Stockholm 2016: Challenges in Design and Construction of an Innovative and Sustainable Built Environment, September 21, 2016 - September 23, 2016, Stockholm, Sweden.

Park, P., El-Tawil, S., Park, S. Y. 2011. Improved geometric design of bridge asphalt plug joints. *Journal of Bridge Engineering*, *16*(1), 158–165. doi:10.1061/(ASCE)BE.1943-5592.0000121

Park, P., El-Tawil, S., Park, S. Y., et al. 2010. Behavior of bridge asphalt plug joints under thermal and traffic loads. *Journal of Bridge Engineering*, *15*(3), 250–259. doi:10.1061/(ASCE)BE.1943-5592.0000056

Partl, M. N., Hean, S. 2011. Experience with Testing and Performance Evaluation of Bituminous Plug Expansion Joints on Concrete Road Bridges. *International Journal of Roads & Airports*, *16*(1), 158–165.

Qian, Z. Q., Akisanya, A. R., Imbabi, M. S. 2000. Effects of geometry on the deformation of asphaltic plug joints subjected to surface tractions. *Journal of Strain Analysis for Engineering Design*, *35*(5), 403–413. doi:10.1243/0309324001514170

Reid, M. D., Imbabi, M. S., Coutellier, D. 1998. Effects of joint geometry on response of asphaltic plug joints. *Journal of Transportation Engineering*, *124*(4), 311–318. doi:10.1061/(ASCE)0733-947X(1998)124:4(311)

Ren, D. Y., Mei, Y. K., Zhang, J. K., et al. 2021. Distinguishing Evaluation of High Temperature Performance Index of Seamless Expansion Joint Asphalt Binder. *Jianzhu Cailiao Xuebao/Journal of Building Materials*, *24*(2), 440–446. doi:10.3969/j.issn.1007-9629.2021.02.030

Shen, G., Savioz, P., Ortmann, D. 2022. *The Modern PU-Based Flexible Plug Expansion Joint for Bridges - The Ideal Solution For City Expressways With Recent Innovations Making Installation Even Faster and More Reliable than Before*. Paper presented at the IABSE Congress Nanjing 2022 - Bridges and Structures: Connection, Integration and Harmonisation, September 21, 2022 - September 23, 2022, Nanjing, China.

Teltayev, B. B., Rossi, C. O., Izmailova, G. G., et al. 2019. Evaluating the effect of asphalt binder modification on the low-temperature cracking resistance of hot mix asphalt. *Case Studies in Construction Materials, 11*. doi:10.1016/j.cscm.2019.e00238

Wang, T., Wang, M., Peng, Z. T., et al. 2020. Service Status and Disease Analysis of Asphalt Pavement of Immersed Tunnel. *Tunnel Construction*, *40*(S1), 429–435.

Xiao, M. M. 2016a. *Research on the Interfacial Mechanics Behavior Characteristics of Asphalt Plug Expansion Joint Pavement*. Paper presented at the 16th COTA International Conference of Transportation Professionals: Green and Multimodal Transportation and Logistics, CICTP 2016, July 6, 2016 - July 9, 2016, Shanghai, China.

Xiao, M. M. 2016b. Mixture composition design and interface properties of asphalt plug expansion joint. *Huanan Ligong Daxue Xuebao/Journal of South China University of Technology (Natural Science)*, *44*(8), 106–113. doi:10.3969/j.issn.1000-565X.2016.08.016

Xiao, M. M. 2016c. Mechanical Behavior Characteristics of Asphalt Plug Expansion Joint Pavement's Interface. *Journal of South China University of Technology(Natural Science Edition)*, *44*(06), 105–112.

Xie, Y. J., Mo, L. T., Su, D. L., et al. 2013. Investigation into fundamental properties of bituminous plug expansion joint filling mixtures containing rubber granules. *Constr Build Mater*, *47*, 984–989. doi:10.1016/j.conbuildmat.2013.06.001

Tunnelling for a Better Life – Yan, Celestino, Thewes & Eberhardt (Eds)
© 2024 The Author(s), ISBN 978-1-032-80042-4
Open Access: www.taylorfrancis.com, CC BY-NC-ND 4.0 license

Analysis and research on seismic effects of immersed tunnel joints of Shenzhen-Zhongshan Link

Zhi Li*, Zheng Jie Chen & Hong Chen
Shanghai Tunnel Engineering & Rail Transit Design and Research Institute, Shanghai, China

ABSTRACT: The immersed tunnel of Shenzhen-Zhongshan Link is the first to adopt the steel shell concrete structure in China, and the immersed tunnel section is ultra-wide, ultra-long and ultra-deep with complicated stress on the element joints under seismic effects. A refined three-dimensional model was established for the elements (Element 2 to Element 5) with significant changes in shallow stratum by the nonlinear time-history analysis method. The model included foundation soil, backfill materials, immersed tunnel structure, GINA gasket, horizontal shear key, vertical shear key, etc. Under the horizontal & transverse seismic and horizontal & longitudinal seismic effects in earthquake fortification and rare working conditions, the unevenness of foundation stiffness and the stress characteristics of GINA gaskets and shear keys are mainly considered. The compression of element joints opening, shear forces of shear keys, and interlayer displacement angles of elements were calculated to verify the safety, water tightness, and overall deformation performance of the element joints under seismic conditions, providing a reference for engineering design.

Keywords: Immersed tunnels, Element joints, Seismic effects, Time-history analysis

1 INTRODUCTION

Immersed tunnels have become an important means of crossing rivers, harbors, and sea due to their unique advantages. Immersed tunnels are generally shallower in depth, more susceptible to seismic effects. Meanwhile, the immersed tunnel is formed by multiple elements and requires very high performance of the sealing, and stress behavior. During the earthquake, the immersed tunnels buried in soil layers are generally less likely to experience collapse like structural damage, but the elements are prone to significant deformation due to their low stiffness, which poses a safety hazard to the normal operation of immersed tunnels. Therefore, the study on the stress deformation at the element joint under earthquake action is of great significance for its seismic safety evaluation.

Today, there has been some research on the overall dynamic response of immersed tunnels under earthquake action and the seismic performance analysis of local refined structures. The nonlinear seismic performance of immersed tunnel structures under deep water were calculated and analysed by establishing a beam and spring model (Anastasopoulos, 2007); an analytical model for the seismic response of the immersed tunnel in Tianjin Haihe River was established, and calculated the stiffness of the steel tension cables, horizontal shear keys, vertical shear keys, and GINA gaskets in the direction of corresponding degrees of freedom, and then conducted the nonlinear spring simulation through superimposed the above equivalent stiffness (Zhang et al., 2011); The dynamic calculation method of the interaction between soil and structure in the immersed tunnel of Hong Kong-Zhuhai-Macao Bridge, and the seismic response analysis method for ultra long immersed tunnels under non-uniform seismic effects were elabrated (Yu et al., 2012); a 3D dynamic time history analysis model of the soil-waterstop-immersed tunnel system were established based on the immersed tunnel of Hong Kong-Zhuhai-Macao Bridge, in which the waterstop was simulated by elastic rubber material (Qiu et al., 2019).

In this paper, 3D time history analysis method was adopted to accurately simulate the stratum fluctuation changes, treated soil and backfill materials that have a great impact on earthquake response. Spring unit was used to simulate GINA gasket, vertical shear key and horizontal shear key respectively to analyze the stress deformation characteristics of element joints under seismic fortification and rare working conditions, providing references for engineering design.

2 PROJECT OVERVIEW

Shenzhen-Zhongshan Link Project is located in the core area of the middle reaches of the Pearl River,

*Corresponding author: li.zhi@stedi.com.cn

DOI: 10.1201/9781003495505-316

about 30km from Humen Bridge in the north and 38km from Hong Kong-Zhuhai-Macao Bridge in the south. The immersed tunnel of Shenzhen-Zhongshan Link starts from the East Artificial Island at Shenzhen side, runs westward through Dachanwan Channel, Airport Branch Channel, Fanshi Waterway, and ends at the boundary milestone of the bridge and tunnel on the West Artificial Island. The total length of the tunnel is 6845m, of which the immersed tunnel section is 5035m long. The immersed tunnel adopts the monolithic rigid element scheme. The maximum longitudinal slope of the tunnel is 2.98%, the minimum longitudinal slope is 0.4%, and the lowest design elevation of the road surface is -33.786m. The immersed section is divided into 32 elements, with a standard element length of 165m. Five 123.8m long elements are arranged on the side of the east artificial island due to the widening of the cross section, and one 123.8m long section is arranged on the west artificial island. The profile of immersed tunnel is shown in Figure 1, and the cross section of steel shell concrete immersed element is shown in Figure 2.

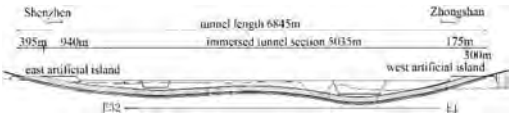

Figure 1. Profile of the immersed tunnel.

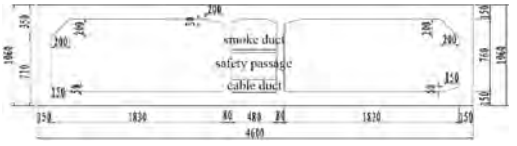

Figure 2. Cross section of the immersed element.

3 TIME-HISTORY ANALYSIS METHOD

The time-history analysis method was applied for this seismic analysis. The "time-history analysis method" is a kind of structural dynamic calculation method which integrates the basic motion equation of structure into the seismic acceleration record and obtains the seismic effect of structure in the whole time history. Since the 1960s, it has gradually developed into one of the general structural analysis methods because of its clear concept and its ability to reflect the influence of the three parameters of ground motion (amplitude, frequency content and ground motion duration) on the structure. The time-history analysis method can be used for a variety of complex analysis cases.

The main analysis steps of finite element time-history analysis method of soil-underground structure were as follows: The appropriate finite element model was established according to the characteristics of the analysis object and model. The appropriate seismic wave was selected when the influence of the three elements of ground motion (amplitude, frequency content, and ground motion duration) on the calculation results should be taken into account. The dynamic time history response of the whole structure model was obtained by applying the ground motion as a load to the finite element model in the way of time history.

4 MODELLING

Based on the analysis of the design drawings and research report of Site Design Ground Motion Parameters, the refined finite element model of soil-structure interaction was considered for the elements (Element 2 to Element 5) of the west slope section. The calculation section were about 660m long, which included the climbing slope section, and the buried depth of the immersed tunnel in this section was shallow. The spatial layout and structural stress were of typical significance.

4.1 *Stratum and backfill*

The main stratum within this calculation section were divided into 5 layers: silt, silty clay, silty sand - medium sand, fully weathered rock and medium weathered rock. According to geological exploration report and the soil shear wave velocity, ②$_{23}$ silt, ③$_5$ fine sand, ③$_6$ medium sand and ③$_8$ gravel sand layers were integrated into silt - medium sand layer. The local small layer was simplified considering the complexity of modelling, as shown in Figure 3. The foundation of Element 2 to Element 5 was considered to be reinforced with deep cement mixing (DCM) piles, with a depth of reinforcement reaching the top of layer ⑥ of fully decomposed granite. The backfill and foundation reinforcement condition refers to Figures 3-4. The stratum calculation parameters were obtained from the research report of Design Ground Motion Parameters of Shenzhen-Zhongshan Link and one-dimensional ground motion response analysis, as shown in Table 1.

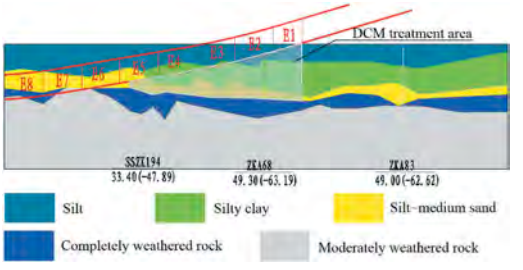

Figure 3. Geological profile of immersed tunnel.

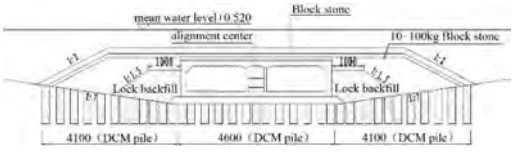

Figure 4. Backfilling and foundation reinforcement of the anti-collision section of west artificial island.

Table 1. Soil layer calculation parameters.

Soil layer	Unit weight (kN/m3)	Dynamic poisson's ratio	Dynamic modulus of elasticity (kN/m^2)
Silt	16.1	0.49	27402
Silty clay	17.1	0.49	56224
Fine~medium sand	18.6	0.49	199520
Completely weathered	25.0	0.49	1439028
Moderately weathered	25.0	0.49	2286524
Lock backfill	24.0	0.49	801024
Block stone	24.0	0.49	450576
DCM reinforcement for silt	20.0	0.49	69601
DCM reinforcement for silty clay	20.0	0.49	142810
DCM reinforcement for fine~medium sand	20.0	0.49	506783

4.2 *Modelling*

4.1.1 *Model establishment*

In the modeling, the shell element was used to simulate elements, the spring element was used to simulate element joints, and the hexahedral and pentahedral solid elements were used to simulate soil. Three element joints were considered in the model.

Modelling length direction: From Element 2 to Element 5, the length was 4×165m=660m; modeling depth direction: From the bottom of Element 5 to the top of Element 2, the elevation ranged from -31.743 to -9.171, with a total of 22.572m, the modeling depth was 50m, and the foundation was medium-weathered rock; modeling width direction: The width of the immersed tunnel structure(B) was 46m, and the expansion range of both sides was 3B respectively, with a total width of 7B=7×46=322m.

In the depth direction, the unit depth the was about 1~1.5m. In the width direction, the unit length was about 3m~4m. In the length direction, unit length was about 5m~10m. The number of model units was 296 948, and the number of nodes was 290 191.

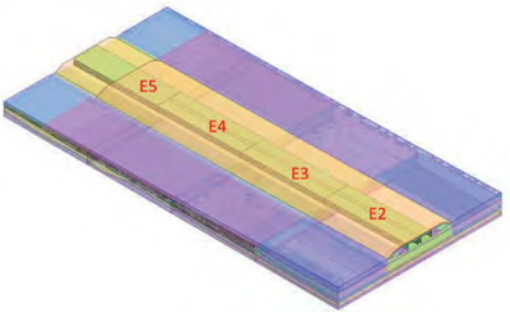

Figure 5. Overall model diagram.

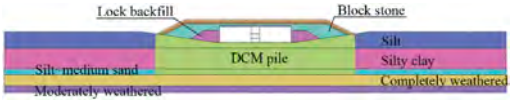

Figure 6. Model cross-section.

4.1.2 *GINA gasket simulation*

Trelleborg's GINA gasket was used, and different types of GINA gaskets were used for different water depths. The basic material of GINA gasket is natural rubber, which is a highly nonlinear elastomer. The equivalent particle - spring model method was used in the calculation. The compression of GINA gasket opening was less than 30mm, and the deformation of GINA was considered to be in the elastic deformation range. Considering that the calculation volume of 3D overall nonlinear time history analysis would be too large, the linear spring unit was adopted for the calculation to simulate GINA gasket, and the initial stiffness under initial compression of the force-compression curve was taken as the calculation stiffness, as shown in Table 2. The simulation of GINA gasket for the model is shown in Figure 8. Stiffness conversion was carried out according to unit length in the calculation.

Table 2. Sheet of GINA stiffness values.

Element Joints	Element 6~Element 5	Element 5~Element 4	Element 4~Element 3
GINA body hardness	62	62	62
Average pressure on GINA gasket at construction stage (kN/m)	939.1	822.8	702.4
Initial deformation (mm)	140.6	134	127.1
Initial stiffness (kN/m/m)	6679	6140	5526

4.1.3 *Shear key simulation*

There were 2 sets of horizontal concrete shear keys (bottom) and 4 sets of vertical steel shear keys (side and middle walls) between the elements. 2 sets of vertical steel shear keys were arranged on the middle and side walls respectively. The steel shear keys on the side wall were connected with the transverse partition inside the steel shell by high-strength bolts, and the steel shear keys on the middle wall were welded directly with the end panel of the steel shell. The bottom slab was provided with 2 sets of horizontal concrete shear keys located in the ballast concrete of the bottom slab of traffic tubes.

Figure 7. GINA gasket + shear key diagram.

For the element joints in Shenzhen-Zhongshan Link, the recommended stiffness value of the vertical steel shear keys of the 2 sets of side walls was 1.3×10^5kN/m, that of the 2 sets of vertical steel shear keys of the middle wall was 1.9×10^5kN/m, and that of the 4 sets of horizontal concrete shear keys was 5×10^6kN/m. The shear key simulation in the model was simulated with 8 separate springs, as shown in Figure 7.

4.1.4 *Boundary conditions*

In the eigenvalue analysis, the 4 sides of the model used vertical constraints, and the bottom adopted fixed constraints. In the dynamic time history analysis, the 4 sides of the model adopted vertical constraints, the bottom adopted vertical constraints and mass elements, and the calculated damping used Rayleigh damping. Through the eigenvalue analysis, the two periods with the highest mass participation were obtained. The characteristic periods of horizontal lateral seismic effects were 0.972s and 0.832s, and the characteristic periods of horizontal longitudinal seismic effects were 0.89s and 0.82s, respectively. The empirical critical damping ratio was 0.05.

5 SEISMIC LOADS AND WORKING CONDITIONS FOR ANALYSIS

According to the Site Seismic Safety Evaluation Report, the seismic response of the immersed tunnel was analyzed by selecting the seismic acceleration of the man-made ground motion of bedrock with the probability of exceeding 10% (fortification earthquake) and 4% (rare earthquake) in 100 years. The time history of seismic acceleration of the site bedrock is shown in Figure 9. The entire seismic wave calculation time could be 35s. The control frequency was considered around 5~10Hz, and the integral time step was between 0.005s and 0.01s. Considering the size of the model and the calculation time, the 3D fine analysis was calculated according to the integral step size of 0.01s. Seismic analysis under fortification earthquake and rare earthquake was carried out respectively, as shown in Table 3.

6 ANALYSIS OF CALCULATION RESULTS

This calculation mainly took into account the compression of element joint opening under horizontal and longitudinal seismic effects, the stress of horizontal shear keys and the interlay displacement angle between elements under horizontal and transverse seismic effects.

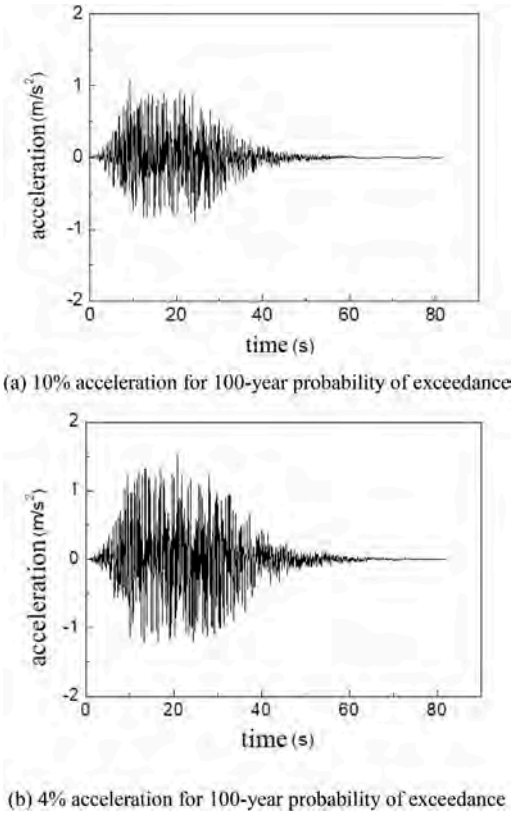

Figure 8. Seismic acceleration time history of site bedrock.

Table 3. Calculated working conditions for seismic analysis.

Calculated working conditions	Seismic wave input direction	seismic effects level	Standard	Amplitude modulation of surface peak acceleration
1	Horizontal and longitudinal	Fortification earthquake	10% for 100 years	160 gal
2		Rare earthquake	4% for 100 years	210 gal
3	Horizontal and transverse	Fortification earthquake	10% for 100 years	160 gal
4		Rare earthquake	4% for 100 years	210 gal

6.1 *Horizontal and longitudinal seismic effects*

The compression deformation of element joint opening under horizontal and longitudinal seismic effects of fortification and rare earthquakes are shown in Figures 9-12.

When the horizontal and longitudinal seismic input was applied, the longitudinal deformation of the element joint was relatively large, while

Figure 9. Envelope value of element displacement under fortification earthquake.

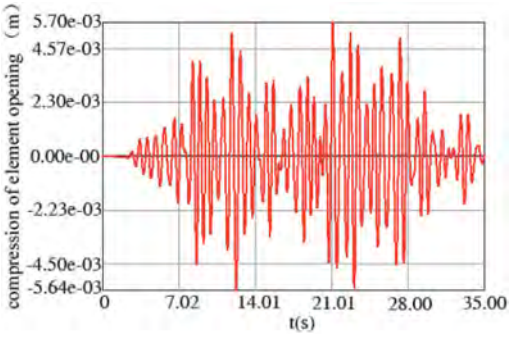

Figure 10. Time history curve of compression of element joint opening under fortification earthquake.

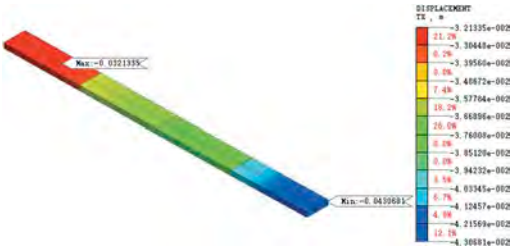

Figure 11. Envelope value of element displacement under rare earthquake.

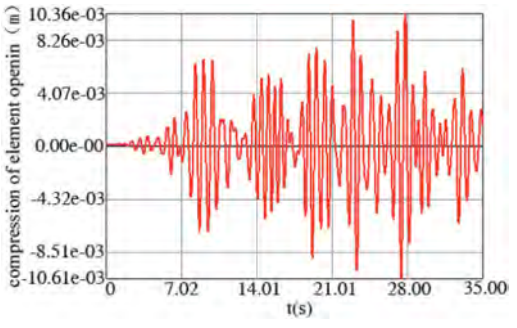

Figure 12. Time history curve of compression of element opening under rare earthquake.

the shearing force of the horizontal and vertical shear keys was relatively small. The main focus was on the deformation of the element joint. According to calculations, the maximum compression and opening of the element occurred at the joint between Element 3 and Element 2, where the elements are shallowest and most significantly affected by seismic effects. Under fortification working conditions, the maximum compression amount was 5.6mm and the maximum tension amount was 5.7mm; under rare working conditions, the maximum compression amount was 10.6mm and the maximum tension amount was 10.4mm. According to the design of reinforcement plan, DCM reinforcement was used for both the ranges from Element 5 to Element 2 and backfilling area, which played good role in controlling the deformation at the element joints. Under horizontal and longitudinal seismic effects, the deformation of the element joint met the water tightness requirements.

6.2 *Horizontal and transverse seismic effects*

The internal force of the horizontal shear key and interlayer displacement difference of the elements under horizontal and transverse seismic effects are shown in Figures 13-16.

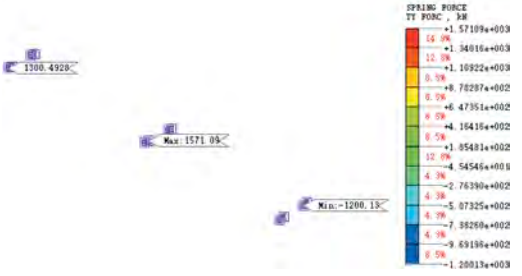

Figure 13. Envelope value of internal force of horizontal shear key under fortification earthquake.

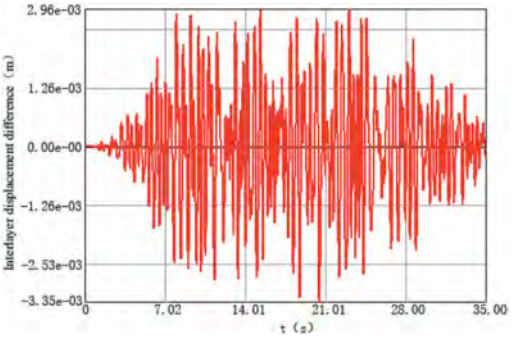

Figure 14. Interlayer displacement difference of elements under fortification earthquake.

Figure 15. Envelope value of internal force of horizontal shear key under rare earthquake.

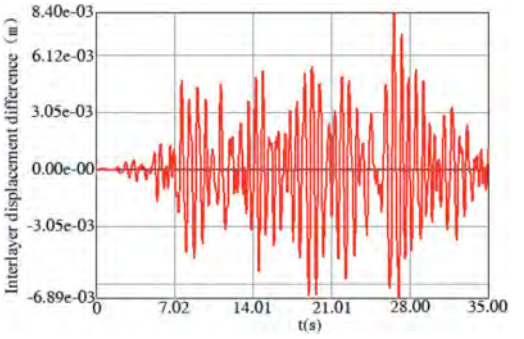

Figure 16. Interlayer displacement difference of elements under rare earthquake.

When inputting horizontal seismic effects, the internal force of the horizontal shear key was relatively large, while the deformation of the element joint and the shearing force of the vertical shear key were relatively small. The main focus was on the horizontal shear key and the interlayer displacement difference of elements. According to the calculations, the maximum internal force of the horizontal shear key under fortification working conditions was 1571kN, and the maximum internal force of the horizontal shear key under rare working conditions was 4417kN. With the consideration of partial coefficient of horizontal seismic effects, the design value should be less than the limit requirement of 34MK for a single shear key. The calculation of the interlayer displacement angle of the elements is shown in Table 4. And the interlayer displacement angle of the elements met the requirements under both fortification and rare working conditions.

Table 4. Horizontal seismic interlayer displacement angle.

Working condition	Horizontal relative displacement DX (mm)	Floor height (mm)	Inter-layer displacement angles	Limit value of interlayer displacement angle
Fortification	3.35	9100	1/2716	1/550, compliance
Rare	8.40	9100	1/1083	1/250, compliance

7 CONCLUSIONS

By establishing a refined 3D dynamic time history analysis numerical model for the immersed tunnel of Shenzhen-Zhongshan Link, the focus was on analyzing the compression of element openings under horizontal and longitudinal seismic effects, internal force of horizontal shear keys under horizontal and transverse seismic effects, and interlayer displacement difference of elements.

(1) Under the action of horizontal and longitudinal seismic effects, the longitudinal deformation of element joint was relatively large, while the internal forces of horizontal and vertical shear keys were relatively small; when the horizontal and transverse seismic input was applied, the internal force of the horizontal shear key was relatively large, while the deformation of the element joint and the internal force of the vertical shear key were relatively small.

(2) Under horizontal and longitudinal seismic effects, the deformation of the element joint met the waterproofing requirements. The maximum compression and opening of the element occurred at the joint of Element 3 and Element 2, where the elements are shallowest and most significantly affected by the seismic effects. The DCM reinforcement in the area from Element 5 to Element 2 had played a good role in controlling the deformation of the element joints.

(3) Under horizontal seismic effects, the horizontal shear key met the design requirements. The interlayer displacement angle of the elements met the specification requirements.

The analysis results provides references for seismic design of similar immersed tunnel structures.

REFERENCES

Anastasopoulos I., Gerolymos N., Drosos V., et al., 2007. Nonlinear response of deep immersed tunnel to strong seismic shaking [J]. Journal of Geotechnical and Geoenvironmental Engineering, ASCE, 133 (9): 1067–1090.

Hai T. Y., Yong Y., 2012. Issues on the seismic design and analysis of ultra-long immersed tunnel [J]. Journal of Shanghai Jiaotong University, 46 (1): 94–97

Jun L. Q., Shun Y. Y., et al., 2019. Dynamic time-history analysis of 3-D seismic response of immersed tunnel [J]. Highway, 64 (2): 256–262

Xu Z., Guan L. Y., Jian H. W., Simplified method and three-dimensional finite element analysis of quake-proof for immersed tube tunnel joints. Chinese Journal of Underground Space and Engineering [J], 2011, 7 (S1): 1292–1297, 1402

Tunnelling for a Better Life – Yan, Celestino, Thewes & Eberhardt (Eds)
© 2024 The Author(s), ISBN 978-1-032-80042-4
Open Access: www.taylorfrancis.com, CC BY-NC-ND 4.0 license

Seismic resilience assessment for longitudinal response of immersed tunnels

Xinxi Li*
Department of Geotechnical Engineering, Tongji University, Shanghai, China

Haitao Yu
State Key Laboratory of Disaster Reduction in Civil Engineering, Tongji University, Shanghai, China

ABSTRACT: Seismic resilience assessment is an important means to evaluate the seismic performance of structures, but the seismic resilience assessment for longitudinal response of immersed tunnels has not been reported yet. Based on the multi-scale model, this paper proposes a longitudinal resilience assessment framework for immersed tunnels. The macroscopic spring-beam model is used to describe the dynamic nonlinear characteristics and the interaction between structure and stratum. And the microscopic refinement model is used to capture the dynamic laws of the relative deformation of joints. Fragility curves are developed at different limit states by nonlinear incremental dynamic analysis procedure with appropriate ground motion, intensity measure and damage measure. The seismic resilience assessment method was modeled by the estimation of restoration functions and the resilience index. Taking an immersed tunnel as an application example, parametric analyses are performed to investigate the influence of the peak ground acceleration and soil-structure relative stiffness ratio. The results show that the residual functionality and seismic resilience decrease significantly with the increase of the peak ground acceleration. And the seismic resilience index increases with the increasing soil-structure relative stiffness ratio. The proposed method can provide reference and basis for seismic risk assessment of immersed tunnel.

Keywords: Immersed tunnel, Seismic resilience, Longitudinal seismic response, Functionality function, Restoration model

1 INTRODUCTION

The damage of tunnels under earthquakes will have an impact on urban traffic, energy, municipal and other aspects. Seismic resilience can be described as the ability to withstand, respond and rapidly recover from hazards. It is a crucial means to evaluate the seismic performance of structures by considering the degree of functional loss and the post-earthquake repair process. Therefore, it is of paramount importance to evaluate the seismic resilience of tunnels.

The conceptual framework of seismic resilience was proposed by Bruneau et al. (2003), and its theory and design have gradually become a research hotspot and applied to buildings, bridges, transportation network and other fields (Alipour & Shafei, 2016; Anwar et al., 2020). At present, the research on the seismic resilience of underground structures mainly focuses on the improvement of structural resistance and self-centring structure, such as the installation of supports at the end of middle columns to increase their deformation capacity (Ma et al., 2018). Chen & Zhou (2019) realized the self-centring of the structure by installing energy dissipation devices between the bottom of the column and the beam so that the damage of the structure under earthquake was significantly reduced. Huang et al. (2022) put forward the seismic resilience assessment process for cross-sectional tunnels in soft soil areas, and explored the influence laws of soil conditions, tunnel burial depth, construction quality and other factors. However, the above research is limited to the cross-sectional seismic resilience study of underground structure. Considering that joints are the weak point of tunnel structures, it is necessary to evaluate the longitudinal seismic resilience of tunnel.

This paper establishes the evaluation method and process of longitudinal seismic resilience of immersed tunnels. Taking the characteristics and joints of immersed tunnels into consideration, fragility curves

*Corresponding author: 2010049@tongji.edu.cn

DOI: 10.1201/9781003495505-317

are calculated and the seismic resilience assessment framework are modelled by the estimation of restoration functions and the resilience index. Taking an immersed tunnel as an application example, parametric analyses are performed to investigate the influence of the peak ground acceleration and soil-structure relative stiffness ratio.

2 SEISMIC RESILIENCE FRAMEWORK FOR IMMERSED TUNNELS

2.1 *Numerical model of immersed tunnel*

As shown in Figure 1, the longitudinal dynamic response analysis of immersed tunnel based on beam-spring model is established. The tunnel is simulated as beam element and the soil-structure interaction is modelled as spring and damping elements. The spring stiffnesses of longitudinal, transverse and vertical formation springs can be expressed by Eq. (1)-(2) (John & Zahrah, 1987). The damping between tunnel and soil can be expressed by Eq. (3)-(4). Non-linear hyper-elastic springs is introduced to simulate the actual non-linear force-deformation behavior of the Gina gasket. And bilinear models are used to describe the structural forms and bearing mechanics of shear keys. Each node and the adjacent end of segmental element is rigid connect, forming a combination of the microscopic refinement model of joints and the macroscopic beam model. The continuity equation is satisfied between the macro and micro models, as shown in Eq. (5) (Zhang et al., 2021).

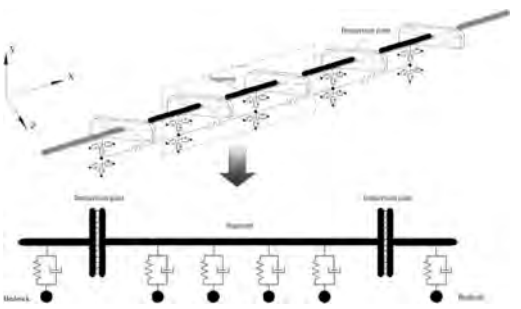

Figure 1. Multi-scale model of immersed tunnel.

$$k_x = k_y = \frac{16\pi G(1-\nu)}{3-4\nu}\frac{d}{L} \tag{1}$$

$$k_z = \frac{2\pi G}{1-\nu}\frac{d}{L} \tag{2}$$

$$C_x = \rho V_s \pi d \tag{3}$$

$$C_y = C_z = \rho V_s d + \rho V_{La} d \tag{4}$$

$$\begin{cases} x'_{O_1} = x'_{S_i} = 0 \\ y'_{O_1} = \sum_{i=1}^{j} y'_{S_i}/j \\ z'_{O_1} = \sum_{i=1}^{j} z'_{S_i}/j \end{cases} \tag{5}$$

Where, L is the wavelength of the incident wave (m); d is the width of the tunnel (m); G is the shear modulus of soi, $G = \rho V_s^2$, ρ is the soil density (kg/m^3), Vs is the shear wave velocity (m/s); υ is the Poisson's ratio; V_{La} is the Lysmer wave velocity, $V_{La} = \frac{3.4}{\pi(1-\nu)} V_s$; O_1 is the end of beam element; S_i is the node of the joint; x'_{O_1}, y'_{O_1}, z'_{O_1} are the coordinates of O_1, respectively; x'_{S_i}, y'_{S_i}, z'_{S_i} are the coordinates of S_i, respectively; j is the number of joint spring elements.

2.2 *Fragility curves*

The seismic vulnerability can be assessed based on fragility curves, that is, the exceeding probability of structural damage measures (DM) exceeding a certain limit state under a given ground motion intensity measures (IM), which can be calculated by Eq. (6) (Liu et al., 2017).

$$\begin{aligned} \mathrm{P}(\mathrm{LS_i}|\mathrm{IM}=im) &= \mathrm{P}(\mathrm{DM}>dm_i|\mathrm{IM}=im) \\ &= 1-\mathrm{P}(\mathrm{DM}<dm_i|\mathrm{IM}=im) \\ &= 1-\Phi\left(\frac{\ln dm_i-\mu_{\ln \mathrm{DM}|\mathrm{IM}=im}}{\sigma_{\ln \mathrm{DM}|\mathrm{IM}=im}}\right) \end{aligned} \tag{6}$$

Where, the limit state *LSi* is quantified by DM and expressed as *dmi*. Eq. (6) calculates the probability of DM exceeding *dmi*, when IM=*im*. $\mu_{\ln \mathrm{DM}|\mathrm{IM}=im}$ and $\sigma_{\ln \mathrm{DM}|\mathrm{IM}=im}$ are the mean and the standard deviation of ln(DM), respectively. And Φ is the standard cumulative normal distribution function.

The limit state represents the maximum expected damage degree of the structure under a specific ground motion intensity, and it can be divided into four types, namely no damage, minor damage, moderate damage and extensive damage. Table 1 shows the definitions of each limit state using the ratio of the bending moment (M) and moment capacity (MRd).

Table 1. Definitions of each damage state.

Limit state	M/M_{Rd}
no damage (LS_0)	1
minor damage (LS_1)	1.5
moderate damage (LS_2)	2.5
extensive damage (LS_3)	3.5

2.3 *Restoration models and resilience analysis*

A reasonable restoration model should be established for seismic resilience assessment, as shown in Figure 2, where $Q(t)$ is the functionality function changing over time. t_0 is the time when the earthquake occurs, and t_1 is the time when the repair is completed. The functionality function between t_0 and t_1 is the resilience curve. Once the form of the resilience curve is determined, the seismic resilience of the tunnel can be quantitatively evaluated. However, the resilience curve needs to consider the influence of many factors, and is closely related to the damage of the component, repair cost, repair priority and other factors, so it is difficult to get a unified form. At present, classical restoration models include linear functions (Bruneau & Reinhorn, 2007), trigonometric functions (Bocchini & Frangopol, 2012), and exponential functions (Cimellaro et al., 2010; Dong & Frangopol, 2015).

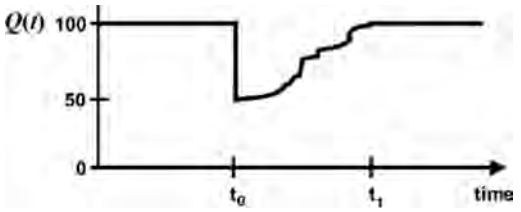

Figure 2. Assessing model of seismic resilience (Bruneau & Reinhorn, 2007).

The resilience index R is given in Eq. (7) to quantitatively evaluate the longitudinal seismic resilience of the immersed tunnel.

$$R = \frac{\int_{t_0}^{t_1} Q(t)dt}{t_1 - t_0} \tag{7}$$

3 APPLICATION

3.1 *Parameters of the numerical modelling*

This research is based on the real project of an immersed tunnel. As shown in Figure 3, the immersed tunnel is composed of 7 concrete elements with a standard length of 108 m. The tunnel structure was modelled as beam elements supported by interaction springs and dashpots, with the cross-section 43 m in width and 9.55 m in height. Concrete Damaged Plasticity model is used to simulate the material of the tube, in which the density is 2500kg/m3, the elastic modulus is 3.15×10^4MPa, Poisson's ratio is 0.2, the initial compressive yield stress is 14.3MPa, the ultimate compressive yield stress is 29.6MPa, and the tensile failure stress is 2.5MPa. Nonlinear hyper-elastic springs are introduced to simulate the Gina gaskets and bilinear models are used to describe the two load-deformation stages of vertical shear keys and horizontal shear keys, as shown in Figure 4.

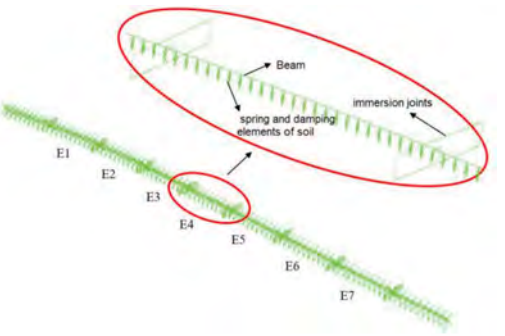

Figure 3. Finite element model.

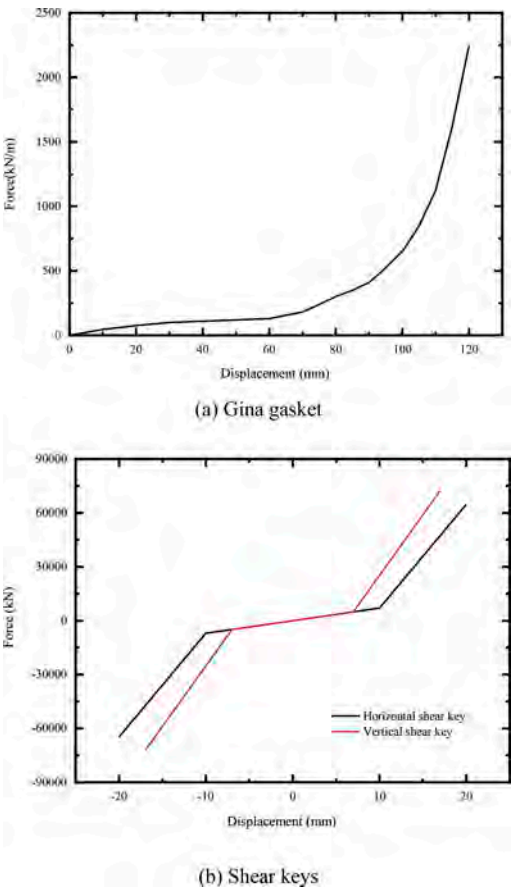

Figure 4. Force-displacement relationship of immersion joint.

The layered soil is equivalent to a homogeneous soil layer with equivalent shear velocity, with a soil density of 2000kg/m^3, shear velocity of 180m/s, and Poisson's ratio of 0.3. The nonlinear characteristics of soil layer are treated by equivalent linearization and calculated by Shake91, a one-dimensional soil layer seismic response analysis program. The curve of shear modulus ratio and damping ratio change with shear strain is shown in Figure 5. Finally, the stiffness and damping of soil spring are calculated by Eq. (1)-(4) according to the equivalent shear modulus.

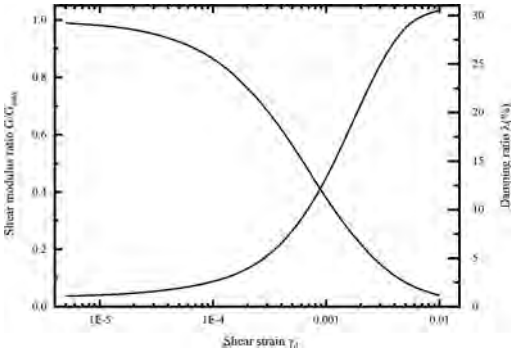

Figure 5. Shear modulus ratio and damping ratio.

In this study, the peak ground acceleration (PGA) is adopted as the IM and the peak relative extension of immersion joints is selected as DM. Based on incremental dynamic analysis (IDA), fragility curves of the four limit states are shown in Figure 6.

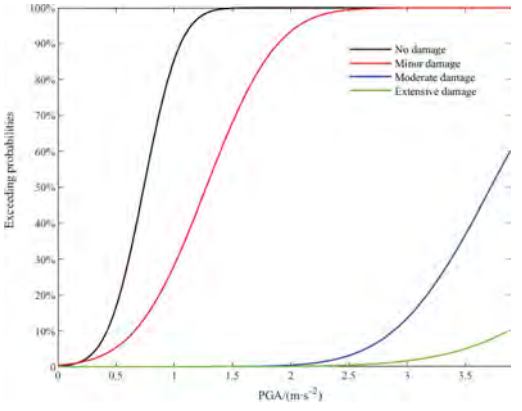

Figure 6. Seismic fragility curves.

3.2 *Resilience assessment*

Functionality function $Q(t)$ is estimated using the method proposed by FEMA (2020), as shown in Figure 7. The resilience curve is obtained based on the best fitting of ATC-13 data, and $Q(t)$' is defined as the average function of the tunnel in the recovery process, as shown in Eq. (8). According to the definition, the functionality function $Q(t)$ under the given IM can be derived, and then the resilience index R can be obtained from Eq. (7).

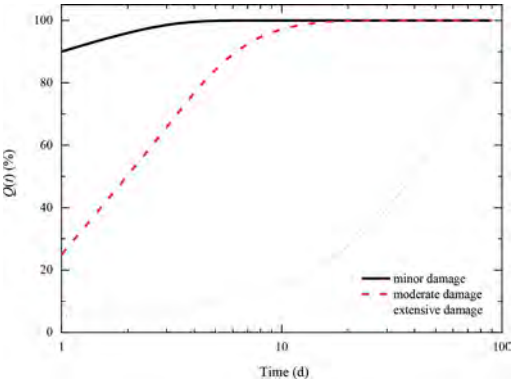

Figure 7. Tunnel restoration curves (FEMA, 2020).

$$Q(t)' = \sum_{i=1}^{3} Q[LS_i|t]P[LS_i|IM] \tag{8}$$

Where, $Q[LS_i|t]$ represents the functionality of the tunnel being in LS_i at time t, which can be obtained from Figure 7. $P[LS_i|IM]$ represents the probability of occurrence of LS_i for a given IM, as defined in the following equations

$$\begin{aligned} P[LS_i|IM] &= P[DM > LS_{i-1}|IM] \\ &- P[DM > LS_i|IM], i = 1, 2, 3 \end{aligned} \tag{9}$$

Where, $P[DM > LS_{i-1}|IM]$ and $P[DM > LS_i|IM]$ are the exceeding probabilities of the DM exceeding LS_{i-1} and LS_i at a given IM, respectively.

3.3 *Parametric analysis*

3.3.1 *Effect of PGA*

The resilience curves for immersed tunnel with different PGAs is presented in Figure 8. It can be known from the figure that the residual function Q (t=0) of the tunnel after the earthquake decreases with the increase of ground motion intensity. And the slopes of the resilience curves change significantly during the 3-5 days of the recovery process. According to Figure 7, the recovery time of minor damage and moderate damage is 3 days and 7 days respectively, that is, after 7 days, the tunnel function is expected to recover 100% in cases of minor and moderate damage, and the resilience curve is only determined by the recovery function of extensive damage. Figure 9 shows the resilience index of

immersed tunnel decreases with the increase of ground motion intensity. Especially when PGA is greater than 0.25g, the resilience index decreases significantly.

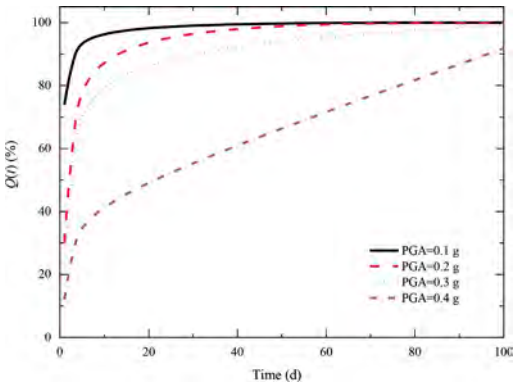

Figure 8. Resilience curves of the recovery of functionality with time for immersed tunnel with different PGAs.

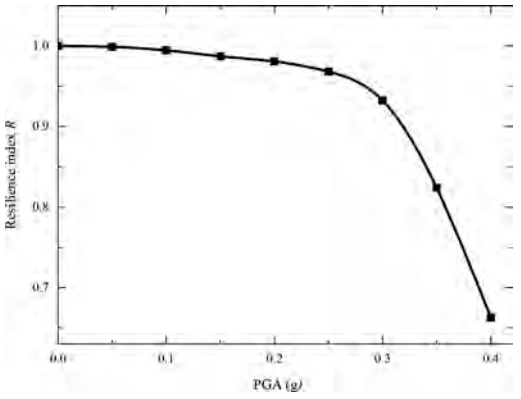

Figure 9. Resilience index of immersed tunnel.

3.3.2 *Effect of the soil-structure relative stiffness ratio*

The soil-structure relative stiffness ratio F is defined as (Wang, 1993)

$$F = \frac{G}{24}\left(\frac{d^2H}{EI_B} + \frac{dH^2}{EI_H}\right) \tag{10}$$

Where, G is the shear modulus of soil; d and H are the width and height of the tunnel, respectively; E is the elastic modulus of the tunnel; I_B is the inertia moment of the top and bottom plate; and I_H is the inertia moment of the side wall.

The soil-structure relative stiffness ranges from 0.0006 to 0.03 in the analysis and the resilience index is shown in Figure 10. It can be seen from the figure that with the increase of the soil-structure relative stiffness ratio, the t resilience index gradually increases, that is, the greater the relative stiffness ratio, the higher the tunnel resilience.

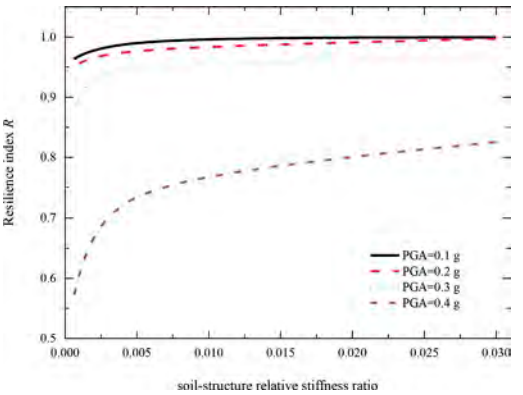

Figure 10. Resilience index with different soil-structure relative stiffness ratios.

4 CONCLUSIONS

This paper established an evaluation method for the longitudinal seismic resilience of immerse tunnel. Based on the longitudinal dynamic response analysis model of multi-scale immerse tunnel, the seismic fragility curve is established. Combined with the recovery model proposed by FEMA, the seismic resilience of tunnel is quantitatively evaluated. Parametric analyses were performed to investigate the influence of PGA and the soil-structure relative stiffness ratio. It is shown that the residual function of the tunnel after earthquake significantly decreases with the increase of PGA. And the seismic resilience increases with increasing soil-structure relative stiffness ratio.

It is worth noting that this paper aims to establish a framework for evaluating the longitudinal seismic resilience of immersed tunnels, but there are still unavoidable limitations. The restoration models need to consider the influence of various factors, which is closely related to the damage situation of the component, repair cost, repair priority and other factors, involving social, technical and economic factors, etc. The model adopted in this paper is a simplified model proposed by FEMA based on the data of California, so a more reasonable functional function recovery model needs to be developed in the subsequent research to consider the tunnel construction, maintenance costs and related uncertainties accurately and quantify them.

REFERENCES

ASTM D2938-95, 1995. Standard test method of unconfined compressive strength of intact rock core specimens. ASTM International, West Conshohocken, PA, USA.

Cairns, R.B., 1965. Infrared spectroscopic studies of solid oxygen. PhD Thesis. University of California, Berkeley, CA, USA.

Guo, R., He, C., Su Z. X., et al, 2011. “Study of shearing mechanical properties of segment joints of shield tunnels. Mode. Tunn. Tech. 48(4), 72–77.

Holt, R.M., Kenter, C.J., 1992. Laboratory simulation of core damage induced by stress release. In: Tillerson, J.R., Waversik, W.R. (Eds.), Rock Mechanics – Proceedings of the 33rd U.S. Symposium on Rock Mechanics (USRMS). A.A. Balkema, Rotterdam, Netherlands, pp. 959–968.

Levinsky, N.G., 1977. Fluid and electrolytes. In: Thorn, G. W., Adams, R.D., Braunwald, E. (Eds.), Harrison’s Principles of Internal Medicine, 8th ed. McGraw-Hill, New York, NY, USA, pp. 364–375.

Vutukuri, V.S., Lama, R.D., 1978. Dynamic elastic constants of rocks. In: Lama, R.D., Vutukuri, V.S. (Eds.), Handbook on Mechanical Properties of Rocks, vol. II. Trans Tech Publications, Clausthal-ZellerfieL, Germany, pp. 236–237.

Alipour, A., Shafei, B., 2016. Seismic resilience of transportation networks with deteriorating components. Journal of Structural Engineering. 142(8), C4015015.

Anwar, G. A., Dong, Y., Zhai, C. H., 2020. Performance-based probabilistic framework for seismic risk, resilience, and sustainability assessment of reinforced concrete structures. Advances in Structural Engineering. 23(7), 1454–1472.

Bocchini, P., Frangopol, D. M., 2012. Optimal resilience- and cost-based postdisaster intervention prioritization for bridges along a highway segment. Journal of Bridge Engineering. 17(1), 117–129.

Bruneau, M., Chang, S. E., Eguchi, R. T., et al., 2003. A framework to quantitatively assess and enhance the seismic resilience of communities. Earthquake Spectra.. 19(4), 733–752.

Bruneau, M., Reinhorn, A., 2007. Exploring the concept of seismic resilience for acute care facilities. Earthquake Spectra. 23(1), 41–62.

Chen, Z. Y., Zhou, Y., 2019. Seismic performance of framed underground structures with self-centering energy-dissipation column base. Advances in Structural Engineering.. 22(13), 2809–2822.

Cimellaro, G. P., Reinhorn, A. M., Bruneau, M., 2010. Framework for analytical quantification of disaster resilience. Engineering Structures. 32(11), 3639–3649.

Dong, Y., Frangopol, D. M., 2015. Risk and resilience assessment of bridges under mainshock and aftershocks incorporating uncertainties. Engineering Structures. 83, 198–208.

FEMA, 2020. Hazus earthquake model technical manual, Hazus 4.2 SP3. https://www.fema.gov/flood-maps/tools-resources/flood-map-products/hazus/user-technical-manuals

Huang, Z. K., Zhang, D. M., Pitilakis, K., et al., 2022. Resilience assessment of tunnels: framework and application for tunnels in alluvial deposits exposed to seismic hazard. Soil Dynamics and Earthquake Engineering. 162, 107456.

Liu, T., Chen, Z. Y., Yuan, Y., et al., 2017. Fragility analysis of a subway station structure by incremental dynamic analysis. Advances in Structural Engineering. 20(7), 1111–1124.

Ma, C., Lu, D. C., Du, X. L., 2018. Seismic performance upgrading for underground structures by introducing sliding isolation bearings. Tunnelling and Underground Space Technology. 74, 1–9.

St John, C. M., Zahrah, T. F., 1987. Aseismic design of underground structures. Tunnelling and Underground Space Technology. 2(2), 165–197.

Wang, J. N., 1993. Racking effect on rectangular tunnels. In: Wang, J. N. (Eds.), Seismic design of tunnels: a state-of-the-art approach. Parsons Brinckerhoff Quade & Douglas, New York, USA, pp. 83–134.

Zhang, S., Yuan, Y., Li, C., et al., 2021. Seismic responses of long segmental immersed tunnel under unfavorable loads combination. Transportation Geotechnics. 30(1–2), 100621.

Tunnelling for a Better Life – Yan, Celestino, Thewes & Eberhardt (Eds)
© 2024 The Author(s), ISBN 978-1-032-80042-4
Open Access: www.taylorfrancis.com, CC BY-NC-ND 4.0 license

Void detection method and its application for steel shell-concrete interface of immersed tube tunnel

Songhui Li & Yan Zhang*
State Key Laboratory of Simulation and Regulation of Water Cycle in River Basin, China Institute of Water Resources and Hydropower Research, Beijing, China

Shaokong Feng
School of Naval Architecture, Ocean and Civil Engineering, Shanghai Jiaotong University, Shanghai

ABSTRACT: In the manufacturing process of sandwich-structured immersed tunnel (SSIT), the self-compacting concrete cannot be vibrated. Therefore, the bonding surface between the steel plate and concrete is susceptible to void defects, and the overall safety of the tunnel will be adversely affected. In this study, we performed void detection on large-scale steel shell-concrete SSITs using the impact imaging method and proposed some void defect control methods. First, the relationship between impulse response and each of the void area and void depth was derived theoretically. Next, a full-size model of a steel shell-concrete SSIT was established. According to the waveform characteristics of shock response measured by the test, an impact response strength index was proposed as a quantitative criterion for void detection. The relationship between the normalized impact response strength and the height of cavitation was fitted, and the quantitative criterion of sinking tube cavitation was put forward. The accuracy rate of test data was up to 87.5%. Using this method, 32 tubes in the Shenzhen - Zhongshan bridge were inspected, and by summarizing the void law, suggestions to improve the casting process were proposed, such as adjusting the casting speed. Meanwhile, the void probability decreased significantly. The proposed method provides an important basis for high - quality construction in SSIT projects.

Keywords: Steel-concrete-steel sandwich composite structure, Void defect, Non-destructive testing, Full scale test, Impact imaging method

1 INTRODUCTION

Immersed tube tunnels are widely used in large underwater tunnelling projects, and have two main structural forms, namely reinforced concrete immersed tubes and steel shell - concrete immersed tubes (Grantz,1997 and Lin et al., 2017). Reinforced concrete immersed tubes have a reinforced concrete structure as the core component of the immersed tube, complex prefabrication and casting processes, and stringent constraints for prefabrication sites (Deng et al., 2002 and Yu et al., 2000). The walls, ceiling slab, and base slab of the shell - concrete immersed tube are assembled in sections using steel components, self - compacting concrete being poured into the interior of the steel compartment after assembly. This structural form is also known as sandwich - structured immersed tunnel (SSIT) (Kimura et al., 2002, Akimoto et al., 2002 and Bowerman et al., 2002). The steel shell of an SSIT serves as the main component for bending and shear resistance and as a waterproof layer. The concrete serves as the ballast and bears the pressure (Liu et al., 2021). The overall structure has several advantages, such as a high carrying capacity, small section size, good waterproof performance, no temperature control crack prevention problems, and construction convenience (Nie, 2019). Among which, the largest being the under - construction SSITs in the world is the Shenzhen - Zhongshan bridge in China (Luttikholt et al., 2022).

The SSIT is cast with self - compacting concrete through the reserved pouring holes and ventholes. Because the self - compacting concrete casting cannot be subjected to vibration, void defects can occur during the casting process and cannot be directly observed. The voids can reduce the carrying

*Corresponding author: zhangyan@iwhr.com

DOI: 10.1201/9781003495505-318

capacity of the structure and lead to local buckling, affecting the overall safety and long - term service life of the structure (Nie, 2019 and Guo et al., 2019). The detection of steel shell - concrete voids has many challenges. First, the thickness of steel plate, as a load - bearing component of the SSIT, is generally more than 14 mm (to meet force requirements), while that of the steel plate even reaches 40 mm at the local position of the ultra-wide tube section. Therefore, void detection must be performed through the thick steel plate to reach the void-defect area and carry details of the defects back to the surface of the steel plate. Second, there are longitudinal and transverse bulkheads, stiffening ribs, and other components in the steel-shell structure that make the structure very complicated. Third, the results of SSIT model tests have shown that with a 14 - mm thick steel shell, local void depths of 10 mm or more are unacceptable in a steel-shell–concrete compartment of size 3.5 × 3 × 1.5 m, and void depths of more than 5 mm had to be avoided in the structural design (Guo et al., 2019). Consequently, the complex form of the thick steel-plate cover, dense distribution of ribs, millimetre-scale detection accuracy, and high detection efficiency requirements are problems that need to be addressed (Liu et al., 2022 and Mizuno et al., 2013).

Researchers have tried to address the high precision and efficiency detection requirements of steel shell - concrete void detection using ultrasonic, infrared thermal imaging, impact elastic wave, acoustic, neutron, and impact imaging methods (Mizuno et al., 2013, Yanagihara et al., 2013, Nishioka et al., 2008, Mitsuo et al., 2008, Chen et al., 2020, Mandal et al., 2012 and Meng et al., 2013). Among them, impact acoustics and impact imaging methods are the only methods that can simultaneously distinguish the type, as well as the area and depth of a void defect. However, some experimental studies conducted in Japan (Nishioka et al., 2008 and Mitsuo et al., 2008) show that when the impact acoustics method is used, the small gap that forms between the steel plate and concrete due to hardening-induced shrinkage may be misidentified as a void defect. In addition, the impact acoustics method demonstrates low efficiency (approximately 30 s/point), and in practical engineering applications, its detection accuracy is generally only 60%–70%. The impact imaging method originates from seismic imaging in petroleum exploration. In this method, an elastic wave field is generated on the surface of the structural component mechanically, e.g., using a steel hammer or a steel ball. The health of the structural component is determined based on the analysis of the reflected waveforms. The application and the effectiveness of this method for void detection in steel shell–concrete SSITs have not been reported.

The aim of this study is to investigate void detection using the impact imaging method and propose methods of void defect control for steel shell–concrete SSITs, and hoping to realize the quantitative detection of millimetre void of thick steel shell-concrete interface. First, the relationship between impulse response and the void volume is derived theoretically. Next, a full-size model of a steel shell–concrete SSIT is established. Finally, the accuracy of the impact imaging detection method is analysed.

2 THEORY

The impact imaging method uses a phase-controlled array to collect the elastic wavefield on the surface of a medium to reflect an image of its internal structure on its surface, before analyzing the spatial distribution characteristics of the full wavefield through inverse mapping.

The normalized free vibration waveform is integrated with respect to time to obtain the impact response strength function, as follows:

$$I(k) = \Delta t \times \sum_{i=1}^{k} (x(i-1) + x(i))/2 \qquad (1)$$

where $I(k)$ is the impact response strength function; Δt is the time interval; k is the number of sample data points obtained during the free vibration test; $x(i)$ is the value of the i-th sampling point; i is the number of the sampling point, where $i = 1,2,3,\ldots,k$.

After the void area at the detection point is obtained through integration, the calculated value is corrected using the actual void area. Once obtaining the corrected void area, the relationship between the impact response strength and the void index of the thick steel shell–concrete can be established.

The void area within a detection area of a thick steel shell–concrete structure is expressed as:

$$\begin{aligned} A_c &= \int\int \psi(x,y)dxdy \\ &= \Psi(x_1,y_1)\Delta s + \Psi(x_2,y_2)\Delta s + \ldots + \Psi(x_3,y_3)\Delta s \\ &= A_{c1} + A_{c2} + \cdots + A_{cn} \end{aligned} \qquad (2)$$

$$\psi(x,y) = \begin{cases} 0, d < 5mm \\ 1, d > 5mm \end{cases} \qquad (3)$$

where A_c represents the void area in the detection area of a thick steel shell–concrete structure; $\Psi(x,y)$ is the discriminant function of the void area at different detection points; x_n and y_n represent the coordinates of the n-th detection point; Δs is line spacing of the detection grid; A_{ci} is the void area at the i-th detection point; d_i is the void depth at the i-th detection point, which is related to the impact response strength and can be expressed as:

$$d_i = -ae^{-bI_i} + c \quad (4)$$

where I_i is the impact response strength at the i-th detection point; a, b and c are constants. Thus, the void volume is the multiplication of the void area and depth.

The positive correction factor between the calculated and actual void area is expressed as:

$$\alpha = A_m / A_c \quad (5)$$

where A_m represents the measured void area, and A_c is the calculated void area. Therefore, the corrected void area is

$$A_c' = \bar{\alpha} A_c \quad (6)$$

where $A_c^{'}$ is the corrected void area, and $\bar{\alpha}$ is the average correction factor calculated based on sampled void defect data.

3 FULL-SCALE MODEL EXPERIMENT

3.1 *Model establishment*

The SSIT comprises a fully enclosed steel shell structure filled with self-compacting concrete. Several transverse and longitudinal partitions are arranged between the inner and outer plates of the steel shell to integrate them into a single force-bearing frame, thereby increasing the overall shear bearing capacity of the SSIT. Furthermore, the entire shell is partitioned into multiple independent compartments, which facilitates the pouring of self-compacting concrete. The full-scale model of an SSIT section and the layout of one compartment are shown in Figure 1. To strengthen the effective bonding and synergistic force between the steel shell and concrete, steel studs and longitudinal T-stiffeners are installed in the top-slab compartments, as shown in Figure 2(b), and multiple longitudinal stiffeners and transverse flat ribs are installed in the bottom-slab compartments, as shown in Figure 2(c). Each compartment is designed with a pouring hole and air vents, as shown in Figure 3.

The full-scale model of the steel shell–concrete SSIT section used in this study is 9.6 m long, 55.4 m wide, and 10.6 m high. The steel shell comprises 14 mm/44 mm steel plates welded together, with the entire shell structure weighing approximately 740 t. Additionally, approximately

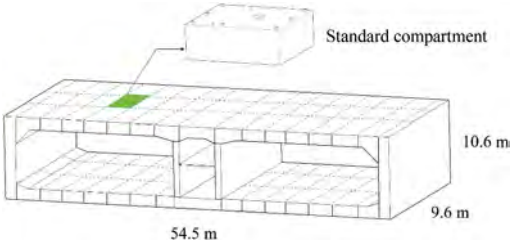

Figure 1. Full-scale model and compartment partitioning of steel shell SSIT section.

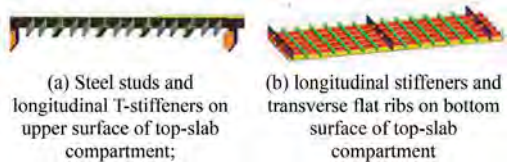

Figure 2. Stiffener components.

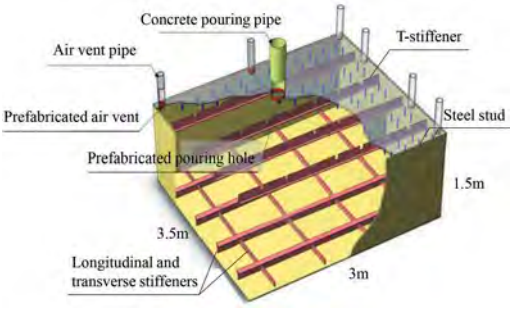

Figure 3. Full-scale model of typical compartment.

1500 m³ of self-compacting concrete was used to independently cast 105 compartments.

3.2 *Material properties and concrete mix proportion*

The material parameters and mix proportions of the self-compacting concrete are shown in Tables 1 and 2, respectively.

3.3 *Detection method*

In the present study, the full-scale model was manufactured, transported, and poured using actual construction

Table 1. Material parameters.

Cement	Fly ash	Slag powder	Fine aggregate	Coarse aggregate	Coarse aggregate	Water	Plasticizer
P II42.5	Grade I	S95	Grit	(5–10 mm)	(10–20 mm)	Tap water	Polycarboxylate superplasticizers

Table 2. Mix proportions of self-compacting concrete.

Material	Cement	Fly ash	Slag powder	Crushed aggregate (5–10 mm)	Crushed aggregate (10–20 mm)	Silica sand	Water	Plasticizer
kg/m^3	270	196	84	339	508	782	171	5.5

methods and processed under typical operating conditions of a steel shell–concrete SSIT. Therefore, the void defects formed naturally during the pouring process without any human intervention. Void detection was performed during the initial setting period of concrete in the poured compartments.

3.3.1 *Data acquisition equipment*

The detection system used in the present experiment is shown in Figure 4. Elastic wave excitation was performed manually using a steel hammer; the excitation frequency ranged from tens to thousands of Hertz. The testing equipment included a medium-high frequency vertical geophone (100 Hz) with a sensitivity of 0.28±5% (V/cm/s), and a US-made high-resolution GEODE seismograph. During data acquisition, the impact strength must remain as consistent as possible. The impact magnitude should be recorded and normalized to eliminate the human factor.

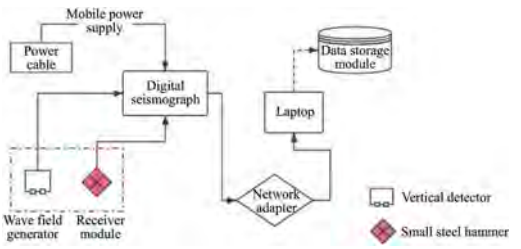

Figure 4. Schematic diagram of testing equipment.

3.3.2 *Data acquisition*

In the present void detection experiment, each compartment of the full-scale model was regarded as a data acquisition unit. The data acquisition process is as follows:

(1) Testing-grid layout: during detection, the elastic wave excitation and data acquisition devices should be applied strictly along the designed grid lines. In each tested compartment, the detection grid lines were arranged along the direction of the T-stiffeners. For a typical compartment measuring 2.8 m × 3.5 m × 1.5 m, the grid line spacing was set to 10 cm, except the areas adjacent to the T-stiffeners, where a denser spacing of 5 cm was used, as shown in Figure 5(b). Therefore, in areas adjacent to the T-stiffeners, a uniform 5 cm × 10 cm grid was used, whereas in the remaining areas, a uniform spacing of 10 cm × 10 cm was used.

(2) Elastic wave excitation and data acquisition: A small hammer was used to hit the steel top-plate of the compartment, generating an elastic wave field in the detection area. A vertical geophone was placed 10 cm away from the excitation location to record the waveform data. A single-point method of data acquisition was adopted along the detection lines, with an acquisition interval of 20.83 μs and a total of 8,192 sampling points. After the stress wave propagation and reflection signal were recorded by the vertical detector, the data acquisition system was shifted to the next detection point while maintaining a constant distance between the excitation and receiving points. In addition, the striking direction and strength were maintained constant. The process above was repeated along the entire grid line, as shown in Figure 5(d).

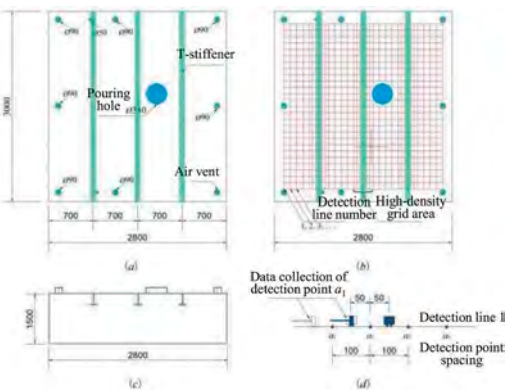

Figure 5. Detection point layout on compartment surface (units: mm).

3.4 *Void characteristics*

3.4.1 *Measurement of void index*

After the initial concrete setting period, the steel shell plates of 10 randomly selected compartments were partially cut open to verify the condition of the poured concrete at those locations. The positions of the selected compartments in the full-scale model are shown in Figure 6. In each compartment, we randomly selected six square grid units (30 cm × 30 cm) to cut open the steel shell. Each grid unit contained 15 to 21 detection points. The void area can be obtained by calculating the number of grid units along the

measuring line, and the void depth can be read using a Vernier caliper and a measuring frame.

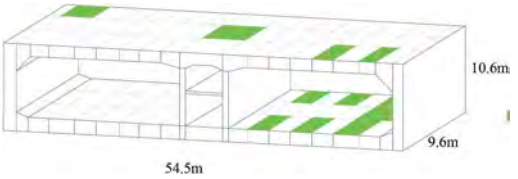

Figure 6. Layout of open compartments in full-scale section model.

3.4.2 *Void defect characteristics*

A typical compartment was selected to determine the condition of the poured concrete. The cutting locations of the steel shell and their corresponding numbers are shown in Figure 7.

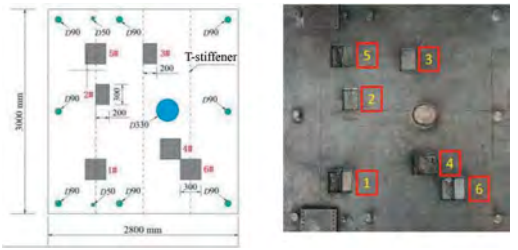

Figure 7. Distribution and numbering of steel shell opening locations in typical compartment.

4 DATA ANALYSIS

4.1 *Impact response strength index*

The impact response strength I defined in Equation (1) can be used as a as a potential discriminant parameter for detecting voids in steel shell – concrete structures via the elastic wave method. In actual signal processing, I can be calculated by integrating the absolute value of the normalized impulse response signal during the acquisition period t. The original signal is composed of a set of discrete equidistant sampling points. Therefore, the integral of the waveform signal can be approximated as the sum of the product of all previous sampling values and the sampling time, as follows:

$$\begin{aligned} I &= \int |x(t)|dt \\ &= \int_0^t |I_1 \sin(\omega_1 t + \varphi_1) + \cdots + I_n \sin(\omega_n t + \varphi_n)|dt \\ &\approx \sum_{i=1}^{i=s} |F_i| * \Delta t, \end{aligned} \tag{7}$$

where F is the waveform amplitude, $\triangle t$ the sampling time interval, i the number of sampling points at time t, and $s = 1,2,\ldots,n$.

4.2 *Correlation between impact response strength and void depth*

The impact response strength index I_i of the detection points at open-shell locations and the corresponding void depths d were analyzed statistically to determine the relationship between the response intensity and void depth; the resulting best-fit curve is shown in Figure 8. The best-fit curve was expressed in Equation (8) with a correlation coefficient (R) of 0.916 and a coefficient of determination R^2 of 0.839.

$$d = -25.58e^{-0.08I_i} + 23.1 \tag{8}$$

Based on the fitting curve, we propose a quantitative criterion for the non-destructive testing of void defects in steel shell–concrete SSITs, as shown in Table 3. Different colors (blue, yellow, orange, and red) signifying different void depths were used to represent the bonding condition between the steel plate and concrete.

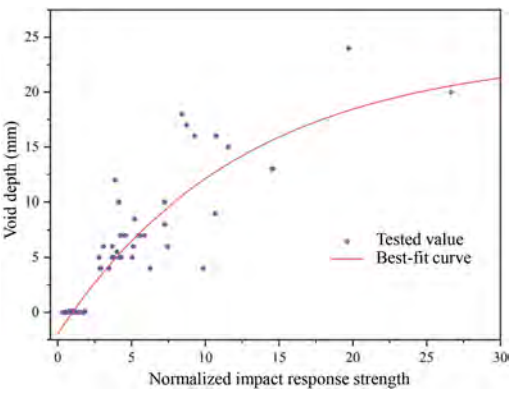

Figure 8. Comparison between detection results and measured data at open-shell locations.

4.2 *Verification of testing criterion*

The void detection was performed again on another 5 model compartments. The steel shell cover of each compartment was cut open in six randomly selected locations for verification. Figure 9 shows the comparison between the detected and actual conditions at six typical open-shell locations. It is evident that the detection results were generally consistent with the actual condition of the concrete surface. The detection results at all 30 open-shell locations were analyzed statistically to determine their accuracy in reflecting the actual condition of the concrete

Table 3. Normalized impact response strength index.

Normalized impact response strength (A)	Color code		Bonding condition	Description
$A \leq 2.3$		blue	Dense	Steel plate and concrete are closely bonded
$2.3 < A \leq 3.3$		yellow	2–3 mm	Steel plate and concrete are not bonded; concrete has a honeycomb-pitted surface; the void depth is 2–3 mm
$3.3 < A \leq 5.0$		orange	3–5 mm	Steel plate and concrete are not bonded; void depth is 3–5 mm
$A > 5.0$		red	5 mm or more	Steel plate and concrete are not bonded; suspected void depth is ≥ 5 mm

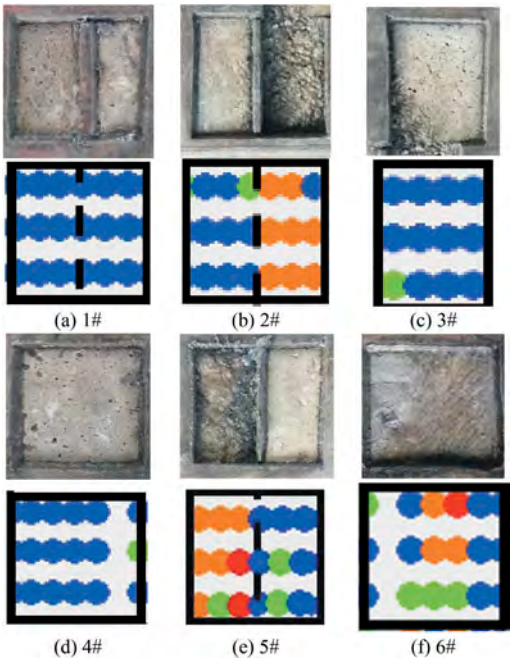

Figure 9. Comparison between normalized impact response strength values and actual condition of concrete surface.

surface. It was discovered that the coincidence rate between the detection results and the actual surface condition was 87.5%.

5 CONCLUSION

The aim of this study was to investigate void detection using the impact imaging method and propose methods of void defect control for steel shell–concrete SSITs. The main conclusions are as follows:

(1) By extracting the impact response energy and waveform processing, the impact imaging method could quantitatively calculate the void area and classify the voids based on a specific depth range.

(2) The void location, area, and depth were determined as metrics to describe the void severity in thick steel shell - concrete immersed tube tunnels, and using four levels for the void depth - namely, 0 - 3, 3 - 5, and > 5 mm - the bonding state of the steel plate and the concrete could be described.

(3) The relationship between impact response strength I and void depth d was established statistically through full-scale model experiments, based on which the quantitative void detection criterion was proposed. The void detection accuracy using the impact imaging method was shown to reach 87.5% through experimental verification.

ACKNOWLEDGMENTS

This work was supported by the R&D Projects in Key Areas of Guangdong Province (Grant no. 20191105), the Five Talents Program of IWHR (Grant no. SD0145B042021), the State Key Laboratory of Simulation and Regulation of Water Cycle in River Basin (Grant no. SKL2022TS15 and SKL2020ZY10).

REFERENCES

Akimoto, K., Hashidate, Y., Kitayama, H., Kumagai, K., 2002. Immersed tunnels in Japan: Recent technological trends. Underwater Technology. Proceedings of the 2002 international symposium on. pp. 81–86.

Bowerman, H., Chapman, J.C., 2002.Bi-steel steel-concrete-steel sandwich construction. Composite Construction in Steel & Concrete IV Conference.

Chen, D., Montano, V., Huo, L., 2020. Detection of subsurface voids in concrete-filled steel tubular (CFST) structure using percussion approach. Constr. Build. Mate. 262: 119761.

Deng, F.J., He, W.Q., 2002. Comparison of the characteristics of steel structure and concrete structure of immersed tube tunnel. Traffic Engineering Science and Technology,pp. 42–48.

Grantz, W.C., 1997. Steel-shell immersed tunnels- Forty years of experience. Tunnelling and Underground Space Technology. 12(1): 23–31.

Guo, Y.T., Nie, X., Tao, M.X., Qiu, S.Y., Tang, L., Fan, J. S., 2019. Bending capacity of steel-concrete-steel composite structures considering local buckling and casting imperfection. Journal of Structural Engineering. 145 (10): 1–04019102.16.

Kimura, H., Moritaka, H., Kojima, I., 2002. Development of sandwich-structure submerged tunnel tube production method. Nippon Steel Technical Report. 86: 86–93.

Lin, M., Lin, W., Liu, X.D., Hanada, Y., 2017.Development and experience of immersed tunnel in Japan. Journal of Waterway and Harbor.

Liu, R.Q., Zhang, G.X., Li, S.H., Feng, S.K., Xin, J.D., 2022. Application of impact imaging method on nondestructive detection of void defects in sandwich-structured

immersed tunnel. Mathematical Problems in Engineering, pp. 1–14.
Liu, R.Q., Li, S.H., Zhang, G.X., Song, S., Xin, J., 2021. Simulation analysis of void defect detection in sandwich-structured immersed tunnel using elastic wave. Shock and Vibration. (4): 1–12.
Luttikholt, A., Doorduyn, A., de Wit, H.D., Li, Y., 2022. Consideration of concrete and steel sandwich tunnel elements. Tunnelling and Underground Space Technology. 121: 104309.
Mandal, A., Baidya, D.K., Roy, D., 2012. Dynamic Response of the Foundations Resting on a Two-layered Soil Underlain by a Rigid Layer. Geotech. Geol. Eng. 30 (4): 775–786.
Meng, C., Feng, S.K., Che, A.L., 2013. Study on the imaging method for detecting defect in high-speed railway embankment. Proceedings, the 11th SEGJ International Symposium.
Mitsuo, I., Kazunori, K., Kengo, Y., 2008. Study on Non-Destructive Testing Method of Steel Plate Concrete Composite Deck by Impact Acoustics. Kawada Tech. Report. Pp. 27.
Mizuno, H., Izumi, Y., Sakagami, T., Matsui, S., Sugiyama, T., 2013. Study on nondestructive testing for steel-concrete composite slab by infrared thermography technology. Structural Engineering Papers. pp. 59a.
Nie, J., 2019. Application of steel-concrete composite structure in ocean engineering. Steel Construction. 35(1): 1–15.
Nishioka, K., Watanabe, Shigemura, D., 2008. Detection of voids on the underside of steel sheet of steel-concrete composite structure using impact elastic wave method (non-destructive inspection/diagnosis). Proceedings, Japan concrete institute.pp. 715–720.
Yanagihara, A., Hatanaka, H., Tagami, M., 2013. Development and application of Non-destructive inspection for steel-concrete composite structures. J. Ihi Technol. 53: 47–53.
Yu, G.Q., Fu, Z.P., 2000. Immersed tube tunnel in Europe and America. Advances in Science and Technology of Water Resources. 20(6): 11–14.

Tunnelling for a Better Life – Yan, Celestino, Thewes & Eberhardt (Eds)
© 2024 The Author(s), ISBN 978-1-032-80042-4
Open Access: www.taylorfrancis.com, CC BY-NC-ND 4.0 license

Assessment of operational limits for tunnel element transport using a shallow draft semi-submersible barge

Meihong Lin*, Zongquan Ying, Wengeng Shen & Xuegang Wang
CCCC Fourth Harbor Engineering Institute Co., Ltd., Guangzhou, China
Southern Marine Science and Engineering Guangdong Laboratory (Zhuhai), Zhuhai, China
CCCC Key Lab of Environmental Protection & Safety in Foundation Engineering of Transportation, Guangzhou, China

ABSTRACT: In order to meet the transportation and installation requirements of tunnel elements in nearshore shallow water environments and overcome the economic problems of prefabrication factories and the installation site of tunnel elements, shallow draft semi-submersible barges are employed for the long-distance transportation and installation of tunnel elements. For offshore installation operations of tunnel elements dominated by waves, the operating limit is typically expressed by allowable sea state parameters, such as the significant wave height (Hs) and spectral peak period (Tp). However, due to their particularity, in-depth research is required to accurately determine the large scale and shallow draft parameters of shallow draft semi-submersible barges. Moreover, the allowable sea conditions need to be evaluated during the planning phase of long-distance transportation and installation. Multiple sources of uncertainties (e.g., weather forecasts, wave spectrum models, and numerical models) must also be considered in the allowable sea conditions to provide safety margins. Based on the response spectrum and failure probability analysis of the operating conditions, this study establishes an adaptability analysis method for tunnel element transportation and installation using a shallow draft semi-submersible barge and evaluates the impact of wind sea and swell sea on its propagation under different directions and propagation directions in the Guangdong–Hong Kong–Macao Greater Bay Area. We also investigate the adaptability of long-distance transportation and installation using a shallow draft semi-submersible barge and assess the construction operation limits of the transportation and installation for tunnel elements. A case study using a semi-submersible barge to transport and install tunnel elements was selected to address these uncertainties in the allowable construction sea conditions, and to subsequently analyse the adaptability and superiority of tunnel element transportation and installation using a shallow draft semi-submersible barge.

Keywords: tunnel element, operational limit, shallow draft semi-submersible barge, response spectrum, failure probability

1 INTRODUCTION

Immersed tube tunnels and shield tunnelling are important types of river crossing channels. The immersed tunnelling method has the advantages of less land occupation, a lower navigation impact, and a fast construction speed compared to shield tunnelling. However, the former also requires a greater amount of construction technology and accurate construction monitoring systems. With the continuous maturity of its construction technology, the construction scale of immersed tunnelling is constantly growing and the construction conditions are becoming more complex. Furthermore, immersed tunnels are typically constructed using dry dock or factory prefabrication. Prefabrication is followed by wet towing or the specialized floating construction of towing ships for floating transportation. However, urban traffic congestion, narrow urban spaces, and the high cost of axis dry docking act as key bottlenecks affecting the construction cycle and cost of immersed tube tunnels. Thus, employing off-site dry docking or factories for prefabrication and long-distance floating transportation to the installation site has become a preferred construction method (Hu, Xie et al. 2015, Quanke, Yongling et al. 2022). Despite this, due to the complex sea conditions and higher requirements for the crack control of tunnel elements, long-distance floating transportation can pose potential risks during construction and have

*Corresponding author: linmeihong@qq.com

DOI: 10.1201/9781003495505-319

a huge impact on the safety of tunnel construction. Therefore, the risk assessment and control of risk factors for immersed tunnel construction are of great significance (Busby and Marshall 2000).

Sudden disastrous weather is an important risk factor during floating transportation (Dong, Li et al. 2023). By analysing the motion behaviour of the tunnel element and installation ship system under different wave, current, and ballast system load combinations, the weather window for the tunnel element can be determined. This consequently ensures that the tunnel element can be safely and accurately transported to the installation site for installation (Huang, Zhang et al. 2016). Thus, in-depth research is required to select the response measures for tunnel element movements under long-term regular and irregular wave actions. This with aid in improving the predictions of the accurate and safe handling of tunnel elements under adverse weather conditions (Song, Zhang et al. 2018).

Despite the current availability of numerous advanced software (e.g., ANSYS AQWA, and OrcaFlex) for the time-domain response analysis of a three-dimensional floating body motion, establishing accurate numerical simulations to predict its six-degree of freedom motion is still highly challenging. Time-domain methods can be inefficient due to their long calculation time and the large number of calculation conditions implemented for long construction windows. Although frequency domain and spectral analyses methods have been applied to the motion analysis of large floating structures, there is relatively little research on the motion of tunnel elements transported by transport vessels (Li, Haver et al. 2021). Combining frequency domain analysis methods with spectral analysis can potentially be used to predict the motion response of tunnel elements.

In this study, based on the frequency domain calculation of three-dimensional potential flow theory and the wave spectrum analysis method, we establish a calculation approach for the motion response spectrum of a semi-submersible barge during transportation. The spectral energy distribution of the shallow draft semi-submersible barge under different wave directions is subsequently analysed, and the boundary conditions of the semi-submersible barge construction are obtained using a probability-based approach. The time series data is then employed to analyse the operability for construction window of the semi-submersible barge.

2 METHODOLOGY FOR THE ASSESSMENT OF OPERATIONAL LIMITS

For the motion response prediction of a semi-submersible barge during offshore construction, it is usually assumed that the semi-submersible barge generally moves in a rigid body under the action of wind, waves, and currents. Current dynamic analysis methods and software used to simulate small amplitude waves on floating bodies are relatively mature, and the calculation results based on commercial software such as ANSYS AQWA have a high accuracy for semi-submersible barge construction analysis. The motion response of a semi-submersible barge is calculated based on three-dimensional potential flow frequency domain theory. ANSYS AQWA solves a set of linear algebraic equations to obtain the harmonic response of a semi-submersible barge to regular waves. These response characteristics are commonly referred to as response amplitude operators (RAO) and are proportional to the wave amplitude. The linear frequency domain motion equations of hydrodynamic interaction structures with frequency correlation coefficients can be expressed as follows:

$$\left[-\omega^2(M_s + M_a) - i\omega C + K_{hys}\right]\left[X_j\right] = \left[F_j\right], \quad (1)$$

where ω is the frequency; M_s is the float body mass matrix; C is the damping matrix; K_{hys} is the hydrodynamic stiffness matrix; X_j is the motion response; and F_j is the external force. Equation (1) can be expressed as $\left[X_j\right] = H\left[F_j\right]$, and $H = \left\{-\omega^2(M_s + M_a) - i\omega C + K_{hys}\right\}^{-1}$.

We determined the $RAO(\omega)$ of the incident waves at different angles acting on the semi-submersible barge through commercial hydrodynamic analysis software such as ANSYS AQWA. The motion response of the semi-submersible barge was then calculated as follows:

$$S_{res}(\omega) = S(\omega)RAO^2, \quad (2)$$

where RAO is the amplitude response operator of the barge motion calculated in equation (1); $S_{res}(\omega)$ is the motion response spectrum; and $S(\omega)$ is the irregular wave spectrum. In offshore seas, the irregular wave spectrum is generally a mixed wave composed of wind waves and swells. The combination of wind waves and swells can be described using a bimodal spectrum, as in equation (3):

$$S(\omega) = S_{wind}(\omega) + S_{swell}(\omega), \quad (3)$$

where $S_{wind}(\omega)$ is the wind-wave spectrum; and $S_{swell}(\omega)$ is the swell wave spectrum.

In addition, the actual sea waves are usually multi-directional and irregular, and the wave energy spectrum function is a function of the wave direction and frequency. The length width ratio of the plane dimensions of semi submerged barges and other construction ships often exceeds 2. Thus, the motion response peak frequency of semi submerged barges in the length and width directions can be different. The different directions and frequency distribution characteristics of irregular wave energy spectra complicate the motion response analysis of semi-submersible barges. During the construction process,

the length direction of semi-submersible barges usually maintains a small angle with the spectral direction to avoid significant rolling motion. However, the characteristics of multi-directional irregular waves may increase the roll. Therefore, it is necessary analyse the motion response characteristics of semi-submersible barges under the action of multi-directional irregular waves. The directional spectrum of multi-directional irregular waves can be expressed as:

$$S(\omega,\theta) = S(\omega)G(\omega,\theta), \tag{4}$$

where $S(\omega,\theta)$ is the multidirectional wave spectrum; and $G(\omega,\theta)$ is the directional distribution function of ocean waves, with

$$\int_{\theta_{min}}^{\theta_{max}} G(\omega,\theta)d\theta = 1, \tag{5}$$

where $[\theta_{min},\theta_{max}]$ is the directional distribution range of the multi-directional wave spectrum. Considering equations (4) and (5), equation (3) becomes:

$$S(\omega,\theta) = S_{wind}(\omega)G_{wind}(\omega,\theta) + S_{swell}(\omega)G_{swell}(\omega,\theta). \tag{6}$$

The influence of frequency can generally be ignored, and the wind wave spectrum can thus be expressed as:

$$G(\theta) = \frac{\Gamma\left(1+\frac{n}{2}\right)}{\sqrt{\pi}\Gamma\left(\frac{1}{2}+\frac{n}{2}\right)}\cos^n\left(\theta-\theta_p\right) \tag{7}$$

Where Γ is the Gamma function, θ_p is the main wave direction. Finally,

$$S_{res}(\omega,\theta) = S(\omega,\theta)RAO^2(\omega,\theta). \tag{8}$$

For semi-submersible barge construction operations within a limited duration, the barge movement within 3 hours can be used as the basic parameter for its operation, and multiple 3-hour windows can be analysed as the analysis conditions for continuous operations. By further assuming that the global maximum is statistically independent and identically distributed, the distribution of N_{3h}=10800/T_z can be expressed as follows:

$$F\left(x_j\right) = \left\{1 - exp\left\{-\frac{1}{2}\left(\frac{x_j}{\sigma_j}\right)^2\right\}\right\}^{N_{3h}}. \tag{9}$$

In order to determine the appropriate extreme sea state, we assume that the probability of the maximum value exceeding the limit $x_{j,lim}$ within 3 hours is less than the selected target failure probability q3h hours. To meet this requirement, the following equation should be met:

$$P\left[x_{j,3h} > x_{j,lim}\right] = 1 - \left\{1 - exp\left\{-\frac{1}{2}\left(\frac{x_{j,lim}}{\sigma_j}\right)^2\right\}\right\}^{N_{3h}} \leq q3h \tag{10}$$

By calculating the motion response index using equation (10), the boundary wave parameters with the limiting conditions can be determined.

3 FLOATING TRANSPORTATION PARAMETERS AND PROCESS

3.1 *Main scale parameters of the semi-submersible barge*

Figure 1 presents the hull shapes of the semi-submersible barge employed in the case study. Table 1 reports the corresponding characteristics. The ship is mainly used for the transportation of large tunnel elements for nearshore tunnel construction. It is also used as a dock to repair ships, as a prefabricated platform for large caissons, for the towing and transportation of large offshore components, and the dispatch and transportation of engineering ships.

The semi-submersible barge selected for the case study is employed as a transportation platform for large tunnel elements. The barge is connected to the dock and a wheel rail type trolley is used to roll and transport the tunnel element from the dock to the loading area of the deck and place it on the support pier. The semi-submersible barge is towed to the diving area by a tugboat to dive. The immersed tunnel element floats and is pulled away from the semi-submersible barge. The semi-submersible barge then begins to float and enters the next working cycle.

The semi-submersible barge has core advantages such as a high cargo capacity, universality, and intelligence, and a strong ballast capacity. Moreover, it has an excellent "wide, flat, and shallow" draft performance. The ship can significantly reduce the amount of channel dredging, avoid the construction of large dry docks, and effectively reduce the construction costs of immersed tube tunnels.

Figure 1. Hull shape of the semi-submersible barge in the case study.

Table 1. Key parameters for the semi-submersible barge.

Parameter (unit)	Value
Length (m)	164
Moulded breadth (m)	65
Moulded depth (m)	10.2
Operational draft (m)	6.0
Displacement (kg)	5E7
Design load capacity (kg)	4.5E7

3.2 *Floating transportation process*

The loading, transportation, unloading, and floating in the foundation trench require strict hydrological and meteorological constraints. The selection of the construction window is a complex process related to the overall project schedule, project risks, and equipment costs. It thus requires comprehensive argumentation and analysis to ensure the safe installation of tunnel elements.

We used the tunnel construction in Tai Shan Bay of Shenzhen as an example. During the transportation process of semi-submersible barges, due to the complexity of the wind, wave, and flow parameters compared to inland rivers, and the resistance to oblique currents, the total floating resistance of semi-submersible barges is usually analysed at different upstream angles and tugboat configurations. The semi-submersible barge transports tunnel elements from Niutou Island through the Rongshutou Waterway to the Lingdingyang Waterway, and subsequently passes through the Tonggu, Shenzhen Public, and Tai Shan Bay Channel Waterways to a dedicated diving pit for the semi-submersible barge (Figure 2). Table 2 reports the angle of each transportation path and Figure 3 depicts an example of the towing system.

Figure 2. Transportation path of the semi-submersible barge of the case study.

Table 2. The angles of each transportation path in the case study.

Transportation Path	The angle between the current direction and the orientation of barge(°)
Rongshutou Channel	12, 168
Lingdingyang Channel	-11, 191
Tonggu Channel	25, 155
Shenzhen Western Channel	0, 180
Tai Shan Bay Channel	0, 180

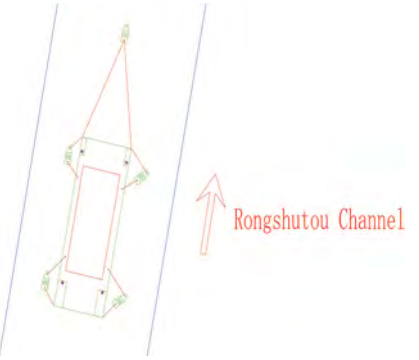

Figure 3. Example of a towing system in the case study.

4 RESULTS

The model for the semi-submersible barge is determined by analysing the wave angles that could potentially be encountered along the entire transportation path, combined with the energy distribution of the wind, waves, and swells. In this section we analyse the construction limiting parameters and construction windows of the semi-submersible barge.

4.1 *Numerical model and parameters*

The model of the semi-submersible barge and tunnel elements is established using ANSYS AQWA. Frequency domain analysis is then performed and the corresponding RAO is obtained. Figure 4 presents the numerical model and Table 3 reports the corresponding calculation parameters.

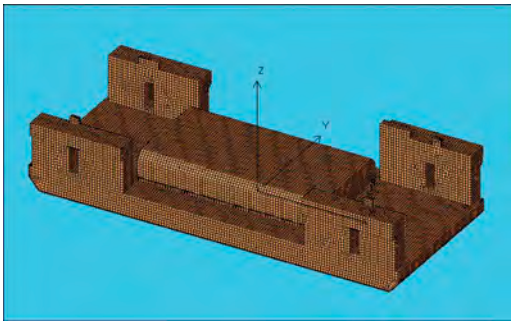

Figure 4. Numerical model.

Table 3. Parameters of the barge.

Parameters (unit)	Value
Tunnel element length (m)	80
Total mass (Kg)	70435900
I_{xx} (kg·m^2)	3.18E10
I_{yy} (kg·m^2)	2.71E11
I_{zz} (kg·m^2)	3.00E11

4.2 *Statistical analysis of sea state parameters*

The waves are affected by many islands in the Pearl River Estuary, and the wave propagation is complex. The SE, SSE, S, and SW waves are the main wave directions in this sea area. The annual maximum wave height (Hm), $H_{1/10}$, H_s and H_z are 2.58 m, 1.81m, 1.43 m, and 0.89 m, respectively, all of which occur in August.

Taking the wave data of March and August 2020 from ERA5 data set of ECMWF as an example, Figures 5 and 6 present the significant wave height (Hs) and spectral peak period (Tp) of the total sea, wind wea and swell sea of the wave data. Although these scatter plots overlap, the swells are generally steeper and have longer periods compared to windy seas. Extreme wave conditions with high Hs values are usually dominated by wind seas, and wind waves and swells tend to occur simultaneously. In addition, the two-month scatter plot clearly reveal that August is more likely to experience severe wave conditions. This is due to the influence of the typhoons Mekkhala and Higos, and indicates significant deviations in the operability of transportation operations across the two months. Based on the data from March, 26.8% of the angle differences between total sea and swell sea exceed 10°, while 8.8% of the angle differences between total sea and swell sea are greater than 30°. Moreover, based on the data from August, 16.5% of the angle differences between total sea and swell sea are greater than 10°, while 2.6% of the angle differences between total sea and swell sea that greater than 30°.

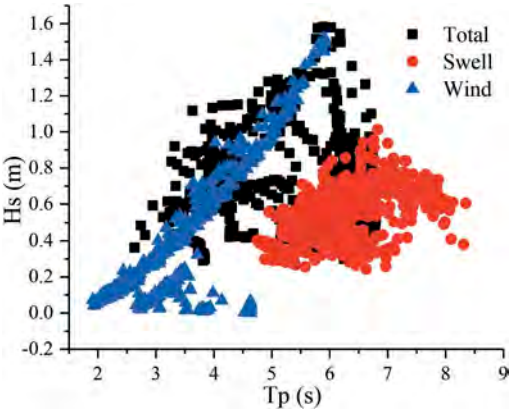

Figure 5. Scatter plot of the sea state parameters for Hs and Tp from March, 2020.

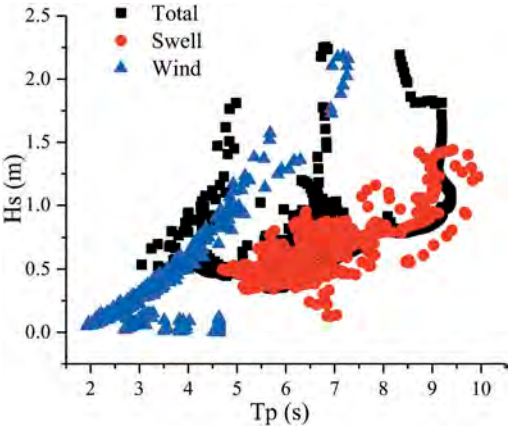

Figure 6. Scatter plot of the sea state parameters for Hs and Tp from August, 2020.

4.3 *RAO Characteristics*

Table 2 reports the natural periods of the barge, which range from 9 to 21 s. The size of the semi-submersible barge is observed to have a strong adaptability to the wave period of 3–9 s in the nearshore sea area (Figure 7 and Table 4). The differences in ship size induce a 1.85 times difference in the natural periods of roll and pitch, with a corresponding increase in the motion response by 4.59 times. Under the action of oblique waves, multiple peaks appear in the motion response due to its coupling effect.

4.4 *Operational limit analysis*

Large variations are observed in the spectral density distribution across the entire wave frequency when using JONSWAP and Torsethaugen spectra. In particular, the response spectrum peak of JONSWAP is close to 5–7 s, while when using the bimodal spectrum, the energy is concentrated around 6–8 s. When the Torsethaugen spectrum is adopted, the spectrum density of the semi-submersible barge is distributed over a wider frequency range. Moreover, the difference in heave response spectrum values between the two spectra types exceeds 1.66 times.

Figure 9 present the operational limits of several incident angles. Due to the misalignment of sea condition and barge direction, the allowable sea conditions are lower than those of the alignment conditions. For wave conditions with Tp values less than 9 s, the misalignment may result in a 30–50% reduction in the maximum allowable Hs values.

4.5 *Operability analysis*

The operability of floating transport operation is defined as the ratio between the length of the operable weather window and the total reference duration. We calculated the monthly construction operability based on equation 10 and using continuous 3-hour operation data of year 2020 from ERA5 data set of ECMWF.

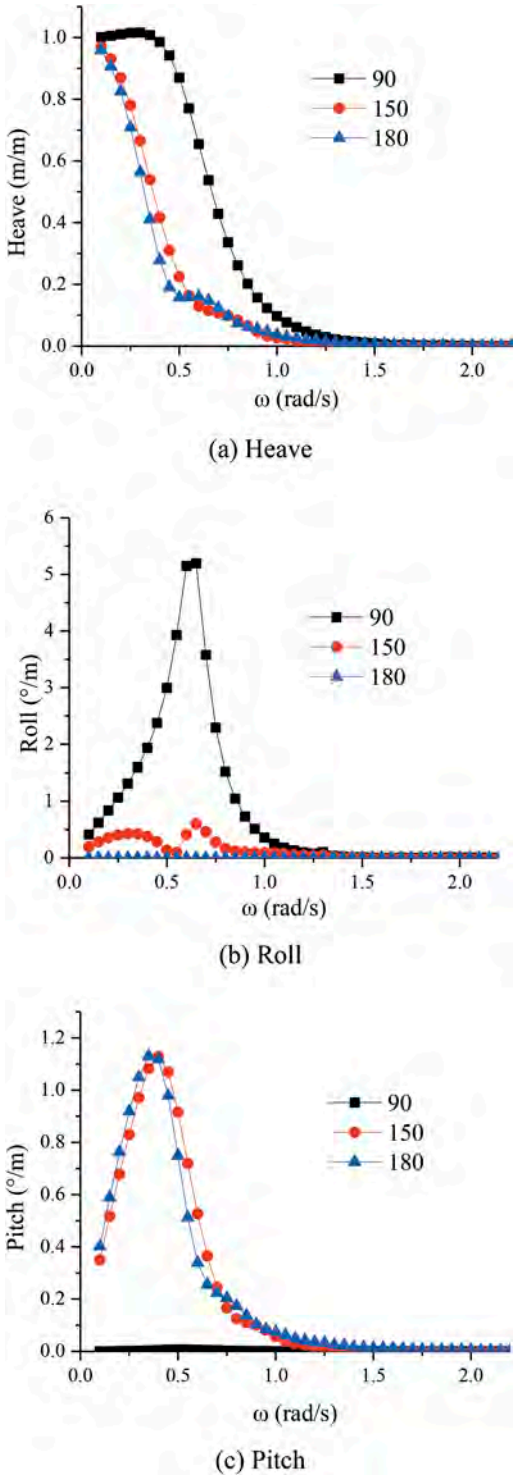

Figure 7. RAOs of the barge for three wave directions (The direction is defined as the angle between the wave propagating direction and the positive X-axis measured anti-clockwise).

Table 4. Natural periods of the barge motion.

Motion	Value (s)
Heave	20.9
Roll	9.6
Pitch	17.9

Table 5 shows the corresponding parameters. Note that due to the strong seasonal variations in sea state data, independent calculations and analysis were conducted on the operability of each month. Operability calculations were performed using JONSWAP (Total sea parameters), Torsethaugen spectra (Separate sea parameters: swell wave + wind wave) and both include

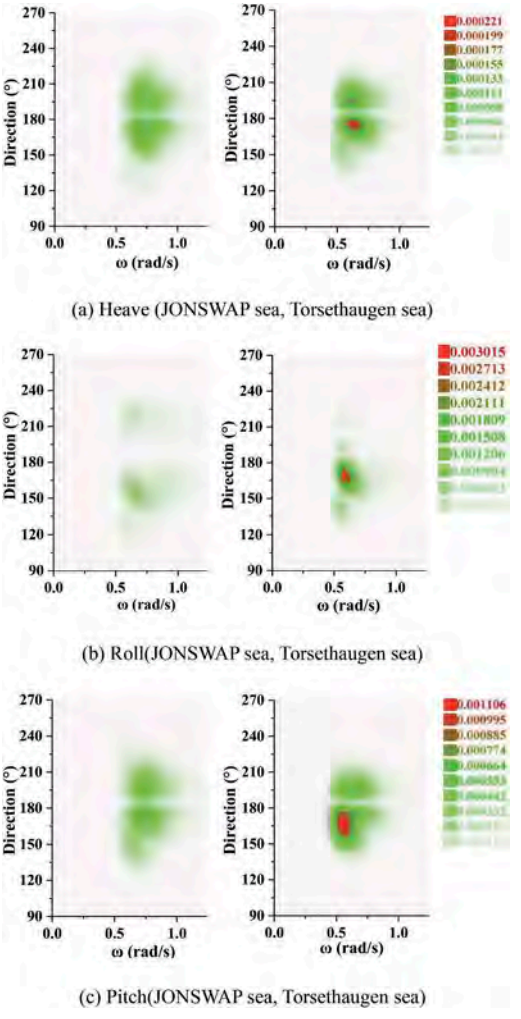

Figure 8. Response spectra for motion, S(ω,θ), with misaligned wind sea and swell sea (total sea: Hs = 1.19 m, Tp = 6.37 s, direction = 172.5°; wind sea components: Hs1 = 1.00 m, Tp1 = 5.04 s, direction = 176°, n1 = 2; swell sea component: Hs2 = 0.65 m, Tp2 = 7.66 s, direction = 162.5°, n2 = 12).

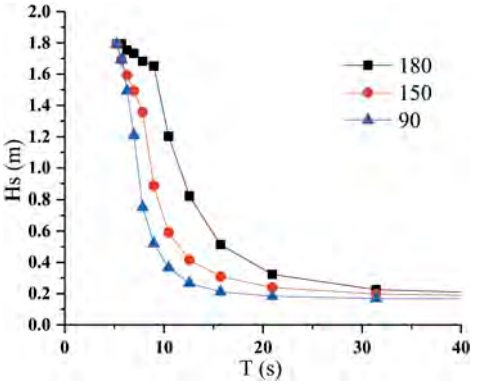

Figure 9. Allowable sea states.

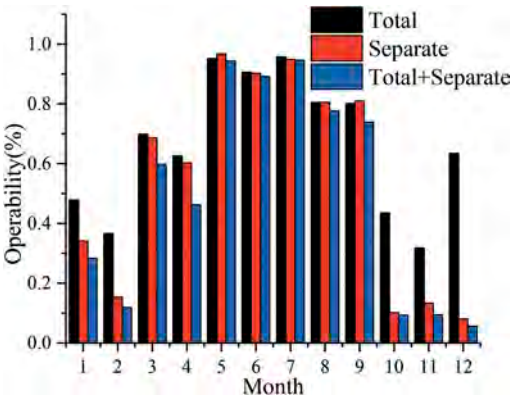

Figure 10. Operability (total sea, separate sea and total + separate sea).

Table 5. Parameters.

Parameter	Value(unit)	Failure probability
Heave	0.1m	0.0001
Roll	1°	0.0001
Pitch	0.5°	0.0001

condition (Total sea + Separate sea), respectively. Adopting both include condition for operability analysis resulted in a 10% reduction in operability during the months 05-09 and a 10% reduction in operability during the months 10~04, and the variability in the operability was higher within months (10~02). The operability in all directions during winter (10–11) was on average below 40%. This reveals that using both include condition for the analysis can account for inconsistencies in the surge direction, and the constructability analysis results are more reasonable.

5 CONCLUSIONS

In order to address the uncertainties in the operational limits caused by different sea state modelling methods, this article adopts a case study that implements a semi-submersible barge to transport tunnel elements. We analysed the characteristic parameters and adaptability to sea conditions of semi-submersible barges, and compared the effects of the wave propagation, wave spectrum types, and directional deviation of wind and swell seas on semi-submersible barges. Following this, we calculated the construction operability. Based on the results, the following key conclusions were obtained.

(1) The design of the semi-submersible barge size has strong adaptability to wave periods of 3–9 s in the nearshore sea area.
(2) The direction misalignment of wind seas and swell seas can enhance the motion response, which subsequently increases the difficulty in controlling the towing system.
(3) Due to the misalignment of the wind sea and swell sea components, the allowable sea conditions are reduced compared to the alignment conditions. For wave conditions with Tp values less than 9 s, misalignment may result in a 30–50% decrease in the maximum allowable Hs value of both containers.
(4) Analysis based on both include condition is able to consider the inconsistencies of surge direction, which increases the reasonability of the constructability analysis results.

REFERENCES

Busby, J. and Marshall C. (2000). Design and construction of the Øresund tunnel. Proceedings of the Institution of Civil Engineers-Civil Engineering, Thomas Telford Ltd.

Dong, S., Li, S., Yu F. and Wang K. (2023). "Risk Assessment of Immersed Tube Tunnel Construction." Processes 11(4): 980.

Hu, Z. n., Xie Y. l. and Wang J. (2015). "Challenges and strategies involved in designing and constructing a 6 km immersed tunnel: A case study of the Hong Kong–Zhuhai–Macao Bridge." Tunnelling and underground space technology 50: 171–177.

Huang, G., N. Zhang, A. W. K. Law, Y. Song and Lin, L. (2016). "Motion response of immersing tunnel element under random waves." Ships and Offshore Structures 11 (6): 561–574.

Li, L., Haver, S. and Berlin N (2021). "Assessment of operational limits: Effects of uncertainties in sea state description." Marine structures 77: 102975.

Quanke, S., Z. Yongling, C. Yue, F. Lei, Y. Yu, S. Zongxian, H. de Wit and Ying L (2022). "Hong Kong Zhuhai Macao Bridge-Tunnel project immersed tunnel and artificial islands–From an Owners' perspective." Tunnelling and Underground Space Technology 121: 104308.

Song, Y., N. Zhang, G. Huang and Sun Z. (2018). "Experimental study on motions of tunnel element during immersion standby stage in long wave regime." Ocean Engineering. 161 29–46.

Tunnelling for a Better Life – Yan, Celestino, Thewes & Eberhardt (Eds)
© 2024 The Author(s), ISBN 978-1-032-80042-4
Open Access: www.taylorfrancis.com, CC BY-NC-ND 4.0 license

Research and application of steel intelligent manufacturing of Shen-Zhong Link steel sandwich immersed tunnel

Hanxin Long*
Guangchuan Shipbuilding Intetnational Limited Company, Guangzhou, China

Weiguo Rui
Shengzhong-Link Administration Center, Zhongshan, China

Yidong Xie
Guangchuan Shipbuilding Intetnational Limited Company, Guangzhou, China

ABSTRACT: As a new production mode, the intelligent manufacturing has become the development direction for the future manufacturing industry. The steel shell used in the Shen-Zhong Link steel sandwich immersed tunnel is characterized by its large volume, comprising 32 pipes with a total weight of approximately 320,000 tons. To meet the project's timeline, the production rate of one pipe per month must be achieved. However, traditional process technologies face challenges in achieving high-quality and high-efficiency construction. Therefore, it is imperative to conduct research and apply intelligent manufacturing techniques to ensure the timely completion of this project. This paper presents the key technologies employed in the intelligent manufacturing of steel shells for the Shen-Zhong Link immersed tunnel. By establishing intelligent manufacturing systems and technical standards for steel shells, developing welding robots based on visual recognition, implementing intelligent coating for large steel structures, and integrating BIM-oriented system integration, the large-scale application of intelligent manufacturing for large steel structures has been successfully realized. Moreover, the application of intelligent production lines demonstrates significant advantages over traditional manual operations in terms of efficiency.

Keywords: Shen-Zhong Link steel, intelligent manufacturing, welding robots, intelligent coating

1 INTRODUCTION

In recent years, there has been a global boom in intelligent manufacturing. Germany, known for its manufacturing prowess, proposed the "Industry 4.0 strategy," while the United States put forward the "advanced manufacturing national strategy." In May 2015, China also launched the "Made in China 2025" plan, aiming to achieve the strategic goal of becoming a manufacturing powerhouse through a three-step approach. Transportation construction plays a crucial role in the manufacturing industry, and technologies such as production execution systems (MES), industrial robots, new sensors, and intelligent control systems have been partially applied in transportation construction. However, there is still a significant gap in terms of interconnection, information integration, and other aspects when compared to advanced production models as previously shown (Wu et al., 2016).

Overall, the level of automation and intelligence in transportation construction is still insufficient. The problem of "information islands" remains prominent, and there is a lack of comprehensive integration, collaboration, and innovation.

The Shenzhen-China Channel project is built on the concept of "integration of the two" and seizes the opportunity presented by the "Made in China 2025" initiative. By combining Internet technology, Building Information Modeling (BIM), and smart engineering, the project focuses on research and applications in intelligent manufacturing for steel shell concrete immersed tube tunnel steel structures. This endeavor aims to enhance manufacturing efficiency and quality, ultimately elevating the level of intelligent manufacturing in the transportation industry.

2 PROJECT OVERVIEW TRANSPORTATION TECHNOLOGY

The Shenzhen-China Passage is another world-class mega project that combines bridges, islands, tunnels, and underwater interconnections, following the Hong Kong-Zhuhai-Macao Bridge as previously shown (Song et al., 2020). The immersed tube tunnel measures 5035m in length and consists of a total of 32 immersed tubes with 1 final joint. The standard pipe section spans 165m, while the curve-widened pipe

*Corresponding author: 29888766@qq.com

DOI: 10.1201/9781003495505-320

section extends to 123.8m. The specific division of joints is as follows: 123.8 + 21×165m + 2.2m + 5×165m + 5×123.8m = 5035m. The Shenzhen-China Passage is the first steel-concrete composite immersed tube tunnel scheme in China as previously shown (Xu et al., 2015). The manufacturing of the steel shells for the immersed tube tunnel is a pivotal process within the entire project, as it plays a crucial role in overseeing the overall progress. Each individual standard steel shell pipe section measures 165m in length, 46m in width, and with a height of 10.6m. The maximum weight of a single section reaches 12,500 tons, resulting in a total steel volume of approximately 320,000 tons

3 SINKING TUBE STEEL SHELL STRUCTURE AND DIFFICULTIES

The steel shell primarily consists of internal and external panels, vertical and horizontal partitions, vertical and horizontal stiffening ribs, and welding nails. The inner and outer panels, along with the vertical and horizontal partitions, are interconnected to create a cohesive structure, forming an independent partition for concrete pouring. The longitudinal stiffening ribs are constructed using T-shaped steel and Angle steel, working in conjunction with the transverse flat ribs to enhance the panel's rigidity. Simultaneously, the longitudinal stiffening ribs and welding nails ensure a secure connection between the panel and the concrete, as depicted in Figure 1.

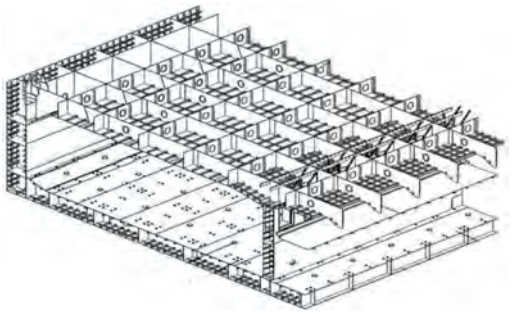

Figure 1. Schematic diagram of basic structure of steel shell.

Based on the structural form and construction process characteristics of Sink steel shells, they are suitable for factory assembly-line manufacturing in large shipyards. However, there are several challenges associated with the construction of Sink steel shells:

(1) Large volume: A single standard pipe section requires approximately 10,000 tons of steel and involves a weld length of nearly 300 kilometers.
(2) Complex structure and manufacturing process: The Sink steel shell comprises numerous independent compartments (up to 1597), with staggered horizontal and vertical partitions and connecting parts. Additionally, there can be up to 15,000 process holes. China lacks mature construction experience in this regard.
(3) High precision requirements pose a significant challenge in the construction of steel shells. The accuracy standards for steel shells are much higher compared to those in the shipbuilding industry and steel box girder manufacturing. Additionally, the use of Q420 high-strength medium-thick steel plates in large quantities presents difficulties in controlling welding deformation.
(4) High anticorrosion requirements are essential due to the severe seawater corrosion at the tunnel site. To address this, a triple anticorrosive approach is employed for the pipe sections, including "reserved corrosion thickness + heavy coating + sacrificial anode block" measures. This involves applying a glass scale paint coating with a dry film thickness of 700~1000μm. The quality of the painting construction plays a crucial role in ensuring effective corrosion protection.

4 INTELLIGENT MANUFACTURING SYSTEM CONSTRUCTION

In accordance with the project's requirements for controlling the overall construction period, the steel shell manufacturing unit for the immersed tube tunnel needs to have the capacity to produce one pipe section per month. Given the challenges involved in steel shell manufacturing, meeting high-quality construction demands using traditional technology alone is difficult. Therefore, it is essential to conduct research and implement intelligent manufacturing techniques for the steel shell of the immersed tube tunnel. This will ensure timely project completion while maintaining high-quality standards. The following sections will outline the development of an intelligent manufacturing system for the project based on the construction process flow of the steel shell and leveraging existing advanced manufacturing technologies.

4.1 *Steel shell construction process*

To fulfill the requirements of intelligent manufacturing for the steel shell, the 165m standard segment is divided into 11 larger segments, each measuring 15m in length along the longitudinal direction. These larger segments are further divided into 22 sub-segments based on left-right symmetry principles along the width direction, as illustrated in Figure 2. Each sub-segment is then divided into four plane blocks, namely the bottom plate, middle wall block, side wall block, and top plate, taking into account the structural characteristics. Additionally, based on the specific structural characteristics of each block, further division into several pieces is made. The primary process flow of steel shell construction is depicted in Figure 3.

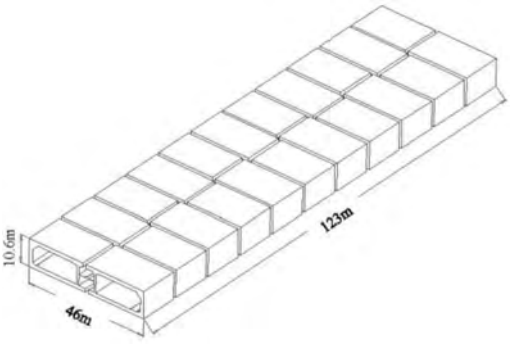

Figure 2. Schematic diagram of steel shell division.

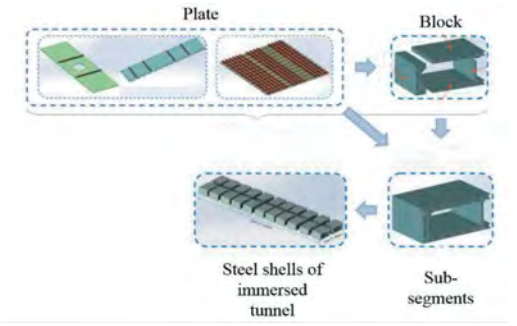

Figure 3. Main process flow chart of sinking tube steel shell structure.

4.2 *Construction of intelligent manufacturing system*

Taking into account the construction process of the steel shell structure and the current level of intelligent manufacturing equipment, a study is conducted on the construction processes of cutting and beveling, sheet assembly, block assembly, and subsection painting in the production of the steel shell structure. Based on the operations involved and their characteristics, these processes can be categorized into five intelligent production lines: the intelligent cutting production line, slice intelligent welding production line, block intelligent welding production line, segment intelligent painting production line, and the workshop manufacturing execution control system (MES). The research and development of the steel shell intelligent manufacturing system focuses on implementing "four lines and one system," utilizing robots and assembly lines for intelligent production.

4.3 *Function and technical index design of "four-wire one system"*

Intelligent cutting production line

(1) The application of plate/profile CNC cutting production lines in the steel shell production unit has reached a relatively mature stage. However, each production line's cutting equipment operates independently, requiring manual allocation and statistical tracking of tasks and production volumes. This manual process significantly limits production efficiency. To address this issue, it is essential to implement intelligent networking control through network system integration technology for the original CNC cutting production lines. This transformation will enable intelligent cutting operations, as illustrated in Figure 4.

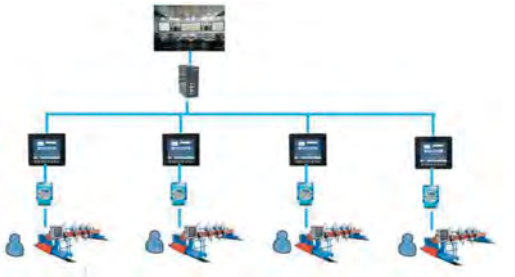

Figure 4. Frame of intelligent steel cutting production line.

(2) The main key technical indicators are as follows:

① Enable networking between CNC cutting machines, profile cutting lines, and the workshop MES system.

② Realize real-time data acquisition and feedback of CNC cutting machine and profile cutting line;

③ Can feedback processing data including cutting steel furnace batch number, cutting part number, cutting time and other information to the information management system.

(2) sheet intelligent welding production line

Based on the analysis of the steel shell structure, it is observed that there are numerous relatively simple sheet parts. With the availability of production line conditions, these parts can undergo manual assembly, followed by 3D online scanning to automatically generate welding procedures. Once the instructions are received, robots can carry out automatic welding operations,as illustrated in Figure 5.

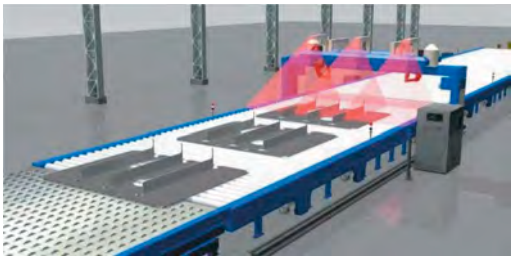

Figure 5. Schematic diagram of sheet body intelligent welding production line.

(3) The main technical indicators are as follows:

① Welding capacity: capable of performing flat fillet welding and wrap fillet welding in the range of 3.5mm to 9mm.;

② The system can accurately position the welding, automatically acquire workpiece information, and generate welding programs automatically.;
③ Realize longitudinal and transverse diaphragm unit stiffening fillet weld intelligent welding;
④ Processing capacity: the size range of the body can be processed is 1500mm-4500mm long, 1500mm-4500mm wide;
⑤ Realize the production line and workshop MES system networking, with online programming function.

(3) block intelligent welding production line

The block intelligent welding production line is primarily utilized for the robotized automatic welding of open block structures within the deep channel. It consists of various stations, including loading, FCB panel installation, longitudinal assembly welding, block intelligent robot welding, repair, pre-outfitting, tire out, and more. The block robot welding system comprises a mobile welding gantry, beam-type walking trolley, and welding robot (including a vertical lifting system), as illustrated in Figure 6.

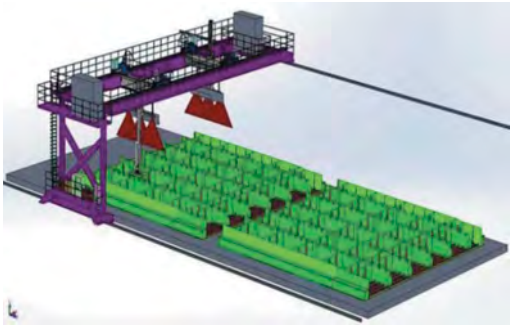

Figure 6. Schematic diagram of the block robot welding system.

(4) The main technical indicators are as follows:
① Able to accurately position the weld, automatically obtain the workpiece information, and automatically produce welding procedures;
② It can realize intelligent welding of vertical and transverse partition board and top and bottom plate structure;
③ Realize the block intelligent welding production line and MES system networking, with offline programming function;
④ Welding capacity: It can meet the 5mm to 12mm foot height of flat fillet welding, vertical fillet welding, cladding fillet welding and no more than 14mm plate thickness of deep penetration welding.

(4) Intelligent coating production line

The outer surface of the steel shell section (top, bottom, side) is flat with a large area and few surface outfitting parts. Utilizing robots for sanding and spraying provides significant advantages. By incorporating sandblasting and painting robots along with a remote control system, intelligent coating of the steel shell subsection is achieved. The intelligent sandblasting and painting workshop can be seen in Figures 7 and 8.

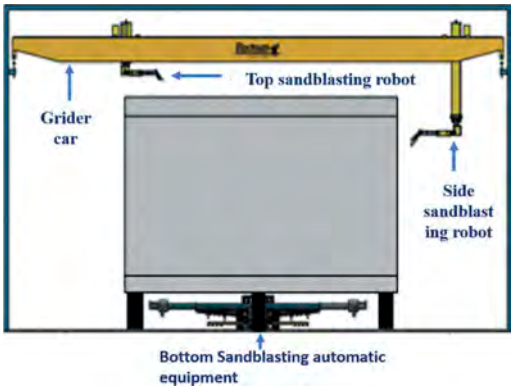

Figure 7. Schematic diagram of intelligent spraying workshop.

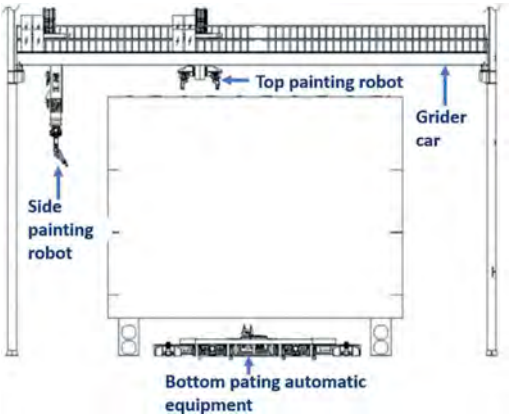

Figure 8. Schematic diagram of intelligent spraying workshop.

(5) The main technical indicators are as follows:
① Can realize the robot automatic sandblasting and automatic spraying.
② Processing capacity: The size range of the bar segment that can be processed: (L × W × H) 15m× (23m-28m) ×10.6m;
③ With offline programming, online monitoring functions, and can be optimized and upgraded during use;
④ Realize intelligent painting production line and workshop MES system networking.

(5) Workshop manufacturing implementation control system

Within the framework of the BIM technology management system, a workshop manufacturing execution system software is developed. This software utilizes the digital workshop integrated management system (MES) as its core and adheres to the unified standard of BIM technical data interface. Through various modules such as basic data management, intelligent engineering

planning, tire frame layout, block transportation management, quality control, equipment management, status Kanban management, etc., the software enables information control over the workshop manufacturing execution process. It further achieves data interconnection by developing a data interface with the intelligent production line and establishes seamless integration with the BIM platform. This ultimately realizes intelligent control over the workshop manufacturing execution process. The functional architecture of the digital workshop Manufacturing Execution System (MES) is depicted in Figure 9.

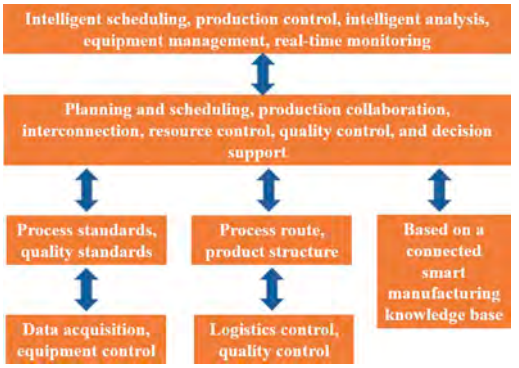

Figure 9. Digital workshop Manufacturing execution system (MES) functional structure.

(6) The main technical indicators are as follows:

① Deploy a wired or wireless network in the production workshop to facilitate the transmission of processing data to each production station through the network;
Through the collection of equipment working status data, to

② achieve the monitoring of the running status of each production line, through the development of data interface, the relevant information into the special management information platform;

③ Realize the information management and control of the workshop manufacturing execution process, and realize the interconnection and interworking of data by opening the data interface with the intelligent production line of blanking processing, the intelligent welding line of sheet body, the intelligent production line of block body and the intelligent painting production line;

④ And the special management information platform to achieve seamless connection, to achieve the intelligent control of the workshop manufacturing execution process;

⑤ With basic data module, production management module, quality management module, resource management module, status Kanban management module, etc;

⑥ 3D digital production design model and drawings are completed and submitted on time, to realize the integration and linkage of MES system and "four lines", and to realize the integration of MES system and special management information platform system.

5 APPLICATION PRACTICE OF INTELLIGENT MANUFACTURING

Currently, intelligent manufacturing has been implemented in over ten steel shell projects. Based on the application results, the "four-wire one system" operates smoothly, and it successfully achieves the intended objectives in terms of functionality, manufacturing quality, and efficiency.

(1) The steel intelligent cutting production line is built upon the existing automatic CNC cutting equipment. By developing networking control software, layout data acquisition systems, and integrating on-site industrial computers, it can automatically receive plate and profile cutting instructions, nesting book data, as well as cutting equipment operating status information and production data feedback generated by the design system. These data are then uploaded to MES (Manufacturing Execution System). Additionally, key production process data can be fed back to the BIM system through an external network, creating an integrated program for automation, management data, Kanban visualization, and intelligent cutting production line, with modules for management, information, monitoring, early warning, analysis, reports, and Kanban.

The implementation of the production line enables the comprehensive deployment of a CNC cutting production line network control system. This addresses issues such as real-time remote monitoring of the cutting production line's status, real-time production progress statistics, and equipment fault alarm analysis. It also introduces an innovative solution for real-time data acquisition and replication of CNC cutting equipment, laying the technical foundation for achieving the "digital twin" of an intelligent cutting production line.

Figure 10. Application of intelligent cutting.

(2) Body intelligent welding production line

The intelligent sheet welding production line incorporates advanced technologies including machine vision analysis, automatic welding path planning, and fully automated and efficient welding. It achieves workpiece identification and online programming through 3D

laser scanning adaptive programming, eliminating the need for importing a 3D model. The line laser enables real-time tracking of the weld, allowing for automatic adjustment of the welding path based on the workpiece's weld straightness deviation.

Figure 11. Application of sheet body intelligent welding in steel shell and ship products.

After conducting preliminary tests and continuous adaptability tests during the production process, the welding of stiffeners in the diaphragm body of the steel shell structure achieves 100% full coverage of 3D scanning and 100% automatic identification welding. The robot welding speed reaches 0.42m/min, enabling 2 door frames and 4 robots to weld synchronously in a single pass. The robot welding demonstrates stable quality, uniform and good weld formation, and can achieve fillet welding, significantly reducing the workload of repair and grinding. Intelligent sheet welding greatly enhances production efficiency and welding quality, providing significant advantages in improving production capacity, reducing labor costs, and minimizing manual polishing tasks.

(3) Block intelligent welding production line

The intelligent welding production line enables robot automatic recognition and welding in complex and narrow spaces composed of vertical and horizontal partitions, longitudinal ribs, and bottom plates. It supports various types of welding such as flat fillet welding, vertical fillet welding, and deep penetration welding. The objective is to facilitate the complete automation and intelligence of the entire process from panel → FCB welding → longitudinal rib assembly → longitudinal rib welding → block component assembly → block component robot intelligent welding → shipping for the sink steel shell blocks.

Figure 12. Application of block robot in product welding.

By incorporating advanced technologies and equipment such as offline programming, three-dimensional simulation, and welding robots, the block intelligent production line facilitates fully automatic collaborative work of multiple welding robots. This results in uniform weld formation, stable welding quality, and a weld inspection pass rate of up to 99.9%. As a result, the workload for grinding and repair is significantly reduced, with approximately 225 hours of grinding saved for a single standard pipe section.

In comparison to the previous manual welding production mode, the block intelligent welding production line has substantially improved the proportion of welding time and efficiency. It has also significantly reduced waste in welding materials caused by excessive welding beads and defect repairs.

(4) Intelligent coating production line

The intelligent painting production line utilizes multiple sandblasting and painting robots to achieve fully automatic collaboration in performing sandblasting and painting operations for subsections of the submerged tube steel shell. It is equipped with a central control system that enables remote monitoring of the entire painting process. The system provides functions such as fault alarms, real-time display of dynamic information on painting working conditions, and parameter data. Additionally, it includes intelligent data collection and processing capabilities. This greatly reduces the risk of physical harm to operators and lays the groundwork for the realization of unmanned painting workshop operations.

Based on the application of multiple pipe sections, the sandblasting robot achieves a sandblasting efficiency of more than 50㎡/h with a single gun, while the painting robot achieves a painting efficiency of more than 150㎡/h with a single gun. These figures represent a significant improvement of approximately 67% and 25% in efficiency compared to manual operations, respectively. The block intelligent production line not only enhances the quality of the process but also reduces labor requirements. It ensures a high level of roughness, uniform paint film thickness, and a high one-time pass rate. Additionally, there is no longer a need for construction work, resulting in a reduction of about 36 hours.

(5) Workshop manufacturing implementation control system

The BIM-oriented Workshop Manufacturing Execution System (MES) has a wide application scope, including the steel shell pipe section cutting workshop, sheet and block site, and intelligent painting production line. By deploying network optical fiber in the steel shell manufacturing area, it enables data processing through the network and monitors the operating status of intelligent production lines. The collected data is then connected to the MES system platform. Through the development of data interfaces within the MES system, seamless integration with design systems, product data management systems, and other information systems can be achieved internally. Externally, timely dissemination of steel shell pipe manufacturing production information to the Shenzhin-China channel BIM

Figure 13. Application of intelligent painting.

collaborative platform is facilitated, opening up the gateway for upstream and downstream data flow and resolving long-standing data "island" issues. This ultimately enables intelligent control over the entire process of steel shell manufacturing.

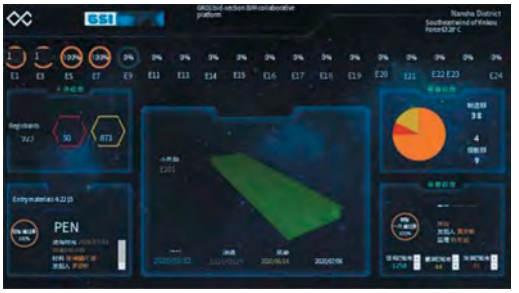

Figure 14. Intelligent production line integrated management and BIM collaborative platform.

Simultaneously, various research efforts are being conducted on BIM technology to ensure efficient connectivity between project planning, implementation, and operation as previously shown (Chen et al., 2020). The aim is to achieve an organic combination of the design system and production management system used by shipyards in steel shell manufacturing with the BIM system. Currently, Shenzhen-China Channel Steel Shell Manufacturing has undertaken comprehensive work related to intelligent manufacturing and BIM information technology for steel shells. This includes the establishment of an information platform (BIM technology-oriented Workshop Manufacturing Execution System (MES), weld three-dimensional mapping, BIM models, and WBS coding) as well as infrastructure development (workshop network, site video surveillance, etc.). Additionally, the application of the Shenzhen-China BIM collaborative management platform is employed. Through the implementation of BIM and information technology, process improvements, and functional verification, the overall system operation has become stable. This has effectively enhanced the level of intelligent manufacturing for steel shells, thereby laying a solid foundation for improving the production quality of steel shells.

6 CONCLUSIONS

Through the research on intelligent manufacturing of steel shells, the application of the "intelligent manufacturing system of steel shells" has been successfully promoted. Moreover, technical standards for intelligent manufacturing of steel shell tube segments have been established. This breakthrough includes key technologies such as online programming of welding robots based on visual recognition, integration of 3D positioning of large steel structure blocks, precise positioning of weld points using lasers, intelligent painting of large steel structures, and BIM-oriented system integration. The intelligent production line demonstrates excellent production capacity and efficiency, meeting the requirements of the steel shell manufacturing schedule. The cutting, welding, and painting processes exhibit stable and reliable quality, offering significant advantages over traditional manual operations. The achievements in this field play a leading and exemplary role in the transformation and upgrading of intelligent manufacturing within the transportation manufacturing and shipbuilding industry.

REFERENCES

Chen Weile, Shao Mingzhi, Song Shenyou, et al, 2020. Research on the index body system of Steel shell Intelligent energy Manufacturing Technology [J]. China Water Transport. 20(8),58–59.

Song Shenyou, Chen Weile, Jin Wenliang, et al, 2020. Key Closing Technique and Challenge of Deep and Middle Channel process [J]. Tunnel construction. 40(1),143–152.

Wu Xiaofeng, Yue Hong, Shi Yao, et al, 2016 CurrentSituation and Trend of intelligent manufacturing and Standardization of shipbuilding industry in China [J]. Ship Science and Technology. 36(5),1–6.

Wu Xiaofeng, Yue Hong, Shi Yao, et al, 2016 Current Situation and Trend of intelligent manufacturing and Standardization of shipbuilding industry in China [J]. Ship Science and Technology. 36(5),1–6.

Tunnelling for a Better Life – Yan, Celestino, Thewes & Eberhardt (Eds)
© 2024 The Author(s), ISBN 978-1-032-80042-4
Open Access: www.taylorfrancis.com, CC BY-NC-ND 4.0 license

Research and application of transportation and landing technology for Shen-Zhong Link super large steel shells of immersed tunnel

Hanxin Long*
Guangchuan Shipbuilding Intetnational Limited Company, Guangzhou, China

Weiguo Rui
Shengzhong-Link Administration Center, Zhongshan, China

Guangfeng Zhang
Guangchuan Shipbuilding Intetnational Limited Company, Guangzhou, China

ABSTRACT: The steel shell volume of the Shen-Zhong Link's steel sandwich immersed tunnel is substantial. To enhance production efficiency and quality, the steel shell manufacturing and concrete pouring are carried out in two specialized factories. Each steel shell weighs approximately 10,000 tons. After manufacturing, it undergoes a ro-ro (roll-on/roll-off) process from land to a barge, then transferred to the concrete pouring plant site. Subsequently, the steel shell is ro-ro'd from the barge to the land workshop for concrete pouring. However, conventional transportation methods pose significant technical and safety risks, leading to potential deformation of the steel shells. In this paper, we present an innovative transportation technology for immersed tunnel steel shells. This approach involves utilizing a rail-type hydraulic car and Self-Propelled Modular Transporter (SPMT) in tandem for combined transportation. By improving the transportation system, calculating and verifying transfer deformations, implementing linkage control between the two systems, and regulating transfer deformation, successful transportation and landing of super-large steel shells for immersed tunnels have been achieved. This method offers advantages such as effective control of shell deformation, flexible layout options, and cost efficiency, thereby serving as a valuable reference for similar large-scale steel structure projects.

Keywords: transportation, landing, rail type hydraulic car and Self Propelled Modular Transporter, deformation control

1 INTRODUCTION

The Shenzhen-China Corridor is a remarkable infrastructure project that connects the motorway expressway of Shenzhen in the east with Zhongshan's Saddan Island in the west. It also links up with the Zhongkai and Eastern Outer Ring Expressways. Spanning a total length of approximately 24km, the section across the sea measures around 22.4km. This project is yet another world-class engineering feat that integrates bridges, islands, tunnels, and underwater connections, following the success of the Hong Kong-Zhuhai-Macao Bridge.

One notable feature of this project is the implementation of the first steel-concrete composite immersed tube tunnel scheme in China. It is also the first time worldwide that the two-way 8-lane super span steel shell concrete immersed tube tunnel structure form has been utilized as previously shown (Song et al., 2020). This innovative approach has established the foundation for controlling the overall project. Specifically, the immersed tube tunnel in the Shenzhen-China Passage project measures 5035m long and consists of 32 immersed tubes, including one final joint. The standard pipe length is 165m, with additional lengths for curved widening pipes measuring 123.8m. The concrete division of the pipe sections is as follows: 123.8m + 21 × 165m + 2.2m + 5 × 165m + 5 × 123.8m = 5035m. Each individual standard steel shell section has a length of 165m, width of 46m, and height of 10.6m, with a maximum weight of 12500 tons.

According to the project plan, a total of 22 ultra-large steel shell of immersed tunnel are manufactured on the platform line of the Shipyard using the Guishan Island plan. After manufacturing, these steel shell are loaded onto barges using a special transportation method known as "over barge." Subsequently, the barges tow them to Guishan Island

*Corresponding author: 29888766@qq.com

DOI: 10.1201/9781003495505-321

Prefabrication Yard, where the steel shell are carefully rolled off the barge and landed using the same transportation method known as "ashore." The steel shell are then transferred to the support system in the unloading area of the precast yard for temporary storage. Once the pouring area is ready, the track trolley within the precast yard transports the pipe section by driving into the bottom of the steel shell, transferring it from the supporting system in the unloading area onto the track trolley, and finally transporting it to the pouring area for concrete pouring as previously shown (Chen et al., 2020).

Transporting the steel shell requires strict control over deformation, with a maximum allowable deformation of 20mm within the 165m × 46m wide range of the steel shell However, the design of the Immersed Tunnel featuring two holes and one pipe corridor results in a weaker transverse structure. Conventional transportation methods used in shipyards often lead to significant deformation during the process of overloading and landing, making it difficult to meet the deformation control requirements. Therefore, it becomes necessary to study a transportation method specifically for super-large immersed tube tunnels, utilizing the existing resources of the shipyard to solve the deformation control problem during steel shell transportation and reduce operating costs.

From the manufacturing of the steel shell to the prefabrication of the immersed pipes, ensuring proper temporary storage of the steel shell in the unloading area and facilitating system conversion are crucial steps in the key lines of immersed pipe tunnel construction. The steel shell sections may remain in the unloading area for an extended period, possibly spanning tens of days. Given the local environmental factors, including prevailing typhoons and adverse sea conditions, it is essential to ensure long-term storage of the steel shell and the safety of system conversion. The design of the support system in the unloading area poses great challenges due to the existing foundation conditions, the performance requirements of the transfer track trolley equipment in the prefabrication yard, and the need for precise control of the steel shell.

2 RESEARCH ON STEEL SHELL OF IMMERSED TUNNEL COMBINED TRANSPORTATION TECHNOLOGY

2.1 *Shortcomings of existing transport overloading and landing methods*

The shipyard platform line is primarily used for shipbuilding purposes and is equipped with self-propelled rail-type hydraulic trolleys for transporting ships on barges. To accommodate the launching of various large and small wide ships, while considering the substantial transverse structural strength of the ships, only a set of trolley tracks are positioned at distances of ±1m and ±7m from the platform line. In accordance with the existing transportation method and accounting for the robust structure of the steel shell, 32 cars are evenly arranged along the track ±7m below the steel shell (refer to Figure 1, Figure 2). Based on the average total weight of the steel shell, which is calculated to be 11,000 tons, each car carries an average load of 344 tons. This is less than 0.8 times the designed load capacity of 500 tons per car, thus meeting the load requirements for each car.

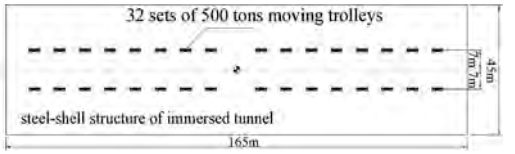

Figure 1. Layout diagram of rail type hydraulic carriage transport pipe section (Plan).

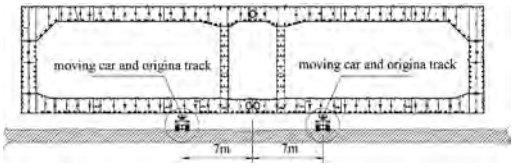

Figure 2. Layout diagram of pipe section for rail type hydraulic carriage (cross section).

The Partran software was utilized to conduct finite element calculations regarding the transportation conditions of the pipe sections. It was determined that the maximum deformation of the pipe section during transportation reached 36.5mm (refer to Figure 3), surpassing the allowable maximum deformation limit of 20mm. Therefore, it was deemed infeasible to employ the existing transportation method.

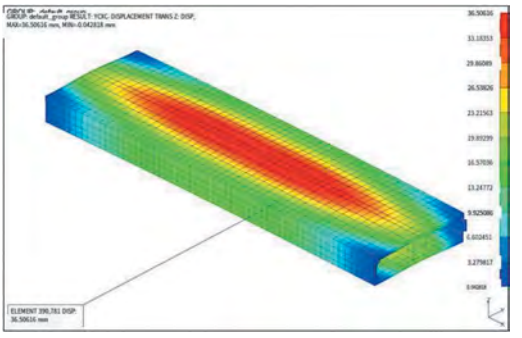

Figure 3. Deformation cloud diagram of pipe section transported by 32 rail-type hydraulic trolleys at ±7m distance (maximum deformation 36.5mm).

2.2 *Technical scheme design of combined transportation*

The existing transportation equipment for horizontal berthing in the shipyard consists of track-type hydraulic cars and tire-type module cars. This includes 40 track-type hydraulic cars with a total load capacity of 20,000 tons, and 136 units of tire-type module cars with a combined load capacity of approximately 4,800 tons. The track-type hydraulic car is equipped with its own power unit and features self-lifting and self-propelling capabilities. It offers a large carrying capacity per unit area and provides cost-effective transportation. On the other hand, the wheeled module car is a hydraulic flatbed vehicle with wheels, widely used for transporting large components both domestically and internationally. While it offers stable performance and flexible usage, its unit area carrying capacity is lower compared to the track-type hydraulic car, and the cost is significantly higher.

Based on the results of finite element calculations, it was determined that the main transverse deformation occurs during the transportation of the pipe sections. This is attributed to the weak transverse structure resulting from the design of two holes and one pipe gallery for the pipe sections. For a pipe section with a width of 46m, the rail hydraulic trolley is only arranged at a distance of ±7m, causing overhangs on both sides and leading to transverse deformation of the pipe section.

The effective solution to this problem involves increasing the transportation equipment on both sides of the pipe section. For instance, adding track-type hydraulic trolleys on both sides would require the destruction of the ground concrete structure and the installation of embedded trolley tracks. In order to maximize the utilization of shipyard equipment resources, avoid additional investments in infrastructure and equipment, and simultaneously reduce the deformation during pipe section transportation, it is proposed to utilize tire module cars at a pitch of ±18.9m along with track-type hydraulic trolleys at a distance of ±7m. This approach facilitates the joint transportation, overloading, and landing of the pipe sections while considering the structural strength of the pipe sections and the barge deck walking channel.

To minimize the transverse deformation of the steel shell, all 136 axes of the tire module vehicles are utilized and divided into four groups, evenly arranged on both sides of the steel shell. Similarly, the track-type hydraulic cars are also organized into four groups, with a total of 32 sets (refer to Figure 1-4 and Figure 1-5). The wheeled module cars serve as auxiliary bearing equipment, providing sufficient bearing capacity to enhance the operational space. They are designated to bear a total weight of 3,000 tons for the steel shell, while the remaining 8,000 tons are supported by the 32 sets of track-type hydraulic cars, averaging 250 tons per car.

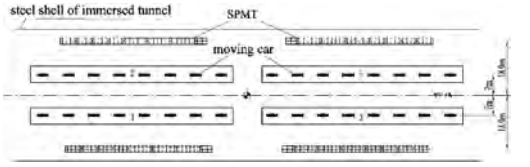

Figure 4. Joint transport of steel shell section laying car by track type hydraulic car and tire type module car (Plan).

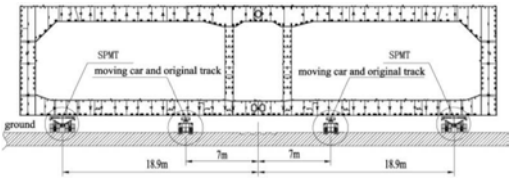

Figure 5. Joint transportation steel shell layout of track type hydraulic car and tire type module car (cross section).

2.3 *Theoretical check calculation*

The Partran software was utilized to evaluate the combined transportation conditions and obtain the calculation results for the deformation of the steel shell as depicted in Figure 1-6. It can be observed that the maximum deformation of the steel shell during transportation is 15.1mm, which satisfies the requirement of a maximum allowable deformation of 20mm. Therefore, the proposed joint transportation scheme is theoretically feasible.

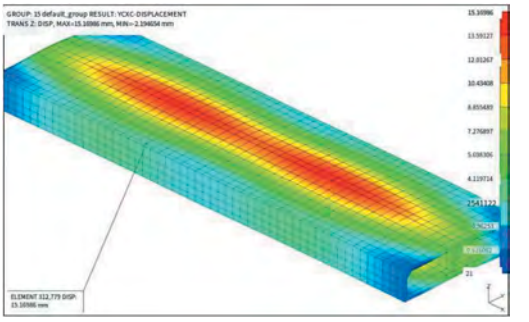

Figure 6. Deformation cloud map of joint transport of the steel shell by rail type hydraulic trolley and tire type module vehicle (maximum deformation 15.1mm).

2.4 *Analysis and solution of technical difficulties*

The local climate of Guishan Island in Zhuhai is characterized by unstable weather conditions, including strong winds and waves throughout the year. The barges docked at the Guishan Island Pouring Plant's wharf experience significant swaying due to these environmental factors. Under such challenging circumstances, it becomes exceedingly difficult to use two sets of equipment for transporting steel shell from the barge to the shore. This is especially true when employing this joint transportation method for

the first time, as it requires both sets of equipment to perform complex joint actions, necessitating the resolution of various technical difficulties.

The transportation of pipes demands high precision, not only in terms of controlling overall deformation within a 20mm limit but also due to the compact design of the casting station. Even a slight deviation in the centerline or flatness during onshore transportation can result in contact with the workshop edge or the pier below. Therefore, ensuring synchronous accuracy in the joint actions of the two sets of equipment is crucial.

To address this challenge, specific operational strategies are formulated based on the performance characteristics of the two sets of equipment. Manual control is employed to achieve high synchronization between the two sets of equipment at key stages. During simultaneous jacking up/down actions, the main strategy involves using the track hydraulic car, which has a large load capacity and sensitive operation, while utilizing the tire module car with a smaller load and better controllability as an auxiliary unit. Pressure monitoring and manual remote control enable the wheeled module car to follow the synchronous jacking/descending movements of the track hydraulic car. When both sets of equipment need to move together, the traction is provided by the tire module car, which boasts strong driving/braking capabilities, while the track-type hydraulic car follows suit. This approach ensures the complete synchronization of the two sets of equipment during their movement.

Based on the aforementioned strategy, the operational process for jointly transporting the track-type hydraulic car and the tire-type module car is formulated.

1) The track-type hydraulic car and the tire-type module car are positioned according to the layout plan at the designated location beneath the steel shell tube section.
2) Only the track-type hydraulic car performs synchronous jacking, lifting the pipe section 10-20mm above the ground. The actual weight of the steel shell is then measured and recorded before placing it back onto the support pier.
3) The track-type hydraulic car is pre-jacked to ensure that all cars are in close proximity to the bottom of the pipe section.
4) The track-type hydraulic cars are grouped based on the center of gravity. Typically, they are divided into four groups (1-4), and the force value for each group is manually set by inputting the difference between the actual weight and the carrying weight of the tire-type module car (3000t) divided by four.
5) The tire-type module cars are also grouped based on the center of gravity, generally divided into four groups labeled as ABCD.
6) The wheeled module car is lifted first, and all ABCD groups lift the same weight until the total load reaches 3000t.
7) Both the tire-type module car and the track-type hydraulic car are simultaneously raised until the steel shell is lifted away from the support pier.
8) The wheeled module car is driven by remote control, with the track-type hydraulic car following behind (clutch open). They transport the pipe section to the barge. During transportation, if there are significant changes in the steel shell orientation, adjustments are made by individually raising or lowering the major groups of the track-type hydraulic car and the tire-type module car.
9) Once the pipe section is in position, it is placed on the pier of the barge.
10) The same method is employed to transport the pipe section to Guishan Island and transfer it ashore.

2.5 *Advantages and application promotion of combined transportation*

The joint transportation method of the track-type hydraulic car and the tire-type module car allows for the efficient utilization of high-quality equipment resources in the shipyard, eliminating the need for redundant investments in equipment and facilities and saving operating costs. This method is not only applicable to the manufacturing project of deep-middle channel submerged tube tunnel steel shells but also highly suitable for promoting and implementing ship barge launching operations in the shipbuilding industry with diverse product types. It effectively combines the advantages of both sets of equipment: The track-type hydraulic car, with its large carrying capacity per unit area, is utilized as the jacking equipment for the ship's fore and stern lines, avoiding the need for extensive tooling. On the other hand, the tire-type module car, with its small carrying capacity per unit area, is ideal for the flat outsole area of the ship's cargo hold which has a larger carrying area. This choice of jacking equipment is not only convenient and flexible but also compatible with any wide ships, including super large marine products.

Figure 7. Layout diagram of the joint transport ship of the track type hydraulic car and the tire type module car.

The successful implementation of this method on the steel shell of the ultra-large submerged tube tunnel in the Shenzhen-Middle Passage not only facilitates the transportation of products from the platform line to the barge but also enables the transportation of products from the barge to the shore. This achievement lays a solid foundation for future closure of the platform line after the construction of products at different

locations, thereby expanding the product business scope of the shipyard's platform line.

Figure 8. Successful transfer of steel shell of immersed tunnel transportation.

Figure 9. Successful landing of steel shell of immersed tunnel on Guishan Island.

3 DESIGN AND RESEARCH OF TEMPORARY STORAGE SUPPORT SYSTEM OF STEEL SHELL OF IMMERSED TUNNEL IN THE UNLOADING AREA

3.1 *Design objectives*

1) The design of the support system should meet the requirements of the original structure's design bearing capacity in the unloading area. The foundation treatment for the unloading area adopts the "PHC pile + cast-in pile" scheme. Concrete piers are installed on top of the piles to serve as the supporting foundation for the steel shell (refer to Figure 2-1). The design bearing capacity of each individual concrete pier should not exceed 200t. Considering factors such as the construction organization, economic cost of the immersed tube tunnel, and other considerations, the existing structure in the unloading area is maintained as much as possible, and major modifications are avoided. The support system is designed using the existing concrete piers to ensure that both the concrete piers and pile foundation can meet the required design bearing capacity during the period of pier lowering and temporary storage of the steel shell.

Figure 10. Layout of cement buttress piers in the unloading area.

2) The design of the support system should accommodate the system conversion requirements. Once the steel shell is transported to the unloading area in the prefabrication yard, it is first unloaded onto the support using the "track type hydraulic trolley + tire type module car" method, and then transferred from the support to the track trolley in the prefabrication yard. This process is known as the steel shell support system conversion. The conversion process of the steel shell support system can be divided into two main stages. In the first stage, the steel shell is unloaded from the "track type hydraulic car + tire type module car" onto the support, where the support surface maintains a consistent elevation. Through the stroke of the equipment cylinders, the full weight of the steel shell is actively placed onto the support. The second stage involves transferring the steel shell from the support to the rail platform car in the prefabrication yard.
3) The design of the support system must meet the precision control requirements for the steel shell. The maximum allowable deviation for the flatness of the steel shell's bottom plate is ±10mm. Therefore, the design of the support system should prevent the bottom plate's flatness from exceeding this allowable deviation value.

3.2 *Design difficulties*

Based on the current structure status of the unloading area and equipment conditions, the design of the support system faces the following challenges in achieving the aforementioned design objectives:

1) The hydraulic jacks used in the track trolley of the prefabrication yard, which were left over from the construction of the Hong Kong-Zhuhai-Macao Bridge, have a limited lifting stroke of only ±25mm. This stroke is insufficient to actively push the steel shell away from the support surface

and complete the second stage system conversion. To address this issue, it is necessary to design a support system with a pressure relief device that can reduce the supporting surface through pressure relief, allowing for the transfer of the steel shell's weight to the rail trolley.

2) During the process of steel shell lowering, the elastic deformation of the middle arch and the sinking of the four corners result in the two ends of the steel shell making contact with the support first. Additionally, the bottom plate may not be perfectly flat (with a maximum allowable deviation of ±10mm). As a result, there is a risk of localized excessive support force during the pier lowering process, which could potentially damage the concrete piers or pile foundation. Effective measures need to be taken to avoid structural overload and mitigate potential damages.
3) The longitudinal spacing between concrete piers on-site varies, with most of them being 5m apart. However, the transverse partitions of the steel shell have a spacing of 3m. Consequently, it is not feasible for each cement pier to correspond directly to each transverse partition of the steel shell. This mismatch can lead to some supports falling on the weaker parts of the steel shell structure (refer to Figure 2-2), resulting in deformation of the steel shell and uneven distribution of support forces.

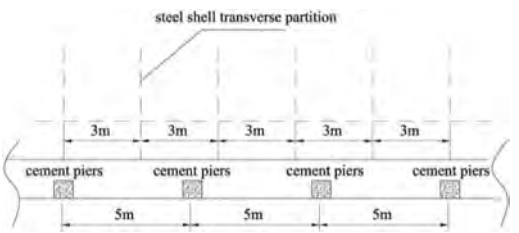

Figure 11. Corresponding relationship between cement piers and steel shell transverse partition (longitudinal section).

3.3 *Design scheme*

In light of the aforementioned design challenges in the support system, an innovative support form has been devised. The specific scheme is outlined as follows:

1) Drawing inspiration from the design scheme of a floating pier used in the shipping industry for inclined ship platforms, the depressible support main structure employed during the construction of the Hong Kong-Zhuhai-Macao Bridge is selected (refer to Figure 2-3). This structure allows for passive support that can be lowered to facilitate pressure relief when converting between the support and the mobile trolley in the unloading area. By sliding down the slope of the depressible support, the weight of the steel shell can be unloaded onto the mobile trolley.

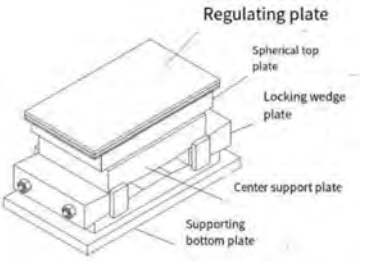

Figure 12. Passive support mode.

2) To mitigate the risk of overloading the supports at the two ends caused by the initial lowering of the piers at the steel shell's four corners, a solution has been devised that does not require altering the existing foundation of the unloading area. Additional piers have been installed to strengthen the foundation at the Shenzhen end of the steel shell, totaling 8 piers in number. Additionally, a total of 12 piers have been strategically placed at corresponding pile positions along the middle section (refer to Figure 2-4). By adding these piers, the safety factor of the supports at both ends of the steel shell has been enhanced, ensuring the safety of the steel shell pier during the lowering process.

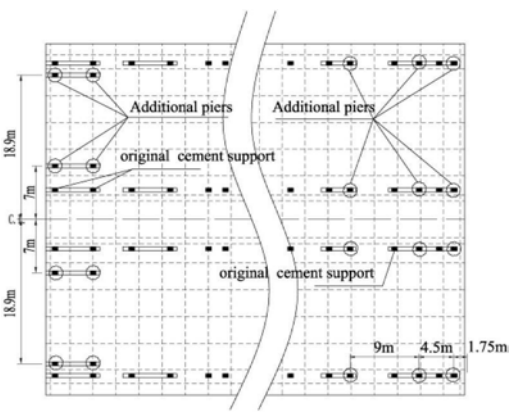

Figure 13. Adding piers at both ends of a steel shell.

3) To prevent deformation of the steel shell caused by the support force point falling on vulnerable areas, two types of supports are designed due to the mismatch between the cement piers and the transverse partition of the steel shell. Firstly, steel piers and passive supports are placed on the cement piers that correspond to the transverse partition of the steel shell. Secondly, passive supports and box beams are placed on the cement piers and new steel piers that do not align with the transverse partition of the steel shell. Additionally, to mitigate uneven support force when

the pier falls as a result of an uneven bottom of the steel shell, a 30mm buffer rubber is installed on top of the support (refer to Figure 14).

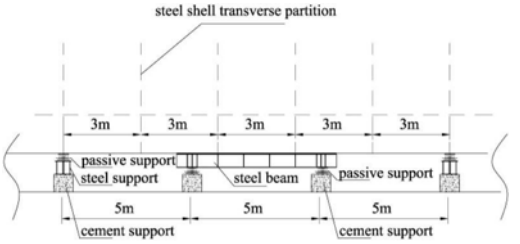

Figure 14. Schematic diagram of the combination of the two support forms.

4) After implementing the aforementioned design, the layout scheme of the support system in the unloading area is illustrated in Figure 15.

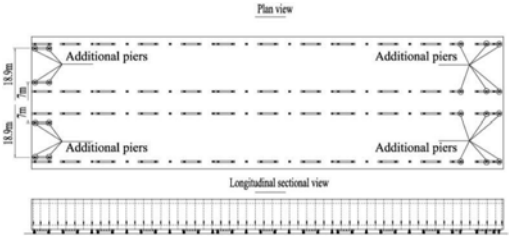

Figure 15. Overall layout of the support system in the unloading area.

3.4 *Finite element calculation check*

To analyze the design effectiveness of the support system, we employ the finite element calculation method for theoretical verification and compare the calculation results under two working conditions: before and after the implementation of this design scheme.

1) Finite element modeling
The MSC PATRAN software was utilized to establish a comprehensive three-dimensional finite element model, encompassing all the key structures of the steel shell. A plate and BEAM composite model was employed to simulate the internal and external panels, vertical and horizontal partitions, platforms, and the web of the main components (girder) of the steel shell using 2D plate units (SHELL). Additionally, 1D beam units (BEAM/BAR) were used to represent components such as bones and reinforcements. Some minor structures that had negligible impact on the calculation results, such as the aggregate end bracket, were not included in the model. The grid was divided based on the spacing of the aggregates, with a typical cell size of approximately 500×500mm. The origin of the model's coordinate system was located at the sealing plate of the Shenzhen end pipe section. Specifically, the X-axis was oriented longitudinally along the pipe section towards the middle end, while the Y-axis pointed to the left in the width direction of the pipe section. The Z-axis originated from the bottom of the pipe section and extended upwards along the height direction (refer to Figure 16).

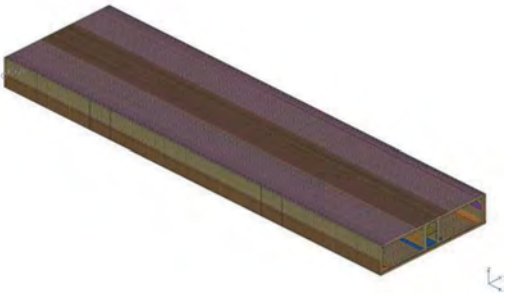

Figure 16. Stereogram of finite element model of steel shell.

2) Calculation results
The MSC NASTRAN program was employed to compare and calculate two scenarios: one before implementing the design scheme (with the steel shell directly resting on the support surface of the cement pier) and another after implementing the design scheme. The following aspects were analyzed:
a) Deformation comparison of the steel shell: The maximum deformation of the steel shell was calculated as 5.97mm before incorporating this design scheme. However, after implementing this design scheme and utilizing the load distribution function of the box beam, the maximum deformation of the steel shell was reduced to 3.74mm.

Figure 17. Deformation cloud picture of steel shell before adopting this design scheme (maximum deformation 5.97mm).

Figure 18. Deformation cloud image of steel shell after adopting this design scheme (maximum deformation 3.74mm).

b) Comparison of vertical forces on concrete support piers. Before adopting this design scheme, the vertical load of 32 of the original 136 concrete piers exceeded the design load by 200t, and the maximum vertical load of a single pier was 404t; After this design scheme is adopted, the maximum load of the original concrete support pier is reduced to 188t, and the load of each pier is more uniform. The comparison of the loading results of each pier is shown in Figure 19 (taking one of the piers as an example).

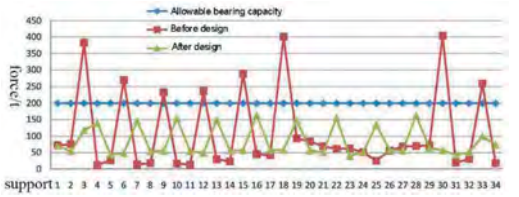

Figure 19. Comparison of vertical stress results of the first column pier.

In summary, the proposed design scheme successfully fulfills both the precision control requirements of the steel shell and the load-bearing requirements of the existing concrete piers. This design approach avoids extensive reinforcement work on the foundation, resulting in cost savings and a shortened construction period. Overall, the support system design scheme effectively meets the project's requirements.

4 CONCLUSIONS

The steel shell tube section of the deep and middle passage ultra-large submerged tube tunnel adopts a new transportation method, which combines rail-type hydraulic cars and tire-type module cars. This approach presents a novel way to transport products from the shipyard platform line. The successful application and popularization of this method not only expands the range of suitable products for the shipyard platform line but also lays the foundation for constructing large-scale marine products on the platform line. It enables the closure of the upper platform after off-site construction of half the ship and facilitates repairs to the ship's upper platform. Furthermore, it provides a reference for leveraging the advantages of shipyard equipment resources in the future and achieving more diversified platform barge launching operations through equipment combinations. This will help promote the integration of shipyard resources and reduce enterprise investment costs.

The innovative design scheme of the support system, based on the current foundation conditions and equipment status in the unloading area of the immersed tube prefabrication yard, not only meets the requirements for converting the support system in that area but also prevents overload damage and deformation caused by uneven local forces acting on the piers and steel shell. This design ensures the long-term storage safety of the steel shell and the smooth conversion process of the system. Additionally, the support system design is rational, avoiding extensive transformations, saving costs, and shortening the construction period. It realizes "factory prefabrication and on-site assembly" of components, while maintaining high construction quality and efficiency that align with project requirements. The design methodology and its application in the support system have significant reference value for the design of support systems in super-large immersed tube tunnels and large components.

REFERENCES

Chen Yue, Chen Weile, Song Shenyou, et al, 2020. Key construction technologies for immersed tunnel of Shenzhen-Zhongshan Link [J]. Tunnel Construction. 40 (4), 603.

JIN Wenliang, Song Shenyou, Chen Weile, et al, 2021. Overview of the overall design of steel shell concrete immersed tube tunnel in Shenzhen-Middle Passage []. China Harbor Construction. 41(3), 35–40.

Song Shenyou, Chen Weile, Jin Wenliang, et al,2020. Key technologies and challenges of Shenzhong Link[J]. Tunnel Construction. 40(1), 143.

Xu Guoping, Huang Qingfei, 2018 Overall design of cross-river passage project from Shenzhen to Zhongshan [J]. Tunnel Construction (Chinese & English). 38(4), 627–637.

Tunnelling for a Better Life – Yan, Celestino, Thewes & Eberhardt (Eds)
© 2024 The Author(s), ISBN 978-1-032-80042-4
Open Access: www.taylorfrancis.com, CC BY-NC-ND 4.0 license

Innovative research on key technologies for dredging construction of immersed tunnel

Dingqiang Ma, Peng Zhang, Zhonghao Li & Yifan Yao
CCCC Guangzhou Dredging Co., Ltd., Guangzhou, China

ABSTRACT: This study seeks to investigate the key technological innovations in the dredging construction of immersed tunnels, with the objective of addressing the challenges encountered during the construction process. We employed a range of research methods including simulation experiments, field observations, and numerical calculations, and combined them with an analysis of the specific characteristics of dredging in immersed tunnel construction. We addressed key issues in the dredging process and implemented a series of equipment and technological improvements at different stages. Specifically, we developed new technologies such as precision dredging equipment for shallow shoals and deep troughs, and environmentally-friendly rock-breaking excavation methods, and applied them to the dredging process of immersed tunnels. The outcomes of the application demonstrate that these innovative technologies not only satisfy the requirements of on-site construction, ensuring that the construction quality meets the design and specification standards, but also enhance the efficiency and quality of the dredging construction. As a result, they provide a more robust assurance for the long-term operation of immersed tunnels. Overall, this study provides in-depth insights into key technological innovations for dredging in the construction of immersed tunnels. We propose a series of new technologies and improvement measures that offer effective reference for research and application in related fields.

Keywords: immersed tunnel, dredging construction, deep water foundation trench, equipment modification, rock drilling technology

1 INTRODUCTION

In recent years, with the completion of Hong Kong-Zhuhai-Macao Bridge, immersed tunnel technology has been rapidly developed and widely used. Immersed tunnel has become an important choice for crossing rivers, lakes and seas today due to its advantages such as shallow burial depth, large traffic capacity, short route, flexible selection of cross-sectional shape, easy quality control of tube element prefabrication and good waterproof effect [1]. By the end of 2020, there were 23 immersed tunnels, accounting for 10% of the total number of underwater tunnels in China. Shenzhen-Zhongshan River Crossing Link Project (hereinafter referred to as "Shenzhong Link") is located in the core area of the Pearl River Delta. The overall design adopts the scheme of "east tunnel and west bridge", with a total length of about 24km and an undersea tunnel of about 6.8km, which is an important transportation hub connecting the Pearl River Delta. The foundation trench dredging construction of Shenzhong Link immersed tunnel is restricted by many factors such as geological conditions, marine environment and navigation safety. The construction conditions are extremely complex and the construction technology is difficult. In view of the difficulties in the construction of Shenzhong Link, innovative researches have been carried out on key technologies for dredging construction of immersed tunnel, and new technologies such as shoal and deep groove accurate desilting, environment-friendly rock breaking excavation, and precision dredging of foundation trench have been developed to further improve the construction level of immersed tunnel dredging and perfect the construction theory and method, which will certainly promote the development of immersed tunnel technology.

2 PROJECT OVERVIEW

The Shenzhong Link immersed tunnel consists of 32 elements of immersed tube, including 26 standard tube elements and 6 non-standard tube elements. The standard tube element is 165m long and 10.6m high. The non-standard tube element is 123.8m long and 10.6m high. The bottom width of the foundation trench in the standard tube section is 50.0m, and that

DOI: 10.1201/9781003495505-322

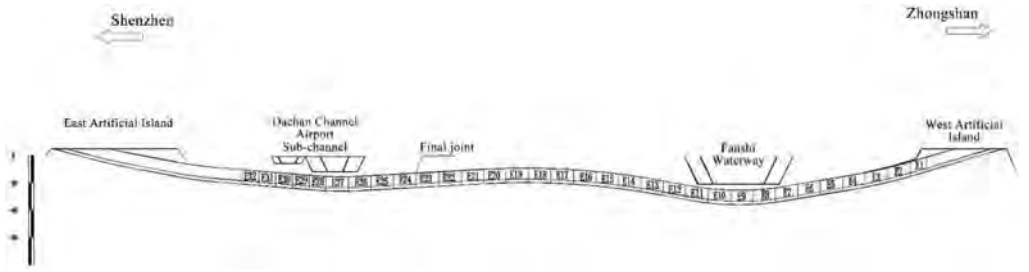

Figure 1. Schematic diagram of vertical section of immersed tunnel.

in the widest section is 59.46m. The standard section and the widest section are gradually connected from 50.0m to 59.46m, with a bottom elevation of -12.76 ~ -37.08m (elevation 85, the same below). Where the trench bottom elevation changes suddenly due to different cushion thicknesses, a gentle slope shall be adopted for transition, which is a longitudinal slope with a gradient not steeper than 1:10. The section of the tunnel foundation trench is complex, and the method of transverse gradation and longitudinal segmentation is adopted, as shown in Figure 1.

3 KEY CONSTRUCTION TECHNOLOGIES AND INNOVATIONS

3.1 *Shoal and deep groove accurate desilting equipment*

The hydrology and sediment in the Shenzhong Link site area are complex. According to the siltation observation test study of trial trench carried out in the early stage, after one-year siltation observation period, the siltation intensity of trial trench in flood season is about 2.0 cm/d, and the natural siltation intensity of foundation trench is at least twice that of Hong Kong-Zhuhai-Macao Bridge, Island and Tunnel Project. Therefore, siltation and desilting during construction period will be one of the difficulties of the Project. In addition, nearby waterway dredging and sand mining operations, disturbance of substrate by large transport ships and abnormal severe weather will cause increased siltation of foundation trenches or even sudden siltation.

In view of the strong back-silting intensity of the Shenzhong Link and the risk that sudden siltation may be caused by surrounding sand mining operations, the special dredging vessel "Jielong" used in the Hong Kong-Zhuhai-Macao Bridge Project has been improved and equipped with a novel dredging construction system with higher construction efficiency and more accurate positioning specifically for dredging operations at the trench bottom before rubble dumping and gravel leveling. The addition of a high-pressure water tank and high-pressure nozzle enables the spraying of water at a higher pressure, effectively enhancing the impact on seabed silt and ensuring more thorough cleaning. Furthermore, by augmenting the power of the dredging pump, the suction capacity for silt is increased to three times that of the Hong Kong-Zhuhai-Macao Bridge Project. This results in a clean water flow rate of 7,000 m³/h, leading to a remarkable improvement in desilting efficiency. We have independently developed a high-precision suction head positioning and monitoring system. This cutting-edge system enables real-time display and bottom-out monitoring of the dredging suction head, effectively addressing the challenge of achieving highly accurate dredging of the foundation trench during construction.

Following the silt suction power increase of "Jielong", the flow velocity at the silt outlet experienced a significant rise, reaching 5.5 m/s. Previously, the conventional loading method involved directly attaching the silt discharge pipe to the side of the silt barge. However, this approach posed a risk of damaging the ship equipment due to high-speed silt ejection, and stable loading could not be guaranteed. To mitigate the risk, a dredging and loading system consisting of T-structure silt discharge pipe, energy dissipation pipe and semicircular buoy has been developed, as shown in Figure 2. An energy dissipation device, equipped with internal ribs, is installed at the silt discharge pipe outlet to make high-speed silt form a large turbulent vortex in the device for energy dissipation. As a result, the flow rate can be decreased to be lower than 2 m/s. This solution ensures the stable loading of the silt, effectively addressing the issue posed by the excessive impact kinetic energy experienced at the silt discharge pipe outlet.

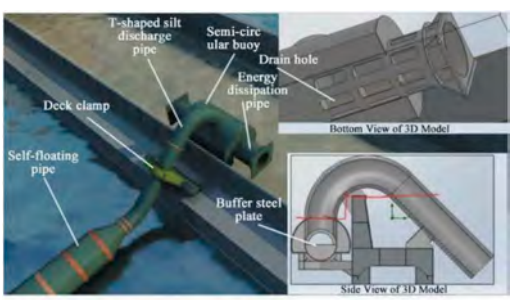

Figure 2. Composition diagram of dredging and loading system.

3.2 *Environment-friendly rock breaking excavation*

According to the design data, there are a large number of completely, highly and moderately weathered rocks within the design elevation range of the foundation trench of Shenzhong Link immersed tunnel, mainly distributed in E6-E12 and E24-E30 tube element sections, which are characterized by wide distribution, deep burial depth and high strength. In dredging operations, conventional underwater blasting technology is typically employed to crush hard rocks within foundation trenches. However, considering the specific circumstances of the construction area being situated within the White Dolphin Nature Reserve and the proximity to Shenzhen Bao'an Airport, along with the high volume of ship traffic, only rock drilling technology can be used for physical crushing of hard rocks.

Rock drilling construction is improved from grab dredger, in which the grab of grab dredger is changed into rock drilling rod. During construction, the rock drilling rod is lifted to a certain height and then falls freely, hits the underwater rocks by its own impact force, and crushes the rocks with longitudinal impact load. This construction method started late, but developed rapidly. It is used in foreign projects such as the Friendship Port Dredging Project and Zawr Dredging Project in Saudi Arabia.

The impact range of vibration wave generated by rock hammer construction is related to the weight and lifting height of the hammer, and the surge wave generated is related to the shape of the rock hammer. The commonly rock hammers include axe type, cylindrical type, quadrangle pile type and quincuncial pile type. Different shapes of rock hammers have different characteristics of impact damage to rocks, and their kinetic energy loss process is also different, as shown in Figure 3.

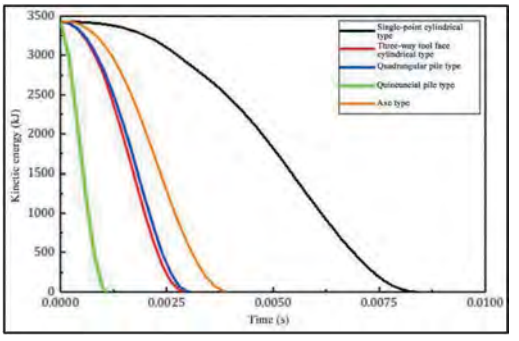

Figure 3. Kinetic energy loss process curve of rock breaking hammers with different shapes.

The main parameters affecting the rock drilling effect include the lifting height of rock drilling rod, row spacing, position spacing of drilling points, and number of drilling. The construction parameters with the best construction effect are mainly determined through single-factor test and multi-factor test. Based on the results of single-factor test and multi-factor test, the influences of various factors on drilling effect and reef removal thickness are studied. The main conclusions are as follows:

1) It is found that the average lumpiness and non-uniformity coefficient are positively correlated with lifting height, row spacing, and position spacing, but are negatively correlated with number of drilling. The fractal dimension is negatively correlated with lifting height, row spacing and position spacing, but is negatively correlated with number of drilling. The reef removal thickness is positively correlated with lifting height and number of drilling, but is negatively correlated with row spacing and position spacing.
2) Through the range analysis of multi-factor test results, it is shown that the primary and secondary order of influence on rock drilling effect is: lifting height > number of drilling > row spacing > position spacing; the primary and secondary order of influence on construction efficiency is: row spacing > number of drilling > position spacing > lifting height, as shown in Figure 4 and Figure 5.
3) Based on the results of multi-factor orthogonal in-situ tests, for moderately weathered granite (strength range: 80.01 MPa ~ 133.63 MPa) at Shenzhong Link site, the optimized drilling parameters under water depth of 40 m are determined as follows: lifting height 27 m ~ 34 m, row spacing about 2.5 m, position spacing 1.4 ~ 1.7 m, and number of drilling 2-3. The damage development and fissure distribution under the optimized parameters are numerically studied. Under the optimized parameters, the damage degree near the drilling point is high, the fissures are relatively developed, the damaged areas between the two rows of drilling points are connected as a whole and in a critical connection state, the fissure connection degree between the drilling points in the position distance direction is high, the rock is effectively broken, the drilling effect is good, the drilling efficiency is high, and the construction effect of the optimized scheme is better.

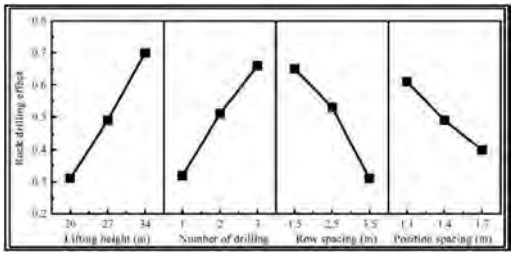

Figure 4. Relationship curve between various factors and rock excavation effect.

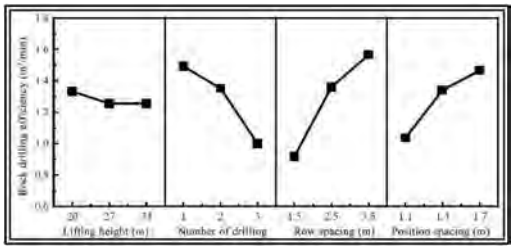

Figure 5. Relationship curve between various factors and rock excavation efficiency.

3.3 *Improvement of precision dredging process for foundation trench*

For immersed tunnels, water leakage between tube elements is primarily attributed to differential settlement, and the control of differential settlement is closely related to the shear keys between tube elements, the setting of water-stop facilities and the bearing capacity of the shear keys. In order to ensure the safe operation of the immersed tunnel within its design service life, the immersed tunnel foundation trench must be accurately dredged under the condition of adapting to large excavation depths, and efforts shall be made to minimize any occurrence of differential settlement from the first step of the foundation trench construction as much as possible.

The difficulties in precision dredging of the foundation trench are mainly reflected in the following aspects:

1) The cross-section design of the foundation trench of the immersed tunnel is complex: multi-stage slopes are set horizontally, with many break angles on the variable slope line, and dozens of combinations of gentle slopes and variable slopes are set longitudinally, making construction difficult. Furthermore, given that the foundation trench depth for large-scale immersed tunnel projects typically exceeds 30m, the range of applicable dredgers becomes limited, and grab dredgers are commonly selected in such scenarios.
2) The elevation deviation standards for excavating the foundation trench surpass the specifications commonly observed in current water transportation engineering practices. It is often the case that conventional large grabs fail to meet the precision dredging requirements, necessitating specific modifications.
3) The connection between the grab and the hull is primarily established through steel wires, constituting a flexible connection. When carrying out foundation trench dredging operations at significant dredging depths, achieving precise depth control becomes notably challenging.

In response to the above difficulties, functions such as over-depth limit and comprehensive deviation adjustment are incorporated into the original dredging control system of the precision dredging ship. As a result, a precision dredging computer measurement and control system has been established, making the construction process visible, controllable and measurable. At the same time, based on the principle of iterative fitting, the system automatically controls the dynamic sinking of the grab through controlling the bucket rope. This facilitates the achievement of a horizontal undulating trajectory curve for the actual soil mass cutting throughout the grab closure process, as shown in Figure 6. The actual construction results substantiate that the plane dimensions and elevation fully meet the design requirements, and the maximum over-depth is controlled within 0.5 m.

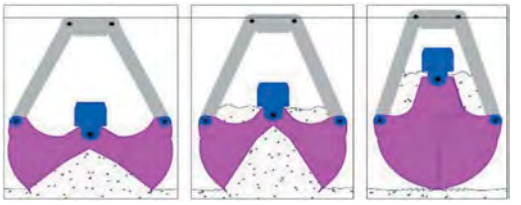

Figure 6. Schematic diagram of the precise excavation function of the grab bucket.

3.4 *High-precision desilting technology for multi-stage slope of foundation trench*

During the installation process of the immersed tube, a gradual accumulation of silt occurs on the slope after the formation and the period of being left alone of the foundation trench. If the thickness of backsilting exceeds the slope's siltation capacity, it can potentially trigger the collapse of the slope, resulting in detrimental consequences to the foundation trench and foundation bed treated through rubble dumping. This, in turn, could lead to quality issues such as differential settlement and unbalanced stress of tube elements after installation. To ensure the protection of the completed foundation trench against slope collapse and dredging construction, it is necessary to accurately desilt the foundation trench slope, which requires high desilting construction accuracy.

The desilting of the foundation trench slope is carried out using a specialized suction drag head fitted on a drag suction dredger. Construction parameters, including the desilting track line and slope desilting control elevation for each layer, are pre-determined based on the slope's post-formation shape and backsilting distribution. To ensure precise movement along the planned track line, the DPDT system is employed to control the vessel. The DTPS provides accurate guidance for drag depth, while the computer-aided dredging decision-making system assists in analyzing parameter variations throughout the desilting process.

At the same time, considering the loose and non-adhesive nature of the silt on the slope, there is no need for drag teeth to mechanically cut the soil.

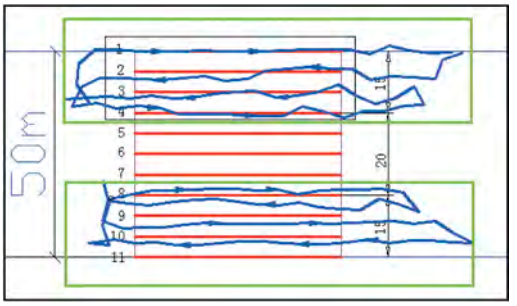

Figure 7. Schematic diagram of actual navigation trajectory of DPDT system.

Instead, only the vacuum of the dredging pump is made use of to absorb the silt from the slope into the hopper through the drag head and suction pipe. Throughout the suction process, intelligent control is employed, utilizing feedback signals such as flow, density and pressure, and the special drag head is used in collaboration to consistently maintain a distance of 500 mm between the suction plane of the movable cover and the seabed during operation. This ensures thorough desilting of the multi-stage slope while effectively preventing damage to the original slope. Compared with traditional construction methods, there is no need to adjust the drag depth according to changes in the slope section, and the drag head can be prevented from damaging the formed slope, achieving the best desilting effect.

4 CONCLUSIONS

To sum up, the equipment technical improvement and innovation measures carried out based on the foundation trench dredging work of immersed tunnel in Shenzhong Link have addressed the difficulties encountered in the construction process, and significantly improved the efficiency and quality of dredging construction. At the same time, consideration has been given to construction, navigation and environmental protection, which promotes the progress of immersed tunnel dredging technology and provides reference for similar projects.

REFERENCES

[1] CHEN Yue. Application and Developing Trends of Immersed Tunnel [J]. Tunnel Construction, 2017, 37 (04): 387–393.

[2] LIN Wei, LIANG Jiezhong, LIU Linfeng, et al. Development and Prospect of Immersed Tunnel and Artificial Island Technology [J]. Tunnel Construction, 2021, 41 (12): 2029–2036.

Tunnelling for a Better Life – Yan, Celestino, Thewes & Eberhardt (Eds)
© 2024 The Author(s), ISBN 978-1-032-80042-4
Open Access: www.taylorfrancis.com, CC BY-NC-ND 4.0 license

Immersed tunnels – knowledge sharing in the past showing the way towards sustainable solutions in the future

Tommy Olsen*
COWI A/S, Kongens Lyngby, Denmark

ABSTRACT: The immersed tunnel technology has seen many developments since the first immersed tunnel projects were constructed more than 100 years ago. New requirements and constraints have led to original and innovative solutions. People and organisations moving from project to project and exchanging experience have led to significant improvements by combining existing local knowledge with expertise from abroad. Growing demand for sustainable solutions now and in the future will require organisations to collaborate and share knowledge about new solutions at an even brisker pace. Throughout modern history, innovations within immersed tunnel technology have been introduced and further developed in later projects, either by the organisation initially presenting the innovation or by other organisations elsewhere. This paper shows examples where immersed tunnel solutions developed on one continent have been further developed with great value in another continent. Selected examples of specific developments are presented in this paper, e.g., steel vs concrete immersed tunnels to fit local constraints, watertight concrete to improve performance, construction of elements under factory conditions to reduce construction time while maintaining or improving quality, and casting elements floating without use of a casting yard due to lack of space and/or access. Knowledge sharing across organisations and cultures is needed to face global challenges. This paper also briefly identifies some of the contemporary challenges regarding immersed tunnel technology, as well as the sustainable benefits immersed tunnel solutions can offer across the world.

Keywords: Immersed tunnel, knowledge sharing innovation, sustainability, concrete technology

1 INTRODUCTION

Let us go back in time to Paris in the period called "Belle Époque" (1871-1914), an idyllic place and time for visionary, scientists, engineers, authors, philosophers and political thinkers, all sharing thoughts and dreams for a new and better world. The era hosted three World Exhibitions (1879, 1889 and 1900), all showcasing mind-blowing innovations, and the one in Paris in 1889 marked the 100-year anniversary of the French Revolution.

Skilled bridge engineer Gustav Eiffel was asked to design a tower to be a landmark for the exhibition, and his project was constructed as a temporary structure. Although at first many Parisians did not like the project, considering it not feasible, useless and even "monstrous", it became one of France´s most distinguished symbols: the Eiffel Tower turned out to be a "valuable asset" for the Parisiennes, initially for telegraph companies and later for tourism. It was the world's tallest structure until it was surpassed by the Chrysler Building in New York in 1930. That goes to show that, when large and innovative structures are planned – also within transportation and mobility – it is difficult to know precisely what a structure will be used for in the future.

Paris was a growing metropolis, with the needs of a modern city. Public transportation comprised steam trains connecting other cities and horse-driven trams. In competition with London, New York, Budapest and Berlin, Paris also wanted an underground metro, and initially six lines were planned. Metro line 4 had to go beyond the Seine River, connecting Châtelet to Saint-Michel Notre-Dame through Île de la Cité. At this location, due to the proximity to the Notre Dame Cathedral, the metro line could not be a bridge; instead, it was designed as a subsea tunnel. Figures 1 and 2 show the tunnel construction with a floating caisson. Constructed in 1905, this stretch of the tunnel was built before the first registered immersed tunnel but is not defined as an such because the casting was on site and not at a remote location later towed in place.

*Corresponding author: tool@cowi.com

DOI: 10.1201/9781003495505-323

Figure 1. Floating caissons, line 4 at Île de la Cité (1905).

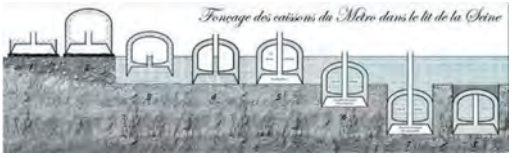

Figure 2. Paris metro, casting of caissons, crossing river Seine.

As inspiration to engineers of today through examples in the past, this paper points to the need for global collaboration and knowledge exchange across fields of engineering and across geographies, to facilitate innovation.

1.1 *Sustainable development for the future*

When designing future infrastructures, it is valuable to know the challenges faced by similar constructions in the past. Most of the lines from the first metros constructed in European cities 100-150 years ago are still in use today.

Metro lines connect residential areas where people live with areas of business and/or recreation. Metros keep the cities moving. In many places in Europe, heavy industries and manufacturing jobs are moving out of the city, where land value generally increases, and new jobs are being created in the service sectors. It is difficult to imagine how metro lines will look 100-150 years from now. However, any future plans must prioritize sustainable development and incorporate the necessary flexibility to ensure their success.

We all know that the construction industry is facing challenges to comply with current and future expectations and requirements to support infrastructures that are more climate friendly, lead to more biodiversity, use more recycled material, allow for higher operational performance, etc., all at the same or lower cost. This paper encourages engineers to look into the past to seek inspiration from when the need and the challenge appeared for the first time, to understand the roots of the problems and the constraints of the past and of today, helping find solutions for the future.

1.2 *Local context and international trade*

Large transportation infrastructures are planned within a local context. Infrastructures are constructed to the benefit of society, most often by public funding. It is commonly accepted in Europe that it is the public that assesses the benefits of a transport infrastructure. In contrast, it is the market that controls the construction cost via competition, and the price is often reduced by elements of innovation.

The examples and perspective of this paper are based on the experience of the author (from Copenhagen, Denmark) and his 30 years working in civil engineering as a specialist in immersed tunnels. It shows project examples that have shaped the industry from a Danish-European perspective. The examples may give indications on the directions for the future of Northern Europe. Other parts of the world have a different background and, therefore, a different path. Globalisation has been an effective facilitator in the dissemination of the development of immersed tunnels for the last 70 years, but it is uncertain how development and knowledge sharing will develop over the next 70.

People, nature, climate, geology, political systems, all contribute to the development of major projects as much as technology itself. We may assume science, technology and cost are the main factors in all decisions, but we should not underestimate that it is people working together and their combined knowledge and experience that decide what will be built and how it will be done. To make significant changes, it is necessary to think and act differently.

Trade routes around Denmark can be traced back thousands of years. The Danish soil consists of sand and clay left by the glacial period that ended some 20,000 years ago, making farming a good source of income. It lacks mountains and has no tradition of mining for resourcing metals, but it is composed of a bedrock of limestone, forming an excellent source of cement-based construction materials.

In the late 1800s, roads, railways and harbours were planned to help the country's economy grow. Danish engineers sought new ways of construction techniques in the United Kingdom, France, Germany, and the United States. Inspired by Hennebique and Monier, the first reinforced concrete bridge in Denmark - Gefionbridge (1896) (Figure 3) - was designed by Professor A. Ostenfeld from the faculty of Structural Engineering, School of Polytechnic (Chr. Ostenfeld, 1976).

2 EARLY TECHNOLOGY, LEARNING TO MASTER

2.1 *First immersed tunnel*

It is accepted that the first immersed tunnel was the Michigan Central Railway Tunnel (1910) in Detroit (Figure 4). Constructed by concrete-filled steel shells, towed, and immersed in place, it was a shallow

Figure 3. Gefion bridge (1896), at Langelinje in Copenhagen.

Figure 4. Michigan Central Railway Tunnel (1910).

alternative (good for a railway) compared to the shield tunnel technology known from the Thames tunnel (1843) and metro lines in London.

2.2 *Danish pioneers learning from working abroad*

In 1900, young engineer Rudolf Christiani graduated from the Danish School of Polytechnics. Aware of a new trend, Professor Ostenfeld recommended Christiani to go to Paris to get some experience in a new composite construction material: *reinforced concrete*. A few years in Paris and in Düsseldorf made Christiani more familiar with reinforced concrete and in 1904, together with his partner Aage Nielsen, he founded the engineering and construction company Christiani & Nielsen (C&N) in Copenhagen.

In 1905, C&N designed and constructed Amtmand Hoppes Bro, the first reinforced concrete bridge for road traffic in Denmark. The company was ready to explore the potential of this new composite material and was able to convince owners, especially owners of marine infrastructures, of its benefits. In Denmark, large quantities of steel needed for construction projects had to be imported and treated to prevent corrosion. Meanwhile, the availability of local cement made reinforced concrete a highly cost-effective alternative.

Aalborg Harbour, in the western part of Denmark, was undergoing expansion; agricultural produce such as meat, corn and dairy products were exported to nearby countries. C&N offered to design and construct a new quay wall of concrete caissons (Figures 5 and 6). Due to his background as a captain of the Naavy, Nielsen was familiar with shipbuilding. That knowledge, and the understanding of scaling up production from shipbuilding, was used as an advantage in the construction of large infrastructures, with repetitive works.

Figure 5. Aalborg Harbour (1906) reinforced concrete caissons.

Figure 6. Aalborg Harbour (1906) launching caissons.

Between 1900 to 1935, Danish contractors opened offices around Europe and were involved in activities with the design and construction of reinforced concrete for civil works, especially within marine works. Engineers of all ages gained a lot of experience that way.

Denmark is a country with more than 443 named islands, 78 of which are inhabited; some are some connected by ferries, some by bridge. During the 1930s, several large bridge projects were planned to replace the slower and weather-sensitive ferries. The first major bridge wasthe Little Belt bridge (1935). At 3,6km long Storstrømmen bridge (1937) (Figure 7) was the longest bridge in Europe at the time, a record it held for 30 years.

With experience from projects outside Denmark, it was a challenge taken on by Danish designers and contractors. C&N oversaw the substructure and concrete foundations cast inside steel caissons, using compressed air to access the foundation (see Paris metro earlier). The steel structure came from English company Dorman Long (Tyne Bridge, Memorial Bridge Bangkok and Sydney Harbor Bridge). As earlier, this large project

Figure 7. Storstrømsbridge (1937).

provided new knowledge and experience to a new generation of engineers (marine works, repetitive production, prefabrication, and pre-casting at scale).

2.3 *Maas tunnel*

In The Netherlands, also in the 1930s, another important infrastructure had been planned for a while: a fixed link, a road crossing river Maas in Rotterdam, in one of the largest harbours in Europe. The project was tendered out by the Engineering Department of the City of Rotterdam, who was open to alternatives and new technology, focusing on reducing the cost and time and with desire to learn from leading innovations.

The project was tendered with two alternatives: as a suspension bridge or as an immersed tunnel of two circular tubes of steel, similar to the concept that had been developed and used in the US since the Detroit Michigan Central Railway Tunnel inception.

At the time, a short reinforced concrete immersed tunnel of 120m for pedestrian traffic had already been constructed in Berlin (Der Spreetunnel at Friedrichagen, 1927). For the Mass tunnel, a reinforced concrete alternative was proposed by C&N in a joint venture with a group of Dutch contractors. The alternative was accepted by the owner, and construction started in 1937. The Maas tunnel project (Figure 8) was completed and opened to traffic in 1942 (Rasmussen, 1987). Table 1, based on ITA database, shows immersed tunnels since 1910.

Table 1. Immersed tunnel around the world.

Years	America	Europe	Asia and Australia
1900-1920	3	0	0
1920-1940	2	1	0
1940-1960	9	1	1
1960-1980	11	19	12
1980-2000	4	25	12
2000-2020	3	17	14
2020-2024	0	1	?
Total	32	64	39

2.4 *Deas Island and Havana immersed tunnels*

The story about the construction of the Maas Tunnel went around the world. Here are the words of the Chief Engineer of the Maas Tunnel, M. Lassen-Nielsen, who was based in Rotterdam at the time:

"Christiani & Nielsen's interest in the traffic problem was first aroused ten years ago by Mr. George Massey, a very enterprising man, who owns a machine shop in a small town in the vicinity of Vancouver, Mr. Massey read an article on the tunnel under the River Mass in Rotterdam and wrote to the company to find out if a similar tunnel could be built under the Fraser River. Correspondence with Mr. Massey continued for many years until, in 1955, Mr. Lassen-Nielsen went to Vancouver to investigate the matter on the spot. As a result of this investigation Christiani & Nielsen decided to collaborate with Foundation of Canada Engineering Corporation Limited (Fenco), the executive Vice-President of which is Mr. Per Hall." (Lassen-Nielsen, M., 1959).

In 1956 the agreement to design and construct the Deas Island tunnel was made (Figure 9). Again, work was done in collaboration between the local construction companies and the international immersed tunnel specialists. Around the same time, an immersed tunnel was planned in Cuba, crossing the Havana harbour, constructed by French company Grand Travaux de Marseille (G.T.M).

Figure 8. Maas tunnel.

Figure 9. Deas Island Tunnel (1958).

2.5 *European immersed tunnels in the 1960 - 1970*

After the success of the Deas Island tunnel and Havana immersed tunnels - both projects involving European contractors - and with the economic stability and growth in Europe, there was a boom in the construction of immersed tunnels in Europe starting up in the 1960.

See Table 2 for a list of worldwide immersed tunnels in the period 1958-1969. New technologies were developed, and some immersed tunnels had multiple functions, as concrete casting allowed for a flexible cross section with several tubes and several functions. Some of the new immersed tunnels were constructed in soft soil conditions and some were placed on piles, like the Tingstad Tunnel in Gothenburg, Sweden.

The first immersed tunnel and first major subsea tunnel project in Denmark, Limfjordstunnel, was opened on the May 6, 1969. The project used the experience gained from the designs and constructions of the immersed tunnel, bridge, and marine projects abroad.

Table 2. Immersed tunnel 1958 -1969.

Europe	Outside of Europe
Rendsburg, Germany	Havana, Cuba
Liljeholmsviken, Sweden	Deas Island, Canada
Coen, The Netherlands	Webster Str, US
Viex Port, France	La Fontaine, Canada
Tingstad, Sweden	Parana, Argentina
Rotterdam metro, The Netherlands	Dojima River, Japan
Ij, Amsterdam, The Netherlands	
J.F. Kennedy (Schelde), Belgium	
Heinenoord, The Netherlands	
Limfjord, Denmark	

Concrete technology had been under development for many years, and in the Netherlands, it was assessed that new immersed tunnels could be constructed without an external waterproofing membrane, as opposed to earlier immersed tunnels. That required concrete without through-going cracks and control of cracks.

The Vlake tunnel (1975) (Figure 10) was the first concrete immersed tunnel built without a waterproofing membrane and the first segmental immersed tunnel (Glerum, 1976). The method was proved to be cost-effective and has been used on immersed tunnels in The Netherlands ever since.

Figure 10. Vlake tunnel, casting with no early-age cracking.

2.6 *Concrete immersed tunnels around the world*

Concrete tunnels have been constructed around the world since the Deas Island tunnel opened in 1958. The Louis-Hippolyte Lafontaine Bridge-Tunnel in Montreal opened in 1967. Cut & cover tunnels with 4 or more road lanes are often provided with permanent transverse prestressing. This immersed tunnel in Canada, like the Havana tunnel, also had permanent transverse prestressing; until recently, very few immersed tunnels have made use of permanent transverse prestressing.

The company Per Hall, involved in Deas Island and Louis-Hippolyte immersed tunnels, used the experience from Canada in the first immersed tunnel in Hong Kong, the Cross-Harbour tunnel (1972), where a monolithic concrete tunnel was a cost-competitive alternative compared to the initially proposed steel solution option.

Note the first immersed tunnel in Japan was the Dojima River (1969), inspired by US steel shell type, much driven by seismic considerations which are not relevant for immersed tunnels in Northern Europe.

The concrete method used on the first immersed tunnel in Hong Kong has been used on all six immersed tunnels constructed in Hong Kong since 1972. The first immersed tunnel in Australia was the Sydney Harbour Tunnel (1992), also using concrete type, with inspiration taken from the immersed tunnels built in Hong Kong.

A specially constructed concrete immersed tunnel was the Singapore cable tunnel (1986), a project that gave inspiration to the later Øresund tunnel (2000). Inspired by Øresund, The Busan-Geoje immersed tunnel was constructed between 2004-2010. It was the first immersed tunnel in South Korea and the first segmental concrete tunnel in Asia, (Figure 11) (Olsen 2009).

Figure 11. Busan-Geoje immersed tunnel, casting yard.

It was a brave decision to use segmental concrete immersed tunnel in South Korea for the first time. It followed the European practice, relying on high-quality concrete, and differed significantly from the practices adopted in Hong Kong and China, based on monolithic elements with a waterproofing membrane, or steel shell used in Japan.

The concept of segmental concrete immersed tunnels was introduced in China with the Hong Kong – Zhuhai – Macao immersed tunnel (2018), with successful outcome.

3 LONG IMMERSED TUNNELS

After the opening of the Deas Island tunnel, confidence built within the industry and companies were ready for the next major immersed tunnel projects. Since the 1930s, it had been a long-term ambition in Denmark to connect more of the many islands of the country, either by long bridges or tunnels. Proposals for fixed links, both at Storebælt (Great Belt) and at Øresund, were put forward, revisioning a proposal made in 1930. A proposal for an immersed tunnel under the Channel (UK-France) was put forward by C&N in 1963.

In the United States, the first major fixed link, the Chesapeake Bay Bridge–Tunnel, a 28,3km fixed link crossing the mouth of the Chesapeake Bay in the state of Virginia, opened in 1964. It replaced ferries that had operated since the 1930s. This fixed link, combining bridges and tunnels with artificial islands, has been the inspiration for many fixed links around the world, in projects like the Great Belt Link (1998) in Denmark and the Tokyo Bay Aqua-line (1997) in Japan.

In 1985 a 2,6km long subsea tunnel was planned in Singapore by C&N (Figure 12). Inspired by segmental bridge construction - an innovative method to increase production rate and maintain sufficient water tightness in concrete quality - a factory-like production set-up was made. A segmental-type immersed tunnel was used (Rasmussen 1987). Young engineers involved in the Deas Island tunnel (1958) were now senior engineers working in Singapore.

A similar type of immersed tunnel for water intake was constructed for the Kilroot power station, in Northern Ireland (1978). Like the Singapore cable tunnel, the segments were cast under factory-like conditions, assembled and post-tensioned on a ship-lift made specifically for the project.

The length of the tunnel elements was 100m, using 29 elements with segments of 3,5m, and 754 segments were used in total. The project served as inspiration for the factory-like construction method for the Øresund tunnel (Figure 13), with same people from the Singapore cable tunnel developing the concepts.

The Øresund tunnel is a combined road and rail immersed tunnel, 3,6km in length, constructed by 20 tunnel elements of 180m. The length and scale required special considerations around the construction methodology of the elements. Two production lines allowed the production of two elements every second month.

Figure 12. Singapore cable tunnel.

Figure 13. Øresund tunnel element fabrication.

When the Hong Kong – Zhuhai – Macao immersed tunnel project was planned in 2008, with a length of 6,0km, considerations were made to construct the tunnel elements either as in Busan (casting yard) or as in Øresund (production lines). Site constraints on one of the available sites on Niutou Island led to the decision to use a production-line setup (Figure 14). The tunnel element length of 180m was selected, similar to Øresund and Busan, in a total of 33 tunnel elements.

The Femern tunnel, with 18km of length, is under construction and uses experience from concrete immersed tunnels from the last 65 years.

Figure 14. Hong Kong – Zhuhai – Macao element factory.

4 SHORT SPECIAL ELEMENT IMMERSED TUNNELS

On another scale, with a different type of complexity, we find a shorter special type of underwater tunnel like the Paris metro, where the immersed tunnel type can be made to fit a specific element construction method or to fit the ground conditions. An example from the Stockholm metro, the subsea tunnel at Liljeholmsviken (Chr. Ostenfeld 1968) had a shallow alignment, with the immersed tunnel element structurally spanning like a bridge beam (Figure 15).

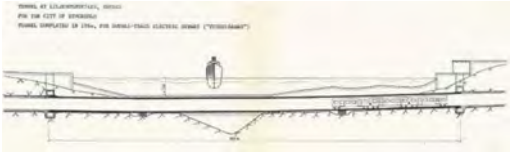

Figure 15. Liljeholmsviken immersed tunnel.

Figure 16. Söderström immersed tunnel.

Söderströmstunnel (Glückert 2014), located close to Liljeholmsviken, is a more recent example. Steel shells were constructed several hundred kilometres away, in Estonia, and towed on a barge to Stockholm, Sweden for installation. The method was developed to handle specific constraints on-site with limited water depth and with an opportunity to optimise cost and risk (Figure 16). The tunnel elements on Söderström were placed on piles, naturally inspired by bridge design and construction.

5 CONCLUSION

This paper delineates some important steps taken in the evolution of immersed tunnel technology when transferring between continents, emphasizing the preservation of core principles including waterproofing, durability, joints, and longitudinal performance.

Highlighted innovations in immersed tunnels (IMT):

Now: Very long immersed tunnel: 18km, Femern tunnel,

2016: Steel shell concrete IMT floating: Söderströmtunnel,

2000: Gravel bed for concrete IMT: Øresund tunnel,

1986: Production line: Singapore cable tunnel,

1975: Segmental construction: Vlake tunnel,

1964: Immersed tunnel for Fixed link: Chesapeake tunnel,

1942: Concrete monolithic: Maas tunnel,

1910: First immersed tunnel: Michigan central railway.

Innovation and knowledge sharing is important for the development of sustainable solutions.

The past shows that changes are made when inspired by other fields of engineering and across geographies. While learning from the past, new thinking can guide us towards the future. Some lessons learned:

1) *Knowledge sharing and technology implementation follow people and organisations more often than what can be heard, taught and read about.*
2) *Owners shall be open to new ideas, and willing to take risks on new technologies to make noteworthy changes.*
3) *Globalisation is a facilitator for knowledge sharing, striking a good balance between collaboration and competition between organisations in the global market.*

Future sustainable immersed tunnels need innovation within low-carbon materials based on renewable energy, recycling, equipment electric powered and much more.

As an industry, we should celebrate owners, consultants, contractors, suppliers, and influenced stakeholders for being brave in promoting new technologies. Had it not been for curious persons like the late George Massey in Vancouver, Canada, and M. Lassen-Nielsen, Chief engineer of C&N in Rotterdam and the Engineering Department of the City of Rotterdam, the owner of the Mass tunnel, the immersed tunnel technology, at least in Northern

Europe, would have developed in a completely different direction.

Question: Who are the "George Masseys" and "M. Lassen-Nielsens" of today, to inspire a culture of innovation and develop it for future immersed tunnel projects?

ACKNOWLEDGEMENTS

The author would like to thank Niels Iversen, former Technical Director of Christiani & Nielsen, for inspirational discussions and showing a way through extensive use of CN Post - with technical articles from C&N projects during the years - how the development of new technology in the past, can be an inspiration for the development of new technology now and in the future.

REFERENCES

Chr. Ostenfeld, 1976. Christiani & Nielsen, Danish Pioneers of Reinforced Concrete, Polyteknisk Forlag.

Chr. Ostenfeld & W. Jønson, 1968, Tunnel Projects design by Chr. Ostenfeld & W. Jønson, Consulting Engineers.

Gimsing, N.J., Iversen C. 2001. The Tunnel, The Øresund Technical Publication, published by Øresundsbro Konsortiet.

Glerum, A., Rigter, B.P., Eysink, W. D., Heins, W.F., 1976. Motorway tunnels built by the immersed tube method, Rijkswaterstaat Communications, No. 25.

Glückert, J., Johansson, C., Odgaard S.S., 2014. Floating Construction of an immersed tunnel – Söderströmstunnel, Proceeding of WTC 2014, Foz do Iguacu, Brazil.

Lassen-Nielsen, M., 1959. Deas Island Tunnel, CN Post No. 47 November 1959.

Olsen, T., Jackson P., Lee J.S. 2009. Construction of the Busan-Geoje immersed tunnel from the designer's view point, Proceeding of Strait crossing 2009, Trondheim, Norway.

Rasmussen, Nestor S., Jensen O.P., Jørgensen Steen, 1987. Undersea cable tunnel, Singapore, IABSE report.

Rasmussen, Nestor S., L. Gravesen, 1987. A Milestone in Tunnelling: Rotterdam's Maas Tunnel Celebrates its Fiftieth Anniversary, Tunnelling and Underground Space Technology, Vol. 8, Number, 1993.

Tunnelling for a Better Life – Yan, Celestino, Thewes & Eberhardt (Eds)
© 2024 The Author(s), ISBN 978-1-032-80042-4
Open Access: www.taylorfrancis.com, CC BY-NC-ND 4.0 license

Small-scale model test for the dynamic behavior of submerged floating tunnels considering the coastal connection with subsea bored tunnels

Joohyun Park*, Seok-Jun Kang, Jun-Beom An, Jin Kim & Gye-Chun Cho
Department of Civil and Environmental Engineering, Korea Advanced Institute of Science and Technology (KAIST), Daejeon, Republic of Korea

ABSTRACT: Due to the displacement imbalance between the submerged floating tunnel (SFT) and the subsea bored tunnel, the coastal connection of the SFT has weak stability. Therefore, it is necessary to accurately analyze the dynamic characteristics of the SFT by considering the interaction between the ground and the tunnel structure in the coastal connection. In this study, a small-scale model test was performed to evaluate the effect of ground-tunnel interaction on the dynamic characteristics of an SFT in the coastal connection due to horizontal displacement induced by the dynamic behavior of the SFT. In the model, the coastal connection has been simplified to a situation in which a bored tunnel and SFT were connected on a cliff-shaped coastal ground. The experiment was performed by changing the horizontal displacement of the end of the SFT. The vibration of the SFT was induced by impacting the outer side wall of the SFT with a hammer. The vibration response of the SFT was measured using accelerometers. The measured time domain acceleration response spectrum signal was converted to a frequency domain signal through fast Fourier transformation (FFT), and the natural frequency of SFT was analyzed. As a result, the horizontal displacement caused deformation in the ground around the bored tunnel and reduced the ground stiffness. Depending on the induced strain, the natural frequency of SFT decreased linearly, then nonlinearly in the form of an exponential function, and then tended to converge. It has been experimentally confirmed that ground-tunnel interaction in coastal connections affects the dynamic characteristics of SFT. Therefore, to accurately predict the dynamic behavior of a SFT, it is essential to reflect ground deformation and nonlinear characteristics considering the interaction between the ground and tunnel at coastal connection.

Keywords: Natural frequency, Soil-structure interaction (SSI), Acceleration response, Fast Fourier transformation (FFT), Experimental method

1 INTRODUCTION

Bridges, subsea bored tunnels, and immersed tunnels are known as representative infrastructures used to cross the sea or river. However, they have the problem of being greatly affected by the geotechnical factors of the construction site. In particular, when the seabed is deep, they require excessive construction costs and practical limitations (Jiang et al. 2018). Recently, as an alternative, research has been actively conducted on submerged floating tunnels (SFT), in which a tunnel module floats at a specific water level through mooring and tethering methods. They have the advantage of being less affected by meteorological factors above the water. Still, they behave dynamically under the influence of tidal currents in a maritime environment, so accurate analysis is required (Long et al., 2009). For SFTs to provide a path between lands, they must be connected to the ground (Xiao and Huang 2010). In Figure 1, a representative schematic diagram of the coastal connection for the connection between the bored tunnel and the SFT is presented. Unlike SFT, which has relatively dynamic behavior, a bored tunnel is constrained by the surrounding ground. Due to the displacement imbalance between the SFT and the bored tunnel, the coastal connection of the SFT has poor dynamic stability, so this characteristic must be considered when the SFT is connected to the ground through the connection with the bored tunnel (Kang et al., 2020).

In previous literature considering coastal connection, research on earthquake excitation in SFT was conducted (Xiao and Huang, 2010). Still, there was a limitation in assessing the boundary condition only as a bearing element. The soil-structure interaction (SSI) plays a crucial role in determining the response

*Corresponding author: joohyun.park@kaist.ac.kr

DOI: 10.1201/9781003495505-324

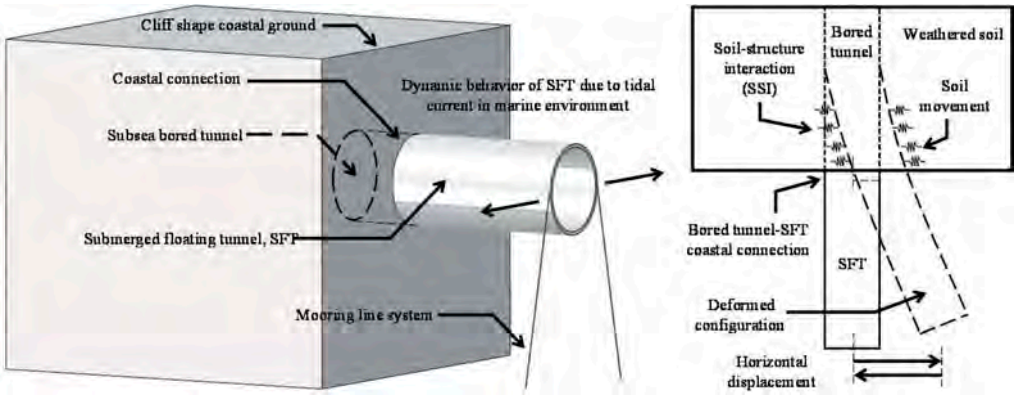

Figure 1. Schematic diagram of coastal connection for connecting subsea bored tunnel and submerged floating tunnel.

of structures to static or dynamic loading. This influence extends beyond the soil behavior alone and encompasses the structural response under load (Kavitha et al. 2016). Therefore, a comprehensive analysis should consider both soil characteristics and structural features. The effect of connection stiffness at the end of the SFT on the natural frequency of the SFT system was determined through an experimental study conducted by Park et al. (2021). Kang et al. (2020) performed a numerical analysis to assess the stress concentrations at coastal connections when subjected to static conditions. They found that implementing a coastal connection with a flexible joint could effectively mitigate the stress concentration at this junction. Park et al. (2022) conducted a series of parameter studies by numerical methods to confirm that the resonant frequency of the SFT system can be controlled by implementing a ring-type joint between the SFT and the boundary. Kang et al. (2023) employed a three-dimensional numerical analysis to assess the impact of coastal connection design in the presence of dynamic loading conditions. However, the previous studies have not effectively determined the alterations in dynamic characteristics while accounting for the interaction between soil and the tunnel structure. According to Doebling et al. (1998), ground condition alterations impact the vibration characteristics of structures. Hence, the assessment of changes in dynamic properties with a variety of SSI can be conducted through an analysis of the free vibration response of the SFT. Therefore, the current study aims to experimentally analyze the effect of changes in soil-tunnel interaction on the dynamic characteristics of SFT in the coastal connection due to horizontal displacement induced by the dynamic behavior of SFT. A small-scale model was used to simulate the coastal connection between the bored tunnel and SFT. The experiment was performed by changing the horizontal displacement of the end of the SFT. The vibration of the SFT was induced by impacting the outer side wall of the SFT with a hammer. The vibration response of the SFT was measured using accelerometers attached horizontally to the impact inside the SFT. The measured time domain signal was converted to a frequency domain signal through FFT, and the natural frequency of SFT was analyzed.

2 EXPERIMENTAL STUDY

In this study, an experimental study was conducted using a small-scale model to evaluate the dynamic characteristics of a submerged floating tunnel considering the coastal connection with the subsea bored tunnel. In the experiment, a rope was used to simplify the SFT module floating in the water by a mooring line system. When designing an SFT in practice, various buoyancy weight ratios (BWR) are considered, but in experiments, only the case where BWR is 1 was considered. Using water has the advantage of considering various BWRs and the effect of hydrostatic pressure. However, this has the limitation that it complicates the behavior of SFT and makes it difficult to clearly understand the interaction with the ground in the coastal connection. In addition, actual SFT exhibits various dynamic behaviors depending on load combinations in the marine environment, but the most dominant behavior during operation is lateral behavior due to tidal current. Therefore, only horizontal displacement was considered in the model test. A model test was performed to observe changes in the natural frequency of SFT due to horizontal displacement caused by the dynamic behavior of SFT. The main goal was to analyze the effect of soil-tunnel structure interaction on the dynamic characteristics of SFT at coastal connection.

2.1 *Small-scale model test setup*

The setup for the small-scale model test consisted of a subsea bored tunnel, a coastal ground restraining it, and a submerged floating tunnel connected to the bored tunnel and supported by a rope at one end (Figure 2a). The rope was connected to a crane to

simulate the horizontal displacement caused by the dynamic behavior of the SFT. To model the cliff-shaped ground, a soil box combined with a separable bulkhead was used. The bulkhead was installed at the boundary of the coastal connection to distinguish between the bored tunnel and SFT. Polyethylene sheets, characterized by their elastic properties, exhibit deformation in response to the behavior of SFT and concurrently serve as a barrier to prevent the loss of ground materials and water. Polyethylene sheets were utilized around the tunnel to allow the tunnel and surrounding ground to interact according to the dynamic behavior of the floating tunnel (Figure 2b). To measure the acceleration response of the SFT, sensors were attached to the inner side wall of the tunnel in the horizontal direction parallel to the ground (Figure 2c).

2.1.1 *Weathered soil ground*

A soil box was manufactured to simulate the conditions under which a tunnel was constructed on soil, and the width, length, and height of the box were 100 cm, 100 cm, and 90 cm, respectively (Figure 3a and 3b). To enhance visibility, acrylic was employed as the material for the soil box. The ground was modeled as weathered granite soil widely distributed in Korea. This proves effective for assessing tunnel interaction, demonstrating substantial strength and self-support when compacted to the optimal moisture content. As shown in Table 1, the soil has a passing quantity of #200, a sieve passing rate of 2.31%, a uniformity coefficient (C_u) of 3.47, and a curvature coefficient (C_c) of 0.94. It is classified as poorly graded sand (SP) by the Unified Soil Classification System (USCS).

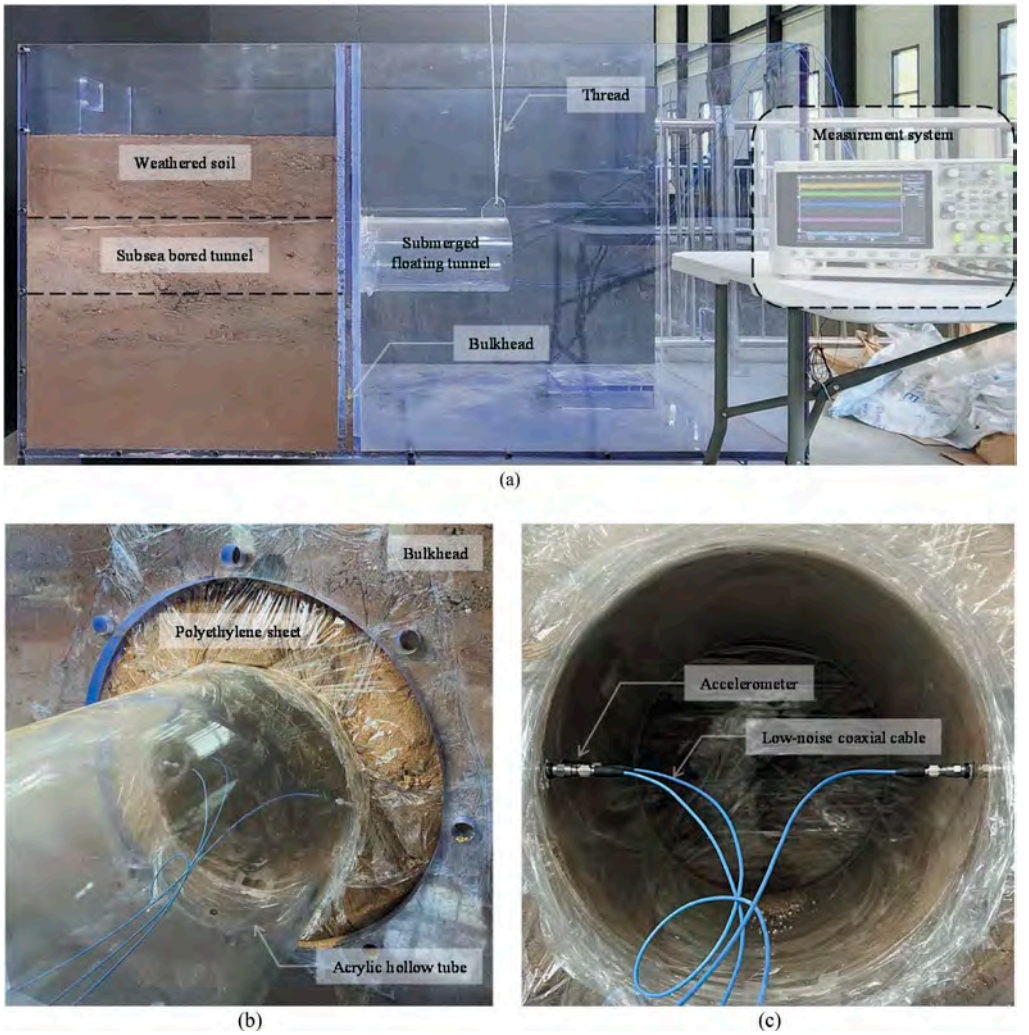

Figure 2. Small-scale model test setup for experimental study: (a) overall view; (b) coastal connection; (c) Acceleration measurement.

Considering the optimal moisture content, a standard compaction hammer modeled the ground using sand with a water content of 15%.

Table 1. Index property of weathered soil.

Specific gravity [-]	2.67
D_{60} [mm]	1.25
D_{30} [mm]	0.65
D_{10} [mm]	0.36
Passing quantity of No. 200 [%]	2.31
Coefficient of uniformity, C_u	3.47
Coefficient of curvature, C_c	0.94
USCS	SP
Water content [%]	15

*USCS: Unified Soil Classification System

2.1.2 *Tunnel structure*

The tunnel was modeled as an acrylic hollow tube with the physical properties shown in Table 2. The diameter, length, and thickness of the tunnel were 25 cm, 150 cm, and 1 cm, respectively (Figure 3a and 3b). Since the distance between the tunnel axis and the ground surface, C, is 37.5 cm, the shallow tunnel condition C/D = 1.5 was considered. The tunnel structure consisted of a 100cm bored tunnel section confined by weathered soil and a floating tunnel section protruding 50cm outside the bulkhead (Figure 3b). The end of the bored tunnel was fixed to the wall of the soil box. The end of the floating tunnel was supported by a rope connected to the crane so that the dynamic behavior of the SFT could be simulated through crane operation.

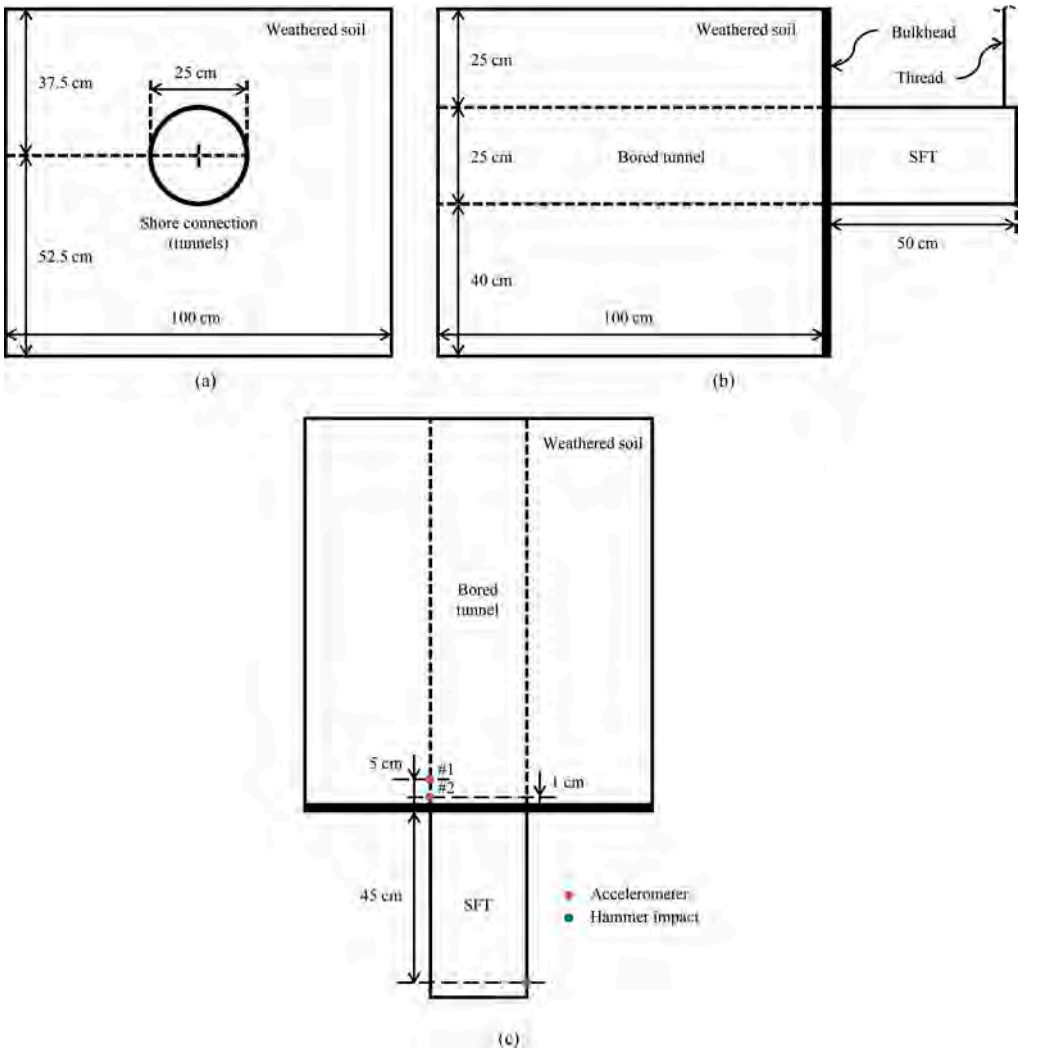

Figure 3. Schematic diagram of small-scale model test setup: (a) front view and (b) side view (c) top view and sensor location.

Table 2. Physical properties of acrylic.

Density [kg/m^3]	1200
Elastic modulus [GPa]	3
Shear modulus [MPa]	890
Poisson's ratio [-]	0.35
Tensile strength [MPa]	73
Yield strength [MPa]	45

2.2 *Measurement and analysis system*

The measurement system to determine the dynamic response characteristics of the floating tunnel was configured as shown in Figure 4. Inside the tunnel, an accelerometer was attached in a direction parallel to the hammer impact and horizontal to the ground. The accelerometers were located 5 cm and 1 cm from the bulkhead toward the bored tunnel (Figure 3c). A hammer with a length of 20 cm and a weight of 0.5 kg was freely dropped from a 45-degree point and struck in a direction parallel to the tunnel. A widely used rubber tip was selected for the hammer to measure the response in the low-frequency region.

To measure the fine-scale vibration response of the structure, two accelerometers (353B18, PCB Piezotronics, NY, USA) with a sensitivity of 10 mV/g and capable of measuring accelerations of up to 500 g and frequencies of 1 Hz to 10 kHz were used. After hammer impact, the signals measured by the accelerometer were filtered, amplified, and acquired by a signal conditioner (482C54, PCB Piezotronics, NY, USA), oscilloscope DSOX3024T, Keysight Technologies, CA, USA), and a laptop computer. Noise elimination was achieved through a signal conditioner, ensuring the acquisition of high-quality signals. During this process, the signal underwent amplification to facilitate the reception of the target signal in the time domain. Furthermore, the utilized oscilloscope was specifically configured to capture free vibration data resulting from hammer impact, encompassing the triggering system. The recorded time domain data was converted to frequency domain data through fast Fourier transform (FFT) using MATLAB (MathWorks, MA, USA). From the results obtained after filtering by removing random noise through a low-pass filter and a high-pass filter, the pre-dominant frequency was evaluated as the natural frequency of the SFT. Additional data processing included improving the quality of the FFT data through offset processing and zero-padding.

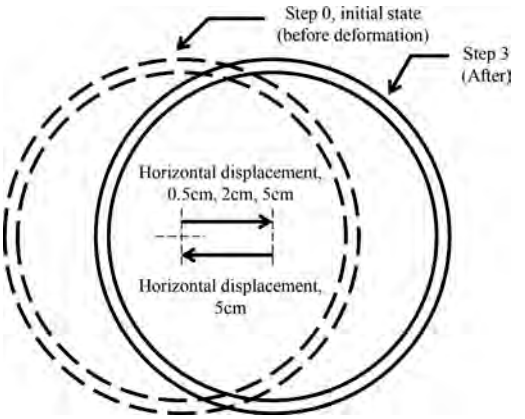

Figure 5. Horizontal displacement at the end of SFT by step.

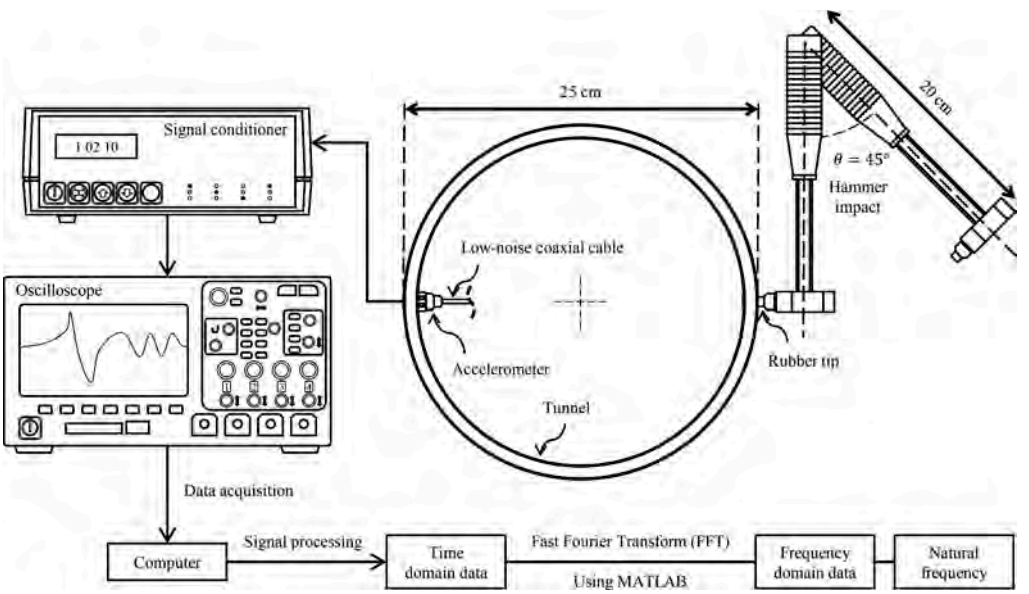

Figure 4. Measurement system.

Table 3. Small-scale model test procedure.

Step 0	Initial state: static equilibrium with the soil confinement
Step 1	A state where the horizontal displacement of the end of the SFT is 0.5cm (+ 0.5 cm)
Step 2	A state where the horizontal displacement of the end of the SFT is 2.0cm (+ 1.5 cm)
Step 3	A state where the horizontal displacement of the end of the SFT is 5.0cm (+ 3.0 cm)
Step 4	A state in which the end of the SFT returns 5cm in the opposite direction. (- 5.0 cm)

2.3 *Test procedure*

In the small-scale model test procedure, the assessment of natural frequencies was conducted for four distinct horizontal displacement states, ranging from step 0 (the initial step) to step 4 (the final step), as illustrated in Figure 5 and summarized in Table 3. Up to step 3, the state where horizontal displacement at the end of SFT of 0.5 cm, 2 cm, and 5 cm occurred in the same direction was evaluated. In step 4, the condition with a return of 5 cm in the opposite direction was assessed. To minimize the influence of changes in rope tension, a 0.5 cm unit was adopted.

3 EXPERIMENTAL RESULTS AND DISCUSSION

After performing a small-scale model test, the signals measured at each step were compared and analyzed. Figure 6 presents time domain data acquired through the measurement system (Figure 6a) and frequency domain data processed through FFT (Figure 6b). As shown in the time domain result, the amplitude of free vibration of the SFT model due to the impact load showed a transient response in which the amplitude decreased exponentially with time.

Due to the influence of sensor location, the response was observed first from sensor 2, which was installed closer to the hammer impact. Nevertheless, as shown in the frequency domain graph in Figure 6b, it was found to have similar natural frequency values. This means that the natural frequency of the SFT system was well captured. The natural frequencies evaluated for each step are presented in Table 4. As the step increases, the natural frequencies of SFT gradually decreased as the step progressed and showed a tendency to converge. The natural frequencies from sensor 2 offering the same trend as sensor 1.

The results of plotting the natural frequencies of the SFT obtained at each step according to horizontal displacement are presented in Figure 7a. As a horizontal displacement of 0.5 cm occurred from step 0 to step 1, the natural frequency of SFT tended to decrease linearly. The natural frequency is reduced due to an additional horizontal displacement of 1.5 cm from step 1 to step 2. As the horizontal displacement increased by 3 cm from step 2 to step 3, there was a decrease in the natural frequency. However, the rate of decrease diminished significantly, indicating a tendency towards gradual convergence. These results can be confirmed more clearly through the natural frequency reduction rate results according to the accumulated horizontal displacement presented in Figure 7b. In step 3, where the maximum displacement occurred, the natural frequency reduction rate of SFT was found to be 15.49% in sensor 1 and 13.48% in sensor 2. There

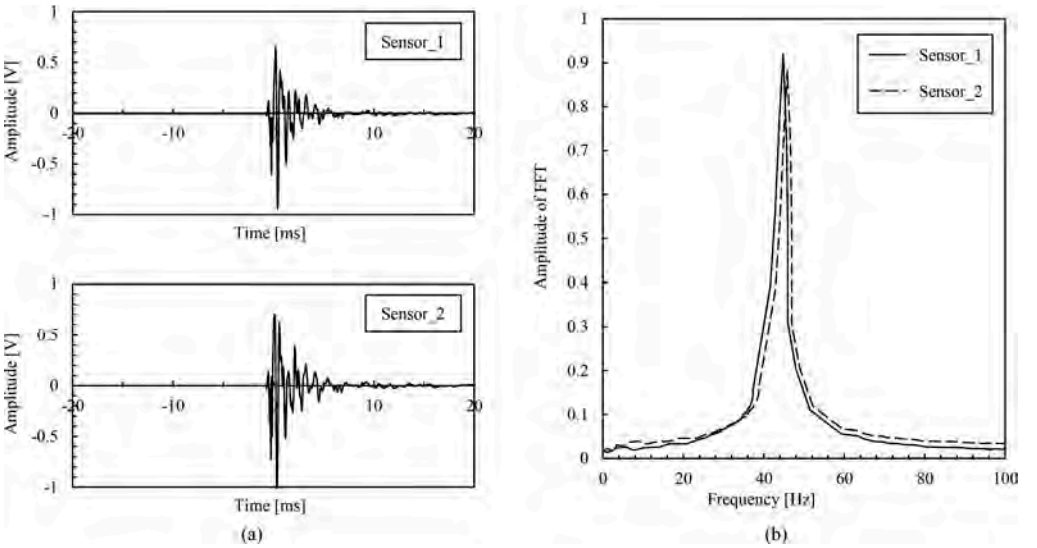

Figure 6. Measured signals: (a) time domain data and (b) frequency domain data.

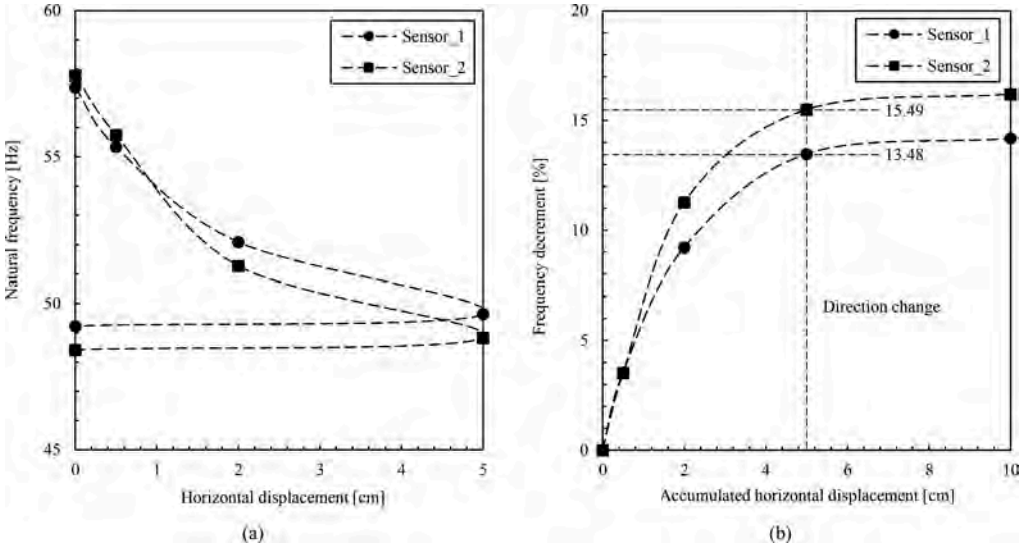

Figure 7. Natural frequency of SFT evaluation results at each step: (a) natural frequency of SFT according to horizontal displacement and (b) natural frequency reduction rate according to accumulated horizontal displacement.

Table 4. Natural frequency of SFT for each step.

Step #.	Horizontal displacement [cm]	Natural frequency by sensor_1 [Hz]	Natural frequency by sensor_2 [Hz]
0	0	57.37	57.78
1	0.5	55.34	55.75
2	2	52.08	51.27
3	5	49.64	48.83
4	0 (Return)	49.26	48.42

was a slight decrease even after the direction change, but it generally tended to converge. This can be explained by the fact that plastic strain induced in the soil occurred in the process of generating the maximum horizontal displacement.

The results of the experimental study indicate that the dynamic properties of SFT are changed by soil-tunnel structure interaction (SSI) at the coastal connection. This is consistent with the literature (Kavitha et al. 2016), as an increase in horizontal displacement causes soil deformation around the tunnel, which leads to a decrease in confining pressure and the natural frequency of the structure interacting with the surrounding ground. A substantial horizontal displacement from stage 0 to stage 3 leads to a significant compressive force on the ground in the direction of the SFT movement. Conversely, in the opposite direction, the ground undergoes stretching, resulting in reduced confinement. The reduction in confining pressure at the SFT-ground interface leads to a decrease in the natural frequency of the SFT. Consequently, plastic strain is induced around the SFT, leading to plastic permanent displacement. This means that even in the process of returning to the initial state from step 3 to step 4, the natural frequency of the SFT is not recovered and is still reduced to a converged value, which can be inferred that permanent deformation has been caused in the soil. It was experimentally confirmed that the dynamic behavior of SFT causes permanent deformation and a decrease in the confining pressure of the ground at the coastal connection and that the resulting SSI also affects the dynamic properties of SFT.

4 SUMMARY AND CONCLUSIONS

In this study, a small-scale model test was performed to evaluate the effect of ground-tunnel interaction on the dynamic characteristics of an SFT coastal while the horizontal displacement occurs. The experiment was performed by changing the horizontal displacement of the end of the SFT. The main conclusions obtained through this study are summarized as follows.

1) As the horizontal displacement of the SFT increases, the natural frequency of the SFT appears to decrease, and SSI at the coastal connection affects the dynamic characteristics of the SFT.
2) The behavior of the SFT impacts the magnitude of ground deformation, and the consequent confining pressure influences the change in natural frequency.
3) The excess dynamic behavior of SFT may cause permanent deformation in the soil, resulting in the natural frequency of SFT not being recovered after being reduced.

ACKNOWLEDGMENTS

This work was supported by a grant (RS-2023-00245334) funded by Korea of Ministry of Land, Infrastructure and Transport (MOLIT). The first author and fourth author are supported by the Innovated Talent Education Program for Smart City from MOLIT.

REFERENCES

Doebling, S. W., Farrar, C. R., and Prime, M. B. 1998. A summary review of vibration-based damage identification methods. Shock and vibration digest. 30(2), 91–105.

Jiang, B., Liang, B. and Wu, S. 2018. Feasibility study on the submerged floating tunnel in Qiongzhou strait, China. Pol. Marit. Res. 25, 4–11.

Kang, S. J., Kim, J. T., and Cho, G. C. 2020. Preliminary study on the ground behavior at coastal connection of submerged floating tunnel using numerical analysis. Geomech. Eng. 21(2), 133–142.

Kang, S. J., Lee, M., An, J. B., Lee, D. H., and Cho, G. C. 2023. Dynamic behavior of submerged floating tunnels at the coastal connection considering the use of flexible joints. Geomech. Eng. 33(1), 101–112.

Kavitha, P. E., Beena, K. S., and Narayanan, K. P. (2016). A review on soil–structure interaction analysis of laterally loaded piles. Innov. Infrastruct. Solut., 1, 1–15.

Long, X., Ge, F., Wang, L. and Hong, Y. 2009. Effects of fundamental structure parameters on dynamic responses of submerged floating tunnel under hydrodynamic loads. Acta Mech. Sin. 25(3), 335–344.

Park, J., Kang, S. J., and Cho, G. C. 2021. Dynamic characteristics of submerged floating tunnel affected by coastal connection. In The 2021 World Congress on Advances in Structural Engineering and Mechanics (ASEM21). IASEM, KAIST, KTA, SNU DAAE.

Park, J., Kang, S. J., Hwang, H. J., and Cho, G. C. 2022. Numerical study on the resonance behavior of submerged floating tunnels with elastic joint. Geomech. Eng. 29(3), 207.

Xiao, J. and Huang, G. 2010. Transverse earthquake response and design analysis of submerged floating tunnels with various coastal connections. Procedia Eng. 4, 233–242.

Tunnelling for a Better Life – Yan, Celestino, Thewes & Eberhardt (Eds)
© 2024 The Author(s), ISBN 978-1-032-80042-4
Open Access: www.taylorfrancis.com, CC BY-NC-ND 4.0 license

Mechanical behaviors of steel-concrete-steel immersed tunnel composite structures

Shenyou Song
Shenzhen-Zhongshan Link Administration Center, Zhongshan, China

Xin Nie, Jiansheng Fan, Yutao Guo & Hanshuo Zhang*
Department of Civil Engineering, Tsinghua University, Beijing, China

ABSTRACT: The development of large urban agglomerations has led to a demand for large-scale infrastructure construction. In response to this trend, the immersed tunnel structures has been evolving towards longer spans and deeper burials. Compared with traditional reinforced concrete structures, steel-concrete-steel immersed tunnels have gradually demonstrated their advantages of high load-bearing capacity, good waterproof properties, and low construction site requirements. The immersed tunnel of the Shenzhen-Zhongshan Link is a typical application of steel-concrete-steel immersed tube tunnel. However, due to the lack of application cases and relevant studies on this type of structure, the load-bearing mechanism of steel-concrete-steel structures is unclear. This has brought great challenges to the design and construction of the immersed tunnel of the Shenzhen-Zhongshan Link. This study is based on sufficient structural experiments, and the structural mechanism of the steel-concrete-steel immersed tube tunnel has been studied in terms of bending and shear resistance. The study has fully considered the multi-axis effect of concrete, multi-mechanism shear resistance and has developed a complete calculation method for steel-concrete-steel immersed tunnels. This paper provides comprehensive guidance for the design and construction of engineering structures with similar forms.

Keywords: Immersed tunnel, Steel-concrete-steel composite structures, Structural mechanism, Experimental study, Bearing capacity

1 INTRODUCTION

With the development of the economy, human activities are gradually expanding to the underground and marine domains. The exploration of these new areas will provide more space, resources and opportunities. To meet the transportation needs in the underground and marine domains, the immersed tunnel structures, with low environmental disruptions and little climate dependencies, have been widely utilized in engineering projects (Chen, 2017).

The concept of immersed tube tunnels originated in the United States and later saw significant development in Europe and Japan (Grantz, 1997). Traditional immersed tunnels can be classified into two categories: reinforced concrete tunnels and steel-concrete composite tunnels. However, it was not until the 1980s that a new type of structure, known as the steel-concrete-steel tunnel structures, emerged (Tomlinson et al., 1989). Compared to traditional type, the steel-concrete-steel tunnel offers several advantages including smaller size, material savings, increased load-bearing capacity, improved earthquake resistance, and better resistance to explosive impact. Steel plates can serve as concrete formwork during construction and provide both structural support and waterproofing during operation. Due to these numerous advantages, the steel-concrete-steel tunnel structure has become one of the most promising development directions for future immersed tunnels.

The steel-concrete-steel immersed tunnel structure is relatively novel with limited research and application. Existing methods for the bending and shear capacities calculation, as well as some related research, are as follows.

In terms of bending capacity, the relevant regulations generally adopt the classical plastic design method based on section equilibrium (Bowerman et al., 2000). However, research has also indicated that steel-concrete structures may exhibit other brittle failure modes when subjected to bending moments

*Corresponding author: zhang-hs22@mails.tsinghua.edu.cn

DOI: 10.1201/9781003495505-325

with improper design (Xie et al., 2007). By installing steel end plates, a combination effect can be achieved between the steel and concrete, promoting ductility and enhancing bending capacity (Wang et al., 2016).

The initial calculation method for shear capacity referred to concrete design theory and involved summing the capacities of the concrete and steel portions (Narayanan et al., 1994). For combination immersed tube tunnels without reinforcement, the diaphragms were considered as the reinforcement, and the shear capacity was calculated separately for longitudinal and transverse diaphragms. The larger value between the two cases was taken as the design capacity. Further studies have shown that the effect of flange dowel action on structural shear capacity is significant, and the original calculation method tends to be conservative (Yan et al., 2015).

The immersed tunnel of the Shenzhen-Zhongshan Link has a total length of 5,035m. The standard section consists of a double eight-lane configuration with a width of 46.0m and a maximum water head of 38m. To meet the construction requirements of this extra wide and deep-buried immersed tunnel, the steel-concrete-steel immersed tunnel structure has been adopted. However, the design traditional approach cannot be directly applied to the Shenzhen-Zhongshan Link. On one hand, the the immersed tunnel structure approximates a plane strain state, and the influence of multi-axial stress needs to be considered when calculating the bending capacity. On the other hand, the utilization of diaphragms introduces multiple shear transfer paths within the structure.

To address the issues of unclear mechanisms and inappropriate calculation methods for the steel-concrete-steel immersed tunnel structure, this study focuses on the immersed tunnel of Shenzhen-Zhongshan Link and establishes a comprehensive set of stress mechanisms for the structure, including bending and shearing. Through numerous experimental tests, the accuracy of these mechanisms is verified, resulting in a practical and reliable design calculation method for the load-bearing capacity.

2 BENDING CAPACITY WITH MULTI-AXIAL EFFECTS

This section focuses on the critical components of the steel-concrete-steel tunnel structure and investigates its bending mechanical characteristics by experiments. Seven large-scale bending tests were conducted to analyze the bending mechanism considering the multi-axial effect and validate the calculation methods.

2.1 *Bending experiment*

The bending test layout is shown in Figure 1, and the specimen parameters are shown (Table 1). The specimen was named as W1-W6 and W8. The height of the specimen is 800mm, the span is 6000mm, the width is 600mm, the upper flange thickness is 6mm, the lower flange thickness is 10mm, the axial diaphragm thickness is 10mm, the transverse diaphragm thickness is 6mm, s_a is the spacing between axial stiffeners, d_G is the height of the concrete void, and f_c' is the compressive strength of the concrete cylinder specimen.

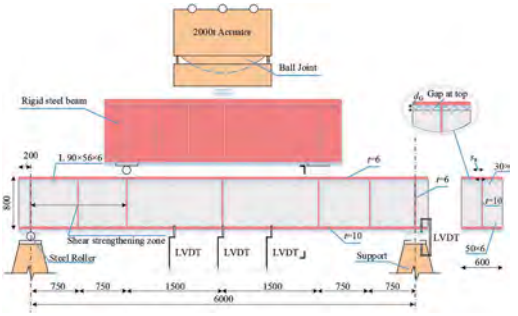

Figure 1. The bending test layout.

Table 1. The specimen parameters of bending test.

No.	Specimen	s_a (mm)	d_G (mm)	f_c' (MPa)
1	W1	250	0	38.8
2	W2	100	0	38.8
3	W3	250	5	38.8
4	W4	250	10	38.8
5	W5	150	0	38.8
6	W6	250	15	20.3
7	W8	100	0	20.3

The final state of the specimen W1 is shown in Figure 2, while the load-displacement curve is depicted in Figure 3. Except for specimen W8, which failed due to the fracture of the lower flange steel plate, the failure of the other specimens was dominated by the crushing of the concrete, accompanied by localized buckling of the upper flange.

Figure 2. The final state of the specimen W1.

In the experiment, most components exhibited good ductility and showed evident confinement between the compressed flange plate and concrete before failure.

2.2 *The mechanism of multi-axis effects in bending*

Some existing design methods consider steel plates as steel bars and assume that they are in uniaxial stress

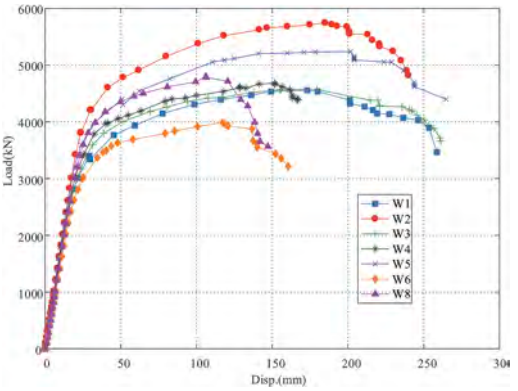

Figure 3. The load-displacement curve of bending experiment.

states. However, in actual tunnel structures that are continuously distributed with considerable length, steel plates are subjected to bidirectional strain states. Concrete supports the flange plate and restricts its transverse deformation, generating transverse stress. Therefore, a multiaxial stress analysis is conducted for the steel-concrete-steel composite tunnel during bending. The yield condition under multiaxial stress states is as follows:

$$\sqrt{\frac{(\sigma_1-\sigma_2)^2+(\sigma_2-\sigma_3)^2+(\sigma_3-\sigma_1)^2}{2}}=f_y \quad (1)$$

Where, σ_i (i=1,2,3) represents the principal stresses, and f_y is the yield strength of steel. Since the thickness of the flange is extremely small, the normal stress out of plane is negligible. Substituting σ_3=0 yields:

$$\sigma_1{}^2+\sigma_2{}^2-\sigma_1\sigma_2=f_y^2 \quad (2)$$

According to Hook's Law:

$$\begin{cases}\varepsilon_1=\frac{\sigma_1}{E_s}-\nu_s\frac{\sigma_2}{E_s}\\ \varepsilon_2=\frac{\sigma_2}{E_s}-\nu_s\frac{\sigma_1}{E_s}\end{cases} \quad (3)$$

Where, ε_1 represents the strain corresponding to the principal stress σ_1; ε_2 represents the strain corresponding to the principal stress σ_2; ν_s is the Poisson's ratio, and E_s is the elastic modulus. Assuming the longitudinal direction as the direction corresponding to σ_1, then ε_2 equals zero.

$$\sigma_2=\nu_s\sigma_1 \quad (4)$$

$$\sigma_1=\frac{1}{\sqrt{1-\nu_s+\nu_s{}^2}}f_y \quad (5)$$

When ν_s=0.3, σ_1=1.125f_y. This result indicates that due to the influence of multiaxial stress, the structure's elastic limit increases by 12.5%. The steel-concrete-steel tunnel structure exhibits bidirectional reinforcement due to lateral constraint.

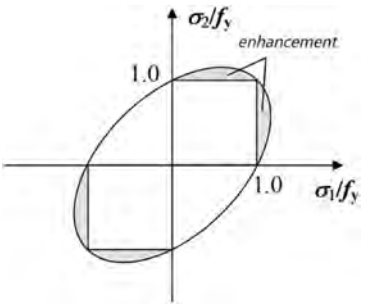

Figure 4. The yield surface of Von-Mises under 2D stress state.

When the structure enters the plastic state, it must satisfy the stress-strain conditions of elastic-plastic mechanics:

$$f=\sigma_1{}^2+\sigma_2{}^2-\sigma_1\sigma_2-f_y^2=0 \quad (6)$$

$$\mathrm{d}\varepsilon_p=\mathrm{d}\lambda\frac{\partial f}{\partial\sigma}=\mathrm{d}\lambda\begin{bmatrix}2\sigma_1-\sigma_2\\ 2\sigma_2-\sigma_1\end{bmatrix} \quad (7)$$

$$\begin{cases}\mathrm{d}\sigma_1=\frac{E_s}{1-\nu_s{}^2}(\mathrm{d}\varepsilon_1{}^e+\nu_s\mathrm{d}\varepsilon_2{}^e)\\ \mathrm{d}\sigma_2=\frac{E_s}{1-\nu_s{}^2}(\nu_s\mathrm{d}\varepsilon_1{}^e+\mathrm{d}\varepsilon_2{}^e)\end{cases} \quad (8)$$

$$\mathrm{d}\varepsilon=\mathrm{d}\varepsilon^e+\mathrm{d}\varepsilon_p \quad (9)$$

Where, $\mathrm{d}\varepsilon_p$ represents the plastic strain increment; $\mathrm{d}\sigma_i$, $\mathrm{d}\sigma_2$ represent the stress increments, and $\mathrm{d}\varepsilon_1{}^e$, $\mathrm{d}\varepsilon_2{}^e$ represent the elastic strain increments. The equations mentioned above take into account that the shear stress and shear strain are assumed to be zero in this state.

When the stress state reaches a stable point, $\mathrm{d}\sigma_1$ =$\mathrm{d}\sigma_2$=0, which implies $\mathrm{d}\varepsilon_1{}^e$=$\mathrm{d}\varepsilon_2{}^e$=0. Consequently, $\mathrm{d}\varepsilon$=$\mathrm{d}\varepsilon_p$. Since $\mathrm{d}\varepsilon_2$=0, we find that $\mathrm{d}\varepsilon_{p2}$=0. Substituting this into equation (7) yields $2\sigma_2$-σ_1=0, σ_2=0.5σ_1, so σ_1=1.155f_y.

This result indicates that, due to the influence of multiaxial stress, when using the plastic design theory, a 15% bidirectional reinforcement coefficient can be used in calculations to consider the enhancement of material performance caused by lateral constraints.

2.3 *Methods for calculating bending capacity*

When the structure is properly designed, it is recommended to calculate the bending capacity using plastic theory:

$$M_u=C_s y_{st}+C_c y_c+C_w y_{cw}-T_w y_{tw} \quad (10)$$

Where, M_u represents bending capacity; $C_s=f_yA_{st}$ is the compressive force of top flange; $y_{st}=h_s-0.5t_t-0.5t_b$ is the distance between the center of the top flange and bottom flange; $C_c=\beta f_c b_c x$ is the compressive force of concrete; $y_c=h_s-t_t-0.5t_b-0.5x$ is the distance from the center of compression in the concrete to the center of the bottom flange; $C_w=f_y x t_{wx}$ is the compressive force of longitudinal diaphragm; y_{cw} is the distance from the center of the compressed section of the longitudinal diaphragm to the center of the bottom flange, which is equal to y_c; $T_w=f_y(h_s-t_t-t_b-x)t_{wx}$ is the tension force of longitudinal diaphragm; $y_{tw}=0.5(h_s-t_t-x)$ is the distance from the center of the tensed section of the longitudinal diaphragm to the center of the bottom flange; A_{st} is the area of top flange; b_c is the width of concrete; h_s is the height of structure; t_{wx} is the thickness of longitudinal diaphragm; t_t and t_b are the thickness of flange; β refers to relevant code; x is the height of the compressed concrete zone which is obtained by:

$$C_s + C_c + C_w = T_s + T_w \tag{11}$$

Where, $T_s=1.15f_yA_{sb}$ is the tension force of bottom flange; A_{sb} is the area of bottom flange.

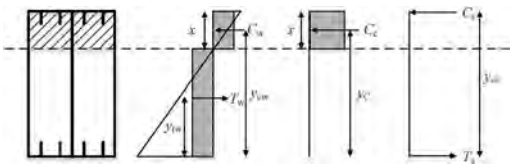

Figure 5. Schematic diagram of bending capacity calculation.

The comparison of relevant calculation methods with experimental capacity is shown (Table 2). The calculation method proposed in this paper demonstrates an improved accuracy of 5%-10% due to a more reasonable consideration of the mechanism. On the other hand, when using the yield strength of steel for calculation, it still yields lower values compared to the experimental results with an average error of -13.9%. This is attributed to the fact that the bending members possess good ductility, resulting in flange entry into the strengthening stage. In actual design, material strengthening is generally not considered, and can be regarded as a safety reserve.

In conclusion, the computation method for bending capacity provided in this paper aligns well with experimental results, with approximately a 10% safety margin reserved.

3 SHEAR CAPACITY WITH MULTIPLE MECHANISMS

This section focuses on the critical components of the steel-concrete-steel tunnel structure and investigates its shear mechanical characteristics by experiments. Sixteen large-scale shearing tests were conducted to analyze the shear mechanism and validate the calculation methods.

Table 2. Comparison of bending capacity calculation (kN).

No.	F_{ut}	F_{uE}	err_E	F_{uJ}	err_J	F_{uP}	err_P
W1	4558	3745	-17.8%	3623	-20.5%	3987	-12.5%
W2	5747	4231	-26.4%	4232	-26.4%	4528	-21.2%
W3	4567	3723	-18.5%	3591	-21.4%	3962	-13.2%
W4	4680	3701	-20.9%	3560	-23.9%	3938	-15.9%
W5	5277	3987	-24.5%	3963	-24.9%	4256	-19.3%
W6	3987	3532	-11.4%	3313	-16.9%	3748	-6.0%
W8	4799	4100	-14.6%	4101	-14.5%	4375	-8.8%
Average		-	-19.2%	-	-21.2%	-	-13.9%

Note: F_{ut} is the experimental result; F_{uE} is the result of European code; F_{uJ} is the result of Japanese code; F_{uP} is the result of method proposed; err_x is the relative error.

3.1 *Shear experiment*

The shear test layout is shown in Figure 6, and the specimen parameters are shown (Table 3). The standard test specimen is half the actual size of the structures. The experiment was conducted with three-point loading mode and simply supported boundary conditions.

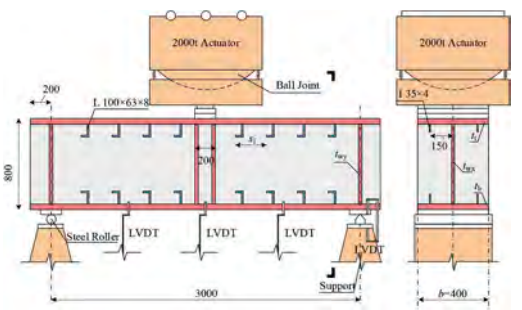

Figure 6. The shear test layout.

The specimen was named as J1-J14 and J16-J17. The height of the specimen h is 800mm; the span l is 1500,3000,3600mm; the width b_s is 400,600mm; the width of concrete b_c is 100,200,400,600mm; the spacing between axial stiffeners s_l is 100,150,300mm; the upper flange thickness t_t is 6,25,30,40mm, the lower flange thickness t_b is 10,25,30,40mm; the axial diaphragm thickness t_{wx} is 6,10,12mm, the transverse diaphragm thickness t_{wy} is 6,10mm; compressive strength of the concrete cylinder specimen f_c' is 20.3,38.8MPa.

The final state of the specimen J1 is shown in Figure 7, while the load-displacement curve is depicted in Figure 8.

Table 3. The specimen parameters of shear test (mm, MPa).

No	b_c	s_w	s_1	t_t	t_b	t_{wx}	t_{wy}	f_{cu}	f_c'
J1	600	1500	300	6	10	10	6	48.5	38.8
J2	400	1500	300	25	25	10	6	48.5	38.8
J3	400	1500	100	40	40	10	6	48.5	38.8
J4	200	1500	300	25	25	10	6	48.5	38.8
J5	100	1500	300	25	25	10	6	48.5	38.8
J6	200	1500	100	25	25	10	6	48.5	38.8
J7	200	1500	150	25	25	10	6	25.4	20.3
J8	200	1500	100	25	25	6	6	25.4	20.3
J9	200	1500	100	30	30	12	6	25.4	20.3
J10	100	1800	300	25	25	10	6	25.4	20.3
J11	200	750	100	25	25	10	6	25.4	20.3
J12	200	750	300	25	25	10	6	25.4	20.3
J13	200	500	300	25	25	10	6	25.4	20.3
J14	400	1500	100	40	40	10	6	25.4	20.3
J16	200	750	300	25	25	10	10	25.4	20.3
J17	200	500	300	25	25	10	10	25.4	20.3

Figure 7. The final state of the specimen J1.

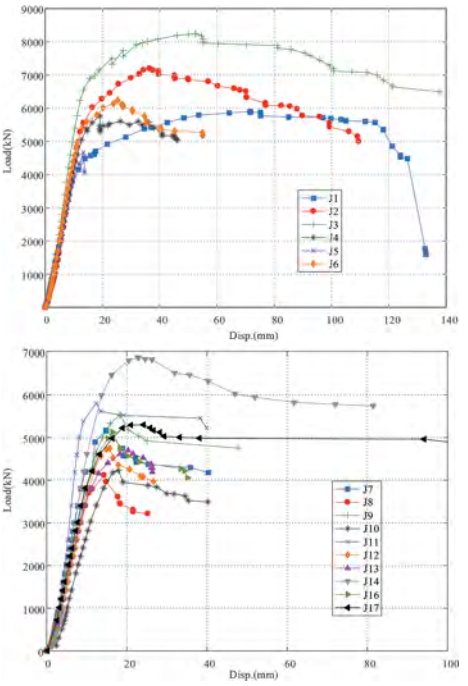

Figure 8. The load-displacement curve of shear experiment.

3.2 *Several mechanisms of shearing*

The shear capacity of the steel-concrete-steel composite immersed tunnel structure is not simply the sum of the concrete and steel parts, but is composed of three anti-shear mechanisms: composite truss, web pure shear, and dowel action.

3.2.1 *Composite truss mechanism*

In steel-concrete-steel structure, the concrete and longitudinal diaphragm are continuously distributed. The concrete experienced inclined compression failure in the experiment, indicating its role as an inclined compression strut. To balance the inclined compression stress, the axial and transverse diaphragm can provide tensile resistance, acting as tension rods. In this truss model, the upper chord is composed of both concrete and top flange, while the lower chord is made up of bottom steel plates. The composite truss mechanism is shown in Figure 9.

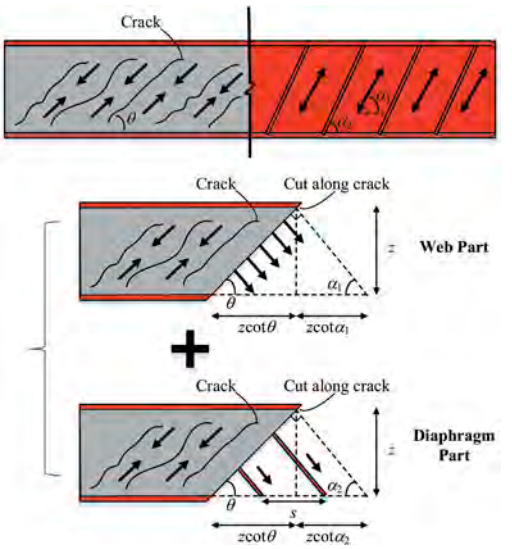

Figure 9. The composite truss mechanism.

The shear capacity of the structure controlled by the inclined strut is given by:

$$V_{uc} = f_{vud} b_c z \tag{12}$$

$$f_{vud} = 1.25 f_c'^{1/2} \tag{13}$$

where V_{uc} represents the shear capacity dominated by the concrete inclined compression strut; f_{vud} is the shear design strength of the concrete in inclined compression strut (JSCE, 2016); z denotes the height of the concrete shear region, which is equal to the height of the concrete when bending moments are not considered.

In the loading process, both longitudinal and transverse diaphragm can reach yielding. The shear capacity dominated by the failure of the tension rod is:

$$V_{ut} = \frac{sin\alpha_1}{\sin\theta} z t_{wx} f_y + sin\alpha_2 \frac{(cot\theta + cot\alpha_2)z}{s_w} A_t f_y \quad (14)$$

where V_{ut} represents the shear capacity dominated by the diaphragm yielding; A_t is the area of transverse diaphragm; θ represent the angle between the concrete strut and the horizontal direction; α_1 represents the angle between the tension rod and the horizontal direction; α_2 represents the angle between the transverse diaphragm and the horizontal direction.

Based on relevant literature and the experimental research conducted in this paper, it is recommended that θ=30°, α_1 = 60°, α_2 = 90°. The shear capacity of composite truss mechanism is as follows:

$$\begin{aligned} V_{truss} &= \min(V_{uc}, V_{ut}) \\ &= \min(1.25 f_c'^{1/2}, \sqrt{3} f_y \frac{t_{wx} + A_t/s_w}{b_c}) b_c z \end{aligned} \quad (15)$$

3.2.2 *Web pure shear mechanism*

It is assumed that the steel material has good ductility, allowing for sufficient stress redistribution between different mechanisms. This allows for the maximum shear capacity to be achieved in possible combinations. In the ultimate shear state, the axial diaphragms first participate as inclined tension rods in the shear truss mechanism. If there is still surplus capacity, they then contribute as steel webs in the pure shear mechanism.

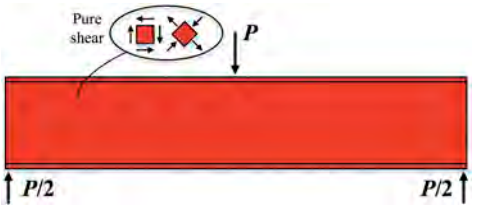

Figure 10. The web pure shear mechanism.

The stress distribution of different shear mechanisms in the longitudinal diaphragm can be illustrated by the Mohr circle shown in Figure 11: Point A represents the ultimate stress in the composite truss mechanism in the direction of α_1, where it is under pure tension; Point B corresponds to rotating state A to the vertical direction, where the normal stress is σ_{rx} and the shear stress is τ_r; Point C represents the superposition of stress state B and the pure shear stress τ_p of the second mechanism, which is the actual stress state in the vertical direction. Based on the Mohr circle and the Von-Mises yield theory, f_t and τ_p satisfy the following equation when the steel yields:

$$f_t^2 + 3 f_t \tau_p \sin 2\alpha_1 + 3\tau_p^2 = f_y^2 \quad (16)$$

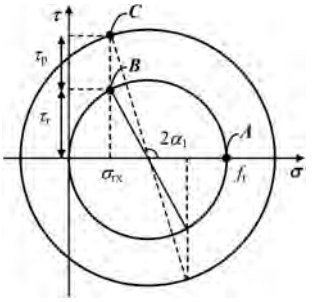

Figure 11. Stress distribution of shear mechanisms in diaphragm.

When θ=30°,α_1=60°,α_2=90°:

$$f_t = \frac{f_{vud} b_c}{\sqrt{3}(t_{wx} + \frac{A_t}{s_w})} \quad (17)$$

$$\tau_p = -\frac{\sqrt{3} f_t}{4} + \frac{\sqrt{12 f_y^2 - \frac{21}{4} f_t^2}}{6} \quad (18)$$

The shear capacity of web pure shear mechanism mechanism is as follows:

$$V_{web} = \tau_p z t_{wx} (\text{if } V_{uc} < V_{ut}) \quad (19)$$

3.2.3 *Dowel action mechanism*

In the steel-concrete-steel immersed tunnel structure, the top and bottom flanges are supported by concrete, similar to longitudinal bars in reinforced concrete. During the shear loading process, the flanges will provide shear resistance through the action of dowelling. The shear capacity of this mechanism is calculated by regression analysis of the experimental data:

$$V_{dowel} = 0.05 f_y b_s (t_t + t_b) \quad (20)$$

where V_{dowel} is the shear capacity of dowel action mechanism; b_s is the width of flanges; t_t,t_b are thickness of flanges.

Based on the above analysis, the total shear capacity V_u of the steel-concrete-steel immersed tunnel structure is:

$$V_u = V_{truss} + V_{web} + V_{dowel} \quad (21)$$

3.3 *Methods for calculating shear capacity*

Based on the experimental data, it is recommended to make the following modifications to the calculation formulas for the shear capacity of two parts: the composite truss mechanism and the dowel action mechanism.

$$V_{\text{truss_n}} = \frac{4.3}{\lambda + 2.4} V_{\text{truss}} \tag{22}$$

$$V_{\text{dowel_n}} = \max\left[\frac{0.24 f_y b_s (0.5 t_t + t_b)}{1000} - 900(\text{kN}), \frac{0.05 f_y b_s (t_t + t_b)}{1000}\right] \tag{23}$$

The theoretical model's predictions for the shear capacity are compared with experimental results in Table 4. The proposed approach has better accuracy, with an average error of 4.0%.

Table 4. Comparison of shear capacity calculation (kN).

No.	V_{ut}	V_{uE}	err_E	V_{uJ}	err_J	V_{u_n}	err_{u_n}
J1	5899	-	-	-	-	-	-
J2	7194	7272	1.1%	4980	-30.8%	7498	4.2%
J3	8249	7281	-11.7%	4980	-39.6%	8040	-2.5%
J4	5765	4202	-27.1%	2490	-56.8%	5748	-0.3%
J5	4674	2458	-47.4%	1245	-73.4%	4849	3.7%
J6	6258	4202	-32.9%	2490	-60.2%	5748	-7.9%
J7	5169	2313	-55.2%	1802	-65.1%	5285	2.2%
J8	4115	2356	-42.7%	1802	-56.2%	4285	4.1%
J9	5529	2326	-57.9%	1802	-67.4%	6114	10.6%
J10	4233	1400	-66.9%	901	-78.7%	4563	7.8%
J11	5801	2313	-60.1%	1802	-68.9%	5786	-0.3%
J12	4744	2313	-51.2%	1802	-62.0%	5333	12.4%
J13	4697	2313	-50.7%	1802	-61.6%	5370	14.3%
J14	6877	4169	-39.4%	3604	-47.6%	7150	4.0%
J16	5123	2313	-54.8%	1802	-64.8%	5380	5.0%
J17	5300	2313	-56.3%	1802	-66.0%	5424	2.3%
Average		-	-43.6%	-	-59.9%	-	4.0%

Notes: 1. V_{ut} is the experimental result; V_{uE} is the result of European code; V_{uJ} is the result of Japanese code; V_{u_n} is the proposed method; *err* is the relative error.

4 CONCLUSION

This paper investigates the steel-concrete-steel composite immersed tunnel structure, with a focus on the bending and shear mechanisms, and the establishment of design methods. The following conclusions can be obtained:

(1) During the bending load process of the steel-concrete-steel composite immersed tunnel, there exists significant constraint between the steel and the concrete, resulting in the steel being in a multi-axial stress state. This effect can improve the actual flexural resistance capacity of the structure.
(2) The shear capacity of the steel-concrete-steel composite immersed tunnel structure is mainly composed of three parts: the composite truss mechanism, the web pure shear mechanism, and the dowel action mechanism. The actual shear bearing capacity of the structure is the sum of the shear resistance provided by these three mechanisms.
(3) A set of bearing capacity calculation methods suitable for practical structure design is proposed, which is well agree with experimental results and superior to existing design methods.

This research addresses key aspects of the bearing capacity of tunnel structures and has significant value on scientific research and practical application

ACKNOWLEDGMENTS

This research is supported by the National Natural Science Foundation of China (52121005). The authors express their sincere appreciation for their supports.

REFERENCES

Bowerman, Hugh, and John C. Chapman. 2000. Bi-Steel Steel-Concrete-Steel Sandwich Construction. In: Composite Construction in Steel and Concrete IV Conference, 656–667. Banff, Alberta, Canada.

Chen, Yue. 2017. 'Application and Developing Trends of Immersed Tunnel', Tunnel Construction, 37, 387–393.

Grantz, Walter C. 1997. 'Steel-shell immersed tunnels—Forty years of experience', Tunnelling and Underground Space Technology, 12: 23–31.

JSCE. 1991. Standard specification for design and construction of concrete structures. Tokyo, Japan.

Narayanan, R., F. J. Naji, and T. M. Roberts. 1994. Design guide for steel-concrete-steel sandwich construction. Volume 1 (The Steel Construction Institute).

Tomlinson, M. J., A. Tomlinson, M. Li Chapman, A. D. Jefferson, and H. D. Wright. 1989. 'Shell composite construction for shallow draft immersed tube tunnels.' in, Immersed tunnel techniques.

Wang, Y. H., J. Y. R. Liew, and S. C. Lee. 2016. 'Ultimate strength of steel-concrete-steel sandwich panels under lateral pressure loading', Engineering structures, 115, 96–106.

Xie, M., N. Foundoukos, and J. C. Chapman. 2007. 'Static tests on steel–concrete–steel sandwich beams', Journal of Constructional Steel Research, 63, 735–750.

Yan, J. B., J. Y. R. Liew, M. H. Zhang, and K. M. A. Sohel. 2015. 'Experimental and analytical study on ultimate strength behavior of steel-concrete-steel sandwich composite beam structures', Materials and Structures, 48, 1523–1544.

Tunnelling for a Better Life – Yan, Celestino, Thewes & Eberhardt (Eds)
© 2024 The Author(s), ISBN 978-1-032-80042-4
Open Access: www.taylorfrancis.com, CC BY-NC-ND 4.0 license

Key technologies of concreting construction of super-wide steel-concrete-steel sandwich immersed tunnel element tubes in Shenzhen–Zhongshan Link

Zong-xian Su*
The Hong Kong University of Science and Technology (Guangzhou), Guangzhou, China

Xu-dong Wu
Poly Changda Engineering Co., Ltd., Guangzhou, China

Chang-liang Zhang & Shen-you Song
Shenzhen-Zhongshan Link Administration Center, Zhongshan, China

ABSTRACT: The immersed tunnel of Shenzhen-Zhongshan Link is the highway immersed tunnel in the world with both the widest element tube and the widest single-carriageway hole. The construction standard is the highway with two-way four lanes (eight lanes total) and some super-wide sections even exceed two-way five lanes (ten lanes total). The width of the standard tubes is 46m and the maximum width of the widest tube is over 55m. The structure adopts the sandwich composite structure filled with high-flow and self-compacting concrete into the double-layer steel shell. The requirements for the tubes prefabrication quality and accuracy are strict. Then it needs some key technologies for the concreting construction of the super-wide tubes, such as the pouring process of self-compacting concrete, intelligent equipment development, deformation control, and so on. The construction organization design is mainly carried out around the conditions of prefabrication inside the dock. The final acceptance measurement data of the widest element tube shows the success of the prefabrication scheme. The experience summary is also drawn at the end.

Keywords: Shenzhen-Zhongshan Link, Immersed tunnel, Sandwich structure, Concreting

1 INTRODUCTION

Although the Hong Kong–Zhuhai–Macao Bridge has been successfully built and opened to traffic, with the sustained and rapid economic development of the Pearl River Estuary, traditional reinforced concrete immersed tunnels can no longer meet the demand for greater traffic flow and more lanes in the future. The Shenzhen–Zhongshan Link is located in the Lingding Sea area about 38 km upstream of the Hong Kong–Zhuhai–Macao Bridge. Its construction standard is the highway with two-way four lanes (eight lanes total) and the widest section even exceeds two-way five lanes (ten lanes total). It is the first large-scale application of steel-concrete-steel composite structure ("sandwich" structure) in tunnel engineering in China.

The sandwich structure immersed tunnels first appeared in Japan, which is a composite structure with hundreds of compartments composed of steel shell, partition, rib, and infilled concrete. With the development of high-flow self-compacting concrete technology and the shortage of land for dry dock, this structure has been developed in Japan. Several sandwich structure immersed tunnels have been built, including the Kobe Port Minatojima Tunnel (1999), the Naha Tunnel (2011), and the Shin–Wakato, Tunnel (2012). Their construction standards did not exceed two-way three lanes (six lanes total) and the longitudinal division did not exceed 10 elements. In terms of length, width, the number of elements, the amount of steel and concrete, and complex construction conditions, the construction scale and difficulties of the Shenzhen–Zhongshan Link have exceeded those of Japan.

The civil works of the Shenzhen–Zhongshan Link immersed tunnel are divided into two sections, and the Steel shell tube manufacturing works are divided into another two sections. Here we present some key technologies of the concreting construction of the widest element tube, which is connected to Shenzhen, such as the pouring process of self-compacting concrete, intelligent equipment development, deformation control,

*Corresponding author: zongxiansu@hkust-gz.edu.cn

DOI: 10.1201/9781003495505-326

and so on. The construction organization design is mainly carried out around the conditions of using a dock in the shipyard for prefabrication. The final acceptance measurement data of the widest element tube shows the success of the prefabrication.

2 PROJECT OVERVIEW

The Shenzhen–Zhongshan Link is a strategic crossing channel across the Pearl River estuary, integrating a super-wide underwater tunnel, super-long span bridges, deep water artificial islands, and underwater interchange. It is also another mega project in China after the Hong Kong–Zhuhai–Macao Bridge (Shown in Figure 1).

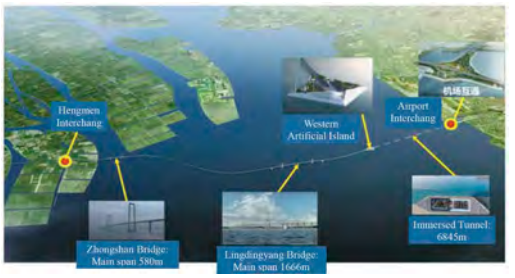

Figure 1. The Route of the Shenzhen–Zhongshan Link.

The immersed tunnel is 5035m long, which is divided into 32 elements longitudinally. The width of the standard tubes is 46m and the maximum width of the widest tube is over 55m. After scheme comparison, taking into account factors such as structural bearing capacity and dredge volume of the foundation trench, the element tube of the immersed tunnel adopts a sandwich composite structure filled with self-compacting concrete inside the double-layer steel shells.

The main dimensions of standard elements are 165m long, 46m wide and 10.6m high. E28 to E32 are in curve elements with ultra-width from 46 to 55.467m and shorter length of 123.8m. Figure 2 shows the cross-section of the element tubes. Each standard element tube consists of 2255 compartments filled in over 29000 m^3 of self-compacting concrete. The non-standard one in curve consists of approximately between 1700 to 2000 compartments filled in over 22500 m^3 of self-compacting concrete. Figure 3 shows the steel shell structure with compartments. The compartments are relatively isolated from each other.

Figure 2. Cross-section of the element tubes.

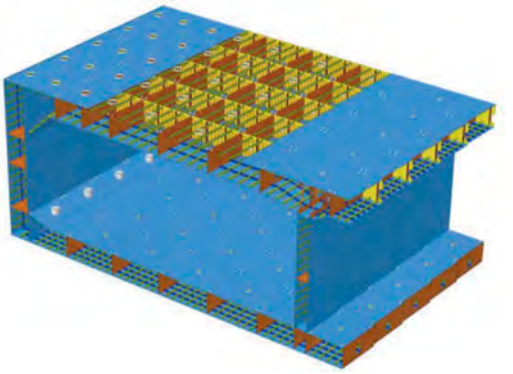

Figure 3. Steel shell structure with compartments.

The closure joint of the immersed tunnel is located between E23 and E24. Then the construction of the immersed tunnel is divided into two contract sections for implementation after the steel shell manufacturing, including concreting, floating, immersion and installation of the elements. The S08 Contract Section is responsible for the implementation of 9 elements from E32 to E24. The steel shell manufacturing is also divided into two contract sections, which are located in the shipyards on Longxue Island in the northwest of the tunnel site with about 21 km floating voyage. Then the S08 contract section rented a portion of the shipyard's dock space for concreting and primary outfitting. The first implemented element of the S08 contract section is the widest element E32, which is connected to the eastern artificial island at the Shenzhen end. It is the most difficult and typical non-standard element tube.

3 CONCRETING SCHEME

3.1 *Construction site*

The element tube prefabrication area is set up in the shipyard's dock, which simultaneously accommodates the overall assembly of steel shells, concreting, and the original shipbuilding work. The steel shell assembly and concreting station of element E32 is arranged in the dock on the northwest side. The information control center, the concrete quality testing area, the concreting equipment layout area, and the outfitting material storage yard are equipped near the dock shore. The route of the concrete transportation is about 1.2km long and the running speed of the concrete delivery trucks should be controlled within 20km/h inside the shipyard. It takes about 5 minutes for the new concrete to reach the quality control room for tests and it takes about 8 minutes for the verified concrete from the quality testing area to the farthest discharge port.

3.2 *Concreting process*

In the dry environment inside the dock, the concreting is carried out after the completion of the steel shell assembly, with a general order of bottom slab, wall and roof.

The bottom slab concreting adopts the process of "Bailey channel + concrete delivery truck + funnel conduit + intelligent pouring vehicle", as shown in Figure 4. The concrete delivery truck travels from the dock shore onto the Bailey channel and stops at the discharge through-hole opened through the channel and the roof of the tube, then the concrete is discharged through the funnel conduit into the hopper of the pouring vehicles inside the element tube. The vehicle adopts a gantry structure and a big pouring hopper. The vehicle moves longitudinally through the rails laid inside the shell tube, and the hopper moves laterally on the main girder of the gantry.

Four sets of pouring vehicles are equipped, which means four pouring points are arranged for the bottom slab concreting. The vehicles can achieve certain intelligent functions such as precise automatic positioning of pouring holes, keeping constant pouring speed, automatic switching of pouring speed, and automatic starting and stopping.

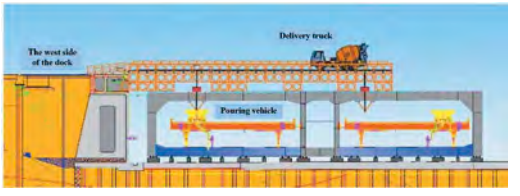

Figure 4. Cross section of the tube with bottom slab concreting.

The concrete pouring of the wall and the roof is located on the top of the element tube, with a relatively open space. Then the flexible folding arm distributors are available and the process of "Concrete trailer pump + concrete distributor" is adopted, as shown in Figure 5. The pumps are placed on the dock shore, and the connecting pipes and the distributors are laid on the top surface of the tube.

Four pouring points are also arranged for the wall and the roof concreting, but six distributors are equipped to reduce the frequency of moving and for emergencies.

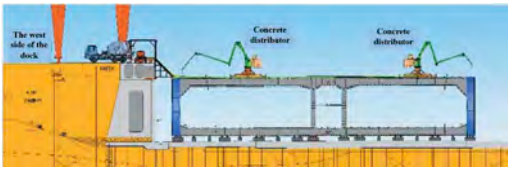

Figure 5. Cross section of the tube with wall and roof concreting.

3.3 *Main control parameters*

Due to the structural characteristics of the steel shell compartments, it is necessary to apply a large amount of high-flow self-compacting concrete without vibration. It is required to have good flowability, filling ability, cohesiveness, passing capacity through gaps, and anti-segregation. After the experimental research of self-compacting concrete in the early stage of the project, the main required performance control indexes of self-compacting concrete are shown in Table 1.

Table 1. Performance control indexes of self-compacting concrete.

Performance	Parameters	Requirements
Filling ability	Slump flow /mm	600~720
	T_{500} expending time /s	2~5
Passing capacity through gaps and anti-segregation	V-shaped funnel passage time /s	5~15
	L-type testing instrument / (H_2/H_1)	≥0.8
Others	Density /(kg/m^3)	2300~2400
	Gas content /%	≤4
	Temperature /℃	≤30, output; ≤32, into the compartment

To ensure that the working performance of self-compacting concrete can be relatively stable within the requirements, it is required that the single truck concrete must be strictly controlled within 90 minutes from discharge of the mixer to finish up. Meanwhile, the pouring inside a single compartment must be strictly controlled within 90 minutes from the start to the completion. Due to the volume of a single compartment (the standard one is approximately 15.75m^3) is greater than the loading capacity of the concrete delivery truck (9m^3), then the compartments that cannot be continuously poured inside must also be completed within the specified time. This requires high synergy and continuity through the production, transportation, and pouring.

After preliminary steel shell compartment model tests and the transverse full-scale model tests, the main control parameters for the concrete pouring into the compartment have been determined:

1) The lower space of the compartment with a thickness of 130cm is poured at a speed of 30m^3/h, while the remaining upper space with a thickness of 20cm is poured at a speed of not more than 15m^3/h.
2) When pouring into the compartment, the distance between the nozzle of the pouring conduit and the concrete upper surface should not be greater than 1m at the beginning, and later it remains not more than 0.5m until the pouring of the compartment is fulfilled.

3) The pouring of the compartment is judged to be completed based on not less than a 30cm rise of the concrete level in the exhaust pipes.

These parameters can be automatically controlled by the intelligent concreting equipment and the intelligent management system.

4 INTELLIGENT CONCRETING EQUIPMENT

4.1 *Variable span pouring vehicles*

As E28 to E32 are in curve elements with variable width, in order to meet the construction requirements of the bottom slab concreting, variable span pouring vehicles have been developed, as shown in Figure 6. The main structure adopts a gantry type and the length of the main girder can be adjusted in four levels. The distance between support legs can be adjusted between 8.45~15.58m, which can make the rail suitable for non-standard element tubes. The pouring hopper can run on the outer side of the support legs, with the main girder in a cantilever-bearing state.

Figure 6. Variable span pouring vehicle.

The vehicle is mainly composed of a main girder structure, an entire structure longitudinal traveling mechanism, a trolley transverse traveling mechanism, a hopper with its weighing system, a pouring speed control module, a discharge control mechanism, and an electrical control system. Its key technologies are the automatic intelligent positioning of the pouring port and automatic speed regulation.

(1) Before concreting the tube, the relative positions of each compartment and the pouring port can be input into the industrial control computer system for storage. When receiving a working instruction for a certain compartment, the PLC(Programmable Logic Controller) drives the vehicle's longitudinal and transverse traveling system (motors and traveling wheels) to travel a specified distance. Then the hopper on the vehicle automatically moves above the designated compartment to achieve coarse positioning. Currently, the deviation between the center of the pouring conduit nozzle and the center of the pouring port of the compartment is within ± 30mm in plane. Subsequently, the intelligent analysis camera, intelligent analysis video server, and intelligent algorithm DSP(Digital Signal Processing) are utilized to achieve recognition. The server calculates the accurate deviation between the two centers and then sends instructions to the PLC for precise positioning. Then the deviation can be achieved within ± 10mm in plane.

(2) The pouring speed control mechanism mainly consists of a concrete storage hopper with a weighing function, an electric control sluice valve, a concrete upper surface level measuring instrument (installed above the exhaust pipes at the compartment corners) and a PLC control system. The measurement of the concrete upper surface level adopts several laser rangefinders, which is an integrated application of various technologies such as laser, electronic, microcontroller control, signal control and processing, precision mechanical, and so on. Since the pouring operation is started, the pouring conduit under the hopper is controlled by PLC to maintain the required distance from the concrete upper surface. The initial speed is set at $30m^3/h$ until the concrete upper surface in the compartment reaches a height of 1.3m(0.2m left). The subsequent pouring speed is reduced to no more than $15m^3/h$. The pouring speed is controlled by the openness of the sluice valve and adjusted based on the reduction of concrete weight inside the hopper and the rising speed of the concrete upper surface inside the compartment.

4.2 *Concrete distributors and delivery pumps*

For the concreting of walls and roofs, the pumping process has higher convenience and efficiency. The distributors are customized based on the size and concreting characteristics of the tubes. The arm frame of the distributor has three arm rods and a total length of 17m, with a maximum pouring range of 16.5m radius. Due to its connection with the metal pump pipe fixed on the top surface of the tube, it cannot move autonomously during the pouring process.

Automatic control of concrete pouring speed is still required. The concrete delivery pumps are upgradable with PLC. The pump speed can be adjusted according to the needs of the pouring speed. The control module inside the machine can receive wireless command signals and adjust the pumping frequency. The rise of the upper surface of the concrete inside the compartment is still monitored by laser rangefinders. The monitoring information will be wirelessly sent to the intelligent management system that integrates various functional modules. After independent analysis, the pouring speed adjustment command is automatically issued to the control module installed inside the machine.

5 INTELLIGENT MANAGEMENT SYSTEM

During the concreting of the element tubes, a series of data, such as concrete production, delivery trucks, concrete performance index, timing, and monitoring information, etc. will be generated. To automatically process these massive data and achieve efficient,

refined, and standardized management of the concreting process, an intelligent management system has been developed. It covers raw material inventory management, concrete production management, concrete index detection, guidance for concrete delivery trucks, intelligent pouring, video monitoring and other processes. It combines BIM, IoT, and intelligent sensing technology to control various terminal equipment, such as the pouring vehicles and pumps, to complete the intelligent concreting task of the element tubes. The map of the construction plant and virtual construction information models of each tube with each compartment are constructed in the management system.

Based on real-time monitoring data, decisions and actions are made and executed in the varying external environments (not traditionally operated automatically according to fixed programs), in order to meet the on-site concreting requirements of the compartments, including the concrete delivery, pouring speed control, automatic extension and contraction of the pouring conduits, automatic stopping of pouring, automatic positioning and so on. At the same time, integrated management of various data can be conducted. Figure 7 shows the interface of the intelligent management system on the central control screen. The lower half of the middle part is the real-time pouring information of the four pouring points, including the current pouring speed, the position of the upper surface of the concrete inside the compartment, and the current real-time status of each compartment of the entire steel tube (poured, in pouring, and not poured). The upper half of the middle part is mainly the real-time concrete delivery truck information, including the current location along the route and the consumed time for the new concrete. The intelligent management system can also guide the delivery trucks to different unloading points based on the concrete allowance at four pouring points.

The intelligent management system adopts an advanced multi-layer technology architecture, which integrates multiple technologies such as C/S (Client/Server) architecture, B/S (Browser/Server) architecture, App, and microservices. The C/S architecture is mainly used for connecting with laser ranging sensors, pouring equipment, radio frequency identification sensor equipment, etc. The B/S architecture is mainly used for system applications and all supporting modules. Apps are mainly applied to iPad monitoring operations at pouring sites, vehicle positioning mobile terminals, and quality detection module mobile terminals. Microservices are used for coupling services between various modules in the system. Establish such an intelligent pouring management system to accurately and efficiently control the equipment and to conduct real-time linkage with concrete mixing stations and delivery vehicles to achieve intelligent production control and dynamic allocation of material transportation. Specifically, the following functions have been developed and integrated into the intelligent management system:

(1) Develop an intelligent pouring system to achieve multi-point collection of the rising height of the concrete upper surface in the compartment and to control the pouring speed based on the height and rising speed, which can drive the developed equipment and can be visually displayed on mobile devices.
(2) Develop vehicle positioning and onboard equipment to collect real-time locations of delivery trucks, visualized on the central control screen, and to receive delivery information, providing guidance to drivers from mobile terminals.
(3) Develop a pouring data management platform that integrates on-site data for real-time analysis and provides early warning prompts.
(4) Established a BIM for the element tubes, utilizing BIM technology to dynamically and vividly display pouring progress and management construction data.

Figure 7. The interface of the intelligent management system on the central control screen.

6 DEFORMATION CONTROL DURING CONCRETING

6.1 *Requirements for prefabrication accuracy of tubes*

The prefabrication of the tubes is divided into two stages: steel shell manufacturing and concrete casting. The concreting of the compartments shall be carried out after the steel shell is inspected and accepted. Before undocking, primary outfitting work shall be also completed, mainly including the installation of ballast water tanks, pipelines and bulkheads.

Table 2 shows the requirements for the inspection and evaluation indicators of the two stages. It can be seen that for the super large tubes with lengths of 123.8~165m and a maximum width of 55m, when the deviation of the steel shell manufacturing is within the allowable limit at the measuring points, the allowable deviation of the subsequent concreting shall reach the millimeter level. In extreme cases, the reduction of the net height of the inner hole shall be controlled within 10mm.

In the past, the concreting sequence of the steel shell in Japan mainly considered the concrete casting afloat. As a single hole contains only two lanes, its cross-sectional deformation is so small that the deformation control is not a constraint factor for design and construction. The simplified longitudinal variable section beam model was used for numerical analysis in the Naha port immersed tunnel project by Kimura, et al. in Japan. The method is to divide longitudinal elements of the tube as a beam and to convert the cross-sections of different casting states into different section moment of inertia (EI) and different load conditions, which are assigned to different positions of the beam body. It mainly solves the problem of overall deflection and longitudinal deformation caused by the floating casting. Muramoto established a 3D finite element tube model for analysis and compared the results with those of the simplified longitudinal variable section beam model, but he did not simulate the stiffeners inside the compartment of the shell.

6.2 *Finite element simulation analysis*

As the first non-standard tube E32 weighs about 68000t (including outfitting) and the standard tube weighs about 78000t after concreting, which exceeded the historical record of shipbuilding weight in the dock of Huangpu Wenchong Shipyard, it is necessary to calculate the bearing capacity of the bottom foundation. At the same time, the foundation deformation will also affect the deformation of the tubes. The finite element model of the tube needs to be provided with the foundation stiffness parameters by the foundation bearing capacity calculation. Therefore, the tube structure analysis and foundation-bearing capacity calculation shall be systematically organized.

As the cross-section of the widest tube is adopted in calculation with 2D FEM in the early design stage, the concreting sequence and spatial mechanical effect are not taken into account. The downward deflection of the roof after concreting is quite large (about 28mm), so for reliability, the original construction drawing design requires the setting of temporary support rods inside the lane hole during the concreting of the roof. In order to further exploit the spatial mechanical effects of the structure and make a good choice of the concreting sequence, 3D FEM is used to create a detailed model of the steel shell-concrete composite structure of the tubes during the construction scheme preparation stage. Shell elements are used to simulate the steel shell, solid elements are used to simulate the concrete, and spring elements are used to simulate the bottom supports. For the first non-standard tube E32, both a full structure model considering the curve widening and an equal-width structure model based on the widest cross-section are established for parallel calculation. Besides, the stiffening ribs inside the compartments can be simulated by beam elements. Figure 8 shows one of the Vertical displacement results.

The concreting process is simulated by the "live-dead element" method. Experiments of compressive strength and elastic modulus of concrete at an early age conducted by Yang W. J. showed that the

Table 2. Quality inspection and evaluation standard for geometric dimensions of prefabrication of element tubes.

Sequence number	Inspection items	Allowable deviation after steel shell manufacturing /mm	Allowable deviation after concreting /mm	Allowable deviation of concreting after steel shell manufacturing in extreme cases /mm
1	Width of tubes	-10, +25	-10, +30	0, +5
2	Height of tubes	-5, +20	-10, +20	-5, 0
3	Length of tubes	±(10+(L-20)/10)	±(15+(L-20)/10)	±5
4	Net width of the lane holes	-5, +15	-5, +20	0, +5
5	Net height of inner holes	-5, +20	-15, +20	-10, 0
6	Longitudinal deflection of tubes	-	±10	±10

Note: L is for Length, value in units of m.

measured elastic modulus of C50 concrete can reach 66.2% in 3 days and 88.2% in 7 days; the elastic modulus of C60 concrete can reach 70.4% in 3 days and 89.1% in 7 days. The measured strength of C50 concrete prepared in this project is close to that of C60 concrete, so in the calculation process, it is simplified to consider that the elastic modulus of the third day is 70%, and that of the fourth day and later is 90%. For the simulation of concreting in each batch, the concrete solid elements on the first day are "killed to dead", the density and elastic modulus of the concrete are not involved in the calculation, then the concrete gravity loads are directly applied to the steel plates at the bottom of the compartments; on the second day, the solid elements are "activated to alive", and the elastic modulus is approximately set to 40%, the concrete gravity loads applied on the steel plates are removed and then replaced by the concrete density of the solid elements; on the third day and the fourth day and later, the elastic modulus of solid elements are set to 70% and 90% respectively.

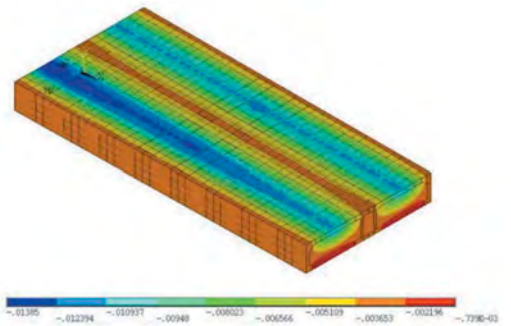

Figure 8. Vertical displacement of E32 /m.

6.3 *Concreting sequence*

As the tubes are concreting inside the dock, it is necessary to complete the concrete filling of the bottom slab as quickly as possible to form a stiffness to facilitate the bearing capacity and reduce the deformation. The overall concreting sequence in the cross-section of the tube is bottom slab → wall → roof. According to the principles of making stress even, reducing load concentration and spacing the adjacent areas of concrete not less than two batches, several trial schemes of concreting sequences are calculated, mainly as follows (without temporary support rods). The sketch maps are shown in Figure 9~11.

(1) Scheme 1: bottom slab concreting sequence① + wall concreting sequence① + roof slab concreting sequence①;
(2) Scheme 2: bottom slab concreting sequence① + wall concreting sequence② + roof slab concreting sequence②;
(3) Scheme 3: bottom slab concreting sequence② + wall concreting sequence① + roof slab concreting sequence①.

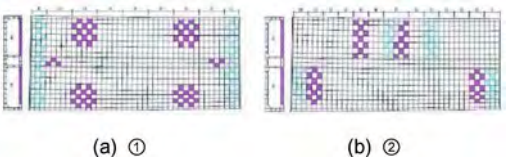

Figure 9. Sketch concreting sequence of the bottom slab.

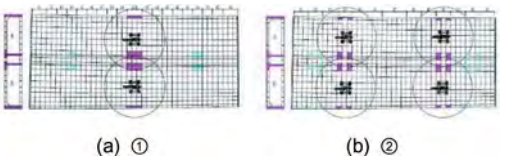

Figure 10. Sketch concreting sequence of the wall.

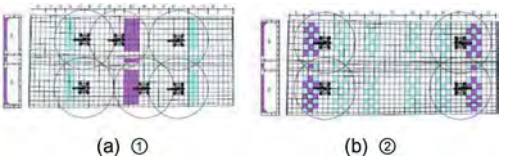

Figure 11. Sketch concreting sequence of the roof.

Preliminary analysis shows that the change of clearance inside the steel shell tube (vertical deformation) during the concrete casting is mainly caused by the self-weight of structural materials, The change of tube in length and width (horizontal deformation) may be mainly caused by temperature effect. Among the acceptance indicators of dimensional accuracy of the tube prefabrication, the control of inner clearance is the most difficult to achieve. In addition, the construction design requires adding temporary support rods inside the tube, which directly affects the construction process and the prefabrication schedule.

In addition, considering that most of the hydration heat of concrete is released in the first 3 days, the concreting batches within 3 days should be spaced out a certain distance, then the influence of hydration heat on deformation is mainly in the local scope. After the temperature drops, most of the temperature deformation can be recovered, which has a limited impact on the overall structure. Therefore, the selection of concreting sequence is mainly based on the calculation of deformation caused by the dead weight of structural materials. During the construction, the concreting has avoided the high-temperature period on summer days (concreting at night). Thus, the temperature effect analysis is taken as the check.

Three back-to-back parallel computations have been organized, adopting the equal-width tube model with the widest dimension, the non-equal-width tube model with actual dimensions, and the equal-width tube model considering the temperature effect during the construction process. The comparison of calculation results for the four listed concreting sequence schemes can be seen in Table 3. On the other hand, the calculation result of reduction in net

Table 3. Comparison of calculation results of concreting sequence schemes (E32).

Schemes	Reduction in net height of inner hole /mm			Times to move the distributors		Times to move the distributors	Estimated duration of concreting /d	Notes
	Calculation 1	Calculation 2	Calculation 3					
1	9.1	9.1	9.21	Wall Roof	30 14	44	20+16 +18=54	Concreting in the jumping area with the transverse strips on the roof.
2	9.2	9.2	9.08	Wall Roof	40 28	68	20+17 +21=58	Concreting in jumping chessboard like on the roof.
3	9.5	9.2	9.56	Wall Roof	30 14	44	18+16 +18=52	Implement asymmetric concreting of the bottom slab based on Scheme 1.

Note: Calculation 1 adopts an equal-width tube model; Calculation 2 adopts a non-equal-width tube model with actual dimensions; Calculation 3 adopts an equal-width tube model with temperature effects considered.

height with temporary support rods is about 7.5mm, but it will cause a delay of one month in outfitting operation inside the dock. Then the concreting sequence scheme 1 is adopted.

7 ACCEPTANCE MEASUREMENT RESULTS AFTER CONCRETING

7.1 *Concreting quality inspection*

After the prefabrication of the steel shell concrete immersed tube is completed, its concreting quality is tested using a combination of impact imaging method for full inspection and neutron method for partial re-inspection. The effectiveness of these two void detection methods has been verified in the previous full-scale model concreting process test. The inspection works are carried out by third-party units entrusted by the owner of Shenzhen-Zhongshan Link. Table 4 shows the statistical results of the void detection for element tubes E32 and E31. It shows that the concreting quality is good and meets the inspection and evaluation standards (including all subsequent tubes). For suspected void areas, there is no need for grouting reinforcement after retesting using the neutron method. The adoption of this concreting process and the introduction of intelligent pouring control can effectively eliminate the adverse effects of human non-standard or inconsistent operations on concreting quality, and reduce the risk of voids which need reinforcement.

7.2 *Geometric dimensions inspection*

Before concreting of the E32 tube, 15 profiles were selected within the steel shell tube (with 3 pairs of inner net height monitoring points set for each lane hole) for acceptance measurement. The maximum and minimum inner net height measurement values were compared with the design values, which were within the allowable deviation range. After concreting, acceptance measurements were carried out again on the 15 profiles, and the maximum variation measured in the net height of the inner hole was -10mm. (The accuracy of the laser rangefinder used is 1mm.) It appeared at the widest end, matching the calculation result. The final qualification rate in length, width, and height is 100%. In addition, the deformation in longitudinal length after concreting is basically within ± 3mm. Under the constraints of the dock bottom supports, the deformation of the tube caused by the temperature effect of concrete hydration heat is mainly reflected in the horizontal direction, with little impact on the final deformation of the overall structure. Table 5 shows the geometric dimensions inspection qualification rates of E32 and E31 after concreting. All the inspection qualification rates are greater than 95% (including all subsequent tubes), meeting the acceptance standard requirements.

8 REMARKS AND CONCLUSIONS

The immersed tunnel tubes E32 to E24 of Shenzhen-Zhongshan Link have been successfully prefabricated with concreting in the dock, especially tube E32, the widest and the first one. Both the deformation control and the concrete filling quality have passed the acceptance with excellent inspection data.

To reduce labor and improve construction efficiency, a self-compacting concreting technology is developed for the steel shell of immersed tunnel element tubes according to the environmental construction conditions. Intelligent concrete pouring vehicles and folding arm distributors have been developed. The information and automation technologies with BIM, IoT and intelligent sensing have been employed, which can effectively reduce the quality risk and mechanical injury caused by human error during the concreting process.

Data statistical analysis shows that through the intelligent self-compacting concreting process, the daily average concreting volume is about 800m^3. The main limiting factor for its efficiency is the impact of

Table 4. Statistics of void detection results of the steel-shell concrete interface of the element tubes (partial).

Element tube number	Bottom slab			Wall			Roof			Ratio of total suspected void area /%
	Number of compartments	Number of suspected void areas	Ratio of suspected void areas/%	Number of compartments	Number of suspected void areas	Ratio of suspected void areas/%	Number of compartments	Number of suspected void areas	Ratio of suspected void areas/%	
E32	697	53	0.0416	205	24	0.0564	533	49	0.0403	0.0431
E31	656	41	0.0289	205	9	0.0214	492	47	0.0403	0.0322

Table 5. Geometric dimensions qualification rates of E32 and E31 after concreting (partial).

Element tube number	Width	Height	Length	Net width of the lane holes	Net height of inner holes	Longitudinal deflection
E32	100%	100%	100%	100%	100%	100%
E31	100%	100%	100%	96.7%	97.8%	100%

daytime temperature during summer on the working performance of concrete. The concreting process and intelligent management system can operate continuously for 24 hours.

By refining 3D FEM numerical analysis and optimizing the concreting sequence, the net height deformation inside the element tubes was controlled within 10mm, and the temporary support rods inside the lane hole were successfully canceled, enabling the initial outfitting operation inside the tube to be started about one month earlier, which can be parallel to the wall and roof concreting.

REFERENCES

Chen Y., Chen W. L., Song S. Y., et al, 2020. Key Construction technologies for immersed tunnel of Shenzhen-Zhongshan Link. Tunnel Construction, 40(4), 603–610.

Jingjun Y., Yoshida H., Yujing A., et al, 2006. Development and construction of filling concrete in Shinwakado tunnel. Proceedings of Civil Engineering. Japan Society of Civil Engineers, Tokyo, Japan, pp. 7.

Kimura H., Kojima I., Moritaka H., 2022. The study on deformation of immersed tunnel element during production works while afloat. Journal of Tunnel Engineering Report, 12, 117–124.

Matsuishi M., Iwata S., 1988. Study on strength of sandwich composite structure composed of steel plate and concrete (Fourth Report). Journal of the Japan shipbuilding Society, 164, 395–405.

Muramoto T., 2001. Deformation analysis of composite type immersed tunnel during self-compacting concrete casting at floating. Journal of coastal center, 1, 73–76.

Shoji T., Yasutoshi L., Tetsurou A., 2003. Application of high fluidity concrete to marine caisson. Concrete Engineering, 41(7), 60.

Song S. Y., Nie J. G., Xu G. P., et al, 2019. Development and application of steel-concrete-steel composite structure in immersed tunnels. China Civil Engineering Journal, 52(4), 109–120.

Su Z. X., Tan L. X., Song S. Y., et al, 2022. Casting deformation control of super-wide steel-concrete immersed tunnel tubes of Shenzhen-Zhongshan Link. China J. Highw. Transp., 35(10), 36–46.

Wei D. J., Chen W. L., Wu X. D., et al, 2022. Development and application of the intelligent concrete pouring trolley in immersed tube with steel shell of the Shenzhen-Zhongshan Link project. Highway, 67(1), 235–240.

Wei X. C., Liu Y. F., Song S. Y., Fan J. S., et al, 2022. Overall deformation of steel-concrete-steel immersed structures during construction stage considering temperature effect. Structures (Oxford), 46, 1055–1066.

Wu X. D., Xi J. J., Liu H., et al, 2022. Intelligent casting technology of self-compacting concrete for steel-shells of Shenzhen-Zhongshan link immersed tunnel tubes. Tunnel Construction, 42(2), 328–335.

Xu G. P., Huang Q. F., 2018. General design of Shenzhen-Zhongshan River-crossing Link project. Tunnel Construction, 38(4), 109–121.

Yang W. J., Wang Y., 2007. A diachronic variation model of compressive strength and elastic modulus of concrete at early age. Journal of China & Foreign Highway, 27(6), 149–152.

Tunnelling for a Better Life – Yan, Celestino, Thewes & Eberhardt (Eds)
© 2024 The Author(s), ISBN 978-1-032-80042-4
Open Access: www.taylorfrancis.com, CC BY-NC-ND 4.0 license

Experimental study on the typhoon resistance by placing Shenzhen-Zhongshan Link immersed tunnel element on the seabed

Shi-peng Sun
Guangzhou Salvage, Guangdong Engineering Technology Research Center of Ocean Engineering and Water Emergency Rescue, Guangzhou, China

Qun-an Ou Yang
Tianjin Research Institute for Water Transport Engineering, National Engineering Research Center for Port Hydraulic Construction Technology, Key Laboratory of Engineering Sediment, Ministry of Transport, Tianjin, China

Wang-hui Li & Jia-jie Ma
Guangzhou Salvage, Guangdong Engineering Technology Research Center of Ocean Engineering and Water Emergency Rescue, Guangzhou, China

ABSTRACT: It is the first time in the world that the immersed tunnel elements of Shenzhen-Zhongshan Link (hereinafter referred to as the "Shen-Zhong Link") is placed on the seabed and resists against typhoon in the semi-open sea area on a large scale. In order to ensure the safety of the immersed tunnel element when stored on the seabed, an experimental study was carried out. Accurate evaluation of the safety and stability of the tunnel element during typhoon period can provide a strong scientific basis for the design of gravel foundation, submerged tunnel load and cable selection. This paper takes different immersed tunnel elements of Shen-Zhong Link as the research objects based on the given undersea deposit layout scheme and dynamic characteristics of the engineering water area. Through qualitative analysis, the most unfavorable wave direction to the stability of immersed tunnel elements against typhoon is determined and then a physical model test of the wave forces of different directions under different conditions of water level, wave height and foundation laying rate was carried out. According to the measured wave forces, given friction coefficient and negative buoyancy, the anti-typhoon stability of the immersed tunnel elements was evaluated.

Keywords: Immersed tunnel elements, Undersea deposit, Typhoon resistance, Foundation laying, Shen-Zhong Link

1 INTRODUCTION

With the accomplishment of the 21st century Hong Kong-Zhuhai-Macao Bridge project, the construction projects of domestic immersed tunnels have been increasing rapidly. There are nearly 20 immersed tunnels under construction or proposed, among which are mainly inland immersed tunnels. According to statistical data[3], the immersed tunnels which have already completed mostly adopts the form of axis dry dock or independent dry dock for batch prefabrication. After the completion of the docking, a series of processes such as tunnel elements floating transportation, mooring, and installation are carried out. Therefore, immersed tunnel production has become a key step of the project construction. Shen-Zhong Link is the first project in China to customize the production of immersed tunnel elements by the form of "prefabricated factory + shipyard". During the construction process, the foundation groove of the tunnel on Shenzhen side was affected by force majeure, resulting in that the first element E32 could not be installed immediately after the prefabrication. In order to make sure that 4 elements of tunnel have been prefabricated before the E32 is settled so that the prefabrication does not occupy the key line, the tunnel element needs to be stored underwater for up to one year in the semi-open sea area of Longxue Harbor, which requires that the safety of the tunnel element at the bottom must meet the working condition of a typhoon once in 50 years.

DOI: 10.1201/9781003495505-327

Due to its large size and water depth limitation in the storage area, the water depth of the tunnel top after sitting on the bottom is small and the force area is large, meaning that the force state during the bottom sitting and typhoon resisting is very complicated. The influences of multiple factors such as ballast, waves, water level, geological conditions etc. should be fully considered. The bulkhead door may be damaged by long-term wave force impact. The tunnel may be affected by the uneven silt substrate in the bottom area, causing large settlement, uneven settlement, and serious deformation. Meanwhile, if the ballast capacity is not enough and the negative buoyancy is insufficient, it would leads to slippage of the tunnel element. In addition, a large amount of silt and the long time storage of the tunnel may lead to a series of problems such as excessive bottom suction and the inability of the tunnel to float smoothly. In-depth analysis of the force on the tunnel element is required through physical model tests or numerical simulations. Based on actual engineering, domestic scholars have carried out a series of force analysis and tests of large-scale structures sitting underwater. Wang Baoxing et al.[4] carried out the research on the "XIWANG" super-large tanker bottom sitting scheme, and conducted a comprehensive analysis on the various factors, calculation methods and hull structure reinforcement methods considered in the new topic of using the method of large ships sitting on the bottom to build offshore isolated building. Under different negative buoyancy conditions and the settlement of crushed stone bed, Shang Qiankun et al.[5] carried out experimental studies on the friction coefficient of reinforced concrete immersed tunnel element model and crushed stone bed. Lin Wei et al.[6] analyzed the sensitivity of friction coefficient to the crushed stone particle size, pressure, direction, area etc. through the pulling, correction operations and movement of adjacent tunnel elements during the tunnel jointing process, combining with the data during tunnel elements pulling operation of the Hong Kong-Zhuhai-Macao Bridge. Through theoretical analysis and experimental methods of different models, Gao Zhanfeng et al.[7] proposed a method to estimate the substrate suction force that different shapes of structures submerged on the seabed need to overcome when leaving the bottom. Shu Ning et al.[8] gave the friction coefficients between the bottom surface of different steel structures and the crushed stone foundation bed through experimental methods.

Although the research results above certainly have guiding significance for the development of similar projects, it is the first time in the world that such a large-scale tunnel element is placed on the seabed in semi-open water area. The immersed tunnel element needs to face the test of the stability by waves in typhoon weather for a long time. In order to ensure the safety of the tunnel element, it is necessary to comprehensively consider the influences of combined factors such as the basic processing of the element, the negative buoyancy control, the strength and direction of the waves, and the terrain around the harbor.

In this paper, the element stored in Longxue habor is taken as the research object. The horizontal wave force and lifting force encountered by the tunnel element under the condition of typhoon once in 50 years are studied, and the friction coefficient is set to be 0.4. At the same time, in order to reduce the cost and increase the foundation groove silt accommodation capacity under the premise that the stability meets the requirements, the stability of the tunnel element under the conditions of different foundation laying rate is also compared and analyzed.

2 PROJECT OVERVIEW

The Shen-Zhong link is a major infrastructure project in China, with unprecedented scale, complex construction conditions and complicated technologies. It is a world class super large tunnel-island-bridge cluster project spanning the Pearl River estuary after the Hong Kong-Zhuhai-Macao Bridge. The total length of the main project is about 24km, with the technical standard of two-way eight-lane is adopted and the designed speed of 100km/h. The overall layout of the project is shown in Figure 1.

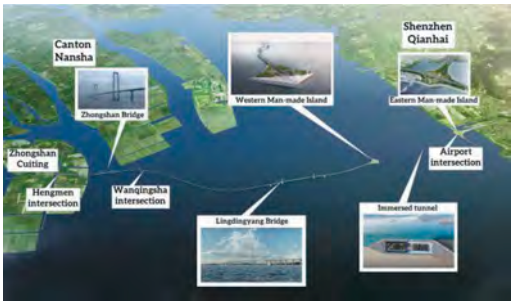

Figure 1. General layout of Shen-Zhong Link.

Figure 2. Top view of the storage area.

The immersed tunnel project of Shen-Zhong link is 6845m long, of which the immersed tunnel is 5035m long, consisting of 26 standard tunnel elements, 6 non-standard tunnel elements and 1 final joint. The tunnel is a combined steel shell-concrete structure type and has a shape of cuboid. The immersed

tunnel element was poured at the site of the Longxue Shipbuilding Base of CSSC. After being assembled in the dock, the tunnel continues to complete the whole-land-wide pour (dry dock pour) in the dock and then is transported out of the dock. Mooring, typhoon resisting and subsequent outfitting operations are carried out in the harbor of Longxue shipbuilding base, beside of the berm pier of Huangpu shipbuilding factory. The harbor has a dredging area of 670m (East-West)×608m (South-North). The top elevation of the bottom sitting area the elevation of the waters bottom where the immersed tunnel gyrate and float are both -12.5m (with the elevation standard of 1985 and the same below).

The layout and bottom sitting storage scheme of the tunnel element which needed a stability appraisal is shown in Figure 3. When the tunnel element sits on the bottom, besides the role of providing uniform support, the foundation could also decrease the suction force between silt and the tunnel bottom. After the berth excavation, the gravel bed with thickness of 1m is needed. When sitting on the bottom, the freeboard of tunnel element can be gradually eliminated by ballasting the tunnel inside the tunnel and then the tunnel could be slowly located on the gravel bed. Continue to increase the ballast to make sure that the negative buoyancy and friction between the tunnel and gravel bed are able to stand the wave force caused by typhoon. Then wait for proper window period to float, moor and carry out secondary outfitting operation. The gravel bed is designed to be 5m shorter than the tunnel in the front and rear each, and 5m wider than the tunnel in the left and right each. In order to hold silt, the form of ridge, which is 1.8m wide, and ridge top, which is 0.3m wide, is applied. Single gravel cushion is shown in Figure 4.

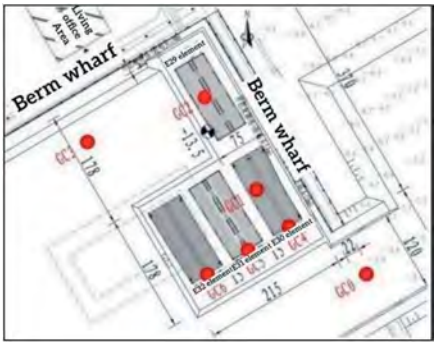

Figure 3. Layout of tunnel and wave data detecting point in the harbor.

3 MODEL DESIGN AND TEST CONDITIONS

3.1 *Experimental conditions*

The layout of wave data detecting point is shown in Figure 3. The experiment would not consider the effect of water flow as the wave speed in the harbor is relatively low. The water level in the harbor is shown in Table 1.

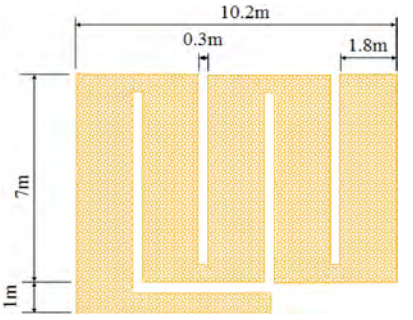

Figure 4. Single gravel cushion.

Table 1. Water level in the harbor.

Object	Elevation(m)
Average water level	0.64
Designed high water mark	1.98
Designed low water mark	-0.73
Extremely high water mark	3.18
Extremely low water mark	-1.36

The average wind velocity at 10m elevation under typhoon is predetermined to be 35.9m/s (within 10 minutes) and 47.4m/s (within 3 seconds). Extremely high water mark of 3.18m, extremely low water mark of -1.36m and wave superposition working condition. once in 50 years are considered to be the combined condition.

3.2 *Parameters of the tunnel*

S08 segment consists of 4 standard and 5 non-standard elements. The standard element is 165m long, 46m wide and 10.6m high while the non-standard element is 123.8m long, 55.5m wide at the widest end and 10.6m high. The cross-section of the element is shown in Figure 5. After the tunnel submerges completely in the water, the maximum of negative buoyancy of standard tunnel element is 10222.8T when the concrete density of the main structure of the tunnel element is taken as the upper limit 2.35T/m3 and the buoyancy of tunnel element drainage is taken according to the lower limit of water severity, while the lower limit value is 7061.9T when the concrete density of the main structure of the tunnel element is taken as the lower limit 2.30T/m3 and the buoyancy of tunnel element drainage is taken according to the upper limit of water severity. While for non-standard tunnel elements, (take E32 as an example) the values are 8956.2T and 6650.5T.

Figure 5. The cross-section diagram of the element.

3.3 *Selection of unfavorable wave direction condition*

To meet the actual needs of the project and shorten the test cycle, it is necessary to test under the most unfavorable wave direction condition. According to the storage plan, the tunnel element is located in the northeast corner of the harbor. According to Figure 3, it can be seen that waves can only come through the northeast-facing gate of the harbor. Given a combined condition of water level and wave height, the wave direction determines the magnitude of the incoming wave energy and the area of the tunnel element directly facing the wave. Take the E wave direction as an example and the red zone is the area of direct action of waves, where forces are relatively large. While the wave force in the indirect action zone is mainly the result of wave diffraction and reflection and the force is relatively small, as shown in Figure 6. The four wave directions ENE~SE that have a large impact on the engineering waters were analyzed and the ESE direction was found out to be the most unfavorable wave direction, as shown in Figure 7. Based on previous calculation, at the entrance gate GC0, the magnitude relationship of the wave features around each direction is: ENE>E>ESE.

With different selections of wave directions, water levels, foundation laying rates etc., there are 30 test conditions in total. Considering that the effective wave height in the E direction that occur once in 50 years at extremely low water levels is very close to that in the ESE direction, there are actually only two wave heights at this water level. See Table 2 for details.

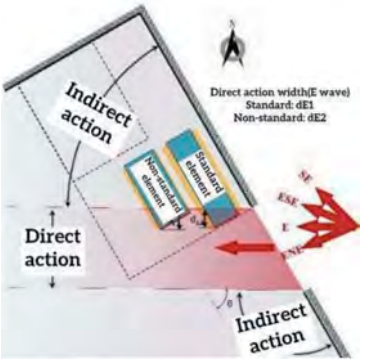

Figure 6. The affected harbor area under ENE~SE wave direction.

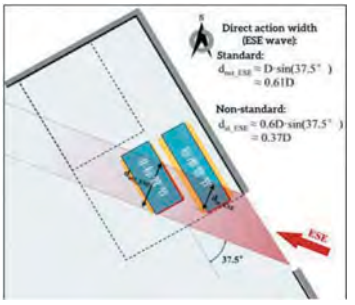

Figure 7. ESE wave vertical projection width.

3.4 *Similarity guidelines*

Given that the immersed tunnel element is a box-shaped blunt body, this test is a physical model test of the force of the structure under the action of wave dynamics. Complying with the "*Wave Model Test Procedure JTJ T234-2001*"[9], the normal physical test model was used. When the model and the prototype meet the similarity of Fu Rude, the similarity of the force on the tunnel element can be ensured. When the stability of the tunnel element meets the requirements under the action of external load, the tunnel element is fixed, and its force is similar to the force of fixed structure under wave conditions. Therefore, when carrying out the force simulation of the tunnel element, it is only necessary to ensure that the tunnel element strictly meets the geometric similarity, and there is no need to ensure that it strictly meets the weight similarity. The scales of each physical quantity are shown in Table 3:

3.5 *Model fabrication*

The model tunnel element is made of waterproof plywood. A reinforced frame is included to ensure sufficient stiffness to avoid significant bending deformation. The bottom foundation of the model is laid with a certain amount of crushed stone according to different working conditions of 50%, 75% and 100% laying rate. Supports for force measurement are installed in the corners. The simulation of the harbor and offshore terrain is completely based on geometric scales and make the terrain in the test pool. Modelling controlled elevation with the pile point method and the control point elevation error is less than ±2mm. The terrain of the model is filled with sand, plastered with cement mortar. See Figure 8.

Table 2. Conditions of test of tunnel element sitting bottom against typhoon.

Condition	Wave direction	Storage location	Tunnel element	Water level	Wave height	Stone foundation laying rate
1-1~3	ESE	Measuring point GC5 berth (The wide end faced the southeast side)	Non-Standard tunnel element E32	Extremely high water mark	2.37m (effective wave height in ENE direction once in 50 years)	50%/75%/100%
2-1~3					2.17m (effective wave height in E direction once in 50 years)	50%/75%/100%
3-1~3					2.00m (effective wave height in ESE direction once in 50 years)	50%/75%/100%
4-1~3					1.12m (effective wave height in ENE direction once in 50 years)	50%/75%/100%
5-1~3				Extremely low water mark	1.03m (effective wave height in ESE/E direction once in 50 years)	50%/75%/100%
6-1~3		Measuring point GC4 berth	Standard tunnel element		2.37m (effective wave height in ENE direction once in 50 years)	50%/75%/100%
7-1~3				Extremely high water mark	2.17m (effective wave height in E direction once in 50 years)	50%/75%/100%
8-1~3					2.00m (effective wave height in ESE direction once in 50 years)	50%/75%/100%
9-1~3					1.12m (effective wave height in ENE direction once in 50 years)	50%/75%/100%
10-1~3				Extremely low water mark	1.03m (effective wave height in ESE/E direction once in 50 years)	50%/75%/100%

Table 3. The scale of each physical quantity in model test.

Variable name	Symbol	Calculations	Scale
Length/Water depth/Wave height	λ	λ	40
Time/Period	λ_t	$\lambda^{1/2}$	6.32
Force	λ_F	λ^3	64000
Pressure	λ_p	λ	40

4 TEST RESULTS AND ANALYSIS

4.1 *Wave force*

4.1.1 *Vertical lift force*

The following reference coordinate system form is defined: The geometric center of the tunnel element is the coordinate origin, the longitudinal southeast direction of the tunnel element is the positive X-axis, the transverse northeast direction of the tunnel

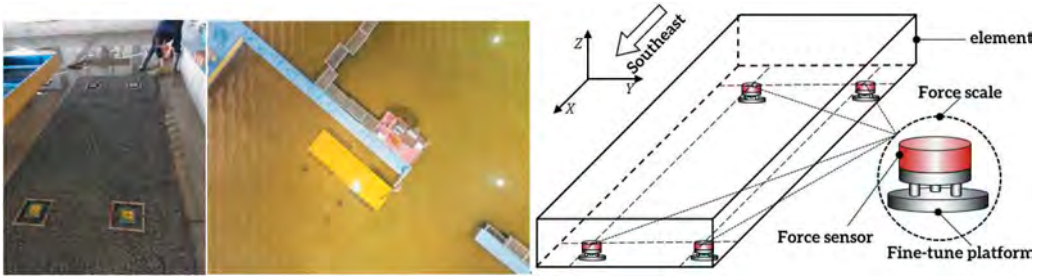

Figure 8. The site model and force support settings.

element is the positive Y axis, and the vertical up direction is the positive Z axis.

The statistical results of vertical lifting force under each working condition of non-standard tunnel element E32 and standard tunnel element are shown in Figures 9 and 10. As the results illustrated, the vertical lifting extreme value is positively correlated with wave height and negatively correlated with the laying rate. Non-standard and standard elements stored in different berths have almost equal lifting forces under the same dynamic conditions, with the non-standard element, which has a small bottom area, slightly larger in general. This is mainly due to the different coverage against the waves at the two berths, which can also explain that GC5 berth is more significantly affected by waves. The extreme value of vertical lifting force of the standard element at each wave height is 5000~9000 kN for extremely low water level and 15000~32000kN for extremely high water level. The most unfavorable lifting force reaches 45% of its lower limit of negative buoyancy. For non-standard element, the extreme value becomes 4000~11000 kN and 15000~37000 kN seperately. And the most unfavorable lifting force reaches 55% of its lower limit of negative buoyancy.

The reduction of the lifting force at the condition of 100% laying rate of the foundation compared with 50% laying rate is shown in Table 4. For non-standard and standard element, the extremum of this index can attain 40% to 60% and 30% to 40% respectively. Both indicate that when the gravel base is fully laid, the sliding resistance of the element could be greatly increased.

4.1.2 *Horizontal wave force*

For non-standard element, the wave force extremum in X direction: 1821~2309kN at extremely low water level, 3450 ~ 5320kN at extremely high water level. In Y direction: 1666 ~ 2358kN (low), 3892 ~ 4609kN (high). General: 2159 ~ 2535kN (low), 4378 ~ 5585kN (high). For standard element, in X direction: 2350 ~ 2876kN (low), 3947 ~ 5862kN (high). In Y direction: 1704 ~ 2055kN (low), 4028 ~ 6220kN (high). General: 2474 ~ 3220kN (low), 4878 ~ 6348kN (high). The test result indicates that the extremum in the X direction, Y direction and its actual direction of the horizontal wave force are all positively correlated with wave height and do not change significantly with laying rate, as shown in Figure 10 to 12.

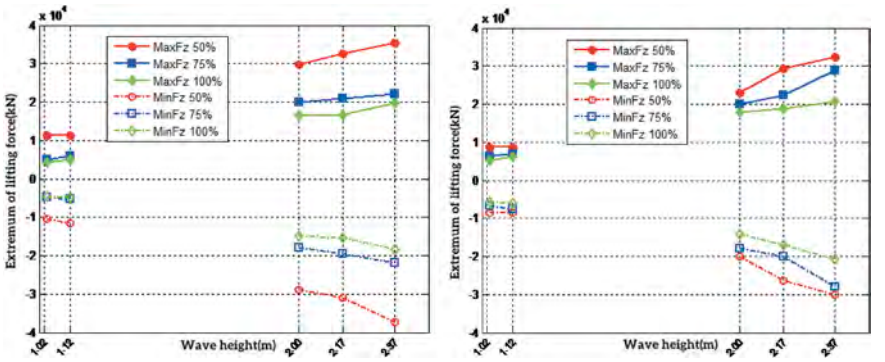

Figure 9. Vertical force extremum V.S.wave height of non-standard tunnel element and standard tunnel element.

Table 4. Reduction of the extremum of vertical lifting force at the condition of 100% compared with 50% laying rate.

		Extremely low water level		Extremely high water level		
Tunnel element type	Water level/effective wave height(m)	Wave height 1.03 m	Wave height 1.12 m	Wave height 2.00 m	Wave height 2.17 m	Wave height 2.37 m
Non-standard E32	Reduction degree (maximum) (%)	62.2	56.9	44.7	48.9	44.1
	Reduction degree (minimum) (%)	56.9	57.9	48.2	50.6	50.6
Standard	Reduction degree (maximum) (%)	38.6	28.6	23.1	35.6	36.5
	Reduction degree (minimum) (%)	34.3	29.5	29.1	36.2	30.9

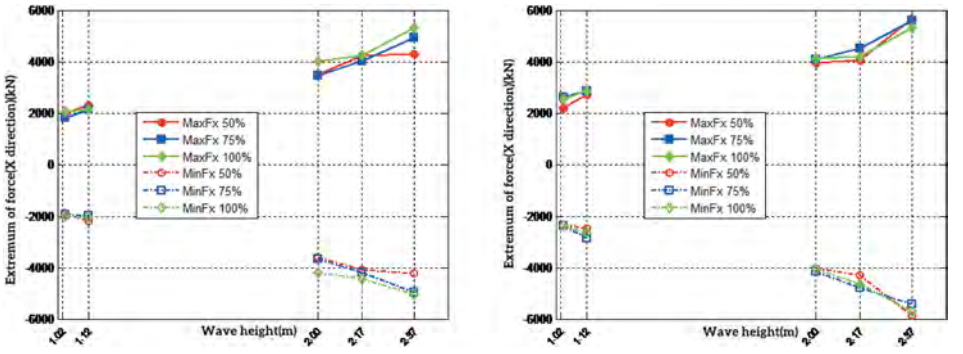

Figure 10. EVI of wave force V.S. wave height(X direction) for non-standard and standard tunnel element.

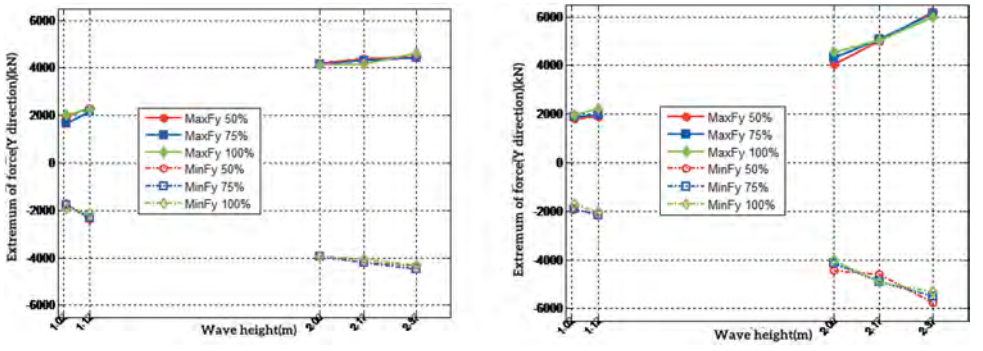

Figure 11. EVI of wave force V.S. wave height(Y direction) for non-standard and standard tunnel element.

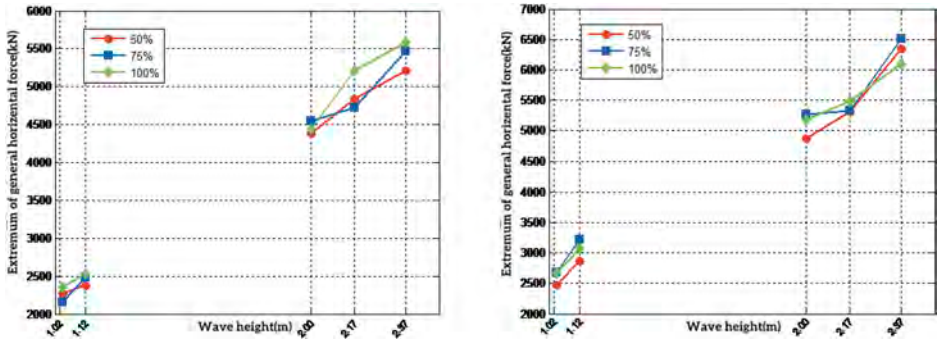

Figure 12. EVI of wave force V.S. wave height(General) for non-standard and standard tunnel element.

4.2 *Stability of the tunnel*

4.2.1 *Analysis method*

Since the lifting force of the tunnel element is less than the negative buoyancy force, the stability analysis of the tunnel element against typhoon mainly considers the performance of anti-slip. Therefore the rigid body limit equilibrium method[10,11] was used. The prerequisite for the tunnel element not to slip is that the static friction between the tunnel element and the foundation is sufficient to overcome the wave force. Assume that the transverse and longitudinal horizontal forces of the tunnel element under the action of waves are F_x and F_y separately and lifting force is F_z.M_x, M_y *and* M_z are the torque around the longitudinal, transverse and vertical directions about the origin of the tunnel element. Then the prerequisite should be satisfied:

$$F_R = \mu(Mg - F_z) - \sqrt{F_x^2 + F_y^2} - \tau_{M_z} BL > 0,$$

among which F_R is residual resistance, that is the difference between resistance and slip force, μ is the static friction coefficient between the tunnel element and the crushed stone bed, M is the negative buoyancy of the tunnel element, g is the gravitational acceleration, B is the element width, L is the element length. The torque M_x and M_y may change the vertical pressure distribution at the bottom of the tunnel element, but not change the total load on the foundation imposed by the element, which is considered to be invalid to the general resistance of the tunnel element. So its impact on the residual resistance force is neglected. τ_{M_z} is the equivalent thrust stress corresponding to the torque M_z in Z direction, which is used to indirectly consider the friction loss of the contact surface caused by suppressing the rotational trend caused by torque. The equivalent thrust stress τ_{M_z} is calculated as follows:

Assuming that the rotational thrust stress is proportional to its distance from the center of the tunnel element, the maximum rotational thrust stress τ_{max} is:

$$\tau_{max} = \frac{|M_z|}{I_z} \cdot \frac{\sqrt{B^2 + L^2}}{2},$$

where I_z is the pole moment of inertia with respect to the Z-axis rotation:

$$I_z = \frac{BL}{12}\left(L^2 + B^2\right).$$

To ensure safety, the maximum thrust stress τ_{max} is used as the equivalent thrust stress τ_{M_z}. The relationship should be satisfied if the tunnel element does not slip:

$$F_R = \mu(Mg - F_z) - \sqrt{F_x{}^2 + F_y{}^2} - |M_z| / \left(\sqrt{B^2 + L^2}/6\right) > 0$$

Divide the left and right ends of the residual resistance calculation formula by μMg to make it dimensionless as:

$$\dot{F_R} = 1 - \dot{F_Z} - \dot{F_{xy}} - \dot{M_z},$$

where $\dot{F_R}$ is dimensionless lifting force: $\dot{F_Z} = F_z/Mg$, $\dot{F_{xy}}$ is dimensionless horizontal thrust stress:

$$\dot{F_{xy}} = \left|F_{xy}\right|/\mu Mg = \sqrt{F_x{}^2 + F_y{}^2}/\mu Mg,$$

$\dot{M_z}$ is dimensionless torque:

$$\dot{M_z} = \frac{6}{\sqrt{B^2 + L^2}} \cdot \frac{|M_z|}{\mu Mg},$$

and $\dot{F_R}$ and is dimensionless residual resistance force:

$$\dot{F_R} = F_R/\mu Mg,$$

when $\dot{F_R} > 0$, the anti-slip stability of the tunnel element meets the requirements and vice versa.

4.2.2 *Stability of the tunnel element under different condition*

For safety, when calculating the anti-slip residual resistance, the negative buoyancy of non-standard and standard element takes the lower limit value. The minimum dimensionless residual resistance under each working condition is shown in Table 5.

It can be seen that the anti-slip stability of the tunnel element meets the requirements under each working condition of the normal combination of the load component. The anti-slip stability of the tunnel element decreases with the increase of wave height, and the decrease of laying rate. At extremely high water levels, the anti-slip stability decreases significantly with the decrease of laying rate. That corresponds to the fact that the increase of lifting force is larger with the decrease of laying rate at extremely high water level.

Table 5. The minimum dimensionless residual resistance when the load components are normally combined.

Water level/effective wave height(m) / Foundation laying rate		Extremely low water level		Extremely high water level		
		Wave height 1.03 m	Wave height 1.12 m	Wave height 2.00 m	Wave height 2.17 m	Wave height 2.37 m
Non-standard E32	50%	0.717	0.706	0.385	0.319	0.296
	75%	0.749	0.725	0.476	0.435	0.386
	100%	0.827	0.831	0.521	0.463	0.416
Standard	50%	0.735	0.689	0.272	0.312	0.190
	75%	0.771	0.750	0.415	0.423	0.369
	100%	0.786	0.737	0.499	0.497	0.436

Table 6. The smallest dimensionless residual resistance when unfavorable extremum of load components occurs at the same time.

Water level/effective wave height(m) Foundation laying rate		Extremely low water level		Extremely high water level		
		Wave height 1.03 m	Wave height 1.12 m	Wave height 2.00 m	Wave height 2.17 m	Wave height 2.37 m
Non-standard E32	50%	0.598	0.556	0.148	0.080	-0.068
	75%	0.637	0.719	0.278	0.156	0.077
	100%	0.734	0.690	0.286	0.266	0.165
Standard	50%	0.624	0.595	0.225	0.011	-0.189
	75%	0.690	0.612	0.252	0.170	-0.093
	100%	0.708	0.618	0.315	0.221	0.157

The probability of the load components reaching an unfavorable extreme value at the same time is very small, however, the possibility of its appearance is not excluded in the long-term effect. When this happens, the smallest dimensionless residual resistance force under different working conditions is shown in Table 6. It demonstrates that at extremely low water level and different laying rates, the smallest dimensionless residual resistance forces of non-standard and standard element both exceed 0.5, which meets the requirement. However, at extremely high water level, the smallest dimensionless residual resistance force might be negative when laying rate is 50% or 75% and the tunnel elements are on the risk of instability. While when laying rate is 100%, that value exceeds 0.15 for every condition and the anti-slip stability meets the requirement.

5 CONCLUSION

The wave forces in all directions are positively correlated with wave height, and the laying rate of the foundation bed has little effect on the vertical outward wave force, but has a significant effect on the vertical wave force.

With the increase of laying rate, the vertical wave force decreases, and the anti-slip stability of tunnel element increases. Under the normal combination of load components, the anti-slip stability of non-standard and standard tunnel element meets the requirements.

In the case of combinations of extreme load components, When the foundation laying rate is 50% and 75%, there is a risk of instability at extremely high water level. And when the laying rate is 100%, the stability can be ensured. Therefore, the recommended laying rate is 100%.

The bulkhead door locates close to the waterway of port gate of the harbor and is easily affected by hydrodynamic action as well as collisions with ships, which deserves high attention. Although the influence of wave growth in closed harbors has been considered, the study does not include experimental analysis of wave evolution during the actual period of typhoon, which is relatively long. According to the experience and other researches, waves in the harbor will evolve from high to low frequency. Besides, the latter stage of typhoon may also be accompanied by surges of low frequency. Therefore, the stability monitoring of the element during the typhoon season should be strengthened, and relevant risk plans should be formulated.

REFERENCES

[1] Lunniss R, Baber J. Immersed Tunnels[M]. Boca Raton: CRC Press, 2013.

[2] Wang MS. Current developments and technical issues od underwater traffic tunnel—discussion on construction scheme of Taiwan strait undersea railway tunnel-[J]. Chinese Journal of Rock Mechanics and Engineering, 2008, 204(11): 2161–2172.

[3] GUO Jianmin, SHAN Lianjun, MA Mingjun. Statistics analysis and development of immersed tunnel tunnels in China[J]. Tunnel Construction, 2023, 43(1): 173.

[4] WANG Baoning, Shu Ning. Study on Scheme for Seating Oil Carrier on Seabed as Isolated Offshore Structure at Nanpu Oil Field 35-2. China Harber Engineering, 2001(05): 20–24.

[5] SHANG Qiankun, WANG Dianwen. Reinforced concrete immersed tunnel element and foundation bed friction resistance test and study[J]. China Harbour Engineering, 2015(7): 46–48.

[6] LIN Wei, YIN Haiqing, ZHANG Jianjun, WANG Xiaodong, SHANG Qiankun, LIN Ming. Full scale observation and test of the frictional force of the concrete element and gravel bed of immersed tunnel[J] Journal of Waterway and Harbor, 2018, 39(S2): 54–60.

[7] GAO Zhanfeng, Study on Calculation Model and Method for Breakout Force of Embeded Objects from Sediments[D].Dalian University of Technology, 2005.

[8] SHU Ning, LI Yanbao, Determining Friction Factor between Gravity Steel Structure and Rubble-Mound Foundation[J]. China Harbour Engineering,2005(02): 32–35.

[9] JTJ/T 234-2001, Wave Model Test Procedure[S].

[10] ZHANG Jinsheng. Discussion on the Rigid Body Limit Equilibrium Methods-A Probe of the Criterion of the Gravity Dam Safety Factor Against Deep Sliding Stability Analysis in the Dam Foundation[J]. Journal of Hydroelectric Enginering, 2005(05): 26–33.

[11] CHEN Geqiang. Analysis of Rigid Body Limit Equilibrium Method[J]. Haihe Water Resources, 1999(02): 18–20.

Tunnelling for a Better Life – Yan, Celestino, Thewes & Eberhardt (Eds)
© 2024 The Author(s), ISBN 978-1-032-80042-4
Open Access: www.taylorfrancis.com, CC BY-NC-ND 4.0 license

Assessing the suitability of coarse sand for the sand flow method in immersed tunnel foundations

Xavier Szadkowski*, Michel van der Molen & Rick Hermsen
Ballast Nedam, Nieuwegein, The Netherlands

Roline Montijn
MH Poly, Bergen op Zoom, The Netherlands

ABSTRACT: This research aims to investigate the feasibility of using coarse sand for the sand flow method in immersed tunnel foundations, with a specific focus on achieving the desired pancake diameter. The study was conducted in the context of the Khor al Zubair Immersed Tunnel project, Iraq, which faces light seismic activity. Traditionally, gravel beds are chosen as foundation for earthquake-prone areas, but the project opted for the innovative and cost-effective sand flow method using coarse sand with specific particle size requirements. The methodology involved conducting sieve analysis on Iraqi sand samples intended for sand flow foundation use. Based on the results, similar materials available in the Dutch market were examined and compared in terms of mineralogy and particle distribution. The relative density range was determined through laboratory tests, using Cone Penetration Test (CPT) values to derive the in situ relative density values. The test setup, comprising a water-filled basin and a modular enclosed plane simulating the tunnel element's underside was used to perform full scale pancakes. Measurements of hydraulic pressures, density, flow rates, and pressures during sand flow were recorded. Subsequently, CPTs were conducted after sand flowing and thereafter the plates were dismantled to make a point-cloud analysis measuring the pancake diameter. The results indicated that the desired relative density could not be achieved, irrespective of using coarse sand or the conventional fine sand typically employed for immersion tunnel foundations. However, the targeted pancake diameter was successfully attained. The conclusion suggests the need for further testing and the consideration of additional adhesives to potentially enhance the liquefaction resistance. Additional full-scale tests are recommended to investigate the feasibility of coarse sand in the sand flow method for immersed tunnel foundations. This research underscores the importance of advancing the sand flow method and exploring alternative materials for immersed tunnel construction in seismic zones.

Keywords: Sand flow, Immersed Tunnels, full-scale model, sand deposit foundation, liquefaction susceptibility

1 INTRODUCTION

The installation of immersed tunnels has significant implications for the surrounding soil. Excavation and backfilling processes during tunnel construction alter the soil structure, leading to uncertainties and increased risks, particularly in earthquake-prone regions. The choice of foundation layer between the trench and tunnel bottom varies, with options including sand, gravel, or grouted foundations, often requiring additional support measures (Lunne et al., 1997; Lunniss & Baber, 2013).

The sand flow method, notably used in recent projects like the Marieholm tunnel in Sweden and the Maasdeltatunnel in the Netherlands, seeks to have each tunnel element supported by subsoil (sand) instead of temporary supports. Sand and water are pumped through embedded pipelines in the tunnel elements' floors. Outflow openings beneath the elements discharge the sand-water mixture, allowing it to settle and form a sand ring at ground level, resembling a "pancake." This process repeats until the sand ring reaches the tunnel element's bottom, generating "rivers of sand" at points of least resistance.

*Corresponding author: x.szadkowski@ballast-nedam.nl

DOI: 10.1201/9781003495505-328

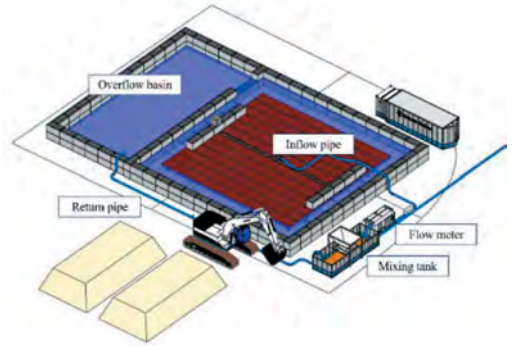

Figure 1. Overview of test set-up.

In the context of Iraq, traditional 0.2mm D50 sand, typically used for foundation via the sand flowing method, is unavailable. Therefore, testing the suitability of the chosen sand is crucial. A similar 0.55mm D50 sand used in the Zhoutouzui Tunnel project in China (Li et al., 2018) is being considered, as it proved non-liquefiable, given the relative density. A full-scale trial test will assess parameters such as pancake radius, uplift pressure, and sand flow rate, crucial for evaluating liquefaction stability. Liquefaction assessment can be accurately accomplished through the extrapolation of cone penetration test values (Lunne et al., 1997). Following the trial test, the sand gradation will be determined, and the addition of cement clinker will be considered if liquefaction is a concern.

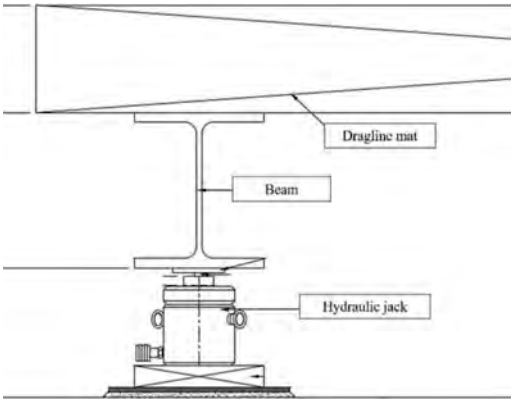

Figure 2. Supports of the dragline mats.

In the design of Immersed Tunnel (IMT) structures, the arrangement of sand flow pipes has been influenced by cautious assumptions based on the Zhoutouzui tunnel test results conducted in China (Li et al., 2018). As a result, the design of the cast-in pipelines has been adjusted, expanding them from two rows to three. However, it is essential to acknowledge that a larger sand diameter can affect the achievable pancake diameter, necessitating a thorough reassessment of these assumptions before proceeding with the sand flow process. This paper aims to provide a comprehensive evaluation of these critical considerations in the design and implementation of IMT structures.

2 TEST MODEL

2.1 *Test set-up description*

The test basin was constructed with dimensions measuring 19 m x 19 m x 1.6 m. It featured twelve watertight steel dragline mats, collectively representing the bottom of a tunnel element, and these mats were supported by two HEM-300 beams positioned atop six hydraulic jacks. The bottom of the steel dragline mats, replicating the tunnel element's base, was precisely set at the same height as specified in the Khor al Zubair Immersed Tunnel design, mirroring the 0.5m separation between the tunnel bottom and the trench top.

To counter uplift forces, sixteen concrete ballast blocks, each weighing 2.4 metric tons, were employed to stabilize the mats. In a separate mixing tank, the creation of a turbulent environment was achieved using jets to thoroughly mix sand and water before being pumped into the primary basin.

The testing encompassed a comprehensive examination of sand materials. Initially, a baseline test was conducted using Zeeuws sand, following the methodology established by Griffioen (Griffioen & van der Veen, 1972). Subsequently, four additional tests utilized Kaliwaal 41, a material chosen after conducting a comparison of the mineralogy and particle distribution of the available Dutch market materials to the Iraqi sand samples intended for sand flow foundation use. These tests aimed to assess material behaviour under varying flow speeds, both increased and reduced from the required flow speed, providing valuable insights into the material's response in different flow conditions.

Figure 1 provides an overview of the test configuration, while Figure 4 presents an image of the test setup after testing Kaliwaal material. For specific details on the arrangement of the hydraulic jacks, please refer to Figure 2.

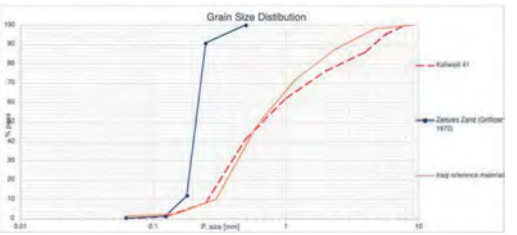

Figure 3. Particle size distribution.

Figure 4. Test set-up after sand flowing Kaliwaal 41.

2.2 *Test materials*

The susceptibility of sand deposits to liquefaction induced by seismic activity (Hashash et al., 2001) underscores the importance of maintaining the quality of sand within artificial sand deposit foundations. To minimize the risks associated with liquefaction, it is essential to utilize well-graded sand free from chemical admixtures and environmental contaminants, as emphasized in prior research (Guanghui et al., 2009). In accordance with the design principles established for the immersed tunnel project, the test sand has undergone rigorous screening to ensure its compliance. As illustrated in Figure 3, the particle size distribution of the sand aligns with the stipulated requirements for test materials, attesting to its suitability for use in the project. Table 1 shows the material characteristics of Zeeuws sand (Griffioen & van der Veen, 1972) and Kaliwaal 41.

Table 1. Material characteristics.

	Zeeuws (baseline)	Kaliwaal 41
D_{50}	$140 < D_{50} < 230$ µm	700 µm
D_{60}/D_{10}	$2{,}3 < D_{60}/D_{10} < 2{,}7$	3,5
x < 63 µm	< 2%	< 2%

2.3 *Test parameters*

A sequence of five sand flow tests was conducted, involving an initial baseline test employing Zeeuws sand. The primary purpose of this baseline test was to verify the functionality of the test setup by aligning its outcomes with the well-established methodology from Griffioen's research, thereby confirming the correct operation of the system.

Subsequently, the remaining tests utilized Kaliwaal 41 material, and they were designed to investigate the optimal process parameters, namely mixture speed and concentration. These parameters were varied to ascertain the most favourable combination. The specific input parameters used for each of the five tests are detailed in Table 2.

The analysed output parameters included:

- Uplift forces
- Pancake diameter
- Pancake build-up
- Sand segregation
- Relative density
- Test set-up operational parameters

For a comprehensive assessment, the measured uplift forces were compared with theoretically determined uplift forces, as outlined in the theory presented by Griffioen & Westersehelde (Griffioen & van der Veen, 1972).

Table 2. Input parameters.

Test	Flow rate (m/s)	Average mixture density (kg/m^3)
1	4.4	n.a.
2	4.8	1131
3	4.7	1152
4	4.1	1129
5	5.6	1109

2.4 *Measurement methods*

The methodology encompassed the comprehensive monitoring of several crucial parameters, allowing for a detailed examination of the test parameters:

1. **Uplift Forces**: Pressure transducers were employed to gauge the uplift forces generated by the sand pancake, which pressed against the cumulative effective weight of the dragline mats and concrete ballast blocks, effectively replicating the conditions beneath a tunnel element.
2. **Displaced Volume and Pancake Diameter**: LiDAR measurement was conducted after the test to determine the total displaced volume and pancake diameter, providing insights into the resulting formation.
3. **Conductivity (pancake build-up)**: In the methodology section, ground conductivity meters (GCM) were employed to capture changes in soil height within a 40cm vertical range at specific x, y coordinates. This methodology allowed for a comprehensive examination of the sand pancake's width and height variations during the test, even underneath the plateau. To optimize data collection, sensors were strategically placed in every other hole (see Figure 5), with the remaining holes reserved for Cone Penetration Tests (CPTs) following the sand flow test. The precise operational steps for the GCM measurements are as follows:

- **Data Averaging**: Data points were averaged over a 3-second time step to mitigate electrical noise.
- **Time Standardization**: To synchronize measurements across all tests, t = 0 s was set as the reference point, considering variations in the start time of measurements.
- **Detection of Sand Passage**: The moment of sand passage past a sensor was determined by a significant drop in the sensor's value, as the conductivity of water markedly differs from that of a sand-water mixture.
- **Linear Analysis**: Employing linear interpolation and extrapolation, the sand height at specific time points was calculated.
- **Data Visualization**: The acquired data points across the vertical and horizontal planes, along with time, were utilized to create a comprehensive 'pancake build-up graph.' This graph visually represents the evolution of the sand pancake over time, providing valuable insights into its development.

4. **Sand Segregation**: Visual inspection of bore holes was employed to assess sand segregation.
5. **Penetration Resistance and Relative Density**: Phase 1 involved a comprehensive assessment of several key parameters, including grain distribution (D50 calculation), maximum proctor density, optimal moisture content, saturation degree, and material settling form. These measurements provided a foundation for subsequent phases of the investigation.

   Phase 2 aimed to establish a calibration line that encompasses different relative densities and compaction conditions. Our goal was to closely replicate a calibration line from a prior study, which featured relative densities of 15, 50, and 70% (see Figure 6). This consistency with past research is crucial for maintaining accuracy.

   The calculation of relative density, a key factor in our study, relies on the penetration resistance data obtained through the Penetrologger Cone Penetration Test (CPT) (Tufenkjian et al., n.d.). These tests were conducted by penetrating the soil through the two rows of lifting holes in the steel dragline mats, with these holes temporarily covered during the sand flow process to ensure uniform test conditions.

   To determine the in-situ relative density (D_r) of the applied sand after the test, we relied on a combination of the well-established relations, such as those formulated by Jamiolkowski (Jamiolkowski et al., 2003; Lunne et al., 1997) and results from phase 1.

   The calculation of relative density is determined by considering the maximum and minimum pore content. The maximum pore content represents loose-poured sand, measuring 1660 kg/m³ at 0.0% moisture, while the minimum pore content reflects the maximum density attained through a weighted proctor test, with a density of 1824 kg/m³ at 10.3% moisture. This approach ensures the accuracy and reliability of our relative density calculations and offers a robust foundation for our study.

   Furthermore, the methodologies that were used in order to assess the operational parameters that were tested during the study are explained as follows:

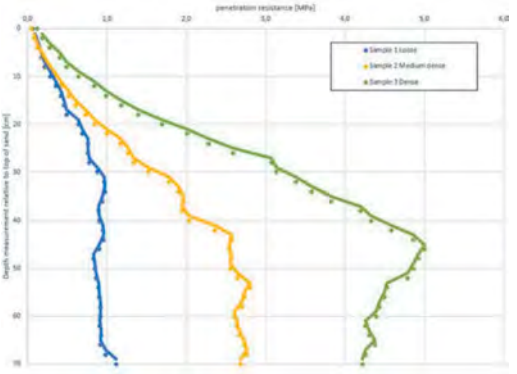

Figure 6. Cone penetration resistance from calibration test.

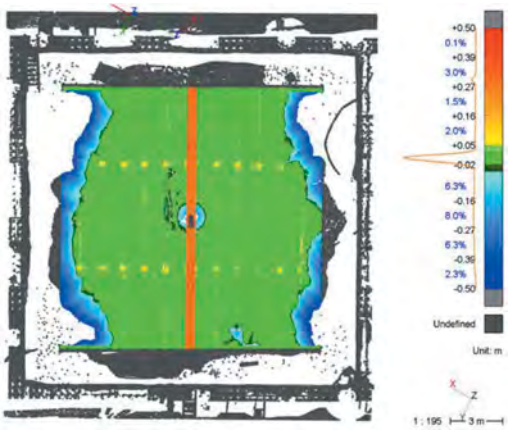

Figure 7. Sandflow test, 4th pancake with Kaliwaal 41.

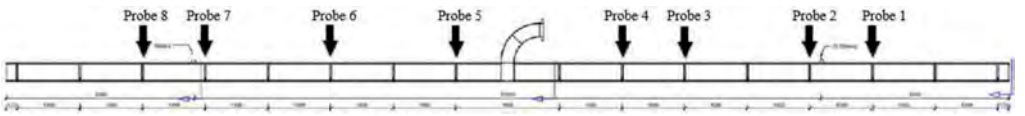

Figure 5. Location of conductivity probes.

6. **Flow Velocities**: Inflow and outflow velocities to and from the mixing tank were consistently monitored to assess the fluid dynamics.
7. **Pipeline Pressure**: Pressure levels within the pipelines connecting to the mixing tank were under continuous scrutiny to maintain stable operational conditions.
8. **Mixture Concentration**: Regular recording of the density of the sand/water mixture was performed to gain insights into the mixture's composition and consistency throughout the experiment.

3 RESULTS

The results section presents key findings related to uplift forces, pancake diameter, build-up, sand segregation, relative density, and test set-up parameters. These results provide insights into the performance and behaviour of sand flow foundations in immersed tunnel construction. They form the basis for our analysis and contribute to the field's advancement.

3.1 *Uplift forces*

The uplift forces were measured during, immediately after and 24 hours after the test. No reduction of uplift forces was measured after 24 hours, which can be explained by the coarse character of the sand material.

The difference of the uplift force before and after the test is presented in Table 3. During test 3, a local breakthrough of the dragline mats explains the large reduction in uplift forces.

The theoretically determined uplift forces (Griffioen & van der Veen, 1972) are also shown in Table 3. It can be concluded that the results were in the same order of magnitude as the uplift forces measured during the tests, but come out lower than measured. The uplift force is highly dependent on mixture density and production speed. The difference between the measured value and the theoretical value could be due to measurement errors in the mixture density. Verification of the theory is not accomplished in this test.

Table 3. Test results.

Test	Uplift force from pancake - neasured (metric tons)	Uplift force from pancake - theoretical (metric tons)	Average diameter (m)
1	15	n.a.	11
2	47	22	15.2
3	33	24	12.7
4	50	21	13.6
5	50	19	16.7

3.2 *Pancake diameter*

The prescribed radius for the Khor al Zubair Immersed Tunnel, set at 7.3 meters (see Figure 7), was successfully attained in two out of the four conducted tests, see Table 3. This achievement suggests an observable correlation between the flow rate and the resultant pancake diameter. Collectively, the test outcomes unequivocally demonstrate the feasibility of achieving the stipulated radius requirement for the immersed tunnel project.

3.3 *Pancake development*

The accumulation of sand pancakes was quantified by measuring their diameter across predefined locations marked by conductivity probes, as depicted in Figure 11. This approach facilitated real-time observations of the pancake formation throughout the duration of the test. Notably, the observed pancake evolution revealed distinct phases. Within the initial 10 to 20 minutes of sand flow initiation, the pancake exhibited a characteristic formation of a central crater. Subsequently, over a span of 40 to 50 minutes from the onset of sand flow, the central crater gradually closed, likely attributed to the consolidation of material around the previously formed ring structure at its periphery. Only after approximately 80 minutes, marking the latter stages of pancake production, did the material completely fill the void beneath the steel dragline mats. Figure 11 illustrates the data generated through the GCM measurements, providing a visual representation of these observations.

3.4 *Sand segregation*

Refer to Figure 9 for a representative depiction of a trial pit. The examination of both the trial pit and the soil samples extracted from each sand pancake reveals a consistent pattern of material segregation that is evenly distributed throughout the pancake's depth. However, it is noteworthy that within the uppermost 5-10 centimetres of the sand pancakes, a prevalence of coarser particles is evident. This phenomenon can be attributed to the washing out of finer particles when the gap between the pancake

Figure 8. Result of Sand flow test with Kaliwaal 41.

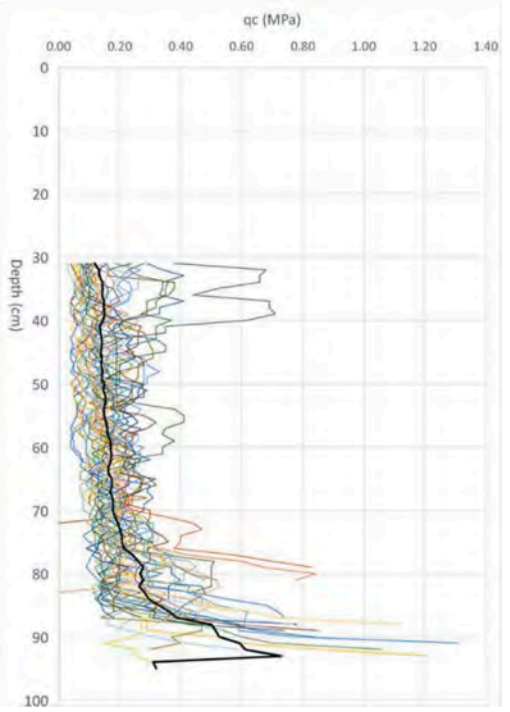

Figure 9. Small trial pit showing homogeneous sand build-up with a coarse top layer.

Figure 10. Cone penetration resistance made in the pancake after sand flowing.

and the tunnel element narrows, leading to an increase in flow velocities. Consequently, these finer particles tend to accumulate in the outer edges of the pancakes, thus contributing to the observed coarser composition in the upper layers.

3.5 *CPT and relative density*

The results of the Cone Penetration Test (CPT) conducted during the initial test utilizing Kaliwaal 41 are graphically presented in Figure 10, with similar outcomes observed in subsequent tests. Figure 10 exhibits a spectrum of coloured lines representing data obtained from various CPT locations distributed across the pancake's surface, as indicated by numbered CPT locations in Figure 5. Notably, the black line signifies the aggregated value of multiple CPT measurements, serving as a comprehensive indicator of the CPT values for this specific pancake. To examine these results, a comparative analysis was performed against the calibration test results depicted in Figure 6. This analysis reveals that the cone resistances consistently exhibit low values, notably falling below the threshold of 15% as indicated by the blue curve labelled 'loose' in Figure 6. Consequently, it can be deduced that the observed cone resistances in this study are generally characterized by a "loose" nature.

4 DISCUSSION

1. Our study reveals the feasibility of creating 7.3-meter-radius sand pancakes using materials akin to Kaliwaal 41. This discovery hints at the potential use of materials falling within the range from Zeeuws sand to Kaliwaal 41 in sand flowing processes for immersed tunnels. This exciting prospect warrants further exploration and experimentation to assess the applicability of a broader spectrum of materials with intermediate properties. Future research could unveil the adaptability of sand flow techniques, accommodating diverse geological conditions.
2. Our research underscores the value of utilizing data gathered during the sand pancake formation, as measured by the Ground Concentration Measurement (GCM), for validating computational

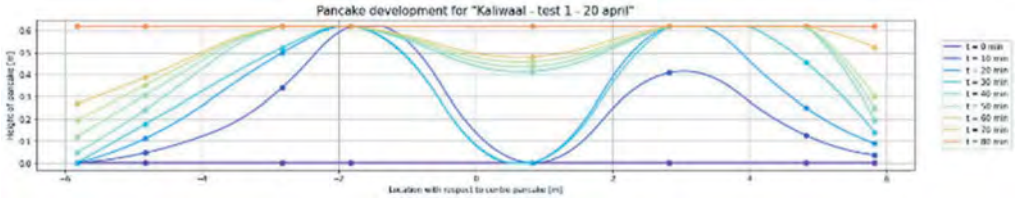

Figure 11. Pancake development using GCM sensors for Kaliwaal 41.

tools like TUDFlow3d. TUDFlow3d, a fully three-dimensional CFD solver, designed for simulating turbulent flow on an engineering scale, stands to gain significant insights from empirical data derived from real-world sand flow operations. This fusion of experimental results and computational modelling holds tremendous promise for enhancing our grasp of sand flow processes, offering the potential for more precise and efficient engineering solutions in the realm of immersed tunnel construction. Collaborative research in this area may pave the way for an enhanced integration of computational fluid dynamics in practical sand flow applications.

3. The determination of relative density through CPT values, as prescribed by (Lunne et al., 1997), has yielded consistently low values. These values are intrinsically linked to a percentage that serves as a basis for assessing material liquefaction susceptibility. Our study has raised concerns about the accuracy of CPT values in representing reality accurately. This prompts the need for exploring alternative methods to determine relative density from CPT data. Furthermore, the determination of relative density in our calibration tests may require further scrutiny to ensure the validity of the obtained values.
   Ensuring a robust calibration necessitates a direct correlation between dry densities and relative densities. The established dry densities for different relative densities, such as saturated (Dr = 0%) at 1660 kg/m³, loose (Dr = 15%) at 1685 kg/m³, medium dense (Dr = 50%) at 1742 kg/m³, dense (Dr = 70%) at 1775 kg/m³, and optimal (Dr = 100%) at 1824 kg/m³, serve as a vital foundation for consistency with prior research and offer a valuable benchmark for future investigations and analysis.
4. Given the indications of liquefaction potential in the applied sand material based on our test results, it is prudent to consider and investigate the incorporation of cement clinker. A forthcoming test will be conducted wherein clinker material will be introduced to Kaliwaal 41. This research avenue holds the promise of shedding light on potential stabilization methods to mitigate liquefaction risks in sand flow applications.

5 CONCLUSIONS

In conclusion, the full-scale sand flow test conducted at the Ballast Nedam premises in Maarssen, Netherlands, provided valuable insights into the feasibility of using an increased grain size for sand flow applications. Several key findings emerged from this study:

1. **Uplift forces:** Uplift forces were examined during and after the tests. No significant post-test reduction was observed, likely due to the sand's coarse nature. Test 3 experienced a notable reduction, attributed to a dragline mat breakthrough. The theoretically determined uplift forces were generally within the same order of magnitude as the measured forces, though measurements exceeded theoretical values. This difference could be attributed to factors like mixture density and production speed, possibly influenced by measurement errors. It's crucial to recognize that this test did not fully validate the theoretical model, indicating the need for further investigation and refinement.
2. **Pancake diameter:** Feasibility of Increased Grain Size: The test unequivocally demonstrated that sand flow with an increased grain size is indeed feasible. The minimum required radius of 7.3 meters was successfully achieved during the tests, suggesting that larger grains can be effectively employed in sand flow applications without compromising the structural integrity of the system.
3. **Pancake development:** Our study employed conductivity probes to monitor sand pancake formation and evolution in real-time. We observed distinct phases, including the initial central crater, gradual closure, and eventual complete filling beneath the steel dragline mats. Figure 11 visually depicts these findings. The experiments revealed that the largest sand pancakes were formed under conditions characterized by relatively high mixture velocities and low sand concentrations. This finding suggests that controlling these parameters can be crucial for optimizing sand flow processes, particularly when larger grain sizes are used.
4. **Sand segregation:** Our examination of the trial pit and soil samples from the sand pancakes indicates a consistent pattern of material distribution throughout their depth. Notably, the uppermost 5-10 centimeters of the pancakes exhibit coarser particle prevalence. This phenomenon results from increased flow velocities and the subsequent washing out of finer particles near the tunnel element interface.
5. **CPT and relative density:** An important aspect of this study was the assessment of the relative density of the Kaliwaal sand pancakes. Based on the data obtained from the calibration chamber tests and penetrologger results, the estimated relative density of these sand pancakes was found to be less than 15%. This low relative density may have implications for the stability and behaviour of the sand pancakes in practical applications.

Overall, the results of the full-scale sand flow test provide valuable information for engineers and researchers interested in utilizing larger grain sizes in sand flow systems. The successful achievement of the required radius and the insights into sand

pancake formation contribute to our understanding of the potential benefits and challenges associated with this approach. Additionally, the estimation of low relative density underscores the need for further research and consideration of factors that may affect the performance and stability of sand pancakes in real-world scenarios. This study serves as an important step toward advancing the field of sand flow technology and offers a foundation for future investigations in this area.

ACKNOWLEDGMENTS

I would like to extend my heartfelt acknowledgments to several individuals and organizations who have played a pivotal role in the development and completion of this research paper. Firstly, I am immensely grateful to Roline Montijn for her invaluable and substantive input, which significantly contributed to shaping the content and direction of this paper. Her expertise and dedication have been instrumental in the success of this project. I would also like to express my appreciation to Rick Hermsen for his fresh and insightful perspectives on various aspects of the paper, which added depth and clarity to our discussions. Furthermore, I extend my sincere gratitude to Michel van der Molen for his expertise, methodical analysis, and invaluable advice throughout the execution of the test and the writing of this paper; his contributions have been indispensable to this work.

Additionally, I would like to extend my gratitude to Ballast Nedam Infra Projects and Daewoo E&C, our esteemed partners in the Khor al Zubair Immersed Tunnel Project, for their generous support and the opportunity they provided us to write and publish this paper. Their collaboration and cooperation have been essential in advancing our research efforts.

Lastly, I extend my thanks to the various subcontractors and suppliers of sensors, materials, and terrain, whose contributions were essential for the successful execution of the test and, ultimately, the completion of this paper. Their commitment to excellence and provision of necessary resources have been instrumental in achieving our research objectives.

REFERENCES

Griffioen, A., & van der Veen, R. (1972). Ontwikkeling en onderzoek ten behoeve van tunnelfundatie door middel van onderstromen. *Overdruk Ingenieur B&W6*. https://repository.tudelft.nl/islandora/object/uuid%3A46ee4d09-45b7-435a-b5ef-e3550567af13

Guanghui, W., Zhiguo, L., Xiaoming, C., & Yan, S. (2009). Sand flowing experiment and experiment result analysis: Case study on Shengwudao Daxuecheng Immersed Tunnel. *Tunnel Construction - Scientific Research Institute under China Railway Tunnel Group Co.*

Hashash, Y. M. A., Hook, J. J., Schmidt, B., & I-Chiang Yao, J. (2001). Seismic design and analysis of underground structures. *Tunnelling and Underground Space Technology*, *16*(4), 247–293. https://doi.org/10.1016/S0886-7798(01)00051-7

Jamiolkowski, M., Lo Presti, D. C. F., & Manassero, M. (2003). *Evaluation of Relative Density and Shear Strength of Sands from CPT and DMT*. 201–238. https://doi.org/10.1061/40659(2003)7

Li, Y., Li, W., & Cui, J. (2018). *Exploration of tube segment uplift through a full-scale model test of immersed tube tunnel foundation treated by sand-flow method*.

Lunne, T., Robertson, P. K., & Powell, J. J. M. (1997). *Cone Penetration Testing in Geotechnical Practice*. https://www.geotashfeen.tech/https://www.geotashfeen.tech/https://www.geotashfeen.tech/https://www.geotashfeen.tech/

Lunniss, R., & Baber, J. (2013). Immersed tunnels. *Immersed Tunnels*, 1–487. https://doi.org/10.1201/B14281/IMMERSED-TUNNELS-RICHARD-LUNNISS-JONATHAN-BABER

Tufenkjian, M. R., Yee, E., & Thompson, D. J. (n.d.). *Comparison of cone and minicone penetration resistance for sand at shallow depth*.

Tunnelling for a Better Life – Yan, Celestino, Thewes & Eberhardt (Eds)
© 2024 The Author(s), ISBN 978-1-032-80042-4
Open Access: www.taylorfrancis.com, CC BY-NC-ND 4.0 license

Ventilation and smoke exhaust technical scheme of super wide section immersed tunnel

Xiujun Yang*
Department of Engineering Physics, Institute of Public Safety Research, Tsinghua University, Beijing, China
Jiaoke Transport Consultants Ltd., Beijing, China

Liang Cheng
Jiaoke Transport Consultants Ltd., Beijing, China

Maohua Zhong
Department of Engineering Physics, Institute of Public Safety Research, Tsinghua University, Beijing, China

ABSTRACT: The Shenzhen-Zhongshan Link immersed tunnel has eight lanes in both directions, which is the widest section immersed tunnel in the world. The special construction form and ultra-wide section of the tunnel pose great challenges to tunnel ventilation and smoke exhaust system. In order to solve the needs of normal operation and fire case, the tunnel is equipped with tunnel environment detection system, main line tunnel normal operation ventilation system, main tunnel independent smoke exhaust system, exit passageway pressurized air supply system, ramp tunnel normal operation ventilation system, ramp tunnel smoke exhaust system, and staircase pressurized air supply system. Pioneering the ultra-wide cross-section smoke exhaust system and device firstly, and the smoke exhaust efficiency was increased by 42 %. This paper provides a technical reference for the setting of ventilation and smoke exhaust system of an ultra-wide section immersed tunnel and other ultra-wide section tunnels.

Keywords: super wide section immersed tunnel, ventilation system, smoke extraction system, New smoke exhaust technology

1 INTRODUCTION

The total length of the Shenzhong Tunnel is 6845m, and the immersed section is 5035m. The tunnel is a two-way eight lane road with a design speed of 100km/h. It connects to artificial islands at each end. The width of the main tunnel has changed from 46m to 69.8m, making it the world's widest cross-section highway immersed tunnel. There is an underwater interchange at the East Artificial Island that intersects with the main tunnel. The smoke exhaust efficiency under ultra wide cross-section conditions[1] and the smoke exhaust arrangement at underwater interchanges and confluences are the main challenges for ventilation and smoke exhaust in this project.

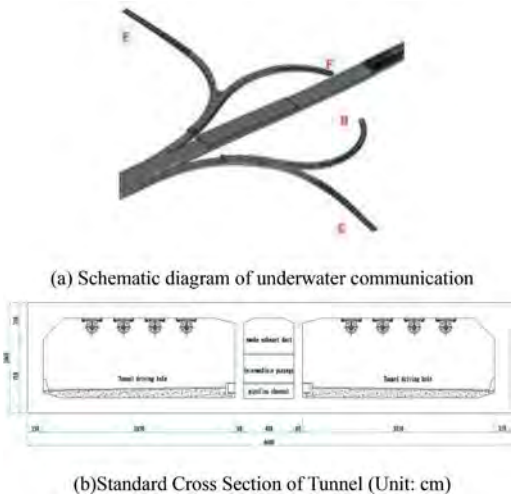

(a) Schematic diagram of underwater communication

(b)Standard Cross Section of Tunnel (Unit: cm)

Figure 1. Cross Section of Underwater Interchange and Tunnel.

2 SYSTEM COMPOSITION

The ventilation system of the Shenzhong Tunnel consists of 8 subsystems: tunnel environment detection system, normal operation ventilation system of the main driving tunnel, independent smoke exhaust

*Corresponding author: yxj21@mails.tsinghua.edu.cn

DOI: 10.1201/9781003495505-329

system, safety passage ventilation system, normal operation ventilation system of the ramp tunnel, centralized smoke exhaust system of the ramp tunnel, pressurized air supply system of the ramp tunnel staircase, and ventilation and ventilation system of the rainwater pump room. The ventilation system design follows the principle of one-time design and phased implementation.

2.1 *Tunnel environment detection system*

By setting detectors (carbon monoxide/visibility/ nitrogen oxide detectors, temperature detectors, wind speed and direction detectors) inside the tunnel, data is provided for normal ventilation and emergency ventilation under normal operating conditions and accident conditions.

2.2 *Ventilation system for normal operating conditions of the main tunnel of the train*

The ventilation and ventilation function in the tunnel is achieved through the action of jet fans and piston air in the tunnel, ensuring the safety and comfort of driving in the tunnel. At the exit of the tunnel, polluted gases are concentrated and discharged from the entrance, causing the concentration of polluted gases in the tunnel site to exceed the standard. The polluted gases are centrally extracted and discharged at high level through wind towers set up on the east and west artificial islands on the exit side of the tunnel.

2.3 *Smoke exhaust system*

By using smoke exhaust fans, smoke is concentrated and extracted through horizontal contact with the flue and side wall smoke exhaust outlets, controlling the smoke diffusion range. Smoke is also discharged through wind towers set up on the east and west artificial islands to achieve the purpose of smoke exhaust and ensuring the safety of personnel escape.

2.4 *Safe passage ventilation system*

Under normal operating conditions, ventilation and air exchange functions are achieved through the pressurized fans on the east and west artificial islands to ensure personnel maintenance needs. Under fire conditions, positive pressure above the pressure in the accident tunnel is achieved through the pressure regulating fans installed in the fan rooms and safety passages of the east and west artificial islands, as well as the pressure regulating fans installed in the safety passage. This prevents smoke from entering the safety passage during fire conditions and ensures personnel escape and rescue work needs.

2.5 *Ventilation system for normal operation of ramp tunnels*

The ramp tunnel is equipped with jet fans to achieve ventilation and ventilation functions for the ramp tunnel.

2.6 *Ramp tunnel centralized smoke exhaust system*

A centralized smoke exhaust outlet is set up at the intersection of E and F ramps, and key smoke exhaust is carried out by opening the electric air valve in the corresponding area during fire conditions.

2.7 *Smoke prevention system for evacuation staircase of ramp tunnel*

A mechanical pressurized air supply system is installed in the evacuation staircase of the ramp tunnel to achieve positive pressure air supply function under fire conditions.

2.8 *Ventilation and ventilation system for rainwater pump room*

The rainwater pump room and distribution room are equipped with mechanical air supply and exhaust systems to achieve ventilation and ensure the normal operation of internal equipment.

3 VENTILATION SYSTEM SCHEME

3.1 *Ventilation system for normal operation of the main driving tunnel*

The normal operation ventilation of the tunnel driving hole adopts a combined ventilation scheme of longitudinal ventilation with a full jet fan and separated vertical shaft exhaust ventilation. Under normal operating conditions, the jet fan is turned on for ventilation and air exchange inside the tunnel. To ensure the air quality at the tunnel entrance, polluted gases are collected and discharged at high altitude through the wind towers on the east and west artificial islands. The wind towers have a height of approximately 30m.

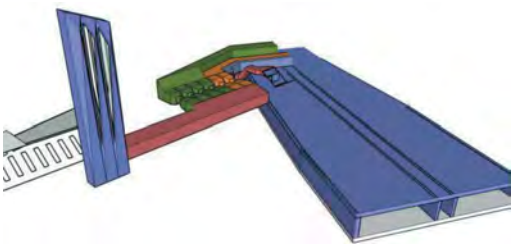

Figure 2. Schematic diagram of fan room in West Island.

3.2 *Smoke exhaust system*

To reduce the length of smoke spread under fire conditions, this project adopts a key smoke exhaust scheme [2]. The immersed tunnel generally adopts a lateral centralized smoke exhaust mode for smoke exhaust [3]. Due to the large cross-sectional width of this

project, direct lateral smoke exhaust cannot meet the safety requirements for personnel evacuation. Through physical model experiments and numerical simulations, a centralized smoke exhaust scheme of "top horizontal connecting smoke exhaust duct (with louvered air outlets at the bottom) and electric smoke exhaust outlets on the side walls" is adopted for the super large cross-section transition section of the main tunnel and interchange underground hub section; Smoke exhaust is carried out by setting a horizontal flue connecting the lateral smoke exhaust outlet of the tunnel at the top of the tunnel. Due to structural safety reasons, the smoke exhaust outlet adopts a group of three schemes. The maximum spacing between horizontal flues is 165m. Adopting a key smoke exhaust scheme that combines top centralized smoke exhaust with lateral centralized smoke exhaust.

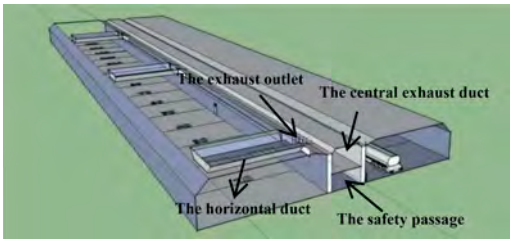

Figure 3. Schematic diagram of smoke exhaust duct setting.

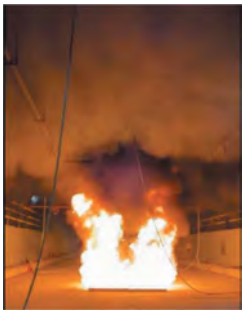

Figure 4. Photos of on-site fire experiments.

According to physical model experiments and numerical simulations, the smoke exhaust efficiency has been verified to be more than 40% higher than that of lateral concentrated smoke exhaust.

3.3 *Safe passage ventilation system*

Under normal operating conditions, a stable airflow is formed by turning on the fans in the east and west artificial islands and the fans in the passage for ventilation.

Under fire conditions, it is used to maintain positive pressure ventilation of the accident tunnel and prevent smoke from entering the safe passage.

3.4 *Ventilation system for normal operation of ramp tunnels*

Under normal operating conditions, the ventilation and ventilation function of the ramp tunnel is achieved by setting a jet fan in the ramp tunnel, ensuring the tunnel operating environment.

3.5 *Ramp tunnel centralized smoke exhaust system*

On the upper part of the ramp tunnel, a mezzanine layer is used for centralized smoke exhaust, and a total of electric smoke exhaust outlets are set up for centralized smoke exhaust.

The ramp tunnel smoke exhaust room is equipped with an independent room for centralized smoke exhaust.

3.6 *Smoke prevention system for evacuation staircase of ramp tunnel*

The smoke prevention system is designed for the evacuation staircase of the ramp tunnel, and a mechanical pressurized air supply system is designed in the front chamber and stairwell respectively to maintain positive pressure in the stairwell and front chamber, ensuring that under tunnel accident conditions, the pressure in the stairwell is greater than that in the front chamber and greater than that in the tunnel.

3.7 *Ventilation system for rainwater pump room*

The underground distribution room and rainwater pump room are equipped with axial flow fan mechanical supply and exhaust systems, which exchange air with the outdoor through the louvered air vents of the island air shaft. Fire dampers should be installed when the air duct passes through the floor slab and firewall, and they should be interlocked with a fire alarm. In case of a fire, the axial flow fan stops running, the fire damper is closed, and the fire control status is switched to.

4 CONTROL STRATEGY

4.1 *Smoke exhaust plan for the main tunnel*

The main tunnel ventilation system utilizes the exhaust duct above the middle passage between the two tunnels, and activates a dedicated exhaust fan to exhaust smoke through a set of horizontal ducts upstream of the fire source, 2-3 sets of horizontal ducts downstream, and side wall exhaust outlets during the period. The wind speed inside the main tunnel is controlled by the jet fans. In cases where smoke exhaust needs cannot be met, an additional set of smoke exhaust outlets can be opened downstream. Further the jet fans are controlled to reduce the wind speed in the main tunnel and the length of smoke counterflow[4] .

When a fire occurs in the dimming section and entrance section of the tunnel, smoke exhaust is carried out by opening the exhaust outlet downstream of the fire source. By controlling the jet fans, the wind speed inside the main tunnel is reduced to reduce the length of smoke counterflow. After the evacuation of upstream tunnel users, it is determined whether to reverse the fans to exhaust smoke from the entrance according to the situation.

The combined air valve in the central exhaust duct is closed under normal working conditions. One end fails, smoke exhaust through the other end fan.

The safety passage ensures positive pressure through a pressurized fan to prevent smoke from entering. Opening the jet fan towards the tunnel ensures positive pressure in the opening area of the safety door and reduces pressure loss in the safety passage.

4.2 *Ventilation and smoke exhaust control scheme for ramp merging section*

Under fire conditions, smoke exhaust is carried out by opening the centralized exhaust outlet downstream of the fire source, and a jet fan 150 meters upstream is also activated to prevent smoke from flowing backwards.

5 CONCLUSIONS

The deep channel underwater tunnel belongs to an ultra wide cross-section immersed tube tunnel, which is also connected to underwater interchanges, making smoke exhaust difficult and smoke control strategies complex. The first proposed method of converting lateral centralized smoke exhaust to top centralized smoke exhaust solves the problem of smoke exhaust efficiency in wide cross-section tunnels. In addition, the smoke control design of other areas ensures the safety of personnel under fire conditions.

ACKNOWLEDGMENTS

Thank you for the support of Guangdong Province Key Field R&D Plan Project: Research and Development of Key Technologies and Equipment for Intelligent Control and Emergency Support of Highway Network Tunnel Engineering Operation Safety (2022B0101070001).

REFERENCES

[1] Deng X H, Song S Y, Cao Z M, et al. Overall Plan for Smoke Extraction System of Submarine Tunnel in Shenzhong Channel [J]. Tunnel Construction, 2020, 40 (08): 1176–84.

[2] Li J M, Tu D K, Li Y F, et al. The smoke exhaust volume and arrangement of smoke exhaust outlets for key smoke exhaust in tunnel fires [J]. Journal of Beijing University of Technology, 2023, 49(03): 363–70.

[3] Xu P, Jiang S P, Xing R J, et al. Full-scale immersed tunnel fire experimental research on smoke flow patterns [J]. Tunnelling and Underground Space Technology, 2018, 81: 494–505.

[4] Tang F, Zhu Y, Chen L. Experimental study on the effect of lateral concentrated smoke extraction on smoke stratification in the longitudinal ventilated tunnel [J]. Fire and Materials, 2020, 44(7): 1004–12.

Tunnelling for a Better Life – Yan, Celestino, Thewes & Eberhardt (Eds)
© 2024 The Author(s), ISBN 978-1-032-80042-4
Open Access: www.taylorfrancis.com, CC BY-NC-ND 4.0 license

Fire prevention and rescue technologies used in ultra-wide cross-section immersed tunnel

Xiujun Yang*
Institute of Public Safety Research, Department of Engineering Physics, Tsinghua University, Beijing, China
Jiaoke Transport Consultants Ltd., Beijing, China

Ling Yin
Jiaoke Transport Consultants Ltd., Beijing, China

Maohua Zhong
Institute of Public Safety Research, Department of Engineering Physics, Tsinghua University, Beijing, China

Liang Cheng
Jiaoke Transport Consultants Ltd., Beijing, China

ABSTRACT: The Shenzhen-Zhongshan Link has a total length of 6845m submarine tunnel and eight two-way lanes. There is an undersea interchange tunnel that intersects with the main tunnel. This project has a high traffic volume, complex traffic organization, high operational risk, and difficult linkage rescue. In order to solve the problem of the operation safety of subsea tunnel, the countermeasures are carried out from the aspects of hazard source control, accident prevention, accident early warning, accident alarm, accident disposal, emergency linkage and so on. An intelligent linkage rescue system for tunnels has been developed to realize rapid rescue linkage with accident scenarios under accident conditions.The fire rescue technology program by this project has a certain reference for the operation safety of other projects.

Keywords: Ultra-wide cross-section immersed tube tunnel, fire, fire rescue, emergency linkage

1 INTRODUCTION

The Shenzhen-Zhongshan Cross-River Link is a significant highway channel crossing the Pearl River Estuary, situated approximately 30km downstream of the Humen Bridge and 31km upstream of the Hong Kong-Zhuhai-Macao Bridge. This extensive cluster project spans a total length of about 24km, featuring a combination of a bridge, an island, a tunnel, and an underwater channel. The subsea tunnel of the Shenzhen-Zhongshan Link measures 6,845m, while the immersed tube section extends 5,035m. The project is scheduled to open to traffic in 2024.

This two-way, eight-lane tunnel is designed for a speed of 100km/h. The width of the main tunnel line varies from 46m to an impressive 69.8m, making it the widest highway immersed tube tunnel in the world. With a considerable traffic volume, a significant proportion of large vehicles, and complex traffic flow, how to ensure the operational safety of this ultra-wide steel shell immersed tube tunnel is the primary issue[1]. Traditional tunnel fire protection facilities mainly provide safety protection by setting up fire hydrants and other facilities in the tunnel, and do not form a full-chain disaster prevention system. In order to ensure the safety of the tunnel, systematic research has been conducted on key technologies, such as hazard source elimination, accident warning and alarm systems, fire smoke extraction, fire extinguishing, emergency rescue and personnel evacuation, and so on.

2 GOALS AND PRINCIPLES OF FIRE RESCUE SYSTEM DESIGN

The design of the tunnel fire rescue system is guided by the principle of prioritizing prevention and integrating prevention with firefighting. During the design stage, aligned with the specified safety objectives, the focus is on ensuring the overall operational safety of the tunnel. This involves considerations such as fire scene design, the configuration of fire rescue equipment, and emergency ventilation plan, etc.

*Corresponding author: yxj21@mails.tsinghua.edu.cn

DOI: 10.1201/9781003495505-330

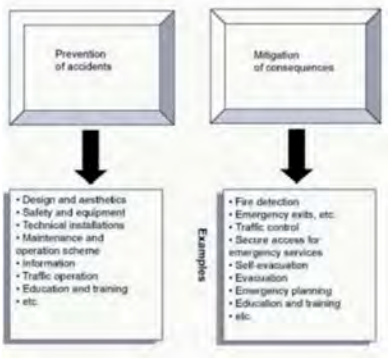

Figure 1. The global safety concept[2].

3 CONTROL OF DANGEROUS GOODS TRANSPORT VEHICLES

Dangerous goods transport vehicles are strictly prohibited from traversing the entire route. The system is integrated with the national key operating vehicle network joint control system to enable dynamic monitoring of vehicles for highway passenger transportation, tourism passenger transportation, hazardous chemical transportation on the platform.

The capture function of the ETC mast is used to collect the data of vehicles, which is compared with the data of vehicles for highway passenger transportation, tourism passenger transportation, hazardous chemical transportation in the national key operating vehicle network and joint control system to confirm the key vehicles. The management platform confirms the precise locations of these key vehicles and tracks the vehicles that entered into the tunnel by using the tunnel's video and digital data, along with twin hardware facilities. Real-time status information is then back to the central platform for display, which significantly enhanced the safety monitoring of key vehicles.

In addition, control is maintained through the management of the road network, employing a combination of 'vehicle face recognition,' 'traffic radar,' and 'video surveillance.'"

4 FIRE ALARM FACILITIES

In the fire alarm system, the tunnel section fire alarm information is categorized into three types:

The first type: dual-wavelength flame detection, manual alarm button, fire hydrant box unpacking, fire extinguisher box unpacking, fire hydrant button signals;

The second type: fiber Bragg grating temperature sensing optical cable alarm signals;

The third type: video smoke detection alarm signals.

The fire alarm controller receives dual-wavelength flame detection, manual alarm button, fire hydrant box unpacking, fire extinguisher box unpacking, and fire hydrant button signals via the bus, and receives fiber grating temperature-sensing optical cable alarm signals through the serial port. The fire alarms in tunnel sections and monitoring station machine rooms form a ring network through optical fiber to realize independent transmission of alarm information and has information transmission channel redundancy. Temperature detection information from the fiber grating temperature-sensing optical cable is transmitted through the industrial Ethernet ring network of the traffic monitoring system. Video smoke detection alarm information is transmitted through the surveillance system. The tunnel fire detection equipment settings are shown in the following table:

Table 1. Table of fire detection equipment layout.

Location	Equipment	Configuration
Driving Passage Inside the tunnel	Dual wavelength flame detector	Staggered arrangement on both sides
	Fiber Bragg Grating Temperature Sensing Optical Cable	Full length
	Video smoke detection	Via cameras
	manual alarm button	Staggered arrangement on both sides
strong current cable channel Inside the tunnel	Fiber Bragg Grating Temperature Sensing Optical Cable	Length settings

5 VENTILATION AND SMOKE EXTRACTION FACILITIES[1,3]

The ventilation and smoke exhaust facilities in the main tunnel serve various critical functions. The ventilation system primarily ensures driving safety and comfort within the tunnel, while the smoke extraction system plays a pivotal role in centralized smoke extraction during fire emergencies. This helps control smoke propagation, safeguard personnel evacuation, and facilitate effective rescue operations. Additionally, the safety passage ventilation system supports normal ventilation operations and positive pressure ventilation during fire incidents.

5.1 *Tunnel ventilation system*

The ventilation system of the main tunnel adopts a ventilation scheme of longitudinal full jet ventilation and split-type exhaust at the tunnel entrance.

5.2 *Exhaust system*

The tunnel is equipped with an independent smoke exhaust duct on the upper level of the central pipe gallery along the entire tunnel length. The exhaust duct is connected to the smoke exhaust fans located on the east and west artificial islands. Approximately every 85 meters, a smoke exhaust outlet is provided,

positioned within the exhaust duct on the side of the pipe gallery in the middle of the main tunnel. The tunnel structure design unit has designed these smoke exhaust outlets in alignment with the civil structure. The outlets are arranged in groups of three.

A top smoke exhaust solution is employed, with an auxiliary flue located at intervals of about 165 meters.

Jet fans within the exhaust duct assist with auxiliary smoke extraction.

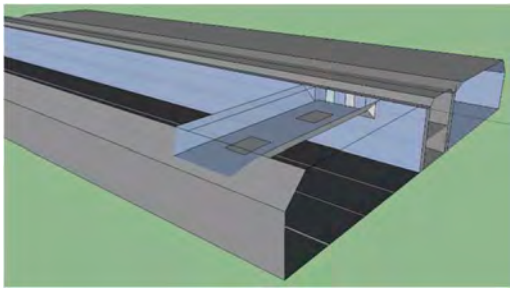

Figure 2. Diagrammatic Sketch of Exhaust Duct Settings in Top Smoke Exhaust Mode with Louver Air Outlets at the Bottom.

Through verification through numerical simulation and model experiments, this method can increase the smoke exhaust efficiency by more than 40%.

5.3 *Safe passage ventilation system*

A safe passage fan room will be established on each of the east and west artificial islands to provide pressurized air supply. Maintain channel positive pressure at 30-50pa through local pressurization.

5.4 *Centralized smoke exhaust system for E and F ramp tunnels*

Independent flue ducts are installed in ramp tunnels for the centralized smoke extraction during fire conditions.

Smoke exhaust outlets placed at the confluence section of the E and F ramp tunnels will be concentrated for smoke extraction. In the event of a fire, the electric smoke exhaust outlets positioned at the corresponding locations will be activated for centralized smoke extraction.

6 FIRE EXTINGUISHING FACILITIES

6.1 *Facilities composition*

In the driving tunnel, the following systems are in place: a foam-water spray combined system, a tunnel fire hydrant system (including a fixed aqueous film-forming foam fire extinguishing device), and a fire extinguisher system.

At the tunnel entrance and in the open section of the tunnel, an outdoor fire hydrant system is installed, which adopts a temporary high-pressure system.

Within the tunnel equipment cavern, a fire extinguisher system is established.

In the tunnel cable channel, fire separation facilities are installed to limit the fire to a certain area and minimize fire losses when the fire cannot be extinguished in time.

6.2 *Foam-water spray fire extinguishing system*

6.2.1 *System composition*

The tunnel is equipped with a foam-water spray fire extinguishing system. This system features water supply pipelines and foam liquid pipelines running along the tunnel. In case of a fire, the water spray pump and foam liquid pump in the affected area are activated to provide water and film-forming foam liquid to the tunnel's foam-water spray combined system.

6.2.2 *System setting requirements*

The application rate of the foam-water spray combined system is ≥6.5 L/(min·m²). The time duration of foam mixture injection is ≥22 minutes, and the time duration of water spray injection is ≥60 minutes. The concentration of the foam mixture is ≥3%, and the pressure at all tunnel-specific foam-water spray nozzles is no less than 0.35 MPa.

Additionally, the maximum spacing between deluge valves is 22 meters, and the working pressure of a single nozzle is 0.35 MPa.

6.3 *Fire hydrant system*

Fire equipment boxes and fire hydrant pipes are installed along the buried section of the tunnel. Outdoor fire hydrants are also placed near the main tunnel entrance and within the open section of the tunnel. In case of a fire, the tunnel fire hydrant pump and outdoor fire pump in the affected area are activated to supply water to the fire hydrants and AFFF fire extinguishing devices inside the tunnel and at the tunnel entrance.

6.4 *Fire extinguisher system*

Fire extinguisher boxes are positioned staggered on both sides of the tunnel lane, with a maximum spacing of 50 meters on one side. Each box contains a dry powder portable fire extinguisher for extinguishing initial fires.

In addition, fire extinguisher boxes are installed on both sides of the safety door at the traffic opening side of the upward tunnel in the safety passage, and dry powder portable fire extinguishers are placed in the boxes.

7 RESCUE FACILITIES AND EVACUATION FACILITIES[4]

Emergency rescue follows a two-level management system: Shenzhen-Zhongshan Link Rescue Command Center — Rescue Stations.

The Rescue Command Center, located at the Ma'an Island Management Center on the Zhongshan side, is responsible for emergency rescue command for all emergencies along the entire route.

Rescue Stations are the specific execution units for rescue operations. In case of an accident, the emergency plan will be activated immediately, and the rescue stations are ready to engage in the rescue operations under the command of the Rescue Command Center.

Each Rescue Station is equipped with rescue facilities. There are three rescue stations along the entire route, located at the West Artificial Island, East Artificial Island, and Management Center on the Zhongshan Side.

The temporary evacuation passage in the middle pipe corridor of the main tunnel has a net width of 2 meters and a net height of 2.2 meters. This passage extends along the entire route with safety doors placed at intervals of no less than 90 meters. In case of an accident, personnel can enter the passage and escape from the opposite tunnel, which directly leads to the safe areas of the east and west artificial islands. Additionally, there are two escape stairs in the underwater interchange. In case of accident, people can enter the passage directly to the ground.

Relying on informatization and intelligent methods and based on accident scenarios, a fire rescue module has been developed. It is founded on event perception, situation prediction, and intelligent equipment linkage, allowing all relevant equipment to be activated with a single click to initiate disaster prevention zone linkage rescue, thereby enhancing rescue efficiency.

Figure 3. Tunnel linkage rescue platform.

8 OTHER FACILITIES

8.1 *Power supply facilities*

In order to improve the reliability of power supply, The 110KV external power supply is sourced from two different superior substations. Moreover, 10KV diesel generators are positioned on the east and west artificial islands as backup power sources. These generators offer support for the fire pump room, basic lighting, emergency lighting, and monitoring equipment.

An EPS (Emergency Power Supply) system is also installed to ensure continuous power supply during emergencies.

8.2 *Lighting facilities*

Within the tunnel, an emergency lighting system is installed to facilitate safe evacuation and rescue operations in case of a tunnel accident.

In addition, side wall light strips span the entire length of the tunnel. These strips utilize varying light colors and flashing frequencies, etc. to convey information about tunnel operating conditions, ensuring drivers and passengers are well-informed throughout their journey.

Figure 4. Diagrammatic Sketch of Side Wall Light Strip in the Tunnel.

8.3 *Communication facilities*

When a fire breaks out in a certain area within the tunnel passage, the operational status of emergency telephones in other areas remains unaffected. Drivers and passengers can use these emergency phones to call the monitoring center or the West Artificial Island Monitoring Station for assistance. Rescuers can also use these emergency phones near the fire site for emergency communications.

Cable broadcast control centers are established in both the monitoring center and artificial island monitoring station to manage broadcasts in the bridge section and tunnel section respectively.

The monitoring center can broadcast throughout the entire bridge section via the cable broadcast system, or broadcast in specific zones for some road sections.

A wireless FM broadcast system is deployed in the tunnel to enable one-way broadcasting. This wireless FM radio can rebroadcast traffic information and content from other radio stations. Furthermore, it can be used to transmit emergency information. Drivers and passengers can access diversion instructions via this radio system.

9 CONCLUSION

The comprehensive design considerations encompassing the removal of potential hazards, fire alarms, fire suppression, smoke extraction, emergency response, and evacuation measures are paramount in ensuring the operational safety of this ultra-wide cross-section immersed tube

tunnel. The findings and outcomes derived from this project are not only valuable for similar tunnel projects but also serve as a reference for the wide tunnel engineering industry.

REFERENCES

[1] Deng XH, Song S Y, Cao ZM, et al, 2020.Overall Plan for Smoke Extraction System of Submarine Tunnel in Shenzhong Channel [J]. Tunnel Construction, 40(08): 1176–84.

[2] Art BENDELIUS,2007.PIARC Committee on Road Tunnels Operation (C3.3).Systems and Equipment for Fire and Smoke Control in Road Tunnel[R]. France.

[3] Yang X,2016. Design Environmental Protection, Energy Saving and Safety Ventilation System of Long Highway Immersed Tunnel [J]. Procedia Engineering, 166: 32–6.

[4] Caliendo C, Ciambelli P, Guglielmo MLD, et al, 2012. Simulation of People Evacuation in the Event of a Road Tunnel Fire [J]. Procedia - Social and Behavioral Sciences, 53: 178–88.

Tunnelling for a Better Life – Yan, Celestino, Thewes & Eberhardt (Eds)
© 2024 The Author(s), ISBN 978-1-032-80042-4
Open Access: www.taylorfrancis.com, CC BY-NC-ND 4.0 license

Quantitative detection method and practice of voids at the interface of steel-shell concrete with complex structure

Hongbo Zhao*, Guoqing Liu, Ziwu Fan, Long Sun, Lingchao Meng & Langlang Wang
Nanjing Hydraulic Research Institute, Nanjing, China

ABSTRACT: This study employs neutron moderation theory to quantitatively detect millimeter-level voids at the interface of steel-shell concrete with complex structures. Experiments were conducted using concrete models varying in moisture content and steel-shell thickness. The results indicate a consistent decrease in the thermal neutron counting rate with increasing void height, demonstrating a strong linear relationship between these variables. The calibration relationship was verified by detecting the known void height between the thick steel plate (40 mm) and the plain concrete block; the maximum difference between the test result and the actual void height was only 2.1 mm. Additionally, the full-scale model of the Shenzhen–Zhongshan Link immersed tunnel was utilized to devise an on-site detection methodology. This involved conducting void detection and subsequent destructive verification tests. The neutron method detection yielded statistical results. The accuracy rate reached approximately 94% at an allowable error of ±2.0 mm. This demonstrates a high level of quantitative identification accuracy for the millimeter-level voids at the interface of the steel-shell concrete with a complex structure in the immersed tunnels. This method has been effectively applied in the formal tubes of the Shenzhen–Zhongshan Link immersed tunnel.

Keywords: steel-shell concrete, void height, neutron method, non-destructive testing, immersed tunnels

1 INTRODUCTION

Steel-shell concrete composite structures are widely adopted in the structural design of immersed tube tunnels (Grantz 1997, Fu 2004), water conservation and hydropower (Wang 2019, Wu et al. 2021, Yang et al. 2018, Wang 2021), bridges (Pan 2018, Zhang 2020, Xu 2021), and other engineering fields owing to their superior properties including high strength, good ductility, fatigue resistance, impact resistance, explosion resistance, and waterproofing, as well as the advantages of labor-saving, material-saving, lightweight erection, and rapid construction (Akimoto et al. 2002, Song and Chen 2005). In the domain of immersed tube tunnels, steel-shell concrete composite structures have evolved from waterproof formwork, which plays a minimal role in structural stress (Gursoy 1995), to steel-shell reinforced concrete structures bearing combined stress (Grantz 1997). The development progressed from stacked stud and channel steel connections (Pryer and Bowerman 1998, Xie and Chapman 2006) to steel–concrete–steel composite structures with longitudinal and transverse partitions (Song et al. 2019). Further advancements include increasing the contact surface angles between the steel shell and concrete as stiffeners, and integrating welding studs with the concrete to enhance the shear connection of steel plate concrete (Shariati et al. 2013).

However, the complex structural design poses significant challenges to the pouring construction of the concrete. This not only requires a sufficiently good fluidity performance of the concrete paste but the concrete must also be ventilated smoothly (Lyu et al. 2016, Penget et al. 2021). Extensive experimental research and engineering practice data reveal that owing to the densely packed and staggered components such as steel shell longitudinal and transverse partitions and stiffeners, concrete is prone to the formation of voids during the pouring process, particularly near the interfaces of these components with the steel and concrete. Early Japanese steel-shell concrete casting tests revealed that the hollowing areas could constitute up to 5% of the total area (Komon et al. 1995). Notably, hollowing significantly impacts the load-bearing capacity of the joint: a 10 mm hollow can reduce the capacity by

*Corresponding author: hbzhao@nhri.cn

DOI: 10.1201/9781003495505-331

a maximum of 16.5%; at 20 mm, this reduction can reach 37.5% (Tang et al. 2020). Consequently, accurately detecting concrete voids beneath the steel shell surface is vital for maintaining the structural integrity and ensuring project safety. An effective detection method can provide essential guidance for the grouting reinforcement.

At present, the commonly used non-destructive testing techniques for detecting the defects of steel-shell–concrete interface voids include the artificial malleting, ultrasonic (Yang et al. 2012, Wang et al. 2021), impact-echo (Yao et al. 2017, Liu et al. 2021), and impact-imaging methods (Tang and Che 2019, Zhang et al. 2022), which are based on the elastic waves theory; as well as the infrared (Liu et al. 2021), γ-ray (Hua 1981), and neutron methods (Zhang et al. 2017), which are based on the radiographic detection technology.

The artificial malleting method judges the voids by the sound of the mallet hitting the steel shell, which is influenced by the subjective experience of individuals, and therefore often used as a qualitative discrimination method for initial screening in the actual detection. Ultrasonic, impact-echo, and infrared methods can often only qualitatively identify the presence of defects within the structure but cannot identify the height of the void defects. The impact imaging method can provide the distribution range of the height of the voids but cannot be used to determine the exact value. The γ-ray method has considerable external radiation damage. Therefore, the protection requirements are incredibly high and the implementation of engineering applications is challenging. The neutron method uses a neutron source to emit fast neutrons that easily pass through the steel plate and concrete to produce detectable thermal neutrons, according to the counting rate and distribution rule of the thermal neutron, which can be detected out of the region and height of the voids. The neutron method can use low-energy radioactive sources. Therefore, relative to the γ-ray method, the protection requirements are lower. Currently, the neutron method is primarily applied in detecting voids in steel-shell concrete within hydraulic structures, specifically in water diversion and transmission pipelines, runner chambers, and volutes of electric generating units. However, there has been no effective research or application of this method in steel-shell concrete immersed tube tunnels.

This study addresses the challenge of quantitatively detecting millimeter-scale hollowing in concrete under a thick steel shell with a complex structure. The proposed method utilizes the principle of fast neutron slowing to investigate the response relationship between the thermal neutron counting rate and the height of hollowing in a steel-shell concrete composite structure. A technique encompassing both hardware and software equipment has been developed for the quantitative detection of such hollowing. Theoretical foundations for this technique were established through indoor calibration tests, enabling the quantitative detection of millimeter-scale hollowing in the steel-shell concrete composite structures. The theoretical non-destructive quantitative detection of millimeter-scale hollowing of complex steel-shell concrete structures is achieved by conducting indoor calibration tests. At the same time, combined with the steel-shell concrete immersed tube foot-scale model of the Shenzhen–Zhongshan Link, a blind on-site lid opening verification test is carried out to demonstrate the accuracy of the neutron method in detecting millimeter-avoidance of steel-shell concrete complex structures. This can provide technological support for the high-quality construction of the century-long quality project of the Shenzhen–Zhongshan Link.

2 DETECTION METHOD AND EQUIPMENT

2.1 *Introduction of the neutron method*

Neutron law quantitative detection of the steel shell concrete interface dehulling is mainly based on the neutron slowing theory, that is, the use of radioactive sources emitted by fast neutrons and the medium atomic nuclei collision, which reduce the energy and decelerate the neutrons, ultimately yielding slow neutrons. The effect of the medium on the fast neutron deceleration and the mass size of atomic nuclei within the medium influence this process. As atomic weight decreases, the deceleration effect strengthens. Hydrogen, with the smallest atomic weight in nature, is the most effective neutron slowing agent. The slowing ability of the hydrogen atoms is 2–3 orders of magnitude larger than that of general soil elements such as oxygen, silicon, aluminum, calcium, magnesium, and iron. Therefore, the slowing and decelerating effect of the medium on the fast neutrons is mainly determined by the amount of hydrogen contained in the medium. Concrete consists of crushed stone, coarse sand, and cement mixed with a specific amount of water. Most of this water reacts with cement to form hydrated water, while a small portion remains in a free state. Both forms of water are uniformly distributed within the concrete. Because concrete is a water-containing material and water molecules contain hydrogen atoms, concrete is a good fast neutron moderator.

Because the fast neutron radiation is easily slowed by "light" but not "heavy," it can easily penetrate the steel-shell concrete structure of the surface of the steel plate and the concrete material below the interaction. This mainly occurs with the concrete contained in the hydrogen atoms, slowing down the formation of the thermal neutrons. The water content is fixed for a particular proportion of the concrete, which affects the formation of thermal neutron density, that is, the thermal neutron counting rate per unit volume of concrete mass. In areas with void defects, the mass per unit volume of the concrete is noticeably lower than

that in the densely filled areas. Consequently, the thermal neutron counting rate in these hollow regions is lower compared to that in the denser parts. Utilizing a neutron source and thermal neutron detector enables the determination of the thermal neutron counting rate in various parts of the inspected object. This approach allows for pinpointing the location of the hollowing plane and measuring the depth of concrete hollowing beneath the steel plate.

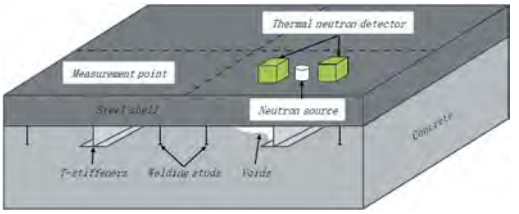

Figure 1. The basic principle diagram of neutron method.

2.2 *Detection equipment for the neutron method*

The detection equipment for the neutron method comprises a neutron source, thermal neutron detector, integrated circuit, battery, antenna, and an operating computer. The neutron source used in this study is an americium-241-beryllium radioactive source, and the thermal neutron detector is a helium-3 orthogonal gas counting tube; the specific parameters are shown in Table 1.

Table 1. Module parameters of detection equipment for the neutron method.

Module	Type	Property parameter
Neutron source	^{241}Am-Be	Cylindrical shape, diameter 16 mm, height 20 mm, activity 1.48 E +9Bq (40 mCi).
Thermal neutron detector	helium-3 orthogonal gas counting tube	Gas pressure greater than 6 atm; Detection efficiency exceeds 50% for thermal neutrons with wavelengths greater than 1 Å; Thermal neutron sensitivity 104 cps/nv.
Battery	Ni-MH	1.2 V, 1200 mAh

2.3 *Correlation calibration*

According to the basic principle of neutron detection, the size of the thermal neutron counting rate (N) at measurement points is related not only to the height of steel plate evacuation (h) below these points but also to the thickness of the steel plate and the actual water content in the concrete material. Therefore, once the steel plate thickness and concrete material water content have been established, the deflation height at the measurement points is determined solely by the thermal neutron counting rate at these points. When combined under specific testing conditions, a distinct correlation emerges between the steel plate, concrete, and structure of internal stiffeners of the object being tested. Establishing this correlation requires calibration before the test.

In this test, steel plates with six thicknesses of 14, 18, 24, 30, 36, and 40 mm were selected. Five types of concrete equivalent media with a background moisture content of 117.8, 192.0, 238.7, 354.4, and 598.1 kg/m^3 were used for 30 combinations of the working conditions. The upper surface of the concrete equivalent medium and the steel plate were closely fitted to simulate the non-dehollowing situation, on which five regular defects were formed by lifting the steel plate to varying heights (5.0, 10.0, 20.0, 30.0, and 50.0 mm). The thermal neutron counting rate for each condition was measured by the equipment for different heights of evacuation.

The correlation between the thermal neutron counting rate and the height of deflection was fitted using the least squares method. A quantitative model (Equation (1)) was established by this process. The model relates the thermal neutron counting rate to the height of the de-voids for the combinations of varying steel plate thicknesses and different background moisture contents in the concrete equivalent media.

$$h = f(N) = \sum_{i=0}^{2} a_i N^i \tag{1}$$

As an example, the calibration curve for a 40 mm steel plate is shown below.

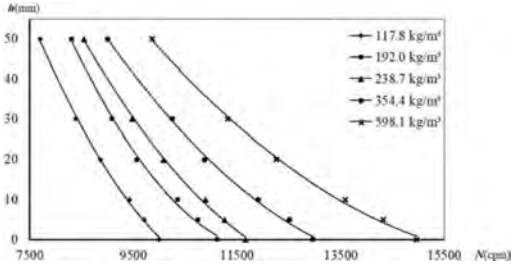

Figure 2. Calibration curve for 40mm thickness steel plate.

The calibration curves show that when the thickness of the steel plate and the background moisture content of the concrete are known, the thermal neutron counting rate is the highest in the absence of de-voids, and it decreases gradually with an increase in the de-voids. Using the thermal neutron counting rate measured during non-decavitation as a baseline, a decrease in this rate indicates an increase in decavitation. The extent of this decrease is directly

proportional to the decavitation size, a relationship crucial for quantitatively identifying the height of decavitation with this method.

3 PROTOTYPE EXPERIMENT

To further test the validity and accuracy of the neutron method for quantitatively detecting the dehulling of complex structures in the steel-shell concrete, a blind check-open lid validation experiment was carried out based on the foot-scale model of the steel-shell concrete immersed tube tunnel of the Shenzhen–Zhongshan Link.

3.1 *Introduction of the full-scale model*

The full-scale model was 9.6m long, 54.5m wide, and 10.6m high; the materials and detailed structures, such as cross-section, compartment dimensions, and stiffeners, were consistent with those of the Shenzhen–Zhongshan Link. The model was divided into 51 compartments on the bottom plate, 12 on the wall, and 42 on the top plate. The top planes of the base and the top plates were welded with a mixture of 14 mm and 40 mm steel plates, the pouring holes (φ 273 × 8mm) were set in the middle of the top planes of the compartment, and the vent holes (φ 89 × 8mm) were set in the corners of the perimeter of the compartments and the T-stiffeners. The C50 high-flow self-compacting concrete was used for the full-scale model and poured without vibration.

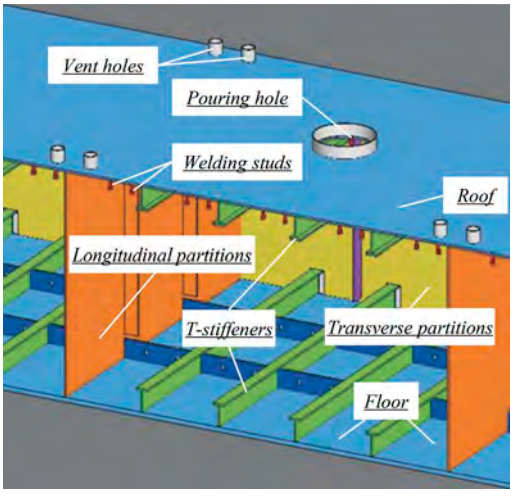

Figure 3. Steel-shell structure diagram of full-scale model.

3.2 *Measurement points division*

The full-scale model test was conducted using each compartment as a test unit, following the final setting of the self-compacting concrete. Variations were observed in the thermal neutron counting rate at the measurement points. These may be attributed to the use of the same concrete batch but with different thicknesses of the top steel shell, various T-stiffeners, and welding studs on the bottom surface of the steel shell. These variations influenced the concrete content within the test scope. To mitigate the impact of these connectors on the test results, the model was divided into measurement lines, with measurement points deployed according to the arrangement of the T-stiffeners and welding studs.

Considering the standard compartment (3.5 m × 3.0 m × 1.5 m) as an example; the T-stiffener spacing was 700 mm, and two rows of welding studs were laid between two T-stiffeners. Measurement lines were arranged along the direction of the T-stiffener with a width of 300 mm for the T-stiffener and 200 mm for the welding studs. This was based on a principle involving a 150 mm range on either side of the T-stiffener. Along these lines, the measurement points were placed at 300 mm intervals, following the same layout rules as that for the T-stiffener. This arrangement was also applied to the cross-partition lines at the measurement points. The layout of the measurement points on the top plane of the standard silo grid, along these measurement lines, is illustrated in Figure 4.

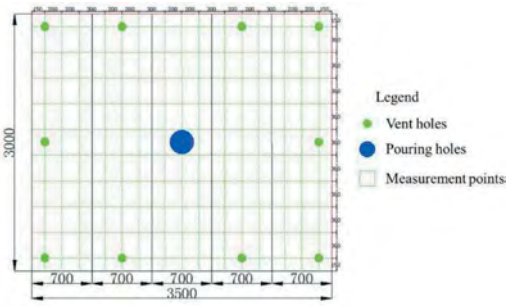

Figure 4. Layout plan of detecting line and point on the top of standard compartment.

3.3 *Collecting data*

Prior to data collection, it was necessary to clean the steel shell surface to remove any debris, including rust, welding slag, and slurry. This step ensured that the surface remained clean, smooth, and free from sand, loose soil, and stagnant water.

A planar model was built in the collection software based on the length, width, and layout of the measurement points; the two-coordinate system was the same, and the equipment was placed in the center of the measurement points of the probe flat, ready for measurement.

The computer was set to a single acquisition time step of 30 s. This setup enabled the activation of specific measurement point positions. By controlling the acquisition button, the thermal neutron counting rate was automatically collected. This process was repeated twice, and the average of these two readings was taken

as the final thermal neutron counting rate measurement value for each measurement point. After the acquisition, the equipment probe was moved to the following measurement point. This was repeated until all the measurement points in the compartment were completed. The above-mentioned three steps were repeated for each compartment.

3.4 *Data processing and analysis*

After completing point-by-point data collection for each bin, the next step was to process and analyze the collected data, which was also performed on a compartment, including the calculation of the baseline value of the thermal neutron counting rate and the normalization factor for the detection condition.

(1) Reference value of thermal neutron counting rate. The reference value of the thermal neutron counting rate is the value of the thermal neutron counting rate of the concrete in a certain structural (T-stiffeners, welded nail) condition without deflation, i.e., each measurement line in the compartment corresponds to a benchmark value. If there is no point on the line of measurement of deflation, the thermal neutron counting rate of all measurement points should be equal to or similar to the benchmark value (there is a certain degree of fluctuation in the value of the thermal neutron counting rate). Therefore, if there is no significant difference in the data along the measurement line, the average value will be used as the benchmark. However, if individual data points are notably lower than this average, it suggests a potential deflation at the corresponding measurement points. These points should be excluded from the data set before recalculating the average value. The base value of thermal neutron counting rate for neutron method detection under working conditions was calculated according to Equation (2).

$$\overline{n_j} = \frac{\sum_{i=1}^{I} n_{ij}}{I} \tag{2}$$

where, $\overline{n_j}$ is the reference value of the thermal neutron counting rate for column j of the detection condition (counts per minute (CPM)), n_{ij} is the thermal neutron counting rate in row i and column j of the detection condition (CPM), i and j $=1,2,\ldots,n$.

(2) Normalization coefficient. In on-site test conditions where the steel plate thickness matches that of the calibration conditions, the reference value for the thermal neutron counting rate in these on-site tests may be lower than that in the calibration settings, owing to the variations in the bottom structures of the steel shell. In this case, it is necessary to normalize the test data before it can be included in the calibration curve of this condition for calculating the void values. Normalization coefficient calculation is given by Equation (3).

$$k_j = \frac{n_0}{n_j} \tag{3}$$

where k_j is the normalization coefficient of the reference value in column j, and n_0 is the reference value for the thermal neutron counting rate of steel plates with the same thickness under the calibration conditions.

The thermal neutron counting rate after normalization of the measurement points can be obtained according to Equation (4).

$$n'_{ij} = k_j n_{ij} \tag{4}$$

where, n'_{ij} is the normalized thermal neutron count rate in row i and column j. This value is introduced in the calibration curve calculation to obtain the value of void height.

(3) Equivalent void height. The void of the calibration experimental design is a regular void defect body formed by continuously improving the steel plate in a state of complete adhesion between the steel plate and the concrete block. Therefore, the void value calculated using the curve is the average of the void values in the measurement points, and we refer to this average value as the equivalent void height. The equivalent void height can be calculated by substituting the normalized thermal neutron count rate into the calibration curve of the corresponding working condition in Section 2.3.

3.5 *Radiation safety*

The neutron sources used to produce three types of radiation, including alpha particles, gamma Rays (photons), and neutrons, The alpha particles are stopped by the source capsule. Only the gamma and neutron radiation can contribute to any occupational radiation exposure. Under normal conditions a full-time operator of the detection equipment will receive less than 1.5 mSv per year, which is lower than the annual dose limit specified in the "Basic Code for Protection against Ionizing Radiation and Safety of Radiation Sources" (GB18871-2002), taking advantage of all available means to limit radiation exposure is always recommended. The three methods of limiting exposure are: (1) Detection equipment has shielding built into the system which reduces the exposure. (2) Anyone working with or near radioactive materials is subject to the limits of occupational exposure and must complete a radiation safety training course. (3) Keep personnel outside the safety distance of 3~5m from the detection equipment when the detection equipment is working. (4) Keep the time spent by the operator around the radioactive source to a minimum and wear a thermoluminescence dosimeter to monitor the irradiated dose.

4 ANALYSIS OF TEST RESULTS

The consistency of the calculated deflation values with the actual concrete deflation was verified by opening the cover of the steel shell. In the foot-scale model, nine compartments in the bottom plate, three in the wall, and two in the top plate were chosen randomly for verification. In each compartment, six measurement points were selected, giving a total of 84 points. To access these points, covers were opened by cutting a small area of the steel shell at each point using carbon arc gas cutting. This method was employed to avoid damaging the interface between the cover and the bottom surface of the steel shell in contact with the concrete, thus ensuring that the concrete surface morphology remained unchanged after the covers were opened.

4.1 *Measurement method for voids*

To the top surface of the steel plate as a reference surface for the measurement of the number of defects, the plasticity of the rubber cement to fill the open cover parts so that it is filled with recessed concrete voids, and then a steel ruler to flatten the surface of the rubber cement, so that it is flush with the reference surface, take out the rubber cement, the use of the principle of overflowing method of obtaining the volume of the rubber cement Q, then the actual volume of the defects V can be calculated by Equation (5).

$$V = Q - l_l * l_w * H \tag{5}$$

where l_l is the cutting length of the steel shell at the opening measuring point, l_w is the cutting width of the steel shell at the opening measuring point, and H is the thickness of the steel shell at the opening measuring point.

Then, the relationship between the measured height h of the open lid deflation at the measurement points and the actual defect volume V is described by Equation (6).

$$\overline{h} = \frac{V}{l_l * l_w} \tag{6}$$

4.2 *Verification results*

The measured void results of 84 open-lid areas were compared with the detection results for validation. We have used the comparison of a typical compartment as an example for illustration.

As shown in Figure 7, #1, #5, and #6 are the open cover positions located on the T-stiffeners structure, #3 and #4 are located on the welded nail structure, and #2 is located on the side of the T-stiffeners leaning on the pouring hole. Among them, the #1 detection result

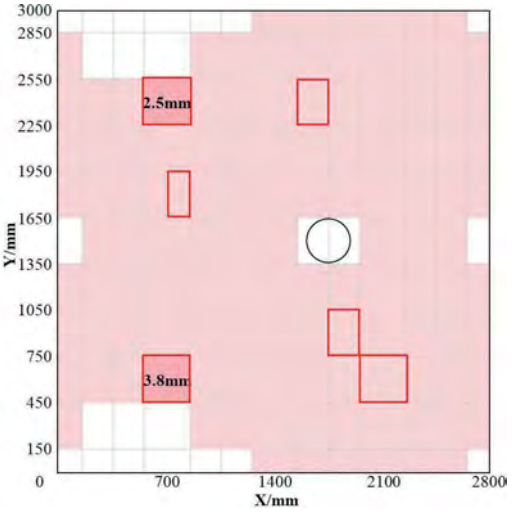

Figure 5. The results of neutron method.

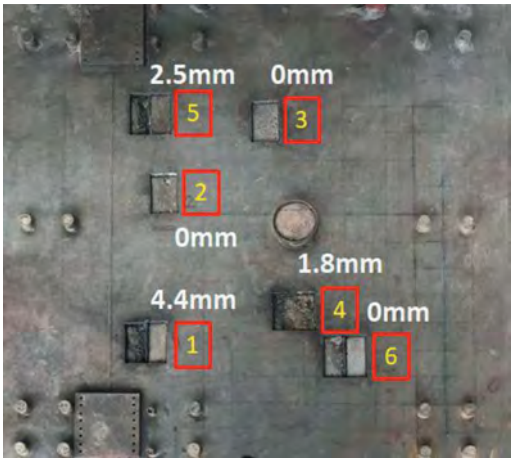

Figure 6. Opening locations at site.

indicated the presence of 3.8 mm voids, whereas the open cover measurement showed 4.4 mm voids, which aligns closely with the detection results. Specifically, these voids are located on the left side of the T-stiffeners, with the right side appearing dense. For #2 and #3, the detection results indicated a dense structure and the open cover test revealed slight honeycomb formation, which are not classified as voids. Thus, these observations correspond with the results of the respective tests. Furthermore, #4 detection result is dense, and the measured void value of the open cover is 1.8 mm, which is slightly inconsistent with detection result. #5 detection result is dense, and the measured void value of the open cover is 1.8 mm, which is slightly inconsistent. The test for #5 revealed a 2.5 mm voiding, which precisely matches the measured hollowing value on the open cover. This consistency underscores the

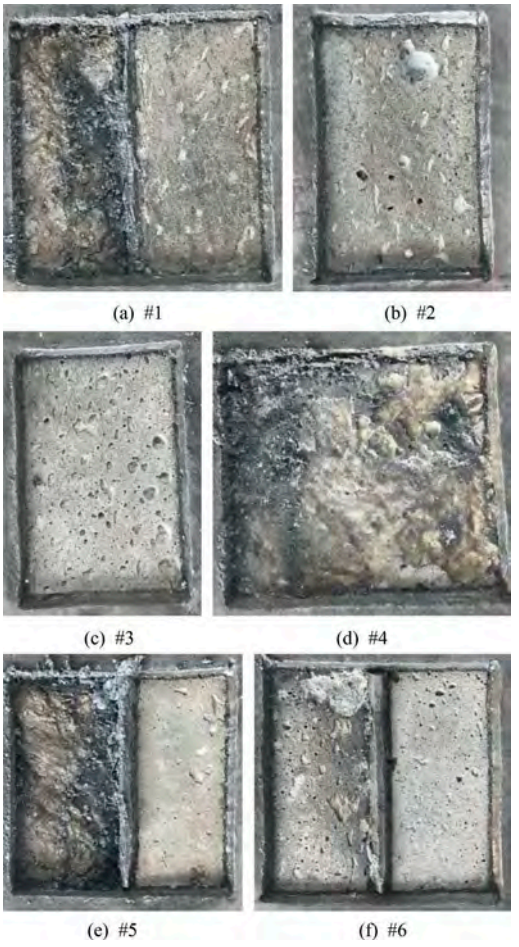

Figure 7. Opening condition of steel case Nos. #1 to #6.

fact that the hollowing is predominantly concentrated on the left side of the T-stiffeners, with the right side exhibiting a denser structure. The #6 exhibits denseness accompanied by a minor honeycomb formation observed during the open-cover test. Notably, the honeycomb formation on the left half of the T-stiffeners appears slightly larger than that on the right half. Additionally, it is important to recognize that the upper right corner of the left half experiences open-cover damage, which should not be classified as a part of the void.

Upon verifying the test results of 84 open cover positions and comparing them to the measured void values of the open cover, it can be determined that the compliance rate for void height reaches 94.0% within an error range of ±2 mm.

5 FORMAL IMMERSED TUBE APPLICATION

The results of the full-scale model cover opening verification test show that the method has met the requirements of formal immersed tube void detection. Therefore, this method was used to quantitatively detect the void height of the suspected void parts screened on the formal pipe sections, and the quantitative detection results were used as the basis for judging whether the void parts needed to be opened and grouted. According to the requirements of the engineering design, grouting reinforcement is required when the equivalent void height of a single measuring point is greater than 5 mm, and when there are two or more adjacent measuring points with equivalent void heights greater than 3 mm across the T- stiffeners, grouting reinforcement is also required.

Using the neutron method, we have completed the detection of a total of 32 formal pipe sections and nearly 100,000 measurement points. Taking the last immersed tube E24 in the east as an example, 39 suspected void parts were screened out in the bottom plate, and 49 in the top plate. The neutron method was used to detect these 88 parts, a total of 2820 measurement points were detected, and the detection results did not find the parts that need grouting reinforcement, only 25 measurement points had a voiding value between 2.5 and 5.0mm, accounting for approximately 0.16 parts per ten thousand.

6 CONCLUSIONS AND RECOMMENDATIONS

(1) Based on the theory of fast neutron slowing, the calibration test was carried out by constructing a regular dehollowing defective body. The relationship between the thermal neutron count rate and the dehollowing height of the steel-shell concrete was constructed using the numerical fitting method, which can reach 99% when a steel plate of 40 mm thickness was used, and thus yield a more satisfactory result.

(2) By integrating the structural design of the steel shell, the intricate steel components located at the base of the shell can utilize the burial rule to systematically arrange the measurement lines for data classification. These lines are then matched with the calibrated thermal neutron count rate benchmark values under normalized working conditions. This approach enables the achievement of millimeter-level non-destructive quantitative detecting of voids at the steel-shell concrete interface, even within complex structural configurations.

(3) The results of the blind open-cap validation test show that the equivalent height of evacuation detected by the neutron method quantitatively conforms well to the actual situation. The compliance rate of the height of evacuation is calculated to be 94.0% for a margin of error of ±2 mm.

(4) The neutron method has been successfully applied to the steel-shell concrete immersed tube tunnel project of the Shenzhen–Zhongshan Link,

completing the test of the critical parts of all 32 official tube sections. The test results not only ensure the quality of the concrete pouring but also serve as important guidelines for the improvement of the structure and the optimization of the construction process.

ACKNOWLEDGMENTS

This work has been supported by the Special Funds for Basic Research Operations of Public Welfare Research Institutes at the Central Level(No. Y122011) and the Guangdong Province KeyField R&D Program Project (No.2019B111105002).

REFERENCES

Grantz W. C., 1997. Steel-shell immersed tunnels—Forty years of experience. Tunnelling and Underground Space Technology. 12(1): 23–31.

Fu Q. G., 2004. Development and Prospect of Immersed Tunnels. China Harbour Engineering. (5): 53–58.

Wang X. Y., 2019. Analysis and Scheme Selection of Pressure Pipeline for Super High Head Power Station. Water Resources Planning and Design. (03): 106–110.

Wu H. G., Gao X. F., Fu D., 2021. Review and Prospect in Research and Application of Spiral Case Structure in Hydropower Plant. Journal of Hydraulic Engineering. 52(07): 770–780.

Yang Y. H., Han X. Y., Min S. H., et al, 2018. Voiding of Steel Lining of Draft Tube of Ertan Hydropower Station and Its Treatment. Dam & Safety. (05): 44–47.

Wang Y., 2021. Study on Treatment of Lining Steel Plate and Concrete Drop of Jilintai Second Stage Hydropower Plant Draft Tube. Shaanxi Water Resources. (07): 229–230.

Pan Z. Y., 2018. Mechanical Analysis on CFSS Bridge Tower Segment Under Debonding Condition. Communications Science and Technology Heilongjiang. 41(12): 99–100.

Zhang X. L., Tian T., 2020. Comparative Study on Seismic Behavior of Steel Tube Reinforced Concrete Bridge Columns and Reinforced Concrete Bridge Columns. Journal of Water Resources and Architectural Engineering. 18(03): 228–233.

Xu Y., Wang Z., Chen Z. Z., 2021. Minimum Concrete Filling Rate of Single Partially Concrete-Filled Steel Tubular Piers. Journal of Tongji University(Natural Science). 49(11): 1546–1555.

Akimoto K., Hashidate Y., Kitayama H., et al, 2002. Immersed tunnels in Japan: recent technological trends. International Symposium on Underwater Technology. Institute of Electrical and Electronics Engineers. New York, America.

Song J., Chen B. L., 2005. Advantages of immersed tube tunnel option in river- or gulf-crossing. Modern Tunneling Technology. 42(3): 28–30.

Gursoy A., 1995. Immersed steel tube tunnels: an American experience. Tunnelling & Underground Space Technology. 10(4): 439–453.

Pryer J. W., Bowerman H. G., 1998. The development and use of British steel bi-steel. Journal of Constructional Steel Research. 46 (1):15–15.

Xie M., Chapman J. C., 2006. Developments in sandwich construction. Journal of Constructional Steel Research. 62(11): 1123–1133.

Song S. Y., Nie J. G., Xu G. P., 2019. Development and application of steel-concrete-steel composite structures in immersed tunnels. China Civil Engineering Journal. 52(04): 109–120.

Shariati A., RamliSulongN. R., Shariati M., 2013. Comparison of behaviour between channel and angle shear connectors under monotonic and fully reversed cyclic loading. Construction and Building Materials. 38: 582–593.

Lyu W. Q., Wang S. N., Lyu H., et al. 2016. Preparation technology of steel shell submerged tunnel used self-compacting concrete. Bulletin of Chinese Ceramic Society. 35(12): 3952.

Peng Y. J., Wu X. D., Liu H., et al. 2021. Intelligent Pouring Quality Control of Steel Shell Concrete Immersed Tube in Shenzhong Link. Construction Quality. 39(11): 27–30.

Komon T, Suzuki Y, Wako T, et al. 1995. Characteristics of powder type high fluidity concrete for filling into submerged tunnel full sandwich structure. Annual Report on Concrete Engineering. 17(1): 191–196.

Tang L., Fan J. S., Nie J. G., et al. 2020. Experimental Study on the Mechanical Performance of Angle Shear Connectors with and without Concrete Gaps. Engineering Mechanics. 37 (10):45-55+115.

Yang J., Han X., Yang K., et al. 2012. Review on Nondestructive Testing Technology of Voids in Concrete Filled Steel Tube. Journal of China & Foreign Highway. 32 (05): 189–191.

Wang J. W., Ma S. N., Liu Z. Y., et al. 2021. Experimental Study on Non-destructive Testing Methods of Voids in Concrete Filled Steel Tube. Joural of Shijiazhuang Tiedao University(Natural Science Edition). 34(02): 38–45.

Yao D. W., You L., Shu L. G., 2017. Application of Impact-echo Method in Steel Lining Void Detection. Site Investigation Science and Technology. (06): 55–58.

Liu W. H., Li J., Yang J. X., et al. 2021. Detection of Concrete Defects in Steel Tube Lining by Impact Echo Method. Nondestructive Testing. 43(11): 47–52.

Liu H., Hou D. X., Zheng G. B., et al. 2021. Infrared Thermography-based Void Detection Technology for Concrete-filled Steel Tubes. Infrared Technology. 43 (11): 1119–1126.

Hua R. Z., 1981. Using γ-Ray Absorption and Scattering γ-Ray Method(γ-γMethod) Measuring Rock(Ore) Density. Geophysical and Geochemical Exploration. (03): 158–164.

Zhang H., Liu G. Q., Liu C., 2017. Study on Application of Quantitative Detecting of Inner Cavity Defect of Concrete Under Steel Plate Lining of Hydro-power Plant. Journal of Isotopes. 30(03): 194–199.

Tunnelling for a Better Life – Yan, Celestino, Thewes & Eberhardt (Eds)
© 2024 The Author(s), ISBN 978-1-032-80042-4
Open Access: www.taylorfrancis.com, CC BY-NC-ND 4.0 license

Research on settlement calculation method for DCM composite foundation of immersed tunnel in Shenzhen-Zhongshan Link

Jia-Jin Zhou
Research Center of Coastal and Urban Geotechnical Engineering, Zhejiang University, Hangzhou, China

Feng-yong Xia
Shenzhen-Zhongshan Link Management Center, Guangzhou, China

Zhuo-Jie Chen & Xiao-nan Gong
Research Center of Coastal and Urban Geotechnical Engineering, Zhejiang University, Hangzhou, China

Di Liu
Shenzhen-Zhongshan Link Management Center, Guangzhou, China

Jian-lin Yu*
Research Center of Coastal and Urban Geotechnical Engineering, Zhejiang University, Hangzhou, China

ABSTRACT: Deep cement mixed (DCM) pile composite foundation was widely used in the immersed tunnels of Shenzhen-Zhongshan Link. The submarine DCM pile composite foundation was characterized by a high replacement rate and large cushion thickness. While there is limited research on the load transfer mechanism and settlement characteristics of DCM pile composite foundation. Based on the field test results, this paper proposed an analytical method which could consider the gravel cushion, DCM pile composite foundation and fully weathered rock layer at the pile base as a co-acting system. Furthermore, the stress and deformation coordination on the contact surfaces between each part of the system was considered. The pile-soil stress ratio and composite foundation settlement calculation equations were derived by analyzing a typical unit body. Finally, the theoretical calculation results were compared with the field test results, and the rationality of the theoretical equations was verified. The proposed theoretical calculation method of submarine DCM pile composite foundation was a theoretical basis for the design of subsequent related projects.

Keywords: Immersed tunnel, Submarine DCM pile composite foundation, Gravel cushion, Load transfer mechanism, Settlement calculation

1 INTRODUCTION

Numerous tunneling projects are emerging with the growing demand for infrastructure construction in China. Currently, Ningbo Yongjiang Tunnel, Ningbo Changhong Tunnel, Shanghai Outer Ring Tunnel, Hong Kong-Zhuhai-Macao Bridge Immersed Tunnel and Shenzhen-Zhongshan Link Immersed Tunnel have been built and are under construction (Yan et al., 2022). The immersed tunnel foundations of the Shenzhen-Zhongshan Link Super Project were the first in China to use large-scale deep cement mixed piles (DCM piles). Previous studies have indicated that excessive settlement or differential settlement in immersed tunnels can affect operational safety (Grantz, 2001). Therefore, it is necessary to investigate the accurate calculation method of composite foundation settlement.

A number of researches on composite foundation settlement calculations have been conducted. Alamgir et al. (1996) derived analytical equations for the calculation of pile stresses, lateral friction and settlement in composite foundations under flexible foundations. Subsequently, Yang (2000) introduced the concept of 'neutral point' and re-assumed the distribution of pile lateral friction. Lyu et al. (2010) improved the displacement mode proposed by Alamgir (Alamgir et al., 1996), and regarded the foundation, cushion, composite foundation and substratum as a co-acting system, and considered the stress and deformation coordination on the contact surfaces between each part of the system is considered. Smith (2005) established

*Corresponding author: yujianlin72@126.com

DOI: 10.1201/9781003495505-332

a simplified method for settlement calculation of rigid pile reinforced embankment according to the results of numerical analysis, while the calculation mode of pile-soil load sharing is not suitable for mixing pile composite foundation. Luo and Lu (2018) developed a non-uniformly varying pile lateral friction distribution model and derived the analytical equations for the settlement and pile-soil stress ratio of a rigid pile composite foundation. Based on the load transfer method, Yu et al. (2022) investigated the stress characteristics and settlement calculation method of concrete-cored cement-soil pile composite foundation by considering the influence of interface relative displacement on interface side friction.

At present, most of the investigations on composite foundations are based on land area conditions. However, many studies have neglected the settlement of the cushion (Alamgir et al., 1996, Yang, 2000, Lu et al., 2010) and rarely consider the coordination of stresses and deformations of the cushion, the composite foundation, and the substratum (Lu et al., 2010). Compared with the traditional land area conditions, the foundation treatment method of thick cushion and high replacement rate DCM pile was applied in the Shenzhen-Zhongshan Link. The results of the field load plate test indicated that the load transfer mechanism and settlement characteristics of composite foundations were influenced by the cushion thickness and replacement rate (Fu et al., 2021). In this case, the traditional methods for calculating the settlement were not applicable. With the development of cross-sea projects, submarine DCM pile composite foundations have been successfully used in the Busan Immersed Tunnel (Olsen et al., 2022) and the third runway of Hong Kong Airport. The immersed tunnel of the Shenzhen-Zhongshan Link is currently at a critical stage of construction. Therefore, systematic research on the load transfer mechanism and settlement calculation method of DCM pile composite foundation is needed.

Based on the results of field load plate tests, this paper considers the effect of thick cushion on the settlement characteristics and load transfer mechanism of composite foundations. Then, the gravel cushion, the composite foundation and the substratum are considered as a co-acting system. From the coupling relationship between the stress and deformation of the three at the interface, the load transfer law and settlement characteristics of the gravel cushion, pile and foundation soil are analyzed. Finally, the rationality of the settlement calculation formula proposed in this paper is verified by comparing the calculation results with the field measured data. The research results can provide reference for the design and construction of DCM pile composite foundation in future submarine immersed tunnels.

2 PROJECT OVERVIEW

The Shenzhen-Zhongshan Cross-Sea Link (referred to as the Shenzhen-Zhongshan Link) is a super cross-sea project that integrates bridges, islands, tunnels and underwater interchange hubs. The Shenzhen-Zhongshan Link is about 30 km from the Humen Bridge in the north and 38 km from the Hong Kong-Zhuhai-Macao Bridge in the south. The total length of the tunnel is 6845 m, and the length of the immersed tube is 5035 m (Yan et al., 2022). The project overview of the Shenzhen-Zhongshan Link is shown in Figure 1.

Figure 1. Overview of Shenzhen-Zhongshan Link project.

The DCM method was applied to the immersed tunnel foundations of the Shenzhen-Zhongshan Link. The construction process for this method was as follows: (1) Calculate and set parameters in the DCM construction ship control system according to the design requirements; (2) The cement slurry was stirred and pumped to the front end of the drill bit by using a slurry preparation and transportation equipment; (3) The cement slurry was injected into the foundation soil that had been fully crushed by the drill bit, and a certain strength of cement soil pile was formed after mixing. Photographs of the DCM construction ship and on-site construction are shown in Figure 2.

DCM piles were arranged in the form of single piles. The diameter of the single pile was 1.3 m, the lapping was 0.3 m, four piles were in a cluster, and the equivalent diameter was about 2.3 m. The longitudinal spacing of single piles was 3 m. The horizontal spacing was categorized into 3 m, 4 m and 5 m depending on the magnitude of the upper loads. The comprehensive replacement rate was 41% to 47.4%. The layout of the DCM piles is shown in Figure 3.

(a) DCM construction ship (b) On-site construction photos

Figure 2. Photographs of the DCM construction ship and on-site construction.

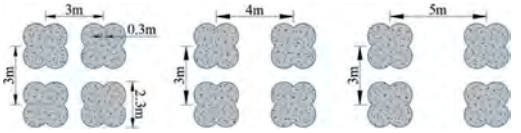

Figure 3. Layout of DCM piles.

Field load plate tests were conducted to investigate the settlement deformation behavior of gravel cushion and DCM pile composite foundations. However, the mechanism of the settlement was not clear (Fu et al., 2021). Therefore, it needs to be further studied by theoretical methods.

3 CALCULATION MODEL AND BASIC ASSUMPTIONS

3.1 *Derivation of calculation model*

The width of the immersed tunnel foundations is large, with a maximum width of more than 55 m. In order to simplify the model, the concentric cylinder formed by a single pile and the soil within its influence range is taken as a typical unit body for analysis. The typical unit body is shown in Figure 4, where a and b are the equivalent radius of a single pile and the soil within its influence range, respectively.

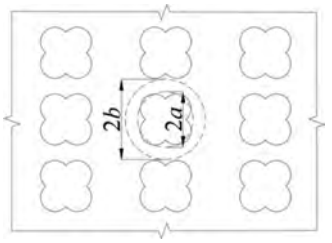

Figure 4. Typical unit body.

It is assumed that the pile and its upper cushion are inner soil columns (radius a), and the soil between adjacent piles and the upper cushion portion above them are outer soil columns (radius b). The b can be obtained by pile arrangement and pile spacing (GB, 2012). The simplified model for the composite foundation of immersed tunnel is shown in Figure 5, where l_c is the thickness below the gravel cushion, and l_p is the thickness of the reinforced area.

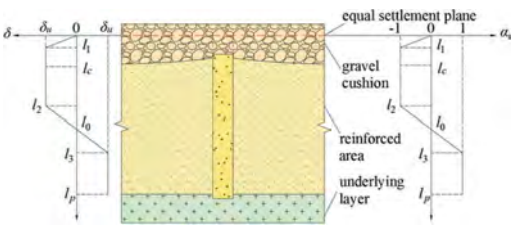

Figure 5. Simplified calculation model.

3.2 *Basic assumptions*

The thickness of the gravel cushion is larger and the compression modulus is smaller. When analyzing the load transfer mechanism, the immersed tunnel foundation can be regarded as a flexible foundation. According to previous studies (Lu et al., 2010), the vertical displacement pattern of soil between adjacent piles can be assumed:

$$w_{si} = w_{pi} + f_{1i}(z)g(r) + f_{2i}(z) \tag{1}$$

$$g(r) = \frac{r}{a} - e^{B\left(\frac{r}{a}-1\right)} \tag{2}$$

Where, z is the depth of the calculated point from the gravel cushion; r is the horizontal distance from the calculation point to the center of the pile; w_{si} is the displacement of soil between adjacent piles, which is a function of r and z; w_{pi} is the pile displacement, which is only a function of z; $f_{1i}(z)$ and $f_{2i}(z)$ are all the undetermined functions with z as the independent variable; B is an undetermined constant; $i = c, s$, corresponding to the gravel cushion and reinforcement area, respectively.

Correspondingly, the ultimate lateral friction of the pile at i can be calculated by equation (3):

$$\tau_{sui} = \beta_i \sigma_v^{'} = \beta_i \left(\sum_{j=1}^{i} \gamma_j^{'} z_j + p_s \right) \tag{3}$$

Where, τ_{sui} is the ultimate lateral friction of the pile at i; β_i is the coefficient of pile lateral friction at i; $\sigma_v^{'}$is the overlying effective stress at the calculated depth; $\gamma_j^{'}$ and z_j are the effective weights and thicknesses of the material above i; p_s is the stress of the outer soil column at the gravel cushion.

The degree of pile lateral friction at i is defined as α_i, which can be calculated by equation (4):

$$\alpha_i = \tau_{sai} / \tau_{sui} \tag{4}$$

Where, τ_{sai} is the lateral friction of the pile at i.

Based on the previous research (Randolph and Wroth, 1979, Evgin and Fakharian, 1997), Luo and Lu (2018) proposed the ideal elastic-plastic model δ_u. In this paper, the pile-soil interaction at the pile-soil interface adopts the model to determine the relationship between τ and δ. With δ_u as the boundary, in the elastic stage, $\alpha_i = 0 \sim 1$, while in the plastic stage, $\alpha_i = 1$. According to the system load transfer law, the distribution of δ and α_i along the depth is obtained, as shown in Figure 6.

By integrating δ at depths $l_c \sim l_0$ and $l_0 \sim l_p$, respectively, the relative pile-soil displacements at the pile top and pile bottom, Δ_a and Δ_b, respectively, can be obtained as follows:

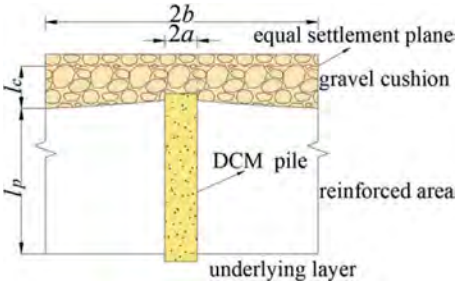

Figure 6. Distribution of δ and α_i along depth.

$$\Delta_a = \frac{(3l_2 + l_3 - 4l_c)\delta_u}{4} \tag{5}$$

$$\Delta_b = \frac{(4l_p - l_2 - 3l_3)\delta_u}{4} \tag{6}$$

Where, $l_2 + l_3 = 2l_0$

4 DERIVATION OF ANALYTICAL SOLUTION FOR COMPOSITE FOUNDATION SETTLEMENT

4.1 *Displacement mode*

According to the previous study (Lu et al., 2010), the distribution function of pile lateral friction is f_{1i}(z). To equalize the pile lateral friction of each segment at the interface, the stress coordination constant φ_i is introduced. φ_i satisfies the following relationship:

$$\varphi_c A_c = \varphi_s A_s \tag{7}$$

Where, $A_i = a\beta_i {G_{si}}^{-1}(1-B)^{-1}$; G_{si} is the shear stiffness of soil between adjacent piles at i.

Let $\varphi_s = 1$, then:

$$\varphi_c = A_s / A_c \tag{8}$$

Similarly, f_{2i}(z) is the slip function at the pile soil interface, which can be obtained by integrating δ along the depth z.

4.2 *Stress equilibrium equation of microelement*

The cylinder with a thickness of dz is analyzed, and its stress distribution is shown in Figure 7.

From the vertical equilibrium equation of the inner soil column element, it can be obtained:

$$\frac{d\sigma_{pi}}{dz} = -\frac{2}{a}\tau_{sai} \tag{9}$$

Where, σ_{pi} is the vertical stress in the inner soil column at i.

According to the vertical equilibrium equation of the outer soil column element, it can be obtained:

$$\frac{d\sigma_{si}}{dz} = \frac{\tau_{si}}{r} + \frac{\partial \tau_{si}}{\partial r} \tag{10}$$

Where, σ_{si} is the vertical stress in the outer soil column at i.

Substituting equations (1) to (4) into equations (10) and taking two partial derivatives for w_{si}, it can be obtained:

$$\frac{d\sigma_{si}}{dz} = h(r)\varphi_i\alpha_i\beta_i\left(\sum_{j=1}^{i}\gamma_j' z_j + p\right) \tag{11}$$

Where, $h(r) = \frac{1}{1-B}\left[\frac{1}{r} - B\left(\frac{1}{r}+\frac{B}{a}\right)e^{B\left(\frac{r}{a}-1\right)}\right]$.

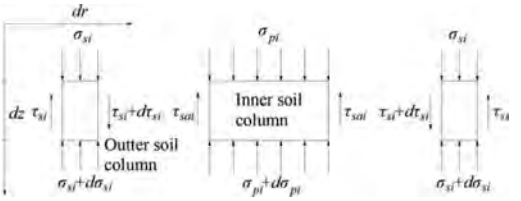

Figure 7. Stress analysis of typical unit bodies.

4.3 *Stress equation for each section*

Substitute equations (3) and (4) into equation (9). Then integrate equations (9) and (11) at each segment. The obtained stress equations for each segment are as follows:

(1) Gravel cushion segment, z=0~l_1

$$\sigma_{pc} = \frac{\varphi_c\beta_c}{3al_1}\left(2\gamma_c' z^3 + 3p_s z^2\right) + M_1 \tag{12}$$

$$\sigma_{sc} = -\frac{h(r)\varphi_c\beta_c}{6l_1}\left(2\gamma_c' z^3 + 3p_s z^2\right) + M_2 \tag{13}$$

(2) Gravel cushion segment, z= l_1~l_c

$$\sigma_{pc} = \frac{\varphi_c\beta_c}{a}\left(\gamma_c' z^2 + 2p_s z\right) + M_3 \tag{14}$$

$$\sigma_{sc} = -\frac{h(r)\varphi_c\beta_c}{2}\left(\gamma_c' z^2 + 2p_s z\right) + M_4 \tag{15}$$

(3) Reinforced area segment, z= l_c~l_2

$$\sigma_{ps} = \frac{\varphi_s\beta_s}{a}\left[\gamma_s' z^2 + 2\left(\gamma_c' l_c - \gamma_s' l_c + p_s\right)z\right] + M_5 \tag{16}$$

$$\sigma_{ss} = -\frac{h(r)\varphi_s\beta_s\gamma_s' z^2}{2} + M_6 - h(r)\varphi_s\beta_s z\left(\gamma_c' l_c - \gamma_s' l_c + p_s\right) \tag{17}$$

(4) Reinforced area segment, $z= l_2 \sim l_3$

$$\begin{aligned}\sigma_{ps} &= \frac{\varphi_s\beta_s\gamma_s' z^2(l_2+l_3)}{a(l_3-l_2)} + M_7 \\ &+ \frac{2\varphi_s\beta_s z(l_2+l_3)}{a(l_3-l_2)}\left(\gamma_c' l_c - \gamma_s' l_c + p_s\right) \\ &- \frac{\varphi_s\beta_s z^2}{3a(l_3-l_2)}\left[4\gamma_s' z + 6\left(\gamma_c' l_c - \gamma_s' l_c + p_s\right)\right]\end{aligned} \tag{18}$$

$$\begin{aligned}\sigma_{ss} &= \frac{2\gamma_s' h(r)\varphi_s\beta_s z^3}{3(l_3-l_2)} \\ &- \frac{h(r)\varphi_s\beta_s\gamma_s' z^2(l_2+l_3)}{2(l_3-l_2)} + M_8 \\ &+ \frac{h(r)\varphi_s\beta_s z^2}{(l_3-l_2)}\left(\gamma_c' l_c - \gamma_s' l_c + p_s\right) \\ &- \frac{h(r)\varphi_s\beta_s z(l_2+l_3)}{(l_3-l_2)}\left(\gamma_c' l_c - \gamma_s' l_c + p_s\right)\end{aligned} \tag{19}$$

(5) Reinforced area segment, $z= l_3 \sim l_p$

$$\begin{aligned}\sigma_{ps} &= -\frac{\varphi_s\beta_s\gamma_s' z^2}{a} + M_9 \\ &- \frac{2\varphi_s\beta_s z}{a}\left(\gamma_c' l_c - \gamma_s' l_c + p_s\right)\end{aligned} \tag{20}$$

$$\begin{aligned}\sigma_{ss} &= \frac{h(r)\varphi_s\beta_s\gamma_s' z^2}{2} + M_{10} \\ &+ h(r)\varphi_s\beta_s z\left(\gamma_c' l_c - \gamma_s' l_c + p_s\right)\end{aligned} \tag{21}$$

Where, M_1 to M_{10} are integration constants, which can be solved based on the stress continuity condition of the inner and outer soil columns at each segment.

4.4 *Settlement calculation of substratum*

The determination of the additional stress at the top of the substratum is critical to its settlement calculation. Substituting $z=l_p$ into equations (20) and (21), the equations for pile bottom stress and soil stress between adjacent piles at the pile bottom plane are obtained, respectively:

$$\begin{aligned}\sigma_{ps}|_{z=l_p} &= -\frac{\varphi_s\beta_s\gamma_s' z^2}{a} + M_9 \\ &- \frac{2\varphi_s\beta_s l_p}{a}\left(\gamma_c' l_c - \gamma_s' l_c + p_s\right)\end{aligned} \tag{22}$$

$$\begin{aligned}\sigma_{ss}|_{z=l_p} &= \frac{h(r)\varphi_s\beta_s\gamma_s' z^2}{2} + M_{10} \\ &+ h(r)\varphi_s\beta_s l_p\left(\gamma_c' l_c - \gamma_s' l_c + p_s\right)\end{aligned} \tag{23}$$

According to equation (23), the average additional stress of soil between adjacent piles at the pile bottom plane can be obtained as follows:

$$\bar{\sigma}_{ss}|_{z=l_p} = \frac{\int_a^b \sigma_{ss}|_{z=l_p} 2\pi r dr}{\pi(b^2-a^2)} \tag{24}$$

According to equations (22) to (24), the additional stresses at the top of the substratum σ_r caused by the pile stresses and the average stresses in the soil between the adjacent piles can be obtained as (Zhao et al., 2010):

$$\sigma_r = m\sigma_{ps}|_{z=l_p} + (1-m)\bar{\sigma}_{ss}|_{z=l_p} \tag{25}$$

Where, m is the area replacement rate; $m= a^2/b^2$.

The compression amount of the substratum w_r is calculated by substituting σ_r into the layerwise summation method (GB, 2011), as follows:

$$w_r = \varphi_r \frac{\sigma_r}{E_r}\left(\overline{\alpha_i} z_i - \overline{\alpha_{i-1}} z_{i-1}\right) \tag{26}$$

Where, φ_r is the empirical coefficient of settlement, which is taken as 0.3 in this paper; z_i and $z_{i\text{-}1}$ are the depth of the substratum bottom and top, respectively; $\bar{\alpha}_i$ and $\bar{\alpha}_{i-1}$ are the average additional stress coefficients at the substratum bottom and top, respectively.

5 CALCULATION RESULTS VALIDATION ANALYSIS

5.1 *Determination of solution conditions and calculation parameters*

The previous literature (Lu et al., 2010, Luo and Lu, 2018) provided a detailed introduction to the solving process of the integral constant M_1-M_{10} and positional parameters l_1, l_2, and l_3. By substituting the integration constants and positional parameters into each stress and displacement equation, the stresses and settlements in each part of the system can be obtained. The pile-soil stress ratio n is determined by the following equation:

$$n = \frac{\sigma_p|_{z=l_c}}{\bar{\sigma}_s|_{z=l_c}} \tag{27}$$

$$\bar{\sigma}_s|_{z=l_c} = \frac{\int_a^b 2\pi r\sigma_{ss}|_{z=l_c} dr}{\pi(b^2-a^2)} \tag{28}$$

Where, $\bar{\sigma}_s$ is the average vertical stress in the soil between adjacent piles at the plane of the pile top.

According to the previous in-situ test results (Chen et al., 2010), the height of the equal settlement surface of the gravel cushion is taken as the net pile spacing in this paper. The ultimate lateral friction degree coefficients of the piles in the gravel cushion and the soil are determined by the β-method (GB, 2011) and were 0.3 and 0.2, respectively. δ_u is determined to be 0.15% by the statistical results of Luo and Lu (2018). Based on the field test results and inverse analysis (Fu et al., 2021), the compression modulus of the gravel cushion is 1.8 MPa under the first stage load and 10 MPa

under the subsequent load. Other calculation parameters are shown in Table 1. Note that the soil parameters between adjacent piles are taken as a weighted average of the thickness of each soil layer within the pile length range.

Table 1. Physical and mechanical parameters of materials.

Material name	γ_{sat} /(kN·m^{-3})	h/m	E_s/ MPa	c'/kPa	φ'/°	v
Gravel cushion	21.0	1.0	10.0	0.1	30.0	0.30
Reinforced area soil	18.4	18.0	5.4	7.9	18.5	0.38
Substratum	20.3	5.0	30.0	18.0	23.9	0.35
CM pile	22.0	18.0	160.0	500.0	30.0	0.25

5.2 *Comparison of settlement calculation results*

The comparison results of theoretical calculation and measured settlement are shown in Figure 8. As seen in Figure 8, the trend of the theoretical calculation and measured load-displacement curves was consistent, and the settlement values were close under each load. Under the first level load (62.8 kPa), the theoretically calculated and measured settlements were 71.2 mm and 64.9 mm, respectively, with a relative error of 9.7%. Under the second level load (112.2 kPa), the theoretically calculated and measured settlements were 91.4 mm and 84.4 mm, respectively, with a relative error of 8.3%. Under the third level load (161.6 kPa), the theoretically calculated and measured settlements were 104.1 mm and 96.0 mm, respectively, with a relative error of 8.4%. Under the fourth level load (211.1 kPa), the theoretically calculated and measured settlements were 116.4 mm and 107.7 mm, respectively, with a relative error of 8.1%. Overall, the difference between the theoretical calculation and the measured settlement was not large. The error was within 10%, and the calculation accuracy satisfied the engineering requirements. In addition, the relative error tended to decrease as the load increased. Therefore, the settlement calculation method of DCM pile composite foundation proposed by this paper is reliable.

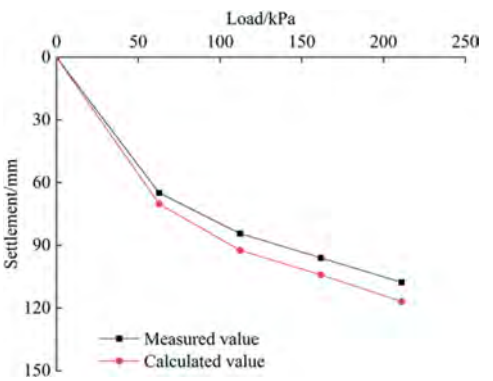

Figure 8. Comparison of settlement calculation results.

5.3 *Comparison of pile-soil stress ratio calculation results*

The comparison results of the measured and theoretical calculation of the pile-soil stress ratios are shown in Figure 9.

As seen in Figure 9, both theoretically calculated and measured pile-soil stress ratios increased with increasing load. Under the first level of loading, the theoretically calculated and measured pile-soil stress ratios were 4.4 and 4.6, respectively, with a difference of 4.1%. At the last level of loading, the theoretically calculated and measured pile-soil stress ratios increased to 7.2 and 7.8, respectively, with a difference of 8.5%. The increase in the pile-soil stress ratio gradually decreased. This is because when the load increases, the pile is subjected to more load due to the adjustment of the cushion, resulting in an increase in the pile-soil stress ratio. However, when the load increased to a certain extent, the adjustment effect of the cushion would reach the limit (GB, 2011). In addition, the error between the theoretically calculated and measured pile-soil stress ratios was within 10%. The results of the theoretical calculations can be considered reliable.

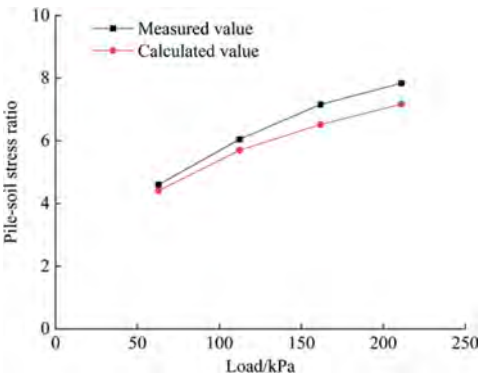

Figure 9. Comparison of pile-soil stress ratio calculation.

6 CONCLUSION

(1) Based on field load plate tests, the effect of thick cushion and high replacement rate on the load transfer mechanism and settlement characteristics of DCM pile composite foundations were analyzed. Each part co-action of the composite foundation system and the coupling relationship of stress and deformation at the system interfaces were considered. Finally, the analytical solution for the composite foundation settlement

of the immersed tunnel in the Shenzhen-Zhongshan Link was obtained.

(2) The analytical solution could comprehensively reflect the characteristics of pile-soil interaction, load transfer law and settlement of each part in the composite foundation system with ultra-thick cushion and high replacement rate DCM piles of immersed tunnel. The calculation results of composite foundation settlement and pile-soil stress ratio were similar to the measured results, with relative errors within 10%.

(3) Submarine immersed tunnel projects have the characteristics of harsh construction environment, large thickness of submarine DCM pile composite foundation cushion and high DCM pile replacement rate. Therefore, the settlement of the cushion and its influence on the deformation coordination of the composite foundation system should be considered in the settlement calculation. To make the calculation results more reliable, the compression modulus of the cushion should be smaller than the design value, and the effective weight as the material weight.

ACKNOWLEDGMENTS

We want to express our gratitude to the support provided by Shenzhen-Zhongshan Link Management Center, China Communications Construction First Harbor Engineering Co., Ltd., China Communications Construction Fourth Harbor Engineering Co., Ltd., China Communications Construction Highway Consultants Co., Ltd., etc.

REFERENCES

Alamgir, M., Mjura, N., Poorooshasb, H.B., 1996. "Deformation analysis of soft ground reinforced by columnar inclusions. Comp. and Geot. 18(4), 267–290.

Chen R.P., Xu Z.Z., Chen Y.M., et al, 2010. "Field tests on pile-supported embankments over soft ground. Jour of Geot and Geoe Engi. 136(6), 777–785.

Evgin, E., Fakharian, K., 1997. "Effect of stress paths on the behaviour of sand steel interfaces. Cana geot jour. 33(6), 853–865.

Fu B.Y., Song S. Y., Xu G.P., et al, 2021. "Study on settlement of gravel cushion and deep cement mixing pile composite foundation. High. 66(5), 65–70.

GB 50007-11, 2011. Code for design of building foundation. China.

GB/T 50783-12, 2012. Technical code for composite foundation. China.

Grantz, W.C., 2001. "Immersed tunnel settlements—Part 1: Nature of settlements. Tunn. and Unde. Spac. Tech. 16(3), 195–201.

Lu W.Z., Yu J.L., Gong X.N., 2010. "Analytical method for pile composite ground under flexible foundation. Chin Jour of Rock Mech and Engi. 29(2), 401–408.

Luo, Q., Lu Q.Y., 2018. "Settlement calculation of rigid pile composite foundation considering pile soil relative slip under embankment load. Chin Jour of High and Tran. 31(1), 20–30.

Olsen, T., Kasper, T., De, W.J., 2022. "Immersed tunnels in soft soil conditions experience from the last 20 years. Tunn and Unde Spac Tech. 121, 104315.

Randolph, M.F., Wroth, C.P., 1979. "Analysis of vertical deformation of pile groups. Géot. 29(4), 423–439.

Smith, M.E., 2005. Design of bridging layers in geosynthetic-reinforced column-supported embankments. PhD Thesis. Virginia Polytechnic Institute and State University, Virginia, CA, USA.

Yan, L., Han, H., He S. H., et al, 2022. "Full-scale model test of bearing capacity of temporary anchorage system for immersed tube in Shenzhen-Zhongshan Link. Chin. Jour. of High. and Tran. 35(10), 47–54.

Yang, T., 2000. "Settlement analysis of composite ground improved by flexible floating piles under road embankment. Chin Jour of Geot Engi. 22(6), 741–743.

Yu J.L., Xu J.C., Zhou J.J., et al, 2022. "Experimental study on frictional capacity of concrete-cemented soil interface of concrete-cored cemented soil column. Chin Civi Engi Jour. 55(8), 93–104.

Zhao M.H., He L.P., Zhang, L., 2010. "Settlement calculation of CFG pile composite foundation based on load transfer method. Rock and Soil Mech. 31(3), 839–844.

Waterproofing and drainage

Taylor & Francis
Taylor & Francis Group
http://taylorandfrancis.com

Tunnelling for a Better Life – Yan, Celestino, Thewes & Eberhardt (Eds)
© 2024 The Author(s), ISBN 978-1-032-80042-4
Open Access: www.taylorfrancis.com, CC BY-NC-ND 4.0 license

Next generation tunnel waterproofing

Yves Boissonnas*
Sika Services AG, Zurich, Switzerland

ABSTRACT: Sika has been developing a new generation of tunnel waterproofing utilizing sheet membranes, watertight concrete technology, and fully bonded basement waterproofing membranes. This waterproofing concept combines systems well established over the last 50 years with an optimized application. The technology using fully bonded membranes in tunnels was first developed in South Korea and successfully applied in many projects. The fully bonded system, which can also be seen as an improved watertight concrete in accordance with the most advanced tunnel waterproofing standards, offers a reduction of the CO2 footprint compared to the regular waterproofing membrane by a factor of 2, and an increased reliability compared to the current system. The application is simplified, reducing the work steps but still using the same well-established technique and know-how. The new generation tunnel waterproofing fits the drained tunnels as well as the pressurized systems. It also replaces the waterbars and control sockets needed in the conventional compartment system.

Keywords: waterproofing, fully bonded tunnel membrane, tunnel lining concept

1 INTRODUCTION

Tunnel waterproofing has been a crucial aspect of tunnel construction for many centuries. Ensuring the protection of underground structures from water ingress is vital for their long-term stability and operational safety. The first traces of waterproofing in tunnels go back more than 4′000 years to the Euphrates Tunnel in the city of Babylon where a cut & cover tunnel was then plastered with asphalt. Bitumen only found its way in some cut & cover constructions but is not used anymore in modern tunneling. Over the years, various materials and techniques have been employed to waterproof tunnels and basements. For instance, in South Korea, where the development has led to the adaptation of the fully bonded membrane systems commonly used in basements, and the optimization of the installation process. In this article, we will delve into the worldwide history of tunnel waterproofing using sheet PVC, TPO (FPO) membranes and watertight concrete, explore South Korea's journey towards fully bonded systems, and explain the technique's advantages. Additionally, we will describe the installation process of this waterproofing membrane in a tunnel.

2 HISTORICAL PERSPECTIVES OF PVC, TPO (FPO) MEMBRANES, AND WATERTIGHT CONCRETE

Modern tunnel waterproofing has come a long way since its inception, with the earliest approaches primarily relying on watertight mortars. Sika was one of the first supplier to develop watertight mortars in 1910. This watertight mortar technology was used 1918 in the old Gotthard railway tunnel opened in 1882, when dripping water had to be controlled to allow the first electrification of the tunnel. Then in the mid-20th century, watertight concrete was a major innovation in tunnel construction, effectively reducing water penetration. However, this method had limitations and was not entirely reliable in providing long-lasting protection against water infiltration. In fact, the constrains of the concrete in

Figure 1. Gei tunnel Switzerland opened in 1967.

*Corresponding author: boissonnas.yves@ch.sika.com

DOI: 10.1201/9781003495505-333

contact with the rock did not allow a concentration of the shrinkage movement in the watertight joints. This leads to cracks within the concrete blocks in-between the dilatation-joints and therefor to water infiltrations.

In the 1970s, the introduction of sheet polyvinyl chloride (PVC) membranes revolutionized tunnel waterproofing practices. The Sika (Sarnafil) membranes were the first to be installed in a tunnel in 1967 to waterproof the Gei Tunnel in Switzerland. PVC membranes offered enhanced impermeability, flexibility, and ease of installation compared to watertight concrete. The flexibility of PVC allowed its adaptation to irregular surfaces and accommodate movements in the tunnel structure, eliminating the risk of cracks leading to leaks.

In the following decades, thermoplastic polyolefin (TPO) membranes emerged as an alternative to PVC. Both PVC and TPO (FPO) membranes contributed significantly to improving waterproofing performance, becoming widely used in tunnel projects around the globe.

These membranes are commonly used in different systems. Firstly, classic drained umbrella waterproofing protecting structure and operation against percolating water and the compartment system widely used in pressurized tunnels. In this system compartments between the membrane and the concrete lining are created by welding waterbars on the membrane to reduce eventual water migration and allow targeted repair injections. Finally, an active control system composed of two membrane layers welded together in compartments and offering the possibility to control the watertightness of the systems by applying a vacuum in the compartment during the construction phase. These compartments can be injected with raisins in case of later water ingress.

3 REASONS FOR TUNNEL WATERPROOFING

There are mainly three reasons to waterproof a tunnel. The most common one is to protect the service from humidity and water. The impact of water on operation can be very diverse like water harming the installations, ice endangering the service, humidity inducing electrical wastage by creeping current and many more. In case of aggressive groundwater, a waterproofing is needed to protect the concrete structure and reinforcement from corrosion. Finally, in some tunnels a waterproofing is needed to prevent any influence of the excavation on the surrounding hydrogeology. Where per example the drainage of the surrounding groundwater leads to settlement at the surface or to protect the phreatic water of tunnel wastewater seeping in the ground.

The waterproofing strategy must meet the needs by installing a pressurized, drained, full round or umbrella waterproofing system. The pressurized system prevents any waterflow in or out of the tunnel and the full water pressure acts on the tunnel lining. A pressurized tunnel waterproofing is common in urban soft ground. This is the trickiest waterproofing concept as water will find and penetrate any defect. Measures must be foreseen to seal or contain any leaks. Drained systems allow the protection of the structure and operation without the full water pressure acting on the tunnel lining. The water inflow can also be reduced by injecting the ground around the excavation changing its permeability.

4 RISK CONSIDERATION ON THE CHOICE OF WATERPROOFING STRATEGY

The waterproofing strategy should be based on a risk management approach. Water inflow and water damages have a huge impact on a tunnel lifecycle cost and the risk can be reduced by installing an adequate waterproofing system. But no waterproofing layer will be 100% failure free. There can be problems with the materials, the handling, the installation, or the design details. Due to the large size of the surface to be waterproofed in a tunnel, even low remaining risks still have a huge impact on the project. If this remaining risk cannot be accepted and controlled, then mitigation measures and/or limitations of the impact of these leakages on the structure need to be planned.

By installing several lines of defense, the risk can be reduced to an acceptable level. For example, compartmentalization into multiple waterproofing sectors can be treated separately by injections to limit water migration and repair any failure. This is a widely used method to reduce the risk. When a punctured membrane is detected, the compartment is injected with resins and the waterproofing layer restored. As these injection systems can be harmed during concreting or due to challenging application, further measures like double membrane layers are recommended, when a fully dry tunnel is mandatory.

Another approach is to reduce the impact of a risk to the minimum. By using fully bonded systems preventing any water migration between membrane and concrete inner lining, the impact of a failure in the waterproofing layer can be reduced to a very localized spot. In case the lining concrete is not watertight at the same and unique spot as the punctured membrane, then a targeted repair by water-tightening the lining with common concrete injection will lead to an elimination of the risk with a high chance of success.

The same risk approach is needed in TBM tunnels with single shell segmental lining. The huge length of installed gaskets will inevitably lead to localized failures and measures need to be planed. Furthermore, the concrete of the segments is directly exposed to any aggressive groundwater reducing the durability of the lining. Some major owners therefore do not accept single shell segmental linings in critical tunnels due to this remaining risk and the challenging mitigation measures.

Figure 2. Fully bonded membrane ready for concrete application.

5 DURABILITY

Nowadays owners require a low impact on the operation by maintenance work. A common request is limited maintenance guaranty on the tunnel lining in the first 100 years. Therefore, the waterproofing needs to withstand these minimum 100 years, offering a full protection of the tunnel structure and operation.

The client on the New Swiss Alp Transversals (NEAT) decided in the late 20th century to set up an expert group to clearly define objective requirements and tests to replicate the 100 years durability of waterproofing membranes in a tunnel. Since the aging process in the PVC or TPO (FPO) membrane is a chemical reaction and the higher the temperature, the faster a given chemical reaction happens, accelerated aging tests were defined. Membranes are put in a hot aggressive water bath for long periods up to one year and the change on membrane properties, like elongation at break, are measured. The reduction on characteristics can then be extrapolated to determine when the end-of-life level will be reached. The goal is for the membrane to fulfil its waterproofing duties throughout the full life cycle coping with any stresses and movements that can occur on the system. These standardized tests were compiled in major tunnel waterproofing standards like the Austrian ÖBV. So far, only the high-quality PVC and TPO (FPO) membranes fulfil the 100+ years durability tests. Other systems may withstand the aging degradation and prevent any water inflow on the long term, but as long as the aging behavior cannot be proven based on objective standardized tests, a risk remains.

Fact is, that the most widespread reasons for refurbishment and repair of tunnels under operation are water induced damages.

6 FULLY BONDED WATERPROOFING MEMBRANES

The turn of the century witnessed the introduction of a revolutionary technique for waterproofing - the fully bonded waterproofing membrane. This membrane is a multi-layered composite sheet with a carrier layer, and a bonding layer.

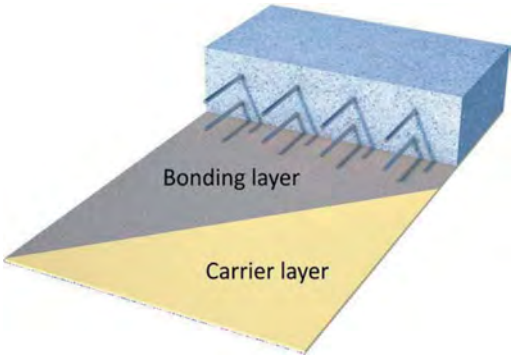

Figure 3. Fully bonded waterproofing membrane.

The (mechanical and chemical) bonding layer provides excellent adhesion to the concrete, creating a continuous waterproof seal. The bond occurs when the fresh concrete is poured against the bonding layer creating a strong connection when hardened. Additionally, the carrier layer provides mechanical protection to the bonding layer, enhancing the system's durability and robustness. The carrier layer consists of a fully watertight TPO (FPO) membrane with a proven durability.

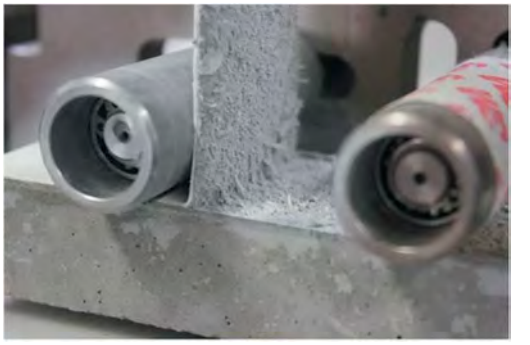

Figure 4. Strong bond between membrane and concrete.

This fully bonded system overcomes the limitations of the earlier sheet membrane technique. It prevents water from migrating between the membrane and the tunnel concrete lining. The

EN standards require a bond resisting to 7 bars water pressure to call it a fully bonded membrane. In practice, the effective bond is higher than the required 7 bars.

The system preventing water migration allows a precise location of any damage in the membrane leading to water leaks through the concrete lining. The bond also offers superior resistance of the membrane to ground movement and mechanical impacts, thereby ensuring the longevity of the tunnel structure.

Figure 5. Crack bridging test.

The fully bonded membranes show high flexibility (bi-axial) and excellent crack-bridging capabilities due to the unique combination of high quality membrane with high elasticity and strong bonding resistance.

Typically, fully bonded membranes are used in basement waterproofing. The thickness of the carrier layer varies between 0.8 mm and 1.2 mm. Sika developed fully bonded membrane with up to 2.0 mm carrier layer designed for underground constructions with higher water pressure. The membrane can be welded like the loose laid membrane without a bonding layer. The fully bonded technology saves the need of compartment systems, the waterbars and the control sockets. The first tunnels using this technology are in South Korea. In South Korea typically a 1.0 mm thick carrier layer is used. A first project using the 2.0 mm carrier layer is the Riedberg Tunnel located in Switzerland.

7 EVOLUTION IN SOUTH KOREA

The evolution of tunnel waterproofing in South Korea coincides with its rapid industrialization and infrastructure development. By the 1980s, as South Korea began constructing numerous underground facilities and tunnels, waterproofing became a critical issue.

Early efforts involved conventional waterproofing methods such as the use of watertight concrete and a sheet membrane. However, these techniques had limitations. For instance, the watertight concrete approach did not entirely prevent water leakage in tunnels, and the sheet membrane method required extensive maintenance due to membrane damage from various construction activities.

By 2015, to overcome these challenges, South Korea started to explore innovative waterproofing solutions and worked towards developing more effective waterproofing systems. This pursuit of excellence led to the introduction of fully bonded systems in tunnel waterproofing. Till today about 4 million m^2 fully bonded tunnel waterproofing membranes were successfully installed in South Korea.

Figure 6. SikaProof®-110.

The fixation of the membrane to the primary rock support was optimized to reduce the work steps and increase ease of application. The membrane including the functional layer can still be hot air welded as in the conventional loose laid membrane system. The quality weld prevents concrete from flowing through poor connections between the different membrane strips when the fresh concrete pushes the membrane into uneven bumps. The fully bonded system addresses issues that plagued older methods, such as the formation of water pathways between sheet membrane and inner lining concrete surface. The blockage of water migration facilitates the localization and repair of leaks as wet spots or dripping cracks coincide with punctured membranes and can easily be fixed with localized concrete injections. Therefore, the system is less sensitive to application quality issues.

The membrane thickness can be reduced to 1.0 mm in comparison to the classic loose laid membrane system, as the membrane works in combination with the inner lining concrete and is not exposed to the same stresses as conventional loose laid membranes. The use of high quality long lasting TPO (FPO) membrane layer allows very long life expectancy of more than 100 years proven by the standardized durability tests.

The system was successfully applied in several South Korean projects among others the Milyang - Ulsan expressway (172′000 m2 in 2020), the Kangjin – Kwangju expressway (155′000 m2 in 2022) or the Ansung – Sungnam expressway (165′000 m2 in 2022).

Figure 7. Tunnel in South Korea with SikaProof®-110.

8 POSITIONING IN RELATION TO TUNNEL WATERPROOFING STANDARDS

Most countries, with extensive tunnel projects, have national standards guiding designers regarding tunnel waterproofing. Clients with large tunnel inventory often have their own additional guidance. As an example, in Switzerland the SIA-272 standard regulates the waterproofing and drainage of underground constructions. In addition, the Swiss Federal Railway as well as the national road authorities specify in addition that no single shell segmental lining is acceptable. Only double shell lining including a waterproofing layer and an inner lining are allowed based on their bad experiences on segmental lining water tightness.

Unfortunately, most standards are outdated and reviewing national standards is slow and time consuming. It is therefore important to clearly position new systems in relation to the existing standards.

The fully bonded membrane can be seen as an "upgraded" watertight concrete. Due to the interaction of the membrane and the concrete, the membrane thickness can be diminished, at the same time the crack requirements for the concrete can be loosen and steel content reduced.

The requirements to prove the durability of the carrier waterproofing layer are defined in most tunnel waterproofing standard with the same tests as for the loose laid membranes. Therefore, the fully bonded membrane complies with the usual requirements in the tunnel waterproofing standards/guidelines, even if the system is not yet described in the latest.

The fully bonded membrane also protects the concrete effectively against aggressive ground water, a constraint that was heavily limiting the use of watertight concrete in underground constructions.

9 SYSTEM DESCRIPTION

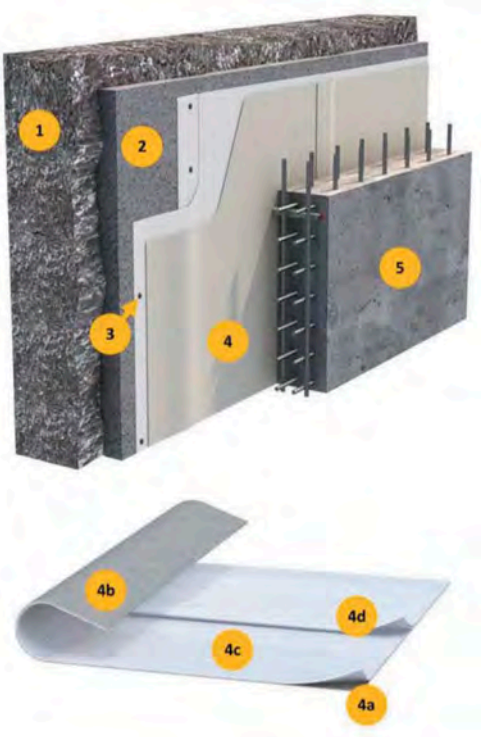

Figure 8. Membrane buildup.
1. Rock
2. Spray concrete
3. Nail fixation
4. SikaProof®-110 waterproofing membrane
   a. EVA-based waterproofing layer
   b. Functional layer for full bond
   c. Geotextile spot-fixed to the waterproofing-layer
   d. Geotextile strip
5. Inner lining concrete

The waterproofing layer is a fully and permanently bonded, flexible sheet membrane waterproofing system. It consists of an elastic polyolefin (FPO) membrane containing a unique hybrid bonding layer on polyolefin (PO) basis, which bonds permanently with the fresh concrete structure. The membrane is a pre-applied waterproofing system that is designed to be installed before the steel reinforcement (if needed) is fixed and the lining concrete is poured. The concrete is cast directly against the membrane system, where the fresh concrete is embedded completely into the hybrid bonding layer and creates a permanent dual bond both mechanically and adhesively.

The dual bond prevents any lateral water migration between the membrane system and the hardened

concrete. The membrane sheets can be hot air welded together to prevent any fresh concrete flowing behind the membrane between the seams. This is possible in conventional tunnel excavation when the membrane is pushed into uneven bumps when pouring the fresh concrete into the vault formwork.

The geotextile on the backside of the membrane is punctually fixed, allowing the full elasticity of the membrane. Conventional waterproofing membranes with a fully laminated geotextile on their back are losing their elasticity due to the geotextile "reinforcement". When the fully laminated membrane is exposed to high stress, the geotextile ruptures locally leading to a local over-elongation of the membrane, as all movements occur at this point.

The punctually fixed geotextile on the back of the SikaProof®-110 fully bonded membrane allows simplified fixing and acts as a cushion layer to protect the membrane from rough substrates. The loose geotextile strips can directly be nailed to the substrate holding the membrane in place.

10 WATERPROOFING CONCEPTS

There are two different waterproofing concepts. One is a drained system preventing any water pressure on the tunnel lining and the other is the pressurized system with the full water pressure acting on the lining.

Figure 9. Drained system.

In the drained system the membrane is installed only in the vault like an umbrella. Drainage pipes are placed in the arch-foots and the membrane stretched down to the drainage. A drainage layer needs to be installed outside the membrane to drain the water down to the drainage pipes. The fully bonded membrane will guarantee a water tightness comparable to class "fully dry" and there is no risk of any water migration along the tunnel inside the waterproofing layer.

The other concept is a pressurized watertight construction. The water does not get drained by the tunnel and the full water head acts on the concrete lining. The membrane is installed fully around the circumference of the tunnel.

Figure 10. Pressurized system.

Due to the water pressure the system is exposed to far more stresses than the drained system. Depending on the hydrostatic water pressure, thicker membranes than used in the drained system are recommended. Although due to the system being fully bond, the membrane thickness remains much lower than the loose laid system. A punctured membrane will have the full water pressure acting locally on the concrete lining. In case of crack or poor concrete quality the water will cause a damp to wettish surface. But this water ingress can be easily fixed by localized concrete water-tightening injections.

In shallow pressurized tunnels a 1.0 mm thick fully bonded membrane is installed on the full circumference and welded together. Commonly the invert is installed in a first step and the vault completed in a second step.

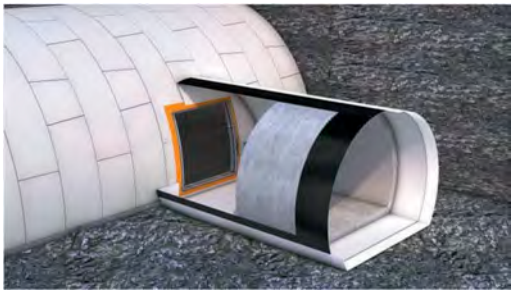

Figure 11. Cross passages in TBM tunnels.

Another typical pressurized waterproofing is used in cross passages between two TBM excavated tunnels with a single shell segmental lining. Here

a fully bonded membrane can be connected directly to the segments using a tape. The 2.0 mm membrane is recommended when facing higher water pressure and due to a better weldability to the tape. The Sikaplan® WT Tape-200 is fixed to the segments with epoxy glue. The fully bonded membrane is then hot air welded to the tape offering a watertight connection between the segments and the membrane. This offers a high level of watertightness at low cost.

11 THE INSTALLATION PROCESS

The speed of waterproofing installation can easily be adapted to the general speed of the tunnel lining installation and is never the critical path.

With the geotextile punctually-fixed to the waterproofing SikaProof®-110 membrane, the application is simplified. At the same time, thanks to its spot-fixing, the geotextile does not act as a reinforcement for the membrane and limiting its elasticity. The elongation at break of the membrane remains unchanged.

Figure 12. Scaffolding for membrane installation.

The installation procedure of the waterproofing system depends on the site conditions. As for all tunnels waterproofing, the installation should be performed by skilled and experienced waterproofing contractors, specifically trained in membrane welding and installation. The membrane is delivered to site in 2.0 to 2.1 meter wide rolls with a length adapted to the construction geometry in order to reduce waist. The 2.0 to 2.1 meters are a common size in waterproofing as this allows an appropriate handling in the tunnel and limits the weight of the rolls.

For the installation, only a nailer, hot air welding equipment and a scaffolding adapted to the size of the tunnel are needed.

The substrate needs to comply with the supplier's requirements for waterproofing membrane installation. The roughness of the primary lining shall be smooth and free of harmful objects like steel fibers and anchor heads. This is to prevent a puncture of the membrane when the membrane is pressed by the fresh concrete against the rock support. A layer of spray concrete without steel fibers and smaller aggregate size is used to reduce the roughness. An evenness of 1:10 (depth D to length L) is needed on the substrate surface. This is to prevent an overextension of the membrane when pushed into bumps by the fresh concrete.

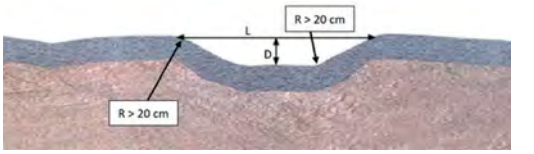

Figure 13. Geometrical substrate requirements.

Due to the fully bonded properties of the membrane the watertightness is less at risk than with loose membranes as the water inflow at a leakage will mostly be blocked by the concrete.

Figure 14. Fixation of the membrane using the geotextile.

The membrane is unrolled, and the attached geotextile fixed with a nail gun to the substrate. First the middle strip (4b, Figure 8) is attached followed by the edges of the geotextile (4c, Figure 8). The next membrane strip can then be fixed parallel with a slide overlap of approximately 10 cm.

Then the two membrane sheets are hot air welded together. Best is the use of an automatic double seam welding equipment. These machines produce two parallel weld seams leaving an air channel in the middle.

This air channel can then be pumped with air and the weld seams checked by controlling the air pressure kept in the channel. Fully bonded membranes can tolerate some insufficient welding due to the restrain of water migration. A quality welding offers

Figure 15. Hot air welding of the membrane.

an additional safety in the system. TPO (FPO) is a thermoplastic, so it can be hot air welded. Combined with the concrete lining the membrane creates a monolithic layer that protects the whole tunnel from water inflow. The welding can also be done manually. The single weld is tested using a screwdriver to control the continuity of the seam.

Figure 16. Test of welding seams.

The tunnel lining formwork can be installed once the waterproofing membrane is completed. The formwork is filled with the fresh concrete and the concrete compacted. Immediately with the pouring of the concrete the functional (bonding) layer starts to interact with the concrete and the bonding takes place. After the concrete has cured the full bonding strength is reached. The gap filling in the crown is recommended after 28 days to prevent any debonding due to injection infiltrating. The gap filling needs to be done with shrinkage compensated mortar to prevent any shrinkage cracks between concrete and mortar.

12 REDUCED INSTALLATION STEPS

This next generation waterproofing for tunnels reduces the work steps for installation from 4 steps to only one step. The installation of the conventional systems needs several work steps. For a pressurized compartment system, in a first step, a cushion layer is installed with the fixation disc, then the membrane is spot welded to the discs and the membrane strips welded together. Finally, waterbars and injection hoses/ports are installed and the waterbars in the crown injected to guarantee the full bedding. Later, any compartment showing water inflow due to a leakage, needs to be injected with raisins.

In drained tunnels with an umbrella waterproofing the drainage layer is attached using the fixation discs. In a second step the membrane is spot welded to the discs and terminated towards the drainage system in the side walls. In a last step the membrane strips are welded, and a protection layer installed where needed.

With the new buildup, the membrane can be installed in one step using the geotextile for fixation. This is a massive reduction of work steps and costs compared to the actual widely used concepts.

13 CONCLUSION

Over the past 60 years, tunnel waterproofing has witnessed significant evolution worldwide. The transition from watertight concrete to sheet PVC and TPO (FPO) membranes marked a substantial improvement in tunnel waterproofing practices. In the last decade only, minor evolutions managed to implement themselves. South Korea's commitment to innovation led to the development and adoption of fully bonded systems, which provide a seamless and reliable barrier against water ingress.

Fully bonded systems offer numerous advantages, including superior watertightness, longevity, and resistance to movement. Their installation process was optimized to reduce the work steps and improve productivity.

The major improvements this new tunnel waterproofing membrane SikaProof®-110 offers are:

- Fully-bonded preventing any water migration
- Weldability of the membrane
- Optimized timesaving fixation

As tunnel construction continues to evolve, it is likely that further innovations will emerge, making tunnel waterproofing even more efficient and reliable, ensuring the safety and sustainability of underground infrastructures for generations to come.

Tunnelling for a Better Life – Yan, Celestino, Thewes & Eberhardt (Eds)
© 2024 The Author(s), ISBN 978-1-032-80042-4
Open Access: www.taylorfrancis.com, CC BY-NC-ND 4.0 license

Mitigation of the sources of infiltration in the segment sealing gasket

Gustavo Bomben*
FAMA, Zoppola di Pordenone, Italy

ABSTRACT: Tunnel watertightness must be ensured during the construction and operation phases to prevent water infiltration, to minimize maintenance and repair costs, keep operational safety and protect vehicles in transit and mechanical and electrical equipment which are in the tunnel.

In the segmental tunnel lining, watertightness is ensured by each component of the support system, that is the precast concrete tunnel segments with their embedded inserts and gaskets positioned around their sides.

They are different types of infiltrations: Infiltration through cracks in concrete; Infiltration in the interface with embedded inserts; Infiltration of the sealing gasket.

In this paper, we examine the innovative measures introduced to minimize the causes that generate water infiltration in the gasket through the study and experimentation of the measures that reduce the breakage of the segments caused by the gasket and the gasket destabilization during the launch of the segment.

Keywords: Tunnelling, TBM, sealing, connection, infiltration

1 INTRODUCTION

In segmental tunnel lining, watertightness is ensured by each components of the support system, that is the precast concrete tunnel segments with their embedded inserts and gaskets.

There may be infiltrations through cracks in the concrete, in the interface with inserts and in the sealing gasket. In this paper, we are examining the latter.

2 GASKET

It is well known that the performance of the gasket, even if of excellent workmanship, can be endangered during the entire construction cycle. However, it is in particular compromised during the installation of the segment.

During the installation, damages of segment edges and segment corners and the expulsion of the gasket may occur; these are the primary causes of infiltration. Therefore, the aim is to provide gaskets difficult to be removed from their position and with low compression loads. In this condition, repair is not needed.

To reach this aim, gasket geometry engineering has been required, that is made possible thanks to experimental virtualization which allows the assessment of the effects of hydrostatic pressure and to consider the effects on concrete.

The other fundamental element is the size of the gasket.

it must also be acknowledged that a better installation of the segments and rings has been achieved thanks to the widespread use of the dowels instead of the bolts.

Moreover, with the use of 3D modelling of the segments and formwork and the numerical control machining, a greater accuracy of the shapes has been achieved and therefore the coupling of the surfaces between the segments and the rings reaches a much more precise and important result.

Before these innovations, it was quite mandatory to use large size gaskets to compensate for the significant misalignments and openings of the joints.

In this new context, excellent results have been reached with the gasket of medium size, gasket of third generation, 29x14, even in tunnels with diameters exceeding 11 meters and with working pressure exceeding 10 bar.

A further element is represented by the choice of the type of gasket installation to the segment which may be achieved:

- either gluing the gasket;
- or incorporating the gasket into the concrete segment.

2.1 *Glued gasket*

Gluing is a complex process that is strongly influenced by several elements: environmental conditions, the skill and the consistency of the operator.

*Corresponding author: Gustavo.bomben@famaspa.it

DOI: 10.1201/9781003495505-334

In this case, health and environmental aspects should not be underestimated.

Gluing is exposed to the risk of widespread detachments, misalignments and displacement of the gasket.

All these phenomena significantly affect gasket performance.

2.2 *Anchored gasket*

The anchored gasket is an innovation of recent years and it has replaced the glued solution as its installation is more solid. It also offers several advantages regarding construction, environment and performance.

The anchored gasket, which has brought considerable benefits, has however evidenced critical issues that must be correctly managed to avoid failures.

The anchored gasket, because of its geometry, increases the application arm of the forces generated by its compression, thus augmenting the loads on the concrete.

Therefore, there are:

- increased risk of broken edges;
- increased risk of broken corners.

In particular, there can be hidden breakages, non-visible but that may occur over time. When they are at intrados, they may have important consequences.

Other damages are due to the manufacturing process.

They are classified as follows:

- Tearing;
- Sinking;
- Edge breaking during handling.

Obviously, for each of these aspects repair techniques have been studied and validated.

The effects of the anchored gasket on the concrete require attention to specific aspects that can be summarized as follows:

1. The position from the segment edge which may cause breakage;
2. The filling rate which represents the ratio between the compressible section of the gasket and the groove in which it is contained at full compression.

We must keep always in mind that rubber is flexible but not compressible.

STUVA suggests that the filling rate should not exceed 95% but it also suggests that, under special conditions, it can reach 100%.

These indications are NOT confirmed by ITA which limits the filling rate to 90%.

My personal experience suggests that we should not exceed, when possible, 80%; this is due to the greater loads that the gasket applied to the concrete.

The third point is:

3. The groove of the anchored gasket which is formed by the gasket, whose construction tolerances directly affect its size with significant effects on its hydraulic performance, and on the risk of segment breaking. This risk is reduced when glued gaskets are used because the groove is realized in the formwork that has lower tolerances.

Table 1. Filling rate.

Filling Rate of T-Joint									Corner Expulsion			Increase of the Volume of the Corner Groove		
Gasket Type	Anchored Profile	Compressible Profile Section	Groove Section	Filling Rate of Linear Profile	Considered Length from the Top	Volume of Compressible Profile - T-Joint	Groove Volume - T-Joint	Filling Rate of the Corner	Length of the Corner Expelled during Launch	Added Volume	Filling Rate of the Corner	Corner Sinking	Increase oft the volume of the Corner Groove	Filling Rate of the Corner
[-]	[-]	[mm²]	[mm²]	[-]	[mm]	[mm³]	[mm³]	[-]	[mm]	[mm³]	[-]	[mm]	[mm³]	[-]
Glue	UG066C	237.2	302.5	78%	100	149370.4	167353	89%	30	7116	94%			
	UG066C	237.2	302.5	78%	50	78210.4	76603	102%	30	7116	111%			
		287.4	302.5	95%	100	175060	167353	105%	30	8621.25	110%			
		287.4	302.5	95%	50	88847.5	76603	116%	30	8621.25	127%			
Anchored - Std Corner	UG066C	237.2	302.5	78%	100	165647	167353	99%	30	7116	103%	2	3016	92%
	UG066C	237.2	302.5	78%	50	94487.01	76603	123%	30	7116	133%	2	3016	107%
		287.4	302.5	95%	100	194329	167353	116%	30	8621.25	121%	2	3016	108%
		287.4	302.5	95%	50	108116.5	76603	141%	30	8621.25	152%	2	3016	122%
- SOFT Corner	UG066C	237.2	302.5	78%	100	152919	167353	91%	30	7116	96%	2	3016	85%
	UG066C	237.2	302.5	78%	50	81759.01	76603	107%	30	7116	116%	2	3016	92%
		287.4	302.5	95%	100	181601	167353	109%	30	8621.25	114%	2	3016	101%
		287.4	302.5	95%	50	95388.55	76603	125%	30	8621.25	136%	2	3016	108%

The filling rate is assessed on the gasket section and its groove section, but this represents only one of the aspects. As a matter of fact, the table summarizes several aspects and assessed the filling rate of both the gasket and the linear section in the T-joint and the positive effects of the innovative SOFT CORNER that brings the profile as close as possible to the top and uses sophisticated injection techniques to reduce the infiltration of hollow parts of the profile. It also takes into account the deterioration effects due to the expulsion of the corner that occurs during the installation. At last, it considers the load containment on T-joint due to the position of the variable-geometry gasket that we will discuss later.

The table assesses the use of both glued and anchored gaskets and traditional and SOFT CORNERS, with filling rate ranging from 78% to 95%.

The assessment of STUVA considers only the filling rate represented in the fifth column but not all the other effects which are very important:

- position of the anchored feet in particular in large gaskets and with high compressive force; in this case, asymmetric solutions may represent a mitigation;
- The asymmetric position of the gasket in the joint which protects it from the compression of the TBM jacks.

2.3 *T-joint*

The T-joint is analyzed according to:

– Compressive force;
– Spalling test.

2.3.1 *The compressive force*

STUVA has established a procedure for the definition of these loads, using a special equipment.

The test involves compressing the longitudinal joint, represented by the two opposing angular structures, to a gap of 2mm. Next, the gasket linear frame, which represents the circumferential joint, is compressed against the two angular structures up to a gap of 0mm.

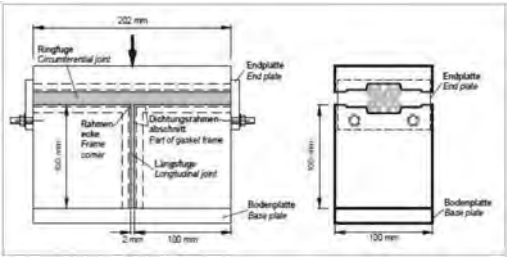

Figure 1. Load and displacement test.

The test detects the load and the displacement.

The compression test of the T-joint, as indicated, involves the closure of the longitudinal joint at gap 2mm. However, this does not represent the real conditions when the longitudinal joints are often closed at gap 0mm.

A different and innovative test establishes a more burdensome procedure with the closure at gap 0mm; moreover, it simulates the expulsion of the gasket in the corner and it measure the consequent loads.

We are now analyzing the variation of the load of the T-joint using both methods.

The test is performed on gaskets of medium size UG018A.

The maximum load measured with STUVA method is 20kN, while using the other method, the load rises to 32kN, an increase of 60%.

Let's now analyze the results with the simulation of the angle expulsion.

During the launch of the segment, in fact, the corners of the gaskets are very often expelled or wrinkled. This creates a concentration of rubber.

The result of this condition is shown in the following graph, where there are also the results of the previous tests.

Table 2. Load deflection test.

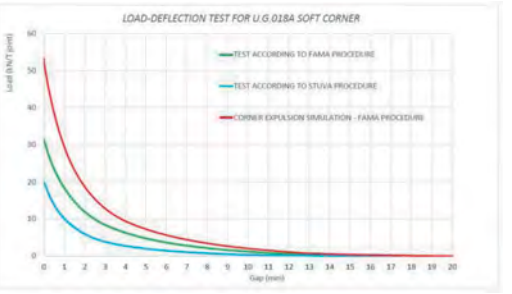

It can be observed that the wrinkling of the corner increases the load up to 52kN compared to the 20kN assessed with STUVA method.

In order to reduce the loads generated by the T-joint, an innovative special corner, SOFT. Here follows a comparison, achieved according to STUVA method, of this corner with gasket corners of the same size on the market.

Table 3. Compression load comparison.

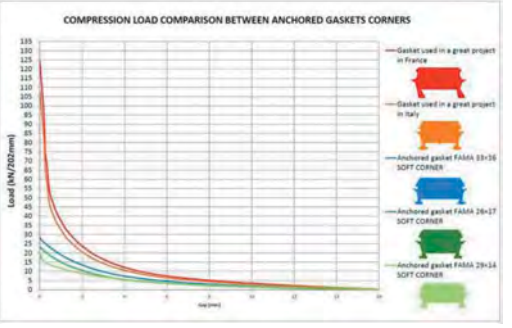

The SOFT CORNERS range from 18kN to 28kN while the corners of similar gaskets on the market have loads which exceed 120kN. It is well known that the higher is the load, the higher is the risk of breaking and therefore of infiltration.

2.3.2 *Spalling test*

The spalling test is performed on concrete blocks having dimensions as illustrated in the following figure, with a characteristic and a determined condition: the blocks have T-joint corners at 90° and, as it occurs with the compression test, the longitudinal joint is closed to a gap of 2mm while the circumferential joint is closed at gap 0mm.

The test is conducted to verify that the edge does not break and the corner does not break.

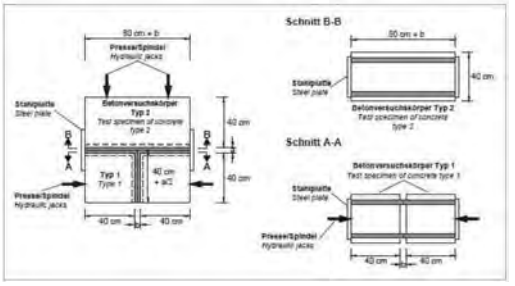

Figure 2. Spalling test.

The influence of the geometry of the segment corner should be examined.

The mechanical resistance of the acute corners is lower than the mechanical resistance of obtuse and right corners. The experience confirms this thesis. In the following graph, relief of the number of broken corners gives data in tunnel, in particular regarding the breaking of the angles.

96% of broken corners are acute and only 4% are obtuse. The broken corners were actually distributed equally between those facing the direction of excavation and those opposing it.

The test was performed with concrete blocks with right and obtuse corners, according to STUVA, and the corners angles and obtuse, according to the project. The test with concrete blocks with right corner is performed according to the STUVA method. The test performed on the concrete blocks with acute and obtuse corners provides a first step that closes the longitudinal and circumferential joint to gap 0mm. In the second test, to consider the load increases due to the gasket expulsion e al wrinkling of the gasket corner, situation that really occurs, it generates a hyper-closure of the circumferential joint to a gap of -2mm to value the safety margins.

The photos show a spalling test performed according to STUVA and according to the innovative methods. It shows that there is no breaking of the corners and there is no breaking of the edges. It

Table 4. Broken corner.

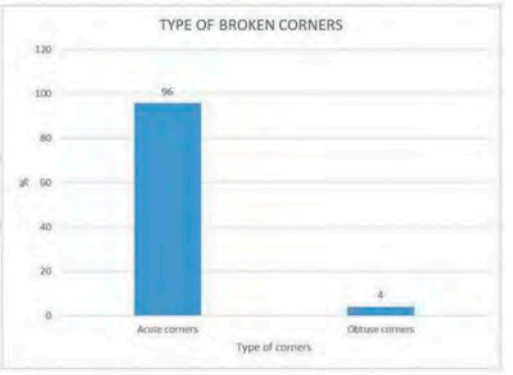

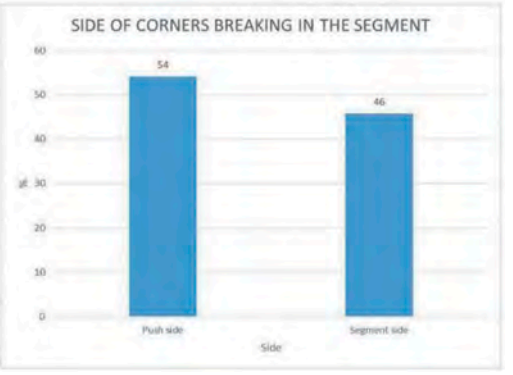

Figure 3. STUVA spalling test.

should be reiterated that the test performed according to the innovative method is much more burdensome than the one performed according to the STUVA method.

3 INNOVATION

Considering the importance of the phenomena concerning the T-joint, the objective is to study solutions that can contribute to reducing the negative effects.

Figure 4. Innovative spalling test.

To reach this aim, we must first assess the filling rate of the gasket and T-joint. STUVA, as already underlined, describes limits of the filling rate that only concerns the linear part of the gasket and does not deal with T-joint. This approach does not create particular problems with glued gaskets while it becomes decisive for anchored gaskets.

In order to assess the filling rate of the T-joint, the profile section is not taken into account, that is a bidimensional dimension, but the volume, that is a tridimensional value, of the T-joint grooves and the volumes of the gasket linear section and the two angular structures, in open and closed joint conditions, are considered.

When examining the volume of the angular structures of the gaskets, both the compact part of the injected corner and the infiltration of the void parts adjacent to the molded corner were taken into account.

The results of this analysis are shown in the table that compares the filling rate of glued gaskets of different sections with the filling rate of similar anchored gaskets (see Table 1).

4 CONCLUSIONS

The glued gaskets have a filling rate in the T-joint ranging from 89% to 116%.

Similar anchored gaskets with traditional corners have a filling rate ranging from 99% to 141%. Thanks to the SOFT CORNER, this value passes to 91%-125%.

This highlights the positive effect of the SOFT CORNER compared to the traditional one but the levels of the glued solution are not reached.

Experience has shown that the T-joint with a low filling rate does not create any particular problems as the exceeding rubber is absorbed by longitudinal displacements of the gaskets surrounding the same joint.

On the other hand, when this rate exceeds a determined limit, this contiguous displacement does not occur sufficiently and therefore there is a volume of rubber greater than the volume of the groove that causes the rupture of the system.

In order to minimize the phenomenon above-described, a particular gasket geometry in the T-joint must be studied in order to contain the filling rate within limits more tolerable by the system. This has been achieved by a gradual retreat of the gasket closer to the corner. This approach has given very important results of the T-joint compression.

It passes from 32kN at standard condition to 10kN with variable geometry, compared to 9kN of the linear section of the gasket.

The hydraulic performance of the variable-geometry gasket is comparable to the standard one. Where special sealing performance levels are required, the variable-geometry angle may be unsuitable and the effects of the loads generated in the T-joints should always be verified by spalling test.

The innovation is therefore a gasket with variable geometry that prevents the expulsion of the corners and the loads on the corners of the segments and therefore less infiltrations.

REFERENCES

Fascicule N. 67 Titre III, 2019. Version commentée du Ministère de la transition écologique et solidaire. Cahier des clauses techniques générales applicables aux marchés publics de travaux de génie civil Étanchéité des ouvrages souterrains. Centre d'Études des Tunnels. Bron, FRANCE.

ITA Report N. 22, 2019. Guidelines for the Design of Segmental Tunnel Linings. Chatelâine, GE, SWITZERLAND.

SIG Working Group 2 Report N. 1, 2019. Damages of Segmental Lining. Milan, ITALY.

STUVA, 2019. Recommendation for Gasket Frames in Segmental Tunnel Linings. Köln, GERMANY.

Tunnelling for a Better Life – Yan, Celestino, Thewes & Eberhardt (Eds)
© 2024 The Author(s), ISBN 978-1-032-80042-4
Open Access: www.taylorfrancis.com, CC BY-NC-ND 4.0 license

Analysis of cement grout hydraulic erosion in a homogeneous fracture

Hongyu Duan* & Liangchao Zou
Department of Sustainable Development, Environmental Science and Engineering, Royal Institute of Technology, Stockholm, Sweden

ABSTRACT: Cement grouting has been widely used in rock tunneling to reduce groundwater inflow by sealing rock fractures. However, the injected cement grout often encounters hydraulic erosion that affects the safety and sustainability of rock tunnels in the long term. Analysis of the long-term hydraulic erosion effect on cement grout in rock fractures is therefore important for the safety and sustainability development of rock tunnel engineering. In this work, a hydraulic erosion model for analyzing cement grout erosion in a homogeneous fracture is established and used to theoretically investigate the transmissivity evolution of the grouted fracture under long-term hydraulic erosion. In the present model, the fracture seepage characteristics, solid erosion theory and mass conversation for water-solid two-phase flow are considered, and the mathematical model as a set of partial differential equations is established. Based on laboratory tests, the key parameters (e.g., erosion coefficient) are calibrated and the erosion model is validated. Numerical simulations are conducted by numerically resolving the mathematical model. The results show that the erosion phenomenon first occurs in the edge areas of the grouted area near the fracture boundary; the erosion area gradually expands toward the center of the grouted area. The porosity and flow velocity significantly increase in the area with relatively strong erosion effects. During the erosion process, the concentration of cement grout gradually increases along the seepage path until a more uniform distribution of cement particle concentration is achieved. Due to the erosion process, the spatial distribution of hydraulic pressure along the fracture direction transforms from a linear distribution to a nonlinear distribution. The effective fracture transmissivity increases nonlinearly along the erosion process. The presented erosion model and analysis results are potentially useful for the safety and durability assessment of rock tunnels.

Keywords: Hydraulic erosion, Cement grout, Homogeneous fracture, Long-term effect, Effective transmissivity, Two-phase flow

1 INTRODUCTION

Cement grouting is a highly effective method utilized in rock tunnel engineering to ensure the safety and stability of tunnels. When tunnelling in areas with poor geological conditions characterized by highly fractured rock, cement grout could be injected into rock fractures to seal them, thereby reducing the permeability of the rock mass and preventing groundwater inflow into the tunnel. However, the sealing effect of cement grout in rock fractures can gradually decrease over time due to degradation processes (e.g., hydraulic erosion), leading to an increase in fracture permeability that poses a threat to tunnel sustainability. Therefore, it is imperative to investigate the long-term evolution of permeability in grouted rock fracture.

Many studies have been conducted on the long-term permeability of cement grouted areas focused on the impact of cement grout composition and groundwater chemical environment. Laver et al. (2013) analyzed the samples taken from the grouted area surrounding a tunnel constructed in the early 1900s, and discovered an increase in permeability within grouted area. The degradation of the cement grout was attributed to cement carbonization and the sulfate reaction between the cement grout and groundwater. Lin et al. (2021) conducted experiments to determine the limited hydraulic pressure of cement grouting materials containing different admixtures and predicted the long-term permeability of cement grouts.

However, the aforementioned studies have not taken into account the long-term hydraulic erosion phenomenon, which is in fact a prevalent phenomenon in nature. Under high hydraulic pressure, solid particles within the rock or soil may detach from their mass skeleton and migrate with fluid flow. A similar effect occurs in cement grouted areas under hydraulic erosion, which has been confirmed by laboratory experiment results (Chan 1986) and in-situ observations (Akagi et al. 2010; Liu et al. 2018). Dekker et al.

*Corresponding author: hongyud@kth.se

DOI: 10.1201/9781003495505-335

(2020) developed an analytical solution for groundwater flow and transport within the cement grouting layer, examined the evolution of hydraulic conductivity in the cement grouted area, and quantified the mass flux and dilution ratio of erosion-related components. Liu et al. (2018) developed a hydraulic erosion model for curtain grouting in fully weathered granite, analyzed the overall response of the curtain grouting during hydraulic erosion, and determined the recommended design value for curtain thickness. Liu et al. (Liu 2022) analyzed the permeability evolution law of the cement grouted area under hydraulic erosion, established the damage evolution model of the cement grout, and obtained the relationship between permeability and damage variables.

The permeability evolution of cement grouted area under the action of hydraulic erosion has been studied in the above literature, but the long-term hydraulic erosion in the rock fracture cement grout has not been paid attention to. For the long-term hydraulic erosion of cement grouted area in fractures, it is necessary to consider more complex boundary conditions of hydraulic erosion, and take the non-Darcy seepage and solid-liquid two-phase flow in fractures into consideration. In order to analyze the sustainability of grouted fracture under long-term hydraulic erosion, a hydraulic erosion model of cement grout erosion in a homogeneous fracture is established in this paper. The model is verified by the laboratory tests, and the evolution law of hydraulic characteristics of rock fractures under hydraulic erosion was obtained. The grout erosion model established and the analysis results have certain guiding significance for the safety and durability evaluation of rock tunnels.

2 MODEL ESTABLISHMENT

2.1 *Model description*

The fracture grout erosion model is illustrated in Figure 1, where x represents the length of the rock fracture, z denotes its width, and a grouted area with a radius of r is positioned at the center of the fracture. The hydraulic pressure on the left side of the rock fracture is p_A, while that on the right side is p_B. Due to hydraulic erosion, fine solid particles in the grouted area migrate from left to right. The seepage area can be partitioned into three zones, namely Zones A, B and C. Owing to the distinct physical phenomena in each zone, diverse forms of governing equations are required to be established. Among them, the analysis of water flow and solid-fluid two-phase flows in rock fractures is required for Zones A and C, respectively, while the hydraulic erosion phenomenon in porous cement grout should be considered for Zone B.

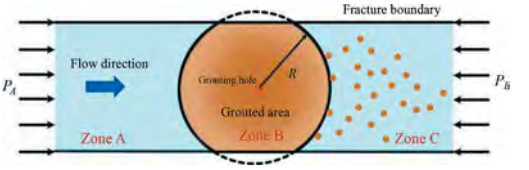

Figure 1. The principle of the hydraulic erosion model for cement grouts.

2.2 *Model assumption*

The model takes into account the following assumptions:

A. The fracture is homogeneous and the surface roughness is not considered.
B. In the process of hydraulic erosion, the cement grouted area is saturated, and it is composed of cement grout skeleton, water and fluidized cement grout particles.
C. The grouting porosity is the effective porosity, and the disconnected porosity is regarded as a part of the cement skeleton.
D. Groundwater and fluidized cement grout particles maintain the same velocity.
E. The chemical reactions between water and rock, as well as water and cement, are not taken into consideration.

2.3 *Governing equations*

For Zone A, according to the cubic law (Zimmerman and Bodvarsson 1996), the permeability k of rock fracture has the following relationship with its aperture e:

$$k = \frac{e^2}{12} \tag{1}$$

According to previous studies, fluid flow in rock mass fractures can be represented by the Forchheimer equation (Zeng and Grigg 2006):

$$-\nabla p = \frac{\mu}{k}u + \rho_W \beta u^2 \tag{2}$$

where p is hydraulic pressure, μ is dynamic viscosity, ρ_W is the density of water, u is the fluid velocity, and β is the non-Darcy factor. In rock fracture, the non-Darcy factor can be calculated by the following empirical equation (Li and Engler 2001).

$$\beta = \frac{1.1 \times 10^{-5}}{k^{1.176}} \tag{3}$$

For Zone B, considering the mass conservation law in the cement grout area during hydraulic erosion, the mass conservation equations for cement grout skeleton (1), water (2) and fluidized cement grout particles (3) are obtained as (Bear 2013):

$$\frac{\partial \rho^{(n)}}{\partial t} + div\left(\rho^{(n)} v^{(n)}\right) = l^{(n)} \quad n = 1,2,3 \tag{4}$$

where $v^{(n)}$ is the actual velocity of different phases, according to Assumption D, $v^{(2)} = v^{(3)}$ .Since the cement skeleton does not move with the flow, $v^{(1)} = 0$. In addition, there is a relationship between the actual velocity of water and the flow velocity:

$$u = \phi v^{(2)} \tag{5}$$

And $l^{(n)}$ is the mass loss rate of phase n, since all fluidized cement grout particles are derived from cement skeleton, so $l^{(1)} = -l^{(3)} = J$, where J is the mass loss rate of cement skeleton, and $l^{(2)} = 0$. $\rho^{(n)}$ is the partial density of phase n, and it can be expressed by Equation 6.

$$\begin{cases} \rho^{(1)} = \rho_s(1-\phi) \\ \rho^{(2)} = \rho_W(1-c)\phi \\ \rho^{(3)} = \rho_s c\phi \end{cases} \tag{6}$$

where ρ_s is the density of cement grout, ϕ is porosity, and c is fluidized cement grout particle concentration. Combine Equations (4)-(6), the mass conservation equations for each phase are obtained:

$$\begin{cases} \dfrac{\partial \phi}{\partial t} - \dfrac{J}{\rho_s} = 0 \\ \dfrac{\partial (1-c)\phi}{\partial t} + div[(1-c)u] = 0 \\ \dfrac{\partial c\phi}{\partial t} + div(cu) + \dfrac{J}{\rho_s} = 0 \end{cases} \tag{7}$$

For the fluid flow in the grouting area, the following equation is satisfied:

$$-\nabla p = \frac{\mu}{k} u + \bar{\rho}\beta u^2 \tag{8}$$

where $\bar{\rho}$ is the average density of the two-phase fluid, which could be calculated by Equation 9:

$$\bar{\rho} = \rho_W(1-c) + \rho_s c \tag{9}$$

For the non-Darcy factor in the grouted area, it can be expressed by Equation 10 (Li and Engler 2001):

$$\beta = \frac{1.15 \times 10^{-6}}{k\phi} \tag{10}$$

According to the previous research (Lee et al. 1996), the permeability in porous media has the following relationship with its porosity:

$$k = k_R \frac{\phi^3}{(1-\phi)^2} \tag{11}$$

where k_R is the permeability parameter. To describe the mass loss rate of cement grout skeleton, there is a constitutive relationship of hydraulic erosion (Vardoulakis et al. 1996).

$$J = \lambda \rho_s (1-\phi)\left(c - \frac{c^2}{c_{cr}}\right) u \tag{12}$$

where λ is the erosion parameter and c_{cr} is a critical value of particle concentration.

For Zone C, the non-Darcy equation is the same as that in the grouting region (Equations 9 and 10), and the equation of fracture permeability and non-Darcy factor is the same as that in Zone A, as shown in Equations 1 and 3. The mass conservation equation for Zone C can be calculated by the following equation (Bear 2013):

$$\frac{\partial c}{\partial t} + div(cu) = 0 \tag{13}$$

And the fracture effective transmissivity can be obtained by (Zou et al. 2018):

$$T = \frac{\bar{u}_{out} L}{e\Delta p} \tag{14}$$

where $\bar{u}_{out}$ is the average flow velocity at the outlet boundary of fracture, and Δp is the difference between the inlet pressure and the outlet pressure of the fracture.

2.4 *Computational conditions*

For the grouted area (Zone B), there are the following initial conditions:

$$\phi(x,y,0) = \phi_0,\ c(x,y,0) = c_0,\ k(x,y,0) = k_0 \tag{15}$$

For the initial condition in Zone C, there is:

$$c(x,y,0) = c_0 \tag{16}$$

Taking the center of the grouting hole as the coordinate origin, the boundary condition for the fluidized grout particle concentration is:

$$c(x_0,y_0,0) = c_0,\ \text{where} \begin{cases} x_0^2 + y_0^2 = R^2 \\ x_0 < 0 \end{cases} \tag{17}$$

And the boundary conditions for the hydraulic pressure are:

$$p\left(-\frac{L}{2},y,t\right) = p_A,\ p\left(\frac{L}{2},y,t\right) = p_B \tag{18}$$

3 CALIBRATION AND VALIDATION OF THE MODEL

Table 1 presents the primary parameters of the model, in which initial porosity, permeability parameter, and erosion parameter are obtained from specific measurements or calibration, and the remaining parameters can be established based on previous references (Ma et al. 2023) or research requirements. Initial porosity is determined through nuclear

magnetic resonance technology, while the permeability parameter is calculated using Equation 11 in combination with initial permeability from testing results. The erosion parameter is obtained through cylinder sample test calibration as described by Ma et al. (2022).

The hydraulic erosion equations in the grouted area constitute the core of the proposed model. To simulate cement grout erosion processes in a laboratory setting, an accelerated test method is employed that involves increasing boundary hydraulic pressure and reducing sample size. A cylindrical cylinder was used to conduct tests lasting 50 hours during which changes in sample quality were monitored and porosity evolution curves calculated. Experimental parameters were then input into the proposed hydraulic erosion equation to obtain calculated results for porosity evolution that could be compared with experimental curves using absolute percentage error (APE) and mean absolute percentage error (MAPE) calculations:

$$APE = \left| \frac{\phi_i - \phi_{ci}}{\phi_i} \right| \times 100\% \tag{19}$$

$$MAPE = \frac{1}{n} \sum_{i=1}^{n} \left| \frac{\phi_i - \phi_{ci}}{\phi_i} \right| \tag{20}$$

where ϕ_i and ϕ_{ci} are testing and calculating the value of porosity at time i (i=1…n).

Table 1. Model parameters.

Model parameters	Value
Fracture length of the, L (m)	3
Fracture width of the, W (m)	0.9
Fracture aperture, e (m)	0.001
Radius of grouted area, R (m)	1
Initial concentration of the fluidized particle, c_0	5×10^{-3}
Critical value of concentration, c_{cr}	0.4
Dynamic viscosity of water, μ (m^2s^{-1})	1.01×10^{-3}
Density of water, ρ_f ($kg\cdot m^{-3}$)	1000
Density of cement grout, ρ_s ($kg\cdot m^{-3}$)	2500
Hydraulic pressure at the left boundary, p_A (MPa)	1
Hydraulic pressure at the right boundary, p_B (MPa)	0
Initial porosity, ϕ_0	0.072
Permeability parameter, k_c (μm^2)	5.12×10^{-10}
Erosion parameter, λ (m^{-1})	2×10^{-5}

Figure 2 Shows the comparison between test and simulation results, demonstrating a high level of agreement between the two. The APE is less than 0.6%, with a MAPE of only 0.28%. These findings indicate that the erosion equations utilized in the proposed model possess strong applicability when simulating hydraulic erosion within grouted areas.

4 RESULTS AND DISCUSSION

4.1 *Evolution of porosity*

The porosity evolution law in the grouted area under hydraulic erosion is illustrated in Figure 3. After 2.5 years of continuous hydraulic erosion, a slight increase in porosity can be observed at the inlet and outlet of water flow at the fracture edge, indicating that some fluidized cement particles have started to detach from the grout skeleton due to water flow. At this time, the erosion effect has only caused a minor impact on the area with a maximum porosity increase of 0.09, indicating that the erosion phenomenon is not significant within 2.5 years. However, after five years of hydraulic erosion, the affected area expanded from the fracture edge to the grouting center and resulted in a maximum porosity of 0.13. Furthermore, seven and a half years later, there was further expansion of the erosion area with an increased maximum porosity of up to 0.23. After 10 years, the grouted area exhibited a maximum porosity of 0.43, which was 4.8 times higher than its initial value. At the same time, hydraulic erosion caused the formation of two high-porosity regions at both ends of the grouted area, with the maximum porosity continuously increasing and the growth rate accelerating over time. Specifically, the maximum porosity only increases by 0.02 in the range of 0-2.5 years, whereas it increases by 0.2 in the range of 7.5-10 years.

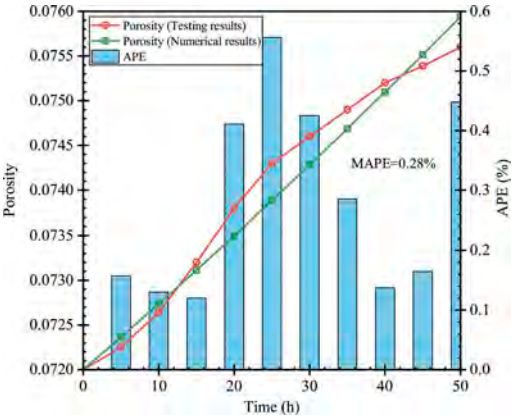

Figure 2. Evolution of porosity of cement grouted area under hydraulic erosion.

4.2 *Evolution of flow velocity*

The evolution of velocity magnitude and direction in the fracture is depicted in Figure 4, where the arrow indicates the direction of velocity and its size is positively correlated with the magnitude of velocity. After 2.5 years of hydraulic erosion,

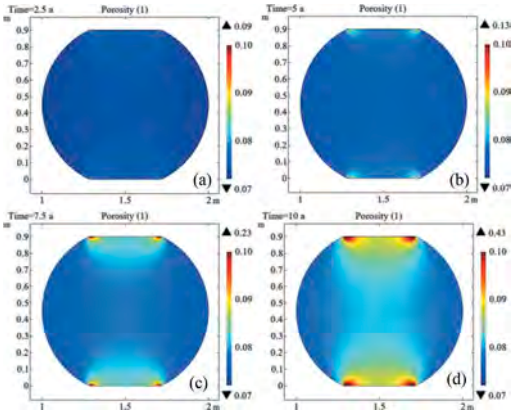

Figure 3. Evolution of porosity of cement grouted area under hydraulic erosion (a) 2.5 years; (b) 5 years; (c) 7.5 years; (d) 10 years.

a high-velocity zone emerged near both ends of the fracture adjacent to grouted areas, where fluid mainly infiltrated or exfiltrated from these zones with a maximum flow rate reaching 0.0086 m/s. At this time, the velocity distribution within the grouted area is relatively homogeneous with no discernible areas of high flow velocity. However, after five years of hydraulic erosion, as this phenomenon gradually intensified, the maximum flow rate increased to 0.01m/s and a small region of elevated flow rates was observed within the grouted area. After 7.5 years of erosion, the maximum flow rate increased to 0.02 m/s and a larger area of high flow rate was observed. Following 10 years of erosion, the maximum flow rate reached 0.06 m/s and a large area of high flow rate can be found in the grouted area. By comparing the magnitudes of vector arrows shown in Figures 4(a) and 4(d), it can be observed that the flow velocity increase significantly both in the grouted area and the rock fracture away from the grouted area. Furthermore, by comparing Figures 3 and 4, it can be inferred that both velocity growth and porosity growth occur at the same location within the grouted area, indicating a significant increase in velocity within areas experiencing hydraulic erosion.

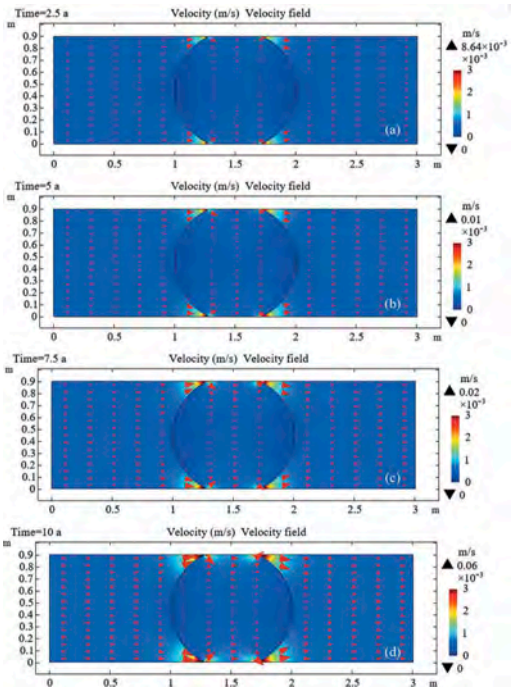

Figure 4. Evolution of flow velocity in the fracture under hydraulic erosion (a) 2.5 years; (b) 5 years; (c) 7.5 years; (d) 10 years.

4.3 *Evolution of cement particle concentration*

The evolution of fluidized cement grout particle concentration under hydraulic erosion is illustrated in Figure 5. After 300 seconds of erosion, a significant increase in grout particle concentration was observed in the rear half of the grouted area, indicating particle aggregation in this region. After 900 seconds, the high grout concentration area migrates towards the fracture, indicating that some cement grout particles have started to exit the grouted area and infiltrate into the rock fracture. A stable grout concentration distribution was observed in the fracture after one year. For the grouted area, the fluidized cement grout particle concentration increased along the seepage path, and the highest concentration was found at the rear of the grouted area. In the fracture area, the concentration is higher in the center than at the boundary. Over a period of 5 years, erosion led to a gradual decrease in grout particle concentration within both the grouted area and fracture, resulting in a more uniform distribution. Throughout this entire process, there was only minimal variation observed in fluidized cement grout particle concentration around 0.005.

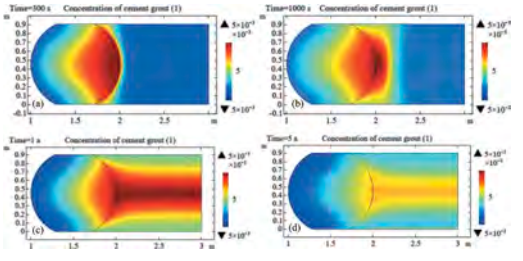

Figure 5. Evolution of cement particle concentration in rock fracture (a) 300 seconds; (b) 1000 seconds; (c) 1 year; (d) 5 years.

4.4 *Evolution of hydraulic pressure*

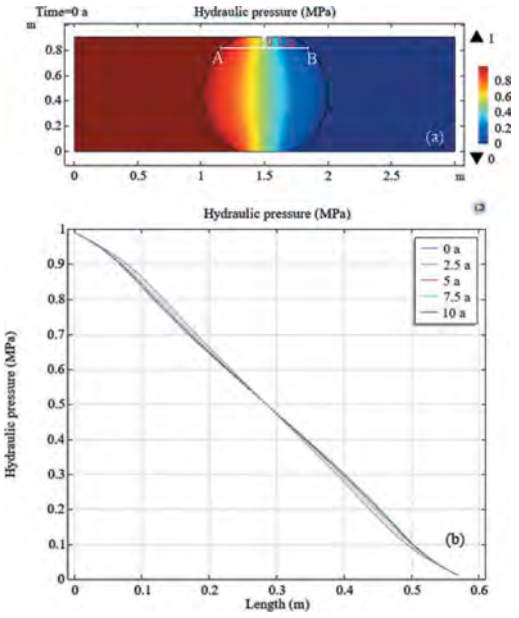

Figure 6. Evolution of hydraulic pressure in grouted area under hydraulic erosion (a) hydraulic pressure distribution in 0 years; (b) evolution curve of hydraulic pressure in line section AB.

Figure 6 (a) illustrates the initial spatial distribution of hydraulic pressure. It can be observed that there is minimal variation in hydraulic pressure within the fracture on both sides due to the fracture's higher permeability compared to that of the grouted area. Meanwhile, the hydraulic pressure gradient is greater at the upper and lower ends of the grouted area near the fracture's edge due to shorter seepage paths, which explains why erosion initially occurs in these areas. In order to further analyze the evolution of hydraulic pressure under hydraulic erosion, taking line segment AB as an example, the evolution curve of hydraulic pressure on this line segment was analyzed (as shown in Figure 6 (b)). It is observed that erosion causes slight changes in hydraulic pressure at each position. In the front half of the grouted area, hydraulic pressure exhibits a time-dependent increase, while in the rear half it shows a decrease. The spatial distribution of hydraulic pressure evolves from linear to nonlinear over time, which can be attributed to erosion effects.

4.5 *Evolution of fracture effective transmissivity*

The evolution of the effective transmissivity of fractures is depicted in Figure 7, which illustrates a 60% increase in the effective transmissivity of fractures over ten years due to hydraulic erosion. This indicates a significant decrease in the water-proof performance of the grouting body and a non-linear growth trend for the effective transmissivity of the fracture. After 3 years, the effective transmissivity growth rate of fracture accelerates due to hydraulic erosion and gradually deviates from linearity. Therefore, it is necessary to consider reinforcing the grouted area at this stage to mitigate this growth trend.

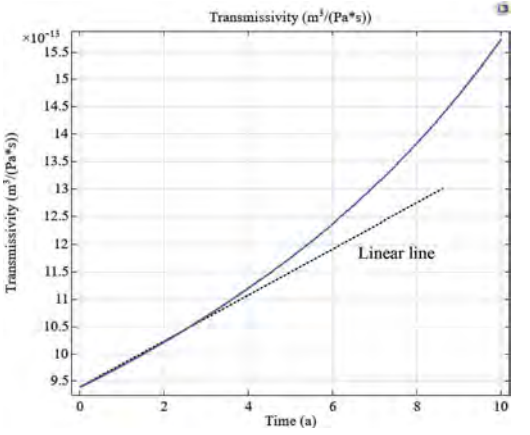

Figure 7. Evolution of effective fracture transmissivity under hydraulic erosion.

5 CONCLUSION

In this paper, we establish a hydraulic erosion model for uniform fractures and verify its accuracy through laboratory tests. The evolution law of hydraulic characteristics in grouted fractures under long-term hydraulic erosion is obtained. The main findings are presented as follows.

The model result is consistent with the accelerated test results. During hydraulic erosion, the APE of the erosion model remains within 0.6%. Based on the model calculations, porosity growth is initially observed near the fracture boundary and gradually expands to include grouting holes. Over time, porosity growth in the grouted area accelerates significantly due to hydraulic erosion. In areas experiencing significant hydraulic erosion, a marked increase in velocity can be observed. In the initial stages of hydraulic erosion, fluidized cement grout particles accumulate at the rear end of grouted areas and gradually enter rock fractures. After 5 years of hydraulic erosion, particle concentration slowly decreases throughout all positions while becoming more uniformly distributed across both fractures and grouted areas. Hydraulic pressure changes minimally at each position, and under the influence of hydraulic erosion, the spatial distribution of hydraulic pressure shifts from linear to nonlinear. The effective transmissivity of the fracture increases with erosion, and after three years, the growth of transmissivity deviates gradually from linearity. Therefore, it is necessary to consider reinforcing the grouting area to curb the trend of transmissivity growth.

At present, we only focus on a generic analysis of the impact of cement grout hydraulic erosion in a homogeneous fracture. The more realistic conditions, such as fracture surface roughness and in-situ hydrogeochemical conditions on the evolution of grouted rock fractures' permeability remain important questions for future study.

ACKNOWLEDGMENTS

This work was supported by Stiftelsen Bergteknisk Forskning (BeFo, Sweden): [Grant Number 447].

REFERENCES

Akagi H, Komiya K, Shibazaki M, 2010. Long term field monitoring of chemically stabilized sand with grouting. International Symposium on Ground Improvement Technologies and Case Histories, SGI'09, pp. 383–387.

Bear J, 2013. Dynamics of fluids in porous media. Courier Corporation.

Chan HT, 1986. Erosion of clay-based grouts in simulated rock fractures. Proceedings of the Canadian Nuclear Society 2 international conference on radioactive waste management, Canada, pp. 821.

Dekker JM, Sweijen T, Zech A, 2020. Groundwater flow below construction pits and erosion of temporary horizontal layers of silicate grouting. Hydrogeol. J. 28(8), 2821–2832.

Laver RG, Soga K, Wright P, et al, 2013. Permeability of aged grout around tunnels in London. Geotechnique. 63, 651–660.

Lee DJ, Chen GW, Liao YC, et al, 1996. On the free-settling test for estimating activated sludge floc density. Water Res. 30(3), 541–550.

Li D, Engler TW Literature Review on Correlations of the Non-Darcy Coefficient. SPE Permian Basin Oil and Gas Recovery Conference, 2001. SPE-70015-MS.

Lin R, Yang L, Pan G, et al, 2021. Properties of composite cement-sodium silicate grout mixed with sulphoaluminate cement and slag powder in flowing water. Constr. Build. Mater. 308, 125040.

Liu J, Chen W, Yuan J, et al, 2018. Groundwater control and curtain grouting for tunnel construction in completely weathered granite. Bull. Eng. Geol. Environ. 77 (2), 515–531.

Liu L, Wang H, Zheng S, et al, 2022. Damage Model and Experimental Study of a Sand Grouting-Reinforced Body under Seepage. Processes. 10(2), 256.

Ma D, Duan H, Zhang J, et al, 2023. Creep-erosion coupling water inrush model of weakly cemented fault rock mass. J. China Coal Soc. 48(6), 2453–2464.

Ma D, Duan H, Zhang J, et al, 2022. Numerical Simulation of Water–Silt Inrush Hazard of Fault Rock: A Three-Phase Flow Model. Rock Mech. Rock Eng. 55(8), 5163–5182.

Vardoulakis I, Stavropoulou M, Papanastasiou P, 1996. Hydro-mechanical aspects of the sand production problem. Transp. Porous Media. 22(2), 225–244.

Zeng Z, Grigg R, 2006. A Criterion for Non-Darcy Flow in Porous Media. Transp. Porous Media. 63(1), 57–69.

Zimmerman RW, Bodvarsson GS, 1996. Hydraulic conductivity of rock fractures. Transp. Porous Media. 23(1), 1–30.

Zou L, Håkansson U, Cvetkovic V, 2018. Two-phase cement grout propagation in homogeneous water-saturated rock fractures. Int. J. Rock Mech. Min. 106, 243–249.

Tunnelling for a Better Life – Yan, Celestino, Thewes & Eberhardt (Eds)
© 2024 The Author(s), ISBN 978-1-032-80042-4
Open Access: www.taylorfrancis.com, CC BY-NC-ND 4.0 license

Seepage and drainage study of underwater tunnel connecting section with combined method

Helin Fu, Kaixun Hu & Yimin Wu*
School of Civil Engineering, Central South University, Changsha, China
National Engineering Laboratory for High Speed Railway Construction, Central South University, Changsha, China

Yong Yu & Wenjun Liu
China Railway Liuyuan Group Co., LTD., Tianjing, China

ABSTRACT: Combined construction with multiple methods is the development trend of underwater tunnels in the future. In the construction process, it is inevitable to encounter the connection problems between different methods. Under high water pressure, it is very important to design the drainage system for the connection parts well. Based on the Zhujiangkou Tunnel of the Shenzhen-Jiangmen Railway, this paper derived the analytical calculation model of seepage considering the drainage system for the connecting section and verified it. It also conducted sensitivity analysis on the main parameters of the drainage system. The results showed that as the circumferential drainage pipe spacing decreased, and the combined parameter of geotextile thickness and permeability coefficient increased, the tunnel seepage flow increased and the lining water pressure decreased. Through the allowable limit water inrush amount, allowable pressure value and economic requirements of the tunnel, the calculation inversion could guide the design of the drainage system for the tunnel connecting section.

Keywords: Underwater tunnel, Combined method, Connecting section, Seepage field, Drainage system

1 INTRODUCTION

Underwater tunnels are transportation channels that expand the urban development space and promote economic development. At present, the construction of underwater tunnels has entered a rapid development stage, and the new development trends are: from single soft soil layer to soil-sand composite layer, from conventional geotechnical to special geotechnical and unfavorable geological conditions, from medium water pressure to high water pressure and ultra-high water pressure, from single method to combination of multiple methods (Li et al., 2017a; Li et al., 2017b). In order to adapt to the new development requirements, more and more underwater tunnels adopt the combined method for construction, and the design and operation process of underwater tunnels have strict requirements on the structural safety and drainage. Excessive water pressure behind the lining and unreasonable drainage structure may cause cracking or damage of the lining, or even sudden water inrush and other safety problems. The traditional seepage law and drainage design of underwater tunnels are no longer applicable to the connecting sections of the combined method, so it is necessary to study the seepage law and drainage system parameters of the connecting sections.

Regarding the seepage field law and drainage system parameters of underwater tunnels, many scholars have carried out research and achieved certain results by means of theoretical analysis, numerical simulation, field measurement, etc. For the research on the seepage field law of underwater tunnels, Zhang et al. (2020) proposed a method to estimate the amount of water inrush into a tunnel by using the superposition principle based on the Tsingtao subsea tunnel and calculated the tunnel water inrush. Su et al. (2017) based on the numerical analysis results, analyzed the relationship between the groundwater level drop height and the tunnel seepage amount, and improved the seepage prediction accuracy. Li et al. (2022) conducted experiments on grouting rings and initial support under different permeability coefficients, and analyzed the influence of support structures on tunnel seepage and water pressure distribution. EI Tani (2003) transformed the relationship between infinite strata and tunnels into two concentric circles through conformal coordinate

*Corresponding author: hukaixun@csu.edu.cn

DOI: 10.1201/9781003495505-336

transformation, thereby optimizing the boundary conditions and making the seepage differential equation easy to solve. Zhu et al. (2019) derived the underground seepage field of double parallel tunnels through conformal transformation. Fu et al. (2021a) extended the conformal mapping technology to calculate the water inrush of tunnel in the fault-affected area, and analyzed the effect of fault on the water inrush. Fu et al. (2021b, 2021c, 2022) analyzed the seepage law and the water inrush of Lianhuashan Tunnel. They considered the relationship between fault and the tunnel position, the influence of surrounding rock permeability coefficient and so on to improve the existed seepage analytical methods. Farhadian et al. (2012) based on Amirkabir Tunnel considering the values of r/h (tunnel radius/ water table height above tunnel) to optimize the analytical equations of groundwater seepage into tunnels. Zhang et al. (2022) based on ABAQUS software platform to analyze the seepage control of the diversion tunnel under high external water pressure. Qin et al. (2022) considered the mutual interference in the seepage fields of subsea twin tunnels and proposed an analytical model for the seepage field of subsea twin tunnels. Liu et al. (2023) regarded the seepage law in lining and grouting area as the non-Darcy seepage, and improved the analytical solutions for the subsea tunnel with Hansbo seepage model. For the research on the design of drainage system of underwater tunnels, He et al. (2017) developed a tunnel seepage model experimental system for the construction and operation periods, and explored the relationship between the tunnel drainage system and the groundwater seepage. Arjnoi et al. (2009) revealed the distribution law of seepage around the tunnel under different drainage conditions. Li et al. (2018) constructed a railway tunnel bottom drainage pressure relief system, which includes a horizontal water collection system, a vertical water conduction system, and a bottom-up drainage system. Based on numerical calculations, they verified the performance of the drainage system. Zhu et al. (2022) equivalently treated the drainage system, calculated the distribution law of external water pressure for shallow buried non-circular tunnels, and promoted the development of the design theory of the drainage system.

In summary, the current research on underwater tunnels with combined construction methods including connection sections is still blank, and the parameters of the drainage system of the connection sections have an unclear impact on the seepage of the connection sections. It is urgent to carry out research on the seepage field and drainage system parameters of the connection sections of underwater tunnels with combined construction methods. A seepage model of the tunnel connection section considering the drainage system is constructed, and the corresponding analytical equations are derived. The equations are verified by degeneration test and numerical simulation, and a sensitivity analysis is performed on the parameters of the drainage system that affect seepage, including circumferential drainage pipes spacing, geotextile parameters, initial support parameters, and grouting ring parameters, in order to guide the design of the drainage system of the connection section.

2 ENGINEERING BACKGROUND

The Zhujiangkou Tunnel of Shenzhen-Jiangmen Railway is located in the downstream of the Pearl River waterway, connecting Humen Town in Dongguan and Wanqingsha in Guangzhou. It is designed and built according to the high-speed railway standard with a design speed of 200km/h. It has a single tunnel with two tracks, a total length of 13.69km, a crossing water section length of about 11km, a maximum burial depth of about 115m, and a maximum water pressure of about 1.06MPa. It is currently the underwater tunnel with the largest burial depth and water pressure in China.

The tunnel adopts shield construction method at both ends and mining method in the middle hard rock section. The shield section has a total length of 6.52km, which is divided into two sections, east and west, with lengths of 3.59km and 2.93km respectively. The middle mining method section has a length of 5.52km. The shield tunnel uses two composite slurry balance shields to start from the shield wells in

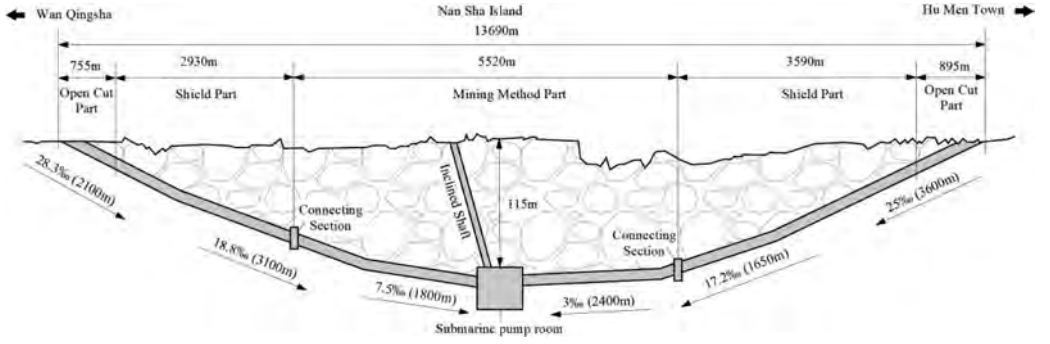

Figure 1. Longitudinal section of the Zhujiangkou Tunnel.

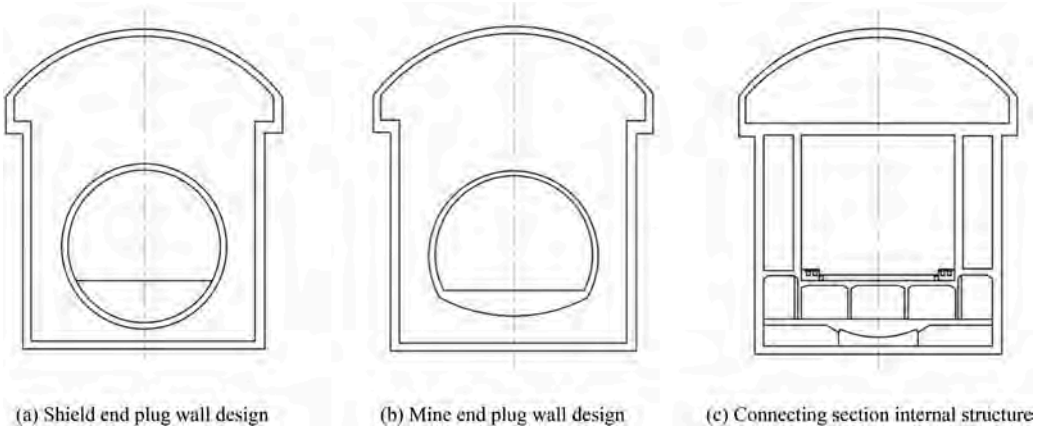

Figure 2. Connecting section structure design diagram.

Humen and Wanqingsha respectively, and disassemble at the boundary of the sea mining method section. The mining method tunnel is constructed through inclined shafts, which are set on the shore of Nansha Island, with a length of 1.16km; the tunnel shore section is mainly constructed by open-cut method, including the ground connection starting point section on the Humen side and the ground connection end point section on the Wanqingsha side, with a total length of about 1.65km. The longitudinal section of the Zhujiangkou Tunnel is shown in Figure 1.

A connecting section is set at the connection position of the shield section and the mining section, which is used to receive and dismantle the shield. The connecting section is built by mining method, and its internal structure and the plug walls on both sides are designed as shown in Figure 2. The construction of the analytical calculation model in the following is based on this design drawing.

3 CALCULATION MODEL

3.1 *Simplification of the connecting section model*

Generally, the excavation seepage of the tunnel is a three-dimensional flow. For the water flowing into the tunnel along the axial direction, the main source is from the front of the tunnel face. For the transverse and radial directions, it mainly comes from the runoff of the tunnel. When the tunnel is excavated for a certain length, the water flow along the axial direction can be approximately ignored, and only the transverse flow of the tunnel water occurs. Therefore, the cross section of the tunnel is usually selected for analysis, and the two-dimensional plane steady-state seepage is studied. According to the design drawing of the tunnel connecting section, the anisotropic tunnel section of the connecting section is simplified, and the cross section of the connecting section is converted into a circular section for solution by using the equivalent area method (Luo et al., 2017). The corresponding calculation equation is shown in Equation (1). Therefore, the seepage model of the tunnel connecting section drawn is shown in Figure 3.

$$r = \sqrt{S/\pi} \tag{1}$$

In the equation, r is the equivalent radius of the tunnel obtained by the equivalent area method, and S is the cross-sectional area of the tunnel.

The inner contour area S of the design drawing is 385.6123m^2, so the derived equivalent radius r is 11.08m.

The following basic assumptions are made for the seepage model of the tunnel connecting section:

(1) In this seepage model, the seepage path of groundwater starts from the surrounding rock, passes through the grouting ring, initial support, geotextile, and then enters the tunnel through the circumferential drainage pipe. The seepage of groundwater conforms to the mass conservation law, is steady flow, conforms to Darcy's law, and satisfies the seepage continuity equation. That is, the seepage amount of groundwater from the surrounding rock to the grouting ring, initial support, geotextile, and then to the circumferential drainage pipe are equal. All the water entering the tunnel is discharged through the circumferential drainage pipe, and the water leakage effect of possible cracks is ignored.
(2) The surrounding rock and lining of the tunnel are isotropic and continuous porous media. When it is assumed that the tunnel burial depth is large and the water level is high, the grouting ring and tunnel lining are assumed to be constant head boundaries, and the corresponding boundary head is calculated at the center position of the tunnel.
(3) The groundwater in the geotextile uniformly infiltrates into the circumferential drainage pipe. In the geotextile, from the middle position of two circumferential drainage pipes to one of them, the head pressure shows a linear distribution. The

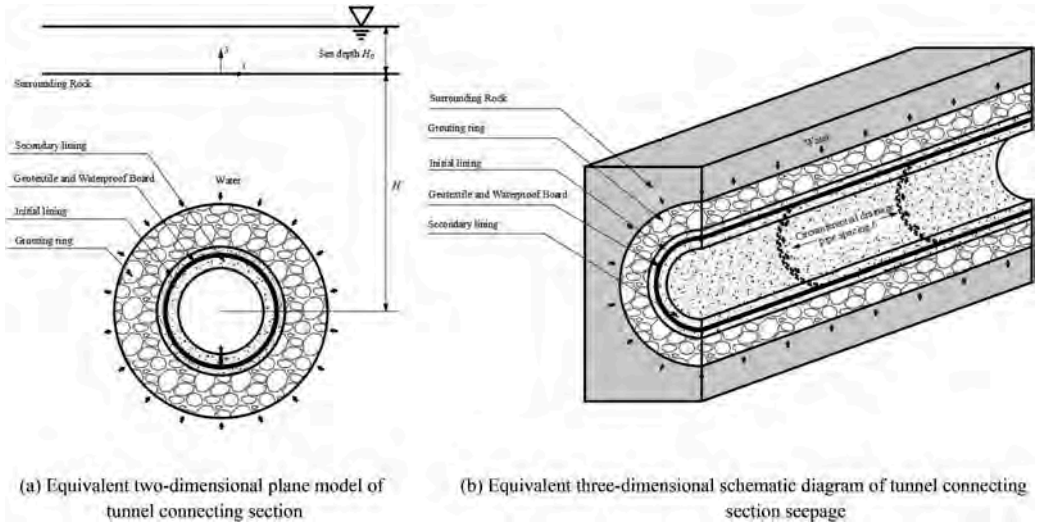

(a) Equivalent two-dimensional plane model of tunnel connecting section

(b) Equivalent three-dimensional schematic diagram of tunnel connecting section seepage

Figure 3. Seepage calculation model diagram of tunnel connecting section.

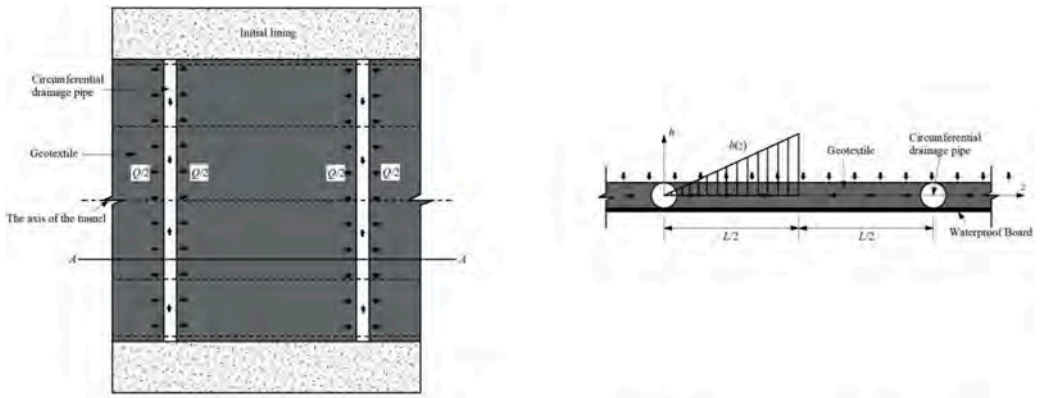

(a) Seepage path in geotextile

(b) Assumed seepage in geotextile at section A-A

Figure 4. Seepage in geotextile of tunnel connecting section.

inside of the circumferential drainage pipe is a free outflow surface (communicating with the atmosphere), with only position head and zero pressure head. According to this design, it can be seen that the water pressure in the geotextile at the middle position between two circumferential drainage pipes is the largest, as shown in Figure 4.

3.2 *Derivation of seepage analytical equation considering the drainage prevention system*

Using the mirror method, the tunnel seepage problem in the half-infinite space is transformed into the superposition problem of the seepage field of one source and one sink in the infinite space in the surrounding rock area. As shown in Figure 5.

According to the superposition principle, the head expression of any point $M(x, y)$ in the surrounding rock area is:

$$h = \frac{Q_r}{2\pi k_r} \ln \frac{R_1}{R_2} + C \tag{2}$$

In the equation, R_1 and R_2 are respectively the distances from point M to the center point of the tunnel and the center point of the mirror tunnel, Q_r is the seepage amount, k_r is the permeability coefficient of the surrounding rock, and C is an undetermined coefficient.

According to the boundary condition, when M is located on the ground line, at this time $R_1=R_2$, the total head $p/\gamma+z=H_0$, so substituting into Equation (2), $C=H_0$ can be obtained. Therefore, the function

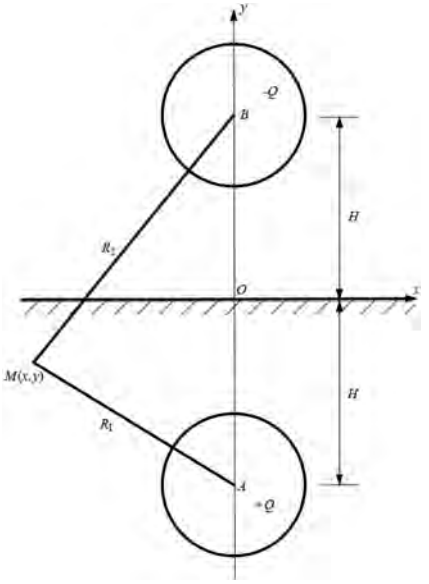

Figure 5. Solving the tunnel seepage problem in half-infinite space by mirror method.

expression of the head pressure h_g at the outer edge of the grouting ring can be analyzed:

$$h_g = \frac{Q_r}{2\pi k_r} \ln \frac{r_g}{2H} + H_0 \tag{3}$$

In the equation, r_g is the outer radius of the grouting ring, H is the distance from the center point of the tunnel to the ground line, and Q_r is the seepage amount of groundwater flowing into the grouting ring from the surrounding rock.

Therefore, the expression of Q_r, which is the seepage amount flowing into the grouting ring, is:

$$Q_r = \frac{2\pi k_r (H_0 - h_g)}{\ln \frac{2H}{r_g}} \tag{4}$$

The seepage between grouting ring and lining should satisfy seepage continuity equation:

$$\frac{\partial^2 h}{\partial r^2} + \frac{1}{r}\frac{\partial h}{\partial r} + \frac{1}{r^2}\frac{\partial^2 h}{\partial \theta^2} = 0 \tag{5}$$

In equation, h is full head of tunnel, which is sum of position head and pressure head, r is polar coordinate radius, θ is polar coordinate angle.

When the tunnel burial depth is large, the head difference between the tunnel crown and the invert is very small, and it can be assumed that the head on the outside of the entire tunnel is equal, and that the groundwater uniformly radially penetrates through the grouting ring and lining, so it is assumed that $\partial h/\partial\theta$=0, then Equation (5) is simplified to:

$$\frac{\partial^2 h}{\partial r^2} + \frac{1}{r}\frac{\partial h}{\partial r} = \frac{1}{r}\frac{\partial}{\partial r}\left(r\frac{\partial h}{\partial r}\right) = 0 \tag{6}$$

Solving Equation (6), the head equation of any point between the grouting ring and lining can be obtained:

$$h = C_1 \ln r + C_2 \tag{7}$$

Assuming that the head at the outer edge of the initial support is h_2, and the head at the inner edge is $h(z)$, several boundary conditions that need to be considered for the model equation can be written as:

$$\begin{cases} BC1 : h|_{r=r_g} = h_g \\ BC2 : h|_{r=r_2} = h_2 \\ BC3 : h|_{r=r_1} = h(z) \\ BC4 : h|_{r=r_0} = 0 \end{cases} \tag{8}$$

Therefore, for the seepage inside the grouting ring, considering boundary conditions $BC1$ and $BC2$, the head equation and corresponding flow rate Q_g expression of any point inside the grouting ring can be solved:

$$h = \frac{h_g - h_2}{\ln \frac{r_g}{r_2}} \ln \frac{r}{r_g} + h_g \tag{9}$$

$$Q_g = 2\pi k_g \frac{h_g - h_2}{\ln \frac{r_g}{r_2}} \tag{10}$$

In equation, k_g is permeability coefficient of grouting ring, r_2 is outer radius of initial support.

For seepage calculation in initial support, considering basic assumptions (2) and (3) of model, from circumferential drainage pipe to middle position of two circumferential drainage pipes, head follows linear distribution. Assuming that head at middle position of two circumferential drainage pipes is h_z, pressure head at drainage pipe is 0, and total head is position head -H, then when $0<z<L/2$, head loaded on waterproof board is:

$$h(z) = \frac{2z(h_z - H)}{L} \tag{11}$$

Take a micro annulus with axial length dz of initial lining. The seepage amount entering geotextile through micro annulus is:

$$Q_{Li} = 2\pi k_c \frac{h_2 - h(z)}{\ln \frac{r_2}{r_1}} dz = 2\pi k_c \frac{h_2 - \frac{2z(h_z - H)}{L}}{\ln \frac{r_2}{r_1}} dz \tag{12}$$

In equation, k_c is permeability coefficient of initial support, r_1 is inner radius of initial support.

Integrate Equation (12) (boundary $-L/2<z<L/2$), obtain calculation equation of per meter seepage amount Q_L entering geotextile from initial support:

$$Q_L = \int_{-\frac{L_1}{2}}^{\frac{L_1}{2}} 2\pi k_c \frac{h_2 - \frac{2z(h_z-H)}{L}}{\ln\frac{r_2}{r_1} L} dz = \frac{2\pi k_c (h_2 - \frac{h_z-H}{2})}{\ln\frac{r_2}{r_1}} \tag{13}$$

For seepage in geotextile, according to basic assumption (2) and (3) of model, for arc length $d\theta$ and longitudinal width L geotextile micro element, seepage velocity v entering circumferential drainage pipe in micro element (water inlet on both sides of drainage pipe) is:

$$v = 2k_z i = 2k_z t \frac{h_z + H}{L/2} = \frac{4k_z(h_z + H)t}{L} \tag{14}$$

In equation, t is thickness of geotextile, k_z is permeability coefficient of geotextile. Per meter seepage amount Q_t entering circumferential drainage pipe from geotextile is:

$$Q_t = \frac{\int_0^{2\pi} v r_1 \mathrm{d}\theta}{L} = \frac{8\pi r_1 k_z (h_z + H)t}{L^2} \tag{15}$$

Because fluid entering grouting ring, lining and tunnel interior satisfies mass conservation law and flow rate equals, derivation can obtain calculation equation for tunnel seepage amount considering drainage prevention system of connecting section:

$$Q = \frac{2\pi(H_0 + H)k_c k_g k_r}{\frac{k_c k_g k_r L^2}{8k_z r_1 t} + k_c k_g \ln\frac{2H}{r_g} + k_g k_r \ln\frac{r_2}{r_1} + k_c k_r \ln\frac{r_g}{r_2}} \tag{16}$$

For tunnel seepage without considering drainage system, water seepage in surrounding rock area and grouting ring satisfies Equation (4) and Equation (10). For seepage calculation in initial support, expression for seepage amount Q_L' is:

$$Q_L' = 2\pi k_c \frac{h_2 + H}{\ln\frac{r_2}{r_1}} \tag{17}$$

Therefore, according to mass conservation law and flow rate equals, combine Equation (4), Equation (10) and Equation (17), derivation can obtain calculation equation for seepage amount without considering drainage prevention system in composite lining:

$$Q' = \frac{2\pi(H_0 + H)k_c k_g k_r}{k_c k_g \ln\frac{2H}{r_g} + k_g k_r \ln\frac{r_2}{r_1} + k_c k_r \ln\frac{r_g}{r_2}} \tag{18}$$

Combine Equation (17) and Equation (18), it can be found that calculation for seepage amount considering drainage prevention system after correction for situation without consideration. Set correction coefficient as λ, then λ expression is:

$$\lambda = \frac{k_c k_g k_r L^2}{8k_z r_1 t} \tag{19}$$

4 MODEL VERIFICATION

4.1 *Model degeneration analysis*

The model degeneration method (Ying et al., 2016) is used to verify the correction equation, that is, the limit of the proposed correction equation is first obtained, and the equation is degenerated into a general case without considering these factors, and then compared with the general characteristics considering these factors. When the difference between the two is small, the model equation is confirmed. The correction equation proposed in this paper considers more parameters of drainage pipe and geotextile than conventional equation, and degeneration analysis is required for corresponding parameters.

4.1.1 *Circumferential drainage pipe spacing*

When the circumferential drainage pipe spacing $L\to\infty$, that is, it is assumed that no drainage pipe is set between the lining, the correction coefficient Equation (19) and seepage amount Equation (16) degenerate into:

$$\begin{cases} \lim\limits_{L\to\infty} \lambda = \lim\limits_{L\to\infty} \dfrac{k_c k_g k_r L^2}{8k_z r_1 t} = \infty \\ \lim\limits_{\lambda\to\infty} Q = \lim\limits_{\lambda\to\infty} \dfrac{2\pi(H_0 + H)k_c k_g k_r}{\lambda + k_c k_g \ln\frac{2H}{r_g} + k_g k_r \ln\frac{r_2}{r_1} + k_c k_r \ln\frac{r_g}{r_2}} = 0 \end{cases} \tag{20}$$

Equation (20) shows that when the circumferential drainage pipe spacing tends to infinity, the correction coefficient tends to infinity, and the tunnel seepage amount Q tends to 0, which can be considered as impermeable structure of lining. This is consistent with the drainage prevention mechanism of composite lining. When no circumferential drainage pipe is set, it is assumed that the tunnel is a fully enclosed non-drainage full-package structure.

When the circumferential drainage pipe spacing $L\to 0$, that is, it is assumed that the inner edge of lining can drain to tunnel, the correction coefficient Equation (19) and seepage amount Equation (16) degenerate into:

$$\begin{cases} \lim\limits_{L\to 0} \lambda = \lim\limits_{L\to 0} \dfrac{k_c k_g k_r L^2}{8k_z r_1 t} = 0 \\ \lim\limits_{\lambda\to 0} Q = \lim\limits_{\lambda\to 0} \dfrac{2\pi(H_0 + H)k_c k_g k_r}{\lambda + k_c k_g \ln\frac{2H}{r_g} + k_g k_r \ln\frac{r_2}{r_1} + k_c k_r \ln\frac{r_g}{r_2}} = Q' \end{cases} \tag{21}$$

Equation (21) shows that when the circumferential drainage pipe spacing tends to 0, the correction

coefficient is 0, and the tunnel seepage amount is consistent with the tunnel seepage amount calculation equation without considering the drainage prevention system in composite lining. Groundwater penetrates through lining and enters tunnel directly.

4.1.2 *Geotextile permeability coefficient*

When geotextile permeability coefficient $k_z \to \infty$, corresponding correction coefficient and tunnel seepage amount equation are consistent with Equation (21). At this time, geotextile in drainage prevention system is equivalent to extension of drainage pipe and plays role of drainage channel completely. Groundwater enters tunnel directly through lining.

When geotextile permeability coefficient $k_z \to 0$, corresponding correction coefficient and tunnel seepage amount equation are consistent with Equation (20). It is equivalent to geotextile being impermeable, that is, a water barrier layer is set up, which makes tunnel impermeable. Tunnel is fully enclosed non-drainage full-package structure.

4.2 *Numerical simulation verification*

ABAQUS software is used to simulate the seepage of the tunnel connecting section. The model construction considers the complete drainage prevention system, including grouting ring, initial support, drainage pipe, geotextile, waterproof board and secondary lining. The model needs to eliminate the influence of size effect, and the size is 150m×30m×200m (length × width × height, the left, right and lower boundaries of the surrounding rock are more than 3 times the diameter of the tunnel from the center of the tunnel, and the upper boundary is the actual burial depth). The physical and mechanical parameters of the model calculation process are shown in Table 1.

Table 1. Model parameters.

Item	Value	Item	Value
Sea level height H_0/(m)	20	Initial support inner diameter r_1/(m)	11.68
Tunnel burial depth H/(m)	50	Secondary lining inner diameter r_0/(m)	11.08
Surrounding rock permeability coefficient k_r/(m/s)	1.2×10^{-6}	Geotextile thickness t/(m)	0.003
Grouting ring permeability coefficient k_g/(m/s)	6×10^{-8}	Geotextile permeability coefficient k_z/(m/s)	3.5×10^{-4}
Grouting ring outer diameter r_g/(m)	16.98	Circumferential drainage pipe spacing L/(m)	5
Initial support outer diameter r_2/(m)	11.98	Circumferential drainage pipe radius r_p/(m)	0.075
Initial support permeability coefficient k_c/(m/s)	6×10^{-10}	Surrounding rock density γ/(kN/m^3)	20

The boundary conditions of the model are: the bottom and the front and rear hydraulic boundaries are impermeable boundaries, the top boundary is permeable and a constant hydrostatic pressure is applied according to the sea level height, and the left and right hydraulic boundaries are through ditch water and the pore water pressure is linearly distributed. The constructed model is shown in Figure 6.

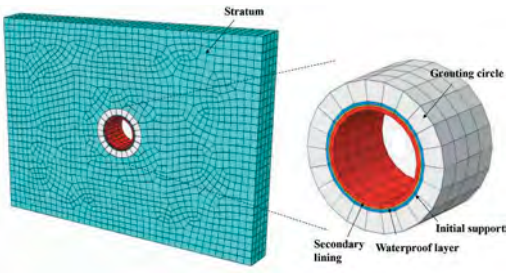

Figure 6. Numerical calculation model of the connecting section.

The calculation verification process considers the change of sea level height, and uses the model to calculate the seepage flow under the sea leve heights of 10m, 20m, 30m, 40m, and 50m, and summarizes them with the calculation results of analytical calculation as shown in Table 2.

Table 2. Comparison of analytical solution and numerical solution calculation results.

Sea level height H_0/(m)	Water inrush Q/(m^3·d^{-1}·m^{-1})		
	Analytical solution	Numerical solution	Error %
10	0.6539	0.6124	6.34
20	0.7629	0.7133	6.50
30	0.8718	0.8141	6.62
40	0.9808	0.9134	6.87
50	1.0898	1.0137	6.98

As can be seen from Table 2, the maximum error between the numerical solution and the analytical solution for the tunnel seepage flow is 6.98%, and the minimum error is 6.34%. The results are consistent, indicating that the analytical results have high accuracy.

5 PARAMETER SENSITIVITY ANALYSIS

For the analysis of the influence of the drainage parameters of the connecting section, the main influencing parameters include the circumferential drainage pipe spacing L, the geotextile parameters k_z and t, the initial support permeability coefficient k_c and

its thickness, and the grouting ring permeability coefficient k_g and its thickness. Therefore, referring to the calculation parameters used in the numerical simulation verification, the control variable method is used to perform the sensitivity analysis of the drainage parameters of the connecting section under multiple factors.

5.1 *The influence of drainage pipe spacing*

Under the condition that other parameters are consistent with Table 1, considering the change of circumferential drainage pipe spacing L, draw the relationship curve between tunnel seepage flow, water pressure of lining and circumferential drainage pipe spacing, as shown in Figure 7.

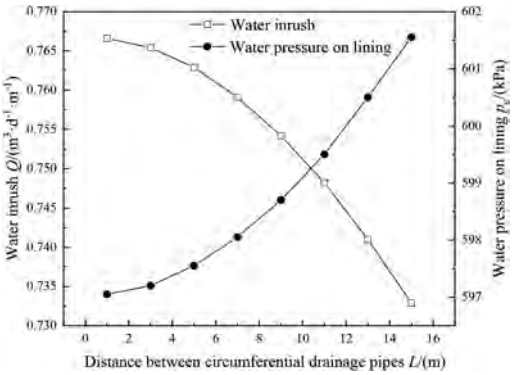

Figure 7. The influence curve of circumferential drainage pipe spacing on tunnel seepage flow and water pressure of lining.

It can be analyzed from Figure 7 that as the circumferential drainage pipe spacing increases, the amount of water drained into the tunnel through the drainage pipe decreases, and the water pressure of the lining increases. The slope of both curves gradually increases, reflecting that the rate of change has been increasing. When the circumferential drainage pipe spacing increases from 1m to 15m, the flow rate decreases by 0.0337$m^3 \cdot d^{-1} \cdot m^{-1}$, and the water pressure of the lining increases by 4.5kPa. Figure 7 shows that the drainage pipe plays a role in draining the tunnel seepage water into the tunnel and reducing the water pressure of the lining.

5.2 *The influence of geotextile parameters*

Under the condition that other parameters are consistent with Table 1, considering the change of geotextile parameter $k_z \cdot t$, draw the relationship curve between tunnel seepage flow, water pressure of lining and geotextile parameter, as shown in Figure 8.

It can be analyzed from Figure 9 that as the geotextile parameter increases, the amount of water flowing into the tunnel increases, and the water pressure of the lining decreases. The slope of both

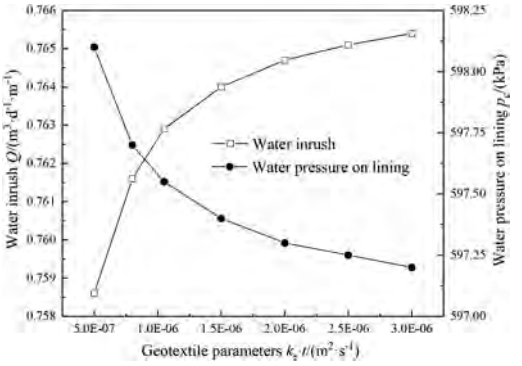

Figure 8. The influence curve of geotextile parameter on tunnel seepage flow and water pressure of lining.

curves gradually decreases, and this effect will gradually weaken and stabilize. When the geotextile parameter increases from 5×10^{-7} m^2/s to 3×10^{-6} m^2/s, the flow rate increases by 0.0068 $m^3 \cdot d^{-1} \cdot m^{-1}$, and the water pressure of lining decreases by 0.9kPa. Figure 9 shows that improving the permeability performance of geotextile will make more water drain into the tunnel and reduce the water pressure of lining, but this improvement is limited. When the geotextile parameter is greater than 3×10^{-6} m^2/s, the effect can be ignored.

5.3 *The influence of initial support parameters*

Under the condition that other parameters are consistent with Table 1, considering the change of initial support permeability coefficient k_c and initial support thickness, draw the relationship curve between tunnel seepage flow, water pressure of lining and initial support parameters, as shown in Figure 9.

It can be analyzed from Figure 9 (a) that when initial support permeability coefficient increases from 5×10^{-11} m/s to 1×10^{-9}m/s, flow rate increases by 1.081 $m^3 \cdot d^{-1} \cdot m^{-1}$, and water pressure decreases by 145.2kPa. Therefore, an increase in the initial support permeability coefficient will result in a decrease in both tunnel seepage flow and water pressure, and the curves show an approximate linear relationship. It can be analyzed from Figure 9 (b) that as initial support thickness increases, both tunnel seepage flow and water pressure decrease. The slope of both curves gradually decreases and stabilizes. When initial support thickness increases from 0.1m to 0.6m, flow rate decreases by 1.3214 $m^3 \cdot d^{-1} \cdot m^{-1}$, and water pressure increases by 181.5kPa. Figure 19 shows that improving initial support permeability performance will make more water drain into tunnel and reduce external water pressure; while increasing initial support thickness will extend path for water to pass through initial support which will reduce amount of water flowing into tunnel but increase water pressure accordingly; there is a limit to effect of initial support thickness; when it is greater than 0.6m, effect can be ignored.

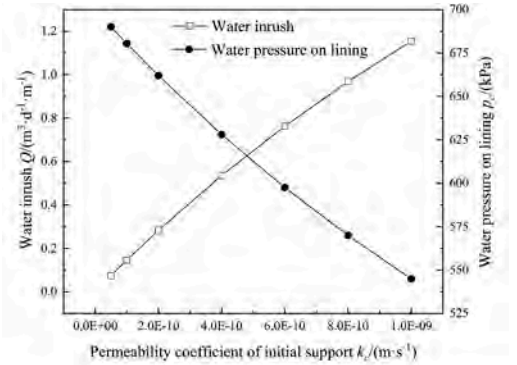

(a) Influence curve of initial support permeability coefficient

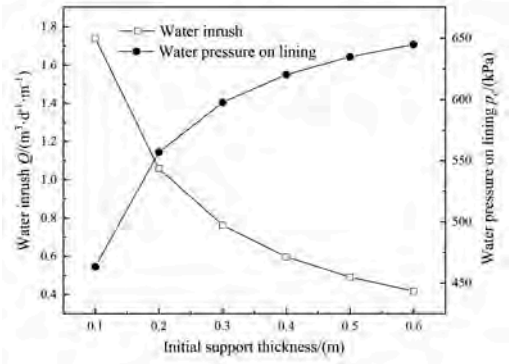

(b) Influence curve of initial support thickness

Figure 9. The influence curve of initial support parameters on tunnel seepage flow and water pressure of lining.

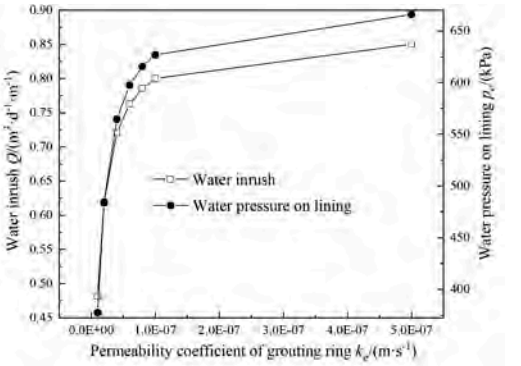

(a) Influence curve of grouting ring permeability coefficient

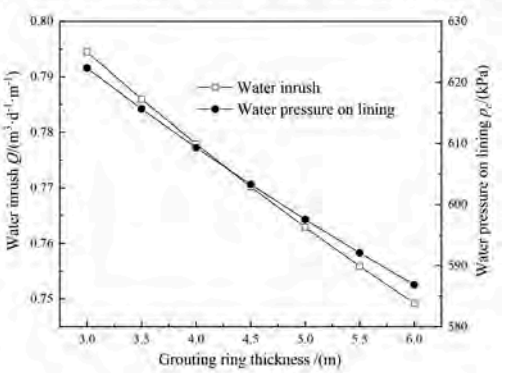

(b) Influence curve of grouting ring thickness

Figure 10. The influence curve of grouting ring parameters on tunnel seepage flow and water pressure of lining.

5.4 *The influence of grouting ring parameters*

Under the condition that other parameters are consistent with Table 1, considering the change of grouting ring permeability coefficient k_g and grouting ring thickness, draw the relationship curve between tunnel seepage flow, water pressure of lining and grouting ring parameters, as shown in Figure 10.

It can be analyzed from Figure 10 (a) that as the grouting ring permeability coefficient increases, both tunnel seepage flow and water pressure of lining increase. The curves first increase rapidly, there is a turning point at k_g=1×10^{-7}m/s, and then maintain a low rate of increase. When the grouting ring permeability coefficient increases from 1×10^{-8}m/s to 5×10^{-7}m/s, the flow rate increases by 0.3684 m^3·d^{-1}·m^{-1}, and the water pressure of lining increases by 288.6kPa. It can be analyzed from Figure 10 (b) that as the grouting ring thickness increases, both tunnel seepage flow and water pressure of lining decrease. The curves show a linear relationship. When the grouting ring thickness increases from 3m to 6m, the flow rate decreases by 0.0453 m^3·d^{-1}·m^{-1}, and the water pressure of lining decreases by 35.5kPa. Figure 10 shows that improving the permeability performance of the grouting ring will make more water drain into the tunnel and increase the water pressure of lining. This improvement effect will be limited by its permeability coefficient. When it is greater than a certain value, the effect is not significant. While increasing the grouting ring thickness will extend the path for water to pass through the grouting ring, which will reduce the amount of water flowing into the tunnel and also reduce the water pressure of lining.

The above parameter sensitivity analysis provides the functional relationship between tunnel seepage flow and various parameters. By combining tunnel drainage limit standard and allowable value of water pressure of lining with economic requirements of improved parameters, reverse calculation and comparison can be performed to determine reasonable drainage parameters for tunnel connecting section and guide design.

6 CONCLUSION

Based on the Zhujiangkou Tunnel of the Shenzhen-Jiangmen Railway, this paper studies the drainage system parameters of the underwater tunnel connecting section of the combined method, proposes a tunnel

connecting section seepage equation considering the drainage system, performs degeneration test and numerical simulation verification on the equation, and conducts sensitivity analysis on the parameters affecting seepage, providing reference for the design of the drainage system of the tunnel connecting section.

(1) The derived seepage equation of the tunnel connecting section considering the drainage system is applicable to the seepage field calculation of underwater irregular section tunnels with large burial depth and high water level, and is also applicable to the seepage field calculation of underwater tunnel connecting sections of the combined method.
(2) Through degeneration test analysis and numerical simulation verification, the difference between analytical calculation and numerical simulation of tunnel seepage flow and water head pressure of lining is small, and the results are consistent. The degeneration test shows that this equation is essentially a modification of the tunnel calculation equation without considering the drainage structure, making the results more accurate.
(3) The sensitivity analysis of drainage parameters reveals the influence of circumferential drainage pipe spacing, geotextile parameters, initial support parameters, and grouting ring parameters on the seepage field of tunnel connecting section. Among them, decreasing circumferential drainage pipe spacing, increasing geotextile parameter, increasing initial support or grouting ring permeability coefficient, and decreasing initial support thickness will increase tunnel seepage flow and decrease lining water pressure. It is worth noting that decreasing grouting ring thickness will also lead to simultaneous increase in tunnel seepage flow and water pressure of lining. Combining tunnel drainage allowable value and economic comparison requirements, calculation inversion can be used to guide design of drainage system parameters for tunnel connecting section.

ACKNOWLEDGMENTS

This research was supported by the National Natural Science Foundation of China (No. 51978667), China Railway Liuyuan Group Co., LTD Technology Project and China Construction Fifth Engineering Division Co., LTD Technology Project (No. cscec5b-TM-2023-65). The authors appreciate the editors and anonymous reviewers for their valuable comments and suggestions.

REFERENCES

Arjnoi, P., Jeong, J. H., Kim, C. Y., et al. 2009. Effect of drainage conditions on pore water pressure distributions and lining stresses in drained tunnels. Tunnelling and Underground Space Technology. 24(04): 376–389.

El Tani M. 2003. Circular tunnel in a semi-infinite aquifer. Tunnelling and underground space technology, 18(1): 49–55.

Farhadian, H., Aalianvari, A., Katibeh, H. 2012. Optimization of analytical equations of groundwater seepage into tunnels: A case study of Amirkabir tunnel. Journal of the Geological Society of India. 80: 96–100.

Fu, H. L., Li, J., Cheng, G. W., et al. 2021a. Semi-analytical solution for water inflow into a tunnel in a fault-affected area with high water pressure. Bulletin of Engineering Geology and the Environment. 80: 5127–44.

Fu, H. L., An, P. T., Chen, L., et al. 2021b. Analysis of tunnel water inrush considering the influence of surrounding rock permeability coefficient by excavation disturbance and ground stress. Applied Sciences. 11(08): 3645.

Fu, H. L., An, P. T., Cheng, G. W., et al. 2021c. Calculation of the safety thickness of water inrush with tunnel axis orthogonal to fault. Arabian Journal of Geosciences. 14 (11):931.

Fu, H. L., An, P. T., Chen, L., et al. 2022. Analysis of the impact of water gushing influenced by the relationship between fault and tunnel position. Journal of Performance of Constructed Facilities. 36(01): 04021106.

Li, P. F., Liu, H. C., Zhao, Y., et al. 2018. A bottom-to-up drainage and water pressure reduction system for railway tunnels. Tunnelling and Underground Space Technology. 81: 296–305.

Li, S. C., Li, X. Z., Jing, H. W., et al, 2017a. Research development of catastrophe mechanism and forecast controlling theory of water inrush and mud gushing in deep long tunnel. China Basic Science. 19(03): 27–43+2+63.

Li, S. C., Wang, K., Li, L. P., et al. 2017b. Mechanical mechanism and development trend of water-inrush disasters in karst tunnels. Chinese Journal of Theoretical and Applied Mechanics. 49(01): 22–30.

Li, Z., Chen, Z. Q., He, C., et al. 2022. Seepage field distribution and water inflow laws of tunnels in water-rich regions. Journal of Mountain Science. 19(02): 591–605.

Liu, X, Wang, D. C., Zhang, Y., et al. 2023. Analytical solutions on non-Darcy seepage of grouted and lined subsea tunnels under dynamic water levels[J]. Ocean Engineering, 267: 113276.

Luo, Q. Q., Li, P., Zhou, B., et al. 2017. Application of Analytic Solution on Tunnel Seepage Field Based on Equivalent Area Method. Science Technology and Engineering. 17(32): 174–180.

He, C., Li, Z., Yang, S. Z., et al. 2017. Development and Application on Mined Tunnel Seepage Model Test System for Construction and Operation Period, China Journal of Highway and Transport. 30: 114–21 and 31.

Qin, Z. G., He, W. G., Zhou, H. G. 2022. Analytical study on seepage field of subsea twin tunnels constructed by NATM. Ocean Engineering. 264.

Su, K., Zhou, Y., Wu, H., et al. 2017. An analytical method for groundwater inflow into a drained circular tunnel. Ground Water. 55(05): 712–721.

Ying, H. W., Zhu, C. W., Gong, X. N. 2016. Analytic solution on seepage field of underwater tunnel considering grouting circle. Journal of Zhejiang University (Engineering Science). 0: 1018–23.

Zhang, L. W., Zhao, D. K., Wu, J., et al. 2020. Prediction of water inflow in Tsingtao subsea tunnel based on the superposition principle. Tunnelling and Underground Space Technology. 97: 103243.

Zhang, Z. J., Zeng, C. P., Li, H., et al. 2022. Optimal Design of the Seepage Control for Xianglushan Diversion Tunnel Under High External Water Pressure. Geotechnical and Geological Engineering. 40: 4595–615.

Zhu, C. W., Ying H. W., Gong X. N., et al. 2019. Analytical research on seepage field of underwater twin parallel tunnels[J]. Chinese Journal of Geotechnical Engineering, 41(02):355–360.

Zhu, Y. M., Yang, H. P., Huang, M. Q., et al. 2022. External hydraulic pressure and invert uplift study in a non-circular shallow tunnel. Tunnelling and Underground Space Technology. 122: 104345.

Tunnelling for a Better Life – Yan, Celestino, Thewes & Eberhardt (Eds)
© 2024 The Author(s), ISBN 978-1-032-80042-4
Open Access: www.taylorfrancis.com, CC BY-NC-ND 4.0 license

Comparison of double shell and sprayed single shell waterproofing methods in tunneling

Ibrahim Uğur Gök* & Ercüment Karahan
Kartun Engineering Consulting and Ltd. Co., Ankara, Türkiye

Bahtiyar Ünver
Department of Mining Engineering, Hacettepe University, Ankara, Türkiye

ABSTRACT: The waterproofing methods used in tunneling can be categorized into two main application types namely, the double shell waterproofing method and the sprayed single shell waterproofing method. DSW (double shell waterproofing) method involves a PVC-membrane placed between the primary reinforcement and the final coating concrete. SSW (sprayed single shell waterproofing) method involves a sprayed liquid membrane instead of a PVC membrane and reinforced shotcrete instead of final coating concrete. This paper presents the application methods and material properties of both waterproofing methods. Performance of both methods were analyzed by means of 2D numerical modelling. DSW and SSW methods were also compared in terms of cost, and occupational health and safety. Both methods meet stability criterion. Although the direct cost of SSW method is found to be a little higher, it is superior in terms of labour requirement. Hence the operation is far safer and faster.

Keywords: Waterproofing in Tunneling, Liquid Membrane, Sprayed Single Shell Method, Double Shell Method

1 INTRODUCTION

During tunnel construction, managing surface and underground water challenges necessitates effective waterproofing for long-term viability. There are currently two waterproofing methods used to prevent water problems that may be encountered during tunnel construction. The Double Shell (DSW) and Sprayed Single Shell (SSW) methods offer solutions. DSW utilizes geotextile and PVC-membrane, placed between primary support and final coating concrete, while SSW employs synthetic or steel fiber reinforced shotcrete for primary support, a liquid membrane for waterproofing, and steel fiber reinforced shotcrete as the final lining, creating a rigid structure. This paper discusses the applications, equipment utilization, and material features of the two waterproofing methods. In addition, a 600-meter long tunnel with three different rock classes is considered as a sample tunnel for comparison of these two methods on the basis of cost, stability, and accident types in terms of worker health and safety. Due to high waterproofing performance of methods, no direct waterproofing comparison is made.

The paper guides engineering decisions for sustainable and secure tunnel construction, ensuring longevity and safety of underground infrastructure.

2 TECHNICAL BACKGROUND AND LITERATURE REVIEW

Waterproofing is a critical aspect in the design of long-term tunnel project. Although effective and cost-efficient, the DSW method has drawbacks, including complex and vulnerable workmanship, limited application areas, and troublesome repair works after construction.

The SSW method has been used in tunneling widely in recent years. This method eliminates the use of PVC-membrane, final cast concrete, and steel mesh. Instead, steel fiber reinforced shotcrete is applied as a primary support and final coating consisting of synthetic or steel fiber reinforced shotcrete. The impermeability is ensured by spraying a liquid membrane in between linings. Considering the differences between the two methods, SSW method can be preferred over the traditional method due to its ease of application and speed, under suitable geological conditions. While it has a higher material cost than the traditional method, it offers greater flexibility in application and is advantageous in terms of occupational health and safety. Furthermore, it can be practically repaired during tunnel construction or operation, making it a viable option (Wu et al., 2017).

*Corresponding author: selam.iug@gmail.com

DOI: 10.1201/9781003495505-337

2.1 *The double shell method*

The DSW aims to waterproof a tunnel by placing a PVC-membrane between two linings.

PVC-membrane, protection geotextile, and the carrying system are mounted on shotcrete with care to avoid future repair difficulties. The preferred membrane should be made of PVC compound, and plasticized for flexibility and durability. It must possess high elongation and tensile strength and withstand high hydraulic pressure.

To protect the membrane during installation, a geotextile membrane can be applied. In cut-and-cover structures, double-sided geotextile is recommended. In case of damage, a thin signal layer with a distinct color and thickness is added to aid detection. The waterproofing membrane can vary in thickness depending on the water presence (Multiplan, 2016).

Two main waterproofing methods used in traditional tunnel construction are, *the drainage system*, which channels water away, and *the barrier system*, which offers continuous water resistance (Sikaplan, 2017).

2.1.1 *Material properties of pvc-membrane*

A complex coating system for waterproofing involves integrating main and auxiliary elements with the support system. The primary elements are the membrane, typically made of PVC-P (Plasticized Polyvinyl Chloride) or TPO (Thermoplastic Polyolefin) compounds. PVC-P is a widely used synthetic plastic polymer that can be made more flexible with the addition of a plasticizer. On the other hand, TPO is a modern polymer with a long service life, resistant to various environmental factors, and doesn't require plasticizers during its production. Polyethylene membranes have also been tested and confirmed to have a long service life and durability (Prişcu, 2013). Waterstop tapes, drainage plates and flanges are used as auxiliary waterproofing elements (Multiplan, 2016).

2.2 *The sprayed single shell*

The SSW method is a more practical alternative method than the DSW method in terms of waterproofing. It involves applying synthetic fiber or steel fiber-reinforced shotcrete to create a stable and rigid structure. After applying the primary support, a liquid membrane is sprayed to form the waterproofing layer. This method provides a smooth appearance to the tunnel lining surface. After the application of liquid membrane, the reinforced shotcrete is reapplied and so the single shell is completed. Using liquid membrane instead of PVC-membrane can speed up the process and reduce the working costs, making it more suitable for challenging surface geometries like T-points (intersections) (Wu et al., 2017).

2.2.1 *Application of liquid membrane*

The liquid membrane is applied in a similar manner of shotcrete using special equipment (Figure-1). Also, it should be applied to a dry and clean surface to ensure optimal performance. The liquid membrane should have a minimum thickness of 3 mm and the smoothness of the surface being applied is essential to create an effective waterproofing layer and material savings (Ma, 2011).

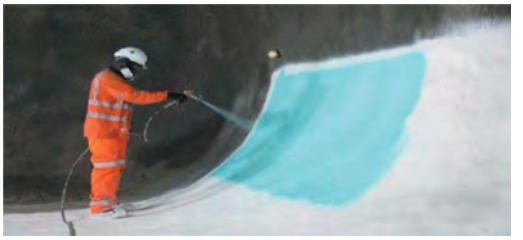

Figure 1. Liquid membrane application on the tunnel surface (Bridgepreservation, 2013).

Besides effective shotcrete application is crucial for achieving an efficient and stable single shell method. The surface should be dry before application, as the liquid membrane can be weakened if it comes into contact with water during the curing process (Wu et al., 2017).

2.2.2 *Material properties liquid membrane*

The liquid membrane used in the SSW is based on a specially formulated EVA (Ethylene Vinyl Acetate) polymer. EVA is chosen for its flexibility, chemical resistance, and high friction coefficient. The degree of elasticity is determined by the amount of vinyl acetate in the chemical formula of EVA. High amount of vinyl acetate decreases hardness of liquid membrane. The material also contains a filling material that contributes to its long-term behavior and curing mechanism, providing long-lasting protection of chemical properties (Wu et al., 2017).

The liquid membrane is designed to create a highly bonded composite support system between the primary and secondary support linings. It adheres firmly to the rough surface of shotcrete. It maintains continuity between the two coatings, regardless of the presence of steel or fiber reinforcement or the use of PVC-membrane. It should eliminate the possibility of mechanical discontinuity and should create a sandwich structure between the outer and inner shotcrete coatings which ensure resistance to rock and water loads (Holter et al., 2014). Unlike PVC, the liquid membrane does not allow water migration between the two sides. It acts as an excellent waterproof barrier, preventing water from passing through the strong polymer chain matrices. The liquid membrane has small pores, allowing water vapor to penetrate and release as steam, avoiding pressure buildup behind the membrane (Wu et al., 2017).

For a leak to occur in single shell system, water must pass through three failure zones: a crack in the primary lining, the liquid membrane, and the

secondary lining. Groundwater cannot migrate over the liquid membrane, making it necessary for all three crack zones to align. In the double shell method, the leak passing through the primary lining is directed to the PVC-membrane and discharged by drainage. Meanwhile, the water pressure on the membrane is carried to the secondary coating concrete.

The strength properties of the liquid membrane are given in Table-1 (Wu et al., 2017):

Table 1. Liquid membrane material and strength properties.

Bond Strength to Concrete	~1.2 MPa
Tensile Strength	1.5 - 3.5 MPa
Elongation	100%
Crack Bridging	>2.5 mm

The liquid membranecan be sprayed directly onto steel inserts or is compatible with coatings using synthetic or steel-fiber reinforced shotcrete on both sides. Its adhesion strength to concrete is 1.2 ±0.2 MPa, while its bond strength to metals is between 0.5 and 1.2 MPa. These properties also allow liquid membrane as part of hybrid waterproofing applications with traditional membrane when it is necessary (Junwei, 2014).

However, the liquid membrane may not be effective in areas with active water intrusion, as small infiltration rates can lead to increased hydrostatic pressure at the concrete/membrane interface, hindering proper hardening and waterproofing. In such cases, it is recommended to remove the water from the environment before applying the liquid membrane. Fast-curing liquid membranes may also be used to prevent leakage if required (Mcdonald, 2009).

3 METHODOLOGY

The study compares the stability of tunnels constructed with SSW and DSW methods in a 600-meter sample tunnel having of A2, B2, and C2 rock classes by using the RS² finite element numerical analysis program under static and dynamic conditions. Besides the stability analysis, the cost analysis of tunnels with three different excavation and support systems were performed and the results were compared for two methods. Finally, these two waterproofing methods are examined in terms of occupational health and safety, based on the types of work accidents during construction.

3.1 *Stability analysis and comparison*

The rock mass parameters of the 600-meter sample tunnel, is divided into three regions having various properties (Table-2). 200- meter long regions were of A2, B2, and C2 classes. The stresses on the shotcrete and on rock bolts are examined respectively, and the tunnel support of these two waterproofing systems is compared by means of 2D numerical modeling. The parameters for the A2 section of the tunnel have the characteristics of the hard rock class. The rock mass parameters of the medium rock class for B2 and the weak rock class for C2 are also determined. In this direction, parameters such as GSI, uniaxial compressive strength (qc), Hoek-Brown failure constants m, s and mi, the density of rock mass (γ), modulus of elasticity of rock mass, and coefficient of disturbance are used. The numerical values of these parameters are given in Table-2.

In addition, the characteristics of the support system and the material parameters of the support units are illustrated in Tables 3 and 4. The finite element model involves 5 stages for the A2 and B2 classes and 6 stages for the C2 class that includes an invert geometry. The tunnel geometry was based on a typical highway tunnel, with a height of approximately 10-meter and a width of 13-meter as the excavation dimensions. It is a double lane, single tube tunnel with an 8-meter platform width (Kartun, 2022).

In the RS² model, the "Initial Loading" is applied as "Gravity Field Stress" since the underground excavation geometry can be modeled with the surface topography. The earthquake acceleration value (a=0.2) used in the dynamic analysis is taken from the Turkey Earthquake Map published by AFAD (Kartun, 2022).

Table 2. Rock classifications and material parameters.

	A2	B2	C2
GSI	65	49	27
Depth (m)	100	100	70
q_c (MPa)	83	55	12
m_i	17	15	12
γ (t/m³)	0.0265	0.0265	0.023
UNDISTURBED ROCK			
E_m (MPa)	18951	14158	405
m	4.871	2.427	0.0035
s	0.0205	0.0035	0.0003
DISTURBED ROCK			
E_m (MPa)	9211	5770	317
m	2.851	1.112	0.442
s	0.0077	0.008	0.0002
Disturbance factor (D)	0.6	0.6	0.2

Results of finite element analysis for each rock class and waterproofing methods reveals that there is no instability problem for support systems of tunnel. Also maximum displacements are in acceptable level in dynamic conditions.

Figures 2 show that total displacements of each rock class in dynamic conditions and maximum displacement is 7.2 cm in C2 class, which is an acceptable value. Also, maximum displacements are 0.7 cm and 0.5 cm for B2 class and A2 class respectively which are quite small.

Table 3. Excavation and support systems.

Support Systems	A2	B2	C2
Rock Bolts Diameter and Type	SN Ø28 cm	SN Ø28 cm	IBO Ø32 cm
Rock Bolts Length and Spacing	Local	4 m Length 2 m X 2 m Spaced	6 m Length 1 m Spaced
Shotcrete Grade and Thickness *Single Shell*	5 cm C25-30 Steel Reinforced	15 cm C25-30 Steel Reinforced	25 cm C25-30 Steel Reinforced
Shotcrete Grade and Thickness *Double Shell*	5 cm C25-30 Non-Reinforced	15 cm C25-30 Non-Reinforced	25 cm C25-30 Non-Reinforced
Wire Mesh Type (The Double Shell)	-	Single - Q221/ 221	Double - Q317/ Q317
Steel Arch Type and Spacing	-	I-100 1.75 m Spaced	I-180 1 m Spaced
Forepoling Spacing and Diameter	0.250 m Spaced, Ø 1.5 Inch Pipes, 2.5 m Overlaped, 5 m Length *Forepole application is used only in the C2 excavation and support class.*		

Moreover, the axial stresses on the bolts were also examined in Figure 3 for C2 class. As seen, the capacity of bolts is enough for induced stresses.

The most important point that should be emphasized for the comparison of DSW and SSW methods according to the numerical analysis is that, as the quality of the rock mass decreases, the feasibility of the utilization of SSW method also decreases. It can be seen from the displacement values and stresses in C2 class excavation and support system.

Therefore, for weak and extreme weak ground conditions, double shell supporting method and traditional waterproofing should be prioritized.

The results of calculations of stresses on shotcrete according to numerical anaylses are given in Tables 5-6-7. Based on these stress values and its calculations, both methods ensure the stability of the tunnel without the secondary shell and final coating (Gök, 2021). Tensile stresses (negative values in Table 5) occurred in C2 class have been disappeared after the completion of both waterproofing methods (Table 6). Besides, the cast concrete coating and secondary sprayed lining in both methods are crucial in terms of closing the waterproofing structure and creating an isolated system. Also, it composes a stable shell against dynamic conditions and provides a smooth appearance.

Although the membrane utilized in double shell method can be considered as a discontinuity between shotcrete and coating concrete, it also creates a mobile and flexible structure that is expected to be more stable under dynamic conditions.

3.2 *The cost calculations and comparison*

The 600-m sample tunnel is divided into 3 rock classes (A2, B2, C2) with 200 meters each to make an accurate and analytical cost comparison.

For both waterproofing methods, each work item is detailed separately, and the cost calculation is made according to the unit price list of the General Directorate of Highways of Turkey. All work items used for this calculation and their descriptions, amounts and application prices are given in Table-8.

Cost calculations are based on 2 main subjects. Such as material and workmanship costs. Material cost includes the amount of shotcrete, metal materials (steel pipe, bolt, reinforcement, etc.), PVC materials (PVC-membrane, drainage pipes, etc.) and coating concrete for DSW method. For the SSW method, steel fiber reinforcement and liquid membrane costs are included. PVC materials, steel mesh and final coating concrete costs are also deducted. The prices used for cost calculations involve both material fees and labor fees of construction.

Table 4. Material parameters of support elements.

Support port Systems	Steel Fiber Reinforced Shotcrete (C20-25)	Non-Reinforced Shotcrete (C20-25)	Bolt		Steel Arch		Wire Mesh		Coating Concrete
			SN Ø28 cm	IBO Ø32 cm	I-100	I-180	Q221/ 221	Q317/ 317	(C25-30)
E (MPa)	28,500	28,500	210,000	210,000	210,000	210,000	210,000	210,000	30,000
Compressive Strength (MPa)	20	20	400	400	400	400	400	400	25
n Poisson Ratio	0.2	0.2	-	-	-	-	-	-	0.25
Cross-Section Area (cm²)	-	-	6.157	8.042	10.60	27.90	2.21	3.17	-
Tensile Strength (MPa)	1.50-2.50*	1.00-2.00	0.16 (MN)	0.25 (MN)	-	-	-	-	1.8

* According to experiments, utilization of steel fiber increases the tensile strength of shotcrete with minimum 20% rate, while it has not an important change on the compressive strength of shotcrete (Shende, 2011).

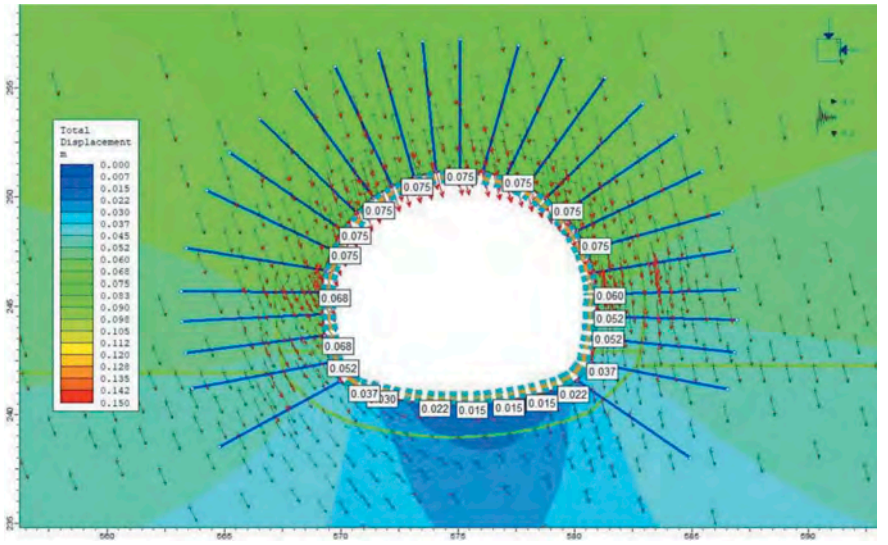

Figure 2. Total displacement of C2 class single shell method in dynamic conditions (Gök, 2021).

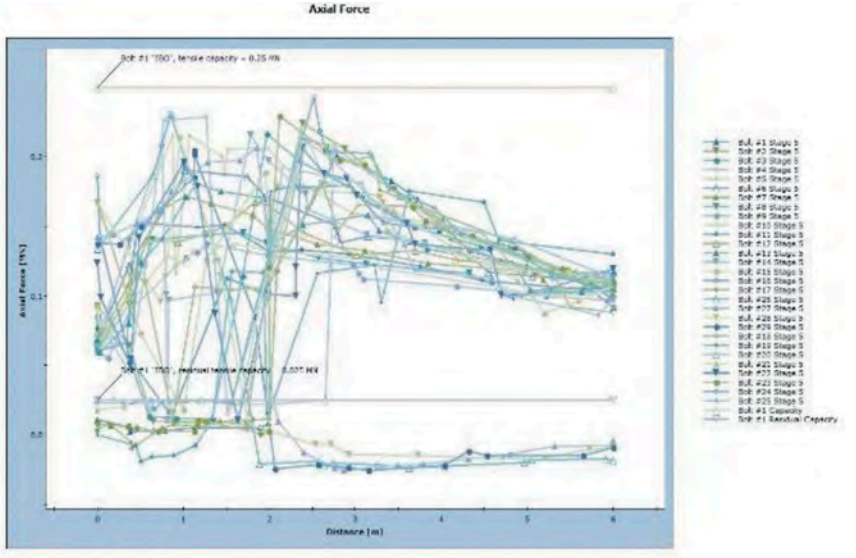

Figure 3. Bolt axial stresses of C2 class single shell method (Gök, 2021).

According to these cost calculations, the 600-meter tunnel constructed with SSW method is is found to be costly. However, the financial difference between the two methods remains very low compared to the total cost of the project which is approximately 2.5%. In addition, labor cost savings resulting from the use of steel fiber reinforcement and liquid membrane instead of mesh and PVC membrane applications are not included in the cost calculation. On the other hand, it is expected that tunnel construction will be accelerated by 20-30% thanks to the elimination of mesh and PVC membrane applications, and this will also directly affect the labor costs (Arıoğlu et al, 2008)

3.3 *The comparison of two waterproofing methods in terms of occupational health and safety of workers*

Occupational health and safety must be prioritized, regardless of the method used during tunnel construction. One of the most significant advantages of the SSW method is the occupational health and safety it offers.

Table 5. Compressive stresses in 3 rock classes for double shell and sprayed single shell without secondary lining (Gök, 2021).

COMPRESSIVE STRESSES				
	The Double Shell (without coating concrete)		The Sprayed Single Shell (without secondary shell)	
	Maximum (kg/cm^2)	Minimum (kg/cm^2)	Maximum (kg/cm^2)	Minimum (kg/cm^2)
A2	129.12	110.88	129.12	110.88
B2	154.00	79.34	157.33	82.67
C2 *Calculated with Maximum Axial Force Value.*	214.48	189.52	214.48	189.52
C2 *Calculated with Maximum Bending Moment*	208.8	-40.80	210.72	-42.72

Table 6. Compressive stresses in 3 rock classes for double shell and sprayed single shell with secondary lining (Gök, 2021).

COMPRESSIVE STRESSES				
	The Double Shell *(+ 40 cm coating concrete)*		The Sprayed Single Shell *(+20 cm secondary shell)*	
	Maximum (kg/cm^2)	Minimum (kg/cm^2)	Maximum (kg/cm^2)	Minimum (kg/cm^2)
A2	13.44	13.22	24.36	23.64
B2	34.60	29.04	58.29	44.57
C2 *Calculated with Maximum Axial Force Value.*	79.55	75.85	116.07	108.37
C2 *Calculated with Maximum Bending Moment*	50.77	13.85	85.78	7.56

When Table-9 and Table-10 are examined, it is clear that the first two main causes of 5,239 work accidents may occur during the application of the DSW method (Müngen, 2011). Also, one of the financial disadvantages of the traditional method is to ensure the occupational safety and health of

Table 7. Shear stresses in 3 rock classes for double shell and sprayed single shell (Gök, 2021).

SHEAR STRESSES				
	The Double Shell *(without coating concrete)* (kg/cm^2)	The Sprayed Single Shell *(without secondary shell)* (kg/cm^2)	The Double Shell *(+ 40 cm coating concrete)* (kg/cm^2)	The Sprayed Single Shell *(+20 cm secondary shell)* (kg/cm^2)
A2	0.40	0.42	0.044	0.084
B2	4.33	4.33	1.18	1.86
C2	12.8	12.8	4.92	7.11

workers who work on the platform and/or scaffold during the application of the DSW method.

It is possible to prevent fatal or injury-inducing work accidents that may occur due to falls from the scaffold or platform during the installation of PVC membrane or steel mesh by choosing the SSW method. Moreover, opting for the sprayed SSW method will provide a significant advantage, both in terms of enhancing worker health and safety and in reducing the optimal costs allocated for worker health and safety.

While applying the liquid membrane, there is a risk of injury or even death due to factors such as hearing loss (noise exposure), eye discomfort (eye contact), or potential equipment malfunctions during the spraying process. However, these risks can also be encountered during the application of shotcrete in the DSW method. These accidents are not related to the type of material but to the spraying mechanism.

4 CONCLUSIONS

In this study, two fundamental waterproofing methods used during tunnel construction are examined. A comparison of DSW and SSW methods is given in terms of operational, stability and cost details. To make a more understandable comparison, two waterproofing methods are applied to a 600-meter-long sample tunnel with rock classes A2, B2 and C2. As a result, it is seen that these two methods have their specific solution proposals under appropriate conditions. It also has been concluded that both methods have advantages and disadvantages. Although SSW method is more costly than the traditional method, it has been determined that this innovative method is quite fast and reliable. According to the results of the finite element analysis, compared in terms of stability, these two methods showed almost no difference in terms of performance in the stationary (static) condition. However, it has been determined that DSW method is more stable in the dynamic state. Since the

Table 8. Cost analysis of double shell and sprayed single shell methods for sample tunnel (Gök, 2021).

No.	Work Item No	Name and Short Description of Business Item	Amount		Application Unite Price ($)	Single Shell App. Cost ($)	Double Shell App. Cost ($)
			Single Shell	Double Shell			
1	2002	Tunneling in A2 rock class with the new Austrian tunneling method (m³)	17,060	17,704	13.67	233,210	242,013
2	2005	Tunneling in B2 rock class with the new Austrian tunneling method (m³)	17,420	18,214	25.64	446,648	467,006
3	2006	Tunneling in C2 rock class with the new Austrian tunneling method (m³)	22,440	23,238	36.47	818,386	847,489
4	2011	Shotcreting in tunnel (m³)	8,970	5,370	28.42	254,927	152,615
5	2012	Non-injection forepoling with 1.5" outer diameter steel pipe in the tunnel (m)	2,240	2,240	14.29	32,009	32,009
6	2013	Injectioned forepoling with 1.5" outer diameter steel pipe in the tunnel (m)	20,160	20,160	14.40	290,304	290,304
7	2016	Installation of 28 mm diameter SN type rock bolt in the tunnel (m)	5,000	5,000	14.39	71,950	71,950
8	2018	Installation of 32 mm diameter IBO type rock bolt in the tunnel (m)	31,80	31,800	24.80	788,640	788,640
9	2021	Coating made of ready-made ribbed mesh steel in the tunnel (Wire Mesh) (tonnes)	0.00	97.40	1,284	0.00	125,117
10	2022	Waterproofing the tunnel (with geotextile and membrane) (m²)	0.00	18,000	14.92	0.00	268,560
11	2024	Making the final concrete lining in the tunnel (m³)	0.00	5,760	46	0.00	264,960
12	3605/A1	Supply and laying of Ø200 mm tunnel type drainage pipe (m)	1,200	1,200	3.84	4,608	4,608
13	18.460/04	Laying of 400 mm diameter spiral wound PVC-based pipe (m)	1,200	1,200	18.71	22,452	22,452
14	3000	Cast cement included in the construction (tonnes) (Final concrete, shotcrete, non-ferrous, ferrous concrete)	6,300	5,435	55.25	348,075	300,283
15	16.100/K-HR	Non-ferrous concrete (Foundation, Base, Base Arch, and Filling Concrete) at every dose in dry (except Bridge foundations) or water in all kinds of construction (m³)	5,884	5,884	31.15	183,286	183,286
16	16.130/K-H	Ferrous concrete at every dose in dry or water in all kinds of construction (m³) - (Cover, Box culvert, etc. concrete/ reinforced)	390	390	80.72	31,480	31,480
17	23.014/K	Fine ribbed steel workmanship of Ø8-Ø12 mm for reinforced concrete (tonnes)	15.60	15.60	1,208	18,844	18,844
18	23.101/K	"Beams, caps, connections" workmanship with profiled iron and sheets (except shipping, including material) (tonnes)	134	134	1,478	198,151	198,151
19	Specific Work Item	Waterproofing the tunnel (Liquid Membrane) (tonnes)	90	0.00	5,250	472,500	0.00
20	Specific Work Item	Steel Fiber Reinforcement (tonnes)	121	0.00	1,418	171,871	0.00
21	Y.27.581	Making a 200 kg cement dose leveling layer (m²)	2,400	0.00	3.13	7,512	0.00
		TOTAL TUNNEL COST				**≅$4.400.000**	**≅$4.300.000**

● *Unit prices are based on TL converted to dollars at a fixed exchange rate.*
● *In both methods, the amount of excavation to be made, the number of support elements to be applied, and the amount of ferrous-non-ferrous cast concrete were calculated from the scaled 'Autocad' drawings.*

Table 9. Distribution of 5239 occupational accidents examined by "accident types" (Main groups), (Müngen, 2011).

Main Groups	Death		Injury		Total	
Accident Type	Number	%	Number	%	Number	%
Human Fall	1,028	42.9	934	32.9	1,962	37.4
Material Drop	251	10.5	278	9.8	529	10.1
Material Splash	10	0.4	211	7.4	221	4.2
Collapse of the Excavation Edge	138	5.8	53	1.9	191	3.6
Collapse of Structure Part	167	7	73	2.6	240	4.6
Electric Shock	293	12.2	80	2.8	373	7.1
Explosives Accidents	50	0.2	82	2.9	132	2.5
Construction Machine Accidents	206	8.6	97	3.4	303	5.8
Other Types of Accidents	255	10.5	1033	36.3	1288	24.7
TOTAL	2,398	100	2,841	100	5,239	100

Table 10. Distribution of 5239 occupational accidents examined according to "accident types" (Subgroups), (Müngen, 2011).

Human Fall - Subgroups	Death		Injury		Total	
Accident Type	Number	%	Number	%	Number	%
From Floor-Platform Edge	248	35.7	190	24.1	439	29.6
From Scaffolding	139	20.0	236	30.0	375	25.3
From Voids in the Structure	99	14.3	71	9.0	170	11.5
From the Roofs	76	11	71	7.8	147	9.9
Level Falls	11	1.6	61	5.1	72	4.9
From the Hand Stairs	21	3.0	40	4.8	61	4.1
From Electric and Telephone Poles	19	2.7	38	2.8	57	3.8
From Fixed Construction Stairs	14	2.0	22	0.5	36	2.4
Other Types of Falls	67	9.7	58	6.9	125	8.4
TOTAL	694	100	787	100	1481	100

SSW method is a more mechanized method than the traditional method, accidents that may occur during PVC-membrane application can be avoided. In the liquid membrane construction phase, occupational safety increases as the labor requirement decreases significantly. When the literature studies, analysis studies, and cost calculations for the 600-meter-long sample tunnel with three different rock classes were examined, the following results were obtained;

-Although PVC-membrane has a low cost and effective waterproofing performance, sprayed liquid membrane can be preferred in terms of ease of application and time-saving.

-Although the use of PVC-membrane is advantageous in projects with standard tunnel walls, it was emphasized that the use of a single shell spraying would be a much more effective method in tunnels with complex geometries or corners. Moreover, the tunnel construction time is expected to be reduced by 35% (23% steel mesh additional >10% liquid membrane) thanks to the use of steel fibre and liquid membrane. This acceleration will provide a cost advantage.

-Groundwater must be completely drained for the SSW system to be efficient, otherwise, it will not be possible to achieve the desired performance.

-One of the biggest advantages of the SSW method is to contribute to occupational health by reducing work accidents.

- "Falling from a platform or scaffolding" or "dropping material" are the most common occupational accidents in construction. Such accidents will not occur in the SSW method, since there is no platform established for PVC-membrane application or a welding machine to be used.

-As the quality of the rock mass decreases, the feasibility of the utilization of SSW method also decreases. For weak and extremely weak ground

conditions, double shell supporting method and traditional waterproofing are recommended.

-These two methods could be used as hybrid thanks to the adhesion of the liquid membrane on the PVC-membrane and the traditional method could be preferred if the water drainage is delayed.

REFERENCES

Arıoğlu, E., Yılmaz, Y. A., & Yılmaz, A. O. (2008). Püskürtme Beton Bilgi Föyleri-Çözümlü Problemler ("Sprayed Concrete Information Sheets- Problems with Solutions" in English), p. 60.

Gök, I. U. (2021). Comparison of Double Shell and Sprayed Single Shell Waterproofing Methods in Tunneling, Hacettepe University, Master of Science Thesis, Department of Mining Engineering, pp. 96–156.

GEODATA. (2017). Chenani-Nashri Tunnel, Application of Sprayed Waterproofing Membrane and Fiber-Reinforced Shotcrete for Final Lining of The Escape Tunnel, p.18.

Holter, K. G., Nilsen, B., Langås, C., & Tandberg, M. K. (2014). Testing of Waterproofing Membranes for Single Shell Sprayed Concrete Tunnel Linings in Hard Rock, p. 10.

Comins, J. (2021). Application of Liquid Membrane. [Website]. Retrieved from https:/ccsbestpractice.org.uk/entries/spraying-of-tunnel-waterproof-membrane/

Junwei, Z. (2014). Waterproofing of a Bored Tunnel by Employing an Innovation Composite Membrane, p. 2575.

International Tunneling Association (2013). ITAtech Report No 2. Design Guidance for Spray Applied Waterproofing Membranes, p. 16.

Kartun Engineering Consulting and Trade Ltd. Co. (2022). atl, pp. 5–28.

Ma, J. (2011). Application of spray-on waterproofing membrane in tunnels. Advanced Materials Research Vols.168-170, pp. 822-826.

MacDonald, M. (2009). Product Evaluation of MASTERSEAL® 345 Application and Specification, pp. 19-21.

Müngen, M. U. (2011). Inşaat Sektörümüzdeki Başlıca Iş Kazası Tipleri. Türkiye Mühendislik Haberleri ("Main Types of Work Accidents in Our Construction Industry. Türkiye Engineering News" in English), Issue 469/34-35, Ankara, 2011/5.

Multiplan. (2016). Membran Uygulama Kılavuzu (Membrane Application Guide in English), p. 23.

Prişçcu, R. (2013). Geotechnical Aspects in Tunnel and Underground, pp. 2–5.

Shende, A. M. (2011). Experimental Study and Prediction of Tensile Strength for Steel Fiber Reinforced Concrete. International Journey of Civil and Structural Engineering, Vol. 1 No.4, pp. 910–915.

Sikaplan. (2017). Waterproofing Sikaplan Membrane Systems For Tunnels, pp. 2–11.

Wu, A., Coppenhall, P., Davies, A. G., & Traldi, D. (2017). Sprayed Waterproofing Membranes on Recent Shotcrete Lining Tunnelling Projects in London, pp. 2–6.

Tunnelling for a Better Life – Yan, Celestino, Thewes & Eberhardt (Eds)
© 2024 The Author(s), ISBN 978-1-032-80042-4
Open Access: www.taylorfrancis.com, CC BY-NC-ND 4.0 license

Constitutive model of aged EPDM rubber in subsea shield tunnel

Chenjie Gong & Chaoran Xie*
School of Civil Engineering, Hunan Provincial Key Laboratory for Disaster Prevention and Mitigation of Rail Transit Engineering Structure, Central South University, Changsha, China
School of Civil Engineering, Central South University, Changsha, China

Yangyang Ge* & Jianrong Song
School of Civil Engineering, Hunan Provincial Key Laboratory for Disaster Prevention and Mitigation of Rail Transit Engineering Structure, Central South University, Changsha, China

ABSTRACT: Ethylene-propylene-diene monomer (EPDM) Rubber gasket, as the key material of waterproof system of shield tunnel joint, will inevitably cause aging damage and reduce waterproof performance with the increase of service time. Moreover, the erosive marine environment will accelerate this damage. Based on the research background of subsea shield tunnel, the accelerated aging test of artificial seawater was carried out, and the attenuation law of tensile properties and the change of micro-morphology of the material were obtained. The constitutive model parameters of the aged rubber material were obtained by fitting, and the accuracy of the results was verified by combining with the finite element model.

Keywords: waterproof performance, shield tunnel, sealing gasket

1 INTRODUCTION

With the rapid development of China's economy and the progress of construction technology, more and more cross-sea and cross-river tunnels are being built. Waterproofing of shield joint is the most critical factor affecting the service safety of shield tunnel. (Ding et al., 2017; Gong et al., 2020) EPDM (Ethylene-propylene-diene monomer) rubber gasket, as the main part of the waterproof system of shield joints, will inevitably cause aging damage with the increase of service time, resulting in leakage accidents. (Shi et al., 2015; Gong et al., 2019) Especially in the erosive marine service environment, the aging of rubber materials will be more significant (Wang et al., 2020).

In order to study the durability of rubber gasket materials, a large number of artificial accelerated aging tests were designed and carried out. Based on thermo-oxidative aging test, unrecoverable damage characteristics (Leng et al., 2021) and molecular structure changes (Li et al., 2020) of gasket rubber materials were analyzed. Based on hydrothermal aging test, mechanical properties (Shi et al., 2015; Johlitz et al., 2020) attenuation law and stress relaxation law (Liu et al., 2022)of rubber materials were studied,, and a series of constitutive models were established to analyze mechanical properties changes of gasket rubber materials under thermo-oxidative aging and hydrothermal aging (Guo et al., 2023; Wang et al., 2023).

In view of the research on the aging properties of rubber gasket materials, the methods of thermal oxygen aging and hydrothermal aging are mainly used, which can not simulate the real Marine service environment. In addition, a large number of studies have focused on the physical and chemical properties of rubber materials after aging, and there is a lack of research on the parameters of the constitutive model of materials after aging in Marine environment.

In this paper, artificial seawater accelerated aging test was designed to simulate the service environment of rubber material in undersea tunnel. Tensile test and scanning electron microscope test were conducted for the rubber material after aging. The constitutive parameters of rubber material after seawater aging were analyzed, and the accuracy of constitutive parameters was verified by finite element model.

2 EXPERIMENTAL METHOD

2.1 *Materials*

The EPDM rubber sample used in this study is produced by Beijing Oriental Yuhong Waterproof

*Corresponding author: 224812345@csu.edu.cn; geyy@yuhong.com.cn

DOI: 10.1201/9781003495505-338

Technology Co. Ltd., and its main performance indexes are shown in Table 1. The samples were cut into standard dumbbells for tensile and aging tests, as shown in Figure 1. The sample has a thickness of 2mm and a length of 75mm. The width of the drawing section is 4mm, and the drawing gauge distance is 20 mm.

Table 1. Performance indicators of EPDM rubber.

Item	Index
Shore hardness/ H_A	67
Tensile Strength T_s/ MPa	≥10
Elongation at break E_b/ %	≥330

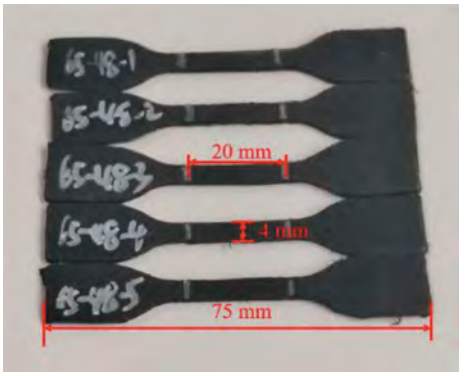

Figure 1. Test samples of EPDM.

2.2 *Seawater accelerated aging test*

For subsea shield tunnel, the gasket is in contact with seawater for a long time. Therefore, the seawater accelerated aging test is designed to simulate its performance changes in the marine service environment. The conditions of seawater accelerated aging test are shown in Table 2. The three aging temperatures are 55℃, 65℃ and 75℃ respectively, and the five aging times are 24, 48, 72, 96 and 168 h respectively.

Table 2. Aging conditions of EPDM sample.

Aging conditions	Index
Aging temperatures/ ℃	55, 65, 75
Aging time/ h	24, 48, 72, 96, 168

Artificial seawater is configured according to ASTM D41141-98(2021). In order to prevent artificial seawater from damaging instruments and equipment, dumbbell samples were put into a high-temperature resistant plastic box filled with artificial seawater, and then the plastic box was put into an SME7000-JY constant temperature water tank for accelerated aging test of samples.

2.3 *Tensile test*

The tensile property of EPDM rubber gaskets was tested on a CMT4104 universal testing machine by following the standard ASTM D412. In the experiment, extensometer was used to measure the deformation of the stretching section, and the standard distance of extensometer was 20 mm. The maximum range of force sensor is 250N, and the loading rate of tensile test is 500mm/min.

The force-deformation curves, tensile strength T_s and elongation at break E_b of five samples in each group were recorded.

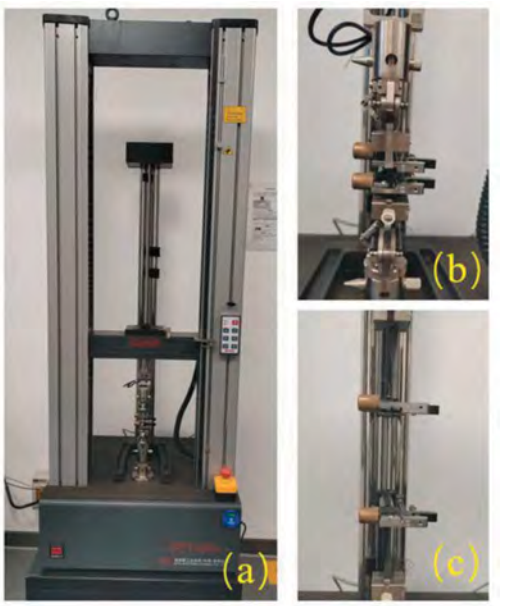

Figure 2. Tensile Test. (a) Universal testing machine. (b) Sample before test. (c) Sample breaking.

2.4 *Scanning electron microscope (SEM) analysis*

The microstructures of EPDM samples were observed with a Quanta 250 FEG scanning electron microscope (SEM) at the acceleration voltage of 15 kV. The surfaces were ion beam sputter-coated with gold with layer thickness of 1–20 nm.

3 TEST RESULTS AND ANALYSIS

3.1 *Mechanical properties*

The average tensile strength T_s and elongation at break E_b of five samples after aging are obtained through tensile test as shown in Figures 3 and 4. Results On the surface, at the initial stage of aging, the tensile strength T_s and elongation at break E_b decreased rapidly, which was due to the molecular chain rearrangement caused by rubber molecular chain scission under the action of thermal-seawater environment. With the

extension of aging time, the tensile strength of rubber is improved, mainly due to the hardening of rubber materials caused by aging. However, after a slight increase, the elongation at break Eb generally shows a downward trend, which indicates that with the increase of aging time, the properties of rubber develop to brittleness, and the higher the aging temperature, the more obvious the decrease of elongation at break.

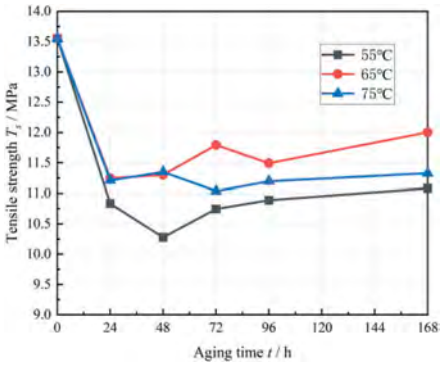

Figure 3. Tensile strength T_s of aged samples.

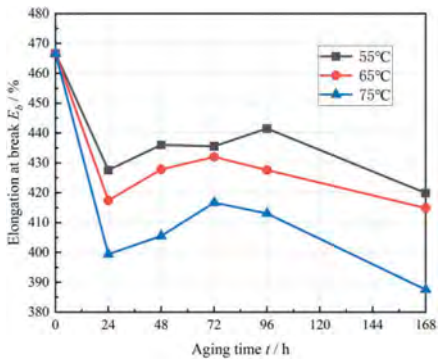

Figure 4. Elongation at break E_b of aged samples.

3.2 *Microscopic surface morphology*

The surface morphologies of EPDM samples after seawater ageing were shown in Figure 5. For the unaged EPDM sample, the surface characteristics are smooth and flat(Figure 5 (a)). At the initial stage of aging, the initial defects on the surface of the sample began to expand, forming some larger holes (Figure 5 (b)). With the extension of aging time, the surface of the sample began to become rough, and the number and size of cracks and defects gradually increased (Figure 5 (c),(d)). This phenomenon may be caused by the volatilization of small molecular additives in rubber materials and the interface between inorganic fillers and EPDM substrate during seawater aging. In a word, seawater aging will lead to structural damage of EPDM rubber material, which will affect the mechanical properties of the samples.

4 COSTITUTIVE MODEL OF SEAWATER AGING RUBBER

4.1 *Mooney-Rivlin model parameters*

Mooney-Rivlin model, as one of the most widely used rubber constitutive models, is suitable for simulating rubber deformation behavior with strain less than 100%. A large number of scholars obtained the model parameters of Mooney-Rivlin by fitting the experimental data, which verified the accuracy of the model. The expression of Mooney-Rivlin model is as follows:

$$W = C_{10}(I_1 - 3) + C_{01}(I_2 - 3) \tag{1}$$

where W is the strain energy density function, and I_1 and I_2 are the two strain invariants of the Green deformation tensor. C_{10}, C_{01} are the material parameters of the Mooney-Rivlin model.

For uniaxial tensile test, the engineering stress σ has the following relationship with the extension ratio λ (Gent, 2002):

$$\sigma = 2\left(C_{10} + C_{01}\lambda^{-1}\right)\left(\lambda - \lambda^{-2}\right) \tag{2}$$

Where λ=1+ε, ε is the strain of tensile test.

Equation (2) can be rewritten as:

$$\frac{\sigma}{2\left(\lambda - \lambda^{-2}\right)} = C_{10} + C_{01}\lambda^{-1} \tag{3}$$

The stretching curve is converted into the form of equation (3), and linear fitting is carried out by least square method. The slope and intercept of the straight line obtained by fitting are C01 and C10.

The calculation of C01 and C10 values at different aging temperatures and times are shown in Figures 6 and 7.

4.2 *Comparison of experimental and simulationresults*

In order to further verify the rationality of the constitutive parameters obtained from the test, the finite element model of rubber specimen tension is established by ABAQUS. The rubber parts in the model have the same size as the experimental materials, and the element type is C3D8R, which is solved explicitly by dynamic method. The meshing of the model is shown in Figure 8.

The boundary conditions of the model are shown in Figure 9, with fixed constraints at one end of the sample and displacement-controlled loading at the other end. The distance between section An and B in the model is 20mm, which is consistent with the extensometer distance of the tensile test. In the post-processing, the displacement difference between the two sections of A and B is extracted as the deformation of the sample.

The constitutive parameters were obtained by fitting in section 4.1, the unaged sample and the

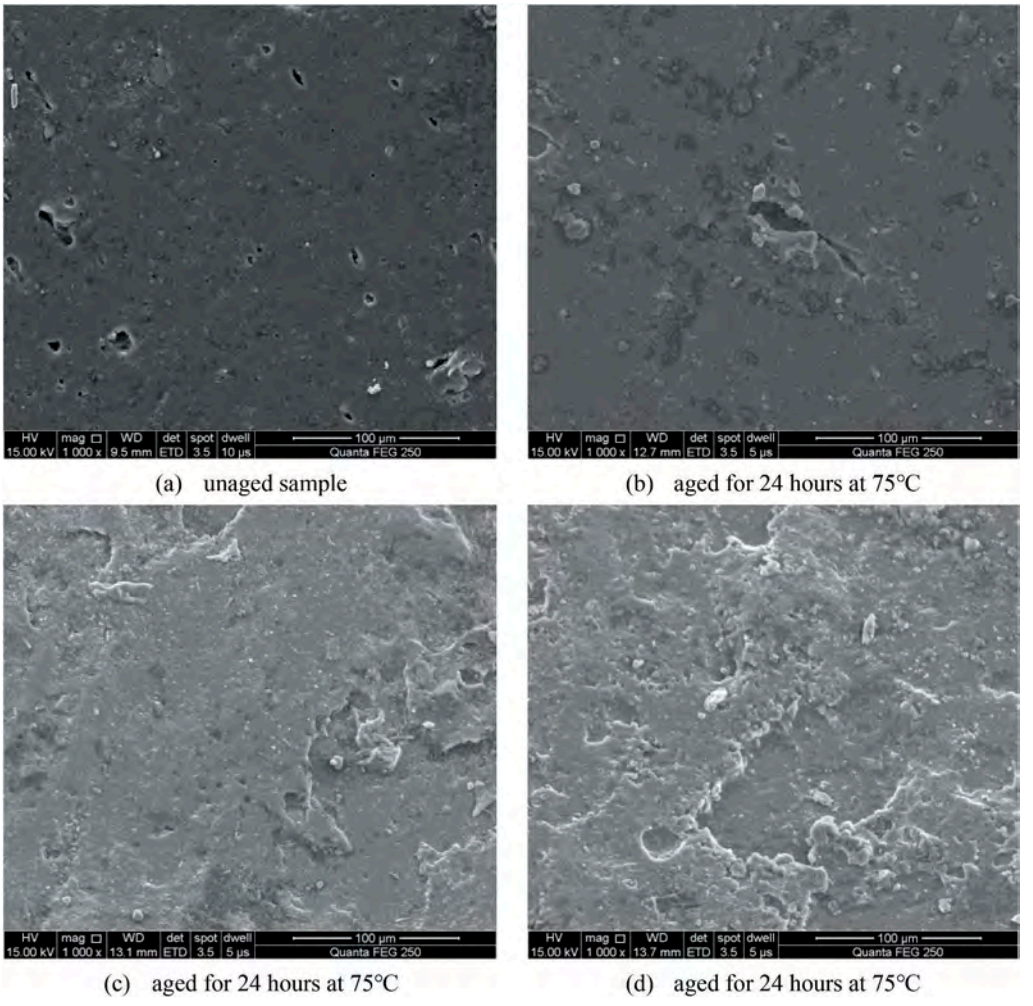

Figure 5. SEM image for EPDM samples after artificial seawater aging (magnification × 1000).

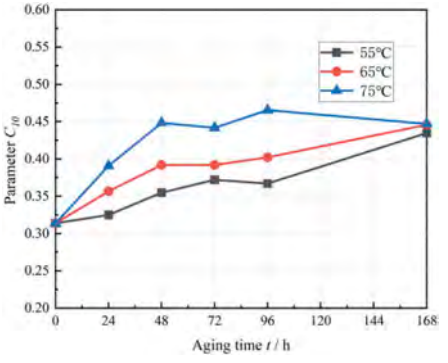

Figure 6. Parameter C_{10} of aged samples.

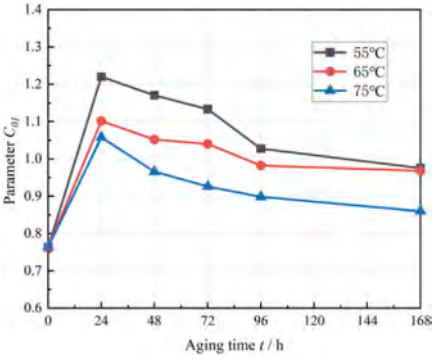

Figure 7. Parameter C_{01} of aged samples.

sample aged for 168 h at 75 ℃ were simulated by finite element method. Figure 10 shows the tested engineering stress-strain curves and finite element method (FEM) results of the unaged sample and the aged samples. The maximum errors of the tested values and FEM simulation of the two samples are 8.07% and 8.54% respectively, which proves the accuracy of the model.

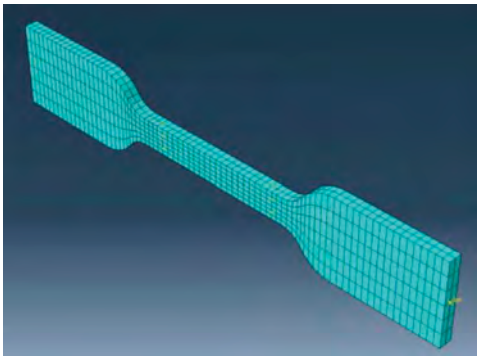

Figure 8. Meshing of finite element model.

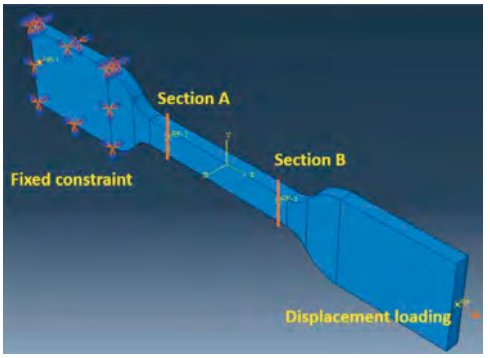

Figure 9. Boundary conditions of finite element model.

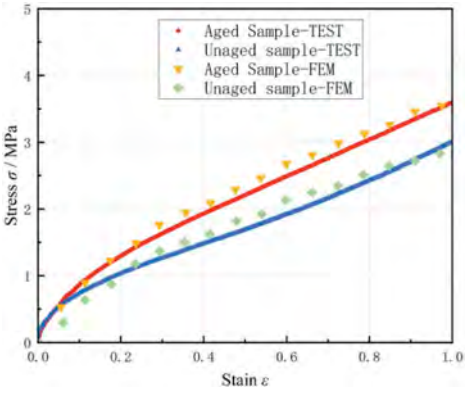

Figure 10. Comparison between test and finite element method (FEM).

5 CONCLUSION

In this work, EPDM rubber, as the main waterproof material of subsea shield tunnel, was subjected to the seawater accelerated aging test and the tensile test after aging. The main conclusions are as follows:

1. After aging, the tensile strength of rubber materials decreased rapidly at first, and then increased gradually due to the hardening effect of rubber.
2. With the increase of aging time, the elongation at break of rubber materials generally showed a downward trend.
3. Seawater aging will damage the microstructure of materials, and then reduce the mechanical properties of materials.
4. The Mooney-Rivlin constitutive parameters of the aged rubber material are fitted by the least square method, and the variation law of the constitutive parameters with aging temperature and time is obtained.
5. The finite element modeling is verified by using the fitted constitutive parameters, and the numerical simulation results can well fit the experimental results, with the maximum error of 8.54%.

ACKNOWLEDGMENTS

We gratefully acknowledge the financial support provided by the National Natural Science Foundation of China (Grant No. 52278421) and the State Key Laboratory of Special Functional Waterproof Materials (No. SKWL-2022KF01).

REFERENCES

Ding, W.Q., Gong, C.J., Khalid, M., et al, 2017. Development and application of the integrated sealant test apparatus for sealing gaskets in tunnel segmental joints. Tunnelling and Underground Space Technology incorporating Trenchless Technology Research. 63(2017), 54–68.

Gong, C.J., Ding, W.Q., Xie D.W., 2020. Parametric investigation on the sealant behavior of tunnel segmental joints under water pressurization. Tunnelling and Underground Space Technology incorporating Trenchless Technology Research. 97(2020), 103231.

Shi, C.H., Cao, C.Y., Lei, M.F., et al, 2015. Time-dependent performance and constitutive model of EPDM rubber gasket used for tunnel segment joints. Tunnelling and Underground Space Technology incorporating Trenchless Technology Research. 50(2015), 490–498.

Gong, C.J., Ding, W.Q., Soga, K., et al, 2019. Failure mechanism of joint waterproofing in precast segmental tunnel linings. Tunnelling and Underground Space Technology incorporating Trenchless Technology Research. 84(2019), 334–352.

Wang, Z.N., Shen, S.L., Zhou, A.N., et al, 2020. Experimental evaluation of aging characteristics of EPDM as a sealant for undersea shield tunnels, J. Mater. Civil Eng. 32 (7), 04020182.

Leng, D.X., Huang, C., Xu, K., et al, 2021. Experimental mechanics and numerical prediction on stress relaxation and unrecoverable damage characteristics of rubber materials. Polymer Testing. 98(2021), 107183.

Li, C.J., Ding, Y.Q., Yang, Z., et al, 2020. Compressive stress-thermo oxidative ageing behaviour and mechanism of EPDM rubber gaskets for sealing resilience assessment. Polymer Testing. 84(2020), 106366.

Musil, B., Johlitz, M., A. Lion, 2020. On the ageing behavior of NBR: chemomechanical experiments, modelling and simulation of tension set. Continuum Mech Therm. (2020) 32127–32146.

Liu, Y.K., Zhang, Q.S., Liu, R.T., et al, 2022. Compressive stress-hydrothermal aging behavior and constitutive model of shield tunnel EPDM rubber material. Construction and Building Materials. 320(2022), 126298.

Guo, J.X., Xu, P.K., Han, X., et al,2023. Ageing behaviour and molecular/network structure evolution of EPDM/carbon black composites under compression and in thermal-oxidative environments. Polymer Degradation and Stability. 214(2023), 110417.

Wang, S.H., Xu, J.S., Li, H., et al, 2023. The effect of thermal aging on the mechanical properties of ethylene propylene diene monomer charge coating. Mechanics of Time-Dependent Materials. 11(7).

ASTM D41141-98, 2021. Standard Practice for Preparation of Substitute Ocean Water. ASTM International, West Conshohocken, PA, USA.

ASTM D412, 2006. standard test methods for vulcanized rubber and thermoplastic elastomers-tension. ASTM International, West Conshohocken, PA, USA.

Mooney M 1940. A Theory of Large Elastic Deformation, Journal of Applied Physics, 11(6): 582–592

Tunnelling for a Better Life – Yan, Celestino, Thewes & Eberhardt (Eds)
© 2024 The Author(s), ISBN 978-1-032-80042-4
Open Access: www.taylorfrancis.com, CC BY-NC-ND 4.0 license

Research and application of joint waterproofing technology for prefabricated metro station structures

Meiqun Huang, Qi Fan*, Xiuren Yang & Lin Fang
Beijing Urban Construction Design and Development Group Co., Ltd., Beijing, China
National Engineering Research Center for Green & Safe Construction Technology in Urban Rail Transit, Beijing, China

ABSTRACT: The industry has placed significant emphasis on the collective waterproof performance of open-excavated prefabricated station structures. This paper examines the impact and control measures of two significant factors, namely "joint opening" and "gasket dislocation", which are closely associated with the waterproof performance of prefabricated structures. The multi-line waterproof technologies of "two gaskets + one injection + one embedding" have been thoroughly demonstrated through a combination of experimental research and monitoring results from actual engineering applications. The research and engineering application demonstrate that the waterproofing of prefabricated station structures differs from that of shield tunnels, not only in terms of waterproof structural measures, but also in various control standards. The waterproof sealing gasket, when subjected to an opening amount of 10mm and a dislocation amount of 5mm, is capable of withstanding a water pressure of 1.0MPa. This meets the performance requirements of the station structure, which is buried at a depth of 30m and needs to resist 2-3 times the water pressure. The gaskets exhibit a residual stress value of approximately 67% after a period of 100 years, indicating their ability to withstand long-term water pressure. The double sealing gaskets exhibit a modest enhancement of 20% in performance. The in performance is enhanced by 30% when performance to using a to single sealing gasket. When water leakage occurs in the outer sealing gasket of the lining, the utilization of double sealing gaskets offers notable advantages. According to the current and ongoing projects, the observed maximum joint opening for the station structure and the maximum surface displacement complies with the standards set for controlling the waterproof performance of the joint. There is no evidence of any leakage occurring at the joint, even in the absence of an external waterproof layer.

Keywords: Prefabricated station, Joint waterproofing, Multi-line waterproof technology, Waterproofing test, Joint opening and dislocation

1 INTRODUCTION

The waterproofing of underground projects, such as subways, has consistently attracted considerable attention from the industry. The subterranean constructions are prone to the extended infiltration of groundwater. If the integrity of the waterproofing system of the structure is compromised, it will not only have a substantial impact on the durability and lifespan of the structure, but also have adverse effects on the functionality of the building and accelerate the corrosion of electrical equipment in the event of groundwater infiltration. Simultaneously, the presence of multiple water leaks can lead to the subsidence of neighbouring layers and have significant implications for the groundwater ecosystem. Numerous engineering projects have provided substantial evidence of the arduous and costly nature of mitigating leakage in subterranean structures.

The occurrence of water leakage in cast-in-place concrete structures of subway stations is a prevalent issue, which has become a persistent problem. According to Xiao (2021), approximately 90% of cast-in-place concrete stations experience leakage issues. The cost of treating leakage water at each station is estimated to be at least several million, with individual stations incurring costs of nearly 10 million. Upon conducting an investigation into the current state of over a dozen river crossing tunnels constructed in Shanghai, it has been observed that the leakage of the prefabricated tunnel sections, constructed using the shield method, is consistently maintained below 0.1L/m2/d. This leakage rate aligns with the waterproof design specifications for river crossing

*Corresponding author: fanqi@tju.edu.cn

DOI: 10.1201/9781003495505-339

tunnels. Furthermore, the majority of leakage points are concentrated at the joints, grouting holes, and bolt holes. However, in the case of cast-in-place concrete tunnel sections constructed using alternative construction methods, there remains a lack of adequate leakage control. This is primarily attributed to the significant leakage observed at the construction joints and contraction joints that are specific to cast-in-place structures (Wu et al., 2013).

The shield tunnel is considered to be the most exemplary fabricated underground structure. The shield method is extensively employed in the construction of tunnel engineering projects in various sectors such as railways, highways, subways, water conservancy, and municipal infrastructure. This construction method is applicable for both land and underwater construction scenarios, as well as diverse engineering geological and hydrogeological conditions. In recent years, the field of shield tunnel construction in China has experienced significant advancements. Notably, there has been a notable increase in the construction of underwater tunnels with large diameters and high water pressure. For instance, the Qiongzhou Strait Tunnel, which has a diameter of 15.9m and experiences a maximum water pressure of 1.7MPa, presents a formidable challenge for ensuring the waterproofing of shield tunnel segment joints (Chen, 2014).

In China, the construction technology of shield tunnel has undergone significant advancements over the past fifty years, starting with the construction of the Dapu Road River Crossing Tunnel in Shanghai in 1965. During this period, the joint waterproof technology has also experienced continuous development, resulting in notable achievements in waterproof theory, gasket material selection, and setting methods (Zhou, 2004). Zhou (2004) provided a comprehensive analysis of the effectiveness, composition, manufacturing process, cost-effectiveness, and current applications of elastic rubber gaskets, water swelling rubber gaskets, and composite rubber gaskets. The study highlighted the growing complexity and diversity of seal section structures in order to meet the rising requirements for segment joint water pressure, opening, and dislocation. It was noted that the porous elastic gasket, which is primarily made of ethylene propylene diene monomer (EPDM), has emerged as the dominant choice in this field. China's current national standard for shield tunnel engineering includes a provision specifying that the waterproof gasket must be constructed using either EPDM rubber or a composite material consisting of water swelling rubber and EPDM rubber. It is noteworthy that the establishment of a comprehensive set of design and construction methods, as well as technical systems, for the waterproofing of shield tunnel segment joints has been achieved. This includes aspects such as design, construction, and quality control, as outlined in the following standards: GB/T51438-2021 (2021), GB50108-2008 (2008), GB50157-2013 (2013), and GB/T51310-2018 (2018).

Following the successful construction of the initial prefabricated station for the Changchun metro, the presence of numerous connection joints has brought attention to the critical issue of waterproofing in the prefabricated station structure. This matter has garnered significant interest within the industry. Currently, there are six operational prefabricated stations in the Changchun Metro. From the operational data collected at the stations, it has been observed that the maximum groundwater level at the site is approximately 1.5 meters below the surface. The prefabricated station structure exhibits a lack of leakage at the joints in the absence of an external waterproof layer. Water leakage was observed exclusively in the arch of the initial test station, attributed to insufficient sealing measures implemented for the longitudinal tensioning channel of the first ring. After a series of timely improvements in each station during the subsequent period, there was no recurrence of a similar phenomenon. The waterproofing of the prefabricated station structure of Changchun Metro has been found to fully comply with the waterproof technical requirements outlined in the design and specifications, successfully achieving the intended objective (Yang, 2022).

2 DESIGN OF JOINT WATERPROOFING FOR PREFABRICATED STATION

2.1 *Prefabricated station joint*

The connection method used for the prefabricated station structure is comparable to that of the shield tunnel, as it employs a dry connection process. The connection of prefabricated concrete components involves the direct alignment and interlocking of joint mating surfaces, which can take various forms including mortise joints, flat joints, or lap joints.

As depicted in Figure 1, the grouted mortise joint represents a novel form of dry joint that has been specifically designed for the prefabricated station lining structure. The connection interface of precast concrete components is designed using a tenon and groove system. After the component joints have been aligned and brought into contact, grout is injected into the enclosed gap area created by the waterproof sealing gasket (or isolation rubber) at the joint through the grouting hole. This process ensures that the contact surface of the joint is completely sealed, resulting in

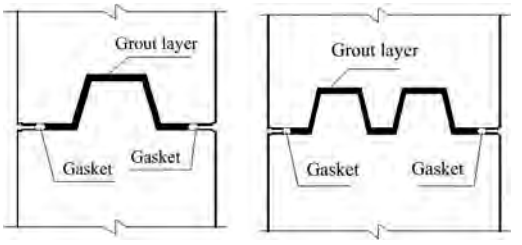

Figure 1. Structure of grouted mortise-tenon joint (single tenon and double tenon).

effective contact. The tenon and groove exhibit complete occlusion, thereby facilitating effective force transmission.

Figure 2 depicts a cross-sectional schematic diagram illustrating the prefabricated station structure of Changchun Metro. The longitudinal joints in the lining structure are formed by 7 internal ring joints. With the exception of the staggered assembly of the arch joint, all other joints are assembled through joints. Among the various joints in the structure, the longitudinal joint of the AB block's bottom plate is secured by applying circumferential prestressed tension. The longitudinal joints of the BC block, CD block, and CE joint on the side wall are primarily compressed by the weight of the components themselves and secured using external bolts. The longitudinal joint of the top arch DE block joint is tightly squeezed through the interaction between the left and right arches, and additional external bolts are employed for locking. The circumferential joints of the station lining structure are formed by inter ring joints, which are assembled through joints and secured by relay type longitudinal prestressed tension.

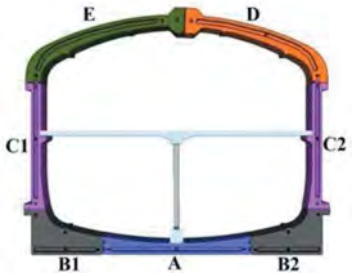

Figure 2. Structural cross section of Changchun prefabricated station structure.

As a crucial structural measure for the precise positioning control of prefabricated station structure assembly, the installation of positioning pin devices is implemented at all joints within and between the rings of the lining structure. Figure 3 depicts a schematic diagram illustrating the positioning pin device. The positioning pin assumes a critical function in the assembly process by guiding the path of component assembly and ensuring precise assembly accuracy.

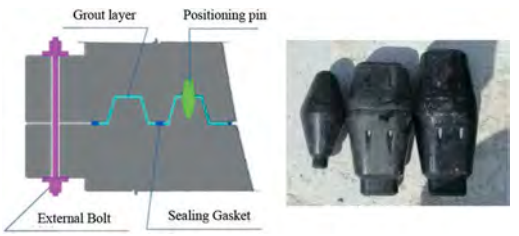

Figure 3. Schematic diagram of locating pin rod.

2.2 *Technical scheme of joint waterproofing of station lining structure*

2.2.1 *Joint waterproofing technical scheme*

The grouting mortising joint of the assembled station lining structure is designed using the technical scheme of "two gaskets + one injection + one embedding" and includes multiple layers of protection. Figure 4 illustrates the schematic diagram of the joint waterproof structure. Two waterproof gaskets are strategically placed at the joint to effectively provide a sealing mechanism. Grout is introduced into the space between the two gaskets in order to establish a seal that is impervious to water. Additionally, an insert is inserted into the caulking to further enhance its waterproofing capabilities. Among the various components, the waterproof gasket functions as the primary barrier against water infiltration, while grouting and other measures are employed as supplementary methods to enhance waterproofing.

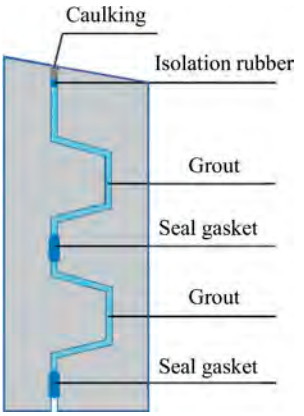

Figure 4. Joint waterproof of grouted mortise-tenon joint.

2.2.2 *Waterproof gasket*

(1) Materials. The two waterproof sealing gaskets utilize the commonly used EPDM elastic sealing gasket as the primary waterproof material. Additionally, water swelling rubber is incorporated to enhance the waterproofing capability, resulting in a composite porous and multi-groove sealing gasket, as depicted in Figure 5. EPDM rubber exhibits excellent microwave heat vulcanization processing ability, as well as notable durability and cost-effectiveness. The incorporation of composite water swelling rubber improves the waterproof capabilities of the sealing gasket. Additionally, the material used in the composite sealing gasket adheres to the applicable regulations outlined in the current national standards.

(2) Classification of Section Type. The circular hole is chosen for the inner hole of the sealing gasket section, while the bottom plate is designed with a consistent groove shape. The width of the bottom structure measures 42mm, while the top structure measures 30mm. The rubber material expands by 2mm when in contact with water, and

the overall height after composite is 18mm. The cross-sectional area of the sealing gasket groove should be equal to or greater than the net cross-sectional area of the sealing gasket, with a ratio of 1 to 1.15. This ensures that when the joint opening is 0mm, the sealing gasket can be completely compressed into the groove.

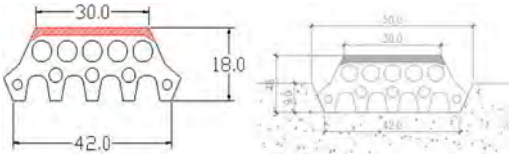

Figure 5. Joint waterproof of grouted mortise-tenon joint.

2.2.3 *Analysis of index of joint opening and dislocation*

Based on the assumption that the joint utilizes a tenon groove structure and is furnished with a positioning pin device, the variation in component manufacturing precision and the intricate configuration of the structure significantly influences the displacement of the sealing gasket and surface misalignment. The disregard of assembly construction and the neglect of the influence of the structural stress state can have significant consequences. The theoretical dislocation amount of the sealing gasket primarily arises from the positioning deviation of the sealing gasket groove center, which is ± 0.5mm, and the positioning deviation of the positioning pin rod center, also ± 0.5mm. Simultaneously, it is imperative to incorporate a reserved gap of 0.5mm for the positioning pin rod, while the theoretical maximum value for dislocation control is 3mm. The theoretical analysis suggests that the extent of surface dislocation in the structure is primarily accounted for by a thickness deviation of -1mm.~During the manufacturing process of the component, there is a deviation of +3mm in the center positioning of the positioning pin rod, with a tolerance of ± 0.5mm. Additionally, a gap of 0.5mm is reserved for the pin rod. The theoretical maximum value for controlling surface dislocation is 6mm. Among these challenges, controlling the precision of component thickness production proves to be difficult, as the allowable deviation value is relatively large. Consequently, this leads to a greater displacement of its control index when compared to the waterproof sealing gasket. From the empirical observation of the project's assembly process, it is evident that the utilization of the positioning pin rod in the joint has resulted in a highly accurate positioning effect. This has led to a relatively optimal control of surface dislocation in the structure, both longitudinally and circumferentially. The measured values typically range between 0.3mm and 4mm.

The measurement of the waterproof sealing gasket, which is located inside the joint, is not possible directly. Instead, it can only be assessed through the surface dislocation index. Therefore, in practical implementation, the control criterion for surface dislocation has been suitably elevated, resulting in the attainment of equal values for both parameters. When designing and conducting performance tests on the waterproof sealing gasket, it is recommended to utilize the surface dislocation standard as a means of control. It is advisable to assign a control index value of 5mm for the surface dislocation of the structure.

3 EXPERIMENTAL STUDY ON WATERPROOF PERFORMANCE OF JOINTS

To assess the waterproof capabilities of the chosen waterproof sealing gasket and establish the corresponding performance parameters, a comprehensive set of tests was carried out on a singular composite sealing gasket in Changchun before the construction. These tests encompassed evaluations of temperature adaptability, water pressure resistance, stress relaxation, and compression load. Figure 6 depicts the schematic diagram of the waterproof sealing gasket and testing device. The test utilizes a sealing gasket measuring 200mm in length, in conjunction with a steel structure testing device featuring an end plate. The speed at which the loading displacement occurs is 50mm/min.

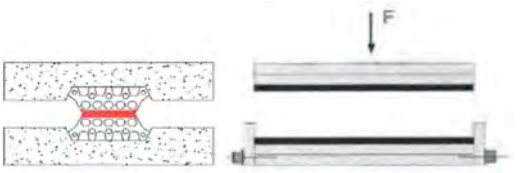

Figure 6. Waterproof sealing gasket and experimental device.

3.1 *Water pressure resistance test*

Based on the above analysis of the control indicators for joint opening and sealing gasket dislocation, in order to study the waterproof performance of sealing gaskets under different splicing conditions, experimental tests were conducted on the waterproof performance of sealing gaskets corresponding to different joint opening amounts under 5 different conditions, including sealing gasket dislocation amounts of 0mm, 5mm, 10mm, 15mm, and 20mm. Figure 7 shows the water pressure resistance curve of a single composite sealing gasket under different opening and dislocation conditions. The analysis of the test results is as follows:

(1) When the joint is opened by 0mm and misaligned by 0mm, the ultimate water resistance pressure of a single sealing gasket is measured to be 2.6MPa. The experimental observation indicates that the joint is completely sealed at this particular moment. Subsequently, additional pressure testing was carried out, revealing an occurrence of adhesive separation between the sealing gasket and the surface of the steel mold

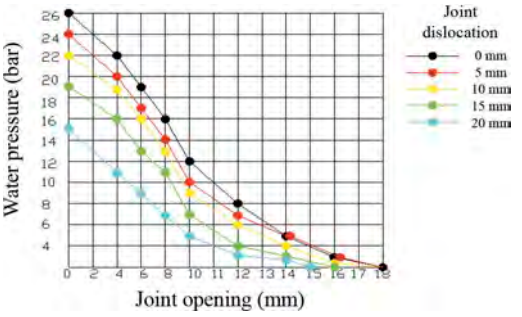

Figure 7. Water pressure resistance curve of single composite sealing gasket under different opening and dislocation conditions.

base. The adhesive's compressive strength limited its capacity to enhance the water pressure resistance of the sealing gasket.

(2) When the joint is opened by 10mm and misaligned by 5mm, the ultimate water resistance pressure of a single sealing gasket is 1.0MPa. This opening and dislocation surpass the prescribed maximum control index of 8mm for joint opening and 3mm for sealing gasket dislocation in prefabricated station structures.

(3) Typically, for underground stations with two or three stories, the depth at which the bottom plate is buried is less than 30m, and the maximum water pressure does not exceed 0.3MPa. According to the test results, it has been determined that the single sealing gasket has the ability to withstand a maximum head pressure of 0.3MPa. When the dislocation reaches 5mm, the permissible opening amount is 16mm. It can withstand twice the maximum head pressure of 0.6MPa. Similarly, when the displacement is 5mm, the allowable opening amount is 13mm. In this case, it can resist three times the maximum head pressure of 0.9MPa. Furthermore, when the displacement is 5mm, the permissible opening amount is approximately 10.6mm.

The influence of the displacement of the sealing gasket on the water pressure performance is less significant compared to the opening of the joint. However, when the displacement reaches 15mm, particularly 20mm, the water pressure performance experiences a notable decline in comparison to other types. This decline is primarily attributed to the width of the sealing gasket. The width of the sealing gasket utilized in the experiment measures 42mm. When the displacement is limited to one-third of the sealing gasket width, the increase in displacement does not have a significant impact on the water pressure resistance performance. However, if the displacement exceeds half of the sealing gasket width, there is a significant decrease in water pressure resistance performance.

According to the pertinent regulations outlined in the current national standards of China, it is imperative for the sealing gasket to adhere to specific performance criteria. This includes the ability to withstand a water pressure that is 2-3 times greater than the buried water head, taking into consideration the maximum opening and estimated displacement as per the design specifications. Based on the analysis and experimental research conducted on the comprehensive opening and displacement control indicators, a performance standard of 0.6MPa for resistance to water pressure is recommended for prefabricated station structures buried at a depth of 30m.~A pressure of 0.9MPa is necessary. The single composite waterproof sealing gasket demonstrates the ability to withstand water pressure of 1.0MPa, while maintaining an opening of 10mm and a displacement of 5mm, thus satisfying the specified requirements.

3.2 *Stress relaxation detection*

The durability of elastic sealing gaskets is significantly influenced by the stress relaxation occurring during long-term compression. In order to ensure the long-term effectiveness of the sealing gasket, it is necessary to conduct stress relaxation testing on the gasket. The present study employed the high-temperature accelerated aging technique to examine the long-term compressive residual stress levels of a singular composite sealing gasket under varying service life conditions. Figure 8 depicts the compressive stress relaxation detector along with the schematic diagram illustrating the stress residual curve. From the stress residual curve, it is evident that the stress relaxation of the sealing gasket exhibits a more pronounced effect in the initial phase, but gradually slows down in the subsequent stages. The residual stress ratios of the sealing gasket after 100 and 200 years are 67% and 63%, respectively.

If the station structure is designed with a buried depth of 30m, in accordance with the standard for withstanding a water head of 100m (1.0MPa), it indicates that the sealing gasket's residual resistance capacity after 100 and 200 years is 67m (0.67MPa) and 63m (0.63MPa) respectively. These values still largely satisfy the specifications' requirements. This observation suggests that the sealing gasket utilized in the experiment possesses the capability to fulfil the prolonged water pressure criteria, thereby demonstrating satisfactory water resistance performance.

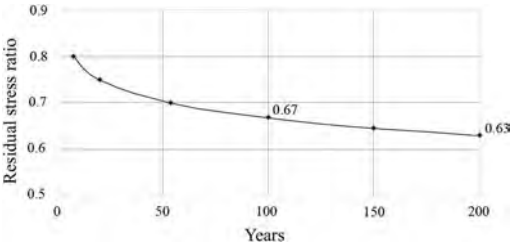

Figure 8. Compression stress relaxation tester of single composite sealing gasket and stress residual curve.

3.3 *Compression load test*

The maximum compressive stress index of the sealing gasket serves as the governing criterion for determining the maximum tensile load designed at each tensioning point of the prefabricated station structure. Compression load tests were conducted under various compression and dislocation conditions. Figure 9 presents the schematic diagram illustrating the compression load strain curve of a solitary composite sealing gasket. The experimental results indicate a significant correlation between the compression amount and the compression load. Specifically, as the compression amount increases, the compression load also increases, demonstrating a nearly linear relationship. On the other hand, the displacement has a minimal effect on the compressive load, particularly when the displacement is less than 5mm, as it is not statistically significant. When the displacement exceeds 10mm, there is an inverse relationship between the magnitude of displacement and the compressive load. When the displacement is 0mm and the compression reaches 16mm, the maximum compression load is 38kN/m. Similarly, when the displacement is 5mm and the compression reaches 16mm, the maximum compression load is 36kN/m. The maximum compressive stress index of a single composite sealing gasket should not exceed 40kN/m.

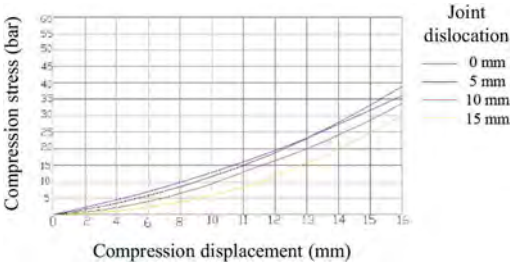

Figure 9. Compression load strain curve of single composite sealing gasket.

3.4 *Research on waterproof performance of dual waterproof sealing gasket*

The design dimensions of prefabricated station structural components are relatively large, and the joint section is also large. Double waterproof sealing gaskets are recommended for installation at the joints. In order to investigate the waterproof performance characteristics of double sealing gaskets, a novel testing apparatus was specifically developed. Comparative tests were conducted to evaluate the waterproof performance of both double and single sealing gaskets under various operating conditions. Figure 10 depicts the schematic diagram of the test apparatus used to evaluate the waterproof performance of dual sealing gaskets. A pressure gauge is incorporated between the inner and outer channels in order to measure the pressure within the outer channel. The initial measurement is determined using a standardized experimental block of a specific thickness, while the displacement measurement is adjusted through the mutual translation of the mold.

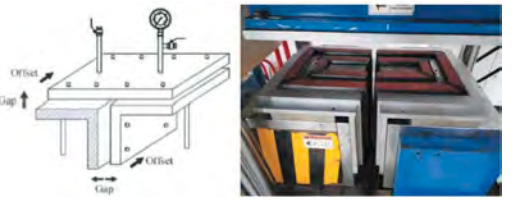

Figure 10. Experimental device of waterproof performance for double sealing gaskets.

The analysis of the test results is presented below:

(1) Comparative Analysis of Water Pressure Resistance. The comparison test conducted to evaluate the water pressure resistance under various working conditions reveals that the double seal gasket exhibits a slight improvement in water pressure resistance compared to the single seal. The improvement rate ranges from 20% to 30% when considering the same opening and displacement.

(2) An experiment investigating the correlation between the opening amount and the opening amount. The experiment aims to evaluate the maximum opening capacity by subjecting the system to various working conditions while maintaining consistent water pressure and displacement. Experiments have demonstrated that, when subjected to identical water pressure and displacement conditions, the maximum permissible aperture of a dual sealing gasket can be augmented by approximately 25% in comparison to a single sealing gasket.

(3) Experiment on the relationship between displacement and distance traveled. In order to conduct the experiment, it is necessary to establish consistent water pressure and opening amounts across multiple working conditions. The objective is to measure the maximum displacement achieved. Experiments have demonstrated that, when subjected to identical water pressure and opening conditions, the maximum permissible displacement of a dual sealing gasket can be enhanced by approximately 30% in comparison to a single sealing gasket.

Based on the aforementioned three sets of test results, it is evident that the dual seal gasket exhibits limited waterproof performance in comparison to the single seal gasket. The improvement rate ranges between 20% and 30%, indicating that the relationship between the two is not simply additive (1+1=2). The significance of a dual sealing gasket becomes apparent when there is a local water inrush from the outer sealing gasket of the lining.

4 CONCLUSIONS

The lining structure of the prefabricated station utilizes a grouting tenon joint, which incorporates a waterproof technical approach known as “two gaskets + one injection + one embedding”. The utilization

of double waterproof sealing gaskets involves the application of EPDM elastic sealing gasket as the primary waterproofing component, while composite water expansion rubber serves as the reinforced waterproofing element. The composite expansion rubber sealing gasket functions as the primary defence mechanism for the joint, with grouting and caulking serving as supplementary defence mechanisms for the joint.

Based on an analysis of the characteristics of prefabricated stations' structure, component manufacturing, and construction technology, as well as an examination of the factors influencing opening and dislocation, this study draws conclusions by considering experimental research on the waterproof performance of sealing gaskets and monitoring results from actual engineering applications:

(1) The waterproofing of prefabricated station structures differs from that of shield tunnels in terms of construction measures and control standards for joint opening and sealing gasket dislocation. Research findings indicate that an initial opening amount of 10mm and a dislocation amount of 5mm serve as appropriate indicators for effectively managing the waterproof performance of joints in prefabricated station structures.
(2) A solitary waterproof sealing gasket, featuring a 10mm opening and a 5mm displacement, exhibits the ability to withstand a water pressure of 1.0MPa. This performance meets the requirements for a station structure that is buried at a depth of 30m and is designed to resist 2-3 times the water head pressure. After a century of utilization, the material continues to exhibit a residual stress level of approximately 67%. Furthermore, it demonstrates the ability to withstand a water pressure of 0.6MPa and exhibits long-term resistance to water pressure.
(3) The double channel waterproof sealing gasket exhibits a relatively modest enhancement in waterproof performance when compared to the single channel sealing gasket, with an improvement rate ranging from 20% to 30%. Nevertheless, the significant advantages of the double channel sealing gasket become apparent when there is a local water inrush in the outer channel sealing gasket of the lining.
(4) The composite porous multi-groove sealing gasket, which exhibits a maximum compressive stress of 40kN/m when fully compressed, can serve as a benchmark for determining the assembled tensile load value of prefabricated structures.
(5) The influence of the displacement of the sealing gasket on the water pressure performance is comparatively less significant when compared to the joint opening. When the displacement is limited to less than one-third of the sealing gasket width, there is no significant decrease in water pressure performance. However, if the displacement exceeds half of the sealing gasket width, there is a significant reduction in water pressure resistance performance.
(6) Given that the waterproof sealing gasket is positioned within the joint, the attainment of accurate measurement and monitoring in practical engineering becomes challenging. When examining the surface dislocation standard that encompasses the dislocation standard of the sealing gasket, the design and performance evaluation of the waterproof sealing gasket can be regulated by considering the surface dislocation.
(7) From the analysis of the structural engineering of prefabricated stations in China, both those that have been completed and those currently under construction, it is evident that the absence of an external waterproof layer does not result in water leakage at the joints. The majority of longitudinal joints in the measured structure have a maximum opening that is consistently below 5mm. However, the longitudinal joint located on the arch top of the station reaches a maximum opening of 6mm. In terms of the measured circumferential seam, the maximum opening is generally controlled below 7mm, although there are some points that reach 8mm. The measured surface dislocation of the structure can be effectively controlled below 4mm, which demonstrates compliance with the joint waterproofing performance control standard.

ACKNOWLEDGMENTS

The authors would like to acknowledge the financial support from the National Key R&D Plan (Grant No. 2017YFB1201104) and Innovative Project of Beijing Urban Construction Group (Experimental Study on a New Prefabricated Underground Station Structure).

REFERENCES

Xiao X. W., 2021 Study on development strategy of engineering leakage prevention and control. Beijing: Department of Civil, Hydraulic and Architectural Engineering, Chinese Academy of Engineering.

Wu H. N., Shen S. L., Ma Y. H., et al, 2013. Investigation and analysis of leakage of Shanghai river crossing tunnel. Chinese Journal of Underground Space and Engineering, 9(03): 663.

Chen K., 2014. Prospects on new technologies of super-large diameter shield machine for Qiongzhou Strait Tunnel. Tunnel Construction, 34(7): 603.

Zhou W. B., 2004. Shield Tunnelling Technology. Beijing: China Architecture& Building Press.

Zhu Z. X., 2016. State of art and Developing Direction of Waterproofing Technology for Sealing Gasket of Shield Tunnel Segment Joints. Tunnel Construction, 2016, 36 (10): 1171.

GB/T51438-2021, 2021. Code for construction and acceptance of shield tunnelling method. China Architecture& Building Press, Beijing, China.

GB50108-2008, 2008. Technical Code for Waterproofing of Underground Engineering. China Planning Press, Beijing, China.

GB50157-2013, 2013. Code for design of Metro. China Architecture& Building Press.

GB/T51310-2018, 2018. Standard for construction of metro engineering. China Architecture& Building Press, Beijing, China.

Yang X. R., 2022. Research and Application of Prefabricated Structure Construction Technology for Metro Station. Tunnel Construction, 42(3): 345.

Tunnelling for a Better Life – Yan, Celestino, Thewes & Eberhardt (Eds)
© 2024 The Author(s), ISBN 978-1-032-80042-4
Open Access: www.taylorfrancis.com, CC BY-NC-ND 4.0 license

Innovative waterproofing system for shallow underground structures

Dmitry S. Konyukhov*, Tengiz E. Kobidze* & Oleg B. Krymov
Mosinzhproekt JSC, Moscow, Russia

ABSTRACT: One of the topical problem of underground construction is the protection of underground structures from water encroachment. The problem is based on the impossibility to apply traditional waterproofing materials for underground constructions (bituminous-polymer rolls, polymer sprayed compositions) on inaccessible exterior insulated surfaces of runway slabs and wall structures constructed in open pits without slots for backfilling. Before the erection of supporting structures, the waterproofing coating is laid on the accessible surfaces of the concrete preparation and "wall in the ground". This eliminates the adhesion of the waterproofing coating on the outer surface of the protected structures and results in the formation of a gap between the waterproofing and the protected structure. In the case of damage or defect of the waterproofing coating, the seeping ground waters migrate uncontrollably along the formed joint and penetrate into the building. The report presents the results of scientific and practical work performed in the Mosinzhproekt JSC to eliminate the mentioned problem, including the development of design and technological solutions using the methods of voile injection and manufacture of a two-layer seamless waterproofing membrane in the building environment as well as making changes to the effective regulatory and technical documents of the Russian Federation.

Keywords: repair system, tunnel, waterproofing, Tunnelling, Metropolitan, Underground Space, Waterproofing, Underground Construction, Ground waters)

1 INTRODUCTION

Among the actual problems of modern tunnelling, an important place is occupied by the prevention or elimination of flooding of underground transport structures during their construction by open and semi-closed methods (hereinafter we will refer to all underground structures as such). In this case, waterproofing protection is completely excluded, which results in the loss of water tightness and maintainability of structures, and violates the conditions of safe operation of such structures.

The reason for this problem is the design limitations in the use of such traditional for underground construction waterproofing materials as bitumen-polymer spreading roll materials and sprayed polymer compositions based on bitumen-polymer composites, polyuria, methylmethacrylate resin – the most widespread and supported by the regulatory framework (CS 120.13330.2012, 2012; CS 122.13330.2012, 2012; PS NOSTROI 2.27.123-2013, 2013).

In accordance with the requirements of the normative document of the Russian Federation (PS NOSTROI 2.27.123-2013, 2013) reliable waterproofing of underground structures is provided by laying a coating of spreading and spraying materials directly on the building envelope from the outside (from the side of groundwater exposure). But adhesive bonding of these materials is achieved only with the surface of the aged ("old") concrete structure, which must be available for such an operation. This can only be enclosing walls built with backfill slots and pavement slabs (Figure 1).

In the case of tray slabs of any kind, walls constructed without backfill slots and press walls for load-bearing 'diaphragm wall', it is necessary (CS 120.13330.2012, 2012; CS 122.13330.2012, 2012):

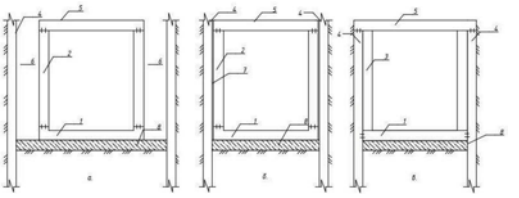

Figure 1. Variety of methods of construction of underground structures made of cast reinforced concrete: *a* – cut and cover method with backfill slots; *b* – cut and cover method without backfill slots; *c* – cut and cover and semi-closed-cut method with slab (cover) spacing discs, with a load-bearing 'diaphragm wall'; *1* – buckle (foundation) slab; *2* – bearing wall; *3* – pressure wall; *4* – excavation wall (in part *b* – bearing structure); *5* – floor slab (cover); *6* – cavities for backfilling; *7* – sliding plane (plane of mutual shift of the walls); *8* – concrete foundation mattress.

*Corresponding author: konuhovds@mosinzhproekt.ru; koba1948@mail.ru

DOI: 10.1201/9781003495505-340

- for the waterproofing of the flume slab, the waterproofing coating shall be placed on the concrete preparation;
- when using the technology of a load-bearing 'diaphragm wall' or without backfill slots, the waterproofing shall be laid on the surface of the 'diaphragm wall', and the 'pressure' or permanent wall shall be tightly pressed against the 'diaphragm wall' to absorb the expected hydrostatic pressure.

  In practice, based on the design standards in question, waterproofing protection of building envelopes on the groundwater side is provided. However, due to the lack of adhesive bonding with the insulated surface, the waterproofing coating is not able to localise seeping groundwater within the through damage and prevent uncontrolled migration of groundwater across the entire outer surface of the protected structure in case of even a single filtration damage to the coating or techno-coating. Experience shows that this leads to an unrecoverable emergency situation, in particular:
- to complete watering of the outer surface of the insulated structure and penetration of groundwater into the structure through the filtering defects of concrete and the reinforced concrete structure itself (cracks, voids, weakened and highly porous areas of concrete, technological and expansion joints, etc.) in the form of leaks of different intensity and wet spots on the inner surfaces of the structure (Figure 2);

Figure 2. Example of water penetration in a monolithic reinforced concrete tunnel lining in the case of open works without backfill slots and with waterproofing based on traditional technological schemes and materials of adhesive fixing to the concrete foundation.

- loss of repairability of the protected structure, as sealing of one or several filtration defects (possible at continuous adhesive connection of waterproofing with concrete base) leads to an increase of hydrostatic pressure of groundwater; the consequence of this is activation of "dormant" filtration defects and appearance of new water spots on other parts of the surface of the watered structure.

To exclude the possibility of such emergency situations, contradictions in the rules of design and construction of waterproofing were eliminated. At the same time, amendments were made to the normative and technical documents of the Russian Federation. These documents establish unified rules for reliable and maintainable waterproofing of underground structures and are based on the need to lay the waterproofing coating by adhesive bonding directly on the outer surface of the protected structures regardless of the availability of access to the isolated surface.

As a result, the use of traditional adhesive bonding materials and technological schemes of their laying for waterproofing of enclosing structures with no access to the external surface remains a possible, but not mandatory technical solution, leading to the arrangement of unreliable and unrepairable waterproofing. In this case, there is an urgent need to introduce into practice waterproofing materials of a new generation that meet the updated regulatory requirements.

2 METHODS AND MATERIALS

The Russian market offers a number of innovative waterproofing materials of domestic and foreign production, providing continuous adhesive bond to freshly laid concrete of protected structures of underground structures without access to the external surface. These are tray slabs, wall structures constructed without slots for backfilling of soil and a pressure wall for a bearing 'diaphragm wall' (Figure 3).

These materials include the following:

1. An origina waterpro-ofing system based on the use of an innovative waterproofing composite material developed by the authors (Underground construction, 2015; Underground construction, 2016) and combining the technical properties of two initial materials, which were adopted as:
- sprayed waterproofing polymer compositions with 'two-sided' adhesion, in particular, ethylene vinyl acetate polymer and bitumen-polymer composite of Flexigum brand, providing normative adhesion (over 0.5 MPa according to CS 120.13330.2012) not only with the base of 'old concrete' covered with a layer of sprayed polymer, but also with the external surface of concrete laid as mortar on the finished waterproofing coating. The ability of durable adhesion of bitumen-polymer waterproofing systems to concrete is confirmed by the traditional character of their use in construction, and EVA-polymer – by many years of experience in the construction of multi-layer monolithic transport tunnels of the closed method of works (Kobidze, 2021);

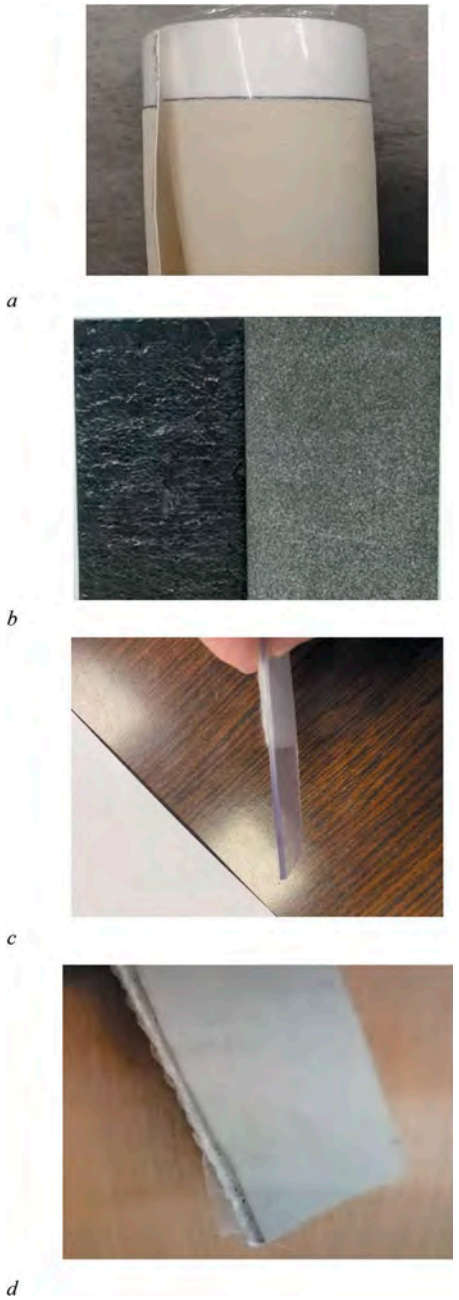

Figure 3. Waterproofing sheet materials (membranes) with adhesion to freshly laid concrete: a – factory-made waterproofing three-layer roll with self-adhesive edges, with surface adhesion layer, including sand sprinkling; b – two-layer roll based on polyvinylchloride membrane with 'implanted' surface layer made of fibre material FiberTex; c – roll based on bitumen-polymer composite (front side with sand sprinkle on the right side); d – seamless two-layer waterproofing coating, produced in construction conditions by applying a surface adhesion layer of sprayed compositions with two-sided adhesion to geotextile reinforcing substrate (base) with an outer polyethylene coating.

- geotextile nonwoven needle-punched material with a density of 250-500 g/m2 (GOST R 53225-2008, 2008), used as a reinforcing and strengthening element of the polymer coating, as well as the underlying fabric-base for the manufacture of two-layer seamless waterproofing coating (polymer membrane with a base) in construction conditions by spraying a layer of waterproofing composition with a thickness of 4-6 mm on the ready-made geotextile underlying fabric.

Application of sprayed composition with two-sided adhesion and its modification in the form of a two-layer polymer seamless membrane with reinforcing base, as well as the possibility of directional regulation of physical and mechanical properties of the waterproofing coating with reinforcing fabric depending on the problem to be solved provide:

- the possibility of using the waterproofing coating without a protective layer of fine-grained concrete when binding the reinforcement frame and subsequent concreting of the trough slab by hardening the surface layer of the coating with reinforcing geotextile fabric (Figures 4 and 5);
- speeding up the process of waterproofing works, reducing their cost and guaranteeing a continuous adhesive bond of the waterproofing coating with the inaccessible outer surface of the trough slab;
- adhesive bonding of the sprayed polymer layer of the two-layer sprayed membrane with the hard-to-reach outer surface of the walls of structures built without backfill slots;
- safety of such coating on the wall surface in case of subsidence of the underground structure, achieved as a result of free suspension of the

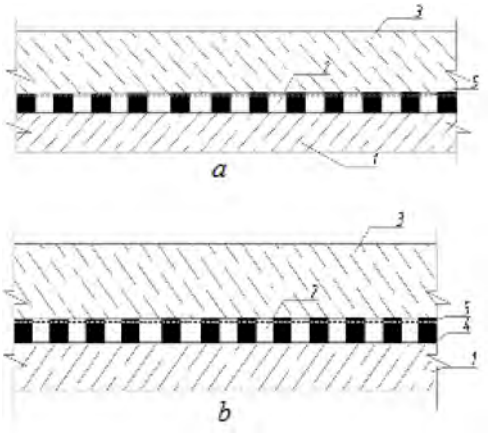

Figure 4. Seamless waterproofing of a tray (foundation) slab with sprayed compounds with double-sided adhesion: a – without underlying layer; b – with underlying layer of nonwoven geotextile; 1 – concrete preparation; 2 – waterproofing layer; 3 – tray slab; 4 – underlying layer of nonwoven geotextile; 5 – nonwoven geotextile reinforcing the surface layer of the waterproofing coating.

a

b

Figure 5. Binding of reinforcement cage over sprayed waterproofing coating with two-sided adhesion with reinforced surface layer of geotextile fabric and without protective layer of fine-grained concrete: a – spraying of waterproofing material with two-sided adhesion on the inner surface of the lining and installation of reinforcing frame; b – binding of reinforcing frame over sprayed waterproofing coating with two-sided adhesion with reinforced surface layer made of geotextile fabric and without protective layer made of fine-grained concrete.

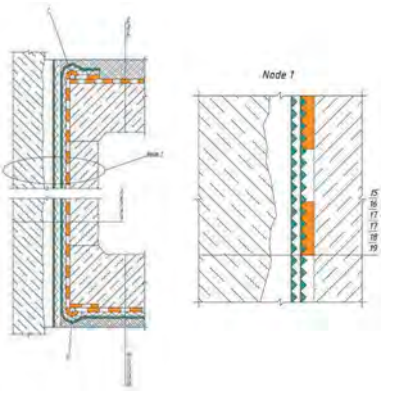

Figure 6. Waterproofing with two-layer sprayed waterproofing coatings with adhesion to freshly laid concrete of the monolithic wall construction of an underground structure without backfill cavities (Node 1): 1 – compensating loop; 2 – protective layer of concrete on mesh; 3 – sprayed waterproofing coating with primary and secondary adhesion; 4 – reinforced concrete floor; 5 – ditch sheeting – 'diaphragm wall'; 6, 16 – levelling layer (if necessary); 7 – two layers of geocomposite material; 8 – waterproofing coating with primary and secondary adhesion applied to the geotextile of the geocomposite material; 9 – reinforced concrete wall; 10 – concrete buckle plate; 11 – protective sand cement screed; 12 – waterproofing coating with primary and secondary adhesion applied to the geotextile of the geocomposite material; sprayed waterproofing coating with primary and secondary adhesion; 13 – geocomposite material; 14 – concrete bedding; 15 – ditch sheeting - 'diaphragm wall'; 17 – geocomposite material (polyethylene film + geotextile, facing a layer of polyethylene film to the 'diaphragm wall'); 18 – sprayed waterproofing coating with primary and secondary adhesion applied to a geotextile geocomposite material; 19 – concrete load bearing wall.

two-layer fabric on the "membrane wall"; in this case, the waterproofing layer of the fabric is facing towards the erected wall, and the strong reinforcing geotextile backing is sliding surface towards the "membrane wall" (Figure 6);

- arrangement of reliable waterproof three-layer wall construction of "sandwich" type by applying a waterproofing layer of sprayed waterproofing with double-sided adhesion to the levelled surface of the bearing "diaphragm wall"; subsequent erection of a "pressure" wall made of monolithic or sprayed concrete in the construction of underground structures using the "diaphragm wall" technology by "top-down" and "bottom-up" methods (Figure 7 and 8);
- reliability of waterproofing, safety of protected underground structures and their maintainability as a result of:

a) adhesion fixing of seamless waterproofing coating directly on external surfaces of protected structures with and without access to the external surface, in accordance with the requirements of CS 120.13330.2012;

b) local character of water penetrations due to continuous adhesive bonding of waterproofing with concrete base. Under these conditions, groundwater penetration into the underground structure is possible when the location of the through damage to the waterproofing coating or process joint and the filtering defect of the enclosing structure coincide. The low probability of such a coincidence increases the operational reliability and safety of underground structures. However, localisation of groundwater in the zone of coating damage and its migration through the filtering defect of concrete simplifies the establishment of a place for local and relatively low-cost work to restore water tightness of the structure by injecting a sealing compound into the filtering defect of concrete.

Technical characteristics of materials and design and technological solutions for the developed

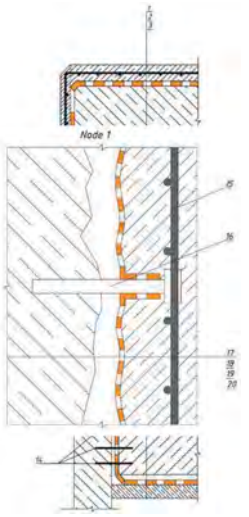

Figure 7. Waterproofing the load-bearing wall of an underground 'diaphragm wall' structure with sprayed polymer compound with two-sided adhesion: 1 – protective layer of concrete on mesh; 2, 7, 12 – sprayed waterproofing coating with primary and secondary adhesion; 3 – reinforced concrete floor; 4 – free length of 'diaphragm wall' reinforcement; 5 – load-bearing 'diaphragm wall'; 6 – levelling layer (if necessary); 8 – pressed wall of concrete on mesh; 9 – anchoring the pressure wall; 10 – buckle plate; 11 – protective sand cement screed; 13 – concrete bedding; 14 – anchoring the buckle plate; 15 – steel mesh; 16 – steel anchor; 17 – load bearing 'diaphragm wall'; 18 – levelling/smoothing layer (if necessary); 19 – sprayed waterproofing coating with primary and secondary adhesion; 20 – pressed wall on mesh.

Figure 8. Experimental stand. Arrangement of the 'pie' of composite waterproof load-bearing 'diaphragm wall' at the stage-by-stage construction of two-layer concrete structure of 'sandwich' type with a middle waterproofing layer with double-sided adhesion: from left to right – model of trench 'diaphragm wall'; levelling layer with anchor releases; sprayed waterproofing layer with double-sided adhesion; reinforcing mesh, sprayed concrete layer.

waterproofing system under construction conditions were confirmed during bench tests and recommended for pilot application at the Moscow Metro facilities.

2. A number of Russian companies act as suppliers of foreign roll waterproofing polymer membranes with the ability to provide adhesive bonding to the inaccessible external surface of protected structures of underground structures. These materials are a polymer with thickness from 2 to 4.5 mm (depending on the raw material – polyethylene, polyvinyl chloride or bitumen-polymer composite, respectively) with a special thin and hardened surface layer that provides:
   – adhesive adhesion (over 0.5 MPa) of the waterproofing coating with the surface of freshly placed concrete of protected reinforced concrete structures erected without access to the external surface;
   – refusal to install a protective layer of waterproofing made of fine-grained concrete and performance of works on binding of reinforcing frame with subsequent concreting of the trough slab immediately after laying of the waterproofing sheet.

Waterproofing coating of the above materials is made by laying rolls of 10-15 cm overlap and sealing them with the formation of technological joints (Figure 9).

Factory readiness guarantees the consistency of membrane quality characteristics, significantly accelerates waterproofing and general construction works, as well as reduces labour and material and financial costs for their implementation, but the device of technological joints requires their qualitative

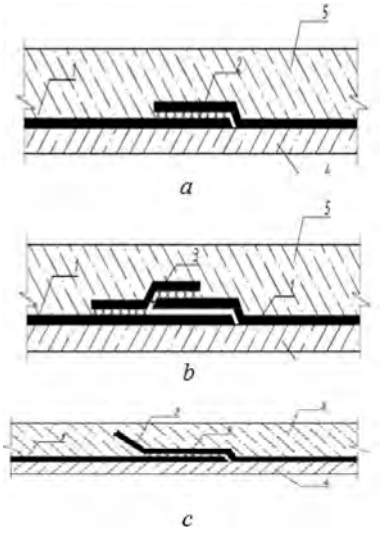

Figure 9. Waterproofing of a buckle plate (base slab) using prefabricated three-ply sheet membranes with 'free' laying and adhesion to freshly-formed concrete. Laying scheme of three-ply sheet membranes with overlapping self-adhesive strips of longitudinal edges (a), cross edges with overlapping adhesive sheets (b) or bitumen-polymer-based membrane Kolfen BSH with overlapping longitudinal edges (c), overlapping of cross edges Kolfen BSH is performed only with overlapping edges for welding: 1 – three-ply sheet membrane; 2 – technological seam of self-adhesive strips of longitudinal edges; 3 – overlapping adhesive sheet; 4 – base concrete; 5 – buckle plate (base slab).

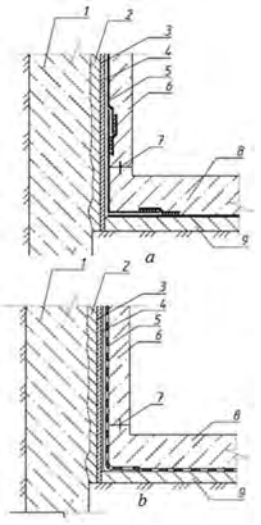

Figure 10. Waterproofing of structures without slots for backfilling: *a* – using factory-made membranes; *b* – using sheet waterproofing with a surface layer of sprayed compositions with two-sided adhesion; *1* – enclosing 'diaphragm wall'; *2* – levelling layer of fine-grained concrete or false wall; *3* – layer of geotextile fabric, expanded polystyrene boards or profiled membranes; *4* – sliding plane; *5* – waterproofing coating; *6* – permanent wall; *7* – waterproof core; *8* – trough slab; *9* – base concrete.

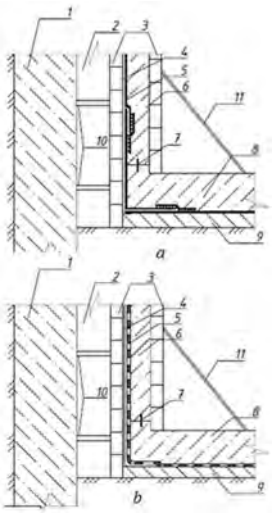

Figure 11. Waterproofing of structures with slots for backfilling: a – waterproofing coating from factory ready rolls; b – waterproofing coating from sprayed compositions; 1 – excavation fence; 2 – slots; 3 – external and internal formwork boards; 4 – geotextile fabric substrate, 5 – waterproofing coating; 6 – monolithic wall structure; 7 – hydrotrench; 8 – tray slab; 9 – base concrete; 10 – telescopic spindles; 11 – frame for one-sided concreting.

performance to ensure the operational reliability of the waterproofing coating.

Figures 10 and 11 show the schemes of waterproofing for underground structures, created without slots for backfilling and with such slots, respectively, with the use of new generation materials under consideration, characterised by the ability of adhesive bonding with freshly laid concrete.

3 CONCLUSIONS

The application of 'pre-installed' waterproofing systems (Kobidze) in underground construction is characterised by the fact that it:

1. has no alternative for the application of adhesion bonded waterproofing coating directly onto insulated exterior surfaces that are not accessible when conventional waterproofing systems are installed;
2. eliminates the need to allocate time for ageing and curing of the concrete base, as well as thorough preparation of its surface for the application of waterproofing coating of adhesive fixing and its protection by a layer of fine-grained concrete before concreting the foundation (trough) slab;
3. accelerates the process and reduces the cost of general construction and waterproofing works, eliminates the possibility of continuous flooding of underground structures, increases the reliability, durability and maintainability of waterproofing coatings and safety of underground structures of open and semi-closed construction methods.

REFERENCES

CS 120.13330.2012. Metropolitans (with Amendments No. 1-4). Updated edition of SNiP 32- 02-2003.

CS 122.13330.2012. Railway and road tunnels (with Modification No. 1). Updated version of SNiP 32-04-97.

CC NOSTROI 2.27.123-2013. Waterproofing of transport tunnels and subways constructed by open cut. Rules of design, production and acceptance of works.

Underground construction, 2015. Patent RU162638U1 16.12.2015.

Underground construction, 2016. Patent RU164721U1 14.01.2016.

Kobidze, T.E., Konyukhov, D.S., 2021. Causes of watering of tunnel structures and innovative 'pre-installed' waterproofing systems for its elimination. *Metro and Tunnels*. No 1. Pp. 18–23.

GOST P 53225-2008, 2008. National Standard of the Russian Federation. Geotextile materials.

CC 75-03, 2023. Mosinzhproekt JSC. Waterproofing of underground constructions of subways for transport purposes, erected by open and semi-closed methods of works. Rules of design and workmanship.

Tunnelling for a Better Life – Yan, Celestino, Thewes & Eberhardt (Eds)
© 2024 The Author(s), ISBN 978-1-032-80042-4
Open Access: www.taylorfrancis.com, CC BY-NC-ND 4.0 license

Tunnel drainage system and the possibility of non-destructive remediation

Juraj Ortuta* & Viktor Tóth
Amberg Engineering Slovakia, s.r.o., Bratislava, Slovakia

ABSTRACT: Tunnels are an important part of our infrastructure. The performed inspections and subsequent analysis show that currently a large percentage of roads are damaged and require remediation work. Due to the high increase in mobility and thus the use of road networks, this is associated with potential risk and the possibility of systematic fatigue damage. Faults in the drainage system are often one of the main reasons that can lead to damage to roads and reduced traffic safety. Therefore, preventive measures can improve the quality and durability of these structures in the long run. However, the issue is insufficiently addressed. In the construction sector, there is missing professional literature, proven technologies, and finally a wider market with an offer of remediation work for drainage systems. Tunnels and, in general, all underground structures are costly and time-consuming. The focus of increased attention already during the design on the protection of the tunnel against water and the subsequent design of drainage with the entire drainage system is more than on the spot. The article discusses the possibility of non-destructive remediation measures to ensure the safe drainage of groundwater using the tunnel drainage system.

Keywords: Drainage, Technical design, Underground water

1 INTRODUCTION

Tunnels, and all underground structures in general, are financially and time consuming. Focusing increased attention during the design phase on the water protection of the tunnel and the subsequent design of the drainage with the entire drainage system is more than appropriate. In the event of design errors in the form of unfinished details or imperfect construction work caused by the contractor, negative consequences can arise, the direct impact of which is the remediation work during the actual execution of the work or even during the actual use. During the operation of the work, the defects become more widespread, and the rehabilitation of the drainage system becomes necessary.

Groundwater levels, inflows and water properties in the rock environment are essential input parameters for any tunnel protection design. External requirements such as the degree of protection and, more recently, the requirement not to deplete the water in the rock environment are also crucial at this point.

The design of tunnel drainage needs to address waterproofing, proper drainage system as well as roadway drainage. Their implementation is about achieving a completely impermeable structure, where neither leakage nor a disproportionate increase in hydrostatic pressure is permissible.

The drainage system is used to capture seepage water, groundwater, and water during the implementation of linear constructions. The distribution of drainage profiles along the Višňove tunnel was determined on the basis of the hydrogeological conditions of the massif, which were investigated during the tunnelling.

Currently, the largest works on the Višňové Tunnel are underway in Slovakia and therefore we would like to give a few examples of damage to the drainage system and possible remediation recommendations. We are aware that the situation in this tunnel is very sensitive, but the problem described is far from being related only to this tunnel, but it is a global problem for both completed, historic tunnels and tunnels under construction.

2 WATER AS A (DIS)FRIEND

During the construction, as well as during the actual use of tunnel structures, we very often encounter the problem of water in the structures as an undesirable element. A detailed investigation of the surface and subsurface hydrology should therefore be carried out before and during construction. If the negative effects of water are not of a temporary nature and persist during the lifetime of the tunnel, they become an obstacle to the operation and maintenance of the

*Corresponding author: jortuta@amberg.sk

DOI: 10.1201/9781003495505-341

tunnel itself. In coined tunnels there is the problem of seepage water, which accumulates in faulted tectonic rocks and creates aquifer zones and can also have a buoyancy effect in places.

The transport of seepage water to the tunnel structure is certain and there the water degrades the tunnel lining by its long-term action. The increased pH of groundwater in contact with alkaline substances (monolithic concrete, shotcrete, or cement grouting) can cause lime to be expelled. Contact with water saturated with carbon dioxide (aggressive water) causes calcium hydroxide to leach out of the concrete and calcium supersaturated water to form, which then forms solid deposits in the drainage systems Figure 1. (This effect is more common in old tunnels with outdated drainage systems.)

Another problem is freezing, which occurs at portal points and in winter operations up to a depth of several tens of metres, causing subsequent weathering of the rock and the tunnel structure itself. The impact of water pressure and the cyclic freezing of the tunnel results in a gradual erosion of stability, possibly leading to deformation and even destruction of the structure, which can endanger human lives and cause considerable financial damage to property. The necessary step is then to close the tunnel and undergo rehabilitation of the systems.

Current trends in infrastructure (especially tunnelling) vary from country to country. Some countries have set regulations or have specific regulations and standards in place for tunnel drainage, while others have no regulations.

In Slovakia, TP 04/2015 Protection of tunnels against water and drainage of tunnels and TKP Part 26 Tunnels are currently in force. These documents indicate to some extent the method of implementation of drainage systems but are not intended to address more demanding hydrogeological conditions.

Figure 1. Water seepage through cracks in the lining.

3 TUNNEL VIŠŇOVE

In the following sections, however, we would like to focus on the drainage system of the tunnels and their rehabilitation. As mentioned earlier, the topicality of the topic is not only related to the upcoming tunnels, but also to the historic tunnels and, of course, to tunnels where construction works are in progress and the back drainage has been damaged.

Currently, the largest works on the Višňové Tunnel are underway in Slovakia and therefore we would like to give a few examples of damage to the drainage system and possible remediation recommendations. We are aware that the situation in this tunnel is very sensitive, but the problem described is far from being related only to this tunnel, but it is a global problem for both completed, historic tunnels and tunnels under construction.

The Višňove tunnel is located on the territory of the Little Fatra mountain range. The Little Fatra is a 55km long mountain range in the northwestern part of Slovakia, extending southeast from Zilina, following the main arc of the Western Carpathians. The main ridge runs from southwest to northeast. The centre of the mountain range is divided by the Vah Riverbed. At this place, the river created a 12km long narrow valley known as Strečnianska Tiesňava. The altitude of the mountain range along the route of the tunnel being designed as well as the already built tunnel ranges from 800 to 1300m.

The drainage system is used to capture seepage water, groundwater, and water during the implementation of linear constructions. The distribution of drainage profiles along the Višňove tunnel was determined based on the hydrogeological conditions of the massif, which were investigated during the tunnelling. During the excavation of the exploratory tunnel, the groundwater inflows were stabilised at the interface between the carbonate rocks and the crystalline bedrock (stationing approx. 2400 m) at 10 -20 l/s (in the karst system it depends on the intensity of atmospheric precipitation). After breaching the two sections of the adit, the total amount of water flowing to the eastern portal is 150 -220 l/s. The conditions during tunnelling were mainly influenced by changes in hydrogeological conditions. Given the permanent drainage effect of the exploration tunnel, smaller inflows were expected. The strongest water inflows were expected at the contact of the Mesozoic fault zone between Mesozoic and crystalline rocks. It was calculated that depending on the rate of atmospheric precipitation, inflows of 20-100 l/s would occur. In other parts, short-term and local inflows of 0.2 -0.3 l/s were assumed. However, local, and isolated inflows to open karst systems as well as discontinuities and fault zones that were not registered during the survey were not excluded. In crystalline rocks, large inflows to the tunnel tubes were expected in the range of 10 to 20 l/s in individual sections (Figure2 and 3). The strongest inflows were already in the first phase of coining and decreased over time to the current level.

Figure 2. Water in main collector.

Figure 3. Damming and groundwater pumping. Preparation for reconstruction.

4 DRAINAGE SYSTEM AS A CRITICAL PART OF THE TUNNEL

The drainage system of the tunnel secures removal of seepage water from longitudinal drainage pipes behind the extrados of the lining and from the roadway bed. From the point of view of the drainage system concept, two systems are used, i.e.:

- drainage system without a main collector,
- drainage system using a main collector.

The drainage system without a main collector is used mainly in shorter and less water-yielding tunnels, where designing external drainage pipes with a sufficient capacity, without negative effects on the design of the lining, is not a problem.

The drainage system using a main collector is used for longer tunnels and for heavily water-yielding tunnels, where the use of external side drains is not effective.

If possible, the use of the drainage system without a main collector is preferred. At this system, locations of the origination of defects in the roadway (at shafts and manholes) and subsequently the necessity for regular repairing them are significantly reduced.

The diameter of the drainage pipes is determined by a hydrotechnical calculation taking into consideration the amount of water flowing from the rock massif to the tunnel. The diameter of the tunnel side drainage pipeline in the meaning of current regulations must be 200mm as a minimum for the drainage system using a main collector and 250mm for drainage systems without a main collector. The diameter of the drainage pipeline in the other parts of the construction with smaller profiles, for example in cross passages, must be 150mm as a minimum. The diameter of the linking pipeline (transverse linking of side drains with the main collector) must be 200mm as a minimum. The diameter of the pipeline draining the roadway bed must be 150mm as a minimum.

The diameter of the main collector of seepage water must be designed with respect to the amount of water flowing into the tunnel from the surrounding massif. The main collector can also fulfil the function of the roadway bed drainage.

5 CHANGE IN THE CONCEPT OF THE DRAINAGE SYSTEM

The decision on the change of the function of the original exploratory gallery was made before the start of the construction of the Višňove tunnel proper. The original exploratory gallery was to come to an end by the excavation of the southern tunnel tube. The decision to change the function of the original exploratory gallery to the function of a drainage gallery was made with respect to the permanently high rate of water inflow into the exploratory gallery and the necessity for a design of the drainage system for the Višňove tunnel using a main collector. The drainage gallery assumed the function of the main drainage collector in the space of the tunnel tubes, which fact allowed for excluding the construction of the main drainage collector in the space of the tunnel tubes. As a result of this change, the directional and vertical alignment of both tunnel tubes and the drainage gallery had to be completely redesigned in both portal sections. The alignment of the southern tunnel tube was shifted more southward, so that the original part of the drainage gallery ran approximately in the centre between the tunnel tubes. The vertical alignment of the tunnel tubes was shifted higher, so that the tunnel tubes were located above the drainage gallery along the entire length of the tunnel, and thus the gravity removal of water from the tunnel tubes to the drainage gallery was ensured. After the portal sections of the gallery with the newly designed alignment were broken through, the original portal sections were filled with backfill concrete, or they came to an end by the breakthrough of the southern tunnel tube (Figure 4, 5).

Drainage boreholes ca 300mm in diameter, outfitted with DN 250mm sewerage tubes, in some areas DN 200mm, were carried out for transferring water from the external drainage of the tunnel tubes to the drainage gallery. The drainage boreholes in the

tunnel tubes are in drainage cleaning niches and transverse linking of the cleaning manholes of the drainage under the roadway is carried out in the locations of the boreholes as a standard.

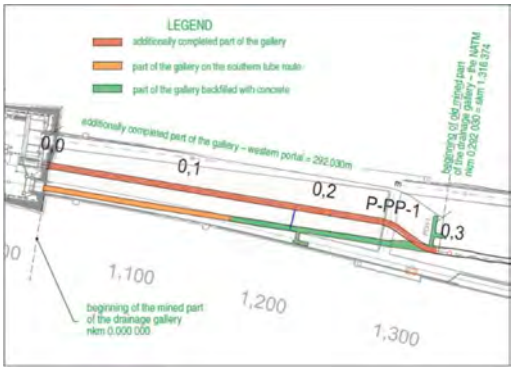

Figure 4. Plan of the portal section of gallery at the western portal.

6 TECHNICAL DESIGN OF THE DRAINAGE GALLERY

The drainage gallery of the Višňove tunnel is located between the northern and southern tunnel tubes along the entire length of the tunnel. It is used as the main collector of the drainage system of the Višňove tunnel and for transferring groundwater from the external side of the drainage of the tunnel tubes to the area of the Višňove tunnel portals. The drainage gallery is formed by four sections, depending on the tunnelling method used and the period in which it the given part was excavated:

1) completion of the part of the drainage gallery from the western portal; the NATM method; section 292.03m long,
2) the original part of the exploratory gallery; the NATM method; section 2799.78m long,
3) the original part of the exploratory gallery; the NATM method; section 3800.22m long,
4) the newly built part of the drainage gallery from the eastern portal; the NATM method; section 554.72m long.

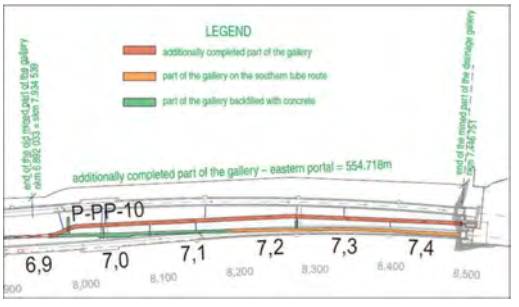

Figure 5. Plan of the portal section of gallery at the eastern portal.

The total length of the gallery amounts to 7446.75m. A permanent extraction points for supplying the fi re water tank will be provided in the drainage gallery. There are 10 vertical service entrances for the maintenance of the tunnel leading to cross passages passable for vehicles (in the locations of emergency lay-bys) and, in the space of joining the drainage boreholes, drainage niches, in which the drainage boreholes are terminated so that they do not extend into the gallery profile, are carried out.

7 DIRECTIONAL AND GRADIENT RELATED CONDITIONS

In the original part, the gallery roughly follows the horizontal and vertical alignment of the tunnel tubes. In the newly built parts, its horizontal alignment is adapted so that the ends at the portals is between the tunnel tubes and the vertical alignment does not collide with the cross passages located closest to the portals.

The longitudinal gradient of the drainage gallery is variable, from 0.1% to 9%. The longitudinal gradient in a major part of the gallery is ca 2.5%. The highest point of the gallery is at chainage km 0.580 83.

The 1.8m wide and 2.2m high drainage gallery cross-section passable for vehicles is designed. The internal shape varies depending on the tunnelling method as follows:

a) The original part of the exploratory gallery – section driven using a TBM: circular profile with radius of 1.55m.
b) The original part of the exploratory gallery – section driven using the NATM: the profile with double-radius (1.75–2.4m).
c) The newly built part of the drainage gallery – section driven using the NATM (Figure 6); profile with double-radius (1.675–2.325m).

A drainage trough with various profiles, depending on the gallery section along which groundwater is led to the portal areas, lies on the drainage gallery centreline.

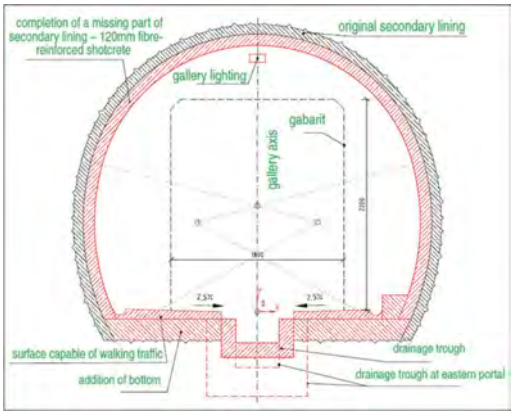

Figure 6. Gallery cross-section – portal sections.

7.1 *Mined part of the gallery structure*

The structure of the mined part of the drainage gallery consists of a double-layer lining with an intermediate drainage and insulation layer. Specifications of the concrete mixtures used differ depending on the period in which the particular part of the structure was built and the standards current in the given period of time. The secondary lining of the drainage gallery is formed by C30/37 grade shotcrete. The secondary lining is applied only in the gallery sections with unfavourable geological conditions and in the newly built portal sections of the gallery. An open waterproofing system is designed for the protection of the drainage gallery against groundwater. The waterproofing consists of a 500mm wide dimpled sheet membrane, which is installed locally, in locations of groundwater inflows through the primary lining. The concentrated groundwater inflows are directed through a short drainage borehole, through a flexible hose to the drainage trough in the gallery bottom.

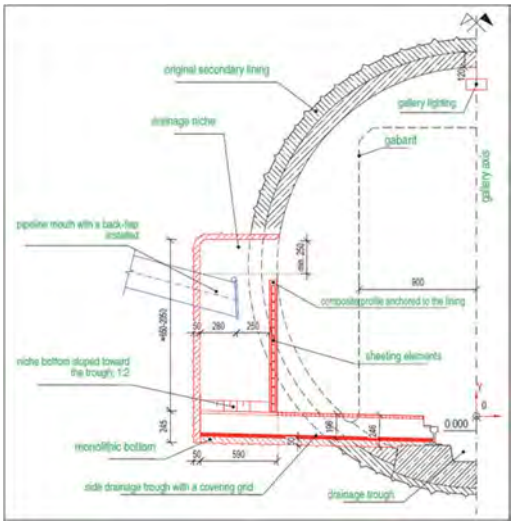

Figure 7. Drainage niche – cross-section.

7.2 *Drainage of the gallery*

In the centre of the bottom, there is a drainage trough with variable cross-section, depending on the gallery section along which groundwater is directed to the portal areas. There, in the cut-and-cover block of the gallery, it is connected to the tunnel drainage shaft.

Local inflows in the gallery are directed to the drainage trough by a collecting system. This system consists of short drainage boreholes, which are carried out in the locations of concentrated inflows, and flexible hoses, which are installed in the lining and lead through the bottom to the drainage trough.

Drainage niches (Figure 7) are designed for connecting the drainage boreholes collecting water from the external tunnel drainage. The niche is 550mm wide as a minimum (Figure 9). There are 62 boreholes between the tunnel and the gallery carried out from the northern tube and 64 from the southern tube. The net height of the niche is adapted separately to each drainage borehole, depending on the level of the connection of the borehole in the drainage gallery. The minimum net depth of the niches is equal to 590mm in the widest location of the gallery. A back-fl ap is installed on the borehole mouth. It prevents the overpressure of air to the external tunnel drainage during ventilation of the drainage gallery. A trough made of precast components is in the bottom of the niche. It is covered by a grating with minimum loading class B125 (part of the pre-cast trough), which is connected to the main drainage trough (Figure 8, 10). The niches are marked by serial numbers, the side of the drainage gallery on which the niche is found, and a complementary marking of the tunnel tube block from which the drainage borehole is carried out.

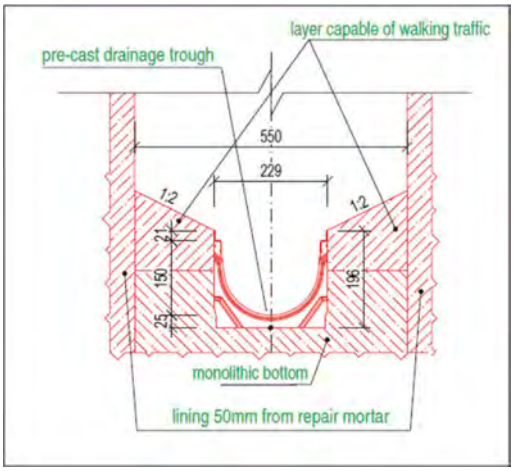

Figure 8. Drainage niche – side drainage trough in drainage niche.

7.3 *Service entrances to cross passages*

With respect to the client´s requirements, entrances in the form of chimneys passable for persons were designed between cross passages and the drainage gallery. In this way, employees of the operation services will be able to enter the cross passages without the necessity for entering the tunnel tubes (Figure 11).

The net cross-section diameter of the passages is 800mm as a minimum in the part of the cross passage bottom and 1400mm in the section passing through the rock massif and the drainage gallery. They are outfitted with composite pipes providing a sacrif cial formwork, and the space between the formwork and the excavation is filled with C30/37

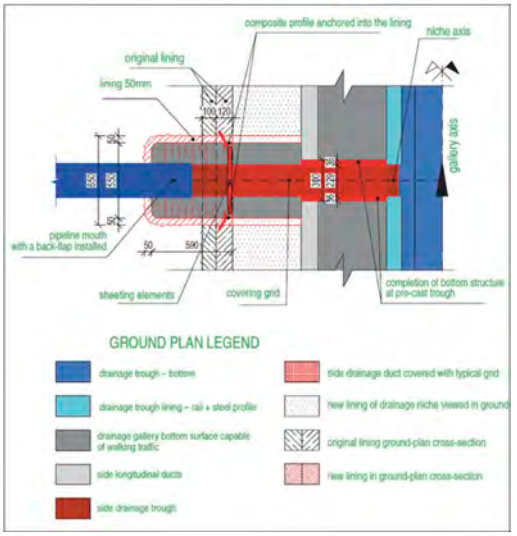

Figure 9. Drainage niche – ground plan.

Figure 10. Completed drainage niche.

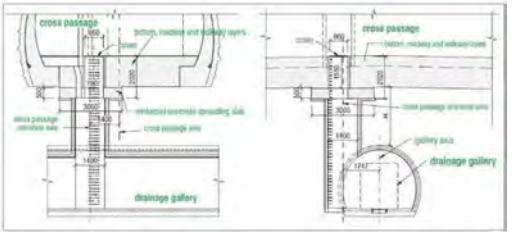

Figure 11. Service entrance passable for persons – longitudinal section and cross-section through the gallery in the location of the service entrance passable for persons.

grade concrete. The entrances are equipped with composite ladders and are closed by an airtight, fi re resistant cover.

7.4 *Closing cross passages and excavation stubs*

The cross passages were considered in the original exploratory gallery design as transverse connections between the southern and northern tubes. With respect to the change in the function of the gallery to the drainage gallery and the changes in the horizontal and vertical alignment of the tunnel tubes, their originally planned function will not be applied, and it will be necessary to close them partially of completely. The cross passages and excavation stubs are closed at the minimum length of 3m from the right-hand wall of the northern tunnel tube (Figure 12).

In the case of a defect of the lining or the bottom of the cross passages, some cross passages were completely closed. The closing involved filling of the space of the cross passages and excavation stubs with cinder cement grout with minimum compressive strength of 10MPa. The unfilled spaces of the cross passages could be used in the future as rooms for storing materials and equipment for the maintenance of the gallery.

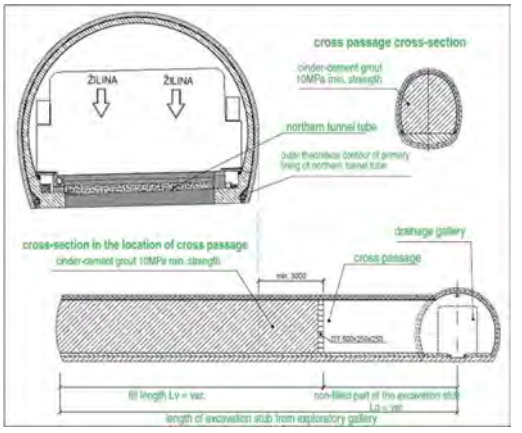

Figure 12. Closing of cross passages.

7.5 *Intersections with cross passages No. 25, 26 and 27*

The vertical alignment of the tunnel route was designed with the aim of minimising possible single-level intersections with cross passages and the existing drainage gallery. A 6.0m difference between the levels of the tunnel alignment and the alignment of the drainage gallery was designed. The level difference H between the bottom of each cross passage and the vault of the drainage gallery depends on the type of the cross passage and its location.

In the case of cross passages No. 25, 26 and 27, the level difference between the cross passage and the drainage gallery is smaller than 2m, therefore it was not possible to use the standard solution to the intersection. For that reason, different solutions were designed for those cases.

In the cases of the cross passages No. 25 and 26, the difference in the levels H was achieved approximately 1.5m from the drainage gallery by increasing the longitudinal gradient of the cross passage up to the maximum value of 10%. For that reason, only local reconstruction of the drainage gallery lining was necessary.

In the case of the cross passage 27, difference between the drainage gallery level while using the maximum gradient reached a value smaller than 0.5m – in the location of the intersection the ground beams of the standard profile extended into the space of the drainage gallery. For that reason it was necessary in the area of the intersection with the cross passage to carry out locally new anchoring of the primary lining of the cross passage using IBO anchors, to reconstruct the lining of the drainage gallery outside the area of the intersection with the cross passage, within the reach of the newly anchored primary lining with IBO anchors and to carry out comprehensive treatment of the drainage gallery lining and foundations of the cross passage in the intersection with the drainage gallery (Figure 13, 14).

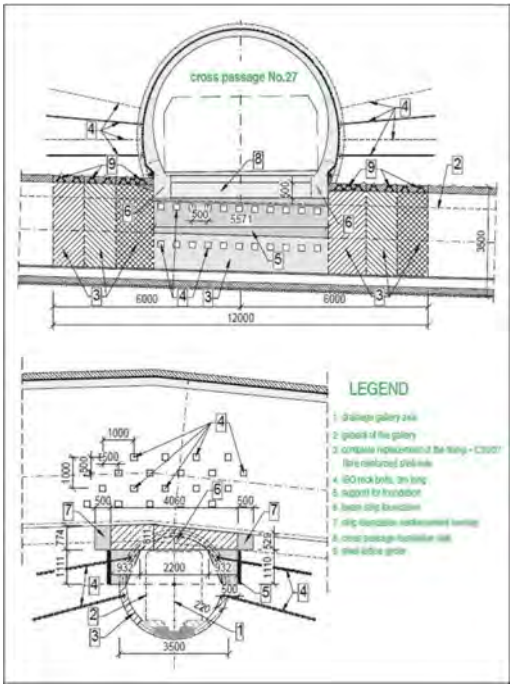

Figure 13. Intersection with cross passage No. 27 – cross-section and longitudinal section through the gallery.

Figure 14. Intersection with cross passage No. 27 – construction phase.

8 CONCLUSION

Changing the main contractor is a rare phenomenon in Slovakia for large infrastructure projects. One of the most important parameters in the selection of a new contractor for the construction of the D1 motorway section Lietavská Lúčka - Višňové - Dubná Skala was the price of the implemented work. The examples presented in this article have also shown that it is often possible to design structures more optimally and with lower investment costs, even without significant negative effects on the safety and durability of the work. In today's economically challenging times, more emphasis should be placed on the use of more efficient designs, which often have fewer negative impacts on the surrounding environment. Unfortunately, investors are often inclined to use less efficient solutions only because fewer contractors have experience with more efficient solutions, and the quality of construction is also problematic for these reasons in such works, but this is often not the fault of the project (although there are quite a few such cases), but the desire of contractors to save in the wrong places, or lack of control by the building supervisor.

Other extremely important factors for designing more optimal solutions are the time available to the designer for design and the reliability of the design inputs. Many times, the designer does not have enough time available to design a particular work and for this reason designs a more massive and expensive structure. Reliability of design inputs is also a frequent problem, given that the results of geotechnical investigations are usually only available in the final stages of design, the area is only sparsely investigated, and the potential variance of design inputs is often too large.

The development of the purpose of the drainage gallery of the Višňove tunnel has undergone dynamic development since its construction, depending on the changing requirements of the client and various designing approaches of the contractor and designing companies. The decision regarding the use of the original exploratory gallery as a permanent object brought an advantage in the exclusion of the main drainage collectors from the tunnel tubes, owing to which the origination of sewerage manholes in the tunnel carriageway was excluded. This decision will have a positive influence on the longevity of the roadway in the tunnel and, at the same time, the necessity for decommissioning this heavily loaded tunnel for the roadway repairs in the future will be excluded, which fact will have significantly positive effect on traffic around Zilina. However, this decision required a design of structural elements which had not been used in Slovak tunnels and the concept of which has not been established in current standards and regulations. In conclusion, it can be stated that it is beneficial that the working, demanding in terms of cost and time, which the original exploratory

undoubtedly is, and the Višňove tunnel will bring indisputable advantages during the operation and maintenance of the tunnel itself.

REFERENCES

Diaľnica D1 Lietavska Lučka – Dubna Skala vrátane tunela Višňove, dokumentácia na realizáciu stavby, Amberg Engineering Slovakia, s.r.o., 2021.

Matejček, A., et. al. Čiastková záverečná sprava: D1 Višňove-Martin, podrobný IGHP formou prieskumnej štôlne pre tunel Višňove, čiastková sprava č.1, Žilina 01/1999.

Coplak, M., et. al. Diaľnica D1 Lietavska Lučka – Višňove – Dubna Skala, Hydrogeologické zhodnotenie vplyvu výstavby, Odborný geologicky posudok, 2017.

TKP 26 – Technicko-kvalitativne podmienky – Tunely, 2017.

Diaľnice a tunely na Slovensku, [on-line], http://dialnice.szm.com/tunnels/Visnove.html, 2018.

Malík, P., Coplák, M. Rozsah infiltračnej oblasti tunela Višňové. Zborník 13. slovenskej hydrogeologickej konferencie "Človek a voda", Brusno 26.-28.10.2005, ISBN 80-969342-1-X.

Barták, J., Pruška, J., Podzemní stavby. 1. vydání. V Praze: České vysoké učení technické, 2011. ISBN 978-800-1047-897.

Barták, J., Přehled klasických metod výstavby tunelů. In: Česká tunelářská asociace (CzTA - ITA-AITES) [online]. Praha: Česká tunelářská asociace ITA-AITES, z. s. a Slovenská tunelárska asociácia ITA-AITES, 1991.

Klepsatel, F., et. al. Výstavba tunelu ve skalních horninách. 1. vydání., V Bratislave: Jaga Group, 2003. ISBN 80-88905-43-5.

Hulla, J., et. al. Predpoklady a skutočnosť v geotechnickom inžinierstve. 1. vydanie, V Bratislave: Jaga Group, 2002, ISBN 80-88905-42-7.

Tunnelling for a Better Life – Yan, Celestino, Thewes & Eberhardt (Eds)
© 2024 The Author(s), ISBN 978-1-032-80042-4
Open Access: www.taylorfrancis.com, CC BY-NC-ND 4.0 license

Step effects of hydraulic pressure of tunnels in loess under high-pressure seepage

Junling Qiu* & Kunjie Tang
School of Highway, Chang'an University, Xi'an, China

Zhihong Zhao
College of Transportation Engineering, Chang'an University, Xi'an, China

Yibin Bai
School of Architecture, Harbin Institute of Technology, Harbin, China

Nianxiao Zhang, Yuhang Chen & Shangxuan Ding
College of Transportation Engineering, Chang'an University, Xi'an, China

ABSTRACT: During metro construction, it is likely to cross the stratum with complex water environment. The great difference of geological conditions in China brings great variations to the properties of immersed soil layer, which has a great impact on the metro tunnel structure. Thus, this paper statistically analyses the cases of water gushing accidents in metro tunnels in China and puts forward the failure modes of immersed surrounding rock. Failure can be divided into three modes: flow sand instability failure, fracture expansion failure and collapse failure. Furthermore, based on typical engineering cases, the structural response characteristics of metro tunnel under various failure modes are further analysed and summarized. This study can provide significant reference information and experience for metro tunnel construction.

Keywords: Metro tunnel, Water environment, Statistical analysis, Failure mode, Tunnel structural response

1 INTRODUCTION

With the construction of underground urban space and rail transit, more and more metro tunnels pass through unfavourable geology(Huang et al., 2021; Liu et al., 2018). The great differences in natural conditions of China brings some difficulties to metro construction. Especially in special stratum such as sand, karst and loess, affected by water environment, the nature and structure of immersed soil changes significantly(Mao et al., 2019; Sun et al., 2021; Wang et al., 2018; Zhang et al., 2021). In the dynamic water environment, sand stratum is prone to flow sand, and the stability is completely lost, resulting in pores or cavities around the tunnel. The stratum crossed by Shanghai metro line 18 is mainly sandy soil. Water gushing accident occurs during tunneling, resulting in deformation and damage of tunnel lining(Fan et al., 2018; Zhao et al., 2021) . Otherwise, during the construction of Yi wan Railway Tunnel, large-scale karst stratum is encountered. Under the pressure water environment, the water-rock interaction leads to the expansion of karst fissures and the outburst of tunnel fissure water. Karst stratum with water-rich caves or poor load-bearing capacity may cause water ingress, mud gushing, formation sliding, tunnel structure damage, or even ground collapse, etc.(Qiu et al., 2019, 2020; Wang et al., 2020). The collapsible loess stratum is prone to collapse after water immersion, which will seriously affect the metro tunnel structure.

Therefore, the change of water environment under complex geological conditions brings difficulties and challenges to metro tunnel construction. In view of the lack of a systematic summary on failure mode of immersed surrounding rock and structural response mechanism of metro tunnel. This paper pays more attention to: (1) propose failure mode of immersed surrounding rock, (2) to summarize and analyse the response characteristics of immersed surrounding rock failure to metro tunnel structure.

*Corresponding author: junlingqiu@chd.edu.cn

DOI: 10.1201/9781003495505-342

2 WATER IMMERSION FAILURE MODE OF SURROUNDING ROCK OF METRO TUNNEL

2.1 *Statistical investigation of metro water gushing accidents*

To study failure mode of immersed surrounding rock and structural response mechanism of metro tunnel, the water gushing cases of metro tunnels in China recent years are statistically analysed in this section. And the common characteristics of the immersion failure of surrounding rock are summarized. Specific statistical analysis is shown in Table 1.

2.2 *Analysis of water gushing accidents in metro tunnel*

2.2.1 *Space analysis*

From the perspective of seven natural geographical divisions in China, the locations of metro

Table 1. Case statistics of water gushing accidents in metro tunnels in China.

Region	Metro name	Cause analysis of surrounding rock failure	Tunnel structure response
Northwest China	Xi'an Metro Line 9	Surrounding rock structure is changed and the strength is reduced after water immersion. Then, the surrounding rock collapse occurs	The arch foot of the tunnel has cracks and large deformation
	Xi'an Metro Line 1		The stress of tunnel sidewall and arch foot increases
	Xi'an Metro Line 2		The stress of tunnel arch bottom increases and deformation occurs
	Xi'an Metro Line 3		The stress on the sidewall of the tunnel increases
	Xi'an Metro Line 4		The bending moment and axial force of tunnel vault increase in the immersion range
	Xi'an Metro Line 2		Tunnel arch foot deformation is large and cracks occur
	Lanzhou Metro Line 1		The stress of tunnel vault and arch foot increases, resulting in deformation
	Xi'an Metro Line 2		The stress on the sidewall of the tunnel increases
	Taiyuan Metro Line 1		Cracks appear at the arch foot of the tunnel, resulting in deformation
	Changsha Metro Line 3		The stress above the tunnel vault is large and uneven deformation occurs
	Kunming Metro Line 5		The stress on the arch foot of the tunnel increases, resulting in cracks
	Guiyang Metro Line 3		Tunnel arch foot damage
Southwest China	Kunming Metro Line 2	Fracture expansion occurs in surrounding rock under high-water pressure	Tunnel arch foot deformation is large and damage occurs
	Guiyang Metro Line 2		The stress on the side wall of the tunnel increases
	Guiyang Metro Line 1		The deformation of tunnel arch bottom is large, and cracks appear at the arch bottom
	Kunming Metro Line 2		The stress on the sidewall of the tunnel increases and the segments produce cracks
Central South Region	Zhengzhou Metro Line 2	Surrounding rock structure is changed and the strength is reduced after water immersion. Then, the surrounding rock collapse occurs	The arch foot of the tunnel has cracks and large deformation
	Zhengzhou Metro Line 3		The stress on the sidewall of the tunnel increases
	Zhengzhou Metro Line 12		The stress on the bottom of tunnel arch gradually increases, and finally the failure occurs

(*Continued*)

Table 1. (*Continued*)

Region	Metro name	Cause analysis of surrounding rock failure	Tunnel structure response
East China	Zhengzhou Metro Line 5	Under the action of hydrodynamic force, flow sand occurs in the surrounding rock, resulting in instability failure of surrounding rock	Tunnel arch foot deformation is large and damage occurs
	Wuhan Metro Line 7		The stress above the tunnel vault is large and uneven deformation occurs
	Shenzhen Metro Line 1		Tunnel arch foot damage
	Guangzhou Metro Line 5		The arch foot of the tunnel has cracks and large deformation
	Wuhan Metro Line 3		The stress above the tunnel vault is large and uneven deformation occurs
	Wuhan Metro Line 6		The stress on the side wall of the tunnel increases
	Guangzhou Metro Line 2		The stress of tunnel arch foot increases
	Foshan Metro Line 2		Compared with other parts, the stress of tunnel vault is larger
	Guangzhou Metro Line 3		The stress on the sidewall of the tunnel increases
	Wuhan Metro Line 4		The stress of tunnel arch bottom increases and deformation occurs
	Shanghai Metro Line 11		A cavity is formed at the top of the tunnel and the stress increases
	Qingdao Metro Line 3		The stress above the tunnel vault increases, resulting in the collapse of the vault
	Nanjing Metro Line 3		The stress on the sidewall of the tunnel increases, resulting in cracks
	Nanjing Metro Line 2	Under the action of hydrodynamic force, flow sand occurs in the surrounding rock, resulting in instability failure of surrounding rock	The stress above the tunnel vault is large and uneven deformation occurs
	Nanjing Metro Line 4		The stress of tunnel arch foot increases
	Hangzhou Metro Line 1		The stress above the tunnel vault is large and uneven deformation occurs
	Hangzhou Metro Line 4		The stress on the sidewall of the tunnel increases, resulting in cracks
	Shanghai Metro Line 15		The stress on the top of the tunnel increases, resulting in large-scale cavities
North China	Tianjin Metro Line 2	Surrounding rock structure is changed and the strength is reduced after water immersion	As the stress on the arch foot increases, the bending moment and axial force of the tunnel lining structure increase within the immersion range
	Beijing Metro Line 10		The stress on the sidewall of the tunnel increases

water gushing accidents are mostly concentrated in the northwest, southwest, central and eastern regions of China (Figure 1). By consulting Chinese geological data, it is found that the stratum in northwestern China is mostly loess. The middle-south and east China are typical sandy soil stratum. While the karst stratum in southwestern China is relatively developed, and there are more rifts, grooves and caves. The occurrence of water gushing hazard in the above stratum not only affects project construction, but also causes huge economic losses.

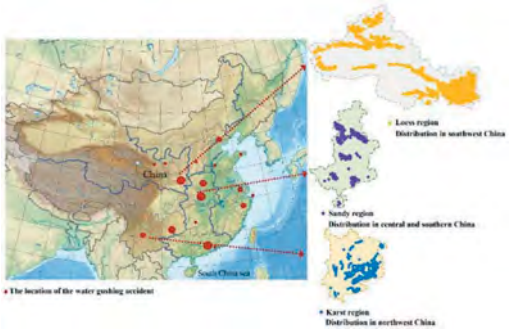

Figure 1. Geographical location of metro water gushing accidents.

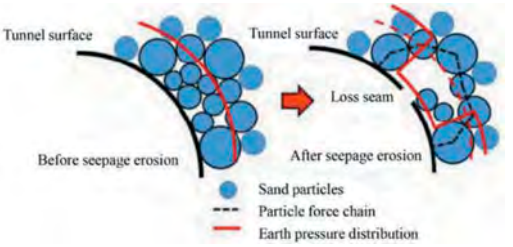

Figure 2. Diagram of earth pressure distribution on tunnel surface (Zhang et al.,2017).

2.2.2 *Cause analysis*

Through analysis and statistics of metro water gushing accidents in China, it can be seen that unstable failure of surrounding rock structure up to 43.6% due to the sand flowing under the action of hydrodynamic force. The instability failure caused by the fracture expansion (FE) of surrounding rock under high water pressure accounts for 17.9%. Collapse failure of surrounding rock after water immersion accounts for 38.5%. Therefore, flow sand instability (FSI), FE and collapse are the main causes of surrounding rock structure damage in water environment.

2.3 *Water immersion failure modes*

According to the above summary and analysis of the statistical water gushing accident cases, from the surrounding rock classification and the causes of immersion failure, failure of immersed surrounding rock is divided into three modes: FSI failure, FE failure and collapse failure.

2.3.1 *Flow sand instability failure*

FSI failure means that the surrounding rock produces flowing sand and loses its stability under hydrodynamic action. The most representative stratum in China is the sand stratum of Wuhan area. Sand is a typical loose granular medium. Under stress conditions strain softening and strain localization will occur in sand. If sand is in dynamic water environment, its physical and mechanical properties will be more complex, which is confirmed by a large number of experimental results in the world (Fang et al., 2019; Zhang et al., 2019).During tunnel construction in the sandy stratum, due to the relatively high mobility of sand, the groundwater is replenished quickly. Under the hydrodynamic action, fine sand particles are brought into the tunnel, resulting in the loss of soil particles in the soil around the tunnel. Dominant channels are formed, and pores or cavities are generated around the tunnel (Long and Tan, 2020).

The loss of sand particles changes the soil particle structure in the particle loss area, and changes the distribution of soil pressure on the tunnel surface. The change process of soil pressure distribution is shown in Figure 2. Before seepage erosion, soil pressure is evenly distributed on the tunnel surface. After the loss joint appears on the tunnel surface, the sand particles are lost and the earth pressure at the loss joint is greatly reduced. The large particles around the loss joint form a force arch (particle force chain) to bear the earth pressure outside the loss area (Zhang et al., 2017). This change leads to the original tunnel surface uniform stress state into uneven stress. Seepage erosion generally occurs in the weakest link of tunnel structure, such as ring joint, longitudinal joint and bolt hole. After the width of the loss joint increases, the amount of particle loss will increase, further exacerbating the change of soil pressure around the loss joint, forming a vicious circle to accelerate the process of seepage erosion.

2.3.2 *Fracture expansion failure*

FE failure refers to the continuous expansion of surrounding rock fractures under the action of water erosion in pressurized water environment. The most representative stratum in China is karst stratum in Guizhou area. The development of karst starts from the dissolution and expansion of the original narrow channel of soluble rock by water flow. The dissolved rock components are continuously taken away through the water flow cycle. The intermittent cracks (voids) of rock mass expand and the connectivity increases, which changes original structure of the rock mass. The increase of permeability further accelerates the seepage of karst water.

Huang et al. (Huang et al., 2021)reported that the overall crack connecting the tunnel and the cave is dominant channel, and the groundwater is transported through the dominant channel. When the water gushing hazard source enters the dominant channel, it is transformed into a hazard body. The formation of dominant channel is essentially the evolution process of solid-liquid-gas coupling of hazard body, which is usually manifested as two failure modes: high-pressure hydraulic fracturing failure and instability failure of filling structure (Li et al., 2017).

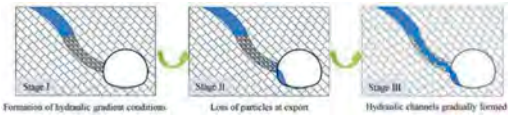

Figure 3. High pressure hydraulic fracturing failure process (Lai et al., 2021).

Lai et al. (Lai et al., 2021) studied the process of water gushing hazard in karst tunnel and the seepage characteristics of surrounding rock. The results showed that the essence of seepage failure is the macroscopic result of the initiation, expansion and penetration of surrounding rock cracks under the action of tunnel excavation disturbance and karst water pressure (Figure 3). In the paper reported by Gao et al.(Gao et al., 2021), it is also mentioned that the initiation, expansion and penetration of cracks in surrounding rock are spontaneous, and finally the water gushing channel is formed by cracks.

Wide cracks, faults, karst pipelines and other unfavorable geological structure, their internal filling medium seepage hazard led to the formation of water gushing channel. Subsequently, fault activation water gushing and karst pipeline filling infiltration instability water gushing occur, which is instability failure of filling structure. For the filled karst tunnel, the seepage failure instability process can be divided into three processes (Figure 4) (Lu, et al., 2017, Li et al., 2017):

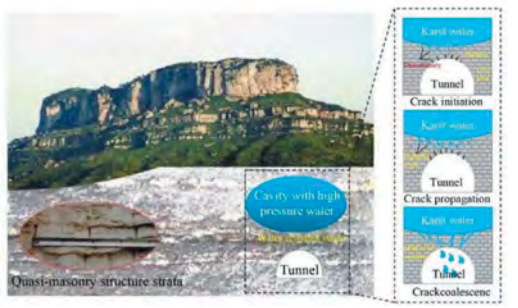

Figure 4. Filling medium overall instability failure schematic diagram (Lu, et al., 2017).

Moreover, Meng et al. (Meng et al., 2020)studied the seepage characteristics of filling karst tunnel structure, and found that water pressure in filling body gradually decreased along the seepage direction of confined water. With the increase of confined water pressure, the average hydraulic gradient and pore water pressure of filling body gradually increase.

2.3.3 *Collapse failure*

Collapsibility refers to the property that the internal structure of soil is destroyed under a certain compressive stress after immersion, and then significant additional subsidence occurs. The most representative stratum in China is loess stratum in Xi'an area. Loess is a kind of special Quaternary sediment formed under dry conditions, which is rich in pores, loose structure, developed vertical joints, and generally has different degrees of collapsibility. The three characteristics of strong water sensitivity, structural plane development and dominant seepage channel of loess determine that loess is prone to collapse after water immersion.

Calcite, clay cementation and silt morphology between loess particles make intact soil metastable under dry condition (Jiang et al., 2012). Collapsibility caused by water immersion is the result of the combined effect of primary and secondary microstructure characteristics (Garcia et al., 2012). The former is a large number of weakly cemented, unsaturated and porous pure clay and clay-silt mixture aggregates, and the disintegration after immersion leads to the collapse of the overall structure. The latter is composed of high porosity, unstable particle contact and clay coating on silt particles. Their synergistic effect leads to collapsibility. The conceptual model of loess collapsibility mechanism is shown in Figure 5.

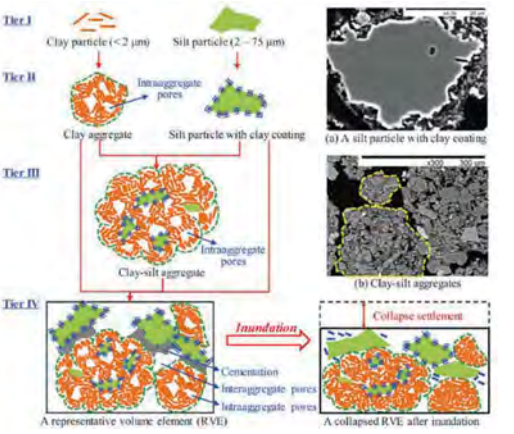

Figure 5. Conceptual model of loess collapsibility mechanism (Garcia Giménez et al., 2012).

To further explore the failure mode of surrounding rock of loess tunnel in hydrostatic environment, Li et al. (Li et al., 2019)carried out a long-term large-area static load immersion test on the surface of tunnel crossing strong collapsible loess stratum. The result is shown in Figure 6. It can be seen from the figure that the water in the test pit mainly infiltrates in the vertical direction, while the horizontal infiltration distance is small. Before the seepage front reaches the buried depth of the tunnel, the shape of the seepage area is elliptical. With the increase of

immersion time, the seepage area extends along the vertical direction. Therefore, the area affected by immersion eventually becomes the shape of 'bulb'. The maximum influence depth of water infiltration is 35 *m*, and the horizontal diffusion distance is about 5 *m*. After the immersion test, a detection ditch with a depth of 3m is excavated near the boundary of the foundation pit. The groove shows that the angle between the seepage line and the vertical direction is approximately 45° in the surface layer. After the infiltration front reaches the buried depth of the tunnel, due to the obstruction of the tunnel structure, water infiltrates into the surrounding rock along both sides of the tunnel and continues to move downward.

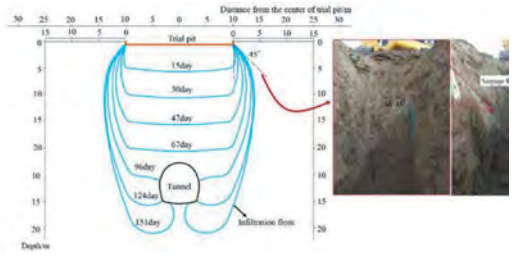

Figure 6. Change process of saturation line in different periods and Form of saturation line in shallow layer (Li et al., 2019).

3 STRUCTURAL RESPONSE CHARACTERISTICS OF METRO TUNNEL UNDER DIFFERENT IMMERSION FAILURE MODES

3.1 *Flow sand instability failure*

Wuhan located in Hubei Province of China has a huge sand stratum. When the shield tunneling passes through the high-water pressure sand stratum, it is easy to cause water gushing accidents, which may lead to serious secondary accidents, such as excessive surface subsidence, even collapse, tunnel structure deformation and damage (Selmi et al., 2020). Relying on a shield section of Wuhan Metro Line 7 as the research object, Ye et al. (Ye et al., 2017) studied the influence of water gushing on the surface settlement and metro tunnel structure when the earth pressure balance shield was excavated in the sand layer. The metro tunnel is mainly located in the Yangtze River valley area, and the groundwater in the surrounding rock is interlinked with the river water. The phreatic area in the surrounding rock is about 0.5 *m*-4.2 *m* away from the surface position. When the tunnel passes through the sandy stratum in the region, it encounters confined water and underground river. Causing water gushing in the tunnel and obvious surface subsidence. The variation of surface subsidence along the horizontal and vertical directions is shown in Figures 7 and 8.

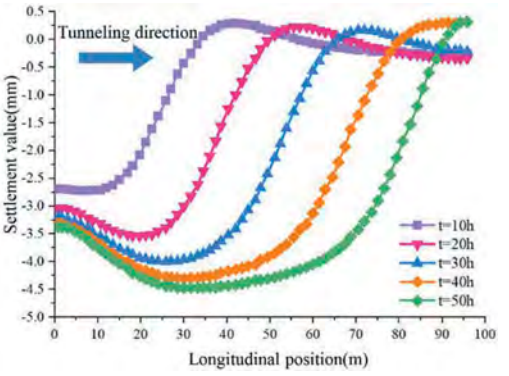

Figure 7. Surface transverse observation axis settlement curve (Ye et al., 2017).

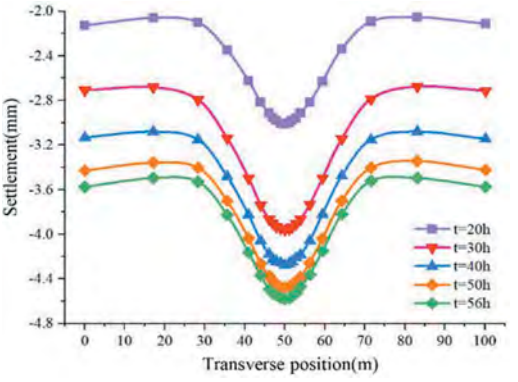

Figure 8. Surface longitudinal observation axis settlement curve (Ye et al., 2017).

According to the distribution of surface lateral settlement, the surface settlement above the tunnel is the largest, which is 4.5 *mm*, and with the increase of time, the surface settlement is larger, the early settlement amplitude is larger, and the later period is slowly stabilized. For the distribution of longitudinal surface subsidence, the surface subsidence near the water inflow location is large, and the influence range is about 50 *m* along the longitudinal direction.

According to the construction situation on site and the geological survey of water gushing section, when passing through the sandy stratum with high-water pressure and rich local water content, the hazards such as segment dislocation and cracking occur frequently. By analysing the influence of different seepage velocity on tunnel structure, the variation trend of maximum deformation, maximum tensile stress and maximum compressive stress of tunnel segment with water inflow is shown in Figure 9. With the increase of water inflow, the deformation internal force of the segment shows a nonlinear growth trend. For the segment structure of the

interval tunnel, affected by the water environment, with the increase of segment internal force, the segment lining develops from the initial crack to the late dislocation and damage, further reducing the stability of the overall structure of the tunnel. The risk of tunnel leakage and local collapse is induced. Therefore, when the tunnel passes through the water-rich sandy soil stratum, especially in the environment of confined water and underground river, to prevent excessive surface subsidence and segment structure fracturing by water pressure, effective treatment measures such as grouting should be taken in time to control the water output in a certain range and prevent the further expansion of the accident.

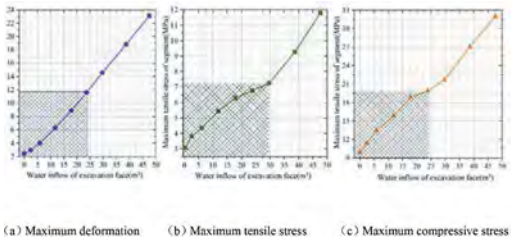

Figure 9. Influence of water inflow on tunnel segment (Ye et al., 2017).

3.2 *Fracture expansion failure*

The water content in karst area is abundant. In the construction process, due to the excavation of tunnel rock mass, the stability of the original hydraulic circulation system or static water body is destroyed, and it is easy to cause karst collapse, karst leakage, underground water gushing and other adverse geological phenomena. Underground engineering such as metro tunnel has great risks in the construction of such stratum. However, for the tunnel structure that has been used as lining, affected by the water environment such as surface rainfall, the cavity previously existing around the tunnel is filled again. If the pores in the cavity are filled with water, the distance between cavity and tunnel is relatively close, surrounding rock between cavity and tunnel is weak or reinforcement effect is poor. At this time, the high-water pressure in the cavity is easy to have a large bias effect on the tunnel, and even the tunnel lining will be partially destroyed, leading to water gushing accident.

Therefore, taking a karst tunnel with hidden cavity at the bottom as the engineering background, Mo (Mo, Y.C., 2011) analysed the response characteristics of water pressure in karst cavity below the tunnel and the spacing between karst cavity and tunnel to the internal force of tunnel structure.

The influence of water pressure in the cavity on internal force of tunnel lining is shown in Figure 10. With the gradual increase of water pressure in the cavity, the axial force of tunnel lining gradually increases as a whole (Figure 10(a)). Especially for the tunnel wall foot position, when the water pressure of the cavity is 0.3 *MPa*, 0.6 *MPa*, 1.0 *MPa* and 1.5 *MPa*, the corresponding axial force of the wall foot lining is-258.2 *kN*, -511.3 *kN*, -844.2 *kN* and-1301 *kN*.

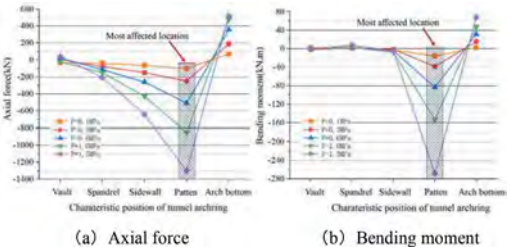

Figure 10. Variation of Internal Force of tunnel lining characteristic position with water pressure in cavity (Mo, Y.C., 2011).

At the same time, the smaller the distance between the tunnel and the solution cavity, the greater the absolute value of the axial force (negative axial force) at the spandrel, side wall and foot of the tunnel, and the greater the absolute value of the axial force (positive axial force) at the top and bottom of the tunnel. The change of the axial force is: foot of the wall > bottom of the tunnel > side wall > arch shoulder > vault. The change of cavity water pressure mainly affects the bending moment of tunnel wall foot, as shown in Figure 10(b), but has little effect on other positions. When the test section is close to the cavity section, the bending moment of the vault and side wall of the tunnel changes little, and the maximum bending moment increment is at the arch foot of the tunnel, followed by the bottom of the tunnel, and the tunnel spandrel is the smallest.

Figure 11 shows the influence law of lining internal force on the variation of cavity spacing between tunnel and karst cave. When the distance between the tunnel and the cavity decreases continuously, the axial force growth law of the tunnel at the characteristic position is different. As shown in Figure 11(a), the axial force of the tunnel wall foot and the side wall increases significantly.

When the distance between the solution cavity and the tunnel is 5.0 *m* and 3.5 *m,* the axial force at the wall foot is-844.2 *kN* and-1053 *kN*, respectively. Compared with the distance between cavity and tunnel 7.5 *m*, the axial force increases 1.4 *times* and 1.8 *times* respectively. In contrast, the increase of axial force at the bottom, spandrel and vault of the tunnel is small. As shown in Figure 11(b), with the decrease of cavity spacing, the bending moment increment of tunnel wall foot and tunnel bottom is more obvious, among which the bending moment

increment at tunnel bottom is the most obvious, while the bending moment increment at tunnel vault, spandrel and side wall is small. For the tunnel lining with large cavity distance, the bending moment and axial force are less affected by the cavity.

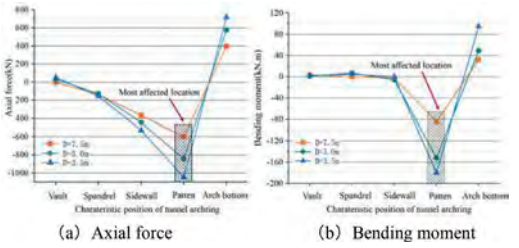

(a) Axial force (b) Bending moment

Figure 11. Influence of the distance between water filled cavity and tunnel on the internal force of lining (Mo, Y.C., 2011).

3.3 *Collapse failure*

In collapsible loess areas, the migration of soil moisture often causes the spatial-temporal discontinuity and spatial heterogeneity of collapsibility, and induces the destruction of tunnel structure (Qiu et al., 2018; Wang et al., 2021). Therefore, to ensure the safety of the loess tunnel structure, Li et al. (Li et al., 2019) revealed the collapsible deformation characteristics of loess tunnel site and its influence on tunnel structure (Figure 12), by measuring and analysing the mechanical response of stratum settlement and tunnel structure during long-term immersion.

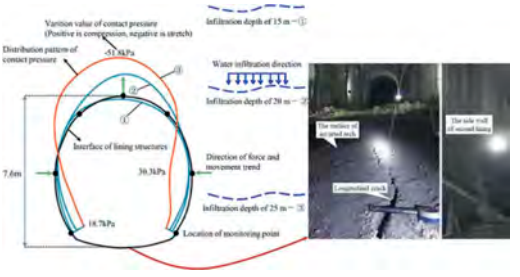

Figure 12. Contact pressure on section XK140 changes with water infiltration depth and Cracks on the tunnel structure (Li et al., 2019).

In the long-term immersion process of the surface above the tunnel, the surface water will infiltrate into the bottom of the tunnel. When the surface water infiltrates near the tunnel depth, the pressure state of the tunnel structure will change due to the collapse of the surrounding loess. The main feature of the change is that the side wall of the tunnel is squeezed laterally by the surrounding loess, and the vault of the primary lining has the trend of upward movement. Meanwhile, the foundation pressure increased significantly, the tunnel structure collapse, and the inverted arch crack.

With the increase of soil immersion conditions around the tunnel, the adverse impact on the tunnel is also more serious. Weng et al. (Weng et al., 2019) improved the water immersion system (WSS) on the basis of the existing CTE, then it was used to carry out centrifugal model tests on a metro tunnel under full-range and half-range foundation soaking conditions with different soaking depths. The results show that half-range soaking is more harmful to the mechanical properties than full-range foundation soaking. The differential deformation caused by half-range foundation soaking is one of the main reasons for the tunnel cracks.

4 CONCLUSIONS

The failure modes of tunnel surrounding rock after immersion in different water environments are proposed based on the case analysis of water gushing accidents in China's metro tunnels. Combined with typical engineering cases, the structural response characteristics of metro tunnels under various failure modes of surrounding rock are further analysed and summarized. The following conclusions can be drawn:

(1) From the surrounding rock classification and the causes of immersion failure, failure of immersed surrounding rock is divided into three modes: flow sand instability failure, fracture expansion failure and collapse failure. Flow sand instability failure: under the action of hydrodynamic force, the soil particle structure in the particle loss area is changed, which changes the earth pressure distribution on the tunnel surface. Fracture expansion failure: under the interaction of water and rock, the fracture of surrounding rock expands, resulting in the weakening of surrounding rock strength and instability failure. Collapse failure: after the collapsible loess stratum is immersed in water, collapse is attributed to both primary and secondary microstructure features.

(2) Under the influence of immersed surrounding rock, the metro tunnel structure has different response regularities. Flow sand instability failure occurs in surrounding rock, the influence on the tunnel structure is mainly concentrated in the vault. Fracture expansion failure occurs in the surrounding rock, the influence on the tunnel structure is mainly concentrated at the arch bottom. When the surrounding rock collapses, the stress on the side wall and arch foot of the tunnel increases in the large area of static water immersion environment, while in the local pressure water immersion environment, the surrounding rock near the water source occurs local collapse, and the stress increases at the arch foot and arch bottom, resulting in uneven deformation.

ACKNOWLEDGMENTS

This work was jointly supported by the National Natural Science Foundation of China (Grant No.51978066).

REFERENCES

Fan, H.B., Zhang, Y.H., He, S.Y., Wang, K., Wang, X.L., Wang, H., 2018. Hazards and treatment of karst tunneling in Qinling-Daba mountainous area: overview and lessons learnt from Yichang–Wanzhou railway system. Environ. Earth Sci. 77 (19).

Fang, Y., Chen, Z.T., Tao, L.M., Cui, J., Yan, Q.X., 2019. Model tests on longitudinal surface settlement caused by shield tunnelling in sandy soil. Sustain. Cities Soc. 47.

Gimenez, R.G., de la Villa, R.V., Martin, J.A.G., 2012. Characterization of loess in central Spain: a microstructural study. Environ. Earth Sci. 65 (7), 2125–2137.

Huang, K., Sun, Y.W., He, J., Huang, X.Q., Jiang, M., Li, Y.J., 2021a. Comparative Study on Grouting Protection Schemes for Shield Tunneling to Adjacent Viaduct Piles. Adv. Mater. Sci. Eng. 2021.

Huang, Z., Zhao, K., Li, X.Z., Zhong, W., Wu, Y., 2021. Numerical characterization of groundwater flow and fracture-induced water inrush in tunnels. Tunn. Undergr. Space Technol. 116.

Jiang, M.J., Hu, H.J., Liu, F., 2012. Summary of collapsible behaviour of artificially structured loess in oedometer and triaxial wetting tests. Can. Geotech. J. 49 (10), 1147–1157.

Lai, Y.B., Li, S., Guo, J.Q., Zhu, Z.G., Huang, X., 2021. Analysis of Seepage and Displacement Field Evolutionary Characteristics in Water Inrush Disaster Process of Karst Tunnel. Geofluids. 2021.

Li, J., Shao, S.J., Shao, S., 2019. Collapsible characteristics of loess tunnel site and their effects on tunnel structure. Tunn. Undergr. Space Technol. 83, 509–519.

Li, S.C., Wang, K., Li, L.P., Zhou, Z.Q., Shi, S.S., 2017. Mechanical mechanism and development trend of water-inrush disasters in karst tunnels. Chinese Journal of Theoretical and Applied Mechanics. 49(1), 22–30.

Liu, X., Fang, Q., Zhang, D.L., 2018. Mechanical responses of existing tunnel due to new tunnelling below without clearance. Tunn. Undergr. Space Technol. 80, 44-52. 90.

Lu, W., 2017. Study on karst water inrush mechanism and treatment method and its engineering applications in tunnels. Shandong University.

Mao, Z.J., Wang, X.K., An, N., Li, X.J., Wei, R.Y., 2019. Water Disaster Susceptible Areas in Loess Multi-Arch Tunnel Construction under the Lateral Recharge Condition. KSCE J. Civ. Eng. 23 (10), 4564–4577.

Meng, Y.Y., Jing, H.W., Yin, Q., Wu, X.J., 2020. Experimental study on seepage characteristics and water inrush of filled karst structure in tunnel. Arab. J. Geosci. 13 (12).

Mo, Y.C., 2011. Research on the effect of concealed bottom water-filled cavity tunnel on internal forces of secondary lining. Hydrogeology & Engineering Geology. 38(05), 31–37.

Qiu, J.L., Liu, H.Q., Lai, J.X., Lai, H.P., Chen, J.X., Wang, K., 2018. Investigating the Long-Term Settlement of a Tunnel Built over Improved Loessial Foundation Soil Using Jet Grouting Technique. J. Perform. Constr. Facil. 32 (5).

Qiu, J.L., Lu, Y.Q., Lai, J.X., Guo, C.X., Wang, K., 2020. Failure behavior investigation of loess metro tunnel under local-high-pressure water environment. Eng Fail Anal. 115.

Qiu, J.L., Qin, Y.W., Lai, J.X., Wang, K., Niu, F.Y., Wang, H., Zhang, G.L., 2019. Structural Response of the Metro Tunnel under Local Dynamic Water Environment in Loess Strata. Geofluids.

Selmi, M., Kacem, M., Jamei, M., Dubujet, P., 2020. Physical Foam Stability of Loose Sandy-Clay: a Porosity Role in the Conditioned Soil. Water Air Soil Pollut. 231 (5).

Sun, W., Liang, Q.G., Qin, SH., Yuan, Y.X., Zhang, T.J., 2021. Evaluation of groundwater effects on tunnel engineering in loess. Bull. Eng. Geol. Environ. 80 (3), 1947–1962.

Wang, X.L., Lai, J.X., Qiu, J.L., Xu, W., Wang, L.X., Luo, Y.B., 2020. Geohazards, reflection and challenges in Mountain tunnel construction of China: a data collection from 2002 to 2018. Geomatics, Nat. Hazards Risk. 11(1), 766–784.

Wang, Z.C., Xie, Y., Lai, J.X., Xie, Y.L., Su, X.L., Shi, Y. F., Guo, C.X., 2021. Designing an innovative support system in loess tunnel. Geomech. Eng. 24 (3), 253–266.

Wang, Z.F., Cheng, W.C., Wang, Y.Q., 2018. Investigation into geohazards during urbanization process of Xi'an, China. Nat. Hazards. 92 (3), 1937–1953.

Weng, X.L., Sun, Y.F., Zhang, Y.W., Niu, H.S., Liu, X., Dong, Y.L., 2019. Physical modeling of wetting-induced collapse of shield tunneling in loess strata. Tunn. Undergr. Space Technol. 90, 208–219.

Ye, Z., Liu, H.B., Liu, W., 2017. Analysis of Influence of Water Inrush at Shield Tunneling Face on Ground Surface Settlement and Internal Stress of Segment. Tunnel Construction. 37(10), 1276–1286.

Zhang D.M., Gao, C.P., Yin, Z.Y., Wang, R.H., Yang, T.L., 2017. Particle flow simulation of seepage erosion around shield tunnel. Rock and Soil Mechanics. 38(S1), 429–438.

Zhang, D.M., Gao, C.P., Yin, Z.Y., 2019. CFD-DEM modeling of seepage erosion around shield tunnels. Tunn. Undergr. Space Technol. 83, 60–72.

Zhang, D.M., Xie, X.C., Zhou, M.L., Huang, Z.K., Zhang, D.M., 2021. An Incident of Water and Soil Gushing in a Metro Tunnel Due to High Water Pressure in Sandy Silt. Eng Fail Anal. 121.

Zhao, C.Y., Lei, M.F., Shi, C.H., Cao, H.R., Yang, W.C., Deng, E., 2021. Function mechanism and analytical method of a double layer pre-support system for tunnel underneath passing a large-scale underground pipe gallery in water-rich sandy stratum: A case study. Tunn. Undergr. Space Technol. 115.

Tunnelling for a Better Life – Yan, Celestino, Thewes & Eberhardt (Eds)
© 2024 The Author(s), ISBN 978-1-032-80042-4
Open Access: www.taylorfrancis.com, CC BY-NC-ND 4.0 license

ITAtech design guidance chapter for composite Sprayed Concrete Lined (SCL) tunnels waterproofed with sprayed membranes

Jiang Su*
AtkinsRealis, Epsom, UK

ABSTRACT: Composite sprayed concrete lined (SCL) tunnels waterproofed with sprayed membranes have been constructed in major tunnelling projects worldwide. The use of sprayed membranes has the potential to reduce the secondary lining thickness significantly. So far, this potential has yet to be fully realised, mostly due to a lack of detailed design guidance. In response, the author has undertaken the task of developing a design guidance chapter for the ITAtech Lining and Waterproofing Activity Group guidance document.

The design guidance chapter begins by presenting various composite lining configurations and provides a flow chart to aid decision-makers in selecting the most suitable lining configuration based on specific ground conditions and project requirements. It further elucidates the impact of composite action and load sharing on tunnel linings, emphasising their significance in achieving optimal lining structural performance. The stress status of the membrane interface under varying loadings is thoroughly explained. The chapter also recommends analysis stages and verification points based on the membrane interface's life-cycle behaviour within the tunnel to facilitate a comprehensive understanding of the design process. Moreover, the chapter explores various numerical modelling approaches for simulating the membrane interface. Project examples and reference literature will not be listed in this paper due to space limitations.

By focusing on key concepts such as composite action and load sharing, as well as addressing practical considerations such as numerical modelling techniques, this design guidance chapter fills a critical gap in the field. It will serve as a valuable resource for professionals engaged in the design and construction of composite SCL tunnels waterproofed with sprayed membranes, enabling them to make informed decisions and enhance the overall efficiency and effectiveness of such tunnel projects. This paper provides a glimpse of the comprehensive design guidance chapter.

Keywords: ITAtech, Composite Lining, Sprayed concrete, Sprayed membrane

1 INTRODUCTION

Composite sprayed concrete lined (SCL) tunnels waterproofed with sprayed membranes have been constructed for major projects worldwide in various ground conditions. Recent example projects include the Crossrail project in London (Su & Thomas, 2015), REM and Blue Line projects in Montreal (Nasri & Vovou, 2023; Nasri et al., 2023), Gevingas rail tunnel in Norway (Holter, 2013), WestConnex New M5 tunnels in Australia (Aitchison et al., 2018). The ground in which those tunnels were constructed ranges from impermeable stiff clay to permeable weak and hard rocks. The lining configurations range from relatively thick lining working as a passive load-bearing shell structure to an active system with relatively thin lining combined with permanent rock bolts that better utilise the inherent rock strength. Both drained and undrained (tanked) waterproofing strategies were used. The wide range of applications of composite SCL tunnels waterproofed by sprayed membranes in different geological conditions demonstrates its versatility. However, there is currently no detailed guidance on the design of composite SCL tunnels waterproofed by sprayed membranes. ITAtech Lining and Waterproofing Activity Group published a guidance document in 2013 (ITAtech, 2013), with only two pages covering the high-level design principles. This has left a wide knowledge gap for tunnel designers to efficiently design this innovative lining configuration to achieve acclaimed benefits, such as reduced lining thickness and improved safety records, etc.

With over 15 years of combined academic research, construction supervision, practical design

*Corresponding author: Jiang.su@atkinsrealis.com

DOI: 10.1201/9781003495505-343

and numerical modelling experience on the composite SCL tunnels, the author has been tasked to develop a new design chapter for the next version of the ITAtech Lining and Waterproofing Activity Group guidance document. This paper provides a glimpse of this comprehensive design chapter. The author hopes the publication of the paper will encourage the exchange of relevant experience and lessons globally and provide more confidence to adopt this innovative lining configuration among clients and designers. This paper presents the key information in the same order as in the proposed design chapter.

2 LINING CONFIGURATIONS

Table 1 lists typical composite SCL tunnel configurations using a sprayed waterproofing membrane as the main waterproofing measure. For completeness purposes, single shell lining configurations waterproofed with sprayed membranes but without secondary lining are also included. The example lining configurations shown in Figure 1 cover stiff clay (e.g., London Clay) and weak rock (e.g., Breccia and Basalt). The lining configurations can be extended to hard rock ground conditions if rock anchors are installed. It should be noted that this table does not list all possible composite SCL tunnel configurations using a sprayed waterproofing membrane. Instead, it intends to provide tunnel designers with information on selecting the most suitable lining configurations.

Table 1. Typical composite SCL lining configurations.

No.	Name
A-1	Undrained sacrificial primary lining
A-2	Undrained hybrid sacrificial primary lining
A-3	Drained sacrificial primary lining
B-1	Undrained permanent primary lining
B-2	Undrained hybrid permanent primary lining
B-3	Drained permanent primary lining
C-1	Undrained single shell lining
C-2	Drained single shell lining

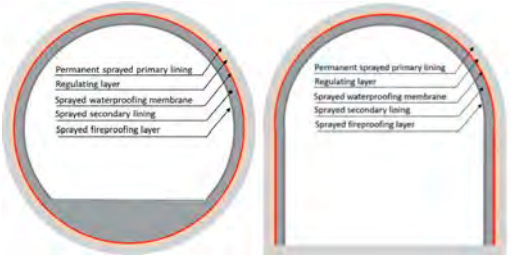

Figure 1. Typical undrained (B-1) and drained permanent (B-3) primary lining configurations.

3 LINING CONFIGURATION SELECTION PROCESS

A lining configuration selection process is shown below in Figure 2. The first column on the left-hand side shows three different levels of watertightness requirements, with the most relaxed requirement on the top and the strictest requirement at the bottom. The second column in the middle asks a key question: With the project ground conditions and local sprayed concrete quality control system, is the permanent primary lining a feasible option? Depending on the answer, the third column on the right-hand side lists suggests lining configurations.

It should be noted that temporary water control measures have been introduced to improve the substrate dryness for tunnels constructed on permeable ground with success. (Bedi et al., 2022; Amoushahi et al., 2022). This has greatly expanded the applicable scenarios for the use of sprayed waterproofing membranes, which were only able to be used in relatively dry conditions previously.

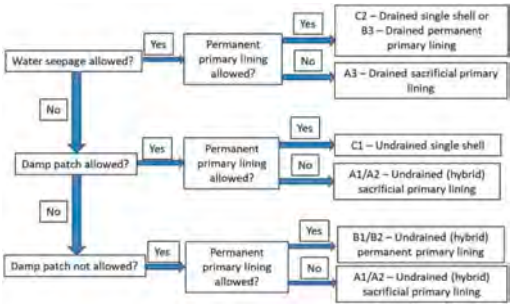

Figure 2. Lining configuration selection process.

4 FUNDAMENTAL ENGINEERING PRINCIPLES

In previous sections, 8no. of lining configurations are introduced. The following section will focus on the B series lining configurations, comprising two layers of permanent linings with sandwiched sprayed waterproofing membranes. This section will first introduce the fundamental engineering principles.

4.1 *Functions of the membrane interface*

A composite shell lining physically comprises primary and secondary linings with sandwiched sprayed membranes. From a structural perspective, there are two interfaces between the membrane and the concrete linings – the primary-membrane and secondary-membrane interfaces. Conceptually, the sprayed membrane and the two interfaces can be together described as the 'membrane interface', which has significantly lower mechanical properties (i.e., strength and stiffness) than the concrete layers on each side

and hence has been the focus of research on the past ten years (Dimmock et al., 2011; Su & Bloodworth, 2014, 2016; Holter, 2016; Diez et al., 2019). The definitions of these terms and the relationships between them are shown in Figure 3. The membrane interface functions on two levels in the composite shell lining, as shown in Figure 4. The first level is to ensure the primary and secondary linings work compositely without failure occurrence at the membrane interface, which is a prerequisite for the second level function. The second level is in the determination of the lining forces (i.e., axial force and bending moment) induced in the primary and secondary linings under various loading conditions as a consequence of the composite action. The following sub-sections will describe the function of the stiffness and strength in both the normal (crossing the membrane) and shear (along the membrane) directions of the membrane interface. The stiffness of the membrane interface follows Hooke's law in this paper.

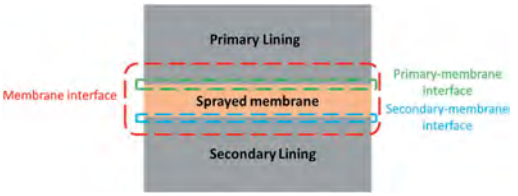

Figure 3. Definition of technical terms in composite shell lining.

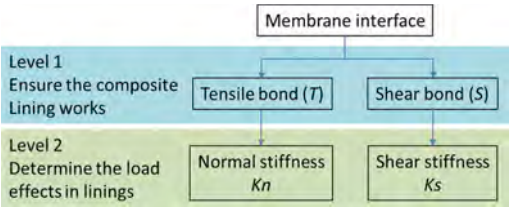

Figure 4. Functions of the membrane interface.

4.1.1 *Normal stiffness*

The normal stiffness describes how well the membrane can transfer both compression and tension (for bonded interface) and compression only (for unbonded interface) between the primary and secondary lining layers. The higher the normal stiffness, the greater the compression/tension is transferred between the two linings.

4.1.2 *Normal strength*

The compressive strength of the membrane interface is usually not a concern from design's perspective. There are three different tensile strengths: adhesive tensile strength between the membrane and the two concrete linings and the cohesive tensile strength of the membrane itself. The stress status related to the normal tensile strength at the membrane interface will be explained later in Section 3.3.

4.1.3 *Shear stiffness – composite action*

Shear stiffness restricts the relative movement between the primary lining by converting part of the global bending moment into a force couple - axial compression and tension in the two linings, depending on the lining deformation curvature. The effect of shear stiffness is also known as "composite action", which refers to the transfer of shear stress across the membrane interface. The composite action significantly affects the stresses in the primary and secondary linings. Figure 5 (Su & Bloodworth 2018) shows the expected stress distributions in fully composite, partial composite, and no composite beams due to M_{global}, assuming Euler bending and linear elastic behaviour appropriate to the pre-cracked state. The key takeaway is that composite structural action induces a combination of local bending moment M and local axial force N in each layer, as illustrated in Figure 6 (Bloodworth & Su, 2018) for the partial composite case. To design an effective composite lining system, it's important to carefully consider the stress distributions that M_{global} will induce. This requires a thorough understanding of the properties and behaviour of each component layer, including their axial stiffness and Young's modulus.

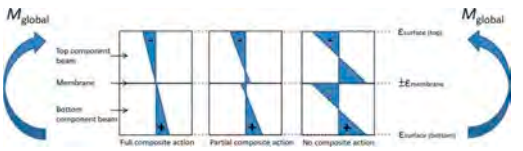

Figure 5. Composite lining stress due to global bending.

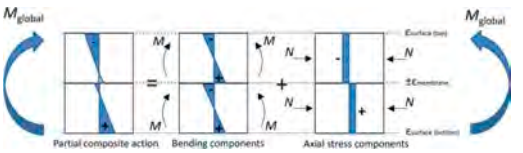

Figure 6. Breakdown of composite lining stresses due to global bending into bending and axial.

4.1.4 *Shear strength*

It is important to ensure the membrane interface has sufficient shear strength to resist external load-induced shear stress. It is essential that neither cohesive shear failure within the membrane material nor adhesive failure at the concrete-membrane interface should occur if the tunnel is designed as a composite lining.

4.2 *Load-sharing effect*

This section explains the load-sharing effect in tunnel lining (1) without and (2) with considering the effect of composite action.

4.2.1 *No considering the effect of composite action*

The load sharing in tunnel linings without considering the effect of composite action can be explained using

Figure 7 (Su & Bloodworth, 2023). The gravity effect and the impact of the membrane shear stiffness (i.e., composite action) are ignored in this example. Only the normal stiffness of the membrane interface is considered. The tunnel has an equal thickness in primary and secondary linings and a 10mm thick sprayed membrane in the middle. When the membrane interface is very stiff, imagined with infinite normal stiffness, it will transfer approximately 50% of the external forces to the secondary lining with effectively zero strain in the membrane. In this case, the deformation of the primary and secondary linings will be the same. The membrane interface will experience the maximum normal stress but the minimum normal strain.

If the membrane's normal stiffness gradually reduces, the primary lining deformation will gradually become greater than the secondary lining. In an extreme case, if the membrane interface has zero normal stiffness (becoming a 10mm air gap between the two linings), the primary lining may take all the external force if its deformation is less than 10mm, and the secondary lining would take none and therefore have no deformation. In this case, the membrane interface will experience the minimum normal stress but the maximum normal strain. This qualitative description is also valid for scenarios where the forces are applied to the sprayed membrane extrados (as would be conceptualised for the groundwater pressure), provided the membrane is still bonded. Besides the normal stiffness of the membrane, the load sharing for a permanent SCL tunnel with a bonded membrane is also affected by the relative lining thickness and the direction of the loading.

Figure 7. Schematic diagram for a composite lining under uniform external loading.

If the membrane is assumed to be unbonded in the long term, based on the pre-construction test of the membrane interface, it can be assumed that the primary lining will resist all the long-term ground loads, and the secondary lining will resist all the long-term groundwater pressure for a fully tanked composite SCL tunnel. This assumption can be used at the preliminary design stage for SCL tunnels constructed in both permeable and impermeable ground. For the latter case, very little long-term consolidation load will be shared by the secondary lining due to the relatively low normal stiffness of the membrane interface when compared to the concrete linings.

4.2.2 *Considering the effect of composite action*

Composite action leads to different short-term and long-term effects on load sharing in tunnel linings.

In the short term, right after installing the sprayed membrane and secondary lining and before any external ground loads or groundwater pressure is applied, the sprayed membrane is bonded to both lining layers. It will restrict the secondary lining movement from the early-age thermal and shrinkage effects. This will usually lead to tensile stress being generated in the secondary lining. The maximum tensile stress usually occurs at the crown and knee position, as shown below in Figure 8 (Su & Bedi, 2019). This stress at the knee position is usually not a concern due to the design of either a construction joint or a full-moment connection. The maximum tensile stress at the secondary lining crown is usually a main concern. The higher the degree of composite action (e.g., the higher the shear stiffness of the membrane interface), the greater the maximum tensile stress at the secondary lining crown. Hence, the greater the risk of secondary lining cracks.

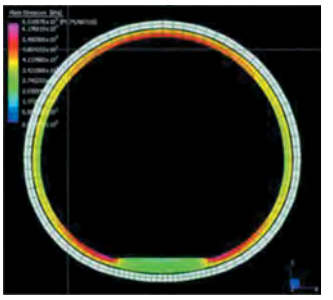

Figure 8. Secondary lining stress under early-age thermal and shrinkage effect for a composite SCL tunnel.

In the long term, after the long-term ground load and groundwater pressure are shared between the primary and secondary linings, the generated bending moment will be partly converted to axial compression and tension force in the primary and secondary linings, as explained previously. The quantity of this conversion is governed by the shear stiffness of the membrane interface. In addition, to understand how much the bending moment will be converted to axial force, it is also important to understand which lining will take the converted compression and tension. Figure 9 (Su, 2022) shows that the composite action-induced axial compression and tension depend on the tunnel lining deformation shape. If the tunnel is elongating horizontally, axial tension will be generated in the secondary lining at the crown and invert and in the primary lining at the axis level. In comparison, if the tunnel is elongating vertically, axial tension will be generated in the primary lining at the crown and invert and in the secondary lining at the axis level.

4.3 *Stress status of the membrane interface*

This section explains the stress status of the membrane interface under (1) early-age thermal and shrinkage effect, (2) external water pressure, (3) long-term consolidation loads, (4) other loads and (5) combined effects.

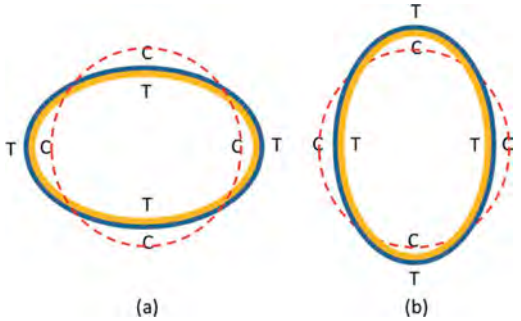

Figure 9. The positions around tunnel lining where composite action-induced tension and compression will occur.

4.3.1 *Stress induced by early-age thermal and shrinkage*

When the secondary lining is installed on the sprayed waterproofing membrane substrate, its early-age thermal and shrinkage effect will lead to a volume contraction of the lining. Due to the double-bonding nature of the sprayed membrane, tensile stress will be generated at the primary-membrane and secondary-membrane interfaces, as well as the sprayed membrane itself.

4.3.2 *Stress induced by groundwater pressure*

The stress states of the sprayed membrane under different groundwater pressure application positions are explained in this section. To facilitate the understanding of this topic, a visual representation of the interaction between the primary lining, sprayed membrane, and secondary lining in response to water pressure is shown in Figure 10 (Su & Bloodworth, 2022). The vertical bars represent the axial stiffness of the primary and secondary linings, which generate internal strains and stresses to resist external loading. The hand holding between the people represents the interface between the membrane and two linings.

In case 1, water pressure applied to the primary lining extrados is resisted by both linings and the membrane. In this case, the linings, membrane, and interfaces are in compression in the normal direction.

In case 2, when water pressure applies to the membrane extrados, the membrane, secondary lining, and secondary interface are in compression, but the primary lining and primary interface are in tension. If the magnitude of the water pressure exceeds the tensile strength between the primary lining intrados and the membrane extrados, debonding will occur. It is important to note that the membrane itself will not be in tension.

When short-term ground loading is superposed on the primary lining, its stress state changes from tension to compression. At the tunnel crown area, the membrane and the secondary interface could be in tension due to the self-weight of the secondary lining. As case 2 introduces tension at the primary-membrane interface and is a more conservative design assumption, its stress status will be used in the following discussion.

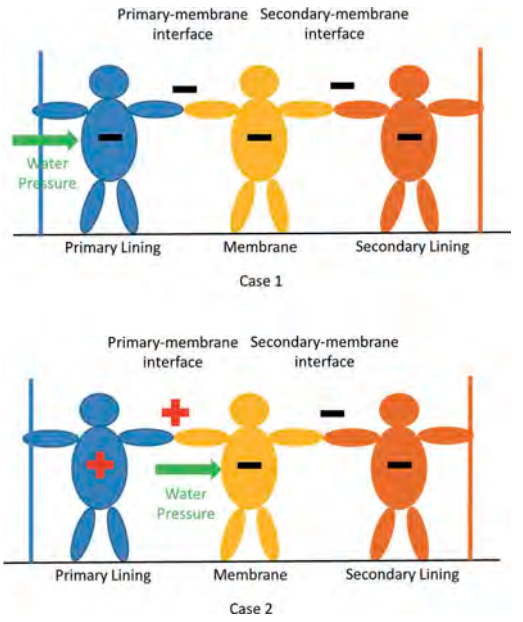

Figure 10. Holding hand analogy for load effects in membrane interface when water pressure on primary lining extrados (case 1) and membrane extrados (Case 2).

4.3.3 *Stress induced by long-term consolidation loads*

If composite SCL tunnels are constructed in impermeable stiff clay, the long-term consolidation will apply loads to the primary lining extrados, introducing compression in both interfaces and the sprayed membrane.

4.3.4 *Stress induced by other loads*

Depending on the individual project requirements and environment, the tunnel lining might experience other types of loads, such as internal downloads loads, etc. This will introduce local tensions in both interfaces and the sprayed membrane.

4.3.5 *Final stress status*

Therefore, the final stress status of the two interfaces and the membrane itself are subjected to the combined effects of the above-mentioned sources. The effect of the first three loadings is shown below in Table 2, with EAT, GWP, and LTC representing early-age thermal and shrinkage, groundwater pressure and long-term consolidation loads.

5 DESIGN OF COMPOSITE SCL TUNNELS

This section first presents the behaviour of the sprayed membrane within a composite tunnel through its whole life cycle, followed by recommended analysis stages. The suggested sprayed membrane properties for numerical analysis are provided as well.

Table 2. Stress status of membrane interface under different loadings.

	EAT	GWP	LTC
Primary interface	Tension	Tension	Compression
Sprayed membrane	Tension	Compression	Compression
Secondary interface	Tension	Compression	Compression

5.1 *Membrane behaviour in composite SCL tunnels*

To ensure optimal performance of the composite lining, the sprayed membrane must remain firmly bonded to both primary and secondary linings under the individual or combined action of compression, tension, and shear. This requirement applies to both short- and long-term scenarios and dry and wet conditions. Dry conditions refer to ambient temperature sprayed membranes with no direct water exposure or low moisture content. Wet conditions refer to sprayed membranes at ambient temperature, either directly exposed to water or with high moisture content.

To achieve this, it is crucial to understand the timeline behaviour of sprayed membranes within composite SCL tunnels. A simplified explanation of membrane behaviour in low-permeability stiff clay or high-permeable weak rock can be found in Figure 11 (Su & Bloodworth, 2023) and the accompanying bullet points. It is important to note that this does not consider the freeze and thaw effects on sprayed membranes. The behaviour of the sprayed membrane can be split into two stages – stage 1 is the loading stage, and stage 2 is the relaxation stage.

Stage 1 starts with installing the membrane and secondary lining with zero membrane shear stress and shear displacement (point a). After this point, the early-age thermal and shrinkage effect occurs, leading to certain stress generated in the membrane. After that, the long-term consolidation effect begins if the tunnel is constructed in impermeable stiff clay. For tunnels constructed in the permeable ground, the dewatering/depressurisation commissioned during the ground excavation and primary lining construction stops. Hence, the membrane interface's normal and shear stress and displacement start to increase.

Stage 1 ends at point b when long-term consolidation is completed for tunnels constructed in stiff clay, and dewatering/depressurisation effects disappear for tunnels in permeable ground. The membrane is still dry and without any creep within stage 1. At this point, the normal and shear stresses are the greatest throughout their lifetime. It should be noted that a certain degree of creep should occur, and the membrane gradually becomes wet during stage 1. However, this figure neglects these effects for demonstration purposes to ensure the maximum interface stresses are obtained.

After point b, creep and moisture movement into the membrane begins. They will reduce the membrane's stiffness, reducing normal and shear stress and increasing normal and shear displacement. These effects continue and, in theory, could finish at either point c or d.

At point c, a small amount of normal and shear stresses is maintained within the membrane, and the normal and shear displacement of the membrane is greater than at point b.

In the theoretical maximum case point d, very little normal or shear stress is maintained within the membrane, and the normal and shear displacement reaches the theoretical maximum value.

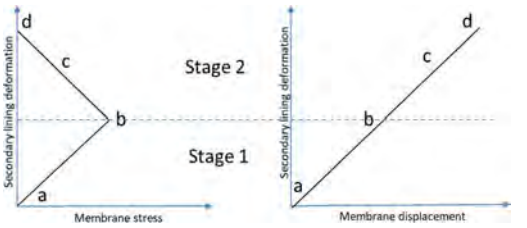

Figure 11. Timeline behaviour of sprayed membrane within a composite SCL tunnel.

5.2 *Recommended analysis stages*

Based on the description of the timeline behaviour of the sprayed membrane above, three stages are suggested to be analysed, and lining and membrane performance are to be checked according to Figure 11.

At point a, check the interface robustness for water pressure on the primary lining extrados. The secondary lining is only resisting its own self-weight and early-age thermal and shrinkage-induced stresses.

At point b, with the dry membrane properties, the membrane interface normal and shear stresses are greatest and should be checked against short-term dry membrane interface tensile/shear strain and stress limits. The interface robustness should be checked by assuming water pressure on the primary lining extrados. Note that this is a theoretical point for the maximum membrane interface stress in an SCL tunnel with a permanent primary lining.

At point c, with the wet membrane properties, the normal and shear strain (displacement) of the membrane interface is the greatest and should be checked against long-term wet membrane interface tensile/shear strain and stress limits. The interface robustness should be checked for water pressure on the membrane extrados. The primary and secondary lining capacity should be checked at each of the above stages. The capacity of the tunnel linings should be checked following the relevant concrete design standard or industry guidance, which will not be expanded here.

5.3 *Selection of interface parameters*

Su and Bloodworth (2016) carried out a comprehensive laboratory testing programme on element specimens cut from composite SCL panels (with

sandwiched EVA-based sprayed membrane) with different primary lining substrate surface preparations and membrane thicknesses, loaded in compression, tension and shear under ambient laboratory climate conditions (e.g., 15-20°C temperature and 40-60% relative humidity) under immediate short-term loading.

The variation in moisture content of the EVA-based membrane observed in field measurements can affect its mechanical properties, as suggested by Holter (2016) and confirmed by Diez et al. (2019). Table 3 provides a range of key mechanical interface parameters for EVA-based membranes in dry and wet conditions. However, it should be noted that the limiting tensile and shear strains under long-term loadings at different stress levels have not yet been determined, and this is an important area for future research. Table 3 lists recommended interface parameters for the sprayed membrane interface, adopting the option 1 modelling approach as mentioned in the next section.

Table 3. Recommended membrane interface parameters.

	Unit	Dry membrane	Wet membrane
Normal stiffness (Kn)	GPa/m	4-8	0.55-0.85
Shear stiffness (Ks)	GPa/m	2-4	0.30-0.35
Tensile strength	MPa	0.8	0.35-1.00
Shear strength	MPa	2.0	Not reported*

* A value of 0.5MPa can be used for modelling purposes, subjected to project testing verification

6 MODELLING COMPOSITE SCL TUNNELS

To effectively simulate composite action in a sprayed membrane interface, commercially available finite element or finite difference software can be used. Closed-form analytical solutions are generally avoided due to the complexity of SCL design, the construction sequence, and non-circular tunnel profiles. "Beam and Spring" models are typically used to simulate the secondary lining behaviour. However, these models cannot realistically simulate the stage construction of the primary lining and complex soil-structure interaction. In more complex situations, such as junctions and caverns with multiple side galleries, 3D models may be used.

For the routine design of SCL tunnels, 2D plane strain modelling is the most common and stress relief factors obtained from detailed 3D modelling experience can be applied. A list of key considerations for simulating composite SCL tunnels is provided in the full design guidance document, which is not included in this paper due to paper length limitations. The following sections will introduce the three key topics in the numerical modelling of composite SCL tunnels: (1) simulation of composite action, (2) simulation of the membrane interface, (3) simulation of groundwater pressure on the membrane, and (4) simulation of early-age thermal and shrinkage effect.

6.1 *Simulation of composite action*

When designing an SCL tunnel with composite action, it's important to use appropriate modelling techniques to simulate the interaction between the primary and secondary lining layers. Traditional 2D beam or 3D shell elements should be avoided as they cannot realistically model the stress distribution through the depth of the linings. Hence, no composite action will be simulated using two beam elements (representing two layers of concrete linings) and one layer of membrane interface. Instead, 2D zones or 3D volume elements should be used for the linings and interface elements for the sprayed concrete-sprayed membrane interface to simulate composite action accurately. It's also important to ensure that sufficient elements are present through the thickness of the linings to model the flexural behaviour and any potential cracking.

When using 2D zones or 3D volume elements to model primary and secondary linings in SCL tunnel analysis, the output is stresses rather than internal force resultants such as axial force and bending moment, which are required for thrust-moment capacity curves used in design verification. To obtain these internal force resultants, 2D beam or 3D shell elements can be attached to the centroidal axis of each lining layer, with negligible stiffness, to follow their deformation. This is known as the "dummy beam" approach. To ensure accurate analysis, it is important to appropriately scale the output of axial force and bending moment during post-processing. Another option is to use built-in functions in some finite element programs to calculate lining forces automatically based on the stresses.

6.2 *Simulation of membrane interfaces*

To effectively simulate composite action in SCL tunnels, the interface used in the numerical analyses must be capable of transferring compressive, tensile, and shear stresses between the two layers of zones or volume elements. Option 1, which uses interface elements, is typically the most suitable for simulating the membrane interface in the composite SCL tunnel. This is because the thickness of the membrane is relatively small compared to the lining thickness. To implement Option 1, normal (cross the membrane) and shear (along the membrane) springs with tension and shear strength cut-offs can be utilised to create interface elements. Figure 12 (Su & Bloodworth, 2019) provides a schematic example of this approach.

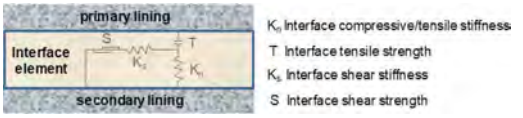

Figure 12. Interface element approach (option 1).

On the other hand, when carrying out numerical calibration against composite beam tests, neither adhesion nor cohesion failure is usually a concern. Instead, the membrane thickness is significant compared with the total lining thickness (e.g., >5% of total thickness), and if ignored, predicted results will differ significantly from laboratory test results. In this case, Option 2 should be adopted with the sprayed membrane simulated with 2D zones or 3D volume elements, as shown in Figure 13 (Su & Bloodworth, 2019). Option 3 is the most comprehensive method to simulate composite action in situations where both the membrane thickness effect and adhesion and cohesion failure mechanisms need to be considered. In this approach, the 2D zones or 3D volume elements representing the membrane are assigned actual material parameters, and the appropriate interface parameters are assigned to each interface element, as shown in Figure 14 (Su & Bloodworth, 2019).

Figure 13. Zone or volume element approach (option 2).

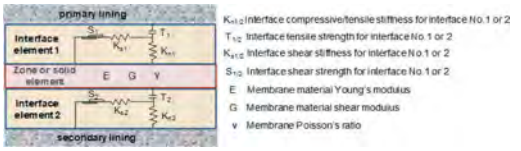

Figure 14. Hybrid approach (option 3).

6.3 *Simulation of groundwater pressure*

The application of groundwater pressure to the extrados of the primary lining was achieved by assigning groundwater within the ground, resulting in the groundwater pressure being applied to the extrados of the primary lining. To move the application of groundwater pressure to the extrados of the membrane interface, a pair of mechanical loads should be applied to the model, as shown in Figure 15 (Su & Bloodworth, 2022). These loads consisted of outward forces that cancelled out the groundwater pressure applied from the soil and inward forces that applied the groundwater pressure at the desired location. The magnitudes of these forces should be automatically calculated as a function of their depth below the phreatic surface in the model. The effect of groundwater pressure-induced membrane interface debonding is not discussed here but can be referred to Su (2023).

6.4 *Simulation of early-age thermal and shrinkage*

The early-age thermal and shrinkage effect of the concrete lining can be simulated by assigning compressive strains with age-dependent concrete

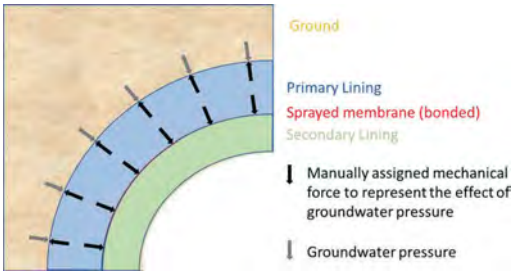

Figure 15. Simulation of groundwater pressure application for bonded membrane using mechanical forces.

Young's modulus in a stepwise approach. Alternatively, an equivalent total strain can be assigned to the matured concrete Young's modulus in a one-step approach to achieve the same effect. The compressive strain is derived from the concrete mix specification and testing performance requirement. Combined with the restraint effect of the membrane substrate, tensile stress at the membrane-concrete interface and the membrane itself, as well as in the concrete lining hoop direction, will be developed, as shown in Figure 8.

7 CONCLUSIONS

This paper provides a glimpse of the updated design chapter for the next version of the ITAtech Lining and Waterproofing Activity Group design guidance document. This design chapter is still under development and review. Hence, new information might be added. Notwithstanding, it is hoped that this paper will serve as a valuable resource for professionals engaged in the design and construction of composite SCL tunnels, enabling them to make informed decisions and enhance the overall efficiency of such tunnel projects. Last but not least, long-term stress and strain monitoring data for composite linings are sought to verify the engineering principles and proposed design approaches.

REFERENCES

Aitchison, B., Oliveira, D., Backhouse, D., Netterfield, R., 2018. Design and construction of a shallow cover tunnel junction using sprayed concrete, Sydney Australia. In: Proceedings of the 8th International Symposium on Sprayed Concrete, Trondheim, Norway, pp.9–23.

Amoushahi, S., Tremblay-Laforce, A., Habimana, J., Thomas, A., 2022. Construction challenges of tunnel waterproofing using spray-applied membranes. In: Proceedings of the Tunnelling Association of Canada Conference 2022. Vancouver, Canada.

Bedi, A., Gupta, S., Trivedi., Pengelley., 2022. Design & Construction of Mumbai Metro Line 3 Sarah Road crossover cavern using permanent sprayed concrete linings. In: Proceedings of the World Tunnel Congress 2022, Copenhagen, Denmark.

Bloodworth, A., Su, J., 2018. Numerical analysis and capacity evaluation of composite sprayed concrete lined tunnels. Underground Space, 3(2), 87–108.

Diez, R., Pound, C., McKibbins, L., Khosravi, N., 2019. Testing of sprayed waterproof membranes and implications for composite action. Tunnelling Journal, Feb/March 2019. 26–33.

Dimmock, R., Haig, B., Su, J., 2011. Spray applied waterproofing membranes–key success factors and development of efficient sprayed concrete tunnel linings. In: Proceedings of the 6th International Symposium on Sprayed Concrete, Tromso, Norway. pp. 110–124.

Holter, K., 2013. Loads on sprayed waterproofing tunnel linings in jointed hard rock: a study based on Norwegian cases.

Holter, K., 2016. Performance of EVA-Based membranes for SCL in hard rock. Rock Mechanics and Rock Engineering, 49(4), 1329–1358.

ITAtech., 2013. ITAtech design guidance for spray applied waterproofing membranes. ITAtech Activity Group Lining and Waterproofing.

Nasri, V., Bakhshi, M., Maurel, G., Saghaee, R., 2023. Montreal metro blue line extension tunnels and caverns. In: Proceedings of the World Tunnel Congress 2023, Athens, Greece. pp. 1640–1647.

Nasri, V., Vovou, T., 2023. Design and construction of the deepest underground station in Canada. In: Proceedings of the World Tunnel Congress 2023, Athens, Greece. pp. 1648–1655.

Su, J., 2022. Adopting “less is more” principle for efficient design of Composite SCL Tunnels. In: Proceedings of the World Tunnel Congress 2022, Copenhagen, Denmark.

Su, J., 2023. A numerical investigation of the lining performance of composite SCL tunnels with debonded sprayed waterproofing membrane. In: Proceedings of the World Tunnel Congress 2023, Athens, Greece, pp. 994–1002.

Su, J., Bedi, A., 2019. Load-sharing effect for sprayed concrete lined tunnels in various ground conditions. In: Proceedings of the XVII ECSMGE, Reykjavik, Iceland. Icelandic Geotechnical Society, Reykjavik, Iceland.

Su, J., Bloodworth, A., 2014. Experimental and numerical investigation of composite action in composite shell linings. In: Proceedings 7th International Symposium on Sprayed Concrete; Sandefjord, Norway. pp. 361–374.

Su, J., Bloodworth, A., 2016. Interface parameters of composite sprayed concrete linings in soft ground with spray-applied waterproofing. Tunnelling and Underground Space Technology, 59, 170–182.

Su, J., Bloodworth, A., 2018. Numerical calibration of mechanical behaviour of composite shell tunnel linings. Tunnelling and Underground Space Technology, 76, 107–120.

Su, J., Bloodworth, A., 2019. Simulating composite behaviour in SCL tunnels with sprayed waterproofing membrane interface: A state-of-the-art review. Engineering Structures, 191, 698–710.

Su, J., Bloodworth, A., 2022. Groundwater pressure induced failure of sprayed waterproof membrane interface in tunnels. Proceedings of the Institution of Civil Engineers – Geotechnical Engineering.

Su, J., Bloodworth, A., 2023. Determination of the stress-strain demand curve of sprayed waterproofing membrane interface in composite SCL tunnels. Tunnelling and Underground Space Technology, 142.

Su, J., Thomas, A., 2015. Design of sprayed concrete linings in soft ground—a Crossrail perspective. Crossrail Project: Infrastructure design and construction, 1, pp.123–136.

Tunnelling for a Better Life – Yan, Celestino, Thewes & Eberhardt (Eds)
© 2024 The Author(s), ISBN 978-1-032-80042-4
Open Access: www.taylorfrancis.com, CC BY-NC-ND 4.0 license

Self healing materials for preventing tunnel crystalline damage: Anti-calcium leaching, mechanical performance, self-healing mechanism

Yueping Tong, Fei Ye, Chongming Tian, Yin Jiang, Junyuan Zhang, Han Wang, Bowen Wu & Xingbo Han
Chang'an university, Xi'an, China

ABSTRACT: The crystalline blockage disease in tunnel drainage systems is closely linked to the calcium leaching process of shotcrete, especially in water-rich tunnels. Groundwater infiltrates the initial support shotcrete through cracks, continuously transporting calcium material from the hydration products of cement into the drainage system. This leads to a significant reduction in the tunnel's drainage capacity and a notable increase in safety and operational risks to the lining structure. In order to reduce the generation of calcium crystallization within the tunnel from the source, this paper employs a deionized water immersion test method. Through the determination of parameters such as the pH value of the leaching solution, calcium ion concentration, mechanical strength, variation rate of crack length, and relative strength recovery, as well as microstructure analysis, it investigates the effectiveness of self-healing materials in improving the resistance of shotcrete to calcium leaching and their applicability in tunnels. The research findings indicate that self-healing materials can effectively enhance the resistance of shotcrete to calcium leaching. The calcium ion concentration in the leaching solution is significantly lower than that of ordinary shotcrete, with a reduction rate of up to 80.72%. Self-healing materials enable the shotcrete to withstand significantly higher bending loads, and they also contribute to substantial improvements in flexural strength and ductility. These materials also exhibit good repair effects on pre-existing cracks in the mortar, with a relative compressive strength recovery rate of up to 88%. Microscopic observations reveal the growth of insoluble micro-crystallizations within the self-healing shotcrete. These micro-crystallizations fill the capillaries and interface cracks in the shotcrete, reducing the seepage pathways between groundwater and shotcrete. This suggests a certain potential for resisting calcium leaching.

Keywords: Tunnel crystallization disease, Preventive measures, Self-healing materials, Calcium dissolution performance, Mechanical properties, Self-healing effect

1 INTRODUCTION

In recent years, a significant number of tunnels worldwide have experienced the phenomenon of crystalline blockage in their drainage systems (Jung et al., 2013; Ye et al., 2021). Due to the fact that these drainage systems are concealed within the tunnel structure, addressing this issue has proven to be a challenging task, causing substantial concerns for tunnel operators and maintenance personnel. The blockage of tunnel drainage systems results in a substantial reduction in the tunnel's drainage capacity. If left uncleared, the water pressure acting on the lining continuously increases, exacerbating pre-existing issues in the tunnel, such as cracks and water infiltration. As the water pressure continues to rise, it may even lead to structural damage, including deformation and cracking of the lining. This poses a significant risk to both the operational and structural safety of the tunnel (Xu et al., 2022).

The crystalline substances found within tunnel drainage pipes are primarily composed of calcium carbonate, often mixed with sediments, cement particles, and other particulate matter. Initially, these substances are relatively loose in texture and can be easily flushed away by water. However, over time, these crystalline materials become more compact, adhering to the interior surface of the drainage pipes, forming a hard and high-strength plate-like structure that is difficult to remove. The main source of crystallization in tunnel drains is the Ca^{2+} leaching process of the shotcrete, and mountain tunnels are subject to seepage fields that allow water from within the mountain to continuously converge into the tunnel. Before groundwater can enter the tunnel drainage system, it must first pass through the

DOI: 10.1201/9781003495505-344

tunnel's initial support shotcrete, a process that is actually the root cause of the crystalline clogging problem in tunnels. As groundwater continuously permeates the shotcrete, calcium-rich hydration products in the shotcrete, such as $Ca(OH)_2$ and C-S-H, undergo dissolution-diffusion processes: $Ca(OH)_2$ (s)→ Ca^{2+} + 2 OH^-, C-S-H (s)→x Ca^{2+} + 2x OH^- + $SiO_2 \cdot n$ H_2O (Lu et al., 2021). This leads to a substantial influx of Ca^{2+} into the tunnel drainage system. When these Ca^{2+} come into contact with the air, they react to precipitate calcium carbonate: CO_2 + $Ca(OH)_2$ → $CaCO_3$↓ + H_2O, CO_3^2 + Ca^{2+} → $CaCO_3$↓, HCO_3^- + Ca^{2+} + OH^- → $CaCO_3$↓ + H_2O, The accumulation of calcium carbonate crystals gradually leads to the blockage of the tunnel drainage pipes.

To address the issue of crystalline blockage in tunnel drainage systems, many researchers have suggested that the solution should start with the concrete itself, considering it as the source of the problem (Dietzel et al., 2022; Tian et al., 2020; Galan et al., 2019). Currently, commonly used approaches primarily involve enhancing the compactness of concrete through the addition of mineral admixtures to improve its resistance to calcium leaching. As shown by Thurmann et al. (2015) investigated the anti-leaching effects of various concrete mixtures and proposed that replacing 30% of cement with materials such as fly ash or slag can reduce calcium leaching by 35%, while substituting 15% of cement with higher-activity volcanic ash can reduce it by 55%. Jiang et al. (2023) studied the impact of different levels of glass powder on concrete's resistance to leaching and found that adding 10% of glass powder led to the least calcium ion precipitation and the densest microstructure in concrete. Harer (2017) suggested that using materials such as fly ash and 7% aluminum sulfate accelerant can significantly reduce the calcium leaching in concrete, leading to a reduction of about 65% in calcium ion release. Tang et al. (2016) employed an accelerated calcium leaching test method to study the effect of slag on the calcium leaching process in cement slurry and determined that a slag content of 40% to 50% reflected the optimal resistance to calcium leaching.

However, as tunnel operations continue for longer durations, the incidence of water infiltration and cracking in tunnels increases. To meet the demand for enhanced durability, some scholars have proposed the application of self-healing materials to cement-based materials to achieve self-repair effects in concrete (Ghosh et al., 2009; Van et al., 2011). As shown by Kim (2011) introduced a self-healing technique for post-cracked concrete performance by embedding polyurethane healing agents in mortar. The results demonstrated that the mortar could recover over 50% of its original strength and stiffness after self-repair. Additionally, due to autonomous crack healing, permeability was reduced by factors ranging from 102 to 104. Tran et al. (2009) explored the effectiveness of developing a self-repair system in ordinary concrete using single-component epoxy resin as the healing agent and hollow tubes as the storage system. The research revealed that repeated self-healing was achievable, with strength partially recovered after four days of healing and fully restored after seven days, with an increase of approximately 30% over the initial values. The post-healing crack strength also exceeded that of standard specimens by 32%. Ahn et al. (2010) investigated the self-healing effect of concrete with mineral admixtures through a recrystallization method in practical applications. The results indicated that concrete cracks autonomously healed after three days, with crack widths decreasing from 0.22mm to 0.16mm after seven days of curing. By day 33, nearly complete self-healing had occurred, presenting a viable method for repairing concrete cracks in tunnels.

In summary, self-healing materials offer excellent durability and crack repair capabilities. However, existing research has predominantly focused on the crack repair and strength enhancement aspects of self-healing concrete, with limited attention given to its resistance to calcium leaching. Therefore, this paper, by incorporating self-healing materials into shotcrete, investigates the variations in calcium leaching resistance, compressive strength, flexural strength, and crack development. Microscopic analysis is employed to validate the optimization mechanisms. The research findings present a novel approach to address crystalline blockage in tunnels and leakage-related cracks in linings.

2 MATERIALS AND METHODS

2.1 *Materials*

The cement used is White Dragon brand cement with a grade of P·O 42.5. The coarse aggregate sourced from the Mahu Stone Factory, while the fine aggregate Hanjiang River sand. Local groundwater is supplied for mixing, and a high-performance water-reducing agent with a 40% water-reducing rate is used. The accelerator selected is a non-alkaline liquid accelerator from Shanxi Budongquan Building Materials Co., Ltd., meeting the GB/T35159-2017 standard. The specific performance characteristics of the HZC-1B non-alkaline liquid accelerator provided in Tables 1 and 2.

The self-healing permeable crystalline material (SHM) is provided by Nanjing Paniel Technology Industrial Co., Ltd. The substance's composition was tested using a PANalytical Axios X-ray fluorescence spectrometer, with the test results shown in Table 3. Performance parameters of the SHM were evaluated

Table 1. Chemical composition and physical properties of cement.

CaO	SiO_2	Al_2O_3	Fe_2O_3	MgO	SO_3	TiO_2	K_2O
59.30	19.80	5.23	2.07	0.87	2.05	0.26	0.79

according to the GB18445-2012 standard, and the test results are detailed in Table 4.

Table 2. The property indicators of accelerator.

Solid content /%	pH	Density (g/cm^3)	Setting time/min		Na_2O /%	SO_4^{2-} /%
			Initial time	Final time		
41.2	2.10	1.43	3:31	7:45	0.72	14.9

Table 3. Chemical composition of self-healing material.

CaO	Na_2O	SiO_2	CaO	Al_2O_3	SO_3	Fe_2O_3	MgO
15.68	35.77	28.41	15.68	9.06	6.43	0.84	0.64

Table 4. Properties of self-healing material.

Fineness /%	Water-reduing rate	Difference of setting time /min	Compressive strength ratio		Penetration pressure ratio
			7d	28d	
3.1	2.4	5	108	118	300

2.2 *Mix proportion*

Large panels of shotcrete were prepared on-site at the Shuang Feng Tunnel in Shaanxi for experimental purposes. The control group utilized regular shotcrete, denoted as "OS," while the experimental group used shotcrete with internally incorporated self-healing material, referred to as "SHS." In this mixture, the sand content was 50%, the water-reducing agent dosage was 1% of the cementitious material content, the accelerator dosage was 4% of the cementitious material content, and the self-healing material was internally incorporated at 3% of the cementitious material content. The shotcrete mix proportions are provided in Table 5.

Table 5. Shotcrete mix proportions/(kg/m^3).

No.	Cement	Sand	Stone	Water	SHM	Sp.	Acc.
OS	410	868	843	183	0	4.1	16.4
SHS	397.7	868	843	183	12.3	4.1	16.4

2.3 *Specimens procedures*

In accordance with GB50086-2001 "Technical Specification for Soil and Rock Anchor and Shotcrete Support," wet shotcrete large panels were produced using the wet-spray method at the tunnel site. The dimensions of the large panel were 450 mm × 350 mm × 120 mm. Before spraying the shotcrete, the large panel test molds were positioned against the wall at a 75º angle with the ground. The nozzle was positioned vertically to the test mold, with a distance between 0.95 m to 1.20 m. After 1 day of forming the large panel, it was demolded, and a multifunctional cutting machine was used to cut the large panel into cubes measuring 100 mm × 100 mm × 100 mm and prisms measuring 100 mm × 100 mm × 400 mm. These specimens were then used for immersion testing. The immersion tank dimensions were 40 cm × 50 cm × 22 cm, and each tank was filled with 19.5 L of deionized water to fully submerge the test specimens, simulating the calcium leaching process of shotcrete. The test process is depicted in Figure 1.

2.4 *Testing method*

2.4.1 *Calcium dissolution test*

At 1 day, 3 days, 7 days, and 28 days of immersion, 1000 mL of leaching solution was collected for analysis. A PXSJ-226 ion meter was employed to

Figure 1. The forming process of shotcrete slab and soaking process.

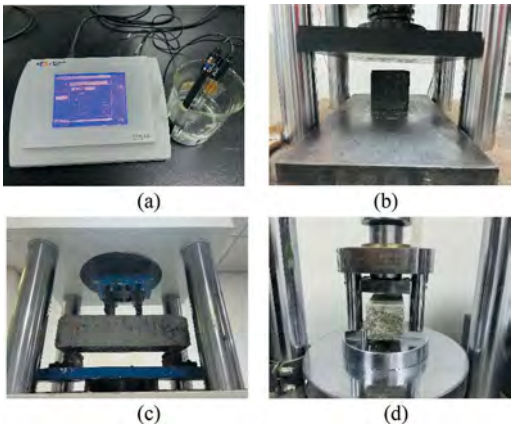

Figure 2. Macroscopic test of the shotcrete specimen (a) Calcium dissolution test (b) Compressive strength (c) Four-point bend strength test (d) Mortar compressive strength tester.

conduct Ca2+ and pH tests on the leaching solution. Each test was performed six times, and after each test, the electrodes were rinsed with deionized water and dried to minimize errors. The average values were then calculated. The testing procedure is illustrated in Figure 2(a).

2.4.2 *Compressive strength and four-point bend test*
After immersing the specimens for 1 day, 3 days, 7 days, and 28 days, the specimens were removed for compressive strength and four-point bending tests conducted in accordance with the GB/T 50081-2009 standard. For the compressive strength test (Figure 2-(b)), the specimen was tested using the servo-hydraulic loading device, and the compressive strength value was calculated based on Equation (1). For the four-point bending test (Figure 2(c)), the DYW-2000 universal material testing machine was used. The flexural strength of the specimens was calculated using Equation (2). Three specimens were tested for each group, and the arithmetic average was determined.

$$f=\frac{\frac{1}{3}\sum_{i=1}^{3}F_i}{\mathrm{A}} \tag{1}$$

Where, f is the compressive strength (MPa); F_i is the peak load of the three specimens (KN); A is the cross-sectional area (mm^2).

$$f_t=\frac{Fl}{\mathrm{bh}^2} \tag{2}$$

Where, f_t is the flexural strength (MPa); F is the peak load of the specimen (KN); l is the distance between the bottom supports of the specimen (mm); b is the width of the specimen (mm); h is the height of the specimen (mm).

2.4.3 *Self-healing crack test*
The testing procedure for evaluating the self-healing effect of self-healing shotcrete cracks is as follows: 1) Prepare mortar specimens measuring 70 mm × 70 mm × 70 mm; 2) After curing for 7 days, apply compressive force to the mortar specimens until cracks appear, as shown in Figure 2(d), and record the compressive strength as the initial compressive strength of the mortar, denoted as I_0; 3) Place the cracked specimens in deionized water and observe the crack healing process. After 28 days, conduct a second compressive strength test, and calculate the relative strength recovery rate using Equation (3).

$$K_I=\frac{I_R}{I_0}\times 100\% \tag{3}$$

Where, I_0 is the initial compressive strength, I_R is the secondary compressive strength after the crack healing process, K_I is the relative strength recovery rate.

2.4.4 *SEM test*
After the specified leaching time, the shotcrete specimens to be tested are cut into small pieces of approximately 0.5 mm in size. Subsequently, these pieces are dried in a drying oven for 24 hours. The dried, electrically conductive samples are then prepared for testing, and their microscopic appearance is observed. The testing equipment used is the Tescan Mira4 scanning electron microscope (SEM).

3 RESULTS AND DISCUSSION

3.1 *Anti-calcium ion leaching of shotcrete*

Based on the pH change curves in Figure 3, it can be observed that both ordinary shotcrete and self-healing shotcrete exhibit relatively high pH values within the first 7 days of leaching, with minor variations. The pH value of ordinary shotcrete is around 11.8, while that of self-healing shotcrete is above 11.4. As the leaching process progresses, the hydration reactions in the shotcrete become more extensive, and secondary hydration reactions occur, consuming a significant amount of alkaline compounds. By the end of the 28-day leaching period, the pH values for ordinary shotcrete and self-healing shotcrete have decreased to 10.3 and 9.9, respectively.

Figure 4. illustrates the changes in Ca^{2+} concentration in the shotcrete. The data indicate that as the leaching time increases, the Ca^{2+} leaching efficiency in self-healing shotcrete gradually decreases. The Ca^{2+} concentration in self-healing shotcrete is significantly lower than in ordinary shotcrete, with a reduction rate of up to 34.69% to 80.72%. Self-healing materials contain a substantial amount of hydrophilic crystalline growth factors. Under conditions of water infiltration, these growth factors move through the internal moisture of the shotcrete,

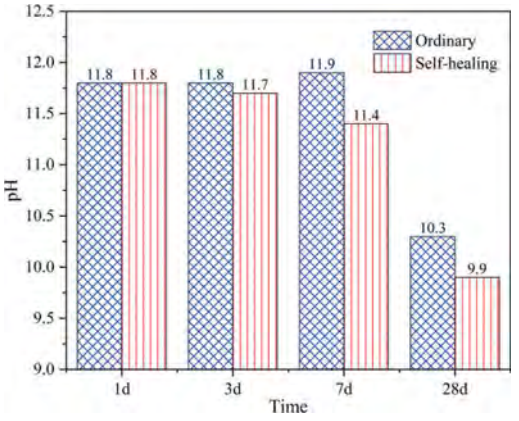

Figure 3. The pH change of the leaching solution.

triggering secondary cement hydration reactions and continuously generating insoluble micro-crystallizations. These micro-crystallizations serve two main purposes: 1) They can penetrate into the capillary cracks within the shotcrete, thereby enhancing the shotcrete's resistance to water permeation; 2) They can fill the pre-existing cracks in the shotcrete or new cracks formed due to leaching, thus cutting off the flow pathways between groundwater and the shotcrete lining. This significantly improves the shotcrete's resistance to calcium leaching, and this process is referred to as the self-healing process, as depicted in the schematic diagram in Figure 5.

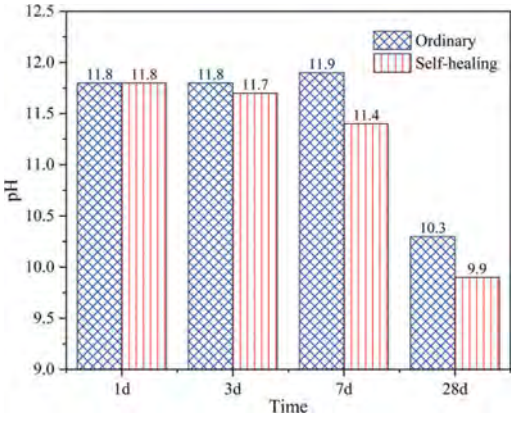

Figure 4. Variation of calcium ion concentration in shotcrete.

3.2 *Compressive strength of shotcrete*

The compressive strength variation of shotcrete is shown in Figure 6. After 1 day of leaching, the compressive strength of self-healing shotcrete and ordinary shotcrete is essentially similar. At 3 days of leaching, the compressive strength of shotcrete increases significantly. By 7 days of leaching, the change in compressive strength is minimal. After leaching for 28 days,

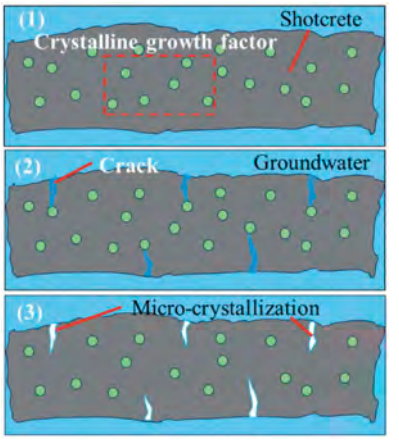

Figure 5. Crystal growth factor healing mechanism.

the compressive strength of ordinary shotcrete and self-healing shotcrete is 31.190 MPa and 30.163 MPa, respectively. Overall, the inclusion of self-healing materials has resulted in a slight reduction in the compressive strength of shotcrete. This outcome may be due to the relatively high content of self-healing materials, which tend to aggregate within the shotcrete, leading to poor homogeneity and limited improvement in the compressive strength of shotcrete.

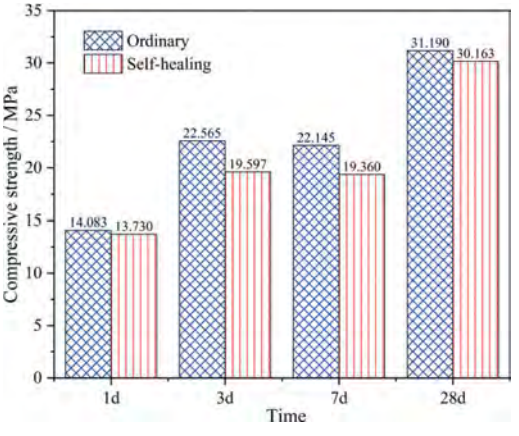

Figure 6. Compressive strength of shotcrete.

3.3 *Bending property of shotcrete of shotcrete*

3.3.1 *Failure pattern*

The fracture morphology of the two types of shotcrete after 28 days of leaching is shown in Figure 7. From the figure, it can be observed that the ordinary shotcrete instantly fractures from the middle portion when it reaches the ultimate load, resulting in an incomplete form. In contrast, the shotcrete containing self-healing materials exhibits a distinct difference in the mode of failure. Before reaching the maximum load, fine cracks appear in the lower middle section

of the specimen and continue to expand, but they do not completely split. Moreover, it is evident that the loading time for self-healing shotcrete is longer, and the appearance of cracks is delayed.

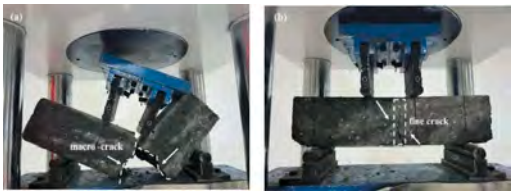

Figure 7. Cracking pattern of (a) ordinary shotcrete and (b) self-healing shotcrete.

3.3.2 *Calculating crack width*

Due to the varying crack failure patterns observed in the shotcrete, it is necessary to quantitatively assess the changes in crack length using Equation (4). Figure 8 illustrates the curve displaying the rate of change in cracks in the shotcrete. In comparison, self-healing shotcrete exhibits a higher rate of change in crack length. This results in longer and more intricate cracks, with the rate of change in crack length increasing by 13.8% to 52.2%. This observation suggests that self-healing shotcrete can accommodate more significant deformations and is characterized by a ductile failure mode. In contrast, ordinary shotcrete exhibits brittle failure, with a smaller load-carrying capacity when subjected to larger crack openings.

$$R_L = \frac{L_1 - L_0}{L_0} \times 100\% \quad (4)$$

Where, R_L is the percentage change in crack length, (%); L_1 is the crack length, (mm); L_0 is the initial specimen height, L_0=100 mm.

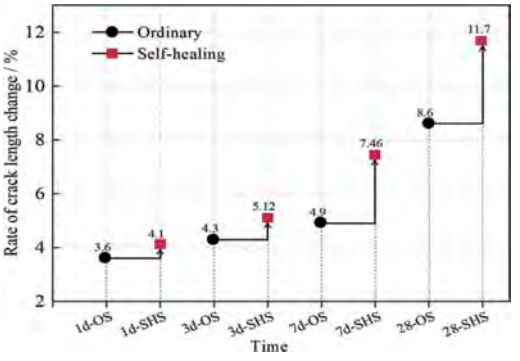

Figure 8. Rate of crack length change of shotcrete at different time.

3.3.3 *Flexural strength*

The variation in the flexural strength of shotcrete is depicted in Figure 9. Both types of shotcrete show an increasing trend in flexural strength as leaching time progresses. However, in comparison, the self-healing material proves to be more conducive to enhancing the flexural strength of shotcrete. At 28 days, there is an 8.3% increase in strength, with the most significant increase occurring at 3 days, reaching 10%. This underscores the fact that the self-healing shotcrete contains a substantial quantity of micro-crystallizations that serve as bridges, reinforcing its toughness and enabling it to withstand higher bending loads, resulting in improved flexural strength (Diego et al., 2023).

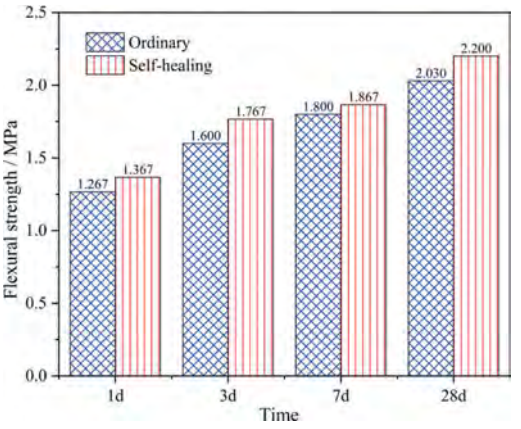

Figure 9. Flexural strength of shotcrete.

3.4 *Self-healing property*

3.4.1 *Crack healing morphology*

The morphology of ordinary mortar and self-healing mortar after prefabricated cracks is shown in Figure 10(a) and (c). When the ordinary specimen is compressed to 88.1 kN, severe damage is evident with large cracks and corner detachment, resulting in poor integrity. In contrast, for the self-healing sample, when subjected to a load of 131.0 kN, only a small crack and a few micro-cracks are observed. After 28 days of immersion, the crack-healing morphology of ordinary mortar and self-healing mortar is presented in Figure 10(b), (d). In the ordinary sample, the original cracks are still clearly visible, showing no healing effect. Conversely, in the self-healing sample, the original cracks and fissures are no longer observable at their initial locations, and large cracks are hardly visible on the surface and sides.

Due to the possibility that micro-crystallizations generated by self-healing materials may form within the shotcrete, assessing the self-healing effect of these materials based solely on changes in surface crack width is not comprehensive (Zeng et al., 2015). Furthermore, the relationship between external changes in crack appearance and the internal self-healing state

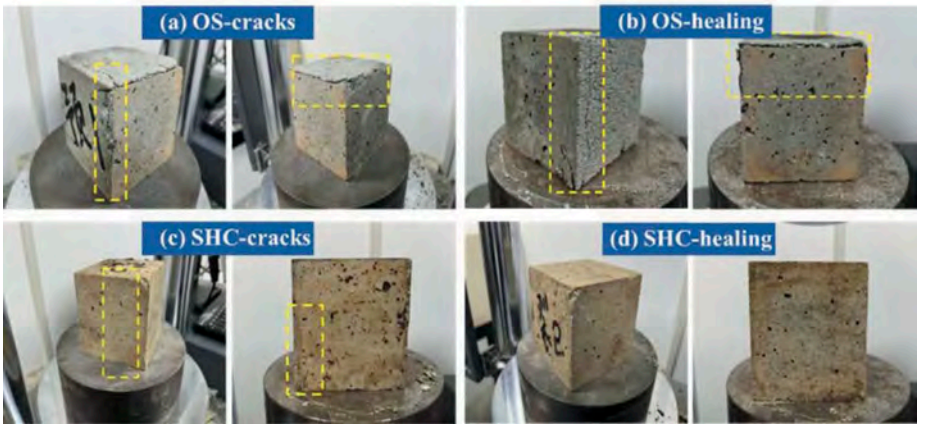

Figure 10. Mortar crack morphology comparison before healing and 28 days healing.

may not necessarily be straightforward. Therefore, the next section provides a more comprehensive evaluation by considering the restoration of mechanical performance.

3.4.2 *Compressive strength of mortar*

Figure. 11 illustrates a comparison of compressive strength before and after healing for the mortar. It is evident that the compressive strength of both the damaged self-healing mortar and the ordinary mortar decreases after 28 days of leaching. However, the self-healing mortar exhibits a smaller reduction in compressive strength, with a post-healing compressive strength that is 3.5 times that of the ordinary mortar. The relative strength recovery rates are 59% for the ordinary mortar and 88% for the self-healing mortar. This indicates that self-healing materials not only facilitate crack healing but also contribute to the restoration of mechanical performance to some extent. This outcome is mainly associated with the inherent characteristics of the healing materials.

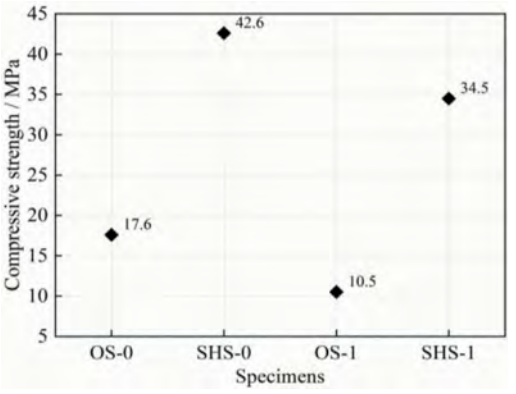

Figure 11. Initial and second compressive strength of specimens.

The self-healing mortar undergo a process of "dehydration-dormancy" to "hydration-activation-crystallization" before and after the creation of cracks. After 28 days, the cracks are substantially healed, resulting in a relatively high compressive strength recovery rate (Victor et al., 1998). This suggests that when groundwater infiltrates the shotcrete in tunnels, self-healing materials play a role in repairing leaching fissures and larger cracks, filling voids created by cracks and defects with generated micro-crystallizations, sealing the cracks, and reducing the risk of calcium leaching (Qian et al., 2010; Yang et al., 2010).

3.5 *SEM analysis*

Figure. 12 presents SEM images of ordinary shotcrete and self-healing shotcrete at 1, 7, and 28 days, respectively. In the early stages, both ordinary and self-healing specimens exhibit plate-like calcium hydroxide and unhydrated cement particles. The ordinary specimen's interface regions show pre-existing cracks, whereas the self-healing specimen's interface is denser. After 7 days of leaching, it is observable that at the crack interfaces of ordinary specimens, cracks are more pronounced, and calcium hydroxide is still present. In contrast, the self-healing specimens have grown a substantial network of micro-crystallizations at the interface, and noticeable cracks are not visible. By the 28th day, the internal structure of the ordinary specimens exhibits short rod-shaped ettringite and C-S-H gel. In contrast, the self-healing specimens primarily consist of fibrous gel. With increasing leaching time, the self-healing specimens shift from localized micro-crystallizations to a substantial quantity of micro-crystallizations. These micro-crystallizations deposit at the surface or interfaces of the paste, forming a network structure (Reinhardt et al., 2003; Chu et al., 2014). This network structure fills the capillaries within the paste and serves as a bridge in the transition zones between interfaces. The internal

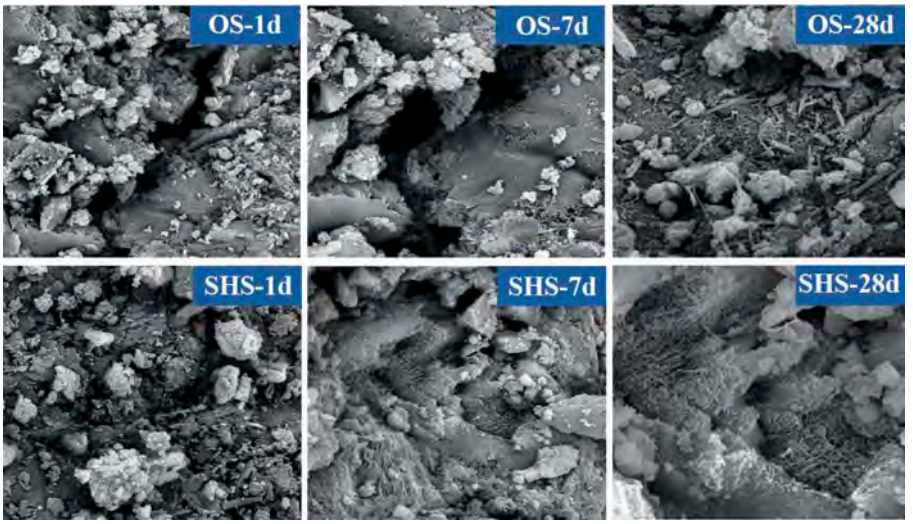

Figure 12. Mortar crack morphology comparison before healing and 28 days healing.

structure of the self-healing specimens appears relatively dense, predominantly filled with a significant number of fine micro-crystallizations generated during different stages (plastic and hardening). Therefore, self-healing materials not only repair early cracks but also inhibit the development of later cracks in shotcrete, ultimately achieving the desired effect of "no cracks, no leakage" (Mihashi et al., 2000).

4 CONCLUSIONS

This paper employed a deionized water immersion method to investigate the effects of self-healing materials on shotcrete, focusing on improvements in calcium leaching resistance, mechanical properties, and crack repair. The main conclusions are as follows:

1) The pH difference between the leaching solutions of ordinary shotcrete and self-healing shotcrete was small. After 28 days of leaching, their pH values decreased to approximately 10.3 and 9.9, respectively. The self-healing shotcrete exhibited significantly lower Ca^{2+} concentrations in the leaching solution, with reduction rates of up to 80.72%.
2) Self-healing materials had a limited impact on improving the compressive strength of shotcrete but enhanced its deformability. Self-healing shotcrete displayed a more ductile failure mode, with crack length changes higher by 13.8% to 52.2%, and a maximum increase in flexural strength of 10% compared to ordinary shotcrete.
3) The incorporation of self-healing materials resulted in the effective repair of native cracks in mortar or concrete and controlled the development of cracks. Self-healing specimens achieved a relative compressive strength recovery rate of 88%.
4) Microscopic analysis indicates that self-healing materials contain a significant amount of hydrophilic crystalline growth factors. These factors lead to the formation of insoluble micro-crystallizations that fill the micro-cracks and interfacial cracks within the shotcrete, resulting in a network structure. The internal structure becomes denser, suggesting that self-healing materials hold potential as a means to resist calcium leaching.

ACKNOWLEDGMENTS

The authors gratefully acknowledge the funding by the National Natural Science Foundation for General Project of China (No. 51878060), and the Fundamental Research Funds for the Central Universities, CHD (300102212706). The colleagues are thanked for the fruitful discussions.

REFERENCES

Ahn T. H., Kishi T.. 2010. Crack self-healing behavior of cementitious composites incorporating various mineral admixtures. J. Adv. Concr. Technol. 8(2), 171–186.

Chu H., Jiang L., Xiong C., et al, 2014. Use of electrochemical method for repair of concrete cracks. Constr. Build. Mater. 73, 58–66.

Dietzel M., Rinder T., Leis A., et al, 2008. Koralm tunnel as a case study for sinter formation in drainage systems–precipitation mechanisms and retaliatory action. Geome Tun: Geome. Tun. 1(4), 271–278.

Diego J D S, Leandro F. M. S., 2023. Understanding the efficiency of autogenous and autonomous self-healing of conventional concrete mixtures through mechanical and microscopical analysis. Cem. Concr. Res. 172, 107219.

Galan I., Baldermann A., Kusterle W., et al, 2019, Durability of shotcrete for underground support–Review and update. Constr. Build. Mater. 202, 465–493.

Ghosh S. k., 2009. Self-healing materials: fundamentals, design strategies, and applications. 1–28.

Harer G., 2017. Measures for the reduction of sinter formations in tunnels[C]//IOP conference series. Mater. Sci. Eng. 236(1), 012071.

Jung H., Han Y., Chung S., et al, 2013. Evaluation of advanced drainage treatment for old tunnel drainage system in korea. Tun. Under. Spa. Tech. 38, 476–486.

Jiang Y. j., Zheng Y., Yu l., et al, 2023. Effect of glass dust on the resistance of concrete to calcium corrosion under contact corrosion conditions. Mod. Tun. Tech. 60(2), 223–229.

Kim V. t., Nele D. b., Denis V. l., et al, 2011. Self-healing efficiency of cementitious materials containing tubular capsules filled with healing agent. Cem. Concr. Compos. 33, 497–505.

Lu G. n., Wang P., Yang Y., et al, 2021. Review of researches on groundwater seepage induced crystallization and blockage mechanism and scale in hibition technology in the tunnel drainage system in karst areas. Mod. Tun. Tech. 58(06), 11–20.

Mihashi H., Kaneko Y., Nishiwaki T., et al, 2000. Fundamental study on development of intelligent concrete characterized by self-healing capability for strength. Concr. Res. Tech. 11(2), 21–28.

Qian S. z., Zhou J., Schlangen E., 2010. Influence of curing condition and precracking time on the self-healing behavior of engineered cementitious composites. Cem. Concr. Compos. 32(9), 686–693.

Reinhardt H. W. Loos M., 2003. Permeability and self-healing of cracked concrete as a function of temperature and crack width. Cem. Concr. Res. 33, 981–985.

Tian C. M., Ye F., Song G. F., et al, 2020. Investigation and snalysis of crystal blockage of tunnel drainage system. Mod. Tun. Tech. 57(05), 66-76+83.

Thurmann M., Astner M., Saxer A., et al, 2015. Precipitations in the tunnel drainage system – optimized shotcrete mix-design. ECI Dig. Arch.

Tang Y., Zuo X., He s., et al, 2016. Influence of slag content and water-binder ratio on leaching behaviour of cement pastes. Constr. Build. Mater. 129, 61–69.

Tran D. P. t., Tay J. S. j., Quek S. t., et al, 2009. Implementation of self-healing in concrete – Proof of concept. The IES Journal Part A: Civ. Struc. Eng. 2(2), 116–125.

Van T. k., De B. n., Van L. d., et al, 2011. Self-healing efficiency of cementitious materials containing tubular capsules filled with healing agent. Cem. Concr. Compos. 33 (4), 497–505.

Victor C. L., Yun M. L., Yin W. C., 1998. Feasibility study of a passive smart self-healing cementitious composite. Compos. Part B: Eng. 29(6), 819–827.

Xu s., Ma e., Lai J., et al, 2022. Diseases failures characteristics and countermeasures of expressway tunnel of water-rich strata: A case study. Eng. Fai. Analy. 134, 106056.

Ye f., Tian C. m., He b., et al, 2021. Experimental study on scaling and clogging in drainage system of tunnels under construction. China J. Hig. Trans. 34(03), 159–170.

Zeng J. j., Fan Z. h., Xiong J. b., et al, 2015. Assessment methods for concrete crack self healing caused by permeable crystallization. Bulle. Chinese Cera. Soci. 34 (10), 3051-3055+3062.

Yang Z. x., John H., He X. d., et al, 2010. Laboratory assessment of a self-healing cementitious composite. Trans. Res. Rec.: J. Trans. Res. Boa. 2142(1), 9–17.

Tunnelling for a Better Life – Yan, Celestino, Thewes & Eberhardt (Eds)
© 2024 The Author(s), ISBN 978-1-032-80042-4
Open Access: www.taylorfrancis.com, CC BY-NC-ND 4.0 license

Analysis of viscous fingering between water and cement-based grout in tunnels

Suihan Zhang*, Fredrik Johansson & Liangchao Zou
KTH- Royal Institute of Technology, Stockholm, Sweden

ABSTRACT: Rock grouting is a common measure to reduce the seepage through conductive fractures in the rock mass around tunnels. Two types of grouting are normally carried, pre-excavation grouting and post-excavation grouting. Pre-grouting, commonly applied in Scandinavian tunnels, is used to seal the conductive fractures around the tunnel before the excavation of tunnel sections. In post-excavation grouting, which is dedicated to seal the remaining leakage in the excavated tunnel sections, the injected grout often encounters large seepage in rock fractures. Previous experiments have shown that the grout can be washed out easily when the grout is fresh even though the injected grout has initially sealed the fracture. One of the most significant phenomena for the water to "break up" the grout is viscous fingering. Viscous fingering occurs when certain conditions enable interface instability between the water and the cement-based grout. In this paper, the authors aim to evaluate if viscous fingering can be avoided under pre- and post-grouting conditions. For this purpose, computational fluid dynamics (CFD) simulations using the software Ansys Fluent is carried out. The simulation results demonstrating viscous fingering between water and cement-based grout are analyzed and discussed. Based on the results, suggestions on the grouting strategy with respect to pre- and post-grouting are provided to deal with the potential issues related to viscous fingering.

Keywords: Rock grouting, Rock tunnelling, Viscous fingering, Yield stress, CFD analysis

1 INTRODUCTION

Excessive water seepage through rock fractures can cause significant problems in rock tunnels in both construction and operation phases. To deal with the excessive water seepage, one of the common measures is to seal the rock mass around the tunnel using cement-based grouting. For instance, pre-excavation grouting (pre-grouting) is commonly applied in Scandinavian tunnels to seal conductive fractures around the tunnel before excavation of tunnel sections. It aims to form a tight zone around the tunnel that ensures the water ingress into the tunnel is within requirements (NFF 2011; Stille 2015). Another common type of tunnel grouting, post-excavation grouting (post-grouting), mainly serves as a remedial measure to seal the remaining leakage after the excavation of tunnel sections.

The pre-grouting in tunnels is usually carried out under the assumption of hydrostatic pore pressure conditions with no seepage flow occurring in the rock fractures (Stille 2015). This implies that the injected grout is not likely to be disturbed by the flowing water in the fractures if the rock fractures are not well connected. However, once the grouted fracture is connected to the excavated tunnel, e.g. via new boreholes, a pressure gradient may build up in the grouted areas causing seepage flow in the rock fractures that can disturb the injected grout. Post-grouting work, on the contrary, often encounters unfavorable hydraulic conditions. The excavated tunnel functions as a well in the rock mass. Therefore, the pressure gradient can be high close to the tunnel, especially if the tunnel is at great depth under the groundwater level. The grout for post-grouting is often injected into fractures or zones with strong water flow and high pressure gradient. This unfavorable environment affects the penetration length of the grout during the injection since erosion constantly occurs (Axelsson 2009; Guo et al. 2020). Even if the fractures were sealed during the injection, the high pressure gradient may still drive the water to disturb the grouted area afterwards.

One of the mechanisms that could potentially disturb the injected grout when pressure gradient exists in the grouted fracture is viscous fingering. Viscous

*Corresponding author: suihan@kth.se

DOI: 10.1201/9781003495505-345

fingering describes a type of interface instability between two fluids when the less viscous fluids is displacing the more viscous fluid (Homsy 1987). This instability, which is also called the Saffman-Taylor instability (Saffman and Taylor 1958) occurs due to the difference in viscosities and presents itself in the shape of fingers in the more viscous fluid. In the context of rock grouting, the groundwater (Newtonian fluid) behaves as the less viscous fluid which can displace the more viscous fluid, i.e. the grout (yield-stress fluid for cement-based grout) after the injection. Coussot (1999) and Lindner et al. (2000) studied the viscous fingering between a Newtonian fluid and a yield-stress fluid in a Hele-Shaw cell (parallel plates similar to a homogeneous fracture replica), but these studies was not performed in the context of water-grout interaction. Funehag (2017) described the risk of viscous fingering after grouting with leaking boreholes penetrating the grouted area. From the observation of an unpublished experimental attempt by the authors to visualize water-grout interaction, viscous fingering initiated in the grout and then developed rapidly until the water penetrated into the grouted area. Significant grout erosion followed up and reduced the grouted area. Apart from Funehag (2017) and this experimental attempt, the viscous fingering between water and cement-based grout has not been specifically investigated elsewhere.

The present study aims to investigate the interaction between water and cement-based grout from perspectives of potential risks for viscous fingering in tunnel grouting. The focus is given to the time window after the injection is finished (grouting pressure relieved). This is the time when viscous fingering is most likely to occur. If viscous fingering is not initiated, the cement-based grout has the time and the space to grow its strength through hardening and thus ensure a satisfactory grouting outcome.

The study is performed through two-phase computational fluid dynamics (CFD) simulations. A sensitivity analysis is performed of the parameters describing the rheological properties as well as the influence from the boundary conditions. The outcome of the present study is to suggest principles for a design strategy to prevent or minimize the effect of viscous fingering between groundwater and cement-based grout with consideration of the rheological properties of the grout.

2 METHODOLOGY

2.1 *Analytical limit state for viscous fingering*

For a typical yield stress fluid, the shear stress in the fluid needs to overcome the yield stress for this fluid to start flowing. The fluid will remain static if the shear stress is lower than the yield stress. Based on this property of a yield stress fluid, groundwater may not be able to displace the fresh grout if the pressure gradient is insufficient. As described in the previous chapter, one of the prerequisites for viscous fingering to occur is one fluid displacing another. Therefore, a limit state where viscous fingering is just to be initiated may exist between water and cement-based grout. This limit state coincides with the limit state for the cement-based grout to start flowing. Based on the work by Coussot (1999), in the context of flow between two parallel plates, the limit state can be written in a simple analytical form as:

$$\frac{\partial P}{\partial x} > \frac{2\tau_0}{b}, \tag{1}$$

where P is the pressure at the interface, x is the flow direction of the displacing fluid, τ_0 is the yield stress of the displaced fluid and b is the aperture between the parallel plates. This limit state will be evaluated

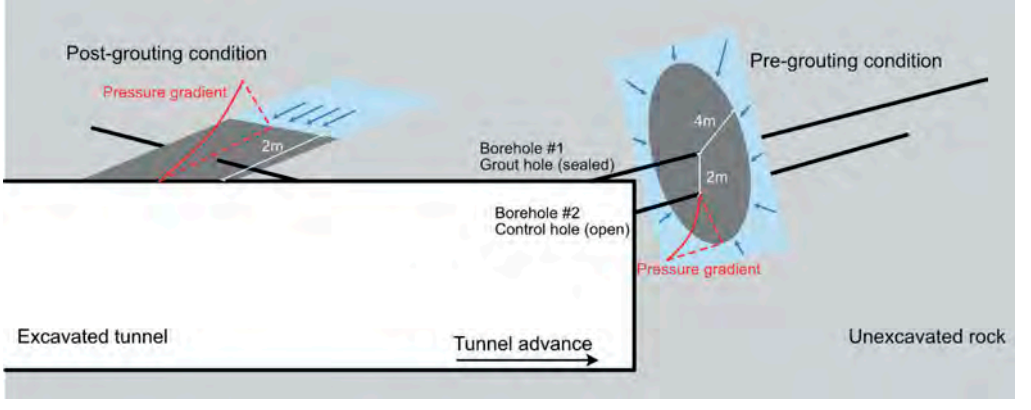

Figure 1. Conceptual model for the risk of viscous fingering after the completion of pre-grouting (right) and post-grouting (left).

against the numerical studies to test whether it can be used to control viscous fingering behavior in cement-based grout.

2.2 *Conceptual model*

Risk of viscous fingering can occur both in pre-grouting and in post-grouting conditions in tunnel constructions. In this study, both scenarios are taken into consideration. The conceptual model for pre- and post-grouting conditions with respects to viscous fingering are illustrated in Figure 1.

Pre-grouting from a tunnel face is commonly carried out in sequences. In difficult grouting conditions where the requirements are higher, multiple rounds of borehole drillings are required including: probe holes to measure the conductivity of the rock mass, additional grout holes to perform grouting and control holes to measure the sealing results. Among these boreholes, the grout holes and the control holes can be drilled after some of the grouting in other holes are finished. The drilling of these boreholes, if they intersects the grouted fractures, will expose the grout to a low pressure, meaning that the groundwater pressure from the inside of the fracture will create a pressure gradient in the grout. Such scenario would also occur if the packer does not stay in the grout holes or the packer leaks.

The tunnel in the conceptual model was excavated 20 m under the groundwater level in Swedish granite with few major fractures. A consistent fracture perpendicular to the pre-grouting boreholes with an aperture of 0.2 mm was assumed in this analysis. This fracture was close to the tunnel face. The pre-grouting has been completed for borehole #1, it resulted in a radial penetration length, I, of 4 meters. The control hole, borehole #2, was drilled 2 meters below borehole #1 and intersected the grouted fracture. The pressure gradient, i, in the grout was thus 10 m/m. The cement-based grout was assumed to behave as a Herschel-Bulkley fluid (Shamu 2021) whose rheological model is defined as

$$\tau = \tau_0 + k\dot{\gamma}^n, \tag{2}$$

where τ (Pa) is the shear stress in the grout, k is the consistency coefficient, n is the flow index and $\dot{\gamma}$ (1/s) is the shear rate. In this study, the rheological model of the grout was simplified with n=1 (also called Bingham model) and thus k becoming the dynamic viscosity of the grout μ_g (Pa·s). The rheological properties of different alternatives of the cement-based grout varies in the analysis following Table 1.

The same tunnel was used for the conceptual model of post-grouting condition as illustrated in Figure 1. A fracture with an aperture of 0.2 mm opened up after the excavation and leakage into the tunnel appears. Post-grouting was thus performed in this fracture to stop the leakage. This fracture was assumed to be surrounded by unconducive rock or grouted areas, thus having closed boundaries. After the fracture was sealed as suggested in Figure 1, a pressure gradient starts to build up in the 2-meter long grout due to the pressure difference between the tunnel and groundwater. The pressure gradient in such case was also 10 m/m. In the conceptual model for post-grouting conditions, the alternatives of the grout also varied in its rheological properties following Table 1.

Based on the criterion in Eq (1), it was not expected that viscous fingering would occur in grout B4 and B5, while viscous fingering to a varying degree were expected in all other grouts in Table 1.

2.3 *CFD analysis*

Ansys Fluent was used in this study for the CFD analysis. The interaction between groundwater and cement-based grout was achieved by involving two phases of fluids, phase 1 being water and phase 2 being the cement-based grout.

In Ansys Fluent, the multiphase flow simulations are performed by solving transport equations of two types of scalars: within the phase and the mixture between phases (ANSYS Inc. 2009). Within phase-j and for an arbitrary k scalar φ_j^k, the software solves the transport equation in the volume which is occupied by the respective phase:

$$\frac{\partial \alpha_j \rho_j \varphi_j^k}{\partial t} + \nabla \cdot \left(\alpha_j \rho_j \vec{u}_j \varphi_j^k - \alpha_j \Gamma_j^k \nabla \varphi_j^k \right) = S_j^k \qquad k = 1, \cdots, N, \tag{3}$$

where α_j is the volume fraction, ρ_j is the physical density, $\vec{u}_j$ is the velocity of phase-j. Γ_j^k is the diffusion coefficient, S_j^k is the source term. The mass flux for phase-j, F_j, is calculated as

$$F_j = \int_S \alpha_j \rho_j \vec{u}_j \cdot d\vec{S}. \tag{4}$$

When the scalar φ^k is associated with the mixture of the phases, the transport equation to be solved is

$$\frac{\partial \rho_m \varphi^k}{\partial t} + \nabla \cdot \left(\rho_m \vec{u}_m \varphi^k - \Gamma_m^k \nabla \varphi^k \right) = S_m^k \qquad k = 1, \cdots, N, \tag{5}$$

Table 1. Rheological properties of different cement-based grouts for conceptual models and for analysis.

Grout number	0 (Basis)	A1	A2	A3	A4	A5	B1	B2	B3	B4	B5
τ_0 [Pa]	3	3	3	3	3	3	1	5	8	10	12
k [Pa·s]	0.05	0.01	0.03	0.07	0.09	0.11	0.05	0.05	0.05	0.05	0.05

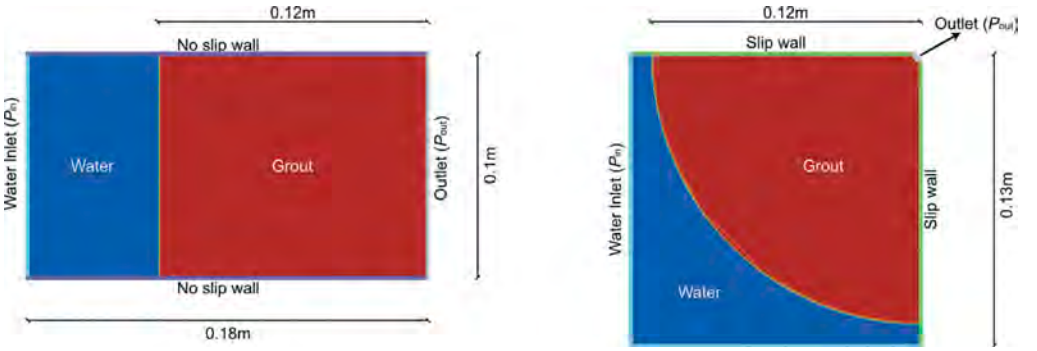

Figure 2. Dimensions and boundary conditions of the models for CFD analysis: (a) Post-grouting conditions; (b) Pre-grouting conditions. Both models are 0.2 mm in the third dimension (fracture aperture).

where the mixture density, ρ_m, can be calculated as

$$\rho_m = \sum_j \alpha_j \rho_j. \tag{6}$$

The mixture velocity, $\vec{u}_m$, can be calculated as

$$\rho_m \vec{u}_m = \sum_j \alpha_j \rho_j \vec{u}_j. \tag{7}$$

The mass flux of the mixture, F_{m}, is calculated as

$$F_m = \int_S \rho_m \vec{u}_m \cdot d\vec{S}. \tag{8}$$

The mixture diffusion coefficient, Γ_m^k, is calculated as

$$\Gamma_m^k = \sum_j \alpha_j \Gamma_j^k. \tag{9}$$

Lastly, the source term, S_m^k is calculated as

$$S_m^k = \sum_j S_j^k. \tag{10}$$

For this study, two 3D models were designed to simulate the rock fractures of interest, as shown in Figure 2. In order to reduce computational time and to increase accuracy, down-scaling was performed based on Eq (1). This equation has indicated that the pressure gradient $\partial P/\partial x$, the yield stress of the grout τ_0 and the fracture aperture b are the controlling parameters. These parameters should thus be the same as in the conceptual models and the other parameters can be scaled down. Therefore, the dimension of the rock fracture was reduced to 0.13 m x 0.13 m for the pre-grouting model (1/4 of the grout disc) and 0.18 m x 0.1 m (length x width) for the post-grouting model, with the unchanged aperture b=0.2 mm.

For the pre-grouting model, the upper and lower boundaries of the fracture models were modelled as no-slip walls while the walls in the aperture direction were modelled as slip walls. On the other hand, all the walls for the post-grouting model was no-slip walls due to that the fracture has closed boundaries. At the initial stage for both models, grout occupied 0.12 m of the fracture and the pressure gradient was achieved by applying the inlet groundwater pressure P_{in} from the inlet edges, which was calculated from the outlet pressure P_{out} and the pressure gradient i:

$$P_{in} = P_{out} + i \cdot 0.12 \text{ m}. \tag{11}$$

In this study, P_{out}=0 Pa and i=10 m/m or 100 kPa/m, which resulted in P_{in}=12 kPa. With a constant inlet and outlet pressure, the flow time in the simulations lasted for 10 s. The behavior of viscous fingering phenomena was recorded during this flow time.

3 RESULTS

The analysis results for both models with all the listed cement-based grouts are summarized in Table 2. In the table, if the grout is washed out after 10 s, the key moment showing typical viscous fingers with their respective time stamps is shown. For the rest of the analyses, the interfaces at 10 s of flow time are shown. All the results are followed by description over: if the grout is pushed back, if the interface is stable, if the viscous fingers are observed.

By comparing the results for post-grouting conditions from Grout 0 and A1-A5, having the same yield stresses, higher viscosity delayed the formation of viscous fingers in post-grouting conditions although it failed to avoid interface instability. It suggests that viscous fingers may still occur after 10 s of flow time for Grouts A3, A4 and A5. For pre-grouting

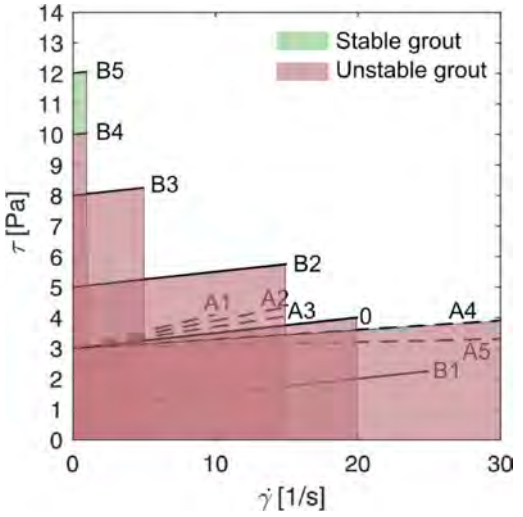

Figure 3. Bingham rheological models of all the grouts in the analyses.

conditions with Grout 0 and A1-A5, the difference made by higher viscosity is not clear apart from Grout A1 which has very low viscosity. No dominant viscous fingers appeared with Grout 0 and A2-A5. Instead, multiple smaller fingers appeared and then disappeared. The possible explanation for such phenomena could be that the small grout outlet limited the flow rate of the grout thus limited shear rate of the grout and the progression of viscous fingers.

Among Grout 0 and B1-B5, the results show that higher yield stress will bring better resistance against grout pushed back and viscous fingering. Especially for Grout B4 and B5, the results coincides with the expectation that viscous fingering will not occur in both cases. Even though the interface is not stable in the pre-grouting conditions, the grout is not pushed back so viscous fingering is not likely to develop further. Compared to the increase of the viscosity, the increase of the yield stress appears to be more effective in preventing the viscous fingering from occurring.

The rheological models of all the cement-based grouts are plotted in Figure 3. All of the lines of the different grout rheological properties start at zero shear rate and end at the approximated shear rate (at 10 s) of each simulation. The highlighted areas between them provide indications on the sufficient grout property to maintain interface stability. The green area suggests that grout is stable (not pushed back and no viscous fingering) while the red area suggests unstable grout. In the specific case shown in Figure 1, the cement-based grout needs to have at least 10 Pa of yield stress to avoid viscous fingering from occurring.

Table 2. Analysis results with different cement-based grouts.

Grout	Post-grouting conditions		Pre-grouting conditions	
0	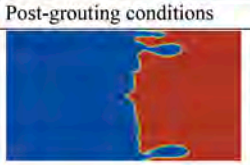	Grout pushed back, unstable interface with viscous fingers (10 s)	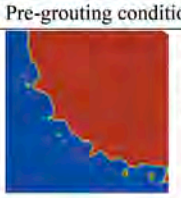	Grout pushed back, unstable interface with viscous fingers (10 s)
A1	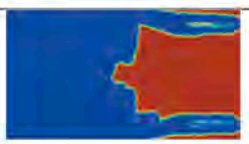	Grout pushed back, unstable interface with viscous fingers (**3s**, washed out at 10 s)	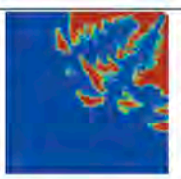	Grout pushed back, unstable interface with viscous fingers (10 s)
A2	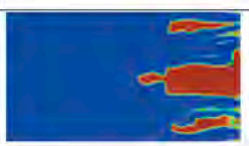	Grout pushed back, unstable interface with viscous fingers (10 s)		Grout pushed back, unstable interface with viscous fingers (10 s)
A3		Grout pushed back, unstable interface with no clear fingers (10 s)	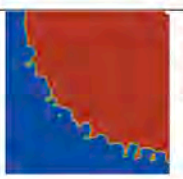	Grout pushed back, unstable interface with viscous fingers (10 s)

Table 2. (Cont.)

A4		Grout pushed back, unstable interface with no clear fingers (10 s)	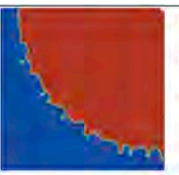	Grout pushed back, unstable interface with viscous fingers (10 s)
A5		Grout pushed back, unstable interface with no clear fingers (10 s)		Grout not pushed back, unstable interface with appearing viscous fingers (10 s)
B1		Grout pushed back, unstable interface with viscous fingers (10 s)		Grout pushed back, unstable interface with viscous fingers (10 s)
B2		Grout pushed back, unstable interface with no clear fingers (10 s)	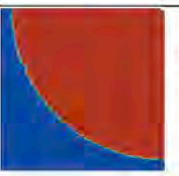	Grout not pushed back, unstable interface with no clear fingers (10 s)
B3		Grout pushed back, unstable interface with no clear fingers (10 s)	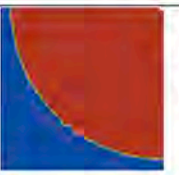	Grout not pushed back, unstable interface with no clear fingers (10 s)
B4		Grout not pushed back, unstable interface with no clear fingers (10 s)		Grout not pushed back, unstable interface with no clear fingers (10 s)
B5		Grout not pushed back, stable interface with no clear fingers (10 s)		Grout not pushed back, unstable interface with no clear fingers (10 s)

4 DISCUSSIONS

4.1 *Risk for viscous fingering in pre-grouting*

The results indicate that the disturbance from viscous fingering was generally less serious in pre-grouting conditions than in post-grouting conditions. The reason for this difference could be that the relatively small open borehole creates a threshold effect of outflow in the pre-grouting analyses, which limit the flow rate of the grout. For pre-grouting conditions, the risk lies in the backflow of the grout into the borehole, this would reduce the grouted area and thus compromise the overall grout results. Water leakage through the open borehole caused by penetrating viscous fingers presents lower risk than anticipated in the case of the conceptual model.

However, significant back flow with viscous fingering would still occur if the viscosity is lower than 0.01Pa·s.

4.2 *Risk for viscous fingering in post-grouting*

Comparing the pre- and post-grouting conditions with the same type of grout, the post-grouting conditions present higher risk with respect to viscous fingering. The grout is more prone to have viscous fingering because the grout is exposed to a wider outlet, which is the entire cross-section between the fracture and the tunnel wall. In post-grouting conditions, the analyses showed the serious disturbance regimes of wash away (A1) and penetrating fingers (A2, B1). If the grout is completely washed away, the excessive leakage into the tunnel will likely to resume to its original level after a certain time; it means that the post-grouting is failed and changes of grouting plan or grout is required. Compared to be washed away, the penetrating fingers may actually cause more problems in the long term since it may easily lead to misjudgment of the grouting results. From the observations in the tunnel, seepage has indeed been reduced. However, until the grout has gained sufficient strength against erosion, seepage water will continuously erode the grout and expand the seepage channel even though viscous fingering has stopped. Although a few studies have been done previously (e.g. Axelsson 2009), the mechanism of grout erosion has not been fully understood. The exact time window before erosion stops is uncertain. The time delay before the worsening seepage is observed can cause extra operations and thus extra costs.

4.3 *Strategy to reduce the risk of viscous fingering*

One can conclude from the results in Table 2 and Figure 3 that higher viscosity and higher yield stress of the grout are beneficial with respect to delay or prevent viscous fingering. Between the two rheological properties, yield stress appears to play a more important role to prevent the viscous fingering from occurring than the viscosity. On the other hand, the viscosity helps delaying the occurrence of viscous fingering. In the particular case of the conceptual model, the yield stress of the grout is preferably higher than 10 Pa to maintain a stable water-grout interface.

High initial viscosity and initial yield stress, however, would compromise the penetrability of the grout, making it harder and slower to be injected. Therefore, it is more reasonable to use ordinary mixes of grout (w:c ratio between 0.6-1.0 in Swedish practice) and to hold the grouting pressure beyond the time needed to seal the fracture. The pressure during the holding time does not need to be as high as during the injection. A pressure that is close to the groundwater pressure would be sufficient. Although this holding time would not give longer penetration length, it would allow the grout to develop strength without being displaced by the flowing water. No displacement indicates no viscous fingering. The exact pressure holding time depends on the actual recipe of the grout. For example, a low w:c ratio and accelerator can shorten the holding time while a high w:c ratio will prolong it. In a real project, pretesting on the grout's strength development over time is thus highly recommended to provide reference to the actual pressure holding time required.

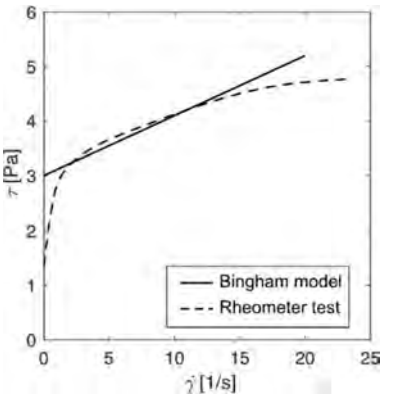

Figure 4. Rheological properties directly from rheometer test and after Bingham fitting.

4.4 *Uncertainties in grout properties*

An important simplification in this study is that the cement-based grout behaves as an ideal Bingham fluid (n=1 in Eq (2)). It, however, may not represent the realistic rheological properties of cement-based grout in reality. As illustrated in Figure 4, the result of a typical rheometer measurement on the grout's properties does not strictly follow the linear Bingham model. Instead, the measured shear stress at low shear rate is much lower than the yield stress with Bingham curve fitting. This fact suggests that the risk of viscous fingering could be underestimated if the Bingham model is used to describe the grout properties.

5 CONCLUSIONS

From the performed numerical analyses in this study, the main conclusions are summarized as follows:

- Viscous fingering poses a risk for both pre-grouting and post grouting conditions in rock tunnel construction. In a worst case scenario, the injected grout can be washed away quickly from the fracture.

- The risk of viscous fingering is higher in post-grouting conditions compared to pre-grouting conditions.
- Higher yield stress can effectively reduce or avoid viscous fingering according to the limit state by Eq (1). In the specific case of the conceptual model, a yield stress of 10 Pa can prevent viscous fingering. Compared to high yield stress, higher viscosity may contribute less in preventing viscous fingering but can delay it.
- A practical suggestion for the grouting design in post-grouting conditions is that the grouting pressure should not be relieved before the grout has gained adequately high yield stress. The exact holding time varies depending on the grout mix. Pretests on the cement-based grout on the development of yield stress is recommended.

ACKNOWLEDGMENTS

The research presented in this paper was supported by the Swedish Hydropower Centre (SVC) (Grant No. VK14170) and the Swedish Rock Engineering Research Foundation, BeFo (Grant No. 440). SVC was established by the Swedish Energy Agency, Elforsk and Svenska Kraftnät together with Luleå University, KTH Royal Institute of Technology, Chalmers University of Technology and Uppsala University. http://www.svc.nu.

REFERENCES

ANSYS, Inc. 2009. *ANSYS FLUENT 12.0 Theory Guide*

Axelsson, M. 2009. *Prevention of Erosion of Fresh Grout in Hard Rock*. Chalmers University of Technology. Gothenburg.

Coussot, P. 1999. "Saffman–Taylor instability in yield-stress fluids". Journal of Fluid Mechanics, 380, 363–376.

Funehag, J. 2017. *Borrhål - hydraulisk gradient och erosion/Leaking boreholes- Hydraulic gradient and Erosion*. BeFo-Rock Engineering Research Foundation, Report 172. (in Swedish).

Guo, Y., Zhang, Q., Xiao, F., Liu, R., Wang, Z., Liu, Y. 2020. Grouting rock fractures under condition of flowing water. Carbonates and Evaporites, 35, 1–15.

Homsy, G. 1987. Viscous Fingering in Porous Media. Annual Review of Fluid Mechanics, 19(1),271–311.

Lindner, A., Coussot, P., Bonn, D. 2000. Viscous fingering in a yield stress fluid. Physical Review Letters, 85(2), 314.

NFF - Norwegian Tunnelling Society. 2011. *Rock Mass Grouting in Norwegian Tunnelling*.

Saffman, P., Taylor, GI. 1958. The penetration of a fluid into a porous medium or Hele-Shaw cell containing a more viscous liquid. Proceedings of the Royal Society of London. Series A. Mathematical and Physical Sciences, 245(1242),312–329.

Shamu, J. 2021. *Rock grouting design: Rheological aspects and radial flow visualizations with ultrasound* KTH Royal Institute of Technology. Stockholm.

Stille, H. 2015. *Rock Grouting - Theories and Applications*. BeFo-Rock Engineering Research Foundation.

Tunnelling for a Better Life – Yan, Celestino, Thewes & Eberhardt (Eds)
© 2024 The Author(s), ISBN 978-1-032-80042-4
Open Access: www.taylorfrancis.com, CC BY-NC-ND 4.0 license

Analysis of cement grout propagation with varying fracture apertures

Liangchao Zou*
KTH Royal Institute of Technology, Stockholm, Sweden
RISE Research institutes of Sweden, Stockholm, Sweden

Giedrius Zirgulis, Ali Nejad Ghafar & Ulf Håkansson
KTH Royal Institute of Technology, Stockholm, Sweden
Implenia Sverige AB, Stockholm, Sweden

Vladimir Cvetkovic
Implenia Sverige AB, Stockholm, Sweden

ABSTRACT: Cement grouting is widely used in rock tunnelling to control groundwater inflow by sealing rock fractures. Accurately predicting grout propagation in rock fractures is crucial for the design, execution, and monitoring of rock grouting in engineering applications. Current methods rely on theoretical models, such as the real-time grouting control (RTGC) method, which is derived based on simplified fracture geometries like smooth parallel plates/disks. However, real rock fractures consist of rough surfaces with variable apertures. In this study, we present a computational model for theoretically predicting the propagation of non-Newtonian cement grout in variable fracture apertures. This model is validated with laboratory test data on grout propagation in a one-dimensional varying aperture long slot (VALS). We also analysed the impact of varying aperture on cement grout propagation processes. Our findings demonstrate that the presented computational model predicts the grout propagation process in this geometry with good accuracy. Moreover, we observed that varying aperture significantly affects the grout propagation process in fractures. The insights provided by our model and analysis results are potentially useful in rock tunnelling projects, specifically for the theoretical analysis of cement grout propagation in rock fractures.

Keywords: Cement grout, Rock grouting, Varying aperture fracture, Real-time grouting control, Propagation length, Two-phase flow

1 INTRODUCTION

Cement grouting serves as a pivotal technique extensively applied in rock engineering projects, encompassing the construction and maintenance of rock tunnels, dams, and underground infrastructures built in or on rock. Modelling of cement grout propagation within rock fractures plays a pivotal role in the holistic approach to designing, implementing, and monitoring rock grouting processes (Stille 2015).

In rock grouting practice, cement grouts are often injected through boreholes, which propagate through connected rock fractures. The cement grouts applied for rock grouting are typically non-Newtonian fluids with yield stress, which are often assumed as Bingham fluids (Håkansson 1993). The rheological properties of cement grouts are important parameters in rock grouting design. It is found that the rheological parameters of cement grouts i.e. yield stress and plastic viscosity, significantly affect propagation lengths in single fractures (Zou et al. 2018).

In the literature, a few analytical and numerical models have been developed to analyse non-Newtonian cement grouts propagation in single rock fractures (Hässler et al 1992; Stille 2015; Zou et al. 2018, 2019, 2020a, 2020b). For simplicity, the fractures are typically assumed as a pair of parallel plates with constant apertures in previous studies. However, all natural rock fractures inherently feature rough surfaces, which causes variable aperture structures. Many studies have shown that fracture surface roughness and variable aperture structures can significantly affect fluid flow and mass transport in rock fractures (e.g., Zou et al 2018, 2019). In particular, Ghafar (2017) conducted grout tests in a variable aperture long slot (VALS) and compared the test results with the analytical solution of the real time grouting control (RTGC) method. It is found that the

*Corresponding author: lzo@kth.se

DOI: 10.1201/9781003495505-346

RTGC method using either the mean mechanical aperture or the hydraulic aperture can overestimate the grout propagation length. However, varying apertures caused by surface roughness have not been considered in previous theoretical and numerical studies on rock grouting and the impact of varying apertures on cement grouts propagation has not been comprehensively analysed.

In this work, we present a two-phase flow model to analyse Bingham cement grout propagation in fractures with variable apertures. This model is validated against a set of laboratory test data conducted by Ghafar (2017), for the first time. The validated model could be helpful for analysing cement grout propagation in natural rock fractures required in design for rock grouting in practice.

2 THEORY AND METHOD

The rheological properties of cement grouts are greatly dependent on water and cement ratios. In practice, the water and cement ratio are between 0.6 and 0.8, where the cement grouts behave as yield-stress fluids, often approximated by the Bingham model, expressed as

$$\begin{cases} \tau = \tau_0 + \mu_g \dot{\gamma}, & |\tau| > \tau_0 \\ \dot{\gamma} = 0 & \text{otherwise} \end{cases} \quad (1)$$

where τ is shear stress, τ_0 is the yield stress, μ_g is the plastic viscosity and is the shear rate.

Assuming that the cement grouts and groundwater are immiscible and incompressible fluids, a two-phase flow model for grout propagation into water-saturated fractures has been developed in previous work (Zou et al 2018; 2019), expressed as

$$\frac{\partial}{\partial \mathrm{x}} T(C) \frac{\partial \mathrm{P}}{\partial \mathrm{x}} = 0 \quad (2)$$

$$u = \frac{T(C)}{2B} \frac{\partial \mathrm{P}}{\partial \mathrm{x}} \quad (3)$$

$$\frac{\partial C}{\partial t} + u \frac{\partial C}{\partial \mathrm{x}} = 0 \quad (4)$$

where C is a phase function (i.e., $C = 1$ denotes the grout phase and $C = 0$ denotes the water phase), t is time, P is pressure, u is velocity, and $T(C)$ is the transmissivity, which is a function of C. For groundwater, i.e., $C = 0$, the transmissivity is given by the cubic law,

$$T(C = 0) = -\frac{2WB^3}{3\mu_w} \quad (5)$$

where B is the half of the fracture aperture, W is the fracture width and μ_w is the viscosity of groundwater. For the Bingham grout, its transmissivity can be determined by the analytical solution of the flow-rate for single-phase flow between smooth parallel plates, expressed as (Zou et al. 2018)

$$T(C = 1) = -\frac{WB^3}{3\mu_g} \left(1 - \frac{z_p{}'}{B}\right)^2 \left(2 + \frac{z_p{}'}{B}\right) \quad (6)$$

where z_p' is half of the plug flow region in the grout phase, which is a function of yield stress and the pressure gradient between the injection inlet and grout propagation front $I(t)$ (Zou et al., 2018)

$$z_p{}' = min\left(\frac{\tau_0 \mathrm{I(t)}}{P_1 - P_{I(t)}}, B\right) \quad (7)$$

where $P_{I(t)}$ is the pressure at the interface. Illustration of the plug flow region for yield stress fluid flow in homogeneous fractures is available in Zou et al. (2018).

The mathematical model for the two-phase flow of cement grout propagation in water-saturated fractures is a set of nonlinear partial differential equations, since the transmissivity for the Bingham grouts is naturally nonlinear. For modeling of grout propagation in fractures with variable aperture structures, the mathematical model is solved numerically by iteration at each time step. In order to track the propagation interface, a novel algorithm by introducing a moving node in each fracture has been developed in Zou et al. (2018). The detailed algorithm of the solution for the two-phase flow of grout propagation in saturated fracture networks and its advantages compared to traditional methods can be found in Zou et al. (2018).

3 RESULTS

3.1 *Laboratory grouting test*

A set of laboratory grouting tests in a varying aperture long slot (VALS) has been performed and presented in Ghafar (2017). We adopt this set of data to validate our computational model presented in Section 2. For completeness, the tests are briefly introduced here; more detailed information can be found in Ghafar (2017).

A long slot with varying apertures is manufactured to conduct the tests. The aperture structure of the varying aperture long slot is shown in Figure 1, where the slot aperture changes from 220 μm to 40 μm with chambers of 500 μm in between. The total length from the inlet to the outlet is 2.88 m. The detailed information on design of the VALS and the monitoring system is available in Ghafar (2017).

The adopted data contain two tests with two types of oil samples, named as SAE20 and SAE50, and four tests with two recipes of cement grouts, named as R1 and R2. The water-to-cement (w/c) ratio is 0.8 for both types of grouts; however, different concentrations of the super-plasticizer were added in the two recipes of cement grouts, i.e., 0.5% and 0.18% by volume in recipes R1 and R2, respectively. The rheological properties of the oil samples and cement grouts are summarized in Table 1.

A constant injection pressure of 15 bar was applied for all tests. The outlet boundary condition is zero pressure (i.e., open to air). Pressure sensors were installed at different locations in the slot. In each test, the grout front was monitored by recording the time interval when each pressure sensor began to rise. All tests were conducted in dry condition, which means that the involved two phases are the oil/grout and air.

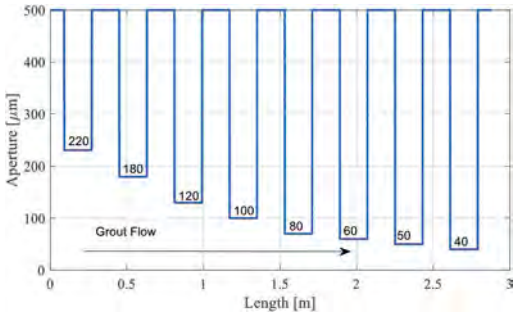

Figure 1. The aperture structure of the varying aperture long slot (VALS).

Table 1. Material properties (Ghafar 2017).

Materials	Density (kg/m)	Plastic viscosity (Pa s)	Yield stress (Pa)
Oil SAE20	880	142.1e-3	0.14
Oil SAE50	950	754.6e-3	0.55
Grout R1	1610	8.3e-3	0.08
Grout R2	1600	5.7e-3	1.01

3.2 *Comparison with laboratory grouting test data*

Using the proposed two-phase flow model, we simulated the grouts propagation in the varying aperture long slot based on the test conditions and using the specific rheological properties. The simulated results of grout propagation with time are compared with the laboratory grouting test data.

Figures 2-5 present comparison of simulated grout propagation over time with test data. In general, the simulated results of propagation length over time match well with the results from the tests, for all cases.

The differences between the repeated tests for the adopted two recipes of cement grouts illustrates the uncertainty in the tests, which could be caused by complexity of rheological properties for cement grouts with additives of super-plasticizers, and filtration of cement particles that are not considered in the presented computational model.

The relatively good agreement between the simulated results and test data indicates that the presented two-phase flow model can reliably predict cement grouts propagation process in fractures with varying apertures.

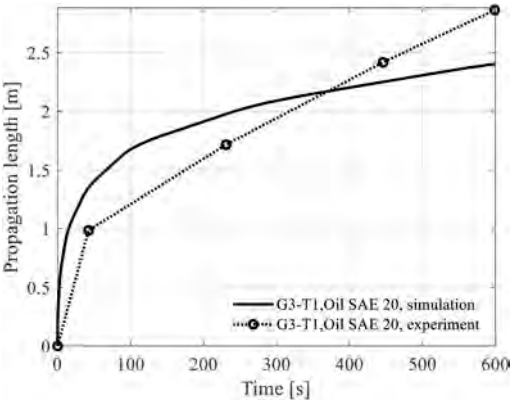

Figure 2. Comparison between the simulated and tested grout propagation over time for oil SAE20.

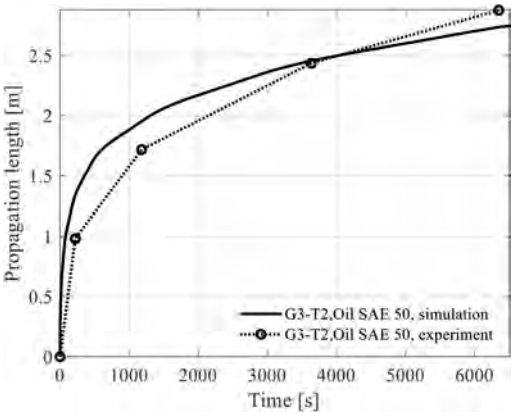

Figure 3. Comparison between the simulated and tested grout propagation over time for oil SAE50.

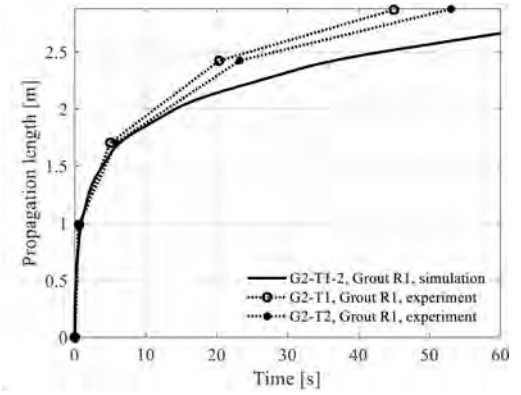

Figure 4. Comparison between the simulated and tested grout propagation over time for grout R1.

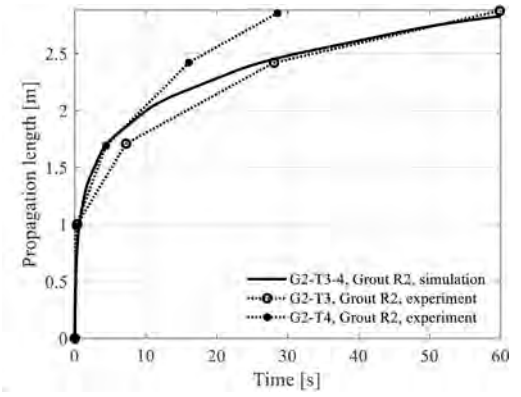

Figure 5. Comparison between the simulated and tested grout propagation over time for grout R2.

4 GROUTS PROPAGATION IN RANDOM FRACTURES

After validation, we aim to use the two-phase flow model to analyse cement grouts propagation in heterogeneous fractures with varying apertures. In the literature, the apertures of rock fractures are often assumed following lognormal distributions based on observation from laboratory and field tests (e.g., Zou et al. 2020). In this work, we randomly generate rough-walled fractures with lognormal distributed apertures, for a generic analysis.

4.1 *Random generation of varying fracture apertures*

We consider 1D fractures with the length of 3m. The lognormal distributed fracture apertures are generated based on correlated Gaussian field, expressed as,

$$\log(b) = \sigma\, MG(0,\ 1, \lambda) \tag{8}$$

where b is the fracture field, σ is the is standard deviation of a lognormal field, *MG* is a Gaussian field with mean 0 and standard deviation 1, and λ is the correlation length. Our previous studies showed that the correlation length has limited impacts on fluid flow and solute transport in fractures compared to the variance. Therefore, in this work we adopt a constant value for the correlation length, $\lambda = 0.15m$, and focus on the impact of variance.

Specifically, we randomly generated varying fracture apertures following lognormal distributions with three values of log-variances, that is,. For the case $\sigma^2 = 0$, the aperture is constant, which is considered here as a reference case. For the cases of $\sigma^2 = 0.1$and0.5, we simulated 50 realizations for each case to obtain a stable statistical analysis. The number of realizations is adopted based on our previous studies using lognormal distributed apertures, which showed that around 20 realizations are adequate to achieve a stable statistical analysis (Zou and Cvetkovic 2020; Zou et al., 2023).

Figure 6 illustrates the assembled cumulative distribution function (CDF) of generated varying apertures for different cases, showing the increasing variation when σ^2 increased from 0.1 to 0.5. Figure 7 illustrates an example of generated aperture geometry for each case.

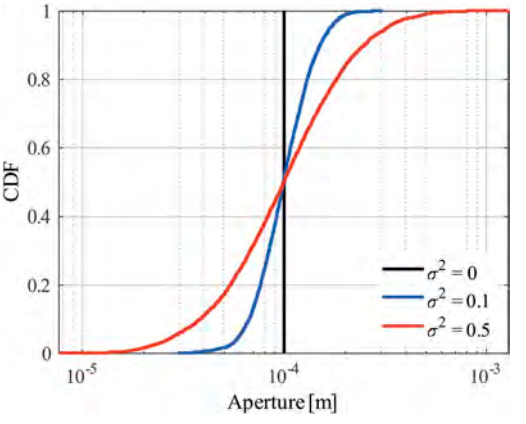

Figure 6. The cumulative distribution function (CDF) for different cases, i.e., $\sigma^2 = 0$ (constant), 0.1 and 0.5.

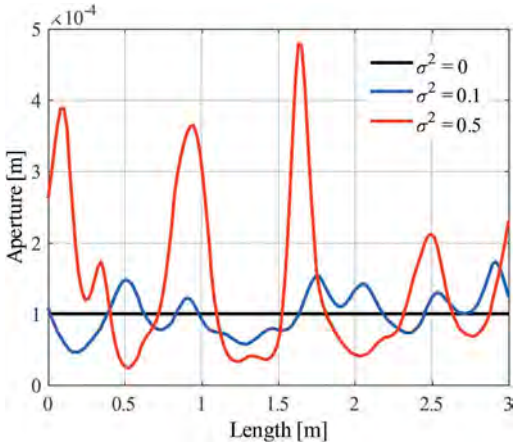

Figure 7. Exemplified randomly generated varying fracture apertures for different cases, i.e., $\sigma^2 = 0$ (constant), 0.1 and 0.5.

4.2 *Evolution of propagation length over time*

The cement grouts propagation in all generated realizations of varying apertures are simulated using the validated two-phase flow model. The rheological parameters for Grout R2 shown in Table 1 are adopted in all simulations.

For a statistical comparison, the median values of propagation lengths for the 50 realizations are presented in Figure 8. The result shows that cement grouts generally propagate slower in varying fracture apertures. In particular, the propagation time is increased over 4 times for the case of$\sigma^2 = 0.5$, compared to the cases of $\sigma^2 = 0$ (constant) and 0.1.

This finding is consistent with previous studies on fluid flow in rough-walled rock fractures (e.g., Zou et al., 2015). The main reason is that the varying fracture apertures can reduce the effective transmissivity and cause additional pressure drop during the cement grout propagation process. This result also indicates that characterization of fracture aperture distributions is important in rock grouting analysis and ignoring the features of varying apertures could overestimate the propagation lengths in practice.

5 DISCUSSIONS AND CONCLUSIONS

In this work, we presented a two-phase flow model for predicting non-Newtonian cement grouts propagation in 1D fractures with varying apertures. This model is validated against a set of laboratory grouting tests in a varying aperture long slot. The validated model is used to analyse the impact of varying aperture on cement grouts propagation in 1D fractures with lognormal distributed apertures.

The results show that the presented two-phase flow model is reliable and can predict cement grouts propagation in more realistic rock fractures with varying apertures. The varying apertures, quantified by variance, can significantly affect the cement grouts propagation process, and ignoring the varying apertures could generally overestimate propagation lengths. Therefore, it is recommended to consider the more realistic apertures structures in fracture characterization for rock grouting analysis in practice.

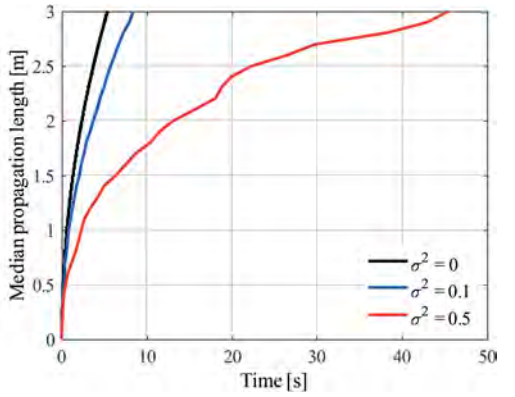

Figure 8. The median propagation lengths for different cases, i.e., $\sigma^2 = 0$ (constant), 0.1 and 0.5.

Although the presented two-phase flow model can be readily used to predict cement grouts propagation in fractures with varying apertures, accurate characterization of fracture apertures remains a challenge. In practice, the distributions of fracture aperture can be obtained from the fracture traces of rock cores or outcrop mapping. The obtained fracture aperture distributions can be used as the input information for the presented two-phase flow model to perform stochastic analysis, as presented in Section 4. Furthermore, the illustrated impact of varying aperture on cement grout propagation length can be potentially used to correct the analytical models with constant apertures, which could be an important topic for the future study.

ACKNOWLEDGMENTS

We sincerely thank the Swedish Rock Engineering Research Foundation (BeFo) for providing the funding for this study.

REFERENCES

Ghafar, A. N., 2017. An Experimental Study to Measure Grout Penetrability, Improve the Grout Spread, and Evaluate the Real Time Grouting Control Theory. PhD Thesis, Royal Institute of Technology, Stockholm, Sweden.

Hässler, L., Håkansson, U., Stille, H., 1992. Computer-simulated flow of grouts in jointed rock. Tunnelling and Underground Space Technology; 7, pp. 441–446.

Håkansson, U., 1993. Rheology of fresh cement based grouts. PhD Thesis, Royal Institute of Technology, Stockholm, Sweden.

Stille, H., 2015. Rock Grouting-Theories and Applications. Vulkan Förlag Stockholm.

Zou, L., & Cvetkovic, V., 2020. Inference of transmissivity in crystalline rock using flow-logs under steady-state pumping: Impact of multi-scale heterogeneity. Water Resources Research, 56, e2020WR027254.

Zou, L., Håkansson, U., Cvetkovic, V., 2018. Two-phase cement grout propagation in homogeneous water-saturated rock fractures. International Journal of Rock Mechanics and Mining Sciences. 106, pp. 243–249.

Zou, L., Håkansson, U., Cvetkovic, V., 2019. Cement grout propagation in two-dimensional fracture networks: Impact of structure and hydraulic variability. International Journal of Rock Mechanics and Mining Sciences. 15, pp. 1–10.

Zou, L., Håkansson, U., Cvetkovic, V., 2020a. Analysis of Bingham fluid radial flow in smooth fractures, Journal of Rock Mechanics and Geotechnical Engineering, 12 (5), pp. 1112–1118.

Zou, L., Håkansson, U., & Cvetkovic, V. 2020b. Radial propagation of yield-power-law grouts into water-saturated homogeneous fractures. International Journal of Rock Mechanics and Mining Sciences, 130 (104308), 104308.

Zou, L., Jing, L., Cvetkovic, V., 2015. Roughness decomposition and nonlinear fluid flow in a single rock fracture. International Journal of Rock Mechanics and Mining Sciences. 04, 2015; 75. DOI: 10.1016/j.ijrmms.2015.01.016.

Zou, L., Selroos, J-O, Poteri, A, Cvetkovic, V., 2023. Parameterization of a channel network model for groundwater flow in crystalline rock using geological and hydraulic test data, Engineering Geology, 317, 107060.

Taylor & Francis
Taylor & Francis Group
http://taylorandfrancis.com

Instrumentation and monitoring/testing and inspection

Taylor & Francis
Taylor & Francis Group
http://taylorandfrancis.com

Tunnelling for a Better Life – Yan, Celestino, Thewes & Eberhardt (Eds)
© 2024 The Author(s), ISBN 978-1-032-80042-4
Open Access: www.taylorfrancis.com, CC BY-NC-ND 4.0 license

Design and development of tunnel liner void detection system

Aixia An
Gansu Highway and Transportation Construction Group Co., Ltd, Lanzhou

Weibin Luo & Guoqin Tian*
Gansu Road and Bridge Construction Group Co., Ltd, Lanzhou

Yinran Xu, Lin Gao & Junxing Zheng
Huazhong University of Science and Technology, School of Civil and Hydraulic Engineering, Wuhan

ABSTRACT: The space between the primary support and secondary lining of tunnel supporting structures is usually backfilled by grouting concrete slurry. Grouting quality significantly affects integrity of supporting structures, and therefore, the safety of tunnels. Several tunnel lining failure accidents have demonstrated that insufficient grouting and grouting defects may cause serious collapse disasters. As such, many non-destructive evaluation techniques have been developed to detect grouting defects, such as ground penetrating radar (GPR). However, these techniques cannot perform a real-time in-construction-process grouting defects and voids evaluation. Therefore, this study aims to develop a novel equipment based on a Raspberry Pi, which can evaluate grouting quality during construction process. This equipment can automatically detect concrete backfill quality by monitoring the conductivity of backfill. Then, the Raspberry Pi connects to the internet and uploads evaluation results in real time. A smartphone application is developed, which can visualize the grouting quality detection results by Raspberry Pi.

Keywords: tunnel second lining, raspberry pi, smart detection, smart construction, internet of things

1 INTRODUCTION

Tunnel second lining refers to the tunnel has been the case of initial support, the use of reinforced concrete and other materials to build the second lining structure of the tunnel, to achieve the role of support and reinforcement, anti-drainage, in order to meet the normal use of tunnels and the requirements of safe operation. When the back of the tunnel lining structure appeared hollow, will cause the second lining for the surrounding rock and supporting structures can not play a protective role, so that the overall rigidity of the tunnel lining and the force state changes, resulting in the stability of the tunnel structure, safety reduction, the lack of internal stability prone to safety accidents, in the external environment, the occurrence of the hollow will be with the cracks, the structure of vibration, the structure of freezing, and the lining itself insufficient thickness and other factors. Insufficient thickness of the lining itself and other factors to occur coupled with the disease, the structure of the overall damage, and ultimately have a significant impact on the safety of the project.[1]. In general, the secondary lining of tunnels is monitored by means of pre-hole grouting, tapping or geo-radar buried in the ground. [2]. Eventually, grouting backfill, anchor reinforcement, liner arch reinforcement, surface part of the reinforcement and other treatment measures will be taken to deal with. The appeal of all the detection methods have a large demand for labor, monitoring is more complex, need to spend a lot of manpower and material resources to carry out, and monitoring has a periodicity, can not always understand the state of the two lining structure and timely safety measures to prevent the occurrence of safety problems and so on.

In order to improve the quality of tunnel engineering and avoid safety accidents. Combine the secondary lining cavity monitoring with sensors to realize the detection of the cavity in the back of the secondary lining of the tunnel, and then transmit it through the Raspberry Pi microcomputer[3],

*Corresponding author: 470065016@qq.com

DOI: 10.1201/9781003495505-347

Processing inspection data, and ultimately uploaded to the cloud, and then through the cloud and mobile data writing and reading through the cell phone or website to view the data, to realize the monitoring of the informationization and real-time, anytime and anywhere to open the app to view the current tunnel lining conditions, as well as real-time grouting situation analysis [4]. When a problem arises, it is possible to notify the relevant personnel in a timely manner to take immediate action to deal with it, prevent accidents from occurring, and minimize safety risks.

2 HARDWARE DESIGN

Figure 1. Detection instrument.

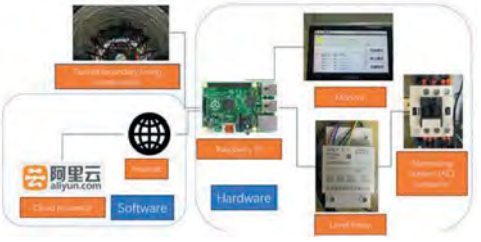

Figure 2. General design of the instrument.

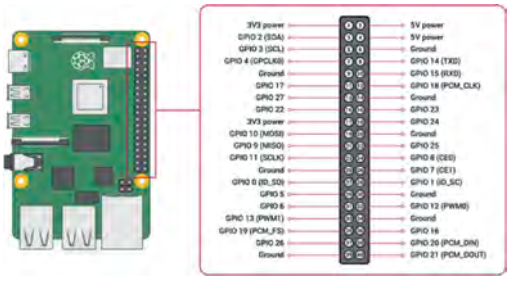

Figure 3. Raspberry Pi GPIO coding.

2.1 *Introduction to the Raspberry Pi platform and GPIOs*

Using the Raspberry Pi platform for the latest release of the fourth generation of products Raspberry Pi 4 B, its performance and the Raspberry Pi 3B + compared to both processor speed, multimedia and memory have been significantly improved[5]. The Raspberry Pi 4B has desktop performance comparable to entry-level x86 PC systems.

The Raspberry Pi 4B features a 64-bit quad-core processor running at 1.5Ghz, up to 4GB of RAM (1GB, 2GB, 4GB, 8GB depending on model), 2.4/5.0 Ghz dual-band wireless LAN, Bluetooth 5.0/BLE, Gigabit Ethernet, USB 3.0, and PoE capability [6]. These configurations provide hardware support for the computerization of secondary lining cavity monitoring. As shown in Figure 2 is a schematic of the Raspberry Pi modules.

The choice to use Raspberry Pi as the main control platform is due to the fact that the Raspberry Pi system has the most powerful GPIO (General-Purpose Input/Output) with 40 pins. As shown in Figure 3 below [7]. GPIO: General Purpose Input/Output Port, through some of its above pins output high level or low level or read out the current state of the pin is high level or low level. Can be through the current state of the high and low levels and computer-related software. Eventually realize the purpose of data interaction, control software and hardware work, read the working status signal of software and hardware. Through the GPIO pin external wires to realize the current circuit to determine whether the successful connection, and ultimately realize the current state of the tunnel secondary lining of the back of the judgment of whether there is a hole [8]. Figure 3 below shows the 40 pins of the GPIO and the code of each pin [9].

The 40 pins of the GPIO is the BCM (Binary Coded Matrix) coded 17 pin GPIO.5 3.3v writing Pi coded 0 number of pins and ground pins for the operation of external wires.

2.2 *Composition of testing instruments*

It adopts a three-level rainproof distribution box, which is equipped with a buzzer alarm, signal light, test button, switch knob, and other devices[10]. Its functions are:

1) When the slurry is full of squeeze signal probe, through the signal probe to the relay action signal, buzzer flash, and alarm signal[11].
2) All components voltage selection DC24V (relay, buzzer, signal lamp), power supply from AC220V through the power converter into DC24V low voltage, to ensure the personal safety of construction workers.
3) A signal probe installed in the vault waterproofing board on the inside, to tower style is appropriate, to ensure good signal contact and normal feedback,

each board has two lining lengths of 12m, along the longitudinal direction of the vault and is equally spaced sequentially laid 6 groups, signal acquisition probe as a monitoring point, 6 groups of signal lines to lead to the distribution box terminals[12]. Terminal order: (11, 12) for the first group, (21, 22) for the second group, (31, 32) for the third group, (41, 42) for the fourth group, (51, 52) for the fifth group, (61, 62) for the sixth group.

4) 6 groups of monitoring point signal probes are connected in series to ensure that all 6 monitoring points are filled with relay action, the distribution box operating panel flash buzzer at the same time issues a warning signal[13].
5) Distribution box operation panel is equipped with a hand/automatic knob switch, automatic response from the probe, relay absorption issued by the warning sound, and manual position only for the role of the test sound warning device.

The selected AC contactor for this study is the Schneider LC1-D25 series, designed for use in AC circuits with a frequency of 50Hz or 60Hz and a voltage of 220V. Primarily intended for long-distance circuit connection or interruption, it can be combined with a thermal relay of corresponding specifications to form a magnetic starter, providing overload protection to the circuit. The operational principle involves the passage of current through the contact coil when the circuit is energized, generating a magnetic field. This magnetic field induces electromagnetic suction in the static iron core, attracting the movement of the dynamic iron core. Consequently, the AC contactor points are set in motion, leading to the disconnection of normally closed contacts and the closure of normally open contacts, creating a synchronized action between the two.

When the coil is disconnected, the electromagnetic suction vanishes, and the armature, released by the release spring, restores the contact point. This action leads to the disconnection of the normally open contact and the closure of the normally closed contact. By controlling the open and closed states of normally open contacts, the main AC circuit can be rapidly interrupted, allowing frequent switching of the high-current control circuit. Contactors find extensive application in controlling electric motors, factory equipment, electric heaters, workhorses, and various power units. Beyond circuit connectivity, contactors also offer low-voltage release protection. Their robust control capacity makes them suitable for frequent operations and long-distance control, rendering them indispensable components in automatic control systems.The main purpose of the electronic display is to serve as an external screen for the Raspberry Pi, allowing the user to program or operate the Raspberry Pi computer by directly connecting the mouse and keyboard to write and enter programs. It also allows the user to observe the results of the operation in real-time and to find out the results of previous measurements on the display. Electronic display through the HDMI interface wire and the Raspberry Pi on the high-definition multimedia interface HDMI interface connection can display the contents of the Raspberry Pi computer, combined with the Bluetooth connection of the mouse and keyboard, the user can be in the Raspberry Pi to carry out a series of operations. Figure 4 below shows the hardware schematic of the instrument.

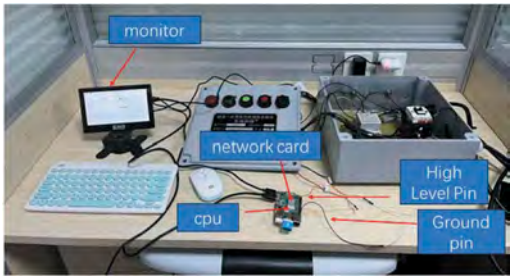

Figure 4. Schematic diagram of the instrument hardware.

3 SOFTWARE AND PROGRAM WRITING

The primary implementation of this program is in Python, focusing on developing and running the test page, including page loading and the transmission process. The procedure begins by entering the test point number and name to initiate testing. Upon circuit access, a returned value signifies a connected circuit, indicating the absence of voids behind the lining. The results are then stored in a designated folder.

In the case of an open circuit, where the circuit is not connected, the program conducts 20 tests at 0.1s intervals. If the internal access test matches the first case, or if the circuit remains unconnected, the program returns the corresponding information, storing pile number, pile name, etc. The test results are dichotomously stored and uploaded to the cloud.

Upon opening the program, historical data is automatically retrieved and displayed on the start page. The latest data is used for monitoring, and the monitoring data is seamlessly uploaded to the cloud for real-time accessibility on mobile devices.

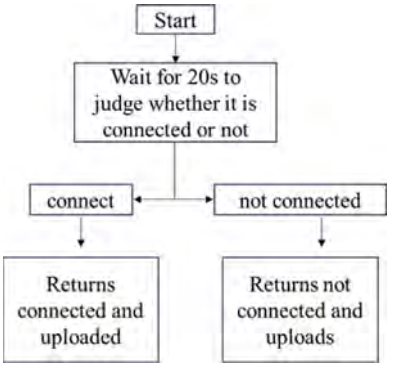

Figure 5. Judgment flowchart.

Page Design For the UI page design, the content to be included in the entry page of the program includes the page size, cover design, loading animation settings, and the running of the program needs to include the start and end key settings, the historical data list, and the latest data table (including the description of the pile number, the pile name, and whether it is full or not).

Utilizing the Tinder statement for UI design, the Label component is employed to exhibit information. Historical and latest data forms are constructed through direct definitions of height, width, and image parameters. The UI interface is crafted to showcase the word "Gansu Tunnel" and tunnel images upon program entry. As the loading figure progresses from 0% to 100%, the word "Gansu Tunnel" is displayed beneath it.

The left section of the UI features a historical data table presenting pile number, pile name, and connection status. On the right, the UI displays the current pile number, pile name for testing, and a start test button, requiring user input. Upon clicking, the program transitions to the operational interface.

4 CLOUD STORAGE OF DATA

To ensure the safety and integrity of the massive data generated during the monitoring of the tunnel's secondary lining, crucial for project safety, effective data management is imperative. Key considerations include data storage integrity, security, readability, easy retrieval, disaster recovery readiness, and timely synchronization, all pivotal for the smooth functioning of the detection system.

Opting for cloud storage presents notable advantages. It allows seamless storage and retrieval, ensuring data security and implementing emergency measures to avert potential data loss and its associated severe consequences. Given the substantial data volume, utilizing traditional storage methods like U disks, CF cards, SM cards, TF cards, and flash memory sticks is cumbersome. Therefore, the study has wisely chosen cloud storage as the preferred method for data storage.

Utilizing an AliCloud server for data storage, the research group invested in this solution to ensure efficient data transmission and retrieval. The choice of AliCloud is advantageous due to its strong endorsement by a major Internet enterprise, ensuring mature technology and robust protection against data disruptions caused by external factors. This server proves effective in safeguarding data privacy. Additionally, it offers convenience and fulfills various requirements essential for this study. The data transfer to the cloud and subsequent retrieval are executed through Python statements, inputted into the Raspberry Pi for seamless storage and access in the cloud.

The data presented in the mobile app's display section showcases historical operational data from testing and commissioning. This historical data, stored both on the Raspberry Pi computer and in the cloud, ensures convenient and timely access via the mobile app. Users can utilize the WeChat mini-program "Crafted Tunnel" to gain real-time insights into various piles within the tunnel, allowing them to understand the current status of the tunnel lining. This approach enables continuous, real-time monitoring of the cavity behind the tunnel lining. Users have the capability to monitor the secondary tunnel lining status in real-time through the software and website, providing a proactive measure against potential hazards.

Front-end and backend development in Java involve a separated approach. In front-end development, we utilized the Element UI component library, Vue framework, and Echarts library. These tools offer high efficiency, flexibility, and ease of expansion. Element UI, based on Vue library's desktop components, allows individual component introduction, reducing the impact on project volume. However, it may require manual code entry, which is manageable for this project due to its simplicity. Echarts, an open-source JavaScript chart library from Baidu, offers rich icon content, compatibility with most browsers, and the flexibility for users to create their charts. It is a valuable asset for chart drawing on the site.

The back end incorporates Spring Boot, MyBatis data interface, and Redis for data caching. Spring Boot facilitates seamless data exchange between the front and back end. MyBatis data interface encapsulates complex SQL database operations, mapping them through Java objects and SQL statements, simplifying the execution of SQL statements in code. This eliminates the need for manual processes like registering the driver, creating a connection, and setting up parameters.

MyBatis connects to the database through a configuration file, enhancing maintainability by avoiding hard-coding issues. SQL statement execution in MyBatis is configured separately from Java code, providing flexibility. MyBatis manages connection pooling and caching, optimizing database interactions for efficiency.

Redis primarily serves as a data cache for temporary storage, crucial for handling the large amount of data generated during the monitoring process in this study. The data is temporarily cached in Redis before being stored in the MySQL database hosted on Alibaba Cloud. MySQL is chosen for its advantages of small size, speed, low cost, and open-source nature. The overall interaction process between the front end, back end, and the cloud is depicted in Figure 6.

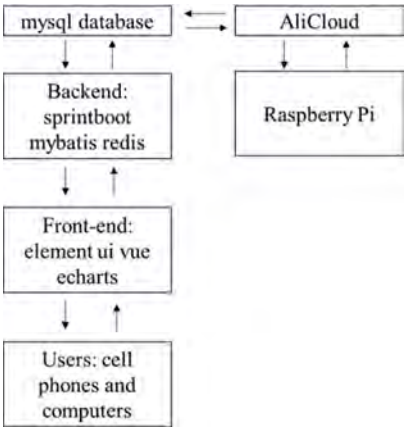

Figure 6. Front and back-end data as well as a cloud interaction process.

5 CONCLUSION

This paper introduces an Internet of Things (IoT) based system for detecting cavities in the secondary lining of tunnels. Leveraging the conductivity of reinforced concrete, the system forms a closed circuit at the connection points, allowing for the assessment of the tunnel lining's condition. If the secondary lining is full without any cavities, the concrete's conductivity maintains a normal circuit, triggering the indicator light, and storing the message "no cavity in the back of this secondary lining section" in the system, subsequently uploading it to the cloud.

Conversely, if there is a cavity in the back of the tunnel's secondary lining, the lack of conductivity in the air interrupts the circuit, preventing the indicator light from illuminating. This absence of a circuit connection indicates the presence of a cavity, prompting the system to store the information "there is a cavity in the back of this secondary lining section" in the Raspberry Pi system. This data is then transferred to the cloud and integrated into the app, allowing users to check the current status of the tunnel's secondary lining at their convenience through the app or web client.

This system design aligns with the current trends in civil engineering and the trajectory of intelligent construction. It not only addresses a wide market but also holds practical significance and social value.

REFERENCES

1. Ye Z, Ye Y, Zhang C, et al. (2023) A digital twin approach for tunnel construction safety early warning and management. Computers in Industry 144:103783.
2. Yu G, Zhang S, Hu M, et al. (2020) Prediction of highway tunnel pavement performance based on digital twin and multiple time series stacking. Advances in Civil Engineering 2020:1–21.
3. Yu G, Lin D, Wang Y, et al. (2023) Digital Twin-enabled and Knowledge-driven decision support for tunnel electromechanical equipment maintenance. Tunnelling and Underground Space Technology 140:105318.
4. Shen Y, Ling J, Li X, et al. (2022) Holistic digital-twin-based framework to improve tunnel lighting environment: From methodology to application. Building and Environment 224:109562.
5. Lee J, Lee Y, Park S, et al. (2023) Implementing a Digital Twin of an Underground Utility Tunnel for Geospatial Feature Extraction Using a Multimodal Image Sensor. Applied Sciences 13 (16):9137.
6. Latif K, Sharafat A, Seo J (2023) Digital Twin-Driven Framework for TBM Performance Prediction, Visualization, and Monitoring through Machine Learning. Applied Sciences 13 (20):11435.
7. Zhao Y, Wang N, Liu Z (2022) An Established Theory of Digital Twin Model for Tunnel Construction Safety Assessment. Applied Sciences 12 (23):12256.
8. Hu W, Zhang T, Deng X, et al. (2021) Digital twin: A state-of-the-art review of its enabling technologies, applications and challenges. Journal of Intelligent Manufacturing and Special Equipment 2 (1):1–34.
9. Chang L, Zhang L, Fu C, et al. (2021) Transparent digital twin for output control using belief rule base. IEEE Transactions on Cybernetics 52 (10):10364–10378.
10. Yang S-W, Kim S-J, Kim S-A (2021) BIM-based Design Automation Tool and Digital Twin Interoperability-Case of the Next Generation Noise Barrier Tunnel. Journal of KIBIM 11 (4):31–41.
11. Sepasgozar SME (2020) Digital twin and web-based virtual gaming technologies for online education: A case of construction management and engineering. Applied Sciences 10 (13):4678.
12. Kaewunruen S, Peng S, Phil-Ebosie O (2020) Digital twin aided sustainability and vulnerability audit for subway stations. Sustainability 12 (19):7873.
13. Ikeda H, Mokhtar NEB, Sinaice BB, et al. (2023) Digital Twin Technology in Data Center Simulations: Evaluating the Feasibility of a Former Mine Site. Sustainability 15 (23):16176.

Tunnelling for a Better Life – Yan, Celestino, Thewes & Eberhardt (Eds)
© 2024 The Author(s), ISBN 978-1-032-80042-4
Open Access: www.taylorfrancis.com, CC BY-NC-ND 4.0 license

Tunnel condition assessment: State-of-the-art

Saleh Behbahani
Lyles School of Civil Engineering, Purdue University, West Lafayette, IN, USA

Jerome Steinkuehler
DIBIT Measuring Technique USA, Inc., Redmond, Washington State, USA

Jamal Rostami*
Earth Mechanics Institute (EMI), Department of Mining Engineering, Colorado School of Mines, Golden, CO, USA

Xiao Wang
Department of Civil Engineering, Hangzhou City University, Hangzhou, China

Tom Iseley
Division of Construction Engineering and Management, Purdue University, West Lafayette, Indiana, USA

ABSTRACT: Asset Management involves meeting the underground infrastructure's current operational demands while moving from being reactive to more proactive. This reduces the dollars spent on crises management by investing in preventing emergencies. This is accomplished by developing an accurate and complete record and understanding of the current state of the underground's assets which include developing an asset registry, condition assessment and developing a plan to maximize the assets' service life. A report which was prepared as part of National Cooperative Highway Research Program Project (NCHRP) 20-07/Task 276, (Development of Guidelines for Rehabilitation of Existing Highway and Rail Transit Tunnels) indicates that water leakage through the tunnel lining has been the majority of the problems. The main reason for tunnel inspections is to identify structural condition by locating and prioritizing structure defects to assure the safety of public traveling in tunnels and protect property. Historically, visual and manual procedures for tunnel inspection have been widely used. Since these procedures are time-consuming and subjective to human error, alternative automated techniques to increase efficiency and reliability in tunnel inspection are needed. This session will review the state-of-the-art of tunnel inspection technologies toward tunnel condition assessment and discuss case studies.

Keywords: Tunnel inspection, Asset management, Photogrammetry

1 INTRODUCTION

Based on the 2020-2021 International Tunnelling and Underground Space Association (ITA) Activity Report, the worldwide tunneling market has an estimated value of around $135 billion annually, growing at a rate of 9 percent per year. This growth rate is significantly higher, approximately 2.5 times, compared to the overall construction market. Furthermore, the passage of the Infrastructure Investment and Jobs Act (IIJA) of 2021 is providing a much-needed financial boost to tunneling projects, which have historically faced significant funding obstacles. This legislation allocates $66 billion over a span of five years to support rail initiatives, with $8 billion specifically designated for the Gateway program. Additionally, funding is being allocated for water and wastewater projects, including those related to combined sewer overflow (CSO) programs.

As tunneling projects continue to grow in length, size, depth, and complexity, there arises an increasing need for thorough and reliable tunnel inspection processes. These inspections play a crucial role in ensuring the safety, integrity, and functionality of the tunnels over their operational lifespan. Regular and comprehensive tunnel inspections are vital for identifying early signs of damage, assessing structural stability, and detecting potential issues that may compromise the tunnels' functionality and safety. The repair cost of tunnels will increase if

*Corresponding author: rostami@mines.edu

DOI: 10.1201/9781003495505-348

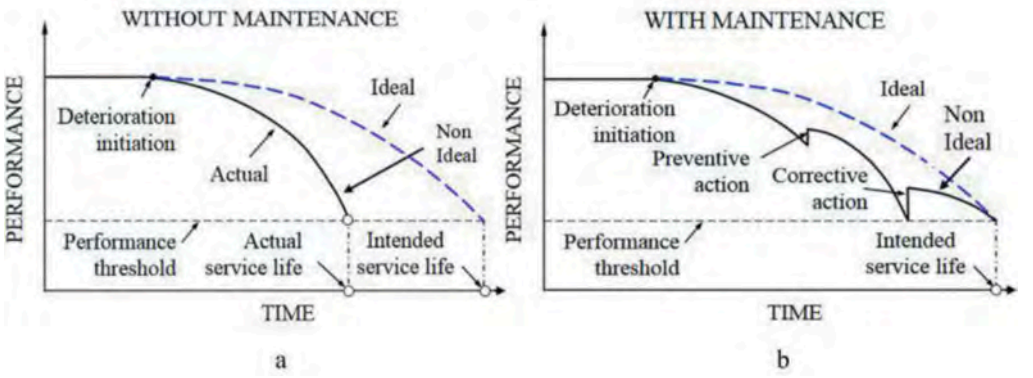

Figure 1. Deterioration curves without (a) and with (b) proper structures maintenance (Chaiyasarn, 2011).

maintenance of tunnels is not satisfactory and timely. Figure 1 illustrates an example of using Level of Service (LOS) in the asset management plan. Figure 1(a) illustrates a deterioration curve without asset renewal activities and the difference between it and the ideal service life of the asset. However, as shown in Figure 1(b), to restore the asset's condition and extend its service life, rehabilitation is needed at specific times to ensure that the asset's condition remains above the desired LOS. With proper structures maintenance, the service life of an asset can be extended to its intended service life.

2 BACKGROUND OF TUNNEL INSPECTION

Throughout history, the assessment of tunnels has predominantly hinged upon visual inspections conducted manually. These long-standing practices, although prevalent, come with inherent drawbacks, notably their laborious nature and susceptibility to human mistakes. Consequently, there exists an urgent requirement for the introduction of cutting-edge automated methodologies capable of not only expediting the inspection process but also elevating the overall dependability of tunnel evaluations. As of the 2020 report by the National Tunnel Inspection Program, the United States boasts a grand total of 526 tunnels. These tunnels can be predominantly categorized into two distinct eras of construction: the initial wave occurred during the 1930s and 1940s, while the second surge coincided with the development of the Interstate Highway System throughout the 1950s and 1960s. Figure 2 provides a visual representation of the top five states in the United States, which collectively house more than 270 tunnels.

Due to easy access, durability, and lower cost precast concrete liners and cast-in-place concrete liner are frequently used as permanent final lining systems in highway tunnels (FHWA, 2015). Figure 3 lists some common concrete defects.

In Specifications for the National Tunnel Inventory manual, which was published by the FHAW in

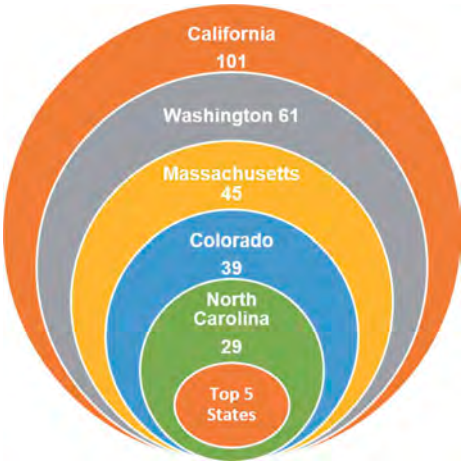

Figure 2. Top five states with majority of tunnels in the US.

2015, four different condition states for tunnel liners have been described and quantified based on the severity of defects. Figure 4 shows these four condition states. Tables 1 describes the definitions of four different condition states for precast concrete tunnel liner (FHWA, 2015).

In tunnel inspection process, detecting and measuring cracks in tunnel lining is vital as cracks are the initial signs of damages to the tunnel structure. It is an arduous task for tunnel inspectors to visually detect and measure cracks in tunnel liners as it is a time-consuming task and subjected to human error. Also, to decrease the downtime during tunnel inspection, monitoring and inspection of tunnel structure usually is conducted during the night time. With advanced inspection technologies and methodologies, engineers and inspectors can closely monitor the condition of the tunnels and implement timely maintenance and repair actions. Additionally, considering the extensive

Figure 3. Some common concrete defects.

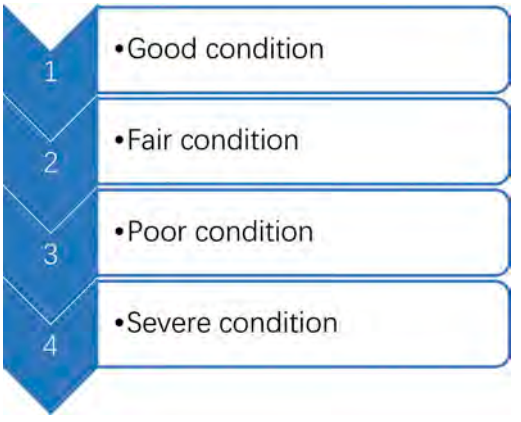

Figure 4. Tunnel liner condition states.

capital investments involved in tunnel construction, conducting regular inspections is a cost-effective approach to preventing major failures that could result in expensive repairs or even partial or complete shutdowns. As the demand for tunnels continues to rise, and as they become more challenging to construct and inspect, investing in state-of-the-art inspection techniques becomes paramount. Traditional tunnel inspections often involve manual and time-consuming methods, requiring a substantial workforce and significant financial investment. However, the process of tunnel inspection can be significantly optimized by leveraging advanced tunnel scanning technologies, such as laser scanners, thermography, and photogrammetry systems (Behbahani et al., 2023). These state-of-the-art systems offer numerous benefits, including cost reduction, time savings, and decreased personnel requirements, making the inspection process more efficient and accurate. By proactively addressing potential issues through regular inspections and adopting cutting-edge inspection techniques, tunnel owners and operators can ensure the long-term performance, safety, and sustainability of these critical infrastructural assets.

3 3D TUNNEL SCANNING SYSTEM

3D Tunnel scanning opens up possibilities to create a digital twin of tunnel tubes with a surface resolution of up to 1 x 1 mm per pixel and a geometric resolution of up to 5 mm. The Altira scanning system, an ultra-light and compact hybrid scanning system developed by Dibit Measuring Technique, records 3D measurements of tunnels. It is a hybrid device equipped with a LiDAR (Light Detection And Ranging) scanner, a photo unit, and an optional thermal unit (also known as infrared or IR cameras). The laser scanner enables precise measurements of the tunnel geometry (Mett et al., 2019). The measurement unit can be mounted on a trolley that is highly adaptable to various settings and can be used in water tunnels, railroad tunnels, and road tunnels. Figure 5 shows the Altira System in subway tunnels on the left and in a water tunnel on the right.

The measurement trolley is manually pushed through the tunnel, allowing the operator to achieve a recording speed of approximately 2-3 mph (Steinkühler et al., 2022). During recording, the operator monitors the measurements on a computer that displays a live cross-section of the tunnel surface. The use of the Altira mobile scanning device can reduce inspection time spent in the tunnel by up to 75%. The raw data will be processed and referenced in Dibit's proprietary software, Dibit-8. This software is specifically designed for processing and analyzing 3D data captured in cylindrical structures such as tunnels (Steinkühler et al., 2022). Dibit-8 is capable of handling large volumes of data and can quickly and seamlessly visualize the 3D scan data in both 3D and 2D views (see Figure 6).

The database "dibit-TIS" (Tunnel Information System) is a core component of the software. In combination with the dibit-Viewer 3D, tunnel data is analyzed and visualized (Steinkühler et al., 2022). The high-resolution data provides inspection engineers with the capability to measure and map cracks with a width as small as 0.3 mm. In fact, all defect locations can be mapped as planes, lines, or points in the software and are actively visible in the viewers. Furthermore, they can be exported to open data formats such as Excel spreadsheets, ASCII point clouds, and AutoCAD scripts (see Figure 7).

Each digital tunnel assessment provides a snapshot of the tunnel's conditions. By comparing the measured data with future scans, changes can be detected (Steinkühler et al., 2022). For follow-up scans, Dibit-8 can display both datasets in parallel within the viewers. This enables users to compare areas of interest, such as

Table 1. Condition state definitions for precast concrete tunnel liner (FHWA, 2015).

Defect	Condition State 1	Condition State 2	Condition State 3	Condition State 4
Delamination/ Spall/Patched area	None	Delaminated. Spall 1 in. or less deep or 6 in. or less diameter. Patched area that is sound.	Spall greater than 1 in. deep or greater than 6 in. diameter. Patched area that is unsound or showing distress. Does not warrant structural review.	The condition warrants a structural review to determine the effect on strength or serviceability of the element or tunnel, OR a structural review has done completed and the defects impact strength and serviceability of the element or tunnel
Exposed Rebar	None	Present without measurable section loss.	Present with measurable section loss, but does not warrant structural review.	
Efflorescence/ Rust Staining	None	Surface white without build-up or leaching without rust staining.	Heavy build-up with rust staining.	
Cracking (Liners)	Width less than 0.012 in. or spacing greater than 5.0 ft.	Width 0.012 - 0.10 in. below spring line or spacing of 1.0 - 5.0 ft.	Width greater than 0.10 in. below spring line or greater than 0.012 in. above spring line or spacing of less than 1 ft.	
Distortion	None	Distortion has received structural review and has been mitigated.	Distortion has received structural review and does not require mitigation.	
Leakage	Dry Surface	Saturated surface indicating seepage may be present or evidence of past seepage.	Fully saturated surface with seepage.	Seepage could range from dripping to flowing.

Figure 5. Altira System in subway tunnels on the left and in a water tunnel on the right. The measuring system is supported by a robust aluminum construction with a specially designed rail/wheel cart. Altira consists of an LED flash-lighting unit (white), cameras, and the LiDAR scanner (gray puck).

cracks and spalls, over time (see Figure 8). Inspection engineers can now observe and objectively describe and map changes on the tunnel surfaces.

Automated interpretation of tunnel lining inspections represents a burgeoning area of research within the fields of deep learning and artificial intelligence. Numerous automated video interpretation systems for sewer pipelines have already been developed, employing Convolutional Neural Networks (CNNs) for tasks such as classification, localization, and object segmentation. However, based on the literature search and interviews with industry experts, it becomes apparent that relatively few studies have focused on the automated interpretation of tunnel lining inspections. To achieve real-time object classification and localization, several advanced models, including You Only Look Once (YOLO), Faster Region-based Convolutional Neural Network (Faster R-CNN), and Mask R-CNN, have been developed. Currently, the authors are actively researching ways to harness recent breakthroughs in deep learning to enhance the accuracy and speed of defect detection in tunnel inspections. Figure 9 provides a glimpse of this ongoing work, showcasing examples of crack detection utilizing YOLOv8, a cutting-edge computer vision model developed by Ultralytics.

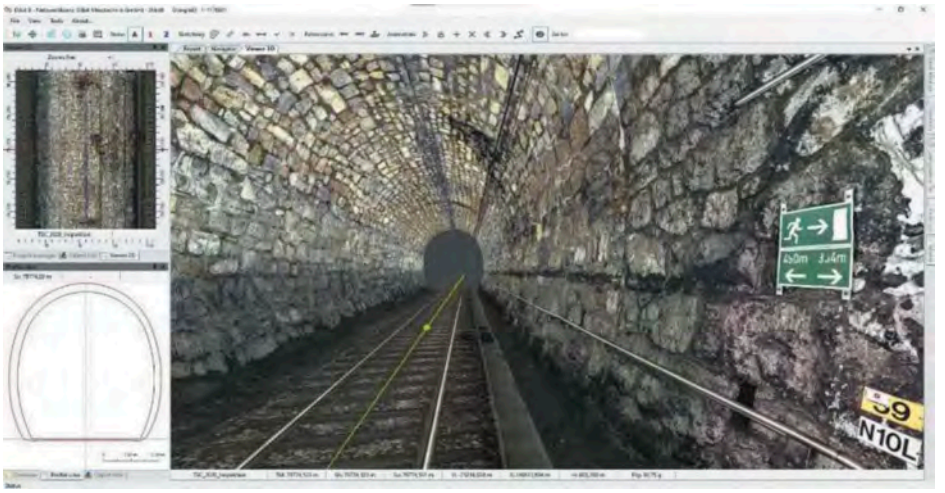

Figure 6. A 3D-view of a railroad tunnel in the Dibit-8 software (center), along with the 2D-view and profile-view at the same location in the tunnel (left).

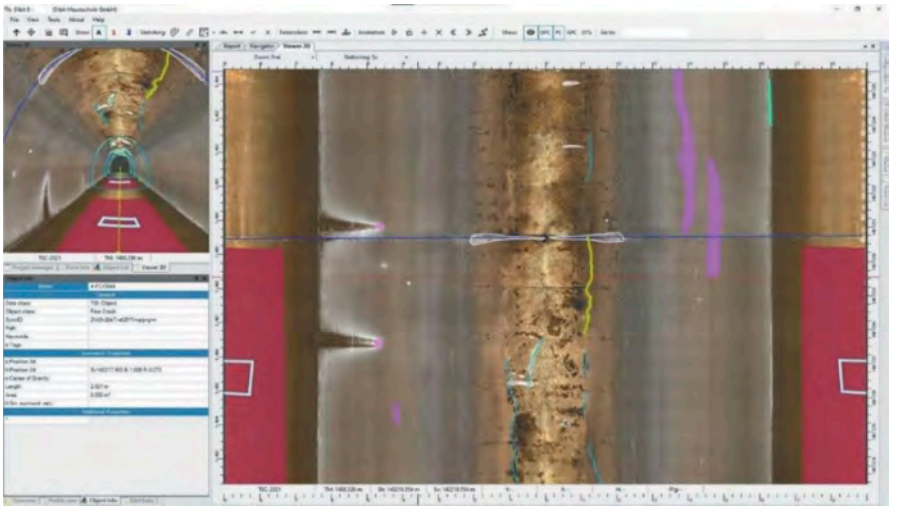

Figure 7. A 2D view of a water tunnel in the Dibit-8 software (center), along with the 3D view and the database (left). Every object mapped in the software is visible in the viewers.

4 CONCLUSIONS

Proactive and comprehensive tunnel inspections are indispensable for safeguarding the longevity and effectiveness of these vital underground infrastructures in an era of unprecedented growth and investment. Neglecting tunnel maintenance can lead to escalating repair costs. The field of tunnel inspections is undergoing a rapid transformation with the integration of advanced scanning technologies such as laser scanners, thermography, and photogrammetry systems. These cutting-edge systems offer a multitude of benefits, including cost savings, time efficiency, and a reduced need for manpower, effectively streamlining the inspection process and elevating its precision to new heights. The adoption of these state-of-the-art inspection techniques enables tunnel owners and operators to proactively address potential issues through routine assessments, thereby ensuring the sustained performance, safety, and long-term sustainability of these vital infrastructural assets. By embracing these innovations, not only do they enhance the efficiency of the inspection process, but they also fortify the overall resilience and dependability of tunnel systems, a crucial consideration in today's ever-evolving and demanding operational environment.

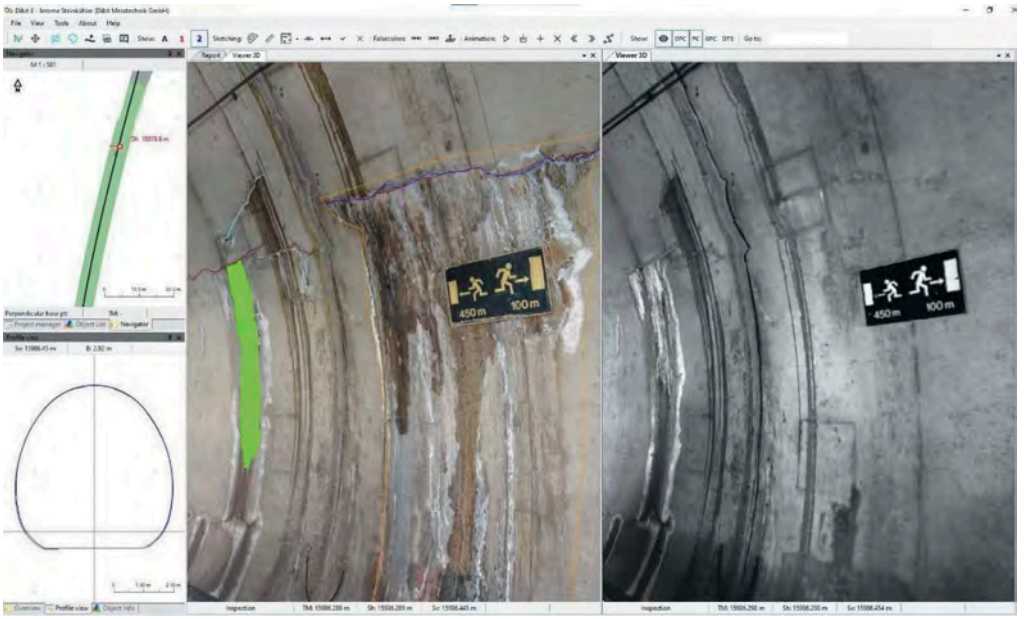

Figure 8. A 3D view of a subway tunnel in Dibit-8 software, scanned in 2021 (left), and scanned in 2015 (right), with crack annotations. Changes in cracks can be readily detected and mapped.

Figure 9. Examples of crack detection utilizing YOLOv8, a cutting-edge computer vision model developed by Ultralytics.

REFERENCES

Behbahnai, S., Iseley, T., Golrokh, A., Hafiz, A., Tabrizi, K., 2023. Tunnel Condition Assessment: State of the Practice. Rapid Excavation and Tunneling Conference (RETC). June 11–14, 2023. Boston, MA.

Chaiyasarn, K., 2011. Damage Detection and Monitoring for Tunnel Inspection based on Computer Vision. Christ's College, University of Cambridge. PhD Thesis. September 30, 2011.

Kontrus, H., Mett, M. 2019. High-speed 3D Tunnel Inspection. 7 S. Proceedings of the Rapid Excavation and Tunneling Conference (RETC) 2019. 16.06.-19.06.2019, Chicago, IL. SOC for Mining Metallurgy. ISBN: 978–0–87335–470–7.

Mett, M., Kontrus, H., Eder, S. 2019b. 3D Tunnel Inspection with Photogrammetric and Hybrid Systems. Proceedings of the 14th International Conference on Shotcrete for Underground Support (ECI SUS XIV), Nong Nooch Gardens – Pattaya, November 17–20, 2019. Thailand.

Specifications for the National Tunnel Inventory Manual. U.S. Department of Transportation, Federal Highway Administration. Publication No. FHWA-HIF-15–006. July 2015.

Steinkühler, J., Mett, M. Heiner, K., Dippold, C., and Latimer, K., 2022. 360-degree, 3D digital assessment of subsurface water infrastructure. Tunneling & Underground Construction, UCA 16 (3): 29–32.

Tunnel Operations, Maintenance, Inspection, and Evaluation (TOMIE) Manual. U.S. Department of Transportation, Federal Highway Administration. Publication No. FHWA-HIF-15-005. July 2015.

Tunnelling for a Better Life – Yan, Celestino, Thewes & Eberhardt (Eds)
© 2024 The Author(s), ISBN 978-1-032-80042-4
Open Access: www.taylorfrancis.com, CC BY-NC-ND 4.0 license

Ground movement due to shaft construction and dewatering at Bengeworth road for the London Power Tunnels 2 scheme

Oliver Brown*, Anna Simic & Joseph Ellis
AECOM, Croydon, UK

ABSTRACT: London Power Tunnels (LPT) Phase 2 is a new purpose-built cable tunnel system which will replace the existing buried cable network in the south of London. This £1 billion National Grid (NG) scheme comprises 32.5km of 3m internal diameter deep underground tunnels and 8 shafts which will help keep Londoners connected to safe and reliable electricity supplies. The tunnels extend from Wimbledon in the West to Crayford in the East, reaching depths of up to 50m below ground level. At Bengeworth Road, a 15m diameter, 30m deep shaft has been constructed to provide a connection to UK Power Network's (UKPN) existing high-voltage electricity transmission network, whilst also providing permanent access and ventilation to the tunnels.

This paper presents the ground surface settlement monitoring data recorded during shaft construction, which is compared against the existing industry standard empirical relationship by New & Bowers (1994), and numerical analysis methods, to evaluate potential risk to adjacent assets. Finite element (FE)/ finite difference (FD) analysis was undertaken to predict ground movements due to the excavation of the circular shaft and associated dewatering within the Lambeth Group and Thanet Sand Formation. Analysis of groundwater drawdown was carried out using MODFLOW and analysis of ground movements due to shaft construction was carried out using PLAXIS, considering the anticipated range of input parameters, e.g. groundwater level and the coefficient of earth pressure at rest (K0). The monitoring data and analysis indicates some variation from the empirical relationship by New & Bowers (1994) and highlights the importance of considering the shaft construction method, site-specific ground conditions and dewatering when making ground movement predictions, particularly when in close proximity to sensitive third-party assets.

Keywords: Tunnelling, Numerical analysis, Simulation, Monitoring

1 INTRODUCTION

London Power Tunnels (LPT) Phase 2 is a new purpose-built cable tunnel system which will replace the existing buried cable network in the south of London. This £1 billion National Grid (NG) project comprises 32.5km of 3m internal diameter deep underground tunnels and 8 shafts which will help keep Londoners connected to safe and reliable electricity supplies. The project will replace three existing high voltage transmission cable circuits from Wimbledon to New Cross, New Cross to Hurst and Hurst to Crayford. The new tunnels extend from Wimbledon in the West to Crayford in the East, constructed by tunnel boring machines (TBMs) in 5 tunnel drives with a precast concrete segmental lining and reaching depths of up to 60m below ground level. Shaft diameters vary between 9m and 15m and are constructed by a variety of techniques including caisson sinking and underpinning with precast concrete segmental lining, sprayed concrete lining and secant piling. The shafts will later be covered by headhouses to provide access and ventilation for the tunnels. The project is currently under construction and due to be completed in 2027. HOCHTIEF-MURPHY Joint Venture (HMJV) are contracted to deliver the Package 2 Tunnels & Shafts and Package 5 Headhouses & M&E contracts on the scheme, and appointed AECOM as permanent works design partner.

At Bengeworth Road, in the London Borough of Lambeth, a 15m internal diameter, 30m deep circular shaft has been constructed to provide a connection to UK Power Network's (UKPN) existing high-voltage electricity transmission network, whilst also providing permanent access and ventilation to the tunnels.

During construction of the shaft, ground movements exceeded predictions. Numerical analysis was carried out to investigate and better understand this behaviour and to estimate final settlements to evaluate potential risk to adjacent assets.

*Corresponding author: oliver.brown@aecom.com

DOI: 10.1201/9781003495505-349

This paper presents the ground surface settlement monitoring data recorded during shaft construction, which is compared against the existing industry standard empirical relationship by New & Bowers (1994), and numerical analysis methods. Finite element (FE)/ finite difference (FD) analysis was undertaken to predict ground movements due to the excavation of the shaft and associated dewatering within the Lambeth Group and Thanet Sand Formation. Analysis of groundwater drawdown was carried out using MODFLOW and analysis of ground movements due to shaft construction was carried out using PLAXIS, considering the anticipated range of input parameters, e.g. groundwater level and the coefficient of earth pressure at rest (K0).

Figure 1. Scheme overview.

2 GROUND CONDITIONS

The Bengeworth Road site is located approximately 1.2km northeast of Brixton, in the London Borough of Lambeth. The ground conditions at the site are typical London Basin strata, comprising Made Ground overlying London Clay Formation, Harwich Formation, Lambeth Group, Thanet Formation and Chalk.

The assumed ground profile at the location of the shaft based on interpretation of historical and recent ground investigation at the site is given in Table 1.

3 GROUNDWATER CONDITIONS

Based on groundwater monitoring data, it was evident that multiple groundwater bodies would be encountered below the Bengeworth Road site. Shallow/ perched groundwater is present in the Made Ground and shallow London Clay where infiltrating surface water becomes trapped on low permeability layers such as the London Clay. The London Clay Formation generally acts as an aquiclude, meaning perched water may also be present in isolated lenses and pockets but not in significant volumes. Perched water posed a risk of localised instability of shallow excavations, particularly in granular materials.

Groundwater is present within the underlying Harwich Formation and in granular horizons within the upper layers of the Lambeth Group (Woolwich and Reading Formations), confined under pressure by the overlying London Clay. Together these strata are referred to as the "intermediate aquifer". The thickness, lateral variation and inter-connectivity of the units in this aquifer varies significantly. Groundwater is also present in the Upnor Formation (the basal deposit of the Lambeth Group), Thanet Formation and Chalk, typically considered as one aquifer and referred to as the "lower aquifer", which is the main water-bearing unit beneath the site.

The groundwater level in the lower aquifer is confined under pressure by the overlying lower permeability strata. Available data suggests the groundwater in the Upnor, Thanet and Chalk Formations are in hydraulic continuity. There is no evidence of hydraulic connectivity between the intermediate and the lower aquifers.

Table 1. Derived ground profile.

Stratum	Top of stratum m bgl	Top of stratum mOD	Thickness m
Made Ground – Cohesive (MG-C)	0	+16.5	3.5
London Clay (LC)	3.5	+13.0	19.8
Harwich Formation (HA)	23.3	-6.8	1.4
Woolwich Formation Upper Shelly Beds – Cohesive (LG-C1)	24.7	-8.2	1.4
Reading Formation Upper Mottled Beds – Cohesive (LG-C2)	26.1	-9.6	1.9
Woolwich Formation Laminated Beds – Cohesive (LG-C1)	28.0	-11.5	3.4
Woolwich Formation Lower Shelly Beds – Cohesive (LG-C1)	31.4	-14.9	0.3
Reading Formation Lower Mottled Beds - Cohesive (LG-C2)	31.7	-15.2	4.7
Reading Formation Lower Mottled Beds – Granular (LG-G2)	36.4	-19.9	1.4
Upnor Formation – Granular (LG-G2)	37.8	-21.3	1.9
Thanet Formation (TG)	39.7	-23.2	12.0
Chalk (CHK)	51.7	-35.2	Not proven

4 GEOTECHNICAL PARAMETERS

The following characteristic geotechnical parameters were derived for the strata present at the site.

Hardening soil model stiffness parameters (Schanz et al., 1999) for the London Clay were derived from oedometer test data available from the site-specific ground investigation.

Table 2. Characteristic geotechnical parameters.

Parameter	Units	MG-C	LC	HA-C
Bulk unit weight, γ_{bulk}	kN/m^3	19	19.5	19.5
Saturated unit weight, γ_{sat}	kN/m^3	20	20.5	20.5
Poisson's ratio, v	-	0.2	0.2	0.2
Coefficient of lateral earth pressure at rest, K_0	-	0.58 - 0.62	0.7 - 1.5	0.9 - 1.5
Undrained shear strength, c_u	kN/m^2	40	40 + 4.4z[1]	130
Drained cohesion, c'	kN/m^2	0	0 - 5[2]	0 - 5[2]
Friction angle (constant volume), φ_{cv}'	°	23	22	23
Friction angle (peak), φ_p'	°	N/A	22	24
Undrained stiffness, E_u[3,4]	MPa	16	16 + 1.76z[1]	52
Drained stiffness, E'[3,4]	MPa	12.8	12.8 + 1.41z[1]	42

Parameter	Units	LG-C1	LG-C2	LG-G2	TG
Bulk unit weight, γ_{bulk}	kN/m^3	19.5	20	20	19
Saturated unit weight, γ_{sat}	kN/m^3	20.5	21	21	20
Poisson's ratio, v	-	0.2	0.2	0.2	0.2
Coefficient of lateral earth pressure at rest, K_0	-	0.7 - 2.0	0.7 - 2.0	0.7 - 1.5	0.7 - 1.0
Undrained shear strength, c_u	kN/m^2	110	125	N/A	N/A
Drained cohesion, c'	kN/m^2	0	0	0	0
Friction angle (constant volume), φ_{cv}'	°	20	20	30	30
Friction angle (peak), φ_p'	°	20	20	32	32
Undrained stiffness, E_u[3,4]	MPa	55	62	N/A	N/A
Drained stiffness, E'[3,4]	MPa	44	50	120	130

1. z = depth from the top of the London Clay, with z = 0m at +13.0 mOD
2. Drained cohesion value assumed when peak parameters are appropriate. Cohesion of 0kN/m2 applied for critical state/ constant volume shearing.
3. Stiffness values for bedrock materials refer to horizontal stiffness. For London Clay, Harwich Formation and Lambeth Group cohesive, E'h=1.5E'v.
4. Stiffness values assume large strain (0.1% to 1.0% strain).

A summary of the hardening soil model parameters derived is provided in Table 3.

Table 3. Hardening soil parameters for London Clay.

Parameter	Units	Value
Tangent stiffness for primary oedometer loading, $E_{oed,ref}$	kN/m^2	12,000
Secant stiffness in standard drained triaxial test, $E_{50,ref}$	kN/m^2	14,000
Unloading/ reloading stiffness, $E_{ur,ref}$	kN/m^2	36,000
Power for stress-level dependency of stiffness, m	-	0.75
Reference stress for stiffnesses, p_{ref}	kN/m^2	200

For completeness, the in-situ stiffness profile obtained with the hardening soil model parameters was compared against the stiffness values derived from empirical correlations with undrained shear strength (c_u). The E_{ur} profile derived showed a good correlation with $E' = 400c_u$ which is consistent with relationships typically used for the proposed method of shaft construction and the anticipated unload-reload behaviour of the over consolidated London Clay.

5 THE BENGEWORTH ROAD SHAFT

The site comprises an area of land within the UKPN Bengeworth Road site where the new shaft has been constructed which incorporates a number of existing structures and utility services (see Figure 2).

Figure 2. Bengeworth road site.

NG are to provide a Grid Supply Point (GSP) to UKPN by developing a 400/132kV substation to feed new and existing 132kV transformers at

Bengeworth Road. The new NG 400kV Gas Insulation Substation (GIS) will be fed via Circuit 1, to be housed within the proposed LPT Phase 2 cable tunnel between New Cross and Wimbledon.

A schematic of the shaft is shown in Figure 3. At the top of the shaft (1m below ground level) is a 1m deep temporary reinforced concrete collar beam used to facilitate construction of a 15m internal diameter, 350mm thick precast concrete segmental shaft lining by the underpinning method. The shaft lining comprises 33 no. 1m deep rings, below which is a 2.2m thick reinforced concrete base slab with mass concrete infill above. The base slab is tapered to provide stability against uplift/ flotation and a temporary sprayed concrete lining (SCL) is used to provide temporary support to the side walls of the base slab excavation prior to casting the base slab.

Figure 3. Bengeworth road shaft schematic.

The underpinning method of shaft construction (see Figures 4 and 5) falls under the Support Before Excavation (SBE) construction category as defined by Faustin et al. (2018).

Figure 4. Bengeworth road shaft lining underpinning.

Figure 5. Bengeworth road shaft lining underpinning.

As part of a wider value engineering exercise, the LPT Phase 2 tunnel alignment was realigned to pass directly through the Bengeworth Road shaft (online shaft) and therefore the shaft incorporated an 8m high, 500mm thick reinforced concrete secondary lining with two portals to transfer forces around the openings. The shaft is then covered by a headhouse to provide access and ventilation for the tunnels.

The lowest excavation level of the shaft is at -19.66mOD which is within the Reading Formation Lower Mottled Beds (LG-C2). Checks of the temporary stability against uplift were carried out in accordance with Eurocode 7 and indicated that groundwater control would be required for both the lower aquifer and intermediate aquifer to control the basal heave risk during shaft excavation.

Groundwater control on site was carried out by HMJV's specialist supply chain partner WJ Groundwater and comprised an array of surface dewatering wells extended down to the Lambeth Group and Thanet Sand (see Figure 6), with provision for probe drilling at the base of the part excavated shaft within the Lambeth Group.

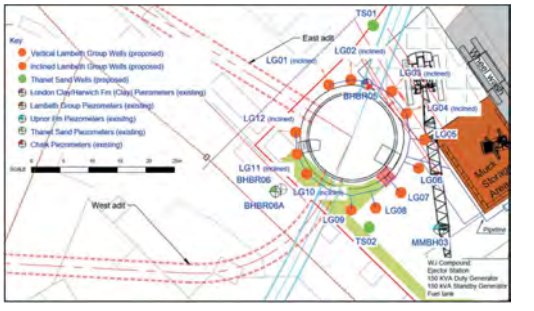

Figure 6. Dewatering well layout.

Throughout the shaft excavation process, HMJV instigated a permit process closely aligned with that

of SCL works, for the underpinning construction, i.e. a Required Excavation Support Sheet (RESS). As well as review of monitoring data, strength testing and survey results (steps, lips, ovality, alignment), regular face logging was undertaken prior to the construction of each ring. This regular review of ground conditions ensured design requirements were closely followed and mitigation measures undertaken if necessary.

6 EMPIRICAL GROUND MOVEMENT PREDICTION

Predicted ground movements due to shaft construction were initially based on the well-known empirical relationship by New & Bowers (1994) between distance from the shaft wall d and the settlement S_d, which has the following equation:

$$S_d = \alpha.(H - d)^2 / H \quad (1)$$

Where, S_d is the settlement at distance d from the shaft wall in m; α is an empirical constant; H is the depth of the shaft excavation in m; and d is the distance from the shaft wall in m.

This is based on data analysed from an access shaft at Heathrow, near London, UK, constructed by caisson-sinking and then underpinning to 16 m depth, and then excavated in 1m steps and lined with shotcrete to 26 m below ground level. For the Bengeworth Road shaft, an α value of 0.0006 was adopted in line with industry practice and the maximum settlement predicted adjacent to the shaft was approximately 22mm.

It was accepted that this relationship would not account for potential dewatering impacts on settlement. Past experience suggested that whilst increasing total settlement values, differential settlements were unlikely to be significantly increased at the location of nearby assets. Monitoring of the shaft lining and nearby assets was carried out in order to review differential settlement in the daily review meetings.

7 ANALYSIS OF GROUND MOVEMENTS

During construction of the shaft, recorded ground movements exceeded the empirical prediction. The layout of monitoring points is shown in Figure 7.

After construction of the 11th segmental shaft ring (excavation depth of approximately 13m), the 3 no. monitoring points installed on the top of the shaft lining indicated between 24 and 42mm settlement compared to an empirical prediction of approximately 8mm maximum settlement for this stage. Whilst differential settlement triggers had not been exceeded, this significant difference prompted

Figure 7. Location of monitoring points around the shaft.

numerical analysis to be carried out to investigate and better understand this behaviour and to estimate final settlements to evaluate potential risk to adjacent assets. The following sections describe the numerical analysis carried out to estimate settlements due to both dewatering and shaft construction and compare the results of the analysis with the empirical predictions and monitoring data.

7.1 *Analysis of ground surface settlements due to dewatering of the Lambeth Group and Thanet sand formation*

Finite difference software MODLOW was used to analyse the groundwater drawdown profile due to depressurisation and dewatering of the Lambeth Group and Thanet Sand Formation. The drawdown estimates were based on the following method and assumptions:

- Hydraulic properties for Thanet Sand Formation and Lambeth Group based upon pumping tests undertaken by WJ Groundwater in 2021.
- MODFLOW model used to simulate the head distribution created by lowering of piezometric pressures in the Lambeth Group and Thanet Sand Formation for a pumping period of between 56 days and 120 days.
- Lambeth Group properties; hydraulic conductivity k = 0.12 m/d, aquifer thickness b = 16.9m, transmissivity T = $2m^2/d$, storativity S = $3x10^{-4}$, initial groundwater level = -6mOD, 12 no. surface well points assumed to lower pressure to -20mOD.
- Thanet Sand Formation properties; hydraulic conductivity k = 4 m/d, aquifer thickness b = 11.5m, transmissivity T = $46m^2/d$, storativity S = $1x10^{-2}$, initial groundwater level = -16mOD, 4 no. surface well points assumed to lower pressure to -22mOD, very low vertical hydraulic conductivity.
- All water is derived from storage (no boundary inflow or recharge).
- Confined system assumed.

Due to the vertical and lateral variability of the Lambeth Group material, and possible 'pockets' of groundwater not in continuity with the main aquifer, it is very difficult to predict the drawdown distribution with confidence. As a result, the drawdown results were an estimate only, and are presented in Figures 8 and 9 below.

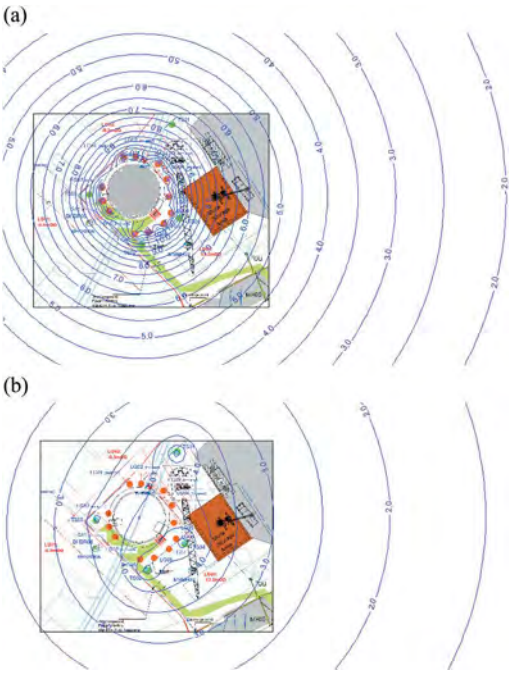

Figure 8. (a) Lambeth Group drawdown contour (metres) after 56 days pumping (b) Thanet Sand Formation drawdown (metres) contour after 56 days pumping.

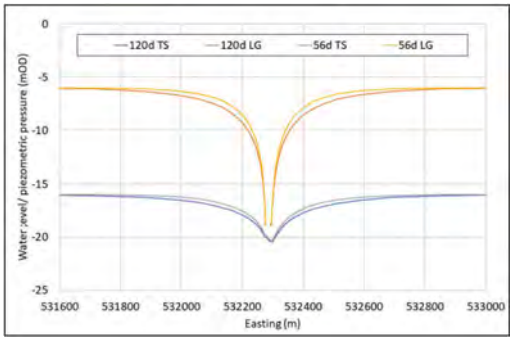

Figure 9. Estimated drawdown after 56 days and 120 days pumping in the Lambeth Group (LG) and Thanet Sand (TS).

The ground surface settlements associated with the above predicted drawdowns were then calculated, based on the following method and assumptions:

- Groundwater drawdown results in a reduction in pore water pressure and hence an increase in effective stress in the ground.
- Settlement was calculated based on reduction of pore water pressure corresponding to predicted drawdown.
- Small strain stiffness (0.1 to 0.01% strain) was assumed.
- For Lambeth Group dewatering, it was assumed that drawdown occurs in the entire thickness of Lambeth Group and Harwich Formation strata and that cohesive strata become drained by the end of pumping. This is conservative but is a reasonable assumption given the permeability of the Lambeth Group and the presence of sand channels and granular lenses.

The settlement estimates are presented in Figure 10 below. The localised effects on groundwater drawdown and associated settlement in close proximity to the pumping wells is ignored for simplicity.

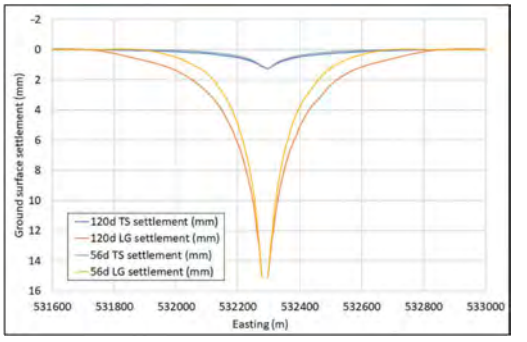

Figure 10. Estimated ground surface settlement after 56 days and 120 days pumping in the Lambeth Group (LG) and Thanet Sand (TS).

7.2 *Analysis of ground surface settlements due to shaft construction*

Finite element software PLAXIS was used to analyse the ground surface settlement due to shaft construction. A 2D axisymmetric model was used (see Figure 11) and considered the anticipated range of input parameters including groundwater level, the coefficient of earth pressure at rest (K0), surface surcharge and undrained (A) or undrained (B) material models (for cohesive materials).

Soils have been modelled using the Mohr-Coulomb (MC) or Hardening Soil (HS) constitutive models (Schanz et al., 1999), depending on the level of ground investigation data available. The stiffness parameters were specified assuming a dominant strain level of between 0.1 and 1% for the underpinning method of shaft construction.

Granular materials were assumed to be drained and cohesive materials were assumed to be undrained in the short-term during shaft construction, which has been modelled using either the

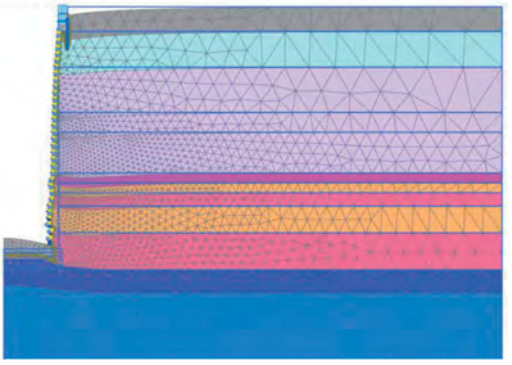

Figure 11. PLAXIS 2D axisymmetric analysis of the shaft.

undrained (A) or Undrained (B) drainage types in PLAXIS. The undrained (A) drainage type uses an effective stress analysis with effective stiffness and effective strength parameters, whereas undrained (B) uses an effective stress analysis with effective stiffness and undrained strength parameters. A summary of the soil models and drainage types adopted for each stratum is as follows:

- MG-C, HA (cohesive) LG-C1 and LG-C2: Mohr Coulomb material model and either Undrained (A) or Undrained (B) parameters.
- LC (cohesive): Hardening soil material model and either Undrained (A) or Undrained (B) parameters.
- LG-G2 and TG: Mohr Coulomb material model with drained parameters.

The segmental lining was characterised by 350mm thick linear elastic two-dimensional plate elements with axial, shear and flexural resistances. The construction of the segmental lining by underpinning was modelled explicitly considering step by step excavation and installation of each 1m deep segmental lining ring. Full face excavation of the shaft was considered with an unsupported excavated depth of 1.5m prior to the installation of each ring. A pin connection between each segmental lining ring was modelled. The temporary reinforced concrete collar beam, permanent base slab and mass concrete infill were characterised by linear elastic non-porous volume elements. The temporary SCL support to the side walls of the base slab excavation were characterised by 100mm thick linear elastic two-dimensional plate elements and assigned isotropic stiffness according to Chang & Stille (1993) to reflect the time-dependent behaviour of the SCL properties, accounting for creep. Construction of the SCL sealing layer was modelled explicitly considering step by step excavation and installation of 1m deep rings, similar to the segmental lining.

It is worth noting that the rate of settlement of the top of the shaft lining was higher up to grouting of the second segmental shaft ring, which had settled by up to 21.9mm (see Figure 12) by this stage.

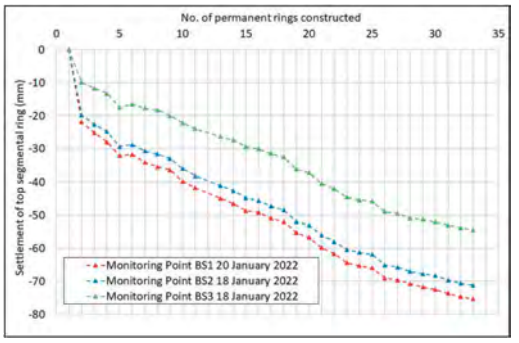

Figure 12. Recorded settlement of shaft top segmental ring.

This increased settlement may have been due to a low strength/ stiffness or more drained behaviour of the MG-C, e.g., a higher permeability/ granular material. It is also understood that there was a delay in grouting behind these rings, which may have caused additional settlement due to the excavated shaft face remaining unsupported for an extended period, partly because of constraints to permitted working time arrangements.

This behaviour was not replicated in the PLAXIS analyses because a reduced strength or stiffness of MG-C was not adopted in the analysis. Instead, in order to allow a more meaningful estimate and comparison of settlements, the maximum monitored settlement of the top of the shaft lining after grouting of the second segmental shaft ring (21.9mm) was used as a starting point (see Figure 13) and added to the PLAXIS analysis settlements for subsequent construction stages.

A comparison of the monitoring survey readings, empirical predicted settlement and PLAXIS 2D analysis settlements is presented in Figures 14-16.

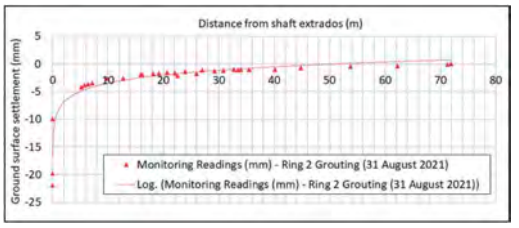

Figure 13. Monitoring readings after grouting of ring no.2.

Figure 15 shows a comparison of the ground surface settlement after installation of permanent ring no. 18. This was the latest stage which did not include the influence of dewatering as it had not yet begun (dewatering settlement is analysed separately in Section 7.1). The analysis results which most closely matched the recorded movements were then used to provide an estimate of the future settlements due to shaft construction to evaluate potential risk to adjacent assets. Note that an extra point has been

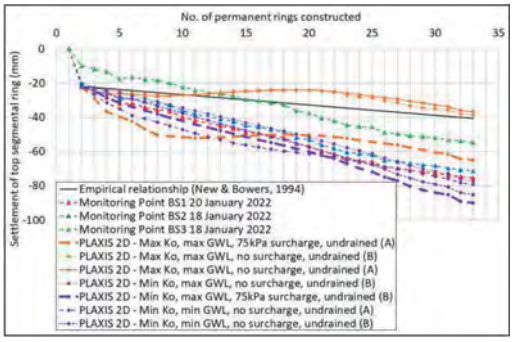

Figure 14. Settlement of shaft top segmental ring (excluding dewatering settlement).

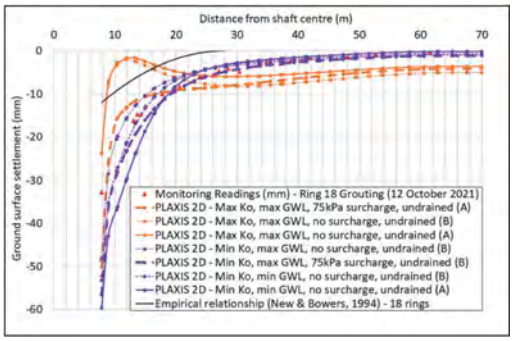

Figure 15. Ground surface settlement after ring no. 18 installation.

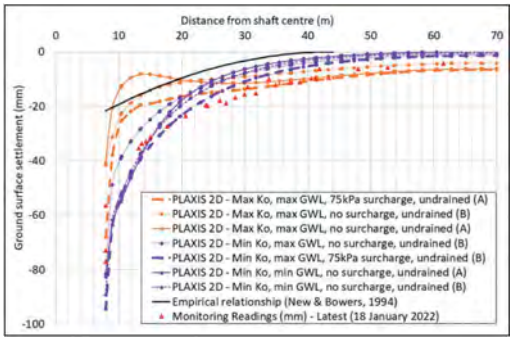

Figure 16. Ground surface settlement after base slab installed.

added to each of the curves to indicate the settlement of the shaft top segmental ring (plotted at the extrados of the shaft lining, i.e., distance from shaft centre = 7.85m) but this is the movement of the shaft lining itself and not the ground surface movement. Figure 15 indicates that for installation of permanent ring no. 18, the PLAXIS analysis case assuming minimum Ko, minimum groundwater, no surcharge and undrained (B) material model was the closest match to the recorded movements, and results of this analysis were then combined with the estimated settlements due to dewatering and used to evaluate potential risk to adjacent assets (see Section 7.3).

Figure 16 shows a similar comparison but for a later stage after the base slab was constructed. For this stage, the recorded movements more closely match multiple PLAXIS analysis cases which assume min K0, however, it should be noted that for this stage, the PLAXIS analysis results do not include dewatering settlements whereas the recorded movements will be influenced by dewatering and therefore a direct comparison cannot be made.

7.3 *Combined estimate of ground surface settlements due to shaft construction and dewatering*

Combined estimated ground surface settlements due to shaft construction and dewatering from numerical analysis are compared against recorded movements in Figure 17.

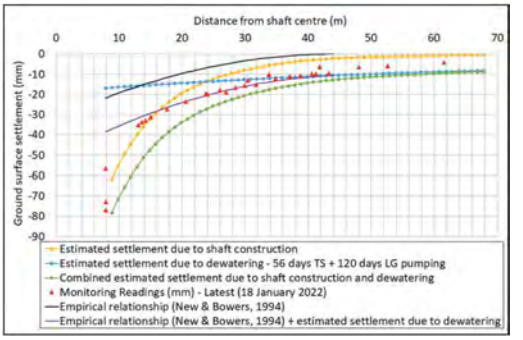

Figure 17. Combined ground surface settlement vs distance from shaft centre after base slab installed.

Estimated settlements due to shaft construction are from the PLAXIS analysis case assuming minimum Ko, minimum groundwater, no surcharge and undrained (B) material model, and the estimated settlements due to dewatering are from the MODFLOW analysis for 56 days Thanet Sand pumping and 120 days Lambeth Group pumping.

These combined settlements were used to evaluate potential risk to adjacent assets by calculating settlements, rotation and angular distortion along the assets in close proximity to the shaft, i.e., 2 sets of cables, the UKPN substation perimeter wall to the north of the shaft and the wall to the south of the shaft. To simplify the assessment, it was assumed that the settlement along the assets is equal to the predicted ground surface settlement.

During shaft construction, ground surface settlements were monitored to check that the impact of shaft construction and dewatering were consistent with the above estimates.

Additional monitoring points were installed in proximity to the shaft, and frequency of monitoring was increased to closely align construction activities with recorded movements. Figure 17 shows that

estimated ground surface settlements due to shaft construction and dewatering from numerical analysis correlate well with recorded ground movements and have a similar profile shape but are slightly higher. Although the recorded ground movements significantly exceeded predictions based on the empirical relationship by New & Bowers (1994), a reasonably good match with recorded movements can be found by combining the empirical prediction with the estimated ground movements due to dewatering, except for approximately one shaft radius away from the shaft where there is a significant difference. However, the movement attributed to the separate activities of shaft construction and dewatering cannot be differentiated from the monitoring data with certainty as both activities were generally progressing concurrently.

8 DISCUSSION AND CONCLUSIONS

During construction of the shaft, recorded ground movements significantly exceeded predictions based on the empirical relationship by New & Bowers (1994). Numerical analysis was carried out to investigate and better understand this behaviour and to estimate final settlements due to both dewatering and shaft construction. The numerical analysis considered several cases covering the anticipated range of groundwater level, coefficient of earth pressure at rest (K0), surface surcharge and undrained (A) or undrained (B) material models (for cohesive materials). Estimated ground movements from the numerical analysis were found to correlate reasonably well with the recorded movements, with the best match generally provided by the PLAXIS analysis cases assuming minimum K0 and the undrained (B) material model.

A reasonably good match with recorded movements can be found by combining predictions based on the empirical relationship by New & Bowers (1994) with estimated ground movements due to dewatering, except for approximately one shaft radius away from the shaft.

The significant increase in settlement at the location of the shaft lining, particularly during construction of the initial lining rings, is thought to be due to a low strength/ stiffness or more drained behaviour of the MG-C, e.g., a higher permeability/ granular material. It is also understood that there was a delay in grouting behind these rings which may have caused additional settlement due to the excavated shaft face remaining unsupported for an extended period.

Overall, the monitoring data and analysis indicates some variation from the empirical relationship by New & Bowers (1994) and highlights the importance of considering the shaft construction method, site-specific ground conditions and effects of dewatering when making ground movement predictions, particularly when near sensitive third-party assets.

ACKNOWLEDGMENTS

The authors would like to thank HOCHTIEF-MURPHY Joint Venture, National Grid and their engineering partners for their collaboration during the design and construction process and for their support with this paper.

REFERENCES

Bond, A., & Harris, A. (2008). Decoding Eurocode 7. Abingdon: Taylor & Francis.

New, B. M. & Bowers, K. H. (1994). Ground movement model validation at the Heathrow Express trial tunnel. Tunnelling ’94, Proc. 7th Int. Symp. IMM and BTS, London, UK, pp. 310–329. London: Chapman and Hall.

CIRIA (1996). Prediction and effects of ground movements caused by tunnelling in soft ground beneath urban areas. Construction Industry Research and Information Association, Project Report 30.

Faustin N.E., Elshafie M.Z.E.B and Mair R.J. (2018). Case studies of circular shaft construction in London. Proceedings of the Institution of Civil Engineers – Geotechnical Engineering Vol 171:5, pages 391–404.

Gaba, A., Hardy, S., Doughty, L., Powrie, W., Selemetas, D. (2017). CIRIA C760 Guidance on embedded retaining wall design. London: CIRIA.

British Standards Institution. (2004). BS EN 1997-1:2004 +A1:2013 Eurocode 7: Geotechnical Design – Part 1: General rules. London: British Standards Institution.

Schanz, T., Vermeer, P.A. and Bonnier., P.G. (1999). The hardening soil model: formulation and verification. Beyond 2000 in computational geotechnics (1999): 281–296.

Chang, Y. and Stille, H. (1993). Influence of early-age properties of shotcrete on tunnel construction sequences. Shotcrete for Underground Support VI, American Society of Civil Engineers (ASCE), pp110–117.

Kundan, R., Daniele, S. and Martin, S. (2023). Challenges of delivering 32.5km of major tunnelling infrastructure in South London (UK), and the influences of an innovative “Enterprise” project delivery model. Proceedings of the Tunnelling Association of Canada (TAC) 2023 Conference.

Tunnelling for a Better Life – Yan, Celestino, Thewes & Eberhardt (Eds)
© 2024 The Author(s), ISBN 978-1-032-80042-4
Open Access: www.taylorfrancis.com, CC BY-NC-ND 4.0 license

Application of Acoustic signal to quantify the damage of the lesser Himalayan sandstone under unconfined compression loading and its implementation in the micromechanical damage-plasticity model

Shubham Chajed*
Research Scholar, Indian Institute of Technology, Roorkee, India

Aditya Singh
Assistant Professor, Indian Institute of Technology, Roorkee, India

ABSTRACT: Space scarcity and population growth are the two reasons for using underground space to improve the quality of human life. Currently, numerous rock tunnels are constructed in the Himalayan region of India. Due to the stress variation, microcracks are generated in the rock, leading to damage. The quantification of damage with the microcrack propagation is essential for the safety and health monitoring of the rock tunnels. The Acoustic Emission (AE) technique is a real-time Structural Health Monitoring (SHM) method. This technique records the micro-physical activities in terms of acoustic signals that occur during the loading of the rocks. The recorded AE signals contain valuable information about the damage and fracture mechanism. In this paper, we have experimented on the lesser Himalayan sandstone under unconfined compression loading to quantify the damage using real-time recorded AE signals. Further, we have implemented the AE-based damage variables to obtain the Himalayan sandstone's nonlinear constitutive behaviour. The present study results encourage utilization of the AE technique, i.e., the non-conventional experimental method for safety and health monitoring of rock tunnels in the Indian Himalayas.

Keywords: Acoustic Emission (AE), Himalayan Sandstone, Damage Quantification, Micromechanical Damage-Plasticity Model

1 INTRODUCTION

In the modern era, space scarcity and population growth are the two main reasons for using underground space to construct shallow and deep underground rock engineering structures. The major rock tunnel projects like subsurface roads, railways, and hydroelectric power projects are constructed in India's sub-Himalaya and lesser Himalaya. These tunnelling projects are the Udhampur-Katra rail tunnel project, Uri hydroelectric project, Parbati stage-II hydroelectric project, Rohtang highway tunnel project, Maneri stage-I and II hydroelectric project, Tehri project, Rishikesh and Karanprayag rail link project, Subansiri hydroelectric project, Laktak project and many others, lies in the Himalayan states of Jammu and Kashmir, Himachal Pradesh, Uttarakhand, Assam, Arunachal Pradesh, and Manipur in India (Goel and Singh, 2017). During the construction and operation of tunnels, local stresses are altered. Due to these changes in the stress state, microcracks are generated in the tunnel's surrounding rock or rock mass. In the case of a rockburst, the stored elastic strain energy that triggers the fracturing processes and damage to the tunnel is released. During the damage evolution, the release of stored elastic strain energy generates a high-frequency elastic wave called the Acoustic Emission (AE) signal (Ishida et al., 2017; Feng et al., 2019).

The AE technique records elastic vibrations in rocks or rock masses caused by the growth or generation of micro or meso cracks. The recorded AE signals contain valuable information about the microcrack generation and fracture processes and are related to the damage evolution of rock under external compressive loading (Shah and Labuz, 1995; Eberhardt et al., 1999; Kim et al., 2015; Du et al., 2020; Chajed and Singh. 2023a, b, c, d). The consequences of damage are inelastic deformation and deterioration of mechanical properties, which results

*Corresponding author: s_chajed@ce.iitr.ac.in

DOI: 10.1201/9781003495505-350

in a nonlinear stress-strain behaviour of rocks (Zhu et al., 2016; Zhu and Shao, 2017). The AE-based damage quantification and its use in constitutive modelling is an area that can be explored in the safety and health monitoring of rock tunnels.

In the current study, we have reported the monitored AE of the lesser Himalayan sandstone under unconfined compression loading for following two objectives: the first objective is to quantify the damage variable of the lesser Himalayan sandstone under unconfined compression loading using acoustic signals; the second objective is to implement the AE-based damage variable for obtaining the nonlinear constitutive behaviour of the lesser Himalayan sandstone using the micromechanical damage plasticity constitutive model.

2 EXPERIMENTAL METHODOLOGY

Experimental work includes the damage quantification of the lesser Himalayan sandstone under uniaxial compression loading using real-time AE monitoring. This section mentioned the rock material, the experimental setup with the AE monitoring system, and the AE-based damage quantification methodology.

2.1 *Rock material*

The Himalayan sandstone employed in the current study is the Devprayag sandstone collected from the Devprayag town of the Tehri Garhwal district, Uttarakhand, India. The Tehri Garhwal district lies in the outer lesser Himalayas.

2.2 *Experimental setup with AE*

The uniaxial compression tests were performed by the servo-hydraulic closed-loop static cum dynamic rock triaxial testing system at the Indian Institute of Technology, Roorkee. The loading capacity of the system is 2000 kN. The test specimens were loaded under displacement-controlled mode with a constant displacement rate of 0.2 mm/min. The load and strain data were recorded by the load cell and strain gauge, respectively, with a sampling rate of 1 Hz. At the same time, the acoustic signals induced by microcracks growth were recorded by an AE sensor with the data acquisition system. The AE sensor was placed at mid-height of the rock specimen. The sampling rate of the AE data acquisition system is 1 MHz. The total test duration was 6 minutes and 41 seconds, with 401 million data points. The schematic diagram of the laboratory AE monitoring system and the positioning of the AE sensor and strain gauge on the Devprayag sandstone specimen are shown in Figures 1 (a, b, and c), respectively. The recorded AE signal is processed using the developed MATLAB program. The processed AE signal is used to quantify the damage of the Devprayag sandstone under uniaxial compression loading.

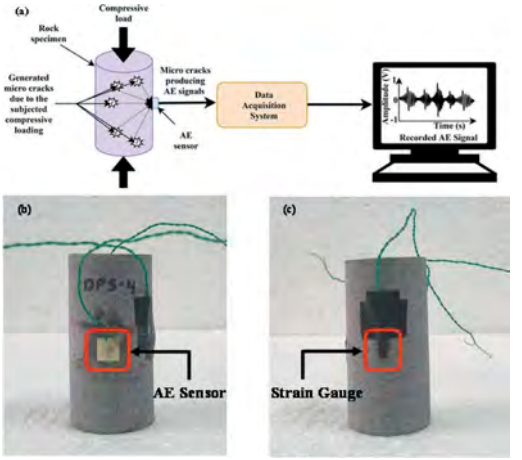

Figure 1. (a) Schematic diagram of the laboratory AE monitoring system, (b and c) positioning of an AE sensor and strain gauge on the Devprayag sandstone cylindrical specimen.

2.3 *Methodology of AE-based damage quantification*

First, we need to denoise the recorded AE signal and determine the different AE signal parameters to obtain the AE-based damage quantification. During the testing, the recorded AE signal will be interfered with by the noise signals from the surrounding environment, transmission media, and vibration induced by the testing machine. In the present study, we have denoised the recorded AE signals using the wavelet transform filtering algorithm based on the local time-frequency analysis method with multiscale wavelet coefficient processing (Yang et al., 2021). Morlet proposed this method in the 1980s. Afterward, the filtered AE signal was used to determine different AE signal parameters, i.e., AE event count, AE ringdown count, and AE event duration. Figure 2 graphically represents a typical AE signature's AE signal parameter. A reader can refer to Chajed and Singh's (2023a, b) articles for more details about determining different AE parameters from a typical AE signature. The obtained AE parameters are used to quantify the degree of rock damage. The AE-based damage variable (d_{AE}) is the ratio of the cumulative AE parameter under a certain stress level to the total cumulative AE parameter until the failure of the rock. In the present study, we have used AE event count (E_{AE}) as an AE parameter for damage quantification of the Devprayag sandstone under unconfined compression loading.

3 AE-BASED MICROMECHANICAL DAMAGE PLASTICITY MODEL

This section briefly presents the formulation of the AE-based micromechanical damage plasticity model proposed by Chajed and Singh (2023b). The proposed model utilized the AE-based damage variable to

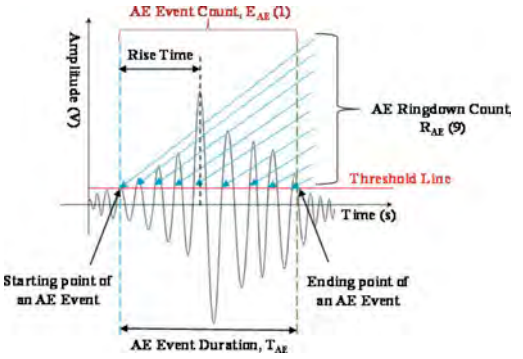

Figure 2. Graphical representation of the AE signal parameters in a typical AE signature (red horizontal line represents the threshold line; blue and green dashed vertical lines are shown as the starting and ending point of an AE event, respectively).

predict the nonlinear stress-strain response of intact rock under Conventional Triaxial Compression (CTC) loading. The model is based on two main dissipation processes: the first one is the inelastic deformation due to friction sliding along the closed microcracks surface, and the second one is the damage due to the growth of microcracks. The friction and damage criteria are presented below based on these two dissipation processes.

3.1 *Friction criterion*

A linear Coulomb-type friction criterion is used to determine the friction-induced inelastic deformation along the closed microcrack surface, and it is given by Eq. (1) as:

$$f(\sigma^d) = \|q^d\| - \zeta p^d \leq 0 \tag{1}$$

where $\boldsymbol{q^d}$ and $\boldsymbol{p^d}$ are the local deviatoric and hydrostatic stress acting on the crack surfaces, respectively, and ζ is the apparent friction coefficient associated with the roughness of the crack surface.

3.2 *Damage criterion*

A strain-energy release rate-based damage criterion is used to determine the damage due to microcrack growth, and it is given by Eq. (2) as:

$$f^d(F^d, d) = F^d - R(d) \leq 0 \tag{2}$$

where F^d is the damage-deriving force associated with the internal damage variables (d), the $R(d)$ represents the resistance to damage evolution of material, and it is given by Eq. (3):

$$R(d) = R(d_{AE})_c \left[\frac{b_2 \eta}{(b_2 - 1 + \eta^{b_2})}\right] \tag{3}$$

where $\eta = d/(d_{AE})_c$ is defined as a dimensionless parameter, $(d_{AE})_c$ represents the AE-based critical damage variable corresponding to the peak stress, $R(d_{AE})_c$ is the AE-based critical damage resistance of rock at $d = (d_{AE})_c$, and b_2 is the material parameter.

3.3 *Yield function*

Coupled the abovementioned two dissipation processes and obtained the final damage plasticity yield function, which is given by Eq. (4) as:

$$f(\sigma) = \|q\| - \zeta p - 2\sqrt{R(d)\kappa} \leq 0 \tag{4}$$

where q and p are the deviatoric and hydrostatic stress, and κ is a model parameter. Zhu et al. (2016) use a similar yield equation for penny-shaped microcracks. In the proposed model, the value of κ is obtained for arbitrarily shaped microcracks using the triaxial compression test and AE data. For arbitrarily shaped microcracks, the value of κ is given by the Eq. (5) as:

$$\kappa = \left[(\sigma_1)_p - \frac{(\sqrt{6} + 2\zeta)}{\sqrt{6} - \zeta}\sigma_3\right]\left[\frac{(\sqrt{6} + 2\zeta)(d_{AE})_c M}{6(\varepsilon_1^{in})_p}\right] \tag{5}$$

where $(\sigma_1)_p$ is the peak stress, $(\varepsilon_1{}^{in})_p$ is the inelastic strain corresponding to the $(\sigma_1)_p$, σ_3 is the confining pressure, and M is given by Eq. (6) as:

$$M = \left(\frac{2}{\sqrt{6}} - \frac{\zeta}{3}\right) \tag{6}$$

3.4 *Constitutive equations for unconfined compression loading (σ_3 =0)*

The final yield function can be written in the form of σ_1 and d, as given by Eq. (7), and the modelled axial strain component is determined by Eq. (8).

$$\sigma_1 = \frac{6\sqrt{R(d)\kappa}}{\sqrt{6} - \zeta} \tag{7}$$

$$\varepsilon_1 = \frac{\sigma_1}{E^s} + d\sqrt{\frac{R(d)}{\kappa}}\left(\frac{2}{\sqrt{6}} - \frac{\zeta}{3}\right) \tag{8}$$

where E^s is Young's modulus of elasticity of rock. A reader can refer to the Chajed and Singh (2023b) article for detailed information and formulation of the AE-based micromechanical coupled damage plasticity model. The experimental results and model validation are reported in the following section.

4 EXPERIMENTAL RESULTS, DISCUSSION AND MODEL VALIDATION

The AE-based damage quantification of the Devprayag sandstone under unconfined compression loading and its model validation results are presented here.

4.1 *AE-based damage quantification of the Devprayag sandstone*

The total 11572 AE event counts are identified within the Devprayag sandstone under uniaxial compression. Based on the normalized cumulative AE parameter concept, the AE event counts are used to quantify the rock's damage variable. Figure 3 shows the damage variable based on the AE event counts of the Devprayag sandstone under unconfined compression loading. The obtained value of the damage at peak stress is 0.0088. This damage is called the AE-based critical damage variable $(d_{AE})_c$. After the peak stress, a sudden increase in the damage variable is observed. Physically, it signifies the generation of macro fractures within the rock. Therefore, we can use these AE-based damage quantification results for the safety and health monitoring of the rock tunnels. Correspondingly, we can implement these AE-based damage variable results for the constitutive modelling of tunnels surrounding rock material.

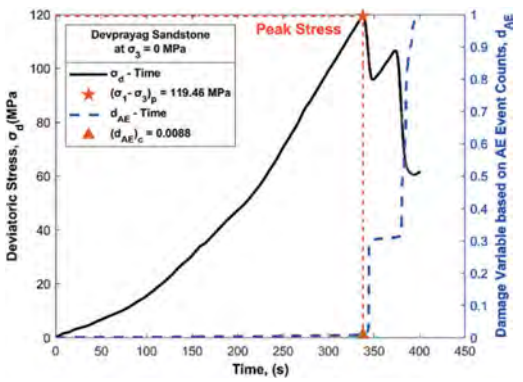

Figure 3. Deviatoric stress-time response of the Devprayag sandstone under unconfined compression loading with damage variable (d_{AE}) based on AE event counts (peak stress, and critical AE-based damage variable $(d_{AE})_c$ is marked the by symbol star and triangle, respectively).

4.2 *Model validation*

The triaxial compression and AE data are used to determine the model parameters. Their values are presented in Table 1.

Table 1. Typical values of model parameters for the Devprayag Sandstone at 0 MPa confining pressure based on AE Event Counts (E_{AE}).

Model Parameters	Values
$(\varepsilon_1^{in})_p$ (%)	0.01
E^s (GPa)	54.13
ζ	0.935
$(d_{AE})_c$	0.0088
κ	1895.733
$R(d_{AE})_c$	0.479
b_2	1.45

We compared the modelled damage variable with the experimentally obtained AE event counts-based damage variable, and the result is presented in Figure 4. It is noticed that the magnitude of the damage variable obtained from the model is close to the experimental data in the pre-peak region. The obtained damage variable is used to get the nonlinear stress-strain response of the Devprayag sandstone under unconfined compression loading.

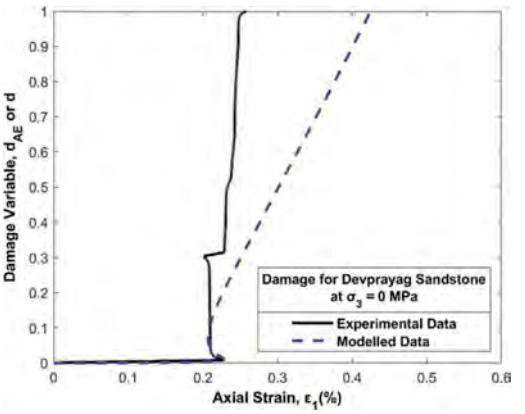

Figure 4. Comparison between the experimental and modelled damage variable-strain response based on the AE event counts for the Devprayag sandstone under unconfined compression loading.

Figure 5 compares the modelled stress-strain response with the experimental data. The model performance is verified by obtaining the class-II nonlinear stress-strain behaviour, similar to the experimentally obtained stress-strain response of the Devprayag sandstone under unconfined compression loading. The class-II stress-strain curve of rock undergoes self-sustaining fracturing and shows the rockburst condition (Akdag et al., 2019).

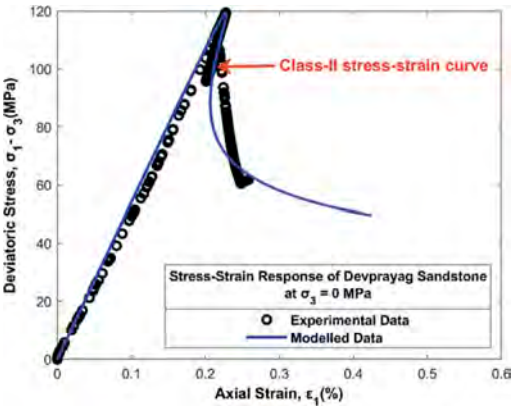

Figure 5. Comparison between the experimental and modelled stress-strain response of the Devprayag sandstone under unconfined compression loading.

5 CONCLUSIONS

In the present study, we performed the AE monitoring of the lesser Himalayan sandstone under unconfined compression loading and quantified the damage variable based on AE event counts. We have observed from the test results that a sudden increase in damage variable occurred after the peak stress. Physically, it signifies the generation of macro fractures within the rock. We have also implemented the experimentally obtained AE-based damage variable for simulating the nonlinear constitutive behaviour of the lesser Himalayan sandstone. The model performance is verified by obtaining the class-II nonlinear stress-strain behaviour of the Devprayag sandstone, similar to the experimentally obtained stress-strain response under unconfined compression loading. It is the first time such a study has been conducted on the Devprayag sandstone in the lesser Himalayan range of the Indian Himalayas. The present study results encourage utilization of the AE technique, i.e., the non-conventional experimental method for safety and health monitoring of rock tunnels in the Indian Himalayas.

REFERENCES

Akdag, S., Karakus, M., Nguyen, G.D., Taheri, A., Bruning, T., 2021. Evaluation of the propensity of strain burst in brittle granite based on post-peak energy analysis. Underground Space, 6(1), 1–11.

Chajed, S., Singh, A., 2023a. Microcrack Source Classification of Rock Salt Under Quasi-Static Unconfined Compression Test Using Acoustic Emission. (In Preparation).

Chajed, S., Singh, A., 2023b. Acoustic Emission (AE) based Damage Quantification and its Relation with AE-based Micromechanical Coupled Damage Plasticity Model for Intact Rocks. (In Preparation).

Chajed, S., Singh, A., 2023c. AE Event Count-Based Damage Evaluation and Its Application in Micromechanical Damage Plasticity Model. 9th Indian Young Geotechnical Engineering Conference (9IYGEC), Aurangabad, India.

Chajed, S., Singh, A., 2023d. Quantified a Damage Degree and Fracture Mechanism of the Subansiri Sandstone under Uniaxial Compression Loading using Real-Time Acoustic Emission (AE) Monitoring. Indian Geotechnical Conference, IIT Roorkee, India.

Du, K., Li, X., Tao, M., Wang, S., 2020. Experimental study on acoustic emission (AE) characteristics and crack classification during rock fracture in several basic lab tests. Int J Rock Mech Min Sci 133, 104411.

Eberhardt, E., Stead, D., Stimpson, B., 1999. Quantifying progressive pre-peak brittle fracture damage in rock during uniaxial compression. Int J Rock Mech Min Sci 36, 361–380.

Feng, X.T., Young, R.P., Reyes-Montes, J.M., Aydan, Ö., Ishida, T., Liu, J.P., Liu, H.J., 2019. ISRM Suggested Method for In Situ Acoustic Emission Monitoring of the Fracturing Process in Rock Masses. Rock Mech Rock Eng 52, 1395–1414.

Goel, R.K., Singh, B., 2017. Tunnels in the Himalaya. In Rock Mechanics and Engineering: Volume 5: Surface and Underground Projects, CRC Press, pp. 69–108.

Ishida, T., Labuz, J.F., Manthei, G., Meredith, P.G., Nasseri, M.H., Shin, K., Yokoyama, T., Zang, A., 2017. ISRM Suggested Method for Laboratory Acoustic Emission Monitoring. Rock Mech Rock Eng 50, 665–674.

Kim, J.S., Lee, K.S., Cho, W.J., Choi, H.J., Cho, G.C., 2015. A comparative evaluation of stress–strain and acoustic emission methods for quantitative damage assessments of brittle rock. Rock Mech Rock Eng 48, 495–508.

Shah, K.R., Labuz, J.F., 1995. Damage mechanisms in stressed rock from acoustic emission. J Geophys Res Solid Earth. 100, 15527–15539.

Valdiya, K.S., 1980. Geology of Kumaun Lesser Himalaya. Wadia Institute of Himalayan Geology, Dehradun.

Yang, Y., Liu, P., Zhou, H., Tian, Y., 2021. A Speech Enhancement Algorithm combining Spectral Subtraction and Wavelet Transform. In 2021 IEEE 4th International Conference on Automation, Electronics and Electrical Engineering (AUTEEE), 268–273.

Zhu, Q., Shao, J., 2017. Micromechanics of rock damage: Advances in the quasi-brittle field. Journal of Rock Mechanics and Geotechnical Engineering, 9(1), 9–40.

Zhu, Q.Z., Zhao, L.Y., Shao, J.F., 2016. Analytical and numerical analysis of frictional damage in quasi brittle materials. Journal of the Mechanics and Physics of Solids, 92, 137–163.

Tunnelling for a Better Life – Yan, Celestino, Thewes & Eberhardt (Eds)
© 2024 The Author(s), ISBN 978-1-032-80042-4
Open Access: www.taylorfrancis.com, CC BY-NC-ND 4.0 license

Tunnel detection and monitoring technology based on terrestrial laser scanning

Yun-Jian Cheng*
School of Civil Engineering and Geomatics, Southwest Petroleum University, Chengdu, China
Chengdu Tianyou Tunnelkey Co.,Ltd., Chengdu, China

Chao Wang & Wen-Ge Qiu
Chengdu Tianyou Tunnelkey Co.,Ltd., Chengdu, China

ABSTRACT: Currently, most of the geometric element detection methods used in tunnel engineering still rely on traditional methods such as total stations and laser profile meters. These traditional sampling methods have potential risks and may ignore some data that constitute hazards. Terrestrial Laser Scanning (TLS) is a new remote sensing technology that provides high-precision and high-density active measurement data even in harsh, unlighted conditions, with lower requirements for the work environment than traditional measurement techniques. Based on TLS, this paper proposes a method for reorganizing tunnel point cloud data and studies tunnel detection (including clearance, smoothness, and lining steel bar installation) and deformation monitoring technology. The proposed method has advantages such as high automation, high precision, and high efficiency, and has been validated in practical engineering, which can improve the quality of tunnel construction. The holographic deformation monitoring method can capture the asymmetric and non-uniform deformation characteristics of the initial support structure and improve the safety of the construction.

Keywords: Terrestrial Laser Scanning, Monitoring, Inspection, Tunnel

1 INTRODUCTION

The detection and monitoring of geometric elements in tunnel sections are necessary and extremely important processes that directly affect the construction quality, progress, cost, and safety of tunnels. Traditional methods for tunnel section detection and monitoring include the use of total stations, cross-sectional detectors, etc. The former can measure the coordinates of any single point, and by comparing the position coordinates with the corresponding position of the designed section, it is possible to determine over-break and intrusion conditions. By monitoring different fixed points over time, the deformation situation of those points can be obtained. The latter method upgrades from one-dimensional single point measurement with a total station to two-dimensional cross-sectional measurement, but fundamentally, it is still a sampling detection method that cannot grasp the construction situation of various parts of the tunnel wall, and it often has a long working time inside the tunnel, which easily affects the normal progress of other processes. Terrestrial Laser Scanning (TLS) is a non-contact active technique for rapidly acquiring dense three-dimensional point cloud data of object surfaces (Cheng et al., 2019). It is considered as a technological revolution in the field of surveying and mapping after GPS technology. This technology can obtain vector coordinates and reflectivity of tens of millions of points within a range of approximately 60 meters in about three minutes. Through post-processing software, including line data and design section initialization, point cloud cleaning, denoising, and registration, accurate results of overall over-break, intrusion, initial support flatness, and tunnel deformation can be obtained. It breaks through the traditional sampling measurement methods and has unique advantages such as high efficiency, high accuracy, and holistic information, as listed in Table 1.

Table 1. Traditional measurement vs TLS.

Items	Traditional measurement	TLS
Efficiency	3-5 mins per single cross-section	40-60 m per station within 3-5 mins
Results	Limited sample testing	Holistic detection
Presentation	2D cross-sections	3D as-built BIM

2 THE WORKING PRINCIPLE OF TLS

TLS technology uses the principle of laser ranging to quickly and extensively acquire the three-

*Corresponding author: by_sky@126.com

DOI: 10.1201/9781003495505-351

dimensional coordinate values, reflectivity, and color information of scanned tunnel arch walls and lining surfaces. The data acquisition speed can reach several tens of thousands to millions of points per second. The collected data is later processed on a computer to efficiently model tunnels. The data collected in the field can provide a basis for subsequent work as original measurement data resources.

At present, to fully utilize the functions of a 3D laser scanner, control software and data processing software are also needed. The control software is built-in software in the scanner, primarily used for data acquisition and processing according to certain requirements. The data processing software is generally provided by other companies, specifically designed for data processing, such as TK-PCAS (Tunnelkey 3D Laser Point Cloud Processing and Analysis System) which has optimal processing speed, learning cost, and scene quantity.

The laser rangefinder uses active laser emission and measures distance based on the laser echo signal, which is the laser reflected from the surface of the tunnel's arch walls and linings. By calculating the corresponding changes in the emitted and received lasers, the distance is determined, and the spatial relative coordinates of the scanned points are obtained. If the coordinates of the survey station are known, data processing software can be used to convert the coordinates to absolute coordinates, i.e., coordinates in the measurement coordinate system. The 3D laser scanner's reflector mirror vertically reflects the laser beam onto the scanned object, and the vertical angle encoder simultaneously measures the vertical rotation angle β (vertical angle) of the mirror. The laser scanner can rotate horizontally 360°, and the horizontal angle encoder simultaneously measures the scanner's horizontal rotation angle α (horizontal angle), thereby obtaining the three-dimensional point cloud data . The scanner scans the target object in all directions through the motion of the transmission device, and a series of processing is conducted to obtain the point cloud data of the tunnel's arch walls and linings. The spatial position of the scanned points relative to the instrument is shown in Figure 1.

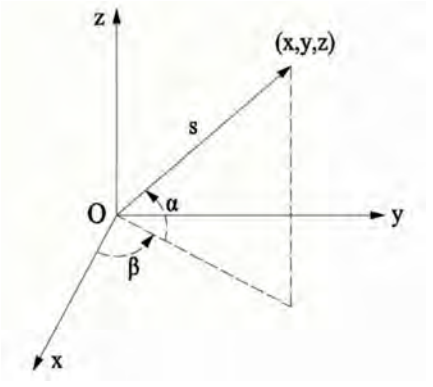

Figure 1. Single point spatial coordinate positioning.

The point cloud obtained above is in relative coordinates and needs to go through engineering coordinate registration in order to have practical engineering significance. After setting up the total station, the center of the prism ball is marked by points, obtaining the coordinates of the prism ball center. At the same time, the scanner scans the back of the prism ball and fits the virtual prism ball center. By using post-processing software, the coordinates from the total station are transferred to the point cloud, with a registration accuracy as high as 1mm.

3 OVER-BREAK AND CLEARANCE DETECTION

After excavation or blasting on the face of the tunnel and completion of debris removal, the excavation face is scanned. TLS technology, with its efficient and holographic features, can quickly obtain the coordinates of all points within the scanning range. The relative point cloud obtained by the 3D laser is converted into absolute point cloud coordinates using a total station, and placed in the corresponding positions of the designed tunnel. By comparing it with the design cross-section, the analysis results of over-break or under-break can be obtained (Cheng et al., 2016). Similarly, scanning detection at the appropriate time can yield results on the intrusion limits of the initial support and secondary lining.

The newly-built Lijiang to Shangri-La Railway (referred to as "LiXiang Railway") is located on the Yunnan-Guizhou Plateau, with a total length of 139.7 kilometers and over 20 tunnels. It starts from the Shangri-La Basin at an elevation of 2400 meters and climbs northwards to the Shangri-La Basin at an elevation of 3400 meters, passing through plateau snow mountains. The surrounding rock stress of the tunnels is complex, and some tunnels experience significant deformation in soft rock, up to the magnitude of meters.

To better understand the deformation of various parts of the tunnel in the circumferential direction, the construction unit used TLS technology to conduct holographic scans and inspections of the areas with significant deformations in the tunnel. Point cloud data was then processed to generate cross-sectional drawings, 2D unfolded drawings (Qiu and Cheng, 2017)., and 3D chromatographic maps. Among them, the 3D model provides the most intuitive display (Duan et al., 2021), differentiating over-break and under-break using warm and cool colors, and indicating the extent of over-break and under-break with varying shades of color. The results allow for a comprehensive understanding of the overall tunnel conditions, providing strong data support for experts in formulating response plans in the next steps.

4 SMOOTHNESS DETECTION

The smoothness index of the initial support of a tunnel refers to the level of unevenness on the

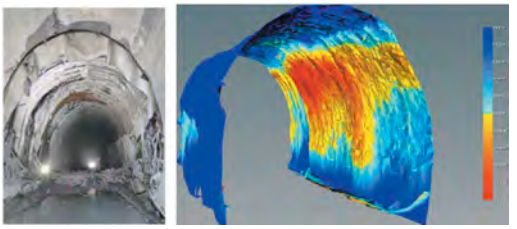

Figure 2. On-site view and three-dimensional laser results of a tunnel on the LiXiang Railway.

surface of the initial support concrete lining. It is an important criterion for tunnel engineering quality acceptance. The smoothness of the initial support directly affects the laying of waterproof membranes, the quality of the second phase lining, and the safety of the tunnel engineering. Excessive smoothness of the initial support surface can cause a decline in the construction quality of the waterproof membranes and the second phase lining, indirectly affecting the water permeability of the tunnel surface and the compactness of the secondary lining, making the tunnel surface more prone to water leakage and the quality of the secondary lining fails to meet the standards.

The traditional method of smoothness detection in railway tunnels involves using a 1-meter or 2-meter ruler to randomly sample different parts of the initial support. If the ratio of depth to length (D/L_t) is greater than 0.05, it is considered to exceed the smoothness standard. This detection method has low accuracy due to the randomness of the selected measurement points, and it is slow and inefficient. When using a total station to measure the smoothness of the initial support surface, the prism mode can greatly affect the measurement accuracy, resulting in a significant deviation between the fitted plane and the actual wall surface. Consequently, the precise smoothness of the initial support cannot be obtained. In addition, the subjective selection of measurement points on the arch wall of the tunnel cannot fully and accurately reflect the condition of the surface of the initial support.

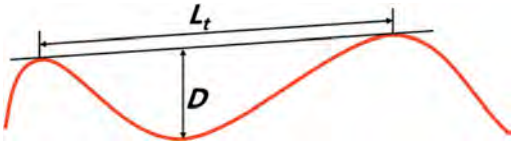

Figure 3. Computing the ratio of depth to length.

By using the achievements of TLS holography, the initial support of the tunnel can be scanned and analyzed for smoothness using the "virtual standard ruler" in the system. Two-dimensional reports and three-dimensional walkthroughs can be generated, and they can be displayed in the section quality inspection module. By setting a threshold, the thermal distribution of the tunnel surface can be displayed, allowing clear identification of abnormal locations and values of smoothness. This provides a comprehensive overview of the smoothness of the initial support, indirectly avoiding quality issues such as lining voids.

To verify the accuracy and efficiency of the three-dimensional laser smoothness detection technology, the Z+F5016 three-dimensional laser scanner was used at the entrance construction site of the Sangyuan Tunnel on the Xi'an to Shiyan High-Speed Railway. The initial support in the section from DK40+671 to DK40+709 was scanned, and more comprehensive smoothness results were obtained by importing the data into post-processing software.

Figure 4. The on-site operation of the Z+F5016 three-dimensional laser scanner.

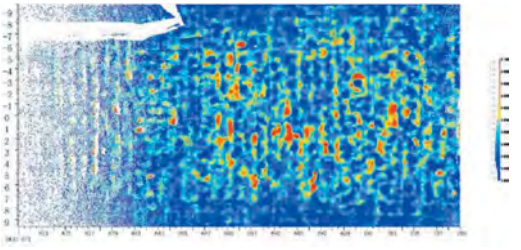

Figure 5. The thermal map of the simulated smoothness calculation results using the virtual ruler method (with the color scale and distribution chart on the right).

The blue region represents a smoothness depth-to-length ratio parameter between 0 and 0.05, the orange region represents a smoothness depth-to-length ratio parameter between 0.05 and 0.1, and the red region indicates that the smoothness parameter exceeds 0.1. The on-site construction personnel can locate the areas of potholes based on the mileage and planar coordinates and carry out corrective measures accordingly, as shown in the Figure 6.

5 REBAR INSPECTION

Before pouring the secondary lining concrete in the tunnel, it is necessary to conduct acceptance

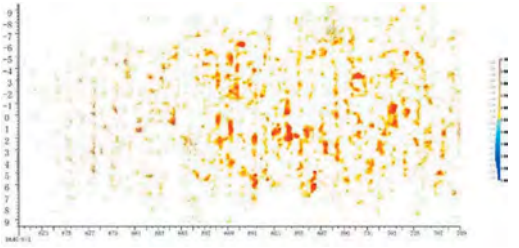

Figure 6. The focused presentation of the areas with potholes.

inspection of the reinforcement in the initial support. The inspection of the geometric elements of the reinforcement includes the diameter, quantity, spacing, etc (Cheng et al., 2023). Due to the tight coordination of tunnel construction processes, inadequate time coordination often leads to the omission of acceptance of this hidden engineering process. However, a three-dimensional laser scanner can scan millions of points in just three minutes. The panoramic point cloud data of the reinforcement can be stored on a computer, and the diameter, spacing, and lap length of the reinforcement can be directly measured from the point cloud data.

To quickly analyze the quality of the reinforcement construction, the software can automatically extract and build a three-dimensional model of the reinforcement based on the characteristics of the lining reinforcement data. The modeling results are shown, and the reinforcement in both circumferential and longitudinal directions of the secondary lining is clearly visible. It makes hidden engineering no longer hidden.

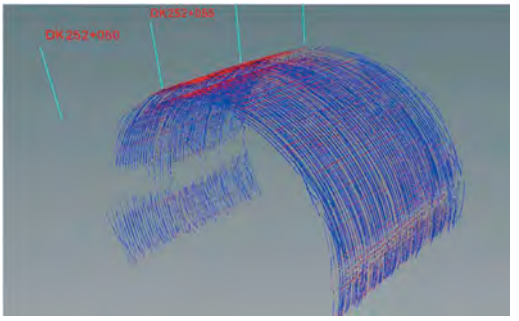

Figure 7. The three-dimensional laser walkthrough of the reinforcement.

Ground Penetrating Radar (GPR) for reinforcement detection is affected by factors such as concrete compaction, antenna fit, and multiple reflections from double-layer reinforcements, resulting in reduced accuracy of radar detection. On the other hand, TLS technology provides intuitive, accurate, and holographic features.

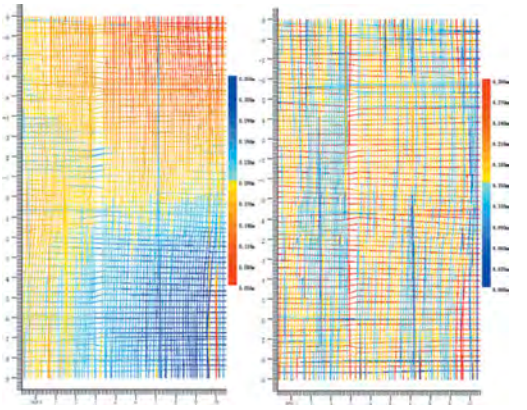

Figure 8. The thickness of the protective layer (left) and spacing between surface reinforcements (right).

6 HOLOGRAPHIC DEFORMATION MONITORING

Deformation monitoring of surrounding rocks in railway tunnels has always been primarily done using total stations. After setting up the total station, the coordinates of the installed reflectors need to be surveyed and collected. Multiple monitoring of the reflectors on the arch can provide information about settlement near the arch. Monitoring the symmetrical reflectors on the arch waist can provide convergence information on both sides of the arch waist. However, traditional methods have several unavoidable limitations due to technological constraints:

1) Difficult to install and protect monitoring points
2) Inaccurate initial values
3) Dust accumulation and re-spraying affecting measurement
4) Influence of light sources
5) Large spacing between monitoring points, poor representativeness
6) Overall deformation and uneven deformation
7) Authenticity of early warning

TLS technology, unlike traditional single-point monitoring, can holographically extract three-dimensional coordinates of various parts of the tunnel. The collected point cloud is compared with the corresponding design section in software to obtain the results of the first scanning phase. Multiple 3D laser scans are performed at different times within the same interval. With the deformation of the tunnel, the deformation of the tunnel can be observed in the multi-phase 3D laser model. This technology allows us to understand the deformation of various positions in the tunnel, avoiding the drawbacks of traditional sampling monitoring. Compared to total station measurements, TLS has the following irreplaceable advantages in deformation monitoring:

1) No need to install reflectors, preventing false alarms

2) High scanning efficiency, fast speed, and no impact on other processes
3) Holistic monitoring and precise control of deformation in various parts
4) Absolute deformation measurement for the tunnel, monitoring overall deformation
5) Evaluation of regional point clouds, providing more accurate information

The Shanenshan Tunnel of the China-Laos Railway has a maximum burial depth of 200m and a total length of 2090 meters. The tunnel site belongs to a tectonic erosion high mountain landform and is affected by the Shanenshan Fault #2 and the Sharabassi Fault, with large undulations in terrain. The strata crossed by the tunnel mainly consist of Carboniferous shales, sandstones, and mudstones. Due to the influence of the Laos-Burma suture zone and regional fault structures, the rock layers are distorted, folded, and fragmented, resulting in uneven deformation of the tunnel. Traditional total stations cannot assess the deformation outside the reflector area. However, using TLS for deformation monitoring can perfectly overcome this limitation.

After the initial shotcrete of the tunnel, the first TLS of the initial support section within the measurement range is conducted. The field scanning should comply with the following requirements:

1) In the deformation monitoring of the clearance, the range of the 3D laser scanner is limited to within 10m in front and back or within one times the diameter of the tunnel (whichever is smaller).
2) In the deformation monitoring of the clearance, the angular resolution should be set to be better than 0.036°. Each station measurement must be registered with a total station and cannot be spliced with targets.
3) The scanning frequency for clearance deformation monitoring needs to be determined based on the distance from the excavation face.
4) Setting up the station for TLS requires the cooperation of a total station. The control points used by the total station are set up on the arch or sidewall closer to the scanning section and on the arch with a longer construction time and almost stable deformation, for verification of the total station's control points.

From August 30th to September 22nd, the monitoring instrument used was the Faro S150 scanner, and a total of 17 scans were conducted. All scans were post-processed using resection method, with two known points observed in the backsight during station setup, resulting in small standard deviations. The holographic settlement and convergence cloud map for the section from DK21+942 to DK21+962 are shown in Figures 9 and 10, displaying the overall settlement and convergence in that section.

To verify whether the accuracy of the TLS in tunnel deformation monitoring meets the standards set by the construction company, deformation monitoring was carried out on the sections of K210 +946 and K210+956. In the holographic deformation monitoring dataset, the monitoring data from the same mileages at the arch crown and arch waist were selected for comparative analysis. As of

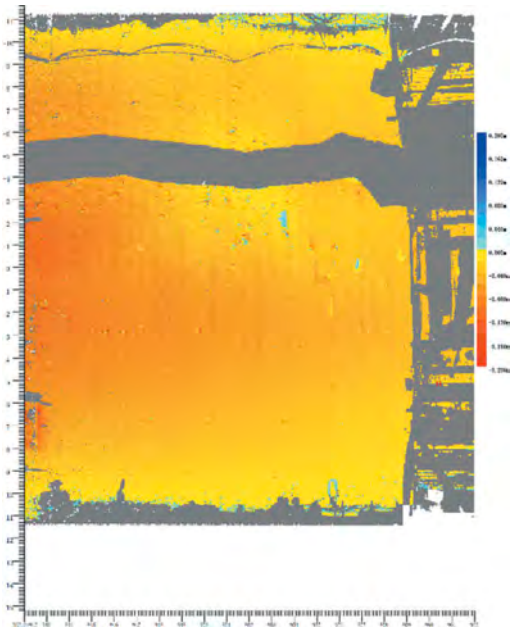

Figure 9. Settlement color map (only showing the final displacement map).

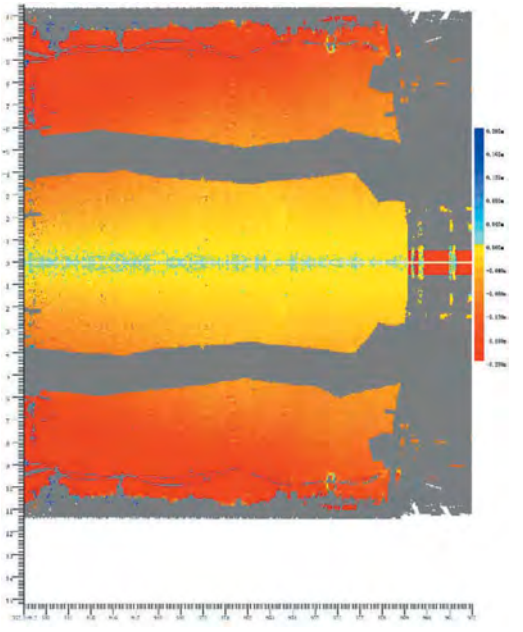

Figure 10. Horizontal convergence displacement color map (only showing the final displacement map).

September 22nd, for the K210+946 section, the maximum cumulative settlement at the arch crown was 65.8mm, while the scanner measured 70mm. The average deviation and mean error between the scanner and total station monitoring data were 2.0 and 5.1, respectively. The maximum cumulative convergence at the arch waist was 199.2mm, while the scanner measured 203.8mm. The average deviation and mean error between the scanner and total station monitoring data were -0.4 and 5.8, respectively. For the K210+956 section, the maximum cumulative settlement at the arch crown was 31.9mm, while the scanner measured 35.3mm. The average deviation and mean error between the scanner and total station monitoring data were -2.6 and 6.8, respectively. The maximum cumulative convergence at the arch waist was 102.8mm, while the scanner measured 112.5mm. The average deviation and mean error between the scanner and total station monitoring data were 1.3 and 8.5, respectively.

7 CONCLUSION

With the widespread application of TLS technology in railway tunnel construction, the use of this technology for detection and monitoring has become increasingly common in the tunnel industry. It has expanded from its initial applications in identifying encroachments and excessive under-excavation to include areas such as initial support alignment, rebar inspection, and holographic deformation monitoring. From the various scenarios and feedback, the following conclusions can be drawn:

1) Ensuring safety: From traditional limited cross-section sampling to holographic deformation monitoring, TLS technology can comprehensively cover all parts of the tunnel and accurately control the overall deformation. When there is non-uniform deformation in the tunnel, holographic area determination can better understand the differential deformations, promptly identify geological hazards, and provide effective data support for changes in construction methods.
2) Quality improvement: Through holographic detection, we ensure that the under-excavation, initial support clearance and smoothness, second lining clearance, and other aspects meet the design requirements before proceeding to the next construction step. By guaranteeing that each process meets the necessary standards, we ensure that the results of each phase during construction meet the design requirements. Compared to traditional total stations, TLS can provide a more comprehensive understanding of the under-excavation and encroachment conditions of excavation, initial support, and lining, while meeting the design requirements. This improves construction quality and speeds up the progress.
3) Cost control: According to statistics, excessive excavation results in concrete wastage of over 3000 cubic meters per kilometer. Through timely holographic detection using TLS, effective data support is provided for concrete preparation, actual consumption statistics, and optimization of drilling and blasting construction processes. This allows for precise concrete preparation and eliminates excessive concrete consumption. Additionally, the three-dimensional laser can accurately determine the precise location and value of the maximum settlement in a specific section. By comparing and summarizing the maximum settlement of continuous sections, the true deformation of the tunnel can be determined, allowing for dynamic adjustments to the reserved deformation allowance in the design. This helps ensure safety and save concrete costs.
4) Efficiency improvement: Three-dimensional laser on-site data collection only takes less than 3 minutes to obtain 40-60 meters of valid point cloud data, which is more than 7 times faster than a total station. This significantly improves on-site detection efficiency. The tunnel quality can be visually displayed through a three-dimensional model and color zoning, enhancing the efficiency of detection. Mid-process control can be implemented for defective areas, saving rework time in the later stages of construction and accelerating the construction progress.

ACKNOWLEDGMENTS

Thanks to Chengdu Tianyou Tunnelkey Co.,Ltd. for their support in data collection and software development.

REFERENCES

Chengdu Tianyou Tunnelkey Co., Ltd., 2023. Tunnelkey 3D Laser Point Cloud Processing and Analysis System. www.tunnelkey.com

Cheng, Y. J., Qiu, W. G., & Duan, D. Y., 2019. Automatic creation of as-is building information model from single-track railway tunnel point clouds. Automation in Construction, 106, 102911.

Cheng, Y. J., Qiu, W., & Lei, J., 2016. Automatic extraction of tunnel lining cross-sections from terrestrial laser scanning point clouds. Sensors, 16(10), 1648.

Cheng, Y. J., Zheng, W. L., & Qiu, W. G., 2023. Reconstruction of tunnel lining rebars from terrestrial laser scanning data. Structural Concrete, 24(1), 563–582.

Duan, D. Y., Qiu, W. G., Cheng, Y. J., Zheng, Y. C., & Lu, F., 2021. Reconstruction of shield tunnel lining using point cloud. Automation in Construction, 130, 103860.

Qiu, W., & Cheng, Y. J., 2017. High-resolution DEM generation of railway tunnel surface using terrestrial laser scanning data for clearance inspection. Journal of Computing in Civil Engineering, 31(1), 04016045.

Tunnelling for a Better Life – Yan, Celestino, Thewes & Eberhardt (Eds)
© 2024 The Author(s), ISBN 978-1-032-80042-4
Open Access: www.taylorfrancis.com, CC BY-NC-ND 4.0 license

Bored tunnels: Automated extraction of segment edge location from scan data

James Douglas*
Business Development, Engineering, Hexagon Geosystems, Warsaw, Poland

Olivier Côté
Reality Capture Solutions Consultant, R-E-A-L.it, Montreal, Canada

Sandeep Jain
Computer programmer and founder of Enable My Team/MobiBiz Ltd., London, UK

ABSTRACT: Bored tunnels normally consist of rings assembled from segments that are bolted together in the tunnel boring machine. Until now the measurement of rings for position, attitude, and rotation has been limited to point-by-point collection by total station or manual extraction from scanned point clouds. The lack of an automatic calculation has limited the application of simple-to-use scanners for bored tunnel measurements to help service the drive-in real time. Furthermore, the value of mapping the segments for the purposes of planning a systemwide installation for new tunnels has been limited by the burden of manually extracting the segment edges from the scanning. The authors will propose and demonstrate that it is now possible to standardize the automatic extraction of quality-controlled segment edge information from a certain density of registered scan cloud using state-of-the-art processing software and by inputting a series of relatively simple-to-define engineering parameters.

Keywords: TBM, scanning, survey, ring, wriggle, systemwide

1 INTRODUCTION

Bored tunnels normally consist of rings assembled from segments. See Figure 1. Bored tunnelling with a Tunnel Boring Machine (TBM) is a process that requires continuous geospatial information for both the machine and the rings as the tunnel is driven in order to optimize the accuracy of the tunnel alignment. Measurement of the rings for position and "attitude" (see below) is normally related to the so-called leading or trailing edges of the ring related to the direction of progress of the tunnelling.

Furthermore, tunnel segments that form the ring normally contain features such as bolt pockets, grout holes and unreinforced edges that are not suitable for drilling into during the later tunnel fit-out stage. In this case, there is an obvious tension between the segment positions and the planned layout of bracketry, bolts, and anchors to support the systems installed in the tunnel.

In both cases, the measurement of segment edges (a ring edge is formed from more than one segment edge) provides the required information. However, despite the uniformity of the environment of a bored tunnel hitherto there has been no automated way of identifying and extracting segment edge positions from scan data to quickly and efficiently provide the information required. Therefore, it is still the case that these measurements are taken manually. This paper will elaborate on the needs for both the tunnel construction phase and the systemwide "fit-out" phase before describing the automated solution using state-of-the-art software that has now been formulated.

2 TUNNEL CONSTRUCTION GEOSPATIAL INFORMATION

The required geospatial information for the bored tunnel drive can be broken down as follows:

(i) Checks on the tunnel guidance system by making comparisons of TBM position and attitude to guidance system outputs.
(ii) Establishment of so-called "lead & look-up" of the last built ring in order to plan the arrangement of segments for the next built ring.

*Corresponding author: James.Douglas@Hexagon.com

DOI: 10.1201/9781003495505-352

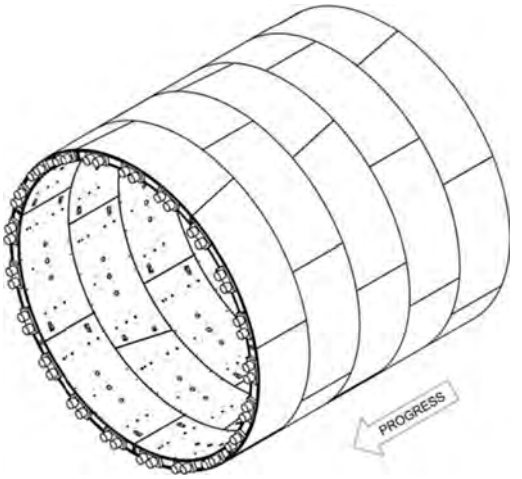

Figure 1. Typical tunnel rings made up of segments.

For the position of both the TBM and rings, several (as well distributed as possible) measurements are taken around the inner lining and a best-fit centre (BFC) is calculated. This is known as a "wriggle" survey. The difference between the best-fit centre to the design tunnel centre (at the measured chainage) in terms of horizontal and vertical offsets from an alignment indicates the misalignment of the TBM or ring at that location. Often tunnel positional tolerances are aggregated to a radial value which is found by taking the square root of the squares of the horizontal and vertical offsets. Radial tolerances for metro tunnels might be as demanding as +/-50mm. TBM "steering" is achieved by varying ram extensions from the rear of the machine pushing off the last built ring. The rings then need to follow the direction of the TBM and a built-in taper on the segment length (in terms of direction of tunnel progress) is employed to make the rings change direction. See Figure 2.

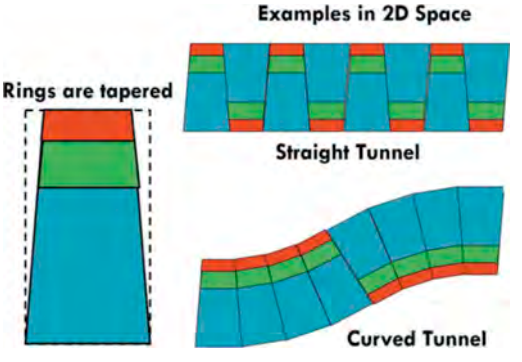

Figure 2. Segment/Ring taper and effects on direction.

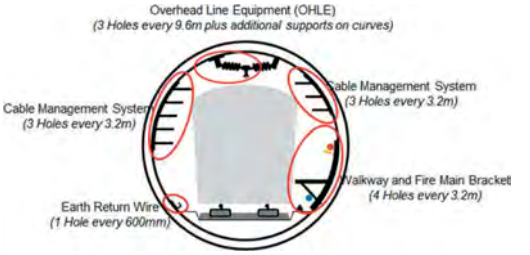

Figure 3. Typical in-tunnel services installed systemwide.

Rings are typically formed of a "key" segment plus two "shoulder" segments and then a number of "standard" segments. The pattern of segments in a ring is constant but the location of the key determines where the taper is. If the taper is at the bottom of the ring, then the top of the ring will be further forward in terms of the direction of progress and the rings will head down. If the taper is on the right-hand side of the ring, then the left-hand side is further forward, and the rings will turn right.

The rings "lead and look-up" (which shall be collectively called "attitude" for the purposes of this paper) are measured in millimetres over the diameter of the ring in the horizontal and vertical (plumb) axes. They indicate the difference of the ring in terms of attitude to the design alignment 3D trajectory of the tunnel. These figures are gathered along the leading edge of the last ring, often using combinations of empirical methods, such as a "plumb bob", with chainage marks. They are used to assess which key location should be next utilised to keep the tunnel in good alignment.

3 SYSTEMWIDE INSTALLATION GEOSPATIAL INFORMATION

After the tunnel has been built it is typical for metros, railways, and other transport systems to require fit-out of the power, mechanical, electrical, and pumped systems that service the use of the tunnel.

For such usage, the in-tunnel installation is itself dimensionally critical. This is primarily to do with the kinematic envelope of the trains/vehicles using the tunnel.

Superelevation (cant) and curvature both affect the cross-sectional position of the vehicle and this in turn forces certain services such as power supply (via overhead catenary or power rail), signalling, and emergency walkway to move with the vehicle in order to interface properly.

Furthermore, the remainder of the services must always be kept clear of the kinematic envelope of the vehicle to avoid clashing and in fact, it is normal for an additional clearance factor to be applied for safety purposes. See Figure 3 for an example of systemwide installation.

4 HISTORY OF SCANNING AND MODELLING TUNNELS

Scanning operational bored tunnels for the purposes of providing clearance and asset inventory has been established for twenty years. The point cloud is sliced into profiles for clearance and the means of collecting bandwidths of data and extracting the most representative (or closest) point for placement in a profile for gauging calculations is already automated.

For CAD modelling on point cloud in a "virtual surveyor" mode, automated extraction of strings representing rails, power lines, continuous structural edges, and boundaries is also already established, although not always used. Feature recognition for vegetation and well-defined point features (e.g., signal aspects) is also available.

In 2004 the Channel Tunnel Rail Link (CTRL) in the UK for the High Speed One line between Paris and London elected to scan the running tunnels from St. Pancras station to Barking portal for the purposes of recording the handover of the tunnels from the civil contractor to systemwide and also to plan drilling for overhead line electrification (OHLE) anchors in the bored tunnel segments. One of the deliverables from the scanning was drilling plans with the guidance given relative to tunnel ring numbers and segment edges. See Figure 4.

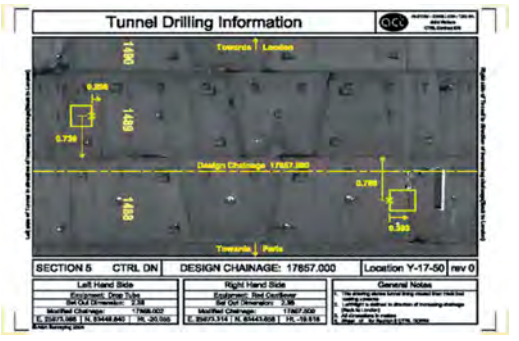

Figure 4. High Speed One OHLE anchor drill plan.

These plans combined modelling of selected segments from the point cloud where they coincided with a planned OHLE position. The anchor position was calculated allowing for vehicle dimensions above the design rails (and incorporated cant and curvature). Where a clash between the drilling and a segment edge was identified a "rule book" of shifts, including potential "knock-on" shifts to adjacent installations, was referenced. In this way, using a trial-and-error process, (which was off the critical path to the site teams for installation,) the fit-out of the OHLE anchors without clashing with "no-drill" zones was resolved in the design office, albeit manually.

In 2015 the London Crossrail project decided to use dedicated semi-automated drilling machines for installing systemwide services in 40 Km of bored tunnel. The installation required around 250,000 holes. In order to resolve the positioning of these holes in bored tunnel segments with "no-drill" zones a full mapping of the segmental lining was required. See Figure 5 for typical Crossrail no-drill zones.

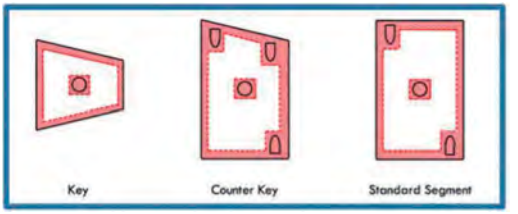

Figure 5. Typical Crossrail no-drill zones in red.

With a full tender process premised on guaranteed delivery dates for information, as well as accuracies and cost, the "state of the art" for modelling the segments was established:

In the most innovative approach at the time, the scanned tunnel was "unwrapped". This means it was projected to a 2D plan (the inner lining when rolled out is, for all intents and purposes, flat), and then the chain of segments for a ring was overlaid and matched manually by a CAD modeller. Once the linework was added to the model the tunnel was projected back from 2D to 3D space. Clearly, this was a significant improvement over drawing each segment edge manually (as per CTRL) but still involved a process that was repeated manually over 25,000 times for the 40 km (the rings being 1.6m long).

The final stages of the Crossrail systemwide drilling project involved the authors formulating algorithms for acceptable drilling patterns that satisfied both the frequency and density required to support the in-tunnel services whilst avoiding the no-drill zones in the segmental lining. Once patterns of drilling were finalised, they were exported to the drilling machines.

Crossrail's drilling machine project was a qualified success: There were challenges with combining so many inputs. Systemwide design, segment edge location, drilling machine parameters, and tunnel geospatial control all had to be input to create guidance. On reflection, there was not enough emphasis on overlaying the finalised drilling patterns on models of the bored tunnel in order to help visualize errors and monitor machine progress. This was partly as a result of the contractual deliverables for the drilling algorithms "only" being tunnel drilling machine inputs which were defined in terms of angles from the zenith and chainage along the tunnel allocated to different drilling arms.

5 JUSTIFICATIONS FOR AUTOMATION OF EXTRACTION

The key cost element of the Crossrail drilling project was the amount of CAD modeller time dedicated to

manual extraction from point cloud data. Despite significant increases in productivity, this was still the same case as for the CTRL project which had been completed ten years earlier. For 40 Km, even when modelling at 20 rings per hour, with assistance from the 2D projection technique, it would require a dedicated modeller for nearly forty working weeks without a break to deliver the required model.

Secondly with Building Information Modelling an ever-greater stipulation for new build projects and existing infrastructure alike, the omission of accurate segment representation in final as-built models of bored tunnels is more and more difficult to justify. However, dedicating skilled CAD modellers to highly repetitive tasks for long periods causes obvious human resource problems.

Thirdly, the uniform nature of the pre-cast segments, in terms of mapping all the characteristics of the lining, lends itself to automated extraction of geospatial position and accurate representation in a CAD model without every feature of every segment being identified. i.e., the position of all bolt pockets and grout holes can be generated from the segment edge positioning by using a library of models for each segment type, attaching them in a "chain" that forms a ring, and matching the chain to the point cloud edges. The "redundancy" afforded in the pattern matching allows the automated extraction to be validated to a high degree of confidence.

Finally, the arrival of a centralised data storage approach to manipulating and processing point cloud has removed the hurdle associated with the amount of data required is considered too great for working efficiently in CAD modelling software. An example of centralised data storage is Leica Geosystems' JetStream™ and their propriety "LGS" file format which reduces file sizes to 5x to 10x smaller than traditional point cloud storage. LGS allows instant loading and rendering of any sized project and when panning and zooming shows "all the points, all the time".

6 A NEW AUTOMATED APPROACH: STAGE ONE

The first challenge with the automated mapping of the bored tunnel segments is the likely presence of significant amounts of in-tunnel equipment, temporary or otherwise, during the data collection stage.

To automatically remove all features from the point cloud, except the inner lining of the bored tunnel, it is necessary to find the best-fit centre of the tunnel rings as a wriggle survey at an interval for which interpolation does not undermine the required accuracy for this data of +/-5 mm. Typically for railway tunnels, this would require a best-fit centre extraction every 5m.

The process of creating a best-fit centre trajectory is as follows: Using the nominal tunnel diameter slices are taken perpendicular to a manually indicated start direction and centre for the tunnel (which is not required to be highly accurate, just "eyeballed".) Each successive slice is assessed for uniformity of radius. Oblique slices will generate an ellipse and will lead to further incrementation of direction at the same

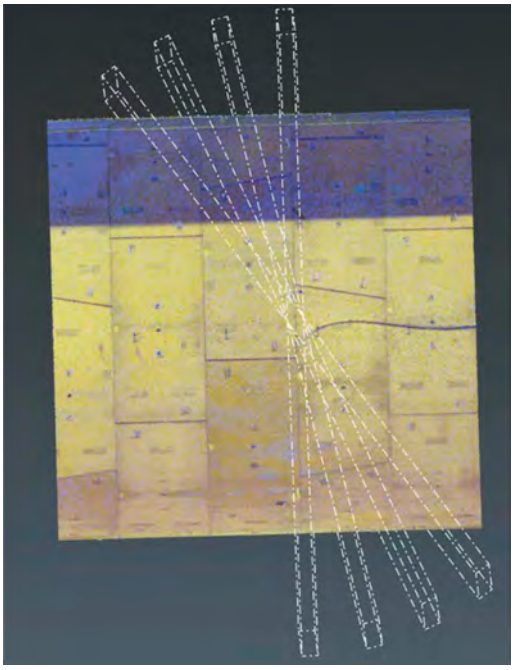

Figure 6.1. Automated iterative process of finding the best-fit centre of the bored tunnel.

Figure 6.2. Oblique slices detected when the diameters or not equal.

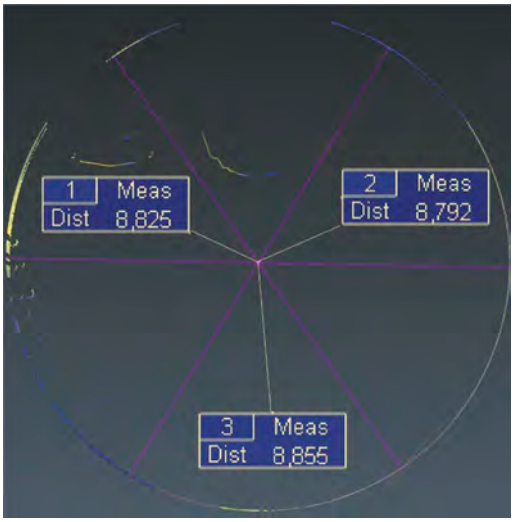

Figure 6.3. Perpendicular slices detected when the diameters or equal, with a certain tolerance.

location until the slice is shown to be circular to the expected tolerances. See Figure 6.

Once the best-fit centre trajectory is found for the tunnel a clean-up of the objects inside the inner lining takes place using a radial "exclusion" which is just inside the "clear bore" for the tunnel.

7 A NEW AUTOMATED APPROACH: STAGE TWO

Segment extraction is possible via more than one automated route.

7.1 *Detection using peaks*

Once the as-built trajectory of the tunnel is established radials can be measured in a perpendicular plane from the trajectory line to the bored tunnel lining. Comparing distances for these radials over appropriate size areas allows the joints for the edges to be detected because at the joint the radial distances are greater than on the segment itself. See Figure 7.

There are three different edges to detect: The "radial" edge that forms part of the leading edge of a ring; the standard longitudinal edge between two segments on the same ring; and the "slanted" edge between the key segment and a shoulder segment on the same ring. Three similar algorithms are needed which slice in a focussed area in order to detect the edges to a resolution that is commensurate with the required accuracy of the segment edge representation in the CAD model (+/1cm). The angle of the slice varies based on the type of edge to detect.

When there is no edge in the slice the radial distances are all very close together in magnitude. If all the distances are ranked from low to high, there is a very high

Figure 7. Radial and longitudinal joints for segment edges.

peak frequency of the same value (c. 98% within a few mm on a well-aligned slice) which we shall call the "centre peak". However when there is an edge inside the area a second "peak" appears for the gap/joint/recess created by the edge and the frequency occurrence of the "centre peak" drops significantly (c.78% on a well-aligned slice). See Figures 8.1, 8.2, 8.3, 8.4.

On this basis as many edges as can be found are extracted. The presence of in-tunnel "furniture", perhaps including a first stage "floor" in the invert of the tunnel to assist in the passage of vehicles, plants, and machinery, means that not all edges for each ring can be seen by scanning. However, as the "chain" of segments in a ring is always the same not all edges need to be detected in order for the as-built position of all the segments to be determined sufficiently accurately. It can be seen that if either of the key segment slanted longitudinal edges is identified all the edges are resolved and additional detection creates redundancy. And if four standard segments are in the chain (as per High Speed Two (HS2) in the UK) then the detection of five successive straight longitudinal edges also resolves the position of the whole ring.

7.2 *Detection using machine learning*

Machine Learning is a type of artificial intelligence that allows computers to learn without being explicitly programmed. Instead, machine learning algorithms learn from data and improve their performance over time. That is: As they are exposed to more data, they become better at identifying patterns and making predictions.

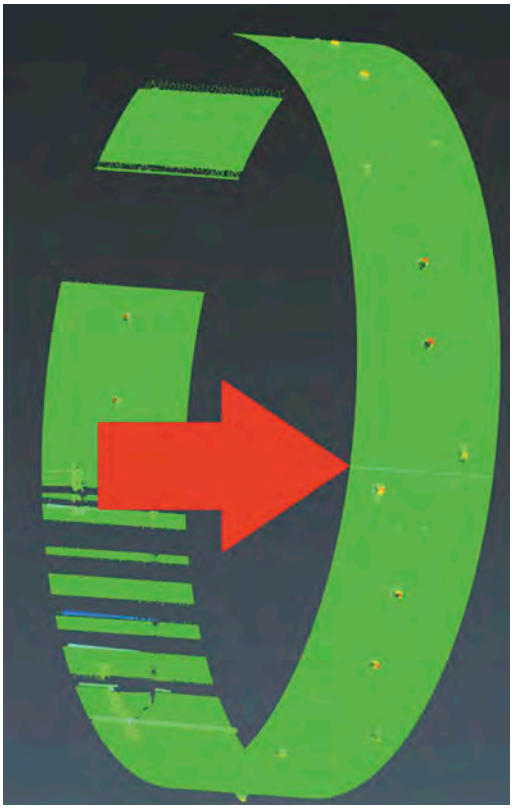

Figure 8.1. Area of interest for the demonstration.

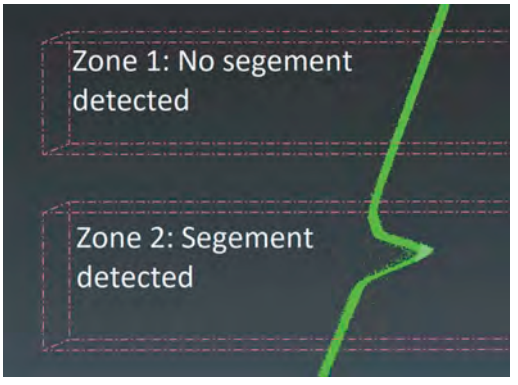

Figure 8.2. View in the direction of the main axe of the areas that will be demonstrated.

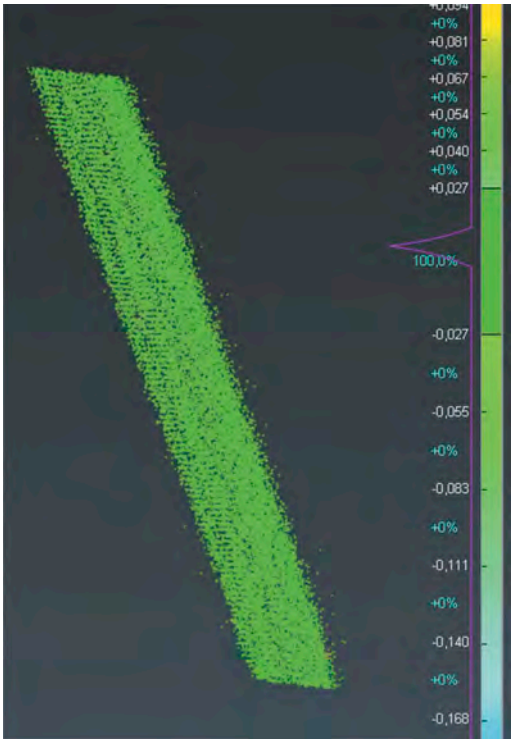

Figure 8.3. Zone 1: 100% of the points are at the same distance from the centre.

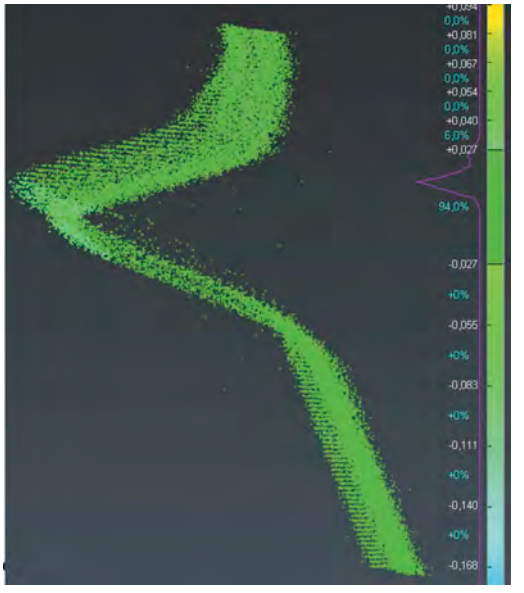

Figure 8.4. Zone 2: A peak of 6% of the points is 0.027 m from the centre.

It is important to remember, however, that machine learning algorithms are only as good as the data that they are trained on. If the data is biased or inaccurate, the algorithm will learn the wrong patterns and make inaccurate predictions.

PointNet++ is a deep learning algorithm used for semantic segmentation of unorganized lidar point clouds. Semantic segmentation aims to associate each point in a 3D point cloud with a class label, (for example bolt, grout hole, radial edge, or longitudinal edge,) with certain characteristics, by sampling, grouping, and then extracting to a new data set with fewer elements.

It is important to be aware of the computational costs and sensitivity to the quality of the input point cloud when using this algorithm.

Clearly in such a uniform environment as a segmentally lined tunnel using PointNet++ to detect segment edges and extract geospatial coordinates at their point ends has a high probability of success.

8 A NEW AUTOMATED APPROACH: STAGE THREE

With the segment edges now described by points with a registered geospatial coordinate they can be compared to the proposed systemwide design for fit-out. In-tunnel positioning is not best described by coordinates because eccentricities in the as-built tunnel position mean that the proposed positions might not intersect with the tunnel lining at all, sometimes missing by hundreds of millimetres.

Instead, positioning is by height above alignment on the sides of the tunnel and horizontal offset left or right of the alignment in the roof of the tunnel.

Ideally, drilling positions are resolved by combining the tunnel as a built position with projected radials from a fixed reference position for the vehicle whose vectors are transformed to coordinates with an origin at the best-fit centre of the tunnel. In this way the intersected position with the as-built tunnel is accurate. See Figure 9.

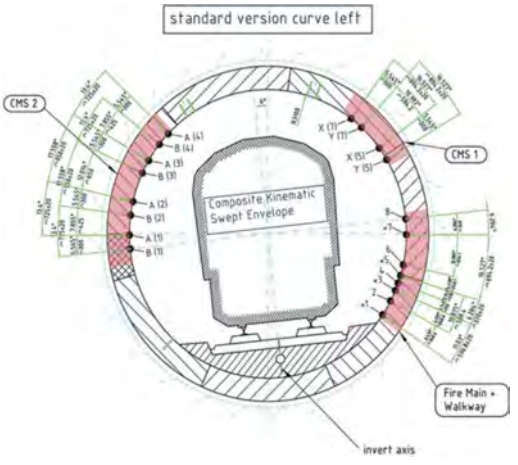

Figure 9. Example of in-tunnel fit-out relative to the vehicle and accommodating as-built position of tunnel lining.

To optimally combine the segment positions with the proposed systemwide layout it is best to consider both in terms of an angle from the zenith and a chainage along the tunnel. If this polar coordinate system is with an origin at the best-fit centre of the tunnel all radial distances will be the same. This completes the transformation of the datasets to a reference system best suited to this environment. See Figure 10.

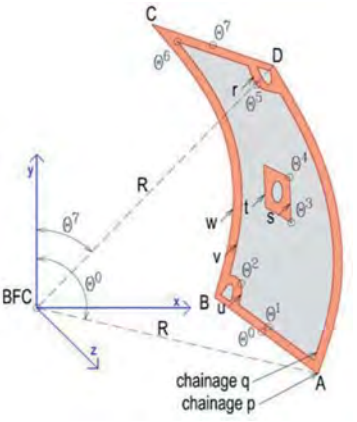

Figure 10. Coordinate system best suited for intersecting drilling patterns with bored tunnel lining.

For the systemwide installation layouts to be resolved in terms of compatibility with the segmental lining and the associated "no-drill" zones a "rule book" of allowable permutations and variations in the fixings is required. These are more than tolerances; they are a series of variables in the detailed design intended to accommodate all possible arrangements on site of segmental lining. It should be borne in mind that the phenomena of machine and ring roll, caused by forces acting on the TBM during excavation, and capable of introducing hundreds of millimetres of unintended rotation in the tunnel lining means that it is possible for longitudinal segment edges to be found at almost any location "around the clock" of the bored tunnel. In past projects, such rules have included the allowable maximum distances between anchors plus the provision of different fixing patterns for the same bracket by providing additional holes in the mounting. Once all the permutations and variations are ranked in order of preference a computer program is written to iterate the fit-out locations for each installation on the whole length of the tunnel. Iteration primarily seeks to find a position at the originally proposed chainage by moving the drilling up or down on the same bracket before considering changing the chainage location. This is because of the "knock-on" effect on adjacent locations in terms of respecting intervals for installation. To manage interval, change a nominal, acceptable "reduced" interval can be employed along with the option to increase the interval where necessary to accommodate changing of a location without any knock-on effects.

9 A NEW AUTOMATED APPROACH: STAGE FOUR

In the case of the Crossrail project, in addition to the "resolution" of the detailed design in terms of its

interface with the segmental lining, there was a need to produce guidance inputs for two bespoke drilling machines. The inputs consisted of chainage and a zenith angle. Because this influenced the output of the fit-out computer program there was a lack of emphasis on "transforming" the guidance data into lay-out "model" data in geospatial project coordinates that could be overlaid on the 3D model of the segment edges to provide comprehendible clash detection. This somewhat denied the most obvious check and balance on what was an easy-to-confuse general arrangement of tunnels where one section looked identical to any other.

In the interim eight years, the now relatively straightforward conversion of drilling data back to points intersecting with the as-built tunnel lining in a 3D model invites new technology such as Augmented Reality, plus automated clash detection between different models in commercially available software such as Cyclone 3DR, multiple opportunities for rapid, independent validation of the outputs ahead of drilling.

10 COST BENEFITS

In the context of systemwide installation for bored tunnels, there are two obvious cost benefits. The first is modelling time, where it is estimated that not less than one week per Km of the bored tunnel would be needed just for manually modelling the segmental lining. The second, less quantifiable benefit, assuming that the systemwide detailed design for layouts is resolved, and there are no clashes with no-drill zones on the segmental lining, is the elimination of delay on-site for the teams and machinery employed to install the bracketry and anchors.

Equally significant but less tangible benefits include the opportunity to refine the component design for in-tunnel fit-out so that remedial or reworks of the components themselves are eliminated. For example, an extra hole in a bracket might be all that is necessary for the component to be compatible with all found cases for the arrangement of the segments on a particular project.

An additional, less tangible, benefit is the completion of the modelling of bored tunnel segment edges for the asset BIM. Previously the modelling of bored tunnels has tended to be limited to best-fit ring representations alongside point clouds without classified features. This situation has denied the mass interrogation of the segmental lining for potential clashes with planned asset maintenance or upgrade operations.

11 CONCLUSIONS

Automated extraction of segment edge location from scan data is the next logical step in the evolution of managing geospatial data for bored tunnels.

The authors are confident it will be proven on the HS2 London-Birmingham high-speed rail project in a "post-processing" mode to optimise the systemwide installation and maximise the digitalisation of the engineering.

Automated extraction is really the only way in which as-built bored tunnels are likely to be analysed for the detail of the segment positions because manual modelling is still considered too slow and monotonous. The option for automated clean-up of tunnels is compelling for all users of the scan data. Furthermore, the extraction and analysis of segment positions are clearly going to optimise some high-risk site operations for systemwide installation in an environment with some extreme challenges in terms of access and logistics. The potential for costly delays in these operations without sufficient planning is very great indeed.

Finally, the automated recognition and extraction of segment edges, and therefore ring position and "attitude", creates an exciting opportunity to use "sentinel" scanners and linked analysis in "near" real-time to export the required "ring by ring" build analysis to the TBM team at the front of the drive. Currently bored tunnel surveying and ring build assessments by engineers are still separate activities. Using a condensed version of stages one and two of the systemwide solution, focussed only on the ring at the front of the drive, all of the required information could be obtained instantaneously in a "single shot" from a geospatially referenced scanner.

ABBREVIATIONS

BFC	Best Fit Centre
CAD	Computer-aided design
CTRL	Channel Tunnel Rail Link
HS2	High Speed Two
LGS	Leica Geosystems
OHLE	Overhead Line Electrification
TBM	Tunnel Boring Machine

REFERENCES

Journal articles

Wren T et al. (2016) Delivering optimum results for ATC on Crossrail. Engineering Surveying Showcase October 2016: pp. 12–13.

Douglas J, Kelly T.A, Jain S (2019) Automated Drilling for Installations inside the Crossrail Tunnels. ICE Publications

Tunnelling for a Better Life – Yan, Celestino, Thewes & Eberhardt (Eds)
© 2024 The Author(s), ISBN 978-1-032-80042-4
Open Access: www.taylorfrancis.com, CC BY-NC-ND 4.0 license

Cavity detection model from GPR images considering reinforcing bars in tunnel segment lining

Chaemin Hwang*, Seunghun Yang, Sangyeong Park, Hojong Kim & Hangseok Choi
Korea University, Seoul, Republic of Korea

ABSTRACT: Since the quality of backfilling the tail void of the segment lining cannot be visually inspected, its evaluation heavily relies on non-destructive testing techniques such as Ground Penetrating Radar (GPR). However, the presence of reinforcing bars (rebars) within the segment lining creates a strong masking effect on electromagnetic waves, making the inspection of GPR challenging. To overcome this limitation, this study considered the scattered and noisy GPR images induced by rebars in the segment lining and proposed an automatic detection model based on the YOLO algorithm. Firstly, numerical analysis using Finite-Difference Time-Domain (FDTD) simulations was conducted to generate GPR images of segment linings with and without the presence of rebars. Subsequently, the YOLOv5 object detection model, which utilizes the convolutional neural network, was trained to detect cavities (i.e., not completely backfilled) behind the segment lining. To enhance the detection accuracy of cavities, the GPR images without rebars were adopted in the training dataset. The model presented in this study successfully detected nearly all cavity signals in the GPR images, and the applicability of the detection model to the on-site GPR results, which are noisier than the numerical results, was further investigated. This advancement contributes to more reliable and efficient quality control of backfilling the tail void of the segment lining.

Keywords: Ground penetrating radar (GPR), YOLOv5, Tunnel segment lining, Object detection, Grout-filled tail void

1 INTRODUCTION

Tunnel segment linings cannot be modified or demolished owing to their size and complexity in tunnel construction. Therefore, non-destructive testing should replace visual inspection for segment maintenance to assess the segment's condition and identify various defects.

One of the defects in tunnel lining structures is cavities. These can result from tunnel deterioration, environmental effects, and improper construction and maintenance. Cavity defects, often found in the backfill grout that fills the tail void during shield TBM excavation, can lead to tunnel degradation, exposing the tunnel to hazards such as leakages and ruptures. Therefore, it is imperative to investigate the presence of cavities in the segment structure to mitigate these tunnel risks.

Ground penetrating radar (GPR) has proven effectively in detecting cavities (Qin et al. 2020). GPR is non-destructive and highly effective, requiring minimal inspection time for the entire survey. However, the propagation of electromagnetic waves is influenced by factors such as antenna characteristics, target geometry, and material properties, requiring specialized GPR measurement and interpretation techniques. Moreover, the interpretation of GPR data can be subjective, leading to different analysis results among experts (Benedetto and Pajewski 2015). Additionally, rebars within the tunnel segment can cause clutter in the GPR image, scattering the hyperbolic signal from the target and making it challenging to distinguish the cavity signal within the backfill grout.

Recently, the prevailing approach has been the use of convolutional neural networks (CNN) to detect underground target signals in GPR inspection results. Various studies have applied automatic object detection algorithms with a CNN structure to GPR images for purposes such as crack detection in pavements (Zhang et al. 2017; Zhang et al. 2020; Liang et al. 2022). Nairit Barkataki et al. (2022) proposed a CNN model to predict the size of buried objects from GPR B-scans.

To overcome the difficulties associated with GPR measurements of tunnel linings, this study employed an object detection algorithm that adopts a CNN to detect the parabolic signals of cavities. The finite-difference time- domain (FDTD) method was used to numerically analyze GPR results with and without rebars in the segment lining. These results were then used as training data to compare and analyze CNN models for the automatic detection of cavities in the grout-filled tail void of a segment lining. The

*Corresponding author: hcm5536@korea.ac.kr

DOI: 10.1201/9781003495505-353

YOLOv5 algorithm was employed to quickly detect objects in the GPR images.

2 CAVITY DETECTION MODEL DEVELOPMENT

2.1 *Database*

In this study, finite-difference time-domain (FDTD) numerical analysis was performed to create a GPR image database for assessing the backfill grout behind the shield tunnel segment lining. In three-dimensional FDTD, the electric and magnetic field components are spatially located in Yee cells and approximated by discretizing Maxwell's equations in time and space, as originally proposed by Yee (1966), as shown in Figure 1.

Maxwell's partial differential equations can be formulated in a three-dimensional Cartesian coordinate system,

$$\frac{\partial H_x}{\partial \mathrm{t}} = \frac{1}{\mu}\left(\frac{\partial E_y}{\partial \mathrm{z}} - \frac{\partial E_z}{\partial \mathrm{y}} - \sigma^* H_x\right) \tag{1}$$

$$\frac{\partial H_y}{\partial \mathrm{t}} = \frac{1}{\mu}\left(\frac{\partial E_z}{\partial \mathrm{x}} - \frac{\partial E_x}{\partial \mathrm{z}} - \sigma^* H_y\right) \tag{2}$$

$$\frac{\partial H_z}{\partial \mathrm{t}} = \frac{1}{\mu}\left(\frac{\partial E_x}{\partial \mathrm{y}} - \frac{\partial E_y}{\partial \mathrm{x}} - \sigma^* H_z\right) \tag{3}$$

$$\frac{\partial E_x}{\partial \mathrm{t}} = \frac{1}{\in}\left(\frac{\partial H_z}{\partial \mathrm{y}} - \frac{\partial H_y}{\partial \mathrm{z}} - \partial E_x\right) \tag{4}$$

$$\frac{\partial E_y}{\partial \mathrm{t}} = \frac{1}{\in}\left(\frac{\partial H_x}{\partial \mathrm{z}} - \frac{\partial H_z}{\partial \mathrm{x}} - \partial E_y\right) \tag{5}$$

$$\frac{\partial E_z}{\partial \mathrm{t}} = \frac{1}{\in}\left(\frac{\partial H_y}{\partial \mathrm{x}} - \frac{\partial H_x}{\partial \mathrm{y}} - \partial E_z\right) \tag{6}$$

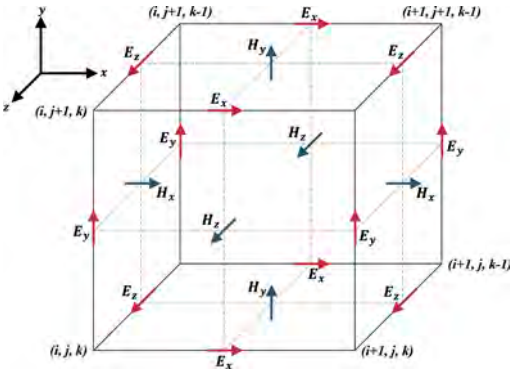

Figure 1. Single FDTD Yee cell geometry of the electric and magnetic field in three-dimensional Cartesian coordinate system.

where E is the electric field (V/m), H is the magnetic field (A/m), ε and μ are the permittivity (F/m) and permeability (H/m) of a material, respectively. Moreover, σ is the electrical conductivity (S/m), and σ^* is the magnetic resistivity.

The FDTD analysis was performed to simulate cavities in the backfill grout using the gprMax program, an open-source Python-based code (Giannopoulos 2005). Material properties of concrete, backfill grout, and air were input as numerical model parameters (Cassidy 2008). Table 1 provides a comprehensive list of material properties used in the FDTD model. Rebars were modelled as a perfect electrical conductor (PEC), meaning their electrical resistance equal to zero. The analysis utilized an 800 MHz GPR transmitted signal with a Gaussian waveform.

Table 1. Electromagnetic properties of materials used in numerical models.

Material	Relative permittivity	Conductivity	Relative permeability	Magnetic loss
Concrete	7	0.005	1	0
Grout	12	0.005	1	0
Air	1.045	0	1	0

To create the dataset for the automatic detection model, the geometry was divided into segments with and without reinforcement. The simulated tunnel lining consisted of a 200 mm thick segment and a 500 mm thick grout-filled tail void, analysed in 2D cross-sections. To prevent overfitting of the detection model, variables like rebar spacing, rebar starting position, cavity position, and the number of cavities were randomized. The rebar spacing in the segment was set to 300 mm, 400 mm, or 500 mm. The number of cavities in the backfill grout varied from 0 to 3, and some cavities were also placed at the boundaries to facilitate object detection for fault waveforms that did not exhibit a complete parabolic shape. In addition, some GPR images without defects were included to reduce false positives in the detection model. The FDTD analysis was performed 100 times for each of the reinforced and unreinforced segment models. Figures 2 and 3 provide an example of the model geometry and B-scan data.

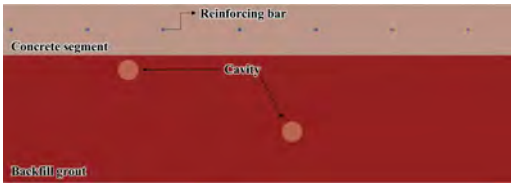

Figure 2. Example of geometry illustration of FDTD analysis model.

Figure 3. FDTD analysis B-scan result of the geometry shown in Figure 2.

2.2 *Detection algorithm – YOLOv5*

YOLO (You Only Look Once), a CNN-based object recognition algorithm, boasts a straightforward training pipeline that allows for rapid learning and prediction while achieving high accuracy compared to existing object recognition algorithms (Redmen et al. 2016; Bochkovskiy et al. 2017).

YOLOv5 consists of three blocks of stages (backbone, neck, and head), the same as the overall structure of YOLOv4, as depicted in Figure 4. In the first stage, it employs the cross-stage partial (CSP) connection method to enhance model learning capabilities, enabling the swift and precise extraction of features. The second stage consists of a path aggregation network (PANet) that integrates feature maps of various sizes to enhance detection performance. In the last stage, the features extracted from the neck are utilized for object detection. YOLO integrates these tasks into a single neural network o achieve rapid object detection.

Several metrics were selected to quantitatively evaluate the predictive performance of the trained model. Precision, which represents the percentage of defects correctly classified by the model as actual defects, and recall, indicating the percentage of actual defects that the model correctly identifies as defects, were employed as performance metrics (Everingham et al., 2015). Precision and recall are defined as follows:

$$Precision = \frac{TP}{TP + FP} \tag{7}$$

$$Recall = \frac{TP}{TP + FN} \tag{8}$$

where true positive (TP) and false positive (FP) are the number of targets correctly and incorrectly classified as positive samples; false negative (FN) is the number of targets that are incorrectly classified as negative samples.

In addition, mAP (mean average precision) is the mean of the average precision (AP) of each class, and AP is defined as follows:

$$AP = \int_0^1 P(r)\, dr \tag{9}$$

This study calculated mAP@0.5, which represents the mean AP when IoU (intersection over union) is set to 0.5, and mAP@0.5:0.95, which represents the mean mAP across different IoU thresholds (from 0.5 to 0.95 in steps of 0.05). The model was trained for 300 epochs using a batch size of 16, with an initial learning rate set at 0.01.

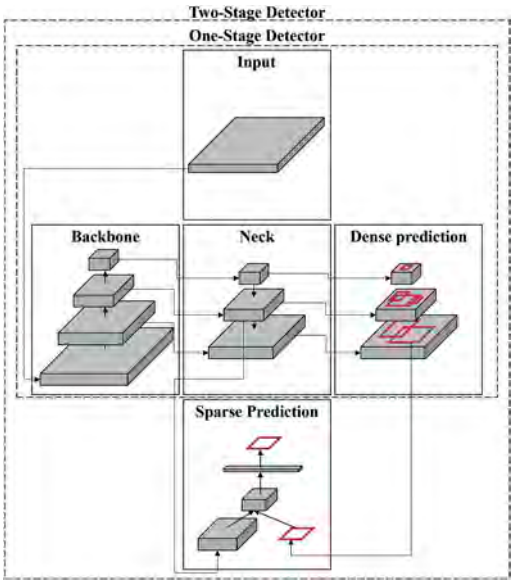

Figure 4. Object detection structure of YOLOv5 (Bochkovskiy et al. 2020).

3 DETECTION RESULTS

The YOLOv5 algorithm was utilized to detect cavities in the backfill grout behind the tunnel segment lining. In this study, three models were constructed according to the configuration of the GPR training dataset: Model A (dataset measured on unreinforced segments only), Model B (dataset measured on reinforced segments only), and Model C (composite dataset of reinforced and unreinforced segments).

Figure 5 initially shows the training and validation results for each epoch for the three models. Here, 'box loss' and 'obj loss' refer to errors in the bounding box and object class, respectively.

The validation loss for the models trained on the different databases consistently decreased as the epoch progressed in all models, indicating that no overfitting occurred. Model A, which exclusively consisted of parabolic signals from cavities without rebar signals, exhibited a low initial loss in the bounding box and object detection. In contrast,

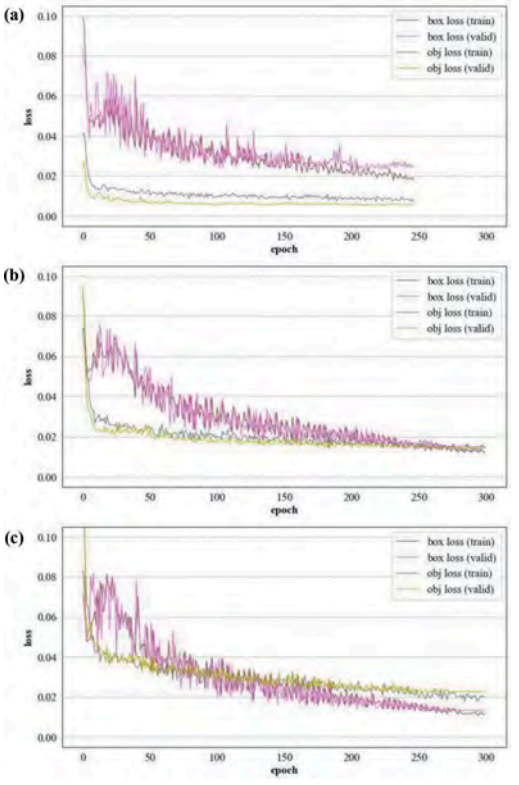

Figure 5. Box and object loss for each model's train and validation results: (a) Model A, (b) Model B and (c) Model C.

Model C, which consists of a composite dataset, suffered some classification losses for rebar and cavity detection in the early epochs but gradually improved during training. Furthermore, two models, except for Model A, completed all 300 training epochs. Model A, however, ceased training early because no improvement was observed in the last 50 epochs.

Figure 6 shows the results of each performance metric for the three models. When the IoU threshold is set to 0.5 for mAP@0.5, all three models exhibit high-performance scores. Nonetheless, Model A records lower scores for the mAP@0.5:0.95 metrics compared to the other two models. This lower performance indicates that Model A struggles to precisely match the bounding boxes of actual object positions with those predicted. This outcome can be attributed to the simplified nature of the configured database and the limitations in feature extraction.

For comparison with each training model, object detection was performed on GPR images that were not included in the training database. First, the results of cavity detection in the backfill grout were compared for unreinforced and reinforced segments. In segments without rebars, all models automatically detected parabolic cavity signals with reasonable accuracy, as shown in Figure 7. The accuracy indicated in the bounding box for the object was slightly higher for Model B and Model C than for Model A.

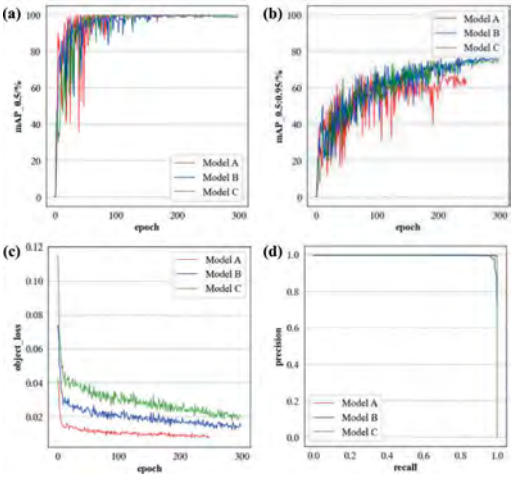

Figure 6. Detection performance results for the three YOLO models: (a) mAP@0.5, (b) mAP@0.5:0.95, (c) object loss and (d) precision-recall curve.

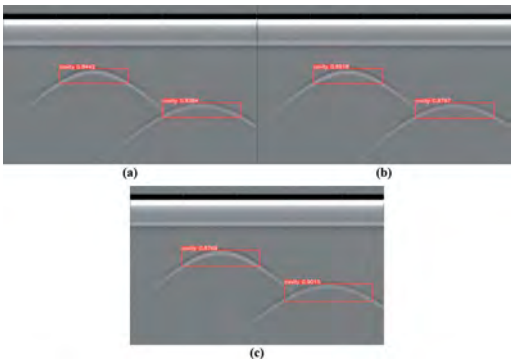

Figure 7. GPR cavity detection results with unreinforced segments for the YOLO model: (a) Model A, (b) Model B and (c) Model C.

Furthermore, all models successfully detected cavities on the rebar segments, as depicted in Figure 8. However, Model A could not detect the parabolic rebar signal in the GPR test image because the rebar waveform was not part of its training, and the cavity detection accuracy was lower than the other models due to the clutter generated by the rebars. Between the remaining two models, Model C, with composite data, showed a 0.0467 and 0.022 higher cavity detection accuracy than Model B.

By acquiring a database of images obtained under different conditions, it is possible to train various GPR images of cavity signals that might be obscured by clutter, resulting in high detection performance.

In this detection test, the detection accuracy was examined when cavities were clustered, and the parabolic cavity signals became noise to each other, that is indistinguishable due to their proximity. The automatic detection results of each model, when three cavities

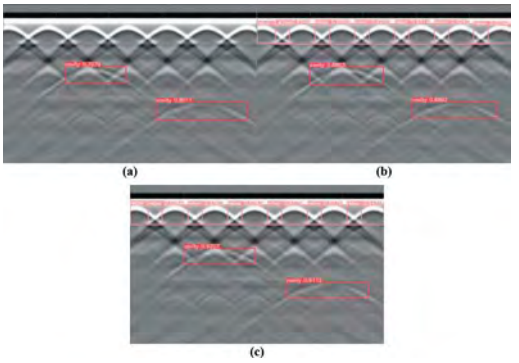

Figure 8. GPR cavity detection results with reinforced segments for the YOLO model: (a) Model A, (b) Model B and (c) Model C.

under the rebar segments were clustered together, are shown in Figure 9. The lowest parabolic cavity signal was significantly masked by the upper rebars and the other cavity signals, resulting in a low detection accuracy.

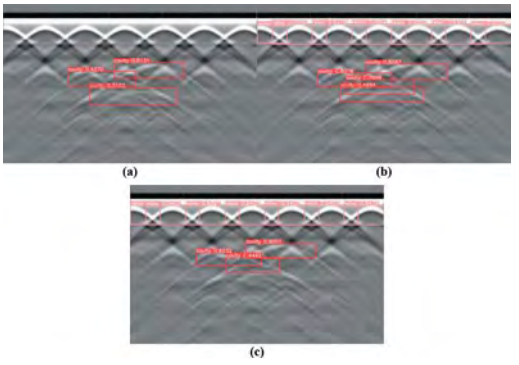

Figure 9. Cavity detection results in GPR images when cavities were clustered: (a) Model A, (b) Model B and (c) Model C.

4 ON-SITE APPLICATION

The cavity detection model was developed using a database generated by numerical analysis. In this section, its applicability was verified by comparing with actual backfilled tail void measurement data. In real-world GPR results, there are target echoes mixed with noise, making it difficult to detect cavities compared to numerical simulation results. The usability of the detection model was evaluated using data from experiments conducted with TBM shield tunnel segments.

The GPR measurement experiment setup is illustrated in Figure 10. Staring from the top, the first layer represents the TBM segment lining without rebars. The second layer consists of soil to simulate the backfill grout, with styrofoam cubes placed at two locations to represent cavities. A MALA GX HDR GPR equipped with a 750 MHz center frequency antenna was used in the test to obtain GPR images, as depicted in Figure 11. In the measurement result used for on-site application verification, two parabolic cavity signals were present, but they were challenging to distinguish due to noise.

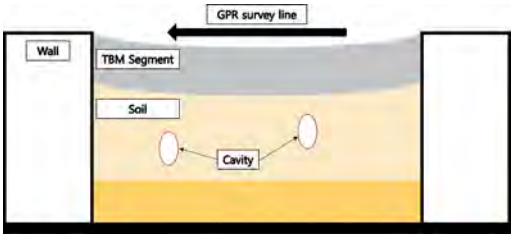

Figure 10. Configuration of a cavity detection experiment for GPR data acquisition.

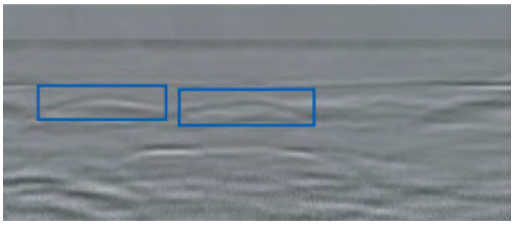

Figure 11. Labeled data for on-site application verification of cavity detection models.

In the analysis of the on-site data using the three detection models, both models A and B failed to detect any reflected signals. Model C, however, managed to detect one of the two cavity signals, albeit with a low detection accuracy of 0.4701, as shown in Figure 12. The reason for these poor on-site applicability results is that the reflection signal obtained by numerical analysis exhibited low noise levels, and the models trained with clean data struggled to perform well in the presence of noise in actual measurement data.

Therefore, to successfully detect cavities within the backfill grout, it is necessary to consider further training the models using realistic GPR data that includes noisy cavity signals. Alternatively, a method that can introduce noise into numerical analysis to generate echoes of reflected signals may contribute to improving the performance of the detection model.

Figure 12. Cavity bounding box and accuracy results in a real-world GPR image for detection Model C.

5 CONCLUSIONS

In a crucial study focused on developing an automatic detection model for cavity defects that occur within grout-filled tail voids behind the shield segment following GPR exploration of lining segments, this research aimed to establish a database consisting of GPR signal results obtained through FDTD numerical analysis. The training database for the CNN model was categorized into three type: measurement results for (1) unreinforced segments only, (2) reinforced segments only, and (3) a combination of unreinforced and reinforced segments. The CNN models were validated by comparing their performance in detecting cavities in test images. The training was performed using the object detection algorithm YOLOv5. The findings can be summarized as follows:

1) Model A performed poorly compared to the other models for mAP@0.5:0.95, one of the performance metrics. Since only GPR images of unreinforced segments were used, a feature map with insufficient variety and detail was extracted. Consequently, it failed to satisfy the high IoU threshold.
2) For validation purposes using GPR test images, Model A showed slightly lower detection accuracy than the other models. This could be attributed to the fact that the training data for Model A did not include the rebar clutter that masks the parabolic cavity signals.
3) The automatic detection model performed poorly under on-site conditions due to the discrepancy between the noise in GPR images and the numerical results. To improve the applicability of the model, future research can concentrate on methods for filtering out clutter in GPR images or simulating noise in the numerical analysis.

ACKNOWLEDGMENTS

This research was conducted with the support of the "National R&D Project for Consecutive Excavation Technological Development Project of Tunnel Boring Machine (RS-2022-00144188)" funded by the Korea Agency for Infrastructure Technology Advancement under the Ministry of Land, Infrastructure and Transport, and man-aged by the Korea University.

REFERENCES

Barkataki, N., Tiru, B., Sarma, U., 2022. A CNN model for predicting size of buried objects from GPR B-Scans. Journal of Applied Geophysics, 200, 104620.

Benedetto, A., Pajewski, L., 2015. Civil Engineering Applications of Ground Penetrating Radar. Springer Cham.

Bochkovskiy, A., Wang, C.-Y., Liao, H.-Y.M., 2020. YOLOv4: Optimal Speed and Accuracy of Object Detection. arXiv:2004.10934.

Cassidy, N., 2008. Introduction to GPR. 12th
Conference on Ground Penetrating Radar (GPR08).

Giannopoulos, A., 2005. Modelling ground penetrating radar by GprMax. Construction and Building Materials, 19(10), 755–762.

Liang, X., Yu, X., Chen, C., Jin, Y., Huang, J., 2022. Automatic Classification of Pavement Distress Using 3D Ground-Penetrating Radar and Deep Convolutional Neural Network. IEEE Transactions on Intelligent Transportation Systems, 23(11), 22269–22277.

Qin, H., Xie, X., Tang, Y., Wang, Z., 2020. Experimental Study on GPR Detection of Voids inside and behind Tunnel Linings. Journal of Environmental and Engineering Geophysics, 25(1), 65–74.

Redmon, J., Divvala, S., Girshick, R., Farhadi, A., 2016. You Only Look Once: Unified, Real-Time Object Detection. 2016 IEEE Conference on Computer Vision and Pattern Recognition (CVPR), 27-30 June 2016. pp. 779–788.

Yee, K.S., 1966. Numerical solution of initial boundary value problems involving maxwell's equations in isotropic media. IEEE Transactions on Antennas and Propagation, 14(3), 302–307.

Zhang, A., Wang, K.C.P., Li, B., Yang, E., Dai, X., Peng, Y., Fei, Y., Liu, Y., Li, J.Q., Chen, C., 2017. Automated Pixel-Level Pavement Crack Detection on 3D Asphalt Surfaces Using a Deep-Learning Network. Computer-Aided Civil and Infrastructure Engineering, 32(10), 805–819.

Zhang, J., Yang, X., Li, W., Zhang, S., Jia, Y., 2020. Automatic detection of moisture damages in asphalt pavements from GPR data with deep CNN and IRS method. Automation in Construction, 113, 103119.

Tunnelling for a Better Life – Yan, Celestino, Thewes & Eberhardt (Eds)
© 2024 The Author(s), ISBN 978-1-032-80042-4
Open Access: www.taylorfrancis.com, CC BY-NC-ND 4.0 license

Combination of modelling and monitoring in assessing stability of a tunnel constructed in highly deformable rock and fragilized by fire

Tohid Kazerani* & Etienne Garin
Department of Transportation & Infrastructure. WSP, Lausanne, Switzerland

ABSTRACT: As one of the major trans-Alpine transport routes between France and Italy, the Fréjus road tunnel is currently the tenth longest road tunnel in the world. It has been constructed in the 1970s by drilling and blasting in a highly deformable Alpine schist which is known for its significant progressive deformation behaviour. During and since the construction, several monitoring campaigns were set to record tunnel's section convergence and stresses in the lining and the ventilation slab. In 2005, the tunnel was subjected to a fire at the Italian side. The aftermath studies suggested that the ventilation slab may have been exposed to temperatures up to 400°C. In addition, following the excavation of a parallel emergency tunnel in the 2010s, a sudden rise to rock deformation was seen where few sections started presenting very concerning section convergences and some minor failures began to appear on the lining. To assess the situation, several rounds of inspection and instrumentation were set that suggested that in some locations the slab could be loaded by the lining movements. The present paper through describing the instrumentation and inspection methodology shows how advanced numerical modelling along with on-time monitoring programme can help assess such a delicate situation. For this purpose, a slip-bond model has been developed for the slab reinforcement based on the recent literature which integrated in a FEM scheme allows to assess the current tunnel state and to predict probable developments in its future behaviour.

Keywords: Fréjus Tunnel, Convergence, Bond-slip model, Visco-elastoplastic, Damage mechanics, Monitoring

1 INTRODUCTION

The current intense circulation across the Alpine underground axes in Europe has made it very difficult to perform major repair or rehabilitation works which by nature require stopping circulation. This situation in the case of Fréjus road tunnel which is excavated in a deformable Alpine schist is much critical, as the tunnel lining has been long exposed to strains exerted by the ground creep movements. In addition, the tunnel has been twice subjected to fire in 2000 and 2005, that the latter incidence, based on the chemical studies done on concrete samples, is believed to have induced very high temperatures into the ventilation slab.

This paper, after presenting a brief history of the asset, describes the monitoring system adopted for the follow-up of the ground movements. Then two models are described: A model to examine the lining behaviour made of plain concrete using a visco-elastic damage constitutive law, and a second model to study the fragilized slab using a bond-slip law developed for the reinforced concrete allowing to consider material properties degradation due to high temperature.

At last, the simulations' results are discussed to show how modelling combined with instrumentation can aid engineer in evaluating the asset current state, and its behaviour in the long run.

2 PROBLEM STATEMENT

2.1 *Fréjus Road Tunnel*

The Fréjus Road Tunnel runs under Col du Fréjus in the Cottian Alps between Modane in France and Bardonecchia in Italy. It is one of the major trans-Alpine transport routes between two countries being used for 80% of the commercial road traffic.

Construction of the 12.8 km long tunnel started in 1974, and it came into service on 12 July 1980, leading to the closure of the motorail shuttle service in the Fréjus rail tunnel. The construction of the tunnel

* Corresponding author: tohid.kazerani@wsp.com

DOI: 10.1201/9781003495505-354

Figure 1. Fréjus road tunnel (right), new second tube (left) and a bypass (SFTRF, 2020).

which is currently the tenth longest road tunnel in the world, cost 2 billion francs (equivalent to €1 billion at 2023 prices).

2.2 *2005 Fire incidence*

The 2005 fire breaks out in a truck carrying tires from France to Italy. The tragedy occurred in the middle of the tunnel where the flames spread rapidly, and made other vehicles be set to fire.

2.3 *2010s Second tube construction*

The European directive on tunnel safety issued in 2004 led to the decision of constructing the road tunnel's emergency gallery at the end of 2009. This was to bring the tunnel into conformity with the obligation for all tunnels in the trans-European network to be equipped with safety shelters no more than 500 m apart.

The main objective of this operation was to increase the number of safety shelters in the Fréjus tunnel from 11 to 34 by building bypasses to the emergency gallery every 400 m on average.

On November 17th, 2014 excavation of the tube, using a tunnel boring machine, was completed (SFTRF, 2020).

This second tube will be opened to single lane traffic (in the direction Italy-France), while the existing tunnel will also be operated for single lane traffic (in the direction France-Italy). This project costs €550 million (2014 value).

3 ROCK MASS CREEP BEHAVIOUR

The existing Fréjus tunnel has been constructed by drilling and blasting. As a result, and as it is the case in most tunnels excavated by this method, the excavation surfaces are very irregular, such that the lining, which was planned to be about 40 to 70cm thick, has been casted with even more than 1m-thick plain concrete (see Figure 7).

Due to the rock mass high creep tendency, the road tunnel was let unlined for few months after excavation to allow it to undergo as much its creep deformation as possible before casting the concrete lining. Nevertheless, in some sections, the creep was that high that required section readjustments before lining.

The tunnel section convergence was recorded during the excavation and the unlined period. Figure 2 shows the variation of these convergences (measured after 1 month from passing the tunnel face by the measurement point) versus the overburden along the tunnel axis.

The measurements showed a significant rock mass creep behaviour particularly at very early days after excavation (the first ten days or so), where rock mass was developing a very rapid deformation toward the tunnel at a rate of around 1cm/day. Though later the creep deformation decelerated, it never stopped such that even after 3 months (when the primary measurements were removed for placing the lining) no sign of stability was seen.

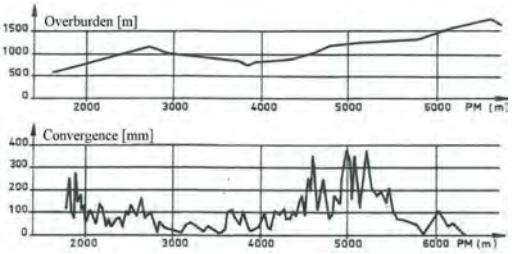

Figure 2. Overburden variation versus 1-month primary convergence for the French side. i.e., the first 6400m of the tunnel.

As seen in Figure 2, the tunnel section convergence does not follow the rock overburden pressure. As a matter of fact, it is more dependent of the local rock mass foliation than its overall stress level. This foliation has a variable dip angle along the tunnel between 10° to 25°.

3.1 *Impact of second tube construction*

The excavation of the second tube and the subsequent change in the rock mass stress state gave rise to the rate of convergence in the existing tunnel. This behaviour was more pronounced where the bypasses were excavated from the second tube toward the tunnel. Due to this issue, new measurement devices including displacement and stress gauges were mounted in 2011along the tunnel liners, inside the new excavations, and over the ventilation slab.

As illustrated in Figure 4, following a general jump right after the second tube excavation (2013 measurements compared to 2007 measurements of Figure 3), except for four places (whereabouts of 2000m, 5400m, 6900m and 7800m), the lining convergence seems to reach again stability. In these four critical places, tunnel behaviour required an enhanced monitoring and numerical analysis which is the subject of the presented study.

3.2 *Lining and ventilation slab overstress*

The lining section lacks a bottom slab (Figure 7). Therefore, against the progressive rock mass creep,

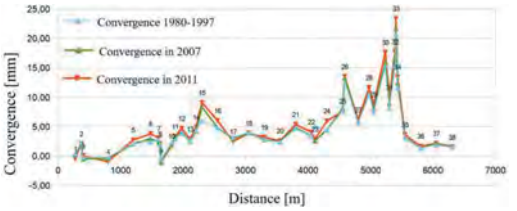

Figure 3. Convergences recorded before the second tube excavation (data for the French side).

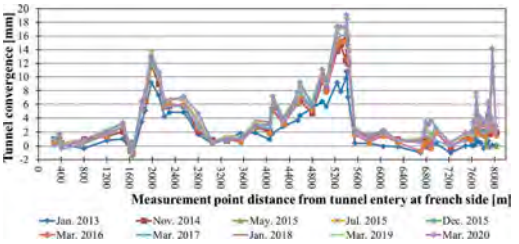

Figure 4. Convergences recorded after second tube excavation (data for the French side. i.e., the first 6400m of the tunnel).

the lining could only resist through two mechanisms: (a) Flexural mechanism, as a result of that the arch crown is compressed at its inner fibre and tensioned at the outer fibre; (b) Ventilation slab reaction, as a result of which the slab is strained axially.

The mentioned compressions have already led to concrete punctual spalling at the arch crown inner surface. As the carried out concrete core samplings confirm a highly resistant material whose mean compressive strength is about 40 to 50 MPa, the arch at the spalling regions should be and have been under very high levels of compression.

In addition, as the tractions induced at the lining unseen outer surface (extrados) may have already exceeded the limited tensile strength of the plain concrete, the liner may have fractured very likely at that surface.

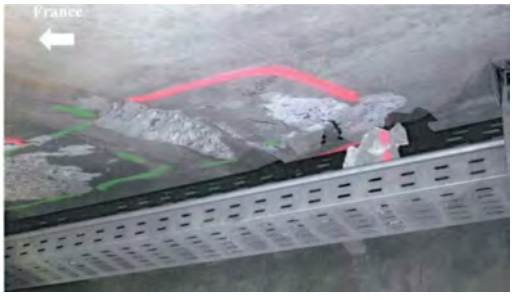

Figure 5. Spalling over in arch inner surface.

From the ventilation slab perspective, the growth of axial strains threatens its stability. Although in French side, the ventilation slab is placed separated from its supports using 1.5cm-thick polystyrene layers, in the Italian side, it was casted in direct contact with the lining.

The in-situ observations at the French side confirm that in some sections the polystyrene layers have been completely crushed and the slab is already touched by the lining.

4 MODELLING

4.1 *Lining: Viscoelastic damage mechanics modelling*

The goal of the study project defined for the asset was to provide a comprehensive picture of the lining currents status, and to put forward solutions to guaranty its long-term durability. For this purpose, a large number of simulations were performed for different parts of the tunnel. This paper only summarizes the modelling fundamentals without going in much detail, and instead it aims at providing the reader with the most important outcomes.

4.1.1 *Rock mass behaviour*

The modelling needed to take creep effects into account due to their importance in predicting structure behaviour. For this purpose, the rock was modelled using a visco-elastoplastic (VEP) law, where rock viscous behaviour is formulated using a series of Kelvin elements as follows, where η is the material viscosity (ZSoil, 2020).

$$\eta\dot{x} + kx = f(t)$$

As a general form, the calculation code allows to define creep displacement as follows,

$$x(t) = x_{ep} + x_{cr} = x_{ep} + \sigma C(t)$$

where, X_{ep} and X_{cr} are the elastoplastic (EP), and creep components of displacement. The latter is formulated do that being dependent of the model stress field through a so-called "*creep function*", C(t). For this study, a logarithmic creep function is opted,

$$C(t) = Aln(1 + Bt)$$

where A and B are the so-called "*creep parameters*" which need to be calibrated using the experimental data. This has been done using the convergence data recorded during excavation works. The rock mass is modelled as a homogeneous isotropic continuum with properties as listed in Table 1.

Table 1. Rock mass characteristics.

Unit weight	Elastic modulus	Poisson's ratio	Friction angle	Cohesion
27 kN/m^3	15 GPa	0.2	40°	5 MPa

4.1.2 *Concrete behaviour*

The lining was simulated using a visco-damage mechanics (VDM) model. The damage mechanism is the one introduced by Omidi and Lotfi (2012). The viscous part of the modelling is defined by the creep formulation proposed in the Eurocode 2 (EN1992-1-1, 2004), where both the long-term deformation and the material maturation (increase in stiffness and strength) are incorporated into the simulation using the equations provided by the Eurocode.

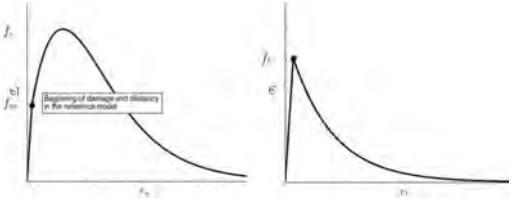

Figure 6. Compressive (left) and tensile (right) behaviours in concrete damage model.

4.1.3 *Model geometry*

In the course of the study, many models were created to examine different aspects of the tunnel. Figure 7 illustrate the geometry of one of the 2D models used in a section presenting the highest current convergence rate.

The modelling was carried out using ZSoil finite elements package (ZSoil, 2020).

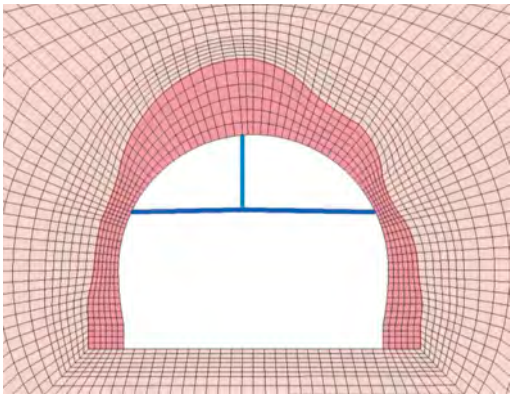

Figure 7. 2D Model geometry with lining varying thickness as a result of excavation by drilling and blasting.

4.1.4 *Validation*

In order to validate the model, the results of a simulation for the tunnel deformations after the construction of the second tube (2010s works) are compared to the in-situ measurements. Note that the creep parameters are calibrated using convergences recorded in the unlined tunnel during the 1970s excavation works.

Figure 8 shows that the model reproduces the tunnel deformations accurately. Note that the

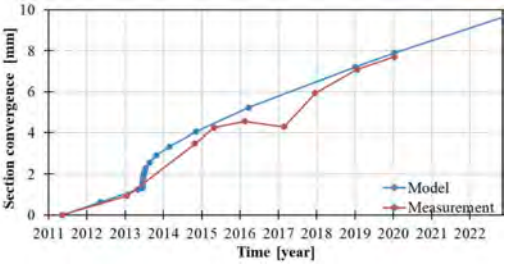

Figure 8. Model comparison with secondary and tertiary convergence measurements.

modelling presents a relatively sharp displacement jump at the second tube excavation, while measurements suggest a more moderate deformation rate. This is because in reality, the confinement effect around the excavation front makes the hole converge less rapidly than the 2D model does which lacks such a confining effect. Apart from this shortcoming, the model can well reproduce the deformation rates before and after construction works.

In addition, lining stress measurements carried out in the arch crown by means of flat jacking suggest that as of 2020 concrete stress at a distance of 30 cm from the surface has been about 8.0 MPa. Figure 9 shows that the model at the same location and at the same concrete age produces the same stress.

4.1.5 *Discussion on concrete creep effect*

The concrete creep behaviour is normally neglected in calculations as it is generally admitted that in terms of stress, material damage behaviour is more important than its creep.

However, when rock creep enters the play, it requires the model to include a large time span of the structure lifetime or even its whole. In such a case, concrete creep becomes important.

Incidentally, the stress relaxation in concrete due to creep has a favourable effect as illustrated by following images presenting the tunnel lining stress once calculated with no creep assumption for the concrete (Figure 10) compared to Figure 9 presenting stresses in the model with concrete creep.

In both figures, the stresses are scaled between 0 and 10 MPa. As seen, while no-creep assumption leads to some unrealistically large areas of overstress (coloured in dark blue) including at the ventilation slab connection point, the model with concrete creep suggests much more reasonable stress values. Note that in the section inspections, not lining failure due to overstress has been reported at the slab support point.

In addition to modelling significance, these results put forward an important practical remedy in dealing with tunnels excavated in deformable rock, that is, the use of light-weight concrete, which is more prone to creep, instead of using normal concrete.

Light-weight concrete can be obtained by using large aggregates with little to no fine aggregates

(pervious concrete), or with a controlled use of gas producing agents in the mixture (porous concrete).

This way, the deformations imposed by ground creep can be absorbed by concrete creep gradually, thereby lining stresses are relaxed.

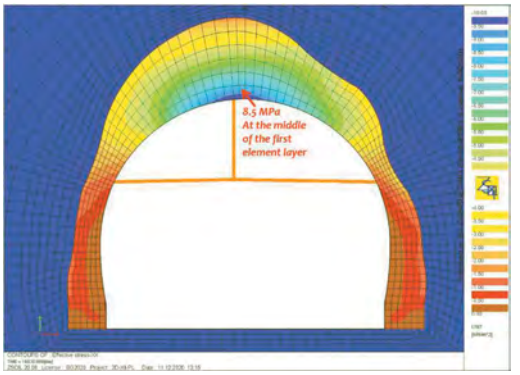

Figure 9. Lining horizontal stress with creep for concrete.

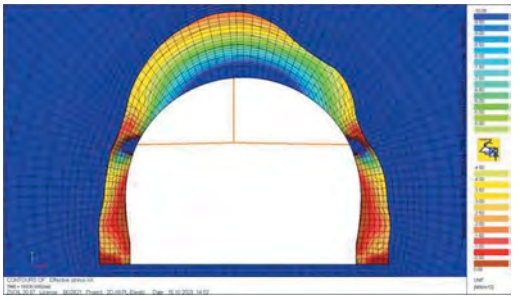

Figure 10. Lining horizontal stress with no creep for concrete.

4.2 *Ventilation slab: Bond-slip model*

This chapter presents the analysis performed to check the current and future state of the slab at location that it has been once exposed to fire in 2005.

This chapter after reviewing the adopted methodology, applies the presented method to the slab and examines its response in post-fire state to deformations imposed by the section convergence.

4.2.1 *General behaviour at low temperatures*

The bond between steel rebar and concrete consists of (a) chemical adhesion, (b) skin friction and (c) interlocking. Chemical adhesion has a negligible effect, which disappears as soon as the initial slippage at rebar-concrete interface occurs. Subsequently, the frictional force generated by the mechanical interlocking of the steel ribs in concrete develops gradually and becomes the main component of rebar's bonding action.

Numerous analytical studies have been carried out to investigate the behaviour of tensioned rebars in concrete at room temperature. These analytical studies provide useful information on rebars deformation process and failure modes. Based on experimental and analytical studies, certain calculation methods have also been established to assess the ultimate bond stress. In addition, numerous studies have attempted to propose a closed-form mathematical expression for the relationship between local bond stress and rebar slip.

The bond-slip stress model which is most widely used in the literature is certainly that specified by Model Code (2010), originally developed by Eligehausen et al (1983).

This slip model defines the local bond-slip relationship by four stress levels as follows:

$$\tau_s = \begin{cases} \tau_{max}\left(\frac{S}{S_1}\right)^m & S \le S_1 \\ \tau_{max} & S_1 \le S \le S_2 \\ \tau_{max} - \left(\tau_{max} - \tau_f\right)\left(\frac{S-S_2}{S_3-S_2}\right) & S_2 \le S \le S_3 \\ \tau_f & S_3 < S \end{cases}$$

where τ_s and s are the bond stress and the slip between the rebar and the concrete; m is a coefficient that defines the ascending branch of the bond-slip curve, set at 0.4 according to the 2010 Model Code.

The results of these tests highlight the fact that, if rebars are sufficiently confined by cover, their failure mainly takes place by a complete pull-out of the rebar after a significant displacement of the latter in concrete, where concrete remains intact (pull-out). On the other hand, when rebars are covered by a relatively thin concrete cover, with or without transversal reinforcement, radial cracks propagating from the bar-concrete interface reach the concrete surface, and failure occurs by splitting the concrete cover (cleavage).

The parameters defining bond stress according to Model Code 2010 are summarized in Table 2 for different failure modes.

For the case of ductile failure (i.e., pull-out or cleavage in concrete reinforced by stirrups), when the slip reaches rebars ribs spacing (l_s), mechanical interlock between steel rebar and concrete becomes negligible, and residual bond stress, τ_f is mainly ensured by the action of friction.

The residual bond stress is set at $0.40\tau_{max}$ in pull-out case, and $0.20\tau_{max}$ for cleavage case. In addition, the interfacial slip corresponding to l_s (in the case of pull-out) and $0.5l_s$ (in the case of cover cleavage) is defined as s_3.

Table 2. Model Code 2010 bond law parameters.

	Pull-out	Cleavage	
Parameter	Sufficient concrete cover	Unconfined rebar (no stirrups)	Confined rebar (with stirrups)
S_1	1.0 mm	0.6 mm	0.6 mm
S_2	s_1+1	s_1	s_1
S_3	l_s	$1.2s_1$	$0.5l_s$
τ_f	$0.40\tau_{max}$	0.00	$0.20\tau_{max}$

In the absence of confining stress around rebars, post-peak bond stress is negligible, thereby τ_f can be assumed null.

The Model Code proposes values for τ_{max}, which depend only on the compressive strength of the concrete (varying between *Lausanne* and $2.0\sqrt{f_{ck}}$ regardless of cover thickness or rebar diameter. For this reason, and given the importance of these parameters, in the present study we rely on the following analytical equation proposed by Gao et al (2019):

$$\tau_{max} = \frac{1.81 c f_{ct}}{\left(1.05 - 3.56d \times 10^{-3}\right) d}$$

Where f_{ct} is concrete tensile strength (MPa) and c and d are cover thickness (calculated from the reinforcement axis) and the rebar diameter, both in mm.

4.2.2 *Bond degradation high temperature*

Estimating the residual bond of steel bars that have been subjected to fire is more complicated than in the case of intact material. This can be explained by the fact that, due to the difference between thermal expansion coefficient of steel and concrete, thermal stresses can occur in the steel/concrete interface at high temperature. If the temperature remains relatively low, the circumferential tensile stress around the rebar will remain lower than concrete tensile strength, and concrete cover will remain intact. However, as temperature rises, tensile stress increases and may reach the material tensile strength, leading to concrete cracking. As a result, in the post-fire state, concrete exhibits partial cracking over a certain radius around reinforcement.

In the literature, several pull-out tests have been carried out to investigate the bond strength of reinforcing rebars during or after exposure to heat (Ergün et al 2016, Bingöl and Gül 2009, Hlavička 2017, Deshpande et al 2020, Yang et al 2018,Yin et al 2011, Ma 2017, Tariq and Bhargava 2020, Zhang et al 2019, and Rashid et al 2019). The results of these tests indicate that bond strength considerably decreases, particularly when concrete temperature exceeds the 400°C limit.

Analytical studies have also been carried out to propose bond-slip models at high temperature (i.e., in the heated state before cooling), like the work of Khalaf and Huang (2019), and also for the bond degradation after exposure to high temperature (i.e., residual bond after cooling), e.g., the study carried out by Wang et al. (2022)

4.2.3 *Bond degradation of corroded reinforcement*

Reinforced concrete structures located in humid areas and exposed to aggressive environments are subject to carbonation and chloride penetration. As corrosion progresses, circumferential tensile stresses induced by the corroded steel expansion, would they exceed the material tensile strength, can lead to concrete cracking and spalling at cover zone, resulting in a loss of bond between steel and concrete.

As tunnels, specially road tunnels, are subject to CO2 emission from cars exhaustion, concrete in these assets is highly prone to carbonisation.

4.2.4 *Empirical models of bond strength degradation*

Experimental study of bond stress degradation of reinforcement after exposure to elevated temperatures has been subject of several scientific investigations. For the present study, we rely on data from one of the most extensive experimental investigations in this field, carried out in 2020 by Tariq and Bhargava. The aim of that study was to investigate the extent to which the bond properties of ductile steel rebars anchored in normal-strength concrete deteriorate under the combination of corrosion and high temperature.

To this end, the bars were exposed to accelerated corrosion to achieve desired corrosion levels in terms of mass loss percentage (2%, 4%, 6%, 8%, 10%, 12%, 14%, 16% and 18%) and then to target temperatures (200°C, 400°C, 500°C, 600°C, 700°C and 800°C). The specimens were tested to failure in pull-out mode to study the sliding behaviour of rebars. The results indicate a significant reduction in bond stress due to the superposition of the two phenomena.

Tariq and Bhargava has not proposed an analytical form for adhesion loss as a function of temperature and corrosion. Based on their results, we have developed a mathematical equation for the maximum residual adhesion stress, which can be expressed as follows:

$$\tau_{max}(T, C) = \tau_{max} \times H(T) \times R(C)$$

Where τ_{max} is the maximum bond stress of an uncorroded rebar at room temperature as given described earlier, and $H(T)$ and $R(C)$ are two statistical functions representing respectively reducing effects of high temperature and steel mass loss due to corrosion:

$$H(T) = \frac{1}{2} - \frac{2.5 \times 10^{-3}(T - 500)}{\sqrt{1 + 2.5 \times 10^{-5}(T - 500)^2}}$$

$$R(C) = \begin{cases} \frac{5}{8} - \frac{25(C-0.03)}{\sqrt{1+2500(C-0.03)^2}} & 20^\circ C < T \leq 200^\circ C \\ \frac{5}{8} - \frac{30(C-0.02)}{\sqrt{1+2500(C-0.02)^2}} & 200^\circ C < T \leq 800^\circ C \end{cases}$$

4.2.5 *Degradation of reinforced concrete properties*

When estimating the slab residual strength, the degradation of concrete and steel mechanical properties, in particular strength and elastic modulus, must be properly assessed.

Elastic modulus degradations of steel and concrete and after fire (AF) can be defined according to the equations proposed by Liang (2008). The equations are given below, where $E_{s.TA}$ and $E_{c.TA}$ are the residual elastic moduli of reinforcement and concrete after exposure to fire. $E_{s.0}$ and $E_{c.0}$.represent the elastic moduli of steel and concrete at room temperature.

$$\frac{E_{s,TA}}{E_{s,0}} = \frac{1}{1 + 0.505 \times (T/1000)^{7.36}}$$

$$\frac{E_{c,TA}}{E_{c,0}} = \frac{1}{1 + 18.5 \times (T/1000)^{2.47}}$$

The permanent degradation in concrete tensile strength after fire is taken into account using the equation below, obtained by Qin et al. (2004) and republished by Wang et al. (2022):

$$\frac{f_{ct,TA}}{f_{ct,0}} = 1.02 - 0.00111T$$

Where $f_{ct.TA}$ and $f_{ct.0}$ are concrete tensile strengths after exposure to high temperature, T, and at room temperature, respectively.

As explained in FIB (2008), the degradations in the compressive strength of concrete during and after exposure to fire must be assumed to be identical, based on a safety approach. These degradations are taken into account by the equations proposed by Eurocode 2, part 1-2 as for siliceous and calcareous aggregates.

4.2.6 *Estimation of the slab post-fire strength*

This section aims at applying the formulation developed above to estimate the ventilation slab residual strength. To reach this purpose, a thermo-mechanical FEM model has been developed in which the presented formulations were applied.

In addition, the equations proposed by Eurocode 2, part 1-2 for change in material thermal properties, i.e., conductivity, heat capacity, and thermal expansion coefficient, were also incorporated into the model, enabling it to automatically simulate the structure behaviour at rising temperature. The simulation is carried out at four temperature levels: 20°C, 200°C, 400°C and 600°C. The simulation aims as examining whether the deterioration in rebar-concrete bond and the materials' strength could have led to a reduction in the structure load-bearing capacity under the transversal compression induced by the tunnel section convergence. To answer this question, buckling strength of the compressed slab under lateral bending due to its self-weight is studied.

The simulation, modelling one metre of the slab length, is carried out under the following assumptions:

- Buckling is taken into account using a second-order approach by applying tunnel convergence in 1-mm steps, where nodal coordinates are updated at each step to incorporate large deformations and geometric non-linearity into calculation.
- Concrete class is assumed C30/37. The elastic modulus and characteristic compressive strength of concrete at 20°C are taken 30 GPa and 30 MPa, respectively.

Figure 11, showing the modelling results for the slab's bending moment and deflection before and after the application of the lateral convergence load (1.0 cm), shows that:

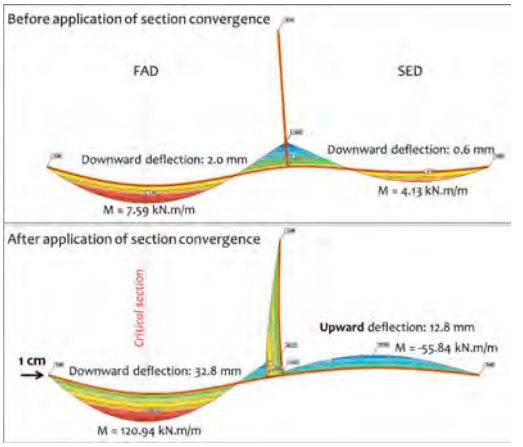

Figure 11. Slab model before and after application of the tunnel convergence load.

- Under the effect of self-weight alone, the two slab spans, separated by the vertical partition, bend downwards and the maximum bending moment occurring at the mid-span on each side is 7.59 kN.m/m (for the resh air duct, FAD) and 4.13 kN.m/m (for the smoke extraction duct, SED).
- As the cross-section in the FAD is wider, it deflects more (Δ_{FAD} = 2.0 mm), so the partition-slab connection point rotates counter-clockwise.
- The applied compression produces two second-order moments ($M = P\Delta$), the larger of which is generated in the FAD ($\Delta_{FAD} > \Delta_{SED}$). This makes the connection point rotate further in counter-clockwise direction under the resulting moment ($P\Delta_{FAD} - P\Delta_{SED}$). Under this mechanism, Δ_{FAD} increases but Δ_{SED} decreases.

The continuation of this mechanism makes the slab span in the SED be deflected upward.

Under section convergence, it is the slab span in the FAD that is subjected to the greatest stresses and is therefore considered to be the critical cross section of the structure.

In this cross section, there are two reinforcement layers: the lower layer comprises 20 mm diameter rebars spaced 20 cm apart, and the upper layer, where reinforcement is provided by two reinforcement positions: one with 10 mm diameter rebars spaced 20 cm apart, and the other with rebars of the same diameter but longer and spaced approximately 30 cm apart.

Figure 12 shows the MN interaction curves (including buckling effect) as calculated for the critical section under different temperature levels. In the same figure, the model results for the evolution of bending moment as a function of normal force exerted by the displacement imposed at the slab support (convergence load) are also presented. These results highlight that:

– As the bond and strength degrade under heat impact, the ultimate bending moment and normal force of the section decrease as a function of temperature.
– The degradation of concrete elastic modulus due to fire has made the slab less stiff at its post-fire state. Consequently, a slab fragilized by fire responds less firmly to convergence-imposed displacements than an intact slab.
– This mechanism by compensating section strength reduction increases the slab's ability to attenuate the imposed deformations and enables it to withstand higher levels of section convergence in post-pic state compared to its pre-fire state. For example, when an intact slab withstands up to 0.6 cm of axial compression, a slab that has been subjected to a temperature of 400°C can withstand displacements as high as 0.9 cm.

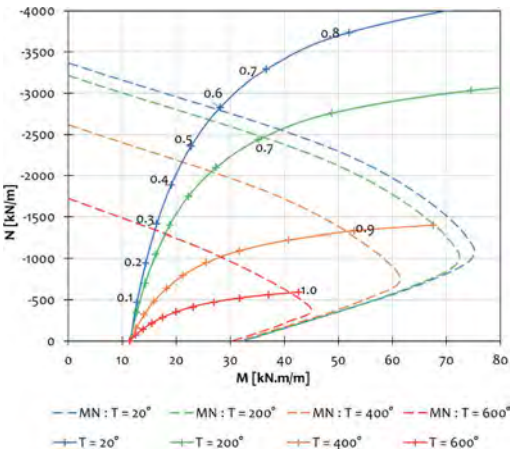

Figure 12. Bending moment - normal force interaction diagram of the slab including buckling (dashed lines) and the curves showing bending evolution as a function of normal force under application of convergence load (solid lines).

ACKNOWLEDGMENTS

The authors would like to thank the Fréjus tunnel French motorway company (Société Française du Tunnel Routier du Fréjus, SFTRF) for its permission to publish the study outcomes. The authors are especially grateful to Monsieur Nicolas Miché of the SFTRF for his kind support during the preparation of the paper.

REFERENCES

A. Ergün, G. Kürklü, M.S. Başpınar. The effects of material properties on bond strength between reinforcing bar and concrete exposed to high temperature. Constr. Build. Mater., 112 (2016), pp. 691–698.

A.F. Bingöl, R. Gül. Residual bond strength between steel bars and concrete after elevated temperatures. Fire Saf. J., 44 (6) (2009), pp. 854–859

fib. Model Code, fib Bulletin 55. The Fédération internationale du béton, Lausanne, Switzerland (2010), p. 2013

R. Eligehausen, E.P. Popov, V.V. Bertero, Local bond stress-slip relationships of deformed bars under generalized excitations, Report No. 83-23, Earthquake Engineering Research Center (EERC), University of California, Berkeley,1983.

É.-L.-V. Hlavička. Bond after fire. Constr. Build. Mater., 132 (2017), pp. 210–218

J. Khalaf, Z.H. Huang. The bond behaviour of reinforced concrete members at elevated temperatures. Fire Saf J., 103 (2019), pp. 19–33

X.L. Gao, N.K. Li, X.D. Ren. Analytic solution for the bond stress-slip relationship between rebar and concrete. Constr. Build. Mater., 197 (2019), pp. 385–397

Y.H. Liang. Statistical analysis and application of high-temperature mechanical properties of the steel bar and concrete, Master Thesis. South China University Of Technology (2008) in Chinese

F. Aslani, M. Bastami. Constitutive relationships for normal-and high-strength concrete at elevated temperatures. ACI Mater. J., 108 (4) (2011), pp. 355–364.

L.K. Qin, Y.P. Song, Y.J. Wang, Z. Zhang, C.J. Yu. Testing research of mechanics characteristics of concrete affected by high temperature. Concr., 5 (2004), pp. 9–11. in Chinese

A.A. Deshpande, D. Kumar, R. Ranade. Temperature effects on the bond behavior between deformed steel reinforcing bars and hybrid fiber-reinforced strain-hardening cementitious composite. Constr. Build. Mater., 233 (2020), 117337

O. Yang, B. Zhang, G.R. Yan, J. Chen. Bond performance between slightly corroded steel bar and concrete after exposure to high temperature. J. Struct. Eng., 144 (11) (2018), p. 04018209

K.F. Yin, Y. Han, Y. Liu. Experimental research on bond strength between rebar and concrete after high temperature. Trans Tech Publ, Appl. Mech. Mater. (2011), pp. 1057–1061

Y. Ma, Experimental study on mechanics properties of concrete structure corroded by chlorine salt afet high temperature, Master Thesis, Guangzhou University, 2017. (in Chinese)

F. Tariq, P. Bhargava. Bond characteristics of corroded pullout specimens exposed to elevated temperatures. Struct., 25 (2020), pp. 311–322

B. Zhang, H. Zhu, J. Chen, O. Yang. Evaluation of bond performance of corroded steel bars in concrete after high temperature exposure. Eng. Struct., 198 (2019), 109479

M.H. Rashid, M. Molla, I.M. Taki. Effect of elevated temperature on bond strength of concrete. Materials Science Forum, Trans Tech Publ., 972 (2019), pp. 26–33

T.C. Wang, W.Y. Gao, L.L. Hu, E. Hamed, Y.L. Bai, J. J. Zeng, J. Yang. Analytical model for predicting the post-fire bond behavior between steel bars and concrete. Construction and Building Materials, 343 (2022), 128129

Fédération Internationale du Béton, 2008, "Fire Design of Concrete Structures—Structural Behaviour and Assessment," Chapter 6: Expertise and Assessment of Materials and Structures after Fire, fib Bulletin 46, State-of-Art Report, pp. 64–95.

EN1992-1-1 (2004) Eurocode 2: Design of concrete structures. Part 1

Omidi, O, and Lotfi, V. (2012) "Continuum large cracking in a rate-dependent plastic-damage model for cyclic-loaded concrete structures". IJNMG, 37:1363-1390, 2012.

SFTRF website, retrieved at https://www.sftrf.fr/uk/index.aspx (2023)

ZSoil (2020). "User manual". ZACE Ltd. Lausanne. Switzerland, retrieved at https://www.zsoil.com/zsoil/ (2020)

Tunnelling for a Better Life – Yan, Celestino, Thewes & Eberhardt (Eds)
© 2024 The Author(s), ISBN 978-1-032-80042-4
Open Access: www.taylorfrancis.com, CC BY-NC-ND 4.0 license

Field measurement of pile transient lateral response to advancing tunnel

C.M. Khoo*
Mass Rapid Transit Corporation, Kuala Lumpur, Malaysia
Universiti Teknologi PETRONAS, Seri Iskandar, Malaysia

H. Mohamad
Universiti Teknologi PETRONAS, Seri Iskandar, Malaysia

B.P. Tee
Smart Sensing Technology Sdn Bhd, Selangor, Malaysia

M.F. Ghazali
Universiti Teknologi PETRONAS, Seri Iskandar, Malaysia

ABSTRACT: A full-scale research study was conducted for the bored tunnelling undercrossed an existing building structure in the Klang Valley Mass Rapid Transit - Putrajaya Line in Kuala Lumpur, Malaysia. The research study, which aims to investigate tunnel-soil-pile interaction and pile responses at various stages of the tunnel excavation by means of full-scale field measurements and numerical analysis, contributed to a more in-depth understanding of the transient effects of shield tunnelling on existing loaded pile. A fully instrumented experimental pile was installed, pre-loaded and monitored in real-time condition throughout the tunnel construction. The in-pile instrumentation comprised of vibrating wire strain gauges, inclinometer and distributed fibre optic sensing using Brillouin Optical Time Domain Analysis (BOTDA). BOTDA is a novel technique of measuring strains in a continuous manner which has inherent advantages over the conventional point-based sensors when evaluating three-dimensional pile deformation such as bending and lateral displacement. This paper presents the setup of the experimental pile, instrumentation regime, field monitoring, interpretation of measurement results and discussion. Tunnelling-induced pile transient lateral responses are examined in detail. It allows engineers to understand the transient behaviour of a loaded pile during tunnel advance.

Keywords: Bored tunnelling, Field measurement, Lateral pile movement, Distributed fibre optic sensor, Tunnel-soil-pile interaction

1 INTRODUCTION

The Putrajaya Line, previously known as Sungai Buloh-Serdang-Putrajaya Line, is the second of three planed mass rapid transit rail lines under the Klang Valley Mass Rapid Transit (KVMRT) Project. The 57.7 km-long alignment covers a span of 13.5 km underground tunnels running through the Kuala Lumpur city centre. Given the dense urban setting, bored tunnelling was adopted for the metro tunnels. The twin 5.8 m I.D. bored tunnels were constructed using closed face tunnel boring machine (TBM) and pre-cast steel fibre reinforced concrete segments. The tunnel route passed underneath, inter alia, about 200 buildings and 30 infrastructures, and divided into 8 tunnelling sections.

A full-scale research site was identified at the Education Quarters located within the central business district of Kuala Lumpur. The tunnels traversing through the Quarters from north-west Hospital KL Cross-over towards south-east direction before arriving at Raja Uda Station (formerly known as Kampung Bharu North Station) as shown in Figure 1.

The southbound tunnel crossed underneath a 5-storey building and faced obstruction from the existing building foundations. The affected piles had to be removed and the underpinning work was carried out in advance of the passage of TBM. The underpinning work comprised of the installation of micropiles capped under a reinforced concrete transfer structure to straddle across the tunnel. Prior arrangement had been made to install an additional 'experiment' micropile to allow for comprehensive in-pile instrumentation and real-time monitoring during tunnel construction.

The research study, which aims to investigate tunnel-soil-pile interaction and pile responses at various stages of the tunnel excavation by means of full-scale field measurements and numerical analysis contributed to a more in-depth understanding of the transient effects of shield tunnelling on existing

*Corresponding author: khoo.cheemin@mymrt.com.my

DOI: 10.1201/9781003495505-355

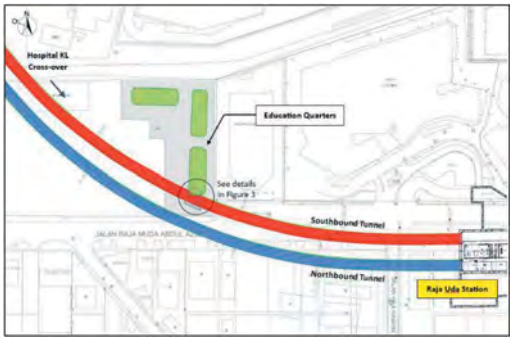

Figure 1. Location plan of the research site.

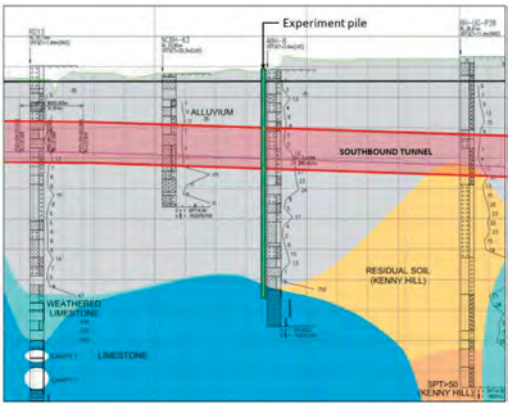

Figure 2. Interpreted geological profile along southbound tunnel.

loaded pile. This paper presents the setup of the experimental pile, instrumentation regime, field monitoring during tunnel advance, interpretation of measurement results and discussion. Transient lateral responses of a loaded pile to advancing tunnel are examined in detail in this paper.

2 SITE CONDITIONS AND SET-UP

2.1 *Ground and hydrogeological conditions*

The site is located within Kuala Lumpur Limestone according to the geological map of Kuala Lumpur (1993 version). Generally, the terrain of the site can be described as flat ground with average level of RL34 m. The site investigation boreholes confirmed the expected regional geological setting, i.e. alluvium overlying limestone bedrock. However, the bedrock levels at the site location were predicted to be erratic and possible cavities due to the inherent karstic features of limestone formation. The alluvium typically comprises interbedded layers of loose sand and soft clay/silt with SPT (standard penetration test) value below 10. Figure 2 shows the interpreted geological profile along the southbound tunnel alignment.

Based on the groundwater monitoring records, the water tables were between 1.3 m and 5.2 m below existing ground level. The general trend observed indicates groundwater drops gradually from RL33.5 m at HKL Cross-over to RL30.5 m at Raja Uda Station. At the research site location, groundwater was found at a depth of 4 m, with typical seasonal fluctuation of ± 0.5 m.

2.2 *Underpinning scheme and pile removal*

The underpinning work consisted of seven 330 mm diameter micropiles capped under a 1 m thick reinforced concrete (RC) transfer structure that straddles across the tunnel. This structure was used to safely support the column loads before the removal of the affected piles. Figure 3 illustrates the plan view and cross-section of the tunnel in relation to the existing building foundation, newly installed underpinning piles and the experimental pile.

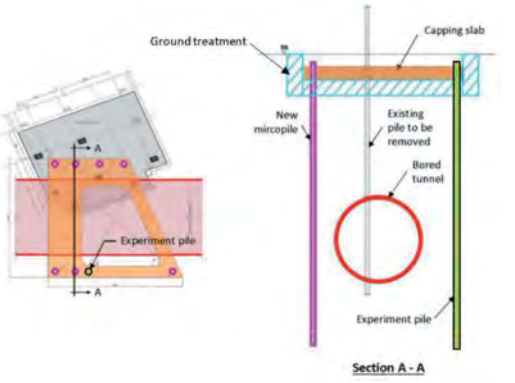

Figure 3. Plan view and cross-section of the underpinning works.

To facilitate the excavation for construction of the transfer structure, ground treatment in the form of jet grout columns (q_u = 600 kPa) was deployed to act as temporary retaining structure together with 1 m thick base grout forming the soffit. Tan et al. (2019) presented the methodology to remove the existing 300 mm RC square piles identified to be clashed with the tunnel.

3 THE EXPERIMENTAL PILE AND INSTRUMENTATION

The experimental pile, having a diameter of 300 mm and located at 1.5 m away from the extrados of the southbound tunnel, is reinforced with API (American Petroleum Institute) pipe of 177.8 mm outer diameter with 10.36 mm wall thickness. The experimental pile was installed to socket 1.5 m into the limestone bedrock at 32.3m below ground level. The micropile (grade G30) design capacity is 600kN.

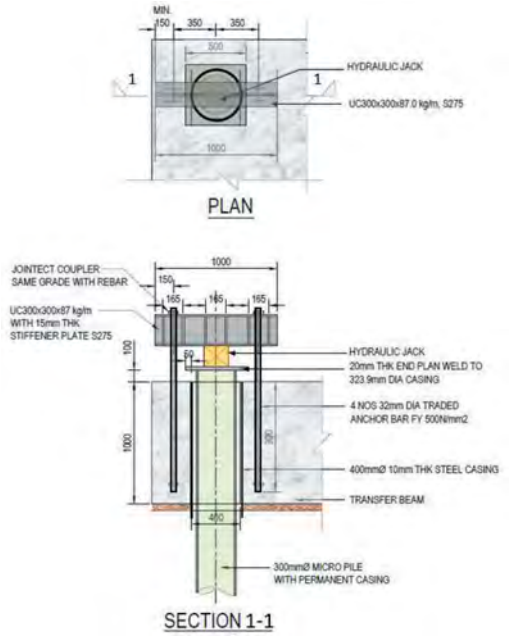

Figure 4. Pre-loading jack configuration.

As shown in Figure 4, a temporary steel casing was left-in until the soffit of ground treatment layer (i.e. 3 m below ground level) to protect the pile head section and to ensure that the cabling survived the construction process. It should be highlighted that the pile head was protruded above the transfer structure within a pre-installed 400 mm dia. 6 mm thick steel sleeve. The pile was preloaded to its working load and maintained throughout the tunnel advance monitoring period. Reaction anchorage method was used to apply the load to the experimental pile. The reaction frame consisted of two UC300x300x87 kg I-beam with 4 nos. of 32 mm dia. SAS (Stahlwerk Annahutte Steel) traded bars anchored into the transfer structure. The hydraulic jack which was used to load the pile to the designated working load was rested between I-beam and the top of a hollow circular end plate welded to the pile head. Load cell was used to measure the amount of load transferred to pile and Linear Voltage Displacement Transducers (LVDTs) installed on an independent reference frame were used to measure pile top settlement in addition to precise optical leveling. During the preloading stage, the jack loads were stepwise increased up to 600 kN, at 10 steps of load increment with 10 minutes withholding time each step, and the strain distribution along the pile was measured. Upon reaching the working load, the applied load was kept constant (i.e. re-jacked if necessary) throughout the monitoring period. In this study, it is assumed that the working load applied to the pile remains constant and does not change because of the tunnel excavation. This assumption may be considered acceptable if the superstructure is flexible and statically determined.

The in-pile instrumentation was essentially designed and arranged in such a manner to provide real-time data on the tunnelling-induced transient pile responses with respect to the pile head vertical displacement, pile shaft horizontal deformation and pile axial load distribution as well as pile internal forces. The instruments installed on experimental pile consisted of both the conventional vibrating wire strain gauges and inclinometer as well as the novel fibre optic distributed sensors. Figure 5 depicts the details of in-pile instrumentation and arrangement.

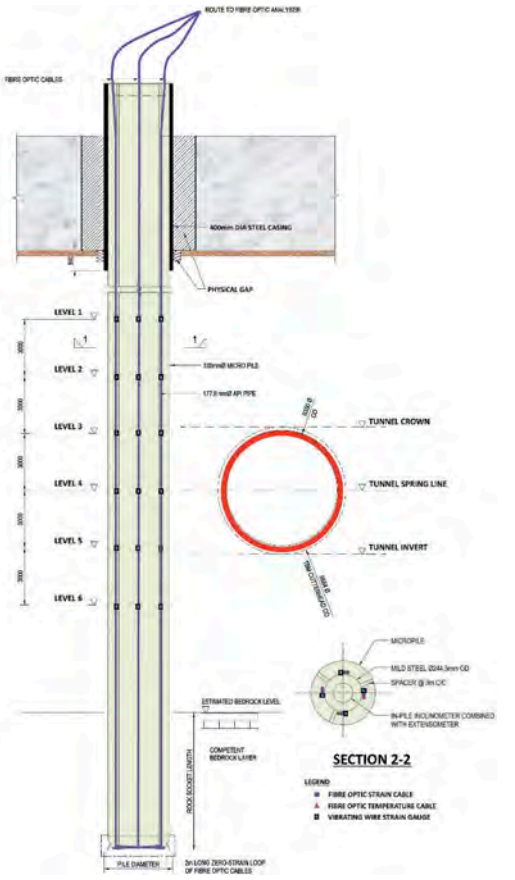

Figure 5. Arrangement of in-pile instrumentation.

Six levels of vibrating wire strain gauges (VWSG) were attached to the pile reinforcement (API pipe). VWSG were placed at every 3 m intervals starting at a depth of 4 m below ground surface in corresponding to each of the important measuring levels, i.e. Level 1 – 6 m above tunnel crown, Level 2 – 3m above tunnel crown, Level 3 – tunnel crown, Level 4 – tunnel spring line, Level 5 – tunnel invert, and Level 6 – 3 m below tunnel invert. Strain gauges were installed at 4 sides (i.e. 2 pairs per level) with each pair positioned to be parallel and perpendicular to the tunnel alignment. The strain gauges were spot

welded on 10 mm steel band before being tied up to the designated levels on API pipe. Unfortunately, not all sensors survived the installation process. Inside the API pile is an inclinometer casing that was pre-installed during the grouting process and provide redundancy for pile deflection measurements.

As one of the key instrumentations, the distributed fibre optic sensing based on stimulated Brillouin scattering (SBS), thorough the so-called Brillouin Optical Time Domain Analysis (BOTDA), is a novel technique of measuring strains in a continuous manner which has inherent advantages over the conventional point-based sensors when evaluating the interaction of the forces between the pile-tunnel structures and the soil (Soga et al., 2008). The sensors can be configured and integrated into the pile to measure three-dimensional deformation such as bending and lateral displacement. It provides more precise information about the pile response over the whole pile length. This method has been successfully employed in monitoring the performance of large civil and geotechnical structures such as piles (Ohno et al., 2002, Klar et al, 2006), test piles (Mohamad et al., 2009, Tee et al., 2016; Tee et al., 2017), retaining walls (Mohamad et al., 2011), bridges and tunnels (Mohamad et al., 2010; Mohamad et al., 2012). The measurement principle and details are described in Mohamad et al. (2009).

The fibre optic sensing cable, consists of a single core single mode optical fibre reinforced with six strands of steel wires and polyethylene cable jacket, was fixed along the two opposite sides of the API pipe with a loose or coiled section at the pile tip before it was extended along each side of the pipe as it was lowered into the borehole. In essence, there are two loops (i.e. A1-A2, B1-B2), four equally spaced at a direction perpendicularly (axis *x*-*x*) and parallel (axis *y*-*y*) with the tunnel alignment. Another pair of temperature sensing cable (T1-T2) was also installed side by side with A1-A2 cable to measure the temperature changes in order to compensate the differential temperature effect to strain reading if any.

In this field measurement, the variations and fluctuations of temperature in the pile were found to be insignificant throughout the monitoring period. Each optical sensing cable used in the field measurement have been calibrated in laboratory with the strain coefficient obtained to be 20 με/MHz. All fibre optic cables were pretensioned aiming to keep it in a straight line along the main axis *x*-*x* and *y*-*y* and hence the positions of sensing sections can be identified when reading from the data trace. The baseline measurement used for the interpretation was performed one month (i.e. 9 April 2019) before the TBM reached the target in order to eliminate all the strain induced by the installation process.

On top of the in-pile instrumentation, settlement markers, inclinometers and piezometers were also installed in the ground adjacent to the experimental pile. The building that the tunnel undercrossed was also closely monitored. Hence, the tunnelling-induced effects and pile-soil-structure responses can be investigated comprehensively. Figure 6 shows the ground and structure instrumentation surrounding the experimental pile. In this paper, only relevant instrumentation data will be presented.

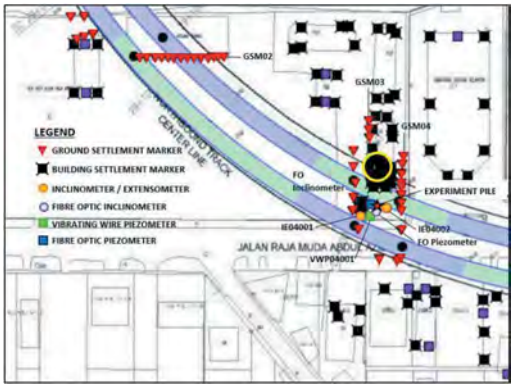

Figure 6. Ground and structure instrumentation.

4 TBM ADVANCE AND ITS DRIVING RECORDS

The installation of the instrumented experimental pile was completed in March 2018 and followed by pile removal work in advance of the passage of the TBMs. Construction activities have been coordinated such that the enabling work does not interfere with the tunnelling activities or in another word, affect the permanent tunnel lining. Consolidation due to piling and ground treatment works was presumed to have completed prior to TBM advance owing to the high permeability of the alluvium sandy soil.

Variable Density (VD) slurry shield machine was selected for excavating the tunnels from HKL Crossover to Raja Uda Station. The VD tunnel boring machine can be operated in four different tunnelling modes and thus perfectly adapted to different geological conditions. It is a further development of the multi-mode TBM, which combines the advantages of the earth pressure balance (EPB) and slurry supported mix-shield modes. Further details can be referred to Schaub & Duhme (2014). In particular, the TBMs were driven in EPB mode at this tunnelling section.

This study focused on the TBM advance for a distance between approximately y = -10D to 10D from the target (i.e. experimental pile) of the southbound tunnel, where y is the distance between the tunnel face to the experimental pile and normalized by the tunnel diameter (D). Distance where the TBM passed beyond the pile is taken as positive. Figure 6 shows the time-location relation of the TBM while Table 1 listed the recorded tunnel mining and ring build dates for the respective locations. In short, this stretch of tunnel was completed from 3 May 2019 to 16 May 2019. It should be taken note that the TBM stopped for planned cutterhead intervention on

6 May 2019 and 7 May 2019, which was carried out in a grout block as indicated in Figure 7. For the purpose of this paper, the solid lines marked on the subsequent charts indicate the time when the face of the tunnel boring machine first arrived at the particular distance, e.g. solid bold line indicates the tunnel face arrived at the experimental pile location. The excavation at the cutting face, the tail void grouting, and the erection of a new lining ring during standstill are taken into account simultaneously.

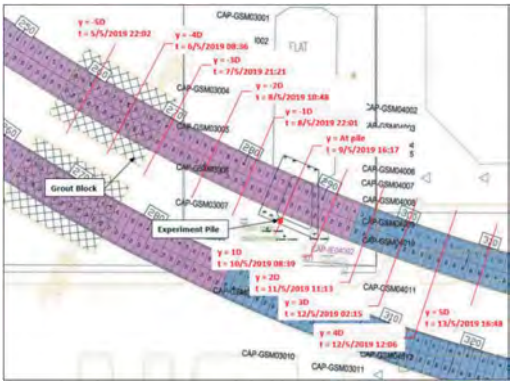

Figure 7. Time-location of the southbound TBM in relation to the experimental pile.

Table 1. Record of tunnel mining and ring build dates.

TBM Location, y	Ring No.	Mining Date	Ring Build Date
-10D	238	3 May 2019	4 May 2019
-5D	260	5 May 2019	6 May 2019
-4D	265	6 May 2019	8 May 2019
-3D	270	7 May 2019	8 May 2019
-2D	276	8 May 2019	9 May 2019
-1D	281	8 May 2019	9 May 2019
At pile	286	9 May 2019	10 May 2019
1D	291	10 May 2019	11 May 2019
2D	296	11 May 2019	12 May 2019
3D	300	12 May 2019	12 May 2019
4D	305	12 May 2019	13 May 2019
5D	310	13 May 2019	14 May 2019
9D	329	15 May 2019	16 May 2019

Generally, a range of face support pressure was provided continuously as the TBM progresses. Figure 8 shows the allocation of the six earth pressure sensors over the cutter head in excavation chamber. Whilst Figures 9(a) and 9(b) shows the recorded individual point pressures and averaged pressure respectively. It is observed that a higher face pressure was applied ahead of the experimental pile. The face pressure was gradually increased from 2 bar (at -3D distance away) to maximum 2.6 bar as the TBM cutterhead reached the experimental pile location and eventually decreased to the normal face pressure at 1D distance away.

Figure 8. Allocation of TBM face support pressure sensors.

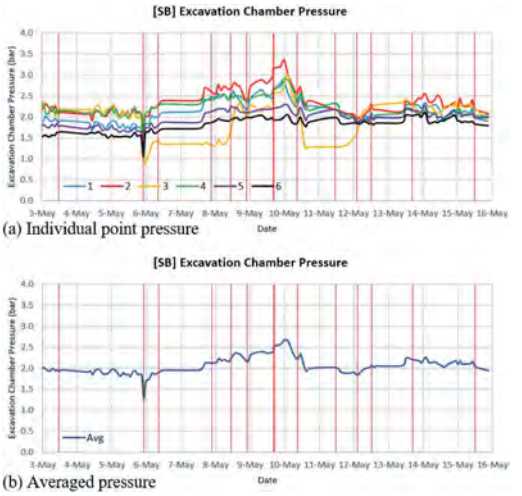

Figure 9. Recorded excavation chamber pressures (a) individual point pressure (b) averaged pressure.

From the Instrumentation Data Management System, the normal range of advance speed was 20 – 50 mm/min with an average of 34.5 mm/min for this length of bored section. Advance thrust forces and advance group pressures were fluctuated between approximate 10 – 17 MN and 50 – 150 bar respectively. The grouting pressure at the grout ports remains relatively constant throughout the tunnel drive with averaged pressures around 30.5 bar. In this paper, the pile lateral response is evaluated with respect to the TBM face pressures only.

5 MEASUREMENT RESULTS AND DISCUSSION

5.1 *Pile axial strains*

All signal responses from the fibre optic sensors were analysed and compared with the readings obtained

from the common method of instrumentation such as VWSG and inclinometer. An overview of the measured axial strain profiles is presented in Figure 10 with reference to the nearest borehole ABH-08 which was sunk at experimental pile location. The strain profiles were processed by averaging the data from four sets of optical cables (see Figure 5) and presented in terms of the date of measurement (daily average) during the TBM advance.

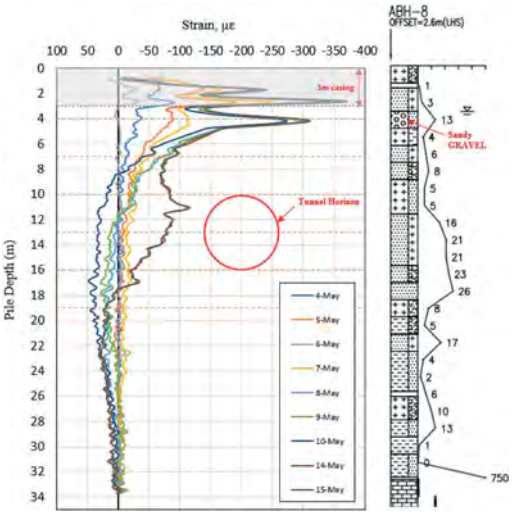

Figure 10. Axial strain profiles measured by fibre optic sensing.

As mentioned earlier, a temporary steel casing was left-in until 3 m below ground level. The cross-sectional area of the pile should be consistent within this area. However, localized strains spike can be observed, and the causes cannot be determined with certainty. It could be possibly due to the laitance that was not being able to be flushed out before the standard length of casing was cut down to 3 m. Localized higher strains have also been observed at approximately 3 m to 5 m deep from the pile top level. This is the depth just below the temporary casing where sandy gravel materials were detected in borehole ABH-08 sunk at the experimental pile location, see Figure 10. Highly possible that some of the soil from this granular layer may had collapsed into the bored hole and contaminated the grout during withdrawal process of the temporary casing. Consequently, integrity of the grout was compromised which directly lower its Young's modulus and contributed to relatively higher strain. Mohamad et al. (2016) demonstrated that typical defects of bored cast-in-situ piles can be identified from distributed strain measurement.

Figure 11 exhibits the transient behaviour of strain profiles in comparison with the VWSG data for four measurement dates which are corresponding to the critical period of TBM advance; (i) Pre-loading stage (-3D/7 May 2019), (ii) Arrival of TBM face (At pile/9 May 2019), (iii) Passing of TBM shield (1D/10 May 2019), and (iv) TBM passed beyond the experimental pile (>5D/14 May 2019). Compressive strain is taken as negative while tensile stress as positive. Excellent agreement between the fibre optic sensors and VWSG measurements on all measurement dates.

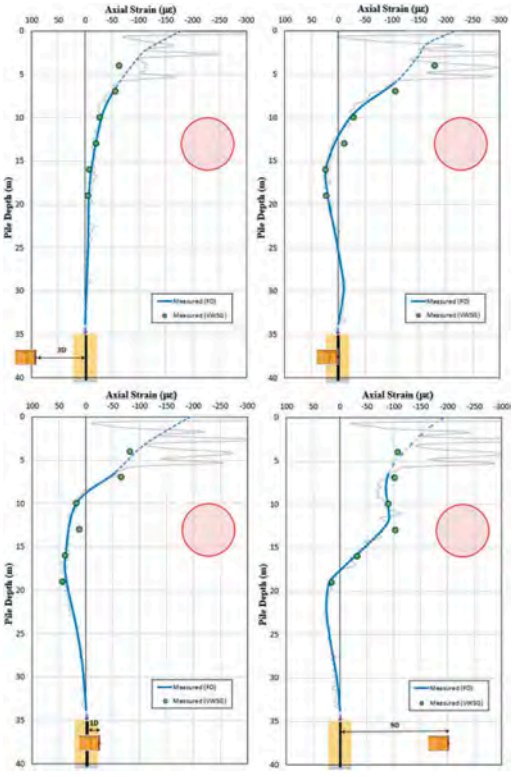

Figure 11. Transient axial strain responses of the experimental pile at different stages of tunnel advance (a) pre-loading stage, y=-3D;(b) arrival of TBM face, y=at pile; (c) passing of TBM shield, y=1D; (d) TBM passed beyond the experimental pile, y=>5D.

It can be seen that axial strains in the experimental pile have responded as the TBM approaching. When the TBM arrived at the pile location on 9 May 2019, tensile strains were started to be detected at pile depth between 12 m and 25 m whereas the upper part of pile was in higher compressive strain. The tensile strain became more apparent and continued to rise above the tunnel axis level as TBM was passing the pile. The tensile strain profile was observed extending upward above the tunnel spring line and reached a maximum value of about 50 microstrains once the TBM (excavation face) had passed beyond the experiment pile. When the TBM shield has been driven completely passed the pile (y > 2D) and the tunnel linings have been erected, the tensile strains within the tunnel horizon

were reverted to compressive strains. The compressive strains increase to a maximum just above the tunnel axis level and stabilised on 14 May 2029 (TBM at y > 5D). The redeveloped compressive strains were higher than the values registered during the pre-loading stage is a clear evident of downdrag (negative skin friction) occurred due to tunnelling-induced ground settlement. The measured strain reached a residual value with the lower portion of the pile, i.e. from 2 m below tunnel invert level remain in tensile state.

All in all, the distributed fibre optic data are better in describing the complete behaviour of the pile as compared to the discrete data of VWSG (Hisham et al., 2023). In this case, the experimental pile had undergone various tension and compressive loadings due to the interacting tunnelling effects.

5.2 *Pile lateral deflection*

The optical fibre strain data can be converted to relative displacement by looking at the curvature changes between two opposite fibres placed symmetrically with respect to the referenced axis. By integrating the curvature once, the inclination/gradient, j of the pile can be calculated; and by integrating it twice, the lateral displacement, u of the pile is obtained as per equations below.

$$j(z) = \int \kappa \, dz + A \quad (1)$$

$$u(z) = \int j \, dz + B \quad (2)$$

In specific, the lateral displacement of the pile is subjected to prescribed displacement at one end and fixed on the other end. For this rock-socketed pile, the tip is taken as reference datum with the zero horizontal and rotational movements and hence the constants A and B were set as zero. Similarly, the computation of pile displacement at any section is not affected by the uncompensated temperature.

Figure 12 shows the interpreted lateral displacement of the pile in two directions. Axis A +ve denotes away from tunnel in transverse direction while Axis B +ve denotes from tunnel face in longitudinal direction. It can be seen that the pile was generally being pushed outward both in transverse and longitudinal directions when the TBM approaching the experimental pile. Once the TBM face had passed the pile, the lateral deflection at tunnel level immediately moved back toward the tunnel as the distance increases before it was released again as shown by the measurements dated 14 May 2019 where TBM at y > 5D. Figure 13 provides a closer view of time-based pile movement path at the six measurement depths.

Further study was also carried out to appraise the ground lateral movements measured from inclinometer IE04002 positioned 1.5 m away from the tunnel extrados. Figure 14 illustrates the measurements

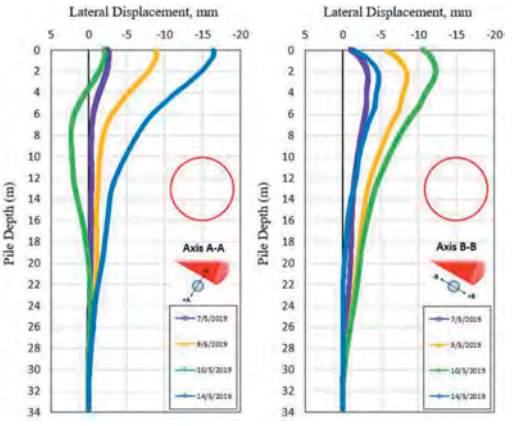

Figure 12. Interpreted pile lateral displacements at different stages of tunnel advance.

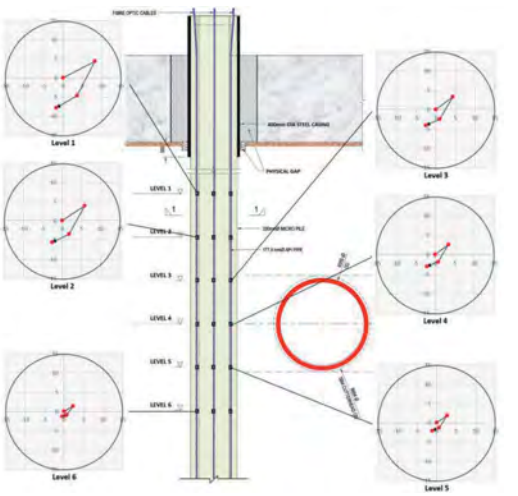

Figure 13. Time-based pile lateral displacements at different depths.

taken between 5 May 2019 and 15 May 2019 with its Axis A-A in transverse direction and Axis B-B in longitudinal direction of the tunnel alignment. Noticeably, the ground has generally moved inward both in transverse and longitudinal directions when TBM approaching the inclinometer location. In contrast, the ground movements reversed outward and being pushed away when TBM arrived at the inclinometer on 9 May 2019. Upon passing of the TBM face, the lateral deflections rebound back with a concave profile observed at the tunnel horizon. This was suspected because of the gaps between the shield and the surrounding ground, including cutter head overcut, conical or telescopic-shaped shield and the tail void. The deflection remained constant for the most part of the monitored period after TBM passed the inclinometer. The data, coupled with the in-pile instrumentation monitoring results, has demonstrated the time-dependent transient behaviour of

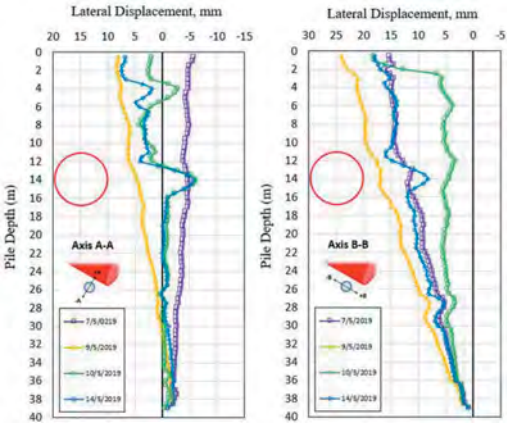

Figure 14. IE4002 inclinometer readings.

pile-soil lateral movements induced by the tunnelling operation.

5.3 *Main findings and discussion*

These emerged observations are in line with the hypothesis of pile movement paths made by Loganathan (2016) for negative face loss case. According to him, when a TBM face pressure is greater than the mobilised earth pressure at the face, the ground, and hence the pile, is pushed away from the TBM face, thereby inducing heave at the surface and subsurface ground movement away from the TBM face. This was evidenced from the measured ground surface heaving as depicted in Figure 15. On the other hand, the measurement of building settlement, as shown in Figure 16, further verified the observations. See Figure 6 for the locations of the instrumentation.

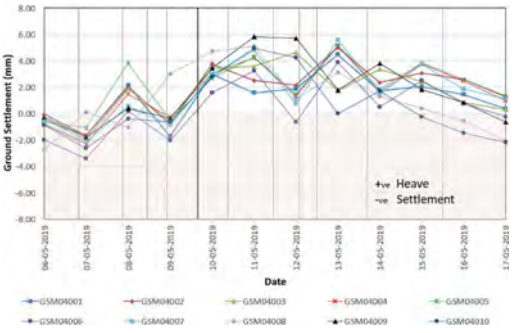

Figure 15. Ground settlements.

When the TBM has passed, a positive shield and tail loss occurs (closing of the physical gap), meaning the ground will move toward the tunnel and followed by dissipation of pore pressure generated due to tunneling, resulting in subsequent ground settlement. It should also be noted that, in some cases, shield pressure and back grouting pressure can be as high as face pressure and piles may not move towards the tunnel.

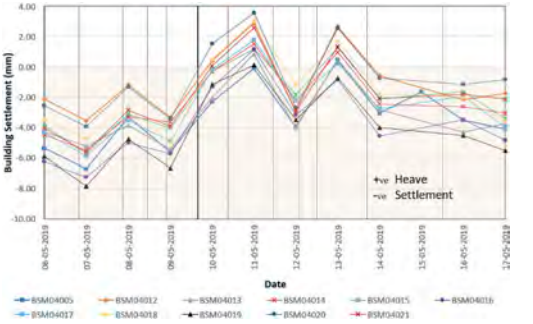

Figure 16. Building settlements.

6 CONCLUSIONS

This paper focuses on the transient effect of pile lateral movements due to TBM advance in a research study. It presented the setup of the experiment pile, instrumentation regime, field monitoring during tunnel advance, interpretation of measurement results and discussion.

Measurement of tunnelling-induced pile lateral movements was successfully demonstrated by using distributed fibre optic sensors via BOTDA and cross-validated with vibrating wire strain gauges and inclinometer. The strain measurements obtained from the fibre optic showed excellent agreement with that derived from VWSG. The in-pile instrumentation data, coupled with inclinometer IE04002 positioned at 1.5m away from tunnel extrados, has revealed the time-dependent transient behaviour of pile lateral movements induced by tunnelling operation.

Based on the tunnel drive and TBM operating parameters described above, the findings supported the hypothesis of pile movement path for negative face loss case as made by Loganathan (2016). It is of great interest for this research study to investigate the transient pile responses to advancing tunnel. It is believed that, if this approach of negative face loss can be adopted at the site coupled with appropriate face pressure control for a safe tunnelling operation, it will bring significance benefits to the tunnelling project by the way of realistic engineering and risk assessment.

ACKNOWLEDGMENTS

The authors are grateful to the management of Mass Rapid Transit Corporation Sdn. Bhd. for their permission to publish this paper and their positive support in the success of this research study. Special thanks to Ir. Dr Ooi Lean Hock of MMC-Gamuda KVMRT (T) Sdn. Bhd. for his insightful suggestions and guidance, without which the large-scale field measurement would not have been possible.

REFERENCES

Klar A., Bennett P.J. and Soga, K., 2006. Distributed strain measurement for pile foundations. Proc. ICE, Geotech. Engineering, 159, No. 3, pp. 135–144.

Loganathan, N., 2016. Design charts: tunnelling-induced effects on adjacent pile foundation. Proceedings of 19th Southeast Asian Geotechnical Conference & 2nd AGSSEA Conference, Kuala Lumpur, Malaysia, pp. 1125–1130.

Mohamad, H., Soga, K. and Bennett P.J., 2009. Fibre optic installation techniques for pile instrumentation. Proceedings of the 17th International Conference on Soil Mechanics and Geotechnical Engineering: The Academia and Practice of Geotechnical Engineering, IOS Press, Vol. 3, pp. 1873–1876.

Mohamad, H., Bennett, P.J., Soga, K., Mair, R.J. and Bowers, K., 2010. Behaviour of an old masonry tunnel due to tunnelling-induced ground settlement. Géotechnique 60, No. 12, pp. 927–938.

Mohamad, H., Soga, K., Pellew, A. and Bennett, P.J., 2011. Performance monitoring of a secant piled wall using distributed fibre optic strain sensing. Journal of Geotechnical and Geoenvironmental Engineering, Vol. 137, No. 12, pp. 1236–1243.

Mohamad, H., Tee, B.P., Ang, K.A. and Chong, M.F., 2016. Characterizing anomalies in distributed strain measurements of cast-in-situ bored piles. Jurnal Teknologi, 78 (8-5), pp. 75–82.

Mohamad, H., Tee, B.P., Beddelee, A.A.A.M., Khoo, C.M., Ghazali, M.F. and Mohd Nasir, M.Y., 2023. Innovations in micropile testing using distributed optical fibre sensors. International Conference on "Case Histories in Geotechnical Engineering; & 4th AsRTC6 Urban Geoengineering Symposium, Bandung, Indonesia.

Ohno, H., Naruse, H., Kurashima, T. and Nobiki, A., 2002. Application of Brillouin scattering-based distributed optical fibre strain sensor to actual concrete piles. IEICE Transaction on Electronics E85, pp. 945–951.

Schaub, W. & Duhme, R., 2014. Multi-mode and variable density TBMs latest trends in developments. Underground Singapore 2014

Soga, K., Mohamad, H. and Bennett, P.J., 2008. Distributed fibre optics strain measurements for monitoring geotechnical structures. 6th International Conference on Case Histories in Geotechnical Engineering (Symposium in honour of Professor James K Mitchell), Arlington, USA.

Tan, Y.C., Teh, W.S. and Gue, C.S., 2019. Special design considerations for underpinning system for existing structures due to tunnelling. Proceedings of ITA-AITES World Tunnel Congress (WTC 2019), Naples, Italy.

Tee, B.P., Mohamad, H., Ang, K.A. and Chong, M.F., 2016. Load test performance of bored pile with distributed fibre optic strain sensing. Proceedings of 19th Southeast Asian Geotechnical Conference & 2nd AGSSEA Conference, Subang Jaya, Malaysia, 31 May – 3 June 2016, IEM, pp. 865–870.

Tee, B.P., Rashid, A.S.A., Abdullah, R.A., Kassim, K.A. and Mohamad, H., 2017. Application of distributed fibre optic sensor in instrumented pile load test. Asean Engineering Journal.

Tunnelling for a Better Life – Yan, Celestino, Thewes & Eberhardt (Eds)
© 2024 The Author(s), ISBN 978-1-032-80042-4
Open Access: www.taylorfrancis.com, CC BY-NC-ND 4.0 license

Model experiment on load-bearing performance and failure process of newly proposed invert to reduce volume of excavation

Yu Koizumi* & Atsushi Kusaka
Public Works Research Institute, Tsukuba, Japan

Nobuharu Isago & Kosuke Kawata
Tokyo Metropolitan University, Hachioji, Japan

Toshiro Otsu & Naoto Mikami
East Nippon Expressway, Saitama, Japan

ABSTRACT: It has been recently reported that ground heaves threatened the stability of road tunnels and the safety of road users during the maintenance stage. Constructing additional invert is effective to reinforce the tunnels, however it would require a lot of time and cost to excavate the bottom of the tunnels using a small machinery if a part of the lanes could be open to the traffic. The purpose of this research is to propose new invert structure that enable to reduce the volume of the excavation. Model experiments were conducted to compare the load-bearing performances between the standard and the 3 newly proposed inverts, for example, the shape of which was flat. As a result, the maximum loads of the proposed inverts, which could reduce the volume of the excavation 30-50%, were slightly over 50% of that of the standard one. It was also found that the failure processes of the 4 test cases were different, therefore they were evaluated in terms of not only the maximum loads but also the capabilities to restrain the ground heave and to transfer bending moment and axial force by analysing the measured deformations and strains of the tunnel models.

Keywords: Ground heave, Reinforcement, Shape

1 INTRODUCTION

Invert is considered as an important support structure to ensure the stability of a tunnel by restraining the ground deformation. Therefore, nowadays, it has been advised to construct it in the area with poor geological conditions during the construction stage in Japan. Table 1 shows the standard combination of support members for a tunnel with standard cross-sectional width, approximately 8.5-12.5m, shown in the technical standard of road tunnel and its interpretation -Part of tunnel structure- (2003). Even though rock class is categorized as CI or CII, namely hard rock, it would be advised to construct invert if rock type is mudstone from the Tertiary, tuff, serpentine and so on. Figure 1 shows an example of support pattern DI of a road tunnel chosen in the area with relatively poor geological conditions. The thickness of the invert would be between 40 and 50cm. The ratio of the radius of the invert to that of the lining is between 2 and 3.

Recently, it has been reported that ground heave occurred in road tunnels during the maintenance stage, resulting in cracks of road pavements and so on as shown in Figure 2. It could threaten the stability of road tunnels and the safety of road users. Such ground heave was more likely to occur in the part of tunnels where invert was not constructed during the construction stage. Constructing additional invert is effective to reinforce such tunnels. On the other hand, it requires a lot of time and cost to excavate the bottom of a tunnel using a small machinery while a part of the lanes is open to the traffic. This would cause the long period of traffic control, leading the inconvenience for road users. The purpose of our research is to propose new invert in terms of its shape, used materials and so on which enable us to reduce the volume of excavation. In this paper, we report the results of 4 model experiments, where the load-bearing performances of

*Corresponding author: koizumi-y573ck@pwri.go.jp

DOI: 10.1201/9781003495505-356

Table 1. Standard combination of support members for a tunnel with standard cross-sectional width (approximately 8.5-12.5m) in Japan (JARA, 03).

Rock class	Support pattern	Standard advance	Rock bolt			Steel arch support			Sprayed concrete	Permanent lining	Invert
			Length	Spacing		Upper half	Lower half	Axial spacing	Thickness	Thickness	Thickness
				Circumferential	Axial						
-	-	m	m	m	m	-	-	m	cm	cm	cm
B	B	2.0	3.0	1.5	2.0	-	-	-	5	30	-
CI	CI	1.5	3.0	1.5	1.5	-	-	-	10	30	(40)
CII	CII-b	1.2	3.0	1.5	1.2	H-125	-	1.2	10	30	(40)
DI	DI-b	1.0	4.0	1.2	1.0	H-125	H-125	1.0	15	30	45
DII	DII	≦1.0	4.0	1.2	≦1.0	H-150	H-150	≦1.0	20	30	50

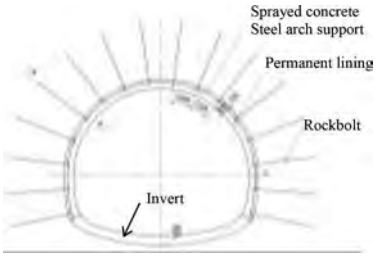

Figure 1. Example of support pattern, DI of road tunnel in japan (JARA, 2003).

Figure 2. Crack of road pavement caused by ground heave.

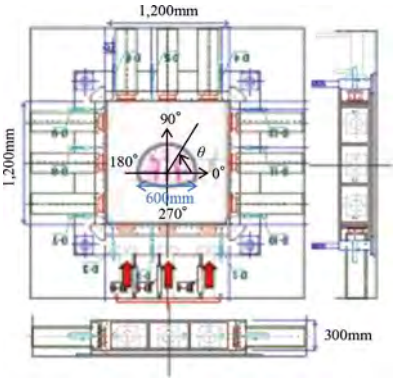

Figure 3. Experimental settings.

3 newly proposed inverts were compared with that of the standard one.

2 MODEL EXPERIMENTS AND TEST CASES

The authors have conducted model experiments where the ground was modelled by steel bars to understand the influence of the shape of invert on its load-bearing performance as reported by Nakazato et al (2022). The widths of the tunnel models in the experiments were approximately 80mm, so we analysed the deformation modes of a series of test cases, but could not analyse them in details. Therefore, in this experiment, we used two-dimensional loading apparatus owned by Public Work Research Institute to load tunnel models, the diameters of which were 600mm as shown in Figure 3. The tunnel models were made of mortar. The thicknesses of their linings were 20mm and the inner diameters R_1 were 280mm. It can be said that the sizes of the models are scale to about 1/20 of an actual road tunnel.

The descriptions of the 4 test cases are shown in Table 2. Case 1 represented the standard invert typically used to reinforce existing tunnels in Japan. Case 2-4 represented newly proposed inverts in this research. We discussed new invert structure which enable to reduce the volume of the excavation in constructing additional invert. Their features were, in short, flat & thick, flat & reinforced and pentagon in the order of Case 2-4. The ratios of excavation volume, R_{ex} were calculated by obtaining the areas below the floor lines of Case 2-4 and comparing them to that of Case 1. As a result, R_{ex} of Case 3 was only 40%. The depth of the pentagonal invert of Case 4 was determined as 48.7mm so that its R_{ex} could be smaller than 70%.

In the experiments, the tunnel model was located in the apparatus as shown in Figure 3, then the outer space of the models was filled with dry sand so that the dry density of the sand was 1.47g/cm^3. The

Table 2. Descriptions of 4 test cases.

Case	Name ・R_{∞}	Descriptions of models and locations of measurements
1	Standard ・ 100%	 The radius of invert is 2.7 times larger than that of arch.
2	Flat & thick ・ 59.5%	 The shape of invert is flat. It is 30mm thick and is 1.5 times thicker than the standard.
3	Flat & reinforced ・ 39.7%	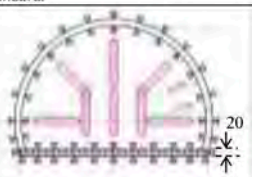 The shape of invert is flat. It is reinforced with copper pipes (φ9.5, t0.8, @50mm)
4	Pentagon ・ 68.1%	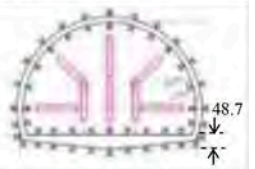 The lower shape is trianglular and the upper shape is flat, considering concrete placement.
		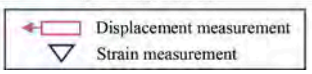

bottom side of the apparatus was loaded by 3 hydraulic jacks. As the displacement increased by 1mm, the loads, displacements and strains were measured. Furthermore, deformations such as cracks on the inner side of the tunnel model were observed through a small window in the cover of the apparatus.

From the uni-axial compression tests using cylindrical specimen of mortar, it was found that the average compressive strength was 22.7N/mm^2, the average Young's modulus was 15.62kN/mm^2 and the average Poisson's ratio was 0.195.

3 LOAD-BEARING PERFORMANCE AND FAILURE PROCESS OF STANDARD AND PROPOSED INVERTS

3.1 *Relationships between load and displacement*

Figure 4 shows the relationships between the sum of loads of the 3 hydraulic jacks and the average displacement of the 3 hydraulic jacks of Case 1-4. It is obvious that Case 1 showed the highest peak load among the 4 cases. In Case 2 and Case 3, the loads decreased once, as for example, the displacement of Case 2 was approximately 24mm, and then they increased again. Figure 5 shows the relationships between the upward displacements of the inner sides of the tunnel models and the average displacement of the 3 hydraulic jacks. It was clear that the trends of Case 2 and 3 were different from those of Case 1 and 4; the displacements of the inner sides of Case 2 and 3 increased rapidly, for example, after the jack displacement of Case 2 was 16mm.

It seemed that Case 1-4 showed the different deformation modes and the failure processes. Thus, the load-bearing performances of Case 1-4 were evaluated in the consideration of the deformation modes and failure processes in the following sections.

3.2 *Failure process of case 1 (standard)*

Based on the analysis of the transition of the displacements and strains of Case 1, its failure process

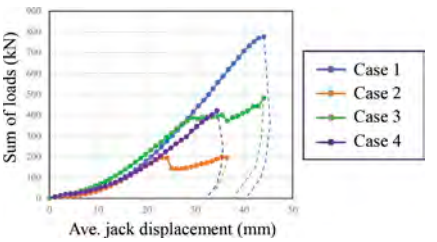

Figure 4. Relationships between load and displacement of case 1-4.

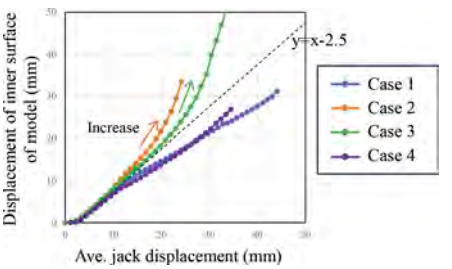

Figure 5. Relationships between displacement of inner surface of model and jack displacement of case 1-4.

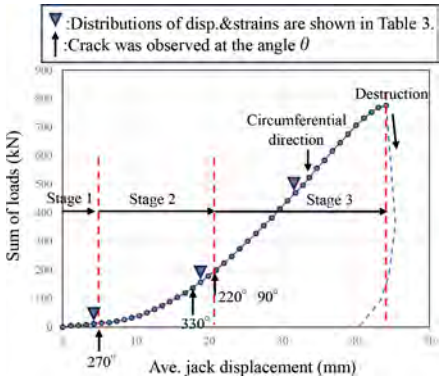

Figure 6. Relationships between load and displacement of case 1.

Figure 7. Deformed tunnel model of case 1.

was divided into 3 stages. Figure 6 shows the relationship between the load and displacement, and the division of the 3 stages. Figure 7 shows the deformed tunnel model at the end of the experiment. Table 3 shows the representative distributions of the displacements and strains of the tunnel model at each stage.

At stage 1, the first crack was observed on the inner side at the centre of the invert (270°). At this stage, the strains of the invert were tensile inside and compressive outside, indicating that the strains of the invert were mainly caused by bending moment.

At stage 2, cracks were also observed on the inner side between the centre and the corner of the invert (330, 220°) as well as of the roof (90°).

At stage 3, as the compressive strains increased on the outer side of the invert and inner side of the arch, the brittle destruction occurred in the end. The compressive strain at the right part of the invert (330°) was approximately 3500 μ just before the destruction occurred. Therefore, it was thought that the shear destruction occurred due to the excessive axial compression.

On another note, the compressive strains at the arch of lining were approximately 2,000 μ just before the destruction occurred. If a piece of lining fell from the arch, it would severely threaten the safety of road users. Thus, it can be said that the results of the measurement here indicate the importance that not only the road pavement but also the arch and the roof have to be inspected carefully in the tunnel where ground heave is observed.

3.3 *Failure process of case 2 (flat and thick)*

Based on the analysis of the transition of the displacements and strains of Case 2, its failure process was divided into 3 stages. Figure 8 shows the relationship between the load and displacement, and the division of the 3 stages. Figure 9 shows the deformed tunnel model at the end of the experiment. Table 4 shows the representative distributions of the displacements and strains of the tunnel model at each stage.

Table 3. Representative distributions of displacements and strains of case 1 at stage 1-3.

Stage	1	2	3
Sum of loads (kN)	11.8	156.9	470.4
Ave. jack displacement (mm)	4.3	18.8	31.8
Displacement of model (mm)	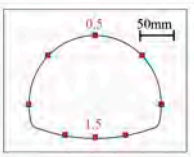	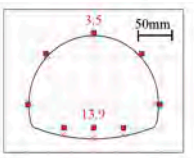	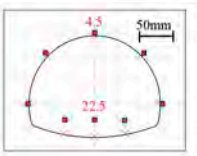
Strain of model (μ)	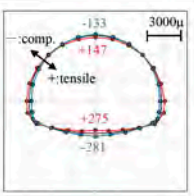	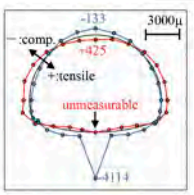	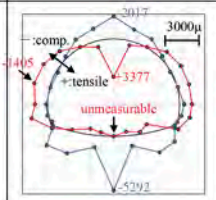

At stage 1, the first crack was observed on the inner surface at the centre of the invert (270°). Hereafter, the strains of both the inner and outer sides of the invert did not increase as shown in Table 4. It was thought that this meaned that the invert of Case 2 became unable to transfer both the axial force and the bending moment after the first crack occurred.

At stage 2, the width of the first crack mentioned above continued to increase, and another crack was also observed on the inner side of the roof as the ground heave increased. From Figure 5 shown in 3.1, the ground heave increased rapidly after the jack displacement was 16mm. This indicated the change of the deformation mode of Case 2, thus it was defined as stage 3 hereafter.

At stage 3, the invert bended notably at its centre. The load decreased once when the jack displacement

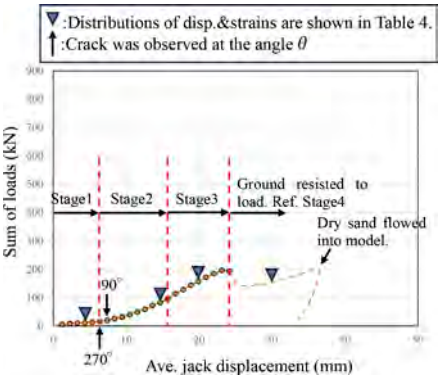

Figure 8. Relationships between load and displacement of case 2.

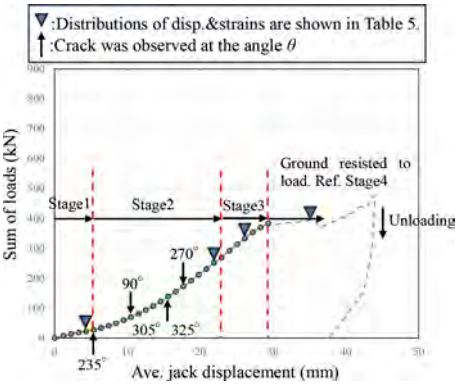

Figure 10. Relationships between load and displacement of case 3.

Figure 9. Deformed tunnel model case 2.

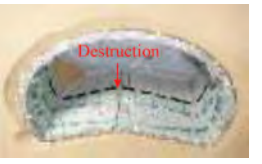

Figure 11. Deformed tunnel model of case 3.

Table 4. Representative distributions of displacements and strains of case 2 at stage 1-3.

Stage	1	2	3	Reference
Sum of loads (kN)	11.8	82.8	156.9	157.6
Ave. jack disp. (mm)	4.3	14.7	19.9	30.2
Disp. of model (mm)	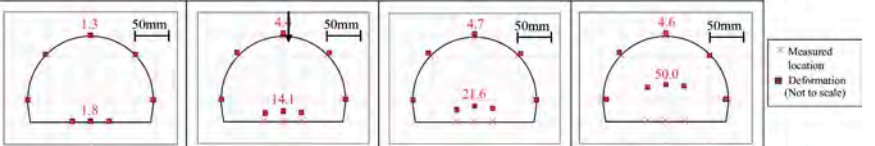			
Strain of model (μ)	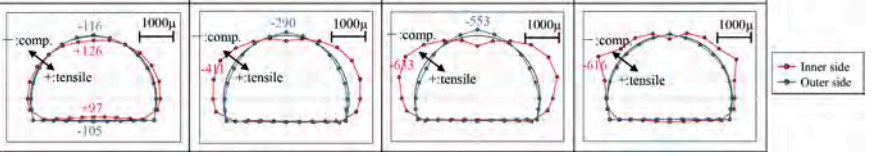			

Table 5. Representative distributions of displacements and strains of case 3 at stage 1-3.

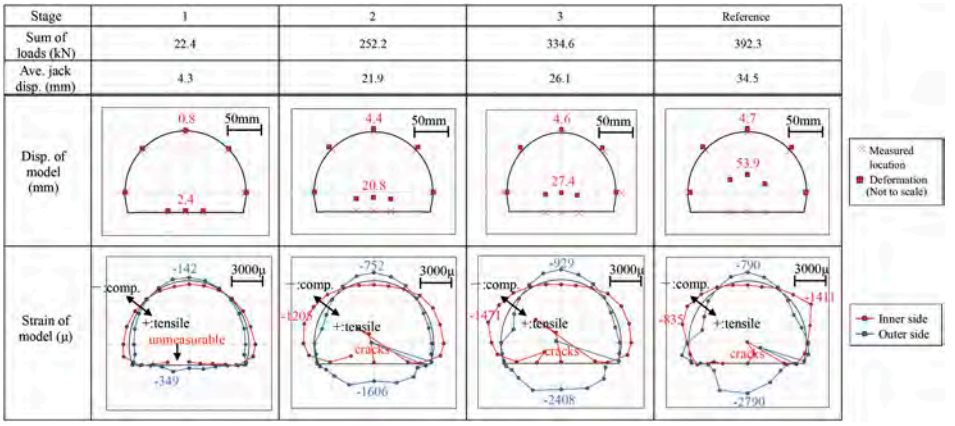

was 24mm, then it increased slowly as shown in Figure 8. It was thought that the load-bearing performance of the tunnel model reduced at this time, then the load was distributed to the ground around the tunnel model. Therefore, the load-bearing performance of Case 2 was regarded as the peak of solid line shown in Figure 8.

3.4 *Failure process of case 3 (Flat and reinforced)*

Based on the analysis of the transition of the displacements and strains of Case 3, its failure process was divided into 3 stages. Figure 10 shows the relationship between the load and displacement, and the division of the 3 stages. Figure 11 shows the deformed tunnel model at the end of the experiment. Table 5 shows the representative distributions of the displacements and strains of the tunnel model at each stage.

At stage 1, the first crack was observed on the inner side of the left part of the invert (235°) although it was assumed that the first crack would occur at the centre of the invert. The tunnel model of Case 3 was reinforced with copper pipes, and the cover of mortar was not completely the same at every location. In this way, the first crack occurred slightly far from the centre of the invert probably because the accuracy of modelling.

At stage 2, as another crack was observed on the inner side of the roof of the model, a lot of thin cracks occurred widely at the invert. Similarly to Case 2, the ground heave of Case 3 increased rapidly after the jack displacement was 23mm, which was defined as stage 3.

Table 6. Representative distributions of displacements and strains of case 4 at stage 1-3.

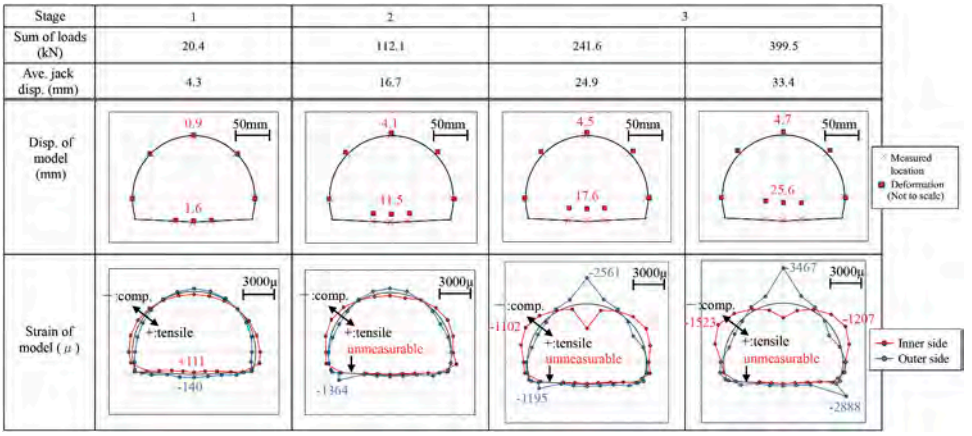

At stage 3, the load increased, and then it became almost stable. It was thought that the load-bearing performance of the tunnel model reduced at this time, following the load was distributed to the ground around the tunnel model, similarly to Case 2. Therefore, the load-bearing performance of Case 3 was regarded as the peak of solid line shown in Figure 10.

The invert as well as the reinforcement pipes were bended at the end of the experiment. The failure process of Case 3 was similar to Case 2, the shape of which was also flat. On the other hand, the stage 2 of Case 3, where the ground heave was relatively restrained, lasted longer than that of Case 2. The strains of both the inner and outer sides of the invert increased at stage 2 and 3, following the model was able to transfer both the axial force and the bending moment to a certain degree. These differences were caused by the effect of the reinforcement of Case 3.

3.5 *Failure process of Case 4 (Pentagon)*

Based on the analysis of the transition of the displacements and strains of Case 4, its failure process was divided into 3 stages. Figure 12 shows the relationship between the load and displacement, and the division of the 3 stages. Figure 13 shows the deformed tunnel

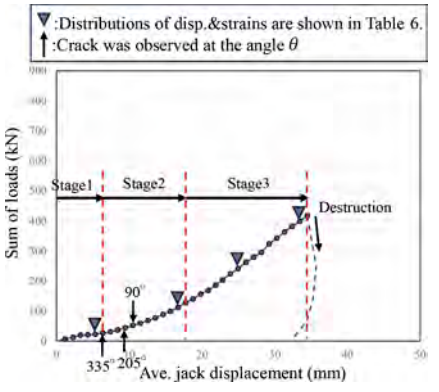

Figure 12. Relationships between load and displacement of Case 4.

Figure 13. Deformed tunnel model of Case 4.

model at the end of the experiment. Table 6 shows the representative distributions of the displacements and strains of the tunnel model at each stage.

At stage 1, the first crack was observed on the inner side of the right part of the invert (335°).

At stage 2, another cracks were observed on the inner sides of the left part of the invert (205°) and the roof (90°).

At stage 3, as the compressive strains on the outer side of the roof and on the inner side of the arch increased, the brittle destruction occurred in the end. At this time, dry sand flowed into the model through the crack at the left part of the invert (205°), but the right part (335°) was also destroyed. As the compressive strain on the outer side at the right part of the invert was approximately 3000 μ just before the destruction occurred. Thus, it was thought that the shear destruction occurred due to the excessive axial compression, similarly to Case 1.

Unlike Case 1-3, a crack did not occur at the centre of the invert in Case 4. Cracks occurred between the centre and the corner of the invert, which resulted in the destruction in the end. This was because the centre of the invert of Case 4 was so thick that the cross-sectional bearing capacity here was large. In addition to it, as the shape of the invert was down to convex, the location of the maximum bending moment was thought to be shifted from the centre of the invert. When it came to brittle destruction, Case 4 was similar to Case 1. However, differences between Case 1 and 4 were also found, for example, strains of Case 4 were relatively small at stage 2 and 3.

3.6 *Comprehensive evaluation of test cases*

The failure processes as well as the deformation modes of Case 1-4 were examined in the previous sections. Figure 14 shows the maximum load of Case 1-4. As the maximum load of Case 1 was expressed as a standard (100%), that of Case 2 was only 25% and those of Case 3 and 4 were slightly over 50%. Furthermore, Table 7 shows the ratio of the maximum load, R_l, the ratio of the volume of excavation, R_{ex} and the R_l/R_{ex}. If R_l/R_{ex} was smaller than 1, it was thought that the disadvantage of the smaller load-bearing performance would predominate the advantage of the smaller volume of the excavation, which was not effective. Among Case 2-4, only the R_l/R_{ex} of Case 3 was higher than 1, and that of Case 2 was the lowest 0.42.

In order to conclude the model experiments, each of the newly proposed invert here, Case 2-4 would be evaluated hereafter. Firstly, the maximum load and the R_l/R_{ex} of Case 2 were the lowest. Furthermore, considering that it became unable to restrain the ground heave and to transfer the bending moment and the axial force after stage 2, the proposed invert of Case 2 would be difficult to put into practice.

The R_l of Case 3 and Case 4 were slightly over 50%. However, as they enable to reduce the volume of the excavation, it would be possibly put into practice in the situation where the potential risk of the ground heave would be relatively low, but the factor of safety against it would need to be improved. The R_l/R_{ex} of Case 3 was higher than that of Case 4. However, the reinforcement would of course

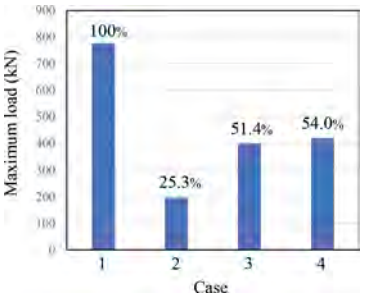

Figure 14. Maximum load of case 1-4.

Table 7. Ratio of maximum load and excavation volume of case 1-4.

Case	Max. load (kN)	Ratio of max. load, R_l (%)	Ratio of excavation volume, R_{ex} (%)	R_l /R_{ex}
1	776.0	100.0	100	1.00
2	196.2	25.3	59.5	0.42
3	398.5	51.4	39.7	1.29
4	418.9	54.0	68.1	0.79

influence the cost and the schedule of the construction work, therefore further investigations would be needed. In addition, copper pipes were located in the centre of the cross section of the invert in this experiment, but such reinforcement structure including its shape and location would need to be considered. Uniquely in Case 4, any crack did not occur at the centre of the invert unlike the other cases, which would need to be investigated by simulating the model experiments by numerical analysis in the future study.

4 CONCLUSIONS

We are developing invert structure which enable to reduce the volume of the excavation in constructing it additionally during the maintenance stage. In this research, the 4 model experiments were conducted to compare the load-bearing performances of the newly proposed invert with that of the standard one, Case 1. Based on the analysis of the measured loads, displacements and strains, the failure process of each case was examined by dividing it into mostly 3 stages. Then the feasibilities of the proposed inverts were examined, paying attention to the maximum load, the reduced volume of the excavation and capabilities to restrain the ground heave and to transfer the bending moment and the axial force.

Case 2 (shape: flat, thickness: 30mm): Its maximum load was only 25% of that of Case 1. Huge floor heave occurred as the invert bended at the crack at the centre of the invert caused by the bending moment.

Case 3 (shape: flat, reinforced with copper pipes): Its maximum load was approximately 51% of that of Case 1. It could reduce the volume of the excavation the most. With the effect of the reinforcement, a lot of thin cracks occurred at the invert but it restrained the ground heave without losing the capability to transfer the bending moment and the axial force in the meanwhile. It must be noted that the floor heave occurred before the invert was destroyed.

Case 4 (shape: pentagon): Its maximum load was approximately 54% of that of Case 1. A crack did not occur at the centre of the invert unlike the other cases. The brittle destruction occurred between the centre and the corner of the invert.

In conclusion, it was found that the maximum loads of the newly proposed inverts were lower than that of the standard one. However, it was advantageous that they enable to reduce the volume of the excavation. Furthermore, the newly proposed inverts could be applied to the area with relatively poor geological conditions where invert would be possibly needed in the construction stage. As the cost of constructing newly proposed inverts would be lower than that of standard one, road administrator could reasonably use them from the viewpoint of preventative maintenance.

We continue to research on the reasonable invert structure and the situations where they could be put into practice. In addition to it, the correspondence between the load in the model experiment shown in this paper and the actual ground heave would need to be further analysed to design invert properly.

REFERENCES

Japan Road Association, 2003. Technical standard of road tunnel and its interpretation -Part of tunnel structure-. Chiyoda, Tokyo, Japan, pp.125–131 (in Japanese).

Nakazato, R., Natsume, T., Kawata, K., Isago, N., Kusaka, A., Koizumi, Y., Otsu, T., 2023. "Mechanical behavior of invert structure with new geometries for simplified construction. Proceedings of the ITA-AITES World Tunnel Congress 2023 (WTC 2023). CRC Press, Athen, Greece, pp. 646–654.

Tunnelling for a Better Life – Yan, Celestino, Thewes & Eberhardt (Eds)
© 2024 The Author(s), ISBN 978-1-032-80042-4
Open Access: www.taylorfrancis.com, CC BY-NC-ND 4.0 license

A noncontact mobil system using camera module for tunnel inspection

Chulhee Lee*, Donggyou Kim & Dongku Kim
Department of Geotechnical Engineering Research, Korea Institute of Civil Engineering and Building Technology (KICT), Gyeonggi-Do, Republic of Korea

ABSTRACT: In the field of tunnel maintenance, computer vision-based noncontact mobile tunnel inspection systems are being developed and used to replace the traditional manpower-based inspections. However, there are existing technical issues regarding its effectiveness mainly due to traffic control caused by the slow inspection speed and motion blur within inconsistent image quality during the high-speed shooting in dark conditions. To efficiently shoot cracks and leaks in tunnel lining walls, it is necessary to optimize the components and requirements for the camera module, which is the core device of the computer vision-based tunnel inspection system. In this study, therefore, the issues and the relevant improvements are defined through indoor shooting tests obtained with area image sensor and light source according to shooting speed. This study developed a high-speed translational rotating panel device capable of simulating driving speeds up to 70 km/h. The device was equipped with a test chart to evaluate image quality. IMATEST® software, one of the reduced reference image quality assessment (RR-IQA) methods, was used to estimate quantitative values for motion blur. The relationship between the exposure speed of the camera and the lighting illuminance was analyzed, and correlations were analyzed to evaluate the optimal image quality. With a higher the camera shutter speed, the darker the image; to compensate for this point, there is a method of increasing the international organization for standardization (ISO) sensitivity of the camera or the lighting illuminance. The results indicate a relationship in which faster exposures darken the image but increase sharpness. In this study, at a shutter speed of 100 us (microsecond), the illuminance of 40,000lux, ISO of 1600, and the F value of 2.8, approximately 120% of motion blur occurred at 70 km/h than at the pause status, and it was difficult to obtain high-quality images through the exposure performance of the camera. Therefore, future studies need to focus on reducing the percentage of motion blur to less than 50% by using fast shutter speed and high luminance lighting.

Keywords: Mobile tunnel inspection, Area image sensor, Light source, Motion blur, MTF (modulation transfer function)

1 INTRODUCTION

Civil engineering structures are designed to be durable for their designated lifetime; however, most tunnels require regular inspections and maintenance to extend their service life. Visual inspection of tunnels has been conducted by human inspectors, and it is generally carried out at night along with high safety risk conditions (Panella et al., 2020). Proposals such as lowering risks to which inspectors are exposed in tunnels, reducing the site inspection time for collecting data, lowering repetitive and labor-intensive work costs, and reducing the time required for simple work by highly skilled inspectors have been increasingly put forward (Attard et al., 2018). In response, there has been continuous research on the development of computer vision-based noncontact mobile systems for more efficient inspection and subsequent maintenance. Especially, computer-vision technologies continuously developed over the last few years have been used to detect damage such as cracks and leaks in tunnels from video images (Huang et al., 2021).

In Korea, three area scan camera-based tunnel scanning systems (KMTL, MTEC, and Deep inspection) have been developed through national R&D to inspect tunnels. They can capture images at a maximum driving speed of 50 km/h, and have software for detecting cracks and damage via deep learning (Lee and Kim, 2023). Camera-based tunnel scanning systems in Japan have been continuously developed since approximately 20 years ago. In 1996, Ukai et al. (1996) first developed a railway

*Corresponding author: lch@kict.re.kr

DOI: 10.1201/9781003495505-357

tunnel scanning system using a line scan camera. Currently, six systems have been registered and used in the New Technology Information System (NETIS) of Japan. The systems that use line scan cameras are MIMM-R, Tunnel tracer, and GT-8K; and the systems that use area scan cameras are MMSD II, TC-3, and eQ Doctor T (NETIS, 2023). The Japanese tunnel scanning system is equipped with cameras and LiDAR to analyze the shape and displacement of the tunnel lining through point clouds. In China, there are tunnel fast detection system (TFS) developed by Wuhan ZOYON company using an area scan camera (Gong et al., 2019), and TDV-H2000 developed by Shanghai TJGEO technology company (Ynag et al., 2018). In addition, Zhejiang Scientific Research Institute of Transport developed the Tunnel Image Fast Acquisition System, which detects cracks of width 0.2 mm from captured images. However, approximately 10% of the errors occur when the crack width is less than 0.3 mm owing to the influences from image processing and pixels, requiring improvements to curb these errors (Wang et al., 2022).

Motion blur is likely to occur in images captured under high speed. It is common in images taken using mobile devices and is caused by camera and subject movements, or a combination of these motions (Abdullah-Al-Mamun et al., 2021). Motion blur is contrasted with sharpness as an important factor to evaluate the quality of images. However, image quality defects such as motion blur have not been considered in previously developed tunnel scanning systems. Image quality is assessed only by subjective (qualitative) evaluation in the human cognitive realm from the video image of the crack width. Quality images are a requirement for high-accuracy damage detection of tunnel lining through deep-learning based on video images; studies on this approach are ongoing. Deep-learning performance depends on the quality of images; it is more important to develop data-quality oriented AI models rather than the AI model development specialized in deep-learning algorithms to meet the high accuracy and precision required for maintenance.

Digital images in image processing systems, such as camera-based tunnel scanning systems, can be degraded at any stage of their life cycles such as image creation, compression, storage, and transmission, resulting in the loss of visual information (Choi et al., 2021). As a result, reliable quality assessment indicators for digital images are required to select high-quality images. Although human subjective image evaluation is reliable, it requires a great amount of time and effort to apply (Dey et al., 2022). Consequently, an objective image quality assessment (IQA) is necessary as it sophisticatedly reflects the image quality perception feature of the human visual system (HSV) (Bae and Kim, 2015). IQA helps objective image quality evaluation by scoring the quality of images. In general, the IQA method can be divided into full reference IQA (FR-IQA), reduced reference IQA (RR-IQA), and No Reference IQA (NR-IQA), depending on the dependence on reference images for quality evaluation (Wang et al., 2004). FR-IQA is a method of measuring image quality by using original images without damage and images with damage. RR-IQA evaluates quality using information that is combined from the damaged images and other damaged images from additional pathways. NR-IQA is a method for assigning a quality score to an image based on only the damaged images without information from reference images (Moorthy and Bovik, 2011).

The required performance of a camera-based tunnel scanning device depends on the driving speed limit per road; the maximum speed of freight vehicles on Korean highways is 80 km/h. Furthermore, a high image resolution of 0.3 mm/pixel or less is required to detect cracks with a width of 0.3mm or less in terms of maintenance. According to such demands, this study aims to develop a tunnel scanning system that can obtain video images of 0.3 mm/pixel at a maximum driving speed of 80 km/h. The recently developed camera-based tunnel scanning systems are used to capture images in tunnels at a completed or prototype stage, and their performance is analyzed. The crucial device in the tunnel scanning system is the camera and lighting, and huge costs are required to re-design and re-develop a device once selected. Consequently, if the performance of cameras and indoor lighting using a device that can simulate driving speeds is tested, it would be possible to reduce trials and errors in the development process.

This study developed a high-speed translational rotating panel device capable of simulating driving speeds up to 80 km/h. The device was equipped with a test chart to evaluate image quality. IMATEST® software, one of the RR-IQA methods, was used to estimate quantitative values for motion blur. The relationship between the exposure speed of the camera and the lighting illuminance was analyzed, and correlations were analyzed to evaluate the optimal image quality.

2 SETUP

2.1 *Proposed approach*

The quality of video images can be generally evaluated by pixel-based metrics such as root mean square error, peak signal-to-noise ratio, or structural similarity index (SSIM). However, these metrics have the disadvantages of first requiring original video images and being poorly correlated with the motion blur level. As for camera systems, modulation transfer function (MTF) is a well-established measure of sharpness (Dinh et al., 2023). Sharpness can be measured by the rise distance of the edges within images. With this technique, sharpness can be determined by the distance of a pixel level between 10% to 90% of its final value. Rise distance is measured in the frequency area, where the frequency is measured in cycles or line pairs per distance

(millimeters, inches, pixels, image height, or sometimes angle [degrees or milliradians]). The relative contrast at a given spatial frequency (output vs. input) is called MTF, which is used interchangeably as spatial frequency response in IMATEST® software. The most common method is to derive MTF from the tilted edge of a standardized test chart. Figure 1 shows the rise distance, and the sharpness of the edge for deriving MTF when motion blur occurs by using IMATEST® (IMATEST, 2023).

2.2 *Experimental setup*

A high-speed translational rotating panel device was designed, as shown in Figure 2, to analyze the performance of cameras and lighting devices through motion blur, which is the image quality, by simulating high driving speed. The maximum rotation speed is 100 km/h, and the speed is adjustable in units of 10 km/h. An eSFR ISO test chart of IMATEST® was attached to the panel to measure MTF. A daylight-colored light-emitting diode floodlighting with a color temperature of 5600 K was placed at a 45° angle in front of the test chart. The used machine vision area scan camera was CMOS image sensor with a resolution of 4096 x 2304. The minimum exposure was 5 μs, and a global shutter was used. The shooting distance was 2 m, and the image resolution was set to 0.2 mm/Pixel.

3 EXPERIMENTAL RESULTS

3.1 *Test condition*

In a conventional single-exposure photograph, moving objects or moving cameras cause motion blur. The exposure time defines a temporal box filter that smears the moving object across the image by convolution

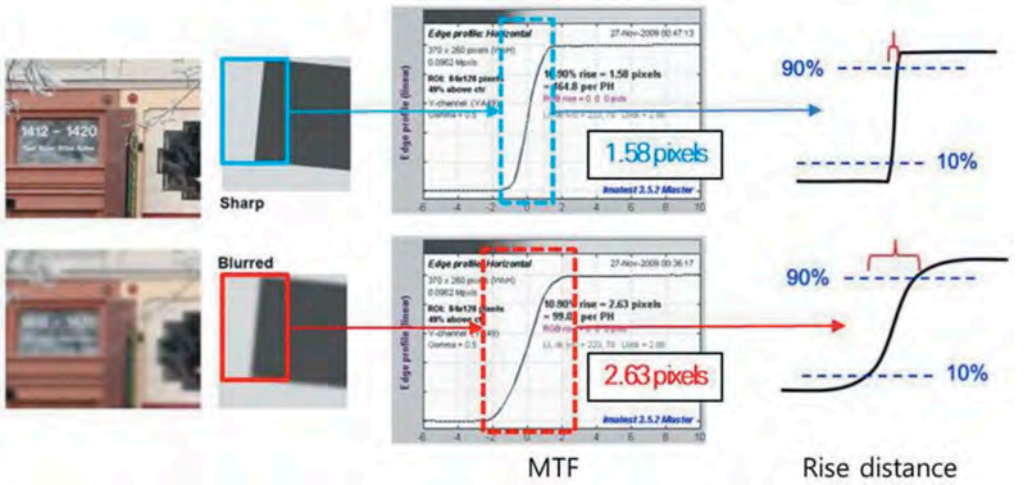

Figure 1. MTF and rise distance graph between sharpness and motion blur (IMATEST, 2023).

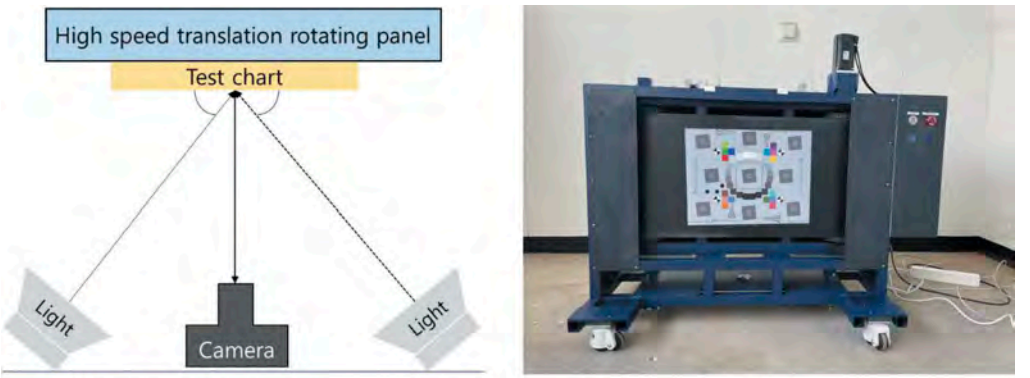

Figure 2. Motion blur capturing on high-speed translational rotating panel in the laboratory.

Table 1. Test condition for capturing motion blur using rotating panel and area scan camera.

Panel speed	Shutter speed	ISO sensitivity	FPS	F-number	Illuminance
0 km/h 10 km/h 30 km/h 50 km/h 70 km/h	250 us 100 us	1,250 1,600	100	2.8	 15,000 lux 40,000 lux

(Raskar et al., 2006). To shoot motion blur, it is important to assume motion and find the fastest exposure time that can make a moving object appear to be motionless. In this study, the lens aperture value F was fixed at 2.8, the shutter speed was set to 250 and 100 us, and ISO was changed to 1250 and 1500, while shooting at a speed of 70km/h. The illuminance of the chart surface was measured with an illuminometer, which was 15,000 and 40,000 lux. By analyzing the MTF of the captured images, this study attempted to identify correlations between the optimal combination of the camera and lighting device. The test conditions are presented in Table 1. The speed of the high-speed translational rotating panel was shifted to 10, 30, 50, and 70 km/h while shooting.

3.2 *Analysis of experimental results*

To analyze the image quality according to the rotating-panel speed variation and the exposure speed of the camera through the quantitative value of motion blur, the shooting took place under the test conditions shown in Table 1 (and Figure 3). The faster the shutter speed, the darker the image; this can be compensated by increasing the ISO of the camera or the lighting illuminance. The results indicate a relationship in which faster exposures darken the image but increase sharpness. In the case of

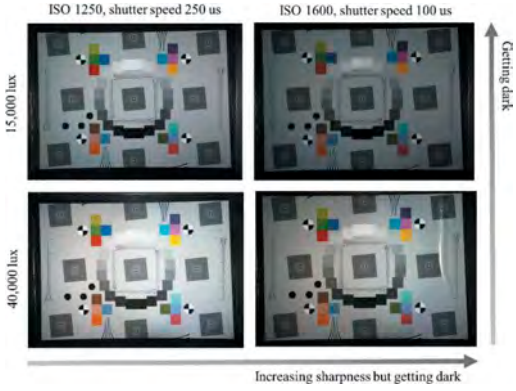

Figure 3. Relationship between shutter speed and ISO.

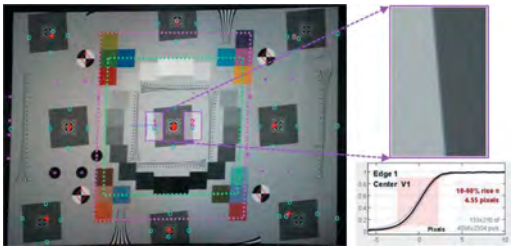

Figure 4. Calculating MTF graph (rise distance) by IMATEST®.

increasing the illuminance from 15,000 and 40,000 lux, the sharpness was improved due to the higher brightness in the image with shutter speed of 100 us. To confirm this, IMATEST® software was used, and motion blur was analyzed in the width (in pixels) at 10 – 90% of the rise distance measured at the center of the eSFR ISO test chart (Figure 4). Figure 5 shows the difference in shutter speed at an illuminance of 15,000 lux. When coming to a halt at a shutter speed of 250 us, the rise distance of MTF was 3.99 pixels, and 19.43 pixels at 70 km/h, indicating that motion blur increased by approximately 388% (Figure 5(a)). At a shutter speed of 100 us, it was 3.81 pixels and increased to 8.46 pixels at 70km/hm, indicating an increase of approximately 122%; it can be observed that the sharpness was improved (Figure 5(b)). When the shutter speed was increased to 100 us, the motion blur was approximately 50% less than that at 250 us.

Figure 6. presents a comparison of the MTF rise distance according to the difference in lighting illuminance between 15,000 lux and 40,000 lux. Figure 6(a) shows the difference in motion blur at a shutter speed of 250 us, and ISO of 1250, and Figure 6(b) present the comparison at a shutter speed of 100 us and ISO of 1600. When the shutter speed is 250 us, the difference in rise distance due to illuminance difference tends to increase as the rotation speed increases. On the other hand, at 100 us, the difference in rise distance due to illuminance difference tends to remain constant. Figure 7 shows the difference ratio in MTF due to illuminance and shutter speed. At 100 us, the MTF difference ratio is relatively constant at 4 ~ 6%, whereas at 250 us, the result of the illuminance difference gradually increases to approximately 11.5% at a speed of 70 km/h.

3.3 *Discussion*

The performance of the core devices (camera and lighting) was analyzed through indoor experiments to develop a camera-based noncontact mobile tunnel inspection system.

Quantitative values of motion blur against sharpness, which is an important factor in IQA, were derived by a high-speed translational

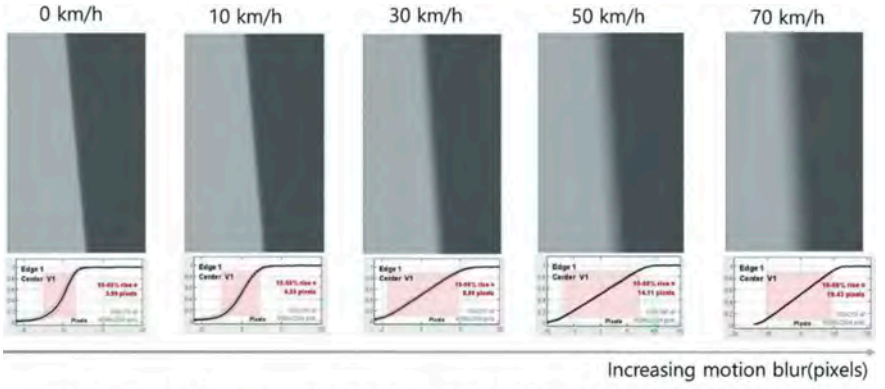

(a) Results of MTF graph (rise distance): shutter speed 250 us, ISO 1250, 15,000 lux

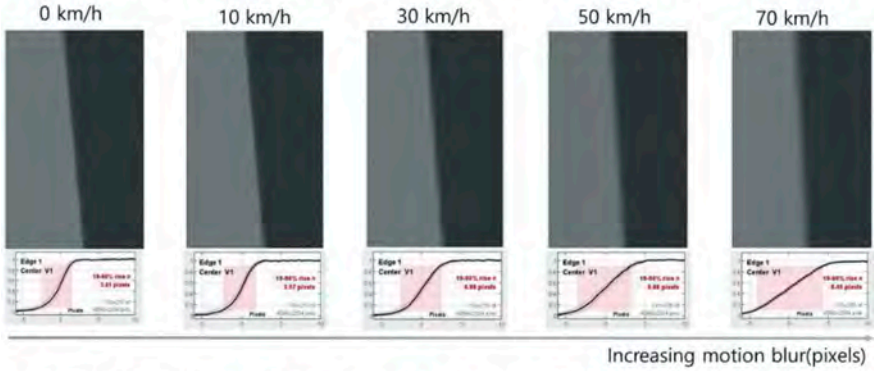

(b) Results of MTF graph (rise distance): shutter speed 100 us, ISO 1250, 15,000 lux

Figure 5. Results of MTF graph (rise distance) on the 15,000 lux.

rotating panel device. The rotation speed and the exposure performance of the camera were compared and analyzed via MTF graphs. The exposure of the camera is determined by the shutter speed, ISO, and the aperture F value of the lens. In this study, the analysis was conducted after setting the following conditions: the aperture F value was fixed at 2.8, the shutter speed was divided into 250 and 100 us to respond to the rotation speed, and the illuminance was divided into 15,000 and 40,000 lux. The results suggest that it is necessary to secure fast exposure performance that can respond to rotation or movement speed to capture clear and high-quality images. In this study, a shutter speed of 100 us was used, and approximately 120% of motion blur occurred at 70 km/h than at the status of pause. Further studies are needed to reduce the rate of motion blur to less than 50% when shooting at high speeds. Furthermore, considering that there are diverse image quality factors besides motion blur such as noise, color accuracy, and distortion, it is necessary to select cameras and lighting devices that consider the image quality in future studies.

4 CONCLUSIONS

This study conducted indoor performance experiments on cameras and lighting devices to develop a camera-based noncontact mobile inspection system capable of obtaining images of 0.3 mm/pixel at driving speeds of more than 80 km/h in a tunnel. A high-speed translational rotating panel device, which can simulate driving speeds of up to 100 km/h, was developed, and the motion blur of the images was measured for comparative analysis using the MTF value after attaching the eSFR ISO test chart. The conclusions drawn from the results of the indoor shooting test are as follows.

1. The higher the camera shutter speed, the darker the image; to compensate for this point, there is a method of increasing the ISO of the camera or the lighting illuminance. The results indicate a relationship in which faster exposures darken the image but increase sharpness.
2. As for a shutter speed of 250 us at an illuminance of 15,000 lux, the rise distance of MTF was 3.99 pixels at a pause status, and it became 19.43pixels at 70 km/h, leading to approximately

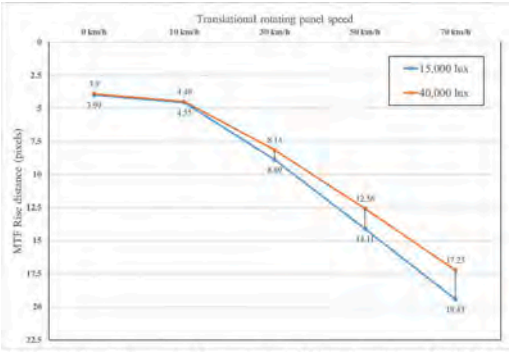

(a) MTF rise distance: shutter speed 250 us between 15,000 lux and 40,000 lux

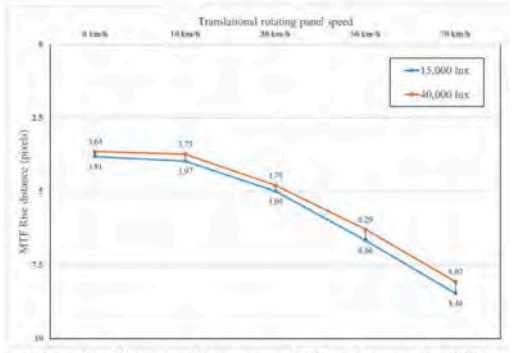

(b) MTF rise distance: shutter speed 100 us between 15,000 lux and 40,000 lux

Figure 6. Comparison MTF graph (rise distance) for shutter speed between 15,000 lux and 40,000 lux.

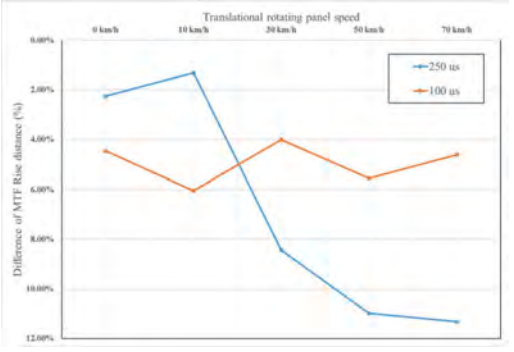

Figure 7. Difference ratio in MTF due to illuminance and shutter speed differences.

388% of motion blur. On the other hand, at a shutter speed of 100 us, it increased from 3.81 pixels to 8.46 pixels at 70 km/h, increasing approximately 122%. It can be considered that the sharpness was improved. Therefore, when the shutter speed increased to 100 us, the motion blur decreased by approximately 50% compared to the status at 250 us.

3. As a result of comparing MTF rise distance due to the difference in lighting illuminance of 15,000 and 40,000 lux, the difference ratio in MTF at 100us was relatively constant (4 ~ 6%), whereas, at 250 us, the result of illuminance difference gradually increased to approximately 11.5% at the speed of 70 km/h.
4. In this study, at a shutter speed of 100 us, the illuminance of 40,000lux, ISO of 1600, and the F value of 2.8, approximately 120% of motion blur occurred at 70 km/h than at the pause status, and it was difficult to obtain high-quality images through the exposure performance of the camera. Therefore, future studies need to focus on reducing the percentage of motion blur to less than 50% by using fast shutter speed and high luminance lighting.

ACKNOWLEDGMENTS

Research for this paper was carried out under the Development of advanced management technology (Total care) for infrastructure (project no. RS-2022-00142566) funded by Korea Agency for Infrastructure Technology Advancement.

REFERENCES

Abdullah-Al-Mamun, M., Tyagi, V., Zhao, H., 2021. "A New Full-Reference Image Quality Metric for Motion Blur Profile Characterization. IEEE Access, 9, 156361–156371.

Attard, L., Debono, C.J., Valentino, G., Castro, M., 2018. "Tunnel inspection using photogrammetric techniques and image processing: A review. ISPRS J. Photogramm. Remote Sens. 144, 180–188.

Bae, S.H., Kim, M., 2015. "Elaborate Image Quality Assessment with a Novel Luminance Adaptation Effect Model. J. Broadcast Eng. The Korean Institute of Broadcast and Media Engineers. 20(6), 818–826.

Choi, S., Jun, H., Shin, S., Chung, W, 2021. "Evaluating Accuracy of Algorithms Providing Subsurface Properties Using Full-Reference Image Quality Assessment. Geophysics and Geophysical Exploration, 24(1), 6–19.

Dey, R., Bhattacharjee, D., Kejcar, O, 2023. No-Reference Image Quality Assessment Using Meta-Learning. In: Sarkar, R., Pal, S., Basu, S., Plewczynski, D., Bhattacharjee, D. (eds) – Proceedings of International Conference on Frontiers in Computing and Systems. COMSYS 2022. Lecture Notes in Networks and Systems, Punjab, India, pp.137–144.

Gong, Y.F., Xiao, M.Q., Wang, S.F., Tang, Z., 2019. "Review and Developing Trend of Railway Tunnel Detection Technology. Railw. Stand. Des. 5, 93–98.

Dinh, H., Wang, Q., Tu, F., Frymire, B., Mu, B., 2023. "Evaluation of motion blur image quality in video frame interpolation. J. Electron. Imaging. 35, 262–265.

Huang, Z., Fu, H.L., Fan, X.D., Meng, J.H., Chen, W., Zheng, X.J., Wang, F., Zhang, J.B., 2021. "Rapid surface damage detection equipment for subway tunnels based on machine vision system. J. Infrastruct. Syst. 27, 04020047.

IMATEST, 2023. https://www.imatest.com/support/docs/23-1/sharpness/ (September 20, 2023).

Lee, C.H., Kim, D.G., 2023. “Non-contact Mobile Inspection System for Tunnels: A Review. J. of Korean Tunn Undergr Sp. Assoc. 25(3), 245–259.

Moorthy, A.K., Bovik, A.C., 2011. “Blind image quality assessment: From natural scene statistics to perceptual quality. IEEE Trans. Image Process. 20(12), 3350–3364.

NETIS, 2023. New Technology Information System, Tokyo, Japan. https://www.netis.mlit.go.jp/netis/ (June 7, 2023).

Panella, F., Roecklinger, N., Vojnovic, L., Loo, Y., Boehm, J., 2020. Cost-benefit analysis of rail tunnel inspection for photogrammetry and laser scanning. In: International Archives of the Photogrammetry, Remote Sensing and Spatial Information Sciences - ISPRS Archives, pp. 1137–1144.

Raskar, R., Agrawal, A., Tumblin, J., 2006. “Coded exposure photography: Motion deblurring using fluttered shutter. ACM Trans. Graph. 25(3) 795–804.

Ukai, M., Miyamoto, T., Sasama, H., 1996. “Development of inspection system of railway facilities using continuous scan image, WIT Trans. Built Environ. 20, 61–70.

Wang, H., Wang, Q., Zhai, J., Yuan, D., Zhang, W., Xie, X., Zhou, B., Cai, J., Lei, Y, 2022. “Design of fast acquisition system and analysis of geometric feature for highway tunnel lining cracks based on machine vision. Appl. Sci. 12, 2516.

Wang, Z., Bovik, A.C., Sheikh, H.R., Simoncelli, E.P., 2004. “Image quality assessment: from error visibility to structural similarity. IEEE Trans. Image Process. 13(4), 600–612.

Yang, J., Liu, X., Liu, X., Zhang, P., Peng, F, 2018. “Review of Rapid Test Vehicles for Highway Tunnel Structure. J. East China Jiaotong Univ, 4, 30–38.

Tunnelling for a Better Life – Yan, Celestino, Thewes & Eberhardt (Eds)
© 2024 The Author(s), ISBN 978-1-032-80042-4
Open Access: www.taylorfrancis.com, CC BY-NC-ND 4.0 license

Tunnel indirect monitoring and damage identification method based on SET-Swin Transformer*

Qi Li, Xiongyao Xie & Kun Zeng
Department of Geotechnical Engineering, School of Civil Engineering, Tongji University, Shanghai, China
Key Laboratory of Geotechnical and Underground Engineering of Ministry of Education, School of Civil Engineering, Tongji University, Shanghai, China

ABSTRACT: Addressing the limitations of current tunnel indirect monitoring and damage identification methods, which struggle with high noise and extensive data, this paper proposes a tunnel indirect monitoring and damage identification method based on SET-Swin Transformer. Initially, an exposition of the principles and procedures of this method is provided. The measured vertical dynamic response slices of the train are simultaneously passed through the corresponding trained classifier to determine the location, type and degree of tunnel damage in one step. Subsequently, the feasibility of this method is validated through model test. Lastly, an efficiency comparison is drawn between this method, employing short-time Fourier transform time-frequency diagrams as algorithm inputs, and the conventional training of convolutional neural networks. The outcomes demonstrate that the proposed method enables a one-step identification of tunnel damage while reducing the composition of the training set and the input data length, with a relatively faster algorithm convergence rate.

Keywords: Model test, Cavity back of tunnel, Fast Fourier transform, Time-frequency diagram, Slice classifier

1 INTRODUCTION

As an important part of urban rail transit, subway plays a vital role in alleviating the traffic pressure in large cities. With the increase of service time, diseases such as uneven settlement, segment deformation, segment peeling, and cavity back of tunnel appear in subway tunnels under the combined action of environmental erosion, material aging, and train cyclic load, which make the maintenance cost of tunnels in operation period increasingly high.

Once the tunnel and its attached structure are damaged, it will seriously affect the travel of residents. If the subway tunnel in operation period cannot be monitored and maintained in time, serious subway accidents are likely to occur. At present, the monitoring of subway tunnels can be divided into manual monitoring and automatic monitoring, among which manual monitoring is time-consuming and laborious (He, 2018). The sensor monitoring system with fixed position can generally only be monitored in some key areas of the tunnel (Yang et al., 2012), and the mobile detection vehicle integrating 3D laser scanner, digital photography and ground penetrating radar technology can only work in the early morning (Yang and Fang, 2017), which is difficult to achieve full-time and full-area monitoring. Therefore, it is of great significance for subway operation safety to find an efficient, economical and full coverage subway tunnel state perception method to detect tunnel damage in time.

In view of the limitations of existing subway tunnel monitoring technologies, Li et al. (2021) proposed an indirect tunnel monitoring method that uses the dynamic response of the service train to identify tunnel anomalies or damage. The proposed scheme is to install the acceleration sensor on the bogie of the service train, collect the vertical dynamic response of the train when the train is running, and determine the tunnel damage by comparing the characteristic quantity of the vehicle body response before and after the tunnel damage.

Li et al. (2021) verified the proposed damage index through theoretical derivation, simplified numerical model and model test. On this basis, Zhang et al. (2022a, b) proposed a damage identification method based on deep learning, and verified the algorithm by obtaining data from the laboratory model. However, Li's method is prone to interference caused by noise and inconsistency of data. Although Zhang uses deep learning to reduce the interference to a certain extent, the proposed VMD-CNN-LSTM method needs to go through multiple classifiers continuously to identify damage location and type step by step. The training set of each classifier contains a lot of cases and the data length of each case is large, which is difficult to adapt to the train test in real scenes.

*Corresponding author: 2310026@tongji.edu.cn

DOI: 10.1201/9781003495505-358

This paper proposes a tunnel indirect monitoring and damage identification method based on SET-Swin Transformer. Initially, the vertical acceleration response of trains undergoes SET to obtain time-frequency diagrams, which serve as input to train slice classifiers within the Swin Transformer. The new measurement data are input into each slice classifier at the same time after passing through the same slice. According to the results of the classifiers, the damage location, type and degree can be determined in one step. Subsequently, a model test is conducted to validate the feasibility of this identification method. Finally, the recognition efficiency of the proposed method is compared with that of the short-time Fourier transform time-frequency diagram as the input of the algorithm and the common convolutional neural network for training.

2 METHODOLOGY

2.1 *SET principle*

Synchroextracting transform (SET) belongs to the post-processing process of short-time Fourier transform (STFT). This algorithm only preserves the time-frequency coefficient of the short-time Fourier transform results on the mid-frequency ridge, thereby removing most of the divergent energy to obtain the time-frequency distribution with higher resolution (Yu et al., 2017). Taking harmonic signal $x(t) = A \cdot e^{i\omega_0 t}$ as an example, synchroextracting transform is mainly divided into three steps:

(1) Perform the short-time Fourier transform on time-domain signal to obtain time-frequency spectrum $G_e(t,\omega)$:

$$\begin{aligned} G_e(t,\omega) &= \int_{-\infty}^{+\infty} x(u)\cdot g(u-t)\cdot e^{-i\omega(u-t)}du \\ &= \frac{1}{2\pi}\int_{-\infty}^{+\infty} \widehat{x}(\xi)\cdot \widehat{g}(\omega-\xi)\cdot e^{i\xi t}d\xi \end{aligned} \tag{1}$$

Where $\widehat{g}(\omega-\xi)$ is the Fourier transform result of the window function $g(u-t)$, $\widehat{x}(\xi)$ is the Fourier transform result of the signal $x(t)$:

$$\widehat{x}(\xi) = 2\pi A\cdot\delta(\xi-\omega_0) \tag{2}$$

Substituting (2) into (1) can obtain the short-time Fourier transform result of the signal $x(t)$:

$$G_e(t,\omega) = A\cdot\widehat{g}(\omega-\omega_0)\cdot e^{i\omega_0 t} \tag{3}$$

The result of formula (3) shows that the time-frequency energy of the signal is mainly concentrated near the frequency $\omega = \omega_0$, and the maximum amplitude $A\cdot\widehat{g}(0)$ is found in the region near this frequency.

(2) Obtain instantaneous frequency estimation $\omega_0(t,\omega)$ based on the phase information of the time-frequency spectrum:

Calculate the partial derivative of the short-time Fourier transform result:

$$\partial_t G_e(t,\omega) = G_e(t,\omega)\cdot i\cdot\omega_0 \tag{4}$$

Further obtain instantaneous frequency estimation:

$$\omega_0(t,\omega) = -i\cdot\frac{\partial_t G_e(t,\omega)}{G_e(t,\omega)} \tag{5}$$

(3) Remove the divergent energy near the instantaneous frequency to obtain a new time-frequency spectrum $T_e(t,\omega)$:

Set extraction operator $\delta(\omega-\omega_0(t,\omega))$:

$$\delta(\omega-\omega_0(t,\omega)) = \begin{cases} 1, \omega=\omega_0 \\ 0, \omega\neq\omega_0 \end{cases} \tag{6}$$

Remove the divergent energy near the instantaneous frequency of the signal in the original time-frequency spectrum to obtain the time-frequency spectrum after synchroextracting transform:

$$T_e(t,\omega) = G_e(t,\omega)\cdot\delta(\omega-\omega_0(t,\omega)) \tag{7}$$

2.2 *Swin Transformer architecture*

Swin Transformer is a network model proposed by Microsoft Research Asia for image classification, object detection and semantic segmentation, which is dedicated to simultaneously solving computer vision tasks and natural language processing tasks (Liu et al., 2021). The model adopts hierarchical design, and the attention calculation is limited to one window by shifted window. On the one hand, the locality of CNN convolution operation is introduced, and on the other hand, the calculation amount is saved.

The architecture of Swin Transformer is shown as Figure 1. The core of the algorithm is to extract image deep features through multiple Block and multiple Patch Merging operations. In each Block, image features are extracted by self-attention mechanism, followed by Patch Merging downsampling to reduce the resolution of feature maps and increase the number of channels.

The specific structure of the Block is shown as Figure 2, which consists of four key modules: Layer Normalization (LN), Windowed Multi-head Self-Attention (W-MSA), Shifted Window Multi-head Self-Attention (SW-MSA) and Multi-Layer Perceptron (MLP). The W-MSA module is used for multi-head self-attention calculation in the window, while the SW-MSA module shifts the window, recombines and integrates features in a local area, and retains the relative position relationship between the windows while obtaining a larger range of information.

2.3 *Damage identification method*

This paper proposes a tunnel indirect monitoring and damage identification method based on SET-Swin Transformer as shown in Figure 3.

Initially, the acquired train dynamic response is filtered based on the results of fast Fourier transform, and the high energy frequency band is retained while

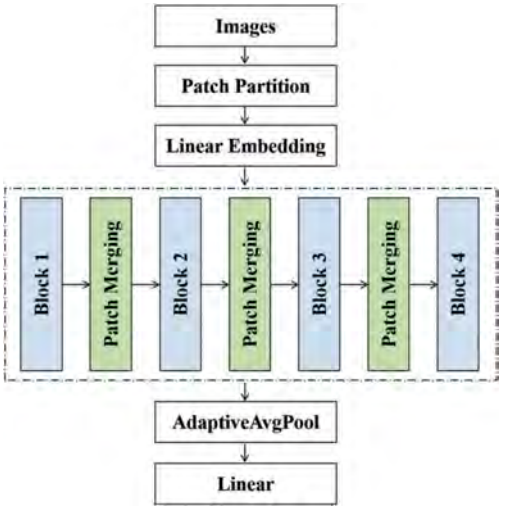

Figure 1. Swin Transformer architecture.

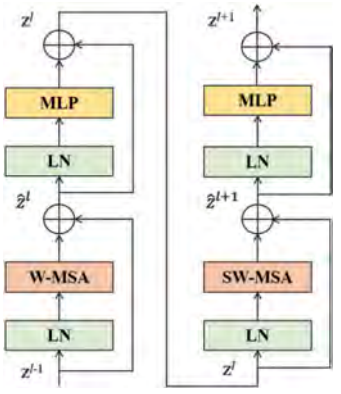

Figure 2. Block structure.

the noise is removed. Then, the denoised signal is sliced according to the actual situation (the real running train can be divided according to the station). When damage occurs in the corresponding tunnel section of a slice, it mainly affects the dynamic response of the train in the slice, but has little impact on the dynamic response of the other slices. Subsequently, SET is carried out on the slicing signals and time-frequency diagram is drawn. The time-frequency diagram is trained as the input of Swin Transformer. A classifier is constructed for each slice, in which the input of each slice classifier is the slice data under the condition of the whole healthy section and the data of different damages in the corresponding tunnel section of the slice.

For the newly acquired train dynamic response, after the same filtering and slicing operation, the time-frequency diagram of each slice data after SET is input into the corresponding trained slice classifier. The results of the slices corresponding to the tunnel section without damage will be output health after the classifier. The type and degree of damage will be output from the slices corresponding to the tunnel section where the damage is located through the classifier, thus realizing the indirect identification of tunnel damage.

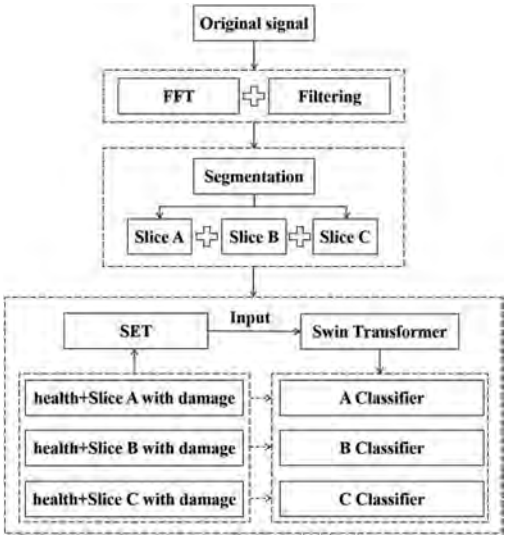

Figure 3. Method flow chart.

3 MODEL TEST AND METHOD VALIDATION

3.1 *Model test*

In order to verify the feasibility of the proposed method, this paper adopted the test system as shown in Figure 4 to carry out the model test. The test system includes sand box, tunnel model, train model, train traction control system and data acquisition system. The tunnel model includes the tunnel structure, track plate and steel track made by 3D printing. The automatic traction and control system includes

Table 1. Test cases.

Case	Damage degree	Damage location
0	—	—
1	1	A
2	2	A
3	3	A
4	4	A
5	1	B
6	2	B
7	3	B
8	4	B
9	1	C
10	2	C
11	3	C
12	4	C

track, motor and chassis, which jointly control the train in the tunnel to do a cycle of uniform speed.

As shown in Figure 4, the wireless acceleration sensor was glued to the train model with AB adhesive in this test, and the sampling frequency was set at 100Hz to continuously collect the triaxial acceleration response of the train. 3D printed resin was placed under the side of the tunnel to simulate the cavity damage. Four resins of different sizes were set in the test to simulate the damage of different degrees (as shown in Figure 5), and the resin was placed on the left, middle and right sides of the tunnel respectively (as shown in Figure 5), in a total of 13 cases as shown in Table 1. The train runned for 15 minutes in each case.

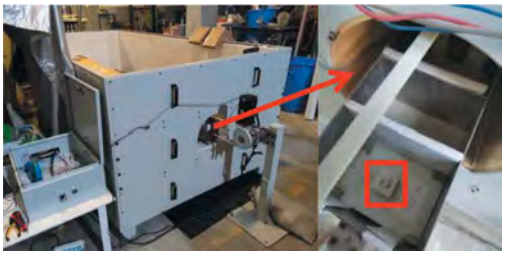

Figure 4. Test system and sensor installation.

Figure 5. Degree and location of damage.

3.2 *Model test data preprocessing*

In this paper, the vertical acceleration response of the train is selected for analysis. Figure 6 shows the first 200s data in case 12, including C→A and A→C directions. Bandpass filtering is carried out according to the fast Fourier transform spectrum diagram of the signal (as shown in Figure 7), and the signal with relatively concentrated energy of 10-20Hz is retained. Further, the original data is segmented according to the acceleration response of the train running direction. Figure 8 shows the acceleration response of the C→A direction after filtering and segmentation. According to the method mentioned in 2.3, the acceleration response in the C→A direction is divided into three slices: 0~2.5s, 2.5~5s, and 5~7.5s, which correspond to the three damage locations respectively, as shown in Figure 9.

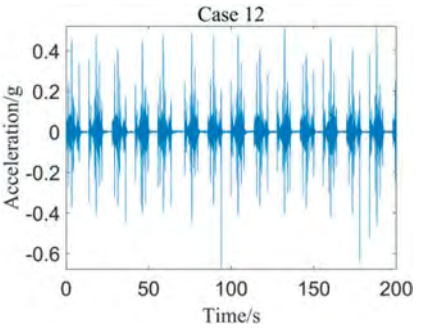

Figure 6. Original signal.

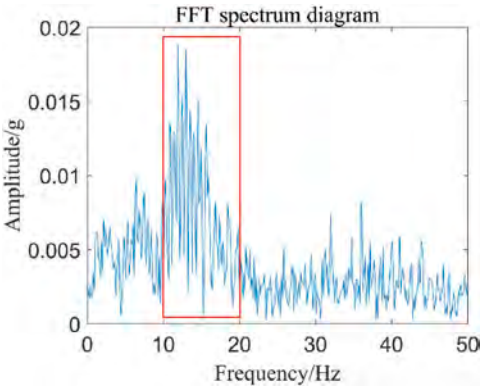

Figure 7. FFT spectrum diagram.

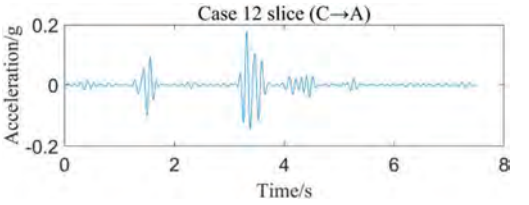

Figure 8. Signal in the C→A direction.

3.3 *Algorithm training and testing*

Figure 10 shows the results of the STFT and the SET, which produces a more energy-focused time-frequency representation. With the time-frequency diagram of SET as input, a Swin Transformer classifier is constructed for each slice. The cases of the training set of each classifier are shown in Table 2. Only the healthy case and the two cases with damage in the tunnel section corresponding to the slice are used for training, and the ratio of training set and validation set is 4:1. In this paper, a pre-trained Swin Tranformer network is used to speed up the training, which has been pre-trained on a larger dataset. Figures 11, 12 show the training results of the B classifier, including training loss, training and validation accuracy.

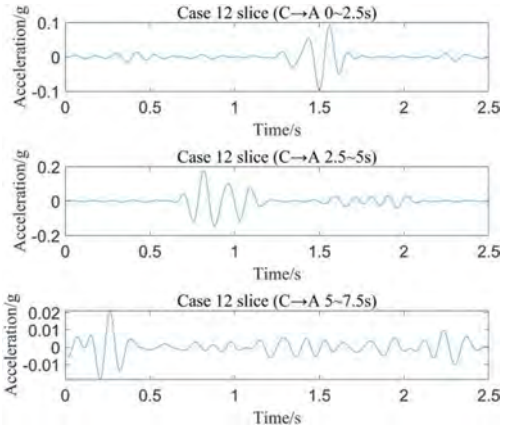

Figure 9. Three slices of signal in the C→A direction.

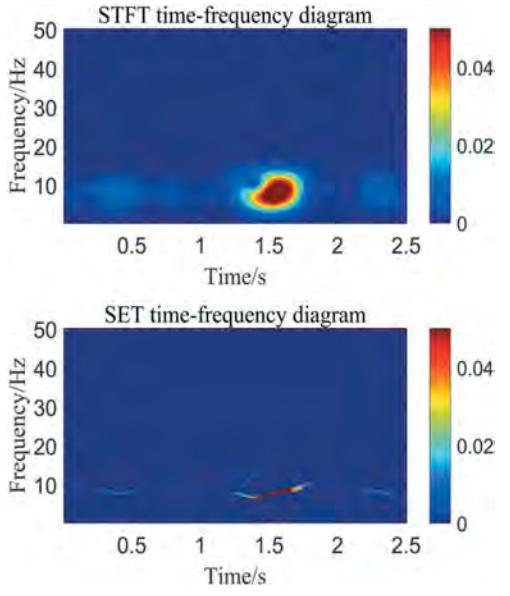

Figure 10. Time-frequency diagram of STFT and SET.

Table 2. Composition of classifier (C→A direction).

Classifier	Time period	Training set cases composition
C classifier	0~2.5s	0, 10, 12
B classifier	2.5~5s	0, 6, 8
A classifier	5~7.5s	0, 2, 4

Three case 4 data that did not participate in the training are tested through the trained classifier, and the test results are shown in Table 3. The data are segmented into three slices and then passed through the corresponding classifier. The results of the C and B classifiers are case 0 (health), while the results of the A classifiers are case 4. The damage location and damage degree identification are realized, which is consistent with the expected results of the method proposed in 2.3, proving the feasibility of the method.

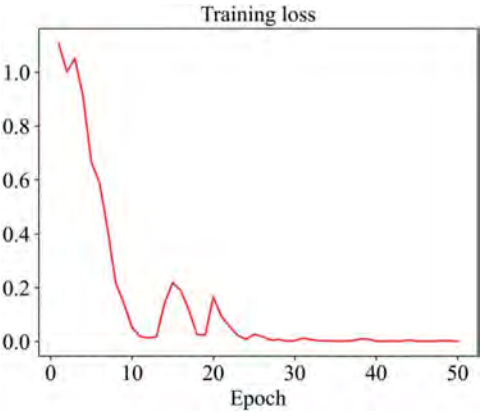

Figure 11. Training loss of the B classifier.

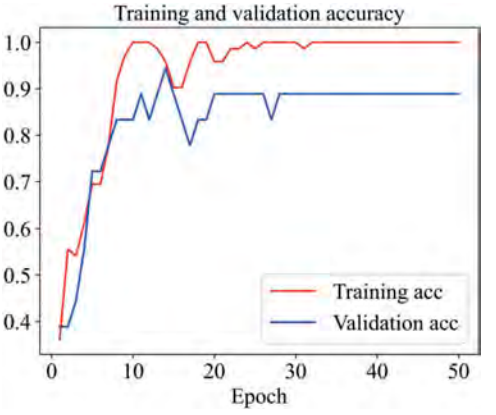

Figure 12. Training and validation accuracy of the B classifier.

Table 3. Test results of new Case 4 data (probability/%).

Classifier	Case	Test result 1	Test result 2	Test result 3
C classifier(0~2.5s)	**0**	**99.9980**	**99.9921**	**99.9991**
	10	0.0017	0.0070	0.0005
	12	0.0003	0.0009	0.0005
B classifier(2.5~5s)	**0**	**80.7251**	**99.9677**	**99.0626**
	6	0.0087	0.0002	0.0009
	8	19.2662	0.0321	0.9366
A classifier(5~7.5s)	0	0.0069	0.0113	0.0027
	2	8.4056	25.7911	0.0550
	4	**91.5875**	**74.1976**	**99.9423**

4 DISCUSSION

As shown in Figure 13, the training loss of the B classifier with the short-time Fourier transform time-frequency diagram as the input of Swin Transformer tends to be stable after 32 epochs, while the training loss of the SET time-frequency diagram as the input of the algorithm (Figure 11) tends to be stable after 24 epochs, which is converging faster.

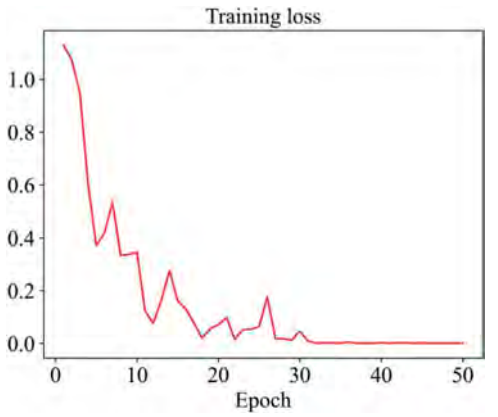

Figure 13. Training loss of the B classifier (STFT-Swin Transformer).

Figure 14 shows the training loss of the B classifier using the commonly used ResNet18 network. Compared with the result of Swin Transformer (Figure 11), the convergence of ResNet18 requires more epochs, and the training loss after 50 epochs is 0.058, which is higher than 0.001 of Swin Transformer.

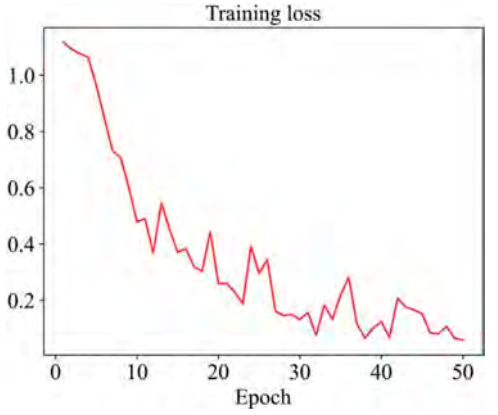

Figure 14. Training loss of the B classifier (SET-ResNet18).

5 CONCLUSIONS

This paper proposes a tunnel indirect monitoring and damage identification method based on SET-Swin Transformer and the feasibility of the method is validated through a model test. The primary conclusions are as follows:

1) Model test results demonstrate that the tunnel indirect damage identification method based on SET-Swin Transformer can achieve one-step identification of tunnel damage location and degree utilizing multiple slice classifiers.
2) In comparison with the previously tunnel indirect monitoring method based on VMD-CNN-LSTM, the classifiers constructed in this paper show reductions in training set composition and data length, allowing adaptability to diverse testing scenarios.
3) Compared with using the STFT time-frequency diagram as the algorithm input and using the commonly used ResNet18 network for training, the proposed method in this paper exhibits faster training convergence and lower loss.

Future work aims to accumulate more data by setting different types and degrees of tunnel damage through model tests to further train the proposed method, and subsequently deploy the algorithm into field applications.

REFERENCES

He, J., 2018. Analysis of subway tunnel disease rapid detection technology. Urban Construction Theory Research (electronic edition), (28): 9.

Li, H., Xie, X., Zhang, Y., et al, 2021. Theoretical, Numerical, and Experimental Study on the Identification of Subway Tunnel Structural Damage Based on the Moving Train Dynamic Response. Sensors, 21, 7197.

Liu, Z., Lin, Y., Cao, Y., et al, 2021. Swin transformer: Hierarchical vision transformer using shifted windows. Proceedings of the IEEE/CVF international conference on computer vision, 10012–10022.

Yang, F., Zhao, J., Liu, Z. M., et al, 2012. Application and analysis of automatic real-time, monitoring in subway tunnel. Journal of Geotechnical Engineering, 34(S1): 162–166.

Yang, L. Z., Fang, E. Q., 2017. Review and development trend of tunnel structure disease detection technology for rail transit. Urban Express Transit, 30(01): 20-25 +76.

Yu, G., Yu, M. J., Xu, C. Y., 2017. Synchroextracting Transform. IEEE Transactions on Industrial Electronics, 64(7): 8042–8054.

Zhang, Y., Xie, X., Li, H., et al, 2022. An Unsupervised Tunnel Damage Identification Method Based on Convolutional Variational Auto-Encoder and Wavelet Packet Analysis. Sensors, 22, 2412.

Zhang, Y., Xie, X., Li, H., et al, 2022. Subway tunnel damage detection based on in-service train dynamic response, variational mode decomposition, convolutional neural networks and long short-term memory. Automation in Construction, 139, 104293.

Tunnelling for a Better Life – Yan, Celestino, Thewes & Eberhardt (Eds)
© 2024 The Author(s), ISBN 978-1-032-80042-4
Open Access: www.taylorfrancis.com, CC BY-NC-ND 4.0 license

Effectual approach to characterize rock fracture: Insight from calculating method of fractal dimension

Bangxiang Li
Geotechnical and Structural Engineering Research Center, Shandong University, Jinan, China
School of Qilu Transportation, Shandong University, Jinan, China

Weimeng Zhang
Geotechnical and Structural Engineering Research Center, Shandong University, Jinan, China
School of Civil Engineering, Shandong University, Jinan, China

Yiguo Xue*
Geotechnical and Structural Engineering Research Center, Shandong University, Jinan, China
School of Engineering and Technology, China University of Geosciences (Beijing), Beijing, China

Kunpeng Li
Geotechnical and Structural Engineering Research Center, Shandong University, Jinan, China
School of Qilu Transportation, Shandong University, Jinan, China

Jianpeng Zhao
ORBBEC, Shanghai, China

Yunjuan Chen
Key Laboratory of Building Structural Retrofitting and Underground Space Engineering (Shandong Jianzhu University), Ministry of Education, Jinan, China

Rui Kong & Gang Wang
Key Laboratory of Ministry of Education on Safe Mining of Deep Metal Mines, Northeastern University, Shenyang, Liaoning, China

ABSTRACT: The characterization of rock fracture is essential for revealing and understanding the fracture mechanism. In this research, the fracture of sandstone is characterized from the perspective of the 3D morphology of fracture surface. The 3D morphology is quantified by two fractal dimension (*D*) calculation methods: cubic covering method(CCM) and surface area method(SAM). The applicability of both methods is verified by two special cases of which one is a 2D plane and another one is a novel surface model with a dimension of 3. However, in actual application, one shortcoming of the CCM rooted in the algorithm is exposed, which introduces a distorted *D* for the surface with a small degree of undulation. On the contrary, relying on a new algorithm proposed to calculate the fracture surface area, the SAM can completely avoid the distortion problem. Based on the SAM, the 3D morphologies of a series of fracture surfaces of sandstone in the conventional triaxial test are quantified. It is observed that *D* has a strong correlation with the fracture mechanism. With the transition of failure mechanism from tension fracture to shear fracture, *D* presents a decreasing trend. The reason underlying this correlation is analyzed. In Discussion, several improved CCMs are introduced, and whether the improvements have solved the distortion problem is verified. The accuracy of the SAM is also evaluated using the Takagi fractal surfaces.

Keywords: Rock fracture, Surface morphology, Fractal dimension, Cubic covering method, Surface area method, Fracture mechanism

1 INTRODUCTION

Rock fracture is one of the key issues in the field of rock mechanics. A better understanding of the rock fracture mechanism is essential to the design and safety of the underground construction. The 3D morphology of the fracture surface is the direct record of the fracture process, and contains amounts of

*Corresponding author: xieagle@sdu.edu.cn

DOI: 10.1201/9781003495505-359

information about the fracture characteristics. Effectively characterizing the 3D morphology of the fracture surface is of great significance to understand and reveal the fracture mechanism.

To date, scholars have done a lot of work on the characterization of the roughness of the surface profile. ISRM recommended that the roughness could be described by the inherent unevenness and waviness of the joint surface relative to its mean plane.(1978; Brady and Brown 2006; Li et al. 2016; Li et al. 2020; Patton 1966; Yang et al. 2001) To quantitatively characterize the roughness, Barton proposed the joint roughness coefficient (JRC) and defined 10 typical joint roughness profiles.(Barton 1973; Barton and Choubey 1977) However, it is highly subjective to quantify joint roughness by visual comparison.(Hsiung et al. 1993; Kulatilake et al. 1995; Maerz et al. 1990) In addition, some scholars proposed statistical parameters to quantify rough surfaces or profiles, which can be categorized broadly into amplitude parameters (Myers 1962; Tse and Cruden 1979), spacing parameters(Sayles and Thomas 1977; Tikou et al. 2000; Wu and Ali 1978; Yu and Vayssade 1991) and hybrid parameters(Chen et al. 2016; El-Soudani 1978; Ge et al. 2014; Tatone and Grasselli 2013; Xue et al. 2020). It should be noticed that the statistical characteristics of the aforementioned parameters are highly dependent on the sampling interval,(Miller et al. 1990) and comparisons between different parameters cannot be performed. Therefore, it is necessary to find an integrated parameter with scale invariance to characterize the morphology of fracture surface. Coincidentally, fractal theory based on the self-similarity of geometry object perfectly meets these requirements.

Since Mandelbrot proposed fractal theory in 1983,(Mandelbrot 1967; Mandelbrot 1977) it has been widely used in the related research of rock mechanics, such as crack propagation pattern(Nara et al. 2006; Yang et al. 2021; Yu et al. 2021; Zhang et al. 2018), rockburst mechanism and prediction(Feng et al. 2016; Feng et al. 2012; Liu et al. 2013; Xie and Pariseau 1993), and pore structure characterization(Ju et al. 2014; Schlueter et al. 1997a; Schlueter et al. 1997b), et al. Numerous studies have shown that the rock fracture surface can be described as a self-affine fractal, and its morphology can be quantitatively characterized by fractal dimension.(Babanouri et al. 2013; Ding et al. 2021; Ehlen 2000; Jafari and Babadagli 2013; Jiang et al. 2006; Raimbay et al. 2017; Xie and Wang 1999b; Xu et al. 2018) However, due to the lack of equipment to obtain the 3D morphology data of fracture surface, the fractal dimension was indirectly determined based on 2D profiles in early studies.(Berry and Lewis 1980; Kulatilake et al. 2006; Liebovitch and Toth 1989; Malinverno 1990; Matsushita and Ouchi 1989; Orey 1970) Considering the anisotropy and heterogeneity of fracture surface, these indirect determination methods are incomplete or even biased. (Archambault et al. 1997; Belem et al. 1997)

With the development of non-contact measurement technologies, the 3D fracture surface reconstruction can be realized. Methods directly determining the fractal dimension were proposed. (Chen et al. 2020; Clarke 1986; Kwaśny 2009; Xie et al. 1998; Zheng et al. 2021; Zhou et al. 2013) Zhou and Xie proposed the cubic covering method (CCM), and successfully employed it to calculate the fractal dimension of a 3D fracture surface.(Zhou and Xie 2003) Zhang et al. pointed out that the complexity and authenticity of fracture surface cannot be well characterized by the CCM and proposed an improved cubic covering method (ICCM), which calculated the number of cubes from a unified reference plane. (Zhang et al. 2005) T. Ai et al. suggested that the CCM and ICCM did not take heights of the intermediate points in the cubes into account, resulting in the fracture surface not being completely covered. Therefore, the differential cubic covering method (DCCM) and relative differential cubic covering method (RDCCM) were proposed.(Ai et al. 2014)

Inspired by the simple "walking divider" method (Goodchild 1982) for quantifying a line, Clark introduced the surface area method (SAM) to determine the fractal dimension of topographic surface.(Clarke 1986) The surface area was calculated by the triangular prism surface area method in which the four nodes and the center point of each grid formed four triangles and the sum of triangle areas on the surface was the surface area. To simplify the calculation of surface area, Xie et al. proposed a projective covering method, in which the grid area surrounded by four nodes was approximately computed by two triangles.(Xie and Wang 1999a)

Theoretically, the fracture surface roughness of self-emulation fractal is only correlated in a limited range(Smith 2014), and different scale ranges may produce different fractal dimension values. Xie pointed out that the fractal dimension estimated in the linear part of the log-log plot of the measurement vs the measured step can represent the roughness of the fracture surface.(Xie et al. 1997) Most previous studies have focused on the calculation of fractal dimension of fracture surfaces and the establishment and correction of calculation methods. The most important aspect in rock engineering practice, however, is that the fractal characterization could be applied to reveal rock fracture mechanism. The applicability of established fractal dimension calculation methods for characterizing rock fracture surfaces has not been discussed, and more importantly, the relationship between fractal dimension and fracture mechanisms has rarely been investigated.

In this study, the CCM are reviewed first. However, when CCM is applied to characterize the rock fracture surface, the distortion problem is exposed. By analyzing the algorithm of the CCM, the cause of the distortion problem is revealed. Then, the SAM is adopted to determine the D instead, in which a new method for calculating the fracture surface area is proposed. Compared to the CCM, the SAM can accurately

identify the small undulation on the fracture surface and avoid the distortion problem. By applying the SAM to a series of fracture surfaces of sandstone in the conventional triaxial test, a negative correlation between the fractal dimension and the confining pressure is observed. This negative correlation results from the transition of fracture mechanism with the variation of confining pressure, and the underlying mechanism for how the fracture mechanism alter the 3D morphology of fracture surface is analyzed. In the Discussion, whether the improved CCMs still suffer from the distortion problems is checked, and the accuracy of the SAM is evaluated using the Takagi fractal surface.

2 CUBIC COVERING METHOD

2.1 *Algorithm of CCM*

The CCM is evolved from the box-counting method (Russell et al. 1980), and their algorithms are similar. Dividing a fracture surface into $n\times n$ grids by a scale of δ, taking the ij-th grid as an example, the elevations of the four nodes are $z_{i,j}$, $z_{i+1,\,j}$, $z_{i,\,j+1}$, and $z_{i+1,\,j+1}$. The elevation difference of the grid is denoted as Δz. Covering this grid by cubes with a size of δ, the number of cubes $N_{i,\,j}$ can be expressed as:

$$\begin{aligned}\Delta z = &\max\left[z_{i,j},\ z_{i+1,j},\ z_{i,j+1}, z_{i+1,j+1}\right] \\ &-\min\left[z_{i,j},\ z_{i+1,j},\ z_{i,j+1}, z_{i+1,j+1}\right]\end{aligned} \tag{1}$$

$$N_{i,j} = F\left(\frac{\Delta z}{\delta}\right) + 1 \tag{2}$$

Where $F(a)$ is the floor function whose value is the maximum integer not greater than a. According to equation (2), the number of cubes $N(\delta)$ required to cover the entire surface can be calculated as:

$$N(\delta) = \sum_{i=1}^{n}\sum_{j=1}^{n} N_{i,j} \tag{3}$$

According to the fractal geometry theory, $N(\delta)$ and δ have the following relationship:

$$_N(\delta) \sim \delta^{-D} \tag{4}$$

Taking the logarithm of both sides of equation (4) gives:

$$lgN(\delta) \sim -D \cdot lg\delta \tag{5}$$

According to equation (5), under the bi-logarithmic coordinate system, $N(\delta)$ has a linear relationship with δ. The absolute value of the slope is the fractal dimension D.

D calculated by the CCM can be related to the dimensions of the 2D plane and 3D solid in the Euclidean geometric space. Firstly, considering a special case in which a 2D horizontal plane A, whose size is $l\times l$, is divided by a scale of δ, the number of grids N_g can be expressed as:

$$N_g = \left(\frac{l}{\delta}\right)^2 \tag{6}$$

Since the Δz of all grids are 0, and each grid only needs one cube to be covered, $N(\delta)$ is equal to N_g. Bring the equation (6) into the equation (5) to get:

$$lg\left(\frac{l}{\delta}\right)^2 \sim -D \cdot lg\delta \tag{7}$$

As δ changes from δ_1 to δ_2, according to equation (7), D can be calculated as:

$$D = -\frac{lg\left(\frac{l}{\delta_1}\right)^2 - lg\left(\frac{l}{\delta_2}\right)^2}{lg\delta_1 - lg\delta_2} = 2 \tag{8}$$

Therefore, the dimensions of the 2D horizontal plane in Euclidean space and fractal geometric space are the same, both of which are equal to 2.

Considering another special case, a horizontal plane B possesses a size of $l\times l$ and an elevation of 0, as shown in Figure 1 (a). In the first iteration, B is equally divided into four grids, and the elevation of the centre node (the red point in Figure 1 (b)) is modified to l. At this time, B is converted to a spatial curved surface with a bulge in the centre, as shown in Figure 1 (b-1). Then, performing the second iteration, the four grids in Figure 1 (b) are further divided into 4 equal parts, and the elevation of the centre node of each grid (the four magenta points in Figure 1 (c)) is modified to l. After performing the third and fourth iterations, the nodes whose elevations are modified to l are marked as orange and yellow points in Figure 1 (d) and (e), and the corresponding spatial curved surfaces are shown in Figure 1 (d-1) and (e-1). Repeating the above process, the spatial curved surface gradually evolves into a cubic solid with a side length of l when the number of iterations n approaches infinity.

In this iterative process, only two types of grids are generated. The first type consists of one node with an elevation of l and three nodes with an elevation of 0 (Figure 1 (f)). While the second type contains two nodes with an elevation of l and two other nodes with an elevation of 0, and the two nodes with

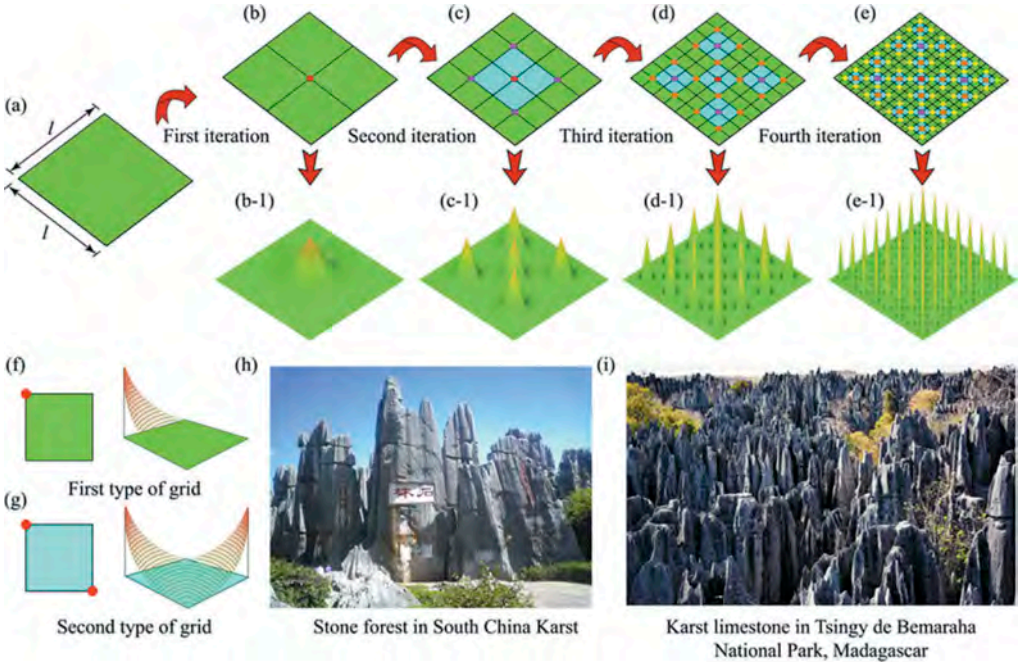

Figure 1. Another special case: (a~e) and (a-1~e-1) evolution of a 2D plane into a 3D solid cube, (f~g) two types of grids in evolution, and (h~i) geological morphologies in nature similar to evolution [Website 1 and 2].

the same elevation are distributed diagonally (Figure 1 (g)). The spatial curved surface after n iterations ($n\to+\infty$) is divided into grids by a scale of δ (Note: δ meets the following condition: $\delta = l/2^m$, $m\leq n$, m, $n\in Z^+$, so do δ_1 and δ_2 in the text below). The numbers of the first type of grids N_1 and the second type of grids N_2 can be expressed as:

$$N_1 = \frac{2}{3}\cdot 4^m + \frac{4}{3} \tag{9}$$

$$N_2 = \frac{1}{3}\cdot 4^m - \frac{4}{3} \tag{10}$$

The Δz of the two types of grids are both l, and the number of cubes N_c required to cover a grid is:

$$N_c = \frac{l}{\delta} \tag{11}$$

The number of cubes $N(\delta)$ required to cover the entire fracture surface is:

$$N(\delta) = \frac{l}{\delta}\times\left(\frac{l}{\delta}\right)^2 = \left(\frac{l}{\delta}\right)^3 \tag{12}$$

Bring the equation (12) into the equation (5) to get:

$$lg\left[\left(\frac{l}{\delta}\right)^3\right] \sim -D\cdot lg\delta \tag{13}$$

As δ changes from δ_1 to δ_2, D can be calculated as:

$$D = -\frac{lg\left[\left(\frac{l}{\delta_1}\right)^3\right] - lg\left[\left(\frac{l}{\delta_2}\right)^3\right]}{lg\delta_1 - lg\delta_2} \tag{14}$$

Therefore, the dimensions of a cubic solid in Euclidean space and fractal geometric space are also consistent and equal to 3.

The morphologies in Figure 1 (b-1) ~ (e-1) are similar to stone forests in Karst Landforms, as shown in Figure 1 (h) and (i). It indicates that the evolution of the spatial curved surface in Figure 1 is not only a hypothetical geometrical model, but supported by some geological morphologies in nature. In addition, any newly proposed method for determining the D of a spatial curved surface should be verified by the above two special cases, and the calculated Ds should be same as the dimensions of 2D plane and 3D solid in Euclidean space.

2.2 *Distortion problem of CCM*

The above proofs show that the CCM have an ability to determine the fractal dimension of any spatial

curved surface whose morphology varies from a 2D plane to a 3D solid. However, when characterizing the 3D morphology of a surface with a small degree of undulation, the CCM suffers from a distortion problem. Taking a fracture surface of sandstone obtained from the true triaxial fracture test (σ_2 =120.3MPa, σ_3=40MPa) as an example, the cause of the distortion problem is analyzed.

The 3D morphology of the fracture surface is shown in Figure 2 (a). It can be observed that there are obvious unevenness and waviness on the surface, and the morphology is quite different from a 2D plane. However, the D calculated by the CCM is 2 (Figure 2 (b)). In other words, the CCM fails to detect the waviness and unevenness and incorrectly identifies the fracture surface as a 2D plane. This distortion problem is related to the algorithm of the CCM.

Figure 2 (c) is the algorithm of the CCM. The number of cubes required to cover a grid depends on $\Delta z/\delta$ (the ratio of the elevation difference to the cube side length). If $\Delta z/\delta$ is less than 1, no matter whether the ratio is 0.01 or 0.99, only one cube is required to cover this grid. It is equivalent to the condition of covering a horizontal grid ($\Delta z/\delta$=0). For a fracture surface with a small degree of undulation, if $\Delta z/\delta$ of all the grids are less than 1 under different scales of δ, the number of cubes required to cover the entire fracture surface is equal to that to cover a 2D plane. Therefore, D is equal to 2. Only when $\Delta z/\delta$ is greater than 1, and two cubes at least are required to cover the grid, will the CCM successfully detect the unevenness and roughness on the fracture surface.

To verify this inference, meshing the fracture surface with different grid numbers, which are 20×20, 50×50, 100×100, 200×200, 500×500, and 1000×1000. The $\Delta z/\delta$ of all the grids are calculated. Based on the value of $\Delta z/\delta$, different colors are assigned to grids, and the color maps of the $\Delta z/\delta$ are generated, as shown in Figure 2 (d).

In general, the maps mainly appear blue and cyan, indicating that in most grids, $\Delta z/\delta$ are not greater than 0.5. When the grid number rises to 200×200, the colors of several grids in the lower left corner approach red. As the number of grids further increases, the color map is basically unchanged.

To better visualize the distribution characteristic of $\Delta z/\delta$, the interval of $\Delta z/\delta \in [0,1]$ is equally divided into 10 sections. The number of grids contained in each section is counted, and its percentage P against the total number of grids is calculated, as shown in the Figure 2 (e).

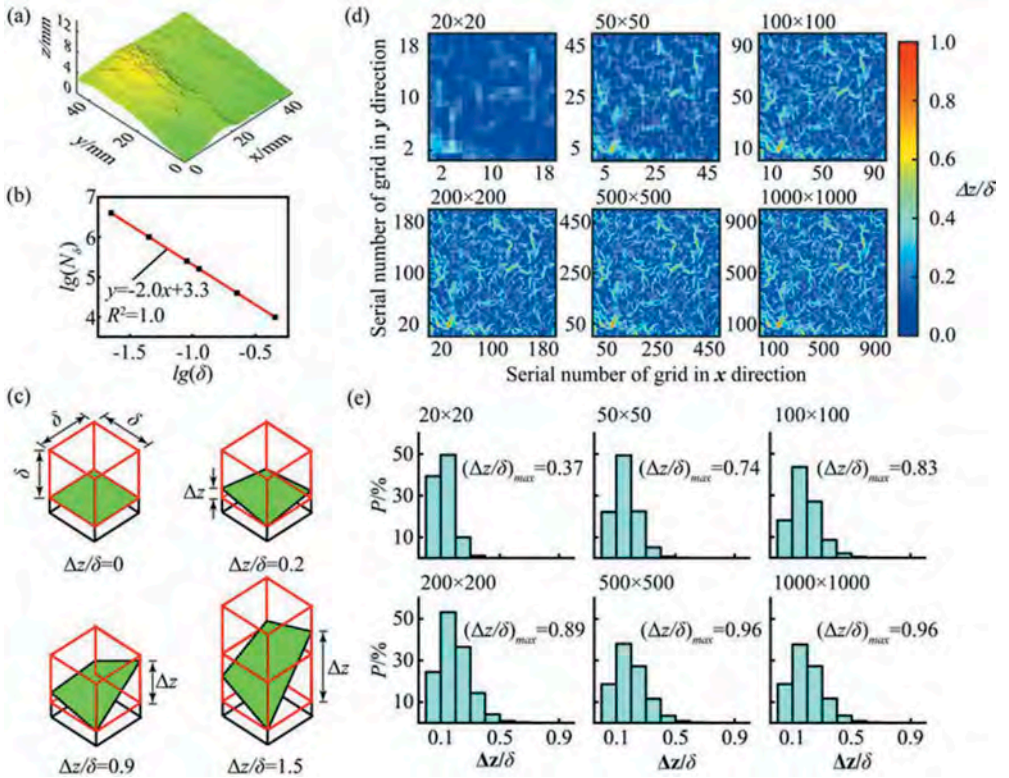

Figure 2. Distortion problem resulting from algorithm of CCM: (a) fracture surface morphology of sandstone, (b) fractal dimension determined by CCM, (c) algorithm of CCM, (d) color maps of $\Delta z/\delta$, and (e) distribution characteristic of $\Delta z/\delta$.

When the grid number is 20×20, all grids are distributed in the interval [0,0.4], and the maximum value of $\Delta z/\delta$ is 0.37. As the number of grids rises to 100×100, the distribution expands to [0,0.9], and the maximum $\Delta z/\delta$ is 0.83. When the number of grids continuously rises to 500×500, the grids are distributed in all intervals, and the maximum value reaches 0.96. With the further increase of the grid number, the distribution interval and the maximum $\Delta z/\delta$ remain unchanged.

The color maps and the distribution characteristics of $\Delta z/\delta$ verify the inference about the distortion problem. As a result, the D calculated by the CCM is equal to that of 2D plane. Therefore, it is inappropriate to characterize the 3D morphology of the fracture surface with a small degree of undulation by the CCM.

3 SURFACE AREA METHOD

To effectively characterize the 3D morphology of the fracture surface with a small degree of undulation, the SAM is adopted instead to determine the D. For the rock fracture surface, the surface area A_s and the grid scale δ have the following relationship (Clarke 1986):

$$A_s \sim \delta^{2-D} \tag{15}$$

Therefore, D can be determined by simply calculating the surface area A_s under different δ.

It is well known that the actual surface area of a fracture surface is almost impossible to be exactly calculated only by the node coordinates. However, when recognizing that meshing is actually a process of differentiating the fracture surface, A_s can be calculated approximatively by the method of surface integral.

Assuming that the fracture surface is continuum and derivable, the elevation z can be regarded as a continuous function $z\ (x, y)$. According to the surface integral, A_s can be expressed as:

$$A_s = \iint \sqrt{1 + \left(\frac{\partial z(x,\ y)}{\partial y}\right)^2 + \left(\frac{\partial z(x,\ y)}{\partial x}\right)^2}\, dxdy \tag{16}$$

The partial derivatives of $z\ (x, y)$ to x and y and the differential elements dx and dy are calculated in the unit of a grid. For the ij-th grid, supposing the coordinates of the four nodes are $(x_{i,\ j},\ y_{i,\ j},\ z_{i,\ j})$, $(x_{i+1,\ j},\ y_{i+1,\ j},\ z_{i+1,\ j})$, $(x_{i,\ j+1},\ y_{i,\ j+1},\ z_{i,\ j+1})$ and $(x_{i+1,\ j+1},\ y_{i+1,\ j+1},\ z_{i+1,\ j+1})$, the dx and dy can be expressed as:

$$dx = \Delta x = x_{i+1,j} - x_{i,j} = x_{i+1,j+1} - x_{i,j+1} \tag{17}$$

$$\mathrm{d}y = \Delta y = y_{i,j+1} - y_{i,j} = y_{i+1,j+1} - y_{i+1,j} \tag{18}$$

While, the partial derivatives of $z\ (x, y)$ to x and y can be expressed as:

$$\frac{\partial z(x,\ y)}{\partial x} = \frac{(z_{i+1,j} + z_{i+1,j+1})/2 - (z_{i,j} + z_{i,j+1})/2}{x_{i+1j} - x_{ij}} \tag{19}$$

$$\frac{\partial z(x,\ y)}{\partial y} = \frac{(z_{i,j+1} + z_{i+1,j+1})/2 - (z_{i,j} + z_{i+1,j})/2}{y_{i,j+1} - y_{i,j}} \tag{20}$$

Then, the grid area $A_{i,\ j}$ can be expressed as:

$$A_{i,j} = \sqrt{1 + \left(\frac{\partial z(x,\ y)}{\partial y}\right)^2 + \left(\frac{\partial z(x,\ y)}{\partial x}\right)^2} \times \left(x_{i+1,j} - x_{i,j}\right) \times \left(y_{i,j+1} - y_{i,j}\right) \tag{21}$$

Accumulating the area of all grids gives the entire fracture surface area A_s:

$$A_s = \sum_{i=1}^{n} \sum_{j=1}^{n} A_{i,j} \tag{22}$$

Similarly, the surface area method is verified by the two special cases in section 2.1. For the 2D plane, according to the equation (19) and (20), the partial derivatives of a grid can be expressed as:

$$\frac{\partial z(x,\ y)}{\partial x} = 0 \tag{23}$$

$$\frac{\partial z(x,\ y)}{\partial y} \tag{24}$$

And the grid surface area $A_{i,\ j}$ is:

$$A_{i,j} = \delta^2 \tag{25}$$

Accumulating the areas of all grids gives the entire fracture surface area A_s:

$$A_s = \sum_{i=1}^{n} \sum_{j=1}^{n} A_{i,j} = \left(\frac{l}{\delta}\right)^2 \times \delta^2 = l^2 \tag{26}$$

At this time, A_s is irrelevant to δ. Bringing A_s into the equation (15) and taking the logarithm on both sides to calculate D:

$$D = 2 - \frac{\log(l^2) - \log(l^2)}{\log(\delta_1) - \log(\delta_2)} = 2 \tag{27}$$

It is obvious that the D of the 2D plane calculated by the SAM is consistent with the dimension in the Euclidean space.

For the second special case, in the first type of grid, the partial derivatives are:

$$\left|\frac{\partial z(x,\ y)}{\partial x}\right| = \frac{l}{2\delta} \tag{28}$$

$$\left|\frac{\partial z(x,\ y)}{\partial y}\right| = \frac{l}{2\delta} \tag{29}$$

The grid surface area $A_{i,\ j}$ is:

$$A_{i,j} = \sqrt{\frac{4\delta^2 + l^2 + l^2}{4\delta^2}}\delta^2 \tag{30}$$

When δ approaches 0, δ^2 is infinitesimal compared to l^2 and can be ignored. Therefore, the equation (33) is simplified to:

$$A_{i,j} \approx \sqrt{\frac{l^2 + l^2}{4\delta^2}}\delta^2 = \frac{l \cdot \delta}{\sqrt{2}} \tag{31}$$

For the second type of grid, the partial derivatives are:

$$\left|\frac{\partial z(x,\ y)}{\partial x}\right| = 0 \tag{32}$$

$$\left|\frac{\partial z(x,\ y)}{\partial y}\right| = 0 \tag{33}$$

The grid surface area $A_{i,j}$ is:

$$A_{i,j} = \delta^2 \tag{34}$$

According to the numbers of the two types of grids N_1, N_2 in the equation (9) and (10), the entire fracture surface area A_s:

$$A_s = \sum_{i=1}^{n}\sum_{j=1}^{n} A_{i,j} = \frac{l \cdot \delta}{\sqrt{2}} \times \left(\frac{2 \times 4^m}{3} + \frac{4}{3}\right) + \delta^2 \times \frac{4^m - 4}{3} \tag{35}$$

Substituting $\delta = l/2^m$ into equation (35):

$$A_s = \frac{4l^2}{3\sqrt{2} \cdot 2^m} + \frac{\sqrt{2}l^2 \cdot 2^m}{3} - \frac{4l^2}{3 \cdot 4^m} + \frac{l^2}{3} \tag{36}$$

When m approaches infinity, comparing to the second term, the first, third, and last terms in equation (36) can be ignored. Equation (36) is simplified to:

$$A_s \approx \frac{\sqrt{2}l^2 \cdot 2^m}{3} \tag{37}$$

Bringing equation (37) into equation (15) and taking the logarithm on both sides to calculate D:

$$D = 2 - \frac{\log\left(\frac{\sqrt{2}l^2}{3} \cdot 2^{m_1}\right) - \log\left(\frac{\sqrt{2}l^2}{3} \cdot 2^{m_2}\right)}{log\frac{l}{2^{m_1}} - log\frac{l}{2^{m_2}}} \tag{38}$$

The dimension calculated by the SAM is the same as that in the Euclidean space. It can be observed that the SAM also have an ability to determine the D of any spatial curved surface whose morphology varies from a 2D plane to a 3D solid.

Then, the SAM is used to determine the D of the fracture surface in Figure 2 (a). The A_s corresponding to different δ are shown in Table 1, and their linear relationship in the bi-logarithmic coordinate system is shown in Figure 3. The D calculated by the SAM is 2.00397, which is significantly higher than that by the CCM. It is proved that the SAM is more effective in characterizing the 3D morphology of the fracture surface with a small degree of undulation.

The reason why the SAM can avoid the distortion problem is its ability to capture the differences in the undulation of fracture surface. Any subtle increase or decrease in the elevations of nodes will be reflected in the A_s, and then alters the linear relationship between δ and A_s, introducing the variation of D.

4 APPLICATION EXAMPLE

4.1 *Effectiveness of SAM*

To further verify the effectiveness of the SAM, the fracture surfaces of sandstone in a series of conventional triaxial tests are selected to analyze, as shown in Figure 4. The Ds of the fracture surfaces are calculated by the CCM and the SAM, as shown in Table 2 and 3. The variation trends of D with the confining pressure σ_c are shown in Figure 5.

With the increase of σ_c, the Ds calculated by the two methods show a decreasing trend. However, the

Table 1. Fracture surface areas corresponding to different grid scales under σ_2=120.3MPa, σ_3=40MPa condition.

δ/mm	9.00	5.62	2.81	1.41	0.70	0.45	0.35
A_s/mm^2	2033.16	2035.52	2039.62	2045.02	2052.37	2056.69	2058.63

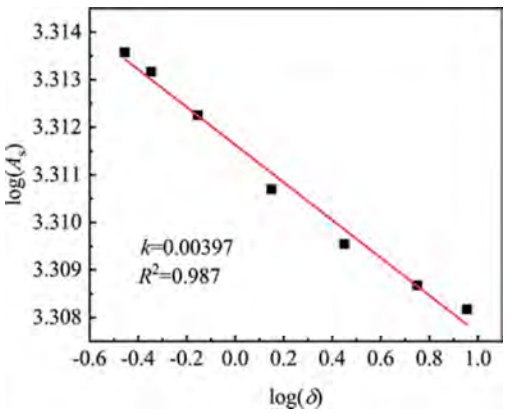

Figure 3. Linear relationship between A_s and δ in bi-logarithmic coordinate system.

*D*s obtained by the SAM are reasonable than those of the CCM.

For the CCM, the variation of *D* presents a step-wise decreasing trend. The distortion problem is reflected not only by the *D*s under σ_c = 40MPa and 50MPa conditions, but also by those under σ_c = 10MPa and 20MPa conditions. Both of the *D*s under σ_c = 40MPa and 50MPa conditions are equal to 2, and the CCM fails to detect the undulations of these two fracture surfaces. While, the *D*s under σ_c = 10MPa and 20MPa conditions are basically equal, which indicates the CCM is unable to identify the undulation difference between these two fracture surfaces.

For the SAM, the undulation difference between the fracture surfaces under σ_c = 10MPa and 20MPa conditions is properly identified. Although the *D*s under σ_c = 40MPa and 50MPa are close, the values are greater than 2, which indicates the undulation is effectively detected.

4.2 *Correlation between fractal dimension and fracture mechanism*

The calculation results obtained by the SAM show that there is a negative correlation between *D* and σ_c, which implies that the increase of σ_c flattens the fracture surface. In order to clarify the mechanism underlying this negative correlation, the fracture surfaces under σ_c = 2Mpa and 50Mpa conditions are selected to identify the microscopic fracture characteristics.

Figure 6 is the SEM micrographs of the fracture surface under σ_c = 2Mpa condition. It is observed that the fracture surface is rough and presents a strong sense of graininess with obvious pits

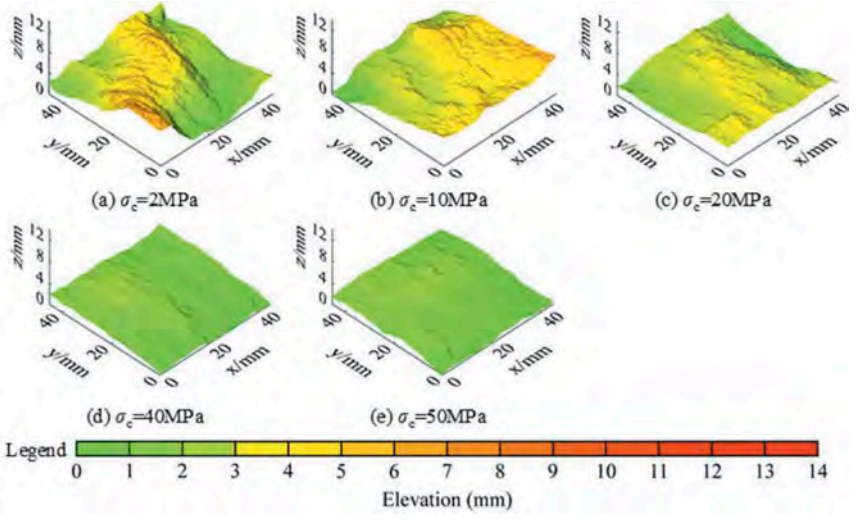

Figure 4. 3D morphologies of fracture surfaces under different σ_c conditions.

Table 2. Fractal dimensions determined by CCM under different σ_c conditions.

σ_c = 2MPa	δ/mm	2.30	0.92	0.46	0.23	0.092	0.046	D=2.00321
	$N(\delta)$	400	2515	10101	40485	253210	1013028	
σ_c = 10MPa	δ/mm	2.30	0.92	0.46	0.23	0.092	0.046	D=2.00064
	$N(\delta)$	400	2501	10014	40077	250562	1002281	
σ_c = 20MPa	δ/mm	2.25	0.90	0.45	0.22	0.090	0.045	D=2.00067
	$N(\delta)$	400	2500	10008	40079	250530	1002202	
σ_c = 40MPa	δ/mm	2.25	0.90	0.45	0.22	0.090	0.045	D=2.00000
	$N(\delta)$	400	2500	10000	40000	250000	1000000	
σ_c = 50MPa	δ/mm	2.25	0.90	0.45	0.22	0.090	0.045	D=2.00000
	$N(\delta)$	400	2500	10000	40000	250000	1000000	

Table 3. Fractal dimensions determined by SAM under different σ_c conditions.

σ_c = 2MPa	δ/mm	9.00	5.62	2.81	1.41	0.70	0.45	0.35	D=2.00910
	A_s/mm^2	2033.16	2035.52	2039.62	2045.02	2052.37	2056.69	2058.63	
σ_c = 10MPa	δ/mm	9.20	5.75	2.88	1.44	0.72	0.46	0.36	D=2.00566
	A_s/mm^2	2131.56	2139.18	2148.84	2155.98	2164.52	2169.48	2171.56	
σ_c = 20MPa	δ/mm	9.00	5.62	2.81	1.41	0.70	0.45	0.35	D=2.00490
	A_s/mm^2	2039.51	2042.53	2049.28	2055.34	2063.59	2069.00	2071.46	
σ_c = 40MPa	δ/mm	9.00	5.62	2.81	1.41	0.70	0.45	0.35	D=2.00360
	A_s/mm^2	2030.33	2031.55	2036.59	2041.39	2047.65	2051.33	2052.95	
σ_c = 50MPa	δ/mm	9.00	5.62	2.81	1.41	0.70	0.45	0.35	D=2.00359
	A_s/mm^2	2028.89	2030.69	2034.37	2039.01	2046.86	2050.01	2051.82	

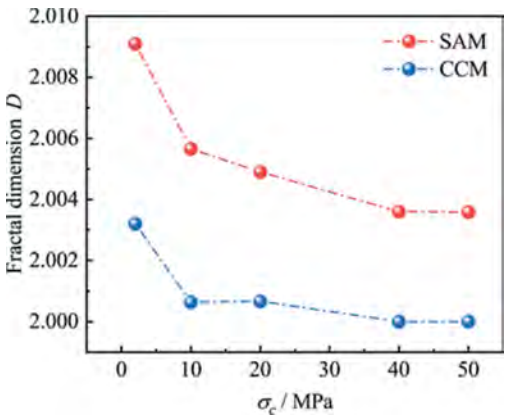

Figure 5. Variation trends of fractal dimension determined by CCM and SAM with increase of σ_c.

(Figure 6 (a)). At the crystal-size scale, the crystalline mineral grains remain intact and present typical intergranular fracture (Figure 6 (b)).

Figure 7 shows the casting thin section micrographs of the fracturing path under σ_c = 2Mpa condition. The blue areas are fracture and voids, and the yellow areas are the mineral particles composing sandstone. Most of the particles on both side of the fracture remain intact. For a few scattered broken grains, a preferred orientation is observed in microcracks that aligned parallel to the direction of the fracture (Figure 7 (b)).

According to the microscopic fracture characteristics in Figure 6 and 7, the fracture mechanism under σ_c = 2Mpa condition is tensile fracture. The fracture propagates along particle interfaces with a weak cementing strength. Due to the spatial randomness and heterogeneity of the cementing strength, the fracture path is tortuous and obvious pits and uplift areas are formed, inducing an increase in the undulation degree of the fracture surface. Consequently, the fracture surface resulting from the tensile fracture possesses a higher D.

Figure 8 is the SEM micrographs of the fracture surface under σ_c = 50Mpa condition. The fracture surface is flat with a large amount of rock powder and debris adhering (Figure 8 (a)). At the crystal scale, the crystalline grains present trans-granular fracture. The sizes and shapes of the broken crystalline grain are irregular (Figure 8 (b)).

Figure 9 shows the casting thin section micrographs of the fracturing path under σ_c = 50Mpa condition. Most of the particles near the fracture surfaces are damaged. Microcracks cross the particles with no preferred orientation (Figure 9 (a)). Meanwhile, the developments of microcracks cross each other and form a diamond cross structure, resulting in the mineral particles being crushed (Figure 9 (b)).

All of the above fracture characteristics showed in Figure 8 and 9 indicate that the mechanism of the rock under σ_c = 50Mpa condition is shear fracture. When

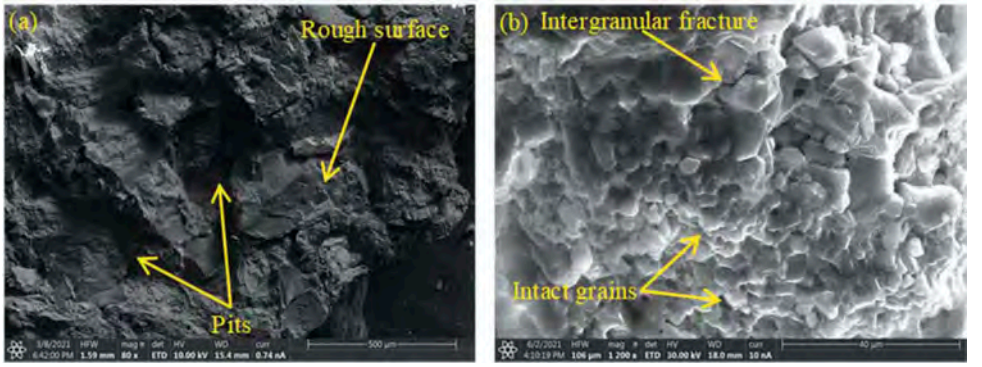

Figure 6. Micrographs of the fracture surface of failed sandstone under σ_c = 2MPa condition.

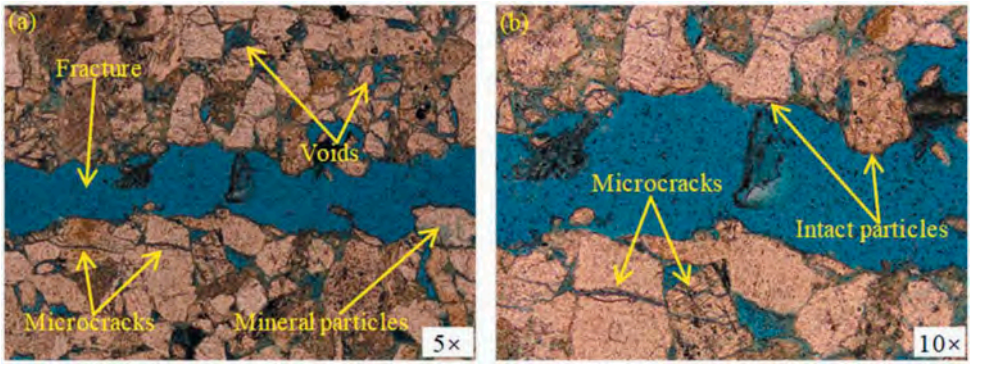

Figure 7. Micrographs of the casting thin section of failed sandstone under σ_c = 2MPa condition.

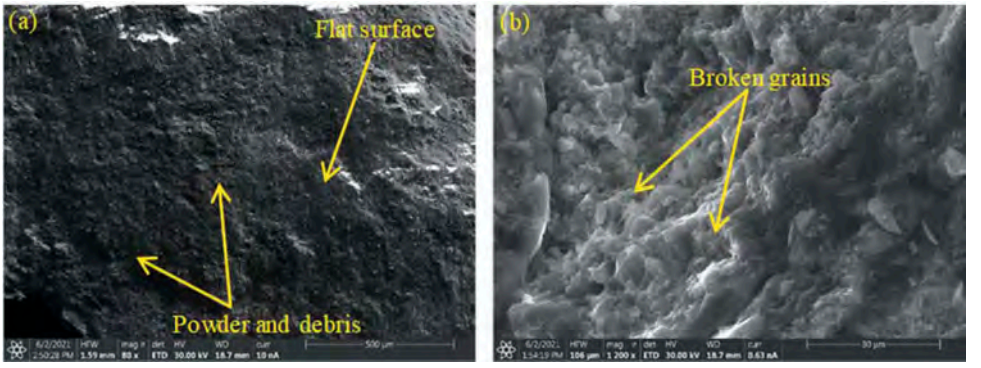

Figure 8. Micrographs of the fracture surface zone of failed sandstone under σ_c = 50MPa condition.

subjected to a strong shearing effect, the fracture propagates along the direction of maximum shear stress, and the large particles on the cracking path are sheared off or crushed. Additionally, the relative slippage and friction abrade away the surface waviness, flattening the fracture surface. Therefore, shear fracture will result in a lower *D*.

Based on the above analysis, it is clear that the reason underlying the negative correlation between *D* and σ_c is the transition of the fracture mechanism. With the increase of σ_c, the fracture mechanism gradually transforms from tensile fracture to shear fracture. (Gao et al. 2019; Yang et al. 2012) The enhancement of shear effect flattens the fracture surface and

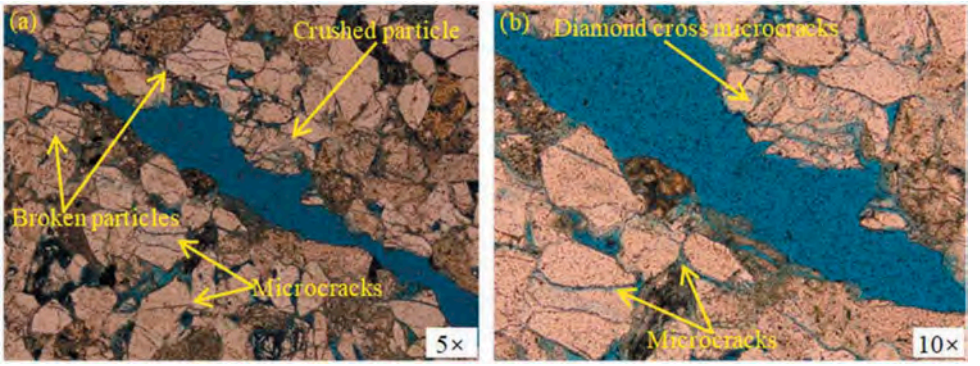

Figure 9. Micrographs of the casting thin section of failed sandstone under σ_c = 50MPa condition.

introduces the decrease of the surface undulation, leading to a lower D.

Inspired by this correlation, D as an index for characterizing the 3D morphology of the fracture surface can be a supplementary means to determine the fracture mechanism. The fracture surface with a larger D is subjected to a stronger effect of tension fracture. Fracture surfaces with approximate Ds share a similar fracture mechanism.

5 DISCUSSION

5.1 *Applicability of the improved CCM*

Several improved CCMs have been mentioned in the Introduction. The purposes of the improvements are to improve the calculation accuracy and stability of CCM. To check whether these improvements help to solve the distortion problems, three improved CCMs which are ICCM, DCCM and RDCCM are chosen to determine the Ds of the fracture surfaces in Figure 5, the calculation results are shown in Figure 10.

For the ICCM and DCCM, with the increase of σ_c, Ds present a rising trend which is obviously not consistent with the undulation characteristics in Figure 5. This is attributed to the fact that these two methods compute the number of cubes covering the fracture surface from a unified reference plane, which brings an overcompensation effect on the cube number. The overcompensation effect becomes stronger with the decrease of the undulation degree, and results in a rising trend of Ds. It is ridiculous that the improvements made by the ICCM and DCCM aggravate the distortion problem rather than solve it.

For the RDCCM, the calculated fractal dimensions are identical to those of the CCM, which implies the improvement made by the RDCCM has no contribution to solving the distortion problem.

Although the above improved CCMs have corrected some shortcomings of CCM on the issues they target, the results show that the improved CCMs are still not suitable for characterizing the 3D morphology of the fracture surface with a small degree of undulation.

5.2 *Calculation accuracy of SAM*

It has been proven that the SAM is an effective fractal dimension calculation method. To evaluate the accuracy of the SAM, the Takagi fractal surface is introduced as the calculation reference.

A Takagi surface is an extension to 2D of the Takagi curve, and can be seen as a superposition of pyramids of various frequencies attenuated by a scaling factor:

$$f(x,y) = \sum_{n=1}^{\infty} b^n \psi\left(2^{n-1}x, 2^{n-1}y\right) \tag{39}$$

Where $1/2<b<1$ and $x, y \in R^+ = [0,1]$. The function ψ, called the generating kernel, is a separable function that consists of the product of two sawtooth function:

$$\psi(x,y) = 2 \cdot D(x,Z) \cdot 2 \cdot D(y,Z) \tag{40}$$

Where D (x, Z) is the distance to the nearest integer of x.

The fractal dimension of the Takagi surface is a known value D_T related to b and given by the following formula:

$$D_T = \frac{\log(8b)}{\log(2)} \tag{41}$$

By assigning a series of values to b, Takagi surfaces with different fractal dimensions are generated, as shown in Figure 11. Then, the SAM is applied to Takagi surface to determine the fractal dimension, which is denoted as D_S. The difference between D_T

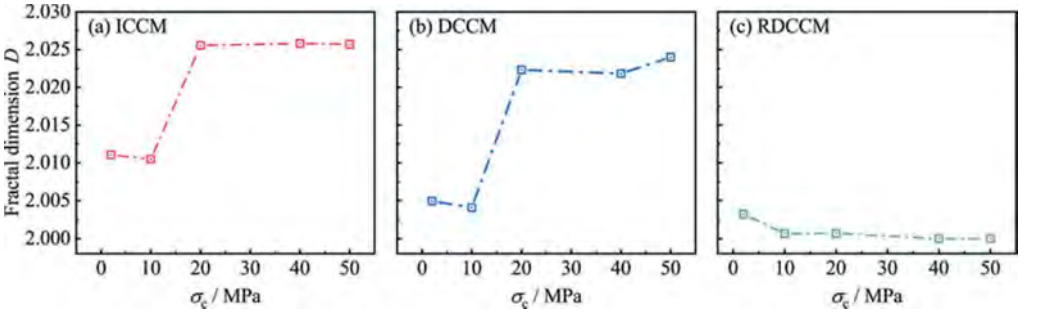

Figure 10. Variation trends of fractal dimension determined by three improved CCMs with increase of σ_c.

and D_S is defined as the error E. The calculation accuracy ε of the SAM is evaluated by the following equation:

$$E = D_T - D_S \tag{42}$$

$$\varepsilon = \left(1 - \frac{|E|}{D_T - 2}\right) \times 100\% \tag{43}$$

The physical meaning of equation (42) is the accuracy of SAM for quantifying the degree to which the morphology of the Takagi surface deviates from that of the 2D plane.

Table 4 is the fractal dimensions of Takagi surfaces calculated by the SAM and corresponding accuracies, and Figure 12 is the comparisons between D_T and D_S. When D_Ts are not greater than 2.40, the values of E are relatively small, and εs are not less than 90%. Once D_T exceeds 2.40, E begins to increase, and ε gradually decreases. Especially, for the Takagi surface with D_T equaling 2.9, ε decreases to 73.33%.

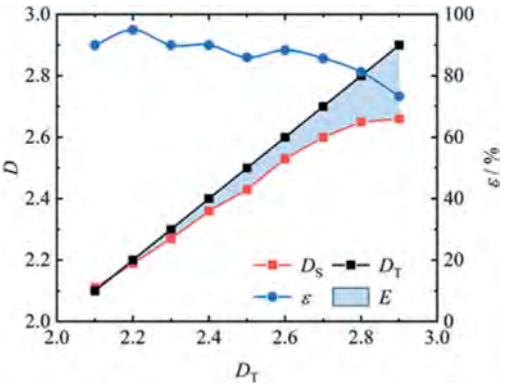

Figure 12. Comparisons between D_T and D_S, and accuracy of SAM.

The results in Table 4 and Figure 12 indicate that the SAM is not a high-accuracy method for determining D of the fracture surface. Nonetheless, considering the Ds of the surfaces encountered in rock

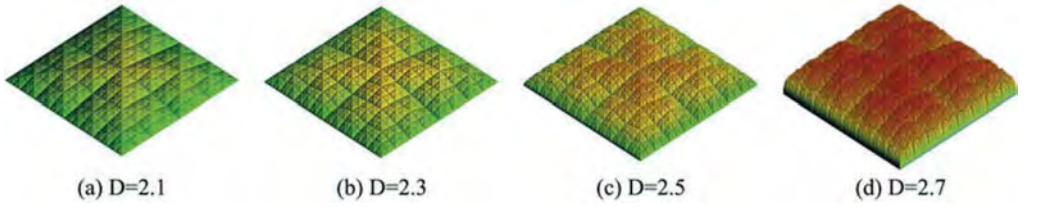

Figure 11. Takagi surfaces with different fractal dimensions.

Table 4. Fractal dimensions of Takagi surfaces and calculated results, errors, and accuracies of SAM.

D_T	2.10	2.20	2.30	2.40	2.50	2.60	2.70	2.80	2.90
D_S	2.11	2.19	2.27	2.36	2.43	2.53	2.60	2.65	2.66
E	-0.01	0.01	0.03	0.04	0.07	0.07	0.10	0.15	0.24
ε	90.00%	95.00%	90.00%	90.00%	86.00%	88.33%	85.71%	81.25%	73.33%

mechanics and engineering are seldom greater than 2.2, the accuracy of the SAM is well enough to characterize the morphology. In addition, the reason for adopting the SAM in this research lies not in its calculation accuracy, but in its ability to effectively identify and reflect the variation trend of the undulation degree of the fracture surface.

6 CONCLUSION

In this study, to seek an effective means to characterize the fracture of rock, the CCM and the SAM are compared by determining the fractal dimension of rock fracture surface. The correlation between the fractal dimension and fracture mechanism is established. The main conclusions can be drawn as follow:

(1) Using the CCM to quantify the 3D morphology of rock fracture surface with a small degree of undulation will result in a distorted D. This distortion problem comes from the algorithm of the CCM, in which the method for determining the number of cubes covering the surface is unable to capture the variation of surface undulation within a size equal to the height of the cube.

(2) Based on a new algorithm for calculating the fracture surface area A_s, the SAM completely avoids the distortion problem. The reason is that any subtle variation in the undulation of the fracture surface will be reflected in the A_s and alter the linear relationship between δ and A_s, which introduces the increase or decrease of D.

(3) There is a negative correlation between the fractal dimension and the confining pressure σ_c which results from the transition of the fracture mechanism with the variation of confining pressure. With the increase of the σ_c, the fracture mechanism gradually transforms from tensile fracture to shear fracture. The enhancement of shear effect induces the undulation degradation of the fracture surface, leading to a lower D.

(4) Fractal dimension can be a supplementary means to determine the fracture mechanism. The fracture surface with a larger D is subjected to a stronger effect of tension fracture. Fracture surfaces with approximate Ds share a similar fracture mechanism.

ACKNOWLEDGEMENTS

The research reported in this paper was financially supported by the National Natural Science Foundation of China (Grant No. 41877239, 51422904, 51379112, 42172310, and 40902084), and the Shandong Provincial Natural Science Foundation (No. JQ201513).

REFERENCES

1978. International society for rock mechanics commission on standardization of laboratory and field tests: Suggested methods for the quantitative description of discontinuities in rock masses. International Journal of Rock Mechanics and Mining Sciences & Geomechanics Abstracts, 15, 319–368, doi: https://doi.org/10.1016/0148-9062(78)91472-9.

Ai, T., Ru, Z., Zhou, H. & Pei, J.L. 2014. Box-counting methods to directly estimate the fractal dimension of a rock surface. Applied Surface Science, 314, 610–621, doi: 10.1016/j.apsusc.2014.06.152.

Archambault, G., Gentier, S., Riss, J. & Flamand, R. 1997. The evolution of void spaces (permeability) in relation with rock joint shear behavior. International Journal of Rock Mechanics and Mining Sciences, 34, 14.e11–14.e15, doi: https://doi.org/10.1016/S1365-1609(97)00046-4.

Babanouri, N., Karimi Nasab, S. & Sarafrazi, S. 2013. A hybrid particle swarm optimization and multi-layer perceptron algorithm for bivariate fractal analysis of rock fractures roughness. International Journal of Rock Mechanics and Mining Sciences, 60, 66–74, doi: https://doi.org/10.1016/j.ijrmms.2012.12.028.

Barton, N. 1973. Review of a new shear-strength criterion for rock joints. Engineering Geology, 7, 287–332, doi: https://doi.org/10.1016/0013-7952(73)90013-6.

Barton, N. & Choubey, V. 1977. The shear strength of rock joints in theory and practice. Rock Mechanics Felsmechanik Mecanique des Roches, 10, 1–54, doi: 10.1007/BF01261801.

Belem, T., Homand-Etienne, F. & Souley, M. 1997. Fractal analysis of shear joint roughness. International Journal of Rock Mechanics and Mining Sciences, 34, 130.e131–130.e116, doi: https://doi.org/10.1016/S1365-1609(97)80001-9.

Berry, M. & Lewis, Z. 1980. On the Weierstrass-Mandelbrot Fractal Function. Proceedings of The Royal Society A: Mathematical, Physical and Engineering Sciences, 370, 459–484, doi: 10.1098/rspa.1980.0044.

Brady, B.H.G. & Brown, E. 2006. Rock Mechanics For Underground Mining. Chapman and Hall, 1993.

Chen, S.J., Chang, J.P., Liu, X.G. & Li, Z.H. 2020. Size effect characteristics of structural surfaces by improved projective covering method. International Journal of Geo-Engineering, 11, 18, doi: 10.1186/s40703-020-00125-0.

Chen, S.J., Zhu, W.C., Yu, Q.L. & Liu, X.G. 2016. Characterization of Anisotropy of Joint Surface Roughness and Aperture by Variogram Approach Based on Digital Image Processing Technique. Rock Mechanics and Rock Engineering, 49, 855–876, doi: 10.1007/s00603-015-0795-x.

Clarke, K. 1986. Computation of the Fractal Dimension of Topographic Surfaces Using the Trangular Prism Surface Area Mehtod. Computers & Geosciences, 12, 713–722, doi: 10.1016/0098-3004(86)90047-6.

Ding, C., Yang, R. & Yang, L. 2021. Experimental results of blast-induced cracking fractal characteristics and propagation behavior in deep rock mass. International Journal of Rock Mechanics and Mining Sciences, 142, 104772, doi: https://doi.org/10.1016/j.ijrmms.2021.104772.

Ehlen, J. 2000. Fractal analysis of joint patterns in granite. International Journal of Rock Mechanics and Mining

Sciences, 37, 909–922, doi: https://doi.org/10.1016/S1365-1609(00)00027-7.
El-Soudani, S.M. 1978. Profilometric analysis of fractures. Metallography, 11, 247–336, doi: https://doi.org/10.1016/0026-0800(78)90045-9.
Feng, X.-T., Yu, Y., Feng, G.-L., Xiao, Y.-X., Chen, B.-r. & Jiang, Q. 2016. Fractal behaviour of the microseismic energy associated with immediate rockbursts in deep, hard rock tunnels. Tunnelling and Underground Space Technology, 51, 98–107, doi: https://doi.org/10.1016/j.tust.2015.10.002.
Feng, X., Chen, B., Li, S., Zhang, C., Xiao, Y., Feng, G., Zhou, H., Qiu, S., Zhao, Z., Yu, Y., Chen, D. & Ming, H. 2012. Studies on the evolution process of rockbursts in deep tunnels. Journal of Rock Mechanics and Geotechnical Engineering, 4, 289–295, doi: https://doi.org/10.3724/SP.J.1235.2012.00289.
Gao, Y., Feng, X.-T., Wang, Z. & Zhang, X. 2019. Strength and failure characteristics of jointed marble under true triaxial compression. Bulletin of Engineering Geology and the Environment, 79, 1–15, doi: 10.1007/s10064-019-01610-2.
Ge, Y., Kulatilake, P.H.S.W., Tang, H. & Xiong, C. 2014. Investigation of natural rock joint roughness. Computers and Geotechnics, 55, 290–305, doi: https://doi.org/10.1016/j.compgeo.2013.09.015.
Goodchild, M. 1982. The Fractional Brownian process as a terrain simulation model. Modelling and Simulation, 13.
Hsiung, S.M., Ghosh, A., Ahola, M.P. & Chowdhury, A.H. 1993. Assessment Of Conventional Methodologies For Joint Roughness Coefficient Determination. International Journal of Rock Mechanics and Mining Sciences & Geomechanics Abstracts, 30, 825–829, doi: 10.1016/0148-9062(93)90030-H.
Jafari, A. & Babadagli, T. 2013. Relationship between percolation–fractal properties and permeability of 2-D fracture networks. International Journal of Rock Mechanics and Mining Sciences, 60, 353–362, doi: https://doi.org/10.1016/j.ijrmms.2013.01.007.
Jiang, Y., Tanabashi, Y., Li, B. & Xiao, J. 2006. Influence of geometrical distribution of rock joints on deformational behavior of underground opening. Tunnelling and Underground Space Technology, 21, 485–491, doi: https://doi.org/10.1016/j.tust.2005.10.004.
Ju, Y., Zheng, J., Epstein, M., Sudak, L., Wang, J. & Zhao, X. 2014. 3D numerical reconstruction of well-connected porous structure of rock using fractal algorithms. Computer Methods in Applied Mechanics and Engineering, 279, 212–226, doi: 10.1016/j.cma.2014.06.035.
Kulatilake, P., Balasingam, P., Park, J. & Morgan, R. 2006. Natural rock joint roughness quantification through fractal techniques. Geotechnical and Geological Engineering, 24, 1181–1202, doi: 10.1007/s10706-005-1219-6.
Kulatilake, P., Shou, G., Huang, T. & Morgan, R. 1995. New peak shear strength criteria for anisotropic rock joints. International Journal of Rock Mechanics and Mining Sciences & Geomechanics Abstracts, 32, 673–697, doi: 10.1016/0148-9062(95)00022-9.
Kwaśny, W. 2009. A modification of the method for determination of surface fractal dimension and multifractal analysis. Journal of Achievements in Materials and Manufacturing Engineering, 33.
Li, Y., Oh, J., Mitra, R. & Hebblewhite, B. 2016. A constitutive model for a laboratory rock joint with multi-scale asperity degradation. Computers and Geotechnics, 72, 143–151, doi: https://doi.org/10.1016/j.compgeo.2015.10.008.
Li, Y., Sun, S. & Yang, H.-W. 2020. Scale Dependence of Waviness and Unevenness of Natural Rock Joints through Fractal Analysis. Geofluids, 2020, 1–18, doi: 10.1155/2020/8818815.
Liebovitch, L. & Toth, T. 1989. A Fast Algorithm to Determine Fractal Dimension by Box-Counting. Physics Letters A, 141, 386–390, doi: 10.1016/0375-9601(89)90854-2.
Liu, J.-p., Feng, X.-t., Li, Y.-h., Xu, S.-d. & Sheng, Y. 2013. Studies on temporal and spatial variation of microseismic activities in a deep metal mine. International Journal of Rock Mechanics and Mining Sciences, 60, 171–179, doi: https://doi.org/10.1016/j.ijrmms.2012.12.022.
Maerz, N.H., Franklin, J.A. & Bennett, C.P. 1990. Joint roughness measurement using shadow profilometry. International Journal of Rock Mechanics and Mining Sciences & Geomechanics Abstracts, 27, 329–343, doi: https://doi.org/10.1016/0148-9062(90)92708-M.
Malinverno, A. 1990. A simple method to estimate the fractal dimension of self-affine series. Geophysical Research Letters - GEOPHYS RES LETT, 17, 1953–1956, doi: 10.1029/GL017i011p01953.
Mandelbrot, B.B. 1967. How Long Is the Coast of Britain? Statistical Self-Similarity and Fractional Dimension. Science (New York, N.Y.), 156, 636–638, doi: 10.1126/science.156.3775.636.
Mandelbrot, B.B. 1977. Fractal Geometry of Nature.
Matsushita, M. & Ouchi, S. 1989. On the self-affinity of various curves. Physica D: Nonlinear Phenomena, 38, 246–251, doi: https://doi.org/10.1016/0167-2789(89)90201-7.
Miller, S.M., Mcwilliams, P.C.M. & Kerkering, J.C. 1990. Ambiguities in estimating fractal dimensions of rock fracture surfaces.
Myers, N.O. 1962. Characterization of surface roughness. Wear, 5, 182–189, doi: 10.1016/0043-1648(62)90002-9.
Nara, Y., Koike, K., Yoneda, T. & Kaneko, K. 2006. Relation between subcritical crack growth behavior and crack paths in granite. International Journal of Rock Mechanics and Mining Sciences, 43, 1256–1261, doi: https://doi.org/10.1016/j.ijrmms.2006.03.016.
Orey, S. 1970. Gaussian sample functions and the Hausdorff dimension of level crossings. Probability Theory and Related Fields, 15, 249–256, doi: 10.1007/BF00534922.
Patton, F.D. 1966. Multiple modes of shear failure in rock. 1st ISRM Congress, 509–515.
Raimbay, A., Babadagli, T., Kuru, E. & Develi, K. 2017. Fractal analysis of single-phase water and polymer solution flow at high rates in open and horizontally displaced rough fractures. International Journal of Rock Mechanics and Mining Sciences, 92, 54–71, doi: https://doi.org/10.1016/j.ijrmms.2016.12.006.
Russell, D., Hanson, J. & Ott, E. 1980. Dimension of Strange Attractors. Phys. Rev. Lett., 45, doi: 10.1103/PhysRevLett.45.1175.
Sayles, R.S. & Thomas, T.R. 1977. The spatial representation of surface roughness by means of the structure function: A practical alternative to correlation. Wear, 42, 263–276, doi: https://doi.org/10.1016/0043-1648(77)90057-6.
Schlueter, E., Zimmerman, R., Witherspoon, P. & Cook, N. 1997a. The fractal dimension of pores in sedimentary rocks and its influence on permeability. Engineering

Geology - ENG GEOL, 48, 199–215, doi: 10.1016/S0013-7952(97)00043-4.

Schlueter, E.M., Zimmerman, R.W., Witherspoon, P.A. & Cook, N.G.W. 1997b. The fractal dimension of pores in sedimentary rocks and its influence on permeability. Engineering Geology, 48, 199–215, doi: https://doi.org/10.1016/S0013-7952(97)00043-4.

Smith, M.W. 2014. Roughness in the Earth Sciences. Earth-Science Reviews, 136, 202–225, doi: https://doi.org/10.1016/j.earscirev.2014.05.016.

Tatone, B.S.A. & Grasselli, G. 2013. An Investigation of Discontinuity Roughness Scale Dependency Using High-Resolution Surface Measurements. Rock Mechanics and Rock Engineering, 46, 657–681, doi: 10.1007/s00603-012-0294-2.

Tikou, B., Homand-Etienne, F. & Souley, M. 2000. Quantitative Parameters for Rock Joint Surface Roughness. Rock Mechanics and Rock Engineering, 33, 217–242, doi: 10.1007/s006030070001.

Tse, R. & Cruden, D. 1979. Estimating joint roughness coefficients. International Journal of Rock Mechanics and Mining Sciences & Geomechanics Abstracts, 16, 303–307, doi: 10.1016/0148-9062(79)90241-9.

Wu, T.H. & Ali, E.M. 1978. Statistical representation of joint roughness. International Journal of Rock Mechanics and Mining Sciences & Geomechanics Abstracts, 15, 259–262, doi: https://doi.org/10.1016/0148-9062(78)90958-0.

Xie, H. & Pariseau, W.G. 1993. Fractal character and mechanism of rock bursts. International Journal of Rock Mechanics and Mining Sciences & Geomechanics Abstracts, 30, 343–350, doi: https://doi.org/10.1016/0148-9062(93)91718-X.

Xie, H. & Wang, J.-a. 1999a. Direct fractal measurement of fracture surfaces. International Journal of Solids and Structures, 36, 3073–3084, doi: https://doi.org/10.1016/S0020-7683(98)00141-3.

Xie, H., Wang, J.-A. & Xie, W.-H. 1997. Fractal effects of surface roughness on the mechanical behavior of rock joints. Chaos, Solitons & Fractals, 8, 221–252, doi: https://doi.org/10.1016/S0960-0779(96)00050-1.

Xie, H. & Wang, J. 1999b. Direct fractal measurement of fracture surfaces. International Journal of Solids and Structures, 36, 3073–3084, doi: 10.1016/S0020-7683(98)00141-3.

Xie, H., Wang, J. & Stein, E. 1998. Direct fractal measurement and multifractal properties of fracture surfaces. Physics Letters A, 242, 41–50, doi: 10.1016/S0375-9601(98)00098-X.

Xu, G., He, C., Su, A. & Chen, Z. 2018. Experimental investigation of the anisotropic mechanical behavior of phyllite under triaxial compression. International Journal of Rock Mechanics and Mining Sciences, 104, 100–112, doi: https://doi.org/10.1016/j.ijrmms.2018.02.017.

Xue, D., Liu, Y., Zhou, H., Wang, J., Liu, J. & Zhou, J. 2020. Fractal Characterization on Anisotropy and Fractal Reconstruction of Rough Surface of Granite Under Orthogonal Shear. Rock Mechanics and Rock Engineering, 53, doi: 10.1007/s00603-019-01974-7.

Yang, L., Yang, A., Chen, S., Fang, S., Huang, C. & Xie, H. 2021. Model experimental study on the effects of in situ stresses on pre-splitting blasting damage and strain development. International Journal of Rock Mechanics and Mining Sciences, 138, 104587, doi: https://doi.org/10.1016/j.ijrmms.2020.104587.

Yang, S.-Q., Jing, H.-W. & Wang, S. 2012. Experimental Investigation on the Strength, Deformability, Failure Behavior and Acoustic Emission Locations of Red Sandstone Under Triaxial Compression. Rock Mechanics and Rock Engineering, 45, doi: 10.1007/s00603-011-0208-8.

Yang, Z.Y., Di, C.C. & Yen, K.C. 2001. The effect of asperity order on the roughness of rock joints. International Journal of Rock Mechanics and Mining Sciences, 38, 745–752, doi: https://doi.org/10.1016/S1365-1609(01)00032-6.

Yu, C., Tian, W., Zhang, C., Chai, S., Cheng, X. & Wang, X. 2021. Temperature-dependent mechanical properties and crack propagation modes of 3D printed sandstones. International Journal of Rock Mechanics and Mining Sciences, 146, 104868, doi: https://doi.org/10.1016/j.ijrmms.2021.104868.

Yu, X. & Vayssade, B. 1991. Joint profiles and their roughness parameters. International Journal of Rock Mechanics and Mining Sciences & Geomechanics Abstracts, 28, 333–336, doi: 10.1016/0148-9062(91)90598-G.

Zhang, S.W., Shou, K.J., Xian, X.F., Zhou, J.P. & Liu, G.J. 2018. Fractal characteristics and acoustic emission of anisotropic shale in Brazilian tests. Tunnelling and Underground Space Technology, 71, 298–308, doi: https://doi.org/10.1016/j.tust.2017.08.031.

Zhang, Y.H., Zhou, H. & Xie, H. 2005. Improved cubic covering method for fractal dimensions of a fracture surface of rock. Yanshilixue Yu Gongcheng Xuebao/Chinese Journal of Rock Mechanics and Engineering, 24, 3192–3196.

Zheng, B., Qi, S., Luo, G., Liu, F., Huang, X. & Guo, S. 2021. Characterization of discontinuity surface morphology based on 3D fractal dimension by integrating laser scanning with ArcGIS. Bulletin of Engineering Geology and the Environment, 80, 2261–2281, doi: 10.1007/s10064-020-02011-6.

Zhou, H. & Xie, H. 2003. Direct Estimation of the Fractal Dimensions of a Fracture Surface of Rock. Surface Review and Letters, 10, 751–762.

Zhou, H., Xue, D. & Jiang, D. 2013. On Fractal Dimension of a Fracture Surface by Volume Covering Method. Surface Review and Letters, 21, doi: 10.1142/S0218625X14500152.

REFERENCE TO A WEBSITE:

1. Yun Chen.https://commons.wikimedia.org/wiki/File:%E7%9F%B3%E6%9E%97%E6%AD%A3%E9%97%A8.JPG
2. Rod Waddington.https://commons.wikimedia.org/wiki/File:Big_Tsingy,_Madagascar_(24082669822).tif

Tunnelling for a Better Life – Yan, Celestino, Thewes & Eberhardt (Eds)
© 2024 The Author(s), ISBN 978-1-032-80042-4
Open Access: www.taylorfrancis.com, CC BY-NC-ND 4.0 license

Research on integrated monitoring platform of composite steel-concrete immersed tunnel

Xingquan Mao & Zhaohui Zhang*
CCCC Highway Consultants Co., Ltd., Beijing, China
CCCC Engineering Big Data Information Technology(Beijing) Co.,Ltd., Beijing, China

Longyun Li
CCCC Engineering Big Data Information Technology(Beijing) Co.,Ltd., Beijing, China

ABSTRACT: Most of the immersed tunnels constructed are reinforced concrete structures in China and overseas, few of which adopt transverse prestressing. Since the 1990s, composite steel-concrete structures have been widely used in Japan. In order to solve the problems of concrete pouring quality and waterproof performance caused by complex force and reinforced concrete joint, composite steel-concrete is used in Shenzhen-Zhongshan Bridge immersed tunnel. The force of composite steel-concrete element is complicated, the inner and outer plates are the main bending members, and the transverse and mediastinal plates are the main shearing members. There is a certain deviation between the theoretical and actual value of foundation settlement. The uneven settlement and local mis movement between different element during the operation period have hidden dangers to the structure safety. In this paper, an integrated monitoring system is established during construction and operation of immersed tunnel, aiming at the problems of large size, complex construction and safe operation of composite steel-concrete element in Shenzhen-Zhongshan Bridge immersed tunnel. This system can realize the continuous and long-term monitoring of key components, and build the digital life cycle of the immersed tunnel. Through the real-time perception of the stress and deformation state of the main structure, the on-line structural safety assessment is realized. Coordinate and optimize construction monitoring and operation monitoring sensor equipment to reduce tunnel monitoring costs and improve monitoring efficiency. The system has been successfully applied in Shenzhen-Zhongshan Bridge immersed tunnel.

Keywords: Composite steel-concrete, Long-term monitoring, Safety assessment

1 INTRODUCTION

In the past 10 years, driven by Chinese government policy such as the Guangdong-Hong Kong-Macao Greater Bay Area, the Planning of the Changjiang River Crossing Channel, and the development of urban construction, China has completed a large number of major and leading highway tunnel projects, such as the Hong Kong-Zhuhai-Macao Bridge (2018), Qingdao Jiaozhou Bay Submarine Tunnel (2011), Shenzhen-Zhongshan Bridge (under construction) and other large-scale tunnel projects. China's tunnel construction has made great innovations and breakthroughs in design concept, construction method, equipment technology and other aspects. At the same time, as an important infrastructure to improve the efficiency of road transportation and road service level, tunnel has been paid much more attention. Compared with other construction methods, immersed tube tunnel has lower requirements on the foundation, and is especially suitable for engineering sites with soft foundation, river bed or seabed which are shallow and easy to excavate the foundation trough by water-based dredging facilities.

In 1910, Detroit built the first immersed tube tunnel for underwater transportation. With the development of reinforced concrete technology, the first reinforced concrete rectangular immersed tube tunnel was built in the Netherlands in 1942. Since then, reinforced concrete rectangular section has gradually become the main section form of immersed tube tunnel. At the end of the 20th century, Japan first adopted steel shell concrete composite structure type immersed tube tunnel. And two immersed tube tunnels of steel-shell concrete composite structure have been built successively. In China, the design and construction of immersed tube tunnel started relatively late. Between 1969 and 1997, five immersed tube tunnels were built in Hong Kong. In

*Corresponding author: neuzzh@126.com

DOI: 10.1201/9781003495505-360

1988, the construction of Ningbo Yongjiang Tunnel and Guangzhou Pearl River Tunnel led to the great development of immersed tube tunnel in China. As of 2022, the number of submerged tube tunnels has been built in China is twenty, the number of submerged tube tunnels under construction is ten, and the number of proposed submerged tube tunnels is six. With the development of China's infrastructure construction and the maturity of immersed tube tunnel design, construction and maintenance technology, China's immersed tube tunnel technology has been in the world's leading level.

In order to solve the problems of concrete pouring quality and waterproofing performance caused by complex force and many reinforced concrete elements, steel shell concrete elements are applied to immersed pipe tunnels in deep and middle passages. Steel shell concrete composite structure is a type of composite structure in which steel shell and concrete work together after filling self-compacting concrete between double steel plates. However, the force of steel shell element is complicated, the inner and outer panels are the main bending members, and the transverse and mediastinal plates are the main shear members. The foundation structure of the whole line is complex and diverse, and there is a certain deviation between the theoretical value and the actual value of the foundation settlement. Uneven settlement and local dislocation between different element during operation pose hidden dangers to structural safety. The above hidden dangers may lead to great changes in the cross section and structural form of immersed tube tunnel, from the early circular cross section gradually developed to octagonal, square, rectangular and polygon cross section forms. Gradually developed from steel shell structure to steel shell and reinforced concrete composite structure, double steel shell/steel structure sandwich composite structure, reinforced concrete structure, prestressed reinforced concrete structure forms.

The construction process of immersed tube tunnel is often complicated. In order to ensure the construction safety, provide the change information of immersed tube timely and accurately, and provide the basis for the determination of construction parameters, the construction monitoring system is very necessary. Li Harting et al. introduced the establishment and operation of the immersed tube tunnel construction monitoring system of the Hong Kong-Zhuhai-Macao Bridge from the aspects of tunnel settlement, joint differential deformation, segment tension and environmental temperature monitoring, etc., and analysed the monitoring data of differential deformation and settlement to verify the reliability of the monitoring system. Similarly, the structural monitoring system during tunnel operation can grasp the structural condition in the use stage in time, providing data support for scientific evaluation and ensuring safety and durability. Li Weiping et al. tested Ningbo Yongjiang immersed tube tunnel during its operation period and evaluated GINA water stop belt. Liu Zhenggen et al. established a real-time health monitoring system of immersed tube tunnel composed of multiple sensors based on the background of Ningbo Yongjiang immersed tube tunnel.

Reinforced concrete structure is used as the main structure in domestic immersed tube tunnel, accounting for 89%. However, the number of immersed tube tunnels with steel shell concrete composite structure is increasing gradually. In view of the problems of large size, complex construction and safe operation of concrete composite structure, the integrated monitoring system of immersed tube tunnel structure during construction and operation is constructed in combination with the actual project of immersed tube tunnel in Shenzhen-Zhongshan Bridge. The continuous and long-term monitoring of key components is realized, and the digital life cycle of immersed tube structure is constructed. Through the real-time perception of the stress and deformation state of the main structure of the tunnel, the on-line structural safety assessment is realized. Coordinate and optimize construction monitoring and operation monitoring sensor equipment to reduce tunnel monitoring costs and improve monitoring efficiency.

2 BASIC OVERVIEW OF IMMERSED TUBE TUNNEL

2.1 *Basic overview*

On the east of the Shenzhen-Zhongshan Bridge is the Hezhou Interchange in Bao 'an District of Shenzhen and on the west is the Hengmen Junction in Zhongshan. It is 24 km long, including 6.8 km long immersed tube tunnel, is the world's first two-way eight-lane underwater immersed tube tunnel. The immersed pipe tunnel is composed of 32 element with a total length of 5035m, the standard pipe section length of 165m and the curve width pipe section length of 123.8m. The final connector is set between E23/E24, and the pipe section is divided into 123.8 (E1) + 22 × 165m (E2 ~ E23) + 2.2m (final connector) + 4 × 165m (E24 ~ E27) + 5 × 123.8m (E28~E32).

The immersed tube tunnel adopts two traffic passageways and one integrated pipe gallery structure. On the left and right side of the main traffic road, the middle pipe corridor from top to bottom are exhaust flue, safety passage and cable passage respectively. The overall external profile size of the pipe section is 46~55.46 m (width) × 10.6m (high). The immersed tube tunnel adopts steel shell concrete composite structure, which is mainly composed of internal and external panels, transverse mediastinum plates, transverse and longitudinal stiffening ribs and welding nails.

2.2 *Characteristics of steel shell immersed tube tunnel*

There are five difficulties in the Shenzhen-Zhongshan Bridge: ultra-wide, changing section width, deep burial, large amount of siltation and poor formation

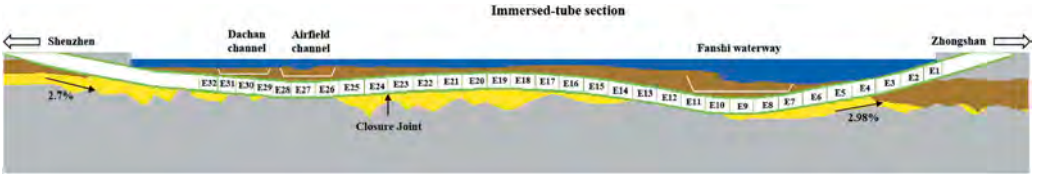

Figure 1. The design profile of immersed-tube tunnel.

stability in the sand pit area. By now, it is one of the most technically difficult projects in the world. The standard section length of the immersed tube is 165 meters, and the displacement is about 80,000 tons. Each of the 32 element uses an average of about 10,000 tons of steel. A single pipe section is composed of more than 2500 independent compartments, which is large in quantity, large in specifications, difficult in process parameter control and construction organization.

Ultra-wide refers to the first in the world that the immersed tube tunnel adopts the two-way eight-lane standard. It's section width reaches 46 meters. Therefore, the design and construction are difficult. Changing section width refers to the tunnel in order to meet the needs of traffic function, set 615 meters of widening section. In order to achieve the goal of multiple submerging in the tunnel, the section of the pipe section is widened from eight lanes in both directions to twelve lanes in both directions. The section width of the pipe section has been widened from 46 meters to about 70 meters. However, according to the current lack of domestic standards, such a large-scale immersed element will bring safety problems.

Deep buried means that the submerged tube tunnel is buried deep. The deepest position of the submerged tube bottom elevation is close to 40 meters from the water surface. Large amount of siltation means that the average rate of siltation in flood season is close to 2 cm per day, and the maximum rate of siltation typhoon period is more than 5 cm per day. Poor formation stability in the sand pit area means that the western island slope section is located in the super-large sand pit. And the regional formation disturbance is serious. The stability is very poor, which causes great difficulties in the excavation of the foundation groove and foundation treatment.

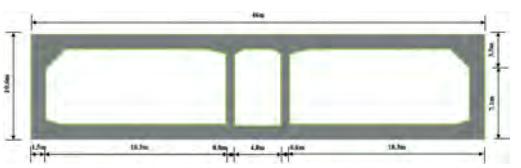

Figure 2. Tunnel cross-section.

3 INTEGRATED MONITORING PLATFORM DESIGN

3.1 *Monitoring content*

The engineering conditions of the tunnel section of Shenzhen-Zhongshan Bridge are very complicated and the environment is relatively bad. The immersed tube tunnel section is located on the weak foundation of the seabed, which is mainly composed of sea sand and sea silt. With the increase of service life, the immersed tube tunnel built in the soft soil layer may cause uneven settlement and local dislocation damage between different elements of the tunnel due to the repeated action of external variable loads such as traffic flow, tide and siltation depth, which brings great hidden dangers to the structural safety of immersed tube tunnel.

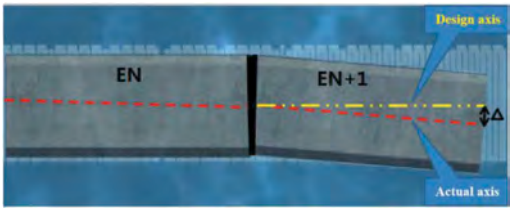

Figure 3. Tunnel attitude monitoring.

A little less, will cause a major accident, and then seriously affect the safety of the tunnel. In order to ensure the safety of tunnel engineering and forecast danger in time, it is very important to monitor and evaluate the safety and stability of tunnel engineering. Through modern detection technology, the establishment of a monitoring system to accurately understand the tunnel conditions, to achieve comprehensive monitoring of the steel shell structure and immersed tube tunnel environment during the construction and operation period, master the stress and deformation of the steel shell structure, and ensure the safety of the structure. Timely detect and forecast the occurrence of dangerous situations, and take engineering emergency measures when necessary.

Figure 4. Monitor content and location.

The main monitoring contents of the Shenzhen-Zhongshan Bridge include: element settlement, deformation, steel shell structure stress, element relative displacement and corresponding environmental temperature. The settlement and deformation of element is an important sign reflecting the stability of sunk pipe structure and surrounding strata. By monitoring the settlement of sunk element, the variation trend of element settlement and deformation can be predicted, and the basis for the precise positioning of new element can be provided. As the main carrier, the horizontal stress, non-uniform settlement and non-uniform force of steel shell element will cause the local stress concentration of steel shell, which will affect the composite system of steel shell concrete and seriously affect the structure. The relative displacement of element is an important index for the detection of uneven settlement and leakage of element in immersed pipe tunnel, which is related to the service effect of the tunnel water stop belt.

3.2 *Integrated monitoring system*

The traditional tunnel monitoring is divided into construction period and operation period. However, due to the problems of inconsistent monitoring subject units and incompatible monitoring equipment, tunnel monitoring has many shortcomings such as data discontinuity, single monitoring system function, data redundancy and inaccurate monitoring results, which can no longer meet the needs of modern large-scale tunnel monitoring automation and intelligence. The immersed tube tunnel in deep and middle channel has some problems such as super width, widening, deep burial and large silt return. Based on this, the overall design idea and system architecture of the integrated monitoring system for tunnel construction operation are studied. According to the special geological and sea navigation conditions of different elements of immersed tube tunnel, a set of construction and operation monitoring system suitable for steel shell concrete composite structure is designed. In the whole life cycle of the tunnel, the functions of the construction and operation stages are different, but interrelated. In this way, the unsafe factors during construction period and operation period are captured, and the state of immersed tube tunnel structure is monitored and evaluated. When there are abnormal changes in the tunnel structure, early warning is carried out to provide data support for the whole life cycle of the tunnel construction, maintenance and management.

In order to meet the requirements of system integration, intelligence and data sharing, the system adopts distributed system architecture to collect the bridge detection data, and transmits the data through the network. The collected bridge health data information is uniformly stored in the data management centre of the system using the database, and provides data support for the tunnel health status assessment. On this basis, real-time monitoring of tunnel health status, emergency information release and early warning are realized. Improve the intelligence of tunnel

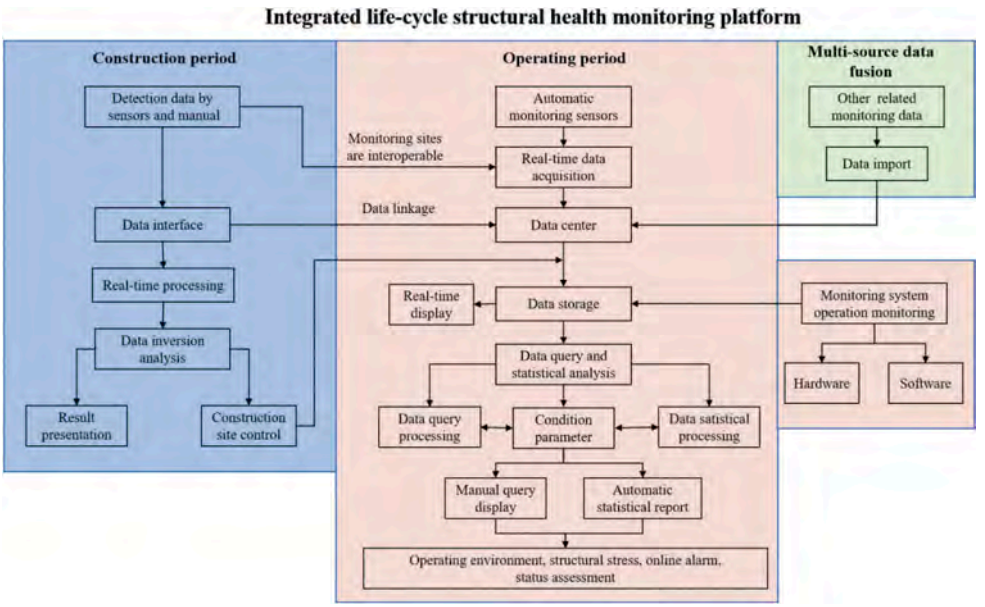

Figure 5. Integrated monitoring platform.

monitoring to ensure the safety and smooth traffic of the Shenzhen-Middle passage. Starting from the time dimension, the system is based on multi-source data fusion, mainly including construction stage monitoring module and operation stage monitoring module.

The main goal of the module in the construction stage is to invert the structure according to the actual construction data and ensure the safety of each pipe section. The main content has the following three aspects. First, the monitoring system database contains design data and sensor layout scheme information, providing basic data support for construction process simulation and construction process control. Second, during the construction phase, all sensors should be arranged according to the designed sensor layout scheme, so as to reduce the disturbance caused by the sensors after completion to the bridge structure and ensure the durability of the sensors. Third, according to the structural characteristics of the steel shell immersed tube tunnel, the focus is on the whole process monitoring of vertical displacement, vertical dislocation, water level displacement, horizontal dislocation, joint relative displacement and corresponding temperature and humidity, structural load and structural internal force to ensure the structural safety during construction. Finally, at the same time, the system saves the construction data as the basic data of the operation stage.

The operation phase module mainly conducts long-term stable health monitoring in four aspects: long-term operating environment, structural state, traffic state and structural disease. The main contents include the following three aspects. First, Automatic monitoring of structural and system damage accumulation and resistance attenuation of immersed tube tunnels in use. Second, assess the safety of the tunnel, provide intelligent early warning of possible damage conditions and even provide repair plans, control the damage, and ensure the safety, integrity, applicability and durability of the structure. Third, develop new conservation management methods, monitoring technologies and corresponding evaluation theories and methods according to their own practices during the use of the system.

4 MONITORING DATA ANALYSIS

On June 11, 2023, the final joint of the world's longest and widest steel-shell concrete immersed tube tunnel, the Shenzhen-Zhongshan Bridge submarine tunnel, was successfully launched, and the penetration measurement results showed that accurate docking with the east section (E24) was achieved. Since the start of the steel shell test section of the submarine tunnel in April 2018, a full five years later, the submarine great wall has finally closed, and the two cities of Shenzhen and Zhongshan have achieved Hand in Hand at the bottom of the Lingdingyang Sea, taking an important step for the opening of the Shenzhen-Zhongshan Bridge. A large amount of measured data has been accumulated during the construction period, and some monitoring data are mainly analyzed now. The monitoring data include the element settlement data (E1-E23), the steel shell stress data (E1, E5, E9, E13, E18, E23, E24, E26, E29, E32), and the element relative displacement data (E1-E11).

4.1 *Element settlement monitoring*

Each pipe section has three settlement monitoring points, which are middle side, Shenzhen side and Zhongshan side. As shown in Figure 6, the settlement of the middle side of E1 pipe section is significantly greater than that of Shenzhen side and Zhongshan side. The vertical displacement of E1 pipe section is less affected during the locking backfill. However, the vertical displacement of element is greatly affected during the covering backfilling period. During concrete placement, the vertical displacement of element is less affected. After covering and backfilling is completed, the maximum settlement occurs in the middle end of the pipe section. Compared with the current maximum cumulative settlement of 51.88mm and the warning value of 56mm, we get that the settlement of E1 element is in a safe state.

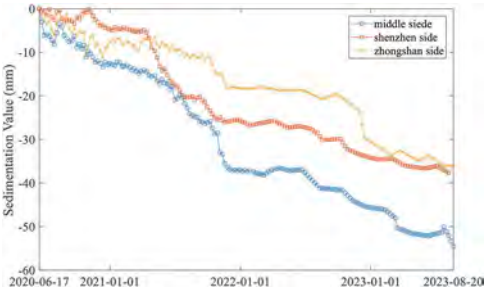

Figure 6. The time history curve of E1 element settlement.

The final joint is located between E23 and E24, so the settlement data of the E23 element needs to be analyzed. The maximum cumulative settlement in the E23 element is -20.06 mm, which is located at the bottom of the pipe gallery in the E23 element. Compared with the warning value (56 mm), the E23 element is in a safe state.

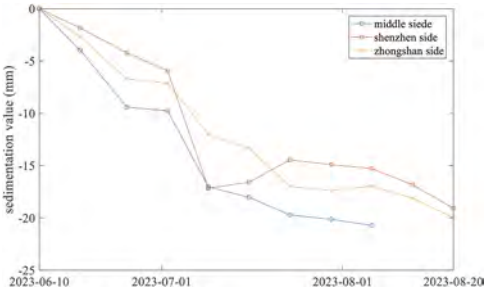

Figure 7. The time history curve of E23 element settlement.

We have successfully monitored the absolute settlement data of all elements during construction. As shown in Figure 8, through data analysis, we get the settlement displacement cloud image of the immersed tube tunnel.

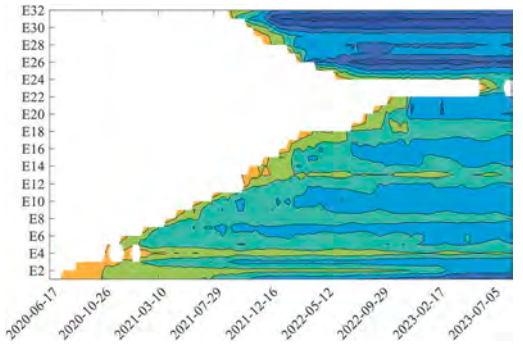

Figure 8. The cloud image of all elements settlement.

It can be seen from the figure that the maximum settlement displacement occurred in the E31 element, and the maximum value was 60 mm. The data show that E31 has a large settlement displacement after settling down. In the subsequent process, the displacement did not change much. The element with large settlement displacement are E1, E3, E6, E10, E16, E20, E26 and E31. So, in the operation monitoring, we should pay more attention to the change of settlement displacement of these immersed tube joints.

4.2 *Steel shell stress*

A total of 10 stress measuring points are arranged for each monitoring section. And each carriageway hole is arranged symmetrically.

As shown in Figure 9, after the sinking of the element, the steel shell in the top plate of the element shows tension, and the steel shell in the side wall on both sides of the element shows pressure. In the process of element backfilling construction, the structural stress increased steadily, no sudden increase was found, and the values of each monitoring point were less than the warning value of 224 MPa, so the element structure was in a safe state. With the completion of tunnel construction, the stress changes were small and the data were normal. The results show that the stress of each steel shell section is symmetrical and the structure does not have significant differential settlement.

4.3 *Element relative displacement*

The relative displacement of element is mainly used as an important index to evaluate the service effect of water stop belt. As shown in Figure 10, the displacement of E1-E2, E2-E3, and E5-E6 is positive, which can be judged as the element is open. And

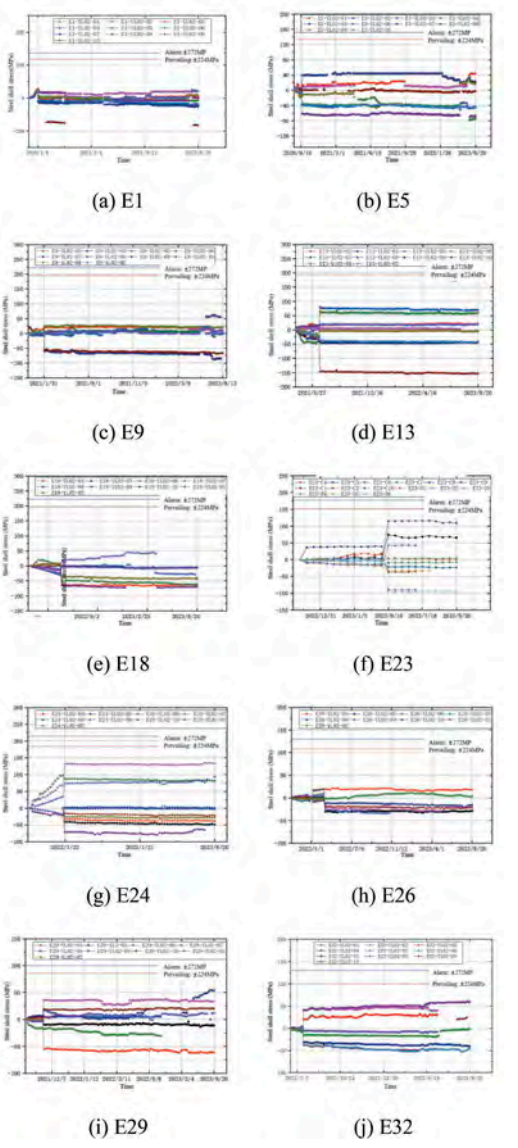

Figure 9. The time history curve of steel shell stress.

affected by the temperature, the immersed element is generally opened in the summer when the temperature is high. The displacement of the E3-E4, E4-E5 is negative, and it can be judged that the element is in a tightened posture. The reason may be affected by the uneven settlement of elements. In the initial stage, the displacement of elements changes greatly, and the maximum value is 25 mm, which occurs at the E1-E2 elements. The change of data in the later period is gradual.

During the construction process, we monitored the relative displacement values of E1~E19 elements. The relative displacement cloud image is obtained by analyzing the data of different element, as shown in Figure 11.

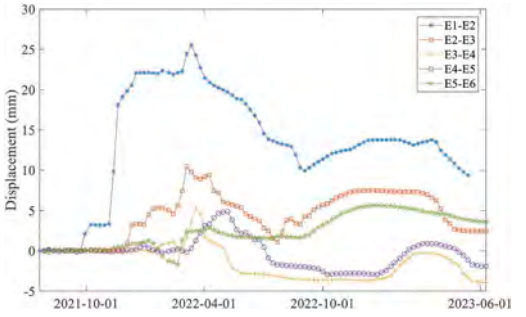

Figure 10. The displacement of E1~E6.

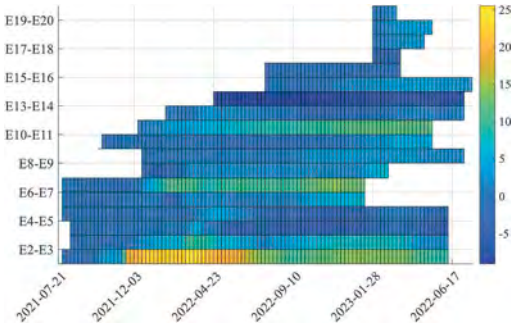

Figure 11. The displacement cloud image of E1~E19.

The tube section with larger opening size are E1-E2, E2-E3, E6-E7, E10-E11. We should pay more attention during tunnel operation. The maximum opening is 25 mm, which does not exceed the displacement limit. The position of the smallest relative displacement occurs at E13-14. The minimum value is -9 mm. The relative displacement of other elements changes little. It can be seen from the data that during the tunnel construction, the relative displacement changes little, and the service effect of the water stop belt is good.

5 CONCLUSIONS

In this paper, an integrated monitoring system was established during construction of immersed tunnel. This system can realize the continuous and long-term monitoring of key components, and build the digital life cycle of the immersed tunnel.

For the settlement displacement, the value in the middle of the element is greater than that at both ends. And the maximum occurred in the E31, and the value was 60 mm. For the steel shell stress, each steel shell section was symmetrical and the stress did not exceed the warning value. For the relative displacement, the maximum value is 25 mm, which occurs at the E1-E2. The smallest relative displacement occurs at E13-14 and the value is -9 mm. The relative displacement changes little, and the service effect of the water stop belt is well.

Through the analysis of element settlement data, stress data and relative displacement data, it can be found that there is no large settlement deformation during the entire construction period of the tunnel. Tunnel joint attitude is maintained well. Stress concentration events did not occur. At the same time, the integrated monitoring platform can integrate multi-source data types well. Through the actual monitoring data, the system has been successfully applied in Shenzhen-Zhongshan Bridge immersed tunnel.

ACKNOWLEDGMENTS

This work was supported in part by National Key R&D Program of China [Grant No. 2023YFC3805705].

REFERENCES

Hong K., Feng H., 2020. Development trends and views of highway tunnels in China over the past decade. China J. Highw. Transp, 33 (12), 62–76.

Li Y., Chen Y., 2011. The importance and technical difficulties of tunnel and island for Hong Kong-Zhuhai-Macao bridge project. Engineering Mechanics, 28(2), 67–77.

Li Z., Wang Q., Chen W., et al, 2018. Innovation and prospect of key technologies of immersed tunnels in China. Tunnel Construction, 38(6), 879.

Lin M., Lin W., Liu X., et al, 2017. Development and experience of immersed tunnel in Japan. Journal of Waterway and Harbor, 38(1), 1.

Yang W., Mao R., Zeng C., et al, 2008. Overview of subsea immersed tube tunnel development in Hong Kong. Modern Tunnelling Technology, 45(S1), 41.

Guo J., Shan L., Ma M., 2023. Statistics analysis and development of immersed tube tunnels in China. Tunnel Construction, 43(1), 173.

Song S., Nie J., Xu G., et al, 2019. Development and application of steel-concrete-steel composite structures in immersed tunnels. China Civil Engineering Journal, 52(4), 109.

Chen S., Chen Y., 2002. Design and construction of immersed tunnel. Beijing: Science Press.

Li H., Xu X., et al, 2015. Construction monitoring system of immersed tunnel of Hongkong-Zhuhai-Macao Bridge. China Harbour Engineering, 35(7), 49–52.

Li W., Wu D., Guo X., et al, 2011. Overhaul design and construction of Ningbo Yongjiang immersed tube tunnel. Modern Tunnelling Technology, 48(1), 82–88.

Liu Z., Hung H., Zhao Y., et al, 2008. Immersed tube tunnel real-time health monitoring system. Chinese Journal of Underground Space and Engineering, 4(6), 1110–1115.

Tunnelling for a Better Life – Yan, Celestino, Thewes & Eberhardt (Eds)
© 2024 The Author(s), ISBN 978-1-032-80042-4
Open Access: www.taylorfrancis.com, CC BY-NC-ND 4.0 license

Study for health monitoring of mountain tunnels operation using distributed fiber optic sensing technology

Hayato Nonaka* & Yasuyuki Miyajima
Kajima Corporation, Tokyo, Japan

Noboru Sakamoto
Yachiyo Engineering Co., Ltd., Tokyo, Japan

Yohei Taira
Kajima Corporation, Tokyo, Japan

Takuji Yamamoto
Advanced Construction Technology Center, Tokyo, Japan

Michio Imai & Konan Koike
Kajima Corporation, Tokyo, Japan

Kinzo Kishida
Neubrex Co., Ltd., Hyogo, Japan

Hiroshi Shinbo
Retec Engineering Corporation, Tokyo, Japan

Junichi Kawabata
Kajima Corporation, Tokyo, Japan

ABSTRACT: In mountain tunnels after construction, structural deformation often occurs due to external forces from the ground. The authors focused on distributed fiber optic sensing (DFOS), which can provide stable and high-density measurement data over a long period of time. DFOS enables quantitative structural health monitoring from construction to operation processes. This contributes rational maintenance management based on the actual condition of the structure. In this study, the installation method, measurement accuracy, and effectiveness of DFOS were considered through tests on laboratory and actual tunnel.

Keywords: Mountain tunnel, Structural health monitoring, Distributed fiber optic sensing, Laboratory test, Field installation

1 INTRODUCTION

1.1 *DFOS for tunnel health monitoring*

In mountain tunnels after construction, structural deformation often occurs due to external forces from the ground. For safe usage of tunnel, structural health monitoring of tunnel is important. Although tunnel deformation is usually monitored using electrical sensors such as strain gauge, the reliability of the measurement data is lost due to reduction of insulation resistance after a few years, which limits the usage in maintenance and management where long-term operation is required.

The authors focused on distributed fiber optic sensing (DFOS) technology, which can provide stable and high-density measurement data over a long period of time along the optical fiber. DFOS enables quantitative structural health monitoring of tunnel from construction to operation. This

*Corresponding author: nonakaha@kajima.com

DOI: 10.1201/9781003495505-361

contributes to the rationality of maintenance and management based on the actual condition of the structure.

In this study, the installation method, measurement accuracy, and effectiveness of DFOS were explored through laboratory tests and application on an actual tunnel.

1.2 *Description of DFOS technology*

DFOS is based on light scattering effects and is divided into three main types; Raman scattering based distributed sensors, Brillouin scattering based distributed sensors, and Rayleigh scattering based distributed sensors. Raman systems are sensitive to only temperature, whereas Rayleigh and Brillouin systems are sensitive to both strain and temperature changes. Table 1 shows general capabilities regarding distance range, spatial resolution and repeatability of popular sensing techniques based on Brillouin and Rayleigh scattering.

Brillouin scattering based DFOS is one of the most popular fully distributed sensing technologies and is mainly divided into Brillouin Optical Time Domain Reflectometry (BOTDR) and Brillouin Optical Time Domain Analysis (BOTDA). Brillouin systems are capable of measuring long distances, which are familiar with monitoring large scale civil infrastructures. However, this sensing technology typically has limited spatial resolution and measurement accuracy.

Recently, Rayleigh scattering based DFOS is receiving increased attention as a monitoring tool for civil structures. The Optical Frequency Domain Reflectometry (OFDR) technique enables high spatial resolution and accuracy measurement, but these measurements are limited in the range of sensing distance. This system is useful in monitoring detailed behavior of structure in the small scale. The Tunable Wavelength Coherent Optical Time Domain Reflectometry (TW-COTDR) technique provides relatively high resolution and accuracy measurement over long distance. The selection of the appropriate DFOS technology must be adjusted depending on the requirements of the actual infrastructure. In this study, TW-COTDR technique is selected for tunnel monitoring which often requires high resolution and long-distance measurement. In the TW-COTDR system, the Rayleigh scattering traces which show random signature obtained at each measurement are compared with the reference state by cross-correlation. The system supplies the Rayleigh frequency shift $\Delta\nu_R$ related to changes of the fiber temperature ΔT or/and strain $\Delta\varepsilon$.

$$\Delta\nu_R = C_{\varepsilon R}\Delta\varepsilon + C_{TR}\Delta T \quad (1)$$

Where, $C_{\varepsilon R}$ is the strain coefficient, and C_{TR} is the temperature coefficient of the optical fiber sensor.

Table 1. Features of different DFOS systems (modified from Monsberger and Lienhart, 2021 and Kishida et al, 2022).

Scattering	Brillouin		Rayleigh	
Technique	BOTDA	BOTDR	OFDR	TW-COTDR
Distance range	≤80km	≤100km	≤0.1km	≤25km
Spatial resolution	≥20cm	≥100cm	≤1cm	≥2cm
Strain repeatability	±2με	±20με	±1με	±0.1με

2 LABORATORY TESTING FOR ACCURACY VERIFICATION

A bending test using beam specimens was conducted to verify the measurement accuracy of strain using DFOS in lining and invert.

2.1 *Test descriptions*

The experiment conducted is a symmetrical four-point bending test. Figure 1 illustrates the structure of the test specimen, a prestressed concrete (PC) beam of cross section 450×360mm and length 4,600mm. Three PC steel wires were arranged linearly 120mm below the beam, and prestress was introduced using the post-tension method to apply stress of 6.0N/mm^2 in the compressive side of the concrete. During the experiment, compressive strength was 49.7N/mm^2, and Young's modulus was 31.5kN/mm^2 for concrete; yield strength was 396N/mm^2, and Young's modulus was 194kN/mm^2 for steel.

To better comprehend the bending behavior, DFOS were installed on the upper and lower sides of the specimen. The sensors were intermittently fixed along the steel with cable ties as seen in Figure 1. In addition, to obtain control data for comparison with DFOS, strain gauges were placed in five locations on the steel, while Linear Variable Differential Transducers (LVDTs) were placed at seven locations on the lower side of the specimen. The load gradually increased, and the sensors took measurements at each loading stage.

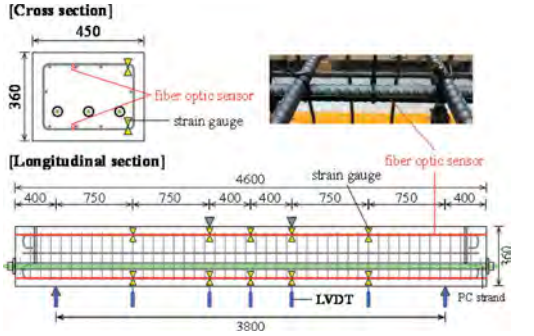

Figure 1. Schematic representation of beam structure and installed sensors (based on Taira et al, 2022).

2.2 *Test results*

Measurements by the DFOS were taken using the Neubrescope NBX-7030, manufactured by Neubrex, using the TW-COTDR method. The measurement interval was set at 5cm, and spatial resolution was 10cm. Figure 2 shows the strains measured by DFOS and the strain gauges (SGs) when load was at 10kN, 70kN, 90kN, prior to fracture. It is observed that compressive and tensile behaviors in response to distribution of bending moment are captured throughout the entire axis, and these measurements confirm that strain increases with load increase. In addition, strain measured through DFOS align with the results obtained from SGs. On the other hand, when load is at 90kN, a difference of approximately 30με occurred on the tensile side. This is presumed to be due to the influence of unobservable cracks. DFOS identify localized strain in several locations. These locations are thought to capture the localized stress concentration prior to formation of cracks, as they match with positions where cracks visibly formed upon further load increment. On the other hand, it is hypothesized that measurements from SGs indicate smaller strain due to stress relief as they do not correspond to crack positions.

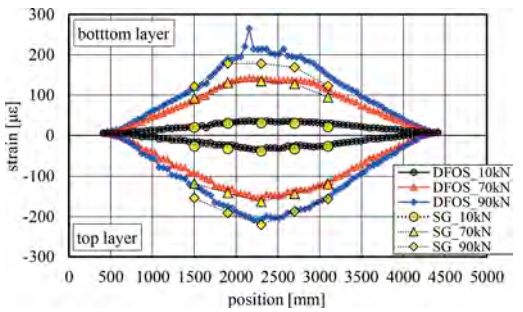

Figure 2. Strain profile along PC concrete beam.

Figure 3 shows displacement distribution calculated from the strain distribution obtained from DFOS. Displacement was determined by calculating the curvature from the strain measured by DFOS on both sides and integrating it twice in the span direction. The displacement based on DFOS conforms with the measurement values shown in the displacement meters, confirming that DFOS can accurately assess deformation caused by bending.

3 TUNNEL MONITORING UNDER OPERATION

To understand the existing condition of the tunnel during maintenance, strain is measured by electrical sensors installed at various points along the concrete lining. Whereas DFOS are installed along the circumferential direction of the tunnel surface, allowing for a more comprehensive understanding of the structure's

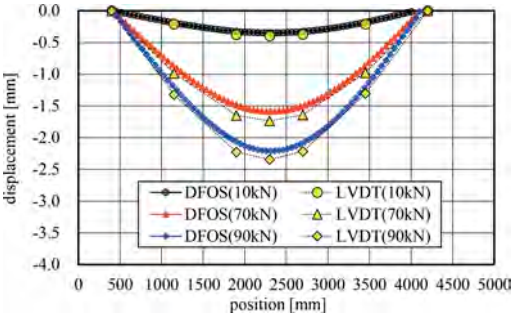

Figure 3. Displacement curves calculated from DFOS strains, measured by LVDT.

behavior. Here, installation of DFOS is assessed in a large-scale simulated road tunnel, and measurement accuracy is verified through a loading test from the tunnel crown.

3.1 *Sensor installation*

Figure 4 shows the three types of fiber optic sensors installed within the simulated tunnel measuring 7.1m in height and 11.2m in width. Two different shapes of sensors are installed using adhesives. The other one variant is tape which reacts to applied primer, with DFOS embedded on the tape enabling immediate attachment to the tunnel wall. The DFOS are placed on top of a fixture positioned across the longitudinal crack that were observed near the crest. It takes 2.5 ~ 3.0 hours to install DFOS along the circumferential direction of the tunnel wall (span of 20m).

Additionally, strain gauges were installed at the crest, the left and right shoulders and at two locations at SL height to verify accuracy. Pi-shape displacement transducers (crack gauges) were placed at the location of the cracks to measure the extent of the crack opening.

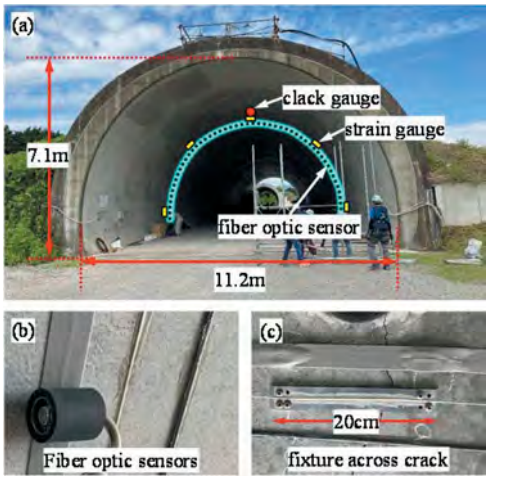

Figure 4. Simulated road tunnel: (a) sensors layout. (b) Fiber optic sensors. (c) fixture across crack.

3.2 *Loading tests*

Figure 5 shows the condition of the load test. A maximum of 47 bags of 1t soil are loaded on top of the tunnel, around the cross-section of the installed DFOS. Measurements were conducted during the loading process, which is divided into 7 loads; and the unloading process, which is divided into 6 loads. The loading step is as shown in Figure 6.

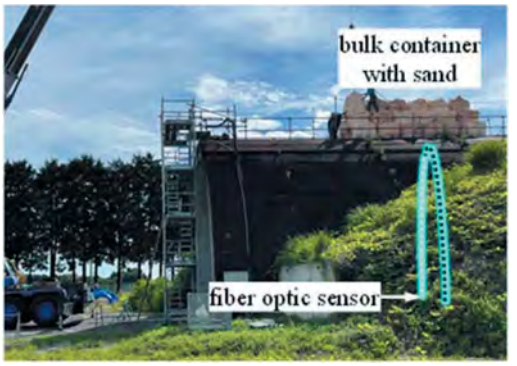

Figure 5. Loading test with bulk container.

Figure 7 shows measurement results from the DFOS and strain gauges when load is at maximum of 47t. The horizontal axis represents circumference length of the tunnel wall, where starting point 0m refers to the south tunnel base, extending along the circumferential direction to the crown at 10m, and ends at the north tunnel base at 20m. Results shows that compressive strain is seen throughout the length of DFOS, except for areas where cracks are observed at the crest, with maximum compressive strain showing at the tunnel shoulders. This is consistent with the general trend of strain with load from the top of tunnel. Furthermore, the strain gauges show similar results with DFOS where maximum compressive strain is measured at the shoulders.

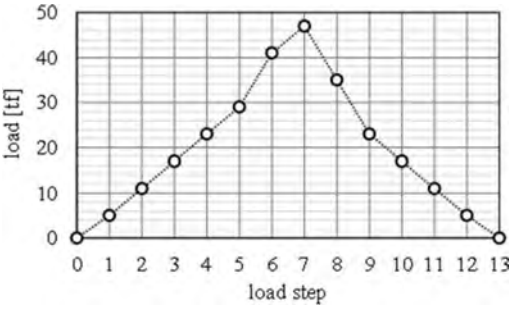

Figure 6. Step of loading test.

Figure 8 shows strain measurement results during the loading and unloading processes at the right tunnel shoulder, which shows maximum strain.

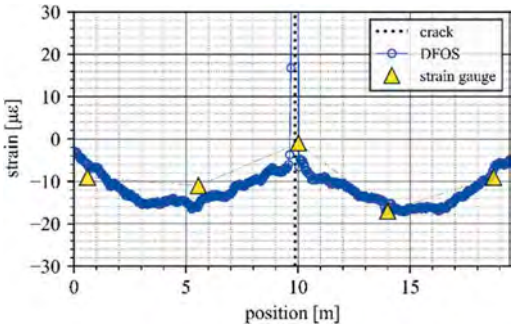

Figure 7. Strain distribution of arch surface in 47t loading.

Compressive strain at both DFOS and strain gauges gradually increased as the loading progressed and showed gradual decrease during the unloading process. However, hysteresis behavior was observed during both loading and unloading processes and a residual strain of about 5με was observed after complete unloading. This is because the tunnel structure was not in complete elastic condition due to crack near the crest. Both the DFOS and strain gauges exhibit a maximum error of 7με. This cause in discrepancy is potentially attributed to the installation environment of the sensors, such as the inhomogeneous nature of the tunnel surface. However, this error is negligible during evaluation of actual tunnel.

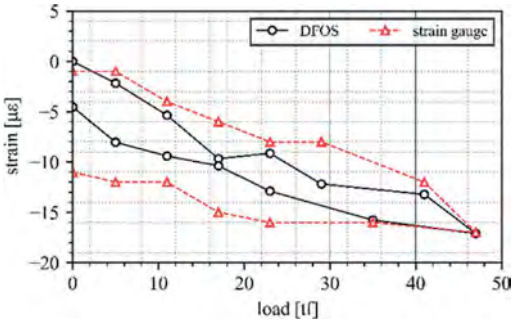

Figure 8. Comparison between DFOS and strain gauge measured at right tunnel shoulder.

Figure 9 illustrates strain distribution around the position of cracks at the crest during the loading process as measured by DFOS. Tensile strain was observed at crack position, gradually intensifying as loading progressed, accompanied by crack propagation. Figure 10 compares the results of crack aperture size calculated from data obtained by DFOS and those measured by the crack gauge. Aperture size obtained from DFOS measurements were calculated by summing the values within the range representing integral of strain that also exhibited tensile behavior. The same trend can be seen in both loading and unloading processes, verifying that DFOS can measure aperture size with the same accuracy as a crack gauge.

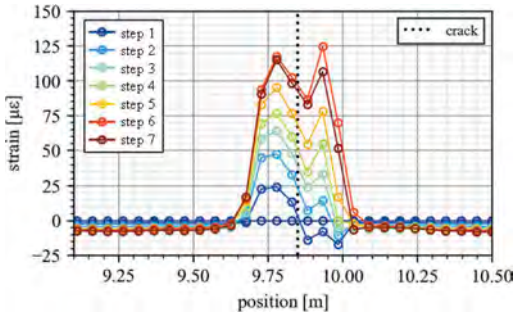

Figure 9. Strain distribution of around crack position.

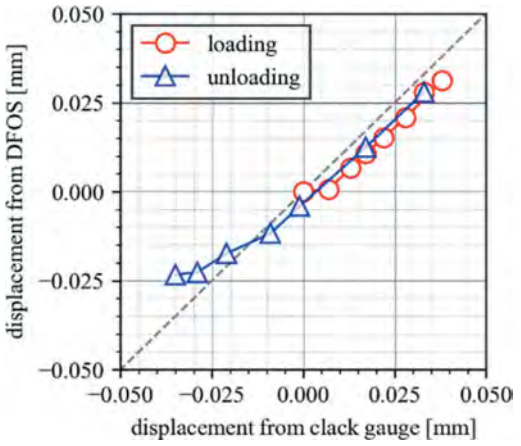

Figure 10. Comparison between DFOS and crack gauge displacement.

4 TUNNEL MONITORING UNDER CONSTRUCTION

The installation of DFOS along the concrete lining of the tunnel wall and invert during the construction phase allow for timely measurement of stress patterns immediately after completion of initial construction. Consequently, it is feasible to manage structural integrity as residual strength. In this section, testing of DFOS installation along the internal concrete lining of the tunnel wall and invert were conducted.

4.1 *Sensor installation*

Complications when installing DFOS directly inside concrete includes bending and tensing of the cable, as well as the possibility of misplacement due to extrusion during concrete casting. As a countermeasure, the DFOS were aligned along the reinforce steel to act as a guide for accurate placement. Figure 11 depicts how DFOS were installed at the invert and at the arch lining. One span of DFOS require approximately 2~3 hours to install at the invert, and 5~6 hours for the lining. The impact of DFOS installation to the construction process is minimal.

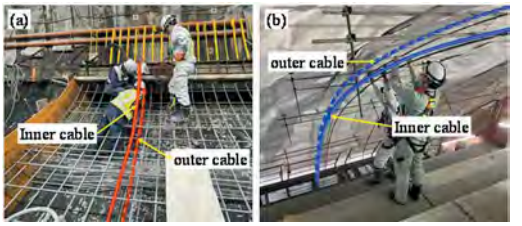

Figure 11. Sensor installation: (a) Invert. (b) Arch lining.

To ensure proper extraction of DFOS, prior planning is necessary as the tunnel wall becomes completely enclosed after concrete was casted at the arch. To avoid disruption to the construction process and operation of the facility, a strategically placed block out box was installed at the invert shoulder. This enables extraction of the sensors from the internal wall at any desired location.

After construction of a tunnel, it is customary practice to install porous ceramic duct within the inspection corridor to facilitate the routing of electrical and communication wires. This allows for the integration of DFOS without the need for installation at the surface. By connecting the extracted DFOS for measurement purpose from the block out box to the communication optic fiber cables within the ceramic pipes, DFOS can be extended all the way to the entrances of the tunnel. Figure 12 provides a visual representation of the DFOS layout during the maintenance phase. Moreover, when measurements from multiple sections of the tunnel are required, a comprehensive observation system can be achieved by connecting these sections to a single measuring device. By combining the installation methods evaluated in this study, utilizing DFOS throughout the lifecycle of the tunnel from construction to operation is possible.

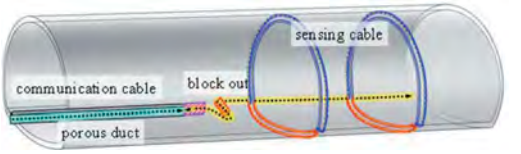

Figure 12. Conceptual diagram of DFOS layout during tunnel maintenance.

4.2 *Monitoring concrete curing process*

Temperature and strain measured during curing of concrete were investigated using DFOS installed at the invert. Figure 13 shows the measurement results taken at the center of the invert for the left lane of the road tunnel. It is observed that temperature rapidly increased by approximately 18°C within two days after placing. Additionally, compressive strain of approximately 50με due to thermal expansion is

observed at the concrete. After hitting the peak, temperature gradually decreased, causing tensile strain due to compression. This confirms that DFOS were able to effectively measure the expansion and compression behaviors after concrete were placed. Similar results were observed in the sensors installed at the arch lining of the tunnel.

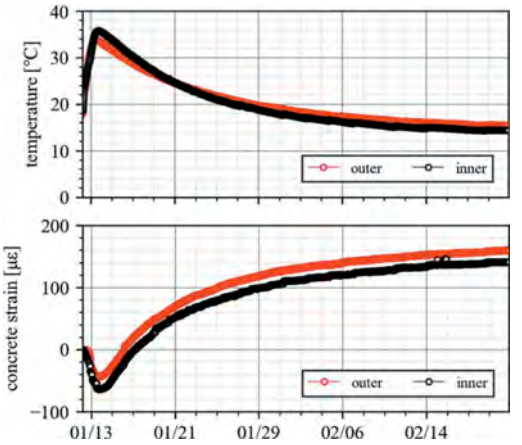

Figure 13. DFOS measurement results. (Curing process at invert concrete).

5 STUDY ON EFFICIENT DESIGN OF COUNTERMEASURES FOR TUNNEL DEFORMATION

An example of remedial construction to countermeasure deformation of concrete lining and invert in road tunnel was examined to evaluate the effectiveness of implementing DFOS in rationalizing remedial construction designs.

5.1 *Description of target deformed tunnel*

The object of this study is a road tunnel constructed using NATM. The specified segment was lined with high-strength steel fiber-reinforced concrete. During construction, a segment of the tunnel that was observed to be layers of weak clay, displayed a maximum displacement of nearly 250mm. The deformation was discovered 20 years after the tunnel was put into service. The extensive fractures were observed along the right concrete arch lining and invert of the tunnel. Although, geological surveys, boring tests and various measurements were conducted, the details of stresses and condition of external forces were not detected. Figure 14 shows the assumed geological condition based on the surveys conducted. Table 2 presents the applied physical properties of the weak ground layers and bedrock grade CII.

As the original case, a 2D skeletal structure analysis was conducted on the deformed segment of the tunnel as shown in the model in Figure 15. The design for reinforcement measures assumed that the same load which caused failure of wall lining and invert would act on the tunnel walls in the future. This yielded the M-N resistance curve shown in Figure 16. A load of 650kN/m^2 was acting on the upper circumference of the tunnel and this was adopted as the design load of the structure. As a result, reinforcement chosen to reinforce the inner section of the wall lining were embedded frames (of thickness 100mm), and internal reinforcement of thickness 250mm for the invert.

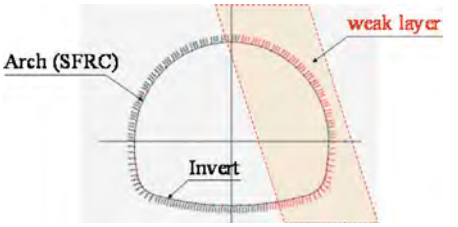

Figure 14. Assumed geological condition.

Table 2. Physical properties.

Rock mass classification	Young's modulus E_0 [N/mm^2]	Coefficient of subgrade reaction K_n [N/cm^3]
CII layer	10,000	197.8
Weak layer	2,300	45.5

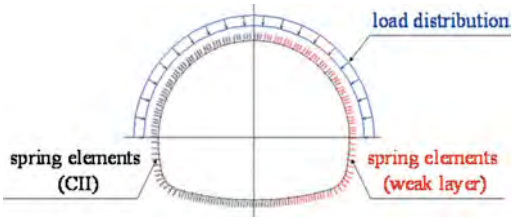

Figure 15. Analysis model (original case).

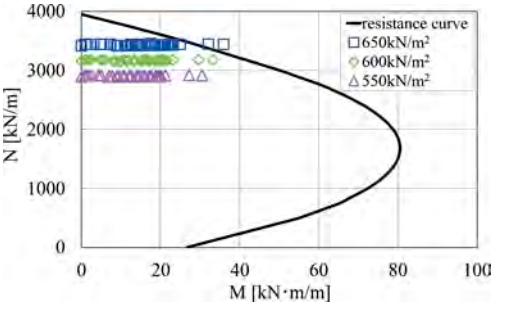

Figure 16. M-N resistance curve (original case).

5.2 *DFOS data for efficient design*

In this section, the remedial construction were designed based on the assumption that stress can be assessed using DFOS embedded in the concrete lining and invert during the construction phase. A 2D skeletal structure analysis was conducted using a tunnel analysis model, when the load is acting on the right side of the weak layer distribution as shown in Figure 17. The remedial construction selected were the same as the actual reinforcement structure; the arch lining section was internally reinforced with embedded frames and internal reinforcement for the invert.

This yielded in the M-N resistance curve shown in Figure 18. As a result, the design load is 500kN/m^2. Reinforcement selected based on this result are the same as in the previous section for the wall lining; internal reinforcement by embedded frames (of thickness 100mm), while internal reinforcement for invert changed from thickness of 250mm to 150mm.

Thus, by continuously monitoring the stress condition of the structure with DFOS, designing appropriate remedial construction is possible.

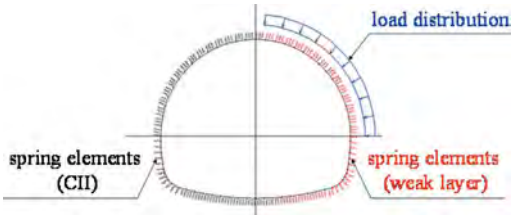

Figure 17. Analysis model (DFOS application assumed case).

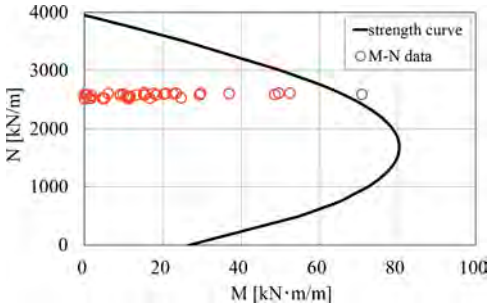

Figure 18. M-N resistance curve (DFOS application assumed case).

6 CONCLUSIONS

This study aims to evaluate the applicability of DFOS in monitoring the structural integrity of tunnels during the maintenance stage. This evaluation was conducted through lab tests, experiments at an actual tunnel, and numerical analysis. Findings from this study are summarized as below.

- Bending tests of beam specimens where prestress was applied shows that DFOS can measure compressive and tensile strains with similar accuracy as strain gauges and is effective in detecting localized strain changes before cracking becomes apparent. Moreover, deflection of the specimens derived from DFOS measurements are equivalent to those obtained from LVDT measurements.
- Load test was conducted on a simulated tunnel where DFOS were installed on the lining surface. The result from this test confirms that DFOS can measure strain with similar accuracy as conventional sensors. Furthermore, it was observed that displacement of cracks calculated from DFOS measurements is consistent with those obtained from crack gauges.
- Implementing DFOS in tunnels have minimal impact on the construction process. In consideration of conducting measurements during the maintenance phase, a wiring method was demonstrated, enabling the installation of DFOS during construction and its retention until after the completion of the tunnel.
- The effectiveness of implementing DFOS was investigated using a case study where a tunnel underwent countermeasure designs against deformation. By assuming that DFOS is capable of depicting stress distribution within the structure, sectional force was investigated. The results revealed that there is potential to implement a more rational and optimized design.

These results indicate that by implementing a long-term stable measurement method such as DFOS, it is possible to accurately measure both local and general behaviors of the tunnel structure. Furthermore, by incorporating DFOS to monitor tunnels, optimized maintenance can be achieved based on the actual conditions of the construction site.

ACKNOWLEDGMENTS

This work was supported by Construction Technology Research and Development Subsidy Program JPJ000094.

REFERENCES

Kishida, K., et al, 2022. “Distributed Optical Fiber Sensors for Monitoring of Civil Engineering Structures” *Sensors* 22, no. 12: 4368. http://dx.doi.org/10.3390/s22124368

Monsberger, Christoph M., and Werner Lienhart. 2021. “Distributed Fiber Optic Shape Sensing of Concrete Structures” S*ensors* 21, no. 18: 6098. http://dx.doi.org/10.3390/s21186098

Taira, Y., et al, 2022. Strain measurement in prestressed concrete beam by distributed optical fiber sensor. – Proceedings of the 77th Japan Society of Civil Engineers 2022 Annual Meeting., CS9-40.

Tunnelling for a Better Life – Yan, Celestino, Thewes & Eberhardt (Eds)
© 2024 The Author(s), ISBN 978-1-032-80042-4
Open Access: www.taylorfrancis.com, CC BY-NC-ND 4.0 license

Development of wear detection device using dye

Yoshie Omae*, Yosuke Imaoka, Hiroshi Ueda & Atsushi Nakamoto
Obayashi Corporation

Rui Fukui
The University of Tokyo

ABSTRACT: A wear detection device using dye has been developed. The dye is installed on the device and is linked with the bit to monitor the depth (amount of wear), and as soon as the predetermined wear amount is reached, the dye is released to the cutting face. The released dye to the cutting face is discharged together with the excavated soil, and the wear amount can be known by checking the coloration of the excavated soil.

In the development of this wear detection device, a preliminary experiment has been conducted to determine the possibility of identifying the colors with mixed soil, and it was found that identification by visual observation and image analysis is possible. Also, the appropriateness of the identifiable amount of used dye and the mechanism of dye releasing to the cutting face under the cutting face pressure was confirmed. To do this, actual site experiments at the two sites with the small and medium-diameter shields were conducted. As a result, it was confirmed that the developed wear detection device using dye can be applied to the actual shield construction sites.

Keywords: Shield, Cutter bit, Wear detection, Dye, Ultraviolet light

1 INTRODUCTION

In shield construction, continuous excavation using the cutter bit which exceeds the allowable wear amount causes troubles such as cutter damage. For this reason, it is important to monitor the wear condition of the cutter bit and manage the excavation. As conventional devices for detecting the amount of cutter bit wear, there are conduction-type wear detection device that detects the amount of wear through electric conduction, and hydraulic wear detection device that detects wear by monitoring the decrease in the hydraulic pressure. These wear detection devices need cables and piping to transmit the wear amount from the cutter face to the inner side of the shield machine. Due to the limited installation space, it is currently difficult to install these detection devices in small-diameter shield machines. Therefore, a wear detection device using dye or odor was developed that does not require cables or pipes. In this paper, an overview of the wear detection device using dye is described. Also, the results of preliminary experiments and site experiments to confirm the applicability of dye, and demonstration experiments using an actual machine are reported.

2 OVERVIEW OF A WEAR DETECTION DEVICE USING DYE

In this wear detection device, the preinstalled dye is released from the cutter bit when the predetermined amount of wear is reached. Since the released dye is discharged together with the excavated soil, the amount of wear can be monitored by checking the coloration of the excavated soil.

2.1 *Dye selections*

After the dye is released, it is removed and collected with the excavated soil. The physical properties of the dye must be naturally harmless taking into consideration the possibility of leakage into the ground or after treatment of the residual soil. Considering the environmental impact, fluorescent tracer dyes, which are used in groundwater flow surveys, were selected as a dye in the wear detection device. The colors are yellow-green (main component: uranine) and red (main component: rhodamine WT), the coloring property is very strong in the water, and visual observation is easy without special equipment. Furthermore, even if the dye diffuses and reaches a low

*Corresponding author: omae.yoshie@obayashi.co.jp

DOI: 10.1201/9781003495505-362

concentration that cannot be confirmed visually, the presence or absence of the dye can be distinghished as it emits light when exposed to ultraviolet (UV) light (Photo 1). These fluorescent tracer dyes have a low impact on the environment and are biodegradable. In addition, water quality analyses have been conducted to confirm that the system meets the drainage and soil environmental standards before application of it in the field.

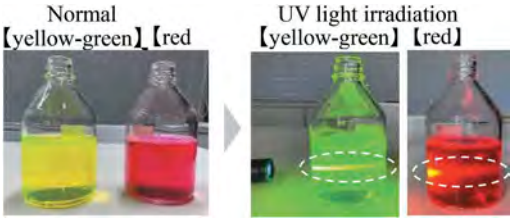

Photo 1. Fluorescent tracer dye (added to water).

2.2 *Dye installation methods*

The dye loading part is inserted at the wear depth that is desired to be monitored (amount of wear), and then the dye is installed. Since it is necessary to release the dye against the cutting face pressure during excavation, the dye is installed under pressure. The dye installation part and the pressurizing part are installed according to the shield diameter and soil quality. For small amounts, they are installed inside the bit, and in the case of large amounts, they are installed in the spoke (Figure 1 and Figure 2). Regardless of whether it is installed inside the bit or the spoke, the dye loading and the pressurizing parts can be installed together near the bit. In this case, as cables and pipes are not required, more wear detectors can be installed than conventional wear detectors.

2.3 *Detection methods*

The dye released by the wear of the bit is discharged into the shield opening together with the excavated soil. Generally, the discharge of dye is detected by visual observation of staff and workers at the belt conveyor, muck car, soil pit, and so on. It can also be detected automatically by image analysis of the excavated soil. A UV light and a remote camera are installed in the location where the brightness of the environment is constant on the excavated soil transportation route inside of the shield tunnel. The excavated soil exposed to a UV light is photographed and the images are analysed using RGB values. The light emitted by ultraviolet light is stronger when the surroundings are dark, and analysis using RGB values cannot be performed correctly if the background color changes. Therefore, the detection equipment is installed in a dark place or dark room where its brightness is constant.

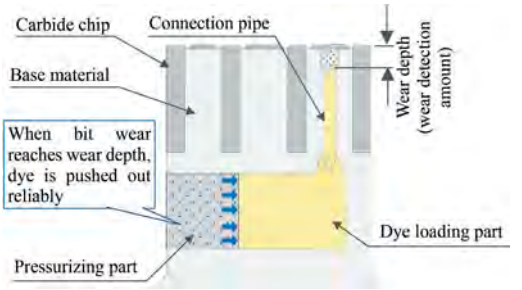

Figure 1. Example of installation inside of bit.

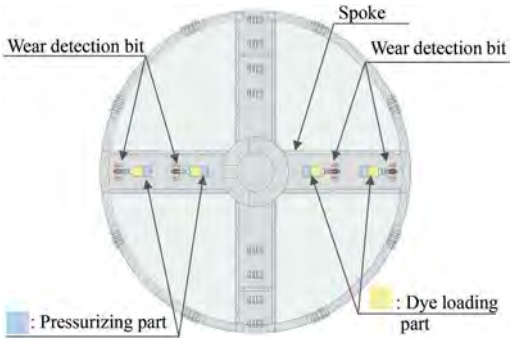

Figure 2. Example of installation in the spoke.

3 PRELIMINARY EXPERIMENTS (CONFIRMATION OF APPLICABILITY OF THE DYE TO THE SOIL)

3.1 *Purpose*

The selected fluorescent tracer dye is a dye used in water flow surveys, and it is known that it is easy to be detected when it is mixed with water. However, it is necessary to verify whether it can be detected even if it is mixed with the excavated soil in the shield.

3.2 *Overview of experiment*

First, a foamed soil (capacity: 5 L) was prepared by the addition of a foaming agent (OL-10) at a concentration of 1.0%, a foaming ratio of 10 times, and an addition rate of 20% to soil having a water content percentage of 12%. Next, red and yellow-green fluorescent tracer dyes (powder) were added to the

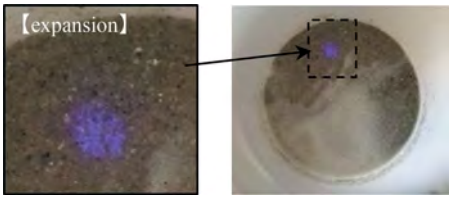

Photo 2. Fluorescent tracer dye (added to water).

foamed soil, and the mixture was stirred and confirmed visually and with a UV light. The foamed soil exposed to a UV light before adding the dye is shown in Photo-2. When it was exposed to a UV light, the color of the blue-purple light appeared to be reflected as it was.

3.3 *Results*

It is known that approximately 10 mg of red and approximately 5 mg of yellow-green is sufficiently visible in case of dissolving a fluorescent tracer dye (powder) in 5 L of water. In this experiment, the status in which 10 mg of each color of dye (powder) was added and stirred was investigated. By comparing the sample with the case before adding the dye, both red and yellow-green were colored, and it was found that the presence of the dye could be detected visually (Table 1). In addition, the coloration did not seem to be the soil itself, but also the foam material and the water such as pore water. When it was exposed to a UV light, the red dye reacted to fluorescent pink and the yellow-green dye reacted to fluorescent yellow-green, compared to the blue-purple color before the dye was added (Table 1). Next, the results of photographing and exposing the dye-containing soil to a UV light in a darkroom are shown in Photo 3. While the soil and the background appeared black, the fluorescent tracer dye emitted red and yellow-green light. From these results, it was found that visual observation can be achieved regardless of the brightness or darkness of the testing location. In the image analysis, it was shown that the presence or absence of the dye can be detected more reliably by exposure to UV light in a dark place.

These preliminary experimental results show that the fluorescent tracer dye is effective as the dye for use in a color-based wear detection device.

Table 1. Status of dye mixed into foamed soil.

	After mixing and stirring	UV light irradiation
Red 10 mg		
Yellow green 10 mg		

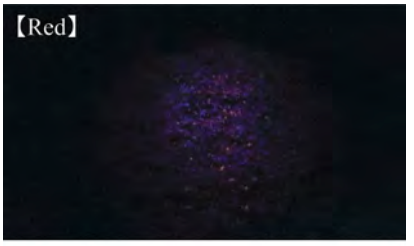

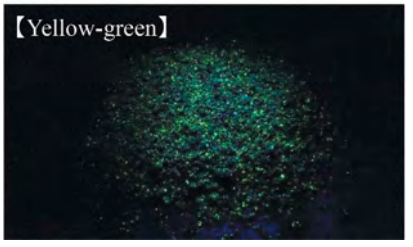

Photo 3. UV light exposure (in dark room).

4 DYE DETECTION SITE EXPERIMENTS (CONFIRMATION OF APPLICABILITY OF THE DYE TO THE SITE)

4.1 *Purpose*

At the medium and small-diameter shield sites, this experiment verifies whether the dye injected into the cutting face can be detected visually and by image analysis. Also, the required amount of the dye to be used should be determined by the injected amount at that time.

4.2 *Experimental methods*

The dye was injected directly into the cutting face, and the color of the soil discharged into the belt conveyor, muck car, and soil pit was confirmed visually and by image analysis. Two fluorescent tracer dyes (liquid), red and yellow-green, were injected into the existing mud additive line by connecting to a manual pump. Injection was performed during segment assembly when excavation was stopped. Since it was difficult to estimate how much the dye would be stirred and dispersed in the chamber, the subsequent injection

Table 2. Outline of the subject shield construction.

	Site 1 (Medium diameter)	Site 2 (Small diameter)
Soil type (experimental place)	sand and gravel・silt・gravel mixed sand	clayey soil
Method of construction	Mud pressure	Mud pressure
Shield outer diameter	φ4.53m	φ2.33m
Chamber volume	Approximately 11.67 m^3	Approximately 0.58 m^3
Method of mucking	Belt conveyer +muck car	Pressure hose +muck car

amount was increased or decreased depending on whether detection was possible or not. Table 2 shows an outline of the two sites where the site experiments were performed.

4.3 *How to confirm the dye*

For visual observation, a muck car at a launch shaft was confirmed visually. For automatic detection, because of different soil removal methods at the two sites, at site 1, a darkroom was set up above the belt conveyor between the screw conveyor and the muck car, and a UV light and a remote camera were installed inside the dark room. The video was taken during the belt conveyor operation and was saved at every second as a stationary image (Figure 3 and Photo 4). At site 2, a UV light and a remote camera were set up 100 m away from the tunnel entrance (Figure 3 and Photo 5). During the passing of a muck car, the system automatically turns off the tunnel lights, takes a video and saves stationary images every second. For image analysis, the taken images were decomposed into RGB, then green and red were binarized, and after that the average brightness value of the binarized image (ratio of white pixels to the total number of pixels after the binarization process) was taken. Therefore, it was possible to emphasize and capture even the slightest part of the green or red colors. For binarization, the middle 127 of the 255 brightness levels of RGB values was set as the threshold. When observing a large variation in the average brightness value, it was determined that there was a possibility of dye discharging. Humans judged visually whether the image contained dye.

Also, at site 1, the soil passes at high speed on a belt conveyor (approximately 1.6 m/s). To investigate the effect of different camera shutter speeds on visual observation by humans and by image analysis, two cameras were installed and they took pictures at two different shutter speeds (1/30 s and 1/100 s).

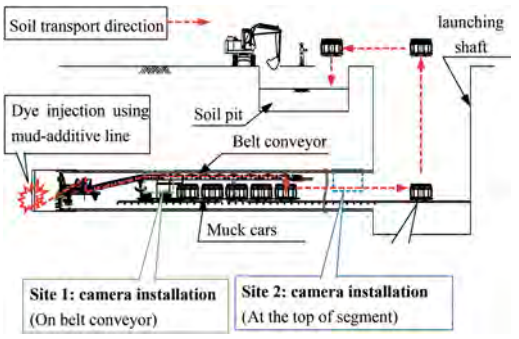

Figure 3. Outline of dye detection locations (camera set up and visual observation) visual confirmation.

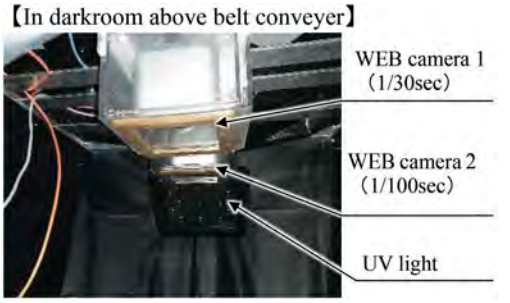

Photo 4. Status of equipment set up at site1.

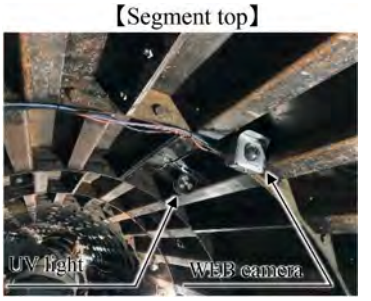

Photo 5. Status of equipment set up at site2.

4.4 *Experimental results*

4.4.1 *Site 1*

Visual observation of the soil with a muck car was sufficiently confirmed with 20 cc red and 40 cc yellow-green (Picture 6). Because of the large amount of sand and gravel, the dye floated to the surface together with the pore water due to vibrations during the transportation of a muck car. Therefore, it was thought that the dye is visible even in small quantities. Also, on the camera's video monitor, instantaneous visual confirmation was possible at 20 cc red and 40 cc yellow-green. The amount of dye injected that could be reliably identified by visual observation of the soil on the muck car, visual observation on a camera's video monitor, and image analysis of stationary images was 200 cc for both red and yellow-green (Figure 4 and Figure 5).

Table 3 shows the differences in images depending on the shutter speed. A faster shutter speed produced clearer images, but the overall image was darker because of the reduced amount of light, and in particular, it was difficult to visually confirm the red color. In the image analysis, it is generally easier to binarize and detect dye mixing when the difference in RGB values is larger and the range of brightness is wider than when the image is clear. Therefore, it was found that a somewhat slower shutter speed is better for both visual observations of stationary images and image analysis, regardless of the soil discharge rate.

4.4.2 *Site 2*

The visual observation of the soil on a muck car showed that it could be slightly confirmed by careful

visual observation with 100 cc red, but because of the clayey soil, the dye was encapsulated in the clay and did not separate and float to the surface, making visual observation more difficult than at site 1. In the case of the 300 cc yellow-green, the visual observation of the soil on a muck car, visual observation on the camera's video monitor, and image analysis of the still images all reliably identified the dye (Figure 6). Because of the small diameter of site 2, it was assumed that a smaller amount of dye could be used to determine that in site 1, but it was found that a larger amount of dye was needed for soil types such as the clayey soil where pore water is difficult to separate in this case.

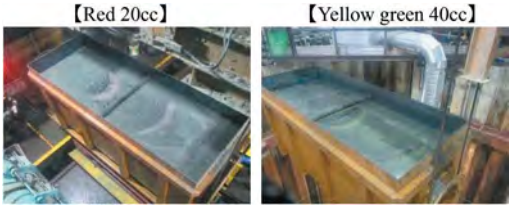

Photo 6. Visual observation of the soil.

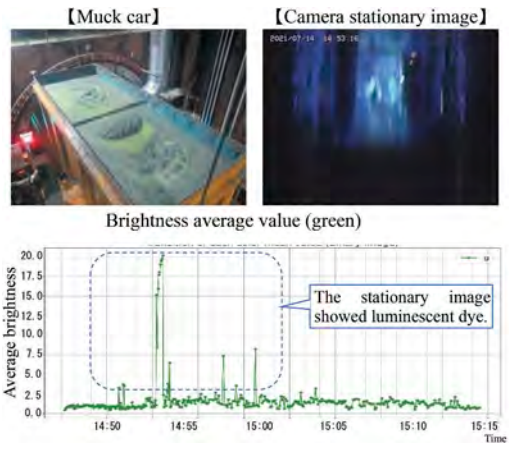

Figure 4. Result of injection of 200 cc yellow-green at site 1

5 DEMONSTRATION EXPERIMENTS

5.1 *Purpose*

This experiment confirms that the dye can be released into the cutting face under the cutting face pressure using the structure of the dye installing and pressurizing parts of the proposed device (spoke-installation type).

5.2 *Experimental methods and results*

When the shield machine was manufactured at site 2, a wear detection device was installed in the spoke

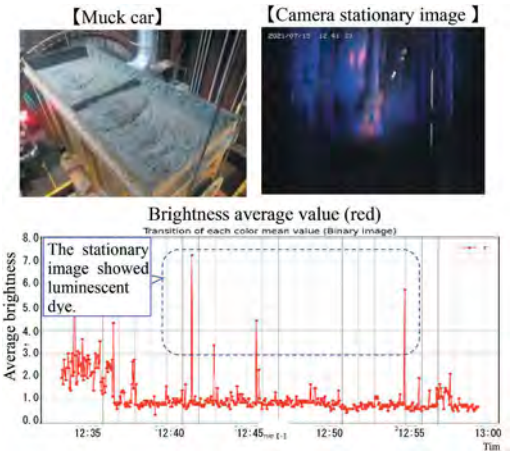

Figure 5. Result of injection of 200 cc red at site 1

Table 3. Shutter speed and image.

	1/30 sec	1/100sec
Red		
Yellow and green		

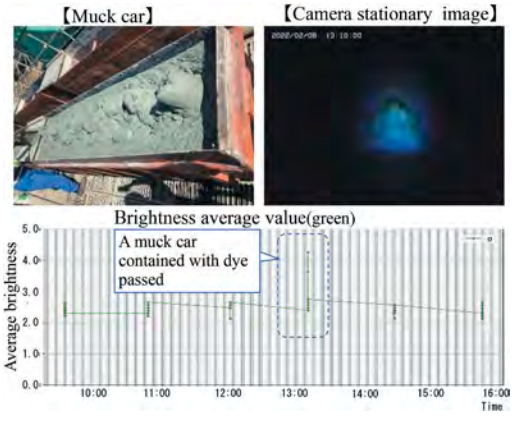

Figure 6. Result of injection of 300 cc yellow-green at site 2.

(installed capacity: 300 cc) with a yellow-green dye of 10 mm wear and a red dye of 35 mm wear. The intended excavation length is approximately 3.8 km (2.5 km + 1.3 km), and the plan is to discharge the

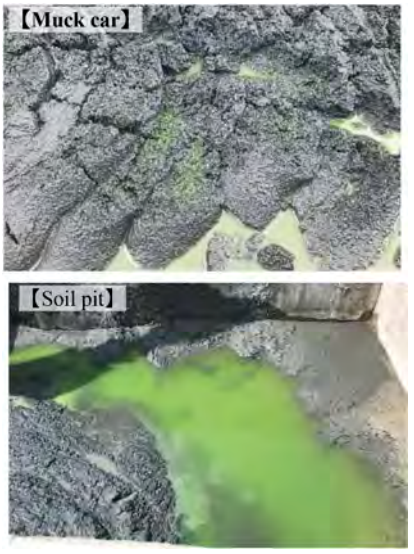

Photo 7. Dye discharging status from the wear detection device installed in the actual machine.

yellow-green dye when excavating approximately 0.9 km and to discharge the red dye when excavating approximately 3.0 km. Currently, 2.5 km has been excavated and the first destination shaft has been reached, and the staff was able to visually detect the discharge of yellow-green-colored soil from a muck car and at the soil pit when it was excavated 1.02 km (Photo 7). After the machine's arrival, a hole in the bit that connects the bit and the dye installation part was also confirmed. As a result, even under the cutting face pressure, the dye is reliably released when the predetermined amount of wear is reached, and it can be easily confirmed from the discharged soil visually. Additionally, it was demonstrated that the system applies to actual constructions.

6 CONCLUSION AND DISCUSSION

It was found that the wear detection device using the fluorescent tracer dye could be visually confirmed, so anyone could distinguish them, and it was also possible to understand the wear by the image analysis. At the medium- and small-diameter shield sites, the sufficiency of the amount installed dye in the spokes, and the applicability to the actual construction were confirmed. However, since the ease of detection varies depending on the soil type, it is necessary to plan the amount of dye installed by considering the soil conditions. Meanwhile, data on the relationship between soil conditions and the required installation amount is planned to be accumulated.

In the case of application to a large-diameter shield, the volume of soil in the chamber is large and the dye may be more diffused. Thus, we will perform experiments to confirm the required installation capacity of dye for large-diameter shields in the future.

In the future, we hope to increase our knowledge by applying this system in the actual construction sites, utilize this device widely and contribute to the prevention of excavation troubles caused by bit wear.

Tunnelling for a Better Life – Yan, Celestino, Thewes & Eberhardt (Eds)
© 2024 The Author(s), ISBN 978-1-032-80042-4
Open Access: www.taylorfrancis.com, CC BY-NC-ND 4.0 license

Structure health sensing network layout and monitoring based on wireless sensor network in undersea tunnel

Linghan Ouyang
Department. of Geotechnical Engineering, Tongji University, Shanghai, China

Hongwei Huang & Dongming Zhang*
Department. of Geotechnical Engineering, Tongji University, Shanghai, China
Key Laboratory of Geotechnical and Underground Engineering of Minister of Education and Department of Geotechnical Engineering, Tongji University, Shanghai, China

Changsong Wang & Shuaida Zhu
Shanghai Research Institute for Intelligent Autonomous Systems, Shanghai, China

ABSTRACT: With the rapid urbanization and the expanding use of subterranean spaces, tunnel structures have gained increasing significance in urban transportation. Given tunnels' permanence once built, assessing their structural health is vital throughout their lifecycle. Wireless Sensor Networks (WSNs) offer self-organization, high data acquisition frequency, low power consumption, and scalability. WSNs, applied in structural health monitoring, autonomously collect and transmit data using routing algorithms over their lifespan. The study focuses on undersea tunnels, known for their long distance, complex cross-sections, and high water-pressure. Taking wireless signal path loss characteristics and structure features into account, a layout for a structural health monitoring network along the tunnel axis was designed. It aims to ensure data acquisition in typical scenarios and maintain system robustness in unfavourable conditions through field experiment. The horizontal convergence of monitored tunnel sections as indicator is analysed detailly with different geological environment and construction method. Field experiment demonstrates that the choice of signal frequency band is important in WSN system deployment and margin of signal strength will be helpful under unfavourable circumstance in maintain the system robust. In cross-sea tunnel, undersea part is more sensitive to disturbance than land part and mining part is more stable than the shield part. Daily fluctuation of the tunnel horizontal convergence has little relationship with the daily change of temperature.

Keywords: Undersea tunnel, Wireless sensor networks (WSN), Path loss, Horizontal convergence, Temperature

1 INTRODUCTION

In recent years, rapid economic development and urbanization in China have led to a significant increase in the scale of tunnel construction and the number of existing tunnels. Tunnel construction and the maintenance of existing tunnels have garnered significant attention due to their wide applicability under complex geological conditions. The widespread use of tunnels provides a convenient means to traverse water, mountains, and other challenging terrain, connecting various parts of cities and significantly reducing transportation time. However, some tunnels under construction and in operation face considerable construction challenges and complex external environments. Complex geological conditions such as high ground stress, water, and weak interlayers are among the external environmental challenges that tunnel construction and operation currently need to overcome. These conditions also introduce certain safety risks during the tunnel construction process and subsequent maintenance and operation.

Monitoring and measurement are fundamental concepts in modern tunnel construction and serve as crucial means to ensure the safety of tunnels during both construction and operation phases (Qian, 2012). With

*Corresponding author: 09zhang@tongji.edu.cn

DOI: 10.1201/9781003495505-363

the development of computer science and communication engineering technologies, tunnel monitoring has gradually shifted from traditional manual monitoring towards automation. Wireless Sensor Networks (WSN) have emerged as a widely recognized monitoring method. WSN were initially applied to the short-term health monitoring of bridge structures (Lynch,2006) and to tunnels latter (Bennet,2010). WSN systems deploy tunnel safety state-aware sensor nodes like inclination nodes and settle-down node inside tunnels to continuously monitor the tunnel's condition and environment in real-time (Huang,2013; Yin and Huang,2015). These sensor nodes transmit monitoring data to gateway and cloud through wireless signals, ensuring that personnel receive timely information regarding structural health parameters. By data analysis, potential safety hazards can be promptly identified, enhancing overall tunnel safety.

Path loss and RSSI (Received Signal Strength Indication) are widely used in evaluation of wireless communication quality (Kalyankar,2020). Taking into account the long-distance structural characteristics of underwater tunnels, wireless transmission frequency bands and the maximum distance between nodes for structural health monitoring network deployment were instructed through field experiments in an effort to optimize the network layout.

2 UNDERSEA TUNNEL HEALTH SENSING NETWORK LAYOUT

2.1 *Project profile*

The Metro Line 8 in Qingdao City, Shandong Province, connects Qingdao North Station and Qingdao Jiaodong International Airport (TAO). The section between Dayang Station and Qingdao North Station is 7.9 kilometres long and the undersea section has a total length of 5.4 kilometres, with the maximum burial depth reaching 56 meters below the sea surface, making it the longest underwater subway tunnel in China at the time. In all the undersea part, the eastern of 2.9 kilometres was constructed using the slurry shield tunnelling method, while the western of 2.5 kilometres was constructed using mining and dual-mode TBM (Tunnel Boring Machine) methods. The different construction methods employed resulted in distinct cross-sectional forms on the eastern and western sides.

This section, as a representative underwater tunnel, underwent field testing of the wireless communication system for the structural health monitoring and the actual deployment of the relevant monitoring systems as described in this article.

2.2 *Wireless signal transmission field experiment*

2.2.1 *Experiment introduction*

The deployment of wireless sensor networks is not only influenced by the monitoring object's location and energy consumption but also by the quality of wireless signal communication. Excessive single-hop communication distances can result in poor signal quality and increased energy consumption. According to relevant regulations from the Ministry of Industry and Information Technology in mainland China, three recommended ISM (Industrial, Scientific, and Medical) wireless signal frequency bands tested in this article for structural health monitoring are 433MHz, 868MHz, and 2.4GHz.

During field experiment, the same part of the tunnel was tested in these three different frequency bands. The receiving end remained stationary while the transmitting end moved away from the receiving end and maintained a signal transmission frequency of 1Hz to simulate real-world structural health monitoring scenarios. The purpose is to determine the maximum transmission distance by observing how path loss changes with distance in different frequency bands within the tunnel environment. When the receiving end is unable to receive signals from the transmitting end, and the transmitting end remains stationary for 30 seconds without reconnection, the distance is considered to be the maximum single-hop transmission distance for that frequency band.

2.2.2 *Experiment analysis*

The experiment was carried out in a 1400-meters-long straight undersea part of Qingdao Metro Line 8 and tests for 443MHz and 868MHz were repeated immediately to confirm the communication ability. It should be noticed that due to regulation, the transmitting power of 2.4GHz is 3 dBm and in comparison, that of other 2 frequency band is 20 dBm. The maximum single-hop transmission distance is shown in Table 1.

Table 1. The maximum single-hop transmission distance.

Test number	Frequency band	Maximum distance(m)
1	443MHz	428
2	443MHz	495
3	868MHz	1286
4	868MHz	1060
5	2.4GHz	207

Signal in high frequency band will perform better in straight transmission. The signal of 868MHz frequency band can reach more than one kilometre in single hop, which is more than twice that in the 433MHz band, suited better to address the transmission requirements in the context of unidimensional long-distance scenarios, such as underwater tunnel deployments.

For the 868MHz frequency band, further field experiment was conducted. Four characteristic positions were selected within the single-hop transmission range, specifically at 500m, 700m, 900m, and 1100m. At each of these positions, the transmitting end remained stationary for 5 minutes (transmitting 300 data packets) to simulate real-world data transmission quality in order to ensure the proper functioning of the

monitoring system after deployment. The path loss of these characteristic positions is shown in Figure 1.

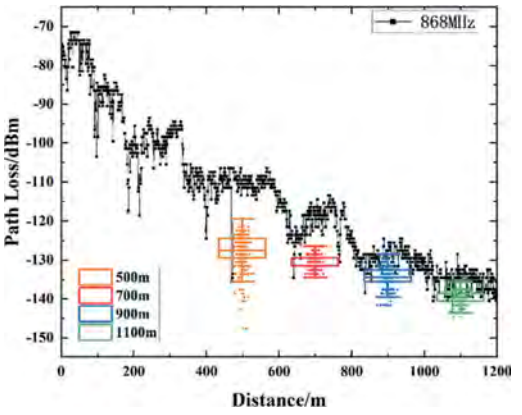

Figure 1. Path loss in 868MHz in field experiment.

According to the Friss formula, which describes signal attenuation in free space, the increase of path loss or the attenuation of signal strength (dBm) is log-dependent with distance.

$$PL = -27.56 + 20\log_{10}(d) + 20\log_{10}(f) \qquad (1)$$

Where, PL is path loss (dBm); d is distance(m); f is frequency of signal (MHz).

The trend is also illustrated in test with a fast decline in near region and a slower decline in far region. Considering the shadow, multi-path effect and obstacle, the curve describing relationship of path loss and distance is not smooth but fluctuates a lot and even in the same position the path loss also alters with time. The median of all the data collected in characteristic position test decline with the increase of distance. However, there is no significant correlation between the fluctuation amplitude and distance of path loss. In other word, it is possible that a node in a much near position malfunction with a node with larger distance functioning well due to the fluctuation. The statistical analysis of characteristic position test is shown in Table 2.

Within the 868MHz frequency band test system, a reception threshold of -112dBm has been configured and this setting ignores signals weaker than this threshold, resulting in packet loss. Based on the 300 data packets, signal at 500 meters is badly influenced by the obstacle and fading, results in strength ranging from -84dBm to -112dBm, namely a nearly 1000-fold difference in milliwatts for transmission power. This observation aligns with rapid and substantial fluctuations in path loss-distance characteristic curve in Figure 1. This variation in signal strength highlights the importance of margin to ensure reliable data transmission in such conditions.

Small signal strength and large variance can detrimentally impact communication quality, notably by increasing the packet loss rate. This conclusion is

Table 2. The statistical analysis of characteristic position test.

Distance(m)	Packet Loss Rate(%)	Signal strength(dBm) Range	Average	Variance
500	1%	[-84, -112]	-92.65	20.2
700	0.66%	[-91, -99]	-94.63	2.867
900	10.7%	[-93, -106]	-99.09	8.217
1100	1%	[-99, -109]	-103.73	2.753

supported by the comparative analysis of data collected at distances of 500m, 900m, and 1100m. The data from 500m, characterized by the highest variance yet relatively high average signal strength, and the data from 1100m, characterized by the lowest average signal strength but small variance, both show favourable packet loss rates due to the low probability of signal strength falling below the threshold. On the contrary, the data from 900m, featuring second lowest average signal strength and second largest variance, reveals a significant deterioration in communication quality, with a packet loss rate exceeding 10%. This adversely impacts the efficiency of the monitoring process.

In this project, despite the potential for single-hop transmission to cover distances exceeding 1200 meters, it is advisable, for the sake of leaving some margin and ensuring monitoring quality, to maintain a separation distance of less than 700 meters between the two nearest nodes.

2.3 *Layout for the monitoring system*

Wireless sensor network for infrastructure health monitoring is a multi-hop ad-hoc network. Consequently, the selection of node locations assumes importance, as these placements are intricately linked to energy consumption, communication proficiency, and the specific attributes of the monitored infrastructure. The undersea tunnel is a typical unidimensional linear structure with long distance and few entrance. The layout aims to build a robust monitoring system with least manned maintenance and monitoring valuable structural health attributes under the limitation of communication ability.

Undersea tunnel of Qingdao Metro Line 8 has some feature like dual construction methods, large depth, long distance and complex geology. Seven monitoring sections are chosen to focus on the influence of longitudinal grade, connected aisle, construction methods and geology which are shown in Figure 2. All the seven sections are divided into two groups according to distance and each group is assigned a gateway to convey and transmit monitoring data into cloud. The gateways are installed between section No.2 and No.3 and near section No.6.

The deformation of tunnel structures is a crucial indicator of safety performance during the operation

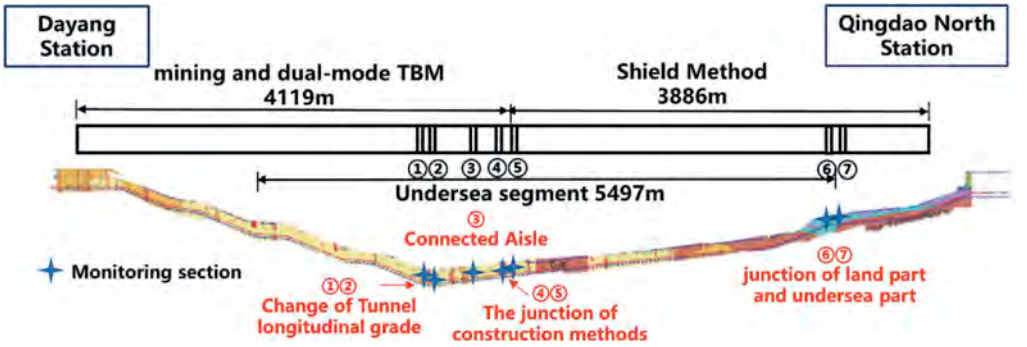

Figure 2. Longitudinal layout for monitoring system.

of tunnel structures. Some safety indicators for tunnels, such as bolt stress, joint separation, and concrete stress, are challenging to obtain. In contrast, changes in tunnel diameter are relatively easy to measure and can be used as a reference for calculating the critical state of other safety indicators through numerical methods (Wang, 2015). Therefore, changes in tunnel diameter are commonly utilized as a key indicator of tunnel cross-sectional safety performance.

Considering that the Qingdao Metro Line 8 undersea part utilizes both shield tunnelling and mining methods for construction, there are significant differences between the cross section of these two construction methods. Tunnels built by shield tunnelling method are typically constructed by immediately connecting and assembling multiple prefabricated segments using bolts after the tunnel boring machine excavation and tunnels built by mining method are initially supported after blasting out the debris and then undergo a secondary lining with shotcrete. Because of the interaction between initial support and secondary lining, monitoring data can only partially indicate the actual deformation of tunnel structures under external loads. Therefore, two omnidirectional inclinometer sensor nodes with laser ranging function are installed in the shield method sections (No. 5,6 and 7) to monitor horizontal diameter changes and settlement at the top of tunnels. In the mining method sections (No. 1,2,3 and 4), only one omnidirectional inclinometer sensor node with laser ranging function is installed to monitor horizontal diameter changes. The detail of sensor nodes layout in cross section is shown in Figure 3 and the parameters of omnidirectional inclinometer sensor node are in Table 3.

3 MONITORING DATA ANALYSIS

Given that the target tunnel is in a state of stable operation and its maintenance is less convenient compared to conventional tunnels, the monitoring frequency has

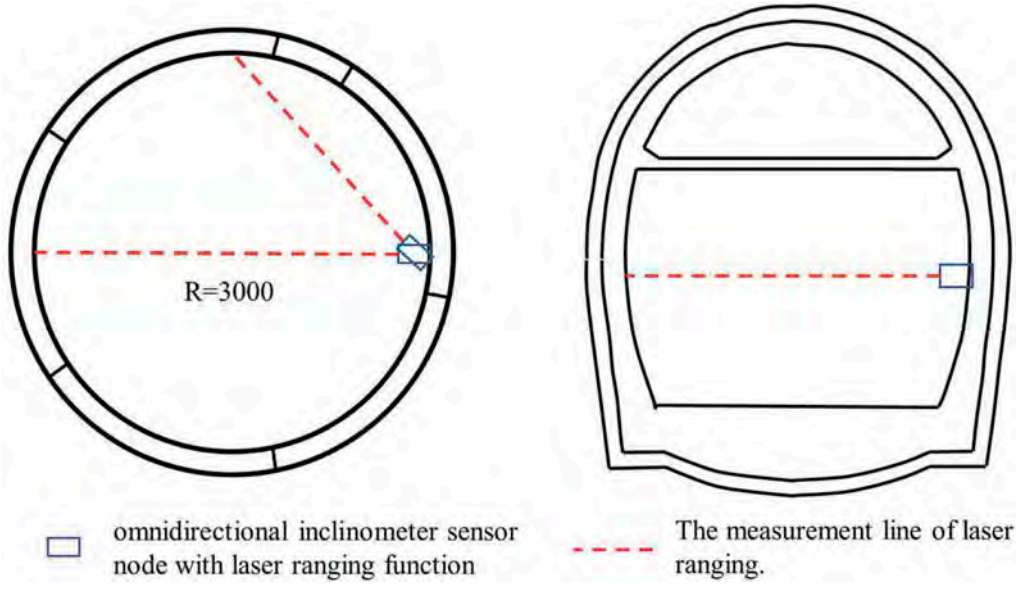

Figure 3. Sensor nodes layout in cross section.

Table 3. The parameters of sensor node.

Node	WISENMESHNET®6F07 inclinometer	laser ranging sensor
Range	-90°-+90°	0.05mm-33mm
Accuracy	0.002°	±1.0mm
Resolution	0.0001°	0.1mm
Weight	Less than 0.65kg	
Size	100mm*100mm*60mm	
Working temperature	-10°C-50°C	
Waterproof level	P6	

initially been established at an interval of once per hour. Notably, the monitoring frequency will be adjusted to once every five minutes during the period from April 10th to May 1st in order to acquire detailed information regarding structural deformation.

3.1 *System reliability and robustness*

Radio connectivity stands as the paramount focal point concerning the reliability and robustness of WSN systems. Despite the WSN monitoring system's configuration as a multi-hop ad-hoc network, all nodes are strategically deployed within 600m. The multi-hop transmission capability functions as a protective buffer, reinforcing the system's robustness against unfavourable conditions.

The data of mesh network demonstrates good results about the radio connectivity. All nodes deployed connect to gateway directly in normal operation and multi-hop transmission capability functions well when the subway trains pass with the electromagnetic environment deterioration. With the distance increasing, the train-influenced signal strength of direct connection is more likely to go down under the threshold and trigger the multi-hop transmission mechanism. To shows how reliable and robust the system is, the packet loss rate and direct connection rate is defined as follow:

$$Packet\ Loss\ Rate = 1 - (n_r/n_s) \quad (2)$$

$$Direct\ Connection\ Rate = n_1/(n_1 + n_2) \quad (3)$$

Where, n_r is number of data packet from the node which cloud received; n_s is ideal number of data packet send by the node; n_1 is number of data packet come from direct connection between nodes and gateway; n_2 is number of data packet send by multi-hop transmission.

The approximate 14000 packet of monitoring data from April 4th to September 13th is analysed about the connectivity. The radio connectivity of each node is shown in Table 4.

Owing to the data packet retention and subsequent retransmission feature integrated into the system's configuration, the packet loss rate will be strictly controlled and be 0 in this system. The node deployment strategy adheres to recommended guidelines, with nodes positioned at a distance less than 700 meters from gateway.

Table 4. The radio connectivity of each node.

Group	Node number	Distance from gateway	Packet loss rate	Direct loss rate
	1	520m	0	0.08%
	2	519m	0	0.44%
		Gateway 1		
1	3	114m	0	0.11%
	4	495m	0	0.18%
	5-1	520m	0	0.81%
	5-2	520m	0	1.09%
		Gateway 2		
	6-1	Less than 20m	0	0.30%
2	6-2	Less than 20m	0	0.50%
	7-1	Less than 20m	0	0.21%
	7-2	Less than 20m	0	0.46%

In most scenarios, monitoring data is routed directly to the gateway, with a diversion to another nodes for transmission assistance occurring only when there is a disruption in the link. The direct loss rate serves as an indicator, quantifying the proportion of data packets transmitted through intermediary nodes rather than being routed directly to the gateway. High direct loss rate means the connectivity margin caused by the multi-hop transmission mechanism functions greatly and the location of this node is not good when considering about the link to gateway.

3.2 *Preliminary monitoring results*

The convergence is a vital indicator of shield tunnel health and excessive horizontal convergence will lead to unfavourable stress condition, shrinking space inside and tunnel disease influencing the safety status and the usage function simultaneously. The sensor nodes in system could provide an unmanned method to monitor the horizontal convergence with high frequency (1 time per hour). For different type tunnels, the threshold of convergence during operations stage varies. With reference to design description and the relevant specifications for shield tunnels, the limit of horizontal convergence in this tunnel is set at 10mm in mining method part and 2‰ outer diameter (13.4mm) in shield method part.

3.2.1 *Undersea section and land section*

The sensor nodes 6-1 and 7-1 are installed to monitor the convergence. There is the air shaft No. 2 between the two cross-sections, with section No. 6 and No. 7 situated at a spatial separation of approximately 25 meters. Notably, section No. 6 lays in the undersea part, while section No. 7 lays in the land part. Except the outer environment, two sections are in similar condition, being good monitoring object for the influence caused by sea. The monitoring data is shown in Figure 4 and the descriptive statistics of monitoring data is in Table 5.

The system error caused by instrument accuracy is inevitably introduced in the monitoring, making the

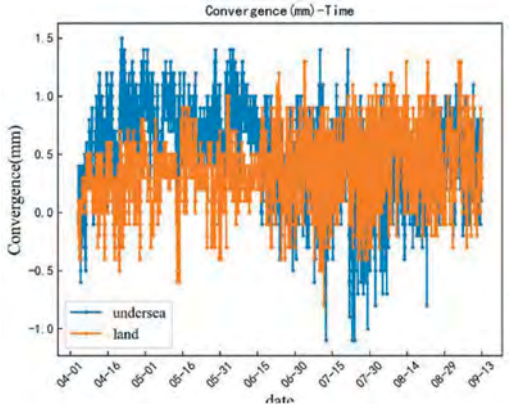

Figure 4. Raw monitoring data of section no.6 and 7.

Table 5. The descriptive statistics of monitoring data of section no.6 and 7.

Monitoring Section	Horizontal convergence (mm) average	variance
No.6 (undersea)	0.700	0.092
No.7 (land)	0.304	0.032

data less creditable. To reduce the impact of instrument error, the Kalman filter algorithm which can real-time denoise data without variation of data size (Kalman, 1960) is introduced in data processing. Kalman filter algorithm predict the state with both physical estimation and measurement and then update the parameter for next prediction, obtaining a more creditable data. The processed monitoring data is shown in Figure 5.

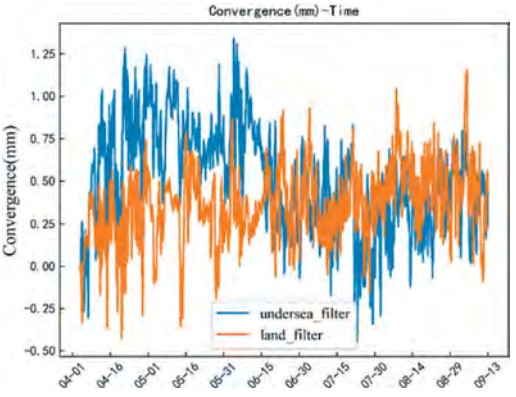

Figure 5. Filtered monitoring data of section no.6 and 7.

The horizontal convergence of section increases about 0.5mm in the past 5 months in both monitored sections. However, there are obvious differences in the trend of change with fast increase and then decrease in undersea section No.6 and slow increase in land section No.7. Hence, in descriptive statistics, the average horizontal convergence delta of section No.6 is more than 2 times of that of section No.7. It can also be found that both sections respond similarly to disturbance but with different amplitude. It is also understandable that undersea section No.6 are more sensitive than the land section No.7 to the influence of semi-day tide of Jiaozhou Bay causing the difference of amplitude. Another potential factor is that the land section is subject to more vertical pressure from upper soil layer which make it less sensitive to the disturbance. The possibility of a periodic trend in the horizontal convergence of the tunnel cannot be ruled out. Therefore, the large peak value of the undersea part (more than 1mm) observed in the monitoring data should be paid attention to in future monitoring.

Before the WSN system installation, the total station-based monitoring is main method to monitor the tunnel deformation. However, due to the extreme length of cross-sea tunnel, manual measurements will take several days. Hence, the manual deformation monitoring will be carried out once a year. The tunnel was put into use in December 2020, so the first monitoring was carried out in January 2021 and latest recorded monitoring was in March 2023. The horizontal convergence of Section No.6 and No.7 increased 0.5mm from February 2022 to March 2023, which showed the same magnitude and trend as deformation monitored by WSN (0.700 for No.6 and 0.304 for No.7 from April 2023 to September 2023). Noticeably, comparing with the designed horizontal convergence, horizontal convergence of Section No.6 and 7 decreases by 2.08 and 2.72, respectively. This can be interpreted to mean that the section reaches a new equilibrium due to the deformation caused earth pressure after the completion of the shield construction and in the long run, the vertical earth pressure is the main load of the section, so the horizontal convergence increases slowly on the basis of the existing equilibrium state. The current deformation level is still far below the deformation threshold, so it can be considered that the tunnel is in a good safety state.

3.2.2 *Shield tunnelling section and mining section*

The sensor nodes 4 and 5-1 are installed to monitor the convergence of different type of section forms due to construction method. At the intersection of the shield and mine construction areas, the section was specially designed and reinforced and no embedded troughs are designed for device installation. Section No.4 and Section No.5 are the first section with the embedded troughs in mining method part and shield tunnelling part respectively with a distance of 25 meters. In the shield section, the internal deformation is directly related to the external load because there are no additional structural layers, however, in the mining section, external load causes the inner deformation through the deformation of first lining and subsequent shotcrete layer which make the monitoring data can not indicate the health condition so effectively. The monitoring data and filtered monitoring data are shown in Figure 6 and

the descriptive statistics of raw monitoring data is in Table 6. Based on current deformation, it can be considered that the section where the construction method is changed is in a good safety state.

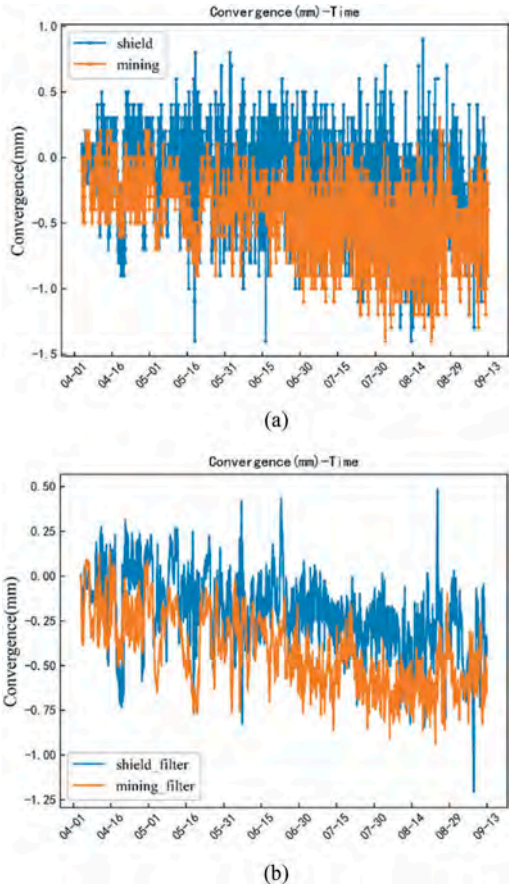

Figure 6. (a) raw and (b) filtered monitoring data of section No.4 and 5.

Table 6. The descriptive statistics of monitoring data of section no.4 and 5.

Monitoring Section	Horizontal convergence (mm) average	variance
No.4 (shield)	-0.138	0.068
No.5 (mining)	-0.302	0.044

The filtered monitoring data of section No.4 and 5 change in a same trend but with different amplitude. The horizontal convergence decreases slightly with about 0.1mm/month. The special structural design and strata reinforcement make the section subject to greater horizontal resistance than the general sections with an unusual decrease in horizontal convergence. The mining section with less variance is in line with the knowledge that structure form make it less sensitive to the outside disturbance and tent to be stable.

3.2.3 *Monitoring data and temperature*

All the monitoring data shows a daily fluctuation and daily temperature change is a potential factor that result in the phenomenon. The installed sensor nodes have extra function of temperature measurement and every data packet has its own temperature data which could be used to analyse the relationship. The R2 was used as an evaluation index of correlation and data from the nodes mentioned in 3.2.1 and 3.2.2 are visualized to show the relationship in Figure 7. The R^2 of monitoring data is shown in Table 7.

The correlation index is too small to take the relationship between monitoring convergence and temperature into consideration and the point in graph also do not show the significant mathematic relationship between convergence and temperature. The laser ranging sensor is not sensitive to temperature changes in the operating temperature range. The daily fluctuation of monitoring data may come from the influence of Jiaozhou Bay semi-diurnal tide and the relationship need further research and analyse.

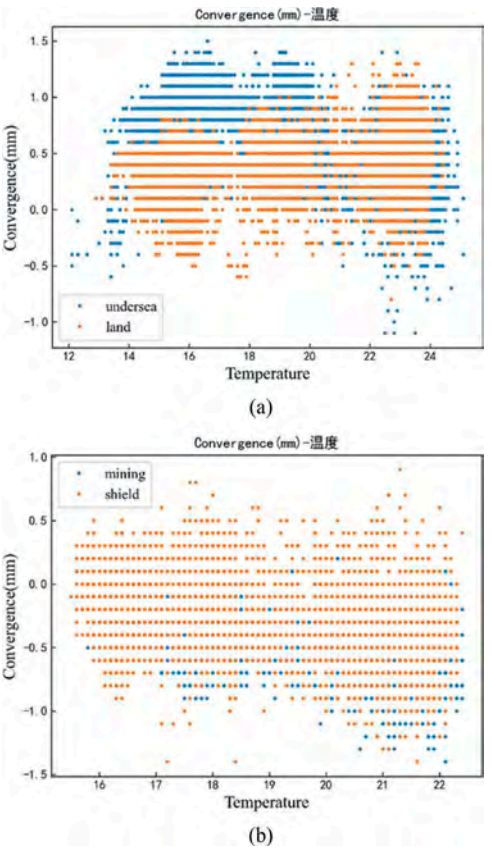

Figure 7. Convergence-temperature graph of (a) section No.6 and 7 (b) section No.3 and 4.

Table 7. The correlation of monitored convergence and temperature.

Monitoring Section	correlation index R^2
No.4 (shield)	0.09
No.5 (mining)	0.30
No.6 (undersea)	0.03
No.7 (land)	0.08

4 CONCLUSIONS

This paper evaluates the ISM band signal transmission path loss characteristic in undersea tunnel field experiment and characteristic position test was carried out for the recommended wireless signal of 868MHz band in order to introduce the influence of shadow fading and obstacles into consideration of the wireless channel quality. Based on the existing configuration of wireless sensor network structural health monitoring system, the recommended maximum single-hop layout distance in undersea tunnel is proposed, and the recommended distance and the undersea tunnel structure character instruct the layout of monitoring system. The approximately six-month monitoring data from system is analyse to study about the structure deformation in different environments. The main conclusions are shown as follows:

1. Limited by the codes and technical configuration, the 868MHz frequency band performs best in the path loss characteristics of the undersea tunnel, the maximum single-hop transmission distance reaching 1200m.
2. Fading and obstacle have negative impact on the wireless channel causing high variance of signal strength and the multipath effect also degrades the communication quality in some areas. To make sure the reliability and robustness of system, a 10dBm margin of signal strength should be considered to remain for potentially unfavourable condition.
3. As an important indicator of tunnel health condition, the convergence of tunnel grow at a speed of 0.1mm/month at the both side of junction of undersea part and land part, but with larger fluctuation in undersea part. Due to the special structural design and strata reinforcement, the convergence at the junction of construction methods decreases slightly.
4. The monitoring data shows significant daily fluctuation and the temperature monitored is verified that no close relationship between convergence and temperature.

It should be noted that the filed experiments only support the conclusion limitedly. Curves and section forms of tunnel will influence the channel in some extent and the pass loss characteristic should take these factors into consideration. Convergence monitoring only last about 6 months and have the possibility missing the annual trend of tunnel which is found in other monitoring project. More data covering longer period is needed to analyse precisely.

ACKNOWLEDGMENTS

This work was supported by the National Key R&D Program of China (No. 2021YFB2600800) and National Key Research and Development Program of China (No. 2021YFF0502200).

REFERENCES

Bennett, P. J., Soga, K., Wassell, I., Fidler, P., Abe, K., Kobayasni, Y., et al,2010. Wireless sensor networks for underground railway applications: case studies in Prague and London. Smart Structures & Systems, 6 (5-6), 619–639.

Huang, H., Xu, R. & Zhang, W.,2013. Comparative performance test of an inclinometer wireless smart sensor prototype for subway tunnel. International Journal of Architecture Engineering and Construction, 2, 25–34.

Kalman, R. E., 1960. A new approach to linear filtering and prediction problems. J. Basic Eng. Mar 1960, 82(1): 35–45.

Kalyankar, S. K., Lee, Y. H., & Meng, Y. S., 2020. Two-slope path loss model for curved-tunnel environment with concept of break point. IEEE Transactions on Intelligent Transportation Systems, PP(99), 1–10.

Lynch, J.P., Wang, Y., Loh, K.J., Yi, J.H. & Yun, C.B., 2006, Performance monitoring of the Geumdang Bridge using a dense network of high-resolution wireless sensors, Smart Mater. Struct., 15(6), 1561–1575.

Qian, Q., 2012. Challenges faced by underground projects construction safety and countermeasures. Chinese Journal of Rock Mechanics and Engineering. 2012, 31 (10):1945–1956.

Yin, J., & Huang, H., 2015. Real time monitoring method for the longitudinal settlement of shield tunnel using wireless inclinometer. Information Technology & Mechatronics Engineering Conference.

Tunnelling for a Better Life – Yan, Celestino, Thewes & Eberhardt (Eds)
© 2024 The Author(s), ISBN 978-1-032-80042-4
Open Access: www.taylorfrancis.com, CC BY-NC-ND 4.0 license

Innovative shaft inspection system for the Gotthard Base Tunnel

Martina Puglia, Peter Spohn & Klaus Wachter*
Amberg Infra 7D, Regensdorf, Switzerland

Leandro Chelini & Shuan Xiao
Amberg Technologies AG, Regensdorf, Switzerland

ABSTRACT: Amberg was commissioned by the Swiss Federal Railways SBB to develop a measurement system and execute an inspection of the 800 m deep Sedrun shaft B at the Gotthard Base Tunnel. A special shaft module equipped with multiple sensors was built to acquire a reliable data base. The inspection and condition assessment were performed based on this data using an in-house inspection and data management platform. This paper presents the innovative measurement system developed and highlights the challenges encountered during this project.

Keywords: Shaft, Measurement, Inspection, Maintenance, Structural Health Monitoring

1 INTRODUCTION

Mobility is a cornerstone of our modern society. It enables us to travel, exchange goods and get in touch with each other. However, the structural infrastructure used for this purpose is subject to a natural ageing process. To assure a long service lifetime and the necessary integrity of such facilities, regular inspections, maintenance and renovation measures must be carried out, all of which involve costs. To make the best use of available financial resources and to ensure the longevity of these important facilities, it is crucial to develop effective maintenance strategies and to create a reliable data basis.

Inspection data provides information about the condition, performance, and potential problem areas of the infrastructure. They thus form the basis for strategic planning of measures and investments. However, depending on the structure and prevailing conditions, the collection of reliable data is not possible with standard tools and calls for new and innovative approaches.

This paper presents the specially developed measurement system developed for the inspection of the Sedrun shaft B at the Gotthard Base Tunnel and highlights the challenges encountered during this project. In the meantime, this system has also been used for the shaft inspection of other tunnel systems in Switzerland.

2 GOTTHARD BASE TUNNEL

The Gotthard Base Tunnel is a symbol of Swiss precision and innovative inspiration, 57 km long at the heart of the Swiss Alps connecting people through the generations to come. It is composed of an intrinsic complex system of tunnels, numerous crossovers, and access tunnels, as well as shafts.

The tunnel is subdivided into the five sections Erstfeld, Amsteg, Sedrun, Faido, and Bodio (north to south). The following Figure 1 shows a schematic overview of the tunnel system.

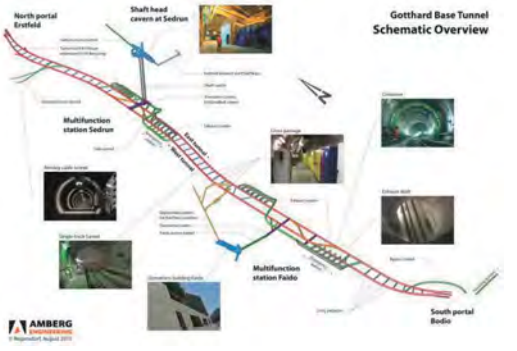

Figure 1. Schematic overview Gotthard Base Tunnel (*Source: Tunnelling the Gotthard, STS Tunnelling Society, 2016*).

*Corresponding author: kwachter@amberg.ch

DOI: 10.1201/9781003495505-364

In the Sedrun section, an intermediate access is provided by a nearly one-kilometer-long access tunnel and two about 800 m deep vertical shafts leading down to the railway tunnel level. In the following, the focus will be led on shaft B in Sedrun (former known as shaft II).

Shaft B is located about 40 m from shaft A in a side niche. The shaft was constructed by raise-boring in the first stage and enlarged to a final excavation diameter of 7.0 m with a shaft boring machine in the second stage. Rock support was composed of wire mesh, rock bolts and shotcrete with steel fibre reinforcement and a layer thickness of 22 cm. The shotcrete serves as both rock support and permanent lining. In order to be able to fulfil its function as an exhaust ventilation shaft even in case of a fire, the shaft was additionally lined with an 8 cm thick shotcrete layer composing polypropylene fibres to ensure fire protection. In case of a fire, the smoke rising through the shaft is directed through an additional inclined tunnel out of the mountain, bypassing the cavern.

In the original concept of Sedrun section, shaft B was not included. The decision for building a second shaft was taken at a later project stage for reasons of construction operations, ventilation, and safety. During the ongoing railway operating phase, shaft B serves as an exhaust air shaft for ventilation in normal operation and in case of an incident. Since this function is crucial for operational safety, the structure must be included in the inspection and maintenance planning for the Gotthard Base Tunnel.

Figure 2. Geological profile of the Gotthard Base Tunnel, with localisation of the Sedrun Shaft (*Source: Tunnelling the Gotthard, STS Tunnelling Society, 2016*).

Built in 1998, shaft B was already operational for almost 18 years when the commercial operation of the Gotthard Basis Tunnel started in December 2016. With its almost 800 m depth, carrying out inspection services is a real challenge in terms of accessibility and health and safety.

During the construction time of the tunnels a heavy-duty hoist and an emergency hoist were installed in the shaft. After completion however, all equipment was deinstalled. As a result, carrying out inspection services in a shaft of this length becomes a real challenge.

In 2019, a pre-inspection of shaft B in Sedrun was performed to conduct several data acquisition tests and gain experience about the shaft environment. It was carried out by staff from Amberg and SBB, who were lowered into the shaft B using the emergency equipment for shaft A.

Due to safety concerns in case of technical malfunctions, further inspections involving personnel in the shaft were forbidden. To overcome this, Amberg was asked by the Swiss Federal Railways SBB to develop an innovative solution for the inspection of Sedrun shaft B.

3 MULTI-CAMERA INSPECTION SYSTEM (MCIS)

To address the challenge given, the first step was to develop an automatic measuring system capable of gathering all the necessary data for an office inspection. To ensure a reliable data set it was defined that the measuring system needed to capture both photos and scan data and provide them with a precise vertical position - a second significant challenge. The third challenge arose from the requirement that the measuring system had to be attached to the crane using only a single rope, making it vulnerable to rotations. To answer these three challenges, the Amberg Multi-Camera Inspection System (MCIS) was developed.

In the following subchapters, the technical solutions for the three challenges highlighted above will be outlined in more detail.

3.1 *Inspection sensors*

Traditionally, Amberg uses laser scanners for inspection data. Hence, the high-performance laser scanner *Amberg Profiler 6012* was the best sensor for integration into the MCIS. This approach had several advantages, including independence from a light source and the elimination of focusing issues to measure the relative diameter of the shaft.

As an additional source of information, six standard single-lens reflex cameras were included in the MCIS to provide high resolution and coloured images of the shaft surface. Given that the radius of shaft B did not change significantly, fixed camera focus was possible. Moreover, six 24 MP full-frame cameras captured significantly more data than a single laser scanner. However, the usage of cameras also necessitated the attachment of a light source to the MCIS. This presented a challenge, not only in illuminating the 6.4 m diameter shaft but also in positioning the light sources carefully to create consistent illumination throughout the shaft surface. Otherwise, over- and underexposed photos would reduce the general data quality in the deep, dark shaft. In the end, 24 LED lights were attached to the system, 12 above and 12 below the cameras, to provide the more than enough illumination.

To power the MCIS, detailed considerations of the necessary electrical power for the 5 V, 24 V and 220 V devices had to be made. Especially the 24 LED lights consume the biggest amount of electrical power. At the current state, multiple battery packages enable the MCIS to acquire data for about 30-40 minutes, which was more than enough time to measure shaft B for two times.

3.2 *Positioning*

It was soon evident that the entire system needed to be time-triggered. The alternative of establishing a data link through cable or radio over the ca. 800 m deep shaft B in Sedrun proved almost impossible. Consequently, all MCIS subsystems had to be controlled by a single computer to generate relatively precise timestamps.

The solution to the second challenge was to measure the relative height of the MCIS by measuring the used length of the steel rope of the crane to lower the MCIS into the shaft. Here an exception to the "one computer controls all devices" concept had to be made since other direct methods were unreliable. The most effective solution involved attaching an optical odometer to the diverter pulley of the crane which could be controlled and observed by a second computer. The odometer logged the revolutions together with an absolute timestamp directly to an internal memory.

3.3 *Rotations*

To counter any rotations caused by the single rope hanging, a highly precise inertial measurement unit (IMU) was required. The *Amberg Measurement Unit 1030* (AMU1030) is designed specifically for measuring rotations and was therefore the ideal solution to master this challenge. This choice was also advantageous as the AMU1030 was already integrated into the *Amberg IMS5000* system, a trolley system used to scan railroad tracks, which also included the high-performance laser scanner *Amberg Profiler 6012*. This ensured the compatibility of the systems used.

4 SHAFT MEASUREMENT AT THE GOTTHARD BASE TUNNEL

4.1 *Data acquisition at shaft B*

The data acquisition for inspecting the shaft B occurred on the 11th and 12th of July 2021, around midnight when a free slot in the train traffic schedule was available. In coordination with Amberg, the SBB provided a special crane with over 800 m of rope and a case for the MCIS installation. Before the measurement, everything was installed and tested on-site. Just before entering the shaft from its top, the MCIS with all its subsystems was initiated, and autonomous data recording commenced.

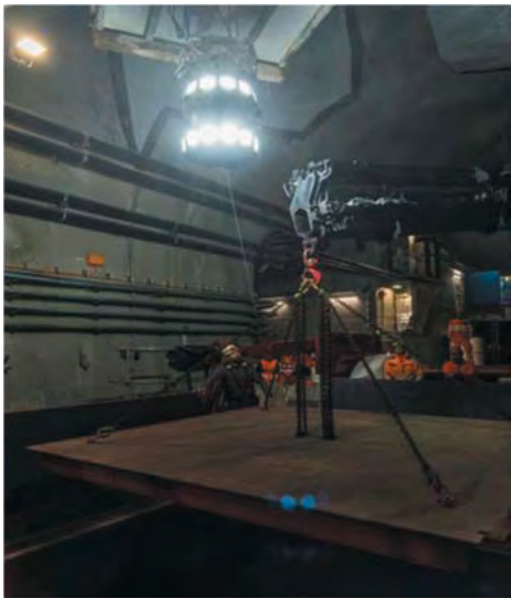

Figure 3. MCIS before entering the shaft B.

The *Amberg Profiler 6012* scanner rotated at 100 revolutions per second, capturing 10,000 points per rotation, resulting in a data acquisition rate of 1 million points per second. Simultaneously, the AMU1030 recorded the MCIS rotation for post-processing correction.

Using the odometer, it was possible to measure not only the depth but also the travel speed, which aimed to maintain a target speed of 0.5 m per second with an accuracy of +/- 0.05 m/sec throughout the entire shaft depth. The speed value was transmitted directly to the crane operator to adjust the speed if necessary.

The camera system was controlled by the measuring computer via a trigger box, capturing simultaneous images from all six cameras at 3-second intervals. Consequently, a series of pictures was taken every 1.5 m, providing a 360° imaging of the shaft. The lenses were manually focused, and each had a focal length of 15 mm, ensuring sufficient overlap for later panoramic image creation.

Within less than an hour, the entire shaft was measured twice, creating over 150 GB of data. The data was stored on a hard drive on site.

4.2 *Data post processing*

After data collection, the first step in post-processing was synchronizing all the timestamps from each different sensor. Since most sensors were controlled by the MCIS computer, only the separate odometer data required synchronization with the MCIS timeline. Scan data and camera data were generally post-processed independently.

Figure 4 below shows the data processing workflow.

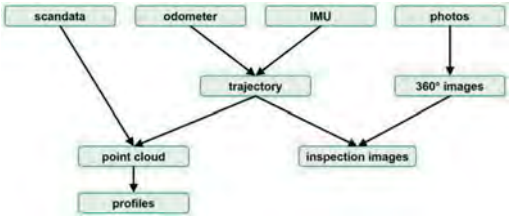

Figure 4. Data processing flow chart.

The odometer data was applied to the scan data to render a tube out of the measured thousands of scan lines during the data acquisition. Subsequently, IMU data was applied to the scan data to correct for rotation movements during data collection. This resulted in a point cloud representing the shaft's geometry accurately from a relative perspective, enabling the extraction of profiles and other data for inspection and other purposes.

The camera data was also post-processed in a similar manner to the scan data. Photo corrections, such as exposure, vignetting, and white balance adjustments, were applied to achieve homogeneous pictures of the shaft surface. Since all photos were taken simultaneously from each camera in sets of six, 360° panoramic images were created using photo-stitching techniques. The final step involved vertically sorting and cropping each panorama picture to generate a complete picture of the vertical shaft surface. Figure 5 below shows the 360° panoramic image at the shaft head: The blue objects are the safety barrier which were installed around the open shaft. Right below the red shaft cover is visible. Under the shaft cover a chamber is visible on the right-hand side. This is the "exhaust" that leads the air to the turbines. The lower part of the images shows the shaft surface with marked defects in blue and red.

Figure 5. 360° panoramic image of the shaft surface.

Based on the referenced point cloud, horizontal profiles of the vertical shaft were created in the software *Amberg Tunnel*. These profiles were centred to the least-square centre point of the measured profile points to best fit the theoretical circle-shaped reference profile for deformation analyses.

5 SHAFT INSPECTION

5.1 *Scope of an inspection*

According to the Swiss standard SIA 469 (1997), an inspection is defined as the determination of the condition of a structure by targeted (usually visual), simple examinations with evaluation of the same.

As a standard procedure, this determination is achieved by a manual inspection of the structure with the aid of adapted access platforms, including simple on-site surveys as crack width measurement and the search for hollow sounding areas with a hammer. All the information collected on site is then displayed in a structural defects map.

In case of an office inspection as performed for shaft B in Sedrun, the quality of the data acquisition is essential for a visual identification of any structural defects. This is assured by using different types of sensors on the MCIS for the acquisition of complementary information for a better inspection and assessment of the structure.

5.2 *Amberg inspection cloud*

For conducting condition assessments, a special inspection and data management software was developed in house – the *Amberg Inspection Cloud* (AIC). This online platform is a comprehensive image-based inspection platform for planning, managing, capturing, and reporting on visual surface conditions. It is designed to act as a single source of information for inspection data allowing for easy visualisation of defects and statistical analysis for every defect category. When uploading inspection data from different points in time, the software allows for a direct defect comparison and thus identification of any development of a defect over time.

More than an inspection tool, the AIC is a conservation management tool as it complements existent data bases of the owners with detailed information about the condition of the structure, showing potential areas of concern. As the data of the inspections over time is centralized and built up on a reliable basis, it becomes possible to predict future needs more accurately.

5.3 *Defect mapping*

Before starting the inspection and defect mapping, the project had to be set up in the AIC. This not only includes the upload of the images but also the definition of the defect catalogue in accordance with the client's standard. For the detailed assessment the shaft was divided in different zones of about 10 m length each.

According to the plans, the shaft was built with a different diameter on the approx. last 9 m at its top at the connection to the shaft cavern, but no dimensions were given. This change of the diameter could be clearly seen and measured from the point cloud data,

allowing for an update of the technical data of the structure.

The mapping of defects in the AIC is performed by an experienced inspector based on a visual inspection of the acquired images. Due to the high-resolution and quality of the data generated by the MCIS, structural defects such as sub-millimetre cracks can be detected. Most importantly, structural defects can be distinguished from any aesthetical or construction caused phenomena.

Figure 6. Detail of the background image generated by the MCIS.

The structural defect map was delivered to the client digitally in the AIC with no further treatment of the data such as CAD drawings being necessary.

5.4 *Condition assessment*

According to the Swiss standard SIA 469, art. 3.22, 3.23 and 3.24., the condition assessment must include an evaluation of the condition of the structure and the determination of any measures to ensure the required safety (structural safety, serviceability, and operational safety). In addition, a forecast of the development of the condition is required.

The defect mapping introduced above is one essential information for the condition assessment. Nevertheless, the data acquired by the MCIS allows for additional analysis.

Based on the georeferenced point cloud, a deformation analysis can be performed. Compared to the perfect circular nominal profile, the measured profile is influenced by slightly changing shotcrete thickness and the roughness of its surface, as much as by the geology that was traversed. The comparison between the circular nominal profile in the calculated centre and the measured profile at shaft B shows profile differences along the shaft. Figure 7 below shows the result of the deformation analysis at position 321.014 m measured from the bottom. The blue dotted line represents the point cloud, the grey circle represents the nominal shaft profile.

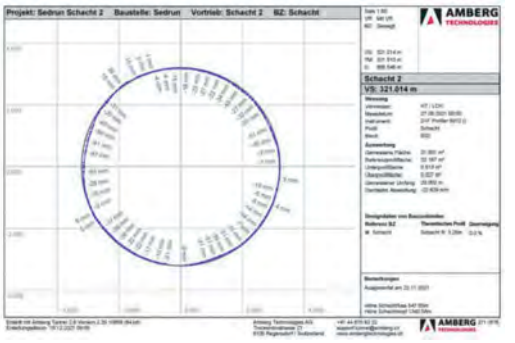

Figure 7. Results of the deformation analysis.

In fact, deformations are not only assessed based on the profiles from the deformation measurements. Deformations due to force redistribution in the rock mass or due to water ingress cause certain damage patterns in the lining, which can be detected by mapping the damages on the images that were taken during the data acquisition. The inspection based on the panoramic images is therefore also decisive for the assessment of the deformations.

The differences between the designed circular profile and the measured one along the shaft were locally up to 100 mm. This would indicate significant deformations. In fact, such deformations would cause cracks in the shotcrete lining. Since no such cracks were found during the defect mapping, it can be concluded that the profile differences are not caused by local deformations but are either due to the construction or any material changes (e.g., calcite concretions).

As a result of the inspection, no severe damages were identified and therefore no structural measures are required. For further inspection it is recommended to collect complementary information about the shaft to refine the condition forecast. This might include a water analysis and some core drilling to obtain further information on the condition of the concrete. All this information will be also useful for planning structural measures in the future.

6 CONCLUSIONS

In this paper an innovative measurement system developed for the inspection of the Sedrun shaft B at the Gotthard Base Tunnel is presented.

The Multi-Camera Inspection System (MCIS) is a data acquisition module equipped with multiple sensors that can be used to collect reliable and high-quality data for inspection purposes.

For the Sedrun shaft B, the digital workflow based on panoramic images and point clouds enabled maximum condition information with minimum risk to people and impact on tunnel operations.

Since its first mission was successfully carried out at the shaft B in Sedrun, the MCIS system has also been used for the shaft inspection of several other tunnel systems in Switzerland.

ACKNOWLEDGMENTS

The authors would like to thank the Swiss Federal Railways SBB for the openness to innovative solutions and the good collaboration in this project.

Finally, the Amberg team thanks Mr Thomas Heiniger for being the mastermind and driving force behind the development of the MCIS.

REFERENCES

Doreau-Malioche J., Paillette F., Puglia M., Spohn P., Frachon S., Poli B.: Tunnel inspections with the aid of high-performance image acquisition tools: an insight on key parameters for a successful detection of structural defects; Proceedings of the ITA-AITES World Tunnel Congress 2023; Athens, Greece, 2023.

Puglia M., Heiniger T., Hewelt T.: Technical report of the main inspection of the Shaft B Sedrun; Amberg Infra 7D, 24.02.2022 (not public).

Sala, A., Wick, R.: Project description – technical data; published in: Ehrbar H., Gruber L.R., A. Sala A.: Tunnelling the Gotthard, section IV Elaboration of the design; STS Swiss Tunnelling Society, 2016.

Spörri D., Meier R.: The shafts at the intermediate access point in Sedrun; published in: Ehrbar H., Gruber L.R., A. Sala A.: Tunnelling the Gotthard, section VI Construction of preliminary lots; STS Swiss Tunnelling Society, 2016.

Swiss standard 469: Conservation of infrastructures; Swiss Society of Engineers and Architects SIA, Zurich, 1997.

Tunnelling for a Better Life – Yan, Celestino, Thewes & Eberhardt (Eds)
© 2024 The Author(s), ISBN 978-1-032-80042-4
Open Access: www.taylorfrancis.com, CC BY-NC-ND 4.0 license

Fault diagnosis system for tunnel boring machines based on electrical energy monitoring

Yuan Qin*, Chengjie Zhang, Sheng Huang, Zhaoyu Wu, Hui Shen & Jun Sun
Shanghai Urban Construction Tunnel Equipment Co., Ltd., Shanghai, China

ABSTRACT: The purpose of this study was to improve the continuity, economic viability, and stability of tunnel boring machines (TBMs) during construction. A comprehensive technical system for electrical energy monitoring, state analysis, and intelligent fault warning was established for the core power components of TBMs, in addition to the development of corresponding software and hardware systems. Based on the electrical energy transmission path of the core power components of the TBM, an effective and reasonable sensing device was installed to collect the data of various electrical, energy consumption, and key physical characteristic parameters. Accordingly, a basic model of the electrical energy consumption and quality of the core power components was proposed. During the operation of the TBM in the construction process, a data chain was established with the tunnel construction parameters, and an algorithm for evaluating the standard energy consumption during the tunnel construction process was established according to the construction conditions. Abnormal states of the core power components were detected, and a comparison analysis was performed between real-time energy consumption, standard healthy state energy consumption, and external state characteristics to determine an intelligent fault identification and warning model for the core power components.

Keywords: Electrical Energy Monitoring, Intelligent Data Collection, Fault Diagnosis System

1 BACKGROUND AND TECHNICAL STATUS

A serial relationship exists between the operation of various systems and equipment of a tunnel boring machine (TBM), and often, a malfunction of one system or device can cause the entire TBM to stop working. Reducing the failure rate of TBMs and pre-diagnosing and pre-eliminating failures are important aspects of maintaining the high efficiency of TBM construction.

Electricity, as a standard way of energy transfer, powers all mechanical equipment on TBMs. By monitoring the electrical energy data, the health state of a TBM can be perceived. Considering the research and development of electrical energy monitoring systems for large equipment, studies have been conducted to identify anomalies from real-time data based on the characteristic energy consumption data and classify them into distorted and non-distorted data. Qualitative and quantitative analyses are then performed to process the data using data mining methods, such as rule-based judgments, cluster analysis, and outlier analysis, to make decisions on issuing alarms upon detecting abnormal data.

However, studies based on TBM electrical energy monitoring are limited. Nevertheless, several theoretical analyses and data simulation explorations have been conducted. For example, researchers have proposed an energy-based analysis method for TBM fault diagnosis for non-catastrophic faults in three fault units: cutterhead, propulsion, and screw machine[1]. Currently, most of the relevant analyses based on tunnel machinery energy consumption monitoring are focused on the energy consumption analysis of individual sub-devices, and research remains at the theoretical and experimental stage, without any precedent studies for comprehensive tunnel applications of TBMs. Therefore, a complete fault diagnosis and online prediction system is required to improve the continuity, economic viability, and stability of TBM construction.

2 RESEARCH ON ELECTRICAL ENERGY HEALTH ASSESSMENT SYSTEM

For intelligent TBMs, information data are defined into four main levels. First level constitutes a comprehensive perception level, wherein sensing technology is utilized to comprehensively perceive

*Corresponding author: qinyuan@stecmc.com

DOI: 10.1201/9781003495505-365

various states of the TBM to ensure data completeness. The second level is the data collection level, wherein preliminary processing is performed on collected data and backups are stored to ensure data integrity. The third level comprises the data sharing level, wherein data is exchanged between various systems to ensure data link reliability. The final level constitutes data mining, wherein various types of artificial intelligence modules are employed to mine and condense various types of data to ensure data usability.

2.1 *Comprehensive sensing of electrical energy data*

Comprehensive sensing of electrical energy data is divided into three parts. The first part is the comprehensive sensing of electrical equipment. This is achieved by integrating various sensing devices to the core electrical equipment of the main operating components of the TBM, such as the high-power motor and its starting circuit that provides power to the hydraulic system. The second part constitutes the comprehensive sensing of electrical energy indicators. To analyze the electrical energy indicators in addition to the conventional current and voltage, it is necessary to collect electrical energy indicators, such as phase angles, high-order harmonics, active and reactive power, and power factor. The third part is the comprehensive sensing of the physical state of electrical equipment, including environmental temperature and data such as motor vibration.

By optimizing sensor selection, improving the range, accuracy, and response speed of the sensing system, and redesigning the sensing system for energy consumption monitoring, core power, and vulnerable components of the TBM, the comprehensive sensing of electrical energy data can be achieved, thereby solidifying the foundation for data analysis and improving the efficiency and accuracy of data analysis.

2.2 *Collection and storage of electrical energy data*

For engineering equipment, such as TBMs, conventional data acquisition systems are developed with the construction object as the main focus, often overlooking the collection of operational state data for mechanical equipment. Therefore, a data acquisition system for equipment needs to be developed.

Generally, the data acquisition system used for construction has an interval of more than 1 s. The data obtained at such a frequency cannot indicate characteristic changes when analyzing equipment failures. Considering the refresh rate of a programmable logic controller (PLC) and the time cycle for communication between the upper computer and the PLC, the data acquisition frequency is differentiated and configured for different targets. The collection interval for routine equipment data is not less than 1 s, whereas the collection interval for captured characteristic fault data of the core system is not less than 0.2 s. At the same time, the time length for capturing characteristic fault data of the core system is not less than 10 s before and after the occurrence of fault. This approach can facilitate the capture of characteristic states and avoid the overloading of the system due to the requirement to record large sets of data.

2.3 *Standard health model and diagnosis*

At the data mining layer, combined with actual construction conditions, big data analysis and machine learning methods are employed to extract feature data closely related to the health state of the TBM. These data are analyzed and refined to extract steady-state and dynamic characteristics of TBM health at different construction states, based on which a standard model for the electrical and mechanical health of the TBM is established. Based on this standard health model, a real-time system is developed to evaluate the health of the TBM and diagnose faults, design a safety architecture for the various systems of the TBM[2], and develop reasonable and effective redundancy schemes and measures to rapidly diagnose and accurately locate faults, improve maintenance efficiency, and reduce equipment failure downtime. By integrating intelligent sensing devices and comparing equipment operating characteristic curves, the relationship and matching of key system and component operating parameters, construction parameters, and environmental parameters of the TBM are further studied. Mechanism models, knowledge engineering, and data-driven methods are adopted to construct fault characteristic parameter judgment models, thereby realizing the fault pre-diagnosis for the key system and components of the TBM[3].

2.4 *Visualization platform based on digital twin technology*

In addition to the standard model, real-time health state data of the TBM, fault diagnosis information, and online prediction results are integrated into a digital platform for visualization. The digital twin model of the TBM is then built using light weighting and model transformation technologies to navigate fault points and guide maintenance.

Figure 1. Health assessment interface.

Figure 1 depicts the energy monitoring module. Considering the real-time and historical analyses of electrical parameters together with the construction conditions, a data chain is established between the energy consumption of key dynamic components and TBM construction parameters to obtain the characteristics of energy consumption changes. A standard construction energy consumption model and dynamic component health assessment model are established, displayed, and analyzed on the platform[4].

3 ENGINEERING PRACTICE

The project relies on the Shanghai-Nantong Railway Cross-River Tunnel Project, which has a total length of 6770 m and uses an 11 m-diameter slurry-balanced TBM designed and constructed by Shanghai Tunnel Engineering Co. The TBM used in this project integrates a health intelligent assessment system and is designed specifically to collect electrical energy data and vibration information of the motor.

3.1 *Sensing system*

The TBM is powered by power transformers with the following parameters: four oil-immersed power transformers with rated capacities of 2500, 1600, 1600, and 1000 kVA and a low-voltage distribution system. Communication modules are present in the power cabinet. The entire TBM electrical energy system can be monitored through the perception system, as shown in Figure 2.

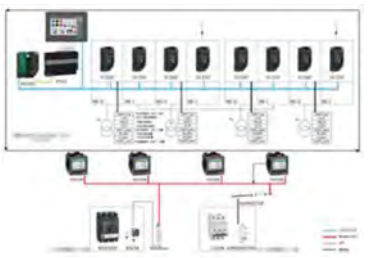

Figure 2. Configuration of the perception system.

The corresponding power supply systems are also tested to determine different specifications for collecting electrical energy data, which are classified and collected.

To obtain the motor vibration and temperature, a vibration sensor with the magnetic suction mounting mode is selected for this design. The sensor has a magnetic base that can be directly attached to the motor. The sensor measures the data via wired Modbus RS485 communication transmission and can collect the vibration data in the horizontal and vertical directions of the equipment as well as temperature[6].

3.2 *Acquisition system*

In this project, a dedicated data collection system is configured for the targeted development of TBM electric power monitoring. The system monitors high- and low-frequency electrical energy data to obtain the data ignored by the conventional TBM data collection system, such as operating data of the electrical energy system, dynamic startup data of the motor, and physical operating state of the motor. These ignored data are essential for diagnosing the faults in the electrical energy system. The data are collected into the on-site database through the data bus and mirrored backup to the cloud to improve the overall system redundancy. Such targeted development renders the data transmitted to the data platform more comprehensive, reliable, and accurate, as shown in Figure 3.

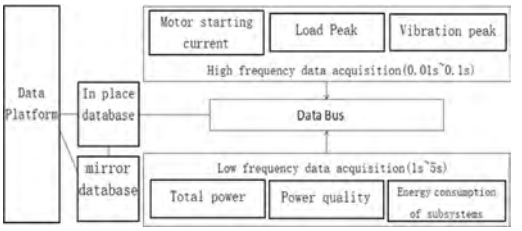

Figure 3. Configuration of the data acquisition system.

3.3 *Data mining module*

Thousands of sensing devices installed in each system of the TBM are responsible for recording real-time data of each device. The transmission and storage of sensor data provide rich data support for the data mining of TBM construction. These real-time construction data of equipment can reflect the faults of the devices themselves and to certain extent reflect the corresponding real-time parameters and even the overall operating state of the TBM. Therefore, using machine learning and deep learning algorithms to fully mine and analyze the shield collection data and visualizing the analysis results, an effective reference can be provided for TBM construction. An abnormal detection model based on deep learning is constructed to monitor the important electrical energy parameters during TBM excavation, learn the behavior and distribution characteristics of electrical energy parameters under normal conditions, and output the corresponding abnormal information of electrical energy parameters when abnormal behaviors different from normal data are detected, providing references for on-site construction personnel to make correct decisions. Additionally, a performance evaluation index and prediction model of shield machine attitude control based on machine learning are constructed to analyze the influence of key parameters on the attitude control performance and assist on-site construction personnel in rapidly identifying the factors that cause abnormalities in TBM control when such abnormalities occur, thereby guiding the advancement of the TBM[7].

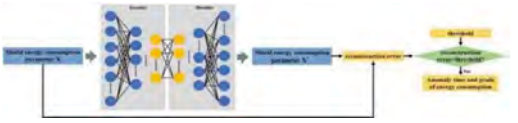

Figure 4. Model for detecting abnormal energy consumption parameters and grading energy consumption level.

In this project, Autoencoder (AE) was used for data mining, which is an artificial neural network that can be used for unsupervised learning.The purpose of autoencoder is to reconstruct the input vector $\hat{X} = (\hat{x}_1, \hat{x}_2, \ldots, \hat{x}_n)$ into an output vector $X = (x_1, x_2, \ldots, x_n)$ with the same dimension.This model typically consists of two main parts, namely an encoder used to map the input vector X to an m-dimensional intermediate vector F and a decoder used to map the intermediate vector F to an output vector. Vector X and vector have the same dimension, that is, n dimension. Here $n \neq m$, and $n > m$.

$$\phi : \mathbb{R}^n \rightarrow \mathbb{R}^m$$

Encoders and decoders can be defined as functions and, $\psi : \mathbb{R}^n \rightarrow \mathbb{R}^m$ and the purpose of autoencoders is to fit an identity function:

$$\underset{\phi,\psi}{arg\,min} ||X - \psi(\phi(X))||^2$$

This definition implies the need for appropriate functions ϕ and Ψ to make the input vector X and the reconstructed output vector $\hat{X}$ as close as possible.

$$F = \sigma(WX + b)$$

In the encoding stage, the autoencoder maps the input vector $X \in \mathbb{R}^n$ to the intermediate vector $F \in \mathbb{R}^n$ using the following function. Here $W \in \mathbb{R}^{m \times n}$ is the weight matrix, $b \in \mathbb{R}^m$ is the bias vector, and σ is the encoding layer activation function.

$$\hat{X} = \hat{\sigma}(\hat{W}F + \hat{b})$$

Finally, calculate the reconstruction error between the reconstructed vector $\hat{X}$ and the original input vector X

$$E(X, \hat{X}) = \sum_{i=1}^{m} ||\hat{\sigma}(\hat{W}\sigma(Wx_i + b) + \hat{b}) - x_i||^2$$

On this basis, the goal of the autoencoder is to minimize reconstruction errors. This is equivalent to learning appropriate weight matrices W and $\hat{W}$, as well as bias vectors b and $\hat{W}$, through gradient descent and backpropagation, to minimize[8] .

3.4 *Visualization platform based on digital twin technology*

The data collected and analyzed are loaded onto a visualization platform based on digital twin technology. These data are distinguished based on their real-time nature, with the first part being the current state of the TBM, which provides information regarding the machine health and fault points to the on-site personnel. The other part is the historical data record, which can serve as a sample for the self-learning of the intelligent system.

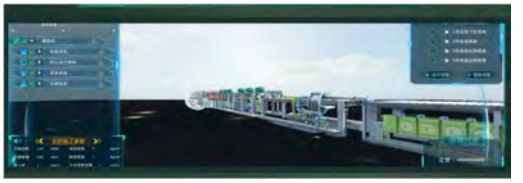

Figure 5. Fault navigation module.

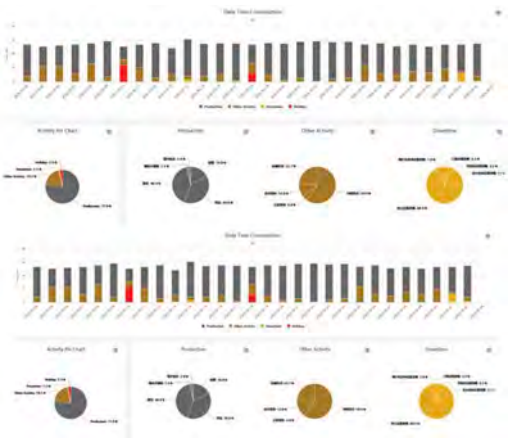

Figure 6. Construction record module.

Figure 5 shows the fault node navigation module in the TBM fault diagnosis platform. Using digital panoramic technology, the entire model and system of the TBM are mapped onto the platform, and the location of the fault points is navigated within the model to help rapidly troubleshoot faults. By studying the energy consumption in different construction states through the platform, parameter optimization strategies are provided to meet economic objectives during the construction process[9].

Figure 6 is the construction record module of the TBM fault diagnosis platform, where the data from the data collection system are linked to the on-site maintenance platform. The intact rate is quantified as the ratio between the time when the equipment is completely normal during construction and the total construction time. This quantitative value is used to

evaluate the design and maintenance effect of the equipment, forming the entire closed loop of fault warning, fault diagnosis, fault maintenance, and feedback during the maintenance and repair process. It provides detailed data support for the full lifecycle management of the TBM[10].

4 EXAMPLE OF FAULT WARNING AND OVERALL EFFECT OF APPLICATION

In the case of the slurry mixing system, the mixing motor stirs the cement slurry to prevent it from solidifying through the reducer. A rubber seal between the reducer and the cement slurry prevents cement slurry from entering the reducer and causing equipment damage. In previous system failures, equipment maintenance was often due to damage to the sealing system, which allowed cement slurry to infiltrate the reducer and cause irreversible damage. As this system operates continuously, such equipment failures directly lead to downtime.

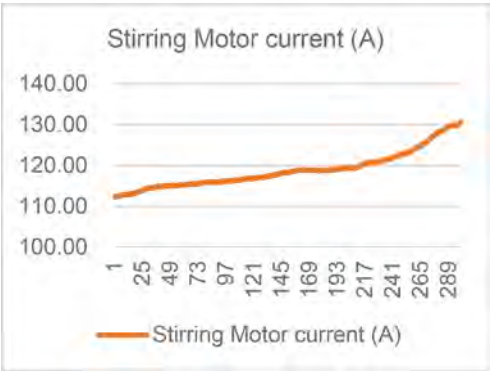

Figure 7. Current of the stirring motor.

After collecting and analyzing the load data of the motor, the average load of the motor is found to slowly increase, as shown in the Figure 7.

At 300 cycles, the health system alerted that the load torque of the motor exceeded the set working threshold. During the shutdown maintenance phase, maintenance personnel performed a targeted comprehensive inspection of the system and found that the parts in contact with the seal and cement slurry had bonded together, and certain parts were damaged. Additionally, the cement slurry tended to enter the reducer. Maintenance personnel immediately replaced the seal, and the system working load was returned within the normal working threshold.

Similarly, in the case of a cutterhead system, the health system found that the fluctuation amplitude of the current of the No. 1 cutterhead motor was larger than that of the other cutterhead motors, which was extremely abnormal. When this characteristic waveform is ignored, a small fault can easily turn into an irreversible major fault, such as damage to the large bearing. With the guidance of the health system, maintenance personnel discovered that the load balance setting of the No. 1 cutterhead motor was not enabled through an inspection of the parameters of the frequency converter. This caused the over-hard mechanical characteristics of the motor, rendering the rotating frequency of the No. 1 cutterhead

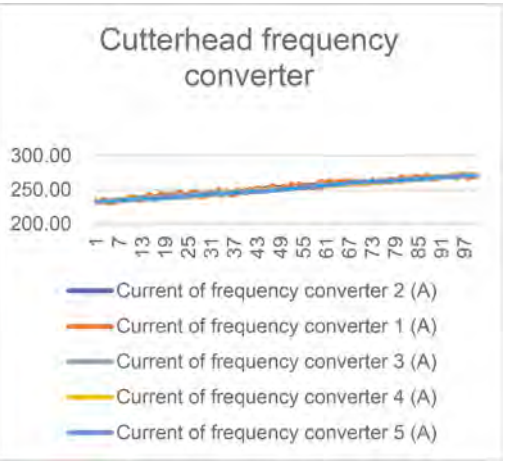

Figure 8. Current of the cutterhead frequency converter.

motor unresponsive to load changes, in contrast to the case of other cutterhead motors. After enabling the load balance function, the system returned to normal.

The stable operation of equipment is a key factor for construction safety. Mechanized equipment, particularly substantially large engineering machinery, such as TBMs, inevitably requires maintenance during construction. The two aforementioned characteristics regarding the fault warning of the system can enable the advance planning and conduction of the maintenance without affecting construction, thereby avoiding sudden interruptions caused by equipment failure. Figure 9 shows statistics on the failure rate of TBMs for three construction projects. In this comparison, the failure rate for TBMs is defined as the ratio of the downtime caused by faults

Figure 9. Comparison of project failure rates.

during construction to the actual construction time. The failure rate of the TBM equipped with the intelligent health system is significantly lower than that of other TBMs of the same diameter.

5 CONCLUSIONS

The proposed system for the health assessment of TBMs is formulated through the integration of multiple disciplines, including artificial intelligence, mechanical engineering, information engineering, and electrical engineering, in the field of underground engineering. It breaks through the framework of conventional passive maintenance of equipment and represents a new generation of active, precise, and real-time health assessment and fault warning system for intelligent equipment. It can be implemented on large equipment, such as TBMs, wherein multiple industrial disciplines, such as civil engineering, mechanical engineering, electrical engineering, information technology, and optics, are involved. The system can effectively integrate multiple disciplines and complex artificial intelligence technologies as well as facilitate the development of intelligent platforms[11].

The fault warning and health assessment of equipment help to enhance the equipment integrity, reduce the downtime caused by equipment failure, improve construction safety, and increase the construction efficiency. These factors can in turn shorten the construction period and minimize the impact on the surrounding environment owing to the specific nature of underground engineering. By improving the construction efficiency, resource utilization can be effectively achieved; construction resource costs can be reduced; and energy conservation and emissions reduction goals can be achieved.

REFERENCES

[1] Zhang Hemeng. Discussion on the key points and measures of large shield construction tunnel construction [J]. China Equipment Engineering, 2023, No.519(05): 252–254.

[2] Huang Shenyuan. Research and application of shield tunnel measurement control technology [J]. Fujian Construction, 2023, No.296(02):78–81.

[3] Li Dawei, Zhou Yuanhang, Ge Yiyuan. Research on shield online monitoring system [J]. Mechanical and Electrical Engineering Technology, 2020, 49(02):106–108+158.

[4] Han Ying. Research on the control and fault diagnosis of the shield machine cutter head electrical system [D]. Xi'an University of Technology, 2018.

[5] Wu Zhaohui, Chang Ying, Li Qing, et al. Research on innovative application of tunnel operation management based on three-dimensional video fusion [J]. Tunnel Construction (Chinese and English), 2022, 42 (1): 154–161.

[6] Sun Zhenchuan, Qian Tongtu, Ren Yingying, et al. Key technology and application research of tunnel boring machine engineering big data management platform [J]. Tunnel Construction (Chinese and English), 2020, 40(6):783–792.

[7] Sun Hao, Jia Lianhui, Wei Xiaolong, et al. Research on fault diagnosis method of atmospheric pressure cutter head shield roller based on machine learning [J]. Tunnel Construction (Chinese and English), 2023, 43(z1): 550–557.

[8] Liu Hongzhi. Review of practical technology for TBM and shield machine equipment status monitoring and fault diagnosis [J]. Tunnel Construction, 2007, 27 (6): 86–88, 97.

[9] Xu Shoutian, Pu Xiaobo. Design of shield ground data acquisition and monitoring system based on OPC [J]. Tunnel Construction, 2009, 29(6):674–677.

[10] Lu Kaizhong. Remote data acquisition of shield machine construction based on SCADA system [J]. Construction Construction, 2014(11):1293–1294.

[11] Chen Gang, Wang Yannian, Li Gang, etc. Development and application of shield data acquisition system based on cloud platform [J]. Computer Era, 2020(3): 5–8,12.

[12] Zhang Huiying, Huang Nantian. Design of electric energy monitoring system based on WSN technology [J]. Electr

Tunnelling for a Better Life – Yan, Celestino, Thewes & Eberhardt (Eds)
© 2024 The Author(s), ISBN 978-1-032-80042-4
Open Access: www.taylorfrancis.com, CC BY-NC-ND 4.0 license

Pivotal role of instrumentation & monitoring in construction of Mumbai Metro Line 3 in an urban setting

Ashish Rawat*
Hindustan Construction Company Limited, Mumbai, India

Ravi Ranjan Kumar & Subodh K. Gupta
Mumbai Metro Rail Corporation Limited, Mumbai, India

ABSTRACT: Instrumentation and Monitoring has played a major role in urban tunnelling and safeguarded the structural stability of the structures in the Zone of Influence of excavations. A thorough monitoring reduces potential risks and enables timely interventions in order that precautionary measures are undertaken prior to any exigencies. Successful completion of a Project without any adversities depends on the veracity of Instrumentation and Monitoring.UGC02 Package of the Mumbai Metro Line 3 comprises of twin-bored tunnels and four stations by cut & cover and conventional drill and blast methods. This stretch is one of the oldest and the most densely populated areas of Mumbai, with heritage structures, some approximately 160 years old and others with an average age of 70 to 75 years adorn the area. Complexities arose during the course of excavations in the form of settlement of structures, apprehensions of depletion of water levels within the premises of Heritage structures, blast induced vibrations during excavation, frivolous claims for damage to property and a number of litigations in courts. An exhaustive Instrumentation and Monitoring regime along the stretch commenced prior to the start of the Metro construction works, which helped in overcoming all complications. The Paper establishes the relationship between the TBM boring operations and a). Tunnel induced settlements, b). Excavation induced vibrations and c). Water level depletion. Effects of settlements in surrounding structures during construction along with corrective and remedial measures are deliberated. Seepage control measures are also discussed. Blasting efficiency and vibration control measures in adjacent structures also find a mention.

Basis the extensive instrumentation including Real-Time monitoring, a successful and timely completion of the Project was achieved despite it being one of the most complex packages in the entire Mumbai Metro Line 3. All litigations won and the local populace convinced through the far-reaching Instrumentation Reports generated.

Keywords: Instrumentation, Real-Time Monitoring, Settlements, Vibration, Water Level Depletion

1 INTRODUCTION

Mumbai Metro Line 3 (MML3) is a 33.5km long underground corridor extending from Colaba to SEEPZ consisting of twin tunnels and 27 integrated stations. MML3 aims at providing a Mass Rapid Transit System that would supplement the existing suburban railway system of Mumbai. UGC02 package with its extent of circa 8km twin tunnels from the Chatrapati Shivaji Terminus (CST) to Mumbai Central Station. UGC02 is the most complex packages in MML3 with 1004 structures in the Zone of Influence, majority of them being in a dilapidated state.

Instrumentation and Monitoring in an urban infrastructure project is of prime importance as it helps to mitigate great risks to life and property. Instruments provide early warning through real time monitoring for any excessive ground settlements affecting the adjoining structures. An important aspect of a thorough Instrumentation regime is that it is a safeguard and provides legal protection against claims by the owners/ residents persisting for damages inflicted to their property during metro construction works.

2 PREPAREDNESS

Series of public hearings were conducted to ward off the resistance from some of the residents and to create a conducive environment for the works to start. Prior to the start of the construction works, an extensive Pre-Construction Building Condition Survey (PCBCS) was conducted as per the Building Damage Classification (Burland 1977). Around 120 structures could not be surveyed due to permissions not being granted by the Owners/Residents and were hence served

*Corresponding author: aashumml3@gmail.com

DOI: 10.1201/9781003495505-366

Table 1. Details of structures in UGC02.

Total Structures	PCBCS completed	Very Severe	Severe	Moderate	Slight	Very Slight	Negligible
1004	884	28	238	417	176	12	13
Heritage Structures: 51/884							
Supported/Repaired Structures prior to Metro Works: 100/884							
Instrumented and Monitored Structures: Approx. 950/1004							
Structurally Audited Structures: 150/884							

notices for granting permissions or owning responsibilities for any damages whatsoever to the structures. Details of the structures and their Classification is provided in Table 1.

Average age of the above structures is 70 to 75 years. Some Heritage structures, which are also places of worship, are nearly 160 years old.

Based on the PCBCS classification of structures, structural auditing of approximately 150 dilapidated structures was completed and the reports shared with concerned authorities. Upon submissions of structural audit reports, structures, which were beyond repairs, were taken up for demolition and the rest were taken up for structural repairs and temporary supports as well.

A comprehensive Instrumentation and Monitoring regime was followed keeping in view the complexity and the close proximity of structures to the excavations. Monitoring of structures along the tunnel alignment and in close vicinity of cut and cover excavations for settlements, cracks, tilt and vibrations was taken up diligently. In addition, ground water level in existing wells and installed Piezometers was monitored during the course of TBM boring and station excavations.

3 COMPLEXITIES DURING THE COURSE OF CONSTRUCTION

TBM mining for the Down Line (Vaitarna-1) started on 6th December 2017 with the breakthrough on 13th August 2019 and the Up Line (Vaitarna-2) started on 24th February 2018 with the breakthrough on 30th April 2020. Few thought-provoking aspects emerged during the course of TBM drive as well as cut & cover construction of station boxes from CST to Mumbai Central.

3.1 *Reported construction induced settlement and consequent damage to surrounding structures*

Several claims on damage to structures cropped up during the course of the construction in UGC02. The claimed damages in forms of cracks and spalling of concrete in most of the structures were refuted with the help of previously prepared PCBCS Reports, which already had these anomalies documented. Litigations in courts of justice were annulled, basis the PCBCS, relevant structural audit and Instrumentation Reports. TBM boring induced settlements recorded along the alignment were bare minimal to a tune of only a few millimetres which were non-significant.

However, specific reference is made to settlement and cracks in a dilapidated structure in close proximity to the Girgaon station for which a litigation was filed associating the damage to metro construction works. The Building Condition Survey conducted a couple of years earlier along with the structural audit and assessment reports proved useful in establishing that the structure was dilapidated prior to the start of the construction works. The Primary reason for the recorded settlement and development of new cracks was therefore in contrary to the claims.

3.2 *Depletion of water levels*

Apprehensions of water level depletion were raised by managing authorities of two 160-year-old Heritage structures, which were important places of worship. Both the structures have four water wells in their premises and the water is considered as 'holy water'. Concerns regarding seepage into the TBM tunnel while boring beneath the structures would deplete or even drain the water out from the 'sacred wells' were raised off and on during the course of tunnelling. Extensive daily monitoring of all the eight wells and standpipes was in place during and after the TBM mining. As a precautionary measure, several recharge wells were constructed in close proximity to the structures to cater to the depletion of water in case the need arose. A relation between the TBM progress in this specific reach and the water level readings was established which is discussed in detail later in this paper.

3.3 *Vibrations during TBM mining*

Geotechnical investigations had established that the proposed Kalbadevi station box consisting of two shafts would encounter hard and compact fresh Basalt rock. Ambiguous claims by the residents of vibrations due to mining in hard compact basalt were negated by vibration monitoring reports carried out in the structures above.

Due to the absence of no-disturbance zones on structures for monitoring of vibrations, several abrupt peaks were observed due to local disturbances, which were inexplicable. Since there were no noise correction options available in the monitors installed, the prerogative was to establish the vibration levels at ground during TBM boring.

A sub-way near the Metro Cinema under which the TBM was to pass through hard compact basalt of Rock Class I to Class II was selected as a disturbance free monitoring zone during the night as the sub-way is non-operational for the public between 2100 hours and 700 hours. Correlation between the Face activity at the TBM and the vibration recorded during the night shift validated the actual vibrations imparted to the surface during mining in hard compact strata. Results of TBM mining induced vibrations are discussed later.

4 INSTRUMENTATION & MONITORING-DATA ANALYSIS

Instrumentation and Monitoring scheme for the UGC02 package was extensive considering the complexity of the alignment, which traversed through dilapidated structures and varied geological formations and a significantly high ground water table.

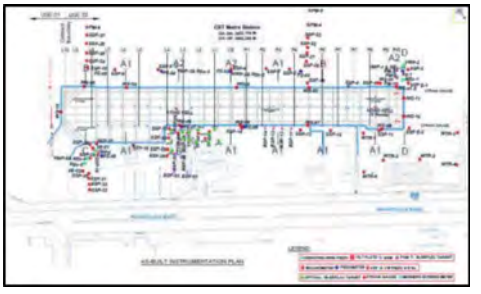

Figure 1. Typical instrumentation - station box.

Figure 2. Typical instrumentation - tunnel section.

All structures within the Zone of Influence (ZOI), which was demarcated as 50m from the centreline of each tunnel and 35m from the station box excavation were included in the monitoring scheme. These structures were monitored for settlement, tilt, vibration and cracks besides Real-Time monitoring. Roads and pipelines were monitored for settlements. Groundwater level monitoring was taken up in installed Piezometers and existing water wells in the ZOI. Some instances with remarkable outcomes are stipulated as below:

4.1 *Settlement graphs*

Settlement issues by residents during TBM mining

Ground settlement due to TBM mining was recorded and were within the design limits in some rare instances. The limited settlements were due to the hard and compact strata encountered during the course of tunnelling. A classic case of settlement not related to TBM mining is discussed below which highlights the remedial measures adopted for settlements and the importance of Instrumentation and monitoring. Several unethical claims by residents were proved frivolous based on the PCBCS Reports compiled some three to four years earlier. Claims of settlements and cracks due to TBM boring were raised on a number of occasions by the residents. On detailed inspection, claims for the newly developed cracks were found to be irrelevant and thus rejected based on the PCBCS Reports and structural audit reports.

4.2 *Ekta society settlement*

A dilapidated structure stood in close proximity to the excavated walls of Girgaon station box. Extensive monitoring of the structure was in place, which started even prior to the start of the construction works. On October 8, 2020, a sharp and sudden drop in settlement was recorded to the tune of (-) 10mm in the installed optical targets and several cracks were observed in the structure. Settlement was also observed on the road adjacent to the structure and despite the fact, that the settlement was not related to the Metro construction works, immediate remedial measures were taken up to minimize the settlement.

Picture 1. Location of ekta society vis-à-vis girgaon station.

Due to minor seepage on the walls of the excavation, cement grouting was initiated at the first instance and was undertaken with refusal pressures of 2 to 3 bars from within the excavation. The structure, because of these grouting measures was uplifted to a certain extent and width of nearly all major cracks was reduced. Optical targets installed in the structure reflect the settlement and uplift depicting the efficacy of the grout. Following pictures depict the condition of cracks immediately upon settlement of the structure and after the uplift and the crack width reduction

Picture 2a & 2b. Crack-1 prior to and after grouting measures.

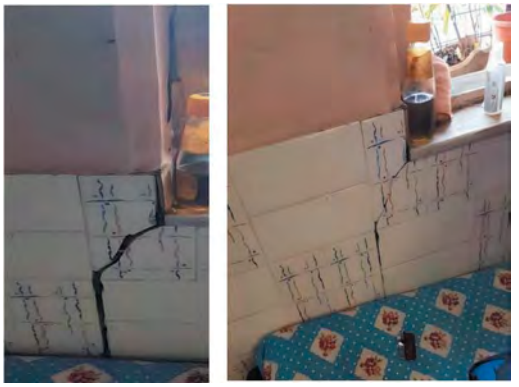

Picture 3a & 3b. Crack-2 prior to and after grouting measures.

The graph representing the settlement and heave of the structure is as shown below. A heave of 13mm from the original position of the specific corer of the structure was observed.

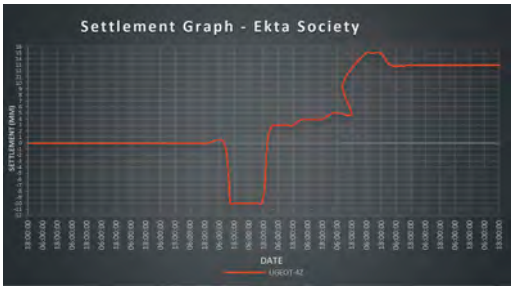

Figure 3. Settlement graph – ekta society.

Thorough scrutiny, to establish the actual cause of the settlement revealed that a leakage in a sewer and subsequent leakage in a nearby water pipe-line was the sole cause of the settlement. Due to the water seepage, ground settlement occurred and thereafter settlement and crack development in the structure. Residents of the building filed a litigation in the court of law claiming that the damage was due to Metro construction. The court of law annulled the appeal basis the dilapidated condition of the structure recorded in the PCBCS reports prior to the start of Metro works. However, crack repairs and strengthening of the structure were undertaken as a mark of social responsibility, which is being adhered to diligently ever since the start of the project.

4.3 *Construction induced ground water depletion*

Behaviour of the ground water table during TBM mining operations can be best exemplified by their manifestations in soft Breccia and hard compact basalt. A major drop in the water table to the tune of 7 to 9m was apparent in soft breccia within a Zone of Influence of 45 to 50m, mined in a span of 7 days.

Figure 4. Location of PZ-18 vis-a-vis TBM rings.

Data from this standpipe for the Down Line, the centre line of which is 24m away and corresponds to Rig No. 856 in the Down Line, recorded a drop from the mining of Ring number 834 and return to original levels after mining of ring number 866 which corresponds to a ZOI of 32 rings or a length of 45m.

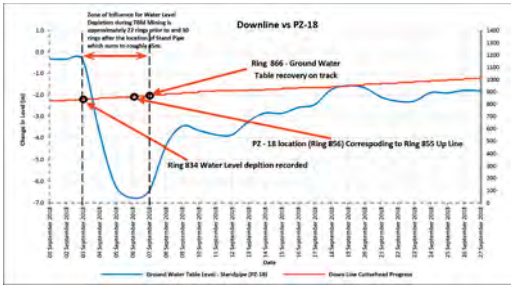

Figure 5. Drawdown in PZ-18 V/S down line TBM progress.

The water level in the standpipe, located at a distance of 12m from the Up Line near ring number 855, started dropping as the TBM started the mining of ring number 823 on February 11, 2019 and continued to drop until the mining of ring number 858. Completing of ring 858 initiated the rise in water level thus demarcating the zone of influence as 35 rings equivalent to roughly 49m in the Up Line TBM.

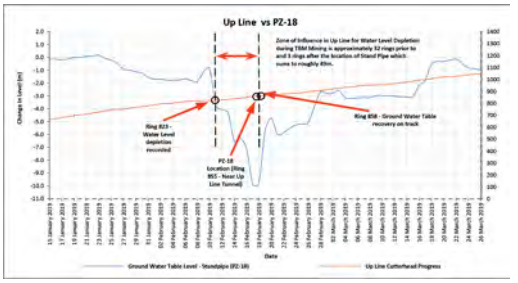

Figure 6. Drawdown in PZ-18 V/S up line TBM progress.

Increase in water level recorded during the course of tunnelling is attributed to the ground recharge by rainwater. Variation in ground water levels during the rainy season and dry spell is to the tune of 3 to 4m.

On the other hand, ground water table was monitored in open wells inside the premises of two heritage structures of prime importance. In contrast to the apprehensions raised by the authorities of the Atash Behram, no water depletion was recorded in any of the eight numbers of 'sacred' wells.

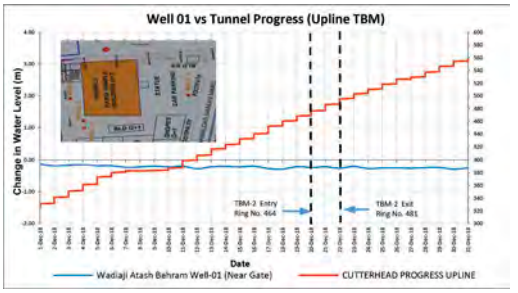

Figure 7. Drawdown in well no. 1 V/S up line TBM progress.

4.4 *Vibrations during TBM boring*

Various claims and counter-claims were raised during TBM mining from CST to Mumbai Central. Vibration monitoring was carried out in structures above the TBM with Instantel vibration monitors. Local disturbances due to their placement in structures were abundant and were reflected in the reports as peaks. Explanations for these abrupt peaks related to local disturbances were not understood by the residents. Subsequently, a disturbance free zone for vibration monitoring was delineated in a nearby subway (Figure 8) and monitoring, during mining under it, was initiated during the night when the subway is closed for public. Face activity of the TBM Mining for Ring number 207 in hard rock, during the shift perfectly correlated with the vibration data recorded during this period. This was further established with the mining of rings 208 & 209. Actual range of vibrations (Peak Particle Velocity) during mining by TBM in hard

Figure 8. Location of sub-way vis-à-vis up line and down line.

and compact basalt can therefore be estimated between 0.182 mm/sec to 0.291 mm/sec.

Vibration monitoring graphs for TBM mining displayed below have demonstrated the accuracy of the data collected in the disturbance free zone with a total disappearance of abnormal peaks in the recorded data. Vibration monitors were placed in the sub-way during the mining of ring numbers 207 and 208 and data from three different units for the mining of ring 207at the same time is similar and most importantly without any abruptly recorded peaks. The data collected was then corroborated with the daily activity reports of the tunnel face. A perfect relation between TBM boring and elevated peaks of vibration and ring building activity reflected as insignificant vibration levels. Three separate Instantel units with Identification Numbers 11694, 11695 and 11207 were installed during the night shift during TBM mining in the subway. Overburden at this particular location was 15m and the subway at a depth of 5m. Thus, the effective depth of vibration measurement was approximately 10m above the tunnel. The correlation of TBM mining and vibrations imparted on Ground are as shown below:

MINING FOR RING NO. 207 (SUBWAY)

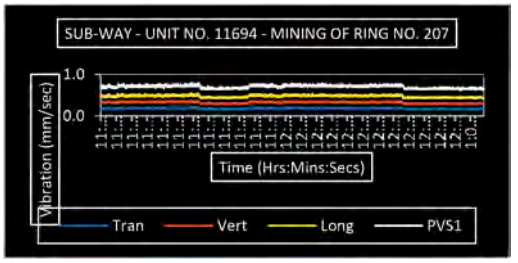

Figure 9. Vibration graph – ring no. 207.

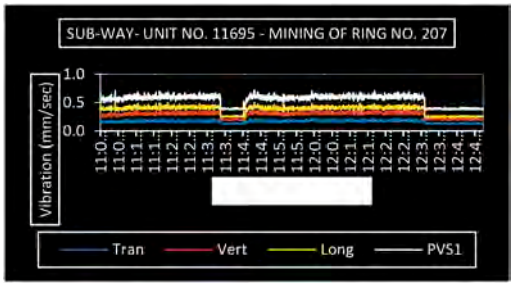

Figure 10. Vibration graph – ring no. 207.

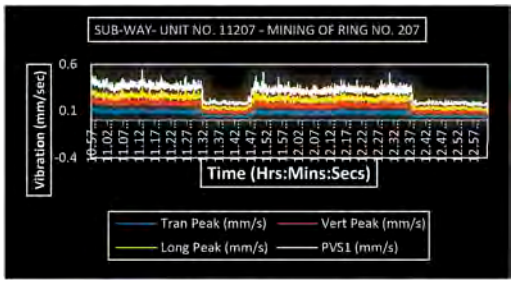

Figure 11. Vibration graph – ring no. 207.

MINING FOR RING NO. 208 (SUBWAY)

5 CONCLUSIONS

This paper deals with three distinctive aspects of the importance of Instrumentation and Monitoring (I&M) during the construction phase of a complex Metro Project. The I&M data is of prime importance

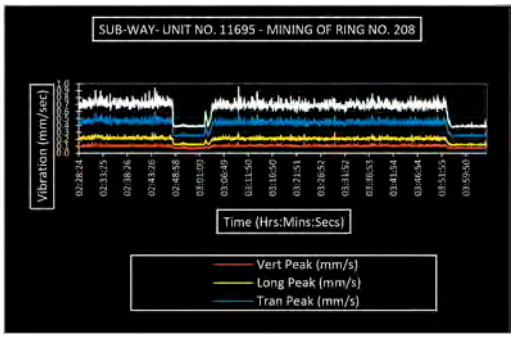

Figure 12. Vibration graph – ring no. 208.

in refuting the frivolous claims by the residents. The three aspects are:

1. Refuting claims for construction induced settlements using Pre-Construction Building Survey reports and reversal of settlements through grouting techniques.
2. Effect of Tunnelling on Ground Water Table and demarcation of a Zone of Influence of approximately 50m in Breccia and
3. Actual vibrations imparted on ground during the course of TBM boring in hard compact basalt in the range of 0.182 to 0.291 mm/sec.

REFERENCES

Burland J.B., Broms B.B., and de Mello V.F.B. (1977). "Behaviour of foundations and structures" Proc., 9th Int. Conf. on Soil Mechanics and Foundation Engineering, II, State of the Art Report, Tokyo, 495–54.

Tunnelling for a Better Life – Yan, Celestino, Thewes & Eberhardt (Eds)
© 2024 The Author(s), ISBN 978-1-032-80042-4
Open Access: www.taylorfrancis.com, CC BY-NC-ND 4.0 license

Geotechnical instrumentation for road tunnels: Success cases in Colombia

Víctor Restrepo*, Héctor Salazar & Jean Piedrahita
Grupo Geoandina, Bogotá D.C, Colombia

ABSTRACT: In this article, the implementation of geotechnical instrumentation systems using Multipoint Borehole Extensometers (MPBX), pressure cells, and strain gauges in two (2) significant road tunnels in Colombia is presented. For one of these tunnels, the records and results obtained during the stabilization of a critical area during construction and recently in its operational phase will be presented. On the other hand, the geotechnical monitoring records of a road tunnel affected by the influence of a landslide are presented. The first case involves a tunnel with a length of 3.50 km, which traverses an active regional geological fault along its alignment. For monitoring purposes, an instrumentation system consisting of six (6) MPBX extensometers, eight (8) NATM-type pressure cells, and eight (8) strain gauges distributed in two (2) critical sections of the tunnel was implemented. This system allowed for recording the deformation behavior of the cross-section, demonstrating the effect of construction phases along its length and its final stabilization, comparing the actual maximum values with those initially estimated using numerical models.

The second tunnel, approximately 700 m in length, is in a fluvio-glacial deposit that has experienced mass movement processes since 2019, affecting the last 200 m of the tunnel. Therefore, an instrumentation system consisting of fifteen (15) MPBX extensometers distributed in three (3) sections of the tunnel was implemented, allowing for a direct correlation between surface rainfall regimes and the surface and subsurface displacement velocity over time. Additionally, an analysis of the current results is included in the context of the expected behavior of the tunnel, particularly after a seismic event occurred near the study area.

Keywords: Tunnel Monitoring, Construction Instrumentation, Geological Fault Instrumentation, Displacement Extensometers, Application of Multipoint Borehole Extensometers (MPBX)

1 INTRODUCTION

During the construction of the Tesalia Tunnel, which is nearly 3.50 km long, in the Department of Caldas, Colombia, one of the most critical engineering challenges was to traverse the Patía geological fault. The excavation had to be carried out with great rigor, at a slower advancement rate, and in a stepwise manner to control potential displacements and convergences that could pose an imminent collapse risk. For this project, two (2) instrumented sections were defined, each equipped with three (3) multipoint extensometers, four (4) NATM-type pressure cells, and four (4) strain gauges. The purpose was to continuously monitor displacement, pressure, and deformation during the excavation process and subsequent tunnel operation.

In the case of a tunnel affected by the landmass degradation process in one of Colombia's most important road arteries, it was necessary to monitor the progress of displacement through three (3) analysis sections, each equipped with five (5) multipoint extensometers. These results were correlated with external observations obtained from Ground-Based Interferometric Synthetic Aperture Radar (GBInSAR) and precipitation monitoring in the area.

This article describes the general aspects of the two mentioned projects, the instrumentation equipment used, its location within each tunnel, and the results recorded during the project phases. It highlights the benefits of precisely monitoring displacement, pressure, and deformation to verify geotechnical behavior and compare it with design premises or other related parameters.

2 SUCCESS CASES OF GEOTECHNICAL INSTRUMENTATION SYSTEMS IN ROAD TUNNELS

2.1 *Overview of the Tesalia Tunnel and the Patía geological fault*

The underground structure is currently in its operational phase and is in an intermediate zone of the

*Corresponding author: vrestrepo@geoandina.net

DOI: 10.1201/9781003495505-367

Western Cordillera, forming part of the Pacific Connection Highway 3 project in the Department of Caldas, Colombia. It consists of the main tunnel and an emergency gallery tunnel parallel to the main one. These tunnels are approximately 3.50 km long and provide a connection between the rural area of El Cairo (entrance portal) and La Libertad (exit portal). Due to its length, it currently stands as the longest tunnel in the Coffee Region of Colombia.

For its construction, the conventional drilling and blasting method was primarily used. However, in areas where geological faults were encountered, mechanical excavations were employed. In the design and planning phase of the underground project, it was projected to cross four (4) geological faults, with the largest and most critical being the Patía geological fault.

The challenge of crossing this latter fault through mechanical excavations necessitated monitoring the subsurface behavior using specialized instruments based on MPBX extensometers, NATM pressure cells, and strain gauges.

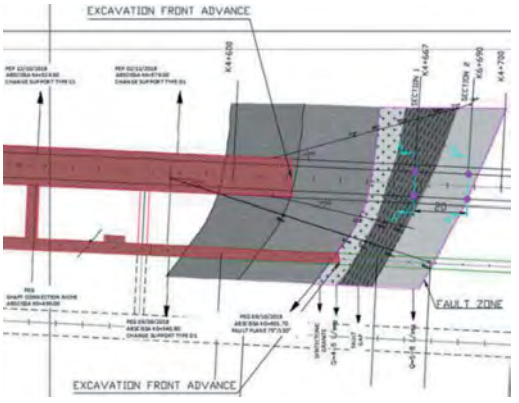

Figure 1. Location of instrumentation stations in the main tunnel.

These instruments allowed for the evaluation of convergence and a possible increase in stresses in 2 sections near the Patía fault, which could indicate zones of rock mass plasticization. Displacement and stress graphs over time were created from the measurements, aiding in understanding and validating stress trends in these sections.

2.1.1 *Installation process of geotechnical instrumentation in Patía fault sections*

Based on the geological-geotechnical models, 2 monitoring stations were defined at abscissas K4 +667.30 and K4+686.70, approximately 20 meters apart, for analysis. For each of these monitoring stations, 3 multipoint MPBX extensometers with vibrating wire technology were installed.

In the extensometer borehole, 3 depths of analysis were defined at 6 meters, 9 meters, and 12 meters. These depths were used to rigorously monitor the main contacts of the Patía fault zone during both the construction and subsequent operational phases.

To construct the borehole or hole for instrument installation, a jumbo-type machinery with a drilling capacity of 12 meters was required.

Figure 2. Drilling process for MPBX extensometers.

The installation of the extensometers was carried out according to the specified lengths, and to eliminate friction between these instruments and the injection mortar, PVC pipes were assembled around the metal anchor bars.

Once the drilling was completed, bars with anchors at the analysis depths were inserted into the holes, and the extensometer head with a vibrating wire extensometric sensor with a range of 100 mm for each anchor bar was installed.

After installing the sensors in the head and securing the head to the ground, grouting was injected through the instrument's tubes.

In consideration of the hydrogeological conditions in the installation area, a waterproofing additive was implemented, allowing the grouting material to set in the presence of water.

This procedure was replicated for each monitoring location in the tunnel's cross-section, which were positioned at the top (keystone), on the left and right sides.

With the injected and set grouting, final adjustments were made to the head, and the initial reading was recorded for each sensor to establish the baseline or reference.

On the other hand, for NATM-type pressure cells with vibrating wire technology, a small excavation was made on the sides of the sections to allow the insertion of 2 of these instruments, oriented radially and tangentially to the tunnel section's geometry.

These pressure cells were anchored to the ground with bolts, and to create a uniform surface between the rock mass and the instrument, waterproof grouting was applied around the cells, followed by sealing the excavation with the same cementitious material, ensuring consistent confinement of the instruments.

Once the grouting had set, the NATM-type pressure cells were pressurized to eliminate any void spaces that could lead to erroneous readings, and initial readings were recorded for monitoring baseline.

Figure 3. Installation of NATM pressure cells.

For monitoring deformations in the sections, 2 strain gauges with vibrating wire technology were installed on each side (left and right) of the section, anchored with bolts in the ground.

Like the NATM-type pressure cells, the instrument was covered with waterproof grouting to create a uniform surface between the rock mass and the sensor.

Figure 4. Installation of strain gauges.

After the instruments were installed, each of these geotechnical monitoring points was centralized using protective pipes and 4-core wiring, allowing the information from the instruments installed per section to be transmitted to recording equipment at strategic locations, facilitating periodic readings without major complications.

These locations were defined on both sides of the tunnel section, centralizing 2 extensometers on the right side and 1 on the left side.

Regarding the tunnel excavation process, initially the stages of execution of the geometry in the upper zone of the tunnel were initially outlined to generate a stabilized surface with which mechanical excavation work could be done.

The excavations of the tunnel front were done using a "mushroom" shape; that is, the upper area of the tunnel section and the central sector of the section was excavated for access to the excavation machine.

The edges were left unexcavated to provide the tunnel section with the necessary stability to facilitate the tunnel excavation and stabilization.

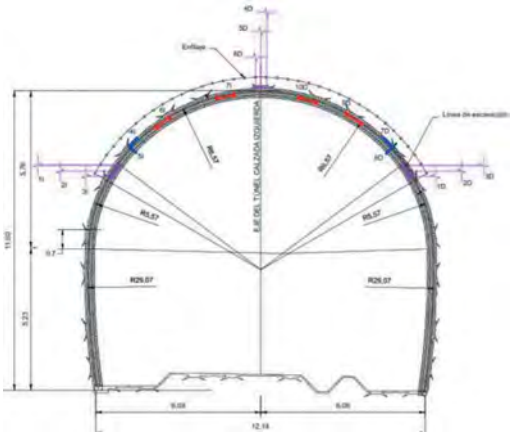

Figure 5. Locations for instruments in sections of the Tesalia tunnel.

After making a tunnel construction advance of approximately 30 m or at the moment when, technically, the stability of the tunnel section was assured, the shoulders were excavated.

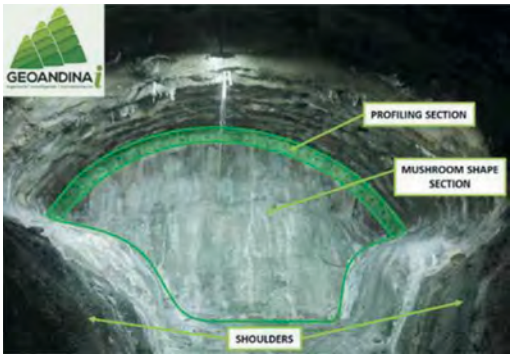

Figure 6. Tunnel excavation section in Patía geological fault - Tesalia tunnel.

2.1.2 *Behavior during the construction and operation progress of the tunnel*

Based on the results obtained from extensometers in different sections of the tunnel, the relative displacements of the rock mass at various depths were accurately evaluated.

The graphs below represent the displacements recorded by extensometers installed in both sections of the tunnel. In the first section (K4+667.30), after 06/10/2019, a change in trend is recorded.

This behavior is primarily seen in the instrument installed at the top of the tunnel section. The event is consistent with the start date of excavation at the work face, during which displacements of approximately 1 mm were observed. Variations in displacements can also be seen starting from 10/30/2019, coinciding with the excavation of the shoulders in the tunnel section.

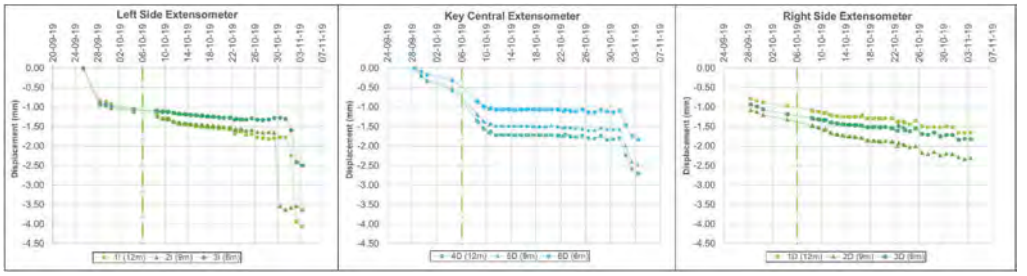

Figure 7. Monitoring results for relative displacements - section K4+667.30.

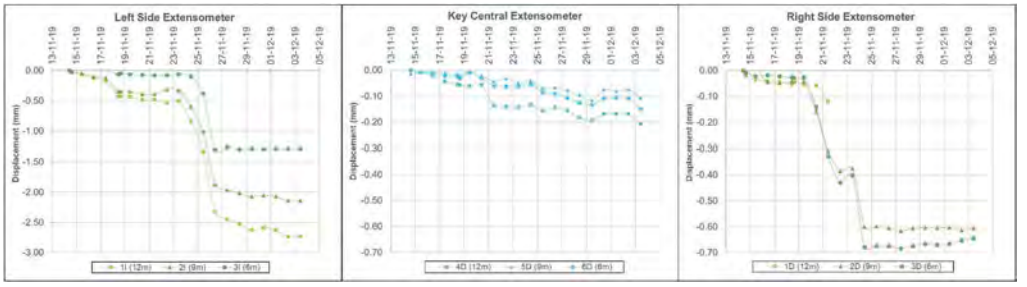

Figure 8. Monitoring results for relative displacements - section K4+686.70.

Similar behavior is recorded in pressure cells (pressure values up to 1.3 MPa) and strain gauges (recordings up to -1650με).

For the second section (K4+686.70), changes in recorded displacements occur starting from 11/17/2019 due to progress in excavation work, with values up to -0.5 mm. Additionally, significant variations in the behavior of extensometers installed on the sides of the tunnel cross-section are recorded between 25 and 26 November 2019, with recordings of up to -2.7 mm.

This coincides with the excavation of the shoulders in the tunnel section, and similar behavior is observed in pressure cells (pressure values up to 0.1 MPa) and strain gauges (recordings up to -2100με).

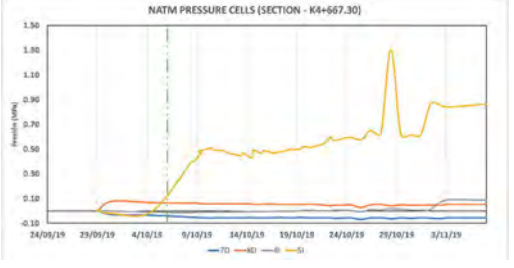

Figure 9. Monitoring results for relative pressures - section K4+667.30 and K4+686.70.

Regarding the conventions used for displacement analysis, positive values represent tensile rock behavior, while negative values represent compressive forces. The rock mass mostly moves the instruments towards the center of the tunnel, causing the extensometers to displace positively relative to the initial position.

For NATM-type pressure cells, positive values were defined as pressure forces on the instrument, and negative readings as depressurization conditions. For strain gauges, positive values in the readings would indicate tensile stresses, and negative values would indicate compressive stresses.

In addition to the previously mentioned relative displacement analyses, unit deformations were validated for each anchor.

These deformations were obtained from the difference between the displacements recorded in one reading and the reading of the same instrument for the immediately preceding record. For the anchor at a depth of 3 m, deformations with respect to themselves were also considered.

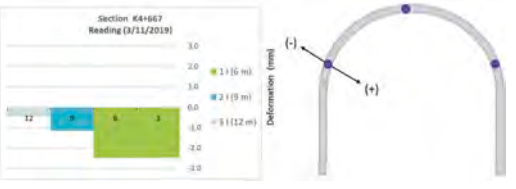

Figure 10. Strains readings to extensometer- section K4 +667.30.

During the monitoring of the tunnel in its construction phase, unit deformations of up to -0.4 mm/m were recorded for anchors at 6 m and 9 m depth. In contrast, for the anchor at a depth of 12 m on the left shoulder,

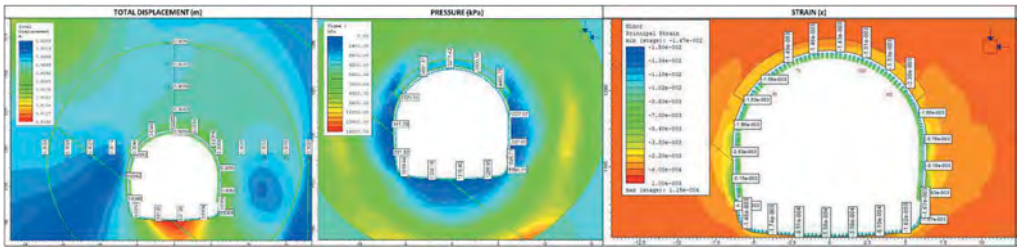

Figure 11. Maximum stress values obtained from numerical modelling.

a unit deformation of approximately -0.18 mm/m was recorded. For the anchors at 12 m from the top of the tunnel section and the right shoulder, positive unit deformations of 0.81 mm/m and 0.20 mm/m were recorded, respectively.

The information obtained through the monitoring of MPBX extensometers in the Tesalia tunnel provided first-hand data to better inform the technical area about the progress processes and other design issues during the excavation and construction phase.

2.1.3 *Comparative evaluation of maximum values*

Based on the numerical models created during the tunnel design stage, it can be observed that the historical records of displacements, pressure, and deformation show stable behavior for both sections, with slight increases in thresholds that do not pose a risk to the stability of the roadway tunnel.

It is also evident that the maximum values recorded are isolated data points without continuity; therefore, they are considered as anomalies or instrumental noise. Hence, the structures built for the Tesalia main tunnel are operating under the initially proposed conditions.

Regarding the lining, based on the simulations, an average maximum displacement of 0.005 m was obtained for the keystone, 0.005 m for the sidewalls, and 0.009 m for the base plate.

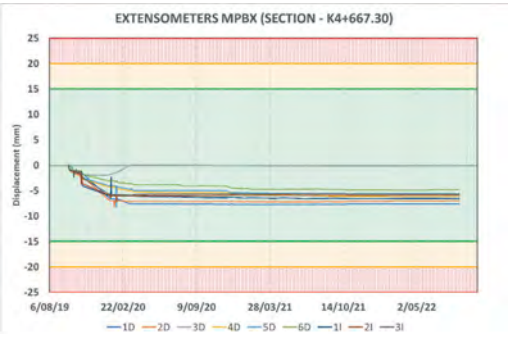

Figure 12. Comparative analysis of thresholds – displacement.

Based on the simulations, estimative calculations were used to determine the stresses to which the primary support would be subjected. These stresses, under static conditions, were recorded on average as 3.70 MPa for the keystone, 0.85 MPa on the sidewalls, and 1.40 MPa on the base plate.

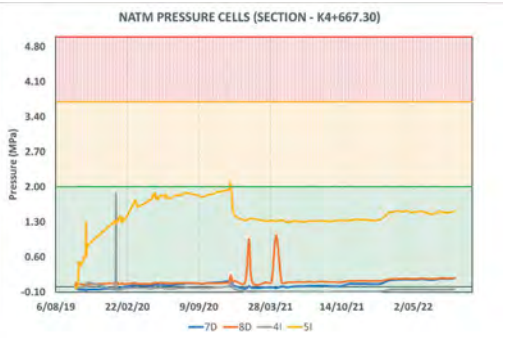

Figure 13. Comparative analysis of thresholds – pressure.

Regarding the presented models, estimative calculations were performed for the unit strains in the tunnel section. These unit strains averaged between -1400 με (microstrains) and -2400 με (microstrains).

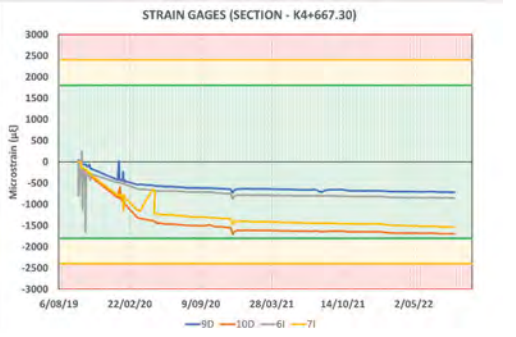

Figure 14. Comparative analysis of thresholds – strain.

2.2 *Overview of Tunnel 13 – Mesa Grande Zone and K58 landslide (Guayabetal)*

In 2013, excavation was carried out using mechanical equipment, without blasting, and in dry conditions for two consecutive roadway tunnels (Tunnel 13 and Tunnel 14), passing through fluvio-glacial terrace material.

Since 2018, significant cracks were identified on the terrace slope, and within Tunnel 13, after 2019, displacement events affecting the normal operation of the K58+000 road section of Vía Al Llano and the planned tunnels were recorded. Due to these landslides, the last nearly 200 m of Tunnel 13 were affected, showing considerable signs of displacement and cracking.

In order to understand the displacement trends and the overall behavior of the underground structure, a geotechnical monitoring system based on MPBX extensometers was installed for three tunnel sections (K57+228, K57+270, and K57+335). From the records obtained through these instruments, the relative displacement between two measurement points for each sensor was estimated.

2.2.1 *Installation process of MPBX extensometers in Tunnel 13*

For each monitoring extensometer well, three analysis depths were defined: 3 m, 6 m, and 9 m, respectively.

Similarly, to the case of the Tesalia tunnel, once the locations of the monitoring points were redefined in the field using a specialized jumbo machine, the respective drillings were carried out to the maximum anchoring depth of 9 m.

Figure 15. Installation process for MPBX extensometers in tunnels.

Following this, a similar installation process was conducted for each of the extensometers. In coordination with the client, the monitoring zones were defined.

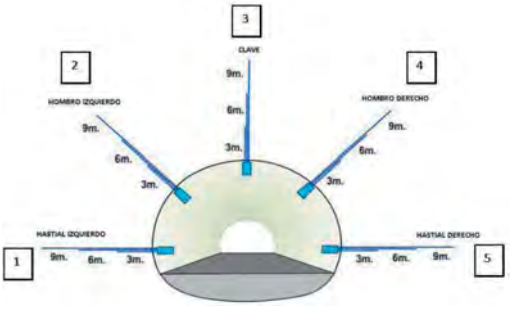

Figure 16. General location of the instruments in the cross section of the tunnels.

Once the installation process of the MPBX extensometer head was completed, the cables and pipes were centralized to carry out readings from the sides of the tunnel using manual switchbox reading equipment.

With the three tunnel sections instrumented, an assessment of the tunnel's behavior was conducted. The instruments installed for this project have a measurement range of 150 mm.

2.2.2 *Results of displacement changes and correlation with rainfall in the area*

Based on the results of the implemented instrumentation system, the behavior of the area where Tunnel 13 was excavated, and which was affected by the earth slide process that occurred on the slope of Mesa Grande, Guayabetal, Colombia, was validated.

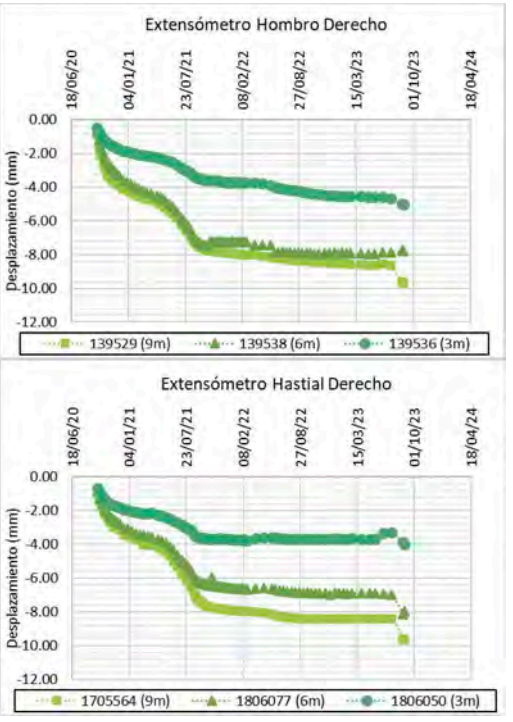

Figure 17. Monitoring results for relative displacements - section K57+228.

The extensometers mainly recorded tensile displacements (negative values), with values of up to -22.63 mm. Generally, maximum displacements were recorded in the sections of the extensometers installed on the left side of the tunnel cross-section.

Sections K57+228 and K57+270 of Tunnel 13 showed occasional compression displacement trends recorded in the left shoulder areas, with displacements of up to 8.20 mm.

Based on climate records (precipitation monitoring) in the Mesa Grande area, a correlation can be observed between increased precipitation and the displacements recorded by the tunnel instrumentation.

According to precipitation data, more than 500 mm of monthly rainfall was recorded in August 2021. During this period, the instruments reported significant variations in ground displacement.

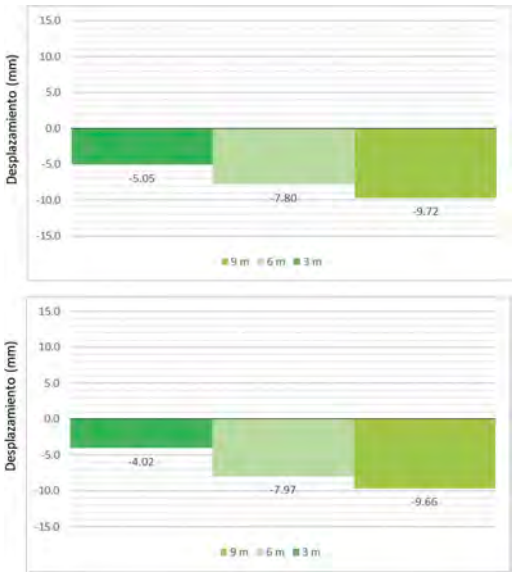

Figure 18. Strains readings - section K57+228.

With the objective of monitoring the surface behavior of the K58 Mesa Grande slope, the installation of a robotic SSR429SAR-X radar station with LiSa technology was carried out.

With the previous monitoring technology, it was determined that, due to the precipitation events that occurred between April and October 2021, a change in trend was evident in the displacements of the material present on the slope.

Therefore, it is possible to conclude scenarios of synchronous behavior between the measurements inside the tunnel and the monitoring of surface displacements using SAR-X terrestrial radar technology (Figure 20).

On August 17, 2023, a seismic event with a moment magnitude of M6.1 was recorded near the municipality of Guayabetal.

Readings were taken from the instrumentation installed in Tunnel 13, and the results of these recordings showed significant variations in displacement trends for each of the tunnel section instruments in the hasty areas.

3 CONCLUSIONS

The implementation of geotechnical instrumentation during the construction and operation of the described tunnels has been essential to obtain on-site data on engineering parameters such as unit strain (strain gages), relative displacements (extensometers) and pressure (NATM cells).

In the case of the Tesalia Tunnel, the instrumentation reading with the advance of the excavation front allowed the dimensioning of the orders of magnitude of deformations and stresses corssing an active geological fault. The changes in stress states were evident during the tunnel excavation of the cross section in different stages and subsequently its stabilization over time to relatively stable final values in expected magnitudes according to the tunnel design numerical models.

Regarding Tunnel 13, affected by the influence of a landslide, a direct correlation was observed between precipitation events in the Mesa Grande area and displacement records inside the tunnel. It was observed that during increased precipitation, the displacement trend is linear and progressive.

After lighter rains, the trend changes from linear to regressive. Additionally, it was noted that after the seismic event with a magnitude of M6.1 near the municipality of Guayabetal, variations in displacement results were recorded for each of the sections of Tunnel 13.

ACKNOWLEDGMENTS

In reference to this article, we wish to express our gratitude to the field and office technical team whose hard work and commitment were paramount to the successful implementation of the monitoring technologies. Their unwavering dedication under often challenging conditions has been an invaluable asset to previous projects and countless other work settings.

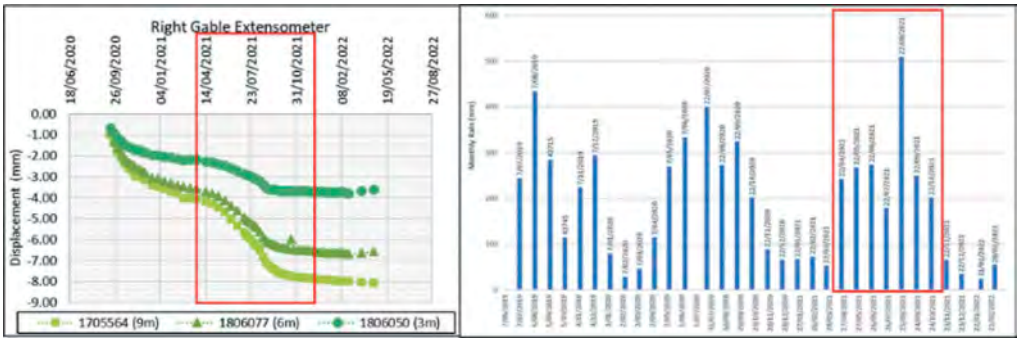

Figure 19. Correlation between the behavior of the tunnel and rainfall in the area.

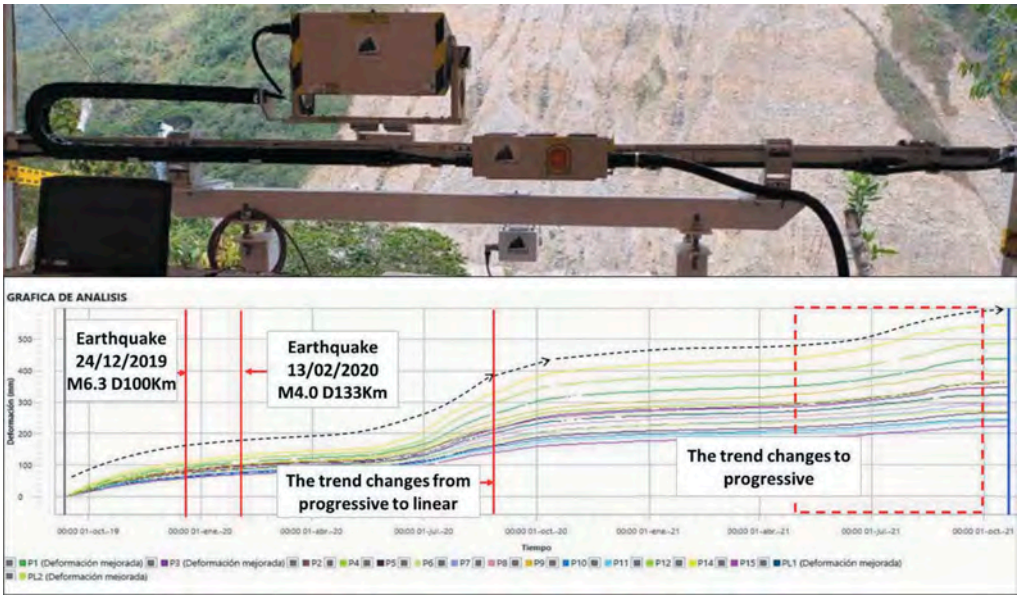

Figure 20. LISA type radar installed for 24/7 slope monitoring and movement behavior on the slope 10/2019 - 10/2021.

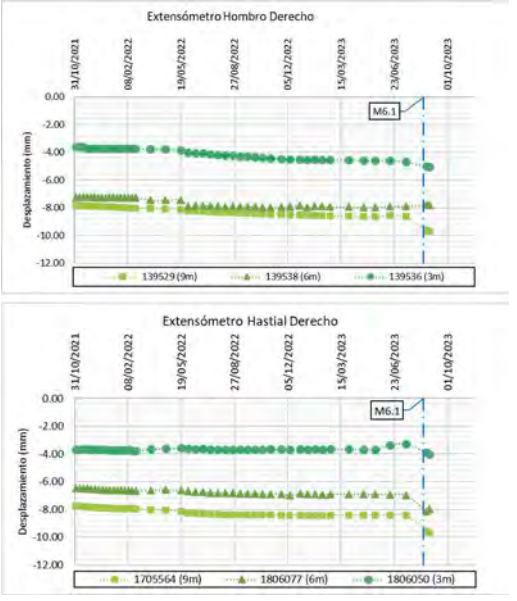

Figure 21. Monitoring after the M6.1 earthquake - section K57+228.

On the other hand, we would like to extend a special thanks to our valued clients, who not only trusted our experience and technical knowledge, but also gave us the opportunity to apply and corroborate these monitoring technologies in real-world situations. Their collaboration and continuous support were essential in all phases of these projects, without them these success stories would not have been possible.

REFERENCES

ITA (2011). Monitoring and Control in Tunnel Construction. Longrine, France: AITES/ITA WG2-Research.

Lunardi, P. (2008). Design and Construction of Tunnels. Milano, Italy: Springer-Verlag Berlin Heidelberg.

Instituto Nacional de Vías, INVIAS. (2015). Manual para el diseño, construcción y mantenimiento de túneles de carretera (Ed 1). Colombia: Ministerio de Transporte.

OGG. (2014). Geotechnical Monitoring in Conventional Tunneling: Handbook. Salzburg, Austria: Austrian Society for Geomechanics.

Do, N. A., Dias, D., Dinh, V. D., & Dao, V. D. (2019). Behavior of noncircular tunnels excavated in stratified rock masses – Case of underground coal mines. Journal of Rock Mechanics and Geotechnical Engineering, 11, 99–110.

Tunnelling for a Better Life – Yan, Celestino, Thewes & Eberhardt (Eds)
© 2024 The Author(s), ISBN 978-1-032-80042-4
Open Access: www.taylorfrancis.com, CC BY-NC-ND 4.0 license

Analysis of laboratory tests for the determination of the clogging risk in mechanized tunnel excavation in fine-grained soils

Diego Sebastiani*
GEEG, Geotechnical and Environmental Engineering Group, Rome, Italy
Department. of Structural and Geotechnical Engineering, Sapienza University of Rome, Rome, Italy

Sara Mangifesta & Armando de Lillis
GEEG, Geotechnical and Environmental Engineering Group, Rome, Italy

Salvatore Miliziano
GEEG, Geotechnical and Environmental Engineering Group, Rome, Italy
Department. of Structural and Geotechnical Engineering, Sapienza University of Rome, Rome, Italy

ABSTRACT: Clogging is one of the main problems encountered in mechanized tunnelling with EPB-TBM in fine-grained soils. This issue is usually addressed by soil conditioning, i.e. the addition of water, foam and other chemical agents during the excavation phase. Over the last two decades, encouraged by the exponential increase of tunnels excavated with EPB-TBMs, many research studies have been carried out, leading to the development of several laboratory tests and classification systems to assess the risk of clogging in fine-grained soils and the effect of conditioning. Nonetheless, due to the complexity of the phenomenon, a number of limitations remain in defining and predicting potential clogging. This also emphasizes the lack of appropriate and widely accepted test standards and the inconsistencies of the classification systems. This paper is part of a larger experimental study on clogging carried out over the last 4 years on more than 20 natural fine-grained soils sampled from real EPB-TBM tunnel projects and subjected to a series of tests aimed at determining the clogging potential. The results of the laboratory tests were systematically compared, highlighting the advantages and limitations of each test and exploring the correlations between them. The results of this investigation, also in light of the great number of tests performed on a wide range of natural soils, can be of assistance in making informed use of the existing laboratory tests and clogging risk classification systems.

Keywords: Clogging, Laboratory testing, Fine-grained soil, Conditioning, Classification

1 INTRODUCTION

Clogging is one of the most critical issues in the excavation of tunnels with Tunnel Boring Machines (TBMs) in fine-grained soils. The phenomenon of clogging is essentially due to the so-called adhering and cohering; the former refers to the forces exchanged between soil particles and metal components of the TBM cutterhead, the latter to the forces exchanged between soil particles (Thewes and Burger, 2005). The occurrence of clogging leads to the increase in torque and consumption and, in extreme cases, to the blockage of the cutterhead.

When excavating with TBMs equipped with Earth Pressure Balance technology, it should also be considered that it is necessary to modify the characteristics of the excavated soil in order to make it suitable for transmitting a stabilization pressure to the excavation face.

This is done by conditioning the soil, that is the addition of water, foam and possibly other additives such as polymers or others. Conditioning, from physical, chemical and mechanical points of view has a number of effects on the excavated soil, mainly summarized as: (1) change in water content and consequently in consistency index; (2) change in the degree of saturation by injection of foam composed mainly of air; (3) chemical modification of the soil with more or less noticeable and lasting effects depending on the chemical composition and dosage of the conditioning agents injected.

For the purposes of this publication, it is important to consider that the conditioning process, in addition to chemically modifying the soil, changes its water

*Corresponding author: diego.sebastiani@geeg.it

DOI: 10.1201/9781003495505-368

content and, consequently, its consistency in a range which is generally considered between the 0.4 and 0.6 (Feinendegen et al, 2010; Hollmann and Thewes, 2013). From this point of view, therefore, it is of particular interest to know the evolution of the clogging phenomenon as the consistency index changes.

The study of clogging should start from the analysis of the characteristics of the soil to be excavated, as the correlation of this phenomenon with certain characteristics, such as the percentage of clay and the plasticity of the soil, is rather well known. Indeed, there are different abacuses and classification schemes in the literature (Thewes and Burger, 2004; Hollmann and Thewes, 2013; Fang et al., 2023) that are quite useful in understanding the "potential clogging" of certain formations based on the analysis of their grain size distribution and Atterberg limits.

To investigate the phenomenon, several tests have been proposed over time, starting with the Hobart mixing test, in the original and later integrated and modified versions (Zumsteg and Puzrin, 2012; de Oliveira et al., 2019), and the pull-out test in flat, conical, and convex versions to assess the clogging potential (Feinendegen et al, 2010; Di Giulio et al., 2018; Spagnoli et al., 2019; Khabbazi et al., 2019). The study of clogging is constantly evolving and new tests and models are proposed annually in an attempt to refine the predictive capabilities of this phenomenon (Chen et al., 2022; Fang et al., 2023).

Each of these tests and models, however, has its advantages and limitations and it is only able to provide a partial view of the problem; therefore, conducting multiple tests and evaluations in parallel can be an effective methodology in order to achieve the broadest and most complete picture possible. Nonetheless, universally accepted procedures for the evaluation of a soil's clogging potential are still lacking.

To fill this gap, an experimental research project has been underway for several years, systematically testing a large number of natural fine-grained soils. The first results of this research project were initially published in Sebastiani et al. (2024), where the results of mixing and pull-out tests were compared, highlighting strengths and weaknesses, and also finding useful correlations between the results of the two tests and between the test results and the clay fraction.

This paper builds on the initial findings by extending the investigation to soils with higher clay content and higher plasticity. The results presented herein also allow to further test the validity of the previous findings against a larger data set.

Testing is currently continuing on an even larger scale and on a wider range of natural soils. Several conditioning agents are also being tested.

2 MATERIALS AND METHODS

As mentioned above, this study builds on the findings reported by Sebastiani et al. (2024) by extending the experimental research to soils with higher clay content and higher plasticity. Samples S9, S10 and S11 were carefully collected at the tunnel excavation depth at three different jobsites and characterized to determine their intrinsic properties.

2.1 *Soil samples*

Table 1 and Table 2 list the grain size distributions and the Atterberg limits of the soil samples determined according to ASTM D6913, ASTM D4318 and AGI Recommendations. *LL* and *PL* represent respectively the liquid and the plastic limit, *PI* the plasticity index and *A* the activity of the clay.

Along with the samples used in this study, the properties of the samples used by Sebastiani et al. (2024), samples S1 to S8, are reported for convenience.

2.2 *Laboratory tests*

The samples were tested to measure their clogging potential (Hobart mixing test and pull-out test). Prior to laboratory testing, the samples were completely dried, quartered and then brought to the desired water content. The tests methods are briefly described below.

2.2.1 *Hobart mixing test*

The Hobart mortar mixer (Figure 1) for soil conditioning testing, described by Zumsteg and Puzrin (2012), is often used to produce a homogeneous clay-chemical paste.

To quantify the clogging potential of soft clayey mixtures, the weight of soil sticking to the mixing tool after mixture preparation can be weighted; the clogging potential increases as this weight increases.

The stickiness ratio λ, which quantifies the tendency of the soil paste to remain stuck on a mixing tool, is defined as:

$$\lambda = G_{MT}/G_{TOT} \tag{1}$$

where G_{MT} is the weight of soil sticking to the mixing tool and G_{TOT} is the total weight of soil involved in the mixing process.

Table 1. Grain size distribution of the soil samples.

Sample	Clay %	Silt %	Sand %
S9	45	42	13
S10	50	38	12
S11	47	51	2
S1	40	60	0
S2	37	43	20
S3	50	42	8
S4	28	52	20
S5	12	38	50
S6	35	65	0
S7	24	51	25
S8	30	58	12

Table 2. Atterberg limits of the soil samples.

Sample	LL %	PL %	PI %	A
S9	57	17	40	0.88
S10	94	33	60	1.21
S11	62	26	37	0.78
S1	40	20	20	0.50
S2	36	21	15	0.41
S3	65	25	40	0.80
S4	48	24	24	0.86
S5	27	19	8	0.67
S6	46	22	24	0.69
S7	35	20	15	0.63
S8	48	19	29	0.97

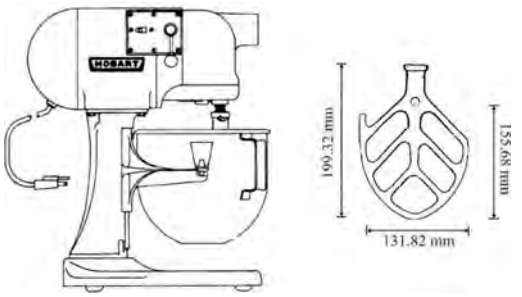

Figure 1. Hobart mixing test equipment.

2.2.2 *Pull-out test*

The pull-out test, in its many variations, is a widely used system for indirectly assessing the clogging potential by measuring the pull-out force registered by a tool first placed in contact with the sample. Different authors, following different approaches, have used this test to measure both the clogging tendency of a soil and the beneficial effects of soil conditioning (Feinendegen et al, 2010; Di Giulio et al., 2018; Khabbazi et al., 2019).

The most common versions of the test are those proposed by Feinendegen et al. (2010), using a conical tool, and by Thewes and Burger (2005), using a flat plate. In this study, the modified version described in Sebastiani et al. (2024) was adopted, essentially applying the same test methods but with a slightly convex plate (Figure 2).

3 RESULTS

In this section, the results of the laboratory tests will be presented and discussed; particular focus will be placed on correlating the results obtained with the water content and I_C value of the soil samples tested.

The following Figures 3, 4 and 5 show the results of the Hobart mixing tests performed on soil samples S9, S10 and S11 at different water contents w (and hence consistency index Ic). The results are interpolated by a Gaussian curve as a function of Ic. The results are well fitted by Gaussian curves for all

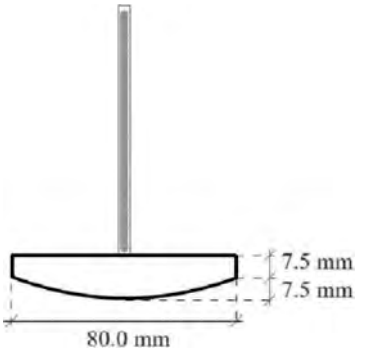

Figure 2. Detail of the pull-out test plate.

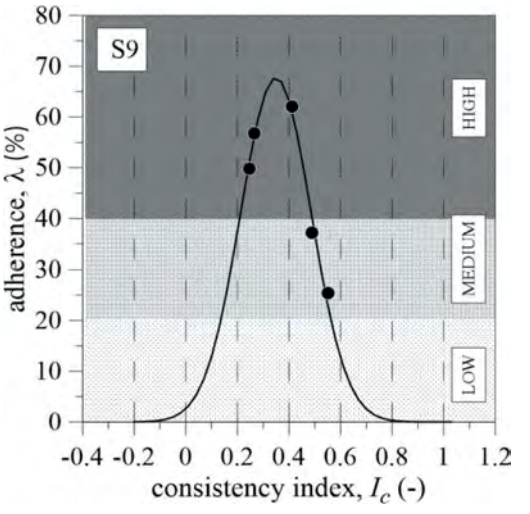

Figure 3. Hobart mixing test results for soil S9.

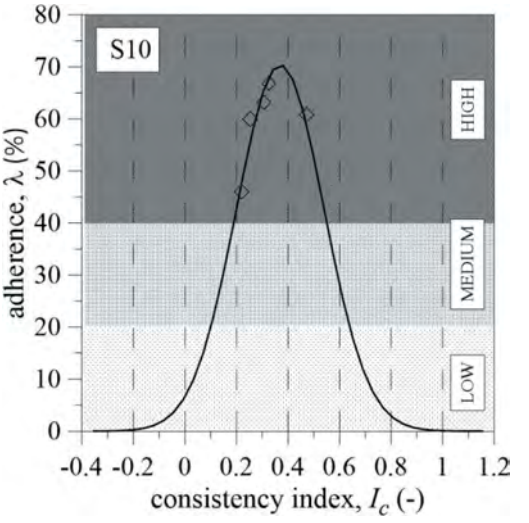

Figure 4. Hobart mixing test results for soil S10.

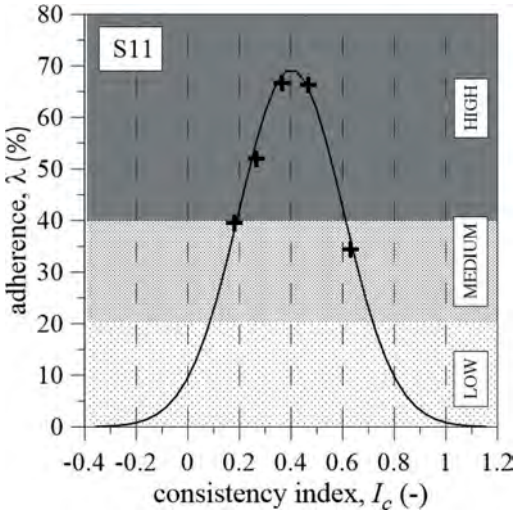

Figure 5. Hobart mixing test results for soil S11.

three soils studied. It should be noted that at high values of I_C there are some difficulties in performing the mixing test, which lead to consider the branch of the curve associated with lower values of *Ic* more reliable (de Oliveira et al. 2019).

Figures 6, 7 and 8 show the results of the pull-out tests carried out on soil samples S9, S10 and S11 at different water contents. Again, the results are well interpolated with a Gaussian curve. It can be noted that these results are substantially in agreement with those of the mixing test in terms of consistency index, with the peak values slightly shifted towards higher values of *Ic*.

Finally, Figures 9 and 10 compare the results of this study with those obtained by Sebastiani et al (2024) in terms of mixing tests and pull-out test results respectively.

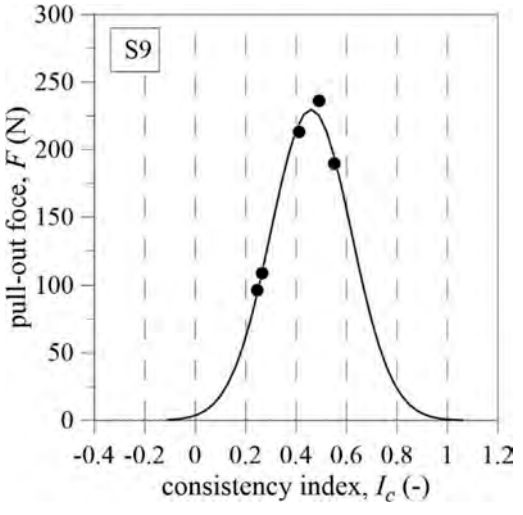

Figure 6. Pull-out test results for soil S9.

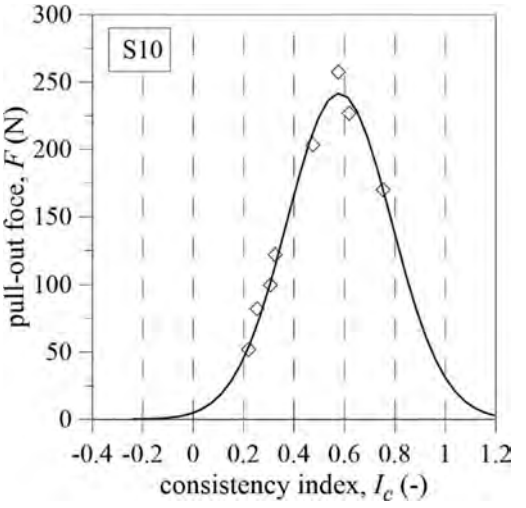

Figure 7. Pull-out test results for soil S10.

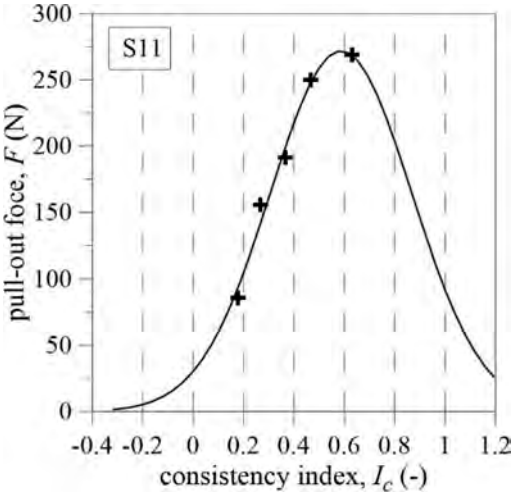

Figure 8. Pull-out test results for soil S11.

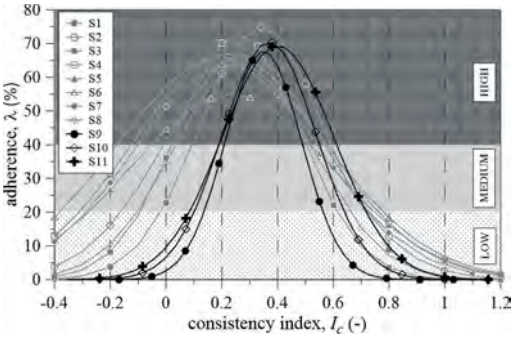

Figure 9. Comparison of the mixing tests results.

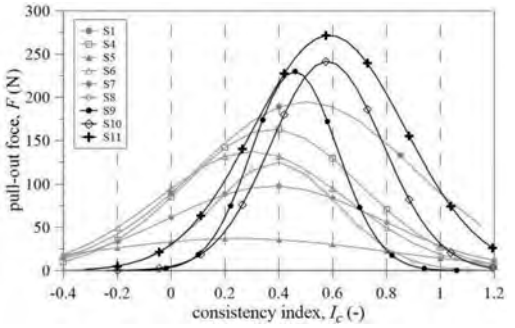

Figure 10. Comparison of the pull-out tests results.

By comparing the results obtained through the mixing tests performed on all the investigated clays, it can be noted that, although the more clayey and plastic soils (i.e. higher *CF* and *PI*) have a slightly shifted peak toward higher consistency indices, there are no remarkable differences in terms of maximum stickiness ratio. Instead, the Gaussian curves obtained through the pull-out tests highlight that as the clay fraction and plasticity increase, the peaks of the curves increase and are slightly shifted toward higher Ic values (lower water content). This results further confirm the effectiveness of the pull-out test in measuring the clogging potential, as it is well known that the clogging risk increases with the clay fraction and the soil plasticity.

4 CORRELATIONS WITH CLAY FRACTION AND BETWEEN TESTS

As said, this study aims to extend the results reported by Sebastiani et al. (2024) to soils with higher clay fraction and plasticity, and also to test the validity of the correlations found in the above study by adding new results to the data set.

The following Figures 11, 12 and 13 show the correlation between the values of peak adherence λ_{pk} and pull-out force F_{pk} estimated through the Gaussian parameters and clay fraction *CF*, overlaid on the interpolation proposed by Sebastiani et al. (2024).

The results show that the correlations remain valid also in light of the new data, accounting for some dispersion of the experimental data. The behaviour shown by the new soils strengthens the experimental bases on which the correlations are based and extend it to fields (i.e. $F_{pk} > 200$ N) that previously could not be reached.

The new pull-out results are in better agreement with the correlations than the mixing tests ones. Pending further investigation, this suggests that the pull-out test is more versatile and more effective in providing a measure of the clogging potential of soils with higher clay content and higher plasticity index.

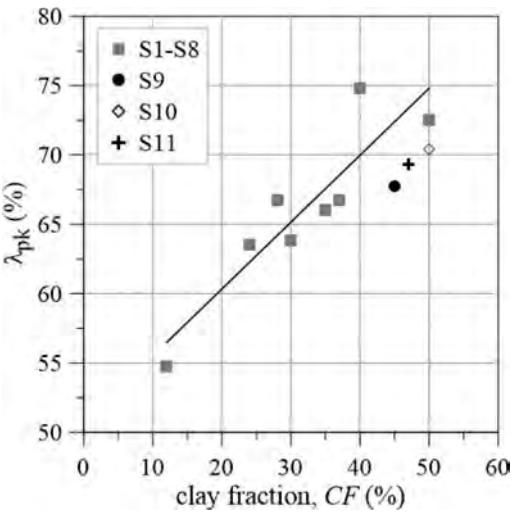

Figure 11. Correlation between estimated mixing peak values and clay fraction.

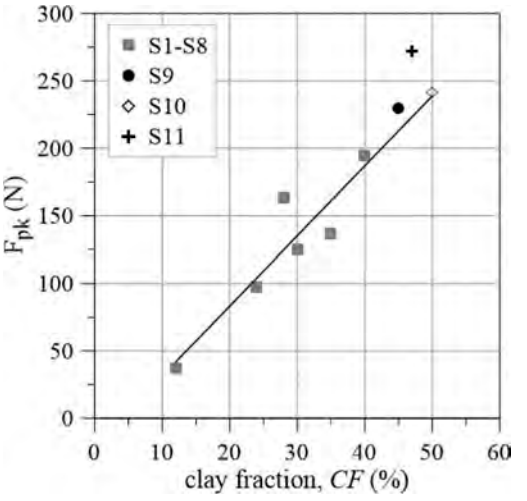

Figure 12. Correlation between estimated pull-out peak values and clay fraction.

5 CONCLUSIONS AND FUTURE DEVELOPMENTS

This paper is part of a larger study focused on the determination of the clogging potential of natural soils through laboratory tests. The research activity carried out, now for several years, has been based on a few basic fundamentals: 1) performing laboratory tests on natural soils from real tunnels and underground works projects; 2) correlating the results of laboratory tests performed to measure the clogging risk to a strong and comprehensive geotechnical characterization and 3) developing laboratory tests in parallel to investigate their limitations and reliability, to compare results and provide useful correlations.

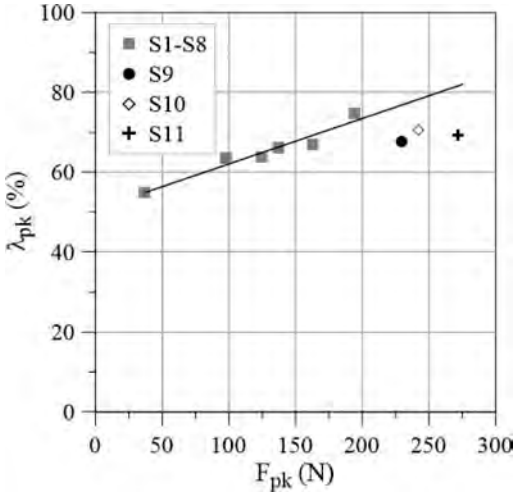

Figure 13. Correlation between estimated mixing and pull-out peak values.

The experimental activity described in this paper aimed to extend the findings of Sebastiani et al. (2024) to soils with higher clay content and plasticity and to test the validity of the proposed correlations in light of the new data.

The new data confirm that:

- gaussian curves well describe the mixing and pull-out results with respect to water content and consistency index;
- the peak of the gaussian curves resulting from the pull-out tests is slightly shifted towards higher values of consistency index than that provided by the mixing tests;
- the pull-out tests shows a greater sensitivity in measuring the clogging potential as its results amplify the differences between various soils.

The results also allowed to:

- the correlation between mixing test results and clay fraction seems to be weaker than that with the pull-out test results;
- extend the validity range of these correlations for F_{pk} values above 200 N;
- find that as the clay fraction of the soil and plasticity increase, the peaks of the curves increase and are slightly shifted toward higher values of consistency index (lower water content)
- observe that the pull-out test is more effective in detecting the increase in clogging potential associated with higher clay content and plasticity index.

ACKNOWLEDGMENTS

The authors would like to thank Dr. Andrea Di Biase for his commitment and contribution in carrying out the experimental laboratory activities presented in this paper.

REFERENCES

Alberto-Hernandez, Y., Kang, C., Yi, Y., & Bayat, A., 2018. Mechanical properties of clayey soil relevant for clogging potential. International Journal of Geotechnical Engineering, 12(6), pp. 529–536.

Associazione Geotecnica Italiana, 1994. Raccomandazioni sulle prove geotecniche di laboratorio.

ASTM D4318, 2017. Standard Test Methods for Liquid Limit, Plastic Limit, and Plasticity Index of Soils. ASTM International, West Conshohocken, PA, USA.

ASTM D6913, 2014. Standard test methods for particle-size distribution (Gradation) of soils using sieve analysis. ASTM International, West Conshohocken, PA, USA.

Avunduk, E., & Copur, H., 2019. Effect of clogging on EPB TBM performance: a case study in Akfirat waste water tunnel, Turkey. Geotechnical and Geological Engineering, 37(6), pp. 4789–4801.

Baghali, H., Chakeri, H., Sharghi, M., & Dias, D., 2020. Effect of Soil Moisture and Granulometry on Soil Conditioning for EPB-TBM Tunneling: Case Study. Journal of Testing and Evaluation, 49(1).

Chen, Z., Bezuijen, A., Fang, Y., Wang, K., & Deng, R. (2022). Experimental study and field validation on soil clogging of EPB shields in completely decomposed granite. Tunnelling and Underground Space Technology, 120, 104300.

de Oliveira, D. G., Thewes, M., & Diederichs, M. S., 2019. Clogging and flow assessment of cohesive soils for EPB tunnelling: Proposed laboratory tests for soil characterisation. Tunnelling and Underground Space Technology, 94, 103110.

Di Giulio, A., Sebastiani, D., & Miliziano, S., 2018. Effect of Chemicals in Clogging Risk Reduction for TBM-EPB Application. In Proceedings of the World Tunnel Congress 2018-The Role of Underground Space in Building Future Sustainable Cities.

Fang, Y., Chen, Z., Song, T., Wang, K., & Zhou, K. 2023. New clogging potential assessment method for conditioned soil based on modified pullout and direct shear tests. Acta Geotechnica, 18(6), 3307–3322.

Feinendegen, M., Ziegler, M., Spagnoli, G., Fernández-Steeger, T. & Stanjek, H., 2010. A new laboratory test to evaluate the problem of clogging in mechanical tunnel driving with EPB-shields. Rock Mechanics in Civil and Environmental Engineering, pp. 429–432.

Feinendegen, M., Ziegler, M., Spagnoli, G., & Fernández-Steeger, T., 2011. Evaluation of the clogging potential in mechanical tunnel driving with EPB-shields. Proceedings of the 15th ECSMGE, Athens, IOS Press.

Hollmann, F. S., & Thewes, M., 2013. Assessment method for clay clogging and disintegration of fines in mechanised tunnelling. Tunnelling and Underground Space Technology, 37, pp. 96–106.

Khabbazi, A., Ghafoori, M., & Cheshomi, A., 2019. Experimental and laboratory assessment of clogging potential based on adhesion. Bulletin of Engineering Geology and the Environment, 78(1), pp. 605–616.

Mori, L., Mooney, M., & Cha, M., 2018. Characterizing the influence of stress on foam conditioned sand for EPB tunneling. Tunnelling and Underground Space Technology, 71, pp. 454–465.

Pirone, M., Sebastiani, D., Carriero, F., Sorge, R., Miliziano, S. & Foti, V., 2019. The management of the soil conditioning process for the excavation of the Rome Metro C line. Proceedings of the World Tunnel Congress 2019 - Tunnels and Underground Cities:

Engineering and Innovation meet Archaeology, Architecture and Art. Naples, Italy.
Sebastiani, D., Di Giulio, A. & Miliziano, S., 2017. La gestione del condizionamento del terreno nello scavo meccanizzato di una galleria con TBM-EPB: risultati di una attività sperimentale. Incontro annuale dei Ricercatori di Geotecnica. Matera, Italia.
Sebastiani, D., Vilardi, G., Bavasso, I., Di Palma, L. & Miliziano, S., 2019a. Classification of foam and foaming products for EPB mechanized tunnelling based on half-life time. Tunnelling and Underground Space Technology, 92, 103044.
Sebastiani, D., de Lillis, A., Di Giulio, A. & Miliziano, S., 2019b, July. Effects of Thickeners Polymers Used in Tunnelling on the Physical and Mechanical Properties of Fine-Grained Soils. In National Conference of the Researchers of Geotechnical Engineering Springer, Cham. pp. 678–685.
Sebastiani, D., Miliziano, S., Vilardi, G., Bavasso, I., Di Palma, L. & Di Giulio, A. 2019c. Chemical interaction between fine-grained soil and foaming agents in tunnelling with TBM-EPB", 17th European Conference on Soil Mechanics and Geotechnical Engineering, ECSMGE 2019 - Proceedings.
Sebastiani, D., de Lillis, A., & Miliziano, S., 2024. A comparison of laboratory tests for the evaluation of clogging risk in mechanized tunnelling. Acta Geotechnica. Accepted for publication.
Spagnoli, G., Feinendegen, M., & Seidl, W., 2019. The impact of mineralogy and chemical conditioning on the mechanical and adhesive properties of clays. In XVII European Conference on Soil Mechanics and Geotechnical Engineering 2019. Geotechnical Engineering Foundation of the Future.
Thewes M., 1999. Adhäsion von Tonböden beim Tunnelvortrieb mit Flüssigkeitsschilden. Berichte aus Bodenmechanik und Grundbau der Bergischen University Wuppertal, (vol. 21) Wuppertal.
Thewes, M., & Burger, W., 2004. Clogging risks for TBM drives in clay. Tunnels &Tunnelling International, pp. 28–31.
Thewes M, & Burger W., 2005. Clogging of TBM drives in clay-identification and mitigation of risks. In: Proceedings of world tunnel congress, Istanbul, pp. 737–742.
Zumsteg, R. & Puzrin, A.M., 2012. Stickiness and adhesion of conditioned clay pastes. Tunnelling and Underground Space Technology, 31, pp.86–96.
Zumsteg, R., Plötze, M. & Puzrin, A., 2013. Reduction of the clogging potential of clays: new chemical applications and novel quantification approaches. Géotechnique, 63(4), pp. 276–286.
Zumsteg, R., Puzrin, A.M. & Anagnostou, G., 2016. Effects of slurry on stickiness of excavated clays and clogging of equipment in fluid supported excavations. Tunnelling and Underground Space Technology, 58, pp. 197–208.

Tunnelling for a Better Life – Yan, Celestino, Thewes & Eberhardt (Eds)
© 2024 The Author(s), ISBN 978-1-032-80042-4
Open Access: www.taylorfrancis.com, CC BY-NC-ND 4.0 license

Information entropy based Robust Sensor Placement (RSP) method for wireless sensing of shield tunnel deformation

Jingkang Shi*
College of Civil Engineering, Fuzhou University, Fuzhou, China

Hongwei Huang
Department of Geotechnical Engineering, Tongji University, Shanghai, China

Zhenchang Guan
College of Civil Engineering, Fuzhou University, Fuzhou, China

ABSTRACT: Structural health monitoring is crucial for ensuring tunnel safety during construction and operational stage. Wireless sensor network (WSN) based monitoring has the advantages of real time and high frequency in data collecting, wireless transferring of data and ease of installation. In real practice, the placement of wireless sensors is needed to be optimized due to the limitation of monitoring cost. Furthermore, shield tunnel linings are subjected to random external loads in operational stage. A robust sensor placement (RSP) scheme should be able to capture the variation of random loads and place the sensors at structural sensitive locations. In order to design a robust sensor placement scheme, this paper proposes an information entropy based optimization method considering the randomness of external loads acting on tunnel linings. The proposed method mainly contains four parts: mechanical model construction, load uncertainty modelling, information entropy calculation and optimization of sensor placement scheme. A case study of Mawan cross-sea passage tunnel is conducted to show the effectiveness of the proposed method. For the large diameter shield tunnel with ten segments, the most sensitive location to external random loads is founded to be 138° (segment B2).

Keywords: Wireless sensing, optimal sensor placement, information entropy; shield tunnel, random analysis

1 INTRODUCTION

Tunnel cross-section deformation is a key factor for evaluating tunnel structural performance (Loganathan and Poulos, 1998; Mair, 2008; Pinto and Whittle, 2014). Therefore, it is crucial to monitor the tunnel cross-section deformation during the construction and operation stages. For shield tunnels assembling with precast segments, the inclination deformation of each segment makes a great influence to tunnel horizontal convergence and joint opening (Wang et al., 2020a). Traditional tunnel structural health monitoring focused on the horizontal convergence and often neglected the segment inclination. Tunnel convergence is an overall indicator and cannot reflect the unsymmetric deformation of lining (Wei et al., 2023).

Wireless sensor network (WSN), having the advantages of easy deployment, reliability, flexibility, real time monitoring, is increasingly used in structural health monitoring (SHM) (Lynch, 2007; Abdulkarem et al., 2020). However, due to the limited cost, wireless sensors are unfeasible to densely deploy in a large scale of infrastructure. Thus, the optimization of sensor deployment scheme is essential to well capture the structural performance during operational stage (Yi et al., 2011). As seen from Figure 1, the operational shield tunnel lining was subjected to adjacent pit excavation (Huang et al., 2019). Wireless tilt sensors were installed at different segments, giving completely disparate monitoring data. The sensors on the right side monitored the segment deformation variation caused by the pit excavation, while the sensor on the bottom-left side could not capture such variation. In this case, the sensor performances were largely dependent on the location they placed. In reality, the pit excavation could not be anticipated before the sensor placement. To systematically evaluate a sensor placement scheme, the uncertain external loads should be carefully modelled. Additionally, there is a need for quantitative standard for assessing sensor performance.

*Corresponding author: jkshi@fzu.edu.cn

DOI: 10.1201/9781003495505-369

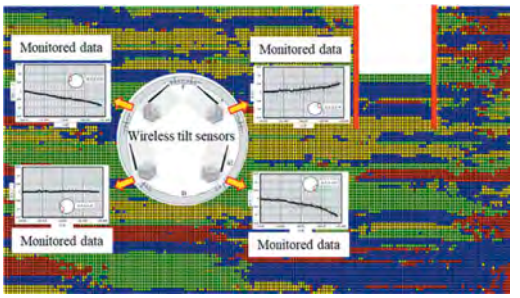

Figure 1. The necessity of RSP for wireless sensing.

In this study, the authors proposed the concept of robust sensor placement scheme (RSPS) and the framework of obtaining RSPS. The RSPS of wireless tilt sensor deployed on shield tunnel lining was took as an example to apply the proposed framework. Information entropy was adopted to evaluate the performance of each sensor placement scheme.

2 THE CONCEPT AND FRAMEWORK OF RSPS

2.1 *The concept of RSPS*

The concept of RSPS was originated from the uncertainty of structural performance which was caused by the uncertainty of external loads. As illustrated in Figure 2, the indeterministic external loads acted on engineering structures in spatial-temporal domain. Thus, the structural responses presented with uncertainty and could be modelled using probability distributions. For point directly measured sensing technique, sensors could only monitor the structural response where they were placed. The sensor measurements varied due to the different placement location. Given the same external loads, the sensor measurements at "Location 1" variated less than the sensor measurements at "Location 2". In the other words, the sensor measurements at "Location 2" were more sensitive to the variation of external loads. "Location 2" gave more information about the change of external loads according to information theory.

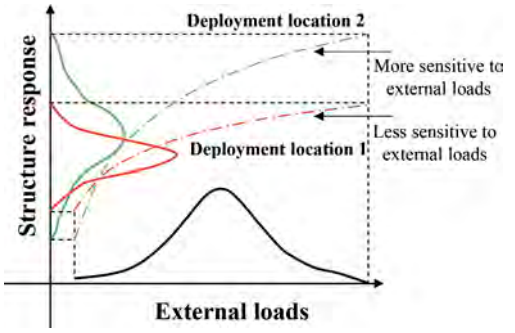

Figure 2. The comparison between different sensor deployment schemes.

More information was expected to be obtained by the installed sensor. The RSPS was the placement scheme which maximized the obtained information confronted with load uncertainty. "Robust" here meant the sensor placement scheme could well capture the variation of external loads. By the adopting RSPS, the overall uncertainty of structural performance was minimized given the limited number of deployed sensors.

2.2 *The framework of obtaining RSPS*

Based on the concept of RSPS, the framework of obtaining the RSPS could be designed. The whole framework consisted of five steps as shown in Figure 3.

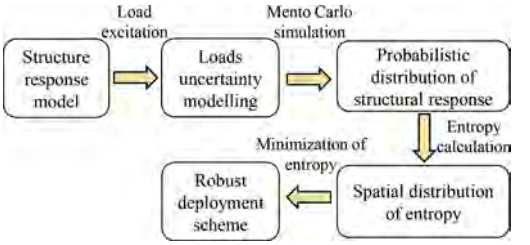

Figure 3. Framework for the determination of RSPS.

Step 1: Established the mechanical model of the structure being monitored. The model must be able to capture the main mechanical properties of the structure and predict the desired structural response. The mechanical model was often an analytical formula or a finite element, finite difference numerical model. The structure itself, together with the different kinds and distributions of loads acting on it, were all included in the mechanical model. To optimize sensor placement scheme, a plausible mechanical model must be established.

Step 2: Modelled the uncertainty of external loads acting on the structure. The load types were usually prescribed. The load level was commonly modelled using one-dimensional or multi-dimensional probabilistic distributions. Random field theory was adopted if spatial variety of load was considered.

Step 3: Using external loads and mechanical models, predicted the desired structural performance indicators, such as internal force and deformation. It was important to sample numerous times for the specified external load distribution in order to acquire the probability distribution of structural response, and then to run a Monte Carlo simulation to do so.

Step 4: Determined the spatial distribution of information entropy by computing the information entropy at various sensor installation places based on the probability distribution of structural response.

Step 5: Placed the monitoring sensors at the location where the structural information entropy was largest so that the structure's overall information entropy dropped most quickly.

3 RSPS OF LARGE DIAMETER SHIELD TUNNELS

3.1 *Mechanical model of large shield tunnels*

This section takes the lining structure of Mawan cross sea passage tunnel as an example to show the effectiveness of the proposed framework. Figure 4 shows the lining structure for Mawan cross sea passage. This shield tunnel has an outer diameter of 15m. Each ring is composed of 10 segments which has a thickness of 0.65m and a ring width of 2m. Among the 10 segments, there are 1 wedge-shaped block with an angle of 12.857 °, 2 adjacent blocks with an angle of 38.571 °, and 7 standard blocks with an angle of 38.571 °. The longitudinal joint is connected using one diagonal bolt. In the longitudinal direction, staggered joint assembly is used to improve the overall stiffness, and 28 longitudinal diagonal bolts are connected between adjacent rings.

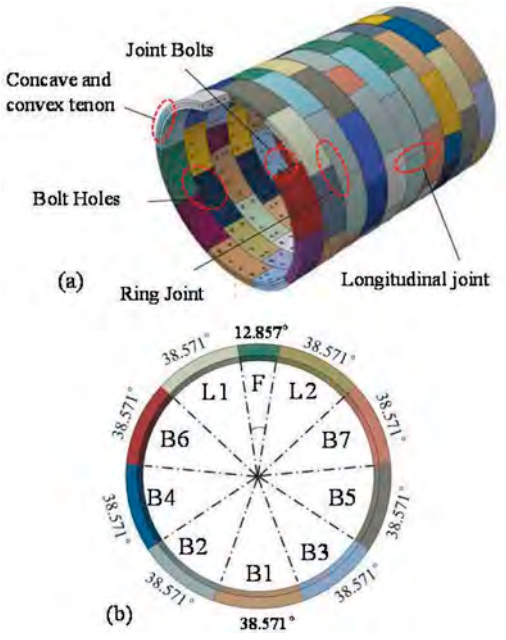

Figure 4. Lining geometry of large diameter shield tunnel.

For the above large-diameter shield tunnel lining structure, previous research has proposed many mechanical models, such as analytical solutions of uniform continuous ring, jointed continuous ring, beam spring model, and shell spring model, as well as refined three-dimensional finite element model. Among the numerous mechanical models of shield tunneling, the jointed continuous ring model proposed by Lee and Ge (2001) is widely used, as shown in Figure 5.

This model simplified the longitudinal joint as an elastic hinge with bending stiffness, and the entire ring structure was equivalent as a continuous jointed ring. Lee and Ge (2001) proposed the load

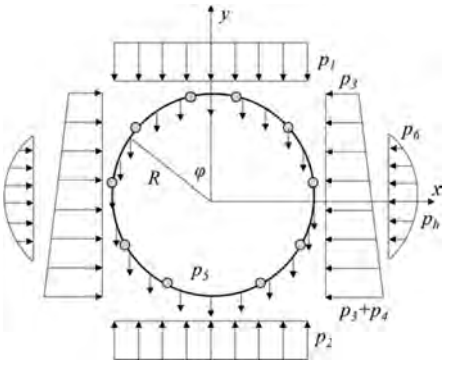

Figure 5. Structural model and loads pattern of the shield tunnel lining.

distribution on shallow shield tunnels during operation based on on-site measured data, as shown in Figure 5. Among them, p_1 is the vertical earth pressure at the arch top, p_2 is the reaction force at the arch bottom, p_3 is the lateral earth pressure at the arch top, p_4 is the difference between the lateral earth pressure at the arch bottom and arch top, p_5 is the self weight of the tunnel lining, and p_6 is the ground resistance. In such a load distribution situation, Lee et al. (2001) used the force method to solve the analytical formula for the internal force and deformation of shield tunnels. Nevertheless, this analytical solution faces difficulties in determining the bending stiffness of joints. In fact, the bending stiffness of a joint varies with the level of internal forces.

To get over the mentioned issue, this paper used the modified analytical solution suggested by Wang et al. (2020b). This modified solution included an analytical model for the joint bending stiffness that created a function of joint stiffness based on the joint's geometrical dimensions, the material properties of the concrete and bolts, the axial force, and the joint's bending moment. The modified solution automatically solved the stiffness at each joint position through iteration, requiring no prior input of joint stiffness.

3.2 *Load uncertainty modelling*

Regarding the mechanical model of large-diameter shield tunnels discussed earlier, only the lateral pressure coefficient K_0 and the ground resistance coefficient K_s required to be taken into account because the burial depth H was typically a constant over the cross-section. For the sake of simplicity, this study made the assumption that the soil in the cross-section was homogeneous and that the uncertainty of K_0 and K_s could be approximated using random variables.

K_0 and K_s were assumed to be two-dimensional normal distributions. The mean and covariance matrix totally described the joint probability distribution of K_0 and K_s. The mean and coefficient of variation (CoV) of the marginal distribution of K_0 is

μ_K_0 and cov_K_0, respectively. The mean and CoV of marginal distribution of K_s is μ_K_s and cov_K_s, respectively. The correlation coefficient between the two random variables is ρ. So the mean vector of the joint probability distribution of K_0 and K_s is μ=(μ_K_0, μ_K_s), and covariance matrix Σ is shown in Equation. (1) as follows,

$$\sum=\begin{pmatrix}(\mu_K_0\times \mathrm{cov}_K_0)^2 & \rho\times\mu_K_0\times\mu_K_S\times\mathrm{cov}_K_0\times\mathrm{cov}_K_S\\ \rho\times\mu_K_0\times\mu_K_S\times\mathrm{cov}_K_0\times\mathrm{cov}_K_S & (\mu_K_S\times\mathrm{cov}_K_S)^2\end{pmatrix} \quad (1)$$

Set ρ=0.5, μ_K_0=0.5, cov_K_0=0.2, μ_K_s =0.5×10^{4}kN/m^3, the joint probability distributions were shown in Figure 6 considering three levels of cov_K_s=0.5, 0.3 and 0.1. The joint probability density of K_0 and K_s tended to be concentrated with the decrease of cov_K_s. 500 sets of K_0 and K_s values were acquired by sampling from each joint distribution.

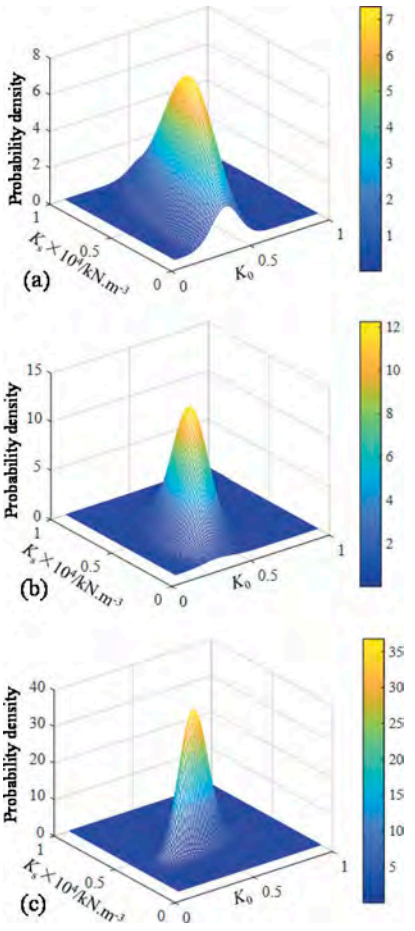

Figure 6. Loads uncertainty modelling using two-dimensional Gaussian distribution: (a) cov_K_s=0.5; (b) cov_K_s=0.3; (c) cov_K_s=0.1.

3.3 *Probability distribution of tunnel deformation*

After obtaining 500 samples of input parameters, Monte Carlo simulation was conducted to acquire the probability distribution of inclination deformation. Took the input parameters H=20m, K_s =5000kN/m^3, μ_K_0=0.6 and cov_K_0=0.3 as an example. The angular coordinates φ characterized the position along the tunnel ring. Tunnel crown tunnel was set as 0° and tunnel invert was set as 180°. The results of six typical positions, namely, φ=10°, 40°, 70°, 100°, 140°, 170° were selected and shown in Figure 7. The probability distribution of inclination deformation at each position could be well fitted with a normal distribution.

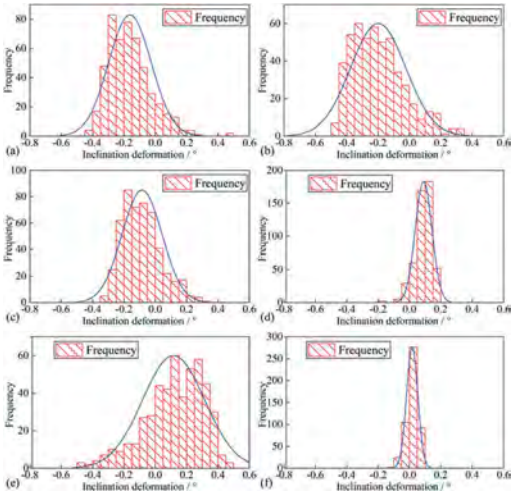

Figure 7. Probability distribution of inclination deformation at different locations along tunnel springline: (a) φ=10°; (b) φ=40°; (c) φ=70°; (d) φ=100°; (e) φ=140°; (f) φ=170°.

As can be seen from the probability distribution in Figure 7, the probability distribution of inclination deformation at at φ=10°, 40°, and 70° was identical, and the probability distribution of inclination deformation at φ=100°, 140° and 170° was identical as well. This kind of similarity for probability distribution was caused by the deformation mode of large-diameter shield tunnels. Shield tunnel cross-section deformation was predominated by segment rotation, which resulting in a "lying duck egg" or "standing duck egg" deformation mode. The deformation probability distribution was identical if the evaluated points were located at the same segment.

3.4 *Determination of RSPS using information entropy*

Based on the deformation probability distribution, it is possible to determine the information entropy at different locations along the lining. Deformation uncertainty is measured by information entropy. The

information entropy of the certain point's inclination deformation increases with the increasing of uncertainty. Deploying monitoring sensors is therefore more essential in order to eliminate uncertainty. The information entropy *En* can be calculated using the following formulas for a particular probability distribution (Shannon, 1948).

$$En(X) = -\sum_{i=1}^{n} p(x_i)\log p(x_i) \qquad (2)$$

Where, *En* is the information entropy; $p(x_i)$ is the probability of deformation range $[x_i\text{-}\Delta x/2,\ x_i\text{+}\Delta x/2]$; n is the number of discrete x_i.

In fact, inclination deformation x_i is a continuous random variable. Integration is needed to accurately calculate the information entropy. This study replaced the accumulation of probability density in a small range $[x_i\text{-}\Delta x/2,\ x_i\text{+}\Delta x/2]$ by the probability $p(x_i)$ of equivalent discrete variable $[x_i\text{-}\Delta x/2,\ x_i\text{+}\Delta x/2]$. Δx is the very small division of deformation range acquired from Monte-Carlo simulation. The information entropy for inclination deformation along tunnel springline was obtained and shown in Figure 8.

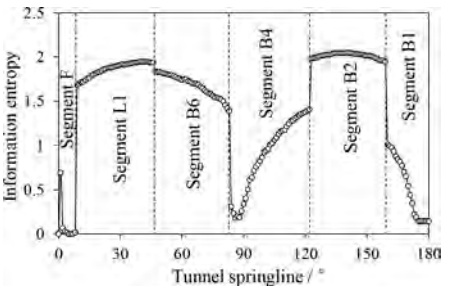

Figure 8. Inclination entropy distributed along the tunnel springline.

As illustrated in Figure 8, block B2 is where the information entropy of the inclination deformation is highest, followed by block L1 and block B6. These three segments have relatively high information entropies, and variance within the same segment is generally modest. Segment B1 and B4 have various information entropies inside the same segment. Therefore, in the case of limited monitoring expenses, priority should be given to installing tilt sensors on segment B2, following with the order of priority being B2, L1, B6, B4, B1, and F blocks. More specifically, the highest entropy within the block B2 was φ=138°.

3.5 *Influence of load uncertainty modelling*

The influence of external load uncertainty modelling on information entropy and RSPS was discussed in this section. As two-dimensional normal distribution was used to model the main uncertainty source K_0 and K_s, the influence of CoV and ρ were investigated. The influence of K_s's CoV was evaluated in Figure 9.

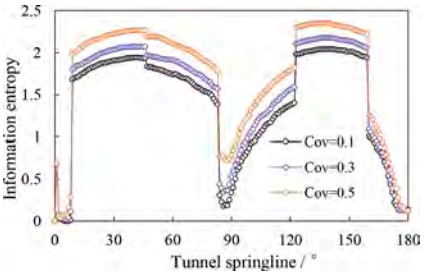

Figure 9. Influence of K_s's CoV on information entropy.

With the increase of K_s's CoV, the information entropy of each point increased, but the overall distribution pattern remained unchanged. The order of information entropy between the blocks was still B2, L1, B6, B4, B1 and F. Similarly, the effect of correlation coefficient ρ between K_0 and K_s on information entropy was investigated in Figure 10.

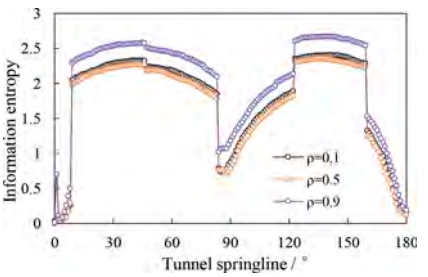

Figure 10. Influence of correlation coefficient ρ on information entropy.

When the correlation coefficient ρ increasing from 0.1 to 0.5, the information entropy change was not significant, but when ρ increasing from 0.5 to 0.9, the information entropy of each point significantly increases. This indicated that reasonable modeling of external loads had a significant impact on the uncertainty analysis of segment inclination deformation. If there were multiple external loads, the correlation of various loads must be reasonably considered. The above analysis indicated that the stronger the correlation between different loads were, the greater the uncertainty of deformation would be. However, the variation of ρ still had no impact on the distribution pattern of information entropy along the tunnel springline.

4 CONCLUSIONS

In real SHM practice, the placement of wireless sensors is needed to be optimized due to the limitation of monitoring cost. The concept of robust sensor placement scheme (RSPS) was proposed in this paper to capture the variation of random loads and place the sensors at structural sensitive locations. In

order to design a RSPS, this study proposed a practical framework. The proposed framework included three steps: the first step was constructing appropriate mechanical models of shield tunnels; the second step was random modelling of external loads acting on shield tunnel lining; the third step was calculating the information entropy based on probabilistic distribution of tunnel deformation. The whole study was concluded as follows.

(1) For the large diameter shield tunnel with ten segments, the most sensitive location to external random loads was founded to be 138° (segment B2). The sensor placement priority was decided according to the information entropy ranking among different segments.
(2) Load uncertainty modelling including the CoV and correlation coefficient ρ had a significant influence on information entropy, however, they had no distinct effect on the information entropy ranking among segments.

ACKNOWLEDGMENTS

This study was funded by the Natural Science Foundation of China (No. 52278399) and the Natural Science Foundation of Fujian Province (No. 2021J01599).

REFERENCES

Abdulkarem, M., Samsudin K., Rokhani F. Z. et al, 2020. Wireless sensor network for structural health monitoring: A contemporary review of technologies, challenges, and future direction. Struct. Health Monit. 19(3), 693–735.

Huang, H. W., Xie X., Zhang D. M., et al, 2019. Multi-sensor data fusion based assessment on shield tunnel safety. Smart. Struct. Syst. 24(6), 693–707.

Lee, K. M. and Ge X. W., 2001. The equivalence of a jointed shield-driven tunnel lining to a continuous ring structure. Can. Geotech. J. 38(3), 461–483.

Lee, K. M., Hou X. Y., Ge X. W. et al., 2001. An analytical solution for a jointed shield-driven tunnel lining. Int. J. Numer. Anal. Methods Geomech. 25(4), 365–390.

Loganathan, N. and Poulos H. G., 1998. Analytical Prediction for Tunneling-Induced Ground Movements in Clays. J. Geotech. Geoenviron. Eng. 124(9), 846–856.

Lynch, J. P., 2007. An overview of wireless structural health monitoring for civil structures. Philos. Trans. R. Soc. A-Math. Phys. Eng. Sci. 365(1851), 345–372.

Mair, R. J., 2008. Tunnelling and geotechnics: new horizons. Géotechnique 58(9), 695–736.

Pinto, F. and Whittle A. J., 2014. Ground Movements due to Shallow Tunnels in Soft Ground. I: Analytical Solutions. J. Geotech. Geoenviron. Eng. 140(4), 17.

Shannon, C. E., 1948. A mathematical theory of communication. The Bell system technical journal. 27 (3), 379–423.

Wang, F., Shi J. K., Huang H. W., et al, 2020a. A horizontal convergence monitoring method based on wireless tilt sensors for shield tunnels with straight joints. Struct. Infrastruct. Eng. 17, (9), 1194–1209.

Wang, F., Shi J., Huang H., et al., 2020b. Modified analytical solution of shield tunnel lining considering nonlinear bending stiffness of longitudinal joint. Tunn. Undergr. Space Technol. 106, 103625.

Wei, G., Feng F., Hu C., et al, 2023. Mechanical performances of shield tunnel segments under asymmetric unloading induced by pit excavation. J. Rock Mech. Geotech. Eng. 15(6), 1547–1564.

Yi, T. H., Li, H. N., and Gu, M., 2011. Optimal sensor placement for structural health monitoring based on multiple optimization strategies. The Structural Design of Tall and Special Buildings. 20, (7), 881–900.

Tunnelling for a Better Life – Yan, Celestino, Thewes & Eberhardt (Eds)
© 2024 The Author(s), ISBN 978-1-032-80042-4
Open Access: www.taylorfrancis.com, CC BY-NC-ND 4.0 license

Design and key features of shaft and tunnel excavation monitoring system implemented in Singapore's Deep Tunnel Sewerage System Phase 2 Project

Aung Ko Ko Soe*, Lai Lynn Woo & Kyi Khin
PUB, Singapore's National Water Agency, Singapore

Poh Chuan Koh
BIENNIES + AECOM JV, Singapore

Angus Maxwell & Elpidio Valdez Jr
Maxwell Geosystems Pte Ltd, Singapore

ABSTRACT: Shaft and Tunnel Excavation Monitoring System (STEMS) developed on MissionOS® is being implemented in Singapore's Deep Tunnel Sewerage System Phase 2 (DTSS2) project to support the construction of 50 km of bored tunnel sewer, another 50 km of link sewer pipe laying, and associated deep shafts, manholes, hydraulic structures, etc. The STEMS is designed to provide centralised data management and integration of various construction and tunnelling data across the project to ensure the adequate level of geotechnical control is achieved on various construction activities. The system is capable of linking up with multiple data sources and devised to deliver quality engineering data with common analytics and reporting capability for risk identification and to assist in decision-making process. Engineering geological data, geotechnical instrumentation data, excavation data, Tunnel Boring Machines (TBM) operation and pipe jacking machine data, construction progress, design information and other relevant data across the projects are taken into the system for processing and integrated into various user definable formats to facilitate quick review, combined analysis and interpretation. The web-based and integrated nature of this centralised processed data management system also has real-time TBM monitoring capability and automatic SMS alerting features. This paper describes the STEMS and highlights the technical capabilities of the system with emphasis on geotechnical control for deep excavation and TBM works.

Keywords: DTSS2, STEMS, Data Management System, TBM, risk identification

1 INTRODUCTION

Since Tunnel Boring Machines (TBM) are more and more used to construct tunnels in challenging environments, such as built-up areas, the predictive risk analysis becomes ever more important (Festa at al. 2012). Recognising the advent of cloud-computing power and applicability of data management systems in predictive risk analysis, Singapore's National Water Agency, PUB implements Shaft and Tunnel Excavation Monitoring System (STEMS) in Deep Tunnel Sewerage System Phase 2 (DTSS2) Project as a centralised integrated data management system for processing, integration and delivery of a large volume of diverse construction and engineering data. The DTSS2 conveyance system has 100 km of deep tunnels and link sewers, of which 50 km is constructed by 19 TBMs via 5 Design & Build contracts. Another 50 km of link sewer pipe laying work being executed by micro TBM and pipe jacking methods will be delivered by 12 Build-Only contracts (Figure 1). Several deep shafts and manhole excavations are also required for construction of hydraulic structures and to launch and receive TBMs.

The DTSS2 tunnel alignments run largely under major expressway corridors at a depth between 35 to 55 m. They are bounded by transportation infrastructures, various buildings, underground structures, and subterranean services. It is known that excavation and tunnelling processes inevitably cause disturbance to surrounding ground and further lead to ground settlement and can even induce severe hazards to structures and services (Yin et al. 2017, Wang et al. 2019, Yin et al. 2020, Zhang et al.

*Corresponding author: aung_ko_ko_soe@pub.gov.sg

DOI: 10.1201/9781003495505-370

Figure 1. DTSS Phase 2 Project Layout.

2021). Therefore, a comprehensive and robust monitoring regime is vital to identify and control the potential risks to ensure the performance and integrity of structures and services in excavation/tunnelling influence zone are not affected.

The TBMs used in the DTSS2 project are heavily instrumented for efficient operation and better control to minimise the risk of over-excavation. Likewise, extensive arrays and several clusters of geotechnical instruments are installed along the tunnelling and pipe jacking corridors for monitoring. As the data acquisition and monitoring are a time-based continuous process, a robust data management system is required for processing and integration of a large volume of captured data, and timely delivery to end-users with appropriate analysis tools for interpretation and to assist in risk identification and decision-making process. All relevant data such as geological data, instrumentation monitoring data, TBM data, construction and excavation data are taken into STEMS's centralised data environment. Therefore, more thorough and comprehensive analysis can be carried out with all vital construction information including those which would not be readily available in conventional systems or hidden in the diverse field data.

2 BACKGROUND

STEMS is developed as a web-based integrated data management system on MissionOS® platform which is designed to work with diverse engineering and construction data. This system is neither a desktop application nor a ready-made software. It is, in fact, a bespoke software and configured based on DTSS2 contract specifications and requirements. This system runs on back-end server and can be assessed by using any popular web browser through internet. STEMS is different from conventional instrumentation monitoring systems or TBM monitoring systems as it also functions as a coordinated and integrated data management platform which bring together various construction data and transform them into useful engineering information. It captures various data directly from their respective sources and process them in a way that everything can be combined and viewed over common parameters such as time series, chainages, etc., in a single common platform (Figure 2).

Nowadays, the availability of megabit-speed internet protocol on large excavation and tunnelling projects in urban environment allows STEMS to interface seamlessly with various data sources. Real-time automatic data are processed and published in real time and notification/alert messages are triggered automatically when pre-set values are breached. STEMS is equipped with tools and functions that are needed for efficient monitoring and analysis. It has various modules covering the key aspects of geotechnical building works such as instrumentation monitoring & data analysis, construction progress monitoring, data visualisation, reporting, TBM monitoring, pipe jacking machine monitoring and quality control plus documentation. Various reports in pre-designed format can also be prepared and generated with readily available information in the system. Other relevant information or documents can also be uploaded and archived systematically for instant access.

Figure 2. Schematic of STEMS configuration.

3 NETWORK STRUCTURE

STEMS is built using standard web scripting languages on a LAMP (Linux, Apache, MySQL, PhP) architecture for server and client-side processing. The architecture is designed as a component-based scalable system allowing a high degree of expandability with flexibility for rapid development without the need for hard coding. It utilises the Amazon Web Service (AWS) server to provide scalable architecture to manage increasing data volume and processing requirements without interruption. For security, data is archived using rolling daily, weekly, and monthly snapshots and can be restored in less than 2 hours. Moreover, a separate local server is installed, and data is mirrored daily.

As shown in Figure 3, STEMS's structure has three layers – underground layer, site layer and web layer. The underground layer constitutes the data from shaft excavations and TBMs. The site layer represents the instrumentation data, drawings, reports, records, and other construction data. The

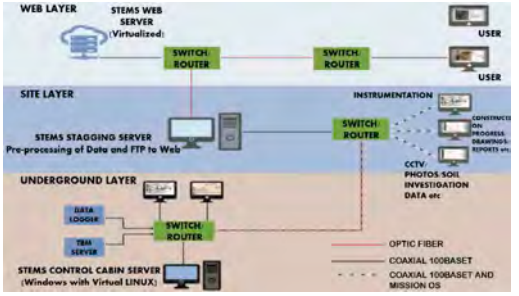

Figure 3. STEMS network structure.

web layer only has STEMS server or cloud server. In that web layer, all data from underground and site layers are processed, stored, and retrieved upon request. Therefore, the web layer is the key component in the structure and subject to strict exploitation, quality control and operational performance.

4 KEY FEATURES

4.1 *Portal*

The main interface in STEMS is the map/drawing window where different types of georeferenced maps/ drawings can be configured to display as a background in it. Aerial images, geological maps, street maps, site plans, combined services plans, instrumentation plans, soil profiles, cross sections, TBM drawings, etc., can be called to display in the map window (Figure 4 & 5). The portal is furnished with basic tools such as zoom controls, digitizer and distance measurement tools, map selection tabs, legend control, drop-pin button and element selection menu.

Figure 4. Main portal with different background maps.

All elements displayed in the map window are interactive. Therefore, key information will be outlined in the information pane and can be further explored when an element is selected. For instance, easting/northing/ ground level, installation depth, review level, calibration certificate (if applicable), installation records and photo attachments will be displayed when an instrument is selected either in the map window or in the data window. Similarly, a complete bore log will be displayed in PDF format and AGS chart when a borehole point or an ID is selected.

Moreover, pins are also available to mark specific locations on the map window interactively. Different pin shapes are available and can be used to indicate shafts, manholes and TBM cutter head intervention locations. The colour of the pin can be changed to indicate the construction status such as active, non-active and temporary. In addition, pins also provide a place to park the documents pertaining to that site and can also publish the time-based information such as daily activity, photographs, records, name and contacts of engineer-in-charge and emergency rescue teams etc. Furthermore, a digitizing tool is also available to draw new elements to identify existing or custom structures to include in 2D sections and 3D models.

Figure 5. Soil profile and TBM drawings shown in map window.

4.2 *Project dashboard*

The project dashboard is a one-stop location which outlines the comprehensive overview of the project. It is designed to provide up-to-date information on construction/tunnelling progress, and the instruments which have recorded substantial readings in past few days. The dashboard tabulates the progress for every shaft/manhole excavation, TBM and pipe jacking drives. The statistics outlined for shaft excavation progress include current excavation level, target excavation level and percentage of excavation completed. For TBM drives, statistics shown in the dashboard are current drive status, ring-built number, head chainage, completed distance, percentage of completion, progress bar and production summary (Figure 6).

TBM daily production chart can also be obtained for any time period. Links are also provided to display TBM locations, soil profile and real-time display of TBM parameters. The TBM progress updates are real time, and each individual progress is automatically consolidated to derive the project wide progress as shown in Figure 7. The total tunnelling and pipe jack distances completed, numbers of shafts/manholes being excavated and completed are tabulated and indicated on the map as shown in the figure below. But this option is only available to authorised users.

Figure 6. Dashboard showing tunnelling progress in a contract.

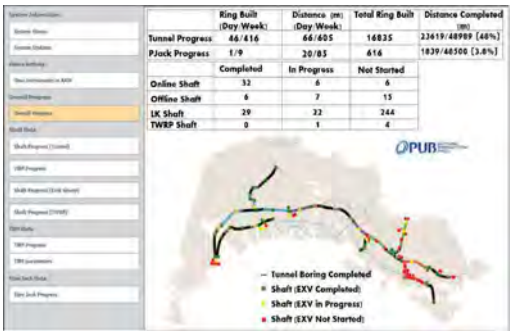

Figure 7. Dashboard showing project-wide construction progress.

4.3 *Instrumentation monitoring data*

Basically, STEMS takes only raw readings from both real-time and non-real-time instruments. Real-time monitoring data are automatically pushed forward to STEMS by respective web servers. Other than manual uploading, non-real-time data can also be transferred electronically through web interface or by emailing to a dedicated email server using a provided template file. Incoming raw data are instantly processed according to respective data models configured in the system. Data models are in fact the calculation templates and each type of instrument have their own data model.

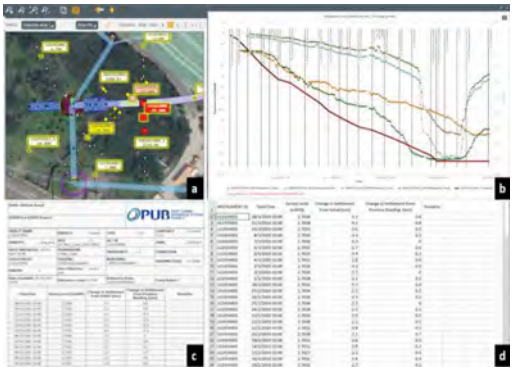

Figure 8. Instrumentation readings formats; (a) highlights and labelling in map window, (b) chart view with construction activity timeline, (c) table format, (d) text format.

They are also used to translate the output results into various units and formats between the graphing engine and the database. Therefore, graphs can be plotted in various engineering units and allow for integration with other instrument readings or excavation depth (Figure 8b). Other than chart format, readings can also be presented in table and text format (Figures 8c and 8d). During the processing, rate of change is also computed to detect spikes and notify the originator for confirmation to avoid erroneous readings. The same algorithm is used to predict when the readings will reach preset threshold values and caption in the chart.

Instruments in array or cluster can also be grouped and enabled to produce section plots to depict the ground movement in relation to excavation progress. Furthermore, it also enables to produce user-defined cross-section in which every object within a user defined distance from a cutting line will be plotted. An option is also available for the section to overlay on the soil profile as shown in Figure 9. So that ground movement/water drawn down can be visualised more clearly and allows the users to observe the risk or identify the area of concern more easily.

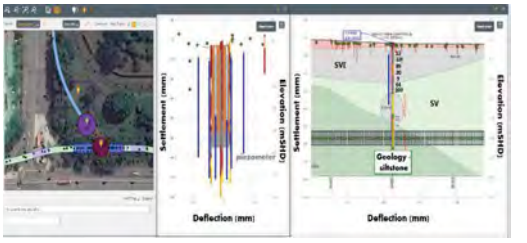

Figure 9. Indication of instrumentation readings in cross-section.

4.4 *Automatic alerts*

When an instrument reading reaches or breaches pre-set threshold limits, SMS and email messages will be triggered automatically to a dedicated group of users. Meanwhile, it will highlight the breached instruments in distinct colour for easy identification in the map window – yellow for alert level (AL), pink for predetermined level (PDL), and red for work suspension level (WSL) (Figure 10). In addition, all breached events are registered in the system and event blogs are created to start interim communication to share views, opinions and justification.

The event blogs are structured to take inputs on description, site activity/observation, other instrument readings in the vicinity, actions taken, recommendation and remarks. Every single input given in the blog is logged and forwarded to all designated emails. This draws an attention from key personnels and helps everyone aware of the development. Then the close out report can be generated and archived in the database. This process is system guided and automated. But no authority is given to end-users to edit

Figure 10. (a) Highlight of breached instruments, (b) breached report.

or delete it. The report format was designed after discussion with all relevant parties across the project.

4.5 *Data visaualisation*

There are a few built-in algorithms to analyse the instrumentation readings and borehole data with different abstraction in STEMS. Interpolation is one of the available features and it uses the Inverse Distance Weighted (IDW) method to draw contours of instrument readings except for inclinometers. In addition, rockhead contour or depth to specific soil layers can also be drawn (Figure 11). The contours are solid filled but they can be overlaid on different backgrounds.

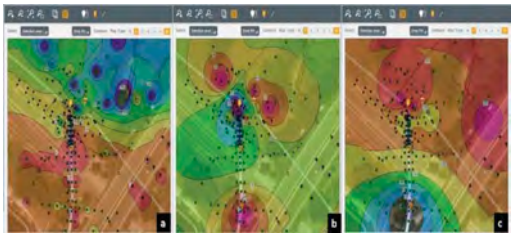

Figure 11. Instrument reading contours, (a) ground settlement, (b) piezometric level, (c) rockhead level.

Similarly, instrumentation arrays or clusters for bored tunnel monitoring can be grouped and preconfigured to compute volume loss using settlement readings (Figure 12a). The calculation methods and applied models used in the system were checked and verified by all project parties during the development stage. On the other hand, the system is also able to identify TBM locations on the soil profile with respect to ring number and chainage (Figure 12b). Therefore, detailed geotechnical condition of current mining stretch can easily be found out.

4.6 *TBM data*

The DTSS2 project deploys 19 TBMs, of which 18 are Slurry Pressure Balance Machines (SPBM) and only 1 is the Earth Pressure Balance (EPB) machine. There are fibre internet connections available to all TBMs. Therefore, STEMS can connect to TBM data

Figure 12. (a) Volume loss (Gaussian curve), (b) automatic display of soil profile at active tunnelling stretch.

servers from all active TBMs through provided IP addresses, usernames and passwords, and streamline the data in real time.

The TBM data are continuous and transmitted with 5 to 7 sec intervals. They are processed and stored in a ring file (last erected ring no is assigned) in the database. A ring file contains clock-synchronised machine data from various sensors on the TBM. These data are designed to display in the main and secondary TBM monitoring tabs (Figure 13 & 14) in real time for TBM operation monitoring.

Figure 13. Real-time TBM monitoring dashboard tabs; (a) key operation parameters, (b) AEM data.

Like other TBM monitoring systems, records of parameters can also be plotted against time, chainage, net stroke or ring number. These parameters are not limited to view within the TBM module itself. They can also be combined with instrumentation data or other information in a single graph over time series axis. Therefore, the effect or the influence of TBM operation parameters on ground movement or their correlation can be studied and identified. Moreover, ring footprints displayed in the map window can be colour coded based on the average value of any operation parameter. As mentioned above, cutter head intervention locations can also be indicated by designated shape of pins (CHI pin). Therefore, all relevant information and documents can be described and attached to CHI pins. Cutter head intervention permits, compressed air dive records, face logs, photographs and cutter head intervention reports etc., are

attached to CHI pins for easy reference. This TBM module greatly assists the tunneling and supervision teams by provision of an efficient real-time monitoring platform.

Figure 14. (a) Operation parameter trend plots, (b) STP data dashboard, (c) STS data dashboard.

4.7 *Pipe jacking machine monitoring*

There are several pipe jacking drives being carried out for the DTSS2 link sewer construction. The machines with a diameter of 2 m and above have onboard data loggers and are connected to STEMS for real-time monitoring (Figure 15). As the number of sensors and instruments on pipe jack machines are much lesser than on TBMs, the parameters streamlined to STEMs are not extensive. Typically, data from the pipe jacking machines come in at 5 seconds interval and key parameters are displayed in the composite dashboard tabs show below. All incoming data are stored in the database and can presented in chart format or retrieved in text format as and when needed.

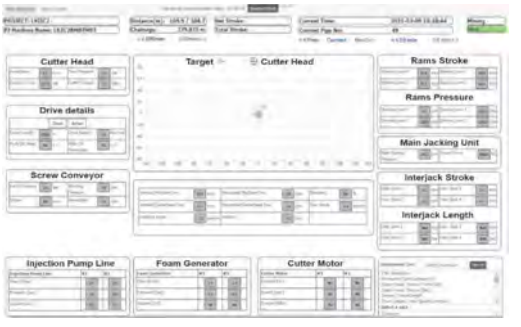

Figure 15. Pipe jacking monitoring dashboard.

4.8 *Reporting*

A Shift reporting tool is also available in the system in order to standardise the reporting format among tunnelling contracts in the whole of DTSS2 project. By using this built-in tool, engineers can prepare a daily or shift report at the end of the day or shift by simply selecting the relevant activities from the list and indicate the timing. For TBM shift reporting, shoving, stoppage and ring building timings will be automatically populated because they are extractable from incoming signals from TBMs. Therefore, it is more accurate than the manual way of doing it in spread sheet or word processing software. Review and approval process is fully online and can be routed automatically to dedicated managers for review and approval. Upon completion, PDF version will be generated and parked in the designated folder with name being given automatically. Another benefit is that it can produce downtime and production statistics from the captured activities and timing. Therefore, end-users can obtain the overview of the production/downtime and be able to develop maintenance strategies to minimise the downtime or improve the production. Figure 16 shows the shift reports generated from the system.

Figure 16. A TBM shift report and downtime data.

4.9 *Others*

STEMS also has direct connections with CCTVs installed at various locations including at TBMs. The links are established by API interface and the footages are stored for 48 hours. Therefore, construction sites and key locations can be monitored in real time without a need to switch over to another platform or input another username or password. Moreover, STEMS is also connected to biometric systems from all 5 tunnel contracts. Thus, manpower on site can also be checked and monitored in real time. In addition, various other metadata such as drawings, photos, soil investigation reports, pre-construction survey reports, CHI reports, weekly interpretative reports, monthly instrumentation reports, weekly meeting minutes, excavation permits, GIBR and TBM protocols reports, etc., are hierarchically saved in the form of a tree menu and can be accessed instantly. This modular menu structure allows systematic documentation and easier to find as needed.

5 DISCUSSIONS

STEMS shows a high versatility in data collection and transparency in processing. The collection and collation of data from different sources and creating a common data environment allow engineers to focus solely on analysis and interpretation rather than processing of data. Real-time access to TBM operation parameters allows managers to monitor

tunnelling operation from anywhere and be able to make prompt and correct instruction. The system is capable of opening and running all real-time TBM monitoring dashboard tabs at any one time without affecting the speed and performance. Table 1 provides the summary of the type and number of real-time connections established in STEMS during the peak period when the system had most number of real time connections. Total data size in STEMS to date is about 6 Terabytes and projected to reach about 8 Terabytes by end of the project.

Table 1. Real-time connections in STEMS.

Real-Time Connection	Total Number	Remark
TBM & STP	17	2 more drives are yet to start
Pipe Jack Machine	15	57 more connections to make
Vertical Shaft Sinking Machine (VSM)	1	Repeated use for 5 shafts
CCTV Camera	213	~50 more to setup
ATMS	12	with 960 prisms altogether
Real-Time Vibration Meter	41	-
Automatic Expressway Monitoring System	9	with 900 reflectorless points
Biometric System	5	-

STEMS users are of different levels: engineers, supervisors, managers, project officers, directors, consultants, and it is therefore designed to support various job roles across the project. Project managers and construction managers can obtain accurate and up-to-date construction progress and be able to visualise it in graphical plots, 2D sections and 3D models. Detailed construction activities, status of TBM drives/pipe jacking drives, their daily/weekly and monthly production can be tracked instantly. CCTV streams and biometric connections are very useful especially for the safety team to remotely monitor high risk operations and identify unsafe behaviours and carry out check/audits on manpower. The system also helps instrumentation teams and design teams by automation and saving of man-hours on processing, reporting and data presentation. Canvas reporting is one of the automations which enables the generation of weekly/monthly factual instrumentation reports, and daily and ring reports. Moreover, various interactive analysis tools are also available and able to generate various integrated cross sections/combined graphs for interpretation and reporting. Likewise, the consolidated TBM monitoring dashboard is found to be very useful as it allows key parameters to be visualised in real time in user-friendly formats. Similarly, report preparation and sign-off procedures are machine driven and thus a need for paper reports is eliminated.

Various reports, drawings, records, permits, photographs etc., are sorted systematically and orderly in respective archive folders for documentation purposes. Therefore, every relevant job role can take part in quality control and document auditing. The instant access to these documents is very helpful for meetings and discussion. Not much time is needed for preparation before meetings because all relevant documents can be opened and presented with a few mouse clicks during the meetings. Latest instrumentation readings, real-time TBM parameters, and volume loss which are key components and subjects of discussion in daily meetings can also be displayed instantly. The induced settlement and TBM operation parameters can be correlated and presented straight away. Furthermore, for instant presentation, interactive canvas tool allows the creation of a content-rich summary report with charts and figures which would be updated automatically with latest readings when reproduced at any later stage. This tool provides significant time savings as well as eliminates a need to export and exchange data. In general, the system interface is user-friendly and even a user who is not familiar with the system can operate it.

The PUB DTSS2 department and its consultant team strictly administers the security and ensure the confidentiality of the data. Performance tests and penetration tests are carried out regularly to check the functionalities and system security. Most importantly, users are only allowed to see their part of the project and some part of the adjacent contracts in interface areas. The project-wide cross contract access is only given to the project directorate office and project management team.

Throughout the project, STEMS plays a crucial role in geotechnical control over various excavation and tunnelling works, and in risk identification process. The summary of its applicability can be summarised as follows.

1. **Data Integration** – The system consolidates data from various sources such as TBM sensors and equipment, geotechnical instruments, geological survey, geotechnical investigation works, excavation and construction activities. It ensures that all relevant engineering data are in one place and can correlate for combined analysis and interpretation.
2. **Data Analysis** – Data analysis, data visualisation, statistical prediction, and trends comparison with all vital information allow to identify potential areas of concern and construction impact to surrounding areas.
3. **Real-Time Monitoring** - Real-time monitoring of tunnelling and construction activities and geotechnical data allows managers, engineers and consultants to get instant updates on how the machines are being operated, and what is happening on sites and underground. Instant access to see operation parameters in real-time provide additional layers of supervision and risk control.

4. **Centralised Data Access** - Stakeholders from different locations can access the data through a web interface. This facilitate collaboration among project teams, even if they are geographically dispersed.
5. **Alerts and Notifications** – These systems can issue alerts notifications via email and SMS when predefined thresholds or conditions are reached or breached. It makes every key personnel be aware of the issue and help to ensure that prompt actions are taken to control the issue within tolerable limits.
6. **Reporting** – System-guided and automated reporting feature make the process simple and easier. It provides accurate updates and summary of project progress, activities, potential issues together with downtime and production statistics in standard and well-structured format. Down-time and production statistics stamped in the report highlight the areas or activities that require improvement such as more maintenance or supervision etc.
7. **Customisation** – Users can customise the system to monitor specific parameters or aspects of the project for automation in the process that are critical to their needs.
8. **Scalability** – The system can scalable to accommodate increasing amounts of data as the project progresses.
9. **Historical data** – The system can archive historical data, which is valuable for post-project analysis, arbitration, and future planning.
10. **Compliance and Documentation** – This assists in maintaining records and documentation required for regulatory compliance, audits and legal purposes as a part of project quality plan.
11. **Cost Saving** – By automation and providing instant access and better visibility into project progress and potential problems the system can help to prevent costly delays and construction mistakes. It is obvious that operator intensiveness is greatly reduced, and significant manpower saving is achieved.
12. **Security** – Robust security features are essential to protect sensitive project data from unauthorized access and cyber threats.

6 CONCLUSIONS

The volume of data and information in underground infrastructure projects is huge and how they are managed and utilised is crucial to identify risks and formulate solutions for mitigation. The biggest source of risk or challenge within major excavation and tunnelling works has often been the ground-related factors and reaching of 65% contribution to overall challenges (Clayton, 2001). Fortunately, digital tools are more and more advanced, and the industry is moving forward. And the way the digital tools is used in underground infrastructure projects is the way to help solving these potential issues and challenges.

In the DTSS2 Project, STEMS has proven its effectiveness not only in managing and delivering substantial quantities of monitoring and construction data from different sources but also in identification and prediction of potential geotechnical risks during excavation and tunnelling works. Data transparency and visualisation are very much improved with more reliable accuracy and loss of information is avoided or minimized. It provides one source of truth which is important for arbitrations and dispute management in the future. STEMS has turned out to be more than an instrumentation monitoring system or TBM monitoring system as it provides optimization and integration potentials with all vital engineering data and information. Workload reduces and time efficiency improves as most part of the process is system guided or automated. Moreover, digitalisation of construction data with centralised storage offers instant access which enables construction managers to make fast and correct decisions and thus positively impact the construction efficiencies.

REFERENCES

Clayton, C.R.I., 2001. Managing geotechnical risk: Time for change. Proceedings of the Institution of Civil Engineers – Geotechnical Engineering, 149(1),3-11.

Festa, D., Broere, W., Bosch, J.W., 2012. An investigation into the forces acting on a TBM during driving – Mining the TBM logged data. Tunnell. Undergr Space Technol. 32, 143–157.

Wang, Z., Yao, W., Cai, Y., Xu, B., Fu, Y., Wei, G., 2019. Analysis of ground surface settlement induced by the construction of a large-diameter shallow-buried twin-tunnel in soft ground. Tunnell. Undergr Space Technol. 83, 520–532.

Yin, W.N., Burd, H.J., Martin, C.M., 2017. Finite-element modelling for the assessment of tunnel-induced damage to a masonry building. G´eotechnique 67, 780–794.

Yin, Z.Y., Wang, P., Zhang, F.S., 2020. Effect of particle shape on the progressive failure of shield tunnel face in granular soils by coupled FDM-DEM method. Tunnell. Undergr. Space Technol. 100, 103394.

Zhang, P., Chen, R.P., Dai, Tian., Wang, Z.T., Wu, K., 2021. An AIoT-based system for real-time monitoring of tunnel construction. Tunnell. Undergr. Space Technol. 109, 103766.

Tunnelling for a Better Life – Yan, Celestino, Thewes & Eberhardt (Eds)
© 2024 The Author(s), ISBN 978-1-032-80042-4
Open Access: www.taylorfrancis.com, CC BY-NC-ND 4.0 license

Research on concrete strength detection method based on digital drilling and machine learning

Rong Wu*
China Railway Construction Heavy Industry Corporation Limited, Changsha, China

ABSTRACT: A concrete strength testing method based on digital drilling and machine learning is put forward in the paper in regards of the problems such as large error, long cycle and high cost existing in the established tunnel concrete strength testing methods. Relying on the energy conservation law and Mohr-Coulomb strength criterion as the theoretical basis, this paper obtains drilling parameters by building an experimental rig to drill concrete blocks for testing. The drilling parameters further function to predict the concrete structural strength through combining theoretical formula and machine learning. As revealed by the study, a big error exists between the calculation results of DP-UCS theoretical model and those of the actual compressive strength. The model is further trained by diverse machine learning methods and tested for validation. According to the results, three machine learning training models are superior to those of DP-UCS theoretical model, indicating that digital drilling test technology can effectively predict concrete strength. Besides, the prediction result of SVM nonlinear regression-based training model differs little from the actual compressive strength of concrete, with an error rate less than 10%, indicating that the model has high accuracy and can serve as a prediction model for the subsequent integrated program of concrete strength digital drilling product detection system.

Keywords: Concrete, Uniaxial Compressive Strength, Digital Drilling, Drilling Parameters and Machine Learning

1 INTRODUCTION

Concrete strength serves as an important index to measure construction quality and ensure construction safety in bridge and tunnel construction. As the main support means of tunnel construction, shotcrete strength test has a significant impact on the stability and deformation control of the tunnel surrounding rock and growth characteristics of surrounding rock pressure. There are numerous concrete strength test methods, including rebound method, penetration method, core drilling method, pull-out method, maturity method and piezoelectric sensor detection method. The rebound method can only measure the strength of concrete surface layer but cannot characterize the internal strength by measuring the rebound value to infer the compressive strength of concrete. The penetration method is easily influenced by the concrete surface condition and the type of concrete aggregate, with errors aroused from such. The core drilling method requires on-site sampling and transportation to the laboratory for uniaxial compressive test analysis, which is cumbersome in operation, long in cycle and high in cost, affecting the integrity of the testing surface and not portable on site. The maturity method and piezoelectric sensor detection method require embedded sensors, which are complex to operate and narrow in scope of application. Moreover, impedance analyzers and other equipment are expensive and bulky, not conducive to field operation. Therefore, it is necessary to develop a convenient, fast and accurate test method suiting concrete strength in tunnels.

Digital drilling test technology [1,2] is a technology to monitor and quantitatively control some parameters while drilling such as penetration rate, rotation speed, torque and propulsion force during drilling. In the current stage, it is mainly used in the realm of rock mechanics and also suitable for concrete strength testing after curing. Sufficient studies have shown that a strong correlation exists between drilling parameters and mechanical parameters such as uniaxial compressive strength. Cohesion, internal friction angle and uniaxial compressive strength (UCS) constitute the basic mechanical parameters of concrete and rock. According to the energy conservation law and Mohr-Coulomb strength criterion, the digital drilling method based on drilling parameters can test the rotating speed, torque,

*Corresponding author: 1239283439@qq.com

DOI: 10.1201/9781003495505-371

propulsion force and other drilling parameters during the drilling process of the drill bit, no matter in the field or laboratory. The test makes the DP-UCS model available to realize effective and convenient testing of concrete strength. According to the research findings of Song Ling et al. [3], the drilling parameters are correlated with uniaxial compressive strength. Sajjad Kalantarib [4] of Isfahan University of Technology in Iran estimated the rock strength parameters using borehole data by carrying out multiple borehole tests as well as calculation and analysis of data, so as to obtain the calculation models between uniaxial compressive strength and cohesion, bit angle (15°), friction angle (contact friction angle) between bit cutting surface and compression fracture zone, friction angle between compression fracture zone and intact rock, and internal friction angle. YASAR et al. [5] put forward empirical formulas for drilling parameters and uniaxial compressive strength through experiments. Wang Qi et al. [6] found that the conventional mathematical model and empirical formula cannot bring about the ideal results esp. when the rock mass quality is poor. Hence, the method of machine learning to obtain more accurate uniaxial compressive strength is a hot research topic for scholars.

This paper establishes a concrete strength prediction model through diverse machine learning and regression analysis methods on the basis of drilling parameters. Compared with the conventional DP-UCS theoretical calculation model, the training model based on SVM nonlinear regression has better accuracy, which is similar to the actual situation of samples, producing high engineering application value.

2 PRINCIPLE ON STRENGTH TESTING OF DRILLING PARAMETERS

The cohesion c and internal friction angle φ of rock and concrete are the most basic parameters characterizing strength properties (referred to as parameters c-φ for short). As revealed by the laboratory tests and numerical simulations, the c-φ parameters of rock is capable of controlling the cutting failure process. Therefore, establishing DP- cφ relationship has the desired feasibility by considering the mechanical analysis of rock cutting failure process.

Traditional indoor tests (uniaxial and triaxial tests) have complicated test steps, long cycle and high cost, and field measurement is infeasible in this case. According to the energy conservation law of cutting and drilling:

Total drilling and rock breaking work W = torque work W_M + pressure work W_F

The energy consumed in the drilling process W = energy in rock cutting and breaking E_C + friction consumption between drill bit and hole bottom E_F, so:

$$W_M + W_F = E_C + E_F \tag{1}$$

Therefore, the quantitative relationship between cohesion c and internal friction angle φ and drilling parameters (DP) such as penetration rate, rotation speed, torque and thrust during drilling is established.

According to the Mohr-Coulomb strength criterion of rock and concrete:

The relationship between uniaxial compressive strength Rc and cohesion C, internal friction angle φ is as follows [7]:

$$R_c = \frac{2C\cos\varphi}{1-\sin\varphi} \tag{2}$$

Then, a quantitative relationship model (DP-UCS model) between drilling parameters and uniaxial compressive strength is established to serve as the basis for strength testing. Scholars at home and abroad have validated through multiple experimental tests.

2.1 *Drilling test scheme*

As shown in Figure 1-3, the test equipment is built with a hydraulic motor drill scheme, including an aluminum profile experimental frame, an optical axis support seat, a hydraulic motor drill and a data monitoring and acquisition system. C10-C60 standard test blocks are used for the test, with the dimension of concrete sample of 150mm*150mm*150mm, as shown in Figure 4. An alloy diamond coring bit with a diameter of 10mm is used. In the test, a single variable is controlled, and a flow valve is used to control the hydraulic motor flow rate to maintain 20L/min. The thrust force is changed by changing the gravity borne by the object. Drilling inspection tests are carried out under different downward pressures, and

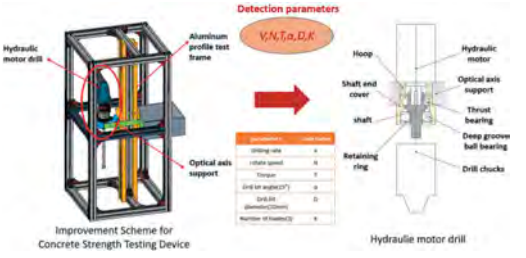

Figure 1. Schematic diagram of test device structure.

Figure 2. Indoor test device.

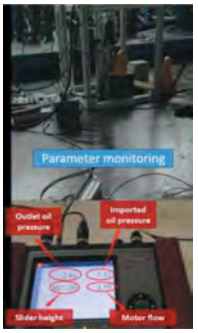

Figure 3. Data monitoring and acquisition system.

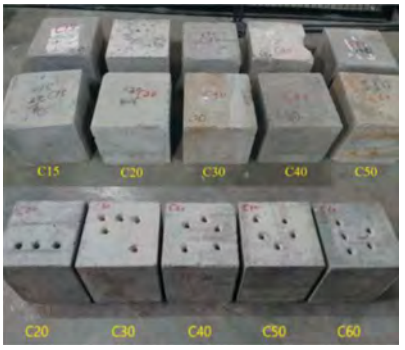

Figure 4. Some concrete samples.

Table 1. Direct monitoring data of test.

Monitoring parameters	Code
Slider height	E
Inlet oil pressure	B
Outlet oil pressure	A
Motor flow	L
Drill bit diameter (10mm)	D
Number of cutting edges (2)	k

multiple groups of repeated tests are carried out for each downward pressure.

The data that can be directly monitored in the test are listed in Table 1 below. Laser displacement sensor is used to measure the rotary cutting speed of drill bit. Torque and rotation speed are calculated from the monitoring data of hydraulic motor (inlet and outlet oil pressure and flow value of hydraulic motor, as well as drilling speed of drill bit, etc.). Combined with the mathematical models of drilling parameters and concrete strength in references [4] and [8], the strength of concrete test blocks is calculated accordingly.

2.2 *Test results*

Some experimental test data are shown in Table 2. The monitoring curves of displacement, flow rate and pressure parameters that are monitored during the experiment are listed in Figure 5.

Table 2. Test data of some hydraulic motor drilling rigs.

Downward pressure/N	Flow rate (L/min)	Pressure difference (bar)	Drilling rate (mm/s)
157	20.29	16.53	0.10
	20.19	16.31	0.05
250	20.83	17.26	0.21
	20.68	17.61	0.22
348	19.83	16.85	0.26
	20.24	17.09	0.20
452	20.11	18.09	0.14
	20.11	17.48	0.20
…	…	…	…

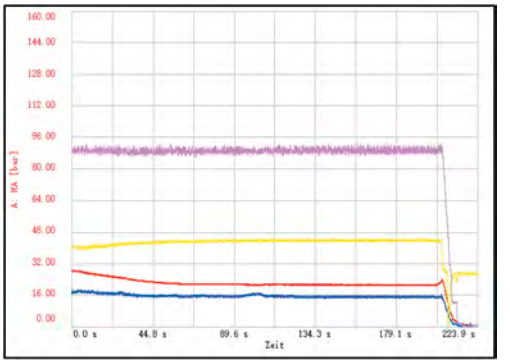

Figure 5. Monitoring curve of displacement, flow and pressure parameters.

The test results are calculated using the drilling measurement models recommended in References [4] and [8], and further compared with concrete uniaxial compressive strength measured by a press. It is found that the error is relatively large and some results have magnitude differences, which impair the reliability of the results. Refer to Table 3 for details.

3 MACHINE LEARNING AND REGRESSION PREDICTION

Due to the inaccurate prediction results of conventional mathematical models and empirical formulas in concrete strength drilling measurement, this paper establishes a concrete strength prediction model through diverse machine learning and regression analysis depending on the original model established with drilling parameters, so as to obtain higher goodness-of-fit.

Machine learning training prediction methods mainly include BP neural network nonlinear regression prediction, SVM nonlinear regression prediction and RBF neural network nonlinear regression prediction. SVM can theoretically approximate any nonlinear function in a global sense, which improves the

Table 3. Comparison of calculation results of different models for drilling measurement.

Test block No.	Literature Model/qc	He Mingming [8] Literature Model/qc	Test strength of press	Errors
C10	-	7.7 MPa	12 MPa	35.83%
C20	550.6 MPa	-	20MPa	2653%
C30	-	32.4 MPa	30.8 MPa	5.19%
C40	38.1 MPa	-	42MPa	9.28%
C50	-	15.6 MPa	58 MPa	73.1%
C50	-	264.6 MPa	58 MPa	356.2%
C60	70.7MPa	-	75MPa	5.73%
C60	255.2MPa	-	75MPa	240.27%

generalization ability of the model by following the principle of structural risk minimization and can obtain better statistical laws even when there are few statistical samples.

To improve the effectiveness of machine learning model training, the experimental equipment shown in Figure 1 is used to increase the data size of borehole test samples for parameter detection while drilling to 119 groups (including 112 groups of training samples and 7 groups of test samples, as shown in Table 4 and Table 5, respectively). Besides, three types of nonlinear regression prediction are adopted to establish a training model.

3.1 *Establishment of BP neural network model*

Artificial neural network is an algorithm simulating the physical structure of human neural network

Table 5. Testing of sample data.

S/N	L/min Flow L/min	Pressure difference/bar	Drilling rate mm/s	Drilling pressure/N	UCS strength/MPa
1	20.4515	1.5812	0.7	181	29.8
2	19.5811	1.5016	1.6	259	29.8
3	19.9492	1.6829	1.7	348	29.8
4	19.7461	1.6651	2.1	460	29.8
5	19.4221	1.8773	2.6	550	29.8
6	20.1088	1.9052	0.8	255	30.8
7	20.0503	1.858	0.8	255	30.8

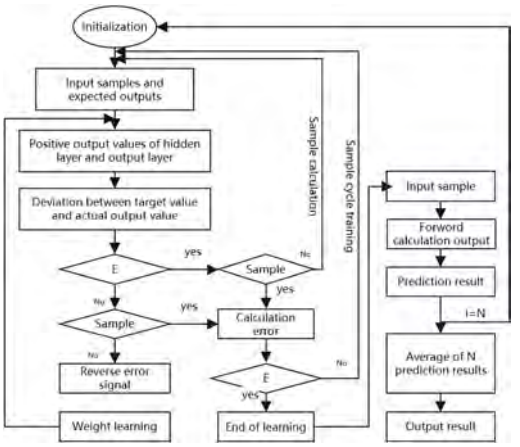

Figure 6. Nonlinear training and prediction logic diagram of BP neural network.

Table 4. Training of some sample data.

S/N	Flow L/min	Pressure difference/bar	Drilling rate mm/s	Drilling pressure/N	UCS strength/MPa
1	20.1205	1.6125	8.58E-05	151	42
2	20.2936	1.6630	0.000289739	151	42
3	20.4502	1.6964	0.000173623	257	42
4	20.1783	1.7352	0.000307768	257	42
5	20.0186	1.7833	0.000347019	257	42
6	20.2837	1.6570	0.000476914	349	42
7	20.3414	1.6800	0.000827469	349	42
∘ ∘ ∘	∘ ∘ ∘	∘ ∘ ∘	∘ ∘ ∘	∘ ∘ ∘	∘ ∘ ∘
103	19.6646	1.5139	0.003	259	29.8
104	19.5811	1.5016	0.0016	259	29.8
105	19.5379	1.4905	0.0016	259	29.8
106	19.9492	1.6829	0.0017	348	29.8
107	19.8499	1.5941	0.0016	348	29.8
108	19.1346	1.9175	0.0023	460	29.8
109	19.3705	1.6143	0.0013	460	29.8
110	19.7461	1.6651	0.0021	460	29.8
111	19.4221	1.8773	0.0026	550	29.8
112	19.6991	1.6501	0.0014	550	29.8

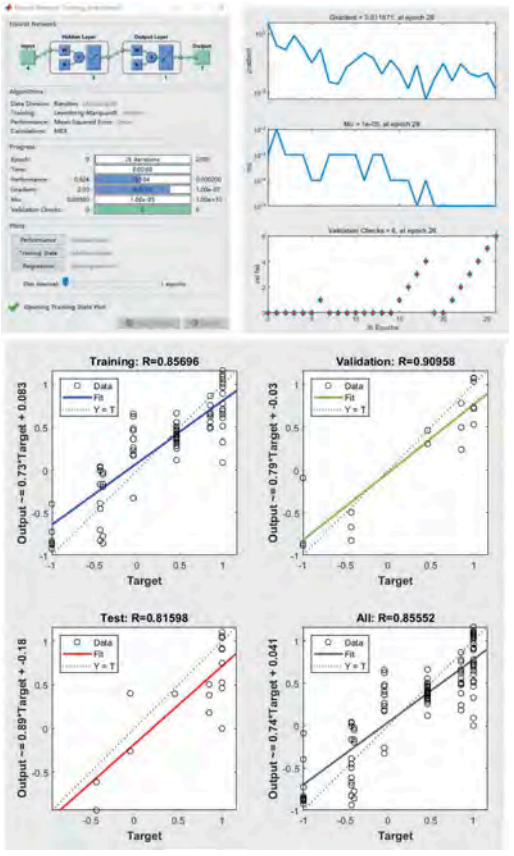

Figure 7. RMP-BP neural network model.

system to enable the neural network system to have partial intelligence of human brain through high-speed simulation calculation of computer. The neural network simulates the uncertain thinking mode of human brain through the process of learning and acquiring knowledge from external environment and using the connection strength of internal neurons to store the acquired knowledge.

The BP neural network in MATLAB 2014a is adopted, with its nonlinear training prediction logic diagram shown in Figure 6.

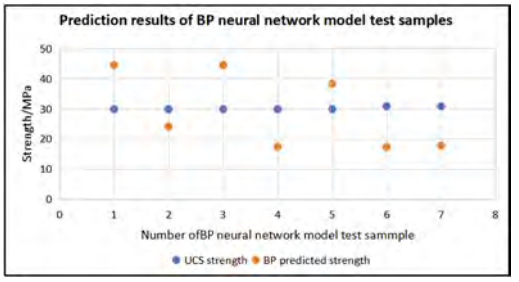

Figure 8. Prediction results of BP neural network nonlinear training model test samples.

Considering the unique characteristics between uniaxial compressive strength of concrete and drilling parameters in experimental boreholes, a BP neural network model for predicting uniaxial compressive strength parameters of concrete is established, which is referred to as RMP-BP model, as shown in Figure 7 for details.

The prediction results of BP neural network nonlinear training model test samples are shown in Table 6 and Figure 8.

As shown by Figure 7, the similarity of the established BP neural network nonlinear regression training prediction model is 90.96%. According to the prediction results of the test samples of the BP neural network nonlinear prediction model for predicting concrete uniaxial compressive strength parameters in Table 6 and Figure 8, the test results

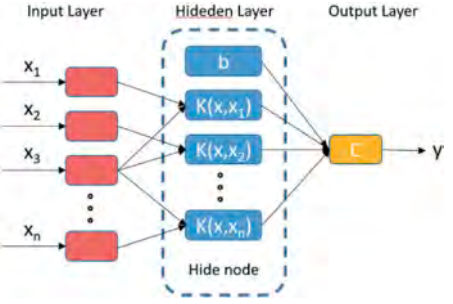

Figure 9. SVM structure model.

Table 6. Comparison of test sample data and RMP-BP training model prediction.

S/N	Flow L/min	Pressure difference/bar	Drilling rate mm/s	Drilling pressure/N	UCS strength/MPa	BP predicted strength/MPa
1	20.4515	1.5812	0.7	181	29.8	44.4302
2	19.5811	1.5016	1.6	259	29.8	24.0695
3	19.9492	1.6829	1.7	348	29.8	44.4302
4	19.7461	1.6651	2.1	460	29.8	17.4362
5	19.4221	1.8773	2.6	550	29.8	38.2532
6	20.1088	1.9052	0.8	255	30.8	17.2657
7	20.0503	1.858	0.8	255	30.8	17.7321

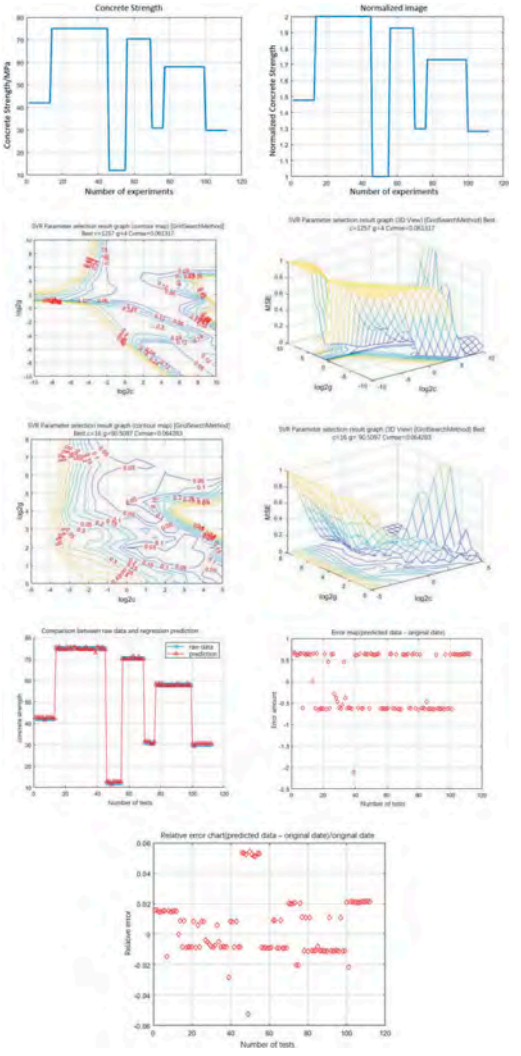

Figure 10. SVM nonlinear regression training model.

however are not ideal due to the great difference between the prediction results and the actual strength value, indicating that the prediction error is large.

3.2 *SVM-based nonlinear regression training prediction*

Support Vector Machine (SVM) can be used for pattern classification and nonlinear regression, mainly aiming to establish a classification hyperplane as a decision surface, so as to maximize the isolation edge between positive and negative examples. The concept of inner product kernel between "support vector" x(i) and input space extracted vector x is the key to construct support vector machine learning algorithm. The support vector machine is composed of a small subset extracted from the training data by an algorithm, with its structural model shown in Figure 9.

Theoretically, SVM can approximate any nonlinear function in a global sense by improving the generalization capacity of the model by following the principle of structural risk minimization so as to obtain good statistical laws even when there are few statistical samples. The non-linear regression training model of SVM based on the training sample data listed in Table 4 is shown in Figure 10.

The prediction results of SVM non-linear regression training model test samples are shown in Table 7 and Figure 11.

As shown by Figure 10, the established SVM nonlinear regression training model has a similarity of 99.6%, with an equivalent error of ±0.06 and a high degree of fit. According to the prediction results of test samples of the SVM nonlinear regression training model for predicting concrete uniaxial compressive strength parameters in Table 7 and Figure 11, there is little difference between the prediction result and the actual strength, with an error rate less than 10%, indicating a higher model accuracy.

3.3 *RBF neural network nonlinear regression prediction training model.*

RBF neural network is the type of feedforward neural network, having the structure resembling that of multi-layer feedforward network, which is a three-layer feedforward network. Basic Rules: RBF functions as the "basis" of hidden elements to

Table 7. Comparison of test sample data and SVM training model prediction.

S/N	L/min Flow L/min	Pressure difference/bar	Drilling rate mm/s	Drilling pressure/N	UCS strength/MPa	SVM predicted strength/MPa
1	20.4515	1.5812	0.7	181	29.8	30.43736
2	19.5811	1.5016	1.6	259	29.8	30.43022
3	19.9492	1.6829	1.7	348	29.8	30.4124
4	19.7461	1.6651	2.1	460	29.8	30.43959
5	19.4221	1.8773	2.6	550	29.8	30.44499
6	20.1088	1.9052	0.8	255	30.8	36.46723
7	20.0503	1.858	0.8	255	30.8	31.38143

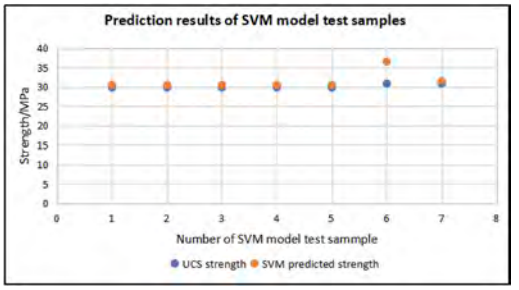

Figure 11. Prediction results of SVM nonlinear regression training model test samples.

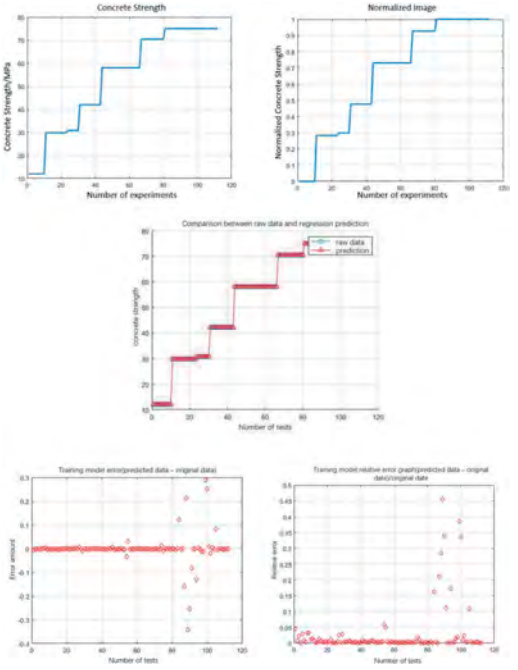

Figure 12. RBF neural network training model.

form a hidden space, and the hidden layer transforms the input vectors and low-dimensional pattern input data into high-dimensional space, so that linear

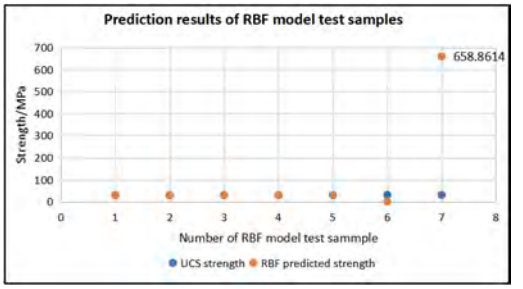

Figure 13. Prediction results of RBF neural network training model test samples.

inseparability in low-dimensional space are linearly separable in high-dimensional space. The RBF neural network is characterized by simple structure, concise training and fast learning convergence speed, which can approximate arbitrary nonlinear functions.

SVM nonlinear regression training model based on the training sample data listed in Table 4 is shown in Figure 12.

The prediction results of RBF neural network training model test samples are shown in Table 8 and Figure 13.

According to Figure 12, the RBF neural network nonlinear regression prediction training model that is established has a high degree of fit, with a similarity of 99.91%. However, as shown in Table 7 and Figure 13, the prediction results of the sample with a drilling pressure of 255N are too different from the concrete strength, and there are some errors in the prediction results.

4 CONCLUSION

(1) The conventional DP-UCS model has great errors as the intensity detection basis. Reasonable selection of machine learning methods and establishment of nonlinear regression models are conducive to improving the accuracy of prediction models;
(2) For BP neural network prediction and RBF network regression, the established model has the

Table 8. Comparison of test sample data and RBF training model prediction.

S/N	Flow L/min	Pressure difference/bar	Drilling rate mm/s	Drilling pressure/N	UCS strength/MPa	RBF predicted strength/MPa
1	20.4515	1.5812	0.7	181	29.8	29.7996
2	19.5811	1.5016	1.6	259	29.8	29.7958
3	19.9492	1.6829	1.7	348	29.8	29.7989
4	19.7461	1.6651	2.1	460	29.8	29.7988
5	19.4221	1.8773	2.6	550	29.8	29.7964
6	20.1088	1.9052	0.8	255	30.8	0.4883
7	20.0503	1.858	0.8	255	30.8	658.8614

degree of fitness more than 90%, but the difference rate of test sample prediction results is high;

(3) According to the prediction results of three machine learning training models, SVM has more accurate prediction results since SVM is a general machine learning method developed on the basis of statistical learning VC dimension theory and structural risk minimization principle, which is mainly used for pattern recognition, classification and regression. It shows multiple unique advantages in solving problems such as small sample, nonlinear, high dimension and local min. value. Consistent with the small number of our data samples, SVM can serve as a predictive model for subsequent product inspection system integration procedures.

REFERENCES

[1] Kahraman S, Bilgin N, Feridunoglu C. Dominant rock properties affecting the penetration rate of percussive drills [J] International Journal of Rock Mechanics and Mining Sciences, 2003, 40(5):711–723.

[2] Yue Zhongqi. Improvement and Perfection of Engineering Rock Mass Quality Evaluation Method by Drilling Process Monitoring (DPM) [J]. Chinese Journal of Rock Mechanics and Engineering, 2014, 33 (10): 1977–1996.

[3] Song Ling, Li Ning and Liu Fengyin. Feasibility Study on Application of Precession Cone Penetration Technology in Harder Stratum[J]. Rock and Soil Mechanics, 2011, 32(2):635–640.

[4] Mohsen Panahandeh, Hamid Hashemolhosseini, Mohammad Reza Eftekhar, et al., Obtaining the strength parameters of concrete using drilling data [J]. Journal of Building Engineering, 2021(prepublish), 102181.

[5] Yasar E, Ranjith P G, Viete D R. An experimental investigation into the drilling and physico-mechanical properties of a rock-like brittle material [J]. Journal of Petroleum Science and Engineering, 2011, 76(3): 185–193.

[6] Wang Qi, Sun Huibin, Jiang Bei, et al. Method for Predicting Uniaxial Compressive Strength of Rock Mass Based on Digital Drilling and Support Vector Machines [J]. Rock and Soil Mechanics, 2019, 40(3): 1221–1228.

[7] Sajjad Kalantari, Alireza Baghbanan, Hashemalhosseini Hamid, An analytical model for estimating rock strength parameters from small-scale drilling data, Journal of Rock Mechanics and Geotechnical Engineering (2019) 135–145.

[8] Mingming He, Ning Li, Jiwei Zhu, et al., Advanced prediction for field strength parameters of rock using drilling operational data from impregnated diamond bit[J]. Journal of Petroleum Science and Engineering, 2020, 187(C).

Tunnelling for a Better Life – Yan, Celestino, Thewes & Eberhardt (Eds)
© 2024 The Author(s), ISBN 978-1-032-80042-4
Open Access: www.taylorfrancis.com, CC BY-NC-ND 4.0 license

Development and application of similar materials to cobble stratum for solid-fluid coupling model test

Wenbo Zan*
School of Highway, Chang'an University, Xi'an, China
Research and Development Center for Loess Mechanics and Engineering Test Technology, Shaanxi Polytechnic Institute, Xianyang, China

Wenjie Zhang
School of Highway, Chang'an University, Xi'an, China
Design and Research Institute of China Railway fourth Bureau Group Co., Ltd., Hefei, China

Qian Yang
Research and Development Center for Loess Mechanics and Engineering Test Technology, Shaanxi Polytechnic Institute, Xianyang, China

ABSTRACT: To study the response characteristics of seepage and stress fields induced by underwater shield tunnelling in cobble stratum, similar materials applicable to model tests were developed from the perspective of solid-fluid coupling similarity theory. Twenty-five test schemes were designed for mix proportions to prepare similar materials using orthogonal test. Therein, 6~8 mesh, 10~20 mesh and 70~140 mesh quartz sand, barite powder and gypsum were used as raw materials, and the aggregate content, fine content, cement-aggregate ratio and coarse-to-fine aggregate ratio were taken as controlling factors. Results show that similar materials have a moderate range of parameters, steady performance, convenient preparation and affordable cost; the content of aggregates and fines are the two critical controlling factors that influence the bulk density; the cohesion is largely determined by the cement-aggregate ratio; the elastic modulus is primarily influenced by aggregate content; and all the factors also exert certain controlling effects on the internal friction angle and permeability coefficient. Furthermore, the regulating effects of silicone oil, liquid paraffin, glycerol and petrolatum on the hydro-mechanical properties of similar materials were investigated. The bulk density is positively correlated with the additive amount of glycerol, and the elastic modulus has a negative correlation with petrolatum or liquid paraffin content. The cohesion increases almost linearly with increasing additive amount of silicone oil and petrolatum, whereas four regulators were unable to regulate the internal friction angle of similar materials. The permeability coefficient sharply decreases with the increasing amount of the silicone oil, liquid paraffin and petrolatum. Lastly, the similar materials were applied to complete the excavation seepage model test in Bahe Tunnel of Xi'an Metro Line 9, it was revealed that groundwater seepage and excavation disturbance together possess the water and sand gushing as well as liner deterioration.

Keywords: Similar materials, Metro tunnel, Orthogonal test, Range analysis, Solid-fluid coupling

1 INTRODUCTION

A special kind of geologic body called as cobble stratum is formed with diverse genesis, complex structure and mixed soil and rock during the Quaternary Period, which is widely distributed in many cities such as Beijing, Chengdu and Xi'an in China. In the past few years, with the rapid development of subway construction, there has been a boom in metro tunnels employing the shield tunnelling method through cobble stratum and water-rich conditions. Particularly for underwater shield tunnels, due to the coupling effect between groundwater seepage and excavation disturbance, the excessive deformation of the formation, water and sand gushing from the excavation surface, instability and

*Corresponding author: zanwb@chd.edu.cn

DOI: 10.1201/9781003495505-372

surface collapse frequently occur (Du et al., 2019; Shi et al., 2021; Wang et al., 2023). For the avoidance and treatment of the foregoing catastrophes, it is hence essential theoretically and practically to study the evolution laws of seepage and stress fields during the excavation process of underwater shield tunnels.

The main research approaches utilized to investigate the mechanism of seepage-induced disasters involve theoretical analysis, numerical simulation and model testing. As a tried-and-true method for resolving challenging geotechnical engineering issues, the geo-mechanical model test can truly reproduce the actual engineering geological and hydrogeological conditions and gather the multi-field information of the entire process of disaster evolution. However, similar materials must concurrently satisfy the similarity criteria of seepage, stress and deformation conditions in the solid-fluid coupling model test (Bai et al., 2020; Chen et al., 2015). Thus, the development of similar materials with a high degree of similarity, reliability and steady performance is a pre-requirement.

The choice of basic materials and material proportions are the key factors that determine the physical and mechanical properties of similar materials. Scholars have carried out numerous investigations utilizing various raw materials to generate a similar material that satisfies the test requirements. Considering the critical influence of mineral composition on the physical and mechanical properties of rock, Lu et al. (2022) and Cui et al. (2022) used standard sand, kaolinite powder, illite powder, ordinary Portland cement, gypsum and iron powder to synthesize the similar materials of white sandstone and red mudstone, which can provide a reference for similar material preparation of other rocks. Luo et al. (2023) developed the similar materials applicable to model tests of reef limestone marine environment, which was composed of the foaming agent, powdered talc, sea sand, cement, gypsum and air-entraining agent. To apply the strength-reduction method to model test, a similar material composed of paraffin wax, quartz sand, and barite powder was developed to simulate the quantitative strength-reduction by temperature change (Kong et al., 2023). To resolve the related problems caused by leakage water of a tunnel in a karst area, Tian et al. (2018) used the fine sand (2 mm in diameter), cement (P.C32.5), clay, barite powder and water mixture as the similar material for limestone, and analyzed the effects of size of cave, inclination of joint plane, distance between cave and tunnel, precipitation, and loading on the pore pressure, soil pressure and displacement.

Although some achievements have been made in the development of similar materials and their simulation testing methodologies, most of them are focused on rock or soil mass and research on the creation and use of similar materials for solid-fluid coupling model experiments in cobble stratum is still rare. Additionally, a great deal of literature merely addresses how to manufacture materials similar to the desired rock and soil based on their own experience and the model's requirements, and research on the regulation of material's physico-mechanical and hydraulic properties is neglected. Therefore, it is an urgent need for systematic research and development on solid-fluid coupling similar materials in cobble stratum.

Based on the investigations of fundamental constituents of similar materials, this paper selected quartz sand with different mesh sizes as the aggregate material, barite powder as the fine material, gypsum as the binder, silicone oil, liquid paraffin, glycerol, petrolatum as the regulator. Through a large number of proportioning experiments, we developed a solid-fluid coupling similar material for cobble stratum and it has a moderate range of parameters, steady performance, convenient preparation and affordable cost. Finally, the similar materials were applied to the excavation seepage model test of Bahe Tunnel in Xi'an Metro Line 9, and the evolution laws of stress and seepage field of the surrounding rock were revealed.

2 SIMILARITY PRINCIPLES

The similarity principles serve as the theoretical basis for conducting model experiments as well as the prerequisite for generating similar materials for model experiments. For underwater shield tunnels, the similarity of geometric, boundary, stress conditions and hydraulic performance must be fulfilled together. The similarity principles are often derived with dimensional analysis, fundamental elasticity equations and solid-fluid coupling theory.

The similarity ratio (C) is the ratio of the same physical variables for the prototype and the model. According to the dimensional analysis method, the similarity ratio of dimensionless physical quantities is 1, and the similarity ratio of the physical quantities of the same dimension is equal. The formula is as follows:

$$\begin{cases} C_\varepsilon = C_\mu = C_\varphi = 1 \\ C_E = C_\sigma = C_c \end{cases} \tag{1}$$

Where ε is strain, μ is Poisson's ratio, φ is internal friction angle, E is elastic modulus, σ is stress, and c is cohesion.

The equilibrium equations for the prototype and the model are:

$$\begin{cases} (\sigma_{ij,i})_p + (f_i)_p = 0 \\ (\sigma_{ij,i})_m + (f_i)_m = 0 \end{cases} \tag{2}$$

Where $(\sigma_{ij,i})_p$ and $(\sigma_{ij,i})_m$ are the stress tensor for the prototype and model, $(f_i)_p$ and $(f_i)_m$ are the volume force tensor for the prototype and model.

The following relationship can be deduced from the equilibrium equations.

$$\frac{C_\gamma C_L}{C_\sigma} = 1 \tag{3}$$

Based on the physical, geometrical equations, as well as the stress and displacement boundary conditions, the following relationship can be derived.

$$\begin{cases} C_\delta = C_\varepsilon C_L \\ C_\sigma = C_E C_\varepsilon \end{cases} \tag{4}$$

The relationship between the model and the prototype variables can be deduced by the solid-fluid coupling mathematical model with a continuous medium, i.e., the seepage equation and the effective stress equation are as follows (Huang et al., 2023):

$$\begin{cases} K_x \dfrac{\partial^2 P}{\partial^2 x} + K_y \dfrac{\partial^2 P}{\partial^2 y} + K_z \dfrac{\partial^2 P}{\partial^2 z} = S \dfrac{\partial P}{\partial t} + \dfrac{\partial e}{\partial t} + W \\ \sigma_{ij} = \bar{\sigma}_{ij} + \alpha \delta P \end{cases} \tag{5}$$

Where K_x, K_y, K_z are the permeability coefficients for the x, y, z directions and K_x=K_y=K_z, P is the water pressure, S stands for the water storage coefficient, e is the volume strain, W is the source and sink term, σ_{ij} is the total stress tensor, $\bar{\sigma}_{ij}$ is the effective stress tensor, α is the coefficient of Biolt effective stress and δ is the Kronker notation.

Based on the seepage equation, the effective stress equation and the equilibrium equation, the similar ratio of the permeability coefficient can be deduced as follows.

$$C_K = \frac{\sqrt{C_L}}{C_\gamma} \tag{6}$$

Where C_K is the similarity ratio of the permeability coefficient, C_L is the similarity ratio of the length, and C_γ is the similarity ratio of the bulk density.

3 MATERIALS AND METHODS

3.1 *Raw materials*

The research object of this similar material simulation experiment is the cobble stratum, which is composed of cobbles, gravel and sand with significantly varied particle sizes. It has the characteristics of coarse particle overlapping, fine particle filling, soil cementation and high permeability. To accurately recreate the sand and water outburst process, the following characteristics are required to be included for new similar materials. (1) Similar materials are manufactured from a mixture of coarse and fine aggregates that guarantee an appropriate framework and porosity. (2) The material has stable physical, mechanical and chemical properties that are not easily influenced by environmental factors including time or temperature. (3) Similar materials should have a wide range of permeability coefficients and excellent adaptability in terms of hydrological properties. (4) The mechanical parameters of the material (e.g., cohesion, angle of internal friction, etc.) vary greatly with the proportions of its composition, facilitating the simulation of complicated and changing geological environments. (5) The materials should be convenient to prepare, mix and shape, as well as simple to maintain with an efficient manufacturing procedure. (6) The materials have a wide range of sources, low cost, and are non-toxic and harmless.

Based on the principles of similar material selection outlined above, the primary goals for making similar materials are overall control and sub-item modification. Since it has stable physical and mechanical characteristics and is not water-insoluble, selecting quartz sand with a 6–8 mesh, 10–20 mesh and 70–140 mesh as aggregates can accurately simulate the complex and diverse grading composition of surrounding rocks. Barite powder with a high specific gravity and high compaction is chosen as the counterweight material, which can be capable of regulating the material's specific gravity. Gypsum is used as the cementing agent because it is simple to use, quick to mold, weak to cement and can more effectively regulate the strength of similar materials. Silicone oil, liquid paraffin, glycerin and petrolatum are sequentially utilized as modifiers to regulate one or several specific parameters and have little or no impact on other parameters.

3.2 *Experimental design*

The orthogonal test is a powerful test approach suitable for multiple factors and levels, which can minimize the number of tests and improve the uniformity of the distribution of test points. Based on the preliminary results of pre-experiment, as well as combined with previous research experience on solid-fluid coupling similar materials, it can be acknowledged that the quantity and particle size of quartz sand, barite powder content and cement-aggregate ratio are all significant factors impacting the material's mechanical and hydraulic properties. In this orthogonal experimental design of similar material proportioning, the aggregate content (i.e., quartz sand content) was chosen as Factor A, the fines content (i.e., barite powder content) was chosen as Factor B, the cement-aggregate ratio (i.e., the ratio of the gypsum to quartz sand content) was chosen as Factor C, and the coarse-to-fine aggregate ratio (i.e., the ratio of the quartz sand

content of the 6-8 and 10-20 mesh to the quartz sand content of 70-140 mesh) was selected as Factor D.

Since this experiment requires a wide range of similar material parameters to be regulated with high precision, each factor is set to a fairly large number of five levels, and the design of the orthogonal test for similar materials is shown in Table 1. The standard orthogonal table $L_{25}(5^6)$ with 6 factors and 5 levels was adopted, and a total of 25 groups of similar materials with different proportions are presented.

Since the regulators used in the similar materials simulation experiments of solid-fluid coupling must be non-hydrophilic, four kinds of materials (i.e., silicone oil, liquid paraffin, glycerol and petrolatum) were selected after reviewing a substantial amount of information on solid-fluid coupling similar materials. On the basis of the above 25 sets of orthogonal tests, the effects of four types of regulators and their additive amount (i.e., 2%, 3%, 4%, 6% and 8%) on the mechanical and hydraulic parameters of similar materials were further studied by employing the single-factor test method.

Table 1. Orthogonal experiments for similar materials.

Level number	Factor A	Factor B	Factor C	Factor D
1	0.20	0.04	2%	0.25:1
2	0.35	0.08	4%	0.5:1
3	0.50	0.12	6%	1:1
4	0.65	0.16	8%	2:1
5	0.80	0.20	10%	4:1

3.3 *Experimental test*

The physical quantities measured in this test include the material's density, elastic modulus, cohesion, internal friction angle, and permeability coefficient. When configuring the similar materials, the quartz sand, barite powder and gypsum powder were firstly mixed, then the weighed water used for mixing was added and finally the appropriate regulators were provided to complete the mixing process until the combining material was homogeneous. The process of preparing the specimens of similar materials was shown in Figure 1.

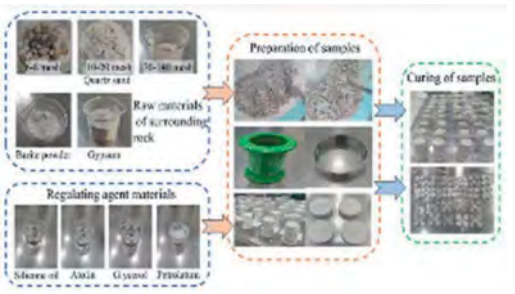

Figure 1. The procedures of preparing the specimens.

A double-opening mold with diameter of 50 mm and height of 100 mm was used to make the cylindrical specimens. The uniaxial compression test was conducted on an electro-hydraulic servo universal testing machine, as shown in Figure 2(a). The specimen was loaded at a displacement rate of 0.02 mm/min along the axial direction. The ultimate failure patterns of the specimen included X-shaped shear failure, single-slope shear failure and tensile failure (see Figure 2(b)). The full stress-strain curve of specimens was obtained, and its slope of the elastic phase was the elastic modulus E.

The cohesive force (c) and internal friction angle (φ) of similar materials were determined by ZJ-4K strain-type direct shear apparatus. The specimens of φ61.8 mm × 20 mm were made by standard ring cutters and were saturated by filling the shear box with water. The direct shear tests were carried out under different vertical pressures of 100 kPa, 200 kPa, 300 kPa and 400 kPa as shown in Figure 2(c). The parameters of shear strength were calculated as follows:

$$\tau = c + \sigma \tan \phi \tag{7}$$

Where τ is the shear force, σ is the vertical pressure.

The permeability coefficient (K) is an important indicator that synthesizes the hydraulic properties of similar materials. Because the permeability coefficient of cobble stratum is commonly large, the TST-70 constant head permeameter was employed to measure the specimen's permeability coefficient as shown in Figure 2(d). The permeability coefficient was calculated as follows.

$$\begin{cases} K_T = \frac{QL}{AHt} \\ K_{20} = \frac{\eta_T}{\eta_{20}} \end{cases} \tag{8}$$

Where K_T is the permeability coefficient of specimen at T Celsius degrees, Q is the volume flow at the time period t, L is the height difference between two pressure measuring holes, A is the test cross-section area, H is the difference in average water level, t is the time, K_{20} is the permeability coefficient of

Figure 2. Physico-mechanical tests of similar materials.

specimen at 20 Celsius degrees, η_T is the dynamic viscosity of water at T Celsius degrees and η_{20} is the dynamic viscosity of water at 20 Celsius degrees.

4 RESULTS AND ANALYSIS

4.1 *Test results of similar material*

The physical quantities of materials including bulk density, modulus of elasticity, cohesion, internal friction angle and permeability coefficient were measured by cutting ring, uniaxial compression test, direct shear test and constant head permeability test. The test results of 25 groups of similar material specimens were listed in Table 3. It can be observed that the variation range of similar material parameters is 16.5-21.1 kN/m3 in bulk density, 3.14-4.63 MPa in elastic modulus, 0.007-0.529 kPa in cohesion, 19.6-38.7° in internal friction angle and 0.003-2.02 cm/s in permeability coefficient. Compared with previous research on the similar materials of geo-mechanical model test, the newly-developed similar materials have a wide range of physical, mechanical and hydraulic parameters and better satisfy the requirements for similar physical modeling tests in cobble formations. Additionally, in accordance with the demands for specific projects, we can flexibly modify the proportions of similar materials to customize the similar materials of solid-flow coupling model test.

Table 2. Test results for similar material parameters.

Number	Bulk density (kN/m^3)	Elastic modulus (MPa)	Cohesion (kPa)	Internal friction angle (°)	Permeability coefficient (cm/s)
1	16.5	3.76	0.038	19.7	2.019
2	18.1	4.63	0.146	21.8	0.258
3	19.4	4.51	0.529	27.9	0.093
4	21.0	4.38	0.185	27.1	0.124
5	20.7	4.08	0.109	26.9	0.231
6	19.4	4.19	0.249	26.8	0.086
7	19.0	4.20	0.102	29.2	0.565
8	20.0	4.03	0.185	35.1	0.093
9	21.0	3.92	0.012	27.8	0.035
10	20.7	4.29	0.376	24.8	0.042
11	18.6	3.97	0.244	26.6	0.164
12	17.8	3.89	0.034	22.3	0.022
13	19.7	4.03	0.061	26.0	0.010
14	21.1	4.00	0.143	21.8	0.045
15	20.4	4.04	0.115	26.7	0.007
16	16.6	3.97	0.224	19.6	0.003
17	18.0	3.56	0.347	20.1	0.010
18	18.6	3.78	0.249	25.2	0.161
19	17.4	3.28	0.185	22.7	0.030
20	20.4	4.01	0.071	38.7	0.032
21	17.1	3.43	0.076	27.1	0.010
22	17.9	3.27	0.282	30.2	0.036
23	17.3	3.31	0.021	33.1	0.006
24	18.6	3.14	0.007	31.7	0.004
25	17.1	3.20	0.070	27.1	0.005

4.2 *Sensitivity analysis involved in parameters*

In this section, range analysis method was utilized to examine the sensitivity of the test results because it has the advantages of simple calculation, an intuitive image and ease of understanding. The magnitude of the extreme difference illustrates the extent to which a specific component influences the material's critical characteristics. The effects of each component of similar materials on parameters including bulk density, elastic modulus, cohesion, internal friction angle and permeability coefficient will be analysed as shown in Figure 3.

It can be seen from Figure 3(a) that the extreme deviations of factors A and B are the largest, whereas those are close and small for factors C and D. This indicates that the two critical controlling factors are aggregates content and fines content, both of which have a significant impact on the sensitivity of bulk density. Figure 3(b) presented the distribution of each factor's impact on elastic modulus. It is noticeable that the factor A has the greatest extreme deviations, while the extreme deviations of the other three factors are close and smaller. This shows that the aggregate content is the main factor that has a significant impact on elastic modulus sensitivity. As shown in Figure 3-(c), the extreme difference of the factor C is much greater than that of other three factors. This means that the cement-aggregate ratio is the most important factor deciding cohesion and its effect on the sensitivity of cohesion is significant. As shown in Figure 3(d), it can be observed that the extreme difference in skeleton content is the biggest, followed by the fines content, which is close to the coarse-to-fine aggregate ratio, and the extreme difference in cement-aggregate ratio is the smallest. In summary, the internal friction angle of similar materials varies significantly with the increasing levels of each factor. Figure 3(e) illustrated each factor's effect on the permeability coefficient. The sensitivity of the permeability coefficient to each factor is in descending order as follows: skeleton content, coarse-to-fine skeleton ratio, fines content and cement-aggregate ratio. Specifically, the permeability coefficients of similar materials increase with increasing coarse-to-fine skeleton ratio, while decreasing with an increase of skeleton content, fines content and cement-aggregate ratio.

4.3 *Effect analysis of the regulators*

To further investigate the regulating effect of different types of regulators and their additive amount on the physical, mechanical and hydraulic parameters of similar materials, Group 9 was chosen from 25 sets of orthogonal tests, and silicone oil, liquid paraffin, glycerin and petroleum jelly were added at 2%, 3%, 4%, 6% and 8% of the total mass, respectively.

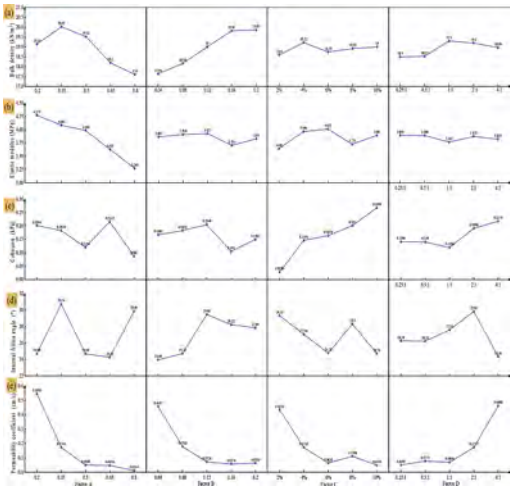

Figure 3. Sensitivity analysis of factors influencing the parameters of similar materials.

The specimen fabrication with the additive regulators and parameter testing were identical to those of the orthogonal test mentioned previously, and the test results are shown in Figure 4.

It can be observed from Figure 4(a) that the bulk density of similar materials is significantly influenced by glycerol, and it gradually increases with the increase of glycerol content. Silicone oil, liquid paraffin and petroleum have a little impact on the bulk density of similar materials, and it presents a fluctuating pattern with the increasing amount of added regulator. As seen in Figure 4(b), liquid paraffin and petroleum have an enormous effect on the elastic modulus of similar materials, yet silicone oil and glycerin have only a minor impact. When more liquid paraffin or petroleum is added, the elastic modulus of similar materials decreases. As shown in Figure 4(c), silicone oil, glycerin and petroleum have a significant effect on the cohesion of similar materials, but liquid paraffin has a negligible impact. With the increase of added glycerol, the cohesion of similar materials shows fluctuating changes, which will not be analyzed detailly. The cohesion of similar materials gradually increases because the amount of silicone oil or petroleum jelly added increases. As illustrated in Figure 4(d), it is difficult to regulate the internal friction angle of similar material even though any of the four regulators was used. Combined with the aforementioned results of the orthogonal test, the skeleton content, fines content and coarse-to-fine skeleton ratio all have a great effect on the internal friction angle of similar materials. It is pointed out that the particle gradation of the materials has a decisive role in the internal friction angle. It can be seen from Figure 4(e) that the permeability coefficient of similar materials is less influenced by glycerol, while silicone oil, liquid paraffin and petroleum have a significant influence on the permeability coefficients of similar materials. With increasing additions of the three regulators (i.e., silicone oil, liquid paraffin and petroleum), the permeability coefficient of similar materials sharply decreases.

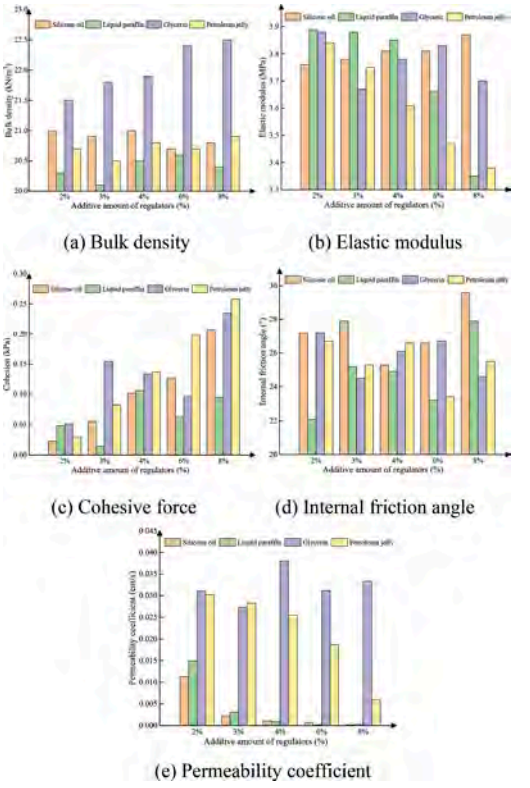

Figure 4 . Effects of four types of regulators and their additive amount on similar material parameters.

5 APPLICATON OF SIMILAR MATERIAL SIMULATION

5.1 *Overview of similar simulation experiments*

Shield tunneling method was employed in Xi'an Metro Line 9 to cross the Ba River between Xiangwang Station and Baliu 2nd Road Station. The diameter of the shield tunnel is 6.0 m, and the depth of the tunnel ranges from 10.0 m to 24.9 m. The left and right tunnels together pass through 124 meters of full-section cobble layer, which has high permeability coefficients, poor stratigraphic stability, complicated constructing circumstances and frequent water and sand outbursts. The process of shield tunneling produces considerable head pressure in the tunnel face, resulting in soil eruption at the screw conveyor, shield tail breakdowns and great increase in safety risk as shown in Figure 5.

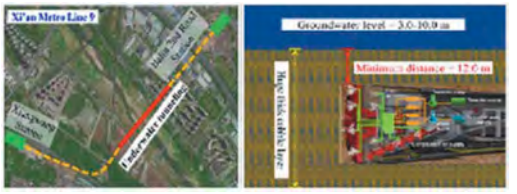

Figure 5. Schematic diagram of underwater shield tunneling in Xi'an Metro Line 9.

To simulate the response of the seepage and stress fields of the surrounding rock during the process of shield tunnelling under the hydro-mechanical coupling effect, a water storage tank with a volume of 1 m^3 was set up above the side of the model box to fulfil the requirements of water pressure and quantity for the experiment. Based on the dimension of model box (1.5 m × 0.5 m × 2.0 m) used in this paper, the geometric and bulk density similarity ratio of the model test were determined to be 1/40 and 1, respectively. Based on the similarity criterion Eq. (1) (3)(4)(6), the similarity ratios of other relevant parameters can be calculated as follows.

$$\begin{cases} C_\varepsilon = C_\mu = C_\varphi = 1 \\ C_E = C_\sigma = C_\delta = C_c = 40 \\ C_K = 6.32 \end{cases} \tag{9}$$

The physical variables measured in this test included pore water pressure, lining strain and surrounding rock stress. The model test device, sensors and data acquisition system are presented in Figure 6. The pore water pressure was measured by DMKY-1 high-precision micro pore water pressure meter with a diameter of 15.8 mm and a height of 21 mm. The lining strain was measured by pasting welding-free strain gauges on the inner and outer surfaces of the PMMA tube, and the dimensions of strain gauges were 10 mm by 5.5 mm. The surrounding rock stress was measured using DMTY-type miniature earth pressure box with a diameter of 16 mm and a thickness of 4.8 mm. All measurement data was recorded by DM-YB 1860 dynamic and static resistance strain instrument.

Figure 6. Model test device and monitoring instruments.

5.2 *Determination of similar material proportions*

Based on a large quantities of material proportioning tests described previously, the similar material proportions employed in this model test were provided in Table 3. The physical and mechanical parameters of the model and prototype surrounding rock were shown in Table 4.

Table 3. Proportioning of similar materials.

Item	Quartz sand (mesh)			Barite powder	Gypsum	Liquid paraffin
	70~140	10~20	6~8			
Percent	21.24%	42.48%	14.71%	19.61%	1.96%	1.8%

Table 4. Material parameters of the model and protype.

Material	γ (kN/m^3)	E (MPa)	c (kPa)	φ (°)	K_t (cm/s)
Model	19.8	3.9075	0.0885	33.7	0.00274
Protype	20.3	147	0.10	36.0	0.09259

Since the structural safety of the lining depends heavily on its flexural capacities, flexural stiffness is hence the key factor to be taken into account when designing for model similarity. According to the principle of bending stiffness equivalence, the lining of the model and prototype tunnel should have similar bending stiffness under the conditions of transverse bending, and their thicknesses should satisfy the following equation.

$$E_m I_m = n^{-3} E_p I_p \tag{10}$$

Where E_m is the elastic modulus of model lining, I_m is the moment of inertia of cross-section of model lining, n is the similarity ratio, E_p is the elastic modulus of protype lining, I_p is the moment of inertia of cross-section of protype lining.

In the practical engineering, C30 reinforced concrete tube were used with an elastic modulus of 30 GPa and a thickness of 30 cm. Thereby, the customized Plexiglas tube has a thickness of 1.5 cm and an elastic modulus of 3.75 GPa, which is calculated by Eq. (10). Additionally, the diameter of the Plexiglas tube employed was 15 cm based on the geometric similarity ratio.

5.3 *Test procedures and results*

Figure 7 illustrated the detailed test procedures for this model experiment. (i) For better sealing and waterproofing, the contact surface between the model box frame and toughened glass was evenly coated with glass adhesive; the waterproof geotextile was laid at the bottom of the model box as shown in Figure 7(a). (ii) As shown in Figure 7(b), firstly, weigh and mix the solid raw materials based on the proportion of similar materials; then, mix the liquid

paraffin with the water; finally, recombine the previously mixed solid components with the freshly mixed liquid paraffin. (iii) The well-mixed model material was filled and compacted in layers to a height of 10 cm per layer as shown in Figure 7(c). (iv) Repeat steps (ii) and (iii) until filling to the reserved tunnel hole, insert the PVC pre-embedded pipe and adhere foam waterproofing tape as shown in Figure 7(d). (v) As shown in Figure 7(e), installing the micro earth pressure box and pore water pressure gauge when filling to the corresponding measurement points. (vi) After the whole model filling was completed, the soil was saturated for 24 hours as shown in Figure 7(f). (vii) Through the gradual removal of the previously buried PVC pipe and the insertion of the organic glass pipe, this experiment reproduces the excavation and support procedure for shield tunnels.

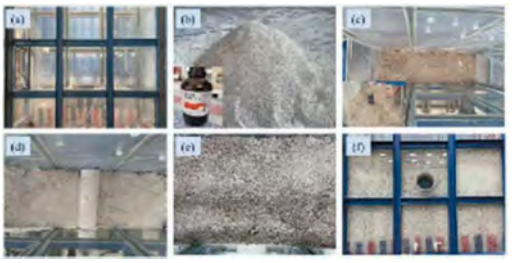

Figure 7. The test procedures for this model experiment.

Figure 8(a) demonstrates the dynamic change curve of osmotic pressure at each measurement point during tunnel excavation and water level variation. As can be observed, the osmotic pressure of each measurement point shows obvious drastic fluctuations due to tunnel excavation and supporting effects, particularly for WS1 nearby the surface and WS5 close to the tunnel border. After that, the osmotic pressure of the surrounding rock exhibits a fluctuating increase when the water level rises. Figure 8(b) shows the dynamic variation curves of vertical stress at each measurement point during tunnel excavation and water level change. During the excavation and support stage, the vertical stress of the surrounding rock shows a fluctuating type of reduction, i.e., the radial stress relaxation phenomenon. Afterwards, the vertical stress of the surrounding rock increased in a stepwise manner as the water level continued to increase. Figure 8(c) illustrates the dynamic variation curves of horizontal stress at each measurement point during tunnel excavation and water level change. It can be seen that the horizontal stress of surrounding rock sharply increases influenced by the disturbing effects of tunnel excavation and support, i.e., the phenomenon of circumferential stress arching. After then, the horizontal stress of the surrounding rock slightly increased as the water level continued to rise.

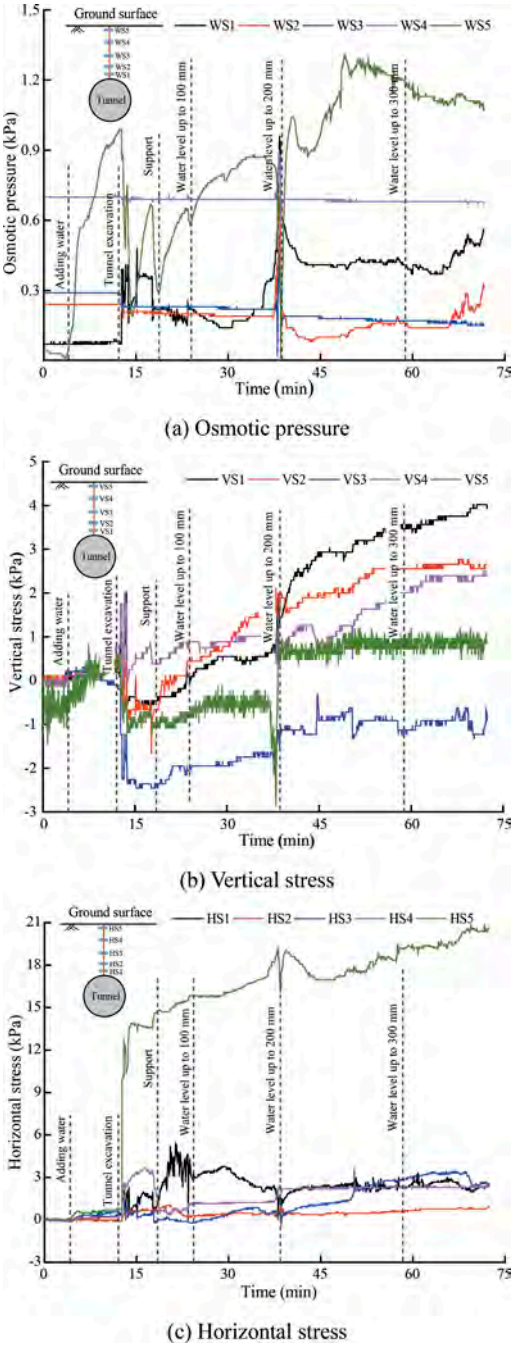

Figure 8. Multiple information of surrounding rock.

The internal force of the model lining can be measured by applying circular resistance strain gauges symmetrically to the inner and outer sides of the lining. The axial force and bending moment of the lining can be calculated by Eq. (11) and Eq. (12), respectively.

$$N = \frac{1}{2}E(\varepsilon_1 + \varepsilon_2)gb\mathrm{h} \quad (11)$$

$$M = \frac{1}{2}E(\varepsilon_1 - \varepsilon_2)gb\mathrm{h}^2 \quad (12)$$

Where N is the axial force of the model lining, M is the bending moments of the model lining, E is the elastic modulus of model lining, ε_1 and ε_2 are the inner and outer strain of the model lining, b is the unit length (1 m) and h is the lining thickness.

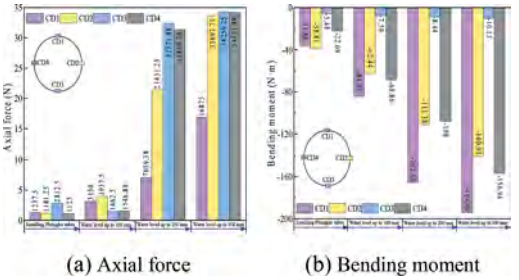

Figure 9. Structure internal force of the model lining.

Figure 9 shows the variations of axial force and bending moment of the lining structure during tunnel excavation disturbance and water level change. At the stages of initial excavation, support and water level up to 100 mm, the axial forces and bending moments of the lining structure were typically low, but they suddenly increased as the water level continued to be greater than 200 mm. In summary, it is obvious that the excavation disturbance and water level changes have significant effects on the distribution of osmotic pressure, surrounding rock stress and internal force of lining structure. Groundwater seepage and excavation disturbance together possess the effect of causing tunnel water and sand gushing as well as liner deterioration.

6 CONCLUSIONS

The similar materials composed of quartz sand with different mesh size, barite powder, gypsum, silicone oil, liquid paraffin, glycerol and petrolatum have a moderate range of parameters, steady performance, convenient preparation and affordable cost. When they were applied to complete the excavation seepage model test in Bahe Tunnel of Xi'an Metro Line 9, it was revealed that groundwater seepage and excavation disturbance together possess the water and sand gushing as well as liner deterioration. This can provide material basis for obtaining good test results and serve as a valuable reference for the selection of solid-fluid coupling similar materials for physical modeling test.

ACKNOWLEDGMENTS

This research was supported by the National Natural Science Foundation of China (No. 52278393 and No. 52208386) and the Projects on Scientific Research Plan of Shaanxi Province Education Department (No. 23JK0314).

REFERENCES

Bai, J., Wang, M., Zhang, Q., et al, 2020. Development and application of a new similar material for fluid–solid coupling model test. Arab. J. Geosci. 13, 913.

Chen, S., Wang, H., Zhang, J., et al, 2015. Experimental study on low-strength similar-material proportioning and properties for coal mining. Adv. Mater. Sci. Eng. 696501.

Cui, G., Zhou, C., Liu, Z., et al, 2022. The synthesis of soft rocks based on physical and mechanical properties of red mudstone, Int. J. Rock Mech. Min. Sci. 151, 105037.

Du, X., Zhang, P., Jin. L., et al, 2019. A multi-scale analysis method for the simulation of tunnel excavation in sandy cobble stratum. Tunn Undergr Sp Technol. 83, 220–230.

Huang, Z, Li, X, Li, S, et al, 2018. Research and development of similar material for liquid-solid coupling and its application in tunnel water-inrush model test. In Chinese Journal of Central South University (Science and Technology). 49(12): 3029–3039.

Kong, C., Gao, X., Ren, S., et al, 2023. Physical model test of tunnel complex surrounding rock progressive failure based on strength-reduction similar materials. Eng. Fail. Anal. 149, 107255.

Lu, H. F., Zhang, K., Chen, J. L., et al, 2022. A study on the optimal selection of similar materials for the physical simulation experiment based on rock mineral components. Eng. Fail. Anal. 140, 106607.

Luo, Y., Tao, Y., Zhang, M., et al, 2023. Experimental study on mix proportions of similar materials to reef limestone. Constr. Build. Mater. 365, 130111.

Shi, J., Wang, F., Zhang, D., et al, 2021. Refined 3D modelling of spatial-temporal distribution of excess pore water pressure induced by large diameter slurry shield tunneling. Comput. Geotech. 137, 104312.

Tian, Q., Zhang, J., Zhang, Y., 2018. Similar simulation experiment of expressway tunnel in karst area. Constr. Build. Mater. 176, 1–13.

Wang, C., Hou, J., Ye X. W., et al, 2023. In-situ monitoring and 3D numerical analysis of reinforced face behavior of tunnel in composite strata by considering randomly-distributed rigid cobble granules. Comput. Geotech. 156, 105263.

Tunnelling for a Better Life – Yan, Celestino, Thewes & Eberhardt (Eds)
© 2024 The Author(s), ISBN 978-1-032-80042-4
Open Access: www.taylorfrancis.com, CC BY-NC-ND 4.0 license

Study on the deformation and stress law of single shell lining in subsea rock tunnels

Wenbo Zhang
China Railway Academy Co., Ltd., Chengdu, China

ABSTRACT: This paper focuses on investigating the performance of a single-layer lining in practical tunnel engineering applications. The study utilizes a test section of a single-layer lining in the Huangdao segment of the Jiaozhou Bay Second Tunnel, China's longest subsea road tunnel. The engineering research aims to validate the effectiveness of a single-layer lining in hard rock tunnel engineering, particularly under grade 3 surrounding rock conditions. The research delves into the mechanical contact characteristics of the anchor-type single-layer lining structure. It also examines the deformation and laws of force governing the interaction between the single-layer lining and the surrounding rock, as well as the overall stability of the support structure. Experimental results indicate that the anchor-type single-layer lining exhibits excellent adhesion and integration with the surrounding rock, with force and deformation remaining within safe allowable limits. The application of a single-layer lining in hard rock tunnels is deemed feasible for ensuring engineering quality and safety. The support structure's operational performance proves reliable, making it suitable for widespread application and promotion in practical engineering.

Keywords: Hard Rock Tunnel, Single-Layer Lining, Force, Deformation

1 INTRODUCTION

The single-layer lining, introduced in the 1970s as a tunnel support system [1], has witnessed significant technological advancements in recent decades. With the refinement of shotcrete construction technology and improved performance quality, its application has proliferated. Nordic countries, including Norway, Sweden, Finland, and others, have widely embraced anchor and shotcrete support as a permanent solution in various tunnel and underground engineering projects, including road tunnels, railway tunnels, subways, underground factories, and sports facilities. Beyond the Nordic region, countries such as Canada, the United States, Brazil, and Chile, along with a notable presence in Asia, particularly in Singapore and Hong Kong, have adopted this method. Additionally, it finds applications in Australia's road and subway tunnels [2]. The construction of shotcrete single-layer lining stands out for its simplicity, eliminating the need for lining trolleys and the laborious installation of geotextiles and waterproof boards. This streamlined construction process not only facilitates easy quality control but also significantly reduces project costs. In geological conditions suitable for its application, the shotcrete single-layer lining demonstrates outstanding promotional value.

In the 1960s, the Cheng-Kun Railway in China successfully employed shotcrete with anchor rod single-layer lining technology in tunnels featuring favorable surrounding rock conditions. Similarly, the Shantou liquefied petroleum gas storage project utilized shotcrete and anchor rod single-layer lining support technology in several tunnels [3]. Notably, the auxiliary adit, spanning a length of 1220m, for the Qinling Tunnel on the Xikang Railway applied shotcrete steel fiber concrete for its single-layer lining [4]. The Gaopeng Gou Tunnel also incorporated 289m of shotcrete steel fiber concrete as a single-layer lining [5]. The Kuanshi Expressway Xiaotuanshan Tunnel employed 30m of wet spray steel fiber and mixed fiber high-performance concrete for its single-layer permanent lining [6]. Single-layer lining was applied in specific segments of the ventilation adit for the Xiaokou Expressway Extra-long Tunnel [7], the ventilation adit for the Baoyi Expressway Hongyanshi Tunnel [8], and the ventilation adit #1 for the Hanglan Expressway Motianling Extra-long Tunnel [9] .

In recent years, China has made notable strides in the research on single-layer lining, including both field applications and a theoretical understanding of the physical properties of lining structures. Yunhua Zhu conducted an analysis of the support structure and surrounding rock stability of wet-sprayed steel fiber concrete single-layer lining using the finite element method [10]. Yilun Zou et al. delved into the mechanical properties of single-layer lining in high-stress tunnels, employing numerical calculations based on the Hoek-Brown criteria [11]. Jianjun Wu

DOI: 10.1201/9781003495505-373

et al. scrutinized the mechanical characteristics of the single-layer lining structure and the stability of surrounding rock in the context of the Heiwu Railway Dabieshan Tunnel [12]. Yisan Deng et al. undertook a comprehensive study on the application of waterproof single-layer lining in the Qingdao Metro [13]. Guoping Du et al. contributed research on the stability of fiber concrete single-layer lining in tunnels, with a specific focus on the forces involved in the working process, including anchor rods, fiber concrete, and their interaction with the surrounding rock [14].

In summary, the aforementioned scholars have conducted extensive studies on the stability characteristics of single-layer lining and its applications in underground engineering. Building upon this existing body of research, the current paper undertakes on-site experiments to investigate the application of single-layer lining with the surrounding rock in hard rock tunnels. The study also examines the deformation and laws of force governing the interaction between single-layer lining and the surrounding rock. The results obtained from these experiments offer valuable references for related engineering projects.

2 PROJECT OVERVIEW

The Jiaozhou Bay Second Subsea Tunnel, strategically positioned between the existing Jiaozhou Bay Tunnel and the Jiaozhou Bay Bridge, serves as a vital cross-sea passage linking the primary urban area of Qingdao on the east bank with the West Coast New Area. The total length of the main line spans 17.48 kilometers, with the tunnel section covering 14.37 kilometers (10.02 kilometers underwater and 4.35 kilometers on land). This tunnel stands as the longest subsea road tunnel in China, plunging to a maximum depth of 115 meters below sea level. As part of the preliminary work for the second tunnel, the Huangdao inclined shaft extends over a total length of 1111 meters. It is comprised of an open-cut section measuring 69 meters and an underground excavation section spanning 942 meters. The cross-section takes on a horseshoe shape, and post-lining, the net width of the bottom surface is 7.0 meters, with a central height of 7.7 meters.

3 FIELD EXPERIMENT

3.1 *Test section support parameters*

The inclined shaft section of the Jiaozhou Bay Second Subsea Tunnel at the Huangdao end, spanning from X1DK0+650 to X1DK0+710, is buried deep and transitions into the underwater section, situated in mildly weathered rock. This segment exhibits local development of joint fractures, and overall stability is deemed satisfactory. While structural fractures with water may be present, the groundwater level remains relatively low. The surrounding rock is classified as level III, with full-section excavation being employed. Key support parameters are detailed in Table 1.

Table 1. Experimental section support parameters.

Content	Parameter Indicators
Support	CF40 Steel Fiber Concrete
	Steel Fiber Dosage: 45kg/m³
	Arch Section Φ22 Multi-layer Anti-corrosion Anchor Rod L=3.0m
	Side Wall Φ22 Multi-layer Anti-corrosion Anchor Rod L=3.0m
Steel Fiber Concrete	Bonding Strength with Rock Mass ≥0.8MPa
	3h Compressive Strength ≥2MPa
	1d Compressive Strength ≥12MPa
	Flexural Strength ≥6MPa Tensile Strength ≥2.7MPa
	Permeability Grade ≥P8

3.2 *Experimental plan*

For a comprehensive understanding of the mechanical changes and deformations in the surrounding rock and support structure post-excavation, it is imperative to select representative sections with typical observation points within the test section. Gathering mechanical data from deformation gauges at these chosen sections enables the assessment of the safety and stability of the tunnel structure. In this experiment, three representative sections were selected, and the milestones and test items are outlined in Table 2. The experiment focuses on anchor rod axial force contact pressure between surrounding rock and shotcrete, and shotcrete stress measurement points. These were strategically placed in areas with significant stress variations, including the crown, arch shoulder, and sidewall. The sensor arrangement is detailed in Table 1. To comprehend the coordinated deformation of the surrounding rock and tunnel structure, deformation measurement points were positioned at the crown and sidewall locations. Each measurement point at these locations was inserted into both the surrounding rock and the shotcrete, as depicted in Figure 2.

Table 2. Test section mileage calculation items.

Measure Section Mileage	Measurement Items	Sensors
DK0+655	Anchor Rod Tension	Rebar Gauge
DK0+682	Contact Pressure between Surrounding Rock and Shotcrete	Pressure Box
DK0+705	Stress in Shotcrete	Concrete Strain Gauge
	Deformation of Surrounding Rock and Lining	

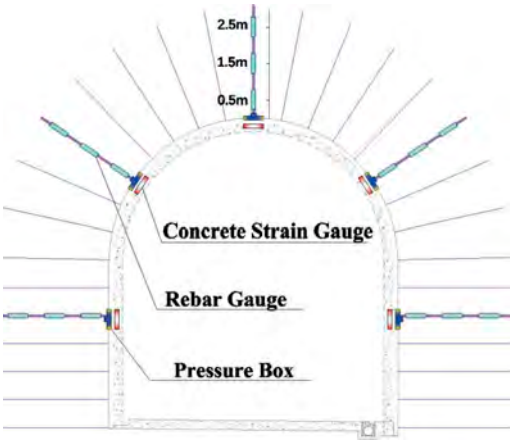

Figure 1. Sensor arrangement in the experimental section.

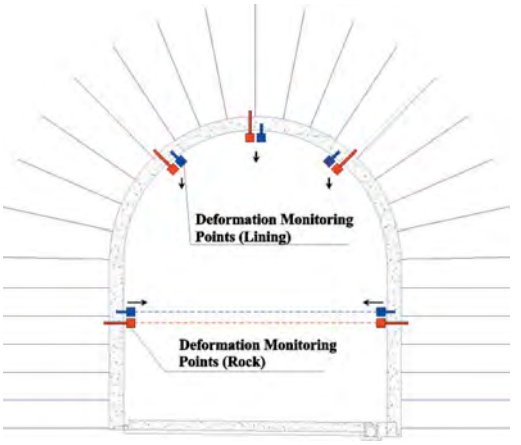

Figure 2. Arrangement of deformation measurement points in the experimental section.

Table 3. Anchor rod tension test results.

Position		Left wall	Left arch foot	Arch top center	Right arch foot	Right wall
DK0 +655	0.5m	13.21	4.55	0.82	0.59	10.31
	1.5m	0.29	1.17	0.02	0.77	0.94
	2.5m	-0.22	1.22	0.83	0.81	1.17
DK0 +682	0.5m	75.35	3.35	0.62	-0.06	6.02
	1.5m	35.58	1.85	-0.15	-0.22	1.44
	2.5m	-7.8	0.49	0.1	0.14	0.65
DK0 +705	0.5m	0.29	0.91	1.03	-0.35	-0.39
	1.5m	-0.08	0.37	0.38	-0.14	0.71
	2.5m	0.09	0.65	-	-0.36	0.02

Note: The axial force of the anchor rod with a "-" value indicates compression, while "+" indicates tension, units "kN".

3.3 *Test results analysis*

(1) Anchor Rod Axial Force

Within the test section, φ 22 multiple corrosion-resistant anchor rods, each with a length of 3 meters, were employed. Five testing points were strategically selected for each section, encompassing the middle of the crown, two arch shoulders (approximately 5.5 meters from the bottom plate), two sidewalls (approximately 2.5 meters from the bottom plate), or two arch feet (approximately 5 meters from the bottom plate). The detailed test results are presented in Table 3.

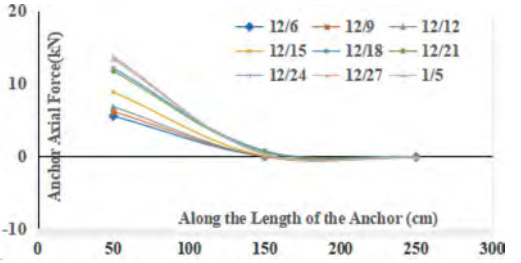

Figure 3. DK0+655 left wall anchor rod axial force.

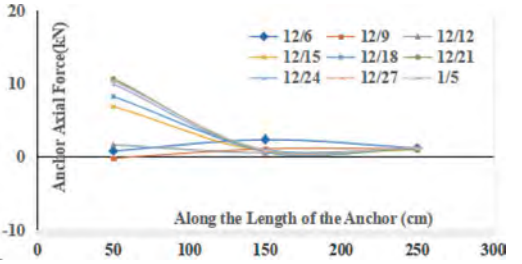

Figure 4. DK0+655 right wall anchor rod axial force.

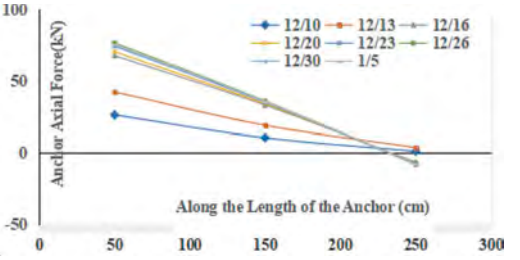

Figure 5. DK0+682 left wall anchor rod axial force.

Test Results Analysis:

➢ The maximum anchor rod axial force recorded in the test section is 75.35 kN, which falls below the ultimate tensile force of the anchor rod body (170 kN). Notably, force values predominantly hover in the range of -1 to +1 kN, suggesting minimal or negligible force impact on these anchor rods due to the surrounding rock. These measured values are

primarily attributed to shrinkage during the solidification and hardening process of the cement mortar.

- ➢ The anchor rods in the test section generally exhibit tension, with axial force variations observed in three distinct stages over time. There is a rapid increase stage in the initial 1-3 days post-construction, where axial force values typically reach 40%-60% of the final stable values. This is followed by a slow fluctuating increase stage spanning the 10-18 days post-construction, with axial force values approaching the final stable values. The final stage involves axial force stabilization after 15-20 days of construction.
- ➢ Considering the distribution of anchor rod axial force, there is a decrease with increasing depth. The force is more pronounced at individual points from a depth of 0.5m to 1.5m, becoming less noticeable at a depth of 2.5m. This suggests that the 0.5m point is within an area where the surrounding rock experiences larger displacement towards the tunnel. It can be inferred that the generally widespread loose zone of the surrounding rock in the test section ranges from 0.5m to 1m, locally extending to 1.5m. Combining this with the loose zone of the surrounding rock, it can be concluded that the depth of anchor rod anchoring into the surrounding rock's elastic-plastic zone is between 1m and 2m.
- ➢ In the DK0+655 and DK0+682 sections, the left sidewall displays more developed joint fractures and slightly lower integrity. The maximum measured points for anchor rod axial force align with these fractured areas, indicating that the anchor rod forces are appropriate for the geological conditions. The results imply that in sections with developed joint fractures and fractured surrounding rock, the anchoring effect of the anchor rod becomes evident.

(2) Contact Pressure between Surrounding Rock and Lining

The focus of this experiment was to assess the variation in contact pressure between the surrounding rock and the lining. Five measurement points were strategically arranged at each section, covering the crown, arch feet (left and right sides), and sidewalls (left and right sides). Detailed test results are presented in Table 4.

Table 4. Contact pressure test results of rock mass and lining.

	Mileage		
Location	DK0+655	DK0+682	DK0+705
Left wall	24.08	21.12	7.23
Left arch foot	13.39	7.67	2.18
Arch top center	17.61	12.82	2.10
Right arch foot	9.99	8.00	12.02
Right wall	9.99	1.47	4.99

Note: Contact pressure with a "+" value indicates compression, while a "-" value indicates tension,units "kPa".

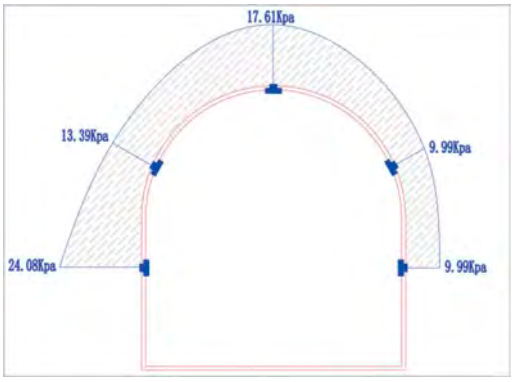

Figure 6. Distribution of contact pressure between rock mass and lining in DK0+655 section.

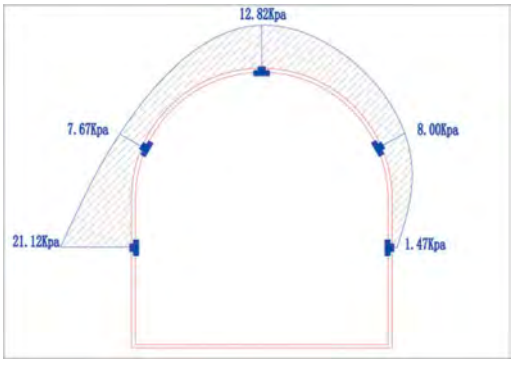

Figure 7. Distribution of contact pressure between rock mass and lining in DK0+682 section.

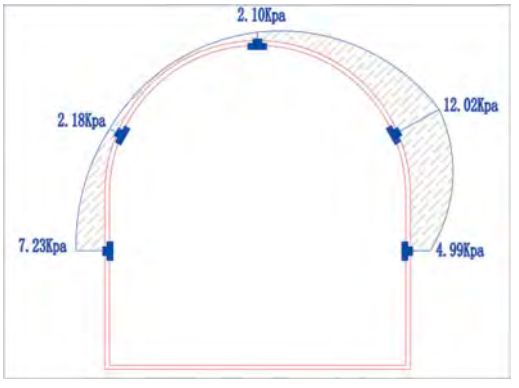

Figure 8. Distribution of contact pressure between rock mass and lining in DK0+705 section.

Analysis of Surrounding Rock and Lining Contact Pressure Results:

- ➢ The contact pressure between the surrounding rock and shotcrete in the test section registers compressive stress, ranging from 1.47 kPa to 24.08 kPa. The maximum contact pressure is

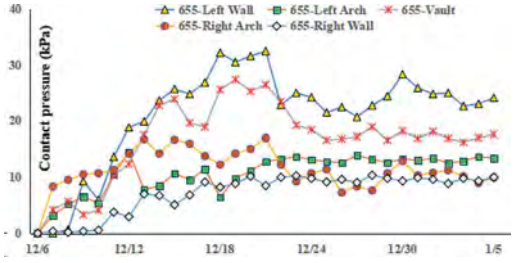

Figure 9. Contact pressure distribution in DK0+655 section.

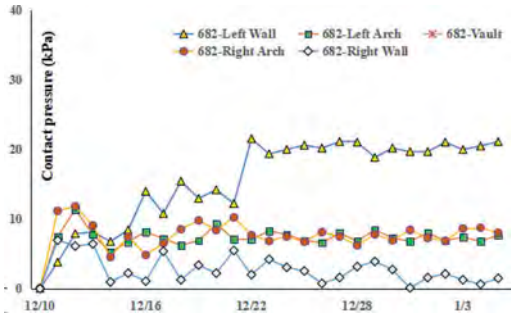

Figure 10. Contact pressure distribution in DK0+682 section.

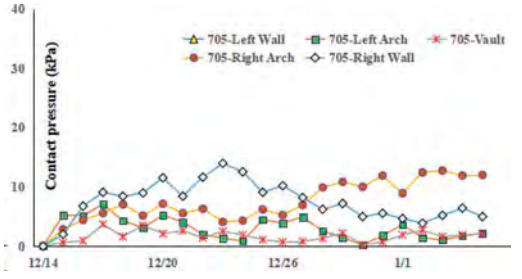

Figure 11. Contact pressure distribution in DK0+705 section.

24.08 kPa for the DK0+655 section, 21.12 kPa for the DK0+682 section, and 12.02 kPa for the DK0+705 section. All absolute values remain below the theoretically calculated design values, indicating a sufficient safety margin in the support structure.

➢ The temporal variation in contact pressure between the surrounding rock and lining unfolds in three stages. There is an early rapid increase stage within 6-8 days post-shotcrete construction, where contact stress values typically reach 60%-80% of the final stable values. Subsequently, a slow fluctuation stage transpires in the 10-20 days post-construction, characterized by continued contact stress fluctuation—some areas exhibit a slow increasing trend, while others show a slow decreasing trend (linked to the redistribution of surrounding rock pressure). The final stage involves contact stress stabilization after 20-25 days of shotcrete construction.

➢ The distribution of contact pressure at each section aligns well with geological conditions and locations where anchor rod axial force is prominent. The left sidewalls of the DK0+655 and DK0+682 sections, marked by more developed joint fractures and a more fractured rock mass, exhibit significantly higher contact pressures between the surrounding rock and lining. Experimental results indicate that in areas with a more fractured rock mass, the synergistic deformation release of surrounding rock pressure by shotcrete with steel fiber and the lining is evident. This underscores the effective support provided by the single-layer lining system comprised of anchor rods and shotcrete with steel fiber.

(3) Shotcrete Stress

This experiment focused on monitoring the circumferential internal stress of the lining layer. Five measurement points were strategically arranged at each section, covering the crown, arch feet (left and right sides), and sidewalls (left and right sides). Sensors were embedded within the steel fiber concrete, and the detailed test results are presented in Table 5.

Table 5. Shotcrete stress test results (MPa).

	Mileage		
Location	DK0+655	DK0+682	DK0+705
Left wall	0.41	-1.02	0.25
Left arch foot	-0.97	0.51	-
Arch top center	0.82	0.68	-1.33
Right arch foot	-2.43	-0.14	0.54
Right wall	0.69	0.07	-0.26

Note: Shotcrete Stress with a "+" value indicates compression, while a "-" value indicates tension,unit "MPa".

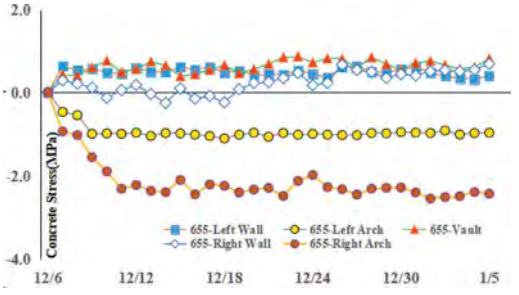

Figure 12. Concrete stress at section DK0+655.

Analysis of Shotcrete Stress Results:

➢ The maximum compressive stress value in the circumferential direction of the resprayed layer in the test section is 2.43 MPa, falling below the design value of 19.1 MPa for the compressive strength of C40 concrete. Similarly, the maximum tensile stress value in the circumferential direction is 0.82

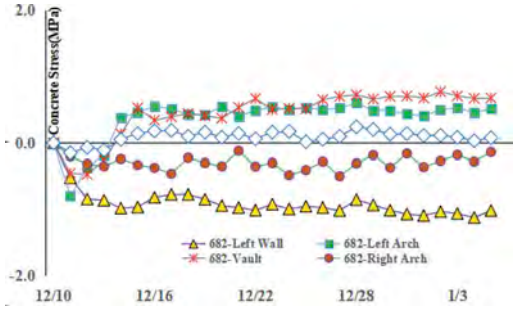

Figure 13. Concrete stress at section DK0+682.

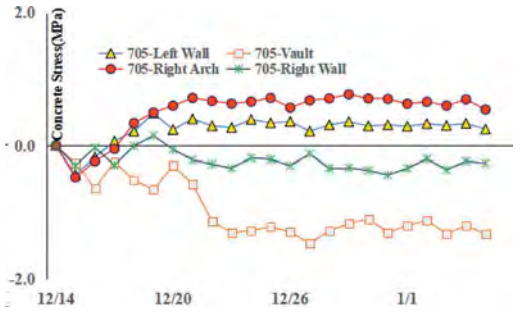

Figure 14. Concrete stress at section DK0+705.

MPa, below the design value of 1.71 MPa for the tensile strength of C40 concrete. These results affirm the safety of the support strength of the shotcrete with steel fiber in the test section.

- Among the measured points, 57% exhibit tensile stress, while 43% show compressive stress. Initially, most points display compressive stress post-shotcrete, gradually transitioning into tensile stress. As shotcrete with steel fiber provides support, internal stresses are generated in the axial and radial directions due to surrounding rock pressure and support resistance, influencing the tangential (circumferential) stress values. Additionally, contact pressure between the resprayed layer and the initial spray layer on the outer side of the resprayed layer can impact internal stress test values.
- Examining the stress change temporal diagram, the evolution of internal stress in the shotcrete lining unfolds in three stages: an early rapid development stage within 6-8 days post-shotcrete construction, a slow fluctuating development stage in 10-25 days post-construction, and a stage where shotcrete stress tends to stabilize after 20-25 days of shotcrete construction (with some stress points exhibiting certain fluctuations after 25 days).
- The locations of the maximum internal stress values vary among sections, and stress values on the left and right sides of the same section display an asymmetrical state. This discrepancy is attributed to differing integrity and deformation of the surrounding rock in various locations, resulting in varying internal stresses generated by the resistance of the shotcrete to the surrounding rock. This underscores the highly effective supporting role played by the resprayed layer.

(4) Deformation of Surrounding Rock and Lining

Deformation monitoring points were strategically positioned on the left and right sidewalls and the crown of the tunnel. At each location, measurement points were established on both the initial support and the surrounding rock to gauge horizontal convergence and settlement of the surrounding rock and lining structure. Notably, three points were selected for settlement measurements at the crown, and one set of convergence measurement lines was chosen for sidewall convergence. Internal measurement points in the surrounding rock were placed at a depth of at least 10cm and not in contact with the shotcrete. Similarly, internal measurement points in the initial support were positioned at a depth not less than 10cm. The detailed test results are presented in Table 6.

Table 6. Deformation test results of surrounding rock and lining in the test section.

		Arch Crown Settlement		Side Wall Convergence	
Mileage	Location	Surrounding Rock	Lining	Surrounding Rock	Lining
DK0 +655	Left	-2.20	-4.40	-1.2	-3.2
	Mid	-3.40	-4.00		
	Right	-3.20	-3.70		
DK0 +682	Left	-1.90	-3.50	-0.4	-0.8
	Mid	-1.50	-2.60		
	Right	-0.60	-4.10		
DK0 +705	Left	-0.70	-2.60	-1.2	-2.4
	Mid	-0.90	-2.90		
	Right	-0.70	-3.30		

Note: "-" values for the arch crown indicate settlement, and "-" values for convergence indicate convergence, unit "mm".

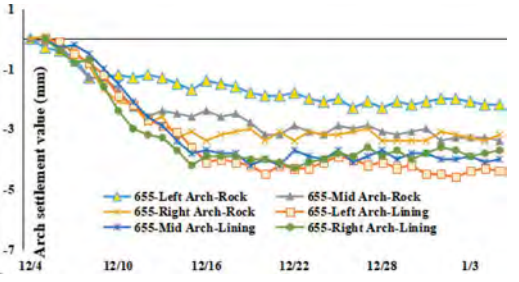

Figure 15. Settlement of surrounding rock and lining arch section at DK0+655.

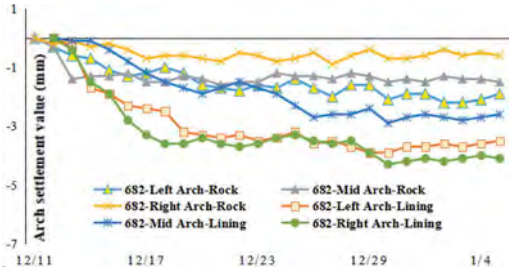

Figure 16. Settlement of surrounding rock and lining arch section at DK0+682.

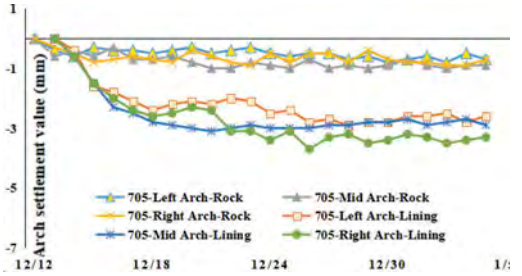

Figure 17. Settlement of surrounding rock and lining arch section at DK0+705.

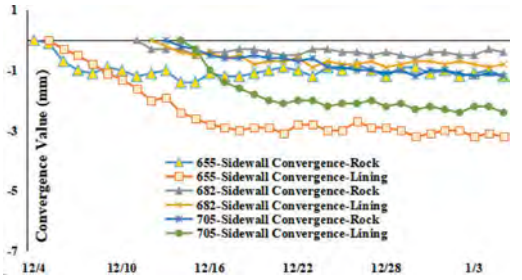

Figure 18. Convergence of surrounding rock and lining side walls in the test section.

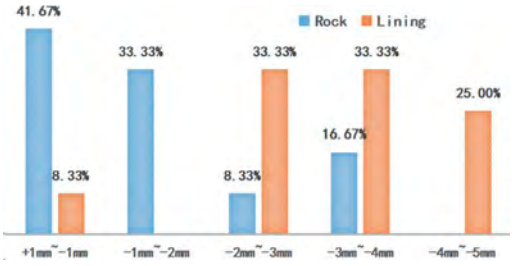

Figure 19. Cumulative deformation distribution of surrounding rock and lining in the test section.

Analysis of Surrounding Rock and Lining Deformation Results:

- The deformation values and deformation rates observed in the test section for the surrounding rock and lining are relatively small, all falling within the design control standards. The average change rates of the surrounding rock crown and convergence range from -0.02 to -0.11 mm/d and -0.02 to -0.05 mm/d, respectively. Similarly, the average change rates of the lining crown and convergence fall within the ranges of -0.12 to -0.17 mm/d and -0.03 to -0.11 mm/d, respectively. These values adhere to the criteria for basic stability of deformation (rate < 0.2 mm/d) .
- Surrounding rock deformation values span from +1 mm to -2 mm, constituting approximately 75% of the total measurement points, with an average cumulative change of -1.49 mm. In contrast, lining deformation ranges from -2 mm to -5 mm, encompassing about 90% of the total measurement points, with an average cumulative change of -3.1 mm. The cumulative deformation of the shotcrete with steel fiber lining surpasses that of the surrounding rock.
- The joint stability of the shotcrete with steel fiber concrete single-layer lining and the surrounding rock is deemed satisfactory. The surrounding rock generally stabilizes its deformation trend 3-5 days after initial data collection, while the lining typically stabilizes its deformation trend 10-15 days after initial data collection. Importantly, the deformation of the surrounding rock stabilizes earlier than the deformation of the lining.

4 CONCLUSIONS AND OUTLOOK

The performance of the single-layer lining support system proves to be excellent for maintaining the stability of the rock surrounding the tunnel. The analysis results lead to the following conclusions:

(1) In areas where joints and fractures in the surrounding rock are more developed and fragmented, the anchor support demonstrates significant effectiveness. The distribution of anchor forces aligns with the surrounding loosened rock. The measured contact pressure between the surrounding rock and the lining is relatively small, indicating the safety of the anchor-sprayed support system in the test section. Contact pressure distribution correlates with the condition of the surrounding rock, with higher pressures observed in areas with more fragmented rock. The variation of 60% to 80% of contact pressure occurs 6 to 8 days after the construction of the secondary spray

layer, stabilizing after 20 to 25 days of construction.

(2) The stress distribution of the sprayed steel fiber-reinforced concrete lining is irregular, signifying that the lining resists the deformation of the surrounding rock and generates different internal stresses. This underscores the effective supporting role of sprayed steel fiber-reinforced concrete. The surface of the sprayed lining exhibits no cracks, and the circumferential tensile/compressive stresses fall within allowable limits, affirming the safety of the sprayed steel fiber-reinforced concrete support strength.

(3) The synergy of deformation between the sprayed steel fiber-reinforced concrete lining and the surrounding rock is satisfactory, with relatively small deformation. The surrounding rock generally stabilizes its trend 3 to 5 days after the initial data collection, while the lining stabilizes its trend 10 to 15 days after the initial data collection. This indicates that the support system of anchor + sprayed steel fiber-reinforced concrete effectively controls deformation, providing robust support.

In summary, the experimental results affirm the feasibility of a single-layer lining under hard rock conditions, ensuring the quality and safety of tunnel engineering. The support structure demonstrates reliable working characteristics and can be widely applied and promoted in the mainline engineering of the Jiaozhou Bay Second Subsea Tunnel and similar projects

REFERENCES

[1] Guan Baoshu Design Main Points in Tunnel Engineering [M]. Beijing: China Communications Press,2003.

[2] Yan Jinxiu. Development trends in world tunneling technology: Safe, economical, green and artistic[J]. Tunnel Construction, 2021, 41(5): 693.

[3] LI Youqiang Application of NMT to Shantou LPG cavern project[J]. WorldTunnel, 2000(6):17–23.

[4] CHEN Zhi Analysis of steel fiber concrete lining compressive and tension strength of Qingling mountain tunnel[J]. Geological Exploration for Non-ferrous Metals, 2001, 4(11):57–59.

[5] Liang Guochen Permanent steel fiber shotcrete construction in Gaobiangou tunnel of XiKang railway [J]. Construction Technology, 2001, 30(5),23–39.

[6] HE Shaohui, MA Wanquan, et al. Permanent single-layer tunnel by fiber reinforced high performance shotcrete and wet-mix method [J].Chinese Journal of Rock Mechanics and Engineering, 2004, 23(20):3509–3517.

[7] Cao Kangjian. Application of fiber reinforced shotcrete in single layer tunnel lining[J].Journal of Water Resources and Architectural Engineering, 2011, 9(3):83–86.

[8] Wang Shicheng. Application Study of Single Layer Lining of Steel Fiber Spraying Concrete of Tunnel Ventilation Slope Well[J].Construction Technology, 2015, 44(S1):233–236.

[9] Du Guoping,Li Xiaohong,SONG Zhanping. Discussion on construction technology of single-layer fiber shotcrete lining [J]. Journal of Highway and Transportation Research and Development, 2010, 6(09):8–12.

[10] Zhu Yunhua. Study on Mechanical Characteristics of Steel Fiber Reinforced Shotcrete and Its Application in Single Layer Tunnel Lining[D].Chongqing University, 2009.

[11] Zou Yilun. Study on Mechanical Characteristics of Single-layer Lining under High Geo-Stress Conditions[J].Modern Tunneling Technology, 2018, 55(S2):129–137.

[12] Wu Jianjun. Study on Mechanical Characteristics of Single-layer Lining of Railway Tunnel Under Condition of Fractured Surrounding Rock[J]. Journal of Railway Engineering Society, 2011, 28(04):53–57.

[13] Deng Yisan, Li Jinming, Li Xiangdong, et al. Application of Waterproof Single-layer Lining in Qingdao Metro Hard-rock Tunnel[J]. Urban Mass Transit, 2023, 26(06):125–130.

[14] Du Guoping. Research on Stability of Fiber Reinforced Concrete among Single Layer Tunneling Lining[D].Chongqing University, 2013.

Tunnelling for a Better Life – Yan, Celestino, Thewes & Eberhardt (Eds)
© 2024 The Author(s), ISBN 978-1-032-80042-4
Open Access: www.taylorfrancis.com, CC BY-NC-ND 4.0 license

Using the acoustic emission and infrared thermal imager to identify the precursor of rock violent failure

Shuaida Zhu*
Shanghai Research Institute for Intelligent Autonomous Systems, Tongji University, Shanghai, China
Department of Geotechnical Engineering, Tongji University, Shanghai, China

Dongming Zhang & Hongwei Huang
Shanghai Research Institute for Intelligent Autonomous Systems, Tongji University, Shanghai, China
Department of Geotechnical Engineering, Tongji University, Shanghai, China
Key Laboratory of Geotechnical and Underground Engineering of Minister of Education, Tongji University, Shanghai, China

Changsong Wang
Shanghai Research Institute for Intelligent Autonomous Systems, Tongji University, Shanghai, China
Department of Geotechnical Engineering, Tongji University, Shanghai, China

Linghan Ouyang
Department of Geotechnical Engineering, Tongji University, Shanghai, China
Shanghai Research Institute for Intelligent Autonomous Systems, Tongji University, Shanghai, China

ABSTRACT: The fracturing of brittle rocks under loading involves an internal energy conversion process within the system. Acoustic emission (AE) and infrared radiation (IR) energy, as two forms of energy, are correlated with the elastic strain energy and dissipation energy of brittle rocks during uniaxial loading. This study introduced an infrared radiation index for the average cumulative radiation energy increment (ΔACRE) based on Stefan-Boltzmann law. AE cumulative Absolute energy and ΔACRE of the samples during loading were obtained separately using AE and infrared thermography systems。The mathematical model for coupling elastic strain energy with ΔACRE, dissipated energy with acoustic emission energy were derived and created. The causes of rock failure under loading were explained from an energy perspective。Based on the theory of energy dissipation, a quantitative analysis index Radiant-AE Energy Ratio (REAER) for rock failure was proposed. It is defined as the ratio between ΔACRE and AE absolute energy, which can be used to predict and identify rock failure and obtain precursor points of failure. This study offers a novel approach to predict rock burst disasters.

Keywords: brittle rock, strain energy, acoustic emission, infrared thermography, precursors of failure

1 INTRODUCTION

Rock bursts often occur during mining, tunnel excavation, and underground construction processes. Due to its sudden, destructive, and unpredictable characteristics, rock burst has become a serious disaster for production and safety. Rock burst is a phenomenon that rock mass releases a large amount of energy instantaneously along the excavation unloading surface (He et al., 2005). Rock is the main carrier of rock burst. Therefore, understanding the evolution process of strain energy during rock deformation and failure at different load stages is of great significance for obtaining precursor indicators of rock bursts and achieving stability monitoring and disaster warning in engineering projects (Zhou et al., 2018).

When rocks are damaged, strain energy is released in the form of elastic waves and heat. Elastic waves propagate rapidly and generate acoustic emission (AE) phenomena (Meng et al., 2014). Heat is transferred from the interior of the rock to the surface, forming an infrared radiation signal (IR). Therefore, the AE and IR characteristics of rocks during damage can help determine the strain energy evolution process during rock deformation and failure (Sun et al., 2017). Previous research on the evolution of AE and

*Corresponding author: 2211056@tongji.edu.cn

DOI: 10.1201/9781003495505-374

IR characteristics during rock loading has achieved many important results. Lin et al. (Lin et al., 2015) examined the mechanisms of crack propagation and failure in granite with defects during uniaxial compression. Li et al. (Li et al., 2010) explored the spatiotemporal evolution of acoustic emission events in both granite and marble. Zhang et al. (Zhang et al., 2018) investigated the failure patterns of anisotropic shale in Brazilian splitting tests, utilizing acoustic emission parameters. Cui (Cui et al., 1993) and Grinzato et al. (Grinzato et al., 2004) studied the thermal radiation characteristics of rocks under load. Wu et al. (Wu et al., 1998) discovered three types of abnormal rock failure characteristics using thermal radiation to study the precursors of rock failure.

However, the relationship between the strain energy under rock loading and the true infrared radiation energy (thermal energy) and acoustic emission energy (mechanical energy) is still unclear. In addition, some scholars have proposed some indicators for determining rock failure precursors based on AE and IR characteristics. Cao et al. (Cao et al., 2020) proposed a quantitative analysis index of energy dissipation infrared radiation ratio (EDIRR). Using the inflection point of EDIRR from horizontal to rapid growth as a precursor point for rock failure. Wu et al. (Wu et al., 2021) used the inflection point of AE cumulative count curve from horizontal to rapid growth as a precursor point for rock failure. However, the monitoring methods used are relatively single, and there are not many studies combining AE with IR. Moreover, the current methods for predicting rock failure are mostly based on observing the trend of changes in indicators, which cannot intuitively and quickly confirm the precursor points of rock failure.

Based on this, this article uses a combination of AE and IR methods to explain the failure process of rocks from the perspectives of infrared radiation energy (thermal energy) and acoustic emission energy, and proposes a new index for efficiently identifying precursor points of rock failure. The research results provide new ideas for predicting the occurrence of rock disasters.

2 EXPERIMENTAL SECTION

2.1 *Sample preparation*

In this study, representative red sandstone samples collected from Hunan Province, China were used. The rectangular size samples having a dimension of 50 × 50 × 100 mm were prepared with high geometric integrity from the same red sandstone block. The faces of the samples were carefully polished to avoid the end non-parallelism and to control parallelism within 0.2 mm. The processed red sandstone is shown in Figure 1(a). Rock samples were divided into 2 groups and each group contain 6 samples. All group samples were kept in laboratory at a room temperature for 48 hours.

2.2 *Experimental equipment*

The rock loading experiment was conducted on a single axis servo rigid testing machine WDW-600 having maximum loading capacity up to 600 kN. The loading rate is 0.15mm/min. The surface temperature of the samples was obtained using a Fotric 618C-L29 IR imager with a resolution of 640 × 480 pixels and a wavelength range of 7.5–14 μm. The capture frame rate of the IR imager is 25 FPS. The AE parameters were obtained using a PCI-2 AE data-acquisition system with a host, 2 signal amplifiers, and 2 AE sensors. The sensor model is R15α and can monitor AE signals with a frequency of 50-400 kHz. The entire testing system is shown in Figure 1b.

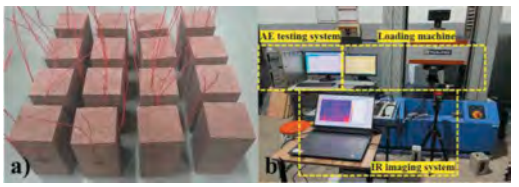

Figure 1. The figures of red sandstone samples (a) and testing system (b).

3 RESULTS AND DISCUSSION

3.1 *Energy evolution process*

Assuming that the compression deformation process of rocks is carried out in a closed system and there is no energy exchange with the outside world. So, the energy change of the system can be obtained from the first law of thermodynamics:

$$U = U^d + U^e \tag{1}$$

Where, U is the total strain energy (J), representing all the energy during the entire process, which can be calculated from the area between the sample stress-strain curve and the coordinate axis; U^e is the elastic strain energy (J), which is the energy stored during rock deformation; U^d is is the dissipated strain energy (J), which can be obtained by the difference between the U^e and the total strain energy U.

Figure 2 shows the relationship of dissipated strain energy and elastic strain energy. According to the study by Zhang et al. (Zhang et al., 2019), the U^e stored during uniaxial loading of rocks can be obtained by formula (2).

$$U^e = \frac{1}{2E_u}\sigma^2 \tag{2}$$

Where, E_u is the unloading elastic modulus; for the convenience of calculation, the elastic modulus is usually used instead of E_u. The elastic modulus in this article is the slope of the linear stage of the stress-strain curve.

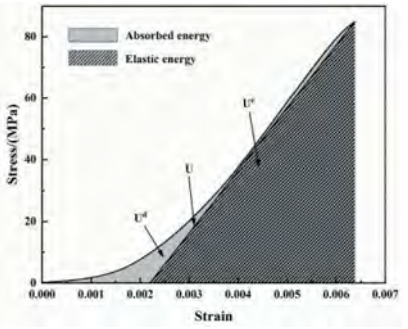

Figure 2. The relationship of dissipated strain energy and elastic strain energy in stress-strain curve.

Figure 3 shows the stress-strain curves and energy evolution-strain curves of the red sandstone samples. It can be clearly seen that as the strain increases, the stress, total strain energy, elastic strain energy, and dissipated strain energy all show an upward trend. According to the changes in stress-strain curves, the uniaxial loading process of red sandstone can be divided into three stages: compaction stage, elastic stage, and brittle failure stage. During the compaction stage, a portion of the input energy provided by the loading machine is converted into elastic strain energy and stored by the rock, while a portion of the energy is released as the primary pores inside the rock are compacted and destroyed. Therefore, the elastic strain energy and dissipated strain energy at this stage slowly increase, and the stored elastic strain energy is much higher than the dissipated strain energy. In the stage of elastic, all the input energy of the loading machine is converted into the elastic strain energy of the rock. Moreover, there are no small cracks or energy dissipation inside the rock, so the dissipated strain energy of the rock remains unchanged. In the stage of brittle failure, the elastic strain energy stored in rocks is rapidly released and converted into dissipated energy.

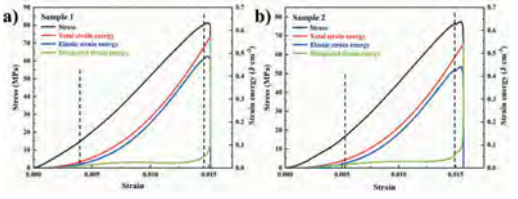

Figure 3. The strain energy evolution curves of red sandstone during uniaxial loading.

3.2 *Infrared Radiation Energy (IRE)*

All objects above absolute zero emit infrared radiation, and its radiation intensity is closely related to material properties and temperature states. During the loading process, the rock generates heat under external forces and emits infrared radiation outward. By using an infrared thermal imager, the temperature state of rocks can be obtained, thereby calculating the IRE. According to thermodynamics, it can be known that the radiation capacity of the red sandstone follows the Stefan−Boltzmann law (Ulhoa et al., 2019). Considering the radiation characteristics of objects, the infrared radiation energy can be calculated using the following formula:

$$IRE(t) = A\varepsilon\sigma\Delta t\mathrm{T}^4(t) \tag{3}$$

Where, *E(t)* is the IRE; ε is the emissivity of the red sandstone, ε≈0.909; σ is the Stefan−Boltzmann constant, $\sigma=5.67\times10^{-8}$ W/(m^2·K^4); T is the average temperature of the red sandstone; A is the area; Δt is the time interval in seconds.

If the IRE corresponding to time t is IRE(t) in the rock loading process, then the variation of the IRE from time t to time t-1 is:

$$\Delta IRE = A\varepsilon\sigma\Delta T^4(\mathrm{t})\Delta\mathrm{t} \tag{4}$$

The average cumulative radiation energy increment during the entire loading process of red sandstone is:

$$\Delta ACRE = \sum_{\mathrm{t_0}}^{\mathrm{t}} \Delta IRE(\mathrm{t}) \tag{5}$$

According to the above equation, the ΔACRE during the entire loading process of red sandstone samples is calculated and plotted in Figure 4. It can be clearly seen that ΔACRE of the sample increases with increasing stress. As the stress has a control effect on IR (Ma et al., 2019), the reduction of rock peak strength will inevitably lead to the change of maximum ΔACRE amplitude.

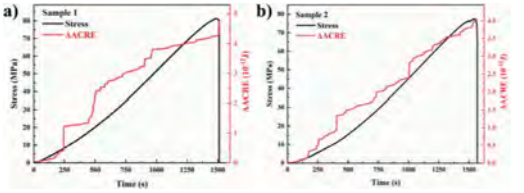

Figure 4. The ΔACRE curves of red sandstone during uniaxial loading.

The relationship of ΔACRE with stress and elastic strain energy during uniaxial loading of rock are shown in Figure 5. The correlation coefficient is more than 0.85 shows a strong linear relationship between ΔACRE with stress. The correlation coefficient is more than 0.90 shows a strong cubic polynomial relationship between ΔACRE with elastic strain energy. The fitting equations are listed in Table 1.

3.3 *AE absolute energy*

When the rock is damaged, the strain energy is released in the form of elastic wave, and the elastic

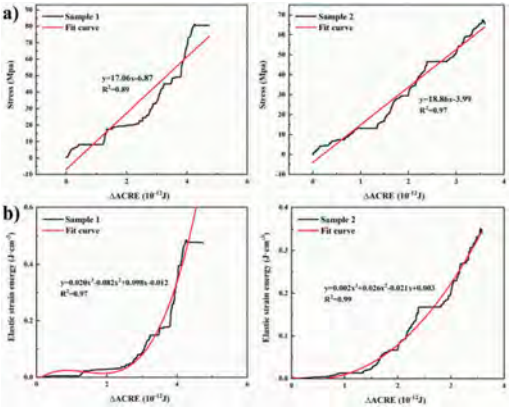

Figure 5. The relationship of ΔACRE with stress (a) and elastic strain energy (b) during uniaxial loading of samples.

Table 1. The relationship of ΔACRE with stress and elastic strain energy during uniaxial loading of samples.

Sample	Relationship equation(ΔACRE-stress)	R^2
1	y=17.06x-6.87	0.89
2	y=18.86x-3.99	0.97
Sample	Relationship equation (ΔACRE- elastic strain energy)	R^2
1	$y=0.020x^3-0.082x^2+0.098x-0.012$	0.97
2	$y=0.002x^3+0.026x^2-0.021x+0.003$	0.99

wave propagates rapidly and produces acoustic emission. Therefore, the AE characteristics of rock during loading are helpful to determine the failure law. Figure 6 illustrates the waveform characteristic of AE signals (Geng et al., 2017). Absolute Energy is the time integral of the square of the signal voltage at the sensor before any amplification, divided by a 10kΩ impedance and expressed in aJ (attojoules, $1aJ=10^{-18}J$). The corresponding physical energy formula is:

$$E = \frac{U^2}{R} \cdot t \tag{6}$$

Absolute energy is not affected by pre gain and can be compared intuitively with energy in physics.

Figure 7 presents the stress-time curves, AE absolute energy and accumulated AE absolute energy of the red sandstone samples. Higher AE energy is associated with more severe rock damage. As shown in Figure 8, the failure process of red sandstone also can be divided into three stages according to AE absolute energy. During the compaction stage (I), microcracks inside the rock rupture and generate a small amount of AE signals, and the accumulated absolute energy slowly increases. In the stage of elastic (II), There is no AE signal inside the rock, and the accumulated AE absolute energy remains basically unchanged. In the stage of brittle failure

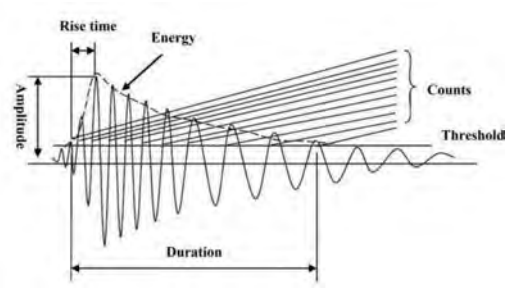

Figure 6. The waveform characteristic of AE signals.

(III), the rock undergoes severe damage, generating many AE signals, and the accumulated AE absolute energy increases exponentially.

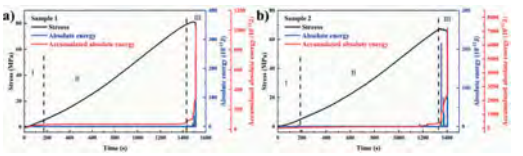

Figure 7. The stress-time, AE absolute energy-time and accumulated AE absolute energy-time curves of the red sandstone samples.

The accumulated AE absolute energy and dissipated energy during the entire loading process of red sandstone samples is calculated and plotted in Figure 8. It can be clearly seen that accumulated AE absolute energy and dissipated energy have the same growth trend over time. It can be interpreted that a part of the dissipated energy is emitted in the form of stress waves.

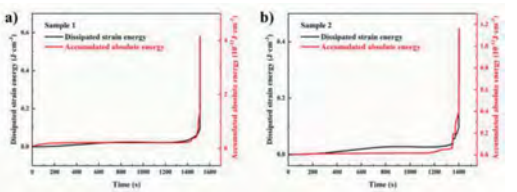

Figure 8. The accumulated AE absolute energy and dissipated energy during the entire loading process of red sandstone samples.

3.4 *Radiation-AE energy Ratio (REAER)*

During the process of rock loading, the increase of elastic strain energy is the process of energy storage in the rock. Its maximum value represents the maximum energy that a rock can store. Continuing to increase the load will result in the release of elastic strain energy. At this point, the elastic strain energy sharply decreases. Dissipated strain energy is the energy dissipated throughout the entire process of

a rock, which remains basically unchanged in the early stage and exhibits an exponential upward trend after reaching the maximum load. The elastic strain energy of rocks is fully transformed into dissipated strain energy. Therefore, the ratio of elastic strain energy to dissipated strain energy can be used as an indicator to predict rock failure. Using the time corresponding to the maximum ratio as the precursor point for failure. According to the research in the previous chapter, it can be seen that ΔACRE can replace elastic strain energy, and AE absolute energy can replace dissipated strain energy. Therefore, the ratio of elastic strain energy to dissipated strain energy can be converted into the ratio of ΔACRE to AE absolute energy, which can be more conveniently and quickly measured in engineering practice.

Using indicator REAER can monitor the process of rock failure under loading in real-time. The calculation formula is:

$$REAER = \frac{\Delta ACRE}{\sum AE\ absolute\ energy} \tag{7}$$

The REAER and stress curves of red sandstone samples under loading conditions are shown in Figure 9. The characteristics variation of REAER curves for rock samples are basically the same. During the compaction and elasticity stages, the REAER of the sample continuously rises to its maximum value. This indicates the beginning of the rock failure stage. During the failure stage, the REAER value continuously decreases until the samples are destroyed. The maximum REAER value of rocks can be considered as a precursor point for rock failure, and the decreasing stage after the maximum REAER value can be used as the criterion to monitor rock failure and instability.

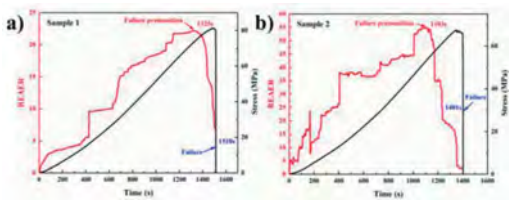

Figure 9. The REAER evolution curves of samples during uniaxial loading.

The failure time, precursor of failure, and leading failure time of rock samples are listed in Table 2. The failure time of sample 1 is 1510 s, the precursor of failure is 1325 s, which 185 s ahead of the failure time. The failure time of sample 2 is 1401 s, the precursor of failure is 1103 s, which 298 s ahead of the failure time. The failure time of sample 3 is 1540 s, the precursor of failure is 1311 s, which 229 s ahead of the failure time. The failure time of sample 4 is 1567 s, the precursor of failure is 1396 s, which 171 s ahead of the failure time. The average leading time reached 220s.

Table 2. The failure time, precursor of failure, and leading failure time of rock samples.

Sample	Failure time /(s)	Precursor of failure /(s)	Leading failure time/(s)
1	1510	1325	185
2	1401	1103	298

4 CONCLUSIONS

This study conducted uniaxial compression tests on red sandstone samples, monitored and analysed the IR and AE characteristics of the rocks to study its failure process. The main conclusions are as follows.

(1) According to the first law of thermodynamics, the energy evolution process during rock loading is analysed. The strain energy during the rock loading process is mainly composed of elastic strain energy and dissipated strain energy. The elastic strain energy undergoes three stages: gentle-rise-sharp decrease, and the dissipative strain energy undergoes three stages: slow rise-constant-sharp increase. Corresponds to the process of rock failure.

(2) According to Stefan-Boltzmann law, the indicator ΔACRE is proposed to reflect the change of stress and elastic strain energy of rock during loading. There is a linear function between stress with ΔACRE. There is a cubic polynomial relationship between ΔACRE with elastic strain energy.

(3) The cumulative AE absolute energy during rock loading is calculated. Compared with the dissipated strain energy, it is found that they have the same change trend, and the dissipated strain energy can be replaced by the cumulative AE absolute energy.

(4) A quantitative analysis index of the REAER was introduced, which can be used to predict violent rock failures intuitively and quickly.

(5) This study not only solves the characterization problem of elastic strain energy and dissipative strain energy during rock loading, but also combines IR with AE, which is more conducive to monitoring and warning of rock failure.

REFERENCES

He M, Xie H, Peng S, et al. Study on rock mechanics in deep mining engineering[J]. Chinese Journal of Rock Mechanics and Engineering. 2005, 24(16): 2803–2813.

Zhou Z, Cai X, Ma D, et al. Effects of water content on fracture and mechanical behavior of sandstone with a low clay mineral content[J]. Engineering Fracture Mechanics, 2018, 193: 47–65.

Meng L, Wang H W, Li X H, et al. Investigation on acoustic emission characteristics in failure process of coal absorbed methane[J]. Journal of China Coal Society, 2014, 39(2): 377–383.

Sun X, Xu H, He M, et al. Experimental investigation of the occurrence of rockburst in a rock specimen through infrared thermography and acoustic emission[J]. International Journal of Rock Mechanics and Mining Sciences, 2017, 93: 250–259.

Lin P, Wong R H C, Tang C A. Experimental study of coalescence mechanisms and failure under uniaxial compression of granite containing multiple holes[J]. International journal of rock mechanics and mining sciences, 2015, 77: 313–327.

Li YH, Liu JP, Zhao XD, et al. Experimental studies of the change of spatial correlation length of acoustic emission events during rock fracture process[J]. International Journal of Rock Mechanics and Mining Sciences, 2010, 47(8): 1254–1262.

Zhang SW, Shou KJ, Xian XF, et al. Fractal characteristics and acoustic emission of anisotropic shale in Brazilian tests[J]. Tunnelling and Underground Space Technology, 2018, 71: 298–308.

Cui C Y, Deng M D, Geng N G. Study on the features of spectrum radiation of rocks under different loading[J]. Chinese Science Bulletin, 1993, 38(6): 538–541.

Grinzato E, Marinetti S, Bison P G, et al. Comparison of ultrasonic velocity and IR thermography for the characterisation of stones[J]. Infrared physics & technology, 2004, 46(1-2): 63–68.

Wu L, Wang J. Infrared radiation features of coal and rocks under loading[J]. International Journal of Rock Mechanics and Mining Sciences, 1998, 35(7): 969–976.

Cao K, Ma L, Wu Y, et al. Using the characteristics of infrared radiation during the process of strain energy evolution in saturated rock as a precursor for violent failure[J]. Infrared Physics & Technology, 2020, 109: 103406.

Wu C, Gong F, Luo Y. A new quantitative method to identify the crack damage stress of rock using AE detection parameters[J]. Bulletin of engineering geology and the environment, 2021, 80: 519–531.

Zhang Y, Feng XT, Yang C, et al. Fracturing evolution analysis of Beishan granite under true triaxial compression based on acoustic emission and strain energy[J]. International Journal of Rock Mechanics and Mining Sciences, 2019, 117: 150–161.

Ulhoa SC, Santos AF, Furtado T F, et al. On gravitational casimir effect and stefan-boltzmann law at finite temperature[J]. Advances in High Energy Physics, 2019, 2031075.

Ma L, Zhang Y, Cao K, et al. An experimental study on infrared radiation characteristics of sandstone samples under uniaxial loading[J]. Rock Mechanics and Rock Engineering, 2019, 52: 3493–3500.

Geng J, Sun Q, Zhang Y, et al. Studying the dynamic damage failure of concrete based on acoustic emission[J]. Construction and Building Materials, 2017, 149: 9–16.

Digital and information technology

Taylor & Francis
Taylor & Francis Group
http://taylorandfrancis.com

Tunnelling for a Better Life – Yan, Celestino, Thewes & Eberhardt (Eds)
© 2024 The Author(s), ISBN 978-1-032-80042-4
Open Access: www.taylorfrancis.com, CC BY-NC-ND 4.0 license

BIM Modelling & reality capture in underground drill and blast caverns

Pedro Rey Antón*, Ivo Jose Ferreira Teixeira, Alessandra Barbetta, Bruna Bezerra Vieira & Fernando Abreu
ACCIONA Construction Brazil

ABSTRACT: Line 6 of São Paulo Metro is a design-build megaproject integrating the simultaneous construction of more than 15 km of TBM tunnel, 15 stations, 17 shafts and around 2km of non-mechanized tunnels and a train yard. The project has being implemented in a consolidated and complex urban environment in the central area of the city, and the northern part of the line was carried out on a granitic hard rock formation under very complex geotechnical conditions, this required the use of drill and blast methods to be excavated. The drill and blast stations concept are based in deep large diameter shafts and caverns, strongly relying on the observational method and toolbox measures, which generates great coordination challenges because the strict and diverse construction tolerances. Therefore the combination of the use of point clouds (generated "in loco" by the survey department) and BIM models was chosen to be able to control and adapt the excavations while coordinating it with other disciplines: civil (primary and secondary lining), architecture, MEP, systems, subcontractors… For the nature of the "fast track" construction method, and the fact it is a design-build project, a lively communication and constant feedback was created between the construction and the design models thought federated models, that is, between the technical office and the construction site. Thanks to this channel, it has been possible to optimize the decision-making process and to perform overall corrective actions in a shorter time span, improving and adapting the original designs, construction methods and generating shorter delays than may have taking place with a traditional method.

Keywords: BIM, Point Clouds, Drill&Blast, decision-making process, Design&Build, Reality Capture

1 INTRODUCTION

Line 6 of São Paulo metro is currently one of the most challenging projects worldwide. Its design-build megaproject integrates the simultaneous construction of more than 15 km of TBM tunnel, 2 km of non-mechanized tunnels, 15 underground stations, 17 shafts and emergency exit points, and large train yard. Its twenty-two trains in operation and two electric substations serve the line. It is important to highlight that while the line faces challenges related with the construction integration within the complex city of São Paulo, a focus is always given to the development of peripherical regions and communities it crosses.

For this article, João Paulo I station will serve as an example (both explanatory and illustrative) on the implementation of the project in three other similar stations and conceptually throughout the line.

The future João Paulo I station encompasses 39.50 m diameter and 41.30 m deep shaft in its underground component, with two 200 m² platform tunnels around 64 meters and 30 meters extension each. The surface of the shafts is around 727 m AOD (Above Ordnance Datum), while the excavation is completed at the 688.8 m level. The station is integrated in a highly dense urban area combining high-rise buildings and small houses in the near vicinity as well as a main artery road and water/drainage infrastructure. All in all, the vibration and excavation control are taken as essential to allow a safe and continuous construction process.

This paper focuses on how BIM methodology and entire processes were established and ran since the early design through the full construction cycle. Emphasis is given on how the Terrestrial Laser Scanning (TLS) point clouds generated from the site were integrated to the BIM models design, adapted construction of BIM models and models from other disciplines in such cases. Through these federated models (design and construction), mitigations, adaptations and improvements were studied and implemented daily through this methodology, adapting the excavation procedures where needed to comply with the strict tolerances.

*Corresponding author: pedro.rey.anton@acciona.com

DOI: 10.1201/9781003495505-375

2 GEOLOGIC AND GEOTECHNICAL ASPECTS

As mentioned previously, due to the particularities of the São Paulo geology the northern part of São Paulo line 6, which is the focus herein is implemented in a heterogenous granitic hard rock formation.

The geology of the João Paulo I station is integrated in the geological context of the intrusive granitoids of the Precambrian Basis covered by quaternary sediments. This granitoids are classified as homogeneous to porphyroids, thin to very coarse and light to heavy gray and red. The relatively high resistance to weathering generates superficial rock elevations and most of the areas are not covered by tertiary sediments having only residual soil below the quaternary deposits.

While the residual soils tend to be essentially soft soils in terms of geotechnical behaviour, the granite due to its formation and weathering patterns present a broad array of Rock Mass Rating (RMR) values, but nevertheless always demanding the use of drill and blast techniques to proceed with the excavation in a reasonable time scale.

2.1 *Local geology and geotechnical profile*

In the station area the stratigraphy can be divided in two major ground types: soil and rock. The soil type can be further divided in two different horizons, the upper one related with quaternary deposits which thickness ranges from 2.0 to 5.0 m and the deeper one with residual soil of granite origin encompassing all three levels of alteration (mature, young, saprolite) and up to 10.0 m thicknesses. Within the residual soil the frequency of boulders is high some of them reaching metric proportions.

Figure 1. 3D schematic geological model study.

In terms of rock excavation two main sub-divisions having different geomechanical behavior were identified. The first one is categorized as small layer of weathered granite (GIra) and is associated with Class V and low Class IV-, while the second category and the vast majority is defined as granite (GI) sub-divided in the remaining RMR classes (IV+ to I).

The rock top in the region is quite irregular, its starting level ranging from 724 mAOD up to 709 mAOD, while up to 10m level difference was identified in the shaft location. The water table is almost at the surface level.

The granite was categorized with a UCS ranging from 34 to 128 MPa and an average of 73 MPa recognizing the need to use drill and blast techniques in the shaft excavation. Additionally, television data from the boreholes allowed an estimation of stereographic projection to identify several main discontinuity families which has a critical aspect of the overbreak probability during the tunnel excavation.

By such a type of geology the selected station concept requires a large diameter shaft which would be excavated in both soil and rock layers interwined with two caverns which would be fully excavated in rock.

2.2 *Excavation concept and construction sequence*

The shaft excavation concept was divided in three types: i) full soil excavation, ii) transition where some part of the shaft would be in soil and rock, and iii) full rock ground. All three types the excavation was partialized by the aplication of a shotcreete primary lining reinforced with steel mesh in the soft soil and transition ground type and macrofibre in the rock part.

To improve the stability conditions and generate a watertight barrier in the soil layer a perimetral ground treatment made by secant jet grouting (JGv) columns was performed. The JGv was designed to have a variable length in accordance with the rock top.

The advancement in the soil-rock transition was predicted to be slower and more complex as the progress rates in rock are much lower than in the soil which requires laborious and carefully controlled drill and blast sequence and the fact that flyrock at such surface level is hazardous. The solution was to create independence between the level where the excavation in the soil would take place and where the rock would still be excavated, meaning that the soil and rock would be excavated in different steps inside the transition area. The remaining excavation of the shaft would be completely carried out in rock and was carried out using the drill and blast method with rock bolts applied as needed in accordance with the local stability conditions.

The tunnel excavation would be performed fully in rock, having a partialization based in crown, bench and invert. A conjugation of shotcreted macrofiber

reinforced primary linning, rockbolts, lattice girders, pipe umbrella, etc. could be used in view of the local conditions and rock behaviour and predicted in the tool box measures defined in the design criteria.

2.2.1 *Blasting schemes and tunnel excavation*

The blasting scheme is a central aspect of the drill and blast methodology. It is always a game of trade-offs, especially in urban areas where vibration limitation is severe and damage to the infrastructures in the surrounding area is not allowed.

The blasting scheme concept was based on the combination of two aspects:

I) smooth blasting and
II) tight net of blastholes with different activation speeds. Additionally small powder factors would be used even with a considerable total amount of explosives.

The "smooth blasting" technique was originated in Sweden after 1950 and consists in the performance of a tight "line drilling" with holes quite close to each other with reduced loading. The objective of this technique is to keep the excavation line as close to the theoretical as possible, minimize overbreak and vibration. The drilling was performed with 'jumbo" and/or pneumatic drilling rig. The explosive type used was packaged emulsion with high water resistance.

While a tremendous effort was made in the blasting schemes to minimize overbreak, lining reinforcements and related issues, the likelihood of its existence in the existing geology was quite high, which could generate a relevant problem in the future in terms of "invading" the space needed for the secondary lining, architecture, MEP, systems, etc.

In order to avoid such problems, which would be translated in costs and time overrun, the implementation of BIM with the 3D scanning since the excavation phase was performed generating specific action plans for each specialty to adapt its design as needed or perform additional civil works to correct the clash. (Bieniawski, 1989) (Teixeira et al., 2023)

3 METHODOLOGY

3.1 *Building information management*

Building Information Modeling (BIM) combines policies, technology and process which altogether constitute a "methodology to manage the essential building design and project data in digital format throughout the building's lifecycle". (Penttilä, 2006)

BIM tools have being increasingly incorporated into collaborative design and modelling processes, with the promise of substantive benefits for the efficiency of the design process. (Hardin & McCool, 2009) This methodology has quickly transformed the way infrastructures and buildings are conceived, designed, constructed, and operated. Although the first concepts of BIM date back to the early concepts of researching in parametric modeling imagined in USA and Europe in late 1970s and early 1980s, the Architecture-Engineering-Construction (AEC) industry practically started to implement it in projects as of the mid-2000s. (Eastman, et al., 2011).

BIM models developed under this methodology contain in their development the geometrical data, and non-geometric data as well. In addition, the following concepts will be achieved: an improved and optimized collaboration, intelligent documentation, access to a single source of information and distributed access and retrieval of building data and high-quality project outcome through enhanced performance analysis, as well as multidisciplinary planning and coordination. (Fischer & Kunz, 2004) (Haymaker et al., 2005) (Haymaker & Suter, 2006) Given the complexity of both the urban and geotechnical aspects, a series of models and studies of the area and the site were carried out where the station was to be built.

3.2 *Design and built project*

It is important to note that São Paulo line 6 project is carried out under the design-built project contract typology. Its design is carried out at the same time as the construction, which is known as "fast-tracking". Normally the construction project is delivered by the traditional method, wherein all activities begin on completion of their predecessors. However, we have become accustomed for some time on seeing the "fast-track" method used on large, complex projects. Fast-tracking consists of carrying out activities, initially considered sequential, in parallel, overlapping their performance. It is considered one of the three most common techniques of scheduling compression or acceleration. Thus, some amount of overlap occurs in this method between pairs of activities such as design and construction. For both project development and construction, a series of BIM models have been developed for each of the disciplines that make up the project.

The main advantage of the design-build approach is that it can implement the orderly intersection and close coordination of work at various stages through the simultaneous performance of design and construction tasks. The success of design projects depends on the quality of the available information. However, unlike crashing and substitution of activities, which usually directly increase project costs, overlapping activities are considered to increase project risk due to increased potential for change and/or rework (Ruby, 1978) (Van der Werf, 2003) which can lead to increased costs and problems such as schedule delay, cost overrun, and quality failure. (Wang & Feng, 2023) (Fazio et al., 1988).

Because of this complexity, decision was made to align the BIM models to the different phases of the project based on the total rework and complexity they generate. A favorable overlap strategy generates the required time savings, while considering both critical and non-critical activities and following the

critical path or adapting to changes if a new critical path emerges.

The use of these BIM models in both design and construction integrated with point clouds application has been used previously and validated in achieving optimization of the schedule of real-world projects.

Therefore, always aligned to the fact that it is a fast-track project, the choice was to combine the use of Terrestrial Laser Scanning point clouds (generated "in loco" by the survey department) and BIM models to be able to control the blasting performance while coordinating it with other disciplines: civil (primary and secondary lining), architecture, MEP, systems, subcontractors… Due to the nature of the construction method and the fact that it is a design-build project, a lively communication and constant feedback was created between the construction and the design models, and between the technical office and the construction site.

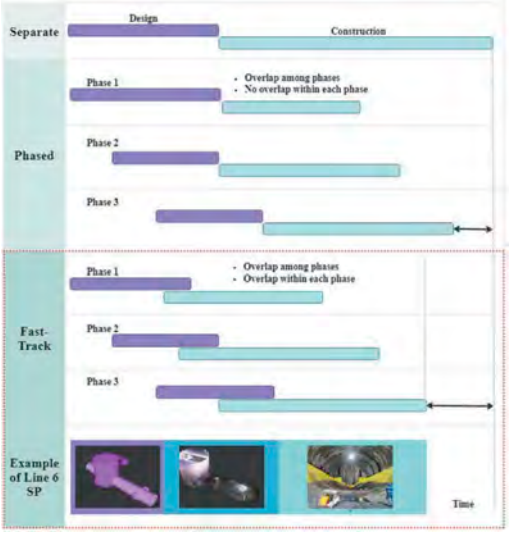

Figure 2. Design/Construction interaction schemes.

3.3 *Overview of laser scanning*

Terrestrial Laser Scanning (TLS) is a new technology that offers the possibility of creating 3D images in a fast way, with high definition and high density of surfaces and built elements.

Looking at it from a practical and economic point of view, this technology has proven to have the ideal characteristics for the incorporation of its use in construction works in general and especially in infrastructure, applying it in multiple uses and providing great benefits. Specifically in the case of tunnel works, it is used by surveyors' teams for surface modelling, profiling, volume calculation and work control. As a result, TLS use has increased even more in this type of projects, however, little has evolved to date in its use in combination with other technologies.

Simplifying the concepts of 3D terrestrial laser scanning very much, in terms of operation and instrument design, it can be perceived as a total station equipped with a servo mechanism and a reflectorless EDM. (Kotsis et al., 2005) In operating mode, the system measurement method takes averages under the system of taking points at a predetermined horizontal and vertical directions controlled by the instrument's control unit. (Lichti et al., 2000) In this way, a large number of points in space, 3D points, are obtained, which are combined by performing the process several times. This set of points is known as a "point cloud". The laser scanner gives the option to place these points in spatial coordinates, with a minimum margin of error. (Berger et al., 2016)

Continuing with this cycle, several point clouds are executed and geo-referenced by least squares-based technique called "Fuzzy Joint", so that they can be joined together between subsequent scan positions performed. Finally, this technique uses overlapped volumes between neighbouring point clouds allowing a full volumetric surface to arise. (Kotsis et al., 2005)

Figure 3. João Paulo I station points cloud.

4 BIM MODELLING & REALITY CAPTURE ON LINE 6

4.1 *Model creation*

Based on the project requirements and baseline information, conceptual BIM models were developed in the early stages of the project by the architectural designer and analysed and validated by the structural and geotechnical designer in conjugation

with the construction company's technical team. For the development, the BIM models were designed in a way that: i) considered both the design of the project itself, ii) particularities of its construction methodology, iii) information for the subsequent use and iv) maintenance in the life cycle of the asset.

Once it was developed and adapted to the needs and requirements of the project, geotechnical and structural designers created the internal and external structural models, based on the architectural models and the construction needs mentioned above. Special emphasis was given to the models of the excavation/ primary structures in view of the construction schedule of the project. The designers' models were coordinated to ensure a seamless and integrated design. At the same time the other designers, especially MEP disciplines, such a HVAC (wet and dry), plumbing, electrical, strain signalling, lighting, or fire protection, started to analyse these models and implement their own design models. Once they were developed, they were also coordinated and retrofitted to the Architecture and Structures models, adapting, and making changes to them as well in an iterative process. The information models already developed includes architectural components, engineering systems for structures, MEP services, as well as details of cross-cutting. In addition, given the fast-track nature of the project, the subcontractors were also brought in at a much earlier stage of the project to ensure the correct functionality and constructability of the project, as well as optimizations. This led them to also developing their own models from the design of the different disciplines, also entering these co-ordination processes at the very beginning.

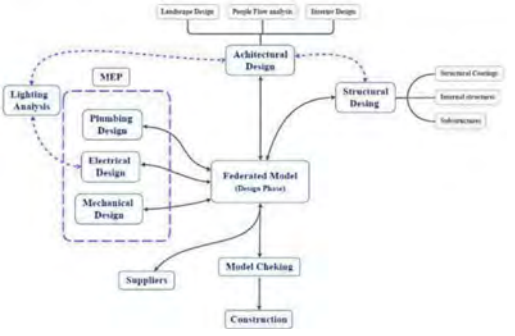

Figure 4. BIM models process. design phase.

Given the magnitude and complexity of the project, the need to introduce multiple BIM uses was prominent. These BIM uses are updated according to the needs required by the work and the construction progress. (Rey & Sedó, 2022)

In such a large project, it is important to analyse and develop the necessary BIM uses, at each site and each case, depending on the necessities of the construction units, different disciplines, work methodologies, etc. The following diagram shows the BIM uses that have been performed to João Paulo I station:

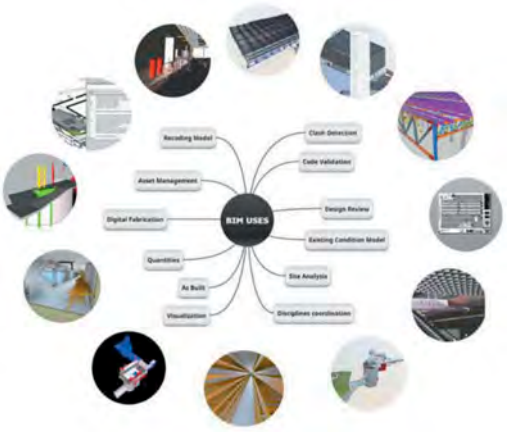

Figure 5. BIM uses.

4.2 *Model coordination*

In this type of large complex construction projects involving multiple parties such as contractors, suppliers and designers proper (model) coordination is fundamental. Many activities are carried out simultaneously, which can generate variations and compatibility issues due to construction, errors, omissions and misunderstandings leading to undesirable results that obligue the need to carry out the rework.

Rework has been a primary cause of cost and schedule overruns in large construction projects (Hegazy et al., 2011). The use of BIM models therefore had to be aligned in all phases linking design and construction aiming at mitigating those reworks. At the start of a project, it could be seen how all the work resides in the backlog of work to be performed. Once the project started to be on track and progressed in its construction, the pace of work is determined while the first objectives are performed. (Cooper, 1993)

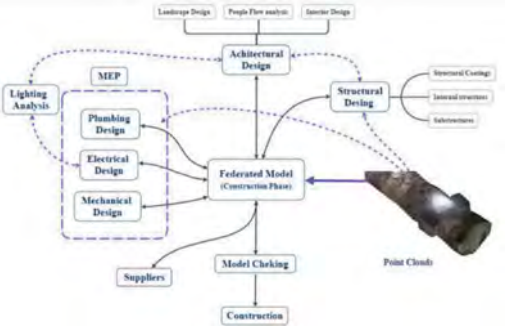

Figure 6. BIM models process. Construction phase.

4.3 *Federated model & point clouds model*

In addition, as explained in the geology section, due to the intrinsic characteristics of the blasting operations, imperfections in the excavation contour would occur in a positive or negative way (overbreak and underbreak). Corrections performed afterwards, especially underbreak correction would cause impact in the schedule as the excavation cycle would not be able to flow.

Thus, the need arose to align the design models according with each specific discipline tolerance, while the construction is carried out almost in "day by day" basis. To allow this, the decision was to have "point clouds" of the performed excavation contour generating realistic topographic models of the construction, that were immediately federated with the design models, thus being able to see the changes from the performance versus the theoretical designed.

In essence, if any change in the design was necessary both for technical and tolerance issues (secondary lining thickness for example), as well as to meet the minimum space requirements of the other disciplines, the federated model would be a decision-making channel and the fundamental workplace to align all the aspects of the construction.

The fractional value of quality determines the portion of the work being done to enter the pool of work really performed, which will never again require the re-doing. The remaining one will need some rework, but during the time that rework remains in a pool which we term "undiscovered rework", work that contains as-yet-undetected errors and is therefore perceived as being performed. (Cooper, 1993)

The creation of this federated model combines the point clouds giving the input of the construction at the moment, together with the design models from the different disciplines these constructability problems was shown also these variations that needed to be eventually "solved".

These types of errors/imperfections natural to this kind of work are traditionally detected "downstream" of the activities and are usually perceived much later. Usually, by then, the dependent jobs have already incorporated and assimilated these issues generating technical and qualitative deviations. Afterwards the level of effort and resources needed to mitigate them are quite high and represent a cost and time overrun that can be quite impactful on such a design and build projects. Sometimes these re-processing are performed again, looping into this cycle of reprocessing once or in additional subsequent times. (Cooper, 1993)

However, they were perceived at a earlier stage in this exercise allowing the proper implementation at each moment of measures to be taken and/or changes to be made. The use of BIM design-build models makes it possible to perceive these hypothetical reworks in advance and to adapt them to accurately re-create, forecast and diagnose the performance in the Project.

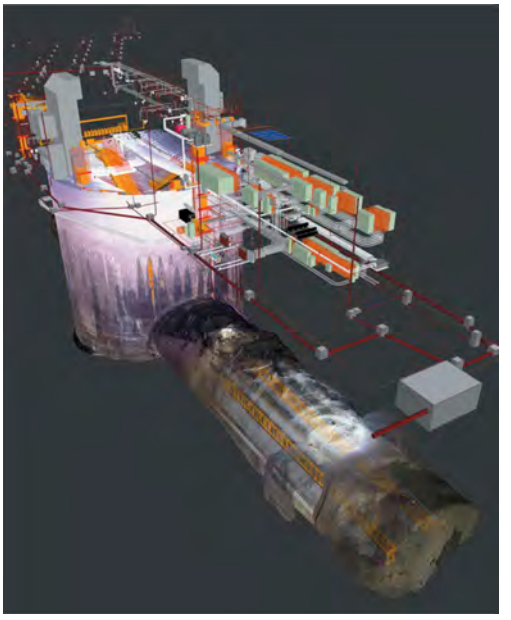

Figure 7. Federated BIM model with point clouds model.

Finally, an additional innovation is the capacity of the technical office to input site relevant data that federates with the rest of the models, while carrying the major responsibility of specialities model coordination. Of course, the prevalence of these work models (realistic – "as-built") over the rest is a sine qua non condition when it comes to coordinating all the disciplines.

5 JOÃO PAULO I EXAMPLE

The concrete case of the deep underground João Paulo I station provides the opportunity to showcase the innovative BIM methodology implemented in São Paulo line 6, as is detailed below with specific examples of the applications carried out on it.

Two major integrations work were carried almost concomitantly while the excavation advances:

i) the first one was to validate and simulate the possible ground improvements and/or lining reinforcements and their impact on the viability of the architecture, systems, and system subcontractors.
ii) the second one was the integration of the point cloud with the spaces resulting from blasting excavation. The most significant case was an important overbreak and underbreak. For this particular item, as explained, modeling certain tolerances and spaceproofing was required, while minimizing the rework such as the excavation of underbreaks that could be "incorporated" in the secondary lining.

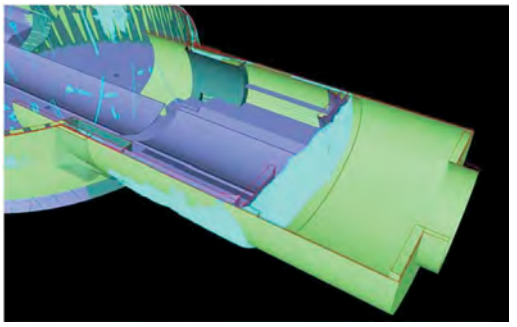

Figure 8. João Paulo I Federated BIM model.

Successful fast-track projects require timely, clear, and high-quality information to be provided to the construction team by the design team. In order to achieve this information on time and on the desired quality, usually the different disciplines involved in the design overlap and optimize each other. This results in the need for bi-directional exchange of information between the dependent design disciplines, sponsored by the point clouds.

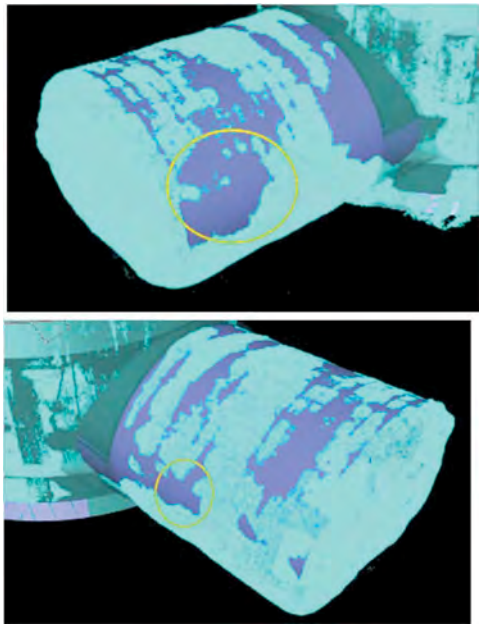

Figure 9. Overbreaks and underbreaks analysis BIM models.

Other case example of this concepts could be seen in the evacuation lateral niches built in the João Paulo I station. Originally these structures were not deemed to be needed and were not foreseen in the overall cavern geometry. Thus, there was an important geotechnical and structural limitation on the sizing and shaping of this lateral tunnel.

While the cavern excavation was already in progress a general task force was done to design and implement such structures in order to deliver a solution that could be still excavated while the main cavern was constructed.

In addition to the strict structural and geotechnic requirements, aspects such as tolerances, headers, escape routes, air extraction, etc., were needed to be taken into account and so decision was to model the space proofing of those points to be able to coordinate, study and consider alternatives; until a coordinated model was achieved, which was finally implemented, and adapted as the blasting was carried out and the scanning was federated and coordinated with the rest of the disciplines, which required further adjustments.

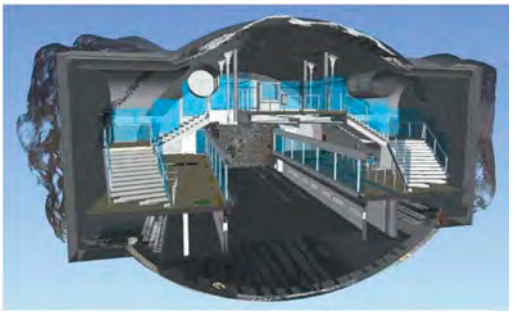

Figure 10. João Paulo I federated BIM model.

In the example of this station, it was made abundantly clear that the discovery of potential rework earlier and immediately avoids a large part of the program-wide disruption, especially in development time impacts. Another advantage of this linkage of design (or construction) models and point clouds models was the possibility of obtaining quantities and measurements, both underbreak and overbreak, which allowed the optimization in construction as well as decisions based on these direct costs.

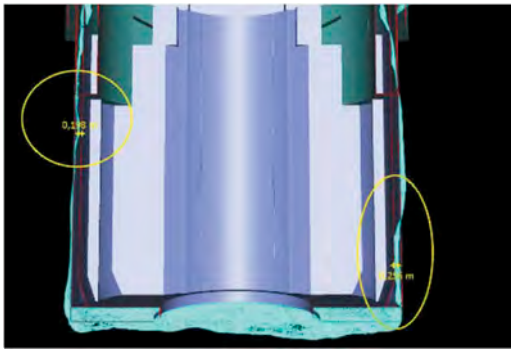

Figure 11. Federated model: structural BIM models & point clouds model.

Finally, it is worth mentioning that in this graphic part, obtaining images of the construction progress at any given moment in conjunction with the design models has helped a lot in the dissemination and clarity of problems, understanding, changes and progress of the work; thus the coordination of the project and its disciplines and the various (and diverse) agents that participate in it become more dynamic, collaborative and manageable.

6 CONCLUSIONS

In this paper we have presented an approach on how the use of point clouds generated on site, federated to the design models, which has allowed us to quantify and mitigate the impact of rework on construction projects.

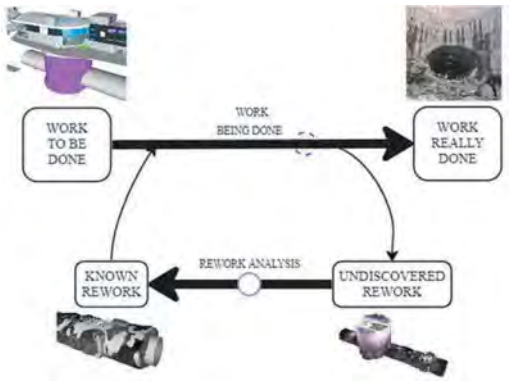

Figure 12. Line 6 - São paulo metro rework cycle.

The use of reality captured for project coordination adds value to the analysis process, since it allows the integration between the construction work and the design in time. Project awareness improves all those involved, since reality captured is a 3D representation of a survey carried out in the field, thus allowing visualization of all the built elements. This allows monitoring the excavation, enabling for example, the verification, quantification, interpretation and mitigation of overbreaks and underbreaks to the extent that there is sufficient space, according to multidisciplinary needs. Additionally, it provides the capacity to visualize the impact of the project changes as well as to extract quantities of the impact of these changes (both positive and negative) and to record rework amount as negative percentage completed of affected activities on the rework dates.

With all this Laser Scanning point clouds and BIM models federation exercise, a complete connection between construction and design, and between the construction site and BIM models, has been performed. This establishes a full collaborative platform, going from design to work and transcending to the subcontractors; having in real time their interaction with the work performed, being able to coordinate and readjust.

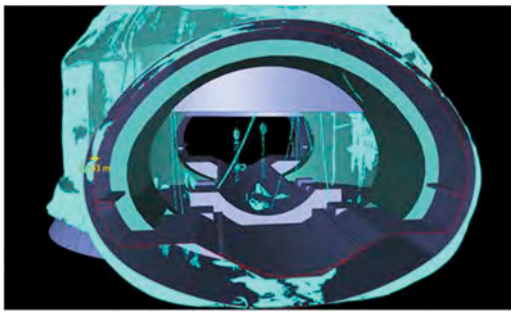

Figure 13. Federated model: structural BIM models & point clouds model.

In summary, this methodology has been exemplary to optimize the decision-making process, based in quantities, and to perform overall corrective actions in a shorter time span, improving and adapting the original designs, generating shorter delays than those taking place in a traditional method.

REFERENCES

Berger, M., Tagliasacchi, A., Seversky, L., Alliez, P., Gael, G. et al., 2016. A Survey of Surface Reconstruction from Point Clouds. Computer Graphics Forum, pp. 27.

Bieniawski, Z.T., 1989. Engineering rock mass classification. New York: Wiley.

Cooper, K. G., 1993. The rework cycle: benchmarks for the project manager. Project Management Journal, 24(1), pp 17–21.

Eastman, C., Teicholz, P., Sacks, R., Liston, K., 2011. BIM Handbook: A Guide to Building Information Modeling for Owners, Managers, Designers, Engineers, and Contractors. John Wiley & Sons. Indianapolis. USA.

Fazio, P., Moselhi, O.,Théberge, P., Revay, S., 1988. Fast-tracking of construction projects: a case study. Canadian Journal of Civil Engineering. 15(4): 493–499.

Fischer, M., Kunz, J., 2004. The scope and role of information technology in construction, Proceedings of JSCE 763 pp. 1–8.

Hardin, B., McCool, D., 2009. BIM and Construction Management: Proven Tools, Methods, and Workflows. John Wiley & Sons. Indianapolis. USA.

Haymaker, J., Kam, C., Fischer, M., 2005. A methodology to plan, communicate and control multidisciplinary design processes. Computer Science

Haymaker, J., Suter, B., 2006. Communicating, Integrating and Improving Multidisciplinary Design and Analysis Narratives. Design Computing and Cognition ’06

Hegazy, T., Said, M., Kassab, M., 2011. Incorporating rework into construction schedule analysis. Automation in Construction,Volume 20, Issue 8. Pp 1051–1059

Kotsis, I., Karamitsos, S., Gikas, V., 2005. 3D Terrestrial Scanning for Tunnel Surveying: Hits and Tips and

comparison with conventional methods. Conference: International Symposium on Modern Technologies Volume: Proceedings of the FIG-ISPRS-ICA

Lichti, D., Stewart, M., Tsakiri, M., Snow, A., 2000. Benchmark tests on a three-dimensional laser scanning system. Geomatics Research Australasia. pp 1–24.

Penttilä, H., 2006. Describing the changes in architectural information technology to understand design complexity and free-form architectural expression, Itcon Vol. 11, Special issue The Effects of CAD on Building Form and Design Quality, pp. 395–408.

Rey Antón, P., Sedó, M., 2022, September 27-29. Line 6 São Paulo Metro Brazil. Resuming the largest infrastructure project in LATAM. Conference session: Autodesk University, New Orleans, USA. https://www.autodesk.com/autodesk-university/class/Sao-Paulo-Metro-Line-6-Resuming-largest-infrastructure-project-LATAM-2022

Ruby, D.I., 1978. Fast-tracking plant projects. Plant Engineering. 32 pp 121–123.

Teixeira I.J.F., Chanquini, C.V., Abreu, F., Messa, P., Partelli, L.B., 2023. Blasting and vibration control for hard rock shafts in urban centers. Expanding Underground – Knowledge and Passion to Make a Positive Impact on the World: Proceedings of the ITA-AITES World Tunnel Congress 2023 (WTC 2023), 12-18 May 2023, Athens Greece, (1st ed.). CRC Press. Pp 1695–1702.

International Symposium on Modern Technologies, Education and Professional Practice in Geodesy and Related Fields, pp. 158–167.

Van der Werf, A., 2003. Risk Mitigation in Fast Tracking Projects. AACE International Transactions.

Wang, T., Feng, J., 2023. Multi-objective joint optimization for concurrent execution of design-construction tasks in design-build mode. Automation in Construction. Volume 156.

Tunnelling for a Better Life – Yan, Celestino, Thewes & Eberhardt (Eds)
© 2024 The Author(s), ISBN 978-1-032-80042-4
Open Access: www.taylorfrancis.com, CC BY-NC-ND 4.0 license

The Sotra Link Project (Norway): An application of the BIM methodology in tunneling design and construction

Guido Barbieri*, Enrico De Panicis, Gianluca Bella & Dario Della Femina
Pini Group SA, Lugano, Switzerland

Andrea Biagi
Sotra Link Construction JV ANS (Webuild Ltd), Knarrevik, Norway

Matteo Giani
Pini Group SA, Lugano, Switzerland

ABSTRACT: The Sotra Link Project (SLP) is one of Norway's priority infrastructure projects. It includes the design, construction, financing, maintenance of several underground and surface structures between Sotra island and the city of Bergen. Among them: 23 tunnel portals, 12.5 km of tunnels and a 900 m-long suspension bridge. This paper deals with the application of BIM approach from the Early Design to the Detail Design of tunnels. The benefits of adopting BIM methodology are shown, and consist mainly of: i) better handling of clashes and inconsistencies; ii) better understanding of effective design choices, resulting in a reduction of errors; iii) better communication between different design teams; iv) a greater level of accuracy, ensuring SLP manageability in each design phase. The evidence of the advantages of BIM approach, also in the Construction Phase, is illustrated. In particular, the focus will be on the excavation of the western portal of Kolltveit tunnel and the first stretch of the Kolltveit tunnel with its technical peculiarities. The result of the excavation compared to the theoretical 3D models will also be shown. The SLP contract was awarded in September 2021 and it is currently in the Construction Phase, while the infrastructure will be opened to traffic in 2027.

Keywords: Building Information Modelling, Tunneling, Computational design, Parametric design, Underground structures, Project database, Rock Support

1 INTRODUCTION

The application of BIM methodology in the design and management of a complex infrastructure project is becoming increasingly relevant and essential to ensure the quality of the project, as well as its manageability over time.

The BIM approach is based on the use of three-dimensional, digital BIM models containing both geometric data and information, which are "comprehensive" and "consistent" and work as a centralized source of data. The adoption of BIM in big civil engineering projects has proved to bring important advantages, among them: a general reduction of design errors, better checking of clashes, better management of the construction and maintenance phases (Barbieri et al., 2023). The current paper deals with the adoption of BIM methodology for a complex infrastructure project in Norway, focusing on the solutions and advantages of BIM in tunnel design and construction.

2 THE SOTRA LINK PROJECT: GENERAL OVERVIEW

The Sotra Link Project (SLP) is a key infrastructure project in the western county of Vestland, Norway. It includes the design, construction, operation and maintenance of a road system connecting the city of Bergen with the island of Sotra. The link includes 9 km of highway, a 900 m-long suspension bridge, 12.5 km of tunnels (Kolltveit, Straume, Knarrvika, Drotningsvik), 19 roads and pedestrian underpasses, 23 tunnel portals, 22 bridges and viaducts, and 14 km of pedestrian and bicycle paths (Figure 1).

*Corresponding author: Guido.Barbieri@pini.group

DOI: 10.1201/9781003495505-376

The Norwegian Public Roads Administration (NPRA) awarded the Public-Private-Partnership (PPP) contract to design, build and operate the project to the "Sotra Link" company (that outsourced the design and construction to the "Sotra Link Construction Joint Venture" SLCJV) in 2021, for a total value of about 2 billion €.

In accordance with the NPRA's BIM guidelines, the BIM approach was adopted for the design process of the entire project (Barbieri et al., 2023).

Figure 1. SLP: rendering of the new bridge (NPRA, 2021).

2.1 *Adoption of BIM in the project*

The adoption of BIM methodology in the SLP is mentioned in the tender documents, where it is clearly stated that the project must be based on BIM models. The models must have a "maturity level" of 3 or higher, as defined in UK's "Government Construction Strategy" documents (BIM Industry Working Group, 2011). This means that the use of BIM models is that of an integrated database that functions as the main source of information of the entire project.

2.1.1 *BIM strategy: The BIM Execution Plan (BEP)*

Implementing a BIM approach in a complex infrastructure project such as the SLP requires a common strategy and a set of rules for the creation and delivery of digital models. The BIM Execution Plan (BEP) is the main document that provides the framework for the BIM project development, in order to meet the Employer's Information Requirements (EIR) requested by the final client of the project (the NPRA). The BEP is prepared by SLCJV with the cooperation of the design team and lays the foundation for collaboration in the BIM project, explaining how project information is managed by each party, the roles and responsibilities of each party, and the exchange of data between parties (ISO 19650-2, 2018). To ensure efficient and comprehensive management of project information, the BEP defines a "BIM Information Strategy", which establishes the framework that enables the delivery and exchange of project information. This strategy is based on an Object Breakdown Structure (OBS), which organizes project data into hierarchical levels (Area, Discipline, etc.; Figure 2).

Responsibility of the BIM and technical coordination for each area is assigned to a specific design company (called a "task team" in the BEP). The exchange of data between task teams during the design phase, as well as coordination and communication between teams, takes place on a digital platform, the Common Data Environment (CDE), which enables collaboration among the various project teams and parties.

Figure 2. OBS structure of the SLP: project Areas.

In the SLP, the CDE consists of several interconnected platforms. Autodesk Construction Cloud (ACC) is the main part of the CDE where all project data is stored: the various task teams produce BIM models containing the data for a specific OBS and deliver it on ACC for review and validation. The "federation" of BIM models is one of the main advantages of BIM methodology, since it allows for the combination of models from different disciplines into a single, comprehensive model of the project (Shivasami et al., 2023). In the SLP, the federation of models follows the OBS structure: each team creates several "Container Models" that link together BIM models related to a certain Area; these container models are then combined into a single "federated" model (the "Coordination Model"), which allows for continuous coordination and inter-disciplinary verification of design data for the entire project.

2.1.2 *Pini Group's responsibilities in the project*

As one of the task teams of the SLP, Pini Group is currently responsible for the design of roads, bridges and structures (together with teams from other companies), as well as for the design of all tunnels in the project, which are located in Areas 02 (Kolltveit), 04 (Straume), 06 (Knarrvika) and 10 (Drotningsvik). These activities mainly concern the geologic characterization of the site, structural/geotechnical design of the tunnels and creation of the BIM models, together with activities on site.

3 THE ADOPTION OF BIM FOR TUNNEL DESIGN

The implementation of BIM methodology for the underground structures in the SLP was based on the integration of all the project data within a centralized project database, consisting of the BIM models and related documentation (drawings and reports), linked together following the Object Breakdown Structure.

To achieve this aim, an integrated processing workflow was set up. The data produced by the various teams of each discipline (geology, geotechnical-structural engineering, road design, etc.) were processed by the BIM Team and integrated in the BIM models. The workflow structure using iterative and automated subprocesses ensured that any changes in design data were quickly integrated into the models.

The data processing workflow is based on the following phases (Figure 3):

1. Production of inputs (geological, geotechnical, structural and road data);
2. Data pre-processing;
3. Implementation of processed data into the BIM models;
4. Upload of BIM models (including the Container Models) to the CDE (ACC) for final review and validation by SLCJV.

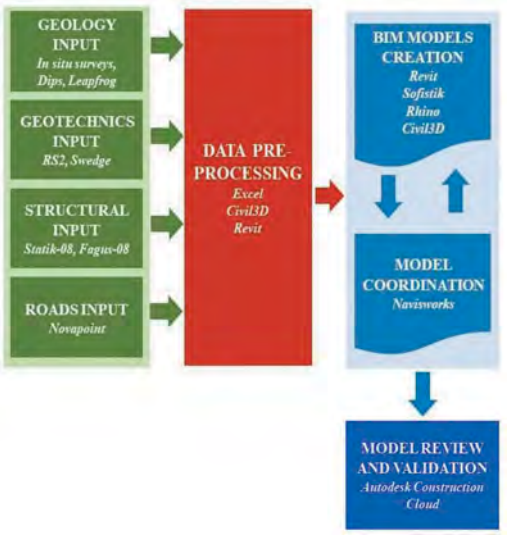

Figure 3. Data processing workflow.

3.1 *Data creation and processing*

The inputs for the BIM models consisted of data belonging to the various sub-disciplines of the underground works design, mainly geological, geotechnical and structural data. These data were integrated into the BIM models to create a consistent database, which served as the basis for continuous quality control of the design.

3.1.1 *Input data*

Geological studies of site conditions resulted in a geological model consisting of homogeneous units, depending on the estimated "Q-value" of the rock masses (Barbieri et al., 2023). This model was created with the support of specialized software, including Leapfrog, which made it possible to produce a 3D model of the main geological units, as well as the position of boreholes and faults, for each project area (Figure 4).

Based on this geological model, homogeneous "rock classes" were then defined along the tunnel alignments, with each class associated with a specific type of "rock support". In the context of the retaining works, tunnel portals and underground structures, the input data for the BIM models (i.e. rock support, shotcrete, bolts, spiling, grouting, formwork geometry, steel reinforcement) were provided by the designers on the basis of Finite Element calculations (Barbieri et al., 2024).

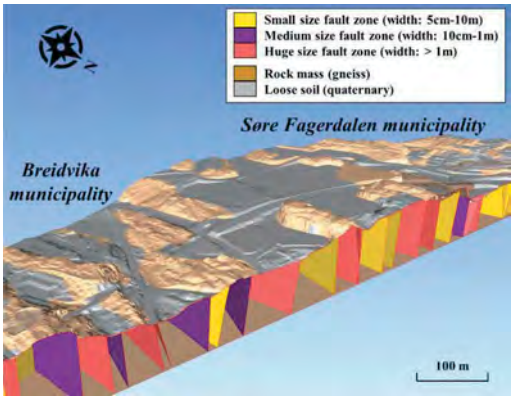

Figure 4. Geological 3D model of Area 10 (Drotningsvik).

3.1.2 *Data processing for BIM models implementation*

Input data to be implemented in BIM models are provided in a variety of file formats (Excel spreadsheets, CAD drawings, etc.) that must be processed to be transformed into information that can be directly used to create BIM models.

The integration of design data into the BIM model is one of the main challenges of an integrated BIM project. For the underground works of the project, the workflow adopted is synthetically shown in Figure 5 and is divided into two phases: a pre-processing of the "raw" data into a form that can be implemented in the BIM environment; and the model creation, which integrates this data into the model.

3.2 *BIM model creation*

The second phase of data implementation into digital models is the creation of the BIM models on the basis of pre-processed data. For the underground works of

the SLP, the BIM platform used was Autodesk Revit 2023, along with special plugins dedicated to infrastructure modelling (Sofistik Bridge + Infrastructure Modeler), visual programming environment used for script creation (Dynamo Revit), and the Rhino.Inside plugin, that allowed an interoperability with the powerful CAD software Rhinoceros and its specific visual programming environment, Grasshopper.

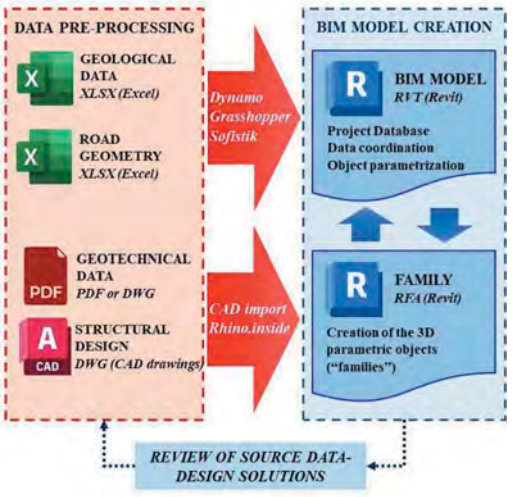

Figure 5. BIM model implementation workflow.

The creation of the BIM models was performed following a strategy consisting mainly of two processes:

1. Creation of classes of parametric objects ("families") in the Revit BIM software environment, which are then used by dedicated Revit plugins to automatically create structural elements along road alignments, following the inputs provided (this was mainly done for the structures of tunnel tubes and ramps);
2. Automatic creation of model elements and implementation of alphanumeric information in the models, through scripts created ad hoc (using Dynamo and Grasshopper).

3.2.1 *Parametric model components: The families*

Parametric objects are the basis of the creation of a digital BIM model of a built environment. Model objects are defined as three-dimensional components representing a specific construction element, which contain data attributes and parametric rules (Sacks et al., 2018). A database of families (i.e., classes of digital objects) was created in the BIM software environment, based on pre-processed design data (in many cases, CAD drawings were imported into a view within the BIM software, to create the family and its parametric rules efficiently). The behaviour of individual instances of these families is governed by parameters that can be manipulated to create a 3D component that faithfully represents the actual construction element.

3.2.2 *Automated modelling workflows*

Parametric families allow the implementation of semi-automated or fully automated modelling workflows, thanks to the parametric nature of these digital objects. Once the library of families has been prepared, the creation of BIM models can be done efficiently, either using scripts created ad hoc, or through specific BIM software plugins that automatically create instances of the families following the pre-processed input data.

In the case of the rock support bolts for tunnel portals, for example, the position and orientation of the bolts are governed by parametric entities within the bolt family (such as adaptive points, numerical parameters for bolt inclination, etc.) After importing the digital model of the rock cut surfaces of the portals, through scripts made with Dynamo and Grasshopper, a set of reference lines was automatically created from the intersection of the laying plans of the bolts and the excavation surfaces. Another Dynamo script was used to create the bolts along the lines, with the desired spacing and bolt inclination according to the design specifications (Figure 6).

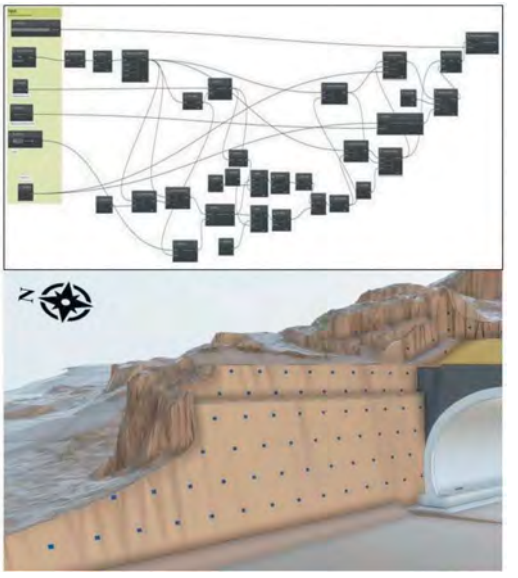

Figure 6. Automated creation of the bolts with Dynamo (Dynamo script; rock support bolts, Kolltveit West portals).

3.2.3 *Parametric modelling of tunnel tubes*

The BIM approach to infrastructure design is proven appropriate when modelling long structures running along an alignment. In this case, parametric cross sections of the various structural components of the tunnel tubes can be extruded to create the BIM model (Sacks et al., 2018). The initial step in creating the

tunnel tube models was to define a set of parametric families, one for each rock class support. The families contain parameters that control the characteristics of the rock support layer, such as bolt spacing and shotcrete thickness. The values of these parameters were set for each rock support class, following the structural indications and according to the adopted excavation method ("drill and blast"). Once the library of families was ready, the Sofistik Bridge Modeller plugin for Revit enabled the automatic creation of each rock support section of the tunnel. The plugin extruded the parametric cross-section families of each structural component of the rock support (shotcrete, bolts, spiles, shotcrete ribs) following the inputs, which consisted of the stations defining the rock support classes and the road geometry data (Figure 7).

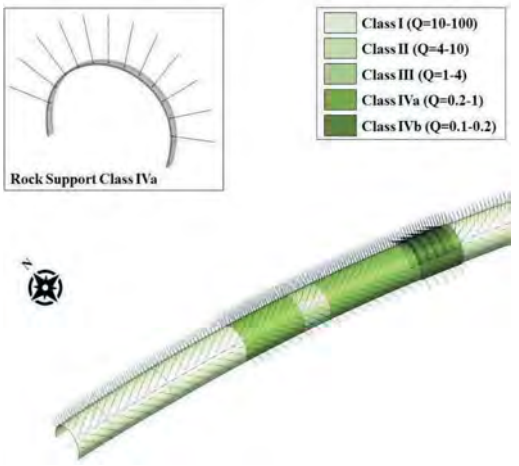

Figure 7. Parametric cross-section family of the rock support of the tube (class IVa); BIM model of the Drotningsvik tunnel tube rock support, with rock support classes shown in false colors.

3.2.4 *Automated implementation of object attributes*

A fundamental feature of the BIM model is that objects not only have a three-dimensional representation, but also carry with them attributes and properties in alphanumeric format, within specific information parameters (Figure 8). The information content of the BIM model is also referred to as LOI, "Level Of Information" of the model and its objects. According to the client's requirements, BIM models are the basis for the construction and maintenance phases of the project. This means that the models must contain all the information needed to manage the various phases of the project. More specifically, the model must allow quantity extraction for the BoQ, and model objects must have special attributes that allow 4D and 5D analysis to be performed on the models.

Figure 8. Information parameters of a rock support bolt (BIM model of the Kolltveit West portals rock support).

Due to the large number of objects in a model (up to about 12,000 elements for the rock support models of the tubes), an automated implementation of the LOI in model elements was required. The "parametrization" of the models (i.e., populating the object parameters with related information) required the use of scripts created ad hoc within the visual programming environments (Dynamo, Grasshopper). To make automation possible, some specific object properties (such as the object's "family name") must follow a codification that allows the use of databases (Excel spreadsheets), containing tables that associate each family with a set of parameter values to be populated in the model objects (Figure 9). The information contained in the database can then be automatically implemented in the parameters of the model objects with a specific Dynamo script (Rich et al., 2023). In this way, the information content of the models can be quickly updated whenever there is a change in the design data.

Family Name	GEO-B01_Boltetype_Bolt-type	GEO-B02_Bolt-staaltype_Bolt-steel-quality
300-BOR-T40-04A_BoltsRockSupport3000mm	Full sementpel bolt [Permanent fully grouted]	B500NC Double corrosion protection
300-BOR-T95-04A_BoltsRockSupportPortal4000mm	Full sementpel bolt [Permanent fully grouted]	B500NC Double corrosion protection
300-BOP-T95-000_BoltsExcavationPort3000mm	Kamstbolt full sementpel [Kamstbolt fully grouted]	B500NC
300-BOP-T95-000_BoltsExcavationPort3000mmAdaptive	Kamstbolt full sementpel [Kamstbolt fully grouted]	B500NC
300-BOP-EXT-000_BoltsExcavationPort3000mmAdaptExtEnd	Kamstbolt full sementpel [Kamstbolt fully grouted]	B500NC
300-BOL-EXT-000_BoltsExcavation3000mmAdaptDrotRampN	Kombinasjonsbolt [CT Bolt fully grouted]	B500NC
300-BOP-EXT-000_BoltsExcavationPort3000mmAdaptDrotRampN	Kamstbolt full sementpel [Kamstbolt fully grouted]	B500NC
300-BOL-EXT-000_BoltsExcavation3000mmAdaptDrotRampS	Kombinasjonsbolt [CT Bolt fully grouted]	B500NC
300-BOP-EXT-000_BoltsExcavationPort3000mmAdaptDrotRampS	Kamstbolt full sementpel [Kamstbolt fully grouted]	B500NC

Figure 9. Part of the database of families attributes for automatic implementation of information in BIM models, showing the bolt families and their information parameters.

4 MODEL FEDERATION AND COORDINATION

Model federation is performed following the hierarchy of container models described in the BEP. The federation process is scheduled every week, to have a constantly updated database of the project.

4.1 *Model federation*

The overall coordination of each project Area is assigned to a specific Area Coordinator, who is the designer (task team) responsible for that Area. Among the responsibilities of the Area Coordinator is the weekly creation of the Area Coordination Model, following the BIM Cycle described in the BEP.

The Area Coordination Model consists of multiple Container Discipline Models, one per designer: each designer creates the Container Discipline Model related to a certain Area by merging all the BIM models related to the disciplines assigned to the designer in that Area. After the Container Discipline Models are uploaded to the CDE (ACC), each Area Coordinator creates the federated Coordination Model as a composition of all the Area's Discipline Container Models, plus the Area's Container Base Model (the model of the Area's existing context). The typical structure of the Area Coordination Model is shown in Figure 10.

The individual BIM models are also regularly uploaded to the CDE for review and validation by the SLCJV. As stated in the BEP, the deliverable BIM models must be in open format (IFC) to enable model interoperability. The models are also georeferenced to allow them to be properly combined in the coordination software environment (Navisworks or Solibri) and on the digital platforms of the CDE.

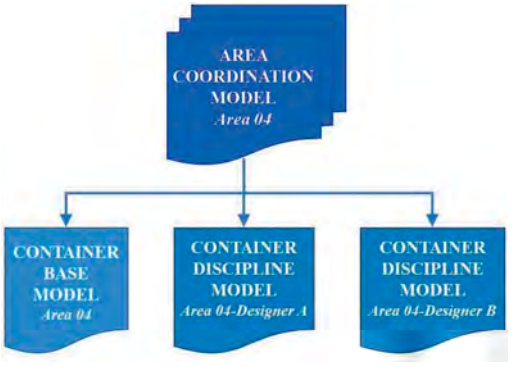

Figure 10. Structure of an Area Coordination Model.

4.2 *Model coordination and check*

Once created, the Area Coordination Models on ACC are combined into a single complete Coordination Model of the entire SLP. This final model is shared on another digital platform of the CDE, BIMcollab, where the project Coordination Model can be inspected and validated by SLCJV and the final client (Figure 11).

One of the main advantages of BIM methodology is the possibility to inspect and verify multiple disciplines in the same model (Shivasami et al., 2023). The Coordination Model on BIMCollab allows for verification of interference between different disciplines, as well as notification of design problems to designers via BIMCollab's "issue" tool, or through the creation of BCF files. This enable designers to adjust their design choices in a timely manner and resolve disciplinary interferences, thus reducing the possibility of problems during the construction phase.

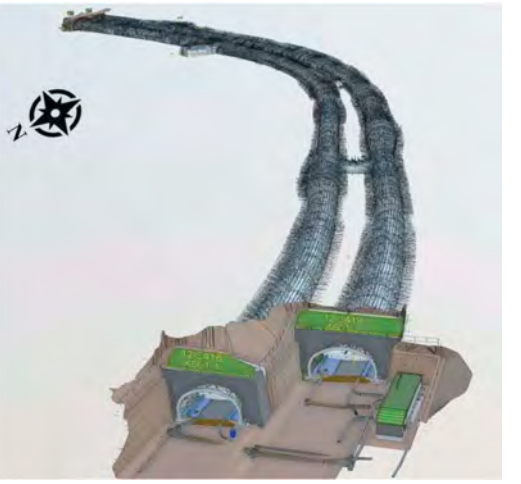

Figure 11. Project Coordination Model (Kolltveit tunnel).

5 BIM AND CONSTRUCTION PHASE

In May 2023, the first tunnel of the SLP, the Kolltveit tunnel, began its construction phase, starting from the West portals (Figure 12). In July 2023, the first blasting was carried out at the West portals of Kolltveit tunnel for the westbound tube.

Figure 12. Kolltveit tunnel, West portals: the construction site in July 2023.

BIM models have proven useful for communication between the design team and the construction team on site and for measuring consistency with the design as the work progressed. Due to local variations in geology from geological prognosis, construction deviations on site were applied in some cases to accommodate unforeseen conditions.

For instance, during the excavation of the West portals of the Kolltveit tunnel, on-site surveys were

carried out with advanced instrumentation and procedures (laser scanning) that enabled the creation of three-dimensional point cloud models of the completed works.

These point clouds files were imported into the model coordination software and then combined with the design BIM models, to verify the adequacy of the built portal pit to the design model. The overlaying of the design BIM model and the point cloud of the finished portal pit is shown in Figure 13. The construction generally followed the design indications in the model, with some variations (especially in the rock cut between the two portals). The westbound and eastbound Kolltveit tunnels also followed the design indication without major variations.

In addition, the use of the point cloud obtained from the laser scanning of the inner lining of the existing old Kolltveit tunnel, which runs close to the new Kolltveit tunnels, allowed the check of the clearance distance between the two infrastructures, in order to make proper design assessments of the impact of tunnel excavation on the existing tunnel.

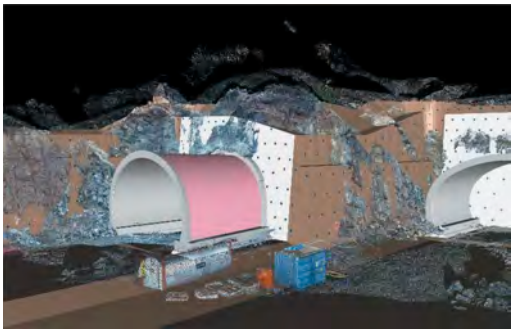

Figure 13. Coordination between the cloud point model and the BIM model of the design phase: Kolltveit tunnel, West portals.

6 CONCLUSIONS

This paper presented a summary of the main aspects of the implementation of BIM methodology in a complex infrastructure project, focusing on the design and construction of underground structures. Compared with a traditional design process based on 2D drawings and non-integrated project data management, the BIM approach for underground works proved to bring several significant improvements in both the design and construction phases. Despite the initial effort to implement BIM-based procedures within the design team, the benefits of BIM became evident as the design phase progressed. The creation of a single comprehensive digital model of the project that worked as single "source of truth" allowed for more precise control of clashes between disciplines and more efficient resolution of design issues. Collaborative workflows on the shared digital platform enabled better communication between task teams and between the design team and the client, reducing the possibility of errors and radical construction variations on site. Moreover, the implementation of information in models (LOI) allowed immediate extraction of project quantities from the models, enabling rapid BoQ updating, and formed the basis for accurate 4D and 5D analysis. In conclusion, the application of BIM methodology to infrastructure projects, despite the initial investment by all parties in terms of intense training, has proven to create a more integrated and collaborative approach to infrastructure, with benefits in terms of increased productivity, reduction of costs due to errors, and improved communication between the stakeholders of the project.

The design and BIM activities of the SLP are currently on schedule. The design phase is scheduled to be completed in 2024, and the infrastructure is expected to be completed in 2027.

REFERENCES

Barbieri, G., Giani, M., De Panicis, E., et al., 2023. BIM and tunneling - a Norwegian application: the Sotra Link Project, ASET & Avestia Publishing (Eds.) – Proceedings of the 8th International Conference on Geotechnical Research and Engineering (ICGRE 2023), Lisbon, Portugal, pp. 1–7.

Barbieri, G., Bella, G., E., Trivellato, E., et al., 2024. Design Challenges in Conventional Tunnelling on the Sotra Link Project in Norway, (Eds.) Proceedings of the World Tunnel Congress (WTC2024), Shenzhen, China, pp. 1–6.

BIM Industry Working Group, 2011. A report for the Government Construction Client Group. Building Information Modelling (BIM) Working Party Strategy Paper. London, UK, pp. 16–17.

ISO 19650-2, 2018. Organization and digitization of information about buildings and civil engineering works, including building information modelling (BIM) — Information management using building information modelling — Part 2: Delivery phase of the assets. International Organization for Standardization, Geneva, Switzerland.

Norwegian Public Roads Administration (NPRA), Alt ligg til rette for at OPS-leverandøren Sotra Link kan sette sine spadar i jorda i 2022 (Online), 2021. Available from: https://www.vegvesen.no/vegprosjekter/riksveg/sotrabergen/nyhetsarkiv/alt-ligg-til-rette-for-at-ops-leverandoren-sotra-link-kan-sette-sine-spadar-i-jorda-i-2022/

Rich, F., Giai Via, C., Bitetti, B. et al., 2023. Tunnel Euralpin Lyon-Turin CO08 – BIM implementation in conventional tunneling, (Eds.) Proceedings of the World Tunnel Congress (WTC2023), Athens, Greece, pp. 2869–2876.

Sacks, R., Eastman, C., Lee, G. et al., 2018. BIM Handbook: A Guide to Building Information Modeling for Owners, Designers, Engineers, Contractors, and Facility Managers, 3rd ed. Wiley, Hoboken, New Jersey, USA, pp. 14-57, pp. 184–186.

Shivasami, A., Lai, D., Dowdell, S., et al., 2023. Early implementation of BIM in large infrastructure projects to manage complex interfaces in a dense urban environment, (Eds.) Proceedings of the World Tunnel Congress (WTC2023), Athens, Greece, pp. 2893–2901.

Tunnelling for a Better Life – Yan, Celestino, Thewes & Eberhardt (Eds)
© 2024 The Author(s), ISBN 978-1-032-80042-4
Open Access: www.taylorfrancis.com, CC BY-NC-ND 4.0 license

INFRA-BIM interoperability for Tunnel Renewal

Maurizio Catapano*, Andrea Poli & Roberto Roncoroni
Tecne Autostrade per l'Italia, Milano, Italy

Ana Reis
Tecne Systra-SWS Advanced Tunneling, Torino, Italy

ABSTRACT: BIM methodology is today the driving force behind an ongoing revolution in the Engineering and Construction sector. In parallel with studies on new tunnels, the engineering company TECNE, part of Gruppo Autostrade per l'Italia (Gruppo ASPI), is implementing the so-called Tunnel Renewal Strategy which aims to propose a new approach to Tunnel Rehabilitation Works. Within this framework, TECNE is developing a proprietary BIM approach to the Design of modernization of existing tunnels based on an interoperable workflow. As the studies cover existing tunnels, the BIM approach depends on the input data available (for example endoscopic video surveys, laser scanner surveys, historical documentation). The BIM project is than developed in different phases according to construction sequence: from the demolition of portions of the existing lining up to the reconstruction phase. This Project & Construction Information Model becomes the basis on which it is then possible to implement the Asset Information Model for Facility Management according to the Asset Information Requirements identified jointly with the concessionaire of the Italian Highway aiming to prototype a digital twin in the perspective of better maintenance planning and integrated infrastructure management.

Keywords: Tunneling, BIM, INFRA-BIM, Tunnel Renewal, Interoperability

1 INTRODUCTION

The Italian motorway network has mainly developed between the 1960s and 1970s. By the end of the 1970s, about 70% of the tunnels of the current ASPI network had been opened to traffic, with an overall development of about 55% of the current network (Tecne, 2023).

Therefore, in compliance with the Italian Guidelines for the management and classification of the risk of existing tunnels, the external linings of the tunnels are subject to surveys. The surveys conducted have shown different types of defects affecting portions of the surface area of the tunnels. Therefore, a project is necessary for the implementation of specific structural renewal interventions on the linings.

Rehabilitation consisted of repairing the interior structure, adding a fire-rated wall to comply with modern standards, optimizing the track alignment, and redesigning the drainage, ventilation and electrical systems.

The purpose of this paper is to present an interoperability workflow for the application of the Infra-Building Information Modelling (I-BIM) methodology during the design of rehabilitation of existing tunnels for Italian Highways.

Figure 1. Tunnels of the current ASPI network.

*Corresponding author: maurizio.catapano@tecneautostrade.it

DOI: 10.1201/9781003495505-377

In the IT field, interoperability is conceived as the ability of a system (software) or an information product (hardware) to exchange data, semantic structures and services with other systems and products, in a reliable and resource-optimising manner, with the aim of ensuring interaction between non-homogeneous systems and platforms and reuse of data by them.

The BIM methodology relies on the above principle, as it is based on an approach grounded on:

- the collaboration between the different players involved;
- information management in a sharing environment.

2 TUNNEL RENEWAL STRATEGY

The objective of ASPI Network's Tunnel Renewal Strategy is the extension of tunnel linings' life cycle (i.e., additional 50 years) through the construction of new, structurally autonomous shell structures, replacing the original linings and ensuring suitable performance in case of seismic events. Given the need to minimise the impact on motorway traffic, the implementation of the programme requires innovative technical and technological solutions, i.e. the optimization of structural interventions, the automation and speeding up of operations, the maximization of work productivity and flexibility in terms of sites and logistics in order to allow rapid work site start-up and dismantling, by only closing at night time.

The TRS defines ASPI's strategic approach to address the modernization and renewal plan of the motorway asset, with specific reference to tunnels (about 600 tunnel-tubes on the network), in an organized manner. The TRS aims at the renewal of the design life of tunnels, by meeting a series of key requirements for the works and through the management of network operations, with a view to identifying the most suitable design solutions according to specific traffic conditions as well as the conditions of relevant work sites.

The main requirements defined in the TRS context are:

- safety for operation (in case of alternation of works/ operation and/or works when there is traffic);
- safety for workers (protection, mechanization);
- minimization of impact on traffic (protection, mechanization);
- prompt intervention (mechanization);
- high structural performance (pre-casting operations, high-performing concrete mix, etc.);
- installation of an effective and durable waterproofing system;
- sustainability (asset preservation, recycling, use of vehicles with low environmental impact, materials with low carbon footprint);
- standardization of solutions.

The TRS design solutions are based on the construction of a new lining that is structurally independent from the original one, which shall be partially demolished, without the reduction of the inner profile of the tube or even with an increase of the profile itself in order to ensure compliance with the minimum cross section necessary as established by the regulations in force. A first view of the basic principles characterizing typological intervention in tunnel lining renewal in terms of structural solutions and construction processes is provided herein.

As mentioned above, any intervention requires the demolition of original linings to the minimum extent necessary for the insertion of a new shell to preserve tunnels' outline, while safeguarding the structural integrity of the residual portion that shall act as a temporary support in the transition period preceding the construction of new linings. To this end, one of the main conditions identifying the application context is the state of stress of existing linings. The presence of compression in existing linings due to the state of stress associated with their selfweight determines the definition of a design intervention.

Demolition may be then carried out by means of low-impact technological solutions, such as milling and hydro-demolition. These methods, also considering that demolition is only partial, offer several benefits in terms of reduction/minimization of the workload that would otherwise be required for rock mass consolidation and support in case full demolition of the crown was to be carried out.

Tunnels covered by the structural renovation plan are generally characterized by the absence of linings waterproofing system, which is typical of ASPI network tunnels built before 1980. Crown and walls were casted directly in contact with the adjoining rock mass, with the possible prior installation of temporary supports.

In order to contribute to the durability of new linings, a waterproofing membrane combined with a compensating geotextile layer between the existing residual concrete lining and the newly built one shall then be inserted. However, the whole sealing system shall guarantee the preservation of the original drainage conditions around the cavity, in order to avoid any possible hydraulic overloading as a result of the intervention or of any changes in the hydrogeological setting established over the years. The insertion of the waterproofing and geotextile layer between the new lining and the original one may result in a slip under shear action.

Because of this possibility and due to the basic design hypothesis of a complete performance decay - in the long run - of the residual portion of the original concrete lining and of any temporary supports installed during the excavation of the tunnel, the total static autonomy of the new lining shall be a priority. Therefore, the latter shall ensure that all the safety requirements needed in the long term and in the various project scenarios (including the seismic one), regardless

of the residual resistant contribution of the existing lining, are met (Mazzola et al., 2023).

3 BIM INTEROPERABILITY FRAMEWORK

TECNE, part of Gruppo Autostrade per l'Italia, has decided to implement the BIM process for the rehabilitation of existing tunnels, providing guidelines on the main documental and technical properties on which the model is based and has chosen to require the production of BIM models in the design and construction phase.

3.1 *Italian legislation and building information modeling*

Interoperability has become increasingly important in recent years. Starting from 2016, where the old public procurement code, under Legislative Decree 50/2016, in Art. 23, par. 13, mentioned the use of interoperable platforms through non-proprietary open formats at the discretion of the Contracting Authorities for new assets, as well as for renovation, upgrading or variants, with priority given to complex works, the use of electronic methods and tools. This guideline was conceived in order not to hinder competition between technology providers and the involvement of specific projects among designers.

Less than 2 years later, the legislator decided to attach more importance to the concept of interoperability; therefore, the Ministry of Infrastructure and Transport issued Ministerial Decree 560/2017 to define the mandatory introduction of the BIM methodology in public procurement. Article 4 of the Decree is fully dedicated to interoperability, requiring Contracting Authorities to use interoperable platforms through non-proprietary open formats, where data must remain connected to multidimensional object-oriented models, as well as being retrievable at any stage and by any operator during the design, construction and management of the intervention, according to open and non-proprietary digital formats.

In 2021, under the 'Governance of the National Recovery and Resilience Plan and Initial Measures to Strengthen Administrative Structures and Speed up and Streamline Procedures' the Ministry of Sustainable Infrastructures and Mobility was required to adopt an autonomous ministerial decree providing for rules and technical specifications for the use of specific electronic methods and tools such as modelling methods for construction and infrastructure in procedures relating to public investments partially or fully financed with the resources provided for by the NRP and the NPCI and the programmes co-financed by the European Union Structural Funds, which was to coordinate with M.D. 560/2017, while remaining separate from it.

Ministerial Decree 312/2021 was therefore introduced, not to alter Article 4 of Ministerial Decree 560/2017, but to transform the term "multidimensional models" into "disciplinary information models and multidimensional aggregates" bringing the concept of interoperability applied to the BIM methodology even closer.

Even the most recent piece of legislation, Legislative Decree 36/2023 for the implementation of Article 1 of Law no. 78, delegating the government in terms of public contracts, in addition to confirming the existing regulatory framework on the subject, it also extends the obligation of interoperability not only to the use of platforms through open formats, but it also requires specific guidelines concerning data and information exchange methods, the provisions relating to the maintenance of the interoperability criteria of the information tools over time, the maintenance of the interoperability characteristics of the information models, the interoperability between works accounting documents and the recording of the controls carried out by the Works Management with the information models.

All the above clearly shows that, over the past seven years, interoperability has evolved considerably, becoming part of the primary objectives of companies wishing to improve and streamline their working procedures based on collaboration facilitated by the exchange of information.

3.2 *Digitalization goals and OpenBIM workflow for existing tunnels*

Since its establishment, Tecne has understood the huge potential of working through the exchange of data and information to make the most of systems and applications chosen based upon its performance requirements.

Furthermore, the legislative framework has over time embraced this trend, especially in those contexts requiring the adoption of digital construction information management methods and tools, in relation to each individual technical-administrative procedure within the contracting authority, for the awarding and execution of public works, services and supply contracts and to ensure maintenance and management of the entire life cycle of the property or infrastructure asset, up to its decommissioning.

Based on the above considerations, Tecne has implemented and invested in OpenBIM tools and expertise, as the method provides a universal approach that fosters collaboration during design, construction and commissioning phases of building construction based on open standards and workflows, capable of:

- promoting a transparent workflow;
- providing a common language;
- providing durable data that can be used throughout the life cycle of the asset.

BIM methodology and tools are designed to facilitate the interoperability of different disciplines, through a system based on open formats (.IFC, .

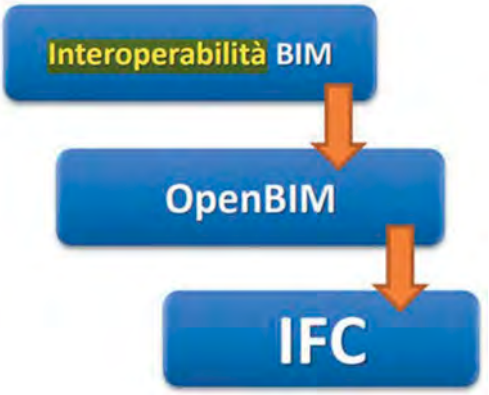

Figure 2. Interoperable workflow based on industry foundation classes format.

BCF, .LandXML, .shp, etc.) that involves every area of engineering from the earliest design stages.

Ensuring a neutral and efficient transfer of information between different disciplines and professionals is now possible thanks to an open format capable of preserving the modelling know-how while maintaining the graphic and alphanumeric information content of the model.

The most popular open formats in BIM modelling are IFC and Land XML.

In order to guarantee interoperability in its processes, Tecne immediately adopted the IFC standard in accordance with the scheme of ISO 16739 and developed its own classification system, associating each type of object with a specific IFC class, distinguishing by discipline and modelling application respecting their specific characteristics.

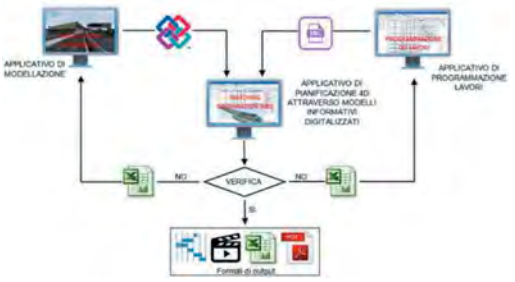

Figure 3. Interoperable workflow with BIM authoring software and work schedule.

Moreover, the company organised its information database by standardising the Property Sets to ensure the transparency and uniqueness of the information transferred in the open format according to the following operational flow:

- breakdown of the project and standardisation of WBS codes;
- compilation of the Property Set by coding each object in the information model;
- transfer of information from the native format to the interoperable IFC (Industry Foundation Classes, ISO 16739-1:2020) format;
- verification and validation of assigned codes through coordination activities (model checking);

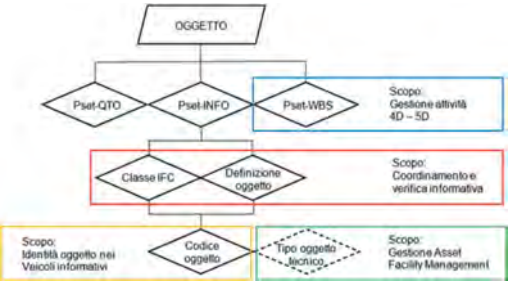

Figure 4. Property set classification for model checking, 4D, 5D and facility management.

The challenge addressed by Tecne is to manage all information assets by applying the processes of verification and coordination (3D), time planning of works (4D) and parametric computation (5D), through information conveyed exclusively by transferring data in open formats according to the diagram in the figure below.

The main data useful to guarantee an information interconnection between processes are retrieved from a well-organised and controlled structure of codes at the various WBS levels assigned to each object, where the structure of any other application (e.g. work programme) must perfectly match the data found within the models, respecting the coding system of the WBS levels and their sequential order.

Such information management is conceived to meet the needs of different BIM uses and must necessarily be subject to a strict verification process of the data structured and organised according to an information flow that Tecne has developed through the support of issues management platforms that allow information exchange by synchronising the information through another type of open format, the BCF (BIM Collaboration Format).

Figure 5. BIM collaboration format for model checking.

The whole co-ordination activity is managed according to a circular flow where the queries stemming from the analysis and verification of the project (so-called Issues) are collected in digital reports (BCFs) via the

Co-ordination software, which in turn generates information exchange according to the steps below:

- the coordination software synchronises the Issues on the information exchange platform through the open BCF format, a true interoperable information carrier. Here, the issues are visualised and commented on by all the operators involved in the project;
- the information exchange platform is then used to download the issues to the modelling software to execute the queries;
- once the operator's queries have been answered, the Issues are again uploaded to the information exchange platform;
- the co-ordination software retrieves the information from the platform and analyses it again, keeping track of all comments.

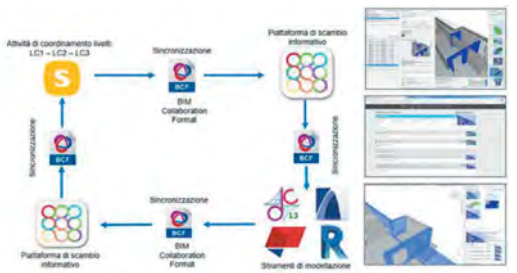

Figure 6. Circular flow of coordination activity and design management.

3.3 *Case study*

In the case studies different interventions design solutions were developed following the BIM methodology. Interventions solutions for Tunnel renewal or structural reinforcement lining that can include voids fillings on the back of the crown, rock bolts, partial or total demolition of the lining, waterproofing and drainage collection system, installation of steel mesh reinforcement, on-site casting of the new lining and/or lowering the road platform.

As a first step, models for the existing state of the tunnel were developed (model containing information about the different cross sections, portals and voids and compress stress model). In compliance with the design solution, the demolition model is developed. Here, the demolition of the lining and sidewalks were designed accordingly with the solutions for the lining rebuilt, as well as the interventions model with all the information and representation of the design solution such as filling of the voids, rock bolts, proposed lining, steel reinforcement mesh, waterproofing and drainage collection system.

For the development of the information models a workflow has been created with a central 3D tunnel model (OTD), capable of connecting with other models such as civil, geological, geotechnical, and steel and concrete (see Figure 7).

This workflow was created with the purpose of connecting all the disciplines involved in the project, so when receiving new input all the disciplines can update simultaneously and be connected.

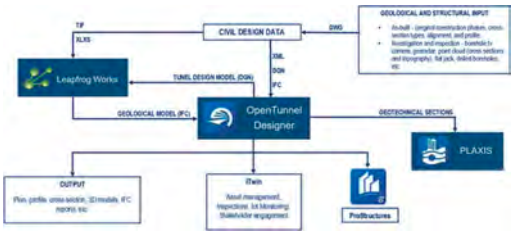

Figure 7. Workflow for the model and design of interventions for tunnel renewal.

The project starts with the analyses of the input data coming from the as-built (original construction phases, cross section types), inspection and investigation (point cloud topography, borehole tv camera, flat jacks, drilled boreholes, defects schedules, etc.). This data is entered in an editable file (xlsx, tif or dwg) in such a way as to allow it to be imported into the modelling softwares and draft models that can provide support for the design of interventions.

The analyses of the existing road and tunnel (tunnel minimum clearance verification) and the reconstruction of tunnel alignments and profiles are performed with a civil software (Civil3D). All the information coming from the civil software is imported as a xml, dgn and IFC file into the 3d tunnel model.

All the data regarding borehole tv camera, flat jacks and topography from the investigations are imported into geologic software (Leapfrog works) as an xlsx file and tif file.This data is used to create a model of the voids that can exist on the back of the crown and to create a flat jack model that shows the concrete compress stress along the tunnel (see Figures 8 and 9).

Figure 8. Voids model (Leapfrog works).

Figure 9. Flat jacks and voids model (Leapfrog works).

The tunnel model can be imported in Leapfrog in a way to have information regarding the tunnel theoretical intrados and extrados.

The models (voids and compress stress models) and topography created in the geologic model are exported in IFC in a way that, in the Tunnel BIM model, the soil meshes, and the voids model will be referenced.

Figure 10. Existing model.

Figure 11. Demolition model.

Figure 12. Tunnel renewal model.

In the tunnel BIM model (OTD), templates of the cross section that contain information about theoretical excavations, sub excavations, lining parts reinforcements and material are created. Templates for MEP elements can also be created, such as hydraulic elements for the drainage and collection of the water coming from the rock mass (see Figure 13).

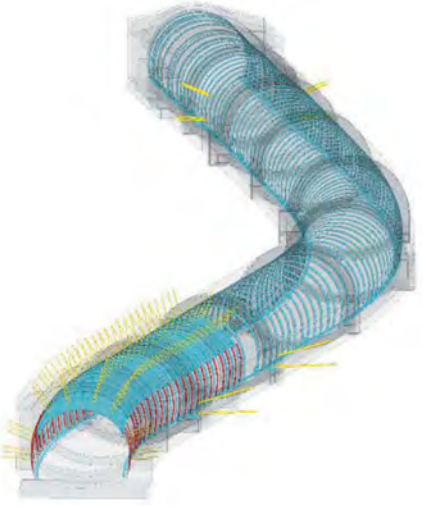

Figure 13. Waterproofing and drainage collection system solution.

Each modelled object is assigned to a WBS levels code to meet the needs of different BIM uses (4D, 5D, 6D) and the verification process.

In the Tunnel BIM model (OTD) analytical sections are created and exported along with the soil into a geotechnical software (PLAXIS 2D), automatically

with scripting files. The geometric tunnel information and reinforcements and soil material are exported into geotechnical software to proceed with the geotechnical verification (see Figures 14).

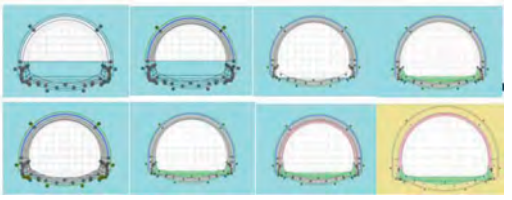

Figure 14. Staged construction for the geotechnical verification (PLAXIS 2D).

In parallel, the tunnel units that were modeled in the tunnel BIM model (OTD) are referenced in the steel and concrete software (ProStructures) where the steel bars and detailed elements of the lining steel mesh reinforcement are drafted (see Figure 15).

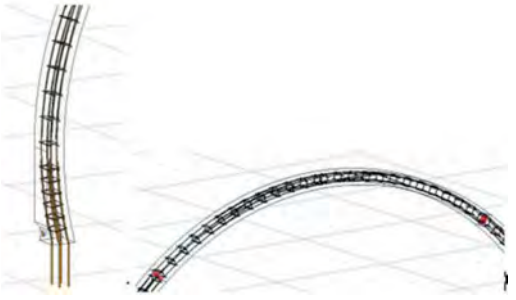

Figure 15. Steel reinforcement mesh model (ProStructures).

From the tunnel BIM model and steel and concrete model plans, profiles, cross sections, reports, schedules, tables etc. are extracted for the project deliverables.

The main software (OTD) creates a model that can be updated into the cloud and be used for different scenarios such as asset management, inspections, IoT monitoring and stakeholder engagement.

4 CONCLUSIONS AND FUTURE WORKS

The application of Building Information Modelling (BIM) in tunnelling projects is nowadays considered the best option as it allows improving design quality, construction schedule and budget by easily implementing many operations. The nature of design-build projects necessitates the use of a smart system able to handle a high volume of data in an efficient way.

BIM procedures can be implemented in Gruppo ASPI to facilitate design, construction and operation processes to form a reliable basis for decisions.

Operating according to the principles of interoperability through open formats only is a difficult and challenging choice, as it can call into question well-consolidated and apparently functioning processes until it is time to deal with a public procurement authority that has reached a level of digital maturity in line with the increasingly interoperability-oriented legal provisions.

Once the choice has been made, and, after better consolidating the whole process, the advantages will become tangible, along with a new awareness of the neutral format as the only form of interoperability capable of ensuring fair data control and validation, a standard that is independent of software house formats and that implicitly ensures the reuse of data over time.

Contracting authorities will soon be required to keep data accessible for a long time avoiding the risks stemming from the relentless evolution of proprietary formats. Moreover, in their role as public bodies, they will be required to make their tenders accessible to as many bidders as possible.

Finally, not to be underestimated is the condition for users and public administrations to freely invest in the technology considered to be the best available option, thus minimising their investments and costs.

Finally, in terms of future works, Gruppo ASPI aims to develop an integrated digital twin for each asset which can be used for managing multiple types of tunnelling data in a comprehensive way by creating a digital twin of the tunnelling project.

REFERENCES

M. Mazzola, M. Giordano, C. Alessio, B. Spigarelli, Autostrade per l'Italia (ASPI) TRS Tunnel Renewal Strategy: The cases of Castello 1 left, San Fermo right and Colle Marino left tunnels, Expanding Underground - Knowledge and Passion to Make a Positive Impact on the World, Proceedings of the ITA-AITES World Tunnel Congress 2023 (WTC 2023), 12-18 May, 2023, Athens, Greece.

Tecne, Autostrade per l'Italia, TRS - TUNNEL RENEWAL STRATEGY, The case of San Fermo right tunnel for sustainability achievement in lining reconstruction works, CERN Tunnel Asset Management (TAM), 27th October 2023, Geneva, Switzerland.

Tunnelling for a Better Life – Yan, Celestino, Thewes & Eberhardt (Eds)
© 2024 The Author(s), ISBN 978-1-032-80042-4
Open Access: www.taylorfrancis.com, CC BY-NC-ND 4.0 license

Design and implementation of a mobile welding robot for TBM cutterhead: Enhancing efficiency, precision, and safety

Peng Chen & Jianfu Chen
China Railway 14th Bureau Group Mega Shield Engineering Co., Ltd

Jianliang Mao*
Southeast University Nanjing Jiangbei New Area Innovation Institute

Jicheng Shu, Minqiang Yang & Shouzhi Guo
China Railway 14th Bureau Group Mega Shield Engineering Co., Ltd

ABSTRACT: In response to the welding needs of cutterheads used in tunnel construction, a cutterhead welding mobile robot has been developed to fulfill the demand for efficient and reliable welding processes. Conventional manual welding methods are time-consuming, labor-intensive, and prone to quality issues and safety hazards. The introduction of welding mobile robots facilitates the automation of the welding process, enhancing precision, efficiency, and ensuring worker safety. The design of the tunnel boring machines (TBM) cutterhead welding mobile robot involves several key steps. Firstly, an analysis of the welding requirements and working conditions for cutterheads used in shield tunneling is conducted. This analysis takes into account material properties, joint configurations, welding parameters, and spatial constraints. Based on this analysis, the mechanical structure, control system, and welding tools of the robot are designed and optimized. Specialized algorithms are developed for weld seam recognition, path planning, motion control, and welding parameter optimization. By utilizing precise visual recognition, path planning, and motion control algorithms, the robot accurately positions itself and ensures consistent welding on cutterhead joints. The design of the TBM cutterhead welding mobile robot holds significant research value. The automation of the welding process has improved welding quality, productivity, and worker safety. Ongoing research aims to further optimize the robot's design and control algorithms, ultimately enhancing its performance and expanding its applications within the tunnel construction industry.

Keywords: Mobile welding robot, Path planning, Weld seam recognition, Welding parameter optimization, Tunnel boring machines cutterhead

1 INTRODUCTION

With the development of industrialization and technological advancements, robotic welding technology has found widespread applications across various industries. It's particularly indispensable in the field of heavy machinery manufacturing. Compared to traditional manual welding, utilizing welding robots in welding tasks not only saves labor costs but also enhances welding efficiency and quality, meeting the diverse requirements of different sectors.

The development of welding robot technology has gone through three stages: teach and playback, low intelligence, and high intelligence [1]. The earliest teach and playback robots executed pre-taught programs for repetitive tasks, demanding high consistency in welding but lacking adaptability. Low intelligence welding robots integrated various sensing technologies, offering some environmental awareness. They could adjust welding paths and parameters based on the actual workpiece conditions, thus improving welding quality. High intelligence welding robots, enabled by digital manufacturing systems and advanced technologies, achieve full welding process automation. This includes scanning, 3D modeling, weld seam recognition, path planning, real-time tracking, and monitoring. Currently, teach and playback and low intelligence welding robot technologies are well-established and widely used in welding applications. In contrast, high intelligence welding robot systems are still in their infancy, with less maturity, limited scope, and higher costs. Nonetheless, they are crucial for realizing the automation, flexibility, and

*Corresponding author: jl_mao@shiep.edu.cn

DOI: 10.1201/9781003495505-378

intelligence of welding manufacturing, representing the inevitable future trend in welding [2].

Tunnel boring machines (TBM) are specialized construction machinery used for underground tunnel excavation, primarily designed for creating tunnels beneath the earth's surface. The key component driving these machines is the cutterhead of the TBM, which plays a pivotal role in the tunneling process [3]. In the manufacturing of the cutterhead, the welding process is extensive. Traditional manual welding methods are not only time-consuming but also lead to lower welding efficiency and quality. Moreover, they pose potential health hazards to the welding operators. To address these challenges [4], this paper introduces a welding system tailored for cutterhead welding in TBM [5], [6]. Utilizing robotic welding offers several advantages. Firstly, it significantly enhances production efficiency and welding speed, ensuring high reliability with the ability to operate continuously, thus guaranteeing welding quality. Secondly, it ensures superior welding quality with a pleasing surface finish, eliminating issues associated with uneven manual welding and reducing the dependence on the skill level of the welder. Finally, robot welding is well-suited for repetitive tasks, often requiring minimal human intervention beyond material supply and monitoring. In the multi-layer and multi-pass welding process of shield tunneling cutterheads, without the support of a vision system, it would typically demand repeated teaching, manual intervention, and could not handle complex groove configurations to ensure weld quality during different layers and passes [7]. Therefore, there's a necessity to introduce intelligent vision-based welding robots to further recognize weld seams.

However, traditional weld seam recognition systems face several challenges, including sensitivity to lighting and environmental conditions, difficulty handling complex weld seams, high real-time demands, the need for manual setup and calibration, and complex data processing requirements [8], [9]. These issues are particularly pronounced in complex tasks such as multi-layer and multi-pass welding. As a result, the field of intelligent welding is increasingly inclined towards utilizing intelligent vision systems, incorporating deep learning neural networks and advanced image processing techniques [10]. These emerging technologies have the potential to overcome the limitations of traditional systems and enhance the accuracy and efficiency of weld seam recognition.

In light of the shortcomings of various conventional approaches, this paper introduces an intelligent vision-based autonomous welding robot with weld seam recognition capabilities. It offers a significant enhancement in welding efficiency and quality for TBM cutterheads. Through a vision system, the robot can instantaneously identify information about weld seam position, shape, and groove, enabling autonomous welding path planning. Consequently, this greatly enhances welding efficiency and quality.

2 BACKGROUND OF MOBILE WELDING SYSTEMS IN TBM CUTTERHEAD WELDING

In the context of TBM cutterhead welding, facing the challenges of massive cutterheads and complex multi-layer, multi-pass welding tasks, the adoption of a mobile welding robot system has become a crucial solution. The background of this project involves the manufacturing and installation of TBM cutterheads, as well as cutterhead cutterbox assembly. Factors such as the enormous size of the cutterhead, multi-piece assembly, various welding bevels, and welding materials increase the complexity and difficulty of welding.

Firstly, the massive dimensions and thickness of the cutterhead necessitate a multi-layer, multi-pass welding process performed by welding robots. The welding robot system must precisely control the movement of the welding torch to ensure welding quality and consistency.

Secondly, various welding bevels need to be considered. In TBM cutterheads, the main bevel types include X-type, Y-type, and K-type. X-type welds are primarily located at thinner cross seams where the cutterheads are joined; Y-type welds are mainly found at the outer edges of the cutterheads, where the steel plates are thicker; K-type welds are predominantly located at the auxiliary support steel plates on the cutterhead's arms that contact the center section of the steel plate [11].

Additionally, considering the scale of the cutterhead, the robot system must have efficient welding capabilities to complete the work within a limited timeframe. The cutterhead's surface can be complex and uneven, so the system needs to accurately control the path to adapt to various surfaces. Since the final size of the cutterhead is massive, the robot system needs to be mounted on a track on the ground to move along the cutterhead's surface for welding.

In conclusion, TBM cutterheads involve complex welding tasks and massive workpiece dimensions, requiring a highly precise welding robot system to accomplish them. This system must not only possess welding capabilities but also take into account factors such as robot motion control, path planning, environmental installation, and welding process parameters to ensure the cutterhead welding is completed smoothly and meets high-quality welding standards. Based on the welding requirements and project background mentioned above, it is advisable to set up a ground track welding experimental platform for various technical tests. The anticipated preview of the final welding project's outcome is shown in Figure 1.

3 TBM CUTTERHEAD MOBILE WELDING ROBOT SYSTEM

The Cutterhead Mobile Welding System developed in this project primarily consists of five main components: the robot body, the visual module, the ground track electrical control system, the welding kit, and

Figure 1. Welding preview image of the TBM cutterhead mobile welding robot.

the welding control software. These components work in synergy to accomplish specific welding tasks. They communicate and exchange data via the Ethernet IP protocol to facilitate functions like arm swinging, visual recognition, precise point control of the ground track system, digital twinning, and the ultimate analysis of welding seam quality. The system's detailed composition is illustrated in Figure 2.

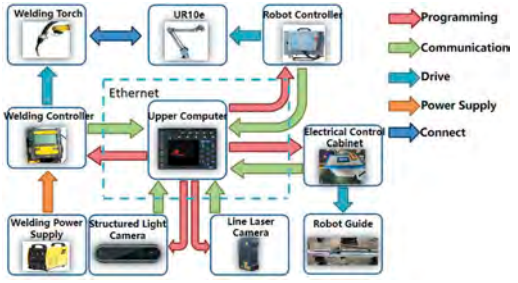

Figure 2. Structure diagram of the mobile welding system.

3.1 *Robot*

The welding robot body uses the UR10e six-axis industrial robot produced by Universal Robots. It serves as the primary motion platform within the welding system and is programmed and developed using URscript language. The robotic arm executes movements based on received welding trajectories. The robot's end-effector, the welding gun, moves to various positions on the workpiece as directed by the robot's motion. Additionally, the robot can receive control commands from the upper-level computer interface. The robotic arm operates alongside human workers in the same workspace and can flexibly adjust its position and orientation to adapt to various working scenarios and requirements. Furthermore, it possesses reconfigurable and programmable capabilities, allowing it to perform different types of tasks.

3.2 *Visual recognition module*

The vision module consists of two main components: the structured light camera and the line laser scan camera. The structured light camera is primarily responsible for coarse welding seam recognition, while the line laser scan camera handles fine seam recognition. For Rough Identification, the structured light camera, specifically the Silver Bull R-132 structured light camera, captures RGB-D images of the welding scene. These images are processed using the CenterNet neural network, enabling rapid and accurate identification of the approximate welding seam location. For Precise Identification, the system utilizes the DeepVision SR-7900 line laser scan camera to generate point cloud images. These point cloud images are further processed by mapping depth information to grayscale images using a linear relationship. The Marr-Hildreth edge detection method is applied to identify the welding seam's edges and create bounding boxes, ultimately extracting detailed welding seam data. This dual-camera system provides comprehensive visual data for precise welding seam recognition, ensuring high-quality welding results.

3.3 *Welding kit*

The welding kit primarily includes a welder, wire feeder, welding gun, and a nozzle cleaning station. The welder employs an Esab welding power source, equipped with overheat, under-voltage, and over-voltage protection mechanisms. It is suitable for various light, medium, and heavy-duty MIG/MAG applications. Standard features encompass built-in optimization curves, arc current, and voltage control, gas checking, 2-step/4-step arc initiation, and inductance adjustment. These functionalities reduce setup time, facilitating high-quality welding results. The Esab wire feeder is an integral component of the welding robot system, responsible for supplying the welding wire to the welding gun. As welding wire serves as the filling material during the welding process, precise control via the wire feeder ensures accurate delivery of the wire to the weld seam, enhancing the automation and precision of the welding process. The TRM605W welding gun is employed for melting the electrode material and forming the weld seam during the welding process. This welding gun employs electric current to heat and melt the electrode material, filling the weld joint with molten metal, establishing a robust connection. The pneumatic welding nozzle cleaner utilizes the SC220ASE model. This essential auxiliary device is mainly utilized for removing slag and impurities from the welding gun nozzle and torch head during the welding process. Its role is to maintain the welding gun in optimal working condition, ensuring welding quality and efficiency.

3.4 *Electrical system*

The electrical control system for the ground track consists of a PLC, ground track modules, servo motors, and associated low-voltage electrical components. The main control PLC used in this system is the Delta DVP-32EH. The primary function of the PLC is to receive, interpret, and execute commands from the upper-level human-machine interface (HMI). These commands encompass settings related to the robot base, including movement, speed, and positioning parameters. The PLC is also interconnected with the servo system to ensure precise positioning and motion control of the robot base. The servo system comprises servo motors, encoders, and servo drives. The servo motor is responsible for driving the motion of the robot base, while the encoder continuously monitors the base's position in real-time. The servo drive adjusts the operational state of the servo motor based on commands from the PLC, enabling high-precision positioning and motion control. Additionally, the electrical system incorporates an upper-level HMI with a touchscreen interface. This interface allows operators to send commands to the PLC via touch inputs, enabling actions such as setting welding positions. It can also provide fault alerts for potential issues that may occur during the operation.

3.5 *Human-machine interaction application software*

The welding software section primarily consists of our self-developed digital twin system and weld seam quality analysis software, as shown in Figure 3.

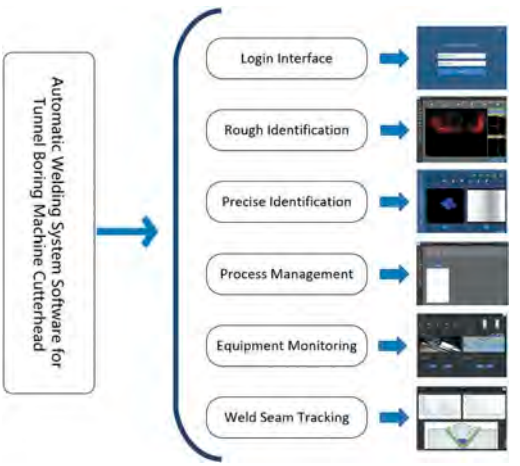

Figure 3. Welding software function overview.

The digital twin system can run synchronously with the actual welding robot. It monitors the welding robot's working status, position, speed, and welding parameters in real-time through sensors and real-time data collection. This allows operators to observe the welding process in real-time on a computer, enhancing control over the welding work. Furthermore, it provides real-time status information for the mobile welding robot, including welding progress, working speed, welding temperature, and other critical parameters, enabling operators to detect and address potential issues promptly, ensuring welding quality. Lastly, the weld seam quality analysis software facilitates a detailed post-weld analysis. This includes welding quality assessment, welding defect detection, and a review of welding parameters. Operators can use this data to refine the welding process and reduce defect rates.

4 THE IMPLEMENTATION OF KEY TECHNOLOGIES IN MOBILE WELDING SYSTEMS

4.1 *Weld seam recognition via multimodal fusion*

The system's core comprises two critical visual systems: a structured light camera and a line laser scanning camera. These two cameras work in synergy, providing the robot with highly accurate welding environment perception and task planning through advanced computer vision techniques. Firstly, the project utilizes two different types of cameras, including the structured light camera for rough welding seam position detection, and the line laser scanning camera for more precise three-dimensional groove data acquisition.

4.1.1 *Implementation of rough identification*

The Rough Identification is performed by the structured light camera. This camera is responsible for capturing RGB-D images of the welding area. The images are transmitted to the upper computer and analyzed using the Centernet convolutional neural network to detect the approximate position of the weld seam [12]. Features processed by residual blocks are readjusted using Channel and Spatial Attention Mechanism (CBAM) (as shown in Figure 4 to reweight the features in both spatial and channel dimensions. These reweighted features are then fused with the features from the decoding layer, allowing the network to make full use of effective features and enhance detection accuracy [13]. The specific process is as follows:

$$\begin{cases} F' = M_C(F) \otimes F \\ F'' = M_S(F') \otimes F' \end{cases} \tag{1}$$

where F is Characteristics of the input; F' is the channel attention and the input features are multiplied by elements to get new features; M_c is the summed result activated by Sigmod to obtain one-dimensional channel attention; F'' is the resulting 2D spatial attention multiplied by the feature map F' by element to obtain a feature map weighted in both the channel and spatial domains; M_s new features F' are subjected to global maximum pooling and mean pooling by space, and the

resulting 2D vectors are spliced and subjected to convolution and Sigmod activation operations to obtain the 2D spatial attention.

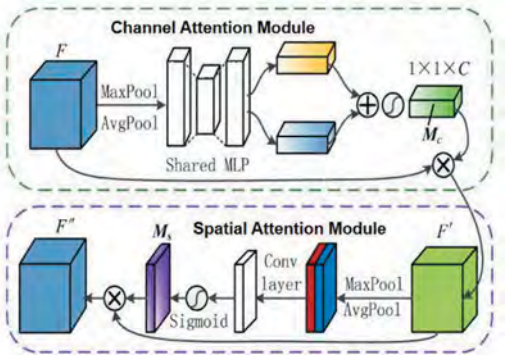

Figure 4. Channel and spatial attention module.

This step is crucial as it provides approximate coordinates and features of the welding area for subsequent tasks. Next, based on the output from the structured light camera, the robot's motion path is planned. This path planning not only ensures that the robot can accurately reach the welding position but also avoids any potential obstacles to ensure safety. The process of Rough Identification is illustrated in Figure 5.

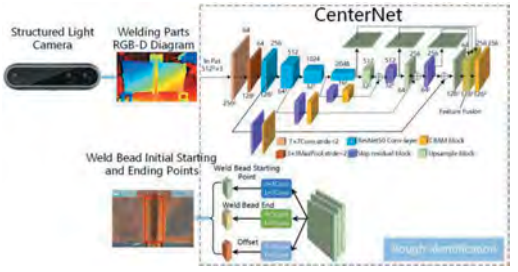

Figure 5. The rough identification process.

4.1.2 *Precise identification implementation*

Precise Identification is achieved through the intervention of a line laser scanning camera. This camera is responsible for high-precision three-dimensional groove data scanning. The scanning is performed using a line laser camera, followed by direct-pass filtering. Simultaneously, it generates a depth-mapped grayscale image and establishes a 3D-2D coordinate index. Subsequently, threshold segmentation is applied to the depth-mapped grayscale image, followed by further morphological processing. Marr-Hildreth edge detection method is then employed to obtain the two-dimensional coordinates of the weld seam [14].

The Marr-Hildreth steps are as follows:

(1) Gaussian filtering:

Gaussian filtering is used to smooth images and reduce the impact of noise. Define *I'(x, y)* as the result of applying a Gaussian filter *G(x, y)* to the input image *I(x, y)*:

$$I'(x,y) = I(x,y) * G(x,y) \tag{2}$$

where * represents the convolution operation.

(2) Laplace operator:

The Laplace operator is used to detect edges in an image. Define *E(x, y)* as the edge strength image obtained by applying the Laplacian operator *L(x, y)* to the smoothed image *I'(x, y)*:

$$E(x,y) = L(x,y) * I'(x,y) \tag{3}$$

where * represents the convolution operation.

(3) Zero-crossing detection:

Zero-crossing detection is used to determine the location of edges.In the context of the edge strength image *E(x, y)*, edge points are determined by comparing the edge strengths of neighboring pixels.

The detected 2D coordinates are combined with the 3D-2D coordinate index previously generated by the low-pass filter. The features of the weld groove are extracted using slope analysis. Once the precise characteristics of the groove are obtained, the upper computer begins the multi-layer, multi-pass welding planning. The Precise Identification process is illustrated in Figure 6.

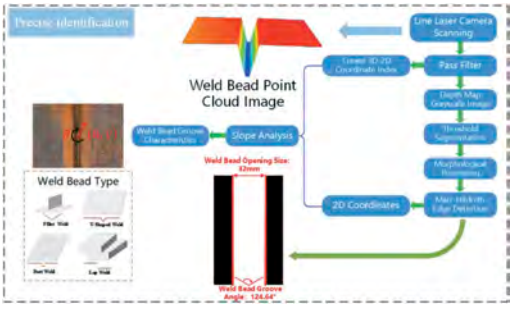

Figure 6. The precise identification process.

4.2 *Calculation of multi-layer multi-pass welding groove layer parameters*

Based on the point cloud data processed from the previous seam recognition step using structured light and line laser scanning, as well as the seam path information, the multi-layer and multi-pass welding path for the robot is planned. Before planning the multi-layer and multi-pass welding, it's essential to determine the seam layout method. There are generally two layout methods: one is the equal-area seam layout, where each seam has the same cross-sectional area. The other layout is the equal-height layout, where each layer of seams has the same height. Each method has its own advantages and disadvantages [15]. In this system, the equal-height seam layout method is selected for planning and design from the perspective of heat input for each layer of seams.

Next, taking the example of multi-layer and multi-pass welding with a flat butt V-groove, after each pass, there will be some welding deformation in the groove. To minimize the deformation caused by the previous pass, it's essential to adjust the welding sequence appropriately. This adjustment is made to balance the heat input at both ends of the groove and reduce the distortion caused by uneven heat input. Typically, there are two welding sequences to consider. In the left pattern, welding proceeds from left to right, which can lead to the accumulation of heat on one side of the workpiece in a short time, potentially causing distortion at one end of the workpiece. In the right pattern, welding begins on both sides before proceeding to the center. This sequence ensures good fusion between the left and right seams and the sidewalls of the workpiece, while also promoting the evenness of the weld layers. However, this sequence may require the robot to travel a distance without welding, leading to a slight reduction in work efficiency. A comparison of these two welding sequences is depicted in Figure 7.

Figure 7. Welding sequence classification.

For the sake of analysis, during the pre-planning process, the cross-sections of the fill welds are simplified into three shapes: triangles, trapezoids, and rhombuses. If a layer has only one weld seam, its cross-section is a triangle. If there are n seams in a layer, the last one is a trapezoid, while the first n-1 seams are rhombuses, where n is greater than 1 [16]. The planning is illustrated in Figure 8.

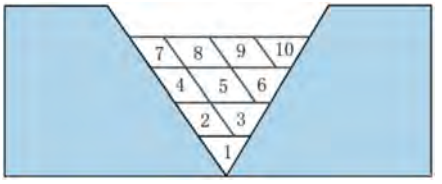

Figure 8. Welding plan.

In the case of the equal-height weld seam layout, where the height of each weld seam is the same in every layer, the steps to determine the position of a single weld seam are as follows. Define h as the height of each weld layer:

$$h = \frac{H}{n} \tag{4}$$

where H represents the groove height/plate thickness, and n represents the number of weld seam layers.According to the triangle theorem, the width W_i of the ith layer can be determined as follows, and the width $W_{i\text{-}1}$ of the i-1th layer is as follows:

$$\begin{cases} W_i = \frac{(i \cdot h)^2}{\cos\left(\frac{\theta}{2}\right)^2 \cdot h} \cdot \sin\theta \\ W_{i-1} = \frac{((i-1) \cdot h)^2}{\cos\left(\frac{\theta}{2}\right)^2 \cdot h} \cdot \sin\theta \end{cases} \tag{5}$$

where θ is the groove angle. Based on the equal-height cross-section of the V-groove, A is defined as the length of the diamond-shaped side of the weld seam in each layer:

$$A = \frac{h}{\sin(\frac{\pi}{2} - \frac{\theta}{2})} \tag{6}$$

The entire cross-section of the weld seam in each layer can be approximated as a trapezoid, where S_T is defined as the area of the trapezoid and can be expressed as follows:

$$S_T = \frac{(W_i + W_{i-1}) \cdot h}{2} \tag{7}$$

The parameter S_T is obtained from the above equation. Define T as the number of weld seams in each layer, with the calculation formula provided as follows:

$$T = \left(\frac{S_T}{A \cdot h}\right) + i \cdot \frac{S_T}{A \cdot h} \tag{8}$$

Define B_T as the length of the lower base of the small trapezoid in the last weld seam of each layer, with the calculation formula provided as follows:

$$B_T = W_{i-1} - \left(\left(\frac{S_T}{A \cdot h}\right) \cdot A\right) \tag{9}$$

By applying all of the above formulas, the necessary parameters for weld seam spatial coordinates can be determined. Coordinates of the spatial position of the j-th weld channel in the i-th layer x_{ij}, y_{ij}, z_{ij}, is:

$$\begin{cases} x_{ij} = \left(x_0 - H_{i-1} \cdot \tan\frac{\theta}{2}\right) + (A \cdot j) + (B_T \cdot j) \\ y_{ij} = y_0 \\ z_{ij} = z_0 + H_{i-1} \end{cases} \tag{10}$$

Based on the analysis of weld bead arrangement described above, the spatial coordinates for each weld bead in every layer can be calculated. UR robot's offset instructions are used for programming and planning. The main approach is to obtain the start and end positions of the weld bead in the first layer based on visual information and plate data. Then, the offset instructions are used to assign positions for other weld beads and introduce any necessary deviation compensation. Additionally, adjustments are made to the welding torch's orientation during the welding process. This significantly reduces the number of teaching iterations in the welding process and enhances welding efficiency.

4.3 *Motion planning for multi-layer and multi-pass welding*

Welding paths and trajectory planning are paramount to ensuring the quality of weld seams. To perform arc-shaped motions, typically, three points are required: two endpoints and one intermediate point. These three points determine a spatial plane, which is used for trajectory planning in that plane. Connecting these three points involves two segments of cubic polynomials. It's essential to ensure that the velocity and acceleration are continuous at the intermediate point to avoid sudden changes in velocity, which would otherwise require infinite acceleration. Increasing acceleration in robot control leads to higher drive currents. Therefore, continuity at the intermediate point is crucial [17]. Assuming that the initial time for each segment of the cubic spline is t=0, and the final time is t=t_{fi} (i=1, 2). Define θ_0 as the initial point, θ_v as the middle point, θ_g as the final point, $\theta_1(t)$ as the first segment of the cubic spline, and $\theta_2(t)$ as the second segment of the cubic spline:

$$\begin{cases} \theta_1(t) = a_{10} + a_{11}t + a_{12}t^2 + a_{13}t^3 \\ \theta_2(t) = a_{20} + a_{21}t + a_{22}t^2 + a_{23}t^3 \end{cases} \tag{11}$$

Applying constraint conditions for each trajectory segment, with the initial velocity and final velocity of each segment being zero, the velocity at the intermediate point [18], and ensuring acceleration continuity, eight constraints can be established as shown in the following equation:

$$\begin{cases} \theta_0 = a_{10} \\ \theta_v = a_{10} + a_{11}t_{f1} + a_{12}t_{f1}^2 + a_{13}t_{f1}^3 \\ \theta_v = a_{20} \\ \theta_g = a_{20} + a_{21}t_{f2} + a_{22}t_{f2}^2 + a_{23}t_{f2}^3 \\ 0 = a_{11} \\ 0 = a_{21} + 2a_{22}t_{f2} + 3a_{23}t_{f2}^2 \\ a_{11} + 2a_{12}t_{f1} + 3a_{13}t_{f1}^2 = a_{21} \\ 2a_{12} + 6a_{13}t_{f1} = 2a_{22} \end{cases} \tag{12}$$

From the eight constraint conditions represented by the eight equations (the first two equations are position constraint conditions for the first segment, the third and fourth equations are position constraint conditions for the second segment, the fifth and sixth equations are constraints for initial and final velocities being 0, and the seventh and eighth equations represent the continuity of velocity and acceleration at the intermediate point) [19], a linear equation system is established with the unknown coefficients, which can be solved to obtain the coefficients for the two segments of the cubic polynomial as follows:

$$\begin{cases} a_{10} = \theta_0 \\ a_{11} = 0 \\ a_{12} = \frac{12\theta_v - 3\theta_g - 9\theta_0}{4t_f^2} \\ a_{13} = \frac{-8\theta_v + 3\theta_g + 5\theta_0}{4t_f^3} \\ a_{20} = \theta_v \\ a_{21} = \frac{3\theta_g - 3\theta_0}{4t_f} \\ a_{22} = \frac{-12\theta_v + 6\theta_g + 6\theta_0}{4t_f^2} \\ a_{23} = \frac{8\theta_v - 5\theta_g - 3\theta_0}{4t_f^3} \end{cases} \tag{13}$$

Following the interpolation algorithm described above, the robot's path and trajectory can be planned, including motions such as the crescent-shaped swing in the welding process of curved or circular weld seams.

5 VERIFICATION OF EXPERIMENTAL RESULTS

In order to verify the stability and reliability of the multi-layer multi-pass welding system, a series of multiple experimental tests were conducted. These experiments focused on different aspects of the system, mainly including the function of the self-developed welding software, the selection of welding process parameters, the effect of visual recognition of weld passes, and the effect of multi-layer multi-pass welding. An experimental test bed was built to conduct experiments on the key functions mentioned above. The results of these experiments will verify the feasibility and stability of the system, as well as help in the further optimization of the system parameters and algorithms and the subsequent upgrading or secondary development, etc., in order to meet various welding scenarios and process requirements. The welding experiment platform is shown in Figure 9.

5.1 *Welding software feature*

The welding software contains the following functions: Rough Identification image display, Precise Identification image display, weld tracking interface, welding parameter monitoring interface and weld quality analysis interface. The main functions are shown in Figure 10.

5.2 *Welding process selection*

Welding process parameters have been repeatedly experimental testing were derived priming layer, filler layer, as well as the cover layer of the required welding current, welding arc voltage and shielding gas flow. Specific as shown in Table 1.

Figure 9. Mobile welding robot experiment platform.

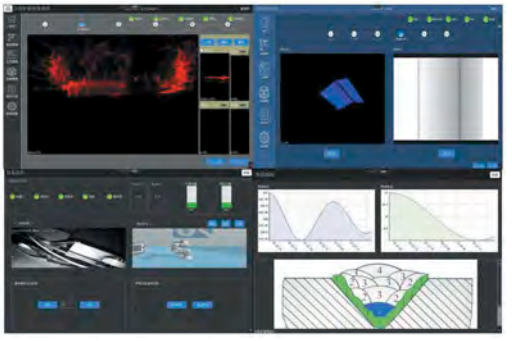

Figure 10. Welding software function demonstration.

Table 1. Welding process parameter table.

weld line	Welding Current/A	Welding Voltage/V	Gas Flow/ L*min^{-1}
underlayer	220-250	25-28	25
filler layer	260-280	30-31	25
covering layer	240-260	28-30	25

5.3 *Weld seam recognition results*

Structured light cameras and line laser scanning cameras play a crucial role in accurate positioning and bevel measurement during the welding process. In the validation session, a series of identification and measurement experiments will be conducted. First, the positioning accuracy of the structured light camera will be evaluated to ensure its reliability in identifying the weld location. Next, a line laser scanning camera will be utilized to acquire bevel data and verify its accuracy. The validation results are shown below.

Figure 11. Rough identification and precise identification results.

5.4 *Multi-layer multi-pass welding results*

In order to verify the welding effect of the system, welding experiments were carried out on the welded plates. The material of the welded structure is Q345B carbon steel with a thickness of about 80mm, which is welded by flat butt welding. Using MAG active gas shielded welding method for physical welding experiments. The welding process is smooth and without anomalies, and the weld filler is uniform. The experimental welds can meet the requirements of the field process. Finally, the Welding results are shown in Figure 12.

Figure 12. Multi-layer and Multi-pass Weld Seam Results.

6 CONCLUSIONS

(1) Through the use of precise path planning and motion control algorithms, the robot is able to accurately position and weld consistently on the cutter head. Automation of the welding process improves weld quality and reduces variability compared to manual welding.
(2) The use of mobile robots increases productivity by reducing downtime and enabling continuous operations.
(3) Implementing welding mobile robots also improves worker safety by reducing worker exposure to hazardous welding environments.
(4) By automating the welding process, the technology improves weld quality, productivity and worker safety. Ongoing research aims to optimize the robot's design and control algorithms, ultimately improving its performance and expanding its applications in the tunnel construction industry.

REFERENCES

[1] Pires, J. N., Loureiro, A., Godinho, T., Ferreira, P., Fernando, B., & Morgado, J. (2003). Welding robots. *IEEE robotics & automation magazine*, *10*(2), 45–55.

[2] Kim, S. W. (2017). Robot Development Trend and Prospect. *Convergence Security Journal*, *17*(2), 153–158.

[3] Su, C., Wang, Y., Zhao, H., Su, P., Qu, C., Kang, Y., & Wang, L. (2011). Analysis of mechanical properties of two typical kinds of cutterheads of shield machine. *Advanced Science Letters*, *4*(6-7), 2049–2053.

[4] Zhu, D., Chen, K., Huang, X. Q., Hou, N., Wang, W. Z., & Huo, J. Z. (2016, December). Finite Element Analysis of a New Welding Structure of Cutter Mount in TBM. In *3rd Annual International Conference on Mechanics and Mechanical Engineering (MME 2016)* (pp. 908–915). Atlantis Press.

[5] Wang, L., Kang, Y., Zhao, X., & Zhang, Q. (2015). Disc cutter wear prediction for a hard rock TBM cutterhead based on energy analysis. *Tunnelling and Underground Space Technology*, *50*, 324–333.

[6] Yu, H., Tao, J., Huang, S., Qin, C., Xiao, D., & Liu, C. (2021). A field parameters-based method for real-time wear estimation of disc cutter on TBM cutterhead. *Automation in Construction*, *124*, 103603.

[7] Muhammad, J., Altun, H., & Abo-Serie, E. (2017). Welding seam profiling techniques based on active vision sensing for intelligent robotic welding. *The International Journal of Advanced Manufacturing Technology*, *88*, 127–145.

[8] Newman, T. S., & Jain, A. K. (1995). A survey of automated visual inspection. *Computer vision and image understanding*, *61*(2), 231–262.

[9] Spencer Jr, B. F., Hoskere, V., & Narazaki, Y. (2019). Advances in computer vision-based civil infrastructure inspection and monitoring. *Engineering*, *5*(2), 199–222.

[10] Xu, Y., & Wang, Z. (2021). Visual sensing technologies in robotic welding: Recent research developments and future interests. *Sensors and Actuators A: Physical*, *320*, 112551.

[11] Yuan, J., Guan, R., Guo, D., Lai, J., & Du, L. (2020, September). Discussion on the robotic approach of disc cutter replacement for shield machine. In *2020 IEEE International Conference on Real-time Computing and Robotics (RCAR)* (pp. 204–209). IEEE.

[12] Lai, Y., Dai, R., Zhou, H., Hou, Z., Chen, H., & Chen, S. (2019). Determination of the Initial Welding Point for Multi-pass Welding Based on Laser Vision. In *Transactions on Intelligent Welding Manufacturing: Volume II No. 4 2018* (pp. 93–108). Springer Singapore.

[13] Xu, F., Hou, Z., Xiao, R., Xu, Y., Wang, Q., & Zhang, H. (2023). A novel welding path generation method for robotic multi-layer multi-pass welding based on weld seam feature point. *Measurement*, *216*, 112910.

[14] Zeng, J., Chang, B., Du, D., Wang, L., Chang, S., Peng, G., & Wang, W. (2018). A weld position recognition method based on directional and structured light information fusion in multi-layer/multi-pass welding. *Sensors*, *18*(1), 129.

[15] Huang, H., Lu, H., Liu, S., Zhang, Y., Zhang, H., & Liu, B. (2021, March). A Novel Robotic Welding Method for Multilayer and Multi-pass Welding Process based on Vision Sensor. In *2021 IEEE 5th Advanced Information Technology, Electronic and Automation Control Conference (IAEAC)* (Vol. 5, pp. 1194–1199). IEEE.

[16] Zhang, H., Lu, H., Wang, S., Zhang, Y., Liu, B., & Huang, H. (2021, March). Welding Path Planning Algorithm for Medium-Thick Plate based on Process Parameters. In *2021 IEEE 5th Advanced Information Technology, Electronic and Automation Control Conference (IAEAC)* (Vol. 5, pp. 1142–1146). IEEE.

[17] Wang, Y., Ma, S., Qin, H., Luan, Y., Lian, Z., & Liu, Z. (2022, November). Robotic medium and thick plate welding planning based on laser vision. In *2022 China Automation Congress (CAC)* (pp. 2356–2361). IEEE.

[18] Zhao, H., Zhang, G., Yin, Z., & Wu, L. (2011). A 3D dynamic analysis of thermal behavior during single-pass multi-layer weld-based rapid prototyping. *Journal of Materials Processing Technology*, *211*(3), 488–495.

[19] Frolov, A. V. (2020, October). Automation the Welding Trajectory Control. In *2020 International Multi-Conference on Industrial Engineering and Modern Technologies (FarEastCon)* (pp. 1–5). IEEE.

Tunnelling for a Better Life – Yan, Celestino, Thewes & Eberhardt (Eds)
© 2024 The Author(s), ISBN 978-1-032-80042-4
Open Access: www.taylorfrancis.com, CC BY-NC-ND 4.0 license

Enhancing management and construction quality for a 5km long sandwich immersed tunnel through digital and intelligent methods

Weile Chen
Shen-Zhong Link Management Center, Zhongshan, China
Guangdong Provincial Highway Construction co., Guangzhou, China

Jian Liu*
Shen-Zhong Link Management Center, Zhongshan, China

ABSTRACT: The transportation infrastructure still holds a vast market with substantial demand, but the traditional construction methods are increasingly insufficient to cater to the evolving landscape of information technology development. Facing the opportunities and challenges of global technological innovation and application, as well as the requirements of high-quality transportation infrastructure, many countries, such as the United States, Germany and China etc, have introduced national policies aimed at advancing digital and intelligent manufacturing. To successfully build a 5-kilometer-long steel-shell immersed tunnel with eight lanes in both directions, it requires many innovations in manufacturing and construction equipment. These include the implementation of four intelligent manufacturing lines and an intelligent management system for steel tube manufacturing, the use of intelligent pouring robots for self-compacting concrete pouring, the employ of intelligent trolleys for moving an immersed element of 80,000 tons, a floating and installation vessel, and an underwater 3D intelligent gravel foundation leveling system. Through a series of innovative approaches, the project has manufactured and installed all 32 elements, along with a final closure. Notably, the lateral accuracy of approximately 50% of the immersed elements has been maintained within 10mm. Digital and intelligent construction methods have proven to enhance manufacturing and construction quality, reduce safety risks, improve construction efficiency, reduce labor costs, and provide a benchmark for future infrastructure projects.

Keywords: Digital construction, Intelligent manufacturing, Concrete pouring, Floating installation, 3D leveling, Integrated vessel

1 BACKGROUND

1.1 *Digital and intelligent construction technology for the infrastructure*

The transportation infrastructure construction industry, one of the largest industries in the world, has been notably slow to adopt standardization and digital and intelligent innovations. In the recent 35 years of global economic and technological development, the application rate of technologies such as Building Information Modeling (BIM) and intelligent manufacturing in the construction field has only reached 60% (including building construction)[123]. In contrast, in the past few years, the utilization of advanced technologies such as cloud computing, intelligent equipment, big data, the Internet, and 5G has surpassed 90%.

In 2015, China introduced the "Made in China 2025" strategy, aimed at enhancing quality and efficiency by accelerating the integration of new-generation information technology with the manufacturing industry. Based on this status quo, the broad prospects for the development of digital and intelligent technologies, point out the direction for future transportation.

At present, China has made significant advancements in cross-sea infrastructure construction technology. The Hong Kong-Zhuhai-Macao (HZM) Bridge, which opened to traffic in 2018, is characterized by its "large-scale, standardization, industrialization, and assembly" approach. However, the infrastructure industry still faces the challenge of integrating digital and intelligent construction technologies with traditional equipment. National major cross-sea projects are urgently needed to drive advancements in "industrialization, digitization, and intelligence" and modern engineering technologies. This will enhance China's

*Corresponding author: tjliujian@hotmail.com

DOI: 10.1201/9781003495505-379

infrastructure construction in the digital and intelligent era.

1.2 *Shen-Zhong Link introduction*

The Shen-Zhong fixed sea link across the Pearl River estuary in China is currently under construction, with an expected opening to traffic in 2024. Connecting Shenzhen in the east with the cities of Zhongshan and Guangzhou Nansha in the west(shown in Figure 1), the 24km link spans over and under the world's busiest shipping channels. It features a suspension bridge with a main span of 1,666m, a cable-stayed bridge with a main span of 580m, and transitions on two man-made islands into a 5km long immersed tunnel and a 485m cut-and-cover section extending from the east landfall near Shenzhen (shown in Figure 2).

Figure 1. Project location.

The link comprises a four-lane highway in each direction, for a total of eight lanes, with a special element of six lanes in each direction. It is designed for a traffic speed of 100km/hr and has a design life of 100 years. The immersed tunnel consists of 32 elements, each measuring 10.6m in height, 46m in width, and 165/123m in length, with a 2.2m long closure joint.

Figure 2. Main structures.

2 INTELLIGENT MANUFACTURING SYSTEM FOR STEEL SHELLS

2.1 *Challenges*

The total amount of steel used for the 32 tubes reaches 320,000 tons, averaging 10,000 tons per tube. The steel plate structure is a composite design, featuring inner and outer panels as the primary flexural elements, along with transverse and longitudinal diaphragms as the main shear components. All these elements are secured together using stiffeners and welding joints (shown in Figure 3). The cumulative length of the weld seams for a single tube section reaches 270,000m. The components required for traffic engineering, electromechanical facilities and other reserved and embedded facilities amount to 32,000 per tube.

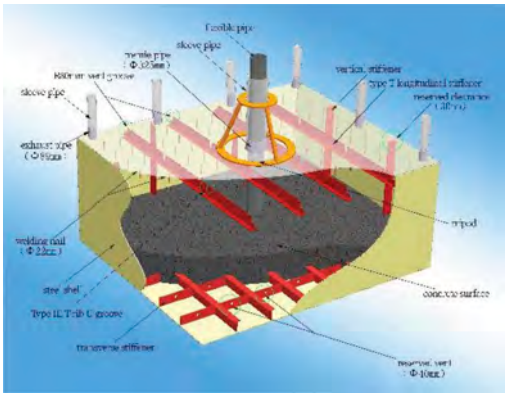

Figure 3. Local details for steel shell.

The geometric tolerance in steel shell manufacturing is set at 10mm between two ends, surpassing the precision requirements of steel box girders and the shipbuilding industry. The inner and outer side panels of the main structure are made of Q420C, with a maximum thickness of 40mm, and the transverse bulkheads constructed from Q390C, with a maximum thickness of 30mm.

To satisfy the overall construction schedule, it was necessary to manufacture one tube per month. Traditional manual fabrication methods for the steel structure proved inadequate for meeting the demands of large-scale, high-efficiency, and high-quality construction required for the Shen-Zhong Link project.

2.2 *Four-lines and one-system*

To promote the convergence of the shipbuilding and transportation industries, a steel shell small segment workshop, a digitized medium segment piggybacking, and an automated large segment assembly production line were studied and developed. Among these, the small segment intelligent manufacturing workshop takes center stage and is referred to as the "four-lines and one-system" intelligent manufacturing production system. This system encompasses a plate/profile intelligent cutting production line, a sheet intelligent welding production line (shown in Figure 4), a block intelligent welding production line, an intelligent painting production line, and an information

management control system. Together, these components enable the intelligent manufacturing of steel shell tubes, enhancing the manufacturing quality and efficiency, and driving technological advancement in both China's transportation and shipbuilding industries.

Figure 4. Intelligent welding line.

2.3 *Achievement*

(1) The utilization rate of steel plates reached 96%, resulting in a savings of 3,436 tons of steel and a total cost reduction of 39.22 million yuan.
(2) The steel intelligent cutting production line improved efficiency and precision in cutting. This led to a total reduction of 594 labor hours required for grinding and repairs per standard tube, equating to a remarkable saving of 19,008 hours for all 32 tubes.
(3) The intelligent welding production line demonstrated a marked improvement in the efficiency and quality of sheet body welding, resulting in a reduction of approximately 192.5 labor hours for grinding and repairs per standard tube. For all 32 tubes, this translated to a substantial saving of 6,160 labor hours.
(4) The block intelligent welding production line made notable strides in both efficiency and welding quality for block assembly. The weld seams were consistently well-formed without the need for additional grinding. In comparison to manual welding, each standard tube can reduce the grinding processing time by about 197.87 hours, resulting in a total saving of 6,331.84 hours for all 32 tubes.
(5) The construction of the intelligent painting workshop for small segments led to a significant improvement in painting quality and efficiency. A centralized control system enabled remote control for automatic sandblasting and paint spraying, increasing sandblasting efficiency by 50% when compared to manual methods.

3 INTELLIGENT CONCRETE POURING ROBOT

3.1 *Challenges*

Each tube requires a substantial volume of self-compacting concrete, totaling 28,000m^3. This places stringent demands on the concrete's working performance, quality stability, casting process, and precise control of pouring speed. Notably, a strict requirement dictates that the gap between the steel panel and the concrete surface must not exceed 5mm, with a heightened sensitivity to temperature.

Traditional pouring equipment heavily relies on manual labor and lacks precision in controlling pouring stop times, often leading to overflows. Additionally, manual measurements are used to control the height of the concrete surface, hindering real-time monitoring and, consequently, compromising the quality of self-compacting concrete pouring. Moreover, traditional pouring equipment requires leveling the tube surface as it moves, which is further complicated by the presence of numerous vent holes, pouring holes, and fixtures on the tube's surface.

3.2 *Concrete pouring robot*

To guarantee the quality of concrete pouring, a self-compacting concrete pouring robot and a control system were studied and developed. These intelligent pouring robots, equipped with various sensors (including temperature sensors, locators, and concrete level rangefinders), are capable of automatic concrete distribution and precise control of the pouring process, ensuring high-quality and controlled pouring speeds.

Based on the BIM technologies, intelligent sensing and Internet of Things technologies, an information management system for the whole process of the concrete pouring was developed. This system covers concrete production, transportation, pouring and testing, and harnesses big data for informed decision-making. It enables real-time monitoring, record-keeping, rapid defect identification, and automatic report generation, and enhances the overall quality of concrete pouring while promoting efficiency. (shown in Figure 5&Figure 6).

Figure 5. System control room.

Figure 6. Intelligent pouring robot.

3.3 *Achievement*

(1) The project has completed the concrete pouring for all the tubes. And the working and mechanical properties of self-compacting concrete for each tube, have met the specified requirements.
(2) Through comprehensive testing, it has been confirmed that the gap between the top surface of the concrete and the inner face of the panel of nearly 2,000 compartments aligns with the project requirements. And the waste rate is only 0.4%. This achievement highlights the project's exceptional levels of automation, pouring quality, and on-site waste rate control.

4 TUBE TRANSPORTATION SYSTEM

4.1 *Challenges*

After the concrete pouring process, each element weighs around 80,000 tons. To meet the requirement of producing one tube per month, the freshly poured tube needs to be transported to the outfitting area within one day to make space for the next one. This involves a transportation distance of up to 220m. Traditionally, a sliding method was employed to move giant components, each weighing over ten thousand tons, such as the 56,000 tons tube of the Oresund Strait Tunnel and the 76,000 tons tube of the HZM Bridge.

However, the equipment used for sliding was both complex and unwieldy to operate. It was challenging to control axis deviation, resulting in low construction efficiency and high operating costs.

4.2 *Digital transportation system*

The immersed element transportation system consists of 200 hydraulic trolleys equipped with wheel rails, each with a maximum load capacity of 800 tons. These trolleys are organized longitudinally into four rows, with each row containing 50 units (shown in Figure 7).

The development of intelligent horizontal transportation equipment and its control system has greatly improved the efficiency of longitudinally moving an 80,000-ton tube. This system features fixed-distance synchronous movement, precise point-to-point parking, self-correction capabilities, self-leveling support, adaptability, and a maximum full-load moving speed of no less than 1m/min.

Figure 7. Transportation trolley.

To achieve self-balance during the transportation of heavy tubes and minimize the impact of uneven track surfaces on tube deformation, a hydraulic three-point support system is utilized. After conducting a risk analysis, to ensure a smooth transportation process and reduce the effects of hydraulic support system faults, two oil circuits, labeled A and B, were implemented. This configuration accounts for potential oil circuit leakage at specific support points in extreme situations. An additional jack is required to support the original weight, necessitating that the entire transportation equipment be able to handle loads up to 2 times the margin (i.e. a maximum load capacity of 160,000 tons).

This system effectively replaces sliding friction with rolling friction, which reduces the friction resistance during the transportation of tube joints. This, in turn, significantly reduces energy consumption while eliminating the need for sliding plates and lubricating oil. At the same time, a control system has been developed, reducing the demand for construction personnel and improving the working environment, resulting in reduced construction costs.

4.3 *Achievement*

(1) Compared to the pushing method involving sliding plates, the number of workers performing each operation has been reduced from 34 to 21. For a single tube, this reduction in labor costs amounts to 78,000 yuan, while management costs are lowered by 300,000 yuan, and consumables expenses are reduced by 690,000 yuan. The cumulative cost saving per tube totals 1 million yuan, achieving considerable economic benefits.
(2) The transportation distance for a single tube is 220m, and the time is shortened from 7 days of

the HZM sliding technology to 4 hours. This significant reduction in time greatly shortens the overall construction period.

5 INTEGRATED FLOATING AND INSTALLATION VESSEL

5.1 *Challenges*

Restricted by the on-site conditions, the construction of immersed elements faces a series of technical challenges. These include transporting the elements over long distance (up to 50 kilometers) with a total weight of 80,000 tons, long-distance lateral towing (up to 5 kilometers), and dealing with high cross-current velocities along the foundation trench. Additionally, precision control is required for the deep-water element immersion and docking, especially under the complex conditions of hydro-logical sediments.

The traditional floating and installation methods are inadequate for meeting the requirements of this project. Consequently, the equipment and installation processes for the 32 tubes must meet exceptionally high standards.

5.2 *Integrated vessel*

Relying on the project, systematic research has been conducted on an integrated vessel for self-propelled transportation, the integrated construction process of floating and the installation of the immersed elements. The development of this vessel hinged on achieving functional integration, merging ship and tube elements, integrating structures, and consolidating power systems. This approach successfully addressed pivotal technical challenges, including ship-element connection technology, automatic trajectory control, resistance to cross-currents, precise positioning of the ship-tube interface, and safety risks during long-distance floating. As a result of these innovations, the efficiency of the floating and installation process more than doubled when compared to traditional technology (shown in Figure 8 & Figure 9).

Figure 8. Integrated vessel.

Figure 9. Control system for installation.

5.3 *Achievement*

(1) The world's first integrated vessel completed the deep-sea precision docking for 22 elements, with approximately 50% of the elements being installed with a lateral deviation of less than 10mm, significantly surpassing the construction standard of 50mm.
(2) This vessel established a groundbreaking element installation pace of one per month, thanks to a systematic overhaul of the immersed element floating and installation process.
(3) The vessel's capabilities included a cruising speed of up to 4 knots per hour, 360° in-situ rotation, and a resistance to cross-current of 1.6 knots.
(4) The vessel managed to reduce the required dredging volume by 15 million cubic meters, thereby enhancing docking accuracy.

6 UNDERWATER 3D INTELLIGENT GRAVEL FOUNDATION LEVELING SYSTEM

6.1 *Challenges*

The pre-paving method for the foundation of immersed tunnel construction has high precision, fast paving speed, and strong quality controllability. The underwater gravel foundation paving and leveling are pivotal technologies in the construction of immersed tunnels.

To accommodate the structural characteristics of immersed tunnels, characterized by their ultra-wide span, variable width, large curvature, deep burial, and demand for high work efficiency, it is crucial to minimize the structural dimensions of the leveling frame. This minimization helps reduce the overall scale and draft depth of the vessel, which is more conducive to maintaining control over the frame's deformation.

6.2 *Gravel leveling system*

The 3D intelligent leveling and dredging vessel is composed of underwater gravel foundation bedding leveling equipment integrated into the working ship (shown in Figure 10). It encompasses vehicle devices, pile leg devices, a leveling funnel, a base frame structure, an electric control system, a measurement and

control system, as well as a skid pipe. The leveling control center, located on the working ship, manages information exchange and control through fiber optic and specialized network transmission cables. The whole process of underwater gravel foundation leveling is characterized by intelligence and full automation.

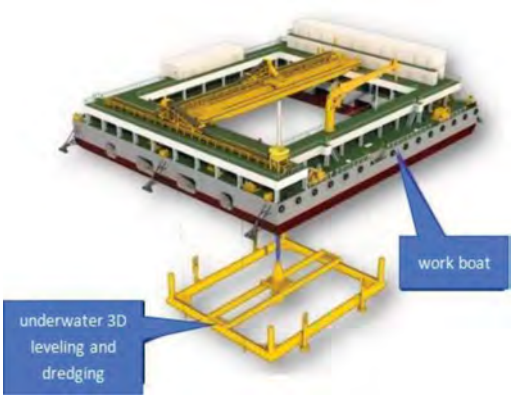

Figure 10. Diagram of 3D intelligent. leveling and dredging vessel

6.3 *Achievement*

(1) Combined with single-beam self-scanning, and verified through underwater probing by multi-beam scanning, it is evident that the surface of the gravel base is smooth, the ridges and furrows are clear, and the leveling precision meets the requirements of ±40mm.
(2) The width of the top of the gravel ridge measures no less than 1.8m, in compliance with the design specifications.
(3) The qualification rate has reached an impressive 98%, exceeding the design requirement of 95%.
(4) Excluding considerations for the entry and exit of the working ship, the leveling of 2 widths can be completed within a single day, aligning with the construction requirements.
(5) Post-immersion measurements for the placement of tubes confirm the elevation control system's authenticity and reliability, underscoring the practicality and effectiveness of the split-width method.

7 CONCLUSIONS

The Shen-Zhong Link immersed tunnel represents a groundbreaking engineering feat, being the world's first two-way eight-lane steel-shell concrete tunnel. This project has presented numerous technological challenges, especially tube manufacturing and immersion for engineers. Through innovation approaches, all 32 elements and one closure joint were successfully installed. The integration of digitized and intelligent equipment played a pivotal role in enhancing the construction process, ultimately improving project quality. Digital and intelligent construction methods have not only elevated the quality of manufacturing and construction, but also mitigated safety risks, boosted construction efficiency, reduced labor costs, and established a benchmark for future infrastructure projects.

REFERENCES

Lin Ming, 2021(09). Intelligent Construction Application and Effectiveness of the HongKong Zhuhai Macao Bridge Island Tunnel Project Management Series No. 8 [J]. Construction Enterprise Management, pp. 81–83 (in Chinese)

Qi Chenglong, Kang Yingeng, Wang Yong, et al.,2022 (03). Intelligent Design and Construction System Scheme for Hangzhou Bay Cross Sea Bridge [J]. Railway Technology Innovation, pp. 30–35 (in Chinese)

Fei Y,Wan-Lin C, Ru-Wei W, et al., 2022. Seismic behavior of prefabricated concrete filled steel tube-bordered monolayer reinforced shear wall[J]. Journal of Constructional Steel Research, pp. 194.

Tunnelling for a Better Life – Yan, Celestino, Thewes & Eberhardt (Eds)
© 2024 The Author(s), ISBN 978-1-032-80042-4
Open Access: www.taylorfrancis.com, CC BY-NC-ND 4.0 license

Digital strategies-driven optimization of infrastructure maintenance: The case study of the rehabilitation of a disused tunnel in northern Italy

Federico Foria*, Emanuele Moschetti & Mario Calicchio
ETS Srl, Via Benedetto Croce, Rome, Italy

Vlad Grigoras & Burak Boyaci
Bentley Systems, Incorporated, Exton

ABSTRACT: In recent years, the planning and design of existing structures have become critical points within civil engineering and infrastructure management. As structures are often built based on design conditions that may no longer align with their current capacity, there is a need to ensure their preservation and meet modern requirements. Building Information Modeling (BIM) has emerged as a valuable solution to addressing these challenges. By utilizing BIM, a technology and methodology that enables comprehensive digital representation of the infra-structure, designers have now the capability to easily identify and mitigate critical points from the early stages of design by using a best practice engineering approach and clash detection technology. In a specific case study, ETS has undertaken the responsibility for conducting the rehabilitation of a disused tunnel with masonry lining in a harbour area. The intervention is within the framework of the connection between the historic harbour of Genoa (Parco Rugna/Bettolo) and Bivio Fegino. The design process has been carried out with digital strategies for infrastructure maintenance that are very fast and minimally invasive. A new tunnel modelling and design solution, OpenTunnel Designer, has been utilized to digitally model and analyze the existing tunnels. Starting from the digital geometric survey, it becomes feasible to generate precise digital replicas of actual structures. This process not only encompasses the replication of the physical elements but also extends to the digitalization of the construction process itself. As a result, a comprehensive digital twin of the infrastructure is created. By adopting this approach, ETS can streamline the assessment and rehabilitation process, ensuring that the historic tunnel meets modern safety standards and preserving its integrity.

Keywords: Tunnelling, TBM, Performance prediction, Simulation, BIM, MIRET, OpenTunnel Designer, Risk management, Existing tunnes

1 INTRODUCTION

1.1 *State of the art*

Infrastructures play a key role in a social and economic life of a country and their strategic value needs to be protected by a solid and reliable plan of maintenance.

The lifespan of tunnel infrastructures is even more longer than other type of structure, and the managing of their aging effects must be a priority for infrastructure owners.

Inspections and diagnosis on structure are the tools in hands of operators that can ensure the asset is guaranteeing safety and structural integrity during the entire operational phase: by a dedicated plan of investigations on infrastructures, it is possible to manage works and repairs that may be necessaries, and verify they are finally effective.

Today standard practise is still based on skills and experience of operators, often equipped only with technical sheets to be filled with analogical information based on each country standards and code. The outcome of the tunnel inspection is usually composed of survey of defects made by a set of photos linked to a location along the tunnel, for the final evaluation for hazard assessment and intervention planning.

This type of analogic approach can lead to the emergence of problems related to data interpretation, human error, inaccuracies in positioning, and insufficient information obtained during inspection, limiting the reliability and reproducibility of the analysis and, most important, invalidating part of the risk assessment.

*Corresponding author: Federico.foria@etsingegneria.it

DOI: 10.1201/9781003495505-380

Moreover, the need to run the inspection works during nighttime and in a rush mode, to reduce the impact on traffic, brings to an increase of risks for workers on the line.

This investigation method, beside the outdated practice compared to nowadays technology, is still the state of the art, it doesn't meet the modern requirement of the civil engineering management and, even worst, a large set of infrastructures world-wide are not checked at all.

As a reference, in China the number of construction accidents shows a rising trend in tunnel projects over the past decade, and it can bring to a public concern in using the infrastructure. Qihu et al. (2016, Qihu et. al) proposed several ways to overcome this problem, including the implementation of the risk management plan by using IT solutions for early warning systems.

1.2 *Innovation*

To overcome old methodologies in latest period the use of BIM technology and the possibility to work on the digital twin of the structure is becoming always more important in the infrastructures field, especially in the operation and maintenance area, as reported also by Qiuchen Lu et al. (2020, Qiuchen Lu et al.).

The implementation of BIM technology requires a framework able to manage the information and to assess the risk management, in order to express its full potential. This is the background used by ETS to implement MIRET approach (Management and Identification of the Risk for Existing Tunnels), to reach the digitalization of the risk management assessment of existing tunnels. The digitalization of the process starts since the beginning of the data acquisition thanks to a mobile mapping instrument developed by ETS and named ARCHITA.

ARCHITA is equipped with a set of instruments like georadar, thermal camera, tunnel scan, laser scanner and lighting system, and it can run an inspection at a speed of 15 to 30 km/h, aiming to a minimization of the time for traffic disruption, increasing of operators safety and improvement of back-office capabilities.

Use of digitalization in the management of asset is a key to improve the infrastructure safety during lifetime, because authorities and operators can base their decisions on more reliable, objective and trusted data, shared in real time with all the actors involved with the workflow. This type of process can also improve the safety of workers on the line.

In the framework of the digitalization for the realization of the Information Modelling (BIM) ETS specialists decided to test the OpenTunnel Designer developed by Bentley Systems (for tunnel modelling) and Leapfrog (for soil modelling) developed by Seequent. Outcomes from this software for digitally model and analyze the existing tunnels, are described in this paper with the case study of the rehabilitation of disused tunnel between the historic harbour of Genoa and Bivio Fegino in Italy, performed by ETS.

2 INTEGRATED APPROACH

The entire method for the improvement of the management of infrastructures safety is an integration of technologies that gives rise to an interweaving of best practices and modern ap-proaches, starting from on-site inspection phase, analysis of data, use of digital representation of the infrastructures, decisions making phase and planning of further inspections.

Also with the help of BIM technology, MIRET approach is able identify and mitigate critical points of the risk management, while using Archita, the elaboration of digital information becomes easier and reliable.

Since BIM approach comes from the field of building structures type, and it is not always applicable to line infrastructures, an innovative tool, OpenTunnle Designer, was used in the process to overcome some gaps related to the digitalization of a line element, like the tunnel.

2.1 *MIRET*

To improve the efficiency and safety of infrastructural works, it's fundamental having tools that can allow proper management and identification of the priorities due to their potential manifestation. The availability and management of information relating to the entire lifecycle of an infrastructural asset may be the innovative element, particularly from a strategic perspective, for infrastructure managers. ETS has started investing in a new approach for the manipulation of the survey-inspection data to get a more objective and dynamic diagnostic, maintenance, and risk assessment to manage existing tunnels (Foria, Ferraro, *et al.*, 2021).

MIRET approaches the analysis of the existing tunnels by focusing on an integrated workflow capable of connecting and manipulating survey-inspection data for diagnostics, maintenance and priorities assessment for the management of existing tunnels.

By repeating the process over time, it is possible to have constant monitoring of the work with the advantage of knowing the infrastructure conditions during its lifetime.

Figure 1. MIRET puzzle chart (Foria, Ferraro, et al., 2021).

2.2 *BIM workflow*

Building Information Modeling (BIM) is a complex system of procedures and technologies to manage building processes.

BIM methodologies, when applied to infrastructure (Infrastructure Building Information Modelling, I-BIM), can offer digital information management, and therefore in a manner that is more effective and can also be used with large-scale infrastructural assets. These methodologies can be successfully applied with considerable advantages in terms of cost reduction and improved management of both material and professional resources (Ciccone *et al.*, 2022).

This process aims to fill and implement the information of the as-built model, through inspection, digitalization and diagnosis of infrastructures to obtain a digital model of the work.

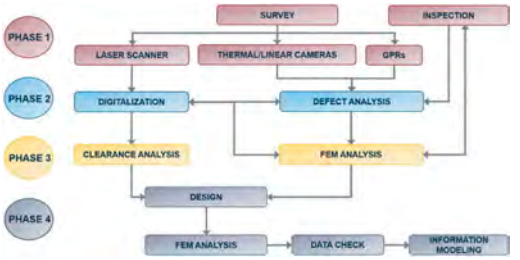

Figure 2. MIRET workflow from survey and inspection to information modelling.

2.3 *Opentunnel designer*

OpenTunnel Designer has been tailored to improve decisions taking process by being able to combine, organize, and manage geotechnical and existing conditions data quickly and accurately. It makes possible to work with soil strata and linear infrastructure data, as well as reference road, rail corridors and bridge structures. Its capabilities include modelling the full excavation shape, excavation tracks, tunnel lining (conventional and TBM type), reinforcements and interior objects. Native modelling tools help you save design time, by making automatic updates as a result of any change made to the tunnel template or alignment geometry. The entire modelling process is done with built-in parametric tools that do not require the use of visual scripting for parametrization, handling complex geometry or geometry transfer from road/rail civil software.

ETS chooses to adopt this workflow early and it also contributed to his development. The process is used for the digitalization and analysis of data for MIRET methodology the progression in machines' computational power allows solutions devised within the artificial intelligence (AI) framework, efficiently applying the knowledge learnt to the collected data.

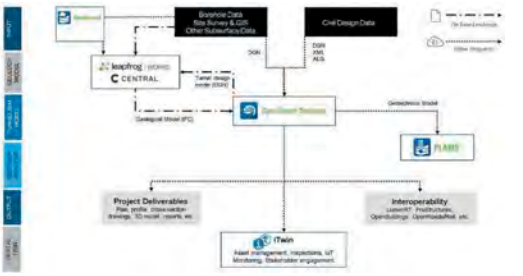

Figure 3. Bentley tunnel design solution workflow.

3 CASE STUDY: DISUSED TUNNEL IN GENOA

ETS, in the framework of the connection between the historical harbour of Genoa, in the "parco Rugno" port terminal, and the "Ex Bivio S. Limbania" worked on the rehabilitaion of the existing and disused tunnel (Galleria Molo Nuovo) with masonry lining. ETS specialists choosed the MIRET approach with the tool provided by Bentley Systems to achieve digitalized, and reliable model of the tunnel.

Building Information Modelling (BIM) is a process that brings data, models and information together, with the goal of coordinating between the different participants in the building process,reducing risk and increasing efficiency. When applied to infrastructure, BIM methods can offer effective digital information management for large-scale infrastructural assets, such as rail tunnels, especially where it is required to capture large amounts of digital information to create an accurate 'as-built' model of the asset in its current state.

Figure 4. Tunnel point cloud model (left) and extracted typical cross section (right).

The project's first phase involved conducting a laser scan of the tunnel interior and then extracting tunnel cross-sections from the point cloud at each point of interest. Using thermal scanning the approximate lining thickness has been identified along the tunnel length.

Using OpenTunnel Designer native tools, the as-built tunnel cross-sections have been created and used for modelling the initial state of the tunnel. The modelling starts by creating a 2D cross section that contains all the necessary elements for creating the 3D model starting with tunnel lining, reinforcement and auxiliary objects. Using the initial point cloud file and the georeferencing capabilities, one can verify if the created BIM model follows the scanned geometry of the actual asset.

Figure 5. As built tunnel section (left) and as built tunnel BIM model (right).

By utilizing intelligent parametric constrained cross-section geometry, 3D models can be updated dynamically, resulting in a significant reduction in modelling time by up to 50% and drafting time by up to 70%.

Based on the proposed design data, the intervention works have been modelled taking into consideration all required design elements. One critical step during the design of intervention works was the assessment of the soil-structure interaction that has been determined using the geotechnical analyzer, PLAXIS. OpenTunnel Designer is able to automatically create design models for PLAXIS 2D/3D using the information from the physical model. This is a great advantage for geotechnical engineers that now can focus on geotechnical analyses and not on creating input geometry for different cases of design.

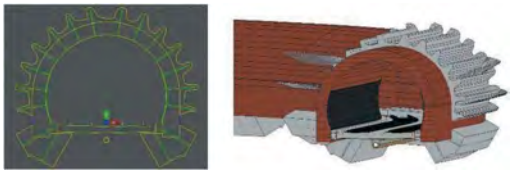

Figure 6. Proposed tunnel section (left) and proposed tunnel BIM model (right).

Improving global infrastructure is vital in tackling climate change, environmental issues, sustaining economies, and enhancing the standard of living. Developing and maintaining a digital twin of a physical asset can be highly beneficial in tunnel renovation and maintenance, and it helps us towards achieving these significant sustainability targets. It was therefore possible to create a digital twin of an existing asset by leveraging the iTwin platform capabilities. Using iTwin Experience the users connect engineering, spatial, and enterprise data in one place to better understand the project characteristics and mitigate risk early on from the first stages of design.

One key component in any construction project is represented by the continuous monitorization of different critical elements that have a high impact on the stability of the structure. iTwin IoT platform enables users to seamlessly incorporate data collected by IoT sensors and condition monitoring devices across infrastructure networks, to measure and visualize changes in asset condition, location, or performance, to optimize processes and/or interventions during construction, operations, and maintenance. By securely incorporating real-time data at scale from hundreds of sensor types, iTwin IoT increases the value of engineering and geotechnical data.

Figure 7. The digital twin of the existing asset with modeled intervention works on iTwin platform.

4 CONCLUSIONS

Digitalization is always more a strategic tool for the improvement of the safety of the infrastructures, and in some cases is also becoming a requirement for calls and competitions.

BIM is a well known tool able to create a digital twin of a structure, but OpernTunnel Designer, a new innovative tool from Bentley Systems, is the game changer tool for infrastructure as tunnels.

The integrated approach of this technology together with MIRET method and ARCHITA instrumentation, developed by ETS srl, gives the possibility to reach the goal of a solid and reliable risk management for existing tunnels maintenance.

Together with the safety improvement, this approach can facilitate the work by reducing the modelling time up to 50%, the drafting time up to 70%, and the 3D geotechnical modelling up to 80%.

Finally, the strict collaboration between different disciplines like geotechnical, drafters and others, combined with the availability of data from the first stage of the project, is a key point for a reliable, reproducible and safe risk management process.

ACKNOWLEDGMENTS

Special thanks to the ETS team that worked on the case study: M.G. Camuti, S. Gazzola, E. Mazza, S. Pantaneschi, C. Petrungaro, V. Sensi, M. Terracciano, L. Terrile. Thanks to M. Brichese for the writing contribution. Thanks also to all who contributes (clients, contractor, supplier) every day in the direction of innovation.

REFERENCES

Foria, F., Ferraro, R., Peticchia, E., Sannino, F. & Miceli, G. 2021. Modélisation des défauts et maintenance des tunnels existants avec une approche novatrice (MIRET): l ' étude de cas de la ligne de chemin de fer Gênes - Vintimille et du métro de Rome. AFTES 2021: pp. 1–10.

Ciccone A., Di Stasio S., Asprone D., Salzano A. & Nicolella M. 2022. Application of openBIM for the

Management of Existing Railway Infrastructure: Case Study of the Cancello–Benevento Railway Line.

Qihu Qian, Peng Lin, 2016. Safety risk management of underground engineering in China: Progress, challenges and strategies. Journal of Rock Mechanics and Geotechnical Engineering 8 (2016) 423e442.

Qiuchen Lu, Xiang Xie, Ajith Kumar Parlikad, Jennifer Mary Schooling, 2020. Digital twin-enabled anomaly detection for built asset monitoring in operation and maintenance, Automation in Construction Volume 118, October 2020, 103277.

Tunnelling for a Better Life – Yan, Celestino, Thewes & Eberhardt (Eds)
© 2024 The Author(s), ISBN 978-1-032-80042-4
Open Access: www.taylorfrancis.com, CC BY-NC-ND 4.0 license

Intelligent technologies and applications on TBM tunnel construction

Weishe Guo*, Kairong Hong & Pan Gao
China Railway Tunnel Group Guangzhou, Guangdong, China

Fengyuan Li
State Key Laboratory of Shield machine and Boring Technology, Zhengzhou, Henan, China

ABSTRACT: In the field of TBM tunneling construction, China Railway Tunnel Group (CRTG) has carried out the exploration and application of intelligent technology including 'one network', 'one platform' and 'six applications'. More specifically, 'one network' refers to one industrial internet of TBM tunnelling construction, which is built by exploring the interconnection of construction equipment and developing an intelligent equipment acquisition terminal for equipment group in tunnel construction based on IoT technology, in order to standardise the digital interface between different equipment. 'One platform' refers to a TBM tunnelling database to standardise the data format, developed through exploring the interaction and fusion of heterogeneous data from multiple sources in tunnel construction, which forms the groundworks for machine learning. Finally, 'Six applications' refers to: (1) intelligent interconnection and collaboration of equipment group in TBM tunnel construction based on IoT technology; (2) intelligent TBM tunnelling based on big data and machine learning; (3) online intelligent detection and diagnosis of TBM status based on sensing and communication technologies; (4) Intelligent assembly of arc components based on automatic measurement and obstacle avoidance perception technology; (5) Intelligent assembly of middle partition wall based on machine vision and automatic measurement technology; (6) non-destructive rapid detection and intelligent identification of tunnel structures based on air-coupled radar, 3D scanning and machine vision technology.

The application of the aforementioned intelligent technologies in the Shanghai Urban Railway Airport Connecting Line Lot 11 Project had achieved the reduction of the number of operating personnel by 18 people per shift and the increase of production efficiency by 16%, and the average advance rate of 460 m/month for a 14 m diameter TBM.

Keywords: TBM Tunnelling, intelligent technology, big data, intelligent tunnelling, Internet of Things (IoT), collaboration

1 INTRODUCTION

By 2022, many tunnels have been built in China, including about 25,000 kilometres of railway tunnels [1], about 22,000 kilometres of highway tunnels [2], about 10,000 kilometres of urban metro tunnels [3], and about 47,000 kilometres of water conservancy/hydropower tunnels and other kinds [4]. At present, infrastructure construction still plays a pivotal role in China's national economy, however, the overall situation of the global economy is not optimistic, and China commits to achieve "Peak Carbon Dioxide Emissions" in 2030 and "Carbon Neutrality" in 2060, all of which have generated an urgent demand for industrial transformation and upgrading and high-quality development [5].

With the rapid aging of China's social population, resulting in the difficulty of construction companies in recruiting workers, the general trend of transformation of technology and production method has forced the tunnelling industry to apply intelligent technology[6] and carry out intelligent construction [7].

In this paper, the ways to enhance the level of intelligent TBM tunnel construction are introduced, focusing on "one network, one platform, and six applications", the role of intelligent technologies in TBM tunnel construction is discussed based on engineering practice, and the prospect and trend of tunnel construction technologies are shared.

2 WAYS TO ENHANCE THE LEVEL OF INTELLIGENT TBM TUNNEL CONSTRUCTION

Normally, the tunnel construction methods include drilling and blasting method [8], TBM method [9], cut-and-cover method and immersed tube method

*Corresponding author: 112899002@qq.com

DOI: 10.1201/9781003495505-381

[10], among which drilling and blasting method and TBM method are the most common.

TBM method is a fully mechanized construction method. The way to improve its intelligent construction level is to make prior knowledge algorithmization [11-12], and to integrate Internet of Things(IOT) technology, with Big Data technology and artificial intelligence technology (AI) on the basis of mechanization construction, and then gradually realize intelligent construction. The path to improve the level of intelligent TBM tunnel construction is shown in Figure 1.

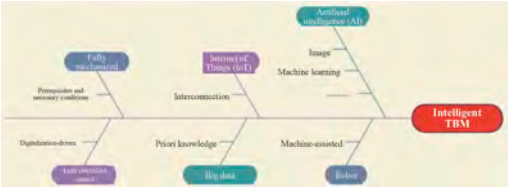

Figure 1. Path to improve the level of TBM tunnel intelligent construction.

3 OVERVIEW OF THE APPLICATION IN PROJECTS

"One network, one platform, and six applications" are the result of a R&D project that has been carried out by CRTG and the Shanghai Rail Transit Airport Link Line Lot 11 is the first demonstration project.

The Shanghai Rail Transit Airport Link Line is an urban railway connecting Shanghai Hongqiao Airport and Pudong Airport with a operation speed of 160Km/h. After completion, the transit time between Hongqiao Airport and Pudong Airport will be shortened from the current 2h to 40min.

The Lot 11 of the airport line is located near Lingkong Road, Chuansha Town, Pudong District, Shanghai. The project scope of works includes a TBM launching shaft in Lingkong Road and a tunnel section in length of 4.721km from Lingkong Road to Resort Station, which is excavated by an air-cushion slurry balance TBM with a diameter of 14.04m. The tunnel internal structures adopting prefabricated assembly design is shown in Figure 2. Among them, the size of three-hole arc-shaped components is 9.5 m × 2.834 m × 2m and the weight is 33.6 t; the size of the middle partition wall is 9.116 m × 0. 4m × 2 m and the weight is 22.65 t.

4 "ONE NETWORK, ONE PLATFORM AND SIX APPLICATIONS" IN TBM CONSTRUCTION

4.1 *"One network" - industrial internet of TBM tunnel construction*

By applying IoT technology, CRTG research team broke through the barriers of multi-type, multi-

Figure 2. Layout of shanghai rail transit airport connecting line project.

protocol and multi-data of engineering equipment used in TBM tunnel construction, developed a series of intelligent acquisition terminals, and created an end-edge-cloud collaborative industrial internet of TBM tunnel construction [13].

In view of the multiple types and multiple protocols of TBM construction equipment, the team solved the problem of equipment adaptive access, developed a series of intelligent acquisition terminals suitable for edge-cloud collaborative processing, and realized the real-time acquisition of PLC data of TBM tunnel group equipment.

For the structured data of TBM mainframe and group equipment, the OPC protocol was adopted to unify ontology models and data interfaces; for semi-structured or unstructured resource data such as geological data and design documents, digitization and vectorization were performed; the fusion of multi-source heterogeneous tunnel construction data was realized, and the big data dictionary was formed.

Based on 5G technology, the end-edge-cloud network architecture was adopted, the data was initially cleaned, processed, denoised, VPN-encrypted and sent to the big data center in the cloud, and the industrial Internet for TBM tunnel intelligent construction was constructed, realizing the data acquisition, fusion and governance of all the elements of TBM construction. The structure of industrial Internet for TBM construction is shown in Figure 3.

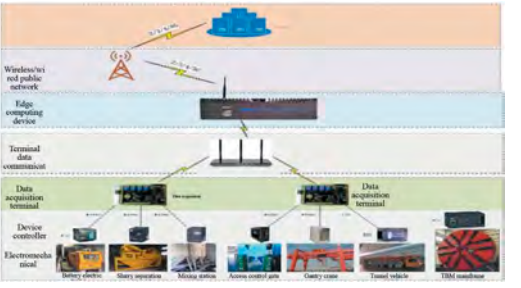

Figure 3. The structure of industrial internet for TBM construction.

4.2 *"One platform" – a TBM construction big data platform*

Based on the industrial Internet structure of TBM construction, a TBM construction big data platform

has been built by adopting Hadoop distributed big data cluster technology architecture and open-source databases such as Hbase and advanced stream processing platforms like Kafka. The data lake governance storage architecture is adopted to process the massive data, which realizes the fusion of multi-source heterogeneous data such as TBM engineering geological, construction environment, group equipment, tunnel structure and so on.

The file security encryption and filtering system is developed in the Platform, which realizes the isolation of client application data. The data calling authority rules solves the problem of customer data privacy and realizes data security, sharing and interaction based on data lake architecture.

The industrial big data platform has the functions of storage, cleaning, and application, from which was developed a system of intelligent monitoring, comprehensive analysis, collaborative management and intelligent application. See Figure 4 for the big data platform for TBM projects. The platform services 590 more projects and accumulates sample data of 152T, which provides the data base and primary platform for the industry.

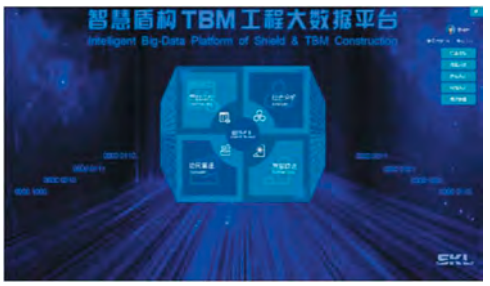

Figure 4. Big data platform of TBM construction.

4.3 *"Six applications"*

4.3.1 *Application 1: Intelligent interconnection and collaborative management of equipment group for TBM tunnel construction*

Based on TBM industrial internet, the intelligent interconnection and collaborative management of equipment group including TBM host, arc-shaped components assembly robot, partition wall assembly robot, material transport locomotive, vertical lifting equipment, slurry treatment equipment, etc, has been achieved.

Based on data governance and fusion technology combined with TBM construction characteristics, the intelligent monitoring of equipment group operation data, comprehensive analysis of parameters, cooperative management and control, navigating tunnelling, and monitoring and command, the cooperative operation of equipment group in TBM construction has been realized, which improves tunnelling efficiency, enhances equipment risk avoidance ability and enhances the comprehensive utility of equipment group.

This application has significantly reduced equipment failure rate and improved equipment use efficiency. By applying this system, the equipment operation and maintenance personnel have been reduced by 5 persons in Shanghai Railway Airport Line Project, and the utilization rate of equipment has been increased by 10% and the construction production efficiency has been increased by 16%.

4.3.2 *Application 2: Intelligent tunnelling driven by mechanism-data hybrid*

Intelligent tunnelling is an artificial intelligence algorithm model that is trained by massive big data such as TBM tunnelling data, equipment data and engineering geological data. After training in the cloud computing center, the intelligent tunnelling model is

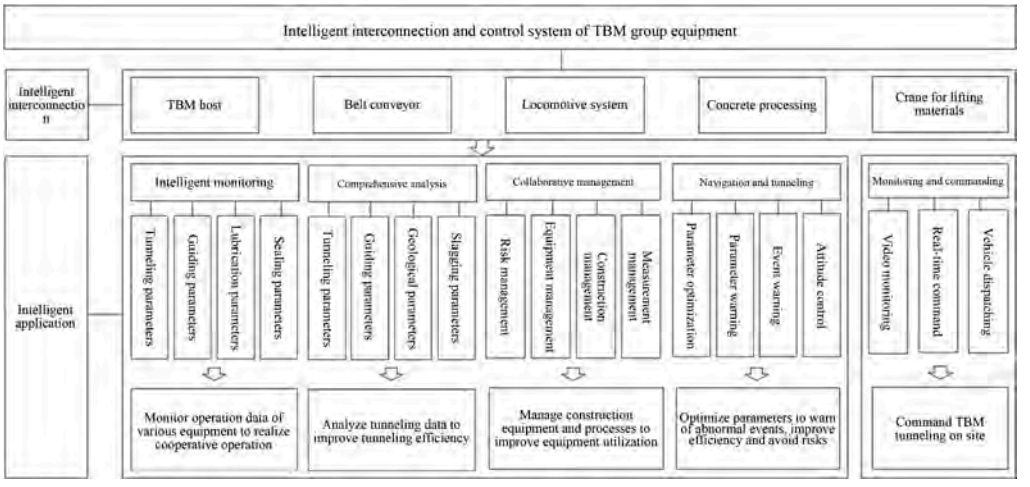

Figure 5. Intelligent interconnection and management system.

deployed on the edge server near the TBM machine [14], and the edge server completes the related calculation and inference tasks with extremely high speed, and then instructs the control terminal to execute tunnelling operations.

The specific principle and process are as follows: Real-time tunnelling data, equipment data and engineering geological data during TBM tunnelling are uploaded to TBM big data platform; and the active tunnelling model, tunnelling parameter recommendation model, attitude control model, abnormal event warning model are trained and managed by the big data platform (see Figure 6 - technical route of TBM active parameter prediction).

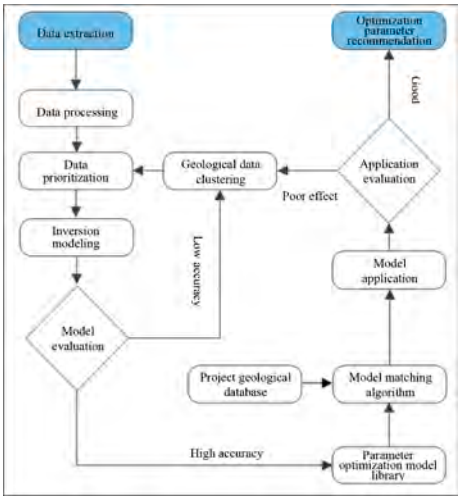

Figure 6. Technical route of TBM active parameter prediction.

After the effect of the relevant intelligent model is verified, it is deployed to the edge server, which provides the TBM control terminal with extremely low-latency intelligent model data service which is not limited by the bandwidth of the communication operators. During intelligent tunnelling, the edge server calculates the relevant intelligent model and immediately transmits the recommended parameters and commands to the control terminal; the control terminal perceived the TBM equipment parameter data in real time in an all-round way, and the edge server carries out light-weight processing on the data and uploads it to the big data platform. This process was repeated continuously in the intelligent tunneling to obtain stable and controllable tunneling parameters and optimal attitude.

The cloud is responsible for the training of intelligent algorithm models, edge for the deployment and feedback of intelligent algorithms, and the end for control and execution. The core of cloud-edge-end architecture is in the cloud, the key is in the edge, and the control is in the end.

The TBM intelligent tunnelling system based on big data was applied to the Shanghai Railway Airport Line Project, and the TBM tunnelling is "under surveillance but unmanned", which reduced two TBM operators per shift. The overall technical route of intelligent tunnelling is shown in Figure 7.

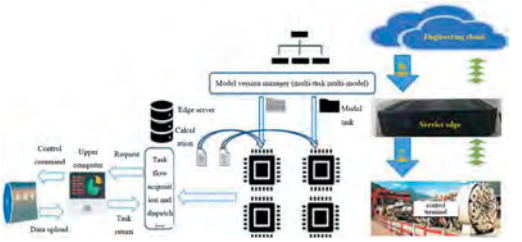

Figure 7. The overall technical route of intelligent tunnelling.

Currently, the algorithm model of intelligent tunnelling is trained by similar historic data and parameter, especially the similar geological data at same region. The research work of combining tunnel advance geological forecast data and historical tunnelling data to train intelligent tunnelling algorithm model is in progress.

4.3.3 *Application 3: Real-time online monitoring and diagnosis of TBM equipment status*

TBM is highly-integrated large equipment, and manual inspection and offline detection can no longer meet its daily maintenance needs. As more TBMs are put into use, real-time on-line monitoring and diagnosis of equipment status is becoming more and more important. Based on sensing communication technology, CRTG develops real-time on-line system for monitoring and diagnosis Principle of TBM status on-line monitoring system is shown in Figure 8.

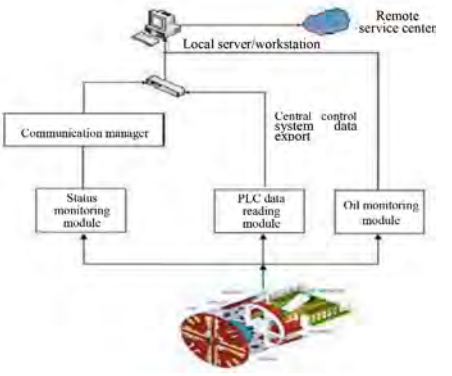

Figure 8. Principle of TBM status on-line monitoring system.

The system can realize automatic acquisition and analysis of (1) vibration, temperature, cutter head torque, bearing running time and other parameters of hydraulic pump unit, main bearing and gear reducer;

(2) viscosity, density, dielectric constant, moisture and laser particle of hydraulic oil; (3) viscosity, moisture, metal particle and laser particle of gear oil.

Based on the big data of TBM operation status, it is feasible to carry out the analysis of equipment operation status, risk and failure early warning and equipment operation trend, etc. The system can protect TBM avoid major losses caused by the damage of core components under complex condition. Figure 9 is the deployment and operation diagram of TBM status online detection system.

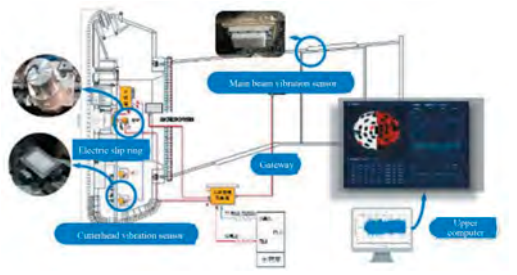

Figure 9. The deployment and operation diagram of TBM status online detection system.

4.3.4 *Application 4: Intelligent assembly of arc components based on automatic measurement and obstacle avoidance perception technology*

The arc-shaped components assembling robot is designed as double-frame structure of main frame and auxiliary frame. The robot consists of main frame, auxiliary frame, fine-tuning platform, hydraulic system and intelligent control system (see Figure-10). Overall dimension is 6530 × 3200 × 2609mm and the weight is 35t. Artificial intelligence technologies such as automatic measurement, obstacle avoidance perception and intelligent algorithm are applied in the robot. Automatic assembly can be realized by only pushing the button.

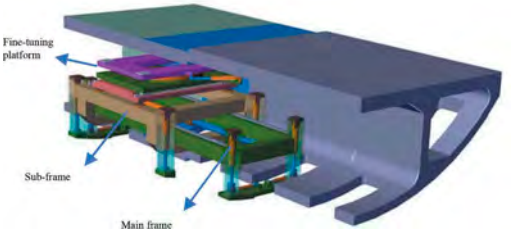

Figure 10. The frame structure of arc-shaped components assembly robot.

The assembly accuracy can be precise to millimeter. Only one person is needed for the operation of the robot, which saves 4 people compared with the traditional assembly. The on-site assembly operation is shown in Figure 11.

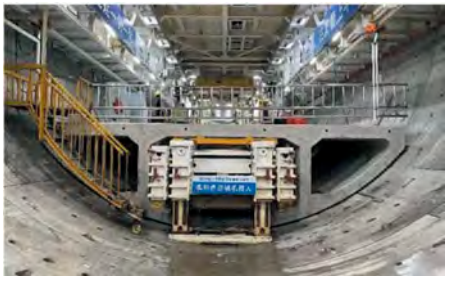

Figure. 11. Arc-shaped components assembly robot on-site operation.

4.3.5 *Application 5: Intelligent assembly of middle partition wall based on machine vision and automatic measurement technology*

The middle partition wall assembly robot is designed as stretchable portal structure, which is composed of main frame, grasping mechanism, stretchable mechanism, rotating mechanism, conveying mechanism, walking system, hydraulic system, intelligent control system and working platform (see Figure-12). The robot is designed as walk-through type with large headroom. The overall size is 11576 × 4350 × 6185 mm, which allows construction vehicles to cross. The dead weight of the robot is 80t.

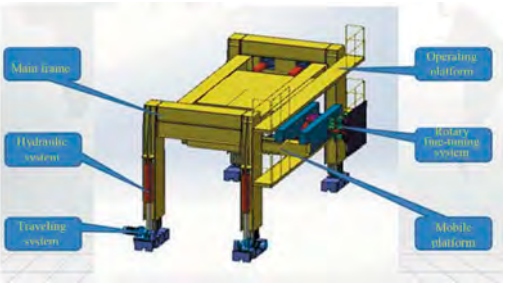

Figure 12. Structure of middle partition wall assembly robot.

Artificial intelligence technologies such as machine vision, automatic measurement and intelligent algorithm are applied in the robot. Only by pushing one button, it will automatically start matching holes, grasping and rotation, which realizes algorithm decision-making and automatic assembly.

The assembly accuracy can be precise to millimeter. Only one person is needed for the operation of the robot, which is 10 times higher in efficiency, and saves 7 people compared with the traditional cast-in-situ operation. The on-site assembly operation is shown in Figure 13.

4.3.6 *Application 6: Rapid non-destructive intelligent detection of tunnel structural health*

The system integrates non-contact multi-channel air-coupled ground penetrating radar, machine vision inspection and 3D laser scanning, which can realize rapid non-destructive detection and intelligent

Figure 13. Partition wall assembly robot on-site operation.

identification of internal damages, apparent damages, geometric and spatial deformation of tunnel lining structures. The intelligent comprehensive detection vehicle is shown in Figure 14.

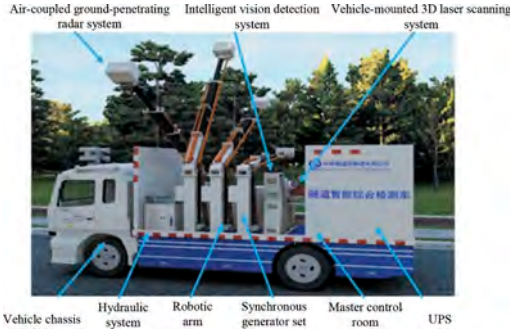

Figure 14. Intelligent comprehensive detection tunnel vehicle.

Comprehensive detection efficiency of air-coupled ground penetrating radar system is 10 ~ 40km/h, which is efficient to detect internal damages of tunnel structures by non-contact detection with detection distance of 0.5~4.5 m.

The machine vision technology can provide a lining crack recognition accuracy of 0.2mm, lining split recognition accuracy of 3mm × 3mm, and water leakage recognition accuracy of 20mm × 20mm; while the 3D laser scanning technology can provide a leakage recognition accuracy of ≤ 20mm × 20mm and a ranging accuracy of ± 1mm. By adopting the modular design, the inspection cabin of the intelligent inspection equipment can be mounted on a vehicle chassis, a railroad flat car and other carriers to perform non-destructive quality testing during the entire life cycle of railroads, highways, urban rail transit and other projects. Figure15 are the on-site operation of TBM tunnel structure detection.

5 SUMMARY OF APPLICATION EFFECT

The above intelligent applications have been applied and verified in the Shanghai Airport Link Line Project, which have achieved the reduction of manpower, increase in efficiency and safety assurance.

Figure 15. On-site operation of TBM tunnel structure detection.

5.1 *Reduction of operators*

The application of Equipment Group Interconnection Collaborative Management System for TBM tunnelling has reduced 6 personnels for equipment operation and maintenance; by using the intelligent tunnelling system, the number of operators is reduced from 3 to 1; 3 operators are reduced after using arc-shaped components assembly robot and 7 operators are reduced after using partition wall assembly robot. A total of 18 operators are reduced in Shanghai Airport Line Project through the above applications. The advantages of intelligent construction technology compared with traditional construction technology are shown in Table 1 below:

5.2 *Efficiency improvement*

These applications have improved the production efficiency of the project by 16% in the Shanghai Airport Line Project. Among them, the equipment group interconnection collaborative management system improves equipment utilization rate by 10%; Compared with the traditional assembly process, the efficiency of the arc-shaped components assembly robot is improved by 3 times; Compared with the traditional operation, the efficiency of the middle partition wall assembly robot is increased by 10 times.

5.3 *Precision and quality*

According to statistics, the accuracy of the tunnel axis after the application of intelligent tunnelling system is significantly improved, as shown in Figure 16; After the application of arc-shaped components and middle partition wall assembly robots, the construction accuracy has been improved from centimeter level to millimeter level compared with the traditional operation method.

Table 1. Comparison of the advantages of intelligent construction technology over traditional construction technology.

Type	Number of workers per shift				Construction Efficiency				Construction Accuracy
	Equipment Operation and Maintenance Management	Tunneling System Operation	construction of arc components	construction of middle partition wall	Equipment utilization rate/%	Average Monthly Progress/ m/month	construction time for arc components/ min	construction time for middle partition wall/ min	Tunnel Alignment Deviation/ mm
Traditional Construction	9	3	4	8	75.2	360	60	386	±50mm
Intelligent construction	3	1	1	1	85.1	420m	22	38	Less than ±10mm

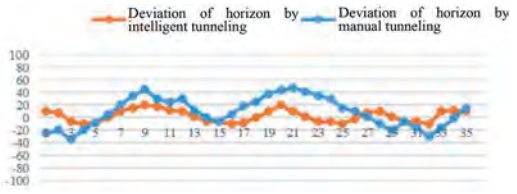

Figure 16. Line chart comparing axis control of intelligent tunneling and manual tunneling.

5.4 *Economic benefits*

After the application of the research results in the Shanghai rail transit airport Link line lot 11, the cumulative economic benefits of 22.98 million RMB have been generated. Among them, labor cost savings of 5.06 million RMB, TBM equipment savings of 16.2 million RMB, water and electricity savings of 1.72 million RMB. After applying intelligent construction technology, the savings in various direct costs are shown in Table 2 as follows.

6 CONCLUSION AND DISCUSSION

In the current situation of global economic development, it is a general trend to study and explore the less human or even unmanned in the construction process by applying the new generation of information technology.

6.1 *Application of intelligent technology and developing intelligent construction is the direction of the high-quality development of tunnel industry*

It is an inevitable trend of society to upgrade construction from mechanization to intelligence. Intelligent construction can improve productivity and realize high efficiency, high quality, energy saving and emission reduction, which is the direction of high-quality development in the industry. The main driving force of the intelligent transformation and upgrading for tunnel construction to intelligence comes from both external and internal aspects. In external aspect, with the rapid development of digital information and intelligent technology and technology spillover, as well as national demands on industrial transformation and high-quality development, the tunnel industry is driven to achieve digital transformation and intelligent construction. In internal aspect, the slowdown of global economic growth, the increasingly fierce market competition, and the aging population have forced the industry itself to take the initiative to develop intelligent construction. In

Table 2. Direct cost savings after applying intelligent construction technology.

Type	Details	Unit Price	Quantity	Subtotal/RMB
labor costs	equipment operation and maintenance management	15000 RMB/month	6person×2.5month	22.5
	construction of arc components	500 RMB/day	3person×296day +4person×83day	61
	construction of middle partition wall	500 RMB/day	7person×118day +8person×98day	80.5
	tunneling system operation	25000 RMB/month	2person×12month	60
	material management	8000 RMB/month	2person×24month	38.4
	project management personnel salary	15000 RMB/month	65person×2.5-month	243.75
TBM equipment rent costs	/	21600 RMB/m	10m×75day	1620
water and electricity costs	/	23000 RMB/day	75day	172.5
total	/			2298.65

this course, enterprises with long-term vision and quick action will take the lead and lay the foundation for their invincible position.

6.2 *"Prefabrication + assembly + interconnection and collaboration based on big data" will become the construction trend*

TBM tunnel can provide favorable innate conditions for intelligent construction, while tunnelling by drilling and blasting with relatively simple geological conditions are also relatively ideal scenes for intelligent construction. The prefabrication of components in factory base on digitalization, and rapid intelligent assembly on site, and the realization of assembly line operation will become the trend of tunnel construction.

6.3 *Intelligent construction will inject new vitality into the tunnelling industry and promote industry upgrading*

In the foreseeable future, tunnel construction will realize the transformation from roughness to precision, from more labor to few or even none, from low-efficiency and high-consumption to high-efficiency and low- consumption. The iterative upgrading of machine learning based on engineering big data will inject enormous vitality into the tunneling industry.

Final words: The Big data platform of TBM construction is definitely an open platform that can be used by the worldwide tunnelling community, including manufacturer, contractor, designer, engineers . And we know that although the application research of intelligent technology in TBM tunnel construction has made some achievements, there is still a significant gap between realizing the goal of TBM tunnel intelligent construction. In order to accelerate the development progress, we are eager to have more TBM equipment connected to the Big data platform of TBM construction. We will provide mature intelligent applications for each connected TBM, such as assisted navigation tunnelling, abnormal event warning, intelligent monitoring, comprehensive analysis, collaborative management, etc.

REFERENCES

[1] Gong Jiangfeng, Wang Wei, Li Xu, et al. Statistics of railway tunnels in China by the end of 2022 and overview of key tunnels of projects newly put into operation in 2022[J]. Tunnel Construction, 2023, 43(4): 721.

[2] Ministry of Transport. 2022 Statistical Bulletin on the Development of the Transportation Industry[N]. China Transport News, 2023-06-16(002).

[3] WANG Fuwen, FENG Aijun. Statistics and development analysis of urban rail transit in China in 2022[J]. Tunnel Construction, 2023, 43(3): 521.

[4] Ministry of Water Resources. China Water Conservancy Statistical Yearbook 2022[M]. China Water & Power Press, 2022.

[5] Chen Jinxiao. Economic Circulations under the "Carbon Peaking and Carbon Neutrality" Goals: Low-carbonization of Economic Circulations and Circulation of Low-carbon Industries[J]. Economist, 2022, No. 285(09): 78–87.

[6] Zhang Wanli, Xuan Yang, Sui Bo, et al. Industrial intelligence, labor structure and industrial structure upgrading[J]. Studies in Science of Science, 2021, 39 (08): 1384–1395.

[7] Zhang Wanli, Xuan Yang. How to Improve the Regional Energy Efficiency via Intelligence? Empirical Analysis Based on Provincial Panel Data in China[J]. Economic Management Journal, 2022, 44 (01): 27–46.

[8] Ma Weibin. Development and Prospect of Key Technology of Drilling and Blasting for Railway Mountain Tunnels[J]. Journal of the China Railway Society, 2022, 44(03): 64–85.

[9] Hong Kairong, Du Yanliang, Chen Kui, et al. Full-face tunnel boring machines (shields/TBMs) in China: History, achievements, and prospects[J]. Tunnel Construction, 2022, 42(5): 739.

[10] Guo Jianmin, Shan Lianjun, Ma Mingjun. Statistics analysis and development of immersed tube tunnels in China [J]. Tunnel Construction, 2023, 43(1): 173.

[11] Ye, XW; Zhang, XL; Zhang, HQ; et al. Prediction of lining upward movement during shield tunneling using machine learning algorithms and field monitoring data[J]. Transportation Geotechnics, 2023, 41(07): 101002.

[12] Bai, XD; Cheng, WC; Wu, B; et al. Shield machine position prediction and anomaly detection during tunnelling in loess region using ensemble and deep learning algorithms[J]. Acta Geotechnica, 2023, 18(11): 6175–6199.

[13] Li, CD; Zhang, W; Zhu, HH; et al. Fast vibration characteristics analysis of an underwater shield tunnel using the accelerometer network enhanced by edge computing[J]. Measurement, 2019, 141(07): 52–61.

[14] Li, YY; Xiao, ZH; Li, JT; et al. Integrating vision and laser point cloud data for shield tunnel digital twin modeling[J]. Automation In Construction, 2024, 157 (01): 105180.

Tunnelling for a Better Life – Yan, Celestino, Thewes & Eberhardt (Eds)
© 2024 The Author(s), ISBN 978-1-032-80042-4
Open Access: www.taylorfrancis.com, CC BY-NC-ND 4.0 license

Research and application of the BIM-based fine management in shield tunnelling construction of rail transit engineering*

Yige Huang & Zhong'an Zhang
Shenzhen Metro Group Co., Ltd, Shenzhen, China

Ke Jia
Shenzhen Metro Construction Group Co., Ltd., Shenzhen, China

Huahui Lai
Shenzhen Municipal Design & Research Institute Co. Ltd., Shenzhen, China

Yuqiong Li
Shenzhen Metro Construction Group Co., Ltd., Shenzhen, China

ABSTRACT: As an essential infrastructure for urban construction and development, rail transit engineering is currently experiencing rapid growth. Considering the future development of cities, shield tunnel construction for urban rail transit is becoming increasingly common. With urban development, the underground environment has become more complex, posing uncertainties for shield tunnel construction, such as intricate geology, underground municipal pipelines, existing underground structures, and operational urban rail lines. Effectively and safely conducting shield tunnel construction has become one of significant challenges in metro engineering. This paper explores a fine management approach for urban rail transit shield tunnel construction using Building Information modelling (BIM) technology. Firstly, BIM technology is applied to integrate various elements along the urban rail transit alignment, creating a comprehensive spatial model for shield tunnel excavation. Then, based on relevant BIM standards and mapping rules, real-time parameters and construction status are linked to the BIM model to facilitate dynamic monitoring of the shield tunnel construction progress. Furthermore, a self-developed BIM-based shield tunnel construction management platform is proposed. This platform advances the "one-map" control of shield tunnel construction in the metro network, and enables remote real-time monitoring of the construction status in a 3D environment. The platform has been applied in the construction and management of Shenzhen Metro Phase IV and its adjustment project, facilitating shield tunnel construction and management in a collaborative 3D environment. This advancement enhances the visualization and digitization of shield tunnel construction, ensuring the quality and efficiency of metro construction, and empowering high-quality urban development.

Keywords: rail transit engineering, shield tunnel construction, BIM (Building Information Modelling), fine management

1 INTRODUCTION

Rail transit engineering is an important infrastructure for city development. The world's first metro project can be traced back to London, United Kingdom, in the year 1863, marking its existence for over 160 years. Across the globe, numerous countries are vigorously advancing their rail transit projects. Considering the city development and the evolution of modern rail transit technologies, an increasing number of cities, particularly those economically developed, are adopting shield technique for the tunnel construction project. The use of shield tunnelling construction can facilitate mechanization and standardization in construction, expediting construction progress. Nevertheless, there are still several issues.

(1) The underground environment is complex, characterized by non-uniform distribution of various geological layers, especially unfavorable

*Corresponding author: 24428412@qq.com

DOI: 10.1201/9781003495505-382

geological conditions, posing significant risks to shield tunnelling construction. Moreover, the presence of pre-existing underground structures and intricate underground pipeline networks in urban areas complicates data collection efforts.

(2) The real-time management of shield tunnelling construction presents difficulties. The existing shield tunnel management systems often use two-dimensional representations and charts to display shield tunnelling construction data. The complex and confined underground environment of shield tunnelling makes data transmission challenging, leading to data issues related to timeliness.

(3) Predicting risks in shield tunnelling construction is challenging. Shield tunnelling construction is dynamic, understanding construction parameters and their development trends typically relies on human expertise, demanding a high level of professional competence.

(4) The aging staff problem in shield tunnelling construction is becoming increasingly severe. The aging problem is profoundly affecting the labor supply-demand structure across various industries, particularly labor-intensive construction industry. It is difficult for aging workforce in shield tunnelling construction to adapt to new technologies and methods.

According to statistics as shown by China Association of Metros (2023), as of the end of 2022, there were 55 cities with operational rail transit systems in mainland China, covering a total distance of 10,287.45 kilometers. Additionally, 50 cities have ongoing rail transit projects. Among them, 98.409 kilometers of rail transit lines are in the construction process in Shenzhen. Furthermore, Shenzhen has received approval for the Fifth Phase of its metro plan, comprising 11 lines, approximately 185.6 kilometers in length. Considering the international index that a network length of 400 kilometers is recognized as a world-class metro, Shenzhen has become the city with a world-class metro.

Facing such a large-scale rail transit construction, the efficient advancement of shield tunnelling operations has become one of the critical challenges in the rail transit engineering. In recent years, Shenzhen Metro has integrated Building Information Modelling (BIM) technology throughout the entire lifecycle of the rail transit engineering. It has also used BIM technology for the fine management of shield tunnelling construction in rail transit engineering. Taking the BIM model as the foundation, various elements along rail transit lines both above and below ground were integrated, and then a three-dimensional (3D), information-rich, and interactive space was developed for shield tunnelling construction. Furthermore, Shenzhen Metro has developed a fine management platform for shield tunnelling construction.

2 LITERATURE REVIEW

In addressing the aforementioned issues, researchers and engineers have undertaken studies and practical efforts for shield tunnelling construction.

(1) Concerning the shield tunnelling excavation model, researchers have explored automated modelling methods for shield tunnelling through using software products such as Revit (Yu et al., 2018) and Bentley (Liu, 2019). Li et al. (2020) employed BIM technology to establish a Tunnel Boring Machine (TBM) information model, including personnel distribution, material transport, and structural layout, and other information. They integrated this model with geological and TBM data to assess shield tunnelling construction risks, visualize risk levels, and aid in risk assessment. Borrmann et al. (2015) employed a BIM+GIS (Geographic Information System) approach to research the semantic modelling method for shield tunnels at different scales, providing a data foundation for macro and micro-level analysis in shield tunnelling management.

(2) In terms of shield tunnelling construction control, Stascheit et al. (2018) studied BIM applications in the design and construction phases of shield tunnelling projects, proposing a construction management and control method based on 3D visualization, digital component-level integration, and multiple data sets. Kiseok et al. (2022) conducted analyses and simulations to optimize shield tunnelling management, considering some aspects such as geological analysis, tunnel curve optimization, and shield envelope surfaces within a BIM-based environment.

(3) Regarding shield tunnelling construction risks, Marco et al. (2023) improved shield tunnelling construction management through the use of a four-dimensional (4D) BIM environment and a safety rule set comprising seven indicators. Zhao et al. (2019) addressed the impact of shield tunnelling construction on surrounding structures. They employed BIM technology and automated detection to analyze deformations after shield tunnelling construction.

(4) As for shield tunnelling construction management platforms, some comprehensive tunnel engineering information systems have been established to collect and manage data throughout the lifecycle. Lin et al. (2018) extended a unified shield tunnel information model based on IFC (Industry Foundation Classes) schema, encompassing data related to tunnel geology, structure, alignment, construction, monitoring and defects. Yu et al. (2016) applied sensor devices for real-time data collection and management, constructing a BIM-based 3D visualization tunnel construction management system. This system enabled dynamic and intelligent

monitoring of materials, equipment, personnel, progress, quality, and safety throughout the entire construction process.

In summary, research and practical applications of BIM technology in shield tunnelling construction have made significant progress. However, there is still relatively limited exploration in the comprehensive and intelligent scenarios through BIM-based environment and BIM data.

3 OVERALL SCHEME OF THE BIM-BASED FINE MANAGEMENT FOR SHIELD TUNNELLING IN RAIL TRANSIT

In response to the aforementioned challenges in shield tunnelling construction management, this study aims at building an integrated 3D space with multi-type data for shield tunnelling construction. A fine management platform for shield tunnelling construction was also developed. This platform refines the management units of rail transit shield tunnelling to meet the demands of various business scenarios. The technical framework and data flow for management are detailed in the following sections.

3.1 *Technical framework*

In this research, a BIM-based fine management technical framework of rail transit shield tunnelling was constructed according to four levels (as illustrated in Figure 1): foundational layer, technical layer, platform layer, and application layer, along with two mechanisms, namely, the standardization and security mechanisms.

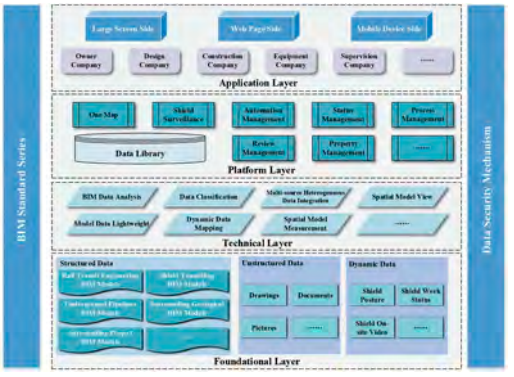

Figure 1. BIM-based fine management technical framework of rail transit shield tunnelling.

3.1.1 *Foundational layer*

The shield tunnelling construction involves surrounding environmental data and its own excavation parameters. Based on data status, it can be categorized into static data and dynamic data. Static data can further be divided into structured data and unstructured data. Structured data primarily includes BIM models of metro stations and tunnels, as well as models of the surrounding geological features and underground pipelines. Dynamic data primarily consists of shield tunnelling monitoring parameters, shield posture and work status during the tunnelling construction. Before shield tunnelling construction, comprehensive collection of above-ground and underground elements provides an accurate data foundation for the fine management of shield tunnelling.

3.1.2 *Technical layer*

The value of BIM technology extends beyond 3D visualization, it also encompasses data computation and analysis. Therefore, data-level processing and analysis of BIM models are necessary. Focusing on the requirements of shield tunnelling management, this layer primarily investigates techniques such as data classification, BIM data parsing, integration of heterogeneous data, spatial model measurement, and develops relevant algorithms and technical engines. This allows for fine management of shield tunnelling construction at the data level.

3.1.3 *Platform layer*

An independent fine management platform of rail transit shield tunnelling was developed. It integrates diverse data from various sources into a database, and contains several management modules such as property management, process management and review management. This platform supports the integration of shield tunnelling construction data from multiple rail transit lines, enabling overall control at the network level.

3.1.4 *Application layer*

With the user authorization, various stakeholders in rail transit engineering, including construction, design, equipment, and other units, can collaboratively manage shield tunnelling on a unified BIM platform. To meet the demands of shield tunnelling construction management across various scenarios, three interfaces have been developed: a large-screen command center, a web-based management portal, and a mobile management application. Specifically, the large-screen command center is designed to meet the requirements of network-level shield tunnel management scenarios, enabling comprehensive oversight, remote command capabilities, and precise control.

3.1.5 *Mechanism*

In the BIM-based fine management process of rail transit shield tunnelling throughout the entire lifecycle, one fundamental task is the integration of BIM model data from the surrounding environment of tunnel projects. To ensure the standardization and uniformity of BIM model data, a series of rail transit engineering BIM standards have been developed, covering aspects like classification and coding, modelling, delivery, and application. Additionally, the mechanism for data security during BIM applications in rail transit

engineering has been established. Measures such as user authorization, data encryption and decryption, and data tracing are implemented to safeguard data security of shield tunnelling management in the rail transit.

3.2 *Management process*

Any accidents involving shield tunnelling equipment during the excavation process can lead to significant economic losses. To ensure the safety, reliability, and compliance of shield tunnelling construction in the tunnel project, an access and management mechanism for shield tunnelling equipment has been established. This mechanism covers the entire process from equipment selection to shield tunnelling excavation management, and ultimately to tunnel breakthrough and equipment removal. The primary management process is illustrated in Figure 2.

Figure 2. Fine management process and data flow of shield tunnelling construction.

3.2.1 *Shield machine selection*

As shown by Song et al. (2022), the selection of shield machines should take into account the characteristics of the engineering project, while ensuring construction safety and project quality, and meeting project deadlines. The primary reference indicators for shield machine selection are the geological and hydrogeological conditions. Typically, in soft geological conditions such as gravelly cohesive soil or soil-like highly weathered mixed granite, considering factors like water height and burial depth, it is recommended to use a slurry balance shield machine. In geological conditions comprising sand layers, silt layers, and other adverse conditions, especially with a high water table, a slurry shield machine is recommended. In cases where the geology is characterized by variable hardness or long stretches of hard rock, an Earth Pressure and TBM Dual-Mode Shield Machine is advisable.

3.2.2 *Shield machine access review*

The platform is responsible for the submission of specialized schemes that evaluate shield machine selection and adaptability, as well as reliability analysis. This process also involves the selection of expert reviewers and other shield machine documents. Prior to the shield machine access review, relevant companies should collect geological survey data and data related to the surrounding environment along the alignment, including existing structures, above-ground and underground structures, pipelines, rivers, etc. This data is then uploaded to the platform, providing a virtual 3D environment for expert reviewers during the shield machine access review. This approach helps address challenges in data collection and presentation during shield tunnelling construction. After expert review and approval of the specialized scheme, the shield machine access permit is issued by the relevant management authorities.

3.2.3 *Shield machine inspection*

Shield machine inspection includes both factory inspection and on-site inspection, with expert participation if necessary. Key aspects of shield machine inspection include the inspection of shield body, cutter head, segment assembly machine, grouting system, and electrical system.

3.2.4 *Shield tunnelling construction control*

According to the requirements of the route design, the construction unit conducts shield tunnelling and segment assembly according to the plan. Utilizing the design line profile and geological information, the construction unit can simulate and analyze the shield tunnelling route, initiating automatic shield machine excavation. During the excavation, real-time monitoring of shield machine excavation status and parameters is achieved through the shield tunnelling fine management platform. Automatic warnings are triggered if excavation parameters deviate from the normal range.

4 INTEGRATION OF HETEROGENEOUS DATA SOURCES AND CONSTRUCTION OF 3D SPACE FOR SHIELD TUNNELLING

When rail transit projects are built in the underground areas of the bustling zone, there are some problems that need to be addressed, including geology (especially adverse geological formations), underground municipal pipelines, underground structures, and existing subway and railway projects. These data sources often belong to different ownership entities, making management interface complex. To ensure the safe and effective excavation of shield tunnelling in such environments, it is crucial to integrate different information along the alignment of tunnel projects. This method can serve as a technical foundation for shield tunnelling construction optimizing, risk mitigation, and other critical aspects of the project.

4.1 *Integration of several heterogeneous data sources*

The surrounding environment data relevant to shield tunnelling construction can be categorized into different types, as shown in Table 1.

Table 1. Surrounding environment data of shield tunnelling construction.

Type	Description	Model Depth
Geology	According to borehole data of field survey, the geological model is simulated by interpolation algorithm.	L3.0 (G3/N)
Underground pipelines	Underground pipelines are created according to drawings of different types.	L2.0 (G2/N2)
Surrounding projects	Based on the collected data, models are created according to different building types, such as existing rail transit lines, existing building foundations, and other existing municipal infrastructure.	L2.0 (G2/N1)

4.1.1 *Information integration*

To develop the effective shield tunnelling method and tunnel construction strategy, it is crucial to consider the conditions along the rail transit alignment. Factors such as the geological and geophysical attributes along the alignment, the distribution of adverse geological conditions, types and dimensions of underground pipelines, and the structural characteristics of existing structures all play a significant role in the shield tunnelling construction. To address issues related to inaccurate, incomplete, and non-standard information along the subway alignment, some attribute information templates were established for geology, underground pipelines, and existing structures. Each participating party is required to collect relevant data and submit to the proposed platform.

4.1.2 *Model standardization*

Before integrating surrounding environment data for shield tunnelling construction, it is essential to generate this data according to uniform standards and specifications. Since there were no standardized guidelines for building geological models, Shenzhen Metro has developed a technical guideline to standardize geological model outcomes. Through this guideline, issues related to the non-standardization and inconsistency of model data, especially for underground pipelines and geological surveys, have been resolved. This not only accumulates standardized urban underground digital assets but also leverages the value of BIM data, improves data reusability, and avoids redundant modelling during shield tunnelling construction. This is particularly valuable for the construction of new lines, where existing geological and underground pipeline data can assist in construction management.

4.1.3 *Depth adequacy*

While there is a high requirement for the depth of tunnel project models in shield tunnelling applications, the surrounding environment models have relatively lower depth requirements. Considering the data application requirements, the depth of surrounding environment models can be appropriately reduced. This is shown in Table 1. For instance, the depth requirement for modelling geological formations due to adverse geological risks can be designated as L3.0, whereas for underground pipelines and nearby existing structures, which only need to exhibit certain geometric characteristics, the model depth for underground pipelines and existing structures can be L2.0. It should be noted that the model depth L1.0-L4.0 employs the expression method specified in the Chinese national standard "Building Information Model Design and Delivery Standard (GB/T 51301-2018)," which is equivalent to LOD 100-LOD 500. By specifying suitable model depths, it not only resolves the issue of varying model depths by different people but also ensures the efficient operation of the BIM platform.

Additionally, by developing data interfaces, monitoring parameters from the shield tunnelling construction can be transmitted to the shield tunnelling fine management platform. This addresses challenges related to transferring data in closed and limited spaces, assisting in the dynamic control management.

4.2 *3D space of shield tunnelling construction*

Based on a unified spatial coordinate system, above-ground and underground model data within the impact range of shield tunnelling construction need to be integrated, constructing a 3D space for shield tunnelling construction, as shown in Figure 3. This 3D space transforms the traditional 2D approach of shield tunnel management, addressing challenges related to complex interference relationships and management difficulties. It makes shield tunnelling construction more precise and more visual.

Figure 3. 3D space of shield tunnelling construction.

4.2.1 *Above-ground and underground visualized space*

Using BIM models as the foundation, this space encompasses various elements of the rail transit project's above-ground and underground components, including geological models, underground pipeline models, and surrounding structure models. It creates a 3D space for monitoring and managing shield tunnelling construction. Project managers can use this visualized space to assess the status of shield tunnelling and potential risks, aiding in optimizing project adjustments. To meet requirements of visible view and data loading, techniques like Level of Detail (LOD) and incremental loading are employed to display elements as needed, meeting the management demands within the 3D space.

4.2.2 *Integrated space with all information*

The 3D space of shield tunnelling integrates various information not only in breadth but also in depth. For example, attributes like stratum numbers, moisture content, porosity, and compressibility modulus of geological bodies are added in the geological model. For underground pipelines, the parameters such as pipeline type, diameter, and material are stored in the model. By integrating comprehensive information in the 3D space, it provides a basis for accurate analysis and prediction of shield tunnelling construction.

4.2.3 *Structured and computable space*

To precisely determine the spatial relationships between the shield tunnelling location and potential risks within the 3D space, measurements techniques for 3D space were studied. The parameters need to be measured include the shield machine's burial depth, the distance between shield machine's cutterhead and building foundations, and the distance between shield machine and adverse geological conditions. Through techniques like capturing the nearest points in the model and calculating distances between two points, a computable 3D space is formed. As shown in Figure 3, it allows for the measurement of the shield machine's burial depth and analysis of spatial relationships between the shield machine and different geological layers.

5 BIM-BASED FINE MANAGEMENT PLATFORM FOR RAIL TRANSIT SHIELD TUNNELLING CONSTRUCTION

To meet the requirements of fine management in shield tunnelling construction, a BIM-based fine management platform for rail transit shield tunnelling construction was developed (hereinafter referred to as the BIM platform). This platform provides technical support for collaborative, digital, and three-dimensional shield tunnelling construction operations for various participating companies. Its main application scenarios are as follows.

5.1 *Data classification and visualization*

In the shield tunnelling management process, data from various participants or of different types needs to be collected, resulting in a wide variety of data sources and formats. To address issues such as unclear data classification, non-standard data representation, and inconsistent integration, a data center was established within the proposed BIM platform. Data is imported after undergoing data cleaning, classified and graded, and a common foundational database for the entire shield tunnelling process was established (as illustrated in Figure 4). It promotes the uniform creation, use, and presentation of shield tunnelling management data.

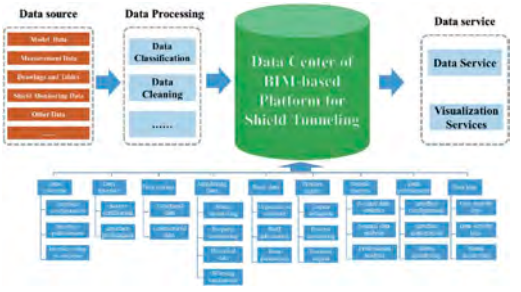

Figure 4. Data classification of data center of fine Management platform for shield tunnelling.

During the shield tunnelling process, data is not limited to the project itself but also relates to the surrounding environment. Relevant data for shield tunnelling management can be categorized into structured data (such as BIM model data) and unstructured data (such as documents and drawings). The parsed BIM models can be divided into geometric information and attribute information, which are stored separately to enhance visualization and data service capabilities. The shield tunnelling process is dynamic, and it requires real-time data storage, such as shield posture, excavation parameters, etc. Historical data storage and data anomaly alert mechanisms can be established after collecting enough data. Maintaining historical data provides a basis for shield control during excavation, while the data anomaly alert mechanism promptly detects shield tunnelling construction issues, allowing for adjustments and optimizations based on historical data to mitigate risks. This research achieves the 3D view of the tunnel project, the dynamical display of shield tunnelling status and parameters, which is beneficial in addressing issues related to two-dimensional management and lagging status updates.

5.2 *"One Map" of shield tunnelling construction*

There may be multiple metro lines under simultaneous construction in the city. Each line's shield tunnelling progress varies, requiring a more scientific and rational approach of network-level shield

tunnelling construction management to avoid impacting the overall quality and progress of the rail transit network. In Shenzhen, there are 12 metro lines under construction in 2023. With the commencement of construction for Shenzhen Metro Phase V, even more lines will be simultaneously constructed. Managing such many shield tunnelling machines simultaneously poses significant challenges.

To address data integration challenges in network-level shield tunnelling management, this study utilized the SuperMap's GIS system as the foundation, and integrated the status of shield tunnelling construction for various railway lines within the "One Map", along with real-time construction data from the sites. By comparing the progress and excavation status of shield tunnelling, it assisted managers in making informed resource allocations for different railway lines, ensuring their smooth progress. Additionally, the "One Map" compiled statistics on risk issues associated with shield tunnelling across all railway lines, aiding project participants in timely risk mitigation. Through the "One Map" approach, it achieved network-level management of shield tunnelling construction from city-wide aspect, as shown in Figure 5.

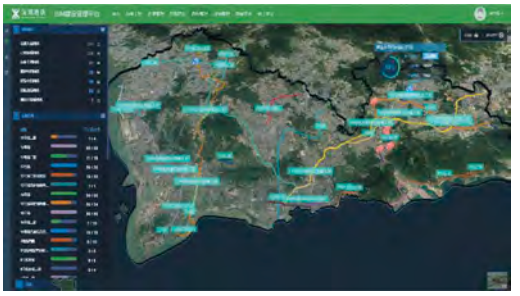

Figure 5. "One Map" of shield tunnelling construction.

To address the macro and micro-level data integration challenges in network-level shield tunnelling construction, GIS and BIM data fusion technology was studied in this paper. It allowed for the rapid transition between GIS data and BIM data through the "One Map". Shield tunnel manager can pinpoint the location of shield tunnelling on specific metro lines, review the progress of the tunnel project, and analyze the interference relationships between surface and subsurface elements within the shield tunnelling range. This facilitates remote control and collaborative management of shield tunnelling construction.

5.3 *Automatic shield tunnelling*

Traditional shield tunnelling excavation and segment assembly plans often require manual calculations based on the design metro line. These processes are highly specialized. The underground construction environment is complex. If there is a deviation from the tunnel's intended alignment, it usually requires a complete redesign based on the original line, which can be time-consuming. To address these issues, an intelligent shield tunnelling technology based on the design route was developed. To analyze the differences among the design line, shield tunnelling line and segment formation line, a predictive model based on shield tunnelling parameters is being developed, using the tunnel project model. This research also involves studying automatic control technology for the shield tunnelling machine system in conjunction with shield tunnelling parameters. The ultimate goal is to establish an intelligent shield tunnelling solution that innovates the tunnelling management approach.

In practical projects, a pilot test of automatic control for the shield tunnel machine has been conducted. The test has shown that under steady-state conditions, the accuracy of shield advance speed control is within ±5 mm/min, the accuracy of soil pressure in the silo is within ±0.1 bar, and the accuracy of shield posture deviation control is within ±3 mm. Figure 6 displays the deviation curves of the main parameters when the shield tunnel machine is in automatic control mode. In the figure, it can be observed that when the predetermined line was used as an input parameter, and the geological conditions along the metro line was applied as boundary conditions, the shield tunnel machine could advance along the spatial line effectively based on the predictive model of shield tunnelling parameters. Additionally, the primary parameters of the shield tunnel machine remain stable in this state.

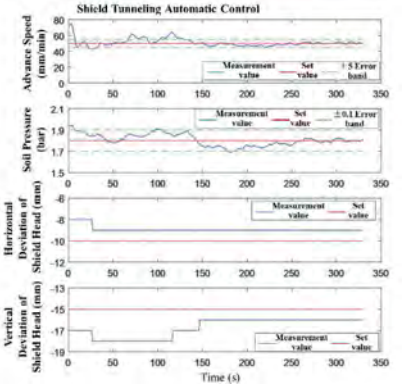

Figure 6. Deviation curve of measurement values and set values of main parameters in shield tunnelling automatic control.

5.4 *Shield tunnelling surveillance*

Status of shield tunnelling machines in different metro lines varies. There are still many problems to be solved, such as data integration difficulties, low visualization, and delayed information transmission, especially during high-risk construction phases like

shield tunnelling construction under existing structures, crossing critical areas, or starting & receiving of shield tunnelling machine. To ensure the safety of shield tunnelling construction and to respond promptly to emergencies, real-time monitoring of shield tunnelling construction is necessary. This study integrates technologies including BIM, AR (Augmented Reality), IoT (Internet of Things), video surveillance, and cloud services to establish an "online + offline" shield tunnelling surveillance mode. Using BIM models as the base, a virtual space of shield tunnelling construction was created in this mode, replicating the construction site at the 1:1 scale. Information is fed back through sensors, surveillance videos, and other media, enabling real-time monitoring of construction status and boring parameters of shield tunnelling. Combining the surrounding environmental conditions presented in 3D space, it intelligently senses construction risks and provides warning alerts through the interaction of AR video and voice, realizing a dual safety surveillance mechanism in the "online + offline" mode.

During the construction, there may be issues like water gushing in the screw machine. Through on-site monitoring and video analysis, a neural network model based on time series analysis was developed, and technology integration of AI (Artificial intelligence) and video was studied for intelligent identification. To identity water gushing issue, its principle is to determine the visual characteristics of object falling at the muck chute. As a result, an online warning system was developed for real-time alerts, reducing risks such as excess spoil discharge and ground collapse.

6 APPLICATION ANALYSIS

6.1 *Data integration*

Since 2019, Shenzhen Metro has been comprehensively promoting the application of BIM technology in Phase Four and Phase Four Adjustment projects. In the initial stages, a series of BIM standards were developed based on project experience, which standardize BIM applications in various project phases. Currently, standardized BIM digital assets have been accumulated, including geological models along metro lines covering 264.92 km, precise real-world models covering 234 km^2, and multiple underground municipal pipelines models along metro lines. These digital assets provide a rich data foundation for constructing the 3D space for shield tunnelling construction. To ensure the uniformity of BIM applications in various business scenarios and facilitate collaboration management on a unified platform, the proposed BIM-based fine management platform for rail transit shield tunnelling construction was embedded in the BIM-based comprehensive application platform, which was independently developed by Shenzhen Metro.

6.2 *Access review for shield tunnelling machine*

To establish a standardized access review mechanism for shield tunnelling machine, Shenzhen Metro has researched and published the "Access Review Management Measures for Shield Tunnelling Machine in Shenzhen Metro". These measures have been embedded within the proposed BIM platform for shield tunnelling management. Before the access review of shield tunnelling machine, participating companies are required to collect information related to geological conditions, underground pipelines, and surrounding structures along the metro line, following the relevant BIM standards. They are then expected to create 3D models and upload to the BIM platform. Through using this information to construct a 3D space for shield tunnelling construction, the platform provides technical support to access review. Based on information concerning geological conditions, underground pipelines, and building structures, the construction company can rapidly assess potential risks during shield tunnelling excavation. This enables them to develop secure and efficient shield tunnelling construction plans.

6.3 *Shield tunnelling construction handover*

In traditional handover procedures for shield tunnelling construction, project managers primarily rely on 2D drawings for technical explanations. It needs highly specialized knowledge to understand complex space relationship and construction technology. Shenzhen Metro has been actively promoting the application of forward-design BIM models during the construction phase, pioneering the use of the 3D-based drawing set in the rail transit field. By using a 3D visual representation, shield tunnelling construction plans and critical milestones can be displayed for construction staff. This approach addresses issues related to inconsistent understanding of the plans, non-intuitive plan representations, and difficulties in grasping spatial relationships. Simultaneously, through binding the staff information to the segments, it can distribute responsibilities to individuals for ensuring the quality of segment assembly. This has led to the implementation of a "real name system" for managing approximately 200,000 segments (approximately 300 km) during shield tunnelling construction.

6.4 *Shield tunnelling intelligent management*

During shield tunnelling construction, the shield tunnelling system transmits real-time excavation status, excavation parameters, and monitoring videos to the BIM platform. Project managers can remotely monitor the shield tunnelling progress, providing a basis for on-site control and resource allocation. Figure 7 illustrates the excavation progress of the tunnel project between Moon Road Station and East Zhou Road Station of Line 13 North Extension. Managers can also

access monitoring cameras at different locations on the shield tunnelling site, observing on-site construction operations and monitoring excavation parameters. In case of data anomalies, early warning alerts are triggered, enabling intelligent risk assessment in shield tunnelling construction and hazard mitigation.

Currently, Shenzhen Metro realizes the real time monitoring of 399 shield tunnelling machines across ongoing projects, ensuring "One Map" management of shield tunnelling. Within the "One Map", the real-time monitoring of key excavation parameters is achieved, and warnings for anomaly indicators such as excavation volume, assembly speed, and soil pressure fluctuations can be automatically reminded. It has accumulated to 2,100 warnings, leading to an 80% reduction in ground collapse rates among tunnel projects.

Figure 7. Fine management of shield tunnelling based on 3D space.

7 CONCLUSIONS

As a critical infrastructure for the city, rail transit engineering has experienced rapid growth in recent years alongside city development. In this paper, the fine management of rail transit shield tunnelling construction was studied based on BIM technology, and a BIM-based fine management platform has been independently developed. This proposed platform integrates diverse and heterogeneous data sources related to shield tunnelling construction, including geology, underground pipelines, and structures. It constructs a computable 3D space for shield tunnelling, providing a data foundation for optimizing and adjusting construction plans. By utilizing structured data from BIM models and real-time excavation data, the "online + offline" shield tunnelling surveillance mode and the shield tunnelling automation mode have been developed.

The achievements have been comprehensively applied to Shenzhen Metro Phase Four and Phase Four Adjustment projects, validating the feasibility and effectiveness. This can serve as a reference for other cities looking to refine their management of shield tunnelling projects.

As Shenzhen Metro Phase Five is about to start, the proposed fine management platform for shield tunnelling construction will be used in more projects. To further enhance its intelligence, efficiency and precision, the future research and applications will focus on the following areas: a) Integration of more comprehensive and abundant urban underground space information; b) Innovation in the application of BIM+5G technology in shield tunnelling for data transmission; c) Deepening the study of the coupling relationship between shield tunnelling 3D space and design line.

ACKNOWLEDGMENTS

This work was supported by the Science and Technology Plan Project of the Ministry of Housing and Urban Rural Development (2020-K-136).

REFERENCES

Borrmann, A., Kolbe, T., Donaubauer, A., et al, 2015. Multi-scale geometric-semantic modelling of shield tunnels for GIS and BIM applications. Computer-aided Civil and Infrastructure Engineering. 30(4), 263–281.

China Association of Metros, 2023. 2022 Annual statistics and analysis report on urban rail transit. Beijing, China.

Kiseok, J., Edward, D., Mehdi, B., et al, 2022. Use of BIM technology for optimization and virtual build of TBM tunnels. Geomechanics and Tunnelling. 15(2), 175–181.

Li, C.B., Xue, Y.D., Fan, Y.Q., et al, 2020. BIM-based quantitative assessment method of tunnel collapse risk in TBM construction. IOP Conference Series: Earth and Environmental Science. 570(4), 042055.

Lin, X.D., Li, X.J., Lin, H., 2018. A GIS/BIM-integrated lifecycle management system for shield tunnel. Tunnel Construction. 38(6), 963–970.

Liu, C.Y., 2019. Research on the BIM technology application of metro interval based on Autodesk and Bentley platform. Journal of Railway Engineering Society. 36 (6), 91–96.

Marco, T., Silvia, L., Monica, C., 2023. 4D approach for urban tunnelling in a BIM environment. Applied Geomatics. 15(2), 337–347.

Song, T.T., Liu, C.K., Chen, F., et al, 2022. Research on the selection and tunnelling adaptability of dual-mode shield/TBM in metro tunnel. Journal of Railway Engineering Society. 39(1), 107–113.

Stascheit, J., Ninić, J., Meschke, G., et al, 2018. Building information modelling in mechanised shield tunnelling - A practitioner's outlook to the near future. Geomechanik und Tunnelbau. 11(1), 34–49.

Yu, G., Hu, M., Gao, X.W., et al, 2016. BIM-based 3D visual construction management system for shield tunnelling. Modern Tunnelling Technology. 53(1), 1-5 +16.

Yu, Z., Lu, Y., Dong, H.F., et al, 2018. Research on automatic modelling method of shield tunnel based on BIM. In: The 4th National BIM Academic Conference in China. Beijing, China, pp. 164–168.

Zhao, W., Wei, Y., Liu, B., et al, 2019. Design and application of automatic monitoring and BIM technology to the construction of shield-bored underneath building. In: Information Technology in Geo-Engineering - Proceedings of the 3rd International Conference ICITG 2019. Guimarães, Portugal, pp. 493–501.

Tunnelling for a Better Life – Yan, Celestino, Thewes & Eberhardt (Eds)
© 2024 The Author(s), ISBN 978-1-032-80042-4
Open Access: www.taylorfrancis.com, CC BY-NC-ND 4.0 license

Innovative design and practice of full life cycle of complex underground engineering equipment based on digital twin

Feixiang Liu*
China Railway Construction Heavy Industry Corporation Limited, Changsha Hunan, China

ABSTRACT: Digital twin is one of the key enabling technologies to implement intelligent construction. According to the characteristics of complex and changeable service environment of typical underground engineering equipment, highly personalized customization and high complexity of equipment itself, based on the continuous pursuit of the digital goal of "stuffing the product into computer, moving the workshop onto computer and building the tunnel on computer", the technological advancement path from digital mock-up to digital twin of underground engineering equipment was put forward. Through the study of key technologies such as high-fidelity modeling and simulation, high-confidence prediction and optimization, and high-real-time data interaction based on digital twin, a new mode of independent innovation design throughout the whole life cycle of complex underground engineering equipment was established. Based on the actual demand, this paper discussed the "three elements" of digital twinning application of underground engineering equipment, described the implementation framework of digital twin, carried out the practice of digital twin technology in the field of large-scale and complex underground engineering equipment, and explored a new way to improve the key service performance of major equipment.

Keywords: Digital twin, Digital, Underground engineering equipment, Full life cycle

1 INTRODUCTION

With the rapid development of a new round of scientific and technological revolution and industrial transformation, the world is in a stage of great transformation from the industrial age to the digital age. The digital economy has become a hotspot for global economic development, and the United States, the United Kingdom, the European Union and other countries have successively put forward digital economy strategies[1]. Promoting the integrated development of digital economy and real economy has become a consensus among governments and industrial circles. Either the National Strategic Plan for Advanced Manufacturing developed by the United States[2], or "Industry 4.0" proposed by Germany[3] or "Made in China 2025 strategy" has taken intelligent manufacturing integrating digitization, networking and intelligence as the core of the new round of scientific and technological revolution, and at the same time intelligent manufacturing has become the common development trend of the world's manufacturing industry at present. The key to intelligent manufacturing lies in the interconnection and integration of the manufacturing information world and the physical world, and the two-way interaction between real world and virtual world based on digital twin provides an effective means[4]. More and more academics and industrialists have regarded digital twin as one of the key enabling technologies to practice intelligent manufacturing[5].

In 2003, Professor Michael Grieves from the University of Michigan in the United States put forward the idea of "virtual digital representation equivalent to physical products", which was officially named as digital twin in 2011[6]. The United States Air Force and NASA adopted this concept and applied it in aircraft design (such as F-15), health assessment, damage prediction, etc.[7][8]. In recent years, the coverage on research and application of digital twin technology has grown exponentially[9]. In October 2019, the United States Navy built the first digital twin for USS Abraham Lincoln[10]; in March 2020, the United States Air Force announced that it was using digital twin technology to safeguard the network security of GPS 2R satellite[10]; the aero-engine enterprises in the United Kingdom and Russia also plan to complete the introduction of digital twin technology in the near future[11]; and domestic aerospace, shipping, machinery, water conservancy and hydropower and other industries are also increasing their attention to digital twin technology year by year[12]-[15]. Some mines and coal mine boring machines, etc. have begun to introduce digital twin technology to realize intelligent construction and management[16]. Moreover, digital

*Corresponding author: wangyongsheng@crchi.com

DOI: 10.1201/9781003495505-383

twin has also been included in the national strategic planning[17]. In April 2020, the National Development and Reform Commission and the Office of the Central Cyberspace Affairs Commission printed and issued the *Implementation Plan on Promoting the "Cloud Application, Data Empowerment and Artificial Intelligence" Action to Cultivate New Economic Development*, juxtaposing digital twin with big data, artificial intelligence, 5G, etc. The State-owned Assets Supervision and Administration Commission of the State Council issued the *Notice on Accelerating the Digital Transformation of State-owned Enterprises* in August 2020, which clearly requires the state-owned manufacturing enterprises to enhance the design and manufacturing level based on digital twin in their digital transformation.

According to the applicable criteria for digital twin proposed by Tao Fei and other scholars[5], the products with high single product value, complex system and process, extreme operating environment and other characteristics are suitable for the application of digital twin, while large-scale complex underground engineering equipment with complicated and changeable service environment and a high degree of personalized customization is highly consistent with the applicable criteria for digital twin. In view of the technical challenges faced by the development of underground engineering equipment, this paper first puts forward the advancement path of digital technology from digital mock-up to digital twin for underground engineering equipment, then introduces the key technologies of digital twin and a new model of independent innovation design based on digital twin throughout the full life cycle of underground engineering equipment, and finally expounds the application value of digital twin technology in solving the technical problems faced by underground engineering equipment through some practical application cases. Based on the requirements of underground engineering equipment, this paper discusses the "three elements" in digital twin application, describes the implementation framework of digital twin technology for underground engineering equipment, and preliminarily realizes the successful verification and practice of digital twin system in the field of large-scale underground engineering equipment in China, thus exploring a new way to improve the core competitiveness of major equipment in China.

2 DIGITAL TECHNOLOGY IS THE ONLY WAY TO DEVELOP UNDERGROUND ENGINEERING EQUIPMENT TECHNOLOGY

2.1 *Technical challenges faced by the development of underground engineering equipment*

After long-term investment in research and development, China's underground engineering equipment has embarked on the road of independent development and made major breakthroughs in key technical bottleneck areas such as main bearings. However, it still faces the following technical challenges:

(1) Difficulty in coupling analysis between equipment and complex and changeable geological environment. Underground engineering equipment has high technical complexity, high interdisciplinary degree and high system integration. The coupling between the equipment system and the geological environment is nonlinear, unstable and unpredictable. Based on the above factors, it is difficult for traditional methods to accurately analyze and optimize the performance of underground engineering equipment in a complex geological environment.

(2) Difficulty in real-time perception and interaction of man-machine-environment. Underground engineering equipment has a high degree of personalization, user attention and participation. It belongs to a typical "multilateral" project such as simultaneous implementation of survey, design and manufacturing, and its development process requires multi-party coordination. However, due to the lack of virtual-real space synchronous mapping and other technologies in extremely harsh service environment, it is impossible to obtain the real status information of equipment in time, and it is difficult to realize man-machine-environment interaction.

(3) Difficulty in accurate prediction and matching of equipment performance. The construction of underground engineering equipment in a complex and changeable high-risk service environment often faces the problems such as unpredictable geological types, life performance and sudden failures, and the "complex mechanism and difficult traceability" of failures result in high risk and high consumption during construction, which greatly limits the service performance of underground engineering equipment.

In view of the above-mentioned technical challenges faced by underground engineering equipment, it is difficult for traditional design ideas and methods to fully support independent innovation and development of products. The independent innovation and development of underground engineering equipment must take a digital way of forward design.

Figure 1. Construction environment diagram of underground engineering equipment.

2.2 *Construction of digital system for underground engineering equipment*

CRCHI has long been committed to the construction of enterprise digital system for high-end complex underground engineering equipment[18]. In 2016, it put forward the digital strategic conception of "stuffing the product into computer, moving the workshop onto computer and building the tunnel on computer", continuously promoted the digital and intelligent upgrading including R&D design, production and manufacturing, marketing service, supply chain, finance, management and operation, promoted the construction and implementation of digital projects such as CAX, CAPP, PLM, ERP, MES and high-performance computing center, and provided a digital environment for the application of digital mock-up and digital twin technology in the R&D design, production and manufacturing stages of products. Meanwhile, CRCHI has also established a product big data platform. By cooperating with multiple underground tunnel construction control business centers, it has developed an IoT platform for underground construction equipment, and connected the underground engineering equipment produced by CRCHI or even third-party equipment to this platform, basically realizing remote monitoring of real-time status information of equipment and intelligent construction assistance and providing network and data support for the application of digital twin technology in the operation and maintenance stage of products.

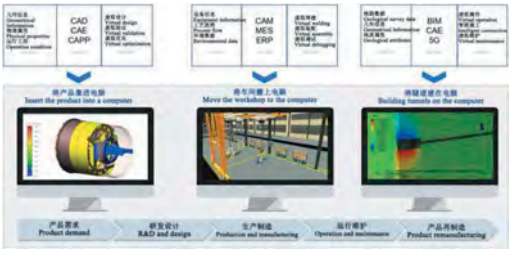

Figure 2. Digitalization objective pursued by CRCHI.

2.3 *From digital prototype of underground engineering equipment to digital twin*

According to the definitions specified in GB/T 26100-2010[19], digital mock-up (DMU) not only reflects the geometric attributes of product objects, but also reflects the functions and performance of product objects in at least a certain field. This paper describes the different development stages of digital mock-up for underground engineering equipment in combination with the elaboration on the evolution process of digital mock-up in Reference[20], as shown in Figure 3. The digital mock-up of underground engineering equipment gradually evolves into one containing functions and physical properties from 2D to 3D in the primary stage with product structure (organizational relationship) and attributes added; moreover, it also reflects real manufacturing information such as production and manufacturing deviation, thus forming a complete engineering design process containing real physical product data. However, due to the lack of data interaction feedback with the manufacturing/service process of physical entities, digital mock-up fails to form a closed loop for iterative design optimization based on real data and cannot solve the problems such as coupling between geological environment and equipment, equipment performance/failure prediction under actual working conditions, intelligent decision-making optimization, etc., seriously restricting the independent innovative design of underground engineering equipment. Therefore, it is necessary to realize data interaction and integration between digital mock-up and physical entity with the help of digital twin technology.

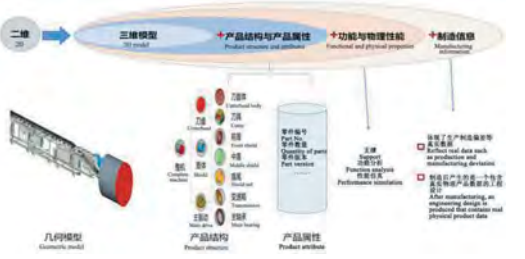

Figure 3. Development stage of Digital Mock-Up (DMU) for underground engineering equipment.

At present, digital twin has no fixed technical system, mode and method[5], and the understanding of digital twin is also different and constantly evolving. The author believes that digital mock-up is a defined ideal product, which reflects human consciousness. Enterprises manufacture the physical products according to digital mock-up, while digital twin describe physical product, which is a combination of digital mock-up and physical entity. Therefore, the digital twin of underground engineering equipment should at least start from "digital mock-up with increased manufacturing information", and the real physical information of physical products is added to the digital mock-

Figure 4. Underground engineering equipment from digital Mock-up to digital twin.

up through sensors, so as to form data interaction and integration between physical product and digital mock-up and realize virtual-real mapping and virtual-real synchronization. Meanwhile, an operation mechanism of virtual-real mutual improvement and mutual iterative update between physical product and digital mock-up has been established through digital twin.

3 INDEPENDENT INNOVATIVE DESIGN OF UNDERGROUND ENGINEERING EQUIPMENT BASED ON DIGITAL TWIN

For complex products, Grieves et al.[6] gave the definition of digital twin: Digital twin is a set of virtual information structures that comprehensively describe potentially produced or actually manufactured products from micro-atomic level to macro-geometrical level. The best result of building a digital twin is that any information that can be obtained by testing the actually manufactured product can also be obtained from its digital twin. However, with the current technology and computing power, it is difficult to realize the digital twin defined above at this stage. In other words, it is difficult to realize a digital twin that can fully map the physical product in real time. Physical product can only be mapped from the required dimension and perspective. Therefore, the application of digital twin can only be obtained from the required dimension and perspective. It can be seen from the definition that the role of digital twin runs through the full life cycle of product such as R&D design, production and manufacturing, operation and maintenance, etc., but it serves the product mainly in the operation and maintenance stage. Based on digital twin, we can obtain the equipment operation condition, predict its service life through simulation and then iteratively optimize the design to form a new model of independent innovative design for the full life cycle of underground engineering equipment and realize the following functions.

3.1 *Operation simulation based on digital twin*

The digital twin can be used to accurately simulate the operation process, behavior and status of underground engineering equipment integrated with the complex service environment in real time. By taking TBM as an example, based on the digital twin of TBM products and tunnel construction environment, it can fully simulate the complex operation process of TBM under arbitrary extreme working conditions and constrained load conditions in virtual environment, analyze and predict the status behavior and task execution success rate of TBM, etc., providing reliable basis for TBM modification before formal service and task execution and decision-making after service.

Figure 5. Operation simulation based on digital twin.

3.2 *Health prediction based on digital twin*

Through the simulation of digital twin and the real-time data collected by sensors, the health status of underground engineering equipment can be diagnosed and predicted to provide guarantee for the safe operation of underground engineering equipment. The underground engineering equipment usually shows the following behaviors during operation: predictable behavior and unpredictable behavior. Predictable behavior is divided into predictable desired behavior and predictable undesired behavior, with the former being a desirable outcome. Unpredictable behavior is also divided into unpredictable desired behavior and unpredictable undesired behavior. The latter belongs to a behavior that needs to be eliminated, which not only seriously affects the normal operation of equipment, but also causes safety accidents of people and equipment. The most important purpose of building a digital twin is to repeatedly simulate operation and accurately predict in virtual space and eliminate the "unpredictable undesired behavior" during the development, operation and maintenance of underground engineering equipment to the greatest extent, thus avoiding unknown catastrophic problems.

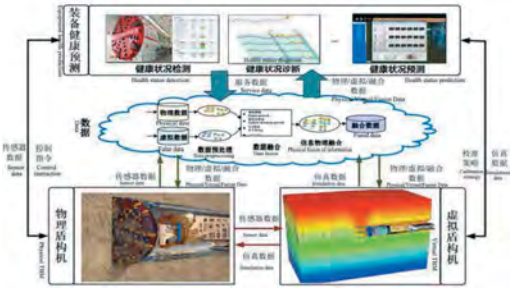

Figure 6. Health prediction based on digital twin.

3.3 *Iterative optimization based on digital twin*

Another important function of digital twin for underground engineering equipment is reflected in the iterative optimization of product life cycle. As shown in Figure 7, sensors collect and sense the status of

physical entity and transmit the data to the virtual twin, and then the virtual twin conducts analysis/reasoning/diagnosis and makes independent decisions to drive the physical entity to accurately execute and optimize the operation scheme, and gradually improve the use value and system stability of the product, thus forming a closed-loop iterative optimization of product life cycle[21]. On the other hand, the data based on digital twin as well as analysis/reasoning/diagnosis results can be fully applied to the development of next generation products, thus realizing iterative optimization of cross-generation products.

Figure 7. Iterative optimization based on digital twin.

4 KEY TECHNOLOGIES OF DIGITAL TWIN FOR UNDERGROUND ENGINEERING EQUIPMENT AND IMPLEMENTATION FRAMEWORK

4.1 *Key technologies of digital twin requiring breakthroughs for underground engineering equipment*

4.1.1 *High-fidelity modeling and simulation technology*

High-fidelity modeling and simulation is the model data basis for building the digital twin of a product[20]. The simulation of digital mock-up is based on the ideally defined DMU, which only plays a guiding role. The simulation of digital twin is based on real physical product, and it is necessary to achieve the fidelity of modeling and simulation with real physical product and real environment. Therefore, the high-fidelity modeling and simulation technology is regarded as an important milestone to realize the digital twin of products, which is also an important feature that distinguishes the digital twin from the digital mock-up. In order to realize high-fidelity modeling and simulation of complex underground engineering equipment, the author believes that there are at least three aspects requiring breakthroughs: mechanical coupling analysis between equipment and rock, soil, etc; full-element modeling and simulation of multiple scales at the complete machine level, component level and part level as well as multiple physical fields such as mechanical, electrical and hydraulic; interface development and real-time data interaction between simulation software for different disciplines.

4.1.2 *High-confidence simulation prediction technology*

One of the important functions of high-fidelity simulation model is to predict its performance and function before the physical prototype is produced, so as to guide design and obtain improved optimization scheme; predict product failure and health status in the operation and maintenance stage of physical prototype, and eliminate unpredictable undesired behavior in advance. The construction environment of underground engineering equipment is highly complex, random and uncertain, and the coupling between equipment and complex and changeable environment makes the high-confidence simulation prediction full of technical challenges while considering the multiple elements such as geological environment and equipment performance. At present, there is no precedent in the industry.

4.1.3 *High real-time data interaction technology*

High real-time data interaction is the material basis for the virtual-real integration of digital twin and physical entity[20]. Mass data will be generated during the manufacturing and construction of underground engineering equipment. Due to the high complexity of the equipment itself, various types of data and extremely harsh construction environment, it is often difficult to collect data on site, integrate heterogeneous data, transmit data in real time, etc. How to realize data acquisition, analysis and control of physical products of underground engineering equipment, as well as high real-time data interaction and application with digital twin is also a key technology requiring breakthroughs.

4.2 *Implementation framework of digital twin technology for underground engineering equipment*

4.2.1 *"Three elements" for implementation of digital twin technology*

As a complex cutting-edge technology, digital twin contains multiple elements. In summary, the core elements are "model, data and software", among which model is the core, data is the foundation and software is the carrier, all of which complement each other. In terms of models, there are the mechanism models including mathematics/physics/chemistry, function, design and analysis, such as GIS/CAE-based coupled simulation model for geology and TBM, and then data analysis models including machine learning model, empirical model and fault model obtained from data acquisition and big data analysis, such as optimization model for muck improvement parameters of Shield Machine based on big data. The comprehensive application of mechanism models and data analysis models constitutes the model source of digital twin. In terms of data, there are the basic model data such as CAX model data and then the physical data collected by sensors.

Both models and data need to be implemented by software. Finally, the whole digital twin technology framework is built with model + data + software as the core elements.

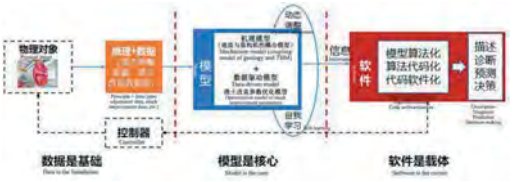

Figure 8. "Three elements" of digital twin.

4.2.2 *Implementation framework of digital twin technology for underground engineering equipment*

The digital thread is regarded as a communication channel for the evolution of product models at all stages. It relies on the business system throughout the product life cycle (as shown in Figure 9), covering various links such as product conception, design, supply chain, manufacturing and delivery. The data from each link, department and system are not isolated but shared through collection, transmission, integration and fusion. Throughout the product life cycle, the digital thread provides access, integration and conversion capabilities for the digital twin of products. Its goal is to run through the product life cycle and value chain, realize comprehensive traceability, information interaction and value chain collaboration, and build a digital environment for the implementation of digital twin technology for underground engineering equipment.

Figure 9. Digital twin implementation basis: Digital thread.

Based on the above analysis, this paper proposes an implementation framework of digital twin technology for underground engineering equipment, which is divided into three aspects: data support, digital mock-up and digital twin platform (providing model and software support) and engineering application, as shown in Figure 10. Digital support consists of a product layer, an acquisition layer and a data layer. PLM, SCADA, MES and collaborative management platform of big data are used to complete the data acquisition and transmission in design, manufacturing, operation and maintenance stages of equipment, providing data support for digital mock-up and digital twin platform. The digital mock-up and digital twin platform consists of a technology layer, a model layer and a software layer. Based on the full life cycle data of underground engineering equipment, the mechanism/non-mechanism models required for digital mock-up and digital twin of underground engineering equipment are constructed by carrying out technical research such as modeling, simulation, prediction and optimization, and the development of digital mock-up software platform and digital twin system of underground engineering equipment is completed, so as to carry out application verification in major national projects such as plateau railway.

Figure 10. Implementation framework of digital twin technology for underground engineering equipment.

5 INNOVATIVE APPLICATION PRACTICE OF DIGITAL TWIN FOR UNDERGROUND ENGINEERING EQUIPMENT

In view of a series of technical challenges such as difficulty in coupling analysis between equipment and complex geological environment, difficulty in real-time perception and interaction of man-machine -environment, and difficulty in accurate prediction and matching of equipment performance caused by the complex and changeable service environment of underground engineering equipment, highly personalized customization and high complexity of equipment itself, CRCHI has set up a technical breakthrough team through industry-university-research cooperation relying on national key research and development projects, taken the lead in breaking through the integrated modeling and simulation technology of large-scale underground engineering equipment and complex geological environment, established an efficient order reduction method for multi-physical field coupling model, overcome the accurate mirroring technology of digital twin driven by construction data online in real time, and independently developed the digital twin system for underground engineering equipment (as shown in Figure 11), covering various types of equipment products such as shield machine, drill jumbo, driving and bolting integration equipment, so as to realize real-time perception feedback and

dynamic decision optimization during equipment construction based on digital twin.

Figure 11. Digital twin system of shield equipment and its functions.

The above technological achievements and digital twin systems have taken the lead in demonstration application in more than ten major projects such as urban subway, plateau railway and large mine, effectively preventing various potential risks in the process of equipment design, manufacturing and service, and significantly improving equipment performance and construction efficiency. The specific application of digital twin in the field of underground engineering equipment is illustrated by two cases below.

Case 1: Real-time prediction of geological environment based on digital twin. In view of the need to obtain geological information in front of the excavation face of shield equipment in time during the construction of a metro project to guide construction optimization, the geotechnical type identification technology based on local tangent space alignment of shield machine operating parameters and Xgboost fusion is studied, and the mapping relationship between historical operation data (cutterhead torque, thrust, etc.) of shield equipment and geological information in front of the excavation face (surrounding rock grade, etc.) is explored by LTSA algorithm. A data-driven high-precision prediction model for geological types of shield equipment construction is developed and integrated into the digital twin system. On this basis, the geological prediction model is driven by the field operation data of shield equipment to realize real-time prediction of geological types and real-time early warning of geological risks.

During the application verification of this metro project, a total of 335 rings were tunneled by the shield equipment. By comparing the real-time prediction results of digital twin system with the on-site sampling test results, the correct number of rings for geological type prediction was 303, with an accuracy rate of 90.4%, which provided strong support for the construction scheme of this metro project to match the geological environment and for making timely adjustment and optimization.

Figure 12. Real-time prediction of geological environment based on digital twin.

Case 2: Intelligent construction of drill jumbo based on digital twin. Aiming at the engineering problems such as over-excavation and under-excavation of working face caused by poor consistency of spatial error distribution in drilling positioning of drill jumbo, we have established the kinematic inverse solution, dynamics and system simulation models of drill jumbo boom, developed the boom deformation compensation algorithm and model order reduction technology to solve the technical difficulties such as poor consistency of spatial error distribution in drilling positioning of drill jumbo construction and difficulty in meeting the high real-time requirements of digital twin, researched the digital twin system for operation and maintenance stage of drill jumbo, and conducted data interaction with enterprise big data platform. In the promoted application of a new plateau railway tunnel, based on the digital twin system, the synchronous action of twin model remotely driven by the actual operation posture parameters (angle, cylinder stroke, etc.) of the boom and the real-time prediction and optimization of boom motion trajectory are realized, and the on-site construction is guided by the feedback control instructions of the twin system. The field measurement data shows that the average deviation between the actual hole position coordinates in automatic drilling of boom and the target hole position coordinates in the blasthole diagram is 4.8 cm, and the construction efficiency of drill jumbo using digital twin system in the same section is increased by 21.5%.

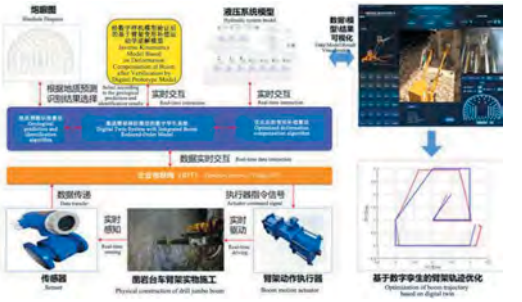

Figure 13. Intelligent construction technology route of drill jumbo based on digital twin.

6 CONCLUSION

(1) In view of the technical challenges faced by the development of underground engineering equipment and in combination with the digitalization process of CRCHI, this paper expounds the advancement path from digital mock-up to digital twin, and proposes a new model of innovative design for the full life cycle of underground engineering based on digital twin.

(2) Furthermore, centered on the key technologies requiring breakthroughs in the application of digital twin for underground engineering equipment and the three elements of "model, data and software", the implementation framework of digital twin technology for underground engineering equipment based on the digital thread is formulated, and the development of digital mock-up and digital twin system for underground engineering equipment is completed.

(3) Through the practical engineering application of digital twin technology for typical complex underground engineering equipment such as TBM, drill jumbo and all-in-one tunneling and anchoring machine, the bottleneck problems such as equipment performance prediction, early warning of construction risks and dynamic decision optimization in complex geological environment faced by underground engineering equipment have been preliminarily overcome, and a closed-loop feedback innovation mechanism based on digital twin throughout the life cycle of underground engineering equipment has been formed to provide a typical demonstration for the promoted application of digital twin technology in large-scale equipment manufacturing industry.

ACKNOWLEDGMENTS

This work was supported by the National Key R & D Plan of China (Grant numbers 2019YFB1705200) .

REFERENCES

[1] BoZhao, et al. Digital Twin White Paper (2020) [R]. China Electronics Standardization Institute, 2020-11.

[2] Holdren J, Power T, Tassey G, et al. A National strategic plan for advanced manufacturing[R]. Washington, DC: the Office of Science and Technology Policy, 2012.

[3] Kagermann H, Helbig J, Hellinger A, et al. Recommendations for implementing the strategic initiative INDUSTRIE 4.0: Securing the future of German manufacturing industry; final report of the Industrie 4.0 Working Group [M]. Forschungsunion, Germany: Office of the Industry-Science Research Alliance, 2013.

[4] Fei Tao, Weiran Liu, Meng Zhang, et al. Five-dimensional Model of Digital Twin and Its Application in Ten Major Fields [J]. Computer Integrated Manufacturing System, 2019, 25(1):1–18.

[5] Fei Tao, et al. Ten Questions about Digital Twin: Analysis and Thinking [J]. Computer Integrated Manufacturing System, 2020, 26(1):1–17.

[6] Grieves M.and Vickers J. Digital twin: mitigating unpredictable, undesirable emergent behavior in complex systems[M]//Trans-disciplinary Perspectives on Complex Systems.Berlin, Germany:Spring-Verlag, 2017.

[7] Glaessgen E, Stargel D. The digital twin paradigm for future NASA and U.S.air force vehicles[C]// Proceedings of the 53rd AIAA/ASME/ASCE/AHS/ASC Structures, Structural Dynamics and Materials Conference. Reston, Va.,USA: AIAA, 2012:7274–7260.

[8] Tuegel EJ, Ingraffea AR, Eason T G, etal, Re-engineering aircraft structural life prediction using a digital twin[J]. International Journal of Aerospace Engineering, 2011, 2011:1–14.

[9] Peigen Li: A Brief Introduction to Digital Twin. http://master.infosws.cn/20200818/38945.html

[10] Xiaohong Li. Development Trend Analysis of Digital Twin Technology in the Defense Field of the United States [J]. Dual-Use Technologies and Products, 2019,12(446): 25–28.

[11] Le Wang, Jun Zhou, Yanlin Cui. Application Analysis of Digital Twin in Aeroengine Field [J]. Aerodynamics, 2020, (5): 63–66.

[12] Leiting Dong, Xuan Zhou, Fubin Zhao, et al. Key Modeling and Simulation Technology of Aircraft Structure Digital Twin. Journal of Aviation https://kns.cnki.net/kcms/detail/11.1929.V.20200615.1314.016.html.

[13] Linli Li, Hao Li, Gu Fu, et al. Multidisciplinary Collaborative Design Modeling Technology for Complex Mechanical Products Based on Digital Twin [J]. Computer Integrated Manufacturing System, 20219, 25(6): 1307–1319.

[14] Guogang Wang, Wenchao Zhao, Yapeng Chen, et al. Application Scheme of Digital Twin Technology in Water Conservancy and Hydropower Engineering Geology [J]. Technical Supervision in Water Resources, 2020, (5): 309–315.

[15] Hongguo Zhang, et al. Digital Twin White Paper (2019) [R]. Beijing: ccidnet.com, 2019-12-19.

[16] Chao Zhang, Xuhui Zhang, Qinghua Mao, et al. Research and Application of Digital Twin System for Intelligent Tunneling Robot in Coal Mines [J]. Journal of Xi'an University of Science and Technology, 2020, 40(5): 813–822.

[17] Zhen Liu. Digital Twin: Gateway to Digital Future of Enterprises [J]. Software and Integrated Circuit, 2020, (11): 10–14.

[18] Feixiang Liu. Exploration and Practice of Digital System for Customized Equipment Manufacturing Enterprises [J]. Science and Technology Management Research, 2019, (7): 127–132.

[19] GB/T 26100—2010 General principles of digital mock-up for mechanical products [S]. Beijing: Standards Press of China, 2011.

[20] Sheng Dai, Gang Zhao, Yong Yu, et al. Development Trend of Digital Product Definition: From Mock-up to Twin [J]. Journal of Computer-Aided Design & Computer Graphics, 2018, 30 (8): 1554–1561.

[21] Min Zhao, Duoxian Zhu. Differentiation and Analysis of Four Terms: Digital Twin, Cyber Physical System, Intelligent Manufacturing and Industrial Internet. WeChat Official Account: Industry 4 Club.

Tunnelling for a Better Life – Yan, Celestino, Thewes & Eberhardt (Eds)
© 2024 The Author(s), ISBN 978-1-032-80042-4
Open Access: www.taylorfrancis.com, CC BY-NC-ND 4.0 license

Research on intelligent construction technology and grading method of railway shield tunnel

Gang Lu
China Railway Engineering Design Consulting Group Co., Ltd., Beijing, China

Tongjun Wang
China National Railway Group Limited, Beijing, China

Jianyou Liu*
China Railway Engineering Design Consulting Group Co., Ltd., Beijing, China

Wanqi Wang
China Academy of Railway Sciences Group Co., Ltd

ABSTRACT: With the development of information technology, automation and artificial intelligence technology, intelligent construction has gradually become the inevitable direction of tunnel engineering development. In order to guide the development of intelligent construction of railway shield tunnel, this paper summarizes the practical experience of intelligent construction of railway tunnel in China and absorbs the latest scientific research achievements of intelligent construction of various industries at home and abroad, and puts forward the principles and objectives of intelligent construction of railway shield tunnel, starting from tunnel survey, design, construction and construction management. The basic requirements, implementation plan and details of intelligent shield tunnel construction are clarified, the classification method and standard of intelligent shield tunnel construction are formulated, and the evaluation system of intelligent railway shield tunnel construction is constructed. At the same time, the composition and function of the visual intelligent management platform of railway shield tunnel are introduced in detail, which provides a hierarchical and step-by-step realization path for intelligent shield tunnel construction. It provides a broad space for the practice of new technologies, new methods, new equipment and new ideas in intelligent tunnel construction.

Keywords: Railway shield tunnel, Intelligent construction, Grading Method, Intelligent management platform

1 INTRODUCTION

With the rapid development of 5G communication technology and AI technology in China, the shield technology is perfecting the adaptability of tunnel construction in different geological conditions and different working conditions, and the continuous improvement of labor cost, the share of tunnel shield (including TBM) construction in railway tunnel construction is gradually increasing, and it may become the mainstream of tunnel construction in our country in the future. According to statistics, by the end of 2021, there are a total of 31 railway shield tunnels in operation or under construction in China, with a total of 303km, and 40 railway tunnels planned to be constructed with the shield method, with a total of 387 km. Shield construction is a factory operation in which segments are prefabricated in the factory, excavation, support, lining and transportation are organized according to the assembly line. With a high degree of mechanization, it has the basis and advantages of intelligent construction. Therefore, research on intelligent construction technology of shield tunnel is of great significance for promoting intelligent and unmanned tunnel construction.

Qinghuayuan Tunnel of Beijing-Zhang High-Speed Railway is located in a densely built area of the city with a complex construction environment. In order to solve the problem of safe passage of large-diameter shield tunnel in dense buildings, China Railway Engineering Design and Consulting Group Co., LTD., together with Beijing Jiaotong University, China Railway 14th Bureau Group Co., LTD., China Academy of Railway Sciences and other units,

*Corresponding author: liujianyou2008@qq.com

DOI: 10.1201/9781003495505-384

carried out the research on intelligent construction technology of shield tunnel. The fully prefabricated assembly technology of shield tunnel has been formed, the intelligent assembly equipment has been developed, the visual intelligent management platform of shield tunnel has been developed, and the intelligent construction technology system of shield tunnel has been established.

In order to unify the technical standards for intelligent construction of railway shield tunnel, commissioned by China National Railway Group Co., LTD., China Railway Engineering Design and Consulting Group Co., LTD., chaired the preparation of Technical Guide for Intelligent Construction of Railway Shield Tunnel, which proposed classification methods and standards for intelligent construction of shield tunnel, laying a foundation for improving the intelligent construction level of railway shield tunnel.

This study clearly puts forward the principles and objectives of intelligent shield tunnel construction, and puts forward requirements for intelligent construction of railway shield tunnel from four aspects: survey, design, construction and construction management. In each aspect, the key process links as technical indicators, according to its degree of intelligence, divided into three levels, respectively, basic intelligence (level I), intermediate intelligence (level II) and advanced intelligence (level III). Therefore, the evaluation index system of shield tunnel intelligent construction is established, and on the basis of the research, the method and process of intelligent evaluation for the whole shield tunnel project are put forward.

2 THE BASIC MEANING OF INTELLIGENT CONSTRUCTION OF SHIELD TUNNEL

Intelligent construction of shield tunnel is to apply advanced technologies such as BIM, GIS, digital twin, visualization, artificial intelligence, 5G communication, prefabrication and assembly to the whole process of shield tunnel construction, and comprehensively improve the digitization, information and automation of shield tunnel in survey, design, construction and construction management. Intelligent decisions and responses should be made to various working conditions and construction risks to achieve safe, quality, rapid and efficient completion of tunnel construction tasks.

According to the actual situation and needs of the project, the intelligent level of the survey, design and construction of the shield tunnel should be predetermined before commencement, and the intelligent results should be evaluated during and after completion.

The intelligent construction level of shield tunnel can be determined according to construction objectives, construction conditions, tunnel characteristics, surrounding environment and other factors. Finally, the intelligent construction of shield tunnel should establish a visual intelligent management platform to realize the centralized and unified management of visualization, digitalization and intelligence in survey, design and construction.

3 THE BASIC REQUIREMENTS OF INTELLIGENT CONSTRUCTION OF SHIELD TUNNEL

3.1 *Survey requirement*

The overall survey work of intelligent construction of shield tunnel should meet the needs of the corresponding intelligent construction grade and provide basic geological data for each process of intelligent construction. The intelligence level and selection index of shield tunnel intelligent construction survey at each stage should be determined according to the actual situation and needs of the project, and the survey work at each stage should be based on the characteristics of shield method and the requirements of intelligent construction grade, so as to provide information support for predicting the impact of engineering activities on the surrounding environment. At the same time, the geological parameters required should be obtained according to the selection of the survey intelligence index and grade in each stage of the survey, so as to meet the needs of intelligent design and construction. The depth of work in each stage of reconnaissance, preliminary test, fixed test, supplementary test and construction survey is gradually increased from the front to the back, and the depth of the corresponding design stage is also gradually increased, and the survey accuracy of the survey work corresponds to the intelligence level, and the unnecessary selection of too high intelligence level in the early stage increases the unnecessary work burden. If the intelligent construction of shield tunnel has special requirements and needs to formulate detailed information model, special investigation or special research should be carried out.

In the investigation of intelligent construction of shield tunnel, the investigation plan and implementation rules should be formulated according to the site, surrounding environment, engineering characteristics and intelligent construction scheme, the geological conditions should be ascertained more accurately, the investigation data should be digitized and a 3D visual information model should be formed, whose scope, form and accuracy should meet the requirements of the predetermined intelligent construction level of investigation.

3.2 *Design requirement*

The intelligence level of the intelligent construction design division shall be determined in the feasibility study stage, the intelligent index of the intelligent construction design division shall be determined in the preliminary design stage, and the design scheme and implementation rules shall be formulated and implemented in accordance with the construction drawing stage. The construction mode of factory

prefabrication and on-site assembly should be adopted preferentially for the main body and auxiliary structure of shield tunnel, which is conducive to realizing the goal of intelligent construction. The influences of embedment depth, geology, surrounding environment, construction technology and other factors should be considered for the main prefabricated components of shield tunnel, and the structural strength, stiffness and stability should be calculated according to the construction stage and the normal use stage.

The intelligent design of shield tunnel should provide the three-dimensional model of prefabricated structure and the selection of shield machine to meet the requirements of the corresponding intelligent construction grade. Intelligent construction design of shield tunnel should adopt BIM forward design, and the accuracy of BIM forward design can meet the requirements of corresponding intelligent construction level, and establish a visual intelligent management platform.

3.3 *Construction requirement*

The intelligent index and grade of the intelligent construction division shall be determined comprehensively by the design unit according to the actual situation and needs of the project, and the construction unit shall, according to the implementation plan of intelligent construction, prepare the implementation rules for intelligent tunneling of the shield tunnel, allocate the necessary machinery (shield) equipment, and equip with intelligent construction software and relevant personnel. The intelligent tunneling construction of shield tunnel should include the matching of tunneling speed and construction group, geological conditions, deformation of risk source, the matching of palm surface pressure and ground deformation, and the linkage of tunneling and advance geological prediction. At the same time, it is necessary to determine the type of shield machine and its supporting equipment, as well as the shield machine starting, receiving and driving scheme. The implementation indicators of the intelligent construction scheme should be reasonably selected according to the project and the actual situation of the surrounding area, and it is not necessarily necessary to select all of them. The implementation rules of intelligent tunneling of shield tunnel should improve the process flow, realization means and control standards.

Finally, the intelligent tunneling construction of shield tunnel should establish the system of tunneling direction perception, comparison analysis of application groups, geological and risk source analysis, ground deformation analysis, advance geological prediction, and include it in the visual intelligent management platform.

3.4 *Management requirement*

The intelligence level of the construction and management division shall be comprehensively evaluated according to the indicators of monitoring measurement and risk control. The intelligent objective of monitoring and measurement should be determined according to the characteristics of the tunnel, construction conditions, surrounding environment and other factors. The requirements of intelligent monitoring and measurement level should be determined in the feasibility study or preliminary design stage, and the type of monitoring and measurement project, the number of sections and the layout method should be determined. An analysis and evaluation system should be established for intelligent monitoring and measurement, and it should be incorporated into a visual intelligent management platform. The statistical function of the data analysis and evaluation system should compare the data directly representing the tunnel state with the overlimit value specified by the existing code or the designed overlimit value to evaluate the tunnel state. The data analysis function of the analysis and evaluation system should realize the charting analysis of the data, and the data directly representing the tunnel state should be displayed through the temporal graphs and spatial distribution charts of stress, strain and displacement. The data analysis function of the analysis and evaluation system should carry out regression analysis on the temporal curve and predict the development trend. For different construction stages, segmental regression should be used for temporal curve fitting.

The risk management and control of intelligent construction of shield tunnel should be carried out in four stages: feasibility study, preliminary design, construction drawing and construction, and the corresponding intelligent indicators and levels should be selected according to the actual situation in each stage. Intelligent risk management and control should be based on monitoring data and combined with other intelligent functions to achieve intelligent risk assessment and dynamic control of construction process risks, and incorporated into the visual intelligent management platform.

4 CLASSIFICATION METHOD OF INTELLIGENT CONSTRUCTION OF SHIELD TUNNEL

Intelligent construction of shield tunnel is to make full use of BIM, GIS technology, digital twin, visualization technology, artificial intelligence technology, 5G communication technology, prefabrication and assembly and other advanced technologies, combined with shield machine. Intelligent objectives of shield tunnel should be determined according to tunnel construction objectives, construction conditions, tunnel characteristics, surrounding environment and other factors, and the overall intelligence of shield tunnel intelligent construction should be initially classified. Then, combined with the overall intelligent construction grade determined in the preliminary design stage, the intelligent level of four divisions (survey, design, construction and management) of shield tunnel intelligent construction should

be determined. Intelligent tunnel construction can be divided into I, II and III levels. Level I intelligence is the basic intelligence, should achieve automatic data upload, automatic sorting, manual analysis, manual decision, manual operation; Level II intelligence is intermediate intelligence, should achieve automatic data upload, automatic sorting, automatic analysis, automatic advice, assist manual decision-making, manual operation; Level III intelligence is advanced intelligence, should achieve automatic data upload, collation, analysis, automatic decision-making and operation.

The intelligent classification standard of shield tunnel is established based on the current technological development status, and the intelligent classification index and standard need to be adjusted according to the future development of artificial intelligence, communication, visualization, construction machinery, machine equipment and other technologies.

4.1 *Survey classification method*

Eight indicators are used to assess the intelligence level of intelligent survey work of intelligent shield tunnel construction. According to the technical accuracy and intelligence perfection of each single indicator, its intelligence level is divided into I, II and III levels. The survey results must be displayed in a three-dimensional digital information model to meet the needs of intelligence in subsequent stages, as shown in Table 1.

4.2 *Design classification method*

The intelligent evaluation of shield tunnel design division adopts 9 indicators. In addition to the traditional items such as shield machine type selection and structural design, intelligent segment design, BIM design and intelligent control design of tunneling process are highlighted, especially the specific

Table 1. Intelligent classification of shield tunnel investigation.

Serial number	Classification index	Level I	Level II	Level III
1	Remote sensing geological interpretation	The mapping scale is 1:50,000, and the spatial resolution should not be less than 10m.	The mapping scale is 1:50,000, and the spatial resolution should not be less than 5m.	The mapping scale is 1:50,000, and the spatial resolution should not be less than 1m.
2	Engineering geological mapping	Engineering geology and hydrogeology mapping should meet the accuracy of 1:10,000 topographic map.	Engineering geology and hydrogeology mapping should meet the accuracy of 1:2,000 topographic map.	Engineering geology and hydrogeology mapping should meet the accuracy of 1:500 topographic map.
3	Existing facility survey	Mainly identify the use of existing buildings (structures), geological diseases, foundation forms, foundation buried depth, etc., the numerical deviation shall not exceed 5m.	Mainly identify the use of existing buildings (structures), geological diseases, foundation forms, foundation buried depth, etc., the numerical deviation shall not exceed 2m.	Mainly identify the use of existing buildings (structures), geological diseases, foundation forms, foundation buried depth, etc., the numerical deviation shall not exceed 0.5m.
4	Stratigraphic lithology and stratigraphic boundary	The accuracy of the decision should not be less than 50%	The accuracy of the decision should not be less than 60%	The accuracy of the decision should not be less than 70%
5	Underground voids and obstacles	The accuracy of the decision should not be less than 50%	The accuracy of the decision should not be less than 60%	The accuracy of the decision should not be less than 70%
6	In-situ testing of formation physical property parameters	The accuracy of the decision should not be less than 50%	The accuracy of the decision should not be less than 60%	The accuracy of the decision should not be less than 70%
7	The physical parameters of formation were tested in laboratory	The accuracy of the decision should not be less than 60%	The accuracy of the decision should not be less than 70%	The accuracy of the decision should not be less than 80%
8	Survey results (required)	The three-dimensional geological information model is established, and includes information such as stratum number, stratum lithology, stratum boundary, geological time, degree of weathering, weathering boundary, basic bearing capacity, conventional parameters, groundwater development degree, type, surface water and groundwater erosiveness, bad geology, special soil and soil.	The three-dimensional geological information model is established, and includes information such as stratum number, stratum lithology, stratum boundary, geological time, weathering degree, weathering boundary, basic bearing capacity, conventional parameters, moisture degree, density state, groundwater development degree and type, surface water and groundwater erosiveness, bad geology, special soil, underground pipeline, etc.	Establish a 3D geological information model, which includes stratum number, stratum lithology, stratum boundary, geological time, weathering degree, weathering boundary, basic bearing capacity, conventional parameters, moisture degree, compaction state, geological origin, lithology description, groundwater development degree and type. Information of surface water and groundwater erosion, bad geology, special soil, underground pipelines, surrounding structures, etc.

Table 2. Intelligent classification of shield tunnel design.

Serial number	Single index	Level I	Level II	Level III
1	Single and double hole selection	Manual comparison	Program assisted manual selection	Intelligent comparison
2	Prefabricated structure (Required)	segment	Segment, rail structure	Segment, subrail structure, accessory structure, track structure
3	Intelligent design of segment structure	Automatically determine the wedge amount, automatically draw the ring three-dimensional map	Automatic wedge measurement, automatic segmentation, automatic drawing of three-dimensional segment segmentation	Automatic determination of wedge, automatic segmentation, automatic determination of detailed structure, automatic drawing of the three-dimensional structure of the segment
4	Intelligent design of shield tunnel profile	Automatic mapping of geology, mileage, slope; Automatic determination of segment type and auxiliary measures	Automatic mapping of geology, mileage, slope; Automatic determination of segment type, auxiliary measures, palm surface pressure, synchronous grouting pressure	Automatic mapping of geology, mileage, slope; Automatic determination of segment type, auxiliary measures, palm face pressure, synchronous grouting pressure, risk type and grade
5	Structural calculation	Three-dimensional structure calculation considering buried depth and geology	Three-dimensional structure calculation considering buried depth, geology and surrounding environment	Fine structure calculation considering burial depth, geology, surrounding environment and construction technology
6	BIM Design (Required)	Lines, strata, sections	Line, stratum, section, segment segmentation	Line, formation, section, segment segmentation, connection, reinforcement, waterproof and other details of the model
7	Dynamic design	Manual dynamic selection of palm surface pressure, synchronous grouting pressure, driving speed and other driving parameters, as well as risk measures	The program assisted the manual decision of the driving parameters such as palm surface pressure, synchronous grouting pressure, driving speed, and risk measures	The program intelligently decides the driving parameters such as the face pressure, synchronous grouting pressure, driving speed and risk measures
8	Shield machine selection	The software provides a list of shield machine types corresponding to the stratum, and manual selection	The software provides the list of shield machine types corresponding to strata, analyzes the pertinence and advantages and disadvantages, puts forward selection suggestions, and makes selection decisions manually	Software automatic analysis intelligent decision selection
9	Visual Intelligent Management Platform (Required)	Two-dimensional information display, shield real-time monitoring, construction video monitoring, monitoring data upload	3D information presentation, monitoring data and construction response prediction	Information display, forecast, dynamic feedback and information construction

requirements for intelligent visual intelligent management platform are put forward. Similarly, according to the degree of intelligence perfection, the intelligence level of each indicator is divided into I, II and III levels, as shown in Table 2.

4.3 *Construction classification method*

Construction is the core link of shield tunnel construction, which has many procedures, complex technology and high technical precision, and is a key part of intelligent construction. The construction process is further divided into five parts: shield equipment, component prefabrication, transportation and lifting, excavation construction, and prefabricated parts assembly. Each part is then divided into I, II and III levels according to its technical details or key process sequence as an evaluation index. Limited by space, only prefabricated parts assembly is taken as an example to illustrate the specific situation of intelligent classification, as shown in Table 3.

4.4 *Management classification method*

The intelligence level of the construction and management division shall be comprehensively evaluated according to the indicators of monitoring measurement and risk control.

(1) Monitoring and measurement of shield tunnel
The intelligence level of shield tunnel monitoring measurement can be divided into I, II and III levels according to 12 indicators, as shown in Table 4.

Table 3. Intelligent classification of shield tunnel prefabricated parts assembly.

Serial number	Classification index	Level I	Level II	Level III
1	Segment identification and selection	Manual selection, manual confirmation	Automatic selection, manual confirmation	Automatic selection and confirmation
2	Segment structure assembly	Manual detection of segment gap, misalignment, manual remote control adjustment assembly	Automatic detection of segment gap, misalignment, manual remote control adjustment assembly	Automatic detection of segment gap wrong table, automatic adjustment assembly
3	Positioning of underrail structure and auxiliary structure	Manual measurements assist positioning	Laser positioning	Automatic identification and positioning
4	Assembly of underrail structure and auxiliary structure	Mechanical manual auxiliary assembly	Manual remote control mechanical assembly	Mechanical automatic assembly
5	Underrail structure grouting	Manual grouting, manual testing	Mechanical grouting, manual testing	Mechanical grouting, automatic testing

Table 4. Intelligent classification of shield tunnel risk management and control.

Serial number	Classification index	Level I	Level II	Level III
1	Working well component stress #	Automatic measurement; Manual collection; Manual upload	Automatic measurement; Automatic collection; Manual upload	Automatic measurement; Automatic collection; Automatic upload
2	Formation deformation #	Automatic measurement; Manual collection; Manual upload	Automatic measurement; Automatic collection; Manual upload	Automatic measurement; Automatic collection; Automatic upload
3	Pressure behind segment #	Automatic measurement; Manual collection; Manual upload	Automatic measurement; Automatic collection; Manual upload	Automatic measurement; Automatic collection; Automatic upload
4	Segment reinforcement stress #	Automatic measurement; Manual collection; Manual upload	Automatic measurement; Automatic collection; Manual upload	Automatic measurement; Automatic collection; Automatic upload
5	Segment stress #	Automatic measurement; Manual collection; Manual upload	Automatic measurement; Automatic collection; Manual upload	Automatic measurement; Automatic collection; Automatic upload
6	Segment working seam change #	Automatic measurement; Manual collection; Manual upload	Automatic measurement; Automatic collection; Manual upload	Automatic measurement; Automatic collection; Automatic upload
7	Water table #	Automatic measurement; Manual collection; Manual upload	Automatic measurement; Automatic collection; Manual upload	Automatic measurement; Automatic collection; Automatic upload
8	Surface, road, underground pipeline settlement *	Manual measurement; Manual collection; Manual upload	Automatic measurement; Automatic collection; Manual upload	Automatic measurement; Automatic collection; Automatic upload
9	Deformation of structures (building)*	Manual measurement; Manual collection; Manual upload	Automatic measurement; Automatic collection; Manual upload	Automatic measurement; Automatic collection; Automatic upload
10	Tunnel deformation *	Manual measurement; Manual collection; Manual upload	Automatic measurement; Automatic collection; Manual upload	Automatic measurement; Automatic collection; Automatic upload
11	Work well deformation *	Manual measurement; Manual collection; Manual upload	Automatic measurement; Automatic collection; Manual upload	Automatic measurement; Automatic collection; Automatic upload
12	Analysis and evaluation system	Data statistics, early warning	Data statistics, early warning and analysis	Data statistics, early warning, analysis and recommendations

Table 5. Intelligent classification of shield tunnel risk management and control.

Serial number	Classification index	Level I	Level II	Level III
1	Risk identification	The program automatically identifies single-factor risks	The program automatically identifies single-factor risks and multi-factor combination risks	The program automatically identifies single factor risk and multi-factor combination risk, and gives the probability of risk occurrence
2	Risk classification	Manual classification	Program aided manual grading	Automatic program grading
3	Risk countermeasure	The program automatically puts forward a list of risk countermeasures and makes decisions manually	The program automatically puts forward risk countermeasures and suggestions, and makes decisions manually	The program automatically puts forward risk countermeasures and analyzes the effect of risk control

(2) Risk control of shield tunnel
The intelligence level of shield tunnel risk management and control can be divided into I, II and III levels according to three indicators, as shown in Table 5.

5 INTELLIGENT SHIELD TUNNEL CONSTRUCTION VISUAL INTELLIGENT MANAGEMENT PLATFORM

Visual intelligent management platform refers to a visual network management platform for collaborative operation and intelligent decision-making based on a unified information cloud platform and a variety of intelligent information integration methods to achieve intelligent construction of railway shield tunnel. At present, the existing railway tunnel construction management system is mainly for construction units. The visual intelligent management platform is a visual unified network management platform of multi-professional cooperation established by applying BIM technology, and carries out systematic management of intelligent tunnel construction. This platform can realize the real-time display of various horizontal profile information, construction video, monitoring data, shield machine parameters, surrounding environment monitoring and other projects; Construction management can optimize and adjust the tunneling parameters, construction organization and risk response measures of shield tunneling machine on this platform. Construction management can carry out progress control, inspection and pricing, quality acceptance and other work on this platform; After the completion of the project, the platform can be used as the basic platform for maintenance and management.

The visual intelligent management platform can realize a series of intelligent requirements, such as: real-time display of the construction progress of each shield machine, detailed record of the comparison between the preset progress and the actual progress of shield construction and the overall completion, statistical analysis of the progress information, and output visual graphics and corresponding reports, as shown in Figure 1. The construction progress indicators of each shield machine can be set within the scope of management authority, and the early warning can be achieved through information push when the progress is abnormal, as shown in Figure 1. The construction parameters of each shield machine in the construction process are displayed in real time, and the manager can realize the remote real-time monitoring of the shield construction process. In the form of time period, the data of material consumption, efficacy, number of advancing rings and mileage in the shield construction process are counted and queried, and can be output in the form of reports. It can upload and download the settlement data of the measuring point, support the query of the accumulated settlement amount and settlement rate curve of single point settlement and multiple settlement points, and output it in the form of a report to push the abnormal data. Empirical formula method, artificial intelligence method, big data processing method and refined numerical modeling methods can be used to analyze the whole process of shield construction based on engineering geological data, construction parameters and monitoring data, so as to obtain the prediction and early warning value of formation deformation during construction and feedback adjustment of later shield construction and a series of reinforcement measures. The plane and section influence areas of risk sources at all levels in each shield section can be displayed by plane plan or three-dimensional model.

Finally, after the completion of the shield tunnel, the construction unit should organize the design, construction, supervision and other units to evaluate the intelligent results. The result evaluation should include the overall intelligent evaluation of the project, as well as the intelligent evaluation of each branch of survey, design, construction and construction management. The scope and items of intelligent results acceptance shall be accepted and evaluated

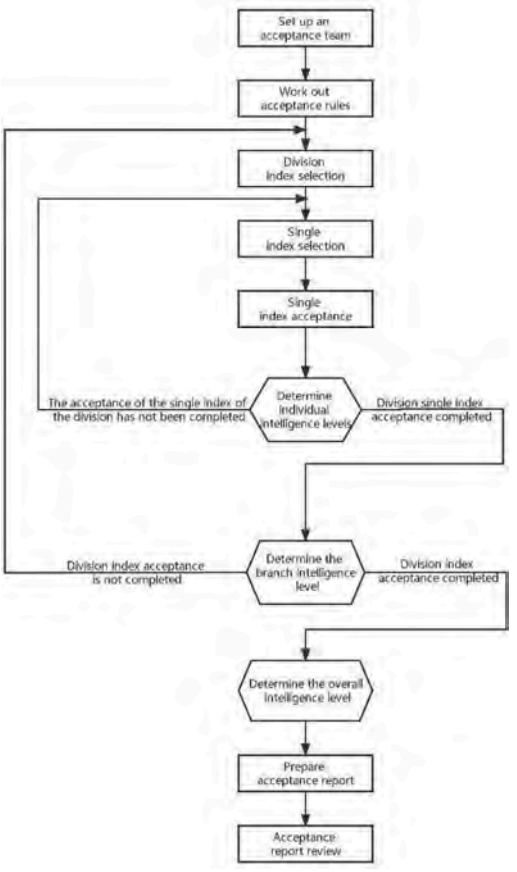

Figure 1. Acceptance process of intelligent achievement of shield tunnel.

item by item according to the intelligent construction implementation plan determined at the construction drawing stage. The acceptance of intelligent results should include the intelligent evaluation indicators proposed in the implementation plan of intelligent construction. The acceptance of intelligent results can be divided into three levels: comprehensive index, partial index and single index. The intelligent management platform can form acceptance reports and transfer them to operation and maintenance. The acceptance of intelligent results should first evaluate the intelligence level of a single index, and comprehensively evaluate the intelligence level of the division index based on all the individual indicators of the division, and comprehensively evaluate the overall intelligence level of the project based on the intelligence level of all the divisions. The acceptance process is shown in Figure 1.

6 ECONOMIC BENEFIT ANALYSIS

The expected increase in the cost of intelligent construction of shield tunnel is mainly reflected in the survey, design, equipment, component prefabrication, transportation and lifting, excavation construction, assembly construction, monitoring and risk control, etc. The increased cost is mainly used for equipment transformation and software development.

The intelligent realization of shield tunnel can greatly reduce labor consumption and save labor cost. Improve the construction efficiency and reduce the construction period; Improve construction safety and reduce accident risk; Improve construction quality and increase quality benefit; Improve the working environment and increase environmental benefits.

To sum up, equipment transformation and software development in the early stage of intelligent construction of shield tunnel will increase a certain cost, but in the later stage, huge benefits will be achieved by reducing labor, improving efficiency, ensuring safety, improving quality and improving the environment, and the overall benefits will far exceed the increased costs.

7 CONCLUSION AND PROSPECT

This paper puts forward the idea of intelligent classification of railway shield tunnel for the first time, puts forward the principles and objectives of intelligent construction of shield tunnel, establishes the evaluation system and evaluation method of intelligent construction, and establishes the classification standard of intelligent construction of shield tunnel. The basic requirements of intelligent construction survey, design and construction of shield tunnel are clarified. This paper mainly discusses the following points:

(1) The basic requirements, implementation schemes and detailed rules of four sub-divisions of intelligent construction of railway shield tunnel, namely, survey, design, construction and construction management are discussed in detail.
(2) The classification method of intelligent construction of railway shield tunnel is proposed, and the intelligent classification evaluation system and evaluation standard are constructed.
(3) Establish an intelligent management platform, realize the visualization of intelligent construction, and carry out systematic management of intelligent tunnel construction.

This paper discusses in detail the basic requirements, implementation plans and rules of the four branches of intelligent construction of railway shield tunnel: survey, design, construction and construction management, summarizes the intelligent classification method of intelligent construction of shield tunnel, establishes a visual intelligent management platform, and provides a broad space for the practice of new technologies, new methods, new equipment and new ideas in intelligent construction of tunnel.

REFERENCES

Tian Siming, Gong Jiangfeng. Statistics of railway tunnels in China up to the end of 2019 [J]. Tunnel Construction, 2020, 40 (2): 1–6.

Gong Jiangfeng, Wang Wei, Zhou Junchao. Statistics and analysis of railway shield and TBM tunnels in China by the end of 2021 [J]. Railway Standard Design, 2022, 66(03):1–5.

Wang Tongjun. Research on Development Strategy of Intelligent High-Speed Rail in China [J]. China Railway, 2019 (1): 9–14.

Wang Tongjun. Overall structure and development prospect of Intelligent Railway [J]. Railway Computer Applications, 2018, 27 (7): 1–8.

He Huawu, Zhu Liang, Li Ping, etc. Research on Intelligent High-speed Rail System Framework [J]. China Railway, 2019 (3): 1–8.

Wang Feng. Development practice and Prospect of intelligent construction technology for high-speed railway in China [J]. China Railway, 2019 (4): 1–8.

Zhao Yong, Lu Gang, Liu Jianyou, Liu Fang. Innovation and Application of Key Technologies in Construction of Qinghua Garden Tunnel on Beijing-Zhang High-Speed Railway [J]. Railway Standard Design, 2020,64 (01): 109-115+136.

Lu Gang, Liu Jianyou, Zhao Yong, Liu Fang, Wang Zhiwei.Precast assembly technology of Under-Rail structure of Tsinghua Park Tunnel on Beijing-Zhang high-speed railway [J]. Tunnel Construction, 2019, 39 (08): 1357–1364.

Technical Guide for Intelligent Construction of Railway Shield Tunnels: Q/CR 9255-2023 [S]. Beijing: China Railway Press Co., Ltd., 2010.

Lu Gang, Liu Jianyou, Zhao Yong, Yue Ling. Intelligent construction technology of Beijing-Zhangzhou high-speed railway tunnel [J]. Tunnel Construction, 2021, 41 (08): 1375–1384.

Wang Tongjun. Evolution of Railway Tunnel Construction Method and Technical System and Prospect of Intelligent Construction [J]. China Railway, 2020 (3): 1–11.

Wang Zhijian Research and Prospect on Intelligent Construction Technology of Zhengzhou-Wanzhou High-Speed Rail Tunnel [J]. Tunnel construction (English and Chinese), 2021, 41 (11): 1877–1890.

Chen Dang, Liu Zai, Liu Jianyou, Fang Qian, Hai Lu. Current situation and Prospect of intelligent construction technology for railway shield tunnel [J]. Tunnel construction, 2021, 41 (06): 923–932.

Tunnelling for a Better Life – Yan, Celestino, Thewes & Eberhardt (Eds)
© 2024 The Author(s), ISBN 978-1-032-80042-4
Open Access: www.taylorfrancis.com, CC BY-NC-ND 4.0 license

The interface between construction site and Tunnel Information Model: The case of the Brenner Base Tunnel

David Marini* & Giuseppe Venditti
BBT SE, Bolzano, Italy

ABSTRACT: The Brenner Base Tunnel is a complex tunnel system and it will require a suitable virtual twin once it becomes operational. In order to achieve this, a Tunnel Information Model of the underground civil works under construction was created, showing the final linings for both mechanised and D&B excavated sections. The correct identification of the level of information required and close cooperation with the construction site are essential elements for this type of virtual reconstruction. A case of synergistic collaboration with the construction phase is seen, for example, with regard to TBM excavation, in which information from the boring machine itself is used for the installed rings. The purpose of this abstract is to present the Information Model approach used for the Brenner Base Tunnel, a strategic project for the future of Europe and the longest underground railway project in the world upon its completion.

Keywords: Brenner Base Tunnel, Tunnel Information Model, TBM excavation, complex tunnel system

1 INTRODUCTION

The Brenner Base Tunnel (BBT) is a flat railway tunnel that connects two States and is the central part of the new Munich-Verona railway corridor, along the extended Scandinavian-Mediterranean corridor within the European

TEN-T transport network. It stretches between Innsbruck (Austria) and Fortezza (Italy) for a total length of 64 km (including the Innsbruck bypass) and will be the longest underground railway link in the world.

The BBT is a complex system of tunnels with a total length of almost 230 km, of which more than 160 km have been completed to date, the main works being the two-line tunnels and the exploratory tunnel (see Figure 1).

It will offer a viable alternative for freight transport and will create a new travel opportunity for passenger traffic.

It is truly a European project, as is shown by the strong confidence the European institutions have shown in this infrastructure project. To date, the European Union has already allocated more than € 1.6 billion to the project, covering 50% of the costs for design and exploration activities and 40% of the costs for construction activities.

Thanks to the new € 700 million tranche of European funding from the Connecting Europe Facility (CEF) European co-financing programme, which BBT SE was able to access following the positive assessment from the European Commission within a recently published call for tenders, all project costs are now borne equally by the European Union (50%) and the two states of Italy and Austria (25% each). The implementation of innovative and forward-looking systems, such as a Tunnel Information Model (TIM) contributed to the positive assessment on the part of the European Commission.

2 OBJECTIVE OF THE TUNNEL INFORMATION MODEL

The objective of the Information Model of the Brenner Base Tunnel project is the digital and information management of the railway infrastructure including civil works, railway superstructure and technological equipment. The Tunnel Information Model (TIM) is methodically integrated into the documentation system of civil and technological works with a transnational view of the project. This requires the setting up of a Project Information Model (PIM), developed during the design (see Figure 2) and construction phases of the different construction lots.

In this specific case, then, we have a TIM generated by the uniform management of information and

*Corresponding author: david.marini@bbt-se.com

DOI: 10.1201/9781003495505-385

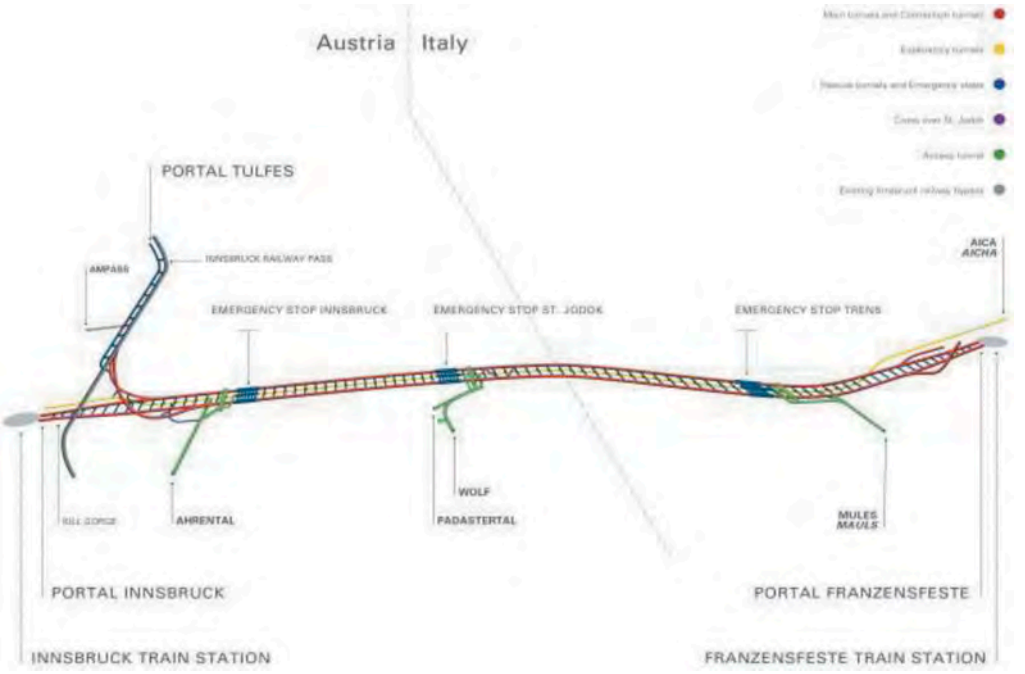

Figure 1. Diagram of the Brenner base tunnel system.

Figure 2. Emergency stop model.

data for the railway outfitting and railway operation phase. The methods applied for the BBT comply with the latest regulatory developments for BIM in Italy and Austria. The consequent improvement in transnational communications also improves and increases the transparency and quality of the project.

The comprehensive and unified management of information and data on the main tunnels leads in the long term to optimised maintenance and fewer breakdowns due to continuous preventive maintenance, as well as fewer disruptions to rail traffic during the operational phase.

3 THE CONSTRUCTION SITE

The construction of the Brenner Base Tunnel requires a careful choice of type sections able to support the stresses induced by excavation. In particular, depending on the excavation method, a final lining consisting of a ring of prefabricated tubbing rings and/or a final lining of cast-in-place concrete is used (see Figure 3).

Figure 3. Final lining, change from single track to double track.

Sections excavated with conventional methods require the final cast-in-place lining with a suitable waterproofing and drainage system.

In excavations with conventional methods, the installed waterproofing system consists, from the outside of:

- levelling layer for the waterproofing;
- dimpled membrane drainage elements supporting the geotextile protection layer;
- protective geotextile with a minimum weight (of 900 g/m²;
- waterproofing sheathing in polyvinylchloride PVC-P or composite geotextile° (see Figure 4);
- PVC protection membrane (or protective layers in the reverse arch);
- Internal and external PVC-P transition strips and elastomer waterstops with steel side seams.

Figure 4. Waterproofing of the dome area for conventional excavation sections.

Depending on the type of structural element, the stretch of the tunnel and the concrete exposure class, stretches excavated using conventional methods mainly require the use of the following compressive strength classes:

- foundations, base slab and invert: C30/37 – C32/40.
- dome: C30/37.
- precast concrete segmental rings: C50/60.

The main components of the concrete used are briefly described below:

- Cement: given the need to guarantee the durability of the work for 200 years, extremely high-performance mixes have been developed to guarantee very low permeability and high resistance to carbonation and chemical attack. Among the various exposure classes, special care was devoted to designing the mixes that must guarantee resistance to sulphate attack, which may only contain cement with a typical maximum content in clinker of 0% C3A (Tetracalcium Aluminate), which can therefore be defined as free of C3A.
- Additives:additives are provided to further increase the performance of the concrete.
- Aggregates:in the Brenner Base Tunnel project, particular importance was given to the environmental impact of producing aggregates to be recycled. If the excavated rock meets the necessary suitability requirements, it is screened and processed in crushing plants.

The prevention of chemical attacks on the concrete has been a particular area of interest. Depending on the type of structural element and the chemical composition and reactivity of the groundwater, assessed in terms of sulphate content, pH, aggressiveness, ammonium content, mercury content and water hardness, exposure classes (XA1, XA2, XA3) which are resistant to chemical attack has been used.

In particular, with reference to the chemical parameters listed above, ranges of values were identified and, based on expectations, a minimum exposure class was associated with each of them. The overall exposure class of the concrete is chosen based on the class associated with the most restrictive parameter.

For sections with emergency evacuation features, highly fire-resistant concrete (CF-ERF) has been used. In addition to the characteristics specified for ordinary concrete in the executive design, the mixture has a polypropylene fibre content. The addition of fibres provides a stiffer and more viscous consistency which can generally be evened out by adding fluidifying additives.

For mechanised excavation in Italy, the lining in the main tunnels consists of a universal type ring composed of 6 ordinary elements plus a keystone. Longitudinally, the tubbing rings are approximately 1.75 m long and 45 cm thick (see Figure 5). The introduction of a universal ring meant the adoption of a monolithic element was created, thus reducing the risk of openings between the joints and guaranteeing better sealing against water infiltration, with a consequent increase in overall performance.

Figure 5. Tunnel lining with universal tubbing rings.

For increased precision in installing the tubbing ring linings, PVC guide bars were installed in the

longitudinal connections between the rings. In order to waterproof the longitudinal joints and the areas between the individual rings of the lining, seals with elastomeric profiles were installed, where necessary, both on the inside and on the outside of the tubbing ring. The longitudinal connection and the alignment between the rings are ensured by means of longitudinal connectors. The connection systems are equally spaced along the circumference and positioned in the middle of the thickness of the tubbing rings.

With regard to the main tunnels, the characteristics of the concrete change depending on whether the tubbing ring is a base slab tubbing ring or part of the ring system. In particular: for the base slab tubbing rings the concrete class C30/37, exposure class XC3/XA1, maximum aggregate size 22 mm and slump S4 is used; for the tubbing rings which are part of the ring system the concrete class C50/60, exposure class XC4/XA2, maximum aggregate size 22 mm and slump S4 is used.

Along the sections excavated by TBM, performance-related and geometric requirements have shown the advisability of using a so-called double lining, i.e. consisting of precast concrete segmental rings and a final concrete lining. Double lining is foreseen in fault zones, in areas where groundwater is particularly aggressive, and in sections that play an important role in case of emergency evacuations (emergency stops, etc.).

4 THE FINAL CIVIL WORKS WITHIN THE MODEL

The different typological sections were developed in such a way as to obtain parametric 3D extrusions that could in turn be used in a versatile manner for the various tunnel sections.

To better meet operational requirements, the modelling was divided into global modelling and typological modelling. Global modelling shows what was actually executed on site and is reported in a unitary federated file (see Figures 6 and 7).

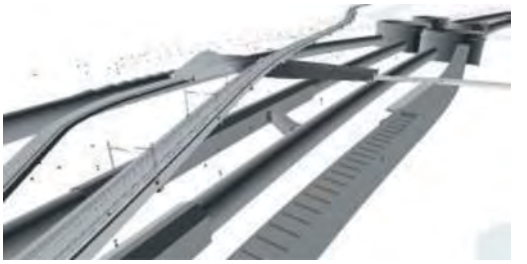

Figure 6. Federated as-built model of the construction lot isarco river underpass.

The global models, besides being a real representation of the finished product, contain specific information on the finished works, such as start and end of casting progressions, mixed-design used, performance characteristics of the cast concrete with the pertinent exposure classes for the different types of works (dome, inverted arch, etc.), non-conformities, technical changes and hyperlinks to the technical documents saved on BBT SE's CDE (see Figure 8). Geological, geotechnical and monitoring information is also present in the global model.

For a better representation of the details of the various section types of the final lining, type models were created which do not contain site-specific details (such as the start and end chainages contained in the global model) but more construction-specific details, such as waterstops, waterproofing layers, geotextiles, etc. (see Figure 9).

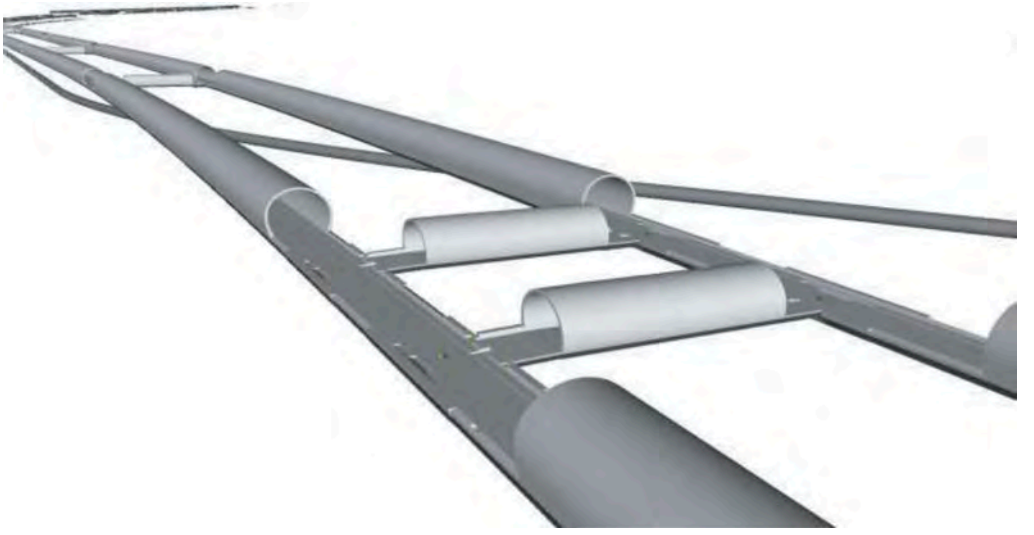

Figure 7. Federated as-built model of the construction lot Mules 2-3 between Mezzaselva and Mules.

Figure 8. Example of global model with an overlay of the laser scan performed on site.

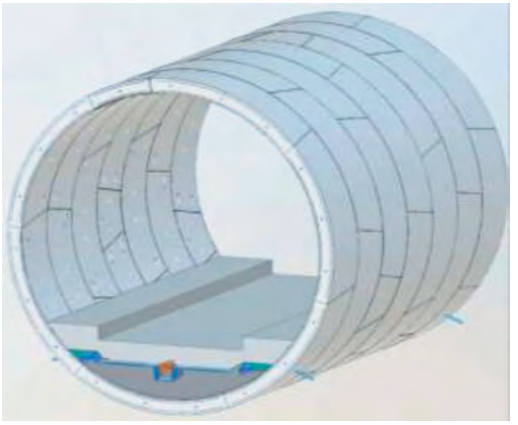

Figure 9. Typological model of the mechanized excavation model.

More specifically, from the modelling of two-dimensional families using generic metric models, we move on to nesting within the generic metric model, using two adaptive points and two reference points. With adaptive points, the sections on the route can be extruded based on the chainages and thus the actual geographical coordinates, whereas with reference points the sections on the route can be seen with the proper rotations.

The adaptive families themselves contain the shared parameters as stipulated by the pertinent level of information needs (see Figure 10).

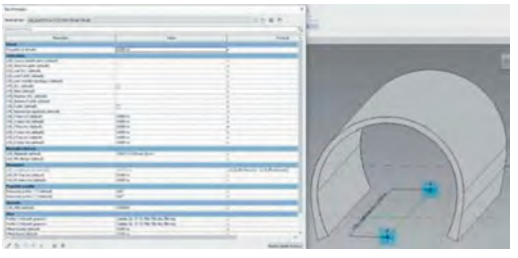

Figure 10. Parametric family pertaining to the dome, for excavation with conventional methods.

In this way, in the adaptive model family, it is possible to assign length and rotation parameters for both two-dimensional profiles, parameters which in turn are calculated directly by visual programming scripts according to the coordinates of the route and with respect to the actual casting lengths executed on site.

Having obtained the three-dimensional sections of each individual element necessary to obtain the federated model (domes, arches, walls, intermediate slabs, side fills, sub-bases, ground and platform pipes, gravel), the modelling of the tunnel sections proceeds by automating the process through visual programming codes.

In this particular case, the code:

- imports the x, y, z coordinates of individual cast sections;
- creation of adaptive points on which to create the segments;
- calculation of the rotations of the start and end profiles of each single cast element;
- extrusion of the ring segment casting as a function of the start and end chainages with the standard section used on site;
- populating the information attributes and document set in each element as required by the level of information need.

For the mechanised excavation of the line tunnels of construction lot H61 Mules 2-3, the type of machine adopted is a double shield TBM, with an excavation diameter of approximately 10.7 m for a section of approximately 14 km for each machine.

The positioning of each individual ring element has been respected, keeping to the assembly diagrams provided for by the project and consistent with the positioning data from the machine's navigation system (VMT). The main data concerns the position of keystone element A. Knowing the position of the key segment from the VMT and knowing the number of possible positions (19 assembly schemes from the design for the line tunnels), it was possible to determine the positions of the remaining ring elements analytically, by automating everything through visual programming scripts (see Figure 11).

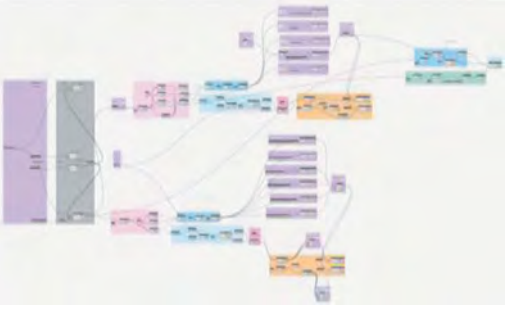

Figure 11. Overview of the script for generating a local model.

Knowing the coordinates of the route and the position of the ring segments and knowing the number of rings between two chainages, modelling proceeded using dedicated scripts according to the route and the related populating of information and document set as per the level of information need (see Figure 12).

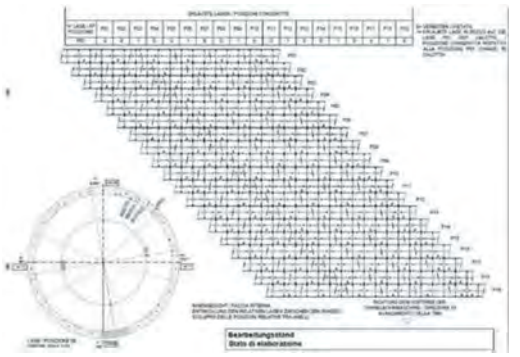

Figure 12. Diagram of precast concrete segmental rings positioning.

For each individual precast concrete segment, for information purposes, its identification code was included as parametric information in the digital model, which allows to trace the production history (see Figure 13).

Figure 13. 6+1 prefabricated segments forming a ring.

5 TECHNOLOGICAL EQUIPMENT AS PART OF THE MODEL

Technological equipment will also play an important role in the Brenner Base Tunnel project in BIM modelling. The information management plan currently drawn up for the final design phase provides clear information on the requirements for the railway superstructure, the electric traction systems, the command and control systems, the mechanical systems, etc. (see Figure 14).

BBT SE's goal is to achieve a unified and complete model which contains both the specialised models for the civil works and specific systems, and the information related to technological equipment.

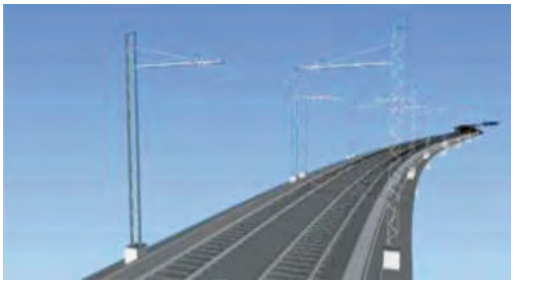

Figure 14. Modelling the railway infrastructure in the open-air section.

6 THE SYNERGETIC FLOW OF DATA TO/ FROM THE CONSTRUCTION SITE

The different information requirements included in the model are identified a priori according to the requirements that arise both during the construction phase of the work as well as during its operation, differentiated for sections built using conventional and mechanised excavation methods, and included in the pertinent information and documentation set.

Thanks to the modelling of the individual concrete cast segments and the precast concrete segmental rings installed by the boring machine, the individual non-conformities (NC) are introduced in the exact detection position, as well as technical modification requests received during construction.

This document set than can be viewed in the modelis connected to the Common Data Environment (CDE) of the project.

A case of synergetic collaboration with the construction phase becomes particularly efficient with regard to the advancement of the TBMs. In the ring segments installed by the TBM, an information set from the excavating machine itself is recorded. These include both information sets in relation to position data (progression, position of the ring segment, etc.), as well as physical and mechanical parameters recorded directly by the tunnel boring machine during excavation (see Figure 15).

Figure 15. TPC command and control screen of the TBM in the Mules 2-3 lot.

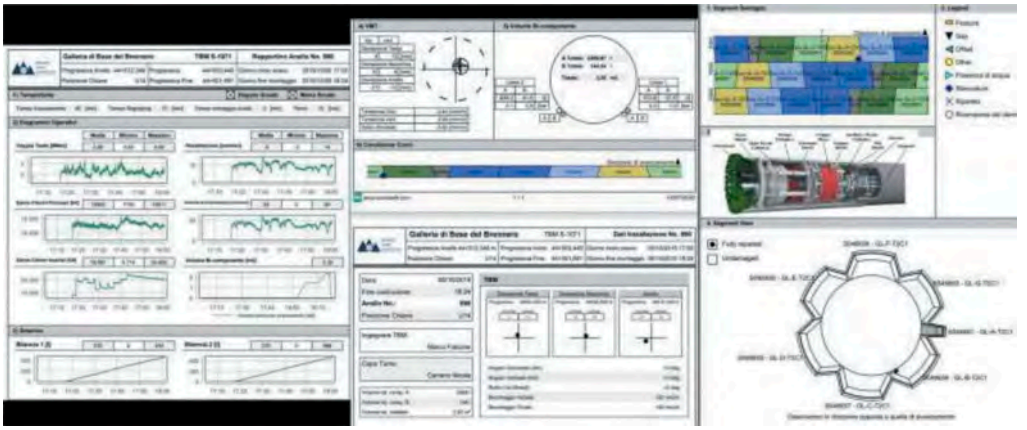

Figure 16. Ring report of a precast concrete segmental ring.

These parameters, acquired approximately every three seconds by the TBM, constitute an effective system for monitoring the condition of the rock mass. Therefore, they are of importance within the project information model. These parameters can be seen in the ring report in the model, and they include: head torque (MNm), penetration (mm/revolution), average spoil weight (t), pea gravel quantity (m^3), horizontal and vertical ring deviation (mm), main and auxiliary cylinder thrust (kN), excavation speed (mm/min) (see Figure 16).

In addition, machine parameters trends are cross-referenced with data from point surveys to define their behaviour as a function of geology. Therefore, in the specific case of the mechanised excavation of the Exploratory Tunnel, the modelling of the TBM segments is supported by the input of reports from the advance drilling.

Core drilling is carried out in the most geologically, geomechanically and hydrogeologically critical portions of the route.

In addition to forward drilling surveys, reports from tunnel face mapping are also put into the model. Geological documentation, which consists of surveys, is of fundamental importance in interpreting some of the measurements that are recorded by TBMs.

The tunnel face mapping carried out on site provides the RMR (Rock Mass Rating) index, always included in the TIM for each chainage survey, which allows the rock to be classified through a score after analysing certain parameters (see Figure 17).

Figure 17. Excavation tunnel face mapping report.

The synergetic flow of data to and from the construction site leads to other information needs, including, by way of example:

- strain-gauge bar monitoring: measurements of deformation/strain on the first-phase lining (shotcrete and ribs) using 5 pairs of vibrating-wire strain-gauge bars welded to the ribs and embedded in the shotcrete;
- load cell monitoring: measurement of deformation/strain on the first-phase lining (shotcrete and ribs), by means of 2 load cells placed below the base of the ribs;
- bolt load sensor monitoring: measurement of the deformations of the rock mass on the contour of the excavation using five radially arranged bolt load sensors;
- convergence monitoring: convergence of 5 reflective targets on temporary shotcrete lining or 2 targets on footings.

All of these data flow into the level of information need, depending on the specific works and the section of the tunnel, according to the latest standards, including ISO 19650 and EN 17412.

7 CONCLUSIONS

For strategic infrastructures such as the Brenner Base Tunnel, a Tunnel Information Model is essential for easier management of the innumerable data generated during construction which can thus be consulted over time, and such a model is also easy to use. In this way, the history of the structure can be tracked throughout its life cycle, which is an effective tool during the operational phase.

ACKNOWLEDGMENTS

We would like to express our sincere thanks to BBT SE CEOs Gilberto Cardola and Martin Gradnitzer, both for their willingness to share the technical experience of the Project and their support of our

active participation in international events in our sector. Our thanks also go to Lisa Terzariol for the translation of this article.

REFERENCES

[1] Marini D., Venditti G., 2022. Tunnel linings made of precast concrete segmental rings - from design choice to installation and performance; Expanding Underground - Knowledge and Passion to Make a Positive Impact on the World, pp. 1346–1356: ISBN 978-1-003-34803-0

[2] Marini D., Catapano M., Squillante A., 2023. The Tunnel Information Model for strategic infrastructure works; CIFI – Ingegneria Ferroviaria 11/2023

Tunnelling for a Better Life – Yan, Celestino, Thewes & Eberhardt (Eds)
© 2024 The Author(s), ISBN 978-1-032-80042-4
Open Access: www.taylorfrancis.com, CC BY-NC-ND 4.0 license

Integrated design of precast concrete linings for mechanized tunnels

Alessandro Menozzi*, Beatrice Tiberi, Daniele Maturi & Roberto Comini
SYSTRA SWS, Trento, Italy

ABSTRACT: Nowadays, metro tunnels represent probably the most sustainable solution for an efficient and environmental-friendly urban transportation, ensuring an optimized use of available land and fostering the development of green livable cities. In this context, mechanized tunnel has become one of the best construction practices, guaranteeing high productivity, safe working environment and small induced surface settlements causing minimal damage to existing buildings.

Considering the cutting-edge digital technologies rapidly evolving in the world of civil infrastructures, an innovative approach has been conceived for the integrated design of precast segmental linings. The developed tool uses basic input data like tunnel alignment and diameter, segments layout and geotechnical profile, to generate the BIM tunnel geometry and the required FEM/DEM structural and geotechnical models.This paper presents the meaningful case study of Grand Paris Metro Line 14, Lot 4, which implements this integrated design strategy and provides an optimized metro tunnel design, overcoming the typical limitations of traditional approaches.

Keywords: BIM technologies, Segmental Lining, Mechanized Excavation, Advanced Simulation

1 INTRODUCTION

Mechanized excavation represents one of the most reliable solutions for tunnels in urban environment. As a matter of fact, this technology is a "unicum" in the world of civil infrastructures, due to the industrialization and standardization of the implemented processes (i.e., segments prefabrication, transportation and installation, TBM driving parameters, implementation of innovative accessories). Furthermore, compared to conventional excavation, TBM-driven tunnels radically reduce construction time, guaranteeing not only a safe and confined working environment, but also an effective quality control.

The integrity of TBM-excavated tunnels mainly relies on their segmental lining, which is obtained by a sequential arrangement of concrete segments adopting a staggered layout for longitudinal joints, in order to guarantee overall stability of the system. This specific structural arrangement activates the typical behavior of reciprocal structures, studied for the first time by Leonardo da Vinci about 500 years ago (Da Vinci, 1519; Da Vinci, 1505).

In this context, an accurate design is fundamental to achieve the expected results in terms of organization and economy of the whole construction process. As in all industrial productions, in fact, the manufacture of segmental lining components is turning into a more and more standardized and refined production chain, implying a non-stop research for time and cost optimizations.

Nowadays, engineers are thus required even more than in the past for a 360-degree integrated knowledge not limited to structural and geotechnical design, but extending to fabrication stages and associated cutting-edge technologies fostering a continuous improvement in the quality and efficiency of the entire process.

1.1 *Traditional design approaches*

The conventional design of tunnel linings has traditionally followed two main approaches (Figure 1): the continuum model and the unidimensional model (hereinafter referred to as "geotechnical" and "structural" models).

The former simulates ground behavior by means of 2D plate elements and concrete lining via continuous beam elements with appropriate axial and bending stiffness. Often, these models also implement contact elements to manage ground-structure interaction.

Unidimensional or structural models, on the other hand, simulate the lining by continuous beam elements: the ground support is accounted for by using compression-only springs, while ground pressure is applied via distributed loads. The second approach allows defining ground loads acting on the lining without the need for a dedicated geotechnical model, as loads can be either obtained by closed-form solutions (Terzaghi, Beniawski, etc.) or by the convergence-

*Corresponding author: amenozzi@systra.com

DOI: 10.1201/9781003495505-386

confinement method. This "beam-spring" model is thus very practical when dealing with multiple load cases (i.e. shrinkage, temperature, traffic, etc.).

Both structural and geotechnical approaches must account for the 3D coupling of consecutive rings and the associated bending moment migration between segments joints, which is a typical behavior of reciprocal structures. This effect is generally addressed in the analysis through an equivalent reduction of lining bending stiffness, according to Muir Wood theory (Wood, 1975):

$$M_0 = M + \xi M = (1 + \xi) M$$

$$M_1 = M - \xi M = (1 - \xi) M$$

$M = (\mathrm{M_0} + \mathrm{M_1})/2$: is the moment calculated with uniform reduced flexural rigidity

$\mathrm{M_2} = \xi \mathrm{M}$: is the design moment transferred to adjacent rings

$\mathrm{M_0} = \mathrm{M} + \mathrm{M_2}$: is the design moment for segments

$\mathrm{M_1} = \mathrm{M} - \mathrm{M_2}$: is the design moment for joints.

The design bending moments for segments (M_0) and joints (M_1) are thus obtained applying the amplification (1+ξ) and reduction (1-ξ) factors to the calculated stress resultants. The main limitation of this approach is related to the correct definition of the redistribution coefficient ξ, which is still too subjective (Pescara and Osgoui, 2014).

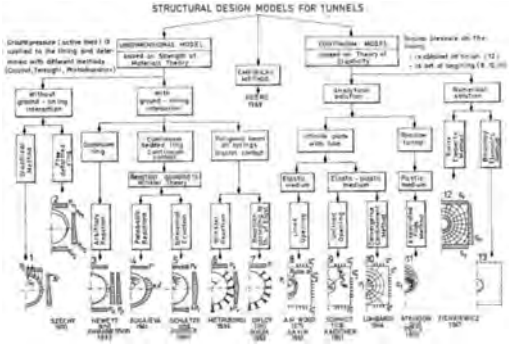

Figure 1. Literature overview of the most accredited traditional analytical models (Iftime, 1994).

1.2 *A new design approach*

Nowadays, the new horizon in civil engineering is represented by the effective implementation of digital technologies, with the aim of developing the so called "Digital Twin" of the infrastructure. This novel design process is strongly characterized by interoperability and collaboration, requiring BIM modeling, implementation of a dynamic and flexible database (conceived to acquire, organize and manipulate data coming from models and processes, in order to perform closed-form analyses and implement automated simulations) and systematic use of nonlinear FE models.

The next sections present in more details the integrated approach implemented and experienced by the authors during their daily engineering practice, and some successful applications within large infrastructure projects.

2 DIGITAL PROJECT - INTEGRATED DESIGN APPROACH

"Digital Project" is the patented name of the innovative approach developed by the authors' Company, which involves a collaborative workflow leveraging BIM technologies, computer programming skills, database potentialities and nonlinear FE simulations. The conceived procedure is summarized in Figure 2.

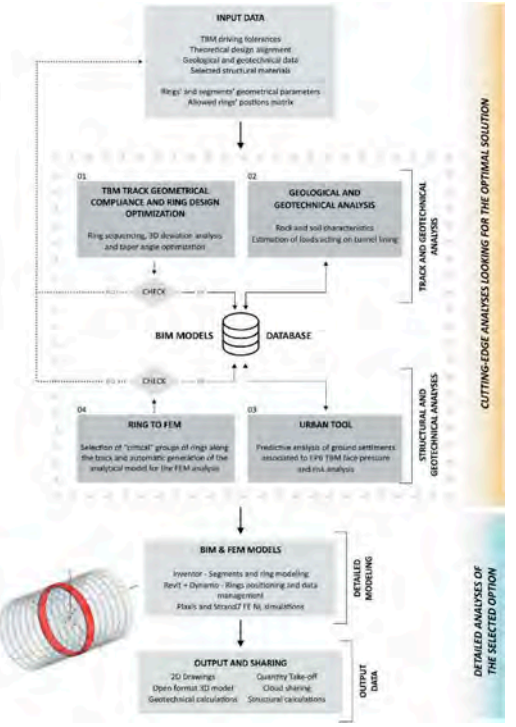

Figure 2. Flowchart illustrating the main steps required for the implementation of "Digital Project.

2.1 *Input data*

A rich set of input data represents the starting point of the described process. In more detail, information can be subdivided between fixed and mutable data.

Fixed (or design) parameters are:

- TBM driving tolerances;
- Theoretical design alignment;
- Geological and geotechnical data;
- Selected structural materials.

Mutable inputs (susceptible to optimization as a consequence of the implemented analysis) are represented by:

- Geometrical parameters of rings and segments;
- Matrix of rings' allowed positions.

2.2 *Cutting-edge analysis looking for the optimal solution*

In order to take advantage of the powerful software packages currently available on the market, in the past years a big effort has been made in developing an integrated tool capable of optimizing the final design solution. This strategy allows engineers to access and manage every piece of information related to the project, thanks to a flexible and dynamic database.

The first step consists in developing the geometrical and informative model, available to the entire working team. The model takes advantage of BIM technologies to perform 3D geometrical evaluations, elaborate design input data, share all relevant information for geotechnical and structural calculations with the database, and visualize in a rational way the obtained results.

As the "engine" of the procedure is represented by the database, considering its importance within the integrated design process, NoSQL technology is used for the core structure, due to its flexibility and dynamism. In more detail, the database is designed to perform specific tasks aimed at supporting the project team in the iterative process of evaluating, validating and designing different solutions, allowing for an interoperable approach to infrastructure design.

The most relevant tools developed and implemented within the Digital Project strategy are briefly described as follows:

01A. Segmental lining geometrical optimization

This tool, conceived with reference to a universal type ring (Guglielmetti et al., 2007), optimizes the ring geometry in terms of taper angle and average length. Thanks to an efficient computational strategy, different options can be quickly analyzed according to the associated taper angle. The obtained results are then post-processed adopting multiple design criteria based on buildability and geometrical compliance.

01B. Evaluation of ring sequencing

The spatial deviation between the theoretical alignment - curvilinear geometry designed by road or rail engineers - and the "real" TBM path - polyline whose elementary unit is represented by ring width - can be analyzed as a function of the size and taper angle adopted for the ring.

By properly varying the input data, a series of analyses should be run using this tool, generating different results that - after a multi-criteria evaluation - allow for the definition of the best choice in terms of minimal deviation and optimized ring positioning. In more detail, the process simulates TBM advancement during tunnel construction, determining the spatial deviation of each ring from the theoretical alignment (calculated considering also the main design constraints, as the allowable ring positions matrix).

Figure 3 Illustrates the implemented strategy and the results obtained for the specific case study described in the following.

02A. Geological and geotechnical data

Geological data are traditionally available in the form of 2D drawings. Starting from geological and geotechnical profiles or from survey information (like boreholes, MASW, etc.), all the meaningful design data are imported into the digital model using specifically developed automatized procedures. Project data typically stored in the database include: georeferenced geological stratigraphy, water table level, rock and soil characteristics, etc.

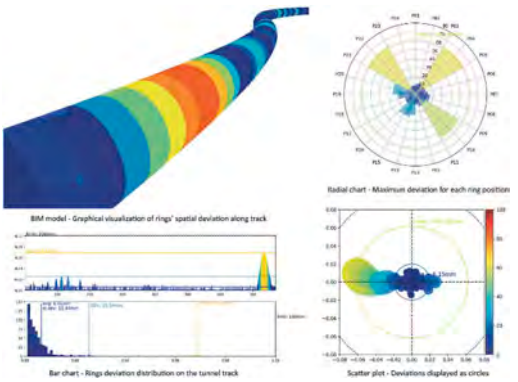

Figure 3. Schematic of the main features of the tool developed for the evaluation of ring sequencing.

03. Predictive analysis of ground settlements and risk analysis

In the context of induced surface settlements due to tunnel excavation in urban areas, the heuristic analysis of the system can be run through the massive implementation of closed-form formulations inferred from the most accredited references in the specific technical literature (Ghensi et al., 2019). SWS Digital Project has been successfully applied in many design cases to perform this challenging task, providing a reliable estimation of the expected ground settlements and a rigorous definition of the optimal TBM EPB face pressure (with the aim of minimizing risk of damage for existing buildings).

On the other hand, a different Digital Project application has been conceived to analyse deep rock tunnels, simulating TBM progress via an iterative analysis of rock mass response to excavation, based on the implementation of Monte Carlo analysis techniques. This application accurately investigates the system sensitivity to the typical uncertainties associated to the choice of design geotechnical parameters.

04. BIM and FE models

Geotechnical and structural engineers finally access the Digital Project database in order to make on-demand FEM models aimed at analysing the most "critical" sections of the alignment.

In particular, the analytical model generation is an automated process developed via the available API of the FE simulation software (in the specific case: Plaxis or Strand7). This approach guarantees reliability and precision, assuring a massive reduction of modelling efforts and allowing to focus mainly on decision-making processes and on accurate result analysis.

Furthermore, another advantage of this integrated approach is the automated coupling of geotechnical and structural models. Soil-lining interface stresses calculated by Plaxis are in fact exported in Strand7, completely defining the load case reproducing the ground pressure effect. The next Section illustrates the strategy implemented for the structural analysis of the concrete lining, together with additional details on FE models.

2.3 *Detailed analysis of the selected option*

The iterative process for defining the optimal design solution terminates with a detailed analysis of the selected option. This task requires the geometrical model of the ring (Inventor), the definition of tunnel coordination model (Dynamo + Revit), the nonlinear geotechnical and structural modeling of the system (Plaxis + Strand7) and the finalization of output files and documents.

One of the most challenging steps of the process is the modeling strategy selected for the automated generation of Strand7 structural models. First, the staggered layout of the ring-set to be included in the analysis is automatically imported in the FEM software from the Revit model.

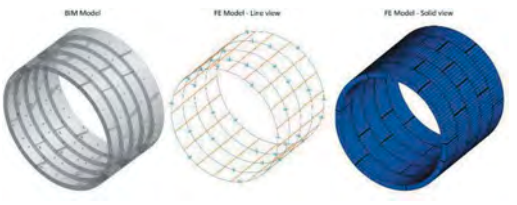

Figure 4. Schematic illustrating the generation of the FE model for a typical ring-set.

"Beam" and "Link" elements are used to reproduce the geometrical configuration of the concrete lining, implementing compression-only supports to model soil-structure interaction. The applied stiffness is calculated using the Vesic (1961) formula:

$$K_R = \frac{E}{(1+\nu)\cdot R}$$

Where: E ground Young's modulus; ν Poisson Modulus of the ground; R outer ring radius.

This approach requires little computational effort, while guaranteeing easily understandable results; in addition, it introduces an innovation simulation of longitudinal and transverse joints. The following sections present this method and compare it with traditional approaches.

2.3.1 *Nonlinear (NL) longitudinal joint model*

The longitudinal joint (i.e., the joint between adjacent segments) is conceived to effectively simulate the nonlinear rotational spring behaviour suggested by JSCE, 2006. This Standard provides iterative analytical formulations in order to simulate the joint behaviour, accounting for the significant correlation between rotational spring stiffness and loading condition.

Joints mainly subjected to compression behave as standard rectangular sections in bending, while joints subjected to tension provide negligible rotational stiffness. These two extreme scenarios highlight the strong dependency of joints rotational stiffness on applied load eccentricity.

The main formulations for rotational spring stiffness are as follows:

Rotational stiffness of longitudinal joints:

$k_\vartheta = \frac{b\cdot a^2\cdot E}{12}$ Closed joint: low eccentricity (e < a/6);

$k_\vartheta = \frac{9\cdot b\cdot a\cdot E\cdot M\cdot\left(\frac{2\cdot M}{N\cdot a}-1\right)^2}{8\cdot N}$ *Partially open joint (a /2 < e < a/6);*

$k_\vartheta = 0$ *Fully open joint (e > a /2).*

Where, b width of the contact area; a height of the contact area; E concrete Young's modulus; M joint bending moment; N joint axial force.

Joint rotation:

$$\alpha = \frac{8\cdot N}{9\cdot(1-2)^2\cdot a\cdot E}$$

Where, $m = M/(N\cdot a)$ represents the eccentricity rate.

As joint stiffness varies with eccentricity, implementing these analytical formulations for each load combination is a time-consuming iterative process (SPRING METHOD):

- STEP1 – FE model solved assuming a rigid joint stiffness (closed joints);
- STEP2 – local evaluation of eccentricity (m) for each joint;
- STEP3 – local evaluation of joint stiffness and manual assignment to the model;
- STEP4 – new run of the FE solver (then back to STEP2).

In order to avoid the above iterations, a nonlinear joint model (Figure 5) is developed, where the

interface between consecutive segments is modeled via a series of rigid links and truss elements accounting for the actual segment thickness. The truss elements, spanning between the rigid links in the contact area, are characterized by a nonlinear stress-strain behavior (the parable-rectangle constitutive law typical of concrete - Figure 6).

A fast convergence of the analysis is ensured by the following modeling choices:

- Consider concrete crushing for $\varepsilon_c > 3.5‰$;
- Assign a negative stress gradient at the compressive boundary of the table;
- Use negligible resistance for concrete in tension;
- Consider both the correct concrete initial stiffness E_{cm} and design resistance f_{cd}.

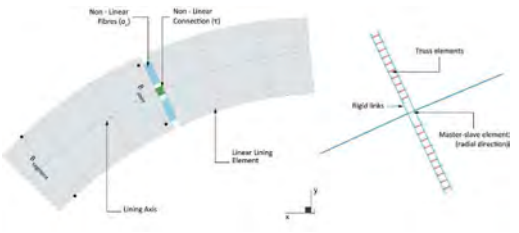

Figure 5. Modeling strategy adopted to simulate the NL behaviour of longitudinal joints.

The analysis convergence automatically implies the joint structural check as well. Thanks to the negative stress gradient at the constitutive law end, in fact, the solver stops in case of concrete crushing at the most compressed fiber or in case of a joint completely under tensile stresses.

This modeling approach has been validated by comparing the FEM output with the analytical results according to the previously listed formulations. In particular, given the joint geometry, concrete class and external axial compression, by progressively increasing the bending moment one can obtain the joint moment-rotation curve, as shown in Figure 6.

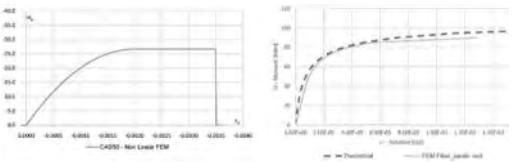

Figure 6. Stress-strain constitutive law (left) and validation results of the proposed modeling approach (right).

2.3.2 *Nonlinear (NL) transverse joint model*

The transverse joint (i.e., the joint between consecutive rings) is conceived to automatically simulate the redistribution of bending moments in multiple rings, without any processing of lining bending stiffness, typical of Muir Wood approach.

A set of tunnel rings is made of multiple components modeled in their actual staggered configuration and connected together via a proper arrangement of finite elements, simulating the bilinear behaviour exhibited by transverse dowels (Figure 7).

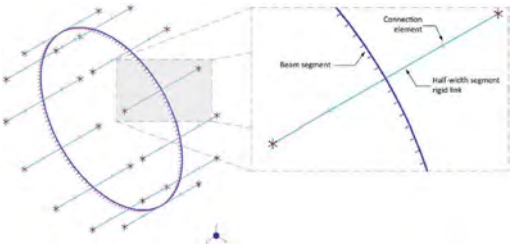

Figure 7. Modeling strategy adopted to simulate the NL behaviour of transversal joints.

At the end of the analysis, the maximum shear force in the dowels must be checked to guarantee compliance with their maximum capacity.

The adopted simulation strategy shows an excellent reliability, as the comparison between FE results and the iterative implementation of the traditional Muir Wood approach yields a bending moment difference less than 2%.

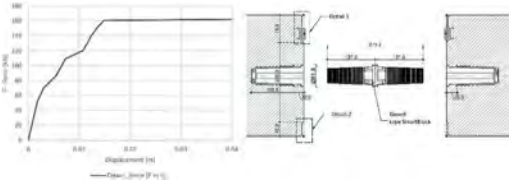

Figure 8. Force-displacement dowel behavior implemented in Strand7 (left) and typical dowel detail for Gran Paris M14 (right).

2.3.3 *Main advantages of the proposed FEM approach*

The proposed FE modeling approach, compared with the traditional Muir Wood approach, offers the following relevant advantages:

- Effective integration with BIM tools, supporting the interaction between different members of the project team and facilitating the implementation of geometry changes during the design phase;
- Precise estimation of the stress field acting in the longitudinal joints, providing valuable information for evaluating gasket water tightness and the overall tunnel sealing performance;
- Automatic redistribution of external forces between adjacent rings, avoiding bending stiffness calibration and manual processing of final results (as required in Muir Wood approach);
- Ability to study non-cylindrical load distribution (typically experienced immediately behind TBM tail shield, where a partial gap filling is extremely probable);

- Ability to perform structural checks for fasteners, guiding rods and concrete compressive stresses directly using the FE model, with significant time save and considerable accuracy improvement; these aspects are essential when multiple stakeholders play a role in the design process, considering that changes can occur even in the final phases of the project;
- In case of large deformations caused by longitudinal joints rotations, ability to considers the beneficial support offered by the contrast of the surrounding ground. This allows significant optimization for tunnels having a small cover (meaning small axial forces and, consequently, large eccentricity values).

3 THE GRAND PARIS M14 LOT 4: A RELEVANT CASE STUDY

The GP M14 Lot 4, about 4km long, is the last section of Paris Metro Line 14, connecting Pont the Rungis Station with Morangis Maintenance Center. In more detail, this project required to design a single double-track tunnel, excavated through a relatively uniform and predominantly clayey soil strata using a 9.0m diameter EPB TBM (also named Koumba).

In this Design & Build contract with a total value of about 200 million EUR, SWS was responsible for the multidisciplinary design of the whole tunnel, providing site support for both temporary and permanent structures.

The application of the integrated design approach allowed for the proper definition of precast lining, suggesting the implementation of a 7+0 universal ring having a mean length of 1800mm and a thickness of 350mm. C40/50 concrete (EN 206-1) and B500C rebars (EN 10080) are the structural material for this project, providing high-performance anchored gaskets, equipped with hydrophilic bars, at all joints between segments. Figure 9 shows the geometry of the adopted segments.

Figure 9. GP M14 Lot 4 precast lining: segments delivered on site (left) and Koumba TBM ready for launching (right).

The limited value of overburden (variable from a minimum of 1.0 to a maximum of 2.0 diameters) and the alignment crossing with very sensitive areas of the city (including Orly airport, roads, bridges, buildings and strategic utilities), more than 400 tunnel sections have been analyzed by the integrated tool. 20 "singular" design sections, identified as the most critical along the alignment, were then automatically generated, and the database populated with a complete set of information regarding: overburden, geological and geotechnical data, water table, presence of buildings/structures and their relative distance from tunnel axis, foundations depth and precast lining characteristics.

This rational and reliable design approach was facilitated by a fruitful collaboration between all stakeholders involved in the project. On the other hand, automation and digital technologies ensured a sensitive improvement in terms of both design quality and efficiency, compared to traditional design approaches.

4 CONCLUSIONS

The integrated design workflow, together with the case study of Grand Paris M14 Lot 4 where this innovative approach was applied, lead to the following conclusions:

- Traditional design approaches of the past cannot compete with innovative procedures in order to reach an optimal design of precast concrete linings;
- Digital technologies, nowadays, can be considered mature enough to be systematically applied for the effective design of infrastructures;
- Interoperable BIM models, if properly developed and managed, can represent one of the most rational options to collect and organize all meaningful project data;
- A flexible database is an essential ingredient for expanding the current limitations identified in all off-the-shelf software that is currently available on the market, making possible a "real" integration between BIM and FEM for both structural and geotechnical problems;
- The massive implementation of closed-form analyses and the automated generation of specific FE models for the most "critical" sections of the infrastructure reduces computational time and increasing the quality and reliability of the project.

REFERENCES

A. M. M. Wood, "The Circular Tunnel in Elastic Ground," Geotechnique 25, No. 1, pp. 115–127, 1975.

DAUB - German Tunnelling Commitee (ITA-AITES), "Recommendations for the design, production and installation of segmental rings," 2013.

F. Maltese, A. Ghensi, G. Eccher and A. Konstantinou, “Digital project: Practical application of an integrated process in TBM tunnel design,” in Proceedings of the World Tunneling Conference, Naples, 2019.
JSCE- Japan Society of Civil Engineers, “Standard Specifications for Tunnelling: Shield Tunnels,” 2006.
L. Da Vinci, Codex Atlanticus, Milan, 1519.
L. Da Vinci, Codex Madrid, Vol. I, Madrid, 1505.
M. Pescara and R. Osgoui, “An integrated design approach for the design of segmental tunnel,” in Proceedings of the World Tunnel Congress, Foz do Iguaçu, Brazil, 2014.
N. A. Do,D. Dias, P. Oreste and I. Djeran-Maigre, “The behaviour of the segmental tunnel lining studied by the hyperstatic reaction method,” European Journal of Environmental and Civil Engineering, 2013.
R. Mahajan, “3 Dimensional Structural Modeling of Segmental Tunnel Lining Using Finite Element Software,” in Australasian Tunneling Society, 2010.
T. Iftime, “Prefabricated lining, conceptional analysis and comparative studies for optimal solution,” in Proc. of the ITA International Congress Tunnelling and Ground Conditions, Cairo, Egypt, 1994.
US Army Corps of Engineers, “Engineering Manual EM 1110-2-2901 Engineering and Design - Tunnel and Shafts in Rock,” Directorate of Civil Works - Engineering and Construction, Washington DC..
V. Guglielmetti, P. Grasso, A. Mahtab and S. xU, Mechanized Tunneling in Urban Areas, Taylor & Francis, 2007.
Working Group No. 2 (ITA-AITES), “Guidelines for the Design of Shield Tunnel Lining,” 2000.

Tunnelling for a Better Life – Yan, Celestino, Thewes & Eberhardt (Eds)
© 2024 The Author(s), ISBN 978-1-032-80042-4
Open Access: www.taylorfrancis.com, CC BY-NC-ND 4.0 license

Data-driven underground construction management: a case study of the Big Circle Metro Line in Moscow

Michail D. Nadot, Valery V. Vyazovoy, Maria A. Lvovskaya & Aleksandr G. Polyankin*
LLC Mosinzhprooekt, Moscow, Russia

ABSTRACT: Underground construction projects are complex and challenging, with the success of such endeavors heavily reliant on efficient management practices. The Big Circle Metro Line (BCML) in Moscow serves as an exemplary case study for the implementation of data-driven techniques in underground construction management. This paper presents an in-depth examination of the BCML project, highlighting the application of advanced automation, Building Information Modeling (BIM), information management, and data-driven technologies to optimize construction processes.

This paper elucidates the integration of data-driven methodologies at each stage of the BCML project, from initial design to operational handover. The strategic application of data-centric decision-making facilitated enhanced collaboration among stakeholders, optimal resource allocation, improved risk management, and increased overall project efficiency.

Key to the project's success was the utilization of BIM for 3D visualization, clash detection, and real-time updates, which ensured a cohesive and adaptive construction approach. Automation played a pivotal role in streamlining repetitive tasks, enabling precision and consistency. Furthermore, robust information management systems were employed to maintain data integrity and accessibility throughout the project lifecycle.

The paper concludes with insights on the transformative impact of data-driven practices in underground construction management. Lessons learned from the BCML project indicate that the judicious use of technology and data can lead to significant advancements in the field, ultimately enhancing the safety, sustainability, and success of underground construction endeavors.

Keywords: Data-driven management, underground construction, Building Information Modelling, automation, information management, project efficiency

1 INTRODUCTION

The construction of subterranean transportation infrastructure is a complex orchestration of engineering, logistics, and stakeholder management. Each phase of development presents unique challenges, amplified by the constraints of working beneath the urban landscape. In recent years, information modeling technologies have emerged as a cornerstone for enhancing efficiency and reducing the inherent risks associated with underground construction projects. This study focuses on the innovative application of these technologies during the construction of seven pivotal metro stations along Moscow's Big Circle Line (BCL).

The BCL project represents a monumental effort to expand Moscow's metro system, serving as a critical case study in the deployment of Building Information Modeling (BIM) and related information modeling tools. The integration of these models facilitated a more collaborative, accurate, and efficient construction process, shifting the industry paradigm toward a data-centric approach. This paper details the key areas where information modeling technologies were harnessed to optimize construction workflows, improve decision-making, and deliver the project with a high degree of precision and efficiency.

2 LEVERAGING INFORMATION MODELLING TECHNOLOGIES AND 3D MODELS IN THE DESIGN AND CONSTRUCTION

The advent of advanced information modeling technologies has significantly transformed the landscape of underground construction projects. In the case of Moscow's Big Circle Line (BCL), these innovations have played a pivotal role in both design and construction phases, ensuring a streamlined, efficient, and cost-effective process. The application of Building Information Modeling (BIM) and 3D models has

*Corresponding author: Polyankin_alex@mail.ru

DOI: 10.1201/9781003495505-387

been central to this transformation, enabling a high degree of precision and collaboration among the diverse teams involved in the BCL project.

Information modeling technologies facilitated a multi-dimensional approach to the BCL's design, allowing engineers, architects, and construction managers to visualize the entire subway line within a virtual environment. This approach provided an intuitive understanding of complex structures and systems before physical construction commenced, thereby reducing the likelihood of costly errors and rework. BIM's capabilities for clash detection were particularly valuable in identifying and resolving potential conflicts between structural, mechanical, electrical, and plumbing systems, which are common in the confined spaces of underground construction.

The use of 3D models extended beyond the design phase, assisting construction teams with planning and sequencing of work. This ensured that construction activities progressed smoothly, with minimal disruption to the urban fabric of Moscow. Additionally, the 3D models were constantly updated to reflect as-built conditions, thereby maintaining an accurate record of the project's evolution over time.

Risk management were also enhanced through the use of BIM and 3D models. Simulations of construction processes and the behavior of structures under various stress scenarios enabled the proactive identification of risky concerns. This allowed for the development and implementation of risk mitigation strategies before the manifestation of any real-world issues.

Moreover, BIM facilitated improved communication and information sharing among stakeholders. With access to a shared model, all parties, including designers, constructors, city officials, and future maintenance personnel, could work from a single source of truth. This level of integration was paramount in managing the complexity inherent in the BCL project and is a testament to the capabilities of information modeling technologies in the realm of large-scale underground construction.

The adoption of BIM and the active use of 3D models in the BCL project not only improved operational efficiencies but also served as a beacon for future projects in the underground construction industry. The case of the Big Circle Line stands as a resounding endorsement of the potential that lies in embracing digital technologies and data-driven methodologies for the enhancement of construction management practices

3 INTEGRATING INFORMATION MODELS FOR ENHANCED CONSTRUCTION EFFICIENCY: A STUDY OF SEVEN METRO STATIONS IN MOSCOW'S BIG CIRCLE LINE

The following sections will dissect the specific applications of information models within the BCL project, beginning with the critical task of collision detection and prevention—a foundational aspect that set the stage for the subsequent successes in construction management and operational execution. Through this exploration, we aim to illustrate the profound benefits that BIM and information modeling can bring to the field of underground construction, potentially serving as a blueprint for future projects around the globe.

3.1 *Collision detection and prevention*

The construction of seven key metro stations within western and eastern sections Moscow's Big Circle Line (BCL) utilized information models to preemptively identify and resolve design conflicts. By integrating BIM technologies, potential clashes between different design elements were detected during the pre-construction stage. This proactive approach effectively minimized delays and reduced the need for on-site rework, ensuring a seamless transition from design to construction.

3.2 *Workfront prioritization and focusing*

Through the strategic employment of information models, project managers were able to predict and prioritize critical work fronts, focusing resources and efforts where they were most needed. The models provided detailed insights into the construction sequence, allowing the team to anticipate and prepare for the next stages of development, bolstering productivity and maintaining project momentum.

3.3 *BIM-Database utilization for author supervision*

On-site author supervision was greatly enhanced by the use of a BIM-database. This centralized repository of project information offered supervisors instant access to detailed, up-to-date data, ensuring that construction adhered strictly to the design specifications. The integration of BIM within the supervision process facilitated informed decision-making and timely interventions, upholding design integrity throughout the construction phase.

3.4 *4D Planning and plan-fact analysis*

The implementation of 4D planning, which integrates the 3D model with the construction schedule, enabled a dynamic analysis of the planned versus actual progress. By visualizing the construction sequence over time, project managers could effectively monitor milestones and manage deviations from the plan, making adjustments as necessary to keep the project on track.

3.5 *Front-of-work and room management*

Information models played a crucial role in the management of construction fronts and spatial coordination within the constrained environments of metro station construction. The ability to visualize and

manage space utilization in real-time helped to avoid conflicts, optimize the use of available room, and ensure that different teams could work concurrently without impeding each other's activities.

4 CONCLUSIONS

The adoption of information modelling technologies across these seven metro stations of the BCL project exemplifies the transformative impact of BIM on underground construction management. These technologies brought about improvements in collision detection, work prioritization, author supervision, planning accuracy, cost control, and spatial management—culminating in a construction process that is more efficient, predictable, and cost-effective. This case study reinforces the value of integrating BIM and information models as standard practice in the complex field of underground construction.

REFERENCES

Eastman, C., Teicholz, P., Sacks, R., & Liston, K. 2011. BIM Handbook: A Guide to Building Information Modeling for Owners, Managers, Designers, Engineers and Contractors. John Wiley & Sons.

Azhar, S. 2011. Building Information Modeling (BIM): Trends, Benefits, Risks, and Challenges for the AEC Industry. Leadership and Management in Engineering, 11(3), 241–252.

Succar, B., & Kassem, M. 2015. Macro-BIM adoption: Conceptual structures. Automation in Construction, 57, 64–79.

Volk, R., Stengel, J., & Schultmann, F. 2014. Building Information Modeling (BIM) for existing buildings — Literature review and future needs. Automation in Construction, 38, 109–127.

Kensek, K. 2014. Building Information Modeling. Routledge.

Liu, Y., van Nederveen, S., & Hertogh, M. 2017. Understanding effects of BIM on collaborative design and construction: An empirical study in China. International Journal of Project Management, 35(4), 686–698.

Charehzehi, A., & Ahankoob, A. 2012. The Role of BIM in Enhancing the Performance of Construction Industry. The Open Civil Engineering Journal 14 (1):388–401

Arayici, Y., Coates, P., Koskela, L., Kagioglou, M., Usher, C., & O'Reilly, K. (2011). BIM adoption and implementation for architectural practices. Structural Survey, 29(1), 7–25.

McGraw Hill Construction. 2012. The Business Value of BIM in Europe: Getting Building Information Modeling to the Bottom Line in the United Kingdom, France and Germany. SmartMarket Report.

Tunnelling for a Better Life – Yan, Celestino, Thewes & Eberhardt (Eds)
© 2024 The Author(s), ISBN 978-1-032-80042-4
Open Access: www.taylorfrancis.com, CC BY-NC-ND 4.0 license

Research on construction collaborative control method based on drilling and blasting tunnel equipment

Qin Nianwen*, Zeng Miaojun & Jiang Weiliang
China Railway Construction Heavy Industry Corporation Limited, Changsha, China

ABSTRACT: Shield method, TBM method and drilling-and-blasting method are the main construction methods of tunnel construction, among which drilling-and-blasting method has outstanding advantages such as wide geological adaptability, low construction cost and flexible construction organization, accounting for some 80% in tunnel engineering. As the drilling-and-blasting method is a step-by-step operation in different processes, various construction method, complex processes, various types of equipment and large personnel needs, it has urgent requirements on construction efficiency, safety and quality, and the complexity and difficulty of construction control are particularly prominent. How to further improve the modern construction capacity of tunnel engineering through mechanical, digital and informational means, and promote the information exchange and transmission among the project participating units has become an urgent problem to be solved. Aiming at the conventional equipment in the construction process of drilling-and-blasting method, this paper systematically carried out the research on the construction collaborative control method based on tunneling equipment, and put forward relevant suggestions on the improvement of equipment data supply capacity, the standardized construction of tunnel network, the interactive sharing of data standardization, and the deepening application of equipment data. And form an intelligent equipment cluster collaborative management and control platform with risk management, construction management, equipment management and quality management as its core functions. The platform has been demonstrated and applied in a number of key projects, with remarkable economic and social benefits, realizing safe, efficient, and high-quality construction of drilling-and-blasting tunnels.

Keywords: underground engineering equipment, intelligent tunnel construction, engineering management, tunnel network, risk warning

1 INTRODUCTION

Main tunnel construction methods include the shield method, TBM method and drilling-and-blasting method. Each method has the working mechanism and application scenarios different from one another. Among them, the shield method is usually used for underwater and soft soil tunneling, and the TBM method is usually used for hard rock tunnel excavation. The drilling-and-blasting method is especially suitable for the geological conditions with uneven hardness by virtue of its wider adaptability. The drilling-and-blasting method is a tunnel construction method based on multi-process cyclic operations such as drilling, blasting, mucking, primary support and secondary lining. By virtue of its significant advantages such as wide geological adaptability, flexible construction organization and high economical efficiency, it has been the main method for mountain tunnel construction, accounting for 80% in tunnel construction. In the worldwide tunnel construction, the number and total length of completed and under-construction tunnels in China rank high. The tunnels under construction and under planning of China show an "ultra-long, ultra-large and ultra-deep" development trend, facing increasing risk geology and extreme construction environment, frequent information exchange and transmission needs among participating organizations as well as increasingly prominent complexity of construction management. In order to achieve the goal of "safe, efficient and high-quality" tunnel construction, it is urgent to improve the construction control capacity of the tunnel equipment in the drilling-and-blasting method and promote the digital and intelligent transformation and upgrading of tunnel construction.

The supporting mechanical equipment of the traditional drilling-and-blasting method has a low degree

*Corresponding author: qinnianwen@crchi.com

DOI: 10.1201/9781003495505-388

of informatization, and cannot meet the requirements of high-quality, high-standard and rapid construction under complex geological environment conditions for tunnel construction, which is mainly reflected in the following aspects. (1) Equipment supply data is insufficient. The control data of the tunnel construction process involves many aspects such as surrounding rock, construction, devices and quality. Traditional construction methods mainly rely on manual paper-based data filling, which is poor in timeliness and lacks intelligent equipment that can sense interactive data in a timely manner, and thus cannot provide quick and accurate data support for comprehensive control of tunnel construction. (2) Network construction is not standardized. As there are many processes in drilling-and-blasting tunnel construction, it is required to frequently relocate various terminals on the tunnel wall based on the construction progress. The multifarious devices, repeated link construction and low modularity of the traditional network deployment method result in difficult network maintenance and low availability, which brings great inconvenience to tunnel data transmission and construction management. (3) There is a lack of uniform requirements for data. The data generated during drilling-and-blasting tunnel construction have multiple sources and great structural differences. Unified interaction standards and application specifications have not been formed according to different data types, and the real-time interaction channel of underlying information is missing between equipment, resulting in information silos. (4) The data processing degree is low. At present, the application of construction control in various countries mainly focuses on tunnel boring machines. Information systems for data monitoring, visualization and analysis of shield tunneling machines, TBMs and large-scale engineering equipment have been established, such as the risk information management system for underground engineering construction that is developed by Italy GeoDATA and the TBM construction plan management and monitoring system developed by Germany ITC Engineering GmbH & Co. However, there is a little study on realizing comprehensive collaborative control of tunnel construction by the drilling-and-blasting method with intelligent equipment as the link.

Therefore, based on the above problems, this paper puts forward targeted suggestions in terms of improvement of the equipment data supply capacity, standardized tunnel network construction, standardized data interaction and sharing as well as deepened application of equipment data. It is suggested to carry out application research around intelligent risk warning, process organization and management, equipment monitoring management, intelligent quality control and other aspects, and to establish a collaborative control platform for intelligent equipment clusters to improve the informatization and intelligent control level of drilling-and-blasting tunnel construction, putting effort into the promotion of intelligent tunnel construction.

2 IMPROVEMENT OF EQUIPMENT DATA SUPPLY CAPACITY

2.1 *Classification of data about tunnel construction control*

The control of drilling-and-blasting tunnel construction involves many aspects such as risk management, construction management, device management and quality management. As shown in Figure 1, risk management focuses on environmental risks, progress risks, geological risks and equipment failures. Construction management mainly focuses on the construction organization level. Device management focuses on equipment state and equipment efficiency data. Quality management focuses on data that can directly reflect tunnel construction quality.

In order to effectively support the core contents of construction control such as risk management, construction management, device management and quality management, the source of data generation must be controlled. Specifically, data needs to be automatically collected, truly recorded and automatically transmitted. Therefore, as an important basis for each construction link, it is the best choice to supply data by equipment. On the whole, the above data can be divided into two types, i.e., real-time data and log data. By carrying various intelligent sensing elements on drilling-and-blasting tunnel equipment, the data perceptibility of equipment is improved.

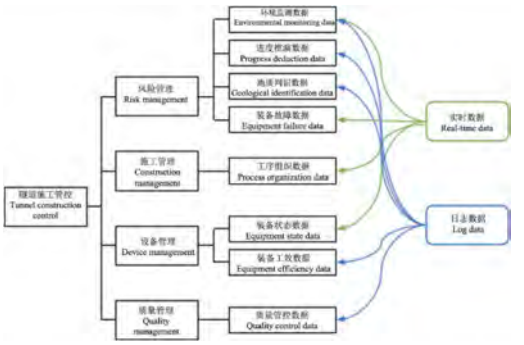

Figure 1. Classification of data about tunnel construction control.

2.2 *Real-time data*

Real-time data includes environmental monitoring data, equipment failure data, process organization data and equipment state data. Their sources are detailed below.

The environmental monitoring data comes from the real-time monitoring of ambient air quality in tunnel construction by each process equipment, including the concentrations of CO, H_2S, CH_4 and other toxic and harmful gases as well as O_2 and dust, to support the application in environmental risk warning scenarios;

Equipment failure data comes from real-time monitoring of device operation state, which is used to improve the equipment failure diagnosis capacity. Different types of equipment have different types of operation failures;

The process organization data comes from the operation mileage, operation tasks, continuous working hours of each operation task and other aspects fed back by each process equipment in real time, so as to realize the automatic recording of the construction process in the tunnel and support the application in construction organization management scenarios by further utilizing the analysis results of geological identification data and configuration information in process plans;

Equipment state data comes from the real-time monitoring of equipment working state, and supports the application of equipment state monitoring scenarios.

2.3 *Log data*

Log data includes environmental monitoring data, progress deduction data, geological identification data, equipment efficiency data and quality control data. Their sources are detailed below.

The environmental monitoring data contained in the log data mainly refers to the monitoring data about tunnel surrounding rock deformation, specifically the multi-scan logs of the tunnel profile in the same mileage range by construction equipment in each process;

The progress deduction data comes from the actual working footage recorded by each process equipment, and supports the application in progress risk warning scenarios based on the project construction plan;

Geological identification data comes from the monitoring records of surrounding rock conditions in front of the tunnel face, including advancing speed, impact pressure, advancing pressure, slewing pressure, slewing speed, water pressure, water flow and other drilling parameters in the borehole log as well as images of the tunnel face, to support intelligent identification of surrounding rock;

The equipment efficiency data comes from the equipment efficiency data recorded in each process, such as the cycle times, cycle footage, cycle time, number of rock drilling holes, concrete spraying volume, number of arch assembly trusses, and number of anchor rod construction, so as to finally realize the efficiency evaluation of all equipment;

The quality control data comes from the detailed operation data of forepoling, drilling, shotcreting, anchor bolts and steel frames recorded by each process equipment. The tunnel construction quality control capacity is improved based on tunnel design data and construction inspection lot standards.

3 STANDARDIZED TUNNEL NETWORK CONSTRUCTION

3.1 *Standardized network device*

In view of the problems of disorder and difficult maintenance in existing tunnel network construction, based on the needs of tunnel informatization construction and application business in the drilling-and-blasting method, standardized and modular network devices are provided, including the base station devices for wireless networking and coverage, vehicle-mounted base station devices for access to wireless networks as well as the intercom, positioning and monitoring devices for various application scenarios. Standardization of network construction is realized through modularization of network devices, as shown in the network master station and slave station modules in Figures 2 and 3, so as to realize standardization of the network bearer, network extension and network management and to reduce personnel maintenance costs.

Figure 2. Introduction to functions of master station.

Figure 3. Introduction to functions of slave station.

3.2 *Standardized tunnel network construction*

3.2.1 *Coverage of key construction areas*

The lining jumbo and waterproof board jumbo that are configured in the secondary lining area of the tunnel in the drilling-blasting method are bench equipment. The excavation construction bench is also arranged in the tunnel excavation area. The position of the bench moves forward continuously with the excavation of the

tunnel face. According to the characteristics of the construction process in the drilling-blasting method, it is recommended to select the network building mode of combining optical fiber wired and wireless devices for mesh networking coverage, as shown in Figure 4.

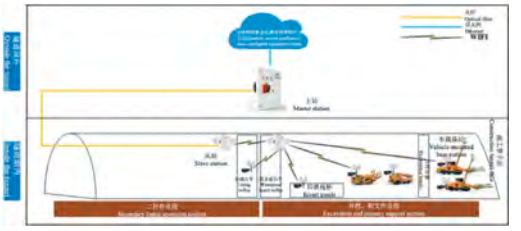

Figure 4. Network coverage of key construction areas in tunnel.

The wired LAN of the optical fiber plus Ethernet is deployed at the construction site, and the master station LAN outside the tunnel is introduced into the tunnel through the optical fiber. Slave stations are arranged on the tunnel wall of the completed lining section to realize tunnel networking. Slave stations for network coverage are arranged on the waterproof board jumbo, and are used for the wireless mesh networking with the slave stations in the completed lining section, so as to realize wireless network coverage of key construction areas of tunnel excavation and support. The tunnel construction equipment ahead can access the wireless LAN through the vehicle-mounted wireless base station to support the two-way communication between underground tunnel equipment and the cloud collaborative control platform, realizing real-time data transmission.

3.2.2 *Full coverage of construction area*

When the tunnel network needs to cover the secondary lining construction area, such as automatic driving application scenarios and man-machine positioning application scenarios, the networking method shown in Figure 5 can be adopted.

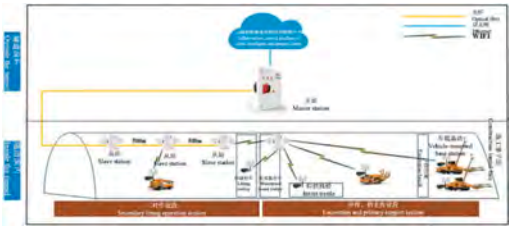

Figure 5. Full coverage of tunnel construction area network.

Compared with the method of fulfilling network coverage of key construction areas only, in this method, slave stations are added at certain intervals in the tunnel lining area, and are wired through optical fibers, so as to achieve full network coverage in the target area.

4 STANDARDIZED DATA INTERACTION AND SHARING

The data about drilling-and-blasting tunnel construction control that are collected by the equipment in each process need to be standardized on the edge side to form various standard data formats. The data is transmitted to the collaborative control platform of intelligent equipment clusters via the above network links in a standardized data interaction mode to support subsequent deepened data application.

4.1 *Standardization of data formats*

For the part of real-time data, a standard representation mode of data is refined and formed according to the common attributes of data, i.e. data message parsing rules, including the data field name, data type, data field index, data field description, data graduation value, data unit and subsystem. After receiving the real-time data message, rapid analysis, efficient storage and flexible use of real-time data are realized according to the data message analysis rules.

The log data part is finally concretized into the construction log, scan log and tunnel face image data of each process. The construction log includes the borehole log, anchor bolt log, vertical arch log, wet shotcreting log and lining log.

In order to facilitate rapid identification and classification of log files, the standard log file name shall include the work section name, operation mileage, operation time and process classification code. In order to quickly index the scan log corresponding to a construction section, it is necessary to add the information about scanning start and end mileages and the code of the scanning section type in the scan log name. For example, a scan log shall be named as: work section name_operation mileage_operation time_scanning start mileage_scanning end mileage_-process classification code_section type code.

In order to quickly analyze, store and apply log files, the text header of a log file shall include the working section name, operation time, operation direction, construction contractor, operation mileage, device information and operation positioning information.

The body of the log file can record and store core data in different dimensions, such as time series, spatial series and operation object series, according to specific construction forms. For example, the text of the lining log records the temperature, liquid level, pressure and other data at different detection positions by time; the text of the scan log records the over-excavation and under-excavation information, absolute coordinate information of sections at different mileage

positions as well as other information by space; the text of logs, such as those of boreholes, anchor bolts and arches, records the construction details of each borehole, anchor bolt and arch in the dimension of the operation object.

4.2 *Standardization of data interaction*

According to the different data types, application scenarios and generation methods, three data transmission modes and acquisition periods of the MQTT protocol, TCP protocol and HTTP protocol are determined.

Among them, the process organization data is connected to the collaborative control platform of the intelligent equipment cluster through the MQTT protocol, and the data is actively uploaded at a rate of 10 seconds/frame;

According to the data message parsing rules, the real-time equipment data can be converted, transmitted, parsed and stored at a rate of 1 second/frame through the TCP protocol;

Log data is actively uploaded to the collaborative management and control platform of intelligent equipment clusters through the HTTP protocol interface after log generation.

5 DEEPENED APPLICATION OF EQUIPMENT DATA

After the reception of the above data, according to the control requirements of drilling-and-blasting tunnel construction, deepened data application is carried out around risk management, construction management, device management and quality management, and four functional modules, i.e., intelligent risk warning, process organization and management, equipment monitoring management and intelligent quality control, are built, providing platform-based services.

5.1 *Intelligent risk warning*

5.1.1 *Environmental risk warning*

(1) Ambient gas monitoring
Based on environmental monitoring data, environmental risk thresholds, such as the concentrations of O_2, CO, H_2S, CH_4 and dust, are set for the collaborative control platform of intelligent equipment clusters. When abnormal environment is monitored, the platform gives an abnormality alarm and pushes the alarm information to on-site operators and construction management personnel in a targeted manner, ensuring the safety of construction personnel.

(2) Surrounding rock monitoring and measurement
Based on the 3D tunnel point cloud scan log obtained by the machine-mounted surrounding rock deformation measurement system, the basis for surrounding rock monitoring and measurement data is formed through preprocessing operations such as slicing and compression of the point cloud. The point cloud data within the specified range around the five key points at the arch crown, spandrels on both sides and hances on both sides is taken. By comparing the changes in over-excavation and under-excavation of multi-scan point cloud data at different time points, the settlement, convergence and other deformation conditions of surrounding rock around the tunnel are analyzed; the deformation rate, deformation amount and other data information of surrounding rock are calculated as the basis for surrounding rock deformation risk; the risk alert threshold is set, realizing the control of surrounding rock deformation risk around the tunnel.

Figure 6. Technical route of surrounding rock monitoring and measurement.

5.1.2 *Progress risk warning*

Risk warning is provided for the construction progress in two dimensions, i.e., excavation and lining, based on the construction log of the whole process.

For excavation dimension, the difference between the construction mileage of the latest borehole log of the drill jumbo and the tunnel portal mileage is calculated as the actual excavation progress. The platform compares the calculation results with the construction plan and progress filled in by the user, analyzes these results, visually displays the results of comparison between the planned and actual progress in the form of Gantt chart, and generates daily, weekly and monthly reports on the construction progress. Additionally, the platform fulfills progress risk warning by setting the risk warning and alert thresholds for excavation progress lag.

For the lining dimension, the difference between the construction mileage of the latest lining log and the tunnel portal mileage is taken as the actual lining progress. By further calculating the spacing distance from different lining construction processes to excavation processes, based on the safety step requirements of different surrounding rock grades and different processes as well as the comparison results of plan and progress, a progress risk alert is provided for the advance or lag of lining processes to assist in construction management decision-making.

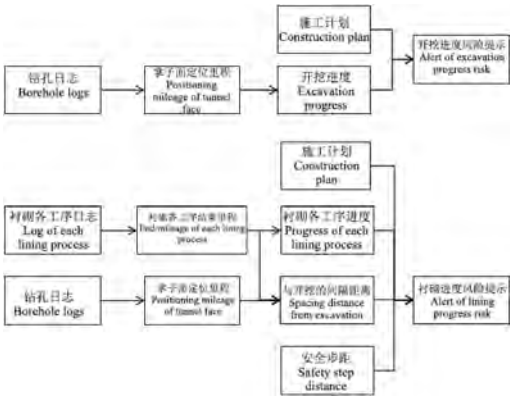

Figure 7. Technical route of progress risk warning.

5.1.3 *Geological risk warning*

Based on the drilling parameters and tunnel face image data collected by the borehole log of the intelligent drill jumbo, the surrounding rock conditions in front of the tunnel face are analyzed and evaluated. First, a sample and tag library of data and images while drilling is established. Threshold filtering, feature dimension ascending, data balance, isolated random forest, image preprocessing and other methods are applied to ensure the high quality of data samples during model training. The intelligent identification method of multi-model fusion surrounding rock based on multivariate features while drilling is adopted to realize the preliminary identification of the surrounding rock grade in front of the tunnel face. On this basis, based on the tunnel face image after adaptive processing, the Canny operator and morphological method are applied to extract the boundary information of the tunnel face. Neighborhood search and boundary aggregation methods are used to automatically connect discontinuous features on the same structural plane, so as to quickly, reliably and objectively obtain the geometrical geological information of the tunnel excavation face and further correct the identification results of surrounding rock based on parameters while drilling. When the identification result of surrounding rock is inconsistent with the design grade of surrounding rock, the platform will automatically give geological risk warning for the front of the tunnel face.

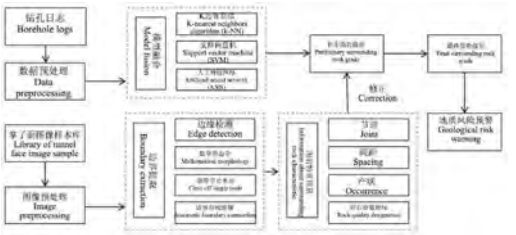

Figure 8. Intelligent identification technology route of surrounding rock.

5.1.4 *Early warning of equipment failure*

Based on the real-time data of equipment and according to the working characteristics of various intelligent equipment, the failure alarm data and failure types collected by intelligent equipment in real time are classified and matched to form failure analysis algorithms for different equipment and failures. The platform pushes the early-warning information about failures to relevant personnel directionally to ensure timely failure disposal, reduce equipment downtime and improve construction efficiency. Additionally, the platform will store and statistically analyze all failure alarm information for users to query and trace back.

5.2 *Process organization and management*

In view of the problems such as poor process connection and long cycle time caused by inadequate process management arrangement on the construction site and operators' failure to respond to process arrangement in time, corresponding algorithms are prepared to identify the current process and process operation results in real time based on the process organization data and the integration of previous processes, so as to realize real-time feedback of processes in the tunnel. Further utilizing geological data and process plan configuration information, the construction scheme setting of the next cycle is adjusted in time, and the subsequent on-site construction equipment and mobilization operation time of various construction personnel are scheduled, ensuring that the construction equipment and construction personnel can enter the site for construction in a timely manner.

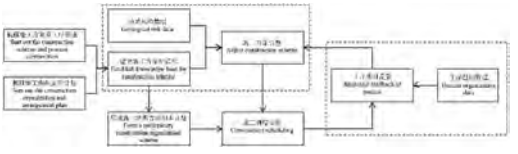

Figure 9. Technical route of process organization and management.

Through the above construction process scheduling, it is possible to optimize the connection time between construction processes, mobilization of construction equipment and mobilization of various construction personnel, so as to improve the efficiency and progress of on-site construction.

5.3 *Equipment monitoring management*

5.3.1 *Equipment state monitoring*

All-round real-time dynamic monitoring of the working state information and position information of various equipment is fulfilled based on basic equipment information, equipment working state data, vehicle-mounted video images and other information, which is conducive to equipment safety control and data tracing.

5.3.2 *Equipment efficiency accounting*

Based on the construction logs and equipment state data dynamically uploaded by the equipment, equipment efficiency evaluation rules are formulated, and equipment efficiency accounting indicators are extracted, including working hours, construction footage, number of logs and failure conditions. Additionally, daily, weekly and monthly equipment construction efficiency analysis reports are generated, so that users can intuitively understand the use and efficiency of equipment construction.

5.4 *Intelligent quality control*

At present, the quality control and inspection during drilling-and-blasting tunnel construction are still mainly based on traditional manual methods. There is a lack of "independent, accurate and efficient" quality control means for tunnel construction. It is difficult to standardize the quality acceptance of "concealed works". This paper aims to fulfill the intelligent control of tunnel support structure quality by analyzing equipment construction data. Based on autonomously-perceived information such as scan logs and whole-process construction logs, the tunnel solid model containing accurate time records is established; by formulating data processing rules and extracting intelligent quality control parameters, the quality control parameter database covering forepoling, drilling-and-blasting excavation, primary support and secondary lining of the tunnel is formed to integrate all elements of tunnel construction quality. Further utilizing the tunnel construction design data of the Design Institute and based on various tunnel construction inspection standards, a digital model for quality evaluation of the time-associated tunnel support structure is established to realize all-round, full-process, real-time and effective feedback based on intelligent operation quality information of equipment.

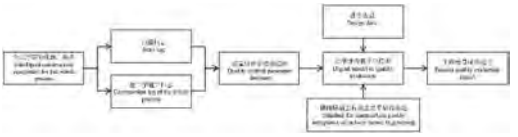

Figure 10. Technical route of intelligent quality control.

6 CONCLUSION AND PROSPECT

The collaborative construction control method based on drilling-and-blasting tunnel equipment focuses on the perception, analysis, decision-making, collaboration, interaction and other key technologies of intelligent equipment, so as to support the intelligent transformation and upgrading of the working modes of key links, such as risk warning, process organization, device management and quality control, during intelligent tunnel construction, which is of great significance for improving the intelligent tunnel construction level.

REFERENCES

[1] LI Jianbin. Current status, problems and prospects of research, design, and manufacturing of boring machine in China[J]. Tunnel Construction, 2021, 41(6): 877.

[2] Shen Weiping, Zhang Jun, Yuan Biao, et al. Research of safety risk management information system for shield tunneling construction in Chengdu metro based on intelligent interconnection technology[J]. Chinese Journal of Rock Mechanics and Engineering, 2019, 38 (S2): 3822.

[3] Wang Zhijian. Research on intelligent construction technology for high-speed railway mountain tunnel: A case study of Hubei section of Zhengzhou-Wanzhou high-speed railway[J]. Journal of the China Railway Society, 2020, 42(2): 86.

[4] YAO Meng. Rock mass intelligent classification based on drilling parameters and SVM [J]. Sichuan Architecture, 2020, 40(5): 149.

Tunnelling for a Better Life – Yan, Celestino, Thewes & Eberhardt (Eds)
© 2024 The Author(s), ISBN 978-1-032-80042-4
Open Access: www.taylorfrancis.com, CC BY-NC-ND 4.0 license

Trusted elements in the digital model of the tunnel

Galina Paskaleva*
TU Wien, Institute of Information Systems Engineering, Business Informatics Group, Vienna, Austria
TU Wien, Research Unit of Building Physics, Institute of Material Technology, Building Physics and Building Ecology, Vienna, Austria

Patrick Beronneau & Thomas Bednar
TU Wien, Research Unit of Building Physics, Institute of Material Technology, Building Physics and Building Ecology, Vienna, Austria

ABSTRACT: The application of Building Information Modelling (BIM) in Tunnelling involves the generation, co-evolution, and maintenance of digital models. This often requires the collaboration of multiple stakeholders on the same digital model over multiple project phases, which, in turn, necessitates the sharing of responsibility for the same model element among those stakeholders. For example, a niche in the tunnel inner lining may be designed simultaneously by a structural engineer, by a fire safety expert who needs to install a fire hydrant in it, and by a HVAC engineer who needs a ventilation control panel in it. Shared responsibility requires trust. Lack of trust often leads to the duplication of models so that each stakeholder can work on a separate model, free from the influence of the work of others. The consequence is a break-down of model continuity and unsustainable usage of personnel and resources. In this work, we present a method for introducing trusted elements into the digital model of the tunnel. This can be accomplished by anchoring those elements to contractually relevant documents, such as the Employer Information Requirement (EIR) according to the ISO 19650 series. Trusted elements can guarantee formally that a certain contractual or technical requirement has been fulfilled, e.g., that the measurement of carbon monoxide for the emergency ventilation system is designed in accordance with ISO 23431. In addition, formal requirements within a trusted element can be tested automatically by the common data environment (CDE) of the project. In case that one stakeholder changes the trusted element so that a requirement is no longer fulfilled, an automatic alert can be issued. We present a standardized workflow for the creation and maintenance of such trusted elements in a digital model on the use case of the design of a ventilation system in a road tunnel.

Keywords: Tunnelling, BIM, Digital model, Trust, Technical guidelines

1 INTRODUCTION

Over the past decades, the Architecture, Engineering, and Construction (AEC) industry, including the tunnelling sector, has been adapting the digital methods originating in automation (Barbosa et al., 2017). These include handling of both geometry and non-geometric, typically highly domain-specific, information (Hegemann et al., 2019). One of the most widely used such methods is Building Information Modeling (BIM) (Laakso and Kiviniemi, 2012; Borrmann et al., 2015). In spite of all these efforts, data integration remains a challenge not only when experts from multiple domains are involved (Haymaker et al., 2000; Lai and Deng, 2018; Rasmussen et al., 2019; Steel et al., 2012), but even within the same domain (Scheider and Kuhn, 2015; Millán et al., 2016).

One of the main goals of BIM is the generation and maintenance of a digital twin (Kaewunruen et al., 2018), a digital counterpart of a built structure that both supplies and receives information from it, thereby regulating its function and reacting to changes in the state of its systems (Lai and Deng, 2018), respectively. Ideally, this digital twin should be a digital model with meaningful interconnections between model elements that carry unambiguous domain-specific semantics (ITA Working Group 22, 2022).

Often however, the digital twin corresponds to the ISO 11354-1 1 definition of a federated model (ITA Working Group 22, 2022). The federated model is simply a set of separate (partial) digital models with possible mappings between them (Leng et al., 2021), i.e., a landscape of heterogeneous syntax and semantics that cannot be easily managed or navigated. For example, querying the relevant information for a particular task, or tracking the direct and indirect effects of a model element update throughout the entire digital twin both necessitate the implementation of specialized views and workflows (Eastman et al., 2011; Hegemann et al., 2019), often embedded in a Common Data Environment (CDE).

*Corresponding author: galina.paskaleva@tuwien.ac.at

DOI: 10.1201/9781003495505-389

1.1 *Motivating example*

This complexity and lack of transparency affects the level of BIM acceptance in the AEC industry in general and in tunnelling in specific (Lehoczky et al., 2022). For example, if during the operational phase of a road tunnel project we need to assess the air quality, different experts may use different technical guidelines, e.g., the ISO 23431:2021 "Measurement of road tunnel air quality", or ISO 4224:2000 "Ambient air — Determination of carbon monoxide — non-dispersive infrared spectrometry method". Those guidelines offer slightly different methods for the evaluation of carbon monoxide presence in air.

On the one hand, ISO 23431:2021, Section 5.5.2 describes the following method for the calculation of gas concentration over a measurement path in *ppm*:

$$c = \frac{c_r L_c}{L} + \frac{c_b (L - L_c)}{L} \qquad \text{(ISO23431.3)}$$

where c_r is the reference test atmosphere concentration in *ppm volume fraction*, c_b is the background pollutant concentration in *ppm*, L_c is the calibration cell length in *m* and L is the measurement path length in *m*. The conversion to *mg/m³* is described in Section 5.7:

$$C_m = \frac{C_v m}{V_m} \qquad \text{(ISO23431.7)}$$

where c_m is the gas concentration in *mg/m³* under the conditions of *standard temperature* and *standard gas pressure* of 101.3 kPa, c_v is the gas concentration in *ppm* volume fraction, *m* is the molecular weight of the gas, and V_m is the molar volume at 0 °C and at *standard gas pressure* of 101.3 *kPa*.

On the other hand, ISO 4224:2020, Section 11 defines the conversion from *ppm* to *mg/m³* for gases in the following equation:

$$\rho_1 = \frac{\rho_2 m_r \ 298 \ p}{24.45 \ T \ 101.3} \qquad \text{(ISO4224.11)}$$

where ρ_1 is the gas concentration in *mg/m³*, ρ_2 is the measured gas concentration in *ppm volume fraction*, m_r is the molar mass of the gas (e.g., 28 *g/mol* for CO), 298 is the standard absolute temperature in *K*, ρ is the measured gas pressure in *kPa*, 24.45 is the molecular volume of 1 mole in l, *T* is the measured absolute gas temperature in *K*, and 101.3 - the standard gas pressure in *kPa*.

The question is, how is an expert to know which guideline has been used and whether it has been applied consistently for all assessments in the federated model? In fact, instead of creating confusion and uncertainty, both of these technical guidelines can be used to create *trusted elements* in a digital model, regardless of its complexity. Our task is to utilise the equations and their parameters as *semantic anchoring points* for the relevant elements of the *digital twin.*

2 APPROACH

Our approach involves the formalisation of guidelines written in a natural language into a graph representation and the subsequent annotation of digital data models with elements of this graph.

2.1 *Semantic anchoring*

Let us have a look at one possible formalisation of both technical guidelines. Figure 1 shows on the right-hand side the graph representation of equation

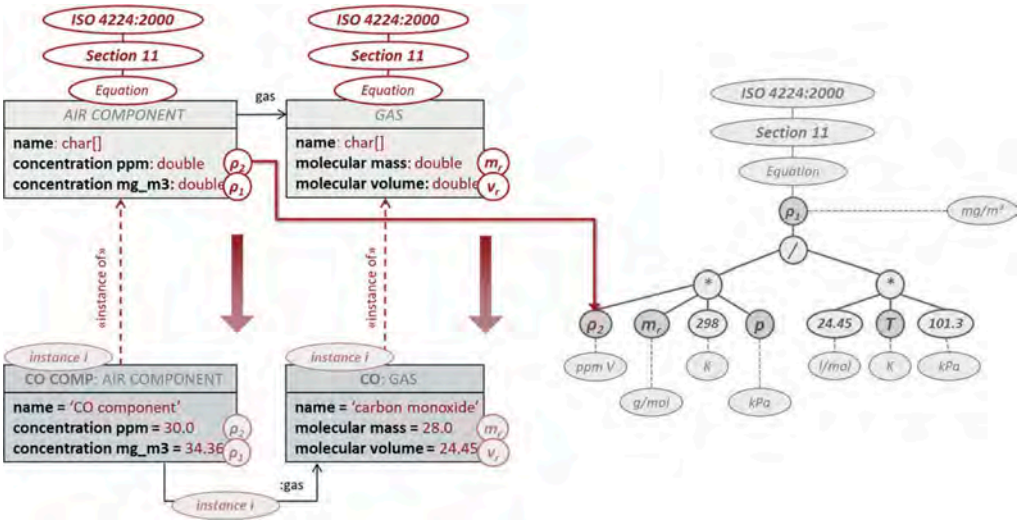

Figure 1. Mapping of a domain model to the ISO 4224:2000 guideline.

ISO4224.11 with both parameters and mathematical operations as nodes. The root of the graph indicates the identity of the guideline, followed by the section and equation (which in this case has no number). Since ρ_1 is a result of division, the only child node of ρ_1 is the corresponding operation, which has two children, both multiplication operations that produce the dividend and divisor, respectively. Each node that contains a parameter or a value has the corresponding unit attached to it, e.g., for ρ_1 it is mg/m^3 These units are by no means just informative. They can be used to describe the *type* of the node they are attached to.

On the left-hand side of Figure 1 is an excerpt of a domain-specific digital model that uses this guideline as a *semantic anchoring point*. In the top row we see the type definitions, for example *AIR COMPONENT* and *GAS*. They tell us that the digital model can save air component objects described by attributes "name", "concentration ppm" and "concentration mg_m3" and referencing objects of type GAS, i.e., gases, which in turn are described by attributes "name", "molecular mass" and "molecular volume". This is by no means a prescription of how such information should be structured, it is just an arbitrary example to illustrate the point that *any* object-oriented data model can be used in the exact same way.

In the bottom row on the left-hand side of Figure 1 we see the instances produced by the type definitions. **CO COMP** is an instance of *AIR COMPONENT* and, consequently, has slots that correspond to the type definition's attributes. For example, attribute "concentration ppm" produces a slot by the same name that carries a specific value (the double 30.0). In the same way **CO** is an instance of type definition *GAS*. The relationship between the type definitions and their instances is represented by the red dashed arrows annotated with *instance of*.

Another type of relationship, between type definitions, is the one between *AIR COMPONENT* and *GAS*, named "gas". It indicates that each air component references a specific gas, i.e., that the air component makes sense only if its definition includes a specific gas, such as carbon monoxide. This relationship can be instantiated as well, as can be observed in Figure 1. There, the instance **CO COMP** references the instance **CO** via the instance of "gas".

Now that we have a digital model capable of holding the information we need in order to comply with ISO 4224, Section 11, we can proceed with making the model elements we just described *trusted*.

The graph representation of the guideline has several features that enable *semantic anchoring* to any of its elements. First, its graph structure makes it easily serializable, e.g., in a common digital format, such as XML. This makes distribution of the formalised guideline or its hosting on a CDE platform quite trivial. Second, the graph structure is efficiently traversable, which presents an advantage in querying both the guideline and any digital model elements attached to it. Third, this structure is well suited for anchoring, since each graph node can play the role of an anchor. This is demonstrated in Figure 1, where both the type definitions and their attributes have been annotated with elements of the graph (see the red labels on the left corresponding to graph nodes on the right). For example, attribute "concentration ppm" of *AIR COMPONENT* has been annotated as "ρ_2" and effectively anchored to the corresponding equation parameter, as indicated by the continuous red arrow pointing to the graph node.

We can observe that the structure of the *domain model on the left does not have to correspond in any way to the structure of the guideline or the equation on the right*, since annotations make the anchoring independent of structure.

Additionally, the anchoring in the type definitions is automatically transferred to their respective instances by the *class – object* relationship characteristic of most object-oriented programming languages.

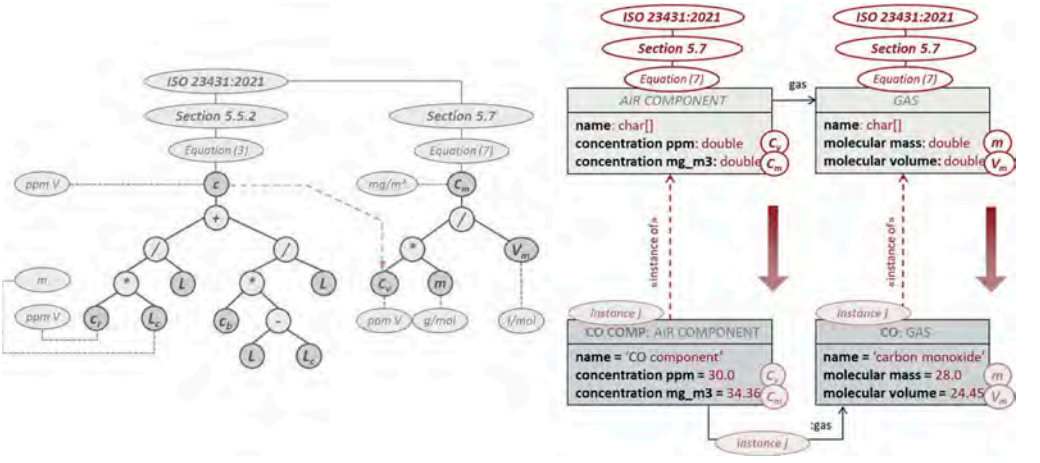

Figure 2. Mapping of the same domain model as in Figure 1 to the ISO 23431:2021 guideline.

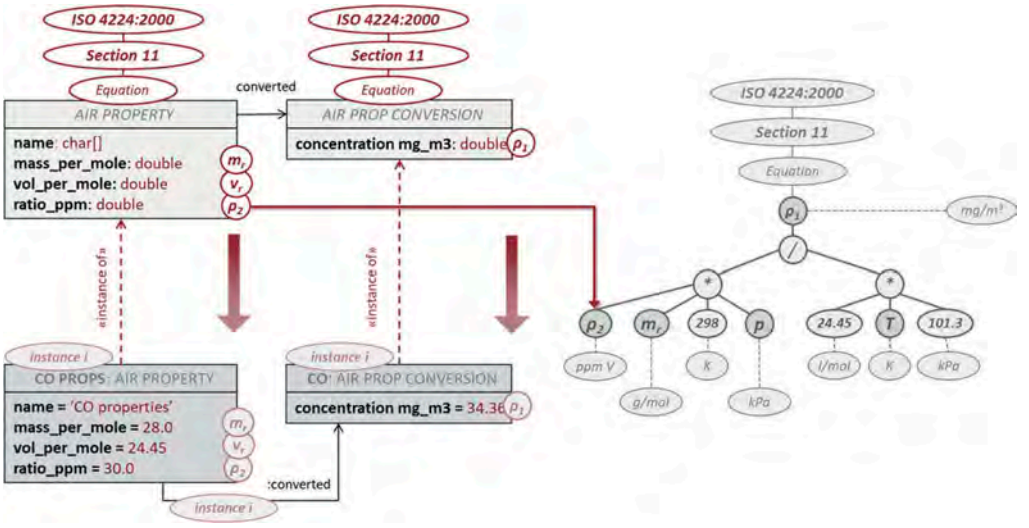

Figure 3. Mapping of a second domain model to ISO 4224:2000 (compare to Figure 1).

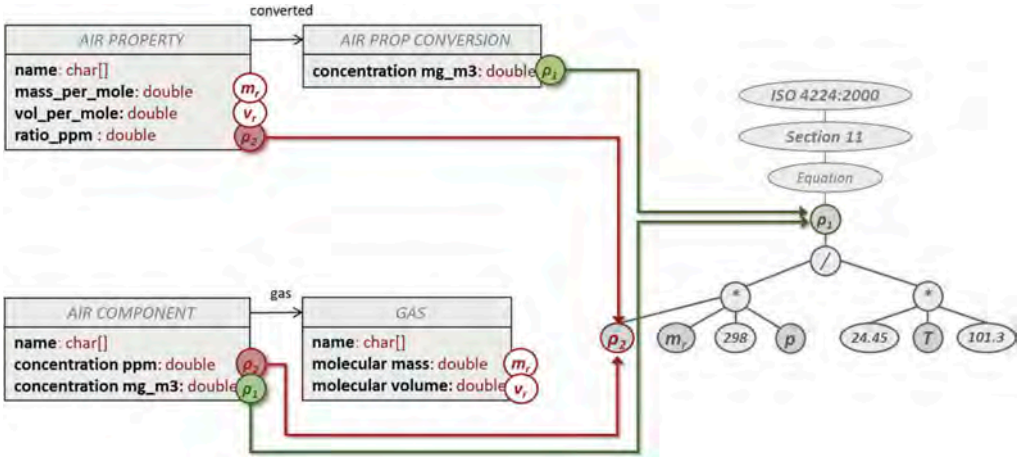

Figure 4. Data integration between two different domain models based on their anchoring to the same guideline equation.

Thus, annotations in the type definitions are sufficient for the annotation of all of their instances, regardless if there are ten or ten thousand of them. Furthermore, grouping of instances that build the same semantic unit are possible via instantiable relationships, such as the one between *AIR COMPONENT* and *GAS* (see the "instance i" labels in Figure 1).

A further example of the semantic anchoring of the same domain model, but this time to the ISO 23431:2021 guideline is shown in Figure 2. Here, we have two formalised equations, equation (ISO23431.3) on the left and equation (ISO23431.7) on the right. This gives us the opportunity to indicate that the result *c* of equation (ISO23431.3) is input *Cv* to equation (ISO23431.7). Otherwise, the domain model now has different annotations that indicate its anchoring to ISO 23431:2021.

It is of note, that these annotations are not mutually exclusive. On the contrary, they exist in parallel. In other words, *the same domain model can be anchored to multiple guidelines* to indicate its compliance to all of them, if necessary.

2.2 *Data integration based on semantic anchoring*

Apart from demonstrating compliance with technical guidelines and providing an automated path towards compliance checking (Jiang and Wang, 2021), this type of annotation allows for automated data integration.

Figure 3 shows a second domain model anchored to the same equation of the ISO 4224:2000 guideline as in Figure 1. Its type definitions differ not only in name, but also in structure from the one we discussed in

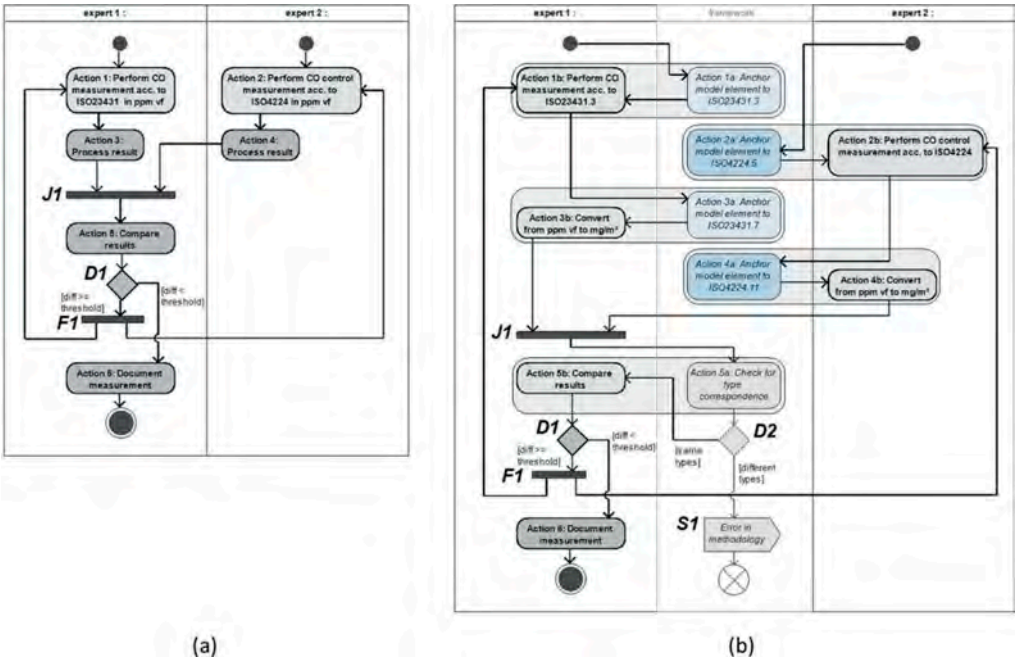

Figure 5. Practical application of semantic anchoring: (a) standard workflow, (b) adapted workflow including anchoring and automated compliance checking.

detail in the previous subsection. However, since the anchoring to the guideline depends only on the guideline's own structure, and not at all on the domain model's structure, the result are the same annotations, but attached to different elements of this second domain model. This is exactly what allows us to find a reliable mapping between the domain models in Figure 1 and Figure 3.

This mapping is shown in Figure 4. Since both the type definitions and their attributes have different names, a mapping based on those cannot be relied upon. A mapping based on their respective *semantic anchor points* on the other hand is both reliable, i.e., *trustworthy*, and can be performed automatically.

Let us look at anchor point ρ_1 first (shown in green in Figure 4), which corresponds to the gas concentration measured in *mg/m³*. This is the result node of the equation in Section 11 of ISO 4224:2000. In the domain model at the top of Figure 4, this anchor point is placed on attribute "concentration mg_m3" of type definition *AIR PROP CONVERSION*. In the domain model on the bottom, the same anchor point is placed on the attribute of the same name in type definition *AIR COMPONENT*.

Analogously, anchor point ρ_2 (shown in red in Figure 4), which corresponds to the gas concentration measured in *ppm volume fraction*, is placed on attribute "ratio_ppm" of type definition *AIR PROPERTY* in the top domain model and on attribute "concentration ppm" of type definition *AIR COMPONENT* in the bottom domain model. We can see that neither name differences, nor attribute grouping within type definitions are of any relevance here. We can transfer or consolidate information along the green or red lines regardless.

2.3 *Guideline-based type safety*

So far, we were concerned with the semantics of the data models. Correct semantics, however, include correct units and unit conversion. In our case, we regard the unit associated with a graph node, e.g. *mg/m³* for node ρ_1 in Figure 3, as that node's *type*. We use the fact that SI units can be subjected to automatic conversion, e.g., *mg/m³* multiplied with *m³* results in *mg*, to provide us with *type safety*. This is based on the formal mathematical methods for calculation with types, or *type reduction*, which proves type correspondence (Bertot and Castéran, 2004). This means that we cannot perform a mapping between, e.g., attributes of type *g/m³* and of type *mg/m³* since *g/m³* cannot be reduced to *mg/m³*. However, mapping between *Pa* and *kg/(m*s²)* is possible. This gives us an additional layer of *trustworthiness*.

2.4 *The workflow*

The methods we outlined in the previous sections can be applied in the following general workflow:

- **Guideline formalisation**: a standardisation body performs a partial or complete formalisation of a guideline;
- **Semantic anchoring**: the domain experts perform a *one-time* annotation of the domain model they utilise for a specific task, which anchors this model to the formalised digital form of the guideline;
- **Creation of trusted model elements**: the domain experts using the above-mentioned domain model instantiate it in the course of their regular work. This causes the anchors attached to the domain model's type definitions to be transferred to each and every instance automatically. All such instances can be regarded as *trusted*.
- **Automatic compliance checking**: Every trusted instance can be subjected to automatic compliance checking against the formalised guideline. This can be particularly useful in a scenario where multiple experts work on the same model and share responsibility for the same model elements. Trusted model elements can be checked for compliance after each significant update, which maintains their role as a *source of trust* in the digital twin.

This workflow can be applied both to a federated as well as to a monolithic digital model. It can run on a single machine or as a part of a CDE.

3 USE CASE MEASUREMENT OF CO CONCENTRATION

Here we give a brief (and simplified) example of the practical application of our approach on the use case of obtaining and recording measurements of CO concentration in a tunnel.

Figure 5(a) shows the standard workflow as a UML activity diagram. It involves two experts who perform measurements independently, according to ISO23431 and ISO4224, respectively. In *Action 1* expert 1 takes one measurement, while in *Action 2* expert 2 takes a control measurement. Following that, each processes the obtained results in *Action 3* and *Action 4*, respectively. The *Join Node* ***J1*** synchronises the information flows and transitions into *Action 5: Compare results*. The result of the comparison is fed to *Decision Node* ***D1***. If the difference between the measurements is less than a predefined threshold, then the result can be regarded as valid and is recorded in *Action 6: Document measurement*, after which the workflow terminates. If, on the other hand, the difference exceeds that threshold, we transition to *Fork Node* ***F1***, which transitions back to *Action 1* and *Action 2*, effectively forcing a repeat of both measurements and, subsequently, of the entire workflow we described this far.

If the difference in the two measurements results not from equipment calibration, or environmental conditions, but from an incorrect application of any of the referenced guidelines, there is a real possibility of this workflow causing an infinite loop, if run in an automated fashion in a CDE. Alternatively, there will be a need for an in-depth manual check for the error to be detected. This problem should be mitigated by the adapted workflow we propose in Figure 5(b).

Here we introduce an additional actor, a framework that applies our *semantic anchoring* approach (see the swim lane between expert 1 and expert 2 in Figure 5(b)). One immediate consequence of this is the splitting of *Action 1* to *Action 5* from the standard workflow we discussed above into two new actions each. For example, before expert 1 can even take a measurement in *Action 1b*, the correct model element for the task is instantiated and anchored to the appropriate equation in ISO23431 by the framework in *Action 1a*. The same applies to *Action 2* from the standard workflow, which is split into *Action 2a* and *Action 2b* in the adapted workflow.

Action 3 and *Action 4* are also split. This time the processing of the results becomes an explicit conversion from *ppm volume fraction* into *mg/m³* (see *Action 3b* and *Action 4b*). But before the experts can perform the conversion, the appropriate model elements are again instantiated and anchored to the relevant equations by the framework in *Action 3a* and *Action 4a*, respectively. This allows us to pass through the *Join Node* ***J1*** with *trusted elements* in our model, which lend themselves to formal checks, e.g., type checking. This is exactly what happens in *Action 5a*. Here, the framework performs a type check. Since anchoring to nodes in an equation allows us to obtain a specific unit, which, as we discussed in Section 2.3, can assume the role of the *type* for the anchored model element, in *Action 5a* we check if the type of the measurement by expert 1 is reducible to the type of the measurement by expert 2. For example, if something went wrong during conversion for one of the experts, we might be comparing *ppm volume fraction* with *mg/m³*. This will immediately produce an error message (see node ***S1*** in Figure 5(b)) and will terminate the workflow, giving the experts involved the opportunity to address the issue without delay. Another possibility is the mishandling of units during calculation, which should also become apparent here, e.g., if we were comparing g/m³ with mg/m³.

All of the above makes the comparison in *Action 5b* more reliable. Due to the utilization of *trusted model elements*, we can claim with some confidence, that if the results differ too much, the likeliest reason is not a data modelling error, but rather a problem with the actual measurement. In addition, the adapted workflow doesn't require the experts themselves to adapt (compare the expert swim lanes in Figure 5(a) and 5(b)). *The only adaptation that takes place is in the technology itself*. This makes the framework we present a good candidate to foster user acceptance and trust in the digital technology in tunnelling (Lehoczky et al., 2022).

4 RELATED WORK

The approach to increasing trust in the digital model of the tunnel we presented in the previous two sections builds on several well-researched concepts.

While there have been many proposals for the utilization of the blockchain technology in communication in the AEC industry (Elghaish et al., 2023; Raslan et al., 2020; Wonjiga et al., 2019), its application in interoperability has been limited to recognising the *presence*, but not the *semantics* of model updates (Xue and Lu, 2020).

On the other hand, graph representations of semantic concepts and the linking between such representations, even when stemming from different domains, shows promise (Witherell et al., 2013; Borrmann et al., 2014; Wang et al., 2023).

In the area of Automated Compliance Checking (ACC) there has been great emphasis on building codes and corporate guidelines as a trust-generating basis for digital models (Häußler et al., 2020; Jiang et al., 2022; Lehoczky et al., 2022).

These are all *a posteriori* approaches, i.e., based on checks of already existing models. However, the most robust approaches, those that provide an *a priori* guarantee of correctness, come from computer science. For example, a formal mathematical proof can guarantee the correctness of a digital model before even one element of it has been instantiated (Bidmeshki and Makris, 2015). This is also where the idea of type safety as a means of providing trust originates (Bertot and Castéran, 2004). It is of note that these approaches come at a very high performance (Bajczi et al., 2022) and maintenance (Sanchez-Stern et al., 2023) cost and are rarely applicable in the large digital models typical of the AEC industry and tunnelling. Nevertheless, in small but critical parts of the model, they can play a significant role.

5 CONCLUSION AND FUTURE WORK

In this paper we discussed a method for ensuring that no matter how complex the *digital twin* of a tunnel may become, it is always possible to ensure that those parts of it that are of critical importance for a certain domain can be designed as *trusted elements*. This trust is based on formalised technical guidelines from the domain itself that provide both *semantic anchoring* and *type safety*. The advantages of this approach include the ability to structure the domain model as required by the expert while at the same time maintaining compliance to a guideline with possibly entirely different structure. In addition, data integration of different domain models can be robust and reliable when built around *trusted elements*. The same method can be utilized to ensure compliance with an Employers Information Requirement (EIR), making parts of the digital twin an *implementation of a formalised contract*. All of this should contribute to increased acceptance of the BIM method in the AEC industry and in the tunnelling sector.

Finally, the approach we presented here handles anchoring to information; in our future work we intend to extend this idea to the geometry of the tunnel, in order to produce *trusted geometry.*

REFERENCES

Bajczi L., Ádám Z. and Molnár V. (2022). C for yourself: comparison of front-end techniques for formal verification, 2022 IEEE/ACM 10th international conference on formal methods in software engineering (FormaliSE), 1–11.

Barbosa F., Woetzel J., Sridhar M., Parsons M., Bertram N., Brown S., Mischke J. and Ribeirinho M. (2017). Reinventing construction: a route to higher productivity, https://www.mckinsey.com/business-functions/operations/our-insights/reinventing-construction-through-a-productivity-revolution, [Online; accessed 17-June–2022].

Bertot Y. and Castéran P. (2004). Interactive theorem proving and program development. coq'art: the calculus of inductive constructions (Brauer W., Rozenberg G. and Salomaa A., editors), Springer, Berlin Heidelberg, Germany, 13–42.

Borrmann A., König M., Koch C. and J. B. (2015). Building information modeling. technologische grundlagen und industrielle praxis, Springer Vieweg, Wiesbaden.

Bidmeshki M. and Makris Y. (2015). Toward automatic proof generation for information flow policies in third-party hardware IP, 2015 IEEE international symposium on hardware oriented security and trust (HOST), 163–168.

Borrmann A., Flurl M., Jubierre J., Mundani R. and Rank E. (2014). Synchronous collaborative tunnel design based on consistency-preserving multi-scale models, Advanced engineering informatics, Vol. 28, No. 4, 499–517.

Eastman C., Teicholz P., Sacks R. and Liston K. (2011). BIM handbook: a guide to building information modeling for owners, managers, designers, engineers and contractors, John Wiley & Sons.

Elghaish F., Hosseini M., Kocaturk T., Arashpour M. and Ledari M. (2023). Digitalised circular construction supply chain: an integrated BIM-Blockchain solution, Automation in construction, Vol. 148, 104746.

Haymaker J., Keel P., Ackermann E. and Porter W. (2000). Filter mediated design: generating coherence in collaborative design, Design studies, Vol. 21, No. 2, 205–220.

Häußler M., Esser S. and Borrmann A. (2020). Code compliance checking of railway designs by integrating BIM, BPMN and DMN, Automation in construction, Vol. 121, No. 103427, 1–24.

ITA Working Group 22 (2022). Chapter 8: classification systems, BIM in tunnelling - guideline for bored tunnels - vol 1, ITA: International Tunnelling and Underground Space Association, Chemin de Balexert 9, 1219 Chatelaine, Switzerland.

Jiang L., Shi J. and Wang C. (2022). Multi-ontology fusion and rule development to facilitate automated code compliance checking using BIM and rule-based reasoning, Advanced engineering informatics, Vol. 51, 101449.

Kaewunruen S., Rungskunroch P. and Welsh J. (2018). A digital-twin evaluation of net zero energy building for existing buildings, Sustainability, Vol. 11, No. 1, 159.

Laakso M. and Kiviniemi A. (2012). The IFC standard - a review of history, development, and standardization, Electronic journal of information technology in construction, Vol. 17, 134–161.

Lai H. and Deng X. (2018). interoperability analysis of IFC-based data exchange between heterogeneous BIM software.", "journal of civil engineering and management, Vol. 24, No. 7, 537–555.

Lehoczky D., Garc D. and Gade P. N. (2022). Adapting the 3s-model for investigating trust in arc solutions in the danish construction industry, Journal of information technology in construction, Vol. 27, 991–1009.

Leng S., Lin J., Li S. and Hu Z. (2021). A data integration and simplification framework for improving site planning and building design, IEEE access, Vol. 9, 148845–148861.

Millán E., Belmonte M., Ruiz-Montiel M., Gavilanes J. and Pérez-de-la-Cruz J. (2016). BH-ShaDe: a software tool that assists architecture students in the ill-structured task of housing design, IEEE transactions on learning technologies, Vol. 9, No. 3, 244–257.

Raslan A., Kapogiannis G., Cheshmehzangi A., Tizani W. and Towey D. (2020). A framework for assembling asset information models (AIMs) through permissioned blockchain, 2020 IEEE 44th annual computers, software, and applications conference (COMPSAC), 529–534.

Rasmussen M., LefranÃ§ois M., Pauwels P., Hviid C. and Karlshøj J. (2019). Managing interrelated project information in AEC knowledge graphs, Automation in construction, Vol. 108.

Sanchez-Stern A., First E., Zhou T., Kaufman Z., Brun Y. and Ringer T. (2023). Passport: improving automated formal verification using identifiers, ACM trans. program. lang. syst., Vol. 45, No. 2.

Scheider S. and Kuhn W. (2015). Applications of conceptual spaces: the case for geometric knowledge representation, Springer International Publishing, Cham, 97–122.

Steel J., Drogemuller R. and Toth B. (2012). Model interoperability in building information modelling, Software & systems modeling, Vol. 11, No. 1, 99–109.

Wang Z., Ouyang B. and Sacks R. (2023). Graph-based inter-domain consistency maintenance for BIM models, Automation in construction, Vol. 154, 104979.

Witherell P., Grosse I., Krishnamurty S. and Wileden J. (2013). AIERO: an algorithm for identifying engineering relationships in ontologies, Advanced engineering informatics, Vol. 27, No. 4, 555–565.

Wonjiga A. T., Peisert S., Rilling L. and Morin C. (2019). Blockchain as a trusted component in cloud SLA verification, Proceedings of the 12th IEEE/ACM international conference on utility and cloud computing companion, Association for Computing Machinery, New York, NY, USA, 93–100.

Xue F. and Lu W. (2020). A semantic differential transaction approach to minimizing information redundancy for BIM and blockchain integration, Automation in construction, Vol. 118, 103270.

Tunnelling for a Better Life – Yan, Celestino, Thewes & Eberhardt (Eds)
© 2024 The Author(s), ISBN 978-1-032-80042-4
Open Access: www.taylorfrancis.com, CC BY-NC-ND 4.0 license

Why is it worth using BIM in tunnelling?

Florent Robert*
CETU, Bron, France

Nataliya Dias
Andra, Châtenay-Malabry, France

ABSTRACT: Digital transformation is underway in the tunnelling sector. BIM (Building Information Modelling) is gradually taking root in our practices in major underground infrastructure projects. Following the impetus given by the French national research project MIN^{n}D for BIM in infrastructures, AFTES (the French association for underground space and works) decided to set up a working group dedicated to new digital technologies for underground works, with BIM at the forefront. The decision has been made to publish a first recommendation to present BIM in an accessible way and familiarise the various players in underground construction with the concept. The recommendation will also set out to meet the expectations of stakeholders: tunnel owners, project managers, construction companies, tunnel operators or maintainers of the structure built using the BIM framework. The recommendation will show the links between the various players and the various phases in the lifecycle of the project, from design through to construction and operation. For this type of approach to be successful, it must be supported by the main player in the construction process: the owner. This recommendation is therefore specifically aimed at project owners, to raise their awareness of the challenges of BIM.

Keywords: BIM, tunnelling, owner, designer, contractor, maintainer

1 INTRODUCTION

A number of countries have made, or are in the process of making, the use of BIM in infrastructure more or less compulsory. This is particularly the case in Italy, the United Kingdom and certain Nordic countries. Some major contracting authorities, such as Luxembourg's rail company, are going even further by requiring the use of libraries of proprietary objects supplied by them and the use of specific software tools. For its part, the German tunnelling association, DAUB, has already put forward several recommendations describing how to use BIM in underground structures [1] [2] [3]. The ITA has also published two guidelines on the use of the ISO 19650 standard [4] [5] and on Bored tunnels [6] in 2022.

In France, there is currently no regulatory obligation to use BIM. There have been incentives in the building sector with the Building Digital Transition Plan (PTNB) in 2015, which has been extended with the BIM 2022 plan, but limited to the building sector. In the infrastructure sector, the French national research project MIN^{n}D [7] for BIM in infrastructures has been working since 2014 to promote the use of BIM in infrastructure. At Andra's initiative, MIN^{n}D has been looking at specific use cases for underground works since 2017 ([8] [9]). Work was carried out on the development of taxonomies and neutral formats, which were then taken to the international level within building SMART International [10].

In 2019, the French Tunnelling Association (AFTES), aware of the challenges and expected benefits of BIM, set up a working group dedicated to new digital technologies, GT 45, to explore the subject. It quickly became clear that we needed to answer the question "why" use BIM for underground infrastructures.

In an attempt to answer this not-so-trivial question, which goes beyond the strictly French framework, the AFTES has drafted a recommendation ([11] currently being published) on the expectations of the main players in the construction industry, be they the project owner, the project manager, the construction company or the operator-maintainer.

2 THE POTENTIAL BENEFITS OF BIM

One of the recurring questions on the subject of BIM relates to the benefits that such an approach can

*Corresponding author: florent.robert@developpement-durable.gouv.fr

DOI: 10.1201/9781003495505-390

bring in relation to the investment made. On this subject, the European Commission has produced a methodological document for calculating the costs and benefits of using BIM in public procurement procedures [12]. This document analyses several types of projects (including infrastructures). Overall, the higher the level of BIM maturity, the greater the benefits in both financial and environmental terms.

Above all, BIM means access to structured information for everyone, at any time, according to pre-established rules. But access to information is not an end in itself; the benefits come from using it to improve project control and limit a whole range of non-quality issues. The models, the digital mock-ups, the information and the data they contain are made available to all those involved in the project, guaranteeing that financial, timescale and/or technical objectives are met.

One of the ways in which BIM can be put to good use is by improving collaboration between teams, by sharing project information in a structured way, and by tracing the decisions made throughout the life of the project, thereby optimising its design, construction and operation. By centralising data (one single source of truth), BIM ensures that up-to-date information is stored and made available. The benefits of BIM are discussed in more detail in paragraph "BIM-related issues for the owner".

Through a more integrated design process, the use of BIM is expected to reduce the number of late design modifications thanks to cross-referenced information updated in real time: correcting a project at the design stage is less costly than a modification during the construction phase. By way of example, BIM makes it possible to detect layout and/or geometry conflicts between different elements from different trades, and to optimise collaboration between the different trades. This is illustrated by the Mac Leamy curves (Figure 1), which show the benefits of early integrated design:

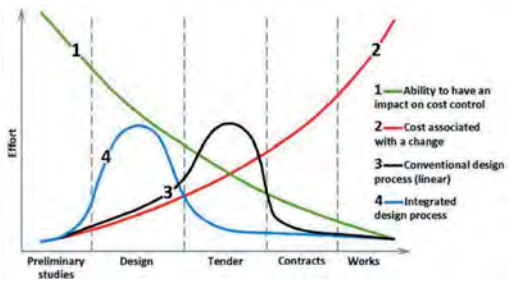

Figure 1. Mac Leamy curves.

Thanks to the integrated design process, it is possible to make some decision changes at an early stage when ability to have an impact on cost control is high and when the cost associated with this change is still low.

BIM also helps to optimise the project because, as a process (with human and technological resources), it enables:

- **Improved performance for everyone involved**, because the use of BIM in their work is a source of efficiency and continuous improvement. Although the benefits for the owner are not necessarily direct and immediate, they are at least indirect, over the long term. Another benefit derived from BIM is that it limits errors, inconsistencies and non-quality, therefore reducing the differences between the initial forecasts in terms of costs and deadlines, the actual timescales and the final cost.
- **Improved overall efficiency** of the project's production system, made up of all the project stakeholders:
  - The implementation of BIM at the overall project level enables easier exchanges of controlled, produced and used data by the stakeholders, each for their own requirements. Not only is this a performance factor for the stakeholders, it also helps the project owner to meet obligations to provide relevant and valid data, providing better visibility and greater confidence in the said owner's control of the project.
  - The collaborative nature of BIM is also demonstrated by the fact that it provides a powerful framework for collaboration and interface management, and guarantees the consistency of the models developed by all the participants, both within and between phases of the project. In this respect, BIM is a way for the owner to reduce the risk of inconsistencies and errors between its various co-contractors and partners, by anticipating and limiting the need to rework the design or construction.

Figure 2. Simulation of the integration of the infrastructure into the landscape (source CETU).

- **Better consideration of the structure's environment** (Figure 2), particularly the physical environment, guarantees greater relevance of the structure, and is also a factor in risk reduction. This is where BIM's power of spatial integration comes into its own. The power of BIM also lies in the ease with which it can be understood. A digital

mock-up is less open to misinterpretation than 2D plans, sections or sketches, forcing everyone to create their own spatial representation.

The benefits can also be seen in terms of **sustainability**, by limiting environmental impact, enabling eco-design at an early stage in the design process, better control of calculations and management of carbon footprints, and optimisation and reduction in the waste of materials used. The health and safety benefits can also be highlighted during the construction and operation phases, through the potential reduction in the number of accidents as a result of better anticipation of design, even though we still lack hindsight on this subject. Finally, the persistence of the data is a tremendous advantage over the lifetime of the project, enabling it to be more durable, reliable, safe and available.

3 SPECIFIC FEATURES OF UNDERGROUND STRUCTURES

Underground structures have specific characteristics that must be taken into account as part of a BIM approach implemented on a project. These include, but are not limited to:

- **The importance of geology, geotechnics and hydrogeology**, and the need to separate factual information from interpretation. In other words, Book A (factual data) and Book B (interpreted data) (cf. recommendations of AFTES WG32 [13] [14]). It should be noted, however, that it is possible to deploy a BIM approach on a project without incorporating these key areas.
- **Georeferencing** is particularly important for underground structures. The structure must be perfectly positioned both on the surface and at depth in order to assess its impact and optimise its location, particularly in relation to its environment (starting with the geology) and the positioning of emerging structures (tunnel portals, ventilation shafts, etc.). In addition, on long structures, the rotundity of the Earth must be taken into account. Some major projects even have their own georeferencing system (for example, the "LTF2004" coordinate system was created in 2004 with the IGN (for France) and the IGM (for Italy) for the Lyon-Turin Euralpine Tunnel).
- **Underground structures can have a complex geometry** and, in addition to the fact that they can be linear, they can interface with volumetric structures (underground stations, etc.) and have variations in geometry (section enlargement, cross-over, connections with shafts, etc.) that are difficult to apprehend in space, making the BIM approach all the more beneficial and effective.
- **Uncertainty**: whatever investigation campaign is carried out, there is still residual uncertainty as to the ground conditions that will actually be encountered, and consequently as to the suitability of the excavation and temporary support methods, and as to the stresses to which the structure will be subjected. The question is how to use digital models of the structure and its environment to better manage this uncertainty, bearing in mind that BIM is not intended to eliminate all risks, but rather to help manage them.
- **Neighbouring structures**: this is a problem that can exist for any structure, and in particular any structure foundation, but which is particularly acute in underground works (urban ones in particular). A virtual 3D model of the planned structure and the existing structures, in which the digital model of the project should play a key role, should make it easier to perceive interferences (primarily geometric but also geotechnical), and facilitate their management. BIM may not be absolutely necessary in this respect, but it does make it effectively possible and on an ongoing basis as the project evolves. Beyond the geometric contact or parametric conflict, there is the question of the wider impact that the structure may have on the surrounding area, and using the BIM model to better assess these impacts.
- **Excavating the ground**: one of the specific features of underground work is that the ground is excavated in order to build the final structure. The features encountered (geology of the face, water ingress, faults, etc.) disappear as the excavation progresses and the support and final lining are put in place. Hence the importance of collecting this information, storing it and using it over time: firstly, during the construction phase, to ensure that the support is appropriate for the geology encountered, and to have reliable information on the conditions actually encountered, particularly in the event of a dispute, then secondly, during the operation/maintenance phase, because in the event of pathologies observed several years after commissioning, archived data related to the ground encountered during excavation can be very useful for diagnosis and the repairs to be implemented.
- **Auscultation**: the structure under construction and the finished structure, including the surrounding area where appropriate, can be instrumented and auscultated. The resulting data must be able to be stored and used at any time during the life of the structure.
- **Temporary structures**: temporary support structures that remain behind the final lining once it has been put in place and that have been determined using the observational method, or technical or reconnaissance galleries or shafts that are subsequently "abandoned". It is important to keep a record of these structures in the event of subsequent intervention, in order to avoid incidents or unnecessary complications.

4 BIM-RELATED ISSUES FOR THE OWNER

Deploying BIM on a project makes it easier for the owner to achieve the objectives it has set for the project, or to aim for higher objectives. This applies to the programming phase of the project, the design phase, the construction phase, and then to the operation of the completed project, and the performance of this operation in terms of cost, quality, deadlines and compliance with expected functionalities.

It is important to note that BIM is not just a matter for each individual; the greater the number of stakeholders involved, the greater the benefit. The project owner will also derive even greater benefits. The owner is in fact the one who has the final say in setting up a BIM approach for the project, and in involving its service providers. It is therefore the quality of the BIM organisation that the owner puts in place for its project that will determine the level of benefits it derives from it. There is no tunnel management or operation company that does not itself have an information system. The data and data structures of this information system are defined during the definition, design and construction phases and are fed into the BIM process. It is therefore essential for the project owner to specify its BIM requirements in order to feed the future information system of those involved in operation and maintenance.

The expectations of the owner with regard to BIM as **a support for project management** are to achieve at least the objectives defined in its BIM policy. The owner establishes contracts with its partners for the development of initiatives that contribute to or even extend these objectives, in accordance with 5 strategic areas of project management for the project owner and with regard to:

- Technical control, quality, performance, safety and environment requirements;
- Cost and deadline control;
- BIM Management and the efficient use of digital mock-ups;
- Consultation, communication and decision-making tool;
- Technical management of assets and configuration management by future operators-maintainers.

With regard to BIM as **a model of data relating to the structure**, describing its physical characteristics, and a digital mock-up of the project representing it, project owner expectations are related to:

- **Quality**: the digital project mock-ups should effectively constitute, at all times, a quality reference database of project management and asset data, i.e. the information contained therein is exhaustive, verified and easily accessible. Digital project models should provide privileged access to such information and the place where it is stored. This will ensure that everyone involved, including the owner, has accurate knowledge of the project, whatever the stage it is at. This implies rigorous management of the model and its successive reference versions;
- **Durability**: the digital mock-ups of the project need to be durable. This implies having them in non-proprietary formats, whose continuity and availability are guaranteed over time, including after completion. In practical terms, this means providing digital mock-ups in a neutral, interoperable format. Today, it is clearly recommended to use IFC formats as they result from the ISO 16739 standard. Note that the data and associated documents (EDM) must also be durable;
- **Interoperability**: that the digital mock-ups of the project are interoperable with other tools or information systems useful to the operation, for the various participants and in particular for the owner, and that they are integrated into the overall information system that the owner uses to manage and operate the project. This means that all those involved in the project, who will be producing data and contributing to BIM, must comply with common requirements in terms of what they produce.

With regard to BIM as **a collaborative tool, expectations are related to**:

- **Sharing**: the expectation is that BIM, digital mock-ups and databases will be effectively shared by all those involved in the same phase of the project, and will be effectively used as a support for collaborative working. By facilitating coordination and collaboration between the players involved, the aim is to improve the overall performance of the project, so that everyone benefits, directly or indirectly;
- **Consistency**: the expectation is that those involved in the project, who are the producers of the information and data making up the BIM, will comply with common standards, which will enable the above-mentioned exchanges on the one hand, and the creation of a consistent database on the other. This is a prerequisite for successful sharing. These include file formats such as IFC (Industry Foundation Classes), which is recommended for digital mock-ups, and BCF (BIM Collaboration Format) for managing BIM subjects;
- **Opposability**: the expectation is that the BIM model thus created can be used as evidence in exchanges between the various players, in terms of its representativeness of the structure. In fact, for a structure that is still in the planning stage, and even once it has been completed, the BIM model contains and enables the manipulation of a much greater quantity of data than is possible with other models. This expectation is therefore driven by a concern for efficiency and consistency. It corresponds to the question of the contractual value of BIM;
- **Transversality or Digital Continuity**: the expectation is that the BIM model created during

one phase of the project's life cycle as deliverables, through the collaborative work of all the players in that phase, can actually be a working basis that is directly integrated by the players in the next phase, as input data.

5 BIM-RELATED ISSUES FOR THE PROJECT MANAGER

From the outset, the project manager needs to be fully aware of the owner's objectives, needs and requirements, which are expressed in part in its Employer Information Requirements or BIM specifications and thus anticipate the following points as far upstream as possible:

- Processes, methods, workflows, exchanges and collaboration, production, verification and validation circuits for digital mock-ups and data;
- Recommendation of the resources needed to successfully complete the project (players, skills, profiles);
- Data coding and structuring, level of information need;
- Tools, softwares, platforms (in particular BIM collaboration platform - BCP or Common Data Environment - CDE) and formats.

Where possible, the project owner must also be aware of the BIM requirements of the future infrastructure manager and maintainer, and where applicable the transport operator, which may differ from those of the project owner, in order to anticipate the best way to return the data. These specifications may, if necessary, be specified later in the life of the project, but in any case, before the specifications for the works that will use them are drawn up. This return of data constitutes the completion of the project and takes the form of the final implementation file (as built), which will be submitted to the operator.

It would be normal for the BIM approach to a project to be set out at the latest when the project management contract(s) is (are) signed, as far as the project owner is concerned, and at the latest during the phase of the award of the works contracts, as far as the future companies holding the works contracts are concerned.

This means that the project owner must be able to provide a framework for this process before launching the call for tenders for the project management team. It can call on the services of an Assistant to the Contracting Authority (ACA) for this purpose.

At the very least, the initial framework should include:

- The designation of the person in charge of the process, who could be called the BIM Project Manager: the project owner or an ACA delegated by the project owner;
- The initial CDE holder: ideally the BIM approach leader;
- Mandatory or priority use cases for the design phase;
- A minimum structure or a principle for structuring the project;
- Specification of interoperable exchange formats at least for the design phase, ideally for the entire project lifecycle;
- The contractual status of the mock-ups for the design phase with regard to the validation of deliverables by the project owner.

However, given the duration of underground works projects and the BIM practices that still need to be refined for this profession, this framework must be able to evolve. In particular, the framework for the works supervision of the project manager could be postponed until the contracting with the construction companies occurs, which would require a modification to the project management contract during the construction phase.

6 BIM-RELATED ISSUES FOR THE CONSTRUCTION COMPANY

In order to achieve the objectives set and to enable the expected uses, all stakeholders involved in a project developed using BIM must have clear and achievable requirements in terms of the information to be provided during the construction phase. The teams in charge of BIM management must define the EIR (exchange information requirements) as defined in NF EN ISO 19650 parts 1 (5.3) and 2, so that the construction company can create and fill in the project information model (PIM) for the construction phase (see Figure 3).

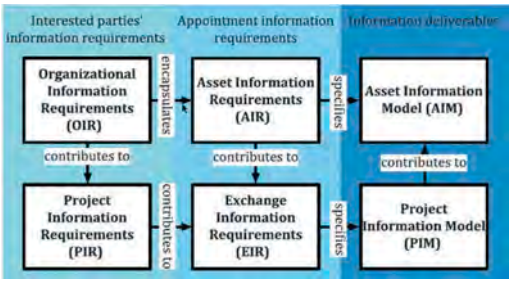

Figure 3. NF EN ISO 19650-1: Hierarchy of information requirements.

The construction company, intervening in the middle of a chain of actions, must have reliable design data, in particular usable 3D models, correctly codified and checked in order to carry out its task.

6.1 *Existing environment data*

The existing environment can be described by 3D models of structures already built, geological and geotechnical models, buried networks (classified and in 3D), and other data sources (GIS, City Information Modelling, databases) in the possession of the owner or the project manager.

For subsurface data, it is important to clearly define the contractual value of the data present in a model (reference must be made to the compendium of factual data (book A) and to the interpreted model (book B)).

For existing structures related to the project, whether or not they have been reworked, it is always useful to have as-built surveys and 3D scans that have been coloured and, if necessary, classified.

6.2 *Model of the structure to be built*

Models of the structures to be built are an essential part of any project. Provided that they are well organised, codified, etc. and where the owner has required the contractor to produce them from the digital design models, they can be used, among other things, to manage quantities in conjunction with the quantity take-off.

It is important to know the degree of reliability or maturity of the data supplied.

The construction company can either develop its own model based on the elements provided in the contract, or retrieve and appropriate the model provided by the owner and produced by the project manager during the design phase. In the latter case, a non-recourse clause should be included in the contract.

7 BIM-RELATED ISSUES FOR THE OWNER-MAINTAINER

7.1 *Owner-maintainer's expectations*

Once the work has been completed, while it is in the operational phase, the "as built" BIM model, also represents a valuable asset for the owner/operator/maintainer from which it can derive multiple benefits:

- Alongside the physical structure, the owner/operator/maintainer will be able to use the "as-built" BIM model to access the verified data that it or its contractors will need for the future management, operation and maintenance of the structure, and ultimately for its dismantling.
- In addition to the data describing the physical structure being built, which is sometimes referred to as legacy data, the BIM can be linked by the owner/operator/maintainer to other tools in its information system, and the model, as a virtual model, can become a particularly ergonomic and powerful access point for data relating to the operation, maintenance and management of the assets that make up its structure. This interoperability enables the development of high-performance applications based on BIM, for the management of these activities, or the control of systems or equipment. This is the digital twin.

The desired interoperability of BIM means that the owner/operator/maintainer must clearly express its requirements for the data model, and the information it expects to find in it, in good time. It can be even more difficult for the owner-builder to do this if the operator or maintainer is only known at a late stage.

It should also be noted that many of the data concerning the as built structure, included in the corresponding BIM model, are not commonly used in the operational phase. For reasons of database size, this leads us to consider that the owner/operator/maintainer can request an additional version of the "as-built" mock-up, purged of data that is not useful for day-to-day operational use.

It should also be emphasised that the foreseeable life of the infrastructure in operation represents the longest period in the life cycle of the structure. In fact, this period is much longer than the initial phase leading from the first sketches to the tender and then to the works.

It should be noted that in certain situations, such as when regulatory compliance work or major renovation operations are being carried out, maintenance operations become a project in their own right, leading to the partial or complete delivery of a new structure. This means that the data needs to be kept up to date as part of the management of an existing asset, and this will undoubtedly require a new organisation to be put in place.

7.2 *Involving the owner/operator/maintainer in the BIM process*

The infrastructure manager must define the data required for the proper management of the infrastructure. By means of a set of specifications, it must specify the organisation of the data it needs to meet its objectives. All this corresponds to the AIM (Asset Information Model) defined by standard NF EN ISO 19650-1 [4]. The AIM is fed by the PIM (Project Information Model) supplied by the works company. Depending on whether or not the infrastructure manager is mature in its BIM approach, the AIM will be integrated very early in the process, or if this is not the case, the manager must be involved upstream in the BIM approach to develop its AIM in order to formalise its requirements and structure the data and models so that they are adapted to its activity.

7.3 *Issues at stake for the owner/operator/maintainer*

Traceability of the various construction phases

One of the special features of underground work is that some of the structures are no longer visible once the work has been completed: the excavated soil, the support and the waterproofing system are no

longer accessible, and only the lining can be inspected. As a result, the BIM model provides access to the information and elements behind or forming part of the tunnel lining.

Points of attention that seem important for the operator and maintainer are as follows (non-exhaustive list):

- The digital model must provide easy access to information, in particular everything behind the concrete lining;
- The digital model should make it possible to trace specific events during the construction phase in terms of geology or difficulties encountered, as these may have an impact on the structure years later;
- The digital model should make it possible to highlight localised particularities (type of lining, dimensions of the structure, geology encountered, etc.) and keep track of the origin of these constructional particularities (design phase, works phase, etc.).

This will be of interest to

- The owner, who wants to know about and monitor the condition of the infrastructure for which it is responsible;
- The operator, who needs to know the information required to operate the infrastructure safely (headroom, gauge, condition of equipment, minimum operating conditions, etc.);
- The maintainer, who needs all this information to carry out its work.

System interoperability

For operators and maintainers, the interoperability of BIM is crucial to making it possible to track assets and maintenance operations on structures and equipment in computerized maintenance management system (CMMS) software. Interoperability will ensure the link between the BIM model and the operating management software. In this respect, it should be borne in mind that the as built model(s) may need to be updated to meet the needs of operations and maintenance, both in terms of the information contained and the level of geometric detail or operations management software. In addition, interoperability must enable information to be transmitted according to the players involved: exchanges between players specify the data to be exchanged.

Operational safety

The use of virtual reality, which is based on the BIM model, may be of interest to external players such as the emergency services. Virtual reality makes it possible to carry out visits to the infrastructure and training staff without having to interrupt traffic (or activity), while guaranteeing that safety personnel have a good knowledge of the structure (see Figure 4). Obviously, the need for real exercises remains. This approach could be taken into account right from the project design phase.

Figure 4. Realistic representation of a safety exercise (source Andra).

Maintenance safety

Virtual reality used as a training medium is an interesting use case, useful for both the operator and the maintainer. In fact, this form of visualisation enables them to familiarise themselves with the infrastructure without having to physically visit the site.

Furthermore, in the case of dedicated modules, it is possible to simulate situations that are considered dangerous without actually being exposed to the risks.

Preparing works to be carried out on the structure

BIM model visualisation tools can be used to:

- Prepare works to be carried out on the structure (safety, security, time saving, better training and efficiency);
- Prepare the phasing of works;
- Check available templates and define works methods;
- Identify storage areas prior to works;
- Define routes;
- Simulate the works before carrying it out in the field.

This is of real benefit to maintainers, who can prepare their work as effectively as possible.

Figure 5. Realistic representation of a tunnel fire (source Andra).

In the case of an intervention during the operational phase (fire drill, for example, see Figure 5), the operator will also be interested in all these aspects, as it will be able to simulate and visualise

the impact of the intervention on the infrastructure for which it is responsible.

Feedback integrated into the design

By including the operator in the design phase, on subjects such as evacuation strategies, smoke extraction, or flooding, the operator will be able to share its experience and provide guidelines for adapting the infrastructure to the use that will be made of it once it is in service.

In addition, by including the maintainer in the design phase, it will be possible to design and build structures and systems that can be easily maintained. For example, the design will avoid cladding structures that prevents inspection of the structure behind them.

The Project Information Model (PIM)

The Project Information Model (PIM) submitted by the construction company, can be sent to the operator and maintainer as soon as the works have been handed over.

BIM should make it possible to improve the operation and maintenance of structures. To make this improvement possible, we need a digital as built model that is adapted to future needs. Involving operators and maintainers early on in the BIM process will ensure that the completeness and quality of the information delivered meet their requirements. Similarly, operators and maintainers will have to indicate their requirements in terms of level of information need. At the same time, the structure of the data will also have to be provided. This requires upstream work to be taken into account right from the start of the project's BIM process.

As far as the completeness of the data is concerned, it is a question of striking the right balance between an abundance of information, some of which will never be used, and a lack of information which would hamper the ability of the operator and/or maintainer to achieve their objectives. This is particularly true of the use of point clouds, the relevance of which for simple structures can be questioned, given the size of the files to be stored.

Traceability of subsequent modifications

For the maintainer and owner, it is important to:

- Be able to modify the model following interventions/modifications made throughout the life of the infrastructure, the aim being to have a digital twin that reflects reality.
- Trace changes in equipment and structures over time and make it possible to specify the date of changes/modifications.

Digital twins

Operation and maintenance require the management of information flows modelling all the states of a structure over time. It is this concept that needs to be integrated very early on in the life of a project.

To date, there are different ways of looking at digital twins, depending on their level of connection (IoT or other), the technological building blocks applied (SCADA, GIS, BIM, CMMS, etc.) and the vision expected of them (web portal, 2D, 3D, cartographic, etc.). Unlike static data models, digital twins are dynamic, "living" entities that evolve over a defined timeframe, or even in real time. This is because the virtual representation of the structure can be connected to the various sensors installed throughout the infrastructure, via a processing system that enables the descriptive, relational or analytical data from the virtual twin and the real structure to be displayed and synchronised.

Once informed of this data, it is possible to use the digital twin to run simulations of interventions, study performance problems and generate possible improvements, all with the aim of generating valuable information that can then be reapplied to the original real physical object.

In this way, the definition of a digital twin specific to the infrastructure to be operated or maintained must be guided by its use, depending on the interoperability of the technological systems in place or to be built. By integrating the digital model into the digital twin, and therefore a geometric and information reality, the latter will have to keep pace with changes in the actual structure by updating the data in the virtual structure.

8 CONCLUSION

Digital transformation is having an impact on our businesses and the way we work, starting with the use of BIM. A BIM approach cannot be improvised, and must be understood and prepared for by all those involved in underground construction, starting with the owner. It is the owner who initiates the BIM approach, who decides whether or not to include it in the contractual requirements, who defines its BIM policy and strategy and who transposes it into its contracts (BIM specifications) with the project manager and the works companies. If the "constructor" project owner does not operate the infrastructure, the infrastructure operator/maintainer must be involved in this process as early as possible. In order to benefit from the advantages of BIM, the project owner (including the infrastructure operator/maintainer) must establish the digital continuity of its operation, define the roles of each party, the nature of the deliverables, what they are expected to achieve and the objectives and uses to which they are to be put.

To this end, the owner must be clear about its strategic objectives, which it has defined and described in its BIM specifications. It must also be clear about who it is entrusting with BIM management and what its responsibilities are. In addition, the owner must be able to require the BIM project manager and the BIM management team to clearly detail the level of information need required, according to the notion of the right level of information (neither too much nor too little), depending on the phase, discipline

and profession of the various people involved in the BIM model.

It is also important not to underestimate the resistance to change that this entails within the structures of the various players, as well as the investment required. A BIM approach, just like a Quality approach or a project to reorganise an entity, whose principles it resembles, must be supported at the highest management level of the players involved, starting with the management for deployment within a legal entity or by the project owner in the case of a project.

REFERENCES

[1] DAUB, Digital Design, Building and Operation of Underground Structures BIM in Tunnelling, 2019.

[2] DAUB, Digital Design, Building and Operation of Underground Structures - Model requirements - Part 1 Object definition, coding and properties, 2020.

[3] DAUB, Digital Design, Building and Operation of Underground Structures Model requirements – Part 3 Ground Model, 2023.

[4] ISO, ISO 19650-1:2018 Organization and digitization of information about buildings and civil engineering works, including building information modelling (BIM) — Information management using building information modelling — Part 1: Concepts and principles.

[5] ITA-AITES-WG22, Recommendations for the Application of ISO 19650 Series during the Delivery of underground Projects and Assets – Information Management Process and Responsibility Matrix – Vol 1, 2022.

[6] ITA-AITES-WG22, BIM in Tunnelling – Guideline for Bored Tunnels – Vol 1, 2022.

[7] MINnD, "Projet National de recherche MINnD (Modélisation des informations interopérables pour les infrastructures durables)," [Online]. Available: https://minnd.fr/.

[8] F. Robert, A. Rallu, C. Dumoulin, N. Delrieu, M. Rives and M. Beaufils, "Building information management for tunneling," in *World Tunnel Congress 2019*, Naples, 2019.

[9] M. Beaufils, S. Grellet, B. L. Hello, J. Lorentz, M. Beaudouin and J. C. Moreno, "Geotechnical data standardization and management to support," in *World Tunnel Congress 2019*, Naples, 2019.

[10] M. Rives, A. Bormann, F. Robert, N. Dias, J. Thoren, G. Brino, H. Shima, J. Weil, J. Hoel, J. Dunn, P. M. A. Vorthon and G. Merkel, "buildingSMART International IFC standards for underground infrastructures," in *World Tunnel Congress*, Copenhagen, 2022.

[11] AFTES, GT45R1F1 BIM en travaux souterrains - Principes généraux (to be published).

[12] European Commission, Calculating Costs and Benefits for the use of Building Information Modelling in Public Tenders - Methodology Handbook, May 2021.

[13] Caractérisation des incertitudes et des risques géologiques, hydrogéologiques et géotechniques – Recommandation AFTES n°GT32R2F1, 2012 – n°232.

[14] Prise en compte des risques techniques dans les projets d'ouvrages souterrains en vue de la consultation des entreprises – Recommandation AFTES n° GT32R3F1, 2016 – n°258.

Tunnelling for a Better Life – Yan, Celestino, Thewes & Eberhardt (Eds)
© 2024 The Author(s), ISBN 978-1-032-80042-4
Open Access: www.taylorfrancis.com, CC BY-NC-ND 4.0 license

Digital automation in the structural modelling process for tunnel linings – A digital tool-based case study

Arjun Shivasami* & Grant Heath
Mott MacDonald, Sydney, Australia

ABSTRACT: Automated design processes are often relied upon for efficacy and innovation in engineering, particularly for complex problem-solving needs in tunnel projects. This paper will present a case study within a project in Australia where SpeedBot's modern digital techniques, including Computational Design (CD) streamlined the modelling process, allowing for various iterations of loading sequences and lining thicknesses to determine the effects of increased loading on a large span cavern. The case study presented in this paper required the structural modelling of a cavern subjected to surcharge loading from aboveground building development, with varying potential loading conditions due to the unknown load path due to the surrounding geology. Multiple structural models were required to analyse best and worst-case scenarios, however, various amendments such as tunnel lining thickness and assumed load dispersion width would need to take place within each model. The time estimated to undertake all required models was significant, however the project did not have the luxury of time. SpeedBot was adopted as a feasible approach to undertake all the required models not only in significantly less time than conventional modelling techniques, but providing a singular modelling approach, improving accuracy. Tunnel designers implemented SpeedBot for the modelling of tunnel concrete linings, through digital collaboration using commonly used commercially available software. This enabled the integration of computational processes, producing output files that can be recognised by Autodesk ROBOT for designers to undertake the required structural analysis. SpeedBot's scripted automation arrangement allowed the first step in the structural engineering process to be automated, significantly reducing modelling time, allowing more time for tunnel designers to analyse output results and focus on first principles for better outcome. The digital tool enabled the designers to compare the potential use of unreinforced vs reinforced concrete linings and promoted optimal solutions in the early stages of design.

Keywords: Tunnel Concrete Linings, Digital Tool, Computation Design, Automation, SpeedBot, Sustainability

1 INTRODUCTION

Designing tunnel support systems is both a complex and extensive process, with structural checks needing to be undertaken for both temporary and permanent support systems. These forms of analysis are resource-intensive and can take weeks for multiple models to be developed and run, consuming large percentages of allocated budgets for the design process. As a minimum, permanent concrete tunnel linings require greater analysis in the form of a bedded beam model using industry-standard structural software and are more time-consuming in terms of structural design than primary support systems, such as shotcrete linings and rockbolts arrangement. Time is also heavily invested during this process for multiple engineers to review the analysis undertaken, requiring collaboration between engineers to determine the approach taken for the analysis and understand the complexity of the model.

This situation was outlined as a potential area for the use of an automation tool during the concept design for one of Mott MacDonald's transportation projects. Additional surcharge loading from a new building to be situated directly above a large span cavern was identified to be a possible risk for the design, giving concerns over the structural adequacy of the permanent lining. To raise concerns further, the additional development loading was in a region of low ground cover above the cavern crown and the load path through the surrounding medium could not be easily determined, requiring multiple analysis options to be conducted. To address these challenges, Mott MacDonald saw opportunities in digital tool implementation into major projects and drew on the capabilities of digital tools in the form of a tool codenamed 'SpeedBot'. The tool leverages the capability of various commercial structural

*Corresponding author: arjun.shivasami@mottmac.com

DOI: 10.1201/9781003495505-391

analysis software's to synchronously automate building multiple bedded beam models representing a 2D tunnel concrete lining, along with the spring stiffness that accounts for the interaction with the surrounding medium. The scripted automation arrangement of 'SpeedBot' proved pivotal in the turnaround of the required modelling, which included multiple models detailing different potential load dispersion sequences due to unknown load paths through the surrounding geology. By implementing scripted automation, significant time was saved by the engineers involved, enabling the analysis undertaken to feed efficiently into further steps like structural design and detailing.

2 SPEEDBOT OVERVIEW

During any structural analysis of tunnel lining, the designers will be required to run a multitude of numerical simulations to understand the performance of the concrete lining and its interaction with local ground conditions, loadings, and their combinations. This becomes critical especially when the properties and behaviour of a given ground are not known, resulting in varying possibilities acting on a tunnel lining. This section of the paper will introduce the concept of automation for structural modelling using SpeedBot and the breakdown of its advantages. A task like this for a single cross section can generally take up to 32 manhours for a designer to complete from start to finish, consuming the focus of the engineer and limiting the time for engineering innovation to be considered during the overall process.

The overall concept of SpeedBot, is to remove significant portions of manual labour from the structural modelling process, highly reducing human errors and allowing tunnel designers to focus their time on research of viable inputs to best change the overall outcome. SpeedBot facilitates Finite Element Analysis (FEA), which is quite complex during model building, to be completed in significantly less time than standard modelling techniques, approximately 12 times faster for a single model to be produced. The approach allows the team to share standardised practice content globally across the organisation, lifting the standard and capacity of other projects and teams.

The benefits of SpeedBot are utilised during the modelling stages when inputs and parameters are to be defined. Through the scripted automation demonstrated in Figure 1, manual inputs for tunnel models, such as tunnel geometry, load patterns and magnitudes, load combinations, materials properties, and spring stiffness, are streamlined and scripted into the physical modelling process producing a completed model within few minutes rather than serval hours when conventional modelling techniques are applied. Tunnel modelling for structural analysis is not a one-cycle process, inputs will need to be changed and altered several times before a model is reviewed and finalised for design. This requires multiple designers to use a significant portion of project budget to develop these models. SpeedBot provides an alternative to applying these changes to the model, providing substantial savings with reduced modelling time.

The most immediate benefit of SpeedBot is the time and cost saving in structural model building and overall design process but in the long-term, it sets a pathway to sustainable outcomes. Building complex geometries into a 2D tunnel model can be difficult and introduces a large potential for human error. By implementing automation tools, the complexity is simplified completing the model building in few minutes and without any potential for human error within structural software during plotting, defining of geometry, loading, combinations, and support stiffnesses. Not only is time saved in the creation of a model, but also in any subsequent model iterations. In the manual development of tunnel models, even the smallest adjustment to geometry requires an almost entire rebuild of the model, but with automation, these changes are incorporated and updated almost instantly and without error. This exponential reduction in design manhours facilitates the designers to focus more on engineering fundamentals rather than spending time on labour-intensive computations and modelling.

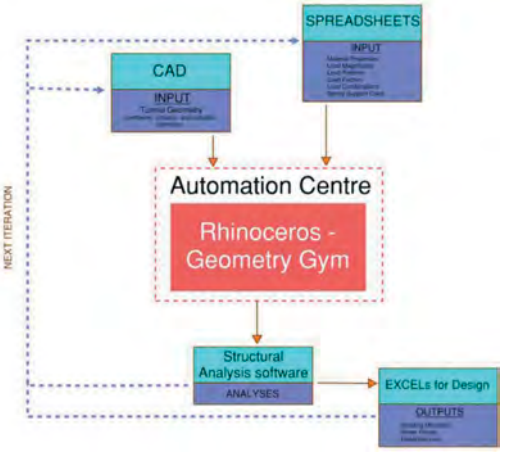

Figure 1. Automation scheme of SpeedBot.

A simplified digital approach provides the designers with more opportunity to do additional sensitivity checks, and trial and error exercises to avoid generalisation and conservatism in the tunnel design, so to a larger extent aiming for optimised and hence the more sustainable solutions. The SpeedBot tool combines the various functionalities of Excel, VBA, Rhino, Grasshopper, and Geometry Gym plugin library to offer an innovative approach to generate 2D tunnel profiles subsequently ready for analysis by structural software. By leveraging the specific capabilities of each application and then linking

them together into a digital workflow, SpeedBot enables efficient tunnel modelling and prepares for quick analysis, reducing human errors and manual effort but ensuring accuracy. A complete breakdown of the various functionalities SpeedBot utilises was documented by Shivasami et.al. (2023) in the paper SpeedBot – A digital tool for automating the structural modelling process for tunnel linings.

3 SPEEDBOT IMPLEMENTATION FOR TUNNEL LINING UTILISATION CHECKS

This section of the paper demonstrates the advantages of implementing SpeedBot into a major transportation project where the structural adequacy of a tunnel permanent lining was investigated for various possible loading conditions that were not originally envisaged in the reference design.

The automated approach to the tunnel modelling offered by SpeedBot and the eventual analysis was implemented during the concept design of one of the major rail transportation projects currently under construction in Sydney. The structural adequacy of a station's permanent lining was under investigation due to an unforeseen addition to the concentrated surcharge loading from a newly proposed overhead building development. The foundation arrangement of the overhead building development in proximity to the tunnel in question is shown in Figure 2. Due to this additional loading, and the uncertain distribution path the loading may take through the surrounding rock, the potential increase in the lining utilisation needed to be checked. However, multiple beam-spring models for each loading circumstance would be time-consuming and expensive. Due to the sudden change, a quick turnaround was needed since the luxury of time was not available, but the prompt technical advice must also be reliable and accurate as it could have potential impact on major contractual decisions. The assembly of one model, due to the complexity and unknown loading conditions can take up to a week to model for a single possible loading condition. For multiple loading conditions, this process can be quite lengthy, requiring multiple tunnel designers to produce multiple models, and introducing different modelling approaches which can lead to a validation process to avoid errors in modelling and misinterpretation of parameters by other tunnel engineers.

The undrained cavern under investigation had a span greater than 25m, a constant 800mm thick concrete lining above the spring line, with very little clearance from the crown of the tunnel to the load point in the ground, of only 3.5m. The loading conditions and magnitudes from the building was known, however the load path possibilities from the structural toe of the foundations onto the cavern were uncertain, resulting in designers assuming the load path through various inclination angles. The load dispersion inclination angles proposed under the footings were 30, 45, and 60 degrees from the underside of the four proposed structural element's foundation, two walls of varying thickness with strip footing and two pad footings supporting column loads. This approach provided more realistic loading possibilities for the surrounding geology while providing crucial information on the lining's behaviour under various loading conditions. In addition, a standalone 20 kPa traffic surcharge was considered as an alternative load case to the new building development to determine which loading case would increase the stress within the tunnel lining.

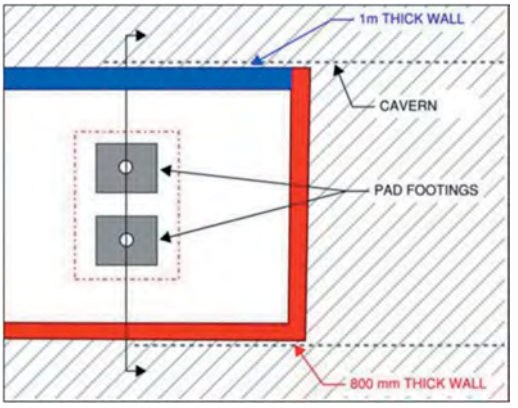

Figure 2. Plan of identified loading conditions on station cavern.

To accurately simulate the conditions in the cavern, the lining was modelled as a series of 500mm straight beam elements 1000mm in depth in the out-of-plane direction, analysed as a beam spring model accounting for appropriate load factors and combinations for Ultimate Limit State (ULS) and Serviceability Limit State (SLS). The geology surrounding the lining was represented as compression-only radial and bi-directional tangential spring support stiffnesses, at increments of 500mm, acting at the supports of the straight beam members. The thickness of the lining members below the spring line were incrementally increased towards the invert of the tunnel at 500mm increments, representing the transition to the invert region of the tunnel.

A specific challenge that designers identified during their preliminary review of the cavern focussed on the concentrated regions of high loading, potentially altering the standard compression/tension zones, and bending moment patterns the lining was originally designed for. Figure 3 illustrates the possible inclination angles of the loading dispersion through the surrounding rock. The identified loading regions on the tunnel lining above the widest span of the tunnel profile showed some regions had very high loading concentration at different locations along the crown of the cavern.

Since the loading inclination angle was not certain, analysing the lining for various potential angles was the only option, otherwise, the design would be incomplete and a high risk if not accurately investigated. The idea of implementing SpeedBot during this phase of the design had positive feedback from the designers, with specific problems and issues being identified as a result, which conventional modelling practices may not have revealed.

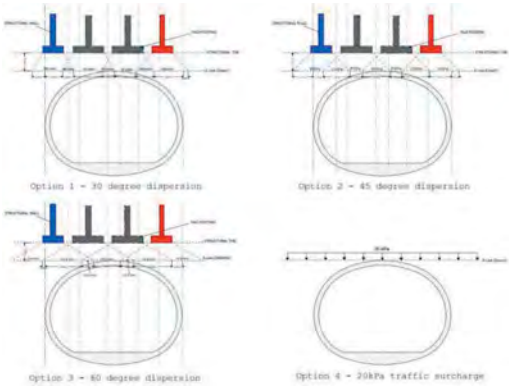

Figure 3. Load dispersion comparison between various options.

The modelling process for this sort of optioneering structural investigation using conventional modelling methods would take a few weeks, including various checks being time-consuming. These requirements include geometry development through AutoCAD, the application of load patterns, manual input of various load factors and combinations, and assigning support stiffnesses within the designated structural software once the tunnel profile has been imported into the structural software. In some instances, the designers chose to build the tunnel profile manually within the structural software which is even more time-consuming. Figures 4 – 7 demonstrate the interface of SpeedBot at different phases of the overall design process, including load combination definition, to results interrogation.

Figure 4. Principal load cases and its pattern definition in SpeedBot through MS Excel interface.

In this case study, the output from SpeedBot was analysed using Autodesk Robot 2022 (ROBOT), that was utilised to investigate the change in forces to the tunnel lining. Loading diagrams, such as bending moment and shear diagrams indicated the regions where significant force increases were situated along the crown and side walls of the lining, while producing result output spreadsheets, documenting the magnitude of loads at each node. These loads are inputted into a pre-determined spreadsheet template, which was created with various structural checks in accordance with BS-EN1992-1-1-2004 for unreinforced concrete and AS5100 for reinforced concrete, including stress/strain, flexural, and shear checks, determining the adequacy of unreinforced concrete. Both unreinforced and reinforced lining solutions were analysed as options and investigated to provide feasible construction options, as designers settled that both options had advantages and disadvantages given the identified loading and design life requirements.

SpeedBot enabled various iterations of loading models to be produced in significantly less time than traditional modelling techniques, allowing varying lining thickness and loading configuration for a proposed unreinforced tunnel lining. Table 1 shows the options tested for each loading configuration, determining the required lining thickness for each loading type, to withstand the additional forces imposed on the lining. As expected, the designers observed that the various loading cases predominantly had tension as a critical force type on the lining, resulting in unreinforced lining suggestions to be of increased thicknesses. Note that Table 1 only shows a small section of the results for the options executed in SpeedBot since documenting the results of all optioneering exercises is out of this technical paper's scope.

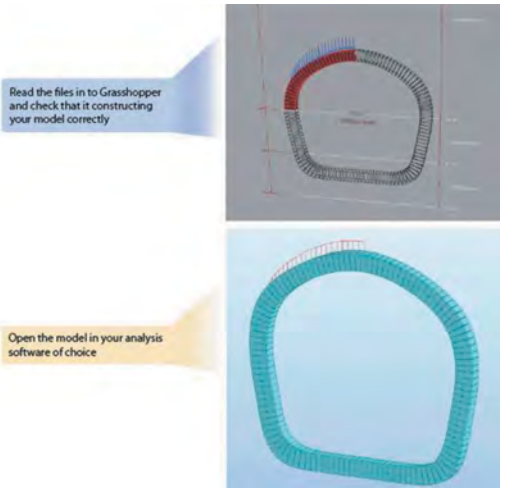

Figure 5. Example of executed automation and transition into Autodesk Robot.

Table 1. Unreinforced concrete lining utilisation at varying thicknesses and loading cases.

	30 Degrees		45 Degrees	
Loading Action	Thickness (mm)	Utilisation (%)	Thickness (mm)	Utilisation (%)
Compression	500	80	500	78
Tension	800	93	850	99
Shear	400	95	400	91
Loading Action	60 Degrees Thickness (mm)	Utilisation (%)	Traffic Surcharge Thickness (mm)	Utilisation (%)
Compression	500	78	500	97
Tension	800	94	900	97
Shear	400	93	400	93

Table 2. Maximum crown deflection for all loading cases at 800mm thick lining.

	30 Degrees		45 Degrees	
Loading Action	Thickness (mm)	Max Deflection (mm)	Thickness (mm)	Max Deflection (mm)
Max. Crown Deflection	800	7.12	800	6.73
Loading Action	60 Degrees Thickness (mm)	Max Deflection (mm)	Traffic Surcharge Thickness (mm)	Max Deflection (mm)
Max. Crown Deflection	800	6.86	800	6.63

The aim of this paper is to demonstrate the capability and the benefits of implementing SpeedBot for tunnel lining optioneering analyses through a case study. Significant time was saved compared to traditional modelling techniques which would take tunnel designers many weeks to complete all the models tested and verified.

To determine serviceability checks for both unreinforced and reinforced concrete linings, the maximum crown deflection was determined for all loading actions at a lining thickness of 800 mm. The maximum deflection identified in Table 2 was identified at the crown of the tunnel profile as anticipated.

Similar to the unreinforced concrete checks, SpeedBot enabled accelerated design checks for reinforced concrete linings using RAPT, determining the required lining thickness and reinforcement to withstand the above load cases. RAPT was used to examine the outputs produced from SpeedBot, in the form of a predetermined template, producing M-N interaction diagrams against AS 5100 to determine the adequacy of the proposed lining thickness and its reinforcement arrangement.

Despite the problem at hand being very specific and the models developed only addressing specific concerns, further optioneering prospects for this case study were identified by designers during the above process. Identified areas for optioneering studies of the developed models included modelling various ground conditions, such as higher/lower groundwater levels or soft ground conditions. The designers opted to use the available data from the identified boreholes within the region of the cavern, recognising the quality of the ground in which the cavern would be encased. This caused alterations to the structural models for various scenarios through the radial and tangential spring stiffness, representing the behaviour of the surrounding geology to the lining. Additionally, different load combinations also impacted the results produced from all models. The various possible load combinations for the analysis were identified and used for the completeness of the study. The ground conditions and load combinations could be altered quickly and tested seamlessly with the implementation of SpeedBot.

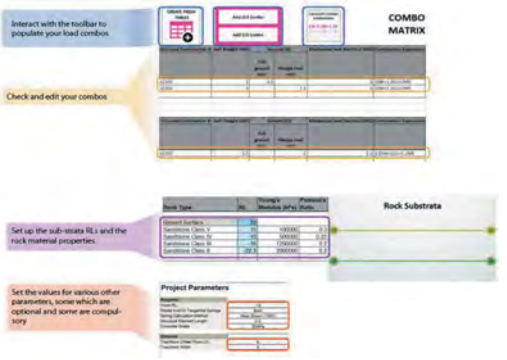

Figure 6. Load factors and its combination definition in SpeedBot through MS Excel interface.

Overall, the lining for the cavern was concluded to be a minimum of 900mm for unreinforced concrete option, and 750mm for reinforced concrete option. The final recommendation was that the lining was to be completely reinforced, citing sustainability interest over increased excavation volume, muck removal and, production of concrete for a significantly thicker tunnel lining, including potential safety considerations for future developments around this location, and increasing surcharge loading during the life cycle of the asset. Concerns were also raised as designers noticed that tensile utilisation was the critical case for all loading cases and the location of the over-utilised beam segments all being located above the spring line i.e., predominantly in the crown and side walls. The lining thickness would be significantly increased in this region if unreinforced, by altering the geometry of the tunnel profile and resulting in a significant increase in excavation and concrete use resulting in higher carbon embodiment.

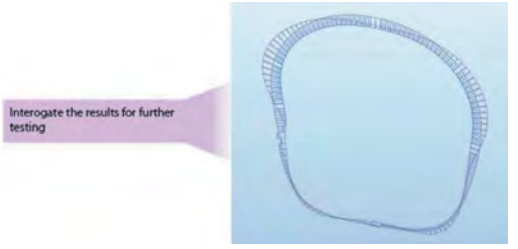

Figure 7. Example of results interrogation in Autodesk Robot.

4 REFLECTION OF DIGITAL TOOL IMPLEMENTATION

This section of the paper will provide a reflection of how SpeedBot not only streamlined the analysis discussed in this paper but how automation tools are advancing the tunnel design space. Outside of SpeedBot's time-saving solutions through advanced automation, reducing lengthy modelling processes, it offers various benefits which further promote the direction the tunnel engineering field could ultimately follow moving forward.

4.1 *Designing resilient and sustainable infrastructure*

The advanced simulations that SpeedBot offers through the automation process for computational engineering greatly impact various conditions of tunnel design, allowing designers to integrate sustainability and resilience conditions into tunnel projects. These considerations include environmental impacts, various design choices, optimisation of resources, and energy efficiency. SpeedBot enabled multiple tunnel lining models to be run much quicker than standard modelling practices, which for the case study presented in this paper, enabled the design of more sustainable linings. This was achieved through various iterations of each model within reasonable timing, varying lining thickness to reduce potential carbon emissions from concrete and steel construction. Tunnel designers also had the ability to spend time on innovation during the early design process without concerns over budget constraints due to the streamlined modelling process of SpeedBot. The streamlined modelling approach allowed designers to focus on engineering basics to attain a highly machine optimised lining section design at specific areas, rather than focussing on generalised lining design, hence supporting good sustainable practices.

4.2 *Efficient and cost-effective solutions*

The most obvious cost-effective solution noticed by designers was the significant reduction in overall modelling and analysis time for multiple loading sequences. Computational digital tools such as SpeedBot utilise algorithms and design tools to optimise the design process, which provides financial and technical benefits. Financial benefits which were observed by designers during the above case study included considerable time savings for multiple model iterations, reduction in software use which can minimise licencing fees for software's that charge on per day of use, and resource optimisation allowing resources to be spread across other projects which benefit the client and consultant. Technical benefits observed by the designers were highlighted by the singular modelling approach in which SpeedBot was developed. The streamlined knowledge transfer allowed multiple designers to follow the modelling and analysis of each load case, allowing collaborative input for result analysis and report writing. This became pivotal during troubleshooting sessions where initial results during the early stages of the design process did not look correct to designers. Implementing a singular modelling approach through SpeedBot enabled peer review sessions regarding the design to be streamlined, as all designers followed the same design and modelling approach, eliminating the need for initial review time and eventual discussions regarding the models produced. All loading cases were addressed using the same approach, providing confidence in the quality of output produced by the designers.

4.3 *Creative and innovative designs*

Conventional engineering practices and technical tools to some extent deter innovation and creativity due to the complexity and time-consuming requirements currently in practice. Enhancing Digital tools such as SpeedBot and harnessing the power of Artificial Intelligence (AI) can allow engineers to push the conventional practice boundaries to develop creative

designs. Conventional designs for tunnel linings for these situations around aboveground developments and high-ground surcharges would dictate an assumption of reinforced concrete linings from the start of the design process. SpeedBot allowed designers the time and resources to swiftly consider other lining options, such as unreinforced or SFRC or bar reinforced linings. Further implementation of digital tools in the form of AI can promote the streamlined design process offered by SpeedBot. Deep Machine Learning (DML) utilises data sets from previous projects to form assumptions and potentially run computational designs without the need for human inputs, allowing designers to encourage innovation through reduced time consumption for initial modelling stages.

5 CONCLUSIONS

Owing to the continuous advancement of technology, engineering consultancies have realised the transformative advantages of incorporating digitalisation in computational design. This approach provides a framework for informed decision-making, promoting collaboration and innovation that leads to superior and sustainable outcomes for the planet. Among the design processes that have benefited from digitalisation, the tunnel design process stands out, with the SpeedBot tool proving valuable in reducing the time spent on modelling. This allows designers to focus on analysing multiple alternative options, leading to more intricate thinking and a broader range of optimisation possibilities.

This paper presented a case study detailing the benefits of SpeedBot in running optioneering assessments for 2D bedded beam models at a high level. Immediate advantages include reduced man-hours and design schedule expeditiousness, while long-term benefits include the elimination of human-instigated errors in structural models and highly refined sustainable results. In this example, the decision to recommend reinforced lining may seem to have a higher carbon footprint, but careful consideration of the required over-excavation, increased muck disposal, and higher concrete volume for unreinforced concrete thickness predicts a more onerous outcome. Additionally, the need to future-proof the lining design for new developments in this location above the cavern has governed the decision for the lining to be reinforced and more flexible.

Moreover, SpeedBot enables the analysis of a greater number of locations along the tunnel alignment, resulting in a more accurate and practical solution that avoids surplus generalisations in the design. This tool is particularly useful for designers who are embracing the digital revolution of tunnel design through automation and Artificial Intelligence (AI). It provides sustainable solutions to tunnel problems and proves invaluable to the field. As engineering continues to leverage advanced technologies and methodologies, the future promises to exceed client expectations and shape a better, more sustainable planet.

ACKNOWLEDGMENTS

The authors greatly acknowledge Mott MacDonald Pty Limited who provided the required funding and encouragement to explore the development of this digital automation tool.

REFERENCES

AS 5100: Bridge Design, 2017. Standards Australia, Sydney, NSW, 2001.

Autodesk Robot Structural Analysis Professional 2022 User's Guide, 2022. Autodesk. https://help.autodesk.com/view/RSAPRO/2022/ENU/?guid=GUID-4A734308-B2F3-4147-A310-BD47C48E9ED1

BS EN 1992-1-1-2004 Eurocode 2: Design of concrete structures, 2004. British Standards Institute, London, United Kingdom, W4 4AL.

Rhinoceros 6 User's Guide, 2019. Robert McNeel & Associates. http://docs.mcneel.com/rhino/6/training-command/en-us/usersguide/Rhino%20User%27s%20Guide%20for%20Windows.pdf.

Shivasami, A, et al. 2023. An overview of SpeedBot – A digital tool for automating the structural modelling process for tunnel linings. Australasia Tunnelling Conference, 2023.

STAAD.Pro V8i (SELECT series 4), 2012. Technical Reference Manual. Bentley Systems Incorporated. http://priodeep.weebly.com/uploads/6/5/4/9/65495087/staad_pro_-v8i_-tutorial.pdf.

Using Strand7, 2010. – Introduction to the Strand7 Finite Element Analysis System. Strand7 Pty Ltd. https://www.strand7.com/downloads/Using%20Strand7%20Manual.pdf.

Tunnelling for a Better Life – Yan, Celestino, Thewes & Eberhardt (Eds)
© 2024 The Author(s), ISBN 978-1-032-80042-4
Open Access: www.taylorfrancis.com, CC BY-NC-ND 4.0 license

Demonstration of parametric analyses in ground models by applying programming logics using a digital tool named ParaRanger

Arjun Shivasami*, Roshan Nair & Lachlan Dunbar
Mott MacDonald, Sydney, Australia

ABSTRACT: The use of numerical analysis routines in tunnel designs has increased with the availability of ample computing power. This has led to development of highly optimal and sustainable solutions that require minimal human effort. This paper discusses the development of a digital tool that streamlines and automates the numerical analysis process for tunnel problems. A digital tool is developed using programming language and third-party packages. It has two components that work together as an interface between the logic and software. The first component is a front-end graphical interface that provides a user-friendly interface for input and output options. The second component interacts with a commercial software to modify the model parameters as specified by the user to perform the calculations and organise the results for subsequent processes. The tool allows for multiple analyses of a single base model without creating multiple models from scratch.

The paper demonstrates use of this tool in an underground tunnel support analysis for a pumped hydropower project. The user-developed geotechnical model for headrace tunnel in RS2 (Rocscience) is used as seed file. The concept stage geotechnical investigation provided large variance in ground parameters, namely strength and stiffness, which was captured as a statistical input. An automated setup created batch files for processing the varying input parameters and tunnel support system. Once the analyses were completed, the displacement and stability factor output matrix template were utilised by the designer to devise tunnel support strategy. This tool is a significant advancement in parametric analyses as it helps to run several sensitivity models with limited human intervention. The tool's ability to organize results in a user-defined and well-formatted manner makes it ideal for informing subsequent numerical analysis. The tool saves time and reduces the cost of running parametric analyses. It suggests innovative solutions with opportunities to manage risks, especially during the early stages of design.

Keywords: Ground models, Digital Tool, Parametric Analyses, Parameters, Automation, ParaRanger

1 INTRODUCTION

Analysis of geotechnical problems requires to simulation of existing ground conditions and envisioned changes in the factors like incidental loads, presence of water and ground properties. Many of these factors are progressively updated and linked to the maturity of the elements in various design phases. Probabilistic analysis approach like Monte Carlo method and Latin hypercube is usually used to deal with such variability and still require development of behavioural models to train the outcomes (Cheng et al., 2019; Mitelman et al., 2023). Many resources are usually spent to develop the process and thereby impacting the meaningful interpretation of output. The variability in parameters leads to complex, time consuming and repetitive process to arrive at design solutions (Yang et al., 2022). During initial concept stages, simpler analysis methods are generally employed aiding interpretation of highly variable geotechnical data and to understand the behavioural pattern resulting in optioneering. Further, in the detailed design stages, the options are evaluated based on more reliable data and refinement of design models occur. During construction, monitoring of the response of ground assist in real-time decision making and risk assessment, allowing for adjustment and improvements as needed (Wiles, 2005). In these design stages, numerical modelling has become an indispensable tool to develop interpretative ground models and carry out the analysis enhancing the precision and reliability while minimizing potential risk (Oreste, 2002). However, more often large amount of information available from

*Corresponding author: arjun.shivasami@mottmac.com

DOI: 10.1201/9781003495505-392

numerical analysis output bias the outcome (Phoon et al., 2022).

In the current form, a common commercial numerical analysis software lacks an in-built ability to generate batch process catering large input variability. Additionally, the post processing outputs are filtered and collated for each parametric analysis. Both tasks require careful handling of large amount of data and potentially prone to human-made errors. These limitations can be addressed by employing additional programming logics that can collaborate with the commercial software to obtain the needed outcomes. Various programming languages can help in generating subroutines which may either directly be incorporated into a software or communicated using third-party digital tools. The digital tools can be programmed to gain access to the numerical analysis software core to automate the process, modify design elements and its properties, filter outputs, present the outputs in desired form. Numerical modelling procedures by using custom-made digital tools can provide superior solutions in comparison to machine learning (Chen et al., 2020).

This paper demonstrates a successful implementation of a digital tool in numerical analysis of underground tunnel. Mott MacDonald's in-house developed tool, ParaRanger, was used to input the variable parameters to a commercial numerical analysis software (RS2 Rocscience) consecutively and perform numerous analyses. The tool was developed with the intention of feeding the parametric input into a developed baseline model, modifying the selected elements in the model, automating the generation of batch files and presenting the desired outputs for post processing.

2 COMPOSITION OF THE STUDY

In a project, numerical analyses of a design element are developed through a systematic process. The process can be summarised into three stages, i.e., pre-processing, numerical simulations, and post-processing. This process is performed iteratively for the variables to optimise the solution and guide the design outcome of the problem. The resource requirements can vary significantly for various components. These requirements can be generalised as shown in Table 1. Nearly 80% of the resources are utilised to carry out pre-processing and numerical simulations, whereas critical task of data visualisation, analysis and interpretation often ends with least resource allotment. There is a need to reduce the manual interventions in

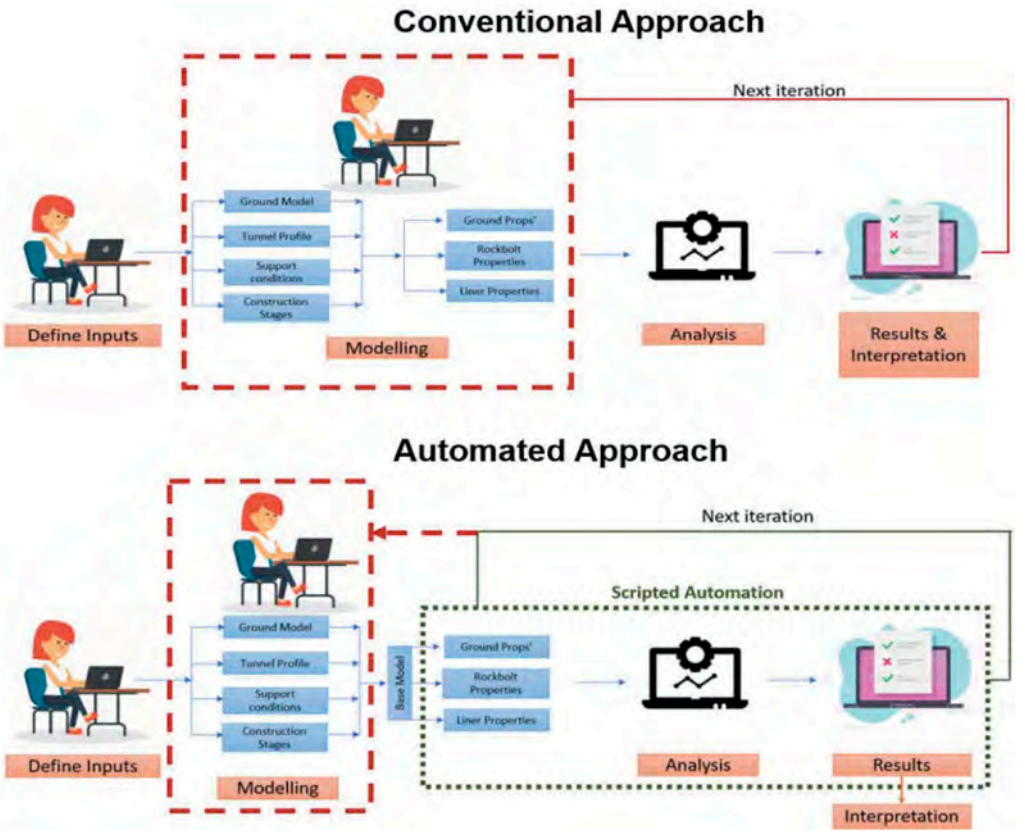

Figure 1. Comparison of automated approach of ParaRanger (Shivasami et al., 2023).

Table 1. Resource requirement for problem analysis.

Stage	Component	Resource requirement
Pre-processing	Problem formulation	50%
	Ground model development	
	Discretisation	
	Error management	
	Data input	
Numerical simulations	Convergence analysis	30%
	Parametric analysis	
Post processing	Visualisation of results	20%
	Optimisation	
	Validation and verification	
	Documentation and reporting	

the first two stages and direct the effort to drive post-processing. Digital tools can contribute to modify this skewed allotment by automation of initial stages and present numerical output in comprehensive format. Shivasami et al. (2023) presented a digital tool, ParaRanger, to aid the numerical analyses through programming language Python. The tools help to reorganise the conventional parametric analyses process through scripted automation (Figure 1).

The digital tool was developed through Mott MacDonald's in-house efforts by integrating an automation scheme to RS2 (Rocscience) software and augmenting the design decisions with well formatted analysis output. ParaRanger was adopted for analysis and design of an underground headrace

tunnel in a Pumped Hydroelectric Energy Storage (PHES) project. The analysis and the outcomes are presented in following sections.

The ParaRanger tool provides a user interface to define the inputs to the numerical software, RS2. A baseline model is initially created by the user which defines the ground conditions, tunnel excavation geometry, boundary conditions, adopted constitutive model and construction stages. This base file is used as a canvas by programming logics in ParaRanger to carry out series of parametric analysis. These parametric analyses represent the combination of design variables such as geotechnical properties of the modelled stratigraphy and ground support (rockbolt and shotcrete) properties. The ParaRanger tabulates the numerical simulation outputs and presents the critical information in both visual and report format. During post-processing, these outputs are then used by the designer to formulate the design. In this study, ParaRanger is targeted to automate data input, generation of batch files (for parametric study), instruct RS2 to process these files and provide a formatted output for swift optimisation and documentation.

3 DEMONSTRATION OF THE PROCESS

It is proposed to excavate a 6m diameter headrace tunnel to connect the water intake structure of upper reservoir to the powerhouse through pressurised penstocks. The underground part of the penstock houses a steel liner to cater for internal water pressure during the operational stage and is not intended to support the loads transferred from the excavated rock mass. The headrace tunnel was required to be designed to fulfil both initial support and long-term support of the excavated ground and to limit ground deformation to the steel liner. The waterway alignment had an invert gradient of about 10-12% towards powerhouse. It was intended to support the excavated ground with combination of shotcrete with steel fibres and fully grouted rock bolts. The annulus between the rock and steel liner was proposed to be backfilled. The tunnel supports are designed to accommodate 100% of the ground loads and considered as a permanent support throughout the design life of headrace tunnel. The geotechnical investigation within the site was limited due to the early stages of the design. The information relied on very limited boreholes drilled around the proposed tunnel and imposed low confidence on the geotechnical parameters along the alignment.

The site featured a complex suite of granites, volcaniclastics and conglomerates which had been transformed by a large-scale geological activity. The true extent of the rockmass affected by the shear zones and other low strength deformed structures was not able to be determined due to lack of available investigative data. The interpreted geological information indicated the natural material on the ground level comprises of residual soil and extremely weathered rock. The overburden above the tunnel was around 12m at the portal and maximum of 40m at the deepest location. The headrace tunnel was intended to be excavated in rockmass (volcaniclastics, greywacke, slate) of varying weathering grade. The ground stratigraphy was interpreted to be 1.5m of soil material, overlying slightly weathered to fresh metasediment for the remaining depth with three distinct structural discontinuities. The stratigraphy was classified into three specific rockmass units as indicated in the Table 2.

It was expected that the tunnel will be under prolonged groundwater head of 30m due to the frequent recharge of upper reservoir. It was anticipated that the block failure will be the predominant failure mechanism and the ground supports in the form of rock bolts and shotcrete may be required to arrest the ground movement. Due to limitation of insitu stress data at the early design stage, a parametric analysis was carried out for KH/Kv values of 0.8, 1 and 1.5. The other loads considered in the analysis included seismic loads, construction loads, excavation sequence loads, long-term permanent loads from the equipment. The design methodology adopted for the

Table 2. Summary of geotechnical parameters.

Parameter	Symbol	Unit	Value					
Classification parameter								
Rock class	-	-	Poor – Rock 1		Fair – Rock 2		Good – Rock 3	
GSI	GS	-	45		60		70	
Q	-	-	$1 < Q \leq 4$		$4 < Q \leq 10$		>10	
Tunnel scale rockmass properties								
Damage Factor (depth = 30m)	-	-	D=0.9	D=0.8	D=0.6	D=0.4	D=0.2	D=0
Cohesion	c	kPa	350	400	860	1100	2000	2200
Friction angle	ϕ	degrees	50	52	61	63	64	64
Tensile strength	Sigma(t)	kPa	30	40	170	240	540	600
Deformation modulus	Erm	GPA	3	3	10	18	27	32

analysis is shown in Figure 2. This paper discusses the numerical analysis carried out in phase 3.

The ParaRanger digital tool was used to develop the ground support system for the headrace tunnel. The assessment involved determination of the required type and quantity of support to construct the headrace tunnel for the uncertain ground conditions. Typical rock support considered included steel fibre reinforced shotcrete and fully grouted Double Corrosion Protection (DCP) rock bolts to resist any imposed deformation on the structure and have an acceptable factor of safety for ultimate limit state design. Considering these design criteria but with a focus on displacement, the project team undertook an assessment to assess the influence of key parameters on deformation.

The rockmass information in Table 2 provided a low confidence data along the tunnel alignment. In order to provide a more definitive design recommendation and evaluate all the risk with variability in data, parametric analysis was carried out to design robust support systems. The parametric analysis included variation to the input parameters as given in Table 3. In each of the listed parameters the support system details were varied which included the bolt length and spacing and shotcrete (liner) thickness.

Table 3. Details of parametric analysis.

First variable (parameters)	Range	Second variable (support system)
Youngs modulus	3-32 GPa	Rock bolt spacing and shotcrete thickness
Cohesion	350-2200 kPa	Rock bolt spacing and shotcrete thickness
Tensile strength	30-600 kPa	Rock bolt spacing and shotcrete thickness

The usual procedure of conducting such parametric assessments is to manually set up a number of finite element models with singular variations between first and second variables. This time consuming and

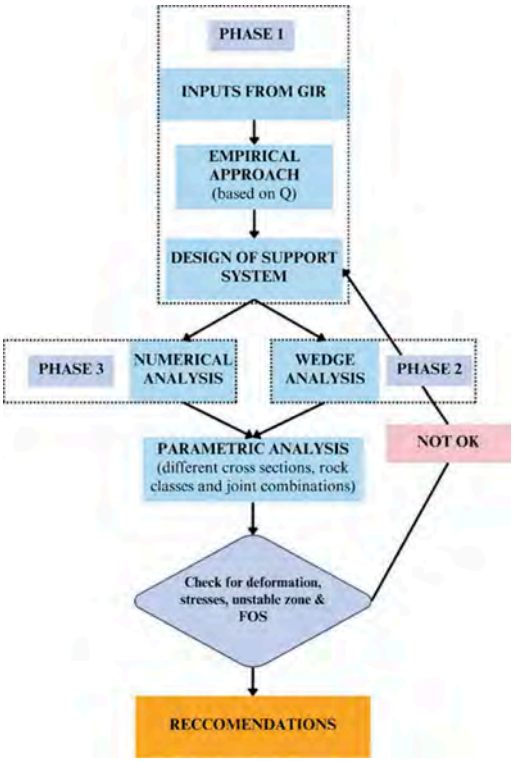

Figure 2. Design methodology for the headrace tunnel.

repetitive process has the potential to introduce error into the analysis as the user must carefully set up the models, change the required parameter, run the model, log, and interpret the data. The use of ParaRanger tool facilitates the above process with significantly lesser user interventions. The user first starts by setting up a 'base case' in RS2 as shown in Figure 3.

In the project, the base case model adopted characteristic strength and stiffness parameters defined by geotechnical interpretive report (GIR). The model was prepared based on the two-dimensional geological model which had two layers namely 'Rock 1′

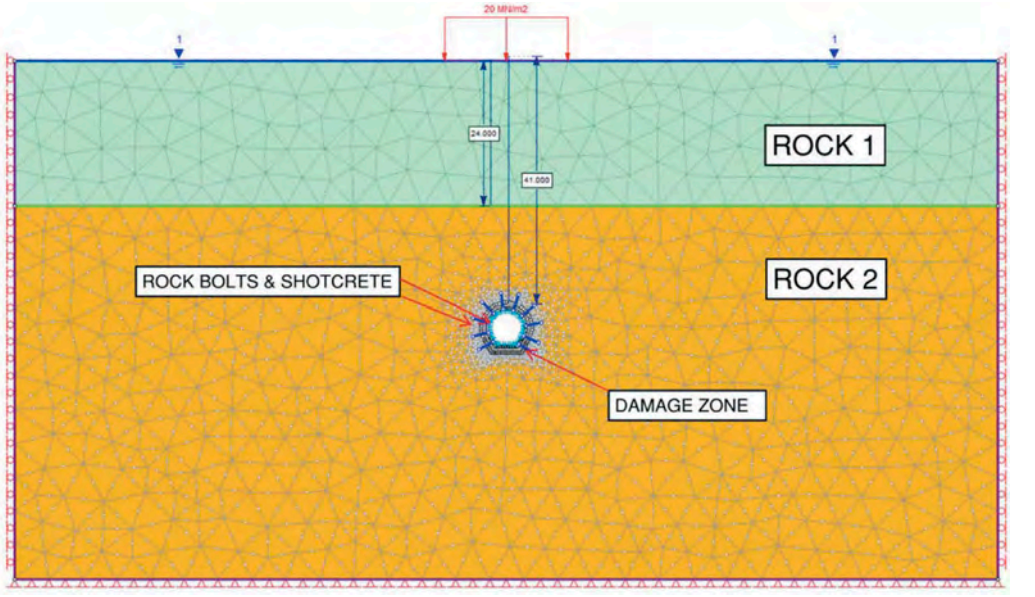

Figure 3. Base case model setup by the user.

and 'Rock 2′ of varying thickness and the geotechnical properties as presented in Table 2. The model was discretised with six-noded triangular elements and mesh gradation within 3 times the tunnel diameter has been set at 1.5m and beyond which graded uniformly up to the boundaries. The horizontal to vertical in-situ stress ratio was conservatively assumed to be unity due to lack of site-specific information. The side boundaries of the model were considered roller in vertical direction, whereas the bottom of model was fixed. The parametric study envisaged to vary the geotechnical properties (i.e., first variable) and support system (i.e., second variable) ensuring all other input to be constant. Further, the ParaRanger input window was used to manipulate the information in the RS2 base model. The Parararanger simulated the geotechnical parameters at pre-set intervals along with pre-defined support system as per the details provided in the input window. A typical input window depicting the iteration for Young's modulus and rock bolt spacing is shown in Figure 4.

The tool triggers the batch analysis of each combination of the parameters. This process fully automates the process that would usually be required to generate individual models. The tool also provides an output selection window which provides a portal for choosing specific output plots along desired path or location (Figure 5).

There are multiple options provided in this form to setup display information on displacements and stresses in the ground, as well as bolt and liner forces and moments. For the study, crown and wall displacements along with structural forces in the bolt and shotcrete was obtained for various parametric analysis as shown typically in Figure 6.

The parametric analysis indicated that the variation of Youngs modulus (stiffness parameter) of the immediate rock stratum influences the displacements around the tunnel than cohesion as expected. The failure mechanism was predominantly structurally controlled as identified from the analysis. Maximum crown displacements are about 9mm for high cover section, whereas wall displacements are negligible. There was localised displacement associated with simulated shear zones in the model. The settlement on the ground surface was observed to be maximum of 2mm to 3mm for low stiffness top layer. Based on the analysis, the support system comprised of 3m long grouted rock bolts at varying spacing of 1.5m and 2.1m for anticipated rockmass of Rock 1 and Rock 2, respectively, whereas for headrace tunnel in Rock 1, spot bolting was recommended. By systematically simulating a wide range of possible ground conditions, it was possible to establish the most critical parameter influencing the design and find an optimised solution. This expedited the user intensive task of running sensitivity analyses and provided more time to carry out post-processing activities.

4 PROJECTED UTILISATION OF THE DIGITAL TOOL AND BENEFITS

Generally, the engineering standards mandates rigorous sensitivity analyses to capture the variation of ground parameters. The on-project demonstration captured that the ParaRanger tool can potentially reduce the user time to undertake model generation (batch process) for sensitivity analyses by 70%. The input-output form provides a good platform for error

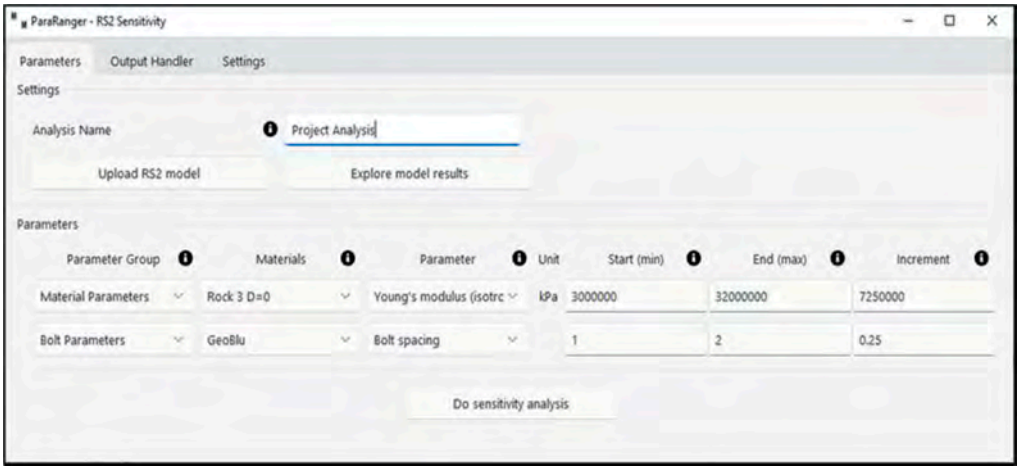

Figure 4. ParaRanger input window defining the variables.

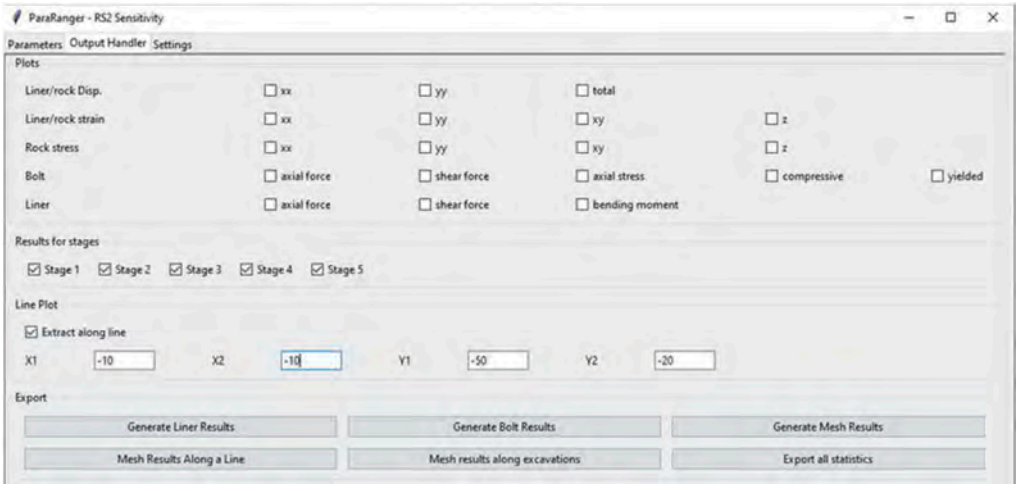

Figure 5. ParaRanger output selection window for post-processing.

elimination. The matrix of desired results aids decision making process and evaluating critical parameters in design. In tight project timelines, these benefits improve efficiency and has financial benefits. In the study, the ParaRanger tool enabled the project team to develop a design solution based on a sound and numerically guided assessment of the ground variability from limited site investigations. The ParaRanger tool is still in development and future development works may include additional functionality to make changes to the geometry of the base case as well as to be able to test strength parameters of soil models other than Mohr coulomb and Hoek brown.

The ParaRanger tool was initially developed to speed up parametric analyses in soil-structure interaction numerical models during a project's early design phases. This is a stage where the inputs required for the numerical models are uncertain, leading to a need for running multiple scenarios with varying ground conditions and associated design necessities. However, with the right knowledge and experience, the same tool can also be used for detailed engineering, resulting in better outcomes. During the detailed design of a project, the level of information available on the ground conditions and parameters is generally rich compared to its early design stages. This gives an opportunity for the designer to refine the tunnel support design further using ParaRanger for a defined ground condition, resulting in a more optimal and sustainable solution.

The process of running repeated analyses is automated through scripted programming, which leads to a huge reduction in time and cost savings. Additionally, ParaRanger directly addresses the most onerous

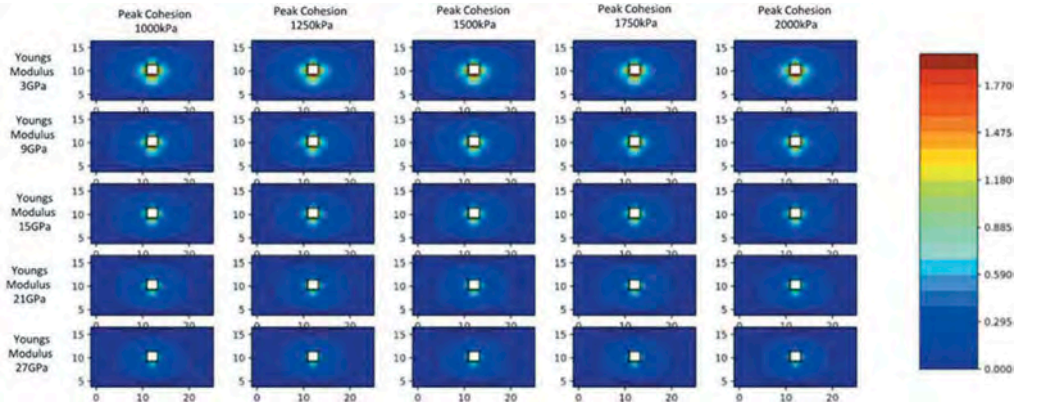

Figure 6. Typical output matrix generated by ParaRanger for post-processing.

task in any parametric analysis, which is carefully documenting the outputs from various numerical models in a unique scale and comparing them to interpret results efficiently. This tool automatically extracts results from various models and prints them into a common unit scale for easy evaluation, taking the designers from a data-rich information-poor state to a data and information-rich state. The tool also enables experienced designers to summarize outputs in an Excel template for advanced design determinations.

Moreover, the manual process of result extraction and interpretation has some degree of human error embodied due to the monotonous nature of the task involving many datasets, which is almost eliminated using this automated digital tool, providing higher confidence and reliability of the design outcomes despite the uncertainty in the input. The current version of ParaRanger focuses on parametric analyses using the commercial software RS2 developed by Rocscience. The next mission for Mott MacDonald's design team is to develop a framework and scheme that can be readily adopted by other ground-based numerical software to benefit from automation in parametric analyses. The ultimate vision for the team is to leverage the vast amount of existing ground data from boreholes and other investigations in an area and implement Artificial Intelligence (AI) in the process. The AI will run an autonomous parametric analysis only based on a possible range of ground parameters from existing ground data and potential support requirements learned from previous projects, with limited to no input from designers, to arrive at a highly optimized but pragmatic solution for a given ground problem.

5 CONCLUSION

Engineering consultancies have a responsibility to prioritize sustainable design solutions that benefit the environment while remaining cost-effective. One promising way to achieve this is through embracing innovation, especially digitalization. Custom digital applications that automate traditional engineering processes have become increasingly popular. Mott MacDonald's ParaRanger digital tool is a prime example of such an application. Its success lies in its ability to reduce ambiguity and increase design reliability. Additionally, it captures valuable data on how the design reacts to various uncertainties in ground conditions and supports requirements during early project stages, which enables appropriate investigations in site and lab procedures to better understand ground uncertainty.

This paper highlighted the effectiveness of the digital tool ParaRanger by presenting a case study that used the tool to test different ground conditions with varying input values, including Young's Modulus, cohesion, and tensile strength. Several parametric analyses were conducted to increase confidence in uncertain ground conditions. Furthermore, different support systems were examined to ensure that the chosen design was reliable and could be implemented with confidence. Overall, the case study demonstrates the potential of ParaRanger as a valuable digital tool for designing and analysing structures in diverse ground conditions. As a result, a well-refined design range for the best to worst ground conditions were developed.

By promoting a digital culture in tunnel engineering, this tool significantly reduces human error and allows for highly optimized solutions. The digitalization of design is an inevitable trend, and tools like ParaRanger are exciting additions to the tunnelling industry and other fields. They are also critical tools for ushering in Artificial Intelligence (AI) into the engineering computation space. Overall, ParaRanger and other digital tools are essential for engineering consultancies seeking to prioritize sustainable design solutions while remaining cost-effective.

ACKNOWLEDGEMENT

The authors greatly acknowledge Mott MacDonald Pty Limited who provided the required funding and encouragement to explore the development of this digital automation tool.

REFERENCES

Cheng, H., Chen, J., Li, J., 2019. Probabilistic analysis of ground movements caused by tunneling in a spatially variable soil, International Journal of Geomechanics, 19(12), http://doi.org/10.1061/(ASCE)GM.1943-5622.0001526.

Chen, C., He, W., Zhou, H. et al. A comparative study among machine learning and numerical models for simulating groundwater dynamics in the Heihe River Basin, northwestern China. Sci Rep 10, 3904 (2020). http://doi.org/10.1038/s41598-020-60698-9

Mitelman, A., Yang, B., Urlainis, A., Elmo, D., 2023. Coupling geotechnical numerical analysis with machine learning for observational method projects. *Geosciences* 13(7): 196. http://doi.org/10.3390/geosciences13070196

Phoon, K.K., Cao, Z.J., Ji, J., Leung, Y.F., Najjar, S., Shuku, T., Tang, C., Yin, Z.Y., Ikumasa, Y., Ching, J., 2022. Geotechnical uncertainty, modeling, and decision making. Soils and Foundations, 62(5), http://doi.org/10.1016/j.sandf.2022.101189.

Yang, W., Liu, H., Zheng, J., and Cui, L., 2022. Reliability analysis of ground movement in tunnelling in spatially variable soil using equivalent parameters. Front. Earth Sci. 10(985882)

Oreste, P.P, 2002. Analysis of structural interaction in tunnels using the convergence–confinement approach, Tunnelling and Underground Space Technology, 18(4), 347–363.

Wiles, T.D., 2005. Reliability of numerical modelling predictions. International Journal of Rock Mechanics & Mining Sciences, 43, 454–472.

Tunnelling for a Better Life – Yan, Celestino, Thewes & Eberhardt (Eds)
© 2024 The Author(s), ISBN 978-1-032-80042-4
Open Access: www.taylorfrancis.com, CC BY-NC-ND 4.0 license

Streamline field management processes to improve labor productivity and reduce material loss

Hirotaka Umeyama*, Shiro Kitagawa, Takumi Arai & Tsuyoshi Fukuda
Shimizu Corporation, Tokyo, Japan

Shunichi Taniguchi
Lightblue Technology, Tokyo, Japan

Fumika Ito
Enzan Koubou co,ltd, Kyoto, Japan

Hisataka Nagamatsu
Kumamoto River and National Highway Office, Kyushu Regional Development Bureau, MLIT, Kumamoto, Japan

ABSTRACT: In recent years, the need to improve productivity including labor savings through mechanization, automation and improvement of the construction method itself, has become an urgent demand of the times, and it is necessary to actively address this issue and establish such technology as soon as possible. In particular, it is necessary to respond to the demand for improved productivity and quality at tunnel mountain sites through management methods that do not rely on conventional experience and sensory perception. Therefore, we have conducted a trial project to improve the productivity of workers and staff at mountain tunnel sites and to reduce the amount of excess concrete during shotcrete installation by using AI-based video judgment technology. This report provides an overview of the trial technology and its results.

Keywords: AI, cycle time, increased productivity, reduced waiting time, carbon neutral

1 INTRODUCTION

Until now, the construction of mountain tunnels has relied on the experience and senses of skilled technicians under the special construction conditions of excavating uncertain ground. However, a shortage of skilled workers is predicted in the near future due to a decrease in the number of workers resulting from a shrinking population and the aging of skilled engineers. Therefore, a management method that does not rely on conventional experience and sense is needed. Under such background, many reports have been accumulated through the application of i-construction and DX promoted by the Ministry of Land, Infrastructure, Transport and Tourism. In this report, we focus on two issues in the construction cycle at mountain tunnel sites: (1) improving the efficiency of construction management work performed by main contractors (hereinafter referred to as "staff") and (2) reducing the amount of shotcrete wasted of during shotcreting. In particular, the second issue sometimes results in insufficient or excess concrete, depending on the skill level of the nozzleman, which leads to the waste of excess concrete. If the amount of concrete required can be quantitatively determined, construction can be performed without relying on experience and sense. Furthermore, the reduction of concrete waste will reduce CO2 emissions and contribute to decarbonization. This report describes the results of this trial project, which was funded by MLIT.

2 OVERVIEW OF TECHNOLOGY

In this paper, three technologies were tested with the aim of improving labor productivity. The trial site was the "Kumamoto 57 Takimurozaka Tunnel West New Construction (2nd phase)" and the Project Client is Kyushu Regional Development Bureau of MLIT. A summary of the site is shown in Table 1.

*Corresponding author: hiro.umeyama@shimz.co.jp

DOI: 10.1201/9781003495505-393

Table 1. Site summary.

Project Name		Kumamoto 57 Takimuro-zaka Tunnel West New Construction (2nd phase)
Construction location		Aso City, Kumamoto Prefecture
Construction period		December 19, 2020 - March 31, 2024
Client		Kumamoto river and national highway Office, Kyushu Regional Development Bureau, MLIT
Contractor		Shimizu-Tokyu-Mori Specified Construction Joint Venture
ConstructionDetails	length	Total length of main tunnel L=2,679m
	cross section	Total length of evacuation tunnels L=3,069m
	Method	Main tunnel 107m^2 Evacuation tunnels19m^2 NATM

Table 2. Work with waiting time.

Target person	Work contents
Worker	Delivery of materials
Worker	Mucking
Staff	Observation of face
Staff	Quality control

2.1 *Technology to reduce waiting time by AI judgment*

This technology reduces waiting time by installing webcams at 40 m behind the tunnel face and near the parking area, using AI to automatically identify the work status based on the images, and then notifying the relevant workers in real time. Judgment is based on the detection of construction machinery working on the face, the combination of construction machinery that appears in each cycle, and the expected order of cycles. The results are notified to staff and workers through the company's SNS. In this trial, the effect of reducing waiting time was verified for the works shown in Table 2.

2.2 *Material loss reduction system*

This system aims to reduce material loss of shotcrete by calculating the discharge volume of shotcrete using AI video judgment, calculating the amount of waste based on the difference from the mixing quantity, and learning the optimum re-bounce rate for the next construction. Figure 1 shows an overview of the system. A vehicle-mounted 3D scanner (Figure 2) is used to measure the shape of the face, calculate the difference from the design surface of the shotcrete, and calculate the required mix volume, which takes into account the rate of concrete bounce during the shotcreting. This mixing rate is automatically notified to the batcher plant via the company's SNS for mixing. The AI camera installed on the shotcreting machine is then used to determine the time required to spray the concrete, which is then multiplied by the hourly discharge capacity of the sprayer to calculate the actual volume of concrete to be sprayed. After the shotcreting, the amount of waste is calculated by calculating the difference between the quantity of mix and the actual quantity calculated by the AI judgment. The amount of waste is re-calculated as a modified bounce rate by learning through a series of repeated cycles. The cycle shown in Figure 1 was repeated to verify the effect of reducing the amount of shotcrete waste.

2.3 *Improving work efficiency by using cloud services*

Figure 3 Shows an overview of this initiative. The information necessary for on-site management is uploaded from existing tunnel construction management software to a cloud server, and measurement results, face photographs, and other data are automatically compiled into reports by using a report generation service. The latest information on measurements and other data is automatically updated, making it possible to immediately check the latest information if it is available on the Internet. In addition, by linking tunnel design and support patterns information necessary for control of management to a data management service on the cloud and inputting the results of formwork inspection, it is possible to process the data from the inspection results and generate forms for control of actual measurements documents. In this trial, the application and effects of the reporting system were examined.

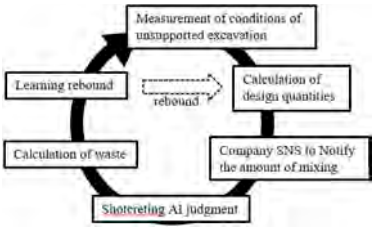

Figure 1. System overview.

Figure 2. Vehicle-mounted 3D scanner.

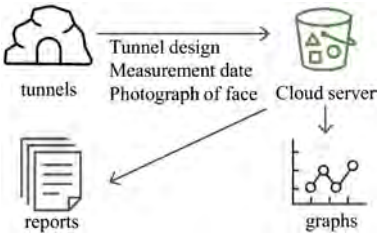

Figure 3. System overview.

3 AI-BASED VIDEO JUDGMENT TECHNOLOGY

The system configuration is shown in Figure 4. Video images from cameras installed in the tunnel are transferred to a PC for AI judgment and analysis, and judgment is performed. After the judgment is made, the results are notified to the company's SNS, and the video data and judgment data are automatically transferred to a cloud server for storage.

3.1 *AI cycle automatic judgment*

Since the combination of construction equipment used in each cycle of tunnel construction is almost similar, AI automatically determines the work to be done by detecting the appropriate construction equipment from the images captured by cameras installed in the tunnel. Figure 5 shows the judgment accuracy of the automatic cycle time judgment system by AI. The figure shows the percentage of actual work that was determined by the AI. For most of the works, the appropriate work content could be determined with a probability of 80% or more. However, the accuracy of the judgment was poor in some cases, such as work F which is support erection and work G which is secondary shotcreting. This is presumably due to the fact that the evaluation accuracy was affected by the tunnels environment (illumination, dust, etc.), since camera images were used for the evaluation. In addition, incorrect judgments were sometimes made when the construction cycle differed from the normal cycle, such as when there was problem occurred.

3.2 *AI judgment of time to shotcreting*

The system detects the arm part from the images captured by two cameras installed on the shotcreting machine and determines its movement to count the time when the machine is actually shotcreting. In the construction of this system, we created an arm detection segmentation model for discharge to detect the arm and determine whether the arm is moving, and created an algorithm that uses the output of the model to make AI judgments. Figure 6 shows the situation of AI detection during shotcrete. Figure 7 shows the accuracy of the judgment of shotcreting time. The time when concrete is being sprayed from the nozzle of the shotcreting machine is defined as the shotcreting time, and the time when concrete is not being sprayed is defined as the time when the shotcreting machine is stopped. The figure shows that the time when shotcrete is actually being sprayed can be correctly determined. The correct answer rate was approximately 80% for each hour of shotcreting, and approximately 90% for the entire work, including the time when the machine was stopped. These results indicate that the AI can determine the time of shotcreting during the work period.

3.3 *Parking area AI judgment*

Judging whether the tunnels are passable or not by image classification based on the images captured by cameras installed in the tunnels' parking areas. The results of the judgment will be notified to the

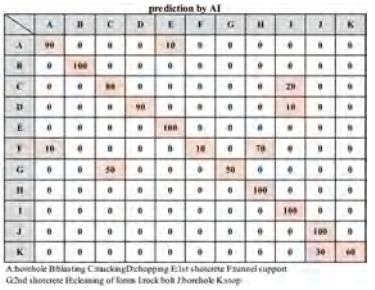

Figure 5. AI judgment accuracy.

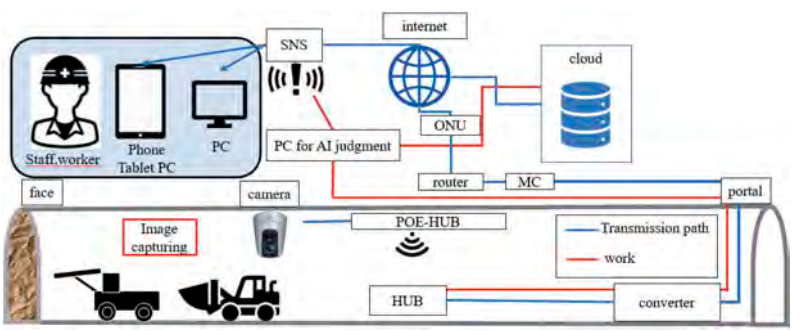

Figure 4. System structure of AI judgment technology.

Figure 6. Identification of shotcreting machine booms by AI.

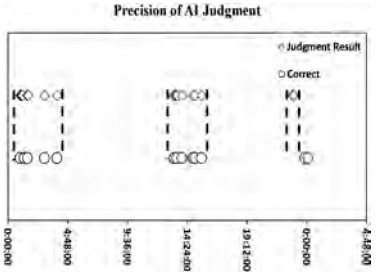

Figure 7. Shotcreting AI judgment accuracy.

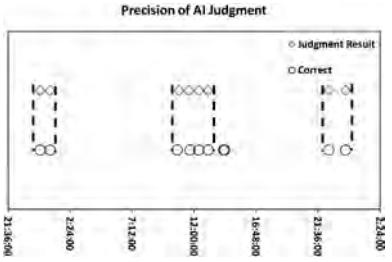

Figure 8. Parking area AI judgment accuracy.

company's SNS. To create this system, an image classification model was created to determine whether the parking area is passable, and an algorithm was created to use the output of the model. Figure 8 shows the accuracy of the AI judgment. The figure shows that the AI was able to determine almost accurately that the tunnel was impassable by detecting the construction equipment. The AI's accuracy rate for determining whether or not the tunnel is passable is approximately 90%.

4 TRIAL RESULTS

4.1 *Reduction of waiting time using AI judgment*

Figure 9 shows an example of the screen shot of the company's SNS notification screen, in which the result of the AI's judgment can be seen. Table 3 shows the waiting time reduced by the trial. The waiting time before the trial was used as the target time for comparison of the trial results after interviewing the subjects. The trial reduced the waiting time for each work by 40% to 60%. In addition, the AI judgment of the parking area reduced the waiting time for material loading and unloading to zero. This technology was found to be effective in reducing the waiting time sufficiently.

4.2 *Reduction of material loss*

A total of 13 trials were conducted in the shotcreting at the trial site. The first to fifth trials were test trials for adjusting the trial environment, etc., and the verification of the trials was conducted from the sixth trial. Figure 10 shows a comparison of the required mix volume obtained by the 3D scanner and the plant mix volume. The variation of the deviation decreased as the trials were repeated, and at the 10th trial, the deviation was 0.01 m^3. Figure 11 shows a comparison of the shotcrete quantity determined by the AI and the quantity calculated from the plant's mixing results. The average error was about 1.2 m^3. The AI judgment of the quantity of shotcrete

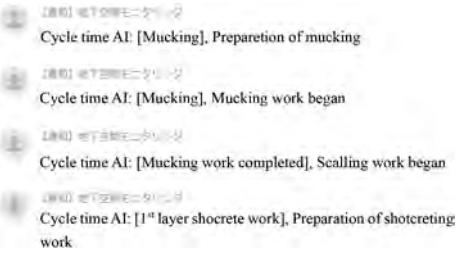

Figure 9. Company SNS notification screen.

Table 3. Work with waiting time.

Target person	Work contents	Previous Waiting time(min)	Trial Waiting time(min)
Worker	Delivery of materials	12	0
Worker	Mucking	37	15
Staff	Observation of face	40	18
Staff	Quality control	23	13

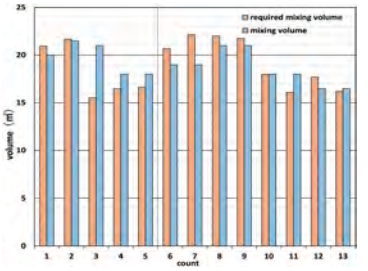

Figure 10. Comparison of mixing volumes.

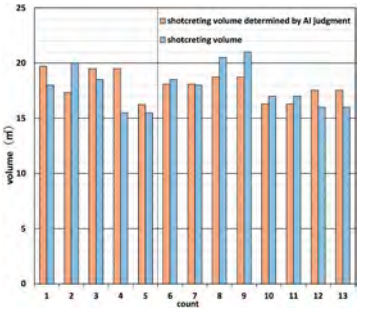

Figure 11. Comparison of shotcreting volume.

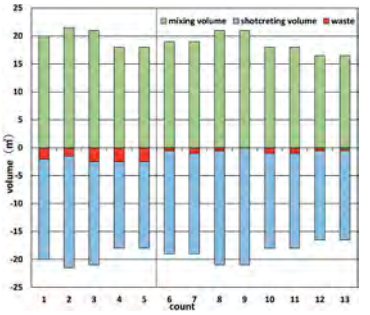

Figure 12. Amount of shotcrete waste.

could be performed within the range that would not cause any problems in construction. Finally, Figure 12 shows the results of the amount of waste. The figure shows that the amount of shotcrete waste decreased after the sixth trial. A comparison of the average amount of shotcrete waste before and after the trial shows that the amount of shotcrete waste was reduced by about 70%. The technology was found to be effective in reducing the amount of shotcrete waste.

4.3 *Improved efficiency of construction management*

This trial focused on the monitoring management, face management, and control of actual management, which are the most frequently performed by the staff, in order to improve efficiency. Figure 13 shows an example of the automatically processed results of tunnel settlement and convergence. The figure shows a graph of tunnel displacements transferred to the cloud using a reporting system. Information such as settlement trends and distance from face is automatically processed and can be accurately graphed. These results can be checked under the Internet environment. This makes it possible to understand the behavior of the ground in a more timely manner. Figure 14 shows an example of a list of photographs of a face. The figure shows a list of face photographs automatically generated by selecting any cross section based on the photo data in the cloud. The photographs of the face are used as materials for selecting appropriate support patterns. Therefore, the amount of time spent by the staff in compiling the photographs of the face could be reduced. To improve the efficiency of control of actual measurements, the cloud-based tunnel design data, support patterns, and other data are linked to automatically create a reporting system for the actual measurements. Figure 15 shows the form selection screen. The measurement result input screen (Figure 16) is created by selecting the construction type and support patterns to be created. By inputting the measurement results, a report converted into a prescribed format (Figure 17) is created. This graphically displays necessary information such as measured values, differences from control criterion, and control criterion. This technology enables direct input of measurement results on site using a tablet terminal or similar device. This reduces the amount of time

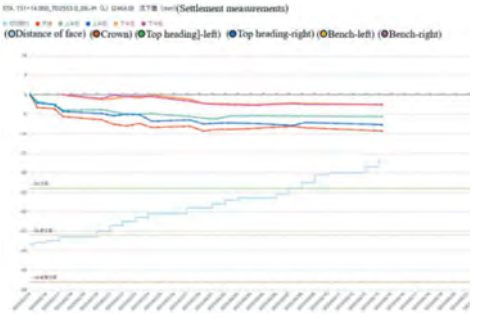

Figure 13. Results of tunnel settlement and convergence.

Figure 14. List of tunnel face photographs.

Figure 15. Report selection screen.

Figure 16. Screen to input measured values.

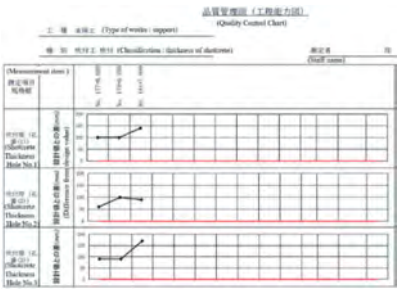

Figure 17. Example of a created report.

spent by staff on control of actual measurements. Although the working time for each staff varies, they spend approximately 15 to 150 minutes/day on construction management. By utilizing cloud services, these works can be automated, and a reduction of up to 150 minutes/day can be achieved.

5 CONCLUSION

Regarding the efficiency of the staff's construction management, the trial technology reduced worker waiting time by up to 22 minutes and staff waiting time by up to 32 minutes. In addition, the use of cloud services can save up to 150 minutes of construction management for staff. Considering these effects, this technology is expected to increase worker productivity by up to 5% and staff productivity by up to 40%. In addition, the use of cloud services can be expected to improve the efficiency of information sharing and the enhancement of construction support through the accumulation of construction data. Meanwhile regarding the reduction in the amount of shotcrete, AI judgment technology reduced the amount of shotcrete waste by 70%. In general, about 270 kg of carbon dioxide is emitted per m3 of concrete during its production process. In other words, the reduction in the amount of shotcrete waste can be achieved to reduce carbon dioxide emissions by approximately 432 kg per construction, contributing to the realization of a carbon-neutral society. Even though it is proven that this technology is expected to improve labor productivity, the trial period was too short to obtain sufficient data. Therefore, we would like to confirm the certainty of labor productivity improvement by continuing the trial over a longer period of time since construction management are not limited to those described in this report. We would like to continue to develop the construction management in order to further improve its efficiency as a whole.

ACKNOWLEDGMENTS

This report is based on consortium formed by Shimizu Corporation, Lightblue Technology, and Enzan Koubou co, ltd, using PRISM budget promoted by the Ministry of Land, Infrastructure, Transport and Tourism (MLIT). We would like to express our deepest gratitude to the people at the Kumamoto River and National Highway Office, Kyushu Regional Development Bureau, MLIT and the consortium members for their guidance and cooperation in this trial.

REFERENCES

H. umeyama, et al, 2023. Efforts to improve productivity using cloud services. JSCE National Convention 78th Annual Scientific Lecture, CS14–39.

S. kitagawa, et al, 2023. Verification of automatic cycle time determination system using video of tunnel excavation work. JSCE National Convention 78th Annual Scientific Lecture, CS14–37.

T. arai, et al, 2023. Trial to Reduce the Amount of Shotcrete Waste. JSCE National Convention 78th Annual Scientific Lecture, CS14–38.

T. fukuda, et al, 2023. Streamline Field Management Processes to Improve Labor Productivity and Reduce Material Loss. JSCE National Convention 78th Annual Scientific Lecture, CS14–40.

T. fukuda, et al, 2022. Development of automated angle control system to improve safety and productivity, ITA-AITES World Tunnel Congress 2022, Copenhagen, Denmark.

T. fukuda, et al, 2023. Development of a ground forecasting system based on the geological and groundwater conditions in mountain tunneling, ITA-AITES World Tunnel Congress 2023, Athens, Greece.

Tunnelling for a Better Life – Yan, Celestino, Thewes & Eberhardt (Eds)
© 2024 The Author(s), ISBN 978-1-032-80042-4
Open Access: www.taylorfrancis.com, CC BY-NC-ND 4.0 license

Research on integrated management platform of shield construction based on digital twin and application in subway engineering

Xuejian Wang* & Jiayuan Wang*
College of Civil and Transportation Engineering, Shenzhen University, Shenzhen, China
Sino-Australia Joint Research Center in BIM and Smart Construction, Shenzhen, China

Yuyu Zhang* & Sili Jiang*
China Railway South Investment Group Co., Ltd., Shenzhen, China

ABSTRACT: To effectively address issues in process of shield tunneling for subway construction, including insufficient real-time monitoring, delayed risk response, and limited visualization. This study proposed an integrated management platform of shield construction based on digital twin, analysed remote communication based on cloud service, real-time risk early warning mechanism in TBM operation, as well as integration approach for multi-source information using BIM and GIS technologies. Finally, taking a subway project as an example in case study, the functionalities of platform is demonstrated, such as virtual tunnel and construction simulation, real-time visualization of operating parameters of shield machine, integrated monitoring of shield machine group, visual display of surrounding stratum information, and risk monitoring and early warning in shield construction. The implementation of this platform can improve efficiency, quality and safety of subway shield construction, and also provide valuable insights for the process control of other shield construction projects.

Keywords: Subway shield construction, TBM (Tunnel Boring Machine), Digital twin, Real-time monitoring, Building Information Modeling (BIM), Geographic Information System (GIS)

1 INTRODUCTION

The shield tunneling method has become a primary construction technique for urban subway tunnels and some railway tunnels in China. In actual subway construction environment, due to complex and varied hydrology and engineering geology of the surrounding strata, and different mechanical properties of soil layer, accidents such as stratum collapse and underground water seepage may occur during the excavation of shield tunnelling, which may cause hidden dangers. However, the current safety and risk control practices for shield tunneling primarily depend on manual surveying on environmental conditions, timely analysis and processing of measurement data to provide information feedback place high demands on workers. Therefore, in terms of construction monitoring, Ye et al. (2013) applied FBG sensing technology to monitor temperature and strain in adverse environments, ensuring the safety of railway shield. Shen et al. (2014) investigated an integrated approach for machine guidance and operation monitoring in tunnel construction. Huang et al. (2018) and Xie et al. (2018), have demonstrated utilization of real-time monitoring systems and platforms in shield tunnelling, specifically in relation to TBM (Tunnel Boring Machine) and surrounding rock or settlement control.

Although the guiding system of TBM can provide a certain degree of guidance and positioning function during operation, it lacks the capability for real-time remote monitoring of shield machine equipment. Other innovative methods were developed by Zhang et al. (2021), Zeng et al. (2022) and Huang et al. (2022) respectively, and were applied to real-time monitoring of shield machine operation and tunnel construction to determine operating status of tunnel boring machines. To ensure safety of tunnel construction, hazards of shield tunnelling were analysed and evaluated (Hyun et al. 2015). Multi-source information fusion technology used by Zhou et al. (2020) for risk assessment and management. Ding et al. (2013) developed a real-time safety early warning system for cross-channel tunnel construction based on IoTs (Internet of Things) technology. The warning of abnormal working status provided by Gong et al. (2021) was utilized to monitor and control the TBM excavation process.

*Corresponding authors: wustwxj@163.com; wangjy@szu.edu.cn; tsjzyy@126.com; jansly@sina.com

DOI: 10.1201/9781003495505-394

Moreover, with development of IoT technology, the application of digital twin technology in construction management (e.g. Boje et al. 2020, Al-Ali AR et al. 2020, Pan and Zhang. 2021, Ye et al. 2022) with great success, including real-time sensing and monitoring, data integration and analysis, simulation and optimization, as well as visualization and collaboration. These can provide more comprehensive and precise construction data and information in real-time, as well as rich management tools and new possibilities for integrated monitoring and control of shield construction.

In this paper, the integrated management platform of shield construction was designed and developed based on digital twin technology, with the application of key technologies and methods of IoT, Building Information Modeling (BIM) and Geographic Information System (GIS), which enables real-time and all-around integrated management and control to improve efficiency, quality and safety of shield construction in subway engineering.

The structure of this paper is as follows: Section 2 describes digital twin based platform architecture of shield construction. Section 3 discusses the key technologies and methods to realize integrated management of shield construction process. In Section 4, the specific implementation and application of platform functionality is shown in a case study. Finally, the conclusion is given in Section 5.

2 DIGITAL TWIN-BASED PLATFORM ARCHITECTURE OF SHIELD CONSTRUCTION

2.1 *Overall framework design*

To improve efficiency, quality and safety of shield tunnel construction in subway project, an integrated management platform using digital twin technology is proposed in this study, overall framework is designed as shown in Figure 1, mainly consists of four levels: physical perception layer, network transmission layer, digital service layer, and management application layer. By adopting a hierarchical design approach, the functional modules of platform are organized to facilitate seamless data exchange and interoperability between layers.

2.2 *Physical perception layer*

During the process of tunnel excavation with TBM, the physical perception layer is mainly responsible for real-time collection of various data and information related to equipment operation and construction environment. In tunnel construction, the shield machine, as a critical mechanical component, is equipped with sensor devices to monitor its operating status parameters such as cutterhead torque, excavation volume, grouting volume, propulsion speed, slurry properties, inclination angle, and

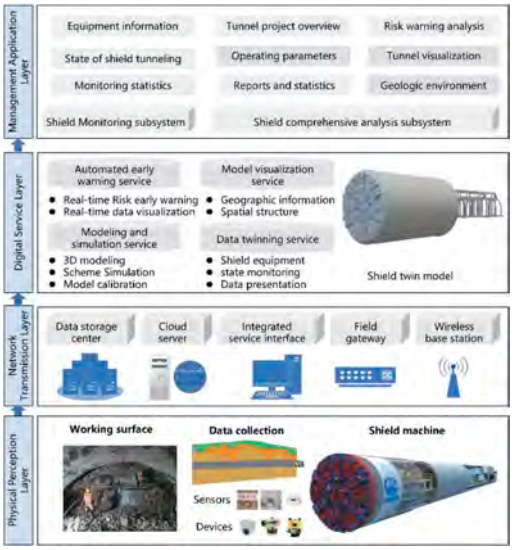

Figure 1. Overall framework of integrated management platform of shield construction based on digital twin.

supervising equipment faults, wear degree in real-time. Combined with tunnel construction working face, various environmental monitoring sensors are required in shield tunnelling process to real-time monitor factors such as temperature, humidity, dust concentration, hazardous gases within the tunnel, as well as data regarding tunnel displacement, deformation, groundwater levels, and soil pressure. sensor sampling frequencies can be set for different monitoring indicators to ensure data accuracy and timeliness. In addition, laser scanners are arranged to scan and capture shape and structure of tunnel cross-section, meanwhile total stations are used for precise positioning and measurement of tunnel size. Cameras installed at site record construction details and changes. These devices and sensors work together to achieve full monitoring during shield construction.

2.3 *Network transmission layer*

Network infrastructures are established to collect various data from perception layer in tunnel construction sites, enabling real-time transmission, storage, and analytics. The 5G, base stations, and onsite gateways are utilized to build wireless communication links both inside and outside the tunnel, facilitating data transfer to remote monitoring servers. Based on system functions and data requirements, a combination of local storage and cloud services is adopted. Large databases such as MySQL and MongoDB are used to manage real-time monitoring data, spatial data, etc. Integrated service interface including Web API (Application Programming Interface), database connections, file transfer protocols, RESTful, and RPC (Remote Procedure Call), which serve

as intermediaries for data transfer and information upload. They are responsible for coordinating and managing communications between different data sources and system modules.

2.4 *Digital service layer*

The digital service layer adopts service-oriented design with different microservices collaborating, including shield tunnel digital twinning, visually modeling and simulation, as well as automated warning and dynamic risk analysis. The visually modeling and simulation service builds digital replicas to simulate actual construction status and predict scenarios, and also adopts BIM and GIS technologies to achieve visualization of construction environment model. The data twin service monitors real-time operational status of TBM equipment. The automated early warning service conducts real-time risk monitoring and alert throughout the entire process. This layer integrates, processes and analyses multi-source data on shield tunnel construction, providing effective support for construction decision-making.

2.5 *Management application layer*

The management application layer is responsible for real-time online interaction between users and the system with the B/S (Browser/Server) mode, which includes the shield monitoring subsystem and shield comprehensive analysis subsystem, integrating multiple functions and configuring virtual environments and data displays based on user needs. The application layer provides specific applications such as report statistical analysis, monitoring and early warning management, risk management and equipment management to support decision-making. Through visual online display, users can intuitively understand the real-time working status of shield machine, tunnel geological condition, environmental indicators, and overall situation at construction site.

3 KEY TECHNOLOGIES AND METHODS

3.1 *Remote communication based on cloud service*

At shield tunnel construction site, some base stations with different functionalities are connected to the gateway to communicate and control various terminal devices and sensors. To ensure secure transmission of data, collected information is sent to monitoring center via a VPN (Virtual Private Network) wireless transmission link. In data storage process, the hyper-converged server technology is utilized to integrate computing, storage and network in physical server. These are then virtualized into logical resources using virtualization technology, and SaaS cloud services are provided in an integrated environment for flexible allocation and management. Based on this, according to monitoring requirements and system design, remote monitoring functionality of shield machine is deployed using containerization and integrated with other business systems. The server deal with data from sensors and monitoring devices through remote desktop services, authorized engineers and administrators can access to monitoring canter using IP address and port, connecting to control room interface of TBM to monitor key data in real-time at construction site, as shown in Figure 2. Notification services are used to send real-time alert messages to relevant staff with SMS, email, or mobile applications, ensuring that issues are addressed promptly.

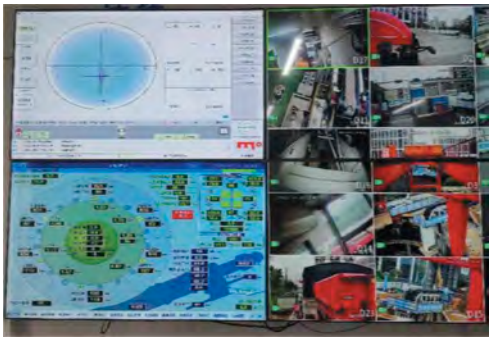

Figure 2. Remote monitoring interface.

3.2 *Risk management and early warning response*

3.2.1 *Risk classification and control*

By identifying and sorting out various potential risks, including TBM failures, changes in geological conditions, and tunnel collapse risks, etc. each potential risk source is analyzed and evaluated to determine its possibility and severity. Based on risk assessment results, the identified risks are categorized and ranked to establish a risk register. Typically, different risk levels indicate the severity of risks, including major, high and low degrees. The identified risks are ranked and divided into high, medium and low risk levels. Based on the risk levels, corresponding emergency plans and preventive measures are formulated for the confirmed risk sources, including risk control measures in construction methods, safety equipment, safety training, contingency plans, special monitoring, etc. For high-risk events, priority is given and more stringent control measures should be implemented.

3.2.2 *Real-time warning and response*

Regarding to key monitoring data such as tunnel geological subsidence, TBM operational parameters, and attitude, a real-time monitoring and warning mechanism has been established, as shown in Figure 3. During this stage, the warning rules including the setting of critical state and threshold values for warning indicators such as rate and cumulative

values, as well as the definition of warning levels. The monitoring system automatically and timely detects collected monitoring data according to warning rules. Once a specific indicator reaches or exceeds the threshold, different warning signals and warning information, including specific response measures and designated responsible personnel, are generated based on different warning levels. These information are communicated to relevant personnel, including manager, engineer, and safety officer, through communication channels such as SMS and application notifications. After receiving the warning information, immediate action needs to be taken at construction site following the established response procedures and measures, which include adjusting direction and attitude of TBM, controlling excavation speed. For high-risk early warnings, stricter control measures such as immediate shutdown and emergency plans will be taken to prevent accidents and ensure project safety.

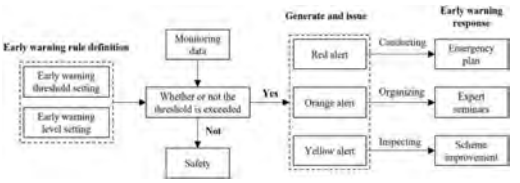

Figure 3. Real-time dynamic early warning mechanism.

3.3 *Information integration with BIM and GIS*

The BIM and GIS technologies play a significant role in integration of multiple source information. By integrating them, more comprehensive and accurate representation of scenes can be achieved. The technical process of BIM and GIS data fusion for visualization as illustrated in Figure 4, involves following steps: In data preparation phase, 3D models of tunnel infrastructure are constructed using BIM tools according to design drawings and engineering demands, various geospatial data, including maps, satellite imagery, and terrain models, will be integrated into a unified geographic coordinate system. In data conversion phase, conversion tools such as FME (Feature Manipulate Engine) or formats like IFC or CityGML are utilized to align GIS data and BIM models within the same geographic coordinate system such as WGS84, CGCS2000. In data association phase, data relevant to specific BIM projects or scenes is selected and extracted. The association between GIS data and BIM models is established based on spatial location, geometric topology relation, and shared attributes or unique identifiers, resulting in formation of an integrated information model. Finally, in process of visualization, the integrated data is utilized for comprehensive analysis and display in a GIS environment, which includes static models such as tunnelling equipment and tunnel structure models, as well as real-time dynamic information from IoT data, such as equipment working status, risk resources at tunnel construction site, enabling construction teams to quickly grasp the site conditions and make timely decisions.

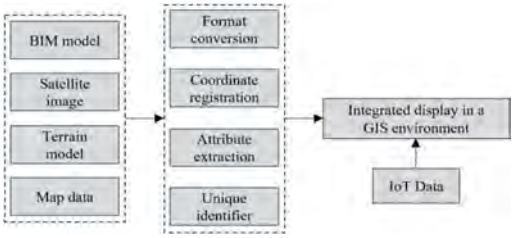

Figure 4. BIM and GIS data fusion for visualization.

3.4 *Digital twin modelling for TBM and tunnel*

The construction of a digital twin model is a critical step to simulate and monitor various aspects of subway tunnel construction. BIM technology has a vital role in efficiently constructing detailed 3D scenes and facility models to enable visualization. The typical workflow involves following steps: First, digital models are usually created using BIM software such as Autodesk Revit, including the mechanical equipment model of TBM, as shown in Figure 5, to simulate the shield construction process.

Figure 5. 3D model of TBM equipment.

Next, for completed tunnel structures, the laser scanner can be used to perform scene scanning and obtain detailed point cloud data, including information about the shape, dimensions, structure, and surface features of tunnel. The point cloud data is then imported into dedicated laser scanning software, such as Faro Scene, to generate an accurate digital 3D model corresponding to physical entity, as shown in Figure 6, and store it in a usable format. This 3D model can be used for assessment of accuracy and inspection of quality defects in tunnel structure. These models can be integrated into BIM platforms as part of digital twin model, and be further enriched with additional information as needed, such as surface texture details, to reflect the actual scene.

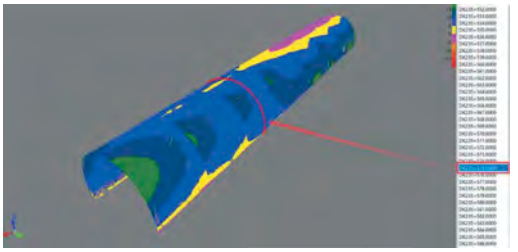

Figure 6. Tunnel 3D model from point cloud.

Additionally, it is necessary to map parameters and state variables from actual scene to model. Through establishing a correlation between characteristics of engineering physical entities and their real-time behavioural processes, including parameter mapping and state variable mapping. By associating real-time data with corresponding elements in the BIM model, this integration enables feedback and synchronization between the physical construction site and the model, realizing a dynamic digital twin for status monitoring in subway tunnel construction.

4 CASE STUDY AND PLATFORM APPLICATION

In major tunnel project of Shenzhen Metro 14, the development and implementation of the proposed integrated management platform for shield construction have achieved comprehensive data collection, processing, analysis and decision support as follows.

4.1 *Virtual tunnel and construction simulation*

In virtual tunnel scene roaming, users can interactively explore the 3D structure of tunnel through a web browser, as shown in Figure 7. The immersive experience enables users to navigate and overview the tunnel layout in detail. Moreover, the assembly of shield segments can be thoroughly checked in virtual environment to verify the accuracy of design. Additionally, the virtual tunnel scene can serve for training new employees, helping them better understand the construction process and tunnel structure, and facilitating effective learning of knowledge.

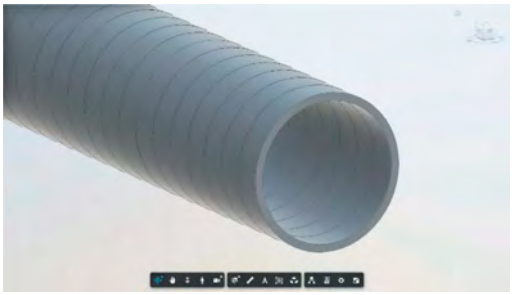

Figure 7. Virtual tunnel scene.

Simulation technology for shield tunnelling is used to analyse the process of shield operation and muck discharge as shown in Figure 8. Based on geological information and exploration data, this technology can simulate potential changes in underground lithology and geological conditions, and predict geological hazards such as geological water inrush, geological faults, and landslides that may occur during construction. The use of construction simulation can empower managers to identify potential risk factors and proactively formulate corresponding safety precautions.

Figure 8. Construction simulation.

4.2 *Real-time visualization of multi parameters*

In construction of earth pressure balance shield, the monitoring parameter provided by platform can show pressure of soil bin in different parts to ensure stability of excavation face and maintain the balance state within safe range. Simultaneously, it can also track and record changes in shield operation and driving parameters, including shield advancing speed, cutter head torque, thrust, cutter head speed and penetration degree, as shown in Figure 9.

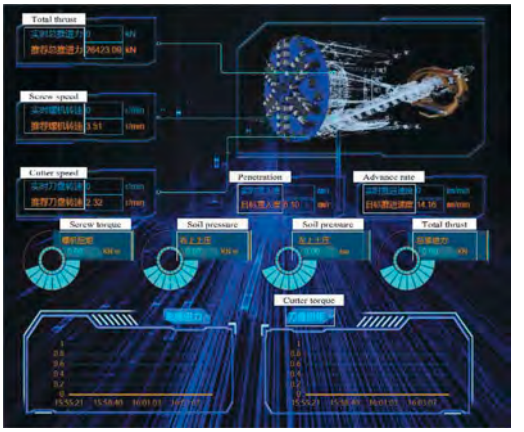

Figure 9. Real-time visualization of operating parameters.

These data allow engineers and operators to tightly control tunnelling speed of shield machine, and adapt to variations in geological conditions. In addition, timely analysis and feedback of monitoring data can facilitate the control of attitude of shield such as tilt and offset, to maintain stability of shield machine throughout construction process.

4.3 *Integrated visualization and monitoring*

4.3.1 *Shield machine group monitoring*

The monitoring system for shield machine group can be integrated with geographic information to provide a spatial representation of each shield machine on a map. Each machine is labelled on the map, and users can click on the label to enter the real-time monitoring interface of each shield machine and view its operational status. When an alarm or fault occurs in the shield machine, corresponding marker on the map will flash, attracting operator's attention to the issue, as shown in Figure 10. A comprehensive overview of all the shield machines in group enables the operator to quickly identify and check the number, location, operating status of shield machines, and resolve any problems that may arise to ensure the safety of shield construction.

Figure 10. Working plane location of shield machines.

4.3.2 *Surrounding stratum information display*

The position tracking of shield machine and updating of its tunnelling status, as well as information display on stratum cross section and geological environment change along the line are shown in Figure 11. By using different colours to mark and highlight the stratigraphic and geotechnical features of current tunnel section, the management personnel can intuitively access this information and assess any environmental risks that may arise during shield construction, and guide shield excavation and driving accordingly.

4.4 *Risk monitoring and early warning*

During operation of shield machine, potential risk events are predicted through risk identification and

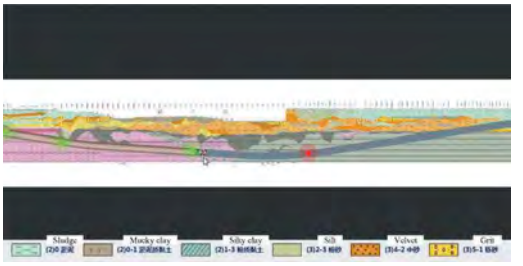

Figure 11. The working plane of shield machine group.

assessment, as shown in Figure 12. One such potential risk is the accumulation of muck in chamber, and corresponding preventive measures are formulated to address this issue. Meanwhile, to mitigate this risk, real-time monitoring of shield machine's working parameters, such as thrust and propulsion speed. Once the potential risk event or parameter abnormality is detected, the platform will timely issue warning signals. In such cases, notifications are promptly sent to engineer and safety personnel at site. By taking proactive measures to timely address potential risks, the construction team can effectively manage operation of shield machine and maintain a safe working environment.

Figure 12. Real-time visualization of operating parameters.

5 CONCLUSIONS

According to current situation and technical requirements of subway shield construction management, the framework for integrated management platform of shield construction based on digital twin was proposed in this study. Firstly, the platform utilized remote monitoring and cloud service for real-time transmission of monitoring data. Then, a whole-process risk monitoring and early warning mechanism was established to enable early detection and response to risks arising from geological conditions and shield machine status. Furthermore, through the integration of BIM and GIS technology, real-time analysis and visualization of information on geological conditions, surrounding environment, and shield machine working process were discussed. Finally, through a case study, the application of this platform has been verified in informatization, visual management of shield

construction. However, despite digital twin technology facilitates comprehensive management practice of platform in subway engineering, further considerations for integrating more advanced monitoring and intelligent technologies, such as data-driven decision-making analysis based on big data, are required to enhance safety and efficiency of tunnel construction.

REFERENCES

Al-Ali A R, Gupta R, Zaman Batool T, et al. (2020). "Digital Twin Conceptual Model within the Context of Internet of Things." Future Internet, 12(10), 163.

Boje C, Guerriero A, Kubicki S, et al. (2020). "Towards a semantic Construction Digital Twin: Directions for future research." Autom. Constr., 114, 103179.

Ding, L. Y., Zhou, C., Deng, Q. X., et al. (2013). "Real-time safety early warning system for cross passage construction in Yangtze Riverbed Metro Tunnel based on the internet of things." Autom. Constr., 36, 25–37.

Gong, Q., Wu, F., Wang, D., et al. (2021). "Development and application of cutterhead working status monitoring system for shield TBM tunnelling." Rock. Mech. Rock. Eng., 54, 1731–1753.

Pan, Y., Zhang, L., (2021) "A BIM-data mining integrated digital twin framework for advanced project management." Autom. Constr., 124, 103564.

Huang, X., Liu, Q., Liu, H., et al. (2018). "Development and in-situ application of a real-time monitoring system for the interaction between TBM and surrounding rock." Tunn. Undergr. Sp. Tech., 81, 187–208.

Huang, X., Liu, Q., Liu, B., et al. (2022). "Development and in-situ application of a real-time cutting tool forces monitoring system in TBM tunnelling." Tunn. Undergr. Sp. Tech., 124, 104453.

Hyun, K. C., Min, S., Choi, H., et al. (2015). "Risk analysis using fault-tree analysis (FTA) and analytic hierarchy process (AHP) applicable to shield TBM tunnels." Tunn. Undergr. Sp. Tech., 49, 121–129.

Shen, X., Lu, M., Mao, S., et al. (2014). "Integrated approach to machine guidance and operations monitoring in tunnel construction." In Proceedings of the International Symposium on Automation and Robotics in Construction (pp. 1). IAARC Publications.

Xie, X., Wang, Q., Shahrour, I., et al. (2018). "A real-time interaction platform for settlement control during shield tunnelling construction." Autom. Constr., 94, 154–167.

Ye, X. W., Ni, Y. Q., & Yin, J. H. (2013). "Safety monitoring of railway tunnel construction using FBG sensing technology." Adv. Struct. Eng., 16(8),1401–1409.

Ye Z, Ye Y, Zhang C, et al. (2023). "A digital twin approach for tunnel construction safety early warning and management." Comput. Ind. 144, 103783.

Zeng, L., Shu, W., Liu, Z., et al. (2022). "Vision-based high-precision intelligent monitoring for shield tail clearance." Autom. Constr., 134, 104088.

Zhang, P., Chen, R. P., Dai, T., et al. (2021). "An AIoT-based system for real-time monitoring of tunnel construction." Tunn. Undergr. Sp. Tech., 109, 103766.

Zhou, H., Zhao, Y., Shen, Q., et al. (2020). "Risk assessment and management via multi-source information fusion for undersea tunnel construction." Autom. Constr., 111, 103050.

Tunnelling for a Better Life – Yan, Celestino, Thewes & Eberhardt (Eds)
© 2024 The Author(s), ISBN 978-1-032-80042-4
Open Access: www.taylorfrancis.com, CC BY-NC-ND 4.0 license

A study of digital quantitative evaluation system for the safety risk management in the construction activities of transportation hubs

Renxue Wen
Sino-Railway South Constructing Group Co Ltd, Shenzhen, China

Dongjian Gao*, Wenwu Yang & Wingfei Mou
AECOM, Hong Kong, China

ABSTRACT: This article systematically quantifies the main characteristic indicators of production factors '5M1E' in the construction of large and complex urban transportation hubs through the classification and rating management of construction safety risks and the information management of on-site hazard investigation mechanisms. Preliminary assessment is firstly carried out, focusing on the general conditions of the construction site, to identify the items of high-risk category. Based on the overall risk assessment, conduct comprehensive fuzzy hierarchical calculation and analysis of the multi-level influence degree (weight) on the hazards derived from the high-risk factors that might lead to major safety accidents. The analytical outcome will be further used for detailed quantitative assessment and hierarchical management of high-risk work breakdown structure (WBS) elements, which ultimately ensure the mitigation and control of major construction safety accidents.

Keywords: Construction safety, Factor quantification, Digital risk assessment, Refined management

1 INTRODUCTION

The utilization and development of urban underground space (UUS) are essential to address the increasingly severe situation of the scarcity of urban land in China. Underground space is usually used for underground transportation, underground service facilities, underground complex, and underground municipal infrastructure (Cheng et al., 2019). For underground transportation, such as subway, rapid transit etc., transportation hubs are usually constructed below the ground surface in urban area as well. However, underground engineering projects usually bear high risk and extreme complexity due to large-scale investment, long construction period, complicated construction technologies and massive social and environmental impact, etc. (Qian & Rong, 2008). Therefore, competent and adequate strategies should be developed and implemented to address the risks in the construction of underground transportation hubs. Categorization of risks on a project should be applied in order to acquire a more sophisticated and comprehensive understanding to benefit and raise efficiency for the development of measures to cope with potential negative consequences. Usually, risks can be divided into "market-related", "technical", and "institutional", etc. and previous research shows that the majority of risks could be tackled by the means of management instead of technology, which is usually more widely reckoned as the foremost attribution of risk response (Roger & Donald, 2001). For mega engineering projects especially of which the construction is subject to substantial uncertainties, a well-rounded systematic evaluation of risks accounting for sufficient factors and variables is the foremost step in the process of risk management. An appropriate methodology for risk evaluation should be carefully considered and selected by decision-makers of projects. According to relevant studies, the main evaluation methodologies that have been developed include: Hazard Examination, Analytical Method of Hazard and Operation, Expert Investigation, FMEA Method, Fault Tree Analysis (FTA), PRA method, Analytical Hierarchical Process (AHP) and MODM method, Influence Diagram (ID), Bayes Network (BN) etc. (Cao & Xu, 2005).

Each method for evaluation has its own advantages and weaknesses and particular attention has to be given with regard to the development of risk management methodology for a specific project. Analytical Hierarchical Process (AHP) was created in 1970s by T. L. Saaty, who was a prominent operations research analyst. It used pair comparison to determine judgement matrix and the weights of different variables based on the eigenvalues of the matrix (Saaty, 1980). This method is featured by combining both quantitative and qualitative principles and is widely adopted for

*Corresponding author: Jason.gao@aecom.com

DOI: 10.1201/9781003495505-395

cost-performance analysis, resource allocation, conflict analysis in a whole variety of industries (Saaty, 1993). This study focuses on improving the efficiency of risk management in construction projects, which contain a multitude of uncertain variables and multi-level decision making and management mechanism. Therefore, Analytical Hierarchical Process (AHP) is adopted as the core technique in the development of the assessment methodology in this study to cope with the challenges. Fuzzy Comprehension Evaluation (FCE) is used to revise AHP so that the evaluation results could be represented mathematically. Also, Fault Tree Analysis (FTA) is implemented for deducing the root causes of risks and hidden dangers based on the analytical results.

At present, engineering risk level assessment is mainly based on the risk probability level and risk loss level matrix for risk level assessment. However, engineering risk assessment is mainly based on qualitative and empirical methods in practice. Due to the fact that the risk probability level is difficult to quantify. This method usually depends on Engineering Judgement, which requires experts in relative fields with extensive experience and knowledge to provide the input for the assessment. Furthermore, qualitative and empirical assessment cannot cater for the accuracy and practicality in the ever-changing construction industry, which generates an urgent need to convert the traditional methodology to a dynamic one with the means of quantification. Combining the rapidly developing technologies of digital engineering and Building Information Modelling (BIM), the characteristics of various elements of construction projects (i.e. safety risk causing factors) are able to be quantified and evaluated in a standardized procedure.

With accurate risk assessment approaches, an overall managerial framework should be established to connect "evaluation" and "response". Mature management systems for safety and risk have been established with the development of major infrastructure projects, such as Hong Kong-Zhuhai-Macau Bridge, over the course of decades (Yang & Hu, 2016). The philosophy of whole-process risk management has been proposed by Yang et al. (2018), which has been examined and improved in the subsea tunnel construction projects. Similar to underground projects, subsea tunnelling is also featured by high-intensity of risk and a well-schemed whole-process management workflow which is embedded in planning, feasibility study, design, tendering, construction, handover and operation stages, and ensures corresponding actions can be taken effectively and timely.

This study is aiming at using mathematical means combining the application of digital technology to facilitate the workflow and outcome of risk management in mega construction projects such as underground transportation hubs. It investigates the risk impact on the Casual Chain of individual work units, which are described using Risk Breakdown Structure (RBS) and WBS respectively under various working conditions and environmental conditions and analyse and calculate the safety risk values based on the multi-level classification of the construction work and quantitative assessment. Lastly, the mechanism of hierarchical management of construction safety risks is established on the assessment results. A software program is developed and elaborated in this study to substantiate the theoretical proposition of dynamic risk management.

2 LOGICAL RELATION OF CONSTRUCTION SAFETY RISK FACTORS

Systematic risk management is essential for managing risks effectively and the initial step is to identify valid risk factors for future analysis (Park et al., 2017). The two major sources of safety risks of engineering construction are: unsafe behaviours of people and unsafe states of things, which are in logical conjunction ('AND'). People's behaviour (Man) could be further divided into individuals and organizations, which are in logical disjunction ('OR'). The unsafe state of things includes factors of Machinery, Method (construction methods), Environment, Materials, and Management (construction/project management), which are in logical disjunction ('OR'). In a construction unit, the risk values of factors of Man, Machinery, Environment, Method, Material and Management (so called '5M1E') will affect the high and low safety risks of the construction unit. As shown in Figure 1, assuming that R_M, R_{MC}, R_{ML}, R_{MD}, R_E, and R_{MG} are risk functions for Man factor, Machine factor, Material factor, Method factor, Environment factor, and Management factor, respectively, the system risk function R_{WBS} (x) for a certain Work Breakdown Structure (WBS) is a combination of 'AND' and 'OR', denoted as:

$$R_{WBS}(x) = (R_M(x) \cup R_{MG}(x)) \cap (R_{MC}(x) \cup R_E(x) \cup R_{ML}(x) \cup R_{MD}(x)) \quad (1)$$

3 TECHNICAL ROADMAP FOR SAFETY RISK QUANTITATIVE EVALUATION

Based on the workflow of typical risk management in project management, the Technical Roadmap for safety risk evaluation is developed by including the quantitative methodology. The procedure mainly consists of five steps:

1. Risk identification: to identify general risks in the holistic perspective;
2. Digital quantification of risk factors: to calculate the weights of risk elements classified into six risk factors ("5M1E");
3. Quantitative risk assessment: to calculate the risk values for high-risk items based on the results of step 1 and step 2;

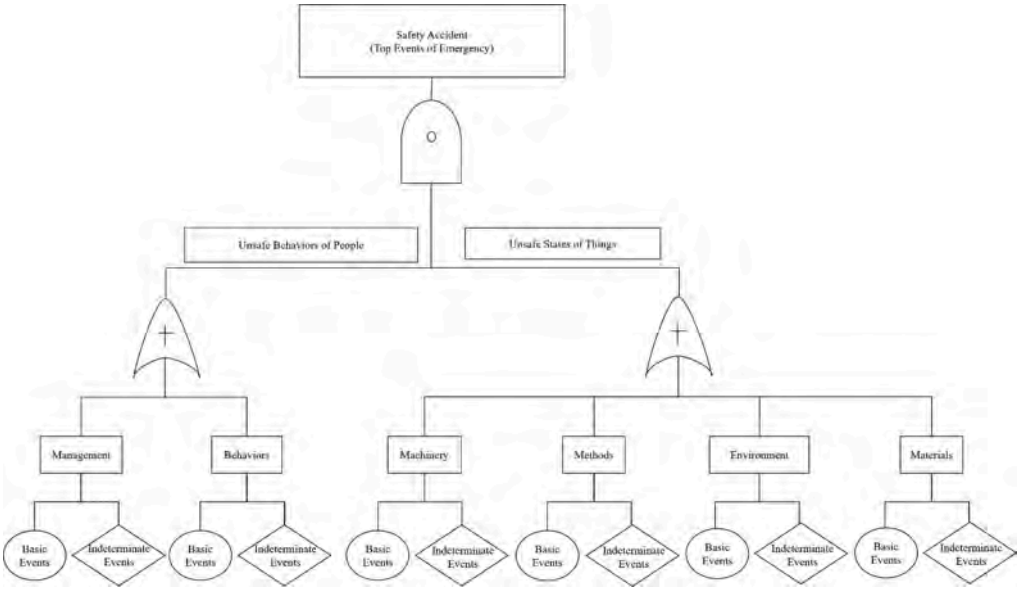

Figure 1. Typical fault tree analysis of construction risk accident.

4. Risk classification management: to continuously manage risks and prioritize high-risk elements;
5. Dynamic management and risk elimination: to develop plans and take measures to mitigate, eliminate and monitor risks.

4 SAFETY RISK FACTOR QUANTIFICATION STANDARD

Risk identification investigates in both internal and external risks of projects. Following the process of "risk identification → risk analysis → risk assessment → risk disposal", the '5M1E' elements of potential risk accidents in construction projects are quantified and evaluated sequentially. Application of Fuzzy Interpretative Structural Modelling (FISM) analysis method to identify potential sources of risk that may lead to accidents, as shown in Figure 3.

Based on existing relevant codes, regulations and standards, as well as analysis of historical accidents in the industry, a multi-dimensional and multi-indicator quantitative evaluation is conducted for each element. For example, the safety ability of construction workers is divided into four dimensions: skill quality, physiological quality, psychological quality, and construction environment. Each dimension is further divided into multiple indicative elements. At present, the content and indicators of digital quantitative assessment for safety risk management include: man factor (R man): 32 elements for individuals and 28 elements for teams; Machinery factor (R machinery): 28 elements; Environmental factors (R environment): 27 elements; Method factor (R method): such as 11 elements for foundation pits; Material factor (R material): 6 elements; Management factor (R management): 45 elements.

5 RISK FACTOR QUANTIFICATION

The quantitative evaluation of each risk factor will adopt the fuzzy mathematics theory, establish a three-level fuzzy comprehensive judgment model and carry out risk evaluation level by level. The multi-level Analytic Hierarchy Process (AHP) will be used to determine the weight of factors at all levels and finally determine the risk level. Using the feature root method to obtain the relative weights of each level, the calculation process is as follows:

The equation of R_i is:

$$R_i = \sum_{i=1}^{n} \sum_{j=1}^{m} C_{ij} \cdot r_{ij} \tag{2}$$

For major risk source (items), for specific construction work units, according to WBS-RBS risk matrix structure analysis and dynamic iterative quantitative assessment of "5M1E" elements:

$$R_{WBS(i)} = \sum_{i=1}^{6} K_{RBS(i)} \cdot R_i \tag{3}$$

where R_i is the risk value of a "5M1E" element, and $K_{RBS}(i)$ is the impact weight coefficient of each risk factor.

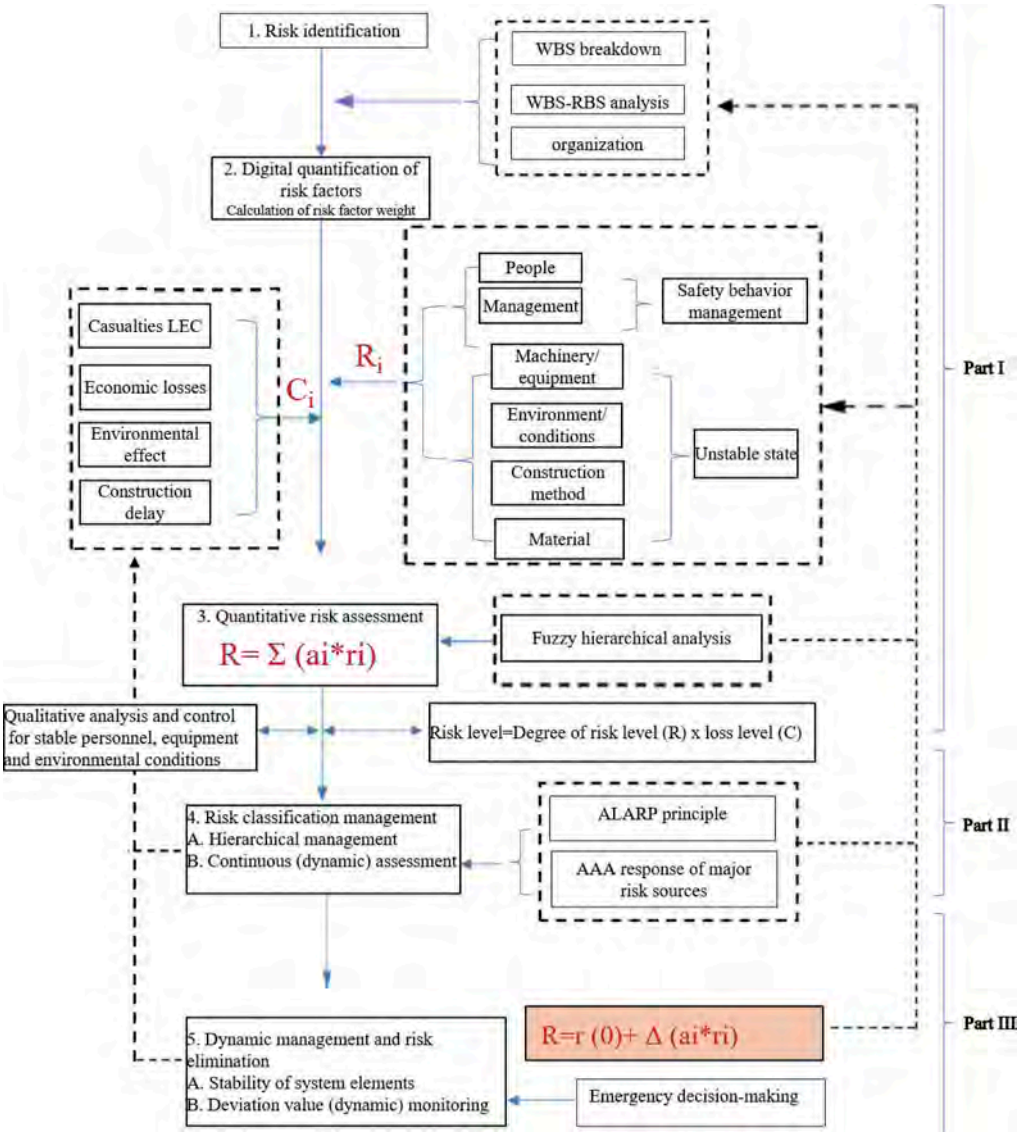

Figure 2. Typical safety risk quantitative evaluation management Framework.

6 DEVELOPMENT OF SAFETY RISK INFORMATION MANAGEMENT SYSTEM

We have developed a safety risk information management system software program using Python 3.9 programming language and SQLite 3 database for construction process. The architecture of the system consists of four levels: 1) Information Display; 2) Application Support; 3) Capability Support; 4) Interface and Transmission, as shown in Figure 5. The system is featured for extension functions of Data-driven analytics, GIS/BIM and IoT for smart construction (Yang & Xia, 2018). The data and information during construction are stored in the system's database on demand. Users will use the interface to input, exchange and display information. The quantitative assessment of risk is based on data in the database, and is analysed through risk analysis algorithms in various application modules. The quantitative evaluation results are displayed in the system interface through values, charts, visualization methods, etc., as shown in Figures 6 and 7. Construction managers or other responsible staff for safety management can refer to the evaluation results of the system to properly manage construction safety risks and develop corresponding emergency response strategies.

Figure 3. Risk Factor – Fuzzy Interpretative Structural Model – Analytical Network Process (FISM-ANP).

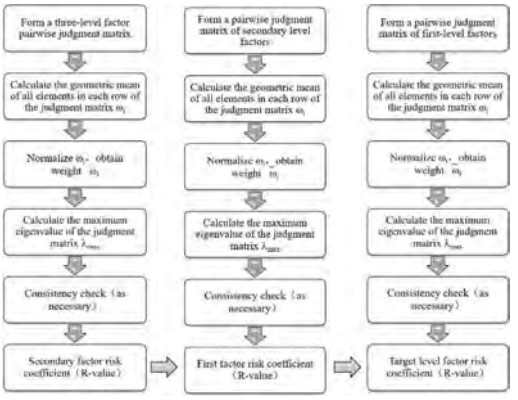

Figure 4. Flowchart for the analytical hierarchical process.

7 APPLICATION OF THE SYSTEM IN A MEGA TRANSPORTATION HUB PROJECT

The Shenzhen Huangmugang (HMG) Hub Project is the reconstruction and expansion of a mega comprehensive transportation hub located at one of the most active areas in Shenzhen, China. It is an interchange station for metro Line 7, Line 14 and Line 24 and integrates Bus & Taxi Services, Pedestrian & Bike Transportation, and underground commercial space. Due to the complicated construction process of underground structural system transfers, interface with existing structures and utilities as well as ground stability during construction of a 40m deep excavation below ground, effective risk control measures are crucial to be implemented throughout the whole construction phases in order to address the enormous potential engineering risks especially those related to safety. Therefore, the Safety Risk Information Management System is applied in this project to improve the safety management for the whole construction activities.

The framework of the system consists of two major stages: 1. overall qualitative risk assessment (at the global level) of the project prior to the construction commencement; 2. quantitative evaluation for Level I (extremely high risk level) and Level II (high risk level) based on the overall risk assessment results. Figure 8 illustrates a typical quantitative evaluation for various factors and overall risk level.

The two stages are further broken down into several steps. Step 1 is to evaluate the project at the holistic level, where the construction type is defined and high-risk items (Levels I and II) are identified by applying relevant codes. Step 2 is to divide high risk items using Work Breakdown Structure (WBS) and Risk Breakdown Structure (RBS). With the developed algorithm, quantification analysis can then be performed, and the risk values are quantified at Step 3. The situation in a construction project would usually be varying constantly, and step 4 implements the

Table 1. The influential weights of construction quality of workers.

Level 1 Indices	Level 2 Indices	Influence Weights	Level 3 Indices	Influence Weights
Man factor	B1 Skill Quality	0.365	C1 Years of experience	0.058
			C2 Expertise level	0.387
			C3 Safety knowledge	0.355
			C4 Risk response ability	0.200
	B2 Physiological Quality	0.125	C5 Age	0.068
			C6 Physical condition	0.199
			C7 Fatigue	0.733
	B3 Psychological Quality	0.233	C8 Responsibility	0.078
			C9 Focus	0.619
			C10 Communication	0.115
			C11 Self-control	0.188
	B4 Construction Environment	0.277	C12 Construction noise	0.041
			C13 Construction lighting	0.058

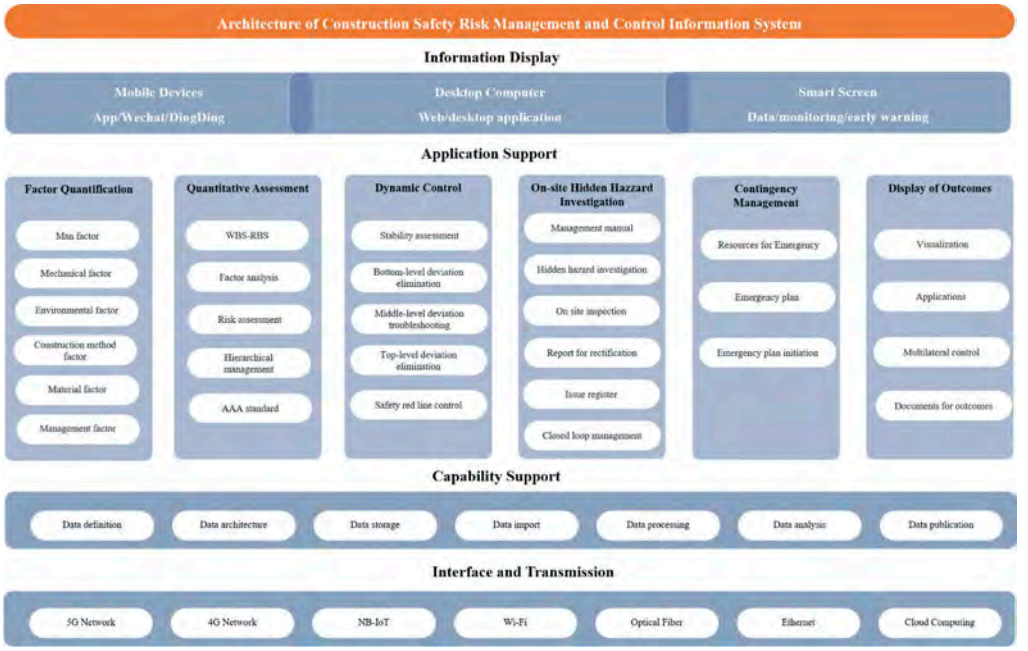

Figure 5. Architecture of safety risk information management system.

Figure 6. Interface of the information system for preliminary assessment and BIM model display.

Figure 7. Interface of the information system for safety risk assessment.

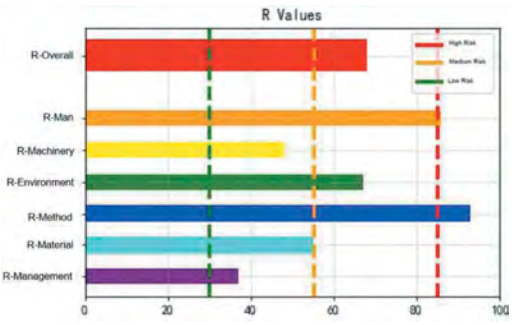

Figure 8. Illustrative evaluation result of safety factors (man, machine, material, method, environment and management).

dynamic evaluation process to cope with the updated site situation where new risks could emerge and level of severity could change. Elimination of hidden hazard exists throughout the whole process of a construction project, which includes tracing back to the root causes with Fault Tree Analysis (FTA) and the timely response according to contingency plans developed based on relative standards. The procedural steps are shown in Figure 9.

In the construction of HMG project, three construction sites are divided and safety risk management is performed based on the work fronts and phasing conditions. At the early stage of the project, safety risks are identified on the scale of the holistic construction area and phases, where 480 items are

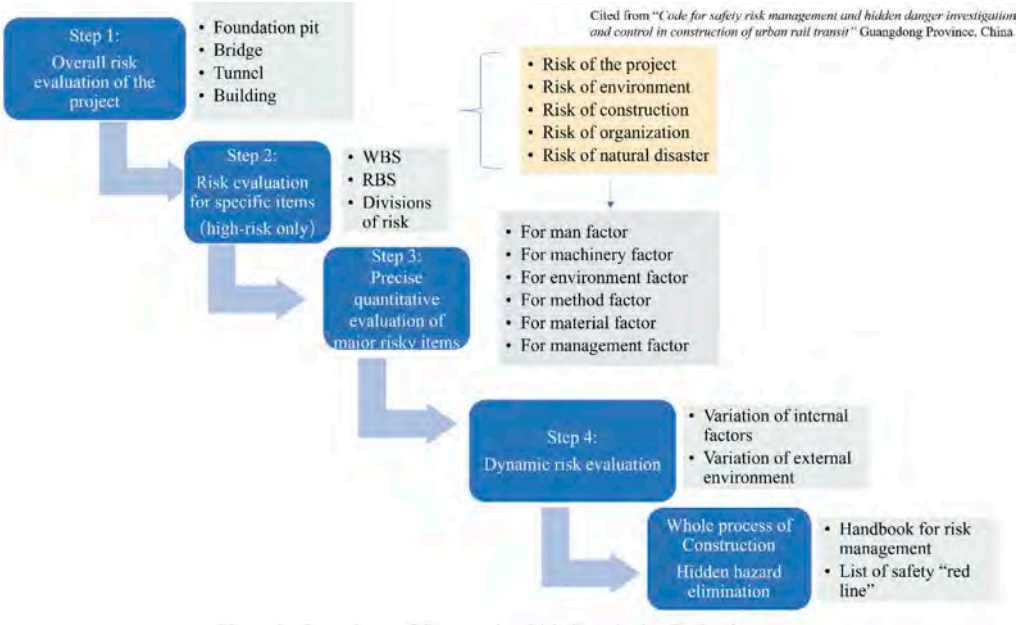

Figure 9. Procedures of construction risk quantitative evaluation.

from site I, 173 items are from site II, and 198 items are from site III. The program was used to analyse the risk items that have been identified and the preliminary assessment results show that there are four high-risk items: 1. geological fault risk; 2. V-shape columns risk; 3. Line 7 existing structure risk; 4. deep excavation risk. Further quantitative assessment and FTA are conducted, the analytical results are provided to the contractor, and several special measures are then developed and implemented accordingly, including removal of existed structure walls, top-down excavation, application of V-shape columns, and application of advanced tunnel reinforcement, etc.Despite the well-rounded risk management considerations, a few incidents still occur due to the lag of the implementation of the construction measures/contingency plans by the contractor. For example, 6 months after starting to apply the system a sudden seepage of ground water occurred at the fault zone identified by the system with the assistance of a 3D geological model. This incident is a proof that our risk identification methodology is valid. However, the lesson learned is that risk response time is also an essential factor in terms of the efficiency of the risk control. Additional features could be added to the system so that required response time window could also be suggested in conjunction with identified hidden hazards. The overall construction work of HMG has been successfully completed without major safety accidents in October, 2022.

8 CONCLUDING REMARKS

With increasing complexity and scale of construction projects in this modern era, conventional risk management means, which mainly relies on empirical analysis, will need to be geared up. The study proposes to use quantitative methodology to address the challenges in that regard. The algorithms of Safety Risk Quantitative Evaluation Management are derived considering the logical relationship of construction safety factors. Through the systematic and quantitative analysis of six 'risk factors' in construction projects, a quantitative risk assessment procedure with multiple steps are developed. Dynamic risk management is also realized based on assessment results with the corresponding risk-elimination and response mechanism. The authors integrate all the aforementioned concepts and developed a software program named Safety Risk Information Management System to facilitate the management workflow. The application of this system in the HMG Transportation Hub project in Shenzhen has shown that it could effectively quantify and evaluate major safety risks in such large-scale and complex construction projects, and predict the Causal Chain of construction safety risks, and achieve effective prevention and control of safety risks, significantly improving the quality and effectiveness of safety risk management.

Further development of the system's extension functions of Data-driven analytics, GIS/BIM and IoT, would be meaningful for smart construction.

REFERENCES

Cao, Y., Xu, W, 2005. Research Progress for Systematic Engineering Risk Evaluation Methodologies. Engineering Science, vol. 7, No.6, pp. 88–94.

Cheng, G., Wang, R., Zhao, M., et al., 2019. The Status and Trend of the Development and Usage of Domestic Municipal Underground Space. Earth Science Frontier, vol. 26, No.3, pp. 39–47.

Miller, R., Lessard, D., 2001. Understanding and Managing Risks in Large Engineering Projects. International Journal of Project Management, vol. 19, pp. 437–443.

Park, K., Lee, S., et al., 2017. Construction Management Risk System (CMRS) for Construction Management (CM) Firms. Future Internet 2017, 9, 5; doi:10.3390 /fi9010005.

Qian, Q., Rong, X., 2008. The Status, Issues and Advices for the Safety Risk Management of Underground Engineering Projects in China. Chinese Journal of Rock Mechanics and Engineering, vol. 27, No.4, pp. 649–655.

Saaty, T. L., 1980. The Analytical Hierarchical Process. New York: McGraw2Hill, 1980.

Saaty, T.L., 1993. Decision Making for Leaders: The Analytic Hierarchy Process for Decisions in a Complex World. China Economic Publishing House, 1993.

Yang, W., Hu, L., 2016. Study of infrastructure engineering safety management system and development. Proceedings of Engineering Management Forum 2016, Page 365–369.

Yang, W., Tsang, C., et al., 2018. Whole-Process Risk Management of Subsea Tunneling [J]. Proceedings of the Institution of Civil Engineers - Civil Engineering, ISSN 0965-089X | E-ISSN 1751-7672. https://doi.org/ 10.1680/jcien.18.00015.

Yang, W., Xia, X., et al., 2018. Prospect of Digital Transformation and Engineering Technology Development. The 12th China Engineering Management (Smart Cities) Forum and the 4th China Smart Cities International Exposition Series Forum 2018, Shenzhen, 317–321.

Tunnelling for a Better Life – Yan, Celestino, Thewes & Eberhardt (Eds)
© 2024 The Author(s), ISBN 978-1-032-80042-4
Open Access: www.taylorfrancis.com, CC BY-NC-ND 4.0 license

Research on data management and analysis of BIM technology

Yang zhaofeng*
Department of Geotechnical Engineering, Wuhan China Geo University, Wuhan, Hubei, China

ABSTRACT: BIM technology is the soul of information and digital. Accompanied by the development of big data, cloud computing, Internet of Things, artificial intelligence and other cutting-edge technologies, the digitisation and informatisation of BIM technology is also in constant depth.BIM technology, as an important supportive technology for digital construction, plays an active guiding role in infrastructure projects. This paper provides new thinking and solutions for the construction of tunnels and underground projects through the data management and analysis of BIM technology in the construction of tunnels and underground projects. It is not only the key to the future field of urban underground space, but also an important trend in the development of global digitalisation and information technology.

Keywords: BIM technology, digitalisation, information technology

1 INTRODUCTION

BIM is leading the way in a technological revolution that the engineering and construction industry is currently undergoing a technological revolution, and BIM is constantly changing the way the construction industry builds and collaborates. The core value of BIM technology lies in the ability to extract the information of the building model and use it in the process of project management such as cost, schedule, quality, and safety, breaking the information island barriers of all parties involved in the construction and realizing the data sharing of the whole process of the construction project.

2 BIM TECHNOLOGY IN BRIEF

2.1 *Definitions*

The full English name of BIM is Building Information Modeling, which is more consistently translated as Building Information Modelling in China. BIM technology is a data-based tool applied in the construction industry, which integrates all kinds of project-related information through parametric models, and shares and transmits them during the whole process of the construction project, and plays an important role in improving productivity, saving costs and shortening the construction period. It plays an important role in improving productivity, saving cost and shortening construction period, etc.

The U.S. National BIM Standard defines BIM in three parts: 1) BIM is a digital representation of the physical and functional characteristics of a facility (construction project); 2) BIM is a shared knowledge resource, a process for sharing information about this facility and providing a reliable basis for all decisions made during the full life cycle of the facility from conception to demolition; 3) during different phases of the facility, different stakeholders collaborate by inserting, extracting, updating and modifying information in the BIM to support and reflect their respective responsibilities.

2.2 *Characteristics*

2.2.1 *Completeness of model information*

Distinguished from traditional CAD 2D plan drawings, it contains complete building information such as equipment name, structure type, construction process, cost, manpower and machinery.

2.2.2 *Relevance of model information*

The objects in the model recognise each other and when one of them changes, all the objects associated with it are automatically updated.

2.2.3 *Consistency of model information*

Consistent model information at different stages eliminates the need to repeat inputs and avoids errors caused by inconsistent information.

*Corresponding author: 954689932@qq.com

DOI: 10.1201/9781003495505-396

2.3 *BIM-based project data and information management*

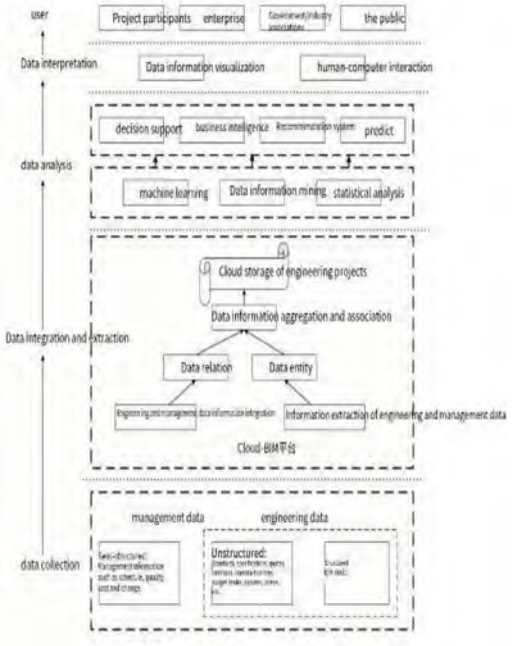

Figure 1. BIM-based project data and information management.

BIM-based project data and information management collects, extracts and integrates heterogeneous data sources at different stages of a project in real time, while also storing the data in logically centralised but physically heterogeneous cloud storage, and analyses the stored data using appropriate data analysis techniques to generate rich reports and analysis data, from which it extracts useful knowledge and presents the results to end-users in an appropriate way as a basis for decision-making in engineering project management, as shown in the figure below. As shown in illustration, it is divided into the following steps: data collection, data extraction and integration, data analysis, and data interpretation.

3 DATA MANAGEMENT AND APPLICATION OF BIM TECHNOLOGY IN THE SPECIALISED FIELD OF TUNNELLING AND UNDERGROUND ENGINEERING

BIM technology is the soul of information and numbers. The information management for the tunnelling and underground engineering profession is geared towards the consideration of the whole life cycle, with data flowing within the respective phases on the one hand, and between the phases on the other. Through the systematic management of the whole life cycle surface information and monitoring and measuring data, it can provide the basis of accurate decision-making for project decision-making. Adopting computer AI, VR and BIM information technology to build a 3D tunnel and surrounding rock environment information model, and developing a cloud BIM platform that can realise information storage and query, 3D visualisation, engineering hydrogeological information reproduction, real-time feedback of design and construction monitoring data, and real-time sensing of safety risks, It provides a new idea and solution for the construction of tunnel and underground engineering.

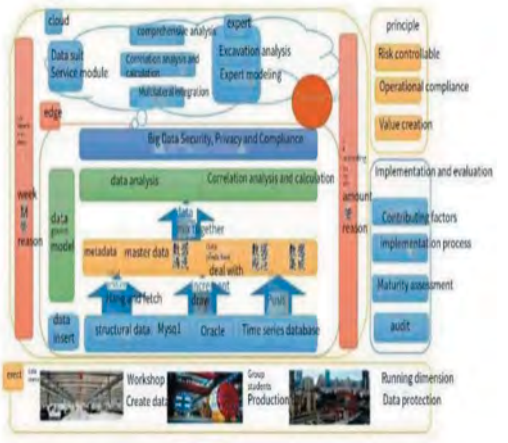

Figure 2. Architecture for managing data and information through the life cycle.

3.1 *Application of information technology in tunnel and underground construction based on BIM technology*

3.1.1 Digital design methods are a continual improvement in the planning process for tunnel construction. Such developments include rule-based system implementations, concepts for integrating data across documents and models, and new evaluation methods that utilise digital design capabilities. For planning purposes along the tunnel construction route, the integration of hardware and software products such as touch tables and virtual reality devices enables decision makers to be directly involved in the planning process. In the tunnel construction practice and planning phase, the process is simplified through the adoption of the Building Information Modelling BIM concept and the use of geometric BIM sub-models as a basis for structural analysis. As the construction industry transitions to digitalisation, information technology IT plays a huge role in large-scale projects for tunnel construction. Different IT applications are used at different stages of the project and stored in multiple formats. In addition, computer-aided design CAD,

for example, has had a clear impact on the way project data is presented. However, using IT tools that are standalone applications with limited interoperability with other platforms, data cannot be exchanged between applications and information sources in a project, and due to the lack of compatibility, information can be exchanged with errors and also lost. The emergence of Building Information Modelling BIM solves the problems associated with decentralised data management.BIM provides an innovative and collaborative solution that enables organised and efficient workflows throughout the entire project lifecycle: planning, design, construction, operations, maintenance and possibly later demolition phases. BIM technology can connect information databases with parametric 3D models to better visualisation, coordination and management of construction projects, thus reducing construction costs and errors. For this purpose, the Tunnel Information Model TIM was developed and integrated to improve the usability and compatibility of the structural tunnel simulation with the BIM methodology.

3.1.2 In BIM-based approaches, information is used as a basis for decision-making and project management. Certain information can only be processed by exploring constraints and dependencies. Relevant information can be decomposed and structured through so-called interaction chains. An interaction chain can be defined as a series of interrelated processes that can depend on each other and whose results can be directly used to evaluate relevant project constraints. The execution of an interaction chain requires the provision of relevant information. This includes available product data as well as interim simulation results. In order to manage this information, a 4D information model has been developed. In tunnelling projects, information is often time-dependent and distributed across different systems and various data formats. Based on the BIM concept in the field of tunnel construction, the Tunnel Information Model TIM creates a comprehensive container for tunneling projects and allows the integration of interaction chains for project evaluation.

3.2 *Digital research application based on BIM technology in the construction of tunnels and underground projects*

The study of digital design of tunnel routes is one of the most important studies in tunnel construction. Comparison of different route options allows cost-effective planning and reduces project risks. Often, variations in route options are effective because the criteria allow for alternative methods and need to be evaluated by experts. The weighted decision matrix method is used to evaluate the variables of such options, and a certain number of route options are studied before the best route option is selected. The most important element of the variables in tunnel design is the impact on the environment, such as critical settlements in protected areas or collisions with underground structures. Traditionally, a route consists of a route and a gradient. The route describes the alignment of the line in a two-dimensional plane, while the gradient adds elevations based on the current curve section. The combination of these two design perspectives creates a three-dimensional line that can subsequently be used for element placement in a BIM-based process. Below are some of the methods used in the digital design of BIM tunnel lines.

3.2.1 *Integrated platform*

The Tunnel Information Modelling TIM framework has been adapted and further developed into an integrated platform. The platform advances the TIM framework by including route planning methods, integrating BIM and GIS data, and creating an interactive planning environment. The framework has been designed to utilise roomware products, primarily touch table devices, to enable collaborative, interactive and continuous exploration of planning variables. A key feature of the integrated platform is therefore the multi-touch interaction with the planning environment, which allows for real-time updating of planning variables in a collaborative environment.

3.2.2 *Lines in parametric tunnel design*

In BIM-based projects, lines are used to position elements relative to the path and inclination of the line axis. In road and railway projects, for example, they are used to generate street and railway systems semi-automatically, including technical equipment and information about ground stripping on the construction site. However in projects in the field of tunnels lines are used to generate tunnel models with cross sections and design parameters as a reference for the modelling process. By using line and cross-section information to generate tunnel models in mechanised tunnelling, the process of aligning elements to lines relies on a series of transformations applied by the system. These models are exported as industrial base class IFC models and can be used for infrastructure information delivery and visualisation of tunnel excavation. A prototype example of the IFC Tunnel Extension is used here to create semantically correct tunnel models and line alignments for data exchange.

3.2.3 *Collaborative exploration with roomware products*

The process of planning indoor equipment routes relies on the feedback and knowledge of experts. In a synergistic environment, the results of planning, design and evaluation can be directly justified. The benefits of a synergistic approach here can lead to significant improvements in the decision-making process for line selection. For example it can reduce the number of planning variables and shorten development times by directly implementing changes. In order to realise the application of the synergetic approach to route planning, interactive exploration on a touch-table device is required. Such an indoor device can be surrounded

and interacted with by a group of people. In order to handle user interactions, planning applications running on such devices need to integrate multi-touch strategies and simplify the planning process to enable semi-automatic re-evaluation of modified routes. With this aim a set of multi-touch strategies is investigated and implemented into the integrated platform. These touch strategies are mainly designed to handle simultaneous multi-touch interactions of the user on groups of areas and locking on touch interactions with elements that are far from the user's viewpoint. Thus with each interaction, the line can be modified and planned using touch and the updated line will be re-evaluated in real time and the results visualised for validation of the interactive planning tool.

3.2.4 *Integration of BIM and GIS*
The platform mainly considers the integration of documents and models used in the BIM and GIS domains, which are often considered as integrated approaches. This is because their information complements each other in the context of the spatial environment. However the concept of integration of BIM and GIS is usually used as an umbrella term to differentiate the integration approaches in terms of the scope and purpose of the information considered, and is categorised according to the integration effort and the terminology used. Considering this approach, the integrated platform belongs to the classification of the integration based on instance level information, and the differences in this classification perspective and links are based on the use of queries with spatial reasoning. The considered documents and models include map data such as cadastral data, built environment, terrain and ground models. However, the integration of the BIM and GIS domains proves to be challenging due to the differences in the format, level of detail and scope of the considered data, and the fact that the documents and models may differ in the level of development including various geometric representations.

3.2.5 *Rule-based line evaluation and data acquisition*
When exploring the integrated environment, rule-based exploration can add value to the information acquisition process and be used to check constraints and requirements. Considering the overlay nature of documents and models in the BIM and GIS domains, spatial reasoning methods can be applied. The context of the route plan is also incorporated into the reasoning approach, thus creating range-rich relationships between elements. These relationships were then used to query information between documents and models, enabling a semi-automated assessment of relevant requirements and constraints. Further research examined the application of the decision-making model to the selection of a single vs dual tunnel system and the selection of a tunnel boring machine. A query highlights a set of elements which can then be evaluated in more detail. For direct visual feedback, these results can be selected and coloured, allowing for visual validation and subsequent integrated investigation.

3.2.6 *Constraints and requirements*
Examine these range-specific requirements and develop a valid set of variables. These variables are evaluated using assessment criteria, such as risk assessment and cost estimation. Interactive results from settlement analyses and building damage risk assessments can be integrated in the evaluation process. The decision-making process in the field of tunnelling can be significantly improved by using decision models, which consist of rules for reasoning in a decision-making system. In the field of tunnelling, this study shows that decision models can enhance the decision-making process and that the weighting of individual criteria affects the evaluation results, which also applies to route analysis and selection.

3.2.7 *Utilising semantic web methods*
The use of semantic web technologies and methods allows the integration of data from the BIM and GIS domains. Since it is considered that data from BIM and GIS domains will lead to a mixture of 2D and 3D representations, these representations can also be defined in different coordinate reference systems CRS. Geometries in the Semantic Web are usually represented using the WKT representation, which is a concise and streamlined version of the most important geometric representations. By utilising WKT-CRS, i.e. the WKT representation extended to handle geometries defined in different CRSs, the geolocation of these elements can be handled naturally. This approach of using the Semantic Web for correlating data and obtaining relevant information has been validated by many studies . Incorporating this spatial reasoning approach into an integrated platform enables semi-automated query execution on documents and models for data acquisition and evaluation. This concept in been elaborated and implemented to establish context-rich relationships between documents and models by including constraints and requirements in the query process.

3.2.8 *Applications for decision-making and review*
In the decision-making process for the selection of a route, it is common to use different route variants to be compared based on assessment criteria, for example using a weighted decision matrix approach. The method considers the assessment and comparison of a range of constraints and requirements to select the preferred variant, e.g. based on a cost-effectiveness examination . Such an assessment method is based on the characteristics of the planning environment and the relevant data. In order to identify the relevant data for carrying out the expedition, the spatial environment must be examined. By using Semantic Web technology, several semi-automated data acquisition cases can

be executed. These filtered subsets can be highlighted to provide visual feedback on the results. As these queries take into account the constraints and requirements of the route planning process, they can be incorporated into the decision-making process by integrating the results as relevant information for the expedition criteria in the methodology.

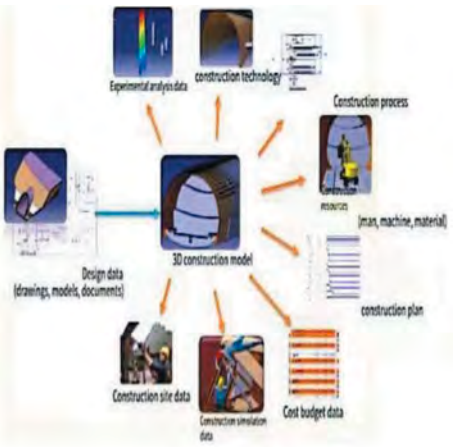

Figure 3. Integrated tunnel solution based on BIM.

4 CONCLUSIONS AND TRENDS, OUTLOOK

At present, with the gradual improvement and application of BIM technology in the construction industry, BIM data will be widely used in the whole life cycle of buildings, and even radiate to the management of the entire digital twin city. From a technical point of view, it is predicted that if BIM semantics and knowledge are widely understood and applied in the future, and continue to accumulate and refine, BIM is likely to be closely integrated with artificial intelligence technology, injecting new vitality and impetus into the sustainable development of the construction industry, and also bringing greater transformative innovation to our work and life. In summary, BIM technology not only promotes the progress and upgrading of existing technologies, but also affects the change of production organization mode and management mode, and promotes the change of people's thinking mode. Through this paper, it is understood that BIM technology is not only the key to the field of urban underground space in the future, but also an important trend in the development of global digitalization and information technology.

REFERENCES

1. Le Yun,Zheng Wei,Yu Wende. Research on data management of engineering projects based on Cloud-BIM[J]. Journal of Engineering Management, 2015, 29(01):91–96.
2. LI Yingpan, MA Xiaofei, LIANG Xin, DENG Yu. Research on green construction information management based on Cloud-BIM[J]. Construction Technology, 2016, 45(18):48–53.
3. Wang Tongjun, Evolution of China's Railway Tunnel Construction Methods and Intelligent Construction Technology System and Prospect, China Railway.

① National BIM Standard (NBIMS), First Edition;
② Shanghai Building Information Modelling Technology Application Guidelines (2017 Edition).

Tunnelling for a Better Life – Yan, Celestino, Thewes & Eberhardt (Eds)
© 2024 The Author(s), ISBN 978-1-032-80042-4
Open Access: www.taylorfrancis.com, CC BY-NC-ND 4.0 license

A study on 3D reconstruction of tunnel based on NeRf: A case study of Shanghai Metro Line 18 Tunnel

Zhaohui Zheng* & Yadong Xue
Key Laboratory of Geotechnical and Underground Engineering of Education Ministry, Tongji University, Shanghai, China
Department of Geotechnical Engineering, Tongji University, Shanghai, China

Yongfa Guo
Kunming Survey, Design and Research Institute Co.,Ltd, Yunnan Kunming, China

Jie Liu
China Railway Kunming Group Co., Ltd, Yunnan Kunming, China

Lan Zhao
Shanghai Institute of Technology, Shanghai, China

ABSTRACT: The subway tunnel is a crucial component of urban rail transportation systems. With the rapid development of urbanization, the focus on tunnels has shifted from construction to operation, making effective and convenient tunnel inspection vital for ensuring safety. This paper introduces a novel method called Neural Radiance Fields (NeRF) for achieving efficient and accurate 3D tunnel reconstruction. The method offers a new solution direction for visualizing the tunnel interior and enables remote inspection, enhancing tunnel safety analysis and evaluation capabilities. This study determines device parameters and data acquisition methods through indoor pre-experimental investigations, employing three computer vision evaluation metrics: PSNR, SSIM, and LPIPS. An image dataset of a subway tunnel was acquired within Shanghai Metro Line 18, spanning from Guoquan Road Station to Fushun Road Station. Subsequently, gamma correction was applied to address uneven brightness in the tunnel image set. Then, by utilizing the Colmap software, the camera pose trajectory within the tunnel interiors was computed, which served as a crucial component of the Nerf algorithm. Finally, a high-quality 3D tunnel model was constructed based on Nerf algorithm, enabling immersive exploration and inspection of the tunnel. Compared to traditional Structure-from-Motion (SfM) reconstruction methods, the speed and quality of tunnel 3D reconstruction based on Nerf have been significantly improved. This work provides a possibility for efficient tunnel surveillance and maintenance.

Keywords: Shield tunnel structure, 3D reconstruction, Image acquisition, Visualization

1 INTRODUCTION

The development and use of urban underground space has brought new vitality into the development of tracks and underground buildings, among which, the metro is the focus of underground space construction in major cities because it can solve the huge pressure brought by daily heavy traffic, improve the city's land use rate and save land resources. However, with the increase of metro service time, the tunnel lining structure due to geological environment changes, vehicle load impact, their own material properties, etc., will inevitably produce a variety of diseases, mainly manifested as: water seepage, lining cracks, joints, joints open, tube sheet misalignment, longitudinal uneven settlement, tube diameter convergence deformation, and so on (Fang et al., 2022). These diseases will not only reduce the service life of the tunnel, but also bring great safety hazards. It can be seen that the use of efficient and reliable testing equipment and technology to detect tunnel defects in a timely manner is the only way to rule out potential safety hazards in tunnel structures in advance,

*Corresponding author: 937742775@qq.com

DOI: 10.1201/9781003495505-397

so as to safeguard the safety of the public in their daily travel (Cui et al., 2022).

As one of the most popular research directions in the field of computer vision, 3D reconstruction technology provides a new solution direction for the visualisation of shield tunnel disease detection and identification. The first stage of 3D reconstruction is about the application of stereo vision technology: Stentoumis et al. (2015) invented a tunnel inspection device based on binocular stereo vision technology, which is able to realise 3D reconstruction of tunnel surface lining. However, this device can only realise the reconstruction of the tunnel within a local area, and the reconstruction speed is slow, so there is still much room for improvement. The second stage of 3D reconstruction is about the application of 3D laser scanning technology: Xie & Lu (2017) took the lead in using terrestrial laser scanning technology (TLS) to develop a new set of 3D modelling algorithms, which can pre-process the raw point cloud data acquired by TLS, extract the tunnel axes, carry out the coordinate conversion, and ultimately generate a 3D model of the tunnel. The third stage of 3D laser scanning is about the application of Structure from Motion (SfM):Xue et al. (2021)proposed a new method for 3D reconstruction based on the SfM method and Direct linear transformation (DLT) method. This method gives the point cloud data scale information, which lays the foundation for future disease quantification and tunnel service performance evaluation based on point cloud data. However, when using this method to reconstruct the shield tunnel as a whole, the constructed model contains a large number of holes, the modelling quality is poor, there is a problem of missing information, and the detection and quantification of disease information is not achieved.

However, with the rapid development of deep learning technology, voxel-based 3D reconstruction technology has gradually become the mainstream of 3D reconstruction technology with its advantages of high efficiency and high accuracy, and Neural Radiance Fields (NeRF) is one of them. Therefore, this paper is based on the NeRF technology for the left shield tunnel of Shanghai Metro Line 18 to carry out visual three-dimensional modeling experiments, to help the visual display of shield tunnel disease detection research which lay the foundation for the realization of the future remote inspection of shield tunnels.

2 METHODOLOGY

The core idea of the NeRF algorithm is to represent a static 3D scene as a deep fully-connected neural network without any convolutional layers, with the aim of achieving new view synthesis for complex scenes(Barron et al., 2021). For a particular static scene, images containing camera positions and camera parameters are provided as a training set to motivate the neural network to predict a scene model with good continuity. Finally, by inputting any camera position and orientation, the neural network can synthesise a new view by volume rendering.

2.1 *NeRF neural network structure*

The NeRF algorithm constructs a Multi-Layer Perception (MLP) neural network. The input of the neural network is a 5-dimensional vector $(x, y, z, \theta, \varphi)$ including the position of the observation point in the absolute coordinate system $x = (x, y, z)$ and the viewing angle of the camera $d = (\theta, \varphi)$; the output is the RGB colour $c = (r, g, b)$ and density $\sigma$of the corresponding position (voxel).

In practice, the position vector $\boldsymbol{x}$ is first fed into the MLP network, which outputs the voxel density$\sigma$and a 256-dimensional intermediate variable, and then the intermediate variable and the viewpoint vector $\boldsymbol{d}$ are fed into an additional 128-dimensional fully connected layer to predict the RGB colour vector. Figure 1 shows the specific structure of the NeRF algorithm.

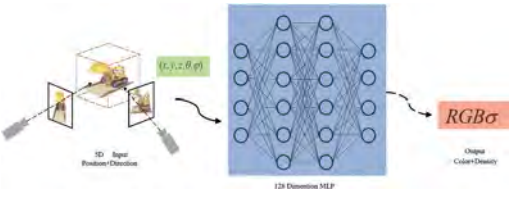

Figure 1. Specific structure of the NeRF algorithm.

2.2 *Volume rendering with radiance fields*

NeRF represents a 3D static scene as an MLP neural network, so that a new view can be synthesised for 3D reconstruction by simply asking for the density $\sigma$and RGB colour $\boldsymbol{c}$ of any point (voxel) in space (Pumarola et al., 2021). When the static scene is imaged by a camera with a known position and viewpoint orientation, each pixel on the resulting 2D image actually corresponds spatially to the projection of all consecutive spatial points on a ray emanating from the camera as the origin, and therefore all points on this ray need to be integrated using the voxel rendering algorithm, as shown in Figure 2.

Voxel density$\sigma(x)$ is the differential probability that a ray terminates at an infinitesimal particle at location$x$, which can also be interpreted as the opacity of a point at that location(Mildenhall et al., 2020). And when a virtual camera observes along a particular direction, the points on its observation ray are continuous, so the colours of the pixel points on its corresponding imaging plane can be obtained by integrating the colours of the points on the observation ray. Marking the camera location as the origin o and the camera's observation direction vector as $\boldsymbol{d}$, the observation ray can be expressed as $r(\mathrm{t}) = o + \mathrm{t}d$, and the near boundary of the

observation ist_n, and the far boundary is t_f.The colour of the pixel$C(r)$corresponding to this observation ray is shown in equation (1) and equation (2).

$$C(\mathrm{r}) = \int_{t_n}^{t} T(t)d(\mathrm{r}(t))c(\mathrm{r}(t),d)dt \tag{1}$$

$$T(t) = exp(-\int_{t_n}^{t} \sigma(\mathrm{r}(s))ds) \tag{2}$$

The function$T(t)$represents the cumulative transmittance along a ray from$t_n$tot_f,which is the probability that the ray will travel from$t_n$to$t_f$without hitting any other particle.

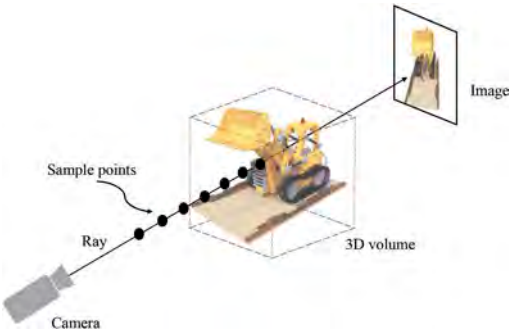

Figure 2. Voxel rendering process.

In practice, the number of consecutive points on each ray is infinite, so numerical approximations are needed to select the sampling points. A common method for rendering discrete voxel meshes is the deterministic product method, thus, N points are uniformly sampled in the region of integration for continuous integration. However, this method is not applicable to the MLP neural network in NeRF, because a fixed sampling habit will cause the MLP network to learn only at definite discrete points, which is not conducive to improving the resolution of the NeRF algorithm. For this reason, NeRF uses a stratified sampling approach, where the region on the ray to be integrated is first divided uniformly into N parts, and then uniformly randomly sampled from the N small regions as shown in equation (3).

$$t_i \sim u[t_n + \frac{i-1}{N}(t_f - t_n), t_n + \frac{i}{N}(t_f + t_n)] \tag{3}$$

Hierarchical sampling ensures that the MLP learns in a continuous manner even when only discrete points are captured, thus guaranteeing the continuity of the NeRF representation of the scene. The classical body rendering algorithm can therefore be reduced to a summation form as shown in equation (4) (5) (6).

$$\widehat{\mathrm{C}}(\mathbf{r}) = \sum_{i=1}^{\mathrm{N}} \mathrm{T_i}(1 - \exp(-\sigma_i\delta_i)) \tag{4}$$

$$T_i = \exp\left(-\sum_{j=1}^{i-1} \sigma_j\delta_j\right) \tag{5}$$

$$\delta_i = t_{i+1} - t_i \tag{6}$$

2.3 *Sampling methods from coarse to fine*

The Neural Radiation Field represents a 3D static scene as an MLP neural network and is able to synthesise new views by a classical voxel rendering algorithm that can obtain the density and RGB colour of any voxel in space. However, in order to achieve high-resolution modelling of complex scenes, two further improvements need to be introduced: i) positional coding to help the MLP network represent high-frequency functions, and ii) a multilayer voxel sampling procedure to ensure continuity of the NeRF algorithm's representation of the scene.

2.3.1 *Positional encoding*

Rahaman et al. (2019) have shown that deep learning networks prefer to learn low frequency functions, so introducing position vector $\boldsymbol{x}$ and viewpoint vector $\boldsymbol{d}$ directly into the MLP network leads to poor performance in synthesising colours and geometries for high-resolution new views. Instead, mapping the inputs to a higher dimensional space first before they are passed to the network using position coding can effectively fit the high frequency changing data.

Reformulation function $F_\theta$as a composition of two functions$F_\theta = F_\theta^{'} \circ \gamma_j$, in this case$\gamma$is a mapping from the real number field R to a higher dimensional spaceR^{2L}, $F_\theta{}'$is still the same simple MLP network mentioned.

2.3.2 *Hierarchical volume sampling*

The classical voxel rendering algorithm operates on the principle of sampling uniformly on the rays emitted by the camera and performing a summation computation on the N sampled points. This rendering strategy is inefficient in the first place, as there is a large amount of space and occluded regions that do not contribute to the rendering that are also subjected to the sampling computation; and the fixed sampling convention causes the MLP network to learn only at definite discrete points, which is not conducive to improving the resolution of the NeRF algorithm.

Therefore, the NeRF algorithm adopts the sampling principle of stratified volume sampling, thus, a multilayer voxel sampling method from rough to fine according to the proportion of the samples contributing to the final rendering effect, as shown in Figure 3. The specific implementation steps are as follows: firstly, sparsely collect N_c sample points by stratified sampling method, and perform rough mesh rendering on these sample points.

The normalised probability density function can be regarded as the probability density function along the ray direction, which reflects the distribution of the static scene in the ray direction, that is, the degree of contribution of the sampling points to the final rendering effect. Based on this probability density function, the inverse transformation sampling method is used to sample another$N_f$sampling point, so as to realise the weight sampling.

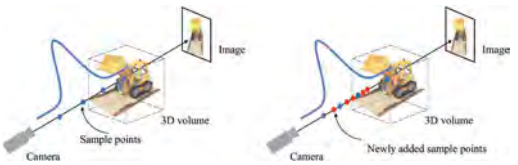

Figure 3. Multilayer voxel sampling method from coarse to fine.

3 PRE-EXPERIMENTAL VALIDATION

3.1 *Equipment selection*

The main factors affecting the imaging of the lens are the focal length and aperture size, which together determine the depth of field of the captured image, which refers to the clear scope of the image can be determined by the lens. Near the focal point of the lens, the image points show a conical convergence and then spread to form a dispersion circle. The size of the dispersion circle determines the degree of clarity of the image. The radius of the dispersion circle gradually increases as the distance of the centre of the dispersion circle from the focal point increases, and when the clarity of the image can no longer be ensured at a certain critical position, the dispersion circle is called the permissible dispersion circle. The distance between the centres of the front and back dispersion circles is called the depth of focus, while the corresponding field of view distance on the other side is called the depth of field.

Equation (7) represents the formula for the depth of field.

$$DOF = \frac{2f^2 \cdot F \cdot \delta \cdot D^2}{f^4 + (F \cdot \delta \cdot D)^2} \tag{7}$$

The specific requirement of equipment selection is to ensure that the camera's nearest shooting point falls within the depth of field range area. By analysing the imaging factors, it can be known that the nearest shooting distance of the shooting system is determined by the focal length of the lens. When the focal length is smaller, the range of view of the lens will be larger. Therefore, a wide-angle lens should be used during the process of picture acquisition of the shield tunnel.

Through comprehensive consideration of multiple brands and models of camera lenses on the market, this paper finally chose the Sony FE 14mm f1.8 GM 14GM lens, as shown in Figure 4. The lens is a compact and lightweight ultra-wide-angle, large-aperture, fixed-focus lens with two built-in XA (Super Aspherical) lenses and two XD linear motors. It offers excellent image resolution while maintaining constant focusing accuracy.

Figure 4. Sony FE 14mm f1.8 GM 14GM Lens.

Take the shield tunnel from Shanghai Line 18 Guoquan Road Station to Fushun Road Station as an example to verify the feasibility of the Sony FE 14mm f1.8 GM 14GM lens as a shield tunnel image acquisition lens:

Sony FE 14mm f1.8 GM 14GM lens with a built-in image sensor of 43mm * 36mm and a focal length of 14mm.

From this, the field of view of the lens can be calculated as shown in equation (8).

$$\alpha = 2acr\tan\left(\frac{21.5}{14}\right) = 113.86^\circ \tag{8}$$

The inner diameter R of the shield tunnel is 5.5m, so the closest distance in the picture is 1.8m.

$$d_{\min} = \frac{\frac{R}{2}}{\tan\left(\frac{\alpha}{2}\right)} = \frac{2.75}{\tan\left(56.93^\circ\right)} = 1.79m \approx 1.8m \tag{9}$$

The focusing distance is taken as 3m, the aperture is selected as f1.8 maximum aperture, and the foreground depth is calculated as 3m by equation (10).

$$DOF_1 = \frac{F \cdot \delta \cdot D^2}{f^2 + F \cdot \delta \cdot D} = \frac{1.8 \times 43 \times 3000^2}{14^2 + 1.8 \times 43 \times 3000} \approx 3m \tag{10}$$

The above calculations show that the depth of field of the Sony FE 14mm f1.8 GM 14GM lens can cover the entire area within the field of view of the filming equipment, which can be applied to the 3D

reconstruction data acquisition requirements of shield tunnels, which are one-dimensional linear structures with narrow space and long depth.

Another requirement to ensure the reconstruction accuracy of the Neural Radiation Field (NeRF) algorithm is to obtain high-resolution image data, and the clarity of the image is determined by the performance of the camera, so another important task in the selection of filming equipment is to choose a camera with high sensitivity performance that is compatible with the lens. Sony FE 14mm f1.8 GM 14GM lens is E-mount, so Sony A7R4 α7R IV A7RM4 camera is chosen to go with it.

3.2 *Test programme determination*

After selecting the model of the filming equipment, it is necessary to further determine the image acquisition method. Considering that the structure of the corridor is similar to that of the tunnel, which is a linear structure with long depth and small lateral dimensions and the lighting conditions are similar at night. So the corridor is selected as the object of this pre-test for 3D reconstruction, and the quality of the reconstructed model is compared with that of the different schemes, so as to guide the image acquisition scheme of the field test.

The modelling object of the pre-experiment is the indoor corridor on the fourth floor of the Southwest Eight dormitory building of Tongji University and the longitudinal cross-section of the corridor is approximately rectangular, as shown in Figure 5.

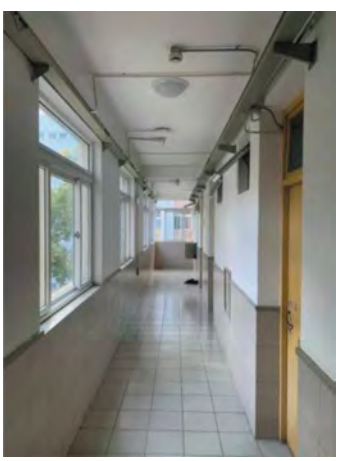

Figure 5. Dormitory corridor.

3.2.1 *Image acquisition method*

The first acquisition method records video along the corridor in the longitudinal direction and then extracts the images through the frame extraction algorithm, screening and deleting jittery and blurred images. This scheme has the highest acquisition efficiency and the frame extraction algorithm can set the interval between images by itself, with the highest degree of superposition between images. The limitation of this scheme is that it is impossible to set the exposure time so when the lighting conditions are poor, the acquired images will be polluted by lots of interference points and the image quality is not high.

The second acquisition method is to take an image every 1m along the longitudinal direction of the corridor. The advantage of this scheme is that the clarity of the image set can be ensured during the image shooting process and the brightness of the image under poor lighting conditions can be compensated by extending the exposure time. But the limitation is that the shooting angle is fixed and it is not possible to obtain the observation image of the target scene at multiple angles.

The third method is to take multi-angle shots along the corridor longitudinally, one shot at each shooting point at 45° intervals from left to right and the interval between adjacent shooting points is taken to be 2 m. The advantage of this scheme is that it can obtain the observed images of the target scene at different observation angles, which improves the accuracy of the MLP network in the neural radiation field algorithm in the representation of the target scene. The limitation is that the angle needs to be adjusted when shooting, which is less efficient.

3.2.2 *Comparison of different acquisition methods*

The model obtained after 3D reconstruction of the acquired corridor images using the NeRF algorithm is shown in Figure 6.

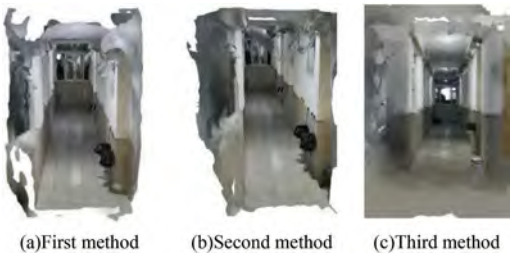

Figure 6. NeRF reconstruction results.

In this paper, three classical image evaluation metrics in the field of computer vision, namely PSNR, SSIM and LPIPS, are cited to evaluate the 3D models obtained from the above three image acquisition methods. Among them, the peak signal-to-noise ratio PSNR is in dB, and the larger its value is, the lower the distortion of the image is, and the image is about close to the original. The interval range of structural similarity SSIM is [0,1] and the closer its value is to 1, the more similar the two images are. And the smaller the value of Learning Perception Image Block Similarity LPIPS, the more similar the two images are.

Table 1. Comparison of reconstruction results.

Method	PSNR/(dB)	SSIM	LPIPS
First method	12.54	0.376	0.577
Second method	12.72	0.365	0.558
Third method	15.83	0.403	0.621

As can be seen from Table 1, the multi-angle photo-taking method (third method) has the best evaluation effect among the above four evaluation indexes. In addition to this and combined with the reconstruction model visualisation evaluation, although the basic structure of the corridor can be reconstructed by using different acquisition methods, the model texture generated by using the third method is smoother with the least number of collapses or depressions of the plane, the least number of transition zones and the portrayal of model details is closer to the real state, so the final image acquisition test of the shield tunnel lining structure will adopt the image acquisition method of taking pictures from multiple angles (third method).

4 CASE STUDY OF SHANGHAI METRO LINE 18 TUNNEL

4.1 *Image acquisition process*

The test object of this paper for data collection of shield tunnel is the left shield tunnel of the section from Guoquan Road Station to Fushun Road Station of Shanghai Metro Line 18. The line map of Shanghai Metro Line 18 and its internal lining structure are shown in Figure 7.

Figure 7. Interior lining of the metro.

According to the analysis of the results of the pre-experiment, it can be seen that the use of multi-angle photography can obtain the observation results of the target scene in multiple angles, which can help the NeRF algorithm to better reason and restore the reconstructed target's three-dimensional model. In addition, the acquisition method is simple and easy to promote, compared with the previous use of 3D laser scanning, which does not require a complex operation process or high test costs. And the acquisition method is very efficient and can cover a long distance of the shield tunnel, which can meet the real-time requirements of the tunnel inspection. Therefore, the image acquisition test for the tunnel lining structure also adopts the method of multi-angle shooting.

Due to the long exposure time, a tripod is needed to fix the camera in order to eliminate the blurring of the effects caused by shaking during the shooting process. As the selected tunnel section is a turning section, the track has a certain slope. So after setting up the tripod, it is also necessary to level the tripod according to the bubble.

After completing the debugging of the camera and the erection of the tripod, the debugged camera parameters are used to take preliminary shots of the tunnel and view the image effect in real time. When the camera's parameters are set to ISO value 640, shutter time 2.5s, aperture size f5.6, the resulting image is basically no noise, full-frame clarity to meet the test requirements, so the shield tunnel image acquisition test throughout the whole to maintain the above parameter settings. The field test finally captured 184 clear and effective images, each with a resolution of up to 9504 × 6336 pixels.

4.2 *Image enhancement pre-processing*

In order to save energy and reduce emissions, only one side of the tunnel is equipped with lighting sources, resulting in uneven brightness and darkness in the captured raw images and the lining information in the dark areas can not be revealed. Therefore, it is necessary to pre-process the original image with image enhancement to recover the hidden lining details in the dark part, so as to improve the reconstruction model effect. In this paper, the gamma transform method is used to perform image grey scale transformation. The principle is to perform an exponential transformation on the grey values of the image and restore the lining information in the dark part by adjusting the valueγ. As shown in the Figure 8, the best image enhancement effect is achieved when $\gamma = 0.6$.

4.3 *Camera trajectory solving*

From 2.2, we know that the input to the NeRF algorithm is a 5-dimensional vector that includes the coordinate position of the observation point in the absolute coordinate system and the observation angle of the camera, so the camera's position and trajectory need to be measured before carrying out the NeRF reconstruction.

When the camera shoots the target scene at different positions, it obtains the image A, image B and image

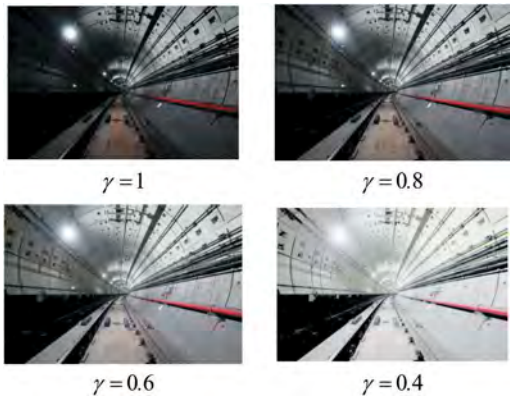

Figure 8. Image enhancement results.

C of the same feature point of the target scene under different observation angles. And each change of camera position can be regarded as the superposition of the effect of camera's translation of a certain distance and the rotation of a certain angle, so the essence of the camera trajectory solving is to request solving the transformation matrix of the change of the camera's position when shooting each image.

In this paper, we use colmap to solve the camera trajectory, and the result is shown in Figure 9, in which the red four-pronged cone represents the position of the camera where the image is taken, and the direction of the bottom of the four-pronged cone represents the camera's orientation. Finally, the information containing the camera internal reference and trajectory is converted into a json file.

Figure 9. Camera trajectory solving results.

4.4 *NeRF 3D reconstruction*

After the above json file containing the camera internal reference, trajectory information and the pictures of the shield tunnel structure processed using gamma transform are obtained, a 3D model of the shield tunnel in various 3D forms can be produced, as shown in Figure 10.

Figure 10. NeRF modelling of shield tunnels.

The NeRF model of the shield tunnel was compared with the 3D reconstruction model obtained from the conventional SfM method and the results are shown in Table 2.

Table 2. Comparison of NeRF and SfM methods.

Method	NeRF	SfM
Reconstruction Efficiency	High	Time-consuming
Memory footprint	Moderate	More
Point cloud density	Moderate	Intensive
Point cloud quality	Higher	Average
Reconstruction scope	Large	Smaller
Texture details	Approximate reproduction of details	Rich texture, high reproduction
Remaining functions	Ability to composite new views	None

Table 2 shows that the two different 3D reconstruction methods, NeRF and SfM, have their own advantages and disadvantages in the 3D reconstruction of shield tunnels. Compared with SfM, the reconstruction speed of NeRF technology has been improved a lot and NeRF reconstruction adopts a hierarchical sampling volume rendering method, which greatly reduces the memory occupancy rate of computing devices. In addition, the NeRF model has a higher point cloud quality, a larger reconstruction range, and more importantly, it is able to achieve the synthesis of new views, which has a broader research prospect in the future.

5 CONCLUSION

Based on the basic principle of NeRF, this paper summarises and puts forward a new method applicable to the 3D reconstruction of shield tunnel structure by exploring the image acquisition scheme of tunnel lining structure through equipment selection

and conducting corridor pre-tests. The feasibility of the above method is verified by carrying out NeRF 3D reconstruction experiments on the left shield tunnel of the section from Guoquan Road Station to Fushun Road Station of Shanghai Metro Line 18. Finally, the NeRF reconstruction method is compared with the traditional SfM method, which highlights the superiority of the NeRF reconstruction method more intuitively.

ACKNOWLEDGMENTS

The authors wish to thank the support from Key Technology R&D Plan of Yunnan Provincial Department of Science and Technology (Grant No. 202303AA080003).

REFERENCES

Barron, J. T., Mildenhall, B., Tancik, M., Hedman, P., Martin-Brualla, R., & Srinivasan, P. P. (2021). Mip-NeRF: A Multiscale Representation for Anti-Aliasing Neural Radiance Fields. 5855–5864.

Cui, P., Ge, Y., Li, S., Li, Z., Xu, X., Zhou, G. G. D., Chen, H., Wang, H., Lei, Y., Zhou, L., Yi, S., Wu, C., Guo, J., Wang, Q., Lan, H., Ding, M., Ren, J., Zeng, L., Jiang, Y., & Wang, Y. (2022). Scientific challenges in disaster risk reduction for the Sichuan–Tibet Railway. Engineering Geology, 309, 106837.

Fang, X., Yang, J., Xiang, M., Zhang, X., & Li, L. (2022). Model test and numerical simulation on the invert heave behaviour of high-speed railway tunnels with rainstorm. Transportation Geotechnics, 37, 100891.

Mildenhall, B., Srinivasan, P. P., Tancik, M., Barron, J. T., Ramamoorthi, R., & Ng, R. (2020). NeRF: Representing Scenes as Neural Radiance Fields for View Synthesis (arXiv:2003.08934). arXiv.

Pumarola, A., Corona, E., Pons-Moll, G., & Moreno-Noguer, F. (2021). D-NeRF: Neural Radiance Fields for Dynamic Scenes. 10318–10327.

Rahaman, N., Baratin, A., Arpit, D., Draxler, F., Lin, M., Hamprecht, F., Bengio, Y., & Courville, A. (2019). On the spectral bias of neural networks. International Conference on Machine Learning, 5301–5310.

Stentoumis, C., Loupos, K., Doulamis, A., & Amditis, A. (2015). A computer vision system for tunnel inspection. SEE Tunnel: Promoting Tunneling in SEE Region.

Xie, X., & Lu, X. (2017). Development of a 3D modeling algorithm for tunnel deformation monitoring based on terrestrial laser scanning. Underground Space, 2(1), 16–29.

Xue, Y., Zhang, S., Zhou, M., & Zhu, H. (2021). Novel SfM-DLT method for metro tunnel 3D reconstruction and Visualization. Underground Space, 6(2), 134–141.

Machine learning

Taylor & Francis
Taylor & Francis Group
http://taylorandfrancis.com

Tunnelling for a Better Life – Yan, Celestino, Thewes & Eberhardt (Eds)
© 2024 The Author(s), ISBN 978-1-032-80042-4
Open Access: www.taylorfrancis.com, CC BY-NC-ND 4.0 license

Development of a hard rock TBM performance prediction model using RMR input parameters

Ameneh Dardashti*
Department of Geology, Faculty of Science, University of Isfahan, Isfahan, Iran

Jamal Rostami
Earth Mechanics Institute, Colorado School of Mines, Colorado, USA

Rassoul Ajalloeian
Department of Geology, Faculty of Science, University of Isfahan, Isfahan, Iran

Jafar Hassanpour
School of Geology, College of Science, University of Tehran, Tehran, Iran

Alireza Salimi
ZETCON Ingenieur GmbH, Berlin Branch, Germany

ABSTRACT: Despite the widespread use of TBMs in tunneling projects, accurate estimation of TBM performance, especially in various geological conditions, can still be challenging. Comparing the most common rock mass classification systems, the RMR classification system shows a better correlation with the TBM penetration rate, due to using uniaxial compressive strength (UCS) as an input parameter in this classification system. RMR parameters are available in most tunneling projects, but it should be noted that the RMR system, was developed to classify the rock mass conditions in terms of tunnel stability and support design, and the effective parameters were selected accordingly. So, when the target is to use the RMR input parameters to predict the TBM performance, modifications should be made in the parameters. This study is offered a new TBM performance prediction model based on the input parameters of the Basic RMR in different rock types, through machine learning-based regression analysis. The proposed model has been developed based on the analysis of a comprehensive database of TBM performance in various rock types. Because different rock types have different fabrics and respond differently to shear forces, incorporating the effects of rock type into performance prediction models can improve the accuracy of estimates, for this reason, the lithology parameter is also included in the model. The model can be practical, especially in the design phase of a tunneling project.

Keywords: Machine learning, Performance prediction, Regression analysis, RMR classification system, TBM performance

1 INTRODUCTION

Since the use of tunnel boring machines (TBMs) requires major investments and high levels of geological risk, therefore, after determining the geological characteristics of the tunnel route and selecting the appropriate machine, the TBM performance should be estimated in the existing geological conditions. TBM performance prediction models consist of two main groups of theoretical and experimental models. The theoretical models have been developed based on the laboratory cutting tests; however, considering the restrictions in the generalization of these stages in the laboratory due to the complexity of the interaction between the rock mass and the machine, these models have not been able to implement all the factors affecting the machine performance. The experimental models have been developed using field data from the machine's performance in different geological conditions, and they have the advantage of naturally taking into account all the effects caused by the ground and the machine. On the other hand, with the development of different machines with different capabilities, the application of these models comes with limitations. In addition, given the fact that the presented models have been developed for specific ground conditions, they

*Corresponding author: am.dardashti@gmail.com

DOI: 10.1201/9781003495505-398

cannot be generalized to all geological conditions. In recent years, some researchers have used computer modeling and machine learning (ML) techniques in order to develop experimental models for prediction of the machine performance, including Grima et al. (2000), Yagiz and Karahan (2011), Jahed Armaghani et al. (2017), Koopialipoor et al. (2019), Salimi et al. (2019), and Zhou et al. (2020). AI techniques is considered as a good idea for estimation and modeling due to no need for formulation, their dynamicity, as well as the possibility of including the more effective parameters. According to recent studies, there is a high correlation between predicted and actual values of machine performance in ML-based methods (He et al., 2022).

In addition, some research has been done to predict TBM performance based on existing rock mass classification systems. Due to their simplicity, universal acceptance, and availability of effective parameters, these classifications are considered as suitable methods for estimating the TBM performance. Compared to the most common rock mass classification systems, RMR shows a better correlation with the TBM penetration rate, which is due to the use of uniaxial compressive strength (UCS) of intact rock as an input parameter in this classification system (Salimi, 2021). It has been also mentioned in previous studies, including Hassanpour et al. (2009, 2011) and Salimi et al. (2016). According to Rostami (2016), the most important geological characteristics that affect the TBM penetration rate are rock strength (UCS or BTS), joint frequency, direction, and condition, as well as rock abrasiveness. Exception of rock abrasiveness, which controls the disc cutter wear and thus the utilization, the other parameters are the same as those used in the RMR classification system. Thus, it is reasonable to be able to use the existing RMR rock mass classification system with some modifications in order to predict the TBM performance. It should be noted that the RMR system, like other rock mass classification systems, was developed to classify the rock mass conditions in terms of tunnel stability and support design, and the effective parameters were selected accordingly. So, if the target is to use the input parameters of the RMR system to predict the TBM performance, there is a need to modify the parameters and their weightings (Salimi, 2021). The main goal of this study is to investigate the possibility of using input parameters of the RMR rock mass classification system for estimating the TBM performance using ML algorithms.

Previous studies show that an increase in rock mass quality usually leads to a decrease in the TBM penetration rate. However, the weak condition of rock mass does not help to increase the penetration rate, as it causes instability. Thus, it is clear that the TBM penetration rate indicates a large dispersion compared to the rock mass classification systems. Sapigni et al. (2002) achieved a quadratic relationship between penetration rate (*m/hr*) and RMR system, which has also been confirmed in Hassanpour et al. (2011).

Sapigni stated that the correlation of the machine penetration rate with the RMR is significant, but it cannot be used for numerical prediction because the RMR does not consider the rock-machine interaction parameters. He pointed out that the rock type affects the TBM performance so that with the same TBM in different rocks with identical RMR, lower penetration rates are obtained in stronger rocks, indicating that factors related to rock type, e.g., texture, schistosity, and tensile strength can significantly influence the chip formation mechanism. Therefore, the conventional RMR system is not enough to predict TBM performance.

Today, with the development of ML algorithms and new data analysis methods, new studies have been conducted with the help of these methods to use the parameters of rock mass classification systems in predicting TBM performance e.g. Salimi et al. (2019) and Gholami et al. (2012). This study attempts to provide relationships for the prediction of TBM performance in different geological conditions with the help of ML algorithms, using the input parameters of the RMR system, which were measured in all the studied tunneling projects.

2 STUDIED PROJECTS AND DATA COLLECTION

To develop empirical equations for the estimation of TBM performance in different geological conditions using input parameters of the RMR system, the boring data from different tunneling projects were collected and compiled into a database. Operational data and the actual machine performance, as well as the engineering geological characteristics of related rock mass in different geological conditions, have been collected in this database. Tables 1 and 2 itemize the main characteristics of 10 TBM tunneling projects in the database. The database contains 523 tunnel sections, which are typically between 5 and 20 meters long, consisting of several excavation cycles, and reliable operational data of the machine and engineering geological characteristics of rock mass are available in these sections. The recorded data of these sections have not had many fluctuations, and the machine's performance has not faced a specific and unknown problem. The studied tunneling projects include Yinsong water supply tunnel, lot 4 and Yinhan water conveyance tunnel in China (Gong et al., 2021), MINAS water conveyance tunnel in Ecuador (Gong et al., 2021), Manapouri second tailrace tunnel in New Zealand (URS Company, 2003; Hassanpour et al., 2011), Maroshi - Ruparel water supply tunnel in Mumbai, India (Jain et al., 2014) and Zagros water conveyance tunnel, lot 2 (Hassanpour et al., 2009; 2016), Karaj-Tehran water conveyance tunnel, Lot 1 (Hassanpour et al., 2010; SCE company, 2006), Ghomrood water conveyance tunnel, Lots 3 & 4 (Hassanpour et al., 2009; 2011; SCE company, 2004), Kerman water conveyance tunnel, Southern Lot (Pourhashemi et al.,

Table 1. Lithology and geological characteristics of the studied tunneling projects in the database.

No	Projects	Geological zone	Formation	Lithology	Tunnel Length (*km*)	Available data (*km*)	Max. overburden (*m*)
1	Yinsong water supply tunnel, Lot 4 (China)	-	-	Granite (4423 m), Diorite (1547 m), Limestone (3161 m), Tuffs (890 m), Sandstone (356 m), Slate (546 m), Tuff sandstone (884 m)	20.2	11.807	< 300
2	Yinhan water conveyance tunnel (China)	-	-	Phyllite (1200 m), Carbonaceous phyllite (509 m), Phyllite and meta- sandstone (3554 m), Amphibole-quartz schist (1067m)	19.98	6.33	1500
3	MINAS water conveyance tunnel (Ecuador)	-	-	Tuffs (1736 m), Diorite (3148 m), Tuffs and adamellite (402m)	11.392	5.286	600
4	Manapouri second tailrace tunnel (New Zealand)	-	Paleozoic metamorphic and igneous rocks of the Fiordland Complex	Gneiss, Calc-silicate and quartzite and the intrusive rocks (Gabbro and Diorite)	10	9.7	1200
5	Maroshi-Ruparel water supply tunnel (India)	Deccan traps (Lava flows of Basaltic rocks)	Upper traps (Upper Cretaceous to Lower Eocene)	Fine compact basalt, Porphyritic basalt, Amygdaloidal basalt, Pyroclastic rocks (Tuff, Tuff breccia) and Intertrappeans (Shale)	12.24	5.83	82
6	Zagros water conveyance tunnel, Lot 2 (Iran)	Zagros Simply folded zone	Carbonate-Argillaceous rocks of Pabdeh, Gurpi and Ilam Formations	Limestone, Shale and Limy Shales	26	15	650
7	Karaj-Tehran water conveyance tunnel, Lot 1 (Iran)	Central Alborz	Pyroclastic rocks of Karaj formation	Tuffs, Shaly and Sandy Tuffs, Agglomerate	15.9	8.7	600
8	Ghomrood water conveyance tunnel, Lots 3 & 4 (Iran)	Sanandaj-Sirjan metamorphic belt	Jurassic metamorphic rocks (low to medium grade) and Cretaceous Limestone	Limestone, Shale and Sandstone, Slate, Phyllite, Schist with Quartzitic veins	21.5	15	700
9	Kerman water conveyance tunnel, Southern Lot (Iran)	Sahand-Bazman magmatic belt (Urumieh-Dokhtar zone)	Tertiary volcanic, pyroclastic and plutonic rocks	Andesite, Andesitic Basalts, Tuff, Rhyolite, Granodiorite, Agglomerate	19.2	5.5	940
10	Golab water conveyance tunnel (Iran)	Sanandaj-Sirjan metamorphic belt	Sedimentary and Igneous rocks of Eucen to Jurassic	Periodic series of argillite shale and metamorphic sandstone, schist and amphibolite	10	8	-

2021) and Golab water conveyance tunnel (Fatemi, 2016; ICE, 2009) are in Iran.

The lithology and geological characteristics of the studied tunnels are summarized in Table 1. As seen in this table, these projects account for a wide range of geological conditions, and in terms of lithology, they contain all types of igneous, sedimentary, and metamorphic, as well as pyroclastic rocks. A wide range of engineering geological characteristics can also be identified in the rock mass along the tunnels. It has been identified from weak and crushed to massive and integrated rock masses, and from rocks with little abrasion to highly abrasive rocks. Due to the extensive geotechnical characteristic of rock mass in the compiled database, it is possible to develop a comprehensive model for predicting the TBM performance in various geological conditions.

Table 2 shows the characteristics of the TBMs used in the studied projects. The TBMs in the tunneling projects, including Karaj (lot 1), Zagros (lot 2), Ghomrood (lot 3 & 4), Kerman (Southern lot), Golab tunnel in Iran, and MINAS in Ecuador are similar to each other to a large extent, and all of them are double-shields (Telescopic). Two machines used in the Yinsong and Yinhan projects in China are open machines. The machine used in the Manapouri is different from other

Table 2. Characteristics of TBMs used in the studied tunneling projects.

Project	Yinsong water supply tunnel, Lot 4 (China)	Yinhan WCT (China)	MINAS WCT (Ecuador)	Manapouri second tailrace tunnel (New Zealand)	Maroshi-Ruparel water supply tunnel Mumbai, (India)		Zagros WCT, Lot 2 (Iran)	Karaj-Tehran WCT, Lot 1 (Iran)	Ghomrood WCT, Lots 3 & 4 (Iran)	Kerman WCT, Southern Lot (Iran)	Golab WCT (Iran)
					Maroshi-Vent hole stretch	Vakola-Vent hole stretch					
TBM type	Open TBM	Open TBM	Double shield	Main beam open TBM	Hard rock Gripper TBM	Hard rock Gripper TBM	Double shield	Double shield	Double shield	Double shield	Double shield
TBM diameter (*m*)	7.93	8.02	5.67	10.5	3.6	3.6	6.73	4.65	4.525	5.275	4.495
Number of cutters	56	50	37	68	31	31	42	31	36	37	35
Cutter diameter (*inch*)	17″, 19″	19″	19″	17″	17″	17″	17″	17″	17″	17″	17″
Average cutter spacing (*mm*)	71	82.2	78	90	62	62	90	90	75	72	75
Maximum thrust force (*kN*)	23,260	27,488	11,000	27,101	3,828	3,828	28,134	16,913	18,000	20,000	20,000
Rated torque (*kN.m*)	8410	7661	2916	9860	225	185	4450	1029	802	1200	802
Rotational speed (*RPM*)	0 ~ 7.6	0 ~ 7.3	0 ~ 9	0 ~ 5.07	0 ~ 14	0 ~ 12	0 ~ 9	0 ~ 11	0 ~ 10	0 ~ 10.9	0 ~ 12

projects, an open TBM with a diameter of about 10 *m*, which is two times greater than the diameter of the machines used in other projects. In the studied tunnels, the machines have flat cutter heads, cutter head diameters ranging from 3.6 to about 10 *m*, disc cutter diameters of 432 *mm* (17 *inches*) and 483 *mm* (19 *inches*), and average cutter spacing of 62 to 90 *mm*.

3 THE DATABASE

Researchers have introduced various indicators to evaluate TBM performance. The field penetration index (FPI), introduced by Nelson et al. (1983), has been successfully used to establish the correlation between rock mass characteristics and TBM performance (Salimi et al., 2019). FPI is calculated by dividing the disc cutter load (Fn in *kN*) by the penetration rate (P in *mm/rev*). This index integrates the effects of penetration rate, disc cutter load, and revolutions per minute (RPM) into one factor. FPI is a machine-independent parameter that can be calculated and integrated from the boring data of machines of different sizes, types, and cutter loads, making it a suitable choice to evaluate TBM performance in this study due to its simplicity, measurability, and scalability across different machine sizes.

While rock mass classifications are generally designed to estimate rock mass behavior, load distribution, and design tunnel support, they are not specifically tailored for predicting machine performance in mechanized tunneling. Therefore, classification systems often include some parameters that may not be necessary for estimating the boreability properties of the rock mass, such as groundwater conditions, joint orientation, and stress-related parameters. In light of this, Hoek and Brown recommended using only the first four parameters of the RMR classification system to determine the rock mass boreability properties, comparable to what is done in GSI (Geological Strength Index) to estimate rock mass characteristics (Hoek et al., 1995; Hoek and Brown, 1997). This approach allows for a more focused evaluation of TBM performance.

The RMR classification system utilizes six parameters, including the uniaxial compressive strength (UCS), the rock quality designation (RQD), joint spacing (Js), joint surface conditions (Jc), groundwater situation, and adjustment concerning joint orientation versus the tunnel axis, to determine the geomechanical condition of the rock mass. Each parameter is given a specific rating based on the relevant tables, and the sum of the ratings of the six parameters is known as adj-RMR. The Basic RMR is obtained from the sum of the ratings of the first five parameters, where the direction of the joints is not adjusted. Also, RMR'_{89} is calculated the same way as the Basic RMR, just the groundwater situation is always considered dry, and its rating is counted 15.

Based on previous studies, Basic RMR and RMR'_{89} have shown a stronger correlation with TBM performance compared to adj-RMR, indicating that adjusted parameter of joint orientation does not significantly improve the correlation (Sapigni et al., 2002; Hassanpour et al., 2011; Salimi et al., 2019). The joint orientation parameter primarily relates to the stability conditions of the rock mass and does not directly indicate the ease or difficulty of tunnel boring. Although joints depending on their orientation with tunnel axis, play an important role in the propagation of cracks during excavation, previous studies indicate that establishing a clear relationship between joint orientation and machine performance is challenging (Salimi, 2021; Hassanpour et al., 2011). In fact, in blocky and layered rock masses with two or three similar joint sets (Isotropic rock mass), the joint orientation effect can be assumed to be very insignificant. The orientation of discontinuities can only affect the machine performance in cases where a main and dominant joint set, such as heavily layered and schistose rocks (Anisotropic rock mass). In this case, when the machine advances parallel to the dominant joint set, the cracks are propagated vertically to the joint surfaces and reduce the penetration rate. When the machine advances perpendicular to the dominant joint set, the rock fracture is created in line with these joint surfaces. This mode usually has the most suitable penetration conditions, as discontinuities help to create and expand cracks between two adjacent disc cutters.

In the compiled database, the majority of tunnel sections are situated in isotropic or relatively high isotropic rock masses, and the effect of joint orientation on machine performance is deemed insignificant. While recognizing the important role of joint orientation in the propagation of cracks during excavation, due to the challenges in finding the relationship between joint orientation and performance, and considering the isotropic rock masses in the database that were not appropriate to assess this parameter, the adjustment parameter of joint orientation was excluded in development of empirical equations for TBM performance prediction using RMR input parameters in this study.

To determine the parameters Js and Jc in the RMR system, the critical joint set, which has the most significant impact on tunnel stability, must be considered. In this study, since the data were collected from mechanized tunneling projects, the critical joint set that influences machine penetration rate was identified. The α angle, representing the orientation between the critical joint set and the tunnel axis, was calculated based on the orientation of layering or schistosity surfaces, if present, or the joint set with the most significant impact on penetration rate ($\alpha = 45° - 70°$) in some cases in the studied projects.

According to Hassanpour et al. (2009), groundwater condition is not a directly influential parameter on the machine penetration rate. However, the mere presence of water, regardless of its quantity, can weaken the strength of the rock mass. Moreover, a high flow of water can wash away the filling materials within joints, further reducing the strength of the

rock mass. Interestingly, groundwater indirectly plays a positive role in increasing the machine penetration rate by altering the rock mass and reducing the strength of both the rock mass and the joint filling materials. Laughton (1998) and Nelson (1983) have also studied the effect of groundwater conditions on TBM performance and found that it often affects the advance rate (AR) rather than the penetration rate (P) through machine utilization. The instability of the tunnel walls is often associated with groundwater flow into the tunnel, and this is the reason for the inclusion of Gw in the RMR system. Accordingly, the groundwater condition parameter was omitted in the modeling process for developing experimental equations in this study. Ribacchi and Lembo-Fazio (2005) argued that given that the RMR classification is usually performed during the excavation of a tunnel, a more simple procedure would be to adopt a slightly modified RMR indicated as RMRP, for which a fixed value of 15 (dry condition) is given to the partial rating of groundwater condition and no correction factors related to joint orientation are applied. Eventually, two parameters of groundwater condition and joint orientation were eliminated in developing empirical equations for TBM performance prediction using RMR input parameters in this study.

It should be noted that in the weighting scheme of the RMR system, the groundwater conditions and the uniaxial compressive strength (UCS) carry equal weights. However, Salimi et al. (2019) demonstrated that the effects of these two parameters on the penetration rate and TBM performance are significantly different. By utilizing the principal component analysis (PCA) method and conducting multiple analyses with various input parameters to obtain the most influential parameters, it was found that UCS, RQD, joint spacing (Js), and joint surface conditions (Jc) have the most significant impact on TBM performance (Salimi et al., 2019).

Moreover, Farrokh et al. (2012) and Salimi et al. (2019) proposed the rock types in the form of Rock Type Code (RTC) as an input parameter in the model for prediction of the TBM performance, because the rock texture, including the cement type, the cementation degree, the shape and size of the grains, affects the machine penetration rate significantly. According to the results of sensitivity analysis and parametric study of the model proposed by Fatemi et al. (2016), the RTC parameter has a great impact on estimating the rock mass boreability. Thus, considering the previous studies, RTC was added to the model input parameters for the prediction of the TBM performance. Seven categories of Rock Type Code (RTC) classified by Hoek and Brown (1980) and Stevenson (1999) were used in this study (Table 3).

In this table, the first four categories are sedimentary rocks, the fifth is metamorphic, the sixth is igneous, and the seventh is volcanic and pyroclastic rocks. It is worth mentioning that although gneiss is a metamorphic rock, it behaves similarly to granite, especially when it has weak foliation, and accordingly, it is included in the G category in this study. Due to the absence of karstic limestone in the database, the K category has been removed.

Table 3. Classification of rock types (RTC) in the database (modified from Hoek and Brown, 1980).

Rock Type	Code
Claystone, mudstone, marl, slate, phyllite, argillite	C
Sandstone, siltstone, conglomerate, quartzite	S
Limestone, chalk, dolomite, marble	L
Karstic Limestone	K
Metamorphic rocks such as gneiss and schist	M
Coarse igneous such as granite and diorite	G
Fine volcanic such as basalt, tuff, and andesite	V

As mentioned, four parameters of Basic RMR, i.e., UCS, RQD, Js, and Jc, as well as, RTC were used as initial input parameters to develop the experimental relationships for TBM performance prediction through the ML-based regression analysis. The frequency percentage of tunnel sections of different RTCs in the studied database is shown in Figure 1. Since the joint condition parameter (Jc) is qualitative and descriptive, it's defined based on the partial rating in RMR classification system (0 - 30) in this study. The statistical analysis of the machine performance parameters (FPI and P) and the input parameters used in the modeling (UCS, RQD, Js, and Jc) are summarized in Table 4. In the studied database, there is a wide range of FPI from 2.14 to 150 (*kN/cutter/mm/rev*) and penetration rates from 1.5 to 41.4 (*mm/rev*).

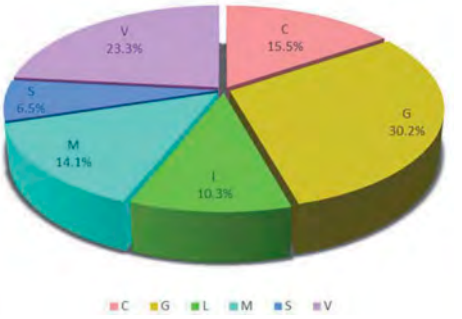

Figure 1. The frequency percentage of different RTCs in the studied database.

Since the rock texture, both grains and matrix directly affect the physical and mechanical properties of the rock, it is expected that in rocks with the same lithology, the machine performance be similar, which is why more focus is on the lithology in this study. Based on the lithology category (RTC), six lithology categories (RTC) are defined based on the available tunneling project data, including:

Table 4. Statistical analysis of TBM performance parameters and four input parameters of BRMR.

	N	Min.	1st Qu.	Median	Mean	3rd Qu.	Max.	Variance	Std. Deviation	Skewness	Kurtosis
FPI (*kN/cutter/mm/rev*)	523	2.14	10.49	16.68	26.37	31.50	150.0	689.11	26.25	2.31	5.89
P (*mm/rev*)	523	1.50	4.50	7.80	8.78	11.10	41.39	36.86	6.07	1.96	5.32
UCS (*MPa*)	523	4.25	38.50	65.0	80.93	120.0	300.0	3357.05	57.94	0.86	0.29
RQD (%)	523	10	45	75	67.15	90	100	708.02	26.60	- 0.53	- 1.03
Js (*m*)	523	0.03	0.13	0.28	0.37	0.43	2.00	0.11	0.33	1.92	3.84
Jc (Partial rating in RMR)	523	4	10	16	16.05	20	30	30.17	5.49	0.21	- 0.62

- 81 tunnel sections in Class C (claystone, mudstone, marl, shale, slate, phyllite, argillite) with FPI_{max} = 24 (*kN/cutter/mm/rev*)
- 158 tunnel sections in Class G (coarse igneous such as granite, diorite, pegmatite, gneiss) with FPI_{max} = 150
- 54 tunnel sections in Class L (limestone, chalk, dolomite, marble) with FPI_{max} = 58.26
- 74 tunnel sections In Class M (metamorphic rocks such as amphibolite, schist, calc-silicate) with FPI_{max} = 77.2
- 34 tunnel sections in Class S (sandstone, siltstone, conglomerate, quartzite) with FPI_{max} = 73.82
- 122 tunnel sections in Class V (Fine volcanic such as basalt, rhyolite, andesite, tuff, pyroclastic) with FPI_{max} = 141.33

As expected, the highest FPI values were observed in igneous rocks (G), while the lowest values were measured in weak sedimentary rocks such as argillite (C).

4 METHODS

In this study, to develop empirical relationships based on input parameters of the RMR classification system, machine learning methods including regression algorithms, were implemented. The currently used AI-based models for TBM performance prediction have been based on supervised learning techniques. In these approaches, input and output parameters are trained to the algorithm, the structure of predictive models is constructed, and then the best model is selected to analyze the relationship between independent and dependent variables. In ML, mathematical algorithms try to optimize a function which is a combination of independent variables, so that the value predicted by the function becomes close to the actual value of the dependent variable. In this research, the dependent variable of machine performance (FPI) is predicted by the use of the independent variables, including the four input parameters of Basic RMR, i.e., UCS, RQD, Js, and Jc, as well as, RTC. Since the dependent variable of FPI is continuous, regression algorithms are suitable for modelling. First, the classic regression algorithm and then more recent algorithms, including Stepwise Regression and Regularization algorithms, i.e., Lasso and Ridge Regression algorithms, are implemented on the dataset. For this purpose, the data is divided into two parts, Train and Test/Validation, and different models are applied to the Train dataset. Different generations of ML algorithms have been implemented to approach the best model so that the model generalizability is satisfied and the model works well on the data outside the range of input data and predicts correctly. If two linear regression hypotheses have been established, generalization is provided (Hastie et al., 2009).

Correlation analysis provides a general overview of the relationship between the independent variables and the dependent variable (FPI). The scatterplot and correlation matrix between variables are presented in Figure 2. As expected, the highest correlation was observed between UCS and FPI (0.74) and joint spacing (Js) and FPI (0.78), which had the greatest impact on the machine performance, followed by RQD with 0.62 and then Jc with 0.38. Previous studies including Robbins 1992, Laughton

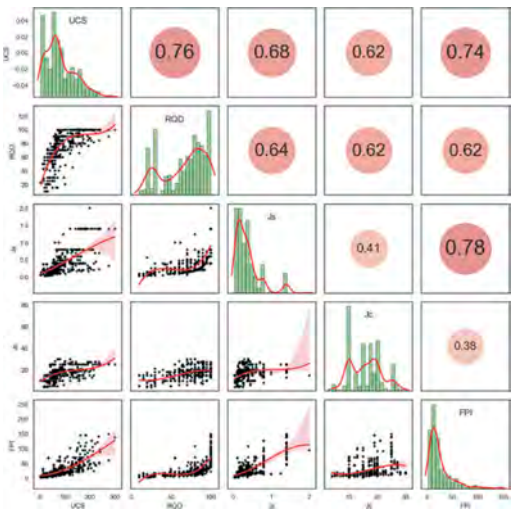

Figure 2. The scatterplot and correlation matrix between independent and dependent (FPI) variables.

1998, and Hassanpour et al. 2011, 2016, also show that UCS is a very important factor in rock boring by TBM. The correlation between independent variables themselves should also be considered because it may cause multicollinearity between variables and affect the regression coefficients, for example RQD has a correlation of 0.64 with Js, which is due to the effect of the discontinuity spacing in defining the RQD. It is important to note that the relationship between all independent input variables and FPI is positive, and with the increase of each independent variable, FPI increases.

5 DEVELOPMENT OF EMPIRICAL RELATIONSHIP FOR TBM PERFORMANCE PREDICTION

Data-based empirical relationships are widely used to predict target variables based on independent variables. In recent years experimental relationships have been valuable in rock engineering projects, because they are more practical compare to complex theoretical analyses. To develop the empirical equations of machine performance prediction, the regression algorithms were implemented on the Train dataset, which includes the FPI as the parameter for evaluating TBM performance, and the Basic RMR parameters (UCS, RQD, Js, and Jc) as well as lithology category (RTC). In this way, the input parameters of the Basic RMR system, which are often available in various tunneling projects, will be used to estimate the FPI. Since ML-based regression analysis enabled the modeling of categorical parameters in regression algorithms, the lithology category (RTC), a qualitative and categorical parameter, was included in the modeling. According to Rostami (1997), by calculating logarithmic regression, instead of linear regression, power functions are developed, and this makes the equations in boundary conditions be estimated with less error. Equation (1) is the best model obtained from training regression algorithms on the Train dataset with R^2 about 0.82. The equation was obtained to predict FPI in different lithologies, and the RTC coefficient was determined for each lithology.

$$FPI = 6.066\ (UCS)^{0.25}(RQD)^{0.22}(J_S)^{0.4}(J_C)^{-0.15}(RTC) \quad (1)$$

($R^2 = 0.82$)

where FPI is Field Penetration Index (*kN/cutter/mm/rev*), UCS is uniaxial compressive strength (*MPa*), RQD is Rock Quality Designation in percentage (0 - 100 %), Js is joint spacing (*m*), and Jc is joint condition in Basic RMR system and defined based on the partial rating in RMR classification system (0 - 30). As mentioned, the joint set which has the greatest impact on the TBM penetration rate, was used to determine the Js and Jc.

The T-test results of Equation (1) indicate that the P-value of Jc is greater than 0.05, and this parameter is not signified, and it is better to be removed from the model. This decision is justified as Jc correlation with FPI was inferior to that of the other parameters. Upon removing Jc, the model was optimized, resulting in Equation (2) with the same performance (R^2 = 0.81). In Equation (2), FPI is estimated accurately by utilizing the three input parameters of Basic RMR and the RTC coefficient proportional to the lithology, as outlined in Table 5. The specific values of RTC in Equation (2) are detailed in Table 5. It is worth noting that in the G and V categories, which encompass a wide range of rock strengths, the tunnel sections were analyzed separately based on strength (below 150 *MPa* and above 150 *MPa*). The corresponding RTC coefficients were obtained for each strength range. Therefore, when using Equation (2) for the G and V categories, attention should be given to the UCS value, and the appropriate RTC coefficient should be used to predict FPI.

$$FPI = 5.173\ (UCS)^{0.22}(RQD)^{0.19}(J_S)^{0.41}(RTC) \quad (2)$$

($R^2 = 0.81$)

Another critical point is that the multicollinearity of the parameters could cause the T-test results to be unreliable because the regression coefficients may not be correctly estimated. Multicollinearity of variables in statistical analysis and machine learning is detected using the Variation Inflation Factor (VIF), and VIF>10 indicates strong multicollinearity in regression (Hastie et al., 2009). The VIF of all independent variables in Equations (1) and (2) were smaller than 10. Then, the model is exposed to the Test dataset. Figure 3 illustrates the measured FPI versus the predicted FPI using Equation (2) for both Train and Test datasets, providing a visual representation of the model's performance.

Table 5. The values of RTC in Equation (2) (RTC table is modified from Hoek and Brown, 1980).

Rock Type	Code		RTC
Claystone, mudstone, marl, slate, phyllite, argillite	C		1
Sandstone, siltstone, conglomerate, quartzite	S		1.598
Limestone, chalk, dolomite, marble	L		1.325
Karstic Limestone	K		-
Metamorphic rocks such as schist	M		1.202
Coarse igneous such as granite, diorite, and gneiss	G	G_1 (UCS < 150 *MPa*)	1.177
		G_2 (UCS ≥ 150 *MPa*)	1.848
Fine volcanic such as basalt, tuff, andesite, and pyroclastic	V	V_1 (UCS < 150 *MPa*)	0.8
		V_2 (UCS ≥ 150 *MPa*)	1.876

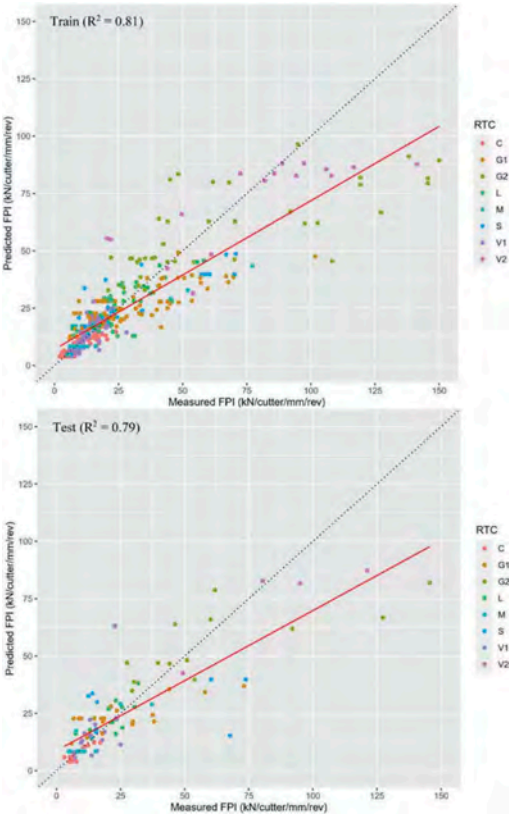

Figure 3. The measured FPI versus the predicted FPI via Equation (2) for Train and Test datasets.

6 CONCLUSION

Various experimental models have been introduced to predict the TBM performance, and many efforts have been made by various researchers to predict the TBM performance based on rock mass classification systems. The RMR classification system shows better correlation with the penetration rate of TBM, which is due to the use of UCS as the input parameter of this system. The RMR like other classification systems, has been developed to analyze the tunnel stability and support design, and the selection of effective parameters has also been accordingly. So, if the goal is to estimate the TBM performance, changes should certainly be made to the parameters. In this study, the input parameters of the Basic RMR (UCS, RQD, Js, and Jc) and lithology category (RTC) were utilized to estimate the Field Penetration Index (FPI) through machine learning-based regression analysis. This equation can be easily used to predict FPI in all rock types accurately.

REFERENCES

Armaghani, D. J., Mohamad, E. T., Narayanasamy, M. S., Narita, N., Yagiz, S., 2017. Development of hybrid intelligent models for predicting TBM penetration rate in hard rock condition. Tunnel. Under. Space Technol., 63, 29–43.

Farrokh, E., Rostami, J., Laughton, C., 2012. Study of various models for estimation of penetration rate of hard rock TBMs. Tunnel. Under. Space Technol., 30, 110–123.

Fatemi, S.A., 2016. Prediction of TBM penetration rate by rock mass classification system. Ph.D. Thesis, Tarbiat Modares University, Tehran, Iran.

Gong, Q., Lu, J., Xu, H., Chen, Z., Zhou, X., Han, B., 2021. A modified rock mass classification system for TBM tunnels and tunneling based on the HC method of China. Int. J. Rock Mech. Min. Sci., 137, 104551.

Grima, A., Bruines, M., Verhoef, P. N. W., 2000. Modeling tunnel boring machine performance by neuro-fuzzy methods. Tunnel. Under. Space Technol., 15(3), 259–269.

Hassanpour, J., Ghaedi Vanani, A.A., Rostami, J., Cheshomi, A., 2016. Evaluation of common TBM performance prediction models based on field data from the second lot of Zagros water conveyance tunnel (ZWCT2). Tunnel. Under. Space Technol., 52, 147–156.

Hassanpour, J., Rostami, J., Khamehchiyan, M., Bruland, A., 2009. Developing new equations for TBM performance prediction in carbonate-argillaceous rocks: a case history of Nowsood water conveyance tunnel. Geomech. Geoeng. Int. J, 4, 287–297.

Hassanpour, J., Rostami, J., Zhao, J., 2011. A new hard rock TBM performance prediction model for project planning. Tunnel. Under. Space Technol., 26, 595–603.

Hastie, T., Tibshirani, R., Friedman, J., 2009. The Elements of Statistical Learning, Data Mining, Inference and Prediction. Springer New York: Springer Series in Statistics: 2nd Edition, 745p.

He, B., Armaghani, D.J., & Lai, S.H., 2022. A Short Overview of Soft Computing Techniques in Tunnel Construction. The Open Construction & Building Technology Journal, 16(1), 1–6.

Hoek, E., Brwon, E.T., 1980. Underground excavations in rock. London: The Institute of Mining and Metallurgy.

Hoek, E., Kaiser, P.K., Bawden, W.F., 1995. Support of underground excavations in hard rock. Balkema, Rotterdam.

Hoek, E., Brown, E.T., 1997. Practical estimates of rock mass strength. Int. J. Rock Mech. Min. Sci., 34(8), 1165–1186.

Jain, P., 2014. Evaluation of engineering geological and geotechnical properties for the performance of a tunnel boring machine in Deccan traps rocks-a case study From Mumbai, India. Ph.D. thesis, Indian Institute of Technology Bombay, India (Unpublished).

Koopialipoor, M., Nikouei, S. S., Marto, A., Fahimifar, A., Jahed Armaghani, D., Mohamad, E. T., 2019. Predicting tunnel boring machine performance through a new model based on the group method of data handling. Bulletin of Engineering Geology and the Environment, 78 (5), 3799–3813.

Laughton, C., 1998. Evaluation and prediction of tunnel boring machine performance in variable rock masses. Ph.D. Thesis, The University of Texas, Austin, USA.

Pourhashemi, S. M., Ahangari, K., Hassanpour, J., Eftekhari, M., 2021. TBM performance analysis in very strong and massive rocks; case study: Kerman water conveyance tunnel project, Iran. Geomech. Geoeng. Int. J, https://doi.org/10.1080/17486025.2021.1912410.

Ribacchi, R., Lembo Fazio, A., 2005. Influence of rock mass parameters on the performance of a TBM in a Gneissic Formation (Varzo Tunnel). Rock Mech. Rock Eng., 38 (2), 105–127.

Robbins, R.J., 1992. Large diameter hard rock boring machines: state-of-the-art and development in view of alpine base tunnels. Felsbau, 10 (2), 56–62.

Rostami, J., 1997. Development of a force estimation model for rock fragmentation with disc cutters through theoretical modelling and physical measurement of crushed zone pressure. Ph.D. Thesis, Colorado School of Mines, Golden, Colorado, USA.

Rostami, J., 2016. Role of rock mass classification in TBM performance prediction, Where Are We Now, Where Are We Heading. International Conference on Tunnel Boring Machines in Difficult Grounds (TBM-DIGS), Istanbul–Turkey.

Salimi, A., 2021. Investigation and Evaluation of Rock Mass Characteristics for Development of New TBM Performance Prediction Model in Hard Rock Conditions. Ph.D. Thesis, Stuttgart University, Germany.

Salimi, A., Rostami, J., Moormann, C., 2019. Application of rock mass classification systems for performance estimation of rock TBMs using regression tree and artificial intelligence algorithms. Tunnel. Under. Space Technol., 92, 103046.

Salimi, A., Rostami, J., Moormann, C., & Delisio, A., 2016. Application of non-linear regression analysis and artificial intelligence algorithms for performance prediction of hard rock TBMs. Tunnel. Under. Space Technol., 58, 236–246.

Sapigni, M., Berti, M., Behtaz, E., Busillo, A., Cardone, G., 2002. TBM performance estimation using rock mass classification. Int. J. Rock Mech. Min. Sci., 39, 771–788.

Yagiz, S., Karahan, H., 2011. Prediction of hard rock TBM penetration rate using particle swarm optimization. Int. J. Rock Mech. Min. Sci., 48(3), 427–433.

Tunnelling for a Better Life – Yan, Celestino, Thewes & Eberhardt (Eds)
© 2024 The Author(s), ISBN 978-1-032-80042-4
Open Access: www.taylorfrancis.com, CC BY-NC-ND 4.0 license

Performance analysis of supervised algorithms on encoded data for predicting tunnel strain classes

Abhinav Dewangan*
The University of Queensland – Indian Institute of Technology Delhi Academy of Research (UQIDAR), New Delhi, India
Department of Civil Engineering, Indian Institute of Technology Delhi, New Delhi, India
School of Civil Engineering, The University of Queensland, Brisbane, Australia

Dipti Ranjan Sahoo
Department of Civil Engineering, Indian Institute of Technology Delhi, New Delhi, India

Jurij Karlovsek
School of Civil Engineering, The University of Queensland, Brisbane, Australia

ABSTRACT: Rapid urbanisation and global callout for sustainable and resilient underground infrastructures, especially transportation and railway tunnels, are possible through digitalization approaches. Machine learning is one approach that has been used to classify and predict the solutions to a given set of problems through supervised and unsupervised algorithms. This paper proposes analysing the supervised algorithms' performance to classify the Tunnel strains and checking the strength of agreement (SOA) for the assessment metrics. These algorithms are Tree based (Decision Tree and Random Forest), Functional based (Logistic Regression and Linear Discriminant Analysis), and Margin based (Support Vector Machines: One vs One). To improve the feature dimension in the input data the encoded feature inputs are used: Rock Type, Location, and Tunnel names along with considering conventional feature inputs: Diameter, Cover Depth, Q-value, and Support Stiffness. The functional based algorithms have shown the best efficacy with improved feature space in these experiments. The improvement in accuracy for predicting training class labels with max. SOA: 0.81 observed as 14-26% whereas for testing class labels with max SOA: 0.52 observed as 8-12%. This study would contribute towards improving the performance of supervised algorithms with better feature space and reduce errors in classification of tunnel strains by these digital methods.

Keywords: Tunnel, Digital Methods, Prediction Feature Space, Tunnel Strain Classification, Strength of Agreement (SOA)

1 INTRODUCTION

The global demand of sustainable and resilient underground infrastructure eying for rapid urbanisation is being lead from the front by transportation and railway tunnels. The digital engineering has the calibre to cater this global call out very smoothly and rapidly. And Machine Learning is one the digital engineering aspect which strong arms the decision-making process based on the prior experience and training. This approach has shown very promising and trustworthy results in its other areas of its applications such as medical, material, management, economical, technological and communications (Ali et al. 2020; Mienye and Sun 2021). The machine learning is found to be trained and tested in tunnel and rock engineering in many literatures.

In the current trends of development of machine learning predictions for Tunnel hazards, the tunnel squeezing has caught the special focus by Chen et al. 2020; Fathipour-Azar 2022; Feng and Jimenez 2015. The tunnel squeezing is a phenomenon dependent on time involving the creep of the soft and weak rock mass especially in a highly structurally stressed environment. In this condition the tunnel walls tend to move inwards due to redistribution of stress after excavation and finally contracting the excavated cross-section. The extent and scale of squeezing depends lithological conditions, rock mass in-situ mechanics and strength.(Sheil et al. 2020; Zhang, Li, and Wang 2020). Unplanned or excessive reduction in the tunnel cross-section affects the equilibrium and stability of the tunnels. This imposes a serious safety and economical risks to the tunnel construction. Therefore,

*Corresponding author: abhinav.se19@gmail.com

DOI: 10.1201/9781003495505-399

Table 1. Summarised supervised algorithms for tunnel strain class prediction with feature space.

Literature	Feature space	Data points	Classifying Algorithm	Multiclass
Shafiei et al. 2012	H,Q	198	SVM	2
Sun et al. 2018	H,Q,D,K	117	M-SVM	3
Feng and Jimenez 2015	H,Q,D,K, SSR	166	BN	2
Ghasemi and Gholizadeh 2019	H, Q, D	115	KNN	2
Chen et al. 2020	H,D, K, SSR, GC	154	DT	3
Huang et al. 2022	H, Q, D, K	178	SVM-BP	2
Zhou et al. 2022	H, K, D, Q, e%	114	WOA-SVM	3
Current Study	H, Q, D, K, Tunnel name, Lithology, location	117 (Sun et al. 2018) dataset	Multiple classifiers (refer Table-2)	3

strength of agreement and accuracy in the prediction of tunnel strain will be having an important contribution towards tunnel construction.(Sheil et al. 2020).

Monitoring the tunnel squeezing through convergence is an important aspect in the conventionally and mechanically excavated tunnels. The envelopes of wall convergence could be recorded by monitoring equipment system. This data would be then utilised to assess and select the appropriate design and supporting structures of tunnel. (Huang et al. 2017). Although the monitoring approach is one of the very effective approaches, but it was found to be very difficult to predict the actual convergence. (Zhou et al. 2023). The relationship between convergence, lithological properties, rock mechanics and strength are nonlinear which were being tried to corelate by numerous literatures using empirical relationships, numerical expressions, statistical methods, and inference systems. (Fathipour-Azar 2022). Although, each system has their own constraints and limitations if the application is generalised for the real-world problems. In contrast ML has been applied to many Tunnel engineering problems to predict the strain or the convergence of the tunnel walls such as Sun et al. 2018 applied the M-SVM approach using the H, D, Q, and K predictors and Chen et al. 2020 using the decision tree approach utilising the H, D, K, SSR, and GC predictors. The other approaches followed by several leading researchers could found in the Table 1 below for predicting the strain or convergence of the tunnel walls using different classifiers.

Following the similar trend, in this study it is aimed to classify the strain in to 3 classes non-squeezing, squeezing and severely to extremely squeezing strain ranging from class 1 to class 3. The novelty in this approach is the utilisation of the data boosting methods by introducing the bias due to tunnel name, location, and lithology of the ground. This approach is found to be contributing towards improving the precision of prediction and strength of agreement with the classification made using different algorithms. Especially in the functional based algorithms with good measure. The algorithms tested in this study are Tree based (Decision Tree and Random Forest), Functional based (Logistic Regression and Linear Discriminant Analysis), and Margin based (Support Vector Machines: One vs One). These algorithms are described in detail in section 3 of this paper. In these algorithms the tree based, and margin-based methods are most used approaches found in the literature (Fathipour-Azar 2022; Feng and Jimenez 2015; Lu, Cheng, and Chen 2020; Sun et al. 2018). The functional based algorithms are only tested by Fathipour-Azar 2022 where the accuracy of the methods are found to be very low and unsuitable for such predictions of Tunnel strain classifications. Thus, the requirement of improving such methods and checking their final strength of agreement from training to predictions is being aimed in this study.

2 DATASET DESCRIPTION & PREDICTING FEATURES

In this study a dataset from Sun et al. 2018 with 117 datapoints are used to train and test the proposed approach for supervised algorithms. These datapoints were curated from different worldwide case studies and literatures where tunnel squeezing is the prime criteria. Based on the (Hoek and Marinos 2000) criteria where the tunnel squeezing is partitioned into total five groups from non-squeezing strain to extremely squeezing strain, here in this case that has been considered from non-squeezing strain to severe (up to extremely) squeezing strain and considered as three groups. These groups are defined as three cases from 1 to 3 and varying from $\varepsilon<1\%$, $1\%<\varepsilon<2.5\%$, and $\varepsilon>2.5\%$ respectively as shown in the Figure 1 which are the output classes as well. To verify this segregation the datapoints are conventionally trained with the decision tree based on (Fathipour-Azar 2022) approach where strain is considered as one of the inputs. The verified segregation plot could be observed from the decision tree plot where the segregation points are 2.48%, and 1% tunnel strains.

The primary input features used in this study are diameter of tunnel (D), cover depth of tunnel (H), stiffness of tunnel supports (K), and rock quality

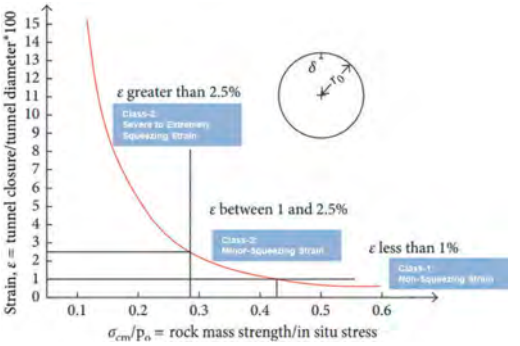

Figure 1. Tunnel Squeezing classification adapted from Hoek and Marinos 2000; Sun et al. 2018.

index for excavated tunnel (Q). These are considered based prior study by Chen et al. 2020; Fathipour-Azar 2022; Sun et al. 2018. The additional features which are introduced in this study to improve the predicting capabilities of the conventional machine learning supervised algorithms are Rock Type, Location, and Tunnel names as the bias in the system. As it is observed in the data set it covers the large range of rock types and tunnels worldwide. In the dataset the case-1 to 3 datapoints are 28,16, and 49 respectively with total of 93 as training datapoints and 24 testing data points in the similar ratio after randomising and splitting. The partitioning of training and testing dataset for this study is done in 80% & 20% respectively. Also, in this study the K-fold cross validation is performed to evaluate the optimum hyperparameters of the supervised algorithms. This evaluation has been carried out after performing the fold sensitivity study. This fold sensitivity study allows to check the optimum fold at which the highest accuracy could be achieved. This provides the freedom to analyse the dataset as per its own baseline instead of following other literature. The 5-fold cross validation is found to be the optimised fold for finding the optimised hyperparameters of the supervised algorithms in this study for the dataset chosen.

3 SUPERVISED ALGORITHMS

This section provides the overview and brief description of the supervised algorithms used in this study. As discussed the Sun et al. 2018 dataset in this study is tested on the 4 sets of experiment. With the experience from Chen et al. 2020, Sun et al. 2018 and Zhou et al. 2022 studies the high efficacy algorithms such as decision tree and support vector machines are chosen in this study to check their efficacy to predict the tunnel squeezing class. Based on these, the other tree-based algorithms such as random forest and XG boost are also being part of this experiments along with logistic regression and linear discriminant analysis which are functional based algorithms. Thus, there are total six algorithms which are being chosen to test in this study and assess their performance based on different performance assessment metrics. These algorithms are all available online and can be easily downloaded from python sklearn official network (https://scikit-learn.org). The combination of experiments followed in this study are given in the table-2 below. The algorithms used in this study are briefed as follows:

3.1 *Tree based algorithms*

It works on the principle of recursive partitioning of the dataset into subsets at nodes and creating tree like models where end node (i.e., leaf node) gives the label or class predicted from the hyperparameters used for training. The split at the node occurs based on the least error and maintaining homogeneity of the subset. The fully grown tree with fixed nodes would be able to predict and classify the datapoints into desired classes. These trees are prone to overfit the training dataset making the classification very complex, so the pruning techniques are employed by providing the constraints on tree depths, and number of leaf nodes. The ensemble methods like random forests and gradient boosting methods are also used. The random forest works on the principle of growing forest with many

Table 2. Test combinations and planned experiments for this study.

Algorithm Family	Test Combinations	EX1	EX2	EX3	EX4
Tree based	i. Decision Tree (DT) ii. Random Forest (RFDT) iii. XG Boost (XGBDT)	Default	Default + DB	Default + CV	Default + DB + CV
Function based	iv. Logistic Regression (LOGRE) v. Linear Discriminant Analysis (LDA)				
Margin based	vi. Support Vector Machines: One vs One (SVMOVO)				
		Experiments			

Where:
Default parametric space of classifier [H, Q, D, K]: Default (Conventional features)
Data Boosting [Tunnel Name, Lithology, Location]: DB
Grid search 5-fold Cross-Validation: CV

classification trees which classifies based on the input vectors and votes for a particular class. The result of the forest choice would be from most voted class. (Hastie, Friedman, and Tibshirani 2001).

In this study the decision tree, random forest, and gradient boosting (XG boost) methods are employed as Tree based supervised algorithms.

3.2 *Functional based algorithms*

It works on the principle of defining a hypothesis based on the input features and target variables or classes in the linear regression function. Here the decision boundary distinguishes between class k and l with the sets of input feature points for which $\widehat{f_k}(x) = \widehat{f_l}(x)$ where the dataset is divided into k classes, and it's fitted as a linear or nonlinear function. Here since the input feature space is divided into regions of constant classification and piecewise hyperplane decision boundaries. Here the regression approach is a member of a class of methods that model discriminant functions $\delta_k(x)$ for each class and then classify the x to the class of the largest value for its discriminant function. (Hastie et al. 2001)These functions could be linear discriminant, quadratic discriminant, regularised discriminant, and logistic regression. The classification in these methods is done based on maximum likelihood of any class with least error. The likelihood functions here are developed using the conditional likelihood which specifies the conditional distribution and appropriate for multinomial distribution for any N number of observations.

In this study the linear discriminant analysis and logistic regression analysis methods are utilised for tunnel strain classification. Since these methods are observed to be performing poorly in Fathipour-Azar 2022 study and could be further improved with data boosting feature space as done in this study.

3.3 *Margin based algorithm*

In margin-based algorithm, support vector machine in this case, the decision boundary is chosen to be the one for which the margin is maximised. In this method the optimal decision boundary also known as hyperplane in this case maximises the margin between datapoints of different classes. It works on the principle of finding the best hyperplane which distinguishes the data points into k classes by using the support vectors. Mathematically linearly separable datasets described by $w^T x + b = 0$ where w: weight vector perpendicular to hyperplane, x: input data and b: bias term. The distance between the hyperplane and support vector is computed as the margin and inversely proportional to weight vector ($||w||$). Maximising the margin translates in to minimising the norm of the weight vector and satisfying the constraints. The SVM can also be extended to nonlinearly separable data using the kernels. It implicitly maps the inputs into a higher dimensional space making it linearly separable. This approach allows the SVM to handle the nonlinear and complex classification very well. (Bishop 2006).

In this study the kernel tricks are used in the support vector machines with one vs one strategy for the tunnel strain classification. The results observed in the experiments are discussed in detail in the section 6 of this paper.

4 PERFORMANCE ASSESSMENT METRICS

In this study to evaluate the performance of different algorithms developed for this paper are assessed on these metrics: Accuracy, Precision, Recall, F1 score, and Cohen's kappa metric (strength of agreement: SOA). From the confusion matrix (CM) as shown below the true positive (TP), false positive (FP), true negative (TN) and false negative (FN) are used to evaluate the algorithms on these metrics. Where TP and TN are the cases when the predicted and actual class of the data point matches i.e., the right classification of a certain class, and FP and FN are the cases when the predicted class is misclassified. For e.g.: If a data point is of actually class-1 and it is classified or predicted as class-1 then it's the case of TP, or if it is classified as class-2/3 it is the case of FN. Also, if as per the actual classification it is class2/3 and it is classified as same then its TN or else FP with reference to class-1 classification. The representation of these metrics mathematically are as follows:

	Actual	*Class-1*	*Class-2/3*
CM = Confusion Matrix		*TP*	*FN*
		FP	*TN*
		Class-1	*Class-2/3*
		Predicted	

Trace (CM) = TP + TN
Sum (CM) = TP + FP + TN + FN
Accuracy = Trace (CM)/ Sum(CM)
Precision, P = TP/(TP + FP)
Recall, R = TP/(TP + FN)
*F-measure = 2P * R/(P +R)*
Where:

Cohen's kappa (Cohen 1960; Tallón-Ballesteros and Riquelme 2014)

$$= \frac{N\sum_{i=1}^{m} CM_{ii} - \sum_{i=1}^{m} Ci_{corr} Ci_{pred}}{N^2 - \sum_{i=1}^{m} Ci_{corr} Ci_{pred}}$$

TP = True Positive; *TN* = True Negative
FP = False Positive; *FN* = False Negative
N = Total data points in confusion matrix (CM)
Also, *N = Sum (CM)*
CM_{ii} = i^{th} diagonal element of confusion matrix (CM)
Ci_{corr} = Sum of all elements in the i^{th} row of the correct or actual class
Ci_{pred} = Sum of all elements in the i^{th} column of the predicted class

The Cohen's kappa metric which is also called the strength of agreement for the predicted classes with respect to the actual classes is a statistical test, which was initially used for inter-rater reliability. Now a days it is utilised for comparing the accuracy of Machine learning algorithms to any random classifier. (Mienye and Sun 2021). The expression given above for the multiclass classification scheme is adapted from (Cohen 1960; Tallón-Ballesteros and Riquelme 2014) and its interpretation for multiclass for this study is referred to (Wardhani et al. 2019). In this interpretation different scales of strength of agreement are detailed as follows:

Table 3. Cohen's Kappa Analysis (Wardhani et al. 2019).

Kappa score range	Strength of Agreement
<0.00	Poor
(0.00, 0.20]	Slight
(0.20, 0.40]	Fair
(0.40, 0.60]	Moderate
(0.60, 0.80]	Substantial
(0.80, 1.00]	Almost Perfect

5 PROPOSED APPROACH

In this study as discussed earlier a total of six algorithms are chosen to test and assess their performance based on different assessment metrics. For these algorithms along with the data available as the conventional inputs such as depth (H), Diameter (D), Rock quality index (Q-value), and Support Stiffness (K), the text inputs such as the Tunnel name, lithology and location inputs are proposed to be used in this study. These informational and numeral inputs will improve the predicting capability of the machine learning models which is a hypothesis for performing this study. The flow chart of the process of performing the training and then predictions in this study is given in the Figure 2 below. In this flow chart the start to end process has been detailed. It is a generalised flow chart for this study. For the EX1 and EX3 the text inputs will not be utilised and hence those steps to be ignored in especially EX1 and EX3 tests. And sensitivity test for K-fold cross validation has also been proposed as a part of this study. Since, it has been observed in other literature that K-fold cross validation is being performed based on prior experience and literatures referred. Whereas the K-fold cross validation could be limited to certain number of folds to have an optimum performance of the model because each dataset performs differently on each model and hence the sensitivity study could actually help in fixed K-folds for respective dataset. For this dataset the 5fold cross validation is found to be optimum and proposing the same for future use of this dataset.

6 RESULTS AND DISCUSSION

6.1 *Assessment results*

As discussed in the previous section there are 4 sets of experiments in this study where with each step the predicting capability is assumed to be improved.

6.1.1 *EX1 results*

Starting with the first set of experiments the training accuracy of the tree-based algorithms are found to be perfectly fitting all the data points in the training with accuracy of 100% and testing accuracy of 75%, 75%, and 83% for DT, RFDT, and XGBDT respectively. Whereas the accuracy for LOGRE, LDA and SVMOVO are found to be 71%, 63% and 71% for training dataset and 63%, 54%, and 54% for testing dataset respectively. Similarly, looking at SOA metric for tree-based algorithms in both training and testing dataset it is varying from substantial SOA to almost perfect SOA except for XGBDT performance on testing dataset which is in moderate SOA range as observed from the Figure 4 to 7, whereas for both functional based and margin-based algorithm its varying from fair SOA to moderate SOA.

6.1.2 *EX2 results*

In this experiment the training accuracy of the tree-based algorithms are found to be perfectly fitting all the data points in the training with accuracy of 90.3%, 97.8%, and 97.8% and testing accuracy of 75%, 75%, and 70.8% for DT, RFDT, and XGBDT respectively. Whereas the accuracy for LOGRE, LDA and SVMOVO are found to be 84.9%, 89.2% and 88.2% for training dataset and 70.8%, 66.7%, and 62.5% for

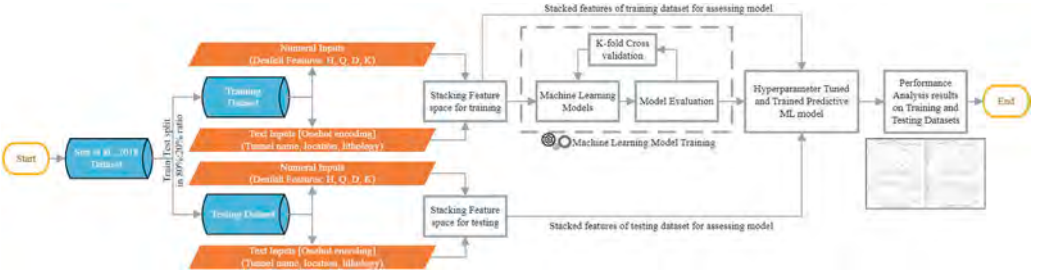

Figure 2. Flowchart for proposed approach in this study.

traindata_X

Proposed data boosting with conventional features

Strain observed

	D (m)	H (m)	Q	K (MPa)	e (%)	Tunnel	Location	Rock type
105	5.4	217.5	0.013	1217.16	25.54	Chameliya hydroelectric project headrace tunne...	Nepal	Dolomite
33	5.0	276.0	0.250	940.00	0.77	Khimti 1 hydroproject A3 ch200	Nepal	Gneiss and schists
30	4.0	225.0	0.140	1430.00	0.24	Khimti 1 hydroproject A4 ch503	Nepal	Gneiss and sericite schists
56	5.8	550.0	1.700	9.81	2.66	Maneri stage 1 tunnel	India	Siliceous phyllites
48	4.6	440.0	0.050	3.97	10.04	Giri-Bata tunnel	India	Crushed phyllites
...	...	...	...	...	...	...	...	...
113	5.4	222.6	0.015	1217.16	1.20	Chameliya hydroelectric project headrace tunne...	Nepal	Foliated phyllite
67	8.7	550.0	0.029	39.13	2.30	Kaligandaki "A" HRT	Nepal	Graphitic phyllite
64	6.8	337.0	0.006	22.58	3.10	Tala HRT, Bhutan	Bhutan	AGO (adverse geological occurrences): complete...

93 rows × 8 columns

Conventional features

Figure 3. Proposed data boosting feature space along with conventional feature space.

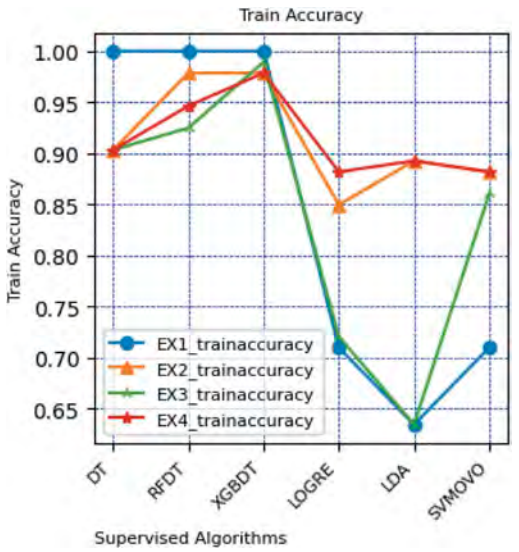

Figure 4. Training Accuracy plot for different algorithms.

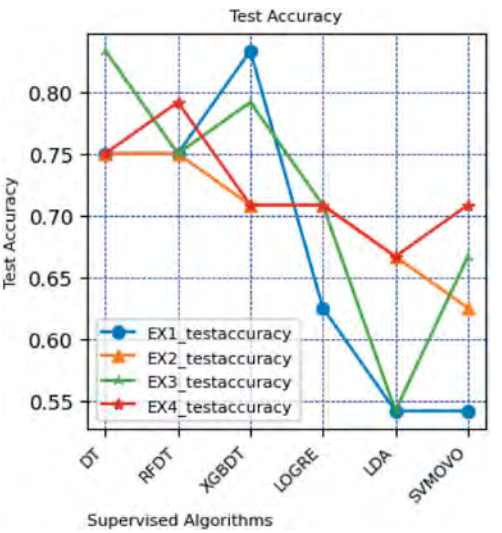

Figure 5. Testing Accuracy plot for different algorithms.

testing dataset respectively. Similarly, looking at SOA metric for tree-based algorithms in both training and testing dataset it is varying from substantial SOA to almost perfect SOA as observed from the Figure 6 and 7, whereas for both functional based and margin-based algorithm its varying from moderate SOA to substantial SOA.

6.1.3 *EX3 results*

In this experiment the training accuracy of the tree-based algorithms are found to be perfectly fitting all the data points in the training with accuracy of 90.3%, 92.5%, and 98.9% and testing accuracy of 83.3%, 75%, and 79.2% for DT, RFDT, and XGBDT respectively. Whereas the accuracy for LOGRE, LDA and SVMOVO are found to be 72%, 63.4% and 86% for training dataset and 70.8%, 54.2%, and 66.7% for testing dataset respectively. Similarly, looking at SOA metric for tree-based algorithms in both training and testing dataset it is varying from substantial SOA to almost perfect SOA as observed from the Figure 6 and 7, whereas for both functional based and margin-based algorithm its varying from moderate SOA to substantial SOA. Exceptionally for LDA the SOA for both training and testing is in fair SOA range only.

6.1.4 *EX4 results*

In this experiment the training accuracy of the tree-based algorithms are found to be perfectly fitting all the data points in the training with accuracy of 90.3%, 94.6%, and 97.8% and testing accuracy of 75%, 79.2%, and 70.8% for DT, RFDT, and XGBDT respectively. Whereas the accuracy for LOGRE, LDA and SVMOVO are found to be 88.2%, 89.2% and 88.2% for training dataset and 70.8%, 66.7%, and 70.8% for testing dataset respectively. Similarly, looking at SOA metric for tree-based algorithms in both training and testing dataset it is varying from

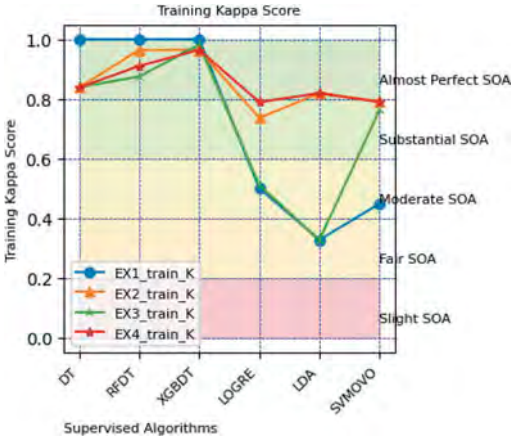

Figure 6. Kappa score plot for training dataset.

substantial SOA to almost perfect SOA as observed from the Figure 6 and 7, whereas for both functional based and margin-based algorithm its varying from moderate SOA to substantial SOA. Exceptionally for LDA the SOA for both training and testing is in fair SOA range only.

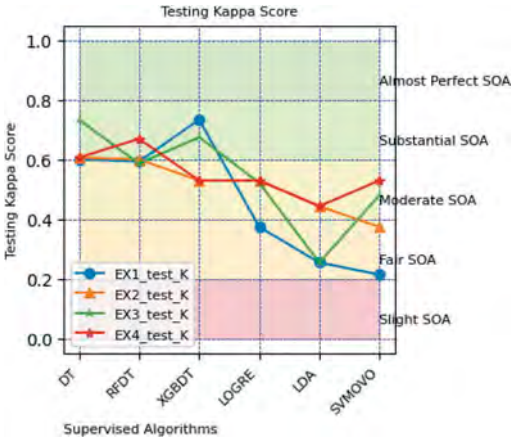

Figure 7. Kappa score plot for testing dataset.

6.2 *Discussion on patterns recognised*

- The improvisation observed from the EX1 to EX2 performance of the algorithms are: for both functional and margin-based algorithms both train and testing accuracy along with kappa score are improved as observed from the Figure 6 and 7. These improvement in accuracy are 14% to 26% in training and 8% to 12% in the testing dataset as observed in section 6.1.1 and 6.1.2. Also, for the tree-based algorithm the accuracy and kappa score for both training and testing has been observed to be reduced a little because of introduction of new inputs as one hot encoding which might not be performing well in the feature space of these algorithms.
- While comparing the EX1 to EX3 results it is observed that all algorithms have improved their accuracy and kappa score. Especially the DT accuracy on testing has been improved by 8% and kappa score by 13% and for the margin-based algorithms the testing accuracy has been improved by 11% and kappa score has been improved by 27%.
- In comparison between the EX2 and EX3 results the functional based and margin-based algorithms are performing better in EX2 along with XGBDT which is a tree-based algorithm and other tree-based algorithms are performing better in EX3 in both training and test phases.
- In the last phase EX4 the functional based algorithms LOGRE and LDA are improved greatly improved as compared to EX1 where their testing kappa score was very low in the range of random prediction only (<0.25), in the EX4 it came in the moderate SOA range by improving from 0.25 to 0.443 and 0.214 to 0.529 SOA along with improved testing accuracy from 62.5% to 70.8% and 54.2% to 66.7% respectively. While the testing accuracy for the SVMOVO improved from 54.2% to 70.8% with change in SOA from 0.214 to 0.529 SOA which are very good improvement both qualitatively and quantitatively. But, in the tree-based algorithms only RFDT has shown some improvement in testing accuracy from 75% to 79.2% and in terms of SOA from 0.593 to 0.669 SOA whereas both DT and XGBDT has shown slight decrease in their performance indicating towards unsuitable feature space for them. Here the precision signifies the TP predictions in the respective class whereas the recall signifies the TP in that overall class actually and F1 signifies the trade-off between these two. As observed from the Figure 8 for precision the class-2 strains are not well recognised in all the algorithms whereas in the recall and F1 score plot especially for SVMOVO and LDA it is behaving like binary class prediction only in EX1 results. In the EX4 results finally this class got some recognition and false predictions are decreased. As the misclassifications observed during the EX1 are as shown in the Figure 9 below compared to the EX4 results in the form of confusion matrix for better understanding.
- In the initial patterns observed in this study the 8 & 10-fold cross validation were adapted referring to previous studies by Chen et al. 2020; Fathipour-Azar 2022; Sun et al. 2018 but while performing the experiments it has been observed that choosing a fold for cross-validation might sometime reduce the overall accuracy of the algorithm and the requirement of optimum fold for cross validation was felt. So, a sensitivity study is performed as part of fold optimisation technique to have an optimum result and check the optimum performance of the algorithms as shown in Figure 10.

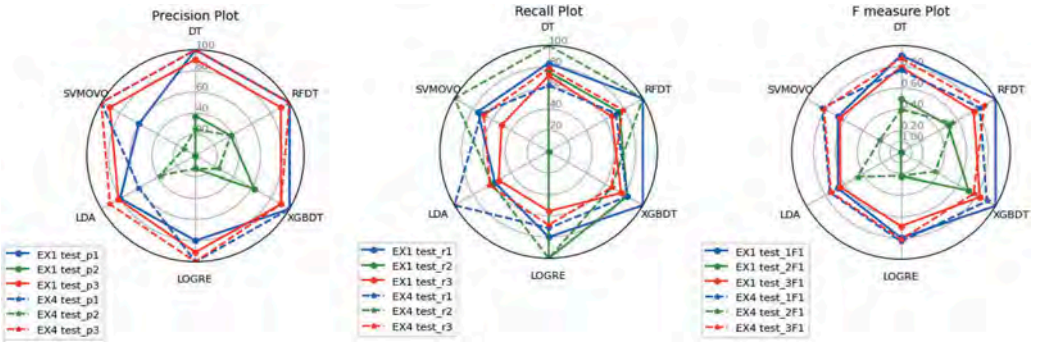

Figure 8. Precision, Recall, and F-measure plot for EX1 and EX4.

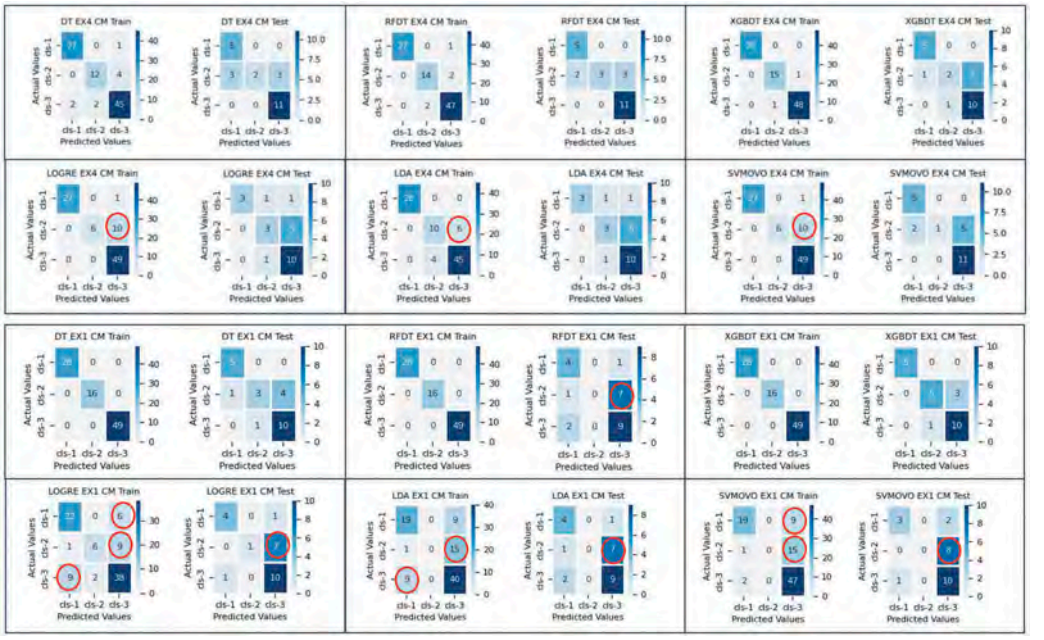

Figure 9. Confusion Matrix plot for EX1 and EX4 performance on training and testing dataset (Misclassifications >5 marked in red).

7 CONCLUSIONS

The major conclusions found in this study are:

- Hypothesis for data boosting encoded parameters is found to be true substantially for functional based algorithms and slightly for Random Forest (Tree based algorithm)
- The contribution of the new encoded parameters is evident from the EX2 tests in the initial phases.
- The overall improvement in accuracy for functional based algorithms for predicting training class labels with max. **SOA: 0.81** observed as **14-26%** whereas for testing class labels with max **SOA: 0.52** observed as **8-12%**.
- 5-fold CV found to be optimum in a **sensitivity study on K-fold cross-validation (CV)**
- Also, the precision, recall and F measure in predicting TP in class-2 & trade-off between the other classes in overall classification is greatly recognised in this study as observed from Figure 8.

Hence this study is contributing towards improved performance of supervised algorithms with better feature space in tunnel strain classification by digital methods.

ACKNOWLEDGMENTS

The authors would like to acknowledge the funding provided for this research by The University of Queensland-Indian Institute of Technology Delhi Academy of Research (UQIDAR) and computational

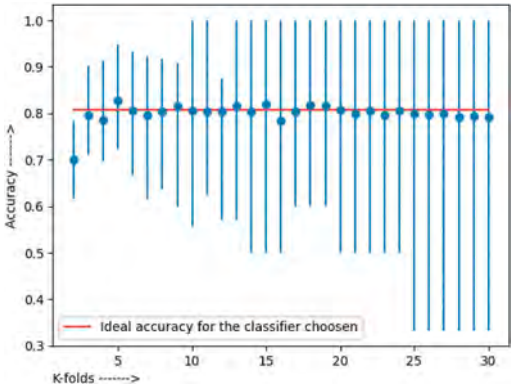

Figure 10. Sensitivity test plot for K-fold cross validation.

facility provided by Heavy Structures Laboratory, Department of Civil Engineering, Indian Institute of Technology Delhi. This work is a part of research project code – UQIDAR305.

REFERENCES

Ali, Farman, Shaker El-Sappagh, S. M. Riazu. Islam, Daehan Kwak, Amjad Ali, Muhammad Imran, and Kyung Sup Kwak. 2020. "A Smart Healthcare Monitoring System for Heart Disease Prediction Based on Ensemble Deep Learning and Feature Fusion." *Information Fusion* 63 (April): 208–22. doi: 10.1016/j.inffus.2020.06.008.

Bishop, Christopher M. 2006. *Pattern Recognition and Machine Learning*. Vol. 49. Springer Science and Business Media B.V.

Chen, Yu, Tianbin Li, Peng Zeng, Junjie Ma, Edoardo Patelli, and Ben Edwards. 2020. "Dynamic and Probabilistic Multi-Class Prediction of Tunnel Squeezing Intensity." *Rock Mechanics and Rock Engineering* 53(8):3521–42. doi: 10.1007/s00603-020-02138-8.

Cohen, Jacob. 1960. "A Coefficient of Agreement for Nominal Scales." *Educational and Psychological Measurement* 20(1):37–46. doi: 10.1177/001316446002000104.

Fathipour-Azar, Hadi. 2022. "Multi-Level Machine Learning-Driven Tunnel Squeezing Prediction: Review and New Insights." *Archives of Computational Methods in Engineering* 29(7):5493–5509. doi: 10.1007/s11831-022-09774-z.

Feng, Xianda, and Rafael Jimenez. 2015. "Predicting Tunnel Squeezing with Incomplete Data Using Bayesian Networks." *Engineering Geology* 195:214–24. doi: 10.1016/j.enggeo.2015.06.017.

Ghasemi, Ebrahim, and Hasan Gholizadeh. 2019. "Prediction of Squeezing Potential in Tunneling Projects Using Data Mining-Based Techniques." *Geotechnical and Geological Engineering* 37(3):1523–32. doi: 10.1007/s10706-018-0705-6.

Hastie, Trevor, Jerome Friedman, and Robert Tibshirani. 2001. *The Elements of Statistical Learning*. New York, NY: Springer New York.

Hoek, Evert, and Paul Marinos. 2000. "Predicting Tunnel Squeezing Problems in Weak Heterogeneous Rock Masses." *Tunnels and Tunnelling International Part* 1 (December):1–22.

Huang, Hong wei, Yan jie Zhang, Dong ming Zhang, and Bilal M. Ayyub. 2017. "Field Data-Based Probabilistic Assessment on Degradation of Deformational Performance for Shield Tunnel in Soft Clay." *Tunnelling and Underground Space Technology* 67(October 2016): 107–19. doi: 10.1016/j.tust.2017.05.005.

Huang, Zhen, Minxing Liao, Haoliang Zhang, Jiabing Zhang, Shaokun Ma, and Qixuan Zhu. 2022. "Predicting Tunnel Squeezing Using the SVM-BP Combination Model." *Geotechnical and Geological Engineering* 40(3):1387–1405. doi: 10.1007/s10706-021-01970

Lu, Yu Tong, Peng Cheng, and Zhi Guang Chen. 2020. "Design and Implementation of the Tianhe-2 Data Storage and Management System." *Journal of Computer Science and Technology* 35(1):27–46. doi: 10.1007/s11390-020-9799-4.

Mienye, Ibomoiye Domor, and Yanxia Sun. 2021. "Performance Analysis of Cost-Sensitive Learning Methods with Application to Imbalanced Medical Data." *Informatics in Medicine Unlocked* 25:100690. doi: 10.1016/j.imu.2021.100690.

Shafiei, A., H. Parsaei, and M. B. Dusseault. 2012. "Rock Squeezing Prediction by a Support Vector Machine Classifier." *46th US Rock Mechanics/Geomechanics Symposium 2012* 1(December 2014):489–503. doi: 10.13140/RG.2.1.3836.3040.

Sheil, Brian B., Stephen K. Suryasentana, Michael A. Mooney, Hehua Zhu, Bryan A. McCabe, and Kevin G. O'Dwyer. 2020. "Discussion: Machine Learning to Inform Tunnelling Operations: Recent Advances and Future Trends." *Proceedings of the Institution of Civil Engineers: Smart Infrastructure and Construction* 173 (1):180–81. doi: 10.1680/jsmic.2020.173.1.180.

Sun, Yang, Xianda Feng, and Lingqiang Yang. 2018. "Predicting Tunnel Squeezing Using Multiclass Support Vector Machines." *Advances in Civil Engineering* 2018:17–20. doi: 10.1155/2018/4543984.

Tallón-Ballesteros, Antonio J., and José C. Riquelme. 2014. "Data Mining Methods Applied to a Digital Forensics Task for Supervised Machine Learning." *Studies in Computational Intelligence* 555:413–28. doi: 10.1007/978-3-319-05885-6_17.

Wardhani, Ni Wayan Surya, Masithoh Yessi Rochayani, Atiek Iriany, Agus Dwi Sulistyono, and Prayudi Lestantyo. 2019. "Cross-Validation Metrics for Evaluating Classification Performance on Imbalanced Data." *2019 International Conference on Computer, Control, Informatics and Its Applications: Emerging Trends in Big Data and Artificial Intelligence, IC3INA 2019* 14–18.

Zhang, Junfei, Dong Li, and Yuhang Wang. 2020. "Predicting Tunnel Squeezing Using a Hybrid Classifier Ensemble with Incomplete Data." *Bulletin of Engineering Geology and the Environment* 79(6):3245–56. doi: 10.1007/s10064-020-01747-5.

Zhou, Jian, Yuxin Chen, Chuanqi Li, Yingui Qiu, Shuai Huang, and Ming Tao. 2023. "Machine Learning Models to Predict the Tunnel Wall Convergence." *Transportation Geotechnics* 41(April). doi: 10.1016/j.trgeo.2023.101022.

Zhou, Jian, Shuangli Zhu, Yingui Qiu, Danial Jahed Armaghani, Annan Zhou, and Weixun Yong. 2022. "Predicting Tunnel Squeezing Using Support Vector Machine Optimized by Whale Optimization Algorithm." *Acta Geotechnica* 17(4):1343–66.

Tunnelling for a Better Life – Yan, Celestino, Thewes & Eberhardt (Eds)
© 2024 The Author(s), ISBN 978-1-032-80042-4
Open Access: www.taylorfrancis.com, CC BY-NC-ND 4.0 license

Automatic classification and segmentation of tunnel cracks based on deep learning and visual explanations

Yong Feng*
Urban Mobility Institute, Tongji University, Shanghai, China

Xiaolei Zhang
Department of Geotechnical Engineering, Key Laboratory of Geotechnical and Underground Engineering of Ministry of Education, Tongji University, Shanghai, China

Shijin Feng
Urban Mobility Institute, Tongji University, Shanghai, China
Department of Geotechnical Engineering, Key Laboratory of Geotechnical and Underground Engineering of Ministry of Education, Tongji University, Shanghai, China

Yong Zhao
Department of Geotechnical Engineering, Key Laboratory of Geotechnical and Underground Engineering of Ministry of Education, Tongji University, Shanghai, China

Yihan Chen
Urban Mobility Institute, Tongji University, Shanghai, China

ABSTRACT: Tunnel lining crack is a crucial indicator of tunnels' safety status. Aiming to classify and segment tunnel cracks with enhanced accuracy and efficiency, this study proposes a two-step deep learning-based method. An automatic tunnel image classification model is developed using the DenseNet-169 in the first step. The proposed crack segmentation model in the second step is based on the DeepLabV3+, whose internal logic is evaluated via a score-weighted visual explanation technique. Proposed method combines tunnel image classification and segmentation together, so that the selected images containing cracks from the first step are segmented in the second step to improve the detection accuracy and efficiency. The superior performances of the two-step method are validated by experiments. The results show that the accuracy and frames per second (FPS) of the tunnel crack classification model are 92.23% and 39.80, respectively, which are higher than other convolutional neural networks (CNN) based and Transformer based models. Also, the intersection over union (IoU) and F1 score of the tunnel crack segmentation model are 57.01% and 67.44%, respectively, outperforming other state-of-the-art models. Moreover, the provided visual explanations in this study are conducive to understanding the "black box" of deep learning-based models. The developed two-stage deep learning-based method integrating visual explanations provides a basis for fast and accurate quantitative assessment of tunnel health status.

Keywords: Tunnel crack, Deep learning, Image classification, Semantic segmentation, Visual explanation

1 INTRODUCTION

Due to the issues of traffic congestion and increased population, numerous transportation infrastructures have been constructed and operated during the past decades (Jiang et al., 2023; Feng et al., 2023). With advantages such as high construction efficiency, high flexibility, low resource consumption, and minor environmental disturbance, tunnels have been widely used and become the core infrastructures (Zhang et al., 2023). However, the tunnels in service, as geotechnical infrastructures, are inevitably subjected to the joint action of adjacent excavation disturbance, untimely maintenance, deterioration of materials, temperature variation, improper construction, and groundwater (Feng et al., 2023). Various defects, such as crack, leakage, and spalling, often occur on the tunnel linings, necessitating timely inspection and management.

Numerous statistical results show that lining crack is one of the most severe defects in tunnel engineering (Huang et al., 2022). The occurrence of cracks on the lining surface will affect the reliability and integrity of the tunnel structure to an extent, thereby causing water leakage, concrete corrosion, and

*Corresponding author: fengyongtj@tongji.edu.cn

DOI: 10.1201/9781003495505-400

reduced lining-bearing capacity of tunnels. Without limiting their expansion, cracks may lead to serious safety accidents (Zhou et al., 2023). Hence, it is necessary to carry out regular crack inspections to ensure the long-term stability and safety of the tunnels. Traditionally, tunnel crack detection relied on manpower. However, the necessity of active use of intelligent recognition technology for tunnel lining cracks has been emphasized due to the low accuracy, low efficiency, high subjectivity, and high risk of manual visual inspections. Deep learning, especially convolutional neural network (CNN), which has made a paradigm shift recently, provides unprecedented opportunities to facilitate fast, accurate, and automatic recognition of tunnel lining cracks.

In the past, many researchers have delved into CNN-based approaches for tunnel lining crack identification. Huang et al. (2018) established a two-stream algorithm based on FCN, where one stream was employed to segment the cracks by sliding-window-assembling operation, and the other was used to segment leakages by resizing-interpolation operation. Yang et al. (2018) also adopted FCN to semantically identify and segment pixel-wise cracks at different scales, and then utilized traditional digital image processing techniques to quantitatively measure the morphological features of cracks. Miao et al. (2019) proposed a novel semantic segmentation by integrating the UNet with squeeze-and-excitation and residual learning blocks to segment crack and spalling defects. Following the same design paradigm, Hou et al. (2021) and Dang et al. (2022) also improved the UNet through adding residual learning units to complete the tunnel lining crack segmentation task. In the work of Gao et al. (2019), an optimal adaptive selection model (RetinaNet-AOS) based on RetinaNet was developed for semantic segmentation on tunnel lining crack images. Xu and Yang (2019) implemented crack identification by means of Mask R-CNN, which has been widely used in the field of tunnel lining defect detection. Similar to the tasks completed by the Mask R-CNN, Zhao et al. (2021) presented an improved PANet model to obtain refined crack segmentation results, achieving complete separation of cracks from the lining backgrounds. After that, Zhou et al. (2022) applied YOLOv4 enhanced by EfficientNet and depth-wise separable convolution to detect three types of tunnel lining defects, i.e., crack, water leakage, and rebar-exposed. Considering the excellent detection performance of the YOLO series models, Liu et al. (2022) coupled YOLOv5 with a transfer learning technique to localize the cracks in the road tunnel lining images.

Based on the above, it can be summarized that existing studies have achieved outstanding results in tunnel lining defect identification by investigating more perfect algorithms or improving existing ones. However, in real-world applications, it is common that image acquisition devices acquire a large amount of lining image data, including abundant normal (defect-free) images and anomalous (crack) ones. The existing engineering requirement is to efficiently, accurately, and automatically identify cracks from massive amounts of tunnel image data, which has become a considerable and urgent challenge for previous research. Most of the available studies directly treat the crack recognition problem as a single-attribute classification or separately strive to find the locations or areas of the cracks as a localization or segmentation problem. To address these limitations, this study proposes a tunnel lining crack recognition framework in a two-stage manner, which combines image classification and segmentation. The purpose of tunnel lining image classification is to determine whether the image contains cracks, while the aim of tunnel lining crack segmentation is to extract cracks from backgrounds in crack images, which are different in definition. Image classification is much easier than crack segmentation. Specifically, the image classification task classifies the tunnel lining images as defect-free or crack ones, while the segmentation task getting the crack pixels from images is much more complex and time-consuming. Consequently, a tunnel lining image classification model named DenseNet-169 is adopted in the first stage to classify and save the images containing cracks. Another tunnel lining crack segmentation model called DeepLabV3+ is exploited in the second stage to process the crack images and isolate the cracks from backgrounds.

Nevertheless, deep learning models also have deficiencies and limitations, such as being considered as 'black box' models, which have trouble in explaining physically and rely heavily on hyperparameter settings. To account for mechanisms behind the 'black box' of the crack segmentation model and build trust in deep learning models, this study employs an advanced visual interpretation technology, i.e., score-weighted class activation mapping (Score CAM) (Wang et al., 2020). The motivation behind Score CAM is to generate heatmaps highlighting meaningful regions to intuitively explain the CNN-based models' internal mechanism.

2 METHODOLOGY

2.1 *Framework for tunnel lining crack identification*

This study designs the tunnel lining crack recognition framework in a two-stage manner, which is shown in Figure 1. In the beginning, the tunnel lining images collected from practical tunnel engineering are fed into the automatic classification stage, where an image classification model is responsible for selecting and saving crack images from massive tunnel lining image data. Specifically, the DenseNet-169 model takes the lining image as an input and outputs two probabilities to determine whether the image belongs to a crack or defect-free image. Subsequently, the images containing cracks are further input into the second stage to isolate the cracks from the backgrounds. That is, the DeepLabV3+ model is dedicated to identifying the pixels belonging to cracks in the

images. Through these two stages, cracks' locations and geometric shapes are extracted with high precision and efficiency. The deep learning models employed in each stage are described in detail in the following subsections. Moreover, a CNN explanation step is also incorporated into the overall framework to understand the operational mechanism of the segmentation model and build trust in CNN.

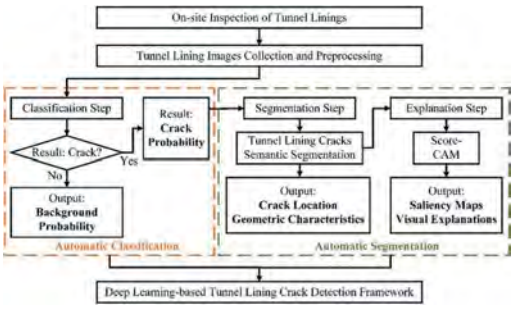

Figure 1. Pipeline of tunnel lining cracks identification.

2.2 *Tunnel lining image classification model*

Powered by the successful application of dense convolutional network (DenseNet) (Huang et al., 2018), this study employs DenseNet-169 as the automatic classification model for tunnel lining images in the first step. DenseNet is a type of convolutional neural network that directly connects all layers (with matching feature-map sizes) with each other for maximum information flow between layers in the network. In particular, each layer obtains additional inputs from all preceding layers and passes on its feature maps to all subsequent layers, as observed in Figures 2 and 3.

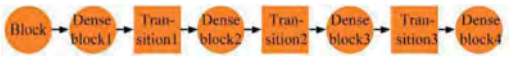

Figure 2. Architecture of DenseNet.

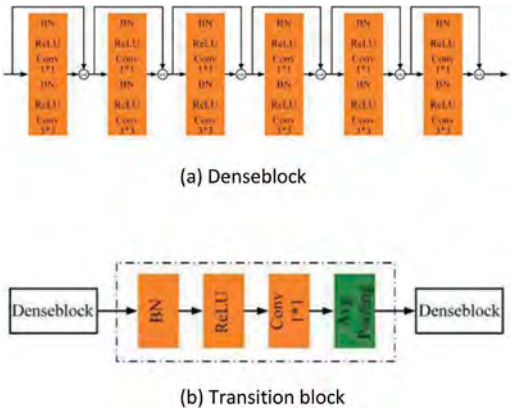

Figure 3. Details of modules in DenseNet.

DenseNet is a multi-stage architecture where the first stage consists of a standard 7×7 convolution, batch normalization, ReLU activation function, and maximum pooling, followed by four stages consisting of Denseblocks and three stages composed of Transition blocks, and finally, a global average pooling layer and a fully connected layer responsible for outputting the predictions. DenseNet-169 is one of the DenseNets, containing 6, 12, 32, and 32 Denseblocks in four stages, respectively. It is worth pointing out that the cross entropy function is chosen as the model's loss function.

2.3 *Tunnel lining crack segmentation model*

After selecting images containing cracks from a large number of tunnel lining images, a crucial task is to segment the cracks from the images in an end-to-end and pixel-to-pixel manner. To this end, DeepLabV3+ (Chen et al., 2018) serves as the crack segmentation model in the second step. Like most semantic segmentation models, the DeepLabV3+ model comprises an encoder and a decoder, with the overall architecture shown in Figure 4.

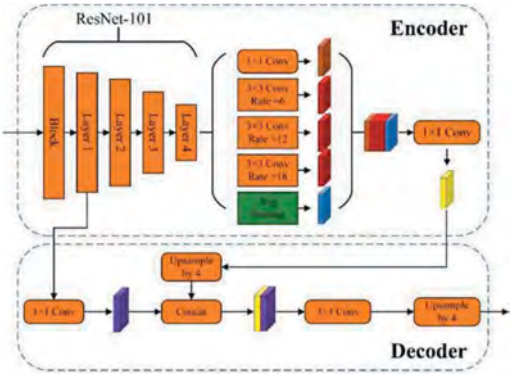

Figure 4. Overall architecture of the DeepLabV3+ model.

ResNet-101 (He et al., 2016) is used as the backbone structure to extract shallower features containing spatial information and deeper features containing semantic information for tunnel lining cracks. Concretely, the ResNet-101 includes a 'Block' for downsampling operation with a factor of four, followed by 'Layer 1′, 'Layer 2′, 'Layer 3′, and 'Layer 4′ for feature extraction. The innovation of the DeepLabV3+ model is the atrous spatial pyramid pooling (ASPP) in the encoder. Discontinuity problem is prevalent in crack segmentation tasks. The reason for this phenomenon is the loss of multi-scale information about the cracks. To compensate for this deficiency, the ASPP structure is created with multiple dilated convolutions. For a dilated convolution with a dilation rate of d and kernel size of N, the receptive field reaches the same as that of a standard convolution with a kernel size of (N-1)×d+1. As a result, dilated

convolution is capable of increasing the receptive field while maintaining the size of the feature maps, thereby reducing the loss of crack feature information caused by consecutive convolution and pooling down-sampling operations. In ASPP, three dilated convolution operations with dilation rates of 6, 12, and 18 conduct multi-scale sampling on the feature maps output by ResNet-101. In addition, the ASPP integrates a 1×1 standard convolution operation and an average pooling operation, which together with the dilated convolutions, form feature maps containing multi-scale information about the cracks. A 1×1 convolution then processes the features to realize further feature extraction and dimensionality reduction. In the decoder, the shallow features generated by 'Layer 1′ of ResNet-101 are collected and then concatenated with upsampled deep features obtained from ASPP. Skip connection enables the deep learning model to combine local spatial features of cracks with global context information, thus further relieving the discontinuity problem in crack segmentation. Fused features are then subjected to successive 3×3 convolution and 4× bilinearly upsampling operations to restore the size of the original input image and produce the final semantic segmentation result.

Last but not least, the loss function is also crucial in segmenting tunnel lining cracks. Tunnel lining cracks are slender and small targets in the image compared to the background. To put it differently, the crack pixels are much less than the background pixels in tunnel lining images. Therefore, the imbalanced data will make the segmentation model biased towards the background class rather than cracks. To address this issue, dice loss is selected as the loss function of the DeepLabV3+ model.

2.4 *Visual explanation methods*

As described before, this study aims to understand and explore the mechanisms behind the 'black box' of the crack segmentation model. An advanced visual interpretation technology, i.e., Score CAM, is leveraged, and its detailed processing steps are as follows.

Given the CNN model (i.e., DeepLabV3+ in this study) $Y = f(X)$ that takes X as an input and outputs a scalar result Y. We select a targeted convolutional layer l in f and the corresponding activations as A. Define the *k-th* channel of A_l as A_l. Given a known baseline input X_b, the contribution of A_l to Y is expressed as follows.

$$C(A_l^k) = f(X \circ H_l^k) - f(X_b) \tag{1}$$

$$H_l^k = s(Up(A_l^k)) \tag{2}$$

where $Up(\cdot)$ represents the up-sampling operation of A_l into the input size. $s(\cdot)$ denotes the normalization operation converting each element in the input matrix to the interval [0, 1].

For a class of interest c (i.e., crack in this study), Score-CAM$L^c_{Score-CAM}$is defined as follows.

$$L^c_{Score-CAM} = ReLU(\sum_k C(A_l^k)A_l^k) \tag{3}$$

Define a weight coefficient$\alpha_k^c = C(A_l^k)$, then the equation (3) can be abbreviated to equation (4).

$$L^c_{(Score-CAM)} = ReLU(\sum_k \alpha_k^c A_l^k) \tag{4}$$

Based on the above steps, visual heatmaps can be acquired to understand the crack segmentation model's internal structure and decision-making mechanism.

3 DATA

All experiments in this study were carried out based on an open-source dataset named NUAACrack-2000 (Qiu et al., 2022; Zhang et al., 2021), where the tunnel lining images were captured in China. On the basis of the NUAACrack-2000, two datasets were established: one was exploited for training and testing of the DenseNet-169 model, and the other for training and testing of the DeepLabV3+ model.

Figure 5 illustrates the typical crack and defect-free images in the image classification dataset, and Table 1 summarizes the number of different types of images. A total of 1942 images with a pixel size of 512×375 were divided into training set, validation set, and testing set according to a ratio of 7:2:1.

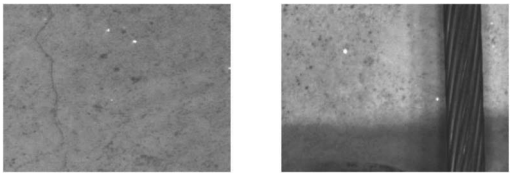

Figure 5. Examples of tunnel lining image classification dataset.

Table 1. Dataset for image classification experiment.

	Training	Validation	Testing	Total
Background	333	94	47	474
Crack	1029	293	146	1468
Total	1362	387	193	1942

After that, 1468 crack images and their ground truths made up the semantic segmentation dataset, as shown in Figure 6. Each crack image corresponds to a label, which was used to supervise the training of the segmentation model. These crack images were also partitioned based on the holdout approach in a ratio of 7:2:1. That is, 1028 images were used for training, 294 images for verification, and the remaining 146 images for testing.

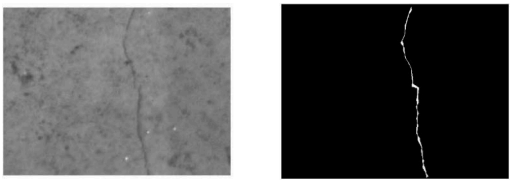

Figure 6. Examples of crack segmentation dataset.

4 EXPERIMENT

The experiments in this study mainly involve two parts: image classification and crack segmentation. In the first part, the image classification dataset was utilized to train and test the DenseNet-169 model. In the second part, the crack segmentation dataset was used for the training and testing of the DeepLabV3+ model. Comparative experiments with other dominant models and visual explanations were also included in this section.

4.1 *Experimental environment*

Experiments were conducted under the computer configurations of the Windows 10 operating system, one NVIDIA GeForce RTX 3090 graphics processing unit (GPU), and one Intel Core i9-12900KF central processing unit (CPU). Python 3.8.12, Pytorch 1.12.0, CUDA 11.6, and CUDNN 8.3 constitute the computation software environment.

4.2 *Tunnel lining image classification experiment*

4.2.1 *Evaluation criteria*

This study adopted two commonly used measures, accuracy and frames per second (FPS), to evaluate the performance of the classification model.

4.2.2 *Model training and testing*

To accelerate training speed and save computational resources, all images in the classification dataset were resized to 224×224 before being input into the model. The batch size was set to four; that is, the model processed four images simultaneously in each iteration. To ensure the convergence of the model, the training epoch is determined to be 100. The learning rate is another important hyperparameter. For the purpose of finding the global minimum of the deep learning model, a dynamic learning rate schedule was adopted instead of a constant learning rate. Specifically, the initial learning rate of 0.005 was decreased every ten epochs with an attenuation factor of 0.1. After completing training, the performance evaluation of the model was performed on 193 testing images. Figure 7 intuitively displays the predicted results of the DenseNet-169 model on several images in the testing set. As seen in Figure 7, the deep learning model automatically outputs two probability values for each image and then determines the image's category. The first row in Figure 7 lists four images classified as background, and the second row shows the examples identified as crack images. Through calculation, the accuracy of the DenseNet-169 model reaches 92.23%, and the FPS reaches 39.80.

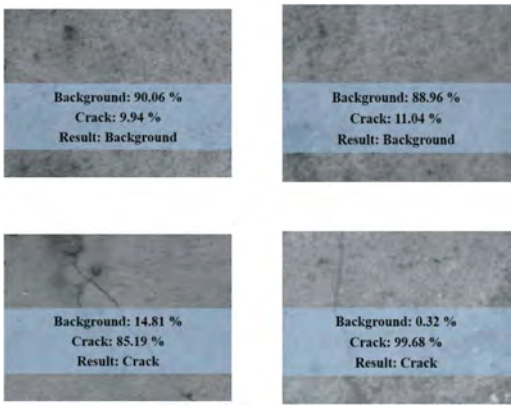

Figure 7. Predictions of DenseNet-169 on several testing images.

4.2.3 *Comparison with other models*

For the sake of further evaluating the classification performance of the DenseNet-169 model for tunnel lining images, six state-of-the-art deep learning models were implemented for comparison. The models used for comparison include CNN-based models and visual Transformer-based models, namely DenseNet-201, EfficientNet-B0, ResNet-50, ResNet-101, Swin Transformer, and Vision Transformer. As reported in Table 2, the DenseNet-169 outperforms the other six deep learning models in terms of accuracy, as reflected in the 2.07%, 16.58%, 17.10%, 18.65%, 16.58%, and 16.58% improvement over DenseNet-201, EfficientNet-B0, ResNet-50, ResNet-101, Swin Transformer, and Vision Transformer.

Table 2. Results of image classification experiments.

Models	Accuracy (%)	FPS (f/s)
DenseNet-169	92.23	39.80
DenseNet-201	90.16	35.60
EfficientNet-B0	75.65	40.77
ResNet-50	75.13	60.22
ResNet-101	73.58	51.68
Swin Transformer	75.65	42.48
Vision Transformer	75.65	69.64

DenseNet-169 incorrectly classified 12 crack images as defect-free images. As for Swin Transformer and Vision Transformer, these two models wrongly classified all defect-free images as crack images, resulting in the lowest accuracy. The reason for this is inferred to be twofold: on the one hand, the small size of the classification dataset used in this

paper prevents the self-attention mechanism in the visual Transformer from realizing its potential, and on the other hand, the imbalance in the number of positive and negative samples leads to a bias in the recognition ability of the models towards the crack images.

From the perspective of the running speed of the models, the FPS of DenseNet-169 is higher than that of DenseNet-201 but lower than that of other models. Improving the running speed of the classification model deserves further research in the future.

4.3 *Tunnel lining crack segmentation experiment*

4.3.1 *Evaluation criteria*

This study exploited four metrics widely used in semantic segmentation tasks, i.e., precision, recall, F1 score, and Intersection over Union (IoU), to comprehensively assess the crack segmentation models.

IoU and threshold d were introduced to compare the similarity between two arbitrary cracks. For crack images, the IoU between the segmented crack and ground truth was calculated to judge whether the crack has been detected. Generally, the threshold d was set to 0.5 (Liu and Wang, 2022). In this study, when the IoU is greater than 0.5, it is considered that the model has detected out the crack; otherwise, it is not. IoU also served as the primary evaluation indicator for segmentation models in this paper.

4.3.2 *Model training and testing*

During the training process, the original images were first resized to 512×384 pixels, which would not cause a large amount of calculation and is easy to work with. Accordingly, the batch size was set as 8. The learning rate was also dynamically adjusted, with a value of 0.001 for the first 50 epochs and 0.0001 for the last 50 epochs. A total of 100 rounds of training ensured the convergence of the crack segmentation models. After each round of training, the model was evaluated on the validation set, and the training and validation loss curves were recorded in Figure 8. It can be seen from Figure 8 that the training loss declines rapidly over the first ten epochs, then slowly decreases in the next 40 epochs, and stabilizes around 0.2 over the last 50 epochs. Validation loss shows fluctuations in the first 50 epochs and stabilizes in the next 50. Based on the values of the loss function on the validation set, the optimal trained model was determined and saved accordingly.

The best-trained model was tested using crack images in the semantic segmentation dataset, and the results showed that the DeepLabV3+ model achieved 57.01% IoU, 67.44% F_1 score, 62.95% precision, and 82.12% recall. There is a significant gap between the precision and recall of the DeepLabV3+ model. It should be emphasized that deep learning models must detect all cracks as much as possible from the perspective of engineering applications. Hence, it is reasonable to improve the recall of tunnel lining crack segmentation during practical inspection tasks, even at the expense of precision (Ren et al., 2020).

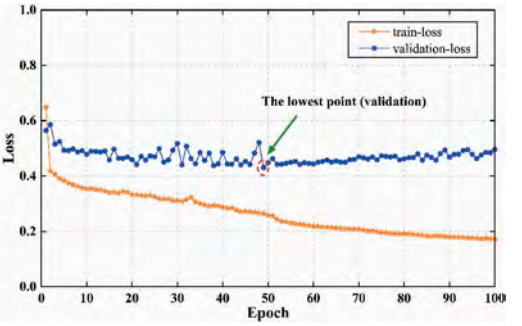

Figure 8. Visualization diagram of loss curves of DeepLabV3+ model during training and validation process.

4.3.3 *Comparison with other models*

Extensive comparative tests were completed to further verify the applicability and superiority of the DeepLabV3+ model in tunnel lining crack segmentation. Four dominant semantic segmentation models, namely DeepLabV3 with backbone ResNet-101, PSPNet with backbone ResNet-50, UNet backboned by VGG-13, and UNet++ backboned by VGG-13 were trained with the crack segmentation dataset for more comprehensive comparisons.

As shown in Table 3, the DeepLabV3+ model obtains the best IoU of 57.01%, which is 1.77%, 5.77%, 0.17%, and 0.59% higher than DeepLabV3, PSPNet, UNet, and UNet++, respectively. Similarly, the precision of DeepLabV3+ is the highest, improved by 2.02%, 3.72%, 0.60%, and 2.64% compared to DeepLabV3, PSPNet, UNet, and UNet++, respectively. The F1 score for DeepLabV3+ is only slightly lower than UNet but higher than the other three models. The recall of the DeepLabV3+ model is lower than that of UNet and UNet++ but 0.83% and 8.52% higher than that of DeepLabV3 and PSPNet, respectively.

Table 3. Results of semantic segmentation experiments.

Models	IoU (%)	F_1 score (%)	Precision (%)	Recall (%)
DeepLabV3+	57.01	67.44	62.95	82.12
DeepLabV3	55.24	66.33	60.93	81.29
PSPNet	51.24	62.18	59.23	73.60
UNet	56.84	67.68	62.35	83.91
UNet++	56.42	67.31	60.31	84.91

Representative testing results predicted by different deep learning models are depicted in Figure 9 to complement the quantitative comparison results above, with the orange dashed box and red dashed box denoting the incorrect and missed detections. From top to bottom of Figure 9, they are the raw images in the crack segmentation dataset, labels, and predicted results made by DeepLabV3+, DeepLabV3, PSPNet,

UNet++, and UNet. The DeepLabV3+ model performs best on the four testing samples, as seen by the comparison of segmentation results of different models. For case 1, the cracks can be accurately isolated by DeepLabV3+ and PSPNet. However, a small section of crack is omitted by DeepLabV3. There are some false detections in the identification results of UNet. UNet++ also has the situation of false detections. For case 2, all models successfully segment the cracks, except for PSPNet, ignoring large sections of the crack. As seen in the third and fourth columns of Figure 9, the features of the cracks do not differ significantly from the background features, posing a challenge for crack identification. In case 3, a small portion of cracks are not segmented by PSPNet and UNet, and a small background area is falsely identified as cracks by UNet++. In case 4, DeepLabV3, PSPNet, UNet++, and UNet have different degrees of missed detections. Additionally, a small portion of background pixels are mistakenly detected as crack pixels. The width of the crack segmented by the DeepLabV3+ model is larger than the actual crack width. Nevertheless, the predicted result retains more edge information relative to the other four models.

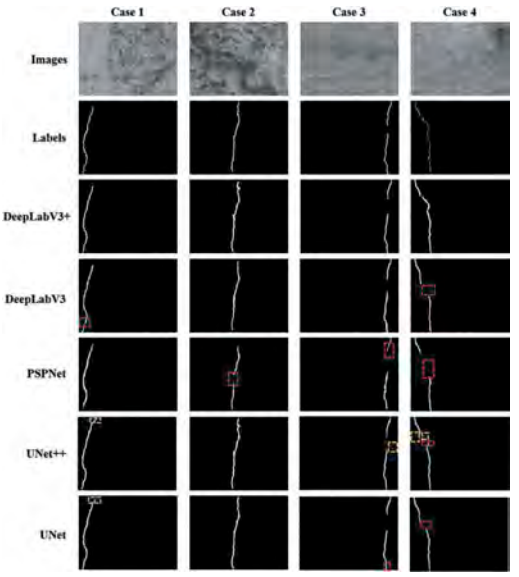

Figure 9. Comparison of prediction performance of different models on the test set.

These quantitative and qualitative comparative results above indicate that adopting the DeepLabV3+ model in the second step of our proposed framework for crack segmentation is effective and superior.

4.4 *Visual explanations*

The heatmaps of some key modules of the DeepLabv3+ model are generated based on the Score CAM technique to focus on the encoding and decoding process of the model and understand the decision-making process. For a brief discussion, Figure 10 presents the heatmaps of the key modules of the DeepLabV3+ model when a single tunnel crack image is used as input. As depicted in Figure 10, the model focuses on the image globally during the encoding process. At the stage of Layer 2, the model pays attention to crack, lining surface, and lighting. Until the stage of Layer 4, the model emphasizes the crack, but the highlighted areas (dark-colored) do not precisely fit the crack. During

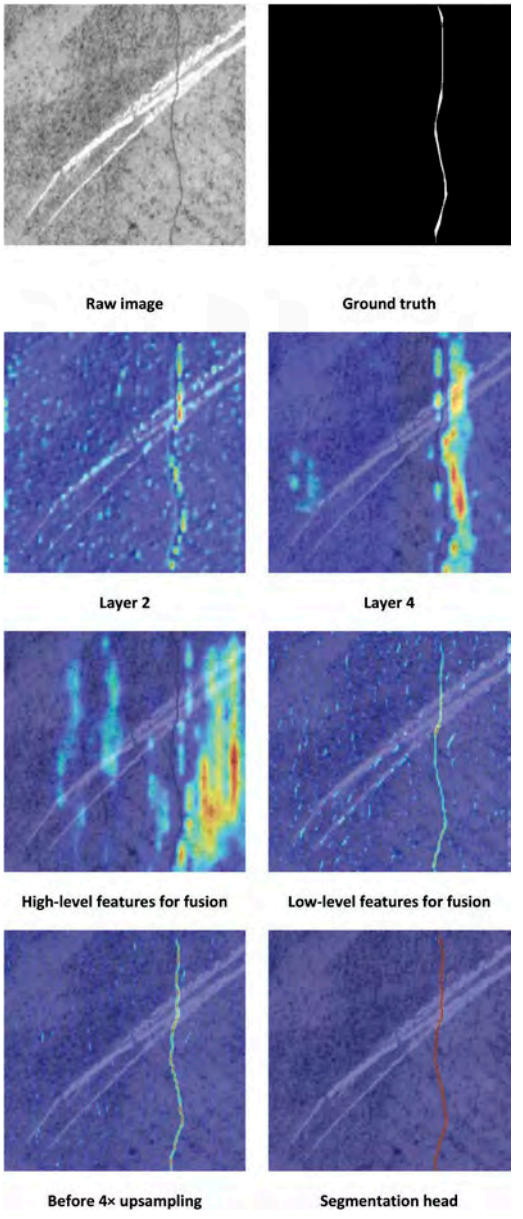

Figure 10. Visual explanations for several key modules of the DeepLabv3+ model based on Score CAM.

decoding, the DeepLabV3+ model gradually focuses on the crack itself. Another interesting finding is that the low-level and high-level feature maps used for the concatenation operation shown in Figure 4 present completely different heatmaps. The heatmaps demonstrate that high-level feature maps focus on the global features of the tunnel lining image due to the inclusion of strong semantic information, while low-level feature maps focus on local regions of the image, confirming that shallower feature maps contain rich spatial information.

5 CONCLUSION

This study proposes a two-step deep learning-based method for the automatic classification and segmentation of tunnel cracks. DenseNet-169 serves as the tunnel lining image classification model in the first step, through which the crack images can be separated and saved from massive image data. In the second step, the DeepLabV3+ model is employed to separate cracks from backgrounds in the crack images. An advanced visual explanation technique is integrated into the two-step method to understand the 'black box' of the crack segmentation model. The superiority and rationality of the two-step method are demonstrated through extensive comparative experiments. DenseNet-169 achieves 92.23% accuracy, which is improved by 2.07%, 16.58%, 17.10%, 18.65%, 16.58%, and 16.58% over DenseNet-201, EfficientNet-B0, ResNet-50, ResNet-101, Swin Transformer, and Vision Transformer. The FPS of DenseNet-169 reaches 39.80, exceeding that of DenseNet-201. For DeepLabV3+, an IoU of 57.01% is obtained, which is 1.77%, 5.77%, 0.17%, and 0.59% higher than DeepLabV3, PSPNet, UNet, and UNet++, respectively. Furthermore, the provided visual explanations show that the segmentation model focuses on the image globally during the encoding process and gradually focuses on the crack itself during the decoding process. Another interesting finding is high-level feature maps focus on the global features of the tunnel lining image due to the inclusion of strong semantic information. In contrast, low-level feature maps focus on local regions of the image, confirming that shallower feature maps contain rich spatial information.

There are still some flaws that need to be addressed in the future. Firstly, it is urgently required to introduce model light-weighting techniques to accelerate the image classification models. Secondly, essential image pre-processing or post-processing approaches need to be incorporated into the crack segmentation process to eliminate the complex environmental interference, thus obtaining refined segmentation results. Thirdly, expanding the tunnel lining image classification and crack segmentation datasets to guarantee higher generalization and robustness of the models. Besides, deep learning-based models should be integrated into intelligent detection devices, such as unmanned aerial vehicles (UAVs), to realize automatic and real-time detection of tunnel lining cracks.

ACKNOWLEDGEMENTS

Much of the work described in this paper was supported by the National Key Research and Development Program of China under Grant No. 2020YFC1808105, Science and Technology Commission of Shanghai Municipality under Grant No. 21DZ1204400, and the National Natural Science Foundation of China under Grant No. 42372335. The writers would like to greatly acknowledge all these financial supports and express their most sincere gratitude.

REFERENCES

Chen, L.-C., Zhu, Y., Papandreou, G., Schroff, F., Adam, H., 2018. Encoder-Decoder with Atrous Separable Convolution for Semantic Image Segmentation. http://arxiv.org/abs/1802.02611

Dang, L.M., Wang, H., Li, Y., Park, Y., Oh, C., Nguyen, T. N., Moon, H., 2022. Automatic tunnel lining crack evaluation and measurement using deep learning. Tunnelling and Underground Space Technology 124, 104472. https://doi.org/10.1016/j.tust.2022.104472

Feng, S., Feng, Y., Zhang, X., Chen, Y., 2023. Deep learning with visual explanations for leakage defect segmentation of metro shield tunnel. Tunnelling and Underground Space Technology 136, 105107. https://doi.org/10.1016/j.tust.2023.105107

Feng, Y., Zhang, X., Feng, S., Chen, H., Zhao, Y., Chen, Y., 2023. Improved SOLOv2 detection method for shield tunnel lining water leakages. Journal of Intelligent Construction 1, 9180004. https://doi.org/10.26599/JIC.2023.9180004

Gao, X., Jian, M., Hu, M., Tanniru, M., Li, S., 2019. Faster multi-defect detection system in shield tunnel using combination of FCN and faster RCNN. Advances in Structural Engineering 22, 2907–2921. https://doi.org/10.1177/1369433219849829

He, K., Zhang, X., Ren, S., Sun, J., 2016. Deep Residual Learning for Image Recognition, in: 2016 IEEE Conference on Computer Vision and Pattern Recognition (CVPR). Presented at the 2016 IEEE Conference on Computer Vision and Pattern Recognition (CVPR), IEEE, Las Vegas, NV, USA, pp. 770–778. https://doi.org/10.1109/CVPR.2016.90

Hou, S.K., Ou, Z.G., Qin, P.X., Wang, Y.L., Liu, Y.R., 2021. Image-based crack recognition of tunnel lining using residual U-Net convolutional neural network. IOP Conf. Ser.: Earth Environ. Sci. 861, 072001. https://doi.org/10.1088/1755-1315/861/7/072001

Huang, G., Liu, Z., van der Maaten, L., Weinberger, K.Q., 2018. Densely Connected Convolutional Networks. http://arxiv.org/abs/1608.06993

Huang, H., Li, Q., Zhang, D., 2018. Deep learning based image recognition for crack and leakage defects of metro shield tunnel. Tunnelling and Underground Space Technology 77, 166–176. https://doi.org/10.1016/j.tust.2018.04.002

Huang, H., Zhao, S., Zhang, D., Chen, J., 2022. Deep learning-based instance segmentation of cracks from shield tunnel lining images. Structure and Infrastructure Engineering 18, 183–196. https://doi.org/10.1080/15732479.2020.1838559

Jiang, Y., Wang, L., Zhang, B., Dai, X., Ye, J., Sun, B., Liu, N., Wang, Z., Zhao, Y., 2023. Tunnel lining detection and retrofitting. Automation in Construction 152, 104881. https://doi.org/10.1016/j.autcon.2023.104881

Liu, F., Wang, L., 2022. UNet-based model for crack detection integrating visual explanations. Construction and Building Materials 322, 126265. https://doi.org/10.1016/j.conbuildmat.2021.126265

Liu, J., Zhao, Z., Lv, C., Ding, Y., Chang, H., Xie, Q., 2022. An image enhancement algorithm to improve road tunnel crack transfer detection. Construction and Building Materials 348, 128583. https://doi.org/10.1016/j.conbuildmat.2022.128583

Miao, X., Wang, J., Wang, Z., Sui, Q., Gao, Y., Jiang, P., 2019. Automatic Recognition of Highway Tunnel Defects Based on an Improved U-Net Model. IEEE Sensors J. 19, 11413–11423. https://doi.org/10.1109/JSEN.2019.2934897

Qiu, J., Yan, X., Wang, J., Guo, Y., Wei, M., 2022. Crack extraction from single tunnel image based on fully convolutional neural network. Computer Engineering and Science 44, 845–854. https://doi.org/10.3969/j.issn.1007-130X.2022.05.010

Ren, Y., Huang, J., Hong, Z., Lu, W., Yin, J., Zou, L., Shen, X., 2020. Image-based concrete crack detection in tunnels using deep fully convolutional networks. Construction and Building Materials 234, 117367. https://doi.org/10.1016/j.conbuildmat.2019.117367

Wang, H., Wang, Z., Du, M., Yang, F., Zhang, Z., Ding, S., Mardziel, P., Hu, X., 2020. Score-CAM: Score-Weighted Visual Explanations for Convolutional Neural Networks. http://arxiv.org/abs/1910.01279

Xu, X., Yang, H., 2019. Intelligent crack extraction and analysis for tunnel structures with terrestrial laser scanning measurement. Advances in Mechanical Engineering 11, 168781401987265. https://doi.org/10.1177/1687814019872650

Yang, X., Li, H., Yu, Y., Luo, X., Huang, T., Yang, Xu, 2018. Automatic Pixel-Level Crack Detection and Measurement Using Fully Convolutional Network: Pixel-level crack detection and measurement using FCN. Computer-Aided Civil and Infrastructure Engineering 33, 1090–1109. https://doi.org/10.1111/mice.12412

Zhang, J., Chu, W., Tu, W., Su, H., Lu, S., Xu, Y., 2023. Computer Vision-based Monitoring Method for Differential Settlement of Shield Tunnels. J. Phys.: Conf. Ser. 2519, 012057. https://doi.org/10.1088/1742-6596/2519/1/012057

Zhang, Y., Li, X., Qiu, J., Zhai, X., Wei, M., 2021. GFU-Net: A Deep Learning Approach for Automatic Metal Crack Detection, in: Zhang, H., Yang, Z., Zhang, Z., Wu, Z., Hao, T. (Eds.), Neural Computing for Advanced Applications, Communications in Computer and Information Science. Springer Singapore, Singapore, pp. 375–388. https://doi.org/10.1007/978-981-16-5188-5_27

Zhao, S., Zhang, D., Xue, Y., Zhou, M., Huang, H., 2021. A deep learning-based approach for refined crack evaluation from shield tunnel lining images. Automation in Construction 132, 103934. https://doi.org/10.1016/j.autcon.2021.103934

Zhou, Z., Zhang, J., Gong, C., 2023. Hybrid semantic segmentation for tunnel lining cracks based on Swin Transformer and convolutional neural network. Computer aided Civil Eng mice. 13003. https://doi.org/10.1111/mice.13003

Zhou, Z., Zhang, J., Gong, C., 2022. Automatic detection method of tunnel lining multi-defects via an enhanced You Only Look Once network. Computer aided Civil Eng 37, 762–780. https://doi.org/10.1111/mice.12836

Tunnelling for a Better Life – Yan, Celestino, Thewes & Eberhardt (Eds)
© 2024 The Author(s), ISBN 978-1-032-80042-4
Open Access: www.taylorfrancis.com, CC BY-NC-ND 4.0 license

TBM machine parameters estimation: From design approach to on-field results. A concrete example based on Kalman Filter approach

Cosimo Iasiello*
Tunnel advisor, Systra-SWS, Rome, Italy

Julio Rodríguez-Sánchez
Project Manager, Ayesa Paseo de la Reforma 284, Mexico City, Mexico

ABSTRACT: The use of the TBMs (tunnel boring machine) is increased in the last decades because of the efficiency and safety during the excavation process. Moreover, the TBM solutions is widely preferred by Contractors to reduce the risks during the construction, have lesser economical deviation from the forecast costs and time. To ensure lower construction cost and higher project safety, it is necessary to adjust the operating parameters of the TBM depending on the geological conditions. The method for improving the adaptability of the TBM is to utilize real on-time monitoring data to predict the future operating values of the TBM. There have been several studies on the prediction of operating parameters. Among them, prediction of the thrust force and torque have been considered one of the important research projects. A study applying random forest (RF) was also conducted based on heterogeneous in situ data. Recently, some works using machine learning (ML) techniques have been reported to effectively analyse complex field data. Based on data collected from the field, some authors employed gene expression programming (GEP) to predict thrust-related parameters, while others used support vector regression (SVR) in hard rock conditions. The aforementioned works are, however, bases on predictions based on experimental data (normally in one single tunnel) or on empirical dataset with the same geological parameters. The aim of this paper, so, is to provide a prediction of the TBM machine parameters to be used during design stage employing the so-called Unscented Kalman Filter (UKF) and be used by the average engineers. The approach employed will take as starting point the average formulations (semi-empirical and analytical) giving a guide to manage the ranges of values based on stochastic approach. The methodology will be applied to a practical example in four HSR (High-speed railway) tunnels in the northern Italy.

Keywords: Tunnelling, TBM, Performance prediction, Back-analysis, Kalman Filter

1 INTRODUCTION

Tunnel boring machines (TBMs) are widely used in areas with considerable urbanization for power supply, water supply, and subway construction. However, the adaptability of the TBM for the future environment is sometimes limited by geological conditions such as rock fracturing, faulting, spalling, squeezing, and high-water pressure (see for instance [1] and [2]). To ensure lower construction cost and higher project safety, it is necessary to adjust the operating parameters of the TBM depending on the geological conditions. The method for improving the adaptability of the TBM is to utilize TBM monitoring data in real time to predict the future operating values of the TBM. There have been several studies on the prediction of operating parameters. Among them, prediction of the thrust and torque have been considered one of the important research issues (see for instance [3], [4], [5], [6], [7] [8] and [9]). Recently, some works using machine learning (ML) techniques have been reported to effectively analyse complex field data. Based on data collected from the field, Naghadehi et al. [10] employed gene expression programming (GEP) to predict thrust-related parameters. Salimi et al. [11] used support vector regression (SVR) in hard rock conditions. A study applying random forest (RF) was also conducted based on heterogeneous in situ data [12]. The aforementioned works are, however, bases on predictions based on experimental data (normally in one single tunnel) or on empirical dataset with the same geological parameters. It is known that different machine parameters may be the sign of the different geological parameters and, indeed, of

*Corresponding author: cosmeiasiello@gmail.com

DOI: 10.1201/9781003495505-401

different type of rings, normally depending of the reinforcement placed. The aim of this article, so, is to provide a prediction of the TBM machine parameters to be used during design stage employing the so-called Unscented Kalman Filter (UKF) (see for instance [13] and [14]) approach taking as reference the torque force measured during the TBM tunnel execution.

2 CASE APPLICATION

The project consisted in the new HSR (High speed-railway) between Milan and Ventimiglia in northern Italy. The tunnels have been bored by a Herrenknecht TBM single shield. The machine had a total length of 150 meters including the back-up; an excavation diameter of 11.8 m, an external diameter of 11.54 m and a net inner diameter of 10.74 m; an installed power of 4,000 kW supplied by 10 engines to rotate the cutterhead; a maximum tunnelling speed of 100 mm per minute. The reinforced concrete lining is composed by 7 segments, 6 segments and one keystone. The ring length is 1.7 m and it has been designed to assume right and left positions within the tunnel (taped ring). The segments thickness is 0.4 m while the height of contact between joints is 0.17m. The segments were designed with conventional steel bars reinforcement concrete. The lining geometrical definitions are collected in Table 1:

Table 1. Lining geometrical definitions.

Parameter	Unit	Value
Outer Diameter	m	11.54
Segmental Thickness	m	0.40
Ratio thick/outer diameter	-	1/28.85

Figure 1 shows the cover, respect to tunnel crown, for the 4 tunnels depending on the GSI values. The dataset employed in this paper is around 4500 rings. The maximum cover is around 350 m while the minimum is around 20 m. GSI (geological strength index) varies from 15, for fault areas, till 55.

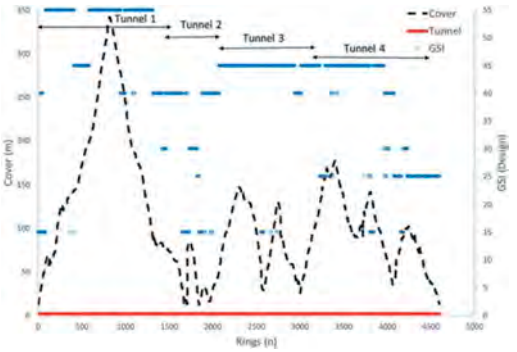

Figure 1. Ring Dataset in function of cover and GSI value.

During detailed design, 145-point load tests were carried out to better estimate the direct standard laboratorial uniaxial compressive tests and indirect tests such as the PLT. There have been different attempts to provide an empirical index-to strength conversion factors between the UCS and Is(50), to reveal their correlations and demonstrate practical application (see for instance references from [15] to [18]). Figure 2 shows the distribution of Is(50).

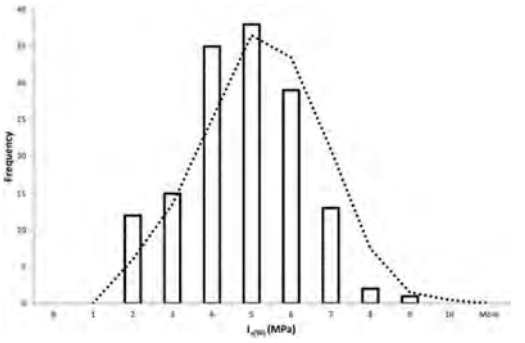

Figure 2. Distribution of Is50 values.

These correlations are very important to estimate the UCS and hence, the TBM machine parameters; in fact, in technical literature there are many examples how to correlate UCS with field penetration index (FPI), as collected in [19], with specific energy as shown in [20], or to calculate the cutting force exerted by the TBM as suggested by [21], or the estimate the penetration rate (PR) as demonstrated in [22] and finally, as suggested in [23] depending on the torque as shown in Figure 3.

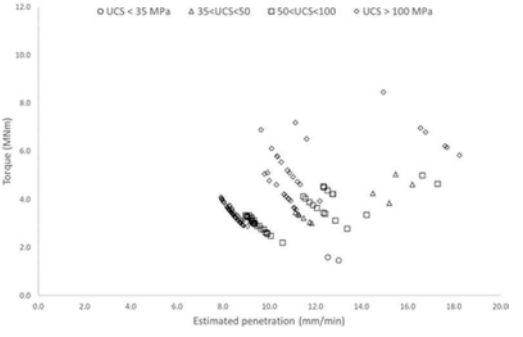

Figure 3. Estimated penetration as function of Torque based on UCS values.

The methodology followed in the detailed design was:

1. Estimation of the UCS values for rock mass based on PLT tests or another specific test
2. Use the correlations between UCS and PR

3. Calculate the penetration (mm/min) as function of PR (mm/round) based on technical literature data (see for instance [24] and [25])
4. Correlate the penetration with Torque, specific energy, and Thrust force

This methodology allows to calibrate the ranges of values for TBM machine parameters and, so provide the designed countermeasures forecast; for example, depending on the geological conditions, it is possible to vary the quantity of reinforcement within the segments. However, the data extrapolated from the UCS, although very useful during the design stage, are related only to a small dataset and could not give a complete picture of the excavation of the tunnels. The approach followed in this paper was to use the partial information from the design to double check the design estimation and, at same time, forecast the possible deviations. The approach employed to analyse the data was through the Kalman filter.

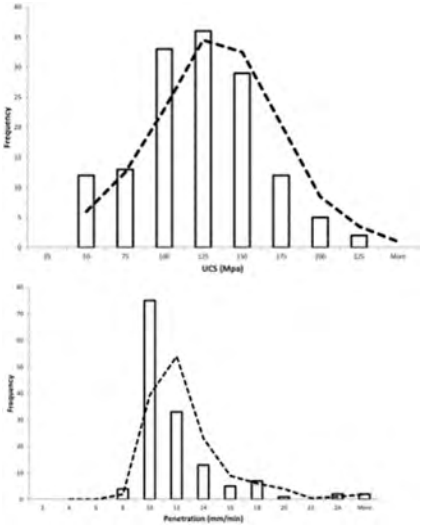

Figure 4. Distribution of designed values of UCS and penetration.

3 KALMAN FILTER METHODOLOGY

The Kalman Filter is a mathematical tool for finding the best estimate for the state of a system in a discrete time process that is assumed as a linear stochastic differential equation ([11]). Following the approach of [15] we could consider the following discrete nonlinear time system:

$$x_{k+1} = f(x_k) + w_k \tag{1}$$

$$y_k = h(x_k) + v_k \tag{2}$$

where $x_k \in \mathbb{R}^{n_x}$ is the unknown state of the system and $y_k \in \mathbb{R}^{n_y}$ corresponds to the output data. In this paper x_k are:

- A: estimated penetration during design stage (mm/min)
- B: UCS data from design stage

Whereas y_k are the observed TBM machine parameters.

In order to provide an adequate initial model, all previous information on the input parameters x_k must be assessed. This previous information will come with an associated error of modelling w_k that can be represented probabilistically by means of a multivariable Gaussian probability density function with zero mean and covariance matrix Q_k. In this paper, the implicit error in the input parameters is represented by the initial standard deviation as shown below.

On the contrary, the error related to monitoring measures (v_k) is usually given by the manufacturer of the TBM, so it also turns out to be an independent and Gaussian random variable, with zero mean and covariance matrix R_k. The nonlinear functions f and h represent the dynamic process and the measurement model, respectively. The estimation of the state consists in elaborating an outlook of x_k employing y_k for each time k. For this reason, the interest of the user should be focused on obtaining the probability distribution function (PDF) of x_k conditioned to y_k or, in other words, the probability of reproducing the observed measurements (TBM machine parameter) with a particular set of input parameters. The probability of a parameter set given the observations is:

$$p(x_k|\mathrm{Y}_{k-1}) = \int p(x_k|x_{k-1})p(x_{k-1}|\mathrm{Y}_{k-1})dx_{k-1} \tag{3}$$

The application of the Bayes Theorem to the observations leads to the updated equation of the parameters set, which is:

$$\mathrm{p}(x_k|\mathrm{Y}_k) = \frac{p(y_k|x_k)p(x_k|\mathrm{Y}_{k-1})}{p(y_k|\mathrm{Y}_{k-1})} \tag{4}$$

Where:

$p(x_k|Y_k)$ is the probability of a certain estimation for the set of geotechnical parameters given the observed measures. This term is also known as the a-posteriori PDF

$p(y_k|x_k)$ is the probability of computing the observed measures through the NLFEA given a certain set of geotechnical parameters.

$p(x_k|Y_{k-1})$ is the probability of a certain estimation for the set of geotechnical parameters given the previous observed measures. This term is also known as a-priori probability

$p(y_k|Y_{k-1})$ in equation (4) is the normalised probability or so-called scale factor so the $p(x_k|Y_k)$ could be between 0 and 1.

In this way expressions (3) and (4) represent the fundamental estimation of the Bayesian system of the equations (1) and (2) depending on time k. The approach is depicted schematically below:

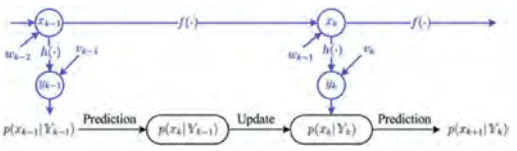

Figure 5. Principles of Bayesian Filter.

However, equations (3) and (4) cannot be used in a simple way to find the PDF of a random vector belonging to a very nonlinear system, since a computationally demanding random sample simulation procedure must be adopted. This issue can be addressed by using the first two statistical moments (mean and covariance) of a Gaussian probability density function assumed for the parameter vector xk. This procedure then aims for finding the PDF of the parameter's estimation. In this case, so, the search problem turns easier to solve by implementing the approach previously mentioned, with the unknown parameter standing for xk at time k. The new equations (3) and (4) can be expressed in terms of the Kalman filter as the predictions:

$$\hat{x}(k|k-1) = E[(f(x_{k-1}|\mathrm{Y}_{k-1})] \tag{5}$$

$$P^{x}_{(k|k-1)} = Cov[(f(x_{k-1}|\mathrm{Y}_{k-1})] + Q \tag{6}$$

and the updated formulation can be expressed as:

$$\hat{y}(k|k-1) = E[(h(x_k)|\mathrm{Y}_{k-1})] \tag{7}$$

$$P^{y}_{(k|k-1)} = Cov[(x_k|\mathrm{Y}_{k-1})] + R \tag{8}$$

$$P^{xy}_{(k|k-1)} = Cov[x_k, (h(x_k)|(\mathrm{Y}_{k-1})] \tag{9}$$

$$\hat{x}(k|k) = \hat{x}(k|k-1) + P^{xy}_{(k|k-1)}(P^{y}_{(k|k-1)})^{-1} (y_k - \hat{y}(k|k-1)) \tag{10}$$

$$\hat{x}(k|k) = \hat{x}(k|k-1) + P^{xy}_{(k|k-1)}(P^{y}_{(k|k-1)})^{-1} (y_k - \hat{y}(k|k-1)) \tag{11}$$

As shown in Figure 6, the Kalman filter employs a repetitive prediction-update procedure to obtain the mean and covariance of xk from measurements. Equations (8), (9), (10), (11) and (12) show how this implementation depends on the determination of the mean and covariance of the random state vector through the nonlinear functions f (·) and h (·).

Figure 6. Principle of Kalman Filter technique.

However, in the case of nonlinear systems, as those commonly encountered in Geotechnical Engineering, the problem is more complicated, and has attracted a lot of research in recent years. Thus, different families of Kalman Filters have been developed for non-linear systems, with three clear outstanding algorithms: EKF (Extended Kalman Filter), UKF (Unscented Kalman Filter) and EnKF (Ensemble Kalman Filter). In this work, the so-called Unscented Kalman Filter (UKF) or, for a better understanding, the Kalman Filter with the application of the Uhlmann transform, has been used. This technique is based on the so-called Unscented transform (UT), which uses deterministic points to trace the mean and covariance of a random variable transformed to a nonlinear system (see for instance ref [26]). The basic idea of the method is to represent the probability distribution of each random variable by means of a set of points (sigma points) deterministically chosen in such a way that the mean and covariance are represented. Then, it is possible to propagate these sigma points through the nonlinear function, obtaining a new set of points that are then used to obtain the mean and covariance of the transformed variable utilizing a weighting procedure.

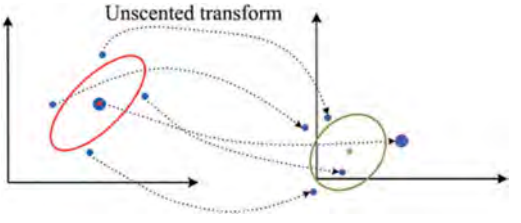

Figure 7. Uhlmann unscented transformation based on reference [12].

The procedure is to generate a first set of points considering the initial mean and covariance (red ellipse in Figure 7) and, subsequently this system is projected through a nonlinear function to generate a new set of sigma points which are used to calculate the new mean (the "star" point at the right of Figure 7) and its covariance (ellipse in Figure 7). In order to develop the UKF, it is necessary to apply the Uhlmann transform, both in the prediction and update processes,

which involves state transformations of the nonlinear functions f and h, respectively.

4 RESULTS

The relationship between the measured and estimated penetration is shown in Figure 8 with R2 of 0.78. The main differences are related to the extreme values (low and high values) and these differences are not quite interesting because they are not attributable to the lack of reliability of the methodology but to specific issues highlighted on field.

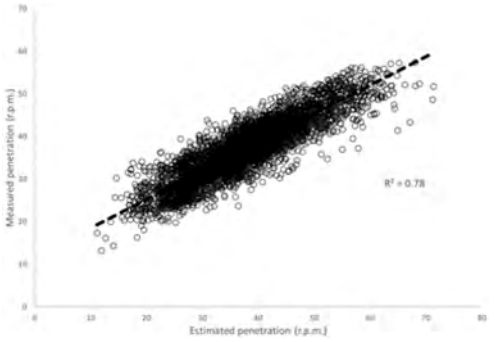

Figure 8. Correlation between estimated and measured penetration (r.p.m).

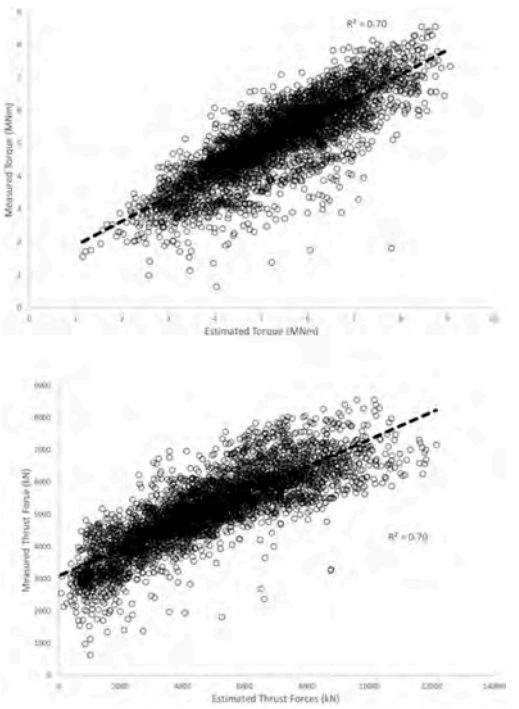

Figure 9. Correlation between estimated and measured Torque (MNm) and Correlation between estimated and measured Thrust Force (kN).

Figure 9 shows the same correlation for the Torque values. In this case the R2 value is quite lower because the methodology employed was not able to forecast the on-field problems, which are clearly highlighted as the lower points in the figure.

5 CONCLUSIONS

From the above considerations, the following conclusions can be drawn:

- The estimation of the TBM machine parameters during the design stage is very important to efficiently forecast the geological conditions during the excavation tunnelling. The most employed methods are the so-called semi-empirical methods.
- From the back-analysis carried out through the application of probabilistic estimators (Unscented Kalman Filter, UKF) it is concluded that this technique constitutes a powerful and versatile calculation tool that, quickly and accurately, allows to obtain very satisfactory adjustments. During the iteration process of the UKF, it has been possible to observe the special relevance of the maximum and minimum limits of each parameter to be estimated and entered in the filter.

The proposed methodology, based on Kalman filter, due to its robustness and versatility can be employed by the designers to efficiently forecast the TBM machine parameters during design stage in abeyance of field data.

REFERENCES

[1] Delisio, A.; Zhao, J. A new model for TBM performance prediction in blocky rock conditions. Tunn. Undergr. Space Technol. 2014, 43, 440–452.

[2] Rostami, J. Performance prediction of hard rock Tunnel Boring Machines (TBMs) in difficult ground. Tunn. Undergr. Space Technol.2016, 57, 173–182.

[3] Maidl, B.; Herrenknecht, M.; Maidl, U.;Wehrmeyer, G. Mechanised Shield Tunnelling; John Wiley & Sons: Berlin, Germamy, 2013.

[4] Wang, L.; Gong, G.; Shi, H.; Yang, H. Modeling and analysis of thrust force for EPB shield tunneling machine. Autom. Constr. 2012, 27, 138–146.

[5] Zhang, Q.; Su, C.X.; Qin, Q.H.; Cai, Z.X.; Hou, Z.D.; Kang, Y.L. Modeling and prediction for the thrust on EPB TBMs under different geological condi-tions by considering mechanical decoupling. Sci. China Technol. Sci. 2016, 59, 1428–1434.

[6] Gertsch, R.; Gertsch, L.; Rostami, J. Disc cutting tests in Colorado Red Granite: Implications for TBM performance prediction. Int. J. Rock Mech. Min. Sci. 2007, 44, 238–246.

[7] Cho, J.-W.; Jeon, S.; Jeong, H.-Y.; Chang, S.-H. Evaluation of cutting efficiency during TBM disc cutter excavation within a Korean granitic rock using linear-cutting-machine testing and photogrammetric measurement. Tunn. Undergr. Space Technol. 2013, 35,37–54.

[8] Yagiz, S. New equations for predicting the field penetration index of tunnel boring machines in frac-tured rock mass. Arab. J. Geosci. 2017, 10, 33.
[9] Hassanpour, J.; Firouzei, Y.; Hajipour, G. Actual performance analysis of a double shield TBM through sedimentary and low to medium grade metamorphic rocks of Ghomrood water conveyance tunnel project (lots 3 and 4). Bull. Int. Assoc. Eng. Geol. 2021, 80, 1419–1432.
[10] Naghadehi, M.Z.; Samaei, M.; Ranjbarnia, M.; Nourani, V. State-of-the-art predictive modeling of TBM performance in changing geological conditions through gene expression programming. Measurement 2018, 126, 46–57.
[11] Salimi, A.; Rostami, J.; Moormann, C.; Delisio, A. Application of non-linear regression analysis and artificial intelligence algorithms for performance prediction of hard rock TBMs. Tunn. Undergr. Space Technol. 2016, 58, 236–246.
[12] Sun, W.; Shi, M.; Zhang, C.; Zhao, J.; Song, X. Dynamic load prediction of tunnel boring machine (TBM) based on heterogeneous in-situ data. Autom. Constr. 2018, 92, 23–34.
[13] Ceravolo, R., De Stefano, E., Matta, et al: "Unscented Kalman Filter for the indentification of passive control devices" Research and Applications in Structural Engineerig, Mechanics and Compution- Zigoni (ED.) 2013 Taylor & Francis Group, London, ISBN 978-1-138-00061–2
[14] Hommels, A. and Molenkamp F., "Inverse analysis of an embankment using the Ensemble Kalman filter including heterogeneity of the soft soil", Proc. of Sixth Eur. Conference on Numerical Methods in Geotechnical Engineering, 6/8 September 2006, Graz (Austria).
[15] E. Broch and J. A. Franklin, "The point-load strength test," International Journal of Rock Mechanics and Mining Sciences & Geomechanics Abstracts, vol. 9, no. 6, pp. 669–676, 1972.
[16] International Society for Rock Mechanics (ISRM), "Suggested method for determining point load strength: ISRM Common testing methods," International Journal of Rock Mechanics and Mining Sciences, vol. 22, no. 4, p. 112, 1985.
[17] K. Tsidzi, "Point load-niaxial compressive strength correla- tion," in Proceedings of the 7th ISRM Congress, W. Wittke and R. Balkema, Eds., vol. 1, pp. 637–639, Lisbon, Portugal, September 1991.
[18] P. Grasso, S. Xu, and A. Mahtab, "Problems and promises of index testing of rocks," International Journal of Rock Me- chanics and Mining Sciences & Geomechanics Abstracts, vol. 30, no. 5, p. 278, 1992.
[19] Nelson P. P., T. D. O'Rourke, and F. H. Kulhawy, "Factors affecting TBM penetration rates in sedimentary rocks," in Proceedings of 24th US Symposium on Rock Mechanics (USRMS), pp. 227–237, Keystone, Colorado, June 1983.
[20] Sanio H. P, "Prediction of the performance of disc cutters in anisotropic rock," International Journal of Rock Mechanics and Mining Sciences & Geomechanics Abstracts, vol. 22, no. 3, pp. 153–161, 1985.
[21] Fukui K. and S. Okubo, "Some attempts for estimating rock strength and rock mass classification from cutting force and investigation of optimum operation of tunnel boring ma- chines," Rock Mechanics and Rock Engineering, vol. 39, no. 1, pp. 25–44, 2006.
[22] Innaurato N, Oggeri C, Oreste P. "Validation techniques in tunnelling: the complementary approach of modelling, monitoring and excavation performance evaluation". Proceeding of the AITES-ITA 2001 World Tunnel Congress, 2001, p 217–26
[23] Bilgin N., C. Balci, H. Tuncdemir, S. Eskikaya, M. Akgul,".The performance prediction of a TBM in difficult ground condition," in Proceedings of AFTES Journees d'Etudes Internationales de Paris, pp. 25–28, Paris, France, October 1999.
[24] Maidl, Ulrich & Comulada, Marc. (2011). Prediction of EPB shield performance in soils. Proceedings - Rapid Excavation and Tunneling Conference. 1083–1091.
[25] Armaghani D, Yagiz S, Mohamad E D, Zhou J: "Prediction of TBM performance in fresh through weathered granite using empirical and statistical approache" Tunnelling and Underground Space Technology, Volume 118, 2021,104183, ISSN 0886–7798, https://doi.org/10.1016/j.tust.2021.104183.
[26] Julier S. J. and J. K. Uhlmann, "Unscented filtering and non-linear estimation," in Proceedings of the Ieee, vol. 92, no. 3, march 2004 isbn 0018-9219/04

Tunnelling for a Better Life – Yan, Celestino, Thewes & Eberhardt (Eds)
© 2024 The Author(s), ISBN 978-1-032-80042-4
Open Access: www.taylorfrancis.com, CC BY-NC-ND 4.0 license

An intelligent decision support system for tunnel structural defects maintenance with combining knowledge graph and deep learning

Fei Jia* & Yadong Xue
Key Laboratory of Geotechnical and Underground Engineering of Minister of Education and Department of Geotechnical Engineering, Tongji University, Shanghai, China

Qingsong Zhang
Geotechnical and Structural Engineering Research Center, Shandong University, Jinan, China

Liqing Qu
Qingdao Guoxin Jiaozhou Bay Second Submarine Tunnel Co., Ltd, Qingdao, China

ABSTRACT: Under the current large-scale operational tunnels, tunnel structure maintenance is an important issue and requires complex decision making, especially involving rapid perception and analysis of structural defects. However, traditional manual inspection and experience driven maintenance decision methods are low efficiency, prone to subjectivity, and gradually unable to meet the engineering requirements. Thus, an intelligent decision support system (DSS) for tunnel structural defects maintenance is present in this paper to realize automatic decision making for tunnel structural defects maintenance. Firstly, a deep learning model for tunnel structural defects detection based on YOLOv8 is built to quickly identify the category and location of defect in an image via supervised learning. Then, a Knowledge Graph (KG) is constructed to store the related maintenance knowledge exist in unstructured format (i.e., standard) through ontological approaches. Besides, the structured data reflecting tunnel structural state (i.e., defect location) can also be added to KG. Finally, on account of the model recognition results, a semantic reasoning language is adopted to automatically inference the optimal maintenance decision from the KG. An evaluation of the DSS is additionally performed to validate rationality and effectiveness of the methodology, the results show that the DSS can achieve reasonable maintenance decision for tunnel structural defects.

Keywords: Tunnel maintenance, Defects detection, Decision making, Computer vision, Graph database

1 INTRODUCTION

With the increasing development of transport infrastructure, railway tunnels (e.g., subway tunnels) have become an important part of urban transit system. However, due to the complex underground surroundings, various structural defects (e.g., leakage, crack) may appear during tunnel operation. Regular inspection and timely maintenance are necessary to guarantee tunnel serviceability. Currently, this task is mainly implemented by manual based method, which is time consuming, subjective, and gradually unable to meet the engineering demands under current large-scale operational tunnels. Thus, it is required to develop a more intelligent and efficient detection and maintenance decision method (Xue et al., 2018).

In recent years, deep learning techniques have been widely used in the field of civil engineering (Wang et al., 2023; Li et al., 2023; Fu et al., 2023; Xue et al., 2022; Yu et al., 2021). Owing to the powerful representative ability of deep learning model and strong hardware (graphics processing unit, GPU), given different data as input, the model can be trained iteratively to complete corresponding task. Xue et al. (2018) firstly developed a Moving Tunnel Inspection (MTI-100) equipment to achieve automatic tunnel defects images acquisition. Then the VGG (Simonyan et al., 2015) and Faster R-CNN

*Corresponding author: jiaruofeihan@163.com

DOI: 10.1201/9781003495505-402

(Ren et al., 2015) models were in turn utilized to perform defects classification and detection, demonstrating the feasibility of deep learning methods. Huang et al. (2018) adopted two fully convolutional network (FCN; Long et al., 2015) to separately segment crack and leakage contours in images collected by MTI-200a, and realized better performance than traditional digital image processing methods. Zhao et al. (2020) used Mask R-CNN (He et al., 2017) instance segmentation model to segment leakage and the number of pixels including in segmented area were employed to quantify defect. Xue et al. (2020) adopted Cascade R-CNN (Cai et al., 2021) to realize finer leakage segmentation, and designed a field experiment to construct a conversion formula between pixel number and defect area. Zhao et al. (2021) took the crack discontinuities into account, added a semantic branch to PANet (Liu et al., 2018) to refine the crack segmentation performance and designed an algorithm to compute crack length and width. Zhou et al. (2021) considered the depth of spalling defect and adopted a laser scanner to generate RGB-D format images, D^3Net (Fan et al., 2021) was then used to segment spalling and calculate the defect volume. The above research mainly utilized different models for each defect, while there are multiple defects present meanwhile in the real context, and thus a model for recognizing two or more defects is necessary.

Based on various defect data, including leakage area, crack length etc., it is also important to evaluate the defect severity and decide maintenance measures. Li et al. (2017) selected six kinds of common defects and conducted 40 samples to regress a tunnel serviceability index (TSI) formula for tunnel condition evaluation through expert rate and partial least squares (PLS) method. Chen et al. (2019) further considered the influence of additional factors (e.g., buried depth, age), constructed a Multiple Indicators Multiple Causes (MIMIC) model to quantify the influence and optimize the original TSI. Zhu et al. (2021) took the subjective factors of expert annotation and insufficient samples in original TSI into account, proposed a cloud based random forests (CRFs) model to solve the two problems and reconstruct TSI through semi-supervised learning. Liu et al. (2023) considered the complex interactions among key performance indicators (KPIs), combined pair copula constructions (PCCs) and Bayesian networks (BN) to assess subway tunnel state. Though different tunnel structure evaluation methods have been studied and maintenance measures are decided for each evaluation level, it is mainly some advice about whether to maintain. However, it may be more applicable to directly determine how and what to maintain for serving the practical engineering by combining decision making with defect detection.

Accordingly, an intelligent decision support system (DSS) is constructed in this study to determine reasonable maintenance methods for three common tunnel structural defects (leakage, crack, and block). This system mainly consists of two parts, one is a deep learning model to detect defect location and category in image and provide a coarse quantification information, the other is a knowledge graph storing detection results and maintenance standard to decide defect maintenance method automatically. The rest of this paper is formed as follows. Section 2 introduces the data acquisition method and deep learning model for defects detection in detail, followed by the construction of maintenance knowledge graph in Section 3. Then Section 4 displays the model training process and maintenance decision results, and finally Section 5 concludes the study.

2 RAILWAY TUNNEL STRUCTURAL DEFECTS DATASET AND DETECTION MODEL

With a defect image as input, the purpose of detection model is to predict defect location and category in the image. Generally, the model can be divided into two parts, backbone and head. The former is used to extract feature maps containing high-dimensional semantic information from images. And the latter predicts several bounding boxes and corresponding category probability vectors for each point on feature maps. Based on the difference between predictions and ground truths (GTs), model parameters are iteratively updated during the training process through gradient backpropagation, which is also called supervised learning. Thus, dataset has an important impact on the model performance, sufficient images are necessary to guarantee steady training process and powerful recognition capability.

2.1 *Data acquisition*

As shown in Figure 1, the cross sections of a single hole double track railway tunnel with different

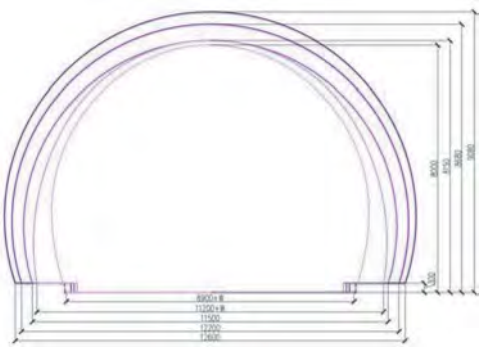

Figure 1. The cross sections of a single hole double track railway tunnel with different design speeds (mm).

design speeds are quite distinct, and the section size is relatively large, requiring a general and efficient image collection measure. To this end, a comprehensive detection device is designed and developed to achieve rapid acquisition of railway tunnel structure images (Figure 2). Taking line scan camera as the main component, the basic acquisition module is established by combining with light source, memory card and other supporting facilities, and totally six modules are adopted to form the detection device. Finally, the main body is mounted on a track engineering equipment to realize movable inspection.

Figure 2. The comprehensive railway detection device.

Considering the large section size of railway tunnel, full section inspection in single operation may require larger device size, more detection modules, and higher resource consumption etc., a special device structure is designed considering the characteristics of round-trip inspection. As shown in Figure 3 (a), for an interval tunnel inspection, the detection device covers half of the structure in a single operation from the beginning to the end. Then on the way back, the device covers the other half by rotating the device horizontally as shown in Figure 3(b). Owing to the special design, the device cost can be significantly reduced, and this design may also be extended to the inspection of other large section projects.

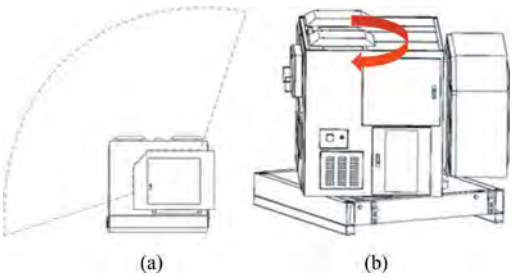

Figure 3. Image acquisition process for a single hole double track railway tunnel. (a) Image acquisition range of single operation. (b) Detection device rotation for image acquisition of another half cross section.

To verify the above work process, an inspection operation is carried out in a railway tunnel in southern China (Figure 4) at a speed of 40 km/h. The sample images collected by each module is shown in Figure 5, indicating that this inspection process is reasonable and the image quality is relatively superior. Besides, each image is named and stored as 'R_N_I', where R means the device operation direction (s or x), N represents the module number, and I is the number of images collected by a module. After locating defect in an image, the absolute defect location in tunnel can then be determined. Finally, 3624 images with a resolution of (8192×4096) are collected.

Figure 4. Inspection process in a single hole double track railway tunnel.

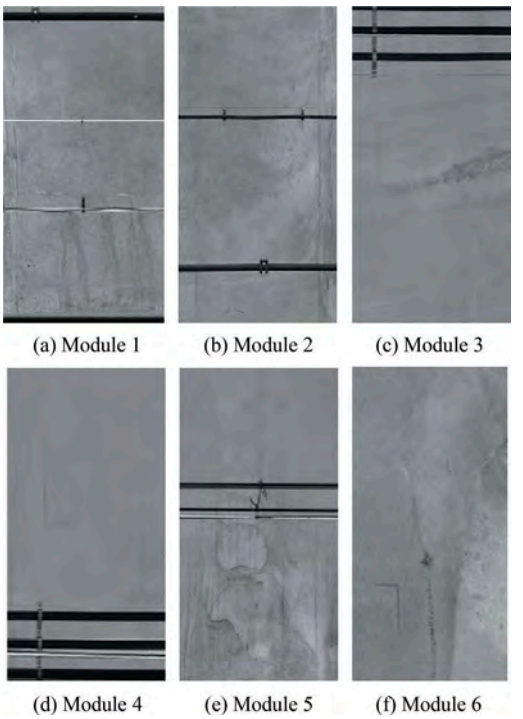

Figure 5. Images collected by each module.

2.2 *Data processing and annotation*

Due to the powerful computation ability of GPU, though deep learning model can efficiently extract features from images, it is still difficult to directly analyse such a large image (8192×4096). Hence, a crop algorithm is performed on an image to obtain 8 images with a resolution of (2048×2048), indicating that the dataset is expanded by 8 times. In addition, each cropped image is named as 'R_N_I_i_j', where i and j represent the row and column number in the original image.

As shown in Figure 6, taking three common railway tunnel structural defects (leakage, crack, and block) as detection object, LabelMe, a general annotation tool, is utilized to label defect location and category in these cropped images through manual annotation. Finally, the railway tunnel structural defect dataset contains 4454 labelled images for training deep learning model.

Figure 6. Railway tunnel structural defect images.

2.3 *Defects detection model*

With the rapid development of computer vision technology in the field of deep learning, multiple models have been proposed to achieve the aim of fast and accurate recognition. Currently, YOLOv8 (Glenn, 2023) is a state-of-the-art (SOTA) model for various vision tasks, and thus is used in this study to detect railway tunnel structural defects.

The overall model architecture is shown in Figure 7. In the backbone, the input image is handled in a series of convolutional blocks to get a feature map containing abundant semantic information. Then a feature pyramid structure is constructed to combine feature maps of different granularity in the head, finally three feature maps are generated to separately detect targets at different scales. For more details, please refer to (Glenn, 2023).

The aim of training a deep learning model is to obtain a group of optimal model parameters, which can make model realize satisfactory detection performance. Thus, a loss function is necessary to perform gradient backpropagation. The loss function of YOLOv8 contains three parts, classification (L_{cls}), regression (L_{box}), and confidence (L_{conf}), as displayed in (1).

$$
\begin{aligned}
L_{cls} &= -\frac{1}{b}\sum_{i=1}^{b}\frac{1}{n_i}\sum_{j=1}^{n_i} y_{ij}\ln(\hat{y}_{ij}) \\
L_{box} &= \frac{1}{b}\sum_{i=1}^{b}\frac{1}{n_i}\sum_{j=1}^{n_i}(1 - IoU(GT_{ij},\ Pre_{ij})) \\
L_{conf} &= -\frac{1}{b}\sum_{i=1}^{b}\frac{1}{n}\sum_{j=1}^{n_i} s_{ij}\ln(\hat{s}_{ij})
\end{aligned}
\tag{1}
$$

where b is the batch size; n_i is the number of positive samples; y_{ij} is the GT class label; $\hat{y}_{ij}$ is the predict class label; IoU is the intersection over union between GT and Pre boxes; n is the size of feature map; s_{ij} is the GT foreground label; $\hat{s}_{ij}$ is the predict foreground label.

The final loss function is formed as (2).

$$
L = \lambda_{cls}L_{cls} + \lambda_{box}L_{box} + \lambda_{conf}L_{conf} \tag{2}
$$

where L is the final loss function; λ_{cls}, λ_{box}, λ_{conf} are the balanced parameters.

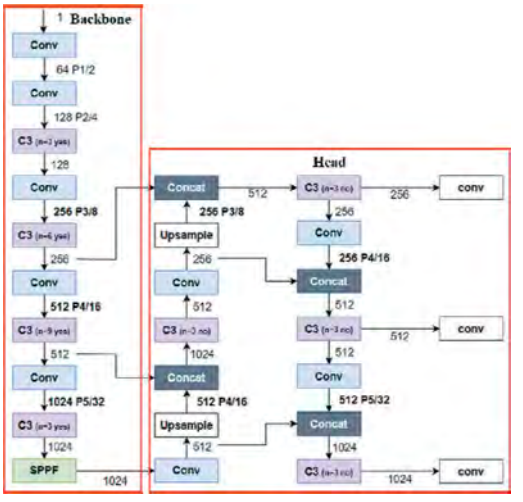

Figure 7. YOLOv8 detection model architecture.

3 KNOWLEDGE GRAPH FOR DEFECTS MAINTENANCE

Traditional methods mainly depend on workers to determine specific maintenance measures for different defects according to relevant standards. While the rationality of measures largely hinges on personnel experience, which may be low efficiency and insufficient to meet the operational requirements. Thus, a defects maintenance knowledge graph is constructed to realize information integration, query, and decision support analysis.

The knowledge graph was proposed by Google in 2012 and was established to improve the search engines performance. At present, knowledge graph (KG) has become one of the important ways for organizing and representing knowledge in the era of big data, and is a key technology for achieving cognitive intelligence (Peng et al., 2023). KG is a structured semantic knowledge base that uses network structures to describe concepts, entities, and their relationships in the real world. The basic unit of KG is an entity-relation-entity triple, as well as the entity and its related attribute value pairs. By pre-defining entities, relationships, and attributes, machines are able to understand and process data in this knowledge form, which is also called ontology design.

3.1 *Ontology design*

Ontologies represent a formal description of concepts and their relationships, allowing modelling a knowledge graph for a specific domain or task (Dimitrova et al., 2020). Hence, ontology design is to determine the concepts and attributes contained in the domain for the requirements of domain knowledge. Besides, the relationship between entities also needs to be defined, and different types of entities may have different relationships for specific domains. In this study, the ontology design for railway tunnel structural defects maintenance is completed in a top-down manner mainly through human knowledge and expert experience (Zheng et al., 2021).

Given that the aim of this KG is to perform maintenance decision for railway tunnel structural defects, the ontological classes are conceptual abstracts of similar entities within the tunnel defects maintenance. Therefore, it can be concluded that the knowledge required for tunnel structural defects maintenance includes the identification of operational tunnels, maintenance methods, and structural segments. Then the ontological classes needs be further categorized to satisfy the maintenance requirements. For instance, an operational tunnel contains several segments and some maintenance methods are defined in relevant standards. Thus, defects information is obtained for each segment with deep learning technology, and maintenance methods for different defect and severity are extracted by expert experience. In addition, the entity properties related to tunnel structural defects are also defined in the ontology design. As shown in Figure 8, the designed ontology displays the relationships between ontological classes by connecting edges in dashed line form, and the solid line represents ontological class properties.

3.2 *Graph construction*

Based on the above ontology design, structured data (i.e., defects detection results) and unstructured

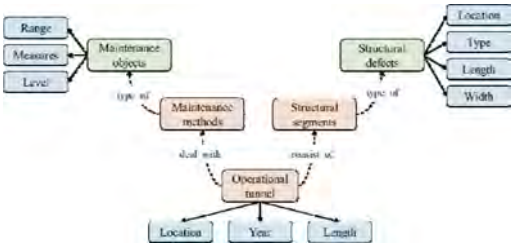

Figure 8. Ontology design for tunnel structural defects maintenance.

knowledge (i.e., maintenance standards) are transferred and stored in a unified knowledge base. For the structured data, after predicting defect location and category, the detection results are stored in the format required in the ontology design. While for the unstructured knowledge, it is mainly summarized and extracted from maintenance standards through human experience. Table 1 displays the severity definition of crack in standards, it is required to manually convert it into a structured storage format (e.g., json, csv).

At present, there are mainly three kinds of knowledge graph storage methods, traditional relational database, RDF triplet database and graph database. Since graph database is a kind of ideal KG management tool where knowledge is stored in graph structure and more intuitive, Neo4j graph database is adopted in this study to store data, which is open-source and uses Cypher language to operate, manage and visualize the graph (Pang et al., 2023).

Table 1. Evaluation standard of segment crack health.

Crack width (mm)	Evaluation standard
[0, 0.2)	Level 1
[0.2, 0.5)	Level 2
[0.5, 1.0)	Level 3
[1.0, 2.0)	Level 4
≥ 2.0	Level 5

4 RESULTS OF DSS FOR DEFECTS MAINTENANCE

4.1 *Defects detection performance evaluation*

Model training is a process of continuous iteration and updating, a regular evaluation is necessary to judge the training state and decide when to stop. Thus, Dataset is usually divided into three parts, train, validation, and test. During the training process, the train set is used to update model parameters and model performance is evaluated on validation set, the trained model can be further evaluated on test set by visualizing detection results. The ratio of three sets in this study is 8:1:1 shown in Table 2.

Table 2. Composition of three sets.

	Defect count			
Name	leakage	crack	block	Image count
train	2150	1980	362	3638
validation	414	156	26	450
test	210	151	23	366

As shown in Table 3, with comparing prediction with label, model detection results can be divided into four categories, and two evaluation indexes are formed as (3). However, given that the total number of targets is fixed, the two indicators show a state of fluctuation and growth. To this end, mean average precision (Lin et al., 2014; mAP) is adopted to comprehensively evaluate defects detection performance., which is also widely used in the filed of deep learning to compare and assess model performance.

Table 3. Model prediction categories.

	Label	
Prediction	Positive	Negative
Positive	TP	FP
Negative	FN	TN

$$Prediction = \frac{TP}{TP + FP}$$
$$Prediction = \frac{TP}{TP + FN} \quad (3)$$

As shown in Figure 9, to determine the optimal model parameters, the recognition performance is evaluated on validation set after each epoch. Finally, the loss and mAP values tend to be stable, and the optimal mAP value is 0.722 at a detection speed of 35 frames per second (FPS). Some model recognition results on test set are also displayed in Figure 10, indicating that the model achieves satisfactory accuracy.

4.2 *Maintenance decision results*

According to the above graph construction process, as shown in Figure 11, the defect detection results are automatically transferred and stored in structured format (csv in this study). While for the unstructured knowledge in maintenance standards, the entities and relationships are extracted and constructed

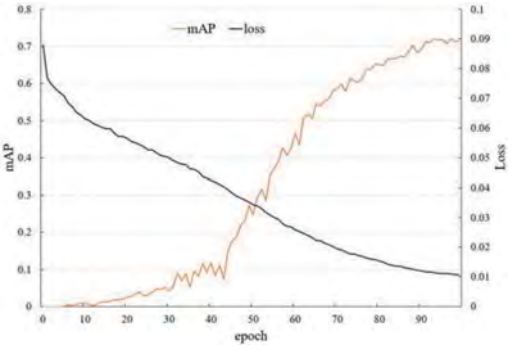

Figure 9. Defects detection model training process.

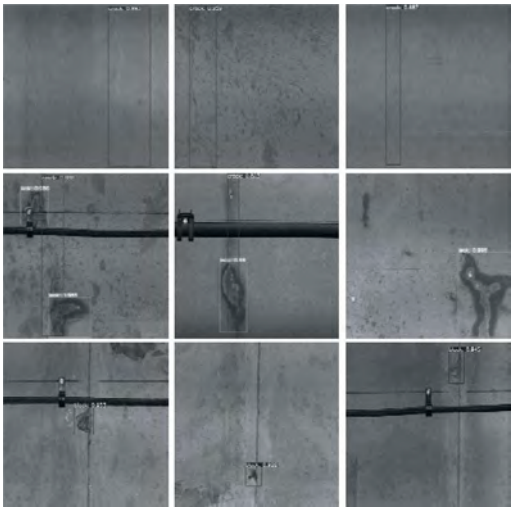

Figure 10. Model recognition results on test set.

Segment	Defect	Type	DefectLoc	SegmentLoc	DefectDirection	DefectInfo
s_1_1006	s_1_1006_0	crack	[1518, 943, 3842, 1521]	650.9376	-1	0.6705
s_1_1006	s_1_1006_1	crack	[5310, 846, 8192, 1324]	650.8788	-1	0.618
s_1_1006	s_1_1006_2	crack	[3898, 930, 5724, 1232]	650.8772	-1	0.5298
s_1_1010	s_1_1010_0	crack	[2867, 1064, 3463, 1465]	657.504	-1	0.2011
s_1_1010	s_1_1010_1	crack	[1538, 675, 5896, 958]	657.3248	-1	1.4464
s_1_1010	s_1_1010_2	crack	[6177, 91, 7127, 655]	657.1476	-1	0.3093
s_1_1014	s_1_1014_0	crack	[1958, 2062, 5895, 2634]	664.9912	-1	1.3319
s_1_1014	s_1_1014_1	crack	[6849, 34, 7254, 637]	663.686	-1	0.3034
s_1_1014	s_1_1014_2	crack	[6085, 2072, 6292, 2466]	664.8598	-1	0.1246
s_1_1014	s_1_1014_3	crack	[7898, 2316, 8190, 3033]	664.6216	-1	0.2168
s_1_1015	s_1_1015_0	crack	[4657, 153, 6490, 461]	665.3132	-1	0.5204
s_1_1015	s_1_1015_1	crack	[648, 3838, 5832, 4096]	666.7772	-1	1.4523
s_1_1016	s_1_1016_0	crack	[5390, 2222, 5861, 2711]	667.8152	-1	0.1901
s_1_1016	s_1_1016_1	leakage	[160, 451, 6959, 1420]	667.2028	-1	1.9017
s_1_1016	s_1_1016_2	leakage	[1021, 1572, 8192, 2136]	667.5704	-1	2.0078
s_1_1017	s_1_1017_0	leakage	[1, 842, 8148, 2370]	669.1096	-1	2.2812

Figure 11. Defect detection results in structured format.

manually in Neo4j (Figure 12). Finally, the railway tunnel structural defects maintenance knowledge graph is visualized in Neo4j (Figure 13), the entity properties and relationships are constructed as defined in Figure 8.

With the constructed knowledge graph, the semantic reasoning language (Cypther) is used to query, analyse, and make decision for railway tunnel structural defects. For example, as displayed in

Figure 12. Defects maintenance graph in Neo4j.

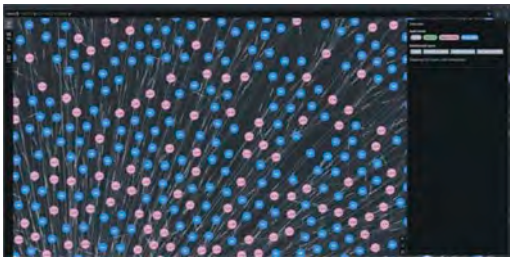

Figure 13. Defects maintenance knowledge graph visualized in Neo4j.

Figure 14, the code "match a=(:Tunnel)-[:CONSIST_OF] →(:Segment)-[:HAD_DEFE CT]→(:Defect {Type:'crack'}) return a" returns all crack defect results. Then, to further realize maintenance decision for defects, the code needs to construct the relationship between defects information and maintenance standard, such as "match (a:Defect {Type:'crack'}), (b:Level {name:'cracklevel'}) where a.Width > b.rangemin and a.Width < b.rangemax return a.ID, b.num". As shown in Figure 15, what (ID, Loc) and how (Level num) to maintain crack defects can be quickly and automatically decided, proving the efficiency of decision support system for railway tunnel structural defects maintenance.

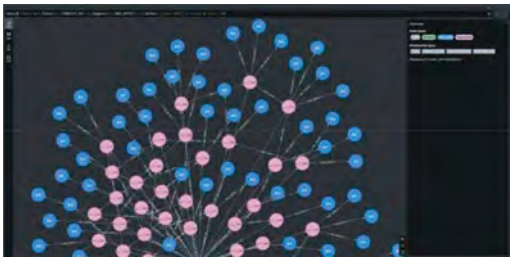

Figure 14. Crack defects displayed in Neo4j.

5 CONCLUSIONS

In this study, an intelligent decision support system is constructed for tunnel structural defects maintenance. This system mainly contains two parts, a deep learning model for defects detection and a knowledge graph for maintenance decision making. It can store both structured detection results and unstructured maintenance standards and realize automatic defects maintenance decision making through a semantic reasoning language. The main conclusions are as follows.

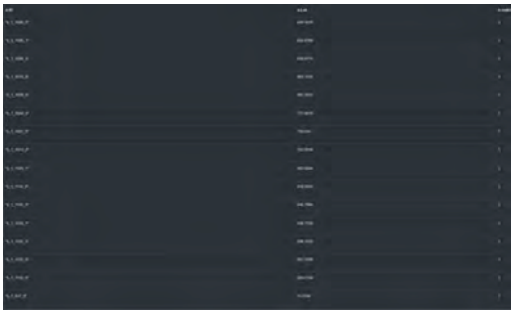

Figure 15. Maintenance decision results for crack defects.

(1) A comprehensive detection device is designed to efficiently collect defect images by considering the characteristics of round-trip inspection, and the absolute image location in tunnel is determined in proper naming rules. Furthermore, the absolute defect location can be automatically obtained with YOLOv8 defects detection model.
(2) Ontology design is the fundamental step of constructing knowledge graph and generally is developed in a top-down manner for domain task. For tunnel structural defects maintenance, based on three top classes, operation tunnel, maintenance segments, and maintenance methods, the ontology can be completed by extracting concepts from detection results and maintenance standards through expert knowledge.
(3) Graph database is a powerful and intuitive knowledge graph form to store structured and unstructured data defined in ontology. According to the entity properties and relationships, semantic reasoning language is utilized to realize automatic decision making for tunnel structural defects maintenance.

ACKNOWLEDGMENTS

The authors would like to express their sincere gratitude to The National Key R&D Plan of China [grant number 2021YFB2600805] for funding this research.

REFERENCES

Cai Z, Vasconcelos N, 2021. Cascade R-CNN: High Quality Object Detection and Instance Segmentation. IEEE Transactions on Pattern Analysis and Machine Intelligence, 43(5): 1483–1498.

Chen X, Li X, Zhu H, 2019. Condition evaluation of urban metro shield tunnels in Shanghai through multiple indicators multiple causes model combined with multiple regression method. Tunnelling and Underground Space Technology, 85: 170–181.

Dimitrova V, Mehmood M O, Thakker D, et al., 2020. An ontological approach for pathology assessment and diagnosis of tunnels. Engineering Applications of Artificial Intelligence, 90: 103450.

Fan D, Lin Z, Zhang Z, et al., 2021. Rethinking RGB-D Salient Object Detection: Models, Data Sets, and Large-Scale Benchmarks. IEEE Transactions on Neural Networks and Learning Systems, 32(5): 2075–2089.

Fu R, Cao M, Novák D, et al., 2023. Extended efficient convolutional neural network for concrete crack detection with illustrated merits. Automation in Construction, 156: 105098.

Glenn J, 2023. YOLOv8. https://github.com/ultralytics/ultralytics

He K, Gkioxari G, Dollar P, et al., 2017. Mask R-CNN. Proceedings of the IEEE International Conference on Computer Vision. Venice, Italy: pp.2961–2969.

Huang H, Li Q, Zhang D, 2018. Deep learning based image recognition for crack and leakage defects of metro shield tunnel. Tunnelling and Underground Space Technology, 77: 166–176.

Li J, Yuan C, Wang X, 2023. Real-time instance-level detection of asphalt pavement distress combining space-to-depth (SPD) YOLO and omni-scale network (OSNet). Automation in Construction, 155: 105062.

Li X, Lin X, Zhu H, et al., 2017. Condition assessment of shield tunnel using a new indicator: The tunnel serviceability index. Tunnelling and Underground Space Technology, 67: 98–106.

Lin T Y, Maire M, Belongie S, et al., 2014. Microsoft COCO: Common Objects in Context. Computer Vision – ECCV 2014. Zurich, Switzerland: pp.740–755.

Liu S, Qi L, Qin H, et al., 2018. Path Aggregation Network for Instance Segmentation. Proceedings of the IEEE Conference on Computer Vision and Pattern Recognition. Salt Lake City, Utah: pp.8759–8768.

Liu W, Shao Y, Li Chen, et al., 2023. Development of a non-Gaussian copula Bayesian network for safety assessment of metro tunnel maintenance. Reliability Engineering & System Safety, 238: 109423.

Long J, Shelhamer E, Darrell T, 2015. Fully Convolutional Networks for Semantic Segmentation. Proceedings of the IEEE Conference on Computer Vision and Pattern Recognition. Boston, Massachusetts: pp.3431–3440.

Pang H J, Li S Y, Dai L F, et al., 2023. Intelligent Metro Shield Tunnel Structure Assessment Based on Knowledge Graph. Trends on Construction in the Digital Era. Guimarães, Portugal: pp. 476–489.

Peng F L, Qiao Y K, Yang C, 2023. Building a knowledge graph for operational hazard management of utility tunnels. Expert Systems with Applications, 223: 119901.

Ren S, He K, Girshick R, et al., 2015. Faster R-CNN: Towards Real-Time Object Detection with Region Proposal Networks. Advances in Neural Information Processing Systems: Vol. 28. Montreal, Canada: pp.1–9.

Simonyan K, Zisserman A, 2015. Very Deep Convolutional Networks for Large-Scale Image Recognition. International Conference on Learning Representations. The Hilton San Diego Resort & Spa: pp.1–14.

Wang W, Su C, 2023. Deep learning-based detection and condition classification of bridge steel bearings. Automation in Construction, 156: 105085.

Xue Y, Cai X, Shadabfar M, et al., 2020. Deep learning-based automatic recognition of water leakage area in shield tunnel lining. Tunnelling and Underground Space Technology, 104: 103524.

Xue Y, Jia F, Cai X, et al., 2022. An optimization strategy to improve the deep learning-based recognition model of leakage in shield tunnels. Computer-Aided Civil and Infrastructure Engineering, 37(3): 386–402.

Xue Y, Li Y, 2018. A Fast Detection Method via Region-Based Fully Convolutional Neural Networks for Shield Tunnel Lining Defects: A fast detection method via region-based fully convolutional neural networks for shield tunnel lining defects. Computer-Aided Civil and Infrastructure Engineering, 33(8): 638–654.

Yu A, Mei W, Han M, 2021. Deep learning based method of longitudinal dislocation detection for metro shield tunnel segment. Tunnelling and Underground Space Technology, 113: 103949.

Zhao S, Zhang D M, Huang H W, 2020. Deep learning–based image instance segmentation for moisture marks of shield tunnel lining. Tunnelling and Underground Space Technology, 95: 103156.

Zhao S, Zhang D, Xue Y, et al., 2021. A deep learning-based approach for refined crack evaluation from shield tunnel lining images. Automation in Construction, 132: 103934.

Zheng X, Wang B, Zhao Y, et al., 2021. A knowledge graph method for hazardous chemical management: Ontology design and entity identification. Neurocomputing, 430: 104–111.

Zhou M, Cheng W, Huang H, et al., 2021. A Novel Approach to Automated 3D Spalling Defects Inspection in Railway Tunnel Linings Using Laser Intensity and Depth Information. Sensors, 21(17): 5725.

Zhu M, Zhu H, Guo F, et al., 2021. Tunnel condition assessment via cloud model-based random forests and self-training approach. Computer-Aided Civil and Infrastructure Engineering, 36(2): 164–179.

Tunnelling for a Better Life – Yan, Celestino, Thewes & Eberhardt (Eds)
© 2024 The Author(s), ISBN 978-1-032-80042-4
Open Access: www.taylorfrancis.com, CC BY-NC-ND 4.0 license

Prediction of disc cutter wear considering ground conditions and TBM operating parameters

Yun Seong Kang, Se Jin Park, Ji Hye Hwang, Ju Pyo Hong & Tae Young Ko*
Kangwon National University, Chuncheon, Korea

ABSTRACT: Tunnel boring machines (TBMs) are being exceedingly used in tunnel projects to minimize noise and vibrations during excavation. The disc cutter, which is a tool mounted on the cutterhead of a TBM, continuously interacts with the ground because of the rotation of the cutterhead, resulting in inevitable wear. Because replacing the disc cutter involves substantial time and cost, it significantly reduces the operation and excavation rates of the TBM and impacts the total time and cost of the TBM project. Thus, accurate prediction of cutter wear or lifespan is crucial. In this study, we estimated the coefficient bearing rate (mm/km), which is an index for quantifying wear, considering both the ground conditions and operating parameters of the slurry TBMs. To address the issue of insufficient uniaxial compressive strength (UCS) data, we first performed UCS prediction, followed by prediction of the Coefficient Wearing rate. The estimation of the Coefficient Wearing rate utilizes machine learning techniques, such as the k-nearest neighbors, Support vector machine, random forest, gradient XGBoost, LightGBM, and CatBoost. The entire dataset was divided into five training/test sets for the purpose of five-fold cross-validation. The model performance was evaluated using the coefficient of determination (R^2) and root mean square error (RMSE), with the hyperparameter optimization process conducted via five-fold cross-validation. The average R^2 and RMSE values for the LightGBM on the test data were 0.624 and 0.00791, respectively. Finally, to evaluate the feature importance of the prediction models, a SHapley Additive exPlanation (SHAP) analysis was conducted.

Keywords: Disc cutter, Wear, TBM, Operation parameter, Machine learning

1 INTRODUCTION

Nowadays, tunnel boring machines (TBMs) are being increasingly used in tunnel projects to minimize noise and vibration during excavation. One of the most critical aspects of the TBM projects is the lifespan and wear of the TBM disc cutters (Mahmoodzadeh et al., 2021). The disc cutter, which is a tool mounted on the cutterhead of a TBM, continuously interacts with the ground because of the rotation of the cutterhead, resulting in inevitable wear. Because replacing the disc cutter involves substantial time and cost, it significantly reduces the operation and excavation rates of the TBM and significantly affects the total time and cost of the TBM project (Kim et al., 2022). Thus, the accurate prediction of cutter wear and lifespan is crucial.

Recent studies have increasingly focused on utilizing artificial intelligence to predict the wear and lifespan of disc cutters in the TBMs. Mahmoodzadeh et al. (2021) employed geological conditions, TBM operating parameters, and machine-learning algorithms to predict the lifespan (H_f, m^3/cutter) of disc cutters in Gripper TBMs. Similarly, Elbaz et al. (2021) used geological conditions, TBM operating parameters, and a group method of data handling (GMDH)-type neural network to predict the lifespan (H_f) of disc cutters in the earth pressure balance (EPB) TBMs. Kim et al. (2022) utilized the TBM operating parameters along with machine learning and deep learning techniques to predict the cutter lifespan and wear rate (%) of the Slurry TBMs. However, there is relatively limited research on predicting the wear of disk cutters in the Slurry TBMs considering both the TBM operating parameters and geological conditions. In this study, we estimated the Coefficient Wearing rate (mm/km), which is an index for quantifying wear, considering both the ground conditions and operating parameters of the Slurry TBMs.

2 DATASET ESTABLISHMENT

In this study, the data from the tunnel projects in Singapore were used. The project involved the excavation of an approximately 5.53 km long tunnel, which was divided into two sections. Both the sections were excavated using the TBMs with identical

*Corresponding author: tyko@kangwon.ac.kr

DOI: 10.1201/9781003495505-403

specifications, which are referred to as TBM #1 and TBM #2, respectively. The specifications of the TBMs are listed in Table 1. The overall geological composition of the tunnel predominantly consists of the Bukit Timah Granite, with some sections passing through the Kallang sediment and mixed ground (Figure 1). TBM #1 excavated a section of approximately 3.14 km, where geological investigation estimated that the rock, soil, and mixed zones were 2670 m, 377 m, and 94 m, respectively; TBM #2 excavated a section of approximately 2.21 km, with the rock, soil, and mixed zones estimated to be 2120 m, 44 m, and 44 m, respectively. The operational data from the TBM used in this study were collected at excavation intervals of approximately 20 mm. Geological conditions were characterized using the weathering grades (G1–G6) obtained from the face logging performed during the CutterHead interventions (CHIs) and uniaxial compressive strength (UCS) values obtained from the drilling investigations. The weathering grade for the entire tunnel section was classified based on Approach 2 of Section 6 in BS5930:1990, and the weathering grades and their characteristics by grade are described in Table 2 (BS 1999). The weathering grades for the entire tunnel section varied from G1 to G5; however, the G6 grade was not observed.

The wear of the disc cutters was measured in millimeters based on the reduction in the radius of each disc cutter observed during the CHIs.

The UCS is frequently used as an input variable in various studies to predict the disc cutter wear and serves as a key indicator of geological conditions (Agrawal et al., 2022; Ding et al., 2022; Elbaz et al., 2021; Kang et al., 2022). In the projects examined in this study, 27 UCS data points were obtained for the section TBM #1 and 22 for section TBM #2 through drilling surveys. This is significantly inadequate compared with the TBM operation data recorded every 20 mm of excavation and cutter wear data obtained from the 203 cutter head inspections (CHIs). To address this data scarcity issue, the UCS values for areas where operation data were recorded were first predicted using the available operation and UCS data. Subsequently, the predicted UCS data were utilized to predict the disc cutter wear.

Table 1. Summary of TBM and disc cutter specifications.

TBM type	Slurry
TBM diameter	6.9 m
Torque	0–6, 250 kN·m
Thrust force	0–51, 200 kN
Cutterhead rotation speed	0–6 rpm
Number of disc cutter	48
Disc cutter diameter	483 mm

Table 2. BS5930:1990 approach 2 weathering classification.

Geo-notation	Grade	Classifier	Typical characteristics
G1	I	Fresh	Unchanged from original state
G2	II	Slightly weathered	Slight discoloration, slight weakening
G3	III	Moderately weathered	Considerably weakened, penetrative discoloration; large pieces cannot be broken by hand
G4	IV	Highly weathered	Large pieces cannot be broken by hand; Does not readily disaggregate (slake) when dry sample immersed in water
G5	V	Completely weathered	Considerably weakened; Slakes; Original texture apparent
G6	VI	Residual soil	Soil derived by in situ weathering but retaining none of original texture or fabric

3 UCS PREDICTION

To predict the UCS, a database was constructed under the assumption that the UCS values were consistent within an approximate 50 mm range centered around the points where the drilling surveys were conducted.

3.1 *Data preprocessing*

3.1.1 *Selection of parameters*

During the tunnelling process carried out by the TBM, approximately 2000 operation parameters, including the thrust force, torque, and cutter head rotation speed, were recorded at approximately

Figure 1. Geological profile of TBM tunnel project.

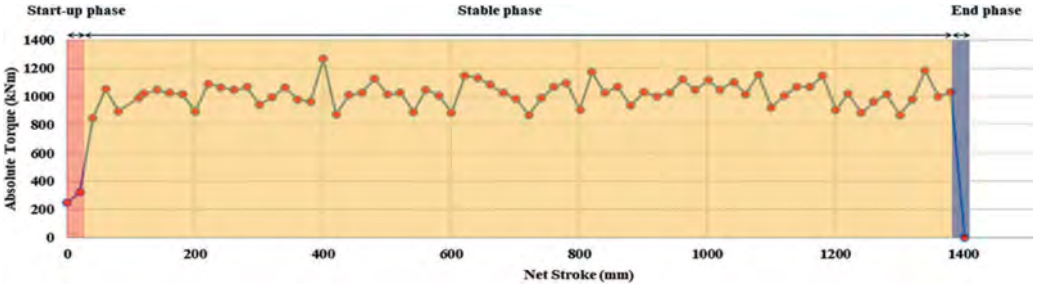

Figure 2. Variations in absolute torque during excavation.

20 mm advancement intervals. Using an excessive number of input variables can complicate the predictive models based on machine-learning algorithms and increase the computational time. Therefore, it is essential to eliminate the variables, which are not significant in predicting the UCS. In this study, the thrust force (TF), torque (TQ), cutterhead rotation speed (CHRS), and advance rate (AR) were chosen as the input variables to reflect the interaction between the cutterhead and excavation face. Additional variables like the bearing thrust force (BTF) and feed pressure (FP), which are related to the face pressure, as well as the feed flow rate (FFR) and discharge flow rate (DFR), which correlate with the stress state of the surrounding ground, were also selected (Xu et al., 2023). Furthermore, the field penetration index (FPI) is a performance evaluation metric for the TBM and can be calculated using Equation 1. Bejari and Hamidi (2013) and Hassanpour et al. (2011) demonstrated a significant correlation between the FPI and UCS. Based on these findings, the FPI was selected as the input variable for the UCS prediction model.

$$FPI(kN/cutter)/(mm/rev) = \frac{F_N(kN/cutter)}{penetration(mm/rev)} \quad (1)$$

Where, F_N is the normal force per disc cutter (kN/cutter).

3.1.2 *Extraction of stable phase*

During the excavation of a single ring, approximately 1.4 m in length, the TBM operation data typically vary continuously. These variations can be broadly categorized into the start-up, stable, and end phases (Figure 2). From the TBM operation data for a single ring, the start-up phase was removed because the TBM operates in an unstable condition, and the end phase was also removed because it corresponds to the periods when the TBM is not excavating (Xu et al., 2023). The start-up phase was defined as the interval from the beginning of the excavation cycle to the point where a 20 mm advance occurred. Records were removed if any of the input variables had a value of zero or less or if they were missing. Descriptive statistics for the variables used in predicting the UCS are summarized in Table 3.

Table 3. Statistical summary of variables in UCS prediction model.

Variables	mean	std	min	max	count
TQ (kN·m)	1011	210	447	1780	242
CHRS (rpm)	3.12	0.59	0.83	3.99	242
TF (kN)	22940	3116	6280	29837	242
BTF (kN)	9212	2514	3546	13541	242
FP (kPa)	388	72	274	545	242
FFR (m^3/min)	6.81	0.26	6.07	7.45	242
DFR (m^3/min)	7.15	0.22	6.45	7.61	242
AR (mm/min)	9.14	3.98	2.08	25.33	242
FPI ((kN/cutter)/(mm/rev))	84.98	52.25	8.48	307.68	242
UCS (MPa)	78.28	32.97	17	144	242

3.1.3 *Data splitting and scaling*

For training and validation of the UCS prediction model using supervised machine learning algorithms, the entire dataset was randomly divided into five subsets. In each iteration, four subsets were used for the training data, and the remaining subsets served as the test data. This process led to the creation of five combinations of the train and test datasets. Some machine learning algorithms, such as the k-nearest neighbors and support vector machines, can be influenced by the differing magnitudes of the input variables. To mitigate this problem, the MinMax scaling was applied to each of the five train and test sets.

3.2 *Methodology*

In this study, various supervised machine learning algorithms, including the k-nearest neighbors (KNN), support vector machine (SVM), random forest (RF), extreme gradient boost (XGBoost), categorical boost (CatBoost), and light gradient boosting machine (LGBM), were employed for the UCS prediction models. Each model was individually trained using five training sets. Hyperparameters for each of these models were optimized using the tree-structured Parzen estimator (TPE) Bayesian

optimization. During the optimization process, each training set was divided into five folds, and five-fold cross-validation was conducted for optimization. The performances of the optimized prediction models were evaluated using the coefficient of determination (R^2) and root mean squared error (RMSE).

$$RMSE = \sqrt{\frac{1}{n}\sum_{i=1}^{n}(y_i - \hat{y}_i)^2} \quad (2)$$

$$R^2 = 1 - \left\{\sum_{i=1}^{n}(y_i - \hat{y}_i)^2 / \sum_{i=1}^{n}(y_i - \bar{y}_i)^2\right\} \quad (3)$$

Where, y_i is the i^{th} actual value; $\bar{y}$ is the mean of the actual values; $\hat{y}_i$ is the i^{th} value predicted by the model.

3.3 *UCS prediction results*

The performance evaluation results for each model are summarized in Table 4. The highest average prediction performance for the test set was observed for the KNN, followed by the CatBoost in the second place. Although both the KNN and CatBoost demonstrated high average predictive performance on the test set, the standard deviation of the prediction performance for the KNN model was relatively higher than that of the CatBoost, indicating that the CatBoost provides more stable predictions. To perform the UCS predictions for the entire range, both the high average prediction performance and model stability must be considered. Therefore, the CatBoost was selected as the final UCS-prediction model. Using the final model, UCS predictions were made for the entire range, in which the operation data were recorded. The average UCS values from the five models were used to determine the final UCS predictions.

Table 4. Performance summary of UCS prediction models.

Model	Test RMSE mean	std	Test R^2 mean	std
KNN	9.36	2.310	0.91	0.042
SVM	26.94	2.597	0.30	0.174
RF	15.03	1.095	0.78	0.045
XGBoost	11.55	1.602	0.87	0.043
CatBoost	11.01	1.011	0.88	0.030
LGBM	13.52	1.522	0.83	0.048

4 DISC CUTTER WEAR PREDICTION

Disc cutter wear prediction considers only the normal wear of the face cutters. Using the data on the radius reduction for disc cutter numbers 13–36, as measured from the 203 CHIs, the Coefficient Wearing rate (CW) was calculated. The CW is obtained by dividing the reduction in the disc cutter radius (mm) by the distance traveled by the specific cutter and expressed as:

$$CW(mm/km) = Cutter\ wear(mm)/Cutter\ rolling\ distance(km) \quad (4)$$

4.1 *Data preprocessing*

The TBM operation data were filtered to include only the stable states, as outlined in Section 3.1.2, and the average values for each CHI were utilized. Geological conditions were also averaged across the CHI to match the CW data. Owing to the measurement errors in assessing the cutter wear, the CW data may contain noise. To address this issue, data points with a CW value of 0.1 or higher were initially excluded, as they were not considered to be representative of normal wear-related data. Subsequently, within each CHI, outliers in the CW variable were identified using the isolation forest technique, and records deemed as outliers were removed. Amoun et al. (2017) revealed that among the TBM operation data, parameters such as the TF, TQ, AR, and cutter rotation speed (CRS) significantly influence the cutter wear. Accordingly, these variables were selected as the input features. Additionally, the FP, which is related to the face pressure, normal force per disc cutter (Fn), cutter seal grease temperature front (CTF), and cutter seal grease temperature rear (CTR), which are relevant to the force and temperature acting on the disc cutters, were selected as the input features. For the geological conditions, the estimated UCS from Section 3 and the weathering Grade (G1–G5) were selected as the input variables. The categorical variable, the weathering grade, was converted into numerical data using one-hot encoding. Descriptive statistics for the variables used to predict the CW are summarized in Table 5.

Table 5. Statistical summary of variables in CW prediction model.

Variables	mean	std	min	max	count
CTF (°C)	42.98	11.92	25.28	89.16	1686
CTR (°C)	34.90	6.93	20.60	52.56	1686
TQ (kN·m)	1009	108	644	1502	1686
CRS (rpm)	26.82	8.47	4.68	46.56	1686
TF (kN)	22855	2904	12623	29470	1686
FP (kPa)	372.42	72.64	209.06	546.44	1686
AR (mm/min)	9.26	2.99	2.77	19.75	1686
Fn (kN/cutter)	209.38	44.66	84.85	319.16	1686
UCS (MPa)	81.12	14.02	38.56	108.89	1686
CW (mm/km)	0.02045	0.01294	0.00219	0.08870	1686

The complete dataset was divided into training and test sets, and MinMaxScaling was applied following the procedure detailed in Section 3.1.3.

4.2 *Methodology*

A CW prediction model was developed using the KNN, SVM, RF, XGBoost, CatBoost, and LGBM algorithms. Hyperparameter optimization and performance evaluation were conducted using the same methods employed for the UCS prediction.

To investigate the importance of the input variables used in the CW prediction model, a SHapley Additive exPlanation (SHAP) analysis was conducted. SHAP, proposed by Lundberg and Lee (2017), is a method for evaluating the importance of variables in predictive models, which utilize algorithms, such as machine learning. The SHAP value (ϕ_i) was calculated as:

$$\phi_i = \sum S \subseteq N\{i\} \frac{|S|!(N-|S|-1)!}{|N|!}[f(S\cup\{1\}) - f(S)] \quad (5)$$

Where N is the set of all the features; S is the subset of N except for the ith feature; $f(S \cup \{i\})$ is the conditional expectation of the predictive model when including the ith feature; $f(S)$ is the conditional expectation of the predictive model when excluding the ith feature.

Calculating the SHAP values requires substantial computational resources as the number of features increases. Methods, such as the Kernel SHAP and Tree SHAP have been proposed to approximate the SHAP values. The Tree SHAP method exploits the internal structure of tree-based models to calculate the SHAP values accurately and quickly (Lundberg et al., 2020).

4.3 *CW prediction results*

The performance evaluation results for each model are listed in Table 6.

Table 6. Performance summary of CW prediction models.

	Test RMSE		Test R^2	
Model	mean	std	mean	std
KNN	0.00833	0.000268	0.581	0.047115
SVM	0.00965	0.000730	0.440	0.060054
RF	0.00805	0.000472	0.611	0.03276
XGBoost	0.00783	0.000440	0.630	0.043621
CatBoost	0.00798	0.000451	0.617	0.038959
LGBM	0.00791	0.000398	0.624	0.034377

The XGBoost model exhibited the lowest average test RMSE of 0.00783 and highest average test R^2 of 0.630. The LGBM followed closely, with the second-lowest average test RMSE of 0.00791 and second-highest average test R^2 of 0.624. Regarding the standard deviation of the test RMSE, the KNN, LGBM, and XGBoost models were ranked in the ascending order. Similarly, for the standard deviation of the test R^2, RF was followed by the LGBM, and CatBoost. In conclusion, the LGBM model was found to have relatively high performance and stability compared with the other models. A comparison between the CW values predicted by the LGBM models and actual CW values is shown in Figure 3.

Feature importance analysis for the LGBM was conducted using the Tree SHAP. Figure 4 shows the mean absolute SHAP values of the input features used in the LGBM.

A higher mean absolute SHAP value indicates a more important feature of the prediction model. In the LGBM, the order was CTR > TQ > AR > CTF > FP. This indicates that the cutter grease temperature (rear and front sides), torque, advance rate, and feed pressure are utilized significantly in predicting the CW in the LGBM models.

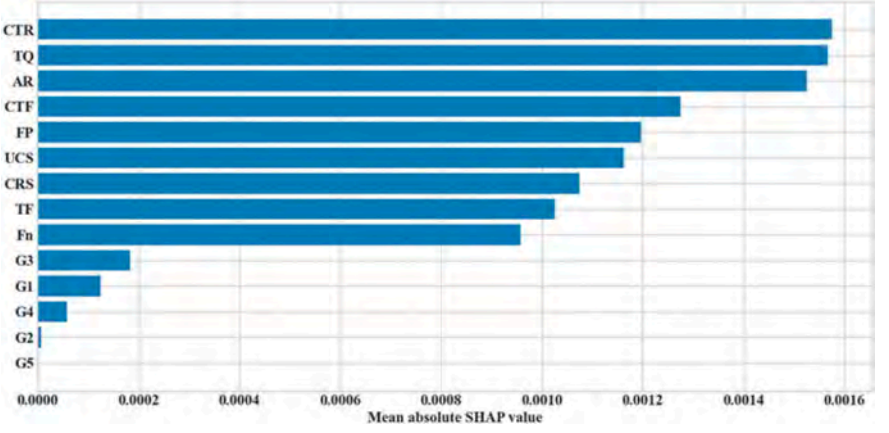

Figure 3. Plots of LGBM models.

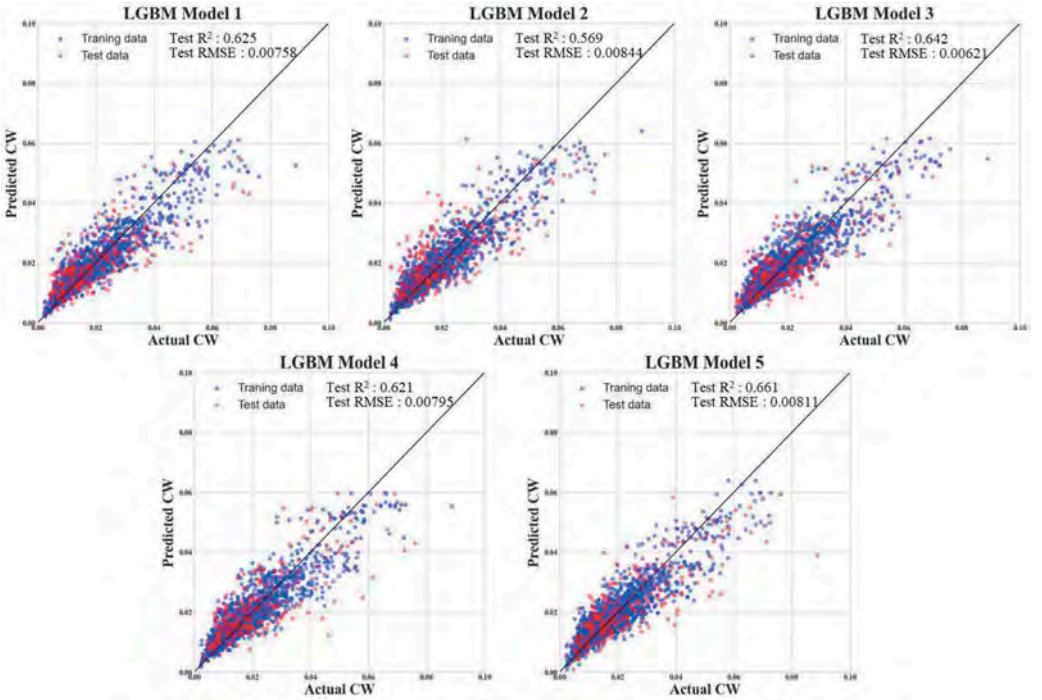

Figure 4. Mean absolute SHAP values of LGBM models.

5 CONCLUSIONS

In this study, we predicted the Coefficient Wearing rate (CW) of a slurry TBM by considering its operating parameters and geological conditions. Owing to the relative scarcity of the UCS data compared to other operations and CW data, we first predicted the UCS using the operation data and drilling survey results to address this data limitation. Subsequently, the CW predictions were performed using the complete dataset. The conclusions drawn are as follows:

(1) For the UCS prediction, we performed data preprocessing activities, such as selecting the input variables, extracting the stable states, and partitioning the data, followed by the MinMaxScaling. We created the UCS prediction models using six supervised machine-learning algorithms (KNN, SVM, RF, XGBoost, CatBoost, and LGBM) and compared their average predictive performances. The CatBoost model displayed relatively high prediction accuracy for the test data, with an average RMSE of 1.001 and an R^2 score of 0.88. Owing to its superior predictive performance and stability, the CatBoost model was selected for the UCS prediction across the recorded sections of the operation data.

(2) The CW prediction models were developed using the input variables CTF, CTR, TQ, CRS, TF, TQ, FP, AR, Fn, weathering grade (G1–G5), and UCS, employing algorithms, such as the KNN, SVM, RF, XGBoost, CatBoost, and LGBM. Upon comparing the performance of these models, the XGBoost model exhibited the lowest average test RMSE of 0.00783 and highest average test R^2 of 0.630. The LGBM followed closely, with the second-lowest average test RMSE of 0.00791 and second-highest average test R^2 of 0.624. Regarding the standard deviation of the test RMSE, the KNN, LGBM, and XGBoost models were ranked in the ascending order. Similarly, for the standard deviation of test R^2, the RF was followed by the LGBM, and CatBoost. In conclusion, the LGBM model was found to have relatively high performance and stability compared with the other models.

(3) Upon analyzing the feature importance using the Tree SHAP for the LGBM models, the top five important features were found to be the CTR, TQ, AR, CTF, and FP. This indicates that the cutter grease temperature (rear and front sides), torque, advance rate, and feed pressure are utilized significantly in predicting the CW in the LGBM models.

(4) In this study, the mean values of the operation data and geological conditions for each CHI interval were utilized to predict the cutter wear. Therefore, it did not adequately account for the variability in the operating conditions. Future research could use algorithms capable of handling time-series data to properly consider such variability, potentially improving the accuracy of cutter wear prediction.

ACKNOWLEDGMENTS

This work was supported by a National Research Foundation of Korea (NRF) grant funded by the Korean government (MSIT) (No. NRF-2022R1F1A1063228).

REFERENCES

Agrawal, A.K., Murthy, V., Chattopadhyaya, S., Raina, A., 2022. Prediction of TBM Disc Cutter Wear and Penetration Rate in Tunneling Through Hard and Abrasive Rock Using Multi-layer Shallow Neural Network and Response Surface Methods. Rock Mechanics and Rock Engineering 55(6), 3489–3506.

Amoun, S., Sharifzadeh, M., Shahriar, K., Rostami, J., Azali, S.T., 2017. Evaluation of tool wear in EPB tunneling of Tehran Metro, Line 7 Expansion. Tunnelling and Underground Space Technology 61, 233–246.

Bejari, H., Khademi Hamidi, J., 2013. Simultaneous effects of joint spacing and orientation on TBM cutting efficiency in jointed rock masses. Rock mechanics and rock engineering 46, 897–907.

Bs, B., 1999. 5930: 1999 Code of practice for site investigations. British Standard.

Ding, X., Xie, Y., Xue, H., Chen, R., 2022. A new approach for developing EPB-TBM disc cutter wear prediction equations in granite stratum using backpropagation neural network. Tunnelling and Underground Space Technology 128, 104654.

Elbaz, K., Shen, S.-L., Zhou, A., Yin, Z.-Y., Lyu, H.-M., 2021. Prediction of Disc Cutter Life During Shield Tunneling with AI via the Incorporation of a Genetic Algorithm into a GMDH-Type Neural Network. Engineering 7(2), 238–251.

Hassanpour, J., Rostami, J., Zhao, J., 2011. A new hard rock TBM performance prediction model for project planning. Tunnelling and Underground Space Technology 26(5), 595–603.

Kang, T.-H., Choi, S.-W., Lee, C., Chang, S.-H., 2022. A Study on the Prediction of Disc Cutter Wear Using TBM Data and Machine Learning Algorithm. Tunnel and Underground Space 32(6), 502–517.

Kim, Y., Hong, J., Shin, J., Kim, B., 2022. Shield TBM disc cutter replacement and wear rate prediction using machine learning techniques. Geomechanics and Engineering 29, 249–258.

Lundberg, S.M., Erion, G., Chen, H., DeGrave, A., Prutkin, J.M., Nair, B., Katz, R., Himmelfarb, J., Bansal, N., Lee, S.-I., 2020. From local explanations to global understanding with explainable AI for trees. Nature machine intelligence 2(1), 56–67.

Lundberg, S.M., Lee, S.-I., 2017. A unified approach to interpreting model predictions. Advances in neural information processing systems 30.

Mahmoodzadeh, A., Mohammadi, M., Ibrahim, H.H., Abdulhamid, S.N., Ali, H.F.H., Hasan, A.M., Khishe, M., Mahmud, H., 2021. Machine learning forecasting models of disc cutters life of tunnel boring machine. Automation in Construction 128, 103779.

Xu, D., Wang, Y., Huang, J., Liu, S., Xu, S., Zhou, K., 2023. Prediction of geology condition for slurry pressure balanced shield tunnel with super-large diameter by machine learning algorithms. Tunnelling and Underground Space Technology 131, 104852.

Tunnelling for a Better Life – Yan, Celestino, Thewes & Eberhardt (Eds)
© 2024 The Author(s), ISBN 978-1-032-80042-4
Open Access: www.taylorfrancis.com, CC BY-NC-ND 4.0 license

Leakage prediction and post-grouting assessment in headrace tunnel of a hydropower project

Tek Bahadur Katuwal*
Norwegian University of Science and Technology (NTNU), Trondheim, Norway
Tribhuvan University, IOE, Pashchimanchal Campus, Pokhara, Nepal

Krishna Kanta Panthi
Norwegian University of Science and Technology (NTNU), Trondheim, Norway

Chhatra Bahadur Basnet
Tribhuvan University, IOE, Pashchimanchal Campus, Pokhara, Nepal

Sailesh Adhikari
Norwegian University of Science and Technology (NTNU), Trondheim, Norway
Tribhuvan University, IOE, Pashchimanchal Campus, Pokhara, Nepal

ABSTRACT: In the Himalayan region, tunnels are often constructed through complex and varying geological formations having rock mass with higher degree of jointing, faulting, folding, and weakness/shear zones. Such rock mass condition significantly increases the rock mass permeability which enables a higher possibility of water leakage into and out of the headrace tunnels built for hydropower projects and is a challenging situation for tunnel stability. Therefore, comprehensive leakage assessment and effective pre- and post-grouting application are essential in hydropower tunnels. In this research, the water leakage was predicted by using three machine learning approaches such as Support Vector Regression (SVR), Decision Tree (DT) regression, and K-Nearest Neighbors (KNN) models. The water leakage/inflow was predicted in one of the hydropower tunnels based on the geological condition of rock mass, rock mass quality, and hydro-geological conditions. The effective post-grouting method was applied to mitigate the potential water leakage and to enhance the rock mass quality and stability of the hydropower tunnel. It was observed that the injection grouting technique helps to make tunnels less permeable, reduces instability conditions, and ensures the long-term safety and structural integrity of the hydropower tunnels.

Keywords: Complex geology, Machine Learning, Leakage, Stability, Post-grouting

1 INTRODUCTION

The tunnel construction in the Himalayan region faces severe tunneling challenges due to the complex geological conditions characterized by a higher degree of jointing, high degree of faulting, folding, weathering, and the presence of weakness/shear zones within the rock mass (Panthi 2006). These complex geological conditions are due to the consequence of active tectonic activities in the region. These conditions significantly increase rock mass permeability and make headrace tunnels of hydropower projects susceptible to water leakage. Thus, groundwater inflow and leakage are the most common and challenging issues in hydropower tunnelling projects in the Himalayan region (Panthi 2006). Water ingress into these tunnels not only affects the stability of the tunnel but also poses operational and safety risks, which could lead to project delay and huge economic loss (Panthi and Nilsen 2010). Therefore, an accurate water inflow/leakage assessment is essential for timely measure and control of water inflow/leakage, and the selection of appropriate grouting techniques to enhance the strength of rock mass and to secure stability of water tunnels.

Many researchers highlight the use of analytical, empirical, and numerical techniques and theoretical frameworks for the prediction of water ingress and grouting capability. However, it is challenging to predict the accurate amount in tunnelling projects (Holmøy 2008 and Stille 2015). To mitigate these limitations, machine learning (ML) techniques could be an appropriate approach to predict the water inflow/leakage and to decide effective grouting

*Corresponding author: tek.b.katuwal@ntnu.no

DOI: 10.1201/9781003495505-404

measures. However, this is challenging due to the limited availability of field data related to rock mass properties, structural geology, groundwater level, project topography, and effective stresses.

This paper attempts to present different machine learning (ML) approaches for comprehensive assessment and prediction of water inflow/leakage, and the application of injection grouting to reduce water leakage and enhance tunnel stability in the headrace tunnel of 54 MW Super Dordi Hydropower Project (SDHEP).

2 PROJECT BACKGROUND

2.1 *Brief about SDHEP*

The Super Dordi Hydropower Project "Kha" (hereafter referred to as SDHEP) is a Run-of-River (ROR) project, which is located at Dordi Rural Municipality, Lamjung District, Gandaki Province of Nepal, which is about 188 km northwest of Kathmandu. Geographically, this project area is located between Longitudes 84°34'15" E and 84°31'00" E, and Latitudes 28° 18'43" N and 28°16'20" N. The project is a high-head scheme with a gross head of 638 m and has a design discharge is 9.9 m^3/sec. The total installed capacity of this project is 54 MW. The main components of this project are low-head diversion dam (18.5 m X 3.3 m), D – shaped gravel trap (36 m X 4 m X 2.3-4 m), double-chamber desander basins (123 m X 11 m X 13 m), D – shaped headrace tunnel (2.8 m Dia and 5.2 km length), surge shaft (6 m Dia. and 49 m height), pressure shafts (2.2 m dia. and 1052 m long including penstock branches to two turbines), underground powerhouse (51.3 m X 15 m X 29.6 m), tailrace tunnel, and access tunnel (PHCPL 2022). In order to address the challenges associated with frequently occurring high tectonic activity and the risk of landslides, and to ensure long-term stability, the major water conveyance structures such as the desander, headrace tunnel, surge shaft, penstock shaft, powerhouse cavern, and tailrace tunnel are strategically constructed underground.

2.2 *Project geology*

Geologically, the SDHEP area is located in the Higher Himalayan range. The major rock types are schist and gneiss as shown in Figure 1. Predominantly, the geological composition of the area consists of banded gneiss with schist partings (Adhikari et al. 2023, Katuwal et al. 2023). These geological formations extensively appear in the Higher Himalayan region, spanning from east to west across the entire Himalayan range.

The upper part of the headrace tunnel (HRT) encountered the slightly to moderately weathered and medium foliated strong gneiss. A relatively short stretch of the tunnel section encountered fresh to slightly weathered gneiss, which is more dominant with quartz content. Likewise, the downstream section of HRT, surge shaft, penstock shaft, and powerhouse cavern encountered the slightly to moderately weathered and medium foliated strong gneiss. Mainly, the bended gneiss with occasional schist parting is encountered along the alignment of the headrace tunnel. The topography of the project area is covered by mainly two soil types, i.e., colluvial and alluvial soil. The colluvial soil consists high content of fine silt and clay which is exposed on the surface of the HRT alignment. Likewise, the surface of powerhouse and headworks are exposed to alluvial soil which consists of predominantly coarse-grained material such as sand, gravel, cobble, and boulder.

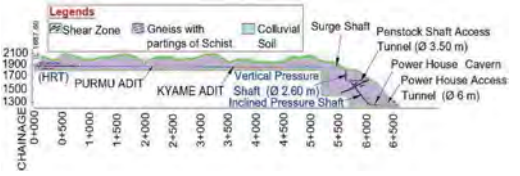

Figure 1. Longitudinal Profile of SDHEP.

3 MACHINE LEARNING TECHNIQUES

Nowadays, machine learning (ML) techniques have been widely applicable to predict water ingress in tunnel projects. The ML approach shows good performance in predicting water inflow/leakage in tunnel projects (Mahmoodzadeh et al. 2023). Therefore, in this paper, three ML regression models such as Support Vector Regression (SVR), Decision Tree (DT) regressor, and K-Nearest Neighbors (KNN) are used to predict the water inflow/leakage at the SDHEP headrace tunnel. These regression models help to predict the dependent variables from several features or independent variables. The most appropriate regression model has been established by comparing the eight statistical indices such as R-squared (R^2), Mean Absolute Error (MAE), Mean Squared Error (MSE), Root Mean Squared Error (RMSE), Relative Root Mean Squared Error (RRMSE), Mean Absolute Percentage Error (MAPE), Mean Relative Error (MRE), and Variance Accounted For (VAF). For this purpose, the research methodology is set up mainly with four components such as dataset preparation, model selection, training and validation of selected model, and result analysis and discussions.

3.1 *Database study*

To predict the water ingress/leakage in the hydropower tunnels, it is necessary to collect the filed data and select the effective parameters. Therefore, in this case study, the number of datasets and types of effective parameters such as Rock Quality Designation (RQD), Joint number (Jn), Joint Roughness (Jr), Joint alteration number (Ja), Q-Classification value (Q), static head (h), overburden (H), shortest distance from the tunnel to topography (d), and specific discharge (q),

average Lugeon Unit (LU) are collected based on actual data received from the project. The summary of the field datasets is presented in Tables 1 and 2, which are used for training and testing parameters. These tables depict the statistical description of selected parameters by defining the minimum, standard deviation, maximum, mean values, and different percentile values.

Table 1. Field datasets for rock mass quality.

	RQD	Jn	Jr	Ja	Q
Count	175	175	175	175	175
Mean	62.17	6.19	1.57	1.55	7.77
Std	9.52	1.17	0.3	0.55	5.69
Min	30	3	1	1	1.1
25%	55	6	1.5	1	3.33
50%	65	6	1.5	2	6
75%	70	6	1.5	2	10.24
Max	80	9	3	3	30

Table 2. Field datasets for topography and water inflow.

	h (m)	d (m)	H (m)	q (lit/min/m)	LU
Count	175	175	175	175	175
Mean	11.3	139.35	173.5	3.52	1.61
Std	7.86	20.53	21.7	6.21	2.82
Min	0.19	63	120	1.28	0.56
25%	3.39	128.5	163	1.95	0.91
50%	14.61	138	170	2.26	1.05
75%	19.96	150	179	2.88	1.3
Max	20.56	191	231	59.51	27.3

3.1.1 *Correlation analysis*

In machine learning, the correlation heatmap is often used to establish and visualize the strength of relationship (multicollinearity) between the multiple feature variables and dependent variables. The accuracy of the predicted model is significantly influenced by the multicollinearity numerical values. In this heat map, Color-coding cells make it easy to see how variables are related with a quick look.

In this research, the correlation heatmap analysis (using the Pearson correlation coefficient) was performed between collected database from the head-race tunnel. This process illustrates the interrelation between independent features and dependent variable. The range of this analysis lies within [-1, 1]. A high value of [+1] means these variables are highly correlated and have a high positive effect and vice versa. In Figure 2, the positive correlation value of 0.62 is seen between the RQD and Q-value, which is remarkable since an increase in the RQD value will give an increased quality of rock mass. The Figure also depicts that the rate of water ingress/leakage positively correlated with the overburden, and joint alteration number. On the other hand, parameters such as RQD, Q-value, and joint roughness are inversely correlated. Moreover, Figure 2 indicates that the correlation between the available datasets seems relatively low. This may be due to the fact that the water ingress and grout consumption are also influenced by variables such as persistence, joint volume, spacing of joints, and infilling material characteristics.

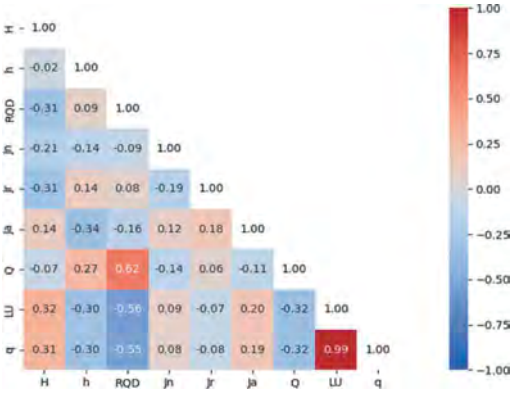

Figure 2. Correlation matrix for database.

3.1.2 *Principal Component Analysis (PCA)*

The PCA is a multivariate statistical approach that is used for the dimensionality reduction of project databases. For this purpose, the principal components have been established to describe the linear combination of features and to define the variation in the selected database. Figure 3 illustrates the screen plot of principal components for the ingress/leakage of water. This Figure clearly explains that 90% of selected database variance is explained by the six major principal components. The variability of each variable in these principal components are presented in Table 3.

Table 3. A Summary of principal components coefficients.

Variables	PC1	PC2	PC3	PC4	PC5	PC6
h	-0.27	-0.15	-0.44	-0.35	0.29	-0.54
H	0.15	0.04	-0.58	0.5	0.41	0.13
RQD	-0.4	0.23	0.31	0.01	0.23	0.45
Jn	0.19	-0.28	0.55	-0.13	0.53	-0.32
Jr	-0.21	0.62	-0.03	-0.2	-0.29	-0.34
Ja	0.16	0.34	0.26	0.63	0	-0.49
Q	-0.39	0.37	0.02	-0.01	0.54	0.07
LU	0.5	0.32	-0.06	-0.28	0.16	0.09
q	0.49	0.33	-0.06	-0.3	0.15	0.13
Eigenvalues	2.89	1.50	1.34	1.11	0.82	0.78
Variability (%)	31.88	16.52	14.78	12.26	9.08	8.57
Cumulative (%)	31.88	48.40	63.18	75.77	84.53	93.10

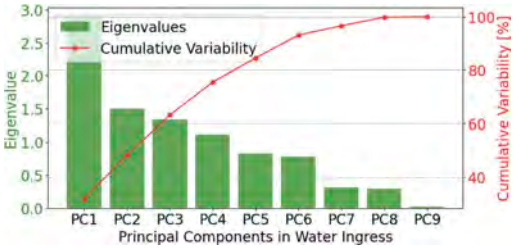

Figure 3. Screen plot for Principal Components.

3.1.3 *Variance Inflation Factor (VIF)*

Dimension of the given data set is primarily reduced by the PCA analysis without quantifying the multicollinearity. To address this limitation, the Variance Inflation Factor (VIF) has been applied. The correlation strength between the independent variables has been established by using the VIF. Moreover, the VIF can provide information about the severity and presence of multicollinearity in the databases, which is illustrated in Table 4. The VIF = 1 indicates no multicollinearity between the selected variables. When the value of the VIF is greater than 10, it is a sign of a high degree of multicollinearity between the variables and it will be problematic in the regression models, therefore, eliminating these features will be easier for regression analysis. However, the selection of independent variables depends upon the selection of the regression model (Cheng et al. 2022). In this research, all parameters are considered for the establishment of a regression model.

Table 4. A summary of Variance Inflation Factor (VIF).

For q	H	h	RQD	Jn	Jr	Ja	Q	LU
VIF	45.9	4.3	65.3	25.1	31.5	11.8	4.8	4.9

3.2 *Data distribution*

The selected datasets have been organized into distinct plots to enable quick visualization and enhance understanding. To accomplish this, box plots were initially generated for the chosen datasets. It was observed that the Jn, Jr, and Ja datasets displayed limited data variability and were not well-distributed. To address this limitation, the plot performance has been enhanced by incorporating both box and histogram plots for the selected datasets as shown in Figure 4. Histograms display how data is distributed in terms of shape and frequency. In contrast, box plots are useful for a rapid assessment of central tendencies, data spread, and the presence of outliers.

In Figure 4, except the box plot data of h, and RQD, the data are out of the middle of the box. Therefore, to address this issue and combine both of these distribution representations into a single plot,

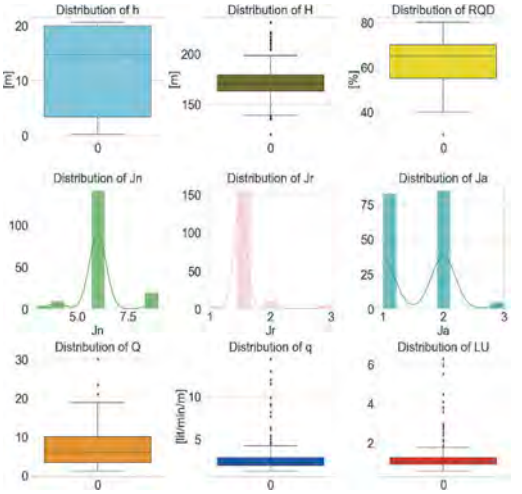

Figure 4. Multivariate data visualization of selected parameters.

the violin plot is found to be a more effective choice for visualizing of data that has multiple peaks or a skewed distribution. Likewise, a violin plot is the configuration of the data set that enhances clarity and understanding. Moreover, the violin plots illustrate the summary of statistics and probability density function (or density) of each feature and dependent variables. Figure 5 illustrates the distribution of the statical quartile summary of filed data set. In these Figures, a wider region of density plot indicates the more frequent occurrence and vice versa.

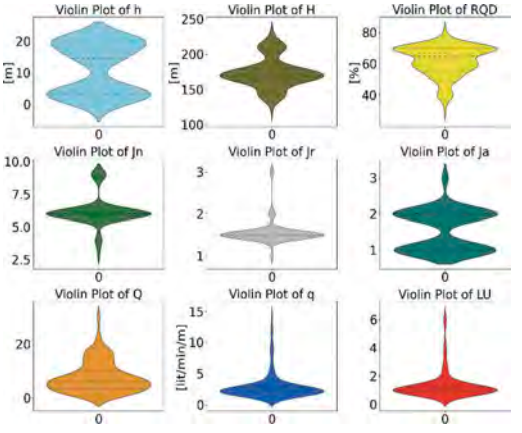

Figure 5. Datasets distribution in violin plot.

3.3 *Data normalization*

Data normalization constitutes a fundamental process within the domain of machine learning (ML). This procedure is essential due to the inherent variability in the dimensions and units of input data,

which can fluctuate with changing input data. The act of normalization serves to rescale all input features and variables to a uniform scale. Table 1 and 2 depicts that the range of specific discharge varies from 1.28 lit/min/m to 59.51 lit/min/m, whereas the joint alteration number (Ja) varies from 1 to 3 and the height of overburden varies from 120 m to 131 m. This indicates that the magnitude of input variables are in different scales. Therefore, data normalization should be conducted for better correlation and prediction of machine learning models.

3.4 *Statistical analysis of selected model*

Statistical evaluation of selected model plays a crucial role in understanding and predicting the efficient model for headrace tunnels of hydropower projects. Therefore, various statistical indices such as R-squared (R^2), Mean Absolute Error (MAE), Mean Squared Error (MSE), Root Mean Squared Error (RMSE), Relative Root Mean Squared Error (RRMSE), Mean Absolute Percentage Error (MAPE), Mean Relative Error (MRE), and Variance Accounted For (VAF) are calculated by using Equation 1 to Equation 8, respectively. The linear correlation between the predicted and actual values is established by using R^2.

$$R^2 = 1 - \frac{\text{sum of squared regression (SSR)}}{\text{sum of squared total (SST)}} \quad (1)$$

$$\text{MAE} = \frac{1}{n}\sum_{i=1}^{n} |y_i^a - y_i^p| \quad (2)$$

$$\text{MSE} = \frac{1}{n}\sum_{i=1}^{n} \left(y_i^a - y_i^p\right)^2 \quad (3)$$

$$\text{RMSE} = \sqrt{\frac{1}{n}\sum_{i=1}^{n} \left(y_i^a - y_i^p\right)^2} \quad (4)$$

$$\text{RRMSE} = \sqrt{\frac{1}{n}\sum_{i=1}^{n} \left(\frac{y_i^a - y_i^p}{y_i^a}\right)^2} \quad (5)$$

$$\text{MAPE} = \frac{1}{n}\sum_{i=1}^{n} \left|\frac{y_i^a - y_i^p}{y_i^a}\right| * 100\% \quad (6)$$

$$\text{MRE} = \frac{1}{n}\sum_{i=1}^{n} \left|\frac{y_i^a - y_i^p}{y_i^a}\right| \quad (7)$$

$$\text{VAF} = 1 - \left|\frac{va\left(y_i^a - y_i^p\right)}{var\left(y_i^a\right)}\right| * 100\% \quad (8)$$

Where, actual and predicted values of variables are represented by y_i^a and y_i^p respectively, and n in the equations is the total number of datasets that are used in selected machine learning models.

4 WATER INFLOW PREDICTION MODEL AND RESULTS

In this study, Support Vector Regression (SVR), Decision Tress (DT), and K-Nearest Neighbors (KNN) models are applied for the assessment and prediction of water ingress in the headrace tunnel of SDHEP in Anaconda version 3.6 with computation in Python.

4.1 *Support Vector Regression (SVR)*

Support Vector Regression (SVR) is a machine-learning technique specifically adapted for predicting water ingress in the headrace tunnel. It connects the capabilities of support vector machines to model and predict water ingress into hydropower tunnels, which supports rock engineers to make well-informed choices for effective management and mitigation of water ingress challenges. The Figure 6 illustrates the water inflow prediction by using this SVR model.

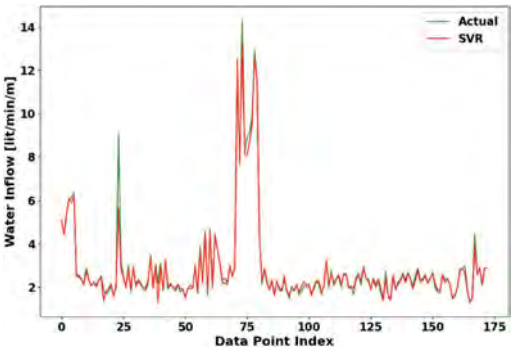

Figure 6. SVR model for water inflow prediction.

As Figure 6 indicates, there is a good correlation between the model and different dependent variables. Table 5 provides information about the statistical indices R^2, MAE, MSE, RMSE, RRMSE, MAPE, MRE, and VAF which are evaluated as 0.99, 0.09, 0.02, 0.12, 0.05, 3.47, 0.48, and 99.6, respectively, where the SVR model indicates high degree of accuracy. Therefore, this ML model has a good capacity for the prediction of water leakage/inflow in hydropower tunnels.

Table 5. A summary of statistical indices of SVR model.

R2	MAE	MSE	RMSE	RRMSE	MAPE	MRE	VAF
0.99	0.09	0.02	0.12	0.05	3.47	0.48	99.6

4.2 *Decision Tree (DT)*

A Decision Tree (DT) is the most widely used predictive model for regression analysis in the context

of hydropower tunnels to forecast and assess the probability of water ingress. It's a visual representation of a decision-making process that considers various factors and their interactions to determine the probability of water inflow/leakage in/from the tunnels. This tool helps rock/tunnel engineers make decisions to prevent and manage water ingress effectively, ensuring the safety and efficiency of hydropower operations.

The Figure 7 illustrates the comparison between the actual field data set and the water inflow prediction by using this DT model. Likewise, Table 6 establishes the statistical indices R^2, MAE, MSE, RMSE, RRMSE, MAPE, MRE, and VAF which are evaluated as 0.97, 0.14, 0.08, 0.29, 0.10, 4.67, 0.98, and 97.6, respectively, which indicate that the DT models have a good capacity for the prediction of water inflow. The statical indices indicated that this model presents a good correlation with the features and dependent variables.

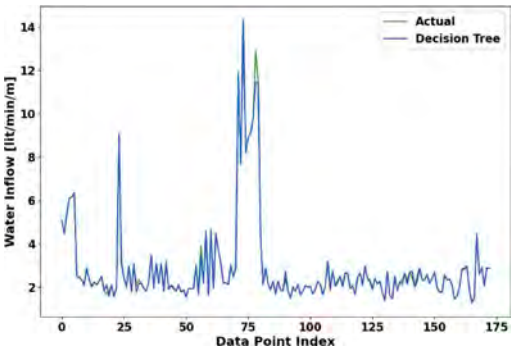

Figure 7. DT model for water inflow prediction.

Table 6. A summary of statistical indices of SVR model.

R2	MAE	MSE	RMSE	RRMSE	MAPE	MRE	VAF
0.97	0.14	0.08	0.29	0.10	4.67	0.98	97.6

4.3 *K-Nearest Neighbors (KNN)*

A K-Nearest Neighbors (KNN) is the most widely used predictive model for regression. Figure 8 illustrates the comparison between the actual field data set and the KNN prediction model for water inflow in the case tunnel project. Table 7 demonstrates the statistical indices R^2, MAE, MSE, RMSE, RRMSE, MAPE, MRE, and VAF which are evaluated as 0.89, 0.45, 0.38, 0.61, 0.22, 17, -1.22, and 88.9, respectively. The statical indices indicated that this model presents a good correlation with the features and dependent variables. All outcomes indicate that the KNN models have a good capacity and are acceptable for the prediction of water inflow in hydropower tunnels.

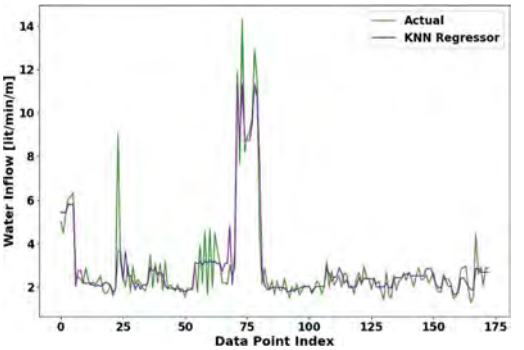

Figure 8. KNN model for water inflow prediction.

Table 7. A summary of statistical indices of SVR model.

R2	MAE	MSE	RMSE	RRMSE	MAPE	MRE	VAF
0.89	0.45	0.38	0.61	0.22	17	-1.22	88.9

5 GROUT CONSUMPTION

Post-grouting technique is very often used to control water leakage from headrace tunnels of hydropower projects in the Himalayan region. The measurement of the Lugeon value, which assesses rock permeability, plays a pivotal role to evaluate the effectiveness of post-grouting. At SDHEP, the post-grouting technique was used to control potential water leakage from the headrace tunnel. The post-grouting technique involves the injection of cement grout into the surrounding rock mass to achieve substantial sealing of joints and discontinuities and reduce permeability. A typical drill hole pattern adopted while post-grouting is illustrated in Figure 9. This Figure demonstrates the drill hole length, and drilling pattern in both the hill and valley sides of the headrace tunnel are shown. Likewise, a detailed description of the parameters associated to post-grouting is illustrated in Table 8.

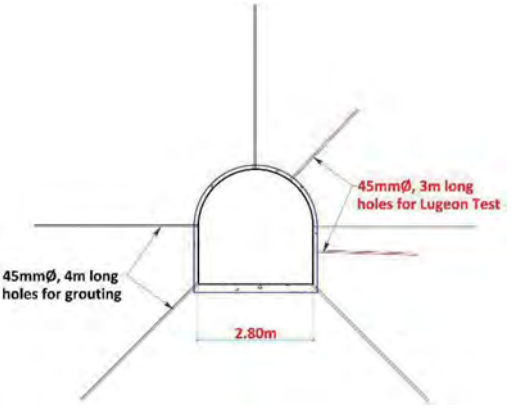

Figure 9. Detail illustration of drill hole arrangement.

At SDHEP the post-grouting not only enhanced the structural integrity of the rock mass but also established a water-resistant barrier, thereby minimizing the risk of water leakage from the tunnel. Consequently, the combination of post-grouting and the reduction in Lugeon value ensured the long-term structural integrity and operational reliability of the water tunnel.

Table 8. Parameter for Injection Grouting.

Parameters	Values
Drill hole length (m)	4
Drill hole diameter (mm)	45-48
Packer diameter (mm)	42
Placement of Packer inside (m)	2
Minimum Grouting Pressure (bar)	4-6
Grout pressure at seepage area (bar)	15
Bentonite (%)	5
Plasticizer (%)	1.5-3
Retarder (if mixed outside) (%)	1.5
W/C ratio	1:1

5.1 *Grout consumption assessment*

The effective post-grouting work is very challenging since it is extremely difficult to achieve targeted pressure without losing unnecessary extra grout material. Therefore, the effective post-grouting work is a challenging task since the grout take is significantly affected by the rock mass properties, topographical condition, structural geology, joint infilling material, groundwater level and effective rock stress conditions. The summary of the field datasets is presented in Table 9, which illustrates the rock mass class (RMC) count and statistical variation of selected parameters that defines minimum, maximum, mean values, standard deviation, and different percentile values.

The pairwise data relationships between different parameters used in grout consumption assessment are illustrated in Figure 10. The Figure shows pairwise plot or scatterplot matrix. This plot helps to visualize and explore different independent and dependent variables. The plot can describe how different variables are relative to each other based on different types of rock mass classes. Moreover, the plot provides a quick overview of the relationship between grout consumption (GC), joint aperture (e), hydraulic

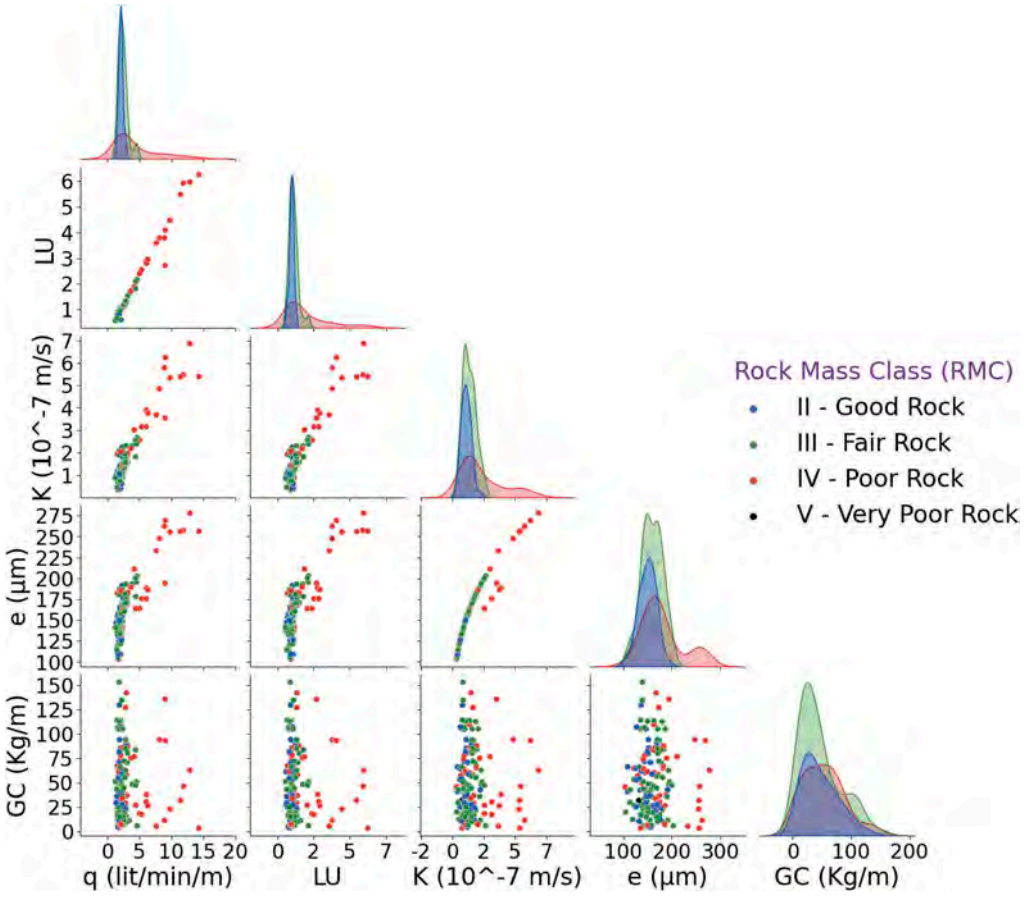

Figure 10. Grout consumption data relationship.

Table 9. Field Datasets for Grout Consumption.

	q (lit/min/m)	LU	K (10^-7 m/s)	e (μm)	GC (Kg/m)
Count	173				
RMC	II = 44, III = 78, IV = 50, V = 1				
Mean	2.88	1.32	1.57	162.04	47.91
Std	2.09	0.95	1.11	30.43	33.68
Min	1.28	0.56	0.35	103.25	3
25%	1.94	0.91	0.94	143.45	22.5
50%	2.24	1.05	1.28	158.78	41.5
75%	2.86	1.26	1.71	174.39	66
Max	14.31	6.26	6.86	277.92	153

permeability (K), Lugeon unit (LU), and water ingress (q) for rock mass class (RMC) II, III, IV, and V. For example, in the context of rock mass classified as Type IV, a high degree of fracture aperture can significantly increase the hydraulic permeability of the rock mass. As the Lugeon unit, a measure of permeability increases, it signifies a higher propensity for water ingress from the hydropower tunnel. Consequently, to mitigate this condition and ensure the stability of the tunnel, large quantities of grout material may be necessitated to seal the fractures and reduce water leakage. Therefore, the matrix is a valuable tool for gaining insights and is particularly useful when dealing with multivariate data, as it offers a quick and comprehensive overview of the relationships between variables, helping in the initial stages of data exploration.

The relationship between water leakage, Lugeon unit, and grout consumption is shown in Figure 11. Likewise, the relationship between hydraulic permeability, hydraulic aperture, and grout consumption is illustrated in Figure 12.

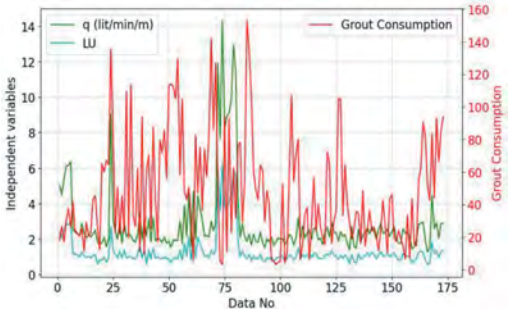

Figure 11. Relationship between water inflow, Lugeon unit, and grout consumption.

6 RESULT ANALYSIS AND DISCUSSION

The water leakage and grout consumption assessments were made on the headrace tunnel of SDHEP. The assessment was conducted using field datasets

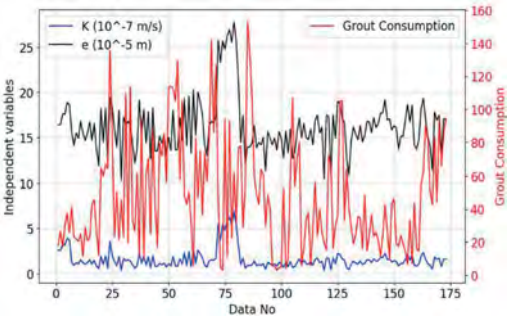

Figure 12. Relationship between hydraulic permeability, hydraulic aperture, and grout consumption.

related to the rock mass quality, hydro-geological conditions, Lugeon unit, and grout consumption.

6.1 *Result comparison of water inflow prediction*

Various machine learning models were employed to predict water leakage from the headrace tunnel. The prediction was then compared to actual datasets. All models demonstrated acceptable and good predictive performance individually. However, it is essential to compare and rank these models to enhance the reliability of selected models. To achieve this, statistical indices were used to evaluate and categorize the performance of each model as good, better, or best, with respective weightings of 1, 2, and 3. The overall ranking of each model was determined by summing assigned weights. Table 10 illustrates the comparative ranking of selected models. The table shows that the SVR, DT, and KNN models perform best, better, and good performance, respectively to predict the ingress of water.

Table 10. Comparison of Water inflow predicted models.

Parameter/Model		SVR	DT	KNN
R^2	Value	0.99	0.97	0.89
	Weightage	3	2	1
MAE	Value	0.09	0.14	0.45
	Weightage	3	2	1
MSE	Value	0.02	0.08	0.38
	Weightage	3	2	1
RMSE	Value	0.12	0.29	0.61
	Weightage	3	2	1
RRMSE	Value	0.05	0.10	0.22
	Weightage	3	2	1
MAPE	Value	3.47	4.67	17
	Weightage	3	2	1
MRE	Value	0.48	0.98	-1.22
	Weightage	3	2	1
VAF	Value	99.6	97.6	88.9
	Weightage	3	2	1
Remarks	Total Weitage	24	16	8
	Rank	1	2	3

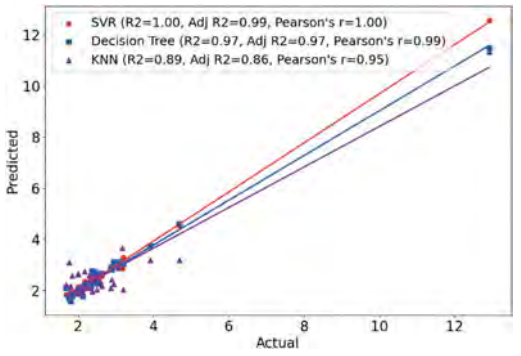

Figure 13. Actual and prediction results in comparisons.

The performance of the selected models is compared using statistical tools such as R-squared, Adjusted R-squared, and Pearson's r value. The actual test database and predicted results of the selected ML models are presented in Figure 13. In the Figure, SVR shows the strongest correlation between the predicted and actual databases, followed by the DT and KNN regression models. Moreover, Pearson's r measures how closely the data points in the scatterplot cluster around a straight line. The authors found that the SVR model quantifies a strong linear relationship between variables, followed by the DT and KNN models. However, all selected ML models establish a strong relationship between actual and predicted variables.

6.2 *Result comparison of grout consumption*

In the above section, the relationship between different independent variables such as water inflow, Lugeon unit, hydraulic permeability, and hydraulic aperture are plotted with grout consumption volume. These curves show fairly good correlations between these parameters in most of the chainage and rock mass conditions. In some parts, the results show unusual tendencies. However, after injection grouting the ingress of water is fully controlled and the headrace tunnel is well-functioning. Hence, the post-injection grouting was successful and has significantly reduced the water leakage potential and rock mass permeability and improved the rock mass strength, and enhanced tunnel stability.

7 CONCLUSION

A comprehensive overview of water ingress/leakage in the headrace tunnel of SDHEP was conducted based on the field data consisting of geology, hydrogeology, and injection grout parameters. After that, thorough data interpretation, statistical correlation, and regression analysis were performed using machine learning algorithms to predict water leakage from the headrace tunnel. It has been observed that machine learning techniques may be successfully used to assess the water ingress potential of the headrace tunnels of hydropower projects. Different machine learning regression models, such as Support Vector Regression (SVR), Decision Tree (DT), and K-Nearest Neighbors (KNN), have demonstrated the ability to predict water inflow/leakage in the water tunnel. As the field continues to evolve, the integration of machine learning in the management of water tunnels may prove to be a helpful tool for assessing tunnel stability challenges.

ACKNOWLEDGMENTS

This research was supported by NORHED II Project 70141 6; Capacity Enhancement in Rock and Tunnel Engineering at the Pashchimanchal Campus (WRC), Institute of Engineering (IoE), Tribhuvan University (TU), Nepal. The authors like to acknowledge NORAD, Norway for funding the project. In addition, the authors are thankful to the management of Peoples Hydropower Company (P) Ltd for providing access to map and collect necessary information and data related to SDHEP.

REFERENCES

Adhikari, S., Panthi, K. K. & Basnet, C. B. 2023. Stability issues associated with the construction of underground caverns of Super Dordi Hydropower Project, Nepal. 15th ISRM Congress 2023 & 72nd Geomechanics Colloquium, Schubert & Kluckner (eds.) © ÖGGAt: Salzburg Congress, Austria, pp. 1199–1204.

Cheng J., Sun J., Yao K., Xu M., & Cas Y. 2022. A variable selection method based on mutual information and variance inflation factor. Spectrochimica Acta Part A: Molecular and Biomolecular Spectroscopy, 268, 120652.

Holmøy, K. H. 2008. Significance of Geological Parameters for Predicting Water Inflow in Hard Rock Tunnels. Ph.D. Theses at NTNU 2008:291. Norwegian University of Science and Technology, Trondheim, Norway. ISBN 978-82-471-1284-7.

Katuwal, T. B., Panthi, K. K. & Basnet, C. B. 2023. Challenges associated with the construction of vertical and inclined shafts in the Himalayan Region. 15th ISRM Congress 2023 & 72nd Geomechanics Colloquium, Schubert & Kluckner (eds.) © ÖGGAt: Salzburg Congress, Austria, pp. 1199–1204.

Mahmoodzadeh A., Ghafourian H., Mohammed A. H., Rezaei N., Ibrahim H.H. & Rashidi S. 2023 Predicting tunnel water inflow using a machine learning-based solution to improve tunnel construction safety. Transportation Geotechnics, 40, 100978.

Panthi, K. K. 2006. Analysis of Engineering Geological Uncertainties Related to Tunnelling in HimalayanRock Mass Conditions. Ph.D. Theses at NTNU 2006:41. Norwegian University of Science and Technology. ISBN 82-471-7825-7.

Panthi, K.K., Nilsen, B. 2010. Uncertainty Analysis for Assessing Leakage Through Water Tunnels: A Case from Nepal Himalaya. Rock Mech Rock Eng 43, 629–639.

PHCPL, 2022. Progress Report of Super Dordi Hydropower Project. Peoples Hydropower Company (P) Ltd., pp.1–55.

Stille, H. 2015. Rock Grouting - Theories and Applications. BeFo – Rock Engineering Research Foundation. ISBN 978-91-637-7638-0.

Tunnelling for a Better Life – Yan, Celestino, Thewes & Eberhardt (Eds)
© 2024 The Author(s), ISBN 978-1-032-80042-4
Open Access: www.taylorfrancis.com, CC BY-NC-ND 4.0 license

A novel machine-learning model for estimating disc cutter life in TBMs considering individual cutter travel lengths

Dongku Kim*
Department of Geotechnical Engineering Research, Korea Institute of Civil Engineering and Building Technology (KICT), Gyeonggi-Do, Korea

Youngjin Shin
R&D division, Hyundai Engineering & Construction, Seoul, Korea

Donggyou Kim & Chulhee Lee
Department of Geotechnical Engineering Research, Korea Institute of Civil Engineering and Building Technology (KICT), Gyeonggi-Do, Korea

Kibeom Kwon & Hangseok Choi
School of Civil, Environmental & Architectural Engineering, Korea University, Seoul, Korea

ABSTRACT: The replacement of damaged or worn disc cutters in tunnel boring machines (TBMs) leads to significant costs and downtime, affecting TBM utilization and advance rates. Therefore, accurately estimating disc cutter lifespan is crucial for efficient TBM deployment in tunnelling projects. In this study, a novel machine-learning-based prediction model designed to forecast disc cutter wear, taking into account individual cutter travel lengths was proposed. The model was implemented using the cutter head intervention (CHI) report from the hard rock excavation section of Daegok-Sosa tunneling project in Korea. Incorporating 9 wear-inducing factors, the developed model demonstrated exceptional prediction accuracy for the single-ring excavation lengths. The proposed model is expected to improve existing disc cutter lifespan prediction methodologies and reduce associated costs and time impact.

Keywords: Disc cutter wear prediction, Machine Learning, EPB TBM Tunnelling

1 INTRODUCTION

The global use case of tunnel boring machines (TBMs) in the tunnelling industry has surged, attributed to their superior performance in ensuring safety and environmental sustainability. Earth Pressure Balance (EPB) TBMs, in particular, are utilized in fine-graded ground conditions where the balance of earth pressure is maintained to prevent ground collapse and to control the advancement of the machine. One of the critical components of TBM is the disc cutter, which plays a pivotal role in the excavation process. These cutters, essential for rock-breaking, undergo wear during TBM operations, necessitating timely replacements to maintain efficiency. Thus, accurately predicting cutter lifespan is crucial for cost-effective tunnelling (Hassanpour et al., 2015).

Several researchers developed disc cutter wear prediction models in TBMs, primarily based on empirical data from past tunnelling projects. Notably, the Colorado School of Mines (CSM) and the Norwegian University of Science and Technology (NTNU) models are well-known. The CSM model, grounded in the Cerchar abrasivity index (CAI), offers a semi-theoretical approach (Rostami, 1993; 1997), while the NTNU model is more empirically driven, utilizing extensive field data (Bruland, 1998). Despite these models, predicting cutter wear remains challenging due to the variability in geological conditions and TBM specifications. Many models, while effective in specific projects, falter in broader applications, emphasizing the absence of a universally applicable model.

Given the complexities of disc cutter wear, influenced by diverse geological conditions and TBM operational nuances, there's a growing interest in applying machine learning (ML) for predictions. Recent advancements in ML, as showcased by studies like Kim et al. (2020) and Mahmoodzadeh et al. (2021),

*Corresponding author: dkkim22@kict.re.kr

DOI: 10.1201/9781003495505-405

have demonstrated promising results in predicting cutter wear. Specifically, the Random Forest(RF) method has shown high accuracy in wear predictions. However, a gap remains in predicting wear across different disc locations, highlighting the need for more comprehensive models to predict the individual cutter wear amount instead of the average disc cutter wear.

This research investigates into machine learning-based prediction models, focusing on the random forest (RF) method, to predict the individual cutter wear amount accumulated during a single ring excavation length. Specifically, the wear of individual disc cutters were incorporated for the first time to factor the travel lengths of each disc cutter. Encompassing geological conditions, TBM operational data, and cutter wear records, total of 17,947 datasets were employed to train and test the cutter wear predicting model.

2 SITE DESCRIPTION

2.1 *Overview of project and machinery*

The Daegok–Sosa railway project spans 18.4 km, linking the Sosa–Wonsi railway to the western coast and enhancing the railway grid in northwest Seoul, as shown in Figure 1. It encompasses two parallel tunnels, each 2.7 km, with a section of 1.2 km beneath the

Figure 1. Construction plan overview.

Han River at depths between 25–55 m. To navigate these challenging terrains, two earth pressure balance (EPB) shield TBMs were employed, featuring inner and outer diameters of 7.0 m and 7.7 m. Key TBM specifications are demonstrated in Table 1.

Table 1. Key specifications of EPB TBM.

Specification [Unit]	Range
Torque [kNm]	7510-12,843
Maximum thrust force [kN]	66,523
Rotational speed [rpm]	0-3.7
Segment length [m]	1.5
Power [kW]	2080 (13x160)

2.2 *Geological conditions*

Situated in the Gyeong-gi massif, the tunnel area is characterized by a Precambrian gneiss complex and granite intrusions from the Jurassic era. The alignment reveals a mix of alluvial deposits, including sand, silt, and clay, with granite and gneiss layers, as shown in Figure 2. Notably, the gneiss and granite exhibit high abrasiveness, indicated by Cerchar abrasivity index (CAI) values of 4–6. The tunnelling encountered mixed geological formations, segmented into mixed ground, hard rock, and soft ground sections. This research primarily delves into the hard rock sections located between chainage 4800–5600, to analyse on the abrasive wear rate of disc cutters during the hard rock zone excavation.

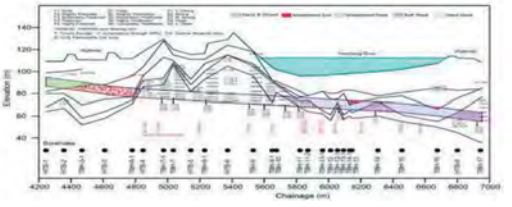

Figure 2. Geological layout along the alignment.

3 DISC CUTTER WEAR CHARACTERISTICS

The Daegok–Sosa tunnelling project utilized a dome-shaped cutterhead, as depicted in Figure 3. This cutterhead was fitted with a mix of disc cutters, scrapers, and buckets. Fifty disc cutters were positioned at the cutterhead's forefront, with three distinct types based on their location: center, face, and gauge cutters. The majority were face cutters, spaced 90 mm apart. All single cutters were 18 inches, with a hardness of 55–58 kN on the Rockwell hardness C scale (HRC).

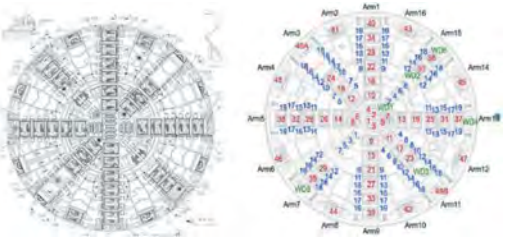

Figure 3. Cutter shape of the EPB TBM.

During the TBM tunnelling, cutting tools wear out due to ground interaction. Disc cutters apply force to rocks, causing chipping. They're also equipped to manage boulders in soil sections. While disc cutters excel in hard rock and dense soils, scrapers are suited for softer grounds, and rippers for medium-dense

terrains. These tools face wear from abrasive materials, leading to both normal and abnormal wear patterns. In mixed geologies, disc cutters undergo varied conditions in a single rotation, causing unbalanced loads and potential abnormal wear. Wear severity relates to the cutter's travel length and penetration rate. If not replaced timely, a damaged cutter can hinder construction progress (Wang et al., 2015).

Figure 3 showcases the locations of disc cutters (marked in red), which can relate to the travel length of each disc cutter. Wear is proportional to penetration and travel length. The travel length is derived from the cutter's radial positions and tunnel advancement. In theory, center and face cutters need more replacements with increased travel length, while gauge cutters wear out faster due to their design (Liu et al., 2017). The CHI interval is vital as TBM excavation downtime occurs during inspections. Sometimes, downtime costs surpass cutter replacement costs. Hence, cutters might be replaced before reaching their wear limit to maintain efficient cutterhead performance.

4 DISC CUTTER WEAR DATABASE

The predictive database for TBM cutter wear was developed by integrating data from the CHI reports, geological survey reports, and TBM operational logs. Due to discrepancies in the data sources, data preprocessing was essential to ensure the consistency in the type and measurements of the input data. For the purposes of this study, the target database was formulated based on the wear amount for each disc cutter per ring. The input database encompassed factors affecting disc cutter wear, including TBM operational metrics and geological factors.

4.1 *Disc wear measurements*

Data on the wear of face and gauge cutters in hard rock sections were sourced from the CHI reports between 30–65. For the consistency of the input data, eight center disc cutters replacement data were removed from the analysis. In addition, abnormal wear data such as the flat wear, chipping, and mushrooming were omitted. Similarly, four CHI reports with major errors were ignored. Lastly, occasional missing data were filled using the linear interpolation method. The interquartile range (IQR) technique was applied to the final database to remove outliers. As the result, the disc cutter wear amount of the face and gauge cutters for each ring excavation length was obtained. The final filtered database has 17,947 entries with wear data varying between 0–1.091mm per ring excavation.

To relate the disc cutter wear per ring excavation, this study identified 9 significant factors rooted in correlations established by prior research (Frenzel et al., 2008; Amoun et al., 2017; Plinninger et al., 2018; Mahmoodzadeh et al., 2021). The operational factors of the EPB TBM encompass five primary controls: rotational speed, torque, thrust force, advance rate, and chamber pressure. Geological aspects at the excavation forefront are captured by the rock quality designation (RQD) values taken at the tunnel's crown. Further geological data includes the distances from the tunnel crown to the groundwater table level (GWL) and the cover depth. This geological information was sourced from a longitudinal profile containing 54 borehole survey reports.

5 MACHINE LEARNING MODEL IMPLEMENTATION

5.1 *Random forest algorithm*

The model to predict disc cutter wear was designed using the Random Forest (RF) algorithm. This ensemble machine learning strategy derives its predictions by averaging the results of multiple decision trees. When benchmarked against other machine learning approaches, the RF model showcases enhanced generalization and a robust mechanism to prevent overfitting. This is largely due to its bagging technique, which synergizes bootstrap sampling with aggregation, repeatedly drawing n random subsets from the main dataset to craft a variety of decision trees. The cumulative result from these trees, represented in Equation 1, offers the final prediction.

$$y = \frac{1}{n}\sum_{i=1}^{n} y_i(x) \tag{1}$$

The efficacy of a machine learning model's prediction is influenced by its input data and hyperparameters—internal configurations that steer the learning journey. This research fine-tuned the RF model by adjusting four key hyperparameters, which are n_estimators, max_depth, min_samples_split, and min_samples_leaf. Furthermore, a grid search approach was utilized to determine the most suitable hyperparameter blend, with the potential combinations.

5.2 *Model implementation*

To implement the wear predicting RF model, the disc cutter abrasion prediction database was reconfigured to align with the abrasion data per unit ring distance. This involved integrating data from CHI reports, geological surveys, TBM operational logs, and tunnel design documentation. The consolidated database housed 17,947 entries, each comprising 9 wear-influencing factors and wear metrics per ring. Subsequently, the RF model was developed, optimizing hyperparameters based on the input datasets. The database was split, allocating 80% for model training and the remaining 20% for performance evaluation.

During the training phase, a 5-fold cross-validation method was adopted to neutralize any potential biases in the input data. This entailed partitioning the training data into five segments. While four segments served as training data, the remaining segment was used for model validation. This validation rotation was conducted five times, ensuring each segment had a turn in the validation role.

The performance of the ML regression models was evaluated using three metrics: RMSE, MAE, and R^2, as depicted in Equations (2)–(4). RMSE provides the square root of the averaged squared errors, whereas MAE computes the average disparity between predicted and true values. A lower RMSE or MAE signifies a more precise prediction of disc cutter wear. On the other hand, R^2 measures the linear association between the predicted and true values, with its value ranging between 0 and 1. A higher R^2 suggests enhanced prediction accuracy of the ML models.

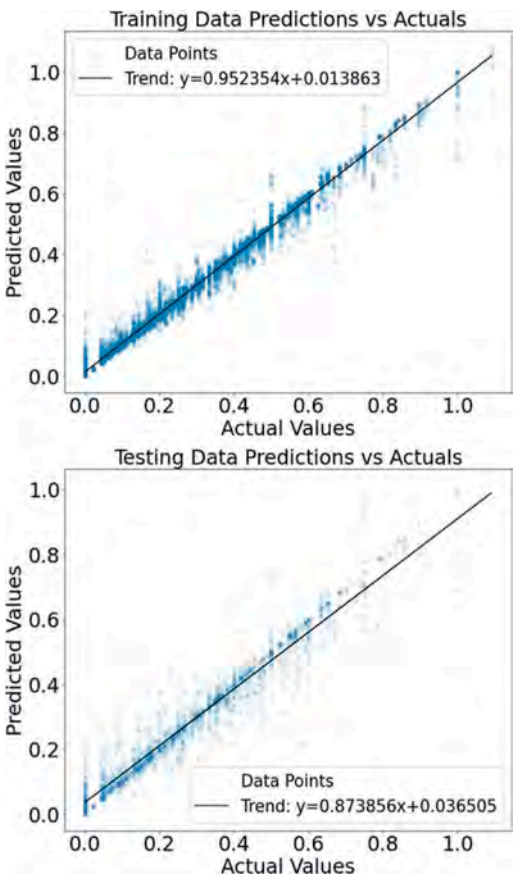

Figure 4. Prediction performance on the training and testing data.

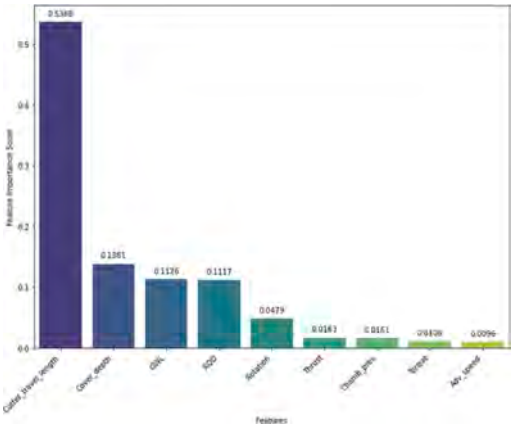

Figure 5. Feature importance scores.

$$\mathrm{RMSE} = \sqrt{\frac{1}{N}\sum_{i=1}^{N}(y_i - \hat{y}_i)^2} \tag{2}$$

$$\mathrm{MAE} = \frac{1}{N}\sum_{i=1}^{N}|y_i - \hat{y}_i| \tag{3}$$

$$R^2 = 1 - \frac{\sum_{i=1}^{N}(y_i - \hat{y}_i)^2}{\sum_{i=1}^{N}(y_i - \hat{y})^2} \tag{4}$$

5.3 *Feature importance*

Feature importance analysis delves into the relative significance of each attribute in determining an ML model's performance. By pinpointing dominant predictors, it sheds light on inherent data patterns. Within the framework of the RF model, the significance of each feature is ascertained by assessing the reduction in data impurity when the feature is split. In this research, we scrutinized the feature importance scores from the RF model to discern the impact of each factor inducing disc cutter wear.

6 RESULT AND DISCUSSION

The RF model's predictive capability was assessed by experimenting with various hyperparameter combinations, identified through the grid search technique. As the result from RF training, the ideal hyperparameter combination was identified as max_depth = 20, min_samples_leaf = 1, min_samples_split = 2, and n_estimators = 105. Figure 4 illustrates the precision in predicting cutter wear for training and testing datasets, respectively. Results using three metrics, RMSE, MAE, and R^2, are 0.024 mm, 0.012 mm, and 0.987 for training and 0.059 mm, 0.031 mm, 0.918 for test, respectively. The proposed model's predicted the disc cutter wear per ring

excavation with accuracy of 0.059 mm, which surpasses the RMSE result of 107.3554 m^3/cutter noted in Mahmoodzadeh et al.'s 2021 study.

Considering the average CHI range in the hard rock layer (CHI from 30 to 65) is 16 rings, the test RMSE implies the RF model can predict cutter wear between each CHI with a precision close to 1 mm; specifically, 0.059 mm multiplied by 16 rings equals 0.944 mm. Moreover, the R^2 value for the test outcomes stood at 0.918, markedly superior to values presented in prior research (Delisio and Zhao, 2014; Hassanpour et al., 2014; Koppl et al., 2015; Liu et al., 2017; Ren et al., 2018).

Figure 5 depicts the feature importance scores obtained from the RF model. The cutter travel length took the lead with a score of 0.54, suggesting the highest potent link to disc cutter wear. Geological elements, namely the cover depth, GWL, and RQD, secured scores above 0.11. This hints at a more pronounced association with disc cutter wear in contrast to the TBM operational metrics. Within the realm of TBM operational factors, rotation speed ranked highest, trailed by thrust force, chamber pressure, torque, and advance speed sequentially. It's noteworthy that the geological data employed in this study was sourced from a restricted set of sites. Consequently, the geological data gaps between survey points were bridged using linear interpolation.

7 CONCLUSION

This research employed the RF algorithm to implement a machine learning-driven model for predicting disc cutter wear per ring excavation. The formulated model provides forecasts of cutter wear for each ring excavation, taking into account the specific travel lengths of individual disc cutters. Using 17,947 datasets from the Daegok-Sosa EPB TBM project and considering 9 factors influencing cutter wear, the model underwent training and validation. From the findings, following conclusions are driven:

1) The RF-based disc cutter wear prediction model showcased superior predictive prowess, registering an RMSE of 0.059 mm and an R^2 of 0.918 for the test set. By factoring in each disc cutter's travel length, along with 14 other wear-influencing elements, the model adeptly predicts cutter wear over a singular ring excavation span.
2) The feature importance analysis pinpointed the cutter travel length as paramount in forecasting disc cutter wear. This was followed by geological and TBM operational elements. The notable gap in importance scores between the cutter travel length and other factors underscores its pivotal role in wear prediction.
3) This paper introduces a model for predicting disc cutter wear that integrates individual cutter travel lengths through machine learning. It's recommended to deploy this model across a broader spectrum of projects, refining it based on outcomes to bolster its universality. Subsequent research can evolve the model to encompass irregular wear patterns in disc cutters and cater to other tunnel segments like mixed-face areas.

ACKNOWLEDGMENTS

Research for this paper was carried out under the Development of advanced management technology (Total care) for infrastructure (project no. RS-2022-00142566) funded by Korea Agency for Infrastructure Technology Advancement.

REFERENCES

Hassanpour, J., Rostami, J., Zhao, J., Tarigh Azali, S., 2015. TBM performance and disc cutter wear prediction based on ten years' experience of TBM tunnelling in Iran. Geomechanik und Tunnelbau, 8, 239–247. https://doi.org/10.1002/geot.201500005

Rostami, J., 1997. Development of a force estimation model for rock fragmentation with disc cutters through theoretical modeling and physical measurement of crushed zone pressure Doctoral thesis, Colorado School of Mines, Golden, CO, USA, 38.55–64.

Rostami, J., 1993. A new model for performance prediction of hard rock TBMs. In: Bowerman, L.D., Monsees, J.E. (Eds.), Proceedings of the 1993 Rapid Excavation and Tunneling Conference, United States.

Bruland, A., 1998. Prediction model for performance and costs. In: Norwegian TBM Tunnelling, Norwegian Tunnelling Society (NFF), Oslo, pp. 29–34.

Kim, Y., Hong, J., Kim, B., 2020. Performance comparison of machine learning classification methods for decision of disc cutter replacement of shield TBM. Journal of Korean Tunnelling and Underground Space Association, 22, 575–589. https://doi.org/10.9711/KTAJ.2020.22.5.575

Mahmoodzadeh, A., Mohammadi, M., Ibrahim, H.H., Abdulhamid, S.N., Ali, H.F.F., Hasan, A.M., et al., 2021. Machine learning forecasting models of disc cutters life of tunnel boring machine. Automation in Construction, 128, 103779. https://doi.org/10.1016/j.autcon.2021.103779

Wang, L., Kang, Y., Zhao, X., Zhang, Q., 2015. Disc cutter wear prediction for a hard rock TBM cutterhead based on energy analysis. Tunnelling and Underground Space Technology, 50, 324–333. https://doi.org/10.1016/j.tust.2015.08.003

Liu, Q., Liu, J., Pan, Y., Zhang, X., Peng, X., Gong, Q., 2017. A wear rule and cutter life prediction model of a 20-in. TBM cutter for granite: a case study of a water conveyance tunnel in China. Rock Mechanics and Rock Engineering, 50, 1303–1320. https://doi.org/10.1007/s00603-017-1176-4

Frenzel, C., Käsling, H., Thuro, K., 2008. Factors influencing disc cutter wear. Geomechanik und Tunnelbau, 1, 55–60. https://doi.org/10.1002/geot.200800006

Amoun, S., Sharifzadeh, M., Shahriar, K., Rostami, J., Azali, S.T., 2017. Evaluation of tool wear in EPB tunneling of Tehran Metro, Line 7 Expansion. Tunnelling and Underground Space Technology, 61, 233–246. https://doi.org/10.1016/j.tust.2016.11.001

Plinninger, R.J., Alber, M., Düllmann, J., 2018. Rock mass-scale factors with an influence on tool wear in the mechanized tunnelling process in hard rock. Geomechanik und Tunnelbau, 11, 157–168. https://doi.org/10.1002/geot.201700068

Delisio, A., Zhao, J., 2014. A new model for TBM performance prediction in blocky rock conditions. Tunnelling and Underground Space Technology, 43, 440–452. https://doi.org/10.1016/j.tust.2014.06.004

Hassanpour, J., Rostami, J., Azali, S.T., Zhao, J., 2014. Introduction of an empirical TBM cutter wear prediction model for pyroclastic and mafic igneous rocks; a case history of Karaj water conveyance tunnel, Iran. Tunnelling and Underground Space Technology, 43, 222–231. https://doi.org/10.1016/j.tust.2014.05.007

Köppl, F., Thuro, K., Thewes, M., 2015. Suggestion of an empirical prognosis model for cutting tool wear of hydroshield TBM. Tunnelling and Underground Space Technology, 49, 287–294. https://doi.org/10.1016/j.tust.2015.04.017

Ren, D.J., Shen, S.L., Arulrajah, A., Cheng, W.C., 2018. Prediction model of TBM disc cutter wear during tunnelling in heterogeneous ground. Rock Mechanics and Rock Engineering, 51, 3599–3611. https://doi.org/10.1007/s00603-018-1549-3

Tunnelling for a Better Life – Yan, Celestino, Thewes & Eberhardt (Eds)
© 2024 The Author(s), ISBN 978-1-032-80042-4
Open Access: www.taylorfrancis.com, CC BY-NC-ND 4.0 license

Segment segmentation of tunnel ring point clouds using 3D deep learning

Wei Lin*
Department of Geotechnical Engineering, College of Civil Engineering, Tongji University, Shanghai, China
Laing O'Rourke Centre for Construction Engineering and Technology, Department of Engineering, University of Cambridge, Cambridge, UK
State Key Laboratory of Disaster Reduction in Civil Engineering, Tongji University, Shanghai, China
Key Laboratory of Geotechnical and Underground Engineering of the Ministry of Education, Tongji University, Shanghai, China

Brian Sheil
Laing O'Rourke Centre for Construction Engineering and Technology, Department of Engineering, University of Cambridge, Cambridge, UK

Xiongyao Xie & Kang Li
Department of Geotechnical Engineering, College of Civil Engineering, Tongji University, Shanghai, China
State Key Laboratory of Disaster Reduction in Civil Engineering, Tongji University, Shanghai, China
Key Laboratory of Geotechnical and Underground Engineering of the Ministry of Education, Tongji University, Shanghai, China

Gang Niu
CCCC Strait Construction Investment Development Co., Ltd., Fuzhou, China

ABSTRACT: Scanned point clouds are high-value digital assets for the inspection and evaluation of tunnel structures. Segment segmentation of scanned point clouds is a prerequisite for measuring the deformation of segments. However, the semantic enrichment of point clouds can be time-consuming and labour-intensive. 3D deep learning (DL) has emerged as a viable means of analysing point clouds. To that end, this paper describes the development of an annotated high-quality and large-volume point cloud dataset for subsequent training and evaluation of 3D DL models. Data augmentation methods, including rotation and feature extending, are proposed to prepare the dataset, ensuring that features of the point clouds can be effectively captured by the 3D DL models. Data experiments are carried out using the popular 3D DL network 'PointNet++' to compare the influences of different data augmentation methods and network parameters. Satisfactory segmentation accuracy (mean interaction over union ~ 90%) is achieved by optimizing data augmentation methods and network parameters. The proposed automatic segmentation method shows promise to improve the efficiency of tunnel ring point cloud processing and facilitate the deformation inspection of segments.

Keywords: Point cloud, Segmental tunnel lining, 3D deep learning, Segmentation

1 INTRODUCTION

Segmental tunnel linings are common support structures for metro tunnels and other large-diameter utility tunnels. Segmental linings are prone to deformation (Lin, Xie, *et al.* 2022, Lin, Li, *et al.* 2023) arising from intensive adjacent construction and uncertain soil properties which can be difficult to predict. An accurate assessment of existing deformations is fundamental to rigorous structural analysis of these assets (Chang *et al.* 2023, Xie *et al.* 2023). However, the traditional methods, such as total stations (Lin, Li, *et al.* 2022), settlement gauges (Xie and Tang 2018), and convergence gauges (Wang *et al.* 2021) can only capture limited point-wise displacements which do not always reflect the full deformation field.

Laser scanning is a powerful means of capturing abundant spatial data. The reliability of extracting

*Corresponding author: linwei9612@outlook.com

DOI: 10.1201/9781003495505-406

deformations of segmental tunnel linings from point clouds has been well-documented (Roca-Pardiñas *et al.* 2014, Xie and Lu 2017, Lin, Xie, *et al.* 2023). The semantics of point clouds are prerequisites for automated deformation calculation. Heuristic algorithms have been developed to segment tunnel point clouds but are highly dependent on tunnel design and construction information (Yi *et al.* 2019, Duan *et al.* 2021). The emergence of 3D deep learning (DL) provides a promising fully automatic way to realize semantic segmentation of point clouds without any project-/site-specific algorithms (Soilán *et al.* 2020, Xie *et al.* 2020). Although applying 3D DL networks to tunnel point clouds is gaining attention (Ji *et al.* 2023, Zhou *et al.* 2023), the application of 3D DL to segment-wise segmentation has not yet been achieved.

To realize automatic segment segmentation of point clouds, a well-annotated point cloud dataset is proposed and utilized to train and evaluate 3D DL models. Data normalization and sampling are adopted to ensure the effective utilisation of point cloud features. Using the popular 3D DL network, 'PointNet++' (Qi *et al.* 2017), experiments are performed to compare the influences of data augmentation methods and network parameters on the segmentation performance.

2 DATASET

The point clouds in the present dataset are scanned by terrestrial laser scanners (TLS) from two in-service shield tunnels located in Wuxi, China and denoted T1 and T2 (see Figure 1). The shield tunnels are hierarchically composed of rings and segments. Each ring consists of six segments, including one key segment, two adjacent segments, and three standard segments. The rings are connected by staggered circumferential joints (Liu *et al.* 2017). The inner diameter and length per ring are 5.5 m and 1.2 m respectively.

The TLS used for scanning is the Leica C10 which acquires high-quality point clouds with a scanning noise (root mean square error) of < 0.5 mm for scanning distances < 50 m. The point clouds are scanned from 31 scanning stations without overlaps. All possible elements and noise, including cables, pipes, rails, walkways, and other non-structural elements, are considered in the present dataset. The total number of scanned rings is 738 equating to a total length of 885.6 m. The total number of scanned points is 439,178,993. Each point comprises the following features: (a) three values for the Cartesian coordinates and (b) one value for intensity (ranging from 0 to 1). The Cartesian coordinates are recorded as the relative positions of scanned elements to the laser scanner (original point).

To train and evaluate the performance of 3D DL networks on segment segmentation, the scanned point clouds are manually annotated. The point cloud annotation follows a top-down workflow, as shown in Figure 2. For the annotated point clouds, T*l*-*m*-*n* is adopted to denote each subset of the data where *l*, *m* and *n* refer to the tunnel number, scanning station number, and ring number, respectively. An exemplar annotated point cloud is presented in Figure 3, where all the labels are displayed in different colours. Label 0 denotes the points of non-structural elements and noise. Label 1 to label 6 represent different segments within each ring. Label 1 stands for the key segment and the rest of the segments are all assigned non-zero labels sequentially according to the installation positions (counterclockwise). The class proportion of all the point clouds in the dataset is shown in Figure 4, where the imbalance distribution of classes can be observed due to the complex environment of in-service tunnels.

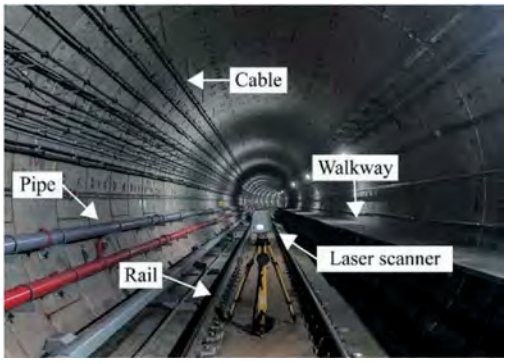

Figure 1. The field scanning of segmental tunnel linings.

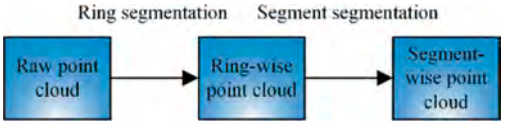

Figure 2. The adopted point cloud annotation workflow.

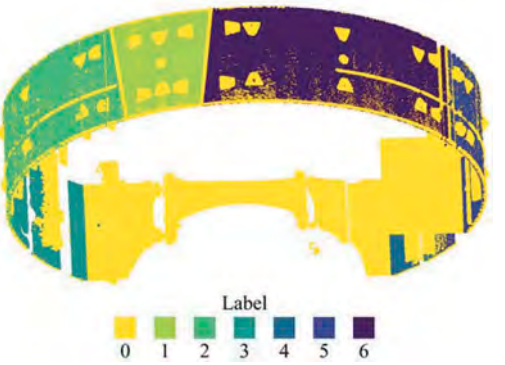

Figure 3. An exemplar annotated point cloud (T2-4-301).

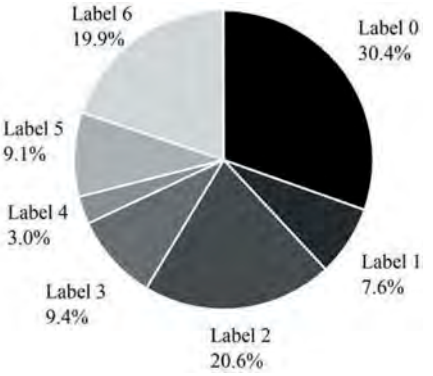

Figure 4. Class proportion of the dataset.

3 METHODOLOGY

3.1 *Data normalization*

Data normalization (Garbin *et al.* 2020) is critical to ensure the DL networks learn the features without being affected by possible disturbances, such as scale effects. Hence, the annotated point clouds are normalized for both Cartesian coordinates and intensity. The Cartesian coordinates are proportionally scaled to ensure that the values are within the interval −1 to 1. The values of intensity are normalized by applying a min-max filtering scaler as follows:

$$i_a = \begin{cases} 0, i_0 < i_{\min} \\ \frac{i_0 - i_{\min}}{i_{\max} - i_{\min}}, i_{\min} \le i_0 \le i_{\max} \\ 1, i_0 > i_{\max} \end{cases} \quad (1)$$

where i_0 is the original intensity value, i_a is the augmented original value, and $i_{\min}$ and $i_{\max}$ are the given thresholds (1% percentile and 99% percentile are adopted here respectively). The results of this exercise for intensity normalization are shown in Figure 5. It is demonstrated that the intensity values are more diversly distributed in the interval −1 to 1 after the intensity normalization.

3.2 *Data sampling*

Point cloud sampling is usually adopted before training and evaluation to improve computational efficiency. Algorithms for data sampling require careful consideration to strike a balance between efficiency and fidelity (avoiding excessive information loss).

Two sampling algorithms are popular in the literature (Qi *et al.* 2017, Hu *et al.* 2022): 'random sampling' (RS) and 'farthest point sampling' (FPS). RS randomly selects individual points for removal where each point has the same probability of being sampled. FPS iteratively returns the farthest point from the sampled points and performs distance

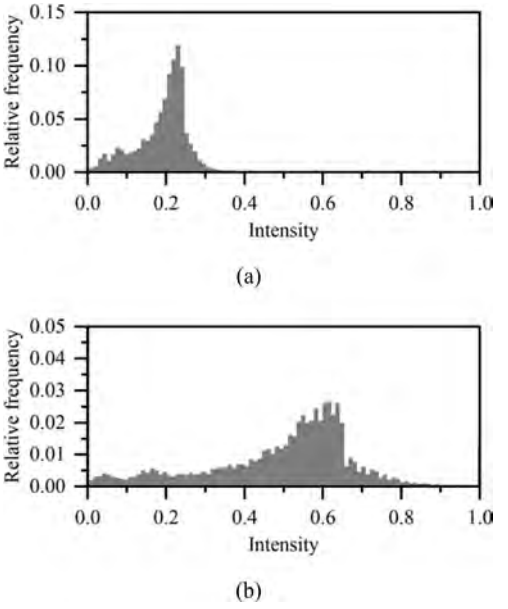

Figure 5. The intensity distribution of ring-wise point cloud (T1-1-21): (a) before normalization and (b) after normalization.

updating. However, the two algorithms have significant drawbacks: (a) RS does not ensure spatial homogeneity of the sampled points and (b) FPS causes high computational costs. Another sampling algorithm, 'grid sampling' (GS) (Sun *et al.* 2022), achieves a good balance between spatial homogeneity and computational efficiency while the sampled number of points can not be determined for GS. By GS, the point clouds are divided into voxels of the same size, and then the point closest to the centre of each voxel is returned as the sampled point. To take advantage of GS whilst controlling the sampled number of points, the 'grid-random sampling' (GRS) approach is proposed. The GRS algorithm is performed in two stages: (a) The point clouds are sampled with the GS algorithm given an approximated voxel size and (b) the sampled point clouds are then randomly sampled to the required number of points.

RS, FPS, and GRS are applied to ring-wise point clouds to compare the influence of the sampling methods on information loss, as shown in Figure 6. The same exemplar ring-wise point cloud consists of 3,694,229 points and is downsampled to 12,288 points. The voxel size selected for GRS is 37.5 mm. It can be observed that the RS returns unevenly distributed points while FPS preserves the most information. GRS outperforms RS as it preserves more details. The computational time of the three algorithms is provided in Table 1. FPS takes about 17 times the computational time of GRS. Considering both efficiency and fidelity, GRS is adopted for sampling point clouds before model training and evaluation.

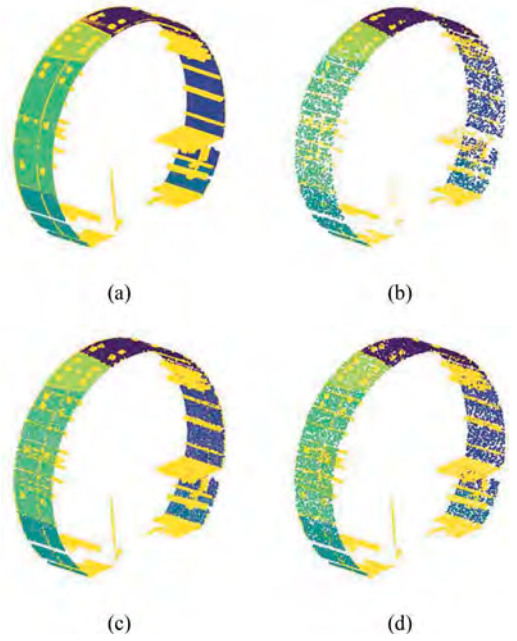

Figure 6. Sampling results of the ring-wie point cloud (T1-1-20): (a) the raw ring-wise point cloud, (b) RS, (c) FPS, and (d) GRS.

Table 1. The computational time of sampling algorithms on the ring-wise point cloud (T1-1-20).

Sampling algorithm	Computational time*/s
RS	3.39
FPS	87.11
GRS	5.12

* The computational time is calculated on AMD Ryzen 7 5800H CPU.

3.3 *Data augmentation*

For point clouds, rotation is the most common way to augment data (Qi *et al.* 2017). After sampling, the ring-wise point clouds are randomly rotated to generate augmented point clouds. The number of point clouds augmented from each original point cloud is denoted C_a.

The rotation can be performed within the x-y plane only or arbitrally in 3D space, as follows:

$$\begin{pmatrix} x_r \\ y_r \\ z_r \end{pmatrix} = R_z(\alpha)R_y(\beta)R_x(\gamma)\begin{pmatrix} x_0 \\ y_0 \\ z_0 \end{pmatrix} \tag{2}$$

$$R_z(\alpha) = \begin{pmatrix} \cos\alpha & -\sin\alpha & 0 \\ \sin\alpha & \cos\alpha & 0 \\ 0 & 0 & 1 \end{pmatrix} \tag{3}$$

$$R_y(\beta) = \begin{pmatrix} \cos\beta & 0 & \sin\beta \\ 0 & 1 & 0 \\ -\sin\beta & 0 & \cos\beta \end{pmatrix} \tag{4}$$

$$R_x(\gamma) = \begin{pmatrix} 1 & 0 & 0 \\ 0 & \cos\gamma & -\sin\gamma \\ 0 & \sin\gamma & \cos\gamma \end{pmatrix} \tag{5}$$

where x_0, y_0, and z_0 denote the original Cartesian coordinates, x_r, y_r, and z_r denote the rotated Cartesian coordinates, R_z, R_v, and R_x are the rotation matrix along axes z, y, and x, respectively, and α, β, and γ are random rotation angles along axes z, y, and x, respectively (β and γ equal 0 for 2D rotation).

Another rotation strategy denoted 2.5D rotation, is proposed for comparison, which performs the rotation within the *x-y* plane first and then rotates the ring-wise point clouds along the fitted cylindrical axis of tunnel rings. The 2.5D rotation is performed as follows:

$$\begin{pmatrix} x_r \\ y_r \\ z_r \end{pmatrix} = R_z(\alpha)R_n(\delta)\begin{pmatrix} x_0 \\ y_0 \\ z_0 \end{pmatrix} \tag{6}$$

$$R_n(\delta) = \begin{pmatrix} n_x^2(1-\cos\delta)+\cos\delta & n_xn_y(1-\cos\delta)-n_z\sin\delta & n_xn_z(1-\cos\delta)+n_y\sin\delta \\ n_xn_y(1-\cos\delta)-n_z\sin\delta & n_y^2(1-\cos\delta)+\cos\delta & n_yn_z(1-\cos\delta)+n_x\sin\delta \\ n_xn_z(1-\cos\delta)-n_y\sin\delta & n_yn_z(1-\cos\delta)+n_x\sin\delta & n_z^2(1-\cos\delta)+\cos\delta \end{pmatrix} \tag{7}$$

where R_n is the rotation matrix along the fitted cylindrical axis and δ is the random rotation angle along the fitted cylindrical axis. Different ranges of random δ are compared, i.e., −180° to 180°, −15° to 15°, and −7.5° to 7.5°, denoted group L, group M, and group S respectively.

To fully exploit the implicit features in the point clouds for model training, the normals of individual points are provided as expanded features. Given a point in the point cloud, the normals are calculated using the following steps: (a) search the five points nearest to the given point, (b) fit the local plane described by these five nearest points, and (c) calculate the of the fitted plane.

Each ring-wise point cloud is rotated C_a times to generate several point clouds for training. To determine the effects of rotation strategies on the segmentation performance, five experiments are performed, where C_a equating to six is adopted. Then, different values of C_a — 6, 9, and 12 — are compared to further determine the best implementation of the data augmentation.

3.4 *Network parameter*

There are two main network parameters in PointNet ++, namely the neighbour radius and the number of neighbours, which control the receptive field of the network. The neighbour radius defines the region of sampling in each feature aggregation layer whilst the number of neighbours defines the number of points to be sampled. With a set of network parameters as the baseline, neighbour radius and neighbour number are both varied as shown in Table 2.

Table 2. The compared perception field parameters.

Model No.	Compared parameter	Layer	Neighbour radius	Neighbour number
P1	Baseline	1	0.1, 0.2, 0.4	32, 64, 128
		2	0.4, 0.8	64, 128
P2	Neighbour radius	1	0.05, 0.1, 0.2	32, 64, 128
		2	0.2, 0.4	64, 128
P3		1	0.01, 0.02, 0.04	32, 64, 128
		2	0.04, 0.08	64, 128
P4	Neighbour number	1	0.1, 0.2, 0.4	16, 32, 64
		2	0.4, 0.8	32, 64
P5		1	0.1, 0.2, 0.4	64, 128, 256
		2	0.4, 0.8	128, 256

3.5 *Model training and evaluation*

All models in the present experiments are trained and evaluated using NVIDIA A100-SXM-80GB GPUs. The training set and test set are split randomly, following the 80/20 rule to ensure rigorous model evaluation, as shown in Table 3. All the trained models are evaluated on the test set.

Table 3. The split of the training set and test set.

Tunnel No.	Scaninig station No. in the training set	Scaninig station No. in the test set
T1	1, 2, 3, 5, 6, 7, 8, 9, 10, 11, 13, 14, 16, and 17	4, 12, and 15
T2	1, 3, 4, 5, 6, 7, 8, 9, 11, 12, and 13	2, 10 and, 14

OA (overall accuracy) and mIoU (mean interaction over union) are employed to evaluate model performance, calculated as follows:

$$OA = \frac{\sum_{j=1}^{M} (TP)_j}{N} \tag{8}$$

$$mIoU = \frac{1}{M}\sum_{j=1}^{M} \frac{(TP)_j}{(TP)_j + (FP)_j + (FN)_j} \tag{9}$$

where M is the number of classes, N is the number of points, and TP, FP, and FN denote true positive, false positive, and false negative predictions respectively. Among the two metrics, mIoU represents the most reasonable evaluation for class-imbalanced datasets and is thus adopted as the priority metric.

4 RESULTS

Table 4 presents the OA and mIoU of PointNet++ trained with different rotation strategies. Using 2D (x-y) rotation, the mIoU reaches 0.869, outperforming other rotation strategies. This may be due to the most realistic augmented point clouds generated by 2D rotation since the tunnel axis is usually within the horizontal plane. By providing the normals of each point in the point clouds, the OA and mIoU further increase to 0.936 and 0.874 respectively, boosting the segmentation performance.

Table 4. The evaluation metrics of PointNet++ trained with different rotation strategies.

Model No.	Rotation strategy	OA	mIoU
R1	3D rotation	0.919	0.836
R2	2D rotation	0.933	0.869
R3	2.5D rotation — L	0.921	0.838
R4	2.5D rotation — M	0.929	0.858
R5	2.5D rotation — S	0.931	0.864

The evaluation metrics of different augmented point cloud numbers are listed in Table 5, where the normal are included as features. The larger number of augmented point clouds leads to better segmentation performance whilst the time consumed for training increases proportionally to the training set size, as indicated by the corresponding OA and mIoU values. By increasing the number of augmented point clouds to 12, the mIoU improves to 0.883.

Table 5. The evaluation metrics of PointNet++ trained with different numbers of augmented point clouds.

Model No.	C_a	OA	mIoU
N1	6	0.936	0.874
N2	9	0.939	0.880
N3	12	0.940	0.883

The best-performing data augmentation strategy — 2D rotation, C_a equating to 12, and using normals as expanded features — is adopted when comparing network parameters. Table 6 presents the segmentation performance for different network parameters. By narrowing the neighbour radius (Model P2), the mIoU is increased to 0.897 compared to the baseline. A similar improvement is observed when increasing the number of neighbours (Model P5). Additionally, an experiment adopting the neighbour radius from Model P2 and neighbour number from Model P5 results in a mIoU of 0.887. This shows that the combination of optimised individual parameters does not necessarily guarantee an optimised overall result. Figure 7 presents the visualized segmentation results for Model P1 (baseline), Model P2, and Model P5. Compared to the baseline, the segmentation performance is improved around the segment boundaries by adjusting the network parameters.

Table 6. The evaluation metrics of PointNet++ trained with different network parameters.

Model No.	Network parameter	OA	mIoU
P1	Baseline	0.940	0.883
P2	Neighbour radius	0.947	0.897
P3		0.941	0.889
P4	Neighbour number	0.934	0.871
P5		0.945	0.894

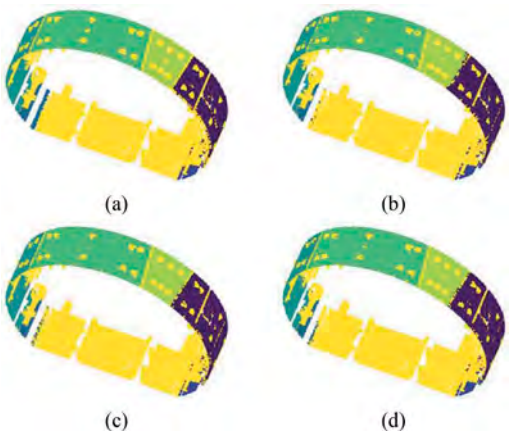

Figure 7. Exemplar segmentation result (T1-4-203) of (a) ground truth, (b) Model P1, (c) Model P2, and (d) Model P5.

The ovalisation fitting (Xie and Lu 2017) is performed and the error between manually processed and automatically processed point clouds is shown in Figure 8. It is observed that ovalisation fitting on both the long axis and short axis achieves submillimeter accuracy. The mean error of ovalisation orientation is 0.7°, showing satisfactory results. Further, the segment segmentation of point clouds enables the per-segment deformation fitting. The per-segment deformation fitting result is shown in Figure 9. The overall trend of per-segment deformation is in line with the ovalisation pattern. However, the per-segment deformation fitting reveals a more high-fidelity deformation description since the differential deformation between segments is captured.

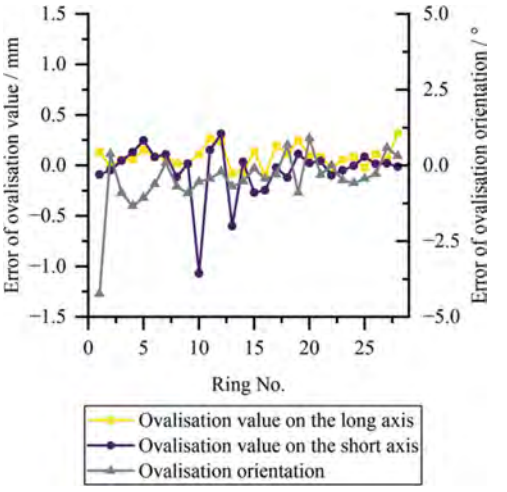

Figure 8. Ovalisation fitting error on the point cloud (T1-4) segmented by Model P2.

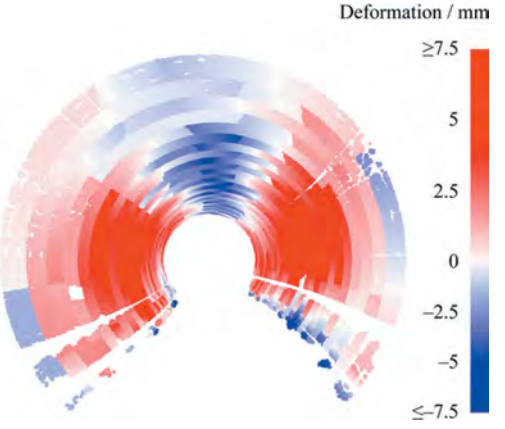

Figure 9. Deformation fitting result of per-segment deformation on the point cloud (T1-4) segmented by Model P2.

5 CONCLUSIONS

Using a richly annotated tunnel point cloud dataset, experiments were conducted to explore the feasibility of 3D DL for segment-wise segmentation. The influence of data augmentation methods and network parameters on the segmentation performance was also investigated by comparative experiments.

A novel sampling algorithm, GRS, was proposed, to an optimal trade-off between fidelity and efficiency. GRS shows the advantages of low computational costs whilst providing a fidelity-preserving performance similar to FPS. It is noted that GRS is computationally extremely efficient, representing only 5.9% of FPS.

2D rotation was shown to be the most effective data augmentation strategy, outperforming 3D rotation and the proposed 2.5D rotation. By calculating the normals of points as expanded input features, the segmentation performance was also improved. Besides data augmentation, the network parameters have a notable influence on the segmentation performance of 3D DL models. smaller neighbour radius and larger number of neighbours, both related to the receptive field, resulted in superior segmentation performance.

In this paper, a viable method for tunnel point cloud segmentation using 3D DL was demonstrated and ways to improve the segmentation performance were also provided. The present study enables the automatic segmentation of ring-wise point clouds, allowing the per-segment deformation fitting and providing high-fidelity deformation inspection.

The proposed method applies to per-ring point clouds, which means that efforts for segmentation between rings remain to be addressed. The segmentation of the original point clouds will lead to the fully automation segmentation of segmental tunnel lining point clouds while involving the challenge of segmenting more large-scale and complex scenes.

ACKNOWLEDGEMENTS

This work was supported by the National Natural Science Foundation of China [grant numbers 52038008, 52378408], the China Scholarship Council [grant number 202206260174], the Science and Technology Commission of Shanghai Municipality [grant numbers 20DZ1202004, 22DZ1203004], and the State Grid Shanghai Municipal Electric Power Company [grant number 52090W220001].

This work was performed using resources provided by the Cambridge Service for Data Driven Discovery (CSD3) operated by the University of Cambridge Research Computing Service (www.csd3.cam.ac.uk), provided by Dell EMC and Intel using Tier-2 funding from the Engineering and Physical Sciences Research Council (capital grant EP/T022159/1), and DiRAC funding from the Science and Technology Facilities Council (www.dirac.ac.uk).

REFERENCES

Chang, J., Zhang, D., Huang, H., and Jia, J., 2023. A hybrid sensing of rotation-induced stress of segmental lining during shield tunneling via WSN and surrogate numerical modeling. *Tunnelling and Underground Space Technology*, 140, 105315.

Duan, D.-Y., Qiu, W.-G., Cheng, Y.-J., Zheng, Y.-C., and Lu, F., 2021. Reconstruction of shield tunnel lining using point cloud. *Automation in Construction*, 130, 103860.

Garbin, C., Zhu, X., and Marques, O., 2020. Dropout vs. batch normalization: An empirical study of their impact to deep learning. *Multimedia Tools and Applications*, 79, 12777–12815.

Hu, Q., Yang, B., Xie, L., Rosa, S., Guo, Y., Wang, Z., Trigoni, N., and Markham, A., 2022. Learning semantic segmentation of large-scale point clouds with random sampling. *IEEE Transactions on Pattern Analysis and Machine Intelligence*, 44 (11), 8338–8354.

Ji, A., Zhou, Y., Zhang, L., Tiong, R.L.K., and Xue, X., 2023. Semi-supervised learning-based point cloud network for segmentation of 3D tunnel scenes. *Automation in Construction*, 146, 104668.

Lin, W., Li, P., and Xie, X., 2022. A novel detection and assessment method for operational defects of pipe jacking tunnel based on 3D longitudinal deformation curve: A case study. *Sensors*, 22, 7648.

Lin, W., Li, P., Xie, X., Cao, Y., and Zhang, Y., 2023. A novel back-analysis approach for the external loads on shield tunnel lining in service based on monitored deformation. *Structural Control and Health Monitoring*, 2023, 8128701.

Lin, W., Xie, X., Li, P., Xiao, B., Lu, X., Feng, B., Jin, P., and Hu, Y., 2022. Prediction of settlement induced by tidal fluctuation for underwater shield tunnel during service based on historical monitoring data. *In*: *2022 8th International Conference on Hydraulic and Civil Engineering: Deep Space Intelligent Development and Utilization Forum (ICHCE)*. 1042–1047.

Lin, W., Xie, X., Zhou, B., Li, P., and Wang, C., 2023. Refined perception and management of ring-wise deformation information for shield tunnels based on point cloud deep learning and BIM. *In*: *Proceedings of the Eighth International Symposium on Life-Cycle Civil Engineering (IALCCE 2023)*. 3991–3998.

Liu, X., Dong, Z., Bai, Y., and Zhu, Y., 2017. Investigation of the structural effect induced by stagger joints in segmental tunnel linings: First results from full-scale ring tests. *Tunnelling and Underground Space Technology*, 66, 1–18.

Qi, C.R., Yi, L., Su, H., and Guibas, L.J., 2017. PointNet++: Deep hierarchical feature learning on point sets in a metric space.

Roca-Pardiñas, J., Argüelles-Fraga, R., de Asís López, F., and Ordóñez, C., 2014. Analysis of the influence of range and angle of incidence of terrestrial laser scanning measurements on tunnel inspection. *Tunnelling and Underground Space Technology*, 43, 133–139.

Soilán, M., Riveiro, B., Balado, J., and Arias, P., 2020. Comparison of heuristic and deep learning-based methods for ground classification from aerial point clouds. *International Journal of Digital Earth*, 13 (10), 1115–1134.

Sun, Y., Zhang, S., Wang, T., Lou, F., Ma, J., Wang, C., and Gui, C., 2022. An improved spatial point cloud simplification algorithm. *Neural Computing and Applications*, 34, 12345–12359.

Wang, F., Shi, J., Huang, H., Zhang, D., and Liu, D., 2021. A horizontal convergence monitoring method based on wireless tilt sensors for shield tunnels with straight joints. *Structure and Infrastructure Engineering*, 17 (9), 1194–1209.

Xie, J., Huang, X., Zhang, Z., and Jin, G., 2023. Cohesive zone model-based analyses of localized leakage of segmentally lined tunnels. *Frontiers of Structural and Civil Engineering*, 17 (4), 503–521.

Xie, X. and Lu, X., 2017. Development of a 3D modeling algorithm for tunnel deformation monitoring based on terrestrial laser scanning. *Underground Space*, 2, 16–29.

Xie, X. and Tang, G., 2018. Effects of curved shield tunnelling adjacent to existing power tunnel. *European Journal of Environmental and Civil Engineering*, 22 (S1), s164–s178.

Xie, Y., Tian, J., and Zhu, X.X., 2020. Linking points with labels in 3D: A review of point cloud semantic segmentation. *IEEE Geoscience and Remote Sensing Magazine*, 8, 38–59.

Yi, C., Lu, D., Xie, Q., Liu, S., Li, H., Wei, M., and Wang, J., 2019. Hierarchical tunnel modeling from 3D raw LiDAR point cloud. *Computer-Aided Design*, (114), 143–154.

Zhou, Y., Ji, A., Zhang, L., and Xue, X., 2023. Attention-enhanced sampling point cloud network (ASPCNet) for efficient 3D tunnel semantic segmentation. *Automation in Construction*, 146, 104667.

Tunnelling for a Better Life – Yan, Celestino, Thewes & Eberhardt (Eds)
© 2024 The Author(s), ISBN 978-1-032-80042-4
Open Access: www.taylorfrancis.com, CC BY-NC-ND 4.0 license

Forecasting the driving speed of the TBM using machine learning algorithms

Mark Miller*
Department of Civil Engineering, Southwest Jiaotong University, Chengdu, Sichuan, China
Department of Bridges and Tunnels, Institution of Railway Track, Construction and Structures, Russian University of Transport (RUT MIIT), Moscow, Russia

Yong Fang, Hu Luo, Yubo Wang, Guowen Xu & Biao Leng
Department of Civil Engineering, Southwest Jiaotong University, Chengdu, Sichuan, China

Sergey Kharitonov & Vladimir Akulich
Department of Bridges and Tunnels, Institution of Railway Track, Construction and Structures, Russian University of Transport (RUT MIIT), Moscow, Russia

Yuyang Ma & Fuqing Zou
China Railway 14th Bureau Group Corporation Limited, Jinan, Shandong, China

ABSTRACT: This article explores the possibility of using machine learning algorithms to predict the speed of a tunnel shield complex. The description and principles of the algorithms are presented. The dataset obtained from the Ziyang Line Project was adapted for the set purpose by means of preprocessing operations. From the results obtained, it is evident that the XG Boost algorithm demonstrates the best predictive ability (R2=0.809; RMSE=5.708) for the stated problem.

Keywords: TBM, Driving speed prediction, Machine learning

1 INTRODUCTION

Tunnel boring machines (TBMs) have revolutionized the way underground tunnels are constructed, allowing for faster and more efficient excavation than by using traditional methods. However, the speed of a TBM depends on a variety of factors, such as the type of soil, rock, and water encountered during excavation, as well as the machine's design and operational parameters. Accurately predicting the speed of a TBM can help optimize its performance, reduce costs, and improve safety during tunnel construction.

Figure 1. TBM ZTSE82000.

In recent years, machine learning (ML) algorithms have shown great potential in predicting the performance of TBMs. By analyzing large amounts of data from previous tunneling projects, ML models can identify patterns and correlations between various parameters and the TBM's speed, enabling more accurate predictions.

2 PROJECT DESCRIPTION

The Ziyang line project starts from Futian Station on the south side of Tianfu International Airport and ends at Ziyang North High-speed Railway Station in Ziyang

* Corresponding author: millermark.swjtu@yandex.ru

DOI: 10.1201/9781003495505-407

City. The total length of the line is 39.37 km, of which the underground section is 9.77 km, including 4 stations and 4 tunnels. The strata where the tunnel passes through are mainly moderately weathered mudstone and sandstone, and locally strongly weathered mudstone and sandstone. The outer diameter of the shield tunnel lining is 7900 mm, the inner diameter is 7100 mm and the thickness of the tunnel segment is 400 mm. ZTSE8200 TBM (Figure 1) is used for the tunnel construction.

3 MACHINE LEARNING

Machine learning is a branch of the science of artificial intelligence that studies methods for constructing algorithms capable of learning. It is based on the idea that a system of such algorithms can learn to identify patterns and make decisions with minimal human involvement. Machine learning is at the intersection of mathematical statistics, optimization methods and classical mathematical disciplines, but also has its unique field of research related to the problems of computational efficiency and retraining. Many methods have been developed as an alternative to classical statistical approaches and are closely related to information extraction and data mining.

Within the framework of TBM driving speed prediction, the ability of machine learning to solve a regression problem is used, in which an algorithm based on an initial dataset predicts the value. Moreover, machine learning methods have been widely used in various fields of civil engineering, such as tunnel settlement prediction (Yan et al., 2020; Hu et al., 2019.), intelligent surrounding rock classification (Liu et al., 2018; Yang et al., 2021; Zhao et al., 2022) and tunnel crack identification (Liao et al., 2022; Dang, L. et al., 2022).

3.1 *Linear models*

3.1.1 *Ordinary least squares*

Ordinary Least Squares (OLS) linear regression is a statistical method used for modeling the relationship between a dependent variable and one or more independent variables by fitting a linear equation to observed data. The goal is to find the line of best fit, which minimizes the sum of squared differences between the observed response and the response predicted by the linear model. The method provides an estimate of the coefficients of the linear equation, which can be used to make predictions about the response variable based on new observations of the independent variables.

3.1.2 *Lasso regression*

Lasso regression is a type of linear regression that adds a regularization term to the loss function being optimized. This term, known as *L1* regularization, helps to prevent overfitting by penalizing large coefficients in the model. The objective function in Lasso regression is defined as follows (McNeish, 2015):

$$L^{Lasso}(\beta) = Y - X\beta^2 + \lambda W^T\beta \tag{1}$$

Where L is the loss function, Y is the target vector, X is the design matrix, β is the vector of coefficients, n is the number of observations, and λ is the regularization parameter. The first term of the objective function is the mean squared error, which is the standard loss function for linear regression. The second term is the *L1* regularization term, which is the sum of the absolute values of the coefficients. The regularization parameter, λ, determines the strength of the regularization and is typically chosen using cross-validation.

Lasso regression has the property that some coefficients equal to zero. This means that Lasso can be used for feature selection, as it effectively removes the least important variables from the model. The *L1* regularization term also has the effect of shrinking the coefficients towards zero, which can help to reduce the variance of the model.

In practice, Lasso regression can be implemented using optimization algorithms such as coordinate descent, sub-gradient descent, or the LARS (Least Angle Regression) algorithm. Lasso regression can also be used in combination with other types of regularization, such as ridge regression, to create an elastic net model.

Lasso regression is a useful tool for linear models with many features, particularly when the number of features is larger than the number of samples. However, it is important to keep in mind that Lasso can be sensitive to the scaling of the features, thus it is often recommended to standardize the variables before fitting the model.

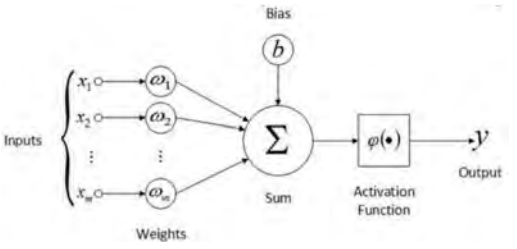

Figure 2. Simplified model of an artificial neuron.

3.1.3 *Ridge regression*

Ridge Regression is a type of regularized linear regression algorithm that aims to minimize the residual sum of squares between the predicted response and the true response by adding a penalty term to the loss function. This penalty term, called "*L2* regularization", helps to reduce the model complexity and avoid overfitting. The regularization term is the sum of the squares of the coefficients, multiplied by a hyperparameter alpha, which determines the strength of the regularization. Larger values of alpha result in a more restricted

model with smaller coefficients, while smaller values result in a less restricted model with larger coefficients. The optimal value of alpha is usually determined by cross-validation. Ridge regression is well-suited for cases where the number of predictors is large compared to the number of observations, or where some predictors are highly correlated.

3.1.4 *Polynomial regression*

Polynomial Regression is a form of regression analysis in which the relationship between the independent variable x and the dependent variable y are modeled as an nth degree polynomial. In polynomial regression, the independent variable is raised to a power to create a new set of predictors, which can model non-linear relationships between the dependent and independent variables. The model is trained using a training dataset, and the coefficients of the polynomial are estimated using optimization techniques such as gradient descent. The goal is to find the polynomial that best fits the data, as measured by an appropriate error metric. Once the model is trained, it can be used to make predictions for new data points.

3.2 *Artificial neural network*

Artificial neural network (ANN) is formed by several neurons as an information processing unit serving as the basis for the performing of a function in accordance with its task (Fausset L., 1994.). A neuron is an element that calculates an output signal using a particular rule from a set of input signals. It consists of weights inputs, a function of summation, a function of activation and output (Figure 2). Neurons can be connected to each other in different ways, but the essence of the neural network always remains the same — transmitting information ahead.

Thus, the input data is sent to the hidden layers for computing. Finally, the last hidden layer sends the processed information to the output layer. In this study, fully connected neural network is used, in which each neuron of one layer is sequentially connected to each neuron of the subsequent layer, including the input, hidden and output layers (Figure 3). Different weights describe the different influence of neighboring neurons on a particular one. These parameters are configured by the network itself during training. The weighted sum of the input data is transmitted to the hidden neurons, where it is transformed using the activation function. The process of obtaining output data is described by the equation:

$$Y_k^{n+1} = f\left(\sum_{i=1}^{N} X_i^n w_{ki}^n + b_i^n\right) \qquad (2)$$

where Y_k^{n+1} is output of unit k in the nth layer, f is the function of activation, X_i^n is the input vector, w_{ki}^n is a weight vector, b_i^n is the bias weight.

The initial values of the weights are often set randomly, and the training of the neural network is the selection of weights — backpropagation algorithm.

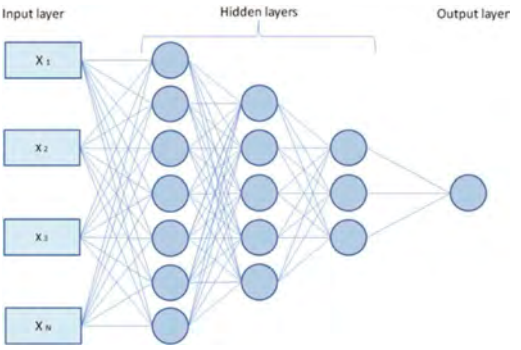

Figure 3. Schematic of an artificial neural network.

Application of the network training rules for backpropagation consists of two stages: feedforward and backward propagation. A set of training examples called training set is given on the network. This training set is represented by a feature vector called the associated input vector with an output that is the target of the training. In other words, the training set consists of an input vector and a target output vector. Exodus from the network is an actual output vector. Next, a comparison is made between the actual output produced and the target output by reducing the two outputs. The result of the reduction is an error. Errors are used to make changes to each weight by repropagating it. Any weight changes that occur can reduce errors. Cycle weight changes (epochs) are carried out in each training set so that the 50 stop is reached, when the set number of epochs is reached or when a set threshold value is passed. The backpropagation network training algorithm consists of 3 stages:

1. The feedforward stage. The input layer is first calculated by summing the weight and bias values up to the output layer using a predetermined activation function.
2. The stage of feedback (backpropagation). The difference between network output with the desired target is calculated, which is then referred to as an error. Next is the back-propagation phase, the error factor is propagated backward, starting from the corresponding line directly with the units in the output layer.
3. The stage of updating the weights and biases. The last phase is modifying the weights to reduce occurred errors (Afandi et al., 2022.).

3.3 *Decision tree*

The decision tree is an effective tool for data mining and predictive analytics. It helps in solving

classification and regression problems. The decision tree is a hierarchical tree structure consisting of a "If … then …" rule. Due to use the training set, the rules are generated automatically during the training process. The rules are generated by generalizing a set of individual observations (training examples) describing the subject area. Therefore, they are called inductive rules, and the learning process itself is called the induction of decision trees. In the training set, a target value should be set for the examples, since decision trees are models created based on supervised learning. Two types of trees are distinguished by the type of variable: classification tree, when the target variable is discrete, and regression one, when the target variable is continuous.

The root node, or the decision node, represents an option that will occur in splitting all records into two or more mutually exclusive subsets. Internal nodes, or random nodes, are one of the possible options available at this stage of the tree structure; the upper edge of the node is connected to its parent node, and the lower edge is connected to its child nodes or leaf nodes. Leaf nodes, or end nodes, are the final result of a combination of decisions or events (Figure 4).

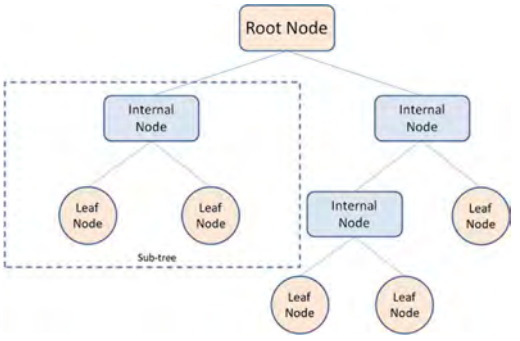

Figure 4. Schematic of a simple decision tree.

Before compiling the model, the most significant input variables shall be identified fist, and then based on the status of these variables the records at the root node and at subsequent internal nodes shall be divided into two or more categories or "bins". Characteristics entropy, Gini index, classification error, information gain, gain ratio and twoing criteria (Patel, Upadhyay, 2012.) are related to the degree of "purity" of the resultant child nodes (i.e., the proportion with the target condition) and used to select between different potential input variables. This splitting procedure continues until pre-determined homogeneity or stopping criteria are met. In most cases, not all potential input variables will be used to build the decision tree model and in some cases a specific input variable may be used multiple times at different levels of the decision tree (Song, Ying, 2015.).

3.3.1 *Classification and regression tree (CART)*

The CART (Classification and Regression Tree) algorithm recursively divides the original data set into subsets that become more and more homogeneous with respect to certain features, resulting in a tree-like hierarchical structure (Breiman et al., 1984.). Division is carried out on the basis of traditional logical rules in the form of IF (A) THEN (B), where A is some logical condition, and B is the procedure for dividing a subset into two parts, for one of which condition A is true, and for the other it is false.

At the first iteration, the root node of the tree is associated with the most optimal conditional judgment, and the entire set of objects is divided into two groups. Two branches can also branch off from each subsequent parent node to the descendant nodes, which in turn are associated with the boundary values of other most suitable variables and determine the rules for further splitting (splitting criterion). The final nodes of the tree are the "leaves" corresponding to the solutions found and combining all the objects of the training sample divided into groups.

The described process refers to the so-called "greedy" algorithms that strive, regardless of anything, to build the most "bushy" tree (also "deep tree"). Naturally, the more extensive and bushier the tree, the better the results of its testing will be on the training sample, but not as successful on the test sample. Therefore, the constructed model must also be optimal in size, i.e. contain information that improves the quality of recognition, and ignore the information that does not improve it. To ensure this, it is common to "prune" the tree (tree pruning) – to cut off branches where this procedure does not lead to a serious increase in errors.

It is impossible to find an objective internal criterion that leads to a good compromise between error-free and compact, thus the standard mechanism for optimizing trees is based on cross-validation (Loh, Shih, 1997). To do this, the training sample is divided, for example, into 10 equal parts: 9 parts are used to build a tree, and the remaining part plays the role of verification aggregate. After repeating this procedure many times, the tree that showed the best result during cross-validation is selected from a certain set of candidate trees that have a practically acceptable range of model quality criteria.

$$RMSE(y,\hat{y}) = \sqrt{\frac{1}{n}\sum_{i=1}^{n}(y_i - \hat{y}_i)^2}$$

3.3.2 *Random forests (RF)*

Random forest is a method invented after CART by Leo Breiman, which is based on the use of a committee (ensemble) of decision trees (Breiman, 2001.). The essence of the algorithm is that at each iteration a random sample of variables is made, after which, on this new sample, the construction of a decision tree begins. At the same time, "bagging" is performed — a sample of random two-thirds of observations for

training, and the remaining third is used to evaluate the result. This operation is performed hundreds or thousands of times. The resulting model will be the result of a "vote" of a set of trees obtained during modeling.

3.3.3 *XGBoost regression*

XGBoost (short for eXtreme Gradient Boosting) is a popular implementation of the Gradient Boosting algorithm. It is an efficient and effective machine learning algorithm for solving regression and classification problems. XGBoost is a tree-based ensemble model that works by building a sequence of decision trees. The model makes an initial prediction based on the mean of the target variable. It then adds a new decision tree that is trained to predict the residuals of the previous trees.

The process is repeated until the residuals are reduced to a minimum or until a predefined maximum number of trees is reached. The final prediction is the sum of the initial prediction and the predictions of all the decision trees. To avoid overfitting, XGBoost uses regularization techniques like *L1* and *L2* regularization and also incorporates early stopping, which allows the model to stop building new trees when it is no longer improving the performance on the validation set.

3.4 *Statistical accuracy measurement*

When using forecasting machine learning models, there is always some degree of uncertainty. The accuracy and correctness of the prediction results are characterized by the magnitude of the prediction error, which shows the difference between the actually measured value and the predicted one. In this study, the accuracy and forecasting power of the models were measured by two indicators: the predictive coefficient of determination R2 and the root mean square error (RMSE):

$$R^2(y,\hat{y}) = 1 - \frac{\sum_{i=1}^{n}(y_i - \hat{y}_i)^2}{\sum_{i=1}^{n}(y_i - \bar{y})^2},\ where\ \bar{y} = \frac{1}{n}\sum_{i=1}^{n} y_i \tag{3}$$

$$RMSE(y,\hat{y}) = \sqrt{\frac{1}{n}\sum_{i=1}^{n}(y_i - \hat{y}_i)^2} \tag{4}$$

Where $y, \hat{y}$ are actual and predicted value, respectively.

3.5 *Dataset*

The dataset is recorded by a computer using data from a TBM during its operation. Initially, the dataset was a table with 280 columns and 212,000 rows for tunnel lining rings numbered 0 to 777, representing various parameters of the TBM and its operation. After applying the data preprocessing procedure, a table with 14 columns (13 features and the speed rate column) and 11169 rows is obtained. Preprocessing operations include removing 5% of the data from the beginning and end of the set to exclude the possible influence of the initial and final conditions at the start and end point of the record. Further, since the regression problem is being solved to predict the speed of the TBM, all rows with zero speed value are also removed from the data set. Finally, out of 280 features, the main 13 ones are used, which have the greatest impact on the speed value. The main selection criterion is the condition under which the value of the correlation score of a particular feature for the speed should be greater than or equal to 0.3. The most significant features are total thrust (correlation score is 0.78 with the driving speed of the TBM), propulsion pump outlet pressure (0.75), speed of the screw conveyer (0.75), working status of shield machine (0.7), screw conveyer blade torque (0.6) and screw engine cylinder pressure (0.6). The distributions of these features and of the TBM's driving speed are illustrated in Figure 5.

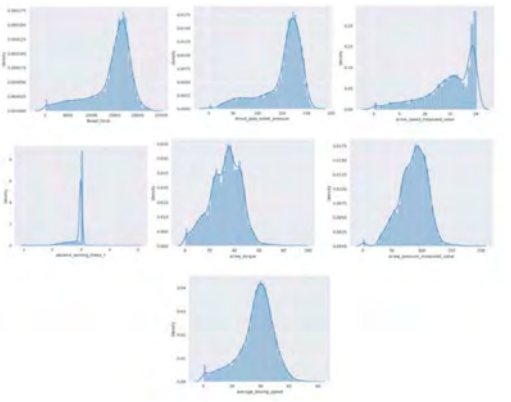

Figure 5. Density distributions of the data.

3.6 *Results*

To determine the reliability of the proposed machine learning solutions, solving algorithms are trained with a training set. The entire volume of data is randomly divided in training (80%), validation (10%) and test (10%) sets by leave-one-out method.

Figure 6 shows the results of comparing actual measurements and predicted values. Each graph contains dot diagrams, which are plotted relative to the line y=x and show correlation between predictions of the models and measured shield driving speed. XG Boost regression model has the best predictive ability with the values R2=0.809 and RMSE=5.708; worst of all, as expected, the decision tree model copes with the prediction with the values of R2=0.626 and RMSE=7.979.

It should be noted that the dataset used by the algorithms is compiled in such a way that each row contains the values of the features and the target

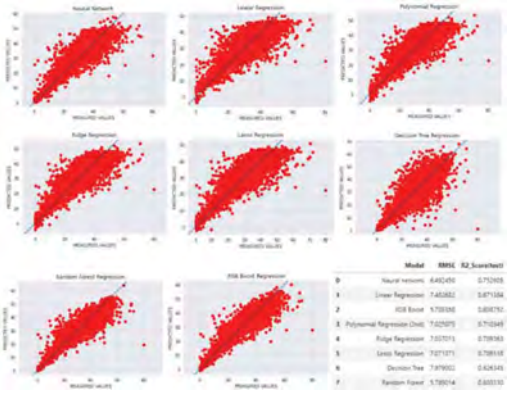

Figure 6. Predictions, R2 score and RMSE values.

variable at a specific time *ti*, for which the correlation coefficients are described above. For successful forecasting, a condition is necessary under which the features obtained at time *ti* allow obtaining the value of the TMB driving speed at time $tj=ti+\Delta t$.

The dataset was modified in such a way that the features at *ti* are compared with the target variable at *tj* with $\Delta t=10$ *mins,* which led to a redistribution of the correlation matrix: the coefficient for thrust force decreases dramatically, while the coefficients bentonite flow increases significantly. For a more detailed study of these dependencies and the derivation of general patterns, it is necessary to use more data from various construction sites.

4 CONCLUSIONS

This study shows that machine learning techniques can be used to accurately predict TBM driving speed, thereby improving tunnel excavation efficiency. A theoretical description of machine learning algorithms is given. The data collection process for the study is discussed, which involved collecting in-situ data from a TBM excavation project in China. Then the data is processed, polished and prepared for machine learning analysis. Finally, several machine learning algorithms are applied to the data, including linear regression models, decision trees models, and neural network to predict TBM driving speed. The results show that XG Boost algorithm outperformed the other algorithms in terms of accuracy, achieving an R2 score of 0.809. Overall, the study highlights the potential of machine learning for improving the efficiency and accuracy of tunnel excavation. Authors hope that presented findings will encourage further research in this area and help to advance the field of tunnel engineering.

ACKNOWLEDGMENTS

Partial funding for this study was provided by the National Natural Science Foundation of China (52078428) and Development and application of big data comprehensive monitoring system for shield construction projects (2018-B06). We also would like to express our gratitude to China Railway 14th Bureau Group Corporation Limited, for sharing the project data and providing us with an opportunity to learn from the people involved into this project.

REFERENCES

Afandi A. et al., 2022. “Prediction of temperature in 2 meters temperature probe survey in Blawan geothermal field using artificial neural network (ANN) method”. Case Studies in Thermal Engineering. 38(1):102309 DOI:10.1016/j.csite.2022.102309.

Breiman L., 2001. “Random forests”. Machine Learning 45 (1). P. 5–32.

Breiman L, et al., 1984. Classification and regression trees. California: Wadsworth Belement; 1984

Dang, L. et al., 2022. “Automatic tunnel lining crack evaluation and measurement using deep learning”. Tunnelling and Underground Space Technology, Volume 124, 2022, 104472, ISSN 0886-7798, https://doi.org/10.1016/j.tust.2022.104472.

Fausset L., 1994. Fundamentals of neural network: architectures, algorithms and applications. Prentice Hall.

Hu M, et al., 2019. “Modern Machine Learning Techniques for Univariate Tunnel Settlement Forecasting: A Comparative Study”. Mathematical Problems in Engineering, Hindawi, 2019: 7057612.

Liao, J. et al., 2022. “Automatic Tunnel Crack Inspection Using an Efficient Mobile Imaging Module and a Lightweight CNN”. IEEE Transactions on Intelligent Transportation Systems, doi: 10.1109/TITS.2021.3138428.

Liu H. et al., 2018. “Method for surrounding rock mass classification of highway tunnels based on deep learning technology”. Chinese Journal of Geotechnical Engineering, 40(10):1809–1817.

Loh, W., Shih, Y., 1997. Split selection methods for classification trees.

McNeish, D., 2015. “Using Lasso for Predictor Selection and to Assuage Overfitting: A Method Long Overlooked in Behavioral Sciences”. Multivariate behavioral research, 50(5), 471–484. https://doi.org/10.1080/00273171.2015.1036965

Patel, N., Upadhyay, S., 2012. “Study of various decision tree pruning methods with their empirical comparison in WEKA”. Int. J. Comput. Appl. 60 (12).

Song, Y., Ying, L., 2015. “Decision tree methods: applications for classification and prediction”. Shanghai Arch. Psych. 27 (2) 130.

Yan K, et al., 2020. “Tunnel Surface Settlement Forecasting with Ensemble Learning” Sustainability 12(1):232. https://doi.org/10.3390/su12010232

Yang, G. et al., 2021. “Intelligent Rating Method of Tunnel Surrounding Rock Based on One-dimensional Convolutional Neural Network”. Journal of Intelligent and Fuzzy Systems 42 (3) p. 2451–2469.

Zhao S. et al., 2022. “Intelligent Classification of Surrounding Rock of Tunnel Based on 10 Machine Learning Algorithms”. Applied Sciences. 12(5):2656. https://doi.org/10.3390/app12052656

Tunnelling for a Better Life – Yan, Celestino, Thewes & Eberhardt (Eds)
© 2024 The Author(s), ISBN 978-1-032-80042-4
Open Access: www.taylorfrancis.com, CC BY-NC-ND 4.0 license

Intelligent tunnel asset management of CERN underground facilities

Vanessa Di Murro*
European Centre of Nuclear Research CERN, Geneva, Switzerland

Aohui Ouyang
European Centre of Nuclear Research CERN, Geneva, Switzerland
University College Cork, Cork, Ireland

John Andrew Osborne
European Centre of Nuclear Research CERN, Geneva, Switzerland

Zili Li
University College Cork, Cork, Ireland
Massachusetts Institute of Technology, Cambridge, MA, USA

ABSTRACT: Maintenance strategy and routine inspections play a crucial role in the management of the large-scale infrastructures built at the European Laboratory for Particle Physics (CERN), which hosts more than 80km of underground tunnels with particle accelerators and beam lines. Most tunnels are not accessible during beam operation. Signs of ageing tunnel defects have been observed during tunnel inspections, particularly in tunnels constructed many decades ago. In the light of the safety of CERN personnel and the operational lifetime of CERN tunnels, the implementation of smart monitoring tools is essential for data automation and remote inspections.

In this paper, an overview of the advanced monitoring technologies that are implemented for the inspection of CERN underground tunnels is presented. This includes the state-of-the-art monitoring tools, robotic mounted imaging, unmanned aerial vehicles (UAV) and fibre optic sensors. The frontier analysis is conducted via artificial intelligence technology, machine learning, graphic based deep learning, and photogrammetry. The feasibility of the above-mentioned methodologies has been tested in CERN underground areas, providing instrumental data for the CERN's tunnel asset management.

Keywords: Monitoring, Tunnel Asset Management, Artificial Intelligence

1 INTRODUCTION

The European Laboratory for Particle Physics (CERN) located on the Franco-Swiss border, hosts the most powerful particle accelerator ever built, the Large Hadron Collider (LHC) (Figure 1). Physics experiments with high energy particle collisions are carried out in 100m deep tunnels, excavated in a sedimentary rock, called the red molasse, which comprises irregular sub horizontal bedded sequence of marls and sandstones (Fern et al., 2018) (Figure 2).

Due to the radioactive environment created in the particle collisions, most CERN's underground areas are inaccessible throughout the year. Only during scheduled periods, such as the Year End Technical Stop (YETS), tunnel access is allowed, which enables upgrades and maintenance activities to be carried out. As a result, it is very challenging to visually inspect CERN infrastructures, calling for exploiting smart and remote tools for comprehensive geotechnical analysis.

This paper presents the state-of-the-art monitoring technologies used in tunnels at CERN. It also describes the emerging technologies in the field of structural health monitoring and focuses on their benefits and challenges.

2 CERN UNDERGROUND FACILITIES

The underground network built at CERN comprises of around 80km of tunnels, shafts and experimental caverns with some structures built more than 50 years ago, thus exceeding their structural design life.

Recent inspections have clearly shown signs of tunnel lining deterioration with time due to tunnel distress, water leakage and concrete spalling.

*Corresponding author: vanessa.di.murro@cern.ch

DOI: 10.1201/9781003495505-408

Several challenges are encountered by the Tunnel Asset Management (TAM) team at CERN during the inspection campaigns:

- Very large-scale underground infrastructure with short inspection window.
- Unavailability of tunnels during operations of particle accelerator experiments, which make the tunnel environment radioactive during operation. For safety reasons, civil engineers can only inspect the underground areas and undertake repairs during the YETS, of 1-2 months duration.
- The radiation environment also limits the use of electronic devices for monitoring CERN infrastructures, as most commercial devices are not radiation tolerant.
- Restricted access: underground areas can only be accessed by CERN personnel equipped with personal safety protection kit and specialized training.

The implementation of remote and automated monitoring techniques plays therefore a crucial role for the management of large underground assets such as those found at CERN.

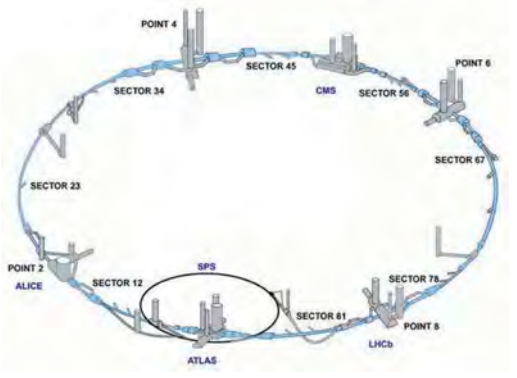

Figure 1. CERN schematic layout (photo credit CERN).

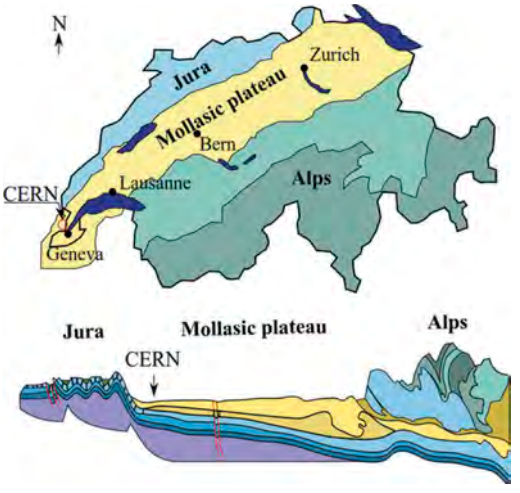

Figure 2. Swiss geology: CERN location (Fern et al., 2018).

3 MONITORING TECHNOLOGIES

The use of intelligent defect detection of tunnel lining surfaces has enabled CERN engineers to overcome a series of challenges related to the limited accessibility to underground areas and obtain instrumental data using different innovative methodologies. The overview of technologies and results are presented hereafter.

3.1 *Computer-vision based remote crack detection system*

Cracks serve as an early sign of deterioration of aging underground infrastructure. Cracks are the main defect encountered at CERN. To undertake remote inspection and enable monitoring during the accelerator experiments, advanced robotic solutions or image-based crack monitoring methods were developed at CERN (Ouyang et al., 2023, O'Brien et al., 2023).

Two robotic solutions are used to collect image data remotely in different scenarios. For monitoring the tunnels, the telemanipulated robot, the CERNbot, mounted with a coordinated camera rigs can be used. This is a modular robot developed by the Robotics team at CERN, enabling real time collection of tunnel lining images at different vertical tunnel positions (Di Castro, 2019) (Figure 3a). In the LHC 27km ring, the customised Tunnel Inspection Monorail (TIM) can also be used for image collection (Figure 3b).

For the monitoring of CERN shafts, an unmanned aerial vehicle (UAV) is adopted, which will be discussed in more detail in Section 3.2.

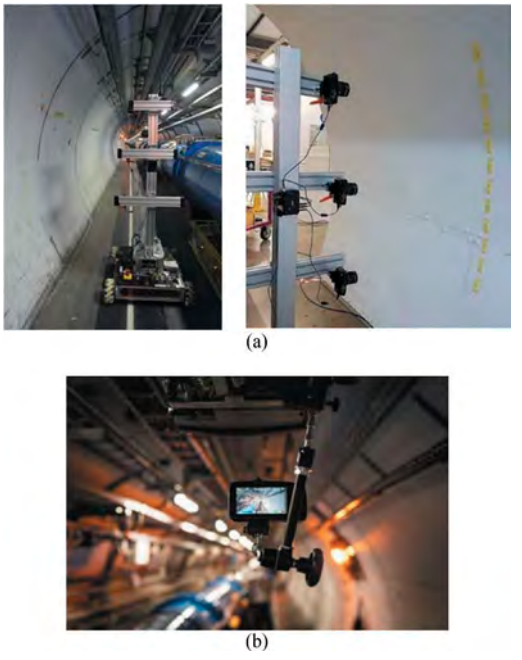

Figure 3. The customised advanced robotic solution (CERNbot) used for crack detection (Ouyang et al, 2023), (b) Tunnel Inspection Monorail (TIM).

Images are taken with overlaps and those images captured by the coordinated camera set in consecutive inspection spots are utilized for the creation of the panorama.

The mosaicking process is conducted by the Speeded-up Robust Features (SURF) algorithm which extracts invariant points in the overlap areas of adjacent images and stitches them all together. The stitched panorama enables a wider field of view, as shown in Figure 4.

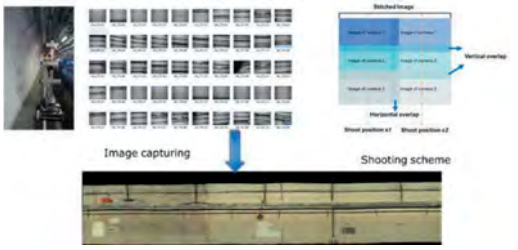

Figure 4. Image stitching for panorama (Ouyang et al., 2023).

To achieve automated crack detection at pixel level, the deep learning model, Deeplab V3 plus, is finetuned on the collected image data base, using transfer learning. As shown in Figure 5, cracks of small patch images are segmented out at pixel level. The cracks on the high-resolution panoramas are separated out with the smooth blending method, as shown in Figure 6. More details of this research can be found in Ouyang et al. (2023).

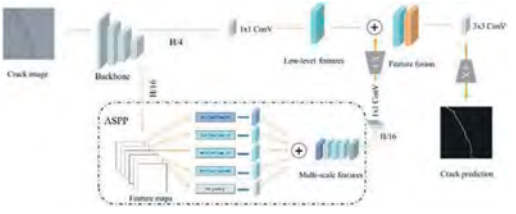

Figure 5. Deeplab V3 plus for automated crack segmentation.

Figure 6. Crack spatial layout after the detection.

Overall, the adoption of a computer-vision based study has reduced the need for human presence in the tunnels as it automates the image collection.

This tool also enables a quick assessment of the general condition of CERN tunnels, it facilitates the identification of the most severe crack damaged tunnel chainages, with sectional crack percentage, as shown in Figure 7a. In addition, the crack spatial patterns also reveal two different tunnel deformation modes for the circular LHC tunnel and the straight TT1 tunnel (Figure 7b).

The assessment of the tunnel structural behaviour enables the TAM team to plan well in advance of any mitigation measures to be implemented during the YETS and, hence, minimise the time on site and inform in the decision-making process for maintenance activities.

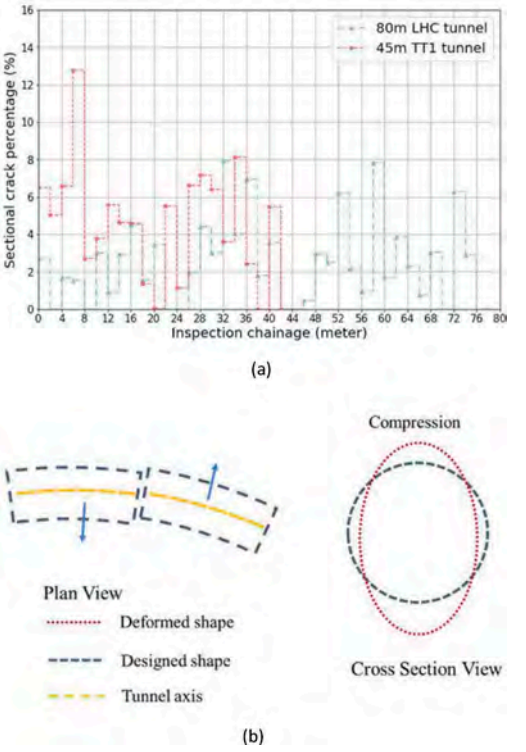

Figure 7. Crack statistics: (a) crack density distribution and (b) two observed tunnel deformation modes (Ouyang et al., 2023).

3.2 *Unmanned Aerial Vehicle (UAV) for defect detection*

The CERN underground infrastructure also includes several shafts, which cannot be visually inspected by the CERN TAM team. It is therefore crucial to adopt innovative monitoring solutions to assess the condition of the shafts.

The use of an unmanned aerial vehicle (UAV) enables to inspect the condition of CERN shaft efficiently and quickly.

A pilot monitoring trial using a drone was carried out in March 2023 for a 10m diameter shaft (PX84) at the Large Hadron Collider Point 8 (LHCb experiment site) by using one of the latest version of the

Elios 3 drone produced by the Flyability company (Figure 8a, b).

The Elios 3 drone was driven remotely by an experienced team from Flyability. The collected images showed the cracks and calcite deposits on the shaft lining (Figure 8c). Water leakages were also visible through a thermal analysis (Figure 8b).

(a)

(b)

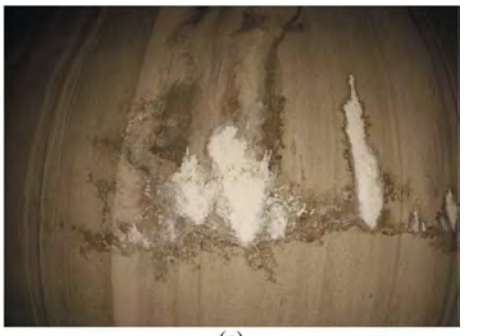

(c)

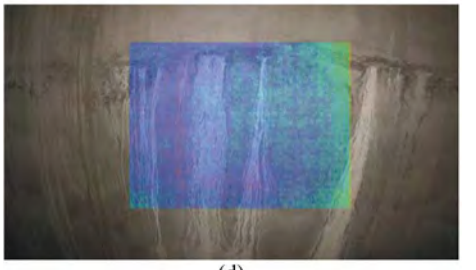

(d)

Figure 8. Drone trial of CERN shaft PX84: (a) drone image, (b) image of the shaft, (c) calcite deposits on the shaft lining, (d) thermal analysis (Flyability).

Processed images taken by the drone allow for automated fault detection of the shaft structural condition, with the aim of assessing its status and, hence, plan any repair works needed.

3.3 *Distributed Fibre Optic Sensors (DFOS) for strain and temperature measurements*

Distributed fibre optic sensors (DFOS) have been extensively used in various projects for monitoring the performance of civil engineering infrastructures such as tunnels (Di Murro et al. 2019, Mohamad et al., 2012, Soga et al. 2017). Among the different monitoring technologies, the use of DFOS seems to be the most appropriate for understanding the behaviour of CERN tunnels. Optical fibres have the advantage of being small in size, as well as being immune to the electromagnetic influence associated with the high energy of the LHC. They also enable the monitoring of long tunnel distances. However, the properties of the optical fibre and its behaviour can change depending on radiation levels. For such environments, an accurate study is required, and radiation resistant optical fibres may need to be adopted.

A monitoring installation using DFOS was trialed for the long-term performance of the concrete-lined tunnel TT10 (Figure 9). Several circumferential fibre optic loops have been deployed (Di Murro, 2019).

Figure 9. View of TT10 tunnel (Di Murro, 2019).

Figure 10. Omnisens FO analyser used in CERN tunnel.

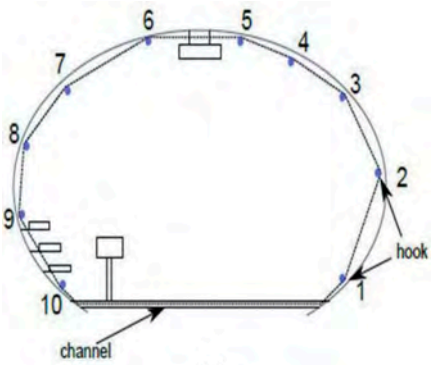

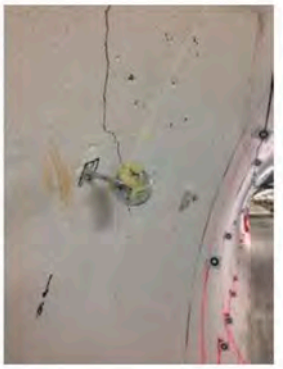

(b)

Figure 11. FO field installations: (a) Cross-section of the circumferential strain cable loop, (b) Method of attachment of optical fibre: pulley wheels (Di Murro, 2019).

The FO strain data was collected by attaching both ends of each FO installation to a Brillouin optical time domain analysis (BOTDA) interrogator, manufactured by Omnisens company (Figure 10).

The FO cable was attached to the tunnel lining at discrete locations by using a gauge-length method which makes use of a series of hook-and-pulleys, with the hook screwed into the tunnel lining surface and the FO cable passing along the pulley (Figure 11a, b). The gauge length method can only measure strain if the optical fibre is sufficiently pre-tensioned, without leaving any slack sections.

An example of FO data results is shown in Figure 12. The continuous axial strain measurement along the tunnel circumference is plotted against the cable distance for a monitoring period of 3 years. A sinusoidal-shaped strain profile with tension (positive strains) at tunnel spring line and compression (negative strains) developed along the tunnel lining, suggesting a vertical tunnel ovalisation as the mechanism of deformation many years after construction.

Overall, the research carried out by Di Murro (2019) shows that the examined tunnel sections exhibit a slow development of strain continuously with time over the monitored period of three years.

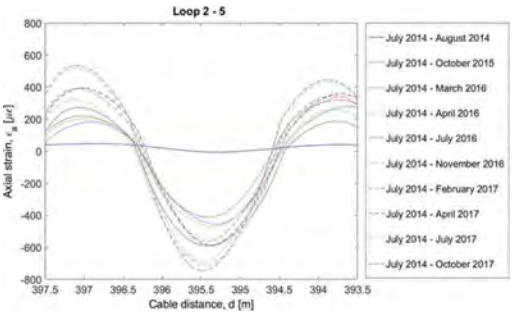

Figure 12. FO data results: strain measurements along the tunnel circumference (Di Murro, 2019).

4 CONCLUSIONS

This paper presented an overview of the smart and emerging monitoring technologies implemented at CERN for the monitoring of CERN underground assets. Ageing tunnels are exhibiting some structural distress over time, resulting in tensile cracks, spalling and water leakages.

Given the large extent of CERN's underground network, the use of intelligent monitoring technologies plays an important role. Advanced robotic solutions have shown that automated images of the tunnel lining surfaces can be collected for crack detection and quantification.

Moreover, to assess the structural condition of shafts, the use of an unmanned aerial vehicle (UAV) has enabled efficient and quick inspection of the shaft defects.

Additionally, the benefits of distributed fibre optic sensors for the strain measurements of a tunnel were also presented and discussed. Optical Fibres used in the structural health monitoring field not only provide continuous strain and temperature data with time, but also allow to understand the mechanism of tunnel deformation remotely.

Overall, by adopting automated and remote monitoring tools, large data sets can be collected and processed, minimising the subjectivity of visual inspection by engineers and overcoming the limited access to CERN areas.

The implementation of the above-mentioned monitoring technologies has improved the inspection of CERN facilities with time and has enabled better planning of repair works.

ACKNOWLEDGMENTS

This research is supported by a grant from the European Organization for Nuclear Research (CERN) for Tunnel Asset Management project. This funding is greatly acknowledged. The authors also appreciate the image data collected and shared by the BE-CEM -MRO section at CERN.

REFERENCES

Bay, H., Ess, A., Tuytelaars, T. and Van Gool, L., 2008. Speeded-up robust features (SURF). Computer vision and image understanding, 110(3), pp.346–359.

Di Castro, M., 2019. A novel robotic framework for safe inspection and telemanipulation in hazardous and unstructured environments, Industriales.

Di Murro, V., 2019. Long-term performance of a concrete-lined tunnel at CERN, Cambridge University.

Di Murro, V., Pelecanos, L., Soga, K., Kechavarzi, C., Morton, R. F. and Scibile, L., 2019. Long-term deformation monitoring of CERN concrete-lined tunnels using distributed fibre-optic sensing. Geotechnical Engineering Journal of the SEAGS & AGSSEA 50(1).

Fern, E.J., Di Murro, V., Soga, K., Li, Z., Scibile, L. and Osborne, J.A., 2018. Geotechnical characterisation of a weak sedimentary rock mass at CERN, Geneva. Tunnelling and Underground Space Technology, 77, pp.249–260.

Kechavarzi, C., Soga, K., de Battista, N., Pelecanos, L., Elshafie, M.Z. and Mair, R.J., 2016. CONTENTS AND PRELIMINARY PAGES. In Distributed Fibre Optic Strain Sensing for Monitoring Civil Infrastructure: A Practical Guide (pp. i–xviii). ICE Publishing.

O'Brien, D., Osborne, J.A., Perez-Duenas, E., Cunningham, R. and Li, Z., 2023. Automated crack classification for the CERN underground tunnel infrastructure using deep learning. Tunnelling and Underground Space Technology, 131, p.104668.

Ouyang, A., Di Murro, V., Cull, M., Cunningham, R., Osborne, J.A. and Li, Z., 2023. Automated pixel-level crack monitoring system for large-scale underground infrastructure–A case study at CERN. Tunnelling and Underground Space Technology, 140, p.105310.

Mohamad, H., Soga, K., Bennett, P.J., Mair, R.J. and Lim, C.S. (2012). Monitoring Twin Tunnel Interactions Using Distributed Optical Fiber Strain Measurements. Journal of Geotechnical and Geoenvironmental Engineering, American Society of Civil Engineers, Vol. 138, No.8, pp. 957–967.

Soga, K., et al. (2017). Distributed fibre optic strain sensing for monitoring underground structures—Tunnels case studies. Underground sensing, S. Pamukcu and L. Cheng, eds., 1st Ed., Elsevier, Amsterdam, Netherlands.

Xiao, Z., Osborne, J.A., Perez-Duenas, E. and Li, Z., 2020. The effect of pore water pressure on structural performance of CERN concrete-lined tunnel.

Tunnelling for a Better Life – Yan, Celestino, Thewes & Eberhardt (Eds)
© 2024 The Author(s), ISBN 978-1-032-80042-4
Open Access: www.taylorfrancis.com, CC BY-NC-ND 4.0 license

Research and practice of digital lean construction mode of tunnelling based on shield self-driving technology

Liefeng Pei & Huiming Wu
Shanghai Tunnel Engineering Co., Ltd, Shanghai, China

Min Hu*
SHU-SUCG Research Centre for Building Industrialization, Shanghai University, Shanghai, China
SILC Business School, Shanghai University, Shanghai, China

Jing Lu
SHU-SUCG Research Centre for Building Industrialization, Shanghai University, Shanghai, China
School of Mechatronic Engineering and Automation, Shanghai University, Shanghai, China

Bingjian Wu
SHU-SUCG Research Centre for Building Industrialization, Shanghai University, Shanghai, China
SILC Business School, Shanghai University, Shanghai, China

Gang Li
Shanghai Tunnel Engineering Co., Ltd, Shanghai, China

ABSTRACT: With the development of machine learning and intelligent control technology, shield self-driving technology is gradually moving from the laboratory into the engineering field. However, tunnel construction is a systematic project. Highly efficient, high-quality construction must be achieved by improving the shield tunnelling capacity and strengthening the synergy of equipment performance, material supply, transportation capacity, and other aspects. Based on analysing the critical problems of shield tunnel construction management, this paper proposes the idea of adopting lean construction to improve the tunnel construction management level. By taking advantage of shield self-driving technology and digital platform, the paper builds a tunnel digital lean construction mode by optimizing the processes, materials, equipment, personnel, and space, tracking and evaluating the effect in real-time, analysing the cause and coordinating various aspects to ensure that the entire construction is always in an efficient state of operation. The tunnel digital lean construction mode has been applied to the JCXSG-12 tunnel section of Shanghai Airport Line. Compared with the traditional construction mode, it can significantly reduce the influence of various human factors, lower labour costs, accelerate the construction process, decrease environmental pollution and mechanical loss during the construction process, and improve project safety, quality, and efficiency. It provides a new way for underground space construction and development.

Keywords: Tunnel, shield self-driving, digitalization, lean construction

1 INTRODUCTION

With the increasing demand for underground space development, there is a new demand for safety, quality, and efficiency in tunnel construction. Therefore, the research of self-driving of shield machines has become a hot spot in recent years to realize the goal of efficient, high-quality, and safe construction during shield tunnelling. However, the self-driving of the shield machine can only partially solve the tunnelling problem because tunnel construction is a systematic project. In addition to shield tunnelling, it also requires the cooperation and support of other links, such as segment transportation, muck transportation, and equipment maintenance. Problems in any one section or step will lead to decreased construction efficiency and increased project risk. Therefore, how to carry out scientific tunnel construction management has become the focus of attention. From the perspective of construction management, there are two types of problems in tunnel construction management: 1) Deviation in the implementation of the technical plan, such as poor supervision of construction quality and risk, which causes various types of

*Corresponding author: minahu@shu.edu.cn

DOI: 10.1201/9781003495505-409

accidents, such as axial deviation, ground settlement, and tunnel leakage. 2) Inadequate management of resources, such as a mismatch between the equipment configuration and the production schedule, and the project suffers from unnecessary waiting situations. 3) Inefficient synergy among the project personnel: personnel's differences in access to information lead to problems in cooperating.

To solve the problems of tunnel project management, researchers have worked from information sharing, risk management, schedule management, and multiple perspectives. Breaking the barriers of communication and synergy among various links around information sharing has been a hot research topic in recent years. People adopt the Internet (Li, 2013), BIM (Yu, 2016; Zhou, 2021), and GIS (Zhang, 2021) technologies to converge and visualize construction data from various sources and different data structures, which promotes the flow and understanding of information and facilitates analysis and supervision. Risk management is the critical point of tunnel construction. People use failure knowledge (Junichi, 2005), risk database (Huang, 2006), WBS-RBS theory (Zhao, 2023), and other methods to establish risk identification, assessment, tracking, and decision-making for the construction process and build a risk management system for tunnel construction. Quality, schedule and cost management are the core of engineering project management. People carry out process supervision and control around the quality control target (Zhou, 2021; Chen, 2004) and introduce the PDCA method for quality management (Song, 2010). Combined with the process flow and technical points of the shield method, technicians monitor, analyse, and control the construction process according to the requirements of construction quality control (Wang, 2021), budget and cost settlement (Xiao, 2018), and optimize the progress and resources of the project by using the construction simulation software (Yang, 2007) and the network planning diagrams (Han, 2019) to improve the construction progress and cost control of tunnelling project. These studies have promoted the improvement of tunnel construction management. However, the current research results still have many problems in practical application: 1) The research is often only from a certain point of view, and the scope of monitoring, evaluation, management, and decision-making is too broad to refine the description and consideration of the complex correlation between various types of information, various steps, and various kinds of goals. 2) The simple sharing of information lacks the deep integration of the task execution and resource layers and cannot promote work implementation. 3) Accurate management decisions must rely on timely and complete information and accurate and reliable forecasts, which traditional project management techniques do not have. As a result, the bottlenecks in tunnel construction management have yet to be effectively solved.

To solve the above problems, the most critical is around the tunnel construction tasks, accurate planning, dynamic scheduling of resources, and strict task implementation. Lauris Koskela proposed to apply lean management to the construction industry, and in 1993, he first proposed "Lean Construction" at the IGLC (International Group of Lean Construction) conference. Lean construction (Koskela,2002) emphasizes more accurate scheduling, effective work distribution, closer collaboration, refined budgeting, and more humanized project management processes. Traditional shield construction is limited by technology, and lean construction is difficult to implement in actual projects due to the lack of process delicate and precise capabilities. Therefore, we adopt the lean construction management idea with the digital technology of the shield self-driving system to realize accurate prediction and execution and promote the implementation of the lean construction management mode. Taking workflow as the core of project management, we connect the three links of planning, scheduling, and execution to establish a new tunnel construction organization and management system with accurate judgment, rapid response, and smooth execution so that the tunnel construction process can adapt to all kinds of changes, realize the optimal integration of resources, lower costs, ensure quality, shorten the construction period, strengthen collaboration, reduce all unnecessary waste, and create more project value of the project.

2 RELATED WORKS

2.1 *Lean construction*

Lean Construction (LC) originates from Lean Manufacturing, which is the application of Lean Manufacturing theory in the construction industry. The Transformation-Flow-Value (T-F-V) theory is the basis of Lean Construction (Koskela, 2000). It states that:1) Production can be seen as a transformation process from input to output, and production management is to break down this process into a number of basic elements and realize these elements as efficiently as possible. 2) Production is seen as a flow including waiting, inspection, movement, and other ineffective activities, so production management is to minimize the ineffective flow. Production management is to reduce the ineffective flow. 3) Production is the realization of customer needs (Value), then production management is equivalent to the customer's requirements accurately reflected in the design and to make the production and design based on requirements to maintain consistency. It can be seen that lean construction needs to achieve is to meet or exceed the design requirements in the project implementation, eliminate waste, and pursue the perfect process cantered on the value stream.

2.2 *Shield self-driving*

Shield self-driving refers to a series of means, such as independent perception, autonomous planning,

assessment decision-making, and automatic control, in which the shield machine automatically performs operational steps such as rock and soil excavation, shield tunnelling, synchronized grouting, and shield tail grease pressure injection, and completes the tasks of tunnel axial control and ground settlement control while ensuring the safety of the project (Hu, 2022). Shield self-driving is centred around project design requirements and value realization and is a core part of the tunnel construction workflow. Therefore, with self-driving as the core, it can provide timely and refined decision-making and execution support for tunnel lean construction.

Table 1 shows the relationship between shield self-driving and construction management's production elements, workflow, and value realization, using a common earth pressure balance shield as an example.

As can be seen from Table 1, through the prediction and planning of critical elements based on shield self-driving technology, it is possible to refine the quantity, time, and location of production elements such as equipment, materials, and labour, and make a detailed plan for the maintenance of equipment, materials, personnel arrangements and the execution of ancillary tasks. By digital means, it can compare the deviation between the refined plan and the actual execution, quickly detect unnecessary waiting and waste in the workflow, and combine with value assessment, timely detection, and early warning of quality and safety problems in the construction process, and dynamically optimize and correct the entire workflow.

3 LEAN CONSTRUCTION FOR SHIELD TUNNELLING

3.1 *Shield construction process analysis*

Shield tunnelling is a cyclic, assembly-line operation process. The most central processes are soil cutting, segment assembly, slurry injection, and Muck transportation. Figure 1 shows the back-and-forth relationship within and between these four processes. As can be seen from the figure, there are many conditional nodes in this process, and the status of the nodes will directly affect the efficiency of the shield construction. The tasks in the orange background of the figure are affected by these nodes, in other words, constrained by various types of space, resources, and equipment. The tasks in the blue background of the figure are provided by the self-driving control system, including tunnelling planning, segment selection and assembly solution, slurry and grease injection plan, and soil transportation plan, which is calculated based on the tunnelling planning. It can be seen that with self-driving technology, the forecast of the amount of resources, time, and space requirements can be depicted in more detail than before, which means that the

Table 1. T-F-V in the perspective of shield self-driving.

	Transformation			Flow	Value
	Task Element Prediction and Plan (Quantity,Time,Space)				
Shield Self-driving Task	Materials	Equipment	Labor	Process Evaluation and Improvement	Value Goal and Realization
Cutting Advancing	Segment, Ancillary materials such as rails and piping	Shield, Crane, vehicle in Tunnel	Supervisory Coordinator, Assembly Team, Maintenance Team, Surveying Team	Advancing Duration, Assembly Duration, Downtime	Improving Advancing Speed, Tunnel Quality, Environmental safety
Soil Conditioning	materials for soil improvement, such as foaming agents.	/	Materials Clerk	Waiting Time, Failure Duration	Improving Advancing Speed Decreasing Energy consumption
Muck Discharge	/	Crane, Vehicle in Tunnel, Off-site transportation	Transportation team, lifting team, Materials Clerk	Transfer Duration	Improving Advancing Speed
Slurry Injection	Slurry	crane vehicle in Tunnel Off-site transportation	Transportation team, lifting team, Materials Clerk	Waiting Time, Slurry usage and effectiveness	Improving Environmental safety, Reducing Material Cost
Shield tail grease Injection	Grease	crane. Vehicle in Tunnel, Off-site transportation	Transportation team, lifting team, Materials Clerk	Waiting Time, Slurry usage and effectiveness	Improving Tunnel Safety Reducing Material Cost

supporting things can be arranged earlier and more accurately according to the plan. This reduces the unnecessary waiting of each conditional node due to unsatisfied states.

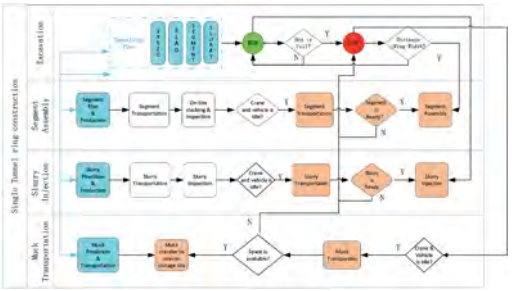

Figure 1. Tunnelling process by shield self-driving.

3.2 *Material requirement planning*

As seen in Figure 1, resources are the most crucial issue affecting the continuity of shield tunnel construction. Three main types of resources are needed for shield construction: materials, equipment, and space. Materials include tube sheets and slurry, equipment includes crane, vehicle, and truck, and space refers to the location needed for temporary stacking of segments and slurry. Therefore, it is essential to determine each resource's preparation time and amount based on forecasting and planning.

Shield self-driving system can predict a reasonable advancement speed based on the surrounding strata, tunnel alignment, and shield machine efficacy, combines historical or pre-engineering data, defines the advancement plan for the next phase (50-100 rings), calculates the types and quantities of each type of resource and constructs an information list table. Based on the tunnel tunnelling plan and resource list table, determine the uncertainty of the advancement speed and resource status, analyse the probability of their occurrence, and further adjust the resource ordering and equipment maintenance plan. The resource requirement planning process is shown in Figure 2.

3.3 *Tunnelling plan optimization*

Another constraint of shield tunnelling comes from the working space because the space inside the tunnel is limited. Even if there are enough resources, many jobs can not be carried out simultaneously in the same working space, which will cause conflicts. Therefore, this paper adopts the line of balance method (LOB) (Sarraj,1990), which is a resource-driven scheduling system for projects with repetitive activities to analyse the occupancy of the construction workspace. Meanwhile, we designed two indicators, Workflow-Idle-Rate and Equipment-Load-Unbalance-Rate, to evaluate the continuity and smoothness of the advancement process.

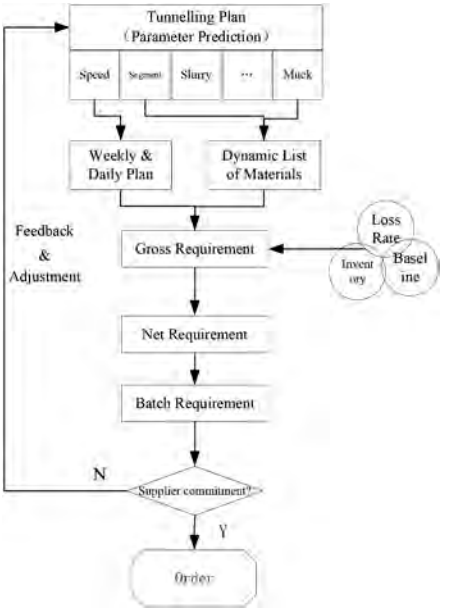

Figure 2. Resource requirements under shield self-driving.

3.3.1 *LOB graph*

In contrast to the critical line method and Gantt charts, the LOB method utilizes clear and easy-to-understand graphics that consider the flow process of tasks through different construction units while showing the productivity and time period of each task. Figure 3 shows the flow of tasks in different workspaces during tunnelling construction. As seen in Figure 3, due to the workspace limitations and the different work efficiency of each task, there will inevitably be the problem of task discontinuity, which will significantly impact the project's progress and cost. Therefore, from the perspective of lean construction, the process or technology of the tasks must be appropriately modified to reduce the waiting time between tasks so that the whole excavation process is always in a stable and smooth state, which is also beneficial to reduce the equipment failure rate and improve the quality of the project.

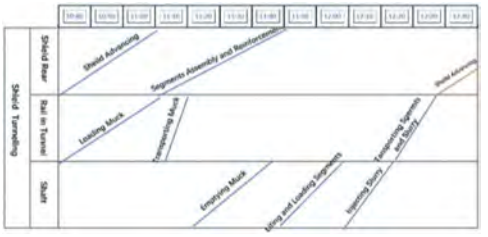

Figure 3. LOB graph of shield tunnelling.

In Figure 3, although the working space shows that the processes are connected as seamlessly as possible,

in reality, the disposal of muck and slurry injection at the shaft occupied a long time, leading to a long waiting time for the shield machine and the vehicle and a lack of production efficiency. Therefore, improving the process flow in the working shaft area is very important.

3.3.2 *Optimization indicator*

1) Workflow-Idle-Rate

Workflow-Idle-Rate (IR) is used to measure the idleness (degree of continuity) of the workflow in the ring, see Equation 1. It is mainly used to analyse the relationship between the ring's tunnelling processes and reduce the single-ring tunnelling time.

$$IR = it/t \times 100\% \tag{1}$$

where.

t: working time, is the time interval from the start of a single-loop workflow to the end of all processes in a single loop; idle time,

it: waiting time is the total waiting time during the working time.

2)Equipment-Load-Unbalance-Rate

Equipment-Load-Unbalance-Rate (UBR) is used to measure workflow equipment workload. On the premise that the advancement time in the ring has been optimized, it ensures the balance of daily, weekly, and monthly planned tasks, which makes the operation of the equipment and workforce in a stable state, reduces the equipment failure rate and improves the quality of the project.

$$\mathrm{UBR} = \frac{\sqrt{\frac{\sum_{i=1}^{N}\left(t_i-\bar{t}\right)^2}{N}}}{\tilde{t}} + \frac{\sqrt{\frac{\sum_{i=1}^{N}\left(tw_i-\overline{tw}\right)^2}{N}}}{\widetilde{tw}} \tag{2}$$

Where,

t_i : is the working time of the ith ring,

tw_i : is the interval time between the ith and the (i +1)th ring,

$\bar{t}$: is the average time to complete a single ring of N rings,

$\overline{tw}$: is the average waiting time between rings of N rings,

N : total tunnelling rings,

$\tilde{t}$: is the standard time to complete a single ring,

$\widetilde{tw}$: is the standard waiting time between two rings.

In this way, according to the LOB graph, with the optimization goal of minimizing the combined idle rate and imbalance, we optimize the processes in the tunneling process and, based on the standard advancement time determined by the automated advancement system, and inconjunction with the current status of the resources, we arrange for the ordering of materials, the maintenance of the equipment, as well as the personnel and vehicle schedules into the determination of the shield advancement plan, to achieve the fine-tuning cooperation of the various collaborating parties.

4 ENGINEERING APPLICATION

4.1 *Engineering background*

The Airport Line of Shanghai Rail Transit City Line, with a total length of 68.627km, is a fast-track Corridor of Shanghai that connects the two airports, and it is also a crucial railroad between Shanghai and the outside of the town. The JCXSG-12 tunnel section of the Airport Line from 7# wind shaft to Lingkong Road conversion shaft, which is 5.7km long, and the shield will cross 48 Class I and Class II risk points along the tunnel designed axis. The geographic graph of the section is shown in Figure 4, and the tunnel is constructed with a 9.3m "Zhiyu" self-driving earth pressure balance shield (Figure 5). Compared with the traditional shield, the "Zhiyu" Shield can quickly judge its state and recognize the surrounding environment, autonomously carry out propulsion planning, determine the advancing speed, thrust, torque, zonal oil pressure, and grouting volume, and other vital parameters, dynamically control the shield to do a series of actions such as cutting, attitude correction, pressure balance, grouting, improvement, etc., to complete the whole process of automatic tunnelling.

Figure 4. Shanghai airport line (JCXSG-12).

Figure 5. "Zhiyu" shield.

4.2 *Other supporting methodology*

In addition to planning and optimizing the tunnelling process and resources using "Zhiyu" shield self-driving techniques, some management tools are required to ensure that lean construction becomes a reality from concepts. The following supporting methods were adopted in the project:

4.2.1 *Last Planner System (LPS)*

Considering the shield advancing as the last process, and according to the idea that the demand of the latter process pulls the former process, we gradually determine the space, equipment, and material demand of the former process based on the needs of the advancement process. The "last planner system" emphasizes pull-type management, releasing daily, weekly, and monthly demand plans through the project cooperative group, coordinating all relevant divisions to participate in the execution of the project plan in depth, thus reducing unnecessary work and waiting time, and maximizing the speed of construction progress. In this way, the tunnel segment production company carries out more accurate production and scheduling, the shield machine and vehicle maintenance team do maintenance according to the downtime gap to minimize unnecessary waiting time, and the project management department contacts the muck transportation service provider in advance according to the production plan to avoid affecting the project schedule because of the problem of muck discharge.

4.2.2 *Just in Time (JIT)*

The just-in-time production system is based on a refined advancement plan, and standardized personnel time, location, and operation requirements are established in project management, preventing redundant operations from interfering with engineering work. With people, materials, and machines arriving on time and a stable work rhythm in each section, not only are workers able to operate more skillfully, but also various types of waste, such as unnecessary movement of items, are reduced, and high quality, low cost, and low resource consumption are realized.

4.2.3 *Activity-Based Costing Management (ABCM)*

The project brings cost management together in every live operation of tunnel tunnelling. Through continuous operation improvement, waste can be reduced, and project costs can be lowered. The operation cost is managed along with the tunnelling process. According to the self-driving system's evaluation system, the effect and cost of soil improvement, shield propulsion, synchronized grouting, and grease injection operations are continuously adjusted. During the advancement process, the automatic control model is dynamically optimized, and the operation cost calculation and analysis are integrated into the whole construction process to continuously transform and maximize self-driving decision-making and control ability. In this project, the average shield propulsion speed was increased from 75mmm/min at the initial stage to 95mm/min at the later stage, while the energy consumption of shield propulsion per unit distance was reduced by 25%.

4.2.4 *6S on-site management*

Site management is the guarantee of lean construction. Therefore, the 6S on-site management theory is adopted in the project through organizing (SEIRI): discard unwanted items; reorganizing (SEITON): make it possible to get the things you want at any time; cleaning (SEISOU): always keep tidy; cleaning (SEIKETSU): always maintain the state of organizing, cleaning, reorganizing; quality (SHITSUKE): comply with the established rules; safety (SAFETY): establish the concept of safety first to ensure the smooth implementation of the project.

4.3 *Application effects*

The whole tunnel was propelled by self-driving, with an average speed of 84.8 mm/min throughout the tunnel, and created a record for the fastest single-day and single-month shield tunnelling of the same class in March 2023, with 19 rings in a single day and 829.8 m (461 rings) in a single month (Figure 6). As can be seen from the Figure 6, the shield machine always maintains a high advancement mileage, and only on March 9, 27 and 28 the number of advancement rings was less. This was due to the fact that the shield machine and the vehicle had reached the required maintenance time and mileage, and needed to be shut down for maintenance, which is a normal part of the production schedule.

During the shield advancing process, the absolute average value of shield attitude deviation is less than 40mm, and the maximum value of cumulative ground settlement is less than -13mm-3mm. The quality of the formed tunnel is good, the tube sheet misalignment and tube sheet gap are controlled within 3mm, and the amount of tube sheet uplift is controlled stably, ensuring "zero accident" in tunnel construction and "zero leakage" in the tunnel of 78,000 square meters. In addition, the energy consumption of the cutting part of the automatically controlled unit advance distance is 25% lower than that of the manual control, and the overall failure rate of the shield machine is 0.48%. After tunnel construction, when the shield was returned to the factory for maintenance, it was found that the shield machine had a good performance, and the wear and tear of each component was very small.

Figure 6. Shield daily advancement rings (March 2023).

5 CONCLUSION

Shield self-driving technology not only solves the problem of lack of experienced technicians and reduces the labor intensity of site operators but also

is an opportunity to change the production mode of the tunnel industry. This paper fully uses the advantages of self-driving technology, combining digital technology with lean construction methods in tunnel engineering project management. Through construction process standardization, resource demand plan refinement, and promotion plan optimization, together with the LPS, JIT, ABCM, and 6S on-site management, this paper significantly improves the production efficiency and quality, reduces the cost and energy consumption in JCXSG-12 tunnel construction of the Shanghai Airport Line, which reflects the advantages of combining the self-driving technology and the lean construction.

This research is just a beginning. The continuous development of digital and intelligent technology not only promotes the improvement of tunnel construction technology but also changes the tunnel construction management mode and injects new vitality into the development of underground engineering.

ACKNOWLEDGMENTS

Grant to the Engineering Project Departments of Shanghai Tunnel Engineering Co., Ltd. for support and assistance in applying the “Zhiyu” self-driving system.

REFERENCES

Chen BX,Yi GH, 2004. Research on the application of rapid construction management technology for long tunnels. Journal of Railway Engineering, 3,5–12.

Han X. 2019. Study on Progress Control of Tunnel Tunnelling Construction. PhD Thesis. Jiangsu University of Science and Technology, Jiangsu, China.

Hu M, Wu B, Zhou W, et al. 2022. Self-driving shield: Intelligent systems, methodologies, and practice. Automation in Construction, 139: 104326.

Huang HW, Zeng M., Chen L, et al. 2017. Development of Shield Tunnel Construction Risk Management Software Based on Risk Database (TRM1.0). Journal of Underground Space and Engineering. 2017(z1):6.

Junichi, Kitahara, Kazuhito, et al. 2005. Development of an assessment system of total construction cost and its application to the shield tunnel constructions in urban area. Journal of Construction Management, JSCE.12: 273–281.

Koskela L, Ballard G, Howell G, et al.2002. The foundations of lean construction. Design and construction - building in value, Butterworth-Heinemann Ltd, London, England. pp211–226.

Koskela L. 2000.An Exploration Towards a Production Theory and its Application to Construction. Vtt Publications, 408.

Li X, Zhu H. 2013. Development of a web-based information system for shield tunnel construction projects[J]. Tunnelling and Underground Space Technology. 37 (6):146–156.

Xiao SH. 2018. Analysis of Cost of Super Large-diameter Subsea Shield Tunnel. Tunnel Construction, 38(6): 907–914.

Song TT. 2010. Quality Management Based on PDCA Method in Metro Shield Tunnel. Modern Tunnelling Technology. 47(3): 24–28,62.

Wang W. 2021. Quality Control Measures of Metro Tunnel Shield Method Construction. Engineering and technical studies.

Yang S, Wei Z. 2007. Tunnel Engineering Construction Schedule Analysis and Management Based on Visual Simulation. Journal of Tianjin University (English Edition).13(002):131–136.

Yu G, Hu M, Gao XW, et al. 2016. BIM-based 3D visualization aid system for shield tunnel construction management. Modern tunnel technology. 53(1):6–12.

Zhang JX. 2021. Study on the application of project management of large-diameter public-railway joint shield tunnel based on BIM technology. Journal of Engineering Management. 35(2):5.

Zhao K.2023. Risk management of tunnel construction under complex geological conditions. Engineering construction and design, (14):pp221–223.

Zhou X. 2021. Comprehensive Management Strategy for Tunnel Construction Quality Inspection and Monitoring. Journal of Architectural Research and Development.

Zhou Y, Wang C, Yuan B,et al. 2021. Research on Visual Management Technology of Tunnel Construction Process Based on BIM Technology. Advances in civil engineering.

Tunnelling for a Better Life – Yan, Celestino, Thewes & Eberhardt (Eds)
© 2024 The Author(s), ISBN 978-1-032-80042-4
Open Access: www.taylorfrancis.com, CC BY-NC-ND 4.0 license

Study on machine learning method for supporting conventional tunnel engineering judgement

Kazuo Sakai*, Shuntaro Miyanaga & Masahito Yamagami
Taisei Advanced Center of Technology, Taisei Corporation, Kanagawa, Japan

ABSTRACT: The authors have been studying design methods in the conventional tunneling for rational and economical selection of support structures and optimal blasting using machine learning algorithm. In the methods, Measurement While Drilling (MWD) data of charging holes on the face are used as input variables. Those data are recognized as "big data" and are automatically collected at several centimeter intervals by the computer-assisted drilling rigs. The proposed method using quantitative MWD data could realize those designs with more consistency and swiftness than conventional ways where decision is emphasized by site engineer's subjective observations of rock mass appearance. This paper reports a case study of analyzing geotechnical information and the MWD data obtained from an actual tunnel project. First, neural network algorithm learning MWD data were constructed. That made it possible for rock mass classification to be used as a basis for the tunnel support selection. The method provided the classifications consistent with geologist's interpretation with more than 70 % regarding rock mass strength, weathering and alternation, and fracture spacing. In addition, random forest algorithm learning MWD data were tested to estimate the explosive volume for a round of blasting. As a result, using both averaged MWD data on each hole and their statistical analysis results, it was confirmed that the explosive volume was predicted with 90 % accuracy.

Keywords: Measurement While Drilling, Neural Network, Random Forest, Rock mass classification, Explosive volume

1 INTRODUCTION

In recent construction industries, productivity enhancement has been one of the high-priority issues as a measure against the prolonged work environment and the labor shortage resulted from declining birthrate and aging population problem in Japan. We, Taisei Corporation, have been developing a remote control or automation system of heavy machinery for the tunnel excavation, making use of the recent enhancement of in in-tunnel network environment and up-to-date sensing technologies with the aid of IoT. In future, we believe that those developments will contribute to realizing excavation and support works only by a single miner, which are normally conducted by a group of people consisting of 5 to 6 workers today in Japan.

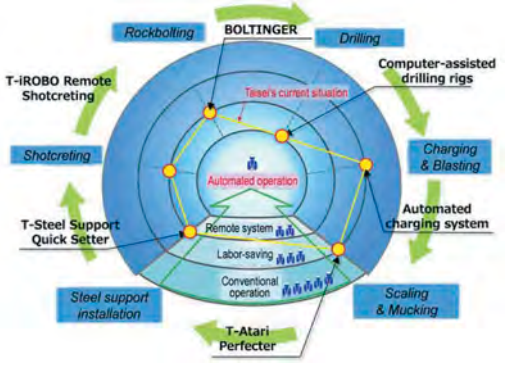

Figure 1. Taisei's current development status for the automation of tunnel excavation.

Figure 1 conceptually represents the Taisei's current development status for the remote or automated tunnel excavation works. It consists of drilling, charging, blasting, mucking, scaling, installing steel supports, shotcreting, and rockbolting. For the drilling of explosive charging (and occasionally rockbolt) holes, the computer-assisted drilling rigs are applied. The rigs and drifters can be automatically operated as designed beforehand. In addition, the rigs are equipped with the Measurement While Drilling (hereinafter called MWD) function which records positions of drilling bits and loads acting on the drifters. Though recordable data may vary depending on manufactures the rigs, they are represented by the parameters, such as

*Corresponding author: skikzo01@pub.taisei.co.jp

DOI: 10.1201/9781003495505-410

Table 1. Specifications of XE3C manufactured by Epiroc.

Epiroc Computer-assisted drilling rigs "XE3C"	
Exterior view	
No. of Rig/ Basket	3 rigs and 1 basket
Drifter model	COP 2238+
- Hammering power	22 KW
- Hammering rate	4,380 bpm
- Rotation speed	215 rpm
Positioning system	Dedicated geodetic method with Leica system
MWD fuction software	Under Ground Manager

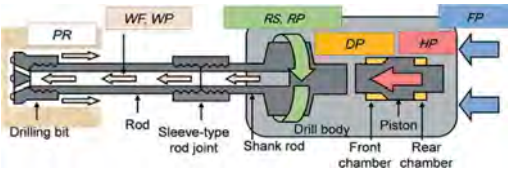

Figure 2. Drilling process and recorded MWD data (After Hashiba et al. 2017).

penetration rate (m/min), feed pressure (MPa), rotation pressure (MPa), and so on. These parameters are considered effective for assessing the rock mass conditions to be blasted and excavated.

For example, Schunnesson (1996) showed the correlation between the MWD data and RQD observed at rock masses in Glödberget, Sweden. Schunnesson (1998) also discussed the necessity of parameter normalization to take influences from the operator and drill control system into consideration, so that remaining data used to characterize the ground conditions only reflect variations of rock mass properties, such as hardness, fracturing and weathering. Eldert et al. (2022) analyzed the correlation between normalized MWD data and Q-parameters with the multilinear regression analysis. They also proposed a prediction method for rock supports by the holistic visual approach on the MWD data. Commonly applied in Japan is the estimation for rock mass conditions ahead of the tunnel face with the drilling energy (specific energy of cutting) calculated from MWD data (Yamashita, 2008). The drilling energy is defined as the specific energy to break one unit volume of rock. In the meanwhile, the rock mass classification with another index of normalized drilling velocity ratio has also been proposed (Kuwabara, et al. 2008). Furthermore, the drilling energy is calculated from the MWD data of a computer-assisted drilling rigs and used not only for rock mass classification on the face but also for blasting design in the subsequent excavation rounds (Fukuda et al., 2020). These studies indicate that the MWD data can support the quantitative engineering judgment for the tunnel construction. The MWD data obtained by the computer-assisted drilling rigs are regarded as "big data": with several centimeters interval in the depth direction for every drilling hole in every blasting round. Therefore, the authors have been developing the design methods in the conventional tunneling for rational and economical selection of support structures and the optimal blasting using machine learning algorithm which is considered suitable for effectively analyzing big data and identifying uncertain correlations. The proposed method using the quantitative MWD data could realize those designs with more consistency and swiftness than conventional ways where the decision is emphasized by site engineer's subjective observations of rock mass appearance. Using the MWD data obtained by a computer-assisted drilling rigs produced by Epiroc, this paper reports two case studies to evaluate rock mass classification which is a basis for the tunnel support system, then to estimate explosive volume for a single blasting round, which is a key parameter in the appropriate blasting design.

2 COMPUTER-ASSISTED DRILLING RIGS AND MWD DATA

To realize the efficient drilling and the minimum over-excavation blasting leading to the reduction of required concrete for tunnel support, the computer-assisted drilling rigs called XE3C manufactured by Epiroc was applied to the Atoda tunnel construction project where the tunnel mainly passed through the tuff breccia in the Southern part of Japan. Table 1 shows the representative specifications of XE3C. The MWD function software called Underground Manager records the following MWD data which are also conceptually shown in Figure 2:

- Hole position and depth (m)
- Penetration rate (*PR*) (m/min)
- Hammering pressure (*HP*) (bar)
- Feed pressure (*FP*) (bar)
- Dumper pressure (*DP*) (bar)
- Rotation speed (*RS*) (rpm)
- Rotation pressure (*RP*) (bar)
- Water flow rate (*WF*) (l/min)
- Water pressure (*WP*) (bar)

Prior to the machine learning analysis, distribution of the raw MWD data was investigated. Through the daily face observation and documentation in the Atoda tunnel project, the rock mass conditions were classified as CII and DI in compliance with the rock classification system for road tunnels in Japan (JSCE, 2007). In the first half

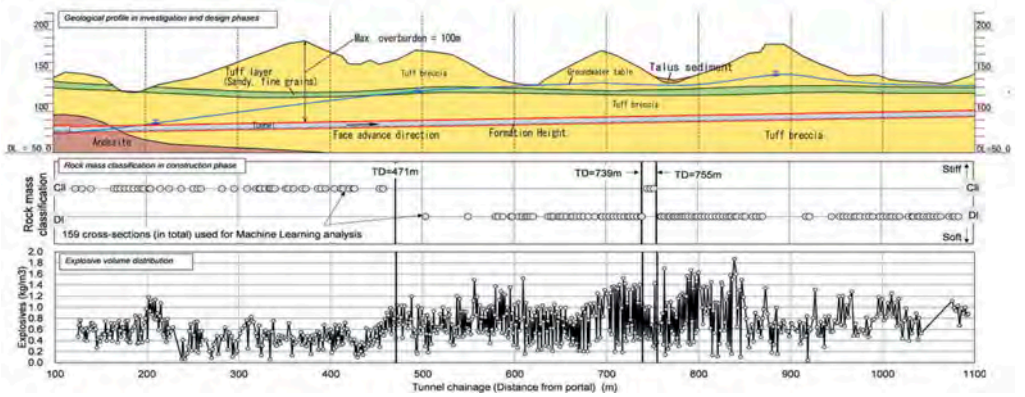

Figure 3. Construction records (top: geological profile, middle: rock mass classification, bottom; explosive volume distribution).

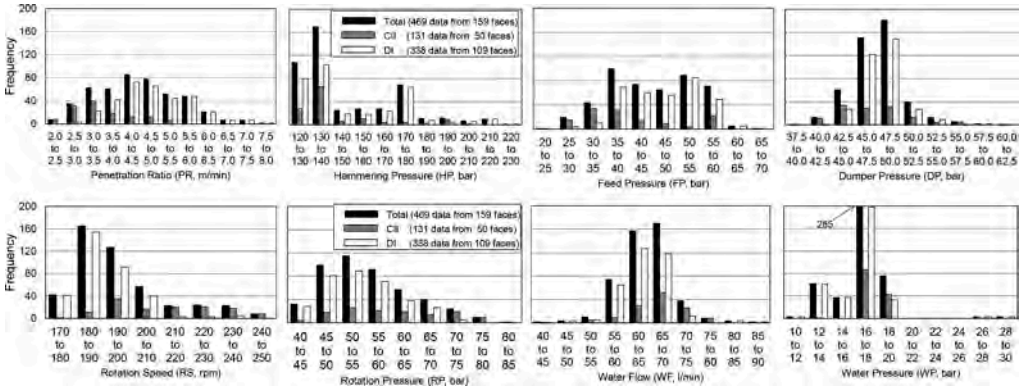

Figure 4. Frequency distribution of MWD data (average data in each area: top, left bottom, and right bottom).

of the excavation length, the tunnel encountered relatively stiff andesite and tuff breccia classified CII and a round length of 1.2 m was applied. After the tunnel face passed the location 471 m from the portal, the tunnel encountered weathered rock repeatedly crossed by vertical discontinuities with slickenside, potentially leading to face instability problems. Therefore, the round length decreased to 1.0 m and the support system corresponding to class DI was selected. Figure 3 represents the geological profile of the Atoda tunnel in the investigation phase together with the construction results of the rock mass classification and the distribution of used explosive volume along the tunnel chainage. Figure 4 shows frequency distributions of the MWD data obtained for 159 observed and documented excavation faces. Each face was separated into three parts: top heading, left and right bottoms. It should be noted that the MWD data in those graphs are averaged values for holes drilled in those three parts. Also note that the data deeper than 50 cm only were analyzed. This is because the computer program is set to work at low speed and low pressure regardless of rock mass conditions to restrict harmful vibration effect from the drilling bit at the initial drilling stage. The normal drilling began at least after the bit reached a depth of 50 cm.

The graphs of penetration rate and feed pressure in Figure 4 indicate that slower rate and lower pressure were recorded in stiffer rock mass conditions (CII) than those in softer conditions (DI). Meanwhile, the peak of rotation speed in class DI was lower than that in class CII. Clear differences were not identified in the other indices.

In the following chapters, machine learning algorithms using the raw MWD data with characteristics explained above are experimentally constructed to examine the accuracy of estimation for the rock mass classification and explosive volume in the Atoda tunnel where the actual judgement was made based on the observations by site engineers and miners.

3 ROCK MASS EVALUATION BY ARTIFICIAL NEURAL NETWORK ALGORITHM

3.1 *Conditions of Artificial Neural Network*

Artificial Neural Network (hereinafter called ANN) generally consists of input, intermediate, and output layers. It provides objective output variables evaluated from explanatory variables in the input layer through intermediate layers. Neurons in the input and

output layers denote the numbers of explanatory and objective variables respectively. In this study, the explanatory variables are 8 MWD data, and objective variables are 6 face observation items for rock mass classification (Table 2): compressive strength, weathering and alternation, crack intervals, crack conditions, water inflow and water induced deterioration. Strike and dip in is not an objective variable in this study, since it can be judged only by visual inspection on the face. The number of layers and neurons in the intermediate layers can be arbitrary determined. In this study, 4 layers and 50 neurons were experimentally applied. An ANN algorithm was constructed in TensorFlow, one of the machine learning libraies. The activating function was a ramp function (ReLU). The ratings of each observation item in the output layer were classified by the Softmax function.

The Softmax function is often used in multiclass classification problems and gives probabilities of the answer that belongs to each rating. Therefore, the rating of each observation item with the highest probability is regarded as the estimation result in this study.

Table 2. Observation items for rock mass classification (JSCE, 2007).

Observation item		Rating					
A. Compressive strength (N/mm²)	Uncondined compressive strength	100 or more	100 - 50	50 - 25	25 - 10	10 - 3	3 or less
	Point load	4 or more	4 - 2	2 - 1	1 - 0.4	0.4 or less	
	Rough guide for strength in hammering	Hard to break when placed on the ground and strongly hammered	Breakable when placed on the ground and strongly hammered	Breakable when held by hand and hammered	Breakable when hit with another rock of the same type	Partially breakable using two hands	Crushable when force is applied with a fingertip
	Rating	1	2	3	4	5	6
B. Weathering and alteration	Rough guide for weathering	Generally fresh		Weathered or altered along the crack	Weathered or altered to the rock core	Weathered into soil or unconsolidated soil	
	Rough guide for hydrothermal alteration	No alteration observed		Clay observed in the crack due to alteration	Decreased strength observed at the rock core due to alteration	Remarkable alteration into soil or clay	
	Rating	1		2	3	4	
C. Crack intervals	Crack intervals	d ≥ 1 m	1 m > d ≥ 50 cm	50 cm > d ≥ 20 cm	20 cm > d ≥ 5 cm	5 cm > d	
	RQD	80 or more	80 - 50	60 - 30	40 - 10	20 or less	
	Rating	1	2	3	4	5	
D. Crack conditions	Crack opening	Tightly closed	Some of the cracks open (less than 1 mm wide)	Many of the cracks open (less than 1 mm wide)	Open (1-5 mm wide)	Open to the width of 5mm or more	
	Substance in cracks	None	None	None	Thin clay (5 mm or less)	Thick clay (5 mm or more)	
	Crack roughness and slickensides	Rough	Smooth	A limited slickenside	A highly polished slickenside		
	Rating	1	2	3	4	5	
E. Strike and dip	Strike perpendicular to tunnel axis	1. Reverse dip of 45 to 90 degrees	2. Reverse dip of 20 to 45 degrees	3. Regular/reverse dip of 0 to 20 degrees	4. Regular dip of 20 to 45 degrees	5. Regular dip of 45 to 90 degrees	
	Parallel with tunnel axis			1. Dip of 0 to 20 degrees	2. Dip of 20 to 45 degrees	3. Dip of 45 to 90 degrees	
Evaluation by water inflow and water-induced deterioration within 10 m from the face (Deterioration shall be evaluated considering existing and possible future deterioration.)							
F. Water inflow	Status	No inflow or water seeping per tunnel 1 liter/min.	Water dripping or 1 to 20 liter/min.		Water locally inflowing at 20 to 100 liter/min.	Water extensively inflowing at 100 liter or more per tunnel 1 liter/min.	
	Rating	1	2		3	4	
G. Water-induced deterioration	Water-induced deterioration	None	Loosened		Weakened	Washed out	
	Rating	1	2		3	4	

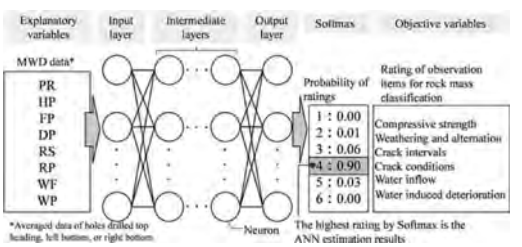

Figure 5. ANN for estimating the rating of observation items.

For the training and validation process, the complete data set which consists of 469 data from 139 cross-sections (131 data in class CII and 338 data in class DI) were divided into 332 data for training (CII: 66 data, DI: 266 data) and 137 data for validation (CII: 65 data, DI: 72 data). The number of trainings was 1000 times. Figure 5 conceptually represents the ANN structure in this study.

3.2 *ANN results of rock mass quality estimation*

Table 3 shows the accuracies of ANN in each observation item. They are calculated by all validation data, by data in class CII, and by data in class DI, respectively. Note that accuracy is defined as the ANN in the validation process that gives corresponding answers to actual observation results judged by engineers at the site. The result of ANN in each observation item can be interpreted as follows.

The accuracy of compressive strength was 73.7 % in total. However, there was a considerable difference between accuracies in class CII (56.9%) and class DI data (88.9%). The difference in accuracies of weathering and alternation was similar. The accuracy was 83.3 % in the class DI data, relatively higher than 64.6 % in the class CII data. Accuracy of crack intervals was also in the same tendency. One of the reasons accuracies in class CII did not reach that in class DI might be that the number of training data in class CII was not sufficient to acquire satisfying accuracy. In other words, additional training data included in class CII class could improve accuracy. On the other hand, the accuracy of water inflow in class CII was 84.6 %, close to the accuracy in total, and exceeded that in class DI (76.4 %). The preferable score of accuracy could however be derived from the conditions that all the observation results in class CII and most in class DI were categorized in rating "1" meaning "No inflow or water seepage not exceeding 1 liter/min" (refer to Table 2). The ANN using drilling data obtained in the tunnel with varying water inflow should be further studied in terms of its accuracy. Accuracy in crack conditions and water induced deterioration were 35.0 % and 54.0 % respectively, and neither were satisfactory. It might have come from more similar distributions in classes CII and DI than those of other items. Meanwhile, it has been proposed in existing research (Schunnesson, 1996 and 1998) that the quantitative fracturing index calculated from the MWD data variation indicates the existence of fractured zone. Further investigations are required, especially in crack conditions as to whether the increasing input data in other tunnels, change in data preprocessing methods, and change in ANN structures can contribute to accuracy improvement.

3.3 *Evaluation of softmax*

Table 4 shows accuracy difference according to the maximum Softmax value. Here, the maximum

Softmax value is the largest figure in Softmax among ratings in each observation item. Whereas accuracy is the probability is in which the rating with maximum Softmax value is consistent to the actual observation result. For example, in the compressive strength column, there were 117 ANN results with the maximum Softmax values higher than 0.900. Ninety-one out of 117 results, *i.e.*, 77.8 % provide right answers. In the same manner, 66.7 % of results with maximum Softmax value of 0.700 to 0.899 and 36.4 % of those with the values lower than 0.699 give right answers. It could be interpreted the higher the maximum Softmax value the ratings have, the more reliable the ANN results. Accuracies of weathering and crack intervals which were relatively high in total as discussed in previous section scored good, such as 76.0 % and 68.8 % respectively when the maximum Softmax value is higher than 0.900. There was a similar tendency in the accuracy of compressive strength. The site engineer could therefore judge whether it is possible to apply the ANN results to the final decision for actual construction strategy on the basis of the

Table 3. The accuracy of ANN in each observation item.

		Observation items					
Accuracy		Compressive strength	Weathering/ Alternation	Crack intervals	Crack conditions	Water inflow	Water induced deterioration
Rock mass class	Total (137 data)	73.7% 101)	74.5% (102)	65.7% (90)	35.0% (48)	80.3% (110)	54.0% (74)
	CII (65 data)	56.9% (37)	64.6% (42)	56.9% (37)	30.8% (20)	84.6% (55)	75.4% (49)
	DI (72 data)	88.9% (64)	83.3% (60)	73.6% (53)	38.9% (28)	76.4% (55)	34.7% (25)

* The figures in parentheses are the number of data to which ANN gives correct answers for each observation item.

Table 4. The difference of accuracy in Softmax value.

		Observation items					
Softmax		Compressive strength	Weathering/ Alternation	Crack intervals	Crack conditions	Water inflow	Water induced deterioration
Softmax value	Higher than 0.900	77.8% (91/117)	76.0% (95/125)	68.6% (83/121)	33.3% (42/126)	81.7% (107/131)	53.9% (69/128)
	0.700 to 0.899	66.7% (6/9)	50.0% (4/8)	66.7% (6/9)	50.0% (3/6)	33.3% (1/3)	66.7% (4/6)
	Lower than 0.699	36.4% (4/11)	75.0% (3/4)	14.3% (1/7)	60.0% (3/5)	50.0% (1/2)	33.3% (1/3)

* The figures in parentheses are the number of data in which Softmax showed the values higher than the indexed value, over the number of data to which ANN gives correct answer for each observation item.

Table 5. Correlation matrix for randomly selected holes.

Correlation analysis result								
	PR (dm/min)	HP (bar)	FP (bar)	DP (bar)	RS (r/min)	RP (bar)	WF (l/min)	WP (bar)
PR	1.0000	0.6701	-0.0542	-0.3710	-0.1433	0.1912	-0.3940	0.4639
HP	0.6701	1.0000	-0.1185	0.2834	0.1745	-0.4637	-0.2247	0.2912
FP	-0.0542	-0.1185	1.0000	0.1091	-0.2305	-0.0220	0.2611	0.5760
DP	-0.3710	0.2834	0.1091	1.0000	0.6992	-0.5993	-0.0711	0.0882
RS	-0.1433	0.1745	-0.2305	0.6992	1.0000	-0.1124	-0.5622	0.0055
RP	0.1912	-0.4637	-0.0220	-0.5993	-0.1124	1.0000	-0.1037	0.1229
WF	-0.3940	-0.2247	0.2611	-0.0711	-0.5622	-0.1037	1.0000	-0.3971
WP	0.4639	0.2912	0.5760	0.0882	0.0055	0.1229	-0.3971	1.0000

Table 6. Results of PCA for different inputs.

PCA results			
	PCA variance ratio explained		
Input variables	Complete data set	Chainage 411 m	Chainage 755 m
Raw data of PR, HP, FP, DPRS, RP, WF and WP	PC1 = 31.0 % PC2 = 22.2 % PC3 = 15.1 % PC4 ~ omitted	PC1 = 31.2 % PC2 = 18.4 % PC3 = 13.9 % PC4 ~ omitted	PC1 = 38.2 % PC2 = 17.6 % PC3 = 12.9 % PC4 ~ omitted
Average in each hole ofPR, HP, FP, DPRS, RP, WF and WP	PC1 = 42.0 % PC2 = 26.5 % PC3 = 13.6 % PC4 ~ omitted	PC1 = 30.0 % PC2 = 23.2 % PC3 = 14.7 % PC4 ~ omitted	PC1 = 36.2 % PC2 = 24.4 % PC3 = 14.0 % PC4 ~ omitted

The PCs of higher than PC4 provide insignificant variance's explanation and are abbreviated

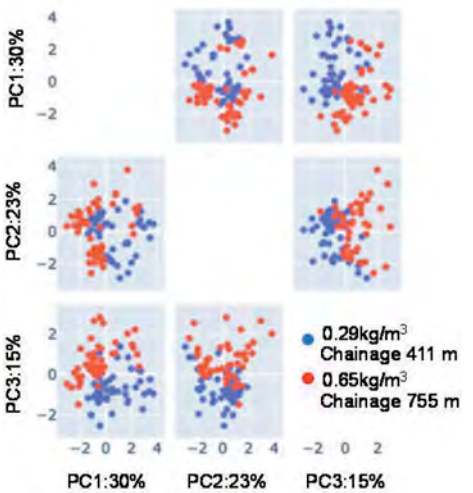

Figure 6. Graphical presentation of PCA results for the MWD data at selected cross-sections.

Softmax value. On the other hand, in the observation items of crack conditions and water induced deterioration with relatively low accuracies in total, the effectiveness of the Softmax value in supporting engineers' judgement could not be clarified, as indicated in the case of crack conditions where the evaluated accuracy was only 33.3 % even when the maximum Softmax value was higher than 0.900.

4 EXPLOSIVE VOLUME ESTIMATION BY RANDOM FOREST REGRESSION

4.1 *Data processing*

Data processing includes some statistical analyses of the data to determine possible constraints in applying various analytical methods and to detect data imbalance. Specifically, correlation analysis and principal component analysis (hereinafter called PCA) were conducted and the results are described in this section.

The correlation analysis was performed to discover and quantify the degree of dependence in the drilling parameters during drilling operation effort (single borehole). The knowledge gained from the correlation analysis could help to prepare the data to meet the expectations of machine learning algorithms, such as linear regression, whose performance will degrade if the input data are significantly correlated.

Table 5 shows the correlation matrix for MWD data (except for drilling positions) constructed by randomly selected 1000 drilling holes from cross-sections 122 to 1026 m of tunnel chainage. Note that the correlation coefficients in the matrix were calculated only in the normal drilling stage (deeper than 50 cm) of each drilling hole. The highest correlation coefficient in Table 5 was 0.699 between the dumper pressure and the rotation speed. Thus, it is not able to conclude that the MWD variables are strongly correlated each other. Therefore, the correlation coefficients in the lower red triangle in Table 5 were extracted and used as explanatory variables together with raw/averaged MWD data for the Random Forest Regression analysis to be described in next section.

Data clustering was performed with PCA. The method is one of the most popular methods to reduce the data attributes to a smaller (and therefore more manageable) number of components (or variables) by obtaining the most significant parameters for variations and preserving as much of the data's variation as possible. It seems to be the most commonly applied method for any MWD data analysis (Qiu et al., 2022).

Table 6 compares the PCA (Principal Component Analysis) variance ratios of the raw and averaged

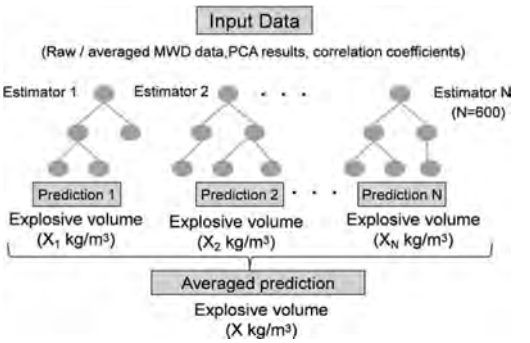

Figure 7. RFR structure for estimating explosive volume.

Table 7. Summary of RFR.

RFR results			
	Performance		
Input variables	RMSE (kg/m^3)	MAPE (%)	Accuracy (%)
Raw MWD data	0.05	13.4	86.6
PCA outputs	0.09	22.1	77.9
Raw MWD data & PCA outputs of raw MWD	0.06	14.3	85.7
Averaged MWD data	0.05	11.2	88.8
PCA outputs of averaged MWD	0.08	21.1	78.9
Averaged MWD data & PCA outputs of averaged MWD	0.03	7.5	92.5
Correlation analysis results	0.05	12.1	87.9
Averaged MWD data & Correlation analysis results	0.03	7.4	92.6

MWD data for explanatory variables. Referring to the complete data set column in the table, first three principal components (PC1, 2 and 3) explain 68.3 % (= PC1 + PC2 + PC3) of data variation with the use of the raw MWD, while this becomes 82.1 % when the averaged data are used. From the comparison, it is clear that the low dimensional representation could be achieved better when the analysis is done on the drilling data averaged per drilling hole. Results from one PCA on the averaged MWD variables were color-coded to the target variable, that is explosive volume as shown in Figure 6. The visualization shows a good separation between the two cross-sections where considerably different volume of explosives were used, even the first three PCs only explain a input data variation of 70%. Therefore, those first three PCs were further used for RFR together with the original MWD data and correlation coefficients.

4.2 *Random Forest Regression (RFR)*

Random Forest (RF) is one of the most popular machine learning methods and helps to reach a predicted result through the combination of outputs from several decision trees. RF is normally applied to two problems such as classification and regression problems. To check whether it's feasible to use the MWD data to optimize the volume of explosive materials used in tunneling, a predictive random forest regression model was developed. The model predicts the total volume of explosive material per m^3 of the excavation in 147 cross-sections at tunnel chainages between 579 and 777 m. Different combinations of inputs were set up for the predictive model training, including a set of inputs with results from the correlation analysis and PCA. For the training and validation process, the complete dataset, which consists of the 147 cross-sections, was divided into input and validation groups randomly with a ratio of 9:1. To guarantee that sections with varying amounts of explosives are included in the validation set, the split-train RF, prediction, and validation procedure were performed multiple times.

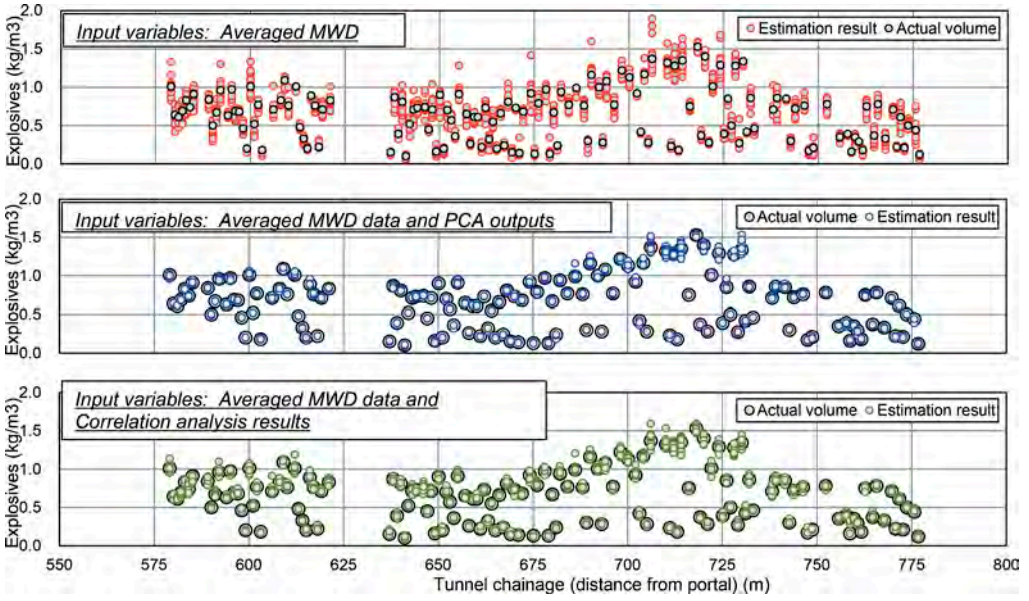

Figure 8. Comparison between estimation results of RFRs and actual explosive volume.

That resulted in multiple outputs for each section. For the settings of RFR, almost the default setting of SciKit Python library was used. The number of estimators was set to 600 because the greater number of estimators did not necessarily improve the result. Figure 7 conceptually explains the constructed RFR model in this study.

Table 7 shows the summary of the RFR analyses. The root means square error (RMSE), mean absolute percentage error (MAPE) and accuracy are calculated as follows and are used to evaluate the models' performance.

$$RMSE = \sqrt{\sum_{i=1}^{n} \frac{(\hat{y}_i - y_i)^2}{n}} \quad (1)$$

where, $\hat{y}_i$ is an estimated i-th value, y_i is actual i-th value and n is the number of samples.

$$MAPE = \frac{1}{n} \sum_{i=1}^{n} \left| \frac{\hat{y}_i - y_i}{y_i} \right| \quad (2)$$

$$Accuracy\ (\%) = 100 - MAPE \quad (3)$$

First, comparing the accuracy of "Raw MWD data = 86.6 %" and "Averaged MWD data = 88.8 %" in the table 7, the input variables using averaged data gave better accuracy. The same tendency was also observed in the comparison between "Raw MWD data & PCA outputs of the raw MWD data = 85.7 %" and "Averaged MWD data & PCA outputs of the averaged MWD = 92.5 %". These outcomes might come from the fact that the PCA results using the averaged MWD data on each drilling hole had higher summation of the first three principal components and that the variation in inputs explained better than by the PCA results using raw MWD data.

Second, comparing the accuracy of "Averaged MWD data = 88.8 %" and "Averaged MWD data & PCA outputs of averaged MWD = 92.5 %" or "Averaged MWD data & correlation analysis results = 92.6 %", the latter cases using statistical values in addition to the averaged MWD data give greater accuracies. These indicate that the statistical values of PCA or correlation analysis contribute to improving the prediction because they might be regarded as additional variables explaining and characterizing MWD data well.

Figure 8 compares the actual and the predicted explosive volume distribution along the tunnel chainage in three cases of RFR using averaged MWD data and statistical inputs. Note that, in the graphs, there are some estimated results in each case (as clearly seen results using the averaged MWD data) because different combinations of input variables were set up for predictive model training, dividing the training and validation data into two groups with a ratio of 9:1. It is clear that the explosive volume can be estimated better when the statistical values of PCA and the correlation analysis are combined with the averaged MWD data, than using the averaged MWD data only in the prediction analysis.

5 CONCLUSIONS

In this study machine learning algorithms were constructed, and their accuracies were examined in which the objective variables of rock mass classification on the tunnel face and the required explosive volume for blasting were estimated by the explanatory variables of the MWD data obtained by the computer-assisted drilling rigs. Those engineering judgements for the conventional tunnel construction used to be conducted by fully trained engineers and miners. ANN for estimating rating of observation items from the MWD data by XE3C produced accuracy of more or less 70 % for the parameters such as compressive strength, weathering and alternation, and crack intervals. However it gave low accuracy on the parameters such as crack conditions and water induced deterioration. This result may suggest that the MWD data mainly consisting of speeds of drilling bits and loads on drifters could be related with strength related parameters of drilled object, but might difficulty in predicting water or crack conditions.

In addition, the RF algorithm could also estimate the actual explosive volume with a small error when the statistical values like principal component analysis results for explanatory variables are applied with the original MWD data. Taking these learned results into consideration, the authors believe that a machine learning algorithm could possibly assist quantitative MWD data acquisition for engineering judgements in tunnel construction which used to be carried out by site engineers and miners.

In this study site engineers' qualitative face observation records and actual explosive volume on the basis of visual inspections and previous experience were regarded as objective variables for respective training of the machine learning algorithms. Therefore, they may still include inaccurate observation records or excessive blasting results which could lead to unnecessary over-excavation in cross-sections and inappropriate advance in the longitudinal direction. In the future studies, applying quantitative data like physical properties of rock or over-excavation measurement results by a 3-D laser scanner as objective variables, the authors would like to improve supporting tools for conventional tunnel engineering judgement which can contribute to construction productivity and safety.

ACKNOWLEDGMENTS

The authors are grateful to Ass. Prof. Takafumi Kitaoka at Kansai University for fruitful discussions and great assistance with the development of Neural Network algorithm in this study. We also thank to Prof. Thomas Marcher and Ass. Prof. Alla Sapronova at Graz University of Technology for estimating the explosive volume by Random Forest Regression algorithm.

REFERENCES

Eldert, V., Funehag, J., Saiang, J. D. and Schunnesson, H., 2020. Rock Support Prediction Based on Measurement While Drilling Technology, Bulletin of Engineering Geology and the Environment, Vol. 80, pp. 1449–1465.

Fukuda, T., Arai, T., Kakimi, K. and Matsumoto, K., 2020. Development of an Automated Angle Control System to Improve Safety and Productivity. Proc. of 37th Int. Sym. on Automation and Robotics in Construction (ISARC 2020), pp. 134–138.

Hashiba, K., Fukui, K. and Koizumi, M., 2017. Drilling Process with Hydraulic Percussion Rock Drills, Journal of MMIJ, Vol.133, No.9, pp. 223–229 (in Japanese with English abstract).

Japanese Society of Civil Engineers, 2007. Standard specifications for tunneling - 2006: Mountain tunnels, chapter 3, pp. 60–70.

Japanese Society of Civil Engineers, 2007. Standard specifications for tunneling - 2006: Mountain tunnels, chapter 7, p. 244.

Kuwabara, T., Hata, K., Inagawa, Y. and Hirakawa, Y., 2008. Evaluation of Geological Characteristics Ahead of the Tunnel Face Using Both Conversion analysis of Non-Core Drilling Parameters and New Parameters "Normalized Drilling Velocity Ratio", Journal of tunnel engineering (in Japan), No.18, pp. 1–10, (in Japanese with English abstract).

Miyanaga, S., Yamagami, M., Sakai, K. and Kitaoka, T., 2023. Tunnel Face Stability Evaluation Method by Means of ANN with Measurement While Drilling Data, Proc. of 49th Sym. on Rock Mechanics, pp. 69–74 (in Japanese with English abstract).

Qiu, M. F. –q., Yang, Ji, Z. and Shi, Z, -r., 2022. Using Principal Component Analysis to Judge the Response of Measurement While Drilling Parameters to Rock Mass Characteristics, 8th Int. Conf. on Hydraulic a Civil Engineering: Deep Space Intelligent Development and Utilization Forum (ICHCE), pp 795–799.

Sapronova, A. Sakai, K. Miyanaga, S. Johannes Unterlass, P. Soliman, A. A. F. E. and Marcher, T., 2023. MWD data analysis for optimization of tunnel excavation, Proc. 15th ISRM Congress 2023 & 72nd Geomechanics Colloquium (printing).

Schunnesson, H., 1996. RQD Predictions Based on Drill Performance Parameters. Tunnelling and Underground Space Technology, Vol.11, No. 3, pp. 345–351.

Schunnesson, H., 1998. Rock Characterization Using Percussive Drilling. Int. Journal of Rock Mechanics and Mining Sciences, Vol. 35, No. 6, pp. 711–725.

Yamashita, M., Fukui, K. and Okubo, H., 2008. Prediction of the rock properties ahead of a tunnel face by percussive long-hole drilling, Vol. 4, No. 1, pp. 9–13.

Tunnelling for a Better Life – Yan, Celestino, Thewes & Eberhardt (Eds)
© 2024 The Author(s), ISBN 978-1-032-80042-4
Open Access: www.taylorfrancis.com, CC BY-NC-ND 4.0 license

Assessment of TBM performance in different types of rocks using supervised learning techniques

Hanan Samadi
MSc., School of Geology, College of Science, University of Tehran, Tehran, Iran

Jafar Hassanpour*
PhD., Associate Professor, School of Geology, College of Science, University of Tehran, Tehran, Iran

Jamal Rostami*
PhD., Professor, Earth Mechanic Institute, Department of Mining Engineering, Colorado School of Mines, USA

Armin Moghbeli
Rahsaztarh Consulting Engineers Co., Tehran, Iran

ABSTRACT: Precise and reliable evaluation of the performance of tunnel boring machine (TBM) is of utmost importance in order to mitigate the risks associated with the substantial capital costs and intricate planning involved in tunnel construction. To address this issue, a total of ten distinct computational techniques have been developed, encompassing supervised and unsupervised learning models based on statistical, machine learning, fuzzy-based, genetic approaches, and deep learning algorithms. The models were implemented using a comprehensive database consisting of five features, namely cutterhead rotation speed, rate of penetration, cutter load, uniaxial compressive strength, and rock quality designation. The data utilized in these models was collected and generated from a specialized database containing multiple tunnel sections from five selected projects, encompassing a wide range of lithological units with varying compressive strength of sedimentary, igneous, and metamorphic rocks. The results of the analysis revealed significant correlations between variables geomechanical properties of rocks and operating machine parameters with TBM performance (TBM-ROP). Various loss functions and evaluation metrics were employed to assess the performance and accuracy of the applied methods. Notably, the outcomes of the proposed models exhibited satisfactory and reliable accuracy, with all models exhibiting an R-squared value above 0.70 and loss function values approaching zero. The results demonstrated that the supervised learning algorithms, particularly the DNN model, yielded the most precise outcomes for ROP (R^2 = 0.97; RMSE = 0.00004; MAPE = 0.00000).

Keywords: Hard rock TBMs, TBM performance prediction, Supervised and unsupervised learning, Computing machinery techniques

1 INTRODUCTION

In the context of planning tunnelling activities involving tunnel boring machines (TBMs), it is imperative to make well-informed assumptions and judgments at various stages of the project. Of particular importance is the rigorous evaluation of TBM performance, as this assessment greatly influences critical aspects such as project planning, cost management, and the overall viability of the project for decision-makers. Any miscalculations in project performance can lead to unexpected expenses, project delays, and diminished profitability (Gokceoglu, 2022) and even viability of the whole project cost and schedule.

The process of tunnelling involves inherent risks and uncertainties, which are influenced by factors such as the characteristics of the TBM, the geological conditions of the rock mass, and the operational parameters. Consequently, successful tunnelling projects necessitate meticulous decision-making and planning processes (Adoko et al., 2017).

Numerous researchers have highlighted the significance of predicting metrics such as the rate of penetration (ROP), advance rate (AR), and penetration per revolution (PR) for accurate estimation of TBMs operating in hard rock conditions. In order to achieve this objective, studies have focused on three prediction techniques: theoretical, empirical, and

*Corresponding author: hassanpour@ut.ac.ir; rostami@mines.edu

DOI: 10.1201/9781003495505-411

soft computing approaches (Rostami and Ozdemir, 1993; Gong and Zhao, 2009; Hassanpour et al., 2011).

Theoretical models employ cutting forces and laboratory cutting tests to establish formulas based on force equilibrium. While these models provide a fundamental understanding of rock fragmentation, they do not entirely capture the complexities of real-world rock conditions (Rostami and Ozdemir, 1993; Bilgin, 2016; Elmo and Stead, 2021).

One highly utilized model for predicting TBM performance is the NTNU model, developed by Blindheim (1979) based on research conducted at the Norwegian University of Science and Technology. Bruland (1998) updated the NTNU model with field data, resulting in one of the most extensively used empirical models for TBM tunnelling. Rostami and Ozdemir (1993) developed a predictive model for estimating the cutting force of disc cutters, which was subsequently enhanced by Rostami (1997, 2013), and by Yagiz (2002) to account for rock mass properties. Barton (2000) conducted a comprehensive review of various TBM tunnelling projects and developed the Q_{TBM} model, which utilizes the Q rock mass classification system to estimate TBM performance parameters including ROP, utilization factor (U%), and AR.

The second approach, based on field performance observations, takes into account the geomechanical conditions at the excavation site (Hassanpour et al., 2011). Researchers have proposed and implemented various statistical methods, grounded in mathematical principles, for predicting TBM performance. Sapigni et al. (2002) and Gong and Zhao (2009) conducted nonlinear regression analyses to explore the empirical relationship between the rock mass rating (RMR) and penetration rate. Hassanpour et al. (2011) established multiple relationships between rock mass parameters such as RMR, rock quality designation (RQD), joint spacing, and uniaxial compressive strength (UCS), and found that a combination of RQD and UCS provides the most accurate prediction of TBM performance. However, Grima and Verhoef (1999) pointed out that statistical methods lack reliability in accurately defining complex and non-linear systems, and their predictability is affected by outliers and distant points in the database.

The third approach, which utilizes artificial intelligence (AI) and computing techniques, has gained significant popularity in recent years to address the complexity of predicting TBM performance (Benardos and Kaliampakos, 2004). The identification of factors influencing TBM performance and its parameters is a common challenge that can be effectively addressed using AI and machine learning (ML) methods. The use of these techniques, such as artificial neural networks (ANNs) has become extensively employed in tunnelling projects to predict TBM driving and operational parameters, and have shown promising and reliable outcomes (Zhao et al., 2007; Gao et al., 2020).

Several models have been proposed for predicting TBM-ROP using support vector regression (SVR) (Okubo et al., 2003; Minh et al., 2017). Furthermore, other successful approaches described in previous studies include ANN, fuzzy logic, and particle swarm optimization (PSO) (Khandelwal and Singh, 2009; Jain et al., 2014). Liu et al. (2019) introduced a tailored version of SVR (single-purpose SVR) for TBM performance forecasting, and their proposed model outperformed the basic SVR model. Zhou et al. (2021) proposed innovative composite predictive models, drawing inspiration from the extreme gradient boosting (XGB) mechanism, to forecast TBM-ROP. They explored various optimization algorithms to enhance the XGB model, and their findings indicated that the PSO-XGB model is the superior predictive model for TBM-ROP prediction.

The present research endeavours to develop, train, test, and analyse the capabilities of ML, DL, fuzzy-based, and genetic approaches. The present study introduces the following novel contributions:

- The research investigates the effectiveness of ten types of supervised and unsupervised learning techniques included radial basis function, k-nearest neighbourhood neural network, multi-layer perceptron, support vector machine, support vector regression, gene expression programming, fuzzy inference system, deep neural network, extreme learning machine, and multivariable regression in the reliability analysis of TBM penetration rate in different rock conditions (a wide range of lithological units with varying compressive strength of sedimentary, igneous, and metamorphic rocks).
- This research examines the impact of multicollinearity in the database on the performance, accuracy, and overfitting of the developed models.
- The study formulates the hypothesis statement for reliability analysis and employs hypothesis tests to select the appropriate research hypothesis.
- Various analyses, including importance ranking, score analysis and regression error characteristics curve, are conducted to identify the optimal performance soft computing models for the reliability analysis of TBM performance.

Generally, the study aims to utilize supervised predictor models to predict TBM-ROP. To accomplish this, a big database comprising necessary data from five tunnelling projects is employed to predict and calculate the target driving TBM parameter based on input parameters, including operational parameters of the boring machine and geomechanical properties of intact rocks and rock masses. The performance of the models is evaluated using superior loss functions associated with artificial intelligence.

The significance of this research lies in its ability to effectively address a range of concerns faced by

operators in the construction of deep tunnels in hard rock conditions. By considering various factors such as the selection of an appropriate TBM, geotechnical characteristics along the tunnel face, and ensuring safe construction practices, this study provides valuable insights and guidance for operators.

2 PROJECT DESCRIPTION

The data utilized in this research was collected and generated from a specialized database containing multiple tunnel sections from several selected projects, encompassing a wide range of lithological units with varying compressive strength of sedimentary, igneous, and metamorphic rocks. A comprehensive investigation was conducted using geomechanical and machine data from five tunnelling projects, including the Zagros water conveyance tunnel lot 2, Manapouri second tailrace tunnel, Ghomrood water conveyance tunnel lots 3 and 4, Karaj water conveyance tunnel lot 1, and Kerman water conveyance tunnel, southern lot. The combined length of these projects amounts to 92.6 km.

A summary of the primary characteristics of these TBM tunnelling projects is presented in Table 1, while the geomechanical parameters of tunnelling projects are presented in Table 2.

Table 1. Main characteristics of tunnelling projects.

Projects	Tunnel length (km)	Available data (km)	TBM type	TBM diameter (m)
Zagross WCT (Lot 2)	26	5	Double shield	6.73
Ghomrood WCT (Lots 3 & 4)	21.5	15.7	Double shield	4.52
Karaj WCT (Lot 1)	15.9	8.2	Double shield	4.66
Kerman (Southern Lot)	19.2	6	Double shield	5.27
Manapouri Project	10	9	Open TBM	10.05

3 DATABASE DEVELOPMENT OF TBM FIELD PERFORMANCE

This section provides a principal component analysis (PCA) to develop the database. PCA is a statistical procedure used for analysing multivariable data in order to identify the principal components. It is common to highlight variations and reduce the dimensionality of the data. In this study, the PCA was conducted on both the output and input parameters to calculate the variance ratio, which indicates the extent to which TBM performance parameter is influenced by geomechanical properties and other operating parameters affecting TBM driving factors. Figure 1 represents the variance ratio of each component. It is noteworthy that the utilization of four features demonstrates the highest variance ratio (above 84%), signifying that it is the most favourable model for calculating TBM driving parameter (TBM-ROP) in terms of statistical analysis. In addition, Figure 2 displays the component transformation matrix using the Varimax with the Kaiser normalization rotation method and component plot in rotated space.

Table 2. Geomechanical parameters of tunnelling projects.

Projects	UCS (MPa)	RQD	GSI	RMCI	RMR
Zagross WCT (Lot 2)	15-150	45-95	30-70	12-120	39-65
Ghomrood WCT (Lots 3 & 4)	25-150	10-100	30-80	4-170	43-76
Karaj WCT (Lot 1)	30-150	10-100	15-85	6-150	27-73
Kerman (Southern Lot)	170-300	100	90-92	160-300	87-89
Manapouri Project	100-225	70-100	-	71-239	51-76

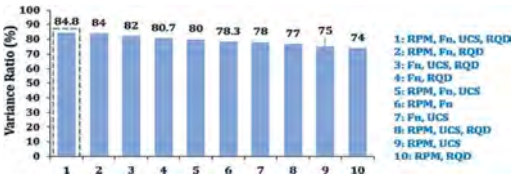

Figure 1. Variance ratio of each component and groups of defined features.

Table 3. Summary results of statistical analysis of parameters recorded in the database.

	Unit	Min.	Max.	Skew.	Med.	Var.
RPM	-	2.5	11.9	1.27	5.48	4.2
UCS	MPa	20	300	0.629	98	4792.4
RQD	%	10	100	-0.85	79.25	736.3
Fn	tonf	24.8	2919.5	-0.16	15.83	28.03
ROP	m/h	0.35	5.88	0.371	2.39	2.172

Thus in order to construct the database for this study, various machine operational and driving parameters, as well as geomechanical properties, were defined. The operational parameters consisted of the cutterhead rotation speed (RPM) and cutter load (Fn), while the geomechanical properties of the rocks were represented by the uniaxial compressive strength (UCS) and rock quality designation (RQD).

Additionally, the mechanical properties of the boring machine were represented by the cutterhead diameters. The collected dataset was categorized into five lithological units based on the formation and engineering geological properties. Table 3 presents statistical indices derived from the dataset under investigation.

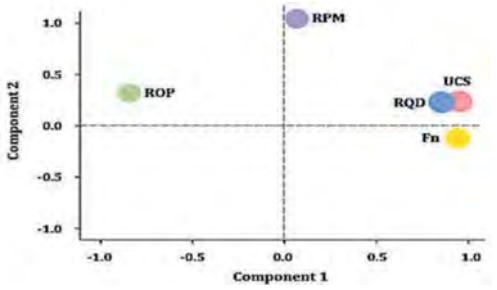

Figure 2. The component transformation matrix using the Varimax and component plots in rotated space.

Subsequently, laboratory tests, daily operating records, and TBM data logger were recorded for each excavation ring and engineering geological units, resulting in a dataset of 177 data points (collected from five tunnelling projects which indicates in Table 1) that included four parameters influencing the TBM performance. The dataset was divided into 90% for training and 10% for testing the supervised learning models. Figure 3 presents boxplots that categorize the defined parameters within the database. This visualization allows for a comparative analysis of these parameters across different strength, enabling researchers to identify any variations or outliers that may exist.

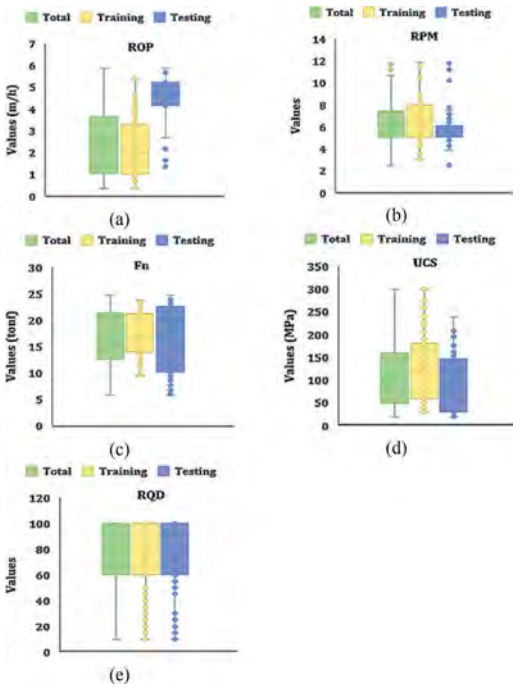

Figure 3. Boxplots diagrams based on each defined parameters within the database (total data, training and testing subsets).

4 EMPIRICAL MODEL

The scatterplot matrix of specified parameters in the database of TBM-ROP is shown in Figure 4 to visualize the linear correlations between the dependent and independent variables, including operating parameters of machine and rock geomechanical properties.

In case of multi-variable regression analysis, four parameters (refer to Table 3) are employed as independent variables and the TBM performance parameter as dependent value to assess the influence of each variable on the TBM-ROP using forward stepwise regression analysis (FSR). The proposed empirical formula to calculate TBM-ROP is presented in Equation 1.

$$\mathrm{ROP(m/h)} = \zeta + \mathrm{MP} + \mathrm{GP} \quad (1)$$

Where ζ is a constant factor: 3.661

MP, operating machine parameters: MP = 0.264 RPM – 0.019 Fn

GP, geomechanical properties: GP = − 0.01 UCS + 0.021 RQD

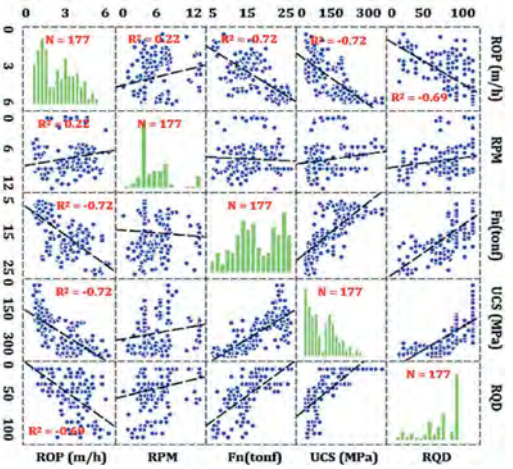

Figure 4. The scatterplot matrix and histograms of considered parameters in the estimation of TBM-ROP.

Figure 5 provides the correlations between the measured TBM-ROP with the calculated results based on the developed empirical formula. The predicted and measured results of this parameters is plotted in Figure 6 showing a good agreement between measured and predicted values for TBM-ROP.

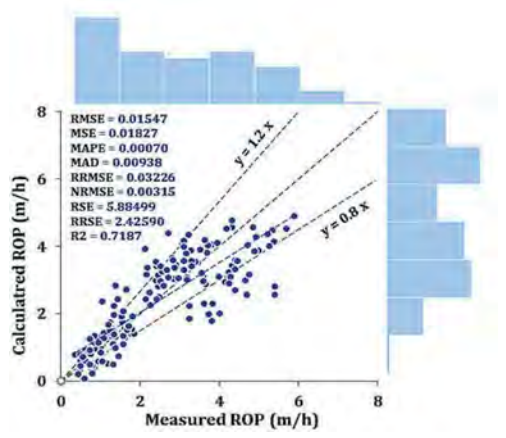

Figure 5. Correlation between measured and predicted values of TBM-ROP.

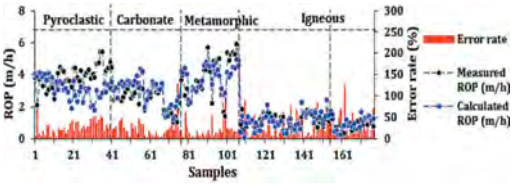

Figure 6. Comparison of measured and predicted values of TBM-ROP by considering different lithological unit.

5 SUPERVISED LEARNING ALGORITHMS

In tunnelling projects with complex physical and geological conditions and multiple input factors, supervised learning techniques such as machine learning, deep learning, genetic approaches, neural networks, and fuzzy-based models have become increasingly popular. The incorporation of these supervised learning algorithms has proven effective in enhancing the accuracy and efficiency of TBM performance estimation models in mechanized tunnelling applications.

This section presents the results of several utilized algorithms for TBM penetration rate, including least-squares support-vector machine (LS-SVM), support vector regression (SVR), Takagi-Sugeno fuzzy model (TSF), gene expression programming (GEP), extreme learning machine (ELM), deep neural network (DNN), multi-layer perceptron neural network (MLP), k-nearest neighbors (KNN), and radial basis function (RBF). Detailed information regarding the tuned parameters and hyper parameters for each applied technique for TBM-ROP is presented in Table 4.

The selection of these algorithm for analysis is justified by several reasons.

- They offer an innovative solution to complex problems through its novel approach to encoding and decoding information.
- They reduce the risk of overfitting by employing a regularization parameter that controls the model's complexity and prevents it from fitting noise in the data.
- These algorithms are well-suited for handling large datasets, as employ a kernel and non-linear trick that allows for data transformation into a higher-dimensional space. This flexibility enables them to effectively handle non-linearly separable datasets.
- The bilingual notation employed in following models provide a unique and effective strategy for addressing complex problems. As another point, these algorithms are renowned for their fast and efficient learning speed, which is particularly essential in tunnelling projects, where timely predictions are crucial for decision-making.
- These algorithms exhibit fast convergence, requiring fewer iterations compared to other machine learning algorithms to achieve the desired level of accuracy.
- They boast a strong theoretical foundation that guarantees convergence and optimality under specific conditions.
- These algorithms are applicable to various learning scenarios, including batch learning, sequential learning, and incremental learning, making them versatile tools for predicting target parameters in diverse tunnelling settings and experimental setups.
- They are valuable tool in various applications in time series forecasting.

To evaluate the performance of the developed models, various loss functions and evaluation metrics have been proposed. These metrics serve the purpose of quantifying the disparity between the predicted and actual TBM-ROP values, as well as assessing the predictive capability of the algorithms.

Figure 7 depicts the correlation between the actual and predicted values of TBM-ROP. As a sensitivity analysis, Figure 8 presents the predicted importance ranking for TBM-ROP using three machine learning algorithms (KNN, RBF, MLP). Also, the lower-dimensional projection of the predictor space considering three input factors (Fn, RPM, RQD) based on KNN network is indicated in Figure 9.

To assess the accuracy of the machine learning networks, loss functions were utilized to measure the deviation between the predicted outcomes and the actual measured values. These measures include the normalized root mean square error (NRMSE), root relative squared error (RRSE), relative root mean square error (RRMSE), mean bias error (MBE), root mean squared logarithmic error (RMSLE), and log cash loss (LCL). These loss functions enable a quantitative evaluation of the predictive capabilities of the machine learning models (Table 5). The evaluation of these loss functions consistently yielded excellent results for the TBM-ROP in the

training and testing subsets, indicating the models' ability to predict TBM performance based on input data derived from input features. These evaluations are integral in determining the potential of machine learning techniques in tunnelling engineering. The findings demonstrate a strong agreement between the predicted TBM performance values generated by the machine learning networks and the measured data.

Overall, this study showcases the use of loss functions and subsequent evaluation of machine learning models' accuracy in predicting parameters for future TBM performance analysis. These techniques can serve as a basis for further research that incorporates machine learning models into tunnelling applications.

Figure 10 effectively illustrates the overall ranking results of the various machine learning models. It is evident that the DNN and ELM models emerge as the most robust and accurate models when considering both the training and testing comprehensive ranking, in contrast to the other machine learning models for TBM-ROP.

Further comprehensive evaluations of the prediction results of multiple soft computing techniques for TBM-ROP was conducted using normalized error analysis, as depicted in Figure 11. This Taylor diagram assesses the performance of the applied algorithms based on the method prediction results, normalized standard deviation, normalized root mean square error, and variance.

Table 4. The structure and description of applied supervised learning models in this study for TBM-ROP.

Model	Description and structure
GEP	General information: Number of chromosomes = 33, Head size = 8, Number of genes = 3, Linking function = addition Genetic operators: Mutation rate = 0.04, IS Transportation rate = 0.1, RIS Transportation rate = 0.1, Inversion rate = 0.1, One-point recombination rate = 0.3, Two-point recombination rate = 0.3, Gene recombination rate = 0.1, Gene transposition = 0.1 Numerical constants: Constants per gene = 2, Data type = Floating-Point, Upper bound = 10, Lower bound = -10
LSSVM	Coupled simulated annealing results: gam = 0.24203, F (x) = 0.68622, obtained hyper parameters F (x) = 6.86226E-01 Optimization routine: Simplex, cost function = leaveoneoutlssvm, kernel function = lin-kernel
ANNs	Epoch = 500 iteration, time = 0:00:02, performance = 0.000151, gradient = 0.000461, Mu = 0.0001, validation check = 0 at epoch 500, neurons in hidden layers = 7, 13, 17, 22, 30, 40

(*Continued*)

Table 4. (*Continued*)

Model	Description and structure
	Algorithm = training, Levenberg-Morquardt, calculations = MEX Train FCN = trainlm, train param = 1*1 struct, performance = 1*1 struct, derive FCN = default-deriv, divide FCN = dividetrain, divide mode = sample
TSF	Name = TakSug 60, type = Sugeno, one method = prod, or method = prober, imp method = prod Agg method = max, Defuzzy method = wtaver Input = 1*4 struct, output = 1*1 struct, rule = 1*17 struct, RR2 = -16.98
RBF	Hidden layer activation function = Softmax, Output layer activation function = Identify Relative error = 0.379, Training time = 0:00:01.12, Hidden layer = H (1) to H (5), Hidden unit width = 0.53 -0.604, Number of units = 290 Error function = sum of squares, Rescaling method for scale dependents = Normalized
KNN	Normalized scale features, K= 5, Distance computation = Euclidean Metrix Prediction for scale target = Mean of nearest neighbour values, Set seed for mersenne Twister = 0, Focal = Yes
MLP	Number of units = 278, Hidden layer = 2, Number of units of hidden layer 1 = 20, Number of units of hidden layer 2 = 15, Rescaling of covariance = Adjusted normalized Activation function = Sigmoid, Relative error = 0.094, Training time = 0:00:00.25 Initial learning rate = 0.4, Momentum = 0.9

Table 6 was presented to enhance its content by providing summaries and detailed information on various soft computing methods found in the literature. As depicted in the table, numerous studies have employed machine learning and deep learning techniques to predict the penetration rate of tunnel boring machines (TBM) using a limited number of models, while this study employs several intelligent networks. This present investigation has yielded more accurate and reliable results compared to previous research. The training and testing subsets of this study exhibit an RMSE range of 0.00 to 0.58 and 0.00 to 0.61, respectively, whereas previous studies have reported an RMSE range of 0.02 to 1.02. It is worth mentioning that the detailed review and analysis of the aforementioned studies can be found in their respective articles listed in the references section.

It is necessary to mention that the physical and mechanical characteristics of machines, including the diameter of the cutterhead, disc cutter diameters and spacing, back-up systems, number of disc cutters, and distance of cutters from the center of the cutterhead, remain unchanged

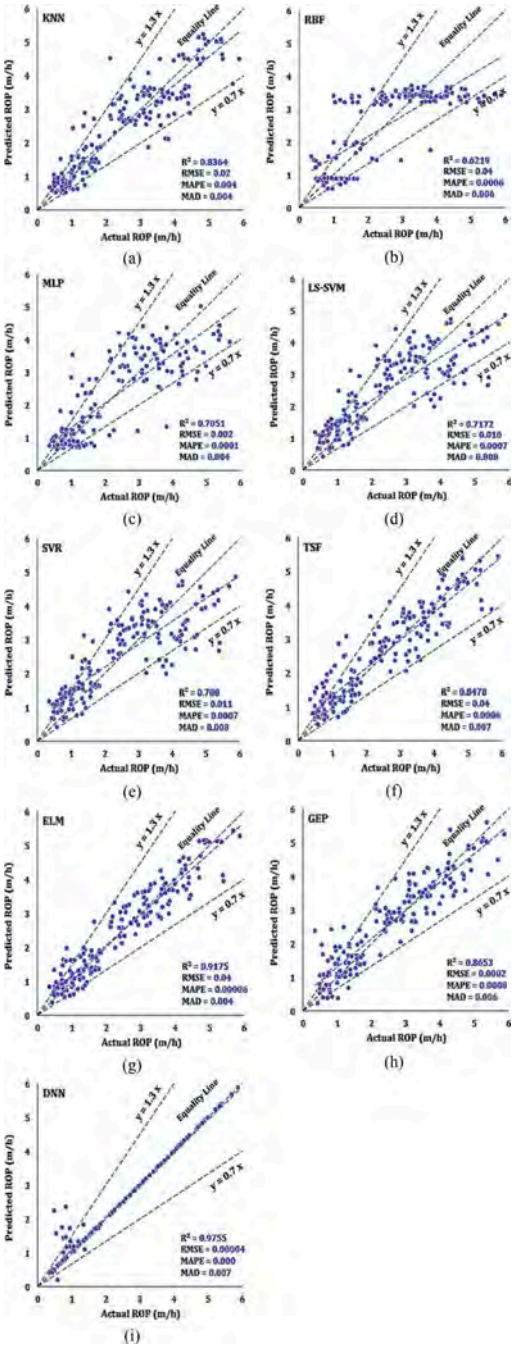

Figure 7. Comparison of the supervised learning predictions with the actual monitored data for TBM-ROP.

during excavation. Consequently, these factors are not suitable for incorporation into smart models that rely on machine learning or deep learning algorithms. In general, constant factors cannot be effectively utilized in the development of intelligent networks, as these networks are unable to be trained using constant factors.

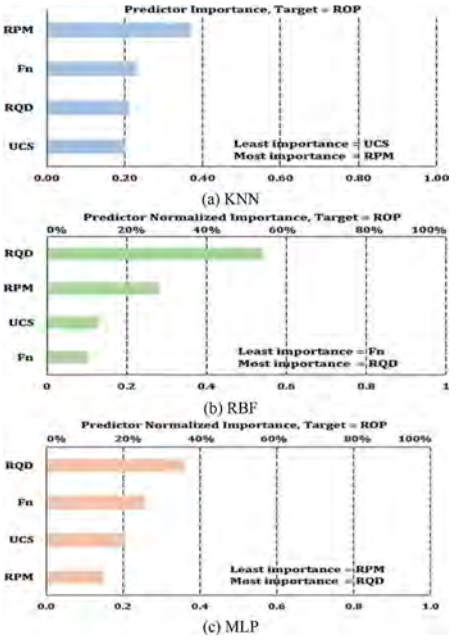

Figure 8. The results of predictor importance ranking based on three smart networks.

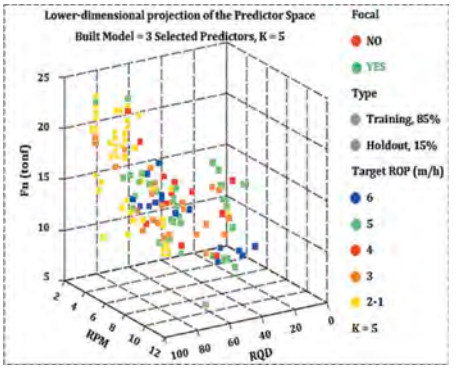

Figure 9. The lower-dimensional projection of the predictor space with K = 5 based on KNN.

Figure 10. Intuitive display of comprehensive ranking of ten applied models.

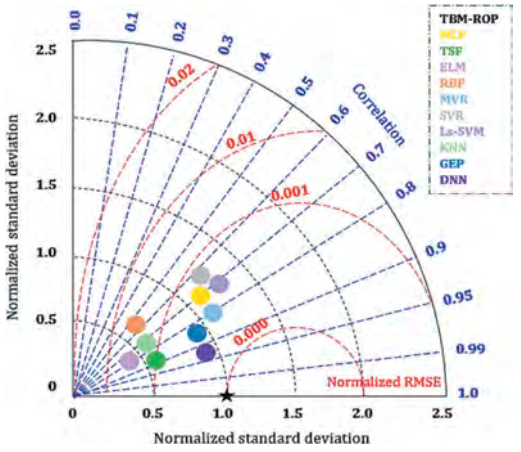

Figure 11. Taylor chart for comparison of multiple supervised and unsupervised models to predict TBM-ROP.

6 CONCLUSIONS

This study primarily aimed to predict the TBM-ROP within diverse rock types, ranging from sedimentary to igneous and metamorphic, with varied uniaxial compressive strengths. To achieve this, statistical analysis and supervised learning algorithms were employed to develop computational models for estimating TBM performance. These models relied on a variety of geomechanical parameters and operating factors pertaining to the machine. The dataset was carefully categorized by rock type, ensuring rational distribution intervals were defined for the geomechanical factors considered. Relationships between chosen parameters were thoroughly examined, leading to the formulation of new equations using the unsupervised regression statistical method. Additionally, machine learning, deep learning, genetic approaches, and fuzzy-based algorithms were developed to predict TBM performance.

By evaluating the performance and accuracy of models using various evaluation metrics, reliable and satisfactory results across all models were observed. These results were evident in R-squared values exceeding 0.70 and the convergence of loss function values towards zero. Remarkably, supervised learning algorithms, particularly the DNN exhibits exceptional precision and reliability in predicting TBM-ROP.

These findings, coupled with the potential application of computing machinery techniques, offer promising avenues for accurately estimating TBM performance. Furthermore, they enhance our understanding of machine driving parameters within different rock types, spanning a wide range of strength levels. It is important to note that the proposed prediction algorithms effectively estimated TBM performance, aligning consistently with the measured data.

In conclusion, this research has effectively demonstrated the efficacy of employing computational techniques to evaluate TBM performance. The insights gained from this study are valuable for mitigating risks, optimizing construction

Table 6. Details of soft computing models available in the literature to predict TBM performance and comparison with current study.

Reference	Inputs	Method
Grima et al. (2000)	RPM, TF, D_c	ANN
Benardos and Kaliampakos (2004)	RQD, RMR, k, N, WTS, WZ	ANN
Shao et al. (2013)	DPW, α, UCS, PSI	ELM LS-SVM PLS GP
Zhou et al. (2021)	USC, RQD, RMR, BTS, TF, WZ, RPM	GWO-XGB PSO- XGB MFO- XGB KNN
Samadi et al. (2022)	UCS, RPM, Fn	GEP
This study	RPM, UCS, RQD, Fn	MLP, RBF, KNN, ELM, DNN, SVR, LS-SVM, TSF, GEP

Table 5. The results of loss functions in the development of AI models (both training and testing dataset).

	RRMSE	NRMSE	RRSE	MBE	RMSLE	LCL
KNN	0.008	0.004	2.494	-0.002	0.034	0.112
RBF	0.024	0.012	2.147	-0.003	0.017	1.471
MLP	0.024	0.000	8.097	0.002	0.009	0.001
LSSVM	0.031	0.002	2.404	-0.004	0.005	0.198
SVR	0.031	0.002	2.401	-0.004	0.005	0.198
TSF	0.027	0.007	1.831	-0.002	0.079	0.167
ELM	0.024	0.002	2.075	-0.001	0.012	0.041
GEP	0.027	0.000	0.643	-0.001	0.005	0.092
DNN	0.000	0.000	0.001	0.000	0.000	0.000

planning, and ultimately facilitating efficient and successful tunnel construction projects, particularly those affected by similar geomechanical variables.

REFERENCES

Adoko, A.C., Gokceoglu, C., Yagiz, S., 2017. Bayesian prediction of TBM penetration rate in rock mass. Eng. Geo. 226, 245–256. https://doi.org/10.1016/j.enggeo.2017.06.014

Barton, N., 2000. TBM Tunnelling in jointed and faulted rock. Balkema, Rotterdam. p.173.

Benardos, A.G., Kaliampakos, D.C., 2004. Modelling TBM performance with artificial neural networks. Tunnel Under Space Tech. 19, 597–605. https://doi.org/10.1016/j.tust.2004.02.128

Bilgin, N., 2016. An appraisal of TBM performances in Turkey in difficult ground conditions and some recommendations. Tunnel Under Space Tech. 57, 265–276. https://doi.org/10.1016/j.tust.2016.01.038

Blindheim, O.T., 1979. Bore ability predictions for tunnelling. Ph.D. Thesis. Department of Geological Engineering. The Norwegian Institute of Technology.

Bruland, A., 1998. Hard rock tunnel boring. Ph.D. Thesis. Norwegian University of Science and Technology, Trondheim.

Elmo, D., Stead, D., 2021. The role of behavioural factors and cognitive biases in rock engineering. Rock Mech. Rock Eng. 54, 2109–2128. https://doi.org/10.1007/s00603-021-02385-3

Gao, X., Shi, M., Song, X., et al, 2020. Recurrent neural networks for real-time prediction of TBM operating parameters. Automat. Const. 98, 225–235. https://doi.org/10.1016/j.autcon.2018.11.013

Gokceoglu, C., 2022. Assessment of rate of penetration of a tunnel boring machine in the longest railway tunnel of Turkey. SN Applied Sciences, 4. https://doi.org/10.1007/s42452-021-04903-y

Gong, Q.M., Zhao, J., 2009. Development of a rock mass characteristics model for TBM penetration rate prediction. Inter. J. Rock Mech. Min. Sci. 46, 8–18. https://doi.org/10.1016/j.ijrmms.2008.03.003

Grima, M., Verhoef, P.N.W., 1999. Forecasting rock trencher performance using fuzzy logic. Inter. J. Rock Mech. Min. Sci. 36, 413–432. https://doi.org/10.1016/S0148-9062(99)00025-X

Hassanpour, J., Rostami, J., Zhao, J., 2011. A new hard rock TBM performance prediction model for project planning. Tunnel Under Space Tech. 26, 595–603. https://doi.org/10.1016/j.tust.2011.04.004

Jain, P., Naithani, A.K., Singh, P.N., 2014. Performance characteristics of tunnel boring machine in basalt and pyroclastic rocks of Deccan traps–a case study. J. Rock Mech. Geo. Eng. 6, 36–47. https://doi.org/10.1016/j.jrmge.2013.11.003

Khandelwal, M., Singh, T.N., 2009. Prediction of blast-induced ground vibration using artificial neural network. Inter. J. Rock Mech. Min. Sci. 46, 1214–1222. https://doi.org/10.1016/j.ijrmms.2009.03.004

Liu, B., Wang, R., Guan, Z., et al, 2019. Improved support vector regression models for predicting rock mass parameters using tunnel boring machine driving data. Tunnel Under Space Tech. 91, 102958. https://doi.org/10.1016/j.tust.2019.04.014

Minh, V. T., Katushin, D., Antonov, M., et al, 2017. Regression models and fuzzy logic prediction of TBM penetration rate. Open Eng. 7, 60–68. https://doi.org/10.1515/eng-2017-0012

Okubo, S., Kfukie, K., Chen, W., 2003. Expert systems for applicability of tunnel boring machine in Japan. Rock Mech. Rock Eng. 36, 305–322. https://doi.org/10.1007/s00603-002-0049-6

Rostami, J., Ozdemir, L., 1993. A new model for performance prediction of hard rock TBM. Proceedings of RETC. In: Bowerman, L.D. et al. (Eds.), Boston, MA. 793–809.

Rostami, J., 1997. Development of a force estimation model for rock fragmentation with disc cutters through theoretical modelling and physical measurement of crushed zone pressure. 38, 56–64. Golden, CO, USA: Colorado School of Mines.

Rostami, J., Sepehrmanesh, M., Gharahbagh, E. A., et al, 2013. Planning level tunnel cost estimation based on statistical analysis of historical data. Tunnel Under Space Tech. 33, 22–33. https://doi.org/10.1016/j.tust.2012.08.002

Samadi, H., Hassanpour, J., Tarigh Azali, S., 2022. Developing GEP technique for prediction of EPB-TBM performance in limestone strata. TBMDigs 2022, Austria, 158–164.

Sapigni, M., Berti, M., Bethaz, E., Busillo, A., & Cardone, G. (2002). TBM performance estimation using rock mass classifications. International Journal of Rock Mechanics and Mining Science, 39, 6, 771–788. https://doi.org/10.1016/S1365-1609(02)00069-2

Shao, C., Li, X., Su, H., 2013. Performance prediction of hard rock TBM based on extreme learning machine. In: Lee J., Lee M.C., Liu H., Ryu JH. (eds) Intelligent Robotics and Applications. ICIRA 2013. Lecture Notes in Computer Science, vol. 8103. Springer, Berlin, Heidelberg. https://doi.org/10.1007/978-3-642-40849-640

Yagiz, S., 2002. Development of rock fracture and brittleness indices to quantify the effects of rock mass features and toughness in the CSM Model basic penetration for hard rock tunnelling machines. Ph.D. Thesis. Department of Mining and Earth Systems Engineering, Colorado School of Mines, Colorado, USA, p. 289.

Zhao, Z., Gong Q., Zhang Y., et al, 2007. Prediction model of tunnel boring machine performance by ensemble neural networks. Geomech. Geoeng. 2(2),123–128. https://doi.org/10.1080/17486020701377140

Zhou, J., Qiu, Y., Armaghani, D., et al, 2021. Predicting TBM penetration rate in hard rock condition: A comparative study among six XGB-based metaheuristic techniques. Geosci. Front. 12, 101091. https://doi.org/10.1016/j.gsf.2020.09.0

Tunnelling for a Better Life – Yan, Celestino, Thewes & Eberhardt (Eds)
© 2024 The Author(s), ISBN 978-1-032-80042-4
Open Access: www.taylorfrancis.com, CC BY-NC-ND 4.0 license

Hyperspectral imaging features for concrete compressive strength assessment: Experimental study

Changsong Wang*
Shanghai Research Centre for Autonomous Intelligent Systems, Tongji University, Shanghai, China
Department of Underground Engineering, Tongji University, Shanghai, China

Hongwei Huang
Shanghai Research Centre for Autonomous Intelligent Systems, Tongji University, Shanghai, China
Department of Underground Engineering, Tongji University, Shanghai, China
Key Laboratory of Geotechnical and Underground Engineering, Ministry of Education, Shanghai, China

Mingliang Zhou
Department of Underground Engineering, Tongji University, Shanghai, China
Key Laboratory of Geotechnical and Underground Engineering, Ministry of Education, Shanghai, China

Shuaida Zhu
Shanghai Research Centre for Autonomous Intelligent Systems, Tongji University, Shanghai, China
Department of Underground Engineering, Tongji University, Shanghai, China

ABSTRACT: Traditional tunnel lining strength detection techniques are mostly contact-based and have lower detection efficiency. This study introduces hyperspectral imaging technology to rapidly identify lining strength from machine vision perspective. It involves collecting spectral data of samples with different strengths using two different wavelength hyperspectral cameras and employs machine learning algorithms to identify concrete compressive strength. Hyperspectral imagery was acquired from the surfaces of concrete specimens, resulting in spectral datasets encompassing both the [400-1000nm] and [900-1700nm] spectral ranges. Machine learning models were formulated to predict concrete compressive strength, both with raw spectral data and data that had undergone Savitzky-Golay (S-G) pre-processing. The findings indicate that satisfactory outcomes were achieved, either without pre-processing or through S-G pre-processing in isolation. Furthermore, the research explored the impact of different spectral wavelength ranges on concrete compressive strength assessment. Notably, the [900-1700nm] dataset exhibited a significant enhancement in the model's determination coefficient (R2) in comparison to the [400-1000nm] dataset. Lastly, a comprehensive analysis of the performance of Principal Component Regression (PCR), Partial Least Squares Regression (PLSR), and Least Squares Support Vector Machine (LSSVM) models was undertaken across various datasets. This culminated in the identification of the most suitable predictive model for concrete compressive strength assessment, accompanied by the computation of model evaluation metrics. This study has opened up new avenues for non-destructive testing of tunnel lining structure strength.

Keywords: Hyperspectral imaging, Tunnel lining, PCR, PLSR, LVSSVM, Compressive strength

1 INTRODUCTION

Concrete compressive strength plays a pivotal role in determining the mechanical performance of concrete. Variations in the source of concrete components, changes during the production process, and the physical properties of concrete directly impact its mechanical performance (Bullard et al., 2019). Among the methods for measuring concrete compressive strength, the uniaxial compressive strength test is considered the most accurate approach. On construction sites, core extraction and pull-out tests are two commonly used methods for testing the compressive strength of concrete (ASTM C42/C42M-18a., 2018). With the core extraction method, a concrete core is obtained by drilling into the concrete structure at a selected location, and its compressive strength is tested (ASTM C1583/C1583M-13., 2013). During a pull-out test, a metal disk is attached to the concrete surface using a strong adhesive. After a short curing period, the metal disk is vertically pulled out from the surface, and the pull-out force can be used to calculate the compressive strength of the concrete structure. Both core extraction and pull-out tests are destructive and have the potential to damage the integrity of the concrete structure.

*Corresponding author: 2211053@tongji.edu.cn

DOI: 10.1201/9781003495505-412

In addition to these methods, the quality and compressive strength of concrete can also be assessed through non-destructive and non-invasive methods (Qasrawi et al., 2000), including ultrasonic pulse velocity (Hassan et al., 2012) and Schmidt hammer tests (Szilágyi et al., 2011), among others. However, after the rebound hammer test (Rojas-henao et al., 2012), the concrete surface exhibits numerous small indentations (Mesbah et al., 2002), which can have a noticeable impact on the appearance of the concrete. Ultrasonic testing (BS 1881-203 1986), on the other hand, is limited in on-site applications due to the influence of voids, cracks, and reinforcement (Popovics et al., 2005). While these methods aid in predicting estimates of compressive strength, the data obtained does not directly provide information about the physical properties and performance values of concrete (Malhotra et al., 2004).

Hyperspectral imaging (HSI) has been introduced as a non-invasive detection technique for characterizing the composition of materials in civil engineering (Eismann et al., 2012). HSI is a subclass of spectral imaging. Spectral imaging typically involves capturing the reflected spectral information from objects to acquire their characteristics (Zaini et al., 2016). For example, a common camera captures visible RGB (Red, Green, Blue) light to gather information about objects, representing simple broadband spectral imaging. In contrast, hyperspectral imaging is based on the use of numerous narrow spectral bands in image data technology (Arita et al., 2001). Unlike the broad channels of broadband imaging, hyperspectral imaging divides a particular spectral band into many very narrow channels, providing detailed spectral information across many bands that the human eye cannot perceive. Hyperspectral cameras effectively collect three-dimensional data cubes, as show in Figure 1. When imaging concrete structures in a two-dimensional space, hyperspectral systems simultaneously acquire one-dimensional spectral information (Kohri et al., 2010). For each pixel, hyperspectral information is collected through multiple channels. Using machine learning methods to analyze concrete hyperspectral data, we can rapidly and cost-effectively determine concrete compressive strength (Brook et al., 2011).

The goal of this study is to rapidly identify the compressive strength of concrete lining structures by using a portable hyperspectral camera to capture the optical reflectance spectra. The focus of this paper is on developing a compressive strength recognition model based on hyper-spectral data of concrete in different wavelength ranges. Various machine learning algorithms are employed to establish the correspondence between optical reflectance spectra and concrete compressive strength. Specifically, concrete samples of five different strength gradients are prepared using different types of silicate cement. For each group, hyperspectral information is collected after standard curing for 28 days, and the compressive strength of the samples is tested. This data is used to establish regression models linking hyperspectral data of different types of concrete samples to their compressive strength.

2 EXPERIMENT SETUP

2.1 *Sample preparation*

Five concrete samples with different strengths were prepared using ordinary Portland cement labelled C20, C30, C40, C50 and C60, as shown in Figure 2. They are a mixture of water, Portland cement and river sand with a water-cement ratio of 0.5. Pour the mortar mixed with cement of different grades into a standard cubic mold with a size of 100 mm ×100mm×100mm. Two samples of each strength are made, for a total of 10 samples. Use plastic cloth to pad the mold to prevent surface cracking due to shrinkage. All samples were cured in a standard curing cabinet at a temperature of 23± 3.0 °C and a relative humidity (RH) of 90 ± 5%. After curing for 28 days, remove the mold and check the size and shape of the sample. Wipe and polish the surface of the specimen to avoid surface stains affecting the collection of hyperspectral information.

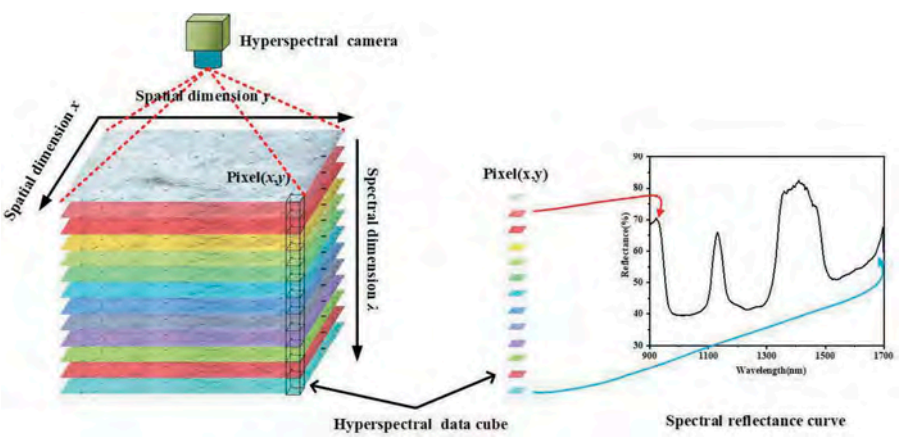

Figure 1. The working principle of hyperspectral imaging.

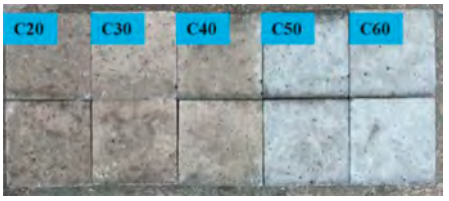

Figure 2. Concrete specimens used in experiments.

Hyperspectral camera scans and uniaxial compression tests followed. For each type of mortar mixture, uniaxial compression testing was performed according to ASTM C39/C39M-18.2018 to obtain the uniaxial com-pressive strength of each sample.

2.2 *Hyperspectral scanning*

Figure 3 shows the test setup for hyperspectral scanning of a sample using two hyperspectral cameras with different spectral ranges. The spectral range of the FS-23 camera is 400-1000nm and the spectral resolution is 2.5nm. The spectral range of the FS-25 camera is 900-1700nm and the spectral resolution is 8.0nm. The camera was fixed on a tripod, and the hyperspectral camera was set directly in front of the concrete sample at a distance of 1.2 m from the sample surface to obtain better resolution for close-range imaging. A white calibration plate with 80% reflectance is placed above the sample. The hyperspectral camera is calibrated by collecting and processing white reference data. The camera is connected to a laptop with data collection software for setting camera parameters and collecting Scan data. After obtaining the corrected reflection hyperspectral image data, ENVI software is used to extract the reflection spectrum of each pixel in the image for subsequent analysis.

Before hyperspectral scanning, the hyperspectral image is calibrated by collecting and processing reflectance data from a white reflectance calibration board, which provides an 80% reflectance curve across the entire wavelength range. As the principles behind hyperspectral imaging resemble those of conventional cameras but with an expanded wavelength range, the impact of temperature and sample smoothness on spectral data is minimal. Subsequently, adjustments to the camera distance and light source are made based on the calibration board until 60% of the saturation light intensity is detected. Insufficient light intensity may generate too many defective pixels, impeding mathematical corrections.

2.3 *Hyperspectral data analysis methods*

Hyperspectral image data cubes of concrete specimen surfaces were acquired by using two types hyperspectral cameras. However, due to significant noise in the original hyperspectral data, the Savitzky-Golay (SG) smoothing algorithm was first applied to smooth the raw spectral data (Ma et al., 2016). Subsequently, three machine learning models, namely, Principal Component Regression (PCR), Partial Least Squares Regression (PLSR), and Least Squares Support Vector Machine (LSSVM), were developed for predicting the compressive strength of

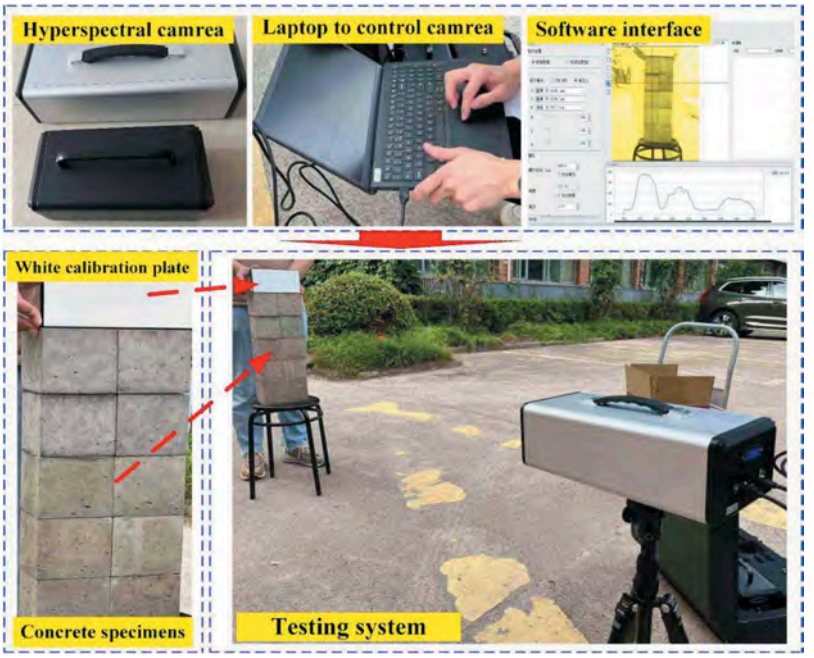

Figure 3. Test setup on concrete specimens using sunlight, hyperspectral camera, laptop and white calibration plate.

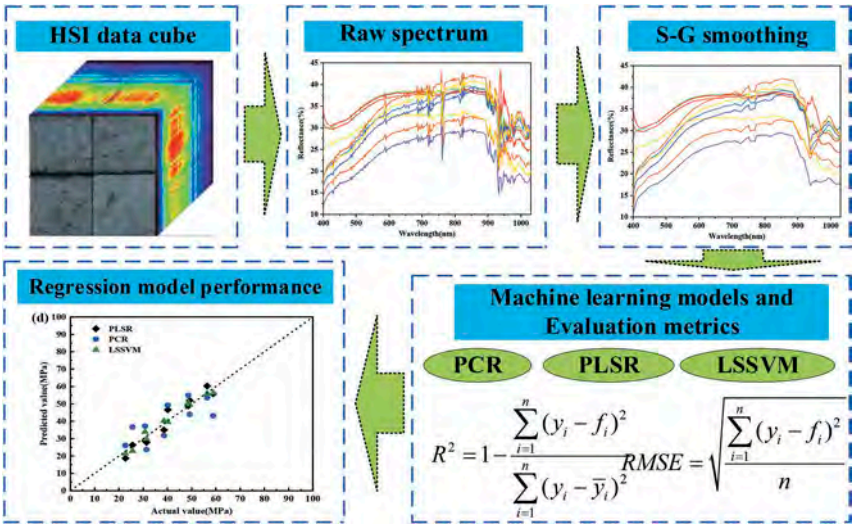

Figure 4. Hyperspectral data analysis process.

the manufactured concrete specimens, as shown in Figure 4.

In this study, 80% of the spectral reflectance data were used for training the models, while the remaining 20% were reserved for testing the prediction models. PCR, PLSR, and LSSVM algorithms were all trained using MATLAB to construct the predictive models. The prediction models were then evaluated using the determination coefficient (R^2) and root mean square error (RMSE) to assess their predictive performance, ultimately identifying the best predictive model.

2.3.1 *Data preprocessing*

Smoothing filtering is one of the commonly used preprocessing methods in spectral analysis. The most direct result in hyperspectral data is to remove the "burrs" of the spectrum, improve the smoothness of the spectrum, and reduce noise interference. This study uses Savitzky-Golay filtering, that is, S-G filter smoothing, which mainly uses polynomials for data smoothing. Based on the least squares method, it can retain useful information in spectral data and eliminate random noise. The two main parameters in the SG smoothing algorithm are the polynomial fitting order N and the sliding convolution frame size F. F is an odd number and satisfies F-1>N. Choosing the correct parameters N and F is important to ensure better smoothing results. A large N and a small F may lead to overfitting due to the noise in hyper-spectral data, whereas a small N and a large F may lose information because the smoothing window is too large to smooth out the characteristic peaks in the spectrum.

2.3.2 *PCR*

Principal component regression (PCR) is a dimensionality reduction technique that transforms a set of highly correlated independent variables into a set of mutually independent variables with no linear relationships (Chang et al., 2011). These transformed variables are called principal com-ponents, and they can capture most of the information from the original data. PCR is commonly used when there are too many independent variables or when strong correlations exist among them.

In this study, each spectral data consists of 256 channels of data. PCR is used to project the concrete compressive strength and its corresponding spectral response matrix into a new space to build a prediction model. It extracts principal components from the compressive strength and spectral response matrix, aiming to maximize the correlation between the principal components extracted from the compressive strength and the spectral response matrix.

2.3.3 *PLSR*

Partial least squares regression (PLSR) builds a prediction model by considering spectral information and sample true values, and obtains latent variables and eliminates useless variables through dimensionality reduction (Cheng et al., 2017). This study employs Partial Least Squares Regression (PLSR) to project concrete strength and the corresponding spectral response matrix into a new space to establish a predictive model. Principal components are extracted from concrete strength and the spectral response matrix, with the aim of maximizing the correlation between the principal components extracted from concrete strength and the spectral response matrix. This approach identifies multi-dimensional directions in the spectral response matrix space that explain the maximum variance in the concrete strength space. Below is the algorithmic workflow for predicting concrete strength using hyperspectral data implemented with PLSR algorithm.

Let X_0 represent the original hyperspectral data, forming an N×m matrix, and Y_0 denote the concrete strength, constituting an N×1 matrix, where N signifies the number of sample pairs, and m corresponds to the number of channels in the hyperspectral data. After undergoing standardization procedures, which involve mean subtraction and division by the standard deviation, the resulting datasets are represented as matrices X and Y.

Assume that the first principal component vectors of X and Y are denoted as w_1 and c_1, respectively, then w_1 and v_1 can represent the first pair of principal components t_1 and u_1 as follows (Cheng et al., 2017):

$$\begin{aligned} t_1 &= Xw_1 \\ u_1 &= Yc_1 \end{aligned} \tag{1}$$

The underlying idea behind PLSR is to maximize the correlation between t_1 and u_1 while maximizing their respective variances. This can be mathematically formalized as follows (Cheng et al., 2017):

$$\begin{cases} <t_1, u_1> = <Xw_1, Yv_1> = w_1^T X^T Y v_1 \Rightarrow \max \\ w_1^T w = \|w_1\|^2 = 1, v_1^T v_1 = \|v_1\|^2 = 1 \end{cases} \tag{2}$$

By utilizing the Lagrange multiplier method, w1 can be obtained as the eigenvector corresponding to the largest eigenvalue of the symmetric matrix $X^T Y Y^T X$, and c1 can be obtained as the eigenvector corresponding to the largest eigenvalue of $Y^T X X^T Y$.

Following the principal component regression concept, X and Y can be separately regressed on their respective principal components t_1 and u_1 as follows (Cheng et al., 2017):

$$\begin{aligned} X &= t_1 p_1^T + F \\ Y &= u_1 q_1^T + G \end{aligned} \tag{3}$$

Where $p_1 = (p_{11}, p_{12}, \ldots, p_{1m})^T$ and $p_1 = (p_{11}, p_{12}, \ldots, p_{1m})^T$ are the parameter vectors in the multiple-to-one regression models, and F and G are the residual matrices. Exploiting the correlation between t_1 and u_1, Y can be regressed on the principal component t_1 of X as follows (Cheng et al., 2017):

$$Y = t_1 r_1^T + H \tag{4}$$

Following the previously described approach for regression, this process is iterated repeatedly until the residual F reaches the desired accuracy or the number of principal components has reached the upper limit (the rank of the initial X), at which point the algorithm terminates.

For a new input data point x, you can first compute its various principal components. Then, by substituting these components into the equation $y = t_1 r_1^T + t_2 r_2^T + \ldots + t_k r_k^T$, you can calculate the predicted value for vector y.

2.3.4 *LSSVM*

LSSVM (Least Squares Support Vector Machine) is an advanced variant of the Support Vector Machine based on statistical theory (Wang et al., 2005). It has found successful applications in various domains, including data regression, pattern recognition, time series forecasting, among others. The LSSVM algorithm involves mapping data from the original feature space to a high-dimensional space, replacing inequality constraints with equality constraints, and solving the minimum loss function in the high-dimensional space to obtain a linear fitting equation. The specific implementation process is as follows:

For a given set of training data (x_i, y_i), where $x_i = (x_{i1}, x_{i2}, \ldots, x_{id})^T$ is a d-dimensional input vector, y_i is the corresponding output data, and N is the total number of training data. To map the input space to the feature space, a nonlinear function $\varphi(x_i)$ is used. The modeling form of the nonlinear function estimation is as follows (Wang et al., 2005):

$$f(x) = b + \langle \phi(x), w \rangle \tag{5}$$

Where, w is the weight vector, b is the bias term, and the symbol <·> denotes the inner product operation.

Based on the principle of minimizing prediction errors, the regression prediction problem is formulated as an optimiza-tion problem (Wang et al., 2005):

$$\begin{aligned} &\min J(w, e) = \min\left(\frac{1}{2}\|w\|^2 + \frac{1}{2}\gamma \sum_{i=1}^{N} e_i^2\right) \\ &s.t. y_i = \langle w, \phi(x_i) \rangle + b + e_i i = 1, 2, \ldots, N \\ &\gamma > 0 \end{aligned} \tag{6}$$

Where, γ is the regularization parameter used to balance the model's complexity and accuracy, and e_i represents the regression error between the actual and predicted values of the output.

To address the optimization problem mentioned above, the corresponding Lagrangian function is constructed as follow (Wang et al., 2005):

$$\begin{aligned} L_{LSSVM} &= \frac{1}{2}\|w\|^2 + \frac{1}{2}\gamma \sum_{i=1}^{N} e_i^2 \\ &- \sum_{i=1}^{N} \alpha_i \{\langle w, \phi(x_i) \rangle + b + e_i - y_i\} \end{aligned} \tag{7}$$

Where α_i is the Lagrange multiplier.

Setting $\partial w = 0, \partial b = 0, \partial e_i = 0$ and $\partial \alpha_i = 0$ yields the following conditions for the optimal solution to the problem:

$$\begin{aligned}
&\frac{\partial L_{isSNM}}{\partial w} = 0 \rightarrow w = \sum_{i=1}^{N} \alpha_i \phi(x_i) \\
&\frac{\partial L_{1ssVM}}{\partial b} = 0 \rightarrow \sum_{i=1}^{N} \alpha_i = 0 \\
&\frac{\partial L_{LSSM}}{\partial e_i} = 0 \rightarrow \alpha = \gamma e_i \\
&\frac{\partial L_{LSVM}}{\partial \alpha_i} = 0 \rightarrow < w, \phi(x_i) > + b + e_i - y_i = 0
\end{aligned} \tag{8}$$

By eliminating w and e_i, the four linear problems can be simplified to (Mall et al., 2015):

$$\begin{bmatrix} 0 & E^{\mathrm{T}} \\ E\,\Omega & +\frac{1}{\gamma}E \end{bmatrix} \begin{bmatrix} b \\ \alpha \end{bmatrix} = \begin{bmatrix} 0 \\ y \end{bmatrix} \tag{9}$$

Where, $y = [y_1, \ldots, y_N]^{\mathrm{T}}$, $\alpha = [\alpha_1, \ldots, \alpha_N]^{\mathrm{T}}$,and Ω is a symmetric N×N matrix of kernel functions.

$$\Omega_{ij} = K(x_i, x_j) = \phi(x_i)^T \phi(x_j) i, j = 1, 2, \cdots, N \tag{10}$$

Where $K(x_i, x_j)$ is a kernel function that satisfies Mercer's condition. Kernel functions have the ability to reduce the computational complexity in high-dimensional spaces and play a crucial role in constructing high-performance least squares support vector machines.

Therefore, the LSSVM model can be represented as (Mall et al., 2015):

$$\begin{aligned}
y(x) &= \langle w, \phi(x) \rangle + b \\
&= \sum_{i=1}^{n} \alpha_i \phi(x_i) \cdot \phi(x) + b \\
&= \sum_{i=1}^{n} \alpha_i K(x_i, x) + b
\end{aligned} \tag{11}$$

The Radial Basis Function (RBF) kernel is a widely adopted kernel function, defined as follows (Mall et al., 2015):

$$K(x_i, x_j) = \exp\left(-\frac{\left\| x_i - x_j \right\|^2}{2\sigma^2}\right), \sigma > 0 \tag{12}$$

Where σ represents the bandwidth of the kernel function.

These two hyperparameters, γ and σ, have a significant impact on the performance of the LSSVM model and need to be carefully determined.

2.3.5 *Model validation*

The R^2 and RMSE are two commonly used metrics to evaluate the performance of regression models.

R-squared is a statistical metric used to measure the goodness of fit of a regression model, and its values typically range from 0 to 1. A higher R-squared value indicates that the model can explain a greater proportion of the variance in the target variable, indicating a better fit. Conversely, an R-squared closer to 0 suggests that the model's explanatory power is weaker, indicating a poorer fit. The formula for calculating R-squared is:

$$R^2 = 1 - \sum_{i=1}^{n} (y_i - f_i)^2 \Big/ \sum_{i=1}^{n} (y_i - \bar{y}_i)^2 \tag{13}$$

Where y_i represents the observed values of the target variable, f_i is the model's predicted values, and $\bar{y}_i$ is the mean of the observed target variable.

RMSE is a metric used to measure the prediction error of a regression model. It represents the square root of the average of the squared differences between the model's predicted values and the actual observed values. Smaller RMSE values indicate lower prediction errors and better model fit. The formula for calculating RMSE is:

$$RMSE = \sqrt{\sum_{i=1}^{n} (y_i - f_i)^2 \Big/ n} \tag{14}$$

RMSE provides an intuitive measure of the size of prediction errors and is often used for model comparison and assessing prediction accuracy.

3 RESULTS AND DISCUSSION

3.1 *Hyperspectral information*

Figure5 displays the raw spectral data obtained using a hyperspectral camera and the spectral data after being subjected to S-G smoothing. It is evident that, compared to the original spectral reflectance curve, the smoothed spectral reflectance curve eliminates the spikes caused by environmental or machine noise, while preserving most of the characteristic peaks for subsequent compressive strength prediction. For each type of mortar strength, ten samples were prepared, and the surface of each sample was scanned. Thirty spectra were extracted from a 100 mm × 100 mm surface area, resulting in a total of 300 spectra. Spectra were collected exclusively from the sample surface area to mitigate errors arising from non-uniform spots.

Figure 5 presents the surface spectral information of concrete specimens acquired using a hyperspectral camera in two different wavelength ranges: 400-1000nm and 900-1700nm. In the figure, the curves of different colors represent the surface spectra corresponding to samples with different compressive strengths. It is evident that both wavelength ranges exhibit significant differences in spectral curves concerning concrete compressive strength. As the compressive strength increases, the spectral reflectance curves also change.

As shown in Figure 5(b), within the 880nm-960nm range, the reflectance exhibits the most significant

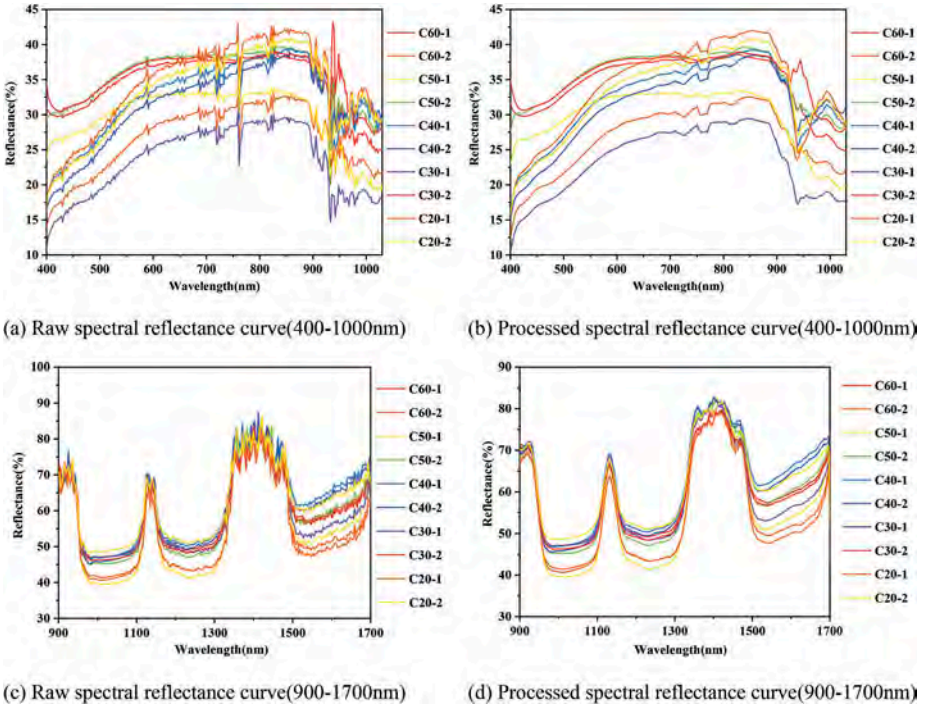

Figure 5. The reflectance spectra of concrete specimens: raw and processed.

fluctuations with compressive strength. This range can be considered the spectral sensitive wavelength for concrete compressive strength. In Figure 5(d), within the [980nm, 1100nm], [1200nm, 1300nm], and [1500nm-1700nm] interval, the spectral reflectance all displays noticeable variations, further confirming the feasibility of using spectral information to characterize concrete compressive strength. To further investigate the relationship between spectral reflectance and compressive strength, it is necessary to continue introducing machine learning methods for the exploration of high-dimensional spectral data.

3.2 *UCS test results*

After the curing period, all concrete samples underwent hyperspectral analysis before undergoing standard uniaxial compression testing. The test specimens were positioned on the platform of a servo-controlled testing machine (WDW-600C Hydraulic Servo Testing Machine) and subjected to a loading rate of 0.2 mm/min until complete failure, yielding the uniaxial compressive strength for each sample, as shown in Table 1. This results serves as the foundation for sub-sequent hyperspectral predictive analyses.

3.3 *Regression prediction results*

Using reflectance spectra acquired from hyperspectral cameras in two different spectral ranges, namely 400-1000 nm and 900-1700 nm, as independent variables, and ten compressive strengths of concrete samples as dependent variables, PCR, PLSR, and LSSVM regression models were established both on the raw spectra and spectra after S-G processing. Table 2 displays the predictive performance results of the regression models under the optimal pre-processing conditions.

Table 1. Concrete specimens uniaxial compression test results.

ID	UCS(MPa)	ID	UCS(MPa)
C20-1	22.61	C20-2	25.62
C30-1	31.46	C30-2	30.85
C40-1	38.53	C40-2	40.17
C50-1	49.28	C50-2	48.67
C60-1	58.91	C60-2	56.44

Regarding the pre-processing methods, as shown in Table 2, for the [400,1000] dataset, the results after S-G processing significantly improved the predictive performance of the PLSR and LSSVM models. The determination coefficient R^2 of PLSR increased from 0.83 to 0.94, and RMSE decreased from 5.88MPa to 1.53MPa, while LSSVM's R^2 increased from 0.94 to 0.99, and RMSE decreased from 6.04MPa to 0.71MPa. In contrast, the effect on the PCR model's predictions was relatively small, with R^2 and RMSE remaining around 0.50 and 10.0MPa, respectively. For the [900,1700] dataset, S-G processing had a slight positive impact on the PCR model's predictive performance but did not significantly improve the predictions of the PLSR and LSSVM models. Overall, the original full-

Table 2. Compressive strength prediction performance based on different regression models.

Spectral Wavelengths	Pre-processing Method	Regression Model	R^2	RMSE(MPa)
[400-1000]	Raw	PCR	0.53	9.70
[400-1000]		PLSR	0.83	5.88
[400-1000]		LSSVM	0.84	5.04
[400-1000]	S-G	PCR	0.51	9.94
[400-1000]		PLSR	0.88	5.53
[400-1000]		LSSVM	0.89	4.71
[900-1700]	Raw	PCR	0.37	11.24
[900-1700]		PLSR	0.92	3.81
[900-1700]		LSSVM	0.95	3.07
[900-1700]	S-G	PCR	0.53	9.71
[900-1700]		PLSR	0.93	3.73
[900-1700]		LSSVM	0.97	2.37

spectrum data provided satisfactory results with little or no need for pre-processing, or with a single pre-processing method.

As shown in Figure 6, overall, both PLSR and LSSVM models achieved determination coefficients (R^2) of above 0.80 for both datasets, indicating reliable predictive accuracy. In contrast, the PCR model had a lower R^2, not exceeding 0.53, suggesting relatively lower precision. Notably, the LSSVM model performed the best on both datasets. In the [400-1000] dataset, LSSVM and PLSR achieved R^2 values of 0.99 and 0.98, with RMSE values of 0.71MPa and 1.53MPa, respectively, while the PCR model had an R^2 of only 0.53 and an RMSE of 9.70MPa. In the [900-1700] dataset, the LSSVM model (R^2=0.97, RMSE=2.37MPa) slightly outperformed the PLSR model (R^2=0.95, RMSE =3.07MPa), while the PCR model's performance remained suboptimal, with an R^2 of 0.53 and an RMSE of 9.71MPa.

In summary, hyperspectral technology combined with machine learning algorithms can effectively detect concrete compressive strength. The results suggest that both LSSVM and PLSR algorithms provide the best predictions, while the PCR algorithm's predictive performance is comparatively modest, possibly due to its strong linearity in principal component extraction. Simultaneously, these relationships also indicate that hyperspectral technology can be used to predict the compressive strength of concrete. These relationships can be applied to predict the strength of concrete structures.

4 CONCLUSIONS AND FURTHER WORK

This study employed two hyperspectral cameras with distinct wavelength ranges to capture images of concrete samples made with different cement types (C20, C30, C40, C50, C60). Machine learning models were developed using hyperspectral data from different wavelength ranges to predict concrete compressive strength. The specific conclusions are as follows:

1. The study examined the impact of spectral pre-processing methods on concrete compressive

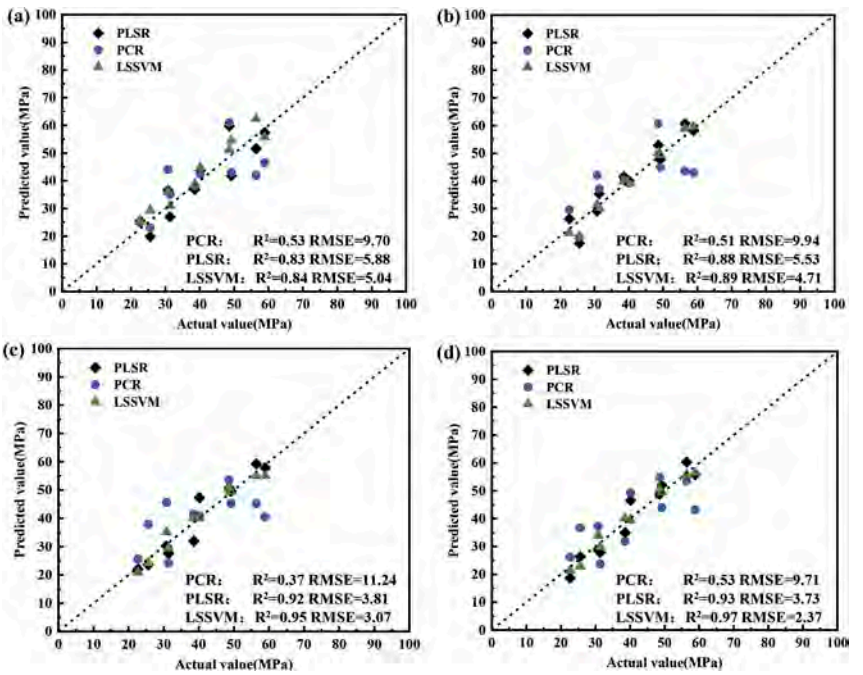

Figure 6. Plots of actual values versus predicted values of concrete compressive strength:(a) Raw[400-1000nm] dataset, (b) S-G[400-1000nm] dataset, (c) Raw[900-1700nm] dataset, (d) S-G[900-1700nm] dataset.

strength prediction. It was observed that the original full-spectrum data performed well without any pre-processing or with a single S-G pre-processing step.

2. The study explored the influence of different spectral wavelength ranges on concrete compressive strength prediction. Machine learning models were applied to two datasets: [400-1000nm] and [900-1700nm]. Notably, the [900-1700nm] dataset showed signi-ficantly improved model performance.
3. A comparison of different models revealed the best model for concrete compressive strength prediction. LSSVM and PLSR models performed exceptionally well in the [400-1000nm] dataset, while the LSSVM model excelled in the [900-1700nm] dataset, achieving a high level of accuracy.

The hyperspectral camera will be utilized to scan concrete samples designed with various mix proportions and subjected to diverse environmental exposures to identify their compressive strength. Expanding the hyperspectral reflectance dataset to encompass as many specific types as possible, such as aging and erosion, will continuously update and enhance the machine learning model for strength identification. The hyperspectral camera, installed on tunnel detection equipment, will conduct on-site concrete lining structure strength assessments. This enables rapid identi-fication of the compressive strength of concrete linings under authentic field conditions, facilitating accurate analysis of structural damage and ensuring safety.

ACKNOWLEDGMENTS

The work described in this paper was supported by the National Key Research and Development Plan (No.2021 YFB2600804), Tongji University Interdisciplinary Joint Research Project (No.2022-3-YB-12, No.2023-2-YB-07).

REFERENCES

J.W. Bullard, H.M. Jennings, R.A. Livingston, et al, 2011, Mechanisms of cement hydration, Cem.Concr. Res. 41, 1208–1223.

ASTM. Standard test method for obtaining and testing drilled cores and sawed beams of concrete. American Society for Testing and Materials (ASTMs) C42/C42M-18a, 2018.

ASTM. Standard test method for tensile strength of concrete surfaces and the bond strength or tensile strength of concrete repair and overlay materials by direct tension (pull-off method). American Society for Testing and Materials (ASTMs) C1583/C1583M-13, 2013.

A.M.T. Hassan, S.W. Jones, Non-destructive testing of Ultra High Performance Fibre Reinforced Concrete (UHPFRC): a feasibility study for using ultrasonic and resonant frequency testing techniques, Constr. Build. Mater. 35 (2012)361–367.

B. Abdul Hussein Ali, Assessment of Concrete Compressive Strength by Ultrasonic Non-Destructive Test. 2008.

L. Rojas-henao, J. Fernández-gómez, J.C. López-agüí, Rebound hammer, pulse velocity, and core tests in self-consolidating concrete, ACI Mater. J. 109 (2012)235–243.

K. Szilágyi, A. Borosnyói, I. Zsigovics, Rebound surface hardness of concrete: introduction of an empirical constitutive model, Constr. Build. Mater. 25(2011) 2480–2487.

ACI Committee 228. In-Place Methods to Estimate Concrete Strength Reported. Am Concr Inst, 2003, pp. 44.

H.Y. Qasrawi, Concrete strength by combined non-destructive methods simply and reliably predicted, Cem. Concr. Res. 30 (2000) 739–746.

N. Delatte, D. Fowler, B. McCullough, High early strength bonded concrete overlay designs and construction methods for rehabilitation of CRCP. Res Rep2911-4, 1996.

H. Mesbah, M. Lachemi, P. Aitcin, Determination of elastic properties of high-performance concrete at early ages, ACI Mater. J. 99 (2002) 37–41.

G. Washer, P. Fuchs, Ultrasonic testing of reactive powder concrete, IEEE Trans. Ultrason. Ferroelectr. Freq. Control 51 (2004) 193–201.

J. Popovics, Ultrasonic testing of concrete structures, Mater. Eval. 63 (2005)50–55.

H. Yıldırım, O. Sengul, Modulus of elasticity of substandard and normal concretes, Constr. Build. Mater. 25 (2011) 1645–1652.

V. Malhotra, N. Carino, Handbook on Non-destructive Testing of Concrete, 2nded., CRC Press, 2004.

BS 1881-203. Testing Concrete. Recommendations for Measurement of Velocity of Ultrasonic Pulses in Concrete. Br Stand Institute, UK 1986.

M.T. Eismann, Hyperspectral Remote Sensing, SPIE Press, Bellingham, Washington USA, 2012, pp. 1–20.

N. Zaini, F.V.D. Meer, F.V. Ruitenbeek, B.D. Smeth, F. Amri, C. Lievens. An alternative quality control technique for mineral chemistry analysis of Portland cement-grade limestone using shortwave infrared spectroscopy, Remote Sensing 8 (2016) 950–966.

J. Arita, K. Sasaki, T. Endo, Y. Yasuoka, Assessment of concrete degradation with hyper-spectral remote sensing. The 22nd Asian Conference on Remote Sensing, Singapore, 2001, pp. 5–9.

M. Kohri, T. Ueda, H. Mizuguchi, Application of a near-infrared spectroscopic technique to estimate the chloride ion content in mortar deteriorated by chloride attack and carbonation, J. Adv. Concr. Technol. 8 (2010) 15–25.

A. Brook, E. Ben-Dor, Reflectance spectroscopy as a tool to assess the quality of concrete in situ, J. Civil Eng. Constr. Technol. 8 (2011) 169–188.

ASTM. Standard test method for compressive strength of cylindrical concrete specimens. American Society for Testing and Materials (ASTMs) C39/C39M-18,2018.

Chang C W, Laird D A, Mausbach M J, et al. Near-infrared reflectance spectroscopy–principal components regression analyses of soil properties. Soil Science Society of America Journal, 2001, 65(2): 480–490.

Ma J, Sun D W, Pu H. Spectral absorption index in hyperspectral image analysis for predicting moisture contents in pork longissimus dorsi muscles. Food chemistry, 2016, 197: 848–854.

Cheng J H, Sun D W. Partial least squares regression (PLSR) applied to NIR and HSI spectral data modeling to predict chemical properties of fish muscle. Food engineering reviews, 2017, 9: 36–49.

Wang H, Hu D. Comparison of SVM and LS-SVM for regression[C]//2005 International conference on neural networks and brain. IEEE, 2005, 1: 279–283.

Mall R, Suykens J A K. Very sparse LSSVM reductions for large-scale data[J]. IEEE transactions on neural networks and learning systems, 2015, 26(5): 1086–1097.

Tunnelling for a Better Life – Yan, Celestino, Thewes & Eberhardt (Eds)
© 2024 The Author(s), ISBN 978-1-032-80042-4
Open Access: www.taylorfrancis.com, CC BY-NC-ND 4.0 license

An energy-efficient tunnel ventilation control algorithm combining dynamic neural network and fuzzy control

Haiying Wang* & Zhi Li
School of Engineering Machinery, Chang'an University, Xi'an, Shaanxi, China

Yingzhi Zhang & Jinxuan Zhang
Shaanxi Transportation Holding Group Co., Ltd. Xi'an, Shaanxi, China

ABSTRACT: The tunnel ventilation system plays a crucial role in reducing the concentration of harmful gases and enhancing visibility within tunnels, ensuring the safety of vehicles and personnel. To address the high energy consumption issue resulting from the lack of control algorithms and dynamic environmental perception in traditional tunnel ventilation systems, this paper introduces a novel energy-efficient control algorithm for tunnel ventilation by combining dynamic neural networks with fuzzy control techniques. The proposed algorithm employs nonlinear autoregressive neural networks (NAR) and nonlinear autoregressive neural networks with external input (NARX) to predict the traffic flow rate $TV_{(t+1)}$ and carbon monoxide concentration $CO_{(t+1)}$ within the tunnel at the next time, thereby detecting the tunnel environment in advance. The tunnel ventilation energy-efficient fuzzy control model employs the predicted value of $CO_{(t+1)}$ concentration e_{co} and its change rate Δe_{co} as inputs and determines the number of fan openings and fan speeds of the tunnel ventilation system as outputs. The control signals are updated at equal time intervals. By considering the dynamic variations in traffic flow and carbon monoxide concentration within the tunnel, the algorithm judiciously sets the appropriate number of fan openings and fan speed for energy-efficient tunnel ventilation control. Furthermore, an energy consumption calculation model for tunnel fans is established. Simulation calculations are conducted on the tunnel ventilation energy consumption using the proposed algorithm. The results demonstrate a 14.4% energy savings in comparison to traditional fuzzy control algorithm that rels on actual measured CO values as inputs.The integration of dynamic neural networks and fuzzy control in tunnel ventilation control presents a promising approach to enhance energy efficiency. The algorithm's ability to predict and adapt to changing tunnel conditions leads to substantial energy savings and improved overall performance, making it a valuable contribution to the field of tunnel ventilation control.

Keywords: Tunnelling, NAR neural network, NARX neural network, fuzzy control, ventilation Energy-efficient control

1 INTRODUCTION

According to statistics, by the end of 2022, there were 24,850 highway tunnels in China, with a total length of 26.7843 million meters, indicating an increase of 1,582 tunnels and 2.0854 million meters compared to 2021. Among them, there were 1,752 extremely long tunnels, spanning a total of 7.9511 million meters, and 6,715 long tunnels, totaling 11.7282 million meters (Ministry of Transport, 2021, 2022). Tunnel ventilation systems are employed to expel harmful gases such as CO and SO2, which pose threats to the safety of passengers, generated by vehicles during transit. The extended length of tunnels imposes higher demands on tunnel ventilation control systems. Traditional tunnel ventilation control systems operate with fixed numbers of fan openings and speeds during operational periods, lacking the ability to dynamically adjust the fan start quantities and speeds based on real-time vehicle traffic and tunnel environmental data. This deficiency results in elevated tunnel ventilation energy consumption. Therefore, reducing tunnel ventilation energy wastage and enhancing the system's capability to perceive and respond to environmental changes have become focal research areas of concern for scholars both domestically and internationally.

The ventilation control of tunnels is generally designed according to the *Design Guidelines for Highway Tunnel Ventilation* (JTG/T D70/2-02—2014). The methods of ventilation control have evolved from manual or indirect control to the current automatic

*Corresponding author: whying@chd.edu.cn

DOI: 10.1201/9781003495505-413

ventilation mode, employing techniques such as expert experience, fuzzy control, and neural network control. (Zhang et al. 2016) achieved intelligent tunnel ventilation control using a fuzzy control method. By predicting smoke concentration for multiple consecutive time intervals, the degree and trend of variations in the predictive result sequence were input to a fuzzy controller to control the duration of tunnel fan activation. (Yu et al. 2017) using an iterative learning algorithm, automated the optimization of parameters for fuzzy PID control of tunnel ventilation fans. This facilitated real-time adjustment of fuzzy PID input parameters, gradually approaching the desired trajectory by altering inputs to enhance fan control precision. (Li 2017) utilized feedforward neural networks and fuzzy control theory, constructed a feedforward intelligent fuzzy control system for tunnel ventilation. It took pollution concentration prediction increment, actual pollution concentration, and control objectives as inputs and output the required increase or decrease in fan groups. (Chu et al. 2010) employed an Actor-Critic structure and natural gradient, introduced a novel reinforcement learning method for tunnel ventilation control, enhancing control accuracy. Mostafa et al. (2013) proposed a tunnel ventilation scheme based on Fuzzy Analytical Hierarchy Process (AHP), selecting the optimal tunnel ventilation method through final weight calculations. Zhang et al. (2017) introduced a PLC-based tunnel ventilation control system, enabling indirect timed control of tunnel ventilation. (Wang et al. 2018) combined cloud services and big data, developed a tunnel ventilation control system using data analysis to enhance control accuracy. (Jiang et al. 2018) used ventilation simulation software to simulate the ventilation system status of extremely long tunnels under various driving conditions, derived ventilation control measures for different vehicle speeds. (Xing et al. 2018) designed a tunnel monitoring system using force control configuration software, enhanced tunnel ventilation control system efficiency. (Wu et al. 2017) designed a control algorithm based on adaptive assessment, established a mechanical model and using a neural network for fan control, enhanced tunnel ventilation control robustness. (Wan et al. 2019) conducted a comprehensive analysis of ventilation calculation parameter ranges and optimization of ventilation methods, aiming to exercise control over the scale of ventilation systems from the very outset of design. By minimizing civil and electromechanical engineering investments and reducing operational costs, achieved energy-efficient effects successfully. The aforementioned ventilation control approaches primarily employ learning algorithms, fuzzy control algorithms, and feedforward neural networks for control. Typically, the predicted concentration and measured concentration of pollutants as inputs, while the number of fan openings or groups is selected as output for tunnel fan control. The application of these methods has, to a certain extent, enhanced ventilation effectiveness and reduced energy consumption. Traffic flow is a major factor causing changes in pollution concentration. However, the above studies do not consider pollution concentration changes caused by traffic flow as the primary variable. Such feedback-based control methods, detached from traffic flow and carbon monoxide concentration changes, exhibit lag and maintain higher energy consumption levels. Thus, rapid sensing and dynamic prediction of tunnel ventilation environmental parameters, using predictive quantities as inputs for adaptive control, will elevate the intelligence of ventilation control and achieve energy-saving effects.

The CO concentration within the tunnel is correlated with tunnel traffic flow. In enhancing the perception and predictive capabilities of tunnel environments, (Qian et al. 2021) designed and developed a highway tunnel environmental perception system based on the Internet of Things (IoT) and cloud computing. The system integrated sensors for harmful gases, temperature, pressure, visibility, and wind speed and direction within the tunnel to achieve real-time cloud storage and monitoring of tunnel environment data. Lv et al. (2013) employed the nonlinear approximation abilities of BP and RBF neural networks to comprehensively extract CO concentration information features within the tunnel. An optimal mean square error and weighted fusion algorithm were then utilized to further integrate and predict CO concentrations. (Ren et al. 2022) designed an adaptive control ventilation system for tunnel construction based on RBF neural networks. This system established the relationship between fan operating frequency and tunnel environmental parameters through the RBF neural network, achieving controlled adjustment of tunnel fan air supply. (Wang et al.2018) proposed a fan frequency prediction algorithm based on BP neural networks, determined the number of activated fans through frequency prediction. (Li et al. 2022) employed RBF neural networks to explore the relationship between tunnel fire scale and critical velocity. By using RBF neural networks to train and validate, achieving intelligent control of tunnel fans in fire environments.

From the application of abovementioned neural network prediction methods in tunnel ventilation control, it can be observed that both BP and RBF neural networks exhibit lower predictive accuracy. This is due to their static learning nature, lacking feedback, memory, and time-delay capabilities. The parameters of tunnel ventilation environment, such as traffic flow and CO concentration increment, form a nonlinear time series. Accurate prediction requires anticipating increments based on the historical data from previous time steps and incorporating it into the calculation of the next time step prediction. (Zhu et al. 2020) applied the NARX dynamic neural network to short-term traffic flow prediction at intersections, achieving a high prediction accuracy of 91.59%. (Zhao et al. 2015) predicted daily flow rates of underground karst rivers using the NARX neural network, effectively capturing trends and dynamic characteristics. Yang et al. (2018) established an NARX neural network prediction

model, trained it with time series data of multi-intersection traffic flow in road networks, and achieved good prediction results for the following day's vehicle count. These studies indicate that the NARX dynamic neural network exhibits better adaptability and predictive efficiency in addressing predictive problems related to nonlinear time series data, making it suitable for predicting nonlinear time series data like CO and traffic flow.

In conclusion, this paper proposed a novel tunnel ventilation energy-efficient control algorithm that combines NAR-NARX dynamic neural networks with fuzzy control, aimed at achieving dynamic and real-time control of tunnel ventilation. This approach is utilizing both NAR and NARX to predict traffic flow and carbon monoxide concentration values. The predicted value of carbon monoxide concentration C0(t+1), along with its rate of change, are then input into the energy-efficient fuzzy control algorithm. This integration achieves control over the number of activated tunnel fans and their rotational speeds. The algorithm demonstrates the ability to proactively respond to changes in tunnel ventilation environmental data, facilitating dynamic fan control and ultimately achieving energy-efficient effects.

2 METHOD OF TUNNEL VENTILATION ENERGY-EFFICIENT CONTROL ALGORITHM

The NAR traffic flow prediction model is based on the monitoring data from traffic flow sensors installed at the tunnel entrance during the current period, enabling the prediction of traffic flow for the next period. The NARX CO concentration prediction model utilizes current period CO concentration monitoring data along with NAR traffic flow prediction data to forecast the CO concentration for the subsequent moment. The tunnel ventilation energy-efficient fuzzy control, guided by predefined fuzzy control rules, accomplished the control of the number of wind turbines and rotational speed within the tunnel. The fan energy consumption model performs energy consumption calculations for variable-frequency jet fans operating within the tunnel, facilitating a comparison of energy consumption across different control strategies and an evaluation of energy-efficient effects.

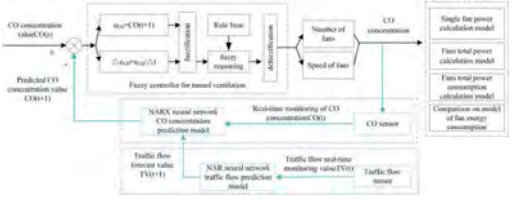

Figure 1. Framework of tunnel ventilation energy-efficient control algorithm combining NAR-NARX dynamic neural network and fuzzy control.

2.1 *NAR-NARX dynamic neural network prediction model*

(1) NAR traffic flow prediction model

The NAR traffic flow prediction model comprises an input layer (traffic flow monitoring values), a hidden layer, and an output layer (predicted traffic flow values), as depicted in Equation (1). The NAR traffic flow prediction model utilizes the output value from the previoustime step as the input for the current time step and introduces a time delay component, implying the output values TV(t+1) has a tightly connection with the previous n output values.

$$TV(t+1) = f[TV(t), TV(t-1), TV(t-2), \ldots, TV(t-n)] \tag{1}$$

Where, *TV(t+1)* represents the predicted traffic flow output at the next time step, *TV(t)* indicates the current monintoring traffic flow value at the current time step *t*, *TV(t-1)* rdenotes the monintoring value of traffic flow at the previous time step, *TV(t-n)* represents the monintoring value of traffic flow at the previous n time step, and *f* is the nonlinear mapping function of the neural network.

(2) The NARX CO concentration prediction model

The structure of the NARX CO concentration prediction model comprises input, hidden, and output layers. The input layer encompasses traffic flow forecast values and real-time CO concentration monitoring values, while the output layer yields the predicted CO concentration. This architecture is illustrated in equation (2). Notably, the model introduces a feedback information transmission component between the output and input layers, in addition to the conventional temporal delay elements. This feedback mechanism, achieved through combinations of distinct input variables, effectively realizes the prediction of CO concentration values for the upcoming time step.

$$CO(t+1) = f[CO(t), CO(t-1), TV(t)\,TV(t-1)] \tag{2}$$

Where, *CO(t+1)* denotes the output of the NARX dynamic neural network, representing the predicted CO concentration. *CO(t)* represents the CO concentration monitoring value at the current time step. *CO (t-1)* denotes the CO concentration monitoring value at the previous time step. *TV(t)* signifies the current traffic flow forecast value. *TV(t-1)* represents the traffic flow forecast value from the previous time step. *f* is a nonlinear mapping function, capturing intricate nonlinear relationships between inputs and outputs.

(3) Prediction Process of the NAR-NARX Dynamic Neural Network

The establishment of NAR-NARX dynamic neural network prediction model is depicted in

Figure 2. Initially, an open-loop NAR-NARX prediction model is developed, wherein input samples are sequentially divided into training, validation, and testing sets. Subsequently, the open-loop NAR-NARX model is trained using the training set. Once the desired level of accuracy is achieved, the open-loop NAR-NARX prediction model is transformed into a closed-loop NAR-NARX prediction model. Lastly, the predictive performance of the closed-loop NAR-NARX prediction model is evaluated on the validation set. If the performance criteria are met, further assessment of its predictive accuracy is conducted on the testing set to mitigate overfitting. In case of overfitting, the NAR-NARX prediction model is retrained or its topological structure is optimized, iteratively refining it until satisfactory predictive accuracy is achieved on both the validation and testing sets.

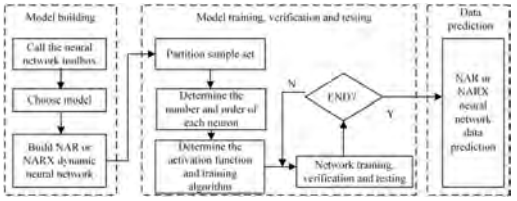

Figure 2. Prediction process of the NAR-NARX dynamic neural network prediction model.

2.2 DESIGN OF TUNNEL VENTILATION ENERGY-EFFICIENT FUZZY CONTROLLER ALGORITHM

The tunnel ventilationenergy-efficient fuzzy controller is of the two-input two-output type, utilizing fuzzy logic control that employs fuzzy sets and fuzzy inference to derive control rules. The implementation process of the tunnel ventilation energy-efficient fuzzy control algorithm is outlined as follows:

(1) Definition of Input and Output Variables for the Fuzzy Controller.
The tunnel ventilation energy-efficient fuzzy control model takes the predicted value of CO concentration e_{co} and its change rate Δe_{co} as inputs and the number of operating fans and fan speed of the tunnel ventilation system as outputs.

(2) Definition of Fuzzy Sets for input and output variables.The domain of the predicted CO concentration $e_{co}$is set as [0, 100], while the change rate Δe_{co},the fan speed and the number of fan opening are set as [-200, 200], [0, 2900], and [0, 6], respectively. Lingustic terms are represented by seven fuzzy states:{NB, NM, NS, ZO, PS, PM, PB}, with Gaussian membership function is defined by Equation (3).

$$y = e^{\frac{-(x-c)^2}{2\sigma^2}} \tag{3}$$

Where, x represents the left and right limit of the membership function curve, c indicates the center of the membership function curve, σ determines the "width" of the curve.

(3) Construction of Fuzzy Logic Control Rule Table
Fuzzy control rules typically consist of "if condition, then result" statements, describing a series of control strategies and objectives. Fuzzy control rules can be expressed using Equation (4):

$$if\ A\ is\ PB\ and\ B\ is\ ZO\ then\ C\ is\ PB \tag{4}$$

(4) Fuzzy Inference
A specific fuzzy inference algorithm is applied to the established fuzzy logic control rules to deduce the required control parameters. The Mamdani algorithm is adopted due to its independent treatment of each component in the fuzzy system's fuzzification process. The Mamdani algorithm is represented by Equation (5):

$$R_K = A_K \times B_K \tag{5}$$

Where A_K and B_K are two distinct inputs, and R_K is the output.
The overall fuzzy relationship matrix composed of Mamdani algorithm is shown in Equation (6).

$$R = \mathrm{U}_{K=1}^{N} R_K \tag{6}$$

The specific values N depend on the number of fuzzy rules.

(5) Defuzzification to obtain the output value
The fuzzy values obtained through inference cannot be directly applied to control. They must be converted into precise control signals to execute control operations on the actuators. Common defuzzification methods include the maximum membership method, centroid method, and weighted average method. The centroid method is selected in this study for its smoother output reasoning control. It relates minor changes in input signals to corresponding output variations. The centroid method is formulated as shown in Equation (7):

$$C(k) = \frac{\sum_{i=1}^{m} x_i \mu_N(x_i)}{\sum_{i=1}^{m} \mu_N(x_i)} \tag{7}$$

2.3 *Energy efficiency evaluation of tunnel ventilation control algorithm*

This energy consumption model is utilized to compute the operational energy consumption of jet fans under different control methods, enabling an assessment of energy-saving effectiveness.

Calculation of Rated Power p_{Rated} for a Single Jet Variable Frequency Fan:

$$p_{Rated} = \frac{Q * p}{3600 * 1000 * \eta 0 * \eta 1} \tag{8}$$

Where Q is the air flow rate, p is the total pressure of the fan, η_0 the total efficiency of the fan, typically ranging from 0.75 to 0.85, in accordance with relevant standards, η_0=0.8, η_1 is the mechanical efficiency, set to 1 as the jet fan is directly connected to the motor,.

The total pressure p is composed of static pressure p_{sp} of the fan and the dynamic pressure p_{dp} of the air. The calculation formula is given by:

$$P = p_{sp} + p_{dp} = p_{sp} + 0.5 * v^2 \tag{9}$$

Among them, p_{sp} is the static pressure at the working environment of the jet variable frequency fan (atmospheric pressure), p_{dp} is the dynamic pressure and v is the outlet air velocity.

As the jet variable frequency fan responds to control signals emitted by components like the fuzzy controller over discrete time steps, the fan speed and number are adjusted in real-time. Considering the continuously changing fan speed, the formula for calculating the variable frequency power consumption of a single jet variable frequency fan p_{fc} is as follows:

$$P_{fc} = P_{Rated} * \frac{n_{fc}}{n_{Rated}} \tag{10}$$

Where, n_{fc} is the variable frequency fan speed, n_{Rated} is the rated fan speed.

The total power consumption P_i of jet variable frequency fans within the tunnel is calculated as follows:

$$P_i = P_{fc} * n \tag{11}$$

Where, n is the real-time fan activation fron the fuzzy controller at the time step i.

The total energy W_T consumed by the jet fans under the fuzzy control algorithm is calculated by:

$$W_T = \sum_{i=1}^{m} P_i * t_i \tag{12}$$

Where, t_i is the operational time interval of the jet fan which is set to 15min, and m is the number of time intervals.

The calculation of Energy-efficient efficiency of the jet fans is shown in formula 13:

$$\eta = \frac{Q_T - W_T}{Q_T} \tag{13}$$

Where, Q_T represents the energy consumption of tunnel fans under traditional fuzzy control inputs, and W_T represents the energy consumption of tunnel fans when the NARX neural network prediction data is used as fuzzy control inputs.

3 CASE STUDY

3.1 *Tunnel and data acquisition*

The case study is based on a tunnel with a total length of 2772 meters, equipped with a designed total of 6 fans. Sensory data is gathered through sensors placed within the tunnel, capturing four days' worth of traffic flow and CO concentration data, resulting in a total of 384 data sets. The data collection interval is set at 15 minutes. The dataset of neural networks is partitioned according to a ratio of 5:2.5:2.5. As a result, the training set encompasses 192 groups of data, while the validation and testing sets encompass 96 groups each.

This comprehensive study aims to evaluate the performance of the proposed control algorithm by comparing the energy consumption results obtained from the fuzzy control approach with those from the reference experiment.

The jet fan utilized within the engineering tunnel is the SDS-7.1-2P-6-33 model. The fan's rated rotational speed is 2900 r/min, with an airflow volume of 12.7 and an air velocity of 40.6 m/s. Carbon monoxide concentration serves as the target parameter for tunnel ventilation control. According to the "*Highway Tunnel Design Code*", the selected carbon monoxide concentration control value for the engineering tunnel is set at 100.

3.2 *Tunnel traffic flow prediction and analysis using NAR neural network*

The number of nodes in the input layer and output layer of the NAR neural network is determined based on the quantity of sample data. Experimentation was conducted with varying numbers of hidden layer nodes ranging from 5 to 15. Through this process, the optimal number of hidden layer nodes, resulting in the least disparity between predicted and monitored traffic flow values, was determined to be 8. A delay order of 1:6 was adopted, implying that the traffic flow monitoring values from the preceding 6 time intervals significantly influence the prediction for the subsequent moment. The simulated results are illustrated in Figure 3. The obtained coefficient of determination for the training, validation, and testing phases were 0.96094, 0.97436, and 0.95099, respectively. The comprehensive coefficient of determination (R1) stood at 0.95967. The average error in the predictions of the testing dataset was determined to be 96.12%, which aligns with the precision of neural network training and validation, effectively achieving the intended outcome.

3.3 *Prediction and analysis of tunnel CO concentration based on NARX neural network*

The parameter configuration process for the NARX neural network follows the same procedure as that of the NAR dynamic neural network. Specifically, the hidden layer contains 15 nodes, and the temporal order extends from 1 to 8.To establish a robust CO concentration prediction model using the NARX

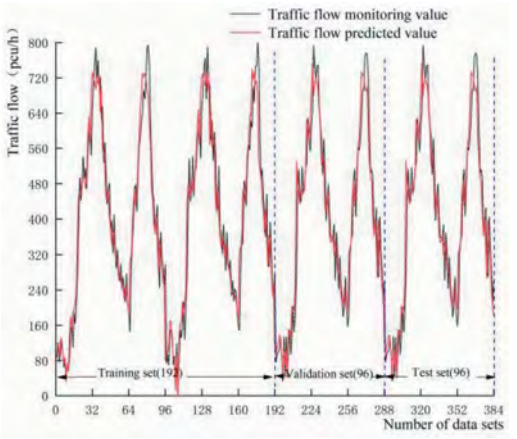

Figure 3. Simulation results of traffic flow prediction model based on NAR neural network.

neural network, a series of steps is undertaken, including model training, validation, and testing. The outcomes of these processes are illustrated in Figure 4. The computed R2 values for the training, validation, and testing phases are 0.93389, 0.9201, and 0.95441, with an comprehensive coefficient of determination (R2) of 0.93407. These metrics serve as indicators of the model's predictive capabilities and validation performance. Furthermore, the predictive accuracy is quantified by evaluating the average error of the test dataset's predictions, resulting in a value of 93.88%. This level of accuracy effectively fulfills the demands of CO concentration prediction, thus aligning with the initial expectations and achieving the intended outcomes.

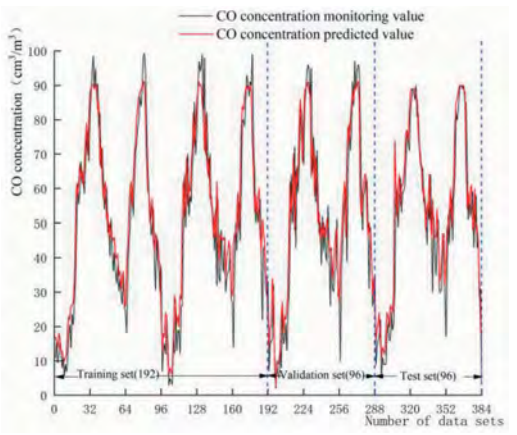

Figure 4. Simulation results of CO concentration prediction model based on NARX neural network.

3.4 *Simulation and analysis of fuzzy control of tunnel ventilation*

In accordance with Section 2.2, Table 1 outlines the fuzzy linguistic terms associated with the input and output variables, along with corresponding ranges of linguistic values.

Table 2 established the fuzzy control rules for the tunnel ventilation system using Equation (4). These rules form the foundation of the fuzzy logic-based control strategy, guiding the system's response to varying conditions and ensuring efficient tunnel ventilation and air quality management.

In order to provide parameters for subsequent calculations of tunnel ventilation energy consumption, simulations were conducted separately for two approaches: the proposed tunnel ventilation fuzzy control method that combines NAR dynamic neural network predictions and the traditional tunnel ventilation fuzzy control method. These simulations were carried out using the validation and test datasets to obtain the number of operating fans and fan speeds.

For the proposed method, the fuzzy control model inputs are based on the CO concentration predictions and their change rate obtained from the NARX CO prediction model in Section 3.3. In contrast, the traditional tunnel ventilation fuzzy control method uses actual CO concentration measurements and their rate of change as inputs.

The simulation results from both approaches provide the essential information regarding the required number of operating fans and corresponding fan speeds to achieve the desired level of ventilation control. These results are visually depicted in Figure 5.

It is evident that the proposed method demonstrates notable advantages in the peak of CO concentration levels. During peak CO concentration periods, the algorithm effectively reduces the number of operating fans while maintaining a consistent fan speed. This achievement stems from the integration of NAR dynamic neural network-based predictions for traffic flow and CO levels. By effectively forecasting these variables, the approach enables advanced perception of the tunnel environment, facilitating intelligent optimization of fan count and speed.

3.5 *Calculation and analysis of fan energy consumption*

In this section, we delve into the calculation and analysis of fan energy consumption within the context of tunnel ventilation. The primary objective is to evaluate and compare the energy efficiency of the proposed NARX combined fuzzy control approach with the traditional fuzzy control method.

Taking into consideration the simulation outcomes derived from Section 3.4, This study employ the relevant equations outlined in Section 2.4 to compute the energy consumption associated with fan operation for both the proposed NARX combined fuzzy control approach and the traditional fuzzy control method.The calculated energy consumption values are then visually presented in Figure 6.

Table 1. Range of fuzzy linguistic variables corresponding to Input and Output variables.

	input variable		output variable	
Variable word set	CO concentration e_{CO}(cm^3/m^3)	CO concentration change rateΔe_{CO}	Number of opreating fan	Fan Speed (r/min)
NB	(0, 25)	(-200, -100)	(0,1)	(0,725)
NM	(12.5, 37.5)	(-150, -50)	(1,2)	(363, 1088)
NS	(25, 50)	(-100, 0)	(2,3)	(725, 1450)
ZO	(37.5, 62.5)	(-50, 50)	(3,4)	(1088,1813)
PS	(50, 75)	(0, 100)	(3,4)	(1450, 2175)
PM	(62.5, 87.5)	(50, 150)	(4,5)	(1813, 2538)
PB	(75, 100)	(100, 200)	(5,6)	(2175, 2900)

Table 2. Fuzzy control rules for the number of opening fans and the fan speed for tunnel ventilation.

		Change rate of CO concentration Δe_{CO}						
rules		NB	NM	NS	ZO	PS	PM	PB
CO concentration e_{CO}	NB	NB/NB	NB/NM	NB/NS	NB/ZO	NM/PS	NS/PM	ZO/PM
	NM	NM/NB	NM/NM	NM/NS	NM/ZO	NS/PS	ZO/PM	PS/PM
	NS	NS/NB	NS/NM	NS/NS	NS/ZO	ZO/PS	PS/PM	PM/PB
	ZO	Z0/NB	ZO/NM	ZO/NS	ZO/ZO	PS/PS	PM/PM	PB/PB
	PS	PS/NM	PS/NS	PS/ZO	PS/PS	PM/PM	PB/PB	PB/PB
	PM	PM/NS	PM/ZO	PM/PS	PM/PM	PB/PB	PB/PB	PB/PB
	PB	PM/ZO	PM/PS	PB/PM	PB/PB	PB/PB	PB/PB	PB/PB

Through Figure 6, we can discern the energy consumption differences between the proposed approach and the traditional method. This graphical representation serves as a powerful tool for conveying the efficiency advantages of the proposed method in terms of energy conservation and sustainability in tunnel ventilation operations.

Taking into account the continuous operation of the tunnel ventilation system, we calculate the cumulative energy consumption for both the proposed NARX combined fuzzy control method and the traditional fuzzy control method. The total energy consumption under the NARX combined fuzzy control approach $w_T$is calculated to be 3441 kWh, while the total energy consumption under the traditional fuzzy control algorithm Q_T is calculated to be 4020 kWh.

Applying Equation (13), the Energy-efficient efficiency is computed 14.4%, indicating 14.4% reduction in energy consumption achieved through the implementation of the proposed approach compared to the traditional fuzzy control algorithm. This substantial energy consumption reduction underscores the potential of the proposed NARX combined fuzzy control method to significantly enhance the energy efficiency of tunnel ventilation systems, thereby contributing to more sustainable and environmentally conscious operational practices.

By conducting a comprehensive analysis of fan energy consumption, we gain insights into how the proposed NARX combined fuzzy control approach optimizes energy usage in comparison to the traditional method. This analysis contributes to a broader understanding of the practical benefits of implementing advanced control strategies in tunnel ventilation systems, ultimately leading to enhanced energy savings and more sustainable operational practices.

4 DISCUSSION

(1) When employing NAR (Nonlinear AutoRegressive) neural networks and NARX (Nonlinear AutoRegressive with eXogenous input) neural networks for prediction, the rational configuration of parameters constitutes a critical aspect in ensuring prediction accuracy. The characteristics of hidden layer nodes indicate that deeper hidden layers theoretically enable neural networks to better fit functions, often resulting in improved predictive performance. However, excessively deep layers may lead to overfitting issues and heightened training complexity, impeding model convergence. When dealing with non-linear time series data with dual inputs, NARX neural networks necessitate a greater number of hidden layer nodes and delay steps, rendering them more intricate compared to NAR networks. Therefore, within this study, multiple calculations were conducted for both NAR and NARX networks with hidden

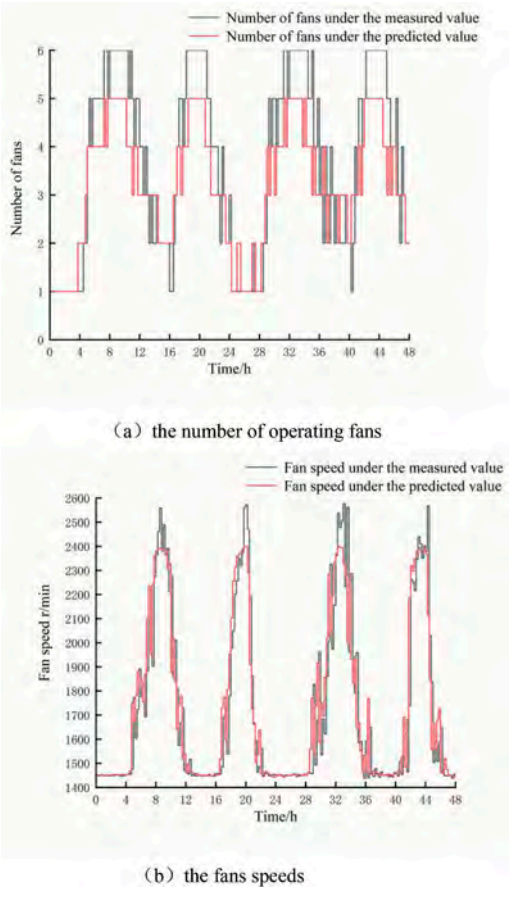

Figure 5. Comparison of the proposed NARX combined fuzzy control and traditional fuzzy control.

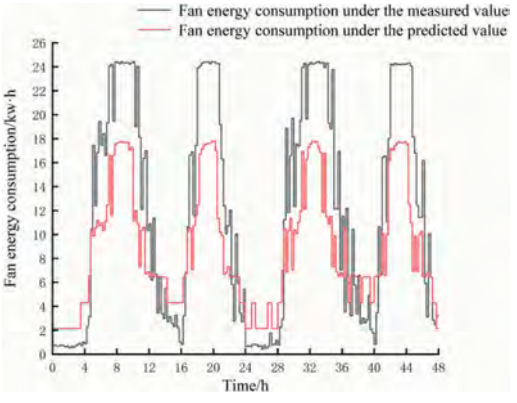

Figure 6. Fan energy consumption Comparison of the proposed approach and traditional fuzzy control.

layer quantities ranging from 5 to 15, to ascertain optimal parameter settings. Specifically, for the NAR traffic flow prediction model, a network with 8 hidden layer nodes and a delay order of 1:6 was selected, while for the NARX CO concentration prediction model, a network with 15 hidden layer nodes and a delay order of 1:8 was chosen. These parameter configurations yield favorable predictive accuracy.

(2) The CO concentration within the tunnel is directly proportional to the traffic flow. The fuzzy controller operates by adjusting the number of working fan units and their rotational speed based on the CO concentration. Conversely, fluctuations in CO concentration correlate positively with the number of fan units and their rotational speed. By incorporating the predicted CO concentration values and their rate of change as inputs to the fuzzy controller, adjustments to the number of fan units and speed are made proactively, prior to significant fluctuations in CO concentration. This proactive adjustment aims to anticipate imminent spikes or drops in CO concentration, thus effectively mitigating abrupt changes in fan operation and minimizing abrupt transitions in the fan's opening and closing.

(3) By comparing energy consumption when incorporating CO concentration predictions and rate of change as fuzzy control inputs, a 14.4% reduction in energy consumption is achieved. The fan counts and speeds demonstrate proactive adjustments before sharp CO concentration fluctuations, resulting in noticeable energy savings during peak and fluctuating CO concentration periods. The dynamic control strategy's benefits are prominently reflected in energy savings.

(4) The current study focuses on a lengthy tunnel scenario. Further verification of the model's responsiveness is required in longer tunnels with more fan units and complex traffic flow conditions.

5 CONCLUSIONS

In this study, a comprehensive method is explored and proposed. The NAR model is used to predict the traffic flow, and the NARX model is used to predict the CO concentration by combining the predicted value of traffic flow and the measured value of CO, and then the fuzzy controller is applied to realize the dynamic and accurate control of the tunnel ventilation system to achieve the goal of energy saving. Through the analysis of actual data and experimental verification, the following conclusions are drawn:

(1) NAR model shows high accuracy and prediction performance in traffic flow prediction. The model can effectively capture the historical pattern and trend of traffic flow, and provide a reliable input for the subsequent prediction of CO concentration; The NARX model combines the predicted value of traffic flow with the

measured value of CO, and predicts the CO concentration and its changing trend successfully. This provides key information for the intelligent control of the tunnel ventilation system, enabling the system to adjust in real time according to the predicted results.

(2) Through the introduction of fuzzy controller, this study realize the dynamic accurate control of tunnel ventilation system. The fuzzy controller intelligently adjusts the opening number and speed of the fan in advance based on the predicted CO concentration and its variation, thus realizing the predictability of the ventilation effect and the optimization of the air supply volume. This method can not only effectively reduce the accumulation of CO concentration, but also significantly reduce energy consumption, providing a feasible solution for tunnel ventilation management.

(3) This study demonstrated an integrated prediction and control method, which realized the intelligent regulation of tunnel ventilation system and achieved the goal of energy saving. This method not only improved the efficiency of ventilation, but also made a positive contribution to the sustainable development of urban transport infrastructure. Future research can further optimize the model and control strategy to adapt to the needs of different situations and environments, providing more beneficial innovations in the field of intelligent traffic management.

ACKNOWLEDGMENTS

This research was funded by the Traffic Research Project of the Department of Transport of Shaanxi Province (Grant Nos. 18-33X and 21-04K).

REFERENCES

Ministry of Transport, 2022. 2022 Transport Industry Development Statistical Bulletin [N]. Transport Finance and Accounting. China.

Ministry of Transport, 2021. 2021 Transport Industry Development Statistical Bulletin [N]. Transport Finance and Accounting, China.

Zhang X. S., Jin, T., Lin, D., 2016. Research on Multi-parameter fuzzy Control of Expressway tunnel ventilation System [J]. *Journal of Chongqing Jiaotong University* (Natural Science Edition), 35(4): 20–24.

Yu F. S., Meng X. L., Cui L. Z., 2017. Research on tunnel traffic risk control Algorithm based on Fuzzy PID Iterative Learning [J]. *Electronic Measurement Technology*, 40(4): 5–8.

Li Z..P., 2017. Research on risk control system of Maanshan Long Expressway tunnel [J]. *Chinese Journal of Underground Space and Engineering*, 13(S1): 400–403.

Chu B., Park J., Hong D. 2010. Tunnel Ventilation Controller Design Using an RLS-based Natural Actor-Critic Algorithm [J]. *International Journal of Precision Engineering and Manufacturing*, 11(6).

Mirhedayatian M., Jelodar M. J., Adnani S., et al, 2013. New Approach for Prioritization in Fuzzy AHP with an Application For Selecting The Best Tunnel Ventilation System [J]. *International journal of advanced manufacturing technology*, 68(9): 2589–2599.

Zhang X. Y., 2017. Research on ventilation energy-efficient System of highway tunnel under PLC [J]. *Science and Technology Wind*, 261.

Wang, J., Liu X.N., Meng Y.P., 2018. Intelligent control system of tunnel ventilation based on Big Data [J]. *Science and Technology Wind*, 30–31.

Jiang X.P., Mao Y S.Y., Xie Z.Y., 2018. Research on operation optimization of complex tunnel ventilation system in extra-long city[J]. *Tunnel Construction*, 38 (9): 1471–1479.

Xing Y.L., Zeng S.L., 2018. Research and implementation of tunnel intelligent monitoring system[J]. *Electromechanical Information*, pp. 54–55.

Wu,K., Yang Q. M., Kang, C., et al, 2017. Adaptive Critic Design Based Control of Tunnel Ventilation System with Variable Jet Speed [J]. *Journal of Signal Processing Systems*, 86: 2–3.

Wan J.G., Peng J.S., 2019. Discussion on optimal design of ventilation and energy saving in highway tunnel operation[J]. *Modern Tunnel Technology*, 56(S2): 471–477.

Qian, C., Deng M.S., Li H.X., et al, 2021. Design and implementation of highway tunnel environment perception system[J]. *Tunnel Construction*, 41(9): 1502–1508.

Lv Y.H., Wang, Q., 2013. Research on prediction of CO concentration in tunnel based on neural network information fusion[J]. *Information Technology*, 37(9): 128–131.

Ren, T., Liao, Y., Chen J., et al., 2022. Adaptive control ventilation system for tunnel construction based on RBF neural network[J]. *Chinese Journal of Underground Space and Engineering*, 18(S1): 404–411.

Wang Z.Y., Meng X.L., 2018. Construction tunnel ventilation control algorithm based on MIV feature screening and BP neural network[J]. *Software Guide*, 17(6): 100-101+105.

Li, X., Chen X.L., Li Y.Z.,et al., 2022. Research on intelligent control model of highway tunnel ventilation under fire conditions[J]. *Highway Traffic Technology.* 38(6): 156–162.

Zhu X.Y., Li D.L., Tian Y.Q., et.al, 2020. Short-term intersection traffic prediction based on NARX neural network[J]. *Journal of Shandong University of Technology*, 34(6): 65–69.

Zhao L.J.,Xia, Yen., Yi L.X. ,et.al, 2015. Daily flow prediction of karst underground river based on NARX model[J]. *Water Resources and Power*, 33(5): 19-21-25.

Yang Q.K., Wang X.H., 2018. Design of traffic control system based on multi-intersection prediction and real-time timing cooperation[J]. *Computer Measurement and Control*,26(12): 93–96.

Tunnelling for a Better Life – Yan, Celestino, Thewes & Eberhardt (Eds)
© 2024 The Author(s), ISBN 978-1-032-80042-4
Open Access: www.taylorfrancis.com, CC BY-NC-ND 4.0 license

Intelligent surrounding rock classification and mechanical parameters analysis method based on drilling parameters of tunnels

Mingnian Wang, Siguang Zhao*, Wenhao Yi & Xin Peng
School of Civil Engineering, Southwest Jiaotong University
Key Laboratory of Transportation Tunnel Engineering of Ministry of Education, Southwest Jiaotong University

ABSTRACT: Drilling parameters such as excavation speed and pressures are automatically recorded by the drilling jumbo during the drilling process in a tunnel face constructed by blasting and drilling method. These parameters are characterised by automatic data collection, direct interaction with the surrounding rock, high data density within the surrounding rock, non-interference with tunnel construction, and low requirements for the tunnel environment. As a result, leveraging drilling parameters for intelligent identification of surrounding rock quality was of significant potential. To set up the intelligent surrounding rock classification and analysis of mechanical parameters, an extensive dataset comprising 5220 samples was built encompassing drilling parameters, surrounding rock grades, and mechanical parameters from tunnel engineering projects such as Zhengzhou-Wanzhou high speed railway, Yichang-Xingshan high speed railway. Firstly, a standardized data cleaning and features mining methodology was established, considering the multi-scale distribution characteristics of drilling parameters in a tunnel face. Then, the typical machine learning algorithm was employed to construct an for intelligent classification model of surrounding rock. Subsequently, the theoretical models were developed for mechanical parameters such as surrounding rock elastic modulus, uniaxial saturated compressive strength using drilling parameters with the use of uncovering the coupling mechanism of "impact-rotation" in rock breaking by the drilling jumbo. The result demonstrated that the accuracy of intelligent surrounding rock classification in grade II, III, IV, and V could exceed 90%. In addition, the identification error of uniaxial compressive strength and elastic modulus of surrounding rock was also within the acceptable range, with better performance in harder rock.

Keywords: Tunnel, Drilling parameters, surrounding rock, classification, Analysis of mechanical parameters, Machine learning, "Impact-rotation" rock breaking.

1 INTRODUCTION

Before a tunnelling project starts, a site investigation is performed to determine the in situ surrounding rock conditions. The information on the surrounding rock quality evaluation is then used to determine tunnel design and construction schemes (Zhou et al., 2014). Generally speaking, surrounding rock quality evaluation includes surrounding rock classification and mechanical parameter analysis. The popular surrounding rock classification systems include the Q method (Barton et al., 1974), the surrounding rock rating (RMR) method (Bieniawski, 1979), the Geological Strength Index (GSI) method and the basic quality index (BQ) method (Lin, 1999). In the construction of railway and highway tunnels in China, the surrounding rock is classified into grades I–VI according to its quality (from high to low, respectively). In the stability analysis and support design of tunnel surrounding rock based on elastic deformation assumption, uniaxial compressive strength and elastic modulus are the most commonly used surrounding rock mechanical parameters.

At present, the surrounding rock classification and rock parameter analysis methods used in the field are mostly the combination of qualitative and quantitative tests and manual experience. Since these methods often have limited availability of information (surface mapping, geophysical profiles, limited bore holes, etc.), the surrounding rock classification may be inaccurate. To solve this dilemma, a more thorough and detailed investigation could be performed, but reaching significantly higher resolutions is expensive and time-consuming. In contrast,

*Corresponding author: mt_guang@163.com

DOI: 10.1201/9781003495505-414

measurement while drilling (MWD) (Schunnesson, 1996) technology has natural advantages in terms of obtaining surrounding rock quality information during borehole drilling. Under MWD, enormous amounts of quantitative data can be obtained from most of the area of the tunnel face quickly and automatically, with no requirements on the environment of the tunnel and without interfering with the construction process (Rai et al., 2016). The MWD technology documents the response of the drilling parameters (e.g., penetration rate, operational pressures, rotation speed, flushing flow) while drilling (Schunnesson, 1996), thus providing an objective and reliable method for assessing surrounding rock conditions ahead of the tunnel face (Schunnesson, 1996; Schunnesson, 1998; Van Eldert et al., 2020).

MWD is a useful technique for gathering data with which to characterize the mechanical of the surrounding rock. A large number of studies have shown that multiple drilling parameters were effective in estimating some mechanical properties of rock, such as uniaxial compressive strength (Kalantari et al., 2018; Mostofi et al., 2011; Rodgers et al., 2017), rock texture and hardness (Bameri et al., 2021), rock shear strength (Kalantari et al., 2018; Rodgers et al., 2017; Rodgers et al., 2019), and internal friction angle (Kalantari et al., 2018). Besides, several studies have shown that the drilling parameters can be used to estimate the characteristics of the surrounding rock, such as joints or fractures (Manzoor et al., 2020; Rajib et al., 2017; Schunnesson, 1998), rock interfaces (Sugawara et al., 2003; Tan et al., 2007), rock quality designation (RQD) (He et al., 2020; He et al., 2021; Schunnesson, 1996) and hydraulic conductivity of surrounding rock (He and Li, 2022; He et al., 2022). On these basics, some good results have been achieved in many existing surrounding rock classification systems, such as the surrounding rock rating (RMR) method (Galende-Hernández et al., 2018), the Q method (Van Eldert et al., 2021; Van Eldert et al., 2020), and the BQ method (Zhao et al., 2022).

In order to further improve the level of geological analysis of surrounding rock based on drilling parameters, in this paper, we extensively collected massive drilling parameter data by full using of the industrial advantages of large-scale mechanized construction in China. On this basis, artificial intelligence and theoretical analysis methods were used to establish the intelligent classification model and the mechanical parameters analytical formula of surrounding rock, so as to realize the intelligent, rapid and accurate analysis of the surrounding rock grades and surrounding rock mechanical parameters on site.

2 DATA SOURCE

In this study, an sample include the drilling parameters, the surrounding rock grades and the mechanical parameters of surrounding rock in tunnel face. The samples of this study were collected from 12 tunnels of the Zhengzhou-Wanzhou railway project and the Yichang-Xingshan railway project in Hubei province, China.

2.1 *Drilling parameters acquisition*

The drilling parameters include four categories: (i) penetration velocity (V_p, m/min), the rate at which the drill bit penetrates the rock mass; (ii) hammer pressure (P_h, bar), a measure of the impact pressure of the bit against the rock mass; (iii) rotation pressure (P_r, bar), defined as the pressure of the bit against the rock necessary to maintain the required rotation; and (iv) feed pressure (P_f, bar), a measure of the hydraulic pressure inside the cylinders necessary to keep the bit in contact with the bottom of the hole. The drilling parameter data were collected automatically by an intelligent drilling jumbo at equal depth intervals of 2 cm. (Figure 1) (Zhao et al., 2022).

Figure 1. Automatic acquisition for the drilling parameters.

2.2 *Surrounding rock grades determination*

There are six classes of surrounding rock, grades I-VI, where grade I represents the best quality of surrounding rock, and grade VI represents the worst. And the information for the surrounding rock grades was collected manually by the geological sketch method according to the degree of hardness, integrity, groundwater state, crustal stress state and major weak structural surface (Figure 2).

2.3 *Surrounding rock mechanical parameters test*

The analysis object of uniaxial compressive strength and elastic modulus of surrounding rock of tunnel face surrounding rock based on drilling parameters described in this paper is the surrounding rock of face surrounding rock, which is the mechanical parameter after the impact of structural plane cutting, which is commonly expressed by the rock integrity coefficient.

Figure 2. Manual acquisition for the surrounding rock grades.

However, the field mechanical parameter test object is mostly rock, so it is necessary to test the integrity coefficient of surrounding rock. The modification of surrounding rock integrity coefficient to rock mechanics parameters is referred to Equation (1)- Equation (2). The integrity coefficient of surrounding rock is realized by means of wave velocity measurement, and the calculation is referred to Equation (3).

$$R_b = K_v R_c \tag{1}$$

$$E = K_v E_c \tag{2}$$

$$K_v = (V_{pm}/V_{pr})^2 \tag{3}$$

Where, R_b is uniaxial saturated compressive strength of surrounding rock; R_c is uniaxial saturated compressive strength of rock; E_c is elastic modulus of rock; E is elastic modulus of surrounding rock; K_v is integrity index of surrounding rock V_{pm} is elastic longitudinal wave velocity of rock; V_{pr} is elastic longitudinal wave velocity of surrounding rock.

Based on this, the field test of surrounding rock mechanical parameters is carried out in the typical section. It includes uniaxial compressive strength and elastic modulus of rock (Figure 3), elastic wave velocity of rock (Figure 4) and surrounding rock (Figure 5).

2.4 *Sample size statistic*

As shown in Figure 6, there were 5220 samples for intelligent surrounding rock classification were collected These samples cover four surrounding rock grades (II, III, IV, and V) and nine main lithologies (dolomite, sandstone, limestone, shale, and mudstone).

And among these 5220 cycles, we selected 15 typical cycles for rock mechanics parameters testing, including five types of rocks, namely granodiorite, dolomite, limestone, sandstone and mudstone, which represent different degrees of rock hardness.

Figure 3. The test of uniaxial compressive strength and elastic modulus of rock.

Figure 4. The test of the elastic wave velocity of rock.

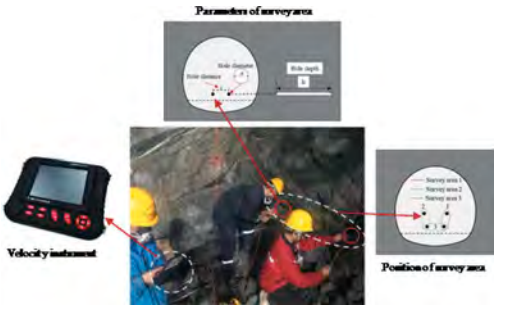

Figure 5. The test of the elastic wave velocity of surrounding rock .

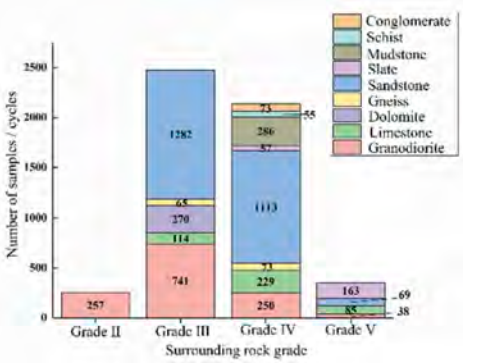

Figure 6. The test of the elastic wave velocity of surrounding rock.

3 INTELLIGENT SURROUNDING ROCK CLASSIFICATION

3.1 *Data preprocessing*

3.1.1 *Data cleaning*

The MWD data were collected continuously during drilling. These machine data normally contain some faulty, biased, or unrealistic values due to the nature of the drilling process, sensor errors, or machine safety systems (anti-jamming). These erroneous data points must be removed prior to assessment of the surrounding rock conditions (Van Eldert et al., 2020).

Through investigation and analysis, each drilling parameter may include two kinds of outliers along the depth of the borehole.

- At the beginning of the borehole (about 0.3–0.5 m), to ensure a straight hole through this disturbed surrounding rock, collaring is normally performed with great care (Manzoor et al., 2020), i.e., lower pressure (P_f and P_r) and speed (V_p), before these parameters are gradually increased to their normal levels (Figure 7, marked with 'Type I'). These drilling parameters recorded at the start of the borehole are not related to the characteristics of the surrounding rock. Therefore, these recorded samples were removed from the input data (Manzoor et al., 2020). Specifically, the drilling parameters from the first 0.5 m of the borehole were deleted in this study.
- Sensor errors or machine safety systems (anti-jamming) cause the drilling parameters to occasionally appear too large or too small (Figure 7, marked with 'Type II'). Fortunately, in high-resolution datasets, more extensive filtering can be applied without losing the general pattern of the data, as the data quantity minimizes the effect of removing abnormal data points. Therefore, the highest and lowest values can be removed by some conservative statistical approach (Van Eldert et al., 2020).

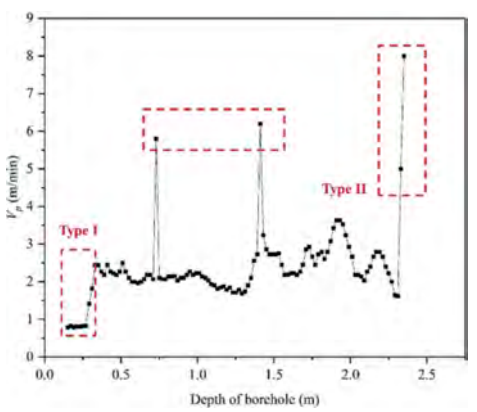

Figure 7. Scatter diagrams of typical borehole drilling parameters.

In this study, the boxplot method was used to determine the criteria of outliers (Dawson, 2017). The box diagram method determines the non-outlier interval according to the quartiles, as defined by Equation (4).

$$[Q_1 - 1.5IQR, Q_3 + 1.5IQR] \tag{4}$$

Where, Q_1 is the first quartile, Q_3 is the third quartile, and IQR is equal to Q_3 minus Q_1.

In summary, the non-outlier intervals for sample data cleaning were shown in Table 1.

Table 1. The non-outlier intervals for sample data cleaning.

Drilling parameters	V_p (m/min)	P_h (bar)	P_f (bar)	P_r (bar)
Non-outlier interval	[0.00, 5.50]	[64.50, 196.50]	[4.50, 112.50]	[17.00, 153.00]

3.1.2 *Feature mining*

In machine learning, feature construction is the extraction of useful features from raw data, which can help the model to discover patterns and laws hidden behind the data and enable the model to make correct predictions

Generally, 200-300 boreholes are arranged at tunnel face for each full-section excavation cycle, and the lengths of the boreholes are about 2-5 m. One set of drilling parameters is collected every 2 cm for each borehole in the longitudinal direction, and about 100-250 sets of drilling parameters are collected from each borehole. A total of approximately 20,000-50,000 sets of drilling parameters are collected from each excavation cycle. The high density and quantity significantly differentiate the drilling parameters collected by the tunnel face boreholes from those collected by the mining drilling equipment and oil drilling equipment. The drilling jumbo records 20,000 to 50,000 data points like a 'CT scanner' in an excavation cycle. Statistical features expansion is the process of statistically analyzing all the drilling parameters at tunnel face. Common statistical features are mean value, quartiles, standard deviation and coefficient of variation. The mean value is the sum of all the data in a dataset divided by the number of data, and is calculated as Equation (5).

$$u_c = \frac{\sum_{i=1}^{n_c} c_{c,i}}{n} \tag{5}$$

Where, u_c is the mean value of feature number c at taget tunnel face; $c_{c,i}$ is eigenvalue of feature number c at data point i; n is the number of data points for the feature number c at target tunnel face.

Quartiles are values arranged from smallest to largest, and are divided into four equal parts at the three division points. Quartiles include the first quartile, second quartile and third quartile, and are denoted by $Q_{1,c}$, $Q_{2,c}$, and $Q_{3,c}$. The standard deviation is an index that describes the degree of dispersion of each observation value from the mean value. The standard deviation is calculated as Equation (6).

$$\sigma_c = \sqrt{\frac{\sum_{i=1}^{n} (c_{c,i} - u_c)}{n}} \tag{6}$$

Where, σ_c is the standard deviation of feature number c at target tunnel face.

The coefficient of variation is calculated as Equation (7).

$$c_{v,c} = \frac{\sigma_c}{u_c} \tag{7}$$

Where, $c_{v,c}$ is the coefficient of variation of feature number c at target tunnel face.

With Equation (5) - (7), the six statistical features of the rock drilling parameters (u_c, $Q_{1,c}$, $Q_{2,c}$,$Q_{3,c}$, σ_c, $c_{v,c}$) can be determined, and the drilling parameters of any tunnel face have 24 features.

3.2 *Machine learning model*

The surrounding rock classification model was constructed by Extra Trees (ET) algorithm, which solves the classification problem by first generating multiple random cut-off thresholds for each feature, and then selecting the best threshold for classification (Figure 8).

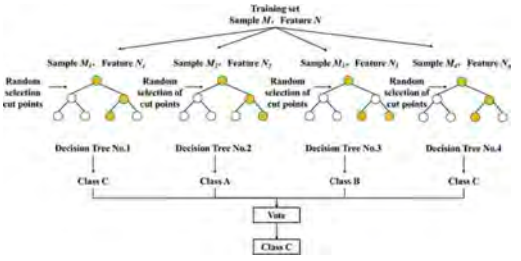

Figure 8. Schematic diagram of ET algorithm.

The key steps include dataset partitioning and oversampling, feature normalization.

3.2.1 *Dataset partitioning and oversampling*

The proportion of training set and prediction set should take into account the needs of model training and the effectiveness of model evaluation. In order to facilitate model performance evaluation, it is considered to set the same number of samples of each surrounding rock level in prediction set. Therefore, according to the distribution of each level of surrounding rock in the samples, the grade II surrounding rock with the least number of samples is mainly considered, and the number of samples of each level of surrounding rock in prediction set is determined to be 50 (accounting for about 20% of the total number of samples in the grade II set). The distribution of samples after splitting is shown in Table 2.

Table 2. Details on the dataset division of models.

Grade Dataset	II	III	IV	V	Total
Training set	207	2422	2086	305	5020
Prediction set	50	50	50	50	200
Total	257	2472	2136	355	200

Referring to machine learning classification, when the difference in the number of samples of all the classes is too large, the training model will pay too much attention to the sample characteristics with a greater proportion, so the classification effect of the samples with a smaller proportion is not ideal. This is called the problem of sample imbalance. These data sets cover four class of surrounding rock, and each class contains 207, 2422, 2086 and 305 samples belonging to the imbalance sample set. The sample imbalance problem is usually solved by three methods of the undersampling, oversampling and sample weight adjustment (Zhao et al., 2022). In this study, the sample imbalance in the surrounding rock classification set is not significant; however, to improve the generalization ability of the model, the ADASYN method is used for feature oversampling (Pan et al., 2022). The oversampling criterion is that the number of samples in each class is exactly equal. The sample sizes of the training set before and after oversampling are given in Table 3.

Table 3. Sample sizes of the training set before and after oversampling.

Grade Training dataset	II	III	IV	V	Total
Before	207	2422	2086	305	5020
After	2422	2422	2422	2422	9688

3.2.2 *Feature normalization*

Considering the influence of the absolute values of the drilling parameter features on the model parameters, the dataset is processed using the feature

normalization. Feature standardization is the conversion of feature data to a distribution with a mean value of 0 and a standard deviation of 1, the feature normalization method utilized in this study is expressed as Equation (8).

$$x' = \frac{x - \mu}{\sigma} \tag{8}$$

Where, x is any set of feature data; x' is any set of normalized feature data; u is the mean of the training set feature data; σ is the standard deviation of the training set feature data.

3.2.3 *Prediction result*

In the final evaluation of the model performance, the precision, recall, and accuracy were adopted for a comprehensive evaluation. They were calculated according to the confusion matrix.

The confusion matrix of intelligent classification model in prediction set was shown in Figure 9. And the precision, recall, and accuracy were shown in Table 4.

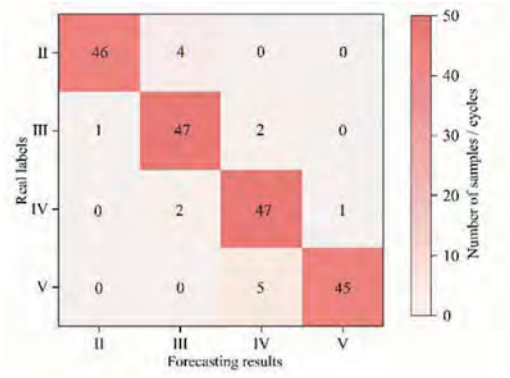

Figure 9. The confusion matrix of intelligent classification model.

Table 4. Model performance in prediction set.

Performance index	Rock Grade	Performance
Precision	II	97.9%
	III	88.7%
	IV	87.0%
	V	97.8%
Recall	II	92.0%
	III	94.0%
	IV	94.0%
	V	90.0%
Accuracy	-	92.5%

As shown in the Table 4, the precision, recall were above 90%, except for the precisions of grade III and grade IV surrounding rock. In particular, the precision of grade II was greater than 95%. And the final accuracy was 92.5%. Thus, the intelligent classification model of surrounding rock based on drilling parameters has high practical value.

4 MECHANICAL PARAMETERS ANALYSIS

4.1 *Analysis principles and methods*

According to the laws of thermodynamics, energy is the essential feature of the physical process of matter, and the destruction of matter is a state instability phenomenon driven by energy.

It can be seen from the drilling process of the drilling rig that the drilling system does work to the surrounding rock through the drill. When the output energy of the mechanical work reaches the energy storage limit of the surrounding rock, the surrounding rock releases energy in the form of elastic deformation, crack expansion, and cuttings bursting, forming holes and reaching a new stable equilibrium state. The total energy output of the drilling system can be called mechanical specific energy under the condition of breaking rock per unit volume per unit time. Existing studies have shown that under external load, the input mechanical energy and heat energy are mainly used for the elastic deformation of surrounding rock, that is, the input energy of external load is mainly converted into the elastic deformation energy of surrounding rock.

At the same time, the mechanical specific energy can be expressed by drilling parameters, and the elastic deformation energy of surrounding rock is also related to the mechanical parameters of surrounding rock.

Therefore, the mechanical parameters of surrounding rock can be analyzed by drilling parameters according to the following Equation (9)-Equation (11).

$$E_{\text{mse}} = f_1(V_{\text{p}}, P_{\text{h}}, P_{\text{f}}, P_{\text{r}}) \tag{9}$$

$$U^e = f_2(E, R_b) \tag{10}$$

$$E_{\text{mse}} k_e = U^e \tag{11}$$

Where, E_{mse} is mechanical specific energy; U^e is elastic deformation energy of surrounding rock; E is elastic modulus of surrounding rock; R_{b} is uniaxial saturated compressive strength of surrounding rock; $f_1(\cdot)$ is the functional relationship between mechanical specific energy and four drilling parameters; $f_2(\cdot)$ is the functional relationship between elastic deformation energy and elastic modulus, uniaxial compressive strength.

The key is the calculation of energy indicators, containing mechanical specific energy during drilling and elastic deformation energy of surrounding rock.

4.2 *Energy indicators*

4.2.1 *Mechanical specific energy during drilling*

According to the principle of mechanical motion of drill jumbo, E_{mse} is the mechanical work done by drilling jumbo per unit volume of rock, and is the sum of hammer specific energy, feed specific energy and rotation specific energy. The drilling specific energy, hammer specific energy, feed specific energy, rotation specific energy calculation method were as following Equation (12)- Equation (18).

$$E_{mse} = E_{fse} + E_{hse} + E_{rse} \tag{12}$$

$$E_{fse} = \frac{E_f}{V_p \frac{\pi D^2}{4}} \tag{13}$$

$$E_{hse} = \frac{E_h}{V_p \frac{\pi D^2}{4}} \tag{14}$$

$$E_{rse} = \frac{E_r}{V_p \frac{\pi D^2}{4}} \tag{15}$$

$$E_f = \frac{\pi D_f^2 P_f V_p}{8} \tag{16}$$

$$E_h = \frac{P_h \pi D_{hB}^3 S_h}{8} \sqrt{\frac{\pi P_h S_h (D_{hA}^2 - D_{hB}^2)}{2 m_h (2D_{hA}^2 - D_{hB}^2)}} \tag{17}$$

$$E_r = P_r V_r q_r i_r \tag{18}$$

Where, E_{hse}, E_{fse}, E_{rse} is hammer specific energy, feed specific energy and rotation specific energy respectively; E_h, E_f, E_r is the work done by the hammer mechanism, feed mechanism and rotation mechanism on the surrounding rock per unit time respectively; D, D_f, D_{hA}, D_{hB} is diameter of the drilling bit, feed piston, hammer piston rear end, hammer piston front end respectively; m_h is mass of hammer piston; S_h is hammer distance; i_r is reduction ratio;q_r is hydraulic motor displacement.

4.2.2 *Elastic deformation energy of surrounding rock*

The surrounding rock unit of a unit volume undergoes deformation under the action of external loading machinery. Assuming that there is no heat exchange between the process and the outside world, and all the output energy of the machinery is converted into the internal energy of the surrounding rock, the work done by the external loading machinery is converted into the dissipated energy of the surrounding rock and the elastic deformation energy of the surrounding rock. Therefore, the total energy generated by the external loading machinery is U. According to the first law of thermodynamics, Equation (19) can be obtained.

$$U = U^a + U^e \tag{19}$$

Where, U is the total specific energy generated by the external mechanical action; U^a is the dissipated specific energy of the surrounding rock; U^e is the elastic deformation specific energy of the surrounding rock.

Taking the typical stress-strain curve of the surrounding rock under pressure as an example, the dissipative energy of the surrounding rock is manifested in the form of surrounding rock loss and plastic deformation, and the elastic deformation energy of the surrounding rock is manifested in the form of surrounding rock elastic deformation. The relationship between elastic deformation energy and dissipative deformation energy per unit volume of surrounding rock is shown in Figure 10.

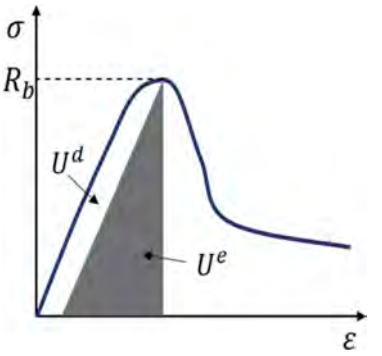

Figure 10. The relationship between elastic deformation energy and dissipated deformation energy of surrounding rock per unit volume.

In the process of impingement, propulsive and rotary rock breaking by all computerized three-arm drilling rig, the surrounding rock mainly suffers from compressive brittle failure, and the mechanical work is mainly converted into elastic deformation energy of surrounding rock. Therefore, the dissipated energy of surrounding rock in the process of mechanical work is ignored in this paper.

According to elastic mechanics, considering the average effect of surrounding rock along the principal stress direction (compression direction), the elastic deformation energy of surrounding rock per unit volume is calculated in Equation (20).

$$U^e = \frac{R_b^2}{2E} \tag{20}$$

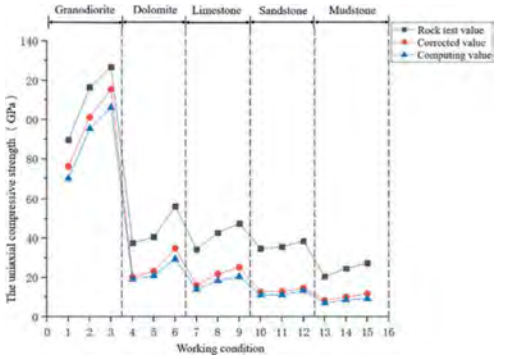

Figure 11. Uniaxial compressive strength testing results, corrected results, model computing results.

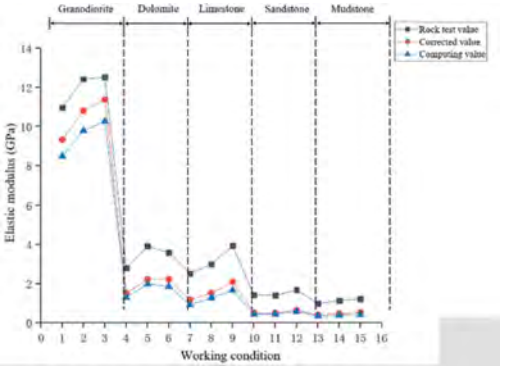

Figure 12. Elastic modulus testing results, corrected results, model computing results.

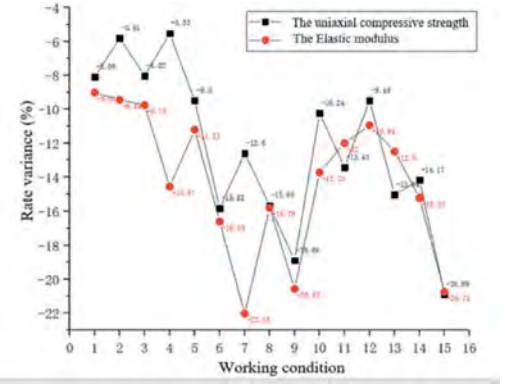

Figure 13. Difference rate between corrected and model computing results.

4.3 *Field demonstration result*

The uniaxial compressive strength and elastic modulus testing results, corrected results and model computing results of the surrounding rock of the tunnel face are shown in Figure11 and Figure 12. The difference rate between the corrected results and the model analysis results is shown in Figure 13.

As shown in Figure11 - Figure 13, compared with the theoretical analytical model and the test results of surrounding rock mechanical parameters, the difference rate of the analytical results of the uniaxial compressive strength of the surrounding rock on the tunnel face ranged from -5.52% to -20.89%, and the difference rate of the analytical results of the elastic modulus of surrounding rock on the tunnel face ranged from -9.01% to -22.03%. The analytical results of the model were all smaller than the test results of surrounding rock mechanical parameters, and the difference rates of the analytical results of uniaxial compressive strength were generally smaller than that of the analytical results of elastic modulus. The analytical difference rates of uniaxial compressive strength and elastic modulus of granodiorite with greater hardness were only -5.81%–8.08% and -9.01%–9.75% respectively within 10%.

They also showed that the analytical results of hard rock are more accurate than those of soft rock. The main reason is that the elastic deformation energy of hard rock is relatively high in the process of deformation and failure. In the failure process of soft rock, the elastic deformation energy and dissipative deformation energy are almost at the same level, but the dissipative energy increases rapidly when the failure is approaching, and the energy dissipation is the main process, so the calculation method of the dissipative energy of surrounding rock needs to be further considered.

5 CONCLUSIONS

Based on the massive drilling parameters from 5220 cycles, an intelligent classification model and mechanical parameters calculation formula were developed.

The conclusions of this study can be summarized as follows.

(1) The drilling parameters were feasible to achieve the classification of surrounding rock after data cleaning and feature mining. The proposed intelligent surrounding rock classification model by using ET algorithm exhibited a high performance. The precisions for each surrounding rock grade exceeded 85%, the recalls for each surrounding rock grade exceeded 90%, and the overall accuracy was 92.5%. Therefore, the intelligent model based on drilling parameters is feasible and reliable for intelligent surrounding rock classification.

(2) The relations between uniaxial compressive strength, elastic modulus and mechanical specific energy during drilling process was deduced, and an analytical model of uniaxial saturated compressive strength and elastic modulus of tunnel face surrounding rock was established based on drilling parameters. The field test showed that the difference rate of uniaxial compressive strength

analysis was -5.52%–20.89%, and the difference rate of elastic modulus analysis was -9.01%–22.03%. The analytical results of the model were all smaller than the test results of surrounding rock mechanical parameters. The analytical results of hard rock are more accurate than those of soft rock.

ACKNOWLEDGMENTS

The authors are grateful for the support from the National Natural Science Foundation of China (51878567, 51878568).

REFERENCES

Bameri, A., Cheraghi Seifabad, M., Hoseinie, S.H. 2021. "Laboratorial studies for the prediction of rock texture and hardness using vibration measurement while drilling". B.Eng.Geol.Environ. 80(11), 8311–8318.

Barton, N., Lien, R., Lunde, J. 1974. "Engineering classification of surrounding rockes for the design of tunnel support". Rock. Mech. 6(4), 189–236.

Bieniawski, Z.T., 1979. "The geomechanics classification in rock engineering applications, 4th ISURROUNDING ROCKM Congress". ISURROUNDING ROCKM, Mechanics, Montreux, pp. 41–48.

Dong, N., Zhao, L., Wu, C.H., Chang, J.F. 2020. "Inception v3 based cervical cell classification combined with artificially extracted features". Appl. Soft. Comput. 93 (2020), 106311.

Galende-Hernández, M., Menéndez, M., Fuente, M., Sainz-Palmero, G. 2018. "Monitor-While-Drilling-based estimation of surrounding rock rating with computational intelligence: The case of tunnel excavation front". Automat. Constr. 93(1), 325–338.

He, M., Li, N., Yao, X., Chen, Y. 2020. "A New Method for Prediction of Rock Quality Designation in Borehole Using Energy of Rotary Drilling". Rock. Mech. Rock. Eng. 53(7), 3383–3394.

He, M., Zhang, Z., Li, N. 2021. "Prediction of fracture frequency and RQD for the fractured surrounding rock using drilling logging data". B. Eng. Geol. Environ. 80(6), 4547–4557.

Kalantari, S., Hashemolhosseini, H., Baghbanan, A. 2018. "Estimating rock strength parameters using drilling data". Int. J. Rock. Mech. Min. 104(1), 45–52.

Lin, Y. 1999. "Study of BQ formula in national standard of qunatitative classfication for basic quality of surrounding rock". Chin. J. Geotech. Eng. 21(4), 102–106.

Manzoor, S., Liaghat, S., Gustafson, A., Johansson, D., Schunnesson, H. 2020. "Establishing relationships between structural data from close-range terrestrial digital photogrammetry and measurement while drilling data". Eng. Geol. 267(1), 105480.

Mostofi, M., Rasouli, V., Mawuli, E. 2011. "An estimation of rock strength using a drilling performance model: a case study in blacktip field", Australia. Rock. Mech. Rock. Eng. 44(3), 305.

Pan, X., Jia, R., Huang, J., Wang, H., 2022. "A resistance outlier sampling algorithm for imbalanced data prediction". Intell. Data. Anal. 26, 583–598.

Rai, P., Schunnesson, H., Lindqvist, P.-A., Kumar, U. 2016. "Measurement-while-drilling technique and its scope in design and prediction of rock blasting". Int. J. Min. Sci. Techno. 26(4), 711–719.

Rodgers, M., McVay, M., Horhota, D., Hernando, J. 2017. "Assessment of rock strength from measuring while drilling shafts in Florida limestone". Can. Geotech. J. 55 (8), 1154–1167.

Rodgers, M., McVay, M., Horhota, D., Sinnreich, J., Hernando, J. 2019. "Assessment of shear strength from measuring while drilling shafts in Florida limestone". Can. Geotech. J. 56(5), 662–674.

Schunnesson, H. 1996. "RQD predictions based on drill performance". Tunn. Undergrsp. Tech. 11(3), 345–351.

Schunnesson, H. 1998. "Rock characterisation using percussive drilling". Int. J. Rock. Mech. Min. 35(6), 711–725.

Van Eldert, J., Funehag, J., Saiang, D., Schunnesson, H. 2021. "Rock support prediction based on measurement while drilling technology". B. Eng. Geol. Environ. 80 (2), 1449–1465.

Van Eldert, J., Schunnesson, H., Johansson, D., Saiang, D. 2020. "Application of measurement while drilling technology to predict surrounding rock quality and rock support for tunnelling". Rock. Mech. Rock. Eng. 53(1), 1349–1358.

Zhao, S., Wang, M., Yi, W., Yang, D., Tong, J. 2022. "Intelligent Classification of Surrounding Rock of Tunnel Based on 10 Machine Learning Algorithms". Appl. Sci. 12(5), 2656.

Zhou, H., Zhang, C., Li, Z., Hu, D., Hou, J. 2014. "Analysis of mechanical behavior of soft rocks and stability control in deep tunnels".J. Rock. Mech. Geotech. 6(3), 219–226.

Tunnelling for a Better Life – Yan, Celestino, Thewes & Eberhardt (Eds)
© 2024 The Author(s), ISBN 978-1-032-80042-4
Open Access: www.taylorfrancis.com, CC BY-NC-ND 4.0 license

Investigation on surrounding rock quality prediction based on incomplete multi-source dataset and tree-augmented naive Bayesian network

Chen Wu* & Hongwei Huang
Key Laboratory of Geotechnical and Underground Engineering of Ministry of Education, Tongji University, Shanghai, China
Department of Geotechnical Engineering, Tongji University, Shanghai, China

HaiBo Tong
College of Electronic and Information Engineering, Tongji University, Shanghai, China

Mingliang Zhou
Key Laboratory of Geotechnical and Underground Engineering of Ministry of Education, Tongji University, Shanghai, China
Department of Geotechnical Engineering, Tongji University, Shanghai, China

Le Zhang
Broadvision Engineering Consultants, Kunming Yunnan, China

Yue Tong
Qingdao Conson Second Jiaozhou Bay Subsea Tunnel CO., LTD, Qindao, China

ABSTRACT: In this research endeavor, a novel and improved Swin Transformer (ST) model is employed to discern and segment disease features, such as cracks, weak interlayers, and leakage on rock tunnel faces. The outcomes of the conducted tests, utilizing a newly curated imageset, elucidate that the recognition and segmentation performance achieved by the improved ST model markedly surpasses those of conventional ST, Unet++ and Unet models. For the quantitative segmentation of rock features and geological sketches, an improved ST model serves as the foundation for establishing a multi-source Tunnel Face Feature (TFF) dataset. This dataset encompasses rock feature parameters, physical-mechanical parameters, and tunnel design parameter. Nevertheless, due to temporal and spatial constraints in procuring on-site information for rock tunnel faces, the simultaneous acquisition of complete parameters becomes a challenging endeavor. To address the incompleteness of the TFF datasets, a Tree-augmented Naive Bayesian Network (TAN BN) is meticulously devised. The proposed TAN BN exhibits a commendable validation accuracy of 92.9%, while the trained TAN BN attains a test accuracy of 89.33%. These outcomes underscore the precision and efficacy of the proposed TAN BN model, particularly when confronted with incomplete datasets. Furthermore, the study presents results from a sensitivity analysis, elucidating the significance of input parameters.

Keywords: Rock mass quality, Computer vision, Incomplete multi-source dataset, Improved Swin Transformer, Bayesian networks

1 INTRODUCTION

The assessment of surrounding rock quality plays a pivotal role in shaping the excavation and support scheme design for rock tunnels. It constitutes an indispensable foundation for evaluating the stability of surrounding rocks, formulating cross-sectional shapes, devising construction methodologies, and determining supporting structures. Consequently, the precise evaluation of surrounding rock quality has perennially been a focal point of scholarly attention and practical consideration among on-site engineers. (Aksoy et al., 2012; Chen and Liu, 2007; Rehman et al., 2019).

*Corresponding author: wylzj9@163.com

DOI: 10.1201/9781003495505-415

Historically, the prevailing classification methods for surrounding rock have been categorized into three distinct types, predicated upon their qualitative and quantitative attributes: namely, the qualitative classification method, the quantitative classification method, and the qualitative-quantitative hybrid method. Including: RMR (Bieniawski, 1988), Q system (Mechanics, 1978), RQD (Deere, 1963) and GSI (E. et al., 1997; Hoek and Diederichs, 2006), etc. Due to differences in the selection of systems and parameter among different evaluation methods, as well as the complexity and anisotropy of tunnel engineering geological conditions (Petronio et al., 2007), these methods are difficult to fully reflect the actual situation and can only reflect the quality of tunnel surrounding rock from one or more aspects (Chen and Liu, 2007), resulting in inaccurate evaluation and prediction of rock mass quality (Chen et al., 2013; Zhou et al., 2021). Therefore, it is necessary to develop more comprehensive and accurate methods for predicting surrounding rocks quality.

In the course of evaluating the surrounding rock quality on rock tunnel faces, numerous characteristic parameters, encompassing water leakage, cracks, weak interlayers, and mechanical properties of surrounding rock, necessitate collection and documentation at the site. For on-site engineers tasked with the observation and recording of said characteristic parameters, exposure to freshly exposed surrounding rock poses an undeniable risk. Moreover, the manual recording of these characteristic parameters relies on human expertise and skills, introducing potential subjectivity and imprecision into the prediction of surrounding rock quality. In response to the aforementioned challenges of insecurity and inaccuracy, it becomes imperative to propose an intelligent, non-contact methodology for acquiring characteristic information about the surrounding rock. Computer vision (CV) models emerge as an automated, non-contact approach for extracting information from images. The application of CV technology has become increasingly prevalent as an intelligent and quantitative means of extracting characteristic parameters from rock tunnel faces (Chen et al., 2022; Chen et al., 2020; Yusoff et al., 2023). Nonetheless, the CV methodologies employed by predecessors predominantly consist of existing CV models, lacking targeted enhancements tailored to the nuanced characteristics of diminutive parameters like water leakage, fracture traces, and weak interlayers against complex backgrounds. This deficiency results in suboptimal accuracy and generalization performance in tasks involving identification and segmentation. Hence, there exists a substantive rationale to ameliorate the existing CV models. Moreover, owing to constraints inherent in on-site construction protocols, spatial limitations, and varying lighting conditions at rock tunnel face sites, a principal shortcoming of extant approaches for predicting rock mass quality lies in the formidable challenge of attaining comprehensive datasets. To surmount this limitation, a novel Bayesian Network (BN) is posited as a solution for predicting rock mass quality. BNs, by nature, exhibit inherent strengths in managing conditional dependency relationships among recorded and unrecorded random variables within a statistical model (Lauritzen, 1995), hence making it a reasonable choice in classification and prediction process of rock mass quality. Besides, although BNs have been widely applied in geotechnical engineering (Huang et al., 2012; Jimenez-Rodriguez and Sitar, 2006; Song et al., 2012), they have not yet been applied to predict the surrounding rock quality.

In this study, an improved ST model is utilized for the acquisition of quantified CV parameters pertaining to rock tunnel faces. Furthermore, the establishment of a multi-source TFF dataset is undertaken, encompassing CV parameters, alongside physical, mechanical, and design parameters of the surrounding rock. Subsequently, a novel TAN BN is introduced to accurately prognosticate the quality of surrounding rock, even when confronted with incomplete data within the multi-source TFF dataset. The RMR system (Bieniawski, 1988, widely embraced at the international level, serves as both a benchmark and an output reference for the proposed TAN BN.

2 SEGMENTATION OF CV PARAMETERS

2.1 *Improved CV model*

The ST model, distinguished by its integration of shift windows, layered computing, and self-attention mechanisms within the realm of CV (Liu et al., 2021), has demonstrated superior outcomes compared to the majority of CNN models in the segmentation of tunnel disease features. Notably, the model's parameter count is considerably lower than that of the Vision Transformer (VIT). The ST model has found successful application in the automatic recognition and segmentation of tunnel disease information, encompassing phenomena such as water leakage and fractures (Meng et al., 2023; Zhou et al., 2023). However, the segmentation performance of small-scale features at the boundaries of diverse disease information is not notably optimal. Unet models, renowned for their proficiency in handling small-scale targets or images featuring intricate boundaries, often exhibit commendable performance. Consequently, this study endeavors to enhance the ST model by incorporating aspects of the Unet model. This integration is undertaken with the aim of ameliorating the segmentation task performance related to small-scale feature information on rock tunnel faces.

Figure 1 illustrate the detailed architecture of the improved ST model. Specifically, the structure of the Unet model has more advantages for processing small-scale information. Refering the excellent structure of Unet, the U-shaped structure is employed in the improved ST model. Simultaneously, the ST block establishes relationships between patches within pre-partitioned windows, effectively reducing computational memory overhead. However, this method to

some extent weakens the global modeling ability of the model. This also leads to unsatisfactory performance of the ST model in identifying and segmenting targets with small-scale features and complex boundaries such as water leakage, fractures, and weak interlayers. To compensate for the loss of feature resolution brought by ST, a CNN module that can leverage detailed high-resolution spatial information is employed to enhance the information exchange of pixels on small-scale features and complex boundaries.

Inspired by the U-shaped architectural design, the self-attentive feature encoded by ST is then upsampled to be combined with different high-resolution CNN features skipped from the encoding path, for enabling comprehensive and accurate pixel information extraction. Such a design allows the improved ST to preserve the advantages of ST and also benefit rock mass characteristic segmentation. Specifically, the rock mass image first traverses multiple CNN blocks, and the features procured at each layer are retained for skip connections. The features obtained from the final layer are transferred to the enhanced Attention Block after linear projection. The hidden feature is simultaneously inputted into the ST Block, extracting global and local level information respectively. The two resulting hidden features are stacked and undergo feature fusion via Conv3x3ReLU. Through the stacking of multi-level Attention Blocks, the model attains a superior feature extraction capability for image data. Lastly, we reshape the acquired hidden feature, merge it with the previously obtained feature via skip connections, and obtain the final semantic segmentation result through the Segmentation Head.

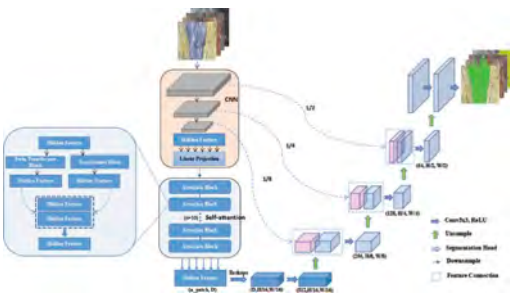

Figure 1. Detailed architecture of the improved ST model.

2.2 *Establishment of TFF imageset*

To efficiently obtain an adequate number of high-definition images of tunnel faces and subsequently acquire quantitative segmented characteristic parameters, an adaptive digital camera acquisition system is established in conjunction with an on-site lighting system during the tunnel construction process. This digital camera system comprises a Canon EOS 6D2 camera, tripod, tape, illuminometer, laser range-finder, and thermo hygrometer. Moreover, the system is equipped with a light source consisting of two LED dropout lamps. This image acquisition system is primarily applied in two categories of rock tunnels, specifically the Second Submarine Tunnel in Jiaozhou Bay, Qingdao, China and the Meng-ping mountain tunnel, Yunnan province, China, which can strength the representativeness and robustness of established imageset.

A novel imageset is established based on the tunnel face images of two tunnel projects obtained by the adaptive digital camera acquisition system. Specifically, to quantitatively obtain geometric and quantitative information of water leakage, fractures, and weak interlayers in the imageset. The length and width of each image can be calibrated by a tape measure. More than 1000 raw images were collected from various tunnel sites in Qingdao second submarine tunnel and Yunnan Meng-ping mountain tunnel. Following the previous work (Chen et al., 2021a; Jose et al., 2020), these raw images are then carefully selected and cropped into 2000 smaller images (512×512 pixels). The raw images are manually labelled via Labelme software.

For the purpose of enriching the imageset established in this section, data augmentation methods have been employed. Such as mirror transformation, random rotation, and random amplification are performed (Chen et al., 2021a; Chen et al., 2021b; Perez and Wang, 2017). Furthermore, the number of various characteristic parameter images in the imagenet processed by the above image augmentation methods are illustrated in Table 1. In this imageset, 80% of the images are utilized for training and the remaining 20% will be evenly allocated to the validation and testing sets.

Table 1. Images distribution in the imageset.

Different parameters	Total number	Number of training set	Number of validation set	Number of test set
Water leakage	6000	4800	600	600
Fractures	6000	4800	600	600
Weak interlayers	6000	4800	600	600

2.3 *Experimental settings and results*

The improved ST is subjected to evaluation on the TFF imageset, specifically for tasks related to the segmentation of water leakage, fractures, and weak interlayers. In the conducted segmentation experiments, the improved ST undergoes training for 100 epochs, initialized with a learning rate set at 0.0001. All models are implemented using the PyTorch platform. The model outputs manifest as probability maps in our experimental setup, which can be transformed into semantic segmentation results by

identifying the category with the highest probability at each position. Concurrently, segmentation experiments are conducted using the conventional, unenhanced ST, along with Unet++ and Unet models, all introduced under the same TFF imageset and experimental conditions. Figure 2 illustrates the visually intuitive segmentation results pertaining to water leakage, fractures, and weak interlayers.To evaluate the impact of different categories of water leakage on the surrounding rock quality, it should be pointed out that for the leakage characteristics on the rock mass, not only the segmentation task has been completed, but also the classification task has been completed. Combined with the RMR systems and previous studies (Chen et al., 2022; Zhou et al., 2021), the states of rock tunnel faces are divided into five types (Bieniawski, 1988), namely Anhydrous state image (1), Wet state image (2), Dropping state image (3), Flow state image (4), Spray state image (5). Furthermore, it is evident that the improved ST model demonstrates a superior capacity to accurately predict both the small-scale features and intricate boundaries associated with water leakage, fractures, and weak interlayers, surpassing the performance of the other three CV models.

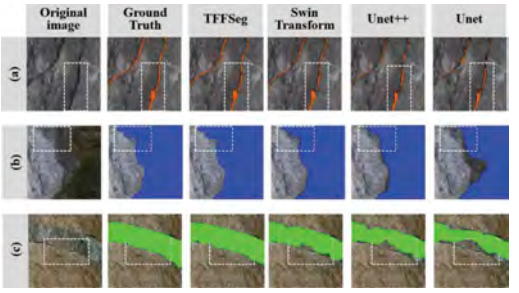

Figure 2. Comparison of qualitative results between improved ST and other frequently utilized CV models.

3 ESTABLISHMENT OF MULTI-SOURCE TFF DATASET

3.1 *Bayesian network*

BN, also known as belief network, or directed acyclic graphical model, is a probability graph model, which was first proposed by Judea Pearl (Pearl, 1986). The nodes in the directed acyclic graph of BN represent random variables, which can be observable variables, hidden variables, unknown parameters, etc. Variables or propositions that are believed to have a causal relationship (or non-conditional independence) are connected by arrows. If two nodes are connected by a single arrow, it means that one node is "parents" and the other is "children", and the two nodes will generate a conditional probability value. On the contrary, the absence of an arrow between two variables indicates their conditional independence (David and Heckerman, 1997). Naive BNs require that children nodes remain independent of each other, but this is often not the case in geotechnical engineering. In view of this, a TAN BN (presented in Figure 3, X is the input variable and Y is the output variable) that allows for a certain correlation between child nodes under the parent node is proposed to improve the applicability and predictive accuracy of the BN.

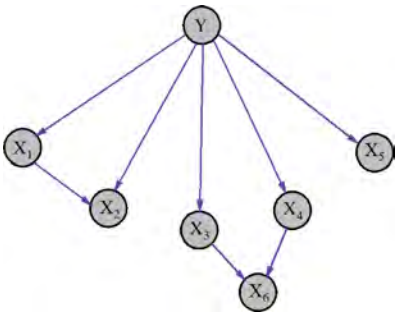

Figure 3. Schematic diagram of BN.

3.2 *Introduction of different parameters*

To comprehensively evaluate the quality of surrounding rock. A multi-source TFF dataset containing CV parameters, physical and mechanical parameters, and design parameter is established in this work. The parameters of water leakage, fractures, and weak interlayers of great concern to some commonly applied international rock mass quality evaluation systems (Bieniawski, 1988; E. et al., 1997; Mechanics, 1978). The acquisition methods of considered parameters in these prediction systems often rely on human observation and experimental records at rock engineering sites, which is dangerous and easily influenced by engineer experience. To address this drawback, a non-contact improved ST model is employed in this paper to intelligently obtain parameters such as water leakage, cracks, and weak interlayers on the rock masses. Specifically, in the multi-source TFF dataset proposed in this section, the water leakage parameters identified based on the improved CV model include Ground water category (GWC) and Ground water area (GWA), fracture trace parameters include Trace density (TD), Trace intensity (TI) and Trace number (TN), Average trace interval (ATI), Maximum trace length (MTL), and weak interlayer parameters include Weak interlayer area (WIA). In addition, guided by previous research (Ietto et al., 2018; Zhou et al., 2021), Uniaxial compressive strength (UCS), Weathering degree (WD) and Tunnel buried depth (TBD) with potential influence on RMR system are obtained in this multi-source TFF dataset, which can further enhance the precision and robustness of predicting the surrounding rock quality in this work. Below is a brief introduction to these parameters.

3.3 *Data discretization of the incomplete dataset*

Nine various categories of parameters (GWA, TD, TI, TN, ATI, MTL, WIA, UCS and TBD) in the proposed multi-source TFF dataset are continuous. Due to the limitations of BN in processing continuous data (Jensen and Nielsen, 2007), the characteristic parameters of rock mass obtained through quantitive calculation are discretized. Owing to the RMR classification system divides the quality of surrounding rock into five levels equidistantly based on the empirical formulation (Bieniawski, 1988), each continous parameter in this work also adopts the principle of equidistance division for discretization. Meanwhile, the intervals defined for the nine continous parameters considered are demonstrated in Table 2.

Table 2. Intervals applied to the continuous parameters in the TFF dataset.

Parameters	Set of intervals
GWA intervals	Zero/ (0, 8.64]/ (8.64, 17.28]/ (17.28, 25.893]
States of GWA	Zero, Small, Medium, Large
TD intervals	[0, 26.7]/ (26.7, 53.4]/ (53.4, 80.1]/ (80.1, 106.8]
States of TD	Very small, Small, Medium, Large
TI intervals	[0, 6.84]/ (6.84, 13.68]/ (13.68, 20.52]/ (20.52, 27.36]
States of TI	Zero, Small, Medium, Large
TN intervals	[0,16.72]/ (16.72,33.44]/ (33.44,50.16]/ (50.16, 66.88]
States of TN	Very small, Small, Medium, Large
ATI intervals	[0.05, 0.2075)/ [0.2075, 0.365)/ [0.365, 0.5225)/ [0.5225, 0.68]
States of ATI	Very small, Small, Medium, Large
MTL intervals	[0.22, 0.6375)/ [0.6375, 1.055)/ [1.055, 1.4725)/ [1.4725, 1.89]
States of MTL	Very small, Small, Medium, Large
WIA intervals	Zero/ [0,4.35)/ [4.35,8.70)/ [8.70,13.05]
States of WIA	Zero, Small, Medium, Large
UCS intervals	[0,16.72)/ [16.72,33.44)/ [33.44,50.16)/ [50.16, 66.88]
States of UCS	Very small, Small, Medium, Large
TBD intervals	[11, 99.50)/ [99.5, 188)/ [188, 276.5)/ [276.5, 365]
States of UCS	Very small, Small, Medium, Large

Due to limitations in the on-site space, process arrangement, and construction data storage of the tunnel working face, it can be seen that not all parameters in the multi-source TFF dataset have a quantity of 140. Some parameters are incomplete, which will affect the precision of prediction tasks based on this multi-source TFF dataset. It is known that BNs have advantages in processing incomplete data (Li et al., 2017; Nikovski, 2000). Therefore, it is reasonable to establish a Bayesian model that can learn the internal laws and conditional probability from incomplete datasets.

4 ESTABLISHMENT OF TAN BN

4.1 *Structure of the BN*

The initial phase in constructing a Bayesian Network (BN) involves determining its network structure, a process that demands careful consideration of the conditional independence and dependency relationships among various input parameters. Once the BN structure is defined, the next crucial step is to establish the degree of correlation between input parameters, specifically, the conditional probability of one parameter given another (David and Heckerman, 1997). For the sake of predicting the surrounding rock quality based on BN. The surrounding rock quality in the work is divided into five levels (I, II, III, IV and V) according to the RMR system (Bieniawski, 1988). The RMR value calculated by the tunnel engineer on site and reviewed by the tunnel expert is set as Y. Similarly, the evaluation parameters can be represented as X= (GWC, GWA, TD, TI, TN, MTL, ATI, WIA, UCS WD and TBD) in the incomplete multi-source TFF dataset. Then, the 140 sets of available data in the multi-source TFF dataset are collected to train the BN established in this work. It is usually arduous to achieve in the application of rock mass quality prediction, as some parameters measured from rock mass are generally not independent of each other. To address this limitation, a novel TAN BN is proposed in this paper. To determine the structure of tree augmentation, correlation analysis is conducted between eleven parameters in the multi-source TFF dataset. The correlation analysis results are demonstrated in Figure 4, which illustrate that the correlations between GWA and GWC, TI and TD, TN and ATI are 0.645, 0.503, -0.788. The absolute value of correlation between other parameters are less than 0.5, indicating a low mutual influence between them (Dancey, 2007; Loozen et al., 2013).

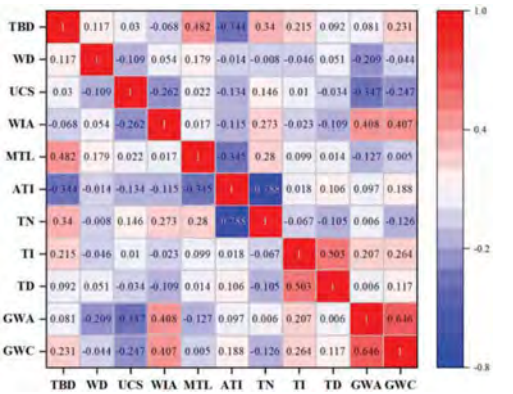

Figure 4. The correlation analysis results of the eleven parameters in the established multi-source TFF dataset.

Therefore, considering the correlation analysis results between the eleven parameters, the TAN BN is selected to improve the prediction performance of surrounding rock quality in this work (Friedman et al., 1997). A tree structure is employed to approximates the interaction between different parameters, where each parameter has a maximum of two parent nodes (Jiang et al., 2005). The structure of the TAN BN applied in this work is illustrated in Figure 5, this network can learn the information of eleven parameters in the multi-source TFF dataset. The reason for TAN BN introduced is that its prediction precision is higher than that of naive Bayesian classifier, and its structure is also relatively simple (Li et al., 2017). It should be emphasized that not all groups of data in this multi-source TFF dataset have complete eleven parameters, and some data groups have less than 140. However, the TAN BN proposed in this work still has the ability to learn CPTs from incomplete datasets and achieve prediction of surrounding rock quality.

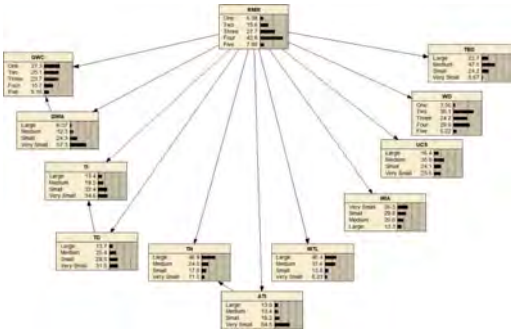

Figure 5. The framework of the proposed TAN BN.

4.2 *Training and validation of BN*

The TAN BN model established can learn the inherent laws of eleven parameters in the incomplete multi-source TFF datasets. To be specific, Netica software (Corporation, 1998) and expectation maximization (EM) algorithm (Dempster, 1977) are applied to assess the quality of rock mass. Simultaneously, the conditional probability between different nodes in the TAN BN can also be investigated. Next, import multi-source TFF datasets into BN for training and validation. The training result of the TAN BN is described in Figure 5. The validation set of the multi-source TFF dataset consists of 28 sets of data, and the confusion matrix of the validation results based on the proposed TAN BN is described in Figure 6. The diagonal data in this table represents correctly predicted data and its prediction precision is 92.9%, which demonstrates the effectiveness of our proposed TAN BN in this work.

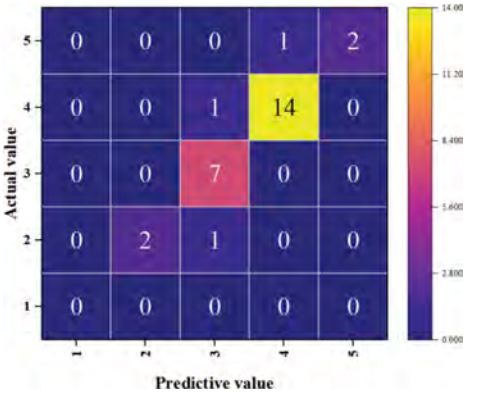

Figure 6. Validation result of the proposed TAN BN.

5 TEST PROCESS AND DISCUSSION

5.1 *Test with new cases*

To assess the efficacy of the proposed TAN BN with a novel dataset derived from a tunnel site, 27 sets of data are newly acquired through the application of the improved ST and geological sketches from the Qingdao Jiaozhou Bay Second Submarine Tunnel. These datasets are subsequently employed in the testing phase of the TAN BN, and the resultant test outcomes are delineated in Figure 7. Notably, only three cases out of the 27 are predicted inaccurately, yielding a prediction precision of 89%. This outcome underscores the precision and reliability of the TAN BN model established in this study. However, it is imperative to emphasize the limitations inherent in the actual surrounding rock quality of the tunnel under excavation. it is crucial to acknowledge that it does not encompass the entire spectrum of RMR levels.

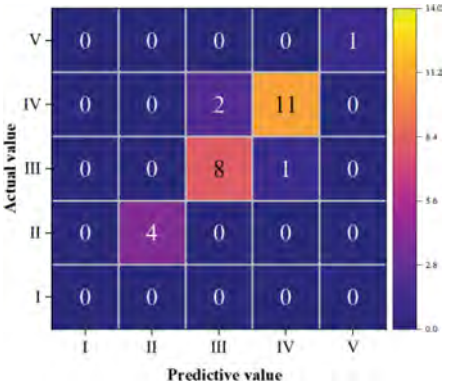

Figure 7. Test results of surrounding rock quality in actual tunnel cases.

5.2 *Sensitivity analysis*

For the sake of measuring the influence of different parameters on the output results of the TAN BN, this work conducted sensitivity analysis of eleven parameter in the multi-source dataset. The commonly used mutual information (MI) (Shannon and Weaver, 1949) and variance reduction (VR) (Pearl, 1991) in Netica software are employed to evaluate the contribution rates of eleven input parameters. Furthermore, the impact of input parameters on rock mass quality is comprehensively measured by MI and VR from two dimensions: mutual influence and error reduction. And the sensitivity analysis results based on Netica software are presented in Table 3.

The "percentage" list shows the contribution percentage of each input node to the "RMR" node; For example, the contribution rate of the node "ATI" to the overall mutual information is equal to 20.6%, which is calculated as 0.41136/1.99604×100%, ATI has the highest contribution rate to the overall mutual information among all input parameters. The contribution rate of node TN to Variance Reduction is 18.6%, and its calculation process is 0.37174/1.99604×100%, ATI has the highest contribution rate to Variance Reduction. The above results indicate that ATI and TN are the parameters that have the greatest impact on the RMR of rock tunnel surrounding rock.

Table 3. Sensitivity analysis results of various parameters in the TAN BN.

Parameters	Mutual Information	Percent (%)	Variance Reduction	Percent (%)
ATI	0.41136	20.6	0.0711840	13.7
TN	0.37174	18.6	0.0643037	12.4
TD	0.22369	11.2	0.0288107	5.6
UCS	0.18647	9.34	0.0100531	1.9
TBD	0.18112	9.07	0.0162280	3.1
MTL	0.12540	6.28	0.0070414	1.3
GWA	0.11189	5.61	0.0083081	1.6
WIA	0.11081	5.55	0.0132595	2.6
WD	0.09691	4.85	0.0077459	1.5
TI	0.08634	4.33	0.0067288	1.3
GWC	0.08486	4.25	0.0059351	1.1

6 CONCLUSION

An improved ST is applied to achieve the task of quantitatively segmenting the characteristic parameters. A multi-source dataset containing CV parameters, physical and mechanical parameters, and design parameters is established. A novel BN is proposed to predict rock masses quality.

Firstly, a multi adaptive electronic image acquisition system and an TFF imageset are established. And the ST model is improved to incorporate the advantages of Unet structure being more sensitive to small-scale features. Extensive experiments demonstrated that the improved CV mode significantly outperformed the previous state-of-the-art methods.

Secondly, to evaluate the surrounding rock quality, eleven parameters are considered to build a multi-source TFF dataset. Some parameters in this multi-source TFF dataset are incomplete.

Third, a novel TAN BN is proposed to overcome the drawback of incomplete dataset and predict the probability of rock mass quality given (probably partial) information in the multi-source TFF dataset. The TAN BN is learned, with the aid of EM algorithm, using an incomplete database with 140 sets of parameters. The validation accuracy of the learned TAN BN is 92.9%. Testing results illustrate that the prediction precision of the rock mass quality is 89%.

Ultimately, a sensitivity analysis to identify the input parameters with a higher influence on rock mass quality has been conducted. Results suggest that ATI is the most influential parameter.

REFERENCES

Aksoy, C.O., Genis, M., Aldas, G.U., et al, 2012. A comparative study of the determination of rock mass deformation modulus by using different empirical approaches. Eng Geol 131, 19–28.

Bieniawski, Z.T., 1988. The rock mass rating (rmr) system (geomechanics classification) in engineering practice, Symposium on Rock Classification Systems for Engineering Purposes.

Chen, C.S., Liu, Y.C., 2007. A methodology for evaluation and classification of rock mass quality on tunnel engineering. Tunn Undergr Space Technol 22, 377–387.

Chen, J., Huang, H., Cohn, A.G., Zhou, M., Zhang, D., Man, J., 2022. A hierarchical DCNN-based approach for classifying imbalanced water inflow in rock tunnel faces. Tunn Undergr Space Technol 122, 1–9.

Chen, J.Y., Zhang, D.M., Huang, H.W., et al, 2020. Image-based segmentation and quantification of weak interlayers in rock tunnel face via deep learning. AUTOMAT CONSTR 120.

Chen, J.Y., Zhou, M.L., Huang, H.W., et al, 2021a. Automated extraction and evaluation of fracture trace maps from rock tunnel face images via deep learning. Int J Rock Mech Min 142.

Chen, J.Y., Zhou, M.L., Zhang, D.M., et al, 2021b. Quantification of water inflow in rock tunnel faces via convolutional neural network approach. AUTOMAT CONSTR 123, 103526.

Chen, P., Yu, H., Xie, K., et al, 2013. Combination evaluation method for classification of surrounding rock quality of tunnels based on support degree. Chinese Journal of Geotechnical Engineering 35, 2233–2237.

Corporation, N.S., 1998. Netica Application User's Guide. Norsys Software Corporation, Vancouver, BC, Canada.

Dancey, C.P., 2007. Statistics Without Maths for Psychology. Statistics Without Maths for Psychology.

David, Heckerman, 1997. Bayesian Networks for Data Mining. Data Mining & Knowledge Discovery.

Deere, D.U., 1963. Technical description of rock cores for engineering purposes.

Dempster, A.P., 1977. Maximum likelihood from incomplete data via the EM algorithm. Journal of the Royal Statistical Society 39.

E., Hoek, and, E., T., Brown, 1997. Practical estimates of rock mass strength. International Journal of Rock Mechanics & Mining Sciences.

Feng, X.D., Jimenez, R., 2015. Predicting tunnel squeezing with incomplete data using Bayesian networks. Engineering Geology 195, 214–224.

Friedman, N., Dan, G., Goldszmidt, M., 1997. Bayesian Network Classifiers. Machine Learning 29, 131–163.

Hoek, E., Diederichs, M.S., 2006. Empirical estimation of rock mass modulus. Int J Rock Mech Min 43, 203–215.

Huang, H.W., Zhang, J., Zhang, L.M., 2012. Bayesian network for characterizing model uncertainty of liquefaction potential evaluation models. Ksce Journal of Civil Engineering 16, 714–722.

Ietto, F., Perri, F., Cella, F., 2018. Weathering characterization for landslides modeling in granitoid rock masses of the Capo Vaticano promontory (Calabria, Italy). Landslides 15, 43–62.

Jensen, B., Nielsen, T., 2007. Bayesian Networks and Decision Graphs. Bayesian Networks and Decision Graphs.

Jiang, L., Zhang, H., Cai, Z., Su, J., 2005. Learning tree augmented naive bayes for ranking, International Conference on Database Systems for Advanced Applications.

Jimenez-Rodriguez, R., Sitar, N., 2006. Inference of discontinuity trace length distributions using statistical graphical models. Int J Rock Mech Min 43, 877–893.

Jose, J.M., Sindagi, V., Hacihaliloglu, I., Patel, V.M., 2020. KiU-Net: Towards Accurate Segmentation of Biomedical Images using Over-complete Representations.

Lauritzen, S.L., 1995. The EM algorithm for graphical association models with missing data. Computational Statistics & Data Analysis 19, 191–201.

Li, N., Feng, X., Jimenez, R., 2017. Predicting rock burst hazard with incomplete data using Bayesian networks. Tunnelling & Underground Space Technology Incorporating Trenchless Technology Research 61, 61–70.

Liu, Z., Lin, Y.T., Cao, Y., et al, 2021. Swin Transformer: Hierarchical Vision Transformer using Shifted Windows, 18th IEEE/CVF International Conference on Computer Vision (ICCV), Electr Network, pp. 9992–10002.

Loozen, G., Ozcelik, O., Boon, N., Quirynen, M., Teughels, W., et al, 2013. Inter-bacterial correlations in subgingival biofilms: a large-scale survey. Journal of Clinical Periodontology 41, 1–10.

Mechanics, I., 1978. SUGGESTED METHODS FOR THE QUANTITATIVE DESCRIPTION OF DISCONTINUITIES IN ROCK MASSES. Int J Rock Mech Min 15, 319–368.

Meng, Z.C., Zhang, H.D., Guo, D.D., et al, 2023. Defocused calibration for large field-of-view binocular cameras. AUTOMAT CONSTR 147.

Nikovski, D., 2000. Constructing Bayesian networks for medical diagnosis from incomplete and partially correct statistics. Knowledge & Data Engineering IEEE Transactions on.

Pearl, J., 1986. A Constraint Propagation Approach to Probabilistic Reasoning. Machine Intelligence & Pattern Recognition 4, 357–369.

Pearl, J., 1991. Probabilistic Reasoning in Intelligent Systems: Networks of Plausible Inference. Morgan Kaufmann Publishers.

Perez, L., Wang, J., 2017. The Effectiveness of Data Augmentation in Image Classification using Deep Learning.

Petronio, L., Poletto, F., Schleifer, A., 2007. Interface prediction ahead of the excavation front by the tunnel-seismic-while-drilling (TSWD) method. Geophysics 72, G39–G44.

Rehman, H., Naji, A.M., Kim, J.-j., et al, 2019. Extension of tunneling quality index and rock mass rating systems for tunnel support design through back calculations in highly stressed jointed rock mass: An empirical approach based on tunneling data from Himalaya. Tunn Undergr Space Technol 85, 29–42.

Shannon, C.E., Weaver, W., 1949. The Mathematical Theory of Communication. Philosophical Review 60.

Song, Y.Q., Gong, J.H., Gao, S., et al, 2012. Susceptibility assessment of earthquake-induced landslides using Bayesian network: A case study in Beichuan, China. Computers & Geosciences 42, 189–199.

Yusoff, I.N., Ismail, M.A.M., Tobe, H., et al, 2023. Quantitative granitic weathering assessment for rock mass classification optimization of tunnel face using image analysis technique. Ain Shams Engineering Journal 14.

Zhou, M., Chen, J., Huang, H., et al, 2021. Multi-source data driven method for assessing the rock mass quality of a NATM tunnel face via hybrid ensemble learning models. Int J Rock Mech Min 147, 104914.

Zhou, Z., Zhang, J.J., Gong, C.J., 2023. Hybrid semantic segmentation for tunnel lining cracks based on Swin Transformer and convolutional neural network. COMPUT-AIDED CIV INF.

Tunnelling for a Better Life – Yan, Celestino, Thewes & Eberhardt (Eds)
© 2024 The Author(s), ISBN 978-1-032-80042-4
Open Access: www.taylorfrancis.com, CC BY-NC-ND 4.0 license

Machine learning-informed soil conditioning for mechanized shield tunneling feature engineering, model selection, and uncertainty quantification

Xiao Yuan*
School of Civil Engineering, Central South University, Changsha, PR China
Tunnel and Underground Engineering Research Center of Central South University, Central South University, Changsha, PR China

Shuying Wang
School of Civil Engineering, Central South University, Changsha, PR China
Tunnel and Underground Engineering Research Center of Central South University, Central South University, Changsha, PR China
MOE Key Laboratory of Engineering Structure of Heavy Haul Railway, Central South University, Changsha, PR China

Tongming Qu
Department of Civil & Environmental Engineering, The Hong Kong University of Science & Technology, Clearwater Bay, HKSAR, China

ABSTRACT: Soil conditioning plays a crucial role in shield excavation. This paper presents a systematic set of intelligent machine learning-based methods for soil conditioning in shield excavation, focusing on data, algorithms, and applications. Additionally, an active learning-based uncertainty quantification strategy is proposed to understand the reliability of the model prediction results without knowing the true value. The results demonstrate that (1) feature engineering and the selection of machine learning models offer a framework and methodology for automated research on soil conditioning in earth pressure balance (EPB) for data and algorithm perspectives, respectively. (2) Machine learning for soil conditioning should fully consider the influence of historical soil conditioning parameters on the prediction results. (3) The active learning-based uncertainty quantification strategy possesses exceptional capabilities in identifying the reliability of model prediction results. This can effectively enhance the application of machine learning for the automation of EPB shield tunneling.

Keywords: EPB shield tunnel, Soil conditioning, Feature engineering, Machine learning, Time-sequence problem, Uncertainty quantification

1 INTRODUCTION

EPB shield machines, favored for safe, efficient, and cost-effective underground subway tunnel construction in cities, transform excavated soil into a paste-like support medium. This paste balances pressure at the tunnel face, blocks unintended soil inflow, and facilitates quick, settlement-free tunneling (Hu et al. 2020). However, in complex strata, EPB machines face challenges like cutterhead "mud cake," rapid cutter wear, screw conveyor blockages, difficult soil discharge, and severe pressure fluctuations. Adapting these machines to various strata necessitates soil with suitable fluidity, plasticity, and compressibility. Soil conditioning is thus crucial (Vinai, Oggeri, and Peila 2008, Wang et al. 2021).

Significant advancements have been made in soil conditioning technologies (Mori, Mooney, and Cha 2018), with soil additive injection emerging as the most effective. These additives are categorized into water, foam, dispersants, clay minerals, and flocculants. While water and foam suit many strata, dispersants, clay minerals, and flocculants target specific conditions like high viscosity, particle scarcity, and water-abundant coarse grains, respectively. These insights guide engineers in additive selection, yet precise, real-time adjustments in their use remain a challenge.

*Corresponding author: 17310169484@163.com

DOI: 10.1201/9781003495505-416

Lab and on-site experiments are the main methods to study soil conditioning, yet they tend to trail behind the actual shield excavation's progress. Differences in pressure and void conditions between lab-tested soils and those in actual excavation environments complicate the application of these results in the field. Consequently, engineers and operators typically depend on past experience for decision-making. This reliance on human judgment for operating complex machinery like EPB machines presents risks. There's a pressing need in shield engineering for innovative, automated solutions to enable precise and efficient decision-making in soil conditioning.

Machine learning offers a revolutionary approach to improving soil conditioning practices in shield tunneling. Various machine learning algorithms have proven effective in addressing challenges in mechanized tunneling engineering. These include predicting ground settlement induced by excavation (Zhang, Chen, and Wu 2019), stratigraphic conditions (Zhao and Wang 2020), and predicting mechanical parameters such as shield thrust (Kong et al. 2022), cutter torque (Cachim and Bezuijen 2019), excavation speed (Shangxin et al. 2021), and soil chamber pressure (Gao et al. 2020). In the context of soil conditioning, Lin et al. (Lin et al. 2022) compared various machine learning models, finding the random forest algorithm to be particularly effective. Despite these advancements, numerous unanswered questions remain in achieving automated soil conditioning during EPB shield tunneling.

This research focuses on developing a comprehensive machine-learning workflow for soil conditioning in EPB shield tunneling, illustrated with a case study from a construction site. It delves into crucial steps of data-driven soil conditioning, including feature engineering for noisy on-site data, model selection, and uncertainty quantification.

2 BACKGROUND OF THE PROJECT

This research utilizes a construction project from Hefei's No. 7 subway line in Anhui Province to demonstrate a machine-learning approach to soil conditioning in EPB shield tunneling. The shield machine deployed here has a 6.48-meter diameter and can boring 4 to 10 rings daily, each approximately 1.5 meters long. Its data acquisition system captures 206 parameters, including both active (shield thrust, foam injection, screw conveyor speed, etc.) and passive (cutter and screw conveyor torque, etc.) control parameters, recorded at one-minute intervals throughout the excavation, lining installation, and shutdown phases.

The initial 100 rings of the tunneling process, identified as the shield driver's adjustment phase, often show irregular data patterns. Thus, for machine learning, data from rings 100 to 530 are used, amounting to 255,323 raw data samples. However, the sparsity of geological boreholes, compared to the continuous tunneling, leaves many locations with unknown geological parameters. To address this, linear interpolation is employed to estimate these parameters between boreholes, based on the assumption of consistent geological characteristics within the same stratum. This approach ensures each excavation data set is paired with corresponding geological parameters for machine learning analysis.

3 FEATURE ENGINEERING

The efficacy of a machine learning model is capped by the quality of its data. Transforming raw, unprocessed data into a format that more effectively reveals underlying patterns, feature engineering is a crucial phase in the machine learning process. Properly executed, it enables the model to extract accurate information from data, significantly enhancing its predictive power.

3.1 *Data preprocessing*

3.1.1 *Identifying missing values*

Data gaps due to equipment issues or human errors can skew model training. This study fills missing values with averages of neighboring data, assuming proximity in value.

3.1.2 *Stable excavation section identification*

A significant portion of the shield machine's data, recorded every minute, includes non-excavation phases. For example, only 180 out of 1,361 data sets recorded in the 160-165 ring rang were relevant to excavation. Direct use of such imbalanced data can bias the learning process and strain computational resources. By analyzing the excavation process, non-representative beginning and end sections are excluded, reducing the data from 255,323 to 4,305 sets for efficient machine learning.

3.1.3 *Outlier detection*

Outliers, identified traditionally by box plots or normal distribution, are located using K-Means clustering and the "3σ principle." This approach addresses multivariate data outliers, with the optimal number of clusters determined based on the objective function's response to varying cluster numbers.

3.1.4 *Noise reduction in excavation data*

Vibrations from the shield cutterhead create noise in sensor data. This study employs the Butterworth filter for noise reduction, with the filter order and cutoff frequency tailored to the dataset. The Fourier transform and energy spectral density graph help determine the optimal cutoff frequency, enhancing data quality for analysis.

3.2 *Feature selection*

Once data is pre-processed, feature selection focuses on identifying key elements crucial for soil conditioning. These are categorized into tunneling and geological parameters. Informed by an understanding of

tunneling dynamics, nine tunneling parameters pertinent to soil conditioning are chosen: cutterhead rotation speed, cutter torque, average soil pressure in the excavation chamber, shield excavation speed, penetration rate, shield thrust, screw conveyor rotation speed, screw conveyor torque, and soil pressure as measured by sensors on the screw conveyor. Geological parameters encompass all features detailed in the geological survey report.

3.2.1 *Min-Max scaling for data*

To ensure model prediction accuracy isn't skewed by varying feature magnitudes, Min-Max Scaling is employed for feature normalization. This scaling technique adjusts all feature values to fall within a [0,1] range, maintaining proportionality while equalizing scale.

3.2.2 *Ranking feature importance*

(1) Principle of feature selection

To address the shortcomings of the traditional boosting algorithm, which is less efficient in the environment of large-sample and high-dimensional data, Ke et al. (Ke et al. 2017) proposed a new type of boosting algorithm, Lightgbm, which introduces GOSS (Gradient-based One-Side Sampling) and EFB (Exclusive Feature Bundling) techniques on the basis of the original boosting algorithm., Gradient-based One-Side Sampling) and EFB (Exclusive Feature Bundling) techniques.The GOSS technique removes most of the data with small gradients and uses only the remaining small portion for the estimation of information gain, thus avoiding the influence of the long-tailed portion of the low gradients. The EPB technique refers to the bundling of the mutually exclusive features to reduce the number of features. In addition, the lightgbm model also uses Histogram and Leaf-wise strategies to greatly improve the prediction speed of the model. The Histogram strategy (Figure 1) directly saves the discretized values of the features, which greatly reduces the memory usage. Leaf-wise is a more efficient leaf-splitting and growing strategy, which, compared with the conventional splitting by layers, the strategy each time from all the current leaves, to find the split gain of the largest leaf split again, and so on, its splitting process is shown in Figure 2.

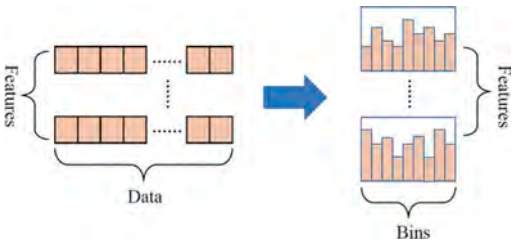

Figure 1. Histogram algorithm.

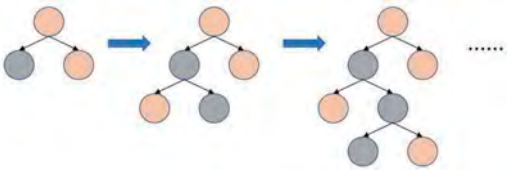

Figure 2. Leaf wise grown strategy.

(2) Feature selection method

Step 1, take shield tunneling parameters and geological parameters as input parameters and target parameters as output parameters.

Step 2, use Lightgbm algorithm to establish the regression model, and adjust the hyper-parameters of the model to improve the accuracy.

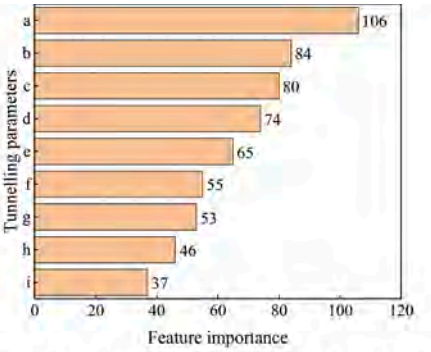

(a) Tunneling parameters (a: the rotation speed of cutterhead; b: the average soil pressure in the excavation chamber; c: shield thrust; d: the rotation speed of the screw conveyor; e: cutterhead torque; f: penetration rate; g: the torque of the screw conveyor; h: soil pressure on the surface of the screw conveyor; i: shield excavation speed)

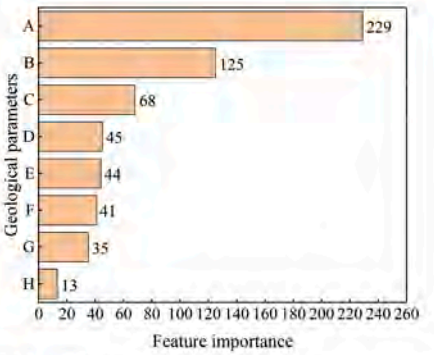

(b) Geological parameters (A: natural water content; B: saturation; C: liquid limit; D: modulus of compressibility; E: frictional angle; F: cohesion; G: plasticity index; H: plastic limit)

Figure 3. Feature importance ranking via the Lightgbm algorithm.

Step 3: After determining the optimal model, machine learning is carried out, and the weights of the shield tunneling parameters and geological parameters are output in the model and sorted accordingly.

The final feature importance ranking is shown in Figure 3.

3.2.3 *Feature correlation analysis*

To streamline the input features for machine learning and boost efficiency, the study conducts feature correlation analysis, building upon the feature importance outlined in Section 3.2.2. This involves using the Pearson correlation coefficient method to evaluate relationships between shield tunneling and geological parameters. Features exhibiting strong correlations (Pearson coefficient absolute value over 0.8) and validated physical linkages see less important ones removed.

4 MACHINE LEARNING MODELS FOR DECISION-MAKING OF SOIL CONDITIONING SCHEMES

Various machine learning models, each adept at different mapping relationships, are evaluated for their suitability in addressing soil conditioning challenges in shield tunneling. Considered models include:

- Gradient Boosting Decision Tree (GBDT): An iterative approach using decision trees, GBDT is effective in both classification and regression. It aggregates outcomes from multiple trees to derive final results.
- Adaptive Boosting (AdaBoost): Similar to GBDT and part of the Boosting ensemble method, AdaBoost refines the model by adjusting weights of incorrectly classified data, while GBDT focuses on negative gradients for improvement.
- Random Forest: This ensemble method involves random data sampling for multiple decision trees (weak learners), with their predictions combined through voting for the final output.
- K-Nearest Neighbor (KNN): KNN identifies the nearest neighbors of a new sample and predicts its value based on the average target values of these neighbors.
- Support Vector Machine Regression (SVR): SVR constructs regression models using the principles of support vector machines. It aims for optimal hyperplane fitting, differing from traditional regression methods.

Each model is trained with the best hyperparameters, identified through Bayesian optimization (up to 50 iterations). Given the foam's persistence in the excavation chamber, historical soil conditioning parameters (e.g., foam liquid and air flow) are considered in two distinct training strategies. Model performance is evaluated using the decision coefficient R^2 and the variance of prediction error σ^2 (Equations (1) and (2)). Higher R^2 values (near 1) and lower σ^2 values indicate better model performance and more stable error variation.

$$R^2 = 1 - \frac{\sum_{i=1}^{n} (y_i - f(x_i))^2}{\sum_{i=1}^{n} (y_i - \bar{y})^2} \tag{1}$$

$$\sigma^2 = \sum_{i=1}^{n} \left((y_i - f(x_i)) - \frac{\sum_{i=1}^{n} (y_i - f(x_i))}{n} \right)^2 \Big/ n \tag{2}$$

where y_i represents the actual values of the sample points, $f(x_i)$ denotes the model's predictions, $\bar{y}$ is the average true value across all samples, and n indicates the total number of samples in the test set.

Table 1 presents the predictive outcomes of various machine learning models, leading to the following insights:

i. Incorporating historical soil conditioning parameters substantially enhances the performance of all machine learning models.
ii. With the addition of historical parameters, all models exhibit comparable R^2, suggesting that high-quality input data enables different models to achieve similar predictive accuracy.
iii. Despite achieving similar predictions, there are minor variations in σ^2, indicating differences in prediction error stability. The Gradient Boosting Decision Tree (GBDT) model shows the lowest prediction error variance (σ^2), making it the most stable option.

Table 1. Comparison of predictive outcomes across various algorithms.

Algorithm	R^2 (without historical variables)	σ^2 (without historical variables)	R^2 (with historical variables)	σ^2 (with historical variables)
GBDT	0.8736	0.3324	0.9991	0.0023
AdaBoost	0.6041	1.0397	0.9932	0.0178
Random Forest	0.8740	0.3311	0.9959	0.0106
KNN	0.9652	0.0915	0.9988	0.0029
SVM	0.8097	0.4906	0.9982	0.0045

5 COMMITTEE ACTIVE LEARNING-BASED UNCERTAINTY ASSESSMENT IN MODEL PREDICTIONS

Machine learning models, typically trained and validated on familiar data distributions, face uncertainty when applied to construction projects with unknown data distributions. It's often unclear if these models will make interpolative or extrapolative forecasts (Guo et al. 2023). This uncertainty about the reliability of predictions hinders the transformative impact of advanced machine learning in soil conditioning and automated EPB shield tunneling. To tackle this problem, this section introduces an active learning strategy for estimating the uncertainty of machine learning predictions, enhancing confidence in addressing real-world engineering problems.

5.1 *Overview of active-learning for uncertainty estimation*

The core idea of this study is that the accuracy of a model's prediction is proportional to the scope of its training data. The wider the data space, the more intrinsic laws the model learns and the more accurate its predictions of unknown data. Machine learning models rely on a large number of training parameters, but usually have only one objective function. As a result, model training results vary for different initial parameter values. If multiple models give similar and consistent predictions with the same training set and hyperparameters but different random seeds, the predictions are considered reliable. On the contrary, if the prediction results vary widely, it indicates that the model has not sufficiently learned the relevant laws and its prediction reliability is low. The steps of the method are shown in Figure 4.

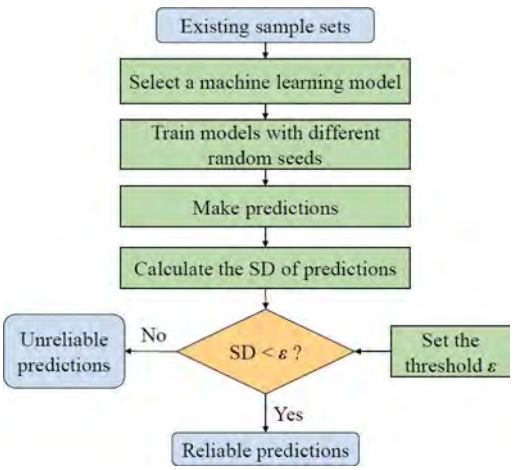

Figure 4. Active learning-based uncertainty recognition flow chart for model predictions.

5.2 *Validation of the uncertainty assessment approach*

In this study, in order to validate the effectiveness of the proposed uncertainty estimation method based on active learning, a dataset in the Geng~Qing interval was selected for the experiment. The 10% sample points with the largest and smallest variance were compared and analyzed. The results (see Table 2) show that with the same number of agent models, the average relative prediction error of the 10% samples with larger variance is always higher than that of the samples with smaller variance. In addition, as the number of agent models increases, the error of the sample with larger variance increases while the error of the sample with smaller variance decreases. This demonstrates the link between the standard deviation among agent models and prediction accuracy.

The ranking relationship between standard deviation and relative error was further analyzed for different numbers of agent models. As shown in Figure 5, when the number of agent models is small, the relationship between the two is not obvious. However, as the number of models increases, the relationship becomes clearer, showing a positive correlation. By defining the effective prediction region (defined by y=0.7x vs. y=1.3x), it is observed that as the standard deviation increases, the number of effective prediction points falling within this region also increases, indicating that the relative error ordering of the sample points is roughly in line with the standard deviation ordering, and the error range is controlled to be within 30%.

Table 2. Analysis of predictive precision across diverse agent model quantities.

	Relative prediction error across diverse agent model quantities (%)	
Number of agent models	10% of data points exhibiting the lowest standard deviation	10% of data points featuring the highest standard deviation
3	0.0094	0.0519
4	0.0087	0.0525
5	0.0084	0.0529
20	0.0034	0.0958
50	0.0033	0.0975
100	0.0033	0.1043

6 CONCLUSIONS

This study explores the intelligent enhancement of EPB, focusing on three key challenges in shield soil conditioning: (1) Strategies for supplying high-quality data to machine learning models, (2) Selecting appropriate machine learning models for EPB soil conditioning based on engineering field data, and (3) Methods for assessing the accuracy of model predictions in the absence of known true values and deciding if expert

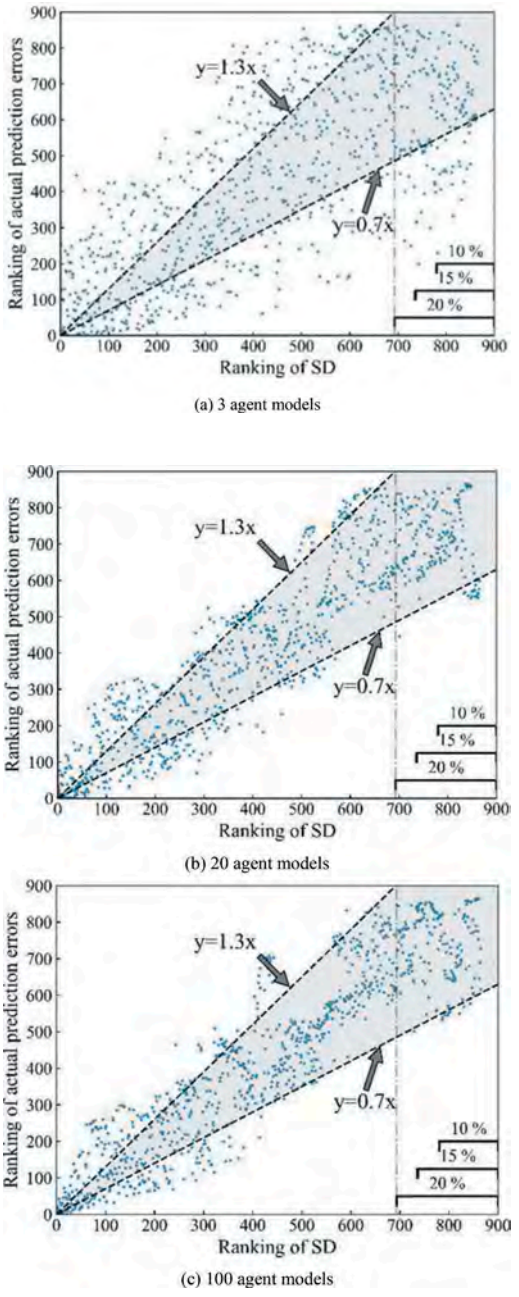

Figure 5. Correlation between standard deviation and relative prediction error across diverse agent model quantities.

input is necessary for further guidance. Key discoveries of the research are outlined below.

The paper presents a systematic approach to feature engineering for EPB soil conditioning, establishing a foundational framework for machine learning data processing. This approach enhances the effectiveness of subsequent machine learning models.

Using data-driven correlation analysis, the underlying mapping rules between parameters in shield tunneling can be effectively revealed, and the strong and weak correlations within parameters can be quantitatively judged. In addition, on the basis of considering the existence of a certain time stability of the foam, comparing the machine learning performance of soil conditioning under different test conditions, it is found that the inclusion of historical soil conditioning parameters can significantly improve the model performance..

In terms of model selection, GBDT, despite having similar efficacy to other common models, shows the lowest variance in prediction error, indicating more stable errors. Therefore, GBDT emerges as the most suitable machine learning model for soil conditioning.

The research demonstrates the effectiveness of an active learning-based uncertainty identification strategy. This approach is particularly advantageous in scenarios where it's uncertain if the distribution of the dataset to be tested aligns with the training set. It enhances engineers' confidence in the predictions of machine learning models and aids in their practical application in significant projects.

REFERENCES

Cachim, Paulo, and Adam Bezuijen. 2019. "Modelling the Torque with Artificial Neural Networks on a Tunnel Boring Machine." *Ksce Journal of Civil Engineering* 23 (10):4529–4537. doi: 10.1007/s12205-019-0302-0.

Gao, Min-Yu, Ning Zhang, Shui-Long Shen, and Annan Zhou. 2020. "Real-Time Dynamic Earth-Pressure Regulation Model for Shield Tunneling by Integrating GRU Deep Learning Method With GA Optimization." *Ieee Access* 8:64310–64323. doi: 10.1109/access.2020.2984515.

Guo, Jingjing, Qian Wang, Shu Su, and Yiting Li. 2023. "Informativeness-guided active learning for deep learning-based facade defects detection." *Computer-Aided Civil and Infrastructure Engineering* 38 (17):2408–2425. doi: 10.1111/mice.12998.

Hu, Qinxin, Shuying Wang, Tongming Qu, Tao Xu, Shuo Huang, and Haibo Wang. 2020. "Effect of hydraulic gradient on the permeability characteristics of foam-conditioned sand for mechanized tunnelling." *Tunnelling and Underground Space Technology* 99. doi: 10.1016/j.tust.2020.103377.

Ke, Guolin, Qi Meng, Thomas Finley, Taifeng Wang, Wei Chen, Weidong Ma, Qiwei Ye, and Tie-Yan %J Advances in neural information processing systems Liu. 2017. "Lightgbm: A highly efficient gradient boosting decision tree." 30.

Kong, Xiangxun, Xianzhang Ling, Liang Tang, Wenchong Tang, and Yifan Zhang. 2022. "Random forest-based predictors for driving forces of earth pressure balance (EPB) shield tunnel boring machine (TBM)." *Tunnelling and Underground Space Technology* 122. doi: 10.1016/j.tust.2022.104373.

Lin, Lin, Hao Guo, Yancheng Lv, Jie Liu, Changsheng Tong, and Shuqin Yang. 2022. "A machine learning method for soil conditioning automated

decision-making of EPBM: hybrid GBDT and Random Forest Algorithm." *Eksploatacja I Niezawodnosc-Maintenance and Reliability* 24 (2):237–247. doi: 10.17531/ein.2022.2.5.

Mori, Lisa, Mike Mooney, and Minsu Cha. 2018. "Characterizing the influence of stress on foam conditioned sand for EPB tunneling." *Tunnelling and Underground Space Technology* 71:454–465. doi: 10.1016/j.tust.2017.09.018.

Shangxin, Feng, Chen Zuyu, Luo Hua, Wang Shanyong, Zhao Yufei, Liu Lipeng, Ling Daosheng, and Jing Liujie. 2021. "Tunnel boring machines (TBM) performance prediction: A case study using big data and deep learning." *Tunnelling and Underground Space Technology* 110. doi: 10.1016/j.tust.2020.103636.

Vinai, Raffaele, Claudio Oggeri, and Daniele Peila. 2008. "Soil conditioning of sand for EPB applications: A laboratory research." *Tunnelling and Underground Space Technology* 23 (3):308–317. doi: 10.1016/j.tust.2007.04.010.

Wang, Haibo, Shuying Wang, Jiazheng Zhong, Tongming Qu, Zhengri Liu, Tao Xu, and Pengfei Liu. 2021. "Undrained compressibility characteristics and pore pressure calculation model of foam-conditioned sand." *Tunnelling and Underground Space Technology* 118. doi: 10.1016/j.tust.2021.104161.

Zhang, Pin, Ren-Peng Chen, and Huai-Na Wu. 2019. "Real-time analysis and regulation of EPB shield steering using Random Forest." *Automation in Construction* 106. doi: 10.1016/j.autcon.2019.102860.

Zhao, Tengyuan, and Yu Wang. 2020. "Interpolation and stratification of multilayer soil property profile from sparse measurements using machine learning methods." *Engineering Geology* 265. doi: 10.1016/j.enggeo.2019.105430.

Underground caverns/underground space use

Taylor & Francis
Taylor & Francis Group
http://taylorandfrancis.com

Tunnelling for a Better Life – Yan, Celestino, Thewes & Eberhardt (Eds)
© 2024 The Author(s), ISBN 978-1-032-80042-4
Open Access: www.taylorfrancis.com, CC BY-NC-ND 4.0 license

Planning and support estimation of underground powerhouse in the Himalayas

Sailesh Adhikari*
Norwegian University of Science and Technology, Trondheim, Norway
Tribhuvan University, IOE, Pashchimanchal Campus, Pokhara, Nepal

Chhatra Bahadur Basnet
Tribhuvan University, IOE, Pashchimanchal Campus, Pokhara, Nepal

Krishna Kanta Panthi
Norwegian University of Science and Technology, Trondheim, Norway

Tek Bahadur Katuwal
Norwegian University of Science and Technology, Trondheim, Norway
Tribhuvan University, IOE, Pashchimanchal Campus, Pokhara, Nepal

ABSTRACT: Underground structures like tunnels and caverns have major advantages in hydropower projects. Tunnels are used for transporting the water from the intake to the tailrace outlet through the turbines whereas caverns primarily serve the purpose of powerhouse, transformer caverns, and settling basins. The site selection of the underground cavern is an important task to be considered to optimize the rock support and cost. Design aspects regarding stability and functionality are governed by the location, orientation, shape, and size of the caverns. Similarly, the choice of support for a particular geological condition and type and quality of rock mass needs to be carefully assessed during planning and implemented during the construction. This article discusses the location design and rock support requirement of the underground powerhouse cavern of the Super Dordi Hydropower Project in Nepal. The project lies in the lower boundary of the Higher Himalayan rock formation. The powerhouse cavern has a length of 39 m and has width (span) and height of 14.5 m × 28 m, respectively. The rock support measures predicted during planning are modelled using 2D numerical modelling tools. The study on monitored data and numerically modelled data are compared and discussed.

Keywords: Underground Space, Support Characteristics, Deformation, Powerhouse Cavern, Himalayan Rock Mass

1 INTRODUCTION

The use of underground spaces has significantly increased in various engineering projects. The development of underground spaces has advantages like no impact on the landscape, very little or almost no disturbance to the surface human activities and resources, higher safety level, etc. It is particularly important in places where natural hazards like landslides and earthquakes are bound to occur. Nepal, a mountainous country, suffers various hazards posing a challenge to develop various infrastructure projects. Having a high potential for hydropower development, the sustainable development of the various structures for hydropower plants is the major issue to be addressed by the engineers in Nepal. The best alternative to protect structures from natural calamities like landslides and earthquakes is to make the components underground. The varied geological conditions and challenging terrains demand special attention to the construction of underground structures in Nepal. The tectonically active rock mass in the Himalayan region has the presence of weak, highly deformable, and anisotropic rock mass with a high degree of weathering and fracturing (Panthi and Nilsen, 2007), posing challenges for the construction of tunnels and caverns. Location, orientation, geometry, complexity of access tunnels, and geological conditions are major factors to be considered

*Corresponding author: sailesh.adhikari@ntnu.no

DOI: 10.1201/9781003495505-417

during the evaluation of stability and planning of underground structures (Rathore and Panthi, 2017). Project-specific characteristics like size, shape, location, and orientation influences the design of caverns and tunnels. (Panthi, 2006). Further, the stability is dependent on the rock mass quality, in-situ stress, and groundwater conditions.

The Himalayan Mountain series was formed due to the subduction of the Indian plate to the Tibetan plate. There are five major subdivisions of the tectonic boundaries in the Himalayan region. The major subdivisions from the southern belt towards the northern belts are the Gangetic plane (Terai), Siwaliks zone, Lesser Himalayan zone, Higher Himalayan zone, and Tibetan-Tethys zone. These divisions span approximately in the NW-SE directions. The subdivisions are separated by the boundaries of the main frontal thrust (MFT), main boundary thrust (MBT), and main central thrust (MCT). These tectonic zones are all characterized by special lithology, tectonics, geological structures, and geological history and are made up of different rock types (Panthi, 2006). Figure 1 shows the simplified geological map of Nepal with the geological and tectonic boundaries.

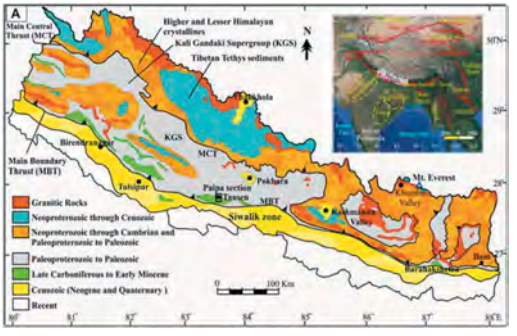

Figure 1. Geologic subdivisions of Himalayas (ref. Khatri et al., 2021).

In the lower boundary of higher Himalayas, i.e. near MCT (project site location of the present case study) the rocks of highly sheared, intensely deformed, and mylonitized green-schist and schistose mica gneiss are present (Robyr et al, 2002). Rock masses in the Himalayan region are influenced by faulting, folding, schistosity, and jointing to varying degrees representing geological complexity (Basnet and Panthi, 2020). In underground openings, the excavation-induced response of the rock mass may arise instability conditions. This paper discusses the design and support estimation of the powerhouse cavern of Super Dordi Hydropower Project (SDHP) located in Lamjung district of Nepal. The project lies in the higher Himalayas zone about 10 km north of MCT. The dimension of the powerhouse cavern is about 39 m × 14.5m × 28m. The powerhouse cavern has an arched roof and vertical walls. The dimensions of the powerhouse were optimized to accommodate the turbine, distribution pipes, and other construction areas based on the dimensions of the various machinery components.

2 BRIEF DESCRIPTION OF THE PROJECT

SDHP is a run-of-river type hydropower project with an installed capacity of 54 MW. The project has a gross head of 638 m. The project lies in the lower boundary of the higher Himalayan rock formation and facilitates a diversion weir (18.5 m long) and intake, double-chambered underground settling basin caverns (each having approximate cross-section area 113 sq. m), gravel trap (33.5 m long), headrace tunnel (4.7 km long), access tunnels, surge shaft (49 m high and 6 m diameter), penstock shafts (1052 m long), powerhouse cavern, and tailrace tunnel. Most of the civil structures of the project are underground except the diversion weir and switchyard. The project area consists of medium to high-grade metamorphic rocks like schist and gneiss and the feasibility study showed that there was no severe geological risk associated with the project (PHCPL, 2012). Figure 2 shows the project layout plan of SDHP with the location of different components of the hydropower project.

Initially, the powerhouse was proposed to be at the surface instead of underground. However, during the earthquake in April 2015, there was a small landslide near the uphill area of the old powerhouse site. The powerhouse will store heavy machinery and expensive equipment; thus, it was too risky to build the powerhouse on the surface. Eventually, it was decided to build the underground powerhouse instead of the surface powerhouse (Panthi, 2018). During construction, a shear band of about 10 to 20 cm was encountered near the powerhouse cavern location. The cavern location was further pushed by about 40m inside the mountain to minimize the impact. The alignment of underground structures is an important parameter to be addressed during the construction of tunnels and caverns. Poor alignment will lead to unusual overbreak, water ingress, and increased risk to health and safety (Katuwal et al., 2023). The rock mass encountered in the powerhouse cavern was of good quality. Two main joint sets with occasional random joints were mapped. These joints have medium persistence, spacing varying between 2.5 to 3m, and tight fillings with clay and silt. The orientation of the powerhouse cavern is N45E and is favourable in terms of major joint sets. Figure 3 shows the joint rosette with a cavern length axis (Panthi, 2018). The rock mass was relatively dry in the powerhouse area with exceptions in the locations from chainage +025 to +030m where minor dripping of water was seen causing dry to damp conditions. The site selection of the powerhouse cavern is suitable in terms of major critical factors influencing the stability and support systems applied in the cavern.

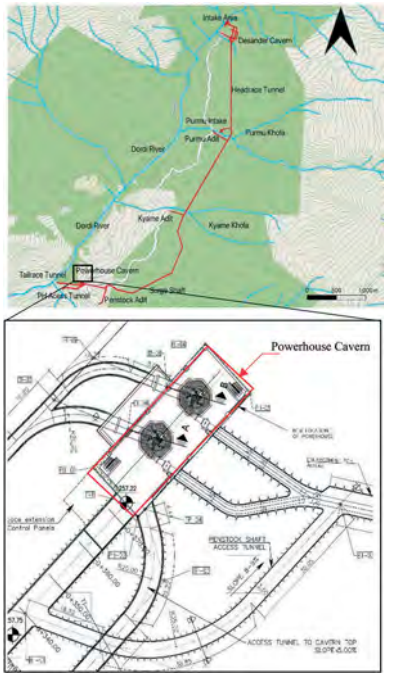

Figure 2. Project layout of SDHP.

Figure 3. Joint rosette of the powerhouse cavern.

3 ROCK MASS QUALITY PARAMETERS

The rock parameters are established based on the geological mapping, laboratory test results of the intact rock, and some empirical relationships. Rock mass strength and deformation modulus, and choice of failure criteria govern the design of underground caverns. The geometry and rock support provided for the powerhouse cavern are shown in Figure 4. The three-layer fiber-reinforced shotcrete, with a final thickness of 15 to 20 cm depending upon rock condition and systematic bolting was provided as rock support. The rock bolts were installed in two stages. The first stage consisted of 5 m long cement grouted rock bolts of 25 mm diameter placed at the staggered arrangements at the spacing of 3m. In the second stage, 8 m long cement grouted rock bolts with 25 mm diameter were provided at a spacing of 3 m in a staggered pattern.

3.1 *Intact rock properties*

The laboratory results of the rock core samples from the project area show the mean uniaxial compressive strength of the samples was 112.6 MPa with a standard deviation of 8.65 MPa. Similarly, Young's modulus was 48.53 GPa with a standard deviation of 5.05 GPa. The average Poisson's ratio of the intact rock was 0.33 and the unit weight of the rock was found to be 2.7 t/m^3.

3.2 *Rock mass properties*

The strength and deformability properties of the rock mass are important parameters for modelling the tunnels and caverns. Additionally, the presence of weakness zone, shear zone, and 3D topography are influencing parameters to model the caverns (Adhikari et al. 2022).

3.2.1 *Rock mass quality*

The rock mass quality was assessed using Q-system of rock mass classification (Barton et. al., 1974). Table 1 shows the range of values and typical mean for the different parameters mapped at the cavern for the determining overall rock mass quality class.

The Q value of the rock mass ranges from 10 to 12 with the typical mean value of 10.5. This indicates the rock mass at the powerhouse cavern is of good quality.

3.2.2 *Compressive strength of rock mass*

Various researchers have provided different relationship between intact rock strength and rock mass strength. The most common ones are Bieniawaski (1993), Hoek et al. (2002), Barton (2002) and Panthi (2017), listed in Equations 1 to 4, respectively.

$$\sigma_{cm} = \sigma_{ci} \times \exp\left(\frac{\mathrm{RMR} - 100}{18.5}\right) \text{ and } \mathrm{RMR} = 9 \times \ln \mathrm{Q} + 44 \quad (1)$$

$$\sigma_{cm} = \sigma_{ci} \times \left[\exp\left(\frac{\mathrm{GSI} - 100}{9}\right)\right]^{a} \quad (2)$$

$$\sigma_{cm} = 5\gamma\left[\frac{\sigma_{ci}}{100} \times Q\right]^{1/3} \quad (3)$$

$$\sigma_{cm} = \frac{\sigma_{ci}^{1.6}}{60} \quad (4)$$

The results of the rock mass strength achieved by the above relationships is illustrated in Figure 5. Based upon the field mapping results and site conditions the value of GSI was considered 60.

It can be seen from Figure 5 that the empirical relationships from Bieniawaski (1993) and Hoek et al. (2002) give a lower value for the rock mass strength whereas the empirical relationships by Barton (2002) and Panthi (2017) give a higher values. For the

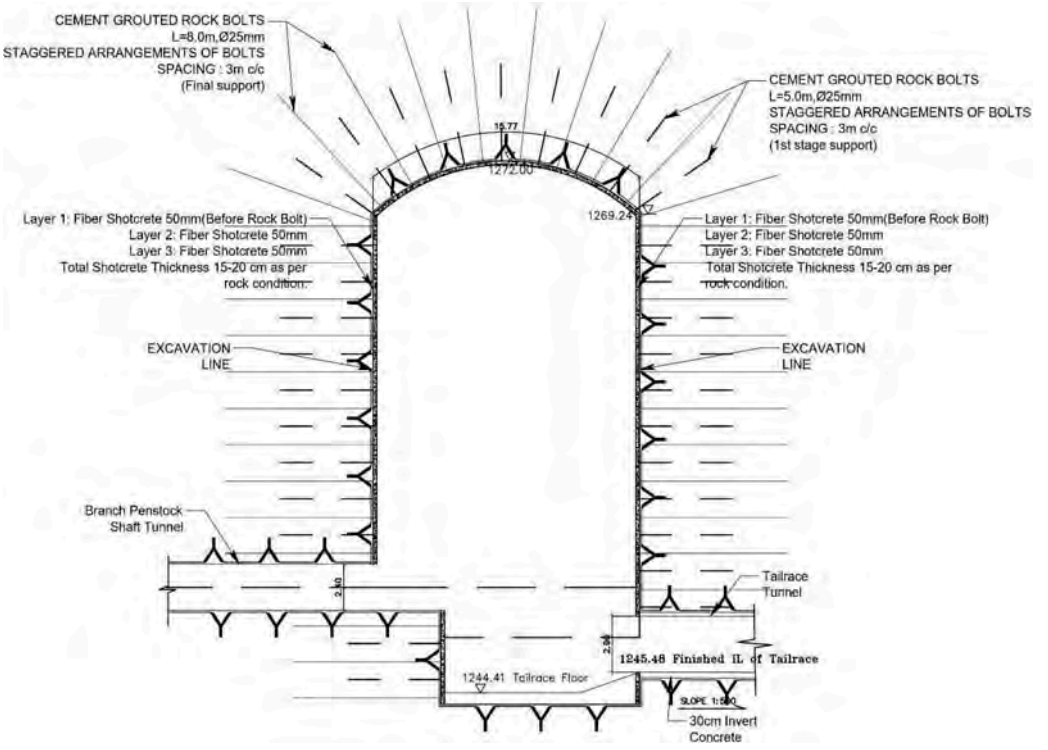

Figure 4. Support system provided in powerhouse cavern.

Table 1. Q-system of rock mass classification.

Parameters	Symbol	Value	
		Range	Typical Mean
Rock Quality Designation	RQD	60 – 80	70
Joint Set Number	J_n	3 – 6	4
Joint Roughness	J_r	1.5 – 3	2
Joint Alteration	J_a	2 – 4	3
Joint Water Reduction	J_w	0.8 – 1	0.9
Stress Reduction Factor	SRF	1	1
$Q = \frac{RQD}{J_n} \times \frac{J_r}{J_a} \times \frac{J_w}{SRF}$		10 – 12	10.5

homogeneous and relatively strong rock mass like at SDHP, the relationship between the intact rock strength and the strength of rock mass provided by Panthi (2017) is considered to be relevant and applicable. Unlike other relationships to compute the rock mass strength, the relationship is mainly based on lab-tested data and has no dependency on the rock mass classification system. Hence, the method eliminates the dependency on several other subjective parameters that depend upon the judgment of the engineer. Thus, an average rock mass strength is taken as 31.94 MPa for further analysis.

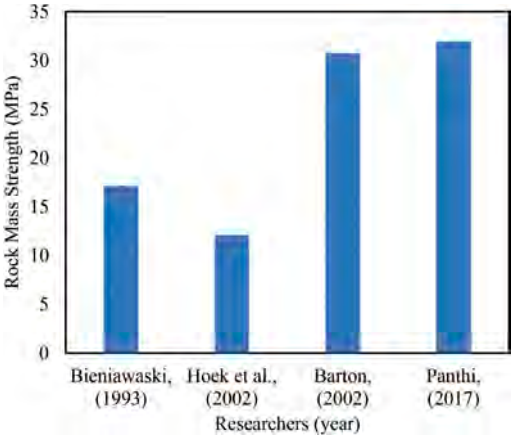

Figure 5. Rock mass strength by empirical relationship.

3.2.3 *Deformation modulus of rock mass*

The deformation modulus of the rock mass is also computed by the empirical relationship owing to the higher cost and measurement difficulties in the in-situ conditions. Like the compressive strength of rock mass, various researchers have provided the empirical formula to calculate the deformation modulus of rock mass. The relationship established by Bieniawaski (1978), Hoek et al. (2002), Barton

(2002), and Panthi (2006) is given from Equations 5 to 8 respectively.

$$E_m = 2RMR - 100 \tag{5}$$

$$E_m = \left(1 - \frac{D}{2}\right)\sqrt{\frac{\sigma_{ci}}{100}}\, 10^{\left(\frac{GSI-10}{40}\right)} \tag{6}$$

$$E_m = 10 \times \left(\frac{Q \times \sigma_{ci}}{100}\right)^{1/3} \tag{7}$$

$$E_m = E_{ci} \times \left(\frac{\sigma_{cm}}{\sigma_{ci}}\right) \tag{8}$$

In the above equation, E_m is the deformation modulus of rock mass, E_{ci} is the Youngs' modulus of the intact rock and σ_{ci} is the strength of the intact rock. The value of the deformation modulus obtained from the empirical relationship is illustrated in Figure 6. It is observed that the relationship provided by Bieniawaski (1978) provides the highest value of the deformation modulus and the relationship by Hoek et al (2002) and Panthi (2006) provides almost similar values. In this article, the deformation modulus obtained from Equation 8 proposed by Panthi (2006) is considered. The relationship is more suitable for the isotropic, homogeneous, and massive rock mass from the Himalayas. The deformation modulus of the rock mass computed is 13.76 GPa and is used as an input parameter for the numerical modelling of the cavern.

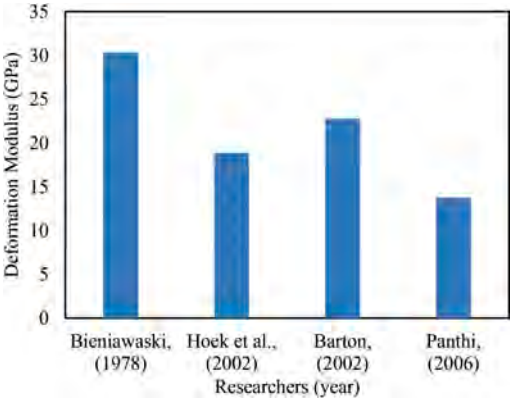

Figure 6. Deformation modulus by empirical relationship.

3.3 *Hoek Brown parameters*

GSI values are calculated by using the Q-systems' parameters using the following relationship (Hoek et al., 2013).

$$GSI = \frac{52(J_r/J_a)}{1 + (J_r/J_a)} + \frac{RQD}{2} \tag{9}$$

GSI was computed in the range of 53 to 63, which also matched the field mapping results to compute GSI. Hoek-Brown constant m_b, s and a are dependent upon the rock mass characteristics. These parameters are computed using the relationship from Equation 10 – 12.

$$m_b = m_i \times e^{\left(\frac{GSI-100}{28-14D}\right)} \tag{10}$$

$$s = e^{\left(\frac{GSI-100}{9-3D}\right)} \tag{11}$$

$$a = \frac{1}{2} + \frac{1}{6}\left(e^{-\frac{GSI}{15}} - e^{-\frac{20}{3}}\right) \tag{12}$$

Based on the site conditions during excavation and the chart provided by Hoek (2007), the value of the disturbance factor (D), which is dependent upon the blast damage to the contour is considered 0.6. Similarly, a GSI value of 60 and m_i value of 23 are considered to obtain the m_b, s, and a parameter. The residual GSI is assumed to be 20.

The values obtained for the disturbed and undisturbed zone are (m_b = 5.512, s = 11.7×10^{-3} and a = 0.503) and (m_b = 2.998, s = 3.86×10^{-3} and a = 0.503), respectively.

4 EVALUATION OF ROCK STRESSES

The in-situ rock stresses are generated due to the combination of gravitational load with tectonic stresses, topographic stresses, and residual stresses. According to Panthi (2012), the vertical and horizontal stresses on the rock mass can be computed as:

$$\sigma_v = \gamma H \tag{13}$$

$$\sigma_h = \frac{\nu}{1-\nu} \times \sigma_v + \sigma_{tec} \tag{14}$$

In the above equations, γ is the density of the rock, H is the overburden height, ν is the Poisson's ratio, and σ_{tec} is horizontal the tectonic stress in the rock mass.

In-situ stresses are measured by different methods like hydraulic fracturing, flat jack test, 3D overcoring test, etc. For the horizontal tectonic stress, no direct test was performed in the field. Instead, the horizontal tectonic stress of 4.5 MPa was assumed based on the tectonic stress of the headrace tunnel of the Upper Tamakoshi Hydropower Project (UTHP) (Panthi and Basnet, 2018) and Parbati-II Hydropower Project (Panthi, 2012) located in a similar tectonic regime and geological formation of the Higher Himalaya (Adhikari et al., 2023). From the World stress map the orientation of the tectonic stress is approximately N10E at the project location site. The

total horizontal stress is computed by resolving the tectonic stress and the horizontal stress due to gravity. Figure 7 shows a simple illustration of the computation for in-plane and out-of-plane horizontal stresses acting on the cavern. The angle between the horizontal tectonic stress regime and the cavern is 35°. The in-plane horizontal stress and out-of-plane horizontal stress are given by Equation 15 and Equation 16 respectively (Basnet and Panthi, 2020).

$$S_{yy} = S_{Hmax}\cos^2\theta + S_{Hmin}\sin^2\theta \quad (15)$$

$$S_{xx} = S_{Hmax}\sin^2\theta + S_{Hmin}\cos^2\theta \quad (16)$$

Based on the above data and the relationship provided in Equation 13 – 16, the in-situ stress parameters for the rock mass of the powerhouse cavern are summarized in Table 2.

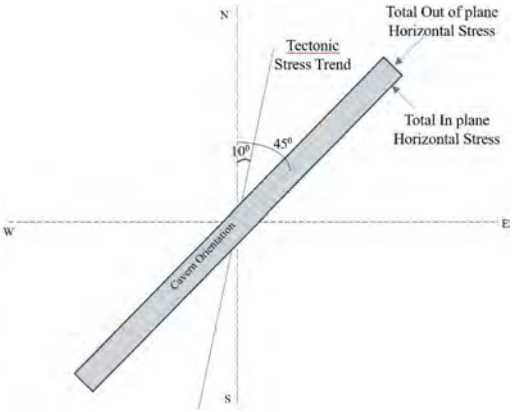

Figure 7. Illustration of the total horizontal stress for the cavern.

Table 2. In-situ stress parameters for rock mass of cavern.

Parameters	Value	Unit
Overburden Depth (H)	335	meters
Poisson's Ratio (v)	0.31	-
Tectonic Stresses (σ_{tec})	7.5	MPa
Tectonic Stress Trend	N10°E	-
Cavern Alignment	N45°E	-
Unit Weight of Rock	2.7	t/m^3
Total Vertical Stress	9.05	MPa
Total Horizontal Stress	11.56	MPa

5 NUMERICAL MODELLING OF THE CAVERN

Numerical modelling of the powerhouse cavern is done by using the finite element method using RS2. The cavern is simulated as a continuum model where the whole rock mass is considered as a single homogeneous mass. The principal stresses and their orientations are computed by creating the valley model. Further, these stresses are then used as input parameters in the box model to compute the deformation and the support details of the cavern.

5.1 *Valley model to determine stresses in the rock mass*

The valley model as per the site condition is shown in Figure 8. This 2D model considers the topographic effects and the horizontal tectonic stress effects. The resolved stress in-plane and out-of-plane are given as input to compute the principal stresses. The results show that the value of major principal stress (σ_1) is 10.80 MPa, and minor principal stress (σ_3) is 6.27 MPa. The direction of the major principal stress to the horizontal axis is 55°. These values are adopted to compute the deformation in the powerhouse cavern by creating the box model of the cavern.

5.2 *Rock support details of the powerhouse cavern*

The support details as shown in Figure 4 are provided to the model of the powerhouse cavern. The supports provided are fiber-reinforced shotcrete, concrete, and systematic rock bolts, the details of which are summarized in Table 3.

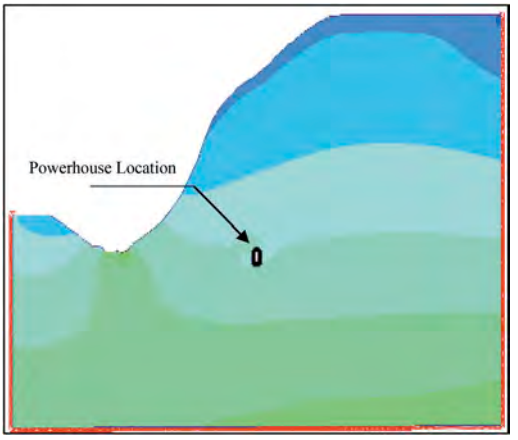

Figure 8. Valley model to compute principal stress for the cavern.

5.3 *Powerhouse cavern model*

The cavern model for powerhouse is made by taking the external boundary of the rock mass as 5 times the size of the cavern excavated. The disturbed zone of 2 meters from the excavation face is considered. The box model of the powerhouse cavern is shown in Figure 9. The support parameters and the stress parameters discussed previously are given as input to the model.

Table 3. Support parameters for cavern.

Shotcrete and Concrete Details:		
Support	Shotcrete	Concrete
Type	Standard Beam	Standard Beam
Compressive Strength	30 MPa	30 MPa
Tensile Strength	5 MPa	5 MPa
Poisson's Ratio	0.3	0.3
Rock Bolt Details:		
Support		Bolt
Type		Fully Bonded
Diameter		25 mm
Length		5m and 8m
Tensile capacity		0.1 MN

The crown of the powerhouse is at 1272 m from the mean sea level. The deformation was obtained numerically in the elevation 1267.6 m of the powerhouse cavern. The reading was computed in this location because the deformation in the powerhouse cavern was recorded using borehole extensometers at these locations. The deformation contour of the cavern is shown in Figure 10. The deformation obtained from numerical modelling and the borehole extensometer are shown in Table 4. The deformation values obtained from numerical modelling vary with the site-measured data but lie within an acceptable limit. The values are obtained for the chainage 15m from the instrument location.

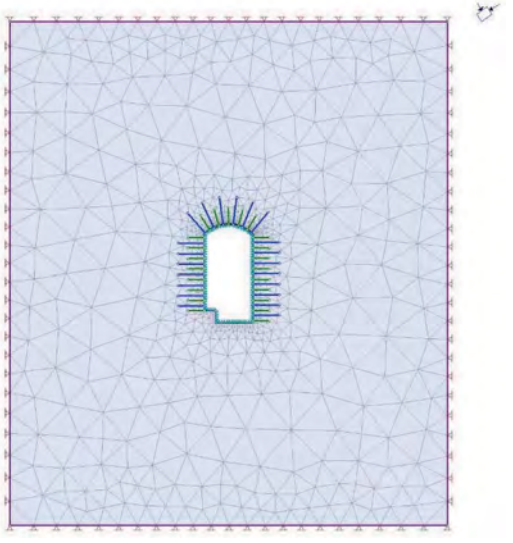

Figure 9. Box model of the cavern.

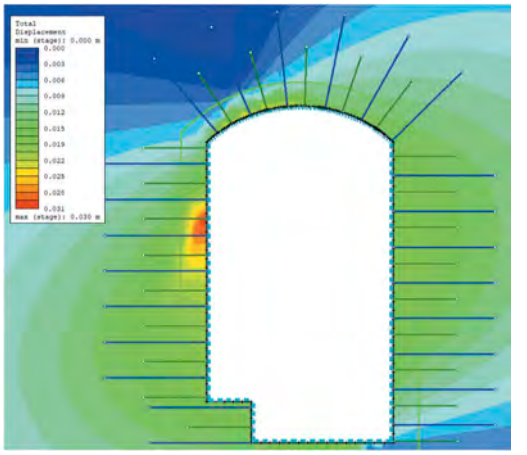

Figure 10. Deformation contour on the cavern.

Table 4. Deformation on the cavern.

Elevation	Wall	Numerical model value	Field Reading
1267.60 m	Left	6 mm	5.7 mm
	Right	5 mm	1.12 mm

6 DISCUSSIONS

The planning of a powerhouse cavern is dependent upon various factors like geometry (shape and size), topography, in-situ stress conditions, rock mass strength, rock mass quality, etc. These parameters must be properly assessed before excavating underground structures like tunnels and caverns. Field mapping and numerical modelling are the key steps to plan the initial support system and determine the magnitude and orientation of principal stresses. The deformation values obtained from the numerical model and the site measurement show the variation in the reading. It is mainly because deformation is affected by parameters prevailing in 3D conditions (geometry, topography, in-situ stresses, etc.). However, in the numerical modelling, only 2D finite element model is considered which lacks the exact situations of the ground conditions based on 3D parameters. Nevertheless, the magnitude from numerical modelling and site does not differ significantly to cause stress-induced instability in the caverns. Thus, 2D numerical model can be used as a tool to predict the deformation behaviour of the underground openings.

7 CONCLUSIONS

This paper discussed the geological conditions, layout, and location of the powerhouse cavern, used rock support, and the deformation characteristics of

the rock mass surrounding the powerhouse cavern of Super Dordi Hydropower Project located in the lower boundary of the higher Himalayan rock formation at Lamjung district of Nepal. The planning and design carried out for this cavern were very suitable in terms of shape, size, and potential weakness zone. The cavern is now in use and no significant deformations and other challenges in the applied rock support are seen at the site. The support provided is sufficient to make the cavern long-term stable and will serve its functional purpose for many decades to come.

ACKNOWLEDGMENTS

This research was supported by NORHED II Project 70141 6; Capacity Enhancement in Rock and Tunnel Engineering at the Pashchimanchal Campus (WRC), Institute of Engineering (IoE), Tribhuvan University (TU), Nepal. The authors acknowledge NORAD, Norway for funding the project and providing financial help for site visits and conducting this research. The authors are also thankful to People's Hydropower Company (P) Ltd. for providing necessary data to publish this work.

REFERENCES

Adhikari, S., Panthi, K.K. & Basnet, C.B., 2023. Stability issues associated with the construction of underground caverns of Super Dordi Hydropower Project, Nepal. ISRM 15th International Congress on Rock Mechanics and Rock Engineering – Challenges in Rock Mechanics and Rock Engineering, Salzburg, Austria, ISBN 978-3-9503898-3-8

Adhikari, S., Basnet, C.B., and Shrestha, G.B., 2022. Rock Excavation and Support for an Underground Powerhouse Cavern at Super Dordi Kha Hydropower Project, Nepal. Proceedings of 12th IOE Graduate Conference, Vol. 12, pp. 291–298 ISSN: 2350-8914

Barton, N., Line, R. & Lunde J., 1974. Engineering classification of rock masses for the design of tunnel support. Rock Mechanics, Vol. 6, pp 189–236, https://doi.org/10.1007/BF01239496

Barton, N., 2002. Some new Q-value correlations to assist in site characterization and tunnel design. International Journal of Rock Mechanics and Mining Sciences, Vol. 39, No. 2, pp. 185–216, https://doi.org/10.1016/S1365-1609(02)00011-4

Basnet, C.B., Panthi, K.K., 2020. Detailed engineering geological assessment of a shotcrete lined pressure tunnel in the Himalayan rock mass conditions: a case study from Nepal. Bulletin of Engineering Geology and the Environment. No. 79, pp. 153–184, https://doi.org/10.1007/s10064-019-01544-9

Bieniawaski, Z.T., 1978. Determining rock mass deformability: Experience from case histories. International Journal of Rock Mechanics and Mining Sciences & Geomechanics Abstracts, Vol. 15, No. 5, pp. 237–247, https://doi.org/10.1016/0148-9062(78)90956-7

Bieniawaski, Z.T., 1993. Classification of rock masses for engineering: The RMR-system and future trends. Comprehensive rock engineering, J. A. Hudson ed., Vol. 3, pp. 553–573, https://doi.org/10.1016/B978-0-08-042066-0.50028-8

Hoek, E., Torres, C. C. and Corkum, B., 2002. Hoek-Brown failure criterion – 2002 edition. Proceedings North American Rock Mechanics Society Meeting. Toronto, Canada.

Hoek, E., 2007. Practical Rock Engineering. www.rocscience.com

Hoek, E., Carter, T.G. and Diederichs, M.S. 2013. Quantification of the Geological Strength Index Chart. 47th US Rock Mechanics/Geomechanics Symposium, San Francisco, CA, USA

Katuwal, T.B., Panthi, K.K. & Basnet, C.B., 2023. Challenges associated with the construction of vertical and inclined shafts in the Himalayan Region. ISRM 15th International Congress on Rock Mechanics and Rock Engineering – Challenges in Rock Mechanics and Rock Engineering, Salzburg, Austria, ISBN 978-3-9503898-3-8

Khatri, D.B., Zhang, W., Fang, X., Meng, Q., Zhang, T., Zhang, D. and Paudayal, K.N., 2021. Rock Magnetism of Late Cretaceous to Middle Eocene Strata in the Lesser Himalaya, Western Nepal: Inferences Regarding the Paleoenvironment. Frontiers in Earth Sciences, Vol. 9, pp. 1–15, https://doi.org/10.3389/feart.2021.744063

Panthi, K.K., 2006. Analysis of engineering geological uncertainties related to tunnelling in Himalayan rock mass conditions. Doctoral Thesis, Norwegian University of Science and Technology 2006: 41, Norway, ISBN 82-471-7825-7

Panthi, K.K. and Nilsen, B., 2007. Uncertainty analysis of tunnel squeezing for two tunnel cases from Nepal Himalaya. International Journal of Rock Mechanics & Mining Sciences, Vol. 44, No. 1, pp. 67–76, https://doi.org/10.1016/j.ijrmms.2006.04.013

Panthi, K.K. and Basnet, C.B., 2018. A dynamic analysis of in-situ stress state at the Upper Tamakoshi Hydroelectric Project area, Nepal. Hydro Nepal: Journal of Water, Energy and Environment, No. 23, pp. 42–47, https://doi.org/10.3126/hn.v23i0.20824

Panthi, K.K., 2012. Evaluation of rock bursting phenomena in a tunnel in the Himalayas. Bulletin of Engineering Geology and the Environment, No. 71, pp. 761–769, https://doi.org/10.1007/s10064-012-0444-5

Panthi, K.K., 2017. Rockburst prediction methods and their applicability. Rock Burst - Mechanism, Monitoring, Warning and Mitigation Elsevier/Butterworth-Heinemann, pp. 381–385

Panthi, K.K., 2018. Super Dordi KHA Hydropower Project in Nepal Follow up and Field Visit Report, Department of Geosciences and Petroleum, NTNU Norway.

PHCPL, 2012. Project Summary & Memorandum of Information. Synopsis Report of Dordi, Nepal, Peoples Hydropower Company (P) Ltd. pp. 1–56

Rathore, A., & Panthi, K. K., 2017. Evaluation of Powerhouse Cavern for the SachKhas Hydroelectric Project in Himachal, India. Hydro Nepal: Journal of Water, Energy and Environment, No.20, pp.23–30. https://doi.org/10.3126/hn.v20i0.16485

Robyr M., Vannay J. C., Epard J. L. and Steck A., 2002. Thrusting, extension, and doming during the polyphase tectonometamorphic evolution of the high Himalayan crystalline zone in NW India. Journal of Asian Earth Sciences, Vol. 22, No. 30, pp. 221–239, https://doi.org/10.1016/S1367-9120(02)00039-1

Tunnelling for a Better Life – Yan, Celestino, Thewes & Eberhardt (Eds)
© 2024 The Author(s), ISBN 978-1-032-80042-4
Open Access: www.taylorfrancis.com, CC BY-NC-ND 4.0 license

A conceptual framework for the creation of an integrated planning system for the strategy of implementing technologies for underground urban construction

Valeriy Agafonov
MISIS University of Science and Technology, Moscow, Russia

Dmitriy Konyukhov*
MISIS University of Science and Technology, Moscow, Russia
Mosinzhproekt JSC, Moscow, Russia

Elena Kulikova
MISIS University of Science and Technology, Moscow, Russia

ABSTRACT: Development of an underground building in the conditions of a dense urban building imposes increased requirements for safety of construction works. There is a problem of creation of a system of complex planning of an appropriate technology. The present report is devoted to forming the conceptual bases of such a system. Proceeding from the analysis of accumulated experience, the conclusion was made that the system of complex strategy planning of underground building technologies should be based on methodological achievements in the building management, on scientific and technological strategies of development of underground space volumes, on a new level of investment attractiveness, competitiveness and industrial and ecological safety. In a number of cases it allows providing safety of the existing development without additional strengthening of building structures or anti-damage measures constitutes the conceptual basis of the considered system and creates fundamental conditions for its successful implementation.

Keywords: Tunnelling, Metropolitan, Underground Space Development, Strategic Planning, Urban Underground Construction

1 INTRODUCTION

The integrated development of the underground space of a metropolis is the formation of a system of elements functioning throughout the life cycle of a structure. It acts as a natural-technical geosystem and consists of a number of interrelated elements.

The problem of underground space development can be considered from different points of view depending on the tasks set, the complexity and labour intensity of which is determined by many factors: mining-and-geological, hydrological, ecological, economic, technological, etc. However, in any case the successful solution of this problem is possible only if there is a detailed and developed strategy for the organisation of underground space development, providing all stages of this process, starting with planning and design and finishing with decommissioning of the exhausted underground structures.

At present, one can distinguish the following strategic directions in the organisation of urban underground space development: directive (dictated by necessity), resource (exhaustible, non-renewable, requiring strict accounting of natural resources), urban planning (provides interconnection of planning and development of territories and underground space), social-and-environmental (solution of relevant problems of megacities).

In the first case, the location of a facility underground is not determined by urban planning or socio-economic factors, but by mining-and-geological, technological, technical-and-economic or strategic considerations.

In the resource-based strategic approach, underground space is seen as a resource whose development must be subject to certain requirements and rules, i.e. underground space is a medium for the processes of various forms of human activity to take

*Corresponding author: konuhovds@mosinzhproekt.ru

DOI: 10.1201/9781003495505-418

place. This resource also includes areas of space intended for future use. It also includes natural cavities available in underground space, used excavations, which have exhausted their operational resource and functional purpose, underground objects, decommissioned for whatever reason, in which, subject to certain regulated requirements, underground structures of other purpose can be placed. The city of Kansas City (USA) is a successful example of such an approach.

The strategic urban planning approach takes into account the relationship between the planning and development of surface areas and the planning of underground development. This approach is usually implemented in the planning of the underground construction of large cities and megacities, whose further development due to the lack of territories on the surface is largely determined and linked to the development of underground space. Examples include the large Russian megacities of Yekaterinburg and Moscow.

In the last decade, another alternative strategy for the development of underground space has become increasingly relevant and is gaining momentum – the socio-ecological one, primarily aimed at solving the social and environmental problems of megacities. As part of this strategy, office and residential infrastructure and office and residential premises are increasingly being formed in underground space.

One of the most important components instead of the above-mentioned strategic directions in the organisation of underground space development is the strategy for implementing urban underground construction technology.

It follows from the experience of active development of Moscow underground space that underground construction affects the ecology of the underground space and the state of the hydrogeological environment, provokes formation and development of adverse geomechanical and geotechnical situations leading to emergencies and man-made disasters. Moscow is experiencing significant structural changes in the geological environment, and the natural resource potential is no longer able to provide its 'status quo'. About 48% of the territory of the city is located in areas of geological risk, 12% – in areas of potential geological risk and only 40% of the territory is characterized as stable..

2 METHODS AND TECHNOLOGIES

Algorithmic filling of organizational and management decisions structure of urban underground building technologies' development planning includes the allocation of priority nomenclature of priority objects, selection of spatial location, selection of time trend of construction, setting the order of projects implementation, setting the methods of preparation of intervening massif, selection of construction technology. From the analysis of experience and peculiarities of existing methodology of creation of complex strategy planning system of underground city building technologies' implementation (Agafonov, V., Zaitseva, E., 2019, Bannister, F., Connolly, R., 2014, Bryson, J.M., Crosby B.C., 2014, Roghanian, E., Alipour M., Rezaei M., 2017) one can draw a fundamental conclusion that building technologies should be implemented proceeding from the existing methodology and methodological support in the field of building activity management and taking into account elements of scientific and technological strategy of underground space volume development which was developed on the basis of breakthrough methodology of design.

Organizational and managerial mechanism of underground building technologies realization strategies can be considered as a set of algorithmically interconnected blocks – dynamic management processes. They include an analysis of the internal and external environments for the implementation and operation of underground construction technologies, goal-setting, selection and justification of construction technology based on related priorities (fundamental principles) of resource allocation and an algorithm of actions, regulatory rules for the implementation of construction geotechnology, taking into account geotechnical risks, assessment and monitoring the implementation of construction geotechnology with a possible adjustment of the progress of implementation, with a change in the sources and amount of funding, as well as the terms of their life.

It is important that the development strategy of both individual components and the underground space as a whole should be based on scientifically substantiated planning of the development of urban underground construction technologies in the short, medium and long term, to ensure the required level of technogenic safety..

3 RESULTS AND DISCUSSION

One of the aspects of technotronic safety is technological safety which determines the degree of protection of population, buildings, structures and the environment from threats associated with the implementation of new and existing technologies in production activities, including underground construction. The variety of factors complicating the mining operations requires special approaches to the organization of underground construction, the use of modern construction technologies and quality control of their performance. These approaches should take into account specific character of underground space development consisting in permanently changing mining-and- geological and hydrogeological conditions within the limits of structure, in high requirements to environmental protection and safety of underground construction works and in maximum reduction of the impact of underground building on

the environment, etc. Underground construction in Moscow with open excavation has an average of 4–5 existing buildings in the influence zone and 17–20 buildings and structures per 1 km of the tunnel length which is under construction as well as operating utility lines, and in some cases metro facilities and other underground ones (Konjukhov, D., Polyankin, A., 2019).

In general, the main shortcoming of the current system of integrated planning of the implementation strategy of urban underground construction technologies is the high number of accidents in construction (about half of the total number of accidents), the primary reason being the violation of work technology and regulations. In this regard, the main task of construction quality management is to ensure its safety. Therefore, when assessing the quality of construction works in the system of integrated planning of the strategy for the implementation of urban underground construction technologies, indicators that make it possible to evaluate the reduction of reliability and durability of structures in relation to the design values would be applied.

As a consequence of the above, an adjustment, transformation and development of a comprehensive strategy planning system for urban underground building technologies, taking into account the density of urban development, geotechnical monitoring and innovative technical solutions for geotechnical risk management within the management support system for underground urban development are required.

4 CONCLUSIONS

Measures to manage technological safety of underground construction should be based on the following principles:

- integration – integrated impact of new construction and works technology on natural-technical, social, economic, ecological systems;
- preventability – assessment of technological impact should be carried out at the design stage and taken into account in decision-making. The essence of this principle is to prevent negative technological impacts on the natural-technical system and related technical, social and economic consequences;
- alternativeness, which is the identification and analysis of alternative construction methods that minimise impacts on the natural system and the rest of the system;
- prioritisation, meaning prioritising construction safety over all other factors;
- credibility, which defines benchmark and limit values for observations;
- compatibility – planned construction should not undermine quality of life and adversely affect the existing natural and technical system;
- flexibility – the process safety management system should be capable of adjusting process parameters at all stages of the project life cycle.

As a method of managing technological safety in underground construction, interactive control of the parameters of mining operations (Konjukhov, D., 2022) can be applied, which ultimately makes it possible to quantify the feedback of the existing development on the parameters of underground construction technologies, to increase the competitiveness and investment attractiveness of the projects under implementation, taking into account the interests of all parties involved.

REFERENCES

Agafonov, V., Zaitseva, E., 2019. Fundamental Organizational Procedures for Designing the Functional Structure of a Cement Enterprise. Science and Business: Ways Forward 11, 37–40.

Bannister, F., Connolly, R., 2014. ICT, Public Values and Transformative Government: A Framework and Programme for Research. Government Information Quarterly, 31(1), 119–128.

Bryson, J.M., Crosby B.C., 2014. Bloomberg L.: Public value governance: Moving beyond traditional public administration and the new public management. Public Administration Review, 74(4), 445–456.

Konjukhov, D., 2022. Interactive control of technological parameters of double-track underground tunnel driving. Gornyi informatsionno-analiticheskii bulletin, 5, 84–94.

Konjukhov, D., Polyankin, A., 2019. Ensuring the safety of the existing buildings during the construction of the underground in Moscow. Tunnels and Underground Cities: Engineering and Innovation meet Archaeology, Architecture and Art. Taylor & Francis Group, London.

Roghanian, E., Alipour M., Rezaei M., 2017. An improved fuzzy critical chain approach in order to face uncertainty in project scheduling. International Journal of Construction Management, 18, 1–13.

Tunnelling for a Better Life – Yan, Celestino, Thewes & Eberhardt (Eds)
© 2024 The Author(s), ISBN 978-1-032-80042-4
Open Access: www.taylorfrancis.com, CC BY-NC-ND 4.0 license

Deep powerhouse caverns design development and challenges – Snowy 2.0 experience

Ivan Ching*
SMEC Pty. Ltd., Sydney, NSW, Australia

Mark Diederichs
Queen's University, Kingston, Ontario, Canada

Ben Chapman & Giancarlo Cardone
Snowy hydro Limited, Cooma, Australia

ABSTRACT: Snowy 2.0 is a major renewable energy infrastructure project currently under construction in Australia. Upon completion, the project will increase the generating capacity of the existing Snowy Hydroelectric Scheme by 2200 MW, making it the largest source of renewable energy in Australia. The Power Station Complex (PSC) is located at about 750m below ground in sedimentary rocks with two main caverns, the Machine Hall (MH) and the Transformer Hall (TH) connected by axillary tunnels. During the preliminary design stage, the post-peak behaviour of rock mass and global stability of the caverns has been studied and confirmed the layout of the PSC. Situating in structured ground with significant in-situ stress, it is expected that the rock discontinuity-controlled mechanism is governing the design of rock support. The support system relies on systematic rock bolts to form reinforced rock arch for temporary and long-term stability. The shotcrete lining is designed as "skin" to resist localised wedges between rock bolts. In construction, the observational approach has been adopted to verify the design based on encountered conditions and ground response. This paper summarises the experience from the preliminary design to the construction stage. The engineering challenges and the risk control measures from the owner's engineer perspective are discussed.

Keywords: Snowy 2.0, Hydropower, Deep caverns

1 INTRODUCTION

1.1 *Snowy 2.0*

Snowy 2.0 is a major renewable energy infrastructure project currently under construction in Australia. Upon completion, the project will increase the generating capacity of the existing Snowy Hydroelectric Scheme by 2200 MW, making it the largest source of renewable energy in Australia.

The project links two existing reservoirs, Tantangara (elevation 1231 m) and Talbingo (elevation 546 m), through 27 km of waterway tunnels and an underground power station equipped with 6 Francis pump-turbine units. The project also includes 1.3 km of shafts and 10.4 km of access tunnels. Figure 1 presents the concept of Snowy 2.0 pumped storage project.

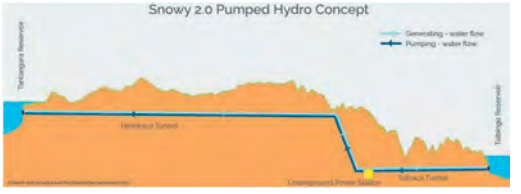

Figure 1. Snowy 2.0 pumped storage project concept (source: FGJV).

The project is owned and operated by the Snowy Hydro Limited (SHL). The design and build contract has been awarded in 2019 to the principal contractor Future Generation Joint Venture (FGJV) and a Design Joint Venture (DJV) has been appointed by the contractor to carry out the

*Corresponding author: Ivan.Ching@smec.com

DOI: 10.1201/9781003495505-419

engineering design for civil and mechanical and electrical works.

1.2 *The power station complex*

The Power Station Complex (PSC) is located at about 750m below ground in sedimentary rocks with two main caverns, the Machine Hall (MH) and the Transformer Hall (TH) connected by the axillary tunnels. The 251m long, 32m wide and 52m height Machine Hall will host six units of pump-turbines, motor-generators, main inlet valves. The Transformer Hall where the six main transformers, draft tube valves and cooling water equipment are located, is 217m long, 20m wide and 46m height. The distance between the two main caverns is 60m. There are two Main Access Tunnels (MAT and ECVT) and six Isolated Phase Busbar (IPB) tunnels which house the electrical equipment required between the motor-generators and the main transformers. The IPB tunnels are 10m wide and 14.5m high. The pillar width between IPB tunnels are 18m to 19m. The layout of the PSC is shown in Figure 2.

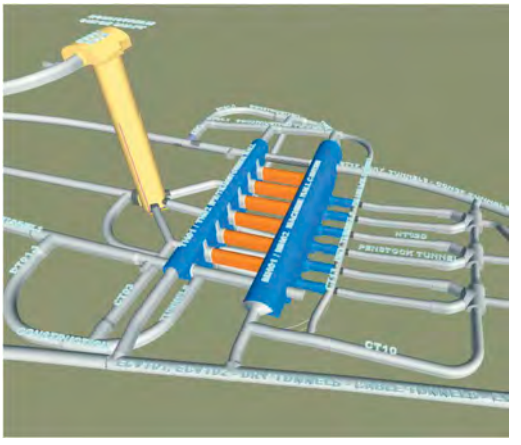

Figure 2. Snowy 2.0 Power Station Complex Isometric View (MH and TH in blue; IPB in orange).

2 ROCK MASS

The PSC is within the Ravine Beds geological unit (Suer label as per Geological Survey of NSW) and this has been sub-divided into the Ravine Beds West (RBW) formation. The lithology is interlaminated and interbedded siltstone and sandstone. There are interbedded sequences of sandstone and conglomerate, to 20 m thickness, which appear to lens out laterally. The core samples from borehole BH5105C-W1 (Figure 3) indicates approximate 500mm of highly fractured cores in cavern horizon. Sheared defects appear to be both parallel and oblique to the bedding, likely associated with the folding of the bedded strata. The bedding is indicated by oriented core data to dip at about 35-45° towards the ENE, being obliquely across the long axis of the cavern (Figure 3).

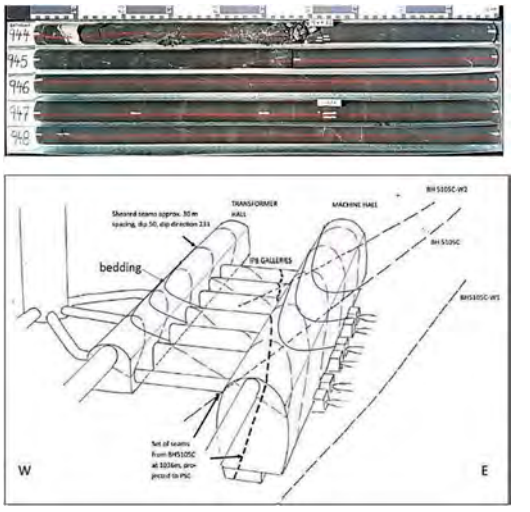

Figure 3. Typical interlaminated siltstone and sandstone within the PSC area (Top); 3D geo-structural model based on available SI data (Bottom).

3 DESIGN DEVELOPMENT AND OPTIMIZATION

3.1 *Rock mass post peak behaviour*

To confirm the layout of the PSC caverns and the overall excavation dimensions, the first optimization of the geotechnical design was carried out in 2020. The acceptance criteria for rock pillar performance were developed collaboratively by the owner and the contractor. A reduction in overall excavation dimensions was achieved while maintaining minimum safe pillar widths for overall cavern stability (Diederichs et al 2022). This was achieved through FLAC continuum modelling. In this approach, the rock mass is modelled as an equivalent continuum material. The rock mass parameters are determined following the Hoek-Brown failure criterion, the global behaviour of the excavations is assessed. Figure 4 presents the FLAC3D modelling of the owner's engineering team.

According to Hoek (2006), it is required to consider the post-failure characteristics of the rock mass when using numerical models to investigate the progressive failure of rock mass. In the analysis, the plasticity theory shall be adopted, and the Hoek-Brown failure criterion shall be treated as a yield criterion. The suggested post peak behaviour of rock mass is presented in Figure 5.

Based on the study of Walton et al (2019) where an extensive triaxial testing database of intact core is established to examine the residual strength of different rock types. The observed stress–strain behaviour

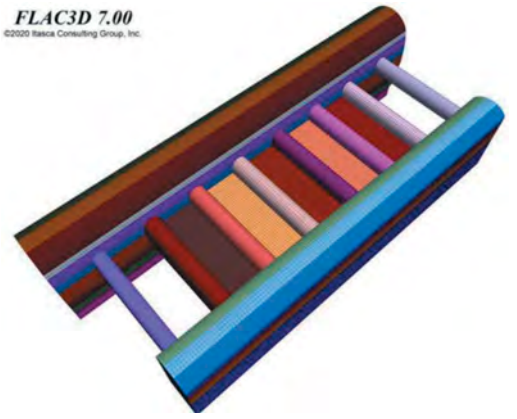

Figure 4. FLAC3D modelling to access the rock pillars stability and rock mass post-failure parameters.

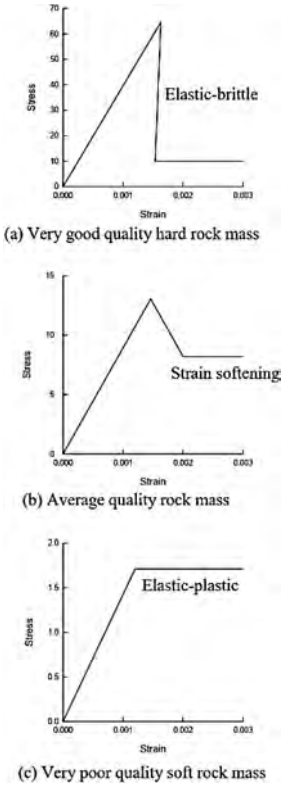

Figure 5. Suggested post failure characteristics for different quality rock masses (after Hoek 2006).

of rocks in compression tests can be separated into the four phases: (i) pre-yield; (ii) post-yield but pre-peak; (iii) post-peak weakening; and (iv) the residual state. The rock behaves from initially elastic to short term frictional strengthening; followed by weakening due to cohesion loss and facture growth; and finally, the strength reduction reaches constant with further straining. The result for sedimentary rocks from the study suggests the proposed post peak parameters can be optimised and a revised set of peak, post peak and residual strength parameters are used in the design.

The sensitivity analysis shows the design criteria such as rock mass plasticity and stability of rock pillars between caverns are very sensitive to the rock mass modulus (peak and residual) as well as the post peak strength evolution and dilation. Figure 6 and 7 present the comparison of the predicted rock mass plasticity around the cavern excavations and the rock pillars between the IPB tunnels using "peak&residual" and "peak,post-peak&residual" rock mass weakening behaviour in the model. The rock support elements are not explicitly modelled in the simulation. It is noted that the rock support cannot reduce the yield zone or pillar plasticity by a large amount in the continuum model. However, the support can reduce the post-yield displacements by reducing the plastic strain in the rock mass without failing as support elements or systems.

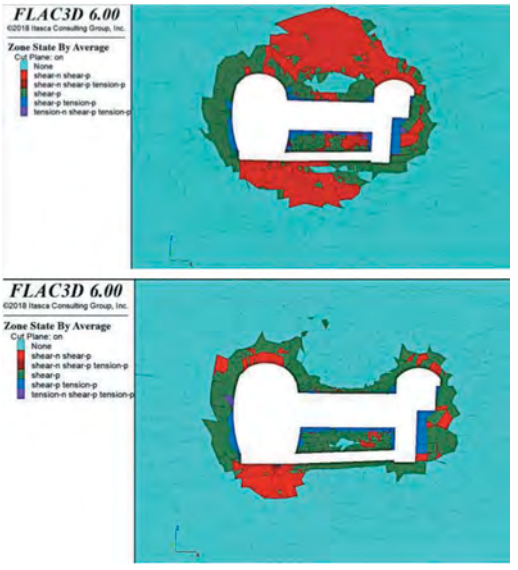

Figure 6. Predicted rock mass plasticity around the main caverns for "peak&residual" behaviour (Top); "peak, post-peak&residual" behaviour (Bottom).

3.2 *Excavation and support philosophy*

A reference design for the cavern complex was initially carried out by SMEC in 2017. The excavation and support concept comprised a combination of rock reinforcement and shotcrete. The support system was designed as "drained".

In the detailed design, a consistent design philosophy of the cavern support system (Figure 8) has been adopted. The systematic rock bolts form a reinforced

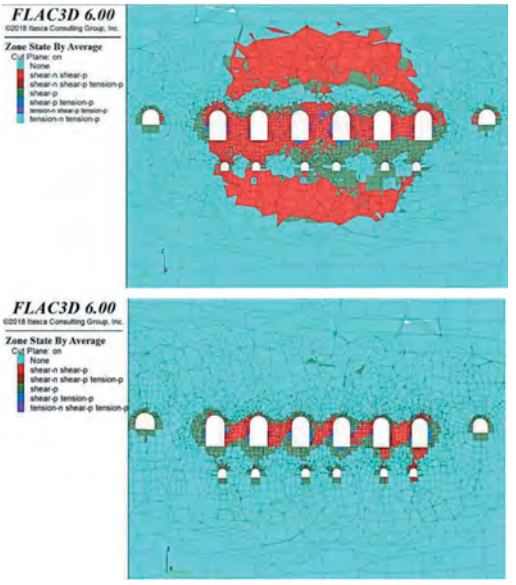

Figure 7. Predicted rock mass plasticity around the IPB tunnels for "peak&residual" behaviour (Top); "peak, post-peak&residual" behaviour (Bottom).

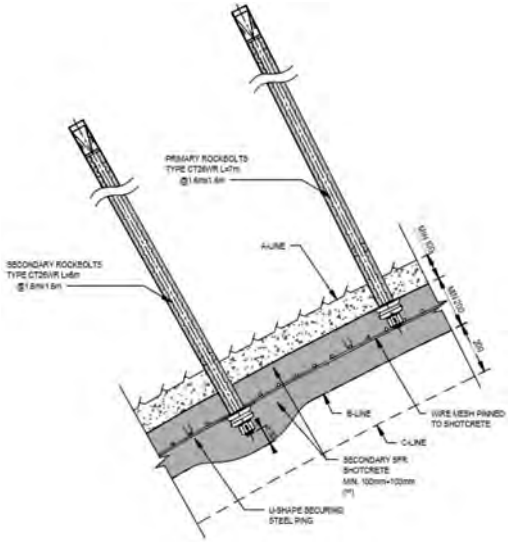

Figure 8. PSC cavern rock support system (after DJV).

rock arch around the excavation and supporting itself. The primary rock bolts are installed after each round of excavation to maintain the stability during excavation and provide a "supported" ground for personnel entry. The installation of secondary bolts shall be delayed as much as possible to minimise the impact from ground deformation to meet the durability requirement. The steel fibre and mesh reinforced shotcrete lining has the primary function as "skin" to protect the rock face and rock bolts from weathering and durability consideration. The shotcrete lining is also designed to resist localised wedges between rock bolts. The addition of polypropylene fibres to the shotcrete mix is to ensure the performance under fire design cases to fulfil the employer's requirement. Shell action of shotcrete lining is not expected as the waviness of excavation profile cannot be guaranteed by the drill and blast excavation method.

To realise the "drained" concept, a systematic drainage holes (102mm diameter, 10m long and 6m spacing) around the caverns and IPB tunnels is proposed in the detailed design. Groundwater inflow is expected to pass through the drainage system into the caverns and discharged to the Talbingo Reservoir. Such that the full hydrostatic load can be avoided in the ground support design. A drainage tunnel CT13 with drain curtain (systematic 73mm diameter drill holes) is proposed to situate between the Machine Hall and the manifolds to cut off the water pressure thus limit the inflow into the PSC structure. To achieve the groundwater inflow requirement, pre-grouting and/or post-grouting may be necessary depending on the encountered ground conditions.

Two types of Double Corrosion Protection (DCP) rock bolts from the manufacturer DSI, i) DSI CT-M33 and; ii) DSI High Strength CT26WR (details in Table 1) were proposed and considered as the permanent secondary rock support initially. An internal assessment using FLAC3D continuum model was performed to investigate the impact on the bolts installed in the cavern crown due to ground relaxation and deformation during benching. The influence of cavern excavation staging and timing of bolt installation were also considered in the modelling.

Table 1. List of major risk items and control measures.

Bolt Details	CT-M33	CT26WR
Nominal Diameter	32 mm	26.5 mm
Bar Cross Section	804 mm²	552 mm²
Yield Strength	383 kN	524 kN

In this assessment, the 8m long 1.6mx1.6m pattern rock bolts were explicitly modelled as cable elements installed in the crown of the caverns. Following the envisaged construction sequence delaying the completion of secondary bolts as much as possible to minimise the deformation imposed by the displacement of the rock mass, the 3D analysis included all the excavation staging and the development of bolt force up to the excavation completion. Figure 9 shows the CT-M33 bolts in the crown started picking up load from stage 3 benching (where the crown bolt installation competed) and reached its yield limit at stage 8 prior to the excavation complete. The prediction from the continuum model only considered the

effect due to elevated in-situ stress and rock mass relaxation. The localised effect from rock discontinuities shear displacement on the rock bolts could not be reflected by the model. The result also revealed that the bolt yielding zones (Figure 9) were concentrated at the upstream and downstream sides of MH and TH due to the influence of in-situ horizontal stress. The predicted bolt force was generally higher at the middle (pillar 3 and 4 locations) of the caverns because of the stress redistribution around the cavern openings and a higher rock mass deformation had resulted. In the current design, CT26WR rock bolts are proposed as the cavern secondary support.

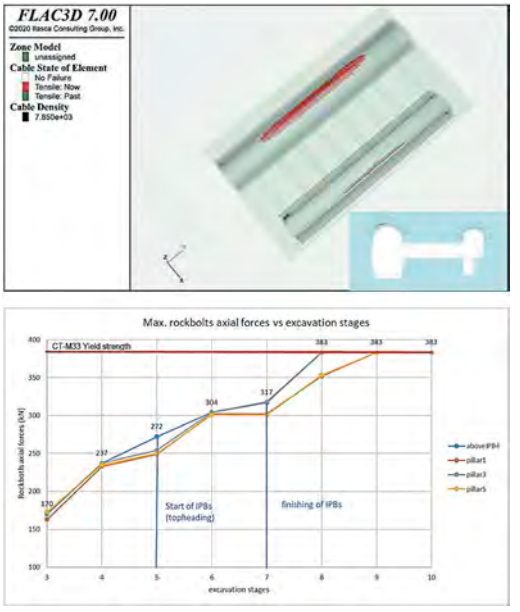

Figure 9. Predicted status of CT-M33 rock bolts in the crown after excavation completed (Top); Predicted bolt force development at different excavation stages (Bottom).

3.3 *Rock support failure mechanism*

With the combination of the elevated in-situ stress and the observed sheared defects of rock mass, the shear displacement failure mechanism of rock reinforcement is expected to be the main driver of potential instability in the caverns. The displacement of rock blocks along sheared joints due to ground deformation can yield a grouted bolt locally where it crosses the rock joints. The bolt will be loaded by a combined action of tensile and shear forces induced by the shear displacement. The ultimate load is depending on the inclination of the rock bolt crossing the rock joint. A study (Chen and Li, 2015) conducted to test the performance of rock bolts under combined pull and shear loading by applying a load in a direction deviated from the bolt axis between zero degree (pure pull) and 90 degree (pure shear). Figure 10 presents the results from the tests suggests that the ultimate pull load (tensile capacity) is decreasing while shear load and inclination angle increase.

Discrete element analysis with rock discontinuities and rock bolt structural elements modelled explicitly allows quantitative assessment of this failure mechanism. DJV utilises 3DEC discontinuum models (Figure 11) to estimate the shear displacement of rock joints and the effect on the rock bolts. Two design criteria for the rock bolts are defined (Khodr et al 2023), 1) Maximum strain: 2.5% for the primary rock bolts and 1.5% for the secondary rock bolts; 2) Maximum bolt shear displacement: 20 mm for durability and 35 mm for structural integrity of the primary and secondary rock bolts. To verify the rock bolt performance under the proposed design criteria, rock bolt preproduction tests are developed and carried out in the laboratories (Figure 12 and Figure 13).

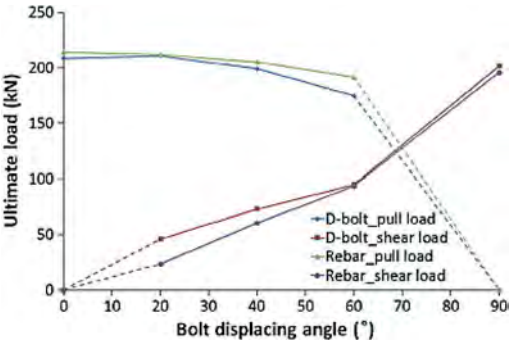

Figure 10. Maximum pull and shear displacement components versus the loading angle (after Chen and Li, 2015).

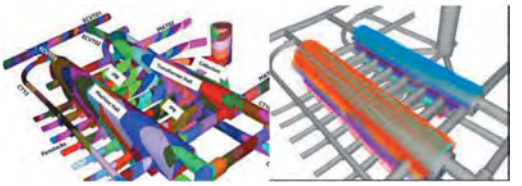

Figure 11. 3DEC discontinuum model – Rockbolts Explicitly Modelled (Source: Khodr et al 2023).

In the double shear tests, the double corrosion protection system of CT26WR bolts at 20mm shear displacement retained its long-term performance. The test samples were sectioned after the tests and indicated that limited number of sub-millimetre perforations, the internal and external grout coverage to the sheath maintained. For the bolts in the 35mm shear displacement tests, the results showed the number and size of perforations in the sheath was significant, the long-term durability was not guaranteed (Figure 12). However, the structural integrity of the bars was retained and fit for its intended purposes.

Figure 12. Double shear test of bolt (Top); CT26WR after 35mm shear displacement (Middle); Load-displacement curves of CT26WR double shear tests for 20mm and 35mm limits (Bottom).

Test samples of CT26WR bolts with a total length of 1m long were prepared for the double embedment tests (Figure 13). Two types of joint arrangements: 900-100 mm and 500-500 mm were considered for the preparation of samples to investigate the different behaviour of bolt under tensile load. To monitor the deformation of the bolts along the encapsulation length and determine the strain of bar at different locations with applied axial tensile load during the test, all samples were instrumented with strain gauges affixed prior to encapsulating the bolts. Figure 13 presents the test results for the CT26WR

Figure 13. Double embedment elongation test (Top); Sectioned CT26WR after 2.5% strain elongation (Middle); Load-displacement curve of CT26WR double embedment test for 2.5% strain limit (Bottom).

500-500 arrangement for 2.5% strain limit. The load-displacement curve showed a linear relationship initially. Until the applied tensile load reached around 520kN, a ductile behaviour of the steel bar started developing as the load increase. The

observation was consistent with the high strength CT26WR bolts yield property.

4 RISK CONTROL

A series of design workshops among the contractor, the designer and the owner's engineer were carried out to resolve the design review comments and discuss the risk items and control measures. The main concerns related to the verification of design assumptions; the confirmation between the predicted, actual and acceptable effects and; the contingence measures to control risks and uncertainties were focused. In general, these concerns can be addressed by applying the observational method and a better understanding of the ground conditions by further site investigation plan. Table 2 lists the major risk items, possible consequences and control measures.

Table 2. List of major risk items and control measures.

Risk items	Possible consequences	Control measures
Design input parameters	Under-design; support failure; tunnel collapse	Insitu geomechanical tests to confirm the design parameters; design model calibration based on observed ground responses; incorporate encountered rock features in the design model
Unexpected ground conditions	Support re-design; construction delay	Horizontal core along the full length of cavern heading; change of excavation sequence to start with exploratory central heading; provisional contingence/poor rock support
Permanent rock bolt performance	Long term durability issues; cavern instability	Change of excavation sequence and delay the installation of bolts to allow displacement and stress release; re-bolting at critical areas
Rock pillars integrity	Pillar overstress; cavern instability	Additional inclined boreholes to investigate the pillar conditions; Instrumentation monitoring to confirm the design prediction
Creep effect	Excessive cavern deformation	Monitoring to confirm the design prediction

4.1 *Observational method*

"The Observational Method (OM) is a process in which acceptable limits of structural and geotechnical behaviour are established. In addition, performance predictions, monitoring, review and modification plans, are fully prepared. The design is checked for robustness before construction starts. During (and after) construction, the results from monitoring are reviewed against the predictions and robust modifications are introduced where appropriate." (CIRIA R185, 1999).

In this project, the application of OM fulfils the Employer's Requirement (ER) of design verification. The acceptance criteria of rock bolts and the design limits of geotechnical parameters which dictate the expected ground behaviour are established during the design. The design predictions on both support performance and ground behaviour based on expected conditions are conducted. Monitoring strategy to capture the actual support performance and ground response is developed. Before construction, further site investigation (section 4.2) and rock bolt pre-production tests (section 3.3) are performed to check for robustness and performance requirement. Contingence support arrangement is prepared as "toolbox" for poor ground conditions/unexpected conditions that outside the design limits during the CHT excavation.

Design hold points (HPs) and witness points (WPs) system (Table 3) was developed to review and verify the predictions. The difference between HPs and WPs is that HPs must be released by the confirmation from the designer prior to the commencement of next construction stage.

Table 3. List of design hold point and witness point.

HP/ WP	Construction stage	Objectives
HP0	Central heading tunnel (CHT) excavation prior to side slashings	To verify the expected ground conditions and predicted behaviour
HP1a	CHT excavation at TBM tunnel crossings	To verify the geological conditions of the rock slab between the CHT and TBM tunnels
HP1	Complete excavation of top heading (CHT and side slashings)	To verify the expected ground conditions and predicted behaviour. To identify the critical areas for specific shear displacement monitoring
WP1	Complete excavation of 1st benching	To review and update the geological conditions and shear displacement monitoring
HP2	Complete excavation of 2nd benching	To identify areas where re-bolting is required and confirm rock pillars conditions based on additional boreholes

(*Continued*)

Table 3. (*Continued*)

HP/ WP	Construction stage	Objectives
WP2	Complete excavation of 4th benching	To review and update the geological conditions and shear displacement monitoring
HP3	Complete excavation of 6th benching and IPB tunnels	To verify the predicted pillar behaviour and support performance
HP4	Complete caverns excavation	To review and confirm the actual ground behaviour and support performance
HP4a	Complete caverns excavation	To review and confirm the effects on TBM tunnels

Back-analysis will be carried out at HP1 to HP4. The 3D numerical design model will be calibrated based on instrumentation monitoring data and geological mapping/investigation of encountered conditions. Critical areas under significant effect of shear displacement will be identified, additional shear displacement monitoring scheme will be implemented in these areas. Together with the input from the refined 3D model, the planned re-bolting strategy will be confirmed. The behaviour of the rock pillars between the IPB galleries will also be re-assessed at HP3 by the model. At the time of writing, the CHT excavations for the MH and TH have been commenced (Figure 14). The HP0 and HP1a are under processed.

4.2 *Additional site investigation*

The primary purpose of the investigation is to confirm the geotechnical design parameters adopted for the detailed design. In particular, the rock mass deformability modulus, in-situ stress status, the rock discontinuities pattern and the joint properties are focused. In-situ stress tests by over-coring are carried out inside the horizontal core drilling along full length of the TH. In-situ Direct Shear strength test (DST) of rock discontinuities and Plate Load Test (PLT) (Figure 15) are performed inside the niches constructed in proximity of the caverns. The core recovery drilling along the TH is completed and assessed prior to the commencement of CHT excavation to confirm the actual ground conditions are in the expected range. Five inclined boreholes are proposed drilling from the top-headings of MH and TH to investigate the IPB tunnels rock pillars conditions prior to benching.

Figure 14. CHT excavation face.

Figure 15. In-situ plate load test.

5 CONCLUSION

This paper has covered the experience of design development and constriction of deep powerhouse cavern of Snowy 2.0 project from the owner's engineer perspective. In structured ground with elevated in-situ stress, the global stability of excavation governed by the layout of the caverns and IPB galleries is the primary consideration. The post failure behaviour of rock mass is playing an important role in the stability assessment. The rock reinforcement is designed as the main support element maintaining the temporary and permanent stability. The failure mechanism is discontinuity-controlled, and the rock

bolt performance is governed by bolt shear and strain-based criteria established. Rock bolt pre-production laboratory tests (Double shear tests and Double embedment elongation tests) are developed to verify the performance of bolt under the proposed acceptance criteria. Risk control by applying observational method to confirm the actual conditions within the range of design predictions. With the back-analysis of numerical modelling based on the encountered rock features and ground response observed, critical areas with special attention/additional support measures or re-bolting can be identified and properly managed.

ACKNOWLEDGMENTS

The authors acknowledge the permission granted by SHL to publish this paper. The authors also acknowledge the contribution of the colleagues from SHL, FGJV, DJV and SMEC on the project.

REFERENCES

Abou-Kheir, S., Brogiato, A., Lignier, P., Lambrughi, A., Decarli, G., Diederichs, M., Ching, I. & Frontini, D. 2023. Assessment of the creep behavior of siltstone for the Snowy 2.0 hydropower station using multistage uniaxial and triaxial creep tests. 15th International ISRM Congress 2023 & 72nd Geomechanics Colloquium, Salzburg, October 09th - 14th, 2023

Chapman B. Yee M., Gomes A.R.A. 2019. Engineering challenges of the Snowy 2.0 pumped storage project. ITA-AITES World Tunnel Congress WTC2019, Naples, Italy - Tunnels and Underground Cities: Engineering and Innovation meet Archaeology, Architecture and Art – Peila, Viggiani & Celestino (Eds), Taylor & Francis Group

Chen, Y. & Li, C.C. 2015. Performance of fully encapsulated rebar bolts and D-Bolts under combined pull-and-shear loading. Tunnelling and Underground Space Technology 45 (2015) 99–106.

Diederichs, M., Miller, D., Chapman, B., Ching, I. & Gomes, A. 2022. "Snowy 2.0 Pumped Storage Scheme: Rock Engineering Challenges in Tunnelling and Cavern Construction", Proceedings of the 2022 Tunnelling Association of Canada Conference, Vancouver, B.C., Canada

Gomes, A.R.A, Chapman, B., Diederichs, M. & Ching, I. 2023. Conceptual Framework of the Snowy 2.0 Pumped Storage Project (PSP) Geotechnical Baseline Report (GBR) for underground works. ITA-AITES World Tunnel Congress WTC2023, Athens, Greece - Expanding Underground - Knowledge and Passion to Make a Positive Impact on the World – Anagnostou, Benardos & Marinos (Eds), Taylor & Francis Group

Gomes, A.R.A, Chapman, B., Chapman N. and Cortes, F. 2021. Development of the Geotechnical Baseline Report for the Snowy 2.0 Pumped Storage Project, ATS 2020 +1 Tunnel conference, Melbourne.

Hoek, E. 2006. Practical rock engineering.

Khodr, S., Tonioni, P.L., Lignier, P., Lambrughi, A., Diederichs, M., Ching, I. & Lazzarin, F. 2023. Design criteria for caverns under high stress rock conditions for Snowy 2.0 Power Station Complex. ITA-AITES World Tunnel Congress WTC2023, Athens, Greece - Expanding Underground - Knowledge and Passion to Make a Positive Impact on the World – Anagnostou, Benardos & Marinos (Eds), Taylor & Francis Group

Lignier, P., Tonioni, P.L., Blaise, A.N., Lazzarin, F., Gallera, R. & Ching, I. 2023. Snowy 2.0 hydro power station complex – The design's evolution of the PSC caverns, from preliminary to detailed design. AFTES International Congress 2023, Paris, 2-4 October 2023

Nicholson, D., TSE, C. & Penny, C. 1999. The observational method in ground engineering – principles and applications. Report 185. CIRIA. London. 214p.

Walton. 2019. On the residual strength of rocks and rock masses. Rock mechanics and rock engineering 52:4821–4833

Tunnelling for a Better Life – Yan, Celestino, Thewes & Eberhardt (Eds)
© 2024 The Author(s), ISBN 978-1-032-80042-4
Open Access: www.taylorfrancis.com, CC BY-NC-ND 4.0 license

Minimising impacts on the local habitat in relocation and construction of a large cavern for track crossover at Acharya Atre Chowk Metro Station of the Colaba-Bandra-Seepz (Line 3) in Mumbai, India

Subodh Kumar Gupta*, Rajeshkumar Mittal, Maheshkumar Dange & Rohit Tilak
Mumbai Metro Rail Corporation Limited, Mumbai, India

ABSTRACT: Mumbai Metro Rail Corporation Ltd is implementing Colaba-Bandra-Seepz (Line 3), a 33.5 Km fully underground metro rail project, in Mumbai, India. The landscape of Mumbai has been formed over a period by joining seven islands through multiple land reclamations in the 19th century. The Line 3 is substantially in South Mumbai, which is the old and historic part of the city. It is a narrow land mass and congested, with sea/ creek on three sides. Road space is less compared to the population density and traffic congestions are norm rather than exception. As a result, major underground intervention is challenging on technical, social, and logistic grounds. In the approved project, track crossover was part planned at the Science Museum Station. However, at execution stage, local authorities refused permission for excavation of the portion of this area due to its potential impacts on a major civic water tunnel that was passing beneath and reservations to relocation of underground grid cables of 220 KV infringing the site. This resulted in exploration of either an alternative method of construction at the planned location or relocation of the crossover nearby to meet operational needs. The adjoining station of Acharya Atre Chowk was also a difficult site, being constructed in a residential and commercial locality and below a busy major arterial road with a junction of 5 roads on one side. There were massive civic utilities limiting further elongation of the station box to accommodate the crossover. This paper explores alternate options examined to arrive at the most appropriate solution. It delves into how, working closely with local community and technical experts, the finalised option of a large cavern was designed and executed in a sustainable way by minimizing social impacts on the local habitat while meeting the operational requirements expected from the crossover.

Keywords: NATM, Metro3, Crossover, Turnouts, Mumbai

1 INTRODUCTION

Mumbai Metro Rail Corporation Ltd, a Joint Venture company of Government of India and the Government of Maharashtra state, has undertaken Colaba-Bandra-SEEPZ (Line-3) Metro line construction in Mumbai, India. Civil infrastructure construction work of this 33.5 Km long fully underground line is divided in seven contract packages. The subject work is part of Package 03 of these seven packages and being implemented by a joint venture of M/s Doğuş İnşaat ve Ticaret A.Ş(Turkey) and M/s Soma Enterprise Limited(India).

A crossover cavern of 106m length, 11m high and 18m wide has been constructed below E. Moses Road between under-construction Science Museum and Acharya Atre Chowk Stations. This road carries heavy city traffic. A crossover is a track structure that permits transfer of trains from one line to another and is an operational necessity. There are limitations related to curves and slopes/grades in the track alignment that have to be factored in to locate a crossover.

This location of track crossover was not originally envisaged at this location and, in a way, was fait-accompli as no other alternative location could be found within acceptable operational parameters after the authorities refused permissions for construction for this facility at the original location. Also crossover could not be shifted adjacent to Acharya Atre Chowk due to presence of junction of five roads with massive utilities beneath it. Construction of cavern for the crossover at this location faced challenges of shallow ground water table, highly weathered to moderately weathered rock strata (Breccia), presence of civic utilities and high-rise buildings in close vicinity. The site would also have had negative impact on local habitat if proper precautions were not taken during implementation due to its being in the midst of residential and commercial localities, and a crematorium.

*Corresponding author: subodh.gupta@mmrcl.com

DOI: 10.1201/9781003495505-420

2 ORIGINAL PLAN

As per original proposal in the Contract, the crossover structure is planned at the north end of the Science Museum Station, Mumbai, India with Cut and Cover construction method. The crossover structure is planned to be a part of the main station box structure. The length of station box was indicated to be 363m out of which 162m length was allocated to the crossover. The box structure is placed on either side of a T- shaped road junction called Rakhangi Junction and crossover is planned at one end of it. Multiple entry/exit structures are planned on either side of the roads of the T-shaped junction. Extent of civic utilities at this junction is highlighted in the inset.

Figure 1. Location plan for station and crossover.

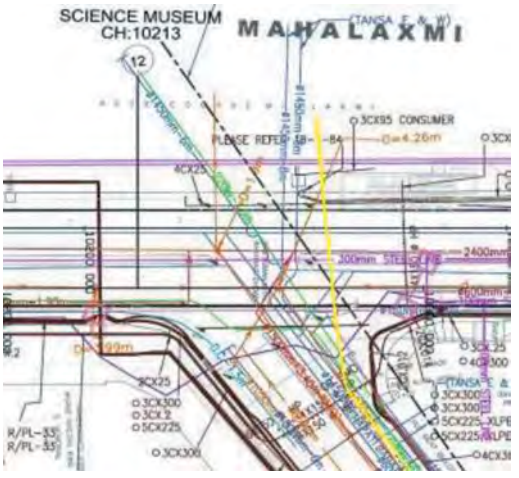

Figure 2. Science Museum Station vis-a vis Rakhangi Junction. Civic utilities at the junction shown in the inset.

After the contract was awarded and utility management scheme was finalised and submitted to the utility owning agencies, two reservations from authorities were received. There were other impediments also to deal with as below:

1) Local Municipal Corporation advised shifting of station box away from their 45 m deep water main tunnel that was crossing the site due to its potential effect on the structural safety of this water main. [Pressurized water main tunnel of 6m diameter, M 20, 300 mm RCC Concrete lining, water pressure of 12 bar]
2) Local power distribution authorities communicated their inability to divert 220 KV power cables passing at shallow depth from this site.
3) A 9 m wide double barrel RCC box barrel drain at the junction of Rakhangi chowk cannot be laterally shifted due to other obligatory civic utilities.
4) Area had many trees that had to be factored in to avoid felling.
5) Underground tanks of a Petrol pump to be relocated.

There is a hospital for old age people, a Christian and Muslim cemetery on one side while a Racecourse on the other.

In view of various conflicting limitations and complexities the Employer (MMRC) and the General Consultants explored various options proposed by the contractors and decided to shift the Science Museum station about 350m away from the Rakhangi junction towards north from the existing location without the crossover component to reduce its longitudinal length. It was also decided to shift the crossover to the adjoining station by making modifications in the existing plans of that station.

This paper will now discuss various alternatives that were explored to arrive at above decisions.

3 SOLUTIONS PROPOSED

Option 1: Rakhangi junction area to be crossed with a NATM structure of 136 m length for crossover while the main station box structure shifted by 350 m towards North.

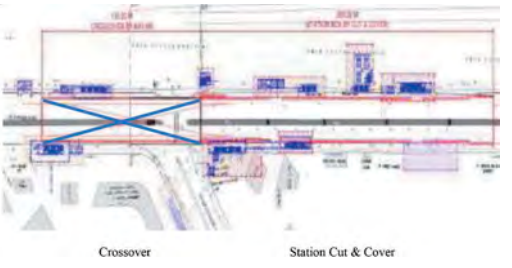

Figure 3. Conceptual plan for option 1.

Geological conditions at this location – on same location, methodology of construction has been modified from Cut & Cover to NATM with similar geological conditions.

Advantages – Minimum land acquisition, minimum tree felling, minimum impact on traffic, minimum utilities diversion.

Disadvantages –

1) Likely higher settlement due larger crossover cavern in weaker ground.
2) Longer construction timeline due to related impacts on TBM scheduling for the remaining tunnel length.
3) More bureaucratic reservations and complexities in monitoring of the water main tunnel that would now have been below the cavern instead of initial concept of Cut and Cover box.
4) Logistic limitations as station portion also to be utilised as the access shaft for the NATM cavern thus having adverse impact on the project timelines.

Option 2: Crossover to be shifted towards South of the Rakhangi junction, junction area to be crossed with two individual NATM tunnels and the Station box shifted towards North.

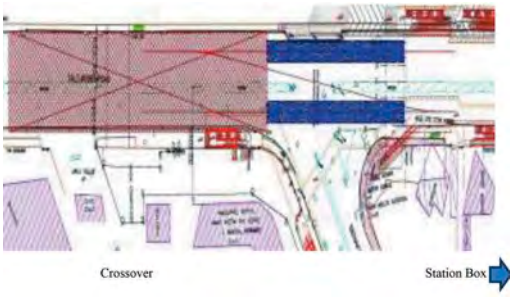

Figure 4. Conceptual plan for option 2.

Advantages – Simultaneous construction of NATM Tunnels from either side, ease of construction and logistic movement.

Disadvantages –

1) Longer construction timelines due to sequencing of NATM tunnel and Cut & Cover structure of the crossover.
2) A separate TBM shafts for undertaking tunnelling between the crossover and up to Mumbai Central Metro Station towards south.
3) Water main tunnel safety related concerns still remains for the municipal authorities even though the cavern size has reduced.
4) Logistic limitations as station portion also to be utilised as the access shaft for the NATM cavern thus having adverse impact on the project timelines.
5) Higher costs due to additional NATM and Cut & Cover construction for crossover and tunnel.
6) Sufficient space not available to divert 9 m wide double barrel storm water drain. Traffic diversion sequence to be complex due to space constraints.

Option 3: A staggered scissor crossover by widening a TBM tunnel by NATM (Downline-169.28 m, Upline-114.16 m) on the south end of the adjoining Acharya Atre Chowk Station

Figure 5. Conceptual plan for option 3.

Geological at the location is predominantly Grade III & IV Breccia weathered rock.

Advantages – Location below the road. No tree felling, no impact on traffic, no utilities diversion.

Disadvantages –

1) NATM cavern with variable tunnel profile and higher number of construction stages
2) for logistic movement, no separate access is available for construction of NATM cavern. Station (Cut & Cover) to be utilised as the access shaft affecting project timelines.

Option 4: Crossover cavern in the mid-section by widening the TBM tunnels by NATM between the Science Museum and Acharya Atre Chowk Station to have a single cavern for both the tracks.

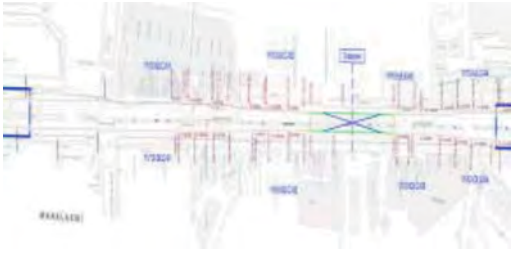

Figure 6. Conceptual plan for option 4.

It is similar to the Option 3 except that the crossover was moved midsection to have benefit of marginally better geological conditions to contain settlement on the surface. Advantages/disadvantages in this Option were same as of the Option 3.

Option 5: Crossover cavern in the mid-section by widening a TBM tunnel by NATM between the Science Museum and Acharya Atre Chowk Station with a logistic shaft on the median area of the road. This is to be a single cavern for both the tracks.

A shaft at the site of NATM cavern would remove logistical and timeline constraint to a large extent as against Option 3, 4 and 5 but still pose problems of traffic management and handling of construction logistics from a small shaft in the middle of the road even if a component of road is taken over for construction purposes.

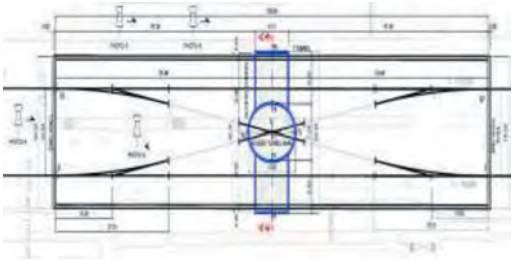

Figure 7. Conceptual plan for option 5.

Option 6: Crossover cavern near the Acharya Atre Chowk station by widening a TBM tunnel by NATM with a logistic shaft on the footpath of the road.

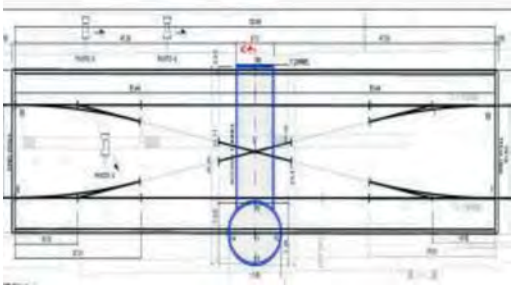

Figure 8. Conceptual Plan for Option 6.

This option is considered superior to the previous option in terms of handling traffic and construction logistics even though few trees on the kerb side would be affected and were to be fell.

Option 7: Crossover cavern of 106 m length near the Acharya Atre Chowk station by widening a TBM tunnel by NATM with a logistic shaft the adjoining plot owned by the Municipality and agreed to be given on temporary basis. This is to be a single cavern for both the tracks.

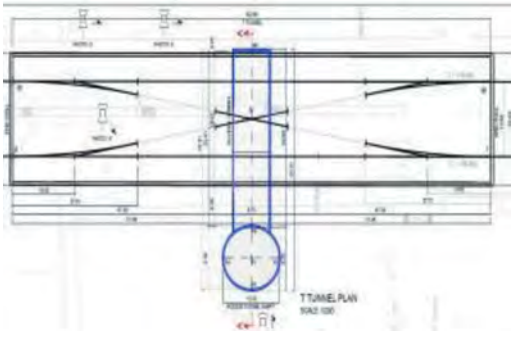

Figure 9. Conceptual plan for option 7.

An appropriately sized vacant plot, belonging to the Municipality for a future requirement of the Worli cemetery, was identified. Authorities agreed to spare the plot temporarily for the purpose of the shaft and for managing construction logistics.

By further optimisation in the metro track alignment the UP-Line tracks were brought closer to the Down Line Track. This helped in reducing the cavern size as well as in reducing the length of the crossover, thereby that of the cavern.

Advantages-No utilities, no impact on traffic being away, no interdependencies on construction sequence for shaft, TBM tunnel work or with the adjoining station construction.

Disadvantages- bureaucratic delay for land

Result of examination of various options led to selection of the most suitable size and location for crossover. This resulted into a solution that was beneficial because of no utilities were to be tackled, no traffic diversion to be implemented and the logistic management was easier. Dependency of construction of cavern on the TBM tunnelling and that of the station was also avoided.

Figure 10. Aerial view of shaft during construction.

Figure 11. Access shaft for crossover.

Figure 12. During excavation.

Figure 13. Crossover end wall shotcrete.

Figure 14. Waterproofing & rebar work in progress.

Figure 15. Overt rebar fixing work in progress.

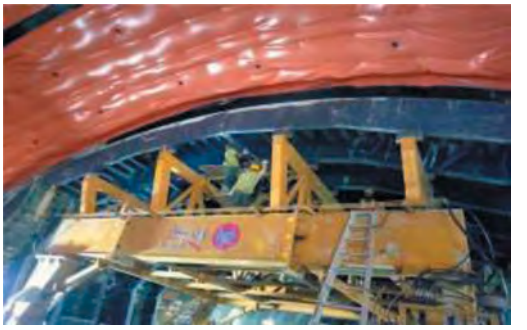

Figure 16. Gantry fixing for final lining.

Figure 17. Final NATM cavern.

4 CONCLUSION

The fate-accompli situation resulted from the concerns of the municipal authority could be addressed in the most optimum method by analysing 7 options and selecting the most appropriate one, i.e **Option 7** by a fairly joint effort by the Employer, the Contractors and the General Consultants. The Crossover cavern construction works has been completed and the experience during construction ratified the assumptions. The entire Metro Line 3 works will be completed by July 2024.

The project could be done with least impacts on the local habitat, civic utilities and other facilities like cemeteries, which were all factored in while taking the decision and thus contributed in sustainable development and preservation of local ecosystems.

REFERENCES

R.Mittal, M. Dange, R. Tilak 2022. Construction of Crossover Acharya Atrey Chowk using TBM and NATM Technology on Mumbai Metro Line 3, Tunnelling Asia 2022.

S.k Gupta, S. Trivedi. 2022. Design and construction of Mumbai Metro Line3 Sahar Road crossover using permanent sprayed concrete.

U.S Virat, M. Molina 1998. Conventionally Excavated Crossover Tunnel Designing Mumbai Metro Line -3.

Tunnelling for a Better Life – Yan, Celestino, Thewes & Eberhardt (Eds)
© 2024 The Author(s), ISBN 978-1-032-80042-4
Open Access: www.taylorfrancis.com, CC BY-NC-ND 4.0 license

Innovation practice of indoor space of rail transit hub

Liwei Ji*, Yanqiao Li & Kaiqi Wei
China Railway Design Corporation, Tianjin, China

Yongzhong Deng & Yongyu Fu
Shenzhen Metro Construction Group Co., Ltd, Shenzhen, China

ABSTRACT: With the development of the city, the development of underground space and the construction of underground buildings are paid more and more attention. In the past, the underground space represented by the subway station is often low, narrow, cold, damp, the space shape is uniform, the demand of urban space development and the limitation of space environment form a distinct contradiction. Rail transit hub is the urban transportation function body most closely connected with the city. It provides travel services for a large number of citizens every day. Its large volume, long construction cycle, large investment and long service life, which has a profound impact on urban development. Its architectural space is in urgent need of further innovation to provide high-quality travel services for citizens. Based on the construction practice of Huangmugang Hub and Gangxiabei hub, this paper summarizes the design experience from the aspects of underground building lighting, building space configuration, and green plant planting, so as to provide reference for the innovation of indoor space of underground buildings.

Keywords: Rail transit, Indoor space, identifiability, Natural environment

1 FOREWORD

At present, the construction of large transportation hub in China is in the stage of rapid development, and the corresponding demand for underground space development and utilization is increasing. The scientific and reasonable utilization of urban underground space can effectively relieve the tension of urban ground space. As a space resource with huge potential in the city, the construction of rail transit hub also makes the underground space more deeply integrated into the urban space system. Facing the vision of sustainable development of urban space, how to establish an efficient, high-quality and three-dimensional underground space and improve people's use experience has become one of the problems that need to be considered recently. Based on the construction examples of Shenzhen Huangmugang hub and Gangxibei hub, this paper analyzes the interior space design of underground hub station, and provides case reference and innovative experience for the space construction of urban underground rail transit hub.

2 PROJECT OVERVIEW

Huangmugang transportation hub project is located in Futian District, the central urban area of Shenzhen. It is an important transportation node serving Huaqiang-step global intelligent terminal innovation center and Bagualing financial technology center, the original regional transportation was five road cross and four layer overpass, with complex traffic organization, severe urban fragmentation, difficulty for citizens to cross the street, and prominent travel safety issues, which have had a significant impact on the urban landscape and citizens' lives.

Figure 1. Location map of Huangmugang Hub.

In order to optimize city function of the area, improve the traffic efficiency in the area, build high quality of urban development space, the municipal

*Corresponding author: 18824652@qq.com

DOI: 10.1201/9781003495505-421

government decided to take advantage of the construction of the Huangmugang subway on Line 14 to demolish the Huangmugang overpass, and comprehensively improve the municipal transportation (road and rail transportation), land use, slow system for comprehensive improvement. The emergence of transportation hub plays an extremely important role in the optimal allocation of transportation resources, the construction of urban landscape and the service experience of citizen life. At the same time, important infrastructure projects such as the Shenzhen Sports Center, the Second People's Hospital, and Huafu Village around the area have included expansion and renovation projects in the planning and construction, which will inevitably enhance the future transportation demand of the area. Driven by these dual updates, Shenzhen is coordinating the development of tracks, roads, surrounding plots, and underground spaces, striving to build a new era urban hub that is ecological green, open and coordinated, and integrated with stations and cities.

Figure 2. Situation of the base before construction.

Figure 3. Future hub and urban living room.

3 CURRENT SITUATION AND DESIGN IDEAS

3.1 *Analysis of the hub status quo*

The surrounding environment of Huangmugang Hub is complex, including schools, hospitals, sports centers, large communities, parks, office buildings, etc. The above-ground traffic is a four-storey overpass, and the underground traffic is Metro Line 7. Due to the existence of the interchange, the urban function and landscape in the whole area, the slow traffic system is poor, the mixed traffic situation of people and cars is serious, and the connection between the subway and other surrounding facilities is not smooth, which cannot be well supplemented.

Figure 4. Poor slow traffic system.

Figure 5. Severe mixed traffic of people and vehicles.

Figure 6. Urban landscape fragmentation.

In addition, the Sports Center of the city around the hub will be expanded, and the expansion project will be positioned as the high-level competition center in the Pearl River Delta and the leisure and fitness center serving the citizens; the beds of the reconstruction project of the Second People's hospital will be increased from 1500 beds to 2500 beds, and the shantytown reconstruction project of Huafu Village will implement the requirements of expanding industrial space and enriching the industrial supporting facilities of residential area, and the important urban renewal project to promote the integration of industry and city. Therefore, the hub construction should be closely combined with the surrounding urban renewal, to shape a fusion of urban functions.

3.2 *Design ideas*

In response to a series of current problems, we are considering how to reduce the number of ground structures while ensuring traffic flow during design, and ensure smooth operation of the slow moving system? How to improve the area environment, enhance the vitality of the area, and maximize the urban efficiency through the hub construction? We incorporate the TOD concept into the construction of

the hub, shape the design concept of "Quality Oriented Development", and sort out the elements of the area from both the above ground and underground parts, breaking them down one by one. We propose corresponding strategies and implementation plans, and ultimately build the hub as a new node in the area, enhancing the charm of urban space and improving the travel experience of citizens, promoting high-quality urban development.

Firstly, in order to achieve Quality Oriented Development, we have implemented a series of development strategies for the over-ground space: (1) Lightweight the ground building. As an urban hub, it is necessary to consider whether the need to strengthen the presence of the hub based on the surrounding environment. The urban buildings around Huangmugang Hub area are dense. In order to fit the whole construction environment, the ground buildings should be minimized as far as possible to ensure the open and smooth vision of the area. (2) Establish a new image. Due to the fact that Huangmugang Hub is located at the intersection of five cross roads, as the gathering point of the roads, the image of the hub can enhance the attractiveness of the area, so as to play a role in driving the social and economic benefits of the area. (3) Build a green ecological network. The spatial form in the southeast and northwest of the area where Huangmugang Hub is located is long and narrow and has a sense of extension. We can introduce green plants in various directions and extend to the surrounding ecological parks to achieve a green axis network, and rely on the green axis to build a slow traffic system in the area, achieving the experience of citizens traveling under green shade.

Secondly, in order to improve the traffic function, avoid the adverse effects of ground structures on the underground space, and create a new form of underground space, we have implemented a series of development strategies for the underground space: (1) Strengthen the traffic nodes, improve the walking environment of the underground core space, and build open three-dimensional traffic nodes. (2) Strengthen the mobility of returning, connect the underground with the above-ground space through the sunken square, improve the walking space environment on the ground, and achieve the return tour through the underground space, thereby promoting the enhancement of urban vitality integration of urban functions. (3) Urban functional integration. Combined with the various urban functions around the hub, the underground space and the sunken square, so as to achieve the complementary effect of space shaping and promote the process of urban renewal around the hub.

Finally, we aim to build a model of urban renewal and create a vibrant city as the means to create an innovative space that blooms the senses of citizens.

4 STRUCTURE SHAPING IN SPACE

Combined with the design concept and the current situation of the hub, we reconstructed the traffic organization of the area. By adopting the three-layer traffic mode of the upper bridge, the ground traffic and the lower tunnel, we created the slow traffic system space underground, so as to improve the travel environment of the citizens in the area.

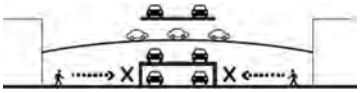

Figure 7. Schematic diagram of slow traffic in the base before construction.

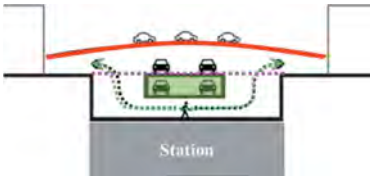

Figure 8. Schematic diagrams for improving slow traffic.

From the perspective of shaping the underground space of the hub, due to the closed and introverted characteristics of the underground space, we should pay attention to the open design in the space design, so that each space can penetrate into each other and broaden the space boundary. The internal space of Huangmugang hub is easy to be blocked and lifeless because the vertical and horizontal direction is set up with the underpass tunnel and the upper span bridge. In order to improve this situation, we innovate in the design of ground bridge and sunken tunnel, open the middle area, and set up a skylight in combination with the ground environment, so that sunlight can reach the internal space of the hub through the bridge, ground and tunnel to the hub of the internal space. In addition, in order to achieve the further openness of the space, in the vertical design, each layer is equipped with a continuous atrium, so that the space and space penetrate, expand the openness of the space, and also make the sunlight throughout the underground space through the atrium, so as to reduce the sense of closure of the underground space. In the horizontal direction, the transfer hall of Huangmugang hub is surrounded by sunken squares, the fire glass between indoor and outdoor area, make indoor and outdoor contact on the line of sight, to broaden the boundary of the space. It also makes the citizens through the sunken square to complete the ground underground slow traffic system space back, improve citizens travel experience. A variety of design elements and techniques are combined to create a tall and extended open space, greatly alleviating the sense of depression of the space.

As a transportation hub space, in addition to considering the openness of space, identifiability is also one of the elements of space design. It can be convenient for pedestrians to judge the direction in the open space, so as to improve the efficiency of passengers. The improvement of spatial identification

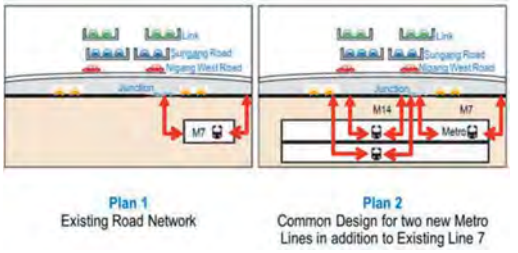

Figure 9. Design mentality 1.

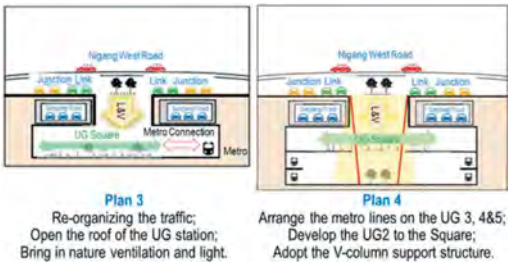

Figure 10. Design mentality 2.

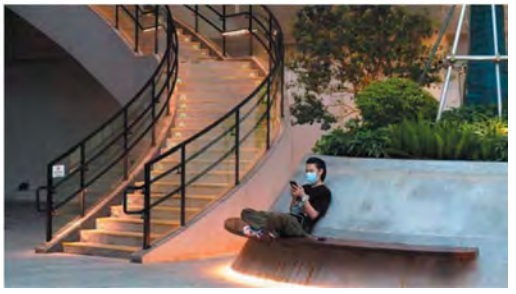

Figure 11. Real scene of sunken square of Huangmugang Hub.

Figure 12. Real scene of atrium space of Huangmugang Hub.

can be accomplished either by shaping the nodal space or by adopting special construction elements. In the space design of Huangmugang hub, the east-west fish belly shaped sinking tunnel is incorporated into the space according to local conditions, formed a suspended inter-layer running through the underground layer of the whole junction. And connect it to the forth layer of rectangular platform form underground, naturally formed the east-west V-pillar support system. The V-pillar runs through the entire transportation space of the first to fourth underground layers, making it one of the most distinctive structural elements of Huangmugang Hub. It not only shapes a charming spatial structure, but also improves the recognition of the hub space, allowing passengers to determine their location and destination direction through the position of the V-pillar on any floor, greatly improving passenger travel efficiency and achieving a balance between open space and directional space required for transportation.

Figure 13. Real view of V-pillar of Huangmugang Hub.

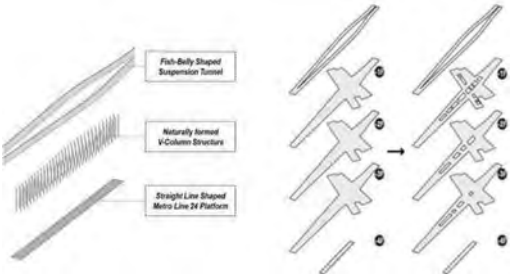

Figure 14. V-pillar formation and atrium formation process.

5 CONSTRUCTION OF THE INDOOR MICRO-ENVIRONMENT

Underground space itself is closed and easily detached from natural elements. Therefore, the design of underground space environment should fully consider human needs, pay attention to the introduction of natural elements, create a pleasant underground space environment, and reduce the sense of difference of indoor and outdoor transition as far as possible.

5.1 *Light introduction into the transit hub*

Introducing natural light into underground space design is one of the commonly used space design techniques. We have also fully considered the impact

of natural light on the environment in the design of the Huangmugang Hub and Gangxiabei Hub.We have set up skylights as much as possible and set up sunken squares, introducing a large amount of natural light from the entrance and top of the hub, allowing people to feel the changes in the spatial environment brought about by sunlight in the underground space, and experience the atmosphere of the natural environment like standing on the ground.

Figure 15. Location of skylight location of Gangxiabei Hub.

Figure 16. Annual average quantity analysis of the first and four underground layers of Huangmugang Hub.

5.2 *Bring in the wind into the transit hub*

Underground space compared with the ground environment has thermal stability, but due to the rock and soil characteristics, condensation water is easily generated inside the structure, giving people a feeling of dampness. Moreover, the air flow in underground spaces is generally poor. Therefore, air conditioning systems are often used in modern rail transit underground hub spaces to regulate indoor temperature and humidity, reducing discomfort. In the design process of Huangmugang Hub, we fully considered the differences in air between the above ground and underground spaces. Multiple sunken squares were installed around the large space, and the upper part was equipped with openable skylights to encourage outdoor air to enter the room and form convection, thereby generating wind and alleviating the dull feeling of the space itself.

5.3 *Introduce the green into the transit hub*

In addition to the introduction of natural light and air, the introduction of green plant landscapes is also an important means to enhance the ground feel of underground spaces. It extends the natural environment outside the building in the form of landscape green plants into the underground space environment,

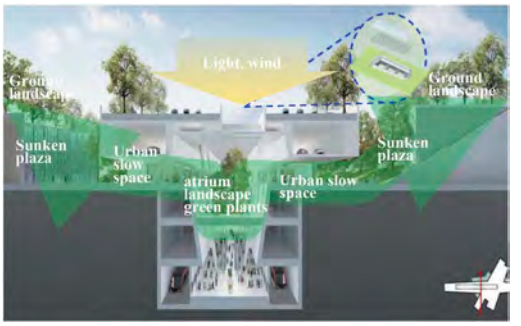

Figure 17. Schematic diagram of "bringing the wind into the city" of Huangmugang Hub.

blurring the boundary between indoor and outdoor humanities and nature, reducing the sense of isolation between indoor and out door spaces, and enhancing people's sense of scale identification with open spaces. In the design of the Huangmugang Hub, the introduction of green plants is also an important means of establishing a connection with nature. By utilizing the light resources brought by skylights, simulating and analyzing the light angle and intensity, plant varieties and planting environment, more than 30 types of green plants were planted indoors, with a planting area of 1200square meters. A miniature garden landscape was constructed, and combined with the atrium space, the ecological functions of plants were utilized. At the same time, it form a staggered layout of green plant planting, establish a healthy and natural green system in the underground environment, improve the comfort of the space, break the concept of indoor and outdoor, and create a comfortable ecological environment for waiting for cars under the shade of green.

Figure 18. Schematic diagram of green plant planting in Huangmugang Hub.

6 SUMMARY

As an important mode of transportation, rail transit is increasingly infiltrating people's lives. As a gateway to the area and even the city, rail transit hubs are gradually moving towards a trend of functional diversification and integration, with the goal of meeting the travel needs of users. This has achieved the coordinated layout and efficient operation of various functional spaces in the hub area. The internal

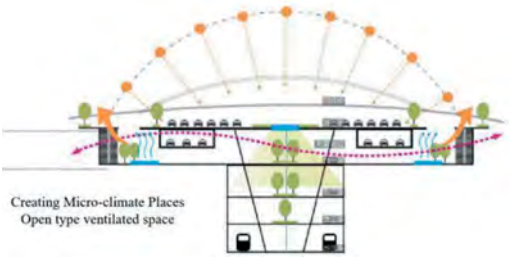

Figure 19. Micro-environment construction of Huangmugang Hub.

Figure 20. Relationship between green plant planting and skylight and atrium in Huangmugang Hub.

environment serves as an important catalyst for people's experience and feedback perception, and space design and innovation are urgent. In the space design of Huangmugang Hub and Gangxiabei Hub, we have combined the inherent conditions of the underground hub to create an open and recognizable transportation space. At the same time, we fully consider the environmental characteristics of underground buildings, and from the perspective of people's psychological needs. We adjust the indoor micro-environment to improve the lack of natural light, lack of air circulation, and monotony of space, attempting to create a space atmosphere that is indistinguishable above and below the ground. At the same time, exploring the development and utilization direction of underground resources also hopes to provide beneficial references for the high-quality development of large transportation hub areas in China.

REFERENCES

Zhang Yan. Study on Integrated Development and Utilization Planning of the Integration of Urban Overground and Underground Space[J]. Intelligent Building & Smart City, 2023(09): 41–44. DOI: 10.13655/j.cnki.ibci.2023.09.012.

Lu Z, Weizhao Q, Xiujuan Y, et al. Dispersivity Identification and Modification with Lime of Soil in Huaaopao's Water Conservancy Project[J]. Geotechnical and Geological Engineering, 2022,40(11).

Dar Al Arkan ties up for key projects in region [J]. Gulf Construction, 2021.

UW Dairy Innovation Hub project up and running [J]. Western Farm Press, 2021.

UW Dairy Innovation Hub project up and running [J]. Southwest Farm Press, 2021.

You Xinhua, He Guangyao, Wang Qiangxun, Zhang Lei. Current Status and Development Trend of Urban Underground Space in China [J]. Tunnel Construction, 2019, 39(02):173–188.

Hong Kairong. State-of-art and Prospect of Tunnels and Underground Works in China[J]. Tunnel Construction, 2015,35(02):95–107.

Wang Bo. Exploration and Practice of the Development and Utilization of Urban Underground Space [D]. China University of Geosciences Beijing,2013.

Wan Hanbin. THE STRATEGY RESEARCH ON URBAN UNDERGROUND SPACE IN HIGH-DENSITY AREA [D]. Tianjin University,2013.

Wang Mengshu. An Overview of Development of Railways Tunnels and Underground Works in China [J].Tunnel Construction, 2010,30(04):351–364.

Lin Yan. Study on the Integration of Building Complex with Urban Transportation [D]. South China University of Technology,2008.

Kong Jian. The Research of"Humanization"Design in the InternalSpace of Metro Station [D]. TongJi University, 2007.

Lu Jiwei, Han Jing. Systematization of Mass Transit Station Area and Urban Design [J].Urban Planning Forum, 2007(02):32–36.

Tunnelling for a Better Life – Yan, Celestino, Thewes & Eberhardt (Eds)
© 2024 The Author(s), ISBN 978-1-032-80042-4
Open Access: www.taylorfrancis.com, CC BY-NC-ND 4.0 license

Hexane section and its section combination honeycomb type underground structure system. Design and implementation of the program study

Qianou Jiao, Lin Guo* & Wenjie Chen
China Railway Shanghai Design Institute Group Corporation Limited Tianjin Branch., Tianjin, China

ABSTRACT: In view of the current domestic and abroad underground project due to the lack of overall planning, design and construction and form a single section, mutual sharing, its system lead to underground space, low utilization rate, zipper excavation, put forward a new hexagon section and by its section combination honeycomb underground engineering structure system design scheme. Comprehensive use of numerical simulation, model test, theory derivation and other means, the hexagonal section and section combination honeycomb underground engineering structure system simulation analysis, and the traditional underground engineering system structure stress, economic and functional analysis, put forward all kinds of honeycomb underground engineering system applicable scope and conditions, design and calculation method and feasible construction scheme, to guide the engineering application of the structure system.

Keywords: hexagon, honeycomb underground structure system, double and multiple compartments, correction coefficient, prefabricated segments

1 INTRODUCTION

With the rapid development of society and economy and the continuous intensification of the urbanization process, the contradiction between urban development and the shortage of land resources is more prominent. The development and utilization of urban underground space resources has become one of the important directions of the social sustainable development, especially in the urban rail transit and municipal pipeline laying. At present, the design sections of underground tunnel and comprehensive pipe gallery in China are mostly rectangular or circular sections, in which the circular section is more reasonable, with small thickness, and the section space is wasted, but the force is poor, especially the corner and cross parts, so thick beams and large reinforcement are needed. The advantages and disadvantages of circular and rectangular conventional sections are relatively obvious, which cannot achieve a better balance in force and space utilization. At the same time, the phased implementation of multi-line interval, especially for the near construction of double circle and multi-round tunnel, it is necessary to take protection measures for their respective projects and reserve enough safe distance, which will cause a lot of waste for underground engineering quantity and space. In order to realize the underground tunnel and comprehensive pipe gallery structure stress and space utilization balance, improve the overall structure performance at the same time reduce cost, realize the intensification of underground space utilization and the optimization of underground engineering construction process, can the traditional pipeline "plane staggered layout" into "three-dimensional centralized layout", greatly increase the utilization efficiency of underground space. Mr. Qian Qihu, an academician of the Chinese Academy of Engineering, once wrote that "the underground comprehensive pipe corridor is of great significance to promoting the new urbanization, strengthening the shortcomings of urban infrastructure, and realizing the transformation of urban development mode"[1].

In nature, honeycomb is hexagonal in nature, and theory proves that this form uses the least material, occupies the largest spatial area, and has the best structural stability[2]. Therefore, we proposed the honeycomb underground engineering structure system of hexagonal section and its section combination, mainly including single cabin hexagonal structure, upper and lower double cabin combined structure, four cabin combined structure, seven cabin combined structure, etc. This paper will focus on the combined structure of hexagonal single cabin and four cabin.

2 FORCE STUDY OF THE HEXAGONAL STRUCTURE

2.1 *Force characteristics of the hexagonal single-cabin structure*

The longitudinal length of the tunnel and pipe gallery structure is usually very different from the section size, which can be considered as a plane strain problem in

*Corresponding author: 1933156821@qq.com

DOI: 10.1201/9781003495505-422

the calculation, so this paper makes a numerical analysis through the two-dimensional plane strain model. The calculation section is calculated on the premise of meeting the subway limit of type A vehicle, and the buried depth is 18m. (Figure 1)

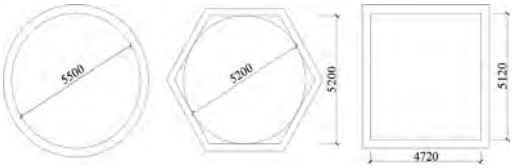

Figure 1. Three sectional dimensions.

The soil in the model of this paper is simulated using the modified Cambridge configuration[3,] In the calculation of the typical silty clay layer parameters in the urban area of Tianjin, a single soil layer is used for calculation and analysis. The specific physical and mechanical parameters of the soil are shown in Table 1.

Table 1. Corrects the calculation parameters of the Cambridge model.

	γ (kN/m3)	Es (kN/m2)	Y	λ	κ	M	e	k0
Powder quality clay	19.4	5.31	0.3	0.0476	0.005	1.139	0.758	0.5

The tunnel structure is simulated by equivalent stiffness method, assuming that the concrete structure has been in the elastic deformation stage in the construction process, and the elastic modulus reduction method is adopted to reflect the stiffness weakening of the underground structure in the construction process. In the model, the underground structure is simulated by beam unit. The thickness of different forms of tunnel structure is taken as 350mm, and the elastic modulus is taken as 80% of the C50 concrete modulus value (Ec50=34.5GPa), that is, E=0.8×Ec50=27.6GPa, and the Poisson ratio is 0.2.

2.1.1 *Hexagonal underground structure, the calculation results*

(1) The hexagonal single cabin structure is deformed in the horizontal direction of the underground structure, showing a horizontal stretching shape, especially at the inflection point of the left and right sides of the largest displacement value, reaching 3.9mm. Due to the effect of the upper soil pressure, the top of the underground structure has a downward deformation, and the maximum settlement of the roof span is 3.9mm; the bottom has an upward deformation due to the unloading of the soil, the maximum uplift of the bottom span is 5.2mm, and the underground structure is in a compressed state. Under the action of soil surrounding pressure, the underground structure is horizontal tensile vertical compression deformation, the maximum tension amount is about 7.8mm, and the compression amount is 9.1mm, the value is relatively close. (Figure 2)

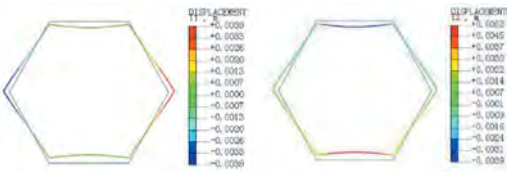

(a) horizontal distortion (b) vertical deformation

Figure 2. Distribution of hexagonal underground structure.

(2) The axial pressure of the underground structure at the left and right corners is the largest, reaching 968 kN, but because the horizontal soil pressure is less than the vertical, the axial pressure of the top and bottom plate of the horizontal distribution structure is the minimum, which is 535 kN. Because the stress concentration is easy to occur at the corner, the maximum shear force occurs at each corner of the structure, with the maximum value of 451 kN. The maximum bending moment of the inner side of the underground structure occurs in the middle position of the top and bottom plate, and the maximum value is 226 kN.m. From the underground structure of the vertical deformation distribution can be found, under the action of upper soil pressure of the upper part of the underground structure downward deformation, and the soil discharge rebound, the lower part of the underground structure of the upward deformation, lead to the underground structure vertical compression, and the compression effect of the extrusion on the corner of the structure, the structure in the lateral moment of the maximum, the maximum value of 398 kN.m. (Figure 3)

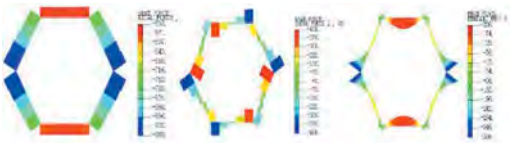

(b) (a) Axial force (b) shear force (c) bending moment

Figure 3. Internal force distribution diagram of the hexagonal underground structure.

2.1.2 *Comparative analysis of the force deformation of three different forms of underground engineering structures*

The vertical displacement values in Table 2 are the maximum absolute value in the structural settlement

or uplift value. Through the numerical comparison in this table, it can be found that the hexagonal underground structure and the circular tunnel both show the relative deformation of vertical compression and horizontal stretching, and the displacement and relative deformation value of the structure are also relatively close. The rectangular pipe corridor is different from the other two in terms of horizontal deformation, and the deformation value is relatively large. It can be seen that under the same net area, the stiffness of the circular tunnel is close to the hexagonal underground structure, while the stiffness of the rectangular tunnel structure is slightly worse.

Table 2. Summary of the calculated results for the three different structural forms.

	circular tunnel	The hexagonal tunnel	Rectangular pipe corridor
horizontal shift /mm	3.6	3.9	1.4
vertical displacement /mm	5	5.2	6.4
Horizontal to relative deformation/mm	7.2	7.8	-2.8
Vertical relative deformation of the region/mm	-8.2	-9.1	-12.2
pulldown /kN	1011	968	846
Inner-side bending moment/kN.m	164	226	333
Outer bending moment/kN.m	149	398	470
shear force /kN	129	451	633

Note: 1. The relative deformation value is positive for stretching and negative for compression.
2. The vertical displacement is the maximum absolute value in the settlement or uplift value

In terms of internal force comparison, the circular tunnel bears larger axial pressure with smaller bending moment and shear, which can give full play to the compression capacity of concrete structure, and the structural force is reasonable; the rectangular tube tunnel bears the smallest axial pressure and shear, especially at the structural corner; The hexagonal underground structure is in the intermediate state of the three structural forms, and the internal force is larger than the circular tunnel, but less than the rectangular tube tunnel. Both hexagonal underground structure and rectangular pipe corridor have corners, which is easy to produce stress concentration. The internal force in this position is large, so more attention should be paid in the design.[4]

Comparing the distribution of bending moment of circular tunnel, hexagonal underground structure and rectangular pipe corridor, the larger range of bending moment requires a larger structural section and reinforcement, and the larger range of rectangular tunnel will be much larger than the hexagonal underground structure. From the above analysis, it can be seen that the hexagonal underground structure is much better than the rectangular pipe corridor than the rectangular tunnel in terms of force and reinforcement, and is more reasonable than the circular tunnel in terms of function use.

2.2 *Comparison of the force-bearing deformation characteristics of hexagonal underground structures under different buried depths*

Through the comparison of Table 3, it can be found that for the hexagonal underground structure, except for the uplift of the roof, the vertical displacement of the other cases is the subsidence of the roof plate and the uplift of the bottom plate. With the increase of the buried depth, the settlement of the roof gradually increases, while the uplift of the bottom plate does not change much, and the overall vertical relative deformation increases. The maximum horizontal displacement, vertical relative deformation and horizontal relative deformation of the structure all increase linearly with the increase of the buried depth.

In terms of the internal force of the structure, the lateral bending moment is always greater than the medial bending moment, and the lateral bending moment of the structure increases more obviously as the buried depth increases. This is mainly because the lateral bending moment occurs at the corner of the left and right sides of the structure, and the extrusion effect of the surrounding soil is more serious. The maximum axial force, maximum shear force and maximum bending moment of the structure also show a trend of linear increase with increasing burial depth.

2.3 *Comparison of hexagon underground structure with circular tunnel and rectangular pipe gallery*

In terms of structural deformation, the deformation values of circular tunnel and hexagonal underground structure under different buried depths are relatively close, indicating that the stiffness of these two structural forms is similar. The rectangular tube corridor is larger than the other two in vertical displacement and vertical relative deformation, especially under the condition of deep burial, the difference of the maximum deformation value is more obvious, indicating that the stiffness of the rectangular tunnel structure is relatively poor, especially it is not suitable for the situation of large buried depth. It should be pointed out that the horizontal displacement and horizontal deformation of the rectangular tube corridor are relatively small. According to the above analysis, this is mainly caused by the deformation of the inner structure of the rectangular structure under the horizontal soil pressure, which is opposite to the horizontal deformation characteristics of the other two structures.

Table 3. Summary of structural deformation and stress results under different burial depths.

	displacement /mm					bending moment /kN.m			
depth of burial /m	roof subside	baseboard rise	Vertical phase To the deform-ation	haunch dis-placement	Level phase To the deformation	The inner bending moment (Central top and bottom)	The lateral bending moment (Two sides of the corner)	Axis force/ kN	shear force / kN
6	1	5.8	4.8	2.2	4.4	112.9	182.2	380.9	182.2
12	-2	5.3	7.3	3.2	6.4	175.4	298.2	677.9	323.9
18	-3.9	5.2	9.1	3.9	7.8	225.9	397.8	957.9	450.8
24	-5.3	5.3	10.6	4.5	9	266.2	486.3	1250.1	571.3
30	-6.3	5.4	11.7	4.8	9.6	299.5	567.1	1525.5	687

Table 4. Comparison table of the calculation results under different buried depths.

Structure buried depth / m	Structural type	horizontal shift /mm	vertical displace-ment /mm	Horizontal to relative deformation/ mm
6	circular tunnel	2	5.8	4
	hexagon tunnel	2.2	5.8	4.4
	Rectangular pipe corridor	0.4	6.1	0.8
12	circular tunnel	3	5.2	6
	hexagon tunnel	3.2	5.3	6.4
	Rectangular pipe corridor	0.9	6.1	1.8
18	circular tunnel	3.6	5	7.2
	hexagon tunnel	3.9	5.2	7.8
	Rectangular pipe corridor	1.4	6.4	2.8
24	circular tunnel	4.1	5	8.2
	hexagon tunnel	4.5	5.3	9
	Rectangular pipe corridor	2	7.9	4
30	circular tunnel	4.4	5.4	8.8
	hexagon tunnel	4.8	6.3	9.6
	Rectangular pipe corridor	2.6	9.2	5.2

Structure buried depth/m	Structural type	Vertical relative deformation of the present form/mm	pulldown / kN	bending moment /kN.m	shear force / kN
6	circular tunnel	4.4	405	105	67
	hexagon tunnel	4.8	380	219	182
	Rectangular pipe corridor	5.7	366	258	291
12	circular tunnel	6.6	713	161	103
	hexagon tunnel	7.3	678	358	324
	Rectangular pipe corridor	9.3	612	415	468
18	circular tunnel	8.2	1011	197	129
	hexagon tunnel	9.1	958	477	451
	Rectangular pipe corridor	12.2	846	563	633
24	circular tunnel	9.5	1301	222	148
	hexagon tunnel	10.6	1250	584	571
	Rectangular pipe corridor	14.7	1068	700	786
30	circular tunnel	10.4	1587	239	164
	hexagon tunnel	11.7	1526	681	687
	Rectangular pipe corridor	16.8	1283	828	929

This stress of the three structural forms does not change with the depth. In addition, with the increase of structural buried depth, the internal force difference between circular tunnel and hexagonal underground structure and rectangular pipe corridor is more obvious. Especially in terms of bending moment and shear force, the maximum bending moment ratio of the three structures is 1:2.1:2.5, and the maximum shear ratio is 1:2.7:4.8; when the buried depth increases to 30m, the maximum bending moment ratio has increased to 1:2:8:3.5, and the maximum shear ratio has even increased to 1:4.2:5.7. Therefore, the stress performance of hexagonal tunnel has great advantages than that of rectangular tunnel.

In conclusion, the deformation of the circular tunnel structure is relatively small, and the force is more reasonable, which is suitable for different burial depths. However, when the circular tunnel does not meet the requirements of functionality or other aspects, the hexagonal underground structure is close to the circular tunnel, and the deformation and range of the force is relatively small, especially in the case of deep burial, its advantages are more obvious. But in the structural design, it is necessary to focus on the corner position, especially on the left and right corners.

3 COMPARISON OF THE FOUR-CHAMBER HONEYCOMB UNDERGROUND STRUCTURE WITH THE CALCULATION RESULTS OF DIFFERENT STRUCTURES

The underground structure of the four-cabin is more suitable for the multi-functional combination of pipelines, subways and roads. Referring to the combination form of honeycomb structure, the following two combination forms are preliminarily conceived for the hexagonal four-cabin underground structure. (graph 4)

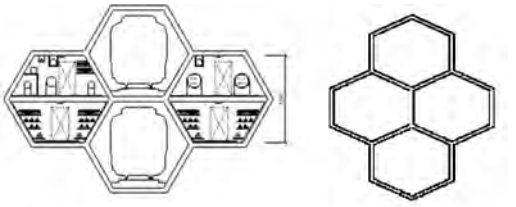

(a) Four-cabin structure form 1 (b) four-cabin structure form 2

Figure 4. Combined type of the four-cabin structure.

Using the finite element model, through the overall comparison in Table 5, the stiffness of the large area circular tunnel is the worst, so its deformation value is the largest among various structures. And the rectangular tunnel can effectively reduce the deformation of the structure, so the deformation is relatively smallest. The deformation of the hexagon four-cabin structure is in the middle, and the vertical direction is slightly larger than the rectangular pipe corridor, while the difference of the horizontal deformation is relatively large.

Compared with the internal force of the structure, the large area circular single-line tunnel bears the largest axial force, but the bending moment and shear force are relatively small, which can give full play to the compressive ability of concrete, so the force is the most reasonable. The rectangular duct gallery bears the least axial force, but the bending moment and shear force of both forms are relatively large, which is unfavorable to the force of the structure. Compared with the rectangle, the four-module combination of the hexagonal underground structure has a slightly larger axial force, but the bending moment and shear force are relatively small, and the force is more reasonable. Therefore, the hexagonal four-cabin structure has more advantages than the rectangular pipe corridor.

Table 5. Summary of the calculation results of various and different structural forms.

	Hexagon and four-cabin combined form one	Hexagon and four-cabin combined form two	circular tunnel	Rectangular four cabin Combination pipe gallery	Rectangular four cabin The parallel pipe gallery
horizontal shift /mm	7.2	6.1	9.8	3.2	1.8
vertical displacement /mm	11.5	10.8	14.3	10.3	9.1
pulldown /kN	2012	1839	2117	1950	1777
Inner-side bending moment/kN.m	319	343	147	314	314
Outer bending moment/ kN.m	513	428	122	697	663
shear force /kN	569	707	75	801	750

Note: The vertical displacement is the maximum absolute value in the settlement or uplift value

4 HEXAGONAL UNDERGROUND STRUCTURE TRANSVERSE STIFFNESS EFFICIENCY, AND BENDING MOMENT CORRECTION COEFFICIENT

The hexagonal underground structure determines the value of the horizontal bending stiffness efficiency η through the line loading mode and the comparison with the numerical simulation, and then uses the numerical simulation to calculate the bending moment correction coefficient ζ in the online loading mode of the staggered assembly hexagonal underground structure. The following conclusions are mainly obtained:

(1) In the online loading mode, both the model test and the numerical simulation results show that the change of the structure diameter increases linearly with the increase of the load. The bending stiffness efficiency η of the model test has a large error in the small load and gradually stabilizes with the increase of the load, while the bending stiffness efficiency η of the numerical simulation does not change with the increase of the load[5].

(2) In the online loading mode, the variation of bending stiffness efficiency η in the through-seam assembly model test is 0.613 to 0.736; the corresponding numerical simulation results is 0.619 to 0.684; the bending stiffness efficiency η of the off-seam assembly model test is 0 to 0.861, and the η variation of the corresponding numerical simulation results is 0.847 to 0.891. The model test is close to the calculation results of the numerical simulation..776

(3) In the real loading mode in sand, the resistance of the soil around the structure has a ring effect on the hexagonal underground structure, which will limit the opening of the structural joint and reduce the weakening effect of the joint on the whole structure. Therefore, when the buried depth is greater than 1.5D, the transverse stiffness efficiency η of the misseam and through-seam assembly structure tends to be stable. With the increase of buried depth, the greater the resistance of the soil around the structure, the stronger the hoop effect on the structure, so the lateral stiffness of the structure becomes more efficient η.

(4) The transverse stiffness efficiency rate of the wrong-joint assembly structure η is larger than that of through-seam assembly, but the gap between the stiffness efficiency rate of through-joint and wrong-seam assembly η is gradually decreasing with the increase of buried depth. In the real loading mode in sand, the range of transverse stiffness efficiency of through joint assembly is 0.515~0.806, and the range of transverse stiffness efficiency of through joint assembly is 0.651~0.919. In the actual engineering design, the transverse stiffness efficiency η can be selected according to the research results of this article.

(5) In the real loading mode in sand, after the internal soil of the structure is dug out, the structure of the three assembly modes of misjoint assembly, joint assembly and complete ring will bulge due to the extrusion of the side and the lower part, and this uplift phenomenon will weaken with the increase of buried depth. The complete ring structure has the least deformation, the through-seam assembled structure is the largest deformation, and the mis-seam assembled structure is in between, which is the same as the deformation law in the line loading mode.

(6) The bending moment of the two adjacent rings of the line loading mode and the misseam assembly structure in the real loading mode changes periodically by 180° along the hexagonal underground structure, which is mainly determined by the bending moment correction coefficient ζ of the misseam assembly structure. When the joint moment correction coefficient of the middle ring is large, the bending moment decay of the middle ring and the increase of the adjacent ring are dominant, while the joint moment correction coefficient of the middle ring is small, that is, when the joint moment correction coefficient of the adjacent ring is large, the bending uation of the adjacent ring and the increase of the bending moment of the middle ring is dominant. The ζ values calculated in this study ranged from 0.19 to 0.4, which is close to the ζ of the existing circular tunnels.

5 CONSTRUCTION METHOD OF HEXAGONAL SECTION AND HONEYCOMB UNDERGROUND STRUCTURE

The construction method of the new hexagonal underground structure system can refer to the conventional circular and rectangular pipe corridor structure. However, due to the particularity of its section form, it should be adjusted on the basis of common construction methods.

The construction of hexagonal underground structure mainly includes two kinds of open excavation method and dark excavation method, open excavation method includes cast-in-place method and prefabrication method, and dark excavation method includes pipe jacking method and shield method. Among them, the open excavation method is suitable for underground structure projects with new urban areas and roads, or with subway, elevated and underground roads; the open excavation method is suitable for urban center or projects with large buried depth, especially if the existing structures are not suitable for open excavation method.

The construction method of the hexagonal underground structure should be decided comprehensively according to the geological conditions of the site, the surrounding environmental conditions, the economic investment of the structure construction, the construction period and the local construction experience.

Based on the shape characteristics of the hexagon underground structure, can be combined with the inclined pile foundation pit supporting new type of hexagon underground structure system, on the one hand, can combine the shape of the hexagon underground structure and inclined pile, improve the utilization of space, on the other hand also can effectively solve the open foundation pit cost is high, using the support of foundation pit excavation construction inconvenience.

6 PIPE STRUCTURE AND CONNECTION MODE OF HEXAGONAL SECTION AND HONEYCOMB UNDERGROUND ENGINEERING

According to the hexagonal underground structure method described above, it can be found that because this new structure belongs to the special-shaped section, the site pouring operation is difficult, so the most reasonable way is to use the prefabrication method for construction. However, the prefabrication method is limited by the volume of the pipe section, and it is inconvenient to transport and install it when the pipe section is too large and heavy. If the whole pipe section can be divided into several segments for on-site assembly, it can not be limited by the volume of the pipe section and effectively solve the above construction problems.

6.1 *Structural type of prefabricated tube segments*

precast segment should adopt integrated form, simple structure and high strength, by making the curved segment and "Y" segment with positive hexagonal corner structure, to avoid the splicing surface between prefabricated segment in the corner position, the disadvantages of low structural strength, make the splicing of hexagon underground structure strength is higher, assembling speed is faster. At the same time, by adjusting the length of each side of the curved segment and the splicing method between the segment ring, different connection forms of "open joint connection" and "wrong joint connection" can be realized to meet the design and construction requirements under different circumstances. (Figure 5)

Figure 5. Precast segments assembled into single cabin structure and prefabricated segments assembled into seven cabin structure.

The corner of the hexagonal underground structure is easy to form stress concentration. For prefabricated types and segments, according to the stress characteristics of the structure, the inner sides of the left and right sides of the segments can be treated when making segments, and then assembled in the field to solve this problem.

6.2 *Pipe segment connection mode*

Bolt holes are opened on the side edge of the prefabricated segments. During assembly, holes are opened on the two sides of the prefabricated segments for the bolt for fixation, so as to form a longitudinal seam and ring between the prefabricated segments. At the same time, the front and rear ends of the prefabricated segments also open holes for bolt penetration and fixation, so that the connection between the front and back rings to form a ring seam. (graph 6)

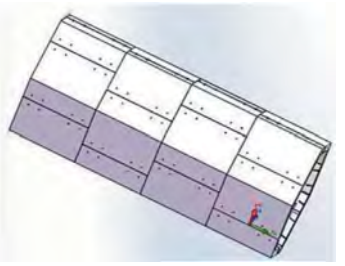

Figure 6. Schematic diagram of misjoint assembly.

7 CONCLUSION AND OUTLOOK

The new hexagonal section and its section combination honeycomb underground structure system has obvious advantages in spatial integration. The whole system unifies the planning, design and implementation of underground engineering, reserving precious space for the urban intensive development. The system can combine the left and right lines, the transfer line interval, the comprehensive pipe corridor and other underground space engineering into the upper and lower overlapping system, the left and right parallel system, etc. The honeycomb system of the hexagonal monomer inside the system can also be flexibly arranged and separated, providing the possibility of infinite creative combination for the underground space engineering.

On the basis of this study, more comprehensive model test and field test can be conducted for different size single cabin structure and multi-cabin system, which can further improve the design method of the hexagonal underground structure. In the construction, the matching shield and pipe jacking equipment and auxiliary facilities needed in the construction process should be developed to meet the needs of the hexagonal underground structure system.

REFERENCES

[1] Qian Qihu. Construction of urban underground comprehensive pipe corridor to transform the urban development mode [J]. Tunnel construction, 2017,37 (6): 647–654.

[2] Zhao Xianwei. Analysis of the mechanical properties of the deformable honeycomb structures [D]. Harbin: Harbin Institute of Technology, 2013.

[3] Schofied AN, WORTH C P.Critical state soil mechanics[M].London: McGraw Hill, 1968.

[4] Meng Wei. Study on the force-bearing deformation characteristics of hexagon pipe gallery and combined structure [J]. Construction technology, 2019,48 (18): 120–124

[5] Feng Kun, He Chuan, Xia Songlin. Experimental prototype of transverse stiffness efficiency of large section shield tunnel structure [J]. Journal of Geotechnical Engineering, 2011,33 (11): 1750–1758.

Tunnelling for a Better Life – Yan, Celestino, Thewes & Eberhardt (Eds)
© 2024 The Author(s), ISBN 978-1-032-80042-4
Open Access: www.taylorfrancis.com, CC BY-NC-ND 4.0 license

Harnessing the potential of underground space for climate-neutral cities: Energy geostructures in metro tunnels

Azad Koliji*, Etienne Garin, Tohid Kazerani, Benjamin Schenk & Jade Senn
WSP BG Consulting Engineers, Lausanne, Switzerland

ABSTRACT: In recent decades, the transition towards sustainable energy has emerged as a crucial challenge in the development of cities and infrastructure. The utilization of eco-friendly technologies that harness renewable energy sources plays a pivotal role in constructing low-carbon buildings and infrastructure. In this regards, energy geostructures present a groundbreaking and versatile technology that can address the challenge. By integrating geothermal heat exchangers in underground structures, energy geostructures offer the potential to serve as heating and cooling systems for various infrastructures. This paper examines the possible incorporation of energy geostructures within the tunnel lining of an under-development future metro line in Lausanne, Switzerland (vd.ch/métros). In general, the urban texture and the proximity of energy consumers provides an opportunity for significant heat recovery, potentially offering a substantial energy source for the surrounding inhabited areas. In the present case, this opportunity needs to be further evaluated with the uncertainties linked to the geology, hydrogeology, temperature variation and the adjacent urban energy consumption. Advanced thermomechanical analyses of the tunnels, equipped with heat exchangers, are carried out to demonstrate the mechanical feasibility of utilizing these structures as energy geostructures. A finite element model with thermodynamic coupling is employed, combining the mechanical forces arising from earth pressure and the expansion of marlstone layers with the thermal forces generated by temperature variation. Conducted in the early stages of the project, theses analyses allow determining the additional thermal forces exerted on the tunnel structure, assessing the resulting impact on the supporting structure, and ultimately verifying the feasibility of integrating these geothermal structures into the new tunnels while minimizing costs and construction timelines. The multidisciplinary study is commissioned by the State of Vaud, the regional authority, which is leading the project in collaboration with the regional public transportation system and the City of Lausanne.

Keywords: Energy geostructures, urban underground, metro tunnels, numerical modelling

1 INTRODUCTION

In recent years, the global demand for energy has exhibited continuous growth, driven by strong economic expansion and burgeoning populations. As per the findings of the International Energy Agency's World Energy Outlook (IEA's WEO), it is projected that worldwide energy demand will experience a further 10% increase between 2019 and 2030 (IEA 2020). In parallel, it is expected that global CO2 emissions will not surpass 2019 levels until 2027, despite the anticipation of demand returning to pre-Covid-19 levels in early 2023. This observation underscores the shift in the energy mix, with renewables emerging as resilient components in the post-pandemic recovery.

The initiatives implemented by governments under the Sustainable Development Scenario (SDS) are steering energy systems onto a different trajectory, with the prospect of reducing CO2 emissions to below 27 Gt by 2030 (IEA 2020). It is becoming increasingly apparent that an accelerated transition to renewable energy sources, as previously outlined in the "Alternative World Energy Outlook" (Zittel & Schindler 2007), is essential to meet the requirements of sustainable societal development.

In the context of energy considerations, the intelligent utilization of underground space for tapping into renewable geothermal energy sources represents an innovative solution in pursuit of the Sustainable Development Goals (SDG), which have been embraced by all United Nations Member States (UN 2015, specifically SDG no.7, 9, 11, and 13).

Within this context, energy geostructures present an innovative solution that combines the utilization of renewable geothermal energy with the structural components situated in underground spaces (Koliji et al. 2022). In the case of metro lines, the heat generated by the metro traffic could also contribute in

*Corresponding author: azad.koliji@bg-21.com

DOI: 10.1201/9781003495505-423

sourcing thermal energy. The core concept of energy geostructures revolves around integrating the primary heat exchangers of ground-source heat pump (GSHP) systems within the foundation and retaining elements, such as piles and diaphragm walls used for tunnel linings (Soga & Rui 2016).

While conventional shallow geothermal energy systems like geothermal probes are commonly employed in building construction, the use of energy geostructures is a relatively recent development, with its inception dating back to the mid-1980s. Nevertheless, this approach still encounters challenges in terms of planning and construction. Despite a growing number of energy geostructure installations worldwide (Laloui & Rotta Loria, 2019), the paucity of data from real-world installations remains a significant limitation. This dearth of information hampers the formulation of design optimization strategies and guidelines for future installations (Zannin et al. 2020a).

This paper presents a study on the possible incorporation of energy geostructures within the tunnel lining of an under-development future metro line in Lausanne, Switzerland (vd.ch/métros). It looks to different aspects related to the geology, hydrogeology, temperature variation and the adjacent urban energy consumption, and examines the possible thermomechanical effects of geoenergy activation on the structure of the tunnel.

2 ENERGY GEOSTRUCTURES

To gain a deeper insight into the potential contribution of energy geostructures to sustainable societal development, it is instructive to examine energy consumption patterns. Across various sectors within European Union countries, residential and commercial buildings collectively account for approximately 38% of the total final energy consumption (IEA 2017, as depicted in Figure 1). Focusing specifically on residential and commercial buildings, nearly 25% of energy consumption is dedicated to heating and cooling purposes (Eurostat 2018). It is worth noting, however, that only a limited portion of this energy is derived from renewable sources.

When we consider renewable energy sources for heat generation, geothermal energy represents just 7% of the total share (as illustrated in Figure 2, IEA 2017), even though it stands as the Earth's second most abundant primary energy source (Lee, Speight, & Loyalka, 2007). The relatively low utilization of geothermal energy in this context can be attributed to various technical challenges tied to exploration, construction, operation, and energy storage. Consequently, there exists considerable untapped potential for leveraging geothermal energy as a direct source for heating and cooling in buildings. Within this context, energy geostructures emerge as a pivotal player, capable of fulfilling this role.

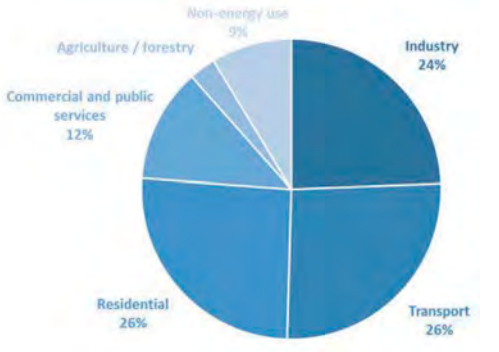

Figure 1. Total final energy consumption by sector in the EU (data from IEA 2020).

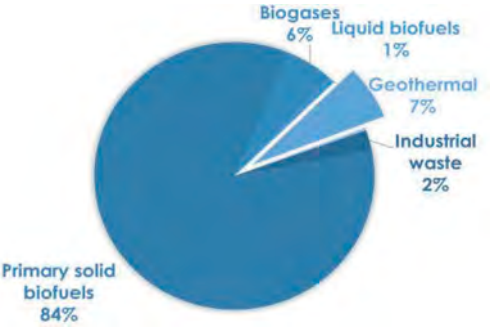

Figure 2. Share of renewable energy sources in heat generation (data from IEA 2020).

Energy geostructures seamlessly integrate the functions of structural support with those of geothermal heat exchange systems within the foundational and shallow subterranean components of infrastructure. These innovative constructs offer a cost-effective, intelligent solution that has demonstrated its effectiveness as a low-emission method for heating and cooling operations in both building and infrastructure contexts (for instance, as highlighted by Sutman et al., 2020). Sterpi et al. (2020) have also presented diverse thermal performance characteristics associated with diaphragms and slabs, shedding light on their versatility.

Furthermore, it is worth noting that the implementation of energy geostructures has resulted in minimal thermally-induced deformations, as evidenced by the observations made at the Lainzer U2 line in Vienna (Brandl, 2016).

3 LAUSANNE NEW METRO LINE

3.1 *Project overview*

Following the significant economic growth in the Lemanic arc region in western Switzerland, several infrastructure projects have been developed in the region with the purpose of achieving a sustainable

solution for population mobility needs. In a decade, the landscape of Lausanne, a city of 140,000 residents, and the Swiss canton of Vaud will undergo significant transformation. The city's mobility will be revolutionized by the introduction of the new M3 metro line, entirely underground, linking the city's central railway station to a brand-new eco-friendly district that is poised to accommodate 8,000 residents and create 3,000 job opportunities in 10 years (Schneider 2022).

Figure 3. Plan view of the existing m2 (pink) and the new m3 (blue) metro lines in Lausanne (Courtesy of Axes Forts).

Figure 4. Longitudinal profile of m3 tunnel (Schneider 2022).

The new M3 line, spanning 3.6 kilometers, will be a fully dual-track underground route connecting the central station to "La Blécherette", situated to the north of the town (see Figure 3 & 4). This line is slated to feature a total of seven stations. Its stars from an existing M2 line metro station, passing through an existing cross-station which needs to be expanded to accommodate m3 line, and then

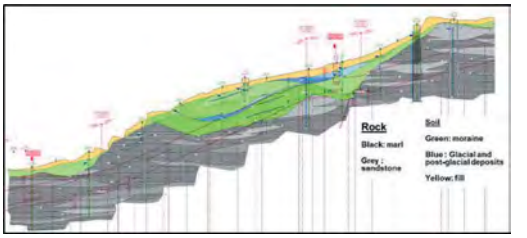

Figure 5. Geological profile of m3 tunnel.

continues its way to the north through new stations. These new stations have been designed with user convenience in mind, emphasizing shallow platforms to facilitate swift entry and exit. In addition, a depot will be constructed at the end of the line to house the train sets.

3.2 *Geology & geotechnics*

One of the key issues in the study of underground energy geostructures is the geology and hydrogeological condition. The new metro line in Lausanne is located in a mixed geological condition along its alignment. However, the interaction with surface air temperature can be expected.

The geology of the section under study is mainly composed of a surface fill material lying on moraine soil layer, and on higher depth on molassic rock.

4 ENERGY GEOSTRUCTURES ASSESSMENT

4.1 *Background*

With the aim of promoting sustainable development and use of renewable energy sources, it was decided to explore the possibility of integrating energy geostructures in the tunnels and underground stations of the new metro line in Lausanne.

In this regards, initial feasibility studies were carried out to assess the thermal potential of energy geostructures implementation and the corresponding effects on the structures. Results of the preliminary feasibility studies showed a potential interest in terms of energy production (Meghari 2022). However, integrating heat exchanger systems in the tunnels and underground structures could also have potential construction and structural impacts. Therefore, it has been decided to carry out further advanced analyses to evaluate potential thermo-mechanical effects on the structure and to assess the impacts on the construction methodology, planning and costs.

4.2 *Thermo-mechanical approach*

Advanced thermo-mechanical coupled analyses are carried out using finite element methods. It combines

Table 1. Thermal material properties.

Parameter	Unit	Concrete	Fill	Moraine	Molasse
Thermal conductivity	$\lambda\ [W/(m^{\circ}C)]$	1.8	0.6	1.8	2.5
Specific thermal capacity	$C\ [MJ/(m^{3\circ}C)]$	880	1.4	2.0	2.1
Thermal dilatancy coefficient	$\alpha\ [1/^{\circ}C]$	10^{-5}	$3.3x10^{-6}$	$3.3x10^{-6}$	$2.3x10^{-5}$

the thermal induced stresses with those coming from tunnel excavation and swelling effects. The thermodynamic approach follows a three-step procedure:

i. Using a thermal model, the initial thermal condition around the tunnel is set up through internal BC (air temperature inside the tunnel) and external BC (surface air temperature and far field temperature).
ii. The liquid temperature inside heat exchangers is imposed, allowing heat diffusion inside the pipes, concert and surrounding ground.
iii. A mechanical model takes the thermal fields and introduce it in the analyses of the stress-strain behaviour. The thermo-mechanical effects are then combined with the mechanical load cases including tunnel sections with and without swelling pressure.

This approach combines the elastoplasticity coming from both mechanical and thermal loading. The total strain increment does reads as follows:

$$\dot{\varepsilon}_{ij} = \dot{\varepsilon}_{ij}^{Me} + \dot{\varepsilon}_{ij}^{Te} + \dot{\varepsilon}_{ij}^{Me} + \dot{\varepsilon}_{ij}^{Tp}$$

in which the superscript, e and p denotes elasticity and plasticity; and M and T denote mechanical and thermal part respectively.

5 NUMERICAL MODELLING

5.1 *Model set up*

The numerical modelling is carried out using finite element code ZSoil. A 2D section of the tunnel is modelled including the tunnel support and lining as well as different geological layers. Concrete is modelled as linear elastic material while elasto-plastic constitutive models are used for soil and rock layers. Figure 6 shows the 2D cross section of the model.

Thermal material properties, reported in Table 1, are taken from previous studies, and are largely based on the literature.

If it is decided to implement geostructures in the project, specific tests are to be carried out in the next stages of the project to confirm or adjust theses parameters.

5.2 *Modelling phases*

Simulations are carried out in three phases:

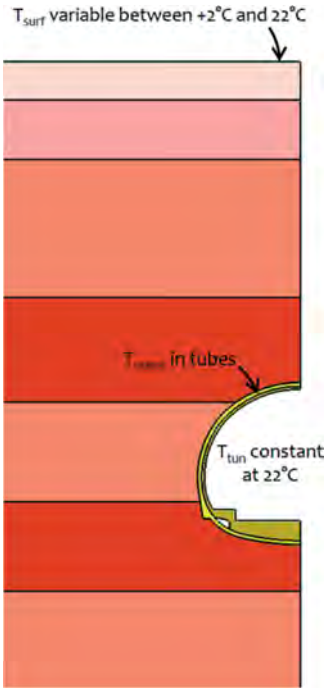

Figure 6. 2D section of the finite element model.

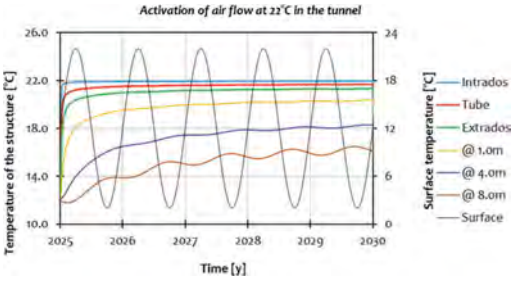

Figure 7. Tunnel construction with constant air temperature inside the tunnel over 5 years (indicative duration) - distances are given with respect to the tunnel vault.

a- Initialization of thermal field in the ground by seasonal variation of surface air over 10 years;
b- onstruction phase during which the tunnel air temperature is constant for 5 years (Figure 7);

c- Geothermal activation with seasonal variation of water inside the heat exchanges pipes over 25 years (Figure 8).

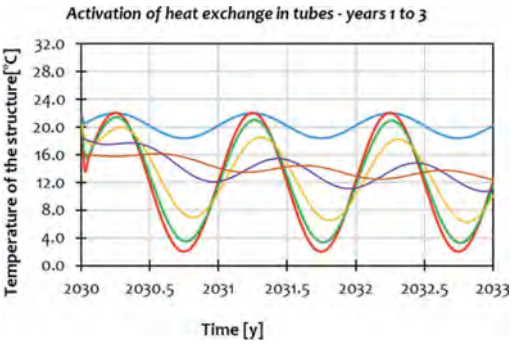

Figure 8. Activation of thermal exchange in the pipes (the first 3 years over 25 years – indicative duration).

5.3 *Result of thermal analyses*

Results of thermal analyses, in terms of temperature variation in the tunnel lining and the surrounding ground, are presented in the following figure for summer and winter.

In both cases, a temperature gradient can be observed along the thickness of the tunnel. This effect, more pronounced in winter, will results in thermal induced stresses in the concrete.

5.4 *Result of thermomecanical analyses*

The temperatures fields obtained from the thermal analyses of the previous section are taken into mechanical analyses to obtain the thermal induced stresses. The results, in terms of thermal induced stresses are presented in the following figure. These stresses are calculated directly from a thermo-elasticity constitutive model for the concrete. It can be noted that the values of these stresses, themselves, are not very high and still far from the concrete strength. However, these stresses are to be combined with those coming from mechanical analyses and assessed for the critical load cases with swelling pressure of the rock.

Results of the combined thermomechanical analysis for the most critical case with rock swelling pressure shows the concrete stress exceeds the strength on the lower parts of the tunnel wall. Accordingly, additional reinforcement is required in these zones to sustain the loads coming from activation of heat exchangers. It should be noted that the integration of heat exchanger pipes, themselves, results in a reduction of concrete mass which is considered to be insignificant.

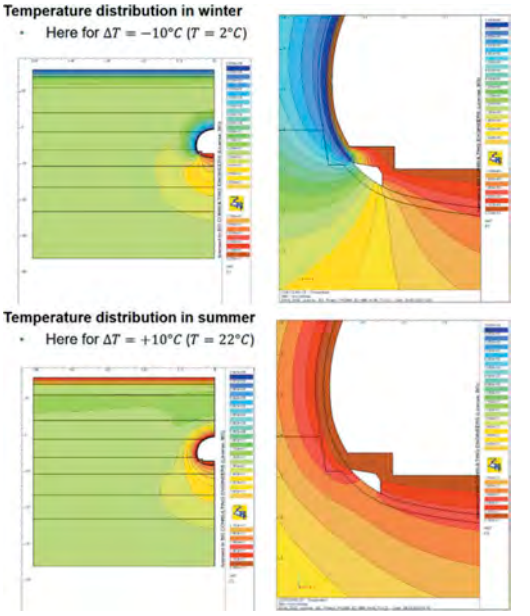

Figure 9. Temperature distribution in the tunnel lining in winter (up) and summer (down).

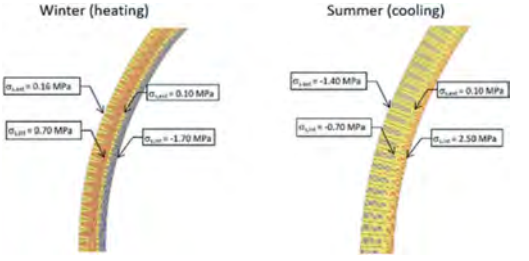

Figure 10. Thermal induced radial stresses in the tunnel lining in winter (left) and summer (right).

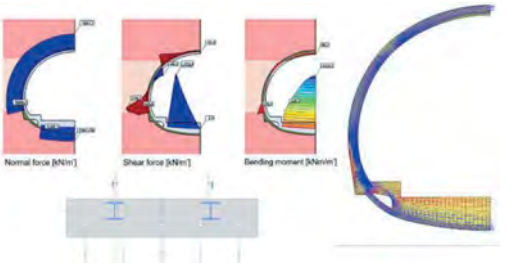

Figure 11. Tunnel support and lining taking the swelling pressure of the rock. Results presented in terms of normal forces, shear forces, bending moment and principal stresses in the concrete.

6 COST AND PLANNING

Results of this study showed that the tunnel lining needs to be reinforced with two layers of B754 mesh (ϕ=12 mm @ s=150 mm), while the support system also requires reinforcement with the same mesh, but only at the base of the walls. For the support system, a mesh layer of 2 meters in height should be installed at the base of each wall. This could influence the total cost and planning of the project. The installation rate for the mesh is 50 square meters per hour with a team of two workers, plus one hour of logistical work per day for approximately 80 days. This work could be conducted in parallel with the lining process, where various workshops follow one another along the tunnel's length. A half-day of production loss should be considered for coordination and coactivity. Based on 12 weeks of lining work for each tunnel, an extension of the overall project duration by 6 days should be expected for each tunnel. On the other hand, the installation of the support reinforcement mesh could not be done in parallel. This would add 5 minutes to each meter of advancement, resulting in an additional 3 days per tunnel. Hence, each tunnel would be expected to experience a two-week extension in the project duration, a relatively short period of time with respect the total construction time. Moreover, according to these first results, to be confirmed in further studies, the additional costs for reinforcing the civil engineering structures of the tunnels to withstand geothermal-induced stresses are reasonable and relatively low compared to the total construction cost.

7 CONCLUSIONS

This study has shown that thermal constraints vary almost linearly with the temperature variation applied to the heat transfer fluid. The greater the applied temperature difference, the more significant the generated stresses.

Regarding the resistance of the tunnel section, the reduction in surface area due to the presence of heat transfer tubes with a diameter of ϕ=40 mm and a spacing of e=40 cm is practically negligible.

As for the lining, it is subjected to tensile forces during the summer. Therefore, it is necessary to rely on the tensile strength of the sprayed concrete or lightly reinforce the support to ensure structural safety. In both cases, a relatively straightforward solution is available. There is no need to alter the structural system or the thickness of the lining due to the additional thermomechanical stresses.

Concerning the support system, thermal activation during the winter generates tensile stresses. In the short term, considering the contribution of hangers, the support system could accommodate all load combinations for temperatures above T_tub=2°C and ensure structural safety.

In the long term, without taking into account the contribution of hangers for the typical profile, however, the strength is exceeded. In this case, it is also possible to reinforce the monolithic section quite easily, especially by considering the tensile strength of the sprayed concrete lining or using passive reinforcement for the lining. Long-term loads then also remain acceptable. Like the lining, it is possible to maintain the currently planned structural system without changing the thickness of the support.

This study thus demonstrates the feasibility of utilizing thermal energy in tunnels for the given cubic meters, provided that the support and lining are reinforced for tensile strength with fibers or passive reinforcement.

At this stage, the possibility of integrating energy geostructures into the future Lausanne M3 metro tunnels is still under study, with a focus on the the benefit-cost ratio. Apart from design considerations, several other issues should be still addressed including the question if this energy project can be ready in time to be integrated into the construction of the M3 metro, or whether an operator interested in running such an energy infrastructure can be found. To date, the final decision by the project owner to implement these geostrutcures has not yet been taken.

ACKNOWLEDGEMENT

The authors acknowledge the permission granted by the client State of Vaud, in collaboration with the regional public transportation system and the City of Lausanne, to publish the main results of the present study. The authors also acknowledge the contribution of members of the Joint-Venture DAVEL for their collaboration on the civil and architectural studies of the project www.vd.ch/métros.

REFERENCES

IEA (2020) International Energy Agency - World Energy Outlook 2020, IEA, Paris https://www.iea.org/reports/world-energy-outlook-2020.

Zittel, W., Schindler, J. (2007), Alternative World Energy Outlook 2006: a possible path towards a sustainable future, D. Yogi Goswami (Ed.), Advances in solar energy, vol. 17, Earthscan, UK, USA, pp. 1–44.

United Nations Department of Economic and Social Affairs. (2015) Transforming our world: the 2030 Agenda for Sustainable Development, United Nations, A/RES/70/1.

Soga, K:, Rui, Y., (2016), Energy geostructures, Advances in Ground-Source Heat Pump Systems, Editor(s): Simon J. Rees, Woodhead Publishing, Pages 185–221, ISBN 9780081003114.

Laloui, L., Rotta Loria, A.F., 2019. Analysis and Design of Energy Geostructures - 1st Edition. Academic Press.

Zannin, J., Ferrari, A., Larrey-Lassalle, P., Laloui, L., 2020a. Early-stage thermal performance design of

thermo-active walls implemented in underground energy infrastructures. Geomech. Energy Environ.

IEA (2017) - International Energy Agency – World Energy Balance, Data and Statistics, https://www.iea.org/regions/europe.

Eurostat (2018), Statistical office of the European Union, Energy Data https://ec.europa.eu/eurostat/web/energy/data.

Lee, S., Speight, J., & Loyalka, S. (2007). Handbook of alternative fuel technologies (Vol. 2). CRC Press.

Sutman, M., Speranza, G., Ferrari, A., Larrey-Lassalle, P., Laloui, L., 2020. Long-term performance and life cycle assessment of energy piles in three different climatic conditions. Renew. Energy 146, 1177–1191.

Koliji A., Rigaud E., Kazerani T., Zannin J., Ferrari. A., Laloui L., Use of underground space as renewable energy source for a sustainable society, WTC 2022.

Sterpi, D., Tomaselli, G., Angelotti, A., 2020. Energy performance of ground heat exchangers embedded in diaphragm walls: Field observations and optimization by numerical modelling. Renew. Energy, Shallow Geothermal Energy Systems 147, 2748–2760.

Brandl, H., 2016. Geothermal Geotechnics for Urban Undergrounds. Procedia Eng., 15th International scientific conference "Underground Urbanisation as a Prerequisite for Sustainable Development" 12-15 September 2016, St. Petersburg, Russia 165, 747–764.

Zannin, J., Ferrari, A., Pousse, M., Laloui, L., 2020b. Hydrothermal interactions in energy walls. Undergr. Space.

Loveridge, F., McCartney, J.S., Narsilio, G.A., Sanchez, M., 2020. Energy geostructures: A review of analysis approaches, in situ testing and model scale experiments. Geomech. Energy Environ. 22, 100173.

Schlosser, T., Schmidt, M., Schneider, M. and Vermeer, P. A., 2007. Potenzial der Tunnelbaustrecke des Bahnprojektes Sttutgart 21 zur Wärme- und Kältenutzung, Universität Stuttgart.

Adam, D. and Markiewicz, R., 2003. Nutzung der geothermischen Energie mittels erdberührter Bauteile - Teil 3: Ausführungsbeispiele und Neuentwicklungen. Österreichische Ingenieur- und Architektenzeitschrift (ÖIAZ), 148(1).

Baujard C., and Kohl Th. Evaluation of the Potential Use of Geothermal Heat Exchangers in the CEVA Tunneling Project, Proceedings World Geothermal Congress 2010, Bali, Indonesia, 25-29 April 2010.

Kohl, T. and Hopkirk, R.J., 1995. "FRACTure" a simulation code for forced fluid flow and transport in fractured porous rock. Geothermics, 24(3): 345–359.

Laloui, L. and G. Steinmann (2002) Finalisation du module de l'EPFL pour les tests de réponses (in French), ENET_Swiss Energy, Nº220188.

Mattsson, N.; G. Steinmann; L. Laloui (2008). Advanced Compact Device for the In-situ Determination of Geothermal Characteristics of Soils. Energy and Buildings, Vol. 40, pp. 1344–1352.

Meghari, M. (2022). Intégration des géostructures énergétiques au futur projet de métro lausannois m3 – Étude de faisabilité. Programme: Stratégie Énergétique 2050 dans les transports publics (SETP 2050). Office fédéral suisse des transports.

Schneider, M (2022). Development of Automated Metro Lines M 2 and M 3, Swiss Tunnel Congress 20222.

Tunnelling for a Better Life – Yan, Celestino, Thewes & Eberhardt (Eds)
© 2024 The Author(s), ISBN 978-1-032-80042-4
Open Access: www.taylorfrancis.com, CC BY-NC-ND 4.0 license

Research on complete technologies for the construction and utilization of super large caverns in Hong Kong

Yifeng Li, Zhengqiang Hong*, Wei Li & Fei Xu
China State Construction Engineering (Hong Kong) Limited, Hong Kong SAR, China

ABSTRACT: In response to land scarcity and the increasing environmental needs in Hong Kong, the construction of public facilities has begun to seek underground space development. One of the first major projects leading the long-term sustainable cavern development in Hong Kong is the Relocation of Sha Tin Sewage Treatment Works to Caverns. The layout and sizes of the caverns must be arranged according to the functionality of the treatment facilities. Taking Sha Tin Caverns as an example, this paper will critically review the main characteristics of underground treatment methods and present the idea of a complete and total solution for the construction of such caverns, focusing on key points such as the construction methodology, implementation of new technology and management for such large caverns. This paper will also discuss the prospects of future relocation of sewage treatment plants to caverns.

Keywords: Complete technologies, Super large caverns, Construction methods, Implementation of new technology, Management method

1 INTRODUCTION

As an important component of municipal engineering, sewage treatment plants play indispensable roles in purifying wastewater, reducing pollution, improving urban ecological environment, and improving residents' quality of life. However, it should also be noted that traditional aboveground sewage treatment plants have negative social and environmental impacts such as excessive land occupation, severe secondary pollution, and negative impacts on the land value of surrounding areas. With continuous development of the economy, cities boundary is gradually expanding, land resources are becoming increasingly scarce, and environmental requirements are becoming more stringent. As such, underground sewage treatment plants (USTPs) have demonstrated clear advantages over traditional STPs in terms of reasonable utilization of underground space, freeing land resources up, odor free, significantly lesser noise pollution, and even somehow making the landscape less attractive - all of which has promoting effects to relocate STP underground. USTP have ushered in new development opportunities.

1.1 *Development of USTPs worldwide*

The development and utilization of underground space has a history of more than 150 years (Bao et al., 2003), and USTPs have also developed well in the past 80 years. So far, there are more than 200 USTPs in stable operation (Wang et al., 2017), which are widely distributed in more than 10 countries and regions, generating enormous economic, environmental and social benefits for the local communities.

Europe has a long history of constructing USTPs. As early as 1932, Finland began constructing of the world's first USTP near Helsinki, and completed the project in 1970 (Herranen, 2001); Sweden leads the world the construction technology and operation experience of USTPs among the world, and all sewage plants in Sweden are USTPs; Norway, Netherland and other counties also constructed lots of USTPs.

In Asia regions, Hong Kong built the first USTP in 1991 in Stanley; other countries and regions started constructing USTPs around 2000 to relocate existing sewage treatment facilities into caverns due to land scarcity.

The current development of USTPs are shown in Table 1 (Tan et al., 2006, and Zhu, 2015).

*Corresponding author: Zhengqiang.hong@cohl.com

DOI: 10.1201/9781003495505-424

Table 1. Current development of USTPs.

Completion Year	Project/ City	Country/ Region	Type of USTP
1964	Bekkeläget	Norway	Cavern/ Tunnel
1969	Käppala	Sweden	Full-underground
1979	Dokhaven	Netherland	Full-underground
1991	Stanley	Hong Kong, SAR of China	Cavern/ Tunnel
2005	Incheon	South Korea	Semi-underground
2008	Kakolanmäki	Finland	Full-underground
2009	Tiantanghe, Beijing	China	Semi-underground
2016	Futian, Shenzhen	China	Semi-underground
2017	National high-tech Industrial Development Zone, Qingdao	China	Full-underground

1.2 *Relocation of Sha Tin Sewage Treatment Works in Caverns in Hong Kong*

In order to overcome the problem of land scarcity in Hong Kong, the Civil Engineering and Development Department (CEDD) of the Hong Kong Government has commenced the "Long-Term Strategy for Cavern Development - Feasibility Study" in 2012. And the study has recommended, among others, the formulation of a territory-wide strategy for sustainable cavern development in the form of Cavern Master Plan (CMP). One of the main features of the CMP is the delineation of suitable sites within all areas of Hong Kong for cavern development, termed Strategic Cavern Areas (SCVAs), and the first major projects leading the long-term sustainable cavern development in Hong Kong is the Relocation of Sha Tin Sewage Treatment Works in Caverns (Sha Tin Caverns, STC).

The STC is about 14 hectares, resides within Nui Po Shan, Sha Tin, Hong Kong. Due to the scale of the STC (serving 800 thousand residents, which is 10% of Hong Kong's population) and unique arrangement of the treatment plants, the layout and sizes of the caverns must be arranged according to the functionality of the treatment facilities, which leads to the largest cavern being 32m high and 32m wide. Drill and Blast Method (DBM) is adopted in this project in order to excavate the largest blast face in Asia.

This paper takes STC as an example to illustrate the construction methods, latest technological applications and management methods applied in the construction process of modern super large caverns.

2 CONSTRUCTION METHODS

The main construction works of STC include the excavation of main caverns, installation of piling works, and buildings of the ventilation facilities and effluent pipelines. The subsequent Chapter 2 of this paper outlined with the construction methods such as blasting and installation of support system of caverns in detail.

2.1 *DBM on super large blast faces*

The largest blast face inside STC has a width of 32 m and a height of 32 m. The blasting operation of each face has to be divided into three stages, namely the top heading, middle bench, and invert, whose average area of face size reaches 300 m^2, making it a rare super large cross-sectional blast face in Hong Kong, even globally. And the rest of the main-cavern blast faces all exceed 200 m^2 (see Figure 1, over 200 blast holes with 8.9m high and 30.52m wide of top heading). Millisecond blasting is applied in the construction of main cavern structure.

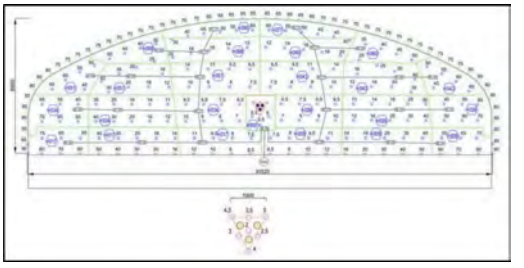

Figure 1. Typical blast face.

To apply DBM on these super large blast faces, precise blasting design and calculation were carried out to determine the size and spacing of blast holes, as well as the sequential blast order of selected explosive holes.

2.1.1 *Pre-blasting*

For DBM, the pre-blasting process mainly involves probing ahead and advanced ductile grouting. The engineering geologists will check and review the ground material from probing (to make sure rock strength is sufficient for blasting), and after confirming that the anticipated ground condition is suitable for blasting, he/she will communicate the findings to blasting engineer, and the blasting engineer will update the blast design accordingly (blast hole pattern, spacing, size, quantity of explosives etc.).

2.1.2 *Blast holes design*

Two Three-arm Tunnel Drilling Rigs (Jumbo) are used to drill cut holes, production holes, perimeter holes as well as holes for rock bolt installation. Compared with the traditional blast holes drilling method (using pneumatic hammer drills), the diameter of STC's cut holes and production holes (as well as

perimeter holes) reached 102 mm and 51 mm respectively; The maximum instantaneous charge (MIC) weight can reach 2 kg/m, and the advance length is maintained at approximately 5 m; Simultaneously, all blasting adopts millisecond method, and a blasting surface of about 300 m^2 can be completely detonated by all explosives within 10 seconds, thus greatly improving the efficiency of construction.

In terms of hole spacing, due to the large diameter of the drilled holes, the quantity of explosives in each hole is also large, therefore the hole spacing need to be larger than that of traditionally drilled holes. The spacing between each production holes is generally over 1 m, and the spacing between perimeter holes is generally over 0.5m. In other words, only one hole is required for every 1.03 m^2 of the blast face on average.

2.1.3 *Explosives*

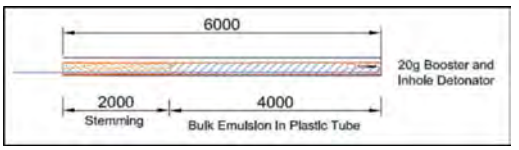

Figure 2. Typical explosive design.

According to the statutory requirements in Hong Kong, the cartridge explosives, bulk emulsion explosives, booster, detonating cords, in-hole delay, non-electric detonators, surface/bunch detonators, electric detonators, electronic initiation system etc. are selected for blasting.

In order to maximize efficiency, enhance economical operation, and control misfire rate, this method only uses non-electric and electric detonators. For any single blasting, electric detonators are only used at the initiation point, and non-electric detonators are used in all subsequent blast holes.

As mentioned in Chapter 2.1.2, the designed MIC for 51mm diameter blast hole can reach 2 kg/m, this is equivalent to 10 kg for one blast hole of 5 m in length, all the while ensuring that environmental impact are within required limits (Section 2.2). Compared to the traditional method of drilling a 38mm diameter blast hole with a length of 3 m, the charge weight for 5 m hole is increased by approximately 3 times.

Figure 2 Shows the typical design of explosives.

2.1.4 *Blast delay design*

Due to the limitations of the product, the delay device will have a tolerance of about 2 % during blasting. Therefore, when designing the delay of millisecond blasting, the larger the time interval between the outer holes, the more it can ensure that the blasting is carried out from the core to the perimeter. In the design of the maximum blast face, the maximum delay of the outermost perimeter hole is 9,000 ms (i.e. 9 s, see Figure 1). As such, all blasts are guaranteed to be completed within 10 seconds.

2.1.5 *Comparison with traditional blast design*

The blasting method comparison between the super large blast face in STC and traditional blast face (using air hammer drill) are shown in Table 2.

Table 2. Comparison of blast design.

Parameters	Traditional Design	Design of STC
Dia. of Blast Holes	32~50 mm	51 mm
Spacing of Production Holes	0.7~0.8 m	> 1 m
Blast Holes per Square Meter of Blast Face	1.8	0.97
Length of Blast Holes	< 4 m	5 m
MIC	< 5 kg	10 kg
Explosive Factor	1.2~2.4 kg/m^3	1.2 kg/m^3
Demanded workers	1 per air hammer drill	1 Jumbo operator

2.2 *Monitoring system*

During the blasting process, two main indicators are measured: peak particle velocity (PPV) and air overpressure (AOP). The outcomes of these two indicators would help to update the next blast design. The thresholds of the two indicators are shown in Tables 3 and 4, respectively.

Table 3. PPV thresholds.

Condition	Threshold
Alert	90 % of the PPV Limit
Action	95 % of the PPV Limit
Alarm	100 % of the PPV Limit

Table 4. AOP thresholds.

Condition	Threshold
Alert	118 dBL
Action	119 dBL
Alarm	120 dBL

After blasting, continuous ventilation is required to ensure the air quality inside the cavern. The concentration of five gases are measured, namely oxygen, methane, hydrogen sulphide, carbon monoxide, and radon. In the meanwhile, 0.5 cm/s of wind speed inside cavern is required.

2.3 *Temporary and permanent support with rock bolts*

The quality of rock mass for the STC project general ranges between Grade I or Grade II (Grade I being massive, usually unjointed and stable), representing

excellent geological conditions. Hence, for the first time, a new rapid support system was adopted in the construction, which uses a combination of temporary shotcrete, permanent grouted rock bolts, and permanent shotcrete to replace the conventional steel arch support. It has the benefits of cost saving, high efficiency and high flexibility for different blast faces and geological conditions.

2.3.1 *Geological mapping*
After mucking out, geologists would carry out geological mapping of the blast face to estimate the quality of the rock mass, and specify any prescribed reinforcement measures or require re-scaling according to the mapping result. The Geologists will determine the Q-value of the exposed rock mass based on NGI-Q System (NGI, 2015, see Equation 1) using individual parameters such as the degree of jointing, joint shear strength, and condition of rock active stress

$$Q = \frac{RQD}{J_n} \times \frac{J_r}{J_a} \times \frac{J_w}{SRF} \quad (1)$$

Where RQD is Rock Quality Designation; J_n is joint set number; J_r is joint roughness number; J_a is joint alteration number; J_w is joint water reduction factor; and SRF is stress reduction factor.

2.3.2 *Temporary shotcrete*
Safety shotcrete of 50 mm applied to unsupported face immediately after mapping. Temporary support shotcrete installed based on the determined support level.

2.3.3 *Rock bolts installation with modified Jumbos*
Traditional method of installing rock bolts uses Anchor Drilling Rigs to drill holes, followed by manual handling of the bolts on elevated working platforms to slowly insert bolts into the holes. This method meets the requirements of safety, efficiency and quality on small blast faces.

However, for super large blast faces such as STC, where the size is approximately 20 m wide (maximum 32 m), 10 m high, and 5 m deep, most rock bolts have a length longer than 6.3m. The actual installation process requires two elevated working platforms and four skilled workers to manually handle rock bolts at two heights of 8 m and 6 m; Simultaneously, a banksman is required to conduct unified dispatch and command on the ground (Figure 3). The larger the space, the lower the efficiency using the tradition method.

To address the aforementioned difficulty, Tunnel Drilling Rigs (Jumbos) are modified and used to replace manual handling (Figures 4 and 5). Firstly, input the coordinate and orientation information of rock bolt holes into the rock drilling rig for drilling; Then, replace the drilling rig with installation tools, and automatically insert rock bolts into the drilling hole according to the coordinate and orientation information.

2.3.4 *Permanent shotcrete*
After the installation of rock bolts, permanent shotcrete construction should be carried out more than 40m away from the blast face to form a complete permanent support structure.

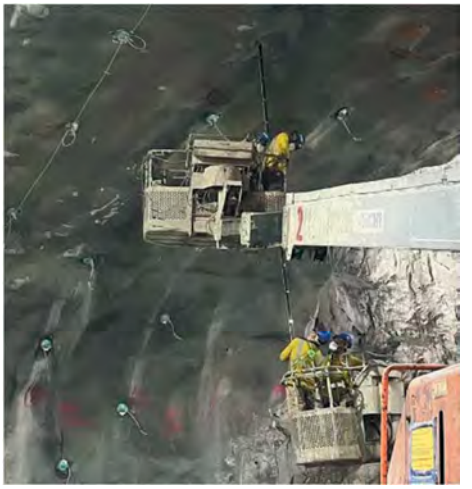

Figure 3. Traditional rock bolt installing method by manual handling.

Figure 4. Modification of Jumbo.

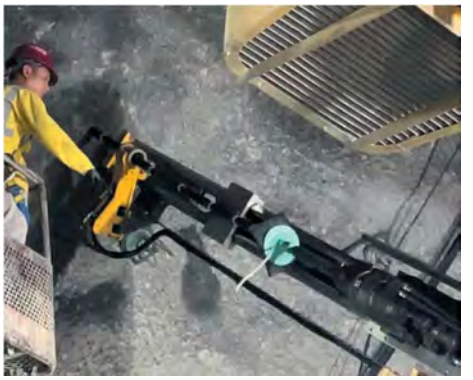

Figure 5. Automatic rock bolts installation by Jumbo.

3 TECHNOLOGY APPLICATION

3.1 *BIM technology*

BIM is adopted to achieve building information integration, and carries out collaborative work and management throughout the entire lifecycle of STC in design, construction organization design, and construction, achieving the goal of efficient transmission of engineering information, improving work efficiency, and reducing costs and increasing efficiency.

3.1.1 *Digital works supervision system*

The BIM Digital Works Supervision System (DWSS) used in STC is a self-designed system that includes four modules: Request for Inspection (RFI), Site Diary System, BIM360 Doc and Safety Inspection System.

The RFI system is developed to issue acceptance application for head office's approval and file management. This system greatly shortens the process and file volume, making it easier for both Project Manager and Main-Contractor; The Site Diary System is adopted to help contractors record construction activities, resource logs, data analysis and storage management (Figure 6); The BIM360 Doc visualizes BIM and bind electronic records to BIM components; And the Safety Inspection System helps recording safety issues.

These four systems form the DWSS, creating more flexibility for both Project Manager and Main-Contractor, reducing paper consumption and improving work efficiency.

Figure 6. Site diary of daily labour.

3.1.2 *Information technology in management*

The information technologies used in the construction management of STC mainly include BIM Deepening Design, BIM Construction Process Management, BIM+Survey and BIM+IoT (Internet of Things).

The BIM Deepening Design conducts structural deepening design and directly converts BIM models into construction drawings (Figure 7); The BIM Construction Process Management sets site planning and layout for each construction stage based on BIM model, and allows the visualisation of the construction process (Figure 8) as well as any technical clarification; BIM+Survey helps the survey team save half of the time, and provides design information of terrain and site model (Figure 9); And BIM+IoTallows management department aware of the power consumption and lighting control of the site (Figure 10).

CMIT greatly improves the quality of disclosure, the management of drawings and documents, and can also handle the workload of one site clerk.

3.2 *Application of DfMA and MiC*

3.2.1 *Design for manufacture and assembly (DfMA)*

DfMA is an acronym for Design for Manufacture and Assembly. In order not to occupy public roads while transporting boulder and rock from blasting, a temporary crane bridge was designed at the site preparation stage of STC for transporting. The temporary steel bridge adopts DfMA method, whose main components are produced and welded in the factory, transported to the site and lifted in place for assembly. This method saved 2 months of construction time and reduced road closure to 2 nights.

Another structure adopting the DfMA method is overhead ventilation ducts (OHVD, Figure 11). After completing all excavation of the cavern, a set of permanent ventilation structures are to be built and handed over to the next stage. The OHVD consists of combination of precast/semi-precast elements and cast-in-situ elements, where the precast/semi-precast parts adopt DfMA method. Due to the large volume of structures to be built, the application of DfMA greatly reduces the construction time compared to conventional cast-in-situ method.

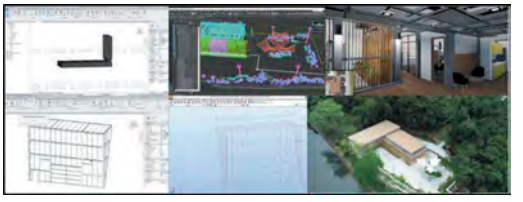

Figure 7. BIM deepening design for MiC.

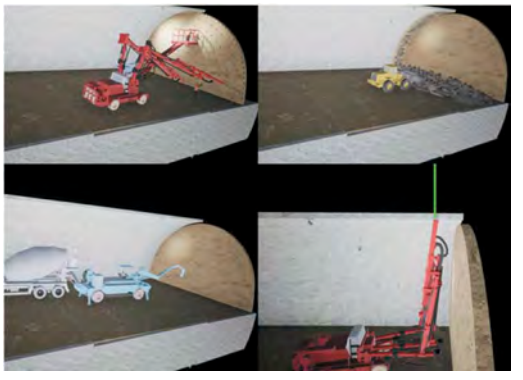

Figure 8. BIM construction process management.

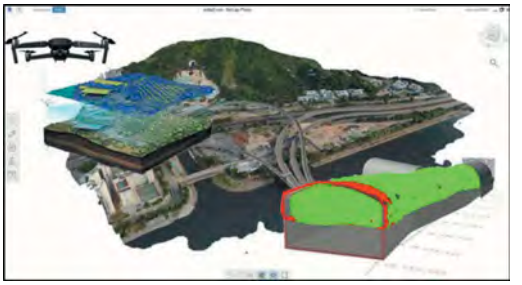

Figure 9. BIM+Survey.

Figure 10. BIM+IoT.

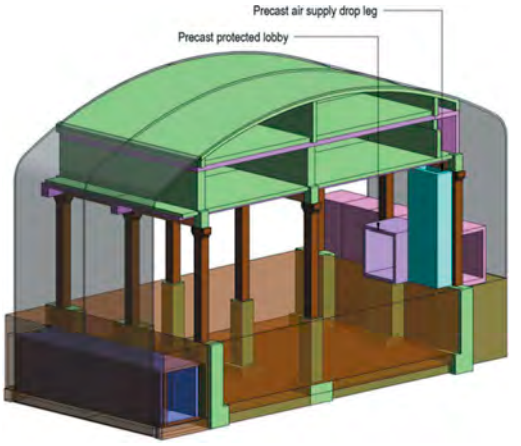

Figure 11. Design of overhead ventilation ducts.

3.2.2 *Modular integrated Construction (MiC)*

MiC, standing for Modular Integrated Construction, is one of the most important aspects of DfMA, mainly focusing on housing facilities. The Community Liaison Centre (CLC) of the STC project was built using MiC technology. All 14 modules were produced in Zhuhai and transported to Hong Kong. They were lifted and assembled within two days to reduce the impact on surrounding residents. By adopting MiC, it has saved labour costs and achieved early completion within the limited construction period during the COVID epidemic.

3.3 *Construction assistance software*

Several construction software were adopted during the construction of STC. For example, all Jumbos are equipped with iSure, a computer program which helps tunnelling construction and drill and blast process control. It produces all the data needed for optimized drilling and blasting cycle; For shotcrete, Real-time Spraying monitoring System was used. This system adopts a laser scanner to scan the surface of the shotcrete and generate a point cloud data. The comparison results between the point cloud data and the design surface can be obtained within 2 seconds, guiding the spray operation, reducing material waste and rework, and greatly reducing the workload of the survey team (Figure 12).

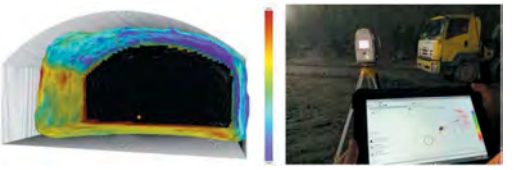

Figure 12. Real-time spraying monitoring system.

4 MANAGEMENT

4.1 *Establishing 5G/Wi-Fi and IoT system*

STC conducts research on the construction of 5G base stations and Wi-Fi networks on site, and established the first on-site 5G base station in Hong Kong to provide networks for the whole cavern (Figure 13). Based on 5G base stations and Wi-Fi networks, STC established Internet of Thing (IoT) System on site, including AI CCTV System, UWB Positioning, AMS System, Intelligent Weight Bridge System, etc, enhancing the efficiency of management.

4.1.1 *AI CCTV system*

AI detection involves processing image data captured by cameras through a certain algorithm and comparing it with known objects in the database; Next, the algorithm will identify objects that are similar to existing objects in the database and return the results.

The AI CCTV used in STC detects unsafe behaviour, wheel cleanliness, and marks out the restriction area to keep unrelated staff away by sounding alarm (Figure 14).

4.1.2 *UWB positioning technology*

The Ultra-wideband (UWB) Positioning Technology is a type of indoor positioning technology with high development prospects. It has advantages such as strong penetration, low power consumption, good multipath resistance, high security, low system complexity, and the ability to provide precise positioning accuracy. Therefore, UWB positioning technology can be

applied to the positioning, tracking, and navigation of stationary or moving objects, including people indoor, with very accurate positioning information.

4.1.3 *Air monitoring system*

Air Monitoring System (AMS) is adopted to detect air flow velocity, temperature, humidity, and level of the usual five confined space gases, namely oxygen, methane, hydrogen sulphide, carbon monoxide and radon, especially after blasting. The thresholds of each kind of index are shown in Table 5.

Figure 13. First On-site 5G Station (Outside/inside Caverns).

Figure 14. AI CCTV Detection.

Table 5. Air quality thresholds.

Item	Unit	Threshold
Oxygen	%	19.5~22
Methane	%LEL	≤ 10
Hydrogen Sulphide	ppm	≤ 10
Carbon Monoxide	ppm	≤ 25
Radon	Bq/m^3	≤ 100
Air Flow Velocity	m/s	≥ 0.5
Wet Bulb Temperature	°C	≤ 27

4.2 *Low-carbon construction management*

The STC project aims to achieve the goal of reducing carbon emissions during the construction process. To achieve this goal, permanent electricity stations were installed instead of generators; reasonable methods to handle blasted boulders and innovating construction processes were carried out; Simultaneously utilizing automatic sprinkler systems, environmental monitoring, blasting doors, and reprocessing of environmentally friendly wood into furniture were also put into effect to achieve the goal of reducing waste and pollution emissions during the construction process. In addition, the construction team conducted a carbon emission inventory of the project, seeking feasible paths for ultra-low carbon construction, and realizing the responsibility of the company and the project to society and environmental protection.

5 PROSPECTS OF FUTURE RELOCATION OF SEWAGE TREATMENT PLANTS TO CAVERNS IN CHINA

5.1 *Feasibility of constructing USTPs in China*

According to the National New Urbanization Plan (2021-2035) released by the National Development and Reform Commission (2022), with the increasingly severe resource constraints and the comprehensive delineation of urban development boundaries, the scale of newly added construction land is controlled to within 29.5 million acres. It is also imperative to transform urbanization development from time oriented to quality oriented. Underground sewage treatment plants fully occupy underground space and efficiently utilize state-owned resources, both of which are in line with the trend of urban development in China.

"Ecological civilization and green health" is one of the guiding principles of urban planning in China. Underground sewage treatment plants not only meet the basic environmental needs of sewage treatment and pollutant discharge standards, they also eliminate the hidden dangers of secondary pollution such as odor and noise. They are an important component of ecological civilization construction.

5.2 *Advantages of Cavern-based USTPs*

(1) Release ground spaces for multipurpose

The released spaces can be used as a comprehensive office building in the factory area for personal use, as well as to build parks, green landscapes, and other buildings to beautify the environment. It can also be developed into projects such as parking lots etc. Foreign experience can be referenced to build profitable projects to further improve economic benefits.

(2) Reduce secondary pollution

When located in caverns, with the surroundings isolating the noise and odor generated during equipment operation, the sewage plants creates almost no secondary pollution, and zero impact to the environment outside caverns.

(3) Stabilize the operation of sewage plants

Traditional sewage treatment plants are susceptible to variation of temperature, and biological

treatment may not operate properly in low temperatures. The characteristics of thermal expansion and contraction of building materials can also cause pipeline system failures when temperature changes are significant. The sewage treatment plant built in a cavern is underground, with a relatively constant temperature and less affected by the external environment, which can ensure the stable operation of the system. Finland, Norway, Sweden and other countries are located in high latitudes and have cold winter temperatures. Therefore, these are also considerations for vigorously developing underground sewage treatment plants.

5.3 *Disadvantages of Cavern-based USTPs*

The construction of sewage treatment plants in caverns usually requires deep excavation, as well as the construction of pre-construction vehicle access channels, which is relatively difficult and costly compared to traditional aboveground sewage treatment plants; In addition, setting the main body of the factory in cavern will have a significant negative impact on natural ventilation and lighting. In order to ensure the health of underground workers, it is necessary to increase ventilation, lighting and other equipment, thus significantly increases the operating costs after being put into use.

5.4 *Summary*

With the further growth of China's economy and the acceleration of urbanization, urban development planning will start from a higher level. Focusing on the future development of the city, adhering to the principle of adapting to local conditions, selecting the scale and address of underground sewage treatment plants reasonably, developing more underground space usage in the factory area, strengthening integration with the surrounding environment, paying attention to the connotation of sustainable development and ecological civilization construction, promoting the coordinated development of the city's economy, society, and ecology in all aspects. The future development of sewage treatment plants constructed in caverns is expected.

6 CONCLUSION

This paper first reviewed the main characteristics of underground treatment methods. Taking the Sha Tin Caverns as an example, this paper presented the idea of a complete and total solution for the construction of such caverns, focusing on key points such as the construction methodology, implementation of new technology and management for such large caverns. This paper also discussed the prospects of future relocation of sewage treatment plants to caverns.

ACKNOWLEDGMENTS

This paper is sponsored by the Technology Research and Development Project of China State Construction International Cooperation (No. CSCI-2023-Z-17).

REFERENCES

Bao, T., Zhu, K., Liu, X., 2003. Overview of Urban Underground Sewage Treatment Plants at Home and Abroad. Chinese Journal of Underground Space and Engineering, 23(3), 335–340.

Wang, Y., Sun, S., 2017. Primary Exploration of Engineering Design of Underground Sewage Treatment Plant. Environmental Science Survey, 36(5), 55–58.

Herranen, T., 2001. Vettä ja elämää: Helsingin vesihuollon historia 1876-2001. Helsingin vesi: Helsinki.

Tan, X., Tang, L., Guo, D., 2006. Analysis and Prospect of Underground Sewage Treatment Plant. Chinese Journal of Underground Space and Engineering, 2(8), 1313–1319,1345.

Zhu, F., 2015. Development and Enlightenment of Underground Wastewater Treatment Plants at Home and Abroad. Urban Roads Bridges & Flood Control, 2015 (12), 62–65,71.

Norwegian Geotechnical Institute, 2015. Rock Mass Classification and Support Design. Oslo, Norway, 10.

National Development and Reform Commission, 2022. National New Urbanization Plan (2021-2035).

Tunnelling for a Better Life – Yan, Celestino, Thewes & Eberhardt (Eds)
© 2024 The Author(s), ISBN 978-1-032-80042-4
Open Access: www.taylorfrancis.com, CC BY-NC-ND 4.0 license

Challenges in planning, design, and construction of the underground power plant station cavern Kühtai 2

Alex Morocutti*
Pini Group, Innsbruck, Austria

Peter Wetzlinger
Swietelsky Tunnelbau, Salzburg, Austria

Rupert Steiger
TIWAG – Tiroler Wasserkraft AG, Innsbruck, Austria

ABSTRACT: The new pumped storage power plant station Kühtai 2 including the underground machine and transformer cavern, the new headrace tunnels and the new Kühtai reservoir comprising collection, connection and investigation tunnels produce renewable energy flexibly and on demand and will serve to the intermediate storage of electricity from other renewable sources. The project is situated in the middle of the Alps in Kühtai, Tirol, Austria and is part of the expansion group "Sellrain-Silz" power plants. Once completed, its purpose is to provide autonomous and environmentally friendly renewable energy.

The most important components of the new Kühtai 2 project comprises an underground power station, a headrace tunnel that connects the new Kühtai reservoir with the existing reservoir, the new Kühtai rockfill dam with a usable storage capacity of about 31 mio m³ and the excavation of a 25.5 km long stream adduction tunnel with hard rock TBM.

The focus of this paper is a comprehensive description of the design considerations and the challenges faced through the excavation of the underground power station built completely in a rock cavern, designed for pumped storage operation. The machine cavern has dimensions of length/width/height 65/26/40m and the parallel situated transformer cavern has dimensions of 55/14,5/19m. These caverns were excavated with drill and blast method through different access tunnels different points of attack. This article shows the exciting particularities and challenges that were encountered during planning, design, and construction of the caverns.

Keywords: Cavern excavation design, construction experience, drill and blast, pumped storage

1 PROJECT OVERVIEW

The Austrian company TIWAG-Tiroler Wasserkraft AG that mainly generates electricity from hydropower is currently expanding the existing Sellrain-Silz power plant group with a second upper stage unit, consisting of the Kühtai reservoir, the Kühtai 2 hydropower pump storage plant. First planning and drafting of environmental impact and assessment declaration of the new power plant begun in 2006. In June 2016 the environmental impact assessment has been approved by Tyrolean government and in June 2019 the legal effective has been approved from federal administrative court, so the preliminary work started in September 2019. The main construction works of the plant started in April 2021. The overall facility is scheduled to be commissioned in the mid of 2026. The project includes headrace and tailrace tunnels as well as a 25 km long water adduction tunnel to the reservoir excavated by an open gripper TBM. The power plant is housed in an underground cavern and will have an installed capacity of 140 MW in turbine mode and 130 MW in pump mode.

The power cavern is situated between the existing reservoir Finstertal and the new Kühtai reservoir, currently under construction, on the orographic right-hand side of Längental. A 1250 m long inclined penstock and a 525m long tailrace tunnel provide the connection between both reservoirs.

The cavern houses the mechanical and electrical plant components for the turbine and pump operation as well as equipment for the monitoring of the power plant.

*Corresponding author: alex.morocutti@pini.group

DOI: 10.1201/9781003495505-425

The size and the shape of the cavern is optimized to meet geotechnical as well as space requirements of the individual components of the power plant.

Figure 1. Project overview.

Figure 2. Geological situation.

2 GEOLOGY

The project area is in the Ötztal and Stubai Alps, both of them belong to the east alpine crystalline formation. The prevailing rock mass type in the cavern area is biotite-plagioclase gneiss, which is partly heavily folded. The fold axes generally strike in east-west direction. The three dominant fold systems in the cavern roof are 180/15, 180/75 and 210/80. The distance between the individual folds is approx. 20 to 60cm. Due to the complex rock structure, a changing foliation orientation is present in the cavern area.

3 DESIGN PROCESS

3.1 *Study of variants*

During the design process for the Kühtai 2 power plant, two cavern variants (single cavern & double cavern) were compared, taking into consideration the geotechnical requirements as well as the requirements for mechanical and electrical system components and maintenance during operation. Furthermore, it was determined that the cavern should have an inner lining to avoid the use of permanent bolting and permanent shotcrete. The longitudinal cavern axis was selected in such a way that foliation and faulting of the rock mass is orientated transversely to the cavern and unfavorable wedges are avoided.

Variant 1, single cavern solution:

In this variant, all electro - mechanical components such as turbines, transformers and control features should be accommodated in a 72.0 m long, 48.0 m high and 29.0 m wide cavern (Figure 2). In this type of cavern, the two sets of machines are arranged side by side in cross section.

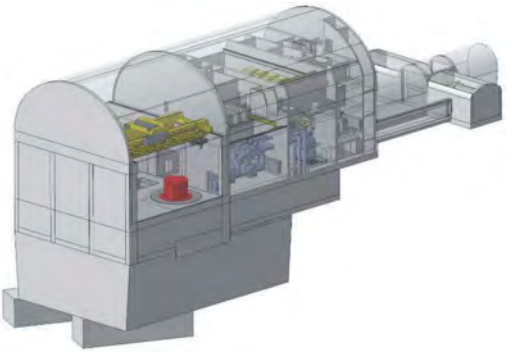

Figure 3. Single cavern solution.

Variant 2, double cavern solution:

In case of the double cavern solution, the machine cavern is 65.0 m long, 40.3 m high and 26.0 m wide. The two sets of machines are arranged side by side along the longitudinal axis of the machine cavern. The transformer cavern has a length of 55.0 m, a height of 17.6 m and a width of 15.5 m. The clear distance between the machine cavern and the transformer cavern is approx. 29 m. The transformer cavern is accessed from the machine cavern via the connection cavern, which is 29.0 m long, 7.5 m high and 6.0 m wide. In addition to the connection cavern, two converter caverns are arranged between the machine cavern and the transformer cavern. The converter caverns are 29.0 m long, 12.0 m high and 9.0 m wide. The size of the remaining rock pillars between the machine cavern and the transformer cavern were selected such, that they are able to resist the concentrated rock pressure. The layout of the double cavern solution is shown in Figure 4.

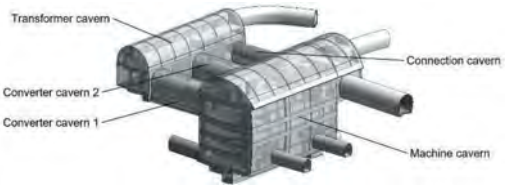

Figure 4. Double cavern solution.

3.2 *Excavation design*

3.2.1 *Excavation sequences*

During the work preparation several variants for the excavation of the caverns were discussed. The task was to work out the most efficient excavation concept based on the geological forecast. This was particularly important for the machine concept as it was not possible to swap selected plants within a short period of time due to the global political and economic environment.

The excavation design supposes that the excavation of the caverns (machine cavern, transformer cavern, converter cavern and the connection cavern) takes place in 5 phases.

Phase 1: All the tunnels surrounding the caverns (access tunnels, drainage tunnels) are excavated in advance of any cavern in order to avoid unfavourable stress redistribution to the main caverns.

Phase 2: An exploratory tunnel is driven at the lowest point. The tunnel serves to verify the geological assumptions in detail and as a mucking tunnel for the lowest level of cavern excavation.

Phase 3: Advancing the top heading of the transformer cavern, followed by the top heading of the machine cavern plus the first bench in the machine cavern and the connection cavern. The next stage is to complete the bench excavation in the transformer cavern and to excavate both converter caverns.

Phase 4: Concreting and anchoring of the crane abutments as well as casting the concrete lining in the vault of the machine cavern is carried out.

Phase 5: Finalising bench excavation in the machine cavern.

3.2.2 *Support measures*

Temporary support measures are applied to avoid progressive loosening of the surrounding rock mass and to retain unstable wedges during the excavation works. The support of the cavern comprising shotcrete and systematic bolting is installed immediately after each round of excavation. The entire cavern complex (machine cavern, transformer cavern, connection cavern, converter caverns 1 and 2) is supported by a 25cm thick shotcrete lining reinforced with two layers of wire-mesh (AQ60) and lattice girders.

Grouted bolts with a length of 9 m, an ultimate load capacity of 440 kN and installed at 1.7 x - 1.7 m centres are used in the machine cavern. In the transformer cavern, in the connection cavern and in the converter caverns 1 and 2 grouted bolts with a length of 6 m, an ultimate load capacity of 440 kN are installed at 1.7 x 1.7 m centres. Near the junctions of the caverns, the bolting pattern is condensed to a spacing of 0.85 x 0.85 m.

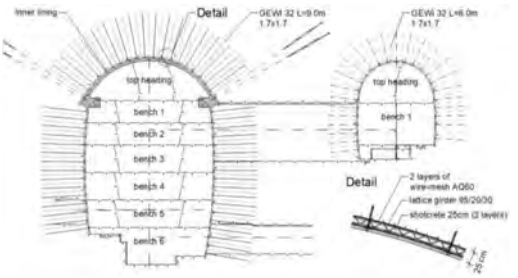

Figure 5. Support measures.

Figure 6. Installing GEWI 32 Anchor bolts 9 m.

The excavation process was supported by an extensive instrumentation and monitoring program existing of

- Extensometers with 3, 5 and 25m meters
- Anchor measuring plates.
- geotechnical measurements (Convergence measurements; Extensometer measurements, Anchor force or pressure measurements)

All the Information was daily available to react quickly to changes.

Figure 7. Geotechnical monitoring of rock bolts.

3.2.3 *Inner lining machine cavern*

The temporary excavation support of the cavern is applied as described in chapter 3.2.2 using shotcrete and systematic bolting. To reduce maintenance efforts during the operation phase, no permanent bolts are installed in the cavern. A 60 cm thick concrete inner lining is placed in the top arch after the excavation of the first bench in the machine cavern instead.

The inner lining consists of 8 individual cast in-situ arch elements with a slot of 50 cm between each element. The slots between the arch elements ensure that hydrostatic pressure cannot build up behind the inner lining. While excavating benches number 2 to 6 in the machine cavern and before the concrete columns are placed under the crane, the elephant's feet and the crane beams, which are situated underneath the top arch, serve as a foundation for the inner lining.

Figure 8. Inner lining works in the machine cavern November 2023.

Figure 9. Slots between the arch elements.

4 CONSTRUCTION EXPERIENCE

A crucial component was the exploratory tunnel which was driven at the lowest point. The exploration tunnel was designed that it could ultimately be used as a drainage tunnel for the five caverns in long term. In advance, important geological discoveries were made during exploratory drilling and geophysical investigations. These results were then incorporated into the drill and blast concept for the five caverns.

The excavation work started on March 16, 2022, in the transformer cavern top heading. This work was completed on April 06, 2022. Subsequently, starting at the beginning of April 2022 until mid-July, the machine cavern roof, the connecting cavern as well as the first bench of the machine cavern were excavated.

The top heading excavation of the machine cavern, the transformer cavern as well as the excavation of the converter caverns and the connecting cavern was carried out in the classic way (horizontal drill and blast in short excavation rounds like 1.70 m) using standard underground construction equipment.

Figure 10. Machine for geological discovery.

Figure 11. Optical Borehole Imager (OBI).

Due to the geological conditions, it was possible to drill and blast the top heading, which originally was divided into three parts, at once. The covered area of the whole top heading was about 204m² and a round length of 1,7m.

The benches in the machine cavern and in the transformer, cavern was excavated using vertical blasting, similar to the procedure in a quarry.

The required vertical blast holes were drilled with a Sandvik ranger surface drill rig. It turned out that the individual blast holes can be produced very precisely and highly efficiently with this device. The round length/bench hight for the vertical benching was until 3.40 m.

The rock mass conditions, and the system behaviour largely corresponded to that anticipated by the design. Only during the excavation work at the elephant's feet in the machine cavern which is later used as an abutment for the crane beam and the inner lining did problems arise due to the sometimes very steep sloping foliation. As a result, parts of the elephant's feet were lost. It was discovered that an elephant's foot is difficult to realize with drill and blast in unfavourable geological conditions. Those parts of the elephant's foot that got lost were subsequently restored using shotcrete and additional bolting. Subsequently bench excavation followed in the transformer cavern, which lasted until the end of August 2022. The excavation of the two converter caverns was completed at the beginning of September. Up to this point, all the construction logistic (mucking and transport of construction materials) was accommodated via the cavern access tunnel.

Figure 12. Excavation works in the cavern in June 2022.

Figure 13. Installing of mechanical part and inner lining.

5 CONCLUSIONS

In the anticipated programme the whole cavern excavation works should be completed in May 2023. In the fact the works were completed in March 2023, so the inner lining works have been started earlier as programmed.

The excavation of the large caverns with notable dimensions in the geological zone of biotite-plagioclase gneiss could be completed without significant problems and in totally safety in according with a sophisticate and detailed planning by the client TIWAG itself.

Demanding preliminary investigation of the geological situation and optimizing size and position of the cavern as described in chapter 2 were also quite important. Also very significant was the optimization of the excavation sequences by contractor in the months of preparatory work before excavation start.

This exciting piece of construction work was only possible thanks to the extraordinary and unique cooperation between client, contractor and site supervision.

The focus actually is on the inner lining and the installation of the mechanical part and equipment of the power plant.

The prospective of the main construction works of inner lining should be completed in second half of 2024.

REFERENCES

R. Steiger, M. R. Henzinger, W. Schubert. 3D numerical stability analysis of a power plant cavern EURO:TUN 2017: Proceedings of the IV International Conference on Computational Methods in Tunneling and Subsurface Engineering

Tunnelling for a Better Life – Yan, Celestino, Thewes & Eberhardt (Eds)
© 2024 The Author(s), ISBN 978-1-032-80042-4
Open Access: www.taylorfrancis.com, CC BY-NC-ND 4.0 license

The use of underground space in greater Kuala Lumpur

Teik-Aun Ooi*
TAO Consult Sdn Bhd, Kuala Lumpur, Malaysia

Chee-Min Khoo
Mass Rapid Transit Corporation, Kuala Lumpur, Malaysia

ABSTRACT: Kuala Lumpur was founded in the late 19th century as a tin mining settlement at the muddy confluence of the Klang and the Gombak Rivers. A century later it has become Malaysia's largest city, its capital and the heart of cultural, financial and economic. It is one of the fastest-growing cities in Asia. Greater Kuala Lumpur, also known as the Klang Valley, extends beyond the boundaries of Kuala Lumpur, it comprises Kuala Lumpur, Putrajaya and 8 districts in Selangor with urban agglomeration of 8.44 million people as of 2020. Given increasing population growth and the rapid pace of development, urban congestion, traffic gridlock and devasting bouts of floodings has become a common phenomenon. The pressing urban phenomenon of metropolis in a developing nation also poses extreme infrastructure needs, which are compounded by inadequate water supply, sewerage and treatment system, and limited parking space, among others. The transformation of Greater Kuala Lumpur into the ultra-modern metropolis has brought along challenges for the town planners and engineers to have innovative underground solutions. This paper discusses the use of underground space in solving the urban problems of Greater Kuala Lumpur/Klang Valley. With a few case studies, it highlights how innovative use of the underground space in Greater Kuala Lumpur can bring more optimal solutions for urban sustainable development and resilience in line with the United Nation's Sustainable Development Goals (SDG).

Keywords: Underground space, Greater Kuala Lumpur, Urban problems, Underground solutions, Sustainable development

1 INTRODUCTION

Kuala Lumpur or KL as it is more fondly called was founded in the late 19th century as a tin mining settlement at the muddy confluence of the Klang and Gombak Rivers. A century later it has become the nation's largest city and serves as the cultural, financial, and economic centre of Malaysia. Rated as alpha world city, it is among the fastest-growing cities in Asia.

Greater Kuala Lumpur extends beyond the boundaries of Kuala Lumpur, it comprises Kuala Lumpur, Putrajaya and 8 districts in Selangor. In 2020, the population of Greater Kuala Lumpur is 8.44 million and it generates about MYR537 billion of the nation's Gross Domestic Product (GDP) (Source: DOSM). This translates to 25 % of the national population contributing more than 40 % of the nation's GDP, proving that Greater KL is indeed the engine of the nation's economic growth. Greater Kuala Lumpur is ranked 10th in Asia's Top 10 cities in Mercer's Quality of Living 2019 survey while the Global Power City Index 2020 ranked Greater KL 14th on its liveability rankings, second in the Asia Pacific region. Figure 1 shows some of the on-going major developments in Greater Kuala Lumpur.

Worldwide, rapid urbanization in developing countries has produced many urban problems such as the need for more affordable housing, traffic congestion, water and power distribution systems, sewerage systems, lack of green space, reduction of air and noise pollution and other population growth issues. The related problem of sprawl away from the urban core strains the environment by creating more traffic gridlock. Greater Kuala Lumpur have all of them, though not in the scale of other Asian nations. Perhaps, it has its own set of challenges – flash floods.

Since 1990s, urban congestion, traffic gridlock and devasting bouts of floodings has become

*Corresponding author: drtaooi@gmail.com

DOI: 10.1201/9781003495505-426

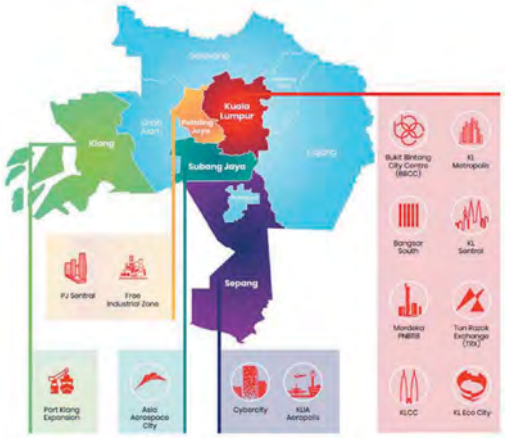

Figure 1. Some on-going major developments in Greater Kuala Lumpur.

a common phenomenon in Greater Kuala Lumpur. On the flip side, we have also seen a lot of major underground space developments especially in transportation (motorways, metros) and public utilities (water supply, sewerage, flood mitigation) in meeting the urbanization needs and challenges, tackling natural hazards and climate change. As a metropolis in the developing world like Kuala Lumpur, ought to take advantage of innovations in engineering and science that will enable them to explore and gain new frontiers in underground spaces as a key element of sustainable development and resilience.

This paper discusses the use of underground space in solving the urban problems of Greater Kuala Lumpur/Klang Valley in view of the rapid growth and unprecedented challenges. With a few case studies, it highlights how innovative use of underground space can bring more optimal solutions for urban sustainable development in line with the United Nation's SDG.

2 STORMWATER RELIEF AND FLOOD MANAGEMENT

Kuala Lumpur (KL) is situated at the confluence of two tributaries of the Klang River and has, from the earliest days, been subjected to flooding. The earliest recorded incident was the flood of 1926 and the largest in recent history was the flood in January 1971 which lasted for 5 days and claimed 32 lives. About 445 hectares of land in the city were inundated to various depths of up to 2 m and the cost of damage was estimated to be in the region of MYR36 million (Abdullah, 2004). The disastrous flood of January 1971 prompted the Malaysian Department of Irrigation and Drainage to establish Kuala Lumpur Flood Mitigation Project which incorporated several engineering options including upstream storage, polder, and pumped drainage, and improving of the drainage capacity of the Klang River and its major tributaries. The increasing pace of development since 1900s resulted in a three-fold increase in the annual discharge of the Klang River at the city centre. The city has been frequently affected by occurrences of flash floods which descend with hardly any warning and totally upset city routine.

In 2001, the Malaysian Government sought proposals for a more effective solution to flooding, to prevent disruption to the city's centre routine during a typical flood event with a duration of three to six hours. The original idea was for a tunnel that would allow floods to bypass the city centre coupled with temporary storage facilities to keep flows downstream of KL within the capacity of the river channel. However, if the tunnel standing empty for most of the time in a year it will not be economical and justifiable expense at public cost. At the beginning of the design stage, an idea to incorporate a road tunnel within the length of the tunnel was proposed to the government to reduce the contribution from public funds and make the project more attractive and more economically viable. A tolled motorway section was integrated into the system to relieve and reduce traffic congestion at the main southern gateway leading to the city centre.

The above ingenuity gives birth to the first of its kind of dual-purpose tunnel in the world – the Stormwater Management And Road Tunnel (SMART). Under the SMART system, excessive upstream water is diverted at the confluence of Klang River and Ampang River into a holding basin. It was then directed to the Taman Desa storage reservoir downstream via the 9.7 km long and 11.83 m internal diameter by-pass tunnel that acts like an underground river, before being released back in stages into the Kerayong River which is a tributary of Klang River. The discharges passing through the city with and without the SMART tunnel are as shown in Figure 2.

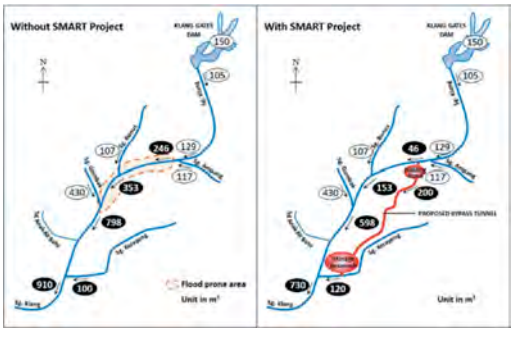

Figure 2. Discharge passing through the city with and without the SMART tunnel (after Abdullah, 2004).

The primary goal of the SMART tunnel was to mitigate flooding caused by heavy rains during the

monsoon reason. By creating a storage tunnel as a release mechanism for the water, Kuala Lumpur can be spared from the expense of flood damages and the retroactive responses to a flood. A second objective of the tunnel was to reduce traffic congestion at the main southern gateway of Kuala Lumpur leading to the city centre. Use of the tunnel also leads to traffic reduction on the above-ground roads. Figure 3 shows an artist's impression of the SMART tunnel. The middle section of about 3 km in length integrates both flood mitigation and motorway purposes.

Figure 3. An artist's impression of the SMART tunnel.

The greatest benefit of the SMART tunnel is that it helps make the city more resilient. In operation for over 15 years now, the SMART tunnel mitigates 45 % of the total flood risks in the Kuala Lumpur, and its activation has saved the city from gridlock and possibly more serious disaster (The Star, 12 February 2022). Because of this infrastructure, areas such as Masjid Jamek area, Dataran Merdeka, Leboh Ampang and Jalan Melaka have witnessed no flooding incidents since SMART tunnel opened in 2007, which has allowed business to operate without interruption. Figure 4 shows the situation before and after SMART activation at Pekeliling area in Kuala Lumpur.

As of December 2021, the SMART tunnel has diverted flood waters on 40 occasions and averted an estimated MYR1.4 billion in public damage (The Star, 22 December 2021). Beyond which, the Department of Irrigation and Drainage's survey concluded that, within the concession period spanning three decades, the SMART tunnel is expected to prevent US$1.58 billion of possible flood damage and up to US$1.26 billion savings from traffic congestion (ITS International, 12 September 2012). The savings are likely to be significantly more since these estimates are only for the duration of the concession. The tunnel has a design life of some 100 years.

That said, the SMART tunnel only diverts water around the critical meeting point from one of the contributing rivers. The increase in the frequency

Figure 4. (a) before SMART activation, (b) after SMART activation at Pekeliling area in Kuala Lumpur (The Star, 22 December 2021).

and intensity of major storms due to climate change coupled with the growing development in other parts of the city could not ensure no flooding will take place or thoroughly protect the city centre. Recently, it was reported that Kuala Lumpur City Hall was working with Department of Irrigation and Drainage to build a high-capacity underground stormwater storage tunnel to overcome the issue of flash floods in the nation's capital (New Straits Times, 3 June 2022). This is one of the long-term solutions to solve the problem for good. Time is of the essence for Kuala Lumpur to take urgent action to create more resilient city that is adapted to the impacts of climate change including flooding.

3 URBAN WATER SUPPLY

One of major problems faced by Greater Kuala Lumpur due to rapid urbanisation – there is not enough water for both daily life and industrial use. According to *Suruhanjaya Perkhidmatan Air Negara* (National Water Service Commission), the total water demand for Selangor, Kuala Lumpur and Putrajaya has more than tripled since 1990. The water supply situation in Selangor and Kuala Lumpur was expected to reach critical levels with water demand envisaged to exceed supply as early as 2014 (Ismail, 2009). Development has been moving forward to ensure water resources in Langat River basin in Selangor to deal with the city's rapidly increasing demand of water. However, efforts to secure resources had not always gone as planned, as demonstrated by such problem as the serious water shortage in the region

for approximately half a year from 1997 to 1998 during the dry season that brought in the haze from Sumatra for the first time (The Edge, 20 April 2009). The Malaysian government considered various plans to address this issue and eventually came to the conclusion that, from the perspective of the amount of water needed as well as cost, it would be best to channel water by constructing a tunnel to the state of Selangor from the stage of Pahang, a water-rich region in the central part of the Peninsula.

In June 2009, Malaysia began a project to build the Pahang-Selangor raw water transfer tunnel as illustrated in Figure 5. It is the longest and biggest tunnel in Southeast Asia and the 8th longest water supply tunnel in the world - a 44.6 km long, 5.23 m diameter tunnel starts at Karak, Pahang, running deep under the ground up to 1,200 m below the Titiwangsa mountain range and hot springs (Ooi & Khoo, 2017). The tunnel would convey 1.89 million litres of raw water daily from Semantan River in Pahang to a new Hulu Langat water treatment plant in Selangor. It has the capacity to convey 27.6 m³ of raw water per second. The great advantage of having the water flow in gravity-driven underground tunnel is that it does not evaporate.

Construction works involved excavation using tunnel boring machines (TBM) for 35 km, while the remaining length was excavated by conventional drilling-and-blasting and by cut-and-cover. The upper and lower ends were excavated by New Austrian Tunnelling Method (NATM). This huge tunnelling project was successfully completed in May 2014 and was able to overcome the various challenges (e.g. Lepoh fault - over 50 m high empty cavern inside a mountain, pressurised spring water that shot out as much as 24.6 cu.m of water per minute, high rock temperature as high as 55 °C, rock burst, etc.) thanks to the strong solidarity of its multinational team consisting of over 1,000 people from 15 countries (Matsumoto, 2013).

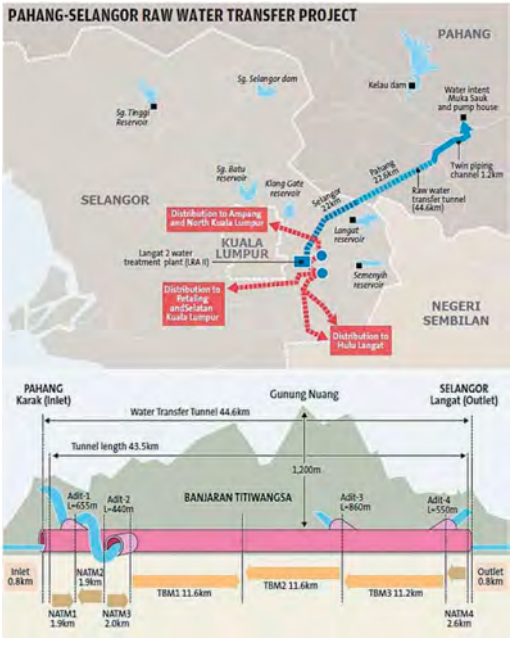

Figure 5. Pahang-Selangor raw water transfer tunnel.

In time, this raw water source from Pahang helps to increase the availability of water resources in the basin to meet the high demand for treated water supply and mitigated the water supply crisis by ensuring that the water source in Langat River is at sufficient level and has a low ammonia level as well as complying with the requirements of the National Standard for Drinking Water Quality Malaysia. The immediate beneficiaries are the people, not only the households but the industries, and factories as well as the agricultural producers. It provides water security for the Greater Kuala Lumpur region, which comprises the capital Kuala Lumpur, Putrajaya and the southern half of Selangor. The tunnel solution is a green initiative – the forest reserves in central Peninsular Malaysia have not been touched by the underground works.

4 URBAN SPRAWL AND PUBLIC TRANSPORTATION

As with most capital cities in the world, urban sprawl has also been a trend in Greater Kuala Lumpur due to abundant work and business opportunities in the city centre. Increased urban sprawl, reduced public transport usage, and increased private vehicle ownership let to massive traffic jams in Kuala Lumpur. Traffic jams in 2018 alone led to economic activity inefficiencies and the country suffered between 1.1 – 2.2 % loss in gross domestic product (GDP) in terms of wasted fuel, carbon emissions, delays, and vehicle maintenance (New Straits Times, 2 January 2020). There is ample evidence linking traffic congestion to environmental degradation. According to Mustapa & Bekhet (2015), the transportation sector accounts for 28 % of greenhouse gases emissions in Malaysia, of which 85 % comes from land transport.

Since 1990s, many phases of the transportation systems have been developed. In 2010, in order to further reduce the traffic congestion in Klang Valley, the Malaysian Government spent billions in new urban rail expansion projects including the 35 km LRT extension – Kelana Jaya Line/Ampang Line, 38 km LRT 3 – Shah Alam Line and the development of Klang Valley Mass Rapid Transit (KVMRT) up to 2030. The KVMRT involves construction of a rail-based public transport network, together with the existing urban rail network, will form the backbone of the public transport system in the Greater Kuala Lumpur/Klang Valley. It consists of three lines linking the capital districts with the centre of the city, aiming to develop a modern and efficient urban metro system in Kuala Lumpur.

Figure 6 shows the existing integrated transit network that primarily serves the area of Klang Valley and Greater Kuala Lumpur. Like all other metro underground railway designed as part of the urban city, the first MRT line implemented is the 47 km Kajang Line, of which 9.5 km is underground tunnels with 7 underground stations. The second MRT line – Putrajaya Line, began fully operations on 16 March 2023, stretches from Sungai Buloh to Serdang and ends at Putrajaya for a length of 57.7 km, of which 13.5 km is underground tunnels with 10 new underground stations. Line 3 - the Circle Line forms the backbone of the metro as it loops around the business districts of the city, it will serve an important role to tie-up and integrate the currently disjointed LRT, KTM and monorail lines. Construction is expected to commence soon.

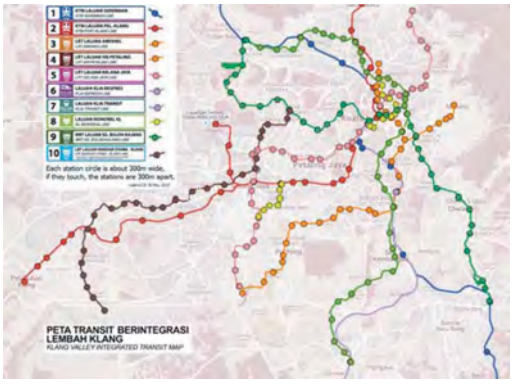

Figure 6. Integrated transit network in Greater Kuala Lumpur.

The completion of the KVMRT Kajang Line and Putrajaya Line not only transforms Kuala Lumpur's underground but also the heart of Malaysia. It changes the landscape of underground space development in Kuala Lumpur significantly as it will generate a sustainable city with greater connectivity. Urban accessibility will be improved through public transportation. Figure 7 shows an example of the upcoming transit-oriented developments (TOD) in downtown Kuala Lumpur. Typically, it entails development of a microcell of the city directly connected to the metro station with TOD buildings rise over and around the station and tunnel.

5 UNDERGROUND SEWERAGE TREATMENT PLANT

In line with Greater Kuala Lumpur's socio-economic development, modern sewage treatment plants have also been developed alongside to treat sewage more efficiently and to accommodate the increase in population, which increases yearly. One of the most modern

Figure 7. Transit-oriented developments in downtown Kuala Lumpur.

plants is the Pantai 2 Sewage Treatment Plant (STP), the country's first and biggest sewage treatment plant as well as the largest in Asia Pacific which was constructed underground and equipped with state-of-the-art green technologies. Previously, the plant used to house an open-air oxidation pond system that could only accommodate 877,000 population equivalents (PE), see Figure 8 (The Star, 22 December 2022). The unfortunate by-products of this service are the water pollution and unpleasant odour that emanate from the facility. Today, the Pantai 2 STP has been upgraded and capable of treating sewage for 1.423 million PE which could cater to a growing population until 2035. The plant can receive sewage flow from a 6,700 hectares Pantai catchment covering central and south-western parts of Kuala Lumpur.

Figure 8. Oxidation ponds at Pantai 2 STP around the year 1984 (The Star, 22 December 2022).

One of the main highlights of the project is that the plant was constructed on the same site as the previous oxidation ponds and comprises two main parts: the fully underground multi-layered sewage treatment facility that goes 17 m deep and the sludge treatment facility above ground developed together with a recreation park right above the underground plant. The park is home to all sorts of sports, leisure and community facilities for the residents and splashes of

lush greeneries and waterways, which spans an area of 12 hectares. The Pantai 2 STP features the use of various green technologies including utilising the skylight concept for the underground plant, effluent reuse, rainwater harvesting and the use of biogas and solar panels to generate electricity. The plant also uses energy-efficient equipment to reduce the amount of electricity consumed. The green technology initiatives adopted help to reduce the carbon footprint and create a sustainable future for all. The overviews of pre-construction and post-construction of the Pantai 2 STP are shown in Figure 9, demonstrating an obvious improvement of the community quality.

Figure 9. (a) Before the construction of Pantai 2 STP, (b) Post-completion of Pantai 2 STP.

With centralisation of sewage treatment at Pantai 2 STP, as many as 140 small plants that produce substandard effluent can be closed, reducing pollution into the Klang River. The Pantai 2 STP was built with sustainability in mind, capitalising on renewable resources for energy and water to reduce wastage and pollution. This new state-of-the-art mechanised underground regional sewage plant has proved to be a model for innovation in concept, design, engineering and construction – setting new standards for sustainable sewage treatment in Malaysia and transforming its surrounding environment. Above and beyond, the Malaysian Government has also committed to a substantial investment in underground infrastructure for several years with the expansion and refurbishment of sewerage facilities throughout the country.

6 UNDERGROUND PARKING AND TRAFFIC DISPERSAL

In Kuala Lumpur, the use of underground space for both commercial retail outlets and car parks had also witnessed a big development. In a growing number of cases, basement car parks are being built for most of the high-rise developments in the city centre. Lately, the trend is observed to be going for large-scale parking towards maximisation of space use and allows complete flexibility in the design of buildings and the disposition of uses and activity at ground level.

The KLCC Underground is noteworthy case study. In the early planning days, the site was earmarked as a "green lung" for the city, with little or no commercial development. However, the enormous potential urban rehabilitation opportunity afforded by the site was also obvious. The compromise was to plan and promote a new city centre surrounding a large park with public amenities. It is the intention of KLCC Master Plan to optimise the land-use treatment for future connectivity and public transportation within the city centre. New planning approach, for example, no provision of podium parking, basement parking wall up to the land boundary lines are specially formulated in the KLCC Master Plan (Figure 10). Notably, the Aquaria KLCC, which has an underwater tunnel, is located just beneath the Kuala Lumpur Convention Centre. KLCC have 5 underground levels of car parks beneath the public park for 5,400 vehicles. In addition, KLCC has also built a few dedicated ingress and egress tunnels to connect the area to the main roads directly, i.e. Jalan Ampang, Jalan Tun Razak. The AKLEH access is unique in the sense that the highway has direct tunnel access to the area's extensive underground parking lot. In 2013, KLCC commenced to construct the new six levels of basement car parks at North-East located underneath KLCC Park to cater for future development.

Figure 10. KLCC master plan with underground connectivity.

Some other similar on-going new landmark developments are the Tun Razak Exchange (TRX), which spread over 70 acres of land, and the 19-acres Merdeka 118 (KL 118) development, both with six levels of underground basements. Both TRX and

Merdeka 118 can directly connect to underground metro stations, see Figure 7. As a lush green tropical heart to the TRX overall master plan – the world largest rooftop 10-acre public park (see Figure 11) lies above the retail with underground basements of more than 20,000 parking bays. The loop tunnel system planned for the movement of vehicles in TRX would enable traffic to bypass inner city roads altogether and divert the traffic underground. The TRX's loop tunnel allows seamless access to and from major highways like SMART tunnel and MEX that bypass the heavy above-ground traffic in Kuala Lumpur and relieve the congestion along Jalan Sungai Besi enhancing TRX's traffic connectivity with the future Bandar Malaysia development.

Figure 11. World largest rooftop public park in Tun Razak Exchange.

The Merdeka 118 development involved construction of the second world's tallest building, 118-storey 678.9 m tall mega skyscraper sits on a common podium containing retail and car parking space over six basement levels and be directly linked from three major roads via underground tunnels. Figure 12 shows the proposed Belfield tunnel in enhancing the connectivity to the Merdeka 118 development.

Figure 12. Belfield tunnel connecting to Merdeka 118.

The TRX and Merdeka 118 due for opening soon will set a new benchmark for large scale, mixed use, sustainable integrated urban underground space development in Asia, enhance Kuala Lumpur's reputation as a highly liveable city.

7 CONCLUSIONS

Since city centre is densely build areas, building underground can relieving pressure on the surface and it can be an attractive solution for solving traffic problems and increasing connectivity. However, use of the underground should not be limited to large scale infrastructure projects. By moving certain facilities below ground, valuable surface area can be preserved for other purposes such as parks, recreational spaces, and commercial developments.

This paper discusses some examples of successful and innovative use of underground space in solving the urban problems of Greater Kuala Lumpur/Klang Valley, yet meeting the urbanisation needs in line with the United Nation's Sustainable Development Goals. For instance, the SMART tunnel provides great flexibility in terms of climate mitigation and road infrastructure, making the city more resilient and sustainable, i.e. SDG 11 – Sustainable cities and communities, and SDG 13 – Climate action. On the other hand, the Pahang-Selangor interstate raw water transfer tunnel and the Pantai 2 underground sewerage treatment plant respectively deliver universal and equitable access to safe and affordable drinking water and access to adequate and equitable sanitation and hygiene for all under SDG 6 – Clean water and sanitation. The recent conceptualisation of underground tunnels to manage urban stormwater detention underneath the Kuala Lumpur city indicate how is Malaysia faring in its battle against climate change towards a sustainable and resilience development goals.

Resilient public facilities are not just a means of delivering services; it is a critical enabler and guardian of sustainable development. Combination of green and grey infrastructure while creating assets, such as parks over the underground facilities, not only as a sustainable solution to urban growth but also provide public amenities that improve quality of life, as is the case in Pantai 2 STP. For all that, underground parking provides intrinsic environmental and recreation benefits to the city such as the case in KLCC Underground, TRX and Merdeka 118 integrated development which has set unparalleled standards with sustainability at its core.

With the continued development of Klang Valley mass rapid transit, making Kuala Lumpur underground a very important connectivity means through the metro stations. Integration in three-dimension is expected to increase over the years, incorporating underground road tunnels, pedestrian and bicycle tunnels, and public transport facilities like light rail or mass rapid transit systems. The use

of underground space for commercial centres will soon see another wave with active retail development coming along with underground metro network likes Singapore.

REFERENCES

Abdullah, K., 2004. The 14th Professor Chin Lecture: Kuala Lumpur: Re-engineering a flooded confluence. In: Ooi, T. A., Chan, S.F., Ting, W.H. (Eds.), Professor Chin Fung Kee Memorial Lectures 1991–2006, The Institution of Engineers Malaysia & The Engineering Alumni Association of the University of Malaya, Malaysia, pp. 277–286.

Ismail, M.T., 2009. The inter-basin water transfer: The Pahang – Selangor water transfer challenges and opportunities. Water Malaysia 2009, International Conference on Water Industry Best Practices, Kuala Lumpur, Malaysia, 19-21 May 2009.

ITS International, 12 September 2012. Success of Kuala Lumpur's dual purpose tunnel. retrieved from https://www.itsinternational.com/its4/its8/feature/success-kuala-lumpurs-dual-purpose-tunnel

Matsumoto, T., 2013. Pahang-Selangor Water Raw Transfer Project – Lot 1-1, Water transfer tunnel and related works. IEM Half Day Seminar on Pahang-Selangor Interstate Water Transfer Tunnel, 15 June 2013, Petaling Jaya, Malaysia.

Mustapa, S.I. & Bekhet, H.A., 2016. Investigating factors affecting CO2 emissions in Malaysian road transport sector. International Journal of Energy Economics and Policy, Vol. 5, Issue 4, pp. 1073–1083.

New Straits Times, 7 January 2020. NST Leader: Urban sprawl. Retrieved from https://www.nst.com.my/opinion/leaders/2020/01/552639/nst-leader-urban-sprawl?

New Straits Times, 3 June 2022. DBKL, Irrigation Dept. to build underground water storage tunnel to overcome flash floods. Retrieved from https://www.nst.com.my/news/nation/2022/06/801876/dbkl-irrigation-dept-build-underground-water-storage-tunnel-overcome

Ooi, T.A. & Khoo, C.M., 2017. The present and future sustainable use of underground space in Malaysia. Proceedings of Southeast Asian Conference and Exhibition in Tunnelling and Underground Space 2017, Subang Jaya, Malaysia.

The Edge, 20 April 2009. My Say: Is a water crisis imminent?. Retrieved from https://www.theedgemarkets.com/article/my-say-water-crisis-imminent

The Star, 22 December 2021. SMART tunnel stretched beyond the max. Retrieved from https://www.thestar.com.my/news/nation/2021/12/22/smart-tunnel-stretched-beyond-the-max

The Star, 12 February 2022. SMART tunnel mitigates 45% of KL floods. Retrieved from https://www.thestar.com.my/news/nation/2022/02/12/smart-tunnel-mitigates-45-of-kl-floods

Tunnelling for a Better Life – Yan, Celestino, Thewes & Eberhardt (Eds)
© 2024 The Author(s), ISBN 978-1-032-80042-4
Open Access: www.taylorfrancis.com, CC BY-NC-ND 4.0 license

SMART tunnel revisited – after 15 years in operation

Teik-Aun Ooi*
TAO Consult Sdn Bhd, Kuala Lumpur, Malaysia

Chee-Min Khoo
Mass Rapid Transit Corporation, Kuala Lumpur, Malaysia

ABSTRACT: Opening on 15 May 2007, the first and one of a kind dual-purpose tunnel in the world – the Stormwater Management And Road Tunnel (SMART) has stood the test of time. It is a nation pride, innovative and a unique solution to the Malaysian capital's long-term traffic and flooding problems. The project was initially incepted primarily to mitigate the recurring floods in the city of Kuala Lumpur since 1971. However, at the design stage, the dual-purpose concept was born from the ingenuity of the project proponents, with a waterway beneath the double-deck motorway tunnel engineered to relieve and reduce traffic congestion at the main Southern Gateway leading to the city centre. The SMART tunnel is touted as a visionary green infrastructure with a sustainable and climate change solution in mind, which helps make the city more resilient. The SMART tunnel clinched the British Construction Industry International Award in 2008 and received the UN Habitat Scroll of Honour Award in 2011 for its innovative and unique management of storm water and peak hour traffic. In April 2015, it was again described by the United Nations as one of the most innovative projects in the world for an urban issue. The SMART tunnel has been listed as one of the top 10 world's greatest tunnels by CNN where the tunnel is expected to prevent billions of dollars of possible flood damage and costs from traffic congestion in Kuala Lumpur's city centre. In operation for more than 15 years now, the SMART tunnel mitigates 45% of the total flood risks in the Kuala Lumpur, and its activation has saved the city from gridlock and possibly more serious disaster. As of December 2021, the SMART tunnel has diverted flood waters on 40 occasions and averted an estimated MYR1.4 billion in public damage, which is expected to continue to save the Kuala Lumpur city from flooding at the time of inclement weather in the foreseeable future. The tunnel has demonstrated the degree of urban underground development Malaysia has achieved and is an example for other developing countries to emulate.

Keywords: SMART tunnel, Dual-purpose tunnel, Innovation, Top 10 world's greatest tunnel, Tunnelling in Malaysia

1 INTRODUCTION

Opening on 15 May 2007, the first and one of a kind dual-purpose tunnel in the world – the Stormwater Management And Road Tunnel (SMART) has stood the test of time. It is a nation pride, innovative and a unique solution to the Malaysian capital's long-term traffic and flooding problems.

The SMART tunnel is no stranger to international recognition. The SMART tunnel clinched the British Construction Industry International Award in 2008 and received the UN Habitat Scroll of Honour Award in 2011 for its innovative and unique management of storm water and peak hour traffic. In April 2015, it was again described by the United Nations as one of the most innovative projects in the world for an urban issue. The SMART tunnel has been listed as one of the top 10 world's greatest tunnels by CNN where the tunnel is expected to prevent billions of dollars of possible flood damage and costs from traffic congestion in Kuala Lumpur's city centre. In operation for more than 15 years now, the SMART tunnel has diverted flood waters on 40 occasions and averted an estimated MYR1.4 billion in public damage, its activation has saved the city from gridlock and possibly more serious disaster (The Star, 22 December 2021). The SMART tunnel is a success. It is unique yet very complex as a whole system though each component has been applied on other projects.

The SMART tunnel is being revisited in this article with a primary objective of re-establishing the associated technical and economic benefits. This article begins with an overview of the project

*Corresponding author: drtaooi@gmail.com

DOI: 10.1201/9781003495505-427

background in the grand scheme of things. The article further elaborated on the tunnel's operations, highlighting the key components and special features driven by opposing needs (alternating wet and dry environments) in the dual-purpose tunnel. Next, construction challenges encountered, and mitigation measures adopted are briefly summarised. It is followed by an appraisal of the technical and economic benefits that have gleaned from this project. The interest in this review is twofold. First, data from the projectile will be documented and support future research with high-quality information. Second, the experience grained, and lesson learnt could assist the engineers in future projects.

2 PROJECT BACKGROUND

Although a booming city and the nerve centre for Malaysia's economy, Kuala Lumpur was built along the flood plains of the Klang River and thus, from its earliest days, has been subjected to flooding. With heightened land development resulting in increased surface runoff coupled with constrictions along the main rivers running through the city, frequent flooding had brought losses and inconvenience to the business district centre of Kuala Lumpur. The earliest recorded incident was the flood of 1926 and the largest in recent history was the flood in 1971 which lasted for 5 days and claimed 32 lives. About 445 hectares of land in the city were inundated to various depths of up to 2 m and the cost of damage was estimated to be in the region of MYR36 million (Abdullah, 2004). The big flood of 1971 prompted the Department of Irrigation and Drainage to establish Kuala Lumpur Flood Mitigation Project. Over the past decade, incidences of major flooding have become more frequent. In addition, the city has been affected by occurrences of flash floods which descend with hardly any warning and totally upset city routine (see Figure 1).

Figure 1. Flash flood in Kuala Lumpur.

In 2001, the Malaysian Government sought proposals for a more effective solution to flooding, to prevent disruption to the city's centre during a typical flood event with a duration of three to six hours. The original idea was for a tunnel that would allow floods to bypass the city centre coupled with temporary storage facilities to keep flows downstream of Kuala Lumpur within the capacity of the river channel. However, if the tunnel standing empty for most of the time in a year will not be economical and justifiable at public cost. At the beginning of the design stage, an idea to incorporate a road tunnel within length of the tunnel was proposed to the government to reduce the contribution from public funds and make the project more attractive and viable. One factor in this evolution was that for liability reasons, the tunnel had to run below government-owned land, which led planners to consider locating the tunnel beneath a road. This led to the idea of integrating a tolled motorway into the project. By allowing a portion of the tunnel to be tolled for traffic, private sector participation in a Public-Private Partnership (PPP) could be secured, reducing the costs of the project for the Malaysian Government.

The above ingenuity gives birth to the first and one of a kind dual-purpose tunnel in the world – the Stormwater Management And Road Tunnel (SMART). Under the SMART system, excessive upstream water is diverted at the confluence of Sg. Klang and Sg. Ampang into a holding basin. It was then directed to the Taman Desa storage reservoir downstream via the 9.7 km long and 11.83 m internal diameter by-pass tunnel that acts like an underground river, before being released back in stages into the Sg. Kerayong which is a tributary of Sg. Klang (Figure 2). The whole system has holding capacity of 3 million m^3 of stormwater – equivalent to 2,000 Olympic-size swimming pools - and able to retain the water until the flood subsides before discharging the water into the downstream river. The discharges passing through the city with and without the SMART tunnel is shown in Figure 3.

The SMART project was developed as a concession. The concession is to operate and maintain the motorway portion of the tunnel. The Malaysian Government maintains ownership of the land and the tunnel itself. The total cost of

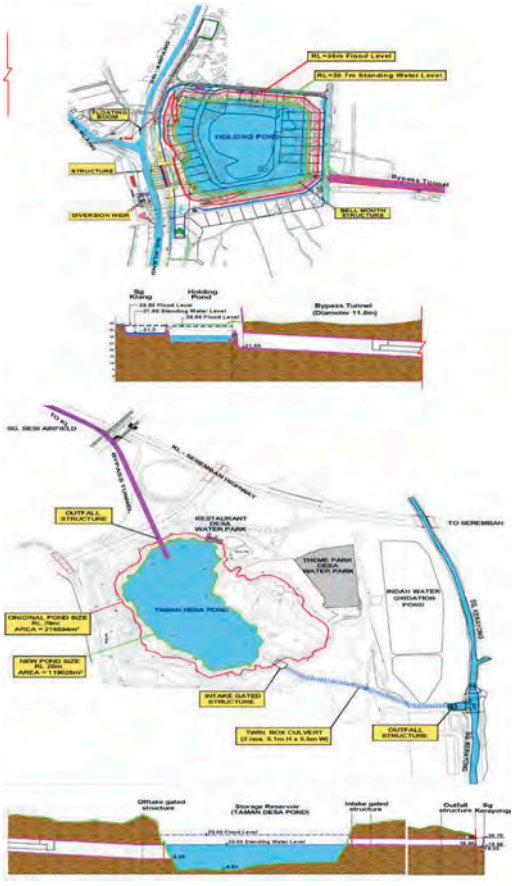

Figure 2. Outline scheme of the flood diversion system.

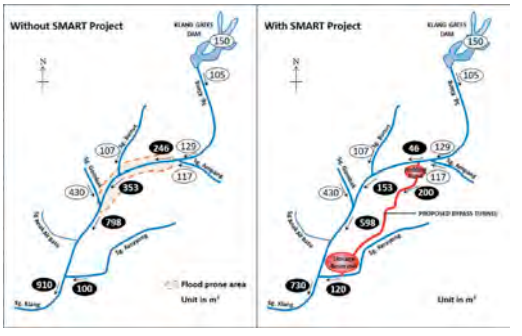

Figure 3. Discharge passing through the city with and without the SMART tunnel (after Abdullah, 2004).

the SMART project was US$514.6 million (MYR1.887 billion). The private sector provided a third of the total funds. In order to recoup the capital investment and operating expenses, the concession charges a toll fee for using the motorway portion of the tunnel.

3 OVERVIEW OF THE SMART TUNNEL

The primary goal of the SMART tunnel was to mitigate flooding caused by heavy rains during the monsoon reason. By creating a storage tunnel as a release mechanism for the water, Kuala Lumpur can be spared the expense of flood damages and the retroactive responses to a flood. A second objective of the tunnel was to reduce traffic congestion at the main southern gateway of Kuala Lumpur leading to the city centre. Use of the tunnel also leads to traffic reduction on the above-ground roads.

The tunnel was divided into two categories that are the stormwater management system and the double deck motorway for vehicles. Figure 4 shows the middle section of about 3 km in length integrate both flood mitigation and motorway purposes. It is key to keep motorists safe from flood water, while at the same time predicting floods early enough to evacuate motorists and convert the tunnel to flood use before the flood peak arrived.

Figure 4. An artist's impression of the motorway.

The motorway traffic is uni-directional, consist of a double decks structure, each carrying two 3.35 m wide traffic lanes and one emergency lane, situated one above other. At each end of the motorway tunnel, there is a Y-junction. One junction allow vehicle to enter/exit the tunnel via ingress/egress section at each end, another junction link to stormwater tunnel (refer Figure 5). The motorway design is only for light vehicles, which is not exceeding 2.55 m height.

For safety reasons, cross-passage decks inside the motorway section placed at 250 m intervals to act as emergency exits, along with ventilation/escape shafts which are placed at 1 km intervals.

3.1 *How the SMART tunnel works*

The SMART system will be operated based on the relationship between flood discharge at the Klang/ Ampang Rivers confluence and the operation status of the motorway. Basically, its operations can be classified into 4 different modes, as illustrated in Figure 6.

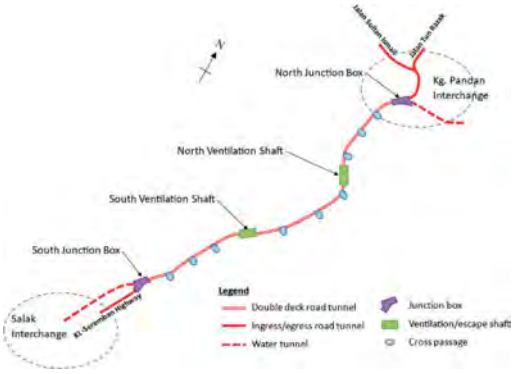

Figure 5. Double road deck motorway tunnel section.

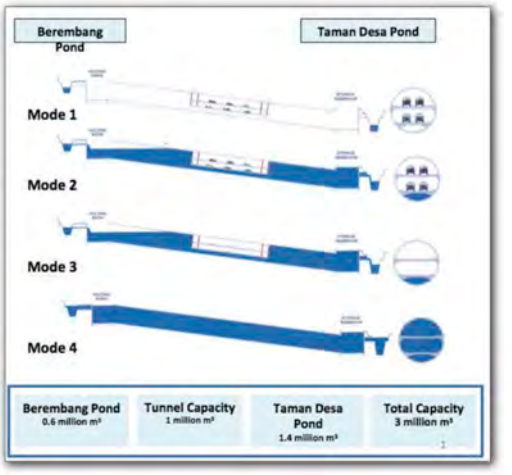

Figure 6. Operation modes (SMART Website).

Mode 1

For most of the time, the road tunnel is opened for traffic under normal conditions (see Figure 7) where there is no storm, no flood water will be diverted into the system.

Mode 2

When the flood discharge exceeds 70 m^3/s, the stormwater tunnel is activated to "semi-open" status by allowing the diversion of excess water into the bypass tunnel in the lower channel of the motorway tunnel. The motorway section operates normally and there is no traffic disruption since only the lowest channel is being used at this juncture.

Mode 3

When major storm event occurs and flood model forecasts a flow rate exceeding 150 m^3/s, the motorway will be closed to all traffic. Sufficient time will be allocated to allow the last vehicle to exit the motorway. Tunnel is on standby mode for stormwater diversion into the motorway component.

Figure 7. The motorway open to traffic (Mode 1 and 2).

Mode 4

The stormwater tunnel is activated to "fully open" status if heavy rainstorm prolongs, usually will be confirmed 1-2 hour after Mode 3 is declared. After making sure all vehicles have exited the motorway, automated water-tight gates will be opened to allow flood waters to pass through the tunnel (see Figure 8).

Figure 8. CCTV images of the SMART tunnel after activation (The Star, 22 February 2022).

After the flood receded and the weather is back to normal, flood water is pumped out of the tunnel and the tunnel is cleaned of mud and small debris. In normal process of cleaning and inspection of the tunnel condition, the SMART tunnel is reinstated within 48 hours after the water channelisation is made and traffic for the motorway section is allowed back for usage as normal thereafter.

During operations, the upstream monitoring facilities and the retention capacities of the two holding ponds together with the tunnel retention capacity provides the system operators at least an hour of warning for the need to close the motorway to traffic and avail it for flood water diversion. Emptying the road tunnel from traffic user will only take between one hour including closing of the gates and cross

passage doors, conducting a walkthrough check and opening the flood tunnel barrier.

3.2 *Key components and special features*

The motorway has all the fittings and safety features in compliance with international and local standards. However, some special requirements are unique to SMART. The entire fitting and road furniture in the motorway is designed to cater for the dual-purpose function of the tunnel. The design philosophy adapted for the road tunnel fixtures and fitting is sufficiently robust to withstand water tightness of 2.5 bars hydrostatic pressure and continuous submergence for at least 24 hours. The bracket design shall withstand the water flow of 5.5 m/s (Santhiman & Looi, 2006).

Two major components to make this tunnel "smart", there are Flood Detection System (FDS) and Traffic Management & Control System (TMCS). FDS is used for forecasting and detect the rainfall and river water at upstream and downstream, it will decide and confirm to close and open the tunnel for flood to bypass. On the other hand, the TMCS is an intelligent system to manage, monitor and control the traffic of the ingress/egress and tunnel.

The status of the primary and essential electrical and mechanical equipment inside the tunnel is continuously monitored, processed, and controlled by SCADA. Having said that, the SCADA monitoring and surveillance system has additional features that are unique in normal motorway tunnel operation. From a central control room which is manned 24/7, over 200 CCTV cameras, linked to an advanced Automatic Incident Detection (AID) system keep watch on every section and can intervene, when necessary, using variable message signs or activation of first responder vehicles and personnel which are on permanent standby (Santhiman & Looi, 2006). The control centre also monitors and operates the 38 sets of air quality monitoring equipment deployed throughout the upper and lower motorway decks. Depending on the equipment returns, four ventilation shafts, each containing 12 number of axial ventilation fans and 2 number of axial pressurized fans, can be activated to provide continued airflow and removal of exhaust fumes (ITS International, 12 September 2012). The ventilation system is integrated with air quality monitoring system and linear heat detection system.

Double set of watertight steel gates at both ends of the motorway, together with surge shafts, were built to prevent damage to the structure caused by surge pressure. As added safety precaution, the opening of flood control gates is not possible without first closing the road gates and vice versa. The two are deliberately interlocked as part of the fail-safe /defect-proof operation. The interlock enabled the dual-purpose operations to be combined safely in a single but dual-purpose structure. Figure 9 shows the upstream stormwater tunnel flood gates at north junction box. Control of the automated flood control gates is also incorporated within the SCADA system.

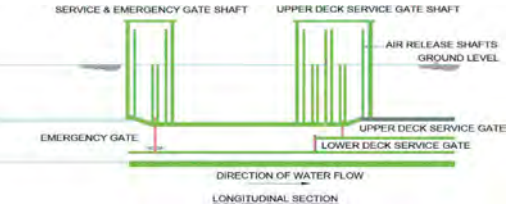

Figure 9. Upstream stormwater tunnel flood gates.

3.3 *Construction challenges*

Construction of the tunnel began on 25 November 2003. According to Special Unit for South-south Corporation's report (2012), construction of the motorway should have been completed in June 2005 and of the stormwater tunnel a year later, but both portions were not completed until mid-2007. The construction posed a number of challenges, primarily related to the unfavourable and highly variable ground conditions particularly the Kuala Lumpur Limestone and ex-tin mining lands. Kuala Lumpur Limestone is well known for its highly erratic karstic features. For more details the reader can refer to Gobbett (1965), Yeap (1985), Tan (2005).

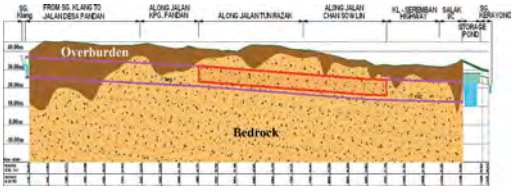

Figure 10. Geological profile along the SMART tunnel (after Darby & Wilson, 2006).

Briefly, as shown in Figure 10, the tunnel traverses 2.5 km of alluvium starting from north end, continuing into 0.7 km stretch of mixed face of alluvium and limestone rock. After, the tunnel alignment passes through limestone again. Overlying the Kuala Lumpur Limestone is soft alluvium and ground disturbed by tin mining (i.e. mine tailings). The last 200 m stretch at the south end, is in residual soils of Kenny Hill formation. The tunnel was bored at shallow depth with the cover to tunnel varied from 0.8 to 1.8 times its diameter (Yeoh & Klados, 2006). On average, the alluvial deposit is generally 4 to 5m thick; typical rock cover to the tunnel lining in limestone is within 3 to 7 m however at karstic areas the unpredictable rockhead may unexpectedly drop to 20 to 30 m. Groundwater table is relatively high at 1.5 to 2 m. Tan (2006) presented a 3D image of the exposed

limestone surface at north ventilation shaft (reproduced in Figure 11). Figure 12 shows an actual site photo taken during excavation at north junction box.

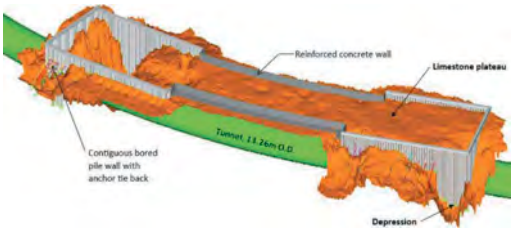

Figure 11. A 3D image of the exposed limestone surface at north ventilation shaft (after Tan, 2006).

Figure 12. Excavation into limestone at north junction box.

Construction of such large diameter tunnel (13.26 m O.D., almost as tall as a four-storey building) with majority of the boring through the highly weathered and extreme karst was the first-time experience in Malaysia. Tunnelling was very difficult, it gave the contractor plenty of headaches, as dozens of sinkholes and mudflows occurred unexpectedly during the construction. According to Klados (2015), 41 numbers of major ground collapses/sinkholes was reported in the construction of SMART tunnel. To a large extend, these incidents was mitigated through careful and deliberate pre-excavation treatment, which largely entails filling up the cavities and voids with grout before the boring machine passes through that stretch. Extensive soil sampling and geophysical tests were conducted to ferret out the anomalies. Ha (2018) documented the challenges and solutions for tunnelling in Kuala Lumpur karst. On the other hand, the initial construction of the launch shaft had also led to higher-than-expected groundwater inflow into the excavation through solution channels. Systematic "preventive" grouting was designed and purposefully carried out to arrest the problem (Raju & Yee, 2006).

This has proved to be unique from the aspect of construction challenges encountered and mitigation measures adopted, which have provided the tunnellers and engineers with a good learning experience in underground construction involving difficult karstic conditions under Kuala Lumpur.

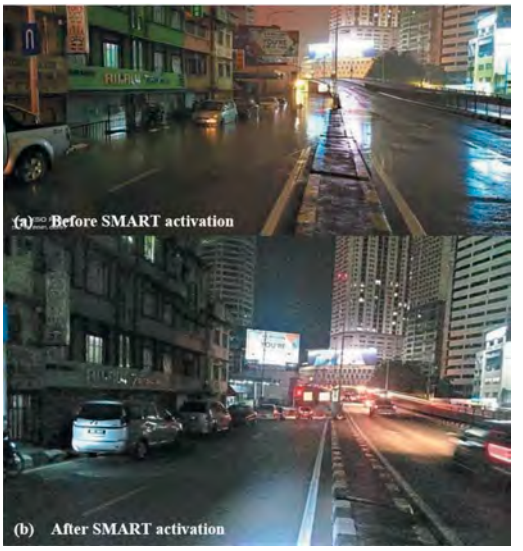

Figure 12. (a) before SMART activation, (b) after SMART activation at Pekeliling area in Kuala Lumpur (The Star, 22 December 2021).

4 RECORD OF PERFORMANCE AND EVENTS

Soon after the SMART tunnel was opened in operation, it faced its first test at the beginning of September 2007, when the motorway needed to be shut down for a major storm. Authorities at the Stormwater Control Center sent the alert to clear the tunnel when the Klang River registered a reading of 70 m^3/s. The SMART tunnel was able to keep the water level of the Klang River below the flood level, preventing a disturbance to the city centre.

In operation for over 15 years now, the SMART tunnel mitigates 45 % of the total flood risks in the Kuala Lumpur, and its activation has saved the city from gridlock and possibly more serious disaster (The Star, 12 February 2022). Because of this infrastructure, areas such as Masjid Jamek area, Dataran Merdeka, Leboh Ampang and Jalan Melaka have witnessed no flooding incidents since SMART tunnel opened in 2007, which has allowed business to operate without interruption. Figure 12 shows the situation before and after SMART activation at Pekeliling area in Kuala Lumpur.

As of December 2021, the SMART tunnel has diverted flood waters on 40 occasions and averted an estimated MYR1.4 billion in public damage. The SMART tunnel diverted 5 million m^3 of water on 18 December 2021 due to continuous torrential rainfall in the Greater Kuala Lumpur area, beyond the tunnel's actual capacity of 3 million m^3 and setting a new record of sorts (The Star, 22 December 2021). This was done by prolonging the diversion period through SMART tunnel and the existing retention ponds, especially the Berembang and Taman Desa retention ponds.

The operation took about 22 hours, some 7 times longer than previous water diversions.

The SMART tunnel is in itself an effective flood deterrent, due to its water capacity and the lag time it creates. It should be noted that SMART tunnel only diverts water around the critical meeting point from one of the contributing rivers. It has no effect on the flow from the other rivers, but it caused the sustained water to flow out. Although the development of SMART tunnel has been considered as successful, however, the growing development in the other parts of the city could not ensure no flooding will take place or thoroughly protect the city centre (Varadharajan & Bailey, 2013).

In terms of its role in traffic relief, SMART tunnel has minimised the journey for cars into Kuala Lumpur city centre from the southern gateway from the normal 20 minutes when using the federal road to only 8 minutes when using SMART tunnel. It serves as traffic dispersal to alleviate the chronic congestion of the southern road arteries of the city. Currently more than 30,000 vehicles use the tunnel daily, helping to ease rush hour traffic by offering an alternative route and cutting driving times (The Star, 11 July 2018).

Putting a financial value to these benefits, the Department of Irrigation and Drainage's survey concluded that, within the concession period spanning three decades, the SMART tunnel is expected to prevent US$1.58 billion of possible flood damage and up to US$1.26 billion savings from traffic congestion (ITS International, 12 September 2012). The savings are likely to be significantly more since these estimates are only for the duration of the concession. The tunnel has a design life of some 100 years.

Soon the SMART tunnel will be directly linked to the Tun Razak Exchange underground parking space, which could accommodate 5,000 car parks to boost the upcoming international business district connectivity (The Star, 12 February 2022).

5 CONCLUDING REMARKS

The dual-purpose SMART tunnel: one for stormwater diversion and second as a traffic dispersal scheme has proved to be unique and first of its kind in the world. By using a public-private partnership, the government was able to effectively lower its costs on a much-needed flood relief tunnel, perhaps kill two birds with one stone. Thus far the SMART tunnel has proven to be a success in meeting its primary and secondary objectives.

Construction of the SMART tunnel is not short of its own set of challenges, the geology in which the tunnel snakes through the city is made of extreme karst. The fact that the road tunnel is designed to flood created novel challenges for the design of the mechanical and electrical systems. The amount of redundancy built in for safety and security to ensure the operation with minimum interruption. Considerable courage, lateral thinking and an entrepreneurial spirit were exercised by all parties to make the concept a success.

Building on the experience gained and technological breakthrough in the industry, the spin-off effects of the SMART tunnel to Malaysia and worldwide tunnelling community were too great to be ignored. Locally, the SMART project has far reaching effect on the development of tunnelling engineering as is evidenced from the innovation of Variable Density TBM (VD TBM), establishment of Tunnelling Training Academy and the local TBM refurbishment plant. This has subsequently led to the in-house development of the world's first autonomous tunnel boring machine (A-TBM), equipped with custom artificial intelligence (AI) control algorithms (New Straits Times, 21 November 2019). Academically, a special session was devoted to the SMART project in the International Conference and Exhibition on Tunnelling and Trenchless Technology 2006 held in Kuala Lumpur in which there are numerous technical papers covering from planning, design, construction to safety issues. There is a wealth of knowledge and experiences shared in the proceedings.

To sum up, the greatest benefit of the SMART tunnel is that it helps make the city more resilient. The SMART tunnel is touted as a visionary green infrastructure built in 2007 with a sustainable, climate change solution in mind. Smart urban infrastructures are included in the United Nation's Sustainable Development Goal (SDG 11 – Sustainable cities and communities), a characteristic intended to be extended to combat climate change. The tunnel has demonstrated the degree of urban underground development Malaysia has achieved and is an example for other developing countries to emulate.

REFERENCES

Abdullah, K., 2004. The 14th Professor Chin Lecture: Kuala Lumpur: Re-engineering a flooded confluence. In: Ooi, T.A., Chan, S.F., Ting, W.H. (Eds.), Professor Chin Fung Kee Memorial Lectures 1991–2006, The Institution of Engineers Malaysia & The Engineering Alumni Association of the University of Malaya, Malaysia, pp. 277–286.

Darby, A. & Wilson, R., 2006. Design of the SMART project, Kuala Lumpur, Malaysia. Proceedings of International Conference and Exhibition on Tunnelling and Trenchless Technology, Selangor, Malaysia, pp. 435–449.

Gobbett, D.J., 1965, The formation of limestone caves in Malaya. Malaya Nature Journal, 19(1), pp. 4–12.

Ha, P.T.T., 2018. Underground MRT in Kuala Lumpur – the inevitable urban transit solution. Journal of The Institution of Engineers, Malaysia, Vol. 79, No. 1, pp. 1–20.

ITS International, 12 September 2012. Success of Kuala Lumpur's dual purpose tunnel. retrieved from https://

www.itsinternational.com/its4/its8/feature/success-kuala-lumpurs-dual-purpose-tunnel

New Straits Times, 21 November 2019. MMC-Gamuda tunnel boring machine wins award in Florida. retrieved from https://www.nst.com.my/business/2019/11/540757/mmc-gamuda-tunnel-boring-machine-wins-award-florida

Raju, V.R. & Yee, Y.W., 2006. Grouting in limestone for SMART tunnel project in Kuala Lumpur. Proceedings of International Conference and Exhibition on Tunnelling and Trenchless Technology, Selangor, Malaysia, pp. 557–581.

Santhiman, M.S. & Looi, H.W., 2006. ITS of SMART. PIARC International Seminar on Intelligent Transport System (ITS) in Road Network Operations, Kuala Lumpur, Malaysia.

SMART Website http://smarttunnel.com.my/smart/what-is-smart/

Special Unit for South-south Corporation, 2012. Report on case study (mixed use tunnel) in Kuala Lumpur, Malaysia.

Tan, S.M., 2005. Karstic features of Kuala Lumpur. Cover story, Jurutera, IEM Bulletin, June 2005, pp. 6–11.

Tan, S.M., 2006. Geotechnical aspects of the SMART tunnel. Proceedings of International Conference and Exhibition on Tunnelling and Trenchless Technology, Selangor, Malaysia, pp. 415–434.

The Star, 11 July 2018, Flood control the priority. retrieved from https://www.thestar.com.my/metro/metro-news/2018/07/11/flood-control-the-priority-kl-motorists-need-to-realise-that-the-smart-tunnel-is-a-storm-drain-first

The Star, 22 December 2021. SMART tunnel stretched beyond the max. retrieved from https://www.thestar.com.my/news/nation/2021/12/22/smart-tunnel-stretched-beyond-the-max

The Star, 12 February 2022. SMART tunnel mitigates 45% of KL floods. retrieved from https://www.thestar.com.my/news/nation/2022/02/12/smart-tunnel-mitigates-45-of-kl-floods

Varadharajan, R.B. & Bailey, C.J., 2013. Performance analysis of the storm water management and road tunnel – SMART in Kuala Lumpur. International Journal of Water Resources and Environmental Engineering, Vol. 5 (7), pp. 410–417. https://doi.org/10.5897/IJWREE2013.0390

Yeap, E.B., 1985, Irregular topography of the subsurface carbonate bedrock in the Kuala Lumpur area. Proceedings of 8th Southeast Asian Geotechnical Conference, Kuala Lumpur, Malaysia.

Tunnelling for a Better Life – Yan, Celestino, Thewes & Eberhardt (Eds)
© 2024 The Author(s), ISBN 978-1-032-80042-4
Open Access: www.taylorfrancis.com, CC BY-NC-ND 4.0 license

Large diameter surge shaft in weak foliated rock mass; excavation and support with real-time investigation and pre-excavation support strategy in the lesser Himalayan Slate

Bibash Parajuli*
PowerChina Chengdu Engin. Corp. Ltd, Chengdu, China

Eirinaios Christakis
Tractebel Engin. GmbH, Bad Vilbel, Germany

Arjun Marasini & Xing-Yi Yang
PowerChina Chengdu Engin. Corp. Ltd, Chengdu, China

ABSTRACT: The underground surge system of Tanahun Hydropower Project (Nepal) comprises a large span vault (29m by 33m) and an 85.5m-deep vertical shaft, excavated in the Benighat graphitic Slate of the Lesser Himalayan sequence. Geotechnical investigation during the tendering stage, and the excavation of a pilot adit provided the basis for the geomechanical parametrisation of the shaft. The encountered geology consists of thin to narrow foliated Slate with frequent intercalations of sheared bands and localised cleavage. The excavation sequence and the temporary support strategy were designed based on 3D numerical analysis, and the assignment of temporary support adopted the Norwegian Q-system. Considering, the residual degree of geological uncertainty and the tectonised nature of the Slate, the excavation was proven a challenging task. To ensure safe excavation and long-term stability, and maintain deformation within permissible threshold, the construction methodology included an iterative process of real-time investigation, pre-excavation measures, and consistent monitoring. Real-time investigation consisted of probe-drilling sessions with permeability tests and televiewer probing, aiming to detect poor quality zones which might compromise stability. Pre-excavation measures comprised high-pressure consolidation grouting, aiming to pre-stress the surrounding rock mass and improve the properties of the excavated sections in advance; followed by active support measures (i.e. pre-stressed anchors in the vault), focusing to the control of plastic zones. Monitoring included convergence stations, load cells, and multi-point borehole extensometers to assess deformation; all of them aiming to validate the performance of temporary supports. Despite the low progress mandated by difficult ground conditions, the excavation of the shaft was successfully completed by adopting the aforementioned observational and conservative approach.

Keywords: Squeezing ground, High-pressure grouting, Slate, Anisotropy, Surge Shaft, Rock support

1 INTRODUCTION

Tanahu HPP is a medium sized storage type hydropower project currently under construction and located in Gandaki Province (central Nepal). The main structures comprise a 140-metres high concrete gravity dam; a 1.45 Km long headrace tunnel that connects the power intake shaft to the underground powerhouse; and an 85.5-metres deep vertical concrete lined surge system, which consists of a Ø6.0m raiser shaft (the first 16.4 metres) and a large diameter (Ø25.5m) surge tank (69.1m) which ends to a vaulted cavern (28.80m x 35.47m).

The surge system is an integral element of a hydropower project that controls the resonance effect that may occur due the sudden closure of turbine valves, and subsequently mitigates water-hammering effect that might lead to the failure of the vertical water conduit (i.e. bursting of the penstock system). Hydraulic transient modelling and the maximum upsurge and downsurge water levels defined the optimal shaft dimensions to function as water hammering attenuator. The designed maximum pressure aiming to withstand pressure fluctuations is 0.9 MPa.

*Corresponding author: bibash.geo@gmail.com

DOI: 10.1201/9781003495505-428

2 REGIONAL AND PROJECT GEOLOGY

The Project is in the Midlands of Nepal, between the Mahabharat Range to the south and the high peaks of the north, at an altitude of +300m to +500m, above sea level.

The entire Project is constructed in the Lower and Upper Nawakot complex formations, a part of the Lesser Himalayan belt. The Surge Shaft is excavated in the Benighat Slates of the Upper Nawakot group. The Slate series overlay the Meso-Proterozoic series of Dhading formation, consisting of grey to light grey, thinly bedded to massive Dolomites, which were also encountered at the west part of the Project's area.

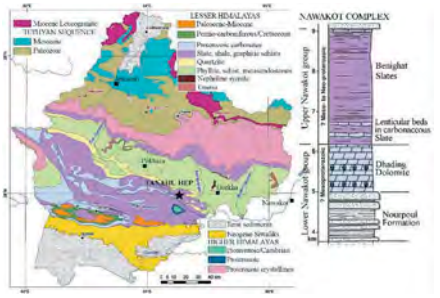

Figure 1. Simplified geological map of the Gandaki region, (after Amatya et al. 1994).

Dhital (2015) describe Benighat Slates as green-grey and light grey, very thinly cleaved, with localised strips of carbonaceous matter, and distinct lamination (from <0.5 mm to 2cm). Cai et al. (2019) consider carbonaceous Slate as special continuous formation, where weak zones parallel to foliation are playing an important role to its anisotropic behaviour.

2.1 *Factual geological regime of surge shaft*

The structure lies beneath a 250m overburden slope, of a 1040m-high Slate massif. The direction of the maximum stress to the horizontal has been measured to 13.0 MPa, with NNE-SSW trend.

The aforementioned general description coincides with the encountered lithology in the vault and the shaft. Based on observations during the excavation stages, the geological regime of the area corresponds to strong to moderately strong (R4-R3), dark greenish grey to dark grey SLATE, slightly decomposed to fresh (II-I), with small-scale fracturing due to mechanical weathering, and presence of graphite. The formation is very narrow (<6mm) to thinly (<100mm) foliated, with random micro-folding features and sheared zones of variable thickness, mainly parallel to foliation. Foliation constitutes the dominant feature, dipping 35°-50°, striking WNW-ESE. It is very closely to extremely closely spaced (<20mm to 60mm), of low to medium persistence (1-10m), smooth to slickensided undulated (V-VI, JRC: 3-9), with tight to very narrow (0-3mm) apertures, with quartzite infillings or graphite with stiff to firm components (S4-S3) and fragments of rock (R2). Open joints are found dry to damp (I-II) with localised spots of low seepage (V), whereas filled joints appear damp to wet with occasional drops (II-III) . Joint surfaces are partially weathered (PW90/100) to unweathered (UW). The geological regime can be characterised as strongly anisotropic, and heavily jointed. Apart from distinct foliation, two major discontinuity sets (J_1: 35°-55°, striking NNE-SSW, parallel to σ_H; and J_2: 20°-40°, striking ESE-WNW, dipping towards σ_H), and several random joints truncate the excavation. The geo-structural features with respect to the shaft are illustrated in Figure-2, below.

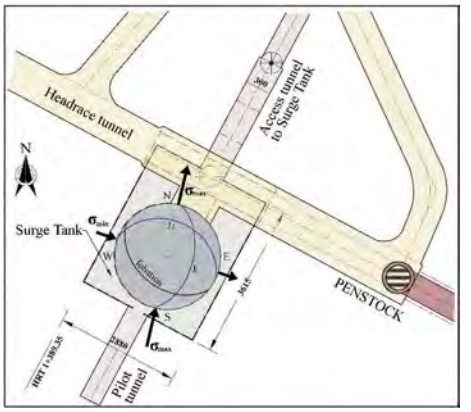

Figure 2. Geotectonic regime of surge shaft.

Furthermore, Alejano et al. (2021) directly link Slate's deformability and strength to the cleavage plane orientations relative to the principal stresses. Sheared zones of various thickness (range between 20-120cm) are mainly expressed parallel to foliation as paraconformities to the normal plane, with micro-scale quasi-folding, distinct moderate cleavage and localised indications of ductility.

3 CONSTRUCTION; CONCEPT AND METHODOLOGY

For the completion of the surge shaft from concept to design and from excavation to support a series of tasks were conducted, as sequential as well as iterative process (whenever this was deemed necessary). At the initial stage for the structure conceptualisation, preliminary information regarding the geological regime was retrieved from the tendering stage desk study, from a number of boreholes and in-situ tests, the detailed geological mapping, and the excavation data from an exploratory adit (i.e. access tunnel). The available baseline information, a collection of investigation data from adjacent vital structures (i.e. underground powerhouse and headrace tunnel), the shaft location,

and the design hydraulic parameters; set the prerequisites for the excavation of the surge system.

With respect to the excavation stages, the anticipated deformability, and the requirements for the temporary support (prior to concrete lining), the design was based on numerical 3D finite element analysis (FEM). For the rock mass classification and the assignment of temporary supports, the empirical Norwegian classification system (Q-value) was adopted. However, considering the anticipated poor rock mass conditions, the geomechanical behaviour of Slate, and aiming to ensure a safe excavation, a series of systematic pre-excavation measures were also introduced. Real-time information was further utilised to adapt temporary support to the needs of the excavated profile. This constitutes an integral part of the observational approach. Such measures included real-time investigation, i.e. vertical and radial probe-drilling; pre-excavation ground improvement with high-pressure grouting; and installation of prestressed anchors (at the shaft's vault). The excavation and temporary support were conducted in stages based on the FEM design; the actual geological conditions; and the response analysis of the surrounding rock mass as this was consistently monitored by a vast instrumentation network. Monitoring evaluation and realistic rock mass classification facilitated the selection of appropriate support which consisted of passive support measures. The aforementioned stages contributed to risk mitigation by improving the surrounding rock mass or by applying confining pressure over the excavated periphery; aiming to form a robust and impermeable uniform shell. Supplementary was the role of pre-excavation grouting, where "supports" focused beyond the excavation boundary.

The observational approach is an iterative procedure that integrates continuous monitoring to the excavation and the support strategy of the underground structure.

3.1 *Design stage*

For the selection of the most suitable location and the apprehension of anticipated rock mass quality, a 437-metres long D-shaped Access Tunnel) was excavated for exploration and geotechnical investigation purposes. In parallel to the Access Tunnel excavation, boreholes were drilled and a series of geotechnical tests (i.e. hydrofracturing, shear stress tests and compressive strength tests) were conducted. Excavation, investigation, and laboratory data constitute the baseline for the parametrisation and design of the geotechnical model, the excavation strategy and the underground support system. The geotechnical parameters which derived during investigation stage and the excavation of the access tunnel are summarised in Table 1, below.

Considering the anticipated foliated Slate and the rock mass quality (poor to very poor, Q: 4.0 to 0.1), a numerical finite element analysis (FEM) was performed, and the 3D model was generated.

Finite element analysis (FEM) indicated that the distribution of plastic zones is strongly affected by the presence of anticipated weak zones, and also

Table 1. Geotechnical parametrisation for design purpose.

Geotechnical parameter	Value range	Test
Unit weight	25-27 KN/m^3 (avg. 26.3 KN/m^3)	Laboratory
Young's modulus	40 GPa	
Poisson's ratio	0.35-0.25	
Shear stress (average)	3.3 MPa	
Residual stress (average)	1.92 MPa	
Uniaxial Compr. Strength	38 MPa	
Cohesion (peak)	0.52 MPa	Block shear tests
Cohesion (residual)	0.51 MPa	
Internal friction (peak)	38.70	
Internal friction (residual)	30.40	
Vertical stress (σ_v)	9.8 MPa	Hydro -fracturing
Maximum stress at horizontal	13.0 MPa (010 deg.)	
Minimum stress at horizontal	4.8 MPa (100 deg.)	

Figure 3. Finite element model (FEM) of surge tank.

demarcates the extent of the plastic zone, 13m beyond the crown. Moreover, the analysis of stresses in the surrounding rock mass provided the estimate for the excepted deformation in the surrounding rock mass, with a maximum vertical displacement of 89mm.

Taking into account the maximum stress concentrations and the resultant maximum deformation, the permanent support of the crown was designed based on the numerical model. With respect to the vertical shaft the numerical evaluation set the baseline for the temporary support

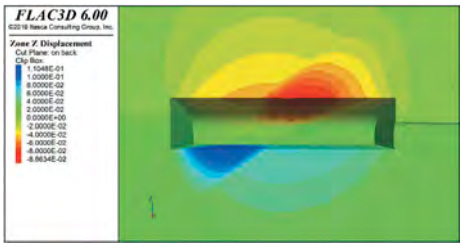

Figure 4. 3D FEM analysis of maximum displacement.

during excavation; whereas the in-situ rock mass assessment and the assignment of support measures adopted the empirical classification system of Q (NGI, 2022).

3.2 *Pre-excavation measures*

3.2.1 *Probe drilling*

The excavation of the exploratory tunnel and the subsequent advancing of shorter pilot tunnel ahead of the surge tank area provided adequate clarity with reference to the geological regime that surrounds the vault and set the principles for a safe excavation strategy.

Considering the intrinsic characteristics of Slate, and aiming to reduce geological uncertainty, probe drilling investigation was conducted over the crown, prior to the phased expansion of the vault. To substantiate penetration data and water pressure tests, supplementary information was retrieved from high-resolution imaging with the aid of camera probing (televiewer).

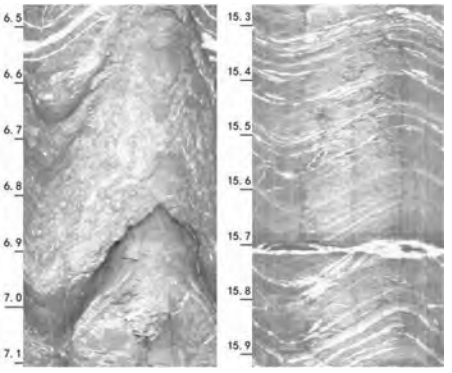

Figure 5. Example of televiewer imaging.

For this stage, 15m-deep probe holes were drilled, to record penetration rates, detect possible weak/shear zones, and assess groundwater regime. In that respect, Lugeon tests were carried out in all 243 holes. During probe drilling sessions, low-pressure ingress (~20 lt/min) was detected at two crown locations. Water pressure tests recorded low to locally very low permeability with values ranging from 0.0 to 3.8 Lu (average 2.4 Lu) which correspond to very tight to tight discontinuities. The average recorded penetration rates range from 0.42m/min to 0.99m/min. The maximum penetration rates were recoded towards the south end part of the crown. Probing penetration rates indicated weak/sheared interlayers in the crown, parallel to the foliation. Provided that the Slate dips with 40°-45°, similar shear zones were expected to be encountered in the shaft, as well.

A similar probing concept (i.e. drilling, recording and testing) was also adopted for the excavation of the shaft, where 20m-long, 20° inclined probe holes were drilled around the shaft perimeter. Each probing session overlapped 5-6m to the next session. Most probe holes in the vertical shaft were found substantially dry, and Lugeon tests indicated very tight to tight conditions (<2.5 Lu).

3.2.2 *High-pressure grouting*

A systematic high-pressure pre-excavation grouting (PEG) programme was designed before every excavation phase. PEG is a direct ground improvement technique that focuses to the modification of discontinuities properties, contributes to the pre-stressing of the surrounding rock mass, reduces hydraulic conductivity, and attempts to enhance the strength of possible weakness zones. Research and project references presented by Barton (2006 and 2011) where pre-injections have been conducted, provide evidence of the adopted practice (i.e. increase of effective RQD, reduction of effective J_n, and improvement of J_a and J_r). Therefore, considering the available pre-excavation information, PEG was proven essential to mitigate geotechnical risk. The basic PEG design considerations are: i) the stress regime, ii) the surrounding lithology and rock mass quality, and iii) the hydrogeological regime; whereas the grouting process criteria are: i) the groundwater behaviour (i.e. seepage and Lugeon data) of a particular probing phase, ii) the penetration rates, and iii) the encountered rock mass conditions during probing. Based on the aforesaid information, the grouting designer will be asked to decide for: i) suitable grout type material, ii) optimal grout mixes, iii) maximum applicable pressure, iv) possible maximum volume limitations, and v) grouting patterns (i.e. depth, hole spacing design, grout-fan geometry, etc.). In that respect, PEG sessions were conducted for the whole surge system, with the use of hydraulic packers set 1.0-1.5m into rock.

Grouts were injected over the entire crown and its sidewalls in radial patterns of 15m-deep holes. The maximum recorded grout take for the deep segments (5-15m) was 89.5 lit/m, and for the shallow segments (1-5m) 78 lit/m. The average injected volume equals to 23.3 lit/m for the deep segments, and 16.8 lit/m for the shallow, accordingly. These figures are considered relatively low, corroborating the low permeability values. Consequently, the injected mixes mainly contributed to the improvement of the weaker layers within the Slate and the overall

pre-stressing of the crown. Injection for all holes was terminated due to pressure limitations. The grout design and injection outcome for the surge tank vault is summarised in the Table 2, and general grouting layout is illustrated in Figure 6, below.

Table 2. Grout design and summary of surge tank vault PEG.

Grout type	Grout mix	Criteria
Microfine cement (MFC)	1.2 to 0.8 water/ cement	<3.0Lu
Portland cement (OPC)	1.2 to 0.8 water/ cement	>3.0Lu
Admixture	Superplasticiser 0.5-2.0%	
Injection criteria		
Pressure	30 bar (5-15m) 15 bar (1-5m)	Pressure refusal
Volume	4100 lit/15m segment	Volume refusal
Injection strategy		
Staged injection	Primary; 4.0m spacing	59 holes; 20130 lit
	Secondary; 2.0m spacing	102 holes; 26403 lit
	Tertiary; 1.0m spacing	66 holes; 13609 lit
	Control; random spacing	16 holes; 3542 lit
Total injected volume		63.7 m^3

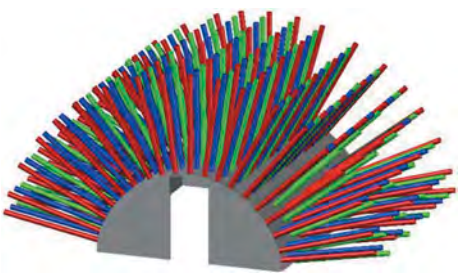

Figure 6. Probing and grouting layout of surge tank vault.

For the injections during shaft excavation, the drilling and grouting of systematic grout fans was adopted. Inclined grout-fans were drilled 20m deep, 1m inside the shaft profile. In order to assure dry excavation for the first 12 metres of the top section, 4 supplementary horizontal radial fans were drilled and grouted, as well. The drilling and injection patterns were linked to the probing results retrieved (i.e. penetration, lugeon tests and televiewer). The vertical spacing between consecutive grout-fans was set to 13-14m (5-6m of overlapping), and the lateral spacing of holes within the same gout-fan ranged between 2 and 4 metres; considering investigation information and observations made during injection (i.e., grout takes, ingress, and penetration).

Lugeon tests were conducted in two sections: i) from 10m to 15m, and ii) from 15m to 20m. Test results also regulated the selection of appropriate grout mix. The selection criteria for cement suspensions was similar to that of the vault. However, the maximum pressure and maximum volume refusal criteria were set to P_{max}=50 bar V_{max}=5000 lit/hole, accordingly. Similar to the vault injection outcome, the injection for all shaft holes was terminated by pressure.

The maximum grout takes were recorded close to the highest shaft sections (first 10m) where the average injection was 21.4 lit/m and the injected volume reached 18.2m^3 (approx. 0.7% consolidation ratio), and the lowest shaft section (28.1 lit/m). With respect to the whole shaft, and considering a theoretical grouting zone (6m around the excavated profile), the average injected grout per drilled metre equals to 18.81lit/m, with an approximate consolidation ratio for the entire profile, 0.45%. The probing and grouting pattern is shown in Figure 7, and the grouting criteria along with the injection data are summarised in Table 3, below.

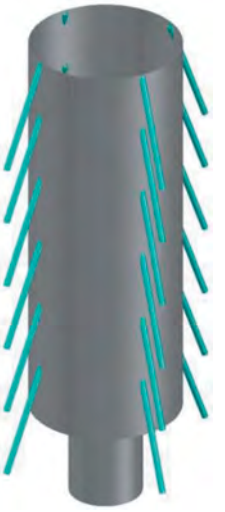

Figure 7. Schematic probing and grouting layout of surge tank.

3.3 *Excavation and support*

3.3.1 *Excavation sequence and advancing*

Considering the shaft and vault dimensions, in conjunction with the actual poor rock mass quality and the anticipated shear zones, the excavation was proven a challenging task which necessitated a conservative advancing. Thus, after the completion of each PEG

Table 3. Grout design and summary of surge shaft PEG.

Injection criteria Pressure refusal Volume refusal Grout fan	 50 bar 5000 lit/20m segment Injection	 Groutability
ST-CG-01 +426.7	42 holes; 5.9m^3 grouts	27.8 lit/ metre
ST-CG-02 +423.7	47 holes; 7.6m^3 grouts	32.2 lit/ metre
ST-CG-03 +420.7	36 holes; 2.3m^3 grouts	12.7 lit/ metre
ST-CG-04 +417.7	36 holes; 2.4m^3 grouts	13.0 lit/ metre
ST-PEG-01 +427.2	33 holes; 11.3m^3 grouts	19.0 lit/ metre
ST-PEG-02 +417.2	19 holes; 3.5m^3 grouts	10.3 lit/ metre
ST-PEG-03 +405.2	38 holes; 6.2m^3 grouts	9.0 lit/metre
ST-PEG-04 +393.2	29 holes; 10.6m^3 grouts	20.3 lit/ metre
ST-PEG-05 +381.2	41 holes; 15.2m^3 grouts	20.6 lit/ metre
ST-PEG-06 +369.2	34 holes; 12.2m^3 grouts	19.9 lit/ metre
ST-PEG-07 +361.5	26 holes; 10.9m^3 grouts	28.1 lit/ metre
Total drilled metres		4900m
Total injected volume		88.15 m^3

session, and taking into account the real-time investigation information, the excavation of the vault was executed in phases, where the timely application of temporary support and short advances were essential limiting factors to undesired occurring deformation.

Four phases consisted of the excavation of the surge vault, which was solely carried out with drilling and blasting.

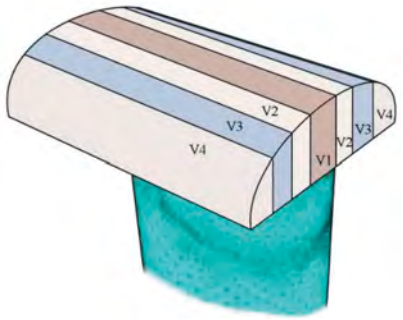

Figure 8. Excavation sequence of Surge Tank's vault.

The first phase (phase-V1) comprised the excavation of a D-shaped central access tunnel (6m span, 8m height) which crosses the area of the cylindrical shaft. To acquire more information regarding the properties of the surrounding Slate, the Access Tunnel was further advanced for 23 metres. The rest phases (phase-V2, phase-V3, and phase-V4) relate to the lateral enlargement of the vault which were carried out in parallel with the execution of PEG sessions, and the installation of the permanent support (crown and sidewalls).

Despite the weak nature of the encountered thinly foliated and cleaved Slate, the excavation and installation of permanent supports of the vault (6655 m^3 total excavated volume) was successfully completed within 5.5 months, without any recorded failure, overbreak, or signs of deformation.

After completing the vault's permanent rock supports, and the casting of the anchored concrete ring at the vault invert, the next stage comprised the phased shaft excavation.

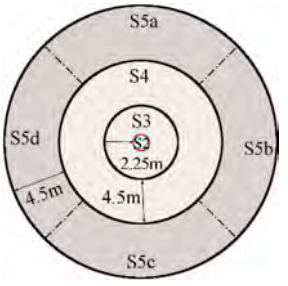

Figure 9. Excavation sequence of surge shaft.

For the first phase (phase-S1), a 0.2m-diameter pilot hole was drilled with the aid of a raise boring machine. During rotary drilling, penetration rates and groundwater behaviour were also recorded, in order to retrieve supplementary information about the underlying rock mass. The next phase (phase-S2) included the reaming of the pilot hole, from bottom to top; resulting to a 1.4m-diameter shaft that was foreseen to facilitate the mucking activity. The main shaft excavation was executed in one or more concentric phases (phase-S3, phase-S4, and/or phase-S5). The rock mass conditions, and in particular the Slate's strength variation, the presence of shear zones, the foliation properties, and the groundwater regime mandated the number of concentric phases, as well as the excavation method (i.e. mechanical or blasting). Due to the encountered weak rock mass conditions, the majority of advances was executed by mechanical means (approx. 97% of the shaft volume).

3.3.2 *Geological regime and as-built support*

In situ rock mass quality assessment and classification were carried out for the entire shaft, according to the NGI standards (i.e. Q-system, span size, purpose of structure, and shape parameters). The corresponding temporary rock supports were also assigned considering the NGI principles (as reference support framework) and the numerical stress and deformation

thresholds, always substantiated by the monitoring output. Taking into account the encountered shear zones, the probing output and the behaviour of rock mass during excavation; in order to assure shaft stability, supplementary support measures were installed in few areas. The encountered lithology and the main geological features are illustrated in Figure 10, below.

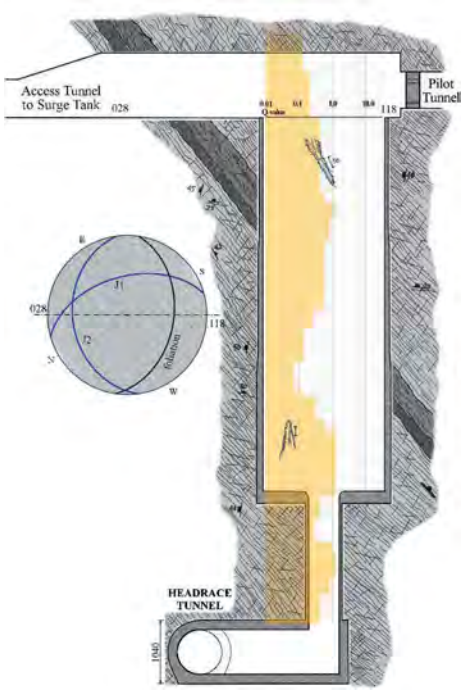

Figure 10. Geological cross-section of Surge System.

Figure 11 illustrates a typical Slate lithology as this was encountered during the shaft excavation.

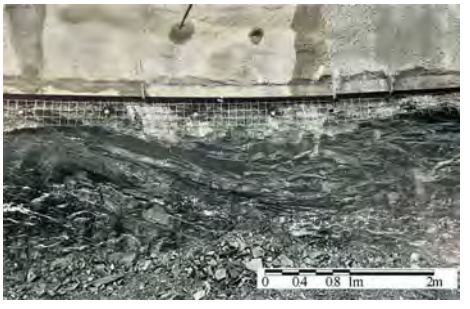

Figure 11. Typical Slate encountered at the South shaft-wall.

The entire structure is allocated in the Slates of Benighat formation, and the engineering geological description of the excavated rock mass is presented in Chapter 2.1. According to the adopted rock mass classification system, rock mass quality is mainly "very poor" ranging between "extremely poor" to "poor" (Q=0.07~1.25). The particular assigned rock mass parameters are summarised in Table 4, below.

Table 4. Rock mass parameters according to Q-system.

Parameter	Description	Range	Freq. value
RQD	Very poor (<15%)	10-15	10
Joint set number J_n	Three sets and random joints and locally heavily jointed	12-15	12
Joint roughness J_r	Smooth undulating to rough planar, locally smooth planar	1.0-2.0	2.0
Joint alteration J_a	Thin clay/graphite coatings, localised thicker (<2mm)	2.0-4.0	2.0
Water reduction J_w	Dry with minor localised drippings.	1.0	1.0
Stress reduction	Medium stress with localised single shear zones	1.0-2.5	1.0

Further to the systematic rock bolts, the surge tank vault was permanently supported with a grid of pre-stressed anchors. With respect to the vertical shaft, the design of temporary support classes comprised a combination of passive measures (i.e. rock bolts, wire mesh, sprayed shotcrete) and confining pressure support types (i.e. lattice girders or H-beams). The permanent rock support of the surge tank vault, and the temporary support patterns for the vertical shaft are summarised in Table 5 and Table 6, accordingly.

Table 5. Design of permanent support for surge shaft vault.

Shotcrete	150mm (fibre reinforced)	
Bolts	Fully grouted passive rock bolts	8.0m Ø32mm 2.0mX2.0m systematic
Anchors	Double corrosion protection pre-tensioned	15.0m Ø47mm; 3.0mX4.0m systematic
Drainage	4.0m, Ø32mm; 4.0mX4.0m systematic	

3.4 *Monitoring*

Considering the dimensions of the surge system along with the encountered geology, a diligent monitoring strategy during all excavation phases was deemed integral for the construction of the entire surge system. Therefore, monitoring instruments were installed in the vault crown, as well as in the shaft walls, as shown in Figure 12.

Table 6. Design of temporary support for surge shaft.

Q-value	Shotcrete	Rock bolts	Steel ring
>50 (RS1)	50mm (plain)	7.0m Ø32mm; spots	N/A
50-8.0 (RS2)	50mm (fibre)	7.0m, Ø32mm; 2.5mX2.5m systematic	N/A
8.0-2.8 (RS3)	80mm (fibre)	7.0m, Ø32mm; 2.0mX2.0m systematic	N/A
2.8-0.8 (RS4)	100mm (fibre)	7.0m, Ø32mm; 1.75mX1.75m systematic	N/A
0.8-0.28 (RS5)	150mm (wire-mesh)	7.0m, Ø32mm; 1.5mX1. 5m systematic	3-element lattice girder
<0.28	200mm (wire-mesh)	7.0 to 9.0m, Ø32mm; 1.0mX1.0m systematic	H-beam

NOTE: Different Excavation Support Ratio (ESR) and downgraded Q-value ranges apply for intersections

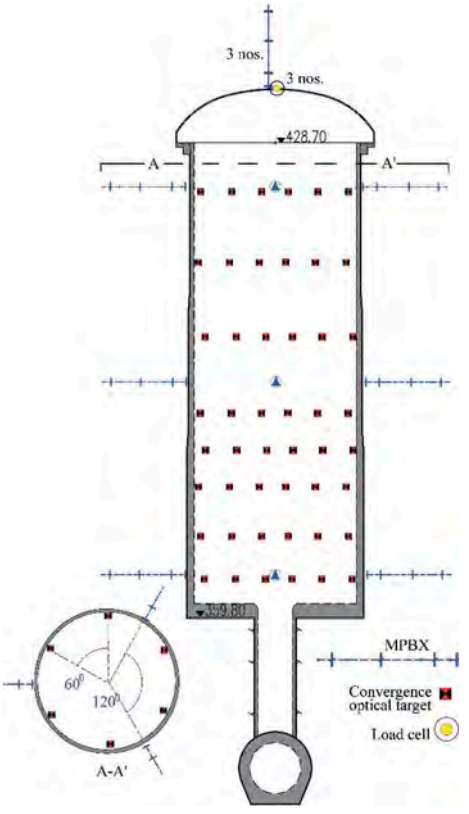

Figure 12. Instrumentation setup of the surge system.

In brief, tree types of instruments were installed:

i) Multi-point borehole extensometers (MPBX) equipped with three displacement sensors (at 2m, 7m and 20m), aiming to monitor displacements and determine the deformation behaviour of the surrounding rock mass.
ii) Load cells at the vault crown, in order to measure the amount of transferred loads to the support element where the instrumented is mounted to. Load cells were mounted to rock anchors.
iii) 6-point optical target stations (convergence stations) were installed in the shaft, where routine geodetic survey readings were providing information about the aggregate deformation during all excavation phases.

A summary of all active instruments utilised for the geotechnical monitoring of the surge system is presented in Table 7, below.

Table 7. Surge tank instrumentation.

Instrument	Location	Behaviour
MPBX	Vault crown; 3 units	Flat trend (max. 7mm) Flat trend (max. 45mm) Flat trend (max. 15mm)
	Shaft +422; 3 units	Flat trend (max. 8mm) Flat trend (max. 8mm) Flat trend (max. 5mm)
	Shaft +394; 3 units	Flat trend (max. 15mm) Flat trend (max. 4mm) Flat trend (max. 6mm)
	Shaft +366; 3 units	Flat trend (max. 8mm) Flat trend (max. 5mm) Flat trend (max. 5mm)
Load cell	Vault crown; 3 units	Flat trend (638KN)
	Flat trend (610KN)	
	Below alarm (808KN)	
Convergence station	Shaft +422; 6 targets	Max. converg. 10-20mm
	Shaft +412; 6 targets	
	Shaft +402; 6 targets	Max. converg. 10-15mm
	Shaft +391.6; 6 targets	
	Shaft +386.6; 6 targets	Max. converg. 10-25mm
	Shaft +381.6; 6 targets	Max. converg. 5-15mm
	Shaft +381.6; 6 targets	

During excavation, damp areas and localised minor seepage (max. seepage <1.0 lit/minute) were observed mainly at the south and southwest shaft walls. The overall ingress estimate for the entire shaft is 5 to 8 lit/min/10m shaft.

4 CONCLUSIONS

The anticipated geological conditions in the Surge Tank system were known to some extent from retrieved information during the design stage, and the excavation stage of the Access Tunnel. However, considering the medium- to small-scale variance within the predominant graphitic Slate, and the observed behaviour of Slate during the excavation of the adjacent underground powerhouse (long-term creeping deformation); a diligent re-assessment strategy was adopted, aiming to mitigate geological uncertainty. This strategy comprised medium-scale pre-excavation investigation tasks in parallel with the excavation and support of the Surge system, alongside with consistent real-time monitoring. Investigation included sequential probe drilling with penetration rate measurements, televiewer probing and water pressure tests (Lugeon permeability tests). The precise allocation and the geometry of weak or shear zones, the detection of excessive groundwater activity, or any other adverse stability factor were the main objectives of this parallel investigation approach.

Probing activities revealed a 6m-thick weak zone that trends parallel to Slate's foliation and consists of a 4m-thick heavily jointed layer which transitions to a 2m-thick shear band. The zone appears at the NNE shaft wall, dipping towards SSW with 45°. In general, the shaft is situated in extremely poor to poor foliated Slate, a specific rock mass quality that necessitated the execution of overlapping pre-excavation grouting fans. The relatively low consolidation ratio (0.42%) indicates that high-pressure injections mainly contributed to the prestressing of surrounding Slate, and the overall improvement of discontinuities. Secondly, it also addressed minor seepage.

On the other hand, permeability tests did not reveal any significant groundwater path that might hamper excavation or influence stability. According to the seepage observation records, areas of minor dripping (<0.1 lit/min) were mainly identified at the SSW area, whereas several damp/partially wet areas are scattered in various locations. All seepage issues were addressed with drainage provisions (i.e. deep drainage holes or shallow relief holes). An indicative example of grout penetration through Slate's jointing system is illustrated in Figure 13.

The anticipated as well as the encountered rock mass quality in conjunction with the intrinsic geomechanical behaviour of the particular graphitic Slate (i.e., slow response elastic-perfectly plastic deformation) advocated to a conservative excavation philosophy. In that respect, blasting activity was constrained in order to eliminate blast damage. Consequently the advancing of the shaft was principally carried out by mechanical means. Further to this, in line with the assessed rock mass quality a considerable part of the shaft (approx. 62%) required the installation of numerous steel ring supports (HEB steel beams or 3-element lattice girders).

Noteworthy is the importance of monitoring during the entire excavation and support process that may act as early-warning system for possible excavation and/or rock support improvements. The recorded strains of the structure during the excavation stage are negligible with normalized trends, and they do not exceed 0.1%.

Figure 13. MFC grout penetration in slate joints (foliation).

The conservative excavation strategy in conjunction with several pre-excavation measures, ensured the safe construction of this large diameter vertical surge shaft. The approach resulted in the reduction of geotechnical risk, a fact which has been also affirmed by the diligent monitoring and careful observation.

REFERENCES

Alejano, L.R., González-Fernández, M.A., Estévez-Ventosa, X., Song, F., Delgado-Martín, J., Muñoz-Ibáñez, A., González-Molano, N., Alvarellos, J., 2021. Anisotropic deformability and strength of slate from NW-Spain. International Journal of Rock Mechanics and Mining Sciences, Volume 148.

Amatya, K. M., Jnawali, B. M., 1994. Geological map of Nepal, Scale: 1:1,000,000. Department of Mines and Geology, International Centre for Integrated Mountain Development, Carl Duisberg Gesellschaft e.V., and UN Environment Programme, Berlin.

Barton, N., 2006. Integrating Q-logging with seismic refraction, permeability, pre-grouting, tunnel and cavern support needs, and numerical modelling of performance. Institute of Engineers, Geotechnical Division, Annual Meeting. Keynote lecture, Hong Kong.

Barton, N., 2011. An engineering assessment of pre-Injection in tunnelling. Keynote lecture. Indian Conf. on Rock Mechanics and Tunnelling. Roorkee, India.

Cai, J., Du, G., Ye, H., Lei, T., Xia, H., Pan, H., 2029. A slate tunnel stability analysis considering the influence of anisotropic bedding properties. Advances in Materials Science and Engineering, vol. 2019, Article ID 4653401, 17 pages.

Dhital, M.R., 2015. Lesser Himalaya of Gandaki Region. Geology of the Nepal Himalaya. Regional Geology Reviews. Springer, Cham. https://doi.org/10.1007/978-3-319-02496-7_9

Norwegian Geotechnical Institute, 2022. Using the Q system: Rock mass classification and support design handbook. NGI, Norway.

Tunnelling for a Better Life – Yan, Celestino, Thewes & Eberhardt (Eds)
© 2024 The Author(s), ISBN 978-1-032-80042-4
Open Access: www.taylorfrancis.com, CC BY-NC-ND 4.0 license

Gangxia North Hub innovation highlights

Xuegang Qie* & Liwei Qi
China Railway Design Corporation, Tianjin, China

ABSTRACT: Gangxia North Hub is the first hub of the Shenzhen Metro Express network, and the first comprehensive transportation hub in Shenzhen to connect 5 subway lines at one time. The hub space is mainly divided into five levels: the ground floor is a sunken plaza and ground structures; The mezzanine is an urban crossing corridor (at the same level as the existing Metro Line 2); The first basement floor is the hub transfer station hall, and the underground space of the east, west and south areas; The second underground floor is the east-west platform and rail area of Line 11 and 14, and the equipment area of Line 10; Three basement levels: Line 10 platform level. Gangxia North underground transfer core area, east, west and south three parts of the underground space. The total length of the hub is about 900 meters from east to west, 620 meters from north to south, and about 235,000 square meters in construction. It is an existing transfer node of Metro Line 2, the newly built Line 10, Line 11 and Line 14, and the commercial development of the underground space of Caitian Road and Shennan Avenue connected by the transfer node, and synchronously connecting the underground space of Line 1 Gangxia Station and Liancheng Xintiandi. Trial operation began on December 28, 2022.

Keywords: Comprehensive Transportation Hub, Innovation Highlights, Urban Public Space, Design Strategy, Urban Underground Space Community

1 PROJECT OVERVIEW

Gangxia North Hub is the first hub of the Shenzhen Metro Express network, and the first comprehensive transportation hub in Shenzhen to connect 5 subway lines at one time.

The hub space is mainly divided into five levels: the ground floor is a sunken plaza and ground structures; The mezzanine is an urban crossing corridor (at the same level as the existing Metro Line 2); The first basement floor is the hub transfer station hall, and the underground space of the east, west and south areas; The second underground floor is the east-west platform and rail area of Line 11 and 14, and the equipment area of Line 10; Three basement levels: Line 10 platform level.

Figure 1. Spatial structure diagram.

Gangxia North underground transfer core area, east, west and south three parts of the underground space. The total length of the hub is about 900 meters from east to west, 620 meters from north to south, and about 235,000 square meters in construction. It is an existing transfer node of Metro Line 2, the newly built Line 10, Line 11 and Line 14, and the commercial development of the underground space of Caitian Road and Shennan Avenue connected by the transfer node, and synchronously connecting the underground space of Line 1 Gangxia Station and Liancheng Xintiandi. Trial operation began on December 28, 2022.

2 THE DIFFICULTIES AND CHALLENGES

Planning and building an all-underground comprehensive transportation hub in the bustling metropolitan area of Shenzhen, carrying the multi-dimensional mission of urban development, while reducing the negative impact on the city during several years of construction, is a major issue facing all participants. As a general contractor of survey and design, CRCC deconstructs the planning and construction goals in different dimensions, and then carries out the logical combination of implementation routes with the goal of high-quality landing, so as to maximize the high-quality completion of the project.

*Corresponding author: Qiexuegang@qq.com

DOI: 10.1201/9781003495505-429

2.1 *Traffic organization and spatial combination*

Rail transit distribution and transfer, bus, slow travel, municipal traffic and other different transportation needs converge here, and the organization of hundreds of thousands of daily passenger flows is the core key of the project. It is necessary to realize the logical undertaking between urban planning, transportation planning and engineering units, and implement the initial requirements to the final engineering practice.

In-depth interpretation of the underground space planning of the central area of Shenzhen, with the help of the planning and construction of the Gangxia North Hub, to build a multi-dimensional urban public space community.

2.2 *Urban integration with rail transit as the core*

Within the area directly or indirectly affected by rail transit construction, urban municipal roads, bridges, green landscapes, underground spaces, public facilities, infrastructure, etc. will be integrated and integrated to build an integrated urban unit.

2.3 *Multi-professional collaborative innovation of comprehensive engineering subjects*

Focusing on the goal of urban quality projects, under the guidance of the innovation of planning and architectural schemes, all relevant technical specialties carry out in-depth coordination and innovation work. Structure, mechanical and electrical equipment, fire protection, civil air defense and other related technical majors carry out cutting-edge exploration in their respective fields, and carry out comprehensive coordination under the overall planning of the project center objectives.

2.4 *Pay attention to systematic industry leadership and pioneering demonstration*

On the basis of the innovation of planning and design schemes, this project should also explore the technological development of the industry, explore and demonstrate the overall innovation of subsequent projects, and reflect the urban spirit based on urban characteristics.

2.5 *Define the cultural and artistic attributes of important public spaces*

Under the mission of realizing the transportation function and promoting urban development, as an important public space in the central area of the city, especially the large-scale underground hub space, the corresponding cultural and artistic attributes should be given through design, so that the public can have a higher quality space experience in the process of traffic travel.

3 INNOVATION HIGHLIGHTS

3.1 *Build a new multi-dimensional urban public space network*

Gangxia North Hub is generally located on the east side of the center of Shenzhen, the central area of Shenzhen. The construction of the hub will connect the surrounding underground space to form a complete underground space network, which will become an important urban public space in Shenzhen.

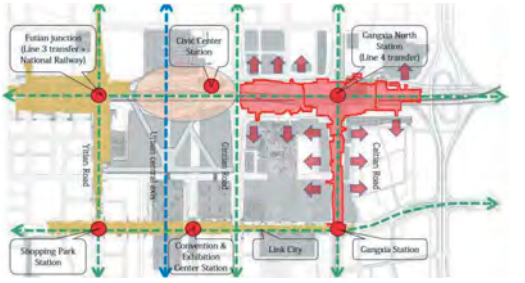

Figure 2. Schematic diagram of underground space planning.

On the basis of building multiple interchange stations, a networked three-dimensional urban space is organized simultaneously. Urban municipal traffic public ring corridor and street passage; Seamless networking of underground space; Sunken plaza and landscape excessive gray space sequence.

3.2 *The design model of "sunken square + underground corridor" was proposed*

As an urban unit without precise boundaries, the exploration of design patterns has been successfully explored in this project, completing the coordinated combination of different sequences. Urban roads have been reconstructed and optimized, the amount of overpasses has been upgraded and upgraded, conventional green belts in the road have been transformed into urban public roadside gently sloped gardens, subway stations are convenient to access and transfer, and underground space and supporting facilities are integrated to form urban units.

Form a hub "connection" city and realize the integrated hub method of road-bridge-station-park-city.

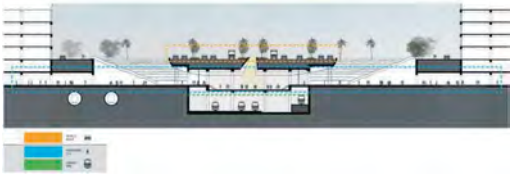

Figure 3. Separated traffic.

3.3 *The largest span underground hub in china, heavy-duty steel beams and concrete slab composite structure*

The three new lines are all stations of the 8A marshall, and the scale of the central hall is beyond the norm based on the need for quick and convenient transfers. According to the special needs of function and space, a structural span of 51.2mX48m was designed. In order to realize the 51.2m underground structure, which is the world's largest span, compatible with the special-shaped space of the daylight, the middle main force member of the super-large span underground structure needs to consider the continuity after disconnection; in addition, the hub is located at the intersection of the main road of the city, and the intersection cannot be severed during the construction process, and the structural system conversion needs to be carried out during the construction. Comprehensively considering different factors, Tsinghua University and Harbin Institute of Technology have carried out a large number of technical and economic comparison work. Finally, considering the influencing factors such as investment control, modeling design, mechanical analysis, implementation difficulty, and adaptability to traffic dredging, it was determined that the flat-plate structure two-way beam steel-concrete composite system was selected as the large-span structural system of Gangxia North Hub.

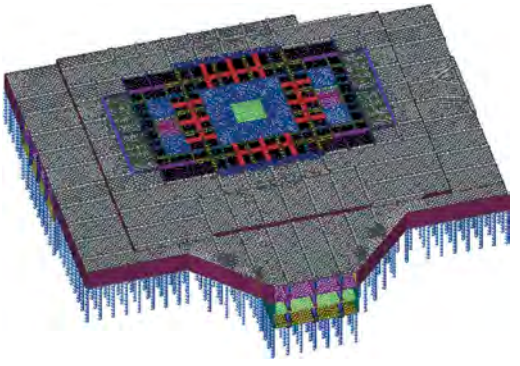

Figure 4. Structural integral model.

Figure 5. Photos of long-span structure on construction site.

3.4 *Developed the glass tunnel system of the platform rail travel area*

Since the opening of the first subway in 1863, the subway has been a weapon to solve urban transportation, with a sense of technology and the future. The industry has been diligently using the language of the times to continue the original characteristics of the subway. Gangxia North Hub has made joint efforts in different dimensions such as material research and development, product customization, structural construction, and design research, and finally realized the glass tunnel in the rail travel area. The traveling process of the train is directly perceived, and at the same time ensures multiple conditions such as earthquake resistance, fire resistance, and pressure resistance. It provides a valuable demonstration of subsequent subway, intercity, railway and other forms of transportation.

Figure 6. Station hall atrium effect diagram.

3.5 *The large-scale underground hub decoration method integrating chinese and western cultural concepts was proposed*

In line with Shenzhen's open and inclusive urban spirit, combined with the special architectural design of Gangxia North Hub, the decoration design creates a conceptual scheme with the theme of "Shenzhen Eye". Implement the design concept of "introducing sunlight into the subway space", and create an

Figure 7. Site atrium effect diagram.

underground space of rail transit hub that can not only reflect Shenzhen's humanistic care but also carry the characteristics of Shenzhen's "convergence, inclusiveness and internationalization". Using the mathematical principle of "Fermat spiral" to design a ceiling design scheme endowed with visual tension, the white spiral converges to the "eye of the sky", reflecting the international style.

4 ENLIGHTENMENT

Human civilization has always been closely related to the development and utilization of underground space, and there are different ways of effective exploration around the world, especially in large cities. Based on the construction process of the subway, Gangxia North Hub has carried out multi-dimensional innovative exploration of planning and design, aiming to expand new ways and methods of development and utilization in the field of underground space. Hundreds of thousands of passengers gather and disperse here every day, and there are also general citizens who carry out various activities in different areas of the underground space. The passage of time never stops, so that people traveling in underground space have a better travel experience, and it is the industry's continuous pursuit to extend more and more suitable activities in underground space. In the continuous iteration of the industry, we will definitely have a better transportation space and lifestyle.

Figure 8. Station hall scene photos.

Figure 9. The story behind shenzhen's eye.

REFERENCES

Qian Qihu et al. 2002., Underground City[M]. Beijing: Tsinghua University Press.

Kevin Lynch, Urban Imagery[M]. Beijing: Huaxia Press. 2001.

Wang Liang, Development and utilization concept of underground space in Huaqiangbei, Shenzhen[J] Tunnel/underground engineering. 2011. 89–92.

Wang Chengfang, Sun Yimin, Sun Xiang, Discussion on underground space development strategy with rail station as the core[C] 2013 Proceedings of the Underground Space Professional Committee of the Tunnel and Underground Engineering Branch of the Chinese Civil Engineering Society. 95–100.

Xia Changqiong, Development and utilization and innovation of underground commercial space in Shenzhen urban rail, building a subway is building a city[C]. Shenzhen: ShenzhenUrban Rail Transit Association and China Academy of Railway Science. 2017. 178–182.

Tunnelling for a Better Life – Yan, Celestino, Thewes & Eberhardt (Eds)
© 2024 The Author(s), ISBN 978-1-032-80042-4
Open Access: www.taylorfrancis.com, CC BY-NC-ND 4.0 license

Contract Korsvägen - part of the new Westlänken Commuter Rail Project in Gothenburg, Sweden. Challenges of drill & blast Tunnelling and cut & cover construction in heterogeneous ground conditions

Klaus Rieker*
Wayss & Freytag Ingenieurbau AG, Frankfurt am Main, Germany

ABSTRACT: The West Link Project in Gothenburg is an 8 km long double track railway line. About 6 km of the section run through a twin-tube tunnel under the city center. An escape/service tunnel, which is accessible for vehicles through access tunnels, runs parallel to the track tunnel in the mined section. There are also three new stations located throughout the city center. Widening from two to four tracks within the stations will make rail operation as efficient as possible. The Korsvägen contract is a 3.2 km long section. It runs through heterogeneous ground conditions, alternating between hard rock and soft soil. The construction elements are therefore: a 700 m long Cut & Cover section, a 1 km long Tunnel, a 300 m long Cut & Cover section, Korsvägen station (constructed partly in an open box and partly within Drill & Blast Tunnel sections) and another 1 km long Tunnel. The joint venture Westlink Contractors (WLC), consisting of construction companies NCC from Sweden and Wayss & Freytag Ingenieurbau AG from Germany were awarded the contract in December 2017. The total bid sum, which also represents the first target price, is the sum of the unit price BOQ of the rock tunnel and the Design & Build price of all other cut & cover structures. The presentation will focus on the drill & blast tunnelling works with cross sections of up to 45 m with a cover of about 8 m only, will highlight the challenges of the open cut & cover temporary works (using different retaining structures) connecting very soft clay to hard rock in the transition areas and touch briefly on the interesting target price model.

Keywords: Tunnelling, Cut & Cover, Target Price, Challenging Geology, Inner City, Design & Build

1 PROJECT OVERVIEW WEST LINK

The West Link aims to increase the transport capacity of the commuter and regional train system, to create more travelling possibilities, to ease passenger flow at the Central station and to eliminate weak links in the current system. Besides the extension of the Central station, two new underground stations will be built - Haga and Korsvägen. This paper however deals further on with the construction section Korsvägen only, highlighted in yellow on the bottom half of Figure 1. The alignment and geology are presented for the whole West Link Project (Figure 2), whereby Korsvägen is on the right hand side.

The Client for the project is the Swedish Transport Authority Trafikverket.

2 KORSVÄGEN CONSTRUCTION SECTIONS

2.1 *Overview*

The Korsvägen project is an approximately 3.3 km long section spanning from the municipality of Mölndal to Lorensberg, a district of Gothenburg. This is also where the boundary line to the Haga construction section lies. The various sections with the project are shown in Figure 3.

Coming from the Mölndal direction, the alignment of the new West Link Tunnel initially runs in Almedal above ground parallel to the European motorway E20 and an existing railway line. In this area, the connection to the existing railway network will be via a trough and tunnel structure. This section is about 700 m long.

*Corresponding author: Klaus.Rieker@wf-ib.de

DOI: 10.1201/9781003495505-430

Figure 1. Overview of West Link Project, Gothenburg.

The next section of the project is the 1,000 m long Örgryte Tunnel, which runs under the European motorways E20/E6 and passes under the residential areas Skår und Örgryte. Just before the transition to the Liseberg cut & cover section, the tunnel passes as well below the Gårda Tunnel, a railway tunnel in operation.

Within the 300 m long Liseberg area, the rock horizon dips down requiring replacing mined tunnelling with cut & cover. Since this area runs through an amusement park, some buildings, including a sports hall, a car park, an access bridge, and various small buildings of the amusement park, had to be demolished first. The Liseberg Amusement Park is the largest in Scandinavia. The excavation pit in this section lies in the Mölndalsån river valley, which is filled with Lera clay.

From Liseberg the construction method changes back to a mining method. This 100 m long section is the trumpet-shaped eastern part of the Korsvägen Station and as well located under the Liseberg

Figure 3. Main construction sections and details.

Amusement Park. At this point, the double-track tunnel changes into a four-track section. Tunnel excavation will be carried out from an access tunnel using the drill & blast method.

The eastern trumpet is followed by the Korsvägen excavation pit. Like the Liseberg excavation pit, it is in a valley filled with Lera clay. The about 100 m long excavation pit will be constructed in two phases by means of secant bored pile walls and steel piles whilst operation of the Korsvägen traffic junction continues on a temporary bridge.

Drill & blast excavation methods will be used for the construction of the second half of Korsvägen station in the direction of the Lorensberg district. After about 100 m the cross section narrows from four to two tracks in the western trumpet-shaped area of the station. In this area caverns for ventilation systems and other technical installations as well as a ventilation shaft and tunnel plus an adit serving later as an entrance gallery to the station must be constructed. The follow-on approximately 1,000 m long Lorensberg Tunnel, which has a double-track cross-section, ends at the boundary line to the Haga construction section. All mined tunnelling in this area will be done from an access tunnel.

Each section (Figure 3) and its challenges will be described in more detail in the following paragraphs.

2.2 *Almedal ramp*

The temporary retaining structure for the trough and tunnel construction consists of about 3,000 sheet piles driven to rock level. Rock dowels and grouting secure the interface. To ensure water tightness everywhere, rock curtain grouting had to be carried out as

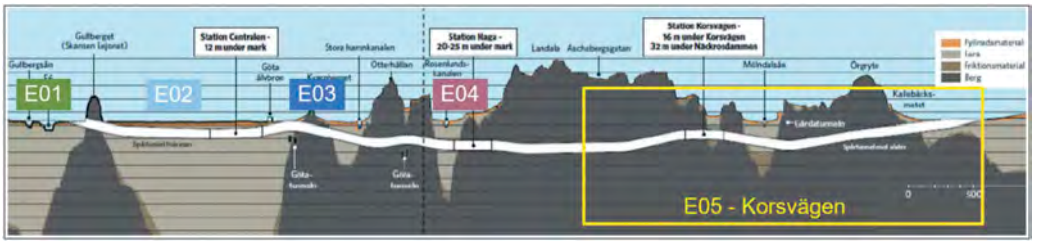

Figure 2. Simplified geotechnical longitudinal section of Gothenburg West Link.

well. Due to the soft soil conditions, the whole area had to be stabilized first by lime-cement soil treatment. Prior to that the existing railway tracks had to be shifted to allow construction to take place. The ramp is squeezed over the entire length between the tracks and the E6 motorway on the other side. The excavation pit was secured by up to three levels of strutting (Figure 4).

Figure 4. Almedal trough and tunnel section.

2.3 *Örgryte tunnel*

The Örgryte track tunnel is excavated via Service Tunnel 209 located just outside the city center of Gothenburg in the Skår residential area. 209 is the intermediate starting point for the construction of the 1,000 m long Örgryte track and a parallel running service tunnel (Figure 5). Both, the track tunnel with an excavation cross-section of approx. 130 m² and the service tunnel with an excavation cross-section of approx. 100 m² will be driven northwards and southwards simultaneously, i.e., four tunnel fronts are operational in this area. Tunnelling works on Service Tunnel 209 started in November 2020. The tunnel section passes as well under sensitive buildings, such as the E-routes 20/6 and the existing railway tunnel Gårda. Granite with strengths of up to 300 MPa are encountered in this section. To-date the southbound Track and Service Tunnels are completely excavated (Figure 6). The northbound excavation is about 80 % complete.

Figure 5. Örgryte track and service tunnel.

Figure 6. Interface Almedal Ramp/Örgryte Track Tunnel.

2.4 *Liseberg cut & cover*

The challenges to overcome in the Liseberg Park area include the existing ramp to the motorway E6 and the historic buildings as well as the Mölndalsan river crossing. The ramp to the motorway had to be demolished and the so-called Rondo, an about 100-year-old building used year-round for performances, had to be partially flattened on one side to make room for the construction pit. An existing restaurant had to be demolished and rebuilt a few meters away to make room on the other side (Figures 7 and 8).

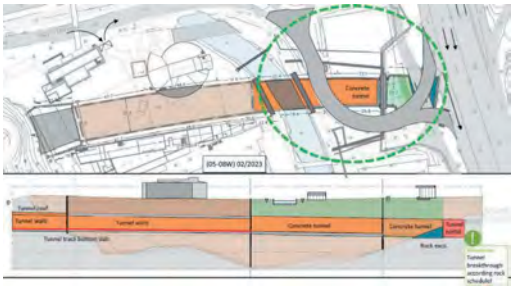

Figure 7. Ramp to E6, Rondo, Restaurant and Mölndalsan River.

Due to the very challenging geology different special foundation techniques came into play over about 300 m in length. Going from East to West, those are: 900 mm interlocking steel pipes, 1,472 mm interlocking steel pipes in the area, followed by diaphragm walls and sheet piles further on. In all areas, watertightness at the toe of the retaining structure must be

Figure 8. Liseberg Cut & Cover Section (grey).

achieved. Rock curtain grouting must be carried out where the rock on either end rises above the final excavation level. The transition to the Liseberg rock tunnel will be achieved with a 25 m long NATM/SCL excavation from within the Eastern Trumpet. Since the river, crossing the alignment, cannot be diverted, blocked or otherwise, a steel trough was manufactured off-site, assembled on site and lifted as one component into place. It rests on a sealing system and the previously mentioned 1,472 mm pipes.

2.5 *Korsvägen station*

Korsvägen station consist of three parts - Station East, Station Mid and Station West (Figure 9).

Figure 9. Station West (left), Station Mid (red), Station East (right).

Station East and West must be excavated via 400 respectively 500 m long access adits with an excavation cross-section of 80 m². Tunnelling works on the city-center access tunnels 206 and 207 began in autumn 2018. With only two blasting times per working day and strict vibration and noise criteria, the excavation cross-section of 80 m² was first subdivided into eleven sections and excavated with a round length ranging from 1 to 2 m. The sensitive buildings in the immediate vicinity (shown in Figure 10) such as the tram line, the Carlanderska Hospital, the Universeum Museum of Natural Science with rare species of fish in large aquariums and other residential buildings directly adjacent to the tunnel portals did not permit longer round lengths. Only after the tunnelling works had successfully commenced, was it possible to optimize the blasting process and change from partial-face excavation to full-face excavation and increase the round lengths to 5 m.

Figure 10. Portals and site installation area of service tunnels 206 (left) and 207 (right), access to Lorensberg and Liseberg.

Figure 11. Abutment walls of access tunnel 206 with the Carlanderska Hospital in the background.

These round lengths, common in Sweden, can be achieved since all tunnel sections built using the drill & blast method are in hard rock.

The subsoil in the mined tunnel sections consists mainly of gneiss with uniaxial compressive strengths between 200 and 300 MPa (Figure 11) shows exemplary the subsoil conditions at access tunnel portal 206, where two of the three portal walls were cut with wire saws to keep noise and vibration loads as low as possible.

Station East

From access tunnel 207, the eastern trumpet was excavated. Due to the large cross-section, 3 pilot tunnel had to be driven towards Station Mid. Prior to taking out the remaining 2 rock pillars, concrete columns must be built in the center pilot tunnel. The construction of these pillars can be seen in Figure 12. Due to the slopping rock level towards Liseberg, the remaining 25 m will be excavated applying NATM/SCL principles from within the trumpet.

Station Mid

The excavation for the mid-section of Korsvägen Station, which lies in Lera clay, will be retained by a combination of a secant pile wall and interlocking 900 mm steel piles (see Figure 13). Some of the surrounding buildings are based on wooden piles, requiring a constant groundwater level of 2 m below ground level. To keep the groundwater level constant

Figure 12. Pillars in the Center Pilot.

during construction the water inflow interrupted by the retaining structure will be pumped out on one side of the excavation and fed back into the soil on the side facing away from the hillside. Permanent water ways will be established within the bottom slab of the station.

Figure 13. Korsvägen station mid construction layout.

Excavation was completed in mid-2023. Currently uplift ankers are being installed and preparation for casting the first section of the base slab are ongoing (Figure 14).

Station West

Station West is being excavated from access tunnel 206. As Figure 9 shows numerous other caverns and tunnels must be excavated in addition to the trumpet and the track and service tunnels running west towards Haga. Some of the caverns are up to 35 m in height. Due to the large cross-section required by the 4 tracks, three pilot tunnels had to be constructed first. As in Station East, concrete pillars have now to be installed in the center pilot prior to taking out the remaining rock pillars. Due to the low overburden in some areas, 6 to 8 m only, intensive grouting works had to be carried out and numerous ankers as rock support had to be installed. Excavation of the service and track and tunnel towards Haga will be completed before respectively after the end of this year.

Figure 14. Korsvägen station mid construction pit.

3 DESIGN

The design for rock tunnelling is provided by the Client. The design for all open excavation is provided by a consultant appointed by the joint venture. As a part of the 3D design of the Design & Build contract, which is carried out concurrently with the construction work, the individual specialist models are joined to form a coordination model that serves to identify discrepancies between the individual specialist designers. Due to the parametric structure of the specialist models, design changes can be implemented efficiently, since the 2D drawings to be derived are automatically updated as views and sections from the model. Once the specialist models have been created using the corresponding authoring software, they are uploaded to BIM360Glue, combined, and automatically converted into the native Navisworks format NWC within the complex software landscape. Finally, detailed attribute and collisions checks are performed via Navisworks. The attributes provide information about release status, calculation reference and quantity of individual components, among other things.

Visualizations support decision-making and create a uniform understanding of the envisaged construction project during the execution phase. The model, which is divided into viewpoints, is also available to site management team members who are away from the site via tablet PCs.

4 TUNNELLING IN ROCK - THE SWEDISH WAY

4.1 *Tunnel cycle*

The working stages on Swedish tunnelling projects are basically the same as on any other conventional tunnelling project. The biggest difference, however, is in the tunnel lining. Normally an in-situ concrete inner lining is used, which is designed as a watertight concrete construction or provided with a sealing layer between the sprayed concrete outer

lining and the inner lining. This type of lining is generally not used on Swedish tunnelling projects. The Swedish tunnelling philosophy is based on using the rock as the final lining as far as possible. To reduce the groundwater and tunnel water inflow during the construction phase, but also permanently in the final state, as far as possible, the tunnelling activities are accompanied by discontinuous cement mortar grouting. The usual tunnelling cycle, consisting of drilling, charging, blasting, ventilating, mucking, scaling, installing of rock support and surveying is extended by operations that are necessary for pre-excavation grouting. The additional operations vary depending on the grouting class. In grouting class 3 the additional operations consist of

1. Drilling the first grout curtain holes
2. Injecting the first grout curtain
3. Drilling the second grout curtain holes
4. Injecting the second grout curtain
5. Drilling for water loss measurements
6. Measuring the water loss in the borehole
7. Evaluation
8. Decision: tunnelling/new injections

As a rule, an injection process is carried out approximately every 15 to 18 tunnel meters. Accordingly, the injection process takes place after every third round in the case of a regular round length of 5 m.

Each grout curtain consists of at least 30 boreholes, depending on the cross-section of the excavation. The boreholes are approximately 30 m long so that the grout curtains overlap. Figure 15 shows the drilling works.

Although the rock prevailing in Gothenburg consists mainly of very competent gneiss and has relatively few fault zones, sealing the fissures and cracks with cement injections as mentioned above is a very complex procedure, which can also have an extreme effect on tunnelling. For example, temperature has a great influence on the curing time of the grouting material, so that the usual curing time of six hours in winter must be extended considerably. In addition, the tunnel grouting process is on the critical path of the tunnelling. If the strict water tightness criterion is not met when measuring the success of the grouting operation, the additional grout curtain has a direct effect on the duration of the tunnelling works.

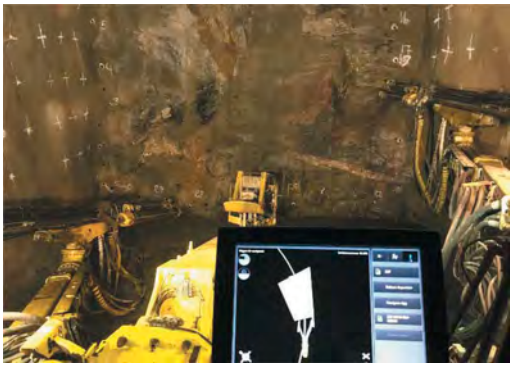

Figure 15. Drilling a grout curtain.

4.2 *Requirements on watertightness*

Since the existing rock is used as a permanent structure and designed with a service life of 120 years, high demands are made on the tunnel lining. The strict water loss criterion should be mentioned in this connection. Once a grout curtain has been completed, six to twelve boreholes are drilled into the working face, depending on the excavation cross-section. Then packers are placed at the borehole and exposed to water pressure. The water loss per borehole must not exceed 0.05 l/min and borehole meter while applying 1 MPa. The total amount of water lost per grout curtain, however, must not be more than 4 l/min.

To meet the requirements, the borehole grout must be capable of withstanding the injection pressure for ten minutes. In addition, a very low injection pressure (approx. 1-10 bar) is specified, which is to prevent the fissures in the rock from splitting apart (see Figure 16). The strict criteria are intended to avoid a permanent lowering of the groundwater level and above-ground settlements that may occur as a result thereof and to reduce the water ingress as far as possible.

Figure 16. Grouting unit during the injection of a grout curtain.

5 PARTNERING

A special feature agreed between the Client Trafikverket and the West Link Contractors Joint Venture is partnering, a collaborative management approach both parties wish to use on the construction project. At the outset of the project, the parties jointly developed a collaboration model comprising five key elements: health & safety, innovations, impact on the surroundings, a common project culture, construction costs and construction time (see Figure 17).

Figure 17. One project culture.

These five keywords represent the goals that each project employee is to incorporate consciously into his or her daily work. One example is the common project culture. Project days are held at regular intervals and everybody from miners to suppliers and external consulting engineers to the project manager are invited to participate.

In addition, team building is also greatly encouraged by the long coffee breaks that are common in Sweden.

The collaboration even goes to such lengths that the Client and the Contractor share the construction offices. Care is taken to ensure that persons having the same position on Trafikverket's side and on the WLC's side share one room. This keeps lines of communication as short as possible and increases cooperation.

6 CONTRACT MODEL

Within the contract, based on the Swedish ABT06 standard, two contract models and two payment mechanisms are used - whereby all open cut structures are executed under a Design & Built Model with a Target Price payment mechanism and all tunnel works are executed under a Built-only model with a re-measured Bill of Quantity payment mechanism.

The total direct and indirect costs of all works are considered variable costs. On top of that, a fixed remuneration is paid. This fixed part must cover some specified costs plus overhead and profit.

Conditions prior to tender submission stipulated that the Fixed Part must not exceed 12 % and that the costs for the tunnels (BoQ-part) must not exceed 30 % of the total variable costs.

Finally, the whole reimbursement model does include a pain/gain mechanism of 80/20. Should the final costs exceed the final target, the overrun would be shared between the Client and the Contractor according to the percentages mentioned, likewise any saving would be shared on the same percentages.

7 SUMMARY

The project mentioned is using a pre-grouting method in the rock tunnel section. The grouted rock formation is the permanent lining for a 120-year life cycle. The conclusion can be drawn that these activities need to be carefully executed to ensure that the requirements are met. Otherwise, groundwater could still infiltrate the tunnels, affecting the settlements of the older properties in central Gothenburg. Due to the complexity of the works and the methods to be carried out, especially considering the varying geology throughout the alignment, a number of challenges had to be met. As of today, all open construction pit retaining structures are completed, rock tunnelling is well under way and constructing the permanent structures in Almedal and Korsvägen Station Mid are underway/have started.

The contract model with a combination of Built-only and Design & Build with different payment mechanisms for the rock tunnel sections and the open excavation areas embedded in a target price payment model poses some manageable challenges.

REFERENCES

Baum, N., Boxheimer, S., Krause, D., Renz, F., 2019 Sprengvortrieb und Spezialtiefbau in Göteborg [Drill & blast and special foundation in Gothenburg]. In: Bautechnik 96, Issue 7, pp 549–557.

Tunnelling for a Better Life – Yan, Celestino, Thewes & Eberhardt (Eds)
© 2024 The Author(s), ISBN 978-1-032-80042-4
Open Access: www.taylorfrancis.com, CC BY-NC-ND 4.0 license

The cross river rail project as a PPP model in Brisbane, Australia. Experiences in cavern construction for 3 underground stations and tunnelling with double shield machines

Klaus Rieker*
Wayss & Freytag Ingenieurbau AG, Frankfurt am Main, Germany

ABSTRACT: Cross River Rail is a new 10.2 km long railway line, comprising of twin 5.9 km tunnels (excavated by TBMs and roadheaders) under the Brisbane River and the city center. It encompasses in addition 4 new stations (3 underground in 280 m long caverns excavated by roadheaders) and ramp structures at both ends as transition points to the existing rail system. Most of the route lies in stable rock such as sandstone, tuff or phyllites. Because of this, and to minimize the impact on the city center during construction, mining methods have been used wherever possible. On 2 stations, temporary access shafts were constructed next to the tunnel alignment due to existing railway lines and pedestrian zones respectively and fully enclosed by temporary buildings to reduce noise and enhance safety. Two station caverns were fully excavated by the time the TBMs reached respective locations. In the third station cavern, only the top heading was excavated and the TBMs mined through the lower cross section. The station caverns will be accessible via entrances located adjacent and will be connected by short tunnels. Construction is being carried out within the framework of a PPP model. The contract was awarded on 1 July 2019. To date, all tunnelling and inner lining works in the caverns are completed; rails in the running tunnels are installed and fit-out works in the stations and tunnels are well underway. The presentation will focus on tunnelling, cavern and shaft construction and the innovative method of casting and installing the mezzanine slab made of precast beams within the caverns.

Keywords: Tunnelling, Caverns, TBMs, Roadheaders, Lining, Precast

1 PROJECT OVERVIEW

As the population of South-East Queensland grows, the current rail network is reaching its capacity limits and is also constrained by a single river crossing in Brisbane and only four inner-city stations. This creates a bottleneck that limits the ability to run more trains.

A new rail link is therefore being built under Brisbane's city centre with the Cross River Rail project. Cross River Rail is a new 10.2 km long railway line from southern Dutton Park to northern Bowen Hills, comprising two 5.9 km tunnels under the Brisbane River and the city center [1]. The main components are four new stations and the associated single-track tunnels as well as the ramp structures at the transition points to the existing rail system (Figure 1).

Most of the route lies in stable rock such as sandstone, tuff or phyllites. Because of this, and to minimize the impact on the city center during construction, mining methods have predominantly been used. Approximately 4 km of the tunnel tubes were driven with two double shield machines. The remaining tunnelling sections, as well as most of the station caverns, were excavated with roadheaders.

At the Albert and Roma Street stations, the TBMs were pushed or driven through the previously (partially) excavated caverns. The access shafts at the individual stations were all enclosed with large sheds to reduce noise emissions and to have as little impact as possible on the surrounding area and enable 24-hour operations.

Furthermore, four caverns at the Boggo Road, Woolloongabba, Albert and Roma Street stations were excavated using roadheaders as well as blasting and rock hammering. Especially at the Albert and Roma Street stations, the mined construction method was necessary to reduce the impact on the densely populated surrounding areas.

The construction project is being carried out within the framework of a PPP model by a joint venture of CPB Contractors, BAM International Australia (with Wayss & Freytag Ingenieurbau AG as internal partner), Ghella and UGL Engineering (CBGU JV).

*Corresponding author: Klaus.Rieker@wf-ib.de

DOI: 10.1201/9781003495505-431

Figure 1. Overview of tunnel excavation. Roadheader tunnels from Woolloongabba to Boggo Road. TBM tunnels from Woolloongabba to Northern Portal.

The contract was awarded on 1 July 2019.

2 STATION CAVERNS

2.1 *Excavation and support*

The caverns of the Albert and Roma Street stations as well as the launch caverns at Woolloongabba were designed with the same internal cross-section. The main differences are the primary and permanent lining as well as the tunnelling and excavation methods used, depending on the station configuration and prevailing ground conditions. Furthermore, the overburden, the location and configuration of the station structure as well as the planned surface development were considered.

All station caverns were excavated using roadheaders. In areas of stable rock, the heading was divided into two sections. In areas with lower strength or where fault zones were present, the excavation of the heading was divided into three sections. Fiber shotcrete and rock bolts were used as support measures. In some support classes, reinforcement mesh was also installed.

2.2 *Roma Street Station*

Roma Street Station is the central connection point for train and bus services in Brisbane and the surrounding area and connection for Suncorp Stadium and the future Brisbane Live arena, both venues for the 2032 Olympic Games. The new station building is being constructed next to the existing bus station, whose operations are maintained during construction. At the beginning of construction, an existing multi-story carpark was demolished, and an acoustic shed was constructed around the temporary access shaft ahead of cavern excavation (see Figure 2). Here, too, the tunnelling work was physically separated from the progressing demolition work and construction of the station buildings.

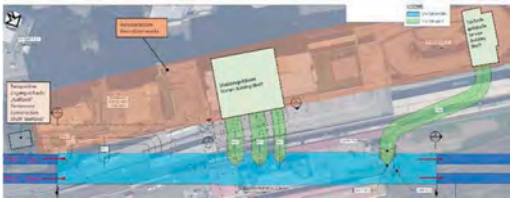

Figure 2. Roma Street cavern and access adits.

The excavation of the cavern took place with roadheaders in the heading, as well as drill and blast in the bench, invert, and the access adits. Here the ground consists of the NFG group with decreasing strength in the northern section of the cavern. After completion of the excavation, the TBMs were pushed through the cavern on rails with a skidding system. The inner lining was then constructed while TBM tunnelling continued. This required a great deal of coordination of the logistics flows within the cavern. For this purpose, one of the existing tunnel tubes was temporarily closed and the supply of the TBM limited to one tunnel by means of multi-service vehicles. Due to the required supply lines and the conveyor belt, only the invert slab could be constructed.

2.3 *Albert Street Station*

Albert Street Station is in the center of Brisbane in a heavily built-up area with many high-rise buildings. Subsequent access to the underground station is via two station buildings that blend into the surface development. During construction, a temporary access shaft with an acoustic shed was built (Figure 3 - Lot 2). In this way, the construction, and logistics processes of excavating the cavern and construction of the station buildings could be physically separated. Due to the confined space in Brisbane's city center, sections of Albert Street were closed to road traffic and a pedestrian gantry enclosure was constructed under the elevated site facility. In this way, pedestrian throughfare could be maintained.

Figure 3. Albert Street cavern and access adits.

The acoustic shed of the cavern's access shaft contained, in a compact space (see Figure 4), the temporary storage and removal of spoil, delivery of all required materials (for example shotcrete, reinforcement), a water treatment plant, a workshop and general storage areas. As the only access point for the excavation of the cavern, the access shaft was a logistical challenge. Material and construction equipment as well as the skip bin for the spoil were lifted into the shaft with the help of a gantry crane inside the hall.

Figure 4. Lot 2 – access shaft to Albert Street cavern and acoustic shed.

The excavation of the cavern in Albert Street is done in sections heading, benching, and invert. In this process, the heading is divided into two sections in the southern cavern and into three sections in the northern cavern. The heading was excavated using roadheaders. The predominant ground was the Neranleigh-Fernvale group (NFG), consisting of phyllites interbedded with quartz layers. The varying rock strength results from the different degrees of weathering of the rock.

The permanent shafts for the station buildings were secured with bored piles and excavated with excavators and drill and blast. The simultaneous blasting in the shaft of Lot 1 with excavation of the cavern and advance of the TBM around and in the Albert Street cavern led to an increased coordination effort between the different teams. In addition, the excavation depth of the Lot 1 shaft had to be limited to ensure the stability of the adjacent rock between the shaft and the tunnel and cavern during the advance of the TBM through the cavern.

2.4 *Woolloongabba start-caverns*

The station in Woolloongabba is the connection of the Gabba Stadium, another venue for the 2032 Olympic Games, to the train network. As the starting point of the mined and TBM tunnels, the construction site facility in Woolloongabba had the largest area. In addition to the logistics areas of the TBM tunnels, the roadheader tunnels and the station building, it included the station box with a temporary access ramp for access to the tunnel drives. After completion of the excavation work and concreting of the base slab, the lower station wall was erected to separate the work on the station building from the logistics of the tunnel drives.

The excavation of the caverns was done with split heading, bench, and invert with roadheaders and with rock hammer. The excavation here was mainly in NFG and Brisbane Tuff in the northern cavern. Defects in the rock of the invert had to be excavated in the area of the later railway line and replaced by concrete.

As shown in Figure 5, mined tunnelling was started in the southern cavern. The TBMs were assembled and started in the northern cavern.

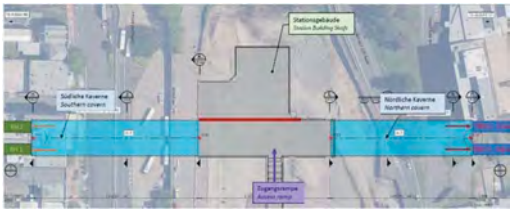

Figure 5. Woolloongabba cavern and station box.

3 MINED TUNNELS

The tunnels from Woolloongabba south to Boggo Road Station were excavated using conventional construction methods with the aid of roadheaders. The primary support of the mined tunnels consists of Swellex anchors and PP fiber shotcrete.

As in the other stations and the start caverns, the predominant ground at the beginning of the excavation is the NFG group with very high strengths in areas with increased quartz veins. In these sections, the excavation method was changed from a pure roadheader excavation to excavation with rock hammer. Here, the profile continued to be trimmed using the roadheaders after the cut length had been reached.

The ground first changed to sandstones and conglomerates and then to Brisbane Tuff. These have significantly lower strengths, so that tunnelling could be carried out entirely with roadheaders. In the NFG area, cut lengths of five meters were achieved, and in Brisbane Tuff 2-5 meter cut lengths were achieved.

The mined tunnels were connected with a total of three permanent cross passages spaced at approximately 250 meters, and three additional temporary cross passages, which were used as logistical hubs during excavation to enable the subsequent construction of the inner lining in the southern cavern and the tunnels.

4 TBM TUNNELS

4.1 *Main drives*

The two 4.2 km long tunnels from Woolloongabba to the Northern Portal were excavated with two double shield machines with an excavation diameter of 7.23 m. The two Herrenknecht machines were already used in the Sydney Metro 2 project with a slightly smaller diameter and were adapted to the required excavation diameter with a new shield and cutting wheel for the Cross River Rail project. The tunnel section includes the two approximately 300 m long station caverns as well as the cross passages 4-16.

From a geotechnical point of view, the excavation can be divided into four sections. The launch at Woolloongabba and the first section were in Brisbane Tuff rock with a strength of up to 175 MPa. Before cross passage 6, there was a fault zone at the transition from Brisbane Tuff to the sandstone and conglomerates with potential water inflow from the Brisbane River and thus marks the starting point of the river crossing. The section of the river crossing extended through the low point at cross passage 7 to the next transition before cross passage 8. From there on, tunnelling was in the NFG grouping. Other features of tunnelling included crossing the Albert Street cavern with little to no overburden, advancing the TBM in the Roma Street cavern using a jacking system and tunnelling towards and at the northern portal with reduced overburden below the tracks of the existing railway network.

The tunnel lining consists of six segments per ring with a large keystone. The main part of the tunnel lining consists of steel fiber segments. Reinforced concrete segments were only used around the cross passages and in the area of the station portals. In addition, highly reinforced segments were installed in the tunnel of the first drive where significant load surcharges were anticipated.

The annular gap was filled with a two-component grout. The segments were equipped with grouting sockets at which a hole could be drilled into the segment shell to further grout the annular gap under pressure at a later stage, if required. These grouting sockets would then be sealed watertight with suitable caps.

Driving in double shield mode allowed simultaneous excavation and ring building. As a result, advance rates of more than 60 m per day were achieved with the TBMs. Due to the fracturing of the layered rock in the NFG, high advance rates were achieved despite high rock strengths. Despite the high quartz content, the wear and tear of the

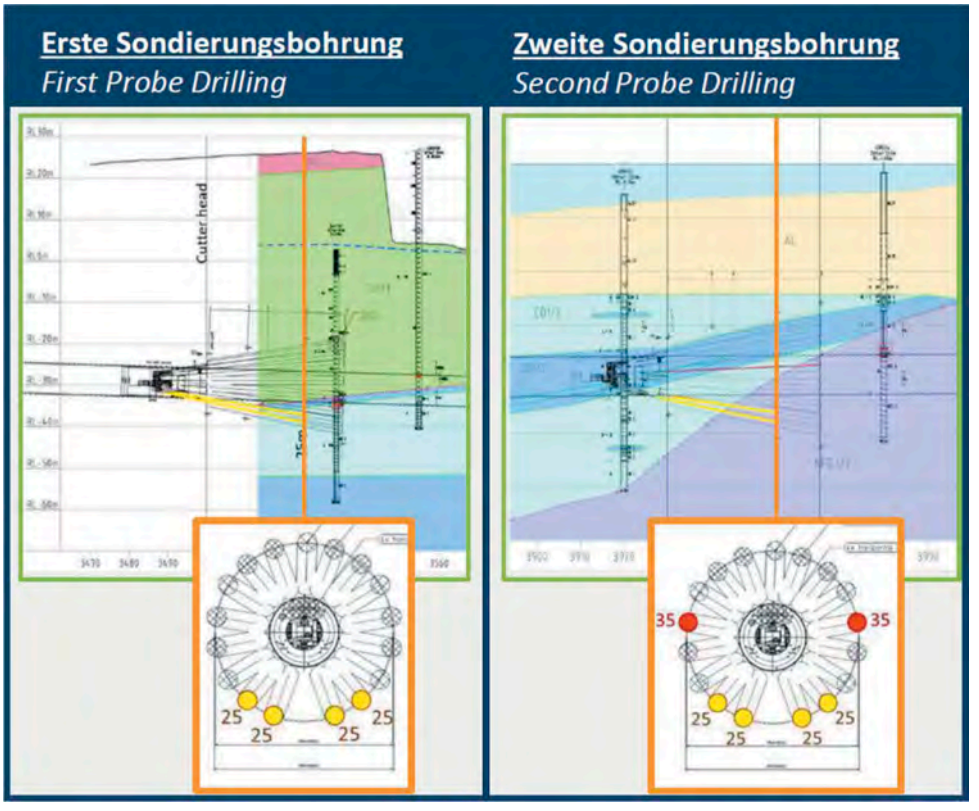

Figure 6. Probe drilling in both fault zones.

excavation tools was also low, with 1-2 maintenance stops per week.

4.2 *Brisbane river crossing*

Prior to confirming the methodology to cross the Brisbane River, the team undertook intensive risk assessments and detailed modelling to ensure all risks could be effectively mitigated. The river crossing was carried out with an open dewatering system. The geotechnical report showed two excavation sections with an increased risk of larger water inflow in the area of the river crossing (see Figure 6).

The first section was in the fault zone at the transition between the Brisbane Tuff and the Aspley Formation consisting of sandstone and conglomerates at the beginning of the river crossing. The second section was located at the end of the crossing between the Aspley Formation and the NFG grouping. Both sections carried the risk of water pathways to the Brisbane River with water inflows of more than 40 liters per second.

Based on the expected water volumes, a multi-stage concept for dewatering during the river crossing was developed:

1. Increased dewatering capacity on the TBM and at the tunnel low point including an emergency dewatering system consisting of additional pumps, pipelines, and an additional sediment pond.
2. Probe drilling in the fault or transition zones.
3. Grouting of the ground to seal the fault zones in the event of increased water ingress from the probe boreholes.
4. Sealing of the TBM: telescopic shield, gripper shoes, muck ring.

Two additional submersible pumps with a pumping capacity of up to 50 liters per second were installed on the TBMs. These were connected to two additional DN150 pipes that drained directly into the sediment pond. One of the pumps was installed in the front shield of the TBM, the second was attached to the Gantry 1. However, the water inflow that occurred was low enough and was pumped out with the standard dewatering.

During tunnelling with TBM 1, probe drilling was carried out up to 35 m in front of the cutterhead at both fault zones. As both fault zones were expected to be at an upward angle to the face, probe drilling was mainly carried out in the bottom of the TBMs (see Figure 6).

In both cases, the drilling parameters and the borehole flushing water showed clear signs that the fault zone had been encountered. In both cases, however, no significant water inflow was measured from the probe boreholes. In addition, during excavation through the two sections and throughout the river crossing, only a small increase in water inflow was detected, which could be managed using standard dewatering. Grouting of the ground and sealing of the shield were therefore not necessary.

4.3 *Albert Street cavern crossing*

The cavern heading was 90 per cent excavated at the time the TBMs arrived, so TBM excavation in the cavern took place with little or no overburden. Figure 7 (left) shows the cross-section of the cavern with the actual state of the excavation depth of the heading.

The low cover caused the rock to break up into large blocks (Figure 7 - right). These were removed as far as possible from the surface with the help of an excavator to prevent damage to the conveyor belt. The ventilation system was adapted during excavation to increase its capacity, with the help of water curtains and scrubbers.

5 MEZZANINE BEAMS AND INSTALLATION

In the three station caverns at Roma and Albert Street as well as at Woolloongabba, the mezzanine level was constructed with precast concrete beams.

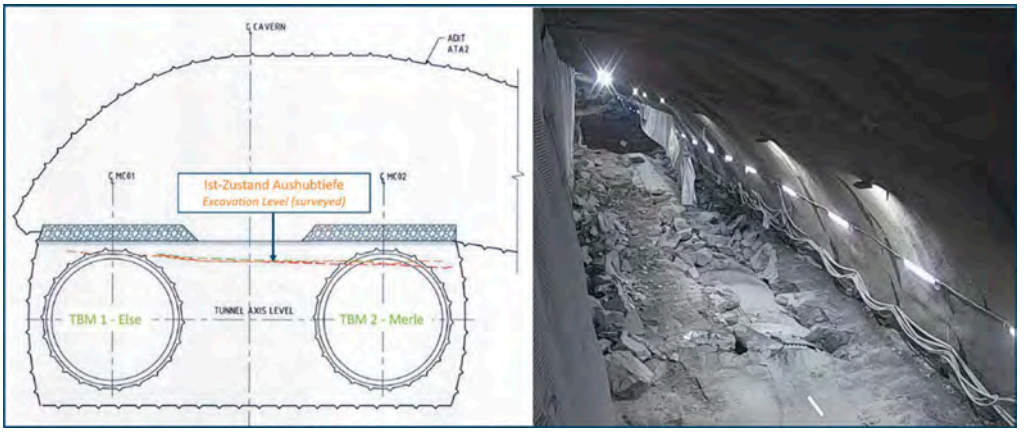

Figure 7. Cavern excavation level. Break-up of cover in Albert Street cavern during TBM excavation.

Figure 8. Mezzanine precast beam factory.

Figure 9. Loader for mezzanine beam installation.

The manufacturing of the beams took place about 400 km south of Brisbane in a dedicated precast yard (Figure 8). Due to the span width of about 20 m and large openings in the mezzanine slab for escalators, an innovative match-cast system was used. Each beam was cast directly against the previous and later installed in the same sequence. Since the beams had to be transported into the caverns via the temporary access shafts, each beam consisted of three sections. For the installation, 2 special loaders (Figure 9) and transport vehicles were manufactured and employed.

6 CURRENT STATUS

TBM Tunnelling on the Cross River Rail project was commenced in early 2021 and completed before the end of the year. All remaining excavation was completed in 2022 in line with project planning. Extensive settlement measurements were carried out in the zone of influence of the tunnel drives. Especially in the heavily built-up inner-city area, the influence could thus be monitored and minimized. Settlements measured in the stations caverns above the alarm values were examined in more detail with all parties involved and no damage was detected throughout tunnelling.

In the Albert Street and Roma Street areas, pedestrian flows were successfully rerouted and enclosed, minimizing the impact in the heavily trafficked inner-city areas. In addition, noise levels and vibration measurements were taken at the surface in the heavily built-up areas. Based on this data, the working hours for certain activities were adjusted. In addition to minimizing the impact on the environment, very great importance was attached to the integrity of the population and neighboring buildings, as well as to occupational safety during construction. Despite the large number of employees and subcontractors, the project had no major incidents.

As of October 2023, all station caverns are fully lined with cast-in-place concrete, all mezzanine precast concrete beams are installed and the fit-out works in the caverns are well underway. Within all tunnels, the tracks are laid and the installation of cables, water mains and safety walkways are well underway. Within all station buildings, fit-out works are ongoing. At the southern end of the project, near Boggo Station, a pedestrian bridge with a cable suspension section in the middle was erected over live railway lines. The northern ramp was already handed-over and overall works are proceeding in line with having 1st Train in the tunnels from there to Roma Street Station in April 2024.

REFERENCES

[1] https://crossriverrail.qld.gov.au/about/project-overview/

Tunnelling for a Better Life – Yan, Celestino, Thewes & Eberhardt (Eds)
© 2024 The Author(s), ISBN 978-1-032-80042-4
Open Access: www.taylorfrancis.com, CC BY-NC-ND 4.0 license

Mechanized shaft sinking with VSM: Developing underground space for U-Park® systems

Peter Schmäh*, Stefan Frey & Marc Peters
Herrenknecht AG, Schwanau-Allmannsweier, Germany

ABSTRACT: In view of the increasing number of megacities worldwide and the growing population living in urban areas, space on the surface is becoming increasingly scarce and correspondingly more expensive. To ease the inner-city parking situation, new space can be developed underground. The Herrenknecht U-Park concept is a combination of mechanized shaft construction using VSM technology and the subsequent installation of an automated parking system with the associated technical equipment.

As a new mechanized solution, the Vertical Shaft Sinking technology (VSM) has been developed to overcome challenging mixed ground conditions, high groundwater tables or economic limits in greater depths. For almost twenty years, the VSM technology has been in operation worldwide to build shaft structures for ventilation, tunnelling operations or mining applications. More than 100 circular shafts have been completed, mainly in difficult, groundwater-bearing soil, in depths of up to 115 meters. The VSM is completely remote-controlled from the surface and covers a diameter range from 4.5 to 18 meters. It meets the key requirements for shaft construction in inner cities: no complex groundwater lowering; maximum production accuracy and safety, both for the site crew and for surrounding buildings; and flexible arrangement of site equipment.

The advantages of mechanized shaft construction with VSM becomes more apparent the deeper the shaft is sunk. Shaft diameter and depth of a Herrenknecht U-Park system are planned and designed according to local requirements in terms of capacity, underground conditions and economic considerations. In Nanjing, the world's first underground parking garage built using Herrenknecht's proprietary VSM mechanized shaft sinking technology went into operation in 2022. This U-Park concept included the construction of two shafts (diameter 12 m, depth 65 m) and the installation of the automated parking system for a total of 200 vehicles on 25 levels.

Keywords: Shaft sinking, drilling, foundations, underground parking

1 INTRODUCTION

The Vertical Shaft Sinking Machine (VSM) was originally developed by Herrenknecht for the mechanized construction of deep launch and reception shafts for microtunnelling. After starting design and testing in early 2004, the first Herrenknecht VSM equipment went into operation in Kuwait and Saudi Arabia in 2006. The machine concept, fully remote-controlled from the surface, as well as its implementation on site proved to be an efficient solution right from the start for the safe and fast construction of shafts especially in difficult, inner-city environment without lowering the groundwater table. Deep shafts can also serve, for example, as ventilation shafts for metro systems, maintenance or collector shafts for sewage, or for underground parking systems as shown in Figure 1. With an increasing number of successful reference projects worldwide, the technology is becoming more and more well-known. The mechanized approach opens up a new technical solution for demanding shaft and foundation construction projects, to the benefit of project owners and planners.

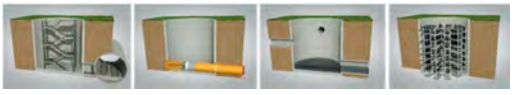

Figure 1. Overview of different applications for VSM.

The latest application of the mechanized shaft sinking with VSM is the construction of deep shafts for underground parking systems, called U-Park®. This automated solution for underground car parking system is ideal for cities with high density population, where the availability of parking places is limited and therefore expensive.

*Corresponding author: schmaeh.peter@herrenknecht.de

DOI: 10.1201/9781003495505-432

2 BENEFITS OF MECHANIZED SHAFT SINKING WITH VSM

Shaft construction companies often encounter difficult geological conditions such as high groundwater tables combined with layers of hard and soft material. The VSM technology can be used in almost all geological formations: from sand and clay to gravel and rock with compressive strengths of up to 140 MPa and below groundwater level with a hydrostatic pressure of up to 10 bar. It masters the main challenges associated with inner-city shaft sinking: safe working conditions for surrounding buildings and the environment, especially regarding potential ground settlement. There is an increased requirement to avoid the lowering of the groundwater level during the construction of shafts in order to avoid the associated settlement, which can affect a wide area. As with using the VSM the water level in the shaft is maintained close to the groundwater level outside the shaft, water flow is prevented which otherwise could cause ground movement. Furthermore, recultivation measures caused by groundwater lowering are not necessary anymore.

In addition, deep shafts and foundation structures need special attention for the safety of the operating personnel. All installations, including the lining erection, are remote-controlled from the surface. No personnel has to enter the shaft until it has reached the final depth and is fully secured. In general, mechanized shaft sinking requires less personnel and machinery on site, which leads to minimized risk exposure.

Simultaneous excavation and shaft lining facilitate high advance rates and shortened overall project duration. At the same time, continuous performance ensures overall high planning reliability for all stakeholders. The lining of a VSM shaft consists of either precast segments or cast-in-situ concrete. As the lining installation is completed on the surface, high quality installation can be accomplished, leading to greater accuracy of the whole shaft structure. In most cases, a secondary, time-consuming lining is not required, resulting in a reduced wall thickness of the shaft and, thus, less soil excavation.

Furthermore, each VSM type is very flexible as its excavation diameter can be adjusted within a specific range. A VSM12000, for example, can cover shafts with inner diameters ranging from 5.5m to 12.0m and is, therefore, a one-time investment for multiple use.

3 VSM EQUIPMENT AND SHAFT SINKING PROCESS

The VSM consists of two main components (Figure 2): the excavation unit and the lowering unit. The excavation unit systematically cuts and excavates the soil and consists of a cutting drum attached to a telescopic boom that allows excavation of a determined overcut. The lowering unit on the surface stabilizes the entire shaft construction against uncontrolled sinking by holding the total shaft weight with steel strands and hydraulic jacks. When one excavation cycle is completed, the complete lining can be lowered uniformly and precisely.

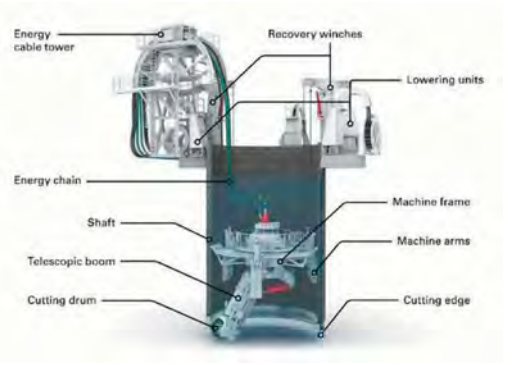

Figure 2. VSM components of equipment.

A slurry discharge system removes the excavated soil with the help of a submerged slurry pump which is located directly on the cutting drum casing. It transports the water and soil mixture through a slurry discharge line to a separation plant on the surface. The whole operation is controlled by the operator from the control container on the surface, without the necessity to view the shaft bottom or the machine. Power supply for the submerged VSM is secured by the energy chain. After reaching its final depth, the VSM is lifted out of the shaft by the recovery winches and the jobsite crane. All installation steps are shown in Figure 3.

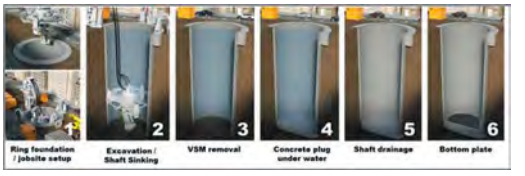

Figure 3. Installation steps of shaft sinking with VSM.

3.1 *The shaft lining*

In most cases, the shaft lining consists of precast concrete segments installed at the surface. The ring building process is comparable to segment lining in tunnelling. The ring is built at the surface with support of a crane. The number of segments depends on the shaft diameter. Ring building work includes the proper connection of the rings by anchors and bolts, which can be handled from outside the shaft. The excavation process of the VSM is not affected by the ring building process. This increases the shaft sinking performance significantly.

Alternatively, in-situ concrete casting of the shaft walls is another solution, especially for larger shaft diameters where segment handling becomes more difficult. In this case, the progress of shaft construction works is slowed down by the necessary time to

build the formwork and the setting time of the concrete structure. The benefit of in-situ casing is the "continuous" structure without joints and the possibility to integrate entire entry and exit structures, e.g. for microtunnelling activities in the shaft walls.

3.2 *Jobsite arrangement in inner-city conditions*

Depending on the space conditions on site, the VSM components can be positioned flexibly to suit local circumstances (Figure 3). As most sites are located in heavily built-up urban areas, the access for logistics, e.g. trucks, ring segment stock or soil disposal, is limited. Special concepts to relocate components such as the separation plant already exist for this purpose and can be discussed if required.

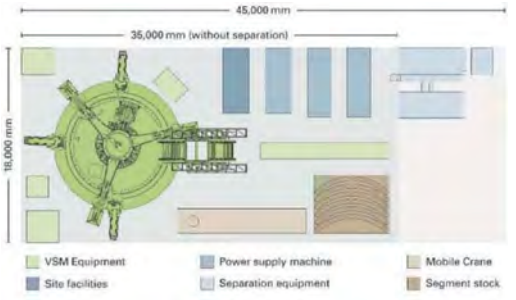

Figure 4. Exemplary layout of a VSM jobsite.

In 2019 and early 2020, a VSM machine has been in operation to sink a total of three shafts in extremely confined space conditions in Barcelona, the capital of Catalonia, Spain. The three shafts with an inner diameter of 9 meters and an outer diameter of 9.8 meters reached a depth of 43.5, 41 and 50 meters. A detailed planning of jobsite logistics was necessary to allocate the key components of the shaft sinking equipment in traffic surroundings and to assure continuous progress at the same time.

Figure 5. VSM Jobsite arrangement in Barcelona.

3.3 *Noise emissions*

An important point to be considered on inner city jobsites are the noise emissions impacts of the construction equipment and the process itself. On a general basis it can be stated, that shaft construction with VSM causes a significantly lower level of noise emissions compared to conventional shaft construction methods. During shaft construction, the main components of the VSM equipment work under water and are supplied with electrical power. Instead of using diesel generators, the electrical power for the VSM jobsite can be provided by the municipal power grid. Thus, a considerable reduction of noise emissions can be achieved.

Within the VSM system the components which create highest acoustic levels are the separation plant and the diesel generator. The flexibility of this equipment makes it possible to place it at a larger distance from the main system components if required, which makes it an advantage highly appreciated not only by contractors but also by residents in these areas.

3.4 *Mobility*

When a VSM is supposed to sink shafts on different construction sites within a city, a quick and smooth mobilization and demobilization of all VSM components and detailed logistics planning can be considered, not only before the construction start of the first shaft, but also for disassembly, transport and installation of the VSM equipment on subsequent locations. After completion of the shaft, disassembly and assembly of the equipment on next location can take place simultaneously, because of the flexibility and compact design of the VSM equipment.

4 THE U-PARK® CONCEPT

In view of the increasing number of megacities worldwide and the growing population living in urban areas, space on the surface is becoming increasingly scarce and correspondingly more expensive. For this reason, urban planners see the future of infrastructure and logistics underground. This applies not only to supply and disposal networks in major cities, but also to the further development of sustainable traffic infrastructure.

To ease the inner-city parking situation, new space can be developed underground – with positive effects on the environment and on people's quality of life. The smart Herrenknecht U-Park concept is a combination of mechanized shaft construction using VSM technology and the subsequent installation of an automatic parking system with the associated technical equipment. The number of parking lots per system depends on the diameter and depth of the shaft and on the expected car sizes (Figure 6).

Figure 6. Shaft sizes and exemplary U-Park® capacities.

In order to use the available space as economically as possible, the shaft diameter and depth of a U-Park system are planned and designed with the respective local requirements, environmental conditions and user-friendliness in mind. Building the deepest possible shafts is a key factor in enabling maximum parking space capacity per U-Park facility and meeting cost-effectiveness requirements.

4.1 *Benefits of the U-Park® concept*

Shifting stationary traffic underground not only alleviates congestion but also offers a multitude of benefits. It effectively eliminates the need for drivers to endlessly circle in search of parking spaces, significantly enhancing the quality of life and safety for both motorists and residents.

This innovative approach also minimizes space requirements, opening up exciting new design and utilization possibilities for above-ground areas, particularly in locations where ground space is exceptionally limited and costly. This concept is particularly advantageous when repurposing outdated parking garages, transforming them into modern, underground parking systems.

Figure 7. Exemplary use of the U-Park® as foundation structure.

4.2 *Shaft construction*

The mechanized shaft sinking approach enables a compact and efficient jobsite setup during construction, as described above, even in tight spaces and densely built-up urban areas. Thanks to the safe mechanized shaft sinking technique, it can be executed in various ground conditions, including high groundwater levels. This makes it a versatile and practical solution for urban mobility challenges. The advantages of mechanized shaft construction become more apparent the deeper the shaft is sunk.

4.3 *Installation of the automatic parking system*

As soon as the shaft is completely finished, the automatic parking system and the technical equipment can be installed. Only the entrance and exit will later be at ground level: in the ground-level reception booth, the intelligent, computer-aided system receives the vehicle from the driver before the driverless car then glides down to a free space in the parking shaft. Matched to the overall capacity of the parking system and arrangement of the platforms, the system manages the parking and removing of vehicles with maximum efficiency and safety. The installation of charging stations for electric vehicles and the integration of car sharing services are also possible.

Access to the parking levels is not necessary and is therefore reserved for service personnel. This reduces the costly installation of lighting and ventilation systems to a minimum. The ground-level access and the simple handover of the car to a closed system not only benefit those with disabilities, but also significantly reduce the risk of property damage or other crimes in some older parking areas.

Figure 8. Surface installations and access design.

The design of the entrance and exit on the surface depends primarily on the size and capacity of the U-Park system. Reception booths can be integrated into new or existing buildings or building complexes and connected to local traffic management. The drive-in booths can be designed to be independent or integrated into building concepts as desired.

4.4 *U-Park reference project Nanjing, China*

The world's first underground parking system built by a VSM mechanized shaft sinking machine went into operation in Nanjing in 2022. The Herrenknecht U-Park for Nanjing concept included the construction of two shafts and the subsequent installation of the automated parking system. The system of two shafts (diameter 12 m, depth 65 m) can accommodate a total of 200 vehicles on 25 levels.

The first shaft was completed in February 2021, the second in May 2021. Installation of the parking system was completed by the end of 2021.

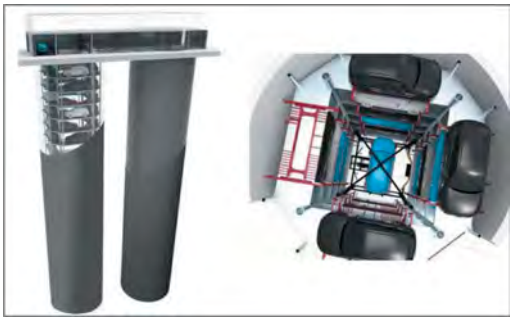

Figure 9. Overview of Nanjing U-Park® concept for 200 cars.

4.5 *Lack of space as major challenge*

The major challenges in Nanjing were the lack of space for placing the equipment, the risks of settlements since several infrastructures, such as offices buildings, were very close to the shafts to be built. Furthermore, a high accuracy of verticality of the shaft installation was required, since the distance between the two shafts was around 5 m.

Figure 10. VSM Jobsite arrangement in Nanjing.

With the implementation of VSM technology, all these challenges could be overcome. Its design was based on the most frequent challenges that clients and contractors face when constructing large-diameter deep shafts in highly populated areas. The modular configuration of some components of the VSM system allow to play with their placement on the jobsite, giving the advantage of reducing the final required footprint, avoiding the necessity of lowering the groundwater level, reducing the risks of settlements and therefore, the risk of damage the infrastructure in the area. Finally, its guidance system together with the lowering system to control each unit individually, allows the system to achieve a very high accuracy of the shafts.

5 CONCLUSION

The current and worldwide trend to construct more and more infrastructure underground, e.g. metro, road and railway as well as a large variety of utility lines, promotes a growing demand for the construction of shafts. With increasing shaft depths and groundwater levels, conventional shaft construction methods reach their technical and economical limits. The efficiency and benefits of mechanized shaft sinking in terms of budget, construction time and occupational safety have led to a total of more than 100 VSM projects where shafts have been successfully sunk. The VSM equipment design has been continuously further developed and adapted to a serve a growing range of applications, with ever larger diameters and in increasing depths.

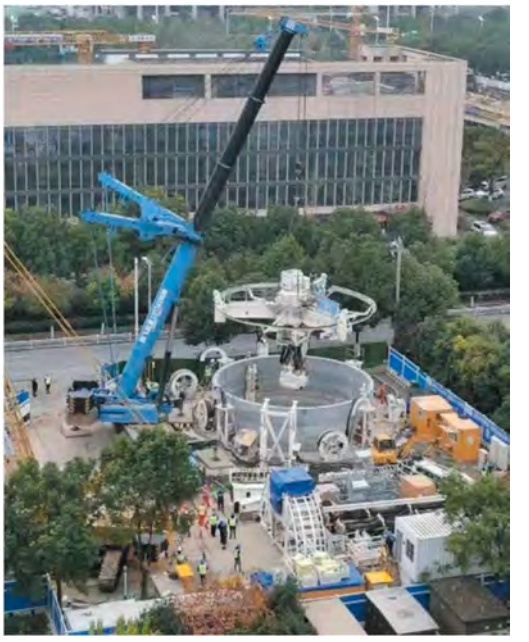

Figure 11. VSM lowered into start section of the first shaft.

Figure 12. Final U-Park® Building, Nanjing.

The future of underground parking facilities in large cities is poised for a remarkable transformation. With the integration of advanced digital processes for parking management, the hassle of finding a parking spot will become a thing of the past. Drivers will be able to effortlessly navigate to available spaces, reserve spots in advance, and seamlessly complete the parking process, all through their smartphones or vehicle systems.

Additionally, charging stations will be integrated into the infrastructure, providing convenient and accessible options for electric vehicle owners to recharge their vehicles while parked. This synergy of smart technology and sustainable mobility solutions will not only ease urban congestion but also contribute to a cleaner and more efficient urban landscape, shaping the cities of tomorrow.

REFERENCES

Schmäh, P., 2023. Game changers – VSM optimizes settlement control. Tunnelling Journal, April-May 2023, p 14–15.

Schmäh, P., Frey, S.; 2019. The role of mechanized shaft sinking in international tunnelling projects. Tunnel Business Magazine, April 2019 issue.

Tunnelling for a Better Life – Yan, Celestino, Thewes & Eberhardt (Eds)
© 2024 The Author(s), ISBN 978-1-032-80042-4
Open Access: www.taylorfrancis.com, CC BY-NC-ND 4.0 license

Snowy 2.0 – Implementation of a "twin numerical model" as computational tool of the "observational method" during the excavation of a large cavern under high in situ stress

Pier Luigi Tonioni*, Antoine Toussaint & Patrick Lignier
Tractebel Engie, Gennevilliers/Lyon, France

Karsten Thermann
Tractebel Engineering, Bad Vilbel, Germany

Angelo Lambrughi
WeBuild Group, Milan, Italy

Ivan Ching
Snowy Hydro Limited, Cooma, Australia

ABSTRACT: Snowy 2.0 is a major hydro power project currently under construction in Australia. This new development will increase the capacity of the existing Snowy Mountains hydro power scheme by 2200 MW, making it the largest source of renewable energy in Australia and one of the largest pumped-storage projects in the world.

The Snowy 2.0 Power Station Complex is excavated at about 720 m depth in high in-situ stresses and fair to good rock mass conditions. During the construction of the two underground caverns, the geological conditions at the basis of the design are systematically and continuously verified thanks to in-situ geological investigations, detailed geological mapping and monitoring measurements, in accordance with the so-called "observational method", allowing to perform design adjustments if and when the actual conditions would be differing beyond the expected design scenarios in a short time.

This article presents the main features of the observational method with a focus on the development of a "twin numerical model" of the Power Station Complex, to be regularly updated during the construction as more information becomes available from the continuing investigations and monitoring.

The development of the "twin numerical model" has for main objective to anticipate the behaviour of possible geological critical areas where the displacement of the rock mass is likely to locally yield the rock bolts which constitute the main support elements of the caverns. Once the possible critical areas are identified, specific monitoring instruments are installed in the most effective way, to identify the rockbolts that may exceed the design criteria.

Finally, depending on the actual monitoring results, remedial measures such as re-bolting may be necessary to comply with the design requirements.

Keywords: Large caverns, monitoring, twin digital model

1 INTRODUCTION

Snowy 2.0 is a pumped-storage hydro project that will generate 2200 megawatts to cover the peak demand of the network connected to the Snowy Mountains Scheme. The project links two existing reservoirs, namely Tantangara and Talbingo reservoirs, through around 27 km of tunnels and an underground Power Station Complex (PSC) at around 720 m depth (Figure 1).

Figure 1. Snowy 2.0 – project alignment.

*Corresponding author: pier-luigi.tonioni@tractebel.engie.com

DOI: 10.1201/9781003495505-433

During low demand hours, the excess of generated energy will be used to pump back the water from the lower reservoir (Talbingo at the western part of the PSC) to the upper reservoir (Tantangara at the Eastern part of the PSC), ensuring the storage of hydro-energy for peak demand hours. Emptying the upper storage reservoir from its full capacity at Full Supply Level could provide approximately 350 GWh of energy.

2 GENERAL CONTEXT

The project is developed and financed by Snowy Hydro Ltd, the owner and operator of the emblematic Snowy Mountain hydroelectric and irrigation scheme. The project construction was appointed to Future Generation, a Joint Venture between WeBuild (formerly Salini Impregilo), Clough and Lane Construction, under an Engineer, Procure and Construct (EPC) contract. Tractebel, together with partners, were contracted by WeBuild to develop the design of the civil works and Voith Hydro to design and procure the electro-mechanical equipment. Within the civil works design consortium, Tractebel is in charge of the design of the Power Station Complex.

The Power Station Complex (PSC) is an underground powerhouse housing six Francis reversible pump-turbines which can operate both in turbine and pumping modes. It includes the following structures: two main caverns, i.e., the Machine Hall (MH) at the eastern part of the complex and the Transformer Hall (TH) at the western part, six Busbar galleries (routing the connection cables between the generation units and the transformers) and six Draft Tubes tunnels (Figure 2).

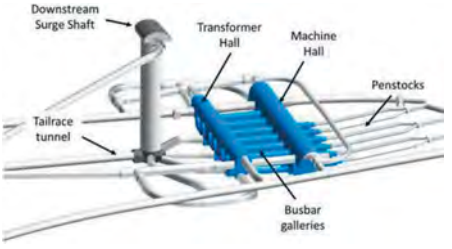

Figure 2. Power station complex (in blue) - general layout.

Other tunnels surround the caverns for waterway, main access, ventilation, emergency egress as well as construction purposes. The main excavation cross sections of the Machine Hall and Transformer Hall are shown in Figure 3.

The maximum length, width and height of the MH are about 250m, 32m and 52m respectively, and for the TH these are about 220m, 20m and 46m respectively. The distance between the two caverns is about 60 m. The six Busbar galleries are

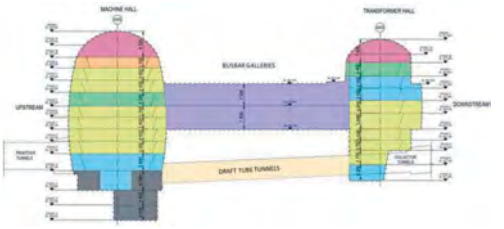

Figure 3. Power Station Complex cross-section.

perpendicular to the longitudinal axes of the MH and TH. The distance between two adjacent Busbar galleries is between 18 m and 19 m. The Busbar galleries are 10m wide and ~14.5m high. The Draft Tube tunnels are ~ 6m wide and ~6.5m high. Two main tunnels (Main Access Tunnel and Egress, Cables and Ventilation Tunnel) provide permanent access to the PSC. Both are excavated from the surface with two TBM of ~10 m diameter. From these main tunnels, Drill & Blast construction tunnels are carried out for the excavation works of the caverns.

3 GEOLOGICAL CONTEXT

The project area is situated within the south-eastern portion of the Lachlan Orogen (Fold Belt) of New South Wales (NSW), which comprises a suite of early Paleozoic Era (550-350 Million years ago) sedimentary, igneous and metamorphic rocks that have developed during several orogenic periods. These periods are associated with extensive faulting and have formed major geological structures through the area.

The Power Station Complex is situated at a depth of about 720 m below ground surface in the Ravine Beds Formation (Figure 4). The main lithology consists of interlaminated to interbedded siltstone/sandstone. Siltstones are predominant.

The rock mass is considered impervious with an average permeability of approximately 10^{-8} m/s.

The main geomechanical parameters considered in the development of the design are given below. They were derived from the outcomes of an outstanding, high quality campaign of geotechnical investigations carried out from the surface:

In-situ stress: the in-situ stresses were defined from over coring and hydro-fracturing/hydro-jacking tests carried out from the surface. The vertical stress at the location of the PSC is around 20 MPa, basically corresponding to the overburden. The major stresses are horizontal, with average values of K_H and K_h of 2.3 and 1.5 respectively.

Unconfined Compressive Strength of the intact rock (UCS): The main parameter governing the UCS value is the lithology. The siltstone being predominant, an UCS characteristic value of ~ 60 MPa was adopted.

Geological Strength Index: The GSI was evaluated from the observation of the boreholes at the

PSC area. Based on the statistical analysis, the average GSI value is equal to 72.

Other parameters such as intact rock modulus (Ei), Poisson ratio and mi were estimated to be 35 GPa, 0.25 and 8 respectively. The joint sets consist of two main families: (i) the bedding joints – almost sub-horizontal –, strongly prevalent, spaced approximately every 2 m, and (ii) tectonic joints – almost subvertical-, more widely spaced. The two joint sets include pre-sheared joints with low friction angle – 25° to 30° - spaced approximately every 10 to 20m. The joints are generally closed. The pre-sheared joints, bedding or tectonic joints, are considered weakness planes. A structural model's scheme of the rock mass is given in Figure 4.

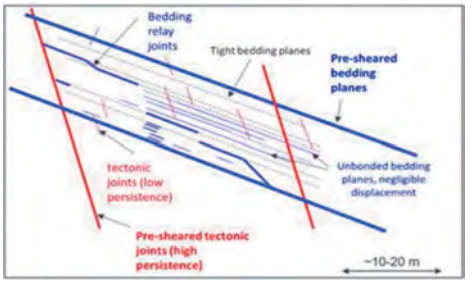

Figure 4. Structural model's scheme of the rock mass.

4 DESIGN APPROACH & CRITERIA

As mentioned in the previous section, the design of the rock support and global stability of the caverns is based on the geotechnical investigations (GIP 2019, 2020 and 2021) available during the design phase (i.e. the PD phase and the DD phase). Design assumptions were made regarding the geological and geomechanical model derived from the investigations.

On the basis of these design assumptions, the Detailed Design was developed to verify the global and local stability of the caverns, as well as the integrity of the rock support, mainly the rockbolts.

The design of the rock support for the PSC was based on the New Austrian Tunnelling Method (NATM), the resistance of the rock mass being preserved and increased by means of point-anchored, fully grouted rock-bolts, reinforcing the rock mass shear strength and multiple layers of steel fibres reinforced shotcrete.

No relevant Code or Standard exists for the design of such large deep underground caverns as the geological and geotechnical conditions govern the stability. Specific design criteria, compatible with the overarching principles of the Australian standards, were therefore defined and agreed with the Employer. The retained design criteria covered the following technical issues:

i. the general rock mass behaviour,
ii. the rock pillars stability,
iii. the rock wedges stability,
iv. the performance and durability of the rock-bolts.

The first three issues are not addressed in this paper. Readers may refer to [7] for a comprehensive discussion of these items.

The verification of the performance & durability criteria of the rock-bolts is developed therein and constitutes one of the main purposes of the "twin digital model".

4.1 *Performance & durability of the rockbolts*

Displacements of the rock mass under high stresses is likely to locally yield the rockbolts, in tension but also in shear when crossing weak geological joints. Rockbolts are verified for their structural integrity and durability. The long-term protection of the rockbolts is ensured by a "double corrosion protection" system, composed of HDPE sheath around the bar and grouting of the gap between the rockbolt and the borehole. After a series of tests, the following design criteria for the rockbolts were specifically defined:

- Maximum elongation strain: 2.5% for the primary rockbolts and 1.5% for the permanent rockbolts, based on an A_{gt} of 7.5%.
- Maximum admissible shear displacement at: 18 ~ 20mm for durability of permanent rockbolt (CT-M24 or CT26WR respectively) and 35 mm for structural integrity of both primary and secondary rockbolts.

5 THE OBSERVATIONAL METHOD

During the construction, the design assumptions are verified based on specific in-situ geological investigations during construction and actual observations (detailed geological mapping and monitoring measurements), also known as the "observational approach" during construction.

The main objectives of the observational approach are:

- to confirm (or update) the geological conditions and model;
- to confirm the validity of the design (for the actual geological conditions and model)
- to provide design adjustments if the actual conditions are differing beyond the expected design scenarios.

This observational approach is based on two processes:

- collecting during construction the geological, geotechnical and monitoring data;

– carrying out a "back analysis" process that involves the analysis of the design components (mainly the mechanical properties of the rock mass and joints, the in-situ stress, the displacements of the rock mass and joints, …) in order to confirm or update the numerical model and if required the design.

In general, the monitoring of the convergences of the caverns constitutes the most significant source of information of a behaviour of the structure during the excavation. To a large extent, the monitoring scheme of the PSC is devised to quantify those kinds of displacement including the direct and undirect measurements of the displacements of the joints and rockbolts. The measurements will be compared to the results of the numerical model of the PSC, potentially leading to adjust some of the geotechnical parameters introduced in the model.

In particular, depending on the actual shear displacement of the rockbolts and joints, re-bolting of some secondary rockbolts may be necessary to guarantee the durability of the support.

5.1 *Design verification by control points*

As part of the observational approach, design control points - **Witness points (WP)** and **Hold Points (HP)** - are defined along the excavation procedure of the caverns and the IPB galleries. The definition and objective of these design control points are presented below:

Witness points

WP are scheduled at specific stages of the excavation where detailed information must be provided to the designer. Relevant tests and monitoring data must therefore be formally documented and provided by the Contractor to be able to follow up the behaviour of the cavern. At this point the construction can continue as planned.

Hold points

HP are scheduled at critical stages of the excavation where specific detailed information must be provided to the designer to check the design and to release those HP to continue the excavation works. Release of the HP by the designer means that the design can be executed *as is* with regards to the actual geological/geotechnical conditions as well as actual monitoring. Construction can proceed only if such confirmation is given by the Designer.

It should be noted that a Witness Point (WP) could become a Hold Point, i.e., in case of identification of unforeseen geological conditions or unforeseen behaviours of the rock mass which would necessitate an immediate adaption of the design at the referred Witness Point. In other words, the principle of the observational method is to be reactive to the actual conditions encountered and therefore, the detailed definition on the HP/WP presented thereafter may be adapted in function of the actual conditions found at site.

A scheme of the HP/WP localization along the excavation staging is given in Figure 5.

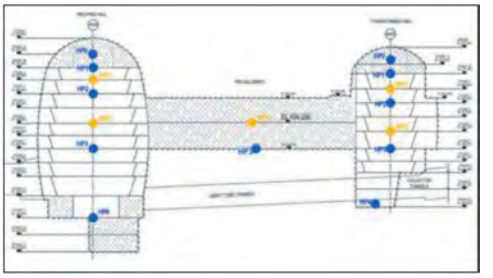

Figure 5. HP/WP along the caverns' excavation staging.

6 TWIN NUMERICAL MODEL & DESIGN ADJUSTMENT

The twin numerical model provides the digital modelling of Power Station Complex. Its main scope is to predict the opportunity of design adjustments at any stage of the caverns' construction. It will also be a powerful tool to assist the Contractor regarding the specific "delayed" sequence of installation of the rockbolts, which has been designed to avoid excessive shearing of the permanent rockbolts.

The level of details of the twin model may vary depending on the analysis to be performed, as well as the type of model itself. In the framework of the Snowy PSC design, a first level of analysis was performed to investigate the spatial relationship between certain parts of the PSC and the main discontinuities detected on site by the geo-structural mapping. This type of analysis was carried out by a "Twin model", developed with Rhino (Figure 6). At the time of writing, this model is continuously updated with the data progressively collected from the detailed geological mapping of the excavation.

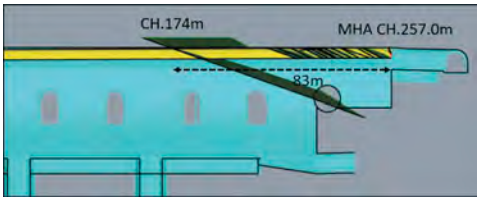

Figure 6. Twin numerical model on Rhino.

A second type of analysis, aimed at identifying the rockbolts exceeding the design criteria, is based on a "Twin model" developed by 3DEC, with a level of detail such to represent both the primary and the secondary rockbolts as well as the main pre-sheared joints at their exact position and orientation (Figure 7).

6.1 *Example of "twin model" for design assumptions verification*

In the framework of the PSC design, a particular attention was given to the intersection between the

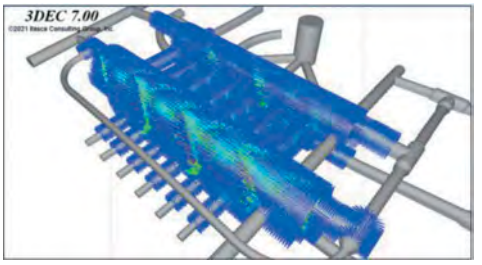

Figure 7. Twin numerical model for rockbolts analysis.

main access gallery MAT01 (ϕ11m TBM tunnel) and the two main caverns. The project features both caverns to be connected by MAT01 during the construction and the service phases. Circulation inside MAT01 must be guarantee as long as possible during the excavation of the caverns (Figure 8) and surrounding galleries, requiring a robust support design.

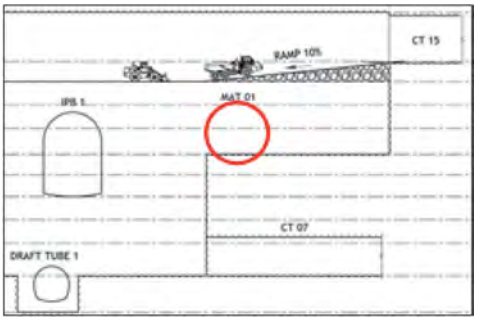

Figure 8. Circulation above MAT01 during cavern excavation.

The numerical model developed for the Detailed Design is a 3DEC model of the whole PSC, which considers the presence of the main joint sets (Figure 9).

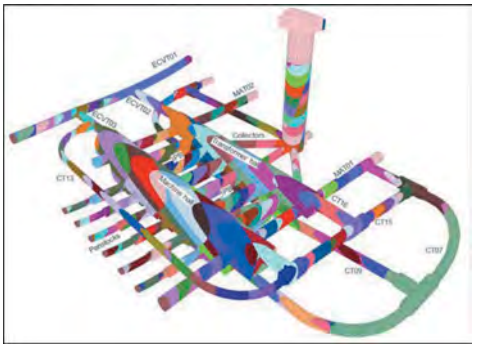

Figure 9. 3DEC Model - geometric hypothesis – 3D view.

Two pre-sheared joint sets, among the 5 joint families, are explicitly represented in the model:

- Bedding joint set: 35° dip, 75° dip-direction and 10 m spacing.
- Tectonic joint set: 75° dip, 125° dip-direction and 20 m spacing.

The remaining joint families were implicitly taken into account, lumped in rock mass parameters.

While developing the 3DEC model of the zone surrounding the MAT01 junctions, the joints positions were adjusted so that a bedding joint and a tectonic joint cross the rock slab in-between Central Heading Tunnel in both MH and TH and the underlying MAT01 (Figure 10).

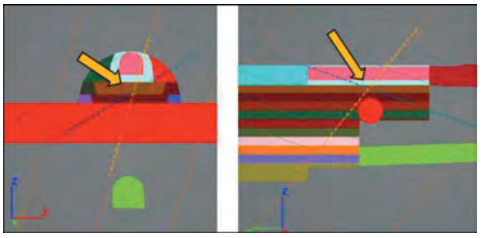

Figure 10. Pre-sheared joints between CHT and MAT01.

This conservative approach, introduced in the numerical model, was adopted as a precautionary measure to maximize the possible rock mass displacements and the wedges dislocation in the surrounding of MAT01 (Figure 11).

In other words, the existence of two joints (bedding and tectonic joints) crossing each other in correspondence of the rock slab in-between the CHT and the underlying MAT01, has to be considered as a sort of "worst case" condition, to be verified in the framework of the HP/WP procedure.

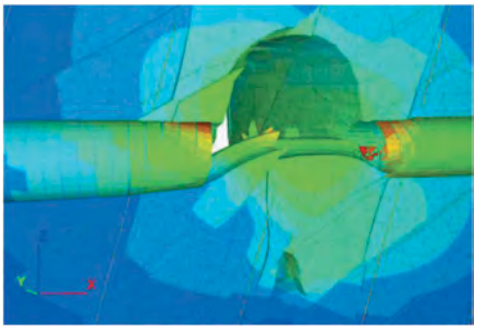

Figure 11. Exaggerate MAT01 displacements induced by MH excavation.

The circumstance described above was the object of a specific Hold Point (HP1a) to confirm that the in-situ geological conditions of the rock

slab in-between the Central Heading Tunnels and the underlaying MAT01 are consistent with the hypothesis assumed for the design (Table 1).

Table 1. Description of the HP01a scope.

WP/HP	Main Objectives	Input required	Home Office Output
HP 1a During the excavation of CHT	Verification of the joint sets intercepting the rock slab in-between the Central Heading Tunnels and the underlaying MAT01.	Routine geological survey focused on the Joint sets.	The output of HP1a shall consist of an "HP1a PSC Report" related to the design of the MAT01/PSC intersection (MH01.3) The report shall confirm that the in-situ geological conditions of the rock slab in-between the Central Heading Tunnels and the underlaying MAT01 are in-line with the conditions assumed for the detailed design (Ref. S2-CIV-PX-MHA-REP -3703) and that the Design Package MH01.3 can be executed *as is*.

The first stage of the verification procedure consists in the joints mapping along the area affecting MAT01.

Due to the joint sets' orientation, the face mapping had to be extended well beyond the area strictly overlaying MAT01 to capture all potential discontinuities passing through the rock slab.

A step further of the verification procedure was based on the data obtained from a long horizontal borehole (250m) drilled all along the TH's central heading tunnel, thus crossing the area of interest above MAT01.

The borehole also allowed to recognize the lithology of the concerned area, as well as the rock mass resistance via several Point Load tests.

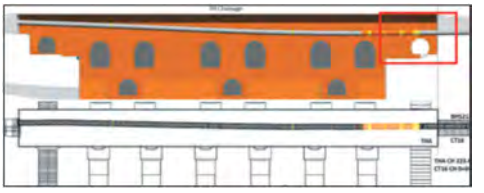

Figure 12. Borehole along TH and area of interest for HP1a.

The development of a "Twin model", using the available data from site, allowed the designer to validate that the actual on-site conditions are consistent with the design hypothesis, so that the "Hold Point 1a" was fulfilled smoothly, without any disruption to site activities.

6.2 *Example of "Twin model" for verification of the rockbolts.*

The re-bolting of the rockbolts is dictated by shear displacement of significant joints, mainly along the pre-sheared bedding joints or tectonic joints.

A preliminary assessment of the required re-bolting was performed by means of a 3DEC full staged PSC "Twin Model", simulating the whole excavation process and the explicit installation of the rockbolts.

At the time of writing, this preliminary "Twin Model" already includes the main pre-sheared joint sets deduced from the previous geological investigation's campaigns. However the final Twin Model is expected to be updated with the joint sets data actually observed on site during the caverns' excavation.

The "Twin Model" analysis suggests the presence of some possible critical areas where re-bolting shall occur because of exceeding the design shear criteria, at the upstream side of the MH, extended between the vault and the sidewall at location of weak pre-sheared joints.

The mentioned critical areas are numbered from 1 to 6 in the following Figure 13.

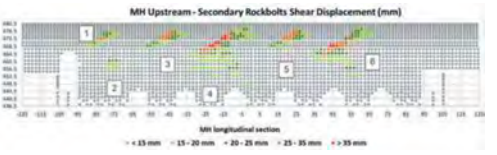

Figure 13. Example of the critical areas assessment.

The results of the in-situ investigations and the data from the monitoring will be considered for updating the PSC Twin Model numerical model, which will be re-run at several stages during cavern excavation – as part as the HP/WP – allowing an early identification of rockbolts (number and location) potentially exceeding the design criteria.

It is expected that rockbolts exceeding the design criteria are related to pre-sheared joints or discontinuities, thus the correct identification of such pre-sheared elements during the excavation process will require special attention and effort.

It is finally noted that even if the general deformation pattern of the PSC is modelled, it is difficult to calibrate the whole PSC numerical model so that all the measurements are in line with each other. Hence, local "Twin Models" are foreseen to be developed, fitting the data collected by the monitoring system in a given area of the PSC through back-analysis in acceptable computational time.

7 CONCLUSIONS

The Snowy 2.0 Power Station Complex is being excavated at about 720 m depth in high in-situ stresses and fair to good rock mass conditions in Australia. During the caverns construction, the geological conditions at the base of the design assumptions are systematically and continuously verified thanks to specific in-situ investigations and monitoring measurements during construction, in accordance with the "observational method", providing time to design adjustments if the actual conditions are differing beyond the expected design scenarios.

The article draws attention on the development of a "Twin Numerical" model of the Power Station Complex, to be regularly updated during the caverns' construction, and allowing to predict the need for design adjustments at any stage of the caverns' construction in a short time.

The level of details of the Twin Model may vary depending on the analysis to be performed; and two cases of application of the Twin Model implemented in the first phase of the Snowy 2.0 caverns' construction are reported as examples.

ACKNOWLEDGMENTS

The authors would like to acknowledge all the peers from Tractebel who contributed to the design of the Snowy 2.0 Power Station Complex over the years.

Authors would like to thank Snowy Hydro Ltd and Future Generation Joint Venture for the intensive and valuable technical discussions that were held along the development of the design.

REFERENCES

[1] Dressel & Diederichs (2021). A numerical investigation on the influence of rockmass parameters and yield mechanics in pillar design, RocScience international conference, the evolution of Geotech – 25 years of innovation, pp. 492–498

[2] Geotechnical Instrumentation and Monitoring Guideline, Version 1.0, Transport for NSW, 20 December 2016

[3] Geotechnical Monitoring in Conventional Tunnelling Handbook, Austrian Society for Geomechanics, 2014

[4] Hoek & Brown (1980). The Hoek-Brown failure criterion and GSI. 2018 edition - Journal of rock mechanics and geotechnical engineering.

[5] Hoek, E., Carranza-Torres, C., Diederichs, M.S., Corkum, B. (2008) – Kersten Lecture: Integration of geotechnical and structural design in tunnelling – Proceedings University of Minnesota 56th Annual Geotechnical Engineering Conference. Minneapolis, 29th February 2008, pp 1–53.

[6] Khodr, Lignier, Tonioni, Lambrughi (2022). Snowy 2.0 – Designing large caverns under high stress rock condition with focus on pillars stability – Tunnels et Espace souterrain – N° 281 – July/ August/Sept. 2022

[7] Khodr, Lignier, Tonioni, Lambrughi, Diederichs, Ching, Lazzarin (2023) - Design criteria for caverns under high stress rock conditions for Snowy 2.0 Power Station Complex – WTC 2023 Athens

[8] Laigle, F. (2015) - General considerations regarding the behaviour and design of large underground caverns - Tunnels et Espace Souterrain –, pp. 339–355, Sept./Oct. 2015

[9] Lignier, Tonioni, Blaise, Ching, Lazzarin, Gallera (2023) - Snowy 2.0 hydro power station complex – The design's evolution of the PSC caverns, from preliminary to detailed design – AFTES 2023 Congress, Paris

[10] Lorig and Varona, P. 2013. Guidelines for numerical modelling of rock support for mines. Ground Support 2013. Perth. p81–106

Tunnelling for a Better Life – Yan, Celestino, Thewes & Eberhardt (Eds)
© 2024 The Author(s), ISBN 978-1-032-80042-4
Open Access: www.taylorfrancis.com, CC BY-NC-ND 4.0 license

Rock engineering in Sweden - Mining, hydropower and railways

Per Vedin*
Swedish Rock Engineering Association, Lulea, Sweden
ITA-AITES World Tunnel Congress 2025, Stockholm, Sweden

Thomas Dalmalm
BeFo Rock Engineering Research Foundation, Stockholm, Sweden
ITA-AITES World Tunnel Congress 2025, Stockholm, Sweden

Johan Brantmark
Swedish Rock Engineering Association, Lulea, Sweden
ITA-AITES World Tunnel Congress 2025, Stockholm, Sweden

ABSTRACT: Rock engineering plays a pivotal role in Sweden's critical infrastructure sectors, including mining, hydropower, and railways. This article provides an overview of the significance of rock engineering in these domains and highlights Sweden's expertise in harnessing the power of its geological formations for sustainable development. Sweden's mining industry relies heavily on the country's rich mineral deposits, particularly iron ore, copper, and zinc. Rock engineering is fundamental in ensuring safe and efficient extraction from underground mines. Sweden's commitment to sustainable mining practices has led to the development of cutting-edge rock reinforcement techniques, ground control strategies, and advanced monitoring systems, making it a global leader in responsible mining operations. Rock Engineering is essential for tunnelling through the country's rocky terrain, enabling reliable transportation even in challenging landscapes. Sweden's rail engineering innovations, including tunnelling methods and rock support systems, ensure the safety and functionality of the railway network and heavy haul transports e.g. iron ore. Due to demand from the mining industry and railway sector Sweden's abundant water resources have made hydropower a cornerstone of its clean energy strategy. Rock engineering is critical for constructing and maintaining hydropower infrastructure, including dams, tunnels, and underground power stations. Swedish expertise in geological mapping, rock mechanics, and tunnelling technologies has enabled the harnessing of hydroelectric potential while minimizing environmental impacts. In conclusion, rock engineering in Sweden is integral to the success of its mining, hydropower, and railway sectors. Sweden's commitment to sustainable practices, coupled with its expertise in geology and engineering, has positioned it as a global leader in these critical industries, serving as a model for responsible resource utilization and infrastructure development all over the world.

Keywords: Sustainability, Tunnelling, Metals, Hydrogen storage, Environmental code

1 INTRODUCTION

In the last century the technique of rock blasting has developed from a manual occupation in which personal skill and intuition plays a great part into a technical science that today can be taught to student's, engineers and workers. A lot of methods and technologies used today worldwide have been development in Sweden according to Langefors, and Kihlstrom, 1978.

The introduction of drills with tungsten carbide bits and modern drilling machines played an important part in the transition to a more automated process. This development accelerated in 1946 as a collaborative effort among large Swedish steel companies to develop materials for rock drilling. The result was the establishment of an association and over time, it expanded its focus to serve the broader rock blasting industry and technology related to underground construction in rock. In 1957 the association changed its name to the Rock Blasting Committee and in 2017, the name officially changed to the Swedish Rock Engineering Association following an expanded collaboration with the Rock Engineering Research Foundation (BeFo).

The Swedish Rock Engineering Association is a non-profit organization that brings together companies involved in the design, construction, and operation

*Corresponding author: pervedin@hotmail.com

DOI: 10.1201/9781003495505-434

of underground facilities and mining, as well as manufacturers of relevant machinery and equipment. There primary activities is to host conferences on rock engineering and rock mechanics and share insights on various topics, and provide information to the public and members free of charge. The association monitors the field of rock engineering accumulating valuable knowledge for the industry and decision-makers.

2 SWEDEN IN BRIEF

Sweden, Figure 1, is a constitutional monarchy with a parliamentary system of government. It covers an total area of about 447 000 square kilometres which makes it the largest country in Northern Europe. Sweden has a population of approximately 10.5 million people and the capital Stockholm is the largest city.

Figure 1. The country of Sweden located in the north of Europe.

In Sweden Education is free and compulsory for all children between the age of 6 and 16 and there is a universal healthcare system that provides healthcare services to all residents. Sweden has one of the highest life expectancies in the world with an average of over 83 years.

Sweden is known various things, awarding the Nobel Prizes, including the Nobel Peace Prize, which is presented annually in Stockholm city hall. When you visit Sweden, you should know the word "Fika". It is a Swedish tradition of taking a coffee break with a snack, often accompanied by socializing.

In northern Sweden, the phenomenon known as the "Midnight Sun" occurs during the summer months, where the sun remains visible throughout the night. This is also the location of the largest iron ore mines in the country.

2.1 *Geology*

The rock underlying much of Sweden is highly suitable for building tunnels and rock caverns. The rock in Sweden comprises of three main units: the Precambrian crystalline basement, the remains of a sedimentary rock cover, and the rocks in the Scandinavian Caledonides mountain range.

The basement is part of a palaeocontinent, Baltica, and comprises of rocks formed during the Precambrian eras approximately 2800-545 million years ago. Most of the sedimentary rocks overlaying the basement to the east of the mountain range were formed in the period from the Cambrian and into the Tertiary period 545-55 million years ago. The sedimentary rocks are fossil-bearing and overlie the crystalline basement. The Scandinavian Caledonides are the remains of and old mountain range 510-400 million years ago when Balitca collided with Laurentia (North America—Greenland). Super-regional thrusts forced up older rocks from the west to from a long mountain range.

2.2 *Sustainability*

Sweden is committed to environmental sustainability, with recycling and eco-friendly practices being common. Sweden is working toward achieving the Sustainable Development Goals outlined in the United Nations' 2030 Agenda. These goals encompass various aspects of sustainability, including poverty reduction, environmental protection, and social equity.

Sustainability goals in Sweden are aligned with global objectives and reflect the country's commitment to environmental, social, and economic sustainability. The sustainability goals reflect a holistic approach to addressing all these challenges. The goals are supported by policies, regulations, and initiatives that aim to make Sweden a model for sustainable development and a leader in addressing global sustainability issues.

In 2022, nearly 98 % of the energy consumption in Sweden came from fossil free energy sources and nearly 70 % of the total energy consumption came from renewable energy sources. Sweden has made significant investments in renewable energy sources, particularly wind and hydropower. The aim is to increase the share of renewable energy in the national energy mix, reducing dependence on fossil fuels.

3 THE ENVIRONMENTAL CODE AND RAILWAY TUNNELS

3.1 *The Hallandsås Tunnel project*

The Hallandsås Tunnel project, initiated in 1992 with an open-face tunnel boring machine (TBM), encountered immediate issues, prompting a shift to traditional drilling and blasting methods. Subsequently, a more significant problem arose as substantial groundwater inflows disrupted the northern tunnels, leading to lowered groundwater levels and well water.

Efforts to seal the tunnel revealed that none of the tested grouting agents could effectively penetrate and seal the finest cracks. Eventually, a chemical grouting agent, widely used in global tunnel projects, was experimented with. This agent contained acrylamide components, initially toxic but rendered harmless through polymerization, making it suitable for sealing fine cracks due to its water-soluble nature.

In October 1997, complications arose as some of the acrylamide failed to polymerize due to abundant groundwater flow and high-water pressure. Consequently, this unreacted acrylamide contaminated nearby streams, resulting in fish mortality and paralysis in cattle that consumed the water. Concerns also extended to local drinking water quality and tunnel workers' safety.

The project came to a standstill in 1997 upon the discovery of acrylamide discharge issues. Further assessments indicated that the drill-and-blast method would introduce substantial water inflows during construction, necessitating a solution. The conclusion was to line the tunnels with enclosed concrete and employ a shielded tunnel boring machine. A vital lesson learned was the importance of prioritizing environmental considerations, control, and public information, BeFo Rock Engineering Foundation and Swedish Rock Engineering Association, 2018.

3.2 *The Environmental Code*

The Environmental Code, implemented in 1999, consolidated various environmental laws with the primary goal of fostering sustainable development, ensuring a healthy and favourable environment for both current and future generations.

Within the Environmental Code, there are overarching regulations concerning responsible planning and execution of subterranean initiatives. These encompass guidelines for land and water management, safeguarding crucial ecological zones, and setting environmental quality standards.

One illustrative instance covered by the Environmental Code involves the extraction of water from tunnels and subterranean caverns, necessitating a permit. A core tenet dictates that all construction endeavours involving groundwater must be formally reported. Furthermore, activities linked to noise and dust emissions during the construction and operation of subterranean facilities can fall under environmentally hazardous classifications in accordance with the Environmental Code.

The Hallandsås Tunnel project serves as a case study illustrating the intersection of infrastructure development, environmental regulations, and the importance of environmental considerations and risk management in large-scale construction projects in Sweden, in accordance with the Environmental Code.

4 HYDROPOWER

Sweden doesn't have much coal and oil, so the focus has been to use more renewable energy sources, being environmentally friendly. This has made Sweden good at finding clean energy solutions. Hydropower has traditionally served as a pivotal pillar in Sweden's industrial progress.

Electricity generation is almost evenly divided between the government, represented by the Swedish State Power Board (Vattenfall), and power companies owned by various entities such as industries, municipalities, and non-governmental bodies. These entities collectively form the Swedish Power Association, established in 1909.

Today, every household in Sweden enjoys access to electricity, and a comprehensive 400 and 220 kV grid system connects Sweden and the Nordic countries. Notably, cooperation among these countries is advantageous due to their distinct power generation mixes.

The design of hydropower stations is contingent upon local natural conditions. Swedish rivers, characterized by flat watercourses and expansive valleys, rarely offer suitable sites for high dams. Consequently, the focus shifts to moderate heads of water from relatively low dams. Favourable geological conditions have made underground power stations coupled with extensive tunnels more cost-effective than multiple above-ground dams and stations along the river.

As a result, a majority of Sweden's hydropower is generated within rock caverns. Depending on circumstances, these underground power stations are positioned near the dam, with water returned to the river through a tailrace tunnel. In some cases, it proves more efficient to place the machine hall downstream to facilitate shorter access tunnels or more favourable transportation gradients.

Economic considerations necessitate minimizing the size of structures and caverns, tailoring machine halls and other rooms to meet maintenance and equipment requirements. The cross-section of tunnels and ducts is chosen to minimize annual energy loss costs due to head losses and reduce initial investment expenses.

Some tunnels are notably expansive, such as the 4-kilometer tailrace tunnel at Stornorrfors with a cross-sectional area of 390 square meters or the tailrace tunnel at Harsprånget, boasting an area of 325 square meters. Power tunnels typically remain unlined, receiving support only in areas with weak rock. Strengthening efforts typically have amounted to 10% to 30% of the tunnel excavation costs. Therefore, for economic reasons, unlined tunnels with larger cross-sectional areas often present a more favourable choice than smaller, concrete-lined alternatives, Winqvist and Mellgren, 1988.

5 MINING IN SWEDEN

5.1 *Sweden's pioneering role in mining*

Mining has deep roots in Sweden, dating back to the Middle Ages when iron ore extraction began in earnest. Today, Sweden boasts a diverse mining sector that includes iron ore, copper, zinc, lead, silver, gold, and other minerals, Table 1. This sector has played a pivotal role in Sweden's industrial development and global economic contributions. Several international mining companies, including Boliden, LKAB, and Lundin Mining, have a significant presence in Sweden, contributing to the global mining industry.

Established in 1637, the Swedish Board of Mines, under royal authority, played a pivotal role in shaping the Swedish mining industry. Initially, it served as an inspection body, overseeing metal production processes. Additionally, the board took on the responsibility of recruiting and training individuals for crucial roles within the mining sector.

Table 1. Production of metals in Sweden in relation to the EU and the World. [Liljenstolpe, C et al].

Type of metal	Production of metals [tons]	Part of production in EU [%]	Part of production in the World [%]
Iron	28 500 000	93	1,2
Lead	79 700	39	1,2
Zinc	250 500	33	1,8
Copper	84 300	11	0,39
Silver	460	20	1,8
Gold	7,2	25	0,23

During the mid-18th century, private mine and works owners united to create a national entity known as the Swedish Iron Masters' Association, which remains active to this day. These two organizations collaborated to synchronize evolving mining techniques. Furthermore, the Swedish Board of Mines played a key role in setting guidelines for the optimal utilization of technology across all mines in the country, Hedström J-O, 2012.

5.2 *Mining innovations and collaborations*

Sweden's mining innovations have global significance. The advancements made in sustainable mining practices, automation, and environmental stewardship are shared with the world. Swedish mining equipment and expertise are in demand internationally, making Sweden a hub for mining innovation and knowledge exchange.

What sets Swedish mining apart is its unwavering commitment to sustainability and environmental responsibility. Swedish mining companies have embraced the challenge of minimizing their environmental footprint and ensuring that mining activities do not harm the delicate ecosystems of the region. This commitment has led to the development of cutting-edge technologies and innovative practices that are transforming the mining industry worldwide.

Swedish mines are at the forefront of automation and digitalization. Mines employ autonomous vehicles, drones, and sensor networks to improve efficiency, safety, and accuracy in exploration and extraction, Liljenstolpe C et al. 2022.

5.3 *Hydrogen storage advances fossil-free steel*

A pioneering project in Sweden, referred to as HYBRIT, has reached a significant milestone by inaugurating the world's first rock cavern storage facility for fossil-free hydrogen gas in Lulea. This marks a groundbreaking development in the journey towards establishing a comprehensive value chain for fossil-free iron and steel production.

The facility has undergone successful pressure tests and demonstrated the ability to operate at a maximum pressure of 250 bar, ensuring the stable and reliable supply of hydrogen for industrial use. By leveraging fossil-free wind power production, this technology addresses the intermittency of renewable energy sources, ultimately contributing to a cleaner steel industry with the potential to store up to 100 GWh of electricity in the form of hydrogen gas.

The HYBRIT initiative, initiated in 2016, is at the forefront of reducing carbon emissions in the global steel industry, pioneering a fossil-free future for steel production. Swedish mines are transitioning towards renewable energy sources. Wind, solar, and hydropower are increasingly used to power mining operations, reducing greenhouse gas emissions.

6 METHODS AND TECHNOLOGIES

The Swede Alfred Nobel and his dynamite played a crucial role in tunnel construction during the late 19th century, notably in the St. Gotthard Alpine railway tunnel from 1872-81. This innovation in rock engineering revolutionized blasting techniques. Pneumatic rock-drilling machines, mounted on rail "jumbos," were further improved, and locomotives driven by compressed air were introduced to remove broken rock.

Despite significant advancements, challenging rock conditions sometimes caused delays and safety issues. Various tunnels, including the impressive Simplon tunnel (19,540 meters) connecting Italy and Switzerland, were constructed during this golden age of railway development. The main tunnel featured a cross-section of 28 square meters and was designed for a single track. A smaller tunnel ran parallel to provide fresh air, with connecting tunnels every 200 meters to maintain a tolerable work environment for laborers.

The construction process involved initially blasting a small section in the main tunnel, followed by widening behind the pilot gallery's face while simultaneously constructing the permanent lining. While rock-drilling machines were employed for the pilot gallery, hand drilling was still necessary elsewhere. The Simplon tunnel's completion in 1905 marked it as one of the most remarkable achievements of the era in tunnel engineering.

Alfred Nobel's dynamite and innovations in tunnelling techniques were pivotal in the development of complex railway tunnels during this period, setting the stage for future advancements in rock engineering. In recent years, Sweden has witnessed several innovations in rock engineering, particularly in the field of underground construction and tunnelling.

7 COOPERATION BETWEEN STAKEHOLDERS

In Sweden, there exists a longstanding tradition of fostering a strong working relationship among the client, consultant, and construction teams, regardless of whether construction is carried out in-house or through contracts. This collaborative approach involves continuous discussions throughout the entire construction process, enabling the adaptation of design and methods to enhance both the project's timeline and cost-efficiency.

In the context of constructing underground power stations, tunnelling plays a crucial role, often dictating the overall project's construction duration. Therefore, it is of paramount importance to seek optimal solutions not only in terms of hydraulics but also regarding tunnelling techniques. This includes adjusting the width/height ratio to match the equipment used and the prevailing rock stress conditions.

Moreover, the selection of the number of tunnel headings is strategic to prevent delays caused by unfavourable rock conditions. To minimize rock damage, overbreak, and head losses, the approach typically involves employing smooth-wall blasting techniques. This comprehensive approach ensures efficient and effective construction processes in Sweden.

8 CONCLUSIONS

Sweden's prominent role in subsurface technology is attributed to a collaborative spirit among all stakeholders, driven by a focus on meeting customer needs and addressing specific challenges. Notable initiatives in this regard include the Swedish Rock Blasting Committee, established in the 1940s, fostering an open exchange of information within the rock construction community.

Today, rock drilling primarily utilizes wheeled or rail-frame jumbos, with hydraulic machines largely replacing compressed-air ones, resulting in quieter operations. Tunnel boring machines (TBMs) have become a permanent fixture for creating circular tunnels. Safety and efficiency have improved with safer blasting agents, ignition methods, and mechanized loading, often employing purpose-built vehicles. Computers play a crucial role in precise work planning, leading to significant improvements in workplace conditions.

Sweden's mining industry is a testament to the potential for environmentally responsible resource extraction. Its commitment to innovation and sustainability has not only contributed significantly to the nation's economy but has also positioned Sweden as a global leader in mining technology and practices. As the world grapples with the challenges of resource scarcity and environmental preservation, Sweden's mining sector offers valuable lessons and inspiration for the mining industry worldwide.

REFERENCES

BeFo Rock Engineering Foundation and Swedish Rock Engineering Association, 2018. Sweden Underground – Rock Engineering and How It Benefits Society. ISBN 978-91-637-7639-7. Åtta45 Tryckeri AB. Stockholm, Sweden.

Geological Survey of Sweden, Hedström J-O, 2012. Bergstaten 375 år. ISBN 978-91-7403-180-5. DanagårdLiTHO AB. Ödeshög, Sweden.

Winqvist, T, Mellgren, K-M, Royal Swedish Academy of Engineering Sciences, 1988. Going Underground. ISBN 91-7082-432-0. Stockholm, Sweden

Liljenstolpe C et al, Geological Survey of Sweden, Statistics of the Swedish Mining Industry, 2022. ISSN 0283-2038. Uppsala, Sweden.

Langefors, U, Kihlstrom, B, 1978. The modern technique of rock blasting. ISBN 91- 20-06104-8. New York, Halstedt Press.

Tunnelling for a Better Life – Yan, Celestino, Thewes & Eberhardt (Eds)
© 2024 The Author(s), ISBN 978-1-032-80042-4
Open Access: www.taylorfrancis.com, CC BY-NC-ND 4.0 license

Integration of stations and cities plan and research on technological innovation of Shenzhen Dayun comprehensive transportation Hub

Ming-sheng Wang*, Chang Liu, Rui-zhen Fei & Wen-rui Liu
China Railway Design Corporation, Tianjin, China

Yong-yu Fu & Yong-zhong Deng
Shenzhen Metro Construction Group Co.,Ltd, Shenzhen, China

ABSTRACT: The transportation facilities of Dayan Comprehensive Transportation Hub have been integrated into development land. In order to break the traditional concept of a clear boundary between rail transit and adjacent commercial buildings, achieve a new hub mode while stitching the land plots on both sides of Longgang Avenue, and further expand the radiation range of the hub, Dayun Comprehensive Transportation Hub requires new ideas, new concepts, and new techniques to achieve true new hub mode of integration of stations and cities, including planning concepts, architectural design, aboveground and underground design of large heterogeneous structural system, and large-scale renovation of existing Line 3 station.

Keywords: Shenzhen Dayun, Transportation Hub, New hub mode, Heterogeneous structural system, Renovation

1 HUB PROFILE

Dayun Comprehensive Transportation Hub is located in Longgang District, Shenzhen City, Guangdong Province, China. It is a large-scale modern comprehensive transportation hub integrating intercity railway, subway, road traffic, bus and slow traffic system, and a fourth-line transfer hub of rail transit. The universiade hub as a passenger "extension" urban infrastructure key nodes, the design of the hub itself and the hub around the "space" and "time" to reconstruct, avoid rail transit hub "island" and urban construction, eventually form the universiade hub super blocks, let the passengers' perception has obvious continuity. The average daily passenger flow of the hub is forecast to be 434,000 person-times per day. Construction is scheduled to start in March 2019 and put into initial operation in October 2022. The total construction area of Shenzhen Universiade comprehensive transportation hub is about 162,200 square meters, with a total investment of about 4.9 billion yuan.

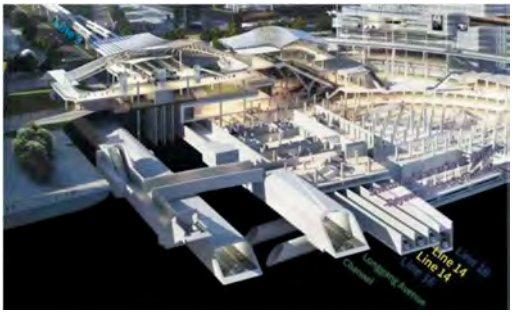

Figure 1. Dayun Hub slice view.

2 HUB PLANNING AND ARCHITECTURAL DESIGN INNOVATION

2.1 *Hub positioning*

Dayun Hub is a comprehensive transportation hub in the eastern region of Shenzhen and an important node

*Corresponding author: Wangmingsheng@crdc.com

DOI: 10.1201/9781003495505-435

on the link between the eastern and western urban agglomerations in the Greater Bay Area. Meanwhile, relying on Dayun Software Town to link Baolong Industrial Park and Apollo Industrial Park, it is an innovative wisdom hub center and an exchange center for gathering industries and talents.

2.2 *New hub mode*

The traditional mode of interconnection between rail transit and surrounding plot development is set independently, and the channel connection is adopted between the two with obvious physical division. The current popular mode, although rail transit is embedded in the development plot, there is still obvious boundary and the connection is still not close enough. Dayun hub adopts the mode of integrating transfer space into the plot development, which makes the rail transit and plot development integrated to achieve mutual nesting and common development.

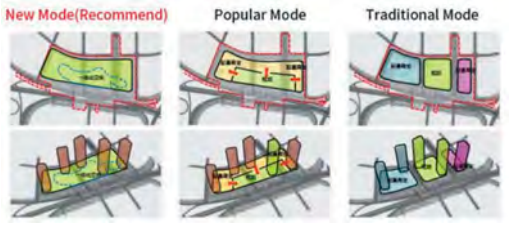

Figure 2. Traditional model comparison chart.

2.1.1 *Hub-based suture space*

The design of the hub makes the main road of Longgang Avenue sink together with the underground structure of the hub. Through the entrance and exit of the first floor, the paid area of Line 3 and the platform of the non-paid area span the Longgang Avenue. The two measures effectively sew up the east and west sides of the plots separated by Longgang Avenue.

2.1.2 *The Line3 will not suspend when the expansion platform is building*

To meet the long-term passenger flow demand of the hub, the hub design built two side platforms while the two sides of the original island platform of Line 3 were not suspended. At the same time, the original canopy was removed, and a large hyperbola canopy covering the platform and the platform of the second floor of Line 3 was built.

2.1.3 *Integration of hub buildings and plot buildings*

In order to break the traditional separation boundary between rail transit and land development, the hub design uses the urban core as an effective separation between rail transit and adjacent commerce, so that the passengers in the commercial land can transition to the traffic core through an urban space, so as to achieve mutual nesting and seamless connection.

Figure 3. Renderings after renovation of line 3.

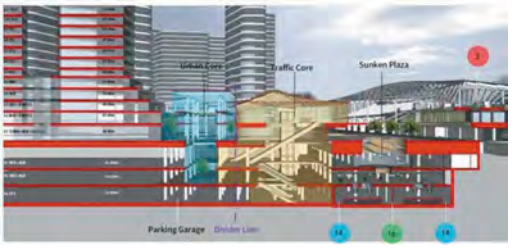

Figure 4. Sliced diagram between urban core and traffic core.

2.1.4 *Vertical transfer of the hub*

The design of the hub adopts vertical traffic core to solve the problem of inconvenient transfer between the elevated Line 3 station and the underground 14,16 and Shenzhen-Dalian intercity stations, effectively improving the comfort of passenger transfer and significantly shortening the transfer time. The height of the elevated transfer is 25m, only 5 minutes.

Figure 5. Scenery photo of traffic core.

3 HUB UNDERGROUND STRUCTURE INNOVATION

3.1 *Underground structure problems that need to be solved to realize the building intention*

For longgang avenue municipal tunnel into the hub construction during the same period, the new line

14,16 Dayun station shall adopt 22m large span roof force conversion, board span nearly 3m soil load but also need to lift nearly 20000 kN axial canopy column on the ground, the roof area also need to in the foundation pit Ming dig construction stage and relief road and construction site, design condition is complex, need to solve the load under the action of load system design problem.

The new foundation pit of lines 14 and 16 is 27~30m deep, 597m longitudinal and adjacent to the Dayun Viaduct station of the existing Line 3. The net distance between the foundation pit and the existing line is only 2.1m, which needs to solve the deformation control problem of the existing lines.

3.2 *Study on the force conversion structure of the joint construction section of the station and the above-ground structure*

The large span structure of the excavated section of the 1-34 shaft cover of Shenzhen Dayun Comprehensive Transportation Hub Project includes the structural part of the conversion section (20-32 axis) bearing the load on the column and the non-conversion section structure (remaining axis) without the load on the column. The scope of this study is the large span structure of the 20-32 axis conversion section, as shown in Figure 6.

The station 20-32 axis of line 14 and Line 16 is built together with the ground structure column with the design scheme of 22m large span beam. The superstructure column is concrete filled steel tube column with a diameter of 1300mm. The layout position of the column is close to the side wall and about 5.1m away.

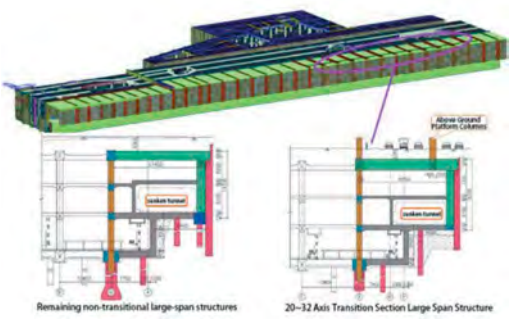

Figure 6. Section diagram of the large-span structure.

Under the premise of selecting the steel concrete beam-column structure system for the stress system of the conversion section, consider the influence of different large span beam conversion nodes on the overall structure, and make the structure design more economical, safe and reliable on the premise of ensuring the strength, stiffness and stability of the structure. Six kinds of large span beam conversion nodes are proposed to be studied: type steel concrete beam scheme, section steel concrete inclined column conversion scheme, steel truss conversion scheme, concrete box beam scheme, steel box combined beam scheme and type steel concrete beam end addition scheme.

All the above schemes can meet the requirements of structural strength, stiffness and stability, but in practical engineering, the influence of structural design on economic conditions, construction difficulty and building effect should also be considered. The advantages and disadvantages of the six schemes are summarized as follows, as shown in Table 1.

Table 1. Comparison table of each conversion scheme.

Project	Plan 1	Plan 2	Plan 3	Plan 4	Plan 5	Plan 6
Description	Girder with rolled steel section en cased in concrete	Inclined column + section steel concrete beam	Steeltruss	Concrete box girder	Steel box-type steel composite girder	Section steel concrete beam with arm
Primary beam section	Wide 3m and high 2.5m	Beam width is 2m and its height is 2m	The total height of the steel truss is 3m, and the truss height is 2.2m	The beam height of 3m	The beam height of 3m	Wide 3m and high 2.5m
Merit	Simple stress; Reliable connection;	Direct force transmission, the beam bending moment is greatly reduced; the bearing capacity is the best.	In light weight; fabricated	In light weight	Advantages of the combined structure; Reduce the beam weight.	Simple stress; Reliable connection; High bearing capacity
Shortcoming		Great influence on B1 chamber; connecting structure Make slightly complex.	The truss height is small, the chord is stressed; the conversion column foot joint connection is difficult;	The connection of beam-column end is complex; the reinforcement is large.	The beam end node connection is complicated; the deflection is relatively large.	Some effect on the B1 room;

As shown in Table 1, the secondary transmission force is the most direct, greatly reduces the internal force of the beam and column, has the best bearing capacity, the best safety and economy, but has a great impact on the indoor function, affecting the overall architectural effect, and the connection structure is slightly complex. Scheme three, scheme four, scheme five although is a new type of conversion structure form, can reduce the structure weight, give full play to the material characteristics, but there are the same design shortcomings, namely the node connection is more complex, construction is difficult, and the existing calculation results show that the beam weight only accounts for 8.5% of the total constant load, so by reducing the trabecam weight to reduce the structure of bending moment, the effect is not obvious. Scheme and six belong to the conventional scheme, but can be seen from the calculation results, through reasonable reinforcement and section design, the bearing capacity, deformation and crack width are meet the requirements of the range, scheme six axillary is further improve the carrying capacity of the structure, and reliable node connection, construction technology is relatively mature, therefore, from the safety, economy and the use of function comprehensive consideration, recommend these two schemes.

In the original structural load composition, the large span beam of the conversion section bears two columns, the load of column A is 7000 kN, and that of column B is 20000 kN. In order to improve the bearing capacity of the large span beam in the lower conversion section of the B column, scheme 6 (steel concrete beam end) is selected as the conversion node of its large span beam, and the load of column A is small, so scheme 1 (steel concrete beam) is selected as the conversion node of its large span beam.

In the current structure load composition, the large span beam under column load into a kind, namely C column load is 15050 kN, compared to before the B column load reduced, so the above six large span beam conversion node scheme and the current column load, choose a scheme (steel concrete beam) as the conversion section structure of large span beam conversion node. The final location of structural members and the dimensions of structural members are shown in Figure 7 and Table 2.

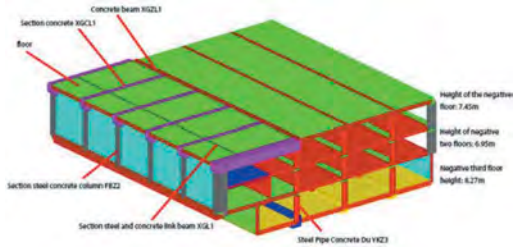

Figure 7. Location of the structural components of the final scheme.

3.3 *Research on the deformation prediction of adjacent existing lines in deep foundation pit construction*

Near the existing Line 3 viaduct, the Dayun Hub is located on the west side of the elevated bridge of Shenzhen Metro Line 3, with a clear distance of about 2 meters, the main foundation pit is constructed by open excavation. The foundation pit of the part of the 1-7 axis at the small mileage end of the station is constructed by cover excavation, and the traffic core is constructed by cover excavation. The retaining structure adopts the supporting form of ground connecting wall, drilling and bite pile (whole meat, meat and vegetable) + inner support, and four supports (three or five partial supports) are set in the foundation pit. The auxiliary structure is constructed by open excavation method or dark excavation method. MIDAS/GTS. In order to eliminate the boundary effect, the length of the soil was 3 times the length of the foundation pit, taking 1200m X, 500m Y and 60m Z. The soil, bridge deck, pier and cap adopt the solid unit, the soil adopts the modified Moore-Kulun constitutive model, the structure adopts the elastic constitutive model; the retaining structure (into equivalent thickness plate), cover plate, floor plate, side wall and side wall adopt the beam unit; the column pile adopts implanted beam unit; the bridge pile; 138501 nodes, 168635 units. The computational model is shown in Figure 8.

Based on the finite element calculation results, Dayun Hub is near the viaduct of Metro Line 3, After excavation of the main foundation pit, horizontal and vertical displacement of cap bridge pile and horizontal and vertical deformation of bridge deck track, The maximum settlement value and the

Table 2. Size of final solution.

Steel-type concrete beam XGCL 1 (High and width, m)	Steel-type concrete beam XGZL 1 (High and width, m)	Steel-type concrete beam XGL 1 (High and width, m)	Concrete roof (thick,m)	Steel-type concrete column FBZ 2 (High and width, m)	Concrete side wall (thick,m)	Steel pipe column YKZ3 (Diameter and thickness, m)
3.0×2.5	1.8×2.7	1.6×2.5	1.2	1.8×3.2	1.0	1.3×0.065

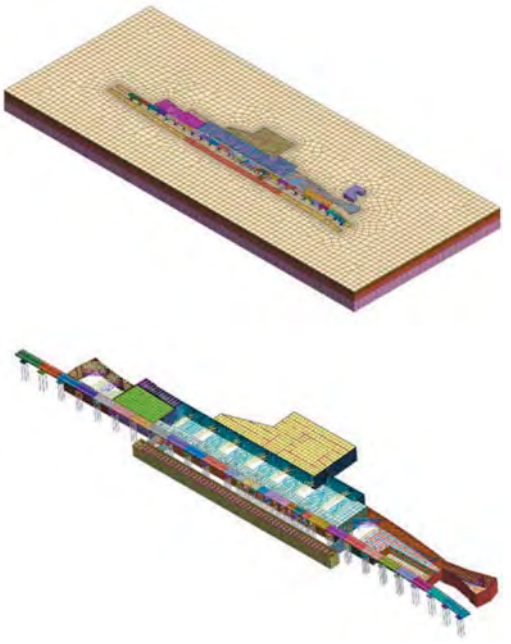

Figure 8. Elevated calculation model of the main foundation pit of Dayun hub near subway Line 3.

maximum horizontal displacement of each construction step cap bridge pile are shown in Figure 4; The maximum settlement value and maximum horizontal displacement of bridge deck piers for each construction step are shown in Figure 5; Taking the representative nodes 711802,711807 (lateral), and 711904 (track) in the model, In accordance with Figure 9, the vertical displacement value on the track should be observed. Subsequently, the change curves for the settlement value, rail deformation difference, and lateral settlement difference should be graphed relative to the construction step . See Figure Figure 10, The calculation results of the pile displacement, pile foundation tilt value, bridge deck pier displacement and track deformation of line 3 in the main construction step are shown in Table 3.

Figure 9. The maximum displacement result diagram of the cap bridge pile of Metro Line 3.

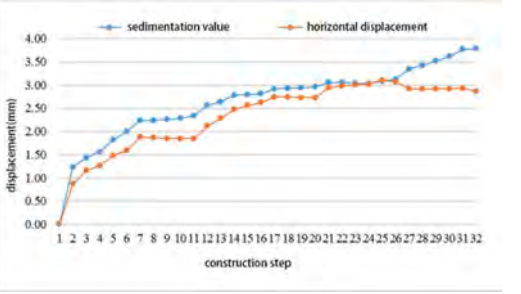

Figure 10. The imum displacement of bridge piers of Metro Line 3.

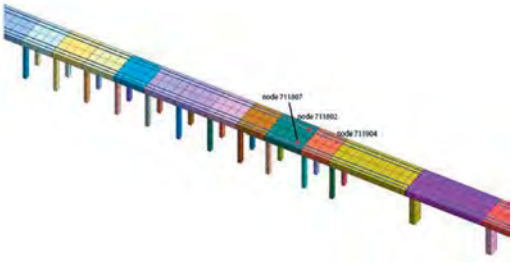

Figure 11. The existing track deformation measurement points of subway Line 3.

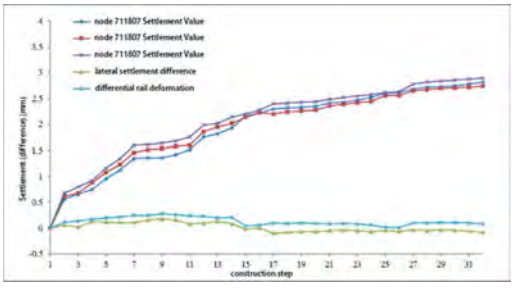

Figure 12. The existing track deformation results diagram of Metro Line 3.

Since AT01~AT12 of Dayun Station of Line 3 is a continuous beam bridge, it is relatively sensitive to the differential settlement between the bridge spans, so the vertical displacement and differential settlement between the bridge spans in each construction stage should be mainly analyzed.

The construction of foundation pit in the open excavation section of large and small mileage has little impact on the vertical settlement of AT01~AT12 piers of Dayun Station. The maximum settlement of cap pile foundation is 1.8mm, which occurs at the bottom of the AT12 pile closest to the foundation pit in the open excavation section of large mileage; the maximum difference settlement of adjacent cap is 0.2mm of AT11 and AT12, the maximum settlement of bridge deck is 1.3mm, and the

Table 3. Summary of the calculation results (cumulative value) of the displacement (deformation) of the viaduct of Metro Line 3.

Displacement \ Operating mode		The foundation pit is excavated to the bottom of the pit	The foundation pit of the station is excavated to the bottom of the pit	Traffic core and Longgang foundation pit excavation to the bottom of the pit	The foundation pit at the open excavation entrance is excavated to the bottom of the pit
Subway line 3 viaduct pile cap displacement	Maximum settlement (mm)	2.06	2.81	2.96	3.62
	Maximum horizontal displacement (mm)	1.27	2.27	2.70	2.49
	Maximum adjacent cap Settlement difference (mm)	0.46	0.63	0.65	0.60
Metro Line 3	Horizontal Displacement/ Pile length (10-5)	3.2	5.7	6.8	6.2
Displacement of the viaduct pier of Metro Line 3	Maximum settlement (mm)	2.23	2.92	3.08	3.77
	Maximum horizontal displacement (mm)	1.87	2.74	3.11	2.93
	Maximum adjacent bridge piers Settlement difference (mm)	0.43	0.64	0.65	0.67
Dedeformation of subway line 3	Monorail longitudinal deformation difference (mm)/10m	0.2	0.2	0.4	0.4
	Horizontal height difference (mm)	0.5	0.7	0.5	0.6

maximum difference settlement of adjacent piers is 0.2mm;

The impact of the construction of foundation pit in the station section on the vertical settlement of AT01~AT12 piers is large but uniform. The settlement of cap bridge piles is not different, the maximum settlement of cap pile foundation is 2.3mm (cumulative value), the maximum difference settlement of adjacent caps is 0.1mm, the maximum settlement of bridge deck is 2.3mm (cumulative value), and the maximum difference settlement of adjacent piers is 0.1mm;

After the completion of the foundation pit and the foundation pit on the east side of Line 3, the vertical settlement of AT01~AT12 piers increases slightly, the maximum settlement of cap pile foundation is 2.4mm (cumulative value), the maximum differential settlement of adjacent caps is 0.1mm, the maximum settlement of bridge deck is 2.5mm (cumulative value), and the maximum differential settlement of adjacent piers is 0.1mm;

The construction of foundation pit at the open dig entrance and exit has a great impact on the vertical settlement of AT01~AT03 piers adjacent to the entrance and exit. The maximum settlement of cap pile foundation is 3.0mm (cumulative value), the maximum differential settlement of adjacent caps is 0.2mm, the maximum settlement of bridge deck is 3.0mm (cumulative value), and the maximum differential settlement of adjacent piers is 0.1mm.

In conclusion, the vertical displacement and settlement difference of each construction stage are

within 5mm of the control value, and the horizontal displacement is also within 5mm of the control value.

The track displacement of existing Line 3 is basically synchronized with the bridge deck, and the monorail longitudinal deformation difference occurs in the construction stage, which is located in the area above HT 43 ~ AT 01 piers, the maximum value of monorail is 0.4mm/10m. The maximum transverse elevation difference occurs in the construction stage of foundation pit of the station, is located in the area above HT 36 piers, and the maximum transverse elevation difference is 0.7mm, which meet the deformation control index.

4 HUB ABOVE GROUND STRUCTURE INNOVATION

In the aspect of hub roof design, in order to make the shape of the roof more beautiful and delicate, the twisted space grid structure system is proposed, and a complete set of analysis and design process is formed, and a new type of joint bearing is applied. In terms of the reconstruction of the existing Line 3, in order to realize the shelter function of the whole process of the transformation of the existing station, it is planned to build a new canopy first, and then dismantle the existing canopy. Special construction method should be adopted to meet the requirements of the protection of the existing stations and the demolition of the existing canopy at the same time.

4.1 *Steel structure system of complex twisted space grid*

The canopy of the Dayun hub is hyperbolic, and the top and side of the roof are gradually transformed in different areas. The vertical lateral force resistance member adopts Y type or straight column type circular steel pipe column, the main beam adopts round steel pipe, and the secondary beam adopts inverted ladder box beam. The columns and the main and secondary beams all present the different section form along with the roof shape, which is light and chic, and perfectly reflects the roof design concept of "Dance of the Bay Area". Each component is made of Q390GJC steel, and the maximum span of the structure is about 36m, as shown in Figure 13.

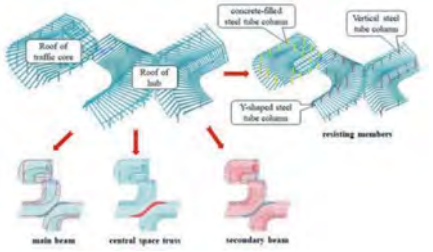

Figure 13. Housing structure composition of the Dayun hub.

Due to the distortion and fluctuation of the canopy form, each structural rod has both the bending force characteristics of the conventional frame structure system beam and the space force characteristics of pressing (pull) bending. It is difficult to find the complete corresponding type of this structure in the division of existing structure forms, so the structure system is defined as "twisted space grid structure" according to its spatial form and force characteristics of components.

In addition, the large canopy beams and columns of the hub are connected by the joint bearing support to release the rotational constraints. In order to realize the "clear purlin" design required by the building shape, the lateral constraint of purlin on the secondary beam is not considered. These special factors all bring greater challenges to the structural design.

According to the shape and stress characteristics of the canopy structure, the overall static analysis, stability analysis, node and support analysis are carried out, and the wind tunnel test is carried out to form a complete analysis and design process to ensure the safety and reliability of the structure design.

In the overall static analysis, the structural stress, deformation calculation and continuous collapse analysis; in the stability analysis, the characteristic buckling analysis and nonlinear buckling analysis were conducted using the finite element analysis software; in the wind tunnel test, considering the recent no interference and future interference, considering 36 wind angles to measure the extreme wind pressure, and the equivalent static wind load is obtained through the wind response calculation and used for the design analysis, as shown in Figure 14.

Figure 14. Wind tunnel test.

4.2 *Application of the new joint bearing support*

The canopy of the Dayun hub chose the scheme of using the centripetal joint bearing support and the angular contact joint bearing support, as shown in Figure 15. These two kinds of joint bearing bearings are different in appearance, but they both belong to the universal hinge, which can release the three-way

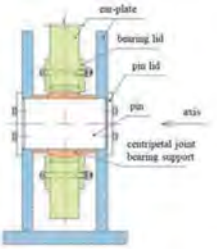

(A) centripetal joint bearing support

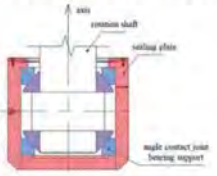

(B) Angle contact joint bearing support

Figure 15. Schematic illustration of both joint bearings.

bending moment and only restrain the three-way translation.

One model is selected: XGJZ-3500-700/1200-0.06, The bearing capacity is 3500 kN, Pull tensile capacity 1200 kN, Axial horizontal shear bearing capacity of 700 kN, The maximum rotation angle of the rotating shaft bearing is 0.06 rad; Two models exist: JGJZ-5300-700/1100-0.06 and JGJZ-3800-700/1300-0.06, 5300 (3800) kN, Axial upward tensile capacity of 1100 (1300) kN, Horizontal shear bearing capacity is 700 kN, The maximum rotation angle of the rotating shaft bearing is 0.06 rad.

The new joint bearing bearing has the following advantages:

1) The beam and column connection is hinged, which can release the bending moment of the junction node and effectively optimize the section size of the nearby rods;
2) The hub canopy spans the existing Dayun Station, and the columns fall on the landscape platform or platform on the east and west sides respectively. There are differences between the two in terms of foundation form, stiffness and settlement, and the uneven settlement problem can be solved through the joint bearing support.
3) The canopy column form is divided into two categories: tree branch type and straight column type. Combined with the shape characteristics, the centripetal joint bearing support and the angular contact joint bearing support are adopted respectively, so as to make it organically combined with the column shape.

Therefore, the use of various forms of universal hinge support on the same canopy steel structure not only solves the stress requirements of the structure itself, but also takes into account the aesthetic effect of the building. The design technique of the support is novel, which provides a new idea for the selection of canopy steel structure support in the future. The site diagram of Dayun hub bearing bearing is shown in Figure 16.

(A) centripetal joint bearing support

(B) Angle contact joint bearing support

Figure 16. Field diagram of two joint bearings.

4.3 *Construction method of mobile protective shed*

The new canopy of Dayun hub is a twisted space grid structure, with many types of rods, complex structure and large weight, so it has high requirements for lifting accuracy. Due to the new canopy across the existing operating elevated station, small parts, small instruments, welding slag and welding sparks may fall in the construction process of high-altitude assembly and welding, and there is a large construction safety risk. In order to ensure the normal operation of the existing Metro Line 3 and the normal operation of the ground traffic on Longgang Avenue, corresponding protective measures must be taken.

To this end, combined with the spatial location relationship, construction requirements, protection requirements and construction period requirements, the construction method of the mobile protective shed is specially designed, as shown in Figure 17. A single mobile protective shed is 22.4m long and 12m wide, and the basic form is arched, with a total of 3 vertical frames. Lay pressed steel plates on both sides and

Figure 17. Schematic diagram of the mobile protective shed of the Dayun hub.

above to play a protective role. Mechanical and electrical equipment are set up at the bottom of the rigid frame column for the function of sliding. At the same time, the track is laid on the two sides of the platform and the extension platform of the new construction, and the mobile protective shed can slide longitudinally along the track. Just the frame is also equipped with lifting hooks, with lifting function.

Two mobile protective sheds are set up in this project, which can cover 22.4m 24m on the plane. On the one hand, the construction technology can form the protective measures of the Dayun station of the existing Line 3, and on the other hand, the canopy of the existing station can be removed, lifted and transported.

The construction method combines the function of the existing station and the demolition of the existing canopy, simple structure, saves materials, avoids the frequent shutdown of existing lines, effectively shortens the construction period, can provide idea and reference for the construction protection of similar reconstruction and expansion projects in the future.

REFERENCES

Guo Haizhu, Zhang Jian, Shi Xiaowei. Analysis of key construction technologies of Shenzhen Metro Dayun Hub Station [J]. Tunnel construction (Chinese and English), 2023,43 (S1): 451–456.

Xie Gannan, Lu Chuang, Fei Jianbo. Numerical analysis of force characteristics of pile foundation in the pit under excavation and unloading conditions —— Take the Dayun Hub Station project in Longgang District, Shenzhen as an example [J]. Engineering Technology Research, 2022,7 (03): 1–4.

Cao Chunbo. Analysis and influence factors of foundation pit excavation on pile foundation of adjacent buildings and control measures [J]. Technology and Innovation, 2021 (15): 126-127 + 133.

Jiao yan yue. Study on the numerical simulation method of the whole process of integrated transportation hub construction based on MIDAS [J]. Technology and Innovation, 2021 (16): 171-172 + 178.

JGJ 7-2010. Technical Specification for Spatial Grid Structure [S]. Beijing: China State Engineering and Construction Press, 2010.

GB50017-2017. Steel Structure Design Standard [S]. Beijing: China State Engineering and Construction Press, 2017.

Tunnelling for a Better Life – Yan, Celestino, Thewes & Eberhardt (Eds)
© 2024 The Author(s), ISBN 978-1-032-80042-4
Open Access: www.taylorfrancis.com, CC BY-NC-ND 4.0 license

Comprehensive development and utilization of underground space of Xiangya Road River-crossing Tunnel project in Changsha City

Hailin Wang, Junqiu Ma*, Xin Zhang & Mi Zhou
Hunan Provincial Communications Planning, Survey And Design Institute Co, Ltd, Changsha, China

ABSTRACT: The Xiangya Road River-crossing Tunnel is an important pathway crossing beneath the Xiangjiang River in the northern part of Changsha City. A 14.5-meter large diameter shield was used to dig the river section of the tunnel, and open cut method was adopted to the river embankment section. This paper aimed to introduce the innovation of the project regarding the comprehensive development and utilization of underground space as follows:(1) The collaborative design and construction problem of long-distance overlapping municipal tunnels and subway tunnels in the urban core area was solved. The open-cut sections of this pathway overlapped vertically with two subway stations. The tunnel was set on the basement floor of the subway station, which makes the best use of underground space. (2) Two underground parking lots (with about 400 spaces) were constructed in the backfilling space above the open-cut tunnel foundation pit, which greatly eased the parking difficulty in the central urban area. (3) The site selection problem of tunnel management building in the central urban area was solved by constructing a semi-underground structure in the Yinpenling Park, which not only met the needs of tunnel maintenance and rescue, but also remained the green area of the park. (4) A multi-point distributed ventilation and emission mode was adopted in this tunnel project, avoiding erecting high wind towers, and realizing the coordination between tunnel environmental protection and urban landscape. The green space of the Yinpenling Park was rationally used, in which 8 decentralized hidden exhaust pavilions were designed.

Keywords: Underground space development, Intensive utilization, Shield tunnels, Foundation pit engineering

1 INTRODUCTION

The Xiangya Road River-crossing Tunnel starts from the intersection of Tongzipo Road and Yuehua Road in Yuelu District in the west to the intersection of Xiangya Road and Furong Middle Road in the east, with a total length of about 4.18 km, which is an important east-west crossing of Changsha City. The geographical location of the project is shown in Figure 1. The Tunnel connects the east and west banks of the Xiangjiang River, and is located in the north comprehensive development belt of Chang-Zhu-Tan city group and on the industrial axis of Chang-Ning-Liu city group in Changsha. The completion of the tunnel would relieve river-crossing traffic pressure in the northern city to a greater extent, specifically in the Yinpanling Bridge to the north and Yingpan Road tunnel to the south of this tunnel, which would connect the isolated lines and surrounding areas, shorten the spatial and temporal distance, improve the quality of the nearby land, and produce economic and social benefits.

Specifically, the Xiangya Road River-crossing Tunnel starts from 290 m to the east of Yuehua Road, and split into 2 sub-lines in the river section. The north line ends at 80 m to the west of Caie Road, and the south line ends at 240 m to the west of Furong Road. The total length of the north line and the south line is 3348 m and 3680 m, respectively. The design speed of the main line tunnel is 50 km/h. A pair of ramps was set up in the west section, the north line exit transferred to the right of Yinshuang Road via

Figure 1. The location of the Xiangya Road River-crossing Tunnel.

*Corresponding author: 253484901@qq.com

DOI: 10.1201/9781003495505-436

Figure 2. The overall layout of the Xiangya Road River-crossing Tunnel and the section of the shield tunnel.

Xiangyue Road, and the south line entrance was arranged parallel to the east of Yinpan South Road. In the east section, the north and south sub-lines were each equipped with one ramp to connect with Huangxing North Road, and the ramps were arranged parallel to the west of Huangxing North Road. The total length of the four ramp tunnels is 1601.11 m, and the design speed is 35 km/h. The connecting roads of the east and west banks of the tunnel are Xiangya Road and Tongzipo Road, both of which are urban trunk roads with a design speed of 50km/h. The middle section of the tunnel adopted a 1400 m long shield tunnel with an outer diameter of 14.5m and an inner diameter of 13.3m (six lanes in both directions), and with a minimum tunnelling radius of 840 m. The shore section was constructed by open excavation method (four lanes in both directions). The maximum longitudinal slope of the tunnel section was 5%, and the section passing through the subway station adopted 0.3% longitudinal slope. The minimum longitudinal slope of the shield section in the middle of the river adopted 0.3%. The minimum cover depth of western and eastern section was 10 m and 8.73 m, respectively. The section of the shield tunnel and the overall layout of the project is shown in Figure 2.

The main challenges of the exploitation and utilization of underground space during the construction of this project can be attributed to: (1) The construction conditions around the project are complicated, as the whole line of the project and Changsha Metro Line 6 have many common and interweaving lines. (2) The tunnel is located in the downtown area of Changsha with precious land resources. (3) The project has high requirements for surrounding environmental protection with plenty of air environment sensitive areas such as parks, hospitals, schools, residential areas and scientific research institutes near the entrance of both sides of the tunnel. Therefore, the impact of the project on the environment was strictly controlled.

Based on the above challenges, this project had carried out some innovations in the comprehensive development and utilization of urban underground space. Firstly, for the collaborative design and construction problem of long-distance overlapping municipal tunnels and subway tunnels in the urban core area, co-construction scheme was exerted. Secondly, the natural formed space above the deep foundation pit of the tunnel was utilized to build a two-story underground parking lot, which alleviated the parking difficulty in the core area of the city. Thirdly, the semi-underground structure in combination with the park landform was adopted to set up tunnel management buildings, which solved the problem of building tunnel management buildings under the land shortage in the central urban area. Fourthly, considering the urban core area and environmental sensitive areas, a multi-point distributed ventilation emission mode was implemented to optimize the air quality at the tunnel entrance, avoid setting high wind towers, and realize the coordination between tunnel environmental protection and urban landscape.

2 THE INNOVATION IN THE COMPREHENSIVE DEVELOPMENT AND UTILIZATION OF URBAN UNDERGROUND SPACE

2.1 *The co-construction of this project and metro stations*

The relative locations of tunnel and subway in this project are shown in Figures 3 and 4. It can be seen the location of this project is similar to Changsha Metro Line 6, and there are many lines interweaving. The Liugoulong Station, Wenchangge station, and the section between The Third Xiangya Hospital Station and The Xiangya Hospital Station of Mertro line 6 almost overlap this project. Moreover, this tunnel crosses Liugoulong Station and Wenchangge Station of Metro Line 6, respectively, occupying the space of basement level 1 of them.

As presented in Figure 5, the section from The Third Xiangya Hospital Station to Liugoulong Station of Metro Line 6 is located below the project, with spacing of 13.8 m~31.6 m. The thickness of the lightly weathered slate cover the subway section is 4 ~ 9m. In the construction of this project, the layered utilization of underground space should be taken into account.

Figure 6. presents the co-construction scheme of this project and Liugoulong Station of Metro line 6.

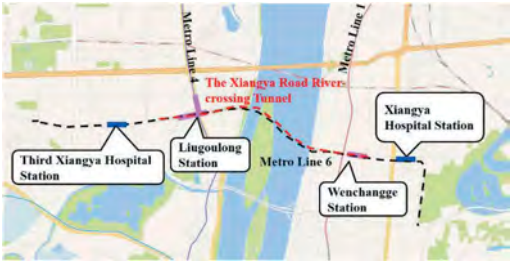

Figure 3. The plane diagram of relative locations of this project and subway.

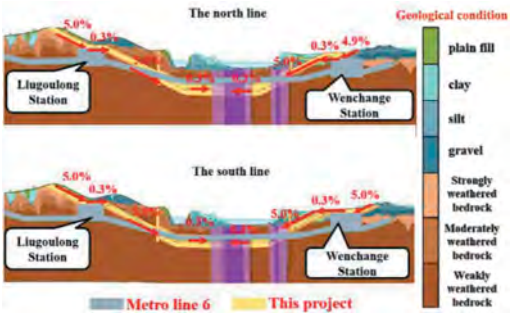

Figure 4. The profile diagram of relative locations of this project and subway.

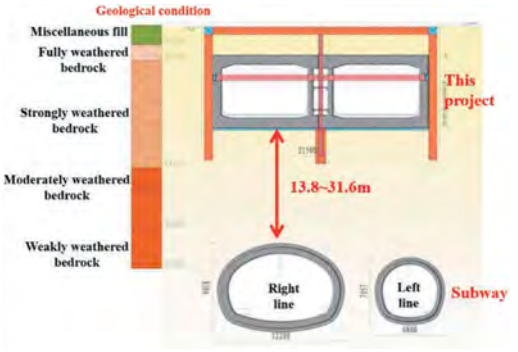

Figure 5. The cross-sectional relationship between the tunnel and metro line 6.

Liugoulong Station is located at the intersection of Tongzipo Road and Yinpan South Road, which is a island station with two underground floors. Moreover, it is also the transfer station for Metro Line 4 and Line 6. The project intersected vertically with Liugoulong Station at the intersection and occupied the basement level 1 (B1) of the station. The B1 of Liugulong Station had reserved 6 lanes.

As shown in Figure7, co-construction scheme was also exerted between this project and Wenchangge Station of Metro Line 6. Wenchangge Station is located to the east of the intersection of Huangxing North Road and Xiangya Road, along Xiangya Road in an east-west direction. Moreover, it is a three-

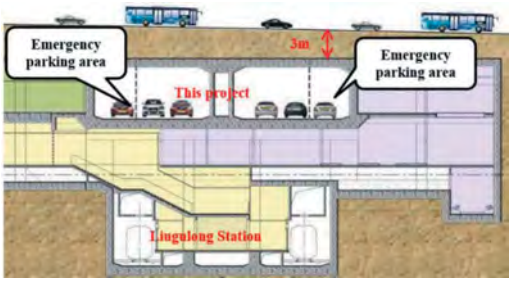

Figure 6. The co-construction scheme of this project and liuguolong station.

storey underground island station with a width of 14 m, which is also a transfer station for Metro Line 6 and Line 1. This project is parallel to Wenchangge Station of Line 6, located on the B1 of Wenchangge Station. The ramp on the north side of the project is above the station and reserved for eastward extension. There was a 2 m mismatch between Wenchangge Station and the south side of this tunnel project. According to the consultation with the Metro Company, the south structure of Wenchangge Station expanded by 2 m to meet the construction requirements of the co-construction.

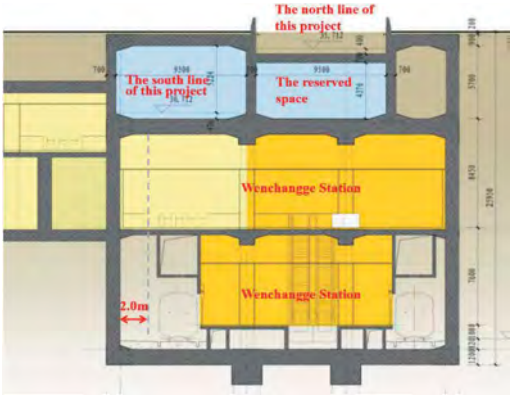

Figure 7. The co-construction scheme of this project and wenchangge station.

The tunnel of this project was arranged along the east-west corridor with Changsha Metro Line 6. The cut-and-cover section on shore of this project and two subway stations were co-constructed and the tunnel is located on the B1 of the subway station. The overlapping sections were arranged by upper and lower layers, and the shield tunnel section adopted separate layout. This project solved the problem of collaborative design and construction of municipal traffic tunnel and subway overlapping long distance in the core area of the city. Furthermore, the multi-layer intensive utilization of the inner space of the narrow traffic corridor in the city was realized.

2.2 *Underground parking lot in the backfill space of the foundation pit*

There was a large demand for parking lots due to the dense population and large traffic flow near the project. However, the project is located in the core area of Changsha City, and the land resources are precious. The development and utilization of aboveground and underground space is one of the main measures for urban land conservation. This project considered the backfill space of the foundation pit above the tunnel to set up two-layer underground parking lot.

The underground parking lot of Xiangya Road River-crossing Tunnel Project is located in the west section of the river, under Tongzipo Road and Yinpenling Park, and above the cut-and-cover section of Xiangya Road tunnel. The east side of the project is close to the scenic belt along the river and Yuxiang Factory of yarn, the south side is the land to be developed, and the west side is Liugoulong Station of Metro Line 4, and Youth Palace of Yuelu District. The project served as a non-profit underground parking lot for minicars and small cars. The total construction area of the parking lot is about 17424.2 m^2, which can provide nearly 400 parking spaces. It is a large parking lot with two vehicle entrances, 7 groups of wind pavilions, 5 safety exits and 3 barrier-free elevators. In order to reduce the impact on the Tongzipo Road, the north side of the Tongzi slope was set to 4 lanes. The renderings of the underground parking lot are shown in Figure 8.

Figure 8. The renderings of the underground parking lot.

This project changed the traditional backfill scheme of open-cut deep foundation pit, and established a comprehensive utilization and development mode of underground space. The natural space formed above the deep excavation foundation pit of the tunnel was utilized to build an underground two-story parking lot (about 400 parking spaces), which reduced the soil covering load of the deep excavation tunnel, optimized the tunnel structure size, reduced the project investment, saved the construction cost of the underground parking envelope, and alleviated the parking shortage in the core area of the city.

2.3 *Tunnel management building of semi-underground structure*

The tunnel management building of this project is located near Yinpenling Park. In order to protect the ecological environment of the park, the project considered the current situation of the park and the underground parking lot and chose semi-underground structure for the tunnel management building. On the premise of meeting the needs of tunnel maintenance and rescue, the construction scheme saved ground and did not affect the overall planning of the park and the area of green space. The plane diagram of the tunnel management building is shown in Figure 9, and the profile diagram of the tunnel management building is shown in Figure 10.

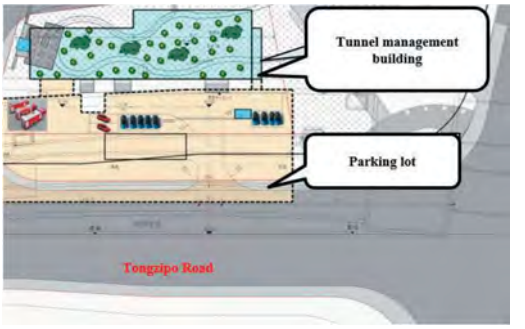

Figure 9. The plane diagram of the tunnel management building.

Figure 10. The profile diagram of the tunnel management building.

According to the requirements of centralized monitoring and management, the land use and the distribution of tunnels, tunnel management building combined with Yinpenling park was designed as covered buildings. The entrance and exit of the building start from the Tongzipo Road, and the roof of the building is covered with about 2-meter-thick soil.

The whole site landscape was integrated into the landscape system of Yinpenling Park. The architectural shape adopted a smooth and soothing style, and

the natural terrain was rationally used in the local area. The plant configuration was further combined to enrich the site landscape. As for the facade design of the building, the environment of the surrounding Yinpenling Park was combined, and the building was fully integrated into the environment by the design of the earth covered building, which reduces the impact on the park. Under the premise of economic rationality, the design was strived to be novel, beautiful, elegant, and modern. The facade adopted a modernist approach with materials of stone, tiles, glass curtain wall, and rainproof louvers. Through a variety of measures, such as virtual-real contrast, rhythm and change, to express the modern, simple and atmospheric characteristics of the building. The diagram of tunnel management building is shown in Figure 11.

Figure 11. The renderings of tunnel management building.

In combination with the landscape of the park, semi-underground structure was adopted to set up tunnel management buildings, which solved the problem of building tunnel management buildings under the land shortage in the central urban area. Located in the park, the tunnel management building with semi-underground structure created a quiet office and living space for users, while reducing the impact on Yinpenling Park and becoming a model of adapting to local conditions.

2.4 *Multi-point distributed ventilation*

Ventilation system is an important part of tunnel. Under normal traffic conditions, the ventilation system should be able to dilute the exhaust gas (CO and smoke) emitted by driving cars, and provide standard ventilation and health conditions for the passenger and maintenance personnel. In the case of a fire accident, the ventilation system should exhaust smoke, control the diffusion of smoke and heat, and provide a certain amount of fresh air for passengers and firefighters staying in the tunnel, so as to facilitate safe evacuation and fire-fighting. In the design of tunnel ventilation, the proper ventilation mode should be selected under the premise of ensuring ventilation effect and energy-saving operation, and saving project investment.

The ventilation mode of urban cross-river tunnel mainly depends on the tunnel length, longitudinal slope, traffic volume and traffic mode. In addition, the environmental protection of the entrance, tunnel construction methods, and fire safety requirements should also be considered. The length of the closed section of Xiangya Road River-crossing Tunnel Project is 3038 m in the north, 3347 m in the south, and 1400 m for shield section in the middle of the river, respectively. There are two ramps on the east and west banks, and the length of the closed sections are 537 m for C ramp, 348 m for D ramp, 204 m for E ramp and 182 m for G ramp, respectively. According to the calculation result of air demand, longitudinal ventilation mode and full longitudinal jet fan were adopted in this project.

There are several environmentally sensitive buildings such as hospitals, schools, residential areas and scientific research institutes near the entrance to both sides of the tunnel, and the concentrated emission from the entrance is bound to affect the surrounding buildings. As shown in Figure12, in order to reduce the impact of concentrated emissions from the tunnel entrance on surrounding buildings along the tunnel entrance, eight decentralized exhaust pavilions were set up in the green area of Yinpenling Park on the West Bank, which covered an area of about 150m^2 on the ground. Each exhaust pavilion was equipped with an exhaust fan with air volume of 40 m^3/s and power of 45 kW. In order to ensure that the length of the smoke exhaust section of the tunnel is not more than 3 km, a smoke exhaust room was set up in the shield shaft of the West bank. Three smoke exhaust fans with air volume of 120 m^3/s and power of 160 kW were arranged in the room, which are responsible for the smoke exhaust of the ramp of the West Bank and the entrance of the main line, as well as the entrance ramp of the main tunnel and the east bank.

Figure 12. Eight decentralized exhaust pavilions were set up in the green area of yinpenling park on the west bank.

In this project, considering the environment of urban core area, the tunnel adopted a multi-point distributed ventilation emission mode to optimize the air quality at the tunnel entrance. The optimized design avoided setting high wind towers, and realized the coordination between tunnel environmental protection and urban landscape. The tunnel entrance is close to the environmentally sensitive buildings. The tunnel ventilation design reasonably adopted the multi-point decentralized emission mode, and eight decentralized concealed exhaust booths were set within the green space of the park to deal with the

diffusion of tunnel pollutants. The emission concentration of pollutants at the exit of the tunnel was controlled, and the risk of affecting the surrounding air environment caused by the centralized emission at the entrance of the main line was effectively avoided.

3 DISCUSSION

The 21st century is the century of underground space development and utilization (Qian, 2007). Vigorously developing and utilizing urban underground space has great strategic significance to address many problems in the urbanization process such as urban land shortage, traffic congestion, and environmental pollution (Cui et al., 2021). Many cities around the world have developed and utilized underground space reasonably, and the development of urban underground space has been a general trend.

Firstly, the development of urban underground space is beneficial for alleviating urban land shortage. The land resources in urban central areas are relatively short, the intensity of land development is relatively high, and the population is concentrated. Therefore, the demand for various urban functions is relatively high, and it cannot be met through ground construction alone, which leads to the imbalance of land supply and demand. Therefore, it is necessary to use underground space to supplement the ground space of urban central area and realize urban redevelopment.

Secondly, the development of urban underground space is beneficial for alleviating urban transportation conflicts. The number of cars in major cities in China continues to grow in recent years, and the huge traffic pressure has caused serious urban congestion, which directly affects the efficiency of social operation. Rationally planning and constructing underground roads can improve the structure of the road network, solve the traffic bottleneck, improve the travel efficiency and relieve the pressure of surface traffic (Jia, 2016).

Finally, the development of urban underground space is beneficial for environmental restoration. Urban central areas are densely built and lacking green space. Through the renewal and utilization of underground space, large facilities such as substations, refuse transfer stations, high-voltage equipment and public transportation platforms can be placed in the underground space to release the public space on the ground and transformed into leisure space, park square and so on. It is conducive to creating living areas filled with bright light and green plants in the ground space, providing a comfortable experience for urban residents (Audi et al., 2020).

On the basis of reasonable protection of various functional spaces, this project focused on the intensive comprehensive development and utilization of underground space, which improved the comprehensive utilization rate of underground space, saved engineering cost and urban land resources, and played a significant role in protecting and coordinating the surrounding environment and landscape. Firstly, the whole line was co-built with the subway, and the technologies such as layered utilization, synchronous co-construction and reserved subconstruction were adopted to solve the collaborative design and construction problems of overlapping and interweaving municipal underwater traffic tunnel and subway in urban areas. Secondly, the underground parking lot scheme saved project investment and provided about 400 underground parking spaces, which greatly alleviated the parking shortage of the surrounding commercial plots and the scenic belt along the river. Thirdly, combined with the Yinpenling Park and the underground parking lot, the tunnel management building was built as a semi-underground structure by using the site height difference in the park, which directly saved land resources of about 2000 square meters. The problem of construction of tunnel management building in the central city was then resolved. Finally, 8 decentralized concealed exhaust pavilions were set up in the green area of Yinpenling Park to avoid setting high wind towers, which realized coordination between tunnel ventilation system and urban landscape.

4 CONCLUSIONS

This project realized the intensive comprehensive development and utilization of underground space by co-construction with subway stations, using the pit backfill space to set up underground parking lot, setting up tunnel management buildings with semi-underground structure by using the elevation difference, and using the park green space to set up dispersed hidden exhaust pavilions. On the basis of guaranteeing all functional spaces, the comprehensive utilization rate of underground space was improved, engineering cost and urban land resources were saved, and the surrounding environment was protected as much as possible.

REFERENCES

Audi, Y., Jullien, A., Dauvergne, M., et al, 2020. Methodology and application for the environmental assessment of underground multimodal tunnels. Transportation Geotechnics, 24, 100389.

Cui, J., Broere, W., Lin, D., 2021. Underground space utilisation for urban renewal. Tunnelling and Underground Space Technology, 108, 103726.

Hunan provincial communications planning, survey & design institute co., ltd., 2018. Preliminary design of Xiangya Road River-Crossing Tunnel Project in Changsha City.

Jia, J., Fang, Y., 2016. Underground Space Development in Comprehensive Transport Hubs in China. Procedia Engineering, 165, 404–417.

Qian, Q. H., 2007. Sustainable civilization and the development of underground space. Science Press, 663–670.

Tunnelling for a Better Life – Yan, Celestino, Thewes & Eberhardt (Eds)
© 2024 The Author(s), ISBN 978-1-032-80042-4
Open Access: www.taylorfrancis.com, CC BY-NC-ND 4.0 license

A broad review of cavern engineering approach in meta-sedimentary rock in Northern Hong Kong

Jeffrey C.F. Wong, Leslie W.H. Tsang* & Hermann H.M. Suen
Geotechnical Engineering Office, Civil Engineering and Development Department, Hong Kong SAR, China

David C.W. Mak*, Franklin K.L. To & Harry H.C. Poon
AECOM Asia Co. Ltd., Hong Kong SAR, China

ABSTRACT: The northern New Territories is being planned for development into one of the important development nodes in Hong Kong. While the flat alluvial plain landform in that region can facilitate future developments, to further optimise the development potential of the new development areas, the mountains flanking the alluvial plain can offer rock cavern development opportunities as an alternative form of land supply to support the overall development, as demonstrated by cavern development in Hong Kong over the past decades. These mountains are composed of the Lok Ma Chau Formation, a meta-sedimentary rock formed in the Palaeozoic period. However, in the past cavern development history in Hong Kong, most of the large-span caverns were built in either granitic rock or volcanic rock. There is also only limited tunnel design and construction experience in the meta-sedimentary rocks and hence the effect of common characteristics of this geology on cavern engineering, such as potentially lower rock strength as compared to that of the igneous rocks, planes of weakness along bedding, high variability in material characteristic over short distances, etc., are largely unexamined in the past.

Given the strategic location, the cavern development potential in the northern part of Hong Kong is expected to gain weight in the future. A broad review of the cavern engineering approach in the meta-sedimentary rocks has therefore been carried out to examine the cavern development potential in this geology with a view to opening up the opportunity for cavern development in meta-sedimentary rocks in the future. The paper presents the findings of the review, which includes a preliminary geotechnical assessment, appraisal of cavern engineering considerations and broad parametric assessment of cavern design, with a particular focus on the feasibility of rock reinforcement approach in the meta-sedimentary rock in the study area.

Keywords: Cavern, Meta-sedimentary rock, Hong Kong

1 INTRODUCTION

The northern area in Hong Kong is one of the important development nodes in the coming future. Near the Hong Kong–Shenzhen Innovation and Technology Park and the San Tin Technopole under planning, the cavern development potential in the mountains flanking these major development nodes is expected to gain weight in the future. These mountains are composed of the Lok Ma Chau Formation, a meta-sedimentary rock formed in the Palaeozoic period. However, the general understanding of this geology is that the rock strength varies widely, with preferred weak planes along the beddings (GEO, 2007), and the general rock strength is potentially lower as compared with granitic/volcanic rock (Arup, 2008). As there was no precedent cavern development in the geology of meta-sedimentary rock in Hong Kong and the available ground information in this area is scarce, the cavern engineering approach in this geology was largely unexamined in the past.

Ho et al. (2020) provided a comprehensive review of rock cavern development and the paradigm shift of the cavern engineering approach in igneous rock geology in Hong Kong. In the past, the most dominant form of permanent support for caverns was the cast in-situ reinforced concrete lining. Yet there is a drive for the use of the rock reinforcement approach, in the form of permanent pattern rock bolt and sprayed concrete, in lieu of the traditional cast in-situ concrete lining in the recent cavern projects. By relying on the formation of reinforced rock arch at the crown of caverns (Bischoff and Smart, 1977), the rock reinforcement approach is considered to be much more cost-effective than the cast in-situ concrete lining (Grøv, 2013) and, therefore, the

*Corresponding author: leslietsang@cedd.gov.hk; David.mak@aecom.co

DOI: 10.1201/9781003495505-437

applicability of the rock reinforcement approach in the concerned meta-sedimentary rock has a significant implication to the cavern development potential from the financial perspective. Nevertheless, the experience of applying the rock reinforcement approach was all in the volcanic/granitic rock in Hong Kong and it is uncertain whether it is suitable in the meta-sedimentary rock commonly found in this area.

To unlock the cavern development potential in the northern area in Hong Kong, a broad review of the cavern engineering approach based on some recent ground investigation (GI) results in the meta-sedimentary rocks has therefore been carried out, which includes a preliminary geotechnical assessment, appraisal of cavern engineering considerations and broad parametric assessment of cavern design, with a particular focus of the feasibility of rock reinforcement approach in the meta-sedimentary rock in the study area.

2 GEOLOGICAL CHARACTERISTICS OF THE STUDY AREAS

The study is conducted on two hilly areas, namely the Lok Ma Chau study area and the Tai Shek Mo study area, as shown in Figure 1, under meta-sedimentary rock conditions in the Northern District of Hong Kong. The Lok Ma Chau study area is situated in the northeast-trending ridge from east of Lok Ma Chau with a maximum height of +143 mPD at the crest and the Tai Shek Mo study area is located in the north-trending ridge of Tai Shek Mo with a maximum height of +163 mPD at the crest.

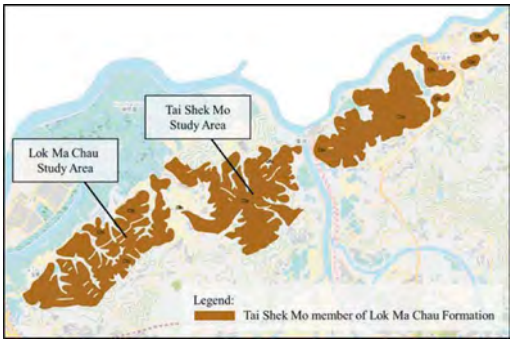

Figure 1. Location plan for the study.

2.1 *Geological characteristics*

Based on the 1:20,000 geological map, the Lok Ma Chau and Tai Shek Mo study areas are predominantly underlain by Tai Shek Mo member (Cts) of the Carboniferous Lok Ma Chau Formation, which comprises meta-sandstone with meta-conglometrate and phyllite.

In reference to the 1:100,000 geological map (GEO, 2016), the Lok Ma Chau and Tai Shek Mo study areas are predominately bounded by the NE-SW and NW-SE trending faults. In addition, some fault gouge materials are also encountered in a few boreholes. The rock head depression and the presence of these fault-related materials shall be indicative of possible fault zones in the study areas. The predominate NE-SW and NW-SE trending with locally N-S trending photolineaments are delineated based on the aerial photo interpretation of the study areas, which may induce potential weakness zones.

In addition, a relatively less persistent and highly anisotropic orientation of foliation and cleavage are observed in the sedimentary rock at a few spots of the study areas in the 1:20,000 geological map (GCO, 1989 and GCO, 1991). Foliation may result in anisotropy rock mass strength, which may lead the shear strength along the foliation to be relatively low, but a higher shear strength perpendicular to the plane of foliation. As a result, there is a possibility to encounter a comparatively large spectrum of shear strength values in the tests. Nonetheless, this is generally local in size and site specified (orientation and excavation scale) concerned.

2.2 *Geotechnical properties*

Based on the geological map and available GI data, meta-sandstone would be the dominant rock type within the study areas. The information from laboratory tests on rock specimens has been reviewed. Based on the laboratory testing results, the uniaxial compressive strength (UCS) of specimens, which are eligible for this test, with material failure identified, elastic modulus and joint shear strength on intact rock specimens have been summarised in Tables 1-3.

Table 1. Summary of uniaxial compressive strength.

	Uniaxial Compressive Strength, UCS (MPa)			
Rock Type	No. of test	Min.	Max.	Avg.
Meta-Siltstone	23	8	164	86
Meta-Sandstone	6	41	220	102

Table 2. Summary of elastic modulus.

	Elastic Modulus, E_i (GPa)			
Rock Type	No. of test	Min.	Max.	Avg.
Meta-Siltstone	17	8	69	49
Meta-Sandstone	3	53	74	64

Table 3. Summary of peak joint friction angle.

	Peak friction angle, ϕ_p (Deg)			
Rock Type	No. of test	Min.	Max.	Avg.
Meta-Siltstone	113	19	56	37
Meta-Sandstone	30	17	49	33

The above available GI data did not differentiate the testing direction in the laboratory testing. Therefore, the above results represent the material strength in a random direction and the anisotropic behaviour due to the foliation/bedding of the meta-sedimentary rock could not be revealed.

The UCS and elastic modulus with the other common rock types in Hong Kong, such as granite and volcanic rocks, have been compared in Table 4. It should be noted that the weathering classification of meta-sedimentary rock is a subject under review recently in Hong Kong. The below table presents all the data of meta-sedimentary rock retrieved at the site without assigning a weathering grade. It can be seen that the maximum and minimum rock strength of the meta-sedimentary stretched considerably but the average rock strength is comparable to that of granitic and volcanic rocks.

Table 4. Comparison of UCS between common rock types in Hong Kong.

	Granite*		Volcanic*			
	Grade II	Grade III	Grade II	Grade III	Meta-Siltstone	Meta-Sandstone
UCS (MPa)	60 to 179	10 to 85	110 to above 300	10 to 120	8 to 164 (avg. 86)	41 to 220 (avg. 102)

(*) Reference from Geoguide 4 (GEO, 2017) and Geoguide 1 (GEO, 2017)

3 BROAD ASSESSMENT OF POTENTIAL FAILURE MODES

Martin et al. (1999), based on Hoek et al. (1995), have worked on the potential failure mode in excavations, as shown in Figure 2. Failure modes in caverns are determined by the characteristics of the rock mass, which is dependent on the strength of the intact rock and Rock Mass Rating (RMR) (Bieniawski 1989), as well as the in-situ stresses.

3.1 *Estimation of Q-value in the study area*

The RMR is estimated based on the approximate relationship between the Q-value and RMR proposed by Bieniawski (1984). The NGI Q-system for rock mass classification and its relationships to tunnel supports were first developed by Barton et al. (1974) and updated by Grimstad & Barton (1993). To characterise the ground condition for cavern design and construction, a range of Q-values have been interpreted in Table 5 using the available existing borehole information.

The Q-value is formulated by multipliers of six rock mass parameters in Equation 1.

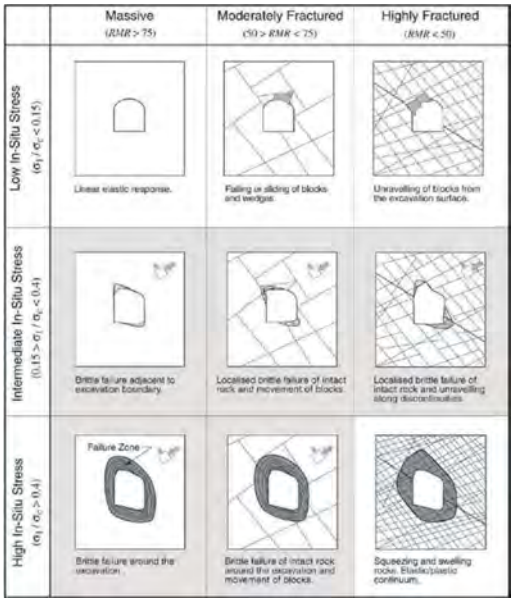

Figure 2. Modes of failure (Martin et al, 1999).

Table 5. Range of Q-value based on ground investigation.

Depth below rockhead	Q<0.1	0.1≤Q<0.4	0.4≤Q<1	1≤Q<4	4≤Q<10	Q≥10
<20 m	12%	13%	16%	51%	8%	0%
≥20 m	8%	1%	2%	48%	28%	13%

$$Q = \frac{RQD}{J_n} \times \frac{J_r}{J_a} \times \frac{J_w}{SRF} \quad (1)$$

The first component (RQD/J_n) describes the relative size of rock blocks. The second component (J_r/J_a) describes the shear strength of inter-block discontinuities. The third component (J_w/SRF) describes the stress conditions.

Further breakdown and examination reveal that the Q-value between 0.7 and 12 would cover about 80% of the estimated ground conditions for depth below rockhead ≥ 20m. By adopting the approximate relationship between Q-value and RMR, the RMR of the meta-sedimentary rocks in the study areas is estimated to be in a range between 40 and 65.

3.2 *Estimation of failure modes in the study area*

According to Table 1, the average UCS of meta-siltstone and meta-sandstone are 86MPa and 102MPa respectively. As discussed in Section 2.3, the laboratory data could not provide the anisotropic parameter and therefore, for the purpose of this broad review, a conservative UCS of the meta-sedimentary rock (UCS = 50MPa) was adopted in the assessment. Although there is no available data about the

principal rock stress ratio, it is conservatively assumed to be 2.5 based on some regional studies (Alan et al. 2012). As a result, the ratio of the maximum principal stress to the UCS would be less than 0.15 at the depth of the assumed cavern crown level in the study areas (i.e. around 70m below ground level) for the above range of principal stress ratio.

Based on the above observations, structurally controlled failures, including falling or sliding of blocks/wedges and unravelling of blocks from the excavation surface, are considered the dominating types of instability for caverns in the study areas in general as the stress level relative to the rock mass strength is generally low, except where localised weaker rock is encountered due to high variation of rock strength. The failure modes of caverns in meta-sedimentary rock in the study areas are estimated to be similar to that in granite and volcanic rocks in Hong Kong in general conditions.

4 CAVERN STABILISATION DESIGN IN HONG KONG

4.1 *Rock reinforcement approach*

Over 80% of the hilly terrain in Hong Kong is underlain by hard igneous rocks with a comparatively higher compressive strength than concrete. The concept of the rock reinforcement approach in cavern design relies on the formation of a rock arch at the cavern crown. The inherent strength and thrust capacity of rock mass are utilised by applying confining stress via systematic bolts. Permanent rock reinforcements in hard rock caverns comprise rock bolts and sprayed concrete. Systematic rock bolts are the main reinforcement and sprayed concrete supports rock wedges between rock bolts (Barrett and McCreath, 1995). On the other hand, spot bolts are installed to stabilise individual blocks and wedges.

4.2 *Deriving support with the NGI Q-system*

For a given combination of Q-value and Equivalent Dimension, the support requirements, such as the required shotcrete thickness and systematic rock bolt spacing for a given rock support class, can be obtained from the NGI Q-system (NGI, 2015) in Figure 4.

The formula proposed by Barton et al. (1977) in Equation 2 is used to determine the initial systematic rock bolt length. Spot bolts for rock wedges shall be assessed separately.

$$L = 2 + \frac{0.15B}{ESR} \qquad (2)$$

where:

L = bolt length in metre.

B = cavern span for crown support in metre (could use the cavern height H for wall support).

ESR = excavation support ratio (safety requirement).

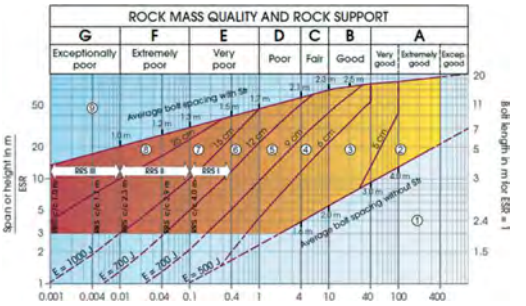

Figure 3. The Q-system rock support chart (NGI, 2015).

Based on Figure 4, for a cavern span of up to 20m in meta-sedimentary rock, rock reinforcement using permanent sprayed concrete and rock bolts would be sufficient to stabilise the ground, while the individual rock blocks would be supported by spot bolts as necessary. Although caverns with a span of more than 30m are becoming very common in Hong Kong, in this assessment, the cavern span is assumed to be 20m, which is considered to be sufficient to accommodate various development needs. This initial cavern supporting system derived from the NGI Q-system and the adopted material capacities are summarised in Tables 6 and 7.

Table 6. Initial rock bolts support for prototype cavern.

Systematic Rock Bolts (Crown)		Systematic Rock Bolts (Wall)		Ultimate Bolt Capacity*
Length	Spacing	Length	Spacing	(kN)
5 m	1.6 m	5 m	1.6 m	482

* The ultimate capacity of a fully grouted bolt, which is required to be 2 times of the working load

Table 7. Initial shotcrete support for prototype cavern.

Shotcrete Thickness (mm)		Shotcrete Strength (MPa)	
Crown	Wall	Flexural	Compressive f_{ck}
130	100	5	37

5 VERIFICATION USING NUMERICAL ANALYSES

On the basis of the methodologies discussed in Section 4, an initial cavern stabilisation system can be reasonably obtained for a single cavern excavation. To further examine the supporting performance under the conditions of multiple cavern excavations, cavern supports derived by the NGI Q-system are verified using numerical analyses. Based on numerical modelling, the permanent rock bolts are checked against their design capacities.

5.1 *General configuration of the prototype caverns*

According to To et al. (2021), the permanent support requirements for rock caverns are more stringent with increasing cavern spans and multiple parallel excavations. Three parallel caverns with 20 m width rock pillars (i.e. 1 × cavern span) between each cavern were assumed in the prototype design for verification. Also, as shown in Figure 5, the cavern in the prototype is assumed to be 20 m (span) × 20 m (height), with a 4 m high roof arch plus a -16 m high straight wall.

Based on the topological setting of the study areas, the ground level is approximated to be +130 mPD. According to the available GI data, the rock-head level is approximately 40m below ground level at +90 mPD. It is considered to have sufficient rock cover of 30 m (i.e. 1.5 cavern span) for the cavern development of a 20 m wide span.

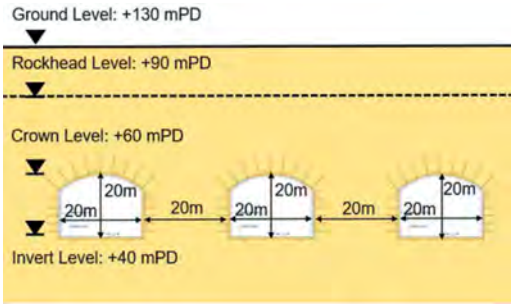

Figure 4. Prototype cavern design (not to scale).

Based on the knowledge from the available data on the rock samples as discussed in Section 2, the geotechnical parameters adopted in the prototype design are summarised in Table 8.

Table 8. Parameters adopted in the prototype design.

Rock type	Q	UCS (MPa)	E_i (GPa)	v
Meta-siltstone	0.7	50	30	0.3
Meta-sandstone		50	65	0.3

5.2 *Verification using numerical simulation*

The commercial 2D finite element method programme (RS2 by Rocscience) was used to conduct the design verification of permanent rock supports for the caverns in moderately to highly fractured ground, as shown in Figure 5.

The rock material (grey in Figure 5) was simulated using the isotropic elastic perfectly plastic model with Generalised Hoek-Brown (GHB) failure criterion for rock mass, which is assumed to be meta-sandstone as it is the dominant rock type with the study areas as discussed in Section 2.3. Rock bolts and shotcrete were modelled using linear elastic structural element. Various modelling stages were assigned to simulate the rock excavation and support installation as illustrated in Figure 6 and Table 9.

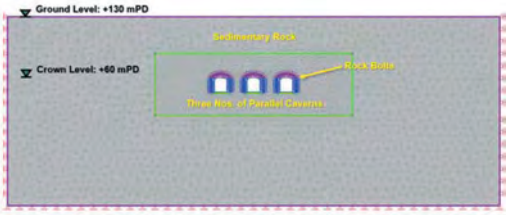

Figure 5. Numerical analysis for multiple caverns excavation.

Table 9. Modelling stage of the numerical analysis.

Stage	Remark
1	Initial stress generation.
2	Core replacement method to mimic the 3D effect of tunnel face support to the surrounding rock mass by retaining portions of the original stress field.
3	Installation of permanent rock bolts and fibre reinforced shotcrete.
4	Full excavation along the rock caverns.

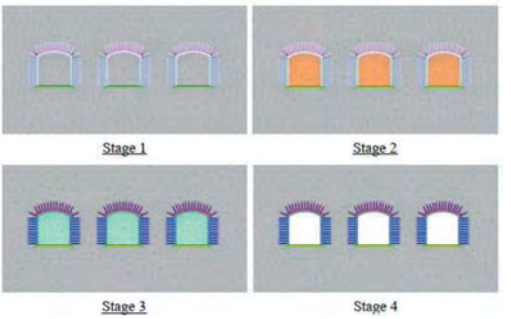

Figure 6. Modelling Stages in numerical analysis.

The estimated maximum bolt force is 111.0kN, which is much lower than the allowable bolt force of 241kN. This indicates that the initial cavern stabilisation design is acceptable in the concerned geology. Nevertheless, due to the characteristics of meta-sedimentary rock (e.g. varying rock quality, rock bedding, etc.), parametric studies have been conducted against different critical parameters which may affect the design of the cavern supporting system.

6 PARAMETRIC STUDIES OF CAVERN DESIGN UNDER META-SEDIMENTARY ROCK CONDITIONS

To further understand the cavern design under different meta-sedimentary rock conditions and allow greater flexibility for subsequent planning, the

design methodology discussed in Section 4 were further examine with the variation of following factors:

i. Rock Mass Quality (Q-value)
ii. Uniaxial Compressive Strength (UCS)
iii. Rock Layering Arrangement

6.1 *Rock mass quality (Q-value)*

Rock mass quality is a critical parameter affecting the support design. The fundamental difference between the use of permanent rock reinforcements and the cast-in-situ concrete lining is the reliance on the strength of in-situ rock mass.

The selected range of rock mass quality for the parameter study in Table 10 is on the conservative side to test the feasibility of rock reinforcement approach.

Table 10. Parametric studies of rock mass quality.

Span	Height	Q-value	UCS
20 m	20 m	0.4 0.7 4	50 MPa

The maximum bolt forces as shown in Figure 7 reveals that the utilisation of the cavern supporting system drops significantly when the Q-value increase from 0.4 to 0.7 (very poor to poor rock quality). The decreasing trend of bolt force becomes steady when Q-value is greater than 0.7 (fair rock quality).

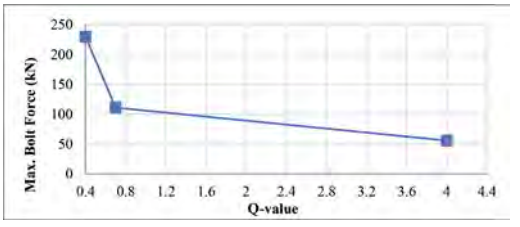

Figure 7. Bolt forces for varying rock mass quality.

6.2 *Uniaxial Compressive Strength (UCS)*

Similarly, UCS is a critical factor in the design of permanent cavern reinforcement. With reference to Table 4, UCS of meta-sedimentary has a wide range from 41 MPa to 220 MPa, and the UCS used in the prototype design is 50 MPa (Table 8). Hence, a range of ±30 MPa was adopted to study the impact when the UCS varies from 20 MPa and 80 MPa respectively, as presented in Table 11.

The maximum bolt forces are shown in Figure 8 that structural forces decrease whilst UCS increasing. It shows that utilisation of bolt at walls is sensitive to UCS, which is similar to the behaviour as observed in Figure 7 for the changes of rock mass quality.

Table 11. Parametric studies of uniaxial compressive strength (UCS).

Span (m)	Height (m)	Q-value	UCS (MPa)
20	20	0.7	20 50 80

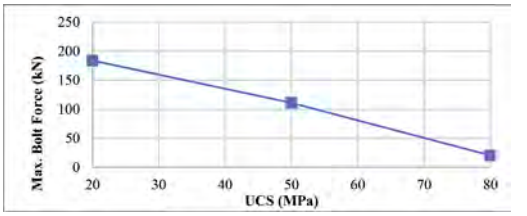

Figure 8. Bolt forces for varying UCS.

6.3 *Rock layering arrangement*

Compared with granite or volcanic rock in Hong Kong, sedimentary rock has the characteristic of rock layering. A study was carried out to examine the impact with respect to the thickness of strata layers and the dipping. To simulate the possible combination of rock layer interfaces crossing the rock bolts at different cavern locations (crown and walls), 5 m and 8 m thick strata layers were assumed based on the available GI data. Based on the published geological map, an average dipping of 30° was noted. For the dipping, horizontal rock layers with 0° and inclined rock layers with 30° were selected for the study. The general arrangement of four numerical models with varying thicknesses and dipping of strata layers are presented in Figures 9-12.

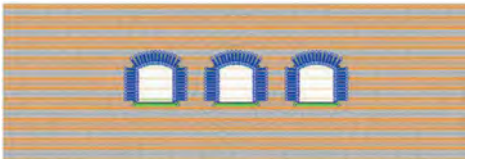

Figure 9. Horizontal and 5 m thick rock layering.

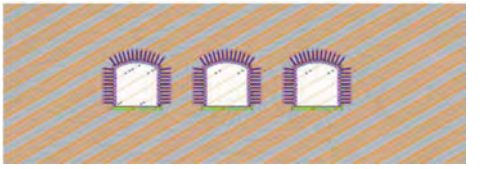

Figure 10. 30 ° Inclination and 5m thick rock layering.

According to Figure 13, the maximum bolt force in the meta-siltstone model is higher than that in the meta-sandstone model. This is because meta-siltstone has lower GHB engineering properties than

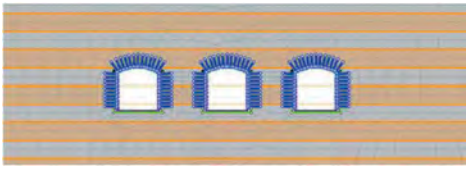

Figure 11. Horizontal and 8m thick rock layering.

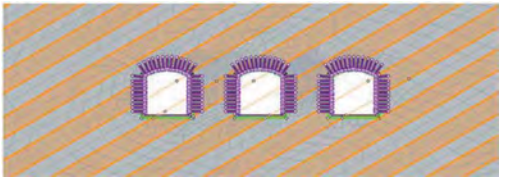

Figure 12. 30 ° Inclination and 8m thick rock layering.

meta-sandstone. With the presence of alternative layering of meta-sandstone and meta-siltstone in various 5 m/8 m thickness and 0°/30° inclination, the corresponding maximum rock bolt forces lay between the upper bound value (meta-siltstone model) and the lower bound value (meta-sandstone model). This outcome reveals that the rock layering arrangement did not significantly affect the utilisation of the cavern supporting system. The homogenous meta-siltstone model would serve as the conservative design case covering the various layering scenarios.

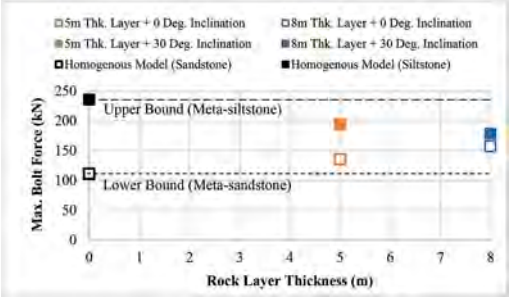

Figure 13. Bolt forces for alternative rock stratum layering.

Nevertheless, amongst the alternative layering models, it is noted that an inclination of 30° incurs is a more critical case. The cavern supporting system requires a higher utilisation. Yet, there was no clear trend observed regarding the impact of 5m/8m thickness.

7 CONCLUSION

An assessment has been undertaken to review cavern engineering considerations and the feasibility of the rock reinforcement approach. A prototype design for cavern development in meta-sedimentary rock was conducted. The performance and utilisation of cavern supports in the prototype design are all within the acceptable range. In addition, parametric studies were conducted with the critical parameters which may bring significant impacts to the cavern support, such as the degree of utilisation of bolt force. It provides a broad understanding of cavern design in meta-sedimentary rock and allows a greater flexibility for subsequent planning and design in the next stage. Nonetheless, the study was carried out based on limited existing GI data without differentiation of testing direction, together with the large variations in meta-sedimentary rocks, including rock strength and bedding arrangement. It is recommended that a more extensive ground investigation and further study on the project site location are required to identify any adverse features in the cavern area.

To conclude, the broad review reveals that, subject to local heavy weathering/fracturing, the rock reinforcement approach is generally feasible for the meta-sedimentary rock in the two concerned study areas, even for ground conditions with special characteristics such as rock layering. Although the cavern engineering conditions in meta-sedimentary rock is still considered to be more complicated as compared to that in the igneous rocks, this review opens up the cavern development potential in this area as it implies that the cavern engineering approach in this geology in general would be similar to those adopted in other igneous rocks in Hong Kong.

ACKNOWLEDGEMENT

The authors gratefully acknowledge the Geotechnical Engineering Office, Civil Engineering and Development Department, the Government of the Hong Kong Special Administrative Region, for permission to publish this paper.

REFERENCES

Arup 2011. Final Report on Enhanced Use of Underground Space in Hong Kong – Feasibility Study. Ove Arup and Partners for Geotechnical Engineering Office, Civil Engineering and Development Department, Government of the Hong Kong Special Administrative Region, Hong Kong, China.

Barrett S.V.L. and McCreath D.R., 1995. Shotcrete support design in blocky ground: Towards a deterministic approach. Tunnelling and Underground Space Technology 10(1): 78–99.

Barton N., Lien R. & Lunde J., 1974. Engineering Classification of Rock Masses for the Design of Tunnel Support. Rock Mechanics, 6, pp189–236

Bieniawski, Z.T., 1984. Rock Mechanics Design in Mining and Tunneling. A. A. Balema, Rotterdam, 272 p.

Bieniawski, Z. T., 1989. Engineering rock mass classifications: a complete manual for engineers and geologists in mining, civil, and petroleum engineering. John Wiley & Sons.

Bischoff J.A. and Smart J.D., 1977. A method of computing a rock reinforcement system which is structurally equivalent to an internal support system. In Proceedings of the 16th US Symposium on Rock Mechanics, Minneapolis, MN, USA (Fairhurst C and Crouch SL (eds)). ASCE, New York, NY, USA, pp. 279–284.

Grimstad E. and Barton N., 1993. Updating of the Q-System for NMT, Proceedings of the International Symposium on Sprayed Concrete, Fagernes, pp46–66

GCO, 1989. 1:20,000 Hong Kong Geological Survey (HKGS) Geological Map Sheet No. 2, San Tin: Solid and Superficial Geology

GCO, 1991. 1:20,000 Hong Kong Geological Survey (HKGS) Geological Map Sheet No. 2, Sheung Shui: Solid and Superficial Geology.

GEO, 2006. 1:100,000 Hong Kong Geological Survey (HKGS) Geological Map of Hong Kong, Web-based Edition.

GEO, 2007. GEO Publication No. 1/2007, Engineering Geological Practice in Hong Kong. Geotechnical Engineering Office, Civil Engineering and Development Department, Hong Kong SAR

GEO, 2018. Geoguide 4: Guide to Cavern Engineering, Second Edition 2018. Geotechnical Engineering Office, Civil Engineering and Development Department, Hong Kong SAR.

GEO, 2019. Geological Reports GR2/2019 – Geology of the Sandy Ridge Area, Northern New Territories. Geotechnical Engineering Office, Civil Engineering and Development Department, Hong Kong SAR

Ho Y.K., Tsang W.H. and Chan C.C., 2020. Rock cavern development in Hong Kong: past, present and future. Proceedings of the Institution of Civil Engineers – Civil Engineering 173(5): 25–31.

Hoek, E., P.K. Kaiser and W.F. Bawden, 1995. Support of Underground Excavations in Hard Rock, Toronto.

Hoek, E., Carranza-Torres, C.T. and Corkum, B., 2002. Hoek-Brown Failure Criterion – 2002 Edition. Proceedings of the 5th North American Rock Mechanics Symposium, Toronto, 7-10 July 2002, 267–273.

Hoek, E. & Diederichs, M.S., 2006: Estimation of rock mass modulus. International Journal of Rock Mechanics and Mining Sciences, Vol.43, Issue 2, pp. 203–215. Elsevier.

Kong, K.W.K. & Garshol, K.F., 2015. Rock Reinforcement Design for Underground Openings. Proceedings of the Underground Design and Construction Conference 2015, The Institute of Materials, Minerals & Mining Hong Kong Branch, Hong Kong 2015. pp. 51–62.

Kwong, K.L. and Wong B.M.L., 2012. An assessment of in-situ rock stress ratio in Hong Kong. HKIE Transactions, vol. 20 No. 1, pp 52–61

Martin, C.D., Kaiser, P.K. & McCreath, D.R., 1999. Hoek-Brown parameters for predicting the depth of brittle failure around tunnels. Canadian Geotechnical Journal, vol. 39, pp 136–151.

NGI, 2015. Using the Q-system: Rock Mass Classifications and Support Design (handbook). Norwegian Geotechnical Institute, Oslo.

To F.K.L., Bridges G.D.C. & Seto A.K.W., 2021. Design Optimization of Permanent Systematic Rock Bolts and Shotcrete Lining for Large-Span Caverns in Hard Rock. Proceedings of The HKIE Geotechnical Division. 41st Annual Seminar. Jointly organized by the

Tunnelling for a Better Life – Yan, Celestino, Thewes & Eberhardt (Eds)
© 2024 The Author(s), ISBN 978-1-032-80042-4
Open Access: www.taylorfrancis.com, CC BY-NC-ND 4.0 license

Key technology for the construction of the Shen-Zhong Link tunnel under the existing operating expressway

Xianping Zhou
Shenzhen-Zhongshan Link Administration Center, Zhongshan, China

Xiaoyong Cheng
Guangdong Province Communications Planning & Design Institute Co., Ltd., Guangzhou, China

Qingshuang Xu
Shenzhen-Zhongshan Link Administration Center, Zhongshan, China

ABSTRACT: Shen-Zhong Link is another bridge-island-tunnel combination project in China after the Hong Kong-Zhuhai-Macao Bridge. The project construction conditions are complex and technically difficult, mainly including a main span of 1666 meters suspension bridge, two artificial island and 6.8 km tunnel, the east artificial island, is China's first large underwater interchange, highway is the construction environment is extremely demanding near both operating highway deep foundation pit engineering, the main line using two-way eight lane highway technical standards.East Artificial Island is a large underwater interchange to realize the traffic transformation between the Shenzhen-China channel and the expressway near the river. It is realized through multiple changes of the structural section. The construction environment is extremely complex. The deep foundation pit project involves the complex external conditions of sea, land, air, passenger terminal, multiple channels, expressway, tight construction period, complex organization and high construction requirements of water environment. Through technical scheme optimization, technical management, site construction management and other technical and management means, the project has formed the technology of the adjacent bridge reclamation, the deep foundation pit protection technology of the existing bridge, and the construction technology of the existing bridge and tunnel. A batch of suitable construction equipment has been developed to form the key technology of tunnel construction of large underwater interchange near and under the existing operating expressway, to provide reference for the construction of the same type of projects.

Keywords: Shenzhen-Zhongshan Link, suspension bridge, subsea tunnel, artificial island, deep foundation pit

1 PREFACE

Deep channel is after the Hong Kong-Zhuhai-macao bridge China another bridge island tunnel cluster engineering, project construction conditions is complex, technical difficulty is big, mainly including the main span 1666 m suspension bridge, two artificial island and 6.8 km long tunnel, the east artificial island, is China's first large underwater interchange, highway construction environment is extremely demanding near both operation of highway filling sand island and island tunnel deep foundation pit engineering, the main line with two-way eight lane highway technical standards.

East artificial island land area of 343,800 square meters, the island with tunnel engineering, rescue wharf, power supply and distribution facilities and related ancillary facilities, the tunnel works include 480 m long weir section tunnel, 855 m long main tunnel on the island, and the four ramp tunnels for traffic conversion. The construction environment is extremely complex, under the existing expressway. East Artificial Island is the gateway project of Shenzhen end, located in the south of Shenzhen Bao'an

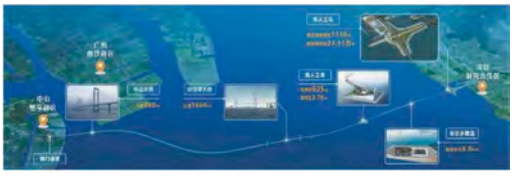

Figure 1. Line bitmap of the deep and middle channel.

DOI: 10.1201/9781003495505-438

Airport, adjacent to Fuyong Airport Terminal, connected to the east of the project, and the complex external conditions of China, including passenger terminal, multiple channels, white dolphin reserve, air pipeline, air route and other water environment. Combined with the characteristics of the project, through technical scheme optimization, technical management, site construction management and other technical and management means, the problems of anti-seepage control and uniform backfill control in the construction stage of deep soft foundation, ultra-deep and ultra-wide foundation pit cluster in the sea area were solved, and the problem of deep foundation pit construction against the small deformation of the structure was solved.

Figure 2. Layout plan of the east artificial island.

2 CONTROL THE DEFORMATION OF THE EXISTING ADJACENT BRIDGE PIERS

The construction of east artificial island is faced with prominent difficulties in large project scale and high environmental protection requirements, and the operation of existing projects such as Baoan Airport and Guangzhou-Shenzhen Yanjiang Expressway cannot be affected in the construction process. The engineering geology is mainly composed of silt and silt soil layer with a small amount of silty clay, 8.0~15.0m thick, backfill sand layer and deep silt layer are distributed in the field, and riprap layer exists in the local area, and it is easily affected by tide, typhoon and rainfall. Under the existing Guangzhou-Shenzhen expressway along the Yangtze River, about 3 million cubic meters of sea sand should be filled within the 40-span pier cap sea area. The ownership unit of the expressway along the river requires that the displacement and settlement of the bridge pier of the expressway along the river shall not exceed 5 mm, which can be said that the control indicators are extremely demanding.

Figure 3. Reclamation of the east artificial island.

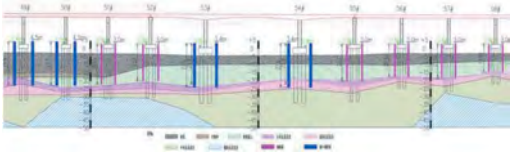

Figure 4. Geological profile of the east artificial island.

2.1 *Carry out special studies on safety evaluation*

According to the characteristics of the implementation of the east artificial island and the island tunnel, the special Study on the safety Evaluation of the impact of the East artificial Island and the Island Tunnel along the Yangtze River was carried out. The proposed plan of the east artificial island project is connected with the existing Guangzhou-Shenzhen high-speed bridge along the River, and the connecting section is originally sea area. In the later stage, the coarse sand and the island wall embankment are constructed to realize the normal use elevation of the artificial island, so as to meet the connection between the buried tunnel and the land viaduct and open tunnel. According to the design, the filling height reaches 7~8m, and the soft soil layer is below the surface of the project area, and the thickness of the soft soil reaches about 10m. Large area sand filling of artificial island, island wall embankment construction, and later building construction in the island will have extremely adverse effects on the adjacent bridge foundation. Large surface overload in sea soft soil area will produce negative friction resistance in the pile foundation, increase the axial force of the pile body, and reduce the vertical bearing capacity of the pile. Meanwhile, large side sand filling will produce additional stress in the soil to move the soil on the side, so that the pile body and even the whole bridge substructure produce additional stress, cause large additional deformation and bending moment of the pile foundation and reduce the horizontal bearing capacity of the pile foundation. Moreover, a large area of sand filling will cause the horizontal and vertical displacement of the bridge substructure, and the large displacement may cause the damage of the bridge substructure, and on the other hand, it may affect the normal use of the superstructure engineering. Project for the above problems, considering the artificial island blowing sand filling process in the pile side, island wall dike construction, island wall inside large sand filling building construction, and the island, and the ramp and the main tunnel foundation pit construction, according to the east artificial island construction of the existing wide expressway bridge pile foundation influence and prevention needs, research: (1) for Ming built sea artificial island and adjacent along the river highway engineering characteristics, clear artificial sand filling on adjacent bridge safety displacement control standard, further guide the project artificial island filling construction and bridge protection. (2) The protection design scheme of the expressway pier along the river adopts the steel plate pile scheme, and the height

difference around the pier is not more than 1m in the process of island building. Analyze and evaluate the highway safety along the river under this working condition. And put forward relevant suggestions for the protection scheme. (3) The island wall structure at the southern end of the east artificial island is located below the expressway along the river. The island wall structure adopts the cement mixing pile composite foundation treatment scheme to analyze and evaluate the safety of the expressway along the river under the working conditions. And put forward relevant suggestions for the protection scheme. (4) Within the range of the concentrated structures on the east artificial island, the stacking prepressure is used for the foundation treatment to analyze the safety of the highway along the river under the working conditions. (5) According to the influence results of different working conditions of the artificial island construction on the adjacent Guangzhou-Shenzhen expressway bridge along the Yangtze River, the key monitoring parts and monitoring and early warning indicators of the Guangzhou-Shenzhen expressway bridge along the Yangtze River are put forward. (6) Through the simulation analysis of the ramp foundation pit construction, according to the calculation results to judge whether the foundation pit excavation affects the adjacent bridge pile foundation, if there is an impact, the degree of impact (mainly from the analysis of the bridge pile deformation and additional bending moment). (7) Through the simulation results of foundation pit excavation and the ultimate additional deformation and additional bending moment value, judge whether the proposed supporting structure of the foundation pit and the bridge pile foundation protection structure can meet the safety requirements of the bridge. (8) According to the position relationship between different ramps and bridge pile foundation, reasonable suggestions are put forward in combination with the design scheme and simulation results. In view of some key technical problems existing in the impact of the large area filling of the east artificial island on the adjacent bridge pile foundation, the appropriate suggestions for bridge protection are put forward.

In order to solve the practical problems in the project and guide the design and construction, based on a large number of theoretical analysis and numerical calculation, the research results consider the engineering practice, combined with the characteristics of the project, focus on the study of the impact of beach siltation, seabed migration, road construction on the adjacent ramp bridge foundation. Finally, according to the simulation analysis of the adverse conditions in the island, such as the sand filling and the dam construction, it is concluded that: (1) due to the soil filling on both sides of the pier alternately, the horizontal displacement of the bridge pile in the sand filling direction will also change alternately, while the horizontal displacement on the other side will increase with the increase of the sand filling thickness. Compared with the calculation results of the unbalanced sand filling between the transverse bridge and the transverse bridge, we find that when the maximum height difference between the left and right sides is always 1m, the sand filling along the bridge has a more significant impact on the adjacent bridge piles. (2) When taking the steel plate pile reinforcement, the steel plate pile is filled first, and then the sand filling outside of the steel plate pile is more conducive to the protection effect of the adjacent bridge pile. The maximum horizontal displacement of the steel plate pile along the bridge is 12mm, while the maximum horizontal displacement along the bridge can reach more than 20mm outside the steel plate pile. It is suggested to fill the steel plate pile with sand first. (3) When the sand is filled in the steel plate pile, the displacement is even greater than 10mm along the bridge, and the impact of the sand filling on both sides of the bridge is much less than 10mm. In the actual construction process, it is suggested to fill sand on both sides of the horizontal bridge, that is, symmetric backfill on both sides of the bridge line. When the backfill thickness reaches 4m, the filling rate should be strictly controlled in the subsequent sand filling process, and it is suggested that the height difference of filling should be appropriately reduced. (4) take steel plate pile first filling sand, one side of the sand filling thickness is greater than 3m, and the other side of the height difference 1m, should strengthen the adjacent pier displacement monitoring, monitoring and warning displacement can be controlled for 5mm, more than 5mm is suggested to stop filling, adjust the filling process or isolation and corrective reinforcement measures, the displacement change of larger condition should reduce the height difference on both sides of the filling, control the balance sand filling construction as far as possible. (5) For the axial force of pile, due to the negative friction resistance, the axial force of pile increases and then decreases with the depth. However, because the piles along the expressway bridge along the river are all rock-embedded piles, the axial load of the pile meets the requirements of compressive bearing capacity. (6) take steel plate pile filling first, for pile bending moment, with the increase of filling thickness, the pile moment is increasing, along the bridge to the thickness of 7m, the other side of 6m pile bending moment, but through the maximum moment section check found that the maximum moment position pile cracks are less than 0.1mm, meet the requirements of engineering safety. (7) take steel plate pile outside filling first, for pile moment, with the increase of filling thickness, the pile moment, along the bridge to both sides or the bridge filling in thickness of 7m, the other side of 6m pile moment, but through the maximum moment section check found that the maximum moment position pile cracks are greater than 0.1mm, does not meet the requirements of engineering safety. (8) By taking the 48 # pier as the typical island pier, during the filling process of the island, after the steel plate pile strengthens and protects the pier, when 7m is filled according to the height difference thickness of 1m, the maximum side shift of the adjacent bridge pile is 5.0mm, and the filling height of one side is 7m and the other side is

6m. Considering the overload of 1~3m, the filling height can reach 8~10m, the maximum horizontal displacement can reach 5.3~6.7mm, and less than 10mm displacement control standard, which can meet the safety requirements of bridge engineering. (9) In the southern end of the island wall area, when steel plate pile is adopted to reinforce the pier, the foundation treatment depth is shallow and the treatment range is small, the dam filling and sand filling have a significant impact on the adjacent 71 # ~75 # piers, and the horizontal displacement is greater than 10mm, and the safety is low. (10) In the island wall area of the southern end, when the steel pipe pile is drilled to reinforce the pier, the foundation treatment depth reaches above the medium weathered rock and the treatment range is from 70 # ~76 # pier area, the dam filling and the adjacent 71 # ~75 # pier are less affected, and the horizontal displacement is less than 10mm, meeting the requirements of 10mm displacement control standard. (11) Due to the geological differences of different piers near the southern island wall, it is suggested that the settlement and horizontal displacement monitoring of the adjacent piers should be strengthened during the island wall construction and sand filling construction in the island, and the filling rate and process should be timely adjusted to ensure the filling balance around the piers as far as possible. It shows that under the action of the dam pile load, the pile foundation of the pier at the embankment corner is subjected to large lateral extrusion pressure, so the multi-layer protection and reinforcement measures of the pier at the embankment corner position should be carried out according to the monitoring results and the actual situation, such as the row pile reinforcement measures.

The results are demonstrated through the study: the horizontal displacement of the backfill in the pile is reduced by 21%, the horizontal displacement of the horizontal bridge is reduced by 61% compared with that of the backfill in the forward bridge, and the horizontal displacement is reduced by 62.5% compared with the 0.5m thick 1m, and the horizontal displacement is increased by 12.5% per 0.1m increase on average.

2.2 *Technical solutions*

Field area exists deep silt layer (8~15m), the physical and mechanical indexes of sea silt formation is poor, high water content, low bearing capacity, easy to touch, easy flow, high compressibility characteristics, backfill construction prone to large area arch, gushing phenomenon, such as directly in the pier and both sides of the backfill, silt layer strength and the resistance to deformation is too low, backfill loading process, will produce the larger range of shape deformation area in foundation soil, make the foundation of too large settlement and lateral displacement. The lateral displacement of soil is an important cause of the additional bending moment and deformation of pier pile foundation. When the additional bending moment and deformation are greater than the allowable value of pile foundation, the pile foundation will stagger and change, reduce the bearing capacity, and the pile foundation will break and destroy in serious cases.

Combined with the research results, it is necessary to take measures to limit the deformation of the silt layer at each pier to avoid the safety risks caused by the island backfill construction and affect the normal use of the piers. From the technical scheme, it is clear that the steel plate pile or steel pipe pile are protected around the pier cap within the influence area of the island, and grasp the data and analyze the development trend, and take timely countermeasures. For symmetrical layered filling on both sides of the existing bridge piers, the force must be uniform, otherwise it is easy to cause partial load, which leads to the displacement of the bridge pier. To solve the bridge area filling sand cannot real-time dispersion of short-term stress concentration problem, innovation adopted the island filling process' sand is method for filling operations, using sand pumping pump will backfill sand filling into the film bag, uniform filling into sand is, a layer a layer evenly spread around the piers, effectively solve the problem of deep silt layer backfill partial load.

Figure 5. Sand backfill by process.

Figure 6. Drainage consolidation.

2.3 *Technical management and construction control*

Through the study, the backfill principle is summarized: according to the horizontal bridge to the backfill, first the inside and outside, the steel plate (pipe) pile, filling to layer, symmetrical, uniform, stratification thickness is strictly controlled at no more than 50cm, the height difference between the left and right sides is controlled at no more than 100cm.

The backfill under the bridge adopts the sand separation device of the sand distributor, and the "7" shaped hole pipe backfill the transverse bridge to the corresponding area. By suction ship + 2 Φ300mm main pipe for backfill sand long distance transportation, each main branch for 2 Φ240mm vice pipe for sand diversion, in the auxiliary pipe port installed sand separator device, both sides are 200mm wide sand, two 100mm wide sand outlet, can effectively ensure the uniform stability of backfill construction, reduce accumulation thickness, all the bottom of the pump pipe are easy to convert backfill working face, a single sand separator

blowing range of 2.5m.4 Φ550mm hole pipes are used at the pipe head of the sand blowing pipe, with 4 Φ150mm sand outlet opened for each pipe. The hole sandblasting distance is 3-5m. The pipe head is fixed by cable to prevent left and right swing. It can control the thickness of a single filling more accurately, and has strong applicability to the backfill construction around the existing bridge structure.

Figure 7. Backfilling of sand division unit.

Figure 8. Backfilling of Figure 7.

The protective steel plate pile of the expressway pier along the river is constructed by static pressure planting pile or without resonance. First, the first steel plate pile is driven into the soil, and then the second steel plate pile is welded with the first section. After the quality of the weld is checked, the whole steel plate pile will be driven to the design elevation.

Figure 9. Hydrostatic pressing pile planting.

Figure 10. No-resonance drilling process.

Drainage is consolidated into an island. After the completion of sand filling island, plastic drainage plate is applied for consolidation and settlement, and then loaded to the design elevation through the combination of blowing, land transportation and direct unloading, and the vibration is washed into the island.

3 DEFORMATION CONTROL OF THE DEEP FOUNDATION PIT OF THE EXISTING HIGH-SPEED BRIDGE

After the completion of the east artificial island island, the island involves the main tunnel and two ramp tunnels under the existing high-speed bridge. In the main tunnel construction, the deep foundation pit about 70m long, 46m wide and 18m deep should be excavated, and the nearest place is only 1.17m from the existing bridge cap. The engineering geology of the site is mainly filled with a small amount of silty clay, 8.0~15.0m thick. There is a riprap layer in the local area, and it is easily affected by tide, typhoon and rainfall. Under the existing Guangzhou-Shenzhen expressway along the River, it involves three times through the existing expressway bridge. The excavation boundary of the tunnel is 62~350cm away from the bridge cap, and the excavation depth of the foundation pit is 8~16m. The ownership unit of the expressway along the river requires that the displacement and settlement of the foundation pit excavation on the expressway pier along the river shall not exceed 5 mm, and the control indicators are extremely demanding.

In the construction process of the ramp tunnel under the east artificial island, H and F ramp and the main tunnel need to pass through the completed main bridge along the river respectively. The open-dug foundation pit of the G and E ramp is also in parallel with the main bridge pier along the riverside expressway, and the local ramp structure is only about 2m away from the pile cap of the bridge along the river. The construction of the ramp foundation pit will cause the imbalance of soil pressure on both sides of the pier pile foundation, leading to the transverse displacement of the pile foundation, and causing certain risks to the normal passage of the expressway along the river. It is necessary to carry out detailed calculation and analysis to determine the protection measures and relevant control standards of the substructure of the main bridge along the river in the tunnel area.

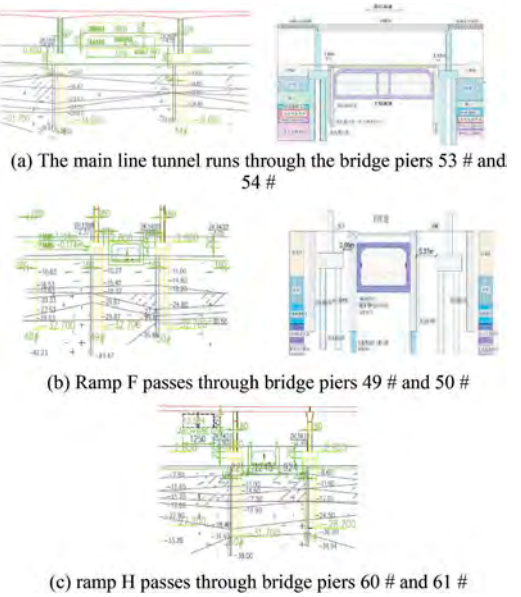

(a) The main line tunnel runs through the bridge piers 53 # and 54 #

(b) Ramp F passes through bridge piers 49 # and 50 #

(c) ramp H passes through bridge piers 60 # and 61 #

Figure 11. Bridge section of the ramp and the main tunnel.

3.1 *Conduct special research on safety evaluation and safety evaluation*

Considering the Shenzhen channel east artificial island and both deep bridge along the river, artificial

island four ramp two parallel with the existing bridge, the main tunnel and the other two ramp under the existing bridge, foundation pit supporting structure distance bridge cap edge, foundation pit excavation depth is larger, excavation of foundation pit excavation is bound to affect the existing bridge, threat to bridge security. In order to ensure the safety of the existing bridge, it is necessary to analyze and evaluate the influence of the ramp foundation pit excavation on the existing bridge, evaluate the support effect and protection effect of the foundation pit supporting structure and the bridge pile foundation protection structure, and put forward reasonable suggestions.

Simulation analysis from the following aspects: (1) according to the existing E ramp foundation pit excavation design drawings, design drawings of high-highway bridge pile foundation and design drawings of bridge foundation protection, the impact of E ramp (parallel bridge foundation) foundation pit excavation on the existing bridge is analyzed. (2) According to the existing F and H ramp foundation pit excavation design drawings, Guangshen and riverside bridge pile foundation design drawings and bridge foundation protection design drawings, the impact of foundation pit excavation of F and H ramp (under bridge foundation) on the existing bridge is analyzed. (3) According to the existing G ramp foundation pit excavation design drawings, Guangzhou-Shenzhen Yangtze River bridge pile foundation design drawings, bridge foundation protection design drawings, the impact of G ramp (parallel bridge foundation) excavation on the existing bridge is analyzed. (4) According to the design drawings of the excavation of the main tunnel, the design drawings of the foundation and the design drawings of the protection of the bridge foundation, the influence of the excavation of the main tunnel (underpass bridge foundation) on the existing bridge is analyzed.

Through the above study, the existing design meets the bridge safety according to the design results, and the reasonable suggestions are as follows:

(1) Calculation and analysis results of piers spanning 53 # and 54 # in the main tunnel project. After review, the compression bearing capacity of the positive section, vertical bearing capacity of pile foundation and pile bearing capacity of the main tunnel pier all meet the requirements. And the following conclusion: ① construction according to the current design, the maximum side of pile foundation cap is 5.84mm, if not considering the cap retaining steel pipe pile, the maximum side of 6.50mm, the displacement increased slightly, the vertical displacement of pile foundation cap is small, the maximum vertical displacement of 4.42mm. The small displacement, consider the retaining steel pipe pile on the vertical displacement, pier and cap displacement overall within the safety range. ② The maximum tensile stress of the pier and pile foundation cap is 0.94MPa, the maximum compressive stress is about 3.95MPa, and the maximum shear stress is 0.53 Mpa, which is within the safety range. ③ The steel pipe pile plays an important role in preventing the lateral deformation of the soil. The maximum lateral deformation of the steel pipe pile is 11.03mm, and the deformation is to the inside of the foundation pit, showing the overall "drum belly" deformation, and the maximum horizontal displacement is near the excavation surface. ④ Four supports, the axial pressure of the third and fourth steel support is the largest, the maximum axial force of the third support is 1518 kN, the maximum axial force of the fourth support is 1430 kN, the overall pressure of each support is within the safe range. The pressure of the lattice column is about 736.2kN, which is also within the safe range. ⑤ According to the calculation results, after the construction of the main line tunnel, considering the precipitation influence of the foundation pit precipitation, the maximum settlement of the surface outside the pit in the model boundary area reaches 1.16cm, which meets the standard requirements, and the maximum uplift at the bottom of the foundation pit reaches 7.77cm. In the actual construction, the detection of the foundation reinforcement effect should be strengthened. ⑥ In order to ensure that the deformation and force of the existing expressway pier and cap pile foundation along the river meet the requirements, the drainage conditions of steel pipe piles on both sides are considered for numerical calculation, and the calculated main structural deformation is taken as the construction limit value, and the warning value is 80% of the limit value. The normal working condition calculation value, standard value, limit value and early warning value are listed as shown in Table 1 below. ⑦ The bearing capacity of the pile foundation of the pier and cap is checked respectively. The bearing capacity of the positive section of the pier is 92499 kN, which is greater than the load of 20785 kN. The bearing capacity of single pile foundation is 80031 kN, and the bearing capacity of pile body is 67682 kN, greater than the load of pile top 8676.5kN. All meet the requirements. The maximum horizontal displacement allowable value of the pile top calculated according to the bearing capacity of the pile foundation is 28.33mm.

Table 1. Construction estimate.

name	Bearing table side shift/mm	Side shift of steel pipe pile/mm
Normal calculation value	5.84	11.03
Drainage on both sides	10.97	11.71
Specification value		27.0 (0.18% depth of foundation pit excavation)
Construction limit value	10.97	11.71
Construction early warning value	8.78	9.37

(2) Calculation and analysis results of F ramp crossing 49 # and 50 # piers. After review, the pressure

bearing capacity of the positive section, vertical bearing capacity of pile foundation and pile bearing capacity of F ramp tunnel all meet the requirements. And concluded as follows: ① as plate support, through the numerical simulation analysis of F ramp shows that the cap will cause stress concentration of cap pile foundation, and lead to the generation of large tensile stress, based on the conditions of 1 and 2 with cap bearing stress is 1.94MPa, greater than 0.5MPa. Large tensile stress may crack the pile foundation and affect the structural safety. In the absence of plate support, the maximum lateral displacement of the pier and pile foundation cap is 8.18mm and 3.59mm respectively, which are still within the allowable range. Compared with the application of plate support, the lateral displacement is only 0.22mm and 1.31mm increased respectively. Therefore, applying the plate support is not the most reasonable construction scheme. ② The maximum transverse deformation of pier and foundation pit. Through calculation and analysis, the maximum transverse deformation of pier under the action of plate support (working condition 1) is 7.96mm respectively, without exceeding the displacement standard value of 25.98mm; the maximum transverse deformation of crown beam and steel pipe pile is 2.42mm and 2.91mm respectively, which does not exceed the displacement standard value of 18.66 mm. After the foundation pit construction, the maximum surface settlement of the soil is distributed on both sides of the pile foundation cap, and the maximum settlement value is 7.68mm, which does not exceed the displacement standard value of 14.00mm. ③ The lateral displacement monitoring warning value of the key parts of the foundation pit of F ramp is set at 80% of the construction limit value. For the horizontal displacement of the steel pipe pile, cap and crown beam top, when the monitoring value reaches 3.73mm, 7.22mm and 2.6mm respectively, the warning should be reminded. ④ The bearing capacity of the pier and cap pile foundation is checked respectively, and the bearing capacity of the pier in the moment plane and perpendicular to the moment plane are 44910 kN and 31919 kN, greater than the load of 5840 kN. The bearing capacity of single pile foundation is 33332 kN, and the bearing capacity of pile body is 27429 kN, greater than the load of pile top 4077.8kN. All meet the requirements. The maximum horizontal displacement allowable value is 35.13mm when the pile foundation section reaches the bearing limit state.

(3) Calculation and analysis results of H ramp crossing 60 # and 61 # piers. After review, the pressure bearing capacity of the positive section, vertical bearing capacity of pile foundation and pile body of H ramp tunnel all meet the requirements. The following conclusions are drawn: during the construction of ① foundation pit, the maximum lateral displacement of the pier top is 8.8mm, and the maximum transverse displacement of the cap is 6.1mm; the maximum vertical deformation of the pier and cap is 1.94mm, which appears on the inside of the cap. The maximum tensile stress of the pier and cap pile foundation is about 0.48MPa, the maximum compressive stress is about 3.30MPa, and the maximum shear stress is about 0.31MPa, all within the safety range. ② The plate support plays a certain role in the displacement control of the cap. The lateral deformation of the cap is reduced by about 0.73mm, but the deformation at the pier can not be well controlled. On the contrary, a large secondary stress is generated in this process, resulting in the large tensile stress and shear stress at the cap. The calculation results of ramp H crossing piers 60 # and 61 # are shown in Table 2. ③ During the construction of the foundation pit, the maximum lateral deformation of the steel pipe pile in the envelope structure is about 7.69mm, the maximum axial tensile stress of the steel pipe pile is 0.65MPa, and the maximum axial compressive stress is 0.79MPa, which is within the safe range. The surface settlement is about 19.42mm, and the maximum lateral deformation of the surface soil is about 20.76mm. ④ In the process of foundation pit construction, the maximum lateral deformation of the crown beam is about 7.42mm, the maximum vertical deformation of the crown beam is about 10.83mm, and the value is small. The maximum tensile stress in the axial stress of the crown is 0.75MPa and the maximum compressive stress is 0.52MPa. The maximum axial compressive stress of the first support is 1.125MPa, and the maximum axial compressive stress of the second support is 11.31MPa. The maximum tensile stress of the main structure is 0.65MPa, and the maximum compressive stress is 2.25MPa. The maximum vertical deformation of the bottom plate is 11.03mm, and the maximum lateral deformation of the side wall is 5.43mm, which is within the safe range. ⑤ It is suggested to give an early warning when 80% of the control standard is reached. The construction limit value and the early warning value are shown in Table 3. ⑥ The bearing capacity of the pier and cap pile foundation is reviewed respectively: the bearing capacity of the pier in the bending moment plane and perpendicular to the bending moment plane is 46659 kN and 34698 kN, greater than the load of 5528 kN. The bearing capacity of single pile of pile is 34374 kN, and the bearing capacity of pile body is 27720 kN, which is greater than the load of pile top and 4044 kN, all of which meet the requirements. According to pile foundation specification and road and bridge code, the maximum horizontal displacement of pile top is 29.3mm.

(4) through the inversion analysis monitoring results, finally suggested as follows: ① because the envelope structure (filling) pile and rotary spray pile of good supporting wall, can effectively control the deformation around the soil to the pit, therefore, should ensure the construction quality of the envelope structure, strengthen the construction quality of testing work, prevent the cross section of the pier pile foundation and the surrounding soil deformation expansion, ensure the safety and stability of the foundation pit. ② The horizontal support of the envelope structure can effectively control the horizontal deformation of the soil. It is suggested that the horizontal support should be performed as soon as possible, and that the

Table 2. H Calculation results of ramp crossing piers 60 # and 61 #.

	displacement /mm		tensile stress /MPa		compression stress /MPa		shear stress /MPa	
Project	Board-free support	Add board support	Board-free support	Add board support	Board-free support	Add board support	Board-free support	Add board support
Pier	8.8	14.8	0.26	1.45	2.29	3.54	0.28	0.75
Pile foundation cap	6.15	5.42	0.48	14.0	3.30	8.19	0.31	2.46

Table 3. Construction limit value and early warning value.

Name	Side shift of steel pipe pile/mm	Side movement of pier top/mm	Bearing cap and pile foundation side shift/mm
Specification value	12.0(0.2% H)	$27.4(5)\sqrt{L}$	
calculated value	7.7	8.8	6.1
Drainage calculation value on both sides	9.4	12.2	10.8
Construction limit value	9.4	12.2	10.8
Construction early warning value	7.5	9.8	8.6

horizontal deformation monitoring of the soil around the foundation pit should be strengthened. ③ Although the bottom plate has been reinforced before the excavation, the uplift of the pit is still relatively obvious after the excavation of the foundation pit. Considering the adverse factors of the high water level of the artificial island, it is suggested to strengthen the detection of the reinforcement effect of the floor, and strictly carry out the construction monitoring of the floor uplift displacement. ④ The foundation pit precipitation has a great impact on the stability of the retaining structure and the surrounding soil, so the reinforcement and drainage scheme during excavation should be scientifically designed, and the effectiveness of the rotary spray reinforcement measures outside the pit and the bottom of the pit should be effectively guaranteed. It is suggested that the precipitation of the foundation pit should be controlled within 1-3m at the bottom of the pit, and the precipitation rate should not be too fast. ⑤ Strengthen the construction monitoring and measurement of foundation pit retaining structure and pile foundation of expressway pier along the river, adjust the construction process and supporting design parameters according to the monitoring results of deformation and stress; strengthen the monitoring of water and soil pressure and groundwater during the construction of working well. When necessary, the slope monitoring of the envelope steel pipe pile should be carried out, and the monitoring measurement forecast and early warning should be strengthened. ⑥ In order to avoid excessive displacement or settlement of the expressway pier along the river, it is recommended to adopt the automatic survey method of measuring robot during the construction period, and give early warning at 80% of the construction control standard, and serve as the basis for the preparation of basic deviation correction and reinforcement process plan. ⑦ Through calculation, the preliminary design of the pier cap and pile foundation surrounding a steel pipe pile as protection, the actual effect is not obvious (such as the main tunnel, as a steel pipe pile and only foundation pit side for steel pipe pile and rotary spray pile, the maximum deformation only 0.66mm), therefore, can consider to reduce the reinforcement strength and parameters (such as steel pipe pile layout sparse or slightly away from the cap, 3m outside), or consider only in close to the foundation pit. ⑧ In the control of F ramp and H ramp foundation pit and along the highway bridge cap lateral deformation, it is recommended that when control deformation measures (such as servo system, support jack or high pressure rotary jet), to strictly strengthen the cap and retaining structure of the lateral deformation monitoring, to ensure the safety and stability of the highway pier and foundation pit along the river retaining structure. ⑨ The force and deformation results of the foundation pit crown beam show that there is some optimization possibility, this calculation, the process, the mechanical parameters and permeability of the foundation reinforcement is given by experience analogy, the next further research based on the field test process sampling analysis, and according to verify the reinforcement parameters on the safety of the existing bridge structure and determine the final process parameters and supporting axial force system.

3.2 *Technical solutions*

The protection design of the affected 49,50,53,54,60 and 61 #. After the completion of the filling of the east island, the foundation pit of F ramp, main tunnel and H ramp will be excavated. According to the supporting scheme of ramp and tunnel foundation pit, the composite pile structure of steel pipe pile + (pouring) pile (in the steel pipe pile) will be adopted. Due to the limitation of construction space near the pier, in order to avoid mutual interference between different construction processes and reduce the construction difficulty, protection measures need to be taken for the pier during island filling and foundation pit excavation, and

the lock steel pipe pile is considered. The specification and depth of steel pipe pile are determined according to the needs of foundation pit support.

Figure 12. Location of the piers of the deep-middle passage and the Yangtze Expressway.

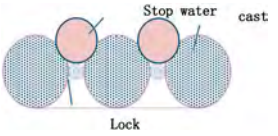

Figure 13. Design schematic diagram.

The 53 and 54 # piers affected by the island filling and the excavation of the main tunnel, steel pipe piles with 1.4m lock diameter and wall thickness of 20mm; 49,50,60 and 61 # piers affected by the island filling and the excavation of F and H ramp tunnel, lock steel pipe piles with a diameter of 1.5m with a wall thickness of 16mm. The steel pipe pile is set along the bridge pier, and the horizontal support is set on the inside to form the combined retaining structure of the locked steel pipe pile + the inner cast-in-place pile + the pile; the silt layer in the bottom and the upper silt layer and the high pressure rotary jet pile are used to monitor the supporting shaft force and the deformation of the foundation pit, control the support shaft force and comprehensively control the safety and deformation of the foundation pit and the protected objects.

Figure 14. Steel pipe pile protection diagram.

Figure 15. Soil reinforcement in passive area.

Figure 16. Steel support servo system.

3.3 *Technical management and construction control*

Enclosure structure technology, in the early island of sand lock steel pipe pile bridge protection measures for steel drum, low headspin drilling hole construction, hole into the lower steel cage using section hoisting measures, after the completion of the bored pile for water stop high pressure rotary spray pile, achieve the purpose of pile water stop, eventually formed lock steel pipe pile + set pile + pile between water stop spin spray pile composite envelope structure, realize "a multi-purpose".

The soil reinforcement technology in passive area affects the scope of foundation pit excavation level of deep silt formation (greater than 3 times the excavation depth). The silt layer at the bottom of the foundation pit and the 15m foundation pit on both sides of the viaduct is strengthened by high-pressure rotary jet pile. By improving the physical and mechanical properties of soil, improving the resistance of soil in the passive area, reducing the deformation of foundation pit supporting structure and enhancing the stability of foundation pit.

The foundation pit support safety scheme is solved by increasing the support axial force servo system. It integrates numerical control hydraulic technology, automatic monitoring technology and Internet of Things technology to monitor the real-time support shaft force and foundation pit deformation. It can regulate the support shaft force according to the foundation pit deformation data, and control the safety and deformation of foundation pit and protection objects in an all-round way. Foundation pit support axial force servo system through the active loading inhibition foundation pit deformation, through the travel of servo system and oil pressure two indicators of double control and timely compensation, can better avoid ordinary steel support in the process of excavation axial force loss, after the envelope structure horizontal displacement has obvious recovery, control effect is more significant.

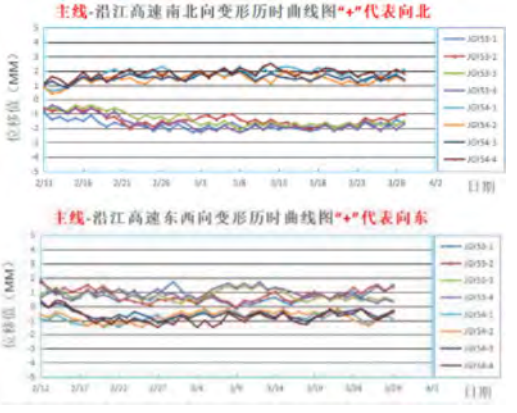

Figure 17. For monitoring data.

Displacement compensation and dynamic deviation correction technology. Make full use of the unloading effect of foundation pit, reasonably adjust the construction sequence to realize the horizontal displacement compensation; active displacement side, rotary jet tracking grouting for the dynamic correction and the deformation limit of the bridge.

Automatic monitoring technology. Leica TM50 automatic monitoring robot is used for all-weather automatic monitoring. In order to reduce the impact of the island on the stability of the observation station, two offshore measuring platforms are set up in the north and south sides of the east artificial island as automatic observation stations.

4 CONCLUSION

1. The deformation control of the piers of the existing adjacent bridge is controlled by the reclamation island. Through targeted project research and actual control, the deformation control index of the reclaimed bridge piers of the existing adjacent bridge is within 5mm, and the measures such as backfill principle and sand separation device should be adopted are effective for the deformation control.
2. Under the both high-speed bridge deep foundation pit deformation control, through the project safety evaluation research and safety assessment and the field more technical control, realized the existing high speed bridge deep foundation pit deformation control index reached 5mm, appropriate use of steel pipe pile, rotary pile water stop, passive area soil reinforcement measures and support axial force servo system way, is effective for control deformation.
3. For the subsequent calculation of soil and water pressure of similar foundation pit supporting structure design in the Pearl River Delta region, it is suggested to comprehensively consider the regional characteristics and influencing factors in order to obtain the quality and stability that meet the requirements.

REFERENCES

Li Zhiqiang, Xue iguo, Qu Liqing and so on. Analysis of the main bad geology and construction risk of the second undersea tunnel in Jiaozhou Bay, Qingdao [J/OL]. Journal of Engineering Geology: 1–12 [2023-08-28].

Li Yungang, Lv Yonggang, Zhang Tao, etc. Key technology of foundation treatment and foundation bed leveling of Dalian Bay Undersea Tunnel [J]. Harbor Construction of China, 2022,42 (12): 91–96.

Liu Jian. Application practice of BIM technology in Dalian Bay Undersea Tunnel Project [J]. China Harbor Construction, 2022,42 (12): 142–147.

Zhou Xianping, Cheng Xiaoyong, Fu Helin, etc. The control effect of the deep and large fault structural zone on the groundwater environment of the tunnel [J]. Journal of Underground Space and Engineering, 2022,18 (S2): 903–909.

Wang Yafei. Research on comprehensive geological survey technology of Jintang undersea Tunnel [J/OL]. Railway standard design: 1–8 [2023-08-28].

Jia Xu, Wang Tao, Sun Yangyang. Detection technology of prefabricated steel shell of immersed tube in submarine tunnel [J]. Harbor Construction of China, 2022,42 (11): 59–63.

Li Gengxin, Bian Jingmei, Bi Ziyang.—— Take Liaoning Province as an example [J]. Pearl River Water Transport, 2022 (16): 58–61.

Guo Yongjian. Research on key technology of Jiaozhou Bay Tunnel in Qingdao [J]. Construction technology (Chinese and English), 2022,51 (03): 42-44 + 58.

Lin Lihua. Research on comprehensive construction technology of water prevention and drainage of large section highway submarine tunnel [J]. Construction technology, 2020,49 (19): 105–109.

Zhang Dingli, Sun Zhenyu, Chen Tielin. Composite grouting technology and its engineering application [J]. Journal of Rock Mechanics and Engineering, 2019,38 (06): 1102–1116.

Huang Mingqi. Research on the construction technology of the complex geological large-section submarine tunnel through the water-rich sand layer [J]. Railway Construction Technology, 2016 (06): 23-26 + 31.

Zhao Xiaomei, Ma Biao, Chen Zhendong, etc. Overall scheme design of large interchange across multi-line railway corridor [J]. Modern Transportation Technology, 2023,20 (03): 34–40.

Bai Yunpeng. Research on key technical parameters of linear design of highway interchange [J]. Transportation world, 2023 (12): 78–80.

Taylor & Francis
Taylor & Francis Group
http://taylorandfrancis.com

Operational safety, maintenance and repair

Taylor & Francis
Taylor & Francis Group
http://taylorandfrancis.com

Tunnelling for a Better Life – Yan, Celestino, Thewes & Eberhardt (Eds)
© 2024 The Author(s), ISBN 978-1-032-80042-4
Open Access: www.taylorfrancis.com, CC BY-NC-ND 4.0 license

The 365 km tunnels assessment along ASPI Motorways Network – Key findings addressing risk analysis procedures and structural conditions evaluation and strategy of interventions

Carlo Alessio, Lapo Baccolini* & Daniele Di Fiore
Tecne Gruppo Autostrade per l'Italia S.p.A., Roma, Italy

Marilisa Conte & Maurizio Mazzola
Autostrade per l'Italia S.p.A., Roma, Italy

Daniele Peila
Politecnico di Torino, Torino, Italy

ABSTRACT: An extraordinary assessment plan, performed on 365 km of motorway tunnels, has been carried out in Italy since 2020 starting with detailed inspections and testing. Hundreds of laser scanning kilometres and ground-penetrating radargrams, thousands of concrete compressive strength tests, endoscope inspections and flat-jack tests have been performed so far. Tens of thousands structural defects were detected and several square meters of temporary safety measures installed as well. This allowed to acquire a significant amount of knowledges about the current condition of the asset.

According to the process defined by the new Italian Regulations, the dataset analysis provides an insight into the condition of the asset, guiding the entire maintenance process. The visual and detailed inspections frequency is driven by the simplified risk analysis outcome and further safety evaluation are designed based on multidisciplinary criticality.

A comprehensive approach, based on in-depth knowledge of the characteristics of the existing tunnel, has been engineered for structural risk, with a focus on tunnel "history" (excavation stages and techniques, construction materials, etc.), design and dimensioning approaches (e.g. Kommerel's graphical method), identified as standard methods for the tunnel construction period from literature review. Additional analyses are carried out for likely local structural failure modes of tunnel lining (punching and flexural strength of residual concrete layers, spalling hazard of concrete thickness anomalies due to temperature variations).

When re-lining is needed, the design of a new shell aimed to ensure at least the same structural performance of the original one is addressed, including seismic loads that were neglected in the original design.

The tunnel assessment, from inspections to re-lining works passing through risk analysis, is an on-going process open to be improved in the upcoming years within a wider asset management strategy.

Keywords: Road tunnels assessment, Detailed tunnel inspection, Asset management dataset, Risk classes, Re-lining works, Existing tunnel analysis

1 INTRODUCTION

Italy has a complex transport system mainly due to its geography and orography. Moving people and goods in the most safe, fast and efficient way is nowadays crucial and strategic at the same time. Road transport mode is historically the most widely adopted in the Country.

In this picture the resilience of the motorway is one of the main objectives that Autostrade per l'Italia S.p.A. (ASPI), the main motorway Concessioner in Italy, is pursuing.

ASPI is actively involved in the maintenance and operation of the asset on behalf of the Ministry of Transport. The main purpose is to ensure travellers, as well as employees, safety and continuity of the operations within a competitive level of service.

An extraordinary assessment plan was launched in 2020 on the road tunnel side, triggering about 365 km of ASPI network (595 tunnels). In 2020, the assessment program was mainly characterized by a reactive approach to maintenance due to few adverse events, one of which is unfortunately well known.

*Corresponding author: lapo.baccolini@tecneautostrade.it

DOI: 10.1201/9781003495505-439

Tunnels were visually inspected and tested through laser scanning (LSC) and ground-penetrating radargrams (GPR) as well as cored to compressive strength of 50 m each.

Many tunnels were visually inspected simultaneously along the motorway. At that time, due to the pandemic, the level of traffic was the lowest ever recorded since many decades and this facilitated construction sites, minimizing the effect on users of the infrastructure.

The reactive maintenance was leading to treatment of structural defects in a short time frame (3 to 6 months) opening several construction sites at the same time, increasing the user related traffic risk when approaching the sites.

A transition from reactive to preventive maintenance approach was then needed among the Organizations and partially promoted by the new Guidelines:

- 23rd August 2022 "G*uidelines for existing tunnel's risk and safety evaluation and monitoring system installation*", referred to as "LLGG" in the following sections.

The new code comes spread in layers (1 to 4) characterized by an increasing level of detail:

- **Level 0** – Asset information such as location, length, lining material, construction age etc.;
- **Level 1** – Asset conditions in terms of scored defect detected during the visual inspection. In this phase, extension (k_1), magnitude (k_2) and severity (G) of the defects are collected in forms for further analyses;
- **Level 2** – The levels 0 and 1 gathered information feeds a process whose purpose is to assign a simplified risk score to each 20 m long segment of the tunnel for each thematic area (structural global and local, geological, seismic, hydraulic and transport related). The score can be low, mid-low, mid-high or high. The six thematic areas (except for hydraulic) are then combined into a global risk rate. Level 2 defines the visual inspection frequency of the asset, by the risk rate associated to structures (both for global and local mechanisms).
- **Level 3 & 4** – Whenever risk rate coming from level 2 is mid-high a preliminary safety evaluation is performed to better investigate the parameters which lead to such rate of risk in the specific thematic area. If the risk rate is confirmed engineering judgement and calculation are put in place to identify the mitigation measures, or eventually monitoring systems, needed to keep the risk acceptable (Level 4). When the risk rate is higher Level 3 is glossed over. At Level 4, the engineered process to residual level of safety evaluation includes calculation and approaches, in some cases, directly derived from the past.

The LLGG multilevel approach helps Organisations like ASPI, with a very large asset portfolio, in prioritizing maintenance and expenditures.

In the following sections the assessment program is described starting from the guidelines approach going through the treatment strategies with an insight to the asset management.

2 ASSET INFORMATION

Risk evaluation and treatment prioritization start from a deep knowledge of the asset. Level 0 is the first step of the assessment process where tunnels affected by the guidelines are analysed to collect the minimum amount of information about (but not limited to) location, owner, designer, length, number of lanes, construction age, structure layout and materials, surrounding conditions of the soil, average number of vehicles per day, percentage of commercial vehicles etc.. Data are collected and printed in standard spreadsheet (Figure 1).

LEVEL 0 Survey form – tunel knowledge

LEVEL 0 Tunnel survey form – **Part 1**

Tunnel general input to define the preliminary risk rate

Figure 1. Standard printout data for Level 0.

The amount of data required is quite large, more than 600 parameters, but the level of detail can be coarse at this early stage. The set of data gained at this stage will be deepened during the subsequent levels. Some of the parameters are directly involved in the simplified risk evaluation of the asset promoted by Level 2 and in the safety analysis of Level 3 and 4.

The Level 0 activity does not require the fulfilling of the 600 requested parameters in a row, it can be accomplished by subsequent runs of digging for knowledge.

3 FIRST INSPECTION

When it comes to Level 1, of the multilevel approach, a first visual inspection is carried out on the asset.

The purpose of the first inspection is to confirm and deepen the data collected at the Level 0, gather further information about the actual geometry and structural characteristics of the tunnel, in addition to assess the degree of deterioration of the liner.

First inspection starts with high pressure water cleaning of the lining surface. In fact, the inner road

tunnel environment is quite aggressive and the exposure of the liner to vehicles smog makes hard to notice any possible evolution of structural defects. Any screen and water-sheet are dismounted in order to have free access to the surface of the concrete (or to inspect the masonry in some other cases).

The inspection is not limited to the tunnel lining only, the access areas of the tunnel and non-structural support elements are analysed as well.

Before Engineers inspect the tunnel, some tests are performed:

- Ground-Penetrating Radargrams (GPR) – a transmitter is used to generate electromagnetic waves across the concrete liner. Waves travel time is measured and distances from obstacles or anomalies inside the concrete detected. The test is used to evaluate the thickness of the liner, the presence of voids or steel rebars and the presence of hidden defects.

The test is performed by longitudinal sections (Figure 2). across the tunnel in central top position and on the sides. A minimum of 3 sections are required for two lanes tunnel, 5 for three lanes one.

- Laser Scanner (LSC) – the travel time of the light emitted by a source, hitting the lining surface and coming back to the receiver is recorded. The output is a cloud of points representing the actual geometry of the tunnel (Figure 3).
- coring for concrete strength – concrete is cored and specimens collected each 50 meters for simple compression testing. The strength of the liner has an impact on the evaluation of the simplified structural risk for local mechanism as well as for the subsequent safety evaluations.

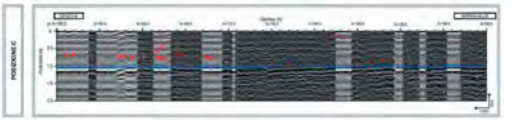

Figure 2. GPR section layout.

During inspection, defects are recorded by position, relative dimensions k_1 (from 0 to 1), intensity k_2 (0.2 – 0.5 – 1.0) and severity G (from 1 to 4).

Defects are listed in a spreadsheet (Figure 4) and represented into a 1 m by 1 m grid plan layout (Figure 5).

k_1 and k_2 are assigned during the inspection whilst G is under the Engineering judgement responsibility who will tag a defect with high severity (G=4) when this could lead to collapse of the structure, mid-high severity (G=3) when leading to an out of service of the asset.

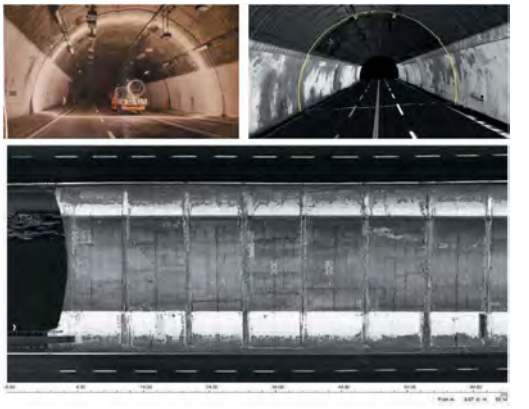

Figure 3. LSC.

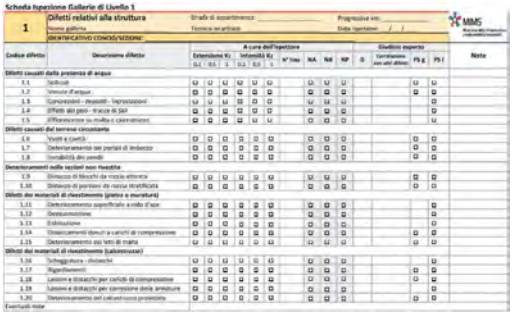

Figure 4. Annex C2.

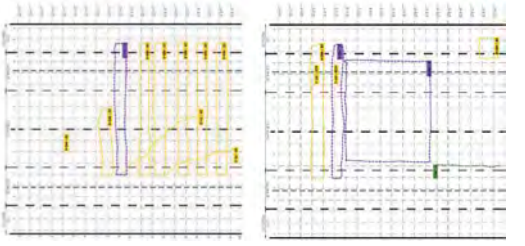

Figure 5. Defect representation.

Defects are then grouped by type in each tunnel element[1] evaluating the size and intensity of the cluster as follows:

$$k_{1,t} = \sum_{i=1}^{n} k_{1,i} \quad (1)$$

$$k_{2,t} = \sum_{i=1}^{n} \left(k_{2,i}.k_{1,i}\right)/k_{1,t} \quad (2)$$

1 A tunnel is usually broken down into 20 m long elements unless geological or structural discontinuities are identified.

$$G_t = \sum_{i=1}^{n} G_i.k_{1,i}/k_{1,t} \quad (3)$$

These parameters are then combined, at Level 2, to have a vulnerability rate (low to high).

4 PRELIMINARY RISK ANALYSIS

The background of knowledge coming from Level 0 and 1 is analyzed at Level 2 to have a simplified indicator of the risk. The preliminary risk rate (CdA) of the tunnel is computed combining hazard, vulnerability and exposure of six different disciplines:

$$CdA = H\ x\ V\ x\ E \quad (4)$$

global structural and geotechnical risk (SGG), local structural risk (SLO), seismic risk (SIS), landslide risk (GEO), transportation risk (STD) and hydraulic risk (IDR). To do so about 60 indicators (primary and secondary) are gathered and combined. Primary and secondary parameters are characterized by a rate (low, mid-low, mid-high, high).

The specific disciplines risk rates are then consecutively combined according to (5) to have the representative risk of the tunnel.

$$\begin{aligned} CdA = \{[(CdA_{SGG} + CdA_{SLO}) + CdA_{GEO}] \\ +[(CdA_{SGG} + CdA_{SLO}) + CdA_{SIS}]\} + CdA_{STD} \end{aligned} \quad (5)$$

Hydraulic stands separately (Figure 6).

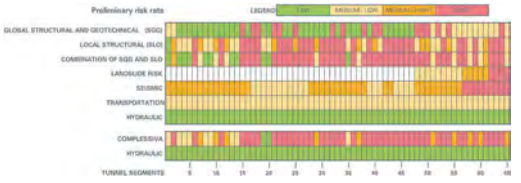

Figure 6. CdA.

The overall risk of the tunnel is represented by the worst one among its sections. The percentage of sections in a specific risk rate classification is calculated and called "*index of diffusion*".

Level 2 allows to preliminary shortlist tunnels based on specific risks. Mid-high to high values of risk lead the disciplines involved to undergo safety evaluation respectively in Level 3 and 4.

In both cases a detailed inspection, including testing, is planned within a year.

Level 3 is focused on the re-evaluation of the CdA concentrating on deepening the board of knowledge gathered at Level 2 whilst, in Level 4, accurate evaluations are carried out to estimate the safety factor of the involved risk disciplines.

During these activities (Level 3 and 4) the asset, is constantly monitored proportionally to its structural criticalities (briefly SGG+SLO CdA) which drive the subsequent visual inspection frequency (both ordinary and detailed).

LLGG also includes a Level 5 analysis, which only applies to strategic tunnels. At this stage, advanced models are put in place to evaluate the resilience of the infrastructure considering the logistic importance of the tunnel itself, analysing the interaction between the tunnel and the transport system of the geographic area and finally studying the consequences of a closure on the social and economic context.

5 DETAILED INSPECTION AND SAFETY EVALUATIONS

5.1 *Detailed inspection*

Detailed inspection has characteristics similar to visual first inspection; nonetheless, it includes some tests previously requested by the company in charge of the activity and results are gathered before entering the tunnel.

Testing is mainly addressed in deepening the knowledge of the areas suspected of hidden deterioration of the concrete liner. Heritage from Level 1 is driving test plans including:

- endoscope (VE) - when GPR provides clues for potential defects under the concrete lining, VEs are then performed by drilling small diameter holes through the liner down to the rock surface. A cctv equipped probe and a tape measure are used to report the layers where concrete, voids or deteriorated concrete are encountered;
- flat jack - stress state of the liner is a needed information for further safety analyses. The concrete surface is cut to measure the displacement of the edges. The original edges position is then restored by applying a flat-jack load;
- pacometer test - a digital tool enabling the detection, the direction and the diameter of the rods in the reinforced concrete in a non- destructive way. It consists of a probe generating a magnetic field and a controller measuring the power dissipated by the metallic object as result of the magnetic induction from the probe. This test can be used to confirm the presence of rebars in specific tunnel sections.

During detailed inspection on site, if any criticality is detected, additional tests and an accurate safety evaluation may be requested to the Process Owner[2].

Level 3, based on the detailed inspection results, investigates deeper the parameters which led to a mid-high specific level of risk.

2 Supported by the Engineering Judgement.

If the risk is confirmed Level 4 is activated for further safety evaluation. In the following sections some of the methods adopted for structural global and local risk are described.

5.2 *Global safety evaluation*

The methods to evaluate the residual safety factor associated to a global mechanism of failure of the structure is strictly linked to the context (presence/absence of primary concrete liner, geological conditions etc…). When the tunnel liner is unloaded, the surrounding soil has good properties (sound rock) and the cross-sectional model is almost symmetric an historical approach to assess liner performance can be adopted. Conversely, finite element analysis is needed to replicate the actual condition of the liner in terms of stress and strain. Here the historical method of "*Kommerell*" is presented, which was widely adopted before '70 to design tunnels in Italy. It is based on a graphic procedure to evaluate the load, and its eccentricity, among the arch sections (Figure 7).

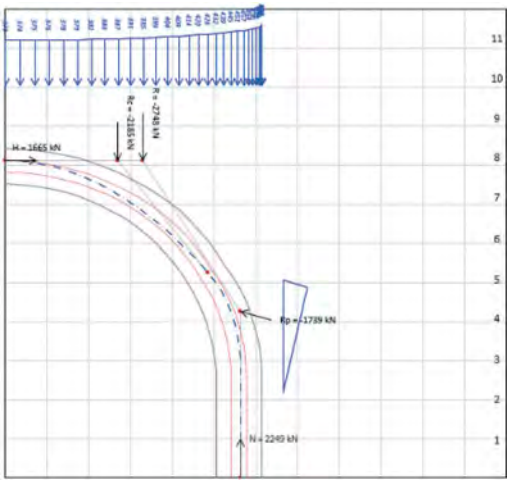

Figure 7. Kommerell method.

The method is based on three main assumptions:

- symmetry of the model (load and geometry);
- sides distributed reaction of the surrounding soil to balance the vertical loads;
- compression of the arch only – the load shall be included in the central t/3 where t represents the thickness of the lining.

The method has been implemented in a user-friendly spread sheet to iterate the calculation increasing vertical loads to the highest compatible with the structure. The thus found load is then compared with the expected one (Figure 8) based on rock mass quality designation (RQD) (Bieniawski).

When the expected load is lower than the maximum one the performance of the lining is adequate and the global failure mechanism unlikely.

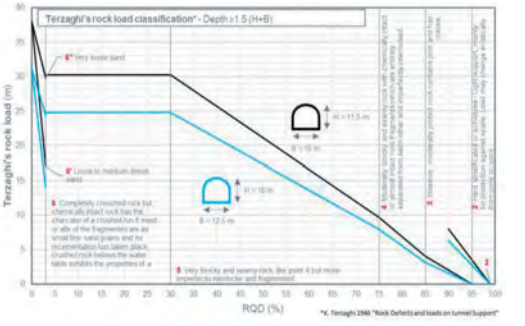

Figure 8. Terzaghi's rock load classification (2, 3 lanes tunnel).

5.3 *Local safety evaluation*

The methods to evaluate the residual safety factor associated to a local mechanism of failure of the structure is strictly linked to the local condition of the lining (construction and exogenous defects). Three methods are used to assess the influence of the anomalies of the concrete lining:

- punching check on the residual thickness;
- bending check on the concrete plate;
- critical temperature variations influence (Aiello et al.).

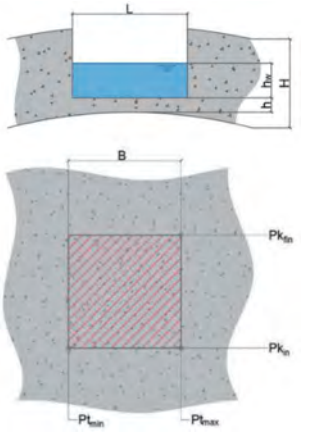

Figure 9. Under thickness of the concrete.

In all cases a thin concrete layer is investigated for likely failures mode and mitigation measures consequently prescribed. Furthermore, that a more comprehensive approach is adopted by the Engineer who is in charge of evaluating the level of deterioration of the asset. Defects distribution, presence of cracks or water leakages and their combination feed

a more complex engineering judgement process that leads to the definition of a monitoring and/or treatment plan on the tunnel.

6 TUNNEL INTERVENTION STRATEGY

Level 4 purpose is to highlight the criticalities and possible solutions in terms of monitoring systems or intervention strategies. Tecne S.p.A., engineering company of Autostrade per l'Italia S.p.A., tends to group intervention strategies with the effect these have on asset conditions:

- IMS – is the treatment approach closer to extraordinary maintenance "*Intervento di Manutenzione Straordinaria*". The aim is to reduce vulnerability for mainly local mechanisms of failure without increasing the strength of the structure.
- IRS – stands for structural reinforcement "*Intervento di Rinforzo Strutturale*". In this, the aim is to reduce vulnerability for global mechanisms and increase the structural strength of the system.
- TRS – stands for "Tunnel Renewal Strategy". The renewal solution is aimed to extend the tunnels life cycle of at least additional 50 years, through the construction of new lining, able to replace the structural function of the existing one and to ensure waterproof condition and suitable performance under seismic events.

The optimal solution to be implemented mainly depends on Organization culture about preventive maintenance, existing lining conditions, impact on traffic, time, costs, waterproofing effectiveness, jobsite organization, reusability of the solution, propensity to innovation.

On a higher organizational level, decision making on tunnel maintenance strategy is moving to a more robust asset management approach also by developing a dedicated tool to compare several alternative intervention scenarios in terms of risk, costs and residual value of the asset.

7 TUNNEL RENEWAL STRATEGY

Due to the early stage tunnel assessment experience mainly based on reactive maintenance, the TRS approach was developed since end of 2021 by the following main steps:

1. analysis of the assessment program and technical solutions applied during 2020/2021;
2. collection of existing tunnel industry state of the art, including bibliographic research, looking for solutions adopted around the word for tunnel rehabilitation both in continuity of operation and closure;
3. definition objectives and requirements of relining works (§7.1);
4. definition of a set of typological interventions and related design methods and verification criteria (§7.2);
5. involvement of construction market to develop mechanized and technologically innovative solutions (§7.3);
6. organizing field tests and application of pilot projects (§7.4);
7. standardization and recurrent applications based on return of experiences coming from pilot projects (§7.4);
8. continuous improvement (§7.5).

7.1 *Objectives and requirements*

The main objectives and requirements defined in the TRS context are:

- safety for operation, especially in case of alternation of works/traffic operation and works during traffic operation;
- safety for workers (protection, mechanization);
- minimization of impact on traffic (protection, mechanization);
- quickness of intervention (mechanization);
- high structural performance (pre-casting operations, high-performing concrete mix);
- installation of an effective and durable waterproofing system;
- sustainability and conservation of the asset by recycling, use of green machine and materials.

Key role to ensure safety conditions and reduce time and traffic impact is played by the minimization of the existing concrete milling, especially when a not negligible stress state is detected in the lining during detailed inspection. This allows also to reduce the supports and soil treatment needed to fulfill the required safety standard during concrete demolition, maintaining low uncertainties regarding rock mass stability.

The minimization of existing concrete milling can be obtained by lowering the road pavement and reducing new lining thickness resorting to high performance materials.

Once the new lining is built, the maintenance of its structural capability is ensured by the mandatory installation of a waterproofing system and drainage system is mandatory to take out water from deterioration root causes during the operational stage.

Every project is accompanied by environmental performance of the works, assessed by LCA methodology, which has become an additional item for designing and choosing between engineering solutions.

7.2 *Typological interventions*

Nine different typological interventions were defined:

A. complete demolishing of existing lining and cast in place of new concrete shell;
B. partial existing lining milling and concrete relining casted in place by precast concrete shell formworks (Figure 10);
C1. C1.partial existing lining milling and relining by high performance shotcrete (Figure 11, Figure 12, Figure 13);

C2. partial existing lining milling and concrete relining by casted in place by modular steel formwork (Figure 14);
D. shallow existing lining milling and relining by implementation of liner plates (Figure 15);
E. existing lining milling and relining by implementation of precast concrete segments (Figure 16);
F. steel liner coupled to existing lining;
G. installation of steel ribs and shotcrete, with or without existing lining milling;
H. platform remodulation (lowering) to avoid existing lining milling combined with inner lining based on previous typological interventions.

Each intervention has been detailed evaluated to define its proper field of application based on a pros and cons analysis and the specific design methods and verification criteria are developed correspondingly.

7.3 *Involvement of construction market*

As part of TRS, the construction market was approached by engaging specialized players by issuing the challenge regarding the development of innovative solutions.

The search for these solutions was mainly directed in the area of materials, seeking innovative materials with high structural performance, as well as in the area of mechanization for the installation of the components of the new lining shell. Not Disclosure Agreements have been signed with the selected companies and suppliers to ensure the exclusive use of the information shared in the design phase, then followed by specific agreements in order to manage future patent developments of original solutions as well.

7.4 *Testing, pilot projects and recurrent applications*

Less than two years from the statement of TRS main steps, all the typological interventions have been preliminary tested and the application of the related pilot projects completed or ongoing.

Deep involvement in the design and testing stage have been extended to members of Construction Company and all the technicians included in the process. It is also demonstrated mandatory training sessions and the availability of detailed method statement for each innovative technologies introduced by the design.

In addition, the daily technical support ensured by design teams during the progress of the works has been crucial to refine typological interventions, fix issues, record feedback and improve products and application processes. In this regard, it is worth to be noticed that the Construction Standards do not provide any facilitation for pilot projects, therefore the process entails unavoidable technical refinement during the works and possible related additional costs.

To date, seventeen TRS projects are under construction and almost half of them are already recurrent applications of the corresponding pilot project.

Figure 10. "*Colle Marino*" tunnel construction site – relining by high strength shotcrete.

Figure 11. "*San Fermo*" tunnel - Field test of shotcrete application.

Figure 12. "*Manfreida*" tunnel construction site – relining by high strength shotcrete.

Figure 13. Relining by high strength shotcrete - Pilot application at "*Manfreida*" tunnel.

7.5 *Continuous improvement*

The next developments of TRS are aimed to the following main goals:

– implementation along the second tube of "*Colle Marino*" tunnel of shields system, to ensure

Figure 14. Relining by high strength fibre reinforced plain concrete - Pilot application at "*Colle*" tunnel.

Figure 15. Relining by liner plates - Pilot application at "*Castello*" tunnel.

Figure 16. "*Poderuzzo*" tunnel - Field test of pre-cast concrete shell implementation.

relining works during the process of two lanes of motorway traffic (Figure 17);

– implementation along the second tube of "*Colle*" tunnel of the innovative steel formworks able to cast in place concrete by continuous extrusion system, in order to speed-up the relining stage (Figure 18);
– finalization the strength tests campaign promoted by construction player involved in TRS process to qualify geopolymer concrete for implementation in relining works (Figure 19).

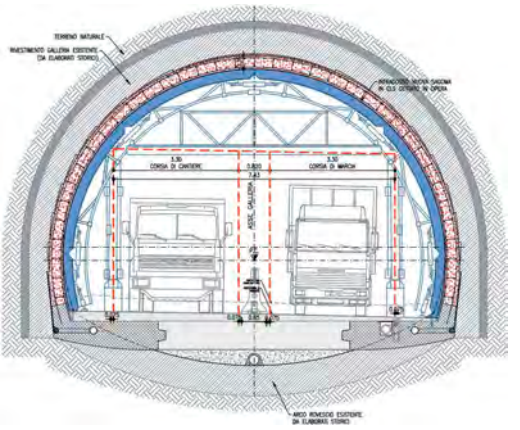

Figure 17. Cross section of shields system.

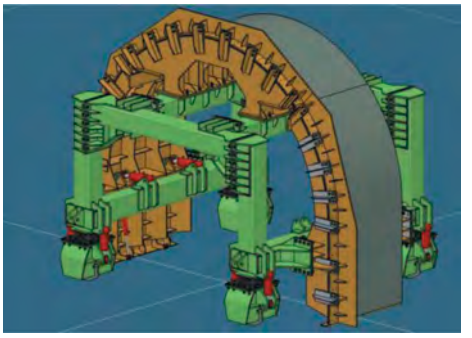

Figure 18. Perspective drawing of the extrusion system.

Figure 19. Geopolymers specimens involved by strength tests.

8 CONCLUSIONS

Tunnel assessment is an on going process for Autostrade per l'Italia S.p.A. The amount of information and experience acquired by its Engineering company

(Tecne S.p.A.) and all the Operators involved in the activities, is constantly growing.

The monetary and economic value of the asset make any effort needed and worthy.

The reactive approach to maintenance has been overtaken and the Tunnel Renewal Strategy is now starting the standardization and recurrent applications stage to extend the tunnels life cycle of at least additional 50 years.

Beyond that, the company is looking forward to embrace a comprehensive tunnel asset management approach including data management, asset condition evaluation and tunnel tailored best intervention strategy going from corrective to preventive maintenance approach.

REFERENCES

D.M. 01/08/2022, n. 247 - Linee guida per la classificazione e gestione del rischio, la valutazione della sicurezza ed il monitoraggio delle gallerie esistenti.

S. Aiello, C. Alessio, L. Baccolini, R. Fantuz, V. De Biagi, B. Chiaia – Analytical study of anomalies in tunnel lining thickness: critical temperature variations, WTC2023, May 12-18, 2023.

Z. T. Bieniawski – Tunnel design by rock mass classifications, January, 1990.

K. Terzaghi – Rock defects and loads on tunnel supports. In Rock tunneling with steel supports, (eds R. V. Proctor and T. L. White) 1, 17–99. Youngstown, OH: Commercial Shearing and Stamping Company, 1946.

L. Desimon – Costruzione delle gallerie – 1953, pp.73–132.

Tunnelling for a Better Life – Yan, Celestino, Thewes & Eberhardt (Eds)
© 2024 The Author(s), ISBN 978-1-032-80042-4
Open Access: www.taylorfrancis.com, CC BY-NC-ND 4.0 license

Conservative rehabilitation interventions of masonry highway tunnels along the historic Genoa-Po valley motorway in Genoa (Italy)

Carlo Alessio, Roberto Pittalis*, Andrea Poli & Giuseppe Attianese
Tecne group Autostrade per l'Italia S.p.A., Genoa, Italy

Bernardino Chiaia
Polytechnic University of Turin, Torino, Italy

Daniele Ferretti, Elena Zanazzi, Lia Ferrari & Eva Coisson
Department of Engineering and Architecture, University of Parma, Parma, Italy

ABSTRACT: The present work deals with the structural safety assessment of existing tunnel masonry linings. Until the introduction of reinforced concrete, masonry linings were the common solution for railway, metro, and road tunnels. As a result, there are still many tunnels with masonry lining that have been in service for more than a century. After such a long time, masonry linings may show signs of degradation due to ageing and the long action of water infiltration may have reduced their strength. For this reason, the safety assessment of existing tunnels is becoming increasingly important, in order to timely identify the criticalities and plan the necessary rehabilitation interventions, but specific regulations are still lacking.

This paper addresses this need by proposing a methodology for the global and local static verification of masonry-tunnel-linings, describing the issues to be addressed and proposing a procedure to define the mechanical properties of the masonry, calibrate the partial safety factors, identify the local vulnerabilities and their priority order. In this process, the scientific literature and normative references developed for cultural heritage masonry structures are taken into account, considering that these tunnels have features and problems similar to old masonry constructions (bridges, porches, vaulted buildings) and that the interventions planned should also have a conservative approach, since these structures represent indeed an important element of the history of our architectural and technological evolution.

Keywords: Cultural Heritage, Masonry infrastructure, Planned conservation, Safety assessment

1 INTRODUCTION

1.1 *Assessment and strengthening of masonry tunnels*

This paper focuses on masonry tunnels, which were the predominant typology in Europe in the 19th and early 20th centuries, before the development of reinforced concrete. For instance, many subway tunnels in Paris and London, as well as the Simplon and Frejus railway tunnels in the Alps, are made in masonry.

Usually, the masonry is made of solid clay bricks, but stone masonry is often used, especially in the lower parts, which are potentially subject to damage by moisture. Brick or stone masonry was the material of choice for the construction of the lining for two main reasons: firstly, because the raw material was often obtained from the excavated material during tunnel construction; and secondly, because bricks have the advantage of being made up of small, easily transported and handled regular units, which were suitable for the construction of arches in confined spaces. However, in order to achieve the required lining thickness, it was usually necessary to construct several layers of brickwork in the side walls and arches with multiple rings, and to use a relatively large quantity of mortar, since the proportion of mortar in brickwork is generally much higher than in good quality ashlar masonry. The thickness of the lining was determined by simple rules of thumb, depending on the type of soil, with light soils generally considered to be self-supporting and heavy soils as requiring support (McKibbins et al., 2009). The

*Corresponding author: roberto.pittalis@tecneautostrade.it

DOI: 10.1201/9781003495505-440

geometric section of the tunnel and subsequent lining were usually related to the excavation and shoring techniques. The thickness and geometry of the lining, therefore, did not descend from structural mechanics but from practical guidance, often described in manuals and regulatory guidelines.

This type of construction has been widely used in Italy since the second half of the 19th century. Currently, due to its morphological conformation (the Alps in the north and the Apennines along the peninsula), Italy has the largest number of road tunnels in the Trans-European Transport Network (TEN-T). Specifically, Italy has well over 1,200 km of tunnels in the ANAS road network, 500 km in the motorway network and 1,200 km in the rail network, with 34 tunnels longer than 5 km (Tunnel, 2023). The problems associated with their preservation and safety are therefore of particular importance, considering their age, which is often a centenary or even more.

In fact, there are numerous scientific studies related to tunnel collapse cases, considering both the census of tunnel damage (Sousa, 2010; CEDD, 2015; Zhang et al., 2016) and the related statistical analysis (Špačková et al., 2013). However, these studies mainly consider two types of causes (Spyridis et al., 2021): the collapse during construction or the damage related to transport accidents followed by a fire. Instead, the present study intends to focus on the analysis of the risk of collapse or damage, both global and local, in masonry tunnels during operation. In fact, many accidents of this type have occurred recently, both nationally and internationally: e.g. Ciclopi, Tenda and Tre Madonne tunnels in northern Italy; Vierzy and Rove tunnels in France. At present, monitoring systems and preventive maintenance activities specific to these infrastructures play a very important role in reducing this type of risk. For this reason, the safety verification of existing tunnels was recently requested in some countries. For example, in Italy, the recent "Guidelines for the classification and management of risk, safety assessment and monitoring of existing tunnels" (DM 247, 2022) require the study of existing tunnels with a multilevel approach that starts from the geometric survey and, depending on the problems found, can reach the static assessment. For the static assessment of masonry tunnel-linings, there are no specific standards, and it is necessary to refer to the code standards for new masonry buildings (DM, 2018) or those for historical buildings (D.P.C.M. 09/02/2011), which, moreover, were mainly developed for seismic problems. In the case of existing bridges, instead, there are specific guidelines for both reinforced concrete and steel (CSLLPP, 2021), or masonry bridges (CNR, 2015), which can also be a useful methodological reference for the static assessment.

In general, the guidelines aim to adopt a preventive approach, both to avoid potentially dangerous situations and to plan maintenance works without having to operate under emergency conditions with long road closures, but there are no clear indications on the quantification of the safety levels and the priority of the interventions.

1.2 *Aims of the research*

Starting from the instructions contained in the DM 247 (2022), written for infrastructures of all ages and types, this research aims to integrate them with approaches derived from the field of architectural conservation and existing buildings static assessment. In fact, at the theoretical level, it is now established that strengthening, when applied to an asset recognised as having historical and/or artistic value, is an essential part of the discipline of architectural conservation and not something separate and autonomous (Di Stefano; D.Lgs. 22/01/2004). For this reason, the analysis will borrow concepts developed for the approach to historical structures (D.P.C.M. 09/02/2011), both from a global point of view, intended to assess the overall structural capacity, and from a local point of view, concerning the material-pathological conditions of the surface. In the first case, the concepts of the Masonry Quality Index (Borri et al., 2019), the Confidence Factor (D.P.C.M. 09/02/2011; D.M 17/01/2018) and, more generally, the methods for defining the mechanical characteristics of an existing masonry are taken up and adapted to the specific case of tunnels, which are characterised by thick masonry built with a curved shape and with a single free face. The local vulnerability associated with surface deterioration (UNI 11182, 2006), which defines a possible risk of detachment of parts of the lining that may interact with the road network, shows similarities with the problems encountered in historic buildings. Similar safety issues were highlighted in all their importance in October 2017, with the fatal accident in the Basilica of Santa Croce in Florence, which triggered a wide-ranging campaign to check the stone facings of monuments in the Tuscan capital (Salvatici et al., 2020; Ceppetelli, 2022). Although there are obvious differences, both in terms of value and operational complexity, in the knowledge and intervention phases, this research aims to propose a possible specific protocol for the study of criticalities in historic masonry tunnels currently in use, for the assessment of their global and local stability conditions and, therefore, for the definition of targeted interventions to resolve criticalities that may pose a risk to vehicle safety, also taking into account the conservation needs of elements recognised as valuable.

The proposed protocol will be tested on two tunnels along the "Genoa-Po Valley Motorway" in Italy, which date back to the 1930s. Since their construction, the works carried out to ensure road safety have been in line with the usual maintenance operations for this type of structure, taking into account only the technical aspects, sometimes to the detriment of the conservation of the material and the perception of the asset. The recognition by the operator, Autostrade per l'Italia, of the specific nature and value of these historic tunnels is now laying the foundations for a different approach to their management.

1.3 *The analysed case study*

1.3.1 *Historical overview of the motorway tunnels*

Aware of the strategic role - both economic and social - played by road communications, the Fascist regime promoted the construction of major infrastructure projects. Among these was the "Genoa-Po Valley Motorway" (*Autocamionale*), which was intended to solve the problem of heavy traffic between the port of Genoa and the hinterland. On August 31, 1932, the preliminary project for the entire motorway between Genoa and Serravalle Scrivia was completed. The works, for a total cost of 218 million lire, were put out to tender on 6 October 1932 and took three years to complete, divided into 22 sections (Pini, 1936).

The motorway had the most modern features for a mountain road at the time and therefore represents an interesting testimony of the evolution of road and tunnel technologies.

1.3.2 *Main features and constructive techniques*

In the Motorway there are 11 tunnels with a total length of 3,002 m, about half of which are in the first 8 km close to Genova. The carriageway is 10 m wide, with two lanes and a platform width of 9.42m, plus margins. The tunnel profile is a horse-shoe shaped with an invert. The construction method used for the tunnels is known as "heading and bench", which involves excavation of a top pilot adit, widening to create space for the vault, excavation of the lower bench, and then construction of the invert (Figure 1).

The thickness of the wall linings varies according to the pressure exerted by the ground, ranging from 0.94 m to 1.60 m for the shell and abutments, and from 0.67 m to 1.07 m for the inverted arch. The linings themselves were constructed using brick masonry for the vaults and inverted arches, and a combination of rubble and brick for the abutments. Only in the central section of the "Littorio" tunnel was a structure of squared stone blocks used.

In the areas where water infiltration occurred on the vault surfaces, waterproofing was carried out by injecting cement mortar under pressure to seal any remaining voids and to divert the water as far as possible towards the abutments. The surfaces were then coated with an external plaster of cement mixed with waterproofing agents (Pini, 1936). The façades were designed with the utmost simplicity: corniches, projections and decorative elements were eliminated, and only a variety of coloured stones were used for decorative purposes. In the "Littorio" and "28 Ottobre" tunnels, the only architectural element is a large Fascist symbol called the *Fascio Littorio* (Figure 2).

1.3.3 *The first tests on two galleries*

The paper focuses on two tunnels built along the "Genoa-Po Valley Motorway": the Campora and Giovi tunnels, 509 m and 910 m long, respectively, both opened to traffic in 1935.

Unfortunately, there is no historical documentation on the design of the Campora tunnel, and for the Giovi tunnel it is incomplete, especially regarding the technical-constructive features of the masonry vaults. In fact, for the Giovi tunnel, the available historical information is derived in part from design drawings for the entrance and exit sections, ventilation shafts, fenestrations and mine work and location of the niches. Construction details are also available but are limited to the basement of the piers.

Additional data have been obtained from the documentation of surface rehabilitation works for the degraded area of both tunnels and related first aid interventions, dating back to the early 2000s (Figure 3). In particular, it was found that the vaults are made

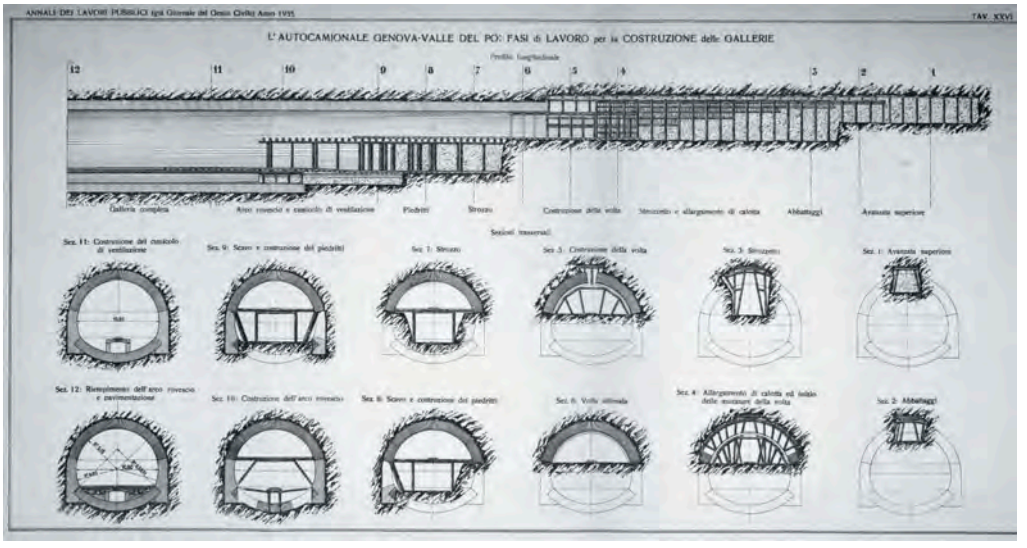

Figure 1. Construction of the masonry lining (CSLLPP, 1935).

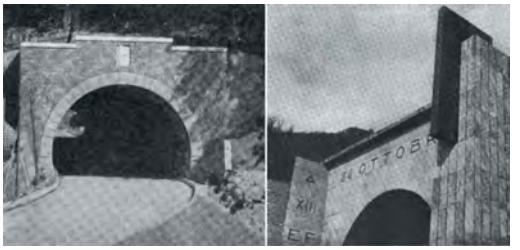

Figure 2. Portal of the Maltempo and of 28 Ottobre tunnels (CSLLPP, 1935).

Figure 3. Detail of the masonry vault and of the first aid intervention.

entirely of brick masonry, plastered in some sections, while the sidewalls are composed mainly of stone masonry.

In 2023, a series of tests were carried out to provide information on the state of conservation of the coating of the two tunnels: laser scanner surveys, thermography, video-endoscopy, single and double flat jacks.

Laser scanner surveys and thermographies provided preliminary and important geometric and diagnostic information about the inspected surfaces. On the vaulted surfaces, there are widespread moisture phenomena that have caused efflorescence, plaster detachment, mortar disintegration and a widespread crack pattern (Figure 4).

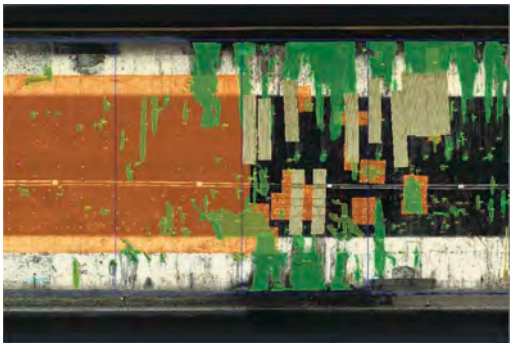

Figure 4. Survey of materials and decay of the Giovi tunnel.

In addition, a settlement in the crown of the vaults was surveyed (Figure 5). Regarding the piers in the Campora gallery, observed degradation is limited only to the plastered surfaces, while in the Giovi gallery there is also widespread mortar deterioration and exfoliation of the stone elements.

On the basis on the above-mentioned surveys, inspection points were chosen for video-endoscopies, which showed the use of full bricks through all the cross section, with no evidence of problematic situations. On the contrary, tests with flat jacks revealed points with a stress state worthy of attention. In fact, for the Giovi tunnel, some tests showed an asymmetric stress state, with compressions on the left haunch and tension on the vault and right haunch, consistently with the asymmetrical geometric deformation surveyed with the laser scanner (orange line in Figure 5). Regarding the Campora tunnel, high stress values are present on the left side of the tunnel and no tension on the crown in two sections (like in normal arches, gravitationally loaded).

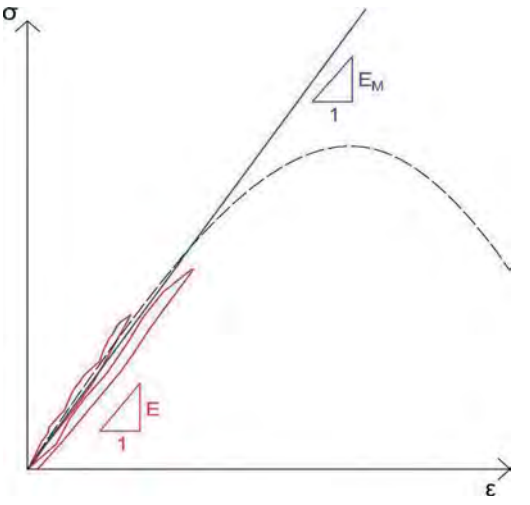

Figure 5. The laser scanner survey highlighted an asymmetrical settlement in the vault of Giovi tunnel.

The inspections described provided qualitative indications and priorities for the inspection activities to be carried out, but the present study aims to integrate these results with more quantitative data to guide the intervention choices.

2 MECHANICAL PROPERTIES OF THE MASONRY

2.1 *Double flat jack tests*

Lining masonry works predominantly in compression, so its safety is determined by the compressive strength of the material. Estimating the compressive

strength of existing masonry is still an open problem. Destructive methods have been proposed in the literature, such as the compression test on undisturbed walls extracted from the masonry, the compression test on cores of appropriate size, and the double flat jack (RILEM 2005, ASTM C1196 2009). In the present work, it was decided to use double flat jacks, as data were already available for the analysed tunnels. For safety reasons, the test was stopped when the measured stress-strain curve began to bend, i.e. before the masonry cracked (Figure 6).

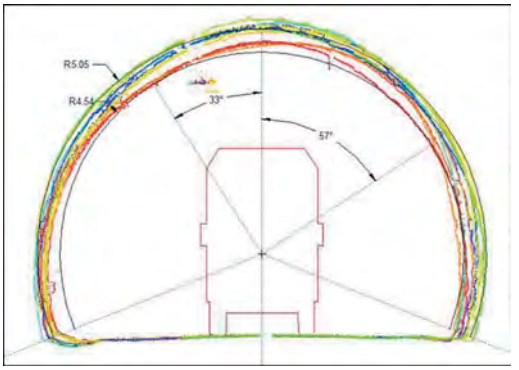

Figure 6. Double flat jack stress-strain curve: for safety reasons, the test was stopped when the measured curve began to bend.

In this case, the test provides a conservative estimate of the compressive strength and the value of the elastic modulus of the masonry E_M. From the latter, the masonry strength f can be estimated using formulae of the type $f = E_M/c$. Using the relationship suggested by EC6 (EC6, 2005), c =1000, and considering a coefficient 0.85 to transform mean strengths into characteristic strengths, gives $f = E_M/850$. It should be noted that the flat jack used in this campaign had a thickness of 200 mm and acted on the intrados of the lining, which has a global thickness of 1200 mm. For this reason, the masonry behind the flat jack constrains the loaded masonry and causes the modulus of elasticity E_M to be overestimated. For this reason, Alecci et al. (2021) proposed a correction factor K for the modulus of elasticity that depends on the ratio between the thickness of the jack and that of the wall. The resistance obtained in this way is still subject to several uncertainties. Firstly, some authors suggest values of c between 250 and 1200 for a solid brick wall, indicating that the correlation between the modulus of elasticity and the strength is not so certain (Costigan et al., 2015). Furthermore, EC6 refers to a secant modulus, whereas flat jacks measure an unloading and reloading modulus, which is generally higher. For this reason, it was decided to estimate masonry strength using also other approaches and to compare and validate the results.

2.2 *Tests on bricks and mortar*

Masonry cores with a diameter of 150 mm were taken from the masonry to characterise the constituents, mortar and bricks. Bricks or parts of bricks were taken from the cores, stoned from both sides and then cut into cubes of 50 mm side. In this way a larger number of samples were obtained, all of the same size, to avoid size-effects (Cabané et al., 2022). The cubes were tested in compression according to EN 772-1 (2011). The normalised strength $f_{b,N} = \delta f_b$ was calculated using the shape factor δ given in EN 772-1 (2011).

The mortar bed joints are approximately 20 mm thick. XRD analysis has shown that the mortar is composed of lime and cement. The mortar was characterised on site using a Gucci penetrometer (Gucci, Barsotti, 1995). Mortar samples of approximately 50 mm x 50 mm x 20 mm were taken from the cores to measure the compressive strength using the UIC double punch test (UIC 778-3R, 2011).

The average strengths of mortar f_m and bricks $f_{b,N}$ can be used to estimate the characteristic strength f_k of masonry using tables or equations. As this is industrial masonry, the power equation proposed by EC6 (2005) for solid bricks and cement mortar $f_k = 0.55\ f_{bN}{}^{0.7}\ f_m{}^{0.3}$ has been used: several authors (e.g., Ferretti, 2020) have shown that this equation also gives reliable results for masonry built with mixed lime-cement mortar, such as the one in question.

Again, the factor of 0.85 proposed by EC6 (2005) was used to divide the characteristic strength f_k to obtain the average strength f. To take into account the fact that masonry consists of several layers, EC6 multiplies the strength by a coefficient 0.8. This coefficient was proposed by EC6 (2005) for buildings and is not necessarily good for the very thick walls of tunnel linings, but cathedrals and towers may also have the same problem.

2.3 *Masonry quality index for tunnels masonries*

The structural behaviour of masonry is influenced not only by the strength of its components, but also by the construction technique of the masonry within its thickness, the texture of the brick (or stone) work and by deterioration: more generally, by compliance with the so-called “rules of the art”. In this study, the empirical approach defined by Borri et al (2015) for calculating the Masonry Quality Index (MQI) is used to rapidly assess the quality of masonry tunnel linings. This is achieved by measuring parameters that indicate whether certain conditions related to the correct and effective construction of the masonry have been met.

The seven parameters to be examined, which can be identified by visual and/or manual inspection, are: (a) the shape of the load-bearing elements, (b) the presence of cross-bonding elements, (c) the horizontal alignment of the layers, (d) the strength of the elements, (e) the size of the elements in relation to

the wall thickness, (f) the offset of the vertical joints and (g) the quality of the mortar. The application of this method to the specific case studies makes it possible to calibrate these parameters in order to take into account the differences in behaviour between vertical thin masonry walls, for which the MQI method was defined, and the curved thick structures of masonry tunnels. In the latter case, the influence of the vault texture (Boni et al., 2022) and the different importance of some parameters under different loading conditions must be taken into account.

Further calibration will be carried out by comparison with the described in-situ tests, in order to refine the formulae proposed by Borri (2015) and to guide the determination of the mechanical parameters of the tunnel masonry, whose parameters can be very variable depending on the technical details analysed in the MQI. The implementation of this method is proposed as a tool to support both the assessment of the safety level of existing tunnels, the definition of the possible inspections needed, and the indications of the necessary reinforcement interventions, also allowing a rapid evaluation of their effectiveness.

2.4 *Decay phenomena*

2.4.1 *Decay phenomena involved in structural weakness*

The alteration of the physical and chemical properties of the materials, such as the disintegration of mortar and the spalling of bricks, is a risk factor for the safety of the tunnel (increasing the possibility of detachment of individual elements) and can have a negative effect on the mechanical behaviour of the masonry, reducing its strength. According to the illustrated glossary of the ICOMOS-ISCS International Scientific Committee for Stone (2008) and Cultural Heritage - Natural and artificial stone Description of the alteration - Terminology and definition (UNI 11182, 2006), the main types of deterioration that affect the properties of the masonry and the risk of detachment of bricks from the tunnel lining can be identified as follows: (a) biological colonization (algae, lichens, moss, mould, plants); (b) deposit (crust, efflorescence, encrustation); (c) material loss (alveolization, erosion); (d) detachment (blistering, bursting, disintegration); (e) cracks (fractures, hair cracks) and (f) deformations.

2.4.2 *Decay survey and in situ analysis*

In the specific case of tunnels, the presence of such deterioration is detected by the evaluation procedure outlined for Level 1 of the 2022 Guidelines (D.M. 247:2022): the catalogue of defects (Annex B) includes the defects associated with the identified deterioration, evaluated in terms of extent (k1), intensity (k2) and severity (G), in order to determine the attention class of the tunnel under investigation.

After an initial qualitative assessment of the existing pathologies, further checks can be carried out using specialised instruments and chemical analyses. In particular, the assessment of the state of deterioration of the masonry, in terms of the reduction of its mechanical properties and consistency, can be carried out by means of rapid investigations such as visual inspections to locate areas of deterioration and define their characteristics; acoustic inspections using mechanical tapping of the surface to detect hidden defects such as detachments, cavities or fractures; and manual inspections to define the surface consistency (i.e. mortar disaggregation). These can be complemented by more detailed investigations such as laboratory chemical analysis to identify materials and degradation agents, georadar and/or thermographic inspections to locate hidden defects, photogrammetric and dynamic laser scanning surveys to check deformations, and pathological material surveys.

One of the objectives of this research is to define an operational protocol for assessing the safety of masonry tunnels through the implementation of a rapid method. Following the approach proposed by CNR-DT 213/2015, the aim is to establish a coefficient for the reduction of the strengths associated with the presence of deterioration and to define the degree of urgency for strengthening interventions in the different areas. This coefficient will be calibrated by comparing the results of in-situ masonry strength tests (single and double flat jacks, drilling energy tests on mortar, and brick sampling for compression test) with expert judgement on the level of deterioration present in the study areas. This makes it possible to estimate the effect of material deterioration on the strength of the masonry and on the risk of detachment.

3 SAFETY ASSESSMENT

3.1 *Global safety*

The original design reports of the lining could not be found. In those days, empirical methods such as Ritter's method and Kommerell's method were used to calculate thrusts (Steiner, Einstein, 1980). Given the actions, the masonry lining was verified using graphical statics methods derived from Mery's method. Today, verification can be conducted by means of non-linear finite element analysis or limit analysis (Tralli et al, 2014). In the latter case, a portion of the lining is studied as if it were a masonry arch. Unlike masonry arches, however, the possible interaction between the lining and the overlying rock can change the collapse mechanism and the position of the plastic hinges, like shown by the laser scanning surveys, in some cases with a possible beneficial effect on the load-bearing capacity. The stresses calculated in this way can be compared with in-situ stress measurements performed with a single flat jack in order to validate the modelling.

For the ultimate limit state assessment, appropriate partial coefficients on actions and material strengths γ_M must be considered. For compressive

strength, the Italian National Annex of EC6 (2005) prescribes a γ_M coefficient between 2 and 3. The value $\gamma_M = 3$ is often too restrictive for existing masonry tunnels. However, this coefficient was defined for the design of walls of new buildings and has no clear probabilistic basis (Lulić et al., 2023). For a sound assessment of tunnel masonry linings, the partial safety factor should be defined taking into account material variability, model uncertainty, and geometric uncertainties. Model uncertainties should include not only the uncertainty arising from the EC6 (2005) equation used to estimate the compressive strength of the masonry, but also the uncertainty of the model used for the global analysis of the arch.

The calculation should be performed for an assigned probability of failure evaluated for an assigned reference period T_R using the reliability index β. This obviously is different for tunnels than for new buildings. By reducing the reference period T_R, for example by prescribing periodic inspections and safety assessments, the β coefficient and consequently the coefficient γ_M can be reduced as already proposed for existing reinforced concrete bridges (CSLLPP, 2021).

3.2 *Local safety*

While ensuring the overall safety of the tunnel, it's important not to overlook the local risk, which corresponds, for example, to conditions of detachment of materials that may interact with the carriageway but do not pose a global instability risk to the structure. The Guidelines (D.M. 247, 2022) provide a procedure for evaluating the level 2 local attention class of structures on portions of tunnels which are 10 m long.

In addition to this procedure, this research aims to define a specific investigative method for assessing in a more detailed way the type and level of risk of detachment of individual elements in masonry tunnels, in order to plan focused rehabilitation interventions to prevent blocks from falling. This proposal draws on the methodologies suggested by Salvatici et al. (2020), Ceppetelli (2022), and Mariotti et al. (2023) for stone masonry facades in monumental buildings: through the visual analysis of the stone surface, the detachment hazard index is determined, allowing for a rapid assessment comparable to that obtained through in-situ investigations. In the case of tunnels, the parameters contributing to the definition of the detachment hazard index should be tailored to the specific case, with primary consideration given to the effects of water, the main cause of deterioration in these structures.

4 CONCLUSIONS AND FUTURE DEVELOPMENTS

The present paper presents a new approach to the local and global safety assessment of historical masonry tunnels, starting from the analysis process proposed in the Italian guidelines for tunnels and integrating some aspects derived from the Italian guidelines for bridges, the Italian guidelines for cultural heritage in seismic areas, and data from the scientific literature in the field of historical masonries mechanical properties, and of monumental façades conservation.

The aim is the quantification of the urgency of the interventions, both from a global structural point of view, and also considering the impact of local degradation and material deterioration. The assessment of the masonry strength has been defined adopting equations and coefficients proposed in EC6 for industrial masonry, considering the presence of large thicknesses and multiple brick layers, applied to the strength of bricks (or stones) and mortars obtained through in situ tests. A possible calibration of the Masonry Quality Index specific for the tunnels conditions was also proposed, to take into consideration not only the blocks and mortars properties but also the effects of the texture and other qualitative parameters that were proved for old buildings to have a high impact on the mechanical behaviour of ancient masonries.

A discussion about the material partial safety factor γ_M to be adopted was also made, considering the possibility of reducing it by prescribing periodic inspections and safety assessments, in line with the prescriptions for Italian RC bridges.

Finally, a proposal was made for the assessment of the level of risk of local detachments, starting from the survey of the materials decays and integrating the data with some on site tests, following a method already used for historical buildings subjected to similar risks of local material detachments.

The results obtained with the proposed method will define a priority list for the interventions and possibly a link between the type and level of risk with the type and urgency of the re-habilitation required, also considering the nominal life of the construction.

Considering these tunnels not only as an important operating infrastructure, but also as a specific typology of historical construction, has made it possible to merge different approaches into a single procedure with one aim: plan the conservation activities on these artefacts in order to preserve them in the best possible conditions, for their future use and for the testimony they represent.

AUTHOR CONTRIBUTION

Conceptualizaton and methodolology: D.F.; E.C.; R. P.; C.A. Investigation: D.F.; Draft writing of the paragraph 1.1; 1.3.3: E.Z.; Draft writing of the paragraph 1.2, 4: C.E.; Draft writing of the paragraph 1.3; 2.3; 2.4; 3.2: L.F.; Draft writing of the paragraph: 2.1; 2.2; 3.1: D.F.; Writing-review: E.C.; D. F.; C.A.; Supervision: D.F.; E.C.; R.P.; C.A.

REFERENCES

Alecci, V., Ayala, A. G., De Stefano, M., Marra, A. M., Nudo, R., Stipo, G., 2021. Influence of the masonry wall thickness on the outcomes of double flat-jack test:

Experimental and numerical investigation. In: Construction and Building Materials, 285, 122912.
ASTM C1196 (2009), 09: Standard Test Method for In Situ Compressive Stress Within Solid Unit Masonry Estimated Using Flatjack Measurements.
Boni, C., Ferretti, D., Lenticchia, E., 2022. Effects of brick pattern on the static behavior of masonry vaults. In: International Journal of Architectural Heritage, 16(8), 1199–1219.
Borri, A., Corradi, M., Castori, G., De Maria, A., 2015. A method for the analysis and classification of historic masonry. In: Bulletin of Earthquake Engineering, 13:2647–2665. (DOI 10.1007/s10518-015-9731-4).
Borri, A., De Maria, A. 2019. Il metodo IQM per la stima delle caratteristiche meccaniche delle murature: allineamento alla circolare n.7/2019. In: Proceedings of the 18th Italian National Association of Earthquake Engineering (ANIDIS), pp. 2–21 (in Italian).
Cabané, A., Pelà, L., Roca, P., 2022. Anisotropy and compressive strength evaluation of solid fired clay bricks by testing small specimens. In: Construction and Building Materials, 344, 128195.
CEDD, 2015. Catalogue of no table tunnel failure case histories (up to April 2015). Hong Kong: CEDD.
Ceppetelli, A., 2022. Le Facciate del cortile dell'Ammanati di Palazzo Pitti a Firenze. Master Thesis. Polytechnic University of Marche, Italy.
CNR-DT 213, 2015. Istruzioni per la Valutazione della Sicurezza Strutturale di Ponti Stradali in Muratura (in Italian).
Costigan, A., Pavía, S., Kinnane, O., 2015. An experimental evaluation of prediction models for the mechanical behavior of unreinforced, lime-mortar masonry under compression. In: Journal of Building Engineering, 4, 283–294.
CSLLPP, 1935. Annali dei lavori Pubblici, Consiglio Superiore dei Lavori Pubblici (in Italian).
CSLLPP, 2021. Guidelines for risk classification and management, safety assessment and monitoring of existing bridges, DM 17/12/2020, n. 578.
D.Lgs. 22/01/2004, n.42. Codice dei Beni Culturali e del Paesaggio, ai sensi dell'articolo 10 della legge 6 luglio 2002, n. 137.
D.M 17/01/2018. Aggiornamento delle Norme tecniche per le costruzioni (in Italian).
D.M. 247, 2022. Linee Guida per la classificazione e gestione del rischio, la valutazione della sicurezza ed il monitoraggio delle gallerie esistenti (in Italian).
D.P.C.M. 09/02/2011. Linee Guida per la valutazione e riduzione del rischio sismico del patrimonio culturale allineate alle nuove Norme tecniche per le costruzioni (D.M. 14 gennaio 2008) (in Italian).
Di Stefano, R., 1981. Analisi Strutturale: Tecniche e Tecnologie, Atti del I° Congresso Nazionale "Consolidamento e Restauro Architettonico", II, Roma, Ed. Kappa, 76.
EC6 (2005), EN 1996-1-1:2005 Eurocode 6: Design of masonry structures - Part 1-1: General rules for reinforced and unreinforced masonry structures.
EN 772-1, 2011. Methods of test for masonry units - Part 1: Determination of compressive strength.
Ferretti, D., 2020. Dimensional analysis and calibration of a power model for compressive strength of solid-clay-brick masonry. In: Engineering Structures 205: 110064.
Gucci N., Barsotti R., 1995. A non-destructive technique for the determination of mortar load capacity in situ. In: Materials and Structures, vol. 28, pp. 276–283.
ICOMOS, 2008. Illustrated Glossary on Stone Deterioration Patterns. ICOMOS, Paris, France.
Lulić, L., Lukačević, I., Skejić, D., Stepinac, M., 2023. Assessment of existing masonry resistance using partial factors approaches and field measurements. In: Buildings, 13(11), 2790.
Mariotti, C., Ruggieri, P., Pozzi, E., Salvatici, T., Centauro, I., Ceppetelli, A., Garzonio, C.A., in press. Governare l'emergenza progettando la cura, tra conservazione materiale e fruizione in sicurezza. Approcci predittivi per Palazzo Pitti a Firenze. Proceedings of the SIRA conference, Naples, 12-14 June 2023.
McKibbins, L., Elmer, R., Roberts, K., 2009. Tunnels: inspection, assessment and maintenance. CIRIA, London.
Pini, G. (Eds.), 1936. L'autocamionale Genova – Valle del Po', Roma.
RILEM (2005), RILEM Recommendation MDT. D. 5: In-situ stress - strain behaviour tests based on the flat jack. In; Mater. Struct. 37 497–501.
Salvatici, T., Garzonio, C.A., Intrieri, I., Pecchioni, E., Centauro, E., Calandra, S., 2020. Monitoring and Evaluation of Sandstone Decay Adopting Non-Destructive Techniques: On-Site Application on Building Stones. Firenze.
Sousa, R. L. 2010. Risk analysis for tunnelling projects. PhD Thesis. Czech Technical University, Prague, Czech Republic.
Špačková, O., Šejnoha, J., Straub, D., 2013. Probabilistic assessment of tunnel construction performance based on data. In: Tunnelling Underground Space Technol. 37, pp. 62–78. https://doi.org/10.1016/j.tust.2013.02.006.
Spyridis, P., Proske, D., 2021. Revised comparison of tunnel collapse frequencies and tunnel failure probabilities. In: Journal of Risk and Uncertainty in Engineering Systems, Part A: Civil Engineering, 7(2), 04021004.
Steiner, W., Einstein, H. H., 1980. Improved Design of Tunnel Supports. In: Empirical Methods in Rock Tunneling–Review and Recommendations, vol. 5, United States. Urban Mass Transportation Administration.
Tralli, A., Alessandri, C., Milani, G., 2014. Computational methods for masonry vaults: a review of recent results. In: The Open Civil Engineering Journal, 8 (Special Issue 2), pp. 272–287.
Tunnel and perforation - www.tunnel-and-perforazioni.it/-news/ (last accessed 2023.02.10)
UIC 778-3R, 2011. Recommendations for the inspection, assessment and maintenance of masonry arch bridges. In: UIC International Union of Railway.
UNI 11182, 2006. Materiali lapidei naturali ed artificiali. Descrizione della forma di alterazione - Termini e definizioni (in Italian).
Zhang, G. H., Jiao, Y. Y., Chen, L. B., Wang, H., Li., S. C., 2016. Analytical model for assessing collapse risk during mountain tunnel construction. In: Can. Geotech. J. 53 (2), pp. 326–342. https://doi.org/10.1139/cgj-20150064

Tunnelling for a Better Life – Yan, Celestino, Thewes & Eberhardt (Eds)
© 2024 The Author(s), ISBN 978-1-032-80042-4
Open Access: www.taylorfrancis.com, CC BY-NC-ND 4.0 license

Colle Marino left tunnel renewal project: The first case-history of full lining reconstruction - from invert to crown - under difficult geotechnical conditions and future developments for working under traffic

Carlo Alessio & Bruno Spigarelli*
Tecne Gruppo Autostrade per l'Italia S.p.A., Rome, Italy

Maurizio Mazzola
Autostrade per l'Italia S.p.A., Rome, Italy

Claudio Ceccarelli
Amplia S.p.A., Rome, Italy

Andrea Poli
Tecne Gruppo Autostrade per l'Italia S.p.A., Rome, Italy

Paolo Iuculano
Amplia S.p.A., Rome, Italy

ABSTRACT: The *Colle Marino left* project, along A14 Bologna-Taranto highway, is the first case, in Italy, of complete reconstruction of existing tunnel final-lining, from invert to crown, over the entire length (960 m). The technical complexity due to the invert demolition in clayey geological context, with overburden of up to 70 m and adjacent tunnel open to traffic, required firstly an extensive geotechnical-survey campaign and systemic concrete-structures investigations, from which significant linings working rates emerged, especially at maximum overburden in higher plasticity clays. The project therefore provided for a careful planning of invert demolition and reconstruction operations, arranged by segments of various lengths at proper spacing, with the adoption of specific demolition-technologies for early-assessment of invert actual working-conditions and structural-disturbance minimization. Specific monitoring procedures and emergency measures have been also established to counteract deformations and existing lining damaging. After complete invert-reconstruction using PP macro-fibers reinforced concrete, temporary re-opening to traffic preceded crown-piers reconstruction adopting pre-cast arch slabs with SCC back-pouring fully waterproofed by TNT+PVC membrane. Construction works, carried out during several H24 tunnel-closure periods (almost 7 months of net activity), included considerable road platform lowering (65 cm) thanks to the absence of altimetric constraints at portals. This solution reduced milling-depth at crown thus strongly mitigating risks associated to demolition of existing concrete lining extensively guarded by temporary steel nailing. General speeding-up of production was therefore achieved. Industrialization of construction processes was ensured thanks to knowledge framework completeness and efficient site-organization. This valuable know-how allowed to plan similar works on adjacent tunnel by granting daily traffic opening, introducing significant technical optimizations for both invert and crown structures. The innovative TLRG system (Tunnel Renewal Work Train) will be adopted to meet workers-safety and automation of main construction processes (milling, waterproofing and high-performance concrete pouring), while ensuring appropriate level of service for highway users.

Keywords: Tunnel linings retrofitting, invert reconstruction, existing tunnel waterproofing

1 INTRODUCTION

The modernization of the Colle Marino left tunnel constitutes the first case of a tunnel in the Italian motorway network subjected to complete demolition and reconstruction of the original definitive linings, from the inverted arch to the crown, over the entire length of the bore. The tunnel, built in the early 1970s, is located

*Corresponding author: bruno.spigarelli@tecneautostrade.it

DOI: 10.1201/9781003495505-441

along the northbound carriageway of the A14 Bologna – Taranto motorway, in the section between the Atri-Pineto and Roseto degli Abruzzi junctions. The intervention implemented is part of Autostrade per l'Italia's Tunnel Assessment Plan aimed at modernizing infrastructural assets and, in particular, represents one of the most significant pilot projects scheduled for the two-year period 2022-2023 on certain tunnels of the network for testing of the so-called Tunnel Renewal Strategy (TRS): this strategy responds to the objective of providing motorway tunnels with a new definitive lining that is structurally autonomous and independent from the original one, renewing the nominal life of the work by a further 50 years.

The scope of application of the TRS interventions specifically consists of tunnels whose original final lining is affected by widespread infiltration phenomena and/or by a structural defects framework and a state of concrete deterioration such as not to guarantee the satisfaction of the minimum performance requirements envisaged by current legislation in the load conditions expected over the life of the work, with particular reference to the effects caused by the action of the earthquake. A salient design element of the TRS interventions consists of the installation of a waterproofing system integrated with all the necessary devices for intercepting, collecting and disposing of infiltrating ground water.

The TRS intervention therefore has the objective of definitively resolving (corresponding to the Vn 50 year scenario) the static critical issues of the tunnel, returning the infrastructure to the operating standard specific to new constructions. The waterproofing of the tunnel involves the elimination of the infiltration phenomena previously present and constituting one of the main causes determining the evolution of the degradation of concrete. The introduction of a new structural shell is usually associated with the complete renovation of the carriageway platform with the creation of a new water collection network (where provided), as well as the installation of all the necessary plant equipment in compliance with the most recent sector regulations (e.g. preparation of underground cable routes with adaptation to the new CEI 64-20 regulation) and network integration needs (e.g. installation of cable ducts for fiber optic networks for telephone operators).

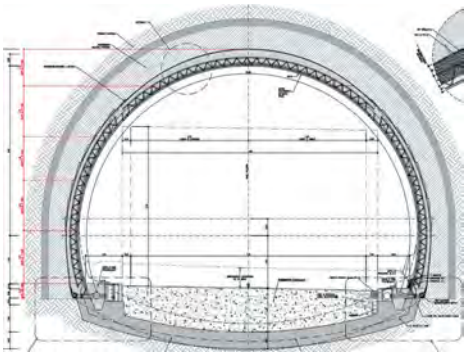

The tunnel is also subjected to a geometric regularization of the intrados profile, with homogenization of the free spaces and elimination of any underprofile resulting from imperfections in the construction of the original definitive lining.

Since the first half of 2022, TECNE has started the planning of pilot TRS interventions to be applied on specific tunnels of the network identified among those most in need of a complete lining renewal operation and at the same time located along motorway sections characterized by traffic volumes compatible with the total interruption (24 hours a day) to traffic over minimum time windows of 2/3 months each, the latter being a necessary condition to actuate the experimental design solutions for the complete reconstruction of tunnel crown as well as, as in the specific case of the Colle Marino left, of the invert.

As part of the TRS strategy, TECNE has developed a series of intervention typologies based on the adoption of different construction solutions for the new definitive lining of the tunnels, making use in particular of technologies recently developed in the underground market, both for the choice of structural materials and waterproofing techniques. By way of example, reference is made to the use of modular elements in galvanized steel for liner plates constituting the new lining, to the use of structural shotcrete with high mechanical performance or of high-resistance fibre-reinforced concrete cast on site, to use of prefabricated structural segments.

In the specific case of the Colle Marino left tunnel, for the new final lining (crown/piers) the solution was identified consisting of an arch of 3 prefabricated slabs with completion casting on the back carried out with high-performance self-compacting concrete. The arch is connected to the invert made of

fiber-reinforced concrete cast on site, through a special shear-key joint reinforced with pre-assembled steel cages.

The following contents retrace the process that led to the development of the design solution, provide a description of the extensive geognostic and structural investigation campaign carried out on the tunnel, illustrate the basic concept of the solution and the dimensioning process and verification of the structures, the most interesting evidence collected during construction is summarized. Finally, the technical-technological contents currently being developed for the modernization project of the adjacent tube, i.e. the right Colle Marino tunnel, are anticipated, the field of application of the "fully operational" TRS strategy resulting from the complete return of experience relating to the pilot intervention conducted on the left tunnel. The structural renewal project of the right bore represents a prototype intervention of works with continuous construction operations, foreseeing the closure to traffic at night and the opening of the tunnel during the day with transit of vehicles underneath a system of shield gantries capable of carry out certain processes simultaneously with the use of the tunnel by users, resorting as far as possible to the automation of the processes.

2 DEFINITION OF THE INTERVENTION ON THE LEFT TUNNEL

The left Colle Marino tunnel, almost entirely made up of the natural section excavated in the consistent clays belonging to the Mutignano Formation (Plio-Pleistocene marine deposits), extends for a total of 960 m, presenting maximum overburden of 70 m. The tunnel, in July 2021, was the subject of a thorough inspection conducted in compliance with the New Inspection Manual issued by the MIT (Italian Transportation Ministry) during the year 2020. From this inspection a severe picture emerged in terms of structural degradation of the original definitive linings for the presence of widespread and persistent cracks in the crown as well as a general state of deterioration of the concrete also determined by the presence of defects which occurred during the casting phase. Furthermore, a good part of the tunnel crown was already protected with previously installed steel wire mesh, precisely because of defects pattern that had emerged over the years. This condition led, in the immediate future, to the use of temporary interventions on the final lining consisting of welded wire mesh coupled in several layers fixed with chemical anchors and, locally, in the most critical sectors, by metal ribs hung from the crown intrados again by chemical anchors (L 450 mm). At the same time, in anticipation of a subsequent and more lasting intervention to resolve the defects, a specific campaign of geognostic investigations was conducted both in the tunnel (continuous core drilling with recovery of undisturbed samples aimed at the geotechnical characterization of the mass as well as the assessment of the mechanical properties of the concrete of the final covering in place), and from ground level (refraction seismic laying with Vp + Vs acquisition, extended to cover the entire longitudinal development of the work). The series of core samples obtained from the invert revealed a critical scenario determined by the modest thicknesses detected (significantly lower than those deduced from the original design documents) and, in particular, by the poor compressive resistance of the cement conglomerate (cylindrical resistance values close to 5 MPa).

The preliminary structural analyzes for the static evaluation of the existing linings confirmed the need to equip the tunnel with a new invert in order to meet the minimum performance requirements required by current legislation, in the specific context of intervention characterized by medium-high seismicity and modest characteristics geomechanics of the soil interacting with the work. Demolition and reconstruction of the invert were therefore included in the design plan for the renewal of the tunnel's definitive linings, according to the logic of the Tunnel Renewal Strategy. Precisely in light of the complex conservation conditions of the tunnel crown subject to the extensive application of temporary protection interventions, the design solution identified by TECNE pursued the objective of significantly reducing the impact of milling operations in the crown sector (confining it between kidneys and the base of the piers), drastically mitigating the potential risk associated with phenomena of uncontrolled detachment of portions of concrete, beyond the theoretical milling profile, triggered by the mechanical demolition/milling of the covering portions incorporating the anchors chemicals for deep fixing of hanging nets and ribs - particularly pervasive in this tunnel - especially in the sections affected by underthickness of the original lining. Furthermore, the deep anchoring bars would have constituted an obstacle to the correct functioning of the milling head, with the possibility of damage and risk of machine downtime.

The total elimination of milling in the central sector of the crown, with the inscription of the new intrados geometry within the profile of the original lining, was achieved as a result of the design choice to implement a significant lowering of the motorway platform (average value 65 cm in roadway axis), permitted by the absence of altimetric constraints at portals (i.e. structures such as bridges, viaduct abutments, underpasses). This option, in the specific case of the Colle Marino sx tunnel, introduces extra costs that are not significant in economic and temporal terms, precisely due to its inclusion in the context of a design solution already contemplating the demolition and reconstruction of the invert. The lowering of the platform made it necessary to design platform altimetric connections with a development limited to within a hundred metres, at each tunnel portal.

3 TECHNICAL CHARACTERISTICS OF THE ORIGINAL TUNNEL

Prior to the development of the design solution, a careful examination of the original design documentation of the tunnel was conducted, as mentioned dating back to the late 1960s, preserved in the Autostrade archives. It was possible to analyze a large number of documents relating to the construction phase of the work, in particular accounting drawings representing in detail the temporary linings (ribs and spritz), the carpentry of the different type-sections applied for the natural tunnel, artificial tunnels and portal (carpentry and armor works). Of particular importance is the availability of the calculation reports of the final linings of both the natural section and the artificial tunnel, from which it is possible to trace the dimensioning and verification approaches of the aforementioned linings, and of the Works Journal useful for the reconstruction of the succession of the construction phases of the the work as a whole, the methods of excavation of the two arches, and any critical issues that occurred in the progress of the works. From this analysis it was possible to deduce how the excavation of the left tube (object of the intervention) was attacked on the Bologna side, anticipating the start of the adjacent tube, adopting the full front advancement technique with systematic installation of reticular ribs (spacing 0.8 /1.00 m) incorporated inside a shotcrete shell 15/ 20 cm thick, probably among the first examples in Italy of full-section excavation considering the year of construction of the work.

The construction sequence therefore included the casting of the walls, the excavation and casting of the invert (unreinforced, thickness 70 cm), the completion of the lining with the crown castings (unreinforced, thickness varying from 70 to 90 cm, depending on the section-type applied). From the examination of the Giornale Lavori there are no particular critical issues during the excavation phase on both arches. The artificial section on the Pescara side extends for approximately 22 m; the work, according to accounting drawings, appears to be entirely reinforced (crown/pier/inverted arch) for the first 14 m, the last 8 m feature exclusively crown reinforcement. The artificial section on the Bologna side, with a total length of 120 m, required very significant excavation excavations. The significant thickness of the filling determined the use of massive structural sections, with crown thicknesses of 120 cm and abutment thicknesses of up to 150 cm at the base. According to the original design documentation, the crowns of the artificial tunnel are reinforced everywhere, while the piers and the inverted arch are reinforced only on the 50 m section starting from the entrance. It is interesting to note the presence of a notch on the valley side of the inverted arch, evidently introduced to counteract the asymmetrical thrust of the earth filling/covering.

4 STRUCTURAL INVESTIGATION CAMPAIGN PREPARATORY FOR EXECUTIVE DESIGN

The tunnel was the subject of a vast campaign of structural investigations preparatory to the detailed executive design of the intervention, in particular to the safe management of the demolition and reconstruction operations of the inverted arch and deep milling of the tunnel piers. The need to have a particularly accurate cognitive framework of the actual thicknesses of the linings (crown/piers and inverted arch), of their work rate, of the physical-mechanical characteristics of the concrete is dictated by the specificity of the intervention context, interacting the tunnel with an averagely consistent clay formation, locally characterized by mechanically poorer sectors from the examination of the results of the extensive geophysical investigation campaign conducted from the surface, precisely in the central part of the tunnel which corresponds to the maximum coverage in crown. This plan consisted in the preparation of approximately 40 investigation sections, placed at a distance of 24 m, where the following tests were carried out:

- N.2 flat jack tests in inverted arch performed inside trenches made on the platform; in particular, the test located on the adjacent tunnel side (hypothesized to be more stressed due to the construction history of the tunnel) was carried out using an innovative method which involves the measurement of the strain value on the surface in correspondence with subsequent cutting steps, with the aim of detect the evolution of the detensioning as a function of the cutting depth. On the opposite side of the inverted arch, traditional tests were conducted (single cycle tests, loading/unloading, with determination of the recovery pressure).
- N. 2 traditional flat jack tests, on the abutments (left/right), at a height of approximately

1.50 m from the pavement level (single cycle tests, loading/unloading, with determination of the recovery pressure);
- N. 2 core drillings passing through the piers (left/right), at a height of approximately 1.50 m from the pavement level, pushed up to the interception of the clay mass, with recovery of concrete samples of the final covering and of the constituent shotcrete the first phase lining (including stratigraphic reconstruction with identification of the thicknesses of the two types of lining).

Throughout the development of the work, ground penetrating radar systems were therefore carried out at the height of the piers, with a specifically defined spectral content for the purpose of reconstructing the thickness of the definitive lining and the pre-lining (since the presence of the reticular ribs was known), also being able "calibrate" the GPR interpretation on the dense series of direct acquisitions consisting of structural core drilling carried out on both the left and right sides with a 24 m spacing.

5 RESULTS OF THE STRUCTURAL INVESTIGATION CAMPAIGN

From the investigation campaign an extremely detailed cognitive picture of the final linings of the natural tunnel emerged. With a frequency of 24 m it was possible to reconstruct the tensional regime acting in the piers and in the inverted arch (associated with similar data already available for the crown sector, key section and kidneys, on the basis of the flat jack tests conducted during the inspection phase in the year 2021), correlating the same to the overburden and the mechanical quality of the soil/rock mass interacting with the tunnel (obtained from the continuous data returned from the surface seismic tests, integrated and calibrated with the evidence of the direct geognostic investigations conducted in the tunnel), as well as the actual concrete thicknesses. To confirm the expected scenario, different sectors of the tunnel were identified with abutments and inverted arches subject to a non-negligible work rate and clearly higher than the tension level associated only with the self-weight of the final linings, a symptomatic situation of a rock mass-structure interaction that has occurred during the excavation phase and, presumably, considering the construction methods deriving from the Work Journal, during the years following the tunnel construction (evolution attributable to the partial physical-mechanical decay of the temporary linings as well as to possible phenomena of stress-strain release in the time, of a viscous nature, occurred in the clayey passages characterized by greater plasticity of the material (and corresponding reduced mechanical characteristics), clearly detectable by the analysis of the Vp-Vs tomographies processed by the seismic refraction survey conducted from the surface.

Of particular importance are the results of the GPR investigations conducted along the piers, as it was possible to identify numerous tunnel sectors with significant under-thicknesses evidently determined by the compensation of tracking errors during the excavation phase. In certain areas, reductions in thickness of up to 50 cm have been recorded compared to the theoretical derivable from historical design documents. The compressive strength of the piers concrete was found to be affected by a modest variability along the development of the tunnel, averaging around 15 MPa (cylindrical strength). Of note is the good quality level of the first phase shotcrete sampled in the core sampling campaign; the simple compression tests returned an average value of 35 MPa.

This evidence significantly guided the process of identifying the design solution and, specifically, the articulation of the operational phases and the scanning of the so-called elementary fields of works-progress of the inverted arch and crown/pier reconstruction.

6 GENESIS OF THE DESIGN INTERVENTION AND ADOPTION OF SPECIFIC TECHNICAL SOLUTIONS

The typical section of the intervention on the natural tunnel was conceived according to the specific construction phases of the work. In particular, the annual arrangement of the windows permanently closed to vehicular traffic, in the reference section (A14, Atri-Pineto/Roseto degli Abruzzi) constituted the main constraint for the organization of the complete renewal works of the definitive coverings of the Opera. This motorway section along the Adriatic coast is affected by particularly intense vehicular flows during the entire summer season and during the main national holidays (Christmas, Easter, All Saints' Day and the Immaculate Conception). The Management of Section 7 has therefore defined the need to guarantee the reopening of the tunnel in the aforementioned periods, consequently determining the distribution and duration of the periods of permanent closure of the tunnel useful for the implementation of the intervention. The most significant time windows in terms of continuous days of closure to traffic of the left tube (northbound) were therefore identified as a priority, for carrying out the intervention with the greatest static commitment of the renewal project, i.e. the demolition and reconstruction of the inverted arch over the entire length of the natural tunnel and approximately 80 m of artificial tunnel, for a total of approximately 900 linear m. This operation was divided into two macro-phases of work: November 2022 (70 m of inverted arch reconstructed on the artificial Bologna side) and January-March 2023 (830 m of inverted arch reconstructed on the entire length of the natural tunnel and on the artificial side Pescara). At the end of the reconstruction of the inverted arch, for the Easter holidays, the Trunk Management requested the reopening of the fornix to vehicular traffic.

The design solution was therefore conceived to allow the return of the work to operation albeit with a partial structural renewal intervention, limited to the inverted arch only: the demolition of the existing inverted arch was therefore carried out with methods aimed at preserving the structures of crown and abutment, making sub-vertical cuts in the base portion of the abutment, extending longitudinally over the entire development of the fornix, both on the right and left side, as well as transversal cuts in an inverted arch, spaced correspondingly to the length established for the elementary field of progress of the works, in order to contain the propagation of the vibrations induced by the mechanical action of the demolition hammer acting on the inverted concrete. The elementary advancement range for inverted arch workings was defined as 6m or 12m based on the evidence of the structural and geotechnical investigation campaign, as well as the results of the longitudinal cutting operations carried out well in advance to pay attention to any resealing phenomena cuts symptomatic of the structures' work rate.

The new inverted arch has a thickness of 45 cm (increased to 60 cm in the tunnel sectors on which a more significant work rate of the linings was measured, in particular in the original inverted arch), and is made with fiber-reinforced concrete casting having Rck 45 MPa (locally reinforced in correspondence with the sectors mentioned above for the application of the increased thickness section).

In order to restore the structural continuity of the coverings during the temporary reopening to vehicular traffic, in the minimum terms of confinement at the foot of the abutment structures freed from the longitudinal cutting and demolition operation of the existing inverted arch, special temporary curbs were introduced connection cast in place against the surface of the longitudinal cut of the abutment and the recess of the cutting key present on both sides of the inverted arch. The interposition of EPS panels and metal sheets on the lateral surfaces of the curbs is functional to the preservation of the concrete of the definitive inverted arch during the demolition operations of the temporary curbs, necessary to proceed with the construction of the new crown covering.

The shell cladding was designed with the aim of minimizing the structural thickness to just 35 cm, adopting prefabricated lattice slabs with lowered geometry to allow easier handling during launching and arch formation. The back casting is made of class C40/50 self-compacting concrete. The waterproofing layer is made up of a layer of 500 g/m2 geotextile and a 2.0 mm thick PVC layer. At the foot of the abutment there is a micro-cracked pipe DN 110 mm, intercepted every 12 m by transversal drains which deliver to the DN200 collector located under the pavement.

A less invasive intervention was adopted on the artificial tunnels, as the original linings were

reinforced, the latter condition causing greater difficulties when milling. The coverings were first subjected to extraordinary maintenance interventions with the aim of resolving all structural defects (remediation of construction defects, sealing of cracks). In order to restore a work with an aesthetic effect in line with that offered by the new crown coverings of the natural tunnel, it was decided to install an internal lining in galvanized steel sheet panels (stiffened with appropriate ribs to achieve suitable rigidity of the elements in launch phase).

7 INTERVENTION DESIGN CRITERIA

The new lining of the crown and inverted arch was sized and verified through detailed numerical modeling which firstly reconstructed the construction phases of the original tunnel (simulating the full face excavation operations followed by the inverted arch excavation) with the aim of calibrating the stress state of the final linings reproduced in the FEM model on the real work rate recorded in the tunnel by the flat jacks installed in the preparatory investigation phase for the executive design of the intervention. The new lining was then subjected to load conditions corresponding to theoretical scenarios identified with a conservative approach, hypothesizing, for example, the total mechanical decay of the concrete of the residual original lining portions after milling, as well as the de-functionalization of the pre-linings (ribs and spritz), i.e. the total absence of load on the new coverings and the concomitant shear deformation generated by the seismic action.

8 MAIN EVIDENCES FROM THE EXECUTION OF THE WORKS

The main evidence returned from the construction phase consisted in the verification of geometries of the existing inverted arch different from those reported in the historical archive documents, frequently revealing under-thicknesses compared to the theoretical value as well as lowered intrados profiles and only partially abutting the walls (with consequent penalization of the theoretical confinement action at the foot of the piers). These results confirmed the strategic layout of the design solution for the integral reconstruction of the inverted arch to respond to the most stringent regulatory requirements in terms of structural performance of the tunnel linings under seismic action. The demolition operations of the inverted arch were accompanied by extensive manual topographic monitoring of the deformations that occurred at the foot of the abutment following the demolition of the inverted arch itself. The design forecast of interception of tunnel sectors interacting with rock mass sectors characterized by more demanding conditions in terms of interaction with the structures was essentially confirmed. This evidence confirmed the validity of the choice to implement an extensive campaign of structural investigations preparatory to the detailed executive planning of the intervention, thanks to which it was possible to reconstruct a detailed cognitive framework on the basis of which to identify the most critical tunnel sectors, guiding the field work and carefully planning the use of protective devices such as the contrasting metal strut.

The synergy between the design group, works management and contractor made it possible to achieve the ambitious objective of demolition and reconstruction of approximately 900 m of inverted arch in the limited time span of 3 months (Jan/Feb/Mar 2023), the first case in a motorway tunnel of the Italian network. The reconstruction work on the crown, which is expected to be completed by March 2024, confirmed the flexibility of the construction solution based on the adoption of prefabricated slabs as disposable formwork, being able to attach multiple work fronts at the same time, to guarantee high production (approximately 350 m of shell in 2 months of work).

9 COLLE MARINO RIGH TUNNEL FUTURE PROJECT DEVELOPMENTS

On the basis of the feedback from the experience gathered from the work carried out on the left tube, the executive project for the similar integral reconstruction of the final linings on the right tube was developed. The intervention involves significant technical optimizations, consisting of the adoption of new inverted arch geometries that are smaller and similar to a slab placed on the intrados of the original building, pursuing the objective of minimizing the demolition of the existing structure (which in any case is totally defunctionalized once the new base slab is completed). The shell lining is made of a cast HPC concrete characterized by the addition of steel and polypropylene fibres, with very high mechanical performance. The main innovation associated with the intervention being designed on the right tube, however, consists of the adoption of a construction system based on work trucks under which vehicular traffic passes during the daytime hours when it is open to traffic.

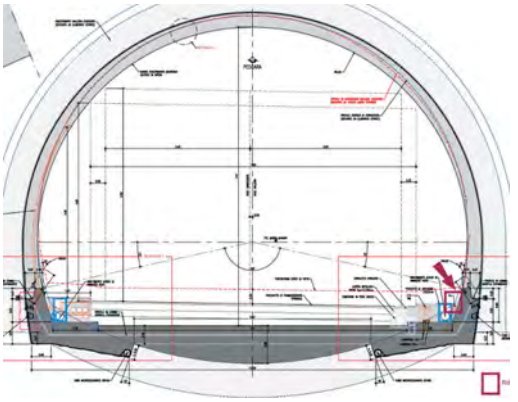

This technology, experimental and in its first application on the motorway network, is aimed at carrying out the works in temporal continuity, regardless of the needs of motorway operations which impose frequent interruptions of the works with associated diseconomies and extensions of the completion times of the interventions and, above all to the increase in safety conditions for users by always being able to guarantee a traffic lane during the day on the roadway on which the tunnel affected by the works is located in the face of the total closure of the fornix to traffic adopted so far for the execution of structural interventions of such importance that it determined the operation of the adjacent barrel in bidirectional mode. The train of wagons consists of a special wagon for milling with dust extraction, a wagon for the automated installation of waterproofing, a wagon with integrated formwork for casting high-performance fibre-reinforced concrete. The train is completed by an invitation wagon which guarantees the correct direction of traffic within the shield, in compliance with the safety conditions established by the technical regulations. The application of this technological solution is expected, on the right tube of the Colle Marino Tunnel, in the first months of 2025.

REFERENCES

Mazzola, M Giordano, C. Alessio, B. Spigarelli Autostrade per l'Italia (ASPI) TRS Tunnel Renewal Strategy: the cases of Castello 1 left, San Fermo right and Colle Marino left tunnels. Proceedings of ITA-AITES World Tunnel Congress WTC 2023, Athens, Greece, 2023, 8th – 13th May

Tunnelling for a Better Life – Yan, Celestino, Thewes & Eberhardt (Eds)
© 2024 The Author(s), ISBN 978-1-032-80042-4
Open Access: www.taylorfrancis.com, CC BY-NC-ND 4.0 license

Lessons learned from longitudinal ventilation worldwide and CFD-based solutions

Ana Belén Amado*
CFD Engineer, Gijón, Spain

Yunlong Zhao
Area Manager China, Gijón, Spain

Encarnación Quesada Ruiz
Marketing Director, Gijón, Spain

ABSTRACT: Longitudinal ventilation plays a crucial role in ensuring safe and efficient operation of underground tunnels. Over the years, Zitron has encountered and overcome various challenges associated with longitudinal ventilation systems in tunnels. This paper presents a comprehensive analysis of the lessons learned from these experiences and explores innovative solutions using Computational Fluid Dynamics (CFD) tools.

The study addresses several critical questions that arise during the design and installation of longitudinal ventilation systems. Firstly, it investigates the optimal spacing between jet fans in tunnels with wide cross-sectional areas. Secondly, the paper investigates the impact of placing information panels in the proximity of jet fans and provides insights into mitigating potential issues. Additionally, it explores the most suitable longitudinal distribution between fan banks to minimize electrical cable usage while maintaining effective ventilation. The feasibility of installing jet fans at tunnel portals is examined, considering the trade-offs between tunnel length, fan quantity, and overall ventilation performance.

Furthermore, it also addresses the challenge of insufficient longitudinal ventilation in existing tunnels through a case study of a tunnel, highlighting successful strategies for improving airflow distribution and enhancing safety.

The results demonstrate the effectiveness of CFD-based tools in optimizing longitudinal ventilation designs, ensuring proper airflow distribution, and validating the performance of the ventilation systems. The lessons learned from Zitron's extensive experience, coupled with the power of CFD tools, provide a valuable resource for engineers, researchers, and professionals in the field of underground infrastructure.

Keywords: Longitudinal ventilation, CFD simulation

1 INTRODUCTION

The design and implementation of longitudinal ventilation systems in tunnels present unique challenges that require careful consideration. This paper presents lessons learned from real-world tunnel ventilation scenarios and proposes innovative solutions using Computational Fluid Dynamics (CFD) tools to address these challenges.

The paper explores several key questions that arise during the design and installation of longitudinal ventilation systems. Firstly, it investigates the optimal spacing between jet fans in tunnels with wide cross-sectional areas. Secondly, it analyses the optimal placement of information panels in proximity to reversible jet fans, considering factors such as airflow distribution and speed. Additionally, it explores the ideal longitudinal distribution to optimize energy

*Corresponding author: anabelen@zitron.com

DOI: 10.1201/9781003495505-442

efficiency and maintain effective ventilation. Furthermore, this paper addresses the challenge of inadequate longitudinal ventilation in existing tunnels through a case study of a tunnel in the Netherlands, showcasing successful strategies for improving airflow distribution and enhancing safety.

The results emphasize the effectiveness of utilizing CFD-based tools in optimizing longitudinal ventilation designs, ensuring proper airflow distribution, and validating ventilation system performance.

2 TUNNEL WITH LARGE CROSS-SECTION

In this tunnel, reversible jet fans with a diameter of 1200 mm and a power rating of 45 kW are installed in pairs. The tunnel's cross-sectional area measures approximately 88.6 m² and is notably wide, as seen in Figure 1. Given the absence of placement restrictions, a Computational Fluid Dynamics (CFD) analysis was conducted to determine the optimal fan spacing for this section.

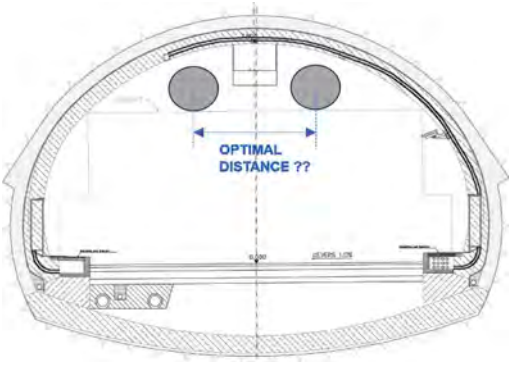

Figure 1. Tunnel cross-section.

Four CFD simulations were performed, varying the distances between fans at 1.8m, 2.4m, 3m, and 5m, aiming to identify which configuration yielded the highest airflow rate or average velocity within the tunnel. Figure 2 and 3 illustrates the results, presenting a plan view and cross-sectional profiles along the tunnel of the different simulations. The colour scale represents velocities ranging from 0 to 10 m/s.

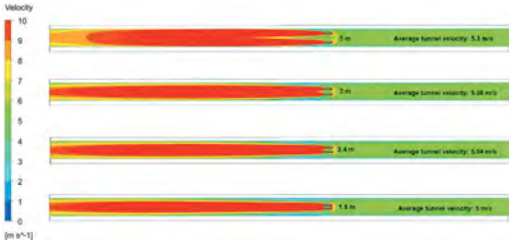

Figure 2. Contours of velocity different simulations.

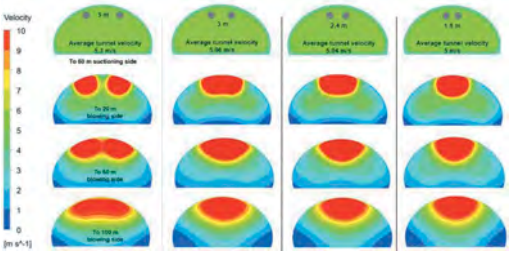

Figure 3. Cross sections of contours of velocity.

The graphical results reveal that greater fan spacing leads to a more favourable average velocity within the tunnel. Consequently, for this particular tunnel with a substantially wide cross-section, the optimal configuration involves placing the fans 5 meters apart. This configuration results in a 5.7% increase in velocity compared to a 1.8 meter spacing, while also there is enough separation for electrical installation trays, as demonstrated in Figure 4, consistent with practices in other tunnels.

Figure 4. Tunnels with significant jet fans spacing.

3 TUNNEL WITH INFORMATION PANELS

During the installation of reversible jet fans in a tunnel, technicians noticed that information panels would be located nearby. These raised questions about whether there would be a change in tunnel velocity and what the optimal distance would be to place the information panels in these circumstances. To address these concerns, Computational Fluid Dynamics (CFD) simulations were conducted. These simulations considered the geometry of the tunnel in question along

with the installed ventilation system, pairs of 1200 mm diameter, 30 kW jet fans, and information panels placed at different distances, ranging from 5 to 100 meters, to gain a broader understanding of what might occur.

In Figure 5, various velocity contours obtained from the CFD simulations are displayed. These contours illustrate scenarios where the information panel is positioned at different distances from the fan on the impulsion side. The colour scale represents velocity ranging from 0 to 10 m/s, with red indicating velocities of 9 m/s or higher. It is observed that in the absence of an information panel, the tunnel exhibits an average velocity of 4.67 m/s. However, when an information panel is placed on the impulsion side of the fans at varying distances, a collision occurs between the fan's jet and the information panel, resulting in a consequent reduction in the tunnel's average velocity. When the panel is positioned 5 meters away, the average velocity decreases by 36%. Conversely, if the panel is placed 100 meters away, there is a 4% reduction in comparison to the average velocity generated without any obstacles.

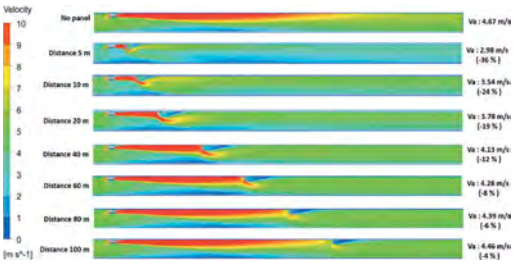

Figure 5. Contours of velocity with information panel on the impulsion side of jet fans.

In scenarios where the information panel is located in the aspiration zone of the jet fans at different distances, Figure 6 illustrates that the reduction in average tunnel velocity due to the obstructive nature of the information panel is much smaller. In fact, the reduction is only 2% less than the velocity without a panel when the panel is situated at 5 meters.

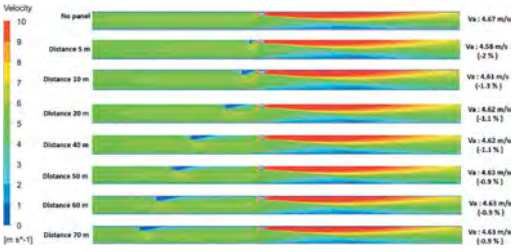

Figure 6. Contours of velocity with information panel on the aspiration side of jet fans.

Based on the results obtained from the simulations, the following solutions are proposed:

In unidirectional tunnels, it is recommended to position the information panels on the aspiration side of the jet fans if possible. This placement minimizes their impact on the tunnel's average velocity.

In bidirectional tunnels, a compromise solution should be sought. Information panels should be placed as far away as possible from the jet fans to minimize their impact on tunnel airflow.

4 TUNNEL AND FAN DISTRIBUTION

This tunnel boasts a length of 505 meters, a cross-sectional area of 166 m², and a 2% gradient. It is an unidirectional urban tunnel with high traffic density. A study conducted for this tunnel indicated the need for 6 jet fans with an inner diameter of 1000 mm and a power rating of 30 kW to fulfil ventilation requirements in both normal and emergency modes. To determine the optimal fan distribution in terms of the average airflow generated within the tunnel and the length of cable used in the installation, simulations using Computational Fluid Dynamics (CFD) were employed. It's essential to note that the electrical technical room was located at the tunnel's entrance.

Four different fan distributions within the tunnel were considered, and the graphical results are depicted in Figure 7. The colour scale represents velocity ranging from 0 to 15 m/s, with red indicating velocities equal to or exceeding 14 m/s.

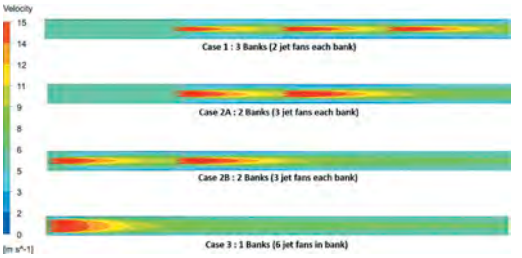

Figure 7. Contours of velocity at fans level for different distributions.

In **Case 1**, the six required jet fans in this tunnel were divided into three banks, with a distance of 12 hydraulic diameters (140 m) from the entrance to the first bank and 10 hydraulic diameters (117 m) between banks, following CETU guidelines. With these conditions, the fans move 850 m³/s of air within the tunnel. Taking into account that the electrical technical room is located at the tunnel entrance, the minimum cable distance required with this distribution would be 1662 m, considering a cost of € 100 per meter (materials + labour), then incurring a final electrical cost of 166.200 euros.

In **Case 2A**, the distribution was modified to consist of two banks of three fans each. The first bank is located 12 hydraulic diameters (140 m) from the entrance, and the second bank is positioned 10 hydraulic diameters (117 m) from the first. This configuration yielded an airflow of 892 m³/s, a 4.7% improvement over the previous case. Additionally, the cable length required was reduced to 1311 m, resulting in a cost of 131.100 euros.

In **Case 2B**, there are still two banks of three fans each, but the position of the first bank has been changed to the vicinity of the tunnel entrance, with the next bank situated 12 hydraulic diameters (140 m) from the entrance. This arrangement guarantees an airflow of 905 m³/s (1.4% more than Case 2A) within the tunnel, with a reduced cable length of 540 m, incurring a cost of 54.000 euros.

Finally, in **Case 3**, all six fans were placed at the tunnel entrance. This configuration achieved 944 m³/s (4.1% more than Case 2B) and required approximately 62 m of cable. However, this option was discarded due to potential safety risks, especially in the event of a fire at the tunnel entrance that could damage most of the fans.

Therefore, the optimal fan distribution, considering the highest airflow achieved within the tunnel, the shortest cable length, and cost-effectiveness, is Case 2B.

However, when the results were presented for approval, it was discovered that the tunnel was not straight but had a pronounced curve, as shown in Figure 8.

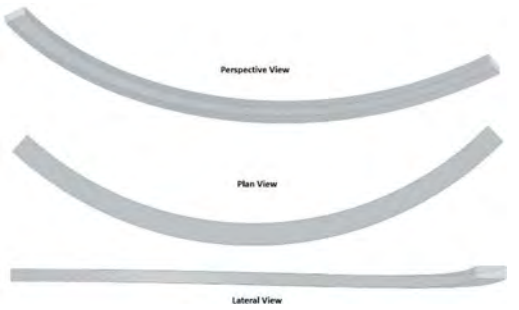

Figure 8. Tunnel geometry.

It was uncertain whether the fluid behaviour would be the same in a curved tunnel, and to avoid assumptions, additional simulations were conducted with the corrected tunnel layout while maintaining the same distribution cases as before. The new graphical results, compared to the previous ones, can be seen in Figure 9.

In **Case 1**, in the curved tunnel with three banks of fans, the airflow when the fans were operational was 838 m³/s. In **Case 2A**, an airflow of 887 m³/s was achieved inside the tunnel. For **Case 2B**, an airflow of 884 m³/s was achieved, and for Case 3, it was 886 m³/s. Choosing **Case 3** is still ruled out as a risky option.

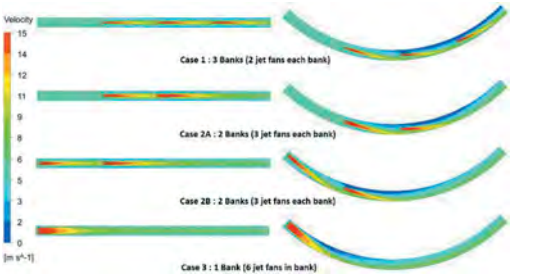

Figure 9. Comparison of velocity contours in straight and curved tunnels.

It is evident that in all cases, the airflow generated is lower than in the straight tunnel due to the reduced effectiveness of the fans' jets when directed toward the tunnel walls.

Although Case 2A in the curved tunnel is slightly better than Case 2B, the reduction in cable length required for Case 2B is considered significant. Therefore, Case 2B remains the best option for fan distribution in this tunnel.

5 TUNNEL WITH VENTILATION ISSUES

This tunnel, situated near an airport, spans a length of 536 meters with a cross-sectional area of 75 m². Inside, there are 19 jet fans equipped with deflectors, featuring a diameter of 700 mm and a power rating of 15 kW. These fans are not evenly distributed but are positioned on one side of the tunnel. Despite its relatively short length and numerous fans, ventilation issues have been observed within the tunnel. Strong winds (~5 m/s) blowing into the tunnel, opposing the ventilation, are a common occurrence. To identify the root of the problem, a Computational Fluid Dynamics (CFD) simulation was conducted to analyse airflow behaviour within the tunnel when ventilation was in operation and wind was acting against it.

In the graphical results obtained from the CFD simulation, as depicted in Figures 10 and 11, it is evident that the velocity distribution within the tunnel is non-uniform, with low velocities and even flow recirculation along the side opposite to the fans.

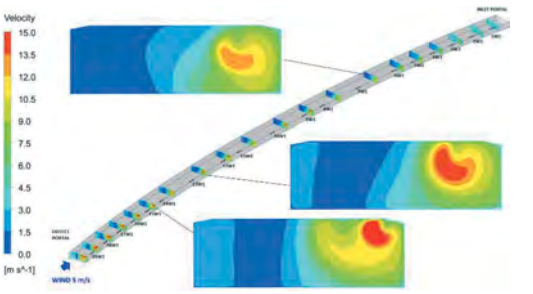

Figure 10. Contours of velocity in different cross-sections.

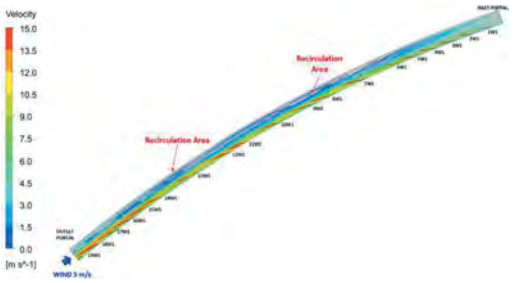

Figure 11. Path lines of velocity inside the tunnel.

Thus, under these conditions, it is confirmed that ventilation is not adequate in all areas of the tunnel, as initially suspected.

As a solution to counteract the wind effect within the tunnel and homogenize the velocity, various fan configurations were tested. The most effective result was achieved by adding two additional fans near the tunnel exit on the side opposite to the others.

Graphical results obtained from the CFD simulation with the added tunnel fans are presented in Figures 12 and 13.

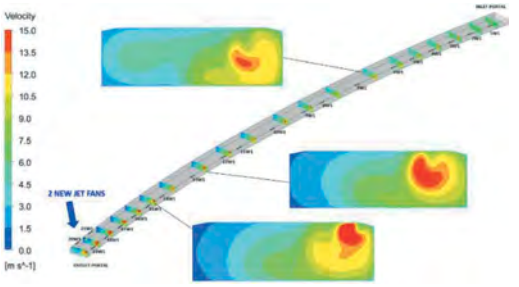

Figure 12. Velocity contours in different cross-sections with two new jet fans.

Figure 13. Path lines of velocity inside the tunnel, including two new jet fans.

These images demonstrate that the installation of two new fans near the tunnel exit, on the opposite side wall from the existing fans, achieves equal or higher velocities exceeding 1.5 m/s in all tunnel sections, effectively eliminating the previous air recirculation issues, even when strong winds at the tunnel portal blow into the tunnel.

6 CONCLUSIONS

The research conducted on tunnel ventilation and the proposed solutions through CFD simulations has yielded valuable insights into addressing specific ventilation challenges in different tunnel scenarios.

For tunnels with a large cross-section, the optimal solution involves placing fans at meters apart. The case study of this paper with 5m increases tunnel velocity by 5.7% compared to a 1.8-meter separation and also separates the fans from electrical installation trays.

In the case of tunnels with information panels, it has been determined that in unidirectional tunnels, placing information panels on the aspiration side of the fans is the optimal solution. This placement has a lesser impact on the tunnel's average velocity. However, in bidirectional tunnels, a compromise solution is needed, with information panels placed as far away as possible from the fans.

In relation to the distribution of fans in tunnels with significant traffic density, the optimal configuration consists of two banks of three fans each, with the first bank located at the portal and the second bank positioned 12 hydraulic diameters from the portal This configuration maximizes tunnel velocity while minimizing the length of cable required for installation. The option of placing all six fans at the tunnel entrance is discouraged due to potential safety risks, especially in case of a tunnel fire.

In the case of curved tunnels, the effectiveness of jet fans is reduced compared to straight tunnels due to the diversion of air towards the tunnel walls. Despite slight variations, the configuration with two banks of three fans each, one in the portal, remains the most practical choice, particularly considering cable length requirements.

In tunnels experiencing ventilation issues due to strong winds blowing against the ventilation direction, adding two additional fans near the exit portal effectively counters the wind effect, achieving velocities of 1.5 m/s or higher in all tunnel sections and eliminating air recirculation, even with strong winds blowing into the tunnel.

In summary, no tunnels are the same and each one has its own challenges, but the use of CFD allows for faster and more reliable solutions. The research provides valuable recommendations for optimizing tunnel ventilation in various scenarios, taking into account factors such as fan placement, tunnel geometry, and safety considerations.

REFERENCES

CETU, 2003. Les dossiers pilotes des tunnels – Ventilation.
PIARC, 2007. Systems and equipment for fire and smoke control in road tunnels.
ANSYS, 2023. Fluent Theory Guide, R1. ANSYS Inc.

Tunnelling for a Better Life – Yan, Celestino, Thewes & Eberhardt (Eds)
© 2024 The Author(s), ISBN 978-1-032-80042-4
Open Access: www.taylorfrancis.com, CC BY-NC-ND 4.0 license

Italian guidelines for the risk classification, safety evaluation and monitoring of existing tunnels: An overview

Andrea Carigi* & Carmine Todaro
Politecnico di Torino, Turin, Italy

Giuseppe Silvestri
Consiglio Superiore dei Lavori Pubblici, Rome, Italy

ABSTRACT: The Italian transport network had a great expansion after World War II and a great number of tunnels were built. After 70 years, those tunnels are approaching their design lifetime. With more than 9000 tunnels extended for 2600 km of underground structures on the Italian national territory, the correct management of this asset is challenging, especially in the context of a complex road network.

To provide an integrated method to monitor and plan the maintenance actions for the different stakeholders on a national scale, a Guideline for the risk classification, safety evaluation and monitoring of existing tunnels has been implemented by the Italian Superior Council of Public Works and is now mandatory for roadways tunnels in Italy.The guidelines are structured in 5 levels with progressively increasing levels of knowledge requirements and detail of the investigation, where level 0 is dedicated to a census of all the available information about the tunnel, level 1 is dedicated to the inspections that have to be carried out with the help a specifically designed defect catalogue. Then, accordingly to the data collected, in level 2 a classification to prioritize further investigations, standard maintenance procedures, or ad hoc designs is regulated through a series of logical operators to ensure that the same classification procedure is used for all the tunnels in the national territory. This last level is subdivided into 6 fields with regard to specific critical phenomena that may lead to a risk to the proper functioning of the tunnel. Then, levels 3 and 4 are respectively dedicated to preliminary and accurate safety evaluations, while the last level regulates the maintenance of tunnels of strategic interest for the nation.

In this paper, a detailed discussion of the structure of the guidelines and about their application is presented.

Keywords: Tunnel, Knowledge, Maintenance, Inspections, Guidelines

1 INTRODUCTION

In the aftermath of World War II, Italy embarked on a plan of infrastructure development, expanding its transport network to accommodate the demands of a growing nation. A crucial component of this expansion was the construction of an extensive network of road and highway tunnels that stretched beneath the complex Italian orography. These tunnels are now nearing the end of their designed lifetimes, having served the nation for over seven decades.

Italian subterranean infrastructure boasts an impressive count, with over 9,000 tunnels spanning an extensive 2,600 km (Pireddu & Bruzzone, 2021). However, the longevity of these critical conduits presents a unique challenge that demands careful consideration and comprehensive management.

As these tunnels have matured over the years, a pressing need has emerged for a holistic approach to their maintenance and safety assessment. The task of ensuring the continued functionality and safety of these subterranean assets has become increasingly complex. In response to this challenge, the Italian Superior Council of Public Works (Italian infrastructure ministery), recognizing the need for a standardized and integrated framework to manage tunnel maintenance, has introduced a Guideline for the Risk Classification, Safety Evaluation and Monitoring of Existing Tunnels (in Italian, “Linee Guida per la Classificazione e Gestione del Rischio, la Valutazione della Sicurezza ed il Monitoraggio delle Gallerie Esistenti”), hereinafter GL2022, adopted by means the Ministry of sustainable infrastructure and mobility Decree 257/2022. This guideline offers

*Corresponding author: andrea.carigi@polito.it

DOI: 10.1201/9781003495505-443

a comprehensive methodology for safety evaluation and continuous monitoring of Italy's existing tunnels. This approach, now mandatory for all road tunnels in Italy, marks a pivotal moment in the nation's commitment to ensuring the enduring safety and efficiency of its underground infrastructures.

In the following pages, we delve into the structure of this guidelines, exploring its structure, fields of applicability and the base philosophy.

2 GUIDELINES 2022

2.1 *Complementary normative*

The GL2022 complement the legislative framework, including Legislative Decree 35/2011 and Legislative Decree 264/2006 which, respectively, address the road and fire safety standards for motorway tunnels. Furthermore, it's worth noting that the technical standards for construction introduced in 2018 (in Italian "Norme tecniche per le costruzioni – NTC2018") remain the primary legislative reference for all design criteria.

2.2 *Field of applicability*

The GL2022 must be implemented comprehensively for all motorway tunnels with a length exceeding 200 meters within the territory of Italy. However, the section pertaining to hydraulic aspects is required also for tunnels with a length less than 200 meters. This exception is primarily driven by the substantial number of underpasses that may be vulnerable to flooding during extreme meteorological events.

Additionally, it's important to note that the GL2022 does not automatically apply to transnational tunnels. The decision is entrusted to the international security committee to establish a consistent method for managing tunnels subject to the regulations of the two nations sharing the infrastructure. This collaborative approach ensures the harmonization of safety standards across international boundaries.

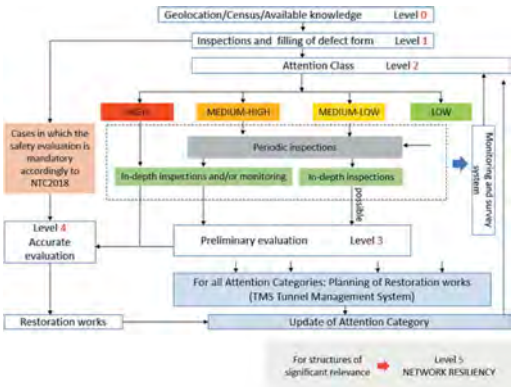

Figure 1. Overall structure of GL2022.

2.3 *General structure*

The articulated structure of LG2022 is summarized with the flux diagram given in Figure 1 and an in-depth analysis is provided in the following sections where are described the various steps (i.e. levels) to be developed.

2.4 *Level 0 – Census*

The acquisition of data for the tunnel census, that constitutes Level 0 of the multilevel approach, involves cataloguing all structures within the guideline's scope. The goal is to obtain detailed information about tunnel geometry, structural elements, and existing analyses to better understand their condition, the surrounding road network, and their location. Data collected by managing entities contribute to creating a national database of tunnels, which must be consistently updated in accordance with the guidelines. The census goes beyond a simple count and aims to achieve a comprehensive understanding of existing tunnels, including all available data related to their condition. Tunnel condition is not solely influenced by structural aging but also by various factors, including environmental conditions, initial design choices, construction methods, and maintenance interventions over time. This process helps prioritize initial visual inspections and initiate Level 1 activities. Moreover, the data collected and subsequent visual inspections allow for identifying cases requiring in-depth safety assessments beyond the Level 2 classification. The acquisition of data for the tunnel census is based on analysing available information and documentation. Retrieving technical and administrative documentation related to the tunnel is crucial to gather necessary information for subsequent preliminary risk assessment. Processing and summarizing these data represent a way to capitalize on resources used in previous studies and investigations during the tunnel's design, construction, and operation phases, and become part of the tunnel's technical documentation. It is essential to conduct thorough research of both technical documents (design, construction, subsequent interventions, etc.) and administrative and accounting documents that document the tunnel's evolution over time. Additionally, it is important to search for data documenting the tunnel's role in the transportation system and its socioeconomic implications, including the road or transportation networks the tunnel is part of, traffic volumes, and available alternatives in case of limitations or closures.

2.5 *Level 1 – Inspections*

Level 1 involves conducting initial inspections on all tunnels catalogued in Level 0 of the census. These inspections are tailored to the specific characteristics of each tunnel and the existing level of knowledge. The primary goal of these initial inspections is to check and to contextualize the data collected during Level 0, gather additional information about the tunnel's geometric and structural features, evaluate the structural

condition, especially for tunnels with limited available information and low knowledge levels. These inspections provide an objective assessment of the tunnel's conditions, including its interior and key structural elements, and require thorough visual examination, which may involve cleaning surfaces for effective assessment of any damages, defects, or infiltrations. The inspection also covers tunnel access areas and non-structural elements such as installations and vertical signage. Visual examinations, supported by portable instruments where necessary, aim to build upon the Level 0 findings and address initial concerns related to the tunnel's characteristics and natural conditions. The Tunnel Officer, with specialist support based on the tunnel's specific features and initial visual inspection findings, should assess whether further, more detailed experimental investigations are needed for defect reconstruction, planning their quantity and location, potentially leading to subsequent in-depth inspections. If specific conditions for the tunnel require additional investigations in terms of quantity and type, as outlined above, the Level 1 phase can still be completed, considering the knowledge gap as a factor that contributes to raising the attention class. This class may be re-evaluated based on the outcomes of subsequent investigations, aligning with the initial attention class priority. During the initial inspection, along with comprehensive photographic documentation and geometric measurements of key tunnel dimensions (where possible), the structural condition is assessed to identify, highlight, and report existing degradation phenomena and defects. Specialized forms or suitable data management systems are utilized for data collection and assessment. These records help identify specific degradation phenomena, their intensity, and extent, which are vital parameters in the Level 2 classification method.

2.6 *Level 2 – Attention category classification*

The classification of tunnels on a territorial scale involves estimating the "risk" factors associated with these structures. In this phase, the risk estimation is simplified and expedited, conducted by expert judgment (the decision-making process, generally multidisciplinary, coordinated by Tunnel Officer) on the basis of data collected in Level 0 and Level 1. The risk associated with tunnels is approximated using the "Attention Class" (CdA). It's important to note that this isn't a comprehensive risk analysis, which should require more complex investigations.

CdA is a tool for setting priorities for further investigations, verifications, controls, and maintenance planning.

The guidelines include four Attention Classes (CdA):

- High
- Medium-High
- Medium-Low
- Low

The CdA value is determined by evaluating hazard, exposure, and vulnerability, based on available knowledge and Level 1 inspections. The CdA cannot be lower than Low Attention Class or higher than High Attention Class.

Various risk types are considered relevant for tunnels, considering their characteristics and the contexts they're in. These risk types include:

- Global structural and geotechnical risks, such as tunnel and geological interactions.
- Local structural issues within the tunnel, including non-structural elements.
- Seismic risk.
- Road-related risk.
- Geological risk related to landslides.
- Hydraulic risk.

These risks independently and define a separate Attention Class for each are analysed. Each Attention Class is uniquely defined based on the three parameters: hazard, exposure, and vulnerability.

The methods for evaluating and classifying these different CdAs are based on logic flowcharts.

After determining the relevant CdAs, they are combined to obtain the overall CdA of the tunnel, which forms the basis for subsequent actions. The classification method is inspired by risk assessment principles.

Each of the primary and secondary parameters required to define the CdA are determined through expert judgment of the Tunnel Officer, considering both the data collected during knowledge gathering and Level 1 visual inspections. Depending on the primary parameter values a class – among Low, Medium-Low, Medium-High, and High – is assigned, with specific criteria for each parameter. Then, these classes are then adjusted based on secondary parameters, which may have two or more classes.

When hazard, vulnerability, and exposure classes are identified, the Attention Class is derived by combining them according to the general scheme shown in Figure 2, applicable to all risk aspects.

Figure 2. General scheme for the CdA determination.

The tunnel divided in stretches with length about 20m and for each of these segments the Attention Class is defined.

The tunnel's Attention Class corresponds to the most critical segments along the route and then a diffusion index (the percentage of tunnel length for each CdA) is added to further characterise the obtained CdA.

It has to be highlighted that a High Attention Class does not mean directly that there is a risk. Rather, it is a condition where additional investigations and

analysis have to be carried out to understand if a risk is present or not.

In Tables 1 to 6 the primary and secondary parameters used for the definition CdA for the different risk types are given.

The Global Structural and Geotechnical Attention Class concerns the possibility of a global collapse of the tunnel as a consequence of the interaction of the structure with the surrounding soil. It involves considering key parameters that influence the structural behaviour of the tunnel, especially concerning the final lining, at a global level, and its interaction with the surrounding rock mass or soil. This entails evaluating parameters related to the magnitude and variations of the applied loads compared to the design predictions for the final lining, as well as factors related to the structural characteristics of the tunnel linings and their level of defectiveness.

Furthermore, due to the global nature of a potential collapse, the potential exposed subjects have been considered, which include both the tunnel users and any structures and infrastructures above the tunnel that may be affected by ground movements.

Table 1. Parameters for the evaluation of Global structural and geotechnical CdA.

	Primary parameters	Secondary parameters
Hazard	Level of knowledge of geotechnical, hydrogeological, and hydraulic characteristics of the mass and reliability of the geomechanical model	Geomechanical characteristics of the rock mass and/or soil, external factors interacting with the tunnel structure.
Vulnerability	Level of defectiveness, type of tunnel, constituent materials, and construction issues	Rate of degradation, presence of circulating water or infiltration, and presence of the waterproofing layer
Exposure	Level of average daily traffic and tunnel length	Heavy vehicles (mass $\geq$ 3.5 tons), maximum design speed, alternative routes, interference with buildings and infrastructure

For the Local Structural Attention Class, the primary concern is the possibility of a portion of the lining or any non-structural component detaching and posing a danger to tunnel users. Unlike the previous Attention Class, which only considers local detachments without consequences for overall stability, this class focuses on conditions, including widespread ones, where portions of the lining may interact with the roadway but do not result in global structural instability.

Table 2. Parameters for the evaluation of Local structural CdA.

	Primary parameters	Secondary parameters
Hazard	Presence of water	Characteristic compressive strength of the lining
Vulnerability	Fracture condition, slab thickness (resulting from construction defects) or presence of internal discontinuities in the lining (such as cold joints, casting inhomogeneities)	Presence of reinforcement, lining history and existing deteriorations
Exposure	Level of average daily traffic and tunnel length.	Heavy vehicles (mass $\geq$ 3.5 tons), maximum design speed, alternative routes

The Seismic Attention Class assesses the potential risks associated with seismic activity on the tunnel, taking into consideration potential local amplification phenomena. In its definition, it was considered that an underground structure, except for portal areas and in case of interference with active faults, is not particularly sensitive to seismic phenomena. It's worth noting that has been included the strategic importance of the structure as an exposure parameter. This is because damage to the tunnel could also affect the emergency response capability for the surrounding area in the event of a seismic event.

Table 3. Parameters for the evaluation of Seismic CdA.

	Primary parameters	Secondary parameters
Hazard	Presence of active faults, susceptibility to landslides, unfavourable geological conditions, Seismic acceleration	Potential local amplification phenomena
Vulnerability	Morphological position, overburden	-
Exposure	Level of average daily traffic and tunnel length	Alternative routes, heavy traffic, strategic importance of the structure

The definition of the Road-related Attention Class considers the key parameters that influence the safety and functionality of the tunnel under normal operating conditions. These parameters encompass aspects related to the tunnel's geometric characteristics, the efficiency of the road surface, its degradation over time, and the volume and composition of

vehicular traffic. Additionally, it includes parameters associated with the operation and management of the road network to which the tunnel belongs.

Table 4. Parameters for the evaluation of Road-related CdA.

	Primary parameters	Secondary parameters
Hazard	Road accidents	Fires
Vulnerability	Road surface defectiveness level, pavement materials	Rate of degradation evolution, design standards
Exposure	Level of average daily traffic and tunnel length	Heavy vehicles (mass ≥ 3.5 tons), maximum design speed, alternative routes

The definition of the Geological Attention Class associated with landslide risk takes into consideration specific parameters indicating the level of the structure's involvement in potential landslide phenomena, both spatially and temporally. In general, artificial tunnels and underpasses in sub-flat areas are excluded from this classification. On the other hand, particular attention should be given to tunnels with low cover and portal areas.

Table 5. Parameters for the evaluation of Geological risk related to landslides CdA.

	Primary parameters	Secondary parameters
Hazard	Slope instability (magnitude, velocity, state of activity)	Mitigation measures or monitoring
Vulnerability	Relationships between the tunnel and morphological conditions: deep instability along the alignment or at the portals, model uncertainty/reliability of the assessment	-
Exposure	Level of average daily traffic and tunnel length	Heavy vehicles (mass ≥ 3.5 tons), maximum design speed, alternative routes, interference with buildings and infrastructure

The Hydraulic Attention Class considers the possibility of aquaplaning caused by flooding of the road, which can result from meteoric contributions and infiltrations from the lining. This class also considers control strategies, focusing on the reliability of capture systems and early alert systems for users. It analyses the causes and identifies the parameters influencing potential flooding phenomena in the structure, defining flooding as any phenomenon that could compromise the functionality and safety of users.

Table 6. Parameters for the evaluation of Hydraulic CdA.

	Primary parameters	Secondary parameters
Hazard	Precipitation intensity, water table level	Contributing surface at access points, hydraulic conductivity of soils, waterproofing deficiency
Vulnerability	Capture system, conveyance system, gravity or lift return system	Capture system blockage, flammable/hazardous liquid collection system, automatic traffic signal system
Exposure	Level of average daily traffic	Transportation of flammable/hazardous liquids, maximum design speed, exposure reduction systems

After defining CdA values for each 20-meter segment of the tunnel, the various CdAs associated with different risk types are aggregated to calculate an overall CdA for each segment. Subsequently, the tunnel's Attention Class is determined by selecting the highest CdA value found (Figure3). A qualification index is then assigned based on the percentage of tunnel segments falling within this highest CdA category.

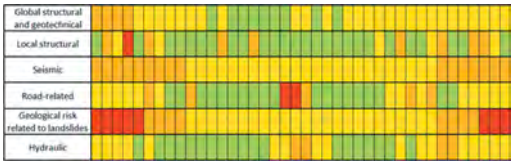

Figure 3. Example of representation of the CdAs along the tunnel.

Table 7. Qualification indexes.

Risk type	CdA	Qualification Index
Global structural and geotechnical	Medium-High	10%
Local structural	High	2.5%
Seismic	Medium-High	40%
Road-related	High	5%
Geological risk related to landslides	High	20%
Hydraulic	Medium-High	10%

2.7 *Level 3 – Preliminary evaluation*

Level 3 preliminary assessment primarily aims to verify the Attention Class assigned to the tunnel in Level 2. It involves a deeper examination of the information obtained in the previous levels, typically based on existing knowledge and data.

The results of the preliminary assessment can lead to two outcomes:

1. Confirmation of a significant risk for the specific context, as previously attributed to the tunnel. In this case, a detailed assessment is necessary.
2. Redefinition of the Attention Class.

If the level of knowledge and available data are deemed insufficient to arrive at a reliable estimate of safety margin, it will be necessary to proceed with an in-depth knowledge assessment and a Level 4 detailed assessment.

2.8 *Level 4 – Deep evaluation*

Level 4 detailed assessment aims to provide a reliable evaluation of the safety margin associated with specific portions of the tunnel or ancillary works, including portals. It also determines whether any mitigation measures are necessary for a specific risk. The reliability of these assessments must be ensured through an adequate level of knowledge. To achieve this, it will often be necessary to plan and carry out additional investigations and measurements, in addition to the data available from previous levels and from the monitoring systems that will be addressed in chapter 2.11.

2.9 *Level 5 – Strategic infrastructures*

Level 5 applies to tunnels considered of significant importance within the road network. For such structures, it is useful to conduct more sophisticated analyses, such as network resilience assessments, by evaluating their transport relevance, analysing the interaction between the structure and the road network to which it belongs, and assessing the consequences of a possible disruption of tunnel operations on the socio-economic context in which it is situated. Due to the importance and the specificity of each of these tunnels, the approach to be used is not specifically regulated by the GL2022 to not constrain the approach of the owner in the management of the infrastructure.

2.10 *Regulatory compliance*

Three main figures are identified in the GL2022: the Tunnel Manager, that is the Body that owns the road or the concession holder, the Tunnel Officer and the Inspector.

The Tunnel Manager must appoint a Tunnel Officer with specific expertise in tunnel management and maintenance. This Officer will oversee and coordinate activities based on the guidelines, under the Operator's supervision.

The Tunnel Officer can oversee multiple tunnels but must have an adequately staffed and skilled operational structure. Also, has to plan activities per the guidelines and coordinate inspections, involving specialists from various disciplines. They must also provide data for the annual tunnel condition report.

Inspections come in different types, as described in Annex 4 of LG2022, and frequencies based on the assigned attention class to the tunnels as described in Table 7.

Table 8. Inspection frequencies.

Inspection	Low	Medium-Low	Medium-High	High
Initial	At the beginning of the Level 1			
Detailed	6 years	4 years	2 years	1 year
Regular periodic	1 year	6 months	3 months	2 months
Post-incident	After a relevant event			

Operators must document inspections with records listing participants and their evaluations. Inspections also cover tunnel-adjacent spaces and specific external zones. If the lining prevents visual inspection, temporary removal procedures should be adopted.

The inspection program considers maintenance and inspection needs from other regulations and aims to minimize impacts on traffic.

Inspections are carried out by competent technical personnel under the Tunnel Officer's coordination. In the absence of in-house expertise, the Operator may engage external entities with competence.

2.11 *Monitoring and investigations*

Monitoring programs must be based on a comprehensive examination of existing information and should be tailored to the specific tunnel's issues, utilizing both direct and indirect types of surveys. Indirect surveys offer the advantage of collecting widespread and non-specific information along the tunnel, usually with relatively quick field operations (high-performance surveys), which is significant for minimizing traffic disruptions.

Measuring indirect physical quantities to correlate with material characteristics and natural formations, as well as assessing their relationships, always requires recourse to direct calibration surveys. This considers the reliability of survey results, which is influenced by the data acquisition phase along with calibration and calibration of the acquisition system relative to the specific conditions and environments in which it operates. It also depends on the processing phase and the representativeness of the adopted reference models and the interpretation phase of the overall measurements, considering direct surveys.

Monitoring programs should also be prepared with specific reference to individual situations, graded, and deepened in relation to the nature and importance of the safety issues identified.

The preparation of investigation and monitoring programs will be coordinated by the Tunnel Officer, who will enlist the expertise of Inspectors and experts while justifying the choices made in relation to specific identified issues.

3 ANNEXES TO GUIDELINES 2022

3.1 *Annex A*

The Annex A contains a "Level 0 Census and Knowledge Sheet" to be compiled for each structure, serving as the initial phase in organizing documentation related to the tunnel. This sheet, signed by the tunnel's manager, provides an assessment of the existing knowledge level and identifies initial indicators of potential hazards, especially those relevant to classifying attention levels. Additionally, the sheet suggests specific areas for in-depth examination during the tunnel's ongoing development. While this document serves as a starting point for determining the initial Attention Class, it will be continuously updated over time to maximize understanding of the structure. To efficiently manage this information, employing a computerized data management system is recommended.

3.2 *Annex B*

The defect catalogue serves as a reference throughout various inspection phases for identifying consistent, comparable, and repeatable elements in tunnels, monitoring their evolution over time, and ensuring the objectivity of defect assessments.

The defect list is categorized into sections, including defects due to water presence, surrounding soil-related defects, deterioration in unreinforced sections, defects in lining materials (stone or masonry, concrete), defects in waterproofing, drainage, and surface water collection systems, defects related to structural elements and tunnel geometry, fire-related defects, defects due to inadequate maintenance, defects related to the road platform, defects in non-structural elements and installations.

The defect level should be evaluated by critically analysing inspection results alongside other available information, either documented or obtained through specialized investigations, using expert judgment. It's crucial for the appointed inspector to gather the necessary elements, through data sheets, to assess the current state of the structure as accurately as possible.

Inspectors should refrain from assessing the causes of defects during inspections, as tunnel contexts often lack straightforward cause-and-effect relationships. Instead, a comprehensive evaluation considering inspection findings and the overall knowledge base, with the inspector collaborating with specialists, should guide the assessment, especially when a single cause can lead to multiple correlated defects or a single defect can have multiple potential causes.

During inspections, inspectors must geographically reference each defect along the tunnel's alignment. Geometrically referencing each defect is essential to clearly identify evolutions of the defects in time.

The assignment of defect severity (G), with possible values from 1 (not severe) to 4 (high-severity) is the responsibility of the Tunnel Officer, based on all inspection findings. Additionally, for each defect type, two parameters should be defined: extension (k1) and intensity (k2), which reflect the defect's spatial spread and magnitude, respectively.

With this information, defect levels can be classified from High, for tunnels with defects that they may lead to the incipient failure or loss of functionality of the structure, to Low for defects that does not pose a significant risk to the structure's overall stability.

3.3 *Annex C*

In Annex C inspection sheets are given. In the header of each inspection sheet, for each element, it is necessary to indicate:

- The tunnel's location by providing toponymic information or the road's name it serves, along with the kilometric progression.
- The identifier of the reference section subject to inspection.
- The date of inspection site visits and the technician who conducted them.

In case the defect is identified on the structure, it is essential to indicate its extent, following the quantitative indicators provided on the specific defect sheet given in Annex B. During the evaluation of the inspection results, these data will be examined to determine the values to be attributed to the defect's extent using the variable coefficient k1 and the defect's intensity using coefficient k2. The potential values for these two coefficients, based on the elements identified during the inspection, are outlined in the defect recording and evaluation sheets (Annex C).

Each defect is associated with a severity (G). The presence of high-severity defects, requiring thorough assessment, may indicate significant and/or immediate structural issues potentially endangering user and employee safety. Therefore, they have a considerable impact on determining the defect class level.

Furthermore, for defects of greater severity, there is the option to indicate whether the presence of such defects could jeopardize the structure's stability and pose a significant risk ("PSg" for a defect affecting the "global" structural response of the structure, and "PSl" for a defect that, although widespread, may lead to local structural crises).

It should be noted that the field inspector should limit themselves to collecting relevant information

for the subsequent defect severity assessment, which will be performed by expert judgment in coordination with the Tunnel Officer.

If a defect listed on the sheet is not identified on the structure, to further characterise the reason why, it should be indicated as follows:

- Use the "NA" box if the defect does not apply to the type of structure and element under examination.
- Use the "NR" box if the defect cannot be detected through visual inspection (e.g., part of the structure is not accessible, etc.).
- Use the "NP" box if the defect is not actually present.

The photo of each defect should be attached to the inspection sheet and appropriately catalogued, numbered, and provided with captions indicating the type of defect, its location, and geometric references within the structural complex.

Finally, each sheet includes a dedicated space for any notes and observations. Emphasis is placed on acquiring as much data as possible during the inspection, so it's important to note any additional relevant information, even if not explicitly indicated in the sheets. This aligns with the primary function of the inspection, which is to record anything potentially useful and meaningful for subsequent evaluations.

In addition to the defect recording sheets, for each tunnel, it is necessary to verify the data from the tunnel census sheet (Annex A) with the main characteristics of the structure identified during the visual inspection, such as structural type, type and material of structural elements, hydro-geomorphological characteristics of the area, rough geometric layouts, and so on. The information collected in this sheet is useful for verifying and confirming the reliability of the data gathered during the initial census and for enhancing the knowledge of the examined structure.

3.4 *Annex D*

Within this Safety Management System, various types of inspections are specified:

1. Initial Inspections
2. Detailed Inspections
3. Regular Periodic Inspections
4. Post-Incident Inspections

The frequency of these inspections is determined based on the infrastructure's Attention Class and environmental conditions.

Authorities overseeing network Operators have the option to conduct their inspections, in addition to those performed by the Operators or other involved bodies.

All inspection findings and observations must be documented, including the use of predefined forms. Detailed inspection reports are required for comprehensive assessments.

Initial inspections are performed when the guidelines are first implemented, upon opening new tunnels, or after major renovations. For existing tunnels, they may also be carried out following significant upgrades or structural changes. These inspections use information gathered from previous activities to establish a baseline knowledge level.

Initial inspections aim to validate the accuracy of available documentation, assess the tunnel's physical and structural characteristics, and evaluate its overall condition. The outcomes determine the tunnel's initial Attention Class, which may lead to further assessments for tunnels with limited data or concerning findings.

Detailed inspections are conducted when specific issues or concerns arise during initial or regular periodic inspections, classifying the tunnel as high or medium-high attention, or as required for in-depth investigations. These inspections may involve the removal of non-structural tunnel linings for comprehensive examinations.

Comprehensive assessments encompass various specialized non-destructive and direct testing methods, including laboratory analysis, to investigate structural components. Advanced technologies like laser scanning, thermography, or ground-penetrating radar may be employed to detect hidden defects or anomalies.

Regular periodic inspections are routine assessments based on predefined schedules, adapted to the tunnel's Attention Class. These inspections are vital to monitor the tunnel's ongoing condition and ensure safety.

Post-incident inspections are initiated following significant events, such as accidents, fires, structural failures, or seismic activity, which could compromise the tunnel's stability. These inspections help assess damage and plan necessary repairs or maintenance.

In summary, various inspection types are integral to maintaining the safety and integrity of road and highway tunnels. They involve a combination of visual assessments, non-destructive testing, and, if necessary, in-depth investigations. The data collected during these inspections inform safety evaluations, maintenance programs, and any required interventions, ensuring the ongoing reliability of tunnel infrastructure.

4 CONCLUSIONS

In conclusion, the introduction of Italy's Guideline for the Risk Classification, Safety Evaluation, and Monitoring of Existing Tunnels (GL2022) represents a significant milestone in the nation's commitment to the preservation and security of its large number of subterranean infrastructures. As we have summarised in this paper, GL2022 is a multifaceted framework, structured across six steps (levels), each with its specific role and purpose.

Level 0 serves as the information repository. Moving up to Level 1, we encounter the initial inspection phase, where the condition and basic characteristics of each tunnel are assessed. Level 2 takes a more nuanced approach, defining the class of attention for each tunnel, considering various parameters and ultimately providing a comprehensive overview of tunnel's status distinguishing across different possible risk sources. At Level 3, the focus shifts towards regular safety assessments, ensuring that these tunnels continue to meet the required safety standards. At the highest operational level, Level 4, in-depth safety evaluations are developed. Level 5 developed for to strategically significant tunnels.

In adopting GL2022, Italy has established a unified and systematic approach to tunnel management, ensuring that the challenges posed by aging infrastructure are met with a comprehensive and forward-thinking strategy.

Through the institution of an observatory for the application of GL2022, it is ensured an increasing level of knowledge also on the compliance practicality and a periodic review of this technical document making this regulation a dynamic and evolving tool, able to adapt to the changing landscape of tunnel maintenance and safety.

REFERENCES

D. Lgs. 264/2006 (2006). Attuazione della direttiva 2004/54/CE in materia di sicurezza per le gallerie della rete stradale transeuropea. (GU Serie Generale n.235 del 09-10-2006 - Suppl. Ordinario n. 195).

D. Lgs. 35/2011 (2011). Attuazione della direttiva 2008/96/CE sulla gestione della sicurezza delle infrastrutture. (GU n. 81 del 8-4–2011).

D.M. Infrastrutture e Trasporti 42/2018 (2018). Norme tecniche per le costruzioni (NTC2018) (G.U. 20 febbraio 2018, n.42)

D.M. Infrastrutture e Mobilità Sostenibili 247/2022 (2022). Approvazione delle Linee Guida per la classificazione e gestione del rischio, la valutazione della sicurezza e il monitoraggio delle gallerie esistenti lungo le strade statali o autostrade gestite da ANAS S.p.a. o da concessionari autostradali (G.U. 23-8-2022, n.196)

Pireddu, A., Bruzzone, S., 2021. "An analysis of the influence of tunnel length and road type on road accident variables" Riv. Stat. Uff., 2, 71–102.

Tunnelling for a Better Life – Yan, Celestino, Thewes & Eberhardt (Eds)
© 2024 The Author(s), ISBN 978-1-032-80042-4
Open Access: www.taylorfrancis.com, CC BY-NC-ND 4.0 license

A computer-vision-based model updating strategy for shield tunnels with cracks

Xiangyu Chang*
School of Civil and Environmental Engineering, Nanyang Technological University, Singapore

Youqi Zhang
Department of Civil Engineering, School of Engineering, Aalto University, Espoo, Finland

Yuguang Fu
School of Civil and Environmental Engineering, Nanyang Technological University, Singapore

ABSTRACT: This paper presents a method that enables a finite element (FE) model of shield tunnels to update the geometric changes caused by cracks, using computer vision (CV) techniques and geometric analyses. Currently, there is a shortage of research on the automatic utilization of tunnel damage detection information for updating FE models. Thus, the objective of this study is to automate the process from tunnel damage detection to numerical analyses in order to quickly evaluate the structural capacity. The Segment Anything Model (SAM) and CV techniques are employed to determine the shapes and dimensions of both tunnel components and damages. Geometric analyses are utilized to develop algorithms that automatically transform coordinates and select elements of FE models for updating the geometric changes. A tunnel segment test is conducted to verify the effectiveness of the proposed technique and algorithms.

Keywords: Shield tunnel, Tunnel cracks, Finite elements model, Computer vision techniques, Segment anything model, Geometric analyses

1 INTRODUCTION

Mass Rapid Transit (MRT) systems, an integral component of urban transportation networks worldwide, rely heavily on tunnel infrastructures (Ye and Liu, 2018). As these subterranean passages play host to countless commuters daily, their safety evaluation during operation becomes a subject of paramount academic and practical importance. As urban populations surged and the demand for efficient transportation grew, so did the complexity and length of these MRT tunnels (Yang et al., 2018). Meantime, over time, the material degradation and damages (i.e., cracks, spalling, and leakage) of tunnel structures can pose challenges in accurately assessing their state. Misjudgement of the structural health status of MRT tunnels could cause unexpected safety problems during operation, such as water intrusion, train derailment, and even geological disasters (Liu et al., 2022; Liu et al., 2021b). Therefore, an accurate assessment of the structural health status of MRT tunnels is essential for understanding the structural behaviour and interactions between the tunnels and their surroundings, as well as ensuring uninterrupted, safe transportation for the public.

Generally, convergence prediction can be carried out through data-driven analysis and numerical methods. Data-driven analysis directly evaluates the tunnel health status based on the measured data. Data analysis tools (i.e., empirical models, statistic models, and machine learning methods) can predict the structural responses, identify the tunnel damage, and detect data anomalies to acquire the overall condition of the tunnel (Chen et al., 2021; Ding et al., 2020; Xie et al., 2021; Zhu et al., 2020). However, the precision of analyses driven by data greatly relies on the quality and integrity of the input data. Inadequate, deficient, or antiquated data has the potential to yield misleading results. Many advanced data-driven models, such as deep learning algorithms, can act as "black boxes," posing a challenge to comprehending the underlying rationale behind their predictions. Alternatively, numerical methods can be used to model the real components of a tunnel and its surrounding environment such as soil, track, and train. These methods solve mechanical equations to determine the tunnel responses, aiding in the evaluation of its safety. During tunnel operation, cracks, spalling, and leakage are the common issues that need to be considered for the assessment of the structural health status (Liu et al., 2021a; Wu et al.,

*Corresponding author: XIANGYU005@e.ntu.edu.sg

DOI: 10.1201/9781003495505-444

2020). It is imperative to ensure that the numerical model (NM) constructed using design files remains up-to-date throughout the duration of the operation period. Currently, a significant challenge for NMs is to model localized damages like cracks, concrete spalling, and leakage within the models. This is primarily because tunnels tend to sustain various forms of localized damages during their operational phase. Manually creating models of these damages is time-consuming, and a resolution that is too coarse may overlook intricate details, while an excessively fine resolution can be costly in terms of computational resources. Therefore, a more efficient approach is needed to accurately simulate local damage in shield tunnels.

In order to achieve automatic updates of the NM with damages, it is typically necessary to perform two primary steps. The first step is the identification of tunnel damages, while the second step entails updating the NM by utilizing the information obtained from the identified damage (Zhang and Lin, 2021). At present, the predominant focus of research lies on the first stage. The development of techniques for identifying structural damage has been enhanced for better accuracy and robustness using various strategies, such as computer vision (CV), structural responses, and natural modes(Ding et al., 2020; Liu et al., 2021b). It is evident that visual information of structures offers a higher level of intuitiveness. This is due to the fact that various structural behaviours, including displacement, damage, and deformation, can be readily identified from the visual data with a high degree of certainty (Chen et al., 2021). Through the utilization of CV algorithms, researchers have successfully devised numerous measurement methodologies within the domain of shield tunnels. For instance, U-Net is a type of convolutional neural network originally designed for image segmentation. It features a distinctive U-shaped architecture that consists of a contracting path to capture context and a symmetric expanding path that enables precise localization (Li et al., 2018). Zhao et al. (2023) developed a hybrid position-channel network by incorporating channel and position attention modules into U-Net to address the crack discontinuity problem in feature channel (i.e., characteristics of the image or feature map) and spatial dimensions. However, CV algorithms, especially deep learning models, require vast amounts of labeled data for training. Gathering and labeling this data is a resource-intensive task. If the training data is not representative of real-world diversity, the algorithm may perform poorly on unseen or underrepresented data, leading to biased outcomes. To overcome such issues, Kirillov et al. (2023) proposed the segment anything model (SAM), which is a deep learning model that has undergone pre-training. This model has the ability to adjust and accommodate various pre-existing and recently developed segmentation tasks by utilizing prompt engineering techniques. Thus, it may be more suitable for detecting the tunnel damages with distinct uncertainties and variability.

To evaluate the residual loading capacities of the tunnels, further developments (step two as mentioned) are needed following the damage detection results. However, this idea is in its early stages as it requires work on damage identification, quantification, localization, alignment, meshing, and further development of modeling methods to solve engineering problems. As a start, some studies attempt to utilize CV techniques (e.g., images, videos, and 3D point cloud data) to update the finite element (FE) model with damages (Korumaz et al., 2017; Zhang et al., 2023). For example, Zhang and Lin (2021) presented a method that enables an FE model to remesh itself for updating the geometric changes caused by structural damages, using CV techniques and geometric analyses. The proposed method utilizes CV techniques to determine the shapes and dimensions of structural components and damages, and geometric analyses to develop algorithms for automatically deleting, generating, and splitting the elements of FE models. Ghahremani et al. (2018) proposed a method using two sets of point cloud data (before and after the damage occurs) to detect the structural damage, quantify the structural change, and generate a solid model of the damage. These results are encouraging since the method can update the geometry of the FE model to consider the structural damage. However, a tunnel segment has a specific cylinder shape resulting in distortion on the image, making it hard to match geometric information in the image with the FE tunnel model. Hence, the additional geometric analysis for both damage images and FE model is required to improve the model accuracy and make it possible to fully automate the procedure of estimating the remaining structural capacity.

In summary, the main contributions of this paper are two-fold. First, a structural damage method based on SAM is proposed to identify tunnel damages on the images. The presented method exhibits superior generalization capacities in multi-task segmentation systems and effectively detects tunnel damages on the image. To the best of the authors' knowledge, SAM has rarely been used in underground structures, and this is the first time to apply it for detecting tunnel damages. Second, an image unwrapping method for tunnel segments is proposed based on CV algorithms to solve segment distortion on the image. The feasibility of the proposed method is validated using the damaged tunnel segment image collected from a loading test. Results show that the proposed model exhibits high precision for updating the FE model based on the identified damages on the image.

2 METHODOLOGY

2.1 *Overview of the method*

The proposed method aims to accurately update the local geometric changes of an FE shield tunnel model caused by structural damages (i.e., crack) using CV techniques and geometric analyses (Figure 1). This approach necessitates two key components: (1) a segmented image that represents distinct elements within the tunnel, such as the tunnel segment,

damages, and the background, and (2) an FE model of the tunnel in its undamaged or original condition. The segmented image can be acquired through the utilization of deep learning models designed for image segmentation, such as U-Net (Li et al., 2018), SAM (Kirillov et al., 2023), or by employing labeling tools. The deletion algorithm employed in this method was introduced by Zhang and Lin (2021).

The pipeline of the proposed method can be summarized into four steps. First, the segmented images representing the tunnel damages are obtained by using SAM. Second, (1) the tunnel segment in the image is unwrapped using CV techniques and (2) the damage on the unwrapped image is also detected by SAM. Third, based on the meshing information (i.e., node list (NL) and element list (EL)) of the FE tunnel model, geometric information is also unwrapped, and the deletion algorithm is applied to calculate the elements and nodes that need to be deleted based on the damage on the unwrapped image. Finally, the updated FE tunnel model is obtained by deleting these corresponding elements.

2.2 *CV algorithms*

2.2.1 *Image segmentation*

SAM is a deep learning model that has undergone pre-training. The purpose of this model is to generate a valid segmentation mask in response to any given segmentation prompt. This model has the ability to adjust and accommodate various pre-existing and recently developed segmentation tasks by utilizing prompt engineering techniques. It is essential to acknowledge that this approach differs from prior research conducted on multi-task segmentation systems. An essential differentiation of this model lies in its capability to perform diverse tasks during inference time, owing to its training in promptable segmentation. In this paper, SAM is applied to extract the tunnel segment information and detect the damage information in the image. Detailed discussions on the SAM can be found in Kirillov et al. (2023), and only a brief introduction to SAM is provided here.

SAM consists of an image encoder, a flexible prompt encoder, and a fast mask decoder (Figure 2). Transformer vision models are utilized to achieve real-time performance (Carion et al., 2020; Li et al., 2022). The components are explained as follows:

(1) Image encoder. An image encoder is employed in order to address concerns regarding scalability and leverage the effectiveness of pretraining techniques. Specifically, a vision transformer (ViT) that has been pre-trained using mean absolute error is minimally modified to accommodate high-resolution inputs. This image encoder is executed once for each image and can be employed before initiating the model.

(2) Prompt encoder. Two categories of prompts, namely sparse (points, boxes, text) and dense (masks), can be employed. Points and boxes are denoted by positional encodings combined with acquired embeddings for each type of prompt and unconstrained text using a pre-existing text encoder from CLIP (Radford et al., 2021). Convolutional operations are utilized to embed dense prompts (i.e., masks), which are then added element-wise to the image embedding.

(3) Mask decoder. The mask decoder effectively corresponds to the embedding of the image, the embeddings of the prompts, and a token produced as output to a mask. This design utilizes a variation of a Transformer decoder block (Vaswani et al., 2017) and subsequently incorporates a dynamic mask prediction head. The altered decoder block employs self-attention and cross-attention in two orientations (from prompt to image embedding and vice versa) to revise all embeddings. After executing two blocks, the mask decoder enhances the image embedding and a multilayer perceptron links the resulting token to a dynamic linear classifier, which subsequently calculates the probability of the mask foreground at every image position.

The model will compute an average of multiple valid masks in the case of an ambiguous prompt. In order to deal with this issue, SAM is adjusted so that it can forecast multiple output masks for a single prompt (Figure 3). It has been discovered that a total of three mask outputs prove to be satisfactory in dealing with the majority of typical scenarios (nested masks tend to have a maximum depth of three: encompassing the whole, part, and subpart).

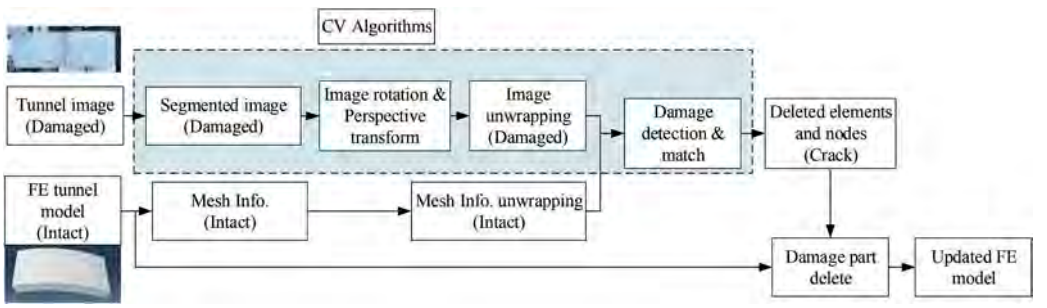

Figure 1. Research framework.

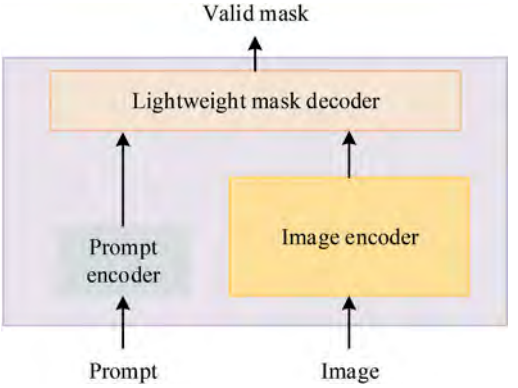

Figure 2. Segment anything model.

Figure 3. Each column shows 3 valid masks generated by SAM from a single ambiguous point prompt (green circle) (kirillov et al., 2023).

2.2.2 *Image unwrapping and damage detection*

A tunnel segment has a specific cylindrical shape resulting in distortion in the image (Figure 4). To precisely align the damage information from the image with the Finite Element (FE) model, the tunnel segment depicted in the image needs to be unwrapped into a rectangular shape. This adjustment allows for an accurate correspondence with the nodes and elements of the FE model, facilitating the acquisition of detailed damage information. In this paper, a six-point method is applied to fully unwrap a tunnel segment. More specifically, A vertical-align algorithm is used to rotate the tunnel segment mask to the standard position (Figure 4). The basic idea of the vertical-align algorithm is to maximize the number of fully black columns of the provided mask. Then, six points around the edges of the segment are detected and positioned, where the corner points (A, C, D, and F) are searched by iterating with the diagonals of the image first (Figure 5).

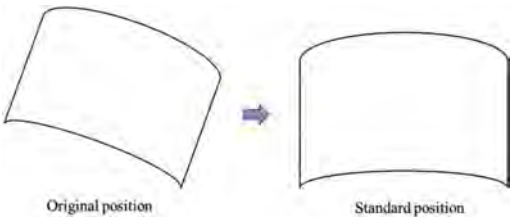

Figure 4. Image rotation.

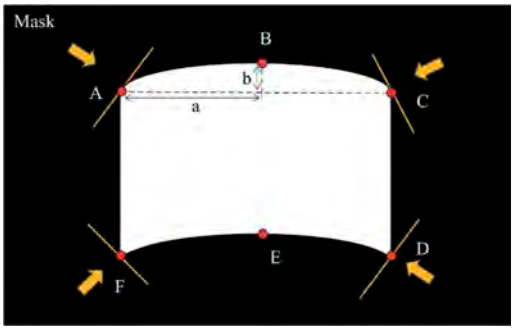

Figure 5. Positions and detection of six points.

The X coordinate for the point B is calculated by:

$$X_B = (X_A + X_C)/2 \tag{1}$$

where X_B is the X coordinate for point B. The column vector $\boldsymbol{Y}_{XB}$ of the segment mask corresponding to X_B is selected and find the first non-zero value of the column vector from the top down as the Y coordinate of X_B (Figure 6).

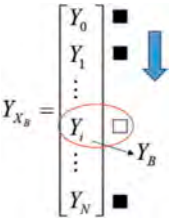

Figure 6. Detection of Y coordinate.

The rationale is the same for the E point: the column vector in the middle of the D and F point first is found and this time the column vector iterates from bottom to top until it finds the first white pixel.

As shown in Figure 5, the tunnel segment consists of two curves ABC and DEF and two vertical lines AF and CD. Vertical lines AF and CD are defined by

the corresponding point coordinates. It is found that an ellipse is a fairly accurate approximation for these curves. Hence, a parametric form of the ellipse could be used to represent these curves:

$$x_e = a \times \cos(t) \tag{2}$$

$$y_e = b \times \sin(t) \tag{3}$$

where x_e and y_e are the coordinates of any point on the ellipse, a and b are the radius on the x and y axes respectively, t is the parameter, which ranges from 0 to 2π radians.

The next step is to unwrap the tunnel segment in the image based on the four edge functions (i.e., left line, right line, top ellipse, and bottom ellipse). Figure 7 shows the technical procedures. First, the lengths of vertical lines and ellipses are calculated using the corresponding point coordinates. Two grid meshes are then built covering cylinder and rectangle surfaces separately. Finally, the information from cylinder surfaces is remapped to the rectangle surfaces by performing the CV algorithms, and the crack in the unwrapping image is detected by SAM.

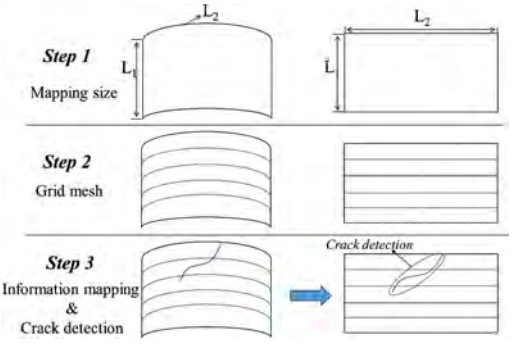

Figure 7. Technical procedures of image unwrapping and crack detection.

2.3 *Geometric match and modelling updating*

2.3.1 *Node and element information unwrapping*

In order to match with the unwrapped image, the coordinates of nodes in the FE tunnel model need to unwrap from 3D to 2D. A coordinate unwrapping method is proposed to obtain the converted 2D coordinates of nodes. Given that the centre of the tunnel segment is at the origin of the coordinates, the coordinate Z remain the same after the coordinate unwrapping. The coordinate X* in the X*-Z coordinate system (unwrapped rectangle surface) can be calculated based on the coordinates x and y in the X-Y coordinate system. Figure 8 shows the process of the coordinate unwrapping method. The coordinate unwrapping method will be introduced in the following part.

As shown in Figure 8 (b), line EF is the unwrapped result of the arc BC. Point D (x_d, y_d) is the midpoint of the lines BC and EF. The angle θ of point (x, y) can be given by:

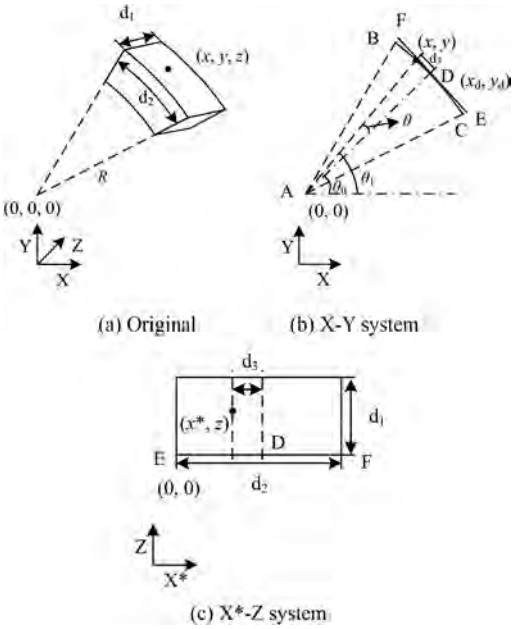

Figure 8. The process of the coordinate unwrapping method.

$$\theta = \begin{cases} \theta_1 - \theta_0, & \theta_1 \geq \theta_0 \\ \theta_0 - \theta_1, & else \end{cases} \tag{4}$$

where $\theta_1 = \arctan(y/x)$ and $\theta_0 = \arctan(y_d/x_d)$. Then, d_3 is calculated by:

$$d_3 = \frac{\theta \cdot \pi R}{180} \tag{5}$$

where R is the radius of the tunnel segment. Finally, the X* of the X*-Z coordinate system can be obtained by:

$$X^* = \begin{cases} \frac{d_2}{2} - d_3, & \theta_1 \geq \theta_0 \\ \frac{d_2}{2} + d_3, & else \end{cases} \tag{6}$$

Therefore, the coordinates (x*, z) of all nodes in the X*-Z coordinate system are solved. It is ready to use the unwrapped damage image and nodes and elements information to update the geometry of the FE model.

2.3.2 *Deletion algorithm of nodes and elements*

The FE tunnel model is modelled by commercial FE software Abaqus. Manual deletion of nodes and elements in affected regions requires precise measurement of the damage dimensions to identify polygons of the damaged area (PDA). It involves recognizing the intersecting nodes and elements with the damage, followed by their removal. This process can be quite lengthy and labor-intensive. Therefore, a more efficient approach is to apply a deletion algorithm, as outlined in Algorithm 1 (Zhang and Lin, 2021).

Algorithm 1. The deletion algorithm of nodes and elements of FE models.

Require: *PDA*, the polygons of damaged areas

Require: *EL*, element list of the intact FE model
Require: *NL*, node list of the intact FE model
Require: *DEL*, empty list of saving the deleted elements
  For element *i* in *EL*:
    If $i \cap PDA \neq \Phi$:
      Add *i* to *DEL*
      Delete *i* from *EL*
  End for
  For *j* in *DEL*:
    For node *k* in *j*:
      If *k* does not constitute any element in *EL*:
        Delete *k* from *NL*
    End for
  End for
Return *EL*, *NL*, *DEL*,

The geometric analyses are conducted through the utilization of the Shapely package, which is firmly grounded in the geographic information system field. In this paper, an FE model is considered akin to a map, allowing for the examination of the spatial connection between nodes and elements using Shapely.

2.3.3 *Tunnel FE model updating*

An FE model updating algorithm is proposed to assess and delete the damage elements on the intact FE tunnel model using its geometric information obtained in the previous section. Finally, the updated FE tunnel model can be obtained after deleting the damage elements.

3 CASE STUDY

To validate the proposed method for automatically updating the geometries of FE models, one lab loading test of a tunnel segment is used. The image should be taken under good lighting conditions. It must include all information from the damaged side of the tunnel segment (including the vertices of the segment and damages). Additionally, the image should be taken from the normal position of the middle surface of the segment to ensure the precision of the information in the image. All the proposed algorithms have been implemented and verified within the Python 3.10 environment. Figure 9 shows the set-up for the loading test. The segment is hinged at the ends and loaded by a vertical jack. The test result is shown in Figure 10. It can be found that a vertical crack is observed in the middle of the tunnel segment.

An FE model of the tunnel segment is established as shown in Figure 11. To demonstrate the updated results with clarity, the mesh employed in this model comprises 823, 143 nodes and 761, 000 elements.

Image segmentation is carried out to obtain the contour of the tunnel segment by specifying the foreground point based on SAM and the segment damage

Figure 9. The set-up for loading test.

(a) Elevation view

(b) Top view

Figure 10. Result of segment loading test.

(a) Solid model

(b) Mesh of FE model

Figure 11. The FE model and mesh of a tunnel segment.

image in Figure 10 (b). Figure 12 shows 3 mask outputs (i.e., whole, part, and subpart) of image segmentation. It is shown that even if there are many other objects around the tunnel segment, mask 2 (part) still provides a good result with a high identification precision of the tunnel segment. Hence, mask 2 will be selected as the mask of the tunnel segment.

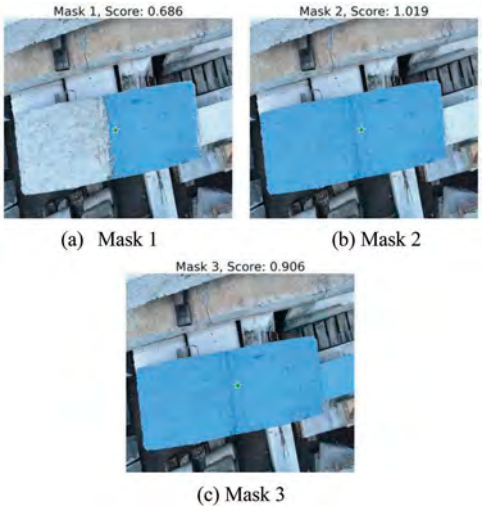

Figure 12. 3 mask outputs of image segmentation from SAM.

The output of each step for image unwrapping is demonstrated sequentially in Figure 13. The whole specimen is seriously damaged after the test, especially in the middle and edges. This will affect the accuracy of the image unwrapping results. However, in practice, cracks and segment edges generally need to be repaired when they are mildly damaged. Finally, Figure 14 shows the crack detection result by SAM in the unwrapped image. It is shown that SAM can detect the crack in the image by specifying proper foreground points.

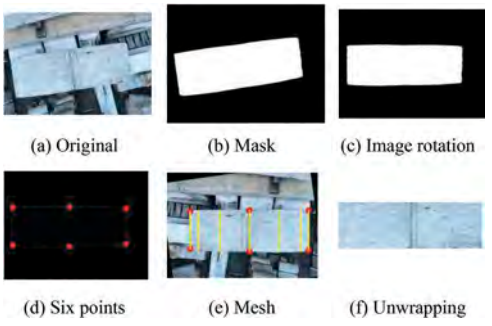

Figure 13. Procedure of image unwrapping processing.

Figure 14. The crack detection result by SAM on the unwrapped image.

Based on the nodes and elements lists of the FE model, the coordinates of nodes are unwrapped from 3D to 2D information. Table 1 shows a part of the results of geometric information unwrapping. Based on the obtained mask of the crack as well as the NL and EL of the FE model, the deletion algorithm is applied to find the nodes and elements that need to be deleted. First, PDA can be generated by using the contour information obtained from the CV algorithms. By using the deletion algorithm, elements in the FE model that have intersections with PDA can be identified. Figure 15 shows the results of intersection elements with damage on the images. Finally, the intersection elements are removed and the FE model becomes in the state as shown in Figure 16.

Table 1. Results of geometric information unwrapping (unit: mm).

Element ID	Coordinates after geometric information unwrapping							
	Node1		Node2		Node3		Node4	
3	0	1900	0	1880	8	1880	8	1900
24	0	1420	0	1400	8	1400	8	1420
25	0	1460	8	1460	8	1480	0	1480
31	0	1580	8	1580	8	1600	0	1600

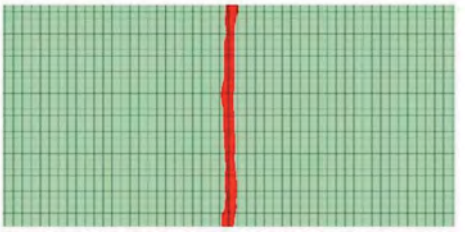

Figure 15. Intersection elements with damage on the images.

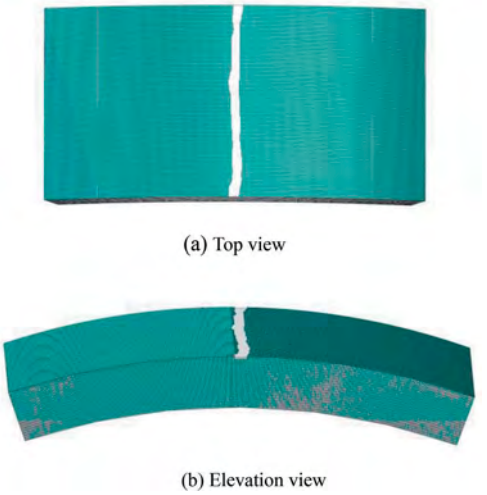

Figure 16. Intersection elements with damage on the images.

4 CONCLUSIONS

In this paper, a computer-vision-based model strategy to update the finite element (FE) model of shield tunnels with cracks. The feasibility of the proposed method is validated through a test on a tunnel segment. The obtained findings are as follows:

(1) The pre-trained segment anything model (SAM) is capable of accurately segmenting the tunnel segment and damages depicted in the image without the need for additional training.
(2) The method of unwrapping an image can perform tasks such as image rotation, detection of six points, creation of a mesh, and mapping of information within the image.
(3) The coordinates of the elements in the finite element model for the 3D coordinate system are converted into 2D coordinates in order to align with the unwrapped image. Subsequently, a deletion algorithm is employed to identify the elements that intersect with the damages on the image.
(4) The proposed approach enables the automatic revision of the FE tunnel model based on damages found in the images using computer vision techniques and geometric analyses. This approach can be effectively employed to evaluate the state of shield tunnels.

ACKNOWLEDGMENTS

This research/project was supported by the National Research Foundation, Singapore under its AI Singapore Programme (AISG Award No: AISG2-TC -2021-001), and The Ministry of Education Tier 1 Grants, Singapore (No. RS04/21). Zhang is financially supported by the Academy of Finland (decision number: 339493).

REFERENCES

Carion, N., Massa, F., Synnaeve, G., et al., 2020. End-to-End Object Detection with Transformers, in: Vedaldi, A., Bischof, H., Brox, T., Frahm, J.-M. (Eds.), Computer Vision – ECCV 2020. Springer International Publishing, Cham, pp. 213–229.

Chen, J., Zhou, M., Zhang, D., et al., 2021. Quantification of water inflow in rock tunnel faces via convolutional neural network approach. Autom. Constr. 123.

Ding, H., Jiang, X., Li, K., et al., 2020. Intelligent Classification Method for Tunnel Lining Cracks Based on PFC-BP Neural Network. Math. Probl. Eng. 2020, 1–12.

Ghahremani, K., Khaloo, A., Mohamadi, S., et al., 2018. Damage Detection and Finite-Element Model Updating of Structural Components through Point Cloud Analysis. J. Aerosp. Eng. 31.

Kirillov, A., Mintun, E., Ravi, N., et al., 2023. Segment Anything.

Korumaz, M., Betti, M., Conti, A., et al., 2017. An integrated Terrestrial Laser Scanner (TLS), Deviation Analysis (DA) and Finite Element (FE) approach for health assessment of historical structures. A minaret case study. Eng. Struct. 153, 224–238.

Li, X., Chen, H., Qi, X., et al., 2018. H-DenseUNet: Hybrid Densely Connected UNet for Liver and Tumor Segmentation From CT Volumes. IEEE Trans. Med. Imaging 37, 2663–2674.

Li, Y., Mao, H., Girshick, R., et al., 2022. Exploring Plain Vision Transformer Backbones for Object Detection, pp. 280–296.

Liu, J., Shi, C., Lei, M., et al., 2021a. A study on damage mechanism modelling of shield tunnel under unloading based on damage–plasticity model of concrete. Eng. Fail. Anal. 123.

Liu, W., Chen, J., Luo, Y., et al., 2022. Long-term stress monitoring and in-service durability evaluation of a large-span tunnel in squeezing rock. Tunnelling Underground Space Technol. 127.

Liu, Y., Chen, H., Zhang, L., et al., 2021b. Risk Prediction and Diagnosis of Water Seepage in Operational Shield Tunnels Based on Random Forest. J. Civ. Eng. Manage. 27, 539–552.

Radford, A., Kim, J.W., Hallacy, C., et al., 2021. Learning Transferable Visual Models From Natural Language Supervision, International Conference on Machine Learning.

Vaswani, A., Shazeer, N., Parmar, N., et al., 2017. Attention Is All You Need.

Wu, H.-N., Shen, S.-L., Chen, R.-P., et al., 2020. Three-dimensional numerical modelling on localised leakage in segmental lining of shield tunnels. Comput. Geotech. 122.

Xie, X., Zhang, D.M., Huang, H.W., et al., 2021. Data Fusion–Based Dynamic Diagnosis for Structural Defects of Shield Tunnel. ASCE-ASME J. Risk Uncertainty Eng. Syst. Part A: Civ. Eng. 7.

Yang, J.-P., Chen, W.-Z., Li, M., et al., 2018. Structural health monitoring and analysis of an underwater TBM tunnel. Tunnelling Underground Space Technol. 82, 235–247.

Ye, Z., Liu, H., 2018. Mechanism and countermeasure of segmental lining damage induced by large water inflow from excavation face in shield tunneling. Int. J. Geomech. 18.

Zhang, Y., Lin, W., 2021. Computer-vision-based differential remeshing for updating the geometry of finite element model. Comput.-Aided Civ. Infrastruct. Eng. 37, 185–203.

Zhang, Y., Xia, B., Taylor, S., 2023. High-resolution 3-D geometry updating of digital functional models using point cloud processing and surface cut. Comput.-Aided Civ. Infrastruct. Eng.

Zhao, S., Zhang, G., Zhang, D., et al., 2023. A hybrid attention deep learning network for refined segmentation of cracks from shield tunnel lining images. J. Rock Mech. Geotech. Eng.

Zhu, M., Zhu, H., Guo, F., et al., 2020. Tunnel condition assessment via cloud model-based random forests and self-training approach. Comput.-Aided Civ. Infrastruct. Eng. 36, 164–179.

Tunnelling for a Better Life – Yan, Celestino, Thewes & Eberhardt (Eds)
© 2024 The Author(s), ISBN 978-1-032-80042-4
Open Access: www.taylorfrancis.com, CC BY-NC-ND 4.0 license

Evolution of safety situation and repair scheme for punctured shield lining

Zhiren Dai & Ruiqing Hu
China Railway First Survey & Design Institute Group Co., Ltd., Xi'an, China
State Key Laboratory of rail Transit Engineering Informatization, Xi'an, China

Zeyu Wang
Jiangsu Ocean University, School of Civil and Harbor Engineering, Jiangsu Lianyungang, China

ABSTRACT: Nowadays, the scale of new city construction and old city reconstruction in big cities is unprecedented. The load capacity and structural durability of shield tunnel are always influenced by exterior workings, especially for the situation of tunnel lining breakage or puncture. And then, the structural safety and normal operation of shield tunnel will be seriously influenced correspondingly. Based on the operating metro tunnel which was punctured by drilling machine accidentally, the stress characteristics of tunnel lining under normal earth pressure are firstly analyzed, then the relevant tension and compression regions of tunnel lining are deeply analyzed and made clear. The specific influences on lining capacity with little range of damage are explained, the advantages and disadvantages of lining repair methods in common use are made clear, and the basic principles of lining repair are also put forward. As for large range of lining damage, the newly built shaft for structure repair is put forward, and the stress characteristics and corresponding safety situation evolution of lining during the whole stage are made clear, from lining damage, to shaft excavation, to structure repair, and to shaft backfilling. The load conversion structure with sharp top and archlike bottom is adopted which can obviously reduce all earth pressure while shaft backfilling. And the working shaft based on the combination of transverse passage and conventional shaft is also proposed to adapt environment requirements. This paper can lead a reference for similar project in future.

Keywords: Shield tunnel, Punctured lining, Stress distribution, Shaft, Load conversion structure, sharp top and archlike bottom, Transverse passage

1 INTRODUCTION

By the end of 2022, the nationwide operational mileage of urban rail transit has exceeded 10,000 kilometers. The investment intense and construction speed of rail transit in major cities have reached new level once and once again. The protection situation of operational rail transit is becoming more and more seriously while the operation miles are becoming longer and longer. Kinds of structural safety hazards are arising constantly during metro operation, although specific protection regulations are issued by local government.

Researches on punctured tunnel and corresponding repair methods are relatively few based on literature. According to the investigation of punctured metro tunnels in different situations, the classification of punctured tunnel and its influences on lining structures are made clear. The common repair methods for damaged lining structures are summarized. The advantages and disadvantages of interior repair method are made clear, and the corresponding selection principle are put forward. And then, key technologies for steel plate reinforcement inside tunnel are made clear. At last, the repair method with outside shaft for large area of tunnel damage is deeply studied. The transverse passage combined with traditional shaft is proposed for tunnel repair as for complex external environment. The lining reinforcement method with cap structure and the load conversion structure with archlike shape are put forward, and the vertical earth pressure can be converted into horizontal load. And then, the force stabilization and long-term durability of lining structure can be ensured.

DOI: 10.1201/9781003495505-445

2 CLASSIFICATION AND SAFETY ANALYSIS OF PUNCTURED SHIELD TUNNEL IN RAIL TRANSIT

There have been cases of rail transit tunnels under construction or in operation punctured by external workings in big cities. Statistics of typical cases are shown in the following table.

Table 1. Statistics of punctured rail transit tunnels and relevant structural repair methods (incomplete statistics).

Region & line	lining puncture	Repair methods
Line 1 in Nanning	Tunnel lining was punctured Train collided with drill bit	Grouting sealing & steel plate reinforcement inside tunnel
Line 11 in Shenzhen	Tunnel lining was punctured by pre-stressed pipe pile at 1 o'clock	Grouting sealing & steel plate reinforcement inside tunnel
Line 10 in Shenyang	Segment joint of lining was punctured	Grouting sealing & aramid fabric cloth reinforcement inside tunnel
Line 1 in Chongqing	Lining of mined tunnel was punctured	Grouting sealing & rebar reconnection inside tunnel
Line 1 in Hangzhou	Segment joint of lining was punctured	Grouting sealing & steel plate reinforcement inside tunnel
Line 7 in Chengdu	Standard segment of line 7 was punctured, 10.4m depth	Shaft & rebar reconnection outside tunnel
Line 8 in Chengdu	Key segment of line 8 was punctured, 11.2m depth	Shaft & rebar reconnection outside tunnel
Line 17 in Chengdu	Key segment of line 17 was punctured, 17.5m depth	Shaft & rebar reconnection outside tunnel
Line 18 in Chengdu	Connecting segment of line 18 was damaged by drilling, 16cm depth of damage was found outside tunnel	Shaft & rebar reconnection outside tunnel

From the table above, as for the punctured tunnel lining by outer workings, shaft and lining repair outside tunnel are always adopted for the relatively better formation in Chengdu, Chongqing and so on. The lining repair methods inside tunnel are adopted in other areas. Rebar reconnection is adopted for the repair of little range, structural repair and steel plate reinforcement inside tunnel are adopted for the repair of large range or segment joint.

2.1 *Classification of punctured shield tunnel*

Tunnel lining is a typical reinforced concrete member which mainly bears bending moment and axial force. According to the distribution of bending moment inside tunnel, the upper half of tunnel can be divided into three regions, namely the tension region, the compression region, and the transition region of tension and compression . As shown in Figure 1.

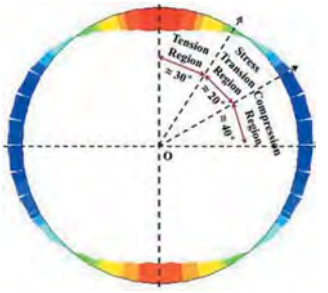

Figure 1. Sketch map of region division for upper half of tunnel based on bending moment distribution inside tunnel.

As for the upper half of shield tunnel, the tension region inside tunnel is distributed within 30 degrees around tunnel vault, namely region I. The compression region is distributed within 40 degrees above tunnel haunch, namely region III. The transition region of tension and compression is distributed within 30 to 50 degrees on both sides of tunnel vault, namely region II. Most of the lining damage and puncture are focused in tension region and the transition region. Based on the statistics, the probability of lining puncture in the tension region is at the highest lever, and the maximum safety influences will be resulted correspondingly.

2.2 *Safety analysis of punctured tunnel lining*

If damaged region is under control after lining puncture, the self-stability of tunnel in short term can be ensured. However, the potential hazards of structure safety are becoming more and more seriously in long term.

2.2.1 *Safety analysis in short term*

The operation of metro line should be recovered as soon as possible after lining puncture. The self-stability of formation and the safety margin of lining structure will be well utilized in this situation. The self-stability of formation above tunnel is mainly depended on the collapse arch which has not been completely destroyed in short term. As for little area of damage, metro tunnel and surrounding formation form a force balanced state, and tunnel safety is still under control in short term.

If large area of lining damage or broken segment joint is encountered, the self-stability of segment can not be ensured especially for the adoption of bent bolt situation. Then, the continuous collapse of shield segment and large area of settlement and deformation of stratum may be resulted.

2.2.2 *Safety analysis in long term*

Lining cracks and fragmentation will develop, and the self-stability of stratum above tunnel will decrease due

to train vibration and redistribution of lining stress, if the repair of punctured tunnel can not be carried out in time. The overall earth column pressure will be resulted if collapse arch reaches ground surface, and tunnel safety will be influenced correspondingly.

1) Influence analysis of crack propagation

Structure capacity and durability of tunnel lining will be influenced in some extent by structural cracks due to exterior action.

As for structure capacity, in the range of crack depth, the binding force between steel bar and concrete will be reduced, and even the function of concrete in crack depth will end. As for structure durability, the thickness of the protective layer of steel bar will be reduced, infiltration process of oxide and carbonate will be accelerated, steel corrosion and expansion cracking will be resulted. As shown in Figure 2.

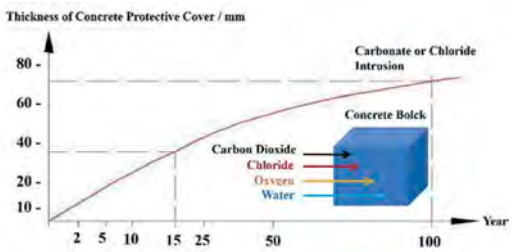

Figure 2. Sketch of durability influences on concrete by corrosive medium with different thickness of protection layer.

2) Influence analysis of the change of earth pressure

The depth of metro tunnel is always more than 10m, the earth pressure of collapse arch above tunnel should be considered correspondingly. One certain tunnel runs mainly in weathered sandstone stratum, and gravel soil and miscellaneous fill lays above. The ground water lever is 3.1m to 5.2m under ground table. The physical and mechanical parameters are shown in Table 2.

Buried depth of one certain tunnel vault is more than double of its diameter, and the earth pressure based on collapse arch should be considered. Lining thickness is 0.35m, reinforced concrete is C50. According to the equivalent calculation

Table 2. Physical and mechanical parameters of stratum.

stratum	γ kN/m³	E_0 MPa	K_0	Poisson's ratio	coefficient of subgrade reaction MPa/m Kv	Kx
Miscellaneous fill	19.0	5	0.65	0.39	10	8
Gravel soil	23.0	55	0.19	0.16	115	90
Decomposed sandstone	20.5	40	0.30	0.23	115	105

model of flexural rigidity, namely E_1I_1=0.8EI, then, $h' = \sqrt[3]{0.8}h = 0.325$m.

According to Terzaghi collapse arch theory, the loose earth pressure can be calculated, namely $p_e = 121.31kPa$. Relevant lateral earth pressure can also be obtained:

$$e_1 = \lambda \cdot (p_e + 20) = 42.4kpa$$

$$e_2 = \lambda \cdot (p_e + 20 + \sum^{\gamma_i} D) = 78.8kPa$$

And the reaction force at tunnel invert is 148.8kPa. Water pressure at tunnel vault is 72kPa, and 134kPa at tunnel invert.

If the earth pressure of all earth column above tunnel is considered, earth pressure is 274.1kPa at tunnel vault. And relevant lateral pressure is 88.23kPa at tunnel vault and 125.4kPa at tunnel invert, and the reaction force at tunnel invert is 297.6kPa.

From Table 3, stress in tunnel vault is relatively small under collapse arch load mode, and tunnel structure is under the state of small eccentric compression. Structure crack can meet requirement without the need of checking calculation. Stress in tunnel vault nearly doubles under all earth column load mode, and structure crack reaches 0.15mm. It can be obviously seen that structure stress and crack width will increase caused by the change of earth pressure mode due to exterior working, especially for large buried depth of tunnel.

From the analysis above, it can be seen that the damage range of tunnel lining is relatively small for

Table 3. Stress and rebar reinforcement at tunnel vault based on loose earth pressure and all earth column pressure.

Operation conditions	Action mode of vertical load	Vertical load	Vault stress/standard combination M	N	rebar mm²	crack width /mm
Undisturbed formation	h_0 height of collapse arch	P_e	63.1	-564.9	1527 6φ18	Satisfied
Tunnel puncture	h all earth column	P_1	132.1	-789.7	1527 6φ18	0.15

exterior working such as geology drilling, the stability of tunnel can be ensured in short term based on the overall capacity of tunnel lining and the constraint of surrounding formation. However, structure durability will severely decrease in long term, and tunnel stresses and crack widths will sharply increase due to the change of earth pressure mode, especially for relatively large buried depth. The repair of damaged tunnel lining should be carried out as soon as possible.

3 REPAIR SCHEME OF TUNNEL LINING IN COMMON AND ITS BASIC PRINCIPLE

3.1 *Feature analysis of repair scheme*

3.1.1 *Classification of common repair scheme*

As for the common repair circumstances of shield lining, based on the repair site, it can be divided into three modes, namely repair inside tunnel, repair from ground, and combined repair. As for structure reinforcement, it can be divided into two types, namely structure self-reinforcement, and structure reinforcement combined with steel plate. Steel plate can also be replaced by aramid fabric cloth or composite cavity.

Figure 3. Steel plate bonded with lining inside tunnel.

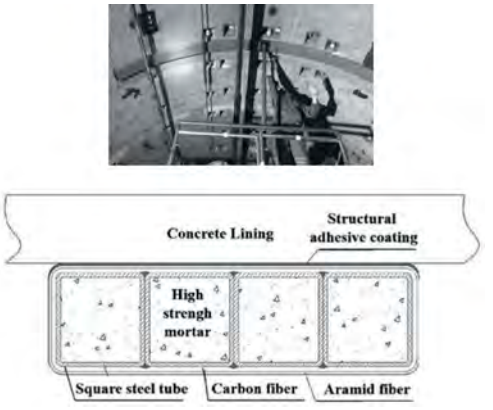

Figure 4. Composite cavity bonded with lining inside tunnel.

3.1.2 *Advantages and disadvantages analysis of common repair schemes*

Steel plate is always adopted in structure reinforcement inside tunnel, the composite cavity is a new reinforcement method. Compared with steel plate, composite cavity is more than 40mm in thickness, and it will result in the risk of equipment and safety operation due to relatively limited space in metro tunnel. And the width of composite cavity is less than 160mm in common, the bonding strength between tunnel and composite cavity is relatively weak. And the bonded surface will open relatively easy in tunnel deformation experiment, and its application is influenced correspondingly.

The steel plate, which is bonded with lining inside tunnel, is corrosive when time goes by. Steel plate should be avoided when obvious corrosive environment inside tunnel is encountered or structure self-reinforcement can meet the requirements. As for the assembly of steel plate inside tunnel, the dedicated device should be adopted in assistance due to its big self-weight, and complex procedure and long construction period will be resulted correspondingly.

The repair measures outside tunnel based on shaft or foundation pit are relatively reliable while the damaged region of lining structure is completely revealed. And little influences will be resulted on metro operation correspondingly. However, excavation period of shaft or foundation pit is relatively long, the earth pressure mode above shield tunnel can be changed due to backfilled soil, the soil arch effect above tunnel will disappear, and the lining safety will be influenced correspondingly.

3.2 *Basic principles of lining repair*

Tunnel repair should be based on the basic principle of lining safety and its durability in the long term. Then, the working time and influences on safety operation of metro tunnel should be reduced to the maximum extent. At last, repair cost and implementation complexity should also be taken into account.

3.2.1 *Principles of lining repair and reinforcement inside tunnel*

Lining repair and reinforcement should be carried out inside tunnel while surrounding stratum has a good self-stabilization and little range of lining damage is found. Meanwhile, steel plate or aramid fabric may also be adopted for overall lining reinforcement in addition. Nowadays, standards of steel plate reinforcement inside tunnel are not inconsistent. However, crack width, damaged area ratio, change of tunnel diameter or ellipticity are the indexes should be considered in general. The relevant indexes are listed in following table, and steel plate reinforcement can be implemented as any index in the following table is reached.

Table 4. Principles and indexes of steel plate reinforcement inside tunnel.

Sequence number	Stratum	Corrosiveness of ground water and soil	Diameter change/ mm	Crack width/mm	Segment misalignment /mm	Damage region
1	Stratum with good self-stability such as hard plastic clay, medium dense and dense pebble soil, medium weathered rock	Microcorrosion	≥120 or ellipticity is more than 20%		≥30	
		Moderate and above	≥70		≥20	
2	Stratum with poor self-stability such as soft soil, weathered and strong weathered rock, loose and denser pebble soil, fine sand and sand soil, saturated soft loess	Microcorrosion	≥100		≥25	
		Moderate and above	≥70	V type crack width ≥0.4mm or penetrated crack width ≥ 0.2mm. Grouting sealing should be implemented firstly for other cracks	≥20	Rectangle side length or diameter of damaged area is larger than steel bar spacing, namely two steel bar will be cut at least
3	Specific stratum such as collapsible loess, fault fracture zone, and soft and hard composite soil.	Microcorrosion	Transverse change ≥80、vertical change ≥100		≥25	
		Moderate and above	≥70		≥20	

3.2.2 *Principles of lining repair and reinforcement outside tunnel*

If tunnel damaged area is relative large or earth pressure mode is obviously changed from collapse arch to all earth column pressure, structure safety and stability can not be ensured by repair method inside tunnel. Then, shaft or foundation pit can be implemented for lining repair. Special structure can be superposed on the damaged lining, and the all earth column pressure can be reduced in other ways.

4 LINING REPAIR SCHEME BASED ON STRUCTURE REINFORCEMENT INSIDE TUNNEL

4.1 *Scheme introduction*

Lining repair and reinforcement inside tunnel can be divided into two types, namely structure self-reinforcement, and steel plate or aramid fabric reinforcement combined with structure self-reinforcement.

If the damage range of tunnel lining is relatively small and little influences on lining safety are found, then structure self-reinforcement inside tunnel can be implemented, and steel bar reconnection and slightly expanded epoxy mortar can be implemented correspondingly. If the damaged range is relatively large, steel plate or aramid fabric reinforcement should be adopted inside tunnel.

4.2 *Key technologies*

Key technologies for structure reinforcement inside tunnel are described as follows.

1) Steel bar reconnection in damaged area should meet the requirement of equal rebar strengthen. And concrete with micro expanded epoxy mortar should be casted in the damaged region.
2) Relocation of trackside facilities or pipeline equipment should be avoided if steel plate is reinforced inside tunnel. The whole lining ring should be bonded with steel plate, and the bull leg should be installed near the track bed, in order to ensure the stability of the whole lining ring.
3) Epoxy slurry should be grouted into the interface of steel plate and lining, and a brand new circle force structure is formed. Aramid fabric can be bonded in damaged area as temporary reinforcement for emergency treatment, in order to restrain further deformation of lining as soon as possible. And steel plate can be bonded as permanent reinforcement.
4) Durability of tunnel lining largely depends on its water resistance. And multi-layer waterproofs can be realized by slurry grouted into surrounding strata inside tunnel and epoxy slurry grouted into segment joints.

5 LINING REPAIR SCHEME BASED ON STRUCTURE REINFORCEMENT OUTSIDE TUNNEL

Shaft or foundation pit is always adopted for structure reinforcement outside tunnel, then the circumstances of damaged tunnel exterior will be totally revealed, and the suitable repair scheme can be confirmed based on the damaged situations of tunnel lining correspondingly.

If exterior environment is relatively complex, and shaft or foundation pit can not be implemented right above the damaged tunnel, then transverse passage and traditional shaft can be combined for lining repair.

5.1 *Repair scheme outside tunnel based on the combination of transverse passage and shaft*

If ground condition is complex and shaft or foundation pit can not be directly implemented right above the damaged tunnel, as for tunnel is beneath operated road or near important buildings in big cities. Then, the ground location of shaft or foundation pit can be leaded to places with relatively good environment conditions based on the adoption of transverse passage. The conventional shaft is divided into two parts correspondingly, which are connected by transverse passage, and lining repair can be implemented from ground surface.

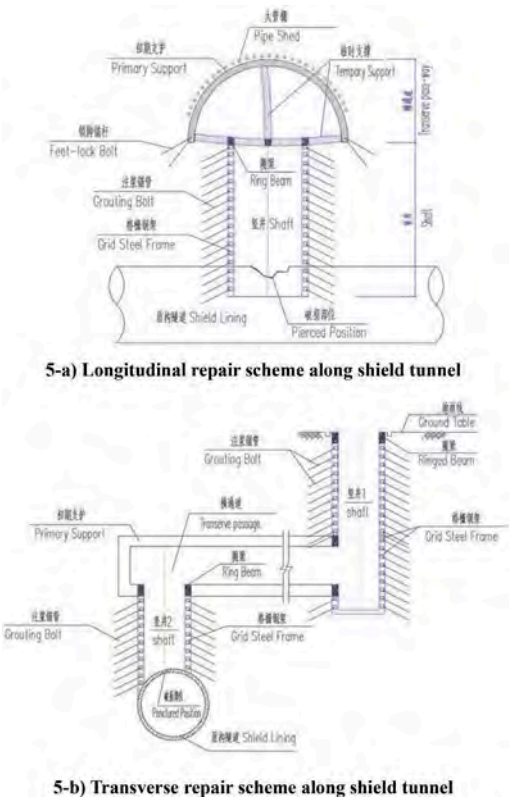

Figure 5. Diagram of lining repair scheme based on the combination of transverse passage and shaft.

5.2 *Repair scheme outside tunnel based on ground shaft or foundation pit*

Shaft or foundation pit can be implemented right above the damaged tunnel if ground condition is permitted. And different types of shaft or foundation pit can be adopted according to the site and size of damaged lining.

(1) Repair scheme for little damaged lining

If only little damaged region of tunnel is found, such as one penetrated crack or lining fragmentation, then small shaft can be adopted for lining repair. The bottom of shaft can be directly set on tunnel lining. The stress converting structure with sharp top and archlike bottom can be set in a certain distance from tunnel vault, and wing angle member is placed at the end of stress transferring structure. Then, the vertical earth pressure resulted from backfilled soil in shaft can be largely converted into horizontal pressure. Lightweight concrete can be taken as backfilling material and the mattress layer which is more than 300mm in thickness can be set beneath the stress converting structure. As shown in Figure 6-a.

The broken steel bar is firstly reconnected in shaft, and micro expanded epoxy mortar is adopted for concrete cast. In order to enhance the effect of structure reinforcement, the superimposed component can be cast in site together with the recovery of damaged lining, namely the cap shaped structure. As shown in Figure 6. Tunnel lining is a typical compression-flexure member, the height of lining compression zone can be enlarged by the cap shaped structure, and the bearing capacity of external loads will be enhanced correspondingly.

(2) Repair scheme for large damaged lining

If large damaged region of tunnel is found, such as several penetrated cracks or punctured area, then larger shaft or foundation pit should be adopted for lining repair. The bottom of retaining pile of shaft or foundation pit can be set more than 3m deeper than tunnel invert. Meanwhile, the load converting structure with sharp top and archlike bottom above tunnel vault can be connected to retaining pile by planted rebar. And the earth pressure based on backfilled soil can be transmitted to deeper stratum. As shown in Figure 6-b.

5.3 *Typical case analysis*

Based on the project case described in Section 2.2, numerical analysis is carried out on the repair of tunnel vault in shaft. MIDAS/GTS is adopted correspondingly, then formation-structure calculation model is established, the displacement boundary condition and the modified Moore-Coulomb constitutive model are adopted. Shaft side-wall, lightweight concrete which is used as backfilled material,

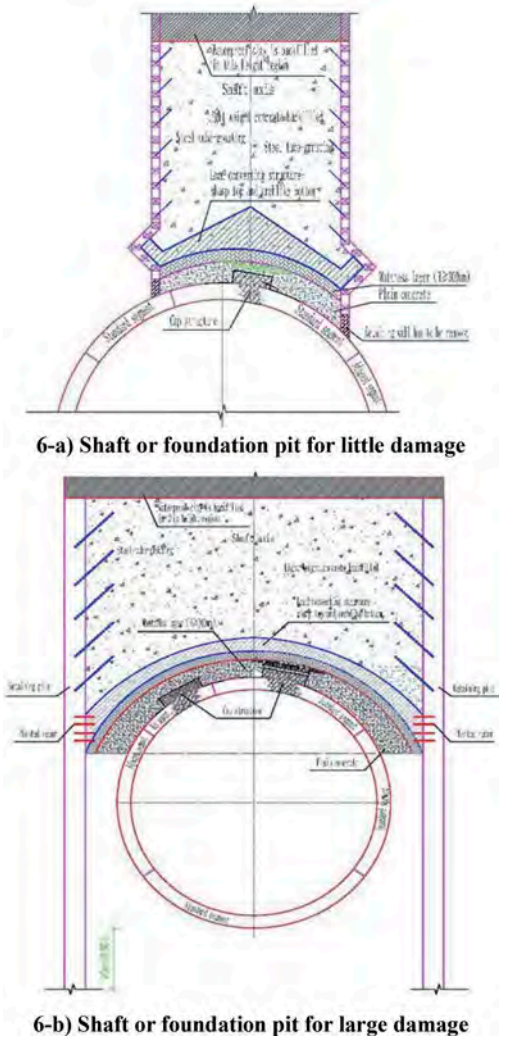

Figure 6. Lining repair scheme based on the combination of shaft or foundation pit.

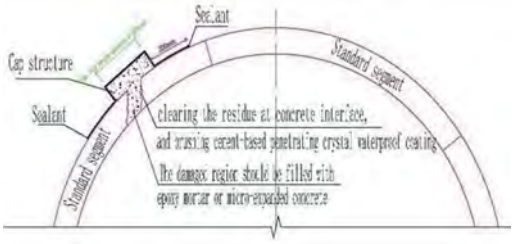

Figure 7. Cap component scheme based on lining reinforcement.

and load converting structure with sharp top and archlike bottom and so on are simulated as solid elements. Tunnel lining is simulated as beam element. Contact element is set between shaft side-wall and backfilled soil. There are 1566 units and 1232 nodes in the numerical model. And the horizontal distance from tunnel haunch to model border is more than the triple of tunnel diameter.

5.3.1 *Stress analysis of tunnel lining*

Stress analysis of tunnel vault is carried out in different construction stages. As shown in Figure 8 and Table 5.

As shown in upper table and figure, the maximum bending moment in tunnel vault reduces due to partially structural fragmentation. Namely the maximum bending moment reduces from 77.5kN.m to 44.3kN.m, and the bending moment in damaged region sharply reduces to 10kN.m. Bending moment of lining near shaft side-wall obviously increases while shaft excavation goes on. And the relevant maximum bending moment reaches 130kN.m when

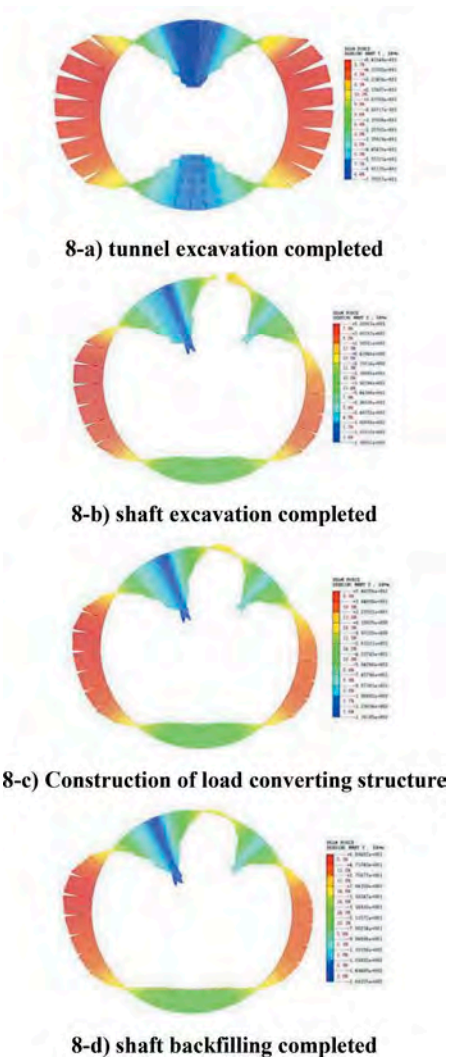

Figure 8. Bending moment diagram of tunnel lining in different construction stage (units: KN.m).

Table 5. Lining stress in tunnel vault in different stage.

Working conditions	Maximum of bending moment		Axial force N/kN
	Value M/kN.m	Location	
tunnel excavation completed	77.5	Tunnel vault	-388.3
Tunnel lining damaged	44.3		-372.9
shaft excavation completed	130.5		-248.3
Cap component construction	130.4	Left side of tunnel vault	-250.8
Load converting structure	139.2		-250.7
shaft backfilling completed	169.2		-264.7

shaft excavation completes and cap component reinforcement begins, the increasing rate is 67.7% correspondingly. However, bending moment in damaged region is still around 10kN.m throughout all stages. With the reinforcement of cap component, bending moment in tunnel vault reaches 169kN.m in shaft backfilling stage. And the correspondingly increasing rate is 30% from shaft excavation to shaft backfilling, and the increasing value of bending moment is 39kN.m. This indicates that partially damage of lining can lead the bending moment transferring from the damaged region to its near sides. As a result, the potential safety hazard of lining near shaft side-wall increases correspondingly due to the increase of bending moment.

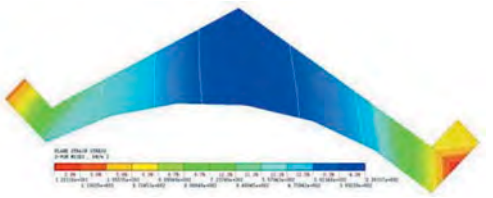

Figure 9. Equivalent stress of load converting structure while shaft backfill completed (units: kPa).

As seen from the change of axial force in tunnel vault, the decreasing rate of axial force reaches 36% from tunnel excavation to lining damage stage, and the value change of axial force is less than 30kN from shaft excavation to shaft backfilling stage.

5.3.2 *Stress analysis of load converting structure*

In order to deeply analyze the function of load converting structure with sharp top and archlike bottom, the stress flow of equivalent stress and maximum principle stress in load converting structure are analyzed during shaft backfilling stage.

As seen from the equivalent stress figure above, the equivalent stress in the middle part of load converting structure is only 226.3kPa, which is nearly equal to vertical earth pressure in the same formation depth. However, the maximum equivalent stress in the wing angle, at the end of load converting structure, reaches 1221.1kPa, namely 5.4 times as in the middle part, even though all parts of the load converting structure nearly lay in the same formation depth. It indicates that the ideal load bearing and converting effect can be ensured based on the load converting structure during shaft backfilling stage.

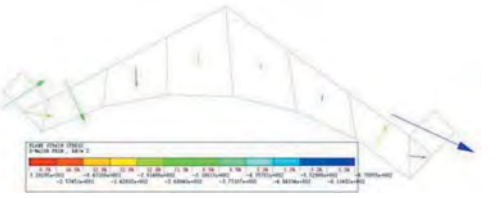

Figure 10. Maximum principle stress of load converting structure while shaft backfill completed (units: kPa).

As seen in the stress flow of maximum principle stress in load converting structure after shaft backfill, the direction of principle stress in wing angle, at the end of load converting structure, rotates. The direction of maximum principle stress in left wing angel shifts from vertical direction to 30 degrees above horizontal direction, and the direction of principle stress in right wing shifts from vertical direction to nearly horizontal direction. It is indicated that vertical earth pressure cased by backfilled soil can be efficiently transferred into horizontal load by the wing angle of load converting structure.

6 CONCLUSIONS

According to the frequent occurrence of damaged lining or punctured tunnel by exterior workings in big cities, this paper made the deep analysis of structure safety cased by lining fragmentation, and the applicability of lining repair and reinforcement methods. Main conclusions can be obtained as follows.

(1) According to stress distribution in top half of tunnel section, the region classification of lining fragmentation is carried out. It is made cleat that the region in 30 degrees around tunnel vault belongs to inner tensile area, the relevant punctured rate is highest, and the influence on tunnel safety is biggest.

(2) If small range of lining damage occurs, self stability of tunnel can be maintained in short term based on the overall capacity of lining and the constraint of surrounding stratum. The earth arch will disappear and the earth pressure mode above tunnel will be influenced when time goes by, and tunnel stresses and lining cracks will sharply increase correspondingly. Structure repair and reinforcement of damaged region should be carried out as soon as possible.

(3) The advantages and disadvantages, and reinforcement principles for lining repair inside tunnel and outside tunnel in common use are summarized. It is made clear that lining repair and reinforcement inside tunnel should be carried out for little damage, such as only one penetrated crack.
(4) As for large area of lining fragmentation, the combination of transverse passage and shaft or foundation pit for lining repair outside tunnel is put forward. The load converting structure with sharp top and archlike bottom, which can obviously make vertical backfilled earth pressure transferred into horizontal load, is put forward. And the influences of all column earth pressure cased by shaft backfilling on operating tunnel will be successfully reduced correspondingly.
(5) As for lining repair in shaft or foundation pit outside tunnel, bending moment of tunnel vault increases and axial force decreases from lining damage stage to shaft excavation stage, and this stress transfer process is very harmful to lining safety. The bending moment in lining repaired region may turn over due to backfilled earth pressure, the stress state of tunnel vault will change from inner tensile to outer tensile, and segment cracks may be enlarged correspondingly.

ACKNOWLEDGMENTS

The approach to lining repair summarized in this paper evolved over a long period in the rehabilitation of several metro tunnels in Chengdu. The authors acknowledge the contribution of colleagues involved in the remedial construction work and the subsequent collaboration of numerous construction practitioners. The authors also acknowledge support from the innovation team for key technology research of Xi'an Metro (2016KCT-07) and scientific research project from FSDI (19-52).

REFERENCES

Dai Zhiren, Lei Shengxiang et al. Key technologies for design and construction of shield tunnels in pebble stratum immersed in water[M]. China Communications Press Co., Ltd. Beijing: 2020.11.

Dai Zhiren, Ren Jian, Li Xiaoqiang, Wang Tianming. Technologies for Shield Tunnel Crossing Underneath Turnout Groups of Railway Turnout Area in Water-rich Sandy Cobble Stratum[J], Tunnel Construction, 2019, 39(6): 1005–1013.

Chengdu Urban and Rural Construction Commission Office. Safety protection guidelines for chengdu urban rail transit facilities. Sichuan, Chengdu, 2018.12.

Bi Xiangli, Liu Xian, Wang Xiuzhi, et al. Experimental study on the ultimate load-bearing capacity of deformed segmental tunnel linings strengthened by steel plates[J]. China Civil Engineering Journal, 2014, 47(11): 128–137.

Fang Zhi, Gong Chang, Yang Jian, et al. Fatigue behavior of reinforced concrete beams strengthened with carbon fiber sheets after creep[J]. Journal of Railway Science and Engineering, 2011, 8(1): 6–13.

Tang Min. Failure mechanism and ultimate bearing capacity of segmental tunnel linings reinforced by steel plates[D]. Shanghai: Tongji University, 2014.

Dai Zhiren, Wan Jun, Hu Ruiqing. Key Technologies for the Application of Large Diameter Shield Tunnel in Urban Railway[J]. Journal of Railway Engineering Society, 2021, 6 (Ser. 273): 75–81.

Dai Zhiren, Wan Jun, Hu Ruiqing. Mechanism and Countermeasures of Structural Cracks and Leakage in Urban Rail Transit[J]. Journal of Railway Engineering Society, 2021, 2 (Ser. 269): 103–108.

Dai Zhiren, Wan Tianming. Research and Discussion of Several Issues on Structural Calculation for Shield Tunnel Lining[J]. Journal of Railway Engineering Society, 2015, 6 (Ser. 201): 45–50.

Liu Xian, Zhang Lele, Li Gang, Zhu Yan. Experimental Study on the Ultimate Bearing Capacity of Shield Tunnel Compositive Cavity Reinforcement[J]. Urban rail transit research, 2015(7): 52–58.

Dai Zhiren, Wang Zeyu, Wan Jun, Hu Ruiqing. Analysis of Breakdown Safety Influence of Urban Subway Tunnel and Its Countermeasures[J]. Journal of Railway Engineering Society, 2021, 12 (Ser. 279): 95–101.

Code for reinforcement design of concrete structure. GB 50367-2013. China architecture & building press, 2013, Beijing.

Standard Property Office of the People's Republic of China. Tunnel spanned system based on pit foundation and arch-covering structure: China, CN 2020 2 0454058.4 [P]. 2020-04-01.

Dai ZHIREN. Study on Mechanism of Segment Crack and Fracture of Underlying Shield Tunnel Caused by Extensive Excavation and Unloading of Ground Surface[J]. China Railway Science, 2017, 38(4): 62–69.

Tunnelling for a Better Life – Yan, Celestino, Thewes & Eberhardt (Eds)
© 2024 The Author(s), ISBN 978-1-032-80042-4
Open Access: www.taylorfrancis.com, CC BY-NC-ND 4.0 license

Smart tunnel in industry 5.0: Improving road tunnel resilience by dynamic risk analysis

Alessandro Focaracci*
Prometeoengineering.it Srl, Rome, Italy

Luigi Martirano & Francesca Zacchei
Università di Roma – La Sapienza, Rome, Italy

ABSTRACT: After the accidents occurred in Mont Blanc, Tauern and St. Gotthard tunnels, safety started to be contemplated as a holistic approach. These events have become a critical issue for politicians and for public, pushing the European Commission to establish the Directive 2004/54/EC, which tackles road tunnels safety and aims to guarantee a minimum safety level to the tunnel users. Technological innovations have led to the tunnel concept evolution from civil works to technological infrastructure, where technology overcomes the geometric-functional limits, increasing its operating capacity. This paper aims to illustrate the fundamental principles of SCADRA (Supervisory Control Acquisition & Dynamic Risk Analysis) system, developed and implemented thanks to EURAM (EUropean Risk Analysis Method) methodology, which assessed the risk of over 600 Italian road tunnel tubes according to the Legislative Decree 264/06, focusing on Industry 5.0 perspective: users and managers' needs (Human-centricity), usage of new green technologies and application of an energy saving strategy (Sustainability), and improvement of tunnels resilience (Resilience).

SCADRA was installed in 3 Italian road tunnels, executing over 130,000 instantaneous risk analyses and this report illustrates the main outcomes and an evaluation for a correct tunnel management during normal operation and emergency situations. SCADRA continuously monitors the tunnel state by gathering the influence variables for tunnel safety and performing a dynamic risk analysis, quantitative and probabilistic, at regular intervals or due to sudden change in the data.

This paper presents the most significant results obtained and identifies possible future developments, in terms of tunnels' safety improvement and conservation, and tunnels' maintenance and management. SCADRA system is therefore a supplementary prevention and safety measure for tunnels management, both during normal operation and in emergency conditions, capable of guaranteeing a real-time monitoring of tunnel risk level.

Keywords: Resilience, Tunnelling, Real Time Risk

1 INTRODUCTION

Italy has an extraordinary formation of its terrain varying from mountains to plains. In order to have an accessible land connection throughout the country that will facilitate the flow of people and goods, the importance of tunnels in road transportation network enters the scene.

After the accidents occurred between 1999 and 2001 in Mont Blanc, Tauern and St. Gotthard tunnels, safety in tunnels started to be contemplated as a holistic approach. These events have become a critical issue for politicians and for public, pushing the European Commission to establish the Directive 2004/54/EC, which specifically tackles the safety in TERN road tunnels (Trans-European Road Network) and aims to guarantee a minimum level of safety to the tunnel users.

In Italy, the European Directive was implemented through the Legislative Decree n.264 of the 5th October 2006, with the purpose of guaranteeing a minimum and sufficient safety level for users in all TERN tunnels, defining a series of minimum safety requirements to be implemented in all tunnels longer than 500 m.

The complexity of an underground structure – environment, planning and construction, safety design, operation and management procedures, etc. – and the fast technological advancement have led to the concept of the "tunnel system".

Due to the accidental events, the European political response and the engineering technique, safety in tunnels has become a central and complex issue involving:

*Corresponding author: alessandro.focaracci@prometeoengineering.it

DOI: 10.1201/9781003495505-446

– Users' behaviour in emergency situations;
– Infrastructure characteristics (construction typology, escape routes, portals, etc.);
– Operational characteristics, such as type and functioning of the equipment installed, including safety measures (fire prevention, ventilation, lighting, etc.).

Technological innovations have led to the tunnel concept evolution from civil works to technological infrastructure, where the installed technology overcomes the geometric-functional limits, increasing its operating capacity.

The purpose of this paper is to illustrate the fundamental principles of SCADRA (Supervisory Control Acquisition and Dynamic Risk Analysis) system, developed and implemented thanks to EURAM methodology and software [1], which assessed the risk of over 600 Italian road tunnel tubes according to the Legislative Decree 264/06, to present and comment the most significant results obtained and to identify possible future developments, in terms of tunnels' safety improvement and conservation and tunnels' maintenance and management.

2 SMART TUNNEL

Smart Tunnel idea [2] comes from the achievement of Industry 4.0, in which there is a strong industrial automation that integrates the most innovative technologies (integrated memories, wireless sensors, integrated actuators and intelligent software), in order to improve the operating and safety conditions and increase the equipment productivity and quality.

Smart Tunnels allow optimal tunnel management during operation and in emergency situations thanks to the installation of traditional and technological sensors and the real-time assessment of tunnels' safety level, as a function of climatic conditions, traffic data and equipment state, in accordance with the Legislative Decree 264/06. Smart Tunnel together with SCADRA system (Figure 1) allow controlling the systems in the tunnel and improving the effectiveness of the operational and integrative measures increasing the safety of the users and producing also other advantages like energy savings and the improved scheduling of maintenance.

Figure 1. Smart tunnel with SCADRA.

SCADRA system was installed in three Italian road tunnels, executing over 130,000 instantaneous risk analyses in real situations and this report illustrates the main results and the considerations that can be drawn for a correct tunnel management during normal operation and emergency situations (Table 1).

Table 1. SCADRA analyses report.

Tunnel	N. of instantaneous risk analyses executed	Hours of analysis [h]
TUNNEL 1	8.640	2.160
TUNNEL 2	92.160	23.040
TUNNEL 3*	28.608	7.152

**Data analysed from 15/10/21 to 10/11/22.*

From the results of the first installations, the Supervisory Control Acquisition Dynamic Risk Analysis (SCADRA system) is proving to be a powerful prevention tool that significantly increases the resilience of road tunnels. Since 2019, the system is installed in tunnels with different structural and technological characteristics and with different environmental and traffic characteristics, and the results are clear and consistent with each other, as shown by the analysis of the data of the first plants.

3 SCADRA SYSTEM

The Supervisory Control Acquisition and Dynamic Risk Analysis (SCADRA) is a system that continuously monitors the tunnel state by collecting the variables that can influence the tunnel safety conditions (equipment and structures state, traffic data and environmental parameters) and performing a dynamic risk analysis, quantitative and probabilistic, at regular intervals or due to sudden change in the gathered data [3]. If the risk level grows towards the unacceptability threshold or in case of anomalous situations (traffic flows increase, equipment deterioration, etc.), SCADRA activates or signals the necessary safety measures in order to restore the required safety level. Instead, if the risk level is low for a certain amount of time, SCADRA suggests energy saving strategies to perform energy management for the lighting and ventilation equipment [4].

SCADRA configuration sets alongside the traditional SCADA, a system of acquisition of all the parameters, that can influence the tunnel management (collecting dated related not only to systems fault and malfunctions, but also on traffic type and intensity, dangerous goods and vehicles presence, air quality, visibility, wind speed, etc.) in order to get information on safety systems operating status, on environmental conditions and on traffic status within the tunnel, necessary for the subsequent dynamic risk analysis. Through the elaboration and analysis of all parameters, obtained from sensors and system,

a continuous safety level monitoring of the tunnel is carried out, performing the Dynamic Risk Analysis at regular pre-established intervals, under normal operating conditions and in emergency case. The equipment installed elaborates an analysis on a series of external input data. These external input data have been divided into 2 macro categories:

– Fixed inputs are the input data related to the tunnel structure, which are not variable over time, unless the structure characteristics or the tunnel systems changes;
– Variable inputs are the input data that may vary over time, such as the weather situation, the vehicular flow data and the actual tunnel systems efficiency (lighting, ventilation, etc.).

SCADRA subsystem acquires, as dynamic inputs, the input data and the parameters necessary for its processing, directly from the SCADA tunnel. The information provided by the sensors and the historical data recorded are processed by the SCADRA through a specific software in order to execute a risk assessment in real time and to determine if the risk is tolerable or if it is necessary to implement further safety measures (Figure 2).

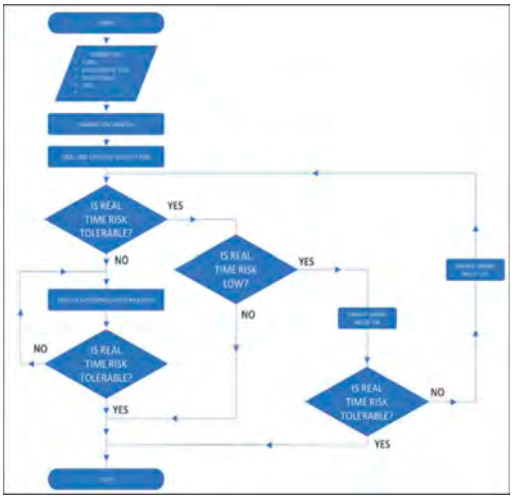

Figure 2. SCADRA flow diagram.

According to the expected level of risk, SCADRA provides a safety management (Figure 3) that can be used for:

– Planning preventive measures, like reducing speed limits, minimum distance among vehicles and prohibition of overtaking for HGV;
– Executing protective measures, such as sending communications to users, fire brigade alert, interruption of the systems energy saving mode.

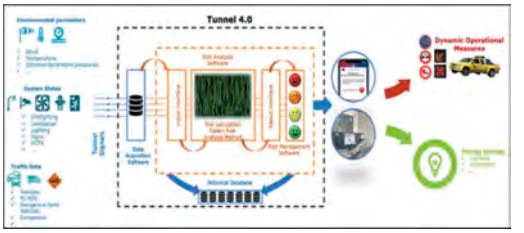

Figure 3. SCADRA system layout.

4 DYNAMIC RISK ANALYSIS (DRA)

SCADRA is based on the Dynamic Risk Analysis (DRA): the data are acquired by technical systems and specific sensors. Afterwards, a processor installed in the server performs the DRA and manages the residual risk (Figure 4).

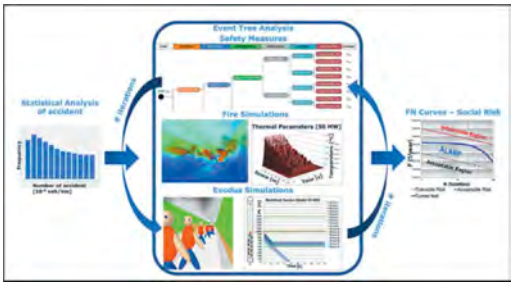

Figure 4. DRA method.

The DRA results are processed in order to classify the value of the risk according to pre-established levels that allow to undertake the appropriate actions associated with them and envisaged in the risk management plan, and it is normally implemented every 10 to 15 minutes, during the operation period, and in case of sudden changes of traffic or environmental conditions and operating level of safety systems.

The risk value is obtained by executing the quantitative probabilistic analysis, according to the method defined by the Italian Law (Italian Risk Analysis Method - IRAM), and the results are represented by the Live Expected Value of Damage (LEVD) and the F-N Curve, which defines the social risk.

The tolerability and acceptability criteria are settled by evaluating the risk level in real time (Live Expected Value of Damage - LEVD) and by comparing it with the reference value, assessed during the tunnel design and approved by the Administrative Authority. If the real time risk becomes relevant, SCADRA starts to manage the technical systems and to introduce effective safety operational measures that can reduce it (Figure 5).

The risk level, calculated as Live Expected Value of Damage (LEVD), has been classified according to 4 categories of instantaneous risk:

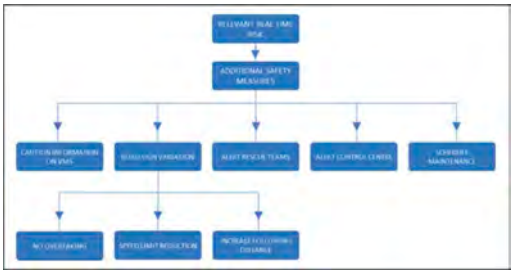

Figure 5. Relevant real time risk.

– Level 1: Low risk level (LEVD continuously below the reference value), which corresponds to optimal safety conditions, where the energy saving mode can also be permitted;
– Level 2: Normal risk level (LEVD close to reference value), which corresponds to standard safety conditions;
– Level 3: Pre - alert level (LEVD is equal to the reference value);
– Level 4: Alert level (LEVD exceeds the acceptable risk level).

The risk levels are represented by a graphical interface, which shows different coloured emoticons according to the real time risk level (Figure 6).

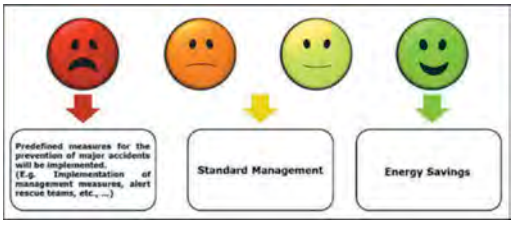

Figure 6. Risk levels.

The graphical interface shows the LEVD trend related to the surveys taken in the last 24 hours and it highlights the significant deviations of the input parameters (Figure 7).

A browser-based graphical user interface was developed in order to be user-friendly to facilitate the control centre operator in the real time risk level monitoring and to easily understand the causes behind the risk level increase and to quickly decide on the necessary safety interventions.

5 SCADRA AND ROAD TUNNEL RESILIENCE

Tunnel resilience has been defined, by PIARC Technical Committee 4.4 "Tunnel", as "The ability to prepare and plan, resist/absorb, recover or adapt more successfully (promptly and efficiently) to the actual or potential negative effects of events or developments affecting the use of a tunnel. In this context, an acceptable level of safety is an essential constraint

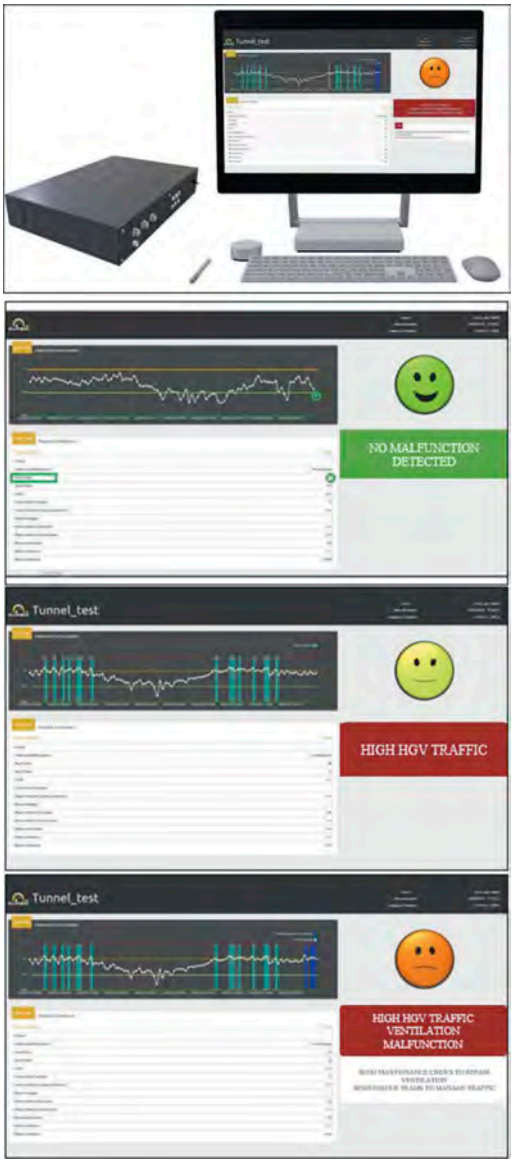

Figure 7. SCADRA interface.

for the availability of the tunnel". SCADRA system installation perfectly fits within improving road tunnel resilience, since it is always possible to know in real time what happens inside the tunnel, the environmental conditions, the traffic data and the system status. Therefore, SCADRA allows to monitor continuously the tunnel risk level (Figure 8) and, if needed, to apply operational measures with the purpose of ensuring the required safety.

Consequently, the system supports the increasing of the road tunnel resilience by preventing and planning safety measure according to every critical situation that might occur. Among all possible applications, it is possible to:

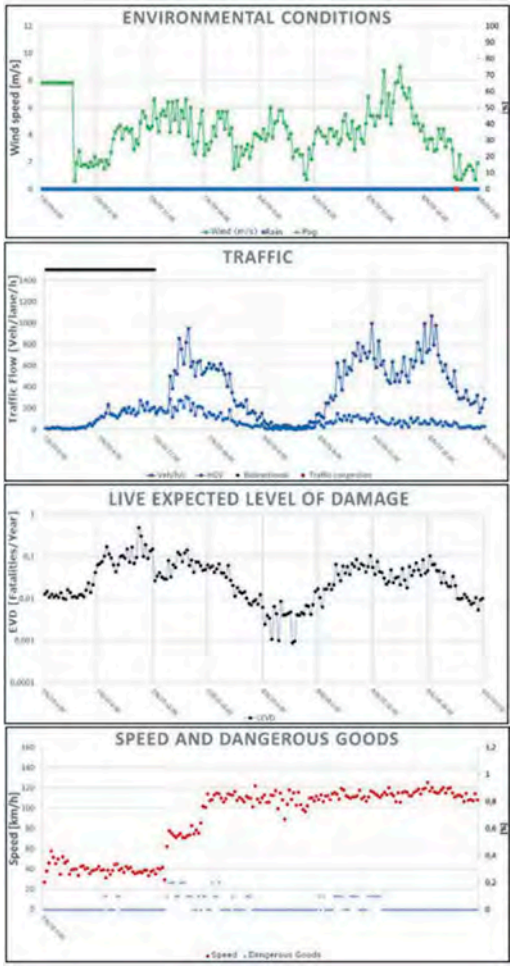

Figure 8. Data collected analysed by SCADRA.

- Pre-alarm the entities involved in the emergency;
- Interrupt of the energy saving mode;
- Identify critical solutions in real time;
- Alert users in critical situations;
- Reduce the evacuation and rescue time;
- Restore the acceptable risk level by intervening on the technical systems or through management operations;
- Plan optimal maintenance, focusing on users' safety;
- Reduce maintenance operating costs and interventions time.

SCADRA system can also represent an effective optimization for the firefighters' management, in order to reduce the instantaneous residual risk in critical conditions, such as congested traffic in a tunnel with longitudinal ventilation. Furthermore, through the continuous acquisition and processing of data, it is also possible to have preventive maintenance focused on user safety, with the aim of reducing interventions, operating costs, intervention times, MTTR (Mean Time To Repair), and system(s) unavailability.

Therefore, SCADRA system allows to operate and manage technical systems improving the effectiveness of operational and integrative measures, by enhancing the maintenance design and planning and considering the users' safety.

6 INSTALLATION RESULTS

SCADRA implementation is quite simple: an industrial PC is installed in the main technical room and connected with the SCADA system and all the necessary sensors. The software installed in the SCADRA allows the DRA execution.

SCADRA cost is compatible with a SCADA system cost, but the obtainable benefits from SCADRA are remarkable as described in the previous paragraphs. In fact, SCADRA has already been successfully installed in unidirectional road tunnels in operation.

The system has been installed in tunnels with different structural and technological characteristics and diverse environmental and traffic characteristics. The main significant data obtained from the tunnels analysis and the main characteristics are summarised in Table 2.

Figure 9 Shows the trend of the LEVD calculated by the SCADRA system in real time for the three tunnels for a period of four days.

It is interesting to observe the excellent consistency of all the data and the risk trend in the different situations which for each tunnel are absolutely different from each other both in terms of type and intensity/ severity.

7 CONCLUSIONS AND FUTURE CHALLENGES

Increasing tunnel resilience is mainly achieved through the search for a continuous improvement in safety during the tunnel operation, by applying the dynamic monitoring of the risk conditions in the tunnel through SCADRA, and targeted maintenance which takes into account the ageing of construction materials and the interaction with the environment, which can endanger infrastructure stability and functionality, as well as the users' safety.

The current technical and technological progress in the field has enabled the safety achievement, for this reason the SCADRA system can be considered a powerful prevention tool that should be integrated in all types of tunnels to increase their resilience. From the applications examined, it has been seen that this system is also suitable for existing tunnels by exploiting innovative low-cost technologies and improving safety in old tunnels thanks to operational measures integrating the systems and, if necessary, replace the lack of requirements.

Italy is the European country with the largest number of tunnels with about 650 km of tunnels in operation on TERN and, worldwide, Italy is second only to Japan for tunnel equipment. Over 600 tunnels

Table 2. SCADRA analyses report.

Tunnel type [-]	TUNNEL 1 Highway	TUNNEL 2 Highway	TUNNEL 3 Highway
N. of tubes [-]	2	2	1
Directionality [-]	Unidirectional	Unidirectional	Unidirectional
N. of lanes [-]	2	2	3
Length [m]	~ 920 m	~ 2000 m	~ 1100 m
Slope [%]	± 0,78 %	± 0,71 %	2,7 %/-2,92%
Ventilation system [-]	No	Yes	Yes
AADT [v/d]	~ 20.000 v/d	~ 20.000 v/d	~ 45.000 v/d
HGV [%]	~ 18%	~ 25%	~ 24%
N. of emergencies exits [-]	1	4	3
Distance between emergency exits [m]	460 m	400 m	300 m

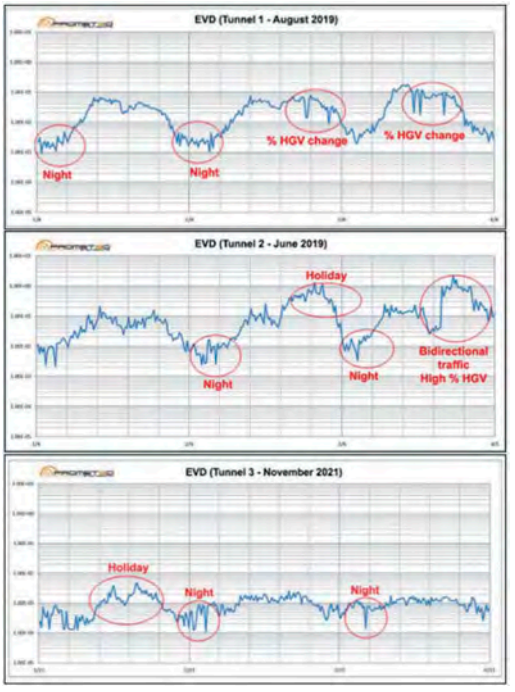

Figure 9. LEVD calculated by SCADRA system.

many of which were built before the 90s and immersed in often very poor soils. This particular feature requires special attention to the theme of resilience of underground works. Therefore, the topics of safety in operation, of a correct structural and plant maintenance and the monitoring of a tunnel play a fundamental role to increase its ability to react or adapt more successfully to the negative effects of events, actual or potential, which affect the tunnel usage.

SCADRA demonstrated to be a supplementary prevention and safety measure for the tunnels management, both during normal operation and in emergency conditions, capable of guaranteeing real-time monitoring of the tunnel risk level. Future developments foresee that the SCADRA will also be able to monitor the structural state of the tunnels and any other structures, such as bridges, viaducts, as well as the presence of any landslides in the surrounding environments (Figure 10).

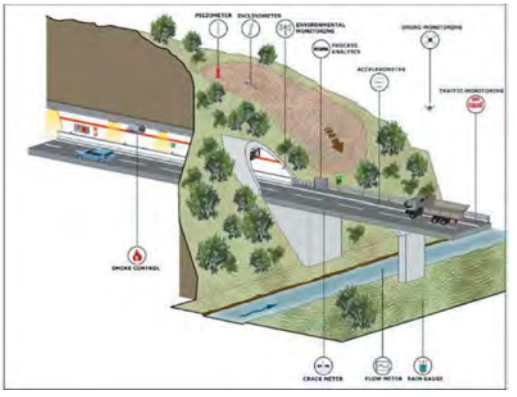

Figure 10. Structural and environmental monitoring sensors.

REFERENCES

[1] Focaracci A., "The methodology of quantitative risk analysis in the application of the Legislative Decree n.264/06", World Tunnel Congress WTC NAPOLI, Napoli, Maggio 2019.

[2] Focaracci A., "Smart Tunnel and Dynamic Risk Analysis", XXVIth World Road Congress Abu Dhabi, 6-10 October 2019.

[3] Focaracci A., "SCADRA: Innovation for Tunnel", IRF Global R2T Conference Las Vegas, NV, 19-22 November 2019.

[4] Focaracci A., "Energy savings in road tunnel. A risk-based approach.", ITA-AITES World Tunnel Congress, WTC2022 and 4th General Assemble Bella Center, Copenhagen 22-28, April 2022.

Tunnelling for a Better Life – Yan, Celestino, Thewes & Eberhardt (Eds)
© 2024 The Author(s), ISBN 978-1-032-80042-4
Open Access: www.taylorfrancis.com, CC BY-NC-ND 4.0 license

Tunnel asset management: Risk analysis through the MIRET approach

Federico Foria*, Gabriele Miceli & Mario Calicchio
ETS Srl, Rome, Italy

ABSTRACT: A high percentage of existing tunnels on heritage infrastructures is currently approaching or already exceeding the expected lifespan, and therefore require periodic and thorough inspections. Tunnel asset management becomes fundamental in order to guarantee the structure's safety and functionality. However, inspections could be problematic due to the danger and difficulty of operating on-site. Proper asset management would require an organized and systematic approach to evaluate and analyze all acquired information and data.

New technologies and methodologies, largely based on the use of mobile technologies and artificial intelligence, make it possible to create a complete digital representation of the infrastructure with reduced impact on traffic. The digital twin and the digital transformation of the processes allow an optimised workflow for the evaluation of the risks, that can be efficiently estimated, identified and mitigated.

Categorizing defects and using artificial intelligence to analyze them, make it possible to obtain a digital representation of the tunnel's state of the art, which allows for timely and effective maintenance intervention planning. Therefore, a new integrated approach, based on logical and coordinated decisions in a digital and multidisciplinary environment, is required. The MIRET (Management and Identification of the Risk for Existing Tunnels) approach allows the digital transformation of asset management, ensuring that existing tunnels meet modern safety standards, preserving their integrity through time and enabling the coexistence of environmental sustainability and technological growth.

By integrating and use efficiently these technologies and methodologies, engineers and professionals can effectively manage ageing infrastructure, improve safety, and ensure the long-term sustainability of critical assets.

Keywords: MIRET, Digital strategies, Survey, Inspection, Planning, Maintenance

1 INTRODUCTION

Infrastructures are crucial and strategic value in a country for both social and economic reasons. Its possibility to create connections and to ensure the movement of people and goods is a key for the development. Ensure the safety and the reliability of the risk management of them is therefore of a high importance and under focus of authorities.

Nowadays the environmental sustainability, together with the social sustainability, is becoming always more and more of a great relevance, and a lot of methodologies, beside the analysis of the safety take in consideration also the impact of the carbon emissions, their mitigation and adaptation to design new processes and products.

As reported also by a paper from Shanghai University (Sun, 2020) there is the need to analyze, integrate and implement tunnel management processes with new, sustainable and reliable tools, in order to ensure safety of operators and the entire society.

Use of digital technologies is one of the most important tools in the hands of people who have the responsibility to manage tunnel maintenance, as reported by a paper of University of Science and Technology of Nanjing (Qihu Qian, 2016).

Working on the management system for the maintenance of existing tunnels is one of the path to reach the goal of a safe, sustainable and even more strategic infrastructure, and it is also the topic we present on this paper.

2 TUNNEL MANAGEMENT AND MAINTENANCE

The planning of resources, environments and the management of existing tunnels are central

*Corresponding author: federico.foria@etsingegneria.it

DOI: 10.1201/9781003495505-447

challenges for industrialized countries. The positive outcome of this challenge, which focuses on coexistence and collaboration environmental sustainability and an exponential technology growth, depends significantly whether objectives are successfully articulated in an understandable, visible, and comprehensive way, and based on clear, repeatable and objective data. This general framework is essential to be able to implement a strategy aimed at the management of existing assets by all the actors involved in the entire cycle of life of the work. A fundamental step forward will be to attribute, especially in the operation phase, a fundamental role to the user, as a single person, a group of people, companies that use and manage the infrastructure, and the environment in which it is deployed and interacts. The user fulfils a socio-economic role that requires greater transparency and possible involvement in the decision-making table. This is possible only with understandable and objective processes. However, a careful and effective management of tunnels that includes all the actors and all the activities related to inspection, planning, design, construction and maintenance is not yet usual. Therefore, proper management would require an organized and systematic approach to evaluate and analyze all the information acquired. ETS srl is moving in this direction, with a new approach based on logical and coordinated decisions in a digital and multidisciplinary environment. The creation of such a scenario requires a dense network of actors and a high concentration of economic, intellectual and technological resources. The summary point of this complex mechanism is MIRET (Management and Identification of the Risk for Existing Tunnels). MIRET is a methodology, a process and a technology for digitalisation, planning and digital and integrated management of existing tunnels. But MIRET is above all a new philosophy "of building", which has conquered the trust of international experts in geo-technical engineering who have awarded its value with the title of best digital innovation at the Ground Engineering Awards 2020 (Digital Innovation), becoming a natural extension in the approach to different projects and flows, from hydrogeological instability to flood risk. The process combines innovative multidimensional mobile mapping survey systems, geotechnical and structural analyses, artificial intelligence and risk, in a common workspace at the service of technical and management table, to aim for a transparent, smart and sustainable system for the planning, design and maintenance of tunnels. The general approach is focused on an integrated workflow capable of linking and manipulating survey-inspection data over time, standardizing processes and languages. This is where the MIRET journey begins, from the surveys, investigations and inspections.

Figure 1. MIRET puzzle chart. Flow of information and their correlation used for the asset management platform starting from survey and inspection and arriving at the Works for Maintenance.

2.1 *Survey and Inspection (SI)*

The current tunnel surveillance system is based on visual inspections, usually conducted on foot or on a trolley with partial or total disruption of traffic. On the one hand, this implies greater attention to the work, on the other hand it creates a situation of discomfort, for users who are excluded from using the infrastructure, for the operators, with a high risk for their own safety, and finally for the managers, who have to face a high resource expenditure. The latest technologies enable survey and inspection of tunnels and infrastructures with Mobile Mapping. These systems can operate at different speeds, depending on the precision and accuracy to be obtained and based on the engineering and management purposes. Mobile Mapping can count on great advantages in terms of speed, efficiency and safety, reducing downtime on the line and moving the activity back office. In this scenario, ETS srl has developed a proprietary Mobile Mapping system: ARCHITA (Foria F. et al., 2019), which in a single pass acquires georeferenced data from several sensors installed on a moving vehicle, and, through the use of appropriate post-processing techniques, allows to obtain a consistent number of information representative of the actual state of the works.

Figure 2. ARCHITA configuration for rail inspection, equipped with tunnel scan, lights, georadar, termal imaging cameras.

ARCHITA is a multidimensional system, ideal for the survey of linear infrastructures, which allows to acquire simultaneous and integrated information with the use of different technologies, such as: laser scanners, georadar, thermal imaging cameras and high-definition photographs.

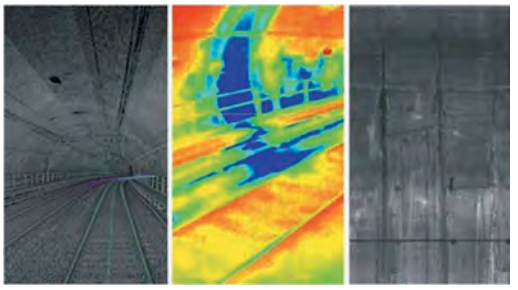

Figure 3. ARCHITA example of data acquisition (from left to right) by: laser scanner, thermal imager, high definition photograph from tunnel scanner.

Data acquisition takes place with limited disruption of traffic flow, as the system allows to survey the entire tunnel at sustained speeds (i.e. 15-30 km/h) with a single pass. The reconstruction of geometry and state of consistency of the tunnel takes place with more objective, clear and repeatable data. These assumptions are essential for the survey and inspection phase, often at the top of the MIRET process, as it can be repeated cyclically, or in post operam phase, to collect and analyze data at different instants of time. This is the only way the inspection can become a tool for monitoring the actual state of the work in order to carry out a predictive and objective analysis.

2.2 *Defect Analysis (DA)*

The thermal-photographic acquisition system installed on ARCHITA, consisting of 3 high resolution linear cameras with 16 LED lights system and 1 thermal camera, allows to obtain a high-resolution photographic reconstruction of the tunnel lining and carry out a detailed defects analysis retrospectively. Key tools of this process are defects catalogues and the relative algorithm for combining the parameters considered, in order to obtain synthetic indices representative of the actual state of the work. Nowadays there is a great variety of catalogues and methods among the clients. There are many differences in the decision-making choices and more generally in the infrastructure management and planning system. MIRET considers the same key tools, but different catalogues and methodologies adopted by the clients are unified in a single standard, which acts as an order system, rather than as a further tool in addition to those available. Subsequently, defects are digitized through a specific software environment in order to obtain output in standard digital formats, ready to be integrated in the following stages.

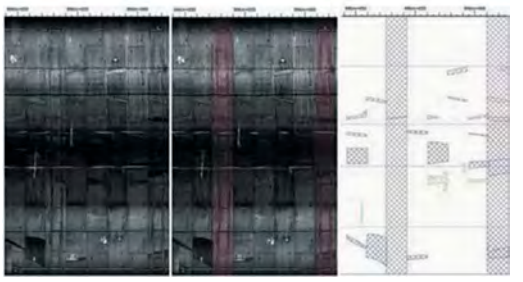

Figure 4. Defect analysis and graphic outputs.

The digitized data can be integrated with data acquired with punctual tests and traditional inspections. Defects are statistically processed and combined in order to obtain easy-to-read indexes, both for the entire tunnel and for sectors of the same. The acquisition of actual state and the digital mapping of defects are part of the standardized, repeatable and objective workflow in the MIRET process which allows a time comparison. Such comparisons also make it possible to generate models on which predictive maintenance is based. Predictive maintenance is fundamental in terms of resource planning and management. The diagnostic process thus becomes repeatable and automatable. ETS srl has chosen to invest in the development of Artificial Intelligence (AI) algorithms for the defect detection (Foria F. et al., 2021a). To date, this algorithm is capable of detecting and segmenting defects related to the presence of water, cracks and detachments, for masonry and concrete. Development starts from the Crack SegNet implementation (Ren, Y. et al., 2020), with a Convolutional Neural Network (CNN) able to automatically detect and segment some defects starting from the analysis of the images. The implementation was done in Python and C++ using Google's Tensorflow software library which, among the available libraries, had the best processing times. Algorithm training was performed on a dataset of 100-1,000 images. Validation and tests carried out on images not used in the training phase show a slight overestimation of defects by AI (10% more on average) than manual detection. Such overestimation has been deliberately calibrated to get ratings that, for the benefit of safety, don't underestimate the problems of the tunnel. Big data therefore becomes smart data, which is then validated by specialized operators. The result is that ETS proprietary software MIRET-Tunnel AI allows line disruption times to be reduced from day/km to h/km.

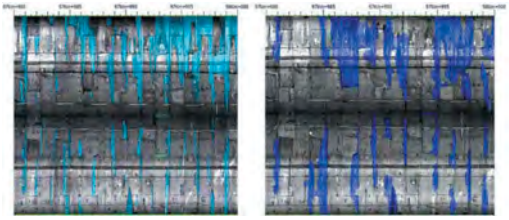

Figure 5. Manual detection vs AI detection. A slight overestimation of defects by AI (10% more on average) than manual detection can be observed.

2.3 *Digitization (DI)*

Digitization (DI) means all those processes which, starting from the Survey & Inspection phase, lead to the creation of a digital model of the work in question. Through the combination of laser scanner and ground penetrating radar of ARCHITA, it is possible to create a 3D model of the tunnel and associate the related information to set up the digital twin in BIM, with the physical and functional characteristics of the work (Foria, F. et al., 2020). In this way, a close relationship can be established between the graphic representation of the model and the technical information that the model is able to store and report with various scales of definition and information. The geometric reconstruction is used as a support tool for the milestones of the MIRET methodology, but also as a check tool in its own right (i.e. transitability checks for limit gauges in the railway sector).

2.4 *Planning and Design (PD)*

Available data and/or milestones (Defect Analysis, Digitalization and Work & Maintenance) underlie the crucial phase of Planning and Design (PD). In this phase, decision-making and design strategies are updated for the purposes of maintenance or management by the clients in a computerized environment (Foria, F. et al., 2020). Even in this case, each line manager makes use of its own flow which identifies the priorities of intervention according to technical and economic considerations. In MIRET, data coming from the mapping of the defects are processed statistically and combined with further parameters (e.g. geological context) which provide descriptive and analytical information on the boundary conditions in which the work is located. These categories are combined with each other through a Spatial Multicriteria Analysis (SMCA). The use of the SMCA is essential in order to have a general picture of the conditions of the tunnel with a structured and repeatable index that takes into account the danger of the phenomena and the vulnerability of the structures (Priority Index), to make comparisons over time and between different works (Foria, F. et al., 2021b). This assessment aims at the management and identification of the risk for existing tunnels (MIRET) for the strategic management of resources and infrastructure assets. To do this, the following categories are taken into consideration: Seismic, Superficial Geology, Deep Geology, Cracks and Water. In order to have a detailed and comparable analysis of the different areas, it was decided to divide the gallery into homogeneous sectors. The analysis described takes place according to the Italian guidelines (cslp.mit.gov.it). The ultimate goal is the management and identification of the risk for existing tunnels (MIRET).

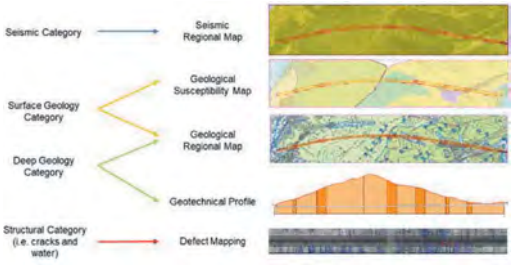

Figure 6. Considered Categories for the identification of risks (Sismic, Surface Geology, Deep Geology and Structural categories).

2.5 *Work and maintenance*

Any cycle of maintenance or intervention on the work passes through the Works and Maintenance phase, where the specific choices determined by the Planning & Design phase are implemented. From the realization of structural interventions to the simple sealing of cracks, this phase contains all the tunnel intervention solutions.

The intervention contributes to the tunnel system, reducing its risk and defining a further moment of analysis of its history. In fact, this gives us a new point of analysis from which to resume the phases of Survey & Inspection, Defect Analysis and heuristically bring together the phase of Planning & Design.

2.6 *Monitoring (MO)*

An effective Monitoring (MO) system provides a continuous source of data allowing a constant input through the different phases. Monitoring allows continuous evaluation, moving the analysis system towards a dynamic structure for asset management by the client and the choices to be made in the Planning & Design phase. This milestone makes it possible to update the parameters taken into consideration for risk calculation over time and to implement a predictive analysis model (Planning & Design phase) and predictive maintenance (Planning & Design, Work & Maintenance phase).

2.7 *Asset management*

The 'MIRETS Platform' asset management project is part of a digital transition context.

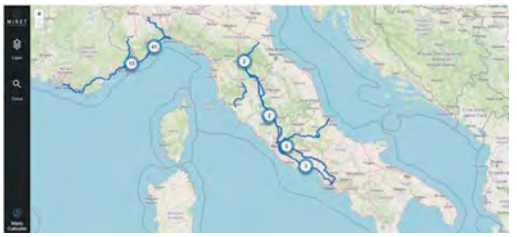

Figure 7. MIRETS Platform example of geolocalized and digitalized information for the management of tunnels in Italy.

It is aimed at creating a product that represents a digital service for analysing data relating to the infrastructure and assessing the risk and context of the same.

A systematic and forward-looking research and innovation strategy is essential to optimize resources in a sustainable way, both in a context of high-level management of infrastructure assets and as a data archiving system.

2.8 *Sustainability of MIRET*

For MIRET process, ETS specialists performed an environmental sustainability analysis to investigate the impact in terms of carbon footprint and social impact of the innovation.

To evaluate the decarbonization of the entire process, MIRET emissions of carbon dioxide were computed, analysed quantitatively and compared with two baselines which represent the most common way to inspect tunnels nowadays, one for rail tunnels and one for highways tunnels, both studied regarding carbon dioxide emissions.

The investigation followed the LCA (Life Cycle Assessment) approach, considering the entire lifetime of the process (the so-called "from cradle to grave"): it considered all the emissions involved from the on-site inspection to the final reporting.

Results show that there is a very interesting save in terms of CO_2 equivalent using the MIRET method, up to 90%, for some types of inspection and their management, thanks to ARCHITA digitalized process and the MIRET data elaboration process. Improvement in terms if safety for workers is also another achieved target for MIRET.

It is registered in risk analysis a reduction on both risk quantity (from 17 to 13 relevant risks) and risk entity (from an average of level 5 risk to a an average of level 3,4). This is a great achievements in terms of social sustainability.

ETS researchers are also working not only on CO_2 equivalent reduction, as a Climate Change effect mitigation, but also on climate change adaptation, by implementation of a tool, named C2Risk, able to identify and helps reliable risk analysis for climate change on infrastructure as railways.

Figure 8. Example of C2RISK tool giving information about vulnerability to climate change of an Italian railway line, in terms of risk for infrastructures.

3 CONCLUSIONS

MIRET's milestones are varied and complex, as well as the connections between its elements. Experience, technique, multidisciplinary, innovation and, above all, balance are required. MIRET's systemic-relational approach draws solutions from cutting-edge technologies, IT structures and processes, linking them to a unified approach of clients, the actual and necessary leaders of resilient change. MIRET is not the answer to the balance question, but one of the main means of conveying it. Deep knowledge and conscious use of resources can make the difference in the impact of a work or its maintenance. Tunnels, bridges, support works, hydrogeological instability and infrastructures are just some of the elements in which engineering and technical value must be the balancer between grey and greenery, applying flexible solutions that aim at the resilience of the work and its perfect integration with the surrounding environment for the duration of the cycle of life (and beyond).

ACKNOWLEDGMENTS

The authors thank the Geotechnics, Geology and Hydraulics Department and the Research and Development Department of ETS for the experience shared which was fundamental in the methodology.

REFERENCES

https://finance-commerce.com/2019/06/the-carbon-footprint-of-modern-construction-is-huge.
https://www.theguardian.com/environment/2011/apr/28/industries-sectors-carbon-emissions.
https://cslp.mit.gov.it/linee-guida-sulle-attivita-di-indagini-ispezioni-manutenzione-e-messa-sicurezza-delle-gallerie.

Foria F. et al., 2019. ARCHITA: an innovative multidimensional mobile mapping system for tunnels and infrastructures. In Smart Underground Space 2019. (https://www.matec-conferences.org/articles/matecconf/pdf/2019/44/matecconf_suslille2019_01005.pdf).

Foria, F. et al., 2020. Galleria Olmata, from survey to construction: an integrated design approach for the renewal of railway tunnels. In World Tunnel Congress 2020.

Foria F. et al., 2021a. Artificial intelligence and image processing in the MIRET approach for the water detection and integrated geotechnical management of existing mechanized tunnels: methodology, algorithm and case study. In Rocscience International Conference.

Foria, F. et al., 2021b. Tunnel defects mapping and maintenance of existing tunnels with an innovative approach (MIRET): the case study of Genova-Ventimiglia railway line and Roma Metro lines. In AFTES 2021.

Ren, Y. et al., 2020. Image-based concrete crack detection in tunnels using deep fully convolutional networks. Construction and Building Materials. Vol. 234.

Yufeng Sun, Min Hu, Shumin Lin, 2021 Green and sustainable tunnel maintenance activities scheduling under uncertainty, Journal of Cleaner Production Volume 297.

Qihu Qian, Peng Lin, 2016. Safety risk management of underground engineering in China: Progress, challenges and strategies. Journal of Rock Mechanics and Geotechnical Engineering 8 (2016) 423e442.

Tunnelling for a Better Life – Yan, Celestino, Thewes & Eberhardt (Eds)
© 2024 The Author(s), ISBN 978-1-032-80042-4
Open Access: www.taylorfrancis.com, CC BY-NC-ND 4.0 license

Tunnel renewal strategy – The evaluation of the advantages through LCA

Sara Frisiani*, Matteo Pierani, Francesca Magnelli, Lapo Baccolini & Andrea Poli
Tecne Gruppo Autostrade per l'Italia S.p.A., Roma, Italy

ABSTRACT: The assessment of the environmental impact of all the phases of a production process, whether related or independent within the entire production cycle, is booming within the world of large road infrastructures and civil engineering.

Considering the relevant environmental impact of construction materials, due both to their production process and to the enormous volumes used, the introduction of the concept of 'Life Cycle Thinking' within the preliminary assessments of a large infrastructure is nowadays strategic and opportune.

The environmental performance of the infrastructure, assessed by Life Cycle Analysis (LCA) methodology, can become a tool for designing and choosing between engineering solutions, as is already the case for technical and economic aspects.

This paper will illustrate the results of an LCA applied to the works to fully relining an existing tunnel, originally built in the 1960s and located in the Tuscan section of the main Italian motorway (A1), managed by the concessionaire Autostrade per l'Italia (ASPI).

The study is focused on the comparison between a traditional solution using standard reinforced concrete and an innovative solution using a special fibre-reinforced concrete, which guarantees better environmental performance and speeds up the maturation of the concrete, guaranteeing, for the same activity, a shorter duration of the construction works.

Keywords: Road tunnels assessment, Re-lining works, Innovative concrete, Construction site, LCA, Environmental impact

1 INTRODUCTION

In 2020 ASPI has launched an extraordinary Tunnel assessment plan, performed on 365 km of motorway tunnels belonging to the Italian highway network, manly built in the 1960s and 1970s by systematic inspections and testing combined with reactive maintenance works.

Within the 3 years (2020-2023) experience the Concessionaire ASPI together with its design agency TECNE has developed the so-called Tunnel Renewal Strategy (Alessio et al., 2022) which provides a new approach to Tunnel Rehabilitation.

Based on the results of detailed inspections and analyzing the development of defects and degradation of the tunnel final lining the effect of water as well as the natural degradation of the concrete and masonry linings, the effect of water has been found as the main driver of deterioration. For this reason, the TRS approach is aimed, not only to the extension of tunnel linings' life cycle of at least additional 50 years, through the construction of new inner shell, able to replace the structural function of the existing one but to integrate an additional waterproofing layer capable to collect mountain water and to insulate the new inner lining form the effect of water.

In order to allow rapid construction site start-up and dismantling and overall construction period thus mitigating the impact on motorway traffic, the TRS has required innovative technical and technological solutions like use of high performance materials, automation and mechanization of operations, the maximization of flexibility in terms of sites and logistics.

The selected case study (Ragnaia II tunnel) is part of a broader plan for the structural renewal of existing tunnels along the Tuscan section of the A1 highway. The Ragnaia II Tunnel, which is approximately 130 m long.

The study presented in this paper aims to analyse the environmental impacts associated with two methods for carrying out the tunnel renewal. Specifically, (1) through the Life Cycle Assessment (LCA) methodology, the impact on various environmental

*Corresponding author: sara.frisiani@tecneautostrade.it

DOI: 10.1201/9781003495505-448

issues will be estimated, with particular reference to climate change, associated with two different design solutions that, with the same structural performance, refer to the use of different materials: a traditional reinforced concrete and a particular fibre-reinforced concrete. Then, the elements related to site logistics are analysed, with particular attention to the sustainability (2) of a solution that, thanks to a greater speed of execution of the work, allows for the minimisation of traffic impacts and road congestion.

2 THE RAGNAIA II TUNNEL

The Ragnaia II Tunnel is a twin bore tunnel located between the ch. 272+428 and the ch. 272+556 of A1 highway. It has a straight alignment and an upward profile toward the North. The relining concerns the right-hand bore.

The tunnel is excavated through conventional method. The tunnel also has two artificial tunnel sections of approximately 7,5 m and 29,8 m in length, respectively, at the Bologna-side and Florence-side entrances. Furthermore, it was built in the 1960s and is characterized by an unreinforced concrete final lining.

2.1 *Solutions compared*

Table 1 shows the technical specifications of the concretesused in the two different design solutions.

Table 1. Technical specifications of the concretes used in the two different design solutions.

Technical specifications	Reinforced Concrete Lining	Fiber-Reinforced Concrete Lining
Concrete strength class	C45/55	C50/60
Concrete exposure class	XD1 XF2 (Tab.4.1.III NTC2018)	XD1 XF2(Tab.4.1.III NTC2018)
Concrete slump class	S5 (UNI EN 206)	S5 (UNI EN 206)
Incidence steel bars	174 kg/m^3	-
Incidence steel fibers	-	40 kg/m^3

In addition to the differences summarised in the table, a further point of divergence between the two concretes concerns the maturation speed. The innovative binder used in the production of fibre-reinforced concrete, in fact, guarantees shorter maturation times of the concrete mix compared to traditional concrete made with CEM IV 42.5R. It is estimated that the time required to cast the innovative concrete is halved (22 days) compared to the time required to lay traditional concrete (44 days).

3 MATERIALS AND METHODS

The quantification and comparison of the sustainability of the two operational methodologies is carried out by implementing a life cycle assessment (LCA). Based on the current ISO standard reference standards (UNI EN ISO 14040 and UNI EN ISO 14040), an LCA study consists of the steps listed below.

1. Goal and scope definition: preliminary phase in which the purpose of the study, the functional unit, the system boundaries studied and the assumptions are defined;
2. inventory analysis: quantification of input and output flows for all the processes analysed;
3. impact assessment: aggregation of the inventory results, using scientific models, into potential environmental impacts;
4. interpretation: analysis of the results obtained.

The four steps of a life cycle assessment are interrelated, making the entire process iterative (Figure 1). In fact, each step is based on the results obtained in the previous step. This promotes the completeness and consistency of the study and any changes made at previous steps are carried over to subsequent levels of the analysis

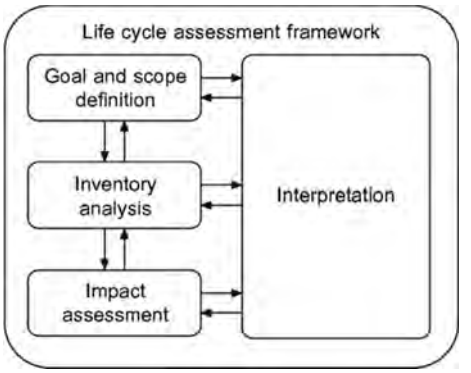

Figure 1. LCA framework - ISO 14040/14044.

3.1 *Goal and scope definition*

This study analyses the environmental implications of two different methodologies used for the lining of the right tube of the Ragnaia II Tunnel. Two different concrete solutions, listed below, were identified for the relining of the structure.

1. Classic solution: traditional reinforced concrete;
2. Innovative solution: concrete with innovative binder and steel fibres.

3.2 *Functional unit*

The term “functional unit” means the reference for the implementation of a life cycle assessment. The functional unit is represented by the portion of the

tunnel affected by the lining, equal to 128 m. The different solutions guarantee the same structural performance and are subject to maintenance at a similar frequency. A unit length was not taken as a reference due to the presence of fixed impacts independent of the linear development of the site.

3.3 *System boundaries*

The system boundaries, where the LCA is carried out, include the production and the construction phase of the material required to provide the lining of the tunnel. The decision not to consider the maintenance and disposal phases was determined by the desire, at this level of the analysis, to give more attention to the construction phase of the lining to compare the environmental sustainability of the construction materials. Specifically, phases of the production of two types of concrete, the production of steel and the production of all elements used in the tunnel lining were included; the site operating equipment, which differed in type and time of use according to the two concrete solutions used, was taken into account; the transport of construction materials to the site was also counted. Figure 2 summarises the system boundaries.

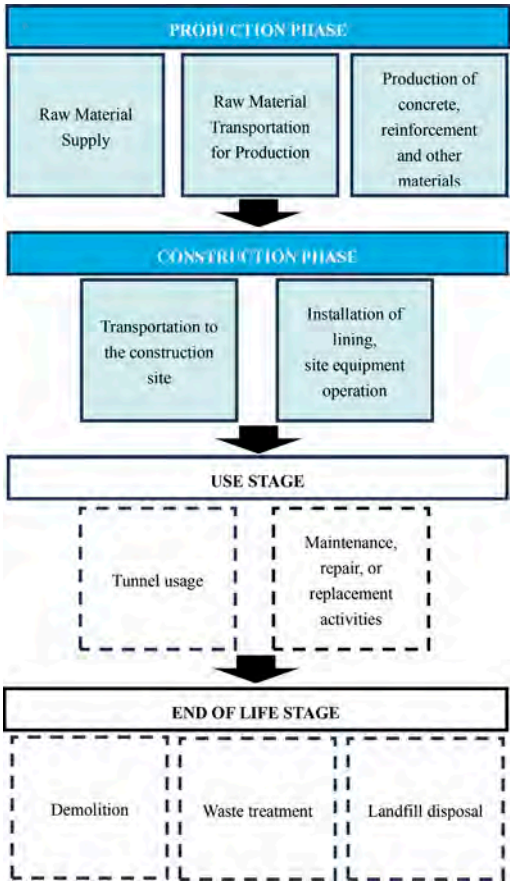

Figure 2. System boundaries. The not colored boxes represent the life cycle phases that are not considered.

3.4 *Inventory analysis*

In this step of the LCA, all input and output material and energy flows are considered for each life cycle phase studied, related to the functional unit. The sum of the emissions of the materials used and the processes implemented, within the system boundaries, constitutes the overall emissions of the tunnel lining process, which are transformed into environmental impacts at a later stage of the analysis. The collection of all emissions, at the selected life cycle stages, constitutes the inventory. In this study, the emissions associated with the different materials and production processes were obtained from the specific production plant or from databases. Listed below is information on how the materials needed to construct the inventory were sourced:

- Concrete with a traditional binder and fibre-reinforced concrete with an innovative binder: the specific production plant directly provided the emissions per cubic metre of the two types of concrete, without allocating the impact between the different constituent materials. Although based on only two individual products, for the purposes of this study, it is considered correct to use the data provided. In fact, it is assumed that they are manufactured at the same production site, and in this way, all variables associated with different production plants, for example the fuels used, the geographical production context or the raw material procurement method, have been eliminated;
- Reinforcing steel bars: the impact of reinforcing steel was quantified using the emissions associated with 1 kg of a generic steel in the ecoinvent v3.6 database (www. ecoinvent.org). This database details the raw materials and energy consumption required to make one unit of material. In the case of steel, its composition was modified to conform to a reinforcing steel produced in Italy in an electric furnace with a recycled steel percentage of 75%, as imposed by the Minimum Environmental Criteria for construction which, although not directly applicable to infrastructures, were taken as a reference for modelling the steel used in the classical solution. Varying the composition of the material changes its emissions.
- Paints, mortars, PVC sheets and geotextile sheets: similar to steel, the impact of these materials is derived from generic elements in the ecoinvent database;
- Transport: Emissions associated with the transport of materials depend on means of transport used, distance travelled and quantity of material transported. The ecoinvent database offers a wide variety of selectable vehicles but, due to focus is mainly on the impact of construction elements, a common vehicle was selected for all materials transported from the different production plants to the construction site. The database expresses

the emissions of the means of transport in terms of "kg·km". This because the emissions of a vehicle increase as the load transported increases and, of course, as the distance travelled. 250 km from the reinforcing steel production plant to the construction site was considered; this value is an average of the distances of two plants that would likely supply the construction site. The impact of concrete transport is quantified not in terms of distance but in terms of the amount of fuel and compressed air consumed by the concrete mixer on the way to the construction site. The quantities of fuel and compressed air are estimated from similar construction sites;

– Fuels: in order to quantify the impact related to the installation of materials and the operation of site equipment, which ensure the correct execution of activities, the quantities of diesel, petrol, electricity, lubricant and compressed air used were estimated from similar construction sites. The emissions reported by the ecoinvent database were associated with these quantities. Also included in this category are the fuels consumed to transport all materials other than steel from the production plant to the construction site: paints, mortars and sheets, as well a as concrete. Table 2 summarises the estimated construction site equipment with relative consumption of diesel and lubricants.

Table 2. Construction site equipment consumption.

Equipment type	Diesel [lt/h]	Lubrificants [lt/h]
Generator set	3,5	0,49
Aerial platform	15	1,5
Truck 4-6 tons	12	1,2
Truck 1,6-4 tons	8	0,8
Compressor for concrete pump, 65 kW	13	0,14
Spritz pump(concrete mixer)	18	1,8
Tanker >18 tons	18	1,8

Table 3 summarises the materials and the relative environmental information collected during the inventory. The emissions of all materials, with the exception of concrete, were taken from average data, modified if necessary, in ecoinvent. The original string by which they are identified in the database is shown.

Table 3. Summary of materials analysed.

Construction materials	Ecoinvent string
Concreteclassic solution	Emissions Modeled from a Specific Manufacturing Plant
Concreteinnovative solution	Emissions Modeled from a Specific Manufacturing Plant
Reinforcing steel	*Steel, low-alloyed {RER}| steel production, electric, low-alloyed | Cut-off, U*
Polyurethane paint	*Alkyd paint, white, without water, in 60% solution state {RER}| market for alkyd paint, white, without water, in 60% solution state | Cut-off, U*
Epoxy paint	*Acrylic varnish, without water, in 87.5% solution state {RER}| market for acrylic varnish, without water, in 87.5% solution state | Cut-off, U*
Two-component background painting	*Acrylic varnish, without water, in 87.5% solution state {RER}| market for acrylic varnish, without water, in 87.5% solution state | Cut-off, U*
Anti-sale siloxane primer	*Polydimethylsiloxane {GLO}| market for polydimethylsiloxane | Cut-off, U*
Mortar	*Cement mortar {RoW}| market for cement mortar | Cut-off, U*
Epoxy filler	*Stucco {GLO}| market for | Cut-off, U*
PVC sheets (2 mm thickness)	*Polyvinylchloride, bulk polymerised {GLO}| market for | Cut-off, U + Extrusion of plastic sheets and thermoforming, inline {GLO}| market for | Cut-off, U*
Water	*Tap water {Europe without Switzerland}| market for | Cut-off, U*
Lubrificant	*Lubricating oil {RER}| market for lubricating oil | Cut-off, U*
Compressed air	*Compressed air, 1000 kPa gauge {RER}| market for compressed air, 1000 kPa gauge | Cut-off, U*
Diesel	*Diesel, burned in building machine {GLO}| market for | Cut-off, U*
Petrol	*Petrol, unleaded, burned in machinery {GLO}| market for petrol, unleaded, burned in machinery | Cut-off, U*
Electricity	*Electricity, medium voltage {IT}| market for | Cut-off, U*

3.5 *Impact assessment*

Impact assessment is the stage in which the emissions collected during the inventory are translated into potential impacts affecting specific environmental components called 'impact categories'. The LCA methodology involves the division of the 'environmental system' into a limited number of categories that are impacted, according to different environmental mechanisms, by the emissions generated in the considered life cycle phases. In this study, the environmental results are expressed according to the impact categories referred to the EN 15804 standard, except for the "climate change" category for which, for the simplicity of communication, the environmental results will be expressed in the aggregate form "GWP".

Each emission collected during the inventory phase is associated with one or more impact categories. Each emission is multiplied by equivalence factors (FE) that express the contribution relative to a reference emission, whose FE is equal to 1 by definition. After the application of the equivalence factors, each impact category will be expressed with a specific unit of measurement.

The association of emissions with specific impact categories, the application of equivalence factors and the sum of emissions within each impact category are performed using the LCA software SimaPro v9.5. This program quantifies the environmental impact by applying the "EN 15804+A2 Method v1.00" calculation method, which expresses the results in accordance with the EN 15804 standard.

3.6 *Interpretation*

The environmental impacts of the two tunnel renewal methods are shown in tabular and graphic form (Table 4 and 5, Figures 3 and 4). The items expressed in the header of the tables include production, transport to the site and installation of the material. The exception is the item "site equipment" which only describes the energy consumption of the vehicles and machinery used during construction, without counting the impact associated with their production and transport to the construction site.

GWP: Global Warming Potential; **ODP**: Depletion Potential of the stratospheric Ozone layer; **AP**: Acidification Potential; **EP-fw**: Eutrophication Potential, freshwater; **EP-mar**: Eutrophication Potential, marine; **EP-ter**: Eutrophication Potential, terrestrial; **POCP**: Formation potential of tropospheric ozone; **ADPE**: Abiotic Depletion Potential for non-fossil resources; **ADPF**: Abiotic Depletion Potential for fossil resources; **WDP**: Water Deprivation Potential.

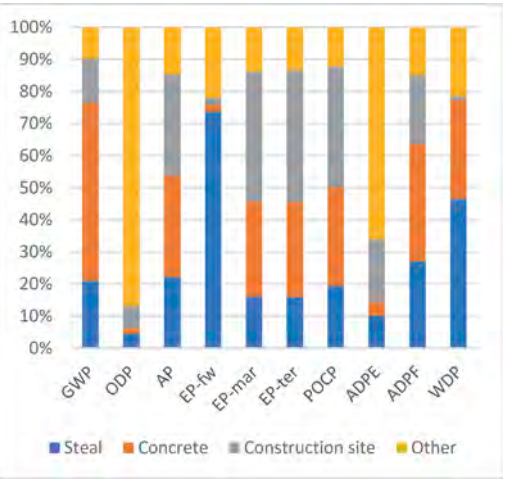

Figure 3. Environmental impact, classic solution - EN 15804+A2 Method v1.00.

Table 4. Environmental impacts, classic solution - EN 15804+A2 Method v1.00.

Impact category (unit)	Steal	Concrete	Site equipment	Other	Total
GWP (kg CO_2 eq)	1,56E+05	4,17E+05	1,02E+05	7,37E+04	7,49E+05
ODP (kg CFC11 eq)	1,59E-02	6,40E-03	2,47E-02	3,10E-01	3,57E-01
AP (mol H+ eq)	7,70E+02	1,10E+03	1,10E+03	5,10E+02	3,48E+03
EP-fw (kg P eq)	5,37E+01	1,62E+00	1,57E+00	1,60E+01	7,29E+01
EP-mar (kg N eq)	1,90E+02	3,53E+02	4,83E+02	1,64E+02	1,19E+03
EP-ter (mol N eq)	2,05E+03	3,86E+03	5,30E+03	1,75E+03	1,30E+04
POCP (kg NMVOC eq)	7,81E+02	1,24E+03	1,52E+03	4,91E+02	4,03E+03
ADPE (kg Sb eq)	1,28E-01	5,34E-02	2,48E-01	8,35E-01	1,26E+00
ADPF (MJ)	1,97E+06	2,67E+06	1,56E+06	1,08E+06	7,28E+06
WDP (m3 depriv.)	4,78E+04	3,15E+04	1,31E+03	2,21E+04	1,03E+05

Table 5. Environmental impacts, innovative solution - EN 15804+A2 Method v1.00.

Impact category (unit)	Concrete	Site equipment	Other	Total
GWP-tot (kg CO_2 eq)	5,46E+05	3,81E+04	7,37E+04	6,58E+05
ODP (kg CFC11 eq)	8,80E-03	9,45E-03	3,10E-01	3,29E-01
AP (mol H+ eq)	2,75E+03	4,06E+02	5,10E+02	3,66E+03
EP-fw (kg P eq)	6,45E+00	7,14E-01	1,60E+01	2,32E+01
EP-mar (kg N eq)	1,05E+03	1,78E+02	1,64E+02	1,39E+03
EP-ter (mol N eq)	1,16E+04	1,95E+03	1,75E+03	1,53E+04
POCP (kg NMVOC eq)	3,06E+03	5,71E+02	4,91E+02	4,13E+03
ADPE (kg Sb eq)	3,17E-01	1,22E-01	8,35E-01	1,27E+00
ADPF (MJ)	4,57E+06	6,03E+05	1,08E+06	6,26E+06
WDP (m3 depriv.)	7,91E+04	6,48E+02	2,21E+04	1,02E+05

GWP: Global Warming Potential; **ODP**: Depletion Potential of the stratospheric Ozone layer; **AP**: Acidification Potential; **EP-fw**: Eutrophication Potential, freshwater; **EP-mar**: Eutrophication Potential, marine; **EP-ter**: Eutrophication Potential, terrestrial; **POCP**: Formation potential of tropospheric ozone; **ADPE**: Abiotic Depletion Potential for non-fossil resources; **ADPF**: Abiotic Depletion Potential for fossil resources; **WDP**: Water Deprivation Potential.

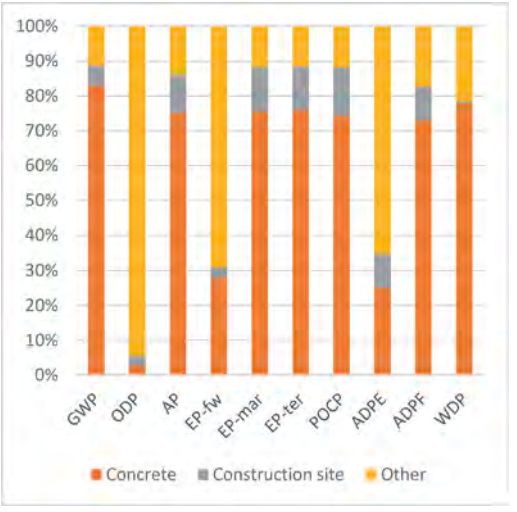

Figure 4. Environmental impacts, innovative solution - EN 15804+A2 Method v1.00.

For almost all categories, most of the impact depends on the production and installation of the concrete, in the innovative scenario, or the production and installation of the concrete and steel in the traditional scenario. It is therefore evident that technological improvement strategies need to be implemented for these two construction materials in order to limit environmental externalities. Globally, it is estimated that around 8% of total CO_2 emissions are due to the cement industry (Supino et al., 2023).

Table 6 compares the aggregate environmental impacts in the different impact categories of the two tunnel renewal solutions. The last column represents the percentage variation of the environmental impact of the innovative solution compared to the traditional solution.

GWP: Global Warming Potential; **ODP**: Depletion Potential of the stratospheric Ozone layer; **AP**: Acidification Potential; **EP-fw**: Eutrophication Potential, freshwater; **EP-mar**: Eutrophication Potential, marine; **EP-ter**: Eutrophication Potential, terrestrial; **POCP**: Formation potential of tropospheric ozone; **ADPE**: Abiotic Depletion Potential for non-fossil resources; **ADPF**: Abiotic Depletion Potential for fossil resources; **WDP**: Water Deprivation Potential.

Half of the categories are more impacted by one or the other solution. The EN 15804 does not allow the application of weights to prioritise impact categories; therefore, it is not possible to discriminate which of the two solutions is more environmentally impactful in absolute terms. However, following the international sustainability goals that aim to achieve climate neutrality by 2050, as mandated by the Paris Agreement, it is appropriate to focus primarily on the "climate change (GWP)" category, which represents the effects of climate-changing emissions. The reference unit is the CO_2 equivalent (CO_2 eq).

Table 6. Environmental impacts, comparison - EN 15804 +A2 Method v1.00.

Impact category	Unit	Traditional solution	Innovative solution	Δ%
GWP	kg CO_2 eq	7,49E+05	6,58E+05	-12%
ODP	kg CFC11 eq	3,57E-01	3,29E-01	-8%
AP	mol H+ eq	3,48E+03	3,66E+03	5%
EP-fw	kg P eq	7,29E+01	2,32E+01	-68%
EP-mar	kg N eq	1,19E+03	1,39E+03	17%
EP-ter	mol N eq	1,30E+04	1,53E+04	18%
POCP	kg NMVOC eq	4,03E+03	4,13E+03	2%
ADPE	kg Sb eq	1,26E+00	1,27E+00	1%
ADPF	MJ	7,28E+06	6,26E+06	-14%
WDP	m3 depriv.	1,03E+05	1,02E+05	-1%

Figure 5 shows that the relining performed with innovative concrete has a reduction in CO_2 eq impact of 12% compared to the operation performed with traditional concrete.

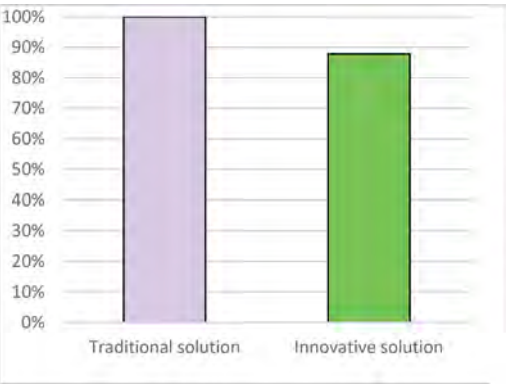

Figure 5. GWP tunnel renewal, comparison - EN 15804 +A2 Method.

Still focusing on the most highly-prioritised impact category, the climate-changing emissions associated with the production and installation of construction materials are presented in Table 7 and Figure 6, Table 8 and Figure 7, on the other hand, express the impact on climate change generated by the use of construction equipment.

Table 7. GWP production and installation of construction materials, comparison - EN 15804+A2 Method.

Impact category	Unit	Traditional solution	Innovative solution
GWP	kg CO_2 eq	6,50E+05	6,23E+05
GWP compared to traditional solution	%	100%	96%

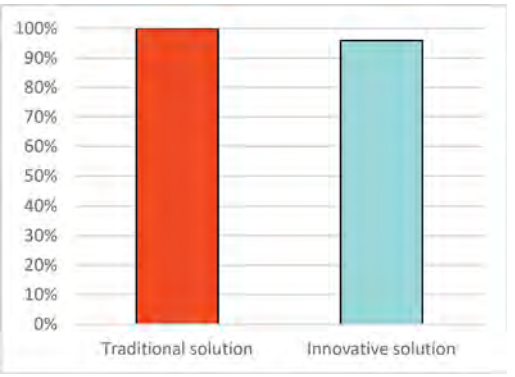

Figure 6. GWP production and installation of construction materials, comparison - EN 15804+A2 Method.

Table 8. GWP construction equipment, comparison - EN 15804+A2 Method.

Impact category	Unit	Traditional solution	Innovative solution
GWP	kg CO_2 eq	9,94E+04	3,51E+04
GWP compared to traditional solution	%	100%	35%

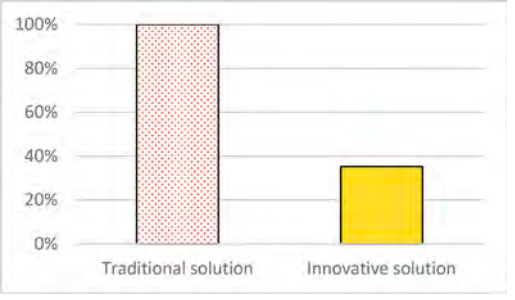

Figure 7. GWP construction equipment, comparison - EN 15804+A2 Method.

The results show that the impact of the construction site is decisive for the quantification of overall climate-changing emissions.

4 SITE LOGISTICS

Environmental impact is not the only element to be analysed to define the sustainability of the intervention under study. In fact, it must also include assessments concerning the social and economic spheres of the sustainability. The parameter used to assess the overall sustainability is time.

The duration of the maintenance work in the two solutions varies depending on the concrete casting speed and the time required to assemble the prefabricated steel reinforcements cage: in the classic configuration, the steel reinforcement is used for the entire covering, while in the innovative solution, only the sidewalls will be reinforced, with a significant reduction in time. The solution using traditional concrete requires an average concrete casting speed of 3 m/day, while the fibre-reinforced concrete casting is at twice the speed of approx. 6 m/day, thanks to the higher maturation speed of the concrete mix, which ensures that the formwork will advance in less time.

Relating the length of the tunnel (128 m) to the concrete casting speed, the paving of traditional concrete takes around 44 days compared to 22 days for fibre-reinforced concrete. Considering also all the other intervention phases and counting a shorter time required for the assembly of the prefabricated steel reinforcements cage in the innovative solution, the relining carried out using fibre-reinforced concrete guarantees an estimated time saving of approximately 50 days compared to the intervention using traditional concrete.

The shorter construction time can be translated into lower environmental, social and economic impacts. In fact, although difficult to quantify in numerical terms, a longer construction phase creates the restriction of the road network with a consequent increase in travel time on the road section. This results in greater emissions for each vehicle that travels on the road interfered with by the construction site (environmental impacts); a reduction in road safety and an increase in noise pollution and stress (social impacts); last but not least, damage to local businesses based on the transport of goods and employees (economic impacts).

5 CONCLUSIONS

This study analyses the environmental impacts of two different ways to carry out the relining works of the right tube of the Ragnaia II Tunnel on the Tuscan section of the A1 motorway, which differ in terms of the type of concrete used: reinforced with steel in the 'traditional' scenario or with an innovative, fibre-reinforced bond in the 'innovative' scenario. The analysis was based on a life cycle assessment (LCA) from the production of the construction materials to the execution of the tunnel renewal.

The study showed that the intervention using fibre-reinforced concrete leads to a reduction in

climate change impacts compared to the solution using traditional concrete. This reduction depends not only on the different concrete mix used and the absence or presence of steel reinforcement, but also on the different number and timing of construction equipment used.

However, it cannot be said that the 'innovative' solution is less impactful in absolute terms due to the absence of standardized weight coefficients to determine the greater severity of the different impact categories. On the other hand, the high casting speed of fibre-reinforced concrete, thanks to the shorter maturation times required, means that relining according to the innovative method guarantees a shorter site duration, with consequent advantages in terms of environmental, economic and social sustainability.

The increase in traffic and road congestion caused by the longer duration of the construction site, although not quantified through LCA analysis in this study, presents objective problems that contribute to making the traditional solution less efficient.

REFERENCES

Aiello, S., Alessio, C., Baccolini, L., Fantuz, R., De Biagi, V., Chiaia, B. – Analytical study of anomalies in tunnel lining thickness: critical temperature variations, WTC2023, May 12–18, 2023.

Ammar Younes, Emad Elbeltagi, Aboelkasim Diab, Giulia Tarsi, Fam Saeed, Cesare Sangiorgi, Incorporating coarse and fine recycled aggregates into concrete mixes: mechanical characterization and environmental impact. Journal of Material Cycles and Waste Management 2023.

Bieniawski, Z., T. – Tunnel design by rock mass classifications, January, 1990.

Desimon, L. – Costruzione delle gallerie – 1953, pp.73–132.

DM 23.06.2022.

EN 15804:2012+A2:2019/AC:2021: Sustainability of construction works - Environmental product declarations - Core rules for the product category of construction products.

Feiz, R., Ammenberg, J., Baas, L., Eklund, M., Helgstrand, A., Marshall, R. Improving the CO_2 performance of cement, part I: Utilizing life-cycle assessment and key performance indicators to assess development within the cement industry. J. Clean. Prod. 2015, 98, 272–281.

Frazão, C., Barros, J.,Bogas, J.A., García-Cortés, V., Valente, T. (2022): "Technical and environmental potentialities of recycled steel fiber reinforced concrete for structural applications".

García-Gusano, D., Garraín, D., Herrera, I., Cabal, H., Lechón, Y. Life cycle assessment of the Spanish cement industry: Implementation of environmental-friendly solutions. Clean Technol. Environ. Policy 2015, 17, 59–73.

Liew, K.M., Akbar, A. (2020): "The recent progress of recycled steel fiber reinforced concrete".

Prè Consultants. Software SimaPro version 9.5.

Qin, X., Kaewunruen, S. (2022): "Environment-friendly recycled steel fibre reinforced concrete".

Stafford, F.N., Dias, A.C., Arroja, L., Labrincha, J.A., Hotza, D. Life cycle assessment of the production of Portland cement: A Southern Europe case study. J. Clean. Prod. 2016, 126, 159–165.

Supino, S., Malandrino, O., Testa, M., Sica, D. (2023): "Sustainability in the EU cement industry: the Italian and German experiences".

Terzaghi, K. – Rock defects and loads on tunnel supports. In Rock tunneling with steel supports, (eds R. V. Proctor and T. L. White) 1, 17–99. Youngstown, OH: Commercial Shearing and Stamping Company, 1946.

Tuladhar, R., Yin, S. (2022): "Use of Recycled Plastics in Eco-efficient Concrete".

UNI EN 206: Calcestruzzo – Specificazione, prestazione, produzione e conformità.

UNI EN ISO 14040:2021. ISO series on Life Cycle Assessment, UNI EN ISO 14040:2021.

UNI EN ISO 14044:2021. ISO series on Life Cycle Assessment, UNI EN ISO 14044:2021

Wang, G.C. (2022): "Electric Arc Furnace – slag use in asphalt paving".

Tunnelling for a Better Life – Yan, Celestino, Thewes & Eberhardt (Eds)
© 2024 The Author(s), ISBN 978-1-032-80042-4
Open Access: www.taylorfrancis.com, CC BY-NC-ND 4.0 license

Development of cementitious repair material for tunnel concrete structures of operating railroad in salt-affected environment

Yoshimi Kose* & Koichiro Miyake
East Japan Railway Company, Tokyo Civil Engineering Technical Center, Metropolitan Division, Chiyoda-ku, Tokyo, Japan

Akira Hosoda
Graduate School of Urban Innovation, Yokohama National University, Hodogaya-ku, Yokohama, Kanagawa, Japan

Makoto Saito
Denka Company Limited, Elastomer & Infrastructure Solution Division, oumi Infrastructure Technology Research Department, Machida-shi, Tokyo, Japan

Hiroyuki Utsugi
TOTETSU KOGYO CO., LTD, Civil Engineering Department, Civil Engineering Division, Shinjuku-ku, Tokyo, Japan

ABSTRACT: Urban railroad tunnels located in seaside areas or near rivers at low tide where affected by leakage water containing chloride ions originated from seawater have been deteriorated particularly in rebar corrosion, while the restriction of repairing work time slot for the railroad structures in the Tokyo metropolitan area due to the quite limited construction time and narrow construction space makes repairing difficult. In addition, conventional patch repair method using polymer cement mortar with nitrite-based admixture has another issue such as slower repairing speed, less sprayable thickness and adhesion performance. Authors have suggested in this paper a newly developed "two-material shot repairing system" with polymer cement fiber mortar to overcome these subjects, by utilizing calcium aluminate powder that performs accelerator as well as chloride ion immobilizer and a liquid accelerator that is to be mixed up just before the spray nozzle. As a result, it was found that the construction cost can be reduced around 30% with keeping fairly same chloride proofing and with obtaining better workability and adhesion performance compared with the conventional patch repairing method.

Keywords: urban railroads, chloride induced corrosion, polymer cement fiber mortar, calcium aluminate admixtures, liquid accelerator, patch repair method

1 INTRODUCTION

In recent years, the proportion of aged infrastructure has tended to increase rapidly. Railroad owners always have the responsibility to supply safe and stable transportation while ensure the structure in proper condition to keep safety, serviceability, and ease of repair work. In addition, there is a demand for more efficient inspection and repair methods in the maintenance and management of railroad structures due to a decrease in the number of employees, lack of well-experienced engineers, increase in the number and frequency of survey points, and reduction of the maintenance and management costs. Tunnels and shafts located on the waterfront of urban railroads and near rivers at low tide are subject to salt damage, and it is necessary to inspect, repair, and improve structures deteriorated by salt damage within the limited working slot and narrow working spaces. Repair methods that can extend the service life of existing structures at a low cost without causing re-degradation of repaired areas are required. Therefore, in this study, the authors decided to develop a new patch repair method using spray mortar for tunnel concrete structures deteriorated by salt damage in commercial urban railroad lines,

*Corresponding author: kose@jreast.co.jp

DOI: 10.1201/9781003495505-449

taking into account the to overcome several issues the above.

2 PREVIOUS STUDIES

Since generally the tunnel structures are unlikely affected by airborne salt and de-icing agents sprayed on roads, there have been quite limited reports on salt damage e.g. in the slab of Shinkansen tunnels and floor slabs of road tunnels by 1990s. Since 2000, intensive investigations have begun however mainly conducted in urban tunnels constructed by open-cut, submerged tunneling, and shield tunneling methods, such as subway, expressway, and power transmission line tunnels, and there are still few reports about repair and reinforcement work in these tunnels. These reports indicate that the salt damage in tunnels often occurs locally in the vicinity of water leakage and at locations where cover thickness for reinforcing bars is thin. Therefore, the patch repair method is effective among many kinds of repairing methods for salt damage of urban railroad tunnels.

Also, constraints in commercial rail line construction include short construction time and small construction space.

Figure 1. Example of work time for commercial railways construction.

As shown in Figure 1, the work time is limited to approximately 90 minutes. In addition, as shown in Figure 2, railway construction limit is set so as not to interfere with train operations, and construction facilities, including temporary facilities, must be located outside the railway construction limit. The time between the completion of the repair work and the start of train operation is short, and the repair method must be easy to apply, exhibit sufficient strength at an early stage, and have sufficient adhesion strength between the repair material and base concrete to stand the wind pressure and vibration caused by passing trains.

After considering these factors, authors concluded that the spraying method is the most superior for our targeted structures. The conventional spraying method

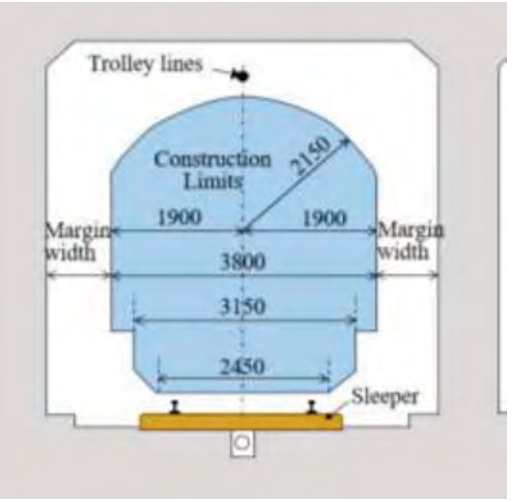

Figure 2. Margins of the construction limit on a commercial railways.

is to use a pre-blended type of polymer cement fiber mortar with chloride proof properties. As shown in Figure 3, This is a method to prevent salt affected using a polymer cement mortar with a mechanism to adsorb chloride ions (Cl^-) and release it with nitrite ions (NO_2^-) by blending a Ca-Al complex hydroxide called nitrite-type hydrocalumite. At present, the effectiveness of this method in terms of durability has been confirmed as shown by Ueda et al.(2012).

On the other hand, it was confirmed that there was room for performance improvement in terms of workability and adhesion under the constraints of this study. Therefore, it was decided to develop a new sprayed mortar utilizing cement mortar, polymers, short fibers, and calcium aluminate admixtures such as rapid hardener and salt fixing material. In this development, a two-material shot method is adopted where the liquid accelerator is added before the spray nozzle. Table 1 shows the performance of the conventional method and the required performance of the newly developed method. The target performance values for workability and adhesion were set based on the construction conditions of the target repair area, while those for durability were set with reference to the performance of the conventional products.

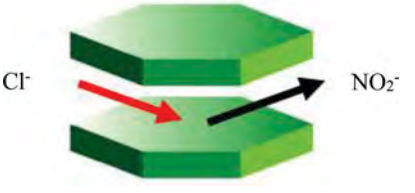

Figure 3. Mechanism of salt adsorption of salt adsorption.

Table 1. Comparison of performance requirements between conventional method and developed method.

Test Items	Conventional method	Developed method
【Construction performance】		
・ Flow value (JIS R 5201)	147mm	160mm or more
・ Set start time	48 minutes	More than 15 minutes
・ Set end time	55 minutes	45 minutes or less
・ Spraying speed	0.2~0.3m^3/hour	0.6~0.7m^3/hour
【Adhesion performance】		
・ Spraying thickness (Upward・ Sideways)	20mm・ 40mm	100mm・ 100mm
・ Adhesion strength (Age of material1hour)	0.2N/mm^2	0.2~0.5N/mm^2
【Durability】		
・ Chloride Ion Penetration Depth	1.8mm	1.8mm
・ Apparent diffusion coefficient of chloride ions	0.37cm^2/year	0.37cm^2/year

3 DEVELOPMENT OF PATCH REPAIR METHOD

3.1 *Spraying equipment*

In developing the method, development of materials was started based on the concept of two-material shot method. In the two-material shot method, mortar and liquid accelerator are pumped in two separated systems, and the mortar is mixed with the accelerator before the spraying nozzle. Compared to the conventional one-material shot method in which the mortar is generally sprayed in one system of pre-blended type mortar, the two-material shot method can maintain mortar fluidity for longer time with having superior pumping performance, and can obtain superior workability. The addition of liquid accelerator instantly solidifies the mortar into a plastic state is the additional feature.

3.2 *Preliminary tests*

In developing the materials, a cement mortar named as “Control” whose concept was shown by Hirama et al. (2016) containing the rapid hardening material shown in Table 2 was used as the basis for testing. Three improved materials were provided such as Improvement 1 with the addition of a polymer for cement, Improvement 2 with the addition of a salt fixing material, and Improvement 3 with both. Ordinary Portland cement, vinylon fiber, and lime-crushed sand were used for all these mortars. Poly-acrylic ester, one of the re-dispersible powder resins, was used as the polymer for cementation. Two calcium aluminate admixtures were used: a rapid hardener, a mixture of $12CaO\text{-}7Al_2O_3$ and anhydrite, and a salt-fixing material (hereafter referred to as CA_2) consisting mainly of $CaO\text{-}2Al_2O_3$. Liquid accelerator were also used, mainly composed of aluminum sulfate.

3.2.1 *Test method*

In order to select the best performance mortar, tests were conducted using the following method to compare properties, using the amount of polymer and CA_2 as parameters.

(1) Fresh mortar property

Flow tests were conducted in accordance with JIS R 5201 "Test Methods for Cement physical" to confirm that the required flowability as a wet shotcrete material could be obtained.

(2) Setting time

In order to confirm the rapid hardening properties that ensure a short construction time and surface troweling time, setting time tests were conducted for

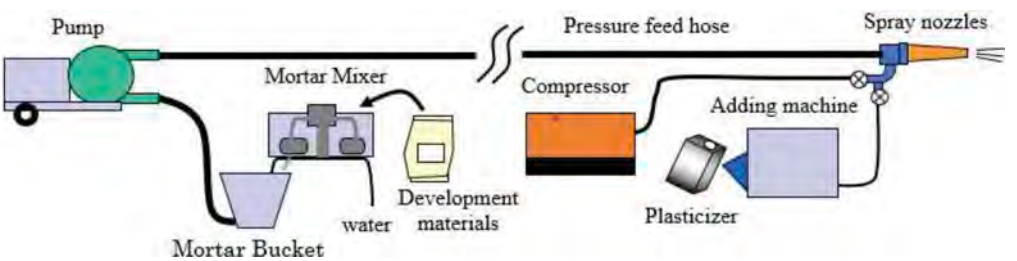

Figure 4. Spraying equipment (2-material shot).

Table 2. Material mix in preliminary test.

No	Product name	density (kg/m^3) water W	cement C	sand s	water-cement ratio W/C(%)	water-reducing admixture (%)	short fiber (%)	redispersible polymer powder (%)	calcium aluminate admixtures quick hardening (%)	fixedchloride ion (%)	liquid plasticizer/ material ratio (%)
1	Control	271	621	1293	44	C×0.05	C×1.6	—	C×10	—	1.1
2	Improvement 1	265	607	1191	44	C×0.06	C×1.6	C×12	C×10	—	1.1
3	Improvement 2	271	621	1229	44	C×0.05	C×1.6	—	C×10	C×10	1.1
4	Improvement 3	263	601	1117	44	C×0.06	C×1.6	C×12	C×10	C×10	1.1

each material in accordance with JSCE-D 102, "Draft Quality Standard for Rapid Setting Agents for Shotcrete (Mortar) and JIS A 1147, "Concrete setting time test.

(3) Length change

Since the initial expansion and drying shrinkage of the materials were considered to have an effect on debonding and cracking, the test for restraint condition was conducted in accordance with JIS A 6202 "Restraint expansion and shrinkage test of expanded concrete". A specimen was taken by spraying the material downward onto a 40 mm x 40 mm x 160 mm formwork in which a restraint device was installed, and finishing with a surface trowel. The specimens were demolded at 1 hour of age, and after that cured in air-dried condition, and the rate of length change was measured with a dial gauge at 1, 3, 6 hours, 1, 3, 7, 14, 21, and 28 days of age.

3.2.2 *Preliminary test results and discussion*

The following are the test results and discussion.

(1) Fresh mortar property

Table 3 shows the results of air temperature, water temperature, mixing temperature, and flow at the time of testing. All of the mixing patterns satisfied the development performance target of a flow value of 160 mm or more.

(2) Setting time

Figure 5 Shows the results of tests using a proctor penetration resistance tester. Table 4 shows the initial and final setting time.

The polymer-added Improvement 1 and Improvement 3 showed open time of more than 15 minutes, which comply with the development performance target. This is thought to be due to retarding effect by the increased amount of water reducing agent in response to the reduced flowability caused by the addition of polymer. The results for the setting end time showed that Improvement 1 and Improvement 3 satisfied the development performance target.

(3) Length change

Figure 6 Shows the results of the length change test. All of the mix showed expansion behavior until around 1 day of age, which is considered to be caused by the hydration reaction of the hardened

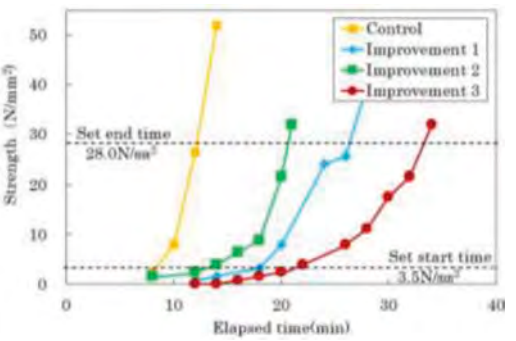

Figure 5. Results of the coagulation test.

Table 3. Test temperature and flow.

Product name	outside temperature (C)	water temperature (C)	material temperature (C)	flow value (mm)
Control	14.6	18.2	18.8	186
Improvement 1	15.4	17.5	17.9	185
Improvement 2	15.7	17.9	18.8	176
Improvement 3	14.8	17.6	18.9	178

Table 4. Starting and ending time.

Product name	time (min)	
	Set start	Set end
Control	8	12
Improvement 1	18	27
Improvement 2	13	20
Improvement 3	22	34

material. The smaller expansion of Improvement 2 and 3 with the addition of salt fixative at 1 day of age is considered to be due to the suppression of ettringite expansion by hydration shrinkage during hydrocalumite formation from the reaction between CA_2, the main component of the salt fixative, and cement hydrates as shown by Fukudome.(2014).

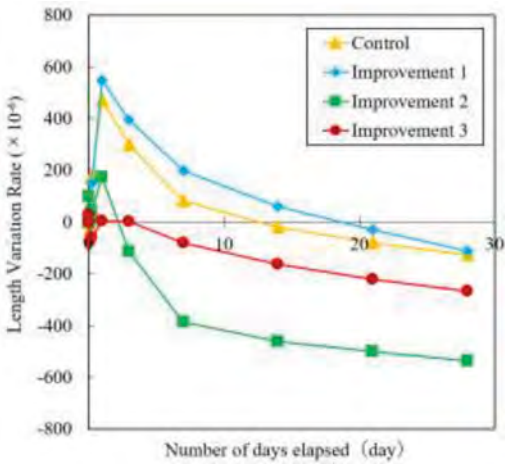

Figure 6. Length change (restraint, air-dry curing).

3.3 *Performance tests*

3.3.1 *Materials to be used*

Since the preliminary test results indicated that Improvement 3 was the material that met the performance requirements, the material used in the performance test was a polymer cement fiber mortar with a calcium aluminate admixture of rapid hardener and salt fixing material.

3.3.2 *Test methods*

To confirm the workability, adhesion, and durability of the developed product, tests were conducted using the following methods to evaluate its performance.

(1) Thickness of the sprayed material

Figure 7 Adhesion test (1 to 24 hours).

By increasing the maximum spraying thickness at the time of construction, it is possible to reduce the construction time and cost. To confirm the maximum thickness of the splayed material, a mortar plate (commercial product with dimensions of 70 mm x 70 mm x 20 mm) with a jig for adhesion test and a wooden frame with a φ60 mm opening shown in Figure 7 is installed on the ceiling surface. The test specimens were prepared by spraying the material upward and then pressing the surface with a trowel to measure the adhesion thickness and adhesion strength for each age of the material. The parameters were 60 mm/layer, 90 mm/layer, and 120 mm/layer, and three specimens were prepared at 1, 2, and 3 hours of age, respectively, to measure the adhesion strength. The curing condition before the measurement was air-drying.

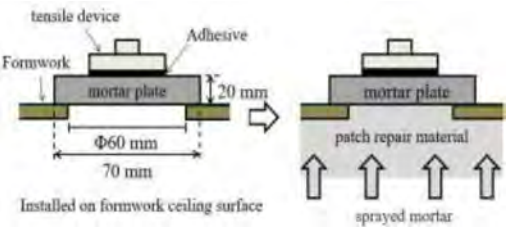

Figure 7. Adhesion test (1 to 24 hours of age).

(2) Workability

Cycle time and spraying volume per hour were measured to confirm the spraying speed, pump frequency, and discharge rate during installation. The sprayed area was 6.4 m^2 (3.2 m high × 2.0 m wide) and the thickness of splayed material was 120 mm. The first layer was 90 mm, the second layer was 30 mm, and the test was divided into two blocks, upper and lower, using a single pipe scaffold.

(3) Chloride penetration resistance

To evaluate the durability of the test specimens against chloride ions after construction, the material was sprayed downward onto a 40 mm x 40 mm x 160 mm formwork, and the surface was trowel-finished. The specimens were then cured in air-dried condition, and at 28 days of age, the specimens were immersed in seawater and the split sections were sprayed with a coloring reagent (0.1 mol/l silver nitrate solution). The depth of chloride ion penetration was measured at 7 locations each at 28, 56 and 91 days after immersion at 5 mm intervals on one side and the average value was used to evaluate the resistance to salt penetration.

(4) Apparent diffusion coefficient of chloride ion

Figure 8 Adhesion thickness test (sprayed thickness: 60, 90, 120 mm)

To evaluate the durability against chloride ions after construction, specimens were prepared as in the salt penetration resistance test and immersed in seawater after age of 28days for 10 months. The concentration of chloride ions in the depth direction was measured by EPMA for the immersed specimens,

and the apparent diffusion coefficient was determined to evaluate the long-term durability.

3.3.3 *Performance test results and discussion*
Test results and discussion are shown below.

(1) Thickness of the splayed material

Only the developed product was tested. Table 5 shows the fresh properties of the product at the time of testing, and Figure 8 shows the test results. The developed product showed high adhesion strength of more than 0.5 N/mm^2 under all conditions of the thickness of splayed material of 60, 90 and 120 mm and ages of 1, 2 and 3 hours.

The developed product can be sprayed upward with a maximum thickness of 120 mm and shows adhesion strength of 0.5 N/mm^2 or higher at an age of 1 hour, ensuring sufficient adhesion strength at the start of train operation on commercial lines.

Table 5. Fresh properties of developed products.

outside temperature	water temperature	temperature of mixed mortar	flow (JIS A 1171)	slump
(°C)	(°C)	(°C)	(mm)	(mm)
11.3	15.8	16.1	169	115

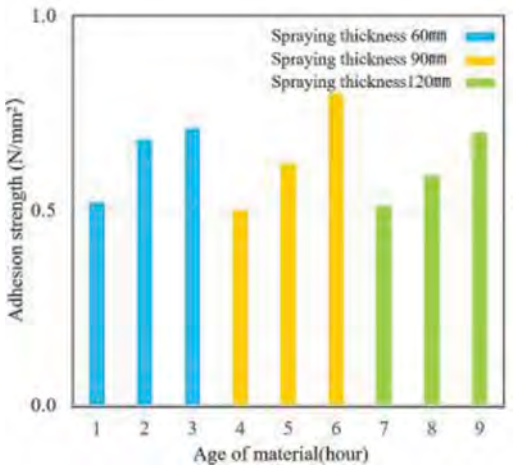

Figure 8. Adhesion thickness test (sprayed thickness: 60, 90, 120 mm).

(2) Workability

Only the developed product was tested. Table 6 shows the fresh properties during the test, Table 7 shows the test results, and Table 8 shows the cycle time. By setting the mixing temperature of the material at 15 to 20°C, the targeted spraying speed of 0.6 to 0.7 m^3/hour and the sprayed volume of 0.77 m^3 within the assumed working time of 90 minutes were confirmed. Figures 9 and 10 show the finished surface after the test, and a certain degree of smoothness was confirmed.

Under the restrictions of only 90 minutes of work time in the commercial railway construction, the developed product can secure a maximum spraying volume of 0.7 m^3/hour and a maximum spraying thickness of 120 mm, which is two to three times greater than the conventional product, enabling 70% reduction in the process related to conventional spraying work. As shown in Figure-11, the construction cost is expected to be reduced by approximately 30%. Specifically, the spraying process for two repair sites with a repair area of 18 m^2 (repair volume of 2.1 m^3) can be shortened from 21 days to 6 days. In addition, since there will be almost no material loss due to rebounding, there will be almost no impact such as scattering on the railways and overhead wires.

Table 6. Freshness of the developed.

outside temperature	water temperature	temperature of mixedmortar	flow (JIS A 1171)	slump
(°C)	(°C)	(°C)	(mm)	(mm)
15.2	22.9	18.7	144	110

Table 7. Results of workability test.

thickness	area	spraying volume	pump frequency	plasticizer-addition volume	spraying speed
(m)	(m^2)	(m^3)	(Hz)	(%)	(m^3/hr)
0.12	6.4	0.77	20	1layer;1.25 2layer;1.00	0.7

Table 8. Cycle time.

time (min)	Spraying		Trowel finish		setup change
0	1st layer lower start	19			
19	〃 finish				scaffolding3
22	1st layer upper start	28			
50	〃 finish				
52	2nd layer upper start ～	10	upper level start ～	19	
60	〃 finish		〃 finish		
71					scaffolding1
72	2nd layer lower start ～	12	lower level start ～	12	
84	〃 finish		〃 finish		
87					total87min

Figure 9. Surface finish after spraying (Upper level).

Figure 10. Surface finish after spraying (Lower level).

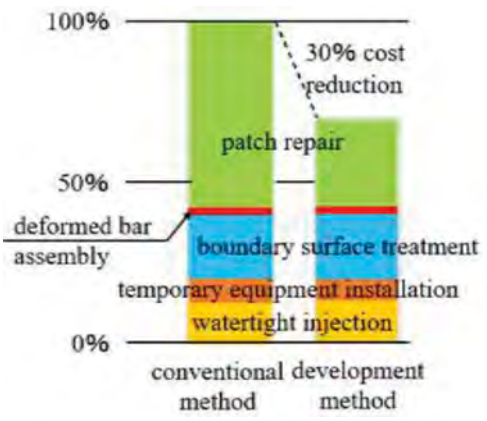

Figure 11. Estimated reduction in construction cost.

(3) Chloride penetration resistance

Table 9 shows the mix of concrete used as a comparison sample (28days of age, The curing condition before the measurement was air-drying) and both conventional and developed products were tested, and the test results are shown in Figure 12. After 91 days of immersion in seawater, the depth of chloride ion penetration of the concrete was 13.4 mm, while that of the conventional product was 1.8 mm and that of the developed product was 1.9 mm. When the chloride ion penetration depth of concrete is considered to be 100%, both the conventional and developed products reduced the penetration of chloride ions by 86%. The developed product showed the same resistance to chloride penetration as the conventional product due to its ability to immobilize soluble chloride ions, as Friedel's salt by the reaction of CA_2, the main component of the salt fixative, with cement hydrate.

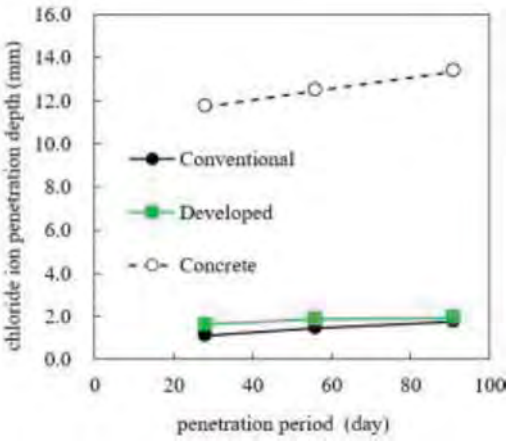

Figure 12. Chloride Ion Penetration Depth Test Results.

(4) Apparent diffusion coefficient of chloride ion

Figures 13 and 14 show the results of EPMA measurements of the chloride ion concentration in the depth direction for the conventional and developed products, and Table 9 shows the analysis results. The developed product showed almost the same performance as the conventional product.

In general, the apparent diffusion coefficient of chloride ions is said to be 5.8 cm^2/year for concrete

Table 9. Concrete mix.

			Unit quantity (kg/m^3)			
cement type	Slump (cm)	water-cement ratio (%)	water W	cement C	sand aggregate S	gravel aggregate G
OPC	12	55	164	299	859	979

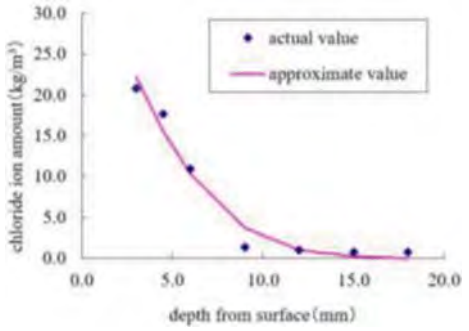

Figure 13. Chloride ion content in depth direction by EPMA (Conventional product).

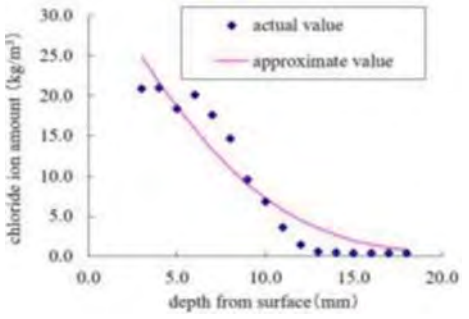

Figure 14. Chloride ion content in depth direction by EPMA (Developed product).

Table 10. Analysis results.

	Apparent diffusion coefficient of chloride ions
Conventional	0.37cm^2/year
Developed	0.36cm^2/year

using ordinary cement and 1.4 cm^2/year for concrete using blast furnace slag as shown by Japan Cement Association.(2008). The measured values are low, ranging from 0.36 to 0.37 cm^2/year for both conventional and developed products, showing high salt barrier properties. The measured values are low at 0.36 to 0.37 cm^2/year for both the conventional and developed products.

4 CONCLUSIONS

Table 11shows the performance of the conventional method and the required performance of the newly developed method as well as the actual performance. A new patch repair method was developed for concrete tunnels deteriorated by salt damage in commercial urban railroad tunnels by taking into consideration construction constraints and the service environment after repair. As a result, the following findings were obtained.

1) A new two-material shot method was developed, in which a reinforced polymer cement fiber mortar is mixed with a calcium aluminate admixture, a rapid hardener and a salt fixative, and a liquid accelerator is added before the nozzle of the shotcrete equipment.

2) Tests were conducted on the workability of the sprayed polymer mortar, and it was confirmed that workability has been improved and construction costs significantly reduced by adjusting fresh properties such as mortar flow and mixing temperature, the amount of plasticizer added, spraying speed, and discharge rate.

3) Adhesion tests of the sprayed polymer mortar were conducted, and it was confirmed that the adhesion strength of the sprayed material and the sprayed thickness at a young age qualified the required performance by optimizing polymer and calcium aluminate admixtures amount in the mortar, amount of liquid accelerator and the spraying speed and discharge rate of the spraying equipment.

Table 11. Comparison of performance between conventional method and developed method.

Test Items	Conventional method	Developed method	
		Performance Requirements	Actual Performance
【Construction performance】			
・ Flow value (JIS R 5201)	147mm	160mm or more	178mm
・ Set start time	48 min	More than 15 min	22min
・ Set end time	55 min	45 min or less	34min
・ Spraying speed	0.2~0.3m^3/hour	0.6~0.7m^3/hour	0.7m^3/hour
【Adhesion performance】			
・ Spraying thickness (Upward・ Sideways)	20mm・ 40mm	100mm·100mm	120mm·120mm
・ Adhesion strength (Age of material 1hour,)	0.2N/mm^2	0.2~0.5N/mm^2	0.5N/mm^2
【Durability】			
・ Chloride Ion Penetration Depth	1.8mm	1.8mm	1.9mm
・ Apparent diffusion coefficient of chloride ions	0.37cm^2/year	0.37cm^2/year	0.36cm^2/year

4) Tests were conducted on the durability of the sprayed polymer mortar, and the depth of chloride ion penetration and the apparent diffusion coefficient of chloride ions were evaluated, and it was confirmed that the performance of the developed product was equivalent to that of the conventional product with high salt barrier performance.

REFERENCES

Fukudome Y: Fundamental Study on Salt Penetration Characteristics of Concrete Mixed with CaO and $2Al_2O_3$, Doctoral Thesis, Kagoshima University, 2014.3

Hirama A, Fukui K, Kawabata Y, Yamagishi T: Development and deployment of surface coating construction method for urban railroad culvert tunnels, Concrete Engineering, Vol.54, No.2, pp.149–155, 2016.2

Japan Cement Association: Report of Concrete Technical Committee, Study on Durability of Concrete with Various Cements, 2008. 3

Ueda H, Mizuno K, Uehara M, Iijima T, Tamai Y: Durability Evaluation of Reinforced Concrete Structure Salt Damage Control Method Using Chloride Ion Adsorbent, Railway Technical Research Institute Report (RTRI REPORT), Vol.26, No.12, pp11–16, 2012.9

Tunnelling for a Better Life – Yan, Celestino, Thewes & Eberhardt (Eds)
© 2024 The Author(s), ISBN 978-1-032-80042-4
Open Access: www.taylorfrancis.com, CC BY-NC-ND 4.0 license

Ventilation for a long underground road tunnel system from a modern perspective

Tsz Kin Lam*
COWI A/S, Kongens Lyngby, Denmark

Ertan Hataysal
COWI UK, London, UK

ABSTRACT: Long road tunnels are becoming a preferred option for the cities to expand the public realm. Therefore, an increasing number of long underground road tunnel systems have been planned and constructed in recent years, with some spanning a length of 10km or more. Such lengths was an issue for the tunnel ventilation system in the past due to the excessive requirements. Nevertheless, the modern vehicle fleet structure includes cleaner engines and electric vehicles which have reshaped the situation recently. This paper discussed the trend of ventilation in long road tunnels from a modern perspective. It covered the transition of ventilation strategy from old to new long road tunnels. It addressed the fundamental principle of ventilating long road tunnels for normal and fire operations and how the tunnel ventilation system has switched from a pollutant driven system to a smoke driven one. The discussion was exemplified on a 10 km long underground road tunnel system for which is a live project in Scandinavia. It included design considerations in pollutant and smoke control; also presented technical challenges in handling airflow in approach ramps.

Keywords: Long tunnels, Tunnel ventilation, Pollutant control, Smoke control

1 INTRODUCTION

For decades, it has been well understood that ventilating a long road tunnel is challenging. Ventilation plays a crucial role in the design of tunnels, requiring a special focus. It affects the tunnel's cross section as it consumes space for air ducts and equipment. It can even affect the profile by incorporating ventilation shafts throughout the tunnel. Therefore, the cost of a tunnel ventilation system is far more than the cost of the mechanical and electrical equipment alone. In reality, it is a huge add-on on top of the cost of the tunnel structure. Nevertheless, the tunnel ventilation system must remain in place to maintain the operational safety and perform during critical incidents.

The main challenge of ventilating long road tunnels was to remove pollutants effectively. The pollutant concentration increases along the tunnel, and it peaks towards the exit portal. This stimulates an increase in the design velocity during normal operation. Which means larger equipment, technical spaces even larger tunnel cross-section.

Today, the vehicle engines are getting cleaner, even there is a trend in replacing the internal combustion engine (ICE) vehicles by the electric ones. It relieves the pressure from the tunnel ventilation system by diluting the in-tunnel pollutants. Some long-span road tunnels which may have seemed impossible in the past have now become more practical and feasible. Now, there are some live road tunnel projects in Scandinavia with overall length of over 10km.

This paper will start with the traditional approach on ventilating long road tunnels. It will discuss how pollutants drive the ventilation system by starting from the basic principles, the characteristics of the predominant ventilation systems and the transition to the modern approaches.

This paper will then provide the details of the transition by the help of quantitative figures on vehicle emissions, and address the consequences on the tunnel ventilation system.

Finally, a future 10km long road tunnel system in Scandinavia will be used as an example to demonstrate the ventilation design in a modern urban example. The challenges about smoke management within this complex tunnel will also be covered.

*Corresponding author: tklm@cowi.com

DOI: 10.1201/9781003495505-450

2 PAST PERSPECTIVE

2.1 *Pollutant driven ventilation systems*

A tunnel ventilation system in a road tunnel primarily serves for two purposes, smoke control and pollutant dilution.

In controlling the smoke, the system is basically dictated by the fire size in the tunnel. The fire size is constant regardless of the length of the tunnel. In a long tunnel, the travel distance of the smoke is also an important issue to be considered.

During daily operation, the vehicle generated pollutants build up in the tunnel. The level of pollutant concentration is directly proportional to both the number of vehicles present in the tunnel and the overall length of the tunnel. Despite the pollutant generation rate varying with changing gradients along the tunnel, the relationship between the pollutant levels can still be simplified and represented by a linear correlation, Figure 1. As the acceptable pollutant level is constant along the tunnel, it becomes more challenging to keep that below the threshold for longer tunnels, especially towards the end.

In the past, the vehicle engine exhausts were worse, which are presented with a steeper line in Figure 1. This was a limiting factor for the tunnel length. Although the distance could extend the length, it would come at a cost such as an interim shaft (if possible) and/or a large ventilation duct.

The smoke control in a fire event was easier to resolve comparing to the dilution of pollutants. Therefore, the ventilation designs were mainly pollutant driven.

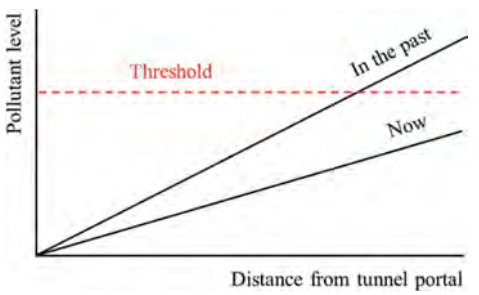

Figure 1. Pollutant levels along a road tunnel.

2.2 *Predominant ventilation strategies*

The vehicle movement in a tunnel generates piston effect and this effect will draw in ambient air from tunnel portals and/or ventilation shafts which helps to dilute the pollutants. If the amount of ambient air drawn is sufficient to dilute the pollutants, the tunnel is self-ventilated.

At the time when the vehicle emissions were high in pollutant concentration, this ideal situation was happening rarely. Therefore, a mechanical ventilation system was required to constantly supply supplementary fresh air from the ambient to lower the in-tunnel pollutant concentration levels. This was comprising a large portion of the operation cost of a road tunnel.

Longitudinal ventilation which only draws ambient air in from tunnel inlet portals was also not feasible for most of the long road tunnels in urban areas. The pollutant concentrations increase linearly towards the exit portal and could easily exceed the threshold value. Therefore, it was required to utilize other ventilation schemes such as fully transverse and semi-transverse as illustrated in Figure 2. These schemes enable introducing fresh air into the system more effectively, as well as reducing the pollution concentrations along the tunnel simultaneously by removing the polluted air from the system.

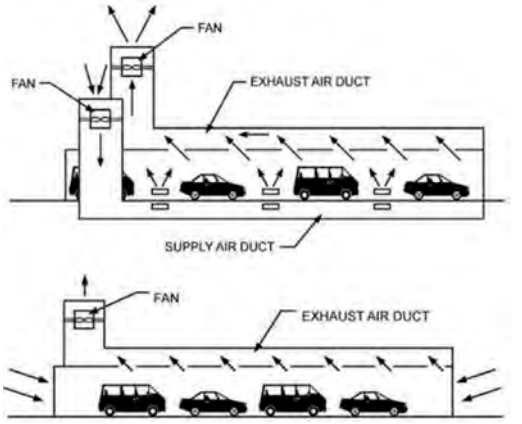

Figure 2. Schematic of fully-transverse (top) and semi-transverse (bottom) tunnel ventilation systems (ASHRAE, 2007).

These schemes require additional ventilation shafts and equipment. It is not always possible to put the ventilation shafts right to the point where the fresh air is supplied from. It depends on geological conditions and other factors. Surely it is easier to place a shaft on land instead of the seabed. Having a ventilation shaft in the middle of the sea can still be achievable; e.g., Hugh L. Carey Tunnel and Tokyo Aqua Line Tunnel. However, it comes at a significant cost.

The air ducts can take up a decent amount of space in a road tunnel. They practically require at least an additional 20% of the tunnel cross section. For long tunnels, the air duct can be even bigger to compensate the huge pressure loss along the ducts due to the long travel distance for the air.

In some tunnels, air purification systems can also be utilized as a pollutant management system alongside with the tunnel ventilation system. The air purification system can also serve as a control measure on the pollutants discharged to the ambient from a tunnel, but this approach involves significant equipment and infrastructure investment.

3 MODERN PERSPECTIVE

3.1 *Cleaner vehicles*

Today, road vehicles are progressively getting cleaner. The European Union (EU) started regulating the vehicle emissions in 1992 by setting up the European emission standards. The standards are staged as legal frameworks applied to all new selling vehicles in EU and they are categorized from EURO 1 to EURO 6. Many countries have already harmonised their legislations in accordance with the EU regulations.

Recently, EU has targeted to ban all new selling ICE vehicles by 2035 and it has been seconded by many countries including the United States and China.

These changes are favourable for longer road tunnels. Improving the vehicle pollutant discharge reduces the emission rates in the tunnels significantly as shown in Figure 1. This enables extending the physical length of a tunnel without exceeding the pollutant concentration threshold.

3.2 *Pollutant emission*

The pollutant emissions from new vehicles are much lower compared to the ones manufactured 20 years ago. World Road Association (PIARC) have a series of publications (PIARC, 1995, 2004, 2012 & 2019) which document a methodology and database to calculate the pollutant levels in road tunnels. Figure 3 shows the trend of the pollutant generation rate from EURO 1 to EURO 6 engines.

Electric vehicles can further lower the emission figures in the tunnels. Even though these vehicles are often considered as zero emission vehicles, non-exhaust pollutants such as particular matter (PM) are still generated by these vehicles. Therefore, ventilation is still required to control this type of pollutants in tunnels.

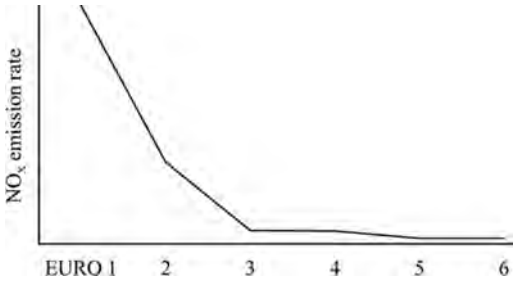

Figure 3. Reduction of NO_x generation rate of gasoline passenger cars from EURO 1 to EURO 6 engines at zero gradient (PIARC, 2019).

3.3 *Fire driven ventilation systems*

The introduction of cleaner vehicles has significantly reduced the levels of pollutants in tunnels. As a result, the ventilation systems in long road tunnels have undergone a transformation and moved away from being a primarily pollutant-driven system.

The changes have shifted the focus on pollutant control and the interventions during a fire incident have become predominant in defining the characteristics of a tunnel ventilation system. The fire incident, being a localized event, is independent from the length of the tunnel; therefore, this removed the key challenges in ventilating the long tunnel sections.

4 CASE: A NEW SCANDINAVIAN ROAD TUNNEL SYSTEM

In recent years, there are a number of long road tunnels planned in Scandinavia. The most significant one is the 18km long Fehmarnbelt tunnel connecting Denmark and Germany. A new road tunnel system has also planned to route the traffic around the city centre in one of the Scandinavian capitals. The tunnel system consists of a 10km long main tunnel and associated ramps along the main tunnel. The overview of the system is presented in Figure 4. This system will be used as a current example case to show how the ventilation system design shifted due to the change in the vehicle fleet.

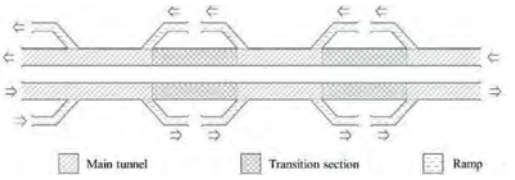

Figure 4. Overview of the new Scandinavian road tunnel system.

4.1 *Baseline ventilation scheme*

The baseline ventilation scheme is longitudinal ventilation using jet fans. It is in general the most cost-effective scheme as it eliminates the ventilation shafts, headhouses and air ducts. In the conceptual design stage, this scheme has been proven to be a robust scheme without any major issues.

4.2 *Pollutant control*

The pollutant analysis in the tunnel reaffirmed the fact that the pollutant control is a lower tier concern in road tunnels nowadays even for long tunnels. By the design year 2035, 46% of passenger cars will be electric and the removal of old ICEs has pushed the in-tunnel pollutant levels far below the threshold.

Nevertheless, the intervention from the tunnel ventilation system is still required in congested traffic scenarios. The critical pollutant has switched from NO_2 to PM which is driven by the cleaner vehicles, as shown in Figure 7. The lowest self-ventilation traffic speed has been reduced from 30km/h to 10km/h in this Scandinavian tunnel.

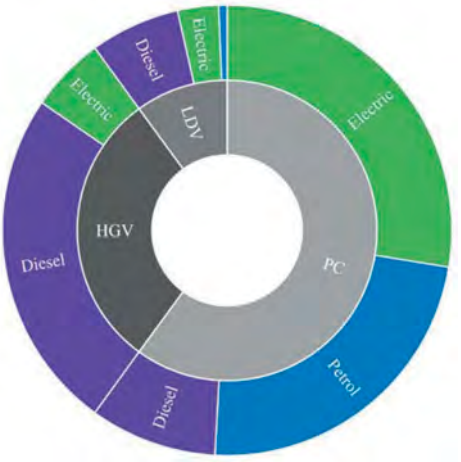

Figure 5. Estimated traffic fleet for the Scandinavian tunnel.

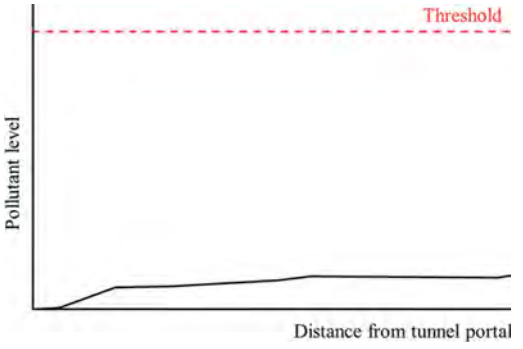

Figure 6. Estimated NO_2 pollutant level in the tunnel at 60km/h.

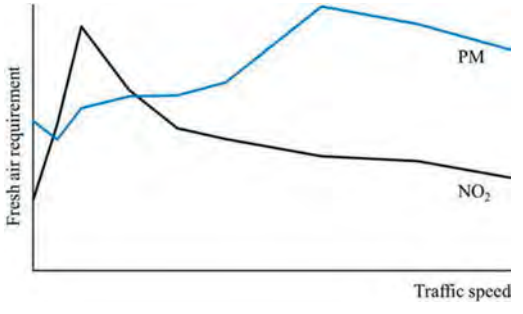

Figure 7. Fresh air requirement to dilute NO_2 and PM in the tunnel at different traffic speeds.

4.3 *Smoke management*

For this tunnel, the ventilation system is completely fire driven. The number of jet fans required to ventilate a tunnel fire is up to three times of that required to ventilate the pollutants generated during normal operation. These figures are given for a critical tunnel section.

The average air velocity is maintained above the critical velocity during a fire incident and it is used as the strategy of smoke management in this Scandinavian tunnel. The tunnel is not a straight single tube, but it is a complex underground tunnel network due to the presence of several ramps spread along the main tunnel. This creates some challenges in applying the longitudinal ventilation scheme in particular in the vicinity of the ramps.

4.3.1 *Short-circuit and recirculation through ramps*

The ramps are approximately 200m in length and the shortest main tunnel section is 2.5km. It is inevitable that some percentage of the air will move in and out of the tunnel network through the ramps rather than following the main air stream within the tunnel. This way the tunnel main airflow short-circuits through the ramps.

In normal operation, the impact of the short-circuit is minimal. Firstly, the fresh air requirements to dilute pollutants is low due to the cleaner vehicles. Secondly, the tunnel air movement is driven by the piston effect from the vehicles. Most of the traffic is in the main tunnel and sufficient air can be maintained to dilute the pollutants. The problem only occurs when the traffic speed reduces and so as the piston effect. The portal winds start to dominate the airflow in the ramps.

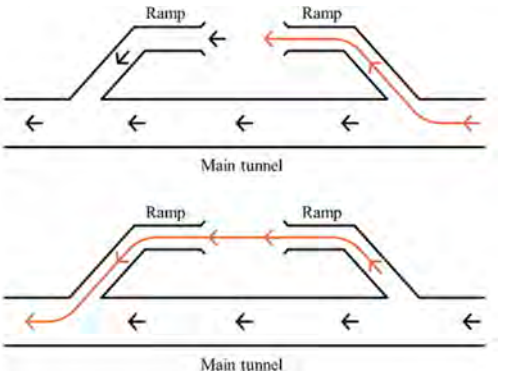

Figure 8. Short-circuit (top) and recirculation (bottom) through ramps and their air path are illustrated in orange arrows.

The airflow short-circuit has a more significant impact on the smoke control within the tunnel. In contrast to a conventional longitudinally ventilated tunnel where smoke is discharged solely through the tunnel portal, the ventilation design in this tunnel should consider whether the smoke goes through the main tunnel or ramps (or both).

The close proximity of the ramps presents an issue where the smoke discharged from one ramp may recirculate back into the tunnel through an adjacent ramp. This creates a potential challenge in maintaining robust smoke ventilation within the tunnel.

4.3.2 *Spatial constraints*

The junction points are located where a two-lane wide main tunnel tube and a one-lane wide ramp connection come together. These junctions facilitate connections to the main tunnel traffic flow. The most challenging part for emergency ventilation is at the transition sections, which are the tunnel stretches located between two junctions. There are a number of these transitions along the main tunnel and they are relatively short in length.

During a fire at a transition section, the short-circuit in ramps is an important issue, since significant amount of the airflow is leaked through the ramps. This results in poor ventilation performance in these sections.

The ventilation scheme in these sections is designed in two steps to overcome the short-circuit issue and remove the smoke in a controlled way.

The first step is to utilise the jet fans in the main tunnel and the ramp sections. This is to adjust the balance between different sections, as shown in Figure 9.

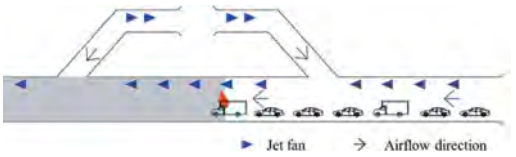

Figure 9. Ventilation scheme to compensate the short-circuit in ramps.

The second step is to optimize the number of jet fans in the transition sections and ramps. This will help boosting the airflow in the transition section. Further, it will improve the system resilience against portal winds in ramps. However, due to spatial constraints only limited number of jet fans can be installed at a certain transition section.

The spatial constraints can be expressed in two dimensions, the tunnel longitudinal span and the tunnel width.

There is a minimum separation between jet fans along the tunnel. The efficiency of jet fan banks will be reduced if they are placed too close to each other. At the transition sections, the distance between jet fans has been lowered to 70m to fit more jet fans whilst keeping the system efficiency at a similar level.

The tunnel width dictates the number of jet fans that can be installed at each location. This dimension is fixed as it is determined by the number of traffic lanes and emergency walkways. The space for jet fans is especially limited in ramps as these only have one-lane traffic. The whole width of the cross section must be occupied to install jet fans at the same location to achieve the necessary thrust. It is also not possible to install more jet fans longitudinally as the ramps are short and there is a need to account for redundancy during a fire event.

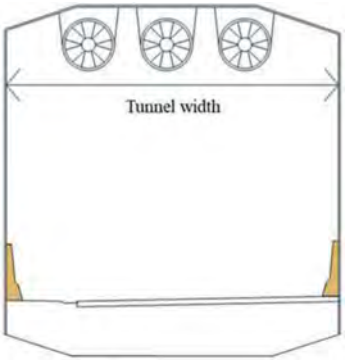

Figure 10. Spatial constraint of jet fans in a single lane tunnel cross section.

4.3.3 *Asset protection*

Depending on the ventilation operation, the smoke can occupy the entirety of the downstream of the fire. Alternatively, it can be discharged through the nearest ramp(s) and the rest of the tunnel can be kept smoke free. These are both shown in Figure 11.

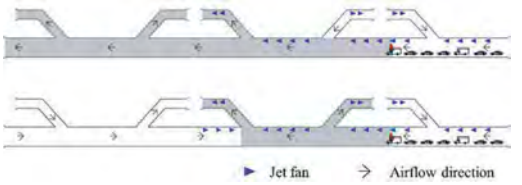

Figure 11. Schematics of two different ventilation approaches and tunnel sections occupied by smoke are coloured in grey.

From an asset protection perspective, it is beneficial to discharge smoke out of the tunnel as soon as possible. In this Scandinavian tunnel, the ramps can be used as a shortcut for smoke discharge and prevent transporting smoke all the way down to the tunnel exit portal. Even though tunnel installations and equipment are fire-rated, insurance and warranty coverage may still be triggered if these equipment have been exposed to fire and smoke. For a long tunnel, this has a serious cost implications considering the amount of equipment.

5 OTHER VENTILATION DESIGN ASPECTS

5.1 *Heat*

Heat build-up can also be an issue in long tunnels, which can be caused by various factors such as vehicles, equipment, metrological and geological conditions. Therefore, it should be looked at and considered in the design of these systems. For example, Yamate Tunnel in Tokyo utilizes a water mist system to bring down the temperature during normal operation.

5.2 *Traffic fleet*

Modern tunnel ventilation designs increasingly align with the progressive agenda of replacing ICE vehicles, particularly in long tunnels. However, some countries already stepping back from their plans.

Electric, hydrogen, and other alternative-powered vehicles are still an emerging research field, making it difficult to predict future issues that may currently go unnoticed. These systems will evolve alongside the changing fleet structure and adapt to ensure a comfortable and safe experience for users.

Therefore, it is important to take into account the recent updates in the traffic fleet and update the emerging risks accordingly.

6 CONCLUSIONS

Due to recent advancements in vehicle technology, the tunnel ventilation systems in long road tunnels have transitioned from a pollutant-driven system to a fire-driven system. This shift is primarily attributed to the widespread use of cleaner vehicles in recent years.

The smoke ventilation is still challenging though; especially, in the long and complex urban road tunnel setup. These tunnels can include networks of ramps connecting to other road systems. In order to create an efficient smoke ventilation system, several key factors need to be taken into consideration such as flow short-circuiting, spatial constraints and heat build-up. It is also key to develop strategies which consider the protection of the assets in long tunnels.

Finally, it is important to ensure that the tunnel ventilation system kept up to date in parallel with the evolving traffic fleet composition. This proactive approach can help alleviate the strain on the systems, leading to safer and more efficient operations.

REFERENCES

ASHRAE, 2007. ASHRAE Handbook - HVAC Applications

PIARC, 1995. Vehicle Emissions Air Demand Environment Longitudinal Ventilation.

PIARC, 2016, Road Tunnels: Complex Underground Road Networks.

PIARC, 2019, 2012 & 2004. Road Tunnels: Vehicle Emissions and Air Demand for Ventilation.

Raza, H., Bilson, M., Li, S. 2022. Analysis of fire-life safety with battery electric vehicles in highway tunnels, Proceedings of the 19th International Symposium on Aerodynamics, Ventilation & Fire in Tunnels, Brighton, UK, pp. 762–776.

Tunnelling for a Better Life – Yan, Celestino, Thewes & Eberhardt (Eds)
© 2024 The Author(s), ISBN 978-1-032-80042-4
Open Access: www.taylorfrancis.com, CC BY-NC-ND 4.0 license

Study on fire smoke exhaust strategy in daliangshan no.1 super-long expressway tunnel*

Fuan Lan, Haiyun Zou & Lingshen Wu
Sichuan Lexi Expressway Co., Ltd, Leshan, China

Yong Wang & Yandan Deng
China Railway Academy Co., Ltd., Chengdu, China

ABSTRACT: Based on the control project of Leshan-Xichang Expressway in Sichuan Province, this paper focuses on the study of the fire smoke exhaust strategy for the Daliangshan No. 1 Tunnel. To address the issues caused by long smoke exhaust distances and inadequate smoke exhaust efficiency at both ends of a single inclined shaft tunnel, such as the rapid spread of smoke and a wide range of hazards, a new fire smoke exhaust mode was studied and designed. Based on this new mode, a civil engineering model for fire smoke exhaust in tunnels was developed, and the smoke exhaust efficiency of this model was predicted and analyzed. Different fire scenarios at various locations within the tunnel were considered, and a one-dimensional analysis approach was used to predict and compare the smoke exhaust efficiency under different strategies. The prediction results of the fire smoke exhaust model efficiency indicate the following: In the original model, certain fire scenarios could not be effectively controlled due to insufficient upstream air flow velocity and downstream smoke exhaust capacity. Smoke stratification and backflow could affect vehicles and personnel upstream of the fire. For fire incidents near the inclined shaft, the original model allowed smoke exhaust through the inclined shaft, which proved to be more efficient compared to using the nearest vehicle cross passage for smoke exhaust. After optimization, the civil smoke exhaust duct featured a cross-sectional area of 9.9 m^2. The smoke exhaust capacity from the smoke outlet above of individual vehicle cross passages was increased, ensuring that any single vehicle cross passage could meet the requirements for fire smoke exhaust. By utilizing the smoke exhaust route downstream, which was closest to the fire location, along with longitudinal smoke induction, it was possible to effectively exhaust all smoke and prevent its diffusion from affecting vehicles upstream and downstream of the fire.

Keywords: fire smoke exhaust strategy, extra-long highway tunnel, single inclined shaft, parallel adit, prediction and analysis

1 INTRODUCTION

In recent years, there has been a rapid development in the construction of extra-long highway tunnels, with increasing scale, providing significant transportation convenience. However, due to the structural characteristics of these tunnels, which resemble narrow and elongated pipes, the risks and safety concerns associated with tunnel fires have become more prominent. To ensure the safety of personnel inside tunnels and to safeguard the socioeconomic aspects, the fire smoke exhaust system has been recognized as a vital component of extra-long highway tunnels. Extensive research has been conducted and the resulting findings have been actively implemented in practice.

In the existing extra-long highway tunnels in China, various ventilation and smoke exhaust schemes are implemented based on factors such as topography, geology, meteorology, and natural environment. The main modes adopted for ventilation and smoke exhaust are longitudinal smoke exhaust, transverse and semi-transverse smoke exhaust, as well as centralized smoke exhaust. Domestic and international scholars have conducted extensive research on different ventilation and smoke exhaust modes. For example, based on the Qinling Zhongnanshan Tunnel, Yu Li, Wang

*Corresponding author: 1294647485qq.com

DOI: 10.1201/9781003495505-451

Mingnian, et al(2009). employed a three-shaft segmented longitudinal ventilation mode. In addition, in the context of a twin-tube unidirectional tunnel, they established, for the first time, ventilation control strategies for tunnels with cross passages in the event of a fire. They also proposed ventilation control benchmarks at different fire locations for tunnels with multiple shafts. Based on the Erlangshan Tunnel, Liu Tong, et al(2006). proposed, for the first time, the use of parallel adits for semi-transverse air supply in a single-tube bi-directional tunnel. This approach was introduced to achieve network ventilation in situations where it is challenging to implement smoke exhaust solely through longitudinal ventilation due to the absence of inclined shafts. Based on the Yunshan Tunnel, Jia Jilin et al(2014). analyzed energy consumption under different angles between the inclined shaft and the main tunnel. They obtained the relationship between ventilation resistance along the tunnel and the inclination angle of the inclined shaft. Zhang Jinglong et al(2012). studied the impact of the angle of ventilation cross passages on the twin-tube complementary ventilation system. Xia Fengyong et al(2014). proposed ventilation modes that can be used in uphill tunnels with varying traffic volumes. Academician Wang Mengshu(2015) also proposed that tunnels with a length of less than 6 km do not necessarily require ventilation shafts or inclined shafts. Based on the Huangjiaoping Tunnel, Xu Baiyang, Liang Shicheng, et al.(2021), developed three smoke exhaust schemes and corresponding smoke exhaust duct structures for extra-long highway tunnels. They analyzed the impact of different smoke exhaust schemes and exhaust duct structures on smoke exhaust efficiency. Ingason et al.(2011) conducted research on single-point and two-point vacuum ventilation systems as well as their effectiveness in controlling tunnel fires and smoke flow. Xu Haozhuo et al., using an orthogonal experimental design, studied the impact of the spacing between smoke outlets and the smoke exhaust rate on the smoke exhaust efficiency of centralized smoke exhaust.

The aforementioned research work demonstrates that investigating suitable smoke exhaust schemes and exhaust duct structures for different extra-long highway tunnels is not only a challenging task but also a crucial aspect of successful tunnel construction and operation.

Based on the engineering project of the Daliangshan No. 1 Tunnel, which is an extra-long highway tunnel with a total length of 15.3 km, and with reference to the ventilation shaft setting as described in Section 4.1.5 of Guidelines for Design of Ventilation of Highway Tunnels (JTGT-D70-2-02-2014), it is typically recommended to have 2 or 3 ventilation shafts for tunnels with lengths between 12000 m and 16000 m. However, due to the unique geographical location of this project, only one combined air supply and exhaust inclined shaft can be accommodated. After analyzing various fire smoke exhaust modes, it was found that the commonly used modes cannot meet the requirements of this project. In response to the challenge of smoke exhaust in the extra-long highway tunnel where only one ventilation shaft can be accommodated, a new smoke exhaust mode was studied and designed in this paper. Based on this fire smoke exhaust mode, smoke exhaust efficiency prediction and comparative analysis of various fire smoke exhaust strategies were conducted. This enables the identification of the optimal tunnel fire smoke exhaust strategy and provides auxiliary references for evacuation rescue and automatic control system schemes.

2 PROJECT OVERVIEW

2.1 *Project scale and overall layout*

The Daliangshan No. 1 Tunnel, a control project of the Leshan-Xichang Expressway in Sichuan Province, features a main tunnel length of approximately 15.3 km. The cross-sectional area of the tunnel for each direction is 68 m^2. The tunnel is designed according to the standards of a twin-tube, single-direction, four-lane highway, with a design speed of 80 km/h. The tunnel is located within the Mamize Provincial Nature Reserve and can only accommodate one combined air supply and exhaust inclined shaft. It is divided into two sections, with lengths of "9+6.3" kilometers, forming a ventilation tunnel. To address the issues caused by long smoke exhaust distances and inadequate smoke exhaust efficiency at both ends of a single inclined shaft tunnel, such as the rapid spread of smoke and a wide range of hazards, it is proposed to adopt a section layout of "left main tunnel - run-through parallel adit - right main tunnel" based on the new fire smoke exhaust mode and design the main model for tunnel ventilation and smoke exhaust accordingly.

Figure 1 shows the main model of the tunnel designed based on the new smoke exhaust mode. The tunnel model includes a run-through parallel adit, the left main tunnel, and the right main tunnel. Between the run-through parallel adit and the main tunnels, there are a total of 16 vehicle cross passages and two multi-functional traffic transition zones (approximately 800 m spacing between adjacent passages, the distance between the vehicle cross passages and the multi-functional traffic transition zones is also 800 meters). Besides, there are 4 cross passages for fresh air supply (with an area of 27 m^2). The space above the run-through parallel adit and the vehicle cross passages is allocated for the tunnel fire smoke exhaust ducts (with an area of 7.1 m^2). The smoke exhaust ducts above the run-through parallel adit and the single inclined shaft are interconnected. Ventilator rooms and related ventilation equipment are installed at the entrances and exits of both ends of the inclined shaft and the parallel adit to ensure effective

ventilation and smoke exhaust in the tunnel. Additionally, two multi-functional traffic transition zones are dividing the tunnel into three sections ("4687 m + 5050 m + 5543 m"). In the event of an accident or maintenance work in one section, it is possible to maintain the traffic capacity of the remaining sections by diverting vehicles through alternative routes.

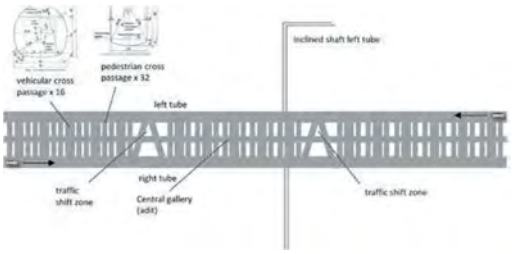

Figure 1. Tunnel plan.

2.2 *Tunnel ventilation system*

The new smoke exhaust mode is based on a combined fire smoke extraction strategy, which combines longitudinal induced smoke exhaust and single-point concentrated smoke exhaust. It aims to control the stratification and diffusion of smoke while efficiently directing the smoke generated by the fire through 1 to 2 designated smoke exhaust ducts for centralized removal. This helps to prevent the impact of fire smoke on vehicles upstream and downstream of the fire.

There are three main smoke exhaust strategies used in the tunnel, including:

1) Utilizing jet fans in the main tunnel to longitudinally induce smoke exhaust and to prevent smoke layer re-circulation and spread.
2) Utilizing the inclined shaft and its associated ventilation equipment to exhaust the smoke generated by tunnel fires to the outside.
3) Utilizing the run-through parallel adit, inclined shaft, and smoke exhaust ducts above the vehicle cross passages, as well as their related ventilation equipment to centralize smoke exhaust and direct the smoke generated by tunnel fire to the outside.

The specific strategy is depicted in Figure 2.

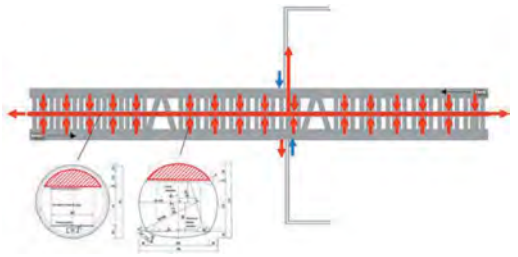

Figure 2. Smoke exhaust path.

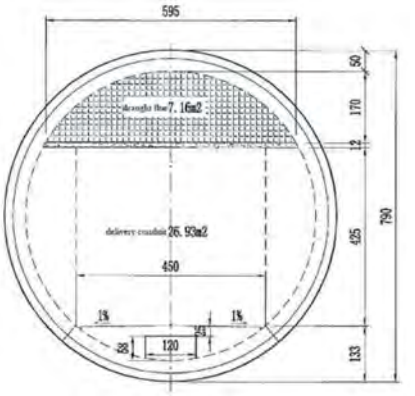

Figure 3. Cross section of parallel pilot tunnel.

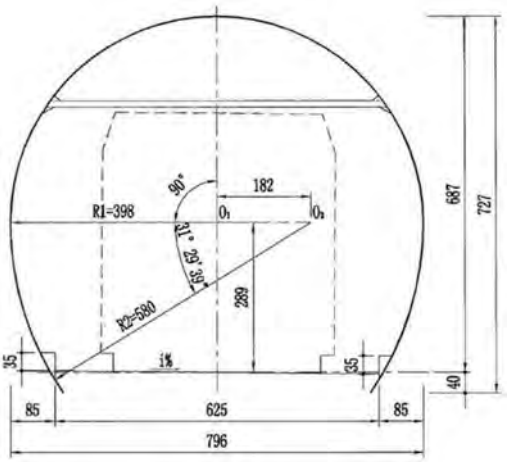

Figure 4. Cross section of vehicular cross passage.

Considering the elongated nature of extra-long highway tunnels, to achieve effective smoke exhaust in the event of tunnel fires, a combined fire smoke exhaust strategy of "inclined shaft + run-through parallel adit" was adopted for fires occurring at different locations within the tunnel. Prediction and analysis were conducted specifically for this strategy.

3 PREDICTION METHOD AND RESULT ANALYSIS

3.1 *Prediction and analysis of fire smoke exhaust efficiency*

This paper is based on the structural model of the Daliangshan No.1 Tunnel. A one-dimensional analysis method, along with the continuity equation, momentum equation (Navier-Stokes equation), and energy equation, was applied to predict and compare

the smoke exhaust efficiency under different fire smoke exhaust strategies for fire scenarios at different locations within the tunnel.

Continuity Equation:

$$\frac{\partial \rho}{\partial t}+\frac{\partial(\rho u)}{\partial x}+\frac{\partial(\rho v)}{\partial y}+\frac{\partial(\rho w)}{\partial z}=0 \quad (1)$$

Momentum Equation:

$$\frac{\partial(\rho v_i)}{\partial t}+div(\rho v_i v)=\rho\left(\frac{\partial v_i}{\partial t}+v_i \cdot gardv_i\right) \quad (2)$$

Energy Equation:

$$\lambda\frac{\partial^2 T}{\partial x^2}+\lambda\frac{\partial^2 T}{\partial y^2}+\lambda\frac{\partial^2 T}{\partial z^2}= c_p\rho\left[\frac{\partial \rho}{\partial t}+\frac{\partial(uT)}{\partial x}+\frac{\partial(vT)}{\partial y}+\frac{\partial(wT)}{\partial z}\right] \quad (3)$$

According to Guidelines for Design of Ventilation of Highway Tunnels (JTGT-D70-2-02-2014), the fire scale was assumed to have a heat release rate of 30 MW. It was assumed that the smoke exhaust equipment at both ends of the parallel adit and that in the inclined shaft would be activated simultaneously to maximize the smoke exhaust capacity. Additional fire prediction scenarios are outlined in Table 1.

Table 1. Predicted fire smoke exhaust scenarios.

	Upstream air velocity (m/s)	Smoke exhaust capacity(m^3/s)	Fire location
Case1	2	136	Far from inclined shaft (upstream location)
Case2	3	204	Near inclined shaft
Case3	2	136	Far from inclined shaft (downstream location)

Figure 5 depicts the predicted smoke exhaust efficiency for fire scenarios at different locations, and the results indicate the following: (1) In case of a fire occurring far from the inclined shaft (upstream location), there is an air-crossing section bottleneck in the smoke exhaust ducts above the run-through parallel adit and the vehicle cross passages, which requires smoke exhaust through the smoke exhaust ducts above two adjacent vehicle cross passage. However, this may result in smoke affecting personnel and vehicles located between the two vehicle cross passages downstream of the fire. If the smoke is adequately controlled in the longitudinal direction, the further downstream spread will be prevented. (2) In case of a fire occurring near the inclined shaft, it is possible to solely rely on the inclined shaft for smoke exhaust. Additionally, the smoke exhaust capacity of the inclined shaft is superior to that of the smoke exhaust ducts above the run-through parallel adit and vehicle cross passages. (3) In case of a fire occurring far from the inclined shaft (downstream location), the smoke exhaust capacity of the smoke exhaust ducts above the run-through parallel adit and vehicle cross passages is insufficient. In this case, the remaining smoke inside the tunnel needs to be extracted from the tunnel portals. (4) When the upstream air velocity is less than 3 m/s, it is not sufficient to control the smoke backflow, which may result in the smoke affecting personnel and vehicles upstream of the fire.

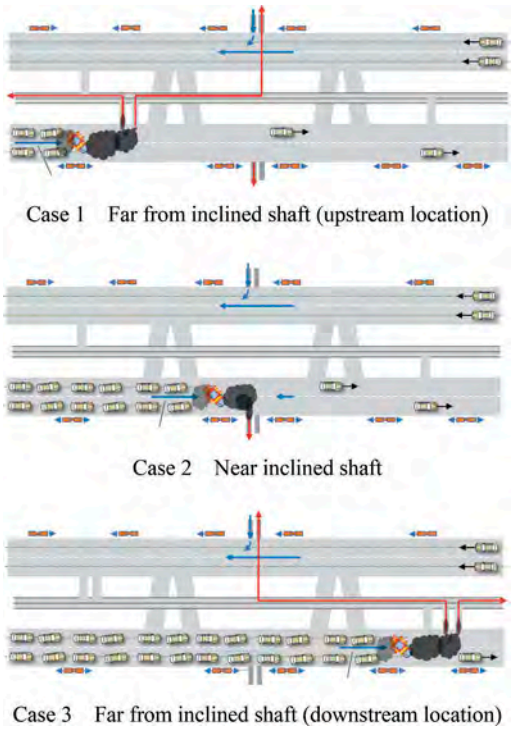

Figure 5. Predicted Smoke Exhaust Efficiency for Different Fire Scenarios at Various Locations (Area of Smoke Exhaust Duct A = 7.1 m^2).

3.2 *Prediction and analysis of optimized fire smoke exhaust efficiency*

Considering the insufficient smoke exhaust capacity of the smoke exhaust ducts above the run-through parallel adit and vehicle cross passages, to meet the smoke exhaust requirements in the event of a fire in the Daliangshan No. 1 Tunnel, which is an extra-long highway tunnel, and to minimize the harm to vehicles and personnel, further optimization research and smoke exhaust efficiency prediction of these smoke exhaust ducts were conducted in this study. The specific fire prediction scenarios are shown in Table 2.

Table 2. Predicted fire smoke exhaust scenarios after optimization.

	Upstream air velocity (m/s)	Smoke exhaust capacity(m^3/s)	Fire location
Case4	3	272	Far from inclined shaft (upstream location)
Case5	3	272	Near inclined shaft
Case6	3	272	Far from inclined shaft (downstream location)

To prevent further downstream spread of the smoke, it is necessary to ensure a critical air velocity of 3 m/s upstream of the fire. Additionally, an air velocity of -1 m/s should be set downstream of the fire to achieve a longitudinal induced smoke exhaust effect.

Figure 6 shows that by increasing the smoke exhaust duct area to 9.9 m^2, the optimized smoke exhaust duct exhibits a stronger smoke exhaust capacity. In the event of a fire occurring far from the inclined shaft, the smoke generated at the fire location can be completely extracted and expelled through the smoke exhaust outlet and air duct above a single vehicle cross passage near the fire source, preventing the smoke from spreading downstream. This reduces the distance of smoke dispersion inside the tunnel, resulting in improved smoke extraction efficiency during tunnel fire incidents.

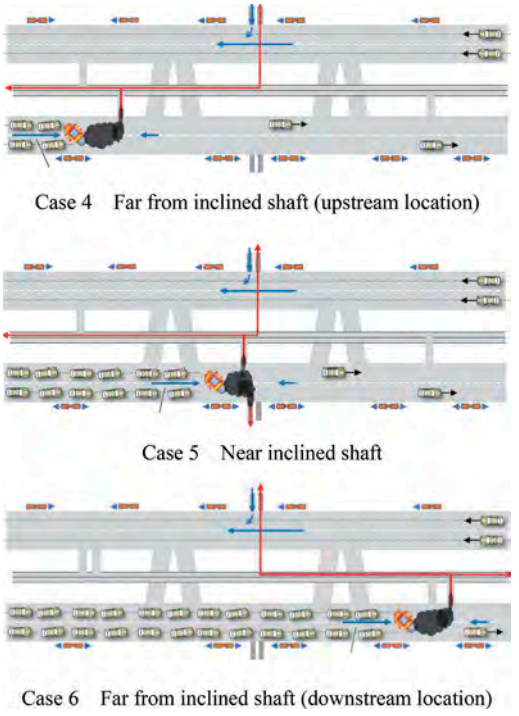

Figure 6. Prediction of somke exhausting effect in different fire conditions (as the area of smoke-extraction duct is 9.9 m^2).

3.3 *Alternate route of fire exhaust smoke*

To ensure effective smoke exhaust in the tunnel during the activation of alternate routes under special conditions, prediction and analysis were conducted for various fire scenarios under the activated alternate route condition. The fire prediction scenarios are outlined in Table 3.

For fires at bidirectional traffic, according to the Austrian design guideline, the jet fans shall be regulated for lower air velocities of approximately 1.0 to 1.5 m/s, with the aim to keep the stratification of the smoke layer intact, and to give people on both side of the fire more time to evacuate. ln this study, according to the amount of smoke from the fire,a representative air velocity of 1.2 m/s was assumed.

Table 3. Predicted fire smoke exhaust scenarios for alternate route.

	Upstream air velocity (m/s)	Smoke exhaust capacity(m^3/s)	Traffic conditions
Case7	1.2	81.6	Full closure of single-track tunnel
Case8	1.2	81.6	Closure of top section of single-track tunnel
Case9	1.2	81.6	Closure of both ends of single-track tunnel

Figure 7 shows the predicted smoke exhaust efficiency under different traffic conditions. The results indicate that: (1) To exhaust a large amount of smoke in the two vehicle cross passages downstream of the fire, the inclined shaft and the parallel adit exit can be used at the same time for smoke exhaust while controlling the longitudinal flow of smoke so that the smoke will not continue to spread downstream. (2) When the upstream air velocity is 1.2 m/s, this speed is insufficient to prevent smoke stratification and the occurrence of smoke backflow. This may result in the personnel and vehicles located upstream of the fire being affected by the smoke.

3.4 *Fire smoke exhaust prediction for optimized alternate route*

In light of the predicted results of fire smoke exhaust for the alternate route described in section 3.3, prediction and analysis were conducted for the

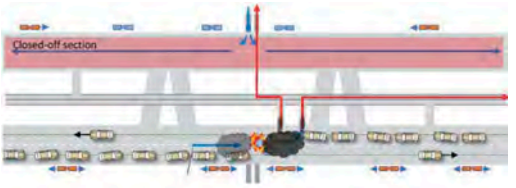

Case 7 Full closure of single-track tunnel

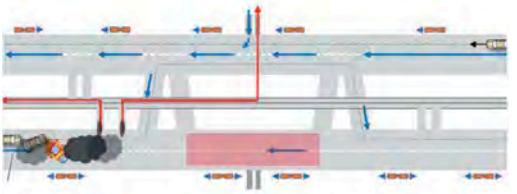

Case 8 Closure of middle section of single-track tunnel

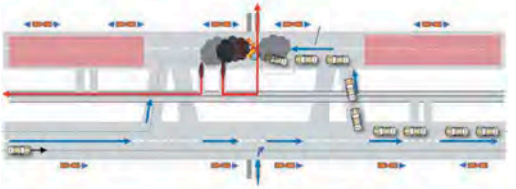

Case 9 Closure of both ends of single-track tunnel

Figure 7. Predicted Smoke Exhaust Efficiency for Different Fire Scenarios at Various Locations on the Alternate Route (Area of Smoke Exhaust Duct A = 7.1 m^2).

optimized alternate route to meet the fire smoke exhaust requirements for the Daliangshan No. 1 Tunnel, minimize potential harm to traffic and personnel, and prevent non-fire areas and closed areas from being affected by smoke. The fire prediction scenarios are outlined in Table 4.

Figure 8 shows the predicted smoke exhaust efficiency under different traffic conditions. The results indicate that: (1) When the single-track tunnel is fully closed, vehicles may be present upstream and downstream of the fire. With the upstream air velocity set at 1.2 m/s, the air velocity is insufficient to control smoke stratification and back-layering, and upstream vehicles may be affected by smoke, but the smoke exhaust capacity is sufficient to discharge all the smoke through the nearest smoke outlet downstream of the fire source, thereby avoiding the impact of smoke on downstream vehicles. This wind speed is only suitable for two-way traffic, whether it is using a smoke outlet or shaft to exhaust smoke, the longitudinal wind speed is 1.2m/s. (2) When the fire occurs on a unidirectional traffic section, setting the upstream air velocity at the critical air velocity can prevent smoke stratification and ensure sufficient smoke exhaust capacity.

Table 4. Predicted fire smoke exhaust scenarios for optimized alternate route.

	Upstream air velocity(m/s)	Smoke exhaust capacity(m^3/s)	Traffic conditions
Case10	1.2	81.6	Full closure of single-track tunnel
	Upstream air velocity(m/s)	Smoke exhaust capacity(m^3/s)	Traffic conditions
Case11	v_{crit}	–	Closure of top section of single-track tunnel
Case12	v_{crit}	–	Closure of both ends of single-track tunnel

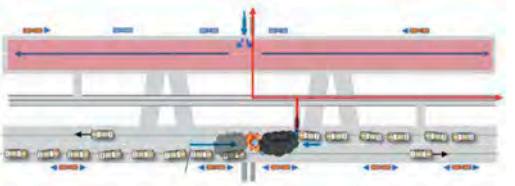

Case10 Full closure of single-track tunnel

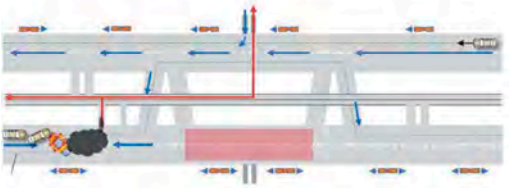

Case 11 Closure of middle section of single-track tunnel

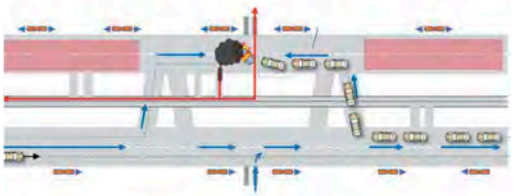

Case 12 Closure of both ends of single-track tunnel

Figure 8. Prediction of smoke exhausting effect in different fire conditions of alternate route (as the area of smoke-extraction duct is 9.9 m^2).

All smoke can be exhausted through a single smoke exhaust outlet, allowing all smoke to be discharged through a single smoke outlet, thus avoiding the impact of smoke on downstream vehicles and personnel.

4 CONCLUSIONS

Relying on the control project of Leshan-Xichang Expressway in Sichuan Province, this paper studied and designed a new fire smoke exhaust mode. A new fire smoke exhaust model was constructed based on this mode, employing a one-dimensional analysis method to predict and compare the smoke exhaust efficiency under various fire scenarios and smoke exhaust conditions at different locations within the tunnel. Major findings were summarized as follows:

(1) The fire smoke exhaust model before optimization cannot provide sufficient smoke exhaust due to the insufficient cross-sectional area of the smoke exhaust duct. Under fire conditions where the fire occurred far from the inclined shaft, the smoke cannot be controlled effectively by sufficient upstream air velocity, leading to stratification and backflow of smoke, which might affect vehicles and personnel upstream of the fire;
(2) For fire incidents near the inclined shaft, the original model allowed smoke exhaust through the inclined shaft, which proved to be more efficient compared to using the nearest vehicle cross passage for smoke exhaust.
(3) For the optimized fire smoke exhaust model, the cross-sectional area of the smoke exhaust duct is increased from 7.1 m^2 to 9.9 m^2. The smoke exhaust capacity from the smoke outlet above of individual vehicle cross passages was increased, ensuring that any single vehicle cross passage could meet the requirements for fire smoke exhaust. By utilizing the smoke exhaust route downstream, which was closest to the fire location, along with longitudinal smoke induction, it was possible to effectively exhaust all smoke and prevent its diffusion from affecting vehicles upstream and downstream of the fire.

Based on the comprehensive analysis and predictions, it is concluded that the proposed new fire smoke exhaust mode is feasible. Through the prediction and analysis of the fire smoke exhaust efficiency, it is proven that the tunnel fire smoke exhaust model developed based on this new smoke exhaust mode exhibits excellent smoke exhaust performance. Furthermore, it can serve as a valuable reference for similar engineering projects.

REFERENCES

China Journal of Highway and Transport editorial office. Review on China's Tunnel Engineering Research:2015 [J]. China Journal of Highway and Transport, 2015, 28 (05):1–65.

CMCT. Guidelines for Design of Ventilation of Highway Tunnels [M] China Communications Press Co., Ltd, 2014

Editorial Department of China Journal of Highway and Transport. Review on China's Tunnel Engineering Research: 2015 [J]. China Journal of Highway and Transport, 2015, 28(05): 1–65.

Haukur Ingason, Ying Zhen Li. Model scale tunnel fire tests with point extraction ventilation [J] Journal of fire protection engineering. Volume 21, Issue 1. 2011. PP 5–36

Jia Jilin. Angle optimization of highway tunnel ventilation shaft[J].Highway, 2014, 59(05):14–18.

Liu Tong, Lai Jinxing, Li Ningjun. Numerical simulation of ventilation in use for Erlangshan road tunnel[J].Chinese Journal of Underground Space and Engineering, 2006 (05):859-862+886.

Li Deying. Simulation experimental study on some influences factors of central exhaust in tunnels based on orthogonal test[D].Chengdu: Southwest jiaotong university, 2002.

Li Baojun, Tao Liangliang, Wang Haoran, et al. Numerical study on the smoke control of single-side centralized smoke exhausting tunnel. [J]. Chinese Journal of Underground Space and Engineering, 2020,16 (S2):912–917.

Qiu Yonghai, Lou Bo, Xu Jianhong, et al. Numerical simulated study of the impact of smoke vent and fire source location on the exhaust emission in case of the tunnel fire[J]. Journal of Safety and Environment,2016,16 (03):51–55.

RVS 09. 02.31,Grundlagen Tunnellüftung, June 2014, 2014.

Wang Yaqiong, Deng Min, Hu Yanjie, et al. Fuzzy control of fire smoke in single highway with subtended traffic[J]. Journal of traffic and Transportation Engineering, 2012,12 (5):13–21.

Wu Dexing, Li Weiping, Zheng Guoping. Comparison of Domestic & overseas design concepts for smoke exhausting in expressway tunnels fires[J]. Technology of Highway and Transport, 2008, 05:113-117+127.

Wu Chenyan, Shi Biming, Peng Wei, et al. Study on smoke back-layering length in highway tunnel fire under semi-transverse smoke exhausting[J]. Journal of Science and Technology, 2021,17(04):92–97.

Xia Fengyong, Xie Yongli, Wang Yaqiong, et al. Complementary ventilation modes of extralong highway tunnel[J]. Journal of Traffic and Transportation Engineering, 2014,14(6):27–34.

Xu Baiyang, Yuan Song, Zhang Sheng et al. Study on smoke exhausting scheme and effect in extra-long highway tunnel[J]. Modern Tunnelling Technology, 2021,58 (S1):513–519.

Xu Haozhuo, Li Yaozhang, Xu Zhisheng. Simulation experimental study on some influences factors of central exhaust in tunnels based on orthogonal test[J].Journal of Railway Science and Engineering, 2018, 15 (10):2590–2596.

Yu Li. Researches on ventilation design and control technology of Zhongnanshan super-long highway tunnel in fire[D].Chengdu: Southwest Jiaotong university, 2009.

Zhang Jinglong, Sun Sanxiang, Li Han. Research on angles of transverse passageways for twin-hole compensatory ventilation system of highway tunnels[J].Technology of Highway and Transport, 2012, 02:109–113.

Tunnelling for a Better Life – Yan, Celestino, Thewes & Eberhardt (Eds)
© 2024 The Author(s), ISBN 978-1-032-80042-4
Open Access: www.taylorfrancis.com, CC BY-NC-ND 4.0 license

Positioning and autonomous control of intelligent hydrodemolition robot

Wei Liang*
China Railway Construction Heavy Industry Corporation Limited, Changsha, China

ABSTRACT: In order to alleviate the unexpected damages and environmental pollution during the mechanical demolition process of underground spaces, we developed a hydrodemolition robot based on the design of end-effector with ultra-high pressure water jet. Aiming at the environment of tunnels, we built the kinematic model of the manipulator and end-effector, the typical operation positions and orientations in the tunnel are simulated and analysed, which can further be used to verify and optimize the mechanical and control parameters. In combination with the trajectory planning of the manipulator and the RTK positioning control of the crawler chassis, the working space and accuracy of the robot in complex tunnel environment are improved. Manual setting and autonomous navigation functions for moving paths and working areas are developed, which can further ensure the operation efficiency and safety of the robot.

Keywords: robot, high-pressure water jet, concrete demolition, kinematic modeling, RTK positioning, autonomous navigation

1 INTRODUCTION

Hydrodemolition, also knHydrodemolition, also known as water jet demolition, is a technology using high-pressure water jets to impact the concrete surface at very high speed and forming a water wedge effect and water hammer effect, so as to peel off the damaged, aged or loose concrete particles [*Montero, R., et. al., 2015,Momber, A., 2011*]. During the maintenance of a tunnel, it is often necessary to demolish the damaged concrete or structures in the tunnel at fixed points, so as to ensure the overall safety and durability. In comparison with traditional mechanical methods, this hydrodemolition technology is featured by many advantages: 1) with water jet demolition technology, the jet direction, target distance, strength and flow rate can be changed to achieve accurate demolition of damaged and deteriorated concrete; 2) the pressure and flow of hydrodemolition are controllable, and the risk of damage to reinforcement and other internal structures is controllable; 3) irregular surfaces can be effectively created with the hydrodemolition technology, contributing to the adhesion of subsequent coating or repair materials; 4) by water jet demolition, the vibration, noise and dust generated in the process of construction will be reduced, making the whole process more environmentally friendly.

The water jet system is combined with the robot operating system to form hydro-demolition robot system. By the water jet system, high-pressure water is transported to the jet mechanism installed at the end of the robot working device through a high-pressure hose to form a high-speed water jet beam, generating strong shooting energy. By the robot operating system, the end spray mechanism is positioned to the demolition point based on the calibrated position information, so as to accurately complete the demolition working task.

Conjet in Sweden has launched a series of products including Robot324, Robot365 and Robot432D, of which Robot 432D is a large-scale concrete removal robot in horizontal working planes [*Fang, X.W., 2019*]. The high-pressure water jet robots produced by Aqua-Jet in Sweden include various models such as 410 and 710, which can realize the operations in horizontal and vertical working planes in narrow spaces to remove concrete from bridges and pavements [*Yang, W.J., 2016*]. NLB in the United States is also one of the R&D manufacturers of high-pressure water jet robots, such as NLB6600 concrete hydraulic crusher, which can achieve different effects according to the specific engineering requirements. For example, where the pressure is lower than 150MPa, only a layer of concrete in about 25mm thick on the surface will be removed to avoid the exposure of reinforcement; its water pressure can be risen up to 280MPa, making it possible to penetrate the concrete layer to completely expose reinforcement [*Xing, J.Z., 2015*]. CITIC Heavy Industries and Giant Hydraulic Tech in China have also launched their own crawler-type high-pressure water jet robots, which are applied to the renovation,

*Corresponding author: liangwei2.zg@crcc.cn

DOI: 10.1201/9781003495505-452

reconstruction and reinforcement of the concrete structures of important buildings such as bridges, dams, tunnels, wharves, airports and power stations [*Cai, S. et.al., 2019*].

At present, most of the hydro-demolition robot technologies integrate various sensors such as advanced 3D scanner and camera, with the function of real-time construction environment feedback; the function of remote operations is also developed to ensure the safety of operators. However, the development of water jet demolition robots is still being confronted with some constraints. For example, the maneuverability of robot in a narrow space is limited, and the robot arm is difficult to extend with increased the risk of collision, causing difficulty to ensure construction safety; secondly, most robots are still manually manipulated for working, with poor vision in tunnels and differences in accuracy and consistency of demolition, causing difficulty to ensure the construction quality and efficiency; in addition, there are safety risks in the short-distance operations of water jet, and it is unadvisable for construction personnel and operators to make close observation and control.

Therefore, it is necessary to accurately model the kinematics of robots to achieve precise operations in narrow or complex spaces, reduce working errors and waste in materials, and improve the construction quality and efficiency; meanwhile, it is necessary to increase the autonomous navigation and autonomous operation functions of robots, which are conducive to enlarging the robots' working range, automatic obstacle avoidance and working area identification, adapting to the diversified tasks and environments, lowering the participation degree of operators, reducing the labor workload and improving the construction safety.

In this paper, the hydro-demolition robot developed by China Railway Construction Heavy Industry Corporation Limited (CRCHI) is introduced, and the modeling of manipulator motions and the planning of working paths are carried out for the robot. In the second part below, the method of modeling each component of the robot is introduced, while in the third part, the motion effect is introduced, and a summary of robot development in the fourth part.

2 MODELING

The hydro-demolition robot SPC-1340A (Figure 1) developed by CRCHI consists of crawler chassis, control module, hydraulic actuator, manipulator and end-effector. Of them, the robot manipulator has four degrees of freedom, and can assist the end-effector to reach different positions and postures around the construction plane circumference; the end-effector has three degrees of freedom, and can realize a variable-angle demolition path with a maximum width of 2 meters on the basis of manipulator positioning; the crawler chassis is strong in comprehensive motion performance, suitable for unstructured construction environment, and able to move to the set working point by itself; the hydraulic actuator powers each of the above-mentioned actuating subsystems.

2.1 *Modeling of manipulator*

The motion of manipulator is of great significance to tunnel maintenance: 1) ensure the accurate removal of concrete; 2) adapt to complex structures and avoid existing obstacles; and 3) improve the construction efficiency. Therefore, the motion of manipulator in the internal space of a tunnel requires precise positioning and trajectory planning, all of which require modeling the kinematics for the manipulator.

As shown in Figure 2, the manipulator has 4 links (Link 1 ~ Link 4), of which Link 4 is connected to the end-effector (Link 5). In the process of manipulator modeling, a fixed coordinate system {0} is set at the proximal end of Link 1 as the base coordinate system; coordinate systems {1} ~ {4} represent each motion joint of the manipulator. It should be noted that joint {2} is a moving subjoint while others are rotating subjoints. Therefore, the DH parameters required for kinematic modeling can be extracted according to the origin and attitude of each coordinate system in Figure 2 and the size of each link (Table 1).

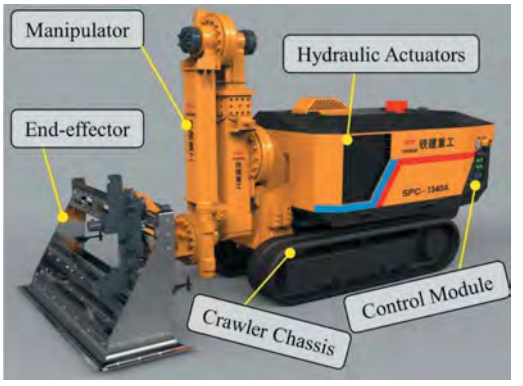

Figure 1. Hydro-demolition robot SPC-1340A designed by CRCHI.

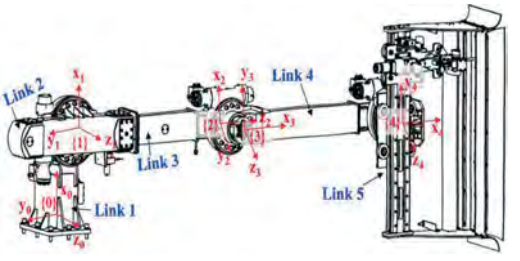

Figure 2. Coordinates of manipulator joints.

Table 1. DH parameters of manipulator and end-effector.

Joint i	α_{i-1} (rad)	a_{i-1} (m)	d_i (m)	θ_i (rad)
1	0	a_1	d_1	θ_1
2	π/2	0	d_2	0
3	-π/2	0	d_3	θ_3
4	0	a_4	d_4	θ_4
5	-π/2	a_5	d_5	0
6	0	a_6	d_6	0
7	π/2	0	d_7	θ_7
8	π/2	0	d_8	θ_8

Note: In the table, $\boldsymbol{\alpha_i}$ means: z_i in coordinate system $\{i\}$ is rotated around x_i by α_i and coincides with z_{i+1} in coordinate system $\{i+1\}$; $\boldsymbol{a_i}$ means: the distance between z_i in coordinate system $\{i\}$ and z_{i+1} in coordinate system $\{i+1\}$ along the direction x_i; $\boldsymbol{d_i}$ means: the distance of x_i in coordinate system $\{i\}$ along the direction z_i relative to x_{i-1} in coordinate system $\{i-1\}$, where d_2, d_5, and d_6 are variable; $\boldsymbol{\theta_i}$ means: the angle of rotation around z_i in coordinate system $\{i\}$.

According to the DH parameters, a homogeneous transformation matrix ${}_i^{i-1}T$ between adjacent joint coordinate systems can be established:

$$
\begin{aligned}
{}_i^{i-1}T &= Rot_{x_{i-1}}(\alpha_{i-1})Trans_{x_{i-1}}(a_{i-1})Rot_{z_i}(\theta_i)Trans_{z_i}(d_i) \\
&= \begin{bmatrix} \cos\theta_i & -\sin\theta_i & 0 & a_{i-1} \\ \sin\theta_i\cos\alpha_{i-1} & \cos\theta_i\cos\alpha_{i-1} & -\sin\alpha_{i-1} & -d_i\sin\alpha_{i-1} \\ \sin\theta_i\sin\alpha_{i-1} & \cos\theta_i\sin\alpha_{i-1} & \cos\alpha_{i-1} & d_i\cos\alpha_{i-1} \\ 0 & 0 & 0 & 1 \end{bmatrix}
\end{aligned} \tag{1}
$$

Further, the homogeneous transformation matrix ${}_4^0T$ of the end connecting joint {4} relative to the fixed coordinate system {0} can be obtained by multiplying each adjacent transformation matrix:

$$
{}_4^0T = {}_1^0T \cdot {}_2^1T \cdot {}_3^2T \cdot {}_4^3T \tag{2}
$$

According to the homogeneous transformation matrix, the position and posture of the end-effector relative to the base coordinate system can be solved by changing the angle of each joint; on the contrary, the rotation angle or moving distance of each joint can also be calculated according to the posture of the end coordinate system as required in construction.

2.2 *Modeling of end-effector*

The pressurized water passes through the nozzle to form a single beam of high-pressure water jet impacting on the deteriorated concrete, and the range of demolition with the nozzle alone is quite limited. Therefore, on the basis of positioning completed by the manipulator, a horizontal reciprocating motion mechanism and an equidistant reversing mechanism are added to the end-effector of the hydro-demolition robot, to expand the working width of the water jet nozzle and improve the uniformity and stability of the operation.

As shown in Figure 3, the whole end-effector is connected to the manipulator end through joint 4, wherein the sliding frame realizes overall left-right translation based on the moving subjoint {5}, increasing the actual working width; meanwhile, through the moving subjoint {6}, the sliding bracket realizes translational motion relative to the sliding frame in the process of demolition; the nozzle is installed on the sliding support, and two hydraulic motors respectively realize equidistant reversing rotation around axis z_7 and continuous working swing around axis z_8.

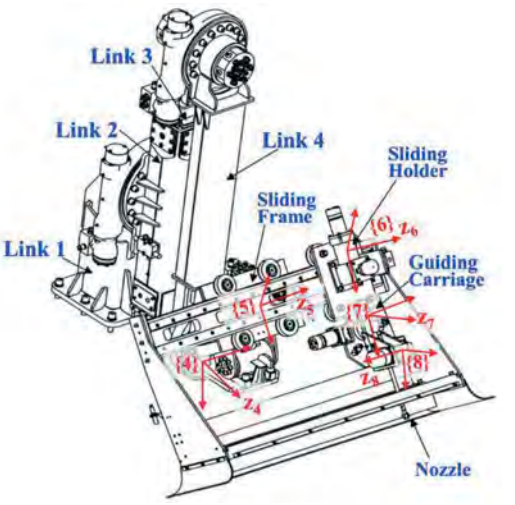

Figure 3. Coordinates of end-effector.

Similarly, the homogeneous transformation matrix ${}_8^4T$ of the nozzle relative to joint 4 and the homogeneous transformation matrix ${}_8^0T$ of the nozzle relative to base coordinate {0} can be obtained according to formula (1) and formula (2) and in combination with Figure 3 and the DH parameters in Table 1. The position and posture of nozzle relative to the base coordinate system has a definite solution relationship, providing a kinematics basis for the positioning of robot for accurate construction in the later stage.

As shown in Figure 4, an eccentrically connected linkage (around axis z_7) is driven by a hydraulic motor to realize equidistant reversing of the nozzle. Stop blocks are added on the left and right sides of the nozzle respectively to effectively fix the demolition angle of the nozzle. The mechanism can ensure that the distance from the nozzle to concrete surface are remained unchanged during the reversing, so as to ensure the consistency of demolition effect; meanwhile, it can prevent the nozzle from being damaged due to collision with the ground and ensure reliable operation of the nozzle.

2.3 *Modeling of crawler chassis*

The forward and backward motion of the crawler chassis can be realized by the motion of crawlers on the left and right sides at a same speed. However, the modeling of crawler chassis steering motion is complex. As shown in Figure 5a, the coordinate system of the chassis in a plane is established with the center of gravity (COM) of the chassis as the origin, the direction of forward motion as the x-axis, and the direction on left side as the y-axis. Points A and B are set at the front and rear ends of the left crawler respectively, and Point D is set at the front end of the right crawler. At this time, if the crawler needs to make steering motion around the instantaneous center of rotation (ICR), the following conditions shall be met:

$$\begin{cases} v_A \neq v_B \\ v_{Ax} = v_{Bx} \end{cases} \tag{3}$$

$$v_{Ay} = v_{Dy} \tag{4}$$

According to Formula (3) and Formula (4), the longitudinal component velocities of all points on the crawler on same side are required to be the same; in addition, the transverse component velocities of two symmetrical points about x-axis on the left and right crawler are required to be the same.

Further, by simplifying the model of crawler motion to a virtual two-wheel differential model as shown in Figure 5b, the following relationship can be obtained:

$$r_c = \frac{v_c}{w_c} = \frac{(v_l + v_r)d_{LR}}{2(v_r - v_l)} \tag{5}$$

Where r_c denotes a radius of rotation (m) at point COM, v_c denotes a linear velocity at point COM, w_c denotes an angular velocity (rad/s) at point COM, d_{LR} denotes a virtual wheel spacing (m), and v_l and v_r denote respectively the virtual left and right wheel linear velocities (m/s, equal to the left and right crawler linear velocities).

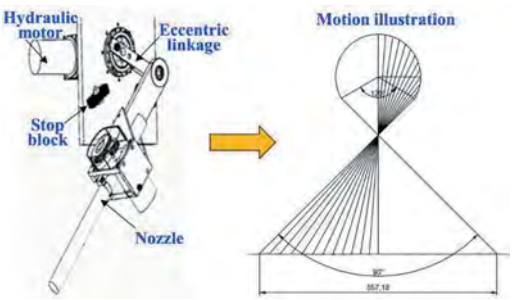

Figure 4. Equal distance switching system.

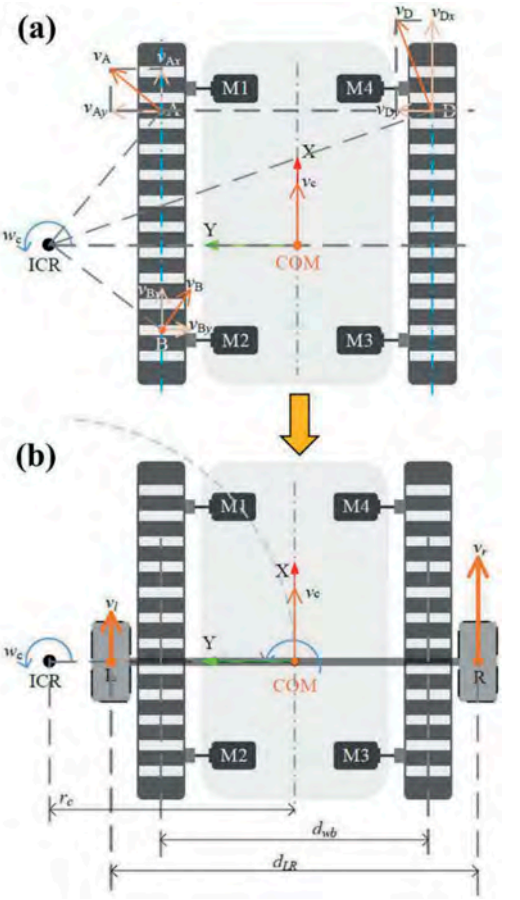

Figure 5. Crawler chassis model, (a) crawler wheel model analysis; (b) equivalent virtual two-wheels model.

Virtual wheel spacing is a complex parameter related to load, friction coefficient, turning radius and center-of-mass position. It is generally obtained through tests:

$$d_{LR} = \gamma d_{wb} \tag{6}$$

Where γ is the dimensionless empirical parameter and d_{wb} is the actual wheel spacing of the robot (m). At this time, the forward kinematic model of the crawler chassis can be obtained as follows:

$$\begin{bmatrix} v_c \\ w_c \end{bmatrix} = \begin{bmatrix} 1/2 & 1/2 \\ 1/(\gamma d_{wb}) & -1/(\gamma d_{wb}) \end{bmatrix} \begin{bmatrix} v_r \\ v_l \end{bmatrix} \tag{7}$$

The inverse kinematic model is:

$$\begin{bmatrix} v_r \\ v_l \end{bmatrix} = \begin{bmatrix} 1 & \frac{\gamma d_{wb}}{2} \\ 1 & -\frac{\gamma d_{wb}}{2} \end{bmatrix} \begin{bmatrix} v_c \\ w_c \end{bmatrix} \tag{8}$$

2.4 *GNSS-based RTK navigation modeling*

A GPS-based GNSS (Global Navigation Satellite System) navigation system is adopted for Robot

SPC-1340A. The ranging principle of GNSS is to obtain the distance between the marked point and the satellite by multiplying the velocity of electromagnetic wave and the time of signal transmission, where time is the key to measurement accuracy. GNSS positioning is based on the principle of distance resection, that is, a spherical surface is established with the satellite as the center and the measured distance as the radius; two points are obtained by intersecting three spherical surfaces formed by three satellites, and the positioning is completed after unreasonable points are excluded geographically.

Since the measuring point has four unknown quantities that are the three coordinates (*x, y, z*) of the position and the clock difference *t*, it is necessary to introduce the fourth satellite to form 4 equations for solving them, so as to obtain the longitude, latitude and altitude of the measuring point.

$$p_i = (x_i - x)^2 + (y_i - y)^2 + (z_i - z)^2 + t \qquad (9)$$

Where *i*=1~4; p_i denotes the relative position of the observation point measured by the *ith* satellite; x_i, y_i and z_i denote the relative coordinates of the observation point measured by the *ith* satellite respectively; t denotes the clock difference (s).

In order to carry out the demolition construction more accurately, it is necessary to further improve the positioning accuracy to centimeter level; and according to the dynamic action process of the robot, the robot should be positioned in real time. Therefore, RTK (Real-Time Kinematic) positioning technology is adopted.

RTK is a relative, dynamic and real-time measurement technology which is realized based on carrier phase. First, the calculation equation based on the observations of carrier phase is as follows:

$$P^i_{s,m} = \rho^i_m + c\left(dt_m - dt^i\right) + \mu_s \cdot I^i_m + T^s_m + \beta_{s,m} - \beta^i_s + d^i_m + \varepsilon^i_{s,m,\rho} \qquad (10)$$

$$\lambda_s \varphi^i_{s,m} = \rho^i_m + c\left(dt_k - dt^i\right) - \mu_s \cdot I^i_m + T^i_m + \lambda_s\left(\delta_{s,m} + \delta^i_s + N^i_{s,m}\right) + d^i_m + \varepsilon^i_{s,m} \qquad (11)$$

Where i is expressed as the satellite number, s and m are expressed as the frequency of the satellite and the receiver of the user; $P^i_{s.k}$ is the original observed value of the pseudorange; $\varphi^i_{s.k}$ is the observed value of carrier phase; ρ^i_m is the distance from the satellite to earth (m); c is the velocity of light in vacuum (m/s); dt_k, dt^i is the receiver clock difference and the satellite clock difference (s); I^i_m is the delay of ionosphere at frequency f1 (m); μ_s is the ionospheric amplification factor between frequencies f_i and f_1; T^i_m is the delay of troposphere on inclined path (m); $\beta_{s,m}$ is the pseudorange delay of the user receiver end at frequency s (m); β^i_s is the pseudorange delay of satellite end at frequency s (m); λ_s is the wavelength (m); $\delta_{s,m}, \delta^i_s$ is the phase delay of satellite and user end at frequency s; $N^i_{s.m}$ is the ambiguity (weeks); d^i_k is other errors unrelated to frequency; $\varepsilon^i_{s\,m\,o}, \varepsilon^i_{s\,m\,\varphi}$ is the measured noise at the same frequency (m).

Based on Formula (10) and Formula (11), for Robot SPC-1340A, 2 stations are used for real-time carrier positioning (Figure 6), in order to achieve the high-precision positioning in centimeter level. The differencing between the observation equations of two different stations is called single difference between stations, and the pseudorange and carrier phase equations for the differencing between two stations m and n through common observation satellite i are as follows:

$$\Delta P^i_{s,m,n} = \Delta\rho^i_{s,m,n} + c \cdot \Delta dt_{mn} + \mu_s \cdot \Delta I^i_{mn} + \Delta\beta_{s,mn} + \Delta d^i_m + \Delta\varepsilon^i_{s,mn,\rho} \qquad (12)$$

$$\lambda_i \Delta\varphi^i_{s,m,n} = \Delta\rho^i_{mn} + c \cdot \Delta dt_{mn} - \mu_s \cdot \Delta I^i_{mn} + \Delta T^i_{mn} + \lambda_i(\Delta\delta_{s,mn} + \Delta N^i_{s,mn}) + \Delta d^i_m + \Delta\varepsilon^i_{s,mn,\rho} \qquad (13)$$

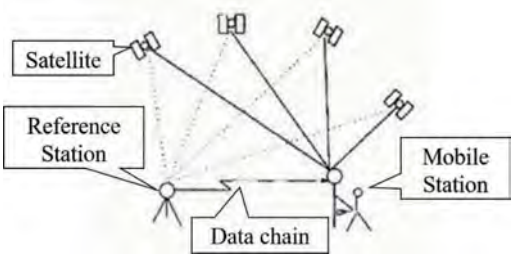

Figure 6. Single differential RTK model between stations.

3 RESULTS

3.1 *Manipulator and end-effector*

By modeling the DH parameters of the manipulator joints and solving the homogeneous transformation matrix of the end connecting joints, Robot SPC-1340A is capable of completing the motions in three degrees of freedom in the plane of workspace. As shown in Figure 7, the manipulator end can complete the motions in three degrees of freedom: horizontal motion, vertical motion and rotation in end posture around axis z_4.

According to the motion of the manipulator position and posture, the posture of end-effector in the working plane is further calculated. As shown in Figure 8, Robot SPC-1340A can adapt to the configuration of various walls in tunnels with a diameter not more than 6 meters, realize the end positioning and complete the demolition operations.

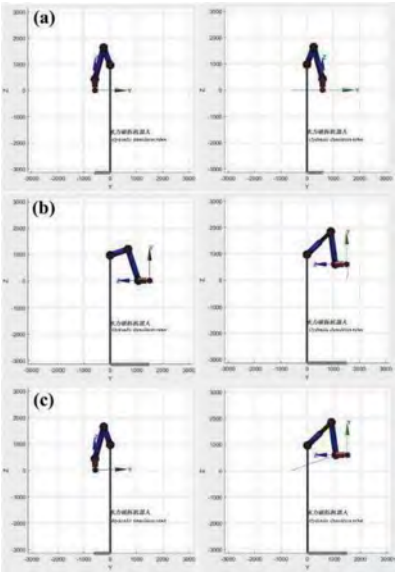

Figure 7. Motions of manipulators, (a) horizontal motion; (b) vertical motion; (c) rotating motion.

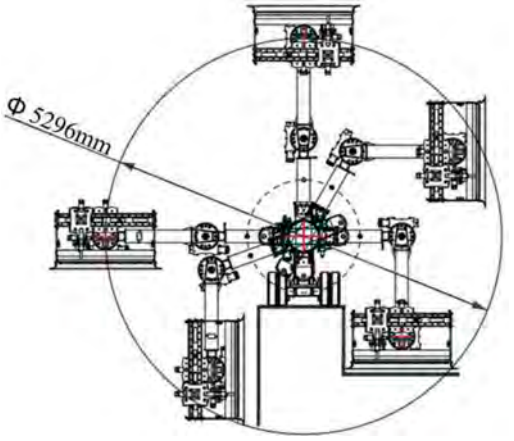

Figure 8. Orientations and Positions of end-effector in the working plane.

3.2 *Robot positioning and automatic operations*

Robot SPC-1340A can automatically complete the positioning, navigation and demolition operations (Figure 9), with the implementation process as follows: 1) complete the robot's own positioning through GNSS system; 2) identify the relative position of a working area to the robot through four marking points; 3) calculate the walking path, working position and actuator posture of the robot based on the kinematic model of the crawler chassis, manipulator and end-effector; 4) carry out the operations based on the GNSS system and planned path.

The human-machine interaction interface on the control panel is shown as Figure 10, where the green line is the robot's walking path, and the yellow line is the demolition + walking route of the robot.

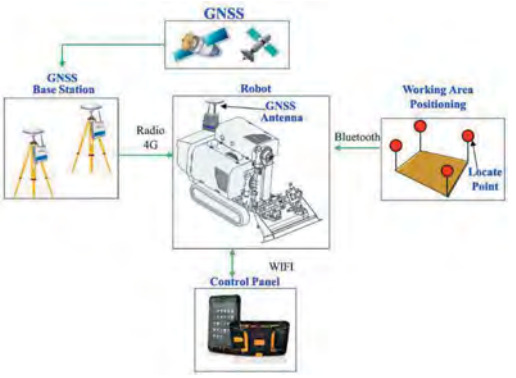

Figure 9. The robot positioning and working area identification.

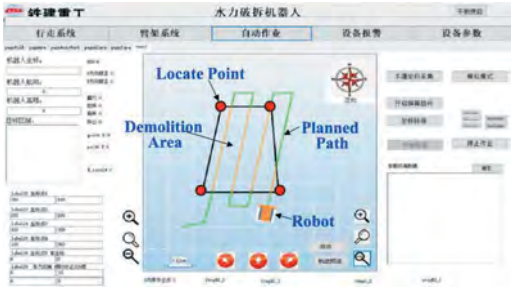

Figure 10. Orientations and positions of end-effector in the working plane.

3.3 *Demolition capability of the robot*

Robot SPC-1340A has been subject to the in-plant hydrodemolition test (Figure 11) and the verification of demolition effect on tunnel maintenance site (Figure 12).

In the process of the in-plant test, under the conditions of water pressure of 160 MPa, flow rate of about 30 L/min, water nozzle aperture of 2.2 mm and frequency of 35 Hz, the demolition finally produced a deep groove in 110 cm long, 21 cm wide and 6 cm deep through three effective travels of the crawler (Figure 11b). The volume of concrete demolished per unit time is about 0.014 m^3/h. Although the test block is nominally a C10 concrete test block, it is poured concrete with more pebbles and higher actual strength.

The industrial field verification was carried out at a tunnel construction site of China Railway 22nd Bureau Group. The track laying of the

construction tunnel was completed. Within about 5.3 m*2.46 m left to and 3.12 m*2.75 m right to the position of lining arch crown and about 100 m from the portal, some defective reinforced concrete needed to be demolished by a depth of 0.5 m and then poured again (Figure 12b). The target concrete strength grade was C50; the concrete specification was 2 m*1.6 m*0.2 m. Under the conditions of water pressure of 160 MPa and flow rate of about 30 L/min, the demolition depth was between 30 ~ 40 cm, and the C50 concrete volume of demolition per unit time was about 0.014 m^3/h (Figure 12c). Meanwhile, Robot SPC-1340A was also verified for its functions of outdoor high-precision positioning in RTK centimeter level, with the functions such as real-time position monitoring, setting and automatic planning of motion route, setting and automatic planning of working area assisting the intelligent operations of hydro-demolition robot.

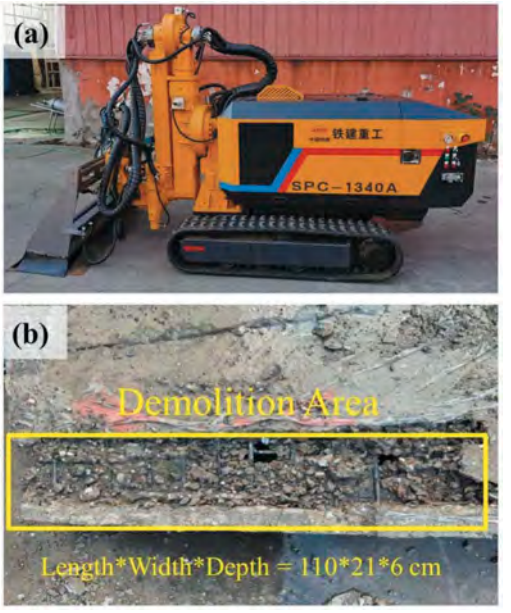

Figure 11. In-plant hydrodemolition test, (a) robot displayed in-plant; (b) demolition area of one swept of nozzle.

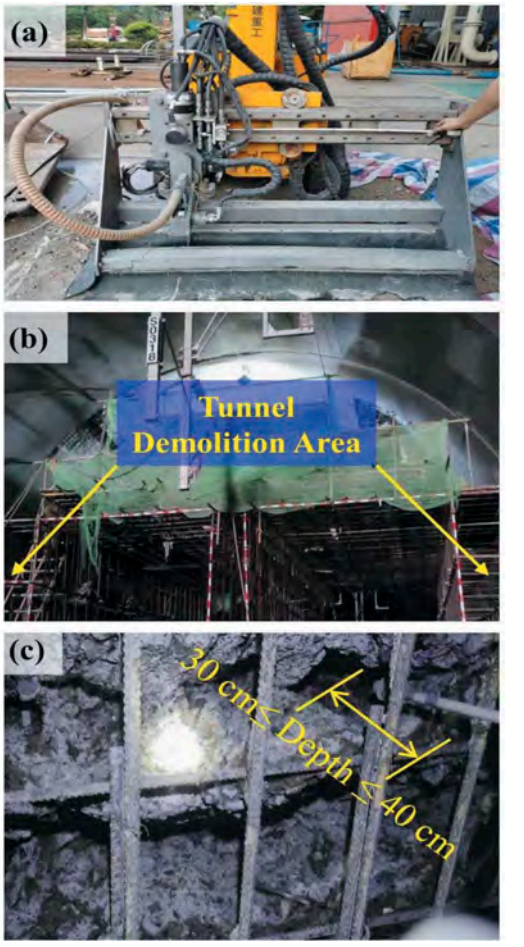

Figure 12. On-site hydrodemolition test, (a) robot displayed tunnel maintenance site; (b) demolition area of tunnel; (c) demolition result of the robot.

4 CONCLUSION

In the field of tunnel maintenance and construction, CRCHI has integrated the traditional water jet technology with advanced robot control technology, developed hydro-demolition robot and related algorithms for intelligent construction operations, and redefined the construction method for removing the deteriorated concrete through the synergistic effect among kinematic modeling, end-effector design, crawler chassis integration and navigation system, thus improving the efficiency, accuracy and safety of construction.

The kinematic modeling of manipulator and end-effector enables the robot to achieve flexible working positions and postures in tunnel spaces. In the process of maintenance, the robot can selectively demolish the damaged parts while retaining structural integrity, which not only adapts to different collective surfaces, but also improves the accuracy and quality of the demolition process, laying a foundation for efficient and accurate restoration of various structures.

The modeling of crawler chassis and the integration of RTK positioning technology bring high maneuverability to the robot in various terrains. It has the ability to autonomously plan paths, avoid obstacles and optimize trajectories. This level of intelligence not only enhances the safety, but also minimizes the human intervention, minimizing the

risk of performing tasks in hazardous or remote environments.

In summary, the collaboration among hydro-demolition robot SPC-1340A, kinematic modeling of robot arm, end-effector design, crawler chassis modeling and navigation system integration can effectively improve the construction efficiency, reduce the waste in materials, enhance the construction safety and protect the critical structures.

REFERENCES

[1] Cai, S., Ma, Z., Skibniewski, M.J. and Bao, S., 2019. Construction automation and robotics for high-rise buildings over the past decades: A comprehensive review. Adv. Eng. Inform., 42, 100989.

[2] Fang, X.W., 2019. Simulation and finite element analysis of new working device of hydraulic demolition robot. Master Thesis. Anhui University of Technology, Maanshan, Anhui, China.

[3] Momber, A., 2011. Hydrodemolition of concrete surfaces and reinforced concrete. Elsevier.

[4] Montero, R., Victores, J.G., Martinez, S., et.al., 2015. Past, present and future of robotic tunnel inspection. Autom. Constr., 59, 99–112.

[5] Xing, J.Z., 2015. Design and Analysis of Ultra-high Pressure Water Jet Emergency Rescue Robot. Master Thesis. Tianjin University of Technology and Education, Tianjin, China.

[6] Yang, W.J., 2016. Design and Research on Hydraulic system of Ultra-high Pressure Water Jet Demolition Robot. Master Thesis. Tianjin University of Technology and Education, Tianjin, China.

Tunnelling for a Better Life – Yan, Celestino, Thewes & Eberhardt (Eds)
© 2024 The Author(s), ISBN 978-1-032-80042-4
Open Access: www.taylorfrancis.com, CC BY-NC-ND 4.0 license

Research on information perception mechanism and evaluation method of tunnel lighting environment

Bo Liang
College of Civil Engineering, Chongqing Jiaotong University, Chongqing, PR China
State Key Laboratory of Mountain Bridge and Tunnel Engineering, Chongqing Jiaotong University, Chongqing, China

Jia'an Niu* & Can Qin
College of Civil Engineering, Chongqing Jiaotong University, Chongqing, PR China

ABSTRACT: The existing tunnel lighting standards are mainly based on physical evaluation indicators, such as luminance and luminance uniformity in photopic vision, which do not fully consider the actual changes of the visual environment when driving in the tunnel, and do not fully reflect the psychological and physiological perception and the behavioral response of drivers. This paper made a systematic study on the information and perception in the tunnel lighting environment, revealed the change rule and relationship between physical information and physiological perception, and proposed a series of evaluation methods of tunnel lighting environment based on information perception, and then verified by numerous static and dynamic information perception experiments. The results show that the tunnel lighting environment is composed of material information and the characteristics of the tunnel lighting environment are represented by physical information. As a coupled human-vehicle-road environment, information perception involves not only the physical information of the tunnel lighting environment, but also the subjective response (i.e. physiological perception) of the driver. Through the comprehensive analysis of the specific relationship between physical information and physiological perception, the information perception mechanism is formed, and the tunnel lighting environment evaluation method based on information perception is further constructed. It provides basis and reference for tunnel lighting environment design.

Keywords: Tunnel lighting environment, Physical information, Physiological perception, Information perception mechanism, Evaluation method

1 INTRODUCTION

At present, China's economy has changed from the stage of rapid growth to the stage of high-quality development of "satisfying people's yearning for a better life". Tunnels play an important role in ensuring smooth traffic and promoting economic prosperity. By the end of 2022, there are 24850 highway tunnels in China, with a total length of 26.7843 million meters (Ministry of Transport of the people's Republic of China, 2022). However, as a kind of semi-closed tubular space structure, the "black hole, white hole" effect of vehicles entering and leaving will cause visual oscillation to the driver (Liang et al., 2020). Drivers obtain information from the outside world through vision, hearing, and smell, of which more than 80% of the outside information perception is obtained through visual perception during tunnel driving (Mehri et al., 2019). A large sample survey of traffic accident causes shows that the proportion of traffic accident causes as the dominant human factor is as high as 92.6% (Shi et al., 2022). Therefore, in the process of driving in the tunnel, how to obtain and correctly perceive the information and make a correct response to the constituent information, especially the lighting environment, is directly related to the safety and comfort of tunnel operation.

Drivers' perception of information involves not only physical information, but also people's subjective reaction, namely physiological perception (Liang et al., 2023). Among them, physiological perception refers to the physiological and psychological response indicators of drivers under tunnel lighting environment, which can also be called biological indicators (Hamedani et al., 2019). Including electrocardiogram (ECG), electromyography (EMG), electroencephalogram (EEG), reaction time, perceived contrast and visual efficacy of a series of indicators (such as pupil

*Corresponding author: ja_niu@163.com

DOI: 10.1201/9781003495505-453

diameter and change rate, fixation, saccade frequency) and so on (Niu et al., 2024). Physical information refers to the definite indicator used to measure material properties and describe matter in different motion states under tunnel lighting environment, which can also be called physical indicator (Niu et al., 2022). Including luminance, luminance uniformity, illuminance, space size, color, traffic flow, speed, visibility and so on. Moreover, the way drivers perceive the lighting environment can be divided into static perception and dynamic perception. The static perception of tunnel lighting environment is the perception mode of tunnel lighting environment under static conditions (Pigliautile et al., 2020). At present, the research on drivers' perceptual characteristics under static conditions is more mature, such as human visual search features, human depth perception features and so on. Dynamic perception in tunnel lighting environment is the way of perception under driving conditions (Zhang et al., 2022). There are two main research methods for dynamic perception: one is dynamic perception in virtual scene, and the other is dynamic perception in real traffic environment.

At present, the design and research of tunnel lighting at home and abroad are mostly focused on the value and evaluation of the physical indicator of lighting environment, without fully considering the driver's physiological perception under the condition of human-vehicle-tunnel lighting environment, and its impact on driving behavior and traffic safety (Qin et al., 2023). The research work and results of tunnel lighting environment are seldom carried out from the point of view of information representation and information perception (Bellazzi et al., 2022), and the dynamic perception mechanism and experimental research are seldom carried out from many aspects, such as driving simulation experiment and real vehicle test. There is no tunnel lighting environment evaluation method considering both physical information and physiological perception (Chihara et al., 2020).

Against the above background, this paper studies the relationship between the physical information of tunnel lighting environment and the physiological perception from the point of view of ensuring safety and comfort, and clarifies the information perception mechanism of drivers in different motion states. A tunnel lighting environment evaluation method based on dynamic perception of biological visual indicator is proposed to provide theoretical basis and evaluation indicator for tunnel operation environment safety, quality improvement and future intelligent lighting.

2 COMPOSITION AND CHARACTERIZATION OF TUNNEL LIGHTING ENVIRONMENT INFORMATION

2.1 *Analysis on the composition of tunnel lighting environment information*

The tunnel lighting environment information is composed as shown in Figure 1.

Figure 1. Sketch of tunnel lighting environment information composition.

2.1.1 *Direct influencing factors*

1) Light source. The light source in the tunnel is one of the important components of the tunnel lighting environment. In addition to the inherent properties such as luminance and light color, the layout of lamps and lanterns is also an important factor affecting the composition of the tunnel lighting environment.
2) Sidewall material. With the improvement of driving safety and comfort requirements in the tunnel, a single concrete sidewall material has been unable to meet the requirements. At present, tunnel sidewall materials can be classified into seven categories: concrete, enamel steel plate, ceramic tile, composite aluminum plate, fireproof material, fiber reinforced concrete board and energy-storage and self-luminous material (Shen et al., 2022).
3) Tunnel vault. As an important part of the tunnel lighting environment, the color of the vault will affect the driver's identification of the tunnel lighting environment and driving comfort.
4) Road surface. As a driving carrier, the road surface is an important part of the tunnel lighting environment. When motor vehicle drivers drive, they feel the road surface luminance visually. Therefore, the lighting design of highway tunnel should meet the requirements of average luminance, total luminance uniformity, longitudinal uniformity, flicker and inducement of pavement centerline.

2.1.2 *Indirect influencing factors*

1) Traffic safety signs. Traffic safety sign setting system includes color, shape, text, graphics, layout, location, structure and materials and other elements, the accuracy and completeness of these information is directly related to the effectiveness of traffic signs.
2) Vehicle characteristics. In addition to the main structure of the tunnel, the composition of the lighting environment also includes the vehicle characteristics such as the size, color, light and

siren of the vehicles in the tunnel. Vehicle color can provide some safety warning information while driving, and whether the lights are normal or not directly affects the driving safety.

3) Guidance signs. The driver is the main factor in driving in the tunnel, improving the visual guidance environment inside the tunnel, keeping the driver within a reasonable range of environmental information, and enabling the driver's visual perception ability to process the driving environment information inside the tunnel, thereby improving the safety of driving.

2.2 *Indicators for characterizing tunnel lighting environment information*

2.2.1 *Physical information*

Describing the physical information of tunnel lighting environment and putting forward the evaluation indicator is not only the key basis for the formulation of tunnel lighting design standards, but also an important basis for tunnel lighting theoretical research.

In the aspect of driving safety, luminance is a physical information that indicates the luminous (or reflective) surface of the luminous body (or reflector). It is the subjective feeling of the light intensity, which determines whether the human eye can see the basic information of the object. Disability glare refers to the occurrence of excessive luminance or excessive luminance change before and after a certain part of the field of vision, which seriously affects the judgment and working ability of drivers in the process of driving, thus leading to safety accidents. Visibility refers to the maximum distance that a person with normal vision can identify the target from the background, which determines whether the driver can clearly identify the outline characteristics of the target from a 20-degree perspective, which is an important factor for safe driving.

In terms of driving comfort, luminance uniformity is an indicator to ensure the visibility and visual comfort of drivers. When the environmental luminance reaches a certain value, the human eye is in an environment with large luminance contrast, so it will be easier to adapt to the environment and identify objects. Uncomfortable glare refers to the repeated high luminance changes in the driving field of vision, which is one of the important causes of visual fatigue, which can lead to the decrease of image clarity and contrast. Color temperature is a general term that indicates that light contains color components. Reasonable color temperature distribution in tunnel lighting environment can shorten the reaction time of drivers and improve driving safety and comfort.

Therefore, as a tunnel lighting environment at a certain speed, the driver's visual perception and judgment of physical information in the process of vehicle driving is obviously different from that in the static state.

2.2.2 *Physiological perception*

When the driver passes through the tunnel, due to the change of the lighting environment and speed in different tunnel lighting areas, the driver's physiological perception changes accordingly, which affects the driver's real perception of the tunnel lighting environment information. and even lead to traffic safety accidents.

Under different light conditions, the changes of ECG can reflect the degree of emotional tension of drivers. The level of skin conductance can show the muscle fatigue accumulated by the driver during driving. EEG signals can record the changes of electric waves during brain activity and indicate the degree of consciousness of the driver. Visual efficacy can describe the influence of the change of tunnel environment luminance on drivers' fatigue and tension, and the degree of difficulty for drivers to obtain tunnel lighting environment information. The reaction time is the time it takes for the driver to identify obstacles and complete braking in the tunnel lighting environment. The perceived contrast can characterize the effects of windshield, atmospheric dispersion, range and luminance of human eye field on drivers' information perception.

Under different speed conditions, the visual spectral sensitivity curve of the driver moves to the short wave direction in advance during dark adaptation, which leads to a change in the dynamic perception state of the visual field luminance of the driver, which in turn affects the driver's driving behavior. The real car test shows that increasing the ambient luminance of the driver in the 20 ° field of view angle in the tunnel can alleviate the driver's tension. As the driving speed increases, the driving task becomes more difficult, the visual task becomes more difficult, and the driver will pay less attention to the road ahead.

3 MECHANISM AND EXPERIMENTAL RESEARCH ON PERCEPTION OF TUNNEL LIGHTING ENVIRONMENT INFORMATION

3.1 *Experimental study on static perception of tunnel lighting environment information*

3.1.1 *Construction of static information perception simulation testing platform*

To test the reaction time of human eyes to random targets on the background under the same lighting luminance (luminance uniformity) and different lighting environments (such as changing background luminance, target contrast, eccentric angle, sidewall material, etc.), an information perception analysis model under static conditions is proposed. The reaction time was selected as the evaluation indicator to study the influence of different lighting environment on the visual efficacy of the subjects. Reaction time directly evaluates the tester's ability to perform visual tasks under different lighting conditions,

which is similar to the completion of visual tasks in the actual visual working environment. Therefore, the visual model based on reaction time can be used to evaluate the information perception ability of highway tunnel lighting environment.

The information perception simulation testing platform under static conditions is shown in Figure 2. It is composed of the target generation of the highway tunnel lighting environment scale model by the photosensitive reaction time measuring device used in the tunnel lighting environment simulation test and the reaction time data acquisition and integrated processing system linked with the reaction time measuring device. The purpose of this paper is to provide the experimental basis for determining the reaction time of the people tested under different sidewall materials.

Based on the information perception simulation testing platform under static conditions, the project team carried out a series of experimental studies, including target perception response time, small target visibility (STV), spectral distribution of tunnel lighting assisted by different materials and so on.

Figure 2. Information perception model under static condition and simulation testing platform.

3.1.2 *Response time test of target perception*

The tunnel lighting uses LED energy-saving light source, and its luminance range can be adjusted (1-15 cd/m^2) to simulate the lighting level of the middle section of the highway tunnel, and the lighting environment of the tunnel can be adjusted according to the two dependent variables of contrast and luminance. According to the position of the target spot, the eccentricity angles of 0 °, 10 °and 20 °are randomly distributed, and the reaction time of target discovery is recorded by timer to simulate the different conditions of middle axis and non-middle axis.

When the contrast C is 0.5 and the background luminance L is 10 cd/m^2, the reaction time of the three test materials with the deflection angle of the sight mark is shown in Table 1. Among them, the reflectivity of cement mortar is the lowest, the energy-storage and self-luminous material is the highest, and the ceramic tile is in the middle. It can be seen from Table 1 that at the same eccentricity angle, the reaction time decreases with the increase of the reflectivity of the sidewall material, and for the same material, the reaction time increases with the increase of the eccentricity angle. The experimental data show that the effect of the increase of the reflectivity of the sidewall material on the reduction of reaction time is more obvious than that of the background luminance.

Table 1. Contrast eccentricity and reaction time when C is 0.5 and L is 10 cd/m^2.

	Reaction time/ms			
Contrast eccentricity/(°)	Cement mortar	Ceramic tile	Energy-storage and self-luminous material	Total reduction of reaction time/ms
0	292.11	262.54	256.37	35.74
10	296.93	275.67	262.81	34.12
20	303.81	292.26	277.48	26.33
Total added value	11.70	29.72	21.11	

3.1.3 *Small target visibility information perception test*

In this paper, cement mortar, ceramic tile and energy-storage and self-luminous material are selected as the sidewall materials of the tunnel. In the tunnel model shown in Figure 2, the composition of the lighting environment such as luminance and color temperature in the tunnel is changed by adjusting the lighting luminance in the model, so as to change the composition information of the lighting environment. Then send out small targets with different information (such as size, position, luminance, etc.) through the small target generator, and take the time needed for the human eye to capture the small target as the experimental data. In this experiment, the laboratory test of small target visibility was carried out by correlation luminance uniformity and discovery time. The visibility curve of small targets under different sidewall materials is shown in Figure 3.

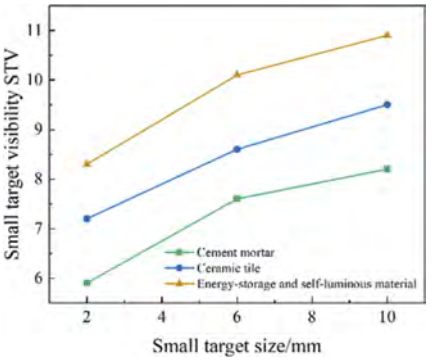

Figure 3. Relationship curves between average luminance of pavement and small target visibility (STV).

It can be seen from Figure 3 that the STV value of small target visibility increases with the increase of small target size, and the growth range of small target visibility (STV) is further increased with the increase of small target size. It also further confirms the common sense that larger obstacles are more conducive to identification in reality.

3.2 *Experimental study on dynamic perception of tunnel lighting environment information*

3.2.1 *Construction and experimental research of a dynamic information perception simulation testing platform*

Based on virtual simulation technology, we have independently developed a simulation testing platform for dynamic information perception (Figure 4). We use a dynamic environment simulation output device to achieve a realistic restoration of the tunnel driving environment in the laboratory, which can be used to conduct indoor research on the safety and comfort of driving environments in different tunnel visual environments.

Figure 4. Dynamic information perception simulation testing platform.

The team conducted a series of experiments on driving dynamic information perception in tunnels based on the dynamic information perception mechanism and the reaction time indicators in visual efficacy theory, and relying on the developed dynamic information perception simulation testing platform.

By recording high-definition videos of 6 extra long highway tunnels at speeds of 60, 70, and 80 km/h, and using a dynamic information perception simulation testing platform, the indoor driving environment was realistically restored to obtain the response time characteristics of the driving process. The reaction time is to simulate the target object with a spot emitter and randomly project it onto different positions in front of the photographic recording road surface. By pressing the brake or pressing the timer, a computer mini program is used to automatically record the time when the driver discovers the spot. The average reaction time of drivers at different distances from the tunnel entrance is shown in Figure 5.

The main experimental conclusions are as follows: 1) Overall, the reaction time shows a process of decreasing first and then slowly increasing; 2) The reaction time at the entrance of the tunnel is relatively long, then rapidly decreases, and the reaction time is the shortest at around 750 meters; 3) The driver's reaction time increases with the increase of tunnel length and driving time, and there are significant fluctuations in physiological and psychological changes during this period; 4) As the vehicle speed gradually increases, the refresh rate of traffic information in the driver's field of view accelerates, the level of danger during driving increases, the driver's attention and vigilance significantly increase, and the reaction time gradually decreases.

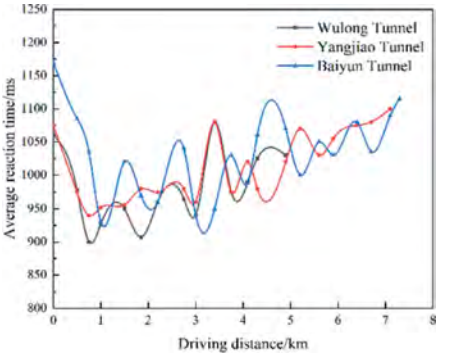

Figure 5. Average response time of drivers at different entrance distances from tunnel.

3.2.2 *Research on dynamic information perception in real vehicle testing*

Based on the Lushan Tunnel, Yeyatang No.1 and No.3 Tunnels in Yunnan, Maoba No.2 Tunnel in Shaanxi, Zhujiadu Tunnel and Shizizhai Tunnel in Sichuan, as well as 13 highway tunnels in Chongqing, including Xianghuang Tunnel, Changchong Tunnel, Nanshan Tunnel, Zhenwushan Tunnel, Cimushan No.1 Tunnel, Bayi Tunnel, and Hengkou Tunnel, a total of 316.24 km of eye movement and physiological indicators were tested for a total of 2004 participants. The study on the eye movement characteristics of drivers based on visual efficacy is to test the eye movement characteristics of drivers driving under different tunnel lighting environments (different lamps, lamp layout methods, etc.) and the same driving conditions during day and night. By analyzing the eye movement characteristics, the changes in eye movement parameters of drivers under different tunnel lighting environments are obtained, The on-site experiment is shown in Figure 6.

Figure 6. Schematic diagram of field test car and pupil area data collection.

1) Analysis of the changing trend of pupil parameters of drivers

To more intuitively characterize the visual load of drivers at the entrance and exit of the tunnel and evaluate the safety of the entrance of the tunnel, on the basis of the widely accepted definition of the visual oscillation time indicator of drivers, and based on the pupil diameter change ratio *PDCR*, the visual oscillation indicator of drivers is modified, and the visual oscillation duration indicator T_{PDCR} is proposed. The entrance section is selected as the research object. at a certain time, the pupil diameter of the driver is d_{i+1}, and the pupil diameter of the previous moment is d_i. The average pupil diameter of the driver during this period is M, and the pupil diameter change ratio *PDCR* is:

$$PDCR = \frac{d_{i+1} - d_i}{M} \tag{1}$$

$$T_{PDCR} = T_e - T_s \tag{2}$$

When the *PDCR* value of a driver at a certain point is compared with the two points before and after, and the fluctuation of the two points is outside the range of ±5% of the pupil diameter change rate and the difference between the two points is more than 10%, the phenomenon of visual oscillation will occur. The first point T_s outside the range of ±5% of the pupil diameter change rate was used as the start of the oscillation for the duration of the visual oscillation, and the first point T_e within the range of ±5% of the pupil diameter change rate was used as the end of the oscillation for the duration of the visual oscillation, as shown in Figure 7.

Figure 7 shows that the ratio of changes in pupil diameter at the inlet and outlet during each time period can be observed. At 9:30 am and 5:30 pm, when the illuminance changes are relatively small, the maximum *PDCR* values at the inlet and outlet are significantly smaller compared to other time periods. Among them, the maximum *PDCR* values at 9:30 am and 17:30 am are only 11.34% and 11.45%, respectively. On the other hand, the maximum (*PDCR*) of the import and export segments in other time periods is generally greater than 20%, and is basically distributed between 20% and 40%; At 13:30, the maximum (*PDCR*) of the entrance section even reached 51.9%. During this period, the maximum value of the illuminance change rate I_c in the entrance section was 3127.637 lux/s, which is the maximum value of the illuminance change rate in the entrance and exit section of the whole day working condition. It can be seen that excessive illuminance change rate has a significant impact on the driver's visual characteristics.

Moreover, drivers at the entrance and exit of the tunnel have different degrees of visual oscillation, but due to the change of illuminance, the duration of visual oscillation T_{PDCR} is different. When the illuminance change is relatively low, for example, the T_{PDCR} of the driver's visual oscillation at the entrance and exit at 9:30 and the exit at 17:30 are 1.22s, 1.68s and 1.28s, respectively, while at the entrance and exit at 10:30, 11:30, 13:30 and 15:30 where the illuminance changes greatly, and at 17:30, the visual oscillation duration T_{PDCR} is more than 2s. At 11: 30, the visual oscillation duration T_{PDCR} of the driver in the exit section is as high as 2.4s. It can be found that the more severe the illuminance difference is, the longer the visual oscillation duration of the driver is, the shorter the visual oscillation duration of the mild illuminance change is, and even there is no visual oscillation phenomenon; it is considered that within a certain range, there is a certain positive correlation between the illuminance difference at the entrance and exit of the tunnel and the visual oscillation duration of the driver.

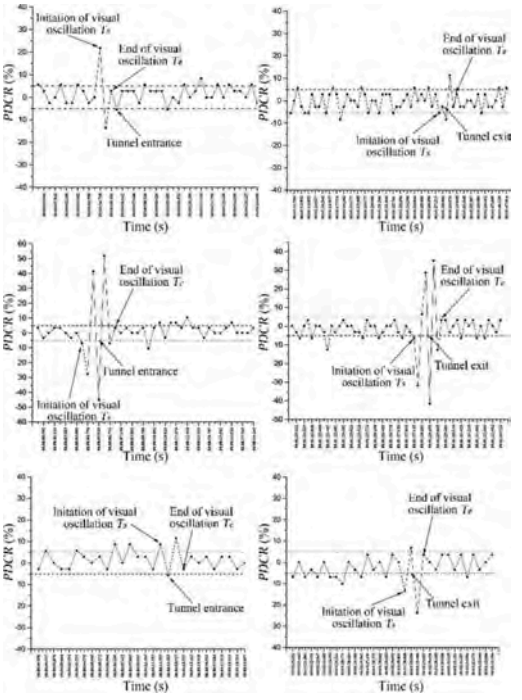

Figure 7. Changing trend of PDCR value at the entrance and exit of the tunnel: (a) 9:30 Entrance, (b) 9:30 Exit, (c) 13:30 Entrance, (d) 13:30 Exit, (e) 17:30 Entrance, (f) 17:30 Exit.

2) Analysis of drivers' saccade behavior.

The saccade parameters include saccade amplitude and saccade speed, which is the breadth of visual range acquisition by human eyes in a period of time, and the saccade speed reflects the speed of visual range acquisition.

$$V_s = \frac{A}{T} \tag{3}$$

Where, V_s is the saccade speed, $°\cdot s^{-1}$; A is the saccade amplitude, °; T is the time of a saccade event, s.

After organizing the analysis of driver's saccade amplitude, it was found that the saccade amplitude of the driver on the entire road section changed slightly at any time, and the overall trend of change was basically consistent. Therefore, a graph of the change in driver's saccade amplitude at 11:30 was drawn as shown in Figure 8:

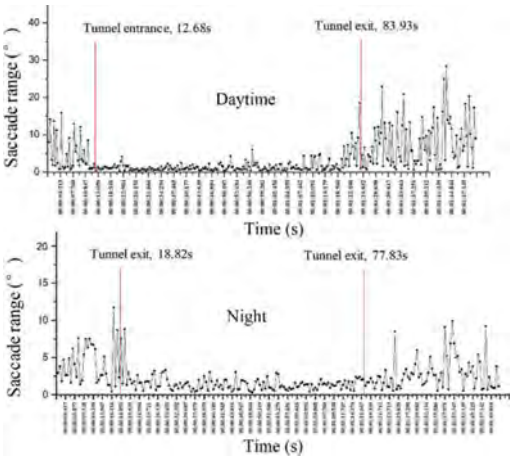

Figure 8. Change in saccade amplitude of the driver.

According to the analysis in Figure 8, it is found that the saccade range of the driver while driving outside the tunnel is basically maintained at 0-30 °. At a distance of 1-2 seconds before the tunnel entrance (i.e. 20-30m from the entrance), the saccade amplitude suddenly decreases, and the saccade amplitude of the driving in the tunnel remains basically at 0-3 °, indicating a small saccade behavior; When approaching the exit of the tunnel, the saccade amplitude increases until it reaches the level of saccade amplitude of the driver in the driving environment outside the tunnel.

The saccade behavior in which the saccade speed is less than 30 °/s is regarded as fixation behavior, so the average saccade speed of drivers in the middle section of the tunnel under daytime conditions is calculated, and the distribution of different saccade speed ranges is drawn as shown in Figure 9. It can be seen from the Figure 9 that 80% of the drivers' eye movement behavior in the middle section of the four tunnels is fixation behavior. The analysis shows that for

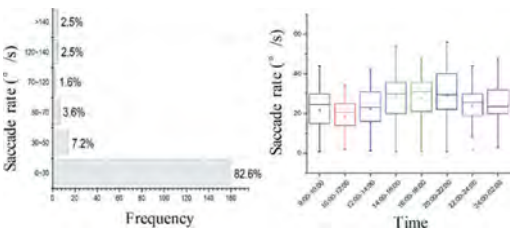

Figure 9. Analysis of saccade behavior of drivers.

the driving environment in the tunnel, because the tunnel is a special semi-closed tubular structure. There is less traffic reference information in the hole, and the saccade speed of the driver is greatly reduced.

4 RESEARCH ON EVALUATION METHOD OF TUNNEL LIGHTING ENVIRONMENT BASED ON INFORMATION PERCEPTION

4.1 *Selection of evaluation indicators and construction of evaluation models*

In this paper, according to the changes of lighting environment in the process of driving through the tunnel, the tunnel section is divided into:

1) Dark adaptation section (scotopic vision): During the day, the driver drives from outside the tunnel to inside the tunnel; The process of driving from the inside of the tunnel to the outside of the tunnel by night drivers;
2) Bright adaptation section (photopic vision): During the day, the driver drives from inside the tunnel to outside the tunnel; The process of driving at night from outside the tunnel into the tunnel;
3) Middle section: The middle section of the tunnel where the luminance remains unchanged in the design of tunnel lighting.

Divide the tunnel driving section into dark adaptation section, bright adaptation section, and middle section. The lighting environment physical indicators for the dark and bright adaptation sections are selected based on the change in illuminance value, while the driver's biological indicators are selected based on the driver's visual oscillation duration indicator (safety evaluation indicator) and saccade speed indicator (comfort evaluation indicator). The selection of physical indicators for the middle section of the tunnel is based on the visibility and illuminance values inside the tunnel. The biological indicators of drivers selected are reaction time (safety evaluation indicator) and saccade speed (comfort evaluation indicator), combined with probability theory 3σ calculate the threshold and evaluation level of each evaluation indicator in principle, and then obtain the safety and comfort rating table for each road section. Based on the functional relationship between various physical indicators of the lighting environment and the biological indicators of the driver, a tunnel lighting safety and comfort evaluation model is constructed to achieve the evaluation of lighting safety and comfort for different sections of the tunnel at different time periods.

4.2 *Research on tunnel lighting environment evaluation based on dynamic perception of biological visual indicators*

Based on the previous test and analysis of the lighting environment physical information and drivers'

physiological perception of the tunnel, the tunnel section is divided into dark adaptation section, bright adaptation section and tunnel middle section according to the changing trend of illuminance, and the safety and comfort evaluation model of each lighting section of the tunnel is constructed.

1) Lighting safety and comfort evaluation model for dark adaptation section of tunnel.

$$\begin{cases} T_{PDCR} = 3.59 * \exp\{-1117.4/(E_c - 397.65)\} \\ V_S = \exp\left(5.12 + 1.81e^{-4}E_c - 6.5e^{-7}E_c^{\,2}\right) \\ x_{vs} = \ln\ V_s \end{cases} \quad (4)$$

Where, T_{PDCR} is visual oscillation duration (ms); E_c is illuminance change value (lux); V_S is saccade speed; x_{vs} is saccade speed.

Table 2. Safety and comfort evaluation table of tunnel lighting (dark adaptation section).

T_{PDCR} / x_{vs}	[0.2,0.74s)	[0.74,1.13s)	[1.13,1.91s)	[1.91,1.23s)	[2.3,2.69]
[4.29,4.55]	A	B	C	D	E
[4.03,4.29)	B	C	D	E	F
[3.51,4.03)	C	D	E	F	G
[3.25,3.51)	D	E	F	G	H
[2.99,3.25)	E	F	G	H	I

(The evaluation level in the evaluation table is divided into 9 levels, A-I, among which A-level has the best driving safety and comfort, followed by B-I evaluation levels where driving safety and comfort gradually deteriorate, and I-level is the worst. The following evaluation criteria are the same.)

2) Lighting safety and comfort evaluation model for bright adaptation section of tunnel.

$$\begin{cases} T_{PDCR} = 3.59 * \exp\{-1117.4/(E_c - 397.65)\} \\ V_S = \exp\left(3.72 + 7.05e^{-4}E_c - 9.48e^{-8}E_c^{\,2}\right) \\ x_{vs} = \ln\ V_s \end{cases} \quad (5)$$

Table 3. Safety and comfort evaluation table of tunnel lighting (bright adaptation section)

T_{PDCR} / x_{vs}	[0.2,0.74s)	[0.74,1.13s)	[1.13,1.91s)	[1.91,1.23s)	[2.3,2.69]
[4.25,4.39)	A	B	C	D	E
[4.39,4.53)	B	C	D	E	F
[4.53,4.81)	C	D	E	F	G
[4.81,4.95)	D	E	F	G	H
[4.95,5.09]	E	F	G	H	I

3) Lighting safety and comfort evaluation model for middle section of tunnel.

$$\begin{cases} T = 1231 - 4.03E + 31.91\tau_R + 0.005E^2 \\ \qquad -144.38{\tau_R}^2 + 0.72E \cdot \tau_R \\ V_S = 24.86 - 0.88E - 64.46\tau_R + 0.009E^2 \\ \qquad +49.6{\tau_R}^2 + 1.45E \cdot \tau_R \\ x_{vs} = \ln\ V_s \end{cases} \quad (6)$$

Where, T is reaction time (ms); E is illuminance value (lux).

Table 4. Safety and comfort evaluation table of tunnel lighting (middle section).

T / x_{vs}	[0.8,0.87)	[0.87,0.94)	[0.94,1.08)	[1.08,1.15)	[1.15,1.22]
[3.86,4.32]	A	B	C	D	E
[3.4,3.86]	B	C	D	E	F
[2.48,3.4]	C	D	E	F	G
[2.02,2.48]	D	E	F	G	H
[1.56,2.02]	E	F	G	H	I

5 CONCLUSION

1) This study elucidates the main factors and transmission methods of highway tunnel lighting environment information representation, comprehensively summarizes the information composition and information characteristics of tunnel lighting environment, and deeply analyzes the direct and indirect influencing factors of information composition. The indicators for characterizing tunnel lighting environment information are summarized from two aspects of physical information and physiological perception.
2) Through indoor static and dynamic information perception simulation testing platforms, combined with a large number of actual vehicle experiments, a series of physiological perception reactions of drivers during tunnel static and dynamic driving processes were analyzed, including reaction time, small target visibility, visual oscillation, and saccade behavior. Further revealed the changing trend and interaction relationship between the physical information of tunnel lighting environment and physiological perception during driving, comprehensively studied and elucidated the information perception mechanism of drivers under different motion states.
3) From the perspective of drivers' perception of tunnel lighting environment information, taking

into account both the physical information of tunnel lighting environment and the driver's physiological perception, a tunnel lighting safety and comfort rating table is proposed. Combining the functional relationship between physical and biological indicators of lighting environment, a dynamic evaluation model for tunnel lighting environment based on biological visual indicators is established.

ACKNOWLEDGMENTS

This study was supported by the National Natural Science Foundation of China (No. 51878107, 52378391), the Project of Chongqing Talent Team (No. 2019-9-95), the Research and Innovation Program for Postgraduate in Chongqing Jiaotong University (No. 2022B0004), and China Scholarship Council (No. 202308500246).

REFERENCES

Bellazzi, A., Bellia, L., Chinazzo, G., et al., 2022. Virtual reality for assessing visual quality and lighting perception: a systematic review, Build. Environ. 209, 108674.

Chihara, T., Kobayashi, F., Sakamoto, J., 2020. Evaluation of mental workload during automobile driving using one-class support vector machine with eye movement data. Appl. Ergon. 89, 103201.

Hamedani, Z., Solgi, E., Skates, H., et al., 2019. Visual discomfort and glare assessment in office environments: A review of light-induced physiological and perceptual responses. Build. Environ. 153, 267–280.

Liang, B., Liang, J., He, S., et al., 2020. Study on lighting environment information perception and experiment method of highway tunnel. Tunn. Constr. 40, 1251–1260.

Liang, B., Niu, J., Zhang, H., 2023. Analysis of driving comfort at tunnel entrance based on saccade path speed. Chin J. Undergr. Space Eng. 20, 1–10.

Mehri, A., Sajedifar, J., Abbasi, M., et al., 2019. Safety evaluation of lighting at very long tunnels on the basis of visual adaptation. Saf. Sci. 116, 196–207.

Ministry of Transport of the people's Republic of China, 2022. Statistical bulletin on the development of transportation industry in 2022. https://www.gov.cn/govweb/lianbo/bumen/202306/content_6887539.htm.

Niu, J., Liang, B., He, S., et al., 2022. Long tunnel lighting environment improvement method based on multiple-parameter intelligent control: Considering dynamic changes in luminance difference. Tunn. Undergr. Space Technol. 128, 104637.

Niu, J., Liang, B., He, S., et al., 2024. Assessment and optimization of tunnel lighting quality based on drivers' visual comfort: From methodology to application. Tunn. Undergr. Space Technol. 143, 105487.

Pigliautile, I., Casaccia, S., Morresi, N., et al., 2020. Assessing occupants' personal attributes in relation to human perception of environmental comfort: Measurement procedure and data analysis. Build. Environ. 177, 106901.

Qin, C., Liang, B., Xiao, J., et al., 2023. Physical characteristics of lighting environment and physiological change of drivers in tunnel. KSCE J. Civ. Eng. 27, 2170–2179.

Shen, Y., Ling, J., Li, T., et al., 2022. Diffuse reflection-based lighting calculation model and particle swarm optimization algorithm for road tunnels. Tunn. Undergr. Space Technol. 124, 104457.

Shi, L., Li, Y., Tao, L., et al., 2022. Sporters' visual comfort assessment in gymnasium based on subjective evaluation & objective physiological response. Build. Environ. 225, 109678.

Zhang, D., Chen, F., Zhu, J., et al., 2022. Research on drivers' hazard perception in plateau environment based on visual characteristics. Accid. Anal. Prev. 166, 106540.

Tunnelling for a Better Life – Yan, Celestino, Thewes & Eberhardt (Eds)
© 2024 The Author(s), ISBN 978-1-032-80042-4
Open Access: www.taylorfrancis.com, CC BY-NC-ND 4.0 license

Research and realization of equivalent lighting environment for tunnels

Bo Liang
College of Civil Engineering, Chongqing Jiaotong University, Chongqing, China
State Key Laboratory of Mountain Bridge and Tunnel Engineering, Chongqing Jiaotong University, Chongqing, China

Can Qin* & Jia'an Niu
College of Civil Engineering, Chongqing Jiaotong University, Chongqing, China

ABSTRACT: Traditional lighting technology is not reasonable enough to improve the quality of tunnel lighting environment. Therefore, it is necessary to further solve the bottleneck problems of energy saving, safety, maintenance under the coupling effect of human-vehicle-tunnel lighting environment. Based on the "non-equivalent characteristics of lighting environment load and visual perception effect" and "the mechanism of equivalent lighting environment affecting driving safety and comfort", this study proposes the theoretical path of equivalent lighting environment combining the effect of multiple light sources and natural light. Through the static and dynamic visual efficacy test, the evaluation method of driver information perception state under the equivalent lighting environment of tunnel is established. By analyzing the change of lighting environment for tunnel under the condition of multiple factors, the specific application method of equivalent lighting environment of tunnel is proposed. The results can providing theoretical and technical references for the realization of safe and energy saving of lighting system for road tunnel, and making positive contributions to the national energy conservation and emission reduction strategy.

Keywords: Road tunnel, Lighting environment, Equivalent lighting theory, Visual perception, Evaluation method

1 INTRODUCTION

As a highly restricted space environment with long depth and strong closure, tunnel must rely on artificial lighting to meet the necessary lighting environment for tunnel traffic (Liang, et al., 2020, Wang, et al., 2016). When drivers pass through the tunnel, they experience the process of alternating cycle mutation of lighting environment and rapid transformation of visual adaptation to light and dark, which is easy to cause visual impairment and lead to traffic accidents (Ma, et al., 2015). Therefore, how to provide a safe and energy-saving lighting environment that meets the visual needs of drivers has become the focus of scholars (Liang, et al., 2019).

The existing lighting specifications for tunnel are based on physical quantity indicators (illuminance, luminance, luminance uniformity) to develop lighting quality evaluation indicators, which is the practice of following lighting specifications for road (JTG/TD70/2-01-2014, CIE88:2004), and does not fully consider the influence of biological quantity (eye movement parameters, physiological parameters, brain electrical parameters) under the tunnel lighting environment. Therefore, the coupling mechanism of human-vehicle-tunnel in operation lighting environment for tunnel is ignored (Yang, et al., 2016, Yan et al., 2022).

Existing studies believe that it is a feasible scheme to achieve traffic safety to improve the lighting power and meet the required physical quantity under the most unfavorable lighting conditions for tunnel (Shi, 2020, Chen, et al., 2006). However, there is a great non-equivalence between the environmental load of lighting and the effect of visual perception for tunnel lighting environment. Although the physical quantity reaches or even exceeds the standard requirements, the overall visual effect of lighting environment is not ideal (Ye, et al., 2022, Liu, et al., 2019).

Many scholars also believe that the degradation of the lighting quality of lighting environment for

*Corresponding author: qinc714@163.com

DOI: 10.1201/9781003495505-454

tunnel is mainly caused by the light decay of lamps. Therefore, the replacement of lamps is often used as the main means to improve the quality, and the influence of the pollution situation and the reflection brightening effect during the operation stage of tunnel sidewalls is not considered (Mehri, et al., 2022, Liang, et al., 2015).

In this study, the theoretical path of equivalent lighting environment combining the combination of multiple light sources and natural light was proposed based on "non-equivalent characteristics of lighting environment load and visual perception effect" and "the mechanism of equivalent lighting environment affecting driving safety and comfort". Moreover, the evaluation method of driver information perception state in equivalent lighting environment for tunnels was established through the static and dynamic visual efficacy test. Finally, based on the analysis of the changes of lighting environment under multi-factor conditions, the realization of equivalent lighting environment for tunnels was built.

2 TUNNEL EQUIVALENT LIGHTING ENVIRONMENT TEST

2.1 *Test device*

According to the common size of existing tunnels, a simulated tunnel with a ratio of 1:10 to the actual tunnel was designed and manufactured. The simulated model is a wooden structure, consisting of tunnel ceiling, movable sidewall panel, road surface plate, lamp support and circuit system. Based on 1:1 physical tunnel, the rule of change of physical evaluation indicators (illuminance, luminance, luminance uniformity) is analyzed from the perspective of tunnel light distribution, spacing of lamps, sidewall material, and type of light source. The simulation tunnel and physical tunnel are shown in Figure 1.

In order to realize the indoor simulation of lighting environment for road tunnel under the coupling condition of multiple lighting factors and the visual efficacy evaluation based on reaction time, combined with the characteristics of visual environment, visual efficacy theory and the reaction time principle of the driver's actual driving condition, the tunnel lighting quality evaluation device and simulation test platform were proposed, which is depicted in Figure 2.

In this experiment, real-car test of biological quantity with a total of 2004 person-times was conducted in 316.24 km of 13 highway tunnels, including Lushan Tunnel, Xianghuang Tunnel, Changchong Tunnel. The biological quantity of drivers driving in tunnels with different materials sprayed on the sidewalls were tested by eye movement instruments, electroencephalographs and

Figure 1. Simulation tunnel and physical tunnel.

Figure 2. Tunnel lighting quality evaluation device and simulation test platform.

physiological instruments, respectively. The collection device and acquisition process is show in Figure 3.

Figure 3. Collection device and acquisition process.

2.2 *Physical quantities test*

Based on 1:10 simulation tunnel and 1:1 physical tunnel, considering the reflection coefficient, lamp layout spacing, lamp installation angle, test voltage, sidewall material, light source type, the physical quantity was explored. The Schematic diagram of lamp layout and sidewall materials is shown in Figures 4 and 5.

2.3 *Static and dynamic visual efficacy test*

In static indoor simulation test, the driving environment of tunnel is simulated by the simulation test platform, and the reaction time is carried out. In the test, the diameter of the red circular spot is 25mm, the background luminance is 2 cd/m^2, the spot appears in the position of the optical eccentricity angle is 0°, 10°, 20° random distribution, the target spot luminance is 6 cd/m^2, 7.2 cd/m^2, 9 cd/m^2.

In dynamic indoor simulation test, in order to study the influence of the lighting environment on the driver's driving, the Nanshan, Zhenwu Mountain and Cimushan in Chongqing was selected, and the driving video of the vehicle passing through the tunnel at a relatively stable speed is recorded from 10:00 to 17:00. Using the tunnel lighting simulation test platform and the reaction time test program, the experimenter interacts was conducting.

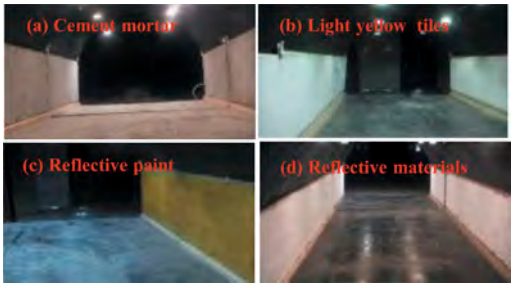

Figure 4. Schematic diagram of different sidewall materials.

Figure 5. Schematic diagram of lamp layout.

3 THEORETICAL PATH OF EQUIVALENT LIGHTING ENVIRONMENT

3.1 *Reduction methods of lighting environmental load*

In Figure 6, the sidewall reflectivity is linear with the illumination uniformity of road surface and wall. For every 10cm increase in lamp spacing, the road surface uniformity decreases by about 0.022. For every 1 increase in lamp angle, the road surface uniformity increases by 0.0016, and for every 1° decrease, the road surface uniformity decreases by 0.0036.

As shown in Figures 7 and 8, under the same lighting conditions, the road surface illumination, luminance and uniformity increase with the increase of sidewall reflectivity. It can be concluded that improving the sidewall reflectivity can improve the lighting environment in tunnels. From the perspective of energy saving, the reflectivity of sidewall materials can be improved to increase the reflected illumination, and then reduce the lighting power of lamps, which is also to meet the original lighting needs. It means that the reflective increment of sidewall coating materials can be used as auxiliary lighting, so as to reduce the lighting environment load and achieve the purpose of lighting energy saving.

3.2 *Visual efficacy analysis in lighting environment*

In Figure 9, the driver's reaction time decreases first and then increases, and the minimum reaction time occurs at the middle measuring point (3 or 4). Because when drivers approach the tunnel, they realize the black hole effect at the tunnel entrance, their attention is enhanced, they are more sensitive to the traffic information around the vehicle, and their reaction time is reduced.

It is revealed in Figures 9 and 10, with the increase of reflectivity increment, the visibility of small targets also increases. It can be concluded that to improve the visibility of small targets can be achieved by improving the reflectivity of sidewall materials. If the number of lamps is reduced or the energy consumption of lamps is reduced, the sidewall materials with higher reflectivity can be used for auxiliary lighting to ensure the visibility of small targets in the tunnel lighting environment.

3.3 *Biological quantity characteristics of drivers*

Figure 11 shows that the heart rate and respiratory rate of different drivers are quite different. After entering the tunnel, the drivers have a higher degree of psychological tension, and the corresponding heart rate and respiratory rate will rise. Moreover, compared with No. 1 tunnel, the heart rate and respiratory rate of drivers driving in No. 3 tunnel are lower, indicating that drivers are more comfortable when driving in No. 3 tunnel sprayed with reflective materials.

It is found from Figure 12 that when drivers drive into the tunnel, due to the narrowing of visual field, the tunnel lighting environment begins to darken, and the proportion of fixation time and pupil area rise sharply, while the saccade range decreases rapidly. When entering the interior zone, due to the relatively dark lighting environment, the proportion of fixation time and saccade range rise slowly, and the pupil area rises to the maximum value. While in the exit zone, the overall luminance of the tunnel increases, and the proportion of fixation time, pupil area and saccade range all show a downward trend. Compared with the daytime, the proportion of fixation time, saccade range and pupil area change less when drivers go from the approach zone to the threshold zone.

It can also be seen from Figure 12 that, in daytime or night, the biological quantity of each zone when drivers drive in No. 3 tunnel are better than those in No. 1 tunnel, which indicates that the lighting environment of No. 3 tunnel is improved after spraying reflective materials, making drivers more relaxed and focused in the driving process, which is conducive to safe driving.

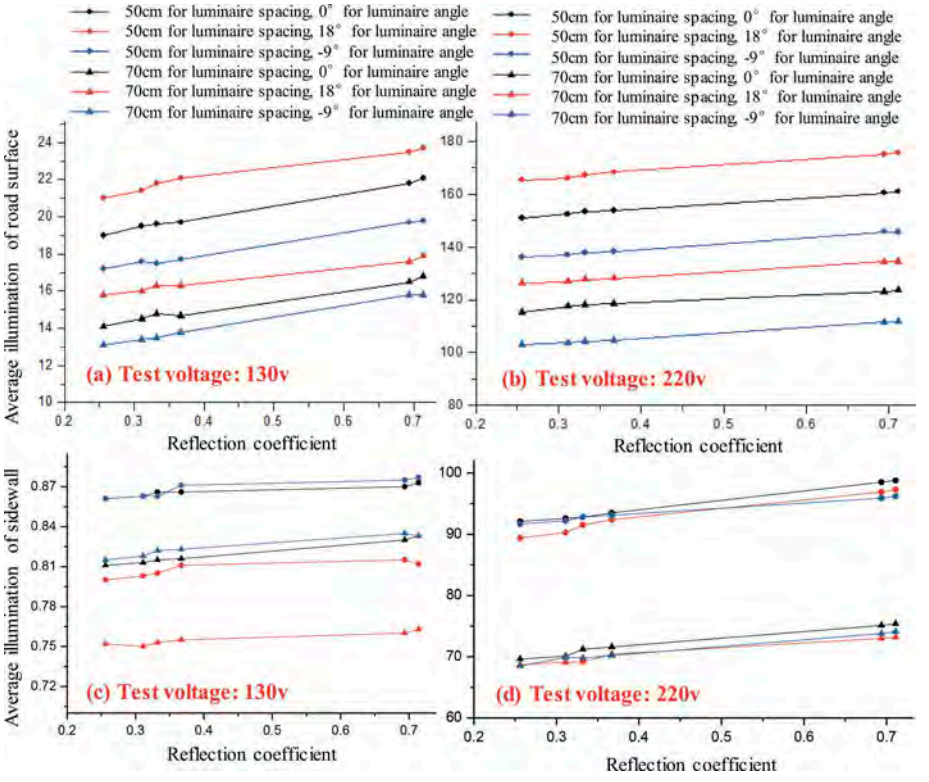

Figure 6. The (a-b) road surface illumination and (c-d) sidewall illumination under different voltage conditions.

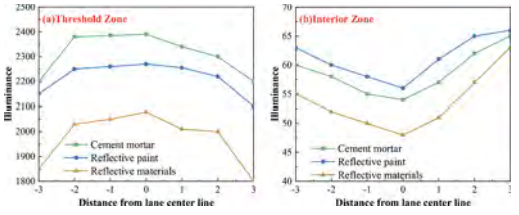

Figure 7. Road surface luminance: (a) threshold zone, (b) interior zone.

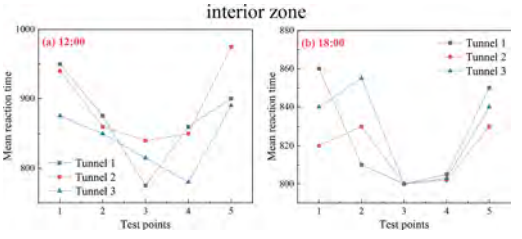

Figure 9. Driver's reaction time: (a) 12:00, (b) 18:00.

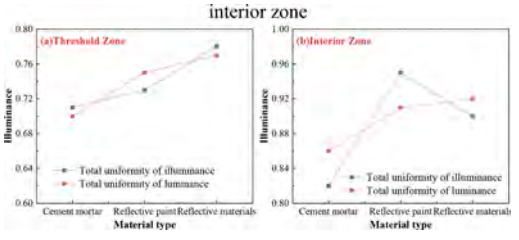

Figure 8. Total road surface uniformity: (a) threshold zone, (b) interior zone.

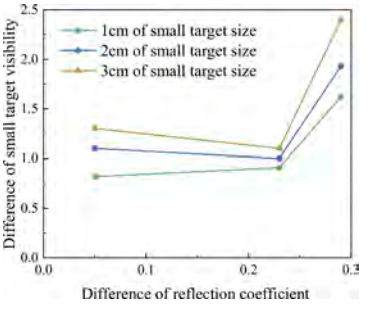

Figure 10. Relationship between reflectivity difference and visibility of small targets.

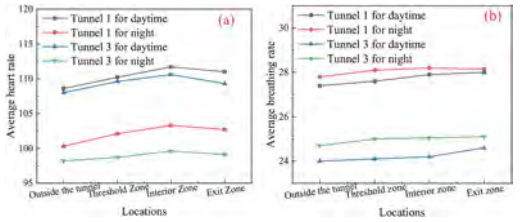

Figure 11. Average heart rate and respiratory rate of drivers during daytime and night.

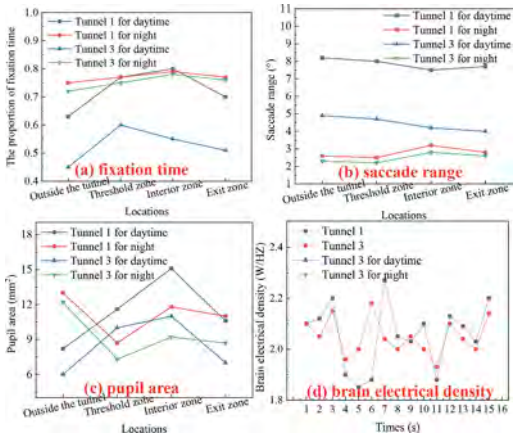

Figure 12. The proportion of fixation time, saccade range, pupil area and brain electrical characteristics of drivers during daytime and night.

3.4 *Realization theoretical path of equivalent lighting environment*

Based on the "non-equivalent characteristics of lighting environment load and visual perception effect" and "the mechanism of equivalent lighting environment affecting driving safety and comfort", the equivalent theory of lighting environment based on the combination of multiple light sources and natural light is proposed. This means that the quality of lighting environment is improved and the lighting environment load is reduced through reasonable matching of lighting environment.

Based on the above research results, one can conclude that the realization of equivalent energy-saving lighting system of tunnel can be realized by adopting measures to improve the quality of the lighting and to reduce the power or energy consumption of the lighting to save energy. Therefore, the methods for realizing equivalent energy-saving lighting are discussed from different perspectives.

(1) Through certain technical methods, the sunlight can replace part of the light source in the tunnel, so as to reduce the energy consumption of tunnel lighting and realize the equivalent lighting of road tunnel. For example, by using solar power generation and photovoltaic technology, the generated electric energy can be directly used as the electric energy of tunnel lighting. Besides, according to the longitude and latitude, orientation and solar altitude of tunnel, the degree and range of the influence of the sunlight on the tunnel can be determined, and then the lamps can be guided to choose a reasonable power for lighting.

(2) Relevant studies have found that under the intermediate visual conditions, the light source spectrum has a great impact on the correct recognition rate of small color targets. For example, the road luminance provided by LED lamp is lower than that provided by HPSL (HPSL), but the correct recognition rate of small targets at each viewing distance is higher than that of HPSL. This shows that compared with HPSL, even if the road luminance is properly reduced, the LED lamp with high color rendition will not affect the correct recognition rate of small color targets, realizing the energy-saving lighting of tunnel.

(3) Tunnel is a semi-closed tubular structure composed of tunnel sidewall and road surface. The sidewall will reflect the light to the road surface once or more, so as to improve the luminance of the road surface. If the sidewall coating material with high reflectivity is used, the light intensity reflected to the ground can be increased, and the increased light intensity can be offset by increasing the spacing of lamps or reducing the number of lamps. Therefore, the number of lamps can be reduced under the condition of maintaining the original lamp design demand unchanged, so as to achieve the purpose of saving tunnel lighting energy consumption.

4 EVALUATION METHOD OF EQUIVALENT LIGHTING ENVIRONMENT

4.1 *Optimization of evaluation indicator*

To ensure that the human eye can better adapt to the changes in the surrounding environment, the pupil needs to adjust the amount of light entering the eye by increasing and decreasing the diameter of the pupil. If the driver's pupil diameter changes too drastically, it will cause it to be unable to see the road conditions ahead. The saccade is an eye movement process that connects two successive fixation behaviors, which can indicate the acquisition width of the human eye to the visual range. The saccade range and saccade speed are the acquisition width and speed of the human eye to the visual range, respectively. Therefore, the pupil and the saccade are used as the evaluation indicator of the equivalent lighting environment in tunnels.

In order to more intuitively characterize the visual load of the driver and the pros and cons of the lighting environment in tunnels, the pupil diameter change ratio (*PDCR*) is proposed.

$$PDCR = \frac{d_{i+1} - d_i}{M} \tag{1}$$

In the equation (1), the pupil diameter of driver at a certain moment is d_{i+1}, the pupil diameter of the previous moment is d_i, and the average pupil diameter at this time is M.

4.2 *Establishment of evaluation method*

4.2.1 *Analysis of pupil diameter*

Figure 13 shows that the pupil diameter of drivers during the daytime driving through the tunnel shows an overall trend of first increasing and then fluctuating slightly, and then decreasing to the value outside the tunnel. When vehicles pass through the entrance and exit of the tunnel at high speed, due to the sharp transition from light to dark, the pupil area of driver changes rapidly, and the rate of change of pupil area increases rapidly.

Figure 13 also shows that the initial pupil diameter of drivers is large at night due to the dark driving environment outside the tunnel, the pupil diameter of drivers shows an overall trend of first decreasing and then increasing, with a small fluctuation in the interior zone. The pupil diameter decreases in the exit zone and gradually increases to the average pupil diameter of drivers outside the tunnel.

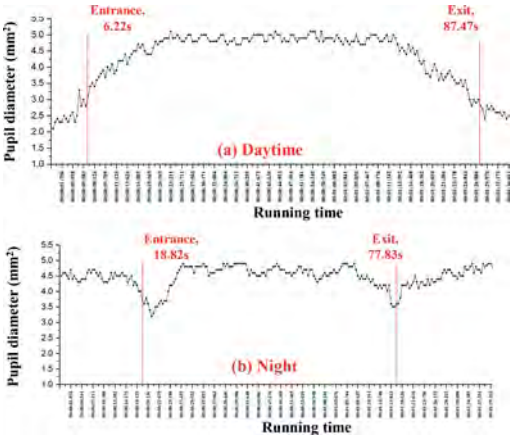

Figure 13. The pupil diameter of the driver in daytime and night.

4.2.2 *Analysis of visual shock phenomenon*

Figure 14 shows that compared with the daytime, visual shock phenomenon still occurs at night, but the degree of visual shock is low and the duration is short. It shows that the driving also causes visual adaptation discomfort under the low illumination outside the tunnel at night.

4.2.3 *Analysis of saccade parameters*

In Figure 15, the drivers' saccade range when driving outside the tunnel during the daytime is basically maintained at 0~30°. In 1~2s before the tunnel entrance, the saccade range suddenly decreases, and

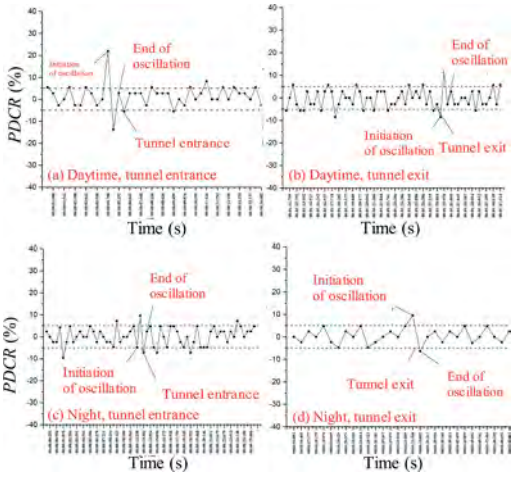

Figure 14. PDCR values of the entrance and exit zone of the tunnel in daytime and night.

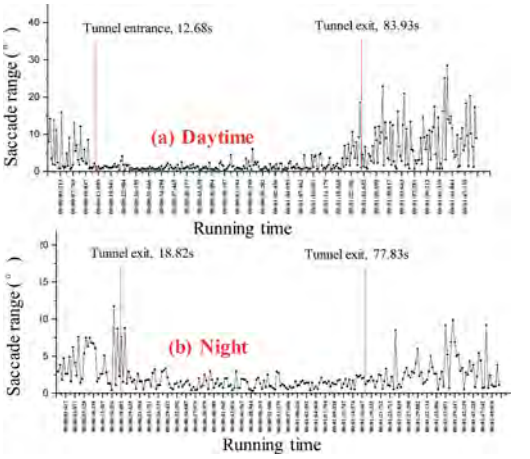

Figure 15. The drivers' saccade range during the day and night.

the saccade range of driving in the tunnel basically stays at 0~3° small amplitude scanning behavior; when approaching the tunnel exit, the scanning amplitude increases until it reaches the level of the scanning amplitude of the driver outside the tunnel environment.

As can be seen from Figure 15, compared with the drivers' saccade range outside the tunnel during the daytime, the drivers' saccade range at night is overall reduced, and the maximum saccade range value of the driver is about 12°, without a large abnormal value of the saccade range.

4.2.4 *Analysis of saccade behavior in the interior zone*

It is illustrated in Figure 16(a), 82.6% of the drivers' eye movement behavior in the interior zone of the

tunnel is fixation behavior. The analysis shows that, because the tunnel is a special semi-closed tubular structure, there is less traffic reference information in the tunnel, and the saccade speed is greatly reduced.

As depicted in Figure 16(b), the overall distribution of the driver's saccade speed is smaller and the average saccade speed is smaller during the 10:00~12:00 when the traffic flow is large and the visibility is low. Moreover, the overall saccade speed is the highest and the average saccade speed is the highest during the 20:00~22:00 when the traffic flow is large and the visibility is best in the tunnel. The distribution of drivers' saccades during other periods with smaller changes in visibility in the tunnel was similar.

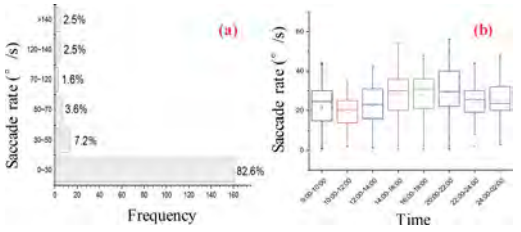

Figure 16. Distribution of saccade speed: (a) frequency, (b) time.

5 REALIZATION APPROACH OF EQUIVALENT LIGHTING ENVIRONMENT

5.1 *Control principle of luminance difference in threshold zone*

5.1.1 *Layout of reflective materials in threshold zone*

Combined with reflectivity, lighting layout and sky factors, the simulation analysis of the layout height of reflective materials in the threshold zone is carried out. Based on the previous research results and the lighting specifications, the three-dimensional simulation is formulated to lay reflective materials in the range of 2m, 2.5m, 3m and 3.5m on both sides of the road. The lighting effect of reflective materials in the entrance in complex lighting environment is comprehensively analysed. The results are shown in Figure 17.

As can be seen from Figure 17, when the reflectivity is fixed, the improvement of reflective materials on road surface illumination and illumination uniformity on sunny days is much greater than that on cloudy and mixed days. With the same sky type and lighting layout, the average road surface illumination and illumination uniformity at the entrance are positively correlated with the reflectivity of reflective materials. The larger the reflectivity of reflective materials is, the larger the average road surface illumination is and the better the illumination uniformity is.

Therefore, the sidewall layout of high reflective materials is conducive to improving lighting quality and achieving the purpose of energy-saving lighting. With the same sky type and reflective material reflectivity, the higher the height of reflective materials layout is, the larger the average road surface illumination and illumination uniformity value of the tunnel threshold zone is. The reflective material reflectivity is fixed. From the perspective of lighting quality and safety, staggered lighting in the tunnel entrance can greatly improve the uniformity of road surface illumination, which is more conducive to driving.

5.1.2 *Optimization of luminance curve in threshold zone*

According to the measurement data of the physical tunnel, the actual luminance peak in different seasons and under different skies and the luminance of threshold zone in a day are obtained. The results are shown in Figures 18 and 19.

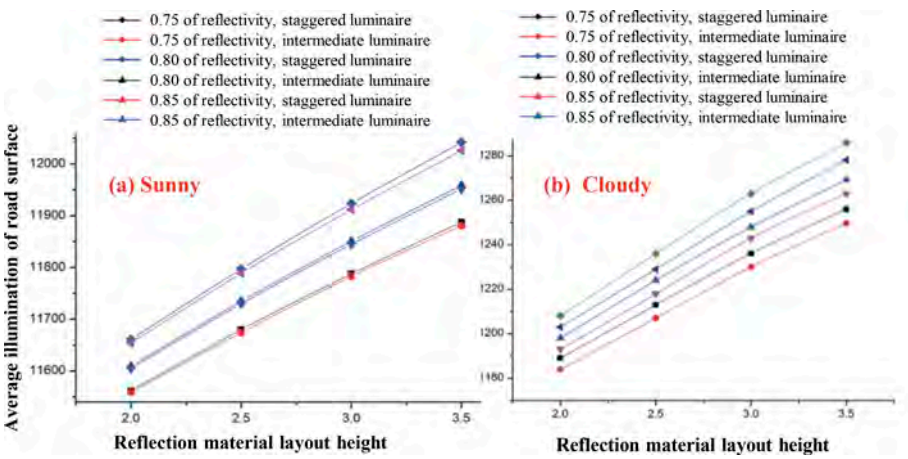

Figure 17. Road surface illumination in south and north directions: (a) sunny day, (b) sunny day.

In Figures 18 and 19, there are great differences in the luminance Lth_1 in threshold zone at noon every day throughout the year. From high to low, it is sunny in summer, sunny in autumn, sunny in spring, cloudy in summer, sunny in winter, cloudy in autumn, cloudy in spring, cloudy in winter, cloudy in summer, cloudy in spring, cloudy in autumn, and cloudy in winter. The luminance peak in cloudy seasons is 0.51-0.63 times of that in sunny seasons.

Based on the above research, it is proposed to set shading vegetation in threshold zone (TH_1) to replace the original artificial lighting and then combined with the grading dimming in threshold zone (TH_2) in the tunnel. It can realize the gradient reduction of natural light lighting in the decrease zone and the smooth transition of lighting luminance inside and outside the tunnel.

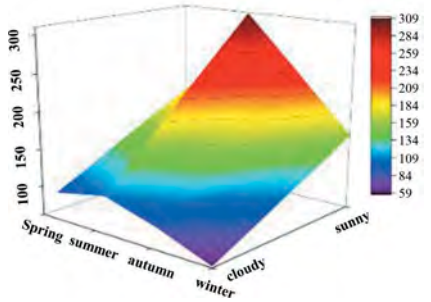

Figure 18. Changes of luminance peak of the entrance in different seasons and under different skies.

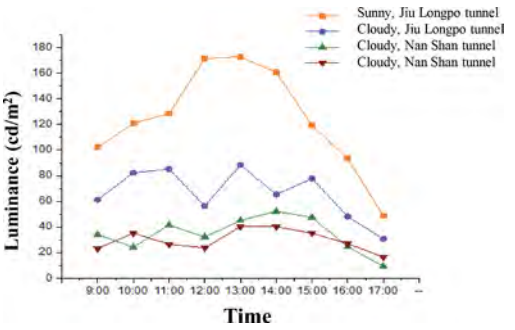

Figure 19. Luminance changes of the tunnel entrance in a day.

5.2 *Reasonable arrangement of equivalent lighting environment*

5.2.1 *Matching analysis of reflective materials and lighting lamps*

As shown in Figure 20, under any lamp spacing condition, the road surface illumination under the condition of reflective materials is greater than that of reflective paint and cement mortar. The increase ratio of road surface illumination under different lamps is MHL, LED and HPSL from large to small. However, when the lamp spacing is 3m, the increase ratio of HPSL is greater than that of LED.

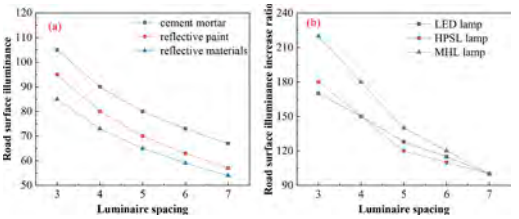

Figure 20. Road surface illumination under different sidewall materials (a) and (b) lamps.

5.2.2 *Matching analysis of vehicle lamps and lighting lamps*

In order to further study the influence of vehicle lamps on the lighting environment with the sidewall material, three types of vehicles (small car, large truck and passenger car) were selected for experimental study, and the lamp spacing was set at 3m. The test results are shown in Figure 21.

As shown in Figure 21, the illumination under vehicle lamp irradiation generally shows a trend of gentle, rapid increase, rapid decrease and gentle, and the rapid change interval is about 5m-15m. For various types of vehicles, the maximum illumination of the lane centerline under the illumination of the vehicle lights is from large to small: bus, car, truck. Moreover, the maximum illumination of the lane sideline under the illumination of the vehicle lights is from large to small: bus, truck, car.

5.2.3 *Comparison analysis of lighting schemes*

As shown in Figure 22, under LED lamp, HPSL and MHP, to achieve the same standard value of road surface illumination, the lamp spacing required by reflective paint and reflective material is greater than the cement mortar. It indicates that the reflective materials was set on the sidewall can increase the lamp spacing on the premise of ensuring the quality of lighting, thus reducing the number of lamps and realizing energy saving of lighting.

Based on the above research results, one can conclude that, under the same road surface illumination value of the three test light sources, the lamp spacing required by reflective material is greater than that required by reflective paint. It shows that the reflective material has a reflectivity 0.2 higher than that of reflective paint, which makes it able to reflect more light energy from the sidewall onto the surface, thus further increasing the lamp spacing.

Besides, under the conditions of 3m~7m lamp spacing, the ratio of lamps reduced by LED with high reflective material is greater than that of HPSL

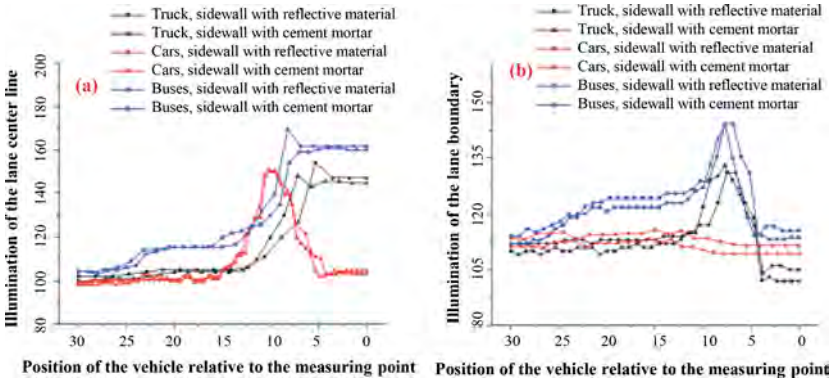

Figure 21. Illumination changes of (a) lane centreline and (b) sideline under vehicle lamp irradiation.

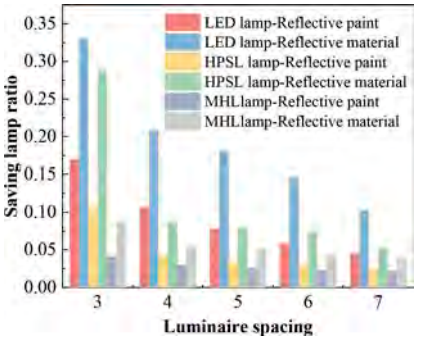

Figure 22. The ratio of saving lamps under different sidewall materials and lamps.

light source with reflective material and MHP with reflective material, indicating that the reflective material has better compatibility with LED light source, which can release more energy-saving space.

6 CONCLUSION

(1) Based on the non-equivalent characteristics of lighting environmental load and visual perception, the quality of lighting environment is improved by reasonable matching of lighting, which reduces the lighting environment load. While meeting the lighting standards to ensure the quality of lighting, the equivalent lighting environment of tunnel based on safety and energy saving is constructed, and the theoretical path of equivalent lighting environment of tunnel based on safety and energy saving is proposed.

(2) Through the simulation tunnel and physical tunnel, static and dynamic lighting environment visual efficacy test, combined with indoor simulation and real vehicle test, from the perspective of the lighting environment load and the equivalent visual perception for tunnel, the evaluation method of driver information perception state is established.

(3) Based on the principle of luminance difference control in the threshold zone, the change of lighting environment under the condition of multiple factors is analyzed, and the specific realization method of equivalent lighting environment in the tunnel is proposed. Besides, the optimization research on the configuration of lighting environment for tunnel is carried out based on the compatibility of lighting lamp, sidewall materials and vehicle lamps.

ACKNOWLEDGMENTS

The work was financially supported by the National Natural Science Foundation of China (grant numbers 51878107 and 52378391), the Project of Chongqing Talent Team (grant number 2019-9-95), and the Research and Innovation Program for Graduate Students in Chongqing (grant number 2022B0004).

REFERENCES

Chen, Y., Tan, G., 2006. Selection of light Source for Highway Tunnel lighting. Light. Lighting. J. 3, 23–25.

CIE 88–2004, 2004. Guide for the Lighting of Road Tunnels and Underpasses. International Commission on Illumination, Vienna, Austria.

JTG/TD70/2-01-2014, 2014. Highway tunnel lighting design rules. People's Communications Press, Beijing, China.

Liang, B., Chen K., He S., et al, 2019. Research on backlight quality based on different visual range. Journal of Chongqing Jiaotong University, Ziran Kexueban, 38(7), 40–47.

Liang, B., He, S., Pan, G., et al, 2015. Research on Road tunnel traffic safety based on new internal materials. Mode. Tunn. Tech. 34(2), 16–21.

Liang, B., Liang, J., He, S., et al, 2020. Experimental research on lighting environment information perception in Highway Tunnel. Tunn. Constr. 40(09), 1251–1260.

Liu, Z., 2019. Optimization design method of inner environment of urban underpass tunnel based on driver's physiological characteristics . PhD Thesis. Hefei University of Technology, China.

Mehri, A., Aliabadi M., Golmohammadi R., et al, 2022. An empirical investigation of disability glare and visibility level during driving inside very long road tunnels, A case study. TUNN. UNDERGR. SP. TECH. 125, 104496.

Shi K., 2020. Study on the influence of tunnel lighting Arrangement on lighting effect. Trans. Energy. Conser. Environ. Prot. 16(04), 134–137.

Wang, J., Hou, L., Wu, P., 2016. BIM-supported tunnel light environment evaluation: A case study on Shanghai Chenxiang Road Tunnel Project. Proc. Int. Conf. Comput. Civ. Build. Eng. 44, 1023–1030.

Yan, G., Wang, M., Qin, P., et al, 2022. Comparative study on drivers' eye movement characteristics and psychophysiological reactions at tunnel entrances in plain and high-altitude areas: A pilot study. TUNN. UNDERGR. SP. TECH. 122, 1–13.

Yang, Y., Ye F., Wang X., et al, 2016. Analysis of ambient illumination and driver pupil area in tunnel cluster. J. S. Univer. Tech. 44(12), 89–96.

Ye, F., Zhang X., Su E., et al, 2022. Research on sidewall decoration of highway tunnel based on driving comfort. Mode. Tunn. Tech. 59(04), 196–203.

Tunnelling for a Better Life – Yan, Celestino, Thewes & Eberhardt (Eds)
© 2024 The Author(s), ISBN 978-1-032-80042-4
Open Access: www.taylorfrancis.com, CC BY-NC-ND 4.0 license

A numerical investigation on the long-term stability of tunnels excavated in the upper stratum of expansive layer

SuJian Ma* & Ying Cui
Graduate School of Urban Innovation, Yokohama National University, Yokohama, Japan

ABSTRACT: Nowadays, the deformation of tunnels during the service period, which occurs after several years or decades of construction, has been reported. The majority of these tunnels were constructed in rock formations with the potential for swelling or weathering. This research focuses on expansive rock as the target type to investigate the long-term stability of tunnels. A long-term seepage model experiment was conducted to study the deformation characteristics of the surrounding soil and tunnel stress response. This experiment aimed to simulate the long-term infiltration of water into the surrounding ground. The experimental results indicate that water infiltration induces swelling of the expansive soil, leading to the deformation of the surrounding ground. When an expansive layer exists beneath the tunnel, differential displacement occurs between the tunnel base and the surrounding ground, developing a significant vertical shear band around the tunnel edge. Initially, deformation occurs at the junction between the surrounding ground and expansive soil. As saturation progresses, deformation accumulates near the top of the tunnel, particularly when it reaches nearly full saturation. The stress distribution on the invert, wall, and crown was investigated. It was found that considerable stress is concentrated at the bottom of the tunnel due to boundary constraints, and a passive pressure acts on the invert at the bottom, causing the incremental pressure acting on the invert to be larger than the expansive pressure of the material. This can be one of the main reasons for invert heave. Furthermore, a corresponding finite element analysis was conducted, incorporating constitutive models capable of simulating the swelling behaviour of the ground. Specifically, the swelling rock model (Wittke-Gattermann & Wittke, 2004) was adapted in Plaxis to replicate the model experiment, aiming to verify the applicability of this model and expand its usage in more complex projects involving swelling strata.

Keywords: Expansive soil, Tunnel, Model test, Simulation, Swelling rock model

1 INTRODUCTION

The rapid development across the globe intensifies the swift progress in the transportation industry, with tunnels serving as pivotal means for interregional connectivity in various modes of land and water transportation. Tunnel construction assumes a pivotal role in the progression of urbanization and facilitation of human connectivity (Asakura, 2003). Tunnel construction plays a crucial role in urbanization and human communication. Despite advancements in the field over the years, it still encounters significant challenges. Tunnels experience structural changes during their service life due to evolving geological conditions, including rock disturbances from excavation and environmental erosion (Zheng et al., 2017). One of the primary factors contributing to tunnel erosion and alterations in the surrounding geology is the ingress of water, which is accompanied by complex stress processes in both saturated and unsaturated geological zones. Research by Usman et al. (2011), Roatesi et al. (2013), and Gschwandtner et al. (2011) has focused on the construction and support of tunnels in complex stress regions. Furthermore, time-dependent deformations, such as creep and swelling, may result in substantial tunnel deformations, potentially leading to instability. Expansive soils, widely distributed in nature, exhibit notable expansion and contraction characteristics, with their high hydrophilic properties making them highly sensitive to changes in water content. Infiltration of water significantly increases their deformations while concurrently reducing their strength. As our understanding of the mechanisms of deterioration remains limited, maintenance of tunnels passing through expansive soil layers primarily relies on safety considerations, prompting the implementation of various reinforcement measures.

Numerous researchers have undertaken extensive investigations into the influence of expansive soils on tunnels through direct means such as field observations

*Corresponding author: sai-ei-mx@ynu.ac.jp; ma-sujian-ft@ynu.jp

DOI: 10.1201/9781003495505-455

and model experiments. Wang et al. (2014), based on field trials and theoretical analyses, elucidated the response patterns of soil pressures around tunnels during the expansive soil swelling process. They proposed a beam-spring model for the pressure load induced by swelling in shield tunnels. Wu et al. (2021), on the other hand, established an indoor experimental model to simulate typical dry-wet cycling conditions. This approach allowed them to study ground failure and instability under tunnel excavation and support conditions in expansive soil environments.

The study of expansive soil constitutive behaviour constitutes a significant portion of theoretical research. A constitutive model for unsaturated soil swelling proposed by Alonso (1990) is widely acknowledged by the majority of researchers. Subsequently, a constitutive theory considering the combination of micro and macro aspects of expansive soil has been detailed (Alonso, 1999), although due to the multitude of parameters and the necessity to consider macro-micro integration, its theoretical rigor is higher than its practical application.

Led by Professor Thomas from NTNU, the swelling rock model exhibits great predictive capabilities regarding the swelling process of expansive rock and soil. Derived from previously established expansive soil theories, this model can simulate the time-dependent anisotropic expansion of rock and soil. A plethora of scholars have employed the swelling rock model to conduct research on expansive soil. For instance, Ammering (2013) proposed an anchor support model under the influence of expansive soil to study the stability of tunnel structures. Hakro (2022) combined laboratory testing with simulations to investigate the impact of in-situ swelling of expansive soil on upper concrete structures. El-Shamy (2019) utilized the swelling rock model to discuss the advantages and disadvantages of different pressure methods and the Huder-Amberg method for testing expansive soil characteristics through pressure consolidation experiments (Huder, 1970). Furthermore, Al-Maamori (2018) employed finite element analysis to examine the effects of time-dependent deformation (TDD) on tunnels constructed using micro-tunnelling technology in the Quaternary shale (QS).

As previously elucidated, several notable studies have been conducted to gain theoretical insights and employ numerical analyses to understand the role of the surrounding ground in tunnel failure mechanisms. Nevertheless, the discussion regarding the extent of the influence of the depth of expansive soils on tunnels has been relatively scarce. Considering this, the present study seeks to investigate the impact of different depths of expansive soil layers on tunnels using the swelling rock model. Building on the research findings of Saqib from 2021 (Ashraf & Cui, 2021), the swelling rock model is employed to examine the effects of varying depths of expansive soil layers on tunnels. The rationality of the modelled approach using the same experimental parameters is validated, and subsequently, the influence of expansive soils at different depths is evaluated.

2 SWELLING ROCK MODEL AND CALCULATION OF PARAMETERS

2.1 *Outline of swelling rock model*

The swelling rock model, originally formulated by Professor Thomas Benz and subsequently expanded upon by Bert Schädlich, is rooted in prior investigations conducted by Wittke-Gattermann & Wittke (2004), Anagnostou (1993), and Heidkamp & Katz (2002). This comprehensive model comprises five fundamental attributes. Significantly, the model can be assumed isotropy within the soil material, requiring the definition of 5 crucial parameters. The constitutive relationship adheres to the Mohr-column (M-C) model with the elastic-perfectly plastic framework.

In addition to its fundamental principles, the computational algorithm utilized in this model derives from three distinct theoretical frameworks: the Wittke model, the Anagnostou model, and a hybrid amalgamation of the two. It is noteworthy that all these theories can be traced back to Grob swelling law, thus furnishing a robust theoretical underpinning for the model computations and prognostications. Grob swelling law is characterized by a logarithmic relationship between the swelling pressure in a loading state and the swelling strain in a one-dimensional (1D) state, as depicted in Figure 1 and Equation 1. Moreover, in order to prevent unbounded expansion of this model, when the loading pressure falls below a specified minimum threshold, the swelling strain is held constant. Within this model, the minimum threshold for σ (stress) is set at -10kPa.

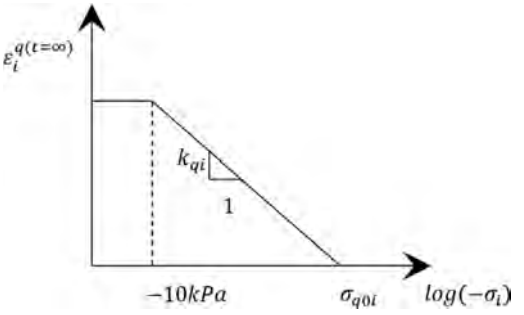

Figure 1. Grob semi-logarithmic swelling law (Grob, 1972).

$$\varepsilon_i^{q(t=\infty)} = \begin{cases} -k_{qi} \cdot \log\left(\frac{\sigma_c}{\sigma_{q0i}}\right) & , \ \sigma_i \geq \sigma_c \\ -k_{qi} \cdot \log\left(\frac{\sigma_i}{\sigma_{q0i}}\right) & , \ \sigma_{q0i} \leq \sigma_i \leq \sigma_c \\ 0 & , \ \sigma_i \leq \sigma_{q0i} \end{cases} \quad (1)$$

(El-Shamy, 2019)

The most direct method for formulating this law entails conducting a series of oedometer tests, where $\varepsilon_i^{q(t=\infty)}$ represents the ultimate swelling strain along

the swelling direction under the given stress, k_{qi} is the parameter associated with swelling and is equivalent to the slope of the swelling curve, σ_i signifies the axial stress aligned with the swelling direction, and σ_{q0i} denotes the maximum swelling stress within the same direction.

2.2 *Parameter determination for swelling rock model*

In this model, where considerations of coupling effects and water infiltration are omitted in favour of an emphasis on isotropic behaviour, the adaptation of the Wittle model (swell ID=1) is prominent. A total of 5 mechanical parameters and 3 swelling parameters are integral to the model. All these parameters, except for swelling parameter A_0, can be rigorously determined through laboratory experiments.

The 5 mechanical parameters align with the M-C model, encompassing the friction angle (φ), cohesion (c), tensile strength (assumed as 0.001kPa to meet interpolation requirements for simulation results, Young's modulus and Poisson ratio. Following calculations based on similar principles, a simulated mixture of bentonite and Toyoura sand is employed for the expansive soil, comprising 75% sand and 25% bentonite. Laboratory experiments, specifically uniaxial compression and direct shear experiments, have yielded a comprehensive presentation of these five mechanical parameters, as shown in Table 1.

Parameters associated with soil swelling encompass the following key aspects: the maximum swelling pressure (σ_{qp} & σ_{qt}), the time-dependent swelling parameter (A_0), and the swelling potential parameters (k_{qp} & k_{qt}). The soil is presumed to demonstrate isotropic behaviour, implying that the values of these parameters in the normal direction are equivalent to those in the tangential direction. The determination of swelling pressure closely follows the methodology outlined in ASTM standard D4546-14 (ASTM, 2013), as depicted in Figure 2. This figure provides a visual representation of the procedural steps employed in the testing method.

Table 1. Model mechanical parameters.

Parameter	Symbol	Unit	Value
Friction angle	φ	°	42
Cohesion	c	kPa	0
Tensile strength	σ_{tens}	kPa	0.001
Young's modulus	E	kPa	4716
Poisson ratio	v	-	0.3

The employed method entails subjecting a saturated soil sample, which has completed its expansion, to a gradual loading process. The ultimate pressure, referred to as the swelling pressure, is determined when the swelling strain has fully recovered to zero. Figure 3 illustrates the results obtained from an oedometer test conducted on an expansive soil sample consisting of 75% sand and

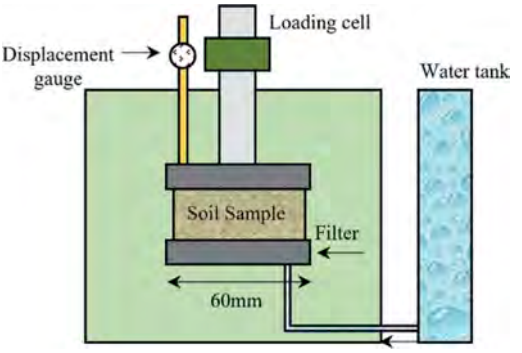

Figure 2. Oedometer test for swelling parameters.

25% bentonite. Notably, the final swelling pressure recorded in this test is measured at 161.72kPa.

Similarly, another critical parameter can be derived through a series of loading and unloading tests using the oedometer test setup. The Huder-Amberg method (Huder, 1970) is specifically employed to measure the swelling potential parameter. As illustrated in Figure 4, swelling potential (k_{qp}) can be calculated based on the results obtained from the loading and unloading recycling tests (set 3 in particular). Equation 2, as depicted, serves as the mathematical expression to determine the swelling potential.

$$k_{qp} = \frac{\varepsilon_i - \varepsilon_u}{\log(\sigma_i) - \log(\sigma_u)} \quad (2)$$

(El-Shamy, 2019)

Where, ε_i and σ_i represent the initial strain and stress before unloading, respectively. And ε_u and σ_u represent the final strain and stress when unloading is completed. Theoretical k_{qp} is calculated to be 0.162, and the final parameter is determined into 0.1 after revision. The swelling parameter A_0 cannot be accurately determined through experimental methods due to the complex and multifaceted influence of various factors. Consequently, it can only be established through a series of iterative trials conducted using the Plaxis model test.

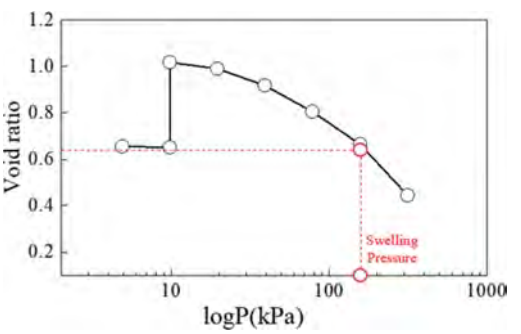

Figure 3. Measurement for swelling pressure.

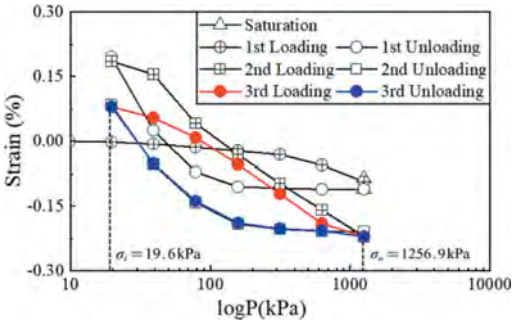

Figure 4. Oedometer test results for loading and unloading recycle.

2.3 *Determination of final swelling parameters*

The validation of the expansive soil model involves initially detecting its properties through soil testing in Plaxis, which includes determining the swelling parameter A_0. However, the ultimate model is established based on physical reality, so verifying the correctness of the swelling model solely through soil tests in Plaxis is not sufficient. Therefore, it is essential to construct a physical model for a more rigorous verification process.

As depicted in Figure 5, the final swelling potential in the laboratory experiment is approximately 22%. When the ultimate parameters are set with A_0 =1, the other two curves nearly coincide. Furthermore, the simulation results exhibit only fractional errors when compared to the actual results. Consequently, the definitive swelling parameters are summarized in Table 2.

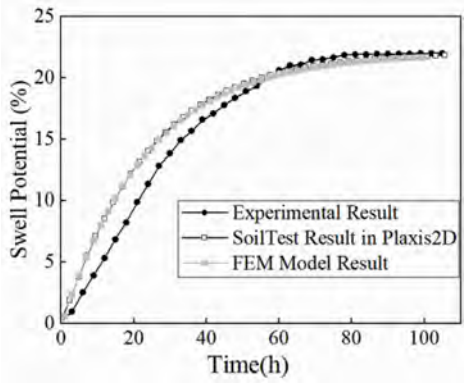

Figure 5. Comparison of time-dependent swell potential between experiment and simulation.

Table 2. Swelling parameters.

Parameter	Symbol	Unit	Value
Time swelling parameter	A_0	1/day	1
Swelling potential	k_{qp}	kPa	0.1
Max swelling stress	σ_{qp} & σ_{qt}	kPa	161.72

3 MODEL TEST AND SIMULATION VERIFICATION

3.1 *Outline of model test and simulation*

The model test was conducted within a chamber constructed from steel and acrylic plates with 600mm in length and height and 200mm in width, as illustrated in Figure 6. To simulate an actual tunnel, a small-scale tunnel, shaped like a horseshoe and constructed from aluminium, was employed. Within this model test, the primary indicators of interest were the pressure exerted on the tunnel lining and the displacement of the surrounding soil. Figure 7 demonstrates the position of load cells (Tokyo Measurement Instruments Lab) at various locations within the tunnel. These load cells were strategically placed around the tunnel lining, crown, invert, wall, shoulder, and spring line. Furthermore, for each of these positions, corresponding symmetric placements were made, denoted as "l" for left, "r" for right, and "c" for centre.

Figure 6. Layout of model test.

In the simulation, the model consists of 3 main components: expansive soil, surrounding soil, and the tunnel. The properties of the expansive soil have been detailed in the second section of this paper. In this experiments, #6 silica sand was utilized, and to maintain consistency, the same parameters as those from the actual experiments were employed.

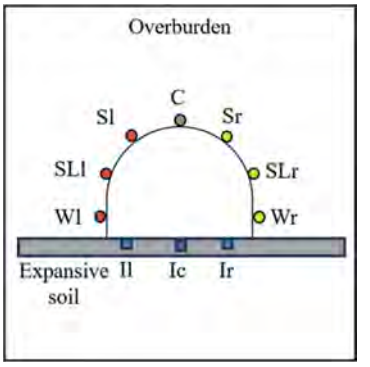

Figure 7. The position of the load cells on tunnel lining.

In this research, the surrounding sand was modelled using the Mohr-Coulomb model. After laboratory testing, the parameters for the sand are presented in Table 3.

Table 3. Material parameters for surrounding sand.

Parameter	Symbol	Unit	value
Friction angle	φ	°	42
Cohesion	C	kPa	0
Young's Modulus	E	kPa	2070

To facilitate the validation process and further research regarding depth, the model has been simplified to a two-dimensional (2D) square configuration. This configuration operates as a plane strain model with dimensions measuring 600mm in both length and height, serving to simplify the model for validation purposes and to facilitate research regarding depth, as illustrated in Figure 8.

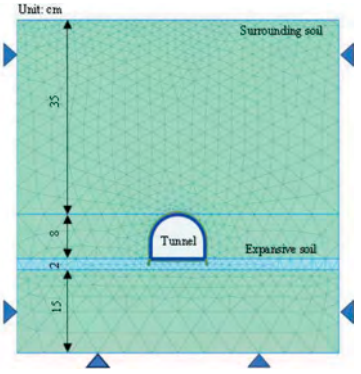

Figure 8. Schematic diagram of the analytical model.

3.2 *Verification of analytical model*

Considering the experimental results, the verification process primarily focuses on two essential aspects: the pressure distribution along the tunnel circumference and the displacements observed in the surrounding soil. To initiate this verification, an initial 0D model, mirroring the conditions of the experiment, is constructed. This model is subsequently subjected to analysis, particularly in assessing the tunnel pressure distribution and the displacements in the surrounding soil.

Given the absence of water throughout the entire process and considering that the soil's swelling process concludes at 100 hours, the calculation period is limited to this timeframe. Figure 9 presents the time-dependent displacements observed in the surrounding soil. Similar to the actual experiments (Figure 10), it is observed that swelling is an ongoing process that depends on time. As time progresses, the displacements on both sides of the model gradually accumulate, with the maximum displacement predominantly concentrated at the surrounding soil edges, ultimately reaching 2.60mm. Similarly, the region surrounding the tunnel remains constrained, and the upper portion of the tunnel remains stationary despite the continuous swelling.

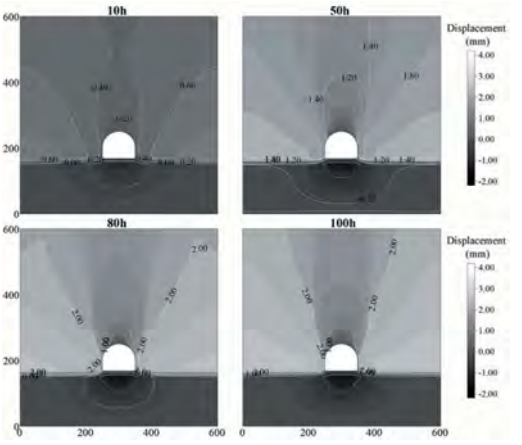

Figure 9. Time-dependent displacement contour around tunnel.

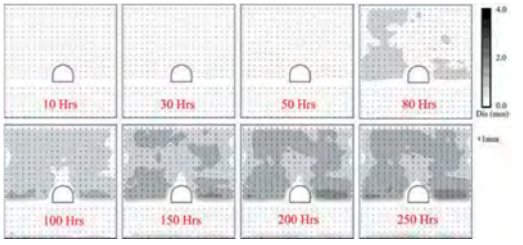

Figure 10. Time-dependent displacement contour of experiment.

Figure 11 illustrates ground movement at a 1D distance from the tunnel crown and displays the ultimate moisture content of the expansive soil upon completion of the process in the experiment. It is significant to note that the displacement of the upper soil is not zero, and this is primarily attributed to the compression exerted by the surrounding soil. The lateral soil compresses the middle soil, and its maximum displacement is 2.83mm, resulting in an increased state of density. As the swelling process continues, the middle soil gradually moves upward.

Upon completion of the test and subsequent measurement of the degree of saturation, it was observed that both sides of the expansive soil had reached full saturation. In contrast, the middle section exhibited a lower degree of saturation, approximately around 80%. Moisture content serves as a demonstration of the variation in swelling potential over time. Similarly, both sides of the model experience completion in terms of swelling; however, the middle section, constrained by the presence of the tunnel, impedes the infiltration of water, resulting in lower displacement compared to the other sections.

Figure 12 represents a comparison of the pressure response within the tunnel during the swelling of the expansive soil between the simulation and the actual experiment. It is evident that the invert, the lower part of the tunnel, is significantly affected by the

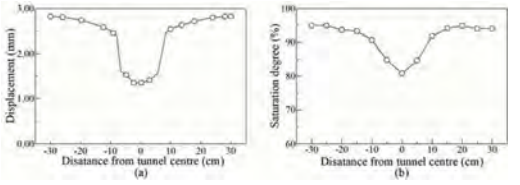

Figure 11. Time-dependent swelling comparison (a) Line cross section Y-direction displacement in simulation (b) Line cross section saturation degree in experiment.

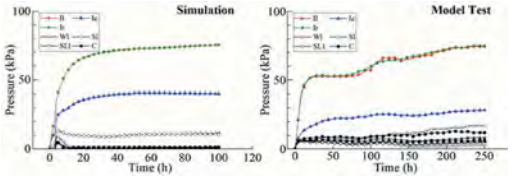

Figure 12. Time-dependent pressure at different sections of tunnel.

swelling process, and it responds to swelling pressure quite rapidly.

However, notable differences exist in the pressure values at the three positions. Specifically, the pressure on the two sides of the invert is similar due to the tunnel symmetrical properties, but the middle part registers lower pressures. The pressure at the edge of the invert initially rises to about 50kPa in the first 20 hours and then steadily increases to reach a final peak of 81.44kPa. This final peak represents 50.58% of the swelling pressure measured by oedometer tests. Conversely, the middle part exhibits an initial increase to 56kPa, followed by a decrease to 46kPa upon nearing completion. This phenomenon appears to be associated with the heave (swelling) of the middle part.

As the swelling progresses, the stress variations between the left and right sides of the invert are relatively large, amounting to 75.6kPa, which corresponds to approximately 46.74% of the swelling pressure, where the error is only 3.84%. In contrast, the middle section of the invert registers a lower stress of 40.32kPa. When compared with the actual experimental results for the invert, these differences between simulation and experiment appear acceptable.

The comparison and analysis conducted in terms of the 0D model between the experiment and the simulation demonstrate that the simulation results, along with the selected parameters, meet the requirements for replication. Further research on different depths will be conducted using simulations with the same parameters.

4 INFLUENCE OF THE DEPTHS OF EXPANSIVE SOIL LAYER

4.1 *Displacement of the surrounding ground*

Figure 13 represents displacement contours for both the 0.5D and 1D cases at four different stages (10h, 50h, 80h, 100h). In both cases, it is evident that the displacement of the surrounding soil continuously increases at the edges of the model. The maximum displacement observed is approximately 2.56mm for the 0.5D case and 2mm for the 1D case, respectively. The final maximum cumulative displacement is concentrated at the left and right edges, consistent with the 0D case. Throughout this entire process, the swelling potential exhibits a time-dependent relationship. Due to the increased thickness of the model, the ultimate strain experiences a slight reduction from the 0D case to the 1D case (2.83mm → 2.56mm → 2.00mm).

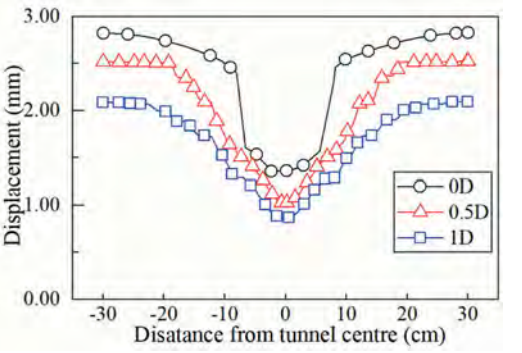

Figure 13. Time-dependent vertical displacement contour around tunnel for (a) 0.5D and (b) 1D.

Figure 14 illustrates the Y-direction displacement distribution of line cross section at a 1D distance from the crown for all three cases. The final maximum cumulative displacement is concentrated at the edge of the model, consistent across all cases. Over the course of the swelling process, the stiffness of the soil located at the tunnel bottom strengthens, leading to an increase in compression stress in this area. When combining this analysis with Figure 13, it becomes evident that the increasing compression stress leads to compression deformation with a negative value in the surrounding soil at the bottom of the expansive soil. Similarly, the movement trend of the surrounding soil shows that the upper soil, located at the crown of the tunnel, undergoes compression due to the movement of the edge soil and then moved by swelling, and the influence range of this behaviour is about 1D (-10~10 cm).

4.2 *Shear deformation of the surrounding ground*

Figure 15 compares deviatoric strain evolution over time between the 0.5D and 1D cases. In the 0D case, where there is no space between the tunnel and the expansive soil, no shear deformation occurs in the surrounding soil.

In the cases of 0.5D and 1D, the shear zone becomes prominently concentrated within the bottom soil adjacent to the tunnel sides. Notably, both the scale and magnitude of shear deformation

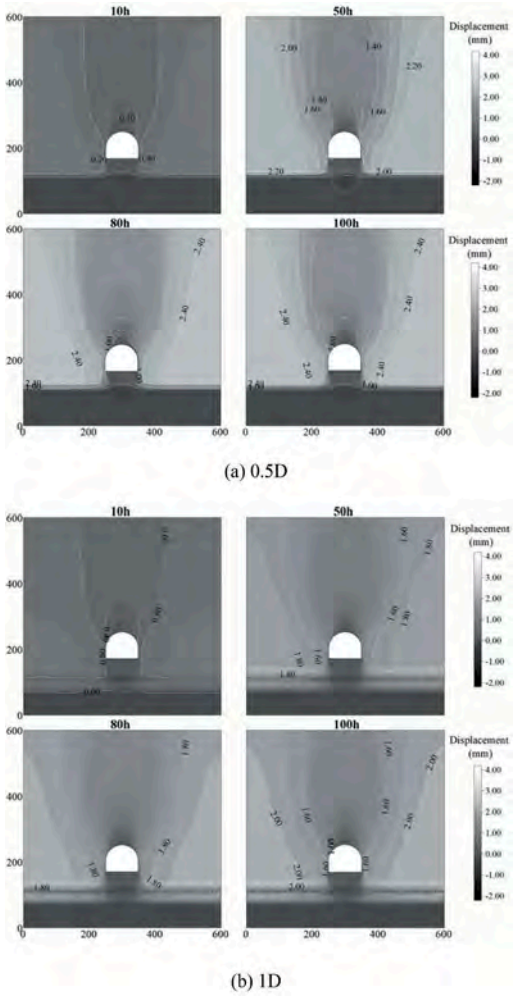

Figure 14. Line cross section Y-direction displacement distant 1D above the crown.

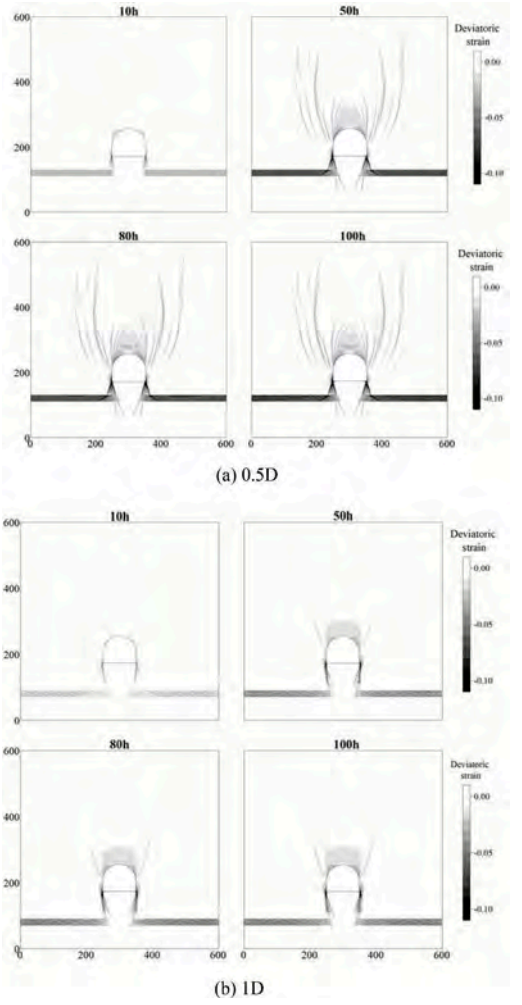

Figure 15. Time-dependent shear development around tunnel for (a) 0.5D and (b) 1D.

exhibit a progressive increase over time. This behaviour can be attributed to the constraints imposed by the tunnel invert, which limit the movement of the bottom soil. In contrast, the soil on both sides of the tunnel remains relatively free to move. Consequently, this non-uniformity in soil movement results in the occurrence of shear deformation along the two sides of the tunnel.

After approximately 10 hours of swelling, the shear zone is initially distributed vertically along the sides of the tunnel. As time progresses, the impact zone expands to cover a wider area. Notably, the shear belt is not a fixed entity; by the 50-hour mark, it stabilizes into a certain width, exhibiting around 20%. Over subsequent time intervals, the shear range experiences minimal variation, and the maximum shear strain value increases only by 1%. Additionally, minor shear strains emerge in the upper surrounding soil starting from the 50th hour, and as time progresses, these strains extend further into the upper soil.

In the 1D case, when compared to 0.5D, the shear zone initially appears exclusively at the base of the tunnel. However, as time progresses to 50 hours, the shear zone begins to connect with the expansive soil, creating a continuous shearing of 17%. Additionally, the increased thickness of the middle soil layer beneath the tunnel prevents shear damage from occurring in the upper surrounding soil. Consequently, the shear area mainly concentrates in the vicinity of the tunnel crown.

4.3 *Time-dependent pressure acting on tunnel lining*

Figure 16 illustrates the variation in tunnel pressure at different points over time. In the initial accelerating stage of 0.5D case, the pressure at edge reaches 121kPa within the first 20 hours and remains steady at 120kPa until completion. The middle part of the invert responds to pressure inferiorly compared to the sides, showing a trend of increasing pressure up to 100kPa at completion. The other points of the

tunnel remain relatively undisturbed, with a maximum pressure of 20kPa.

In the 1D case, pressure at the invert is most intense, with the left and right sides reaching 124kPa within the first 20 hours. The middle invert pressure reaches 100kPa and continues to rise with the swelling process, while the pressure at the tunnel edge shows a slight decrease. At the completion of swelling, the ultimate pressure at these two points reaches 119kPa and 106kPa, respectively. It is evident that the other points of the tunnel remain inactive and sustain a pressure no greater than 20kPa.

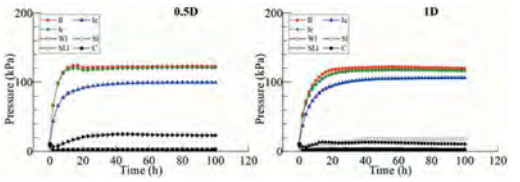

Figure 16. Time-dependent pressure on the tunnel.

When the bottom soil thickness is zero (0D), the maximum pressure registers at approximately 75.6kPa. In contrast, for the cases of 0.5D and 1.0D, the maximum pressures escalate to approximately 121kPa and 124kPa, respectively.

As the depth of the bottom soil increases, it leads to a corresponding rise in soil pressure, as there is an increase in the frictional forces between the bottom soil and the surrounding ground on both sides. This progressive intensification of frictional forces is consistent with the swelling pressure and consequently results in an augmented pressure exerted on the bottom of invert. Consequently, the maximum tunnel pressure experiences a continuous increase, particularly noticeable along both sides of the tunnel.

Likewise, in the context of shear deformation, the predominant shear deformation is concentrated primarily on the two sides of the invert. This phenomenon is another consequence of the augmentation of frictional forces with increasing depth.

5 CONCLUSIONS

(1) Swelling effects induce movement constraints in the surrounding ground at approximately a distance equivalent to one tunnel diameter from both the left and right sides of the tunnel. The maximum displacement occurs at the two sides of the model, and this value decreases as the depth of the expansive soil increases, measuring 2.83mm (0D), 2.56mm (0.5D), and 2.00mm (1D), respectively."

(2) The tunnel constrains the soil beneath it, while the surrounding ground and soil elsewhere tend to freely move upward due to swelling pressure. This leads to noticeable shear phenomena beneath both sides of the tunnel invert, forming a continuous shear zone. As the depth of the expansive soil increases, the shear deformation extends downward, while the shear deformation of the soil in the upper part of the tunnel disappears.

(3) Compared to the pressure at the invert, pressures in other positions are notably lower. As the depth of the expansive soil layer increases, it intensifies frictional forces between the lower soil and surrounding ground on both sides, thereby steadily increasing the bottom pressure from 74.8kPa (0D) → 121kPa (0.5D) → 124kPa (1D).

(4) The expansion deformation of expansive soil is exponentially distributed with time. As the increment of time, the swelling of expansive soil will further strengthen. At a certain stage, there is a substantial surge in the pressure applied to the tunnel. This surge corresponds with an escalation in the movement of the surrounding rock and shear deformation, consequently exacerbating the damage to the tunnel.

ACKNOWLEDGMENTS

This work was supported by JSPS KAKENHI Grant Number 23K04023, the research grant by the Japan Tunnelling Association and the funding of China Scholarship Council.

REFERENCES

Al-Maamori, H.M.S., El Naggar, M.H., Micic, S., 2018. Numerical modeling of time-dependent deformation and induced stresses in concrete pipes constructed in Queenston shale using micro-tunneling technique. Journal of Rock Mechanics and Geotechnical Engineering 10, 290–309.

Alonso, E.E., Gens, A., Josa, A., 1990. A constitutive model for partially saturated soils. Géotechnique 40, 405–430.

Alonso, E.E., Vaunat, J., Gens, A., 1999. Modelling the mechanical behaviour of expansive clays. Engineering Geology 54, 173–183.

Ammering, F.C., 2013. Modelling Swelling Rock Behaviour in Tunnelling.

Anagnostou, G. 1993. A model for swelling rock in tunnelling. Rock Mechanics and Rock Engineering 26 (4), 307–331.

Asakura, T., Kojima, Y. 2003 Tunnel maintenance in Japan, Tunnelling and Underground Space Technology, 18(2), pp. 161–169.

Ashraf, S., Cui, Y., 2021. World Tunnel Congress, WTC2021 and 47th General Assembly Bella Center.

ASTM, 2013. D4546 − 08 Standard Test Methods for One-Dimensional Swell or Collapse of Cohesive Soils 1. ASTM Int. 1–9. https://doi.org/10.1520/D4546-14.

El-Shamy*, A., El-Mossallamy, Y., 2019. Experimental Testing and Numerical Simulations for Typical Swelling Soil in Egypt. IJRTE 8, 4101–4111.

Grob, H.,1972. Schwelldruck im Belchentunnel. Proc. Int. Symp. für Untertagebau, Luzern, 99–119.

Gschwandtner G, Galler R. Einige Gedanken zur gebirgsmechanischen Beurteilung von Untertagebauten. BHM Ber-und Hüttenm? Nnische Monatshefte, 2011, 156 (12):482–486.

Hakro, M.R., Hindu, A., Almani, Z., Habib, A., Zardari, M., 2022. Numerical Modelling of Shallow Foundations on Expansive Shale: A Case Study of Jamshoro, Pakistan. Baltica 80–88.

Heidkamp, H. & Katz, C., 2002. Soils with swelling potential - Proposal of a final state formulation within an implicit integration scheme and illustrative FE-calculations. Proc. of the 5th World Congress on Comp. Mec., Vienna, Austria.

Huder, J. and Amberg, G. 1970. Quellung in Mergel, Opalinuston und Anhydrit (Swelling in marl, Opalinus and anhydrite), Versuchsanstalt Fuer Wasserbau Und Erdbau, Eth Zuerich.

Roateşi S. Analytical approach of the tunnel face effect on the rock-support interface in viscoelastic rock mass //11th International Conference of Numerical Analysis and Applied Mathematics 2013: ICNAAM 2013. AIP Publishing, 2013, 1558(1): 1354–1358.

Usman M, et al. Three Dimensional Load Analysis of Tunnel Linings Including Weathering Processes of the Shotcrete. BHM Berg-und Hüttenm? Nnische Monatshefte, 2011, 156(12):487–491.

Wang,Q.B.et al., 2014. Application of Swelling Shrinkage Mechanism of Swelling Soil in the Tunnel Settlement Control. Chinese Journal of Underground Space and Engineering 10, 1426–1432.

Wittke-Gattermann, P. & Wittke, M. 2004 Computation of Strains and Pressures for Tunnels in Swelling Rocks. Proc. ITA 2004 E14, 1–9.

Wu, Y., et al., 2021. Experimental Study on Strength Characteristics of Expansive Soil Improved by Steel Slag Powder and Cement Under Dry–Wet Cycles. Iran J Sci Technol Trans Civ Eng 45, 941–952.

Zheng, J.-J., Guo, Z.-S., Cui, L., Zhang, J., 2017. Stability analysis of expansive soil tunnel considering unsaturated seepage and moistening swelling deformation. YRock and Soil Mechanics 38, 3271–3277.

Tunnelling for a Better Life – Yan, Celestino, Thewes & Eberhardt (Eds)
© 2024 The Author(s), ISBN 978-1-032-80042-4
Open Access: www.taylorfrancis.com, CC BY-NC-ND 4.0 license

Subway ventilation system design and the importance of predicting the long-term wall surface temperature

Ibrahima Khalil Mbaye*
EUR ING, ing., PEng, Tunnel Ventilation Specialist, Parsons Corporation, Doha, Qatar

ABSTRACT: When designing tunnel ventilation system (TVS) for subway projects, consideration of the tunnel wall surface temperature is very important in quantifying the tunnel air temperature, in order to guarantee adequate and optimal operational conditions for tunnel equipment, thus ensuring their continued performance through their intended lifecycle.

The thermal load within the subway due to the trains' operation plays a key role in the long-term behaviour of the tunnel wall surface temperature. Typical Subway revenue hours period is about 20 hours a day, giving only few hours of rest for the subway without extensive thermal solicitation. The heat accumulated along the revenue hours is absorbed by the tunnel wall and its surrounding soil, preventing the heating of the tunnel environment. In the long term, the surrounding soil will reach its optimum geothermal heat absorption capacity. Consequently, during revenue hours, the heat not being absorbed by the tunnel wall surface temperature, will increase the tunnel air temperature, impacting the equipment operation condition.

The purpose of this paper is to describe the methodology to predict the long-term tunnel wall surface temperature based on the trains operation timetable, by means of unidimensional (1D) numerical simulation, in order to identify the potential appropriate measures such as additional mechanical or passive means of cooling the subway and more stringent specifications on the exposed equipment regarding their operating environment.

Keywords: Tunnel Ventilation Design, Subway, Heat sink, Tunnel wall surface temperature, Long-term simulations, Environment control

1 INTRODUCTION

Below ground level structures, such as caves, refuges, catacombs are generally controlled environment where the air temperature is steady along years. The explanation behind is that there are no major internal heat sources and there is minimal influence of the ambient environment as there is minimal air exchange between the ambient and the underground structures. Subway underground structure is different. There are major heat sources due to dissipating onboard train equipment, besides the fact that trains movement is dragging ambient air from the portals, the natural ventilation shafts and even the entrance when there are no platform screen doors. Other heat sources are related to the lighting, rail technologies, any other potential dissipating equipment installed in the tunnels. These heat sources influence the subway air temperature if the subway tunnel is an uncontrolled environment. This would affect the performance of the equipment installed in tunnel, hence their lifecycle. This paper provides an overview of the influence of these various heat sources on the tunnel wall surface temperature in the long term, hence the tunnel air temperature taking into consideration the associated thermodynamics phenomena. The thermal load induced by the various heat sources is distributed to the tunnels wall surface which then distributed this thermal load to the surrounding soil. The wall and surrounding soil thermodynamic properties along with the depth of the tunnel influence the thermal behaviour of the tunnel air temperature. For the subway, the daily thermal solicitation during revenue service induces heat exchange between the tunnel air, the tunnel wall surface temperature, and the surrounding soil temperature. The surrounding soil heat capacity, also understood as its heat sink represents its budget consumed along the daily revenue service. This paper gives an overview of the consumption of the heat sink under the influence of various factors like the surrounding soil thermodynamic properties, the climate and ambient temperature, the train service daily timetable and its impact on the long-term tunnel wall surface temperature, hence the tunnel air temperature, using common simulation tool Subway Environment Simulation (SES).

*Corresponding author: ibrahimakhalil.mbaye@parsons.com

DOI: 10.1201/9781003495505-456

2 ABOUT THE PHYSICS BEHIND

The subway is generally of a cylindrical shape structure with a layer of concrete, at a certain depth below ground surrounded by soil.

On the one hand, longitudinal air movement due to train movement along with heat dissipation due to the presence of several heat sources occur. The longitudinal air induced by trains movement leads to heat convection thermodynamic phenomenon between the tunnel air and the tunnel wall surface.

On the other hand, the tunnel wall surface exchanges the heat received from the tunnel air along its layer of concrete radially and subsequently within the surrounding soil. The surrounding soil environment is mostly influenced by the ambient temperature.

These thermodynamic phenomena are more elaborated in the following sections.

2.1 *Heat convection phenomenon by forced ventilation*

Convective heat transfer by forced convection occurs when a fluid is forced to flow over a surface by an internal source. In the case of a subway, the fluid is the air dragged by the train piston effect and exchanging heat with the tunnel wall surface. In such situations, thermal balance in a control volume control *Sdx* requires the amount of convective heat transfer between the air and the tunnel wall surface to be equal to the amount of internal energy change in the control volume. The thermal balance equation is given by the following equation:

$$\rho VS(\partial Ttunnel(x)/\partial x)dx = hP(Tw - Ttunnel(x))dx + Qdx \quad (1)$$

With the following parameters definitions:
Tw= Wall Surface Dry Bulb Temperature (°C)

$$\rho = \text{Air density } (kg/m3)$$
$$V = \text{Airflow velocity } (m/s)$$
$$S = \text{Tunnel Cross Section } (m2)$$
$$cp = \text{Specific Heart Coefficient } (J/(kg.K))$$
$$h = \text{Heart Transfer Coefficient } (w/m2/k)$$
$$p = \text{Tunnel perimeter } (m)$$
$$Q = \text{Heart source in tunnel } (w/m3)$$

With the following relationships:

$$h = Nu*\lambda/Dh; Nu = f(Re; Pr)$$
$$Re = \rho * V * Dh/\mu$$
$$Pr = \mu * Cp/\lambda$$
$$\mu = \text{Air Dynamic Viscosity } (N * s/m2)$$
$$\lambda = \text{Air Thermal Conductivity } (W/(m * K))$$
$$Dh = 2*R = \text{Hydraulic Diameter of the tunnel cross section}$$
$$R = \text{Equivalent radius of the tunnel}$$

2.2 *Heat conduction phenomenon*

Conduction heat transfer occurs within an object due to the difference of temperature between its opposite ends. In the case of a subway, heat conduction occurs within the tunnel wall surface and the surrounding soil. Heat conduction occurs along the tunnel lining, generally in concrete, on the one hand, and on the other hand it occurs along the surrounding soil. The pace of the heat transfer by conduction is driven by the concrete and the surrounding soil respective thermal diffusivity noted $\alpha=\lambda/(\rho Cp), inm2/s$.

One dimensional heat conduction along the tunnel lining and the surrounding soil differential equations in polar coordinates can be written as:

$$\partial T(r)/\partial t = \alpha(1/r*\partial T(r)/\partial r + (\partial 2T(r))/\partial r) \quad (2)$$

The initial temperature in any location of the lining or the surrounding soil is the deep sink temperature. The deep sink temperature is the surrounding soil temperature influenced by the yearly average ambient temperature, the surrounding soil thermodynamic properties and its depth. In a subway, before revenue service starts, the surrounding soil is assumed to be stable as well as the tunnel wall surface temperature.

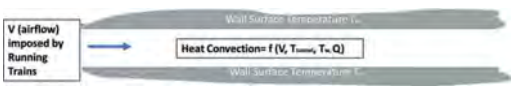

Figure 1. Schematic description of heat conduction phenomenon.

$$Tw(t = 0s) = \text{Deep sink temperature}$$
$$Tsoil \ \& \ lining(t = 0s, \forall r > R) = \text{Deepsink temperature}$$

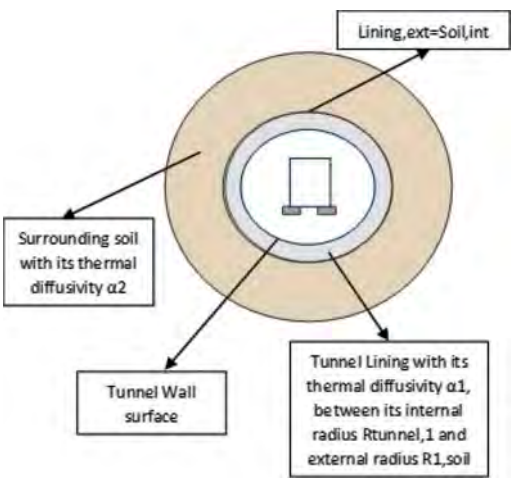

Figure 2. Schematic description of the heat convection phenomenon.

Once revenue service starts, under the influence of the daily thermal solicitation due to numerous trains movement in the tunnel, the temperature at the tunnel wall surface Tw(t) , varies due to the heat transfer by convection, hence the soil temperature in the vicinity of the tunnel T soil(t). Boundary conditions can be defined as:

$$\begin{gathered} h(Tw - Ttunnel(x)) = \lambda lining\ (\partial Tlining(r)/\partial r) \\ Tlining, ext(t) = T\ soil, int(t) \\ \lambda lining\ (\partial Tlining, ext/\partial r) = \lambda soil\ (\partial Tsoil, int(r)/\partial r) \\ Tsoil, r \to \infty(t) = \text{Deep sink temperature} \end{gathered}$$

The following section describes the mathematical model of the heat convection and heat conduction phenomena computed within the Subway Environment Simulation (SES) software.

3 THE 1D ONE-DIMENSIONAL SOFTWARE SES

The Subway Environment Simulation (SES) software latest version 4.1 has been issued in 2002.

The SES computer model provides a dynamic simulation of the bi-directional operation of multiple trains in a multi-track subway and permits continuous reading of the air velocity, temperature, and humidity throughout any arrangement of stations, tunnels, ventilation shafts, and fan shafts.

The SES program comprises four interdependent computation sequences: a train performance subprogram, an aerodynamic subprogram, a temperature/humidity subprogram (thermodynamic subprogram), and a heat sink/environmental control subprogram.

Although all the subprograms are interdependent, the focus of this paper is on the temperature/humidity and the heat/sink environmental control subprograms.

The temperature and humidity of the air throughout a subway system reflect the heat added or removed by underground equipment, trains, and patrons, as well as by the rate of heat exchange across the system walls and by mixing with external ambient air.

The heat sink/environmental control subprogram purpose is to evaluate the interdependent influence of the heat conduction via the surrounding soil and the subway air temperatures.

3.1 *SES Temperature/humidity subprogram*

The thermodynamic subprogram requires input from the train performance subprogram and the aerodynamic subprogram. The thermodynamic subprogram computes several parameters such as the airflow, the average convective heat transfer coefficient for the tunnel wall surface, the rate of sensible and latent heat load due to trains and other heat sources to predict the temperature and humidity in the one-dimensional numerical model. The heat sink being more related to the sensible heat load, the humidity is not elaborated in this paper.

The equation computed by the SES thermodynamic subprogram in a tunnel section/subsegment (i) having its front end defined as (f) and its back end (b) is the following:

$$\begin{aligned} \partial(MCpT_i)/\partial t &= M_{f,i-1}CpT_{i-1} + M_{b,i+1}CpT_{i+1} \\ &-(M_{f,i} + M_{b,i})CpT_i + q_i - h_{w,i}S_{w,i}\left(Ti - Tw_{,i}\right) \end{aligned} \quad (3)$$

Depending on the flow direction in subsegment (i), the mass flow Mf,i is either positive or null, same as Mb,i.

It is noticeable that there is a similarity between equations (1) and (3). The subsegment (i) air temperature rate of change is then based upon known parameters.

3.2 *SES heat sink and air conditioning models subprogram*

The heat sink subprogram uses the output from the aerodynamic and thermodynamic subprogram. The heat sink subprogram carries on an iterative procedure to resolve the tunnel air temperature and the wall surface temperature. The interdependence between the tunnel air temperature and the wall surface temperature drives the requirement for an iterative process. The wall surface temperature is a function of the tunnel air temperature, and the tunnel air temperature is dependent on the wall surface temperature. The iterative process stops when consistent and stable values of the wall surface temperature and the tunnel air temperature are obtained.

The heat sink computation predicts the tunnel wall surface temperature corresponding to the specified month of the year, considering the annual external ambient temperature range (annual amplitude).

The SES heat sink mathematical model, area of concern can focus on the dynamic thermal response matrix (DTRM) and the heat conduction model.

3.2.1 *DTRM model*

The DTRM is based upon 2 levels of derivation, the subsegment derivation which is about the tunnel air temperature prediction in a tunnel section and the node derivation which is about the air temperature at a node. A node is a location along the modelled geometry where 2 or more subsegments meet each other.

Regarding the subsegment derivation model, equation (3) above is considered. An integration of this equation to a Δt corresponding to a period where the tunnel air fluctuates around a mean value, gives the following equation:

$$\begin{aligned} &\int_t^{t+\Delta t} \partial \frac{MCpTi}{\partial t} * dt = \int_t^{t+\Delta t} M_{f,i-1}CpT_{i-1} * dt + \int_t^{t+\Delta t} M_{b,i+1}CpT_{i+1} * dt \\ &- \int_t^{t+\Delta t} (Mf_{,i} + Mb_{,i})CpTi * dt + \int_t^{t+\Delta t} q_i * dt \\ &- \int_t^{t+\Delta t} h_{w,i}S_{w,i}\left(Ti - Tw_{,i}\right) * dt \end{aligned}$$

By considering the system is returning to an original state after a period of Δt, the following assumption has been made: $\int_{t}^{t+\Delta t} \partial \frac{MCpTi}{\partial t} * dt = 0$, hence

$$0 = \int_{t}^{t+\Delta t} M_{f,i-1} CpT_{i-1} * dt + \int_{t}^{t+\Delta t} M_{b,i+1} CpT_{i+1} * dt - \int_{t}^{t+\Delta t} (Mf_{,i} + Mb_{,i}) CpTi * dt + \int_{t}^{t+\Delta t} q_i * dt - \int_{t}^{t+\Delta t} h_{w,i} S_{w,i} (Ti - Tw_{,i}) * dt$$

This equation reflects the balance between the energy flow in tunnel section (i) and the energy flow from upstream and downstream tunnel sections (i-1) and (i+1) as well as the energy absorbed by the tunnel section (i) wall surface and the energy due to steady and transient heat sources. The portion of energy absorbed by the tunnel wall surface and transmitted to the surrounding soil quantifies the heat sink.

Regarding the node derivation model, it is more about the air temperature by predicting the amount of energy leaving a node considering the thermal energy conservation equation.

3.2.2 *Heat conduction model*

The heat conduction model considered by SES heat sink subprogram is similar to the phenomenon described in section 2.2 Heat conduction phenomenon.

The subprogram assumes the tunnel wall surface temperature to be a function of the annual tunnel air average temperature plus the annual thermal amplitude, plus the diurnal thermal amplitude.

Equation (2), already provided above, is applied to each of the 2 regions considered by the subprogram, meaning the lining region and the surrounding soil region.

The initial and boundary conditions are the same as those described in section 2.2 Heat conduction phenomenon.

To resolve the equations and quantify the temperature distribution in both regions, the subprogram divides the temperature into 3 components: a transient component, a yearly component and a diurnal component.

The transient component, which is the major component, is calculated for each of the lining and the surrounding soil layers.

Regarding the lining layer, the transient component T_{trans} (r,t), for $R < r < r_{soil,int}$ is a function of the tunnel wall surface temperature, the deep sink temperature and the unitless parameter $\tau_{lining} = \alpha_{lining} t/R^2$.

The unitless parameter τ allows to derive a coefficient $f(\tau)$ given by Jaeger and Chamalaun (1966). This coefficient is considered in the computation of the transient component of the tunnel wall surface temperature. SES derives the corresponding coefficient for a 30-year period of diffusivity.

The tunnel wall surface temperature is dependent upon the annual average tunnel air temperature which is calculated based on the DTRM model and the annual thermal amplitude.

$$T_{wall} = \frac{T_{annual,average} + T_{deep\ sink} \lambda_{lining} * f(\tau_{lining}) / (h\, Rln\, 10)}{1 + \lambda_{lining} * f(\tau_{lining}) / (h\, Rln\, 10)}$$

Finally, the transient component of the temperature in the lining is given by the following equation:

$$T_{trans}(r, t) = K_1(t) \ln r + K_2(t), R < r < r_{soil,int}$$

The transient component in the surrounding soil layer is also dependent on the deep sink temperature, the temperature at the boundary between the lining and the surrounding soil as well as the unitless parameter $\tau_{soil} = \alpha_{soil} t/(r_{soil,int})^2$.

$$(T_{trans}(r, t) - T_{deepsink})(1 - f(\tau_{soil}) \ln(r_{soil,int}/r)) + T_{deepsink} = K_1 \ln r_{soil,int} + K_2, r \geq r_{soil,int}$$

Details about the mathematical model of the above as well as the annual and diurnal components of the tunnel wall surface temperature can be found in the SES programmers' manual (1975).

4 QUANTIFICATION OF LONG-TERM WALL SURFACE TEMPERATURE AND HEAT SINK

This is about a case study of a one bore bi-directional subway of 9 km circa. with 4 side platform stations fit out with full height platform screen doors and 4 mid tunnel ventilation shafts. The tunnel cross section is about 47 m2. Each of the tunnel portal is connected to the atmosphere.

The metro tunnel ventilation is comprised of station trackway exhaust system and pressure relief shafts at each station end. The mid tunnel ventilation shafts are also operating as pressure relief shaft.

The metro service starts at 5:30 am and finishes at 1:30 am the day after. The peak and off-peak headways are 150 seconds and 300 seconds respectively.

There are 293 trips in each direction with the train fully loaded. The trains are equipped with AC condensers that dissipate heat in the tunnel.

The objective is to quantify the long-term wall surface temperature as well as the heat sink for various types of environment.

The adopted approach is to quantify the long-term wall surface temperature and the heat sink based on the yearly average temperature in these various regions. To do so, it is assessed the acceptability to consider the yearly average temperature instead of the month after month temperature.

As a reminder, the SES heat sink computation predicts the tunnel wall surface temperature for the corresponding month of the year, considering the annual outside temperature range (annual amplitude).

Consequently, the approach is to quantify, for a typical region, the long-term wall surface temperature for the colder month, usually January and the hotter month, usually July, having the same annual amplitude. In conjunction with the latter, the long-term wall surface temperature is quantified using the equivalent yearly average temperature with an annual amplitude equal to 0.

This scenario has been carried out for the Middle East region and the thermal properties of the lining and the soil are described in the following table:

Table 1. Tunnel lining and surrounding soil thermodynamic properties

	Tunnel Lining with a xx mm thickness	Surrounding Dry Soil
Thermal conductivity (W/m/K)	0.8	0.35
Thermal diffusivity (m^2/s)	$7.5 * 10^{-6}$	$2.219 * 10^{-7}$

The obtained results regarding the January, July, and the yearly average tunnel long-term wall surface temperatures are compared.

Looking at the ratio between the average of January and July obtained long term wall surface temperature and the yearly average one, it can be observed that it is in average 0.97.

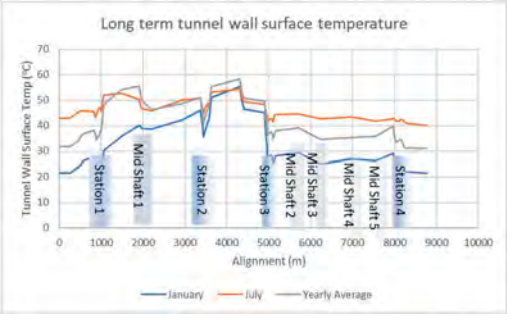

Figure 3. Long-term tunnel wall surface temperature for January, July and yearly average ambient temperatures.

Based on the above, the approach of using the yearly average ambient temperature is acceptable to compare the long-term wall surface temperature of various regions.

4.1 *Average long-term tunnel wall surface temperature based on the region*

For the case study, it has been considered North America, South America, Europe, Africa, Middle East, Oceania, Asia regions.

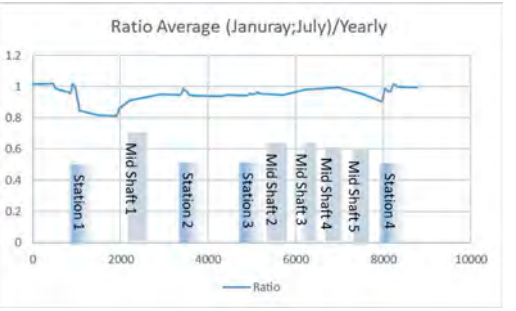

Figure 4. Ratio of the average long term tunnel wall surface temperature obtained based on January and July ambient temperatures by the obtained one based on the yearly average ambient temperature.

The average yearly ambient temperature, in these regions, is given by ASHRAE climatic design conditions (2021) for the following locations:

Table 2. Yearly average ambient temperature in various regions across the world

	Lincoln (Nebraska,US)	Lima (Peru)	Annecy (France)	Dakar (Senegal)	Auckland (New Zealand)	Abu Dhabi (UAE)	Guilin (Guangzhou, China)
Yearly Average Dry Bulb Temperature (°C)	11.2	20.1	11.0	25.1	15.6	28.7	19.8

The average yearly temperature is generally corresponding to the deep sink temperature considering the subway depth below ground.

SES simulations have been carried out accordingly assuming the soil thermodynamic properties to be the same for all these locations.

The obtained long term tunnel wall surface temperature is plotted on the following curve:

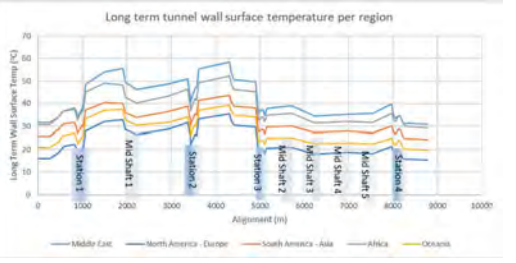

Figure 5. Long term tunnel wall surface temperatures in various regions across the world.

The maximum predicted long term tunnel wall surface temperatures vary between 33°C in region like Lincoln in the US or Annecy in France to more than 55°C in region like the Middle East. The impacted tunnel region is less under influence of outside atmosphere. Where the tunnel is under influence of outside atmosphere, the tunnel wall surface temperature increase is less.

The results, also show that there is a minimum increase of 5°C in the tunnel according to the yearly average temperature and a maximum increase of around 30°C. The equipment installed in tunnel are generally able to operate in a degraded mode at 55°C. The maximum acceptable operating temperature for electrical devices is around 40°C.

This implies that subways for regions like the Middle East, South America, Africa and Asia, are required to be provided means to control the tunnel environment, after a certain period. For region like Oceania, the means to control the tunnel may not be mandatory, but it shall be foreseen a sensitive increase of the temperature in the tunnel after a certain period. While in region like North America and Europe, it is not mandatory to have means to control the environment. It may be a sensitive feeling of temperature increase in tunnel during the summer.

It is important to highlight that the trains are supposed to be equipped with AC, which might not be the case in all these regions and the tunnel is bidirectional. These observations shall be considered in the context of this assumption.

The means to control the environment, when mandatory can be operational from day 1 of the revenue service or after a certain period. In the latter case, this implies the design to account for such means to control the environment. The design shall be carried out not only in terms of operation, power supply and control system, but also in terms of space proofing for the future equipment delivery, installation, and maintenance.

Adequate monitoring devices such as linear heat detector cables laid along the tunnel wall surface at different locations could help to monitor the tunnel wall surface temperature. A threshold could be defined to alert the subway Operator about the necessity to plan for the procurement of the designed means of controlling the tunnel environment.

Besides the tunnel wall surface temperature, the overall heat sink along the alignment gives an indication of the heat sink budget consumption after years of operation.

4.2 *Long term heat sink budget consumption based on the region*

The heat sink magnitudes are among the output provided by SES.

The following curve is providing the heat sink budget consumption along the alignment for a typical revenue operation day, at the beginning of the service with the initial tunnel wall surface temperature:

It can be observed that, at the beginning of the revenue service, the heat sink is much less for region like the Middle East. The reason could be the that the difference between the tunnel air temperature and the wall surface temperature is much less than in the other regions.

One may wonder what the heat sink in these regions would be, when the tunnel wall surface temperature increases.

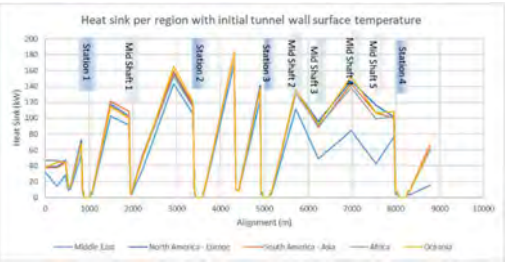

Figure 6. Heat sink with initial tunnel wall surface temperature in various regions across the world.

Simulations have been carried out accordingly to quantify the heat sink when the tunnel wall surface temperature increases for South America region and similar. The analysed tunnel wall surface temperature magnitudes are 26°C and 39°C. The deep sink temperature is still considered same as the average yearly ambient temperature.

The following curve corresponds to the heat sink obtained at the beginning of the revenue service, i.e., the tunnel wall surface temperature initially is equal to the deep sink temperature and the heat sink obtained after the wall surface temperature increases to a magnitude of 26°C and 39°C.

It is observed a decrease in the heat sink due to the increase of the tunnel wall surface temperature. It is important to highlight that when the heat sink is null on this curve, it means, in fact, that the wall is not absorbing heat but rather releasing heat warming up the tunnel air.

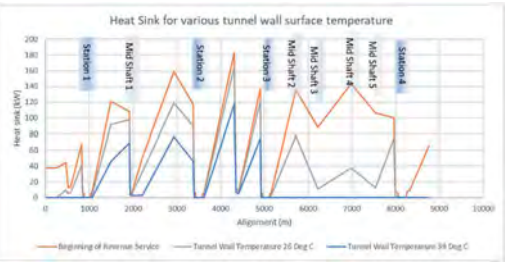

Figure 7. Heat sink with various tunnel wall surface temperatures.

5 IMPORTANCE OF THE SOIL THERMODYNAMIC PROPERTIES

The question which is considered here is whether the soil thermodynamic properties have an impact on the long-term wall temperature or whether it is the tunnel lining thermodynamic properties.

For South America region, comparative analysis has been carried out by increasing the soil thermodynamic properties on the one hand and the tunnel lining thermodynamic properties on the other hand.

The curve below represents the obtained long term tunnel wall surface temperature:

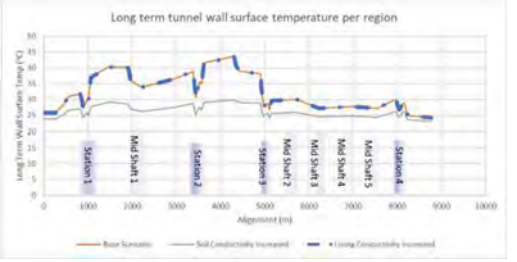

Figure 8. Long term tunnel wall surface temperature with increased lining and soil thermodynamic properties.

The results show that the soil thermodynamic properties have a major influence on the long-term tunnel wall surface temperature. A very conductive soil would consume less heat sink.

The tunnel lining thermodynamic properties do not affect the subway environment thermal behaviour.

6 SUMMARY

After explaining the physical phenomenon occurring in a subway regarding its environment thermal behaviour, after describing the mathematical equations driving the subway environment thermal behaviour and after presenting the equivalent mathematical models computed by SES software, a number of simulations have been carried out to showcase the subway environment thermal behaviour in the long term for various regions across the world.

The analysis show that the daily thermal solicitation due to the trains operation along with the tunnel ventilation configuration and the external ambient conditions drive the subway environment thermal behaviour. The key parameters involved in the subway environment thermal behaviour are the tunnel wall surface temperature and the tunnel lining as well as the surrounding soil thermodynamic properties.

Depending on the region, the long-term tunnel wall surface temperature may require accounting for means of controlling the environment. These means can be operational from day 1 of revenue service or they can be designed to be procured at a later stage. The means can be mechanical equipment such as axial fan, air handling unit. They can also be passive by circulating chilled water pipes along the tunnel wall surface, for instance.

The specifications of the equipment exposed to the tunnel environment could also account for the predicted long-term tunnel air environment.

The study also describes the heat sink magnitudes based on the tunnel wall surface temperature. While the tunnel wall surface temperature increases, the heat sink decreases, and the tunnel is likely to act as heat source warming up the tunnel air.

The study finally shows that the surrounding soil thermodynamic properties have a considerable impact on the subway environment thermal behaviour. The higher its conductivity and diffusivity, the less the heat sink consumption along years of operation, hence the lower the long-term tunnel wall surface temperature.

7 CONCLUSIONS

This paper is about the importance of the subway long-term wall surface temperature and its interdependence with the surrounding soil heat sink.

Depending on the region, means to control the subway thermal environment may be required not to degrade the performance of the equipment installed in tunnel, hence reducing their lifecycle. These means of controlling the subway thermal environment can be either by mechanical cooling or by passive cooling. The increase of the long-term wall surface temperature may have an impact in case of human exposure whether it is about passengers when it comes to train evacuation via the tunnel or is about operators carrying out maintenance activities in tunnel. This subject has not been treated in this paper.

The surrounding soil thermodynamic properties play an important role in the subway long term thermal behaviour. The higher its conductivity and diffusivity, the lower the impact on the subway long term thermal behaviour. This may give perspective for geologist and geotechnical colleagues when it comes to survey the surrounding soil for a subway alignment study.

REFERENCES

ASHRAE, 2021. Climatic design conditions 2021.

ASHRAE Handbook, 2016. HVAC Systems and Equipment.

Subway Environmental Design Handbook, Volume I, Principles and Applications, Second Edition, 1976.

Subway Environmental Design Handbook, Volume II, Subway Environmental Simulation Computer Program, SES Version 4.1, Part I User's Manual, 2002.

Subway Environmental Design Handbook Volume II, Subway Environment Simulation Computer Program (SES) - PART 2: Programmer's Manual, 1975.

Guo, J., Li, A., 2022. "Modelling ventilation and convective heat transfer in deeply buried underground tunnels based on boundary layer theory".

Jaeger, J.C., Chamalaun, T., 1966. "Heat flow in an infinite region bounded internally by a circular cylinder with forced convection at the surface".

Tunnelling for a Better Life – Yan, Celestino, Thewes & Eberhardt (Eds)
© 2024 The Author(s), ISBN 978-1-032-80042-4
Open Access: www.taylorfrancis.com, CC BY-NC-ND 4.0 license

Approach in structural fire resistance of the existing North-South Railway Tunnel in Brussels

Bart De Pauw*
Department of Civil Engineering, Ghent University, Ghent, Belgium
TUC RAIL Ltd., Brussels, Belgium

Carl Timperman & Sébastien Devriese
Department of Civil Engineering, Ghent University, Ghent, Belgium

ABSTRACT: The Brussels North-South Railway Tunnel connects the northern railway station Brussels-North with the southern station Brussels-South as largest Belgian station. The tunnel is a large culvert construction and consists of an integral tunnel structure with 3 parts of two tracks with inner concrete columns making the tunnel a vulnerable part of the Belgium railway network. Although the tunnel of 1946 is a critical spot in the railway network, it does not comply with the current interoperability requirements in safety evacuation and structural fire resistance. A performance-based design approach is adequate to justify an acceptable level of higher structural fire resistance. The rectangular three shaft reinforced concrete tunnel model is setup in Siemens NX 12. Concrete is designed as a non-linear, isotropic, elastic material and the reinforcement is designed as a plastic, isotropic material, both materials follow the law of Von Misses. Two calculation environments are used within the Nastran solver namely, a transient thermal (sol 159) and a linear structural environment (sol 101). Different TT zones are constructed based on the computational fluid dynamics simulation results of a burning M6 train carriage of 600 m tunnel model. This approach results in a more specific and realistic thermal calculation model then those currently described in standards which use oversized benchmark fire curves. The tunnel stability is checked using the structural model based on the data results retrieved from the thermal calculation, leading to identifying zones of concrete damage. Additionally, a manual discretisation method is done to understand better the spalling behaviour during an M6 train carriage fire. An overview of the applied workflow is represented, added with possible extra implementations and improvements that can be done in further research. The paper is a result of a master thesis at the civil Engineering Department of Ghent University.

Keywords: 3D FEM tunnel, thermal calculation, stability check, Siemens NX 12

1 INTRODUCTION

The North-South Railway Tunnel (NSRT) connection has a total length of 1928 meter and exists of sixty-eight tunnel segments. The length of the tunnel segments varies depending on its location. As stated before, in this master thesis, the focus is on the straight tunnel segments sections S1 till S15. These tunnel segments are assumed to have an average length of 21 meters with cross-sections consisting of three tunnel shafts. The tunnel sections S1-S15 and an overview plan of the tunnel with segments is visible in Figure 1. It shows that each shaft has two railway tracks used to travel in both directions, separated by column rows. As a fire source can easily spread from one railway track to another, the space in between the columns was bricked up.

Phase 1 with tunnel segments S1 till S15 of the NSRT-connection, which was constructed between 1936 and 1938, is the subject of the investigation regarding its structural integrity in the event of a fire caused by an M6 train carriage. The M6 train carriage is a type of double-deck passenger train used in Belgium. It is part of the M6 series trains that were introduced in the early 2000s as part of a modernization program for the Belgian railway system and they are designed to be compatible with other types of trains used in Belgium, allowing for greater flexibility in the rail network. The M6 train carriage is given in Figure 2.

The HRR curve of the standard train carriage M6 is used to analyse the impact of the fire on the structural stability. The HRR curve considers the following fire spread scenario. It is assumed that a fire occurs in the lower compartment due to the ignition of a single seat. The fire spread within the M6 train

*Corresponding author: bart.depauw@tucrail.be; bartrm.depauw@ugent.be

DOI: 10.1201/9781003495505-457

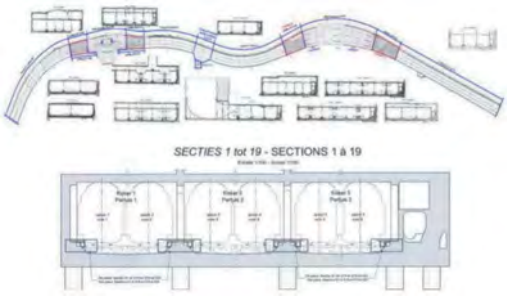

Figure 1. Overview and cross-section plan of the North-South railway connection in Brussels S1-S15.

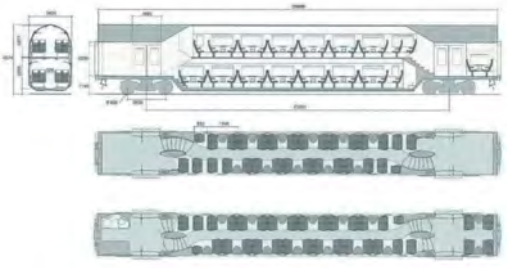

Figure 2. The M6 train carriage - geometry and dimensions.

carriage is limited by the vents and an intermediate door that is opened during an evacuation attempt. Also, half of the total windows in the lower compartment, i.e. 8 out of 16, break. As a result of the broken windows, the fire spreads to the upper compartment of the train carriage, leading to breaking 11 out of 16 windows. The curve consists of two parts. The first part, up to 20 MW, represents the total heat released in the lower compartment, while the second part, from 20 MW up to 35 MW, represents the total heat released by the top compartment after which the fire ramps up to a maximum heat release rate at 37 minutes and later remains constant. The HRR curve is given in Figure 3.

The HRR curve is incorporated into the CFD model to understand the temperature development along the longitudinal direction of the tunnel's concrete surface. Siemens, a finite element software package, is employed to analyse both the thermal and structural behaviour of the tunnel. However, it should be noted that the modelled reinforced concrete material does not account for cracking or spalling behaviour. In the absence of comprehensive data, literature-based criteria are used as assumptions to guide the analysis.

The investigation begins with the creation of a simplified start-up model, which serves as an initial assessment. Subsequently, a longer and computationally demanding 21-meter model (general tunnel model) is developed to better understand the structural response on the fire.

The fire source (M6 train carriage) in the railway tunnel is designed to have a maximum HRR of 35

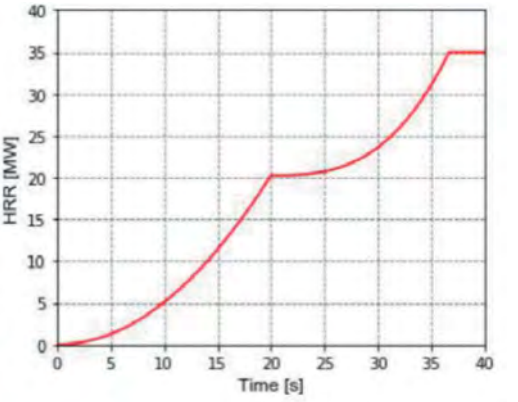

Figure 3. HRR in function of time due to combustion of the M6 train carriage.

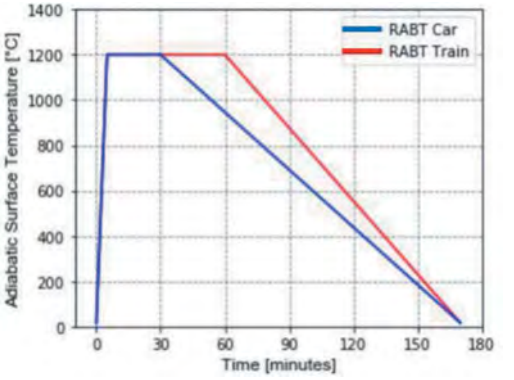

Figure 4. RABT time temperature curves done by design office FESG.

MW as stated above. To consider the increase of temperature in the tunnel, the TT curve is designed based on the "Risk analysis and better targeting (RABT) train" fire curve, visualized in Figure 4. The RABT curve is used for the fire safety design in railway tunnels. It is a risk-based approach that considers the fire load, ventilation conditions and geometry of the tunnel. The RABT curve is the basis for the developing of the M6 curve done by the design office Fire Engineered Solutions Ghent (FESG). Following thorough the study of FESG, the maximum temperature (1200°C) described by the RABT curve can be considered as too conservative for the case study of the NSRT connection. Therefore, the maximum temperature is recalculated to 800°C, based on the results obtained from CFD simulations performed by FESG.

2 ANALYSIS PROCEDURE

The Siemens software, possesses a powerful environment to calculate and analyse heat transport and structural stability through the concrete lining of a three-

dimensional finite element tunnel model. The analysis procedure is represented in Figure 5. The Nastran SOL159 non-linear transient heat transfer analysis type is used to obtain the 3D temperature distribution in the reinforced concrete lining of the tunnel structure. The transition from the thermal analysis to the structural analysis is achieved through a coupled thermal-structural technique. This technique ensures the integration of thermal and structural responses, allowing for an assessment of the tunnel's behaviour under varying temperature conditions. By utilizing this approach, a representation of the tunnel's thermal and structural performance is achieved.

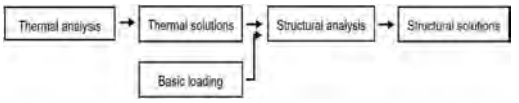

Figure 5. Analysis procedure in siemens.

3 MODEL BUILD-UP

3.1 *Geometry*

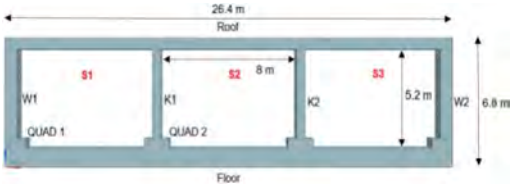

Figure 6. Cross-section of the tunnel model.

To begin, a simplified start-up model is executed consisting of three straight adjacent tunnel shafts, with an inner length of 8 m by 5.2 m and longitudinal length of 1 m. The dimensions and denomination of the different structural parts are displayed in Figure 6. The successful finishing of the start-up model facilitates the base to extend the tunnel with 21 m in longitudinal direction. Three tunnel segments of 21 m are referred to as the general tunnel model. Calculation of the general model requires more powerful computing equipment (32 GB RAM) due to the increase of mesh points.

3.2 *Modelling properties*

Siliceous concrete in the tunnel is represented using hexahedral 8-node volume elements to ensure an optimal fit with the rectangular geometry of the tunnel. The concrete material is assumed to exhibit isotropic, linear elastic behaviour with a compressive strength of C20/25.

The mesh sizes of the concrete shafts vary based on the modelling requirements. An appropriate mesh size accomplishes a balance between calculation accuracy and computational efficiency, aiming to minimize resource utilization and excessive computation time.

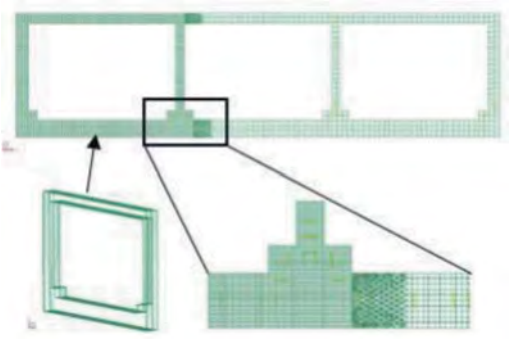

Figure 7. Meshing tunnel model.

In the fire scenario, S1 corresponds to the shaft exposed to the burning M6 train carriage and is modelled using a mesh size of 50 mm. On the other hand, S2 and S3 are equipped with larger 100 mm volume elements, as thermal calculations require less accuracy in those areas. The different mesh sizes are interconnected using 100 mm hexagonal (8-node) volume elements, as depicted in Figure 7. The reinforcement within the model is represented as one-dimensional CBAR elements, which corresponds to a truss behaviour. To optimize computational efficiency, reinforcement is only included in the left shaft. The reinforcement material exhibit linear elastic, isotropic behaviour with a yield strength of 400 MPa and a diameter of 20 mm. Both the concrete and reinforcement materials adhere to the von Mises yield criterion. Temperature-dependent parameters, including mass density, E-modulus, Poisson's ratio, yield strength, ultimate tensile strength, thermal expansion, thermal conductivity, and specific heat, are implemented for both materials.

3.3 *Boundary conditions and soil representation*

To accurately capture the stiff and enclosed behaviour of each segment under investigation, a single boundary condition is applied to the tunnel lining. This boundary condition restricts longitudinal movement at the front and back faces of the entire cross-section. In the model, the surrounding soil is represented as an embedded spring system. A zero-dimensional mesh is created along the outer circumference of W1, W2, and the floor.

The calculation of the spring stiffness depends on the number of mesh nodes and the area affected by the corresponding springs. Based on the mesh modelling described in Section B "Modelling properties", five distinct zones of springs are identified, resulting in five springs, each with normal and shear components. CBUSH-grounded spring elements are utilized to model these springs, with a virtual node assigned with both normal (bi-linear) and shear (linear) stiffness at each mesh node. When a structural component displaces inwards, no resistance from the soil is considered as it cannot generate

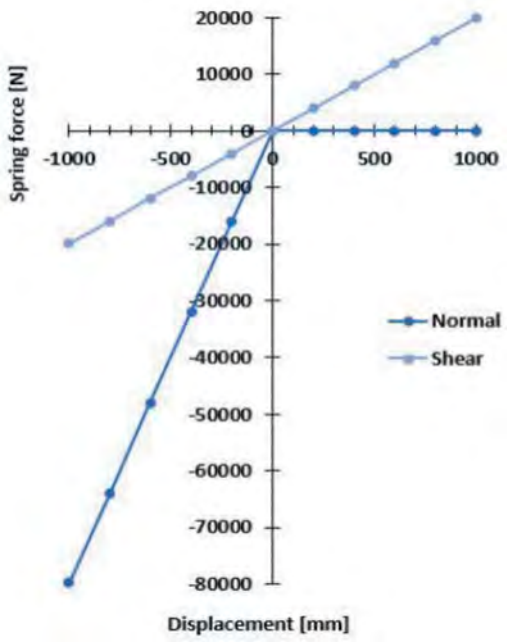

Figure 8. Spring behaviour W1.

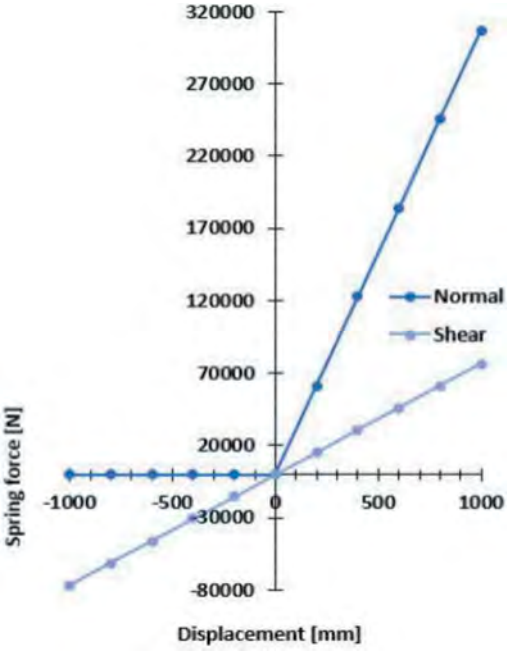

Figure 9. Spring behaviour W2.

tensile forces. However, for outward displacement, the soil provides counteracting forces proportionate to the magnitude of the displacement. The spring behaviour and variations in spring stiffness, as explained above, are depicted in Figure 8 and Figure 9, respectively, for walls W1 and W2.

3.4 *Loading*

Multiple static loads are employed to represent the acting forces on the tunnel and as accurately as possible simulate the interaction behaviour of the tunnel with its surrounding. The implemented forces are self-weight, water pressure and soil pressure. The temperature load data is statically implemented in the structural calculation environment as a three-dimensional temperature distribution through the reinforced concrete, obtained out of the thermal analysis.

4 GENERAL TUNNEL MODEL

The general tunnel model has the attributes as described in paragraph 2. The methodology for the assessment of the structural fire resistance follows three steps: (A) determining the fire scenario with a CFD simulation, (B) performing thermal analysis and (C) performing the structural analysis that considers the thermal load at a certain point in time.

4.1 *Fire scenario and CFD simulation*

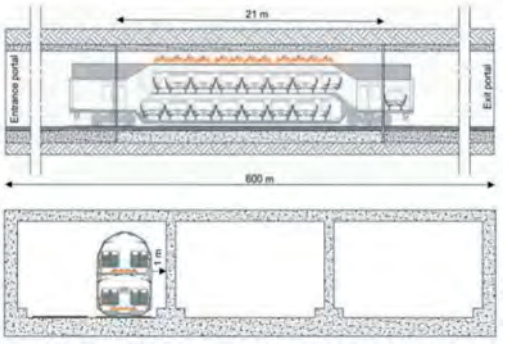

Figure 10. Fire scenario.

The burning M6 train carriage is assumed to be stopped in the middle of tunnel segment 2 and close to the right sidewalk. Furthermore, only one shaft is exposed to a burning train carriage, in particular, the left shaft (Figure 10).

The CFD simulation based on the HRR of the M6 train carriage provides the ability to segregate the roof and walls in temperature zones. The floor is disregarded for analysis purposes. Each zone has a specific TT curve assigned. A total tunnel length of 63 meter, 3 tunnel segments, are investigated on its structural stability. An extended tunnel length analysis is unnecessary due to large decrease in temperatures at greater distance from the centre of the train carriage. The generated TT curves are based on the provided TT curve on the concrete lining by FESG. Figure 11 shows the maximum and minimum TT curves of the roof and walls implemented in segment 2. The fire duration is 170 min (10200 s) and the

maximum temperature is reached after 5 min and is detained for 55 min.

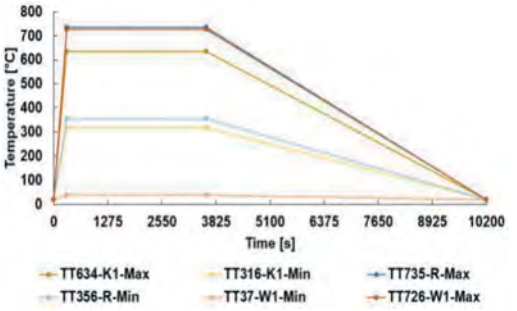

Figure 11. TT-curves of the roof (R), W1 and K1.

4.2 *Heat transfer analysis*

In order to gain a more comprehensive understanding of the three-dimensional heat distribution and its evolution over time, the thermal non-linear calculation method is employed. This computational technique is applied across twelve discrete time increments, which yield valuable data for investigating the time-dependent development of temperature within the reinforced concrete.

4.3 *Structural analysis*

To assess the tunnel's structural stability in ultimate limit state the accidental load combination is applied. The first step in this analysis involves determining the time increment at which the combined internal forces of the concrete and reinforcement are at their maximum. The point in time at which the maximum temperature of the reinforcement occurs and subsequently generates the highest levels of reinforcement internal forces, is at 6000 seconds. The highest internal forces in the concrete are reached at 3600 s. From this, the time increment in which the most severe heat loading of the tunnel is found to occur at 4800 seconds (Figure 12).

In order to assess the structural integrity of the tunnel, the three segments are divided into distinct zones (Figure 13). For the roof and wall structural components W1 and K1, the bending moment lines are compared with their ultimate moment capacity as determined by the NBN EN 1992-1-2 (2005) standard. In cases a part of the bending moment line within such a zone exceeds its ultimate moment capacity then, the part is defined as damaged reinforced concrete and no longer contributes to the local structural stability of the segment. This may result in a potential local collapse of the affected tunnel zone (Figure 14).

The roof zones with 100 % loss of structural capacity are identified as zones 4 to 8, corresponding to a tunnel length of 15 meters. Beyond these zones, it

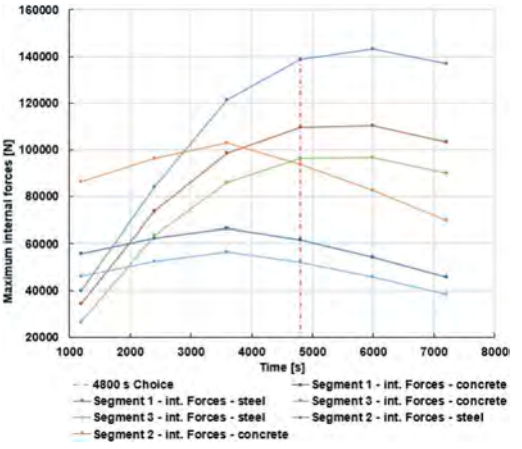

Figure 12. Maximum internal forces in time for the 3 segments.

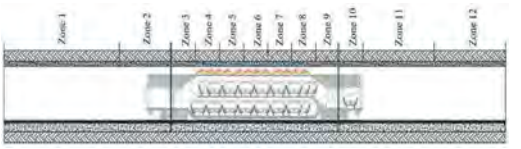

Figure 13. Division of the tunnel into zones in longitudinal direction.

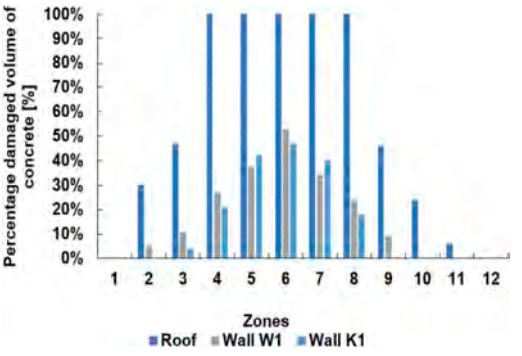

Figure 14. Percentage of concrete damage for each zone.

is noticeable that the percentage of damaged volume of concrete decreases further from the train carriage fire. The maximum volume of damaged reinforced concrete in the walls is 54 %. The damage to the walls is lower because, the fire affects the upper parts more due to the rising hot smoke gases. Interestingly, the wall (K1) closest to the burning train carriage does not exhibit the highest percentage of damaged volume of concrete in every zone. A reason for this is that K1 has a lower stiffness and is connected with two other structural elements. Overall, segment 2 is in the worst condition, while segments 1 and 3 remain mostly intact.

5 SPALLING CONSIDERATIONS

Spalling, the loss of concrete mass during the event of a fire, can compromise the structural stability of the tunnel by reducing the concrete cross-section. Thereby, it allows the elevated temperatures to penetrate deeper into the structure. This induces augmented stresses for both concrete and reinforcement. Unfortunately, implementing spalling directly in Siemens is not possible.

Table 1. Results investigated spalling D300.

Max temperature [°C]	D300 [mm]	Damage Stage	Repairability
456	26	DS3	Clean surface
536	38	DS3	and replace
628	46	DS3	damaged
735	54	DS3	concrete

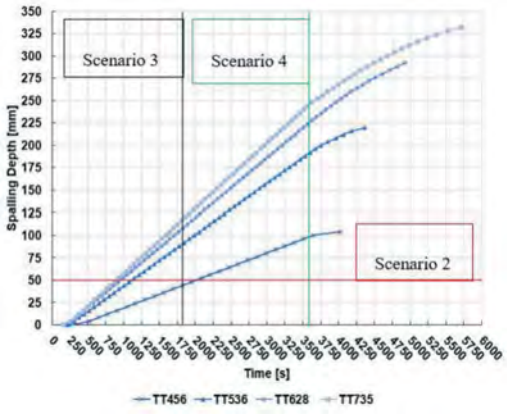

Figure 15. Investigation four spalling scenarios.

To estimate spalling, a manual discretization method based on a conservative temperature criteria of 380 °C is used to evaluate different scenarios. Thereafter, the resulting spalling depths are compared. Although using only a temperature criteria is not sufficient to fully describe this complex phenomenon, it can provide insight in its impact. The TT curve, as well as the specific scenario, have a significant impact on the spalling evolution and resulting spalling depth, observed in Figure 15. An alternative approach to measure spalling depth is the D300 method, which assesses the extent of damage based on the depth of penetration of a temperature of 300°C into the concrete, when subjected to a TT curve. Table 1 presents the repairability of concrete for each TT curve. For every TT curve the repairability result is "clean surface and replace damaged concrete. Figure 16 illustrates a technique depicting the implementation of spalling. The process involves obtaining the depths of spalling in various TT zones, followed by the construction of a reduced model to assess the structural stability of the tunnel. In the general tunnel model spalling is incorporated by assuming the occurrence of scenario 2, where spalling continues until the reinforcement axis. The tensile strength of the reinforcement is reduced with a temperature depending factor, taking into account the decrease in concrete section, reinforcement and concrete strength. By including this consideration for spalling, the results for the roof align with those shown in Figure 14. However, the damaged volume of concrete in zones 2 and 3 increases to 100%.

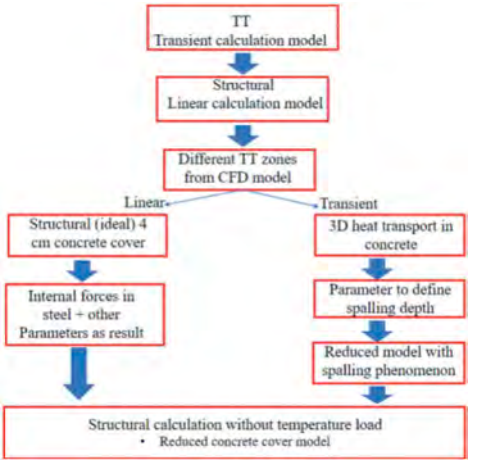

Figure 16. Implementation of spalling in general tunnel model.

6 IMPROVEMENT OF FIRE RESISTANCE

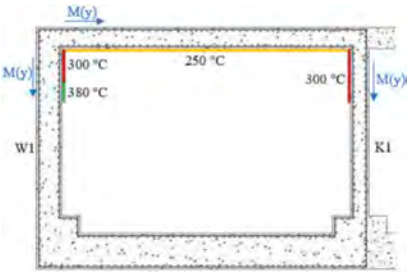

Figure 17. Location and required temperature limit.

Utilizing fire-resistant materials is a highly effective strategy for preventing spalling and enhancing structural stability. The study examines two scenarios: case 1, where the train ignites on the right railway track, and its mirrored counterpart, case 2, with the train igniting on the left railway track. In both cases, a manual iterative procedure is employed to determine the bending moment lines for various combinations of temperature heat loads. Analysis of the bending moment lines reveals that case 1 is decisive, requiring a Roof-Wall combination of 250-300 °C. On the other

hand, case 2 requires a maximum temperature of 380° C. To enhance fire resistance, different fire resistant panels and coatings are assessed, with material thickness identified as the primary parameter influencing the fire resistance. Figure 17 illustrates the specific temperature limits on the concrete lining and their corresponding locations.

7 CONCLUSIONS

Siemens NX 12.0 thermal-structural environment proves to be a valuable tool for investigating fires involving burning M6 train carriages in the NSRT connection. However, it is important to acknowledge that the software has certain limitations when it comes to accurately modelling material and environmental characteristics. By utilizing the HRR curve of the M6 train carriage, a CFD simulation is conducted. This simulation enabled the identification of various TT zones along the concrete lining. Consequently, spalling is discussed, it is established that the depth of spalling is dependent on the specific spalling scenario under consideration. In order to improve fire safety, precise combinations of Roof-Wall (TT) curves are identified to minimize the necessary thickness of fire resistant materials and mitigate the temperature reducing effect. By employing these specific TT curves, the structural impact of a fire is reduced compared to using the RABT curve, resulting in a diminished requirement for fire protective materials. It is also concluded that oversized standard fire curves lead to overestimations in fire protection and structural improvement. However, it is a matter of debate whether intensive computational 3D finite element model calculations are required for implementing fire protection. To reduce costs, fire safety engineering only (mostly) investigates the highest temperatures and not the temperature evolution in longitudinal direction through the tunnel model. Further research can find ways to implement spalling into the NSRT model, to accomplish fire analysis that better represent reality. Improving the structural calculation techniques from the linear SOL 101 to a non-linear environment (e.g. SOL 106) leads to a more correct analysis of the bending moment lines by regenerating the stiffness matrix in every calculation-step. The process of extracting bending moment lines from 3D finite element analysis is a laborious and a time-intensive task that needs to be automated using software code.

ACKNOWLEDGMENTS

The paper is a result of a master thesis at the civil Engineering Department of Ghent University. Special thanks are acknowledged to the students Carl Timperman and Sébastien Devriese, who successfully completed their education as engineers.

REFERENCES

D. Naus A compilation of elevated temperature concrete material property data, p. 328, 2010.

Tunnelling for a Better Life – Yan, Celestino, Thewes & Eberhardt (Eds)
© 2024 The Author(s), ISBN 978-1-032-80042-4
Open Access: www.taylorfrancis.com, CC BY-NC-ND 4.0 license

A seismic damage classification for post-damage assessment of rock tunnels

Dinesh A. Reddy*
Research Scholar, Department of Civil Engineering, Indian Institute of Technology, Roorkee, India

Aditya Singh
Ph.D., Assistant Professor, Department of Civil Engineering, Indian Institute of Technology, Roorkee, India

ABSTRACT: The rock tunnels were partially or completely damaged by earthquakes such as the ones that struck Kern County, Duzce, Chi-Chi, Wenchuan, and many others. The damage degree and classification are important factors in determining how vulnerable rock tunnels are to earthquakes. Based on the amount of damage, researchers modified the damage degree and descriptions in the post-seismic damage classifications of rock tunnels after each seismic event. These classifications are specific to one or a maximum of three seismic events. This suggests that the existing post-seismic damage classifications are not standardized or coherent. In this research study, a seismic damage classification of rock tunnels for post-damage assessment is proposed. This classification is accomplished by utilizing the data of 285 rock tunnels from 26 different earthquakes throughout the world and is the largest seismic damage database of rock tunnels created to date. Further, this classification can be applied to any seismic event as it is linked to seismic and rock parameters. This classification highlights the extent of damage with clarity and can offer a comprehensive account of the performance of rock tunnels after an earthquake. This classification categorizes seven seismic damage levels for rock tunnels ranging from Extremely High (EH) to Lowest (LO). Seismic damages with thorough descriptions are associated with each damage level, along with seismic, rock parameters, and accessibility of the tunnel. This research will help in characterizing the tunnel performance after an earthquake.

Keywords: Earthquake, Rock Tunnels, Seismic Damages, Seismic Damage Assessment

1 INTRODUCTION

The tunnels are one of the major parts of infrastructure for roads, railways, hydropower, and many more. The rock tunnels are generally considered to be seismic resistant and are invulnerable to earthquakes. This traditional point of view was questioned when the tunnels were being posed with risks related to seismicity, especially in the mountainous region. Earthquakes like the 1952 Kern County,1999 Duzce, 1999 Chi-Chi, 2008 Wenchuan, and many more have damaged tunnels to various extents (Dowding and Rozen, 1978; Wang et al., 2001; Wang et al., 2009). A few of the pictorial representations of damaged tunnels are shown in Figure 1. It is evident that the tunnels are also vulnerable to earthquakes. These damaged rock tunnels led to huge social and economic losses. Hence, the assessment for seismic damage to rock tunnels residing in a seismic zone is an important issue for rock and tunnel engineers all over the world. To understand the vulnerability of rock tunnels, various researchers have proposed the seismic damage classification for tunnels after seismic events.

2 PROBLEM STATEMENT

Numerous researchers as detailed in Table 1, such as Dowding and Rozen (1978) categorized seismic damage into three classes. Sharma and Judd (1991) modified Dowding and Rozen's classification by subdividing the first class which is minor damage into slight damage and moderate damage. Asakura and Sato (1996) proposed the damage classification based on the Kobe earthquake. Based on seismic damages to tunnels due to the Chi-Chi earthquake, Wang et al. (2001) modified Dowding and Rozen's classification based on the functionality of the tunnel after the earthquake, observed length, and width of cracks. Yashiro et al. (2007) and Jiang et al. (2010) modified Asakura and Sato's (1996) classification for the tunnels damaged due to Mid-Niigata

*Corresponding author: dinesh_r@ce.iitr.ac.in

DOI: 10.1201/9781003495505-458

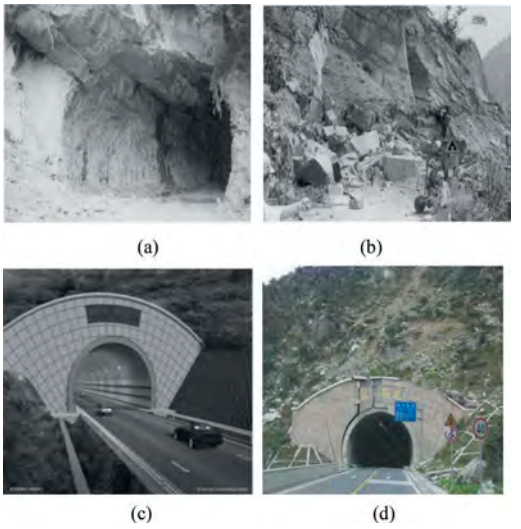

Figure 1. (a,c) Chi-Shue and Taoguan Tunnels before the Chi-Chi, and Wenchuan earthquakes respectively. (b,d) Damages to Chi-Shue and Taoguan Tunnels after the earthquakes (After Wang et al., 2001; Wang et al., 2009; Li, 2012).

Table 1. Literature review of seismic damage classes and classifications of tunnels.

Author	Damage Degree/ Damage Classes
Dowding and Rozen (1978), Owen and Scholl (1981)	No Damage, Minor Damage, and Damage.
Sharma and Judd (1991)	Slight, Moderate, Heavy, and No Damage
Asakura and Sato (1996)	A: Damage Required to Repair, B: Slight Damage, None: No Damage.
Wang et al. (2001), Wang et al. (2009)	A: No Damage/Slight Damage, B: Moderate, C: Severe Damage
Yashiro et al. (2007), Jiang et al. (2010)	A1: Heavy Damage Requiring Repair and Reinforcement, A2: Damage Requiring Repair and Reinforcement, B: Damage not Requiring Repair and Reinforcement, and C: No Damage
Wang and Zhang, (2013), Shen et al. (2014), Yu et al. (2016)	1: None, 2: Slight, 3: Moderate, 4: Severe, 5: Collapse/ Extremely Severe
Shrestha et al. (2020)	Slight, Moderate, and Severe.

Prefecture. Due to the severity of damage to tunnels caused by the Wenchuan earthquake, Wang and Zhang (2013), Shen et al. (2014), and Yu et al. (2016) modified Wang et al. (2001) classification by adding the collapse or extremely severe damage class. The Tunnel Damage (TD) was classified into five classes. Further, Shrestha et al. (2020) modified Wang et al. (2001) classification as the damage was not so severe and was confined to lining cracks and spalling only. The damage degree or damage classes used for all these classifications are shown in chronological order in Table 1.

From Table 1 and the above literature survey, it can be concluded that researchers periodically adjusted the damage classes and descriptions in post-seismic damage classifications based on the quantity and extent of tunnel damage. This suggests that for determining the degree of damage to rock tunnels, there is not a universal or consistent post-seismic damage classification that suits all seismic events. Based on damage data from one or a maximum of three seismic events, the current post-seismic damage classifications are in place (Wang et al., 2001; Wang and Zhang, 2013). These classifications lack a comprehensive understanding of the issue since they are particular to the location and the seismic event that occurred. A significant amount of data on damaged tunnel cases is required in order to evaluate the seismic damage of rock tunnels. To better comprehend the various levels of damage to rock tunnels, a new Post-Seismic Damage Classification of Rock Tunnels is presented in this work. This damage categorization is based on data from 285 rock tunnels damaged as a result of 26 earthquakes, which is the largest post-seismic damage database of rock tunnels in the world. Figure 2 displays the distribution of rock tunnels from each earthquake that were used to create a database. This work is part of Reddy and Singh (2023) and for detailed information on this work, the authors would recommend reading their future journal article.

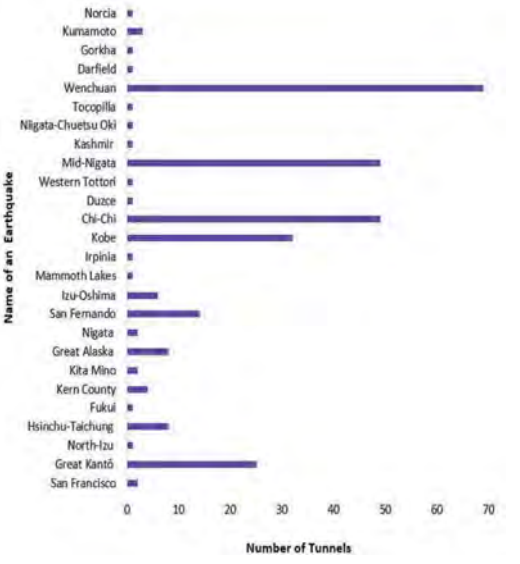

Figure 2. The list of 26 earthquakes along with the number of rock tunnels used in each is listed in the damage database.

3 SEISMIC DAMAGE TO TUNNELS

Earthquake-induced tunnel damage patterns include lining shearing off, tunnel collapse, cracks with different spatial distributions on lining and portals, spalling in the lining, deformation of side walls or inverts, and water leakage (Wang et al. 2021, Wang and Pan, 2022). From the database created, earthquakes like the 1923 Great kantō earthquake, the 2008 Wenchuan earthquake, and others, the damages like avalanches sliding toward the tunnel portal, Rock falls, and portals were completely buried by large slumps of rock/soil mass are observed (Dowding and Rozen, 1978; Wang and Zhang, 2013; Shen et al., 2014). Figure 3 (a-f). displays the visual depictions of seismic damage to tunnels. According to the created database, lining cracks are the most common type of damage observed in rock tunnels (31%), followed by spalling (26%), and the lowest being slope failure-induced collapse (1%). The most severe damage type, shear failure of the lining (7%), has the potential to collapse the tunnels.

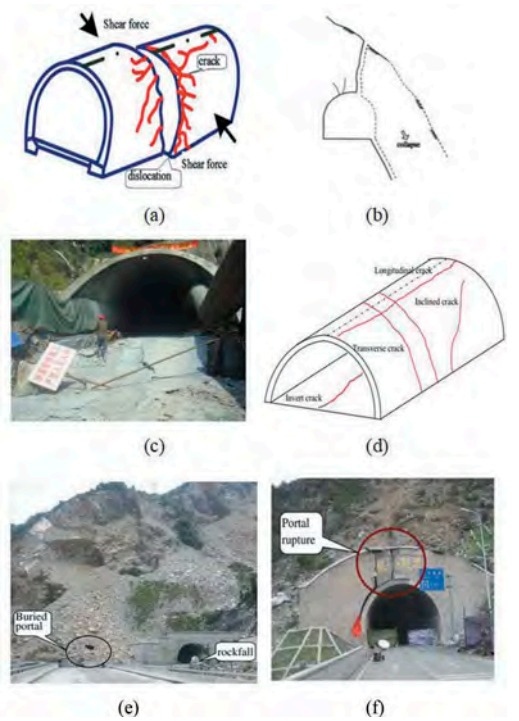

Figure 3. (a) Shear Failure in the Lining (after Shen et al., 2014) (b) Slope Failure Tunnel Collapse (after Wang et al., 2001) (c) Pavement Damage (after Li, 2012) (d) Different patterns of cracks in tunnel lining (after Roy and Sarkar, 2017) (e and f) Types of Portal Damage (after Shen et al., 2014).

4 A NEW POST-SEISMIC DAMAGE CLASSIFICATION OF ROCK TUNNELS

The aim of this research is to suggest a post-seismic damage classification system that can be applied to any forthcoming seismic event of any scale. It is based on the biggest damage database ever assembled. The damage description of this classification uses the amount or extent of damages that were suggested in previous classifications by Wang et al. (2001) and Wang and Zhang (2013). Previous damage descriptions lack information pertaining to rockfalls, slopes, and portals are either sparse. The proposed classification includes a detailed and highlighted breakdown of the damage caused by rockfalls, slopes, and portals in each class. For a new damage classification, a methodical arrangement of damages and damage descriptions taken from the various studies are combined. With comprehensive damage descriptions listed in Table 2, this study presents seven tunnel damage classes for damage degrees: None, Very Slight, Slight, Moderate, Severe, Extremely Severe, and Collapse Classes. In this classification shown in Table 2, the "Very Slight" degree is added for the first time, and the "Extremely Severe" and "Collapse" degrees coexist. In addition, this damage classification provides a qualitative description of parameters such as rock mass, the distance between the tunnel and the ruptured fault zone, as well as a quantitative description of moment magnitude and the accessibility of the tunnel in each class following an earthquake. For more detailed information on this work, the authors would suggest to refer Reddy and Singh (2023)

Table 2. A New post-seismic damage classification of rock tunnels.

DC*/ DD**	Damage Description	Role of Rock, Seismic Parameters, and Tunnel Accessibility
1 / None (N)	No damage is caused due to an earthquake. The tunnel is in an undamaged state.	Found in tunnels in exceptionally competent rock mass, far away from the ruptured fault zone (Mw <6.2). Shortly after the seismic event, the tunnel is readily accessible.
2 / Very Slight (VS)	Very slight cracks (w_c < 3mm, l_c< 1m), Small-scale overhead raveling of rock in mountain tunnels, and no groundwater leakages observed.	Found in tunnels of harder or competent rock mass that are far away from the ruptured fault zone (Mw ≥6.2). Immediately following the seismic

(*Continued*)

Table 2. (*Continued*)

DC*/ DD**	Damage Description	Role of Rock, Seismic Parameters, and Tunnel Accessibility
		event, the tunnel is easily accessible.
3 / Slight (SL)	Cracks (w_c<3mm, l_c< 5m), slight palling, stones falling and stocking up in front of a portal in mountain tunnels, and slight seepage of groundwater can take place.	Found in tunnels of harder or competent rock mass that are far away from the ruptured fault zone (Mw ≥6.2). Immediately following the seismic event, the tunnel is easily accessible.
4 / Moderate (M)	Cracks (3<w_c<30mm, 5<l_c<10m), moderate spalling, deformation in the lining (d_b< 0.25 m), and invert uplift (h_u <0.2 m), moderate rock falls, massive gravel, or many stones stocked up in front of a portal, and dripping groundwater might take place.	Found in softer and harder rock mass tunnels, these tunnels are located close to the ruptured fault zone (Mw ≥6.2). After the seismic event, the tunnel is accessible with numerous signs of caution and regulations.
5 / Severe (SE)	Multiple cracks (w_c > 30mm, l_c> 10m), severe spalling up to a crushed range area of < 2 m^2, a roof can cave in tunnel sections, slight to moderately exposed reinforcement, horizontal dislocation in the lining (d_b < 0.8 m), invert uplift (h_u ≤1 m). Accompanied by portal ruptures, and rock falls, most part of the tunnel portal is buried. The continuous inflow of groundwater.	Found in softer and harder rock mass tunnels or at the interface of rocks, these tunnels are located close to the ruptured fault zone (Mw ≥ 6.2). After the seismic event, the tunnel is not accessible.
6 / Extremely Severe (ES)	a) Continuous cracks at multiple locations (w_c>35mm, l_c>15m), extremely severe spalling up to a crushed range area of >2 m^2, severely exposed reinforcement, extremely severe tilting of concrete blocks, horizontal and vertical dislocation in the lining (d_b< 2 m), and	Found in tunnels with weaker or softer rock masses, tunnels that pass through or are very near to the ruptured fault zone (Mw > 6.5). After the seismic event, the tunnel is not accessible.

(*Continued*)

Table 2. (*Continued*)

DC*/ DD**	Damage Description	Role of Rock, Seismic Parameters, and Tunnel Accessibility
	invert uplift (h_u >1 m). b) Accompanied by portal collapse, Slope failure-induced tunnel collapse, heavy rockfalls, a completely buried tunnel portal, and a continuous inflow of groundwater.	
7 / Collapse (CO)	a) The tunnel can be completely collapsed in the weaker section. b) The lining can be sheared off or dislocated vertically and horizontally to the highest extents (d_b >2 m). Inrush of groundwater.	Found in fault fracture zones in the weaker rock masses and in tunnels passing through ruptured faults (Mw> 6.5). Following the seismic event, the tunnel is unusable and might even be abandoned entirely.

Remarks: DC*- damage class, DD**- damage degree, w_c- Width of Crack, l_c -Length of Crack, d_b- Displacement, h_u- uplift height, M_w – Moment Magnitude.

This damage classification is easy to use, has the potential to be applied to any seismic event due to its connection to seismic and rock parameters, highlights the extent of damage with clarity, and can offer a comprehensive account of how rock tunnels perform after an earthquake. The proposed classification's damage description does not base the amount of damage on a single or few particular seismic events. It is predicated on 26 distinct seismic events, of which the database contains 83% of damaged cases and 17% of undamaged cases. Figure 4 displays the distribution of 285 rock tunnels along with their tunnel damage

Figure 4. The total number of tunnels in each tunnel damage class of the classification.

classes following the application of this classification. In class 3, there are more rock tunnels than in classes 1 and 2, and in classes 6 and 7, there are fewer.

5 CONCLUSIONS

Large-scale seismic damage data are gathered from rock tunnel locations by means of a thorough review of the literature. It served as the foundation for creating the biggest damage database, suggesting new damage classification schemes, and linking to parameters that affect seismic damage to rock tunnels. Additionally, the common seismic damages are noted, clarified, and identified. In summary, the suggested categorization is easy to apply, doesn't necessitate complex computations, can be applied to any given event of any size, and offers a thorough explanation for comprehending the various degrees of damage to rock tunnels following an earthquake. This work is part of Reddy and Singh (2023) and for detailed information on this work, the authors would recommend reading their future journal article.

REFERENCES

Asakura, T. and Sato, Y., 1996. Damage to mountain tunnels in hazard areas. Soils and foundations, 36, 301–310.

Chen, Z., Shi, C., Li, T., Yuan, Y., 2012. Damage characteristics and influence factors of mountain tunnels under strong earthquakes. Natural hazards, 61, 387–401.

Dowding, C.H., Rozan, A., 1978. Damage to rock tunnels from earthquake shaking. Journal of the Geotechnical Engineering Division, 104(2), 175–191.

Jiang, Y., Wang, C., Zhao, X., 2010. Damage assessment of tunnels caused by the 2004 Mid-Niigata Prefecture Earthquake using Hayashi's quantification theory type II. Natural hazards, 53, 425–441.

Li, T., 2012. Damage to mountain tunnels related to the Wenchuan earthquake and some suggestions for aseismic tunnel construction. Bulletin of Engineering Geology and the Environment, 71, 297–308.

Owen, G.N., Scholl, R.E., 1981. Earthquake engineering of large underground structures, prepared for the Federal Highway Administration. FHWAIRD-801195.

Reddy, D.A, Singh, A., 2023. A New Post-Seismic Damage Classification for Rock Tunnels Based on 26 Worldwide Earthquakes. (In Preparation).

Roy, N., Sarkar, R., 2017. A review of seismic damage of mountain tunnels and probable failure mechanisms. Geotechnical and Geological Engineering, 35, 1–28.

Sharma, S., Judd, W.R., 1991. Underground opening damage from earthquakes. Engineering geology, 30 (3-4), 263–276.

Shen, Y., Gao, B., Yang, X., Tao, S., 2014. Seismic damage mechanism and dynamic deformation characteristic analysis of mountain tunnel after Wenchuan earthquake. Engineering Geology, 180, 85–98.

Shrestha, R., Li, X., Yi, L., Mandal, A.K., 2020. Seismic damage and possible influencing factors of the damages in the Melamchi tunnel in Nepal due to Gorkha earthquake 2015. Geotechnical and Geological Engineering, 38, 5295–5308.

Wang, T.T., Kwok, O.L.A., Jeng, F.S., 2021. Seismic response of tunnels revealed in two decades following the 1999 Chi-Chi earthquake (Mw 7.6) in Taiwan: A review. Engineering Geology, 287, 106090.

Wang, W.L., Wang, T.T., Su, J.J., Lin, C.H., Seng, C.R., Huang, T.H., 2001. Assessment of damage in mountain tunnels due to the Taiwan Chi-Chi earthquake. Tunnelling and underground space technology, 16(3), 133–150.

Wang, X., Pan, C., 2022. Review of seismic damage characteristics and influence factors of mountain tunnels. Arabian Journal of Geosciences, 15(6), 478.

Wang, Z., Gao, B., Jiang, Y., Yuan, S., 2009. Investigation and assessment on mountain tunnels and geotechnical damage after the Wenchuan earthquake. Science in China Series E: Technological Sciences, 52, 546–558.

Wang, Z.Z., Zhang, Z., 2013. Seismic damage classification and risk assessment of mountain tunnels with a validation for the 2008 Wenchuan earthquake. Soil Dynamics and Earthquake Engineering, 45, 45–55.

Yashiro, K., Kojima, Y., Shimizu, M., 2007. Historical earthquake damage to tunnels in Japan and case studies of railway tunnels in the 2004 Niigataken-Chuetsu earthquake. Quarterly Report of RTRI, 48(3), 136–141.

Yu, H.T., Chen, J.T., Yuan, Y., Zhao, X., 2016. Seismic damage of mountain tunnels during the 5.12 Wenchuan earthquake. Journal of Mountain Science, 13, 1958–1972.

Tunnelling for a Better Life – Yan, Celestino, Thewes & Eberhardt (Eds)
© 2024 The Author(s), ISBN 978-1-032-80042-4
Open Access: www.taylorfrancis.com, CC BY-NC-ND 4.0 license

The numerical-physical coupling method in investigation of the response of the tunnel structure under fire scenarios

Linxi Wang* & Zhiguo Yan
Department of Geotechnical Engineering, Tongji University, Shanghai, China
State Key Laboratory for Disaster Reduction in Civil Engineering, Tongji University, Shanghai, China

ABSTRACT: Tunnel structures undergo increased safety hazard when subjected to fire, highlighting the critical need to study their structural responses under such scenarios. However, conducting full-scale fire tests in the laboratory is often impractical due to various limitations. The numerical-physical coupling method, which integrates numerical simulation and physical testing, has emerged as a promising alternative for investigating the structural behaviour of the tunnel structure under fire scenarios. In this study, virtual tests are conducted to validate the feasibility of the numerical-physical coupling method under different fire scenarios, including the simple one, where the fire area involves only the key segment affected by thermal conduction, and the complex one, which includes adjacent segments affected by both thermal convection and thermal radiation. The results of the virtual tests indicate that under both scenarios, the material parameters and boundary loads obtained gradually converge towards the reference results as the time steps progress. The final responses gained by the numerical-physical coupling method, including stress fields and displacement fields, are consistent with the reference thermo-mechanical response, with average errors below 5%. The results indicate the promising prospects of the numerical-physical coupling method in investigating the response of the tunnel structure under fire scenarios, while emphasizing the need for future experimental verification.

Keywords: Tunnelling, Thermo-mechanical behaviour, Hybrid fire test, Numerical simulation, Physical testing

1 INTRODUCTION

Fire is one of the main threats affecting the safety of tunnel. A fire incident in a critical infrastructure may cause considerable structural damage, leading to catastrophic losses (Kirkland, 2002; Vuilleumier et al., 2002). The actual response of tunnel is fraught with uncertainties in both material properties and component capacities under extreme fire scenarios, which increases the risk of structural failure. Hence, a well-grounded understanding of tunnel performance, especially the thermo-mechanical characteristics under fire scenarios, is necessary to answer the need for safety requirements.

Various conventional methods have been applied for the investigation of thermo-mechanical behaviour of tunnel structures, including numerical simulation (Maraveas and Vrakas, 2018), component testing (Siemon and Zehfuß, 2017; Yan et al., 2016) and reduced-scale or full-scale testing (Yan et al., 2012). However, the existing methods have their limitations. The component testing fails to reveal the interactions between components and the exact boundary conditions, while the numerical simulation lacks fidelity for structures with unknown or unstable properties. The reduced-scale testing and full-scale testing are considered the relatively credible methods, but are still difficult to faithfully replicate the surrounding loads and thermal boundaries. Inspired by the concept of hybrid test (Takanashi and Nakashima, 1987; Xu et al., 2021) in the seismic field, the hybrid fire test (Mostafaei, 2013a; 2013b), which combines the component testing and numerical simulation, has been introduced. However, existing research on hybrid tests mainly focused on simple frame constructions, making it unsuitable for tunnel structures. Moreover, the stability of hybrid fire tests is also hampered by the split of numerical and physical substructures and the inadequate interaction. To address this challenge, researchers have proposed different improvements to the method (Sauca et al., 2017; Schulthess et al., 2020). Furthermore, several studies (Sauca et al., 2020; Faghihi and Knobloch,

*Corresponding author: 1910332@tongji.edu.cn

DOI: 10.1201/9781003495505-459

2019) have used virtual tests, where numerical simulations of relevant components with real parameter values temporarily replace the physical tests, to investigate the interactions between physical test and numerical simulation.

To fully leverage the advantages of both numerical simulation and physical testing, this research aims to propose a new adaption of the hybrid test as the Numerical-Physical Coupling Method (NPCM), for investigating the behavior of tunnel structure under fire conditions. Subsequently, the feasibility and effectiveness of the NPCM are preliminarily validated via the virtual test.

2 METHODOLOGY OF NPCM

2.1 *Basic concept*

In this paper, the NPCM comprises several modules: the Physical Structure (PS), the Numerical Structure (NS), the Physical-to-Numerical (PtN) module, and the Numerical-to-Physical (NtP) module. In the PS, test components are selected with a focus on parts with unknown material properties and complex stress or thermal conditions, such as weak segments or joints in tunnel structures. Through physical test, the actual performance of materials and components under target conditions is reliably demonstrated. In the NS, numerical simulation is used to simulate the entire structure, considering the interactions between components and providing exact boundary conditions that match the real-time scenario. Different from the existing hybrid fire test method, the NS in NPCM contains the entire structure, including the components which are tested in PS.

For interaction modules, the PtN module aims to adjust the numerical model in NS based on the actual measurements obtained from PS. In this study, the goal is to find the optimal set of parameters that results in the highest similarity between the values on corresponding survey points in PS and NS during the current test step. The modified parameters are suggested to be decided based on sensitivity analysis where the variables that have the most significant impact on mechanical behaviors or measurements can be clarified. On the other hand, in the NtP module, the equivalent loading commands are calculated based on the corresponding boundary stress states of the components in the NS. These commands are then sent to the loading equipment and applied to the tested components in the PS to achieve equivalent loading conditions. In this study, boundary conditions are equivalent and simplified according to Saint Venant's Principle in the NtP module. It is assumed that the static equivalent replacement on the boundary surface only affects the near-end stress distribution within a range of 1 times the thickness of the segment from the adjusted boundary surface, while the far-end stress distribution remains authentic.

In existing hybrid fire test, the components selected for physical tests are excluded from the numerical simulation. The entire structure tends to be treated as separate numerical and physical substructures, interacting only at the intersection of the two parts. Unfortunately, this division of numerical and physical substructures may lead to a lack of interaction between the simulation and test, which can limit the accuracy of the method, particularly for complex structures including tunnel structures, and may even result in divergence. Different from the existing research, the proposed NPCM redefines and reorganizes the division of PS and NS. Moreover, the NPCM focuses on real-time interaction modules, ensuring convergence of both PS and NS through overlapping parts.

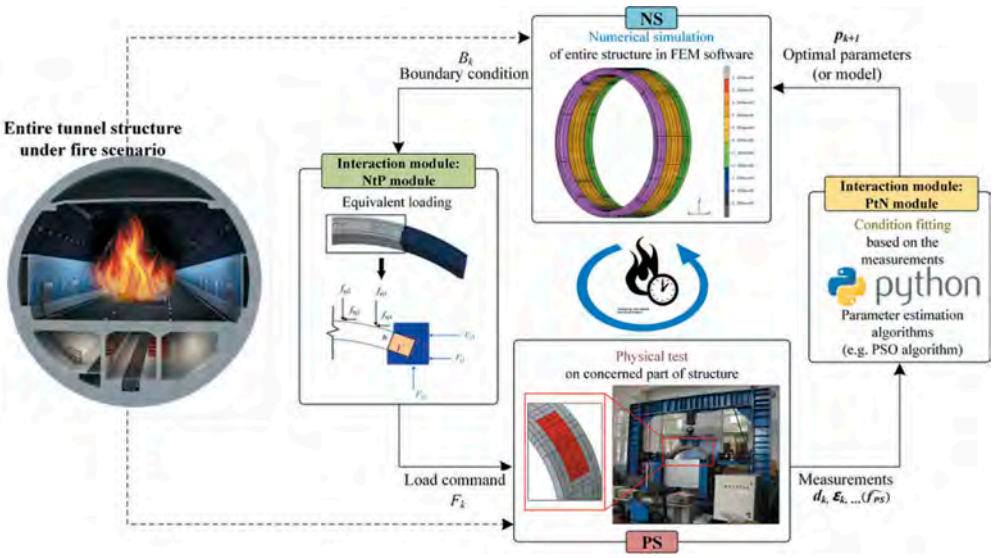

Figure 1. Basic concept of NPCM.

2.2 *Boundary conditions and similarity*

During the NPCM process, component test in PS and numerical simulation in NS progress simultaneously whist the interaction modules provide the adjustment and constraint, ensuring that both PS and NS can converge to the actual response of the structure. The consistency between NS and PS turns out to be the base for NPCT, thus requirement in both boundary conditions and similarity need to be satisfied.

To be consistent with the NS, loads on component should be adjusted to keep the boundary conditions of PS in step as follows:

$$\sigma_{PS}^{B} = \sigma_{NS}^{B} \tag{1}$$

$$\varepsilon_{PS}^{B} = \varepsilon_{NS}^{B} \tag{2}$$

Where σ^B, ε^B represent the stress and strain of certain boundaries and the subscribe *PS* indicates the data from physical structure whilst *NS* indicates the numerical structure.

When the physical field of the overlap part (i.e., numerical part of the physically tested components) in NS turns out to coincide with PS, the NS can then be considered to represent the actual performance of the full structure under target conditions. Therefore, the similarity index, *SI*, is proposed to evaluate the consistency between the two spaces. *SI* should represent the difference of physical quantities and the general expression can be defined as:

$$SI = \sum s(\widehat{f}_{PS}, \widehat{f}_{NS}) \qquad \widehat{f} \in (\widehat{d}, \widehat{\varepsilon}, \widehat{\sigma}, \widehat{F}, \widehat{M}, \ldots) \tag{3}$$

where $\widehat{f}$ represents the field of concerned quantities, which can be chosen from displacement, strain, stress, force, moment, et al. Function *s* evaluates the difference between the data of fields. For ideal conditions, it requires:

$$SI = 0 \tag{4}$$

During the test, the boundary conditions should be satisfied and the *SI* needs to be minimized at each time step. When optimization algorithm is adopted in PtN module, *SI* can serve as the aim object for the evaluation of parameter values.

3 CASE STUDY

To offer a comprehensive demonstration of the NPCM process and primarily validate its feasibility and effectiveness in thermo-mechanical investigation, a virtual test is conducted. In this test, numerical simulations of relevant components with real parameter values temporarily replace the physical specimens (PS) in the investigation of a tunnel structure under fire scenarios.

3.1 *General information*

The prototype structure for the case study is a large, deep-buried shield tunnel. The tunnel has an outer diameter of 15.2 meters and an inner diameter of 13.9 meters. A complete ring consists of ten precast segments, including one top segment, two adjacent segments, six standard segments, and one bottom segment, as is illustrated in Figure 2. Each segment has a thickness of 0.65 meters and a width of 1.2 meters. The segments are made of C60 concrete while reinforced longitudinally with HRB400 steel bars. Adjacent segments are connected with three M36 grade 8.8 angled bolts, totally thirty bolts per ring.

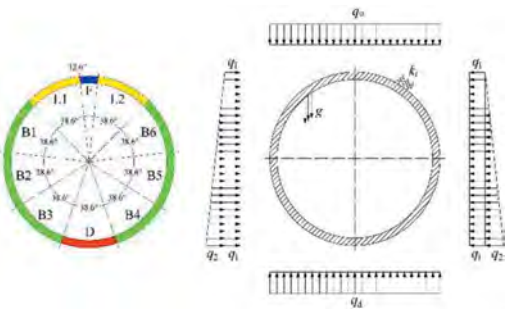

Figure 2. Tunnel construction.

The loads acting on the tunnel lining include the overburden pressure q_u, the subgrade reaction pressure q_d, the lateral uniform earth pressure q_1, the lateral triangular earth pressure q_2 and the gravity g. Accordingly, q_u=651 kPa, q_d=695 kPa, q_1=268 kPa, q_2=142 kPa, g=9.8 m/s^2. The resistance from the surrounding stratum is simulated via non-linear earth spring with compressive stiffness only. The stiffness per unit area, denoted as k_t, is determined based on the foundation coefficient as 19500 kN/m^3.

Two fire scenarios are considered and simulated in the case study, as illustrated in Figure 3. In Case A, only the top segment, which is considered to be directly affected by thermal conduction, is taken into account as the fire-affected area. In Case B, the inner surface of top segment undergoes the thermal conduction while the inner surfaces of the adjacent segments are influenced by thermal convection and thermal radiation. In both cases, the thermal emissivity ε is set as an intermediate value 0.8 according to the European Standards (Cen, 2004) while the surface heat transfer coefficient h is calculated as follow:

$$h = 7.05 \times e^{\left(\frac{T}{372.55}\right)} + 0.84 \quad (5)$$

Where T represents the temperature at the corresponding moment t. The temperature variation on the inner surface due to thermal conduction follows the HC heating curve, as represented by the following formula:

$$T = 20 + 1080(1 - 0.325e^{-0.167t} - 0.675e^{-2.5t}) \quad (6)$$

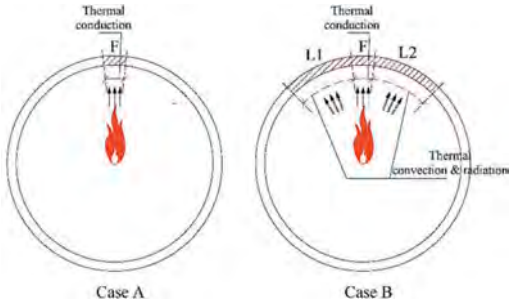

Figure 3. Fire scenarios.

3.2 *Numerical model*

A two-dimensional plane strain model is employed for the calculations. In FE model, the concrete material is simulated via four-node plane strain elements, while the embedded bar is simulated via two-node truss elements. Tied contact is used for the contact between concrete segments and embedded contact is used for the contact between concrete and steel bar.

In the numerical model, both concrete and steel are treated as ideal elastoplastic materials. Their densities remain constant throughout the fire testing process, with values set at 2400 kg/m³ for concrete and 7800 kg/m³ for steel. The thermal conductivity and specific heat capacity of concrete and steel are sourced from European Standards (CEN, 2004). The thermal expansion coefficients are calculated using the formula proposed by Lie (1996) as follows:

$$\alpha_c = (0.008T + 6) \times 10^{-6} \; 20^{\circ}\mathrm{C} \le T \le 1200^{\circ}\mathrm{C} \quad (7)$$

$$\alpha_s = \begin{cases} (0.004T + 12) \times 10^{-6} & T < 1000^{\circ}\mathrm{C} \\ 16 \times 10^{-6} & T \ge 1000^{0}\mathrm{C} \end{cases} \quad (8)$$

Where αc and αs refer to the thermal expansion coefficients of concrete and steel respectively.

At ambient temperature, steel has a yield strength of 360 MPa and an elastic modulus of 200 GPa, while bolts are assumed to have a yield strength of 640 MPa and an elastic modulus of 210 GPa. Both materials share a Poisson's ratio of 0.3. The reduction factors of steel properties under elevated temperature conditions are set based on European Standards (CEN, 2004). Notably, the mechanical properties of concrete at elevated temperatures, such as the elastic modulus and yield strength, can significantly influence structural deformation and internal forces. Thus, these parameters are decided to be modified during the NPCM process, as explained in detail in the subsequent subsection.

3.3 *Set up of the virtual test*

In Case A, testing is limited to the top segment in the PS. However, in Case B, testing involves both the top segment and the adjacent segment, requiring more complex coordination with the overall NS. In both cases, the test duration is fixed at 30 minutes and divided equally into 6 steps. During each step, the parameters of concern are modified in PtN module and interaction between NS and PS is conducted.

Based on existing research findings concerning the mechanical properties of concrete under elevated temperatures, the reduction in its elastic modulus and peak compressive strength at temperature T is modeled as follows:

$$E_0^T = \begin{cases} (1 + a(T - 20))E_0 & 20^{\circ}C \le T \le 800^{\circ}C \\ (1 + 780a)E_0 & T > 800^{\circ}C \end{cases} \quad (9)$$

$$f_c^T = f_c/(1 + 2.5(T - 20)^6 \times 10^{-17}) \quad (10)$$

Where E_0^T and f_c^T refer to the elastic modulus and peak compressive strength of concrete at temperature T, E_0 and fc refer to the elastic modulus and peak compressive strength of concrete at ambient temperature, a refers to the fitting coefficients. During the virtual test, E_0, fc and a are selected as the parameters under modification. In Case B, to consider a more complex scenario, different parameter values are assigned to the concrete material of adjacent segments compared to the top segment, while the parameters of the remaining segments are kept consistent with the top segment. The initial value, reference value and range for modification of each are provided in Table 1. Notably, the parameters are set as the initial values before the virtual test while the reference values remain unknown throughout the test process.

In this virtual test, the standard particle swarm optimization (SPSO) algorithm is selected as the intelligent algorithm for parameter modification in PtN module. In terms of test settings, parameters of the PSO algorithm are selected from experience

Table 1. Values of parameters.

Component	Parameter	Initial value	Reference value	Range
Top segment	$E0$ (Gpa)	25	36	[25,50]
	a	-7.1×10^{-4}	-11.5×10^{-4}	$[-12.7 \times 10^{-4}, -6.93 \times 10^{-4}]$
	fc (Mpa)	25	38.5	[25,50]
Adjacent segment	$E0$ (Gpa)	50	32	[25,50]
	a	-12.5×10^{-4}	-10.0×10^{-4}	$[-12.7 \times 10^{-4}, -6.93 \times 10^{-4}]$
	fc (Mpa)	50	35	[25,50]

and trial run. The population size m and max generation mg are set to 10 and 8, the learning factor c_1, c_2 are set as 2 equally. The SI for optimization is calculated according to the displacement on survey points in both PS and NS as follows:

$$SI = \frac{1}{2N}\left(\sum_{j=1}^{N}\frac{|d_j^{(NS,in)} - d_j^{(PS,in)}|}{|d_j^{(NS,in)} + d_j^{(PS,in)}|} + \sum_{j=1}^{N}\frac{|d_j^{(NS,out)} - d_j^{(PS,out)}|}{|d_j^{(NS,out)} + d_j^{(PS,out)}|}\right) \tag{11}$$

Where N represents the number of survey points on each side; j represents the index of survey point; d represents the displacement on corresponding survey point. Additionally, Superscripts NS and PS indicate the source of measurement data, superscripts in and out indicate the surface where the measurement point is located.

For test segments in PS (simulated via numerical model in this study) and the corresponding components in NS, survey points are uniformly arranged at on both the inner and outer surface of segment. Specifically, there are 7 points on each side for top segment and 11 points on each side for adjacent segment, as illustrated in Figure 4. Notably, in order to mitigate the influence of boundary conditions, two survey points that were originally situated closest to the boundaries on each surface are removed from the adjacent segment.

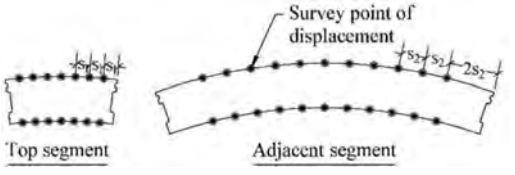

Figure 4. Arrangement of survey points.

The detailed procedures of the NPCM implementation for the virtual test is illustrated in Figure 5.

3.4 *Results and analysis*

The variations of NS and PS during NPCM process for Case A and Case B are illustrated in Figure 6 and Figure 7, respectively. In Case A, the initial values of all parameters deviate by more than 30% from the reference values. However, as the analysis progresses, the modified parameters gradually approach the reference values, with errors of less than 1% by Step 6. Similar trends can be observed in PS. Notably, from Step 3 to Step 4, an evident increase in error is observed due to the changes in reference values for boundary loads, which results from the material degradation. However, subsequent NPCM iterations successfully reconverge the loads to the reference values. In Case B, due to the involvement of multiple test components and parameters, the convergence rate of parameters has slightly decreased. Consequently, the overall error is somewhat higher compared to Case A, but it remains below 5%. In the PS, evident variations in boundary loads occur on both the top segment and adjacent segments in Step 2, resulting in fluctuations in load commands provided by NPCM. The error in bending moments for the adjacent segment reaches a maximum of 22.1%. However, after Step 5, the error of axial forces consistently remains within 0.3%, while the error of bending moments stays within 1.3%, indicating a relatively steady state.

The vertical displacements of survey points on the inner and outer surfaces of target segments are compared both between NS and PS, and between the NPCM results and reference values. The differences are illustrated in Figure 8 and Figure 9. The data for the top segment in Case B is omitted as it closely resembles the conditions in Case A. In Case A, as observed in the figures, middle-region displacements of the top segment are generally consistent between NS and PS, with differences below 0.02 mm. However, displacement differences increase for points near the ends of the segment. Throughout the test progression, NPCM results fluctuate around the reference values. Overall, errors on the outer surface are smaller than those on the inner surface, but their patterns remain largely consistent. In Case B, for the adjacent segment, the boundary effects are relatively significant. In the middle region of both the inner and outer surfaces, the displacements are also

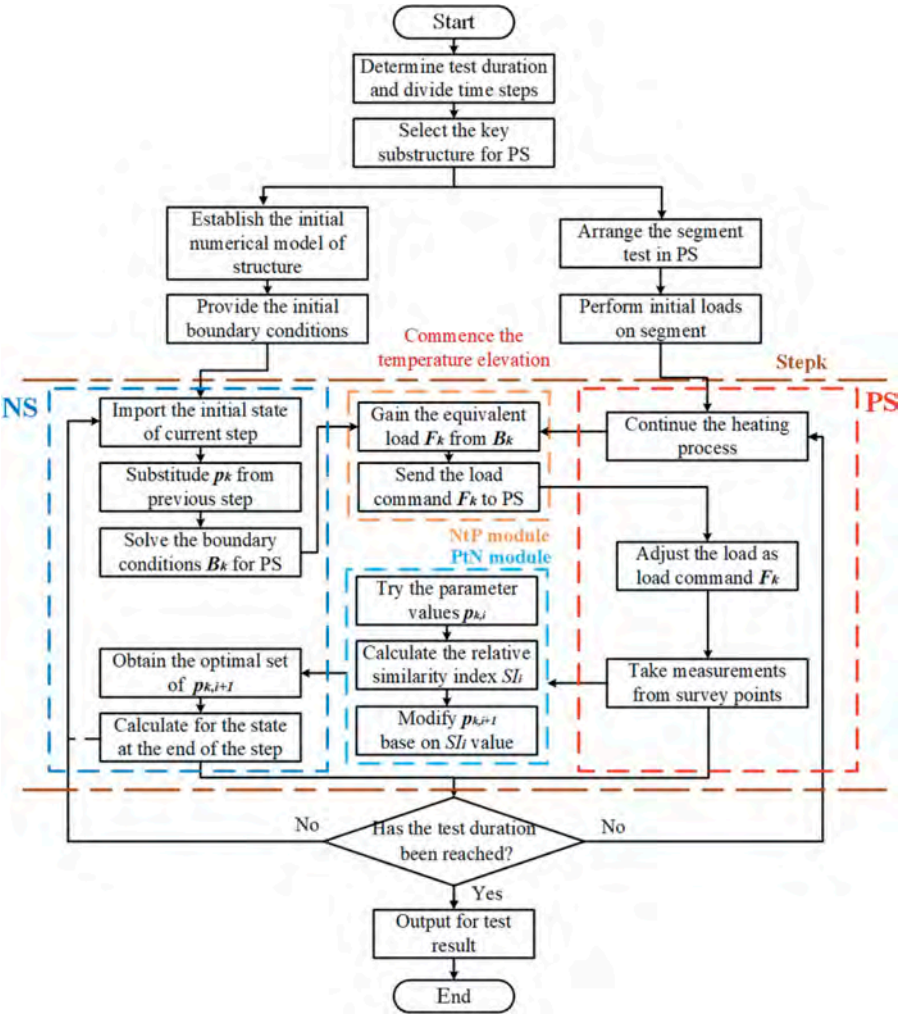

Figure 5. Procedures of NPCM implementation.

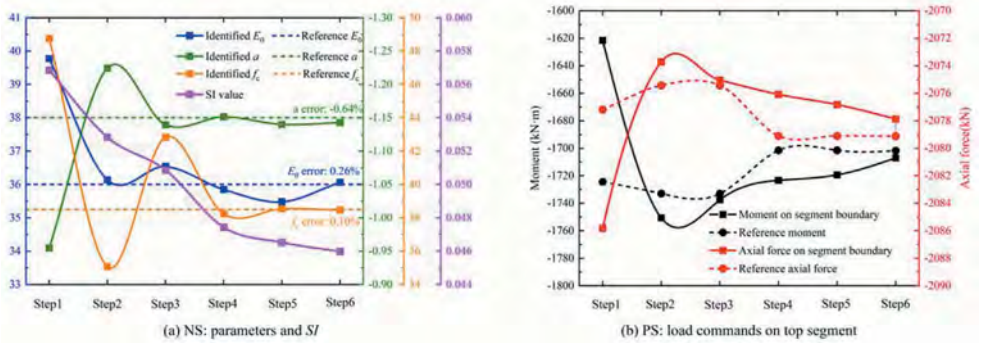

Figure 6. Variation during NPCM process for case A.

consistent, with differences within 0.1mm. Near boundaries, differences between NS and PS increase, with a maximum difference of 0.65 mm. Still, NPCM results closely match reference values with errors below 0.05 mm for most survey points, except for points near the boundary on the inner surface.

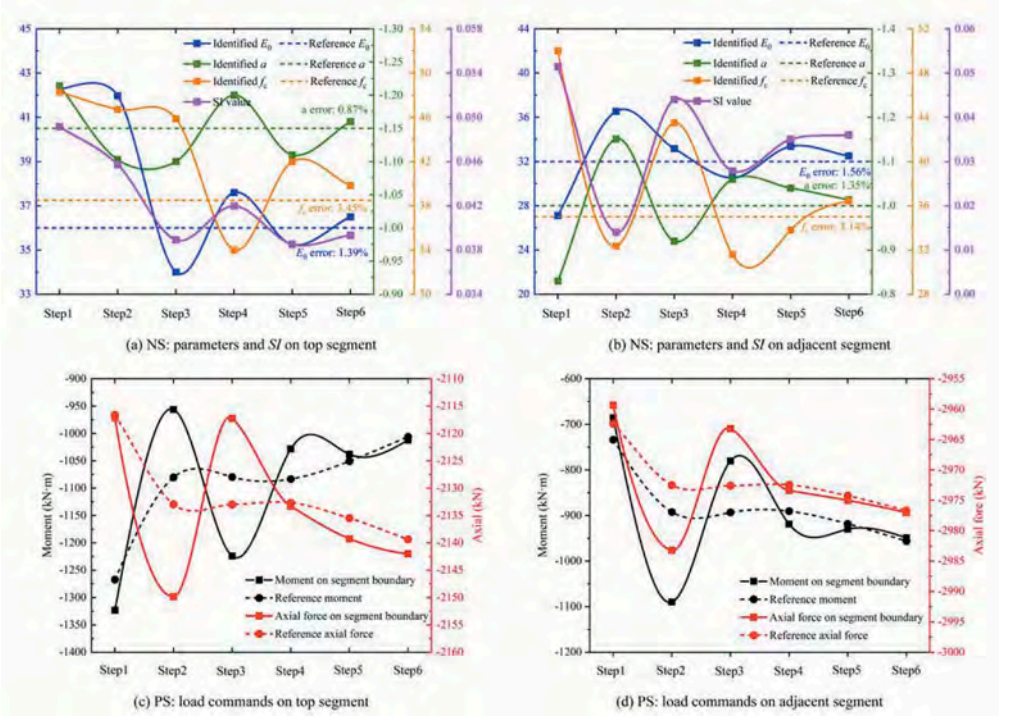

Figure 7. Variation during NPCM process for case B.

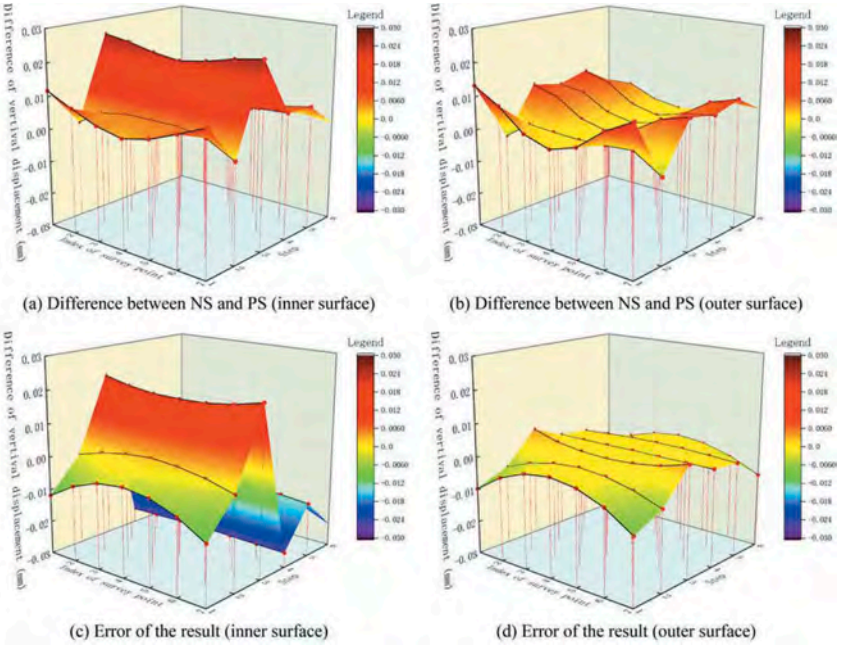

Figure 8. Difference of the displacement on top segment (case A).

The errors of the NPCM results for the entire structure at the end of step 6 are provided in Table 2. For the displacement field and stress field of the overall structure, final errors of less than 5% are exhibited in both Case A and Case B. The proportion of errors exceeding 10% is also found to be below

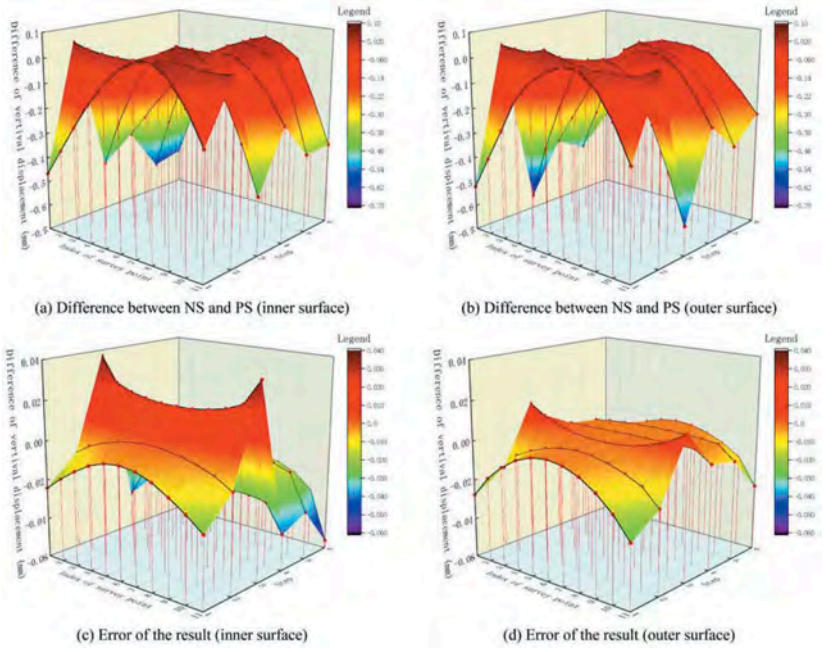

Figure 9. Difference of the displacement on adjacent segment (case B).

Table 2. Final error of NPCM results for entire structure.

	Displacement		Stress	
	Average error	Error rate (>10%)	Average error	Error rate (>10%)
Case A	4.6%	7.7%	3.1%	6.1%
Case B	3.3%	7.0%	5.4%	8.1%

10% in both cases. It can be concluded that in 6 time steps, NPCM effectively provides the actual thermo-mechanical response of the tunnel structure in both Case A and Case B.

In summary, the observed variations throughout the process and the results indicate that the stability of the NPCM may be influenced by boundary effects and the redistribution of forces during the fire test. Nevertheless, despite these influences, the proposed method effectively facilitates a considerably reliable understanding of the actual response of the entire structure by combining physical testing on local components with numerical simulation of structure under different fire scenarios.

4 CONCLUSION

1. A novel NPCM, which combines physical testing with numerical simulation, is proposed in this paper. In the proposed NPCM, the numerical simulation of the entire structure forms the NS whilst the physical test of the concerned component(s) forms the PS. Different from conventional hybrid test, the NS and PS achieve two-way, real-time interaction by specifically designed NtP module and PtN module throughout the test process. This allows for the effective and feasible investigation of the thermo-mechanical behaviour of the entire tunnel structure with relatively low cost.
2. The case study has preliminarily validated the feasibility and effectiveness of the proposed NPCM, with a focus on assessing its stability and accuracy in different scenarios. Despite potential errors arising from factors including the involvement of multiple test segments, the boundary effect and the redistribution of forces, the method demonstrates remarkable stability and accuracy within 6 time steps for both Case A and Case B. When considering the displacement and stress fields of the overall structure, the final errors remain below 5% for both cases. These highlight the potential of the NPCM as a reliable method for investigating the thermo-mechanical behaviour of large tunnel structures.

Admittedly, at this stage, factors such as time delays and experimental errors have not been taken into account. In future research, further validation will be undertaken to evaluate the practical implementation of the proposed method using specifically constructed facilities.

ACKNOWLEDGMENTS

This work was supported by the National Natural Science Foundation of China (Grant No. 52078378) and the Research Fund of State Key Laboratory for Disaster Reduction in Civil Engineering.

REFERENCES

Cen, 2004. Eurocode 2: design of concrete structures., British Standards Institution, London, British.

Faghihi, F., Knobloch, M., 2019. Thermal coupling in hybrid fire simulation, in: Advances in Engineering Materials, Structures and Systems: Innovations, Mechanics and Applications., p 1897–1902.

Kirkland, C.J., 2002. The fire in the channel tunnel. Tunn. Undergr. Sp. Tech. 17, 129–132.

Lie, T.T., Kodur, V., 1996. Thermal and mechanical properties of steel-fibre-reinforced concrete at elevated temperatures. Can. J. Civil Eng. 23, 511–517.

Maraveas, C., Vrakas, A.A., 2018. Design of concrete tunnel linings for fire safety. Struct. Eng. Int. 24, 319–329.

Mostafaei, H., 2013a. Hybrid fire testing for assessing performance of structures in fire—methodology. Fire Safety J. 58, 170–179.

Mostafaei, H., 2013b. Hybrid fire testing for assessing performance of structures in fire—application. Fire Safety J. 56, 30–38.

Sauca, A., Mergny, E., Gernay, T., Franssen, J., 2017. A method for hybrid fire testing: development, implementation and numerical application., 225–234.

Sauca, A., Zhang, C., Chernovsky, A., Seif, M., 2020. Communication framework for hybrid fire testing: developments and applications in virtual and real environments. Fire Safety J. 111,

Schulthess, P., Neuenschwander, M., Mosalam, K.M., Knobloch, M., 2020. A computationally rigorous approach to hybrid fire testing. Comput. Struct. 238, 106301.

Siemon, M., Zehfuß, J., 2017. Behavior of structural tunnel elements exposed to fire and mechanical loading. Journal of Structural Fire Engineering 9, 138–146.

Takanashi, K., Nakashima, M., 1987. Japanese activities on on-line testing. J. Eng. Mech. 113, 1014–1032.

Vuilleumier, F., Weatherill, A., Crausaz, B., 2002. Safety aspects of railway and road tunnel: example of the lotschberg railway tunnel and mont-blanc road tunnel. Tunn. Undergr. Sp. Tech. 17, 153–158.

Xu, Z.D., Dong, Y.R., Chen, S., Guo, Y.Q., Li, Q.Q., Xu, Y.S., 2021. Development of hybrid test system for three-dimensional viscoelastic damping frame structures based on matlab-opensees combined programming. Soil Dyn. Earthq. Eng. 144.

Yan, Z.G., Shen, Y., Zhu, H.H., Lu, Y., 2016. Experimental study of tunnel segmental joints subjected to elevated temperature. Tunn. Undergr. Sp. Tech. 53, 46–60.

Yan, Z.G., Zhu, H.H., Ju, J.W., Ding, W.Q., 2012. Full-scale fire tests of rc metro shield tbm tunnel linings. Constr. Build. Mater. 36, 484–494.

Tunnelling for a Better Life – Yan, Celestino, Thewes & Eberhardt (Eds)
© 2024 The Author(s), ISBN 978-1-032-80042-4
Open Access: www.taylorfrancis.com, CC BY-NC-ND 4.0 license

Research on fire compartmentation of hyperscale public area in underground rail transit hub

Kaiqi Wei* & Liwei Ji
China Railway Design Corporation, Tianjin, China

Yongyu Fu & Yongzhong Deng
Shenzhen Metro Construction Group Co., Ltd, Shenzhen, China

ABSTRACT: With the rapid development of urban rail transit, more and more modern underground rail transit hubs are being planned, constructed or put into operation. The underground hub of rail transit integrates multiple rail lines and various modes of transportation. It has the characteristics of large space volume, complex structure and dense personnel, making it difficult for personnel evacuation and fire rescue in case of fire.Especially when the hub is integrated with other functions such as underground slow space, the hyperscale public area formed brings greater challenges to its own fire protection design. How to integrate the fire protection design of such buildings with safety, economy and rationality has always been a difficult problem for architects to explore. Combined with the construction practice of Huangmugang Hub, Gangxia North Hub and Yujiapu Hub, this paper summarizes the fire protection problems in the hyperscale public area of underground rail transit hub, studies and summarizes the fire protection design experience in the hyperscale public area, such as fire compartmentation, and provides new ideas for the future fire protection design of the hub.

Keywords: underground hyperscale space, rail transit hub, fire protection

1 INTRODUCTION

As the name card of the city and the region, the underground hub of rail transit can not only show the appearance of the city and create a comfortable and beautiful travel environment for passengers, but also have increasingly high requirements for the quality of architectural space, the overlap of functional organization, the convenience of transfer, and the connection with the surrounding land. While improving the quality of hub, it also brings new challenges to the traditional hub fire protection design. How to integrate safety, economy and rationality into the fire protection design of such buildings has always been the theme explored by architects. Recently completed projects such as Gangxia North Hub and Huangmugang Hub in Shenzhen and Yujiapu Hub in Tianjin have explored new fire compartmentation methods, providing new ideas and more possibilities for the fire protection design of future hubs.

2 CHARACTERISTICS AND PROBLEMS OF UNDERGROUND HUB PUBLIC AREA

2.1 *Hyper scale; high space quality requirements*

Large underground transportation hubs often integrate a number of rail lines and a variety of transportation modes into one, assuming the function of traffic conversion, while its public areas also integrate some urban functions such as slow space. In order to meet the characteristics of complex functions and huge passenger flow during peak hours, the public area of the hub is often larger than that of ordinary rail transit stations, and the space quality requirements are high.

Shenzhen Gangxiabian Hub is a comprehensive hub for the transfer of 4 lines of rail transit line 10, 11, 14 and 2, with a total floor area of 41,700 square meters in the public area of the underground three to the mezzanine ring corridor. Huangmugang Hub is a comprehensive transfer hub for Line 7, Line 14 and Line 24. The hub is integrated into the urban walking space, and the public area from the first underground

*Corresponding author: Weikaiqi@qq.com

DOI: 10.1201/9781003495505-460

floor to the fourth underground floor has a construction area of about 63,000 square meters. The comprehensive transportation hub of Yujiapu Station in Tianjin is a large-scale comprehensive hub integrating intercity railway, urban rail transit, bus, taxi and other transportation modes. The total construction surface of the public area connected from the first underground floor to the third underground floor is far beyond the conventional metro station.

In summary, the public area of the three hubs has exceeded the requirements of 5000 square meters of a single fire protection zone and 2.5 times of the public area of the single-line standard station hall in the current norms. Therefore, in order to meet the requirements of the overall fire safety of the building, it is particularly important to organize the fire compartmentation method of the super large public area of the hub under the premise of being a fire protection zone.

2.2 *Low safety performance; difficult evacuation*

Compared with the above-ground buildings, the public space of underground transportation hubs has its own disadvantages. The traditional underground stations have tight space, poor natural lighting and ventilation conditions, poor sense of direction, and poor passenger experience. From the point of view of fire evacuation, the smoke exhaust of underground buildings is not smooth, and the "chimney effect" is easy to form at the evacuation gate during fire, which threatens the evacuation safety of personnel. Underground buildings are mostly artificial lighting, the reliability and visibility are relatively low, especially under the influence of fire smoke visibility is worse, traffic hub underground transfer area personnel flow lines criss-cross, the underground space is not strong direction is easy to make people lost in the state of emergency, resulting in serious consequences.

Figure 1. Traditional underground stations.

2.3 *Atrium space cannot meet the requirements of smoke exhaust*

In order to enhance the internal space effect of the building, the common design method of the hub public area is to set up an atrium on the station hall floor. The current national standards for subway stations are generally based on the fire protection design of the station hall floor as a safe area for evacuation. However, as the hub is equipped with an atrium, the smoke exhaust and evacuation mode of the station are difficult to be completely designed according to the conventional subway station, and the design mode is not clearly stipulated in the current national fire protection technical standards. Whether the station hall floor can meet the requirements of being a safe area needs to be discussed, and it is essential to study the reasonable fire compartmentation of the public area of the station hall.

Figure 2. Atrium space in hub.

3 FIRE COMPARTMENTALIZATION STRATEGIES

A mature research system has been formed in commercial buildings for the oversized fire safety problems in fire protection zones. At the same time, in the ground traffic buildings such as airports, high-speed rail stations and terminal passenger stations, there are more studies on the fire separation of oversized fire zones, and there are more mature solutions. Due to the limitation of function and space layout, the expansion of fire protection zone will inevitably lead to the difficulty of fire prevention and control. Therefore, what kind of fire separation plan should be adopted in the expanded underground public area to achieve the fire safety goal while ensuring the smooth traffic flow of the station hall needs to be further studied.

In the traditional design method of fire compartmentation, the super large underground space is divided into a number of fireresistant partitions less than 5000 square meters, and the partitions are separated by firewalls, which has a great impact on the indoor landscape and is difficult to meet the functional needs of visual transparency.If the fire shutter is used for separation, it is necessary to use a large number of large-span fire shutter. Considering the problem of low reliability exposed in the use of fire shutter and the unreliability of fire protection facilities themselves, this kind of separation is generally not used in the design of fire protection separation in large space public areas.

According to the characteristics of different buildings, Gangxiabian, Huangmugang and Yujiapu transportation hubs have created a series of new methods and new concepts of fire compartmentation, such as fire isolation zone, smoke control zone and subsafety zone. The emergence of these new fire compartmentation strategies makes some architects' space design concepts and fire design better integrated together, using different architectural Spaces to find different fire design solutions, creating a better internal space environment.

3.1 *Fire isolation zone*

Shenzhen Gangxiabian Hub is a comprehensive hub for the transfer of 4 lines of rail transit line 10, 11, 14 and 2, with a total floor area of 41,700 square meters in the public area of the underground three to the mezzanine ring corridor. The design method of fire compartmentation is to use the space form of the mezzanine ring corridor in the public area of the station hall, and set up "fire isolation zone" on both sides of the mezzanine ring corridor as the interface, and divide the station hall into four fire prevention units of less than 5,000 square meters.

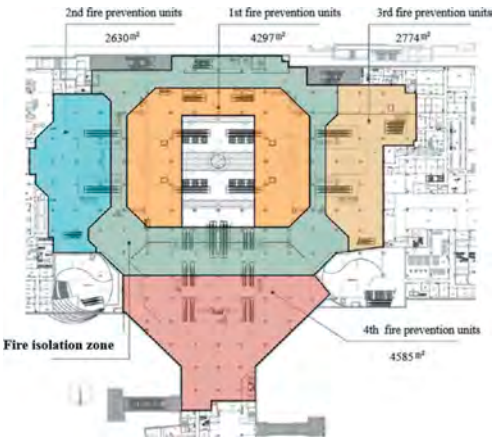

Figure 3. Gangxiabian Hub plan.

Fire isolation zone is a blank area with a certain width. In this area, certain measures are taken to ensure that when a fire occurs on one side, the fire will not spread to the other side of the fire isolation zone.

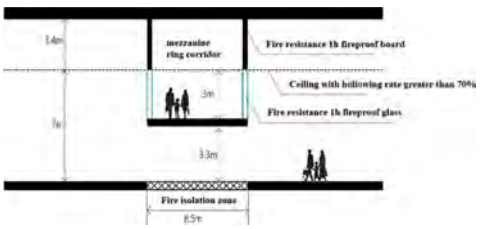

Figure 4. Fire isolation zone.

In order to realize the fire isolation zone as the fire compartmentation method of hyperscale public area in underground rail transit hub, in addition to the use of the natural spatial form of the mezzanine ring corridor, a series of fire protection strengthening measures have been taken.

(1) Enhanced smoke exhaust
The public area of the station hall is naturally divided into four smoke exhaust areas by the fire isolation zone. The mechanical smoke exhaust system is set up according to the area, and the stack start-up mode is adopted to ensure the smoke exhaust reliability of the station hall. Multiple smoke vents are set on both sides of the fire isolation zone, and the calculated smoke exhaust volume is taken as a strengthening measure to ensure that the smoke is effectively blocked at the isolation zone. In case of fire, open the smoke exhaust fan in the corresponding area to exhaust the smoke, and supplement the air through the sunken square and the entrance and exit.

(2) Strengthen fire sprinkler system
Strengthen the fire sprinkler system in the fire isolation zone: In general, the spray intensity is 8L/min·m2, the working area is 160 square meters, and the rapid response sprinkler is used. Enhanced measures were adopted in the Fire isolation zone to increase the functional area to 260 square meters.

3.2 *Smoke control zones*

Huangmugang Hub is a comprehensive transfer hub for Line 7, Line 14 and Line 24. The public area from the first underground floor to the fourth underground floor has a construction area of about 63,000 square meters. The underground floor of the hub will expand the station hall floor area and integrate it into the urban slow walking space, with a construction area of 28,000 square meters. The new concept of "smoke control zone" is put forward by using its own structural spatial relationship.

Firstly, the public area of the hub platform and station hall is divided into smoke bay according to the area of no more than 2000 square meters. On the basis of smoke bay, the public zoning of the station hall is divided into several "smoke control zones" by using the suspended lane structure and other facilities, and between the smoke control zones, the suspended lane structure or the smoke baffle wall with the height of the suspended lane bottom surface are separated.

Considering the small headroom height of the projection area of the suspension lane, its smoke emission can be included in the adjacent smoke bay, and the smoke exhaust is set in the adjacent smoke bay. The smoke exhaust system of the station hall can exhaust smoke from any two adjacent smoke control zones at the same time.

When a fire occurs on the lower floor, the smoke exhaust system of the smoke control zone at the fire is

Figure 5. Huangmugang hub plan.

Figure 6. Suspended lane structure.

started. When the smoke spreads to other smoke control zones and triggers the smoke alarm, the smoke exhaust fans of the corresponding smoke control zone are stacked and started. When a fire occurs in the public area of the underground floor of rail transit, the air supply system, return exhaust fan and platform exhaust pipe in the public area of the station should be closed, the smoke exhaust fan should be opened, and the smoke should be removed by the exhaust pipe of the station hall. Fresh air flows from the entrance to the station hall, and passengers evacuate in the direction of the entrance.

In addition, Huangmugang Hub is an upper and lower overlapping station, and the fire compartmentation between platforms should be considered. The escalator from the third floor underground to the first floor underground station is separated by fire-proof glass with a fire resistance limit of 2h when it passes through the second floor underground. The escalator holes of the underground second floor connecting the underground third floor are separated by fireproof rolling curtains except the escalator entrance, and the other parts are separated by fireproof glass with a fire resistance limit of 2h. The entrance of the escalator in the middle transfer node of the third floor underground is divided by a combined double-track double-curtain curtain with a fire resistance limit of 3h projected along the hole of the second floor underground.

3.3 *Sub-safety zone*

The underground transfer hall of Yujiapu Transportation Hub is mainly used as an evacuation area with less fixed fire load, and the possible combustibles are mainly passenger luggage and temporary kiosks, etc.

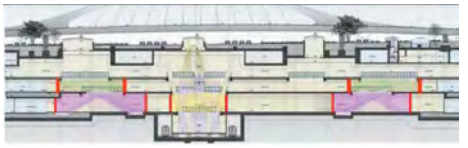

Figure 7. Huangmugang hub section.

The fire risk itself is relatively low, and automatic sprinkler system and smoke exhaust system are set up, so that the underground transfer hall forms a safer transition area for personnel evacuation. In case of fire, the flow of people is evacuated through the transfer hall, which is in line with people's habitual psychology and is not easy to cause chaos. Therefore, Yujiapu Hub will use the transfer hall as a "sub-safety zone".

Commercial room in the transfer hall For the transfer hall, the commercial room is the main area where the fire load is large and the electrical equipment is large. The sprinkler protection fireproof glass system is used to separate the store from the public area, and the fire alarm, automatic sprinkler and mechanical smoke exhaust system are set inside the store. A number of shops connected on the same side are separated from other shops by firewalls to form independent units. Similarly, the national railway waiting area and the transfer hall are also separated by a spray protection fire glass system.

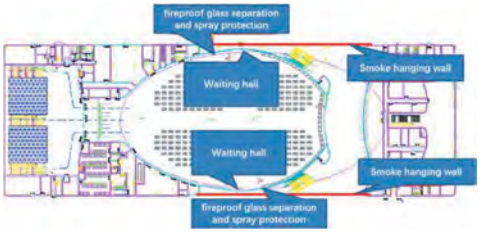

Figure 8. Yujiapu hub plan.

The glass sprinkler system uses water cooling sprinkler head to protect the glass. When a fire occurs, the sprinkler head is heated and opened, and the cooling water is evenly sprayed to the glass, so as to effectively reduce the temperature of the glass and increase the fire resistance time.The combination of fireproof glass and glass sprinkler head is selected on the side of the shop towards the transfer hall, which does not affect the transparent building effect, and also has certain fire prevention ability in the case of fire.

The separation scheme of "fireproof glass separation and spray protection" requires setting up an independent spray cooling system to protect the glass. The spray system adopts a fast response sprinkler, the spacing of the sprinkler is not more than 2m, and the protection length can be determined according to 1.5 times the actual length of the shop with the longest glass pavement along the corridor and is not less than 30m, and the continuous spraying time is not less than 1.5h.

Through the above methods, the fire can be restricted to a certain area as far as possible, so that the impact caused by the fire can be localized and the spread of the fire can be limited.

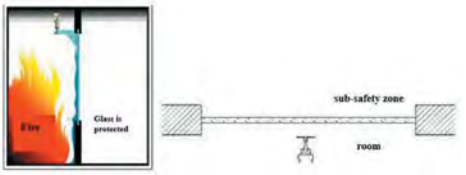

Figure 9. Fireproof glass separation and spray protection.

4 SIMULATION ANALYSIS

In order to scientifically and comprehensively verify the fire compartmentation method mentioned above and the feasibility of safe evacuation of the entire hub, it is necessary to start from the theory of fire engineering, use the calculation simulation software to simulate and analyze the relevant scenes in the building, and finally draw a conclusion.

Firstly, the fire risk of the building should be analyzed, and a reasonable fire scene should be set according to the fire risk. Then, the parameters of fire smoke, temperature and so on are calculated by computer simulation program, and the available evacuation time (T_{ASET}) is obtained. Then, according to the set fire scenario, the corresponding personnel evacuation scenario is set up, and the personnel evacuation simulation software is used to calculate the evacuation situation under the set evacuation scenario, and the necessary evacuation time (T_{RSET}) is obtained. When $T_{ASET} > T_{RSET}$, it can be considered that the fire protection design in the building can ensure the safety of personnel evacuation and is feasible. The following takes Huangmugang Hub as examples for analysis.

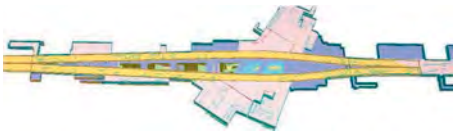

Figure 10. Huangmugang hub fire simulation.

4.1 *Huangmugang hub*

(1) Fire scene setting
Based on the actual situation of Huangmugang Hub, such as the building structure, the distribution of various functional areas and the size of fire risk, a total of 9 fire source locations were set, and 18 fire scenarios were analyzed and determined.

(2) Evacuation scenario setting and simulation analysisThe design principle of evacuation scenario is to find out the most unfavorable situation for safe evacuation of personnel after the fire. According to the situation of Huangmugang Hub, six corresponding evacuation scenarios are set up.

Table 1. Fire scene setting.

Fire scene	Fire source	Scene description	Fire growth coefficient (kw/s^2)	Maximum fire heat release rate (MW)
A1 A0	A	B4F platform	0.01172	1.5
B111 B110 B010 B000	B	B3F rail	0.04689	9.0
C1 C0	C	B3F platform	0.01172	1.5
D1 D0	D	B2F platform	0.01172	1.5
E1 E0	E	B2F platform	0.01172	1.5
F1 F0 F0-1	F	B1F hall	0.04689	3.6
G1	G	D Sunken square	0.01172	1.5
H1	H	1 Sunken square		
I1	I	4 Sunken square		

Table 2. Evacuation scenario summary.

Evacuation scenario	Fire scene setting	Evacuation object	Evacuation path condition
1	A	Passengers in underground fourth platform floor	blocked
2	B	Passengers in underground third platform floor	Normal evacuation
3	C	Passengers in underground third platform floor	Normal evacuation
4	D	Passengers in underground second floor	blocked
5	E	Passengers in underground second floor	blocked
6	F	Passengers in underground first floor	Normal evacuation

In the following, the required safe evacuation time (T_{RSET}) calculated by computer evacuation simulation software for each region is compared with the environment available safety time (T_{ASET}) under each fire scenario

Table 3. Safety judgment of personnel evacuation.

Fire source	Fire scene	area	T_{ASET}(s)	Evacuation scenario	T_{REST}(s)	result
B4F platform	A1	B1F~B4F	>1800	1	1074	safe
	A0	B1F~B4F	>1800		1074	safe
B3F rail	B111	B1F~B4F	>1800	2	672	safe
	B110	B1F~B4F	>1800		672	safe
	B010	B1F~B4F	>1800		672	safe
	B000	B1F~B4F	>1800		672	safe
B3F platform	C1	B1F~B4F	>1800	2	672	safe
	C0	B1F~B4F	>1800		672	safe
B2F platform	D1	B1F~B4F	>1800	3	849	safe
	D0	B1F~B4F	1375		849	safe
B2F platform	E1	B1F~B4F	>1800	4	689	safe
	E0	B1F~B4F	>1800		689	safe
B1F hall	F1	B1F~B4F	>1800	5	672	safe
	F0	B1F~B4F	>1800		407	safe
	F0-1	hall	1285		594	safe
		atrium	>1800		527	
	F0-1*	hall	797		594	
		atrium	>1800		527	

to judge the safety of evacuation in each region.

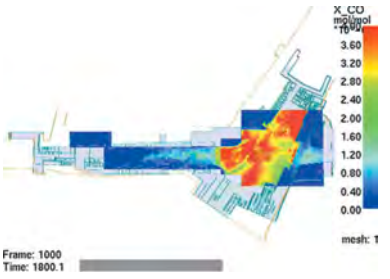

Figure 11. Huangmugang hub smoke simulation.

(3) Summary

According to the analysis results, if the smoke exhaust system is effective, for each set fire scenario and evacuation scenario, the personnel in the building can be evacuated to the safe area through the nearby safety exit before the danger is imminent. When all smoke exhaust systems fail or one of them fails, the available evacuation time of personnel is significantly reduced, and the smoke has a significant impact on personnel evacuation.

The fire compartmentation strategy of the smoke control zone adopted by Huangmugang Hub in the large public area can form an effective separation effect in the fire stage, so as to achieve the purpose equivalent to the fire division and meet the requirements of fire safety.

5 CONCLUSION

To sum up, aiming at the fire protection problem in the public area of the station hall, the three major hubs adopt fire compartmentation measures such as fire isolation zone, smoke control zones, and sub-security zones according to the construction space composition, so as to achieve the purpose equivalent to dividing fire protection zones. Through the design of fire scene and evacuation scene, the computer software is used to simulate and verify the scheme. The results show that the new fire evacuation model of the hub public area meets the requirements of fire safety when the comprehensive fire protection measures are perfect.

From the perspective of architectural space, the above model uses different architectural Spaces to find different fire design solutions and create a better internal space environment. At the same time, these new fire compartmentation methods ensure the continuity and permeability of the public space inside the hub, better create the interior space landscape effect, truly realize the integration of design concept and fire design, and provide new ideas and more possibilities for the future fire protection design of underground hyperscale hubs.

REFERENCES

[1] Wei Wenbin, Liu Songtao, Ou Chen. Fire prevention and evacuation in shared space of subway station hall [J]. Fire Science and Technology, 2015,34 (12):1590–1593.

[2] Li Q. Research on the safety elements of fire separation in vertical overlap of urban underground space functions [J]. Building Technology Development, 2020, 47(12):85–86.

[3] Fang Zhiyong. Application of fire separation technology in building construction [J]. Doors and Windows, 2019(17):248.
[4] Hou Yu-Sheng, Li Yanfeng, Shi Bowei, et al. Fire risk assessment of subway transfer stations [J]. Fire Science and Technology, 2014, 33 (11):1326–1329. (in Chinese)
[5] Li Meng, Fu Yunfei. Discussion on subway fire safety evacuation [J]. Fire Science and Technology, 2011,30 (1): 35–37.
[6] Liu Liu. Fire risk analysis and prevention and control measures of Metro integrated development space [EC]. 2012 China Fire Protection Association Science and Technology Annual Conference proceedings (ii). Beijing: Science and Technology in China Press, 2012:118–120.
[7] Ni Zhaopeng, Lu Shichang, Lai Jianyan. Automatic water jet cooling system protects the tempered glass as Study on feasibility of fire retardant separator [J]. Fire science. 2011, 20(3):l2J–131.
[8] Harold E, Nelson and Frederick W. Mowrer, "Emergency Movement", Boston: Society of Fire Protection Engineers and National Fire Protection Association, 2002: Section3, 367–379.
[9] Vytenis Babrauskas, "Heat Release Rate", SFPE Handbook of Fire Protection Engineering, 2nd Edition[M], Chapter 1, Section 3, Quincy: National Fire Protection Association, 2002.
[10] Huang Xiaolu, Zhang Xiang, Xie Yuanyi. Numerical Simulation of evacuation of shared station hall in Metro transfer station [J]. Fire Science and Technology, 2017,36 (12):1666-1667+1671.
[11] Luo Na, Gao Le, Liu Xiangwei. Smoke control in subway station based on vertical wall and ventilation [J]. Fire Science and Technology, 2019,38 (8):1084–1086.
[12] Nanhua Xiang. Research on fire smoke control in underground station of intercity train [D]. Shenyang: Shenyang University of Aeronautics and Astronautics, 2014.

Tunnelling for a Better Life – Yan, Celestino, Thewes & Eberhardt (Eds)
© 2024 The Author(s), ISBN 978-1-032-80042-4
Open Access: www.taylorfrancis.com, CC BY-NC-ND 4.0 license

Experimental study on the applicability of the combined tunnel ventilation system of complementary ventilation and shaft

Yunxiao Xin & Yaqiong Wang
Chang'an University, Xi'an, China

ABSTRACT: To study the applicability of the combined ventilation system of complementary ventilation and shaft, and the effect of the shaft on complementary ventilation, the tunnel model (1:10) was set up based on the principle of flow similarity. According to the change in wind speed flow field, we carried out reasonable ventilation design when a fire occurred in different parts of the tunnel. The experiment determined the four working conditions by changing the way the shaft was supplied or exhausted and the frequency of the fan. The results show that the air supply shaft can adjust the pollutant concentration, and the smoke exhaust shaft can effectively reduce the smoke exhaust distance. Therefore, a reasonable combination shaft is used in the project to meet the ventilation and smoke exhaust requirements. When a fire occurs in different parts of the tunnel, a reasonable ventilation design is required, which is more energy-efficient.

Keywords: Road tunnel, Tunnel ventilation, Model experiment, Complementary ventilation system, Shaft, Wind speed

1 INTRODUCTION

The construction of highway tunnels has a trend of long and deep development, and a certain slope, which leads to a great difference in pollutant concentration between the uphill and downhill tunnels. Zhang & Tian (2011) put forward the concept of air exchange mode, this method uses the cross channel exchange the air to meet the air quality requirements of the two tunnels. The idea of "two-tube complementary" and the proposal of "air exchange mode" had attracted wide attention. Researchers began to analyze the characteristics of complementary ventilation using different methods, such as ventilation mode, volume, scope, and economic level (Hu et al., 2011; Zhang et al., 2011). Using the method of on-site testing, Wang et al. (2014) analyzed the test data and found the function and existing problems of the ventilation channel under the twin-tube tunnel complementary ventilation mode. Xie et al. (2015) and Wang et al. (2015, 2019) established a scale model based on the similarity theory to verify the feasibility and reliability of the complementary ventilation mode. Adopted finite element simulation analysis method, Ren et al. (2018) studied the effectiveness and influencing factors of the complementary ventilation system with reference to the concentration distribution of particulate matter.

Field testing of highway tunnel ventilation system is difficult and most of them lack measured data. The method of numerical simulation is different from the actual engineering and has unreliability. Therefore, these empirical biases require experimental analysis and physical model are established by taking into the model deflection, test site and technical feasibility. In this paper, the applicability of combined ventilation system with complementary ventilation and shaft is studied in single slope tunnel under unbalanced ventilation condition. Based on the similarity theory, we derived the proportional relationship between prototype and model, and established the scale model test (Li et al., 2011; Liu et al., 2012; Liu D et al., 2015; Zhang et al. 2015). At the same time, we increased the resistance grid can be appropriately to shorten the model length (Lai, 2015).

In view of the insufficiency of the study on the ventilation characteristics of the composite ventilation system in the above-mentioned, we established a 1:10 reduced-scale Ying'erling tunnel model according to the principle of flow similarity. In this paper, we studied the applicability of the complementary and shaft mixing ventilation methods and the effects of shaft on the complementary ventilation. At the same time, when fire occurs in different areas of the tunnel, we have given an appropriate ventilation scheme to provide the theoretical basis for subsequent optimization design.

2 TUNNEL MODEL SCALE

In a ventilation physical model, the mechanic's condition is said to be similar to those in the prototype

*Corresponding author: hapoaaa@foxmail.com

DOI: 10.1201/9781003495505-461

of a highway tunnel, so the three conditions of geometric similarity, motion similarity, and dynamic similarity are satisfied. These three similar conditions constitute similar mechanical phenomena in physical processes. The basics of motion similarity are geometric similarity, and the necessary premise of dynamic similarity is motion similarity. Therefore, if the two systems satisfy the dynamic similarity, the shape similarity and motion similarity of the two systems will inevitably exist.

The long-term air demand of the right tunnel is 1092 m^3/s, and the left is 465.54 m^3/s. The air demand of the two tunnels varies greatly, with a ratio of 2.35. The wind speed in the right line tunnel exceeds 10 m/s. According to the engineering situation, a hybrid ventilation system combined with complementary ventilation with a shaft is proposed. The hybrid ventilation system includes an uphill tunnel, downhill tunnel, air interchange cross-passage, ventilation shaft, etc. The hybrid ventilation system is based on longitudinal ventilation, and the tunnels are connected into a system through two air interchange cross-passages. The abundant fresh air uphill of the downhill tunnel is transported to the uphill tunnel through the air interchange cross-passage to increase the ventilation in the uphill tunnel. The dirty air of the uphill tunnel can transport to the downhill tunnel through the air interchange cross-passage to fully use the surplus air volume of the downhill tunnel to dilute the pollutants and reduce the contaminants at the wind speed in the uphill tunnel. According to the Ying'erling tunnel's air demand characteristics and the disaster prevention and rescue requirements, the complementary ventilation technology meets the daily operation ventilation. The smoke exhaust shaft meets the specification requirements.

Considering the deflection of the model, test site, and technical feasibility, the final ratio of the model is 1:10, including two main tunnels, two complementary cross channels, and one shaft. The main geometric dimensions of the prototype and model are reported in Table 1, and the model diagram is shown in Figure 1.

Table 1. Main geometric dimensions of the prototype and model of Ying'erling tunnel (Units: m).

Item		Prototype	Model
General section	Section height	9.83	0.983
	Section width	10.91	0.109
	Equivalent diameter	9.72	0.972
Ventilation section	Section height	9.83	0.983
	Section width	5.00	0.500
	Section area	44.90	0.449
	Equivalent diameter	6.53	0.653

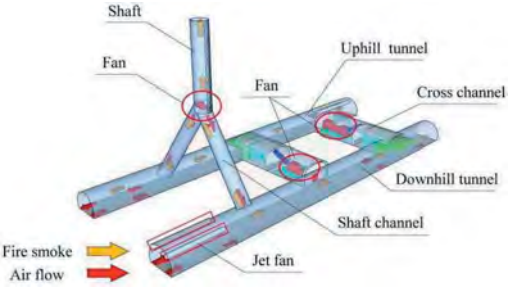

Figure 1. The schematic of ventilation tests system.

In the ventilation system of highway tunnels, the airflow is in a viscous flow state, and the automation simulation of the flow process is one of its main characteristics. After determining the similarity criterion, the values change in a certain range without destroying the similarity between the prototype and the model in the process of automatic simulation. When the Reynolds number $Re < 2320$, $\lambda = 64/Re$, the variation of λ is only affected by Re. In this case, the viscous fluid of incompressibility can be defined as the first self-mode region of pressurized flow.

The Reynolds number critical value of the second self-model area of the physical model system can be calculated according to the theory of self-model area. Experimental studies were conducted by selecting the main tunnel model with a section of normal ventilation. The equivalent diameter is 0.972 m. The air temperature in the laboratory is 20°, and the air density is 1.2047 kg/m^3. Based on the above conditions, the aerodynamic viscosity can be calculated. $V=1.56\times10^{-5}$ m^2/s, so the critical Reynolds number in the second self-model region can also be calculated $Re=2.13\times10^5$. The critical wind speed entering the second self-model region is calculated in Eq.(1).

$$V = \mathrm{Re} \cdot \nu / D = 3.42 m/s \tag{1}$$

3 EXPERIMENTAL DESIGN

The Ying'erling tunnel is 5.6 km long. Considering the technical feasibility, the scale of the test site and other factors, the model ratio is 1:10, and the test model is 560m long. Taking into account the economic and difficult degree of instrument position adjustment, the equivalent friction principle is adopted to establish resistance grids in the appropriate part. The resistance grid can replace the length of the tunnel, thus shortening the length of the model. In each tunnel, 14 resistance grids are added. The resistance grid spacing should not be less than 3D (D is the equivalent diameter) so that it is 3.6m. The final model length is 77 m. Each resistance grid is equivalent to 34.5 m. In the tunnel, the zone between two ventilation complementary cross channels is called a short track, which is

10 m long in the model. The model and fan fit together as a whole through a flexible connection. The layout of the model is shown in Figure 2. Through a Y-shaped structure, the shaft can supply and exhaust air to two main tunnels. The length of the ventilation crossover between the two main tunnel is 3m, and the axis of the complementary cross channel is perpendicular to the axis of the main tunnel. Each model segment is connected by a stainless-steel beam.

Figure 2. Physical model overall layout.

In order to meet the ventilation requirement in the model test, 5 fans are required, three of which were 3 axial fans and 2 centrifugal fans. The power equipment in the cross channel is an SD64-11 series axial fan, and one SDS-112K series axial fan is used in the shaft. At the same time, centrifugal fans are at the entrance of two tunnel models to simulate the natural wind and traffic wind in the tunnel.

The test signal is converted into an electrical signal by the test element. The converter can be connected to the adjustment adapter through a shielded wire, and then connected to the indicator to read the test data. The simulation process of tunnel ventilation physical model test is dynamic, and the section wind speed and wind pressure are constantly changing. Therefore, timely and accurate data collection is very important. The experiment uses PCI 6224 data acquisition cards developed by Ni company of the United States and its supporting development platform LabVIEW (LabVIEW). The system realizes the input, data acquisition, real-time display, storage, playback, and result report output of the test system.

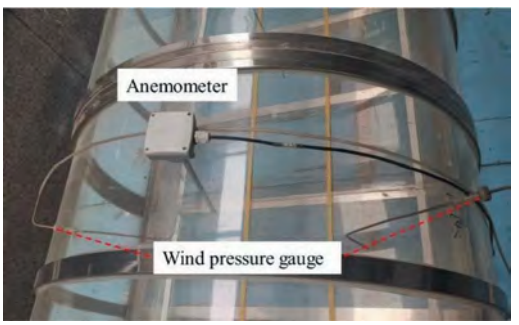

Figure 3. Model test section.

In order to observe the change in wind speed, and control the spread distance of the fire smoke to reduce the impact on the ventilation system, the tunnel is divided into six parts. We measured 10 representative sections, and the test section model and layout are shown in Figure 3. During the test, the centrifugal fan power remained unchanged, and the natural wind was simulated at an average wind speed of 2 m/s. The 2#, 3#, and 5# axial flow fans are adjusted, and the frequency variation of the axial fan is: 20Hz, 25Hz, 30Hz, 35Hz, 40Hz, 45Hz.

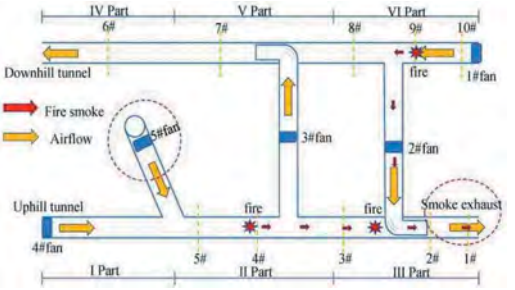

Figure 4(a). Uphill tunnel shafts air supply.

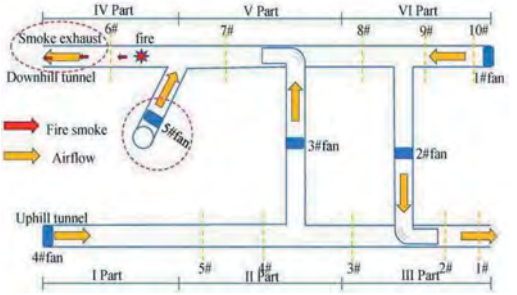

Figure 4(b). Downhill tunnel shafts air supply.

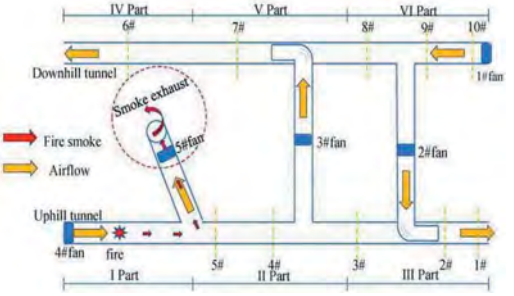

Figure 4(c). Uphill tunnel shafts air exhaust.

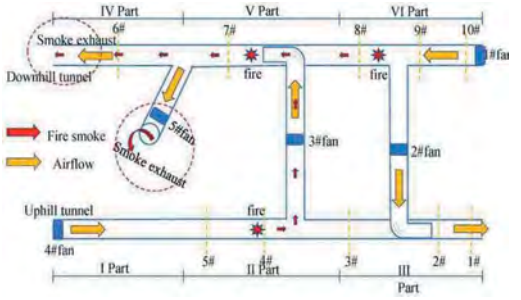

Figure 4(d). Downhill tunnel shafts air exhaust.

The experiment is divided into four operating conditions: the first is uphill tunnel shaft air supply (Figure 4(a)); the second is downhill tunnel shaft air supply (Figure 4(b)); the third is uphill tunnel shaft air exhaust (Figure 4(c)); the fourth is downhill tunnel shaft air exhaust (Figure 4(d)). Each condition is separated into six conditions: 2#axis fan frequency of 20 Hz, 3#axis flow fan at 30 Hz, and the frequency of the 5#axis fan ran from 20 Hz to 45 Hz. So there are a total of 24 small working conditions, and the typical data of each condition is compared and analyzed. According to the change of wind speed field under different conditions, reasonable ventilation design is carried out when different tunnel parts are on fire. The design layout of the ventilation test system is shown in Figure 4.

4 RESULTS AND DISCUSSION

4.1 *The uphill tunnel shaft air supply*

Figure 5 shows that with 5 # fans frequency raised, the variation trend of wind speed of each section is identical. The wind speed of the uphill tunnel increases first, then decreases, and then rises gradually along the tunnel direction. Figure 6 shows that with 5 # fans frequency is raised, the static pressure of each section increases, and the trend is almost identical.

The wind speeds in the 4# and 5# Section increases, while the 3# Section decreases due to the increase in air volume in the cross channel, indicating that the pollutants migrated from the uphill to the downhill. The wind speed of the 1# and 2# section increases, which is to rapidly discharge the pollutants from the outlet of the uphill tunnel. The wind speed of the downhill tunnel increases first and then decreases, then rises gradually and then decreases along the tunnel. The wind speed of the 9# and 10# Sections increases, while the 8# Section decreases due to the increase in air volume in the cross channel, indicating that the pollutants migrated from the downhill to the uphill. The wind speed of the 6# and 7# section increases, which is to rapidly discharge the pollutants from the outlet of the downhill tunnel.

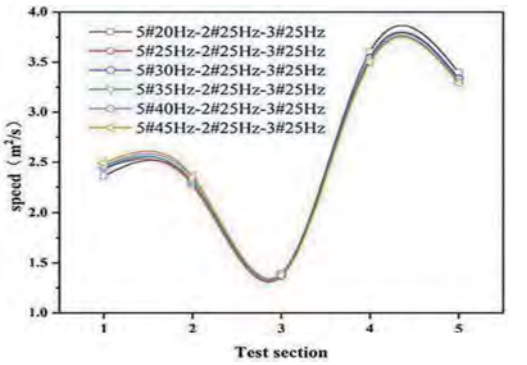

Figure 5(a). Wind speed of uphill tunnel.

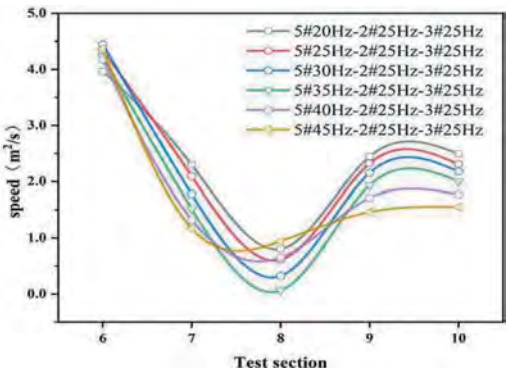

Figure 5(b). Wind speed of downhill tunnel.

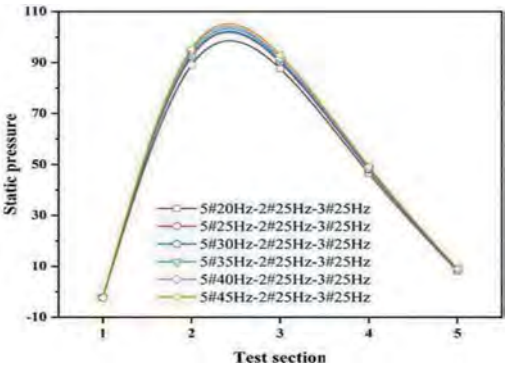

Figure 6(a). Static pressure of uphill tunnel.

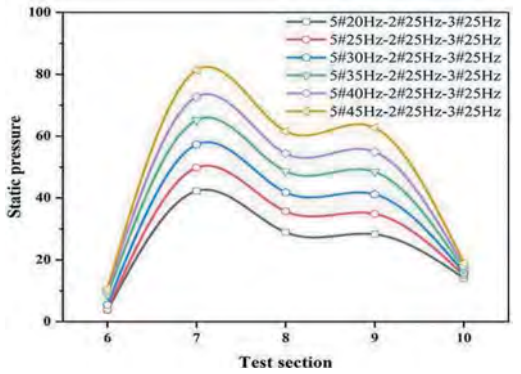

Figure 6(b). Static pressure of downhill tunnel.

The wind speed of the 4# section is 3.495 m/s, and the 3# section is 1.372 m/s. The wind speed of the 4# section is higher than that of the 3# section, which effectively prevents short-track backflow. When a fire occurs in Sections II and III, the difference of wind speed ensures that the fire smoke spreads along the uphill tunnel and is discharged from the outlet quickly.

The static pressure of the 8# section is 61.562 Pa, and the 9# section is 62.706 Pa. The pressure difference between the two sections is small. when the fire occurs in Section VI, in order to shorten the smoke exhaust distance, fire smoke enters the uphill tunnel from the cross channel under the action of 2# fans. Fire smoke will not continue to spread to the downhill tunnel, but will be discharged from the uphill tunnel outlet.

4.2 *The downhill tunnel shaft air supply*

Figure 7 shows that with 5 # fans frequency is raised, the wind speed of each section increases, and the variation trend is identical. The shaft air supply increases the air volume and reduces the concentration of pollutants in the tunnel; the increase of air speed effectively discharges pollutants. The shaft can coordinate with the complementary cross channel to regulate the concentration of pollutants, which can be used in normal operation.

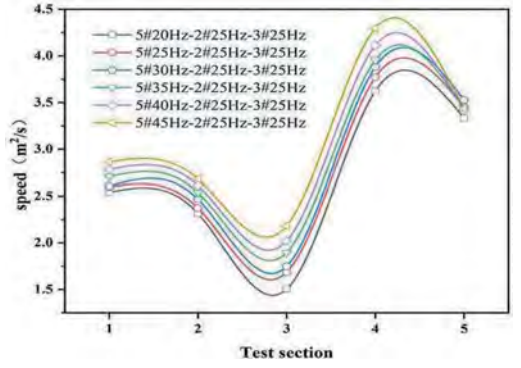

Figure 7(a). Wind speed of uphill tunnel.

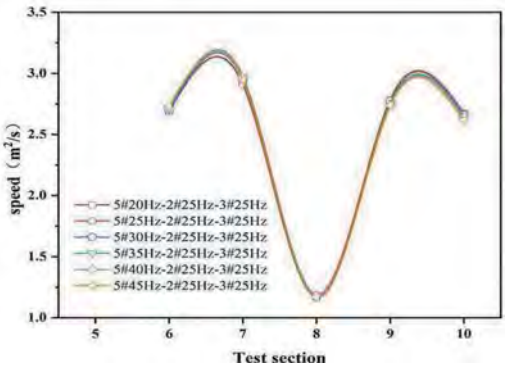

Figure 7(b). Wind speed of downhill tunnel.

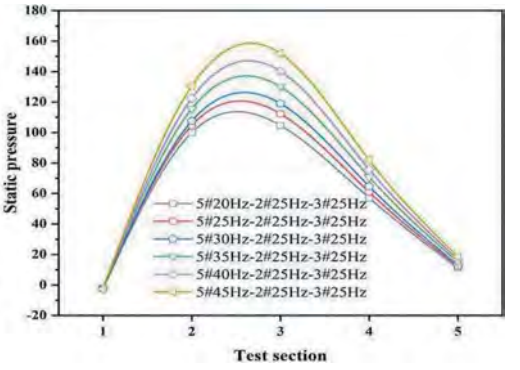

Figure 8(a). Static pressure of uphill tunnel.

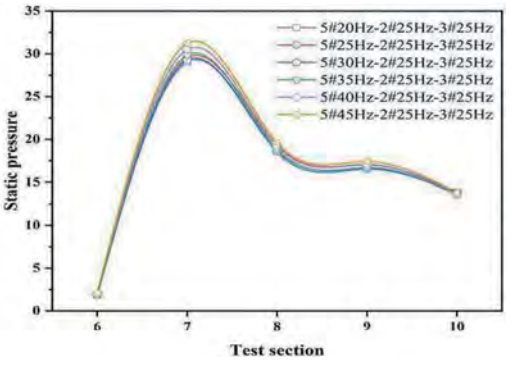

Figure 8(b). Static pressure of downhill tunnel.

Figure 8 shows that with 5 # fans frequency is raised, the static pressure of each section increases, and the variation trend is identical. When the fire occurs in Section IV, the fire smoke discharges from the down tunnel outlet as soon as possible. The static pressure of the 7# section is 31.223Pa, and the 6# section is 2.072 Pa. The static pressure of the 7# section is

greater than the 6# section, which ensures that the fire smoke spreads along the downhill tunnel. The wind speed in the 6# and 7# section increases, ensuring that the fire smoke is quickly discharged from the outlet.

4.3 *The uphill tunnel shaft air exhaust*

Figure 9 shows that with 5 # fans frequency is raised, the variation trend of the wind speed is identical. The wind speed of the uphill tunnel increases first along the tunnel direction, then reduces, and then rises gradually. The wind speed of the downhill tunnel decreases along the tunnel direction, then rises, and then reduces. The wind speed of the 3# section is 1.364m/s, the 4# section is 3.711m/s, and the 7# section is 3.185m/s. The wind speed from the 4# to 3# section decreases rapidly, and the wind speed of the 7# section increases. This explains that the air volume enters the downhill tunnel through the cross channel, which is beneficial to the adjustment of the pollutant concentration of the downhill tunnel.

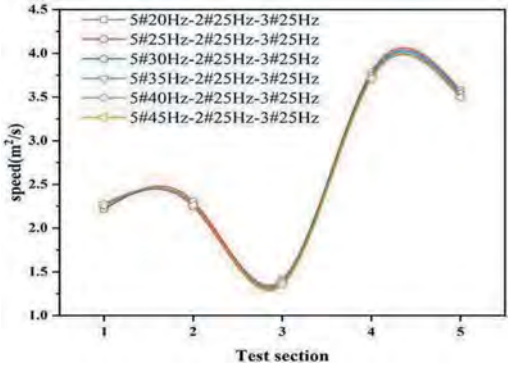

Figure 9(a). Wind speed of uphill tunnel.

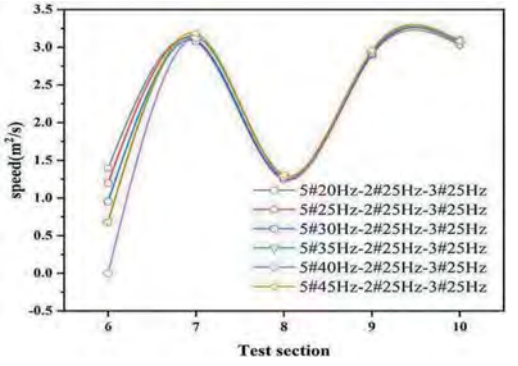

Figure 9(b). Wind speed of downhill tunnel.

Figure 10 shows that with 5 # fans frequency is raised, the static pressure of each section decreases, and the variation trend is identical. When the fire occurs in section I, the fire smoke is discharged from the shaft as soon as possible. The static pressure of the 5# section is 3.498 Pa, and the 4# section is 3.711 Pa. The static pressure of the 4# section is greater than the 5# section, but the change is very small, and the speeds of the two sections are similar. The above conditions ensure that fire smoke does not spread along the uphill tunnel. Under the action of the 5# shaft, fire smoke is quickly discharged from the shaft, which effectively shortens the distance of smoke exhaust.

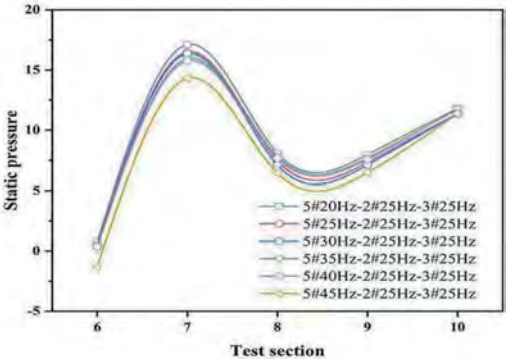

Figure 10(a). Static pressure of uphill tunnel.

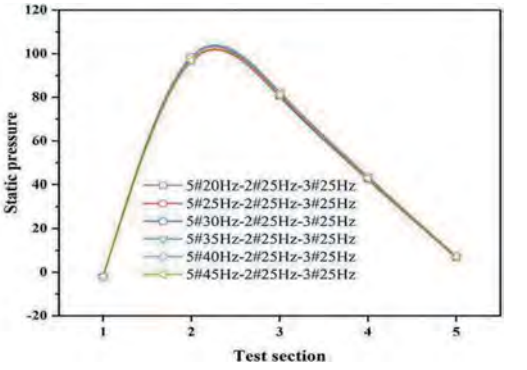

Figure 10(b). Static pressure of downhill tunnel.

4.4 *The downhill tunnel shaft air exhaust*

Figure 11 shows that with 5 # fans frequency is raised, the wind speed in the uphill tunnel decreases, and in the downhill tunnel is stable, and the variation trend is identical. The wind speed of the uphill tunnel increases first along the tunnel direction, then reduces, and then rises gradually. The wind speed of the downhill tunnel reduces along the tunnel direction, then rises, and then decreases.

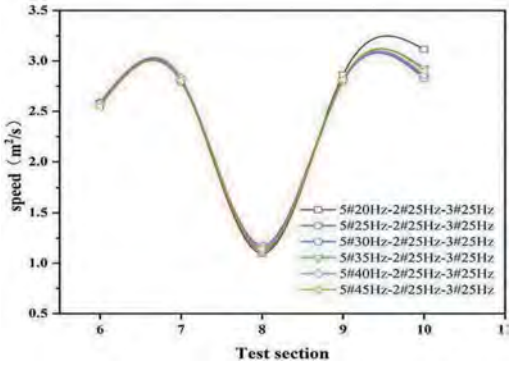

Figure 11(a). Wind speed of uphill tunnel.

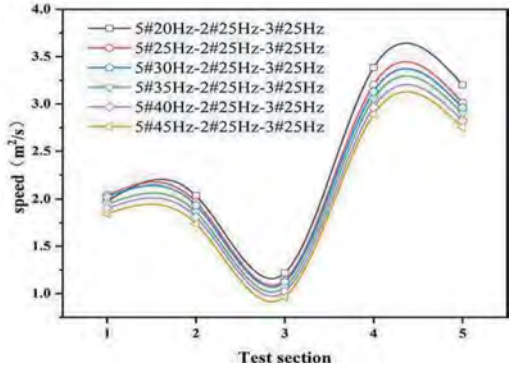

Figure 11(b). Wind speed of downhill tunnel.

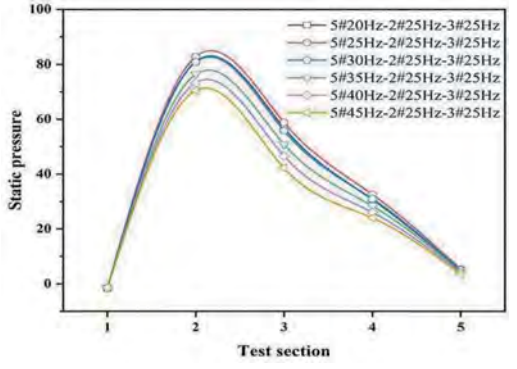

Figure 12(a). Static pressure of uphill tunnel.

Figure 12 shows that with 5 # fans frequency is raised, the static pressure of each section decreases, and the variation trend is identical. When the fire occurs in Section II, the fire smoke enters the downhill tunnel and is discharged from the outlet. The static pressure of the 4# section is 30.757Pa, and the 3# section is 56.814Pa. The static pressure of the 4# section is less than the 3# section, which ensures that

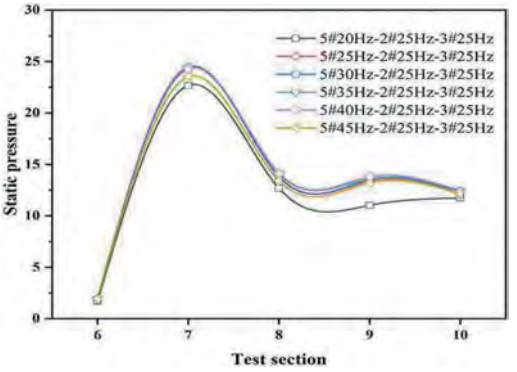

Figure 12(b). Static pressure of downhill tunnel.

the fire smoke will not spread along the uphill tunnel. Under the action of 3# fans, the fire smoke enters the downhill tunnel along the cross channel and is discharged from the outlet quickly. When the fire occurs in V and VI sections, the fire smoke is discharged from the shaft under the action of the 5# fan, which effectively shortens the smoke exhaust distance.

5 CONCLUSIONS

1. The wind speed of 3# Section decreases due to the increase in air volume in the cross channel, indicating that the pollutants migrated from the uphill to the downhill. The wind speed of 1# and 2# section increases, which is to rapidly discharge the pollutants from the outlet of the uphill tunnel. The wind speed of 8# Section decreases owing to the increase in air volume in the cross channel, indicating that the pollutants migrated from the downhill to the uphill. The wind speed of the 6# and 7# section increases, which is to rapidly discharge the pollutants from the outlet of the downhill tunnel.
2. The air supply shaft can regulate the concentration of pollutants by increasing the air volume and wind speed in the tunnel so that pollutants can be quickly removed from the tunnel. The air exhaust shaft can shorten the distance of smoke exhaust, and remove the fire smoke effectively. So, the use of the combined shaft can not only meet the ventilation needs and fire smoke emission requirements but be more energy-saving and cost-effective.
3. When a fire occurs in the I part, the fire smoke is quickly discharged from the shaft when the uphill shaft exhausts. When a fire occurs in the II and III parts, the fire smoke is quickly discharged from the uphill outlet when the uphill air supply. To shorten the smoke distance, the downhill shaft exhaust, the fire smoke that occurs in II enters the downhill tunnel through the cross channel and is discharged from the outlet. When a fire occurs in the IV part, the fire smoke is quickly discharged

from the downhill outlet when the downhill shaft exhausts. When a fire occurs in the V and VI parts, the fire smoke is quickly discharged from the shaft when the downhill air exhausts. To shorten the smoke distance, the uphill shaft supply, the fire smoke that occurs in V enters the uphill tunnel through the cross channel and is discharged from the outlet.

ACKNOWLEDGMENTS

The authors gratefully acknowledge the financial support for this work provided by the National Natural Science Foundation (No.51978059).

REFERENCES

Betta, V., Cascetta, F., Musto, M., & Rotondo, G. (2010). Fluid dynamic performances of traditional and alternative jet fans in tunnel longitudinal ventilation systems. Tunnelling and Underground Space Technology, 25(4), 415–422.

Chen, L. F., Hu, L. H., Zhang, X. L., Zhang, X. Z., Zhang, X. C., & Yang, L. Z. (2015). Thermal buoyant smoke back-layering flow length in a longitudinal ventilated tunnel with ceiling extraction at difference distance from heat source. Applied Thermal Engineering. 78, 129135. Doi:10.1016/j.applthermaleng.2014.12.034

Cascetta, F., Musto, M., & Rotondo, G. (2016). Innovative experimental reduced scale model of road tunnel equipped with realistic longitudinal ventilation system. Tunneling and Underground Space Technology. 52, 85–98.

Hu, Y. J., Deng, M., & Yang, T. (2011) Application Research for the Complementary Ventilation of Dabie Mountains Tunnel. Transportation & Technology. 2011(2).

Lai, J. X., Qiu, J. L., Fan, H. B., Chen, J. X., & Xie, Y. L. (2016). Freeze-proof method and test verification of a cold region tunnel employing electric heat tracing. 60, 56–65.

Liu, Y. N., Xiao, Y. M., Augenbroe, G., Zhou, T. C., Hu, Y. X., Lin, J. Q., & Huang, H. T. (2018). The formation of multi-steady-states of buoyancy ventilation in underground building. Tunnelling and Underground Space Technology. 82, 613–626.

Li, J., Li, Y. F., Cheng, C. H., & Chow, w. k. (2019). A study on the effects of the slope on the critical velocity for longitudinal ventilation in tilted tunnels. Tunnelling and Underground Space Technology. 89, 262–267.

Li, S., Liu, X. F., Wang, J. X., Zheng, Y. L., & Deng, S. M. (2019). Experimental reduced-scale study on the resistance characteristics of the ventilation system of a utility tunnel under different pipeline layouts. Tunnelling and Underground Space Technology. 90, 131–143.

Zhang, Z. Q., Zhang, H., Tan, Y. J., & Yang, H. Y. (2018). Natural wind utilization in the vertical shaft of a super-long highway tunnel and its energy saving effect. Building and Environment. 145, 140–152.

Rui, R., Xu, S. S., Ren, Z. D., Zhang, S. Z., Wang, H., Wang X. L., & He, S. (2018) "Numerical Investigation of Particle Concentration Distribution Characteristics in Twin-Tunnel Complementary Ventilation System," Mathematical Problems in Engineering, vol. 2018, Article ID 1329187, 13 pages, 2019.

Wang, Y. Q., Xia, F. Y., Xie, Y. L., & Hu, Y. J. (2014). Physical Model Experiment on Complementary Ventilation of Extra-long Highway Tunnel. China Journal of Highway and Transport. Vol. 27 No. 6.

Wang, Y. Q., Hu, Y. J., Deng, M., Xia, F. Y., & Xie, Y. L. (2014). Complementary ventilation operational test in large longitudinal slope double-hole tunnel. Journal of Traffic and Transportation Engineering, 2014(5):29–35.

Wang, Y. Q., Xu, S. S., Ren, R., Zhang, S. Z., & Ren, Z. D. (2018). Application of the twin-tube complementary ventilation system in large-slopping road tunnels in China. International Journal of Ventilation. ISSN: 1473-3315 (Print) 2044–4044.

Wang, Z.L., Zhu, L., Guo, X. X., Pan, X. H., Zhou, B., Yang, J., … Feng, L. (2019). Reduced scale experimental and numerical study of fire in a hybrid ventilation system in a large underground subway depot with superstructures under fire scenario. Tunnelling and Underground Space Technology. 88, 98–112.

Xia, F. Y., Wang, Y. Q., & Xie, Y. L. (2015). Design Method and Test of Twin-tunnel Complementary Ventilation for Highway Tunnel. Journal of Highway and Transportation Research and Development. Vol. 32 No. 3.

Zhang, G. P., Lei, B., & Tian, M. L. (2011). Study on air interchange system for road tunnel longitudinal ventilation. Modern Tunneling Technology, 48(1), 42–45.

Zhang, G. P., Lei, B., & Lei, M. L. (2011). Application of air exchange method in longitudinal ventilation of highway tunnel [J]. Modern Tunneling Technology, 2011 (01):48-51+62.

Zhang, G. Z., Liu, S. Y., Zhao, X., Ye, M. X., Chen, R. F., Zhang, H. L., … Chen, J. W. (2017) The coupling effect of ventilation and groundwater flow on the thermal performance of tunnel lining GHEs. Applied Thermal Engineering. 112, 595–605.

Tunnelling for a Better Life – Yan, Celestino, Thewes & Eberhardt (Eds)
© 2024 The Author(s), ISBN 978-1-032-80042-4
Open Access: www.taylorfrancis.com, CC BY-NC-ND 4.0 license

Study on the influence of longitudinal slope on the temperature field inside railway tunnels in cold regions and engineering counter measures

Changxian Yang*
China Railway Design Corporation Limited, Tianjin, China

Siming Tian
China Railway Economic and Planning and Research Institute Co., Ltd., Beijing, China

Zhifu Ma
China Railway Design Corporation Limited, Tianjin, China

ABSTRACT: The frost-resistant fortification length of tunnels in cold areas is highly correlated with experience. Currently, the determination of fortification length is mainly based on engineering analogies, which is not fully combined with the distribution law of temperature field inside the tunnel. By selecting 2 typical tunnel sites with different lengths and slope conditions in the railway projects operating in high latitude and severe cold areas, continuous testing of the longitudinal temperature field distribution in the tunnel was carried out. The temperature field distribution law along the longitudinal direction in the cold areas tunnel was analyzed, and the control equation for the temperature field distribution along the longitudinal direction in the cold areas tunnel was obtained by fitting the curve. Combined with the engineering practice, the temperature standard for frost resistance protection inside the tunnel was verified. The research results show that: 1) The meteorological characteristic parameter values used in the anti-freezing design of tunnels in cold areas should be collected and analyzed based on meteorological statistical data from the area where the tunnel is located for at least 30 years. 2) The relative height difference between the both ends of the tunnel caused by the longitudinal slope of the line is one of the main factors affecting the temperature field distribution inside the tunnel in cold regions.3) The fifth-order polynomial parabolic equation obtained by fitting the longitudinal distribution curve of the average temperature inside the tunnel in January can be used as the control curve equation for the anti-freezing design of the tunnels in cold regions, with the constant term corrected by the average temperature of the coldest month in the region. 4) The length of anti-freezing fortification for the tunnel structure in cold area can be determined according to the temperature inside the tunnel not higher than -15.2 °C, while the fortification length of the thermal insulation drainage and anti-freezing system can be determined according to the temperature inside the tunnel not higher than -13.8 °C.

Keywords: the railway tunnels in cold area, temperature field, engineering countermeasure, dominant factor

1 INTRODUCTION

Unlike the climate in mild areas, cold regions generally experience large changes in environmental temperature every year. The summer environmental temperature may above freezing for a long time, while the winter environmental temperature may below freezing for a long time. This climate change has adverse effects on the tunnel in cold regions, mainly manifested as follows: during the cold season, the anti-drainage system of the railway tunnel needs to consider the possibility of freezing and blockage in the drainage system under continuous negative temperature environment conditions, which is manifested as ice hanging on the lining wall or contact network, and ice accumulation on the roadbed caused by freezing of the drainage ditch. In addition to considering the temperature stress caused by large temperature differences in the tunnel structure, when the tunnel is in a frost heave sensitive formation and the moisture content of the formation exceeds a certain range, or there are local cavities behind the lining and water accumulation inside the cavities, problems such as lining surface cracking, peeling, and falling off occur, which is not conducive to the safe operation of the tunnel. Because of the waterproof and drainage system and structure inside the tunnel in cold regions are greatly affected by the temperature changes inside the tunnel, it is necessary to take targeted measures for structural frost resistance and anti-freezing engineering measures for the waterproof and drainage system based on the distribution and changes of the

*Corresponding author: ycxycxycx007@sina.cn

DOI: 10.1201/9781003495505-462

longitudinal temperature field inside the tunnel according to local conditions.

Relevant engineering technicians and scholars at home and abroad have continuous research on the distribution law of temperature field inside tunnels in cold regions, and have obtained a series of research results. Zhang et al.[1] studied the influence of thermal potential difference and static pressure difference at the entrance of a tunnel on the temperature field changes in cold regions through measured data and numerical analysis. Sun et al.[2]-[4] conducted research on the distribution law of temperature field and buried depth of drainage ditches in cold region tunnels under the condition of thermal fluid solid coupling effect, exploring the influence of initial ground temperature and thermal conductivity of surrounding rock on the distribution of temperature field in cold region tunnels. Li et al.[5] assessed the influence of thermal parameters of surrounding rocks, such as thermal conductivity, specific heat capacity, and freezing temperature, on the radial temperature distribution within tunnels in cold regions. Yu et al. [6] derived a heat transfer model for the airflow temperature field of wind flow in tunnels in cold regions, and explored the effect of ventilation and surrounding rock conditions on the distribution of temperature field within tunnels in cold regions. Guo et al. [7] analyzed the influence and patterns of tunnel length, air temperature, and wind speed on the longitudinal temperature field distribution of tunnels in cold regions through indoor model test.

The summary of the technical research results conducted on the temperature field of tunnels in cold regions can be roughly divided into the following two categories: one mainly combines the relevant theories of heat transfer and derives the temperature field distribution control equation of tunnels in cold regions based on several assumptions, while the other mainly combines the numerical simulation analysis and is supplemented by a small number of on-site temperature data validation to carry out research on the distribution law of temperature field in cold zone tunnels. Due to a series of boundary conditions or assumptions set during the above studies, the conclusions have greater limitations, which are often difficult to fully apply when applied to specific projects of tunnels in cold regions.

Aiming at the above problems, this paper proposes to carry out continuous testing of the longitudinal temperature field distribution inside the tunnel by selecting 2 typical tunnels with different lengths and slopes in high-latitude frigid region railway projects operating in high latitude and severe cold region through research, analysis, and other methods. analyze the temperature field along the longitudinal distribution pattern inside the tunnels in cold regions by measuring the temperature data inside the tunnels. Get the control equation for the longitudinal distribution of the temperature field inside the tunnel in cold region by fitting the curve . The temperature standard for the anti-freezing defense was verified by combining with the engineering practice. It is expected to provide valuable reference for anti-freezing defense of tunnels in cold regions.

2 ANALYSIS OF FACTORS INFLUENCING THE TEMPERATURE FIELD DISTRIBUTION INSIDE TUNNELS

Engineering practice has proved that the temperature field inside the tunnels in cold regions is mainly affected by the combined effects of changes in the surrounding rock temperature field (including the groundwater temperature field) and regional environmental temperature changes, etc. The surrounding rock temperature field is generally in a relatively stable state for a certain time after tunnel excavation, while the ambient temperature in cold region generally cyclical changes over time, which is the main influence of the temperature field changes inside the tunnel. Moreover, this influence is caused by external natural wind flowing along the longitudinal direction of the tunnel, resulting in an overpressure difference in the airflow pressure at the entrance. The thermal potential difference formed by the temperature difference inside and outside the tunnel is superimposed and passes through the tunnel in the form of wind,, heat exchange occurs along the longitudinal and radial directions respectively, thereby changing the temperature field inside the tunnel.

2.1 *Hyperstatic differential pressure effect*

When the height difference between the two ends of the tunnel is not significant, it is usually considered that the air density is a constant. When the atmosphere in the vicinity of the tunnel is at a static state, the air pressure difference formed by the height difference between the two ends of the tunnel can be called the static pressure difference. However, if there is a natural wind outside the tunnel, the airflow pressure difference at the both ends of the tunnel caused by the natural wind direction caused by is called the super-static pressure difference P_{ss}, and its calculation is shown in equation (1).

$$P_{ss} = p_1 - p_2 - \rho g h \tag{1}$$

In the formula: P_1 and P_2 are the air pressure at the both ends of the tunnel, Pa; ρ is the average air density at the both ends of the tunnel, kg/m^3; h is the relative height difference at the both ends of the tunnel, m.

2.2 *The role of thermal potential difference*

The measured data shows that there is generally a significant temperature difference between the inside and outside of tunnels in cold regions. In winter, the temperature inside of the tunnel is generally significantly higher than the ambient temperature outside of the tunnel. At this time, the air outside the tunnel enters the tunnel from the low entrance, pushing the air inside the tunnel out from the high entrance, resulting in a significant buoyancy effect. In summer, the temperature inside the tunnel is generally

significantly lower than the ambient temperature outside the tunnel, which is exactly the opposite of the cold season. The air inside the tunnel flows from the high entrance end to the low entrance and pushes out of the tunnel, forming a sinking effect.

When the temperature changes, the air density will also changes: as the temperature rises, soluble gases fully diffuse, the ambient air pressure decreases, and the density decreases within a certain range. This kind of airflow pressure difference caused by the obvious difference between the ambient temperature inside and outside the tunnel, as well as the relative height difference at the tunnel entrance, can be called as the thermal potential difference. According to the hydrostatic method, the thermal potential difference P_{hot} in the tunnel can be calculated according to equation (2).

$$P_{hot} = (\frac{\rho_1 - \rho_2}{2} - \rho)gh \quad (2)$$

In the formula: ρ_1 and ρ_2 are the air densityat the both ends of the tunnel, kg/m^3; ρ is the air density at the highest air temperature point in the tunnel, kg/m^3; h is the relevant height difference between the both ends of the tunnel, m.

It should be noted that both the atmospheric superstatic pressure difference and thermal potential difference between the two tunnel entrances are related to the height difference of the tunnel entrances, and change in real-time with the meteorological conditions in the region where the tunnel is located, which also leads to changes in the temperature field inside the tunnel in the cold region.

3 SELECTION OF TESTING SITES

Due to the weak solar radiation in the high latitude areas of the northern hemisphere during the winter half of the year, the surface of the Eurasian continent rapidly cooled, and the high latitude areas in Northeast China are affected by the accumulation of cold air in favorable terrain areas such as the Mongolian Plateau and eastern Siberia, forming the main source of cold air in China. In the winter half year, westerly or northwest winds prevail, forming a dry, cold, snowy, and low-temperature climate environment that lasts for about half a year, making it the coldest natural region in China. The Harbin-Mudanjiang high-speed railway in Heilongjiang Province, located in the northernmost part of China, is generally oriented in a west to east direction, which is basically consistent with the main winter wind direction in the region. The project is distributed in multiple tunnels of different lengths and slopes, which is conducive to conducting temperature tests inside the tunnel and comparing and analyzing the influence of different longitudinal slopes on the distribution of temperature fields inside railway tunnels of different lengths.

3.1 *Project overview*

The Harbin-Mudanjiang Railway connects Harbin and Mudanjiang from west to east, the line standard is a high-speed railway with a speed of 250km/h, and the effective area of clearance in the tunnel section is 92m^2. There are a total of 39 double-track tunnels along the line, with a total length of 68.505km. The longest tunnel is the Hufengling Tunnel, with a length of 8.755km. The projects operate EMUs, and during the test period, there are 32 pairs of trains on the Harbin-Mudanjiang Railway.

Combined with the tunnel characteristics of the projects, the Mabei, and Hufengling tunnels of the Harbin-Mudanjiang Railway was selected as typical tunnel sites to conduct longitudinal temperature distribution testing research inside the tunnels. The basic overview of the testing sites is shown in Table 1.

3.2 *Overview of work sites*

3.2.1 *Mabei Tunnel*

The Mabei Tunnel of Harbin- Mudanjian Railway is located in Hengdaohezi Town, Hailin City, Heilongjiang Province, with a total length of 2202 m. The average temperature of the coldest month over the year in the tunnel area is -17.2 ℃, and the maximum freezing depth of the soil is 1.91 m. The plan and longitudinal section of the tunnel are shown in Figure 1.

3.2.2 *Hufengling Tunnel*

The Hufengling Tunnel OF Harbin-Mudanjian Railway is located in Hengdaohezi Town, Hailin City,

Table 1. Overview of temperature testing sites in the tunnel of railways operating in cold regions.

Tunnel Name	Design speed	The name of the railway line	Tunnel length/m	Tunnel alignment	Maximum burial depth/m	The main winter wind direction	Longitudinal Slope Setting	The difference in height of hole/m
Mabei	250km	Harbin-Mudanjiang	2202	Northwest to southeast	141	West, Northwest	Uphill with the wind	16
Hufengling	250km	Harbin-Mudanjiang	8755	Northwest to southeast	275	West, Northwest	Uphill with the wind	103

Note: "-" in the table indicates that the tunnel inlet is higher than the outlet.

Figure 1. Schematic diagram of the plan and longitudinal section elements of the Mabei Tunnel on Harbin-Mudanjian railway.

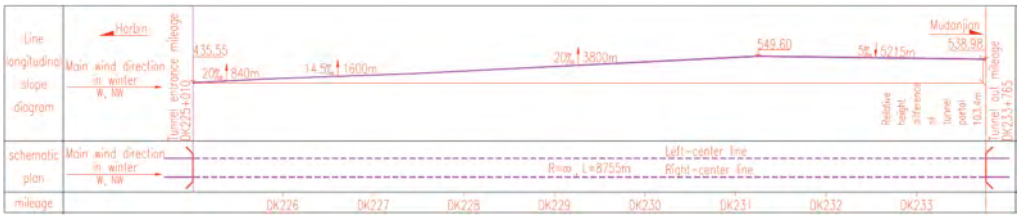

Figure 2. Schematic diagram of the plan and longitudinal section elements of Hufengling Tunnel on Harbin-Mudanjian railway.

Heilongjiang Province, with a total length of 8755 m. The average temperature of the coldest month of the year in the tunnel area is -17.2 °C, and the maximum freezing depth of the soil is 1.91 m. The plan and longitudinal section of the tunnel are shown in Figure 2.

4 TEMPERATURE TESTING PROGRAM IN THE TUNNEL

Due to the characteristics of the Harbin-Mudanjian Railway, have the characteristics of operating EMUs, the line adopts the characteristics of fully enclosed, large machine maintenance and comprehensive maintenance, it is required that the temperature testing instrument in the tunnel has the function of automatically recording data continuously at certain interval. In this test, the Testo174T temperature recorder is selected, which has the ability to automatically record real-time temperature testing data every 30 minutes and store 16,000 sets of data, ensure that the test duration is not less than one winter.

Considering that the tunnel is a linear structure buried underground, the longitudinal test section can start from the first inspection well at the tunnel entrance, and a temperature test section can be laid at every 16 inspection wells (about 480m long) longitudinally.

In addition, in order to ensure the safety of the high-speed EMU operating in the test site, temperature testing instrument can be placed in the communication signal cable trough under certain waterproof measures.

5 ANALYSIS OF TEMPERATURE TEST DATA

5.1 *Analysis of the longitudinal distribution of the temperature field*

Combined with the specific situation of the 2 railway tunnels selected for testing and operation, continuous tests were conducted on the longitudinal distribution of the temperature fields in the 2 tunnels during the winter seasons of 2018~2019. Considering the randomness of temperature changes and the current situation in the field of civil engineering, where the climate environment is generally divided based on the average temperature of the coldest month in the region. After obtaining the effective test data for each test section along the longitudinal distribution of the 2 tunnels, the monthly average temperature of each measurement point was determined according to the arithmetic mean, and the longitudinal distribution curve of the monthly average temperature inside the 2 tunnels were plotted as shown in Figure 2.

Meanwhile, the statistical analysis of the average temperature of the coldest month of the cumulative year in the area where the 2 tunnels are located in comparison with the average temperature of the coldest month (January) of the actual measurement period is shown in Table 2.

From the analysis of Table 2 and Figure 3, it can be concluded that the temperature inside the tunnel of the railway tunnel operating in the high-latitude cold region has the following distribution pattern along the longitudinal direction:

1) Because of the regional meteorological law is obtained through probability and statistical

Table 2. Comparison of the average temperature of the coldest month during the survey period and the measured coldest month.

Tunnel Name	Measured average temperature of the coldest month/°C	Average temperature of the coldest month of the year/°C
Mabei	-9.07	-17.2
Hufengling	-11.69	-17.2

analysis of historical meteorological data, it is generally required that the meteorological statistical period is long enough to obtain relatively stable and representative meteorological characteristic parameter values. Therefore, currently, WMO generally stipulates 30 years as the shortest period for obtaining meteorological characteristic values. As shown in Table 2, the average temperature in January at each measuring point in the 2 typical tunnels during the test period is significantly lower than the average temperature in the coldest month (January) analyzed by the collected. meteorological data in the survey period This indicates that conducting short-period meteorological data testing and analysis of meteorological characteristic parameters near the tunnel site area cannot be directly used to guide the anti-freezing design of the tunnel. Instead, regional historical and multiyear meteorological statistical data should be used to analyzed meteorological characteristic parameters.

2) According to the meteorological statistical data, December to February of the following year is the coldest season in mainland China, with January being the coldest month on the mainland. At this time, the average temperature distribution in the tunnel in the real survey and mapping tunnel in December, January and February along the longitudinal distribution of the three curves of the change law is basically the same, only showing up and down fluctuations. Among them, the temperature field distribution curve in the tunnel is basically at the lowest position in January, which can be used as the control curve for tunnel anti-freezing design.
3) In the cold season, the highest temperature point in the 2 tunnels appeared on the side of the high-end entrance, while the negative temperature section of the entrance at a relatively low-end of the tunnel was significantly longer than that at a relatively high-end of the tunnel, showing

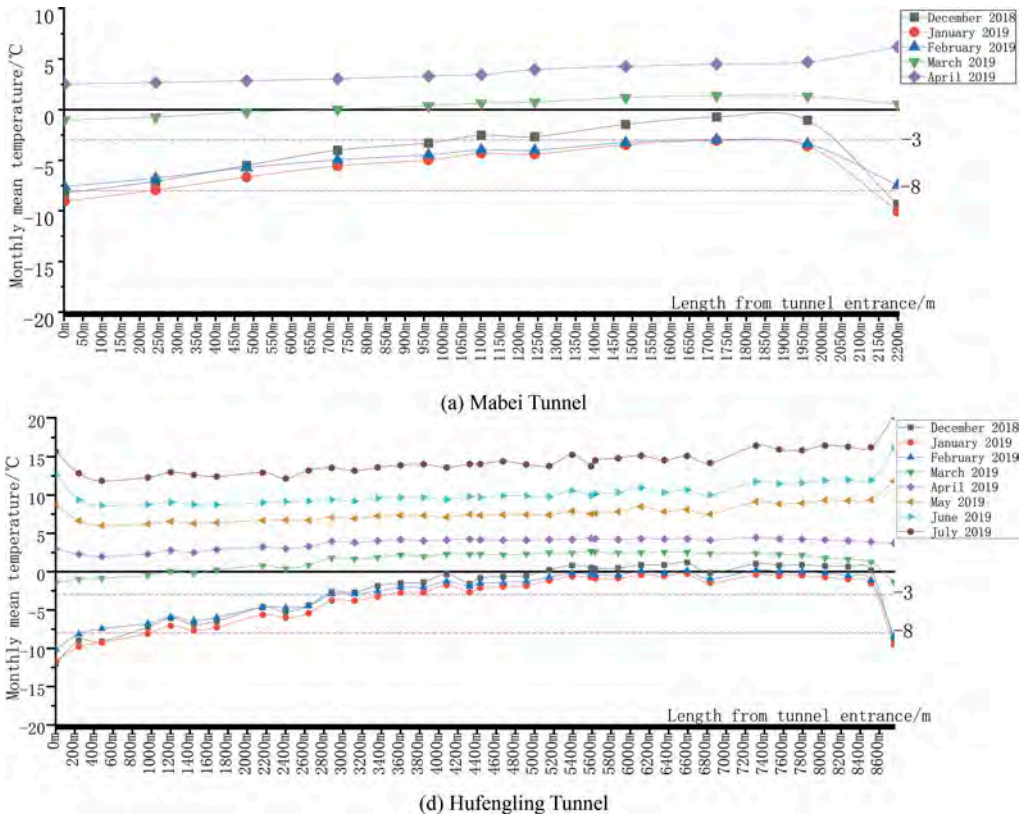

Figure 3. Measured monthly average air temperatures in the 2 operational cold tunnels along the longitudinal distribution curve.

a obvious correlation with the longitudinal slope distribution of the line. The main reasons for the problem are related to the air pressure difference (superstatic pressure difference) caused by the height difference between the two ends of the tunnel, as well as the thermal potential difference caused by the temperature difference between the inside and outside of the tunnel during the cold season. This causes natural wind sources to continuously blow of from the relatively low-end openings to the relatively high-end openings, resulting in a chimney like effect. As a result, the temperature inside the tunnels, which is a longer range from the relatively low-end openings, is more affected by the ambient temperature outside the tunnel. Therefore, the relative height difference between the tunnel at both ends caused by the longitudinal slope of the line is one of the main factors affecting the distribution of temperature field in the tunnel in the cold region.

5.2 *Control equation for temperature field distribution along the longitudinal direction*

The above analysis shows that the temperature distribution curve inside the tunnel in the cold regions obtained in January can be used as the control curve for the anti-freezing design of the tunnel in the cold regions. Moreover, the relative height difference between the both ends of tunnel caused by the longitudinal slope of the line is the dominant factor affecting the distribution pattern of the longitudinal temperature field inside the tunnel in the cold regions. In order to ensure the uniformity of the longitudinal distribution pattern of the temperature inside the tunnels in the cold area, and to overcome the influence of the relative height difference at the tunnel entrance on the longitudinal distribution of the temperature inside the tunnel, the longitudinal distribution curves of the average temperature in the tunnel in January were drawn according to the opening from low to high, and the curve was plotted as shown in Figure 4.

After regression analysis on the longitudinal distribution curves of the average temperature in January in 2 typical tunnels, it was determined that the polynomial Equation (3) could be used for curve fitting, and it has a high correlation coefficient. After fitting, the elements of the longitudinal distribution curve of the average temperature in January in each measured tunnel are shown in Table 3.

$$t_x = t_0 + a_1 x + a_2 x^2 + a_3 x^3 + a_4 x^4 + a_5 x^5 \qquad (3)$$

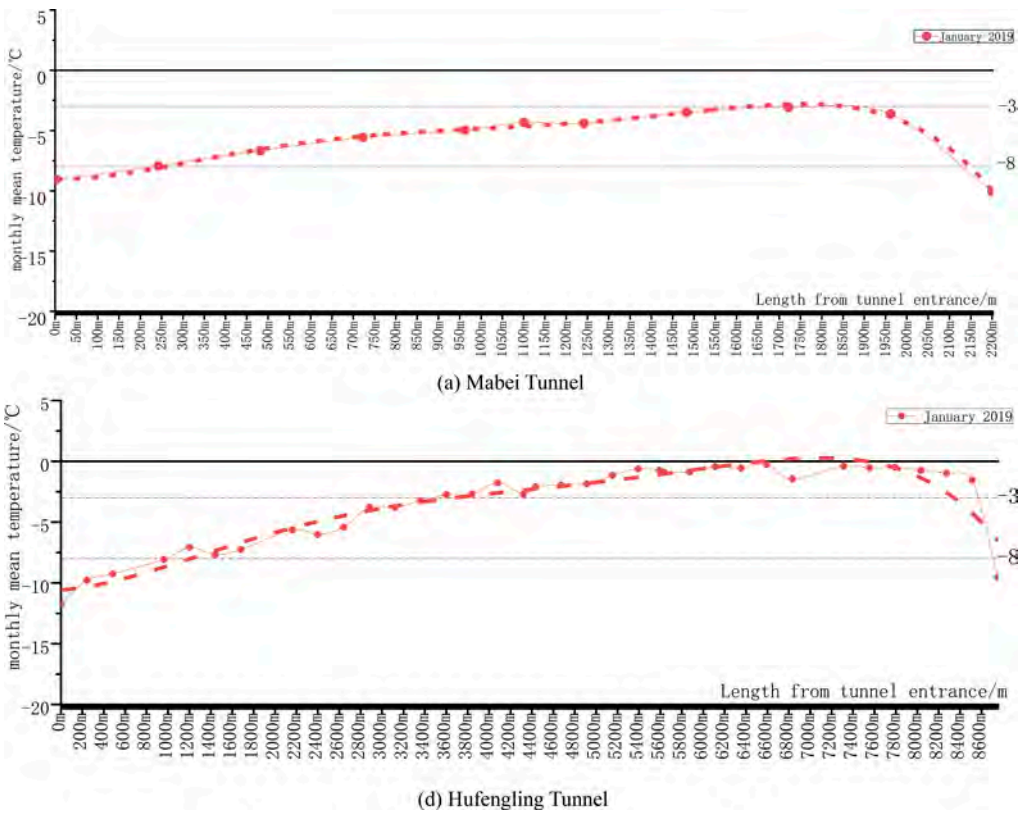

Figure 4. Schematic diagram of the longitudinal distribution curve and regression curve of the measured January average air temperature in the 2 operating cold tunnels.

Table 3. List of elements of longitudinal distribution curves of air temperature in January in railway tunnels of different lengths in high-latitude cold regions.

Curve element								
t_0 /°C	a_1	a_2	a_3	a_4	a_5	Coefficient of complex correlation R_2	Tunnel length/m	Tunnel name
-9.02276	-5.617E-04	2.711E-05	-4.330E-08	2.664E-11	-5.706E-15	0.9893	2202	Mabei
-10.58947	6.273E-04	2.071E-06	-8.205E-10	1.223E-13	-6.375E-18	0.9066	8755	Hufengling

In the formula: t_x - temperature of the tunnel at xm from the low-end opening, °C;t_0 - constant, °C; a_1 - a_5 - are constants, determined by the measured data plotting curve fitting, and the tunnel is located in the geographic location, the relative height difference of the entrance, the flat longitudinal line type, the relationship between the dominant wind direction and the line direction, the enclosing rock geothermal field, the seepage field, and the role of the train piston winds and other factors related to the temperature, °C.

According to the analysis in Tables 2 and 3, it can be seen that the constant t_0 in the curve is the average temperature measured at the tunnel entrance in January. As shown in the previous analysis, the results of short-cycle meteorological data testing and analysis in the vicinity of the tunnel site are unstable and unrepresentative, which can not be used to guide the anti-freezing design of tunnels directly. Instead, multi-year statistical meteorological parameters should be used.

Therefore, the constant t_0 can collect the meteorological data of cities near the tunnel site area for the past 30 years, and the statistical analysis shows that the average temperature of the coldest month in the tunnel site area over the years is used as a meteorological characteristic parameter to modify the derivative into Equation (1). The temperature inside the tunnel, which is used as the anti-freezing engineering measures and defense length for long tunnels in cold regions, is controlled along the longitudinal direction using Equation (4). The temperature inside the tunnel is controlled along the longitudinal direction, as shown in Figure 5, and the curve elements are shown in Table 4.

$$t_x = t_a + a_1 x + a_2 x^2 + a_3 x^3 + a_4 x^4 + a_5 x^5 \qquad (4)$$

6 ENGINEERING APPLICATIONS

In order to adapt the harsh climate environment in cold regions, achieve energy conservation, environmental protection and facilitate maintenance, the tunnels in the cold regions should adopt targeted anti-freezing design in combination with the distribution law of temperature field inside the tunnel. The key technology mainly adopts anti-freezing engineering measures within a certain range of the tunnel entrance.

6.1 *Typical Tunnel Anti-Freezing Design and Operation Practices*

6.1.1 *Anti-freezing measures for insulation and drainage systems*

The main insulation, drainage, and antifreeze measures for the 2 typical tunnels are detailed in Table 5.

6.1.2 *Structural anti-freeze measures*

The main structural frost protection measures for 2 typical tunnels are detailed in Table 6.

6.1.3 *Operational practices*

Since the opening of Harbin-Mudanjiang Railway on December 25, 2018, Mabei, and Hufengling tunnels have been in good operating condition, except for

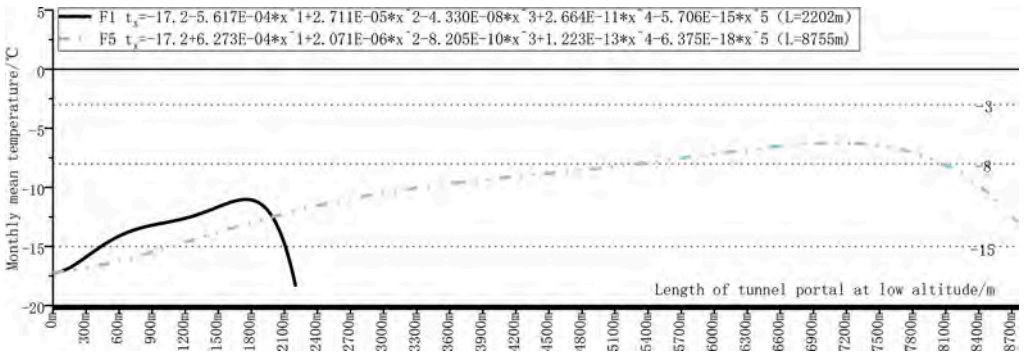

Figure 5. Schematic diagram of temperature control curves along the longitudinal direction in the 2 operating cold-zone tunnel caves.

Table 4. List of elements of control equations of air temperature distribution curve along the longitudinal direction in railway tunnels of different lengths in high latitude cold regions.

curve element								
t_0 /°C	a_1	a_2	a_3	a_4	a_5	coefficient of complex correlation R_2	Tunnel length /m	tunnel name
-17.2	-5.617E-04	2.711E-05	-4.330E-08	2.664E-11	-5.706E-15	0.9893	2202	Mabei
-17.2	6.273E-04	2.071E-06	-8.205E-10	1.223E-13	-6.375E-18	0.9066	8755	Hufengling

Table 5. List of major insulation and drainage measures against freezing in 2 typical tunnels.

Tunnel Name	Center gully	Drainage system behind the lining
Mabei	Installation of deep buried ditch in central with an inner diameter of 80cm through the length of the tunnel	Circumferential φ80 perforated corrugated water permeable blind pipe + longitudinal φ100 perforated corrugated water permeable blind pipe + side wall parts every 12m ~ 16m a width × depth of 0.5m × 0.5m ring gravel blind trench
Hufengling	The inlet and outlet of each 1500m range set up the center of the inner diameter of 80cm deep buried ditch; the rest of the lots set up the use of thermal insulation groove wrapped, the inner diameter of 60cm thermal insulation center ditch	Circumferential φ80 perforated corrugated permeable blind pipe + longitudinal φ100 perforated corrugated permeable blind pipe + inlet and outlet of each 1500m range of the side wall parts every 12m ~ 16m, a width × depth of 0.5m × 0.5m circumferential gravel blind ditch.

Table 6. List of main structural frost protection measures in 2 typical tunnels.

Tunnel Name	Lining frost protection	Lining Temperature Expansion Joints	Radial grouting	Structural insulation
Mabei Hufengling	The lining of the range of 1km from the entrance of the tunnel is C35 reinforced concrete	It is set up in a range of 1km from the tunnel entrance, and which is set up every 100m longitudinally, and the width of the joint is 1.5cm	The III~V grade surrounding rock section is set 1km away from the entrance, and the radial reinforcement arch wall excavation contour line is within 3m range	The tunnel opening and the tunnel body are located in the shallow buried soil and broken stratum section, and the insulation layer of 5cm thick rigid polyurethane insulation board is sandwiched between the initial support of the arch wall and the secondary lining by a double-layer waterproof board

a small number of diseases such as leakage, water and ice. which shows that the anti-freezing measures of the tunnel taken by the design for the meteorological characteristic parameters in the region are basically reasonable.

6.2 *Verification of frost protection design with measured temperature field*

Based on the above analysis, the temperature distribution control equation along the longitudinal direction in 2 typical tunnel openings is determined. Based on the above analysis, the temperature distribution control equation along the longitudinal direction in 2 typical tunnel openings is determined, and the temperature at each typical position inside the tunnel is calculated. Compare the measured temperatures at low and high openings, 1km away from the opening, and 1.5km away from the opening, as shown in Table 7.

According to the analysis of Tables 5-7 and Figure 5, it can be seen that for the Mabei and Hufengling tunnels with a difference in height of 16m and 103m respectively, the ratios of the calculated air temperatures between the low portal and the high portal are 0.93 and 1.32, and that the calculated air temperature ratios for the two tunnels at a distance of 1km from the portals are 1.03 and 2.2 respectively, indicating that the winter air temperature inside the high-end entrance of a long tunnel with a large difference in the relative height of the opening is significantly higher than that at the same location from the low-end entrance. Therefore, the insulation and drainage system and structural frost resistance design of the high-end entrance of a long tunnel with a large slope difference have certain optimization conditions.

Further analysis shows that there were no obvious frost damage problem during the operation period of the 2 typical tunnels, which indicates that the anti-freezing fortification measures and length of the tunnels in the design are basically reasonable. combined with the anti-freezing fortification length of the four

Table 7. List of calculated control temperatures in four typical tunnels.

placement	Calculated temperature inside the tunnel/°C Mabei	Hufengling
Low altitude portal	-17.2	-17.2
1km away from the low altitude entrance	-13	-15.2
1.5km away from the low altitude entrance	-11.6	-13.8
Middle of the tunnel	-12.8	-8.9
1.5km from the entrance of the tunnel at a high altitude	–	-6.3
1km from the entrance of the tunnel at a high altitude	-12.6	-6.9
High altitude portal	-18.4	-13
Low/High	0.93	1.32
1km low/1km high	1.03	2.2

Note: High and low caves are distinguished by the actual elevation of the cave.

tunnel structures are considered as 1km, and the temperature is -15.2 °C ~ -13 °C. Therefore, the anti-freezing fortification length of the tunnel structure in the cold area can be determined according to the calculated temperature in the tunnel is not higher than -15.2 °C, and in the same way, the length of thermal insulation drainage and anti-freezing fortification can be determined according to the air temperature in the cave is not higher than -13.8 °C.

7 CONCLUSIONS AND RECOMMENDATIONS

To analyze the longitudinal distribution law of temperature field inside the tunnel in cold regions, selected 2 typical tunnels construction sites with different lengths and slopes in the railway project of operating in high-latitude and cold region for longitudinal temperature field distribution tests in the tunnel in cold regions, which the continuous test of the longitudinal temperature field distribution in the tunnel obtained the longitudinal distribution control equations of temperature field in the tunnel, and verified the temperature standard for anti-freezing setup in the tunnel through engineering practice.

The main conclusions and recommendations are as follows:

(1) Due to the large dispersion of regional meteorological parameters obtained from the analysis of short-cycle meteorological data, the values of meteorological parameters used in the anti-freezing design of tunnels in cold regions should be collected and analyzed from meteorological statistical data of the region where the tunnel is located for at least 30 years.
(2) The relative height difference between the both ends of the tunnel caused by the longitudinal slope of the line is one of the dominant factors affecting the distribution of the temperature field inside the tunnel in cold regions.
(3) The analysis of the measured data shows that the three curves of average temperature distribution in the tunnel in December, January and February are basically consistent, with only upward and downward fluctuations. Among them, the temperature field distribution curve in the tunnel is basically at the lowest position in January, and the 5th-order polynomial curve equation obtained by curve fitting can be used as the control curve equation for the tunnel anti-freezing design after adopting the average temperature value of the coldest month in the region.
(4) The length of anti-freezing defense fortunnel structures in the cold area can be determined based on the temperature in the tunnel not higher than -15.2 °C, while the length and drainage anti-freezing defense can be determined based on the temperature in the tunnel not higher than -13.8 °C.

REFERENCES

[1] Zhang Chenxi, Xing Dandan, Zhu Yongquan, et al. Study on the Influence of Thermal Potential Difference and Superstatic Pressure Difference on Tunnel Temperature Field in Cold Region[J]. Science Technology and Engineering, 2021, 21 (14):6010–6017.
[2] Sun Keguo, Yang Peng, Chou Wenge, et al, Research on the Temperature Field and the Buried Depth of Drains for Tunnels in Cold Region[J].Journal of Railway Engineering Society, 2017, 34(04):51–57.
[3] Sun Keguo, Xu Yuping, Chou Wenge, et al, On Temperature Field Distribution and the Effects of Surrounding Rock Properties on Tunnels in Cold Regions[J]. Modern Tunneling Technology, 2012, 49 (05): 67–72.
[4] Sun Keguo, Li Si, Xu Weiping, et al, Influence of Thermal Conductivity on Temporal and Spatial Distributions of Temperature Filed in Cold Region Tunnel [J J]. Journal of Southwest Jiaotong University, 2020, 55 (02): 256-264+289.
[5] Li Si, Sun Keguo, Chou Wenge, et al. Influence and Sensitivity Analysis of Surrounding Rock Thermal Parameters on Temperature Field of Cold Region Tunnel [J]. China Civil Engineering Journal, 2017, 50 (S1):117–122.
[6] Yu Li,Sun Yuan, Wang Mingnian, et al. Model and Action Law of Temperature Field of Tunnel in Cold Region Considering Ventilation and Surrounding Rock Condition[J]. Tunnel Construction, 2019, 39 (S2):85–91.
[7] Guo Rui, Zheng Bo, Fang Lin, et al, Model Test Study on Distribution Characteristics of Longitudinal Temperature Field in Tunnels in Cold Regions [J]. Modern Tunneling Technology, 2021, 58(05):129–139.
[8] Ma Zhifu, Yang Changxian. Anti-freezing technology for railway tunnels in cold regions [J].Chinese Railways, 2020(12):74.
[9] Ma Zhifu, Yang Changxian. design standard for thermal insulation and drainage facilities of railway tunnels in cold regions[J].Tunnel Construction, 2019, 39(6):960.

Tunnelling for a Better Life – Yan, Celestino, Thewes & Eberhardt (Eds)
© 2024 The Author(s), ISBN 978-1-032-80042-4
Open Access: www.taylorfrancis.com, CC BY-NC-ND 4.0 license

The impact of landscape belt design inside extra-long highway tunnel on driving comfort: A driving simulation study

Fei Ye
School of Highway, Chang'an University, Xi'an, Shaanxi, China

Jia Liu*
School of Highway, Chang'an University, Xi'an, Shaanxi, China
Department of Bridge Engineer, Hebei Jiaotong Vocational and Technical College, Shijiazhuang, Hebei, China

Wenhao Zhu, Enjie Su, Xiaobao Wen, Xingbo Han, Zhiwei Jiao & Pu Sun
School of Highway, Chang'an University, Xi'an, Shaanxi, China

ABSTRACT: The extra-long highway tunnel shields the surrounding environment, forming a driving environment with monotonous vision and less interference, and long-term driving in an extra-long tunnel has a great influence on driving vision and driving psychology, which is easy to causes visual fatigue and depressive feelings. There are more and more tunnels that are designed with landscape belts to alleviate driving discomfort. However, there are few studies on the landscape design inside tunnel and the mechanism of impact of landscape zones on the human body is unclear. Given this, this paper takes the landscape design scheme of the Qinling Zhongnanshan Highway Tunnel as the benchmark. It adopted the driving simulation test method, taking the driver's pupil and heart rate as indicators to evaluate the impact of landscape belt on driving comfort. The design length and position of the landscape belt in the extra-long highway tunnel were studied. The results show that the maximum length of landscape belt in extra-long highway tunnels should not exceed 3 minutes of driving duration, and the minimum length should not be less than 14 seconds of driving duration; the spacing of landscape belts in extra-long highway tunnels are arranged in a gradually decreasing trend along the tunnel exit direction, which is conducive to increasing driving comfort.

Keywords: Landscape inside tunnel, Driving simulation test, Comfort, Pupil diameter, Heart rate index

1 INTRODUCTION

According to the Statistics Bulletin of the Development of the Transportation Industry in 2022, by the end of 2022, there were 1,752 highway extra-long tunnels in the country with 7,951,100 liner meters (China 2023). The existing specifications refer to tunnels above 3km as extra-long tunnels. With the rapid development of China's highway traffic industry, highway tunnels above 10km are becoming more and more common. Long time's driving in tunnel easily causes visual fatigue, acceleration behaviour and escape psychology, bring hidden dangers to driving safety. Moreover, the inner walls of tunnel generally applied grey-black concrete, and the colour in tunnel is lack of variety, which is easy to cause the driving environment in the tunnel to be monotonous and depressed. Therefore, beginning with the Qinling Zhongnanshan Tunnel, more and more long highway tunnels in our country are decorated with landscape to improve the driving environment inside the tunnel.

In order to study the interaction between landscape and drivers, domestic and foreign scholars have carried out some relevant studies. Vegetation coverage is proportional to drivers' tolerance, and large-area vegetation can improve drivers' driving psychology (Cockowski et al., 2003). When the road environment changes little and vegetation is single, it is easy to cause aesthetic fatigue and driving fatigue conducted by driving simulation experiments (Thiffault et al., 2003). Extensive survey and statistics results of urban roads show that traffic accidents have a large reduction after the improvement of road landscape environment (Mok et al., 2006). The open landscape is the friendliest to driving by analysing driving behaviours as the indicators evaluating driving safety (Antonson et al., 2009). Road environment does have a certain impact on driving behaviours, but a single road condition with beautiful environment will also cause

*Corresponding author: liujialari@163.com

DOI: 10.1201/9781003495505-463

driving distraction (Liu et al., 2009). The landscape types on both sides of the road would bring different driving experience to the driver, but also produce different safety risks by analysing the lateral position and speed of the vehicle (Bella, 2013).

In terms of drivers' physiological characteristics, driving in a single environment will reduce the tension of driving based on the monitoring data of blood pressure and heart rate, but driving in a single environment for a long time will cause certain driving safety problems (Yamakoshi et al., 2009). In order to evaluate the driver's driving state, the methods of auditory test, EEG and ECG index detection were adopted to establish the relationship between the driver's driving state and driving time (Schmidt et al., 2009). The colour brightness of the tunnel entrance had a direct impact on the driver's heart rate, and the proper increase of the heart rate was conducive to the driver's concentration by using the driving simulation experiment method (Tao et al., 2015 a, b).

To sum up, domestic and foreign researches on the interaction between landscape and driver have made some achievements, but they mainly focus on natural landscape, highway landscape and tunnel entrance landscape. However, the research on the influence of landscape design in tunnel on driving comfort is almost in the blank stage. In view of this, based on the design scheme of a extra-long highway tunnel in China, this paper adopts the driving simulation experiment method and uses Eye Tracking Glasses (ETG) and heart rate belt equipment to extract the change rule of the driver's pupil diameter and heart rate when passing through the tunnel, and analyses the design length and design position of the landscape in the tunnel. In order to provide some reference for the landscape design and evaluation of long highway tunnel.

2 SUPPORTED PROJECT OVERVIEWS

Qinling Zhongnanshan highway tunnel has specially set up with three 150-meter-long landscape belts. Through changes in lights and patterns, it creates a "blue sky and white clouds" scene, reducing the driver's monotony in the tunnel and alleviate driving fatigue (Frank et al., 2013; Jensen et al., 1993). The landscape belt inside the tunnel is shown in Figure 1.

Figure 1. Qinling Zhongnanshan tunnel.

3 MATERIALS AND METHODS

3.1 *The experimental schemes of landscape belt*

At present, there is no unified standard for the design position and design length of the landscape belt in the tunnel. The actual design process is relatively random and the driving experience is ignored. Therefore, 2 experiments were conducted intending to study the impact of length and location of the landscape belt on driving experience in the extra-long highway tunnel. The experimental design is as follows:

3.1.1 *Experiment 1*

Based on the basic principles of dynamic vision and traffic psychology, and drawing on the principle of "555" (Jia et al., 2007), with Qinling Zhongnanshan extra-long highway tunnel as a supporting project, two tunnel interior decoration schemes are designed without any decoration and the whole section of blue sky and white clouds decoration in Figure 2. Provide suggestions on the maximum length of the landscape belt and the reasonable design position according to the physiological characteristics of participants.

(a) No decoration

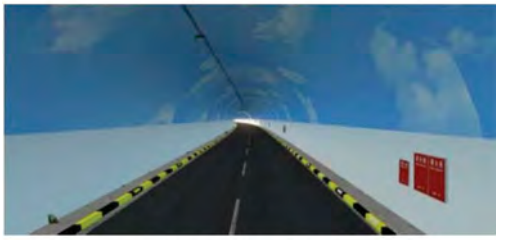

(b) Full decoration

Figure 2. Experiment 1 of landscape design.

3.1.2 *Experiment 2*

The length of this landscape belt of Qinling Zhongnanshan tunnel is 150m. This article uses 150m as a benchmark and considers the driving speed and the driver's dynamic visual characteristics. Three experimental schemes are set, which length of landscape belt are 150m, 300m, and 500m respectively (Figure 3). Each experimental program contains two landscape belts. These schemes are mainly to study the impact of minimum length of landscape belt on driving comfort and safety.

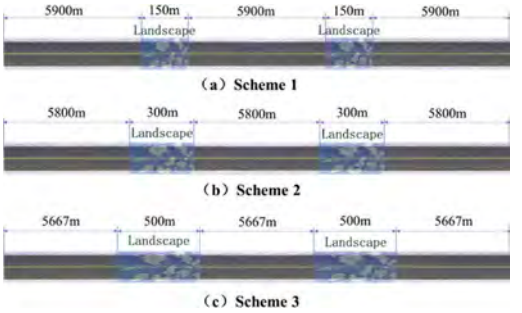

Figure 3. Experiment 2 of landscape design.

3.2 *Experimental installation*

(1) Driving simulator
The experiment uses a self-developed tunnel landscape environment simulation driving simulation system, as shown in Figure 4. The driving simulation experiment system can customize driving simulation scenes, and a random flow of cars will be generated during driving. It greatly restores the real tunnel traffic scene and can simulate the psychological state of real driving to the greatest extent.

Figure 4. Driving simulation equipment.

(2) Eye tracking glasses
In the experiment, the German ETG eye tracker was used to record the participants' eye movement data during driving, as shown in Figure 5. Glasses eye trackers can reduce the interference to participants during the experiment.

Figure 5. Eye tracker.

(3) Heart rate band
In the experiment, a Polar heart rate belt was used to measure the heart rate. The heart rate belt is a Finnish product and reaches the medical level (Figure 6). The heart rate value is a manifestation of the heartbeat, that is, the amplified value of the electrocardiogram (ECG) signal generated by the heartbeat. The electrodes on the chest strap have better anti-interference and are extremely sensitive to ECG signals, so as to obtain accurate heart rate readings.

Figure 6. Heart rate band.

3.3 *Participants*

In this experiment, 20 college students with driving experience were selected as the main subjects. The aesthetic convergence between different groups has been confirmed (Frank et al., 2013; Vodak et al., 1985; Jesen et al., 1993;). Scholar Schroeder H (Schroeder et al., 1981) also pointed out that students' driving feelings can represent the driving feelings of the general public.

3.4 *Experimental process*

(1) Testing resting heart rate
Before the experiment, the participants closed their eyes and sat and rested, and began to test the resting heart rate when they were calm. Each participant tested for 5 minutes, and the average value was taken as the resting heart rate.
(2) Familiar with driving simulation equipment
Inform the participants of the correct operation method of the driving simulator, and ask participants to drive freely for 15 minutes in the road simulation scene, as shown in Figure 7.

Figure 7. Familiarity training of participants.

(3) Eye tracker calibration

After the participants are familiar with the operating methods of the driving simulation system, let them rest for 10 minutes outdoors to restore their normal physical and psychological state. Then perform a three-point calibration of the eye tracker, and the formal experiment can only be carried out after the calibration is qualified. The calibration process is shown in Figure 8.

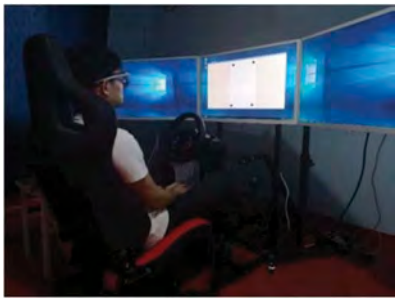

Figure 8. Calibration process of participants.

(4) Formal experiment

After the preliminary work is ready, start the formal experiment. The vehicle started driving 2 kilometres before entering the entrance of the tunnel and stopped after passing through the tunnel. Participants scored based on driving experience. After resting for 15 minutes, continue to the next tunnel driving scene. The test process is shown in Figure 9.

Figure 9. Test scenario.

4 RESULTS AND DISCUSSIONS

4.1 *Maximum length and reasonable position of landscape belt*

(1) Eye tracking data analysis

The eye tracking glasses records data every millisecond thus generating a large amount of data, so the average pupil diameter every 6 seconds is taken as a recording point. The average pupil diameters of the 20 participants in the two scenarios are shown in Figure 10.

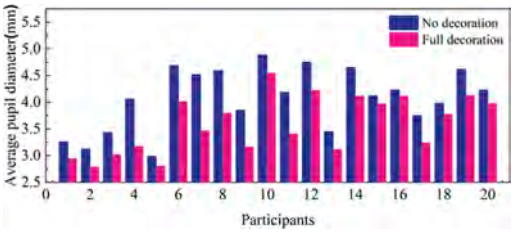

Figure 10. Average pupil diameter of participants.

Due to individual physiological differences, the average pupil diameters of the participants are different, however, the pupil diameter in fully decorated tunnel environment is generally smaller than that in an undecorated tunnel environment. Therefore, full decoration is more comfortable than no decoration (Murata et al., 2001; Choi et al.,2015).

In order to study the driving comfort of the two schemes, the pupil diameter change rate is used for analysis. According to the existing research results (Zhao et al., 2007; Pan et al., 2006; Pan et al., 2005; Zhen et al., 2003), the threshold value of the pupil area changes rate U when the driver is comfortable, tight and very tight during driving is defined as: ①When comfortable, U<20%; ②When nervous 20%≤U≤40%; ③when very nervous U>40%. The shape of the human pupil is approximately circular, so the pupil diameter change rate D_i is used instead of the pupil area change rate for driving safety analysis, which is calculated by the following formula (1).

$$D_i = \frac{d_i - \bar{d}}{\bar{d}} \times 100\% \quad (1)$$

Where, D_i is the pupil diameter change rate of the participant when driving in the tunnel at all times (%); $d_i$is the pupil diameter of the participant when driving in the tunnel at all times (mm); $\bar{d}$ is the average pupil diameter of the participant without driving (mm).

So adjust the driving comfort threshold to: ①When comfortable, D_i<10%; ②When relatively nervous, 10%≤D_i≤18%; ③when very nervous, D_i>10%.Through the analysis of experimental data, it is found that the pupil diameter changes of different participants are consistent, so the pupil data of participant 2 will be analysed below. As shown in Figure 11, the pupil diameter change rate (D_i) of no decorated environment is larger than full decoration, and most of the time, the pupil change rate exceeded 10% for both schemes and even exceeded 18%. indicating that the participant is already in a very nervous and depressed state, so both design schemes have safety hazards.

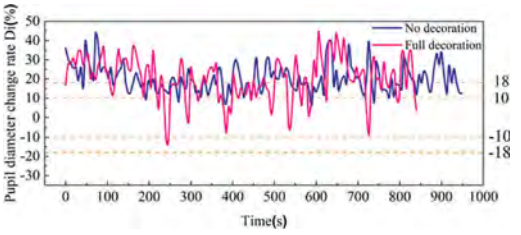

Figure 11. Pupil diameter change rate of participant 2.

In order to further study the changes in the pupil diameter of the participants, the pupil diameter growth rate E_i was used to analyse the relationship between the pupil diameter growth of the participants and the driving duration. The calculation formula is formula (2), and the result is shown in Figure 12.

$$E_i = \frac{e_{i+1} - e_i}{t_{i+1} - t_i} \times 100 \qquad (2)$$

Where, E_i is the pupil diameter growth rate of the participant when driving in the tunnel at time i, (%); e_{i+1} is the pupil diameter of the participant when driving in the tunnel at time $i+1$, (mm); e_i is the pupil diameter of the participant when driving in the tunnel at time i, (mm); $t_{i+1} - t_i$is driving duration, taking 6s in this experiment.

No decoration scheme: After entering the tunnel, the pupil diameter growth rate of the participants fluctuates greatly, and it decreases after 1 minute and 24 seconds. At 6 minutes 18 seconds, the pupil diameter growth rate fluctuates again and continues to 8 Minutes. At 10 minutes and 24 seconds, the growth rate of pupil diameter begins to have large fluctuations until leaving the tunnel exits.

Therefore, it can be considered to set up a landscape belt aiming to reduce the driver's feeling of depression and relieve the driving fatigue where the pupil diameter fluctuates greatly. When entering the tunnel, a landscape belt should be set up to buffer the driving pressure caused by the huge differences in visual environment inside and outside the tunnel. When traveling to the position of 6 minutes 18 seconds, it is recommended to set up a landscape belt. When setting landscape belt in the middle and rear part of the extra-long tunnel, it is recommended that the spacing between landscape belts be gradually reduced.

Full decoration scheme: After entering the tunnel, the driver's pupil diameter growth rate changes slightly; at 1 minute and 42 seconds, the pupil diameter fluctuates briefly. At 3 minutes and 24 seconds, the pupil diameter growth rate begins to change drastically, lasting to 4 minutes and 36 seconds. At 7 minutes and 48 seconds, there was a sudden change again until 8 minutes and 42 seconds. The last big fluctuation occurred at 14 minutes and 42 seconds, until leaving the tunnel exit.

It can be concluded that even if tunnel walls decorated with murals are beneficial to driving comfort, driving fatigue and depressed state will still occur after long-term driving. Therefore, it is not recommended to driving in tunnel decorated with mural exceeding 3 minutes.

Comparing the two design schemes, it is found that when entering the tunnel, the pupil diameter of the full decoration is significantly smaller than that of no decoration, indicating that the use of mural decoration when entering the tunnel will increase driving comfort. Taking into account the "black hole effect", drivers not only need to adapt to changes in light and darkness, but also need to focus on observing the

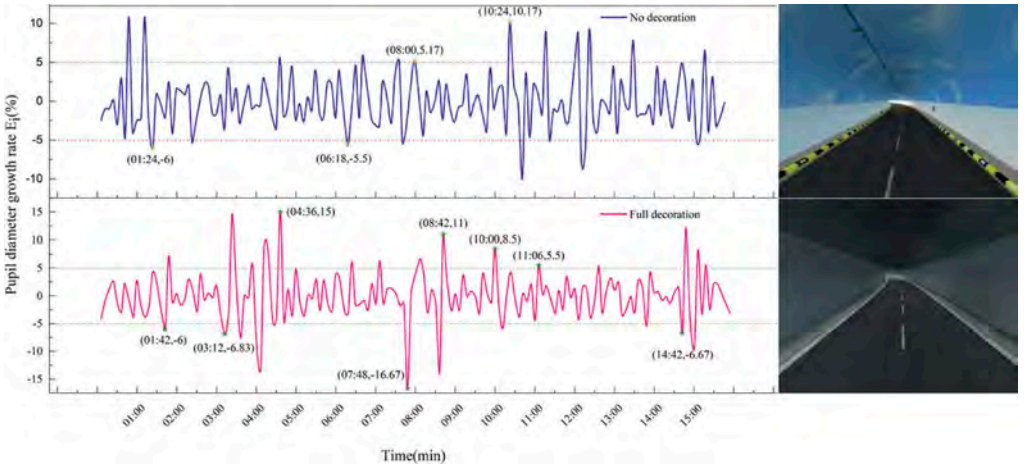

Figure 12. Growth rate for pupil diameter of participant 2.

linearity and road conditions of the road surface, and process various information in a short period of time. Murals would increase the amount of information for driver. It is recommended not to use murals with too bright colors and complex textures at the entrance of the tunnel.

(2) Heart rate data analysis

The heart rate belt records data once every second, and we take the average heart rate every 6 seconds as a recording point. Through data processing, we find that the heart rate change trends of participants are roughly similar. Therefore, the heart rate data of participant 2 will be analysed below. Figure 13 shows the heart rate and heart rate growth rate of participant 2 in the no decorated and fully decorated tunnel environment. It can be seen that in most of the time, the heart rate of the whole section of blue sky and white cloud decoration is lower than that of no decoration.

It also can be seen from Figure 13 that the heart rate growth rate of the no decorated (calculated by formula 3, and the absolute value) is significantly greater than that of the full decorated solution. Whether it is an no decorated or fully decorated tunnel environment, the heart rate growth rate of participants is relatively large. When the heart rate growth rate is greater than 20%, there are already a certain driving safety risk.

$$N_i = \frac{n_{i+1} - n_i}{t_{i+1} - t_i} \times 100 \qquad (3)$$

Where, N_i is the heart rate growth rate of the participant when driving in the tunnel at time i, (%); n_{i+1} is the heart rate of the participant when driving in the tunnel at time $i+1$, (bmp); n_i is the heart rate of the participant when driving in the tunnel at time i, (bmp); $t_{i+1} - t_i$is driving duration, taking 6s in this experiment.

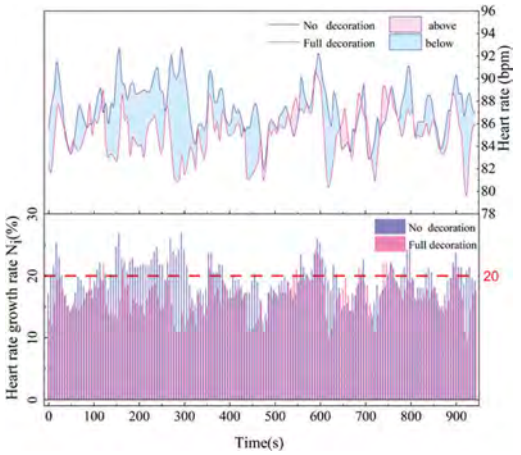

Figure 13. Heart rate curve of participant.

4.2 *Minimum length of landscape belt*

Through data processing, we find that the pupil diameters of participants are roughly similar. Figure 14 shows the pupil 2diameters of participant 2 of each scheme in experiment 2.

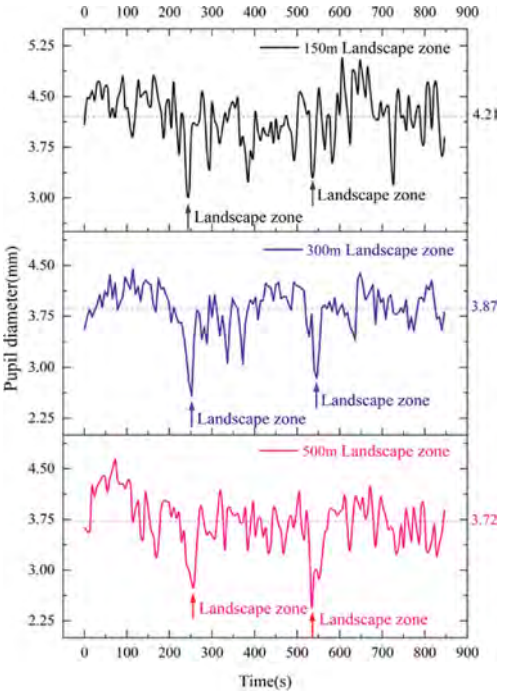

Figure 14. Pupil diameter of participant for different length landscape.

The average pupil diameter of participant 2 in the scheme 1 is 4.2mm, the second scheme is 3.9mm, and the third scheme is 3.7mm. Scheme 1 has the largest pupil diameter, so it is less comfortable than schemes 2 and 3.

In order to analyze driving safety, the normal pupil diameter of the person is measured to be 3mm, and the change rate curve of the pupil diameter is calculated as shown in Figure 15.

It can be seen from Figure 15 that the pupil diameter change rate is the highest under a 150m landscape belt, and most of the time is above 18%. 500m landscape belt is second highest, and most of the time lies between 10% and 18%. 300m landscape belt has the lowest pupil diameter change rate, and most of the time below 10%.

Further analyze the participant's pupil diameter growth rate, as shown in Figure 16. It can be seen that the fluctuation range of the pupil diameter growth rate of scheme 2 and scheme 3 is smaller than that of scheme 1.

It can be seen from experiment 2 that in the 18-kilometer tunnel, the impact of landscape belt of driving comfort with a length of 300m (travel time

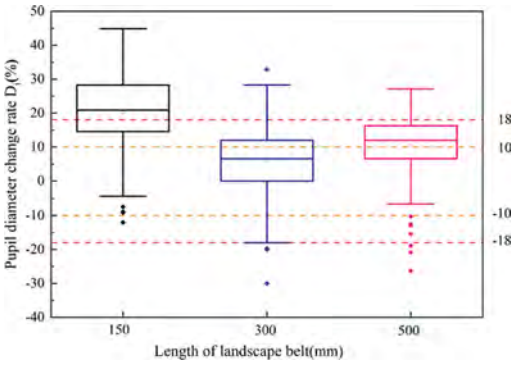

Figure 15. Pupil diameter change rate of participant for different length of landscape.

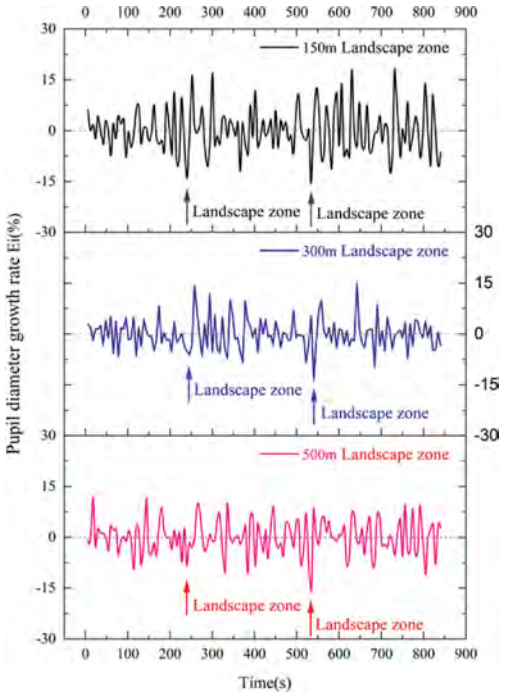

Figure 16. Growth rate for pupil diameter of participant for different length landscape.

of about 14s) and 500m (travel time of about 23s) is better. Landscape belt with a length of 150m has lower driving comfort and a large rate of change of pupil diameter, which poses certain safety risks.

5 DISCUSSION

Analysis of the results of experiment 1 shows that the pupil diameter of drivers in the tunnel varies. When entering the tunnel, pupil diameter changes dramatically and lasts for some time. Pupillary behavior is closely related to psychological stress (Pedrotti et al., 2014). In addition, there is a corresponding relationship between pupil diameter change and visual comfort. The relative variation of pupil diameter is smaller when visual is comfortable (Tian et al., 2020). Therefore, it is suggested to set up a landscape belt at the tunnel entrance to alleviate the huge visual environment difference between the inside and outside the tunnel and alleviate the driver's sense of visual blockade. With the increase of driving time in the tunnel, drivers' escape psychology will gradually increase, and bad mood will become more obvious. It is suggested that the design position of the landscape belt in the tunnel should be arranged at a gradually decreasing distance, and the design location of the landscape belt at the rear of the tunnel should be more compact than the landscape design location in the front half of the tunnel.

It can be concluded from the results of experiment 1 that the setting length of landscape belt should not exceed the driving time of 3min.

The results of experiment 2 show that scheme of 300 and 500 significantly alleviated visual discomfort relative to 150m, while the scheme of 300 perform better than 500. Therefore, it is recommended that the minimum length of the landscape belt in the long tunnel is about 300m, and the driving time can be 14s according to the tunnel speed limit of 80km/h. According to the experimental conclusions, the recommended setting lengths of landscape belts in tunnels with different speed limits are shown in Table 1.

Table 1. Recommended length of landscape in extra-long tunnel.

Tunnel speed limit (km/h)	60	70	80	90
Minimum length of landscape strip (m)	230	270	310	350
Maximum length of landscape belt (m)	300	350	400	450

6 CONCLUSIONS

Based on the Qinling Zhongnanshan Tunnel in Shaanxi Province, two experiments were designed to study the design location and design length of the landscape belt in the extra-long tunnel. The following conclusions were drawn:

(1) Whether tunnel environment is no decoration or full decoration, there is certain safety risks, it is recommended that the same landscape decoration should not exceed 3 minutes of driving time;
(2) It is suggested that necessary decorations should be carried out when entering the extra-long tunnel. As the driver's psychological unease and irritability will increase with driving time in the tunnel, it is suggested that the decorative spacing of landscape belts should be arranged in a decreasing trend;

(3) In the 18-kilometer-long tunnel, recommended length of the landscape belt is 300m (driving duration is about 14s) to 500m (driving duration is about 23s), which could better improve driving comfort. Therefore, it is recommended that the minimum length of the tunnel scenic belt is not less than 14s driving duration.

ACKNOWLEDGMENTS

The authors gratefully acknowledge the financial support provided by the National Natural Science Foundation of China (No. 52078046).

REFERENCES

China, M.O.T., 2023 Transportation overview. https://www.mot.gov.cn/jiaotonggaikuang/201804/t20180404_3006639.html.

Cackowski JM, Nasar JL, 2003. The Restorative Effects of Roadside Vegetation: Implications for Automobile Driver Anger and Frustration. Environment & Behavior, 35(6): 736–751.

Thiffault P, Bergeron J, 2003. Monotony of road environment and driver fatigue: a simulator study. Accident Analysis & Prevention, 35(3): 381–391.

Mok J.H, Landphair H.C, Naderi J.R, 2006. Landscape improvement impacts on roadside safety in Texas. Journal of Architectural Engineering, 78(3): 263–274.

Antonson H, Mårdh S, Wiklund M, et al, 2009. Effect of surrounding landscape on driving behaviour: A driving simulator study. Journal of Environmental Psychology, 29(4): 493–502.

Liu Y.C, Wu TJ, 2009. Fatigued driver's driving behavior and cognitive task performance: Effects of road environments and road environment changes. Safety Science, 47(8): 1083–1089.

Bella F, 2013. Driver perception of roadside configurations on two-lane rural roads: Effects on speed and lateral placement. Accident Analysis & Prevention, 50(JAN): 251–262.

Yamakoshi T, Rolfe P, Yamakoshi Y, et al, 2009. A novel physicological index for Driver's Activation State derived from simulated monotonous driving studies. Transportation Research Part C Emerging Technologies, 17(1): 69–80.

Schmidt EA, Schrauf M, Simon M, et al, 2009. Drivers' misjudgement of vigilance state during prolonged monotonous daytime driving. Accident Analysis & Prevention, 41(5): 1087–1093.

Tao P.P, Shang T, 2015. Landscape color analysis of tunnel entrance based on heart rate index. Journal of PLA University of Science and Technology (Natural Science Edition), 16(05): 471–475.

Tao P.P, Shang T, Zhang H, 2015. Effect of landscape color on drivers' heart rate at the entrance of highway tunnel. Science, Technology and Engineering, 15(14): 219–223.

Frank S, Fürst C, Koschke L, et al, 2013. Assessment of landscape aesthetics—validation of a landscape metrics-based assessment by visual estimation of the scenic beauty. Ecological Indicators, 32: 222–231.

Jensen F.S, 1993. Landscape managers' and politicians' perception of the forest and landscape preferences of the population. Forest & Landscape Research, 1(1): 79–93.

Jia ZR, Guo ZY, 2007. "555" principle and its application in Highway landscape design. Highway, 2007(10): 214–217.

Frank S., Furst C., Koschke L., et al. Assessment of landscape aesthetics—validation of a landscape metrics-based assessment by visual estimation of the scenic beauty[J]. Ecological Indicators, 2013, 32: 222–231.

Vodak M.C., Roberts P.L., Wellman J.D., et al. Scenic impacts of eastern hardwood management[J]. Forest Science, 1985, 31(31): 289–301.

Jensen F. S. Landscape managers' and politicians' perception of the forest and landscape preferences of the population[J]. Forest & Landscape Research, 1993, 1 (1): 79–93.

Schroeder H., Daniel T. C. Progress in Predicting the Perceived Scenic Beauty of Forest Landscapes[J]. Forest Science, 1981, 27(1): 71–80.

Murata A, Uetake A, Otsuka M, et al. Proposal of an index to evaluate visual fatigue induced during visual display terminal tasks [J. International Journal of Human-Computer Interaction,2001,13(3):305–321.

Choi J H, Zhu R. Investigation of the potential use of human eye pupil sizes to estimate visual sensations in the workplace environment[J]. Building and Environment, 2015, 88:73–81.

Zhao L, Hu J, 2007. The Eye Tracking and Driving Behavior. International Conference on Transportation Engineering.

Pan XD, Du ZG, Jiang H, et al, 2006. Experimental study on the relationship between driver's heart rate and blood pressure fluctuation and highway alignment in mountainous area. Ergonomics, (02): 16-18+30.

Pan XD, Yang Z, Zhu ZH, 2005. Relationship between driver's heart rate and blood pressure and curve radius of mountain road. Journal of Tongji University (Natural Science Edition), 2005(07): 900–903.

Zhen K, 2003. Research on highway alignment based on driver's psychophysiological response. Beijing University of Technology.

Pedrotti M, Mirzaei MA, Tedesco A, et al. Automatic stress classification with pupil diameter analysis[J]. International Journal of Human-Computer Interaction, 2014, 30(3): 220–236.

Tian H, Guan T, Cai M. Evaluation model of VDT visual comfort based on pupil diameter[J]. Laser Optoelectron, 2020, 57(15): 300–306.

Tunnelling for a Better Life – Yan, Celestino, Thewes & Eberhardt (Eds)
© 2024 The Author(s), ISBN 978-1-032-80042-4
Open Access: www.taylorfrancis.com, CC BY-NC-ND 4.0 license

Full life cycle multi-hazard scenarios and structural response analysis of metro shield tunnels

Tongsheng Yu, Zhiguo Yan* & Hehua Zhu
State Key Laboratory of Hazard Reduction in Civil Engineering, Tongji University, Shanghai, China

ABSTRACT: The article proposes a method to construct a multi-hazard scenario for the whole life cycle of subway shield tunnels based on a large amount of hazard and defect research data. Taking the tunnel health state field and sudden hazard scenarios as the basic multi-hazard scenario framework, it focuses on summarizing the sudden hazard scenarios that metro shield tunnels may face during the whole life cycle, and gives the determination methods for different tunnels in combination with Bayesian theory. Subsequently, a simplified multi-hazard scenario is employed to analyze the tunnel's structural response. The computational findings reveal that accounting for tunnel defects results in greater structural damage. Moreover, the structural damage is significantly amplified when multiple hazards effects are taken into account, thus underscoring the importance of considering multi-hazard scenarios in the analysis of structural damage.

Keywords: Metro Shield Tunnels, Multi-hazard Scenarios, Structural Analysis

1 INTRODUCTION

MTR tunnels are susceptible to various hazards throughout their operational lifespan, including progressive hazards and material deterioration that occur over time. Additionally, sudden hazards such as earthquakes, train impacts, internal and external explosions, and fires pose significant threats to both the structural integrity of the tunnel and the safety of MTR operations. While numerous studies have focused on analyzing structural damage caused by specific hazards or conditions, the reality often involves a more complex multi-hazard scenario.

On the one hand, as the service time of the tunnel increases, progressive defects and material deterioration will occur in the tunnel structure. At this time, the ability of the structure to resist hazards will be reduced to different degrees compared with the initial period of tunnel construction. For example, Wang et al. (2021) and Liu et al. (2022) investigated the seismic capacity of a tunnel structure considering segment dislocation and material deterioration, respectively, and the results showed that the load carrying capacity of a tunnel in less than optimal health is significantly affected. On the other hand, Hazard scenarios in which multiple sudden hazards act simultaneously or successively on the structure within a short period of time cannot be ignored. Hazard scenarios of this kind have been studied more for superstructures, the most typical case is the fire after an earthquake (Kamath et al., 2015). As for tunnel structures, there are similar cases. For example, the Montreal subway tunnel fire in Canada in 1971 was a typical multi-hazard accident in which the subway collided with the tunnel wall and then caused a fire, and the Baocheng Railway fire in China in 2008 was a continuous hazard accident in which an earthquake indirectly led to a fire, etc. Hazard scenarios such as the above are subjected to multiple forms of hazard loading within a short period of time, including impact, high temperature, cyclic loading and unloading, etc., and the resulting structural damage is usually much larger than that of the case of considering individual hazards. Unfortunately, there has been limited research in this area thus far.

To address this deficiency, a method for constructing multi-hazard scenarios for the whole life cycle of subway shield tunnels is firstly proposed based on a large amount of research data on hazards and defects. Subsequently, it focuses on summarizing the sudden hazards scenarios in the multi-hazard scenarios and gives the method of determining the sudden hazards scenarios for different tunnels. Finally, the damage form and mechanical response of tunnel structure under multi-hazard scenarios are analyzed through a simple case study.

*Corresponding author: yanzguo@tongji.edu.cn

DOI: 10.1201/9781003495505-464

2 FULL LIFE-CYCLE MULTI-HAZARD SCENARIOS FOR METRO SHIELD TUNNELS

Depending on the duration and intensity of hazards, the hazard scenarios in metro tunnels can be categorized into two main types. The first type involves progressive defect and material deterioration that persist throughout the tunnel's life cycle. This type is characterized by low-intensity hazard loads occurring over a short period but persisting throughout the operational cycle. The second type comprises catastrophic loads resulting from natural or accidental factors, such as earthquakes, explosions, fires, vehicle impacts, and combinations thereof forming a catastrophic chain. These events have high-intensity impacts occurring over a short duration, causing significant damage to the structure. However, the probability of their occurrence is extremely low, typically happening once or twice during the tunnel's entire life cycle. Moreover, the two types of hazard loads are essentially uncorrelated. Therefore, the multi-hazard scenario for the full life cycle of a metro tunnel can be represented as a coupled tunnel health state field combined with sudden hazard loads, as depicted in Figure 1.

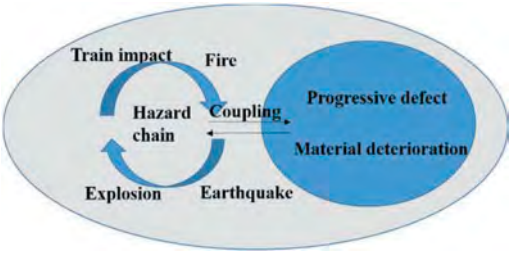

Figure 1. Multi-hazard scenarios for metro shield tunnels.

2.1 *The tunnel state health field*

The description of the tunnel health state field primarily focuses on progressive defect states and material deterioration. Progressive defects encompass longitudinal uneven settlement, radial convergence, cracking (cracks and breaks), misalignment, and water seepage in tunnels. A comprehensive analysis of the parametric state of each defect is provided in an article authored by the same author (Yu et al., 2023). It presents a methodology for generating a progressive defect state field using random field theory. This field serves to describe the potential defect conditions in a tunnel under construction or predict future defect conditions during operation. Figure 2 illustrates a collection of random tunnel condition fields generated for a tunnel under construction, utilizing geological parameters and similar tunnel condition data.

The material deterioration state of shield tunnels encompasses concrete carbonation, tube sheet reinforcement corrosion, and joint bolt corrosion. Among the various joints in shield tunnels, bolts are considered the weakest link, and therefore, bolt corrosion serves as a reference indicator for tunnel deterioration (Liu et al.,2023). Specific strength and cross-sectional variation models for bolt corrosion over time can be found in the literature sources of Ricker (Ricker, 2010).

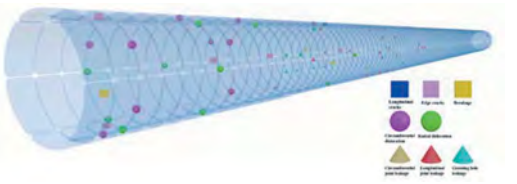

Figure 2. Three-dimensional view of the progressive defect state field.

2.2 *Tunnel sudden hazard scenarios*

In tunnels, there are two primary types of sudden hazard scenarios: single hazards and chains of multiple hazards. While individual hazards have been extensively studied, there is relatively limited research on defining hazard chains, their development patterns, and the magnitudes of hazard loads. A total of 61 cases were investigated and, based on the results, the following hazard chains and typical cases are summarised in Table 1. All case data have been uploaded to the website: https://github.com/yutongsheng/Statistics-of-accident-cases-in-tunnels.git. Based on the above case characteristics, sudden hazards scenarios are categorized into two main types, namely, individual hazards and hazard chains, according to the types of hazards involved and their spatial and temporal distribution characteristics. Among them, the Hazard chain scenarios mainly cover the following two situations. One is that a certain kind of hazard leads directly or indirectly to another kind of hazard. For example, a train derailment impact causes a carriage fire. The other type of scenario is that one type of hazard is repeated in different spaces at the same time, and at the same time there is a causal relationship between them. For example, a fire in a single carriage ignites other carriages or even other trains. The nodes in these hazard chains include earthquakes-(EA), explosions(EX), collision of train (CO), and fires. Due to the substantial variations in spatial distribution and power of the hazard loads, they are further categorized as single carriage fires(SCF), multi-carriage fires(MCF), and multi-train fires(MTF).

Summarizing the data in Table 1, based on historical hazard data, the form of action of sudden hazards contains a total of four individual sudden hazard loads and seven hazard chain loads. Figure 3 counts the percentage of all cases involving the number of different hazard chain nodes, 43.3% of the cases involve only one hazard chain node, and 56.7% of the cases involve more than two hazard chain nodes. This also demonstrates the necessity of considering chained hazard occurrences in multi-hazard scenarios.

Table 1. Typical sudden-onset hazard chain scenarios for shield tunnels.

Hazard scenarios	Count	Typical cases
EA	3	In 1985, the 7.8 magnitude earthquake in Mexico caused structural damage to the subway tunnels.
EX	5	In 2004, terrorist bombings inside the Moscow metro.
SCF	17	In 1994, fire in the shield machine of the Danish metro tunnel, damaging 16 rings of pipe segments.
CO	1	In 1982, Derailment and wall crash on Washington DC subway, USA
EX→SCF	1	In 1981, New York underground, fire after motor failure causes explosion.
SCF→EX	1	In 1996, Fire and explosion in Washington DC Metro.
SCF→MCF	27	In 2003, Daegu underground line 1 fire,destroying all trains.
CO→SCF	1	In 1972, fire in Alexanderplatz underground tunnel, Germany, after derailment and collision with wall.
SCF→MCF →MTF	1	In 2005, a train on line 13 of the Paris metro caught fire, spreading to another train.
CO→SCF →MCF	2	In 1971, the Montreal underground collided with a tunnel, causing a short circuit and a fire that destroyed 24 cars.
CO→SCF→ MCF→ MTF	1	In 1945, London Metro tunnel train collision and fire, resulting in damage to two trains.

Note 1: The article considers only hazards that have an impact on the structure.
Note 2: See above for a description of the hazard chain nodes.

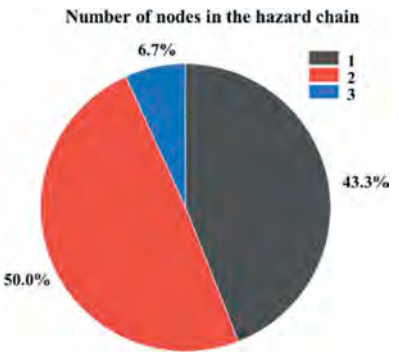

Figure 3. Percentage of number of nodes in different hazard chains.

The data in Table 1 covers the historical cases of major accidents in metro shield tunnels. However, due to the limited number of major hazard cases occurring in metro shield tunnels, the author also investigated a number of hazard cases including road tunnels, railroad tunnels, and metro stations. To add the possible but not historical case situations in subway tunnels, the relevant cases and Hazard scenarios are summarized in Table 2. According to the results of the above analysis, all the sudden hazards scenarios chain relationships that the subway shield tunnels may face are summarized in Figure 4, which contains a total of 6 Hazard scenarios chains, according to which all the possible sudden hazards field scenarios in the subway shield tunnels can be obtained. It should be noted that explosions are categorized into explosions from inside the tunnel and explosions from outside the tunnel according to the location of the source, which are represented by EX-in(Explosion internal) and EX-ex (Explosion external), respectively. As well as although there is a fire → explosion scenario in the aforementioned case study, the subsequent hazard scenarios do not consider this hazard chain. As the main hazard effect affecting the structure in this case is fire, the impact loads caused by the explosion of electromechanical equipment are small and have a limited effect on the structure.

Table 2. Supplement to possible sudden hazards scenarios of hazards.

Hazard type	Hazard scenarios	Existing cases or typical scenarios
Single hazard	Explosion (source outside tunnel)	Bomb attacks against shallow tunnels; explosion of adjacent gas pipeline
Hazard Chain	EA→CO	The 2008 Baocheng Railway was indirectly caused by the Wenchuan earthquake, which led to a train derailment and wall crash, followed by a massive fire and explosion. Subway trains are also subject to such risks.

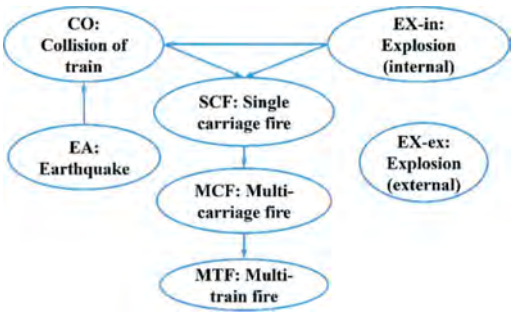

Figure 4. Hazard scenarios and their chain triggering relationships.

Sudden multi-hazard scenarios that need to be considered in metro shield tunnels are given in Figure 4. However, for tunnels with different operating conditions, the types of hazards that need to be considered

may be different. To address this issue, this paper provides a Bayesian network to determine the sudden hazards scenarios that need to be considered specifically for a particular tunnel. The details are shown in Figure 5, which shows that the network consists of eight input node parameters and seven hazard response nodes. For deterministic tunnels, i.e., where all input conditions are known, there are only two scenarios: either some kind of sudden hazard scenario needs to be considered or not. In other words, there is no ambiguity or probability in the deterministic process. In addition, the conditional probabilities of the Bayesian network are determined based on the propagation rules, which are shown in Table 3. Once the values of the eight input parameters are determined, the Bayesian network can be utilized to obtain the corresponding unexpected hazardous situations that need to be considered for that particular tunnel. This approach allows for a more targeted and accurate assessment of the potential hazards facing the tunnel.

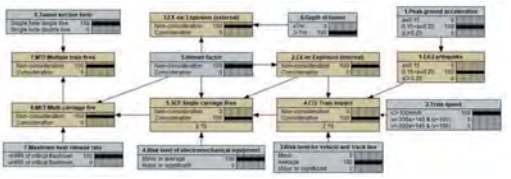

Figure 5. Bayesian network diagram for determining sudden hazards scenarios.

With regard to the rules for taking the conditional probabilities in Table 3, there are several elements that need to be clarified.

(1) EX-in and EX-ex only consider the situation caused by human factors, which are the explosion scenarios caused by terrorist attacks and deliberate retaliation against the community and other factors. The reason for this is that the explosion load caused by the failure of electromechanical equipment is small, much smaller than the impact load caused by the human carrying of explosives, and is not considered for scenarios in which the tunnel structure is the main object of analysis.

(2) Train derailment cases can have various causes, including earthquakes, endogenous explosions, vehicle-related factors (such as wheelset wear, bearing failures, brake cylinder failures), and rail line-related factors (such as track unevenness, turnout damage, rail breakage, tie-breaker damage, ballast bed failure, external barrier intrusion, etc.). Existing standards provide methods for quantitative risk evaluation in such situations. The risk evaluation system for vehicles and rail lines, categorized into four grades (major, significant, average, and minor), can be found in the Measures for the Management of Safety Risk Rating and Control and Hidden Trouble Detection and Management for Urban Rail Transportation Operations (Ministry of Transport of the People's Republic of China, 2019). Figure 5 illustrates the classification rules for train derailment events based on different risk levels, peak ground vibration acceleration, and train running speed. The values for whether to consider derailment

Table 3. Bayesian network node probability propagation rules.

Hazard node	Influencing factors	Probability Transfer Calculation Rules
EA	Regional seismic defense conditions and structural self-resonance periods	Calculate the peak acceleration to be considered according to Code for Seismic Design of Urban Rail Transit Structures (GB 50909-2014)
EX-in	Human factor	Refers to situations of hazards caused by subjective human factors, such as terrorist attacks, deliberate retaliation against society, etc. It is mainly determined by the current level of social stability.
EX-ex	(1) Tunnel depth (2) Human factors	(1)The impact of human factors is the same as the EX-in node. (2) Tunnel depth less than 7m explosion will have an impact on the structural safety of the tunnel, more than 7m is considered to have no effect(Yang et al., 2010) .
CO	(1) Peak seismic acceleration (2) Risk level of vehicle and track line (3) Operating speed (4) EX-in	Whether or not the CO case needs to be considered is shown in Figure 6
SCF	(1) CO (2) Risk level of electro-mechanical equipment (3) Human factors (4) EX-in	Single carriage fire conditions need to be considered when one of four scenarios exists: consideration of human factors, consideration of CO, consideration of EX-in, or high or significant risk level of electromechanical equipment
MCF	(1) SCF (2) Human factors; (3) Maximum heat release rate	(1) MCF is considered when SCF needs to be considered and the maximum heat release rate is greater than the critical power for booming (2) MCF is considered when human factors are considered.
MTF	(1)Tunnel section form (2)MCF	Consider MTF only if you have a single hole with two lines and MCF is considered

events, assuming an average risk level, can be obtained based on the results of Li et al. (2021).

(3) For the MCF node, if the SCF condition needs to be considered, the determination of whether a multi-carriage fire (MCF) needs to be considered depends on whether the maximum heat release rate exceeds the critical heat release rate that can cause the carriage to ignite with a boom. If the maximum heat release rate is below the critical threshold, it is considered that the fire can be controlled within a short period of time and will not result in a multi-carriage fire. Conversely, if the maximum heat release rate exceeds the critical threshold, the possibility of a multi-carriage fire needs to be considered. The calculation of the critical heat release rate for specific carriage ignition can be conducted using the method described by Zhou (2021). The value of the maximum heat release rate can be calculated based on the total amount of combustible materials in the vehicle and the time it takes to reach the maximum heat release rate (Li et al., 2018). However, in human-caused fire scenarios, where additional fuel is usually present, the heat release rate often exceeds the critical threshold for the occurrence of a roaring ignition, and thus the consideration of a multi-carriage fire is necessary.

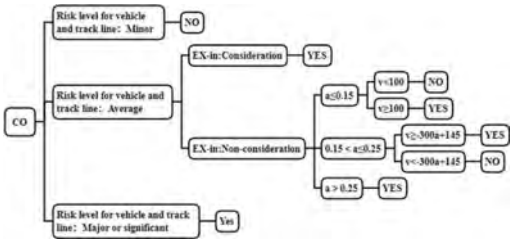

Figure 6. Bayesian network probability transfer rule for train derailment events.

3 CASE STUDIES

Based on the previous analysis, it can be seen that the multi-hazard scenarios that a metro shield tunnel may face throughout its lifetime are extremely complex, but the basic framework is in the form of a tunnel structural health state field superimposed on a sudden hazards field. In this section, the structural response of the tunnel in different health states as well as hazard chain scenarios are considered separately with fire as the main type of sudden hazard. The structural health state simulation includes the tunnel joints opening, the presence of cracks in the tube segments and the material deterioration, while the hazard chain only includes the case where the structure is subjected to train impact followed by a fire, and the specific analyzed cases are shown in Table 4.

The fire load adheres to the BART curve, with a peak heat release rate ranging from 10 to 20 MW, dependent on the specific metro fire scenario under consideration(Li and Ingason, 2016; Shi et al., 2020). The maximum temperature threshold is set at 500°C, and for simplicity, only the capped and adjacent blocks are deemed subject to heating. The numerical calculation model used in the article only considers 3 rings, the width of the tube segment is 1.5m, the section of the tube segment is shown in Figure 7, and the form of through-seam assembling is adopted. The outer diameter of the tunnel is 6.1m, the inner diameter is 5.4m, the depth of the tunnel is 20m, the groundwater is located at 4m below the surface, and the soil pressure is calculated according to the way of soil-water integration. The concrete model is C50, solid unit is used for simulation, the model of this structure adopts the built-in concrete damage plasticity model in Abaqus, the plasticity parameter is shown in Table 5. The compressive and tensile stress-strain relationships are referenced from Appendix C of the Code for the design of concrete structures GB 50010-2010 (2010). The model only embodies the setting of annular rebar, and does not model the hoop bar, the rebar material adopts HRB400E, the upper layer of The rebar material is HRB400E, the upper layer of rebar is 12φ20, and the lower layer of rebar is 10φ22. The truss unit is used for simulation, and it is connected with concrete by built-in way. The bolts are bent bolts M30, mechanical grade 8.8, simulated using solid units, connected to the concrete by means of bolts with both ends built into the concrete, and pretensioned using the method of adjusting the temperature loads applied to them. The thermal parameters of the materials involved in the subsequent simulations, i.e., the specific heat capacity, thermal conductivity, coefficient of expansion, and mechanical properties of the concrete, reinforcement, and bolts as a function of temperature decrease, are described in detail in the literature (Zhang, 2022) and will not be repeated. The ring and longitudinal joints are simulated in the form of contact surfaces, and the normal direction of the contact surfaces is simulated by “hard contact”, and the tangential direction is simulated by Cloumb friction, with the friction coefficient set to 0.4 (Shi et al., 2022; Shi et al., 2016). The numerical model is shown in Figure 8.

Table 4. Multi-hazard analysis working conditions table.

No.	Simulation of working conditions
Case-1	Consider fire only, BART curve, max. temperature 500°C.
Case-2	Consider joints open and heat intrusion in the joint section in the event of a fire.
Case-3	Consider bolt deterioration with a 1mm diameter reduction and a strength discount of 0.9646, followed by fire
Case-4	Consider the initial cracking, followed by fire
Case-5	Consider structural damage from Case-2 to Case, followed by fire
Case-6	Consider structural damage from Case-2 to Case, followed by train impact fire

Table 5. Plasticity parameters in the concrete damage plasticity model.

Parameter	Value
Dilatation angle	30°
Flow potential offset	0.1
Biaxial to uniaxial compressive ultimate strength ratio	1.16
Unvariable stress ratio	0.667
Coefficient of viscosity	0.01

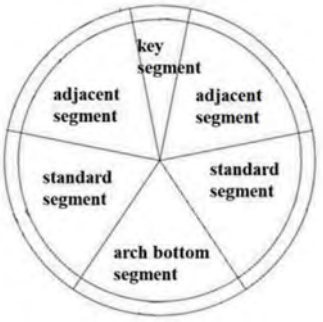

Figure 7. Tunnel section form.

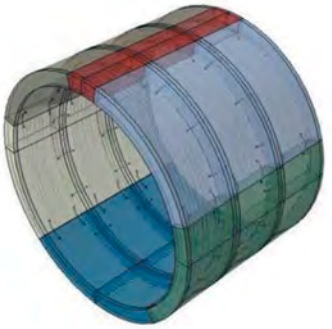

Figure 8. Model schematic.

Figures 9 and 10 compares the temperature field and structural damage with and without joint opening, and it is clear that taking into account the structural base damage has a significant effect on the structural hazard response. The maximum value of concrete compression damage is approximately 0.61 when considering only the fire condition, while the maximum value is approximately 0.90 when all basic structural damage conditions are taken into account.

Comparing the cross-section bending moments of the six cases in Figure 11, it can be seen that the cross-section bending moments under the hazard loading will increase significantly. The different initial damage states also have different effects on the response of the structure at high temperature, and it can be seen that the bending moments of the high temperature response of the structure under the six cases are basically divided into three situations. They are case1, case3 and

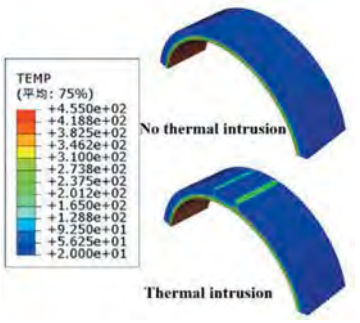

Figure 9. Comparison of temperature fields for case 1 and case 5.

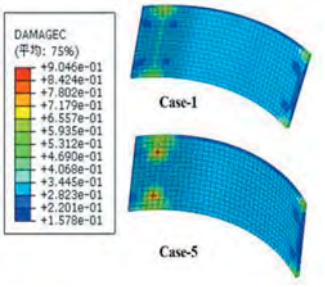

Figure 10. Comparison of damage conditions for case 1 and case 5.

case4 bending moment values are basically the same, case2 and case4 bending moment values are basically the same, and case6 bending moment values are basically the same as case2 and case4 except for the different bending moment values in the interval of 324~342° due to the train impact load. From the above results, it can also be seen that considering the joint opening, the presence of thermal intrusion in the joint portion in the event of a fire has the greatest impact on the high temperature response of the final structure. The reason for this is that the structural damage and bending moments under the six hazard conditions are mainly generated by high temperature effects, and the presence of thermal intrusion will change the temperature field of the structure under high temperature

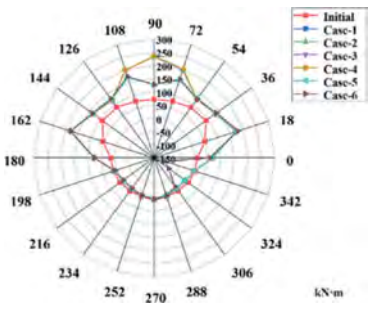

Figure 11. Bending moment for different cases.

loading. While the main impact area of train impact is the standard block, the superimposed impact of the two is essentially smaller because the fire location is mainly the capped block and the adjacent block. Both hazards only affect the damage and structural internal force in the main action region. Similarly, the axial force diagrams for different working conditions in Figure 12 can lead to the same conclusion.

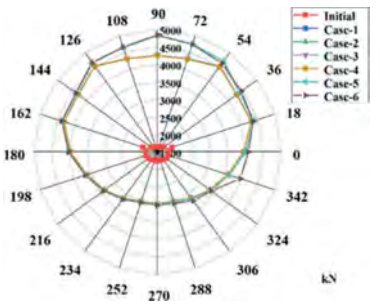

Figure 12. Axial force for different cases.

4 CONCLUSIONS

The article takes the subway shield tunnel structure as the research object, carries out the multi-hazard scenario construction method and structural response analysis research, and mainly obtains the following conclusions.

(1) Based on a large number of hazards and defects research data, the article proposes a method for constructing multi-hazard scenarios during the whole life span of metro shield tunnels. Taking the tunnel health state field and sudden disaster scenarios as the basic multi-hazard scenario framework, it focuses on summarizing the sudden hazard scenarios that metro shield tunnels may face during their whole lifespan, and gives the corresponding determination methods in combination with Bayesian theory.

(2) By conducting a simple case study, the article compares the damage to the structure when considering different multi-hazard scenarios. The calculation results demonstrate that when tunnel defects are taken into account, the structural damage becomes more severe. Furthermore, the structural damage is greater when multiple hazards occur consecutively compared to individual hazards acting alone. This finding highlights the importance of considering multi-hazard scenarios during the analysis of structural damage.

(3) Although the method of determining the multi-hazard scenarios is given, considering the randomness of the hazard loads, the method of taking the value of each hazard load, as well as a variety of hazard loads with correlation, should be further improved.

(4) The case studies of multi-hazard scenarios given in the article are relatively simple, and a more comprehensive investigation of structural response in multi-hazard scenarios should be carried out at multiple scales, such as materials, components and systems.

REFERENCES

Kamath, P., Sharma, U. K., Kumar, V., Bhargava, P., Usmani, A., Singh, B. & Pankaj, P. (2015). Full-scale fire test on an earthquake-damaged reinforced concrete frame. Fire Safety Journal, 73, 1–19.

Li, J. J., Li, H. W., Luo, S. J., & Zhang, H. (2018). Fire heat release rate of subway train based on a simplified 1-D model. Fire Theory Research, (12), 1623–1627 (in Chinese).

Li, J., Lou, Y., Yang, X., & Jin, X. (2021). Nonlinear seismic analysis of a train-tunnel-soil system and running safety assessment of metro vehicles. Soil Dynamics and Earthquake Engineering, 147, 106772.

Li, Y. Z., & Ingason, H. (2016). A new methodology of design fires for train carriages based on exponential curve method. Fire technology, 52, 1449–1464.

Liu, H., Song, K., Ye, Z., Wang, C., & Liu, H. (2022). Seismic fragility analysis of in-service shield tunnels considering surface building and joint-bolt corrosion. Soil Dynamics and Earthquake Engineering, 162, 107455.

Ministry of Housing and Urban-Rural Development of the People's Republic of China (2010). Code for design of concrete structures GB 50010-2010, China architecture & building press, Beijing (in Chinese).

Ministry of Transport of the People's Republic of China. (2019). Measures for the Management of Safety Risk Classification, Control and Hidden Trouble Detection and Management in Urban Railway Transportation Operations. Traffic and Transportation Regulation, No. 7 (in Chinese).

Ricker, R. E. (2010). Analysis of pipeline steel corrosion data from NBS (NIST) studies conducted between 1922–1940 and relevance to pipeline management. Journal of research of the National Institute of Standards and Technology, 115(5), 373.

Shi, C. H., Wang, Z. X., Liu, J. W., Lei, M. F., Peng, L. M., & Peng, M. (2022). Study on ultimate bearing capacity of shield tunnel based on damage model of concrete. Journal of Central South University (Science and Technology), 53(11), 4310–4325 (in Chinese).

Shi, C., Cao, C., Lei, M., Peng, L., & Ai, H. (2016). Effects of lateral unloading on the mechanical and deformation performance of shield tunnel segment joints. Tunnelling and Underground Space Technology, 51, 175–188.

Shi, C., Zhong, M., Chen, C., Jiao, W., Li, J., Zhang, Y., & He, L. (2020). Metro train carriage combustion behaviors–Full-scale experiment study. Tunnelling and Underground Space Technology, 104, 103544.

Wang, G. B., Wang, Y. J., Mu, J. H., & Sun, F. X. (2021). Seismic Performance Analysis of Shield Tunnel Considering Segment Misalignment. Journal of Railway Engineering Society, 38(3):93–101 (in Chinese).

Yu, T., Zhang, Y., & Yan, Z. (2023). A new generation method of tunnel progressive defect status random field (TPDSRF) for subway tunnel structure. Tunnelling and Underground Space Technology, 141, 105340.

Zhang, T. R. (2022). Tunnel in Fire Research on Thermal Properties and Mechanical Behaviors of Large Shield. Modern Tunnelling Technology, 59(5), 202-211 (in Chinese).

Zhou, Y. L. (2021). Study on the heat release rate of the high-speed train fire. (Doctoral dissertation, Chengdu: Southwest Jiaotong University)

Tunnelling for a Better Life – Yan, Celestino, Thewes & Eberhardt (Eds)
© 2024 The Author(s), ISBN 978-1-032-80042-4
Open Access: www.taylorfrancis.com, CC BY-NC-ND 4.0 license

Research on China's extra-long separate construction tunnel emergency evacuation and rescue technology

Yi Yuan* & Shaohua Chen
China Railway First Survey and Design Institute Group Co., Ltd, Xi' an, China

ABSTRACT: For enclosed and lengthy tunnel projects, disasters can lead to significant economic losses and adverse societal impacts. This is especially true for tunnels exceeding 20 km, where the design of disaster prevention, evacuation, and rescue operations is of paramount importance. China's specialized techniques for tunnel emergency evacuation and rescue have evolved alongside the continuous development of tunnel projects in the country. Drawing from exemplary international engineering experiences while considering its unique characteristics, China has formulated its own set of techniques. This article compiles the historical evolution of domestic disaster prevention and rescue efforts and provides detailed comparisons of typical specialized tunnel rescue stations both domestically and internationally. It offers comprehensive discussions on their structural layout, disaster prevention ventilation and smoke extraction systems, electromechanical equipment, and emergency management. By meticulously comparing various parameter technical indicators within the disaster prevention, evacuation, and rescue framework, the article evaluates and summarizes China's proficiency in disaster prevention and evacuation within extra-long tunnels. Furthermore, it delves into an in-depth analysis of the contentious issue of internal crossing line placement within tunnels. This analysis serves as a reference for the design and standard formulation of China's railway tunnel disaster prevention and rescue engineering, while addressing significant controversies.

Keywords: Railway tunnel, Disaster prevention and rescue, Designated evacuation, Emergency rescue station, Crossing line

1 INTRODUCTION

As China's railway network continues to develop, the number of lengthy and large-scale railway tunnels, as well as tunnel complexes, has grown dramatically. These tunnels are becoming increasingly larger in scale. Among the ongoing railway projects, a significant number of extra-long tunnels have emerged. Whether considering individual tunnel lengths or the proportion of tunnel routes, these figures have reached historical highs (Hanley et al., 2022). Given the characteristics of China's railway transportation, including inter-regional and inter-railway bureau (corporation) operations, and long passenger distances, challenges arise for disaster response and evacuation in the case of incidents within enclosed long tunnels. Due to the potential difficulties in rescue and evacuation during disasters and the substantial impact of losses, ensuring operational safety has remained a significant challenge in railway safety operations. China's design, construction, and management entities place great emphasis on disaster prevention, evacuation, and rescue engineering within tunnels. Drawing from successful operational experiences and technological achievements, as well as learning from deficiencies and shortcomings identified in previous designs and emergency drills, these entities have essentially developed a scientific and comprehensive set of emergency evacuation and rescue technology.

China's regulations require a technical and economic comparison between single-bore dual-track and twin-bore single-track configurations for newly constructed tunnel projects that exceed 10 km in length. Currently, for high-altitude railway tunnels, tunnels with a length greater than 15 km are generally advised to adopt separate construction schemes. In cases where a joint construction approach is employed due to specific geological conditions, a connecting passageway should be established. Considering the significant advantages of separate construction tunnels in disaster prevention, rescue operations, and operational

*Corresponding author: yuanyi.yy@crcc.cn

DOI: 10.1201/9781003495505-465

maintenance, the majority of specialized tunnels exceeding 20 km in length have adopted separate construction schemes (Zhao et al., 2021). To further assess the design proficiency of China's long and large specialized tunnels in terms of disaster prevention and rescue, and to understand the current state of railway tunnel emergency evacuation and rescue technology in the country, it is necessary to compile and compare the achievements and successful experiences related to disaster prevention and rescue techniques for these specialized tunnels. This involves identifying deficiencies and shortcomings in the ongoing construction and operation of disaster prevention and rescue engineering, with the goal of enhancing disaster prevention, evacuation, and rescue capabilities within tunnels, improving the reliability of disaster prevention and rescue engineering, and ensuring the operational safety of railway tunnels.

2 THE HISTORICAL EVOLUTION OF RAILWAY TUNNEL EMERGENCY EVACUATION AND RESCUE TECHNOLOGY IN CHINA

Before 1990, China had a relatively small number of tunnels, with few long and large tunnels, mostly consisting of single-track configurations. At that time, extra-long separate construction tunnel emergency evacuation and rescue technology were not common. The earliest involvement in tunnel fire prevention on railways can be traced back to the Daoyaoshan Tunnel on the Hengguang-Fuxian Line. As the construction of the Qinling Extra-Long Tunnels on the Xikang Railway progressed, China's research and design of tunnel disaster prevention began to take its initial steps. A system of measures targeting fire prevention, suppression, and evacuation rescue was adopted, with each railway bureau establishing its respective safety management measures for tunnels.

Entering the 21st century, China saw the emergence of long and large tunnels. A notable project was the Wushaoling Tunnel (20 km) on the Lanwu Second Line. During the construction period from 2003 to 2006, a design scheme emphasizing "fire alarm and designated evacuation" was established. Around the same time, comprehensive research on tunnel emergency evacuation and rescue technology was conducted during the construction of the Taihangshan Tunnel (2005-2009) and the Dayaoshan Tunnel Complex (2005-2009). Emergency rescue stations were established both inside the tunnels and at their entrances. Additionally, comprehensive disaster prevention and operational management techniques were studied for the underwater Shizi Yang Tunnel (2006-2011).

In the past decade, railways have entered a phase of rapid development. With the promulgation of the "Design Specification for Railway Tunnel Disaster Prevention, Evacuation, and Rescue Engineering" (TB10020), tunnels such as Guanjiao, Chenglan, and Lanyu Railways have undergone tunnel disaster prevention, evacuation, and rescue design according to the specification's requirements. International technical consultation has been introduced to enhance and improve disaster prevention and rescue engineering design. The design and implementation of disaster prevention, evacuation, and rescue for long and large tunnels have gradually become standardized and governed by systematic technical regulations.

As of the end of 2021, China Railway Engineering Consulting Group (CRECG), along with the First, Second, and Fourth Railway Survey and Design Institutes, has collectively completed project designs for 127 tunnel emergency evacuation and rescue technology engineering endeavors. These projects encompass a total tunnel length of 9,433.958 km and 929 tunnel structures. Among these, 40 emergency rescue stations have been designed within tunnels, while 123 emergency rescue stations of the entrance type have been established. Furthermore, a total of 958 emergency exits (refuge points) have been included in the designs. In conjunction with achieving disaster prevention and evacuation goals for railway stations, a total of 27 projects have been undertaken, with 5 of them pertaining to underground stations and 22 to entrance stations.

3 DOMESTIC AND INTERNATIONAL EXEMPLARY EMERGENCY EVACUATION AND RESCUE TECHNOLOGY ENGINEERING FOR EXTRA-LONG SEPARATE CONSTRUCTION TUNNELS

3.1 *Domestic exemplary separate construction tunnel emergency rescue station - New Guanjiao Tunnel*

3.1.1 *Tunnel overview*

The New Guanjiao Tunnel spans a total length of 32.645 km and is designed as a twin-bore single-track tunnel with a center-to-center spacing of 40 m. It is the longest tunnel in China's high-altitude regions. The tunnel employs a ventilation and smoke extraction strategy using both tunnel supply air and vertical shaft balanced smoke extraction. It has introduced a technical system for the evacuation and rescue command system and established a design pattern for rescue stations in high-altitude, long tunnels. The construction of the New Guanjiao Tunnel took place from 2007 to 2014.

3.1.2 *Emergency evacuation and rescue engineering design*

The tunnel system has studied the entire process from spontaneous fire occurrence to completing personnel rescue. From an operational and management perspective, comprehensive design integration has

been conducted for civil, mechanical, communication, and fire protection systems.

To ensure the safe evacuation of personnel, an emergency rescue station was established near Shaft No. 6, spanning a length of 550 m. Evacuation cross-passages are located every 50 m within the emergency rescue station. Protective doors have been installed at both ends of all cross-passages, capable of withstanding blast loads of not less than 0.1 MPa and having a fire resistance limit of no less than 3 h. Electrically operated ventilation dampers are positioned above the protective doors, while jet fans are placed at the air-stream facing positions within the 12 evacuation cross-passages. A dedicated smoke exhaust duct has been set up within the emergency rescue station, and a high-pressure fine water mist fire hydrant and emergency telephone are installed at both ends of each evacuation cross-passage. Two sectional contact switches are positioned at the tunnel ends of the twin-bore sections, each serving one tunnel. The comprehensive layout of the New Guanjiao Tunnel 's emergency rescue station is depicted in Figure 1 (Chen, 2016).

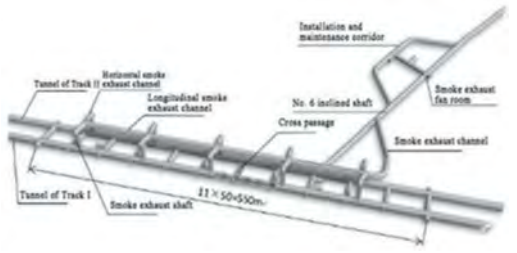

Figure 1. Diagram of the structural layout of the New Guanjiao Tunnel emergency rescue station.

An emergency rescue command center has been established within the Qinghai-Tibet Railway Company to manage the entire evacuation and rescue operation. The command center oversees daily training and drills, as well as emergency response coordination, remote control of tunnel equipment, and monitoring. The main monitoring station conducts centralized remote monitoring of tunnel equipment, tracking relevant parameters, and issuing alarms for various mechanical and electrical equipment malfunctions or anomalies.

Throughout the tunnel, nine guide signs have been positioned along the left side in the direction of travel to accurately guide trains to a smooth stop at the emergency rescue station. Optical image signs are placed at the midpoint of the two cross-passages within the rescue station area, indicating distances in two directions. Directional guidance lines made of reflective material have also been installed.

Fixed lighting, evacuation signage illumination, identification lighting, and evacuation lighting are implemented within the tunnel. Gun-type cameras have been installed at appropriate locations at the entrances of both left and right tunnel bores, in the rescue cross-passages, and near Shaft No. 6. The real-time video monitoring images captured are transmitted to the Qinghai-Tibet Company's emergency command center and the local public security bureau command center.

Within the emergency rescue station area, a smoke exhaust vertical shaft is positioned on the tunnel crown every 100 meters, connected through transverse smoke exhaust ducts that link the vertical shafts with longitudinal smoke exhaust ducts. These longitudinal ducts are further connected to Shaft No. 6, allowing smoke to be expelled from the tunnel. An anti-smoke electrically operated damper within the transverse smoke exhaust duct enables both tunnel bores to share a single smoke exhaust channel (Chen, 2016). A high-pressure fine water mist fire protection system has been installed in the emergency rescue station, along with fire extinguishers placed in various chambers within the tunnel, and firefighting water reservoirs at tunnel entrances.

An electrical phase division has been implemented in the emergency rescue station within the tunnel, near the roof and extending to the power supply arm at the New Guanjiao Tunnel. Prior to activating the fine water mist fire pump for firefighting, the emergency rescue command center issues a command to the traction power dispatching station to cut off power and ground the overhead contact system within the emergency rescue station.

3.1.3 *Summary*

The disaster prevention design of the New Guanjiao Tunnel primarily employs the method of separate construction with designated evacuation and rescue points. In the tunnel, an emergency rescue station is positioned at the main tunnel near Shaft No. 6 for designated evacuation and rescue purposes. Smoke exhaust vertical shafts and ducts are installed on both sides of the tunnel roof, and water-based firefighting is conducted within the rescue station. Smoke extraction and ventilation are managed through the use of separate shafts, ensuring a clear separation between people and smoke within the tunnel.

3.2 *Typical separate construction tunnel: In-Tunnel rescue station - Saint Gotthard Tunnel*

Drawing from comprehensive engineering cases in developed countries including Europe, foreign ultra-long tunnels mostly utilize separate construction methods, with only a few tunnels being constructed using joint methods. The following example of the Saint Gotthard Tunnel will be used to illustrate and analyze this approach.

3.2.1 *Tunnel overview*

The Gotthard Base Tunnel is an exceptionally long railway tunnel traversing the Alps from Basel,

Switzerland, to Milan, Italy. Comprising two parallel single-track tunnels with a center-to-center spacing of 40 m, the tunnel is 57 km in length (57.104 km for the east tunnel and 57.017 km for the west tunnel). A cross-passage is situated every 330 meters along the tunnel. The tunnel features a zigzag longitudinal slope, with a maximum gradient of less than 7‰. Designed for passenger trains, the tunnel allows for a maximum operational speed of 250 km/h. The construction of the tunnel took place from 1996 to 2017.

3.2.2 *Tunnel safety factors and preventive and mitigative measures*

The safety considerations for the Saint Gotthard Base Tunnel primarily encompass various potential hazards within the tunnel environment, including train derailment, fire, train or equipment malfunctions, terrorist attacks, passenger incidents, hazardous material leaks, etc. Among these, fire, due to its high occurrence likelihood and significant impact, has been a focal point of tunnel safety protection. The preventive measures for the tunnel include barring hazardous trains from entering, employing dual tunnels, train signaling, and automatic control systems to prevent collisions, limiting the number of crossover tracks and optimizing their layout to minimize derailment risks, and ensuring freight and passenger trains travel at the same speed to mitigate risks from hazardous material transportation.

Safety zones have been established through the presence of two multifunctional stations, cross-passages every 325 m, and a disaster prevention ventilation system, providing passengers with safe areas and facilitating self-rescue. Specially equipped rescue trains are stationed at tunnel entrances, and simple, standardized emergency management procedures have been formulated and regularly practiced (Zeng and Zhao, 2010).

3.2.3 *Disaster prevention and rescue design scheme*

The disaster prevention and rescue plan for the Saint Gotthard Tunnel employs a designated rescue station model. The east and west tunnels mutually serve as rescue tunnels. Each tunnel has a shaft located in Amsteg and two multifunctional stations in Sedrun and Faido (Figure 2).

The spacing between multifunctional stations is approximately 20 km. Each multifunctional station consists of two emergency stopping stations, two crossover tracks (allowing tunnel segment maintenance with minimal traffic disruption), vertical shafts, and entrances/exits. Each rescue station is about 450 m long, with a platform approximately 2 m wide. Six evacuation cross-passages are evenly distributed, equipped with fire escape doors that can be remotely controlled. Seven smoke exhaust vertical shafts are situated on top of the rescue stations, sealed using exhaust gates.

The multifunctional stations essentially divide the entire tunnel into approximate thirds, serving three main functions. Firstly, trains can switch between the east and west tunnels as required by operational

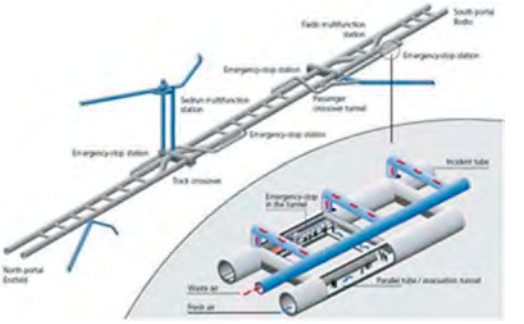

Figure 2. The layout of the Gotthard road tunnel rescue station.

scheduling. Secondly, trains affected by fires that cannot exit the tunnel can halt at the emergency stopping stations within the multifunctional station. Passengers can evacuate into the evacuation passages and wait for rescue at the emergency stopping stations on the non-affected side of the tunnel. Thirdly, both operational and emergency ventilation can reach the emergency rescue station through the vertical shafts and entrance tunnels.

Each crossover track is equipped with specialized doors, as shown in Figure 3. These doors remain closed during normal operations but can be opened when required by dispatching needs.

Figure 3. Fire Door within Crossover Tracks of the Gotthard Base Tunnel.

The Gotthard Tunnel has established behavioral guidelines for both trains and personnel during emergencies in operational conditions. The tunnel's disaster prevention ventilation aims to maintain sufficient positive pressure within the multifunctional stations, preventing smoke from entering the safe tunnel through the opened cross-passages.

The ventilation scheme for emergency rescue stations has been optimized to create smoke-free escape passages and improve self-evacuation conditions (e.g., platform area temperature not exceeding 50°C, CO

concentration less than 150 ml/m³, visibility exceeding 5 meters in the platform area). Disaster prevention ventilation is based on the presence of two multifunctional stations (emergency rescue stations) located within the tunnel at Sedrun and Faido, and it employs different ventilation modes depending on whether a train is stopping at a rescue station or at any other point.

In conclusion, the Gotthard Base Tunnel adopts a dual-track separate construction approach, and its disaster prevention and rescue model involves designated emergency rescue station stops.

4 ENGINEERING COMPARATIVE STUDY

4.1 *Comparison of civil structure, evacuation methods, and smoke exhaust methods in separate construction tunnels*

Both domestic and international separate construction tunnels generally adopt the emergency rescue station stop rescue mode.

For foreign ultra-long tunnels, most employ separate construction methods. Examples include the foreign Saint Gotthard Tunnel and Brenner Base Tunnel. Domestically, tunnels like the New Guanjiao Tunnel, West Qinling Tunnel, and Ping'an Tunnel follow the same pattern. However, there are also single-tube dual-track tunnels exceeding 20 km in length domestically, such as the under-construction Yuntunbao Tunnel and Ganqing Tunnel.

Considering the rescue mode, except for early domestic Qinling Tunnels and the foreign English Channel Tunnel that initially didn't have designated stops, opting for mutual rescue between the two tunnels, both domestic and foreign tunnels now mostly utilize the designated station stop rescue mode. Emergency rescue stations are established for evacuation and rescue, with the distance between them being less than or equal to 20 km.

Both domestic and foreign separate construction tunnels utilize encrypted cross-passages for mutual rescue purposes. In the event of a fire disaster inside the tunnel, trains halt at the nearest emergency rescue station when they cannot exit the tunnel. The evacuation route involves individuals entering the evacuation cross-passages and moving to designated waiting areas for rescue. To achieve smoke separation from people, fresh air is supplied through separate auxiliary adits or isolated auxiliary adit ducts. Within the scope of each emergency rescue station, smoke exhaust vertical shafts and longitudinal smoke exhaust ducts are positioned on the crown of the left and right single-line tunnel sections. Smoke is expelled to the outside through auxiliary adits.

4.2 *Comprehensive comparison of disaster prevention measures*

To conduct a more comprehensive comparison, categorizing by the processes of prevention, mitigating impacts, facilitating evacuation, and promoting rescue, we compare the disaster prevention measures of the foreign Gotthard Tunnel (**A**) and the domestic New Guanjiao Tunnel (**B**). The comparative analysis of their measures is detailed as follows:

- Dangerous Goods Train Management: **A**-Prohibition of dangerous train entry into tunnels; **B**-Handled according to "Railway Regulations on the Management of Dangerous Goods Transportation".
- Collision Prevention: **A**-Train signaling and automatic control system; **B**-Automatic block.
- Maintenance Conditions: **A**-During maintenance, workers only operate in one closed tunnel; **B**-Closure or skylight period.
- Vehicles: **A**-Fire-resistant locomotive vehicles; **B**-Fire-resistant locomotive vehicles.
- Fire Extinguishing: **A**-Rescue station and tunnel entrance water firefighting; **B**-Rescue station high-pressure fine water mist, tunnel entrance firewater pool, tunnel fire extinguisher.
- Disaster Ventilation and Smoke Exhaust: **A**-Partial transverse ventilation, complex system, well-equipped; **B**- Partial transverse, well-equipped.
- Operational Ventilation: **A**-Natural ventilation + jet ventilation, selective opening; **B**-Natural ventilation.
- Travel Guide Signs: **A**-Not specified; **B**-Nine guide signs are placed on the left side along the direction of travel in each tunnel.
- Evacuation Signage: **A**-Evacuation signs; **B**-Directional induction lines made of photoelectric images and reflective materials.
- Illumination: **A**-Emergency lighting system; **B**-Emergency lighting, evacuation sign illumination, identification lighting, evacuation lighting.
- Emergency Communication: **A**-GSM-R radio communication and radio, video collection; **B**-Fixed telephone and video collection, railway-specific mobile communication, public mobile communication.
- Inner Tunnel Crossover: **A**-Installed; **B**-Not present.
- Inner Tunnel Station: **A**-Two multifunctional rescue stations at each location; **B**-One emergency rescue station basic equivalent.
- Rescue Station Spacing: **A**-$\leq$ 20 km; **B**-$\leq$ 20 km.
- Rescue Station Transverse Passage Spacing: **A**-$\leq$ 90 m; **B**-$\leq$ 50 m.
- Platform Width: **A**-2 m; **B**-1.3 m.
- Transverse Passages: **A**-General transverse passage spacing of 325m, 333m; **B**-400-500m.
- Rescue Trains: **A**-Dedicated rescue trains; **B**-Not present.
- Reliability of Power Equipment: **A**-Equipment power supply, cables, etc., meet fire resistance requirements; **B**-Rescue station level 1 power load, other level 2 power load, cables, meet fire resistance requirements.
- Contact Wire Power Off and Grounding: **A**-Segment switching and grounding, remote control;

B-Two contact wire segment switches at rescue station ends, electric phase separation between tunnel stations.

- Equipment Monitoring: **A**-Central control system installed; **B**-Remote monitoring and control.
- Emergency Plans: **A**-Comprehensive; **B**-Comprehensive.
- Command Center: **A**-Operations control center and emergency command post on-site; **B**-Tibet railway company emergency command center.

The above table shows that the disaster prevention, evacuation, and rescue measures of typical projects both domestically and internationally are mostly comparable, with some differences in certain aspects. In the Gotthard Base Tunnel, for instance, four in-track passages are installed (a common practice for long European tunnels), along with dedicated rescue trains. In this regard, some domestic tunnels have only a few high-altitude railways that have planned for backup trains, while others rely on maintenance area backup trains or nearby passenger trains for rescue and evacuation.

The principles for setting up emergency rescue stations, evacuation modes, civil engineering structures, electromechanical facilities, monitoring systems, and emergency management systems are generally consistent for both domestic and international segmented tunnels. Comprehensive disaster prevention and rescue facilities have been established in both cases to meet the requirements for disaster prevention, evacuation, and rescue.

5 ANALYSIS OF INTER-TRACK PASSAGE ISSUE IN SEGMENTED TUNNELS

The significant difference between China and European countries in their ultra-long tunnels lies in the fact that European ultra-long tunnels are all equipped with inter-track passages connecting the left and right tunnel tubes. For example, the Gotthard Base Tunnel in Switzerland and the Lötschberg Tunnel have inter-track passages between the tubes.

On the contrary, Chinese ultra-long tunnels do not have inter-track passages between the tunnel tubes, which differs from the operational safety design in Europe. In light of this, some experts raise the question of whether China's operational safety measures for ultra-long tunnels are less effective compared to Europe. The following analysis aims to provide a comprehensive examination of the necessity of inter-track passages in ultra-long tunnels.

5.1 *Reasons for setting up inter-track passages in Europe*

Channel Tunnel: The entire tunnel is equipped with 4 cross passages to connect the two tracks, allowing trains to switch tracks or reverse (Dai, 2001).

Purpose of inter-track passages in the Gotthard Base Tunnel and Lötschberg Tunnel: When one tunnel requires maintenance, the other tunnel can ensure continuous operation; in case of emergencies, the alternate tunnel offers flexible operational possibilities (Chen, 2006).

From the above discussion and analysis, the purpose of setting up inter-track passages is to enhance the flexibility of transportation and maintenance in tunnels. The decision to transfer trains to adjacent tracks should be determined based on the requirements of maintenance work or the characteristics of incidents occurring within the tunnel.

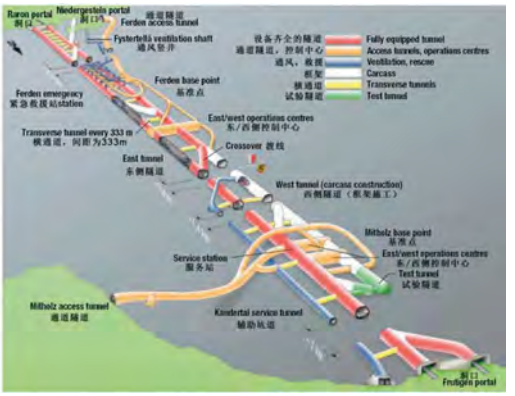

Figure 4. Schematic layout of the Lötschberg tunnel.

5.2 *Safety assurance after implementing the cross-passage system in Europe*

The cross-passages are integrated into the signal system, and the operation of the protective doors (located in the middle of the cross-passage tunnel) is interlocked with the signal system, ensuring safety.

5.3 *Reasons for the absence of cross-passage system in China*

Taking into account the characteristics of railway tunnel projects in China, railway operations, maintenance, and disaster handling regulations, the reasons for not implementing the cross-passage system within tunnels in China are summarized as follows:

(1) China operates its railways on a single line section basis. Currently, there is no need for tunnel stations due to the extended length of tunnels. As a result, the requirement to maintain operations through the installation of cross-passages for long tunnels does not exist in China. Maintenance of equipment is carried out during scheduled maintenance windows, and for dual-bore single-line tunnels, a "V" type maintenance arrangement is commonly adopted where one tunnel bore is under maintenance while the other remains operational. This obviates the need for cross-passages for maintenance purposes.

(2) The railway operation and management practices in China differ from those in Europe. Emergency rescue stations cannot be integrated into the train control system. Consequently, the implementation of a cross-passage system within tunnels cannot be incorporated into the train control system operationally.
(3) When one tunnel bore is affected by a fire, the other safe tunnel bore is required for evacuation and rescue operations. Under such circumstances, the safe tunnel bore cannot be maintained for normal operations, rendering the need for a cross-passage system unnecessary.
(4) After the completion of emergency evacuation and rescue operations, the remaining work within the affected tunnel bore is similar to equipment maintenance. In this scenario, one tunnel bore is used for post-fire disaster relief and recovery operations while the other remains operational. This interval can be maintained in single-line operation mode without requiring a cross-passage system.
(5) If a cross-passage system is installed within a tunnel and a fire incident occurs, activating the cross-passage system would result in the interconnectedness of the two tunnel bores. This would necessitate the installation of complex independent ventilation systems between the two tunnel bores, leading to higher engineering investment, greater technical complexity, higher maintenance requirements, increased operational expenses, and stringent operational demands.
(6) Similar to Europe, there is a shared understanding that the more cross-passages are installed on a line, the less conducive it is to railway operational safety. Therefore, even in the case of the Saint Gotthard Tunnel, efforts are made to control the number of cross-passages. For instance, in the feasibility study of the Wushaoling Tunnel on the Lanzhou-Xinjiang Railway, a cross-passage solution was initially proposed but was later abandoned due to operational safety considerations.
(7) The tunnels with emergency rescue stations and cross-passage systems are typically long mountain tunnels. If cross-passages were to be installed in the middle of such tunnels, it would require strict control of the longitudinal gradient within a certain range near the turnouts. This could have implications for tunnel alignment considerations.

Considering factors such as operational requirements, safety, economic feasibility, and operational management, it is not necessary to implement cross-passage systems connecting the up and down tracks within China's railway long tunnels.

6 CONCLUSIONS

(1) The specific measures of emergency rescue stations in China have continually evolved and improved with the progression of time. The development has transitioned from the early days of single-bore tunnels to the mutual rescue of dual-bore tunnels, and subsequently to the later implementation of "fixed-point evacuation." The designs for disaster prevention and evacuation during various periods have been continuously refined, drawing inspiration from excellent engineering examples abroad. Notably, projects such as the Taihang Mountain Tunnel, the New Guanjiao Tunnel, and the Chengdu-Lanzhou Railway Tunnel have also received international technical consultations, resulting in a constant elevation of technical proficiency. Each of these projects represents the pinnacle of their respective eras.
(2) By comparing the disaster prevention, evacuation, and rescue projects of typical long and large tunnels both domestically and internationally, it is evident that the principles, evacuation modes, civil structures, electromechanical facilities, monitoring systems, and emergency management systems for segmented and fully-bored tunnels are fundamentally consistent. Comprehensive disaster prevention and rescue facilities have been established in both scenarios, fulfilling the requirements for disaster prevention, evacuation, and rescue.
(3) Due to variations in economic development and differences in domestic and international operational management methods, there are certain disparities in the design patterns of disaster prevention, evacuation, and rescue projects. After careful analysis and research, it is concluded that the inclusion of track crossovers near emergency rescue stations is not aligned with China's railway operational management model. In China, the practice of not installing in-tunnel crossovers in segmented tunnels and not dedicating separate rescue trains is consistent with the national context.

REFERENCES

Chen, J.W., 2006. The design and construction of the Lötschberg underground tunnel. China international symposium on high speed railway tunnels. China Railway Society.

Chen, S.H., 2016. The key technologies of the Guanjiao Tunnel of Qinghai-Tibet Railway Xige Second Line. Tunn. Constr. 36(03): 355–372.

Dai, G.P., 2001. Introduction to aerodynamics and ventilation system of English Channel tunnel. Rail. Eng. 1: 3–6.

Hanley, D., Li, J.C., Wu, M.Q., 2022. High-speed railways and collaborative innovation. Reg. Sci. Urban Econ. 93: 103717.

Zeng, M.Y., Zhao, H.D., 2010. Ventilation and disaster prevention technology for the tunnel at the bottom of Gotthard Mountain in Switzerland. High-speed Rail. Tech. 1(03): 42–46.

Zhao, Y., Shi S.S., Tian S.M., et al., 2021. Main engineering technical difficulties and countermeasures for the construction of the tunnel Railway. Tunn. Constr. 41 (07): 1079–1090.

Tunnelling for a Better Life – Yan, Celestino, Thewes & Eberhardt (Eds)
© 2024 The Author(s), ISBN 978-1-032-80042-4
Open Access: www.taylorfrancis.com, CC BY-NC-ND 4.0 license

Concept of a thermoelectric power system in high geothermal tunnel: Preliminary design with numerical simulation

Yong Yuan, Pengyu Cui & Qiling Wang
Department of Geotechnical Engineering, Tongji University, Shanghai, China

ABSTRACT: High geothermal tunnel (HGT) refers to the tunnels where the temperature of surrounding rock mass is higher than 28°C. The normal way for utilizing the heat resource and isolating heat conduction to the tunnel lining is to set up a circular system of ground source heat pump (GSHP). Here, an innovative system to harness geothermal energy with thermoelectric modules (TEMs) was proposed. The proposed system could convert the geothermal energy from surrounding rock into electricity based on Seebeck effect. Conceptual design of the system was introduced firstly. With the help of Multiphysics module of a finite element software, the technical feasibility of the system was verified, and the influences of temperature fields in high geothermal tunnels and parameters of TEM on generation performance were analyzed through numerical simulation. The results can be concluded that (1) The amount of electricity generated by this system was considerable. A thermoelectric power system with 51020 TEMs, occupying an area of 1000 square meters, could reach a maximum output power of 9132 W when the surrounding rock temperature was 90 °C; (2) The generation performance of the system was positively correlated with the temperature difference between the two sides of thermal insulation layer (TIL), and had little to do with the hot side temperature of TIL; (3) The maximum output power of the TEM model first increased and then decreased when the height of TE legs increased. The optimal height of TE legs in high geothermal tunnels was found to be 1.6 mm.

Keywords: High-geothermal tunnel, thermoelectric, numerical simulation, generation performance

1 INTRODUCTION

For the past few years, with the implementation of national major projects such as the West-to-East Power Transmission Project and the Western Development Program (WDP), railway traffic has begun to extend to the mountainous areas with complex geological conditions located in southwest China. Moreover, tunnels tend to be deep-buried and super-long (Ou et al., 2021), and many tunnels have to pass through geothermal anomaly areas. Due to frequent geological activities, these areas have extremely complex geological conditions and abundant geothermal resources (Zhang et al., 2022). Therefore, the emergence of a large number of high geothermal tunnels not only poses challenges for construction, but also provides opportunities for geothermal energy exploitation.

Currently, GSHP is the main method to utilize geothermal energy in tunnels (Walch et al., 2022; Yang et al., 2019, Revesz et al., 2016, Lee et al., 2016). It uses geothermal energy to provide hot water, heating, cooling and other services for buildings. However, GSHP can only utilize geothermal energy through heat exchange (Ogunleye et al., 2020), which somewhat restricts the application range of geothermal energy in high geothermal tunnels. Furthermore, due to the unbalanced heating and cooling loads, the GSHP system may release more heat to the underground during the cooling season than it absorbs from the underground during the heating season, causing a heat imbalance and lowering the performance of the GSHP system (Wang et al., 2010; Yuan et al., 2012). Xi et al. monitored the two-year operating performance and the variation in the underground thermal environment of a GSHP system installed in an office building in Hangzhou. They found that the heat imbalance rate of the system was approximately 24% in the first year and 53% in the second year. Additionally, the underground temperature around the heat exchanger area increased by 1.1 °C after two years of system operation, which led to a decrease in performance of the GSHP system (2017). Therefore, a more stable technology that can utilize geothermal energy in a wider range of applications is required to harness geothermal energy effectively in high geothermal tunnels.

In recent years, thermoelectric (TE) technologies have attracted widespread attention because they can directly convert thermal energy into electrical energy without any noise, vibration or emissions (Wu et al., 2022). This technology bases on the Seebeck effect, which occurs when a temperature gradient is formed along TE materials, causing the migration of charge

*Corresponding author: 2232571@tongji.edu.cn

DOI: 10.1201/9781003495505-466

carriers (electrons in n-type materials and holes in p-type materials) from the hot side to the cold side, thereby generating an electrostatic potential (He et al., 2019a). Compared to other energy converting technologies, TE devices have simple configurations, require no maintenance, operate in a solid-state manner and provide high reliability. These features give TE devices significant advantages in thermal energy harvesting for the recovery of waste heat (Jouhara et al., 2021) and utilization of clean energy (He et al., 2019b). In geothermal energy exploiting field, Li et al. designed a six-layer geothermal-TEG apparatus and tested its generation performance at a geothermal well. The entire six-layer device could generate about 500 W electricity with a temperature difference of about 152 °C (2021). Catalan et al. investigated the suitability of a geothermal thermoelectric generator with passive phase change heat exchangers on the shallow Hot Dry Rock (HDR) field of Timanfaya National Park (Spain). The device has been in operation without maintenance for 2 years now, producing more than 520 kWh of energy (2023). These indicates that thermoelectric technology exhibits a highly stable performance in the field of geothermal energy exploitation.

Since geothermal energy is renewable and stable (Mahmoud et al., 2021), there is always a large temperature difference between the surrounding rocks and the interior of the high geothermal tunnel. Therefore, TE devices can be used to harvest and convert the geothermal energy into electrical energy, which can then be used to power the operation of tunnels. Additionally, employing TE devices in high geothermal tunnels can address the issue of long-distance power supply. The main purpose of this article is to propose a concept for a thermoelectric power system in high geothermal tunnel, verify the feasibility of such a system, and analyze its main influencing factors on power generation performance. The results indicate that the thermoelectric power system is a promising technology for harnessing geothermal energy in high geothermal tunnels.

2 CONCEPT

The thermoelectric power system in high geothermal tunnels consists of thermoelectric modules (TEMs), thermal insulation layer (TIL), heat conducting blocks and bearing modules. Since TIL is generally filled with materials of low thermal conductivity, it can effectively block the heat transferred from the surrounding rock to the tunnel, and a certain temperature difference will be formed between the two sides of TIL. Therefore, based on Seebeck effect, TEMs can be installed in the TIL of the tunnel to convert the heat from the surrounding rock into electricity, which could be stored by the electrical storage module for tunnel operation. The positional relationship of each part of the system is shown in Figure 1.

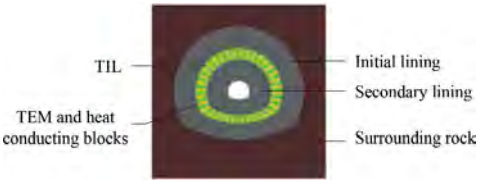

Figure 1. Cross-section diagram of the thermoelectric power system in high geothermal tunnel.

The temperature difference between the two sides of TIL is positively correlated with its thickness, and furthermore, when the thickness is less than 10 cm, its impact on the temperature difference becomes more obvious (Ma et al., 2023). Temperature difference is critical to the generation performance of TEMs, so it is significant to maintain the thickness of TIL during the operation of tunnels. However, thermal insulation materials and TEMs have low compressive strength, making them prone to deformation under the surrounding rock pressure. This deformation leads to a decrease in the thickness of TIL, resulting in a reduced temperature difference between the two sides of TEMs. Therefore, in order to withstand the pressure from surrounding rock and maximize the temperature difference, bearing modules made of materials with low thermal conductivity and high mechanical performance are required. Bearing modules and TIL are arranged alternatively between the initial lining and the secondary lining, as shown in Figure 2. The sizes and spacings of bearing modules are determined based on the surrounding rock pressure.

Figure 2. A design diagram of the thermoelectric power system in the direction of tunnel axis.

A TEM generally consists of many thermoelectric couples, connected by copper strips and packed by two ceramic plates (Luo et al., 2020). The thickness of a single TEM is generally 5 mm, while the TIL usually has a thickness of 5~10 cm. Therefore, in order to make the best use of the temperature difference between the two sides of TIL, it is necessary to add two heat conducting blocks between the ceramic plates of TEM and the tunnel linings, as shown in Figure 3. Through the heat conducting block attached to the surface of the initial lining, heat can be transferred from the surrounding rock to the hot side of TEM effectively. Furthermore, the heat transferred from the hot side of TEMs to the cold side through the couples and medium between the two ceramic plates accumulates at the colder ceramic plate, thereby reducing the temperature difference between the two sides of TEMs. Subsequently, this

heat can be transferred from TEMs to the secondary lining through the heat conducting block attached to it and carried away by the air flow in the tunnels, thus maintaining the temperature difference between the two sides of TEMs.

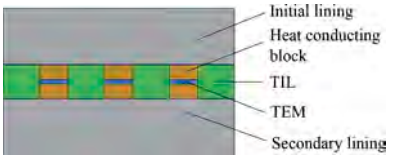

Figure 3. A detailed diagram of the thermoelectric power system in high geothermal tunnel.

The surfaces of the ceramic plates, the heat conducting blocks and the tunnel linings are not smooth planes. There are a lot of tiny bumps and depressions in the planes, so the heat transfer efficiency will be significantly reduced due to point contact. To increase the contact area and reduce the thermal resistance in heat transfer, the gap between these surfaces should be filled with silicone thermal grease or high thermal conductivity graphite sheets. In addition, the temperature difference between the surrounding rock and the air in the tunnel leads to heat transfer from the hot side of TEMs to the cold side. Therefore, the empty space between the two ceramic plates of TEM should be filled with thermal insulation materials to maintain the temperature difference and ensure stable generation performance.

Additionally, the low voltage and instability of the direct current generated by the thermoelectric effect of TEMs do not meet the requirements of general electrical appliances in tunnels. It needs to be boosted and stabilized before it can be used for tunnel operation.

3 MODELING

A finite element software was used to model and simulate the thermoelectric power system in high-geothermal tunnel. A heat transfer model of high geothermal tunnel and a thermoelectric power system model were established during the analysis. By using the former model, the thickness of TIL was decided and the temperature of the both sides of TIL under different temperature conditions of surrounding rock were obtained. These results were then utilized as the temperature boundary conditions for the latter model to verify the feasibility of the thermoelectric power system in high-geothermal tunnels. Subsequently, the influences of temperature difference, the temperature of hot side, and the height of TE legs on the generation performance of the thermoelectric power system were analyzed.

3.1 *Heat transfer model of high geothermal tunnel*

Since the heat transfer in the axial direction of the tunnel is much smaller than that in the radial direction, a two-dimensional(2D) plane model was used. Because thermoelectric power systems are designed to use during the operation of high geothermal tunnels, a steady-state solver was utilized for computation, and only solid heat transfer was considered in this process. The solid heat transfer between the surrounding rocks, linings, and TIL is governing by the following equation,

$$\rho C_P \frac{\partial T}{\partial t} + \nabla \cdot \vec{q} = \dot{q} \tag{1}$$

Where, C_P is specific heat capacity, $\vec{q}$ is heat flux vector, ρ is the density, T is temperature and $\dot{q}$ is the heat generation rate per unit volume.

3.1.1 *Geometric and material parameters*

The geometric parameters and material parameters referred to the literature (Lin et al., 2022). The dimensions of the entire model were 100 m × 100 m. The width and height of the tunnel cross-section were 10.8 m and 8.1 m, respectively. The initial lining had a thickness of 20 cm, while the secondary lining had a thickness of 45 cm. Additionally, TIL was between the initial lining and the secondary lining. The model is shown in Figure 4. The material parameters are shown in Table 1. C25 concrete was used for the initial lining, and C30 concrete was used for the secondary lining.

3.1.2 *Thickness of TIL*

According to the Standard TB 10068-2010, the air temperature in railway operating tunnels should not exceed 28 °C, thus the temperature inside the tunnel was set at 28 °C. The convective heat transfer coefficient of concrete surface was 13 W/m^2·°C. The boundary temperatures of the model were set at 50 °C, 60 °C, 70 °C, 80 °C and 90 °C, respectively and remained constant. The temperature differences between the two sides of TIL for various thicknesses of TIL under different boundary conditions are shown in Figure 5. It can be observed that the temperature difference between the two sides of TIL was positively correlated with the thickness of TIL. However, as the thickness of TIL increases, the impact of TIL on temperature difference gradually diminished. When the boundary temperature of model was 90 °C, the temperature difference was only 9.14% larger when the thickness of TIL was 12 cm compared to when it was 10 cm. Therefore, considering the economy, the thickness of TIL of the model was set at 10 cm in the subsequent numerical simulations. The temperatures of both sides of TIL and the temperature differences between the two sides of TIL under different conditions are shown in Figure 6.

3.2 *Thermoelectric power system model*

A part of the thermoelectric power system in high geothermal tunnel was modeled to analyze the

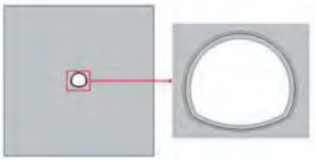

Figure 4. The heat transfer model of high geothermal tunnel.

Table 1. Material parameters of the heat transfer model for high geothermal tunnel.

	Specific heat (J/kg·K)	Thermal conductivity (W/mK)	Linear expansion coefficient	Density (kg/m^3)
Surrounding rock	707	2.3	0.6e-6	2000
TIL	1720	0.0222	1e-5	32
C25 concrete	960	2.94	1e-5	2100
C30 concrete	960	2.94	1e-5	2500

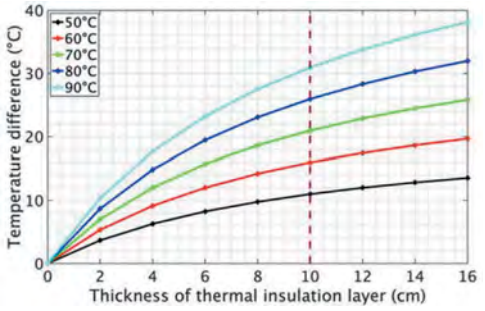

Figure 5. The relationship between the thickness of TIL and temperature difference between its two sides under varying surrounding rock temperatures.

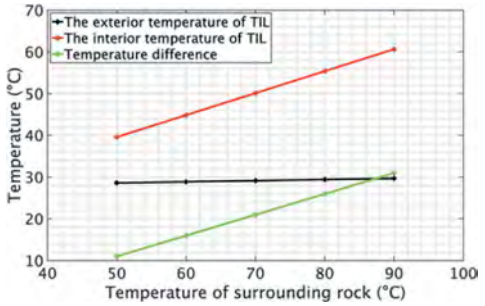

Figure 6. Temperature difference between the two sides of TIL under varying surrounding rock temperature when the thickness of TIL was 10 cm.

generation performance of the system. The thermoelectric effect interface of the finite element software was utilized for research. This interface couples the solid heat transfer field with the electric field. The entire model boundary was adiabatic. Electric charge continuity equation is expressed as follows,

$$\nabla \cdot \left(\vec{J} + \frac{\partial \vec{D}}{\partial t} \right) = 0 \tag{2}$$

where $\vec{D}$ is the electric flux density vector and $\vec{J}$ is the electric current density vector.

The following thermoelectric constitutive equations are used to couple the Equation. (1) and (2),

$$\vec{q} = T[\alpha] \cdot \vec{J} - [\kappa] \cdot \nabla T \tag{3}$$

$$\vec{J} = [\sigma] \cdot \left(\vec{E} - [\alpha] \cdot \nabla T \right) \tag{4}$$

where $[\kappa]$ is the thermal conductivity matrix, $[\alpha]$ is the Seebeck coefficient matrix, and $[\sigma]$ is the electrical conductivity matrix.

The model consisted of TIL, heat conducting blocks and TEMs. The material parameters of TIL were identical to those of the heat transfer model for high geothermal tunnels made in the section 3.1.

The TEM model was based on the geometric parameters of the commercial TEP1-1264-3.4, as provided in the literature (He et al., 2019b). The geometric parameters are listed in Table 2. The thermoelectric material used in this TEM was bismuth telluride, which has the best performance for low-range temperature operations (T<500 K). And the temperature-dependent material parameters were also based on the literature, and are expressed by cubic polynomial functions listed in Table 3. The TEM model consisted of 126 pairs of p- and n-type Bi_2Te_3 legs connected electrically in series by copper blocks, which were used as equivalent substitutes for wires, and thermally in parallel, as illustrated in Figure 7. The ceramic plates of the TEM were made of aluminum oxide. The parameters of the non-thermoelectric materials mentioned above are presented in Table 4.

The TEMs were located in the middle of the TIL, and they were connected electrically in series by copper blocks. An iron block with adjustable resistivity was used as the load resistance. Heat conducting blocks were positioned at both the top and bottom of the TEMs. The heat conducting blocks were made of copper, and its material parameters were the same as those used in TEM models. The voids between the ceramic plates of TEMs were filled with thermal insulation materials. The system model with four TEMs is depicted in Figure 8. The dimensions of the entire model were 66 cm×24 cm ×10 cm. The thermal resistance and electrical resistance at the contact surfaces were 2×10^{-4} m^2KW^{-1} and 6.5×10^{-9} $\Omega \cdot m^2$ respectively.

Table 2. Geometric parameters of the TEM model.

Parameter	Value
Thickness of ceramic plate	0.86 mm
Cross-section dimensions of ceramic plate	40 mm×40 mm
Height of TEM legs	1 mm
Cross-section dimensions of TEM legs	1.5 mm×1.5 mm

Table 3. The cubic polynomial functions of the TE material.

Property	p-type polynomial expression	n-type polynomial expression
Seebeck coefficient (V/K)	$-2.24407\times10^{-11}\times T^3$ $+2.22834\times10^{-8}\times T^2$ $-7.301\times10^{-6}\times T$ $+1.023698\times10^{-3}$	$1.68178\times10^{-11}\times T^3$ $-1.77163\times10^{-8}\times T^2$ $+6.203\times10^{-6}\times$ T-9.54589×10^-4
Thermal conductivity (W/m·K)	$-5.82609\times10^{-8}\times T^3$ $+1.03491\times10^{-4}\times T^2$ $-0.05011\times T+8.726$	$3.76869\times10^{-9}\times T^3$ $+2.81722\times10^{-5}\times T^2$ $-0.02057\times T+5.09531$
Electrical resistivity ($\Omega\cdot m^2$)	$-7.75456\times10^{-13}\times T^3$ $+7.77051\times10^{-10}\times T^2$ $-0.01853\times10^{-5}\times T$ $+1.60117\times10^{-5}$	$-6.04782\times10^{-13}\times T^3$ $+6.09155\times10^{-10}\times T^2$ $-1.715\times10^{-7}\times T$ $+2.11951\times10^{-5}$

Table 4. Parameters of the non-thermoelectric materials.

Material	Density (kg/m^3)	Thermal conductivity (W/m·K)	Specific heat (J/kg·K)	Electrical conductivity (S/m)
Aluminum oxide	3900	35	900	
Copper	8960	400	385	58100000

4 RESULTS AND DISCUSSION

In this section, the generation performance of the thermoelectric power system in high geothermal tunnel under different conditions was obtained through the model established in the previous parts of this paper, and then the factors affecting the generation performance were analyzed, including the temperature difference between the two sides of TIL, the hot side temperature of TIL and height of TE legs.

4.1 *Generation performance*

The temperature differences between the two sides of TIL under different temperature boundary conditions which were obtained in section 3.1 were utilized as the boundary conditions to calculate the generation performance of the thermoelectric power system in high geothermal tunnels. The temperature on the cold side of the model remained constant at 28 °C. Figure 8 shows the open-circuit voltages and maximum output powers of the model with different numbers of TEMs under various temperature conditions of surrounding rock. It can be seen from Figure 8 that the maximum output power and open-circuit voltage are proportional to the number of TEMs in the model. Therefore, to generate electricity on a larger scale, more TEMs are needed. The model with one TEM could generate 0.179 W electricity when the temperature of surrounding rock was 90 °C, and the open-circuit voltage could reach 1.428 V. Based on the simulation results, assuming the TEMs are 10 cm apart, as in the model, we can conclude that a thermoelectric power system with 51020 TEMs, occupying an area of 1000 square meters, could generate approximately 9132 W of electricity when the surrounding rock temperature is 90 °C. Meanwhile, the abundant geothermal energy in the high geothermal tunnel ensures a stable generation performance of the system, making it more attractive. Additionally, a positive correlation between open-circuit voltage and maximum output power with the temperature of surrounding rock can also be observed. This is because when the temperature inside the high geothermal tunnel remains constant, an increase in the surrounding rock temperature will results in a greater temperature difference between the two sides of TIL. Consequently, this enhancement improves generation performance of the TEMs. Therefore, the higher the temperature of surrounding rock, the better the generation performance of this system.

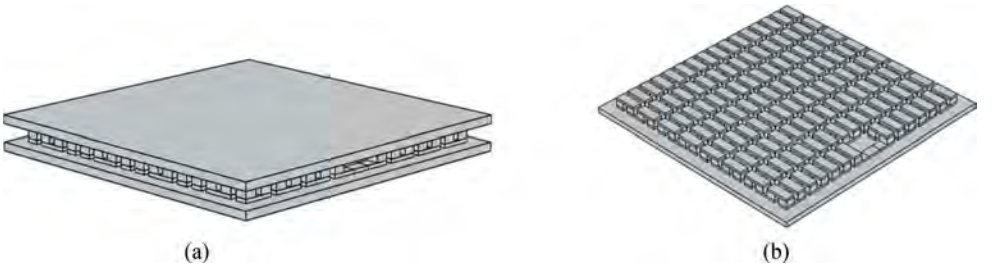

Figure 7. Schematic of the TEM model. (a) Overall diagram of the TEM model, and (b) internal structure of the TEM model.

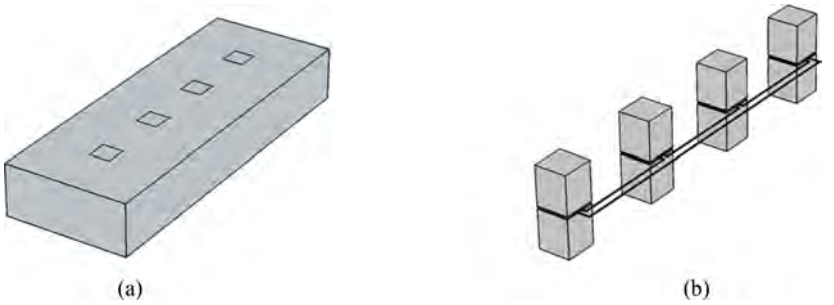

Figure 8. Schematic of the thermoelectric power system model with four TEMs. (a) Overall diagram of the system model, and (b) internal structure of the system model.

The temperature distribution of the model when the surrounding rock's temperature boundary condition was set at 90 °C is depicted in Figure 9. It can be observed that the temperature gradients primarily concentrated in the TEM location in the model, which is mainly contributed to the lower thermal conductivity of thermoelectric materials compared to other materials. Moreover, the temperature variation across the copper heat conductor was 2.62 °C, accounting for only 8.49% of the total temperature difference between the two sides of the model. This indicates that the copper heat conductors are highly efficient in heat transfer, and have almost no thermal loss. Therefore, heat conducting blocks made of high thermal conductivity should be placed between the TEMs and linings to improve generation performance of the system.

4.2 *Effect of temperature conditions*

The temperature of the surrounding rock in high geothermal tunnels varies due to different geological conditions, and the internal temperature requirements for tunnels of various uses also differ. These factors may affect the temperatures at both sides of the TIL. Since the Seebeck coefficient, electrical conductivity and thermal conductivity of thermoelectric materials are temperature-dependent, changes in the temperature on both sides will result in variations in the generation performance of the system. Therefore, this section analyzed the generation performance of the system under different temperature conditions.

The influences of the temperature difference between the two sides of TIL and the temperature at the hot side of TIL on the open-circuit voltage and maximum output power of the model with one TEM are shown in Figure 10. As depicted in Figure 10, the variation in temperature difference between the two sides of the TIL had a great impact on the generation performance of the model. The open-circuit voltage of the model was proportional to the temperature difference. The maximum output power showed a positive correlation with the temperature difference and essentially follows a quadratic function relationship. For example, when the hot side temperature was 60 °C, the open-circuit voltage of the model with a temperature difference of 30 °C was triple that with a temperature difference of 10 °C and the maximum output power was nine times that with a temperature difference of 10 °C. Therefore, in order to improve the generation performance of thermoelectric power systems in high geothermal tunnels, it is necessary to increase the temperature difference between the two sides of the TIL.

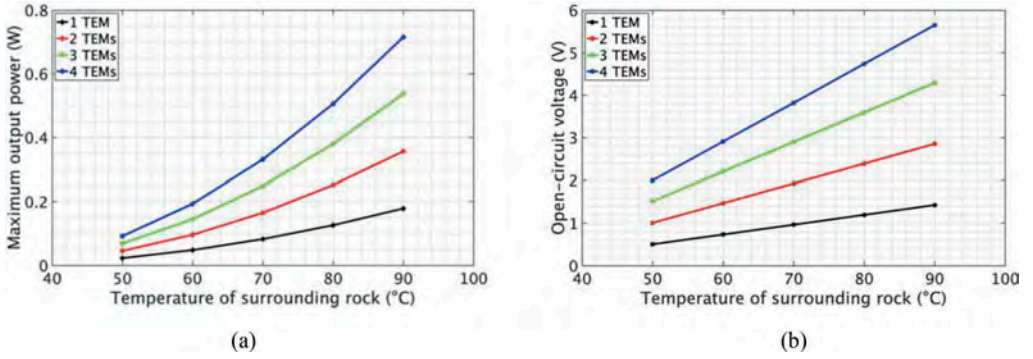

Figure 9. Generation performance of the thermoelectric power system model with different number of TEMs under various surrounding rock temperatures. (a) The open-circuit voltage, and (b) the maximum output power.

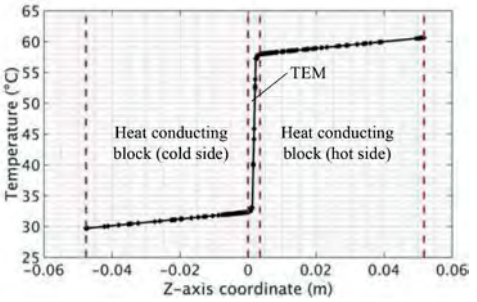

Figure 10. Temperature distribution of the system model when the temperature of surrounding rock was 90 °C.

It can also be observed that under the temperature conditions of high geothermal tunnels, changes in the hot side temperature had little impact on the power generation performance of the model. When the temperature difference between the two sides of the TIL was 30 °C, the maximum output power of the model with a hot-side temperature of 60 °C was only 3.13% lower than that with a hot-side temperature of 40 °C, and the open-circuit voltage differed by only 0.68%. Therefore, as long as there is a sufficient temperature difference for thermoelectric power systems to generate electricity, the same power generation performance can be achieved regardless of the temperatures on both sides of the TIL. This further expands the application range of thermoelectric power systems in the field of tunnels.

4.3 *Effect of height of TE legs*

The generation performance of the thermoelectric power system in a high geothermal tunnel is not only related to the temperature difference but also influenced by the geometric factors of the TEMs. This section analyzes the effect of the height of the TE legs on the system's generation performance.

Figure 11 illustrates the correlation between the generation performance of TEM model and the height of TE legs. It can be observed that the open-circuit voltage of the TEM model was positively correlated with the height of TE legs, while the maximum output power of the TEM model first increased and then decreased when the height of TE

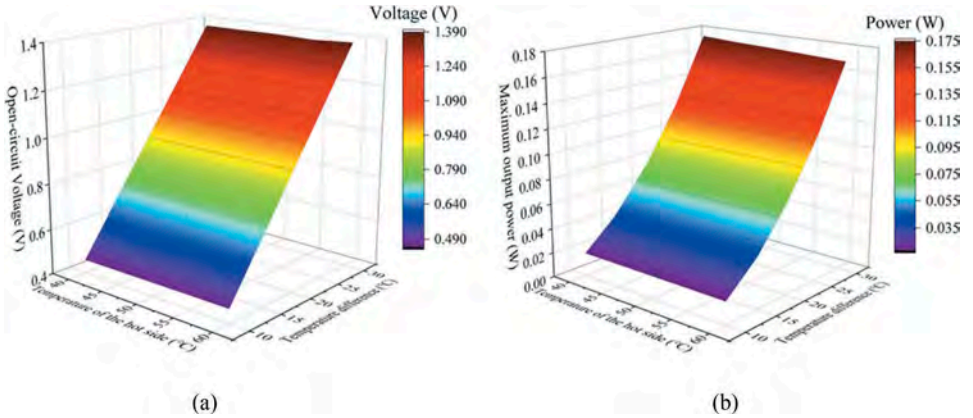

Figure 11. The relationship between the generation performance of the system model with one TEM and the temperature conditions. (a) The open-circuit voltage, and (b) the maximum output power.

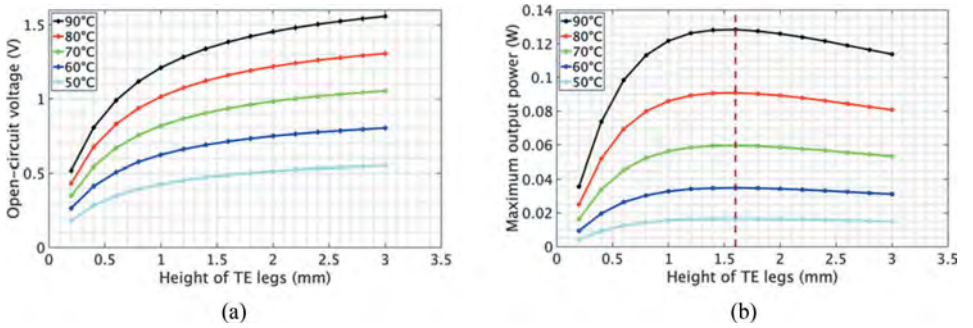

Figure 12. The relationship between the generation performance of the TEM model and the height of TE legs. (a) The open-circuit voltage, and (b) the maximum output power.

legs increased. This is because the height of TE legs is related to the thermal resistance and electrical resistance of the TEM, which have different effect on generation performance. When the height of TE legs increases, both the thermal resistance and electrical resistance increase. As a result, the higher thermal resistance leads to a greater temperature gradient across the thermoelectric couples, resulting in an increased open-circuit voltage of TEM. However, the increase in electrical resistance decreases the maximum output power of TEM. Additionally, according to Figure 15, it can be observed that the optimal height of TE legs was 1.6 mm. When the temperature of surrounding rock was set at 90 °C, the maximum output power of the TEM model with a height of 1.6 mm for the TE legs was 5.51% higher than that of the TEM model with a height of 1.0 mm for the TE legs.

5 CONCLUSIONS

This paper proposes a conception of thermoelectric power system in high geothermal tunnel as an innovative design. To evaluate the generation performance of the thermoelectric power system in high geothermal tunnel, a three-dimensional finite element numerical simulation of the system under various surrounding rock temperatures and number of TEMs was carried out. Meanwhile, the factors that influence the generation performance of the system was analyzed. The results indicates that:

1) Based on the simulation results, we can speculate that a thermoelectric power system with 51020 TEMs, occupying an area of 1000 square meters, could reach a maximum output power of 9132 W when the surrounding rock temperature was 90 °C. The stable performance and considerable electricity generated by the system made the thermoelectric power system a promising way to harness the geothermal energy in high geothermal tunnels and alleviate the power supply problems of these tunnels.
2) The maximum output power of the system was positively correlated with the temperature difference, and they followed a quadratic function relationship. Therefore, increasing the temperature difference is an effective method to improve the performance of the system.
3) The hot side temperature had little effect on the generation performance of the system under temperature fields of high geothermal tunnels. Regardless of the temperature of the hot side, the system can achieve essentially the same power generation performance with a consistent temperature difference.
4) The maximum output power first increased and then decreased when the height of TE legs increased. And the optimal height of TE legs for the system in high geothermal tunnel was 1.6mm.

REFERENCES

Alina W., Xiang L., Jonathan C., et al, 2022. Shallow geothermal energy potential for heating and cooling of buildings with regeneration under climate change scenarios. Energy. 244(PB).

Guang-Zhao O., Yu-Yong J., Guo-Hua Z., et al, 2021. Collapse risk assessment of deep-buried tunnel during construction and its application. Tunnelling and Underground Space Technology incorporating Trenchless Technology Research. 115.

H. Wang., C. Qi., et al, 2010. Improved method and case study of thermal response test for borehole heat exchangers of ground source heat pump system. Renewable Energy. 35, 727–733.

He H., Liu W., Wu Y., et al, 2019. An approximate and efficient characterization method for temperature-dependent parameters of thermoelectric modules. Energy Conversion and Management. 180, 584–597.

He H., Wu Y., Liu W., et al, 2019. Comprehensive modeling for geometric optimization of a thermoelectric generator module. Energy Conversion and Management. 183, 645–659.

Heng Z., Zihan H., Gang Z., et al, 2022. The cooling effect of high geothermal tunnel construction environment: A case of ice and spray method in an extra-long tunnel. International Journal of Thermal Sciences. 178.

Hussam J., Alina Ż., Navid K., et al, 2021. Thermoelectric generator (TEG) technologies and applications. International Journal of Thermofluids. 9(prepublish).

Kewen L., Geoffrey G., Yuhao Z., et al, 2021. Thermoelectric power generator: Field test at Bottle Rock geothermal power plant. Journal of Power Sources. 485 (prepublish), 229266.

Lee C., Park S., Choi H., et al, 2016. Development of energy textile to use geothermal energy in tunnels. Tunnelling and Underground Space Technology incorporating Trenchless Technology Research. 59, 105–133.

Leyre C., Patricia A., Miguel A., et al, 2023. Field test of a geothermal thermoelectric generator without moving parts on the Hot Dry Rock field of Timanfaya National Park. Applied Thermal Engineering. 222.

Luo D., Wang R., Yu W., et al, 2020. Parametric study of a thermoelectric module used for both power generation and cooling. Renewable Energy. 154, 542–552.

Ming L., Ping Z., Yifan J., et al, 2022. Numerical investigation on comprehensive control system of cooling and heat insulation for high geothermal tunnel: A case study on the highway tunnel with the highest temperature in China. International Journal of Thermal Sciences. 173.

Montaser M., Mohamad R., Keith P., et al, 2021. A review of grout materials in geothermal energy applications. International Journal of Thermofluids. (prepublish),100070.

Ogunleye O., Singh M R., Cecinato F., et al, 2020. Effect of intermittent operation on the thermal efficiency of energy tunnels under varying tunnel air temperature. Renewable Energy.146(C), 2646–2658.

Revesz A., Chaer I., Thompson J., et al, 2016. Ground source heat pumps and their interactions with underground railway tunnels in an urban environment: A review. Applied Thermal Engineering. 93, 147–154.

Xi J., Li Y., Liu M., et al, 2017. Study on the thermal effect of the ground heat exchanger of GSHP in the eastern China area. Energy. 141, 56–65.

Yang C., Peng F., Xu K., et al, 2019. Feasibility study on the geothermal utility tunnel system. Sustainable Cities and Society. 46, 101445–101445.
Yuan Y., Cao X., Sun L., et al, 2012. Ground source heat pump system: A review of simulation in China. Renewable and Sustainable Energy Reviews. 16(9), 6814–6822.
Yunfeng M., Linsheng X., Ximei S., 2023. The multi-factor influence of frost resistance and prevention effect of tunnel thermal insulation layer in cold areas. Alexandria Engineering Journal. 78, 15–25.
Zhenhua W., Shuai Z., Zekun L., et al, 2022. Thermoelectric converter: Strategies from materials to device application. Nano Energy. 91.

Tunnelling for a Better Life – Yan, Celestino, Thewes & Eberhardt (Eds)
© 2024 The Author(s), ISBN 978-1-032-80042-4
Open Access: www.taylorfrancis.com, CC BY-NC-ND 4.0 license

Development and application of complete equipment for mechanized construction of defect remediation in existing railway tunnels

Wei Yuan
China Railway Southwest Research Institute Co., Ltd., Chengdu, China

Fengtao Gui
Chengdu Railway Bureau, Chengdu, China

Long Zhang
China Railway Southwest Research Institute Co., Ltd., Chengdu, China

Peng Zhang
Chengdu Railway Bureau, Chengdu, China

ABSTRACT: Aiming at the current technical status that currently treating defects in existing railway tunnels is mainly done by hand with high operation intensity, low efficiency and a lack of safety guarantee, this Paper develops a series of complete equipment for mechanized construction of defect remediation in existing railway tunnels. This series of equipment is able to do self-access to and self-walk on existing railways. Based on modular design concept, drilling, slotting, green cutting, arch installing and concrete spraying modules are designed with a quick functional interchangeability, realizing the mechanized construction of key processes in whole construction process of common treatment technology for tunnel defects, increasing the construction efficiency by 2-3 times when compared with traditional operation methods and reducing the number of operators by more than 50%. In addition, cleaning hole by high pressure water, dust removal by spraying high pressure water and other measures are used to greatly decrease the construction dust discharge and improve the working environment in tunnels.

Keywords: Railways in operation, defect treatment, mechanized construction, complete equipment

1 INTRODUCTION

By the end of 2022, the total operating mileage of railways has reached 155 000 km in China. To be specific, 17 873 railway tunnels have been put into operation, with a total length of 21 978 km as shown by Gong J. F., et al. (2023).With the gradual transition from the peak period of tunnel construction to the peak period of tunnel repair in China, the common defects of water leakage, lining cracking, and back cavity in tunnels are becoming more and more serious. When diseases occur, railway operators often treat them by bolting and shotcreting support or molded lining technology. The main procedures involved include construction of the work platform, drilling of bolt holes, chipping and slotting of lining, installation of bolts and drill rods, fixation of reinforcing meshes, erection of steel formwork, pouring or shotcreting of concrete, spraying of waterproof coatings, etc. At present, the above procedures are still mainly manual operations with low construction efficiency, high operation intensity, and high risks in safety construction, which is obviously difficult to provide operational safety guarantees for the rapidly developing transportation network as shown by Gao J.R., et al. (2018). Based on the above situation, in the paper, a complete set of equipment for treating the defects of operating tunnels was developed targeting the key procedures, such as drilling, chipping, slotting, arch frame installation, and concrete shotcreting, which currently restrict the construction efficiency of treating the defects of operating tunnels as shown by Gao J.R., et al. (2019). For the first time in China, full-face mechanization of the key procedures of treating the defects of operating railway tunnels was realized.

This series of equipment was composed of a guide assembly, a double rotation assembly,

*Corresponding author: 648309437@qq.com

DOI: 10.1201/9781003495505-467

a mechanical arm assembly, a drilling, chipping, and slotting assembly, etc. It could be controlled flexibly due to its high degree of spatial freedom, and had the functions of quickly getting on and off the existing lines and walking by itself, which reduced the construction difficulty and labor intensity of treating the defects of operating tunnels, and improved the construction efficiency, quality, and operation safety. Compared with traditional manual operation modes, by using the developed series of equipment, the construction efficiency of single machine for the bolt hole drilling procedure was increased by 8-10 times, and the number of operators was reduced by more than 60%; the construction efficiency of the lining slotting procedure was increased by 7-8 times, the number of operators was reduced by more than 50%, and the tunnel lining slotting operation was dust-free; under the same construction efficiency of the lining chipping, arch frame installation, and concrete shotcreting procedures, the number of operators could be reduced by more than 80%, and high-pressure water was used for dust settling by spraying, which effectively improved the working environment in the tunnel.

2 EQUIPMENT SCHEME DESIGN

2.1 *Design principles*

(1) The complete equipment for treating the defects of operating tunnels shall have the functions of drilling, chipping, slotting, arch frame installation, and concrete shotcreting.
(2) The complete equipment for treating the defects of operating tunnels shall have the function of walking by itself, and shall not intrude into the rolling stock clearance for railway in the process of entering or exiting the tunnel (in a non-operating state).
(3) The complete equipment for treating the defects of operating tunnels shall be able to avoid the carrier cables and overhead lines to carry out operations on the tunnel roof (drilling, chipping, slotting, arch frame installation, and concrete shotcreting).
(4) The operating range of the complete equipment for treating the defects of operating tunnels shall be able to cover all areas of the circular section the tunnel.
(5) The complete equipment for treating the defects of operating tunnels shall be designed based on the modular design concept, through universal interfaces of different function modules, to realize fast conversion of the functions of drilling, chipping, slotting, arch frame installation, and concrete shotcreting of the multifunctional operation trolley.
(6) The complete equipment for treating the defects of operating tunnels shall be designed with emergency and safety guarantee devices, which can effectively and quickly move the equipment out of the operation area to avoid the impact on train operation in case of equipment failure during operation.

2.2 *Main technical parameters*

(1) Total weight of equipment: 10, 200kg
(2) Operating range of equipment: maximum height 8m, maximum width 6.1m
(3) Total equipment power: 65kW
(4) Drilling range of equipment: 41-102mm
(5) Maximum drilling depth of equipment: 25m
(6) Drilling efficiency of equipment: 1m/min (average)
(7) Chipping efficiency of equipment: $70m^2/h$
(8) Maximum chipping depth of equipment: 20mm
(9) Gouging efficiency of equipment: 0.2m/min (drainage channel with regular size)
(10) Maximum gouging width of equipment: 200mm
(11) Maximum gouging depth of equipment: 200mm
(12) Concrete shotcreting efficiency of equipment: $8m^3/h$
(13) Maximum unit weight of installed arch frame of equipment: 1t
(14) Installation efficiency of arch frame of equipment: 4-5 trusses/h.

2.3 *Scheme design*

The overall design scheme is shown in Figure 1. The equipment was mainly composed of a crawler-type road-rail transport platform, drilling assembly, slotting assembly, chipping assembly, arch frame installation and concrete shotcreting assembly, as well as emergency rescue equipment. Considering cost and safety, a crawler excavator was used as the carrier, and a special guide mechanism was designed to realize the excavator's getting on and off the lines and walking by itself on existing rails. The equipment was more flexible, and it had a short production and manufacturing cycle and high reliability. It was more suitable for the characteristics of small work amount, large number and wide distribution of works of treating the defects of operating railway tunnels.

2.3.1 *Design of the road-rail excavator refitted transport platform*

Considering that the equipment for treating defects needed to crawl along the railway ballast to the track, while taking into account the cost of equipment procurement, it was planned to use the excavator caterpillar chassis, excavator boom, and existing hydraulic control system for reconstruction design, and making full use of the existing equipment. After the defects were treated, the equipment could quickly restore the function of an excavator.

(1) Selection of excavator
The cross-section dimensions and clearance requirements of the tunnels of single-track

railway, while taking account of the flow and pressure parameters of the hydraulic system of the selected excavator. It is recommended to use excavators between 10t and 13t for the tunnels of single-track railway, and 20t excavators for the tunnels of double-track railway.

(2) Design of guide system
The designed guide system used a hydraulic motor of the excavator to provide power with a maximum walking speed of 30km/h and a braking distance of 5m at the maximum operating speed, which effectively shortened the time of preparation for defect treatment in the early stage and scaffolding mobilization and demobilization.

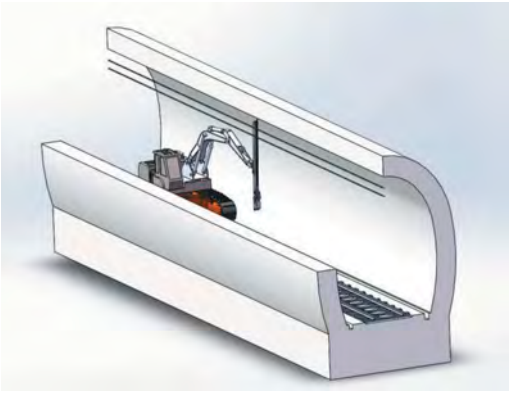

Figure 1. Model diagram of the overall plan of the trolley.

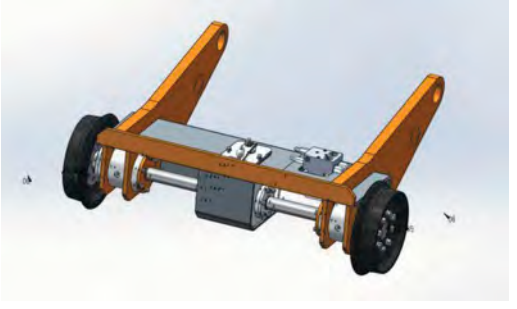

Figure 2. 3D model of rear guide assembly.

2.3.2 *Design of bolt drilling assembly*

(1) Design of propelling beam
According to the cross-section dimensions of the tunnel, the propelling beam was designed to have a total length of 4.5m, and the one-time drilling depth without rod extension was 3.5m, which could meet the design length of most bolts. The maximum drilling depth after rod extension reached 20m. The three-dimensional model of the propelling beam assembly of the rock drill is shown in Figure 3.

Figure 3. Propelling beam assembly.

(2) Selection of rock drill
A hydraulic rock drill was preliminarily selected for drilling. On the basis of thorough research on various rock drills, considering the purchase cost and product performance, the Finnish Doofor DF530 rock drill was selected. The technical parameters are shown in Table 1.

Table 1. Technical parameters of DF530 Doofor hydraulic rock drill.

Model	Rated power	Oil pressure	Flow	Rotation torque	Drilling diameter
Hydraulic rock drill DF530	(kW)	(Mpa)	(L/min)	(N.M)	(mm)
	10	10-13	45-55	70-269	45

(3) Design of double rotation mechanism
In order to adjust the spatial orientation of the rock drill, especially for the construction of radial bolt holes of the tunnel, the pitching motion of the rock drill was adjusted using the rotation bearing and the arm oil cylinder of the excavator. SWE9 rotation bearing was selected based on the weight of the propelling beam to be selected.

2.3.3 *Design of the slotting, chipping, arch frame installation, and concrete shotcreting assembly*

The design of this part mainly includes the design of the universal floating boom and the design of various functional components.

(1) Design of the floating boom
As shown in Figure 4, the floating boom adopted a two-stage telescopic mode and used a hydraulic cylinder to provide power. The telescopic boom end was designed with universal interfaces for the functional components. The telescopic boom had a pitching function, which was used to realize the movement of all functional components along the cross-section of the tunnel. The telescopic boom was also designed with a rotation mechanism, which adopted a rotation support to provide rotation power. When the equipment entered and exited the site, the telescopic boom was parallel to the trolley boom through the rotation mechanism. When the trolley reached a defect treatment

work point, the telescopic boom was rotated parallel to the tunnel cross-section direction through the rotation mechanism.

Figure 4. Floating boom model.

(2) Design of the chipping functional component
As shown in Figure 5, the chipping heads were arranged in quincunx. Compared with traditional manual operations, at each punch of chipping points, the chipping points were even and the chipping depth was controllable. Each hydraulic chipping heads had a retractable mechanism that could realize the self-adaptation of different lining surfaces.

Figure 5. Chipping functional component model.

(3) Design of the slotting functional component
The slotting functional components mainly included a combined-type one-time cutting tool installed on the floating boom, a hydraulic motor driving the tool to rotate, and a mechanical limiting device, etc., as shown in Figure 6.

Figure 6. Slotting functional component model.

(4) Design of the shotcreting component
The design of the shotcreting component is shown in Figure 7. It was mainly composed of a nozzle, a brushing mechanism, a 240° rotation mechanism, and a 360° rotation mechanism, which could flexibly realize shotcreting operations at various angles.

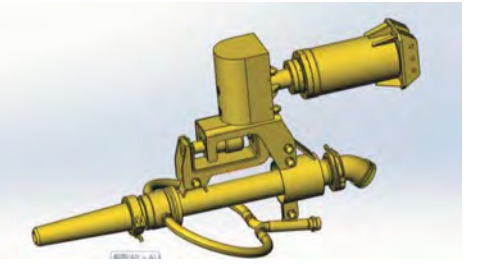

Figure 7. 3D model of the shotcreting component.

(5) Design of the arch frame installation componentThe arch frame installation component is shown in Figure 8. It mainly included a chuck, a pitching mechanisms, a 360° rotation mechanisms, etc., which could install the vault and the arch frame by bypassing the overhead lines.

Figure 8. 3D model of the steel arch frame installation component.

2.4 *Working principle*

(1) Walking and braking of the complete equipment for treating the defects of operating tunnels
The developed complete equipment for treating the defects of operating tunnels was based on a road-rail excavator refitted transport platform (as shown in Figure 9), which adopted a crawler-type and wheel rail-type dual power mode. It realized the function of getting on and off the line and walking by itself on the existing line through hydraulic power switching. When the equipment reached a defect treatment work point, hydraulic braking was used.

(2) equipment for treating the defects of operating tunnels
The developed complete equipment for treating the defects of operating tunnels was designed with

Figure 9. Road-rail transport platform.

a pitching boom, a folding boom, and a telescopic boom. When walking, these booms were collapsed to ensure that the overall size of the trolley did not intrude into the tunnel clearance. When operating, they were expanded to ensure that the scope of mechanization could cover the entire tunnel cross-section (as shown in Figure 10).

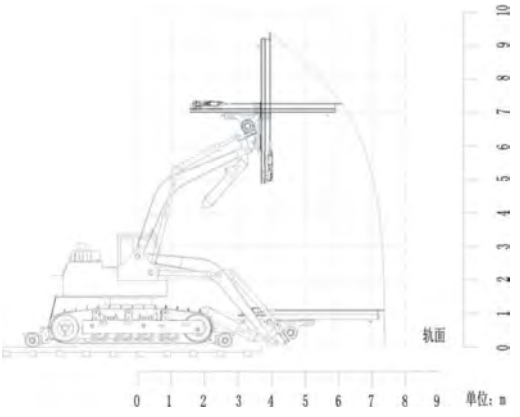

Figure 10. Schematic diagram of the operating range of the multifunctional operation trolley for operating tunnel maintenance.

(3) The principle of switching between different functions of the complete equipment for treating the defects of operating tunnels
The developed complete set for treating the defects of operating tunnels adopted a modular design and shared a common transport platform. The switching of the functions of drilling, chipping, slotting, arch frame installation, and concrete shotcreting of treating tunnel defects could be realized by switching between different functional modules according to the requirements of the tunnel defect treatment procedures.

(4) Principle of efficient drilling of the complete equipment for treating the defects of operating tunnels
The developed complete equipment for treating the defects of operating tunnels realized precise positioning and construction of radial holes on the tunnel vault by replacing drilling functional components, with a 360° double mechanism, and a laser-assisted positioning system. The drilling efficiency of the rock drill was ensured by using control systems such as real-time monitoring of system pressure, anti-trapping drill rod for surrounding rock breaking, and automatic drilling linkage (as shown in Figure 11).

Figure 11. Drilling operation of complete equipment for treating the defects of operating tunnels.

(5) Principle of efficient chipping of the complete equipment for treating the defects of operating tunnels
By replacing the chipping functional component, the developed complete equipment for treating the defects of operating tunnels used an independent air-leg type floating mechanism to drive the hydraulic driven rotary punch-type chipping heads. All chipping heads were arranged in quincunx. Under the action of the floating boom, they could automatically adapt to the tunnel lining surface segment and closely adhered to the tunnel lining surface, and completed the tunnel lining chipping operation under the repeated vibration of the chipping heads (as shown in Figure 12).

Figure 12. Chipping operation of the complete equipment for treating the defects of operating tunnels.

(6) Principle of efficient slotting of the complete equipment for treating the defects of operating tunnels

By replacing the slotting functional component, the developed complete equipment for treating the defects of operating tunnels used a combined-type high-speed rotary concrete cutting head. By adjusting the thickness of the cutter head and the depth of the feed, the mechanical one-time cutting and slotting of the steel arch frame installation groove or drainage channel could be realized. Precise alignment of the cutter head could be realized quickly by using a mechanical arm horizontal state monitoring system and a telescopic boom vertical auxiliary control system (as shown in Figure 13).

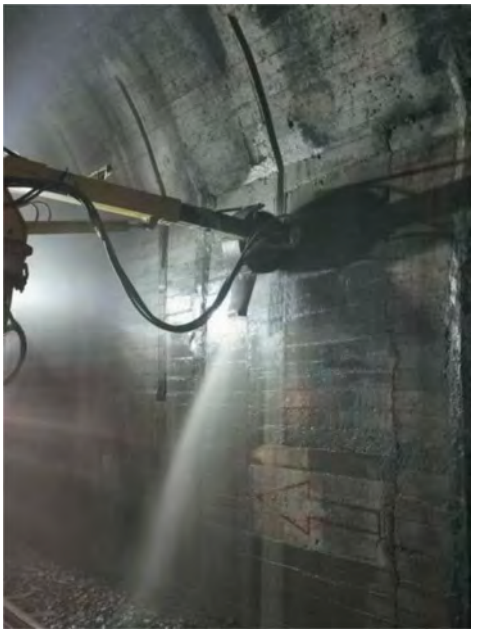

Figure 13. Slotting operation of the complete equipment for treating the defects of operating tunnels.

(7) Principle of arch frame installation of the complete equipment for treating the defects of operating tunnels

By replacing the arch frame installation functional component, the developed complete equipment for treating the defects of operating tunnels realized the alignment, installation, and fixation of the arch frame in the tunnel by using a hydraulic claw to clip the arch frame and adjusting the spatial position of the arch frame through a telescopic mechanical boom, a rotation mechanism, and a pitching mechanism (as shown in Figure 14).

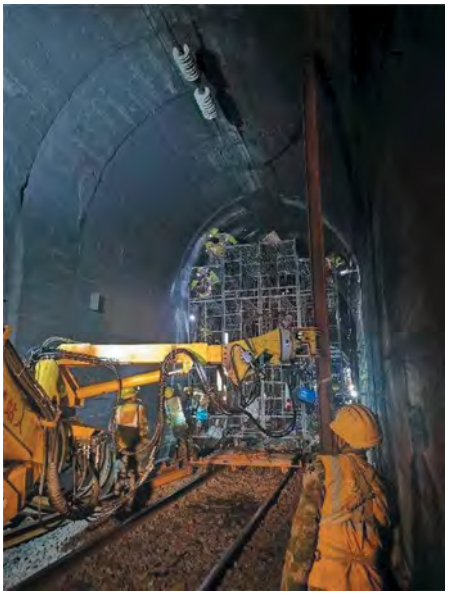

Figure 14. Slotting operation of the complete equipment for treating the defects of operating tunnels.

(8) Principle of concrete shotcreting of the complete equipment for treating the defects of operating tunnels

By replacing the concrete shotcreting functional component, the developed complete equipment for treating the defects of operating tunnels realized concrete shotcreting with remote control through the combination of nozzle rotation and telescopic boom movements (as shown in Figure 15).

Figure 15. Concrete shotcreting operaton of the complete equipment for treating the defects of operating tunnels.

3 ENGINEERING APPLICATION AND ECONOMIC ANALYSIS AND COMPARISON

3.1 *Engineering application*

Up to now, the series of complete equipment for treating the defects of operating tunnels have been applied in dozens of railway tunnel defect treatment projects such as Shanghai-Kunming, Baoji-chengdu, and Neijiang-liupanshui. The on-site applications are shown in Figure 16. The equipment exhibited stable performance, which improved the efficiency of operation, maintenance, and construction, and reduced the safety risk of the construction for treating the defects of the existing railway tunnels.

Figure 16. Photos of the equipment operating on the construction site.

3.2 *Analysis of economic benefits of applications*

Based on the data of the existing traditional manual operation procedures of the project, only the operational benefits of the drilling and slotting procedures were analyzed as shown by Zhang L., et al. (2022).

3.2.1 *Analysis of economic benefits of drilling*

To make the economic comparison and analysis of the mechanized bolt drilling operation and traditional manual pneumatic drill bolt construction operation, statistical analysis was made with the mechanized construction and manual pneumatic drill operation by the same construction team as an example, as shown in Table 2. It can be seen that the mechanized drilling operation is more than 8 times more efficient than the manual pneumatic drill operation.

3.2.2 *Analysis of economic benefits of the slotting equipment*

With the construction of the drainage channel for treating the defects of a tunnel of the Chengdu-Kunming Railway as an example, based on the on-site measurement of the efficiency of manual steel arch frame installation groove of a nearby tunnel, the efficiency of mechanized slotting and manual slotting was compared, as shown in Table 3. It can be seen that the efficiency of mechanized slotting operation was about 6 times that of manual operation, and the former had significant advantages in construction efficiency.

4 CONCLUSION AND PROSPECT

(1) The complete equipment for treating the defects of operating tunnels that integrated functions such

Table 2. Comparison of efficiency and staffing between manual and mechanical slotting.

Compared item	Drilling of traditional manual pneumatic drill	Drilling of mechanized equipment	Remarks
Number of equipment	4 sets	1 set	
Staffing	8 persons (operated by 2 persons per equipment)	1 person	The auxiliary personnel were not counted.
Drilling duration	300min	70min	Pure operation duration
Work amount of drilling	36m (based on average quantity)	66m (based on average quantity)	
Average hole formation efficiency	0.12m/min	0.94m/min	Converted to per linear meter
Average duration of single hole formation	25min	3min	Calculated based on 3m bolt hole uniformly
Working environment	The exhaust noise of drilling was mostly around 120dB, and the oil used for lubricating the rock drill was directly discharged into the air. In addition, high-pressure air cleaning holes were used, which seriously polluted the working environment.	The noise of the hydraulic rock drill was generally below 90dB. High-pressure water cleaning holes were used, which significantly improved the working environment in the tunnel.	

Table 3. Comparison of efficiency and staffing between manual and mechanical slotting.

Compared item	Traditional manual slotting	Mechanized equipment gouging	Remarks
Groove type	Steel arch frame installation groove	Drainage channel	
Preliminary preparation duration	60min	30min	Including mobilization, demobilization and erection duration
Pure operation duration	50min	70min	The machinery did not require scaffolding
Technical parameters of the groove	Groove depth 200mm, groove width 160mm	Groove depth 80mm, groove width 80mm	
Work amount of gouging	0.5m	15m	
Staffing	4 persons	1 person	For manual operation, 2 persons per group, not including auxiliary personnel
Measured gouging efficiency	0.01m/min	0.2m/min	
Comparison of efficiency after converting earthwork	0.016m3/h	0.09m3/h	Efficiency after converting into the same slotting earthwork based on the measured data.

as drilling, slotting, chipping, arch frame installation, and concrete shotcreting, and had the functions of getting on and off and walking by itself on existing railway lines. Corresponding mechanized construction methods and technologies were proposed to improve the efficiency, quality, and operational safety of tunnel defect treatment.

(2) To avoid short board effect, the research and development on mechanized treatment equipment for the defects at the bottom of tunnels are continued to be carried out. After gradually realizing the mechanization of key procedures for defect treatment, the comprehensive rail cars for treating the defects of operating tunnels will be developed actively, which have the function of synchronous and rapid treatment of multiple types of defect, to further significantly improve the efficiency of comprehensive treatment of tunnel defects.

(3) Based on the developed complete equipment for treating the defects of operating tunnels and supporting mechanized construction technology, a rapid repair technology for common flaws and defects of operating railway tunnels will be proposed, forming a technical system for treating the structural flaws and defects of operating tunnels, so as to promote the progress of operating tunnel maintenance technology.

REFERENCES

Gong J. F., et al, 2023, Statistics of railway tunnels in China by the end of 2022 and overview of key tunnels of projects newly put into operation in 2022. Tunnel Construction, 2023, 43(4), 721.

Gao J.R., et al, 2018. State of the Art of Techniques and Equipment for Defect Remediation in Existing Railway Tunnels. Mode. Tunn. Tech. 55(1), 7–16.

Gao J.R., et al, 2019. Research of Equipments for Disease Remediation in Operation Tunnels. Mode. Tunn. Tech. 56(z1), 34–40.

Zhang L., et al, 2022. Researchand Development of the Key Equipment and Construction Technology for the Maintenanee of Operating Railway Tunnels. Mode. Tunn. Tech. 59(S1), 1017–1022.

Tunnelling for a Better Life – Yan, Celestino, Thewes & Eberhardt (Eds)
© 2024 The Author(s), ISBN 978-1-032-80042-4
Open Access: www.taylorfrancis.com, CC BY-NC-ND 4.0 license

Research trend and prospect of reconstruction and expansion technology of existing highway tunnels

Zekun Zhang*
School of Highway, Chang'an University, Xi'an, Shaanxi, China

ABSTRACT: The rapid development of the social economy leads to the increasingly obvious contradiction between highway transportation demand and capacity mismatch, and the reconstruction and expansion of existing highway tunnels has become a long-term effective means to improve the future highway transportation environment. The development trend and research dynamics of highway reconstruction and expansion are clarified through the literature search and statistical analysis of typical reconstructed and expanded highway tunnels. The current situation and shortcomings of the research on highway tunnel expansion schemes are pointed out, and the proposed expansion schemes are put forward based on the scheme comparison. Combined with four typical expansion methods and tunnel expansion coefficients, the proposed construction methods for expanding existing highway tunnels are presented. The research dynamics and shortcomings of mechanical response of surrounding rock, blasting vibration control are described. The application prospects of BIM technology, artificial intelligence technology, and green carbon neutral concepts in the reconstructed and expanded tunnels are proposed. It is pointed out that standardization of construction standards, intelligence of expansion plans, innovation of construction methods are the key research directions in the future.

Keywords: Highway tunnel, Reconstruction and expansion technology, Construction method, Surrounding rock stability

1 INTRODUCTION

In the past 10 years, the annual mileage of road tunnels in China has increased by 1,100 km. Urbanization has brought new challenges to the transport capacity of highway traffic. The capacity of the original tunnels can no longer meet the needs of transport, and tunnel expansion and reconstruction have gradually become an effective method to solve this problem (Li et al., 2012).

Tunnel alteration and expansion refers to the original tunnel whose construction standard cannot meet the traffic demand to be altered and expanded, and the original tunnel structure is removed to realize the expansion of the tunnel section (Peng et al., 2010). Due to the early completion of the tunnel by the design standards and construction level of the limitations of some tunnels construction cycle is short, and the quality of the project is insufficient, resulting in the tunnel operation process of the lining cracks, deformation, water seepage, concrete block spalling and many other defects. Coupled with the influence of highway alignment and urban environment, expanded highway tunnels often face construction problems such as close connection to existing highways, large cross-sections, small clearances, tunnel clusters, and opening to traffic while construction is in progress (Zhang et al., 2020).

Reconstruction and expansion of tunnels will destroy the force balance of existing tunnels, resulting in the accumulation of damage to the surrounding rock, and then deformation and support structure overstressed, poor stability, and other problems (Li et al., 2014), increasing the difficulty of reconstruction and expansion of tunnels. China's research on road tunnel reconstruction and expansion technology is relatively small. It mainly focuses on the basic laws of tunnel expansion construction mechanics based on on-site monitoring and numerical analysis, expansion program and excavation method, and other primary research levels, lack of matching design specifications, and construction basis (Ell et al., 1999). The mechanical response characteristics of the surrounding rock of the reconstruction

*Corresponding author: 993606695@qq.com

DOI: 10.1201/9781003495505-468

and expansion construction, blasting vibration control technology, and monitoring support measures are not enough to explore, which hinders the development of tunnel reconstruction and expansion.

This paper clarifies the research content by reviewing the typical cases of reconstruction and expansion of highway tunnels at home and abroad in the past 20 years. It focuses on the research deficiencies in the reconstruction and expansion tunnel scheme, reconstruction and expansion excavation method, and tunnel surrounding rock stability. Finally, based on BIM technology, artificial intelligence technology, and the concept of green carbon neutrality, it puts forward the key research directions for the future.

2 DEVELOPMENTS AND RESEARCH DYNAMICS OF RECONSTRUCTION AND EXPANSION TUNNELS

2.1 *Development trend*

The earliest origin of tunnel expansion was the railroad tunnels in the 1990s. In order to meet the requirements of train limits and improve the transportation capacity, followed by speed up and expansion of existing railroad tunnels, such as the White Haven and Rockport railway tunnels in the U.S. (Ell et al., 1999), the Rufenen railway tunnel in Switzerland (Deng et al., 1997), the Tower Nominee railway tunnel in Japan (Xian et al., 1996).

At the beginning of the 21st century, the reconstruction and expansion of highway tunnels gradually appeared. Overseas, the Tennozan tunnel (Xian et al., 1996) of the Meishin Expressway in Japan, the original tunnel was reconstructed and expanded due to the deformation and contraction of the cross-section. In 2004-2007, the Nazzano road tunnel (Lin et al., 2018) was widened in Italy, with a cross-sectional area of 158 m^2 after widening. In China, the expansion of the Damaoshan (Zhong et al., 2019) Tunnel on the Quan-Xia Expressway began in 2008. A new four-lane tunnel was built in the middle of the original separated two-way four-lane tunnel, and the original two-lane tunnel on the right was expanded in situ to four lanes, which became China's first four-lane highway tunnel combination reconstruction and expansion project. In 2018, the Housi Tunnel of the Xia-Rong Expressway was expanded from a two-lane to a four-lane tunnel, with a width of 20 m from 9 m, and an expansion length of 1002 m, which is the longest in-situ reconstruction and expansion of highway tunnels in China. In 2019, the Wenling Loushan Tunnel was completed reconstruction and expansion, which became the first case of in-situ reconstruction and expansion around a large cross-section with four lanes expanding to eight lanes in both directions in China (Cheng et al., 2020).

Table 1 summarizes the cases of domestic road tunnel reconstruction and expansion projects in the past 20 years and summarizes the characteristics of road tunnel reconstruction and expansion projects as follows:

Table 1. Typical engineering cases of tunnel reconstruction and expansion.

Type	Scheme		Project name (time)	Forward and backward forms	Tunnel parameters (W×H/m or S/m^2)	Enclosed rock grade/ Excavation method	Causes and characteristics
High-grade	In situ	One-side	Jinji Mountain Tunnel (2013)	Two holes 4 lanes → 8 lanes	S_O: 271.80 m^2 S_L: 481.70 m^2	V: CRD	Increase capacity
			Yuzhou Tunnel (2014)	Two holes 4 lanes → 8 lanes	W_O×H_O: 10×6.79 W_L×H_L: 17.08×8.48	IV: CD	Ease traffic congestion Increase capacity
			Fuzhou Mawei Tunnel (2019)	Two holes 4 lanes → 8 lanes	W_O×H_O: 9×6.86 W_L×H_L: 17.25	II/III: Step method V: CRD	Disease management Increase capacity
			Fuzhou Gushan Tunnel (2019)	Two holes 4 lanes → 8 lanes	W_L×H_L :19.77×13.35	II/III: Step method IV: CD	Disease management Increase capacity
		Two-side	Yangshuo Jingya Tunnel (2015)	One hole 2 lanes → Double linked arches 4 lanes	W_L×H_L: 13.1×5.5;	II: Full section method	Ease traffic congestion Increase capacity

(*Continued*)

Table 1. (Cont.)

Type	Scheme		Project name (time)	Forward and backward forms	Tunnel parameters (W×H/m or S/m^2)	Enclosed rock grade/ Excavation method	Causes and characteristics
		Surrounded	Zhoushan Hai Zhong Zhou Tunnel (2007)	One hole 2 lanes → 2 lanes	W_O×H_O: 10 ×5 W_L×H_L: 16 ×5	V: Step method	Ease traffic congestion Increase capacity
			Wenling Loushan Tunnel (2019)	Two holes 4 lanes → 8 lanes	W_O×H_O: 10.25 ×5 W_L×H_L: 17.25 ×5	IV/V: Twin-side heading method	Increase capacity Small spacing
	Group Combination change Expansion construction		Fujian Dai-MaoShan Tunnel (2010)	Two holes 4 lanes→-Three holes 8 lanes	W_O×H_O: 11.90×9.50 W_L×H_L :19.69×12.30	IV: Twin-side heading method V: CD	Increase capacity Small spacing
			Chongqing Songjiagou Tunnel No. 1(2018)	Two holes 4 lanes→-Four holes 8 lanes	W_L×H_L :20.08×13.40	V: CD	Increase capacity Large section
			Fujian Housi Tunnel (2018)	Two holes 4 lanes→-Three holes 9 lanes	W_O×H_O: 9.2×5 W_L×H_L: 17.75×5	V: Step method V: CD	Increase capacity Small spacing
	Surrounding new construction		Hanjialing Tunnel (2003)	Two holes 4 lanes → 8 lanes	W_L×H_L :19.46×9.75	III/IV: Step method	Increase capacity Small spacing
			DaiPingShan Tunnel (2010)	Two holes 4 lanes→ Four holes 8 lanes	W_L×H_L: 10.5×;	II: Step method	Increase capacity Small spacing
			Guizhou Jiujiawan Tunnel (2017)	Two holes 4 lanes→-Three holes 8 lanes	W_O×H_O: 10.25 ×5 W_L×H_L: 18.50 ×5	V: Twin-side heading method +CD	Increase capacity
Low-grade	In-situ	One side	Anshan Yufoshan Tunnel (2008)	Two holes 2 lanes→ Two holes 4 lanes	W_O×H_O: 7×4.5 W_L×H_L: 12×5.5	III/IV: Step method	Disease management Increase capacity
			S218 Liming Tunnel (2020 under construction)	One holes 2 lanes→ One hole 2 lanes	W_O: 8.5 W_L: 12	V: CRD	Disease management Increase capacity
			Shanxi Pengtougou Tunnel (2009)	One holes 2 lanes→ One hole 2 lanes	W_L×H_L: 11 ×5	V: Step method	Increase capacity
			Fujian Dangfeng Aao Tunnel (2014)	One holes 2 lanes→ One hole 2 lanes	W_O×H_O: 8 ×5 W_L×H_L: 10 ×5	III/IV: Full section method	Disease management Increase capacity
		Surrounded	Lvliang Dongjiagou Tunnel (2008)	Two holes 2 lanes → 4 lanes	W_O: 5 W_L: 11.44	V: Step method	Disease management Increase capacity
			Zibo Heiyu Tunnel (2018)	One holes 1 lane→ One hole 2 lanes	W_O: 5 W_L: 9	V: Step method	Disease management Decorate and beautify

Note: The subscript “O”denotes the original program and “L” denotes the new program.

(1) The number of road tunnels to be reconstructed and expanded will gradually increase. With China's early road tunnels to meet the 25~40 years of service period, many road tunnels are facing reconstruction and expansion. Around 2035, road tunnel reconstruction and expansion will usher in an active period. (2) Highway tunnel reconstruction and expansion can improve capacity and ease traffic congestion. High-grade highway tunnels pay more attention to the quality of highway service and traffic efficiency(Zhang et al., 2022). Low-grade highway tunnels through reconstruction and expansion to solve the problems caused by the service life of the disease and have the role of improving construction standards at the meantime. (3) High-grade highway tunnels are mostly in-situ reconstruction and expansion, and new construction around the dual-hole four-lane expansion of eight lanes is given priority. Low-grade highway tunnels are mostly in-situ reconstruction and expansion to a single-hole, single-lane, two-lane expansion. Its expansion's length and cross-section size are higher than that of high-grade highway tunnels.

2.2 *Research dynamics*

In order to clarify the research dynamics of road tunnel reconstruction and expansion projects, CNIK, SCIE, ASCE, and other databases were searched. Taking "highway tunnel" and "reconstruction and expansion" as keywords, the literature between 1990 and 2021 was searched, and 178 pieces of literature were obtained, which can be divided into seven categories according to the research content, as shown in Figure 1.

Figure 1 shows that before 2010, the road tunnel reconstruction and expansion project was in the beginning stage, the attention to the problems faced by the reconstruction and expansion project was small, and academic research was low. After 2010, the number of road tunnel reconstruction and expansion projects increased, the attention increased significantly, and academic research is at a high level of growth. Analysis of the research content found that the existing research is more concerned about the stability of the surrounding rock, blasting vibration stability and excavation method, construction technology, and program selection. Due to the early stage of tunnel expansion, theoretical research and engineering experience still need to be improved, and we still need to pay in-depth attention to the expansion method, and construction technology. Existing research on the expansion of safety risk assessment and the application of BIM in the expansion of tunnels is relatively tiny. Pre-expansion of the existing tunnel safety assessment and monitoring of the stability of the surrounding rock in the construction process is still the focus of the research.

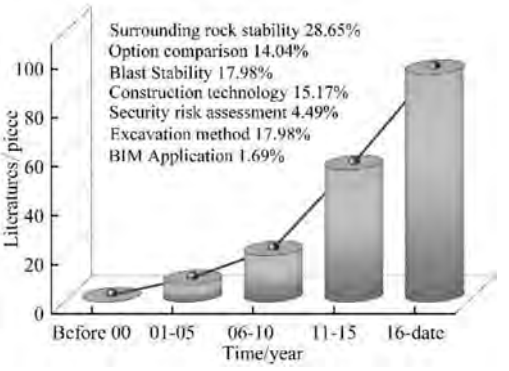

Figure. 1. Research trends in reconstruction and extension tunnels.

3 DYNAMICS OF TUNNEL EXPANSION TECHNOLOGY RESEARCH

3.1 *Dynamics of research on conversion and expansion programs*

3.1.1 *Status of the study of the alteration and expansion program*

According to the division of the reference factors for selecting the reconstruction and expansion program, the current selection mainly includes the construction stability analysis method and the comprehensive social analysis method.

(1) construction stability analysis method

Relying on the Chongqing Goose Ridge Tunnel, Gao et al. (2010) analysed the unilateral in-situ expansion, bilateral in-situ expansion, and the new small-clearance tunnels on the left and right sides respectively. They concluded that the unilateral in-situ expansion is the optimal solution, which aligns with the viewpoints of Zhu et al. (2012). Under topographic factors, Yang et al. (2013) found that the stress state of in-situ expansion is better than surrounding new construction. Using a similar model test, Sun et al. (2012) investigated the construction mechanical behaviours of surrounding in-situ expanded tunnels, unilateral in-situ expanded tunnels, and newly built tunnels. Considering the flow-solid coupling effect, Lai et al. (2019) verified the superiority of the small-clearance expansion scheme in terms of peripheral rock stress, deformation, and protection of groundwater resources.

The above scholars compare the construction stability of different expansion schemes to choose a relatively safe expansion scheme. However, some scholars (Xu et al., 2018) believe that although different expansion schemes have caused a certain amount of deformation of the surrounding rock, they did not affect the tunnel's safety. It can be seen that the construction stability analysis method is an objective quantitative analysis, but there is no uniform criterion for the safety of the expansion plan, and the analysis factors are relatively single, without considering the

interrelationship between the tunnel and the surrounding natural and social environment.

(2) Integrated social analysis method

The integrated social analysis method considers the connection and influence of the expansion program and the environment around the tunnel and has the characteristics of qualitative analysis. Lu et al. (2008) pointed out that the reconstruction and expansion of highway tunnels should meet the requirements of "safety, economy and environmental protection" and fully use the original tunnels to achieve sustainable project development. Zhang et al. (2019) compared and analysed ten kinds of continuous arch tunnel expansion schemes from the perspectives of traffic safety, reuse of the original project, and traffic organization. Wu et al. (2017) conducted an intuitionistic fuzzy preference study of the reconstruction and expansion scheme based on the TOPSIS method and established evaluation indexes for the reconstruction and expansion of mountainous highway tunnels relying on the Xia-long Expressway Reconstruction and Expansion Project, as shown in Figure 2. In addition, Xue et al. (2016) concluded that the unilateral in-situ expansion scheme has the advantages of sufficient space for expansion and a simple support structure, which belongs to the ideal highway tunnel expansion scheme.

The comprehensive social analysis method usually prioritizes factors such as the natural and social environment around the tunnel, project cost, construction period, and traffic volume. It belongs to a subjective qualitative scheme comparison method. For this reason, establishing a comprehensive, integrated quantitative evaluation of the advantages and disadvantages of different expansion programs is the critical research content of the future tunnel expansion program selection.

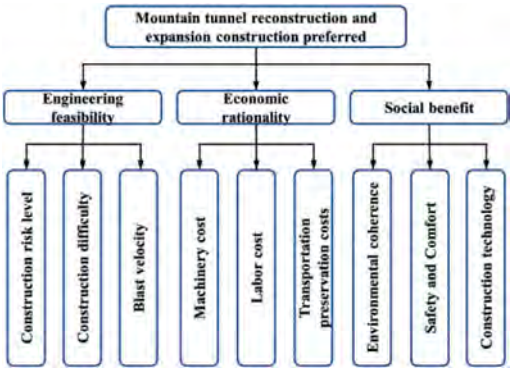

Figure. 2. Evaluation index of expressway tunnel reconstruction and expansion in mountainous areas (Wu et al., 2017).

3.1.2 *Comparative analysis of alteration and expansion options*

Through the general analysis of the typical cases of road tunnel expansion, taking the two-lane road tunnel as an example, the typical expansion schemes are shown in **Table 2** ("a"represents the clearances).

At present, road tunnel expansion mainly involves high-grade and low-grade highway tunnels, and different scenarios of the expansion tunnel affect and determine the selection of the expansion program, which can be seen in Figure 5: For high-grade highway tunnels: (1) When there is enough space for expansion, the magnitude of the highway alignment adjustment is large, and the geologic conditions are poor, it is preferred to select the new surrounding program. (2) When the expansion space is insufficient, and the magnitude of alignment adjustment is small, the in-situ reconstruction and expansion program is preferred. (3) When the surrounding environment is complicated and has many constraints, the combined reconstruction and expansion plan is preferred. (4) The combination expansion or new construction around the program is preferred for highway tunnels with large traffic volumes and high operational demand. Low-grade highway tunnel: Due to the lower construction standards, and smaller traffic volume, the original tunnel disease is relatively prominent, preferred in-situ reconstruction and expansion program. The in-situ reconstruction and expansion program is adopted for municipal highway tunnels with narrow construction space, complex surrounding environments, and many adjacent buildings.

Table 2. Typical engineering cases of tunnel reconstruction and expansion.

Alteration and expansionprogram		Schematic of the program
In-situ reconstruction and expansion	Single	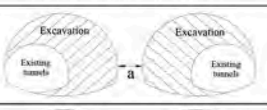
	Bilateral	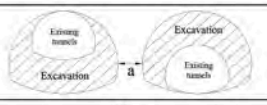
		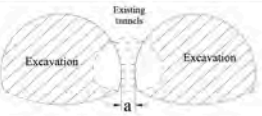
	Surrounding	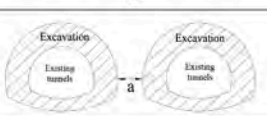
New construction around	Horizontal	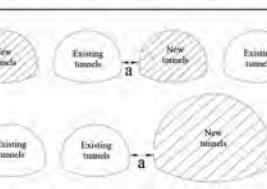
Combined conversion and expansion		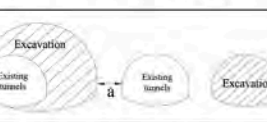

3.2 *Dynamics of tunnel excavation methods for re-expansion and expansion of tunnels*

3.2.1 *Division of excavation methods*

(1) Conventional excavation method

The excavation division of the road tunnel expansion is shown in Figure 3, with the shaded portion being the backfill portion. Unlike conventional new road tunnels, large cross-section road tunnels with poor surrounding rocks are backfilled to the arch waist before in-situ expansion. Then, the widened portion is excavated according to the conventional method, and the backfilled portion improves the pressure on the surrounding rocks and enhances the stability of the tunnel. The double sidewall guide pit, CRD, and CD methods better control surrounding rock stability and deformation. However, the construction procedure could be more convenient, and the construction period is costly, which is suitable for highway tunnels with a large widening section, small clear distance, and poor surrounding rock stability. On the contrary, the full section and step methods have simple construction procedures and are suitable for highway tunnels with small expansion sections and better surrounding rock conditions.

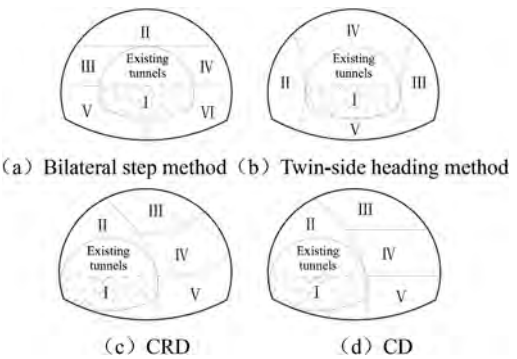

Figure. 3. In-situ expansion and excavation method.

(2) Jump drilling method

The expansion form of the trench jumping excavation method is shown in Figure 4. Tan et al. (2013) combined with the Yuzhou tunnel reconstruction and expansion project to determine the reasonable trenching length and the reserved spacing length of the trench jumping excavation. The slot-jumping excavation method utilizes the original tunnel support structure, which improves the stability of the surrounding rock during expansion excavation, and the slot partition can be used as a new construction section. This method is suitable for highway tunnels with large expansion sections and poor stability of surrounding rock. However, the number of segments using the trench jumping excavation method is larger, which requires higher construction management.

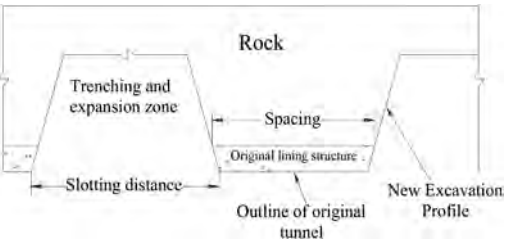

Figure. 4. Jump drilling method.

(3) Layer peeling method

Figure 5 shows the excavation sequence of the layer peeling method, which is more suitable for a unilateral in-situ tunnel expansion program. The tunnel is first divided into longitudinal sections and then expanded horizontally in layers. However, the excavation steps of the layer peeling method are more, and the excavation section should not be too large. The safety and stability of the construction are greatly affected by the width and length of one horizontal excavation. Therefore, determining reasonable excavation parameters is the key to applying this method.

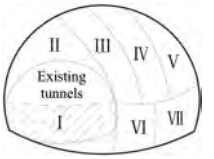

Figure 5. Layer peeling method.

(4) Keep unobstructed expansion method

The biggest problem of tunnel expansion construction is to affect the existing traffic operation. How to reconstruct and expand the tunnel under the condition of keeping the line alive and preserving the traffic is the focus of the research. Tonon (2010) introduced the method of expanding and excavating the tunnel while maintaining the traffic operation and its engineering application worldwide. Zhu et al. (2018) introduced the widening method used in the Nazzano tunnel in Italy, which separates the excavation face from the transportation face by installing a traffic shield. A cutting arm with a unique chain of teeth is installed in front of the shield to cut the broken surrounding rock, and the support tube sheet is installed with the help of a multifunctional mechanical transportation device, as shown in Figure 6. In addition, the tunnel expansion unit combination system was successfully used to expand the Kuckuckslay railroad tunnel in Germany (Vetter et al., 2020), as shown in Figure 6 (b). The "Enlargement of live line tunnel method" was adopted in Japan to expand the Daizo Tunnel (Kamuro et al., 2001).

(a) (b)

Figure. 6. (a) Construction method of Nazzano tunnel (Lin et al., 2018) (b) Tunnel elargement unit combined system (Vetter et al., 2020).

3.2.2 *Excavation method selection*

Considering the construction method of the built-in-situ reconstructed tunnel and the geological conditions of the surrounding rock, the expansion coefficient M is proposed to characterize the degree of expansion of the tunnel section.

$$M = \frac{B_2 H_2}{B_1 H_1} \tag{1}$$

Where: M is the tunnel expansion coefficient; B_2 is the net width of the reconstructed tunnel; H_2 is the net height of the reconstructed tunnel; B_1 is the net width of the original tunnel; H_1 is the net height of the original tunnel.

From equation (1), M is related to the tunnel's clear height and width before and after the reconstruction. The cross-section dimensional characteristics of the road tunnel can be confirmed based on the reconstruction and expansion plan.

Based on the established studies and engineering cases, M can be classified into two levels, as shown in Table 3. Level A has a larger increase in section size, generally adding 1 or 2 lanes to a single tunnel. Level B is mainly found in highway tunnels where only the excavation profile is enlarged without changing the number of lanes due to disease management or upgrading of the roadway grade.

Table 3. Grade table of tunnel amplification coefficient.

M	Level
$1<M<2$	B
$2\leq M$	A

Combined with the constructed projects, the recommended excavation methods under different surrounding rocks and reconstruction grades are shown in Table 4. With the development of construction technology, future reconstruction tunnels are more inclined to the excavation methods with fewer excavation divisions and higher construction efficiency (Zhang er al., 2020)

Table 4. Suggestions for excavation method of reconstruction and expansion of highway tunnel in-situ.

Surrounding Rock Classification	Type	Level	Recommended excavation method
Ⅳ	One side	A	CD/CRD
		B	Jump drilling method/Step method
	Two side	A	Keep unobstructed expansion method/ CRD
		B	CD/ Step method
	Surrounding new construction	A	CD/CRD
		B	Step method
Ⅴ	One side	A	Keep unobstructed expansion method/ CD
		B	Step method
	Two side	A	Keep unobstructed expansion method Twin-side heading method
		B	Step method
	Surrounding new construction	A	Twin-side heading method
		B	Step method

3.3 *Dynamics of surrounding rock stability research in reconstruction and expansion tunnels*

3.3.1 *Characterization of the mechanical response of the surrounding rock*

Surrounding rock stress: In the process of in-situ tunnel reconstruction and expansion, the pressure of the surrounding rock in each part of the tunnel decreases with the demolition of the old lining and the expansion of the surrounding rock in that part of the tunnel, and then increases significantly with the application of the new lining and is significantly asymmetrically distributed, and the axial force of the anchor rods on the outer side of the tunnel is about 4-5 times of that on the inner side. The lining structure of the original tunnel can be used to play the role of temporary support during the expansion process. Local reinforcement measures can be taken for the part with high pressure on the surrounding rock. After the completion of the reconstruction and expansion, the plastic zone of the surrounding rock occurs in the inner side of the arch foot (Shu et al., 2012), the pressure of the surrounding rock generally increases, the structural bias is serious, and the stresses of the surrounding rock in the arch roof and arch waist are large. The compressive stress concentration occurs on both sides of

the tunnel, and the bottom plate and arch top compressive stress is minimal and tends to transition to tensile stress (Cheng et al., 2020). The center rock column is the weakest when the expansion forms a small-clearance continuous arch tunnel, and the upper step excavation has the greatest impact on its stability. Under the influence of the new tunnel, the pressure and stress of the surrounding rock near the center rock column increased significantly. When the clear distance is more than 0.5 times the span, the stress state of the center rock column is less affected by the clear distance (Shu et al., 2012).

Surrounding rock deformation: Influenced by the existing tunnel, the center line of the surface settlement groove curve is slightly shifted to the side of the expansion excavation, showing an asymmetric distribution of "single-peak, skew-normal." When the reconstruction and expansion form a continuous arch tunnel, the surface settlement caused by the excavation of the backward hole is larger, and the maximum settlement occurs on the side of the forward hole. The problem of arch bottom uplift is more prominent when large section tunnels are rebuilt and expanded (Zhang et al., 2019). Sun et al. (2016) establish a mathematical model for the arch displacement of in-situ rebuilt and expanded tunnels:

$$U_R = \left[1 + \exp\left(\frac{x}{0.36R}\right)\right]^{L1} U_R^M \tag{2}$$

Lin Congmou et al. [70] regarded the surface settlement as the superposition of the settlement caused by the excavation of the existing tunnel and the excavation of the expansion tunnel and obtained a mathematical model for predicting surface settlement based on the Peck formula:

$$S(x) = \frac{A_{11}V_{11}}{\sqrt{2\pi}i_1} exp\left(\frac{(x-D_i)^2}{2i_1^2}\right) + \eta\frac{A_2V_{12}}{\sqrt{2\pi}i_2} exp\left(\frac{(x-D_2)^2}{2i_2^2}\right) \tag{3}$$

3.3.2 *Surround rock blasting vibration control*

The blasting excavation of the reconstructed tunnel has a significant impact on the adjacent buildings (structures), so how to reduce the disturbance of the blasting vibration on the adjacent tunnels to ensure the safe operation of the original tunnel is the construction difficulties.

Wang et al. (1996) proposed that the static crushing method applied to the tunnel expansion can achieve the construction effect of no sound and no vibration. Zhang et al. (2010) effectively controlled the blasting vibration caused by the expansion of the Dahuashan small clear-distance tunnel group through the reasonable use of single and compound wedge-shaped hollowing. Liu et al. (2016) found that by canceling the hollowing eyes when blasting in the expansion part, the blasting parameters lower than the standard value of the specification also achieved a better blasting effect. Li et al. (2012) suggested that the blasting speed can be effectively controlled by increasing the number of blasts by installing vibration-damping holes. The contradiction of this method is that with the increase in drilling and blasting, the cumulative damage to the rock mass increases compared to large-scale blasting.

Table 5 shows the peak vibration velocity and the fitting parameters of Sadovsky's formula for the existing reconstructed tunnel. It can be seen that the existing reconstruction and expansion of the tunnel peak vibration velocity and fitting parameters K and α are smaller than the "Blasting Safety Regulations" in the recommended tolerance values.

Table 5. Blasting vibration velocity and fitting parameters.

Surrounding Rock Classification	Project Name	Peak vibration velocity / $cm \cdot s^{-1}$		Sadovsky parameters			
		Measured value	Standardized value	K	Standardized value	α	Standardized value
III	A certain tunnel	0.92	10~20	220.00	150~350	1.6	1.5~2
IV	Yuzhou tunnel	1.96		150.01		1.80	
	Damaoshan tunnel	/		132.71		1.32	
	Jinjishan tunnel	5.71		101.90		1.54	
V	Damaoshan tunnel	15.78		63.23		1.43	
	Loushan tunnel	15.93		125.00		1.39	

4 RESEARCH PROSPECTS

Under the current "Carbon Neutral, Carbon Peak" background, green construction technology has attracted wide attention. With the innovation of artificial intelligence technology, the green construction and rapid construction technology of reconstruction and expansion tunnels will have a broad development prospect. The future development of highway tunnel reconstruction and expansion is expected:

(1) Standardization of construction standards. Based on the active, passive, and forward support methods, we propose excavation and support structure design methods suitable for different peripheral rock conditions. Then, we form norms and standards to guide the expansion tunnels' design, construction, and support.
(2) Intelligent expansion program. Construct an intelligent evaluation system based on artificial intelligence and deep machine learning that considers construction characteristics, social economy, and environmental coordination. Consider using urban civil defense tunnels, air defense tunnels, and other abandoned tunnels to expand and develop urban underground transportation space.
(3) Innovative construction methods. Develop assembly-type large-scale excavation expansion machinery and promote the practical application of the innovative "Bao Tong Expansion and Excavation Method." Combine the concept of "carbon neutral and carbon peak" to propose green reconstruction and expansion technologies. Promote the application of BIM technology in the whole life cycle of reconstruction and expansion tunnels.

5 CONCLUSIONS

(1) In the future, the number of highway reconstruction and expansion tunnels will gradually increase and develop in the direction of large cross-sections, small clearances, and tunnel clusters. The research content is enriched, and construction safety risk assessment and BIM technology application are new research dynamics.
(2) There needs to be uniform uantitative standards for selecting and evaluating road tunnel expansion programs, and there is still a need for comprehensive social analysis combined with construction safety and stability of the program evaluation method. Considering the expansion space, natural and social environment, construction technology, and other factors, a comprehensive comparison of the reconstruction and expansion programs selection is needed.
(3) Common excavation methods for tunnel expansion include the traditional excavation method, jump drilling method, layer peeling method, and expanding the excavation to protect the passage. It should be combined with the tunnel expansion factor and engineering geological conditions to select the expansion excavation method reasonably.
(4) The stress distribution and deformation law of the surrounding rock in the reconstructed tunnel is complicated and variable, which has not yet been involved in deep theoretical research, and few scholars have carried out research on the stability of the surrounding rock in the process of dismantling the original supporting structure.

REFERENCES

Cheng F., Pan X.J., Gong S., et al.,2020. Research on the construction technology of in-situ extension of super large span tunnel with small clear distance. West. Expl. Eng. 32(7), 187–190.

Deng Y.X., 1997. Renovation of the rufenen tunnel of the furka-oberalp railway. World Tunn.1, 57–59+46.

Ell I, Lan L.M.,1999. Reconstruction and extension of the white haven and rockport tunnels. Tunn. Under. Eng.1, 13–25.

Gao G., Liu Y.X., Zhou J.Z, et al.,2010. Study on underground space enlargement options. Mode. Tunn. Tech. 47(6), 1–9.

Kamuro K., Dojo Y., Kageyama M., et al.,2001. The design and construction of road widening under existing tunnel without traffic control. Japan Soci. Civil Eng. 221–232.

Li S.C., Zhao Y., 2012. Spatial deformation mechanism and load release evolution law of weak and surrounding rock during construction of super-large section tunnel with soft broken surrounding masses. Rock Mech. Eng. 31(10), 2109–2118.

Li X.D, Jiang S.P, Liu Y.X., et al.,2014. Blasting vibration control of local expansion of large section tunnel with small cycle distance. Blasting. 31(3), 85–90.

Lin Z., Kai W., Baisong W, et al.,2018. Widening Montedomini tunnel in presence of traffic: evolution of Nazzano method. Tunn. Const. 38(3), 461–467.

Lai Y., Zhang S., 2019. Study on the expansion and excavation method tunnel under the effect of fluid-solid coupling. Under. Space Eng.15(s1), 311–320.

Liu D., Gao W.X., Sun B.P., 2016. Numerical simulation of blasting vibration on existing tunnel extension. Rock Soil Mech. 37(10), 3011–3016.

Lu X.L., Qin Z., Han C.L., 2008. Highway tunnel reconstruction and extension design. Highway. 7, 233–237.

Li X.P., 2012. Design of blasting scheme and monitoring for blasting vibration of shallow embedded enlarged tunnels in small clear distance and large section n. Tech. Highway Trans. 4(1), 86–90.

Liu Q.S., Sun X.S., Su X.J., et al., Optimal analysis of construction schemes for houci extension tunnels with large span. Eng. Jour. Wuhan Univ. 49(4), 544–551.

Peng N., 2010. Study on surrounding rock mechanical response mechanism of in-situ enlarged tunnel. Chongqing: Chongqing University.

Shu Y.G., Jiang S.P., Lei M.L.,2012. Construction mechanics analysis on extension of small interval tunnel. Jour. Chongqing Jiaotong Univ.31(2): 214–217+251.

Sun L.L.,2012. The experimental study and theoretical analysis on mechanical behavior of widening highway tunnel. Xi'an: Chang'an University.

Sun X.S, Dong H.F., Su X.J., et al., 2016. 3D element analysis on mechanical characteristics of surrounding rocks of expansion project: a case study on houci tunnel on Zhanglong-longyan highway. Tunn. Const. 36(1), 52–57.

Tonon F., Asce M., 2010. Methods for enlarging transportation tunnels while keeping tunnels fully operational. Pract. Peri. Struct. Design Const. 15(4), 248–271.

Tan Y.Z., Liu Y.X., Zhou J.W, et al.. 2013. The proper driving footage in the jump-driving method for single-sided tunnel extension. Under. Space Eng. 9(1), 147–154.

Vetter S., Galli M., Steiner P., 2020. Refurbishment of the kuckuckslay tunnel-current experience in the use of the "tunnel-im-tunnel- methode". Geo. Tunn. 13(5), 557–565.

Wu X.G., He P., Su X.G., et al., 2017. Intuitionistic fuzzy optimization of enlargement scheme of highway tunnel in mountain areas based on hamming distance-topsis method. Tunn Const. 37(8), 926–932.

Wang R., 1996. Static crushing method used in tunnel expansion. Coal Mine Blasting. 4, 35–36.

Xue X.B., 2016. Study of the expansion type and stability of highway tunnel change. Chongqing: Chongqing Jiaotong University.

Xu Z.L., Wang G.K., Li Z.C., et al.,2018. Deformation of surrounding rock with in-situ expansion of shallow highway tunnel. Mine. Eng. Rese. 33(3), 52–57.

Xian M.Q., 1996. Transformed from a single track to a double track operating tunnel—hakone tozan railway tower nominee tunnel. World Tunn. 4, 75–80.

Yang L.f., Chen Q.l, Yang Y., et al.,2013. Discrete element analysis of jinjishan tunnel extension alterative scheme. Eng. Jour. Wuhan Univ. 46(3), 339–344.

Zhang J.R, Wu J., Yan C.W., et al., 2020. Construction technology of super-large section of highway tunnels with four or more lanes in China. China Jour. Highway Trans. 33(1), 14–31.

Zhong Y.Q.,2019. Field monitoring and analysis of in-site tunnel extension by three-bench method. Modern Tunnelling Technology. 56(5), 170–179.

Zhang Z.C., Lin C.M., Li J.S., et al.,2022. Construction technology research and prospect of highway tunnel of reconstruction and expansion in China. Tunn. const. 42 (4), 570–585.

Zhu G.Q., Lin Z., Zhu Y.C., 2012. Research on influences of in-situ tunnel extension project on adjacent buildings. Rock Soil Mech. 33(s2), 251–256.

Zhang L., Wang F., 2019. Research on the schemes of multi-arch tunnel in the reconstruction and expansion project. Tunn. Const. 39(s1), 346–354.

Zhang P.S., 2010. Slight vibration controlled blasting technique for damoshan tunnel. Railway Const. Tech. 8, 98–103.

Tunnelling for a Better Life – Yan, Celestino, Thewes & Eberhardt (Eds)
© 2024 The Author(s), ISBN 978-1-032-80042-4
Open Access: www.taylorfrancis.com, CC BY-NC-ND 4.0 license

Reliability study of full jet longitudinal smoke exhaust system for a road tunnel over 5 km long

Xinyue Zhang, Liangliang Tao, Mingrui Luo & Yanhua Zeng
School of Civil Engineering, Southwest Jiaotong University, Chengdu, China
Key Laboratory of Transportation Tunnel Engineering, Ministry of Education, Southwest Jiaotong University, Chengdu, China

ABSTRACT: In China, road tunnels over 5 km utilize shafts for smoke extraction. In order to study the feasibility of full jet longitudinal smoke exhaust for road tunnels over 5 km in length, tunnel ventilation effect tests and fire tests were carried out in a tunnel. Field tests show that when the fire scale is 1.2 MW, the back-layered smoke flow can be effectively controlled by turning on 3 sets of fans downstream of the fire source, with air velocity of 2.4 ~ 3 m/s. When the jet fans are fully switched on, the ventilation step effect is significant, with a maximum air velocity of approximately 7 m/s at each test section. Numerical analysis of the smoke exhaust in the tunnel at a fire scale of 30 MW with different numbers of jet fans on was carried out. In the presence of longitudinal wind, the temperature and CO concentration in the tunnel have less impact on the escape of people upstream of the fire source. When 3 sets of fans are switched on, the flue gas flows backwards and sinks without effective control. When six groups of fans are turned on, the air velocity in the tunnel reached 3.5 m/s, which are able to control the back-layered smoke flow without accelerating the spread of smoke downstream and can provide favorable conditions for personnel evacuation.

Keywords: extra-long road tunnel, tunnel fire, full jet longitudinal smoke exhaust, field test, smoke control

1 INTRODUCTION

In recent years, more and more extra-long tunnels have been built to meet the country's transport as well as strategic needs. By the end of 2020, China had built 1394 extra-long tunnels(Transport, 2022).Due to the special long and narrow structure of tunnels, a fire will bring a great threat to the safety of people inside the tunnel. For the disaster prevention and smoke evacuation of road tunnels, scholars at home and abroad have carried out a large number of studies, mainly focusing on the characteristics of smoke flow(Hu et al., 2008; Tanaka et al., 2021), temperature distribution law(Liu et al., 2021), smoke evacuation efficiency (Tao and Zeng, 2022), personnel evacuation(Zhang et al., 2023) and other aspects.

The specification of "Guidelines for Design of Ventilation of Highway Tunnels" (China, 2014) in China gives the provisions: the tunnel with the length of the unidirectional traffic not more than 5 km can adopt the longitudinal ventilation scheme of the full jet; the maximum travelling distance of the smoke in the tunnel should not be more than 5 km in the fire case. Currently, most road tunnels in China over 5 km utilize shafts for sectional smoke extraction(Wang et al., 2015; Wang et al., 2020; Zhang et al., 2018). The construction of the shaft will greatly increase the cost of the project, and when the geological conditions of the tunnel site area are poor, the construction of the shaft is prone to inducing geological disasters, resulting in casualties(Cao et al., 2020).The possibility of adopting full jet longitudinal ventilation for road tunnels with a length of over 5 km has become an issue of wide concern among experts and scholars.

For the ventilation and smoke exhaust effect of the full jet longitudinal ventilation method, some scholars have conducted research. Li et al (Li et al., 2022) established a numerical model to investigate the influence law of different operation modes of jet fans on the flue gas, temperature and CO concentration in the tunnel. Weng et al (Weng et al., 2020) investigated the effect of different spacing of jet fans on the temperature and wind speed in the tunnel and optimized the spacing according to the tunnel characteristics. Zhang et al (Zhang et al., 2011) conducted smoke evacuation tests in a 6 km long submarine tunnel and found that the use of sectional longitudinal ventilation

DOI: 10.1201/9781003495505-469

can better control the spread of smoke. Cao et al (Cao et al., 2019) conducted field tests and verified that it is feasible to use full jet longitudinal smoke extraction when a 20 MW fire occurs in a tunnel with a length of more than 5 km. In summary, there are almost no full jet smoke extraction tests for road tunnel fires over 5 km.

This paper carries out on-site fire tests relying on the Fenghuangling Tunnel, analyses the smoke spread, CO concentration distribution and temperature changes in the tunnel using numerical simulation software in the case of a 30 MW fire with different numbers of jet fans turned on and the reliability of the more than 5 km highway tunnel using a full jet longitudinal smoke exhaust method was studied, with a view to providing a reference for similar projects.

2 FIELD EXPERIMENT

2.1 *Project overview*

Fenghuangling Tunnel is located in Xinzhou City, Shanxi Province, is located in the mainline section of Xinfu Expressway, the tunnel is a two-hole unidirectional dual carriageway, the left line is 5885 m long, longitudinal slope of 1.8%, the right line is 5760 m long, longitudinal slope of -1.8%, the design speed of 80 km/h. The tunnel adopts full jet longitudinal ventilation, with 44 sets of Φ 1120-37 kW jet fans installed in the left line of the tunnel and 30 sets of Φ 1120-37 kW jet fans installed in the right line.

2.2 *Test scheme*

2.2.1 *Fire source setting*

In this test, two wooden stacks with length, width and height of 2000 mm × 500 mm × 60 mm were set up as combustible materials, erected at a height of 1 m, and diesel fuel was used as fuel to ignite the stacks, and the power of the fire source for the test was about 1.2 MW. The location of the ignition source is shown in Figure 1, and the ignition point is set near the pedestrian crosswalk in consideration of the safety of the test personnel.

Figure 1. Fire source setting.

2.2.2 *Working condition setting*

The longitudinal gradient of the Fenghuangling Tunnel is 1.8%. When a fire occurs, the downslope tunnel is more unfavorable for smoke exhaust, so the right tunnel was chosen to carry out the full jet longitudinal smoke exhaust test. The right tunnel was blocked during the test, and the test conditions were set as shown in Table 1.

Table 1. Working condition setting.

Number	Working conditions	Fan number switched on
1	No fan on	/
2	Switch on 3 sets of reversing fans	1#~3#
3	Switch on 3 sets of forward fans	4#~6#
4	Switch on 1 sets of reversing fans	1#
5	Switch on 1/5th of the number of forward fans	4#~6#
6	Switch on 2/5th of the number of forward fans	4#~9#
7	Switch on 3/5th of the number of forward fans	4#~12#
8	Switch on 4/5th of the number of forward fans	4#~15#
9	Switch on all forward fans	1#~15#

2.2.3 *Test methods*

There are 39 monitors in the Fenghuangling Tunnel, with longitudinal spacing ranging from 100 m to 200 m, which can be used to observe the smoke flow situation in various sections of the tunnel at different moments (Figure 2(a)). In order to observe the smoke flow situation after the fire, two personnel were arranged to photograph and record the smoke flow upstream and downstream of the fire source point respectively. Smoke flow observation stations were set up at the source of fire and at the exit of the tunnel for continuous filming throughout the test (Figure 2(b)).

Four wind speed test sections were set up, as shown in Figure 3, with the fire point located near the #5 pedestrian crossing. Due to the continuous spread of smoke to the downstream of the tunnel after the smoke emission, and in consideration of the safety of the on-site testers, the fourth group of testers was first tested at the dotted line and then transferred to the exit of the tunnel by the vehicle to conduct the wind speed test. The test was conducted simultaneously at each section, with one person reading and one person recording multiple sets of wind speed data.

2.3 *Test results and analysis*

In order to test the smoke removal capability of a full jet fan when a fire occurs in a tunnel over 5 km long, the smoke flow state in the tunnel was observed and the wind speed was tested, and the results are shown in Figures. 4-6, which can be divided into the following five stages of the smoke removal process.

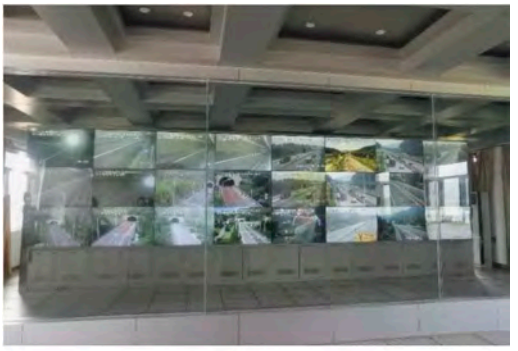

(a) monitoring center

(b) Smoke flow shooting

Figure 2. Records of the smoke flow situation in the tunnel.

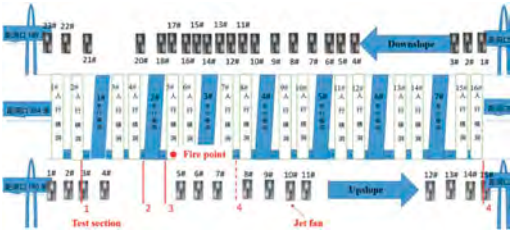

Figure 3. Location of jet fan and test section arrangement.

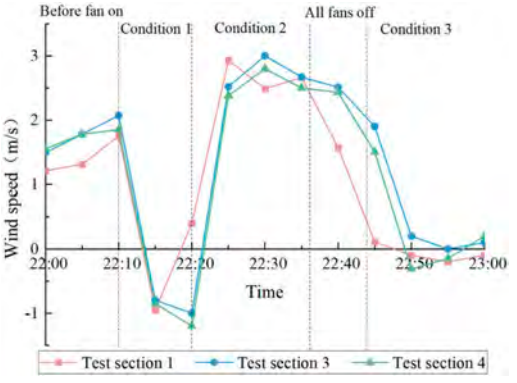

Figure 4. Wind speed change under different jet fan switching on conditions.

Stage before fan on (22:00-22:10): after ignition, all the fire smoke streams flowed in the direction of the tunnel exit due to the influence of the natural wind and without the jet fan on. As shown in Figure 3, the wind speed in the tunnel was measured to be between 1.2 ~ 2.1 m/s during this period.

Condition 1 (22:10-22:20): To reverse the flow of flue gases, switch on the reversing fan set by set. When the 2 sets of reversing fans are switched on, the smoke flow is directed upwards in a vertical direction. The smoke flow was completely reversed after switching on the 3 sets of reversing fans, and the wind speed was measured to be around -1.2 m/s during this period. Thermal buoyancy is the main driver of smoke diffusion as it spreads upstream. Under the influence of thermal buoyancy, the flue gas gradually rises and hits the roof and then spreads radially. Blocked by the roof and sidewalls, the flue gases accumulate downwards, while the buoyancy of the hot flue gases forces them to flow upwards, thus forming a flue gas layer (Figure 5 (a)). In this process, the smoke below the roof is constantly rolled and sucked air, and at the same time by the wall viscous resistance, the smoke flow rate is gradually reduced, resulting in a reduction in the temperature and pressure of the smoke front. The smoke layer close to the fire source is more affected by thermal buoyancy and is denser, while the smoke front is less affected by thermal buoyancy and is sparser (Figure 5(b)).

(a) Initial stage of reverse flue gas

(b) The end of the reverse flue gas

Figure 5. The reverse flue gas on site.

Condition 2 (22:20-22:36): To test the number of fans that need to be switched on to control smoke flow reversal, the forward fans are switched on group by

group. After switching on the 1 set of fans, the smoke stream gradually stood up at the fire point. After switching on the 2 sets of fans, the smoke flow gradually became upright. After switching on 3 groups of fans, the wind speed is between 2.4 ~ 3 m/s, in which the backflow of flue gas can be controlled.

Condition 3 (22:44-23:00): In order to control the continued spread of the smoke flow, the 3 sets of forward fans were switched off at 22:36, and the wind speed in the tunnel began to decrease but remained positive. Group 1# reversing fan was switched on at 22:44, and the wind speed began to drop continuously and reversed around 22:50. At this time, the wind speed in the tunnel is very small, but the smoke flow at the fire point is constantly flowing vertically and spreading, forming a chimney effect.

Smoke extraction stage (23:00 - 00:05 the next day): Turn off the group 1# reversing fan, turn on all the jet fans in the tunnel in turn to exhaust the smoke, at this time the wind speed in the section as shown in Figure 6. Due to the limitations of the test conditions, less data were available for the test section 4 in the Fuping direction. When only 3 sets of fans are switched on, the wind speed in the tunnel is the lowest, between 3.1 and 3.9 m/s. With the increase of the number of jet fan opening groups, the wind speed of each test section increases continuously. For the test section in different locations, the measured wind flow rule of change is consistent, the size of the wind speed difference is not large, this is due to the flow of wind flow is different from the movement of solid matter, between the gas is through the air molecules between the microscopic transmission to achieve. During the actual test, the wind flow at each test section started to change almost simultaneously. The step effect of full jet ventilation in the tunnel is very significant. At 0:00 all the jet fans were switched on, the wind speed at each test section reached about 7 m/s, and the smoke evacuation was completed at 0:05 the next day.

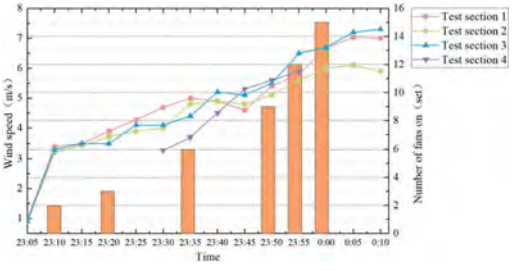

Figure 6. Wind speeds with different numbers of jet fans on.

3 NUMERICAL ANALYSIS OF 30 MW TUNNEL FIRE

3.1 *Numerical modelling*

As shown in Figure 7, the tunnel height is 5 m, the width is 10.25 m, the tunnel length is set to be 600 m, and the fire point is located in the middle of the tunnel. Considering the calculation accuracy as well as the calculation time consuming, grid-independent calculations were carried out and the grid size was set to 0.2 m × 0.2 m × 0.2 m.

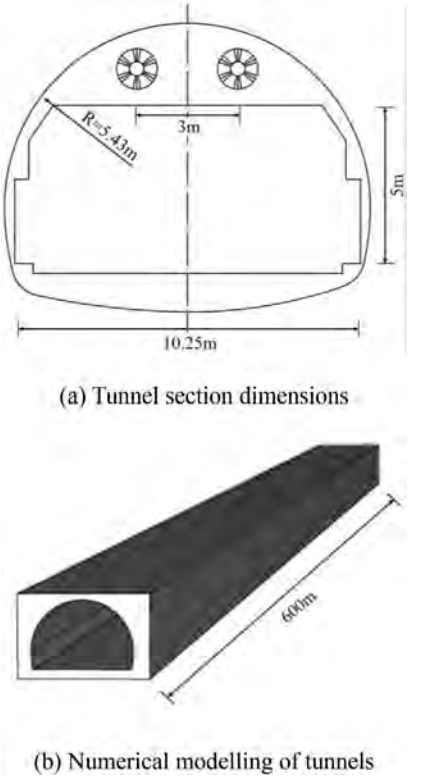

Figure 7. Schematic diagram of the numerical modeling.

3.2 *Working conditions*

Considering the safety of this tunnel field test, it was not possible to carry out a field fire test with a high power source. The effect of smoke evacuation in the tunnel was analyzed by numerical simulation when the power of the fire source is 30 MW. Combined with the results of on-site wind speed tests, the smoke spreading and wind speed in the tunnel were studied under the condition of different numbers of jet fans on.

Table 2. Numerical simulation of working conditions.

Number	Number of fans on/ sets	Wind speed in the tunnel/ (m/s)
1	3	2.5
2	6	3.5
3	9	4.5

3.3 *Results and analysis*

3.3.1 *Flue gas field*

Figure 8 (a) shows the diffusion of smoke in the tunnel when 3 sets of jet fans are switched on, and the wind speed is about 2.5 m/s at this time. At 30 s there was already a reverse flow of smoke. At 60 s the downstream flue gas spreads less than 300 m, and the length of the back-layered smoke flow increases. At 90 s the upstream low-temperature smoke mixed with air sank further, causing unfavorable evacuation of people upstream. At 420 s the upstream flue gas is already close to the ground, and the length of the back-layered smoke flow is more than 100 m, so the spread of the flue gas is not effectively controlled under such working conditions.

When 6 sets of jet fans are opened, the longitudinal wind speed in the tunnel is increased to 3.5 m/s, the upstream flue gas is slightly refluxed at 45 s, and the length of the back-layered smoke flow is unchanged by 60 s. Compared with condition 1, the increase in the number of fans on accelerated the downstream smoke spread, and the length of the downstream smoke spread exceeded 300 m at 60 s. The length of back-layered smoke flow increases slightly at 210 s, and is basically unchanged at 420 s, at which time the flue gas buoyancy and inertia of the gas flow have reached equilibrium (Figure 8(b)). Under this condition, the backflow length is short, the interface between smoke and air is obvious and there is no sinking, which can provide favorable conditions for the escape of people upstream.

When 9 groups of jet fans were switched on (Figure 8(c)), no flue gas backflow occurred upstream at 420 s due to large ventilation rates, but the rate of smoke roll-up of low-temperature air downstream of the fire source was accelerated, and the rate of flue gas diffusion and sinking increased. In comparison, switching on 6 sets of fans can control the backflow of smoke nor accelerate the spread of smoke, and can achieve better control of the fire in the case of a 30 MW fire in the Fenghuangling Tunnel. Meanwhile, the longitudinal wind speed of 3.5 m/s in the tunnel can be used as the control critical wind speed in case of a 30 MW fire.

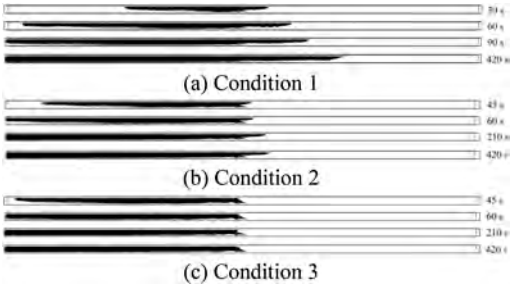

Figure 8. Flue gas diffusion with different number of jet fans on.

3.3.2 *Temperature field*

When a fire occurs, the temperature inside the tunnel will rise sharply. In order to study the safety of personnel evacuation under different conditions of jet fan opening, the temperature change at a height of 2 m inside the tunnel was analyzed, and the temperature exceeding 60 °C was taken as a judgement indicator of the danger of personnel evacuation (China, 2017). Under the effect of longitudinal wind, the temperature at a height of 2 m upstream of the fire point is always less than 60 °C, which is able to guarantee the evacuation safety of the upstream people (Figure 9).

With longitudinal winds, the temperature in the tunnel is greater than 60 °C for a range of 10 m downstream of the fire source and decreases in this range as the number of jet fans switched on increases. Temperatures 10 m downstream of the fire source do not vary much for different numbers of fans switched on. For the range of 10 m ~ 30 m downstream of the fire source, there is a small section of temperature lower than 60 °C at the height

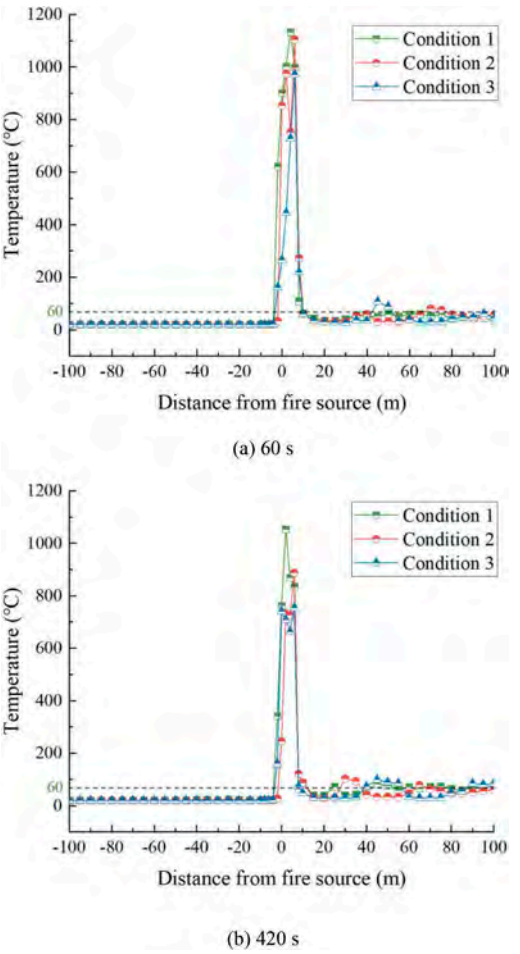

Figure 9. Temperature distribution with different numbers of jet fans on.

of 2 m, which may be due to the fact that the temperature is lowered by more fresh air being sucked in here. The temperature has increased at a height of 2 m outside the 30 m range downstream of the fire source, and is also greater than 60 °C 100 m downstream, so people downstream should drive away from the tunnel as soon as possible.

3.3.3 *CO concentration field*

The environment inside the tunnel is relatively closed, the oxygen supply is insufficient, and in the event of a fire, insufficient combustion is likely to generate a large amount of CO, which poses a threat to the safety of personnel. With longitudinal winds, CO concentrations have little effect on the escape of people upstream of the fire source, and three sets of jet fans on are sufficient to control the CO concentration upstream of the fire at a height of 2 m to less than 50 ppm (Figure 10).

In the presence of longitudinal winds, the maximum CO concentration is concentrated within 10 m downstream of the fire source. At 60 s, the CO concentration at the fire source at a height of 2 m was about 2600 ppm when 3 sets of jet fans were switched on, and about 2000 ppm when 9 sets of jet fans were switched on. At 420 s, the CO concentration at the fire source at a height of 2 m was about 2200 ppm when 3 sets of jet fans were switched on, and about 1700 ppm when 9 sets of jet fans were switched on. The CO concentration decreased as the number of jet fans switched on increased as well as the time. Although the CO concentration is high here, the speed at which people downstream of the fire source drive away from the tunnel is relatively fast and will have essentially no detrimental effect on the escape of people. CO concentrations 10 m downstream of the fire source are slightly higher than upstream, but are still at low values, with a maximum of only 151 ppm, which has a low impact on human safety. Therefore, CO concentration has little effect on the escape of people.

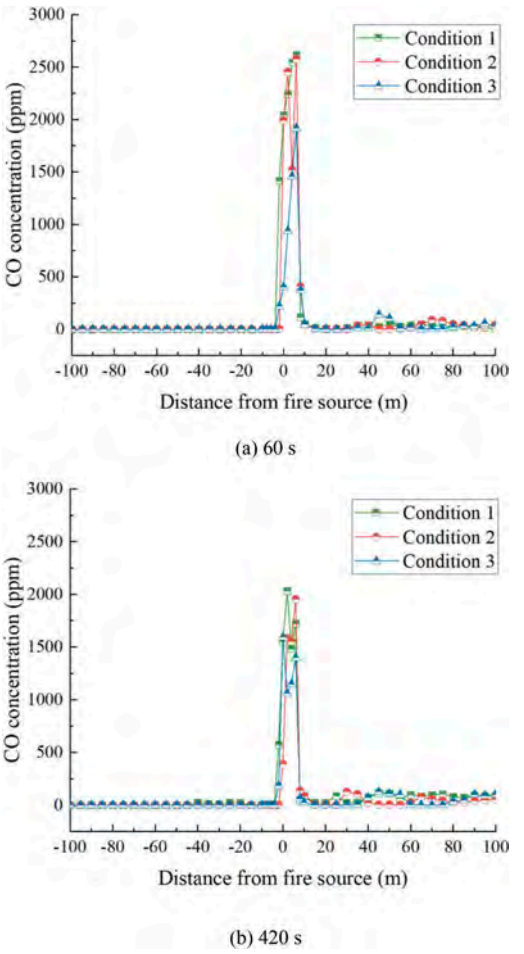

Figure 10. Distribution of CO concentration with different numbers of jet fans on.

4 CONCLUSION

The feasibility of full jet longitudinal smoke evacuation in road tunnels exceeding 5 km has been investigated through on-site fire tests in the Fenghuangling Tunnel and numerical simulation analysis under the condition of switching on different numbers of jet fans, and the following conclusions have been drawn:

(1) For a 1.2 MW fire in the Fenghuangling Tunnel, switching on three sets of fans will be able to effectively control the backflow of smoke, when the wind speed is 2.4 ~ 3 m/s.
(2) When 6, 9, 12 and 15 sets of jet fans are switched on respectively, the wind speed in the tunnel can reach 3.5 m/s, 4.5 m/s, 5.5 m/s and 7 m/s respectively.
(3) During the field test, although the measured natural wind was shown to be the smoke exhaust power, the calculated number of jet fans that need to be turned on when the fire size is 30 MW is 6 groups, which is far less than the number of 15 groups of fans installed in the tunnel. The full jet longitudinal smoke evacuation can provide favorable conditions for the evacuation of people.
(4) In this paper, the reliability study of using full jet longitudinal smoke evacuation in road tunnels over 5 km has been carried out only for the Fenghuangling Tunnel, and the universality of the study needs to be further verified.

ACKNOWLEDGMENTS

The authors gratefully acknowledge financial support for this study from the National Science Foundation of China (No. 52178394).

REFERENCES

Cao, Z.M., Zhang, Q., Chen, J.Z., 2019. Study on super-long-distance longitudinal smoke exhaust test of highway tunnel. Fire Science and Technology 39, 471–474.

Cao, Z.M., Zhang, Q., Chen, J.Z., 2020. Full-Scale Experiment Study on Full-Jet Longitudinal Smoke Exhaustof 20 MW Fire in Yanglushan Tunnel. Journal of Chongoing Jiaotong University (Natural science) 39, 123–128.

China, M.o.T.o.t.P.s.R.o., 2014. Guidelines for Design of Ventilation of Highway Tunnels. China Communications Press Co,Ltd., Beijing.

China, N.R.A.o.t.P.s.R.o., 2017. Code for Design on Rescue Engineering for Disaster Prevention and Evacuation of Railway Tunnel. China Railway Publishing House Co., Ltd., Beijing, pp. 1–67.

Hu, L.H., Huo, R., Chow, W.K., 2008. Studies on buoyancy-driven back-layering flow in tunnel fires. Experimental Thermal and Fluid Science 32, 1468–1483.

Li, F.J., Li, J., Rong, X., et al., 2022. Study on ventilation and evacuation of highwaytunnel fire reversible jet fan based on FDS, in: Dong, L. (Ed.), WTC 2022. China Communications Press Co.,Ltd., Wuhan, Hubei, pp. 481–488.

Liu, B., Mao, J., Xi, Y., et al., 2021. Effects of altitude on smoke movement velocity and longitudinal temperature distribution in tunnel fires. Tunnelling and Underground Space Technology 112.

Tanaka, F., Yoshida, K., Ueda, K., et al., 2021. A simple model for predicting the smoke spread length during a fire in a shallow urban road tunnel with roof openings under natural ventilation. Fire Safety Journal 120.

Tao, L.L., Zeng, Y.H., 2022. Effect of Different Smoke Vent Layouts on Smoke and Temperature Distribution in Single-Side Multi-Point Exhaust Tunnel Fires: A Case Study. Fire 5.

Transport, E.D.o.C.J.o.H.a., 2022. Review on China's Traffic Tunnel Engineering Research: 2022. China Journal of Highway and Transport 35, 1–40.

Wang, L.Y., Guo, J.Q., Wang, M.S., 2015. Study on smoke temperature distribution based on model test in highway tunnel bshaft blow and exhaust ventilation. China civil engineering journal 48, 336–340.

Wang, Y.D., Qin, Z.J., He, Z.W., et al., 2020. Improved Mixed Ventilation Mode Combined Double-hole Complementarity with Blowing and Exhausting Shaft in Highway Tunnel. China Journal of Highway and Transport 33, 106–114.

Weng, M., Obadi, I., Wang, F., et al., 2020. Optimal distance between jet fans used to extinguish metropolitan tunnel fires: A case study using fire dynamic simulator modeling. Tunnelling and Underground Space Technology 95.

Zhang, M.H., Xiao, X.J., Fang, Z., et al., 2011. Experimental studies on fire smoke inthe left line of Xiangan tunnel. Fire Science and Technology 30, 1124–1127.

Zhang, X., Chen, L., Jiang, J., et al., 2023. Risk analysis of people evacuation and its path optimization during tunnel fires using virtual reality experiments. Tunnelling and Underground Space Technology 137.

Zhang, Z., Zhang, H., Tan, Y., et al., 2018. Natural wind utilization in the vertical shaft of a super-long highway tunnel and its energy saving effect. Building and Environment 145, 140–152.

Tunnelling for a Better Life – Yan, Celestino, Thewes & Eberhardt (Eds)
© 2024 The Author(s), ISBN 978-1-032-80042-4
Open Access: www.taylorfrancis.com, CC BY-NC-ND 4.0 license

Resilience assessment of shallow-buried subway stations under earthquake disasters

Chenlong Zhang, Dongming Zhang & Zhongkai Huang*
Key Laboratory of Geotechnical and Underground Engineering of Ministry of Education, Department of Geotechnical Engineering, Tongji University, Shanghai, China

ABSTRACT: This study aims to provide a comprehensive resilience assessment framework for evaluating the robustness and rapid recovery capabilities of shallow-buried subway stations under earthquake disasters. The proposed framework utilizes the ABAQUS software to establish numerical models of relevant subway stations. Subsequently, an extensive numerical analysis is conducted using selected seismic motions to generate vulnerability functions related to Peak Ground Acceleration (*PGA*) for these subway stations. Ultimately, the resilience assessment is completed by considering the vulnerability and recoverability of subway stations. The framework presented in this work contributes to the development of resilience-based design and management strategies for subway networks, facilitating their adaptation to seismic disasters.

Keywords: Subway stations, Resilience, Earthquakes, Fragility, Restoration

1 INTRODUCTION

The underground subway transportation system constitutes a vital component of modern urban transport networks, playing a crucial role in urban economic development and facilitating personnel mobility. In response to the escalating demands of rapidly growing cities, the construction and development of subway transportation systems are progressing at an unprecedented pace. Historically, engineers did not consider seismic design as a mandatory step for underground structures, believing that underground structures were less susceptible to damage compared to their above-ground counterparts (Hashash et al., 2001). However, this confidence was shattered by the catastrophic consequences of severe seismic disasters. A notable example is the 1995 Great Hanshin Earthquake in Japan, which caused extensive damage to underground tunnels, leading to the complete collapse of the Daikai station (Chen et al., 2023). In light of such tragedies, it has become imperative to conduct resilience assessments for critical hubs in urban underground transportation systems, such as subway stations, to mitigate the potential reoccurrence of similar disasters.

The overall reliability of subway transportation systems under seismic disasters has become increasingly challenging to predict (Iida et al., 1996). To enhance the safety of construction and operational services for subway transportation systems and as a crucial component of seismic performance-based design, the theory of seismic resilience has witnessed significant development in recent years (Psyrras et al., 2018). Seismic resilience is typically defined as the ability of a structure to withstand, respond to, and rapidly recover from seismic disasters (Cimellaro et al., 2020). In the context of subway stations, seismic resilience is manifested in specific ways, aiming to reduce economic losses and infrastructure damage caused by disasters, and to achieve the seismic design goal of rapid post-disaster recovery. This concept has gradually been incorporated into the design timelines and operational procedures of relevant transportation infrastructure.

Generally, performance indicators associated with the damaged state of engineering structures are commonly employed to assess the infrastructure's capacity to absorb damage, recover post-disaster, and adapt to new conditions (Argyroudis et al., 2021; Ayyub et al., 2015). These performance indicators are also linked to resilience curves, which further characterize the structural robustness and the speed of post-disaster functional recovery, taking into account the full life-cycle resilience of infrastructure during both construction and operational phases

*Corresponding author: 5huangzhongkai@tongji.edu.cn

DOI: 10.1201/9781003495505-470

(Ayyub et al., 2014; Yang et al., 2019). Currently, resilience assessment frameworks addressing single or multiple hazards have been proposed and extensively applied to various infrastructure systems (Anwar et al., 2020; Ekhlaspoor et al., 2021), including bridges (Argyroudis et al., 2020; Chienkuo et al., 2021), transportation networks (Alipour et al., 2016; Capacci et al., 2002) and other critical engineering structures (Panteli et al., 2017). In the context of tunnels, Huang and Zhang (Huang et al., 2016) considered resilience-influencing factors under extreme loading conditions, refining the stages of tunnel resilience evolution. Huang (Huang et al., 2022). proposed a resilience assessment framework for interval tunnels, specifically designed to evaluate seismic performance in tunnel structures under earthquake disasters. To the best of the author's knowledge, there is currently no quantified resilience framework proposed in the literature for subway stations under seismic disasters.

To bridge the gap between current research and practical needs, this study proposes a practical and feasible resilience assessment framework for subway stations. The framework is applied specifically to a double-deck, double-span subway station exposed to seismic disasters. Furthermore, the research evaluates the robustness and rapid recovery capability of shallow-buried subway stations under seismic disasters. Recommendations for further research are also discussed.

2 STATION RESILIENCE ASSESSMENT FRAMEWORK

The resilience assessment framework for subway stations proposed in this paper consists primarily of three components, as illustrated in Figure 1. Firstly, geological and station-specific physical information is gathered to establish finite element numerical simulations, yielding dynamic response results for the station structure under various seismic loads. Secondly, based on the results of numerical analysis, the relationship between seismic intensity indicators (*IM*) and the probability of station damage states is determined. Finally, the construction of station loss and recovery functions is employed to define the utility function, and the resilience assessment of the station is completed through the integration of this utility function. This resilience framework allows for the evaluation of a subway station's ability to absorb and recover from seismic-induced damage through vulnerability analysis and the development of utility functions. These components will be elaborated upon in subsequent sections.

2.1 *Numerical simulation analysis*

In the numerical simulation analysis section, it is imperative to gather various physical information pertaining to the station under evaluation. This information encompasses station dimensions,

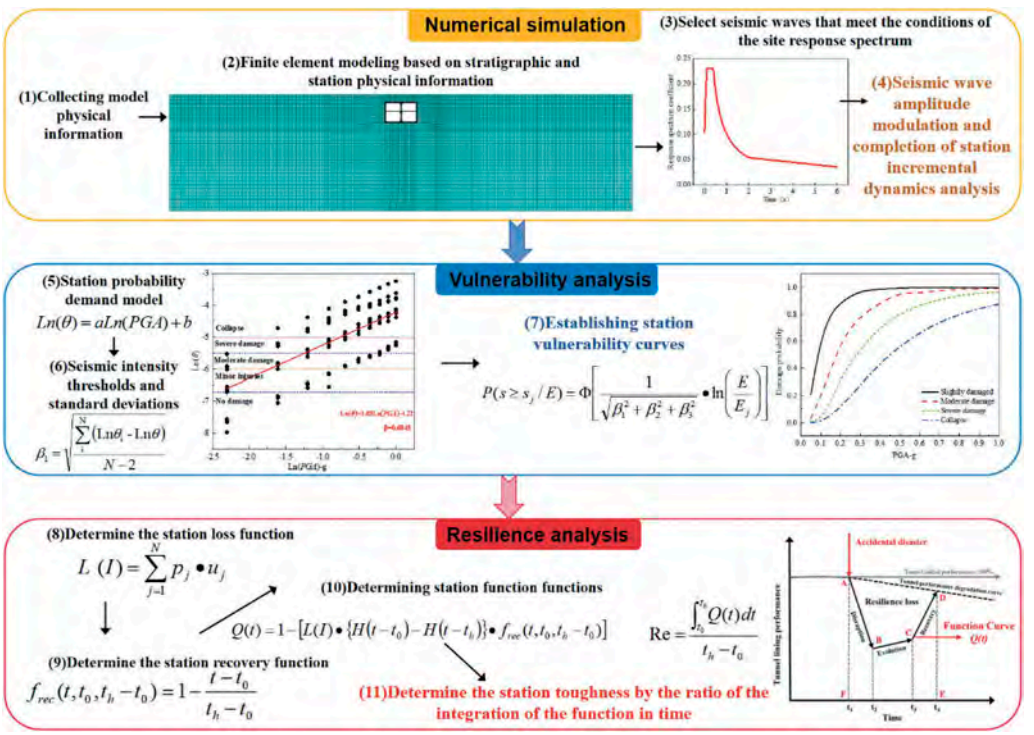

Figure 1. Framework for seismic resilience assessment of metro stations.

reinforcement ratios, material properties, as well as surrounding geological conditions. On this foundation, a finite element numerical model is established. The specific modeling approach is guided by the research methodologies of scholars such as Lysmer and Kuhlemeyer (Lysmer et al., 1969).

Furthermore, it is essential to utilize information regarding the surrounding geological conditions and the geographical location of the station to determine the site response spectrum. This involves selecting 10 or more seismic waves that satisfy the site response spectrum, thereby accounting for the uncertainty associated with seismic loads. Ultimately, the seismic wave amplitudes are adjusted to input seismic loads, completing the incremental dynamic analysis of the station.

2.2 *Vulnerability analysis*

The seismic vulnerability analysis of station structures signifies the probability of surpassing various damage thresholds for subway stations under different intensities of seismic motions. This probability is expressed by Equation (1). Incremental dynamic analysis based on numerical simulation methods is a commonly employed approach to ascertain the seismic vulnerability of subway stations (Hu et al., 2023).

$$F_i(x) = P(S \geq s_i / IM = x), \quad i = 1, 2, \ldots, n \tag{1}$$

In Eq. (1), S is the engineering demand parameter of the station after a seismic hazard, S_i is the threshold value of the i *th* damage state corresponding to the station, IM is denoted as the intensity of the seismic wave, and n is the number of damage states of the station.

Under seismic loading, subway stations primarily experience damage in the form of inter-story displacement, making it the predominant mode of failure. Building upon the success of prior research and applications (Jiang et al., 2023; Jiang et al., 2021), this paper employs the inter-story displacement angle as a measure of damage and an engineering requirement parameter. The calculation formula is expressed as follows:

$$\theta = \frac{W}{H} \tag{2}$$

In Eq. (2), θ is the inter-story drift angle(IDR), W is the horizontal displacement of the station top plate relative to the bottom plate, and H is the station floor height.

The seismic intensity index is crucial for discerning structural damage and conducting vulnerability analyses. Jiang et al. (Jiang et al., 2023) examined 15 seismic intensity indicators, including *PGA*, *PGV,* and *PGD*. They concluded that, for vulnerability analysis of shallow-buried subway station structures, *PGA* is the most efficient and practical intensity measure. Consequently, this paper also adopts PGA as the seismic intensity indicator.

In seismic vulnerability analysis, it is commonly assumed that the structural dynamic response under seismic hazards follows a lognormal distribution (Hu et al., 2023; Huang et al., 2022). Therefore, incorporating Equation (1), the seismic vulnerability function is expressed as follows:

$$P(s \geq s_j / IM) = \Phi\left[\frac{1}{\sqrt{\beta_1^2 + \beta_2^2 + \beta_3^2}} \bullet \ln\left(\frac{IM}{IM_j}\right)\right] \tag{3}$$

In Eq. (3): P denotes the exceedance probability of a station reaching a particular damage state for a given seismic intensity IM; Φ is a standard normal distribution; IMj is the average value of seismic intensity corresponding to different damage state thresholds of the station; β_1 is the standard deviation characterizing the seismic uncertainty; β_2 is the standard deviation characterizing the uncertainty of the construction quality; β_3 is the standard deviation characterizing the uncertainty introduced by the uncertainty of the material and the analysis model standard deviation.

2.3 *Resilience analysis*

The term "seismic resilience," as a professional concept, primarily delineates the robustness and rapid recovery of underground stations amidst seismic disasters. This paper employs well-established analytical definitions widely utilized in the field. The calculation formula is presented as follows (Hu et al., 2023; Huang et al., 2022):

$$\mathrm{Re} = \frac{\int_{T_0}^{T_2} Q(t)dt}{T_2 - T_0} \tag{4}$$

In Eq. (4), R represents the station resilience, $Q(t)$ represents the functionality function of the station during the seismic hazard restoration period, T_0 is the time of the earthquake, and T_2 is the time of the end of the station restoration.

Table 1. Damage status and interlayer displacement angle threshold of subway stations (Du et al., 2020).

Limit states	S_1-No	S_2-Minor damage	S_3-Moderate damage	S_4-Severe damage	S_5-Collapse
Inter-story drift ratio limit (θ)	θ<0.08%	0.08%≤ θ<0.29%	0.29%≤ θ<0.62%	0.62%≤ θ<0.96%	θ≥0.96%

Huang et al. (Huang et al., 2016), through on-site disaster analysis, observed a delay between the occurrence of the disaster and the immediate initiation of repair activities. This interval between disaster occurrence and restoration is defined as an evolutionary phase. Referencing Huang et al.'s (Huang et al., 2016) study, this paper considers the presence of a pre-repair preparation phase, presuming no alteration in station performance during this preparatory period. Figure 2 illustrates the conceptual definition diagram of seismic resilience for subway stations, where T_1 represents the onset of station repair activities.

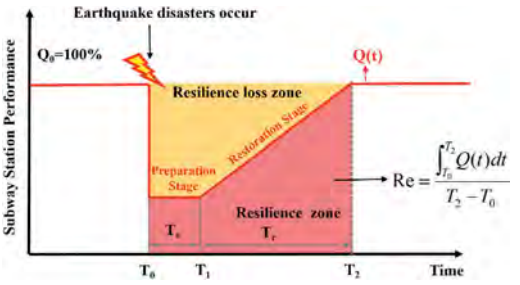

Figure 2. Definition of resilience concept for subway stations.

2.3.1 *Loss function*

When calculating the functionality of structures under seismic disasters, Cimellaro et al.(Cimellaro et al., 2010) propose that a building's functionality can be assessed based on the computation of direct economic losses. This conceptual framework has been extensively employed in studies related to seismic resilience assessment (Hu et al., 2023; Huang et al., 2022; Kassem et al., 2023; Cimellaro et al., 2010). Drawing inspiration from this approach, the structural loss function for the station is formulated as follows:

$$L(I) = \sum_{j=1}^{N} p_j \bullet u_j \tag{5}$$

In Eq. (5): $L(I)$ denotes the station loss function; P_j represents the probability of the station transitioning to damage state j and u_j denotes the repair coefficient required when the station reaches the damage state j. The precise correlation coefficients for this calculation are delineated in Table 2.

2.3.2 *Recovery functions*

The recovery function serves to characterize the repair progress and rate of subway stations during the recovery phase following seismic disasters. The representation of recovery duration and functionality is crucial for assessing seismic resilience (Kassem et al., 2023). Cimellaro et al. (Cimellaro et al., 2010) have pointed out in their research that, due to a lack of information on disaster management and available resources, linear functions are commonly employed to assess building functionality. Therefore, this paper similarly adopts a linear recovery function to characterize the station's recovery process, expressed as follows:

$$f_{rec}(t, T_1, T_2 - T_1) = 1 - \frac{t - T_1}{T_2 - T_1} \tag{6}$$

In Eq. (6), T_1 is the station recovery start time, and T_2 is the end time. The total time required for the recovery process is defined as shown in the following equation[20]:

$$T_r = T_2 - T_1 = \sum_{j=1}^{N} t_j \bullet p_j \tag{7}$$

In Eq. (7): t_j is the time required to repair the station completely when its damage state is j. Detailed insights into the various station damage states and their corresponding probabilities, denoted as P_j. Referring to the Chinese standard "RISN-TG041 -2022 Guidelines for Seismic Resilience Assessment of Urban Engineering Systems" (2022), the required repair times for various damage states of the station are determined, as presented in Table 3.

Table 2. Repair coefficient of stations with different damage states (Huang et al., 2022).

Damage state (DS_j)	S_1-No	S_2-Minor damage	S_3-Moderate damage	S_4-Severe damage	S_5-Collapse
Repair coefficient(u_j)	0	0.10	0.25	0.75	1

Table 3. Repair time of stations with different damage states (RISN-TG041-2022).

Damage state	S_1-No	S_2-Minor damage	S_3-Moderate damage	S_4-Severe damage	S_5-Collapse
Recovery time (Days)	0	0.5	2.4	45	210

2.3.3 *Station function functions*

When establishing the functional function of the station, it is commonly assumed that there is no performance loss before the occurrence of seismic disasters. This implies the exclusion of considerations related to functional degradation due to aging of the subway station. Additionally, it is assumed that the station's performance will be fully restored after the completion of the repair process. The station's functional function can be computed using the formula proposed by Cimellaro et al. (2006), as expressed below:

$$Q(t)=\begin{cases}1-L(I) & T_0<t<T_1\\ 1-[L(I)\bullet\{H(t-T_1)-H(t-T_2)\}\bullet f_{rec}(t,T_1,T_2-T_1)] & T_1<t<T_2\end{cases} \tag{8}$$

In Eq. (8): L(I) and frec(t, T1, T2-T1) denote the station loss function and recovery function, respectively, which will be described in detail in Eqs. (3-7) below; H(x) is the Heaviside step function, as follows:

$$H(x)=\begin{cases}1 & x\geq 0\\ 0 & x<0\end{cases} \tag{9}$$

Based on the subway station functional function formulated in Equation (8), a quantitative assessment of the subway station's resilience index can be obtained by integrating over the time during which performance is impaired. This paper will utilize the actual structural parameters and geological parameters of a specific subway station in Wuhan. The dynamic response process of the station under seismic disasters will be analyzed, applying the seismic resilience assessment framework proposed in this study. This will facilitate a quantitative resilience analysis of the Wuhan subway station.

3 CASE AND MODELLING ANALYSIS

This paper selects a subway station in Wuhan, China, for resilience assessment. The chosen station exhibits a typical double-layer, double-span structure, with a depth of 4.61 meters, an overall width of 21.3 meters, and a height of 13.69 meters. The detailed structural dimensions and cross-sectional reinforcement are illustrated in Figure 3.

The appropriate constitutive relationship accurately reflects the stress-strain behavior of materials. For the characterization of the nonlinear dynamic response process of the station-soil coupled numerical model under seismic loads, the correct choice of constitutive models is crucial for the overall coherence and validity of the paper.

The Concrete Damage Plasticity (CDP) constitutive model is based on isotropic elastic damage and isotropic tension-compression plasticity theories to represent the material's inelastic deformation. It characterizes the stiffness degradation resulting from

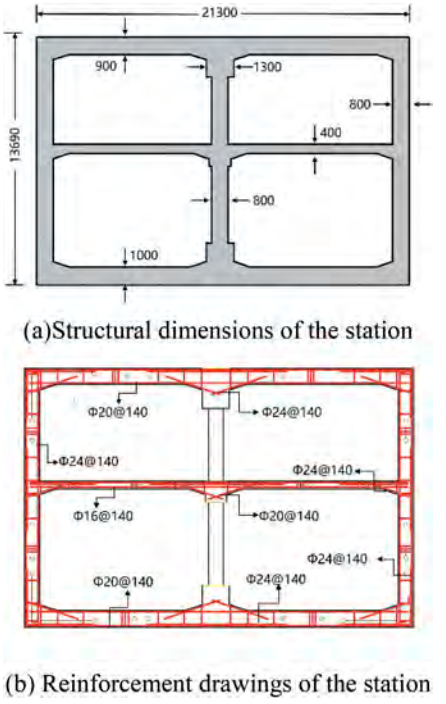

Figure 3. Structural dimensions and reinforcement details of metro station (mm).

damage by quantifying the interaction between damage evolution and plastic slip through the introduction of damage variables . The main structure of the station employs C50 grade concrete. In this study, the CDP constitutive model is selected to simulate the lining, with the relevant concrete material properties set according to the Chinese Concrete Structure Design Code (GB50010-2010) .

The station structure's reinforcement is predominantly composed of HRB335 steel. Following the guidelines outlined in the Chinese Concrete Structure Design Code (GB50010-2010) and relevant research findings, a plastic constitutive model is employed to simulate the behavior of the reinforcement.

The surrounding strata are selected to represent the actual site conditions of the subway station. The Mohr-Coulomb constitutive model is employed to simulate the soil behavior, with the layer thickness of various soil strata chosen as the average thickness from site investigation results. The detailed variations of elastic modulus, unit weight, cohesion, and friction angle with depth across the entire site are depicted in Figure 4.

A finite element numerical model (2D) considering the interaction between soil and tunnel is established using ABAQUS software. The entire numerical model has a height of 74m and a width of 300m. The bedrock position at the bottom boundary

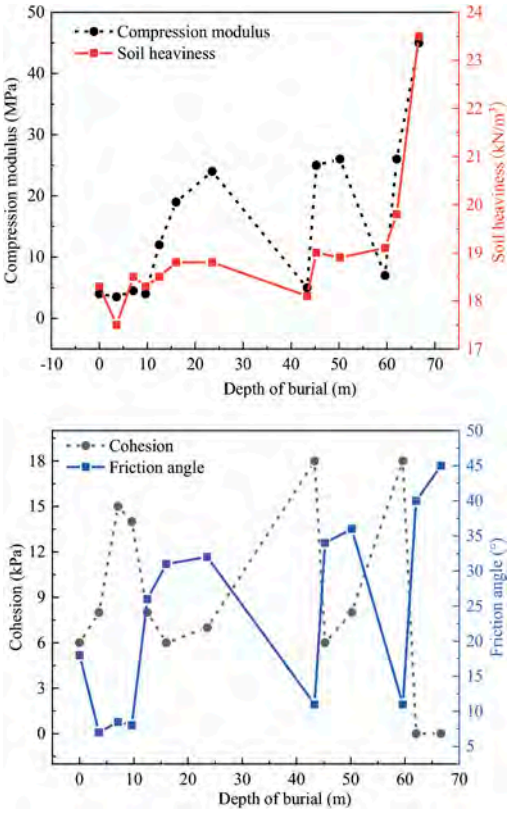

Figure 4. Relationship between soil material properties.

of the model is determined using the method proposed by Lysmer and Kuhlemeyer (Lysmer et al., 1969), treating it as an elastic foundation by appropriately setting dampers. Seismic loading on the model is applied by subjecting the dampers to seismic oscillations. The lateral boundaries of the finite element model are coupled using Motion Projection Constraints (MPC) to ensure simultaneous movement at both ends (Huang et al., 2022). The detailed model dimensions and boundary conditions are illustrated in Figure 5.

The finite element model employs plane strain elements (CPE4R) for both the station and the soil. Steel reinforcement elements are modeled as two-dimensional truss elements (T3D2). The mesh dimensions adhere to the requirements outlined in the study by Lysmer et al. (Lysmer et al., 1969) to ensure grid sensitivity. In terms of interaction, the reinforcement is embedded within the station lining using an embedded approach. The contact between the lining and the surrounding soil is characterized by both normal and tangential behavior. Normal behavior is modeled using a hard contact relationship, while tangential behavior is represented by a penalty function relationship with a friction coefficient set to 0.6 (Huang et al., 2022).

For an accurate assessment of subway station resilience under seismic actions, it is crucial to identify a sufficient and reasonable number of seismic waves. Generally, selecting 10 seismic waves is considered adequate to meet the requirements for computational needs. In this study, ten seismic waves satisfying the response spectrum criteria were chosen from the Pacific Earthquake Engineering Research (PEER) database (https://ngawest2.berkeley.edu/). The seismic waves were selected based on their source site conditions and similarity to the modeled subgrade bedrock. The amplitudes were scaled in increments of 0.1g, ranging from 0.1g to 1.0g. Subsequently, the resulting 100 scaled seismic waves were input into the finite element model to conduct incremental dynamic analysis.

4 STATION RESILIENCE ANALYSIS

4.1 *Vulnerability analysis*

The extracted relative horizontal displacements were used to calculate the inter-story drift angle based on Formula 2. The logarithmic relationship between PGA and inter-story drift angle was plotted, and a linear regression analysis was conducted, as illustrated in Figure 6. According to Figure 6, the probabilistic seismic demand model for the subway station is obtained as shown in Formula 10:

$$Ln(\theta) = 1.365Ln(PGA) - 4.207 \qquad (10)$$

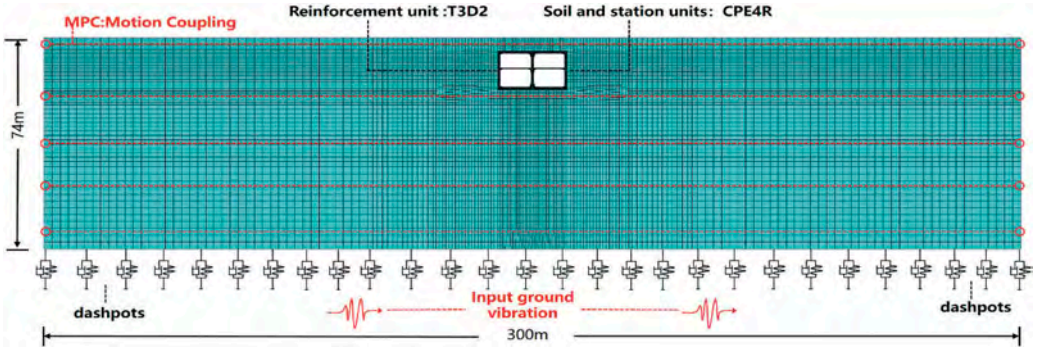

Figure 5. Numerical model dimensions and boundary conditions.

The probabilistic seismic demand model for the subway station represents the evolutionary process of its damage indicators with increasing seismic intensity.

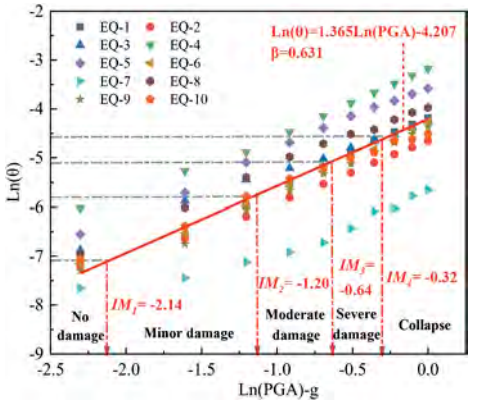

Figure 6. Logarithmic linear regression analysis.

To characterize the uncertainty of seismic waveforms, β_1 was calculated as 0.631 based on Formula 11 and Figure 6. Using Table 1 and Formula 10, the seismic intensity mean values (IM_j) corresponding to different damage state thresholds for the underground station were determined.

$$\beta_1 = \sqrt{\frac{\sum_{i}^{N} (\mathrm{Ln}\theta_i - \mathrm{Ln}\theta)^2}{N-2}} = 0.631 \qquad (11)$$

Based on the obtained values of β_1, β_2, β_3, and the seismic intensity mean values (IM_j) corresponding to different damage state thresholds, the exceedance probabilities for various damage states of the subway station were calculated according to Formula 3, as illustrated in Figure 7. From Figure 7, it is evident that the probabilities of different damage states for the subway station increase with the continuous growth of seismic intensity. When the seismic intensity is below 0.2g, the probabilities of severe damage and collapse are at most 5.4% and 3.8%, respectively, indicating a relatively low threat to personnel and property safety, and limited damage to the subway station. However, when the seismic intensity exceeds 0.4g, the probabilities of severe damage and collapse soar to 14.6% and 20.7%, respectively, highlighting a heightened risk of damage to the subway station, and emphasizing the significance of addressing safety concerns.

4.2 *Function function determination*

The seismic fortification standards in China's "Code for Seismic Design of Buildings" are

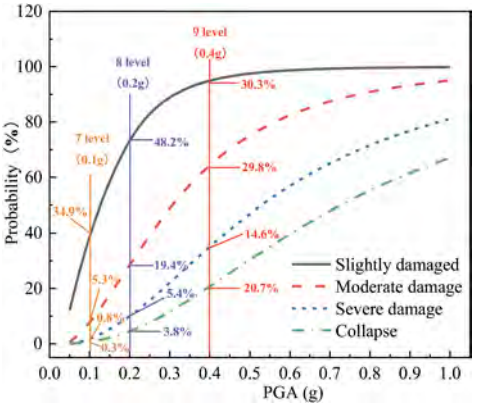

Figure 7. Logarithmic linear regression analysis.

proposed to be 6, 7, 8, and 9 degrees. In this study, fortification standards of 7, 8, and 9 degrees were specifically chosen to assess the seismic resilience of the subway station at the designated location. These fortification standards correspond to I_1 (0.1g), I_2 (0.2g), and I_3 (0.4g) peak ground accelerations (*PGA*s), respectively.

4.3 *Station resilience analysis*

In the event of an earthquake disaster, a preparatory phase exists between the occurrence of the disaster and its restoration due to aftershock disturbances, immediate rescue efforts, and subsequent maintenance activities at subway stations. Huang et al. (Huang et al., 2016) defined this phase as the post-disaster evolution stage. This study posits a correlation between the duration of the preparatory phase for subway station maintenance and the extent of station damage. Specifically, it is assumed that the more severe the station damage, the longer the required preparation time for disaster relief and maintenance. Additionally, the preparatory phase time for subway stations is assumed to be equal to the restoration time.

Based on Equation 4 and Figure 7, the schematic representation of subway station resilience under different fortification standards is illustrated in Figure 8. From Figure 8, it is evident that with an increase in peak ground acceleration (*PGA*), the seismic resilience of the subway station significantly decreases. The primary reason for this decline is the occurrence of severe structural damage in the subway station due to higher seismic intensity. This damage is further reflected in the robustness of the subway station, leading to a reduction in its seismic resilience. It is noteworthy that the seismic fortification intensity for the subway station in this location is 7 degrees. At this seismic intensity, the seismic resilience of the subway station is 0.957. According to the study by Huang et al. (Huang et al., 2022) (as shown in Table 4), the station exhibits high seismic resilience under these conditions.

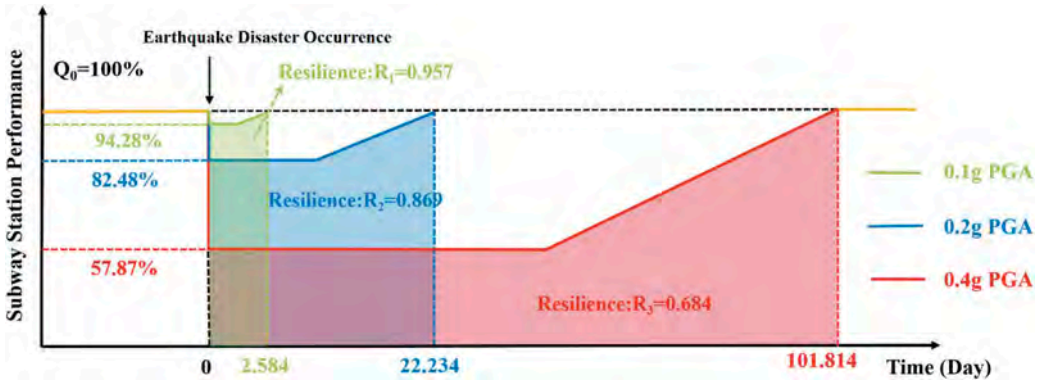

Figure 8. Results of resilience of subway stations under different seismic fortification standards.

Table 4. Definition of resilience grade (Huang et al., 2022).

Grade	High resilience	Moderate resilience	Low resilience
Range	$0.9 \leq R < 1.0$	$0.6 \leq R < 0.9$	$R < 0.6$

5 CONCLUSION

This paper presents a feasible and practical resilience assessment framework for evaluating the robustness and rapid recovery of subway stations in the event of earthquake disasters. The resilience assessment framework adopts inter-story displacement angle as a performance indicator and allows for vulnerability analysis of subway station structures with various configurations, such as single-span multi-story and double-span multi-story structures. It facilitates the quantification of resilience indicators for subway stations.

ACKNOWLEDGMENTS

This work was supported by the Shanghai Science and Technology Committee Program (22dz1201202), the National Natural Science Foundation of China (Grants No. 52108381, 52090082), the Damage Database for Urban Rail Transit Underground Structures and Resilience evaluation algorithm research (TSY2022QT161), and Natural Science Foundation of Chongqing, China (No. CSTB2023NSCQ-MSX0808).

REFERENCES

Argyroudis, S.A. (2021). Resilience metrics for transport networks: a review and practical examples for bridges. Proceedings of the Institution of Civil Engineers - Bridge Engineering.

Ayyub, B.M. (2015). Practical resilience metrics for planning, design, and decision making. ASCE-ASME Journal of Risk and Uncertainty in Engineering Systems, Part A: Civil Engineering, 1(3), 04015008.

Ayyub, B.M. (2014). Systems resilience for multihazard environments: definition, metrics, and valuation for decision making. Risk Analysis, 34(2), 340–355.

Anwar, G.A., Dong, Y., Zhai, C. (2020). Performance-based probabilistic framework for seismic risk, resilience, and sustainability assessment of reinforced concrete structures. Advances in Structural Engineering, 23(7), 1454–1472.

Argyroudis, S. A., Mitoulis, S. A., Hofer, L., Zanini, M. A., Tubaldi, E., & Frangopol, D. M. (2020). Resilience assessment framework for critical infrastructure in a multi-hazard environment: case study on transport assets. Science of the Total Environment, 714, 136854.

Alipour, A., & Shafei, B. (2016). Seismic resilience of transportation networks with deteriorating components. Journal of Structural Engineering, 142(8), C4015015.

Cimellaro, G.P., Reinhorn, A.M., Bruneau, M. (2020). Framework for analytical quantification of disaster resilience. Engineering Structures, 32(11), 3639–3649.

Chienkuo, C., Eiki, Y., & Santoso, D. (2021). Seismic resilience analysis of a retrofit-required bridge considering moment-based system reliability. Structural Infrastructure Engineering, 17(6), 757–778.

Capacci, L., Biondini, F., & Titi, A. (2002). Lifetime seismic resilience of aging bridges and road networks. Structural Infrastructure Engineering, 16(2), 266–286.

Cimellaro, G. P., Reinhorn, A. M., Bruneau, M. (2010). "Seismic resilience of a hospital system." Structural Infrastructure Engineering, 6(1–2), 127–144.

Cimellaro, G. P., Reinhorn, A. M., Bruneau, M. (2010). "Framework for analytical quantification of disaster resilience." Engineering Structures, 32, 3639–3649.

Cimellaro, G., Reinhorn, A., & Bruneau, M. (2006). Quantification of seismic resilience. In Proc. 8th Nat. Conf. Earthquake Eng., 8, 1–10.

Du, X., Jiang, J., El Naggar, M. H., Xu, C., Xu, Z. (2020). "Inter-Story Drift Ratio Associated with Performance Objectives for Shallow-Buried Multi-Story and Span Subway Stations in Inhomogeneous Soil Profiles." Earthquake Engineering and Structural Dynamics, 50, GEM Foundation, PaviaStruct. Control Health Monit., 655–672.

Ekhlaspoor, A., Raissi, D. M., Eghbali, M., & Samadian, D. (2021). Pre-event assessment of seismic resilience index for typical Iranian buildings via a web-based tool. International Journal of Civil Engineering, 1–16.

FEMA. (2009). "Quantification of Building Seismic Performance Factors, FEMA-P695." Federal Emergency Management Agency.

Hashash, Y.M., Hook, J.J., Schmidt, B., John, I., Yao, C. (2001). Seismic design and analysis of underground structures. Tunnelling and Underground Space Technology, 16(4), 247–293.

Huang, H. W., & Zhang, D. M. (2016). Resilience analysis of shield tunnel lining under extreme surcharge: characterization and field application. Tunnelling and Underground Space Technology, 51, 301–312.

Huang, Z., Zhang, D., Pitilakis, K., et al. (2022). Resilience assessment of tunnels: Framework and application for tunnels in alluvial deposits exposed to seismic hazard. Soil Dynamics and Earthquake Engineering, 162, 107456.

Hu, J., Wen, W., Zhai, C., et al. (2023). Seismic resilience assessment of buildings considering the effects of mainshock and multiple aftershocks. Journal of Building Engineering, 68, 106110.

Huang, Z. (2022). "Resilience Evaluation of Shallow Circular Tunnels Subjected to Earthquakes Using Fragility Functions." Applied Sciences, 12, 4728.

Huang, Z., Zhang, C. L., Ma, S. K., et al. (2021). Study of the mechanical behaviour and damage characteristics of three new types of joints for fabricated rectangular tunnels using a numerical approach. Tunnelling and Underground Space Technology, 118, 104184.

Iida, H., Hiroto, T., Yoshida, N., et al. (1996). Damage to Daikai subway station. Soils and Foundations, 36(Special), 283–300.

Jiang, J., El Naggar, M. H., Xu, C., Chen, G., Du, X. (2023). "Seismic fragility analysis for subway stations considering varying ground motion ensemble." Soil Dynamics and Earthquake Engineering, 165, 107705.

Jiang, J., Xu, C., El Naggar, H. M., Du, X., Xu, Z., Assaf, J. (2021). "Improved pushover method for seismic analysis of shallow-buried underground rectangular frame structures." Soil Dynamics and Earthquake Engineering, 140, 106363.

Jiang, J., El Naggar, M. H., Du, X. (2023). "Seismic fragility curves for shallow buried subway stations using pushover-based method." Tunnelling and Underground Space Technology, 135, 105059.

Kassem, M. M., Nazri, F. M. (2022). "Integrated approach between seismic resilience and vulnerability indexes with regularity index for vertical irregularity planar frames risk assessment."

Lysmer, J., & Kuhlemeyer, R. L. (1969). Finite dynamic model for infinite media. Journal of Engineering Mechanics Division, 95, 859–878.

Panteli, M., Mancarella, P., Trakas, D. N., et al. (2017). Metrics and quantification of operational and infrastructure resilience in power systems. IEEE Transactions on Power Systems, 32(6), 4732–4742.

Psyrras, N.K., Sextos, A.G. (2018). Safety of buried steel natural gas pipelines under earthquake-induced ground shaking: A review. Soil Dynamics and Earthquake Engineering, 106, 254–277.

Standard Quota Research Institute of the Ministry of Housing and Urban Rural Development. (2011). "Guideline for evaluation of seismic resilience assessment of urban engineering systems (RISN-TG041-2022)." China Architecture & Building Press. Beijing.

Xiangsheng Chen, Jun Shen, Xiaohua Bao, et al. (2023). A review of seismic resilience of shield tunnels. Tunnelling and Underground Space Technology, 136, 105075.

Taylor & Francis
Taylor & Francis Group
http://taylorandfrancis.com

Contractual practices and risk management

Taylor & Francis
Taylor & Francis Group
http://taylorandfrancis.com

Tunnelling for a Better Life – Yan, Celestino, Thewes & Eberhardt (Eds)
© 2024 The Author(s), ISBN 978-1-032-80042-4
Open Access: www.taylorfrancis.com, CC BY-NC-ND 4.0 license

Development of a tunnel asset management tool from a risk-based approach

C. Alessio, D. Di Fiore* & L. Baccolini
Tecne Gruppo Autostrade per l'Italia S.p.A., Roma, Italy

B. Chiaia
Politecnico di Torino, Torino, Italy

M. Conte
Autostrade per l'Italia S.p.A., Roma, Italy

ABSTRACT: The upcoming challenges in the transport infrastructures industry will surely include the maintenance and rehabilitation of the existing tunnels, furthermore, a consistent approach in accordance with the best practices in Asset Management is key to maintain the tunnels for continued serviceability, defining a proactive and effective maintenance plan within budget constraints. Italy is the second country worldwide in terms of tunnels numerosity. Autostrade per l'Italia S.p.A. operates 595 tunnels, half of them built before 1970. In August 2022, the National regulations introduced a multilevel assessment approach for tunnels, including a simplified risk analysis. In the authors' opinion, these new Standard became crucial to develop of a decision support tool that aims to be robust, and user-friendly. The tool is fed by asset overall information, conditions and defects distribution. Defects are characterized by extension (k_1), intensity (k_2), severity (G) and are used to run the simplified risk analysis in terms of hazard, vulnerability, exposure of six different thematic areas (structural, seismic, geotechnical, etc.). Deterioration models are defined and included based on the age of the tunnel, waterproofing techniques, construction materials etc… Cost and intervention model are included for rehabilitation works as well (TRS – Tunnel Renewal Strategy) and/or "detect and repair" works (IRS/IMS). The tool can assess the current and foreseen monetary value of the asset starting from the gross replacement cost, giving an overview of the tunnels and a medium and highly detailed summary broken down for a tunnel or groups of tunnels. The tool aims to identify and prioritize tunnels that should be maintained in the upcoming years to optimize the lifecycle of the asset based on a short term and a long-term asset management planning analysis towards targeted level of service. A multicriteria analysis will be also included in a future development to account service disruption, reputation, environmental impact.

Keywords: Life Cycle, Deterioration, Risk, Residual Value, Cost Model, Intervention Model

1 INTRODUCTION

The Autostrade per l'Italia S.p.A (ASPI) infrastructural asset is nowadays exposed to climate change effects, seismic and geological hazards and, finally, aging of the materials. ASPI is the major Italian motorway concessionaire in charge for the operation and maintenance of about 595 tunnels.

Aging and deterioration of the infrastructures play a key role in the civil engineering industry also due to the most recent collapses that hardly hit ASPI. These events lead to a new regulation in the bridges and viaducts as well as in the tunnel industry:

- 17th December 2020 "*Linee guida per la classificazione e gestione del rischio, la valutazione della sicurezza ed il monitoraggio dei ponti esistenti*";
- 23rd August 2022 "*Linee guida per la classificazione e gestione del rischio, la valutazione della sicurezza ed il monitoraggio delle gallerie esistenti*", hereinafter referred to as "LLGG";

This scientific work is focused on the development of a decision support tool for tunnel asset management even though the methods and approaches herein analysed are applicable to any kind of civil

*Corresponding author: daniele.difiore@tecneautostrade.it

DOI: 10.1201/9781003495505-471

asset in general. The purpose is to base the tool on the new Guidelines, which represent the common rules for all the Owners/Concessioners of road tunnel asset in Italy.

The new regulation is classified into different layers (1 to 4) characterized by an increasing level of detail:

- **Level 0** – Asset overall information such as location, length, lining material, construction age etc…;
- **Level 1** – Asset condition in terms of scored defect detected during the visual inspection. In this phase extension (k_1), magnitude (k_2) and severity (G) of the defects are collected in forms for further analyses;
- **Level 2** – The levels 0 and 1 gathered information feeds a process whose purpose is to assign a simplified risk score to each 20 m long segment of the tunnel for each thematic area (structural global and local, geological, seismic, hydraulic and transport related). The score can be low, mid-low, mid-high or high. The six thematic areas (except for hydraulic) are then combined into a global risk rate;
- **Level 3 & 4** – whenever risk rate coming from level 2 is mid-high a preliminary safety evaluation is performed to better investigate the parameters which lead to such rate of risk in the specific thematic area. If the risk rate is confirmed engineering judgement and calculation are put in place to identify the mitigation measures, or eventually monitoring systems, needed to keep the risk acceptable (Level 4). When the risk rate is high level 3 is glossed over.

The new regulation is promoting further actions ensure the implementation of more reliable approach to asset management "*Si raccomanda inoltre che detti modelli possano essere anche aggiornati in tempo reale, costituendo quindi un banca dati aggiornata per le necessarie azioni di asset management*".

Italy is the second country worldwide in terms of tunnels numerosity. Autostrade per l'Italia S.p. A. runs 595 tunnels, half of them built before 1970. In this picture, the need for a decision support tool arose within the engineering company of Autostrade per l'Italia Group (Tecne S.p.A).

The decision support tool is feed by the information required by the LLGG among the ones used for the multilevel analyses. Data coming from levels 0, 1 and 2 are necessary to assess the condition of the asset at time 0.

Deterioration models are then implemented to evaluate the foreseen condition of the asset in the most reliable way compatible with knowledges and data available today. The aim is to have a set of models dedicated to specific assets (ie.customized by construction age, liner materials or waterproofing technology).

Cost and intervention models are needed to compare alternative scenarios where Tunnel Renewal Strategy (TRS) or Detect and Repair approaches (IRS/IMS) are possible.

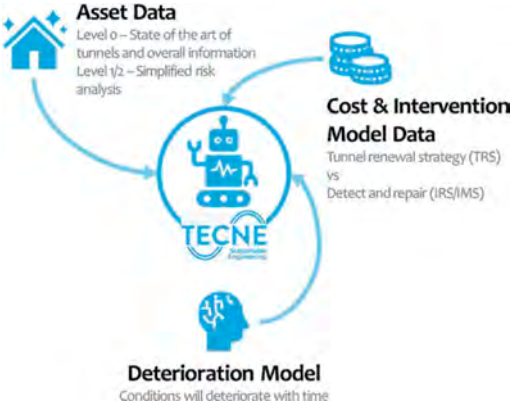

Figure 1. Tool input.

The decision support tool is aimed to compare several parameters such as current and foreseen monetary value of the asset, Capital (CapEx) and Operative (OpEx) discounted expenditures, disruption, environmental impact, effects on reputation etc, in different operating scenarios (including no intervention at all).

Inputs feeds Outputs and vice versa into a never ending loop of asset lifecycle.

Developing a Life Cycle Cost Analysis (LCA) tool brings multiple advantages to the Organization. Herein some of them:

- No bias in the decision making processes concerning intervention planning and design;
- Easy access to the assumptions underlying the algorithm;
- Data driven processes based on the state of the art of the asset management industry.

At this stage, the tool is a mock-up version developed with Visual Basic for Application.

2 ASSET DATA

The LLGG new regulation involves national road tunnels over 200 m long. Autostrade per l'Italia S.p. A. is in charge of the maintenance and management of 595 motorway tunnels, 450 of which have been triggered by the new Guidelines.

LLGG provide a roadmap and a defined timeline for the market operators to fulfil the requirements of each level.

Assets are grouped by age:

- Tunnels built before 1970;
- Tunnels built between 1971 and 1990;
- Tunnels built after 1991.

Timeline is given in the following table:

Table 1. LLGG requirements.

Construction age	Level 0	Level 1 & 2
Ante 1970	Within 3 months	Within 6 months
1971-1990		Within 12 months
Post 1991		Within 18 months

Level 0 need to be fulfilled in 3 months since the LLGG were issued whilst Levels 1 and 2 have different deadlines according with Asset construction age.

As already mentioned, the Guidelines include four main layers (five considering resilience analysis of the transport system) characterized by an increasing level of detail. Collection of the main overall information related to tunnels (Level 0) in a structured database is the first step for the simplified risk analysis. Level 0 includes 617 data that need to be collected in a standard layout and submitted to the Ministry of Infrastructures and Transport.

The set of data includes (but is not limited to) the following list:

- ID number of tunnel, name, location, coordinates, Concessionaire, construction age, designer name, length, lanes number;
- Max speed, curvature change rate (CCR), peak ground acceleration, water table elevation, geology of the area, lining material, presence of rebars, water proofing system, pavements material and international roughness index (IRI);
- Average number of vehicles per day, percentage of trucks and commercial users etc. .

This give a preliminary knowledge of the Asset, where it is located, when it was constructed and so on.

Some of the collected data from Level 0 (about 53) are needed, together with Level 1 visual inspection, to perform the simplified risk analysis (Level 2).

3 SIMPLIFIED RISK ANALYSIS

The purpose of Level 1 and 2 is the evaluation of a simplified risk rate of the asset combination of six different disciplines:

- **SGG** – Global structural and geotechnical risk;
- **SLO** – Local structural risk;
- **GEO** – Geological risk;
- **SIS** – Seismic risk;
- **STD** – Transportation risk;
- **IDR** – Hydraulic risk.

In order to do so about 53 indicators (primary and secondary) are gathered and combined to understand the hazard (H), vulnerability (V) and exposure (E) of each area.

The risk rate, called "Classe di attenzione", ranges from low to high depending on the combination of H, V, E (Figure 2).

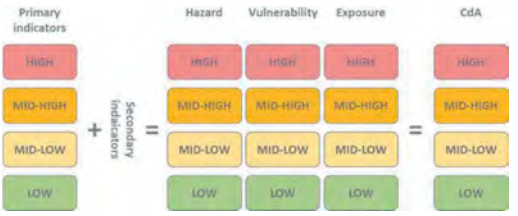

Figure 2. Definition of "classe di attenzione".

Figure 3. Visual inspection.

Vulnerability is mainly linked to condition of the asset. Condition is assessed through visual inspections (Figure 3).

Visual inspection is the first step of Level 1. During the first inspection all the water sheets and screens are dismounted to have an open view of the tunnel liner. The company in charge for the activity, after high pressure watering of the surface, start a close distance inspection hammering and marking all the noticeable structural and water related defects.

Relevant defect clusters are listed and described (with support of case study images) in LLGG – Annex B where some information on the following parameters (to be assigned during inspection) shall be provided:

- **Relative size k_1** – In percentage compared with the characteristic size of the elementary section[1] of the tunnel;

1 A tunnel is usually broken down into 20 m long elements.

- **Intensity k_2** – Can be 0.2 (low), 0.5 (mid) or 1.0 (high) depending on the magnitude of the defect.

Defects are listed in a spreadsheet and represented into a 1 m by 1 m grid plan layout. Defects are then grouped by type evaluating the size and intensity of the cluster as follows:

$$k_{1,t} = \sum_{i=1}^{n} k_{1,i} \quad (1)$$

$$k_{2,t} = \sum_{i=1}^{n} (k_{2,i} \cdot k_{1,i}) / k_{1,t} \quad (2)$$

Where $k_{1,i}$ and $k_{2,i}$ are referred to the defects belonging to the same cluster.

Engineering and expert judgement play a role in the evaluation of the defect's severity (G). G can range from 1 to 4 and has an impact on the results in terms of SGG vulnerability.

Similarly to k_1 and k_2, also G is assigned to each defect and then summarized to have a cluster representative value:

$$G_t = \sum_{i=1}^{n} G_i \cdot k_{1,i} / k_{1,t} \quad (3)$$

These parameters are then combined, at Level 2, to have a vulnerability rate (low to high). For instance, in Table 2, the combination matrix used in the SGG area to assess the condition of the liner.

Table 2. SGG vulnerability combination matrix.

G_t	k_2	k_1		
		0.2	0.5	1.0
1	0.2	Low	Low	Mid-low
	0.5			
	1.0			
2	0.2	Low	Mid-low	Mid-low
	0.5			
	1.0			
3	0.2	Mid-low	Mid-low	Mid-low
	0.5			
	1.0	Mid-high	Mid-high	Mid-high
4	0.2	Mid-high	Mid-high	Mid-high
	0.5			
	1.0			
3 & 4 (critical area[2])	0.2	High	High	High
	0.5			
	1.0			

4 DETERIORATION MODEL

The development and use of an asset is divided into stages. Typically, the sequence of events through the life of the asset progress as follows:

1. concept;
2. design;
3. construction;
4. operation and use;
5. disposal or renew.

Throughout the tunnel lifecycle, the major costs are borne after construction, in the operational phase, and they may excel the initial construction cost.

Prediction on future level of service of the asset (condition/performance) is needed to obtain a benefit during "*operation and use*" timeframe.

Tunnel deterioration is a gradual process through the life of a structure in which routine maintenance and repair actions are performed. While routine maintenance does not improve quality level of a structure but rather keeps it on an operational level repair/remediation works are intended to increase structure performance level (Sandra Skaric Palic et al.).

Define a reliable deterioration model of the Asset is the most difficult goal to achieve for a comprehensive Life Cycle Cost Analysis (LCA).

Tunnel deterioration affects conditions/level of service and depends on many factors (environment, aging of materials, external pressure etc..) and understanding the different implication of asset deterioration is important to address a consistent maintenance plan.

Figure 4 shows the solutions that might be applied across an asset's life cycle.

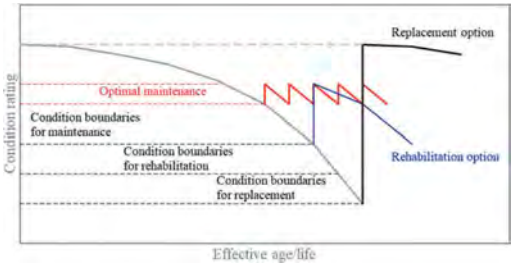

Figure 4. Deterioration and life cycle interventions.

Condition is defined on a scale of 0 to 100 where 100 represents a new tunnel.

Typically, preventive tunnel maintenance processes should be applied while asset is in good condition (Figure 4 – *Optimal maintenance*).

2 Critical area is the projected area of the road on the liner.

Please note that many high regular quality data observations over many years are needed to produce such deterioration curves for infrastructure. The forecast degradation rates may be uncertain, leading to uncertainty as to when intervention is required.

Uncertainties in the decision-making process may be decreased by using information from monitoring which are used to establish triggering thresholds for the structure passing performance levels (Sandra Skaric Palic et al.).

Both deterministic and probabilistic models available which can be used to simulate the structural degradation. The tool is fed by deterministic models but, near future developments could allow the use of both.

Conditions are defined according to the possible mechanism of collapse defined in the new guidelines for a tunnel liner:

- **Global** mechanism, causing failure of the structure.
- **Local** mechanism which results in a temporary "out of service" of the asset.

These mechanisms are covered according to the disciplines SGG and SLO mentioned in the previous section. Increasing in degradation leads to an unacceptable level of service intended as higher structural failure risk both for global and local mechanism.

Not all the parameters affecting hazard, vulnerability and exposure are representative of the structural condition of the asset. Whatever could change in between of two subsequent inspections has a role in the asset condition evaluation.

The parameters affecting SGG and SLO that meet this assumption are:

- **SGG** – Level of structural defect – from LOW (state = 1) to HIGH (state = 4)
- **SLO** – Level of structural defect + Under thickness of the liner – from LOW (state = 1) to HIGH (state = 4).

For instance, SGG condition state evaluation, based on defect affecting global risk of "failure", is shown by Table 2, similarly for SLO.

The degradation of the asset may be accelerated by water leakage, the landslide interference with the lining as well as seismology of the surrounding area.

Conditions are then related to percentage condition bandwidths:

1. From 100% (good as new) to 80%;
2. From 80% to 60 %;
3. From 60% to 40%;
4. From 40% to 20%.

The remaining 20% to 0% is the area beyond the minimum level of service (Figure 5).

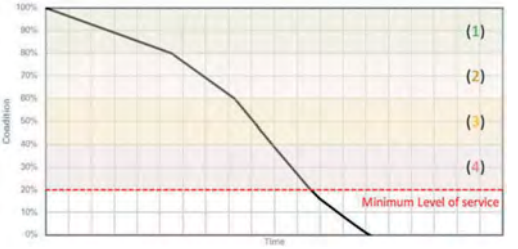

Figure 5. Percentage of condition vs time.

The minimum set of degradation models needed to catch the differences in construction age and waterproof techniques of Autostrade per l'Italia Asset is:

- Ante '70 NO waterproofing;
- '71 to '90 NO waterproofing;
- '71 to '90 with waterproofing;
- Post '91 with waterproofing.

Different degradation should be used for global (SGG) and local (SLO) mechanism for a total of 8 deterioration models.

Unfortunately, the data set available to the scope is not currently sufficient. The new Guidelines were published one year ago and only a first visual inspection was carried out so far for both Ante '70 and '70-'90 tunnels giving an instant picture of the present conditions of the asset. Even if an assumption can be made on the original condition of the asset (100 % when built) the lower condition index (4) cannot be related to a "failure" (many tunnels have one or more section in condition state 4 but still operating). Treatments are usually performed before "failure", so that is difficult to assess the time a section remains in the lowest condition.

Even if often in practice, when it comes to decision making, a simple analysis based on expert judgment of experienced engineers is used to determine the transition into a lower condition level, herein a tentative of fitting degradation curves based on available data is presented.

The Markov model helps assessing the mean time to "failure" of the asset. "Failure" may mean that a section of the tunnel in the worst condition is a strong candidate for replacement or subject to a life extension action such as rehabilitation works (TRS). Markow model makes few assumptions herein mentioned:

1. Condition is determined periodically;
2. Over any single interval, a unit of the asset either remains in same condition state or jumps to one of the other states;
3. The probability of jumping from any one state to any other state is a constant.

The first two of these assumptions are dictated by routine data collection practices so they are easy to

accept. The Guidelines give a visual inspection frequency timeframe based on the risk class SGG+SLO according with Table 3.

Table 3. Inspection frequency according with LLGG.

CdA SGG+SLO	Ordinary inspection	Detailed inspection
Low	12 months	6 years
Mid-low	6 months	4 years
Mid-high	3 months	2 years
High	2 months	1 year

The third one, called the "memoryless assumption" requires more thought. A fourth assumption can be made to simplify the transition state matrix: in the wider time window (12 months) between two inspections the asset moves only from a condition state to the direct following one.

In our case the transition probability matrix is unknown but, it is possible to correlate the present condition of the asset to the starting condition (≈100%) at the age of construction to obtain the transition probability matrix.

The Ante '70 first visual inspections, carried on 173 tunnels in early 2023, has given the condition states distribution of sections that follows (e.g. SGG only NOT previously involved by significant rehabilitation works asset):

21% of sections are in condition 1;
25% of sections are in condition 2;
0% of sections are in condition 3;
54% of sections are in condition 4.

The data set is 59 years old (on average). It is possible to back define the transition probability matrix (for SGG and SLO conditions) which repeatedly multiplied gives the aforementioned states distribution (Figure 6).

The mean time a section of the tunnel stays in the state j can be evaluated as:

$$T_{state,j} = \frac{\log(0.5)}{\log(P_{jj})} \tag{4}$$

where pjj is the transition state probability.

Assuming the mean time in state j it is possible to define a deterioration curve accordingly (Figure 7).

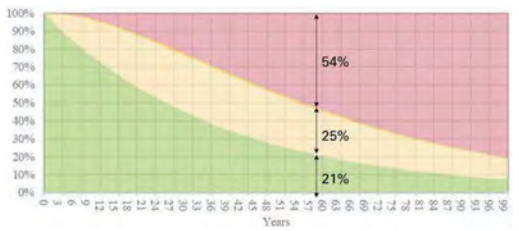

Figure 6. Percentage by condition vs time SGG Ante '70.

The deterioration model assigned to the asset parts (tunnel section) remain the same during life cycle assessment unless a rehabilitation work is performed (TRS).

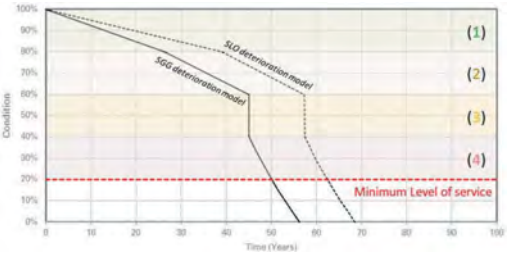

Figure 7. Deterioration model SGG & SLO Ante '70.

In this phase, waiting for the analysis of the data set coming from the first inspection of the clusters '70-'90 and collection of post '91 one, the related deterioration models are assumed by the authors based on the engineering judgement and on the results obtained on the Ante '70 tunnels (e.g. SGG in Figure 8).

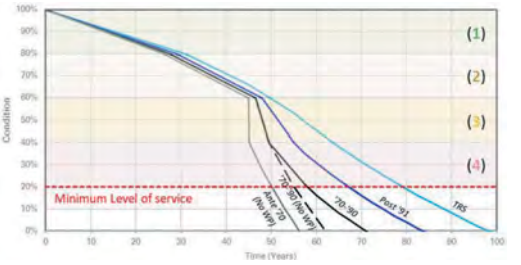

Figure 8. SGG deterioration model of the asset.

The starting condition of a tunnel section at Time = 0, with a condition rate between 1 and 4, is the corresponding bandwidth average (if rate = 4 then condition = 30% etc..) unless the condition rate is the one expected according with the age of the asset (the % starting condition will be evaluated directly on the deterioration curve inside the related bandwidth).

The section deterioration at time > 0 follow the curve of the chosen model.

The decision support tool allows to consider additional effects on degradation of the asset:

a) Landslide interfering with the tunnel – GEO;
b) Seismology of the area – SIS;
c) Water leakages through the lining.

These effects enter the algorithm by speeding up the degradation of the sections by them involved following the equation (5).

$$\Delta_{D,year} = \rho \cdot (Rate - 1) \tag{5}$$

Where ρ is the additional deterioration due to a), b) or c) (e.g. 0.20%/year user defined) whilst *Rate* is the CdA in case of a) and b) (GEO and SIS) or the presence of water leakages for effect no. c).

The choice is left to the user who will eventually include (or not) by checkboxes all (or some) of the additional effects on degradation.

If a TRS is performed effect. c) is automatically omitted by the algorithm from there on.

The main outcomes and benefits of implementing deterioration models in the decision support tool are:

- prediction on conditions of each 20 m long section of the tunnel (both SGG and SLO) enabling intervention strategy based on risk of structural "failure". Any worst section value below "*minimum level of service*" (20% condition) determines the remaining useful life (RUL) of the tunnel;
- prediction on structural risk rate which lead the visual inspection frequency and related costs;
- evaluation of residual value of the Asset.

5 ASSET VALUE

Determining the value of a transportation physical assets is important for both financial reporting and transportation asset management (Spy Pond Partners et al.).

The Figure 9 enhance components of asset value, and helps with the nomenclature that will follow.

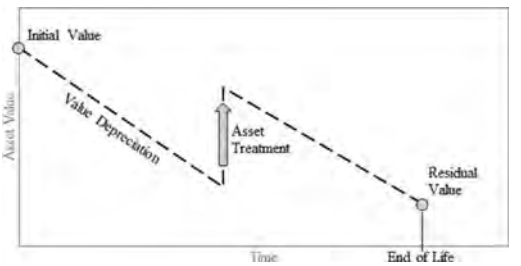

Figure 9. Components of asset value.

In general, there is no single correct way to calculate asset value. Different approaches are reasonable for evaluating initial value of an asset when obtained (or constructed), estimating how value depreciates, establishing how intervention should be considered and what their effects are.

The best approach to calculate asset value depends on how the valuation will be used. Primarily, in tunnel asset management, asset value supports decision regarding investments to maintain and extend the life of the assets; secondary, this information could provide an account of how the organization is spending resources and what is the return in terms of value for the owner of the asset. Asset value could be even used to show how proactive preservation strategy could be more cost-effective than reactive maintenance one.

In general, knowing what a physical asset is worth can be very useful both for supporting asset management and financial reporting.

Testing investment strategies, performing a life cycle cost analysis (LCA), are the main purpose of the decision support tool. The result of a strategy can be summarized by its net present value (NPV). NPV is the sum of the discounted benefits of the strategy less the sum of discounted costs. NPV can be used to compare investment scenarios that result in different condition and remaining useful life (RUL). However, asset value alone is insufficient for prioritizing, it needs to be used in conjunction with cost and intervention models.

Thus far, we have discussed how value can support asset management but not what it represents.

There are mainly three perspectives on asset value:

1. Cost perspective – what does/did it cost to construct and maintain the asset?
2. Economic perspective – what value does the asset provide to travellers and society?
3. Market perspective – where a market exists, for how much can the asset be sold?

For supporting transport asset management, owners tend to use current replacement cost. The cost perspective helps an organization directly relate its expenditures on asset to changes in their value. Also, it is the cost most relevant to an asset manager trying to make decisions that involve spending today's money.

The basic issue with cost perspective is that is flattening the relation between cost and value, e.g. the value derived from spending 10 million in reconstruct a tunnel will be 10 million ignoring benefits generated by the asset on society. However, assuming that an existing asset is worthy of maintenance (and this is the case for motorway's physical assets), the expectation is that its benefits will be equal or exceed its replacement cost.

The purpose of the tool is to support in evaluating intervention-related decisions on the tunnel's lining based on Life Cycle Cost Analysis (LCA). Initial value of the asset will be calculated as Current Replacement Cost of the tunnel according with its peculiarities (lining material, geometry, surrounding soil properties, waterproofing techniques etc..).

6 COST AND INTERVENTION MODELS

One of the key factors of lifecycle cost analysis is the time value of money. In economic decision-making, people value near-term revenue and near-term cost more highly than money that changes hands in the futures.

The mathematical formulas for computing life-cycle cost are well known in asset management applications. The discount factor is calculated from:

$$\delta(t) = \frac{1}{(1+i)^t} \approx exp(-i \cdot t) \; for \; i \ll 1 \qquad (6)$$

Where i is the real discount rate and t the number of years from the instant we want to evaluate different scenarios. In Figure 10 the discount factor for different discount rate.

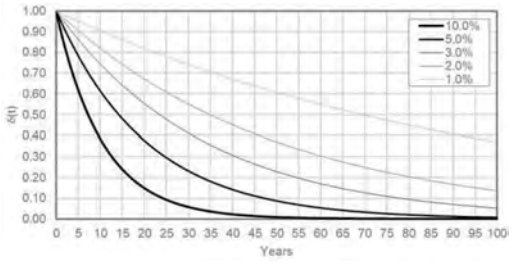

Figure 10. Discount factor for different discount rates vs time.

To compute the net present value (NPV) of future investments, costs, and benefits should be discounted. There are many possible approaches for discounting future benefits and costs, the most common in Italy is the *social rate of time preference* (SRTP) which establishes that there are two effects to consider when selecting the discount rate:

- Pure time consumption;
- Economic growth.

The pure time consumption is purely psychological and accounts for the weight that an individual assigns to future utility compared with present utility. On the other hand, the criteria of economic growth accounts for the fact that as access to resources increases with time, the marginal utility of future investments (costs) becomes smaller (Mauricio Sànchez-Silva & Georgia-Ann Klutke).

The decision support tool allows the user to input the desired discount rate.

Guidelines sets a strict frequency rate for visual inspection of the asset. The frequency is related to the structural risk of "failure" both for global and local mechanisms. Lower is the risk lower will be the number of times visual inspection is required on the asset consequently, lower will be the associated cost.

Reactive or corrective maintenance imply actions after a fault and it relies on data collected mainly through inspections. Proactive or preventive and predictive maintenance is based on probability theory and on the economic assumption that it is better to invest now, to prevent structure damage or its progress, to save money later (Sandra Skaric Palic et al.).

Good management practice should include making optimum use of resources, provide a sustainable program of work and assist in achieving Stakeholders long term policies.

In general, the interventions approaches can be classified in a) "*do nothing repair philosophy*", b) "*regular holding repairs*" and c) "*one off, full refurbishment*".

Three different type of intervention strategy are included in the supporting decision tool:

- **IMS** – Local and relatively small intervention, useful to minimize risk for SLO mechanism mainly (extraordinary maintenance effect);
- **IRS** – Structural reinforcement, higher impact on condition reducing risk for both local and global "failure" mechanisms;
- **TRS** – *Tunnel Renewal Strategy* (Figure 11) – Replacement of the lining with a new one characterized by higher structural performance and strength (impact on condition "*good as new*").

Figure 11. TRS castello I (A10).

For each kind of strategy, the user is required to input the impact on tunnel section conditions +ΔCond (%) in terms of global and local mechanism and the impact on deterioration model.

Treatment strategies entails both capital and operation expenditures. The decision support tool allows for input costs of mobilization and demobilization of construction activities and intervention per tunnel section as well as frequency and cost per tunnel section of ordinary maintenance of the treated areas. Costs for maintenance of intervention can be "*replaced*" when a new treatment is performed or cumulated.

7 SHORT/LONG TERM ASSET MANAGEMENT PLANNING

A case study is here presented to highlight the benefits a life cycle assessment could bring to the organization when different scenarios or strategies of intervention are possible.

Treatments alternatives are so many depending on kind of intervention, timing, number of sections treated per time etc.

A support decision tool is fundamental to analyze and compare as many as possible solutions with a minimum effort of the Practitioner in order to pick the one that leads the organization to its objectives. Herein three scenarios for a relatively short tunnel are presented.

The subject of the simulation is the tunnel "*Rapallo*" right tube, located on the A12 motorway in the Liguria region. The asset is a two-lane tunnel 204 m long (about 11 sections) built in 1969.

The following intervention scenario are applied:

1) "Do nothing";
2) IRS in case at least 5 sections are in condition between 50% and 0% for SGG or SLO risk of "failure"; IMS in case at least 2 sections are in condition between 70% and 50% for SLO risk of "failure"; IRS in each section with conditions lower than 40%
3) TRS in each section with conditions lower than 30%

The purpose is to evaluate conditions/risk, costs (OpEx and CapEx) and residual value of the asset at 2038 (short-term). The analyses are performed on 27 years' timeframe to make some considerations at 2050 as well (long term).

Condition is evaluated for SGG and SLO mechanisms in average and minimum among section values but, here an average of the two structural discipline is presented here to have an overall idea of the structural performance of the asset (Figure 12).

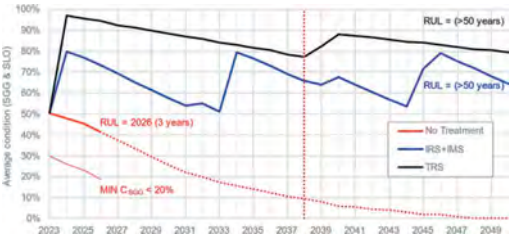

Figure 12. Average SGG & SLO conditions.

The minimum conditions among the tunnel sections is a constrain for the evaluation of the remaining useful life (RUL). The first part of the asset lowering a 20% condition is determining the RUL.

Scenario 1) "*Do nothing*" does not allow for a minimum level of service of the asset up to 2038 (remaining useful life is 3 years). The organization cannot take such a risk and this option should be disregarded immediately at this stage.

In Figure 13 discounted operation expenditures due to visual inspections and maintenance of installed remediation works are plotted. Scenario 1) do not have treatments but, the operation costs are close to scenarios 2) and higher than 3) due to a very strict visual inspection plan given by the high CdA SGG+SLO during the life cycle. Scenario 2) has comparable OpEx due to less inspection but maintenance cost related to performed IMS and IRS. Scenario 3) has very low OpEx since the reconstruction of the liner (TRS) bring back the CdA SGG +SLO to its minimum value.

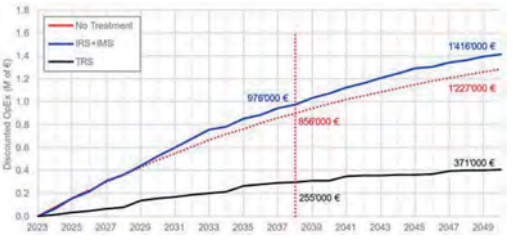

Figure 13. Discounted OpEx.

This is true both at short and long terms whilst discounted total costs (OpEx+CapEx – Figure 14) has a different trend.

Scenario 2) is economically more convenient than scenario 3) at short term whilst at long term the net present cost is approximately the same.

Figure 14. Discounted CapEx + OpEx.

The gross replacement cost of the asset is 4′653′000 € assuming the reconstruction of the liner only. The value of the asset at T=0, since the average condition is 41%, is 1′907′730 € (Figure 15). The residual value after 15 years (short term) is 650′000 € in the scenario 1), 1′117′000 € in scenario 2) and 3′582′000 € in scenario 3).

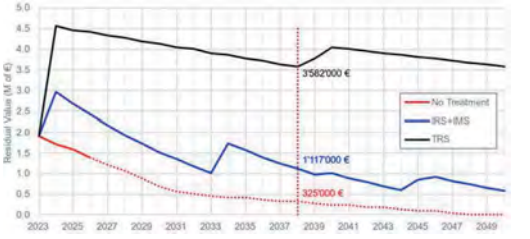

Figure 15. Asset value.

The residual value can be an interesting parameter for the Owner of the asset, also it can be used to justify a specific intervention strategy (e.g. scenario 3) costs 18% more than scenario 2) at 2038 but in the short term timeframe the residual value will be three times higher.

8 CONCLUSIONS

This study highlighted that decision making can strongly be driven by measurable parameters and Asset Management best practices and fundamentals.

The assumptions made are crystal clear and available to the Practitioner who will use the tool to help in planning maintenance and rehabilitation interventions of the asset.

Parameters are in most cases adjustable and free to be modified by the user, leaving a plenty of room for implementation of specific type of intervention and deterioration models.

This work is only a small piece of the toolbox needed to fully embrace the Asset Management practice and many other aspects need to be addressed among the Organization.

On the Engineering side the definition of a proper deterioration models is still an open topic. The approach used is affected by the fact that inspections conducted by the new standard (LLGG) have started recently and evolution of degradation based on defects is still not available. Soon, further inspections on the same asset (or group of tunnels) will be available and could be analysed to better fit a more realistic degradation model. Climate change could also be implemented.

A multicriteria analysis will be included in a future release to address all those aspects not strictly related to cost and value (route criticality for impact of the works on traffic, sustainability, etc..) expanding the criteria of the decision-making process and the stakeholders involved.

REFERENCES

Spy Pond Partners LLC, KPMG LLP, HDR Inc. – NCHRP 23-06 A Guide to Computation and Use of System Level Valuation of Transportation Assets, January 7, 2022, pp.1–2.

Mauricio Sànchez-Silva & Georgia-Ann Klutke – Reliability and Life-Cycle Analysis of Deteriorating Systems, July, 2015, pp.239–242.

Rebecca Hooper, Robert Armitage, Andrew Gallagher, Tom Osorio – Whole-life infrastructure asset management: good practice guide for civil infrastructure, 2009.

Sandra Skaric Palic, Irina Stipanovic, Meho Sasa Kovacevic, Kenneth Gavin – Life cycle management model for tunnels, May 17, 2018 CETRA 2018 – 5th International Conference on Road and Rail Infrastructure, pp.1525, 1528.

Tunnelling for a Better Life – Yan, Celestino, Thewes & Eberhardt (Eds)
© 2024 The Author(s), ISBN 978-1-032-80042-4
Open Access: www.taylorfrancis.com, CC BY-NC-ND 4.0 license

SMART-Systemic approach to risk management of tunnels

Andrés Marulanda E*
INGETEC, Colombia

ABSTRACT: Tunnels are complex systems. To be effective, risk management should adopt a holistic approach to all project activities and stages. If risk management is restricted to certain activities, stages or part conducted only by part of the project team, one the critical links of the project will break, rendering the risk management efforts ineffective. By implementing a systemic approach to risk management of tunnelling projects, synergies arise, and benefits are maximized. For this to be achieved, risk management should be at the core of the managerial processes of all project activities, implemented more as a philosophical approach to managing the project rather than an isolated effort. This paper presents risk management recommendations and best practices to be implemented in all underground project stages, from initiation to dispute resolution mechanisms.

Keywords: Risk Management, Contracts, Emerald Book, uncertainty, differing site conditions

1 INTRODUCTION

We live in a V.U.C.A world: volatile, uncertain, complex, and ambiguous (Winston, 2023). This reality is especially prevalent in underground works projects- and other megaprojects- affected by conflicting interest of project shareholders, uncertain site conditions, long-term regulatory and legal changes, and macroeconomic fluctuations. Yet many of our design and managerial practices for developing complex infrastructure projects assume that we can predict events and situations with certainty in a deterministic matter.

A risk is an uncertain event or condition, that if it occurs, has a positive or negative effect on a project's objectives (PMI, 2021). Thus, risk management is the art and science of identifying, analyzing and responding to risk factors throughout the life of a project to achieve the project's objectives. Given the uncertain nature of tunnelling and underground works, the implementation of rigorous risk management (RM) practices is especially important in this industry.

Risk management has evolved positively in recent decades in most tunneling projects. However, tunneling projects still face significant cost overruns and delays, preventing reaching project objectives (Flyvbjerg, 2003; Kastbjerg, 1994; Murphy, 2008; Thomas, 2009). Hence, risk management practices still have a long way for improvement. Part of the problem can be attributed to a disjointed implementation of RM practices throughout the project cycle. RM is often implemented only in some project stages and activities. However, effective RM requires a systems thinking approach, whereas it is understood that a system fails through is weakest link and the different parts are interconnected. Hence, an approach is required whereas RM is implemented not as a separate activity by some members of the project team, but it is practiced at the core of sound project management practices by all team members throughout the project life cycle. The entire tunnel system and its interrelated components should be considered when analyzing risks and devising strategies for their mitigation. With this approach, RM becomes more a philosophy for delivering and managing the project rather that a project activity. A holistic and systemic approach to RM leads to synergies and amplification of benefits from the implementation of the different tools and strategies in the RM toolbox.

A holistic approach evaluates the risks of tunneling and underground projects throughout the project life cycle as shown in Figure 1.

Figure 1. Holistic approach to risk management throughout the project life cycle.

*Corresponding author: andres@ingetec.com.co

DOI: 10.1201/9781003495505-472

Key practices and considerations for RM applicable during the different stages are presented below.

2 RM DURING THE INITIATION AND PLANNING STAGE

Risk management should start during the project initiation and planning stage by the project Owner or Promotor. Some of the good practices that should be considered during this phase should include:

- Recognize and accept uncertainty, especially epistemic (i.e., knowledge). This should formally be accepted as a reality and not minimized.
- The "Ostrich Approach" to RM should be avoided. Risks do not go away or disappear if we hide our heads in a hole, they need to be identified and managed promptly. The sooner a risk management strategy starts the more alternatives to handle risk are available. As a project matures, uncertainty is typically reduced, but as shown in Figure 2 the influence of the project team diminishes as the project advances. Hence, the early stages of project should have special emphasis in RM given that the greatest positive effect can be achieved early on.
- Risks should be assigned to the party best able to manage them. Project Owners and financiers often minimize the cost to transfer a risk to a contractor. Also, many Owners disregard the fact that a transfer risk does not disappear. If it becomes unbearable to the contractor, an Owner could end up with an unfinished project. Moreover, a sophisticated player does not assume projects risk for free, they normally charge a premium to assume risks. Thus, project Owners should evaluate if transferring risks outside a contractor's control- such a geological risks- is a good practice and in their best interest. Often with such an approach they are materializing a risk and paying for it in advance, even if it does not occur. Also, in many jurisdictions transferring unquantifiable risks exogenous to the contractor contradicts legal dispositions.
- Project Owners should avoid reinventing the wheel. A systematic and rigorous approach to collecting and analyzing lessons learned from other projects should be implemented to improve planning and risk management processes (Marulanda, 2020). Given the uniqueness of each project, the knowledge of projects stays in a tacit and individual way, in a restricted group. A lessons learned process can aid to make this knowledge explicit and collective for the organization.
- ITA's Contractual Framework Checklist for Subsurface Construction Contracts (ITA, 2020) should be consulted. ITA's WG 3 published a recently updated and revised contractual practices checklist for implementing in tunneling projects that the organization believes are fundamental for the success of subsurface construction projects, independently of the form of delivery and risk allocation used. This document can facilitate Project Owners and Consultants the validation of widely recognized and accepted good contractual practices in the tunneling industry.
- A project Owner should assume the risks that is capable of handling and tolerating as a function of its financial capacity, organizational capabilities and strategic policies. Whenever possible, risks outside of its organizational capabilities and control should in principle be transferred to third parties via contractual arrangements, insurance, or financial instruments.
- The ALARP (as low as reasonably practicable) principle should be implemented to analyze and manage risks. Reasonably practicable involves weighing a risk against the trouble, time and money needed to control it.
- It should be recognized that risks are dynamic. A common problem with RM practices is that risks are often identified and analysed in one project stage, but their evaluation is not revised in later stages. As the information related to a risk evolves (i.e. more geotechnical investigations become available), the evaluation of a risk should be reassessed. The responsible person or party to monitor a particular risk should be clearly identified.

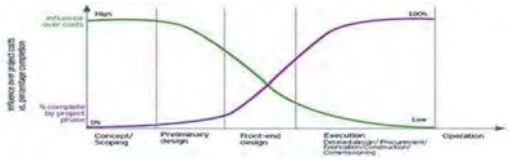

Figure 2. Evolution of influence of the project team to affects costs of a project throughout the project life cycle.

3 DESIGN STAGE

Engineers are trained to be precise. However, in our professional practice, especially when dealing with natural made materials, we seldom have the privilege or capability of precision. This should be openly recognized and acknowledged. Soil and rock mass parameters should not be reported nor used as singular values for analysis and designs, but rather with ranges and statistical variations. By adopting a probabilistic mindset (Watkinson & Konkoly, 2023) we avoid transmitting a false sense of precision.

With today's sophisticated numerical analysis, engineers should exercise engineering judgement to validate the reasonability of complex model results. The well know acronym GIGO (garbage in- garbage out) should not be forgotten. As Ralph Peck, one of the fathers of geotechnical engineering once said, we should be able to validate FEM results with back on the envelope simplified computations.

However expert judgement, in particular for risk assessments, should also be regarded with skepticism as it is often subjective, and subjective to cognitive biases (Hilbert, 2012); Kahneman, 2013; Vick, 2012).

When reporting results, scenario analyses are recommended, combined with sensitivity analysis. Whenever possible, results should be reported with probability of exceedance data. This practice aids to properly communicate variability and uncertainty in a clear way. This is especially important with budget estimates and schedules. Some agencies, such as the WDOT now demand that cost estimates recognize uncertainty and be reported with a probabilistic distribution (Reilly, 2011). Cost estimates should clearly define what level of engineering they are based on. As the level of engineering matures, uncertainty is reduced, but the project budget can increase. If this is not clearly communicated, changes in the project budget throughout the project life cycle can be perceived by the public as lack of diligence by the parties developing the project and not as a normal project maturation. Unfortunately, politicians typically report project budgets without much care of what are the basis for the numbers. Furthermore, project contingencies should not be estimated using rule of thumbs or standard percentages. A project risk analysis should be used to estimate the contingencies with more rigor and substance. Residual risk results after mitigation strategies have been evaluated can serves as the basis for the project contingency.

It is recommended that risk assessments be initially conducted using qualitative analysis. This allows for a more effective investment of limited resources. The project team can devote more resources and refine the risk assessment with quantitative methods of the risks that result to be more critical. Special attention shall be given to "Black Swans" events, low probability events with high impacts (Taleb, 2007). These events are by definition difficult to detect but they could have devastating consequences for the project.

4 TENDER STAGE

The project Owner should aim for a balanced risk allocation. In the long term, an equitable distribution of risks to the party best capable to handle a risk, results in the lowest project cost for the project Owner (See Figure 3).

Figure 3. Conceptual evolution of project costs depending on risk allocation to the Contractor.

One of the most critical risk management decisions in a project is the selection of the procurement strategy. This involves critical strategic considerations, not only legal concerns. No procurement strategy is in general more favorable than others. The desirability of a specific delivery strategy is project dependent, influenced by the specific project risks and the capabilities and experience of the parties involved.

It is recommended that the recommendations and best practices recommended in the Code of Practice for Risk Management of Tunnel Works (ITA/IMIA, 2023) be adopted as early as possible in the project lifecycle. This document aims to reduce significant project losses by recommending and implementing best practices for managing construction risks in underground works. Many insurers demand compliance with the Code provisions as a pre-requisite for procuring insurance in a project involving underground works.

5 CONSTRUCTION STAGE

It is recommended that project Owners consider adopting the "Emerald Book"- Conditions of Contract for Underground Works (2019), jointly developed by FIDIC and ITA, as the basis for the contractual documents for underground works. The ITA has been advocating for the implementation of good contractual practices since the seventies (ITA, 1988, 1996, 2011). Even though many of these recommendations have permeated the industry, unfortunately, the original intend of some of the recommended principles is sometimes misunderstood or modified in the contract documents due to inexperience or lack of skill from individuals drafting the provisions for a tunneling contract. The Emerald Book puts best contractual practices for tunneling projects in a coherent and harmonic contract.

If due to legal restrictions in certain jurisdictions the complete form of contract cannot be adopted, it is recommended that at least the main conceptual aspects behind the Emerald Book be adopted:

- Allocation of ground related risks to the Owner and performance related risks to the Contractor.
- The ground related risk is assigned via the introduction of a Geotechnical Baseline Report (GBR) as the single contractual source for subsurface physical conditions risk allocation.
- The use of a unit rate compensation structure for ground related activities (i.e., excavation and support), including time related costs. Provision of a detailed schedule of baseline performance measures setting out the production rates anticipated for each of the items measured.
- Assessment of the time to carry out the final quantities of work using the baseline performance measures. This will be applied to the time related

items in the bill of quantities and used to assess whether it results in any delay to Completion.

During construction, the use of risk registers as a project management tool should be encouraged. These registers should be reviewed, revised, and monitored on a regular basis, with clear designated responsible parties to monitor and control specific risks. Moreover, the presence of the designer during construction is of utmost importance. The final design and support implemented in a tunnel depend on the actual conditions encountered during construction. The designer should be present during construction to validate and analyze the conditions encountered at the excavation front.

6 DISPUTE RESOLUTION MECHANISMS

The occurrence of disputes will still arise, even in underground projects that are structured with an equitable risk distribution and incorporate the aforementioned recommendations. For that reason, these instruments need to be complemented with dispute resolution mechanisms that promote an equitable, prompt, and cost-effective resolution of claims and disputes. Without them, the benefits and flexibility of the recommended practices will be hindered.

The issues at hand in a differing site condition claim are typically complex and require a deep understanding of the complexity of underground design and construction. Typical drawbacks of litigation include lengthy and costly processes that in the case of large projects can take several years and large amounts of money in legal fees to be resolved. Moreover, judges and juries typically do not possess the knowledge to understand the technical subtleties behind a differing site condition claim. Thus, it is highly recommended that tunneling projects engage a dispute review board (DRB). Depending on the legal provisions in each jurisdiction, the DRB can be an adjudication or recommendation boards. Disputes that cannot be resolved at the DRB level can escalate to and arbitration proceedings.

The analysis of claims is also facilitated if escrow bid accounts are implemented, whereas bid documents are deposited in a confidential account, but can be consulted by the DRB or arbitration panel to understand the consequences of unforeseen conditions.

7 CONCLUSIONS

Uncertain complex systems like tunneling projects require a probabilistic mindset to develop them successfully. Only with such an approach, whereas uncertainty is explicitly acknowledged, can we anticipate the occurrence of unfavorable events and conditions and device mitigation strategies to achieve project objectives. Risk management should be at the core of the managerial processes of all project activities, implemented more as philosophical approach to managing the project rather than an isolated effort. Risk management practices have evolved and permeated the tunneling industry in the last decades, but their implementation is still erratic, not uniform, typically applied only at certain project stages or activities, and assigned to a limited part of the project team. This fragmented approach has diminished the effectiveness of RM practices in tunneling projects. Many tools that support good RM practices have been developed and are available to our industry, we need to extend their use in a holistic and systemic way. Only if we spread RM practices to all tunneling project activities, stages, and team members will the performance record of the industry improve to complete projects complying with the triple project restriction: good quality, on time and meeting the budget.

REFERENCES

Flyvbjerg, B., Bruzelius, N. & Rothengater, W., 2003. *Megaprojects and risk: An anatomy of ambition*. Cambridge University Press.

Hilbert, M. (2012). Toward a synthesis of cognitive biases: how noisy information processing can bias human decision making. *Psychological bulletin*, 138 (2), 211–237.

ITA-IMIA, 2023. Code of Practice for Risk Management of Tunnel Works. 3rd edition. ISBN: 978-2-970143-8-0. ITA Geneva, Switzerland.

ITA, 2021. The ITA Contractual Framework Checklist for Subsurface Construction Contracts. ITA Report No. 25. 2nd Edition. No ISBN: 978-2-9701242-6. Longrine, Avignon, France.

ITA-FIDIC, 2019. Conditions of Contract for Underground Works. Emerald Book. FIDIC, Geneva, Switzerland. ISBN: 978-2-88432- 087–0.

ITA Position Paper on Types of Contracts. 1996. ITA Working Group on Contractual Practices in Underground Construction. Tunneling.

and Underground Space Technology, Vol. 11, No. 4, pp. 411–429. Elsevier Science Ltd.

ITA Recommendations and Contractual Sharing of Risks. 1988. ITA Working Group on Contractual Sharing of Risks. Tunneling and Underground Space Technology, Vol. 3, No. 2, pp. 103–140.

ITA Contractual Framework Checklist for Subsurface Construction Contracts. 2011. Working Group 3 Contractual Practices. N°ISBN: 978-2-9700624-7-9/APRIL 2011.

Kahneman, D. (2013). In Concise Encyclopedia of Economics. Retrieved from http://www.econlib.org/library/Enc/bios/Kahneman.html

Kastbjerg Skamris, M. (1994). Large transport projects–forecast versus actual traffic and costs (Doctoral dissertation, Master's Thesis in International Technology Planning, Aalborg University, Denmark)

Marulanda A. (2021). Using Lessons Learned from Projects to Improve Project Planning and Risk Management. Doctoral Dissertation. ISM, Paris, France.

Marulanda A. (2014). Adapting the FIDIC Standard Forms of Contract for Underground Construction Projects. Proceedings of the World Tunnel Congress 2014 – Tunnels for a better Life. Foz do Iguaçu, Brazil. Brazilian Tunnelling Committee (CBT), Sao Paulo, Brazil.

Murphy, S. P.,2008, July 17). Big Dig's red ink engulfs state-Cost spirals to $22b; crushing debt sidetracks other work, pushes agency.

toward insolvency. *The Boston Globe*. Retrieved from http://www.boston.com/news/traffic/bigdig/articles/2008/07/17/big_digs_red_ink_engulfs_state/?page=3#.

Project Management Institute, 2021. A Guide to the Project Management Body of Knowledge (PMBOK Guide). Seventh Edition. Pennsylvania: Project Management Institute

Reilly, J., Sangrey, D., Gabel, M., Prill, W. & Shibayah., 2011. Emerging Methodologies to Improve Cost and Schedule Estimates Using Rrisk-based Evaluation- The Success of CEVP. *Proceedings of the 2011 Rapid Excavation and Tunneling Conference*. Littleton, Colorado: Society for Mining, Metallurgy and Exploration, pp. 59–72.

Taleb, N. N. (2007). *The black swan: The impact of the highly improbable* (1st ed.). London: Penguin.

Thomas, J. H. 2009. *Managing a metro rail project to avoid cost overruns. (Doctoral dissertation*, *University of Southampton*). Retrieved from http://eprints.soton.ac.uk/195599/

Vick, S.G., 2002. *Degrees of belief: Subjective probability and engineering judgment*. Reston, Virginia: ASCE Press.

Watkinson M., Konkoly C., 2023. Mastering Uncertainty- How great founders, entrepreneurs, and business leaders thrive in an unpredictable world. Matt Holt, Dallas, Tx, USA.

Winston, A., 2023. Resilient, Net Positive Leadership. In Certain Uncertainty- Leading with agility and resilience in an unpredictable world. Ed. Dearlove D. John Wiley & Sons, Hoboken, New Jersey.

Tunnelling for a Better Life – Yan, Celestino, Thewes & Eberhardt (Eds)
© 2024 The Author(s), ISBN 978-1-032-80042-4
Open Access: www.taylorfrancis.com, CC BY-NC-ND 4.0 license

Risk management of tunnel projects: From qualitative to quantitative probabilistic risk analysis

Andrea Antiga*
More Engineering S.r.l., Milano, Italy

Michela Chiorboli
I.C.M.Q. S.p.A., Milano, Italy

Marco Dotti
More Engineering S.r.l., Milano, Italy

ABSTRACT: Tunnel projects involve high capital investments and take a long time to build therefore constitute a major financial challenge for owners. It is impossible to imagine a "zero-risk project". Of course, some projects will be high-risk, while others will have less risk, but all projects are by definition risky. The important thing is not to keep risk out of projects, but to ensure that the inescapable associated risks are at a level which is acceptable to the stakeholders. The use of risk management from the early stages of a project is essential. Risk should be managed through appropriate procedures during planning, design, procurement, and construction. Risk management processes can be significantly improved by using systematic risk management techniques throughout the tunnel project development. Using appropriate techniques, potential problems can be clearly identified such that suitable risk mitigation measures can be implemented in a timely manner. The extent of application of specific procedure as the methods and tools used to support risk management depend on the project development phase and project complexity. Since all projects are exposed to risk, successful projects are the ones where that risk is properly managed. In this paper some ideas of the possible approaches are presented with focus on probabilistic risk analysis.

Keywords: risk assessment, risk mitigation, Monte Carlo simulation, TBM, water inflow, fault zones

1 INTRODUCTION

Tunnel projects involve much higher hazards and risks than any other civil engineering construction.

Statistically, most of the tunnel projects, quite all of them, reported cost overruns and claims in a much greater percentage than other civil construction works.

It is impossible to imagine a tunnel project without risk. Of course, some projects will be high-risk, while others will have less risk, but all projects are by definition risky to some extent. The "zero-risk project" is an oxymoron and a logical impossibility – it does not and cannot exist.

Unmanageable cost escalation and construction time extensions could involve massive difficulties for the stakeholders and could imperil the economic and financial equilibrium of the project.

In this scenario, it is fundamental to develop a plan for risk management in any project, starting from the early phases and then throughout the project life cycle; the efforts must extend throughout the life of a project and must be based on quantitative information that is current and complete.

The goal of risk assessment is not to eliminate all risks from the project. Rather, the goal is to recognise the significant risk challenges to the project and to initiate an appropriate planning response to their management and mitigation.

Project risk management is an art involving careful consideration about uncertainties and risks and relies on sound engineering judgment to plan where to focus energy and resources.

Risk management processes can be significantly improved by using systematic techniques throughout the tunnel project development. Using these

*Corresponding author: a.antiga@more-engineering.it

DOI: 10.1201/9781003495505-473

techniques, potential problems could be clearly identified such that appropriate risk mitigation measures can be implemented in a timely manner.

In this paper an outline of possible approaches is presented focusing on probabilistic risk analysis.

2 RISK MANAGEMENT FRAMEWORK

Risk management is a systematic process of identifying, analysing, planning, monitoring, and responding to project risk over the life of the project. It involves processes, tools, and techniques that help to minimise the probability and consequences of adverse events (threats) and maximise the probability and consequences of positive events (opportunities) throughout the life of the project.

Risk management is most effective when started early in the life of the project, where major decisions such as choice of alignment and selection of construction methods can be influenced and continues throughout the project.

The framework is scalable from small and non-complex projects to large and complex projects.

The overall risk management process is repetitive and cyclical. As the project evolves, some risks will be resolved or diminished, while others may emerge and thus be added. The fundamental risk management steps can be applied throughout the project life cycle. The extent of application of each step, as the methods and tools used to support these steps, depends on the project development phase and project complexity.

It must be recognised that risk modelling is not a precise measurement and cannot be reduced to a rigid process; some features of a model used in a specific case might not be transferred directly to another project.

It is also important to recognise that risk management is not "one-size-fits-all". Since every project has a different level of risk exposure, it is necessary to scale the risk process to meet the risk challenge of each particular project. Projects which are highly risky or strategically important will require a more robust approach to risk management.

In every tunnel project, risk management strategy should be adopted. A recommended strategy is to carry out construction risk assessments at each stage of plan, design, and construction in accordance with the information available and the decisions to be taken or revised at each stage.

In risk management strategy should be included:

- the definition of project objectives,
- a definition of the risk management responsibilities,
- a short description of the activities to be carried out at different stages of the project to achieve the objectives,
- a scheme to be used for follow-up on results obtained by which information about identified hazards (nature and significance) is freely available and in a format that can be communicated to all parties,
- follow-up on initial assumptions regarding the operational phase,
- monitoring, audit, and review procedures.

2.1 *Phases during the life of the project*

The application of risk management during all project stages, from planning, feasibility, and design through to tendering, contract, and then to construction and maintenance, needs to be considered for every tunnel project (Eskesen et al., 2004).

In the planning and design phase the responsibility of establishing a risk policy, the risk acceptance criteria and carrying out risk assessment is the owner alone. In the tendering phase the owner is still the primary responsible party. In the construction phase the primary responsibility moves on to the contractor to establish a risk management system and to carry out effective risk management. The owner should supervise and participate in this work and should further continue to assess and mitigate risks not covered by the contractor.

2.2 *Main steps*

The most common set of processes would include risk identification, assessment, analysis, mitigation, allocation, monitoring and updating.

An important underlying concept of this approach is that the overall process is repetitive and cyclical. As the project evolves, some risks will be resolved or diminished, while others may emerge and thus be added. These steps are continually applied throughout the project implementation period (EN IEC 31010, 2019 and SAEO, 2018). There are six imperative steps to manage project risk.

1. Risk Management Planning. It is a systematic process of deciding how to approach, plan, and execute risk management activities throughout the life of a project. It is intended to maximise the beneficial outcome of the opportunities and minimise or eliminate the consequences of adverse risk events.

2. Risk Identification. It involves identifying and documenting which risks can affect the project and documenting their characteristics.

3. Risk Analysis. It involves the quantitative or qualitative analysis that assesses impact and probability of a risk. It assists in deriving contingency estimates.

Qualitative risk analysis involves assessing risks for probability of occurrence and impact on project objectives. Risks are measured by their "quality". It is fundamental understanding the characteristics of individual risks, analysing their level and prioritising them in order to plan appropriate responses to reduce their negative impacts.

Quantitative analysis is used to analyse the most important individual risks in more detail by assuming different scenarios. Quantitative risk analysis is a way of numerically estimating the probability that a project will meet its cost and time objectives. It is based on a simultaneous evaluation of the impacts of all identified and quantified significant risks.

4. Risk Mitigation. It involves analysing risk response options (mainly acceptance, avoidance, mitigation, transference, or sharing) and deciding how to approach and plan risk management activities for a project.

5. Risk Response. It involves developing options and determining actions to reduce threats or enhance opportunities to project objectives. Actions are identified and assigned to parties that take responsibility for the risk response. This process ensures each risk requiring a response has an "owner." A strategy that is best for each risk must be identified and then select specific actions to implement that strategy.

6. Risk Monitoring and Control. It is the capture, analysis, and reporting of project performance. Risk monitoring and control tracks identified risks, monitors residual risks, and identifies new risks—ensuring the execution of risk plans and evaluating their effectiveness in reducing risk. Risk monitoring and control is an ongoing process for the life of the project.

Figure 1 shows the process described above (SAEO, 2018).

Figure 1. Risk management process.

3 RISK MANAGEMENT OBJECTIVES

Risk can be defined as "*effect of uncertainty of objectives*" (ISO 31000, 2018). Consequently, the first step in the risk management process is not the identification of risk: since risk is defined in terms of objectives, the essential first step is to define those objectives which are at risk. The goal of risk management is quite specific: it is to enable stakeholders to make appropriate decisions in the light of the uncertainties, which could jeopardise objectives of the project.

In principle, risks that could compromise the primary objectives of the project should be examined in the first instance, such as:

1. health and safety of workers and third parties,
2. safeguarding third party property (existing structures, cultural heritage buildings, etc.),
3. preservation of environment (possible land, water or air pollution and damage to flora and fauna),
4. avoidance of the completion,
5. prevention of financial losses and additional unplanned costs.

With reference to the source of the risk, the underground projects must face two broad categories of risks: "technical risks" and "non-technical risks".

Technical risks can be classified in "external" (risks for which stakeholders have no power to act on the source of the risk) and "internal" (risks whose origin is the responsibility of the parties involved in the project, for example arising from contractor methods and means).

Non-technical risks are political and administrative risks, interface, financial, and similar ones.

For instance, in underground constructions, due to the inherent geological uncertainties, including ground and groundwater conditions, there might be significant cost overrun and delay risks as well as environmental risks. Furthermore, for tunnels in urban areas there is a risk of damage to a range of third-party persons and property, which will be of particular concern where heritage designated buildings are involved. Finally, there is a risk that the problems which the tunneling project cause to the public will give rise to public protests affecting the course of the project.

In general, "geo" risks, particularly in the form of unexpected geological conditions, drive time and costs of many underground constructions.

However, it is important to highlight that also contractual disputes are a significant risk factor; indeed, contractual issues are main hazard for tunnel project comparable with geological ones (Avestedt, 2012).

Anyway, even if in modern tunnels advanced technology is used, the final construction cost is still governed by the cost of the tunnel excavation. In first approximation, it is possible to state that excavation cost represents between 60% to 90% of the final construction cost. Therefore, ground conditions represent the largest element of technical and financial risk in tunneling projects and there is an agreement largely unanimous on the concept that "geo" issues are the key cost drivers for tunneling.

In the following pages, probabilistic risk analysis methodologies will be focused, giving an example of the application of the Monte Carlo method to the excavation of a tunnel with TBM in a geological context characterised by the presence of highly tectonised areas with possible significant water inflow.

4 DECISION-MAKING UNDER RISK

The risk assessment phase has as objective the systematic consideration of risk events and has two main points: their probability of occurrence and the consequences of such occurrences. The first determines the probability of a risk occurring (risk frequency); risks are classified along a continuum from very unlikely to very probable. The second judges the impact of the risk should it occur (consequence severity).

Risks affect project outcomes in different ways. Risk effects are usually apparent in direct project outcomes by increasing cost or schedule. Some risks influence the project by affecting the public, public perception, the environment, or safety and health considerations.

In principle, the risk assessment combines both a qualitative and a quantitative assessment. The qualitative assessment is useful for screening and prioritising risks and for developing appropriate risk mitigation and/or allocation strategies. The quantitative assessment is best suited for estimating the numerical and statistical nature of the project's risk exposure.

4.1 *Qualitative risk analysis*

A qualitative analysis is simpler and less costly.

Performing a qualitative analysis of risks and conditions to prioritise their effects on project objectives. It involves assessing the probability and impact of project risks and using methods such as the probability and impact matrix to classify risks into categories of high, moderate, and low for prioritised risk response planning.

Typically, the qualitative risk assessment recognises some risks whose occurrence is so likely or whose consequences are so serious as to justify further quantitative analysis.

A key purpose of quantitative risk analysis is to combine the effects of the various identified and assessed risk events into an overall project risk estimate. Measuring the probability and consequences of risks and estimating their implications for project objectives. Risks are characterised by probability distributions of possible outcomes. This process uses quantitative techniques such as probability-based analysis, sensitivity analysis, and decision tree analysis.

Usually, the overall risk assessment is used to determine cost and schedule contingency values and to quantify individual impacts of high-risk events.

4.2 *Quantitative risk analysis*

Risks do not usually happen one at a time. Instead, they interact in groups, with some risks causing others to be more likely and some risks making others impossible. For the most part, qualitative risk assessment considers risks individually and allows development of a good understanding of each one (although grouping risks into categories can give some insights into patterns of risk exposure). It is however sometimes necessary to analyse the combined effect of risks on project outcomes, particularly in terms of how they might affect overall time and cost. Indeed, this is often the only way to obtain an accurate assessment of the overall risk exposure of the project. This is the purpose of the quantitative risk analysis step, since addressing overall project risk exposure requires use of a quantitative model.

Various quantitative risk analysis techniques are available, including Monte Carlo simulation and decision trees. Monte Carlo is the most popular because it uses simple statistics, it often uses existing project data as its baseline. Decision trees are however particularly useful for analysing key strategic decisions or major option points.

One key aspect of quantitative risk analysis models, which is often overlooked, is the need to include both threats and opportunities. If only threats are considered, then the analysis is limited to modelling the potential downside and the result will always be pessimistic. Since the risk process aims to tackle both threats and opportunities, both must be included in any analysis of the effect of risk on the project.

Monte Carlo methods are probabilistic calculations that use random number generators to draw samples from probability distributions. The objective of the simulation is to find the effect of multiple uncertainties on a value quantity of interest (such as the total project cost or project duration). They can reveal, through sensitivity analysis, the impact of specific risk events on the project cost and schedule.

4.2.1 *Input for risk analysis*

Once the risk factors and other values required for the model have been identified, the values must be assessed. It is rare to have representative historical information that can be used without any human intervention; risk analysis models almost invariably involve some element of subjective estimation. It is usually not possible to obtain data from which to determine the uncertainty of all variables in the model, in order to avoid subjective assessments, because:

- data have never been collected in the past,
- data are too expensive to obtain,
- past data are no longer relevant, or decision makers do not believe they are relevant, and/or
- data are sparse.

The lack of data means that subjective estimates must be made regarding the uncertainty of the variables within the model. Subjective assessments will always be at risk of bias. Even if there is no option but to use them, it is prudent to takes steps to limit or avoid bias.

If risk events are significant enough to be described individually in a model, the probability of each one occurring will have to be assessed.

Probabilistic-based methods require as inputs a probability distribution for the various performance, schedule, and costs risks. Risk variables are

differentiated based on whether they can take on any value in a range (continuous variables) or whether they can assume only certain distinct values (discrete variables). Whether a risk variable is discrete or continuous, two other considerations are important in defining an input probability: its central tendency and its range or dispersion. The mean and mode of an input variable are two alternative measures of central tendency: the mode is the most likely value across the variable's range; the mean is the value where the variable has a 50 percent chance of taking on a value that is greater and a 50 percent chance of taking a value that is lower.

The mode and the mean of two example continuous distributions are illustrated in the Figure 2 (Molenaar et al., 2010).

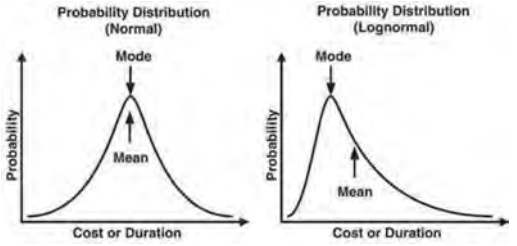

Figure 2. Mean and mode in normal and lognormal distributions.

The other key consideration when defining an input variable is its range or dispersion. The common measure of dispersion is the standard deviation which is a measure of the breadth of values that are possible for the variable. Normally, the larger the standard deviation the greater the relative risk. Probability distributions with different distribution method, which means different mean values and different standard deviation values, are illustrated in Figure 3 (Molenaar et al., 2010).

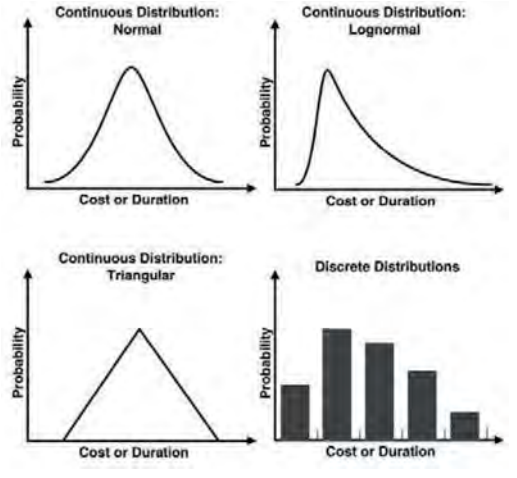

Figure 3. Distributions for risk analysis.

Selecting an appropriate probability distribution is a matter of which distribution is most like the distribution of actual data. For tunnel projects, this is a difficult choice because historical data on unit prices, activity durations, and quantity variations are often difficult to obtain. In cases where insufficient data is available to completely define a probability distribution, one must rely on a subjective assessment of the needed input variables.

Input to Monte Carlo methods requires the user to know and specify probability distribution information; mean, standard deviation, and distribution shape.

4.2.2 *Output of risk analysis*

Figure 4 (Molenaar et al., 2010) shows typical probability output from a Monte Carlo analysis.

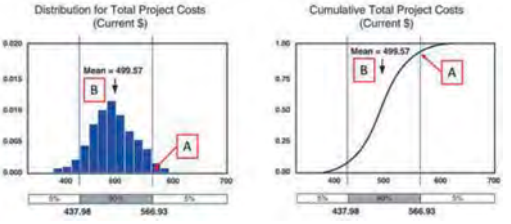

Figure 4. Typical Monte Carlo output for total cost.

The histogram information is useful for understanding the mean and standard deviation of analysis results. The cumulative chart is useful for determining project budgets and contingency values at specific levels of certainty or confidence. In addition to graphically conveying information, Monte Carlo methods produce numerical values for common statistical parameters such as the mean, standard deviation, distribution range, and skewness.

The main output from a Monte Carlo simulation is the s-curve, presenting a cumulative probability distribution of the range of possible values for the parameter being analysed (for example, total project cost, overall duration, end date and so on).

Several elements of useful information can be obtained from the s-curve, including:

- the probability of the project meeting its objectives (taken as the cumulative probability of achieving a given target value, i.e. the 95th percentile as "A" in Figure 4),
- the degree of overall uncertainty in the project parameter, that is standard deviation (derived from the range of possible simulation outputs),
- the predicted "expected value" which would occur on balance if the situation remained unmanaged (taken from the mean value of all possible results, "B" in Figure 4),
- output values corresponding to specific confidence levels (for example, the 95th percentile from the s-curve represents the value for which

we can have 95 per cent confidence of it not being exceeded, "A" in Figure 4).

S-curves can be produced for the overall project, or for interim milestones or specific subprojects, allowing analysis of the components of overall project risk. It is also possible to produce overlaid s-curves, as shown in Figure 4, indicating the cumulative effect of addressing individual risks, showing the relative contribution of planned responses towards overall project risk exposure.

5 APPLICATION OF PROBABILISTIC RISK ANALYSIS

The following is a case history referring to a tunnel construction by double shield TBM. Design is in progress and for reason of confidentiality some data and information will be deliberately simplified. The main frameworks of the project will be presented below.

5.1 *Geological context*

A double shield TBM is planned for the excavation of a tunnel of length 10,000 m.

The excavation of the tunnel affects the following geological formations: arenaceous formations (A) with the best mechanical characteristics and flysch formations (B) with poorer characteristics. In addition, there are some faults and intense fractures zones (C). The water table is present along the tunnel layout in some sections, also affecting fault zones with maximum heads of 20-30 m.

Table 1 shows the compressive strength, GSI and disturbance values representative of the formations defined above.

Table 1. Geological formations and their parameters.

Formation	σ_c [MPa]	GSI
A	30-35	40±5
B	40-45	24±5
C	30-45	18±5

Double shield TBM is not equipped with systems for pressurising the excavation face and consequently for crossing unstable sections and/or below the water table.

Based on the geotechnical characteristics and the depth of the tunnel, different sections with homogeneous deformation behaviour were identified according to the stability conditions, identified in the diagnosis phase for which three stability classes were defined from the highest (A) to the lowest (C).

Figure 5 Shows the main features of each section identified.

ID	Length [m]	Head [m]	Formation	Stability class	Flow rate [l/s]
1	80	-	B	A	-
2	100	-	C	A	-
3	75	-	B	A	-
4	105	-	C	A	-
5	110	5-10	B	B	<50
6	125	-	C	B	-
7	250	5-10	B	B	<50
8	125	-	C	B	-
9	705	-	B	B	-
10	120	-	C	B	-
11	770	10-20	A	A	<50
12	115	-	C	B	-
13	1300	10-20	A	A	<50
14	125	-	C	C	-
15	1150	-	A	A	-
16	100	-	C	C	-
17	475	-	A	A	-
18	85	-	C	B	-
19	370	-	B	A	-
20	1295	20-30	A	A	>50
21	770	-	B	A	-
22	150	20-30	C	A	>50
23	1300	-	A	A	-
24	200	-	B	B	-

Figure 5. Identification of sections with homogeneous behaviour.

5.2 *From qualitative to probabilistic risk analysis*

In the qualitative risk analysis for the tunnel, high level risks were identified in relation to:

1) water inflow in high permeability context,
2) presence of faults/intense fractured areas.

The first one is related to high hydraulic head (up to 20-30 m) in several sections of geological profiles with indications of water inflow and possible unstable behaviour at the excavation face. The second one is related to presence of intense fractured areas with possible face instability also associated with the presence of hydraulic head leading to face instability situations.

Both risks could lead to the possibility of water flows into the excavations even at high pressures potentially jeopardising the regularity of work and safety and the stability of excavations. A quantitative analysis was conducted for risks 1) and 2) above defined for the tunnel.

5.3 *Risk identification and probabilistic analysis*

In order to probabilistically assess the sources of uncertainty inherent in the realisation of the work, a quantitative probabilistic risk analysis was developed using the Monte Carlo method, evaluating the random distributions of costs and times related to the rock improvement works and the excavation of the tunnel.

As explained before, in the Monte Carlo method, the probability that a given event exceeds a certain threshold is defined. This method is based on the random generation of a series of uncorrelated values as a function of an assigned probability distribution. Once the random parameters have been defined, estimates can be derived through one or more simulations.

For this specific case, the variable input data were defined by means of a triangular distribution, which

is established with the following values: minimum, modal, and maximum value. Since there is only limited sample data, triangular distribution was selected. Then, once the parameters have been defined, several iterations are generated according to the assigned distribution (triangular), calculating the result for each iteration. After that, the process can be repeated several times for performing several simulations; for this specific case, 5 simulations were carried out to confirm the validity of the analysis with an appropriate number of simulations, and 10,000 iterations were considered for each of them. Based on previously developed geological and geomechanical assessments, type rock improvement works were identified to be carried out from inside the TBM by means of holes drilled at the section outline of the shield and at the excavation face in the following sections:

- where diagnostic analyses showed a type C behaviour,
- where the water table exists,
- where there are fault zones.

Rock improvement works were distinguished by providing for the possibility of improving the excavation face and introducing variability in absorption of injections, length of overlap and speed of execution (Tables 2 and 3).

Table 2. Characteristics of rock improvement works.

Rock improvement works	A	B	C
# injections along the section outline	32	32	32
# injections at the excavation face	-	10	10
Absorption of injections [%]	18	20	20
Length of overlaps [m]	16	16	12

Table 3. Characteristics of drainage works.

Drainage works	D
# drainage columns	8
Length of column [m]	30
Spacing [m]	15

Figures 6 and 7 show cross and longitudinal sections related to double shield TBM, where it is possible to view how the improvement and drainage works were designed. Quantities and positions are fictitious with respect to how indicated in tables above, but these figures are useful to understand the configuration of excavation by double shield TBM of this case history including rock improvement works; 1.1 indicates the drainage columns, 1.2 indicates injections along the section outline, and 1.3 indicates injections at the excavation face.

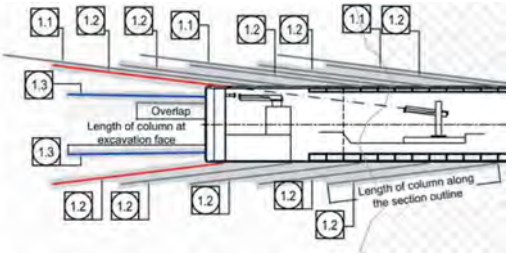

Figure 6. Longitudinal section of TBM.

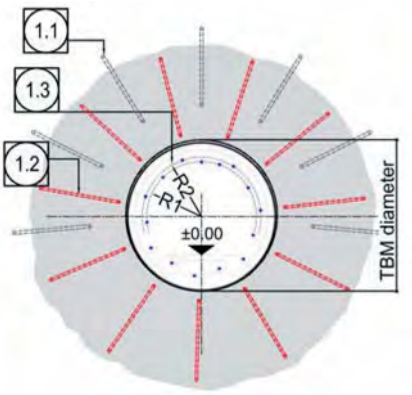

Figure 7. Cross section of TBM.

With reference to Figure 5, the following sections were defined to be improved:

- sections 14, 16: fault and stability class C zones,
- section 20: zones in the presence of water table with flow rates at the face greater than 50 l/s (high permeability),
- section 22: fault zones and presence of water table with flow rates at the face greater than 50 l/s,
- sections 5, 7, 11, 13: zones in the presence of water table with flow rates at the face less than 50 l/s (medium permeability),
- sections 4, 6, 8, 10, 12, 18: fault zones.

The analyses have led to the definition of 5 type solutions for which a combination of the works (defined above) is indicated, according to the geomechanical and hydrogeological conditions of the sections to be improved (Table 4).

To analyse costs and times in probabilistic terms, input data, representing the sources of greatest uncertainty, were included in the analyses as a triangular probability distribution varying from a minimum to a maximum value, such as:

1. length of sections to be improved (Table 5),
2. percentage of application of type works (Table 6),
3. length of overlaps,

4. percentage of absorption of injections,
5. speed of execution of type works,
6. speed of TBM.

Table 4. Definition of the type solutions.

Type solutions	Scope	Section	Type works
1	Fault and unstable zones	14, 16	B, C
2	Presence of w.t. with q>50 l/s	20	A, B, D
3	Fault zones and w.t. with q>50 l/s	22	B, C, D
4	Presence of w.t. with q<50 l/s	5, 7, 11, 13	D
5	Fault zones	4, 6, 8, 10, 12, 18	A

Table 5. Overall length of sections [m].

Solution	Min	Mode	Max
1	90	225	315
2	518	1295	1813
3	60	150	210
4	972	2430	3402
5	310	775	1085

Table 6. Percentage of application of type works.

Solution	Type works	Min	Mode	Max
1	B	95	80	40
	C	5	20	60
2	A+D	90	60	40
	B+D	5	10	15
	D	5	30	45
3	B+D	95	80	40
	C+D	5	20	60
4	No works	80	60	40
	D	20	40	60
5	No works	95	90	60
	A	5	10	40

In addition, the speed of TBM was assumed to be different between the post-intervention sections and the healthy rock sections for which no works are planned (Table 7).

Table 7. Speed of TBM in terms of metres per day.

Speed	Min	Mode	Max
Healthy rock	20	28	35
Post-intervention	15	25	30

5.4 *Results*

By means of a probabilistic analysis it is possible to get the results in terms of costs and time, which depend on fixed and variable parameters. Therefore, the results will be variables, too. Figures 8 and 9 show the variability of TBM + intervention cost. Figures 10 and 11 show the variability of total time taken by the TBM.

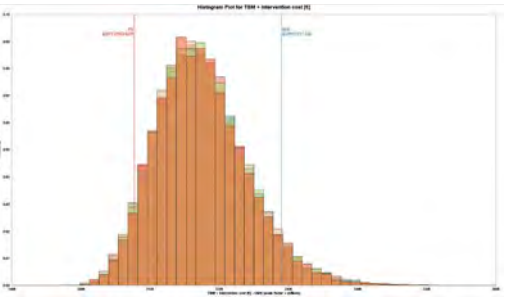

Figure 8. TBM + intervention cost – Histogram.

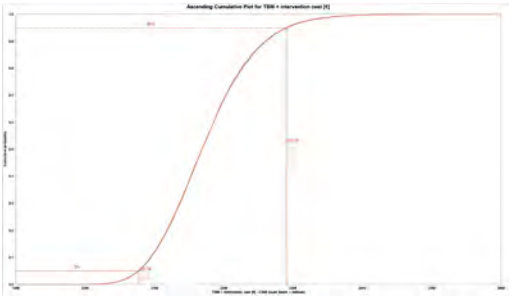

Figure 9. TBM + intervention cost – Ascending cumulative.

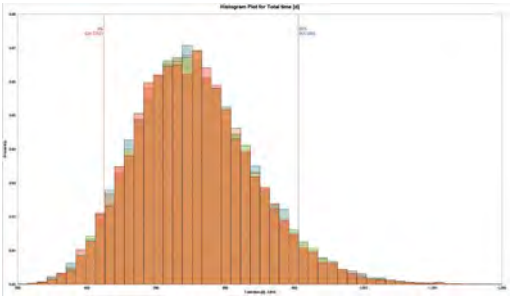

Figure 10. Total time – Histogram.

First of all, it is important to understand where the baseline value (mode) lies in relation to the s-curve, both in terms of cost and time, i.e. considering the parameters as if they were all fixed and none of them

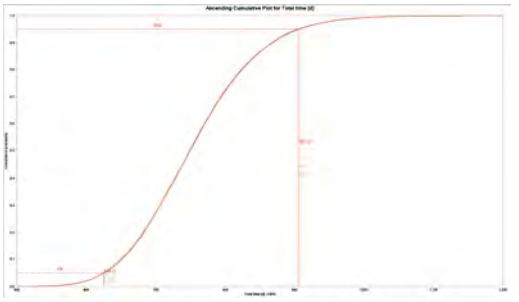

Figure 11. Total time – Ascending cumulative.

variable (no probabilistic risk analysis involved). In this case, the TBM + intervention cost would amount to € 214 million, and the total time would be 701 days. Both cost and time are in the respective s-curves in the cumulative probability of about 30%.

To obtain a cumulative probability of 95% the TBM + intervention cost would have to be about € 229 million.

To obtain a cumulative probability of 95% the total time would have to be about 905-910 days.

This means that in order to have a 95% certainty of covering the TBM + intervention cost and total time, an additional about € 15 million (+7%) and about 200 days (+30%) more than would be achieved without the variable parameters must be taken into account.

This simple example highlights the power of probabilistic risk analysis as a tool that can provide stakeholders with useful elements to evaluate the consistency of cost and time forecasts attributed to a project and thus assess the cost and time contingency amount, develop alternative solutions, or radically change project objectives.

REFERENCES

Avestedt, L., 2012. Comparison of Risk Assessments for Underground Construction Projects – A study about distinctions and common features and suggestions for improvements. Master of Science Thesis. Division of Soil and Rock Mechanics, Royal Institute of Technology, Stockholm, Sweden, pp. 1–79.

Bianchi, G.W., Piraud, J., Robert, A., Egal, E., et al, 2012. Recommendations – Characterisation of geological, hydrogeological and geotechnical uncertainties and risks. Tunnels et Ouvrages n°232, AFTES French Tunnelling and Underground Space Association, France, pp.315–355.

Bravery, P., Cross, S., Gallagher, R., HauteFeuille, O., et al, 2009. Recommendations – A code for practice of risk management in tunnel works. International Tunnel Insurance Group with contribution from ITIG, Tunnels et Ouvrages Souterraines n°214, AFTES French Tunnelling and Underground Space Association, France, pp. 188–205.

EN IEC 31010, 2019. Risk management – Risk assessment techniques.

Engineering and Regional Operations Development Division, Design Office, SAEO, 2018. Project Risk Management Guide – Part I: Guidance for WSDOT Projects – Part II: Guidelines for CRA-CEVP® Workshops. WSDOT Department of Transportation, WA, USA, pp. 1–132.

Eskesen, S.D., Tengborg, P., Kampmann, J., Veicherts T.H., 2004. Guidelines for tunnelling risk management: International Tunnelling Association, Working Group No. 2. Tunnelling and Underground Space Technology, ITA-AITES, c/o EPFL, Bat GC, Lausanne, Switzerland, pp. 217–237.

Hillson, D., 2009. Managing Risk in Projects.

International Standard ISO 31000, 2018. Risk management – Guidelines.

Molenaar, K., Anderson, S., Schexnayder, C., 2010. Guidebook on Risk Analysis Tools and Management Practices to Control Transportation Project Costs. National Cooperative Highway Research Program, NCHRP REPORT 658, National Academies Press, Washington DC, USA, pp. 1–119.

Piraud, J., Bianchi, G.W., Brino, L., Robert, A., et al, 2020. Recommendations – Technical Risk Integration of the Design of Underground Structures Project for the Purpose of Tender Documentation Drafting. Recommendation of AFTES, AFTES French Tunnelling and Underground Space Association, France, pp.1–38.

Sander, P., Becker, S.C., Nübel, K., 2022. Risk Management in Major Tunnelling Projects – Part 1: Basics and Success Factors. Risk Management, Tunnel-online.info, 4/22, Germany, pp.18–23.

Tunnelling for a Better Life – Yan, Celestino, Thewes & Eberhardt (Eds)
© 2024 The Author(s), ISBN 978-1-032-80042-4
Open Access: www.taylorfrancis.com, CC BY-NC-ND 4.0 license

Strong financial and improved procurement strategies for the success of the Grand Paris Express

Alexis de Pommerol*
Société du Grand Paris, Saint-Denis, France

ABSTRACT: Société du Grand Paris was created in 2010. It is in charge of financing, designing, building, testing and commissioning the Grand Paris Express. It's a new fully automated transit network of 200 kilometers. This network is 90% underground, includes four new lines and 68 new stations. A specific financial program was set up by Société du Grand Paris in order to finance the €36bn project: it's based on a 100% Green Bond Strategy and has been successfully implemented since 2018. For the second phase of the project delivery, Société du Grand Paris adapted its contractual scheme and chose design-build contracts. Efficient dialog and updated risk allocation lead to a new generation of contracts meeting performances, costs and planning expectations of all stakeholders.

Keywords: Metro, Deep stations, Green Bond, Design-Build

1 GRAND PARIS EXPRESS PROJECT

During the first decade of this century, Public Transport traffic increased very significantly in the French capital region around the city of Paris. The answer to this raising demand was not to be found in new road or car systems. As in many cities around the world, the Paris region was suffering from social divisions as low-income families were concentrated in some territories that did not offer enough accesses to public transport systems. Several projects emerged at the end of the decade, combining urban planning and transport systems. A dialogue of a rare magnitude took place that reached a significant consensus.

Figure 1. Grand Paris Express network.

In 2010, the French parliament passed the Grand Paris Act and defined the Grand Paris as a urban, social and economic project, based on a new transit system called "Grand Paris Express." A new entity "Société du Grand Paris" was established by this Grand Paris Act that is in charge of financing, designing, building, testing and commissioning the Grand Paris Express.

Grand Paris Express consists of a new fully automated transit network. It combines an extension of one existing Paris Metro Line, Line 14, and four new lines 15, 16, 17 and 18. From the very beginning, it was clear that a significant part of the new sections would be underground. By the end of the first studies, the preliminary design of the Grand Paris Express confirmed that 90% of the 200 kilometers' program would be underground, as 63 of the 68 new stations. The program will also include more than 150 access and/or ventilation shafts as well as six new maintenance centers. The average depth of the network is 35 meters with some stations' platforms at 50 meters under the ground level.

2 GEOLOGY AND CONSTRUCTION

While the overall geology of the "Bassin Parisien" was well documented, it was however clear that Société du Grand Paris would require specific additional geotechnical surveys in order to assess the best possible construction methods for the Grand Paris Express.

*Corresponding author: alexis.de-pommerol@societedugrandparis.fr

DOI: 10.1201/9781003495505-474

Figure 2. Grand Paris Express “carothèque” ».

This enabled the creation of the project geological model and of a specific hydrogeological model, following the G1 and G2 requirements of the French NF P 94-500 standards. A total of 9,800 surveys were carried out for the first delivery phase of the project, with an average depth of 45 meters, the deepest exceeding 100 meters. 21,000 samples were analyzed, 2,400 samples were used to perform laboratory tests and more than 2,000 are now stored in the “carothèque”, the geological library of the Grand Paris Express. All the expertise of the Grand Paris Express community is now available for future construction or research in the Paris area.

Figure 3. March 2022, TBM breakthrough at CMF.

The first Grand Paris Express TBM started its run in 2018 and, by 2020, at its peak, the project required the use of 20 TBM simultaneously. By the end of 2023, more than 100 kilometers had been dug. Mid 2024, first TBM for the second phase of the project delivery (2030-2031) will start digging in the South-Western part of the Paris region.

3 GRAND PARIS EXPRESS FUNDING

Grand Paris Express is a public funded investment. Its first financial source is a dedicated set of additional taxes on specific items such as offices or parking places. These taxes are local which means that only people or companies settled in, working in or visiting the Grand Paris region will contribute to the financing of the Grand Paris Express. In 2022-2023, the total amount collected by these taxes was around €800m. Meanwhile, operations on the Grand Paris Express required a total expense of around €4bn. This was made possible because, according to the Grand Paris act, Société du Grand Paris has also the capability of issuing bonds on the financial markets. Consequently, since 2018, Société du Grand Paris has developed and implemented a strong and efficient strategy that enables the construction of the whole new network in less than 15 years, while it would have probably required more than 50 years if the tax source was the only one available. As of 2030, following global commissioning of the network, construction expenses will be over and the revenue from the taxes will be used to manage and reimburse the total debt of Société du Grand Paris, up to approximately 2074.

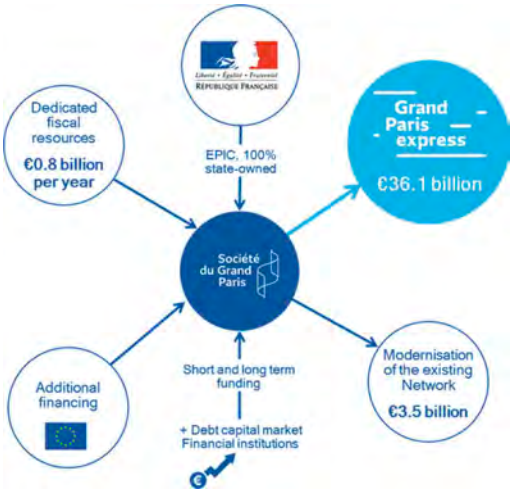

Figure 4. Grand Paris Express funding principles.

Société du Grand Paris was the first global securities issuer to choose a 100% Green financed program through the first international bond program “Green EMTN.” Consequently, Société du Grand Paris reports very precisely on its activities, including specific carbon reports as well as information on the use of excavated materials. Société du Grand Paris’ financial program follow the Green Bonds Principles 2018 standards and are Climate Bond Initiative certified. The initial total CO2 impact of the construction of the Grand Paris Express was 4.4m tons which Société du Grand Paris, following

a complete review with designers and industry, decided to reduce to 3.3m tons in 2021. As early of 2050, the overall impact of Grand Paris Express will be a decrease of 14m tons of CO2. Société du Grand Paris received the 2019 Green Bond of the Year from International Financing Review and the 2020 Green Bond of the Year (supranational, sub-sovereign and agency) from Environmental Finance.

Figure 5. Grand Paris Express debt geography (May 2023).

Construction of the underground sections of the Grand Paris Express results in the excavation of 45m tons of materials. The management of the excavated materials is also key for the appraisal of the project impact. Société du Grand Paris' goal is to reuse 70% of these materials: quarries backfilling or modeling new public areas (parks or public gardens) in the Paris Region. Excavated materials follow strict protocols enabling rigorous and permanent traceability by Société du Grand Paris of their final destination. Water or rail transport is also used for more than 15% of the volumes considered.

Looking at the Grand Paris Express experience, it appears that developing a 100% green financed structure for a transit underground project is possible, considering social and environmental, including decarbonization, management of its construction and future impacts of the network.

4 DESIGN-BUILD CONTRACTING

As a public entity, Société du Grand Paris complies with European and national public procurement regulations that defines scopes of works between employer, designer and contractors, and insists on splitting contracts between design activities and construction activities. In the project first phases, engineering companies carried out the design and supervised construction for the employer, Société du Grand Paris. Interfaces management between the different construction contracts (civil works, tracks, overhead lines, ventilation, power supply, stations' systems…) remains one key issue for the delivery of an efficient transit system. Under this initial scheme, interfaces management is carried out at engineers' and at employer's level, since several engineering entities can be simultaneously active on one line: civil works and stations, systems, rolling stock, maintenance facilities. On this first phase, systems design was ongoing while infrastructure construction had already started. This situation could lead to change orders as well as costs or delays increase. With the overall progress of the design, a first change in the procurement strategy occurred when tracks and overhead lines were added to a civil works contract that initially include only tunnels, stations and shafts.

Following extensive dialog with the industry (engineering and contractors), Société du Grand Paris adapted its procurement strategy in 2018 for the line 15's second phase. The East and West sections of line 15, around 22 kilometers each, will finalize the loop around Paris by 2030-31 when joining the South section (34 kilometers) that will be commissioned end of 2025. These last sections have been procured through four design-build contracts. These include the design and construction of all the civil works (tunnels, shafts and stations) of the project, tracks, overhead line, power supply, stations' and shafts' systems, ventilation, escalators and lifts. Interfaces between all these systems are therefore within one single hand and enable quick and appropriate adjustment in the project implementation and overall planning. Fire detection, ticketing, access control and passenger information design principles remain at employer's level while their detailed design and implementation are in the contractor's hand. Rolling Stock, signaling, Multi Service Network and Platform Screen Doors are kept under employer's management.

Figure 6. Grand Paris Express first Train run (November 2023).

The procurement process included a two-year-long dialog between bidders and the employer. One critical goal of this dialog was the risk allocation between both parties in order to reduce provisions and, eventually, costs of the contracts. The process duration also enabled 1,200 additional geotechnical surveys to be implemented and analyzed, bringing additional information to the bids' risk evaluation.

Based on these supplementary data, the risk allocation in the contracts was clarified: the number of areas where contractors would be able to call for the owner specific responsibility regarding geological context was consequently reduced, to a maximum of 5. Meanwhile, according to bidders' unformal feedback, the contracts costs were reduced, between 5 and 10%. In 2023, Société du Grand Paris awarded the first two design-build contracts for more than €2.5bn each, the last two design-build contracts are to come into force in Spring 2024.

5 CONCLUSION

An anticipative and voluntarist financial strategy, based on a 100% Green Bond program, has been implemented by Société du Grand Paris for the Grand Paris Express to benefit from favorable market conditions and reduce exposure to interest rate and liquidity risks. By the end of 2023, more than 70% of the project budget is financed and secured. At this stage, an initial estimate of the theoretical gain (a lower expense) from this strategy exceeds €5 billion.

Confidence provided by this strong financial structure and continuous dialog, in parallel with additional geotechnical surveys, were key for the success of the adapted procurement strategy as Société du Grand Paris chose design-build contracts for the line 15's second phase. The result can be estimated as reduced contract costs, between 5 and 10%, and, overall, meeting major employer's expectations: global costs, planning and performance.

Tunnelling for a Better Life – Yan, Celestino, Thewes & Eberhardt (Eds)
© 2024 The Author(s), ISBN 978-1-032-80042-4
Open Access: www.taylorfrancis.com, CC BY-NC-ND 4.0 license

A methodology of risk management to urban tunnels and its application to Bogota subway

J. Esteban Alarcón G.*
Universidad de Antioquia, Colombia
University of Brasilia, Brazil

André Pacheco de Assis
University of Brasilia, Brazil

ABSTRACT: Most of tunnel accidents that happened in the last decades have shown that at least 69% of the accidents were related with uncertainties, although some probabilistic methodologies have appeared as a tentative to include such uncertainties; First Order Second Moment (FOSM), Monte Carlo and others. They have shown themselves as insufficient for making decisions on civil projects. Therefore, Risk Management Methodologies (RMM) have appeared to provide better solutions to such necessities by including both the hazard occurrence probability and its associated costs of potential damages, giving a better tool to the decision-making process. This paper presents a RMM and its application to Line 1 of Bogotá Subway (Colombia). As a part of the methodology, a wide and general mathematical expression has been proposed to calculate the total risk expressed in monetary terms. For the application of the proposed methodology, a data compilation was carried out and a spatial database was constructed with geotechnical data and cadastral information of the surrounding urban area of the Line 1 of Bogotá subway. Subsequently, with the collected data, a geomechanical model was generated and probability distribution functions were defined to design variables. The characterized variables were used as an input of a modified Cam-Clay Model and a Finite Element Modelling (FEM) coupled with a FOSM analysis that was carried out to calculate the probability of exceeding control levels of the design variables. The FEM analysis was carried out in a total of 433 runs to both accomplish the FOSM analysis and cover a selected pilot segment of 4,1 km of the total length of the Line 1 of Bogotá Subway. Finally, by using the formulated expression, the total risk in USD/m2 was calculated and the associated map of the study area was built.

Keywords: Risk management methodology, risk analysis urban tunnels, Bogota subway, cost-profit analysis tool

1 INTRODUCTION

This paper presents a Risk Management Methodology (RMM) and its application to Line 1 of Bogotá Subway (Colombia), which is still in concept stage. The methodology incorporates the definition of the Risk Policies, the Qualitative and Quantitative Analysis of the risk and the definition of the Risk Acceptance Criteria, among others. As a part of the methodology, a wide and general mathematical expression has been proposed to calculate the total risk expressed in monetary terms.

For the application of the proposed methodology, a data compilation was carried out and a spatial database was constructed with geotechnical data and cadastral information of the surrounding urban area of the Line 1 of Bogotá Subway. Subsequently, with the collected data, a geomechanical model was generated and probability distribution functions were defined to design variables.

The characterized variables were used as an input of a modified Cam-Clay Model and a Finite Element Modelling (FEM) coupled with a First Order Second Moment (FOSM) analysis that was carried out to calculate the probability of exceeding control levels of the design variables.

The FEM analysis was carried out in a total of 433 runs to both accomplish the FOSM analysis and cover a selected pilot segment of 4,1 km of the total length of the Line 1 of Bogotá Subway. Finally, by using the formulated expression, the total risk in USD/m2 was calculated and the associated map of the study area was built.

*Corresponding author: jestebanalarcong@gmail.com

DOI: 10.1201/9781003495505-475

2 RISK MANAGEMENT METHODOLOGY (RMM)

Risk Management (RM) is a stochastic design methodology with an associated set of processes, which are complementary to the standard design processes. This additional processes are established in order to: define the risk policy, the risk analysis, the risk-transference mechanism, and to take control measures and supervision of the risks. The procedures and components associated are expanded in this section.

The RMM embraces all stages of a civil project and Figure 1 shows those stages and its relationship.

In Figure 2, it is assumed that conceptualization is a part of the basic design, encompassing all stages before tendering. The tender processes can change the position and take place after the detailed design, depending on local tendencies and policies, without affecting substantially the forward discussion.

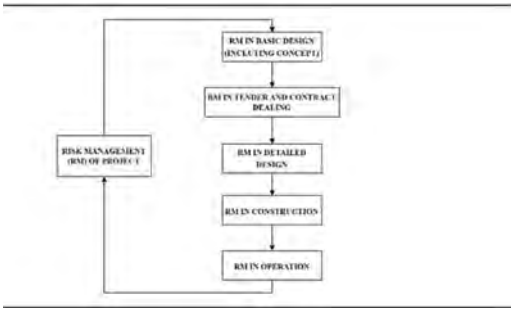

Figure 1. Stages of risk management in a tunnel project.

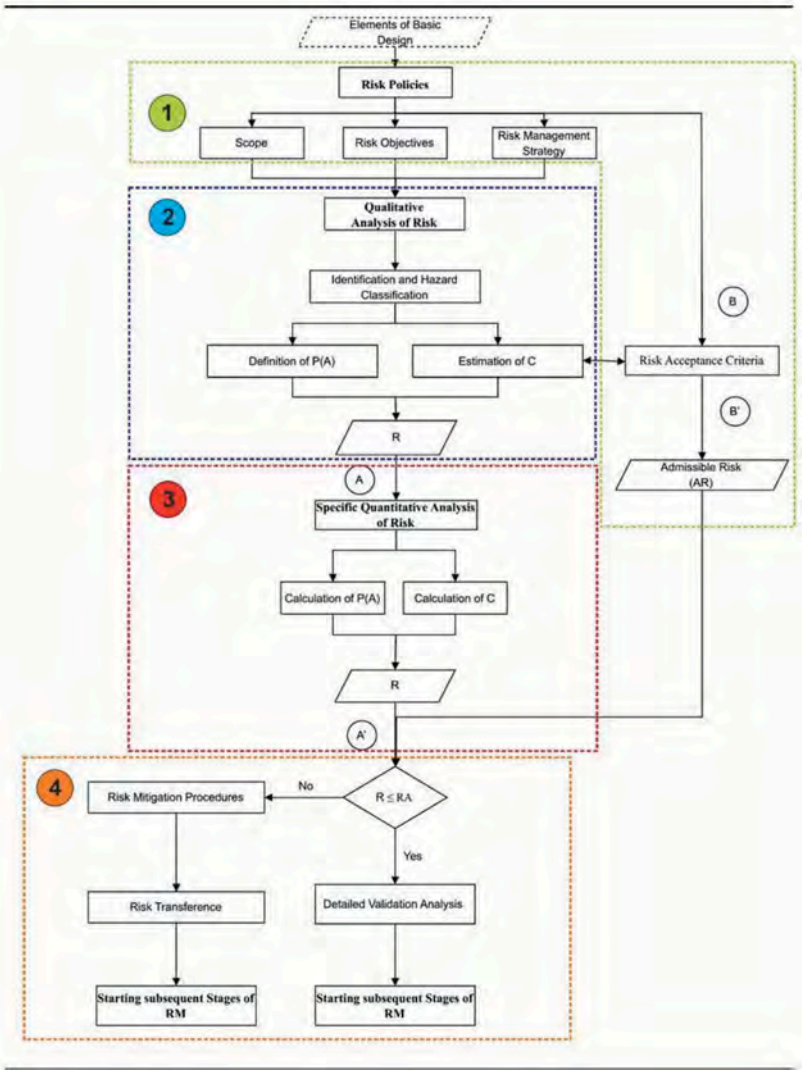

Figure 2. General Risk Management Methodology for a tunnel project in Basic Project Stage.

This paper focuses on the basic design, but, indeed, the methodology can be applied to any design stage or design verification on construction and operation stage no matter the type of civil project. Figure 2 presents the detailed suggested methodology for a RMM in basic design stage.

In Figure 2 four main sets of activities can be seen: risk policies definition; qualitative risk analysis; quantitative risk analysis; and management of the risk.

It is important to highlight that the RM process never ends; it is present in the life span of the tunnel and requires the participation of the owner in all the stages of the project, and the designer, contractor and operator in different stages of it.

The subsequent stages shown in the fourth activity of Figure 2 may be either the tendering and contracting processes or the detailed design, depending on the general requirements of the project and its general configuration.

2.1 *Dimensionality of the risk*

There are several ways to express Risk mathematically (Sturk et al., 1996; Einstein, 1996; Shahriar et al., 2008; Sousa, 2010). However, the simplest way to express Risk is given by:

$$R = P[H].C \quad (1)$$

Where, R is the Risk, P(H) is the probability of occurrence of the hazard H, and C is the consequence of such occurrences.

Risk Management (RM) is a part of a set of processes named infrastructure management, which belongs to a wider process named territory management. To simplify the decision-making process of territory managers, risk must be expressed in monetary terms as suggested by O'Reilly & Stovin (1996) and Eskesen et al. (2004).

By analyzing Equation 1 and given the dimensionless condition of its first component (P[H]), it is necessary to express the consequence (C) in monetary terms in order to express risk in the same way.

Expressing risk in monetary terms represents a big challenge to risk management's specialists because it implies the attribution of costs, for example, to the indemnification for the loss of human life or other social consequences in which quantifications may be quite difficult and uncommon. Nevertheless, monetary expression of the risk is necessary and investigation and academic debate must be oriented in this regard.

2.2 *Acceptability, residual value and risk mitigation*

A context without any kind of risk does not exist. The risk that the project owner is prepared to assume is named Admissible Risk (AR) and it must be defined by the owner by a cost-profit analysis between cost of the mitigation and profits associated with the reduction of the risk.

Nevertheless, some kinds of risks as social and political risks must be analyzed in a wider perspective instead of that cost-profit one. Owner can consider, for example, that certain risks as simply unacceptable.

It is necessary to define AR as a percentage of the cost of the entire project or as an absolute monetary value. For example, 0.5% of the total cost of the project may be recommended as a minimum value of AR.

Risk mitigation process consists on implementing measures in order to reduce risk until the AR level. In civil projects, risk can be reduced by decreasing the P[H] component by improving the design and construction method and/or by controlling the damages, for example, by reinforcing the exposed infrastructure, which implies reducing the probability of occurrence of the consequence. However, due to the nature of some engineering processes, the reduction of the P[H] is not always possible.

Residual Risk (RR) is the remaining total risk after the implementation of mitigation measurements in both design and construction stages. Figure 3 shows a hypothetical relationship between RR, AR, mitigated risks and time of the schedule project before starting operation stage. The shaded area corresponds to the mitigated risk along the time, the dashed line represents the limit given by AR and the area under this line represents the total RR of the project.

2.3 *Temporality of the risk*

Risks are distributed along the time in association with the schedule of a project. As a general behaviour, total risk decreases over time as individual risks are mitigated or never happen, due its random nature. At the end of the construction stage, the total risk reaches a maximum of RR.

2.4 *Risk policy*

All elements considered as input of the basic design are considered in the risk policy definition. Owner must define risk policies and it may indicate (Eskesen et al., 2004):

- scope,
- risk objectives, and
- risk management strategy.

Simultaneously, Risk Policy must define the risk acceptance criteria and, thus, the AR. This process is part of the Risk Management and sre useful in Quantitative Risk Analysis (QRA) as an element of comparing and acceptance of risks.

2.5 *Risk analysis*

Risk Analysis (RA) is the process that consists on the identification and the classification of the main hazards; the calculation of the probabilities of occurrence of hazards; the calculation of the potential

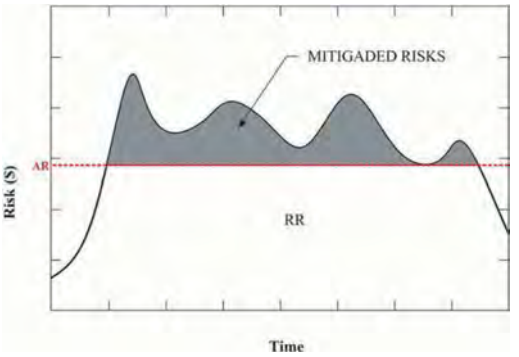

Figure 3. Residual risk, admissible risk and its hypothetical distribution behind the time of the project.

consequences; and of the product between those two components (second and third group of activities in Figure 2).

The Risk Analysis process implies as a first activity the qualitative Risk Analysis (qRA) and as a second activity the Quantitative Risk Analysis (QRA). The qRA is inevitable, but analysts may decide if it is viable to do the QRA, as a function of several conjugated elements, such as, the availability and quality of data; the kind of problem; the scope of the stage of project; and even the knowledgeable expertise of the analysts regarding concepts and tools of RA.

A methodology is called of qualitative or quantitative, depending on the way of determination of the components of Equation 1. A methodology is called of qualitative, when the components P[H] and C are expressed through numerical or adjectival values obtained from the direct specialist inference from his knowledge and practical experience. A methodology is called quantitative when the components of Equation 1 are calculated by engineering and stochastic procedures.

2.5.1 *Qualitative Risk Assessment (qRA)*

It is advisable to carry out a qRA in design stage, even if it is planned to do the QRA, in order to identify the potential hazards and including all the risk classes defined in risk policies definition. This analysis has the objective of both to identify and to classify the main risks of construction stage and to promote a structured basis to basic project stage decisions. Therefore, the qRA conclusions may define the set of risks, which are analysed into QRA, and, then, will be the input of risk management into tender stage (Eskesen et al., 2004).

The qRA process may be carried out by different methodologies of group working, such as, brain storming, Delphi methodologies (Landeta et al., 2011), among others, either as an isolated methodology or as a combination of many of them.

The main goal of qRA is to obtain a matrix, named risk matrix, which allows identifying the most important risks. A risk may be important either when the consequence is high (from a political, social, economic, administrative perspective etc.), when the occurrence probability of the associated hazard is high, or when the combination of those aspects is high. The classification of high depends on the definition of the admissible risk given by the owner. Finally, it is important to consider that the whole matter must be filtered by the specialist who must be able to analyse behind the P(H).C product. A further explanation about what the risk matrix is will be carried out ahead.

To sum it up, the Qualitative Risk Analysis must involve:

- the identification and classification of all the likely hazards;
- the qualification of the probabilities of occurrence of all the set of identified hazards;
- the qualification of potential consequences due the occurrence of identified hazards;
- the calculation of risk matrix and the identification of the risks to be analysed into QRA, by its classification.

Hazards must be expressed through design variables and conditions, in order to carry out a good representation of each hazard, for example, angular distortion (β) may be an adequate design variable, in order to analyse the impact of excavation on buildings, in shallow and brown-field tunnel conditions.

Identified hazards and its occurrence probabilities, just as the potential consequences, must be classified according to the level of represented associated risk in order to help decision-taking process (Eskesen et al., 2004). Such components of risk must be estimated and classified separately. Then, product P(H).C, i.e., the risk, must be classified, as well. This process is named risk classification process.

Classification system may be established into risk policy process as a part of the establishment of acceptancy risk criteria. Frequency classification of P(H), may be carried out by the identification of number of events into a time unit, a length unit (as a kilometer) or the whole construction period.

Regarding a tunnel project in brown-field conditions and in urban environments, there are five main groups of consequences:

1. Physics:
   - directly on works;
   - on third party infrastructure.
2. Socials:
   - human life lost;
   - psychological and morals, for example, familiar structure rupture due the loss of a family member, and social disaggregation;
   - cultural or symbolic effects, for example, the loss of routines and habits of a society.
3. Environmental.
4. Political or project image behind society.
5. Economical-administrative, such as, work schedule delays.

Table 1 shows an example of frequency classification of P(H) and an example of consequences classification.

As already discussed, the main goal of qRA is risk classification and the identification of the main hazards wich can be done through a risk matrix, which is the qualitative representation of Equation 1.

2.5.2 *Quantitative Risk Assessment (QRA)*

After the identification of the main risks in qualitative-risk analysis process, a quantitative analysis over each of them must be carried out. An individual quantitative risk analysis, named by Eskesen et al. (2004) as specific risk analysis, consists on making accurate the qualitative risk analysis by a stochastic approach, the improvement of the elements and methodologies of design, and a detailed evaluation of consequences.

Statistics allows the designation of a probabilistic distribution to data. For example, to discrete events through Poisson distribution; or to continuous events through a Gaussian, logarithmic, or exponential distributions, between others (Chiriotti et al., 2003).

Guglielmetti et al. (2008) highlights probability can be applied to the most of the variables involved in an urban tunnel project such as, geotechnical parameters and construction schedule, among others. Therefore, involved variables in projects, such as, underground characteristics, construction variables, and unpredictable events can be represented by a suitable probability distribution function. It is important taking into account that probability distributions can be determined by statistics procedures or inferred by heuristic processes according to circumstances. Eskesen et al. (2004) describes several heuristic alternatives of analysis if lector is interested in it.

In 1996, Einstein had given a more complete mathematic expression of risk than that of Equation 1. Einstein´s expression considered that consequence can be defined as the product of two components: the occurrence probability of consequence, given an event (Hazard) occurrence, and the cost of the consequences, as it is expressed in Equation 2.

$$R = P[H].P[C|H].C \qquad (2)$$

Therefore, this can get the uncertainties description by considering each consequence as a stochastic variable, and the designation of a distribution to each variable, instead a deterministic value.

Stochastic components of risk can be obtained, for example, by a Monte Carlo simulation, or approximate probabilistic methods such as First Order Second Moment (FOSM) and Point Estimate Method (Rosenblueth, 1975), between others, in order to determine the statistic parameters of probability density functions.

However, risk demands a wider expression than that of Einstein´s. Actually, there are several hazardous events Hi involved in a project. Each of those Hazards involves several kinds of consequences Cj, such as, physic, social, or others, as discussed previously. Therefore, it is suggested the Equation 3 to total risk, when, total potential consequence is the summation of all the set of consequences Ci of a hazard Hi, times conditional occurrence probability of each consequence, given the occurrence of mentioned hazardous event Hi. Thus, total risk is the summation of the multiplication of the probabilities P[Hi] and their associated total consequence $\sum_i P[C_j|H_i].C_j$ associated to the event Hi.

$$R_{TOT} = \sum_i \left\{ \prod_i P[H_i]. \sum_j P\left[C_j|H_i\right].C_j \right\} \qquad (3)$$

Therefore, each hazard Hi will establish an analysis context named Risk Scene (RS). Each RS has an associated risk calculated by the occurrence probability of hazardous event, Hi, and by the set of potential consequences related with. Thus, the total risk can be defined as the sum of the set of risks associated with each RS.

2.6 *Decision taking and risk transference*

Residual risk must be transferred by a procedure named Risk Transference (RT). This transference process must be controlled by the owner of the project to guarantee the reception of the risk by a technical team in the latter stages, and the implementation of mitigation measurements, progressively, until reaching the admissible risk (AR), as discussed in Section 2.2 and Figure 3.

Therefore, risk transference needs specialist preestablishing AR into risk policy procedures. Into basic design process, higher risk than AR must be highlighted as important risks and then analysed accurately in detailed design stage, in order to apply the final measures to reduce them until reaching AR.

The transferred risk to tender stage must be under the acceptable risk. In the same way, risks transferred to construction and operation stages must be also under such criteria. On the other hand, the incorporation of new risks higher than AR should not be accepted into tender stage.

During construction stage, mitigation measures consist on controlling and supervising the identified risk; identifying and calculating new risks; and defining its mitigation measurements. Into operation stage, mitigation measures consist on controlling transferred risk from previous stages.

In construction and operation stages, it is important to implement a modern, automatized, fast response, and fast data access, instrumentation system in order to control the risks.

3 APPLICATION CASE

The Line 1 of Bogotá Subway Project was selected as the application case. Regardless of the fact that there have been several basic designs published in the last 40 years and its alignment has changed a number of times, this case-study´s methodology

was based on the basic design released in 2010, as depicted in Figure 4 (AMB, 2010).

Feasibility design considers a mechanical excavation methodology by using a Tunnel Boring Machine (TBM) of a 10 m diameter tunnel and a general overburden of 20 m.

Study Area has been defined by considering the requirements of future numerical modeling processes, quality and density of information and the alignment of Bogota Subway stablished in AMB design.

Geomorphologically, the region is divided in two areas: one flat located in central area and another mountainous in the east and southeast side of the region. The flat area is the densest inhabited area (FOPAE, 2010).

Geologically, the city is located on a sedimentary deposit which is part of the Bogota Savannah. Bogota is bordered to the west by hills formed by several rock formations, such as, sandstones, claystones and conglomerates.

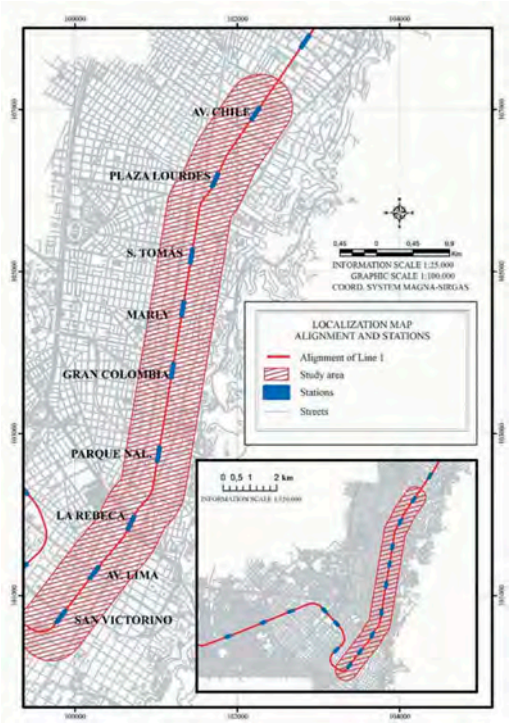

Figure 4. Location of the line 1 of Bogotá Subway (AMB, 2010).

Line 1 of Bogota Subway is planned to be constructed in the transition zone between foothill´s materials and aforementioned sedimentary deposits. It is expected higher vertical than horizontal variability and an alternation between fine and large grading materials as a product of different transport-sedimentation processes.

Bogota Subways is going to be constructed mainly downtown, where the urban context is complex given the different kinds of infrastructures that can be found: historical buildings, large modern constructions, shopping centers, and small commercial and residential buildings.

3.1 *Inputs and data base*

Data collection to apply risk management on an urban tunnel project must be focused on specific and general elements of:

- The environment: anthropic, biotic and physical (Zuquete & Gandolfi, 2004);
- The socio-economic environment.

For the purpose of this paper, the anthropic environment considers all the elements regarding urban environment while the physical environment considers the whole set of elements of the geo-mechanic environment (sub-superficial physical environment) and the elements of the relief, of the hydric network, among others (superficial physical environment). Socio-economic environment refers to the elements that describe the overall aspects of the economy and society, taken from Gross Domestic Product (GDP) per capita, population density, among others.

In consequence, five main sources of information were consulted:

- Agency for Prevention and Emergencies (FOPAE);
- Colombian Geological Service (SGC/ INGEOMINAS);
- Distrital Data Base;
- Bogota aqueduct;
- Bogota Metro Company.

Boreholes were collected by sources and sums up 361 drillings: 214 from the Fopae and 147 from the SGC.

A cartographic database was constructed in order to represent the anthropic, physical and socio-economic environments. In Figure 5 all the aforementioned cartographic elements can be seen.

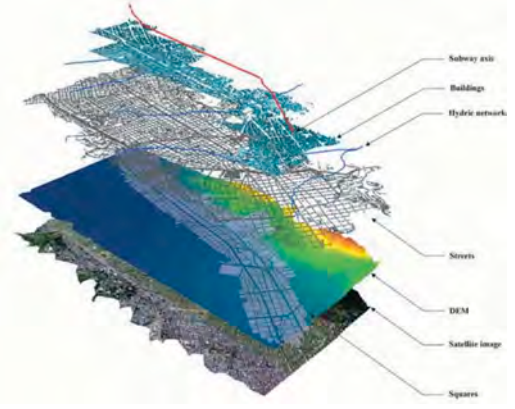

Figure 5. Elements of the anthropic and physic environment.

Figure 6 shows a constructed geomechanical model of the ground using selected geotechnical drilling and RockWorks software of RockWare in context with the Digital Elevation Model (DEM).

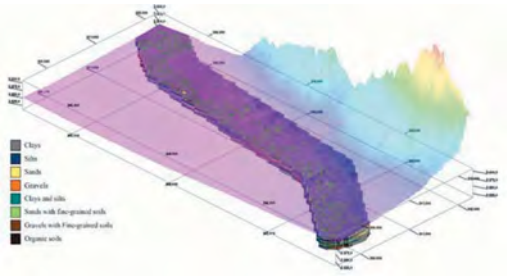

Figure 6. Classified model of subsoil (stratigraphy model) attached to DEM. Vertical enhance: 5X.

3.2 *Geotechnical data base and statistical characterization*

The geotechnical behavior of the ground was studied using the Finite Element Method (FEM) using Cesar LCPC software V5 t and its constitutive model IMOD18. IMOD18 is a modified Cam-Clay model, but it changes the Cam-Clay elastic law for an isotropic linear elastic model. IMOD18 demand the follow input data (Bourgeois et al., 2012):

A statistic characterization of IMOD18 model´s variables was made in order to do a probabilistic analysis of design and technical control variables. A full methodology and procedure presentation of the construction of both the geotechnical database and the statistical characterization of the variables do not concern to this paper.

3.3 *Qualitative Risk Assessment (qRA) to Bogotá Subway*

A Delphi methodology (Landeta et al, 2011) was carried out in order to do the qualitative analysis. A pool of tunnel specialists were put together and were concerned about situations of instabilities, unexpected displacements and, in those cases, a lack of corrective actions, as well as, a the delay in the installation of the lining.

3.4 *Quantitative Risk Assessment (QRA) to Bogotá Subway*

3.4.1 *Risk scenes, hazards and project variables.*

The risk scenes definition was focused on two of the five types of consequences already discussed: physical and social, specifically loss in human life. A quantification of all the other kind of consequences discussed in the previously is a technical challenge, uninvestigated by the scientific community until now, which is beyond this paper´s scope.

As defined by Burland and Wroth (1974 and 1977), angular distortion (β) is related to damages in building and infrastructure, in such a way, distortions greater than 0,002 and 0,007 are related to cracks and minor damage, and structural damages on surrounding buildings, respectively. Mair (2011) highlighted the relationship between the Gaussian Settlement Basin´s relative volume (VSr) and the roof failure propagations to the surface, in such a way, a volume upper than 3% can potentially unleash the aforementioned phenomena. Equation 4 shows the mathematical expression of VSr, where Aexc is the sectional tunnel area.

$$VSr = VS/Aexc \tag{4}$$

Given the urban and geological-geothecnical context, for this paper´s analysis an excavation method based on a Slurry-TBM by using Ibarra et al. (2013) criteria was chosen.

Additionally, due to all the elements pointed out on Delphi´s as part of the qRA, the delay in the installation of the lining is going considered due to a failure if the TBM by a modelling with a typical distension of SEM/NATM excavation method, instead of Slurry-TBM.

In summary, were considered six risk scenes related with six different events:

1. The event of β>0,002;
2. The event of β>0,007;
3. The event of VSr >3%;
4. The event of β>0,002 due to a delay in the installation of the lining due a failure of the Slurry-TBM;
5. The event of β>0,007 due to a delay in the installation of the lining due a failure of the Slurry-TBM;
6. The event of VSr >3% due to a delay in the installation of the lining due a failure of the Slurry-TBM;

3.4.2 *Numerical modelling*

A Finite Element Method (FEM) analysis was carried out in order to do the stress-strain analysis by using the software CESAR-LCPC of IFSTTAR. A state plane of strain was considered.

Into the academic context, only the risks associated to the excavation of the tunnels of study area were analyzed, and specific matters associated with stations' excavation and long-term effects were not considered.

In the context of the Excavation Forces Method programed in the software CESAR-LCPC, a value of the parameter λp (Panet e Guénot, 1982) of 0,1 was defined to the Slurry-TBM standard situation and of 0,67 to the situation of delay of the installation of the lining due to a failure of the TBM situation.

3.4.3 *Probabilistic analysis and probability of occurrence of hazards P[H]*

Four First Order Second Method (FOSM) analysis were carried out: two for VSr and β when λp is 0,1 and two for VSr and β when λp is 0,67. Input

Variables of CESAR-LCPC using modified Cam-Clay model (IMOD18) were considered as the independent variables, and design variables VSr and β were considered as dependent or response variables

3.4.4 *Consequences and P[C|H]*

Table 1 shows a suggested consequence typology related to each event and its P[C|H] values, as well as, the consequences C, both obtained by heuristic approaching in order to show the applicability of the suggested methodology. Those elements were used to the calculus in the example developed in this paper.

The associated cost of each building placed in the study area has been taken from the public information of the city specifically from a public territory gestor named Catastro Distrital.

For the calculation, a mean value for a unit of length of tunnel was considered, obtained from the aforementioned data. The cost of repairing a human life loss was considered as USD 1.000.000, mean values usually used by airlines to repair that condition in air accidents.

Such calculations were attributed to a spatial location and interpolated in order to construct cartographic continuous information of the aforementioned components of the risk. Allowing both a spatial and cartographic calculation of the risk by maps algebra and a cartographic presentation of this variable.

3.4.5 *Individual Risk and Total Risk*

By applying the Ecuation 3 was constructed the map of the risk presented in Figure 7. Each product $P[H_i].\sum_j P\left[C_j|H_i\right].C_j$ was made using cartographical tools. The Total Risk map with the sum of all the considered risks is the onde presented in Figure 7 which shows the urban environment classified according to the zoning of the risk.

3.4.6 *Decision taking and risk transference*

Identified risks will be transferred to the detailed designer and the owner. A mitigation of risks will consist in both depurate and sophisticate the engineering analysis, as well as, cost-profit balances in order to define which risk must be mitigated and its respective engineering procedures of mitigation.

Table 1. Consequence C and probability of occurrence of the consequence P[C|H] given the occurrence of the hazardous event H.

Hazard (H)	Kind of Consequence	P [H| C]	Consequence (C)
β > 0,002	Fissures and minor damage in surrounding buildings	60%	30% of surrounding building cost
β > 0,007	Fissures and minor damage in the own structure	100%	60% of own building cost
	Structural damage in surrounding buildings	60%	1,5 times of surrounding building cost
	Fatal victims inside affected buildings	20%	Human life lost reparation cost times population density
VS > 0,03	Major damage in own structure	100%	Three times of own building cost
	Structural damage in surrounding buildings	60%	1,5 times of surrounding building cost
	Fatal pedestrian victims	50%	Human life lost reparation cost times population density
	Fatal victims inside affected buildings	70%	Human life lost reparation cost times population density

4 CONCLUSIONS

The best tool to handle uncertainties into a civil project, such as an urban tunnel, is the Risk Management (RM) and must be incorporated into engineering stages.

RM of a large-scale civil project, such as, subway projects involve five steps: RM into basic project (including conceptual step), RM into tender and contract negotiation, RM into detailed project, RM into construction and RM into building operation (Figure 1).

Risk must be expressed in monetary terms in order to use it as a cost/profit tool to civil engineering projects such as urban tunnels, therefore, Risk must be given as a likely costs or likely overrun costs.

By using the formulated both methodology and equation it was possible to calculate the risk, expressed in USD/m2, it means in monetary terms, to Bogotá Line 1 subway by using current common projecting and designing information and complementary cartography information common in the most of the city.

The calculation of P[C|H] is one of the most relevant challenges, for the moment and until the development of practical scale engineering formulations, it is possible to use heuristic methodologies, such as, event tree. It is possible assume P[C|H] equal to 1, adopting a conservative perspective of analysis.

To the calculation of P[C|H] to specific soil-structure analysis into a tunnel project is possible to adjust Burd et al. (2000) e Houlsby et al. (1999) work by introducing approximated probabilistic methodologies, however, those approaches can demand a lot of time limiting its use to a whole project.

P[C|H] have a Bayesian nature and such characteristic must be considered. Formulations must be modified by considering aforementioned characteristic.

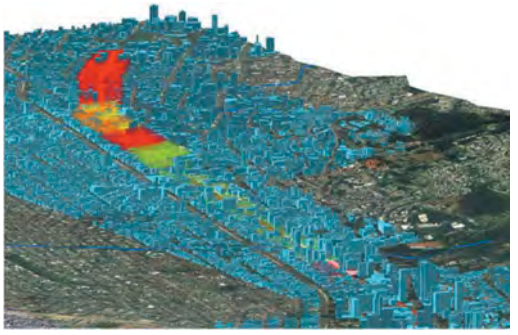

Figure 7. Urban environment and Total Risk zoning – basic design stage.

ACKNOWLEDGEMENTS

Acknowledgements to CNPQ and Capes for founding this investigation, additionally, to Servicio Geológico de Colombia, to Acueducto de Bogotá, to FOPAE and Catastro Distrital for helping in data collecting process.

REFERENCES

AMB (2010). Diseño conceptual de la red de transporte masivo metro y diseño operacional, dimensionamiento legal y financiero de la primera línea del metro en el marco del sistema integrado de transporte publico-sitp-para la c. de Bogota. Relatório, Bogotá, Colombia.

Baecher, G.B., Christian, J.T. (2003). Reliability and Statistics in Geotechnical Engineering. John Wiley & Sons Ltd, Southern Gate, Chichester,West Sussex, England, pp. 605.

Bourgeois, E., Meslat, Ph., Pucheu, M. (2012). CESAR-LCPC. Abridged theoretical manual. IFSTTAR. Montreuil, France.

Burland, J. B.,Wroth, C. P. (1974). Settlement of buildings and associated damage. Proc. Conference `Settlement of structures'. Pentech Press, London, pp.611–654.

Chiriotti, E., Grasso, P., Xu, S. (2003). Annalyses of tunnelling risk: state-of-the-art and examples. Gallerie e Grandi Opere Sotterranee, 69: 35–44.

Einstein, H. H. (1996). Risk and risk analysis in rock engineering. Tunnelling and Underground Space Technology, 11, 141–155.

Eskesen, S.D., Tengborg, P., Kampmann, J., Veicherts, T.H. (2004). Guidelines for tunnelling risk management: international tunnelling association, Working Group N. 2. Tunnelling and Underground Space Technology, 19: 217–237.

FOPAE (2010). Zoneamento da resposta sísmica de Bogotá para o projeto sismo resistente de edificações (em espanhol). Informe Final, Bogotá, Colômbia: 152 p.

Ingeominas & Uniandes (1997). Microzonificación sísmica de Santafé de Bogotá. Relatório, Bogotá, Colombia.

Landeta, J., Barrutia, J., Lertxundi, A. (2011). Hybrid Delphi: a methodology to facilitate contribution from experts in professional contexts. Technological Forecasting and Social Change, 78(9): 1629–1641.

Mair, R.J., Taylor, R.N., Burland, J.B. (1996). Prediction of ground movements and assessment of risk of building damage due to bored tunneling. Proc. Of the international Symposium on Geotechnical Aspects of underground construction in soft ground. Balkerma, Rotterdam, 713–718.

Mair, R.J. (2011). Tunneling in urban areas and effects on infrastructure. Advance in research and practice. Cambridge University.

O'Reilly, M.P, Stovin, V. (1996). Trenchless construction: Risk assessment and management. Journal Trenchless Technol. Vol. 11, No.1, pp 25–35.

Panet, M., Guénot, A. (1982). Analysis of convergence behind face of a tunnel. Proc. Tunnelling'82: 197–204.

Rosenblueth, E. (1975). Point estimates for probability moments. Proceedings of National Academy of Sciences, 72(10): 3812–3814.

Shahriar, K., Sharifzadeh, M, Hamidi, J.K. (2008). Geotechnical risk assessment based approach for rock TBM selection in difficult ground conditions. Tunnelling and Underground Space Technology, 23: 318–325.

Sousa, R. L. (2010). Risk Analysis for Tunneling Projects. PhD thesis, Massachusetts Institute of Technology (MIT), Cambridge, USA: 589 p.

Sturk, R., Olsson, L., Johansson, J. (1996). Risk and decision analysis for large underground projects, as applied to the stockholm ring road tunnels. Tunnelling and Underground Space Technology, 11(2): 157–164.

Zuquette, L. V.; Gandolfi, N. (2004) Cartografia geotécnica. Oficina de Textos, São Paulo, Brasil.

Tunnelling for a Better Life – Yan, Celestino, Thewes & Eberhardt (Eds)
© 2024 The Author(s), ISBN 978-1-032-80042-4
Open Access: www.taylorfrancis.com, CC BY-NC-ND 4.0 license

The use of a reference cost system for contracting underground public works

Eloi Angelo Palma Filho*
DNIT, Brasília-DF, Brazil

Claudio Kazuo Miyazato & Paulo Moreira Neto
ARTERIS, Florianópolis-SC, Brazil

ABSTRACT: The use of reference prices through compositions of unitary prices to contract public road works, within the scope of the federal government in Brazil, began in 1946, in the former National Department of Highways – DNER. As a result of this, in 1992 the Road Costs System – SICRO emerged, which was updated in 2000. In 2017, there was a reform in the System, changing its name to the Referential Costs System, now reaching the Rail and Waterway and bringing, for the first time, references on NATM Tunnels using the classification proposed by Bieniawski and treatment services and consolidation of Underground Works services. Due to its favourable reputation and wide use over decades, SICRO has become the federal reference in the budgeting of public works of transport infrastructure, from which the maximum admissible value for the cost of the enterprise is obtained. However, elements related to underground works have been part of this System for a few years, while other infrastructure elements have already been contemplated there for decades and could be improved by improving their use over time. This article will report on the services contemplated in the Referential Cost System regarding the underground environment, its premises, some evolutions of the first application in a large enterprise and make comments about possible improvements to be made for future uses. As for this practical application, the reference work was the Florianopolis-SC Road Ring, highway BR-101/SC, with construction starting in 2021 of 3 double tunnels totaling 5.4 km and budgeted as US$116.2 million dollars and completion scheduled for December 2023.

Keywords: Budget, Tunnel, Contractual practices, Reference cost system, NATM

1 THE LEGAL CONTEXT

In the context of public contracts, legal regulations in Brazil date back to the times of the Empire. On May 14, 1862, the Decree no. 2,926 was published, which approved "… the Regulation for the auction of services under the responsibility of the Ministry of Agriculture, Commerce and Public Works" (LIMA, DJALBA, 2014). In this regulation, the rite was presented, which at the time was called "competition" and not bidding, but already required a guarantee from proponents of 20% of the budget value. Furthermore, 10% of the measured value was retained in each measurement, which was returned to the constructor after the end of the work guarantee period (which could vary from 3 months to 2 years).

At the time of the Republic, another Decree[1] established the signing of a contract and the holding of a competition as a condition for committing the expenditure. Subsequently, the term "bidding" is presented in Decree-Law 200/1967, which established Competition, Price Taking and Invitation as procedures. In 1986, has been published a new Decree-Law[2], with general rules for bidding and contracts at the federal level, incorporating the modalities of Tender and Auction.

In the post-Constitution era of 1988, which established the Union's competence to legislate on the subject for all entities of the Federation, Law no. 8,666/1993 (BRASIL, 1993) which introduced legislation on Public Administration Tenders and Contracts. This includes the possibility of including the maximum contract price, both global and unitary in the bidding process.

1 Decree no. 4,536/1922.
2 Decree-Law no. 2,300/1986.

*Corresponding author: palmafilho81@gmail.com

DOI: 10.1201/9781003495505-476

In 2011, another legal framework aimed at contracting works and services emerged[3] (BRAZIL, 2011), which created the Differentiated Public Procurement Regime - RDC. The framework which was originally intended only for projects for the 2014 FIFA World Cup and the 2016 Olympic Games, underwent subsequent expansions in scope, enabling its use in different segments.

In 2013, through another Decree[4], rules and criteria were established for preparing a reference budget for engineering works and services, executed from the Federal public budget (BRASIL, 2013). In it, the SICRO cost system is tacitly indicated as a reference for defining the maximum value of the contract.

Finally, in 2021, Law no. 14,133, as new legislation applicable to public tenders and contracts, supplanting the then-current Laws no. 8,666/1993 and no. 12,462/2011. This Law reinforces the role of SICRO as a public reference in the contracting of works, stipulating it as the maximum contract value.

2 THE SICRO REFERENCE COST SYSTEM

The National Department of Transport Infrastructure - DNIT is a Federal Authority created in 2001, with multimodal operations (road, railway, waterways and ports), and succeeded the DNER, National Department of Highways, created in 1937, with operations specifically on highways.

The reference cost system has a history of more than 70 (seventy) years, dating back to a time when works were, in most cases, carried out directly by the administration, and not contracted from the supplier market. This history is shown by ALBUQUERQUE FILHO, 2017.

The main history of the DNER and DNIT cost system is presented below:

1946 - Implementation of the first DNER price tables;

1963 - General price list;

1972 - Launch of the Road Cost Composition Manual;

1980 - Update of the Road Cost Composition Manual;

1992 - Organization of Road Cost Management

1992 - Launch of SICRO 1

1998 - Revision of the Road Cost Composition Manual;

2000 - Launch of SICRO 2;

2003 - Publication of the Road Costs Manual;

2007 - Start of development of the new Construction Reference Cost System (SICRO)

2012 - Recruitment of Getulio Vargas Fundation

2017 - Implementation of the new SICRO.

The DNIT Construction Pricing System is made up of technical manuals describing the pricing methodology, in many cases, with practical examples; description of the composition calculation memory; and payment criteria.

Volume 01 - Methodology and Concepts
Volume 02 - Price Research
Volume 03 - Equipment
Volume 04 - Labor
Volume 05 - Materials
Volume 06 - Rain Influence Factor
Volume 07 – Work site
Volume 08 - Local Administration
Volume 09 - Mobilization and Demobilization
Volume 10 - Technical Manuals
Content 01 - Earthmoving
Content 02 - Paving/Machining
Content 03 - Road Signs
Content 04 - Concrete, Aggregates, Frames, Formwork and Shoring
Content 05 - Drainage and Current Works
Content 06 - Foundations and Retainers
Content 07 – Bridges and Viaducts
Content 08 - Road Maintenance and Conservation
Content 09 - Railways
Content 10 - Waterways
Content 11 - Transport
Content 12 - Complementary Works and Environmental Protection
Volume 11 - Cost Compositions
Volume 12 - Mechanical Team Productions

The Federal Government portal presents a table of services and reference unit prices for each state of the federation.

With this SICRO update in 2017, rail and waterways were incorporated into the system, which already included highway services. Furthermore, the list of services was increased, including, for example, environmental recovery services and Tunnels, whose services can be provided by road or rail.

The methodological concept used by SICRO to obtain the unit reference cost for the execution of a given service considers (DNIT, 2017):

(a) Equipment cycle:

Equipment normally performs operations considered repetitive, that is, it works in cycles. A cycle is understood as the set of actions or movements that the equipment performs from its departure, from a certain position, until its return to a similar position, which marks the beginning of a new cycle.

The time elapsed between two consecutive passes of the equipment is called “cycle duration” or “total cycle time”, which determines an interval during which the equipment performs a certain amount of work.

Quantifying the service performed during a cycle and its total duration is essential to determine the hourly production of the equipment, to size and balance the rest of the equipment that forms a patrol, as well as to calculate the production of the patrol itself.

3 Law no. 12,462/2011.
4 Decree no. 7,983/2013.

(b) Production of mechanical teams:

The production of mechanical teams normally corresponds to that of their main equipment or patrol leader, which conditions the performance of the set of equipment, depending on their different capacities and productions.

Determining the production of mechanical teams is a fundamental element for forming the unit costs of services. The unit execution cost is the relationship between the hourly cost of executing a given service and the production calculated in the same unit of time.

One of the most common practices for pricing road tunnels is determining the costs of inputs and losses and the cost per stay of equipment and labor to determine the overall cost of construction. For this purpose, the duration of each construction stage is calculated with the particularities of the project and external constraints (restrictions on blasting times, available resources, etc.) for different combinations of resources multiplied by the cost of operation and maintenance. The distribution of costs by services is usually just for characterizing events within the analytical structure of the project and determining the financial flow.

In this regard, SICRO innovates by proposing an algorithm for the individual calculation of each service until the construction of the overall value of the project.

The contents of the SICRO Transport Infrastructure Cost Manual, Volume 10 – Technical Manuals, were incorporated into the second edition of the Technical Notebooks, whose SICRO reference is the base month of October 2022. (DNIT, 2022)

2.1 *Tunnels*

SICRO adopts a fictitious tunnel 400 meters long with 4 lanes of cross sections from 20 to 40 m2, from 41 to 60 m², from 61 to 90 m² and above 90 m², geotechnical classification proposed by Bieniawski and typical advances of 0.60m to 4.00m depending on the geotechnical classification.

The productivity coefficients for determining the hourly production of equipment and services were determined by theoretical (productivity declared by equipment manufacturers) and empirical methods (field measurement, technical reference and consolidated historical reference).

Productivity reducing multipliers (efficiency factor) were considered in order to represent the various production losses and discontinuities and multiplier factors corresponding to losses in input consumption.

2.1.1 *Modelling and example*

The referential modelling adopted in the design of the service cost compositions presupposes the execution of the following steps:

- manual installation of electrical systems for tunnel lighting and ventilation;
- drilling holes in the rock mass using an electro-hydraulic jumbo jet;
- manually filling the holes with explosive material using the electro-hydraulic jumbo work platform;
- manual assembly of the detonation circuit;
- rock detonation;
- manual execution of the choco (scalling) with the aid of the electro-hydraulic jumbo work platform;
- slaughter of cuttlefish using an excavator with a hydraulic hammer;
- loading the rock into a dump truck using a tire loader;
- transport of material using a dump truck.

2.1.2 *Hourly production and mechanical team*

The activity is carried out by the following equipment:

- electro-hydraulic jumbo with 3 arms;
- hydraulic excavator with 1,700 kg hydraulic hammer;
- rock tire loader with a capacity of 2.50 m3;
- rock dump truck with a capacity of 12 m3;
- axial fan;
- generator sets.

The hourly production of services was established using the theoretical method, being defined through the application of the following expression:

$$P = H\ x\ \frac{A}{T_c} \tag{1}$$

Where, P is team production (m³/h); H is excavation depth (m); A is the cross-sectional area of the tunnel (m²); Tc is the cycle time of progress in tunnel excavation (h).

a) electro-hydraulic jumbo with 3 arms

Hourly production is established by the theoretical method, being defined by applying the following expression:

$$P = 60\ x\ A\ x\ H\ x \frac{Fe}{Tc} \tag{2}$$

Where, P is hourly production (m³/h); A is the excavation area (m²); H is excavation depth (m); F_e is the efficiency factor; Tc is the total cycle time (min).

b) hydraulic excavator with 1,700 kg hydraulic hammer

Hourly production is established by the theoretical method, being defined by applying the following expression:

$$P = 60\ x\ A\ x\ H\ x\ T_c \tag{3}$$

Where, P is hourly production (m³/h); A is the excavation area (m²); H is excavation depth (m); Tc is the total cycle time (min).

c) rock tire loader with a capacity of 2.50 m3

Hourly production is established by the theoretical method, being defined by applying the following expression:

$$P = 60\ x\ C_{ap}\ x\ F_{ca}\ x\ F_{cv}\ x\ \frac{F_e}{T_c} \tag{4}$$

Where, P is hourly production (m³/h); C_{ap} is capacity of the tire loader (m³); F_{ca} is a load factor; F_{cv} is a conversion factor; F_e is the efficiency factor; Tc is the total cycle time (min).

d) rock dump truck

Hourly production is established by the theoretical method, being defined by applying the following expression:

$$P = 60 \; x \; C_{ap} \; x \; F_{ca} \; x \; F_{cv} \; x \; \frac{F_e}{T_c} \qquad (5)$$

Where, P is hourly production (m³/h); C_{ap} is capacity of the tire loader (m³); F_{ca} is a load factor; F_{cv} is a conversion factor; F_e is the efficiency factor; Tc is the total cycle time (min).

2.1.3 *Payment criteria*

The measurement of underground excavation services for class I to IV tunnels must be carried out in cubic meters, depending on the volume actually extracted, measured and evaluated in the cut (in natura volume).

2.2 *Adjusts already made in the SICRO from its initial application*

Based on the studies for reference budgeting for the construction of tunnel works on the Florianopolis-SC Road Ring, on the BR-101/SC highway, notes were made that resulted in adjustments to the SICRO system, for underground activities.

These adjustments can be checked on the DNIT website.

3 THE FIRST APPLICATION OF SICRO IN TUNNEL WORKS

The pioneering application of SICRO for the pricing of underground works tunnel took place for the concession contract resulting from Notice no. 003/2007, for the so-called "Contorno Rodoviário de Florianópolis-SC", Florianopolis Road Ring project, on the BR-101/SC highway.

As these works were not foreseen in the original contract, their inclusion will require compensation to the concessionaire, which will be done through an adjustment in the toll rate paid by road users. Thus, there are such interventions as public works, which is why the reference value is defined based on official tables, in this case, SICRO.

3.1 *Florianopolis road ring*

The Florianopolis Road Ring is a new highway with 50 kilometers of double lanes and an investment of R$ 3.9 billion or US$ 780 million dollars (Aug/23) consisting of 6 interchanges, 7 double bridges, 20 uneven crossings and 4 double tunnels with the aim of diverting long-distance traffic from the Greater Florianopolis metropolitan region.

The table below illustrates the large numbers of the enterprise.

Table 1. Project numbers.

Soil Excavation: 9,750,000 m3	Rock Excavation: 1.655.500 m3	Asphalt Pavement: 395.400 ton
Geodrain: 3,145,000 m	Concrete: 163,160 m3	Steel Rebars: 9,909 ton

The 4 (four) tunnels of the Florianopolis Road Ring total a length of 7,083.90 m, with a platform for 2 lanes of 3.60 m, shoulders of 3.00 m, sidewalks for escape routes with a clear width of 1.20 m, and distributed as shown in figure x below, with tunnel 4 in the central region of the highway and tunnels 1, 2 and 3 concentrated in the southern section.

Figure 1. Road alignment. Source: Miyazato, 2023.

The tunnels were designed and built using the NATM method in which four typical treatment sections were created for classes I to IV (R1, R2, R3 and R4), 2 sections for soils (S1 and S2) class IV and 3 sections for transitions from soil to rock (M1, M2 and M3) using the Bieniawski classification system – RMR as a reference and showed in Table 2.

The extensive geological investigation shows that 2/3 of the length of the tunnels are predominantly in rock and the other segments in sections of soil or in soil/rock transition, as showed in Table 3.

In rock, a typical section had 135m² of excavation (Figure 2), instead in the soil massive, the typical excavation section presented about 160m² (Figure 3).

Table 2. Classes parameters. ANTT, 2018.

SECTION TYPE	CLASS	MASSIVE	RMR
R1	I	Sound Rock	81 a 100
R2	II	Sound Rock	61 a 80
R3	III	Slightly Weathered Rock	41 a 60
R4	IV high	Weathered Rock	31 a 30
M1/M2/M3/ S1/S2	IV low	Soft Weathered Rock/Saprolite	21 a 30
	V	Saprolite/Residual Rock	<20

Table 3. Massive characteristics. ANTT, 2018.

	TUNNEL 1		TUNNEL 2		TUNNEL 3		TUNNEL 4	
SECTION	EXT (m)	%	EXT (m)	%	EXT (m)	%	EXT (m)	%
R1	0.00	69.2	0.00	65.0	0.00	72.5	0.00	84.5
R2	548.50		590.07		657.31		554.00	
R3	487.00		308.98		414.23		561.50	
R4	321.00		269.60		147.81		273.50	
M1	64.00	30.8	78.87	35.0	17.90	27.5	21.00	15.5
M2	346.50		259.26		92.42		178.30	
M3	0.00		0.00		332.03		0.00	
S2	108.00		0.00		0.00		55.00	
S1	85.00		292.42		19.70		0.00	
TOTAL	1,960		1,799.2		1,681.4		1,643.3	

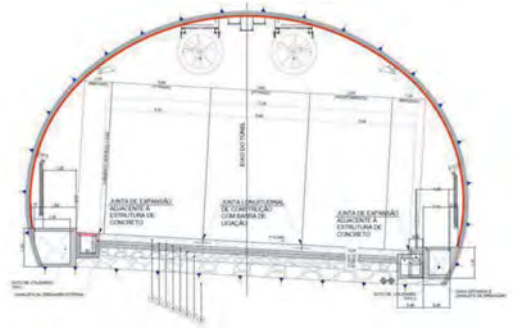

Figure 2. Rock typical section. Source: ANTT, 2018.

3.2 *Pricing the work*

The application of the unit price methodology through the composition of unit prices with the necessary adjustments, the particularities of the Road Ring project brought values to the tunnel budget that are consistent with the historical average prices of the DNIT, as showed in Figure 4.

This represents about US$ 30 million/km, including all costs (land acquisition, design, excavation, support, pavement and security systems).

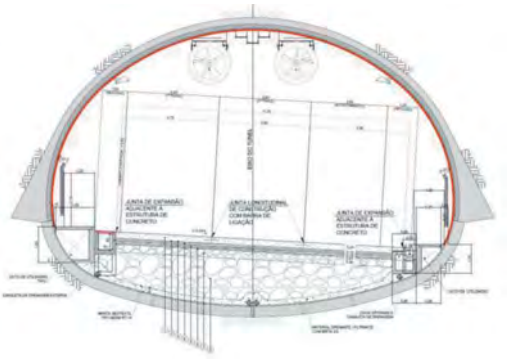

Figure 3. Soil typical section. Source: ANTT, 2018.

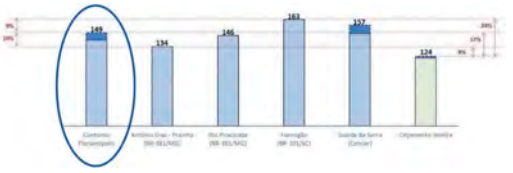

Figure 4. Tunnel pricing, in BRL R$/km, 2021 base.

4 TUNNEL COSTS REFERENCES

It is possible to find information regarding tunnel costs in the bibliography, but in order to relate the cost per kilometer related to the extent of the work, as a rule as shown in Figure 5 and Figure 6.

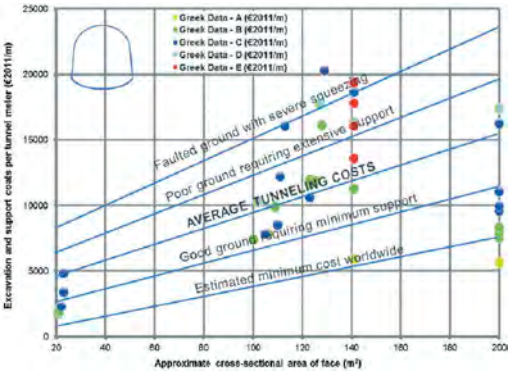

Figure 5. Approximate costs for tunnel excavation and support per tunnel meter according to ground conditions compared with Greek data. Source: Benardos, Paraskevopoulou and Diederichs, 2013.

However, there are no references about cost systems that provide a methodology for calculating the unit costs of underground services in conventional works (sprayed concrete, sequential excavation in soil or rock, rock bolts, steel rebars, lattice girders, etc.).

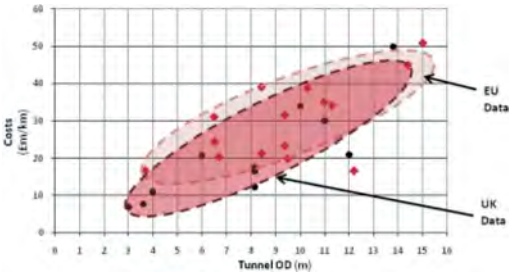

Figure 6. The effects of tunnel outside diameter on unit costs. Source: HM Treasury, 2010.

In Brazil, there is this national reference, regionalized by state, which must be used in public works contracts, as a reference for the maximum value to be paid by the government, with public resources.

5 CONCLUSIONS

The transparent approach with which the methodology is presented, as well as the courage to incorporate improvements in the system and the national coverage for the reference table of services for underground works, brings to the national market means to mitigate risks in contracts.

This is an attempt to increase the chances of completing projects, guaranteeing investments with lower contractual imbalances and transparency for the government structure.

The continuity in the use of the system, the joint work between the Government, the technical environment, designers and construction companies will certainly bring numerous points of improvement.

It is necessary to always remember that the specificities of underground works must always be captured in the budgeting of the works, otherwise it will not be possible to contract them on the market, for which it is essential to fully understand the SICRO methodology and its openness to adaptation to the particularities of each enterprise.

Moving forward, it is understood that the empirical methods used for productivity must be studied in more depth and measured, as well as the assumptions and interfaces between the construction stages.

ACKNOWLEDGMENTS

Our thanks go to DNIT, National Department of Transport Infrastructure and Arteris, the highway concessionaire.

REFERENCES

Albuquerque Filho, L. H. 2017. Novo sistema de custos referenciais de obras – SICRO. Principais inovações e alterações metodológicas - Seminário de apresentação (*in Portuguese*).

ANTT. 2018. Projeto Executivo do Contorno Rodoviário de Florianópolis-SC (*in Portuguese*). Brasília, DF.

Benardos, A., Paraskevopoulou, C., Diederichs, M. 2013. Assessing and benchmarking the construction cost of tunnels.

Brasil, 1993. Law nº. 8,666, of June 21, 1993. Regulates art. 37, item XXI, of the Federal Constitution, establishes rules for Public Administration tenders and contracts and provides other exceptions.

Brasil, 2013. Decree no. 7,983, of April 8, 2013. Establishes rules and criteria for preparing the reference budget for engineering works and services, contracted and executed with resources from the Union budgets, and provides other measures.

Brazil, 2011. Law no. 12,462, of August 4, 2011. Establishes the Differentiated Public Procurement Regime.

Brazil, 2021. Law no. 14,133, of April 1, 2021. Bidding and Administrative Contracts Law.

DNIT. Manual de Custos de Infraestrutura de Transportes (*in Portuguese*). Volume 01 – Methodology and concepts. 2017. Accessed at: https://www.gov.br/dnit/pt-br/assuntos/planejamento-e-pesquisa/custos-e-pagamentos/custos-e-pagamentos-dnit/sistemas-de-custos/sicro

HM Treasury. 2010. Infrastructure Cost Review: Technical Report. <https://assets.publishing.service.gov.uk/government/uploads/system/uploads/attachment_data/file/192589/cost_study_technicalnote211210.pdf>

Miyazato, C. K. 2023. Incorporação das obras dos túneis no contrato de concessão (*in Portuguese*). Presentation made at Simpósio de Túneis Rodoviários. Florianópolis-SC.

Tunnelling for a Better Life – Yan, Celestino, Thewes & Eberhardt (Eds)
© 2024 The Author(s), ISBN 978-1-032-80042-4
Open Access: www.taylorfrancis.com, CC BY-NC-ND 4.0 license

Development of an early contractor involvement selection tool for public owners

Carl Philipp Friedinger*
Bundeswehr University Munich, Neubiberg, Germany

Philip Sander
Bundeswehr University Munich, Neubiberg, Germany
RiskConsult GmbH, Innsbruck, Austria

ABSTRACT: Tunneling projects are complex and large-scale on a regular basis. Consequently, they pose challenges for contractors regarding risk management, cost calculation, and timely execution. These challenges often result in cost and schedule overruns on the part of public-sector owners. An opportunity to remedy these grievances are Innovative Project Delivery (IPD) models. A variation of IPD refers to the early involvement of contractors and suppliers. Early Contractor Involvement (ECI) can take different forms depending on the time of the initiation and the project. The initiation can occur at various points: during the preparation of the project; during the planning phase; and between the planning phase and the construction contract. ECI can influence several aspects positively: improving manufacturing methods; understanding, mitigating, and managing risks; reducing complexity, disputes, and backlog management; cooperation among all stakeholders; on-time execution within budget. This paper aims to identify specific characteristics projects must meet for ECI to be applied successfully. A selection system to determine whether the use of ECI makes sense is developed concerning the requirements of public-sector owners. Firstly, existing and applied forms of ECI are gathered by literature review. Secondly, a qualitative analysis of ECI projects and ECI variations is conducted. Characteristics leading to success or failure are identified by determining the appliance project's success. A selection system for public owners is created to determine whether using ECI is reasonable. Project scale, both financially and in complexity; the application of risk management; timeline; and workforce represent an excerpt of the determined hard characteristics. In comparison, in-house competence and cooperation capability represent soft characteristics. Based on determined characteristics the Contractor Involvement Tool (CIT) is created. The tool helps public owners choose the right variant of ECI for their projects. Therefore, applying the tool to public projects in Germany is the next step.

Keywords: ECI, Integrated Project Delivery, IPD, Project Delivery Model

1 INTRODUCTION

Complex large-scale projects regularly pose challenges to contractors in terms of cost calculation and on-time completion. This in turn leads to cost and schedule overruns on the part of the public owner and the associated negative publicity. One reason for this is the use of traditional project delivery models and unsuitable contracts, both do not meet the special requirements of complex large-scale major projects. Separating mechanisms of these models, coupled with the blinkered pursuit of particular interests, are is one reason of the fundamental problem (Breyer et al. 2020). Innovative project management models offer an approach to counteracting precisely these problems (Becker and Friedinger 2022; Becker and Roman-Müller 2022). Model like the "TIWAG alliance contract", used for a hydroelectric powerplant in Austria, has had a demonstrably positive effect on the construction time (Friedinger et al. 2023a). Prior to that particular project the German government realised the necessity for a change in project delivery, especially the delivery of major projects. Therefore in 2015 a governmental guideline was published to give public owners a helping hand in project delivery and to establish to use of innovative project delivery models. (Bundesministerium für Verkehr und digitale Infrastruktur 2015). Three years later in 2018 another guideline for

*Corresponding author: carl.friedinger@unibw.de

DOI: 10.1201/9781003495505-477

large-scale projects was published, going into detail even more by describing specific methods and instruments, like "integration of execution competence into the planning phase", to enable an improved project delivery. (Bundesministerium für Verkehr und digitale Infrastruktur 2018) So, the use of contractor know-how for the definition and optimisation of performance requirements in the early project stages has proven to be an powerful instrument as is also has an positive impact on project management in a spirit of partnership (Sander et al. 2022). Furthermore, changes in early planning phases have a significantly lower impact on costs and execution time than changes in the construction phase, the use of execution competence in early planning phases is particularly useful (CURT 2004). Thereby, helping to avoid costly planning errors and the overlooking of risks can be minimised (Bourn 2007). The involvement of the executing companies in the planning phase is weidly called Early Contractor Involvement (ECI) (Mosey 2009; Kinlan and Willems 2023). This form of implementation is already being used successfully in other European countries (Haghsheno 2020). The research questions addressed in this paper are:

1. What types and variations of Early Contractor Involvement are used in the public sector and which variations are suitable for public sector clients in Germany?
2. Which project requirements need to be fulfilled for the successful use of ECI?
3. How can the use of ECIs be promoted to public purchasers in Germany?

2 BACKGROUND AND FRAMEWORK

Traditional project management lacks a common and uniform understanding of the project on the part of both the contractor and the client. This leads to misunderstandings, and risks cannot be identified or dealt with in time (Friedinger et al. 2023b). This is partly due to the strict separation of planning and execution (Haghsheno 2020) as well as due to the common procurement practices. The following is a list two of core problems and the associated scientific theories:

First of all, it is impossible to fully complete the tender documents for complex mega projects for the tendering process. At this time point the planning isn't either complete enough or the planner lacks know how to fully plan all aspects of the project. This topic is connected scientific perception of complexity, which itself is a rather new field of research (Bandte 2007). Simple and even complicated systems are describable, whereas complex systems consist of many element, connections and multiple layers. To structure the elements, to connect them in the right way and to identify the relationships between the different layers and the to build a model and simulate the created system is the simplified aim of this research field (ibid.).

Regarding construction projects this approach can be used to structure the planning process, help to involve contractor know-how at the right time and also involve every other stakeholder on point.

Secondly, there is a fundamental conflict of objectives in the two-party system between client and contractor. Companies carrying out construction work are interested in maximising profits, while clients are only interested in the best possible performance of services within the given framework conditions at minimum cost (Faber 2014). This conflict of objectives is exacerbated by an asymmetry of information in favour of the contractor. Related to the situation in construction projects to the principal-agent theory, the information advantage is always exploited to one's own advantage according to the theory (Nister 2005; Faber 2014). In addition to this theory, the hold-up problem describes a problem scenario that also occurs frequently in the construction industry: when the contract is concluded, the actual motives and motivations of the contracting parties are not known to each other, which can lead to opportunistic behaviour in the ex-post contract phase. Dependencies can be exploited through the "lock-in effect" (Picot et al. 1998).

(Nister 2005) describes the development of trust as a solution to the agency problem. A possible solution might be the involvement construction companies at an early stage in the planning. Especially for projects classified as complex, this tends to be highly beneficial (Haghsheno 2020). Thereby, the know-how of the construction companies can be used in this way already in the planning phase. However, a fitting procurement method or model is required.

In Germany, the inclusion of execution expertise in the planning phase is discussed within the framework of partnering models (Hauptverband der Deutschen Bauindustrie e. V. 2005). One model, often referred to as a method, that is regularly used successfully in other countries within and outside Europe in order to utilise contractor know-how in the planning phase is "Early Contractor Involvement (Eadie and Graham 2014; Kinlan and Willems 2023). The implementation of an ECI can promote the following aspects: Use of innovative fabrication methods; Understanding, mitigating and managing risks; Reducing complexity, disputes and backlog management; Cooperation of all parties involved; On-time completion within budget (Bourn 2007). ECI can take different forms. It occurs as a contract model, as an element of a project management form or as a form of award (Walker and Lloyd-Walker 2012). In the private construction industry, a form of ECI known as "preconstruction" is already used in Germany (Smart Construction 2023). These circumstances lead to the third theory, decision theory. It was founded in business administration and enables the development of models that are intended to depict the economic effects of a decision in order to facilitate decision-making (Heinen 1972). In relation to this work, the principles of the theory are applied in the linking of decision criteria for a specific ECI variant.

3 EARLY CONTRACTOR INVOLVEMENT

3.1 *History and definition*

Early Contractor Involvement emerged in the 1990s in connection with project alliances. The term Early Contractor Involvement has a slightly different meaning in each country. In the simplest way ECI describes the involvement of construction companies in the early planning phases of a project. In Australia, the focus is in collaboration between client, planners and contractors is on the early project phases. As the project progresses, relationships evolve towards more conventional and traditional models. Whereas in the United Kingdom (UK), the collaborative nature of the relationship is maintained throughout project delivery (Buchal 2014). In both nations, ECI is regularly a two-stage process. Furthermore, ECI can be an element of another project delivery method or established as a stand-alone project delivery model. The term Early Contractor Involvement covers all variants of the involvement of construction companies in the project initiation phase, for example in an advisory capacity, as well as the examination of a complete planning by a construction company right before the execution phase with subsequent execution (Malvik et al. 2021).

Mostly, however, ECI is understood as a two-stage or there-stage procedure. It may start after the building permit has been granted with a minimum planning stage. In the first stage, a construction company is selected according to criteria set by the client. A price for the construction work to be carried out is not requested at this point, but surcharges for general business costs and profit can be used as decision criteria. Likewise, calculation examples, implementation concepts or partnering concepts can be requested and evaluated by the client. After the selection of the construction company, the planning takes place in the second phase. This can be done together with the construction company or by the latter. In the planning phase, the price for the construction work is determined jointly. It is worth noting that the business relationship does not necessarily have to be continued after joint planning. Some literature points out the actual construction as the third a third phase (Becker and Roman-Müller 2022). However, depending on the contractual agreements made at the beginning, the client can also decide against a follow-up order or to end the cooperation (Riemann 2014; Karasek 2021). The term early contractor involvement is hardly used in Germany. It only appears regularly in connection with or as part of innovative project management models such as IPA (Becker and Roman-Müller 2022). The terms “use of contractor know-how” and “inclusion of execution competence in the planning phase”, which are used in partnership models, among others, are also understood to mean the inclusion of contractors in the planning phase in order to make their knowledge available to the client (Girmscheid 2005; Eschenbruch 2008).

Another definition of ECI was provided in 2022 by the Working Group 194 of the World Association for Waterborne Transport Infrastructure. In its guideline the ECI is described as a strategy that differs from project to project, from client to client, from project framework conditions, budget or time horizon, etc. The ECI is thus the project-specific strategy for the waterborne transport infrastructure. The ECI is thus the project-specific strategy for the meaningful involvement of executing companies in an early project phase. The timing, the depth of involvement and the scope of cooperation vary from project to project. The key points of the ECI strategy also form the framework for the design of the applied ECI model (PIANC 2022).

3.2 *Advantages of ECI*

The use of ECI has the potential to generate numerous advantages in and for project management. However, the application of ECI alone does not automatically lead to project success. The advantages and benefits of ECI must be actively worked out. They depend on the commitment of the project participants, their capacities, their organisational structures and, last but not least, their will to achieve the set goals (Wondimu et al. 2016). The mutual benefit and the associated intrinsic motivation to participate in the Early Contractor Involvement can only be generated if the project participants are involved in the project at the right time and are compensated for the provision of know-how [28, 30]. The following aspects, among others, can be positively promoted through the application of early contractor involvement (PIANC 2022):

- Mutual project understanding
- Reduction of complexity
- Reduction of disputes and supplementary management
- Promotion of cooperation and trust between all parties involved
- Reliable information on costs and execution times
- Fair execution within budget
- Use of innovative and sustainable production methods
- Initiation of a risk management system accepted and supported by all parties involved:
  - Mitigate risks
  - Risk sharing instead of risk allocation by the AG
  - Cost transparency

4 METHODOLOGY

Regarding “Early Contractor Involvement” a systematic literature review was conducted to identify the variations as well as the characteristics of these variations. In particular, a search was conducted for studies on Early Contractor Involvement.

Several research strings were established to search for literature in the search engines Scopus, SpringerLink and GoogleScholar The same search strings were also used on the platforms ResearchGate and Academia.eu. The number of hits was reduced by restricting the search parameters to the field of civil engineering. The actual relevant literature was identified by reviewing the abstracts. By evaluating these collected publications, it was possible to add further thematically relevant literature.

In the course of the literature evaluation, the types and variations of ECI were collected by the analysis of pre-existing studies on ECI. The variations of ECI are subdivided according to when they are implemented in the project. Additionally, the factors and criteria that favour the successful implementation of Early Contractor Involvement are identified. First, these factors are matched with the project properties and then, examined for their feasibility for public clients as they build the base of the selection tool. Based on the results a decision logic is developed and implemented in a new tool. This tool is an software application.

5 FINDINGS

5.1 *Early contractor involvement variations*

(Wondimu et al. 2020) already gives a great overview of the variants by listing 25 different kinds of Early contractor involvement. Within the framework of the systematic literature analysis 15 additional approaches were identified. All together 36 different variants of the early integration of execution competence into a construction project were identified. After identifying that many variants further active research for new forms was stopped.

The variants occur with varying frequency, some were only applied once in practice, others were mentioned several times in the literature. Due to the high implementation effort and the small number of practical implementations as well as the lack of experience reports, the frequency of mention cannot be used for categorisation. However, all identified variants can be differentiated according to time, type, scope and influence of the price on the selection of the contractor. Anyhow, the following list is far from complete as there are still emerging new forms or pre-existing variants under a new name every now end then.

1. Alliance competitive
2. Alliance pure
3. Allowing variant solutions by the bidders during tendering phase
4. Announcing with alternative technical solutions
5. “Bauteam”
6. Construction Management
7. CMR
8. Competitive dialog (CD) procedure
9. Consolation
10. Contractors promote their ideas to the owner in the early phase
11. Cost Led Procurement
12. Design-build contract
13. Design-bid-build contract (DBB)
14. direct contract with front-end phase of projects
15. Framework
16. Front-end partnering process
17. Idea competition
18. Indirect approaches
19. Information meetings
20. Integrated Project Insurance
21. IPD
22. Multiple (dual) TCC/CLP
23. Negotiated procedure
24. Novated design and construction contract
25. Optimization phase after the award
26. Partnering
27. PPP (many sub variations)
28. Public announcment
29. Relational project delivery agreements (RPDAs)
30. Selection based on qualifications and price
31. Selection based on only qualifications
32. Single TCC
33. Supply Chain Collaboration
34. Two-stage TCC/ a tow-stage tender process/ two-stage open book
35. Vladres Model
36. Workshops (with the contractors after design phase but bevor plan approval process starts)

Depending on the ECI model used, an appropriate reimbursement system must be selected for the construction but especially in the case that know-how-transfer from contractor to client takes place. Cost-Plus -Incentive-Fee (CPIF), Cost-Plus-Award-Fee (CPAF), Cost-Plus-Fixed-Fee (CPFF) are suitable reimbursement systems for a joint planning phase. Fixed-Price Prospective Price Redetermination, CPIF, CPAF and CPFF represent a suitable remuneration system for a construction project following early contractor involvement (Becker and Friedinger 2023).

5.2 *Levels of ECI*

Figure 1 illustrates the depth of involvement and the influence of price by distinguishing four levels. Level 1 has the least depth and the smallest scope of cooperation. A construction company is involved in the project planning in an advisory capacity. The public announcement of a major project or participation in the tender process by answering bidders’ questions also fall into this category. Price is the main criterion for selecting the contractor in Level 1 (Friedinger and Becker 2023). Level 2 includes models in which selected companies are invited to bid and there is an intensive exchange between the client and the bidder. At this stage, the contractor may already be involved in the design. A functional tender would be assigned to level 2. Level 3 includes those types of ECI where the contractor is selected

in a two-stage procedure and the design is carried out jointly. At level 4, in addition to the execution. In Level 4, the expertise of other key companies in the supply chain is used in addition to the execution expertise of the construction company. From Level 1 to Level 4, the importance of the construction price in the selection of project partners decreases, while at the same time the risk mitigation increases from Level 1 to Level 4.

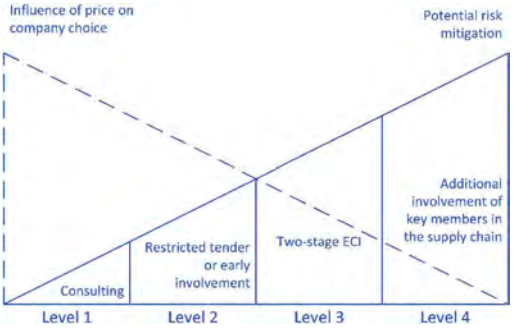

Figure 1. Level of Involvement based on (PIANC 2022).

5.3 *German procurement law*

The volume of construction work for which an ECI makes sense is generally above the threshold for a threshold value for a Europe-wide invitation to tender. In this paper, it is assumed that a Europe-wide invitation to tender is also required for the tendering of an ECI. In accordance with § 119 (1) No. 3-7 of the German Act against Restraints of Competition (GWB) five types of procedure are available: the open procedure, the restricted procedure, the negotiation procedure, the competitive dialogue and the innovation partnership. The rules are specified in the VgV and the VOB/A (Breyer et al. 2020).

If an ECI is to be carried out, it must be taken into account when choosing the award procedure that price must not be the sole decision-making criterion. A procedure must be chosen that allows a decision on the basis of other criteria. Therefore, only the competitive dialogue and the negotiated procedure can be considered for an award in the sense of the ECI.

5.4 *Variants for German public owners*

The 35 identified models were analysed in regards to their usability for Germany Public clients. An important aspect is the. The most important aspect is the compatibility of the variants with German public procurement law.

Apart from a public announcement of a major project, which only aims at arousing the interest of construction companies in a subsequent call for tenders, there is currently no possibility for public contracting authorities to involve construction companies at level 1 in the planning. Level 2 includes types of project management and tendering such as functional tendering. This is of course available to public clients, but by applying these models, their influence on the planning is lost. Although the execution competence is brought in at an early stage of planning, it is not in the way it is thought of in the common understanding of ECI. The “restricted invitation to tender” of Level 2 can be added to a “competitive tendering procedure followed by a restricted procedure” if the bidders’ proposals for optimisation become part of the invitation to tender. However, an ECI in the true sense is not achieved in this way. Only an implementation of your Level 3 model represents an ECI in the true sense. This is mapped within the framework of innovative project management models such as IPA. These innovative models are currently being tested and evaluated in pilot projects. To include the know-how of key companies of the supply chain in the planning in addition to the execution competence, as described in level 4 of the ECI, is too capacity-binding and complex for public clients at the present time. These ECI variants are used e.g. by private clients in the construction of oil rigs (Laryea and Watermeyer 2016; Wondimu et al. 2018; Wondimu et al. 2020; PIANC 2022).

In principle, several ECI variations are compliant with public procurement law and can be implemented. However, their use requires very good knowledge of public procurement law. Additional some variations are rather easy to implement and only turn out to be a form of ECI on closer inspection like the public announcement, like the public announcement.

5.5 *Success factors and criteria*

Early Contractor Involvement is not suitable for every project and every client. In 2016 Wondimu identified six factors (Wondimu et al. 2016):

1. The right timing is crucial, contractors need to be involved early enough. 2.
2. The risk transfer to the contractors must be kept at an manageable level.
3. The contractor must be adequately remunerated for the contribution of his execution competence. This is the only way to create an incentive to transfer know-how to the client.
4. Mutual trust, akin to partnering models,
5. The contractor must have the technical qualification to carry out or evaluate the planning
6. The client must have sufficient competence and capacity.

Furthermore, a consensus on fair risk sharing must be fundamentally anchored. Accordingly, an effective, efficient and sustainable risk management, which is developed in the ECI and continued during construction, is essential. The project must also have a certain

complexity and investment volume to justify the increased effort in the planning phase (Rahman and Alhassan 2012; Nibbelink et al. 2017; Narum et al. 2022; PIANC 2022; Rahmani et al. 2022).

6 CONTRACTOR INVOLVEMENT TOOL (CIT)

6.1 *Purpose and benefit*

The tool provides support for public clients in choosing the adequate form of early contractor involvement for their specific project. It also provides help and additional information for every step to be taken and guides a public client through the complete procurement process.

6.2 *Software application*

In software development one can choose between either a desktop or a web application. For this research a desktop application was chosen. Implementing a standalone application has the following advantages (Sander 2012):

- It is executed directly by the operating system (without a browser as a "man in the middle");
- This allows greater complexity with good performance.
- Concentration on a single platform (Windows) that can be used by all users. users. This is especially true for testing, which does not need to be performed on multiple browsers and operating
- operating systems, which would be very time consuming.
- Possible use of the specific functionality of the operating system and direct cooperation with software packages
- Cooperation with software packages (OFFICE) that run on this system.
- Better availability of GUI elements that can be used to increase usability.
- Connection to a central database is still possible

6.3 *Programming language .NET*

The .NET Framework is an evolution of the Win32 API, which provides access to all the functions of the of the WINDOWS operating system. NET applications access

NET Framework class libraries (file management, graphics output, data processing, etc.). Plus, all of Microsoft's popular programming languages (C#, Visual Basic, C++ and F#) can access the .NET Framework (ibid.). To generate an language-independent code the Common Language Specification (CLS) is used. In this code different languages have equal rights and deliver the same result. Being an open standard the CLS enables the porting of other languages to .NET (Kofler and Nebelo 2008) as shown in Figure 2.

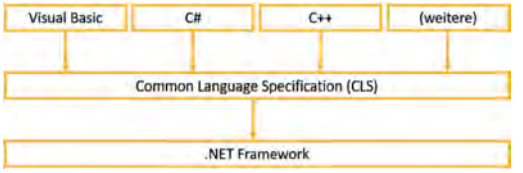

Figure 2. Independent CLS (Kofler 2008).

Additionally .NET applications run independently on Windows systems (Sander 2012), which is a major advantage in usability.

6.2 *CIT in DigiCon*

DigiCon is a software platform developed as part of the "Digital Performance Contracting Center" research project at the University of the Bundeswehr Munich, see Figure 3. The software is still under development. Its aim is to digitally model the mechanisms and processes in public procurement developed in the research project. The Contractor Involvement Tool (CIT) uses the DigiCon platform as a base to model and depict the whole involvement process.

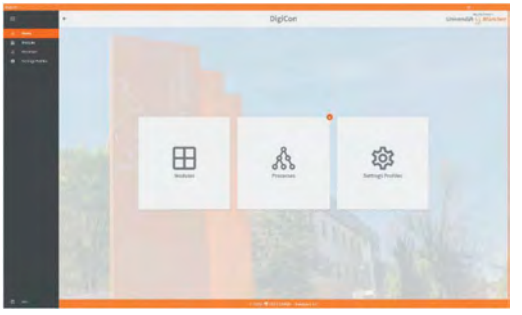

Figure 3. Image of DigCon platform.

DigiCon enables the use to create modules and connect them in a process as they see fit. It also gives the opportunity to choose the logic when combining different modules, shown in Figure 4.

Figure 4. Module creation in DigiCon.

Regarding this research DigiCon as a platform and CIT in particular models a project enquiry in the first place. The enquiry compares the project specifications and properties with the success factors of ECI. Of particular importance are risk management, the client's own expertise and its own capacities. Depending on the result, CIT proposes several suitable ECI variants to the user. The application process is also shown for each variant and additional detailed information can be called up for each individual process step.

The user is responsible for the final selection of the variant, as CIT is not a management tool but a support tool for project management.

7 SUMMARY AND OUTLOOK

The ECI is only suitable for handling large and complex projects, as it entails considerable additional work in the tendering and planning phases. In addition, the client must provide sufficient competence and resources of his own and sufficiently reward the contribution of the execution competence in order to be able to carry out a project successfully with the ECI. Apart from the simple and straightforward variants, which can only be assigned to the ECI on very close examination, the legal regulations in Germany only allow two award procedures for the implementation of an ECI. Nevertheless, it can be stated that the early involvement of construction companies in the planning phase is possible in principle. The next steps are to finish de development of the DigiCon software-platform.

The selection processes must then be precisely defined and modelled in CIT. As soon as CIT is ready for use, it must be tested in practice by public clients. This will hopefully lead to more ECI projects in Germany, which will generate more data on ECI for public owners. However at this point there is more research required regarding the joint planning in ECI as CIT just shows the way to the joint planning. With regard to the transparent settlement with open-book, the joint calculation, the structure of the joint risk management and the risk allocation during the ECI should be examined and described in detail.

ACKNOWLEDGMENTS

This research paper on the project DigiPeC is funded by dtec.bw – Digitalization and Technology Research Center of the Bundeswehr. dtec.bw is funded by the European Union – NextGenerationEU.

REFERENCES

Bandte H, 2007. Komplexität in Organisationen. Organisationstheoretische Betrachtungen und agentenbasierte Simulation. Zugl.: Braunschweig, Techn. Univ., Diss., 2006 u.d.T.: Bandte, Henning: Organisationen und Komplexität: organisationstheoretische Betrachtungen zur angemessenen Handhabung von Komplexität in Organisationen unter Berücksichtigung agentenbasierter Simulation (1. Aufl.). Dt. Univ.-Verl., Wiesbaden, 373 p.

Becker SC, Friedinger CP, 2022. Application of Alternative Contracting Methods for Large Infrastructure Projects as example Project Alliancing. In: (ICPMA) (ed.). Sustainable Mobility Infrastructure (Porto, 2022), 23.05.2022-24.05.2022.

Becker SC, Friedinger CP, 2023. Analyse potenzieller Vergütungsmodelle und Anreizsysteme für die Integrierte Projektabwicklung (IPA), unpublished.

Becker SC, Roman-Müller H, 2022. Integrierte Projektabwicklung (IPA). Schnelleinstieg für Bauherren, Architekten und Ingenieure. Springer Vieweg, Wiesbaden, 61 p.

Bourn J, 2007. Estimating and Monitoring the Costs of Building Roads in England. NAO Information Centre, London.

Breyer W, Boldt A, Haghsheno S, 2020. Alternative m Einheitspreisvertrag für die Vergabe von Bauleistungen durch die öffentliche Hand. Forschungsprogramm: Zukunft Bau, ein Forschungsprogramm des Bundesministeriums desInneren, für Bau und Heimat.

Buchal T, 2014. Early Contractor Involvement (ECI) and its Implementation, unpublished. Technische Universität Prag, Prag.

CURT (Construction Users Roundtable) (ed.), 2004. Collaboration, integrated information and the project lifecycle in building design, construction and operation, Cincinnati, OH.

Eadie R, Graham M, 2014. Analysing the advantages of early contractor involvement. International Journal of Procurement Management, 7 (6), 661.

Eschenbruch K (ed.), 2008. Partnering in der Bau- und Immobilienwirtschaft. Projektmanagement- und Vertragsstandards in Deutschland. Kohlhammer, Stuttgart, 335 p.

Faber S, 2014. Entwicklung eines Partnering-Modells für Infrastrukturprojekte. Ein Beitrag zur Optimierung der Abwicklung von Bauprojekten im öffentlich finanzierten Infrastruktursektor in Deutschland. Zugl.: Kassel, Univ., Diss., 2013. Kassel Univ. Press, Kassel, 241 p.

Friedinger CP, Becker SC, 2023. Early Contractor Involvement für öffentliche Auftraggeber – Chancen für eine effizientere Projektabwicklung, unpublished.

Friedinger CP, Mitteregger K, Sander P, 2023a. Probabilistic Analysis of the Delivery Models Unit Price and Alliance applied at the Project Gemeinschaftskraftwerk Inn with Focus on the Construction Time. In: Schubert W, Kluckner A (eds.). Proceedings of the ISRM 15th International Congress on Rock Mechanics and Rock Engineering & 72nd Geomechanics Colloquium. Challenges in Rock Mechanics and Rock Engineering, October 9-14, 2023, p. 202–207.

Friedinger CP, Sander P, Becker SC, Villinger T, 2023b. Analyse und Gegenüberstellung der Vortriebsdauern von Einheitspreisvertrag und Allianzvertrag beim Druckwasserstollen des Projektes Gemeinschaftskraftwerk Inn. Forschungsbericht, Neubiberg.

Girmscheid G, 2005. Partnerschaften und Kooperation in der Bauwirtschaft. Chance oder Irrweg? Der Bauingenieur, 80, 103–113.

Haghsheno S, 2020. Integrierte Projektabwicklung in Mehrparteienverträgen. Tagung „Bauen statt Streiten", Würzburg.

Heinen E, 1972. Industriebetreibslehre als Entscheidungslehre. Erster Teil. In: Heinen E (ed.). Industriebetriebslehre.

Entscheidungen im Industriebetrieb. (Zweite, durchgesehene Auflage). Gabler Verlag, Wiesbaden, p. 25–75.

Karasek G, 2021. Bauvertrag: Klassisches Modell oder…? In: Agile Digitalisierung im Baubetrieb. Springer Vieweg, Wiesbaden, p. 511–525.

Kinlan D, Willems K, 2023. Applying early contractor involvement in marine infrastructure procurement. TERRA ET AQUA, 169, 6–17. Accessed on 12.06.2023, https://www.iadc-dredging.com/wp-content/uploads/2023/03/terra-et-aqua-169-complete-spread.pdf

Kofler M, 2008. Visual Basic 2008 (1. Aufl.). Addison-Wesley, München, 1344 p.

Kofler M, Nebelo R, 2008. Excel 2007 programmieren. Anwendungen entwickeln und Abläufe automatisieren mit VBA; [sofort einsetzbares Add-in zur Nachbildung der klassischen Menüleiste (7. Aufl.). Addison Wesley in Pearson Education Deutschland, München, 921 p.

Laryea S, Watermeyer R, 2016. Early contractor involvement in framework contracts. Proceedings of the Institution of Civil Engineers - Management, Procurement and Law, 169 (1), 4–16.

Leitfaden Großprojekte, 2018, unpublished, Berlin, 134 p.

Malvik TO, Wondimu P, Kalsaas BT, Johansen A, 2021. Various Approaches to Early Contractor Involvement in Relational Contracts. Procedia Computer Science, 181, 1162–1170.

Mosey D, 2009. Early contractor involvement in building procurement. Contracts, partnering and project management. Ames Iowa, Chichester, West Sussex, 316 p.

Narum KB, Engebø A, Lædre O, Torp O, 2022. Collaborative Project Delivery With Early Contractor Involvement and Target Cost. In: Proc. 30th Annual Conference of the International Group for Lean Construction (IGLC), 27. 07.2022-29.07.2022. International Group for Lean Construction, p. 984–995.

Nibbelink J-G, Sutrisna M, Zaman AU, 2017. Unlocking the potential of early contractor involvement in reducing design risks in commercial building refurbishment projects – a Western Australian perspective. Architectural Engineering and Design Management, 13 (6), 439–456.

Nister O, 2005. Die baubetrieblichen und bauökonomischen Aspekte des Vertragswesens der Projektentwicklung aus der Sicht „Unvollständiger Verträge“. Zugl.: Dortmund, Univ., Diss., 2005, Dortmund.

Partnering bei Bauprojekten - Langfassung, 2005, unpublished.

PIANC, 2022. A framework for a early contractor involvement in infrastructure projects. General Secretariat of PIANC, Brussels, 183 p.

Picot A, Dietl H, Franck E, 1998. Organisation. Eine ökonomische Perspektive (1. Nachdr). Schäffer-Poeschel, Stuttgart, 368 p.

Rahman M, Alhassan A, 2012. A contractor's perception on early contractor involvement. Built Environment Project and Asset Management, 2 (2), 217–233.

Rahmani F, Khalfan M, Maqsood T, 2022. A Conceptual Model for Selecting Early Contractor Involvement (ECI) for a Project. Buildings, 12 (6), 786.

Reformkommission Bau von Großprojekten Endbericht. Komplexität beherrschen - kostengerecht, termintreu und effizient, 2015, unpublished, Berlin, 112 p.

Riemann S, 2014. Ansätze zur Nutzung des Unternehmer-Know-hows bei öffentlich finanzierten Infrastrukturprojekten in Deutschland mit besonderem Fokus auf der Planungsphase. Zugl.: Kassel, Univ., Diss., 2014. Univ. Press, Kassel, 300 p.

Sander P, 2012. Probabilistische Risiko-Analyse für Bauprojekte. Entwicklung eines branchenorientierten softwaregestützten Risiko-Analyse-Systems. Zugl.: Insbruck, Univ., Diss., 2012 (1. Aufl.). innsbruck univ. press, Innsbruck, 207 p.

Sander P, Becker SC, Friedinger CP, Riemann S, Ditandy M, Spiegl M, 2022. Risikomanagement bei Großprojekten im Tunnelbau. Teil 3: Gestaltung von Anreizmechanismen für die Integrierte Projektabwicklung. tunnel, 2022 (04), 12–23. Accessed on 03.01.2022, https://www.tunnel-online.info/de/artikel/tunnel_Gestaltung_von_Anreizmechanismen_fuer_die_Integrierte_Projektabwicklung_3816274.html

Smart Construction, 2023. Realisierung – Smart Construction, 13.06.2023. Accessed on 13.06.2023.

Walker DH, Lloyd-Walker B, 2012. Understanding early contractor involvement (ECI) Understanding early contractor involvement (ECI)procurement forms. In: Smith SD (ed.). Proceedings 28th Annual ARCOM Conference. 3–5 September 2012, Edinburgh, UK. Association of Researchers in Construction Management, UK, p. 877–887.

Wondimu PA, Hailemichael E, Hosseini A, Lohne J, Torp O, Lædre O, 2016. Success Factors for Early Contractor Involvement (ECI) in Public Infrastructure Projects. Energy Procedia, 96, 845–854.

Wondimu PA, Hosseini A, Lohne J, Laedre O, 2018. Early contractor involvement approaches in public project procurement. Journal of Public Procurement, 18 (4), 355–378.

Wondimu PA, Klakegg OJ, Lædre O, 2020. Early contractor involvement (ECI): ways to do it in public projects. Journal of Public Procurement, 20 (1), 62–87.

Tunnelling for a Better Life – Yan, Celestino, Thewes & Eberhardt (Eds)
© 2024 The Author(s), ISBN 978-1-032-80042-4
Open Access: www.taylorfrancis.com, CC BY-NC-ND 4.0 license

Pawtucket CSO tunnel design build - From managing risk and quality to design and construction innovations

Irwan Halim*
AECOM, Chelmsford, Massachusetts, USA

Stephane Polycarpe
CBNA, Pawtucket, Rhode Island, USA

Vojtech E Gall
Gall Zeidler Consultants, New York, New York, USA

ABSTRACT: The Narragansett Bay Commission (NBC) operates Rhode Island (RI)'s two largest wastewater treatment facilities in the United States of America (USA). In 1992, NBC began a three-phase combined sewer overflow (CSO) program to reduce discharges of CSOs to Narragansett Bay. Phase I and II included a 5,030-meter long, 7.9-meter Inside Diameter (ID) rock tunnel, drop shafts, and pump station in Providence, RI. Phase III includes construction of the 3,535-meter long, 9.1-meter ID, deep rock Pawtucket Tunnel. This paper provides an overview of the Pawtucket Tunnel Design Build Project managing design, quality, and risk from base technical concept through final design into construction; highlighting transition of responsibilities amongst the teams engaged. Some lessons learned from the previous phase affecting the current Phase III Project requirements are discussed. This paper further describes some of the implemented design innovations for the large diameter shaft support, precast segmental tunnel lining including at the tunnel adit openings, and design of the liner pipe for the deep vertical drop and vent shafts. Important design considerations and a couple of critical Alternative Technical Concept (ATCs) during the tender impacting the final project design are presented. Finally, the paper concludes with some of the project construction innovations including the elaborate TBM start-up methodology, installations of the deep vertical shaft liner, and microtunneling for the longest adit using Fiberglass Reinforced Polymer Mortar (FRPM) pipes.

Keywords: Tunnelling, Design-Build, TBM, SEM, Risk allocation

1 PROJECT BACKGROUND

The Narragansett Bay Commission (NBC) embarked on a three-phase CSO control program in 1998, aimed at lowering annual CSO volumes and reducing annual shellfish bed closures in accordance with a 1992 Consent Agreement (CA) with the Rhode Island Department of Environmental Management (RIDEM). Phases I and II of the Program, which focused on the Field Point Service Area in Providence, were completed in 2008 and 2015, respectively. The program succeeded in lowering annual CSO volumes and reducing annual shellfish bed closures to levels that are in keeping with a 1992 CA between NBC and RIDEM.

The third and final phase (i.e., Phase III) is focused primarily within the communities of Pawtucket and Central Falls. The implementation strategy prioritizes water quality benefits, while also limiting the financial impact on rate payers. The primary elements include the Pawtucket Tunnel and ancillary underground components including a launching shaft, receiving shaft, drop/vent shafts, adit tunnels, and tunnel pump station. The tunnel system provides volume to store all contributing overflows during a storm event up to the three-month storm for subsequent pump out and treatment. The required minimum storage volume to achieve the defined hydraulic criteria (i.e., no overflows for the three-month design storm, and no more than four overflows per year per outfall for typical year storms) is 221.4 million litres (ML).

The Pawtucket Tunnel is a rock tunnel, 35-m to 47-m below the ground surface, located adjacent to

*Corresponding author: irwan.halim@aecom.com

DOI: 10.1201/9781003495505-478

the Seekonk and Blackstone Rivers in Pawtucket, RI. The tunnel is approximately 3,535-m in length with a 9.1-m inside diameter (see Figure 1). The tunnel is mined with a Herrenknecht dual mode (open/EPB) TBM. The machine is fitted with a hard rock cutterhead and a conveyor to extract muck from the face when it is operated in open mode or a screw conveyor when operated in earth pressure balance (EPB) mode. The lining is made of universal double taper rings of seven fibre reinforced segments, thickness 0.36-meter and 2.0-meter in length. Each segment joint both radial and circumferential is fully gasketed to achieve the water tightness criteria.

Figure 1. Pawtucket tunnel alignment.

The geologic history of the bedrock is complex. The rock originates from fluvial deposits, which characteristically are not laterally continuous. Rock types range from conglomerate to coal with sandstone and siltstone as the predominant rock types. Sequential episodes of tectonic deformation have superimposed structural features including folds, faults, and joints. The Pawtucket Tunnel is constructed mainly in the Rhode Island Formation, a Carboniferous-age sedimentary rock comprised of sandstone and siltstone, with lesser amounts of conglomerate, shale, and coaly deposits. Bedrock is moderately folded and faulted. Bedrock is overlain by a thin layer of glacial till and thick layers of glaciofluvial deposits. Glacial deposits are comprised mainly of sand, gravel, and silt, and are overlain by granular fill.

2 PROJECT DELIVERY

Phases I and II were delivered using the traditional design-bid-build method of project delivery. For the Pawtucket Tunnel Project, NBC selected fixed-price design-build to reallocate inherent risks resulting from the design process, and also to leverage its other benefits to mitigate additional risks:

1. Speed of Delivery – NBC must complete the Pawtucket Tunnel and facilities of the CSO Program in accordance with a consent decree with a regulatory agency. The consent decree includes a milestone date by when the facilities of Phase III must be operational. Design-build allows the procurement of a design-builder prior to final design of the project. It also allows construction to be "fast-tracked" by prioritizing the design of the initial elements of the project such as construction of shafts and starting construction of those elements prior to finishing the design of all elements of the project.
2. Single Point of Accountability – NBC wished to minimize the amount of contractor's change requests resulting from omissions, unclarity, and gaps in interdisciplinary coordination of the design documents. Contractor's requests for change based on omissions, unclarity or gaps in coordination in the owner-provided design results in the expenditure of considerable amounts of owner's time and resources to manage and resolve such requests. Use of design-build relieves the owner of a great deal of involvement in the design change management process.
3. Contractor Involvement in Design Process - Preferences for means and methods of underground construction can vary between contractors. The owner can reduce risk of duplicated design efforts by the contractor related to preferred construction methods by allowing the design-builder to determine the best design to accommodate its means and methods.
4. Price Certainty – As with all capital projects, NBC strongly desired to limit costs for the Pawtucket Tunnel Project to within the contract amount and its contingency. With the exception of differing site conditions, the use of design-build mitigates the risk of cost increases resulting from changes to an owner-provided design.

Although design-build cannot eliminate project risks, it can facilitate the allocation of risk to the party best suited to manage the risk. The assumption of additional risks by the design-builder is likely incorporated in the design-builder's lump-sum price in the form of a contingency.

3 PROJECT CRITERIA

The Base Technical Concept (BTC) design included preliminary design drawings, Geological Baseline Report (GBR), Geotechnical Data Report (GDR), and Environmental Data Report (EDR). The Design Builder (DB) was responsible to developing final design documents for project elements to comply with project criteria for each of the project elements. The

project elements included bored tunnel, large diameter shafts, suction header, drill and blast adit tunnel, and drop/vent shafts. The design was completed in January 2022 to comply with dates in the CA.

The primary functionality of the tunnel is to provide storage of combined sewage during wet weather events to control CSOs. The project criteria require the tunnel provide a storage capacity of 221.4 ML to store CSO generated during the 3-month design flow. The hydraulic criteria are prescriptive specifying vortex style drop shafts with hydraulic capacity to convey peak flows from the 2-year storm.

Durability criteria requires precast concrete segmental lining, internal components, permanent bolts, and associated inserts to be designed for a minimum of 100-year service life. Design and durability analysis considers pH level, chloride content, sulphates and other contaminants in soil, rock, ground water, and future wastewater. Analysis and testing confirmed exposure conditions for service life modelling.

Other key project criteria for the Pawtucket Tunnel included the following:

- Diameter 9.1-m ID
- Slope 0.001 m/m
- Minimum rock cover of two tunnel diameters.

Maximum allowable groundwater infiltration 3.8 litre per minute (lpm) per 305 m of tunnel and 0.38 lpm at any one segment.

4 PROJECT RISKS MANAGEMENT

NBC identified the top five (5) risks to be worker and public safety; TBM mechanical failure; damage to third party building, structures, or utilities due to ground movement during excavation; delay in production or delivery impacting project schedule and milestone completion, and differing site conditions. The procurement commenced in December 2019 prior to risks/issues associated with COVID, supply chain delays, and macroeconomic inflationary pressures. The risks associated with bored tunnel focused on ground conditions, which were baselined in the GBR for Bidding (or GBR-B): methane, water inflow, low strength rock, and potential fault at northern alignment. The GBR-B identified construction considerations attributed to how predominant types of ground are expected to behave in response to construction.

Pawtucket area coal has the capacity to retain high amounts of methane, but geologic history combined with mining and drilling experience indicates that the actual methane content of coal is low. Methane can be adsorbed on organic surfaces of coal and is released by a reduction in hydrostatic pressure. The potential exists for discharge of methane from carbonaceous rock, so excavations in rock were classified as “potentially gassy.”

Rock mass quality generally improves from south to north. For an excavated diameter of 10.2-m, potential collapse in the crown is indicated for some of the alignment in poor rock if not supported properly. To mitigate the risk of roof fallout, the project criteria require tunnel excavation with a shielded TBM and concurrent installation of a permanent lining of gasketed precast concrete segments. The single-pass lining approach minimizes groundwater discharge volumes. This approach mitigates problems associated with localized deposits of weak mudstones and coal, such as loss of bearing on gripper pads, and a soft invert.

A potential fault crosses the tunnel alignment under the river at the northern end of the alignment as was inferred from the change of lithologies from the Rhode Island Formation to the Wamsutta Formation. The GBR-B baselined the fault zone conditions for a total width of 37.5-m. To mitigate the risk of excessive inflows while tunnelling under the river, it is expected that probing and grouting ahead would be needed. The baseline conditions were conservative based on the inability to locate the contact between the two formations during the preliminary geotechnical investigation.

Groundwater inflow was an identified risk due to flow rates encountered during construction of the Phase I Providence tunnel. A secondary risk was impact to NBC wastewater treatment facility from elevated loadings of total suspended solids, pH, and impact to sludge production. Efforts to reduce tunnel dewatering flows became important for both points. The GBR-B baselined the main tunnel drive to cross one or more shear zones. Such locations of high fracture density would produce high inflow rates over a short distance of up to 30.5-m. The baseline for localized heavy inflows is set at a sustained inflow rate of up to 492 lpm per 30.5-m of tunnel, to occur at one interval at an unidentified location. It also baselined the tunnel drive to cross a fault zone under the river. As a baseline, sustained inflows of up to 1,514 lpm per 30.5-m of tunnel may occur within the fault zone. The fracture network related to the fault zone is expected to be directly connected to the river.

The process for modification of the GBR-B to the GBR-C was provided through the Tunnel Design-Build Agreement and was proven to be quite effective. In addition to the GBR, the procurement process also established procedures for Alternative Technical Concepts (ATCs) which are design concepts and/or construction methods that offer alternative approaches to completing the project according to the criteria provided in the RFP. This process was enabled through Proprietary Meetings between the Owner, the Program Manager, and the Design-Builder in an effort to allow the Design-Build team to provide innovation and propose alternatives that suit their preferred design and means and methods and reduce risks. The GBR-B produced for the procurement provided all Design-Build teams with the same set of physical baseline conditions to be used in their design and construction planning during their bid. The process

was set up to allow the selected Design-Build team to provide their interpretations of the various baselines expressed in the GBR-B in developing their design and construction approaches, identifying any gaps, and providing any supplemental information gained through additional geotechnical investigations performed by the Design-Build team. The Owner and the Design-Build team then negotiated revisions to the GBR-B to formulate the Geotechnical Baseline Report for Contracting (GBR-C). The GBR-C reflects the joint understanding of NBC and the selected Design-Build Team regarding the interpreted baselines that are consistent with their design approach, equipment and construction means and methods.

The Design-Builder conducted additional investigations from the surface to revise the baseline within the reach in the GBR for Construction (GBR-C). The Design-Builder successfully located the contact zone between the Rhode Island and Wamsutta formations but with no fault detected and no fractured water bearing features. In addition, a probe at the base of the receiving shaft was drilled in December 2022 with two horizontal probes confirming the contact zone: no apparent faulting along the contact between the two formations, two formations appear to be interfingered, and no significant groundwater inflows. The Design-Builder updated the GBR-C accordingly, identifying TBM operation through this zone to be in open mode.

The Design-Build Team developed a list of ATCs that were discussed at the initial proprietary meetings. The ATCs were proposed to reduce costs or risks to the project. During preliminary design, the vertical profile provided two diameters of sound rock cover over the crown in an area of low rock. The horizontal alignment and shaft locations accommodated property acquisition constraints and operational preferences. The Design-Builder submitted a critical alternative technical concept (ATC) to raise the tunnel elevation and reduce its depth by about 7.6 meter, thereby reducing the amount of rock cover which was approved by NBC. Another important ATC proposed was related to adverse ground conditions near the tunnel pump station (TPS) and launch shaft (LS) locations and was designed to reduce both project risk and costs. The proposed ATC was to relocate the launch shaft to the north along the tunnel alignment and shifting it to the east of the existing shaft. In addition, the TPS was to be moved closer to the launch shaft to be in line with the re-aligned tunnel and to shorten the suction header tunnel. This alternative would move these elements away from the highly fractured rock (potential fault zone) as observed in the Owner's geotechnical explorations.

5 TUNNEL LINING DESIGN

A seven-segment universal tapered ring system was adopted as shown in Figure 2. The tunnel lining ring is 0.36m-thick, 9.2m in internal diameter, and 2m in length, and consists of four (4) regular segments of rectangular geometry, two (2) counter-key segments of right trapezoidal geometry, and one (1) wedge-shaped key segment. All segments will be staggered to avoid creating cruciform joints which could cause leakage and structural distress due to stress concentration. As the key segment cannot always be installed at the tunnel crown, the TBM will need to be able to hold segments in place during ring assembly using an erector and support roller system. The length of the ring was selected by balancing between the constructability factors (ease of transportation, assembly, and ability to negotiate curves) and the utility factors (limiting joint number to reduce leakage and production cost and to increase tunnel advancement rate).

The wedge-shaped key block is often designed as a smaller size piece than other segments because smaller segments are easy to handle. Lately, a large key segment is becoming more accepted in the industry. Our design adopted similar-sized segments. It is advantageous to make all the segments as similar size as possible because of structural and constructability reasons. The longitudinal joints evenly spaced within the ring lead to increased load bearing capacity and reduce ring distortions. The larger key segment also can reduce the size of the regular segments (and therefore the number of longitudinal joints). The segments will not be bolted to each other at the longitudinal joints. This will help increase tunnel advancement rate because some bolting is eliminated. The rings will be connected to each other at the ring joints using fourteen (14) equally spaced dowels. In addition, fourteen (14) pairs of equally spaced shear connectors, i.e., shear bicones with a steel core were specified at the ring joints for centering and shear recovery purposes at the tunnel adit openings.

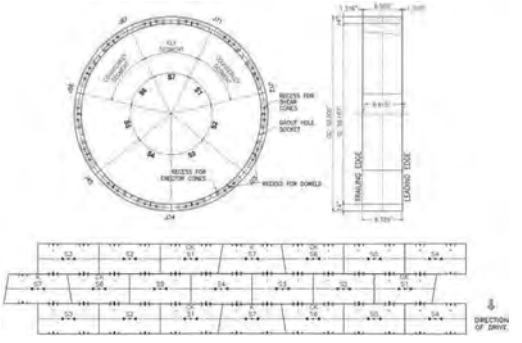

Figure 2. Tunnel lining geometry.

For waterproofing purposes, all-around ethylene propylene diene monomer (EPDM) compression gasket was used. The compression gasket is anticipated to resist maximum 500 kPa of hydrostatic pressure under the design compression and allowable offset scenario. The typical segments are reinforced by steel fibres. The segment thickness was selected to withstand all short-term and long-term loading cases and

service conditions. To achieve the desired 100-year service life, the selected segment thickness includes sacrificial concrete layer to protect the tunnel lining from concrete degradation due to hydrogen sulfide (H_2S) gas from the CSO water. The tunnel lining was designed where loss of the sacrificial layer does not impact the 100-year structural integrity of the lining system.

To demonstrate the adequacy of the adopted tunnel lining design, the stress and deformation of the tunnel lining were evaluated using two-dimensional (2-D) numerical analyses as shown in Figure 3. Total of five analysis sections were selected as representative of variations in overburden depths and anticipated ground and groundwater conditions. Among the five analysis sections, the section with the presence of intensely fractured soft and weak graphitic shale layer that traverse the tunnel alignment was found to govern the design. The graphitic shale layer is approximately 6-meter-thick sub-horizontal layer imbedded within bedrock. The raising of tunnel vertical alignment by 7.6 m resulted in reduction in lining thickness from 0.38 m to 0.36 m and the deletion of the hybrid reinforced (fibre and rebar) segments requirement for the graphitic shale zone.

The analysis was done in stages to evaluate the lining forces and the deformations under various loading conditions that are expected during the construction and throughout its design life. These include the variation of the anticipated groundwater levels, dewatering of groundwater during construction, and crossing of intensely fractured fault zone. The analysis showed that the tunnel lining will be able to withstand the anticipated loads and meet the ring distortion requirement for all these conditions. A seismic analysis was performed to evaluate the effects of seismic waves vertically propagating perpendicular to the tunnel axis. A transverse racking analysis was performed to quantify the racking deformations and their effects on the tunnel lining.

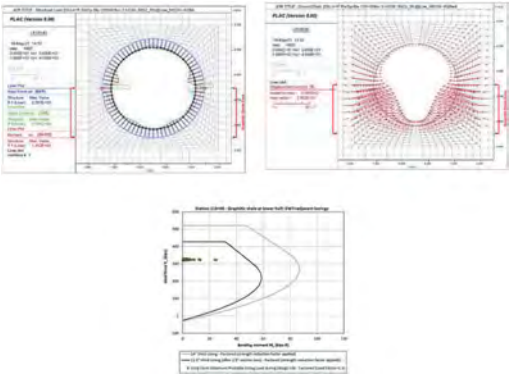

Figure 3. Tunnel lining design verifications.

The segment design was checked against the temporary construction loading scenarios including stripping and handling minimum concrete strength, storage and transportation, erection and TBM thrust rams pushing against the segments, during backfill and contact grouting, and for the TBM gantry load and segment feeder immediately behind the erector. The segment joint design consisted of checking the circumferential dowel system capacity to hold the segments together during erection and maintain gasket compression to adequately seal off the design hydrostatic pressure.

The Pawtucket tunnel is connected to four drop shafts by tunnel adits along its alignment, three of the adits are shown schematically in the above Figure 4. Two adits are planned to be constructed by sequential excavation methods (SEM) and the third will be constructed by microtunneling.

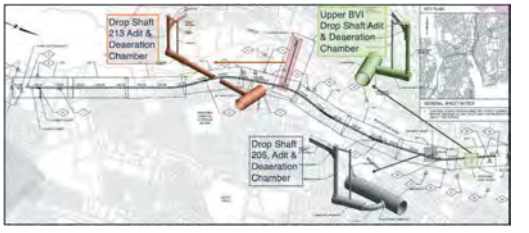

Figure 4. Adits connecting to the bored tunnel.

The SEM tunnel adits will be constructed from the main tunnel by drill and blast with mining outwards towards the base of the drop shaft structures. The third adit constructed by microtunneling will start from the drop shaft location and be jacked into the main tunnel. The final connection between the main tunnel lining and the adits will be achieved by installing a monolithic cast-in-place (CIP) concrete collar around the segment cuts.

At the adit locations in the tunnel, segments will be cut and removed. At these locations the tunnel requires additional bracing to support the temporary forces due to the tunnel wall opening at these locations. Rather than designing the usual external bracing frame at these locations, the opening will be temporarily supported by modified segment rings installed during tunnel construction these rings have additional reinforcement and shear elements included within the specially designed tunnel segments installed along the four rings immediately adjacent to the opening. While the standard lining design along the alignment is pure steel fiber reinforced concrete (SFRC) with two shear dowels installed at each thrust pad, the specially reinforced segments feature a heavy rebar cage in addition to the SFRC as well as 2 additional high-capacity shear cones per segment ring joint installed in the middle of the thrust pads between the shear dowels. The geometry of the specially reinforced segments is equivalent with that of the typical segments.

A staged Finite Element (FE) model was developed for the structural analysis of the lining and collar at the TBM tunnel-adit locations that

considers all the critical design issues, e.g., The in-situ ground pressures, the temporary and permanent ground water loads, the supporting action (or lack thereof) of friction between rings, and the durability of the lining concrete, and the nonlinearities of all the materials involved. An image of the model is shown in Figure 5 below.

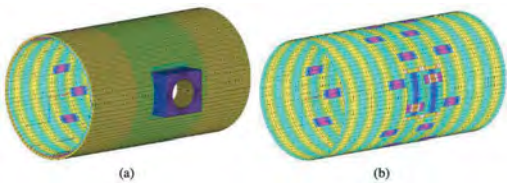

Figure 5. Model of adit connections: a) adit collar; b) isometric view of segmental lining ring.

The structural analysis indicates that, as expected, the most critical case for design is the temporary loading of the segments immediately following the cutting and removal of the lining and before installation of the CIP concrete collar. Specifically, the analysis indicates that the tensile stresses are too high to be carried by steel fibers alone and this resulted in the requirement for additional circumferential rebar reinforcement and shear cones in these special segments.

6 SHAFT DESIGN

Circular secant pile walls were selected as the method of temporary excavation support in soil for the three large diameter shafts, as this method is well suited for the rock depth at each shaft, and due to the need to establish groundwater cut-off. To achieve groundwater cut-off and support lateral soil pressures, secant piles were socketed into unweathered bedrock and designed to have sufficient overlap at depth to form a continuous circular shell, considering installation tolerances. Installation of the secant piles was followed by a pre-excavation grouting program to effectively seal the secant-rock interface. The secant wall design included no internal bracing, allowing for rapid shaft excavation upon completion of the grouting program. In addition, the design excludes the typical ring beam at the bottom of secant piles to save on the final shaft concrete lining thickness in overburden soils.

The analysis model for the temporary secant walls consisted of a circumferential structure of uniform thickness and diameter. Loads to be resisted by the secant walls during excavation included soil and groundwater pressures, as well as localized construction surcharge pressures near the surface. The loading conditions resulted in approximately uniform pressure around the secant wall circumference, increasing with depth. A closed-form solution analysis was used to establish initial dimensions and concrete strength, followed by 3D finite element analyses with soil structure interaction considering various construction surcharge cases. It was determined that an unreinforced circular secant wall of sufficient thickness to resist the pressures in circumferential compression was a feasible option, eliminating the need for steel core beams and internal bracing. Localized, near-surface bending moments resulting from non-uniform construction surcharge loads are resisted by a cast-in-place reinforce concrete ring beam at the top of the secant pile walls.

The project criteria documents recommended initial rock support in the form of grouted rock dowels and wire mesh reinforced shotcrete. Alternatives were considered during detailed design, including use of fibre reinforcement in lieu of wire mesh, and friction bolts in lieu of grouted dowels. After consideration of alternatives and based on the Design-Builder preference, final design was advanced consistent with the initial support system described in the project criteria documents. Initial rock support demand in the large diameter shafts was analysed using wedge analyses, informed by discontinuity data obtained from borehole televiewer logging, and strength parameters determined from laboratory testing conducted during the initial project subsurface investigation and the supplemental investigation. Additional procedural requirements were included in the design, such as line drilling and excavation by mechanical means only near the top of rock to reduce risk of undermining the secant pile SOE system or damaging the grouted cut-off zone. Below this critical zone, the remainder of each shaft was excavated by drill and blast methods.

Fibre Reinforced Polymer Mortar (FRPM) pipes are used for the final drop and vent shaft liners as shown on the Figure 6 below.

Figure 6. Drop pipe installation.

The important design factors for these pipe systems consisted of:

- Ring wall compression, pipe buckling resistance and minimum pipe flexural stiffness for handling purpose.

- Minimum annular grout thickness and strength to act in combination with the pipe inside the shafts.
- Pipe installation method which includes water filling inside the pipe during lowering into the shaft to compensate for buoyancy and hydrostatic pressure, maximum allowed grout lift height, and minimum grout strength gain before the next lift can be placed.

7 TBM START-UP AND LAUNCH SEQUENCES

The Design-Builder have selected a Herrenknecht hybrid TBM with open/closed EPB mode capabilities which presents the advantage of controlling muck management, minimized maintenance and optimized production time. The TBM delivery was completed at the end of June 2022. The 10.3-meter bore diameter TBM has a 14-meter-long shield and a 91-meter-long back-up, comprised of four gantries to supply power to the shield, and connect the utilities and logistics. The shield is composed of 3 main sections with one active articulation. This will enable it to achieve the minimum required curvature of 305-meter radius. The structure and seals are designed for 500 kPa (5 Bar) of pressure.

The 10.3-meter diameter cutter head is designed for hard rock and protected against wear. It is equipped with sixty-four 0.48m disc cutters for high efficiency and reliability in the anticipated conditions. The machine is fitted with a conveyor belt in open mode and a screw conveyor in EPB mode to move muck from the cutting chamber to the Tunnel muck conveyor that will transport the material to the shaft. The face can be closed in less than 10 minutes if required. The dual mode has a real benefit on the Project because it will significantly reduce the need for probe drilling and pre-grouting that a single open mode TBM would require. The selected TBM is shown in Figure 7.

Figure 7. TBM in Herrenknecht factory in January 2022.

The TBM was launched and operated from the Launch shaft located on the main site at the Southern end of the project. It is of 18.9-meter diameter and 47.2-meter deep, excavated within the soil portion inside an excavation support wall made of secant piles and in the rock using drill-and-blast method. When the shaft excavation reaches the level of the tunnel at a depth of 36.6 m a starter tunnel of 70.1 m long, and a tail tunnel of 18.3 m long were excavated by SEM in two stages, top heading and bench. The remainder of the shaft was then completed after the starter tunnel and tail tunnel were excavated. The bottom of the shaft was backfilled, and a trench was kept below the tunnel invert to install the bottom part of the vertical conveyor as shown in Figure 8.

Figure 8. The launch shaft installation during TBM operation.

The TBM was pre-assembled on surface. The 1,665 tons machine was delivered in 82 packages The pre-assembly on the surface made it possible to lower larger assembled TBM sections into the shaft weighing up to 375 tons as shown in Figure 9

Figure 9. 375 tons TBM front shield lowered with the 600 tons crawler crane in the launch shaft.

The main site is set-up to provide the necessary logistic support to the TBM operation. A crawler crane of 350 tons capacity handles the

segments and the services inside the launch shaft. There is sufficient space on top of the shaft to store up to 60 rings, more than a week of anticipated TBM production. The TBM muck is transported from the TBM by a chain of conveyors at a rate of 1,250 tons per hour. The muck is lifted in the shaft using a vertical bucket conveyor as depicted in Figure 10.

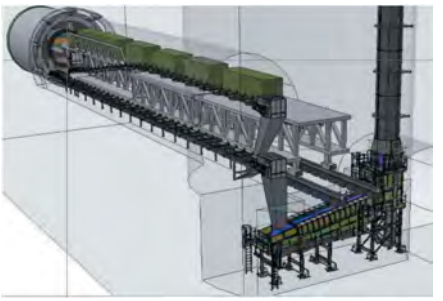

Figure 10. Muck conveyors system in the tunnel and shaft.

On the surface the muck is dropped by a radial stacker in a stockpile accumulating 15,000 cubic yards, the anticipated average weekly quantity excavated by the TBM. The rest of the surface installation comprises a grout plant, electrical distribution, water treatment plant, offices, material storage and workshop. The main launch site is shown in Figure 11.

Figure 11. Main site aerial picture during TBM assembly.

The TBM is set up in the starter tunnel and launched in the second half of September 2022. To minimize the length of the starter tunnel excavation only three gantries are installed initially, the fourth gantry with none-essential services is lowered in the tunnel once the TBM has advanced. The transport of segments in the tunnel is by two multi service (VMS) vehicles shown in Figure 12 that can hold one full ring made of seven segments and one set of temporary services that will be installed in the tunnel to provide fluids, ventilation, and power to the TBM. Tunnelling was started in September 2022 and due to be completed by the end of 2023.

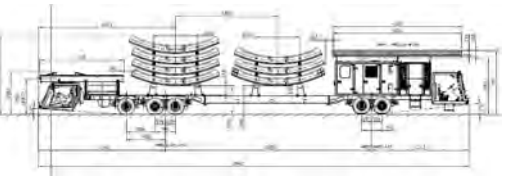

Figure 12. Vehicle Multi Service (VMS) for the segments transport in tunnel.

The Design-Builder self-performed the tunnel liner segments at a facility approximately 40 kilometres from the launch site. Non steam controlled temperature curing is used with production halted during coldest months of the winter.

8 SEM TUNNEL AND ADIT CONSTRUCTION

The Pawtucket project contains several mined tunnels (i.e., main drive, adits). In contrast to TBM tunnelling, mined tunnelling is performed under open face conditions without the aid of a protective shield. As such, to minimize risk, the Sequential Excavation Method (SEM) is employed using separate support classes depending on the expected rock behaviour. The design build delivery allows for a close interaction between the engineer and contractor during tunnelling. This close interaction allows for efficient adjustment of rock support to ensure that what is installed is both safe and economical.

The largest mined tunnel along the alignment is the starter tunnel. The starter tunnel extends northwards from the launch shaft in the direction of the main tunnel and houses the TBM during launch. To further extend the launching area for the TBM, a shorter tail tunnel has been constructed between the launch shaft and the future pump shaft. In addition to these larger mined tunnels, The Pawtucket tunnel will be connected to four drop shafts by smaller adits along its alignment. The adits are "preceded" by a slightly larger deaeration chamber immediately below the drop shafts. When the water is collected in the drop shafts, it flows first through the deaeration chamber and then into the adit.

The final lining of the starter tunnel will be cast-in-place fibre reinforced concrete cast flush with the inner diameter of the TBM tunnel. Fibre reinforced concrete was selected not only out of economy, but to increase robustness of the lining against corrosion, further minimizing risk that significant damage would occur to the as-built-structure over time. The tail tunnel will be completely backfilled.

The longest adit is excavated from the access shaft to the mainline tunnel by microtunneling to mitigate the geological risks inherent to drill and blast mining initially anticipated in the BTC. The adit is over 305 m in length and crosses under the Seekonk River. Additional ground investigations from the surface

were limited by accesses not granted into private properties. The choice of a confined microtunnel TBM prevent the use of pre-excavation grouting and secure the schedule against geological conditions.

Fibre reinforced polymer mortar (FRPM) jacking pipe is used for the 305-m adit to attain the 100-year durability requirement for the project as well as achieving pressures needed on the gaskets. The pipe is 2.4-meter in nominal diameter with a pipe wall thickness of 7.6 cm. The pipe joint is a flush bell and spigot joint which has an allowable safe jacking load of about 1,150-ton and a maximum allowable hydrostatic pressure up to 483 kPa. The MTBM will be retrieved from the mainline tunnel as illustrated in Figure 13 below.

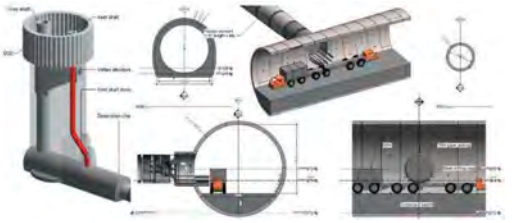

Figure 13. MTBM drive and retrieval from the mainline tunnel.

ACKNOWLEDGMENTS

The authors would like to thank the construction joint venture of CBNA (Bouygues Construction) and Barletta (CBNA-Barletta JV); also known as CB3A for their support in the design work described in this paper. The authors would also like to acknowledge the Narragansett Bay Commission (NBC) as the owner and Stantec Consulting as the program manager of this great project.

Tunnelling for a Better Life – Yan, Celestino, Thewes & Eberhardt (Eds)
© 2024 The Author(s), ISBN 978-1-032-80042-4
Open Access: www.taylorfrancis.com, CC BY-NC-ND 4.0 license

Comprehensive risk management for slurry shield TBM tunneling using fuzzy set theory

Kibeom Kwon*, Minkyu Kang, Hyeontae Park, Yongxun Ma & Hangseok Choi
Korea University, Seoul, Republic of Korea

ABSTRACT: During ground excavation using tunnel boring machines (TBMs), inherent risks stemming from various uncertainties must be addressed. Without effective risk management, construction costs and timelines can significantly overrun, and accidents may occur. However, conventional research approaches have often overlooked uncertainties in expert opinions and TBM tunneling, leading to a limited understanding of risk management outcomes. To address this issue, this study employed the concept of membership degree in fuzzy set theory (FST) to propose a comprehensive risk management model for slurry shield TBM tunneling. The proposed model initially calculated the membership degree for each class concerning impact and probability by comprehensively considering expert opinions. The impact and probability classes with the highest membership degrees were then applied to a risk matrix to determine the risk class. The practical applicability of this model was validated through its application to an actual slurry shield TBM tunneling project. In the risk analysis, the membership degrees of impact and probability were distributed across all classes, with the highest membership degrees being less than half. Notably, these distributions can be comprehensively reflected in the subsequent risk evaluation within the proposed model. All causal combinations related to collapse yielded the risk class of "Significant", indicating the need for countermeasures that can be implemented depending on the situation. Moreover, the risk class corresponding to ground surface deformation, such as surface settlement and heaving/blow-out, caused by shallow cover depth, was determined to be "Significant". In conclusion, the proposed model enhances the reliability of risk management, particularly for tunneling projects with significant uncertainties stemming from various causes, including incomplete site characterization and the utilization of various state-of-the-art techniques. This approach contributes to ensuring both safety and efficiency in TBM tunneling.

Keywords: Tunnel boring machine (TBM), Risk management, Fuzzy set theory (FST), Risk matrix

1 INTRODUCTION

The increasing frequency of tunnel construction has become essential in urban areas characterized by high population density and significant traffic congestion costs (Broere, 2016; Kim et al., 2022). Tunnel boring machines (TBMs) have gained widespread utilization in various tunneling projects, primarily due to their eco-friendliness, stability, and constructability (Hyun et al., 2015; Kwon et al., 2022).

Nonetheless, TBM tunneling comes with inherent risks stemming from various uncertainties, including those related to geology–machine interactions. Proactive risk management is essential to prevent overruns of construction costs and time and mitigate potential accidents such as collapse and mud/water inflow.

Risk, defined as the combined value of impact and probability, is conventionally assessed through expert surveys (Eskesen et al., 2004). This approach involves collecting evaluations of impact and probability provided by experts, and then calculating risk based on these assessments.

A risk matrix has been widely applied in practice due to its simple and intuitive characteristics. Several risk management models in tunneling have introduced the use of the risk matrix (Eskesen et al., 2004; Hyun et al., 2015; Chung et al., 2021). However, these conventional models often require each expert to assign a single class for impact and probability evaluations, which can be challenging. Furthermore, these models typically rely solely on the average or modal opinion when aggregating expert

*Corresponding author: kibb5@korea.ac.kr

DOI: 10.1201/9781003495505-479

assessments, which can hinder the appropriate consideration of uncertainties associated with TBM tunneling.

This study proposes a comprehensive risk management model for tunneling by incorporating fuzzy set theory (FST). FST enables the calculation of membership degrees corresponding to various classes of impact and probability. This approach allows each expert's evaluation certainty to be distributed across multiple classes, rather than restricting it to a single fixed class. Consequently, the risk derived from these distributions comprehensively incorporates the entire range of expert opinions.

2 BACKGROUNDS

2.1 *Risk matrix*

A risk matrix represents a structured methodology employed for evaluating potential risks. This method involves the establishment of a matrix characterized by two fundamental dimensions: impact and probability. Each dimension is divided into discrete classes or levels. The risk class can be determined based on the combination of the evaluated impact and probability classes.

Various forms of risk matrices can be formulated, depending on the criteria used to categorize risk classes. In particular, although the combination of the evaluated impact and probability classes remains consistent, the classification of risk classes can vary for each form of the risk matrix. Figure 1 illustrates the risk matrix adopted in this study.

Risk matrix		Impact class			
		Very-low	Low	Medium	High
Probability class	Very-low	I	I	II	III
	Low	I	II	II	III
	Medium	II	II	III	IV
	High	III	III	IV	IV

Risk class
Negligible (I)
Tolerable (II)
Significant (III)
Intolerable (IV)

Figure 1. Risk matrix adopted in this study.

2.2 *Fuzzy set theory*

Fuzzy set theory (FST) was introduced as a framework to accommodate the inherent vagueness in human cognition when dealing with uncertain information (Zadeh, 1965). In classical set theory, a set possesses distinct boundaries, as depicted in Figure 2(a). In this framework, an element either unequivocally belongs to the set or does not, allowing for the definition of membership degrees as binary values of either zero (non-member) or one (member).

In contrast, a fuzzy set permits its members to exhibit gradual membership degrees within the interval [0,1]. This characteristic arises from the use of an ambiguous set boundary, as illustrated in Figure 2(b).

Once a fuzzy set A is defined on a universe of discourse with elements denoted by x, a membership function can be expressed as $\mu_A(x)$, which takes on values from the interval [0,1] (Wang et al., 2013). Higher values of the membership function correspond to a stronger degree of inclusion of an element within the set.

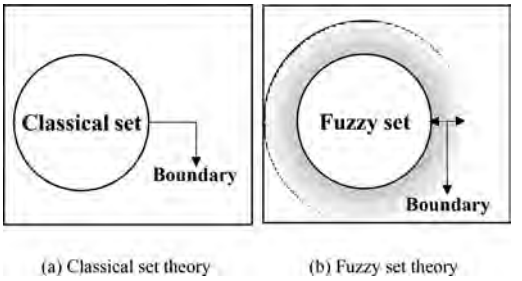

Figure 2. Diagrams of the set boundary.

Various forms of membership functions (e.g., triangular, trapezoidal, and Gaussian membership function) can be employed to represent fuzzy sets, as illustrated in Figure 3. Among these various forms, triangular and trapezoidal functions are frequently preferred due to their straightforward definition, ease of representation, and computational tractability (Thaker and Nagori, 2018).

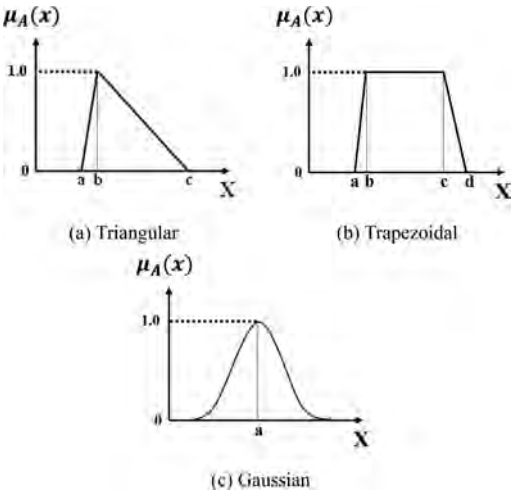

Figure 3. Schematics of the various membership functions.

3 MODEL METHODOLOGY

3.1 *Scope*

In this study, geological sources were exclusively addressed among various types of potential adverse sources, such as design-related sources (e.g., improper design of the cutter head) and operational sources (e.g., insufficient backfill grout). This selective emphasis on geological sources was driven by their

inevitability during tunnel construction and their notable contribution to documented accidents.

Furthermore, the risk evaluations were conducted for each causal combination (i.e., a one-to-one correspondence between sources and resultant accidents). This approach was chosen to account for the fact that the probability of an accident occurring may vary depending upon the specific causal source (Kwon et al., 2023).

3.2 *Risk identification*

In the phase of risk identification, the objective was to identify potential sources, accidents, and the causal combinations relevant to a specific tunnel project. Several methodologies for risk identification have been proposed, with the most common approaches involving comprehensive literature reviews and structured expert interviews (Siraj and Fayek, 2019). Furthermore, it is widely acknowledged that the combination of multiple identification methodologies can improve the reliability of the outcomes (Hillson, 2002). Therefore, this study simultaneously employed literature reviews and expert interviews.

3.3 *Risk analysis and evaluation*

Creating membership functions for each impact and probability class was the initial requirement. In this study, four classes (Very-low [VL], Low [L], Medium [M], and High [H]), two types of membership functions (triangular and trapezoidal), and a total of 12 scores (whole numbers ranging from 1 to 12) were adopted, as illustrated in Figure 4.

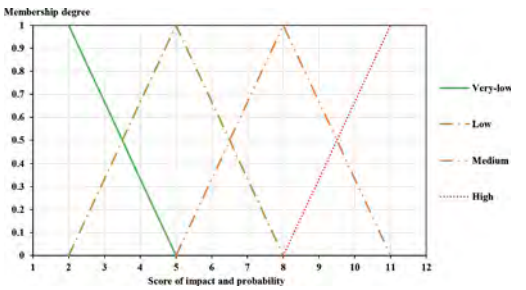

Figure 4. Schematics of the utilized membership functions.

It is important to note that each assigned score for both impact and probability corresponded to a specific membership degree within each class. For example, if a score of 3 was given, the membership degrees for each class would be as follows: VL: 2/3, L: 1/3, M: 0, H: 0.

During the risk analysis, each expert was responsible for assessing the impact of each accident and the probability associated with each causal combination. This evaluation involved selecting one of the available 12 scores. It is noteworthy that, in this study, the evaluated impact of an accident was considered equivalent to the impact of a causal combination containing the same accident. For each impact and probability class, the membership degrees were obtained using Eq. (1), where MD_I and MD_P represent the membership degree of impact and probability, while i, j, and n denote the class, score, and number of expert opinions, respectively.

$$MD_{I,i} = \frac{\sum_{j=1}^{12} C_{I,i,j}}{n}, MD_{P,i} = \frac{\sum_{j=1}^{12} C_{P,i,j}}{n} (i : VL, L, M, H) \quad (1)$$

Risk evaluation determined the risk class based on the evaluation results of impact and probability. In this study, four risk classes were adopted: "Negligible", "Tolerable", "Significant", and "Intolerable". Each risk class entailed a different level of countermeasure necessity, as summarized in Table 1.

For this study, a new risk matrix was developed based on the adopted impact, probability, and risk classes. In this matrix, impact and probability were considered to contribute equally to the overall risk, leading to the establishment of a symmetric risk matrix. For each causal combination, the impact and probability class with the highest membership degree (i.e., i with the maximum of $MD_{I,i}$ and $MD_{P,i}$ in Eq. 1) were applied to the constructed risk matrix, thereby determining the corresponding risk class. The flow chart illustrating the implementation of the proposed model is presented in Figure 5.

Table 1. Degree of countermeasures required for each risk class.

Risk class	Degree of countermeasures required
Negligible	Countermeasures are unnecessary.
Tolerable	Countermeasures not required but can be applied depending on the situation.
Significant	Countermeasures required but cannot be applied depending on the situation.
Intolerable	Countermeasures must be applied.

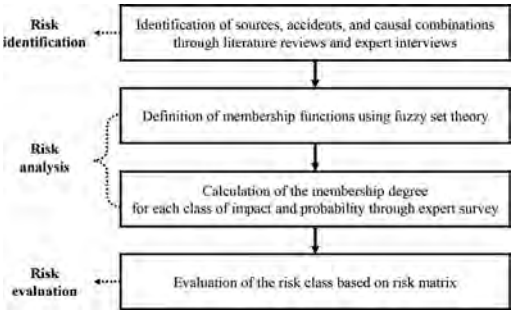

Figure 5. Flow chart of model implementation.

4 RESULTS

4.1 *Site description*

The proposed model was applied to an under-river tunnel project with a total length of 2.86 km. Excavation of this tunnel was carried out using a slurry shield TBM with an excavation diameter of 14.01 m. The ground types encountered along the tunnel alignment was primarily characterized by weathered, soft, and hard rock. The longitudinal geological profile of this site is presented in Figure 6. The outer and inner diameters of the segment lining were 13.5 m and 12.6 m, respectively.

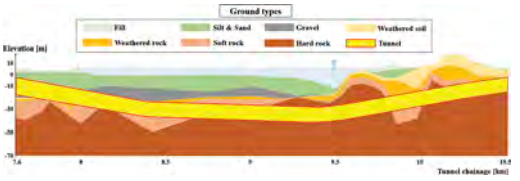

Figure 6. Longitudinal geological profile of the project site.

4.2 *Results of risk identification*

Through literature reviews and expert interviews, seven sources and five accidents associated with the target tunneling site were identified, as summarized in Tables 2 and 3.

Table 2. Identified sources at target tunneling site.

No	Name
1	Faults
2	Shallow cover depth
3	Mixed ground
4	Cross-passage
5	Blocky rock mass
6	High water pressure
7	Weathered ground

Table 3. Identified accidents at target tunneling site.

No	Name
1	Collapse
2	Surface settlement
3	Heaving/blow-out
4	Mud/water inflow
5	Cutter head blockage

Table 4. Identified causal combinations at target tunneling site.

	Causal combination	
Symbol	Source	Accident
CC1	Faults	Collapse
CC2	Shallow cover depth	Collapse
CC3	Mixed ground	Collapse
CC4	Cross-passage	Collapse
CC5	Blocky rock mass	Collapse
CC6	High water pressure	Collapse
CC7	Faults	Surface settlement
CC8	Shallow cover depth	Surface settlement
CC9	Mixed ground	Surface settlement
CC10	Cross-passage	Surface settlement
CC11	Blocky rock mass	Surface settlement
CC12	High water pressure	Surface settlement
CC13	Weathered ground	Surface settlement
CC14	Faults	Heaving/blow-out
CC15	Shallow cover depth	Heaving/blow-out
CC16	Faults	Mud/water inflow
CC17	Cross-passage	Mud/water inflow
CC18	High water pressure	Mud/water inflow
CC19	Weathered ground	Mud/water inflow
CC20	Faults	Cutter head blockage
CC21	Mixed ground	Cutter head blockage
CC22	Blocky rock mass	Cutter head blockage

Subsequently, 22 causal combinations considering the potential causal relationships between the seven identified sources and the five accidents were identified, as summarized in Table 4.

4.3 *Results of risk analysis and evaluation*

A total of 29 experts participated in the survey, and their impact and probability evaluations were compiled. The results of the membership degree for impact and probability classes, derived from these expert evaluations, are summarized in Tables 5 and 6. Using the results from the risk analysis, the risk class for each causal combination was evaluated, as presented in Table 7.

Table 5. Impact results for each accident.

	Membership degree of impact class			
Accident	Very-low	Low	Medium	High
Collapse	0.13	0.18	0.26	0.43
Surface settlement	0.03	0.28	0.46	0.23
Heaving/ blow-out	0.09	0.32	0.45	0.14
Mud/water inflow	0.07	0.38	0.41	0.14
Cutter head blockage	0.16	0.36	0.34	0.14

Table 6. Probability results for each accident.

	Membership degree of impact class			
Causal combination	Very-low	Low	Medium	High
CC1	0.24	0.45	0.24	0.07
CC2	0.20	0.43	0.24	0.14
CC3	0.31	0.45	0.24	0.00
CC4	0.31	0.48	0.17	0.03
CC5	0.43	0.47	0.10	0.00
CC6	0.32	0.31	0.29	0.08
CC7	0.18	0.48	0.29	0.05
CC8	0.14	0.32	0.36	0.18
CC9	0.24	0.43	0.30	0.03
CC10	0.31	0.43	0.23	0.03
CC11	0.24	0.59	0.17	0.00
CC12	0.15	0.47	0.30	0.08
CC13	0.22	0.43	0.31	0.05
CC14	0.18	0.47	0.23	0.11
CC15	0.10	0.36	0.41	0.13
CC16	0.14	0.43	0.40	0.03
CC17	0.29	0.39	0.28	0.05
CC18	0.08	0.45	0.34	0.13
CC19	0.26	0.40	0.30	0.03
CC20	0.20	0.43	0.31	0.07
CC21	0.10	0.48	0.29	0.13
CC22	0.15	0.55	0.26	0.03

Table 7. Results of risk evaluation for each accident.

Causal combination	Impact class	Probability class	Risk class
CC1	High	Low	Significant
CC2	High	Low	Significant
CC3	High	Low	Significant
CC4	High	Low	Significant
CC5	High	Low	Significant
CC6	High	Very-low	Significant
CC7	Medium	Low	Tolerable
CC8	Medium	Medium	Significant
CC9	Medium	Low	Tolerable
CC10	Medium	Low	Tolerable
CC11	Medium	Low	Tolerable
CC12	Medium	Low	Tolerable
CC13	Medium	Low	Tolerable
CC14	Medium	Low	Tolerable
CC15	Medium	Medium	Significant
CC16	Medium	Low	Tolerable
CC17	Medium	Low	Tolerable
CC18	Medium	Low	Tolerable
CC19	Medium	Low	Tolerable
CC20	Low	Low	Tolerable
CC21	Low	Low	Tolerable
CC22	Low	Low	Tolerable

5 DISCUSSIONS

According to Table 5, most of the identified accidents, except for cutter head blockage, had the highest membership degree in the Medium or High categories. This tendency towards sever impact can be attributed to the specific site conditions under the river. For example, accidents like environmental pollution can have more significant consequences when they occur under a river, and implementing countermeasures becomes more challenging.

Regarding the probability, most causal combinations had the highest membership degree in the Very-low and Low categories, except for CC8 and CC15. However, it's worth noting that in some combinations, there was little difference between the membership degree of the highest probability class and the others. For instance, the membership degree difference between Very-low and Low for CC5 and CC6 was 0.04 and 0.01, respectively. In addition, the difference between Low and Medium classes was less than 0.1 for CC8, CC15, CC16, and CC19.

Furthermore, most of the highest membership degrees presented in Tables 5 and 6 were less than half, and the membership degrees were distributed across all the classes except for CC3, CC5, CC11 in probability evaluation. This distribution cannot be considered in conventional risk management approaches where experts select only one impact and probability class, resulting in narrower results that do not consider this level of uncertainty. These results obtained by the proposed model underscore its superior capability in handling uncertainty.

For eight causal combinations (CC1, CC2, CC3, CC4, CC5, CC6, CC8, and CC15), the risk evaluation yielded a risk class of "Significant" (refer to Table 7). In these cases, implementing countermeasures was advised rather than being deemed obligatory.

Except for CC8 and CC15, the causal combinations with the risk class of "Significant" were related to the collapse accident. These results were made by the application of a conservative risk matrix where at least one of the constituent factors, either impact or probability class, was evaluated as High, leading to the derivation of a risk class of at least "Significant".

The remaining causal combinations designated as the risk class of "Significant" (CC8 and CC15) were related to surface settlement and heaving/blow-out, both induced by the same source, which was shallow cover depth. These findings align with expectations, as ground disturbances near the tunnel can easily extend to the ground surface in hazardous zones characterized by shallow cover depth. This has the potential to cause significant damage not only to the tunnel but also to adjacent structures.

6 CONCLUSIONS

This study proposed a comprehensive risk management model for tunneling that combines fuzzy set theory with the risk matrix. To assess its practical applicability, the proposed model was applied to a real under-river tunnel project that utilized a slurry shield tunnel boring machine.

The majority of the membership degrees for impact and probability, as obtained through expert surveys, were distributed across all classes. This distribution results from the comprehensive risk management approach that accounts for the inherent vagueness in expert opinions.

The proposed model can have a significant impact on risk management, especially for tunneling projects with significant uncertainties arising from inadequate site characterization and the application of various state-of the-art techniques. In doing so, it contributes to ensuring the safety and efficiency of TBM tunneling.

ACKNOWLEDGMENTS

This research was conducted with the support of the "National R&D Project for Smart Construction Technology (No. RS-2020-KA157074)" funded by the Korea Agency for Infrastructure Technology Advancement under the Ministry of Land, Infrastructure and Transport, and managed by the Korea Expressway Corporation.

REFERENCES

Broere, W., 2016. Urban underground space: solving the problems of today's cities. Tunn. Undergr. Space Technol. 55, 245–248.

Chung, H., Park, J., Kim, B. K., Kwon, K., Lee, I. M., Choi, H., 2021. A causal network-based risk matrix model applicable to shield TBM tunneling projects. Sustainability. 13(9), 4846.

Eskesen, S. D., Tengborg, P., Kampmann, J., Veicherts, T. H., 2004. Guidelines for tunnelling risk management: international tunnelling association, working group No. 2. Tunn. Undergr. Space Technol. 19(3), 217–237.

Hillson, D., 2002. Extending the risk process to manage opportunities. Int. J. Proj. Manag. 20(3), 235–240.

Hyun, K. C., Min, S., Choi, H., Park, J., Lee, I. M., 2015. Risk analysis using fault-tree analysis (FTA) and analytic hierarchy process (AHP) applicable to shield TBM tunnels. Tunn. Undergr. Space Technol. 49, 121–129.

Kim, D., Kwon, K., Pham, K., Oh, J. Y., & Choi, H., 2022. Surface settlement prediction for urban tunneling using machine learning algorithms with Bayesian optimization. Autom. Constr. 140, 104331.

Kwon, K., Choi, H., Oh, J. Y., & Kim, D., 2022. A study on EPB shield TBM face pressure prediction using machine learning algorithms. J. of Korean Tunn Undergr Sp. Assoc. 24(2), 217–230.

Kwon, K., Kang, M., Kim, D., Choi, H., 2023. Prioritization of Hazardous Zones Using an Advanced Risk Management Model Combining the Analytic Hierarchy Process and Fuzzy Set Theory. Sustainability. 15(15), 12018.

Siraj, N. B., Fayek, A. R., 2019. Risk identification and common risks in construction: Literature review and content analysis. J. Constr. Eng. Manag. 145(9), 03119004.

Thaker, S., Nagori, V., 2018. Analysis of fuzzification process in fuzzy expert system. Procedia Comput. Sci. 132, 1308–1316.

Wang, D., Zhang, P., Chen L., 2013. Fuzzy fault tree analysis for fire and explosion of crude oil tanks. J. Loss Prev. Process Ind. 26(6), 1390–1398.

Zadeh, L. A., 1965. Fuzzy sets. Inf. Control. 8(3), 338–353.

Tunnelling for a Better Life – Yan, Celestino, Thewes & Eberhardt (Eds)
© 2024 The Author(s), ISBN 978-1-032-80042-4
Open Access: www.taylorfrancis.com, CC BY-NC-ND 4.0 license

Geotechnical risks management associated with a tunnel launch in complex geological conditions

C.L. Ng*
AECOM Perunding Sdn Bhd, Kuala Lumpur, Malaysia

C.M. Khoo & N.A. Abdul Rahman
Mass Rapid Transit Corporation, Kuala Lumpur, Malaysia

ABSTRACT: The recent successful completion of the underground section of the Putrajaya Line, Klang Valley Mass Rapid Transit (KVMRT) project, comprises 13.5km of twin bored tunnel with 10 new underground stations, one existing cross-platform interchange station with the Kajang Line; and various ancillary structures including cripple track siding and crossover box, escape shafts, ventilation shafts and tunnel portal. The tunnel was built using 8 variable density (VD) tunnel boring machines (TBMs) and 4 earth pressure balance (EPB) TBMs. One of the critical tunnel drives required a tunnel launch within the Hospital KL crossover box (HKLX), which is not only sited in Kuala Lumpur's notorious karstic limestone but compounded with extremely complex geological conditions such as steep sided trough infilled with unconsolidated clayey materials and presence of complex solution channel networks. The criticality for an early completion of this crossover box structure has significant impacts on the overall tunnel construction programme. However, the many geotechnical challenges faced since the site establishment, such as ground subsidence during borehole investigation, changes in groundwater levels and possible related building settlement has led to the meticulous task of diagnostic investigation, temporary works design enhancement, development of ground improvement schemes and changes in original construction sequence to mitigate these unique set of anticipated geotechnical risks to allow timely completion of the HKLX crossover box for TBM launching. Extensive risk management process, building impact assessment/protection and instrumentation monitoring particularly to verify the performance of the construction was implemented to ensure the works were to proceed in a safe manner. The project was completed on time without incident to facilitate the tunnel launch in achieving the overall planned programme. The case history clearly demonstrated the importance of the deployment of geotechnical risk management/action plan to overcome unusual geological challenges to be faced by geotechnical engineers.

Keywords: Complex geological conditions, Tunnel launching, Kuala Lumpur Limestone, Geotechnical risks, Ground characterization, Ground improvement, Risk management

1 INTRODUCTION

The Putrajaya Line, the second of three planed mass rapid transit rail lines under the Klang Valley Mass Rapid Transit (KVMRT) Project, has been successfully constructed and fully operational on 16 March 2023. The 57.7 km-long alignment covers a span of 13.5 km underground twin tunnels running through the Kuala Lumpur city centre with 10 new underground stations and one existing cross-platform interchange station; and various ancillary structures including cripple track siding and crossover box, escape shafts, ventilation shafts and tunnel portal. Figure 1 shows the underground alignment route map. The running tunnels, measuring 5.8 m internal diameter with 275 mm thick precast steel fibre reinforced concrete segmental linings, were excavated using 8 variable density (VD) tunnel boring machines (TBMs) and 4 earth pressure balance (EPB) TBMs and was divided into 8 sections of tunnel drive.

The project delivery is in the form of Design and Build (D&B). Geotechnical Information Report (GIR) prepared by the Employer's Consultant, including pre-contract ground investigation data and its inferred geological profiles for the project site area, as well as the risk register developed during the reference design stage, were included and form part of the Contract Documents. Under the prevalent Conditions of Contract, full risk of ground conditions and risk management is borne by the D&B

*Corresponding author: chi.ng@aecom.com

DOI: 10.1201/9781003495505-480

Figure 1. Location plan of the underground alignment.

Contractor. The Contract further stated it is the Contractor's responsibility and expense to carry further site investigation and his assessment of ground conditions to fully develop his designs and construction methods for all related activities.

The Hospital KL Crossover/IVS1 (HKLX) is located in between the S14 Hospital KL Station and S15 Raja Uda Station. The HKLX is a two-level multiple track crossover structure, also housing cripple sidings and intervention/ventilation shaft facilities. Besides its operational function, an additional key function of the HKLX box is its use as the 'shaft' for the launch of two TBMs from its east end, and the subsequent retrieval of 2 other TBMs at its west end. The criticality for an early completion of the HKLX box structure has significant impacts on the overall tunnel construction programme. However, the chosen site is not only sited in Kuala Lumpur's notorious karstic limestone but compounded with extremely complex geological conditions such as steep sided trough infilled with unconsolidated clayey materials and presence of complex solution channel networks. The many geotechnical challenges faced since the site establishment, such as ground subsidence during borehole investigation, changes in groundwater levels and possible related building settlement has led to the meticulous task of diagnostic investigation, temporary works design enhancement, development of ground improvement schemes and changes in original construction sequence to mitigate these unique set of anticipated geotechnical risks to allow timely completion of the HKLX box for TBM launching.

This paper presents the detailed examination to establish the geological and hydrogeological model, capturing the geological risks associated with the construction of the HKLX box structure and the various measures adopted to control and minimize the geotechnical risks to an acceptable level. The measures were concluded as effective leading to a safe excavation and successful completion and meeting the overall program.

2 THE SITE AND ORIGINAL DESIGN SCHEME

2.1 *Site location and the surrounding context*

The Hospital KL Crossover (HKLX) site is located at an existing open car park with a few adjacent building structures and hospital facilities, which includes hospital's radicare buildings and offices to the north of HKLX, a power substation in the north-east, Hostel Sejahtera and Hostel Abadi in the south-east and south of HKLX. The hostels are 20-storey high residential quarters for the hospital staff. A river, circa Bunus River, is running along the east boundary. See Figure 2. These structures may be affected by the construction.

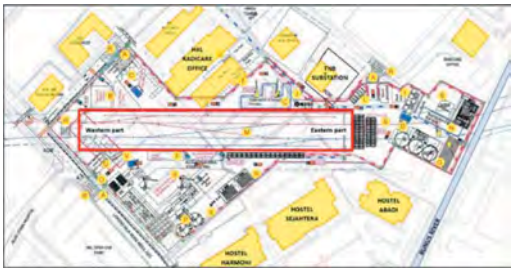

Figure 2. Site context.

Figure 3. Overview of the HKLX site.

The site terrain can be described as flat ground with average level of +34 RLm. The box structure is of approximately 167 m long and 30 m wide and required an excavation of about 20 m below the ground surface. The west end of the box served as a retrieval shaft for the TBMs driven through the Hospital KL station while the other end was for tunnel launching. An overview of the excavation box in relation to the surrounding critical and sensitive buildings is illustrated in Figure 3.

2.2 *General geology of the site*

According to the geological map of Kuala Lumpur (1993 version), the site is underlain by the Kuala Lumpur Limestone formation. Published geological information (Hutchison & Tan 2009) indicates that the bedrocks belonging to Middle to Upper Silurian Age, which typically comprise locally dolomitised grey and white crystalline limestone and marble that is locally interbedded with phyllite and schist. The Kuala

Lumpur Limestone is weakly metamorphosed and is gently folded in places. Superficial deposits comprise man-made fill and underlain by alluvium (Young and Old Alluvium) and saprolite.

Kuala Lumpur Limestone is well known for its highly erratic karst, which is a distinctive terrain developed on soluble carbonate rock. In accordance with Waltham and Fookes (2003), karst weathering observed in Kuala Lumpur is classified as 'Extreme Karst kV' with the associated karst features depicted in Figure 4. Karst features commonly encountered in Kuala Lumpur Limestone include pinnacles alternating with deep troughs, filled and unfilled caves, open and buried sinkholes, open and filled cavities, open and artificially widened vertical discontinuities and limestone floaters, solution channels, overhangs, to name but a few.

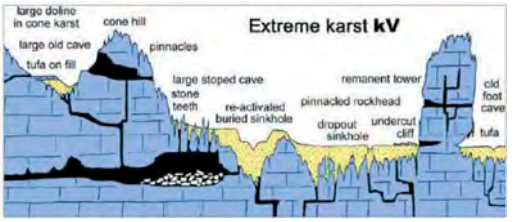

Figure 4. Extreme karst topography (after Waltham & Fookes, 2003).

The problems are further exacerbated by the fact that the limestone bedrock in Kaula Lumpur area is often overlain by weak alluvium or mine tailings, which are also commonly affected by dissolution of the underlying carbonate rocks. Tan (2006) discusses the occurrence of very weak collapsed soil zones immediately above the level of the limestone and refers to these as 'slump zones'. Collapse in soils occurs when either rock caves or other large dissolution features fail under tension or when soil flows into an underlying pre-existing cavity as a result of a change in the groundwater regime. This particular geohazard has significant implications for the formation of sink holes and ground settlement which are considered to represent the greatest risk to the works. The formation of sink holes due to dewatering and construction activities in Kuala Lumpur have been well documented (Tan, 2006).

The nature of this formation is one of the considerable challenges and geotechnical risks for this site. It will be discussed in more detail in the subsequent section with the site-specific data.

2.3 *Original design scheme and construction sequences*

The HKLX box was originally designed to be constructed using bottom-up construction in an area to the east of the box (Gridline 1 – 6) to enable the TBM launch in accordance with the tunnelling programme, and semi-top down in the remaining areas. It was planned to excavate within a strutted diaphragm wall. There will be 4 rows of temporary steel struts and the 1.2 m thick diaphragm will have a toe level of about 20 m below the final excavation level. Cross-lot diaphragm walls will be installed approximately every 15 m along the excavation. A cross section during excavation is shown in Figure 5.

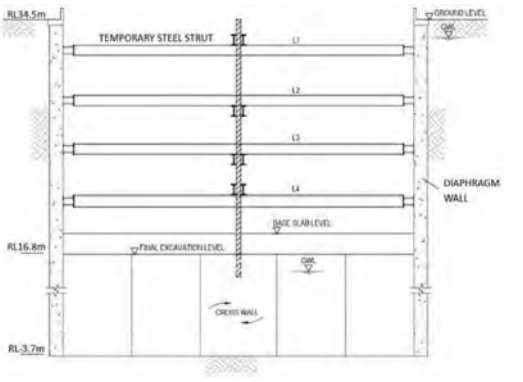

Figure 5. Original excavation support scheme.

The HKLX box was expected to be constructed within superficial deposits above rockhead and the majority of the diaphragm wall which surround the box will also be founded within the superficial deposits, although the rockhead may locally rises above the toe of the wall. Excavation was anticipated to be in ground conditions comprising a mixture of the following materials: man-made fill, recent alluvium, old alluvium.

3 GEOLOGICAL AND HYDROGEOLOGICAL MODEL

3.1 *Geological model*

The three-dimensional structure in karst terrains is often very complex especially when the karst is classified as extreme, as is the case in Kuala Lumpur Limestone. A thorough review of all investigative holes undertaken including exploratory boreholes, rock probing records, grouting records were used to assess the ground conditions at the site. Figure 6 shows the locations and extent of the investigative holes while Figure 7 gives a general idea about the interpreted longitudinal geological profile across the site.

The elevation of the first encounter with limestone varies dramatically within the site, ranging from as high as 18.1 m on the north of HKLX box to as deep as 102.5 m within a relatively short distance. This remarkably contrasts indicates the characteristic of the very rugged top of karst. Figure 8 shows the possible extremely variable rockhead over the HKLX box structure.

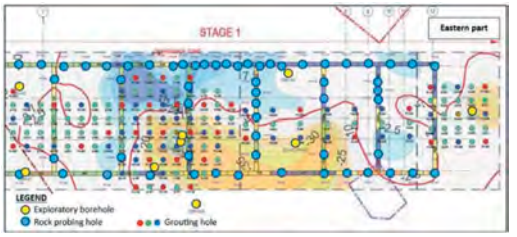

Figure 6. Extent of investigative holes undertaken.

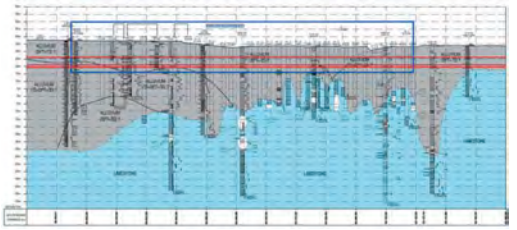

Figure 7. Interpreted longitudinal geological profile.

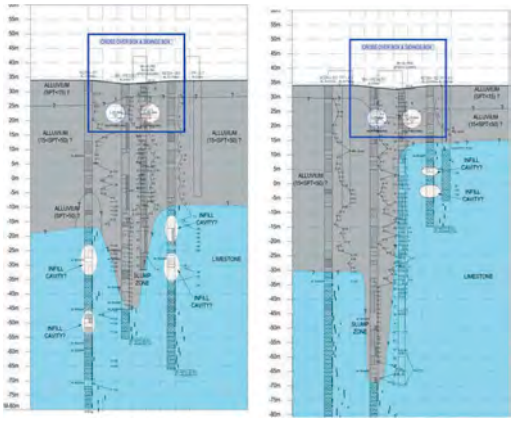

Figure 8. Interpreted transverse geological profile.

Some boreholes indicated slump zones located beneath the eastern half of the box structure, with the deepest was encountered at BH-UG-PB3AR with SPT value less than 4 blows at depth between 69 m and 96 m from ground level. A three-dimensional model was generated as shown in Figure 9 to have better understanding of the slump zones underlying the HKLX box. However, the dramatic variation of rock-head over short distances suggests that zones of slump materials may be expected to be of limited extent and possibly extending in long narrow zones. These zones are mostly likely to be dictated by the original structure of the limestone which has provided under-drainage and affected its dissolution creating cavities, solution channels, and gullies or ravines between ridges and pinnacles of rock.

On review of available information, the superficial deposits comprise interbedded alluvium that is overlain by man-made fill. The nature of the superficial

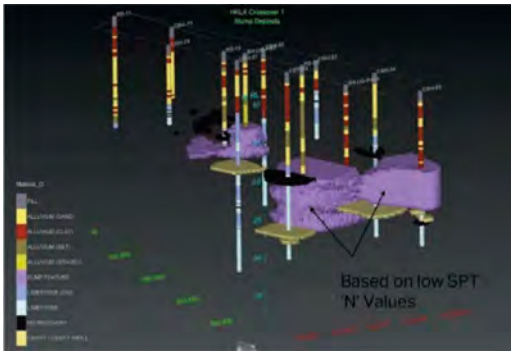

Figure 9. 3D subsurface modelling of slump zones.

deposits is also variable both in terms of material type (clay, silt, sand), and density or strength as identified from the results of Standard Penetration Test (SPT). Typically, SPT values fall in the range of 10 to 50 with a small number of results in excess of 50 for tests carried out to a depth of around 40 m to 60 m below ground level. Below this depth the SPT value at some locations falls rapidly to less than 3. The presence of bedding implies that the soils have been transported and deposited. Nevertheless, there was insufficient information available to differentiate between the soils of the Young and Old Alluvium with any degree of accuracy.

3.2 *Hydrogeological model*

The hydrogeological conditions of the site are generally established based on piezometers and standpipe piezometer installed in the boreholes. The groundwater information obtained during of the boreholes were also assessed carefully. As presented in Figure 10, the measured groundwater levels have been converted into the water pressure at the base of the borehole at the time that the measurement was taken.

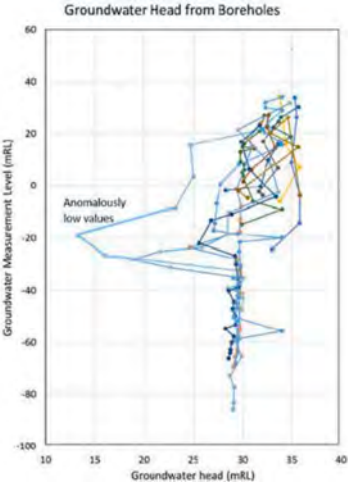

Figure 10. Groundwater level monitoring.

The information suggests that there is a perched water table, hydrostatic to +34 RLm in the upper 25 m to 35 m of the soils, with a general water table in the limestone and the soils immediately above the limestone that is hydrostatic to elevation +27 RLm. See Figure 11.

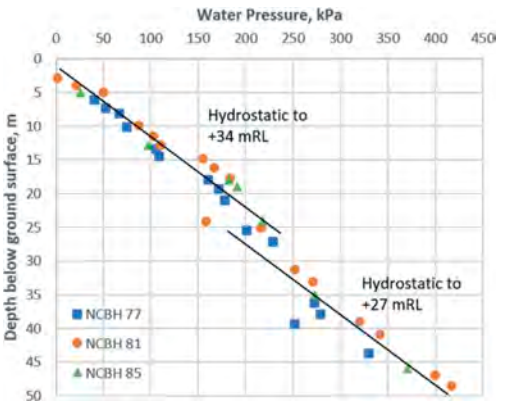

Figure 11. Perched water table condition.

The fact that there appears to be a perched water table at the site indicates that there are relatively lower permeability zones within the upper part of the alluvium, but that the overall mass permeability of the lower part of the alluvium and the limestone is higher (more permeable) than the overlying soils. This has important implications for the design of dewatering system for the HKLX box excavation.

4 GEOTECHNICAL RISKS ASSOCIATED WITH THE CONSTRUCTION

4.1 *Ground subsidence caused by borehole drilling*

At the onset of site investigation, the boreholes showed soil profiles with generally increasing SPT values with depth and then very low SPT values and reports of drilling rods dropping by several metres. The soils with very low SPT values, in particular which lie beneath firmer soils, were identified as slump material and there was a concern there might be an extensive slump zone underlying the HKLX box with karst limestone beneath.

Not only the identification of slump material, but also records of loss of drilling water, and observations of levels of water in boreholes several metres below the surface are indicators of an underlying drainage system within the limestone which was to be expected. Where soils are dispersive and/or erodible, loss of water from boreholes presents a substantial risk of remobilising flow into the underlying drainage system and of developing a sinkhole.

The first recorded instance of a large ground depression with localised subsidence was when extracting drill rods from borehole BH-UG-PB3A as shown in Figure 12. That was one of the boreholes where slump zones were identified. The largest localised subsidence occurred during the drilling of grout hole it was centred around a point about 10 m from the borehole. The maximum settlement was estimated at about 1.5 m, forming a conical depression or sinkhole with a diameter of about 27 m. The estimated volume of the depression was 300 m^3.

Figure 12. Ground depression occurred during soil investigation.

The presence of karst and slump material has serious implications to the HKLX box structure. This includes not only the design principles due to variable ground support but also the risk of ground subsidence both during construction and subsequent operation. Collapse of slump zone outside the HKLX box will cause undue settlement impacting on the surrounding sensitive structures.

4.2 *Unusual ground settlements and building distresses*

During the initial earthworks stage, the hostel structure has unexpectedly registered building settlements and movements that breached the predicted design values. There are areas on either side of the eastern half of the HKLX box, adjacent to Hostel Sejahtera, where there has been ongoing and persistent settlement at least since the surface settlement points were installed prior to major site activities. As an instance, the maximum settlement recorded was already 60 mm during diaphragm wall installation. The trend of large settlement and the speed rate of settlement indicates that settlement may have commenced before start of the monitoring, and that only a proportion of the total settlement has been captured by the settlement points.

Correspondingly, building settlement markers indicate that about 10 mm of settlement occurred at nearest corner of Hostel Sejahtera and up to about 2 mm at side of the building away from the excavation which is considered a significant distance from any work on site. While much of the settlement at the nearest point likely reflects that trenching for diaphragm walling, the further point of settlement was likely to be due to consolidation only.

The ongoing settlements of both the ground and adjacent structures was concerning, and the pattern

of settlement was strongly suggestive of being caused by ongoing groundwater drawdown. This situation has the potential to be worse when the full dewatering scheme for the excavation is in progress.

4.3 *Seepage/dewatering risks*

Most of the standpipes/standpipe piezometers installed at the site have shown a trend of falling water levels since installation, particularly those with any initial reading significantly higher than +27 RLm. The falling water levels in the standpipes are consistent with the standpipes acting as drains, allowing water from the upper, perched water table to drain into the lower aquifer.

Dewatering will be required to lower the water table below the final excavation level and maintain the temporary excavation in dry conditions, therefore preventing base blowout of the alluvial deposits, lowering of groundwater outside the excavation and ensuring the passive pressure support on the diaphragm walls are among the key considerations. From the review of all available data, the possible ground model used for seepage analysis is shown in Figure 13.

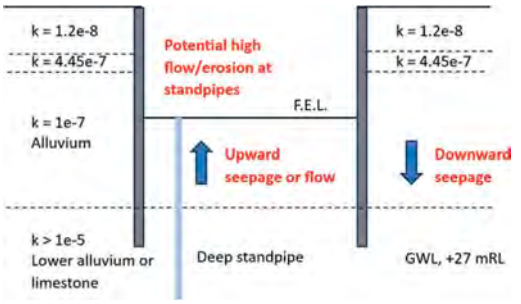

Figure 13. Ground model for seepage analysis.

Based on Figure 13, a number of possible failure mechanisms may occur, such as piping into the base of the excavation due to erosion along the deep standpipes/standpipe piezometers, hydraulic uplift on the base of the upper alluvium exceeding the weight of the upper alluvium in the base of the excavation. If the lower aquifer is deliberately dewatered or is linked to the base of the excavation by the standpipes/standpipe piezometers or wells, then the upper alluvium outside the excavation will be underdrained, potentially leading to further consolidation settlement of the alluvium. On the other hand, significant flow may also occur at steady state conditions through the limestone outside the excavation if preferential high permeability paths, due for example to the presence of cavities, solution channels, and discontinuities in the rock mass, are present within the limestone. Continuous flow through the rock mass from above the limestone outside the excavation may potentially cause loss of fines from the ground overlying cavities with risk of formation of sinkhole if the soil collapses into the cavities.

5 PREVENTIVE AND MITIGATION MEASURES

5.1 *Enhancement of temporary works design*

The main engineering concept underlying the design of HKLX underground structure is load compensation, i.e. it does not impose any load upon the ground on which it is to be founded that is greater than the load to which that ground is already subjected. The foundation system acquires its resistance from subgrade reaction below the base slab plus frictional resistance (outer face) of the diaphragm walls again the soil. The toe level of diaphragm wall was determined according to consideration of toe stability rather than vertical load-bearing capacity in order to minimise the potential for disturbance of the slump zone. Resistance to uplift/flotation shall be provided by the diaphragm walls and cross walls shaft friction.

By taking into account the above factors, the mass of the HKLX structure including its foundations was carefully limited such that there is no net increase in effective soil stress at depth. The box structure has been designed to be robust in addressing the known slump zone risks. It was also in a later stage that the temporary works design was further enhanced by introduction of secondary cross walls resulting to higher structural rigidity towards the eastern end of the box to mitigate the adverse risk of damage to the adjacent structures, in particular the Hostel Sejahtera. See Figure 14.

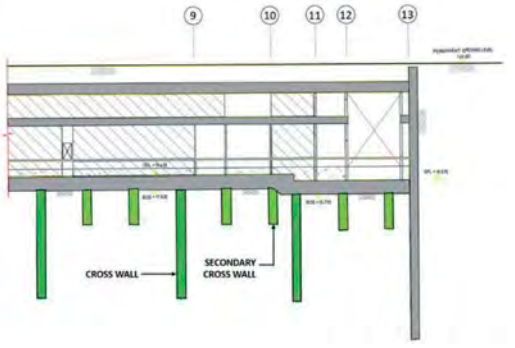

Figure 14. Secondary cross walls added at the eastern portion of the HKLX box.

5.2 *Capping and compaction grouting*

Prior to excavation, extensive compaction grouting had been performed at pre-determined depths and at targeted risk areas, i.e. within the eastern portion of the HKLX box, to address potential ground collapse and/or migration caused by future development and future progression of the karstic subsurface environment.

The proposed grouting mitigation measure is intended to densify the slump zones and to cap the top of the limestone rock head (if encountered) to prevent collapse/flow of fines into underlying

cavities. The slump zone treatment was based on an observational approach of limiting grout volumes or pumping pressures. The grouting will be terminated once the volume or pressure criteria has been achieved through firstly, delineation of slump zone by primary injection points, followed by secondary injection points then tertiary injection points, as necessary. As shown in Figure 15, the grouting has been concentrated in the area where slump zones have been recorded in the boreholes, and particularly where there were large surface depressions when drilling investigation or grout holes.

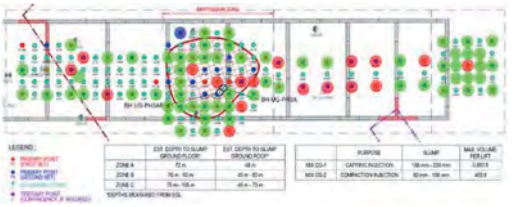

Figure 15. Compaction grouting points.

Similar grouting methods were used, largely successfully, to improve soft mine tailings and karstic cavities for the driving of the SMART tunnel (Raju & Yee, 2011). Although carried out at a much shallower level, this prior experience suggests that compaction grouting can have a beneficial effect in terms of improving soft soils in a karstic environment.

5.3 *Change of construction sequence*

The original planned launching dates were unable to be met due to the unforeseen ground conditions which require a series of ground improvements to be carried out in advance to address the incidents of ground depression/large settlements which happened within the worksite and proximity to the Hostel Sejahtera. In order to avoid further delays to tunnelling program, a proposal was made for new launching arrangement which is from western section of the HKLX box with reduced launch shaft length of 75 m as indicated in Figure 16. This also has beneficial effects as part of settlement mitigation for the eastern section of the box.

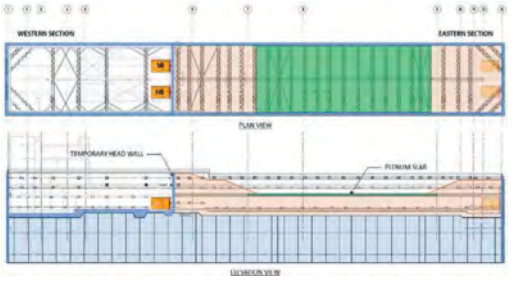

Figure 16. New launching arrangements.

By relocating the launch location about 165 m away from the original location, Hostel Sejahtera will be outside the zone of influence of the TBM initial drive.

The western and eastern sections of the box were constructed with differing excavation and construction methodologies. They were separated by a bulkhead wall located at Gridline 6. Splitting the box in this manner allows the eastern section to be built in a semi top-down construction method that will have reduced ground settlements in comparison to a bottom-up construction method.

5.4 *Pumping test*

As part of a due diligence process, pumping test was conducted prior to bulk excavation at the eastern portion. The primary objectives of pumping test were to evaluate the groundwater regime and the potential adverse impacts that dewatering the excavation may have on adjacent sensitive receivers, in particular Hostel Sejahtera as well as the effectiveness of hydraulic cut-off provided by diaphragm wall. The pumping test was also to help to evaluate whether an impermeable layer and multi-layer aquifer scenario was present.

The pumping test result has eventually verified the presence of a perched water table separated from the sub-artesian aquifer possibly by intermediate low permeability stratum albeit with spatial variance. A degree of vertical hydraulic interconnectivity (drainage paths) has been demonstrated between the upper and lower groundwater regimes. However, the likelihood of significant groundwater drawdown or settlement being induced outside the excavation area during dewatering was anticipated to be limited in view of adequate hydraulic cut-off provided by the diaphragm walls. Besides, the recharge well mitigation measures were already in place and available for immediate activation. Having said that, attention should be given to the potential of encountering high level karstic limestone during excavation and dewatering. The possible presence of preferential flow paths (piping) with the karstic material may potentially adversely impact on the lower aquifer as discussed in section 4.3.

5.5 *Control of construction dewatering*

To facilitate a dry bulk excavation, a suitable dewatering system was adopted to effectively control groundwater and limit settlements within predicted values. In order to avoid the hydraulic uplift failure when the excavation reached deeper level, additional pressure relief wells and piezometers were installed within the excavation zone of the box, as shown in Figure 17, to release the pore water pressure when required. The tip level of the relief well was defined by assuming the aquitard depth ranges beyond 20 m below the surface. The water pressure was calculated according with the highest piezometer head reading measure from the pumping test results.

Figure 17. Provision of piezometers and pressure relief wells.

As precautionary measure, all the existing boreholes and standpipe/standpipe piezometers were sealed with a grout/bentonite mixture to address and sever a potential groundwater connectivity effect across two aquifers by these devices. The areas disturbed by existing abandoned piles were regrouted.

5.6 *Other proactive measures*

Given the magnitude of ground settlements experienced in the initial stage and the timing requirement for other mitigation measures to be implemented, soakaway holes were installed along the existing box culvert between the hostels and the HKLX site. This was a proactive measured in view of the need to recharge as soon as possible, this passive recharge system will potentially allow a quicker recharge to be achieved, utilising existing stormwater and monsoon runoff flows as water sources. These sources were being channelled into a concrete U-shaped channel and discharged into the Bunus River located to the east of the HKLX site. The soakaway holes were intended to capitalise on the monsoon rainy season in lieu of, and in advance of the active recharge wells being installed around the hostels.

At the same time, recharge wells were installed around at spacing of 20 m to 25 m around the hostels. The purpose of these recharge wells was to actively recharge groundwater levels underneath these structures to at least 1 m below original ground water levels or a minimum 2 m recharge in groundwater levels from the existing observed levels as and when required. Other instrumentation includes standpipes and vibrating wire piezometers, combined inclinometer and extensometers, tilt meters, and building settlement markers were installed as per Figure 18.

6 CONSTRUCTION MONITORING

Similar to other underground construction sites in the project, comprehensive instrumentation and monitoring program was undertaken to provide timely feedback and ensure a safe construction.

The general pattern of ground settlement monitored at the site would be consistent with general consolidation settlement, supplemented by local

Figure 18. Groundwater recharge system and instrumentation.

settlement due to diaphragm wall installation, and other activities on site such as bulk excavation and dewatering. Figures 19 and 20 respectively illustrate the typical ground settlement and building settlement profiles for the critical area concerned, i.e. surrounding the Hostel Sejahtera. See Figure 18 for the location of the monitoring points.

Figure 19. Ground settlement profile (GSM16004).

The monitoring data showed the majority of the settlement occurred during the initial earthwork stage and when grouting work was carried out. It was thought that this settlement was due to consolidation of the upper strata, due to drainage of the perched water table in the upper strata into the underlying limestone aquifer. Stabilizing trends were observed after completion of diaphragm wall installation, including the cross walls and secondary cross walls.

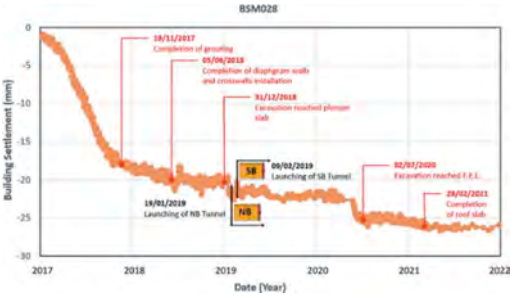

Figure 20. Building settlement profile (BSM028).

With the mitigation measures implemented and the stability of the ground verified by instrumentation-based performance, the excavation at western portion of the HKLX box proceeded with confidence. Both TBMs were successfully launched from the revised location and bored through the temporary slopes and underside of the plenum slab within the HKLX box before break-through the diaphragm wall. From the monitoring results, the ground and building settlements had stabilized with no appreciable further movements after completion of main basic structures of the HKLX box.

7 CONCLUSION REMARKS

The project site area is underlain by KL Limestone formation, where the rockhead is found to be highly irregular and the presence of network of voids, solution channels, slump zones and floaters. The inherent complex geology with extreme karstic features presents the engineer and the contractor with many unique challenges. Risk management and planning for projects in this challenging environment stemming from a full appreciation of the site history, a comprehensive knowledge of the geological and hydrogeological settings of the site. This would allow an assessment of impacts from the construction method and the consequential risks for the development of a robust risk mitigation strategy. It is necessary to supplement the process by effective implementation of the mitigation strategy and continued monitoring to ensure success.

The challenges of the deep excavation in a karstic environment are predominantly related to groundwater inflow through preferential flow paths due to karstic features resulting in consequential impacts form groundwater lowering, ground settlement and sinkholes. The groundwater lowering could induce a profound effect on the underlying slump zones leading to excessive ground settlement giving rise to damages on the nearly structures and the potential overstressing of the permanent underground railway structure.

This paper presented various robust measures to control and overcome the inherent geological risks present for the project. It is believed that comprehensive grouting cut off in the form of compaction grouting below the excavation base in advance of the excavation serves as the primary and most effective measure to mitigate and minimize groundwater inflow, thus maintain the existing hydrogeological setting as far as practicable. Any pre-existed boreholes and old pile foundations within the site remains a preferential seepage path, the importance of carrying out grouting to sealing off these features cannot be overstated. To further control the risk of potential heave of the base due to high piezometric water pressure at depth, passive relief well system was installed, if necessary, the passive relief well can be put into action to lower any excessive water pressure to ensure a stable base.

Other risk mitigation measures pertaining to structural aspect include the provision of cross wall below the formation level to achieve a stiffer box structure to cater for unbalance loads and differential movement resulting from the highly heterogenous site conditions. The permanent structure is designed as a floating structure to maintain vertical load balance and avoidance of additional loading onto the underlying slump zone causing undue settlement. The nearby structures have received strengthening and propping to increase their resilience to ground settlement. Extensive instrumentation and an action plan were deployed for this project to allow ongoing assessment of the monitoring results to ensure the performance of the work.

Upon implementation of the robust mitigation measures, the excavation was completed on time and on program. The TBM retrieval and relaunch was successfully completed in accordance with the program. The case history serves as a testimony to demonstrate how good geotechnical understanding, adequate design provision, exceptional construction planning, good construction practice together with a well plan risk mitigation prerequisite can lead the project to ultimate success on time and in a safe manner.

REFERENCES

Geological Survey of Malaysia, 1993. Bedrock Geology of Kuala Lumpur. Solid Geology, Sheet 94, Series L8010 part of Sheet 94k.

Golder Associates (HK) Limited, 2017. Independent Peer Review of Ground Conditions at Hospital Kuala Lumpur Crossover Box. Report No. 178112005-R001. Submitted to MRT Corporation Sdn. Bhd.

Hutchinson, C.S. & Tan, D.N.K., 2009. Geology of Peninsular Malaysia. University of Malaya and the Geological Society of Malaysia.

Raju, V.R. & Yee, Y.W., 2011. Grouting in Limestone for SMART Tunnel Project in Kuala Lumpur. Proceedings of International Conference and Exhibition on Tunnelling and Trenchless Technology, 7-9 March 2006, Selangor, Malaysia.

Tan, B.K., 2006. Urban Geology of Kuala Lumpur and Ipoh, Malaysia. Proceedings of the IAEG Congress, 7-11 September 2006, Nottingham U K, Paper No. 24.

Waltham, A.C. & Fookes, P.G., 2003. Engineering classification of Karst ground conditions. Quarterly Journal of Engineering Geology and Hydrogeology, Vol 36, No. 2.

Tunnelling for a Better Life – Yan, Celestino, Thewes & Eberhardt (Eds)
© 2024 The Author(s), ISBN 978-1-032-80042-4
Open Access: www.taylorfrancis.com, CC BY-NC-ND 4.0 license

Comparing underground construction risk for urban transportation and hydropower projects – A lender's technical advisor's perspective

Andrew Noble*
WSP, Sydney, Australia

ABSTRACT: With the resurgence of pumped storage hydropower as a key enabler for the world's green energy targets, and with the ever-expanding development of urban tunnels for road and metro transport systems, this paper provides a holistic overview of the key risks related to the underground works for each type of project as viewed from the perspective of the project's lenders' technical advisors. Infrastructure across the globe is increasingly heading underground: in urban areas the competition for affordable space forces many new road and rail systems to be in tunnels. Similarly, in remote, large, pumped storage hydropower projects a significant proportion of the scheme is usually located underground but for differing reasons than urban congestion. The categories of types of tunnelling risks in urban transportation projects are similar to those at remote hydropower projects, but the scale and levels of uncertainties associated with those risks can differ widely. For instance. the frequency of drilled geotechnical investigations, and hence the knowledge gained prior to construction, is an order of magnitude larger in the urban shallow transportation tunnel project where typical depths below ground are less than 50m, whereas in large, remote hydropower the average depth may be several hundred metres and the boreholes be spaced significantly further apart. The paper further explores the role of the Lender's Technical Advisor (LTA) in identifying and mitigating tunnel and underground risks in hydropower projects on behalf of the project lenders. It describes the typical services required to manage the four key phases of: due diligence, pre-financial close, construction financing and operational financing. The paper compares some of the risk management considerations in the planning, design, and construction of tunnels for the conveyance of water versus transportation, from the viewpoint of different stakeholders to the project, but in particular from the project's lenders, and explores the differences in the typical levels of geotechnical investigation undertaken for these two types of tunnel use.

Keywords: Tunnelling, Risk, Financing, Pumped Hydropower

1 INTRODUCTION

When comparing the pre-construction uncertainties in tunnelling ground conditions between urban transport tunnels and remote pumped hydro project, the uncertainties are much higher in the hydro project. The reasons are many but can be distilled into two key causes: a) the opportunities to undertake cost effective geotechnical exploration at the tunnel depth are better in the shallow depth urban transportation tunnel and b) the urban setting provides a wide range of extremely valuable 'bonus' subsurface condition information from previously constructed projects in the locality such as deep foundations for buildings, sewers, deep pipelines, water utility tunnels and rail and metro transportation tunnels. No such bonus information typically exists in remote hydropower projects where the sites are usually greenfield.

Many pumped hydro and hydropower projects have debt funding. In these projects there is usually a lenders' technical advisor (LTA) appointed and embedded in that role representing the lenders, are a wide scope of services, encompassing both engineering and environmental and social aspects. Terminology varies between projects and the LTA role is also known as the Independent Engineer, Bankers' Engineer, Lenders' Independent Consultant, or Independent Certifier. The entity is selected jointly by the lenders and the project developer (the borrower of the loan from the financiers) but is usually contractually appointed, and the LTA's services paid, by the developer.

2 WHAT TUNNELS ARE REQUIRED FOR PUMPED HYDRO?

Pumped hydro is increasingly prevalent in countries where wind and solar renewable energy have expanded. The grid requires stability which is

*Corresponding author: andrew.noble@wsp.com

DOI: 10.1201/9781003495505-481

offered by the near instantaneous electrical power when a pumped hydro scheme starts up in generation mode and it can be used to balance the supply when other supply schemes have fluctuating outputs.

The concept is to use a closed system of stored water, of fixed volume (excluding evaporation from the reservoirs), to generate electricity by allowing water to flow by gravity from an upper reservoir to a lower reservoir through tunnels, shafts (or surface penstock pipes) and turbines. The same water is later pumped up from the lower to upper reservoirs through the same waterway facilities to refill the upper storage reservoir.

No two pumped hydro projects are the same and there is no pre-defined template for what features must be included. In terms of the underground works, a focus of this paper, the differences between the underground elements required for a large, pumped hydro and a conventional generation-only hydropower scheme, are small. This is because the pumped hydro still acts as a conventional hydropower scheme while in generation mode, operating almost the same as a conventional generation scheme. In the pumping mode, when water is pumped uphill back through the same tunnels and shafts waterways, conditions are generally similar and so there are very few material differences in the waterways except for possibly the requirement for additional surge chambers and tweaking of junctions to allow efficient water flow in both directions.

A key aim of the designer for pumped storage schemes is to develop as much head (the pressure differential between upper and lower storage reservoirs) over as little horizontal distance as possible, in other words to minimize the L/H ratio. This is principally for economic reasons and means that the tunnel waterways designer needs to understand the economic driver for the optimum layout.

A high proportion of total civil engineering costs will be associated with the tunnels and shafts in a typical pumped hydro scheme because the head is created within the underground works and the storage reservoir embankments/ dams are usually only low to medium height. Whilst not in the same league as large dams they will likely be categorized for dam safety purposes as 'large dams' due to extreme consequences of failure.

The greater the operating head usually means the greater the constructability challenges. Deep shafts usually more than 300m, and up to 1,000m deep, are often required in such schemes and an obvious optimisation is to consider reducing the total waterway length by making a steeply inclined shaft and shortening the lower tunnel length; conceptually this all makes good sense providing that the time and cost and risks are appropriately considered with experienced constructors during the design phase. A vertical raisebore shaft say 500m deep is far more straightforward than an inclined 60-degree shaft of similar depth although there can be significant cost savings in material costs in shortening the overall waterway lengths especially if the shaft and lower tunnel are to be steel lined, and there are plenty of precedents where the steeply inclined shaft was selected.

3 THE LENDERS' TECHNICAL ADVISOR'S ROLE

The lenders and owner (borrower in this context) will have similar objectives for the project – they each want a successful project delivered safely, on time, and to budget. This is not surprising if we consider that the lenders are effectively the majority owner over the tenure of the loan which is usually 10 to 15 years after the completion of the project.

The LTA represents the lenders across a wide spectrum of technical issues that could arise over the lifetime of their involvement in a project. Flexibility is a key attribute for the LTA, including having the depth of in-house expertise to cope with issues that arise during any of the four key phases of services (due diligence; pre-financial close or 'bankable' stage; construction monitoring; and operations).

The LTA is usually engaged in the pre-financial close stage to undertake a due diligence assessment of the project, once the draft construction contract(s) is available for review, and then continues long after the opening or completion date to monitor the technical and commercial performance of the project.

The lender that engages the LTA is looking for advice on contractual and engineering topics, as well as the growing importance in environmental, social and governance (ESG) matters. With the lenders' reputation at risk if a project fails to follow good ESG practice, the importance of independent monitoring and reporting throughout the construction and operations periods is clear.

The LTA needs to undertake a materiality test for any issues – could it materially impact the lenders' interests? If not, the LTA should not be bringing such issues to the financiers.

4 TYPES OF UNDERGROUND RISKS

4.1 *Overview*

In remote hydro projects which are likely to be located in steep terrain, and possibly sited beneath national parks with restricted access, the available open space for tunnel portal establishment is usually constrained which puts pressure on the environmental management of water management and the siting of adequately sized sedimentation tanks. Achieving a high environmental and sustainability scorecard for the project is important to lenders as most will be committed to supporting projects incorporating ESG good practice and high levels of environmental and social safeguards into their credit approval process. This example is used to provide some balance to the more obvious risk in tunnelling, the ground conditions

uncertainty, which has the potential to dramatically change the time and cost to construct the tunnels.

Lenders will expect the LTA to examine the project in detail to assess that the project will function as planned and produce the revenues needed to meet operating costs and service the debt. Hydropower tunnels earn their position as part of a revenue generating project by delivering water to a generating turbine, whereas a road tunnel earns its payback position through access to vehicles paying toll revenues.

4.2 *Delay in completion*

A major construction delay will likely exceed the cap on the liquidated damages (LDs) for delay applied against the contractor, as beyond those periods, the developer tends to bear most consequential risks (typically the monetary value of caps is 10% of the Contract Price and daily LDs set such that the cap is reached linearly after 6 – 9 months of delay). From general precedents of hydropower tunnels construction in remote locations the lenders may be advised of three broad categories of reasonable expectations of delays:

- 3+ months for a realistic potential delay (statistics show that actually, this is probable)
- 6+ months for the possible delay of an unforeseen event with major consequences
- 12–18 months or more for major unforeseen conditions resulting in an extreme delay (these durations of delay are significant, probably beyond the Sunset Date in the finance agreement and may trigger some form of loan restructure).

The LTA would give an opinion on the probability of occurrence and recommend the level of stress testing to be applied to the borrower's financial model to account for such scenarios.

4.3 *Failure after operations commence*

Tunnelling delays are more likely to occur during construction, leading to a delayed commercial operation date. Unfortunately, however, there are numerous examples of headrace tunnel collapses early in the operational phase which have led to very serious outages in the operational phase and the consequential costs to the owner at this stage are significant. Unlined tunnels, unless located in extremely competent rock, are susceptible to changed conditions at or just beyond the rock inner face, which over time and after subjected to internal water pressure can deteriorate leading to a loss in the self-supporting mechanism.

5 KEY FEATURES OF THE TUNNEL TYPES

5.1 *Urban transportation tunnels*

The dominantly used tunnelling techniques in urban schemes are tunnel boring machines (TBMs) and roadheader; drill-and-blast excavation is used but is much more rare. TBMs are usually well suited for long transportation tunnels and their abilities to navigate the long radii dictated by functional requirements of alignment/ geometrical grounds for road or rail are not normally onerous for TBMs. The typical long tunnel lengths in major transportation projects justifies their use.

In urban settings the depth below surface is modest; typically less than 50m is the norm in relatively level surface urban terrain, and much shallower at stations in the case of rail schemes.

5.2 *Pumped hydro and hydropower tunnels*

5.2.1 *Types and constraints*

The pumped hydro tunnel designers have more geometrical freedom to suit the functionality of the tunnels and can take advantage of the absence of the tighter geometrical constraints applied to the transport tunnel. However, the hydropower pressure tunnels that may appear to be simplistic because they are usually circular and only carry water, not vehicles and passengers, are subjected to a very different set of operational conditions to urban transport tunnels.

5.2.2 *River diversion tunnels*

River diversion tunnels feature high on the risk assessments of hydropower projects: their function is to have a short operational lifespan, say two to three years (up to three wet seasons), while carrying high velocity silt-laden abrasive river water and probably flood debris through the tunnel. These tunnels are normally on the first stage critical path which is governed by seasonal river flows thus placing increased pressures on the organizational skills of the newly mobilized site team.

Unless the project's dam construction phase can withstand a potential delay equal to the length of a wet season or more, a missed river diversion date will be very costly and so the tunnelling schedule is normally non-negotiable. Given that for many projects the actual contractual commencement date is rarely as planned it is even more important to understand the implications of river diversion scheduling. A major project risk with emerging climate change conditions is the early onset of an annual wet season bringing early floods in the river and the construction team needs to have robust contingencies in place.

The designer needs to understand what range of flows and possible debris or siltation loads could be carried through the tunnel. Flat or large-radius inverts are commonly used because they offer advantages for construction equipment and in times of lower dry season diversion flows the erosion forces from heavy silt loads are better distributed over a wider surface. The long-term durability aspects may be of lesser concern if there is to be no future use of the diversion tunnel, however there is

normally at least part of the tunnel that becomes connected to an outlet or is plugged with a flooded section upstream, thereby requiring that the tunnel still be designed for the full project life.

The main duty however is to withstand the high velocity conveyance of the river diversion flows and to ensure that it has a very robust lining that meets the hydraulic requirements and is not adversely affected by erosion from silt or damage from debris. The diversion tunnel will be subjected to relatively low internal pressures during its diversion phase.

5.2.3 *Main waterway tunnels*

Headrace tunnels carry water towards the turbines in generation mode and will operate at low or high internal pressure depending on their setting level below the upper reservoir. In smaller run-of-river schemes some headrace systems adopt open-channel (non-pressurised) flow and may not even be within a tunnel.

The tailrace tunnels, as defined in a conventional hydropower project or in a pumped hydro in generation mode, return the water back to the river (or lower storage reservoir) after passing through the turbines. They operate at a lower pressure than in the headrace system as the turbine-generators extract the energy from the head for the generation of electricity.

These tunnels will likely by fully lined, normally having a circular profile or at least a D-shape with semi-circular crown, lined either in concrete or steel (not shotcrete, this is ill-advised). The adoption of unlined waterway tunnels is now rare on safety during construction grounds, therefore this paper concentrates on those which are fully lined.

5.2.4 *Access and service tunnels and caverns*

Hydropower schemes that contain headrace tunnels, shafts or caverns will require access tunnels and adits. For schemes with a powerhouse cavern there could be several kilometres of tunnels spiralling down from the surface to cavern level. A modern cavern arrangement requires a complex arrangement of various openings: access/ egress adits, ventilation/ cable tunnels, shafts, surge tunnels, etc. Consideration must therefore be given to flooding of the decline during construction or in the operational stage, permanent dewatering arrangements and provision of fresh air to the decline(s) during maintenance inspections. Fire and life safety aspects including emergency egress provisions are also very important considerations.

5.2.5 *Hydropower tunnel construction methods*

TBMs are well suited to most long headrace and tailrace tunnels, typically justified where the length is at least 500 times the diameter, but they are not suited to the scheme's complex warren of tunnels in the vicinity of powerhouse caverns due to the tunnels' steep grades and tight curves.

In remote areas, the use of drill-and-blast tunnels with multiple headings remains the most common method of excavation. When considering, for example, a 20 km length of transfer tunnel of diameter 7 m, there will be clear advantages and disadvantages for both the TBM and drill-and-blast options. The 7 m diameter sits neatly within the constructability comfort zone for both methods, so the decision comes down to scheduling due to its length, economics, logistics and availability of suitably skilled labour and back-up. A 20 km tunnel is too long to be justified for a single TBM given the likely project time constraints that most projects have, so therefore two or three TBMs might be considered viable to meet the schedule and budget. However, the mobilisation of multiple TBMs to a remote area is a major undertaking. With modern computer-controlled drilling jumbos the progress rates in drill-and-blast are impressive, despite the likely need for multiple access adits to be constructed to service the multiple drill-and-blast headings.

6 KEY COMPARISONS OF THE GEOTECHNICAL INVESTIGATION PROGRAMMES

As shown in (Noble 2023a) the differences in the levels of investigations typically undertaken for the two types of tunnels are far apart. The reasons are numerous, and some key reasons are explained in the next sections which consider a simplified example of a 15km long project; a shallow depth urban rail tunnel, comprising twin tubes, and a large and remote hydropower project spanning 15km overall length of waterway tunnels.

For a not dissimilar cost, both projects might undertake a comparable amount of total subsurface drilling, however the targeted and most relevant data obtained from the very deep holes in the hydro project would be significantly less frequently spaced than in the urban rail project.

Let us consider two similarly sized tunnelling projects:

- An underground railway or Metro within a city. 15km length, twin tunnels of 7m diameter, and seven station boxes, average depth to crown below surface of 40m (so six stretches of tunnels between stations each length 2.5km, ignoring station box lengths)
- An underground high-head hydropower (or pumped storage hydro) project: 15km of waterways length, single waterway comprising headrace tunnel, pressure shaft, pressure tunnel and tailrace tunnel, all 7m diameter, varying depth to crown below surface ranging from 100m to 800m.

The railway tunnel project will have relatively easy and cost-effective access to drill holes closely

spaced along the alignment which when added to the existing data knowledge from the built environment such as other tunnels and buildings with deep foundations, the data bank is very large.

The hydro project must start from almost zero existing first-hand knowledge of the conditions at depth. It is unlikely that any nearby projects would have any data at depth and if there were the extrapolation assumptions would be high; and quite likely for there to be nothing at all already available. To reach a tunnel located 800m below the surface will require a hole of slightly longer than 800m deep to be drilled, to obtain the primary data from within the 35m long primary data zone, hence most of its length is 'secondary' and necessary just to reach that zone.

6.1 *Drilled boreholes for urban transportation*

The urban transportation tunnel, either for road or rail, will be in areas where access is generally easily obtained through special permits to undertake drilling. Access can be challenging but normally very achievable, with good access to back-up support.

The urban rail or road tunnelling project will very likely have access to subsurface geotechnical data at an average of much less than 100m spacing along the tunnel, and in some zones have several boreholes concentrated together. For this comparison between the two types of tunnelling projects, consider there are new boreholes funded by the rail project at feasibility or tender stage at 100m spacing along a 15km alignment starting in a CBD and reaching out to the suburbs. This ignores the additional holes for the stations, some of which might even be in caverns, so this baseline data set for the rail project is a low estimate. The average hole depth will be less than 60m (~40m to crown plus the tunnel D plus the 1.5D below the tunnel), making a total drilled length of 8,625m based on 150 boreholes.

6.2 *Drilled boreholes for pumped hydro and hydropower*

Compare the above example with drilled boreholes for the remote hydro project having just ten boreholes planned over the 15km long scheme ranging in depths from surface to tunnel crown from 100m to 800m. Other holes would be needed for service tunnels used to gain access down to the caverns, however this example just compares the power system waterways as it can be simply envisaged as a comparison with the urban rail tunnel example previously described. Eight holes are for exploration of tunnels and caverns at varying depths and two holes are for shafts.

This programme could yield a total drilled length of 4,425m based on 10 boreholes.

6.3 *Why is there such a difference?*

Again from (Noble, 2023a), boreholes drilled in the geotechnical investigation program are planned to target a primary data zone (PDZ) in the vicinity of the tunnel itself. This is to obtain data directly within the envelope of the proposed tunnel opening size plus immediate influence zones surrounding the tunnel opening. For shallow tunnels in the urban setting typically the PDZ will overlap with the whole of the zone above the tunnel up to the ground surface, as data within that entire zone in an urban setting is considered primary as it needs to be modelled for potential interaction between the proposed tunnel structure and the surrounding existing structures, for example to assess the potential surface or subsurface settlements.

For deep tunnels, typically those for hydropower in the several-hundreds of metres depths, boreholes will also yield secondary data as the hole is drilled from the surface to reach the PDZ. Whilst the secondary data is important for building a geological model, it is considered herein as secondary as it has far less direct influence on the tunnel structure design than that generated from the PDZ information.

The above descriptions of primary and secondary data zones are highly simplified but used here to illustrate one of the key reasons why the amount of primary data obtained for remote and deep hydropower tunnels differs so much from the primary data obtained for urban transportation tunnels. Cost of the boreholes and environmental constraints for access for drilling are major factors, but the depth to simply obtain the critical information from within the PDZ is the underlying reason.

6.4 *Cost comparison and value for the effort*

The comparative cost of the two drilling campaigns is not assessed here, however given the relative ease of undertaking 150 shallow depth urban holes with a total drilled length of 8,625m compared to the challenges of mobilizing workers, equipment and consumables to undertake 10 deep remote holes in mountainous terrain with a total drilled length of 4,425m the overall costs may not be too different. However, the urban project yields a magnitude higher degree of frequency of PDZ information. If the cost was similar, the risks must be significantly higher for uncertainty of ground conditions in the hydropower project.

Another metric such as the number of boreholes per km length of tunnel would be for the above examples:

- The rail project: 10 holes per km
- The hydropower project: 0.67 holes per km.

7 RISK MANAGEMENT ON BEHALF OF THE LENDERS

7.1 *Overview*

The preceding sections set the scene that there are usually fairly high uncertainties in tunnelling ground conditions, especially in remote hydro tunnels. The LTA has a core role associated with risk management for the underground works, whether at the initial due diligence phase, throughout the construction phase, or into the operational phase.

The project's contractual arrangement will identify where the risk apportionment lies between the owner and contractor(s). A contracts review will be undertaken, and the LTA will liaise with the lenders' legal advisors in the due diligence phase when several advisors will be undertaking separate due diligence assessments – such as technical, legal and insurances.

As covered in (Plummer 2022a), key findings from the analysis which focused on large hydropower projects in low- and lower-middle income countries suggested that many of the greatest risks associated with large hydropower projects are those that may cause reputational damage to the parties involved, such as social and environmental risks.

7.2 *Geotechnical uncertainty*

Several key issues must be addressed at the outset of a feasibility study or reference design:

- How many boreholes are sufficient?
- How many boreholes are affordable, and achievable, given access constraints?
- What alignment shall we drill, knowing that alignments may change?
- What can we defer to a later stage and leave to the EPC contractor, and would this be a wise decision to take?

These questions arise in most projects, and it requires experience of what is important to make those decisions, but there must be a minimum level of investigation that needs to be done prior to construction tendering, and prior to obtaining credit approval from the lenders.

It is recommended that a two-stage feasibility study is arranged which allows investigations to be tailored towards the preferred options, but there is no avoiding having to invest in some 'at risk' speculative investigations on which to base initial designs (Plummer, 2022a). This is a risk the developer needs to take. A key message from this is that the developer will end up paying to deal with the geotechnical conditions but will ultimately likely pay less overall if more is spent upfront simply because a civil contractor will add a price for the risk element which outweighs the cost of investigations.

For hydropower projects a significant proportion of the risks is in the tunnelling and underground works (McWilliams, 2014) (Plummer, 2022a and Plummer, 2022b), mainly due to uncertain ground conditions associated with the fact that it is significantly more costly, difficult and time consuming to obtain the same level of geotechnical exploration for deep and remote hydropower tunnels than would normally be obtained for shallow depth urban transportation tunnels (Noble, 2023a). Contractually this aspect needs to be made clear as to which party takes the risk of changed ground conditions from the conditions known at contract signing, and the lenders are very keen to understand how the downside scenario risk profile would affect the borrower of their loan (Noble, 2018).

7.3 *Contractual risk and apportionment for price and time uncertainty*

Whichever contractual arrangement is pursued, such as single EPC contract or split contracts, the lenders will look for assurances that the project features are sufficiently developed to be compatible with the contractual mechanism in the construction contract and will look for risk mitigations for cost and time risk such that the borrower is not over exposed. In the case of the tunnelling components of a project this may have a separate contractual mechanism linked to a risk sharing concept, but if this is done the lenders would still want to know the potential downside scenarios for its borrower.

It is reasonable to assume that the differential in pre-construction stage data between the urban transportation tunnel project and the remote hydro project will remain broadly similar throughout all stages of each project. At the initial concept stage, the urban transportation tunnel project will be far ahead of the remote hydro tunnel project in terms of existing knowledge of expected ground conditions, due to the presence of existing city-wide geotechnical data. At best the hydro project will have benefitted from a geological walkover of just the accessible areas, but these are surfaces located several hundreds of metres above the proposed tunnels.

Ultimately the remote hydro tunnels will never match the urban tunnels for metrics on data gathering. Therefore, the contractual mechanisms for tunnelling in the remote hydropower need to be in place for appropriate risk apportionment to deal with the inevitable higher levels of uncertainty than exist in the urban setting. To deal with this there is a growing trend for at least the underground elements of hydropower projects to have a risk sharing mechanism to deal with the inevitable lower levels of certainty in geological conditions.

In large hydropower projects comprising tunnels as well as dams, electro-mechanical works, transmission lines and other supporting infrastructure, the underground works costs may not dominate the entire project cost. However, the unforeseen risks lie mostly here and so a target price type of contract can be developed with only the under-ground works

subjected to such an approach. This gives a better risk apportionment between the employer and the contractor and does make sense given that the owner essentially owns the ground through which the contractor is contracted to excavate.

The relatively new FIDIC form of contract, Conditions of Contract for Underground Works (2019 Emerald Book) is a welcomed new approach which covers risk apportionment of the underground works and is very relevant for use in hydropower. In conjunction with a geotechnical baseline report (GBR), which sets the boundaries of certain geological characteristics as derived from the pre-tender stage site investigation, and thereby sets a trigger level for exceedance, the target price mechanism (TPM) aims to deal with risk apportionment between the owner and the contractor.

8 CONCLUSIONS

The risk profile on the underground works from the lenders' perspective evolves over the life of a hydropower project, from due diligence (pre-financial close) stage, through construction financing and the operation financing, but it does not diminish altogether. Most attention is paid at the pre-financial close phase as this is when the lenders' influence, through the LTA and their other advisors, can impose further risk mitigations if considered necessary.

The LTA role may take a variety of pathways depending on the issues arising on each project. In the author's experience, the major issues are not always of a pure engineering nature, but related to deficiencies in owner's staffing levels, contractor resourcing, scheduling delays or environmental and social aspects.

In urban transportation tunnelling projects, the risks categories are similar to those at remote pumped hydro and hydropower projects, but the scale of those risks due to levels of geotechnical uncertainty can differ widely. The frequency of drilled subsurface geotechnical investigations is an order of magnitude larger in the urban shallow transport tunnel project where typical depths below ground are less than 50m, whereas in large scale and remote hydropower the tunnels may be up to several hundred metres deep. The spacing of drilled holes is therefore significantly further apart in the remote setting. Consequently, the useful data package is far more plentiful in the urban transport project.

For what could be a similar cost in undertaking the two different geotechnical investigation campaigns, the results from the two examples showed that the urban tunnel yielded 4 times the amount of directly targeted PDZ data than the hydropower project, and that PDZ data was distributed 15 times more frequently spaced along the tunnel alignment. This is further evidence that the urban tunnel will have a much lower risk profile for geotechnical uncertainty when compared to the remote hydropower tunnel.

No two transport or hydro projects are the same but there is a compelling argument for the adoption of increased site investigation in the remote hydropower project, together with a compelling case for the adoption of a robust risk sharing contractual mechanism.

ACKNOWLEDGMENTS

Acknowledgements for the insights into this paper are extended to all the project teams and people that I have had the pleasure to work with in the transportation tunnelling and hydropower tunnelling industries worldwide. The experiences and lessons learned formed the basis of what is written.

REFERENCES

McWilliams, M 2014. Geological Risk – Optimal design for risk management. Paper prepared for Hydro 2014 in Cernobbio.

Noble, A.G. 2018. Tunnel and Underground Risk in Hydropower – a Lender's Technical Advisor Perspective. Paper prepared for World Tunnelling Congress 2018 in Dubai. UAE.

Noble, A.G. 2023a. Comparing the issues, risks and levels of geotechnical investigation for remote hydropower tunnels with urban transportation tunnels. Paper presented as an e-poster for World Tunnelling Congress 2023 in Athens, Greece.

Noble, A.G. 2023b. The roles of the Financiers' Certifier in Urban Transportation Tunnels and as the Financiers' Advisor for Hydropower Tunnels. Paper presented at World Tunnelling Congress 2023 in Athens, Greece

Plummer Braeckman et al 2022 Environ. Res.: Infrastruct. Sustain. 2 015006. Financiers' perceptions of risk in relation to large hydropower projects.

Plummer J, Markkanen S 2022. Perceptions of risk in relation to large hydropower projects: a finance perspective.

Tunnelling for a Better Life – Yan, Celestino, Thewes & Eberhardt (Eds)
© 2024 The Author(s), ISBN 978-1-032-80042-4
Open Access: www.taylorfrancis.com, CC BY-NC-ND 4.0 license

Underground risk and ESG aspects in pumped hydro and hydropower projects – What worries the lenders?

Andrew Noble*
WSP, Sydney, Australia

ABSTRACT: Large scale pumped hydro and hydropower projects are complex developments and take several years of planning, design, assessment and contracting, followed by at least 4-5 years of construction, to reach the principal goal of generating electricity. Key concerns for lenders over the project lifecycle are the risks which may eventuate on environmental, social and governance (ESG) aspects and risks to the project outturn cost and completion date. The former are reputational issues, and the latter are financial issues. This paper assesses the question: "What worries the lenders?".

Firstly, dealing with ESG aspects for underground works, these are very wide ranging across the lifecycle of hydro projects. Lenders will typically be involved across four key stages of hydro project development: due diligence phase, pre-financial close ("bankable") phase, construction phase and operational phase. Each phase brings a different focus with the accumulated lenders' risk exposure (a blend of financial, technical, stakeholder and a variety of ESG issues), all ebbing and flowing as the project evolves. The paper explores the changing ESG risk landscape from the perspective of the project lenders.

Secondly, the uncertainty on the outturn cost and completion date are key elements of the techno-commercial risk position for the project. Most uncertainties in large, pumped hydro and hydropower projects tend to lie in the tunnelling and underground works and project-wide geotechnical and geological disciplines, as the ability to explore these thoroughly, for various practical, cost limitations or environmental reasons, is very low in most projects (especially when compared with the levels of ground investigation usually undertaken for large transportation tunnels in urban settings). Significant changes in encountered ground conditions, whether for the dams and reservoirs or in the tunnels and caverns, can lead to cost overruns and delayed completion and hence delayed revenue streams. The paper explains why this is so, explores the financial model stress testing to assess such scenarios, and makes some interesting comparisons from the hydro industry with the levels of exploratory investigations undertaken in large transportation tunnels in urban areas.

The paper explores the above risks through the ESG lens, and the ESG impacts and benefits of tunnels and underground solutions in these large projects.

Keywords: Tunnelling, Risk, ESG, Pumped Hydro

1 INTRODUCTION

Large scale pumped hydro and hydropower projects are complex developments and take several years of planning, design, assessment and contracting, followed by at least 4-5 years of construction, to reach the principal goal of generating electricity. Key concerns for lenders over the project lifecycle are the risks which may eventuate on environmental, social and governance (ESG) aspects and risks to the project outturn cost and completion date. The former are reputational issues, and the latter are financial issues.

The resurgence of pumped hydropower projects in Australia for example, has led to rapid learning curves for developers, most of whom are private entities, and with this the types and scales of development risks across all stakeholders are numerous and large. Coupled with modern and tighter ESG obligations, the pathway is complex. The whole tunnelling industry needs to awaken to tightening ESG requirements across all forms of tunnelling

*Corresponding author: andrew.noble@wsp.com

DOI: 10.1201/9781003495505-482

infrastructure, whether it is for transportation tunnels, water supply, utilities or the expanding field of pumped hydropower.

The uncertainty of the outturn cost and completion date are key risks for the project. The highest uncertainties tend to lie in the tunnelling and underground works, dams, and project-wide geotechnical and geological disciplines, as the ability to explore these thoroughly, for various practical, cost limitations or environmental reasons, is low in most projects. Significant changes in encountered ground conditions, whether for dams and reservoirs or in the tunnels and caverns, can lead to cost overruns and delayed completion and hence delayed revenue streams.

2 KEY ESG ASPECTS

2.1 *Overview of ESG aspects*

The Hydropower Sustainability Assessment Protocol, a product of the International Hydropower Association (IHA) is a tool for assessing projects across a range of social, environmental, technical and economic criteria. It is highly relevant to project developers and to all stakeholders in large hydropower projects which have significant underground works.

Some key ESG risks are presented below.

Environmental risks:

- Flora and fauna impact
- Impacts on water courses, either during construction or over a longer period, from abstraction or water movement and mixing
- Approvals timeline and the risk of having to repeat baseline studies to align with revised engineering approaches.

Social risks:

- Ownership of land.
- Community acceptance.
- The social licence.
- Resettlement or relocation (which are not the same), for example in developing countries.

Governance risks:

- How the project is procured
- What regulatory controls are in place
- Compliance with local and international ESG safeguards guidelines (for example, International Finance Corporation's Performance Standards or the Asian Development Bank's various Safeguards mechanisms).

2.2 *Lenders' credit approval incorporating ESG*

For a project to be successful in bridging the knowledge gap between the feasibility study and the requirements to reach financial close in the most efficient timeline, the feasibility study needs to be a very good study, have clear and defendable options assessment and to have adequately covered all the topics that lenders will require to have been addressed.

Lenders care about whether the project will generate adequate cash to repay the loan plus a margin against lower performing generation. Foremost these days, lenders care deeply about doing the right thing with regards to ESG matters and are very alert to the potential for reputational damage that will result from improperly planned and implemented projects.

In all of the three main types of hydropower (pumped hydro; conventional generation-only reservoir hydropower; and run-of-river hydropower) and across the range of sizes from mini-hydros at <5MW capacity to the mega projects at >2,000MW, the entirety of environmental and social aspects (being the E and S in ESG) have been assessed for decades. The current spotlight on the environmental and social aspects of ESG is therefore not a new approach at all. However, the equal focus on the governance of projects (the G in ESG) has formalised the entire ESG requirement. This formalisation has elevated the importance of ESG to Boardroom levels for all stakeholders in a project – owners, contractors, consultants, lenders, etc., and it continues to be a key element to be satisfied to obtain the Lenders' credit approval for debt funding to a project.

2.3 *The four phases of lenders' involvement*

Lenders will typically be involved across four key stages of hydro project development: due diligence phase, pre-financial close ("bankable") phase, construction phase and operational phase. Each phase brings a different focus with the accumulated lenders' risk exposure (a blend of financial, technical, stakeholder and a variety of ESG issues), all ebbing and flowing as the project evolves.

3 WHAT TUNNELS ARE REQUIRED FOR PUMPED HYDRO?

Pumped hydro is becoming increasingly prevalent in countries where wind and solar renewable energy have expanded. The grid requires stability which is offered by the near instantaneous electrical power when a pumped hydro scheme starts up in generation mode and it can be used to balance the supply when other supply schemes have fluctuating outputs.

The concept is to use a system of stored water, of fixed volume (excluding evaporation from the reservoirs), to generate electricity by allowing water to flow by gravity from an upper reservoir to a lower reservoir through tunnels, shafts (or surface penstock pipes) and turbines. The same water is later pumped up from the lower to upper reservoirs through the same waterway facilities to refill the upper storage reservoir.

Tunnelling for hydropower projects is a very challenging component of the overall development. In contrast to urban transportation tunnelling where the logistics for access and supply of electrical power, water and other essentials are readily available, hydropower projects are usually in very remote locations with challenging steep terrain and all necessary plant, equipment, spares and materials need to be brought in and the site must function as a self-sufficient unit.

For a large scheme the river diversion tunnel(s) are usually on the initial phase critical path to meet the non-negotiable deadline of river diversion before the onset of the next wet season. A newly formed tunnelling crew, once mobilised to the site for the project, will face the first major learning curve of the project's systems and logistics during this first and critical tunnelling activity. This is a challenge at a time when project systems and procedures are still being developed and fine-tuned.

Power tunnels convey the water to the turbines in the powerhouse and are usually on the critical path for the main works, especially if the scheme comprises a powerhouse located within an underground cavern. A modern cavern arrangement requires a complex arrangement of various openings: access/egress adits, ventilation/cable tunnels, shafts, surge tunnels, etc. All of these underground features have an impact to the ESG aspects of the project as they require rock spoil to be removed, possibly processed, and water managed to permit acceptable deposition. The assessment of the treatment and disposal of tunnel spoil and water is one of the biggest ESG aspects to be assessed for underground works for a large hydro project.

4 THE LENDERS' TECHNICAL ADVISOR'S ROLE

The lenders' technical advisor's (LTA) services and scope are always tailored to the lenders' needs for the particular project and their perceived key areas for concern, but with a largely common underlying terms of reference for most LTA roles. The LTA - also commonly termed the Independent Engineer, Bankers' Engineer or Lenders' Independent Consultant - is selected jointly by the lenders and the project developer (the borrower of the loan) but usually contractually appointed and paid by the developer. However, the LTA's selection process is rarely as straightforward as just described, given that the lenders will tend look for experience, reputation, and quality, whereas the developer will additionally be looking for the most competitive price for those services. In most cases the LTA services also include environmental and social monitoring, which is not always obvious from the term 'technical' in the role title. The increased spotlight on ESG issues has tended to increase these tasks within the typical LTA role.

The lenders and owner (the borrower in this context) will have similar objectives for the project – they each want a successful project delivered safely, on time, and to budget. This is not surprising if we consider that the lenders are effectively the majority owner over the tenure of the loan which is usually 10 to 15 years after the completion of the project.

The LTA represents the lenders across a wide spectrum of technical issues that could arise over the lifetime of their involvement in a project. Flexibility is a key attribute for the LTA, including having the depth of in-house expertise to cope with issues that arise during any of the four key phases of services (due diligence; pre-financial close or 'bankable' stage; construction monitoring; and operations).

The LTA is usually engaged in the pre-financial close stage to undertake a due diligence assessment of the project, once the draft construction contract(s) is available for review, and then continues long after the opening or completion date to monitor the technical and commercial performance of the project.

The lender that engages the LTA is looking for advice on contractual and engineering topics, as well as the growing importance in ESG matters. With the lenders' reputation at risk if a project fails to follow good ESG practice, the importance of independent monitoring and reporting throughout the construction and operations periods is clear.

The LTA needs to undertake a materiality test for any issues – could it materially impact the lenders' interests? If not, the LTA should not be bringing such issues to the financiers.

5 TYPICAL ESG CONSIDERATIONS FOR TUNNELS

5.1 *Overview*

Tunnels and other underground works may appear to be quite benign to ESG concerns. They will mostly not be visible at all, except for portals and shaft tops, etc. but their construction, and the potential for underground fire during operation, could lead to major ESG issues if not properly addressed at the design stage.

Some examples of ESG elements which need to be addressed are described below.

5.2 *Environmental*

- Water management: either from groundwater or water used for construction.
- Sediment removal: sediment ponds are required at portals to allow settlement of suspended solids prior to discharge of the water and the removal of the solids.
- Spoil disposal: large volumes normally need to be disposed of in a safe manner. If stockpiled at a remote site, using engineered methods and not

simply tipped to a natural angle of repose of the material.
- Contamination: of groundwater, water bodies or into the environment.
- Spills: of liquids and hazardous materials.
- Noise and disturbances.

5.3 *Social*

- Truck movements: strict monitoring and time of day usage.
- Safety considerations in the communities.
- Worker influx and interactions with community.

5.4 *Governance*

- Contractual requirements
- Conditions Of Approval (COA) linked to the environmental impact assessment
- Ownership and responsibilities for implementing the COAs, i.e. the governance.

6 RISK MANAGEMENT ON BEHALF OF THE LENDERS

6.1 *Overview*

In Project Financing, considerable attention is paid to risk and there are several unique features and risks associated with pumped hydro and hydropower projects that financiers need to be aware of. Lenders will examine the project in detail to assure themselves that the project will function as planned and produce the revenues needed to meet operating expenses and service the debt. The role of the LTA is to identify risks that might influence the viability of the project or affect the borrower's cash flow from the operational revenue and offer strategic advice on how to avoid or mitigate those risks. The lenders expect their technical advisors to point out whether the technology adopted is appropriate and what are the potential or realised items of concern (for instance, the selection of tunnelling methods when faced with a choice between a tunnel boring machine or a drill-and-blast technique).

As mentioned previously, the ultimate objectives of the developer and lender are the same – a successful project that delivers a satisfactory and sustainable financial return. The LTA's duty of care is to the lenders, whose objectives are largely aligned with the developer's.

Delays in completion can be serious events, in particular if the delay period exceeds the cap on the liquidated damages applied to the contractor, as beyond the period when the cap is reached (typically 6–9 months), the developer tends to bear most consequential risks. From general precedents of hydropower tunnels construction in remote locations the lenders may be advised of three broad categories of reasonable expectations of delays:

- 3 + months for a 'realistic potential delay' (this should be considered as highly likely)
- 6 - 12 months for the possible delay of an unforeseen event with major consequences
- 12 – 24 months or more for major unforeseen conditions resulting in an extreme delay.

Such delays are more likely to occur during construction and would therefore impact the completion date. However, instances of headrace tunnel collapses soon after operations commenced made the international headlines and led to very serious delays in operations. Unlike transportation tunnels where imposed loads on the lining hardly change once the vehicles or trains start using the tunnel, in hydropower waterway tunnels the internal and external water pressures are the dominant loads. The watering up of the system and then testing for sudden generation 'trips' which impose high transient pressures on the lining, often several years after constructed, is the first real test on the lining. Linings are mentioned here although the situation can be more severe and uncertain in unlined tunnels; observed stable ground during construction may disguise the softening or other change in characteristic of the rock once wetted, and particularly when the tunnel is dewatered and subjected to a rapid build-up of net external pressure.

Delays to tunnelling may lead to delays in wet commissioning of the station, i.e. if the tunnel and underground works are on the critical path (which they usually are) no water can be made available for trial runs until the waterway is fully connected.

When structuring the conditions of the loan and the payback model, the LTA may recommend that the model is stress tested to take account of the likelihood for delays resulting in consequential delays to the owner's ability to generating revenue and to begin to repay the loan.

6.2 *Geotechnical uncertainty*

Several key issues must be addressed at the outset of a feasibility study or reference design, or at whichever design steps are the predecessors to construction contracting:

– How many boreholes are sufficient?
– How many boreholes are affordable, and achievable, given access constraints?
– What alignment shall we drill, knowing that alignments may change?
– What can we defer to a later stage and leave to the EPC contractor, and would this be a wise decision to take?

These questions arise in most projects, and it requires experience of what is important to make

those decisions. But, there must be a minimum level of investigation that needs to be done prior to construction tendering, and prior to obtaining credit approval from the lenders.

It is recommended that a two-stage feasibility study is arranged which allows investigations to be tailored towards the preferred options, but there is no avoiding having to invest in some 'at risk' speculative investigations on which to base initial designs (Plummer, 2022a). This is a risk the developer needs to take. A key message from this is that the developer will end up paying to deal with the geotechnical conditions but will ultimately likely pay less overall if more is spent upfront simply because a Civil Works contractor will add a high price for the risk element which far outweighs the cost of investigations.

For hydropower projects a significant proportion of the risks is in the tunnelling and underground works (Plummer, 2022a and Plummer, 2022b), mainly due to uncertain ground conditions associated with the fact that it is significantly more costly, difficult and time consuming to obtain the same level of geotechnical exploration for deep and remote hydropower tunnels than would normally be obtained for shallow depth urban transportation tunnels (supported by the paper, Noble, 2023a). Contractually this aspect needs to be made clear as to which party takes the risk of changed ground conditions from the conditions known at contract signing, and the lenders are very keen to understand how the downside scenario risk profile would affect the borrower of their loan (Noble, 2018).

6.3 *A comparison of the hydropower levels of uncertainty with transport tunnelling*

As shown in (Noble 2023a) and summarised in (Noble 2024), a comparison was made between the differences in the levels of investigations typically undertaken for two similarly priced tunnel projects: an urban shallow depth rail tunnel system, and a remote hydropower with very deep tunnels. It showed that the levels of investigation and the amount of data per length of tunnel explored are far apart.

For a not dissimilar cost, both projects might undertake a comparable amount of total subsurface drilling, however the targeted and most relevant data obtained from the very deep holes in the hydro project would be significantly less frequently spaced than in the urban rail project.

In (Noble 2023a) it considered two similarly sized tunnelling projects:

– An underground railway or Metro within a city. 15km length, twin tunnels of 7m diameter, and seven station boxes, average depth to crown below surface of 40m (so six stretches of tunnels between stations each length 2.5km, ignoring station box lengths)
– An underground high-head hydropower (or pumped storage hydro) project: 15km of waterways length, single waterway comprising headrace tunnel, pressure shaft, pressure tunnel and tailrace tunnel, all 7m diameter, varying depth to crown below surface ranging from 100m to 800m.

The railway tunnel project will have relatively easy and cost-effective access to drill holes closely spaced along the alignment which when added to the existing data knowledge from the built environment such as other tunnels and buildings with deep foundations, the data bank is very large.

The hydro project must start from almost zero existing first-hand knowledge of the conditions at depth. It is unlikely that any nearby projects would have any data at depth and if there were the extrapolation assumptions would be high; and quite likely for there to be nothing at all already available. To reach a tunnel located 800m below the surface will require a hole of slightly longer than 800m deep to be drilled, to obtain the primary data from within the 35m long primary data zone, hence most of its length is 'secondary' and necessary just to reach that zone.

The comparative cost of the two drilling campaigns was not assessed, however given the relative ease of undertaking 150 shallow depth urban holes which yielded a total drilled length of 8,625m compared to the challenges of mobilizing workers, equipment and consumables to undertake 10 deep remote holes in mountainous terrain which yielded a total drilled length of 4,425m the overall costs may not be too different. However, the urban project yields a magnitude higher degree of frequency of relevant information in the vicinity of the tunnel itself. If the cost was similar, the risks must be significantly higher for uncertainty of ground conditions in the hydropower project.

Another metric such as the number of boreholes per km length of tunnel would be for the above examples:

– The rail project: 10 holes per km
– The hydropower project: 0.67 holes per km.

7 WHAT MOSTLY CONCERNS THE LENDERS?

7.1 *Overview*

The attempted fast-tracking of pumped hydro development from feasibility stage through to construction presents challenges for the due diligence stage in project finance. If the feasibility study or subsequent early designs have not been as thorough as the lenders may require to satisfy their credit approval processes, or if there are inconsistencies with the environmental impact assessment then delays will occur until the deficiencies are remedied. The lenders' credit approval process follows strict

requirements within defined boundaries of acceptability, especially on modern ESG issues. Depending on the jurisdiction, a variety of safeguard guidelines will be followed, collectively falling under the umbrella of ESG best practice requirements, and especially for those Equator Principles Financial Institutions.

In the case of Australia, many Australian lenders have not previously loaned to pumped hydro projects and will be wary of the risks. A risk evolution graph from the perspective of the lenders aggregating the perceived risks over the timeline of involvement of the lenders and across five key phases is presented in Figure 1. The five phases are: Development, Bankability, Construction, Defects Liability and Operational.

Figure 1. Pumped hydro project risk trend evolution – a lenders' perspective.

The defects liability period is included in the diagram because it represents a duration, usually 2 years, straight after project completion. At this juncture the debt service starts (loan is being repaid) and any teething problems with the plant are most likely to emerge.

7.2 *The greatest perceived risks*

As covered in (Plummer 2022a), key findings from the analysis which focused on large hydropower projects in low- and lower-middle income countries suggested that many of the greatest risks associated with large hydropower projects are those that may cause reputational damage to the parties involved, such as social and environmental risks.

7.3 *Credit approval*

Most lenders have strict requirements to achieve credit approval and if the developer has not understood those from an early stage, i.e., at the feasibility study, there is a likelihood of delays in reaching financial close until the gaps are filled. For environmental and social matters for instance, these assessments can require a very lengthy process of studies that are simply not appropriate for fast-tracking. The gathering of environmental or social baseline data can be at best seasonal but may also be annual or even multi-year, hence a long time is needed. However, providing the lenders' advisors (typically for legal, technical and insurance aspects) are engaged early enough, then in the road to financial closure there are ways to effectively deal with the actions stemming from the LTA's due diligence so that they are prioritised into various categories to be resolved according to their criticality.

On several projects, large and small, the author has used a three-step categorisation to resolve actions arising from the LTA's due diligence:

Category 1 – to be resolved to the LTA's satisfaction prior to Financial Close (which also means prior to the lenders' timeline for achieving credit or board approval)

Category 2 – to be resolved to the LTA's satisfaction prior to First (or subsequent) Drawdown.

Category 3 – recommended actions to be addressed during Final Design or Project Implementation.

What do the lenders need to know?

Among the key issues that lenders need to know to obtain credit approval, the following items tend to dominate:

- Price certainty of the overall development. This is ranked first but it is by no means a guarantee. Just because a single wrap EPC Contract might appear to be less risky for the borrower in the eyes of the lender, there still remain uncertainties in ground conditions and therefore a better approach is to have a good risk apportionment plan.
- Environmental and Social status and the evolution of risks, i.e. the whole ESG position.
- Contractual arrangements and apportionment of risks between the Borrower and contractor(s).
- Engineer-Procure-Construct (EPC) or split contracts?
- Credentials of main contractors and equipment suppliers – have they recent and relevant experience?
- Implications of performance guarantees not being met.
- Accurate timelines for all steps – pre-financial closure; construction; commissioning and buffer times to establish loan sunset dates.
- Operation and Maintenance (O&M) Agreements – in-house or through a long-term services agreement?
- Planning restrictions.
- Grid interconnection and other local infrastructure (roads, quarries, spoil disposal areas, etc).
- Appropriateness of Owner's organisation, competence of its personnel and operational readiness of the completed facility.
- Power Purchase Agreement.

What does the LTA need to know?

The LTA will be required to opine on most of the above issues plus be informed of the following:

- What is the technology being employed; are there any 'prototype' technologies?

- Dam types, dam break assessments and public perception of new dams.
- Who is constructing it, and how is it being built (e.g. tunnels by TBMs or drill-and-blast)?
- What warranties are being provided?
- Once built, will it operate as planned?
- What is the nature of the Power Purchase Agreement; is it robust and are the lenders' interests protected?
- Can the power be delivered efficiently (i.e. is the transmission infrastructure in place)?
- Are the hydrological studies and energy yield assessments sound?
- Is the technical specification appropriate?
- Are the projected costs reasonable and are appropriate contingencies applied?
- What environmental requirements need to be met and social impact mitigation strategies need to be employed to meet Equator Principles and host country regulations?
- What are the completion risks?
- Is the completed facility going to be operated safely and competently, within the bounds of industry norms and the Power Purchase Agreement?

7.4 *The bankability test*

The concept of a 'bankable' feasibility study differs between stakeholders, but it is clear that such a test needs to assess at least the above aspects. Developers are usually optimistic that the feasibility study is completed to a standard that is acceptable to lenders, however that only becomes clear once the lenders have completed their due diligence reviews. The notion of a 'bankable' feasibility study does not merely mean having satisfactory financial and economic metrics – the project needs to pass other gates to be satisfactory to the lenders and to be 'bankable', most notably the ESG compliance test.

Consequently, in the period approaching financial close it is common for the lenders and its advisors to establish a set of conditions precedent (CPs) that are linked to either the financial close or to subsequent disbursements from the loan. The CPs may cover a range of topics such as commercial, contractual, technical, or environmental/social conditions for which the lenders require more comfort that the critical aspects have been, or can and will be, satisfactorily closed out at a set time (some items are mandatory prior to financial close, and others can be left to later milestones such as first or subsequent drawdowns, which would be known as Conditions Subsequent).

To give further reasoning as to why gaps are often identified in reviews of feasibility studies, the notion of a bankable feasibility study is discussed. It is rare to see feasibility studies that claim in their titles to be bankable, and the term is misleading anyway. With definitions ranging from 'likely to make money' to 'acceptable to a bank', no feasibility study at the time of submission to the owner can claim to be bankable until it is accepted by a lender and there are several steps to go through before that occurs. The feasibility study should prove a project's technical and economic viability, but not necessarily the bankability; it is the steps that follow which concern the bankability of the project, not the bankability of the feasibility study report itself.

The bank will decide what is bankable – after all, the bank provides the majority of funds and should be considered as the majority owner throughout the tenure of the loan, assuming a typical 70:30 debt: equity ratio. It is therefore not surprising that the objectives of the owner and the lender are generally aligned – each wants a successful project delivered safely on time and to budget.

The summary issues which determine the bankability are:

- Financial metrics
- Contractual terms and conditions
- Technical engineering
- Risks and risk allocation
- Cost estimate accuracy and levels of contingency
- Environmental and Social compliance, e.g. IFC Performance Standards compliance
- Summary: is the project now deemed "ready to lend"?

To be considered bankable by the banks, the risk allocation needs to be firmly understood and be satisfactory to the lenders. If a lender is comfortable with risk allocation provisions, the more likely it will be willing to keep the equity portion to a lower value. So the contract terms and conditions need to be bankable too. This is clearly a topic beyond the typical feasibility study which brings us to conclude that a feasibility study itself could never reach bankable status in its first edition. Lenders will assess the project holistically, but the factors must be appropriate to the bankability test.

8 CONCLUSIONS

The risk profile on the underground works from the lenders' perspective does change over the life of an hydropower project, from due diligence stage, through construction financing and the operation financing, but it does not diminish altogether. Most attention of course is paid at the pre-financial close phase as this is when the lenders' influence, through the LTA, and other advisors, can impose further risk mitigations if considered necessary.

The LTA fulfils a valued role for the lenders in identifying and making recommendations to mitigate the risks to the lenders, across a range of topics. The LTA has a wide remit in operating essentially as the eyes and ears for the lenders but spends the majority of its effort in the initial stages in ensuring that the total contractual package is appropriately apportioned for risk.

It is rare that a feasibility study in itself is considered bankable; it is the project as a whole which earns this status only after the post-feasibility due diligence and third-party assessments are made and the third party declares the bankability from their standpoint. Unless the terms of reference for a feasibility study were developed to address the key issues that are of interest to prospective lenders, then it remains likely that those lenders during their due diligence process will require additional updates in one or more fields. Those supplementary studies are therefore not part of the feasibility study – they instead form part of a post-due diligence phase, or rather more accurately, a pre-financial close phase. In many cases the price for undertaking additional or supplementary studies are not significant, but the consequential cost in terms of delay to the entire project will be significantly higher.

What is important, is to plan the feasibility study from the outset with the next step in mind, in particular the contracting strategy. If the developer is contemplating taking the large step from feasibility to financial close, assuming the EPC contracting model, this can work but the entire feasibility study should be planned with due consideration in advance of what the lenders will be looking for and ensure there are no gaps.

ACKNOWLEDGMENTS

This paper draws from several other technical papers from the author and is based on his global experiences from tunnelling risks for pumped hydro and conventional hydropower. Acknowledgements for the insights into this paper are extended to all the project teams and people that I have had the pleasure to work with in the tunnelling and hydropower industries worldwide. The experiences and lessons learned from a variety of projects formed the basis of what is written.

REFERENCES

Noble, A.G. 2018. Tunnel and Underground Risk in Hydropower – a Lender's Technical Advisor Perspective. Paper prepared for World Tunnelling Congress 2018 in Dubai. UAE.

Noble, A.G. 2023a. Comparing the issues, risks and levels of geotechnical investigation for remote hydropower tunnels with urban transportation tunnels. Paper presented as an e-poster for World Tunnelling Congress 2023 in Athens, Greece.

Noble, A.G. 2023b. The roles of the Financiers' Certifier in Urban Transportation Tunnels and as the Financiers' Advisor for Hydropower Tunnels. Paper presented at World Tunnelling Congress 2023 in Athens, Greece

Noble, A.G. 2023c. Getting Australian Pumped Hydro moving – what needs to happen after the feasibility study?. Paper presented at Australian national Committee On Large Dams (ANCOLD) 2023 in Cairns, Australia

Noble, A.G. 2024. Comparing Underground Construction Risk for Urban Transportation and Hydropower Projects – a Lender's Technical Advisor's Perspective. Paper prepared for World Tunnelling Congress 2024 in Shenzhen, China.

Plummer Braeckman et al 2022a Environ. Res.: Infrastruct. Sustain. 2 015006. Financiers' perceptions of risk in relation to large hydropower projects.

Plummer J, Markkanen S 2022b. Perceptions of risk in relation to large hydropower projects: a finance perspective.

Tunnelling for a Better Life – Yan, Celestino, Thewes & Eberhardt (Eds)
© 2024 The Author(s), ISBN 978-1-032-80042-4
Open Access: www.taylorfrancis.com, CC BY-NC-ND 4.0 license

Research on risk management and control of undersea tunnel construction based on blockchain technology

Liqing Qu
Qingdao Guoxin Jiaozhou Bay Second Submarine Tunnel Co., Ltd, Qingdao, China

Sihan Liu*
Tongji University, Shanghai, China

Minglun Tan
Qingdao Guoxin Jiaozhou Bay Second Submarine Tunnel Co., Ltd, Qingdao, China

Hongwei Huang
Tongji University, Shanghai, China

ABSTRACT: The multi-subject model of subsea tunnel construction makes information management complex, dynamic, and cross-cutting. At the same time, each department is more willing to keep its own data privacy, and the information exchange and collaboration process across units and departments is relatively vague. This study investigated the work flow of the Jiaozhou Bay Second Submarine Tunnel Project in its construction phase, clarified the functions and responsibilities of the construction unit, survey and design unit, material supplier, supervision unit, etc., and conduct an in-depth study of the current stage of project management. The quality information data in the network uses core technologies such as distributed ledgers, consensus mechanisms, and asymmetric encryption to link multiple subjects of security risk accidents, promote the transparent and efficient flow of information among multiple departments, and provide a basis for the information flow of various organizations to meet the requirements of dynamic risk management during the construction of subsea tunnels can improve the efficiency of risk management and control.

Keywords: subsea tunnel, blockchain technology, risk management

1 INTRODUCTION

With the support of national policies and the growing demands of development, tunnel construction in China is advancing rapidly, and the scale of future development is immeasurable. This also imposes higher requirements on tunnel construction management. Compared to other underground engineering projects, tunnel engineering experiences relatively frequent safety accidents due to the complexity of various uncertainties. These accidents not only result in economic losses for all parties involved but also have significant societal impacts.

The management process of tunnel construction involves multiple stakeholders, including construction units, design units, survey units, supervision units, and others. The construction process encompasses various phases such as construction preparation, portal and adit construction, tunnel excavation, tunnel lining, waterproofing and drainage, ventilation, and dust control. Information sources during construction are extensive, and information exchange is complex. Additionally, construction conditions can change rapidly, making traditional management methods limited in their effectiveness.

To achieve transparency and precision in risk management during tunnel construction using modern advanced information technology, to reduce the frequency of accidents, and to enable dynamic risk management, is of paramount significance for underwater tunnel construction projects. In response to higher construction requirements and standards and the need to improve traditional management models, various entities are gradually incorporating information technology and continuously updating their standardized management processes.

*Corresponding author: 2210345@tongji.edu.cn

DOI: 10.1201/9781003495505-483

However, the traditional management approach, lacking comprehensive planning, can result in inefficient information flow between modules and underutilization of data mining. Additionally, centralized systems rely on absolute trust in specific authoritative institutions, making it challenging to ensure transparency, equitability, fairness, and verifiability during data flow. In case of data fraud or manipulation, the entire centralized system would lose trust, making accountability after accidents even more difficult.

Blockchain technology is an emerging application pattern that combines distributed data storage, peer-to-peer transmission, consensus mechanisms, encryption algorithms, and other technologies. It possesses the characteristics of immutability and transparency, holding enormous potential in anti-tampering and traceability within information management (Nakamoto, 2009; Yuan et al.2016). Blockchain's role in promoting data sharing, optimizing business processes, reducing operational costs, enhancing collaborative efficiency, and establishing a trustworthy system was highlighted.

The integration of blockchain technology can enable monitoring and surveillance devices, such as IoT, to connect, allowing for distributed real-time data and information uploads regarding the security of facilities and equipment. This can reduce manual inspections and enhance work efficiency. Furthermore, through data tracing, blockchain can provide a credible level of information input for individuals, facilities, and hazard rectification in the construction management process. It can offer a verifiable, traceable, and tamper-proof information flow and evidence chain for accident processes (Lu, et al., 2020; Cao, et al., 2019).

Hence, there is an urgent need to holistically plan, establish a risk information database for the tunnel construction process, integrate it into the safety risk information mining and analysis process, construct a tunnel informatization platform, and form a new management model based on this, enabling safety control in tunnel construction, thus achieving information, transparency, and quantified control throughout the construction process.

2 FEASIBILITY OF BLOCKCHAIN TECHNOLOGY IN TUNNEL CONSTRUCTION RISK MANAGEMENT

2.1 *Analysis of risk information issues in the tunnel construction process*

During the tunnel construction process, a significant amount of data can be accumulated. However, the multi-stakeholder nature of tunnel construction often leads to relatively vague and (Zhang, et al., 2013; Zhu, et al., 2022). The transparency and immutability of blockchain technology in data transmission have been effectively applied in monitoring data transmission in the construction process (Liu, et al., 2021; Sheng, et al., 2021; Wu ., et al., 2022; Zhong, et al., 2022; Wu, et al., 2022; Wang, et al., 2022). While ensuring data authenticity, many scholars have proposed integrating blockchain technology with other technologies to expand its application in the construction field (Wu, et al., 2021; Pan, et al., 2022; Yang, et al., 2021). Its application in risk management is relatively less explored, making it necessary to discuss the feasibility of blockchain technology in risk management. A typical block chain including the following key characteristics:

(1) Technical Feasibility: Blockchain technology is a distributed ledger technology that integrates multiple theories and technologies, including asymmetric encryption, P2P networking, smart contracts, and more. Its blockchain structure, with encrypted chained blocks, is used for data verification and storage. P2P technology enables the verification and communication of distributed nodes, while smart contracts allow for automated operations based on complex business logic functions.

(2) Traceability: In the process of transmitting safety information in tunnel construction, safety information primarily exists in the form of signed forms and electronic files, resulting in an inefficient traceability system. However, within each block of a blockchain, there is not only transaction information but also a timestamp (indicating the time of the block's transaction record) and a hash value. All these blocks form a chain-like structure, allowing every block to trace back to the first one. Such a traceability system can provide stakeholders with information about content, source, time, and signatures, serving as the basis for accountability after accidents, enhancing accountability efficiency and capabilities.

(3) Authenticity: Stakeholders in tunnel construction often have motives and behaviors, such as falsifying transaction data, to maximize their interests or avoid accident responsibility. However, the consensus mechanism of blockchain technology requires the approval of all stakeholders for every information change, and transaction content is monitored by all parties, preventing data falsification and improving information authenticity.

(4) Distributed: Storage Many pieces of information in tunnel construction cannot be shared and communicated in real-time among different stakeholders. In a consortium blockchain, each stakeholder has a distributed ledger to store all data, solving the challenge of uneven information distribution. For instance, when an owner initiates a consortium blockchain, other stakeholders join the corresponding chain and complete data and block generation. The survey and design chain records critical safety information or design proposals, the material supply chain records materials supply and testing information, and the monitoring chain records sensor data and approvals.

Considering that tunnel construction risk management involves a large amount of information, a database that can facilitate real-time and transparent information sharing is highly necessary. Blockchain types mainly include public, private, and consortium chains. To ensure that various types of risk information are shared among stakeholders and that information is open and transparent with equal rights and responsibilities, a private chain, which requires specific conditions for information sharing, is not suitable for tunnel construction schedule risk management. Moreover, tunnel construction schedule risk management involves multiple stakeholders, necessitating identity verification for all stakeholders to ensure information security, making it unsuitable for a public chain that is open to all participants. Consequently, the blockchain architecture of a consortium chain is better suited for tunnel construction schedule risk management.

3 ENGINEERING RISK INFORMATION SHARING FRAMEWORK

In the context of tunnel risks, Professor Einstein H. H. from the Massachusetts Institute of Technology (MIT) has long presented valuable theories that provide a theoretical basis for risk analysis in tunnel projects (1974; 1996; Sinfield, & Einstein, 1996). R. Sturk and others applied probability methods and effective statistics in risk analysis to guide highway tunnel projects from the perspectives of reliability and risk (1996). H.M. Tah and V. Carr proposed the five processes of dynamic risk management: risk identification, risk assessment, risk analysis, risk treatment, and outcome monitoring (2001). The application of risk management in tunnel and underground engineering projects in China began relatively late. It wasn't until the early 1990s that Ding Shizhao, an academician of the Chinese Academy of Engineering at Tongji University, explored risk and insurance forms in the Guangzhou Metro Phase I project and the Shanghai Metro Line 1 project. This marked the beginning of research into risk assessment management in China. Huang Hongwei and others suggested that risk assessment typically involves three steps: risk identification, risk estimation, and risk evaluation (2007). These three steps can be improved in terms of information sharing with the help of blockchain technology.

Risk Identification: This involves the process of collecting risk information. Tunnel construction faces numerous risks, such as safety risks like fires, collapses, sudden water inflows, as well as risks related to blasting operations, deformations in surrounding structures, construction organization, and schedule. Each of these risks results from various influencing factors within the risk chain, including factors like inexperienced workers, equipment damage or absence, and inaccurate geological surveys. Based on all possible risks in tunnel construction and their influencing factors, these can be categorized into four types: personnel information, equipment information, management information, and construction environment information. Each unit can classify and synchronize the corresponding information to the blockchain according to its specific needs during the risk identification process, ensuring the authenticity and reliability of the collected information, and providing a stable and reliable data source for risk assessment.

Risk.

Estimation: This stage involves the processing of risk information. It mainly consists of analyzing the likelihood and estimated losses of risk incidents, building upon the risk identification based on blockchain technology. Reliable information sources enhance the credibility of estimation results. In this process, various methods such as the expert scoring method, the analytic hierarchy process, the fuzzy comprehensive evaluation method, and the fault tree analysis method are widely used. Smart contract technology can perform intelligent calculations of risk levels after scoring, thereby increasing the efficiency of the risk estimation process.

Risk Evaluation: This step includes rating risks, ranking them, and making risk decisions, which is the display layer of risk assessment results. Risk levels are assessed and categorized based on the risk probability, losses, and acceptance criteria as specified in the national standard (GB 50652-2011), "Code for Risk Management in Urban Rail Transit Underground Engineering" (hereinafter referred to as "the national standard"). In this stage, blockchain technology is utilized to showcase the conclusions of risk assessment, the responsible personnel for risk assessment, and the weaker aspects of risk impact factors for tunnel construction management personnel to formulate targeted response measures.

The proposed framework for tunnel construction risk information sharing based on blockchain technology is illustrated in Figure 1 and comprises the following modules:

- User Module: This primarily includes various units and departments participating in tunnel construction, such as advanced geological prediction units, survey/design units, construction units, and construction owners. For instance, during the survey and design phase, inaccurate geological surveys may pose a risk, with the responsible units including advanced geological prediction units and survey/design units. The latter are typically information providers, while other units are information reviewers, and there is frequent information exchange between information providers and reviewers.
- Data Acquisition Module: This is used for obtaining data for tunnel risk assessment, and the data source depends on the users.
- Data Storage Module: The data storage module is connected to the data acquisition module and is

used for storing data relevant to tunnel risk management.

- Data Interaction Module: The data interaction module is connected to the data storage module and facilitates the interaction of tunnel risk management data between PC and web interfaces.
- Data Evaluation Module: This module is linked to the data interaction module and is used for risk level assessment based on the results of data interaction.
- Data Visualization Module: The data visualization module is connected to the data evaluation module and is used to retrieve the results of the data evaluation module and present them in a visual format.

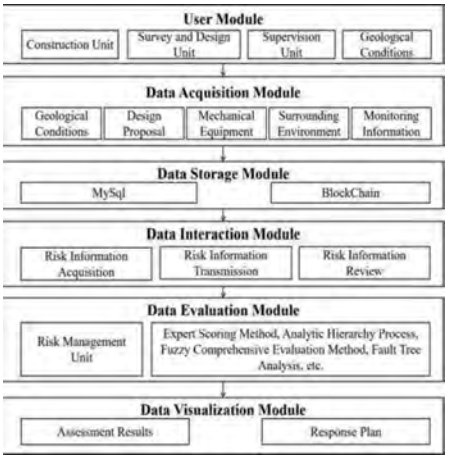

Figure 1. Characteristics of a blockchain-based tunnel construction risk management platform.

4 TYPICAL APPLICATION SCENARIOS

In response to issues such as information sharing and accountability opacity in the risk management process of tunnel fires, a tunnel construction fire risk management platform has been developed based on the Wutong blockchain technology. This platform enables data input, assessment, and user access through a web browser. Leveraging the construction of the second undersea tunnel in Jiaozhou Bay, Qingdao, the construction site of the second undersea tunnel exhibits strong spatial confinement, a high presence of potential combustibles, and challenges in firefighting, posing serious consequences in the event of a fire.

Risk Identification: Taking a specific week in 2023 as an example, the occurrence of unauthorized wiring and the presence of numerous vehicles at the construction site pose significant fire hazards. The possibility of cable wear due to vehicle movement is one of the critical fire hazards for that week. The ongoing installation of geotextiles and waterproof panels involves the use of highly flammable materials such as solid foam and waterproof fabric, representing an important combustible hazard. The current provision of firefighting equipment at the construction site is deemed sufficient. All construction personnel for the week are certified, and there is no smoking or emergency equipment failure reported.

Risk Estimation and Assessment: Relevant information is reported and described by various departments, and the risk control unit assigns scores ($P \in [0,10]$) to the basic events of the week. A higher score indicates a lower probability of the event occurring, and vice versa. Through the platform's information synchronization and probability calculations, the probability of a fire accident occurring during the week is calculated as 0.28, with a likelihood rating of 1.

Accountability Tracing: Events and incidents with lower scores are traced back to responsible individuals, such as inadequate fire spacing or improper cable laying. Detailed event descriptions can be traced through blockchain hashes to the Wutong chain, as illustrated in Figure 2.

The predictive results from the FRC platform indicate a significant likelihood of a fire occurring in the second undersea tunnel, aligning well with the actual conditions of the week. Therefore, the FRC platform is considered effective in predicting the probability of fire accidents, facilitating the organization of daily fire risk management events and accountability tracing following a fire incident to specific events, departments, and units.

Figure 2. Tunnel construction fire risk management platform.

5 CONCLUSION

Risk management in tunnel engineering is a critical aspect of tunnel construction projects. However, due to issues related to the security and legality of information, achieving high-speed, effective, and transparent information exchange during construction processes has been challenging. Blockchain technology, with its unique capabilities such as immutability and data traceability, offers distinct advantages in the field of information management. Therefore, this paper presents the architecture of a tunnel engineering risk management platform based on blockchain technology.

First, we provided a detailed overview of the advantages of blockchain technology in the realm of

information management. Secondly, we proposed the application of blockchain technology in the context of risk assessment, particularly in the three steps of risk evaluation. We believe that blockchain technology enhances the reliability and transparency of risk identification information, ensures the traceability of risk assessment results, and addresses the limitations of traditional risk assessment methods.

The application of blockchain technology in tunnel engineering risk management holds significant potential. Building upon this architecture, further research and development should be carried out to enable the platform to be piloted in actual engineering projects. This will fill the gaps in the current centralized management architecture and promote more efficient and transparent supervision of tunnel engineering risk management.

REFERENCES

Nakamoto, S. (2009). Bitcoin: a peer-to-peer electronic cash system. Available online: https://bitcoin.org/bitcoin.pdf.

Yuan, Y., & Wang, F. (2016). Current Development and Prospects of Blockchain Technology. Acta Automatica Sinica, 42(4), 481–494.

Lu, R., Wang, Z., You, J., et al. (2020). Research on a Blockchain-Driven Information Sharing Framework for Railway Engineering. Journal of Railway Engineering, 37(11), 100–105.

Cao, Y., Su, Z., & Li, N. (2019). Research on the Architecture of a Blockchain-Based Construction Supply Chain Information Sharing Management System. Construction Economics, 40(5), 69–74.

Xu, Q., Chong, H., & Liao, P. (2019). Collaborative Information Integration for Construction Safety Monitoring. Automation in Construction, 102.

Yang, Z. (2019). Research on Deep Integration of Construction Management and Computer BIM Technology. Journal of Advanced Computational Intelligence and Intelligent Informatics, 23(3).

Cryptocurrency Monitoring Website. Available online: http://coinmarketcap.com/, November 24, 2015.

World Economic Forum Survey. Available online: http://www.coinfox.info/news/3184-world-economic-forum-survey-10-of-global-gdp-may-be-stored-with-blockchain-technology-by-2027, February 21, 2016.

Zhang, C., Qiao, M., Li, H., et al. (2023). A Survey of Blockchain Technology Applications in the Construction Field. Journal of Railway Science and Engineering, 20(3), 1105–1115.

Zhu, L., Liang, H., Tang, T., et al. (2022). Empowering Railways with Blockchain: Prospects and Case Analysis. Journal of the China Railway Society, 44(9), 79–86.

Liu, Y., Yang, L., Piao, C., et al. (2021). Key Technologies for Data Sharing in the Safety Monitoring of Railway Construction Based on Blockchain. Journal of Communications, 42(8), 206–216.

Sheng, D., Zhong, B., Luo, H., et al. (2021). Research on the Framework of Worker Information Management in the Construction Industry Based on Blockchain. Construction Economics, 42(10), 89–94.

Liupengfei, W., Weisheng, L., Rui, Z., et al. (2022). Using Blockchain to Improve Information Sharing Accuracy in Onsite Modular Construction Assembly. Journal of Management in Engineering, 38(3).

Botao, Z., Jiadong, G., Lu, Z., et al. (2022). A Blockchain-Based Framework for On-Site Construction Environmental Monitoring: Proof of Concept. Building and Environment, 217.

Haitao, W., Botao, Z., Heng, L., et al. (2022). On-Site Safety Inspection of Tower Cranes: A Blockchain-Enabled Conceptual Framework. Safety Science, 153.

Zhoukai, W., Kening, W., Yichuan, W., et al. (2022). A Data Management Model for Intelligent Water Project Construction Based on Blockchain. Wireless Communications and Mobile Computing, 2022.

Haitao, W., Botao, Z., Heng, L., et al. (2021). On-Site Construction Quality Inspection Using Blockchain and Smart Contracts. Journal of Management in Engineering, 37(6).

Xing, P., Botao, Z., Da, S., et al. (2022). Blockchain and Deep Learning Technologies for Construction Equipment Security Information Management. Automation in Construction, 136.

Yang, Z., Tengyu, W., KaVeng, Y. (2021). Decentralized Management of Construction Site Information Using Blockchain and Smart Contracts. Computer-Aided Civil and Infrastructure Engineering, 37(11).

Einstein, H. H., & Vick, S. G. (1974). Geological Model for Tunnel Cost Model. Proceedings of the Rapid Excavation and Tunneling Conference, 2nd, 1701–1720.

Einstein, H. H. (1996). Risk and Risk Analysis in Rock Engineering. Tunnelling & Underground Space Technology, 11(2), 141–155.

Sinfield, J. V., & Einstein, H. H. (1996). Evaluation of Tunneling Technology using the "Decision Aids for Tunneling." Tunnelling & Underground Space Technology, 11 (4), 491–504.

Sturk, R., Olsson, L., & Johansson, J. (1996). Risk and Decision Analysis for Large Underground Projects as Applied to the Stockholm Ring Road Tunnels. Tunnelling and Underground Space Technology, 11(2), 157–164.

Tah, J. H. M., & Carr, V. (2001). Towards a Framework for Project Risk Knowledge Management in the Construction Supply Chain. Advances in Engineering Software, 32(10–11), 835–846.

Huang, H., Zhu, L., Xie, X., et al. (2007). Risk Assessment of Key Nodes in the Feasibility Stage of Shanghai Metro Line 11. Chinese Journal of Geotechnical Engineering, (07), 1103–1107.

Tunnelling for a Better Life – Yan, Celestino, Thewes & Eberhardt (Eds)
© 2024 The Author(s), ISBN 978-1-032-80042-4
Open Access: www.taylorfrancis.com, CC BY-NC-ND 4.0 license

Study on the major risk control elements under EPC management mode of rail transit

Zheng Shi
Shanghai Tunnel Engineering & Rail Transit Design and Research Institute, Shanghai, China

Jizheng Huang*
BY Civil Engineering Consulting Co., Ltd., Shanghai, China

Lihong Ding
Shanghai Tunnel Engineering & Rail Transit Design and Research Institute, Shanghai, China

ABSTRACT: In order to explore how to control major risks under EPC (Engineering Purchase Contract) management mode, and ensure the smooth progress and safety of rail transit projects, this paper analysed and summarized the major risk control elements from three aspects: relationship between parties facing risks, organizational structure and management personnel through special research and case analysis. Firstly, the relationship between parties facing risks was sorted out, including the relationship between employer, EPC project team, constructor, supervisor, design unit and the introduced third party for risk control. The cooperation and conflicts of opinions between parties ware analysed and solutions ware proposed. Then, the management organizational structure for major risks in EPC projects was discussed. Through investigating the management modes of EPC projects both at home and abroad, a "dual control" management organizational structure with centralized control by EPC project teams and inspection control by third party was proposed. Finally, the core elements of rail transit EPC project management talent ware studied, including project manager, site management personnel and professional technical personnel of the EPC project team. The results show that the relationship between parties facing risks, the management organizational structure for major risks and management talents are the key elements of major risk control in rail transit projects under EPC management mode. Rationalizing the relationship between parties facing risks, building a reasonable management organizational structure of major risk control, and cultivating excellent management talent can effectively control and respond to major risks of rail transit projects, and ensure the smooth implementation of rail transit projects under EPC management mode.

Keywords: rail transit engineering, EPC mode, risk control, element study

1 INTRODUCTION

In order to address the difficulties faced by the lead design unit in the process of EPC transformation, this explores how to control major risks within the EPC management model. It is necessary to study the essential elements for controlling significant risks in the EPC management model for rail transit. In response to issues such as unclear positioning of responsibilities for the lead design unit in EPC transformation, high associated risks, and insufficient management capabilities as shown by Weifeng Chu (2021), it is essential to streamline the relationships related to 'risk,' construct a reasonable organizational framework for managing major risks in EPC projects, and cultivate talented individuals with the necessary management skills. This is to ensure the smooth implementation of rail transit projects under the EPC management model.

2 CLARIFICATION OF THE RELATIONSHIPS AMONG PARTIES FACING RISKS

The domain of the EPC model is Engineering. Hence, participants in the EPC management model should include the engineering owner, engineering contractor, engineering supervisor, design review entity, third-party safety and quality control, and local government regulatory departments. The engineering contractor comprises project management, design teams, civil construction teams, and system equipment installation

*Corresponding author: yiyanghepan@qq.com

DOI: 10.1201/9781003495505-484

teams. In this model, different parties play different roles and responsibilities to ensure the smooth progress and completion of the project.

2.1 *Engineering owner*

The engineering owner (developer) is responsible for establishing project objectives, requirements, and budgets, overseeing the overall progress of the project. Additionally, they need to assist the engineering contractor in external liaison and communication, purchasing insurance, and jointly hiring a third party for safety and quality management.

Compared to traditional contracting models, in the EPC model, the engineering owner delegates most of the rights to the general contracting unit, with a shallower level of involvement in project management. On the other hand, as the engineering owner only needs to contract with the EPC general contracting unit, usually under a fixed total price contract, in comparison to the traditional contracting model, under the EPC model, the engineering owner can have better control over the total investment as shown by Jinrui Zhang (2016).

2.2 *Engineering contractor*

In China, explicit qualifications for EPC general contracting enterprises have not yet been designed. According to relevant policy documents, as long as there is engineering design or construction qualifications that are commensurate with the scale of the project, it satisfies the qualification requirements to become an engineering general contracting unit. As currently, domestic design and construction are mostly independent units, seeking strong alliances and complementary advantages, a model in which qualified design and construction units form a consortium to undertake EPC general contracting has become mainstream in China.

According to the characteristics of the EPC model, the engineering contractor can also be divided into project management, design, construction, and system installation. Depending on the leading unit of the consortium, the project management may come from the design unit or the construction unit.

The function of project management is to coordinate the design, construction, and system installation teams, ensuring the coherence and consistency of the design plans, and providing technical support. They are responsible for procuring major bulk materials, critical equipment, and services needed for engineering construction, ensuring the efficient operation of the supply chain and timely material supply. The function of the design team is to develop detailed engineering design plans, including technical specifications, construction drawings, and quantity schedules. The function of the construction team is to carry out construction, coordinate various trades at the construction site, and ensure construction safety, quality, and progress. The function of the system installation team is to execute system installation.

Specifically, for the design unit acting as the leading entity in the EPC general contracting consortium, besides performing well in their role as a design specialist, they also need to carry out the work of project management. However, at this stage, most design units leading the EPC transformation lack construction site management experience, and some do not even have a sound construction quality or safety management organizational structure. Agreements signed by consortium members are often relatively rudimentary (lacking detailed delineation of rights, responsibilities, and benefits). Design and construction units are individually responsible for their respective engineering contents, lacking awareness and management of each other's work. As the leading design unit, mismanagement could lead to potential joint responsibility due to poor management as shown by Yuan Gu (2020).

Therefore, elucidating the relationship between the design and construction units within the consortium is crucial for risk control in EPC general contracting projects. To achieve this goal, the first step should involve selecting suitable and stable consortium partners, signing comprehensive consortium agreements. Subsequently, establishing a complete risk management organizational structure and having sufficient talent to ensure the project's smooth and efficient completion.

2.3 *Supervision entity*

The supervisory entity is commissioned by the engineering owner to oversee the compliance, quality, and progress of design, construction, and installation schemes, ensuring they adhere to relevant legal standards. In the EPC model, the relationship and positioning of the supervisory entity with the engineering owner and engineering contractor have not fundamentally changed.

2.4 *Design review entity*

Similar to traditional contracting models, the design review entity is responsible for reviewing engineering design schemes to ensure they comply with technical specifications and safety requirements.

2.5 *Third-party safety and quality control*

Operating as a third party in the engineering realm, this entity surveys potential safety and quality haz-

ards in engineering, supervises safety measures at construction sites, prevents engineering accidents, and safeguards the safety of workers and the environment. According to the 'Swiss Cheese Model' as shown by J. Reason (1990), accidents occur when every person in the accident chain makes an error at some point. The stronger the management capability, the more detailed the control granularity, and the healthier the control levels, the easier it is to prevent common accidents. However, they cannot prevent rare accidents and may even amplify the possibility of rare accidents. Independent professional third parties can offer a new dimension and are the best choice for risk reduction implementation.

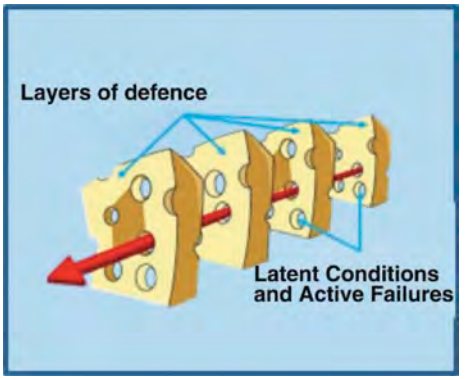

Figure 1. Swiss cheese model.

However, the introduction of third-party risk advisory units can be approached in various ways. In numerous rail transit projects without specific regulations, traditional third-party risk advisory units often face some awkward situations: on one hand, they unavoidably have to point out the shortcomings or even errors of relevant units in specific risk control work; on the other hand, they are commissioned by these units. In past practices, a new approach for introducing third-party risk advisory units has been found. It involves the participation of technical consulting agencies as part of engineering insurance underwriting companies in risk control. This approach both avoids the problems of traditional methods and resolves the inadequacy of technical capabilities within underwriting companies, aligning with the interests of all participating parties.

2.6 *Regulatory departments of local government*

They are responsible for overseeing the project's compliance to ensure it aligns with relevant regulations and standards.

The above are general roles and responsibilities of the various parties in the EPC model. The actual situation might differ based on the specific nature of the project and the regulations of the region. In comparison to traditional models, the major changes in role positioning mainly occur between the engineering owner and the design and construction units within the engineering EPC general contracting consortium.

In a rail transit engineering project, all parties need to work closely together, coordinate effectively, while also clarifying their own roles and correctly delineating rights, responsibilities, and benefits to ensure the project's timely and high-quality completion.

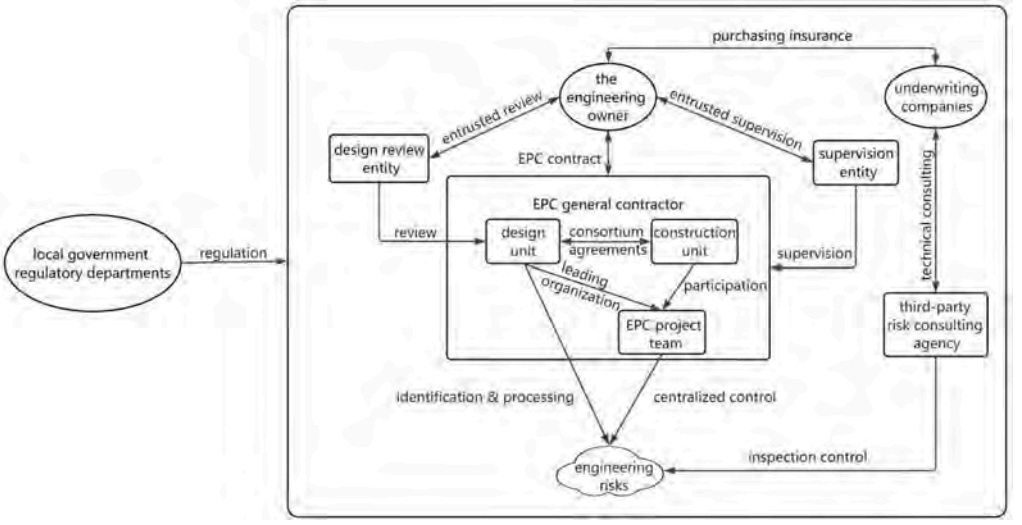

Figure 2. Diagram illustrating the relationships among parties facing risks.

3 RISK MANAGEMENT ORGANIZATIONAL STRUCTURE

3.1 *Risk management organizational structure within the EPC consortium*

According to the analysis in the previous section, the key to controlling risks in railway engineering projects under the EPC model is clarifying the relationship between the design and construction units within the consortium. Therefore, it's essential to establish a comprehensive risk management organizational structure within the EPC consortium to ensure the project can effectively and promptly respond to various risks as shown by Jian Qiang (2011).

3.1.1 *Project senior leadership team*

This includes the project general manager, project executive director, among others, responsible for overall project planning, decision-making, and resource allocation. This team should consist of senior management personnel from various consortium member units, an odd number and not too many in quantity.

3.1.2 *Expert advisory team*

Comprising experts in fields such as law, compliance, engineering technology, risk management, providing professional advice and recommendations to assist in formulating reasonable risk management strategies for the project.

3.1.3 *Risk management committee*

Comprised of the project leadership team, expert advisors, responsible for formulating risk management policies, guiding principles, and reviewing and deciding on significant risks.

3.1.4 *Risk management department*

Responsible for specific risk identification, assessment, control, and monitoring, implementing decisions of the Risk Management Committee. Similar to the project's senior leadership team, the primary personnel of the risk management department should be cross-assigned from various consortium member units. Since the design unit is the lead in the EPC consortium, it's preferable for this department's leadership to be appointed by the design unit. The department should include the following sub-departments or functions:

(1) Risk Identification and Assessment Team: Identifying various potential project risks, performing qualitative and quantitative assessments, prioritizing risks, and identifying significant risks.
(2) Risk Control and Planning Team: Developing response measures and contingency plans for each type of risk, ensuring the project progresses smoothly as per the planned schedule.
(3) Risk Monitoring and Reporting Team: Establishing a risk monitoring system, tracking and monitoring project risks regularly, promptly reporting the status and dynamics of risks to the project's senior management.
(4) Risk Sub-Teams for Each Project Phase: Establishing sub-teams at different project stages, responsible for assessing and managing potential risks specific to each stage, ensuring comprehensive risk control throughout the project.

3.1.5 *Communication and coordination mechanism*

After establishing the leadership team, the risk management committee, and the risk management department within the EPC consortium based on the above principles, it is possible to manage project risk control effectively. However, significant risk management in railway engineering under the EPC management model still requires extensive collaboration from all members involved. Therefore, it is necessary to establish cross-departmental and cross-functional communication and coordination mechanisms to ensure smooth information flow and resource sharing for swift risk response.

3.1.6 *Training and education department*

Responsible for providing training and education regarding risk management to project team members, enhancing the team's understanding and ability to address risks.

3.1.7 *Risk management tools and technical support team*

Offering technical support such as risk management software, data analysis tools, to assist the team in better identification, assessment, and response to risks. This team can adapt to the trend of digitalized risk management, employing more advanced tools to facilitate effective risk management.

It's important to note that the risk management organizational structure for different projects may need adjustments and optimizations based on the project's scale, nature, and characteristics to suit the actual circumstances.

3.2 *Third-party risk consulting agency*

However, the risk control structure involving various units within the EPC consortium, including the engineering owner, supervisory unit, and others, is insufficient. While centralized control is achieved within the EPC project group, it is necessary to introduce an independent third-party professional organization through the engineering insurance institution to participate in risk control activities, serving as a supplement to the entire risk management system, ensuring that the probability of significant and rare risks occurring is minimized.

After the introduction of third-party risk advisory units into railway engineering projects under the

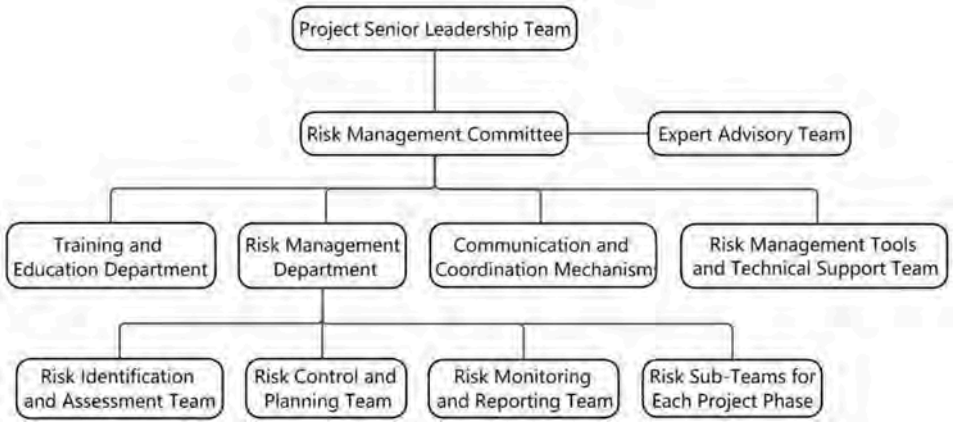

Figure 3. Organizational structure of risk management within the consortium.

design-led EPC model, they need to engage in risk control through a professional and comprehensive process.

3.2.1 *Preliminary preparation*
Collaborating with the EPC project team, gather relevant information and perform risk assessment and classification for different engineering aspects of the rail transit project. Based on the results of the risk assessment, engage in thorough communication with the EPC project team to develop a risk management plan and response strategies. The outcomes should be compiled and presented in a preliminary risk assessment report by a third-party agency. Then, organize a risk survey and briefing meeting involving all relevant stakeholders facing the identified risks.

3.2.2 *Risk operation tracking*
The third-party agency should regularly monitor the project progress. During critical risk-prone periods, pre-selected experts should be communicated with and confirmed by with the EPC project team and engineering insurance agencies.

Prior to the risk survey, prepare a project risk overview and send it for expert review, allowing experts to become familiar with the project in advance.

After the completion of key projects, the third-party agency can conduct a post-assessment of risks. This involves analysing and evaluating the gains and losses of the measures taken by all parties during the significant risk response period, thereby forming effective methods for future similar risk responses.

The third-party agency should also pay attention to the resolution of risk is-sues and can contact experts for confirmation if there are any special problems

3.2.3 *Process risk assessment*
At regular intervals (e.g., monthly or quarterly), the third-party agency can summarize and analyse risk issues for similar projects or compare risk issues across different projects on the same rail line. By analysing and exploring the data, common issues existing in the projects can be identified, facilitating the enhancement of management by the EPC project team and reducing the probability of risk occurrence.

After the completion of key projects, the third-party agency can conduct a post-assessment of risks, analysing and evaluating the gains and losses of the measures taken by all parties during the significant risk response period, thereby forming effective methods for future similar risk responses.

3.2.4 *Value-added services*
In addition to daily risk management, the third-party agency can organize risk management salons for common technical issues and provide emergency response expert services.

3.2.5 *Risk management summary*
Upon the completion of rail transit projects, the third-party agency should com-pile a risk management summary report based on the achievements of comprehensive risk management throughout the entire process, and convene a project risk management summary meeting with relevant parties.

In summary, the combination of a complete risk management organizational structure within the EPC consortium and the involvement of an independent third-party professional organization introduced through the engineering insurance institution constitutes the 'Dual Control Model' of centralized project control and third-party surveillance control.

4 CORE ELEMENTS OF MANAGEMENT TALENTS

Management talents involved in railway engineering EPC projects need to possess a variety of core elements to ensure the smooth and efficient completion of projects. Personnel in the design unit

Figure 4. Framework for risk control services by third-party organizations.

often exhibit strong professional technical capabilities but lack cross-disciplinary comprehensive skills and on-site construction experience. Therefore, the design unit needs to prioritize the cultivation of management talents for railway engineering EPC projects as shown by Xiaodong Zhou (2016). These talents should encompass the following core elements:

4.1 *Professional knowledge and skills*

Project management talents need to be well-versed in relevant fields of railway engineering, including engineering design, construction technology, procurement processes, etc. They should comprehend the technical requirements and standards of the project to effectively communicate and coordinate with various professional teams.

4.2 *Project management skills*

Management talents need to master the fundamental principles and methods of project management, including planning, resource allocation, risk management, schedule control, cost management, etc. They should be able to develop detailed project plans and oversee project execution, ensuring timely, high-quality, and cost-effective project completion.

4.3 *Communication and coordination abilities*

In railway engineering projects, there is a need for external communication with the public and internal coordination involving multiple teams from different professional domains. Therefore, project management talents need to possess excellent communication and coordination abilities to effectively communicate with all stakeholders, resolve issues, manage conflicts, and ensure smooth information flow.

4.4 *Risk management*

Railway engineering projects face various potential risks, including technical, supply chain, and environmental risks. Project management talents need to identify and assess these risks, formulate corresponding risk response strategies to mitigate their impact on the project.

4.5 *Team leadership and management*

Management talents need to demonstrate team leadership and management abilities, motivating team members, guiding them in accomplishing their tasks, ensuring team collaboration, and achieving project objectives.

4.6 *Problem-solving skills*

Throughout project execution, various issues and challenges may arise. Project management talents need to swiftly identify the root causes of problems, find solutions, and take action to resolve issues, ensuring smooth project progress.

4.7 *Compliance and legal awareness*

Railway engineering projects are often subject to various regulations and provisions. Project management talents need to understand relevant laws and regulations to ensure project compliance within legal frameworks and avoid non-compliance.

4.8 *Learning and adaptability*

Technologies and methods in the railway sector are continually evolving. Project management talents need to maintain the ability to learn and adapt to keep up with the latest industry trends and best practices.

In summary, management talents for railway engineering EPC projects need to comprehensively consider various factors including technical, management, communication, leadership, and more to ensure the smooth implementation and successful delivery of projects.

5 CONCLUSION

As the leading entity in the EPC, the design unit, for better risk control of railway engineering projects under the EPC management model, needs to streamline the relationships concerning 'risk,' construct a reasonable major risk management organizational structure for the EPC project, and cultivate excellent talents with management capabilities.

5.1 *Clarifying relationships concerning 'risk'*

The key lies in aligning the relationship within the general contracting consortium and the construction units. This involves selecting suitable and stable consortium partners, establishing detailed consortium agreements, and constructing a complete risk management organizational structure. Additionally, choosing a third-party professional institution as a technical advisory body for the engineering insurance underwriting company is crucial for risk control, thereby aligning the relationship between safety and quality control third parties and the project.

5.2 *Structuring a comprehensive risk management framework for EPC projects*

Internally within the EPC consortium, there should be a complete risk management organizational structure consisting of the project's senior leadership team, a risk management committee, a risk management department, communication and coordination mechanisms, a training and education department, and a risk management tools and technical support team. Based on this, through the engineering underwriting institution, the introduction of an independent third-party professional organization to participate in risk control work serves as a supplement to the overall risk control system, collectively forming a 'dual control model' of centralized project management combined with third-party oversight.

5.3 *Nurturing management-proficient talent*

The design unit needs to emphasize the cultivation of management talents for railway engineering EPC projects, who possess core elements such as professional knowledge and skills, project management skills, communication and coordination abilities, risk management, team leadership and management, problem-solving abilities, compliance and legal awareness, as well as learning and adaptability capabilities.

REFERENCES

Chu, W. F., 2021. Research on Risk Management of EPC Consortium Project Led by Design Institute. MA Thesis. Zhengzhou University, Zhengzhou, Henan, China.

Zhang, J. R., 2016. The Coordination Responsibilities and Management Process of Main Parties in China EPC Project. MA Thesis. Tsinghua University, Beijing, China.

Gu, Y., 2020. The Study on the Management of EPC Consortium Leaded by Design Enterprise. MA Thesis. Zhejiang University, Hangzhou, Zhejiang, China.

Reason, J., 1990. Human error. Cambridge University Press, Cambridge, UK.

Qiang, J., 2011. "On Process Management of Professional Design Institute as the Main Body of the EPC General Contract." Journal of Municipal Technology. 29.06 (2011), 115–118.

Zhou, X. D., 2016. The Belt and Road Practices. China Machine Pres, Beijing, China.

Tunnelling for a Better Life – Yan, Celestino, Thewes & Eberhardt (Eds)
© 2024 The Author(s), ISBN 978-1-032-80042-4
Open Access: www.taylorfrancis.com, CC BY-NC-ND 4.0 license

Tunnel Euralpin Lyon Turin: The design and contract challenges for a modern Alpine base tunnel

Daniele Stocker*
Pini Group, Lugano, Switzerland

Piergiuseppe Gilli
TELT-sas, Torino, Italy

Matteo Falanesca
Pini Group, Lugano, Switzerland

ABSTRACT: The Mont-Cenis base tunnel, part of the TEN-T transport network, is the most important element of the cross-border section linking France to Italy via a 57.5 km rail tunnel. The total excavation length for the construction of the structure is approximately 160 km, 22% of which has already been completed. The tunnel passes through different Alpine geological units with very heterogeneous geological conditions and high overburden, posing particular technical and design challenges. The excavation of the base tunnel will be performed for 75% of the entire length with different types of TBMs chosen on the basis of expected geological risks: Gripper TBMs; Shielded TBMs; Dual-Mode TBMs. Other aspects requiring in-depth design studies concern logistics and the use of excavated materials. On the basis of the agreements adopted by the Inter-Governmental Commission, the work has been divided into 12 main operational sites in order to limit the interfaces among sites and to account for the approval deadlines. The allocation of the main civil works lots has recently been completed. The adopted approach has allowed to maintain a high degree of flexibility in the division of design, construction and supply contracts. This complex project requires thorough design phases, appropriate risk management procedures and the establishment of modern and flexible procurement systems. All these aspects ensure that the economic and time conditions are met, taking into account quality, safety and the environment. Commissioning is planned for 2032.

Keywords: Risk management, Contractual Practices, FIDIC standard, TBM-Tunnelling; High Overburden, Squeezing Conditions

1 INTRODUCTION

As part of the RTE-T transport network, the Mont-Cenis base tunnel (Bufalini et al,, 2017; Stocker an Humbert, 2021) is the key element of the cross-border section linking France and Italy via a 57.5 km high-speed rail tunnel (45 km on French territory and 12.5 km on Italian territory). The construction of the Lyon-Turin rail tunnel (Figure 1), connecting the international stations of Saint-Jean-de-Maurienne and Suse with the existing network, will meet regional, national and European challenges. The existing railway lines, built in the 19th century, no longer meet the demand for freight transport (they are too steep, very twisty and do not meet current rail safety standards). The new Lyon-Turin Euralpine Tunnel project is a mixed passenger/freight project that will overcome the limitations of the current line. For passengers, the project will halve journey times and quadruple capacity. For freight, the Lyon-Turin Euralpine Tunnel will encourage modal shift by making freight transport more efficient and environmentally friendly, and will help to make Alpine road passenger transport safer. The base tunnel consists of two single-track tubes with a centre-to-centre distance of approximately 40 metres, connected by branch tunnels every 333 metres. On the French side, three cut-and-covers (Saint-Martin-La-Porte, La-Praz and Modane) with a total length of about 11 km have already been completed, while on the Italian side, the 7.5 km La Maddalena cut-and-cover has been excavated. Three safety areas are planned along the route (La Praz, Modane, Clarea), connected to the outside by descents. At Modane, the Avrieux shafts will provide

*Corresponding author: Daniele.Stocker@pini.group

DOI: 10.1201/9781003495505-485

ventilation for the future tunnel. Prior to the start of construction, in 2003, the shafts were used to identify the terrain to be encountered during the excavation of the base tunnel and its ancillary structures. During the construction phase, the shafts are used for logistics and ventilation. During the operational phase, in the event of an accident, they will provide access for emergency services and evacuation of victims.

The total excavation length for the construction of the structure is approximately 160 km, 22% of which has been completed (approximately 35 km in total) and 100% of the contracts for the main civil works have already been awarded. Various excavation methods are envisioned, depending on the expected geomechanical conditions, safety and mitigation of environmental impact.

The base tunnel will have a diameter of approximately 10.5 m at the extrados and will be designed to meet safety requirements and to optimise static performance (Figure 2).

The lining along the entire length of the tunnel provides stability during construction and long-term stability for the entire lifetime of the structure (120 years). The final lining is generally unreinforced concrete and is reinforced only in geologically difficult or geometrically complex areas. Water seepage is drained via external drains to a central drain which carries the water out of the tunnel and to the portals.

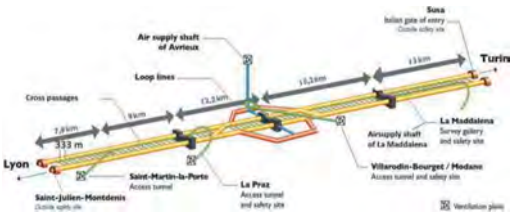

Figure 1. The Mont Cenis base tunnel.

The bi-national Franco-Italian company TELT is the public-sector promoter responsible for building and managing the cross-border section of the future infrastructure. By 2032, the Lyon-Turin line will take one million lorries off the Alpine roads and reduce greenhouse gas emissions by around 3 million tonnes of CO2 equivalent per year. The cross-border section will cost €8.6 billion. It is currently being financed by the European Union (40%), Italy (35%) and France (25%).

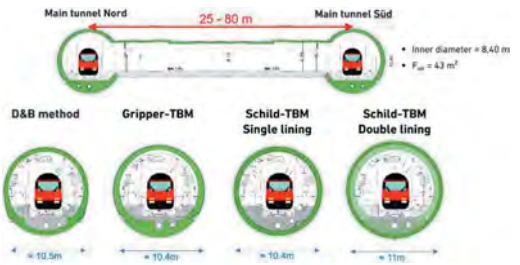

Figure 2. Typical section of the base tunnel.

2 MAIN DESIGN CHALLENGES

The unique challenges of the project have required a great deal of investigations over the years and the design of detailed technical solutions. Various excavation methods are examined, depending on the geomechanical conditions, safety and minimisation of environmental impact. The tunnel crosses several alpine geological units with very heterogeneous geological and geotechnical conditions and high overburden up to approx. 2,200 metres, which poses particular technical and design challenges. Other aspects requiring in-depth design studies include surface logistics, underground logistics and the recycling of the excavated muck.

2.1 *A difficult geological context*

The base tunnel in the cross-border area is located in a very complex geological environment (Humbert, 2015; Monin et al, 2014). This complexity is not only due to the structural aspects, but also to the lithological diversity encountered. In fact, the tunnel is located between the Outer Alps (on the French side) to the west and the Inner Alps (on the Italian side) to the east, separated by the Pennic Front. Figure 3 shows the structural geology of the cross-border area. The geological reference model has been defined along a 4 km corridor along the route and is based on data collected since the 1990s by a series of deep geognostic boreholes along the tunnel axis (to date 357 surveys for a total of 67.7 km of boreholes, 260 km of geophysical surveys), followed by the excavation of the Saint-Martin-La-Porte, La-Praz and Villarodin-Bourget /Modane tunnels (approximately 11 km), the excavation of the La Maddalena reconnaissance tunnel (7. 5 km) and detailed studies for the more complex areas (Monin et al. 2014). Ten macro-zones were identified, two of which are located in loose rock and eight in rock. The maximum overburden is approx. 2,200 metres, with around 40% of the alignment characterized by an overburden of more than 1,000 metres.

Particularly critical zones that require special construction methods are:

- The coal-shale formations of the Houiller Productif, a highly compressive formation in which convergences of up to 2 m occurred in the St. Martin del la Porte tunnel adit;
- The quaternary deposits of the Val Cenischia;
- The highly fissured zones in the Piedmont zone, where high water ingress is expected;
- The asbestos formation in the Piedmont zone;
- Tunnelling in fault zones with large overburden.

From a hydrogeological point of view, more critical conditions are expected than in the other

Alpine base tunnels already built or under construction.

In particular, the expected conditions required the design of technical solutions for high water pressures, minimising the impact on surface sources.

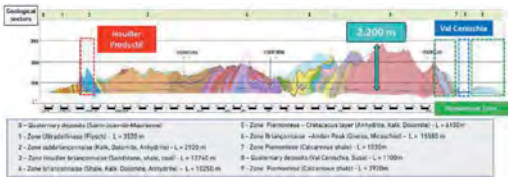

Figure 3. Geological profile main tunnel.

2.2 *Long and deep tunnel*

The design of a long and deep tunnel remains a challenge for engineers today, despite technical and scientific progresses. The complexity of a deep tunnel project lies in the difficulty of anticipating and limiting technical risks from the earliest stages of the project. Given the natural complexity of the geological environment encountered in deep tunnel projects, it is necessary to control the risks and understand the behaviour of the rock mass as well as possible in order to guarantee the safety of personnel and the durability of the structures. The construction of the main tunnel and other underground works will be carried out by alternating several tunnelling methods. Figure 4 summarises the different tunnelling techniques used. As a result, 75% of the tunnel is scheduled to be excavated with TBMs.

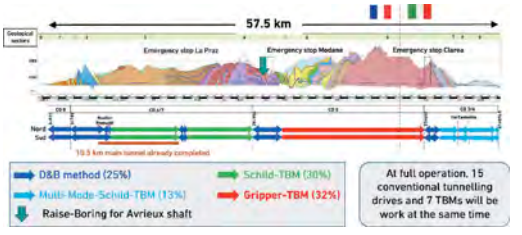

Figure 4. Excavation methods.

The 4 tunnel adits provide access for construction equipment and, at full capacity, 15 D&B headings and 7 tunnel boring machines will be in operation at the same time.

2.3 *Logistic aspects to minimise environmental impact*

An important aspect of the design is logistics, which must not affect production or safety during the construction phase, all in a very restricted environment.

All the construction sites, both in France and Italy, are designed to minimise external impacts (dust and noise) due to the very sensitive public. The sites are located in the Maurienne and Susa valleys, which have a restrictive topography, a high density of infrastructures (energy, industrial, transit) and are locally urbanised (Figure 5). Recycling of the excavated muck from the base Tunnel will limit the transport of the spoils and optimise natural resources. Materials with the required characteristics will be used to produce aggregates for concrete, backfill or landscaping. Approximately 50% of the excavated material will be recycled in this way. Materials will be transported mainly electrically, by conveyor belt and by train.

Figure 5. The example of the Saint-Martin-de-la-Porte site.

3 LOTS AND AWARD OF CONTRACTS

The work was divided into operational sites in order to limit the number of interfaces between the various worksites and comply with the government approval deadlines. The system adopted allows considerable flexibility to be maintained in the allocation of design, construction and supply contracts.

In detail, the works are divided into 12 operational worksites (Figure 6):

- 4 lots for Alpine crossings, subdivided by geographical area, 1 in Italy (CO3/4) and 3 in France (CO5, CO6/7, CO8);
- 1 lot for the ventilation shaft in Avrieux (CO5a)
- 2 lots for the recovery of excavated material in Italy (CO10) and France (CO11);
- 1 lot (CO12) for the railway equipment and safety.

A total of 81 tenders are planned and divided in the following:

- 45 tenders for civil engineering works, divided into four tranches (up to €5 million, between €5 and €50 million, between €50 and €500 million and between €500 million and €1.3 billion);
- 36 tenders for engineering services.

The contracts stipulated between TELT and the companies to which the bids are awarded are "framework agreements" of the mixed (single-award) type. The services can be activated by two means:

- purchase orders: for work already perfectly defined in the contract,
- subsequent contracts: for work that requires additional specifications to those in the initial contract.

Subsequent contracts may only relate to:

- the analysis, sorting and classification of excavated materials,
- the removal of excavated materials to disposal sites,
- earthworks for disposal,
- the construction of structures interfacing with CO 12 (equipment).

All contracts are subject to the rules on the fight against mafia infiltration agreed between the French and Italian governments through the contractual regulations validated by the Intergovernmental Commission and ratified by the French and Italian parliaments, which take precedence over national laws.

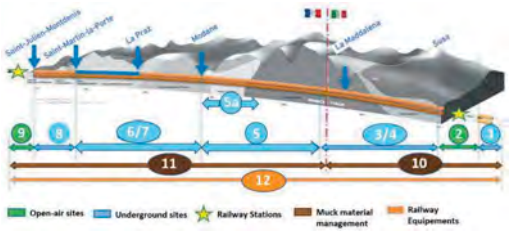

Figure 6. Operational work sites.

The reference information for the main operating underground sites is provided in Table 1.

Table 1. The main underground construction sites.

Operational site	8	6/7	5	5a	3/4
Estimated value	0,23 bn€	1,43 bn€	1,47 bn€	0,22 bn €	1,2 bn €
Indicative length	3 km	23 km	22 km	4 shafts L=500m	9.4 km
Estimated time	70 months	79 months	73 months	52 months	90 months

4 CONTRACT MANAGEMENT

The risk allocation adopted for the TELT project, follows the principles set out in the recent FIDIC-Emerald -Book (FIDIC, 2019; Marulanda and Neuenschwander, 2019). TELT's contracts are of the Design-Build type.

The Tender design is developed by the Client together with his Design engineer and completed by technical reports on the construction methods, phases and technologies proposed by the Bidder.

The organization of technical documents for the tender documentation and for the Contract comply with the GT32R3A2 (AFTES, 2020) and are summarized in the Figure 7. Documents similar to the GDR, based on extensive geological investigations and detailed risk analysis techniques, are developed by the Client's Designer. The Contractor Designer is in charge of the detailed design (DD) and for construction design (FCD), implementing the proposed construction methods, phases and technologies from the tender phase onwards. The site supervision and detail design check is carried out by the Client together with his nominated Designer.

The contract system is mainly based on:

1) the Risk allocation defines the risk type and the owner of the risks;
2) a reference Baseline Schedule which is defined in the tender, with contractual unit rates and items/ quantities on the basis of the expected geology;
3) the time adjustment is recalculated on these bases, according to the effective condition encountered
4) some items (installations and equipment) are defined in terms of duration and are therefore activated in case of EoT.

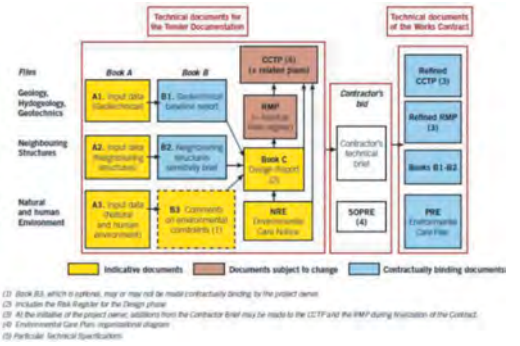

Figure 7. Technical documents for the tender phase according with AFTES GT32.R3A2 (AFTES, 2020).

The contractual time and cost for Excavation, including all necessary support will be adjusted accordingly based on the variations of the physical conditions of the ground encountered within the limits stated in the contractual excavation classes. This adjustment will be performed according to the amounts and production rates stated in the Baseline Schedules in accordance also with FIDIC-Emerald-Book. The contract system included the definition of deadlines, bonuses and contract penalties that could be adjusted on the basis of the effective ground conditions.

The calculation of the estimated construction time is updated periodically for each construction part, usually quarterly.

The construction programme, as shown on the Figure 8, contains the following elements:

- planned construction time: the construction time on which the works contract is based, calculated from the relevant quantities of the bill of quantities at the time the contract is stipulated and the contractor's performance specifications in the works contract as well as from the planned work interruptions;
- Actual construction time: the construction time actually required;

- Construction time for valuation purposes: this construction time is calculated from the contractual quantities and rates on the basis of the geology actually encountered.

After completion of a construction phase, the contractor's advantage or delay can be determined. In the example of Figure 8, the contractor is behind both the target construction time (green) and the construction time for valuation purposes (blue) after construction month 3.

The backlog of the settlement construction time to the target construction time lies within the client's area of risk (difference green - blue). The backlog of the actual construction time to the settlement construction time is within the contractor's area of risk (difference blue - yellow).

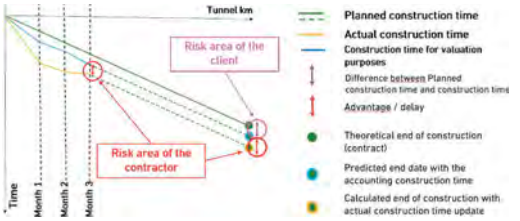

Figure 8. Contractual risk management under normal and exceptional conditions.

Exceptional conditions of execution correspond to situations, not caused by a defect or default of the Contractor, which do not allow the execution of the works subject to the mechanisms of time-adjustment related to the excavations classes fixed in the contract. For the exceptional conditions, the Contractor provides to the Client, within 10 days, all the elements necessary for the assessment of the situation. A Technical Advisory and Mediation Committee (CCMT) may be mobilized by the Client in order to provide an opinion on the effective exceptional nature of the conditions. The entry into exceptional conditions and its date are definitively confirmed by the Client and notified by the Contractor at the latest 4 weeks after. The following flowchart (Figure 9) summarizes the management procedures for normal and exceptional conditions.

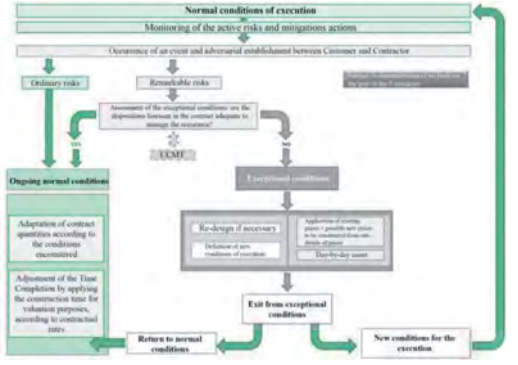

Figure 9. Contractual risk management under normal and exceptional conditions.

Since the main lots are recently awarded or currently in the process of being awarded, there is no direct experience of claims but this possibility seems to be limited only to cases concerning situations not foreseen, and not foreseeable, given the responsibility of the Contractor and its Designer in the development of the DD and FCD.)

5 STATUS OF THE WORKS

In July 2021, all contracts for the entire base tunnel in France were awarded (three lots for a total of 45 km between Saint-Jean-de-Maurienne and the Italian border).

The contracts for the Italian lot (12.5 km between Bussoleno/Susa and the French border) was awarded in August 2023. The international tender for the equipping and technological installations of the tunnel was launched in June 2023. At the end of 2023, the status of the work can be summarised as follows:

- 10 construction sites are operational in France and Italy;
- 35 km, about 22% of the 162 km of tunnels have already been excavated;
- 12 km of the base tunnel have been excavated;
- 10.5 km of the base tunnel between Saint-Martin-la-Porte and La Praz, 9 km of which by Single-shield TBM and 1.5 km by conventional method through the complex formation of Houillier Productif, were completed in April 2022;
- In Saint-Julien-de-Montdenis, the cut-and-cover tunnel, an artificial tunnel that will be the French entrance to the base tunnel, was completed in the autumn of 2021
- In Saint-Jean-de-Maurienne a new temporary multimodal hub station has been in operation since mid-June 2022.
- In Villargondran, consolidation works were carried out on the embankments of the Arc river to protect from floods, as well as to prepare the platform. Work was completed in October 2021.

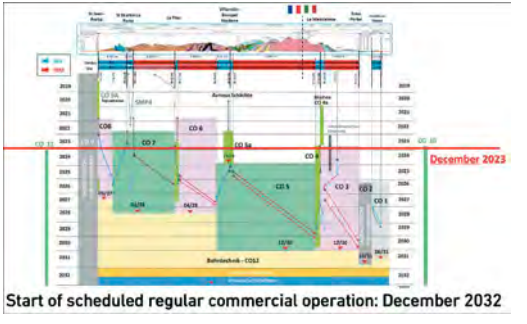

Figure 10. Construction programme.

- In France, the tunnel adit required to start the main construction excavation works were completed: Villarodin-Bourget/Modane (4,000 m, completed in 2007), La Praz (2,480 m, completed in 2009) and Saint-Martin-la-Porte (2,400 m completed in 2010 and 1,800 m completed in 2016)
- In Italy, the Chiomonte exploratory tunnel (Susa Valley, 7,020 m) was completed in 2017.

Overall, more than 2,000 people are currently involved in the construction of this project, including those working in the construction sites and those in services and engineering companies. During the peak of the activities, there will be 4,000 directly hired workers and the same number of people employed in the related supply chain. The following chapters summarize the status of the ongoing work in the base tunnel civil engineering lots.

5.1 *Lot CO8 – Base Tunnel Saint-Julien-Montdenis /Saint-Martin-La-Porte*

The works for the excavation of the base tunnel access, started in December 2022, continue in the 3 km section between the French entrance portal at Saint Julien Montdenis and towards Saint-Martin-la-Porte.

The operations are taking place on the Villard-Clément platform that previously hosted the work for the cut-and-cover tunnel. Excavation in this section will be carried out using the conventional method, by a combination of hydraulic breaker and explosives. The construction site was set up in December 2021 and during 2022 all the necessary equipment was mobilized and the preliminary work for the underground excavation was performed. The work will be spread over 4 years, and will be followed by the completion of the site, entailing the construction of the portal part of the entrance into the mountain that completes the cut-and cover tunnel already built and the restoration of the site to its original state. The works are commissioned to the JV headed by IMPLENIA Suisse and composed of IMPLENIA France/NGE/ITINERA/RIZZANI de ECCHER. Currently about 35% of the work is completed. About 420 m of the first tube and 395 m of the second tube are already excavated (Figure 11).

Figure 11. Excavation works in CO8 lot.

5.2 *Lot CO6/7 – Base Tunnel Saint-Martin-La-Porte*

This construction site for the excavation of the 23 km of the base tunnel between Saint-Martin-la -Porte and Modane proceeds on two work platforms. In total, 43.5 km of tunnels will be excavated, mainly with TBM. Currently about 16% of the work is completed (Figures 12–13). The enlargement of the La Praz tunnel adit for logistic aspects was completed. The excavation of bypass tunnel (currently in progress) will allow the subsequent excavation of the TBM assembly caverns for the two TBM drive through the CO5 lot. In Saint-Martin-la-Porte the technical cavern where the TBM will be assembled is being excavated. The 3 Single-shield TBMs have a diameter of 10.4 metres, 180 metres long and have a total weight of more than 2,000 tonnes with a power of 8,100 kilowatts and 61 cutters.

Figure 12. Excavation works for technical cavern where the first TBM will be assembled.

Figure 13. Excavation works inside the tunnel adit La Praz.

All three shielded TBMs were produced and tested at the Herrenknecht factory in Germany in 2023 (Figure 14).

The first TBM should start excavation by the end of 2024. The works are commissioned to the JV headed by VINCI Construction Grands Projets France and composed of Dodin Campenon Bernard/VINCI Construction France TP Lyon/ WeBuild.

Figure 14. Test of the TBM that will be used to excavate the 9 km of the northern tube of the base tunnel, between Saint-Martin-la-Porte and La Praz at the Herrenknecht factory.

Figure 15. Pilot holes and raise borer machine for the excavation of the Avrieux shaft.

5.3 *Lot CO5a – Avrieux ventilaton shaft*

The construction of the ventilation shafts for the base tunnel is under way. These are four parallel vertical tunnels to be built at an altitude of 1,300 metres. They are very important because they must reach the underground station of Modane (at the foot of the Villarodin/Bourget-Modane slope), 500 metres below, where they will contribute to ventilation and safety. The four parallel shafts with a diameter of 5.2 metres are excavated using Raise Boring Machines, a technology developed in the mining industry specifically for the mechanised excavation of vertical shafts of small diameter. Pilot holes are excavated into the underground caverns at a depth of 500 metres with drilling diameter of 38 cm with admissible tolerance in the vertical 0.46 ‰ or a maximum of 23 cm. Bars are then inserted into the holes, at the ends of the bars the reamers (the heads of the vertical cutters) are mounted, which then go back up and dig the shaft vertically. The excavated material, which falls by gravity, is taken out through the existing tunnel adit. The installation of the rock supports composed of FRC shotcrete and steel ribs for critical section are installed from top to bottom. A final lining of 35 cm in-situ concrete is installed from bottom to top.

The four pilot holes were completed in April 2023. The first shaft was excavated and about 300 m of rock supports are installed. For the second shaft the excavation was completed and the installation of the rock-supports will begin shortly, while boring will start for the third shaft. The safety site tunnels and several technical caverns up to 22 metres in height and 23 metres in width, are also being built underground. They will be used to assemble the TBMs that will then excavate towards Italy. At the end of 2022, the group of companies procured the two tunnel boring machines planned for the excavation of this section. 35% of the works are currently completed.

The works are commissioned to the JV headed by VINCI Construction Grands Projets France and composed of Dodin Campenon Bernard, VINCI Construction France, Webuild e Bergteamet.

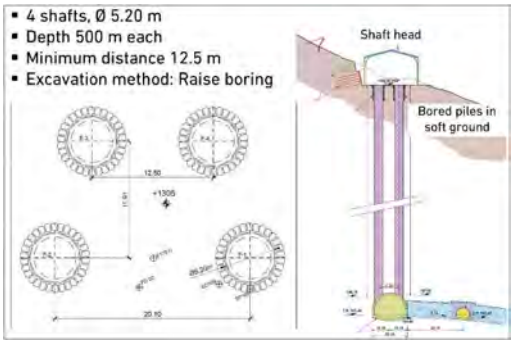

Figure 16. Layout of Avrieux shafts.

5.4 *Lot CO3-4 – Italian main lot*

Preliminary work started in December 2023. In Chiomonte (Susa valley) there is the largest Italian construction site.

The excavation of the niches to facilitate the passage of construction vehicles in the Maddalena 1 tunnel, completed in 2017 (Baldovin et al., 2017), is completed in November 2023. The niches (each 3 m deep and 30 to 40 m long) are constructed every 300-400 m along 7 km. They will transform the tunnel, which was created for exploratory purposes, into an access point for the construction vehicles. In Chiomonte, the construction site for the new junction of the A32 motorway, which will allow the transit of construction vehicles without interfering with the local road traffic is also operational.

Particularly interesting for this lot will be the excavation inside the Cenischia Valley (Figure 17-18). Over a length of around 1 km, the alignment runs through a section with an overburden of approx. 50 m, characterised by the presence of alluvial deposits below the groundwater table with high permeability. The hydraulic pressures are around 5 bar. The alluvial deposits of the Cenischia Valley are classified as sands and gravels with a fine matrix with intercalations and lenses of cohesive material and the possible presence

of larger stones and boulders. The excavation in the quaternary layers and the impossibility of lowering the groundwater level, which is partly due to the built-up area of Venaus, led to the decision to work with a "dual-mode" TBM in this section.

The TBM can be operated both in open mode and in closed mode as a "slurry TBM". The transition zones with mixed face are critical. The segmental lining is 100% tight in this area, the lining must be designed for the full water pressure because no drainage measures are allowed.

In addition to driving the main tunnels, the construction of several cross-passages between the two tubes as well as technical niches is planned in this section.

The cross-passages and technical niches in the loose rock will be excavated using the freezing method. Outside the excavation area, a ring-shaped shell of frozen ground is created, within which the excavation and stabilisation work is carried out. The excavation work may only take place after completion of the freezing phase, which is considered complete when the frozen shell is closed, i.e. when the minimum thickness of 1.00 m required for the project has been reached at an average core temperature of ≤ -10°C.

The freezing system may only be deactivated after the final in-situ concrete lining of the cross-passages has been completed.

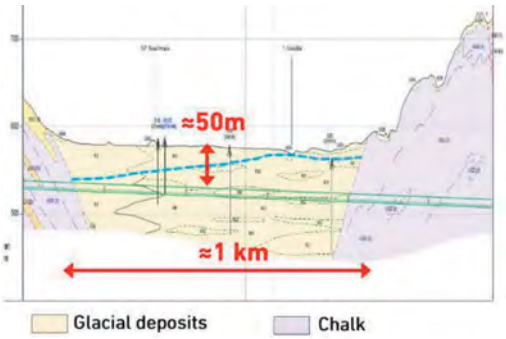

Figure 17. Dual-Mode-TBM excavation inside Cenischia Valley.

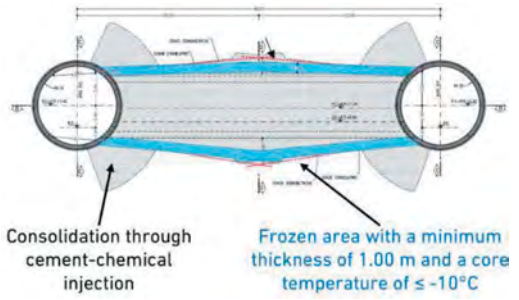

Figure 18. Excavation of the bypass using the freezing method.

6 CONCLUSIONS

The following recommendations can be provided based on the experience of the design and execution of the contracts for the construction of this major underground structure characterised by several complex challenges:

Risk management:

- A fair distribution of risks between contractor and client;
- Control of risks in the planning and construction phase with clear mechanisms for activating corrective measures;
- The client's risk analysis must indicate a possible change in the construction period;
- Control of the interfaces within the lots and among the various construction contracts during all phases of project realization.

Cost management:

- Time-dependent costs must be clearly defined in the bill of quantities;
- A fair allocation of risk between the client and contractor enables quick solutions to be found in the event of changing conditions.

Contractual flexibility:

- Introducing a decision-making tool that can react very quickly to changing conditions;
- Providing the opportunity to implement alternative solutions where appropriate;
- Ensure the consistency and technical quality of the project by rapidly incorporating feedback from experience, using new data acquired during the construction phase to improve the ability to predict the behaviour of the massif and anticipate problems as far as possible, in the interests of efficiency and control of timescales and costs.

Safety and environment:

- Ensuring safety during the construction, operation and maintenance phases;
- Controlling the quality of emissions into the air and aquatic environments, noise pollution for local residents and protecting sensitive environments during the construction and operation phases;
- Managing excavated materials to optimise transport, reuse of materials and use of temporary and permanent disposal sites.
- When the Lyon-Turin line will be operational, over 1 million lorries used for international road transport will no longer be present on alpine roads, thus reducing CO2 emissions by 3 million tons per year.

Quality of the structure:

- Ensure the durability of the structure for 120 years, taking into account the aggressive nature of the soil and water in certain sections;
- Enable the structure to be operated and maintained with minimum intervention.

ACKNOWLEDGMENTS

The authors would like to thank TELT-sas for the permission to publish the data contained in this paper. The authors would like to thank the S2IP site supervision consortium (Setec, Systra, Italferr, Pini Group) for their support.

REFERENCES

AFTES (French Tunnelling and Underground Space Association). 2020. Technical risks integration in the design of underground structures projects for the purpose of tender documentation drafting. AFTES Recommandation. N. GT32.R3A2, pp. 41.

Baldovin, E., De Paola A. Morelli G.L., Gilli P., La Rosa C. 2019. Return of experience following the excavation of "La Maddalena Reconnaissance Gallery"–TBM performance prediction in the Ambin Massif. In: Proceedings of the ITA AITES WTC 2019, Naples, Italy, May 3/9 2019, pp. 616–625.

Bufalini M., Dati G., Rocca M., Scevaroli R. 2017. The Mont Cenis Base Tunnel. of Geomechanics and Tunnelling, suppl. 3. pp. 246–255.

FIDIC (International Federation of Consulting Engineers). 2019. Conditions of Contract for Underground Works - Emerald book - Designed by the contractor according to the reference design by the employer and the Geotechnical Baseline Report, pp. 272.

Humbert E. 2015. Site Investigations Reduce Cost Overruns in Tunnelling Projects. In Proc. Intern. Symp. WTC 2015 Congress and 41st General Assembly May 22-28, 2015, Lacroma Valamar Congress Center, Dubrovnik, Croatia.

ITA/AITES. 2004. Guidelines for tunnelling risk management. ITA, Working Group No.2 Tunnelling and Underground Space Technology, 19, pp. 217–237.

Marulanda, A., and Neuenschwander, M. 2019. Contractual time for completion adjustment in the FIDIC Emerald Book. In: Proceedings of the ITA AITES WTC 2019, Naples, Italy, May 3/9 2019, , pp. 4530–4537.

Monin N., L. Brino, A. Chabert. 2014. Le tunnel de base de la nouvelle liaison ferroviaire Lyon-Turin retour d'expérience des ouvrages de reconnaissance, Congress, AFTES Lyon 2014.

Stocker, D. and Humbert, E. 2021. Tunnel Euralpin Lyon Turin: the design and contract challenges for a modern bi-national Alpine base tunnel. Proceedings of AFTES 2021, Paris.

Tunnelling for a Better Life – Yan, Celestino, Thewes & Eberhardt (Eds)
© 2024 The Author(s), ISBN 978-1-032-80042-4
Open Access: www.taylorfrancis.com, CC BY-NC-ND 4.0 license

Risk limiting in urban tunnel contracts

Harald Wagner*
DHW Consulting Engineers Pte Ltd Bangkok Thailand, Thailand

ABSTRACT: In urban tunnelling, any approach has its limitations in adequately describing the Ground-Structure-Interaction (GSI). Applied approach is of eminent importance in evaluating unforeseeable risks. Tunnel excavation causes disturbance of initial state of stress creating 3-Dimensional-Stress-Regime umbrella like at the tunnel face. Each Simulation of Excavation & Installation of Initial Support shall analyze risks and ground response. Digitisation and engineering based on experience helps to fast-track green underground solutions towards the delivery of UN Sustainable Development Goals (SDG). It helps to limit risks in urban tunnelling and supports contacts with infrastructure industry. Full support is given to "rated criteria" approach at procurement, which has been hailed as a "game changer" for promoting value in procurement. The rated criteria approach underlines the objective of achieving SDG objectives. International procurements shall require use of rated criteria including risk analysis in addition to price as part of bid evaluation.

Keywords: Tunnelling, NATM/TBM, Risk assessment prediction and control, Contract management and foreseeability, Geotechnical Baselines, Claiming procedures and dispute review board, Arbitration

1 INTRODUCTION

Where municipalities have made decisions for Underground Structures, - taking the example of Mass Transport Systems -, there are positive effects. Living quality for the residents is rising as environmental conditions are improving. Where cost analysis includes environmental effects, land value increase etc., Underground attracts more than Above Ground.

Reasons behind are to be discussed and evaluated as they are manifold. In many cities there are historical reasons.

Beginning of public transport on surface started in the middle of the 19th century, when underground technologies in urban areas have been unknown.

Infrastructure projects are investments for the public. Decisions are made by political representatives of the public. Public Authorities are managed by own staff, supported by external experts. Political/economical responsibilities may change, as decisions are reaching far into the future.

It is expected that from nowadays 15 mega cities with population exceeding 10 million, there will be a total of more than 50 mega cities in the year 2050. As a consequence of this development the amount of underground infrastructure will be multiplied with a factor of 5 to 10. While in the past there has been an opinion that underground structures are expensive, in the future we will see a development whereas underground structures will be considered as investment with return to the public, rather than cost.

Figure 1. Global megacities (2010/2050).

While underground structures have been considered in the past of being risky due to some spectacular collapses, the underground industry led by the International Tunnelling Association together with the International Tunnel Insurance Group has responded to that development. Risk Management Guidelines became a standard tool in most tunnel design and

*Corresponding author: drhrwagner@yahoo.com

DOI: 10.1201/9781003495505-486

construction contracts. By managing the risk of underground structures, significant improvements resulted in successful projects, leading to the conclusion, that underground structures are equal in risk and chance.

An integral part of tunnelling is data verification by means of in-situ monitoring of design assumptions made regarding the interaction between the ground and initial support. Collapses happen and contractors claim for not reasonably foreseeable. All subsurface physical data described in tender documents are deemed to be foreseeable, and subsurface physical data outside scope of conditions defined in tender documents are deemed to be Unforeseeable.

The contractor shall be deemed to have based proposals for excavation and lining works on the subsurface physical conditions and ground reactions described in the tender documents irrespective of any discrepancy or ambiguity that may be found between such conditions and/or reactions and conditions described in any data made available.

Physical Conditions mean natural physical conditions and reactions of the ground to excavation encountered, having been Unforeseeable and having an adverse effect on the progress increasing cost of execution. It shall be assessed under measurement of excavation and lining works and adjustment of time for completion and contract price. Even under conditions of actual increasing geotechnical observational data, elimination of Unforeseeable Risks per se would lack factual geotechnical uncertainty in underground construction.

In order to ensure uniform style throughout the papers, all the papers have to be prepared strictly according to the instructions set below. Please review this document to learn about the formatting of texts, table and figure captions, references, and the method to include the indexing information. The full paper in MS Word file shall be written in compliance with these instructions (Full paper template). At a later stage, it will be converted into Portable Document Format (PDF).

2 MASS TRANSPORT TUNNELS

The choice of Tunnel Contract Model is determining design, specifications, and drawings to visualize the structure resulting in a sustainable underground building. Tunnel Designer together with his client is deciding about the future success at the very early project stage. He is at same time the manager of the tunnel construction itself. His decision of contract model, standards, and design, assessing the risks, becomes a management tool in construction. This lecture on tunnel contract models, used standards, site organization, and construction management summarizes the state of the art of contracting for both Conventional and mechanized tunnelling.

A detailed description outlines contractual applications, and construction site organization. Fundamental requirements for contracting tunnel works are knowledges of

- Ground condition evaluation/classification, requirements,
- Decision on the use of standards and specifications,
- Design with staged subdivisions, following project/construction,
- Construction Methods suite for plant, equipment, material,
- Risk Management Plan (RMP), Geotech Baseline Report (GBR),
- Flexible Contractual Models for fair remuneration.

With constantly growing underground infrastructure market, demand for proper designed and contracted Underground Works is continuously growing. Today Conventional Tunnelling (CTM) and TBM Tunnelling are both well suited for tunnelling under difficult, complex, and rapidly changing geological and geotechnical conditions.

Minimizing construction cost by models, driving cross section, driving methods, and lining during the design and construction phases are of the essence. During tunnel excavation simultaneous and joint decision by applied contract model must be realized within predetermined limits to manage flexible response to changing ground and ground behavior conditions.

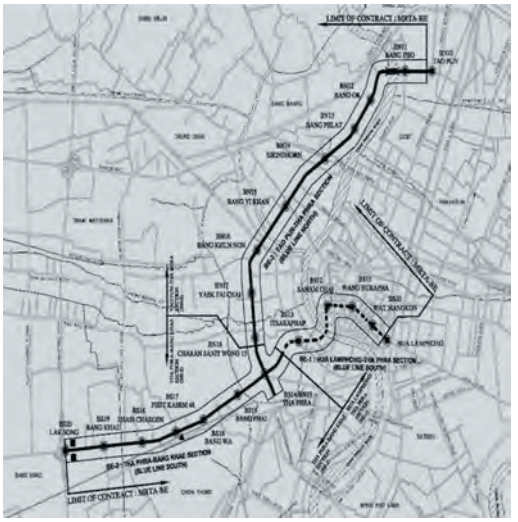

Figure 2. MRTA's blue line extension project in Bangkok (Lay Out).

Tunnels need robust design as well as suitable contract models including suitable standards. Tunnelling needs project specific trained, qualified, and experienced consultants, designers, and contractors. It needs qualified and experienced engineers on site, and qualified and experienced workforce. Contract models shall be able, to cope with changing ground behavior, on base of GBR and RMP. Fair and objective risk management shall be reflected in the contract.

The City of Bangkok has 2 Mass Transport Systems with the Sky Train as an elevated structure dominating the environment of the city where it is built, and the Metro which in the inner urban area is underground, and at the city's Periphery an elevated structure.

Traffic jams in the city and on the roads are daily and omnipresent. Bangkok Municipality's Mass Rapid Transit Authority (MRTA) has therefore decided to invest in further extension of the mass transport infrastructure with the Purple Line having an above ground elevated alignment, and with the Blue Line Extension.

The MRTA Blue Line Extension Project is the 22 km elevated structure with approx. 5 km of Underground Structure. The project is separated into 2 sections, which are Hua Lamphong – Bang Khae section (14 km) and Bang Sue – Tha Phra section (13 km). Hua Lamphong – Bang Khae section contains 7 elevated stations and 4 underground stations. Bang Sue – Tha Phra section contains 10 elevated stations.

The Underground Structure of this project is challenged with complex construction issues around the Old City Area, also known as the Rattanakosin Island. Two underground stations are located inside Rattanakosin Island. These stations need to be constructed using NATM mined methods in order to minimize environmental impact.

Bangkok is a good example but not the only city having both above and underground competing transportation infrastructures. Other examples are the City of Vienna/Austria with U-Bahn (Metro) and S-Bahn (Railway), the City of Hamburg/Germany, New York City/USA et al.

3 URBAN ROAD TUNNELS

Societies worldwide are requesting free mobility, but mobility demands it's toll. Most cities have an urban historical background, and few cities only have, in their core urban structure, streets or roads which are suitable to modern traffic requirements. In fact, most cities have overlapping old fashioned traffic infrastructure with new infrastructure needs and provisions due to increased traffic demand.

Tehran, capital of Islamic Republic of Iran, provides a pioneering example of advanced technical solution in the northern part of the city, in realizing an integrated and intelligent underground urban infrastructure for road traffic and for parking in the alluvial deposits beneath a park.

A total tunnel length of approx. 2 x 3.5 km of unidirectionaladvanced equipped 3-lane tunnels with complex wide span bi-furcations exceeding 200 m2 and lay by areas is under construction using Conventional Tunnelling Technology (NATM) in combination with the Iranian Ribbing Method, which has a century long and very successful tradition in the area.

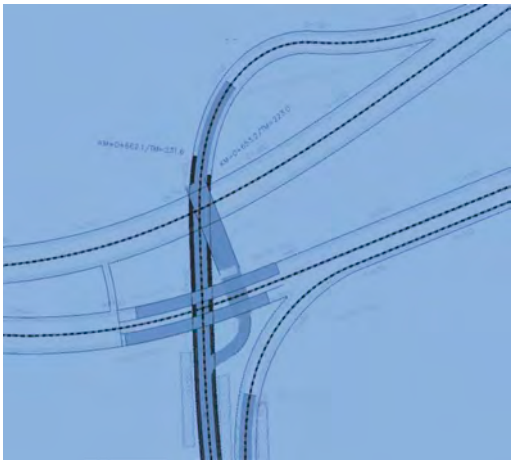

Figure 3. Freedom in underground space use - Bifurcation (Lay Out).

Figure 4. Tehran's urban tunnels (Lay Out).

4 URBAN LORRY TUNNELS

Roads at the beginning of the 21th century and roads one hundert years ago are very different. Traffic in the old days has been fully compatible with living conditions. There was rarely any concern in terms of safety for the neighboring population on the roads under regular traffic conditions. Roads have been used combined, without any hesitation, both for people and for freight traffic.

Roads as a transportation means have reached at the beginning of the 21th century their capacity limits. Serious traffic jams and delays combined with noise, multiple emissions, e.g. carbon dioxide, NOx and fine dust particles, constitute a high risk potential, especially in congested urban area, for urban population, resulting in an increasing demand for separation of people and freight traffic.

Fully automated underground transport concepts can provide freight transport for direct connection between recipient, e.g. department stores in the city centers, and distribution centers located outside the city. In particular in congested urban areas this will serve the distressing of the roads from increasing freight traffic and reduce the environment related problems providing additional surface space.

Due to the use of the underground space this concept offers independence from other traffic infrastructure, traffic jams and unfavorable weather conditions. Transport is managed by computer controlled logistics and is warranting a high freight and destination flexibility.

5 SUMMARY

The world is realizing the shift of economy from rural agrarian to urban service and manufacturing industry. Realisation depends highly on back up infrastructure and energy availability. Requirements are interwoven with developments of underground structures provided by hydro tunnels for energy, metro tunnels for mass transit, road and railway tunnels narrowing communities and underground space development along stressed city centers.

The choice of contracting method and evaluation of tunnel behaviour means balancing the interaction between project owner and contractor, as well as between equipment and ground. For designers guided by FIDIC's Emerald Book, it means production of specs and drawings to visualize a structure which results as a tunnel. The tunnel designers are becoming managers of tunnel contracting including many of its risks, as the choice of contracting and design becomes a management tool in construction.

The paper focuses on principles of tunnel contracting for future Infrastructure and for contract management by design, summarizes state of the art for both conventional (NATM) and mechanized (TBM) tunnelling. Details are provided in regard to Infrastructure and innovative BIM (Building Information Method) technologies, the Choice of Tunnel Contracting, Principles of CTM Tunnelling, Principles of TBM Tunnelling, Monitoring for CTM and TBM Tunnelling, CTM Tunnelling in Soft Ground & Hard Rock.

Issues focus on Underground contracting including claim management, Hydro Tunnelling, Floodwater Control Tunnels, design stages, contractual applications, and construction organization. The ultimate Goal are recommendations for a contract management system and model contract agreement to contribute to accelerated design and construction free of arbitration and disputes.

6 CONCLUSIONS

For Underground Infrastructures in the future a Paradigma Change is to be expected.

As Underground solutions are going to become more attractive, more economic and more safe, even odd surface space is going to receive increased attraction for developers and in consequence will rise in value due to achievements in underground technology.

The lesser above ground infrastructures will require land and space, and the more quality standards of environment will continue to be forced by law, and better life quality is going to be realized.

Underground space use will offer the only sustainable alternative for further development and expansion of living and working.

Within the frame of mega projects, hydro tunnels are going to prevail against open canals. Mass Transport Tunnels are expanding in mega cities with breathtaking progress rates.

Shanghai is giving an example of constructing up to 50 km completed metro sections per year, the majority of which are both mined and open cut tunnels, over the past 15 years.

Freight Tunnels are offering sustainable underground solutions for traffic and transportation problems in urban areas, in separating freight traffic from individual traffic such contributing to the minimization of required storage space of retailers in the cities and to the life quality of the fast increasing global urban population.

The Underground Industry is responding with a clear and positive answer to the question "Why not Underground". It is responding and addressed to sustainable development of a global society.

Underground Infrastructure is growing continuously in the future, providing interesting new challenges for young engineers who are best educated and trained in their profession.

ACKNOWLEDGMENTS

Creative collaboration is spanning decades with ITA International Tunnelling and Underground Space Association's long term Secretary General Claude Berenguier and Executive Director Olivier Villon.

Beyond collaboration with TWB The World Bank, IDB Interamerican Development Bank, ADB Asia Development Bank, and IFC International Finance Corporation, successful collaboration in design and construction has been performed.

Major stake holders of Underground Infrastructures to be acknowledged and highly appreciated are Pravin Karki c/o TWB The World Bank Washington/DC, Julio Lemaitre c/o IFC International Finance Corporation Washington/DC,

Jose Luis Irigoyen c/o IDB Interamerican Development Bank Washington/DC, Vivien Castro Wooldridge c/o ADB Asian Development Bank, Manila/Philippines.

REFERENCES

H. Wagner. “Tunnel Construction Technologies & Risk Practices – Inevitable Risks of Collapses in Construction”. Tunnelling Asia 2022. International Conference on Underground Space – The Need of the Day. 97–110. Mumbai/India, June 27-28, 2022.

H. Wagner. “Urban Underground Space Sustaining Life Cycles”. ITA-AITES World Tunnelling Congress WTC 2022. Copenhagen 2 – 8 September 2022.

H. Wagner. “The Genesis of Underground Engineering”. NBM&CW Tunnelling Technology Publication. October 2022.

27–28, 2022.

H. Wagner. “Urban Underground Space Sustaining Life Cycles”. ITA-AITES World Tunnelling Congress WTC 2022. Copenhagen 2 – 8 September 2022.

Tunnelling for a Better Life – Yan, Celestino, Thewes & Eberhardt (Eds)
© 2024 The Author(s), ISBN 978-1-032-80042-4
Open Access: www.taylorfrancis.com, CC BY-NC-ND 4.0 license

Author Index

Álvarez, C. 1167
Abdul Rahman, N.A. 3623
Abeyawardena, D. 1340
Abreu, F. 2825
Adhikari, R.K. 476
Adhikari, S. 3044, 3149
Agafonov, V. 3157
Aggarwal, P. 1768
Agrillo, S. 164
Ajalloeian, R. 2995
Akulich, V. 3067
Al Haddid, N. 247
Alarcón G., J.E. 3585
Alessio, C. 3303, 3312, 3320, 3557
Al-Khayareen, K.S. 2043
Al-Khayareen, K.S.F.S. 2162
Alsahly, A. 1974
Alvarado, G. 591, 671
Amadini, F. 1875
Amado, A.B. 3328
Amemiya, T. 836
An, A. 2619
An, J.-B. 2442
Anagnostou, G. 451, 2020, 2056
Andrés Marulanda, E. 3567
Anlimah, F. 1383
Ano, T. 848
Anthi, M. 451
Antiga, A. 149, 828, 3572
Antón, P.R. 2825
Anwar, S. 678, 917
Aoki, H. 1340
Aono, Y. 655
Aoyagi, T. 1479
Aoyama, T. 1687
Appleby, B. 1866
Arai, T. 2959
Arora, K. 457
Asanprakit, A. 1446, 1750
Asche, H. 182
Assis, A. 822
Ates, U. 1621
Attianese, G. 3312

Baber, J. 2333
Baccolini, L. 3303, 3371, 3557
Bae, A. 1630, 1860
Bai, H. 493
Bai, X.-D. 2222
Bai, Y. 2575
Bai, K. 1634
Bai, Q. 1356
Bakhshi, M. 158
Bakoš, M. 285
Balakumarasingham, V. 1390
Balci, C. 1641, 1648, 2116
Banda, S. 1902
Bang, J. 685
Bansal, V. 1768
Bao, R. 2376
Baranger, E. 2035
Barbero, E. 1994, 2003
Barbetta, A. 2825
Barbieri, G. 164, 2834
Barret, C. 1207
Barrouillet, E. 1167
Basnet, C.B. 3044, 3149
Bateman, G. 109
Batocchioni, L. 926
Batuman, S. 1768
Bavasso, I. 529
Bazzani, M. 932
Bednar, T. 2927
Behbahani, S. 2624
Bella, G. 164, 2834
Bellardo, L. 760
Bernard, R. 1399
Beronneau, P. 2927
Beyhan, S. 1663
Bezuijen, A. 1682, 2271
Bhasin, R. 941
Bi, X. 2323
Biagi, A. 2834
Bilgin, N. 1641, 1648
Bilotta, E. 877
Bineshian, H. 173
Binnar, D. 1461
Blaise, A.-N. 1126
Bobylev, N. 3, 125
Boissonnas, Y. 2509
Boldini, D. 865
Bomben, G. 2517
Bonfanti, O. 2170
Bono, R. 1792, 1944
Boscaro, A. 1994, 2003
Boursier, T. 28
Bove, F. 8, 2179
Boyaci, B. 2863
Brantmark, J. 3262
Brown, O. 1000, 1199, 2630
Brox, D. 1437
Butt, S.N. 1654
Butterworth, C. 1994

Çalışkan, F. 1594
Çalışkan, U.C. 1663
Cai, Y. 1238, 1806
Caicedo, B. 608
Calicchio, M. 2863, 3365
Caliskan, F. 798
Calleja, M. 1944
Cao, A. 441
Cao, B.T. 1974
Cao, P. 2342, 2358
Cardone, G. 1126, 3160
Cardu, M. 842, 1669
Carigi, A. 842, 3333
Cassani, G. 760, 1935
Catapano, M. 2841
Cavolo, M. 789
Ceccarelli, C. 3320
Çalışkan, U. 1663
Cha, Y. 1475
Chajed, S. 2639
Chang, K.B. 1189, 1967
Chang, J. 1675
Chang, X. 3342
Chang, Y. 946
Chao, H.C. 13

Chapman, B. 3160
Charlesworth, G. 329, 368, 678
Chatoux, E. 1390
Chau, S.F. 182, 1412, 1728
Chayaroon, A. 345, 1446, 1610, 1750
Chelini, L. 2745
Chen, B. 1705
Chen, C. 1784
Chen, C.H. 214
Chen, H. 193, 200, 240, 1705, 2388
Chen, J. 755, 1244, 1276, 1291, 1687, 1694, 1737, 2323, 2848
Chen, K. 2185
Chen, L. 1282
Chen, P. 953, 2848
Chen, S. 3504
Chen, T.H. 214
Chen, W. 1333, 2366, 2857, 3180
Chen, Y. 2575, 2702, 3014
Chen, Z. 193, 705, 711, 1682, 2280
Chen, Z.J. 2388
Chen, Z.-J. 2500
Chen, Q. 1405
Chen, X. 20, 991
Chen, Y.-F. 1698
Cheng, C. 1719
Cheng, J. 1737
Cheng, L. 2483, 2487
Cheng, Q. 1540
Cheng, X. 3290
Cheng, B. 1711
Cheng, W.-C. 2222
Cheng, Y.-J. 2644
Chengzhi, Y. 1902
Cheung, J. 2028
Cheung, T. 1412, 1728
Chiaia, B. 3312, 3557
Chiang, C.E. 209
Chiang, H.T. 209
Ching, I. 3160, 3255
Chiorboli, M. 3572
Chirulli, D. 828
Chiu, I.K. 13
Cho, G.-C. 685, 1475, 2442
Choe, Y. 536, 1630
Choi, H. 536, 1630, 1860, 2658, 3053, 3617
Choi, K. 2035
Chong, J.T. 962
Chou, K.H. 214
Chouhan, M.S. 467
Christakis, E. 476, 3223
Chu, T. 390
Cinelli, M. 529
Coisson, E. 3312
Coli, M. 485, 969
Comini, R. 2910
Conte, M. 3303, 3557
Coppola, P. 828
Copur, H. 1621, 2116
Côté, O. 2650
Coupland, J. 1000
Couturier, F. 28
Cui, H. 711
Cui, L. 1737
Cui, P. 3511
Cui, Y. 1405, 3428
Cvetkovic, V. 2610

Dai, Z. 3350
Dai, G. 705
Dalmalm, T. 3262
Dalvi, S.G. 1418
Dange, M. 3169
Dantas, A. 822
Dardashti, A. 2995
Daudibertières, P. 1390
Davies, B. 1383
Davis, C. 2139
de Almeida, A.M. 579
de Assis, A.P. 3585
de Cabo, M. 220
de Lillis, A. 2771
de Pommerol, A. 3581
de Rivaz, B. 977
del Amo, A. 2139
Deng, Y. 3174, 3394, 3465
Deng, Y.Z. 3267
Deng, Z. 406
Deng, L. 1216
Deng, Q. 983
Denman, D. 1902
Deplagni, E.A. 689
Devriese, S. 3444
Dewangan, A. 3005
Di Fiore, D. 3557
Dias, N. 2935
Dickmann, T. 517
Diederichs, M. 3160
Diez, F. 101
Ding, H. 2358
Ding, L. 3652
Ding, S. 2575
Do, P.N. 732
Dong, Y. 616, 671
Dong, R. 1742, 1806
Dong, X. 991, 1806
Dong, Z. 1429
Doorduyn, A. 2366
Dorji, T. 1437
Dotti, M. 3572
Douglas, J. 2650
Du, L. 1916, 2244, 2253
Du, B. 991
Duan, S. 2323
Duan, D. 493
Duan, H. 2522
Duangsano, O. 1446, 1610, 1750
Dudouit, F. 33
Dumlu, E. 1594
Dunbar, L. 2951
D'Ambrosio, M. 1981, 2179
D'Hondt, C. 182

Eberhardt, E. 300
Ellis, J. 1000, 1199, 2630
Ellison, A. 1207
Ellwood, M. 2139
Emadi, A. 1008
Eratne, S. 1728
Ergin, H. 1663
Ernest, T.E.S. 501
Evtushenko, R.A. 1602

Falanesca, M. 3659
Fan, J. 616, 2450
Fan, L. 1105
Fan, Z. 2492
Fan, Q. 2554
Fang, L. 2554
Fang, Y. 1682, 3067
Fantauzzi, G. 228
Fantini, P. 523, 932
Farshbar, A.R. 1015
Farzay, O. 1669
Fei, R.-Z. 3267
Felice, M.D. 1021
Femina, D.D. 2834
Feng, H. 711
Feng, S. 2400, 3014
Feng, T. 1850
Feng, H.H. 1759, 1828
Feng, Y. 3014
Ferrari, L. 3312
Ferreres, M. 1167

Ferretti, D. 3312
Filho, E.P. 1424
Filho, E.A.P. 3594
Fiore, D.D. 3303
Fischer, O. 315
Flor, A. 523, 1875
Focaracci, A. 3359
Fong, H.M. 1455
Foria, F. 2863, 3365
Forlingieri, L. 1027
Forooghi, M. 1768
Francini, M. 969
Frey, S. 3249
Friedinger, C.P. 3600
Frisiani, S. 3371
Fu, H. 638, 2529
Fu, Y. 3174, 3342, 3465
Fu, Y.-Y. 3267
Fukuda, T. 2959
Fukui, R. 2731

Gakis, A. 1036
Galera, J.M. 220
Gall, V.E. 3608
Galler, R. 396
Galli, D. 1126
Gallo, F. 789
Gallotto, A. 789
Gao, L. 2619
Gao, P. 2868
Gao, S. 890
Gao, D. 2972
Gao, Y.-M. 1777
Garbutt, D. 41
García de Haro, P. 1312
Garin, E. 2664, 3187
Garrido, C. 1167
Gatti, M. 760
Gatti, M.C. 1935
Gavhane, S. 695
Ge, Z. 1784
Ge, Y. 2548
Geng, H. 705
Geng, P. 1244
Gerolymos, N. 323
Ghafar, A.N. 2610
Ghazali, M.F. 2672
Giani, M. 164, 2834
Giannotti, W. 2082
Gilli, P. 3659
Giordano, G. 228
Giovanni, A.D. 1669
Giulio, A.D. 1021
Goh, K.H. 501
Goh, K. 96
Goh, V.C.S. 432
Gök, I.U. 2539
Gomes, A.R. 1008
Gong, C. 2244, 2548
Gong, J. 78
Gong, L. 1092
Gong, R. 368
Gong, X.-N. 2500
González, V. 926
Gopal Madabhushi, S.P. 726
Gopaldasani, V. 1383
Graafhuis, R. 329
Graham, I.T. 591
Grandori, R. 1792, 2049
Grigoras, V. 2863
Grothen, B. 1800
Grøv, E. 377
Gu, Z. 65, 1312
Guan, S. 705
Guan, Z. 2778
Gudžulić, V. 1118
Gui, F. 3520
Guo, B. 1429
Guo, C. 1806
Guo, S. 509, 2848
Guo, Y. 2450, 2985
Guo, L. 3180
Guo, W. 2868
Gupta, S.K. 1418, 1461, 2757, 3169
Gupta, R. 47
Gutierrez, M. 457

Haddid, N.A. 1044
Haigh, S. 1926
Håkansson, U. 2610
Halim, I. 3608
Han, X. 711, 747, 1053, 2593, 3489
Hanaoka, D. 1135
Hangadi, G.C. 1814
Hansson, P. 1159
Hao, S. 857
Hao, M. 718
Hart, M. 2366
Hassanpour, J. 2995, 3095
Hataysal, E. 3388
He, C. 1806
He, D. 1244
He, W. 352
He, C.N. 200, 337, 2349
He, Z. 726
Heath, G. 2944
Hecht-Méndez, J. 517
Hemmi, R. 1469
Hermsen, R. 2475
Hirano, H. 848
Hirata, F. 2082
Hong, J.P. 3037
Hong, K.R. 1759
Hong, K. 2868
Hong, Z. 3194
Höök, C. 946
Hosoda, A. 3379
Hoss, B. 629
Hoss, J. 1820
Hu, C. 1027
Hu, K. 2529
Hu, M. 2309, 3079
Hu, R. 3350
Hu, S. 1820
Huang, C. 616
Huang, H. 806, 1675, 2737, 2778, 2817, 3104, 3131, 3647
Huang, J. 2148, 3652
Huang, L. 755, 1837, 2148
Huang, M. 2554
Huang, S. 1843, 1850, 2751
Huang, W. 1711
Huang, Y. 2876
Huang, Z. 3545
Huo, J. 65
Hwang, J.H. 3037
Hwang, B. 1860
Hwang, C. 2658
Hwang, H.-J. 1475

Iacobini, F. 235
Iacullo, S. 1944
Ianeselli, M. 789
Iasiello, C. 523, 3023
Ibarra, G. 220
Içik, L. 1953
Ide, Y. 1469
Im, S. 685
Imai, M. 2724
Imaoka, Y. 2731
Insam, R. 1561
Inuzuka, T. 1479
Ireland, T. 1728
Isago, N. 836, 1340, 2681
Iseley, T. 2624
Ishaq, M. 1866
Ishii, T. 1517
Ito, F. 1469, 2959

Iuculano, P. 3320
Iwano, K. 1479

Jacques, D. 2012
Jain, S. 1768, 2650
Jakobsen, P.D. 1486
Jarast, P. 57
Javarone, S. 529
Jeng, F.-S. 1698
Ji, L. 3174, 3465
Jia, K. 72, 1837, 2148, 2876
Jia, S. 402
Jia, Z. 1216, 1231, 2294
Jia, F. 3029
Jian, Y.-Z. 1365
Jiang, S. 2342
Jiang, W. 2376
Jiang, Y. 441, 2593
Jiang, H. 292
Jiang, S. 2965
Jiao, L. 2229
Jiao, Q. 3180
Jiao, Z. 3489
Jin, L. 1282
Jin, R. 2202
Jin, W. 1297
Johansson, F. 2602
Jongpradist, P. 345, 1610

Kakimi, K. 1469
Kamada, H. 1687
Kandavorawong, K. 1610
Kang, M. 536, 3617
Kang, S.-J. 2442
Kang, Y.S. 3037
Kapil, S.L. 542
Karahan, E. 2539
Karlin, N. 2108
Karlovsek, J. 3005
Kasal, D. 1875
Kato, K. 1492
Katuwal, T.B. 3044, 3149
Kawabata, J. 2724
Kawata, K. 836, 2681
Kazerani, T. 2664, 3187
Kendall, M. 2108
Khali, R.K. 1499, 1507
Khare, M. 783
Kharitonov, S. 3067
Khin, K. 2784
Khoo, C.M. 2672, 3623
Khoo, C.-M. 3207, 3215
Kikuchi, K. 1062
Kim, D. 2689, 3053
Kim, H. 2658
Kim, J. 685, 1475, 2442
Kim, S. 1630
Kinomura, Y. 1517
Kishida, K. 2724
Kitagawa, S. 2959
Kivliuk, V.P. 689
Kivlyuk, V.P. 65
Knights, M. 41
Ko, T. 13
Ko, T.Y. 3037
Koay, A. 385
Kobayashi, Y. 1517
Kobidze, T.E. 2561
Koh, P.C. 2784
Koh, R. 1814
Koike, K. 2724
Koizumi, Y. 1062
Koizumi, D. 1884
Koizumi, Y. 2681
Koliji, A. 3187
Koma, T. 1517
Kong, R. 2702
Konyukhov, D.S. 65, 689, 1602, 2561
Konyukhov, D. 3157
Korfiatis, G. 1843
Kose, Y. 3379
Kroehong, W. 1610
Krueger, D. 517
Krymov, O.B. 2561
Kulikova, E. 3157
Kumar, A. 47
Kumar, L. 47
Kumar, R.R. 1418, 1461, 2757
Kumar Saw, A. 1526
Kumarasamy, J. 501, 1967
Kumbhar, N. 1893
Kundan, R. 1000
Kuo, K. 390
Kuo, P.S. 209
Kuras, A. 109, 591
Kuroda, C. 1492
Kusaka, A. 1062, 2681
Kwork, D. 2012
Kwon, K. 536, 3053, 3617

Laddakul, A. 2087
Lai, H. 2876
Lai, X.D. 200
Lam, T.K. 3388
Lambrughi, A. 3255
Lan, F. 660, 3394
Le, H.Q. 732
Lee, C. 2689, 3053
Lee, D. 1860
Lee, J. 270
Lees, D. 1902
Lei, J. 72, 2148
Leng, B. 3067
Leone, T. 2020
Li, B. 2702
Li, C. 548
Li, F. 2868
Li, F.-D. 1365
Li, G. 3079
Li, K. 2702, 3059
Li, M. 424, 1044
Li, P. 638
Li, Q. 548, 1326, 1455, 1916, 2244, 2696
Li, S. 747, 857, 2400
Li, W.-H. 2466
Li, W. 493, 1238, 3194
Li, X. 78, 292, 360, 718, 2394
Li, Y. 1258, 1549, 1719, 2229, 2366, 3174, 3194
Li, Z. 638, 705, 2388, 2429, 3073, 3113
Li, Z.Y. 125
Li, F. 556
Li, J. 740
Li, M. 247, 1098
Li, X.X. 240
Liang, B. 3409, 3418
Liang, X. 1926, 2062
Liang, J. 755
Liang, W. 3401
Liao, W. 1742
Lignier, P. 3255
Lim, J. 1814
Lim, K. 1860
Lin, A. 1705
Lin, G. 256, 2202
Lin, Y.C. 13
Lin, F. 2262
Lin, M. 2407
Lin, W. 3059
Lin, Y.J. 209
Lisardi, A. 2170
Liu, C. 3267
Liu, D. 360, 2500
Liu, E. 2342
Liu, F. 2885
Liu, G. 2492

Liu, J. 261, 565, 1071, 1078, 1224, 1297, 2857, 2893, 2985, 3489
Liu, K. 953, 1549
Liu, P. 2215
Liu, R. 424
Liu, S. 3647
Liu, W. 2529
Liu, W.-R. 3267
Liu, X. 1321, 1532, 1549, 1705, 1777, 1784
Liu, Y. 87, 1086, 1540, 2294
Liu, Z. 1092, 1321, 1777
Long, G. 556
Long, H. 72, 2414, 2421
Lorenzi, M. 149
Lou, H. 1694
Lu, G. 261, 1078, 2893
Lu, J. 1098, 2148, 2309, 3079
Lu, M. 193
Lu, S. 548, 572, 660
Lu, Y.Y. 2280
Lucia, A. 149
Lunardi, G. 760, 1935
Lunardi, P. 760
Lund, A.K. 1486
Luo, H. 3067
Luo, M. 1105, 3538
Luo, S. 769
Luo, W. 2619
Lussu, A. 1959
Lv, S. 352
Lv, Z. 1694
Lvovskaya, M.A. 2917
Lyu, Y. 65
L'Amante, D. 228

Ma, D. 2429
Ma, J.-J. 2466
Ma, J. 755, 777, 3276
Ma, T. 2028
Ma, Y. 3067, 3617
Ma, Z. 3480
Ma, S. 3428
Maalouf, T. 158
MacPhail, C. 1383
Magnelli, F. 3371
Magro, J.L. 1944
Mahony, F. 96
Mains, M. 270, 1167, 1953
Maiti, S. 783
Mak, D.C.W. 3282
Malaisree, P. 345
Manabe, T. 416
Mangifesta, S. 2771
Mann, A. 917
Mao, X. 2717
Mao, J. 2848
Marasini, A. 3223
Marazzo, R. 1561
Marini, D. 1561, 1959, 2902
Marotta, M. 1189, 1967
Marottoli, A. 789
Marrazzo, R. 789
Martelli, L. 969
Martirano, L. 3359
Matioszek, D. 28
Maturi, D. 932, 2910
Maxcia, C. 432
Maxwell, A. 2784
Mazzola, M. 3303, 3320
Mbaye, I.K. 3437
Mega, T. 1479
Mendes, T. 822
Meng, D. 424
Meng, L. 660, 2492
Menghini, A. 1994
Mengyan 1429
Menozzi, A. 2910
Mert, A.A. 798
Meschke, G. 1118, 1654, 1974
Mi, W. 1569
Miao, M. 616
Miao, X. 1569
Miaojun, Z. 2920
Miceli, G. 3365
Mikami, N. 2681
Miliziano, S. 926, 2771
Miller, M. 3067
Mitsui, N. 1135
Mittal, R. 3169
Miyajima, Y. 2724
Miyake, K. 3379
Miyanaga, S. 3086
Miyazato, C.K. 3594
Moammeri, H. 1987
Moghbeli, A. 3095
Mohamad, H. 2672
Mohiadeen, M. 1189
Monina, M. 1981
Monteiro, M.D. 579
Montijn, R. 2475
Mooney, M.A. 1112
Mora, C. 1953
Morocutti, A. 3202
Morosi, M. 1027
Moschetti, E. 2863
Mou, W.F. 740, 746
Mou, W. 2972
Muniyandy, P. 1902
Murro, V.D. 3073

Nadot, M.D. 2917
Nagamatsu, H. 848, 2959
Nair, R. 2951
Naito, C. 1112
Nakamoto, A. 2731
Nakano, K. 1517
Nasiri, M. 1987
Nasri, V. 57, 158, 270, 277, 308
Navarro, E. 101
Negro, E.D. 1994, 2003
Neto, P.M. 3594
Neu, G.E. 1118
Ng, C.L. 3623
Ng, N. 2012
Nguyen, X.-P. 1126
Ni, J. 806
Nianwen, Q. 2920
Nie, X. 2450
Nilsen, H. 1486
Ning, L. 584
Nishi, T. 655
Niu, G. 3059
Niu, J. 3418, 3409
Noble, A. 3632, 3639
Nomura, M. 1135
Nonaka, H. 2724
Noorzad, A. 1015
Nordas, A.N. 2020
Nortoft, S. 2179
Núñez, M. 1579

Öztürk, Ö. 1594
Och, D. 109
Och, D.J. 591
Ohmori, S. 1340
Ohno, K. 1492
Okada, W. 1390, 1412
Oliveira, D. 182, 1144
Olsen, T. 2434
Omae, Y. 2731
Ooi, T.-A. 3207, 3215
Oreste, P. 1053
Orlov, K.V. 65
Ortuta, J. 285, 2567
Osborne, J.A. 3073
Oss, A. 1875
Otsu, T. 2681

Ou Yang, Q.-A. 2466
Ouyang, A. 3073
Ouyang, L. 2737, 2817
Ouyang, Z. 1112
Oyama, H. 732
Ozgur, O. 2028

Pakianathan, L.J. 1814
Palombini, M. 529
Pan, J. 109, 591
Pan, H. 72
Panicis, E.D. 2834
Panthi, K.K. 3044, 3149
Parajuli, B. 476, 3223
Park, C. 1475
Park, D.-Y. 685
Park, H. 3617
Park, S. 536, 2658
Park, S.J. 3037
Park, J. 2442
Paschenko, A.I. 65
Paskaleva, G. 2927
Pauw, B.D. 3444
Peach, G. 2043
Peaston, C. 1151
Pei, L. 3079
Peila, D. 842, 2003, 3303
Peng, F.-L. 3
Peng, X. 3122
Pérez-Léon, R. 608
Pesa, S. 932
Peters, M. 3249
Petkov, M. 1159
Petriccioli, A. 2049
Petunina, D.S. 1602
Pferdekämper, Th. 451, 2056
Phienwej, N. 1446, 1750
Phutthananon, C. 345
Pi, D. 1356
Piedrahita, J. 2763
Piemontese, M. 2108
Pierani, M. 3371
Pilbacka, J. 1159
Pires, T. 2082
Pittalis, R. 3312
Poh, C.K. 1189, 1814, 1967
Poli, A. 2841, 3312, 3320, 3371
Polyankin, A.G. 2917
Polycarpe, S. 3608
Pompeu-Santos, S. 116
Poon, H.H.C. 3282
Potnis, S. 467, 629, 783, 1526
Potnis, S. 695
Pranno, A. 235
Psomas, S. 247, 1044
Puglia, M. 2745

Qi, L. 3232
Qiao, W. 1326, 2062
Qiao, Y.-K. 3
Qie, X. 3232
Qin, C. 3409
Qin, Q. 1737
Qin, C. 3418
Qin, Y. 813, 2323, 2751
Qing, E.C. 2349
Qing, W. 598
Qiu, J. 1586, 2575
Qiu, K. 857
Qiu, W. 87, 493, 1086
Qiu, W.-G. 2644
Qiu, M. 1231
Qu, L. 292, 3029, 3647
Qu, T. 3139
Qu, Y. 2349
Quan, Y. 1916
Quiel, S. 1112

Rahjoo, M. 300, 308
Raine, A. 2035
Ramos, G. 1777
Rattia, V. 822
Rauch, F. 315
Rawat, A. 1418, 2757
Reddy, D.A. 3451
Reis, A. 2841
Rejith Kumar, B. 1015
Ren, Z. 2070, 2076
Renault, F. 2099
Restrepo, V. 2763
Rieker, K. 3236, 3243
Rivaz, B.D. 1151
Rizzo, R.E. 485
Robbe, G. 2082
Robbe, G.B. 579
Robert, F. 2935
Rocha, H. 822, 2082
Rocha, H.C. 579
Rodríguez-Rebolledo, J. 608
Rodríguez-Sánchez, J. 3023
Roncoroni, R. 2841
Rossi, F.D. 1981
Rostami, J. 1654, 1866, 2624, 2995, 3095
Roy, M. 1526
Rui, W. 2414, 2421
Ruiz, E.Q. 3328

Sadeghian, S. 671, 917
Saelao, T. 2087
Sahoo, D.R. 3005
Saito, K. 655
Saito, M. 3379
Sakai, K. 3086
Sakamoto, N. 2724
Salak, P. 1036
Salazar, H. 2763
Salimi, A. 2995
Saltarin, S. 1669
Salvador, E. 101
Samadi, H. 3095
Samaniuk, J. 1866
Sampsakis-Bakopoulos, K. 323
Sánchez, J. 1902
Sánchez, S. 1167, 1953
Sander, P. 3600
Santis, F.D. 932
Santos, A. 608
Sarapagdee, K. 2087
Sarathchandran, A. 329
Schenk, B. 3187
Schivre, M. 2099
Schmäh, P. 3249
Schürch, R. 2108
Schwarz, C. 132
Scialpi, M. 2108
Scodeler, B. 1424
Sebastiani, D. 529, 2771
Senn, J. 3187
Serin, A.V. 2130
Shabanimashcool, M. 941
Shan, J. 2376
Shaterpour-Mamaghani, A. 1621, 2116
Sheil, B. 3059
Shen, H. 1244, 2751
Shen, J. 1737
Shen, J.Q. 2349
Shen, W. 2407
Shen, S. 2122, 2130
Shen,, C. 616
Shepherd, J. 182
Sheth, S. 1207
Shi, C. 1231

Shi, M. 1224
Shi, S. 261, 1078
Shi, Z. 337, 1174, 3652
Shi, J. 2778
Shiina, T. 1135
Shimotsu, T. 1884
Shin, Y.J. 1630
Shin, Y. 3053
Shinbo, H. 2724
Shivasami, A. 2944, 2951
Shizawa, T. 1469
Shu, J. 2848
Shuai, X. 1711
Shuyi, W. 1183
Sia, T. 385
Sia, T.J. 2185
Sillerico, E. 2139
Silvestri, G. 3333
Silvestri, M. 828
Sim, A. 1189, 1967
Simic, A. 1000, 1199, 2630
Singh, A. 2639, 3451
Sittiamornporn, N. 345
Soe, A.K.K. 2784
Song, C. 13
Song, J. 2548
Song, P. 1737
Song, S. 2342, 2450
Song, S.-Y. 2457
Song, T. 72, 1837
Song, Y. 65, 2244
Song, C. 352
Song, T. 2148
Sousa, R. 1843
Spigarelli, B. 3320
Spohn, P. 2745
Sposetti, M.A. 2157
Sramoon, A. 1446
Steer, C. 625
Steiger, R. 3202
Steinkuehler, J. 2624
Stocker, D. 3659
Stripp, G. 1987
Stypulkowski, J.B. 2162
Su, E. 3489
Su, S. 1916
Su, J. 1207, 2584
Su, Z.-X. 2457
Suen, H.H.M. 3282
Sugiyama, H. 1687
Sun, J. 2209, 2751
Sun, L. 2185, 2492
Sun, P. 3489
Sun, S.-P. 2466
Sun, W. 292, 1282, 1820, 2202
Szadkowski, X. 2475

Tabata, H. 848
Tafuri, L. 2049, 2170
Taherzadeh, R. 1126
Taira, Y. 2724
Tajik, M. 1768
Takamoto, N. 1687
Tamura, N. 836
Tan, M. 292, 1711, 3647
Tanaka, T. 1884
Tang, K. 1586, 2575
Tang, R. 2253
Tang, Z. 1784
Taniguchi, S. 2959
Tanzini, M. 969
Tao, L. 1105, 1216, 1224, 1231, 3538
Tatebayashi, Y. 836
Tatsumi, Y. 1062
Tee, B.P. 2672
Teixeira, I.J.F. 2825
Thermann, K. 3255
Thompson, P. 2035
Thompson, L.F. 625
Tian, C. 2593
Tian, M. 1540
Tian, S. 78, 360, 1347, 3480
Tian, G. 2619
Tian, H. 647
Tiberi, B. 2910
Tilak, R. 3169
Timperman, C. 3444
Tirpude, S. 1893
To, F.K.L. 3282
Todaro, C. 842, 1669, 2003, 3333
Toi, H. 368
Tomaszewski, M. 2179
Tomita, T. 848
Tomoto, S. 1135
Tong, H. 3131
Tong, Y. 2593, 3131
Tonioni, P.-L. 1126
Tonioni, P.L. 3255
Tóth, V. 2567
Toussaint, A. 3255
Trinh, N. 377
Trivellato, E. 164
Tsang, C.K. 385, 2185
Tsang, L.W.H. 3282
Tseng, H. 390
Tumac, D. 2116
Turmo, J. 1777

Ünver, B. 2539
Ueda, H. 2731
Umeyama, H. 2959
Unteregger, D. 1561
Upadhye, C. 629
Utagawa, N. 1492
Utsugi, H. 3379
Uygur, P. 1594

Valdez, E. 2784
Valiante, N. 1021
van der Molen, M. 2475
Vecchione, G. 789
Vedin, P. 3262
Veeresh, C. 96, 501, 1455
Venditti, G. 1561, 1959, 2902
Viazovoi, V.V. 1602
Vieira, B.B. 2825
Vigil, H. 2043
Vinogradov, S.N. 65
Vishwakarma, S. 1461
Vogt, G. 1634
Vonghirunyika, P. 1610
Vougioukas, E. 871
Vyazovoy, V.V. 2917

Wachter, K. 2745
Wagner, H. 3668
Walker, N. 591
Wan, Z. 857
Wang, B. 660
Wang, C. 1258, 2209, 2644, 2737, 2817, 3104
Wang, D. 368
Wang, G. 2702
Wang, H. 78, 638, 2193, 2280, 2593, 2280, 3113, 3276
Wang, J. 402, 1719, 256, 2209, 2316, 2965
Wang, K. 406
Wang, L. 2492, 3456
Wang, M. 638, 882, 1267, 1347, 2244, 3122
Wang, N. 1250
Wang, P. 711
Wang, Q. 402, 3511
Wang, S. 1276, 1291, 2070, 2076, 2215, 3139

Wang, S.H. 214
Wang, S.Y. 1828
Wang, T.-T. 1698
Wang, T. 65, 2893
Wang, W. 78, 2893
Wang, X. 441, 572, 660, 2323, 2407, 2624
Wang, Y. 598, 1540, 1569, 2070, 2076, 2376, 3067, 3394, 3472
Wang, Y.J. 1297
Wang, Z. 1224, 3350
Wang, M.-S. 3267
Wang, Q. 1244
Wang, X. 2965
Wang, Z. 1238
Wangdi, S. 1437
Watanabe, T. 1062
Wei, F. 2253
Wei, K. 3174, 3465
Wei, R. 396
Weiliang, J. 2920
Weiß, C. 396
Wen, R. 740, 746, 2972
Wen, X. 3489
Wetzlinger, P. 3202
Whitman, E. 2139
Wilhelmstoetter, F. 1036
Wong, J.C.F. 3282
Woo, L.L. 2784
Wu, B. 2222, 2309, 2593, 3079
Wu, H. 2309, 3079
Wu, J. 548
Wu, L. 3394
Wu, M. 2342
Wu, X.-D. 2457
Wu, Z. 2751
Wu, C. 3131
Wu, R. 2792
Wu, Y. 2529

Xia, F.-Y. 2500
Xia, Q.W. 337
Xia, T. 747
Xia, Z. 402
Xiao, M. 292, 406, 1276, 1282, 1291
Xiao, S. 2745
Xiao, Y. 572, 1705
Xiao, X. 2229
Xie, W. 2316
Xie, X.-Y. 1174
Xie, X. 769, 906, 2696, 3059
Xie, Y. 2414
Xie, B. 406, 1297
Xie, C. 2548
Xin, G. 556
Xin, Y. 3472
Xing, S. 1429
Xing, X. 1092
Xing, Y. 1333
Xu, C. 406
Xu, F. 3194
Xu, G. 3067
Xu, H. 1737
Xu, J.-F. 1174
Xu, Q. 3290
Xu, W. 1297
Xu, Y. 2619
Xu, Z. 424
Xu, M. 416
Xue, G. 1276, 1291
Xue, L. 65
Xue, S. 2209
Xue, Y. 647, 2985, 2702, 3029

Yalal, S. 1507
Yamagami, M. 3086
Yamagishi, T. 1479
Yamamoto, S. 1687
Yamamoto, T. 2724
Yan, C. 953
Yan, G. 139
Yan, Z. 1276, 3456
Yan, K. 1303
Yan, S. 2209
Yan, Z. 3497
Yang, F. 256
Yang, H. 755
Yang, J. 2148
Yang, L.W. 1828
Yang, M. 2848
Yang, Q. 2209, 2800
Yang, S. 2658
Yang, W.W. 740, 746
Yang, W. 2972, 1737
Yang, X.-Y. 3223
Yang, X. 1250, 2554
Yang, Y. 877, 1916, 2244, 2253
Yang, Y.D. 1828
Yang, C. 2239, 3480
Yang, W. 865
Yang, X. 1967, 2262, 2487
Yang, Z. 1312
Yao, P. 476
Yao, Y. 2429
Ye, F. 747, 1053, 2593, 3489
Ye, L. 2076
Ye, Y. 1321
Ye, F. 711
Yensri, P. 1750
Yi, W. 3122
Yin, L. 2487
Yin, R. 1326
Ying, K. 747
Ying, Z. 2407
Ying, G. 1333
Yiouta-Mitra, P. 871
Yonjoho, T. 1610
Yoshida, S. 1135
Yoshikawa, S. 655
Yu, D. 1837
Yu, H. 2394
Yu, L. 200, 337, 882, 1267, 1347
Yu, T. 3497
Yu, W. 548
Yu, Y. 352, 598, 1549, 2529
Yu, J.-L. 2500
Yuan, W. 3520
Yuan, Y. 877, 3504, 3511
Yuan, Z. 1105
Yuan, J. 432
Yuan, X. 3139
Yuvaraju, P.V. 1015

Zacchei, F. 3359
Zamberlan, I. 132
Zan, W. 2800
Zanazzi, E. 3312
Zanichelli, A. 1027
Zendaki, Y. 1974
Zeng, K. 2696
Zeng, X. 1326
Zeng, Y. 1105, 3538
Zenti, C.L. 760
Zhai, S. 1340
Zhang, C.-L. 2457
Zhang, C. 1291, 2751, 3545
Zhang, D. 806, 865, 1258, 1675, 2817, 3545
Zhang, G. 2421
Zhang, H. 1231, 1569, 2253
Zhang, J. 718, 777, 806, 1297, 3113, 1569, 2593
Zhang, L. 806, 897, 3131, 3520

Zhang, M. 1569
Zhang, N. 2575
Zhang, P. 2429, 3520
Zhang, Q. 556, 3029
Zhang, S. 2376, 2602
Zhang, W. 2702, 2800, 2809
Zhang, X. 441, 882, 1267, 3014, 3276, 3538
Zhang, Y. 360, 1216, 1347, 3113, 2400, 2965, 3342
Zhang, Z. 261, 2717, 2323, 2876, 3528
Zhang, Z.G. 2185
Zhang, B. 2280
Zhang, C. 2271, 2286
Zhang, D. 2737
Zhang, H. 2450
Zhang, J. 877, 1837
Zhao, J. 2702
Zhao, L. 2985
Zhao, S. 857
Zhao, W. 1356
Zhao, X. 1916
Zhao, Y. 139, 261, 1078, 1916, 3014, 3328
Zhao, Z. 660, 2575
Zhao, H. 897, 2294, 2492
Zhao, S. 3122
Zhao, Z. 890
Zhaofeng, Y. 2980
Zhen, C.L. 906
Zheng, H. 1112
Zheng, J. 256, 598, 2619
Zheng, R. 1333
Zheng, Z. 2985
Zhong, M. 1967, 2487
Zhong, X.-C. 1365
Zhong, X. 1850
Zhong, J.-L. 1365
Zhou, J.-J. 2500
Zhou, J. 65
Zhou, M. 3104, 3131, 3276
Zhou, X. 2062, 2070, 2076, 3290
Zhou, Y. 1429
Zhou, Z. 1742, 1850
Zhou, M.B. 2302
Zhou, W. 2309
Zhu, D. 769
Zhu, H. 3497
Zhu, S. 2737, 2817, 3104
Zhu, T. 139, 1540
Zhu, W. 2316, 3489
Zhu, Y. 598, 2323
Zhu, H. 1373, 2215
Zimbaldi, A. 1935
Zirgulis, G. 2610
Zou, F. 3067
Zou, H. 3394
Zou, L. 718, 2522, 2602, 2610
Zou, M. 906
Zurdo, J. 1579

Taylor & Francis
Taylor & Francis Group
http://taylorandfrancis.com